Encyclopedia of Nuclear Magnetic Resonance

Editors-in-Chief
D. M. Grant and R. K. Harris

Historical Perspectives

COSY Spectra: Quantitative Analysis

Alex D. Bain

McMaster University, Hamilton, Ontario, Canada

1	Introduction	1
2	COSY on a Two-Spin System	1
3	Larger Spin Systems	7
4	Fast Pulsing Artifacts	7
5	Conclusions	7
6	Related Articles	7
7	References	7

1 INTRODUCTION

The COSY[1] experiment (Figure 1) is probably the single most important two-dimensional NMR experiment. The experiment provides a homonuclear chemical shift correlation: if two spins are connected by a scalar coupling, then the COSY spectrum will show a pair of symmetrical cross peaks between the diagonal peaks of two spins (see ***COSY Two-Dimensional Experiments***). Although the SECSY experiment was often used for homonuclear correlation,[2,3] COSY is the one that has survived. It is the simplest pulse sequence, requires no prior knowledge of the spin parameters, is the easiest to analyze theoretically, provides some of the most useful structural information, and is probably the most widely used 2D experiment. For these reasons, there are several variations on the basic experiment. To begin with, a 2D experiment is not just a pulse sequence but also the associated phase cycling sequence, so that must be considered. COSY has also been the subject of many theoretical investigations. The information that it provides is often simply qualitative (on what is coupled to what), but it is important to understand the quantitative basis of COSY as well.

A quantitative analysis of COSY is needed to understand the conditions under which the experiment will work. Many spin systems have a variety of coupling constants ranging from large geminal couplings of 15 Hz or more, through typical vicinal couplings of a few Hz, down to long-range couplings of a fraction of a Hz. Under what circumstances will these couplings show up as cross peaks in a COSY? In a complex system, a multiplet will consist of several splittings corresponding to couplings to several different spins. What are the intensity ratios within a multiplet? Do any new frequencies appear in f_1? In a COSY cross peak connecting two spins, how does the active coupling (the one between the two spins in question) appear relative to the passive couplings to the other spins in the system? What happens if the flip angles or the phase cycling sequence is changed? What happens if the spin system does not reach equilibrium between pulse sequences? What is the role of phase cycling and quadrature detection? These are just some of the questions that arise from a detailed examination of the COSY experiment.

Understanding the COSY experiment is relatively easy since it is such a simple experiment. The manipulations are straightforward matrix operations and no more difficult than simple spectral analysis. COSY can also serve as a prototype for all multidimensional experiments, since it illustrates many of the principles seen in more complex techniques. In this article, we discuss a simple COSY experiment on a two-spin system in detail. This will cover many of the points raised in the previous paragraphs and serve as a basis for a discussion of more complex systems.

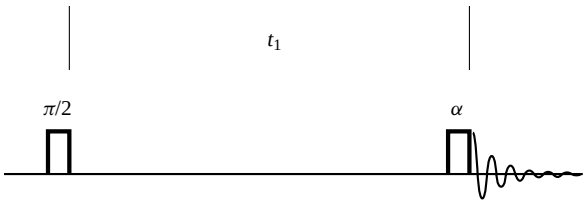

Figure 1 COSY pulse sequence. The initial $\pi/2$ pulse excites the spin system which evolves during the regularly-incremented delay t_1. The second pulse is called the mixing pulse and may have any flip angle, α. For many applications, $\alpha = \pi/2$ or $\alpha = \pi/4$

2 COSY ON A TWO-SPIN SYSTEM

The simplest system has two spins $\frac{1}{2}$, labeled A and B, with Larmor frequencies of ν_A and ν_B. These spins are scalar-coupled with a coupling constant of J, so the spectrum consists of two doublets. Figure 2 shows the energy levels and the allowed transitions. We assume the coupling is weak, so that all four lines in the spectrum have the same intensity. These four lines in the spectrum correspond to density matrix elements which oscillate at these four frequencies. The four lines will all mix with each other in a COSY, so there will be 16 lines in the two-dimensional spectrum. We can study the frequencies, intensities, and phases of these 16 lines by following the modulation of the basic spectrum in the 2D experiment.

2.1 Basic Theory

For any line in a spectrum at frequency ν(in the rotating frame of reference), there are two associated oscillating density matrix elements. These can be thought of as the x and the

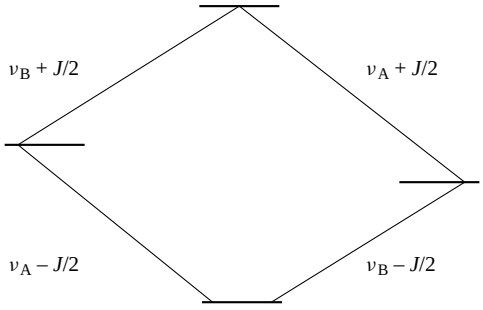

Figure 2 The energy levels of a two spin-$\frac{1}{2}$ system and the allowed single quantum transitions. The two spins, labeled A and B, have Larmor frequencies ν_A and ν_B, and are scalar coupling with a coupling constant of J

y magnetization, or as two counter-rotating magnetizations rotating at the appropriate frequency. We choose the latter picture, and denote the two density matrix elements as $|+\nu)$ and $|-\nu)$. Any coherence associated with the density matrix element $|+\nu)$ will evolve during a delay time, t, as $e^{+i\nu t}$. The terms positive and negative, strictly speaking, refer to the coherence level, a quantum number associated with each coherence. Of course, the frequencies may themselves be either positive or negative with respect to the carrier frequency, and coupling constants may have either sign. This provides the mathematical description of the rotating magnetization.

2.2 Excitation and Evolution

The COSY experiment consists of an excitation pulse, an evolution time t_1, a mixing pulse, and then detection. We will assume that the spin system is in equilibrium at the start of the sequence. The $\pi/2$ excitation pulse in Figure 1 creates coherence corresponding to the four lines in the spectrum, which we will allow to have unit intensity, for simplicity. There will be four positively-rotating elements and four negative ones. These will evolve during the evolution time, so that at the end of t_1 the positively-rotating density matrix elements are given by equation (1).

$$\left.\begin{aligned} |\nu_A + J/2) &= e^{+i(\nu_A + J/2)t_1} \\ |\nu_A - J/2) &= e^{+i(\nu_A - J/2)t_1} \\ |\nu_B + J/2) &= e^{+i(\nu_B + J/2)t_1} \\ |\nu_B - J/2) &= e^{+i(\nu_B - J/2)t_1} \end{aligned}\right\} \quad (1)$$

Similarly, the elements at negative frequency are given by equation (2).

$$\left.\begin{aligned} |-\nu_A - J/2) &= e^{-i(\nu_A + J/2)t_1} \\ |-\nu_A + J/2) &= e^{-i(\nu_A - J/2)t_1} \\ |-\nu_B - J/2) &= e^{-i(\nu_B + J/2)t_1} \\ |-\nu_B + J/2) &= e^{-i(\nu_B - J/2)t_1} \end{aligned}\right\} \quad (2)$$

The mixing pulse in the COSY experiment ends the evolution. The effect of this pulse is the key to the experiment, determining what frequencies will appear in f_1 and with which intensities and phases. In general, the calculation of the effect of a pulse with general flip angle and phase on a general spin system is quite complex and beyond the scope of this article. The simple evolution during a delay, as above, is relatively easy to picture, but the effect of a pulse is the subject of several theoretical descriptions for pulse NMR.[4,5]

2.3 Frequencies in a COSY Spectrum

The mixing pulse should not introduce any new frequencies into the spectrum, so that any frequency that appears in f_1 in a COSY spectrum should also be there in the simple 1D spectrum. The 1D spectrum may be quite complex (see ***Analysis of High-Resolution Solution State Spectra***), but regardless of how complicated the spectrum is no new frequencies will be present in f_1. The principal assumption behind this sweeping statement is that the spin system should be in equilibrium before the pulse sequence starts. This assumption is seldom true in routine practice of COSY. Artifacts[6] are quite common in COSY spectra, but these artifacts are usually simple multiples of the genuine f_1 frequencies. A more detailed discussion of these artifacts and strategies to suppress them is given later.

The reason that no new frequencies are introduced is that only single quantum transitions are excited and detected. A nonselective pulse acting on any spin system in equilibrium will produce only single quantum transitions: the normal equilibrium spectrum. If we ignore relaxation effects, the single quantum transitions will evolve only amongst themselves during the delay. Even though the mixing pulse may create all orders of multiple quantum coherence, only single quantum coherence can be detected directly. In fact, quadrature detection implies that only one of the two senses of precession will be detected, so that only one of the two sets, equation (1) or equation (2), will be observed. Hence, a two-pulse experiment like COSY acting on a spin system in equilibrium will only involve single quantum transitions.

The fact that frequencies in f_2 become frequencies in f_1 means that there is a symmetry to the COSY spectrum.[7] Cross peaks should always occur as symmetrically placed pairs about the main diagonal. This is a very powerful result. It can help us in sorting out genuine cross peaks from artifacts, since artifacts are very seldom symmetrical.

2.4 The Mixing Pulse

In the COSY experiment, where we are dealing only with single quantum coherence, the effect of the pulse is relatively simple. For a weakly coupled spin system subjected to pulses whose flip angles and phases are multiples of $\pi/2$, product operator methods are the most popular approach. In this article, we will take a more general approach in order to see what happens when we go beyond the simple systems. The possible frequencies of lines in f_1 are defined by the one-dimensional spectrum for all types of spin systems and flip angles/phases of the mixing pulse. We must calculate the intensities and phases of the lines under these circumstances.

The effect of a pulse is best handled by using the angular momentum properties of the spin system. A pulse is equivalent to a rotation of the frame of reference (see ***Radiofrequency Pulses: Response of Nuclear Spins***) and angular momentum functions, or spherical tensors, provide a natural basis for describing what happens during a rotation. For any spin system we can convert to a spherical tensor basis, and then the effect of a pulse is simply given by a Wigner matrix element, independent of the details of the spin system.

Among the single quantum transitions, the pulse can take a positive frequency and mix it with the other positive frequencies; it can take a positive frequency, reverse its sense of precession and mix it with the negative frequencies; or it can put a rotating magnetization back up on the z axis. We will ignore the magnetization put back along z and then treat each of the two other cases separately.

The matrix that takes the positive frequencies into the negative frequencies is given by equation (3). Equation (4) gives the matrix which takes the positive frequencies into themselves.

$$\begin{bmatrix} \frac{1}{2}\sin^2\frac{\alpha}{2}(1+\cos\alpha) & \frac{1}{2}\sin^2\frac{\alpha}{2}(1-\cos\alpha) & \frac{\sin^2\alpha}{4} & \frac{-\sin^2\alpha}{4} \\ \frac{1}{2}\sin^2\frac{\alpha}{2}(1-\cos\alpha) & \frac{1}{2}\sin^2\frac{\alpha}{2}(1+\cos\alpha) & \frac{-\sin^2\alpha}{4} & \frac{\sin^2\alpha}{4} \\ \frac{\sin^2\alpha}{4} & \frac{-\sin^2\alpha}{4} & \frac{1}{2}\sin^2\frac{\alpha}{2}(1+\cos\alpha) & \frac{1}{2}\sin^2\frac{\alpha}{2}(1-\cos\alpha) \\ \frac{-\sin^2\alpha}{4} & \frac{\sin^2\alpha}{4} & \frac{1}{2}\sin^2\frac{\alpha}{2}(1-\cos\alpha) & \frac{1}{2}\sin^2\frac{\alpha}{2}(1+\cos\alpha) \end{bmatrix} \tag{3}$$

$$\begin{bmatrix} \frac{1}{2}\cos^2\frac{\alpha}{2}(1+\cos\alpha) & \frac{1}{2}\cos^2\frac{\alpha}{2}(1-\cos\alpha) & \frac{-\sin^2\alpha}{4} & \frac{\sin^2\alpha}{4} \\ \frac{1}{2}\cos^2\frac{\alpha}{2}(1-\cos\alpha) & \frac{1}{2}\cos^2\frac{\alpha}{2}(1+\cos\alpha) & \frac{\sin^2\alpha}{4} & \frac{-\sin^2\alpha}{4} \\ \frac{-\sin^2\alpha}{4} & \frac{\sin^2\alpha}{4} & \frac{1}{2}\cos^2\frac{\alpha}{2}(1+\cos\alpha) & \frac{1}{2}\cos^2\frac{\alpha}{2}(1-\cos\alpha) \\ \frac{\sin^2\alpha}{4} & \frac{-\sin^2\alpha}{4} & \frac{1}{2}\cos^2\frac{\alpha}{2}(1-\cos\alpha) & \frac{1}{2}\cos^2\frac{\alpha}{2}(1+\cos\alpha) \end{bmatrix} \tag{4}$$

These equations are valid for any flip angle, α, of the mixing pulse applied to a weakly coupled spin system. For $\alpha = \pi$, note that the matrix in equation (4) vanishes completely and the only elements in equation (3) that survive are the ones that connect the two lines in each doublet together: elements (1,2), (2,1), (3,4), and (4,3). This is the mixing in the multiplets that gives rise to J-modulation in spin echoes (see ***Two-Dimensional J-Resolved Spectroscopy***).

The simple COSY experiment involves a $\pi/2$ mixing pulse, so we must include the effects of both matrices. Since we detect only one sense of precession, say the positive one, we need only calculate the coherences that contribute to that set. Therefore, to describe what the mixing pulse does, we multiply the coherences in equation (2) by the matrix in equation (3) — these are the coherences with a negative coherence level going into the positives. The result of this is given in equation (5).

$$\begin{aligned}
|\nu_A + J/2) &= \tfrac{1}{4}[+e^{-i(\nu_A+J/2)t_1} \\
&\quad +e^{-i(\nu_A-J/2)t_1} + e^{-i(\nu_B+J/2)t_1} - e^{-i(\nu_B-J/2)t_1}] \\
|\nu_A - J/2) &= \tfrac{1}{4}[+e^{-i(\nu_A+J/2)t_1} \\
&\quad +e^{-i(\nu_A-J/2)t_1} - e^{-i(\nu_B+J/2)t_1} + e^{-i(\nu_B-J/2)t_1}] \\
|\nu_B + J/2) &= \tfrac{1}{4}[+e^{-i(\nu_A+J/2)t_1} \\
&\quad -e^{-i(\nu_A-J/2)t_1} + e^{-i(\nu_B+J/2)t_1} + e^{-i(\nu_B-J/2)t_1}] \\
|\nu_B - J/2) &= \tfrac{1}{4}[-e^{-i(\nu_A+J/2)t_1} \\
&\quad +e^{-i(\nu_A-J/2)t_1} + e^{-i(\nu_B+J/2)t_1} + e^{-i(\nu_B-J/2)t_1}]
\end{aligned} \tag{5}$$

Added to this is the result of applying the matrix in equation (4) to the coherences in equation (1). The contribution of the positive coherences is given by equation (6).

$$\begin{aligned}
|\nu_A + J/2) &= \tfrac{1}{4}[+e^{+i(\nu_A+J/2)t_1} \\
&\quad +e^{+i(\nu_A-J/2)t_1} - e^{+i(\nu_B+J/2)t_1} + e^{+i(\nu_B-J/2)t_1}] \\
|\nu_A - J/2) &= \tfrac{1}{4}[+e^{+i(\nu_A+J/2)t_1} \\
&\quad +e^{+i(\nu_A-J/2)t_1} + e^{+i(\nu_B+J/2)t_1} - e^{+i(\nu_B-J/2)t_1}] \\
|\nu_B + J/2) &= \tfrac{1}{4}[-e^{+i(\nu_A+J/2)t_1} \\
&\quad +e^{+i(\nu_A-J/2)t_1} + e^{+i(\nu_B+J/2)t_1} + e^{+i(\nu_B-J/2)t_1}] \\
|\nu_B - J/2) &= \tfrac{1}{4}[+e^{+i(\nu_A+J/2)t_1} \\
&\quad -e^{+i(\nu_A-J/2)t_1} + e^{+i(\nu_B+J/2)t_1} + e^{+i(\nu_B-J/2)t_1}]
\end{aligned} \tag{6}$$

The final result is the sum of equations (5) and (6), to give the expressions in equation (7).

$$\begin{aligned}
|\nu_A + J/2) &= \tfrac{1}{4}[+\cos(\nu_A + J/2)t_1 + \cos(\nu_A - J/2)t_1 \\
&\quad -\sin(\nu_B + J/2)t_1 + \sin(\nu_B - J/2)t_1] \\
|\nu_A - J/2) &= \tfrac{1}{4}[+\cos(\nu_A + J/2)t_1 + \cos(\nu_A - J/2)t_1 \\
&\quad +\sin(\nu_B + J/2)t_1 - \sin(\nu_B - J/2)t_1] \\
|\nu_B + J/2) &= \tfrac{1}{4}[-\sin(\nu_A + J/2)t_1 + \sin(\nu_A - J/2)t_1 \\
&\quad +\cos(\nu_B + J/2)t_1 + \cos(\nu_B - J/2)t_1] \\
|\nu_B - J/2) &= \tfrac{1}{4}[+\sin(\nu_A + J/2)t_1 - \sin(\nu_A - J/2)t_1 \\
&\quad +\cos(\nu_B + J/2)t_1 + \cos(\nu_B - J/2)t_1]
\end{aligned} \tag{7}$$

This is the modulation of the lines resulting from the simple pulse sequence in Figure 1. The modulation is a cosine modulation, with the diagonal peaks (the peaks due to mixing within a multiplet) $\pi/2$ out of phase with the cross peaks, and the two cross peaks of opposite sign. Since this is a cosine modulation, a real Fourier transform (as distinct from a complex one) will extract the data. Depending on the phase correction used, the diagonal peaks will be dispersion in both dimensions and the cross peaks will be absorption in both f_1 and f_2. This is the basic COSY experiment (note that no phase cycling was done), but there are problems with it and many variations have been developed.

2.5 Different Types of COSY

The different types of COSY experiment generally do not change the basic pulse sequence in Figure 1, but rather vary the associated phase cycling scheme and the way that the data are transformed. One of the problems is that the cosine modulation in equation (7) cannot distinguish between positive and negative frequencies, so quadrature detection in f_1 is not possible. In itself this is not too much of a problem, since quadrature detection in f_1 does not give any signal to noise ratio advantage.[8] However, the lack of quadrature detection in f_1 in a homonuclear experiment prevents its use in f_2 where there is an advantage to its use.

Historically, the first solution to the problem was to use a complex FT, that is to use $e^{i\omega t}$ in the transform rather than $\cos(\omega t)$. When applied to the data in equation (7), this gives peaks at both positive and negative frequencies, since $\cos(\omega t) = 1/2(e^{i\omega t} + e^{-i\omega t})$. These peaks were called P-type and N-type peaks.[2] One or other of these can be removed by phase cycling — repeating the same pulse sequence, but with different phases in the pulses[9,10] (see ***Phase Cycling***). This removes (usually) the positive-to-positive transfer given by equation (6), so that the data have a complex modulation

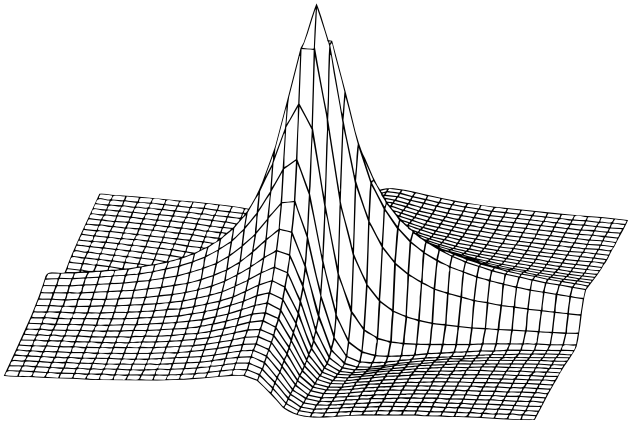

Figure 3 The so-called 'phase twist' lineshape often encountered in COSY spectra. In the center of the line the lineshape is pure absorption, but in the wings in each dimension it becomes more dispersion-like

given by equation (5). The disadvantage of this method is that the lineshapes no longer have a pure phase, but rather a so-called phase twist in which the phase in one dimension changes as one moves across the other dimension. Figure 3 shows the phase twist lineshape. This phase problem can be circumvented by the use of pseudoecho, or sine-bell type apodization functions, and a magnitude calculation rather than a phase correction after the 2D FT. This form of the COSY experiment is very popular and very simple to set up and process.

Figures 4, 5, 6, 7, and 8 show typical results from such an experiment on the molecule serine. Serine is a convenient sample for experimenting with 2D NMR since the chemical shifts of the protons can be easily manipulated by changing the pH of the solution.

Two other solutions to the quadrature detection problem keep the pure phase lineshapes. One is effectively to move $f_1 = 0$ through the use of the time proportional phase increment (TPPI) and still use a real FT.[11] The other method is to collect a parallel data set that is phase-shifted, so that there is true complex data in both dimensions. In this case, a complex FT can be used in both domains.[12] Both methods are widely used and except for some minor details in the baseline the two are essentially equivalent.[13]

The final problem is to make all of the lines, both cross peaks and diagonal peaks, the same phase. If we use a double quantum filter in the mixing pulse,[14,15] this achieves the goal of a homonuclear correlation with pure absorption lines.

For the analysis of the fine structure within a multiplet, the COSY experiment with phase sensitive transforms and double quantum filtering is the method of choice. For quick, qualitative experiments to determine a rough connectivity network, the magnitude calculation COSY is quicker to set up and process (in fact it can easily be set up automatically by the spectrometer). Depending on what sort of information is required, one of these two experiments is used in most cases.

2.6 Intensities of Cross Peaks and Digitization Effects

The fact that the two elements in the cross peak in equations (5) and (6), are of opposite sign is a general one: the cross peaks always have zero net intensity if the acquisition begins

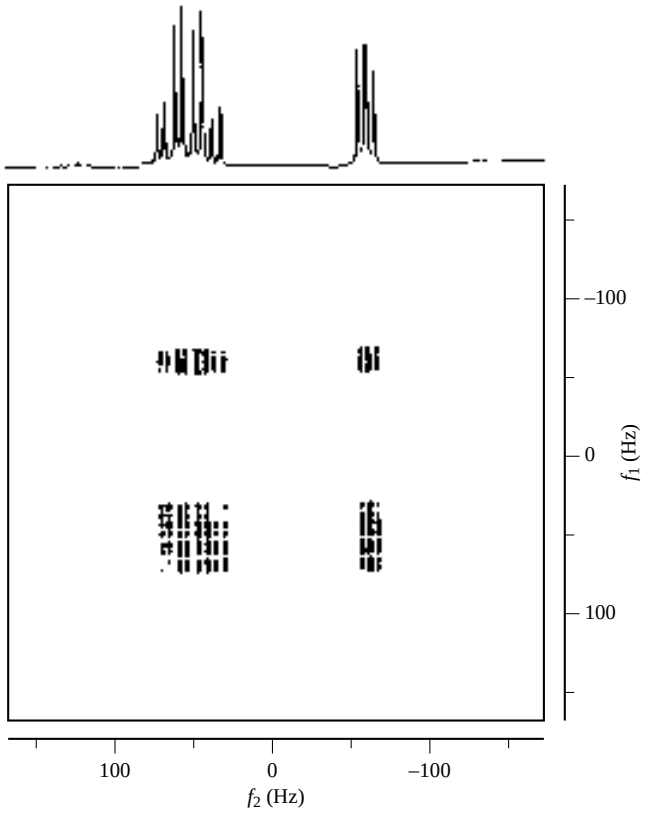

Figure 4 Magnitude calculation COSY on serine, $NH_2CH(CH_2OH)(COOH)$, in D_2O at pH 10 at a spectrometer frequency of 300 MHz. The mixing pulse had a flip angle of $\pi/2$. The raw data consisted of 256 FIDs of 1 k data points, which were Fourier-transformed using an unshifted sine-bell squared apodization in both dimensions. The spectral width in both dimensions was 338 Hz, giving a digital resolution of 0.66 Hz per point. The α proton in serine is at low frequency and the two β protons, β and β', are 0.339 and 0.410 ppm to high frequency at this pH. The measured coupling constants are $J_{\alpha\beta} = 5.9$ Hz, $J_{\alpha\beta'} = 4.3$ Hz, and $J_{\beta\beta'} = -11.2$ Hz

immediately after the mixing pulse. For a weakly coupled AX system as above, the ratio of the peaks is 1: − 1. For more complex multiplets, the relative intensities can be built up from the AX case as for 1D spectra. For equivalent spins, Pascal's triangle can be used so that for the cross peak in an AX_2 system the ratios of the peaks are 1:0: − 1 and the peaks in an AX_3 system are in the proportion of 1:1: − 1: − 1. These ratios will be evident in a phase sensitive COSY, but a magnitude calculation COSY will mask the signs of the peaks.

In a more complex spin system, the distinction between active and passive couplings becomes important. Within a given set of cross peaks, representing the correlation between spin A and spin X, the J_{AX} is the active coupling. This coupling will appear as an antiphase arrangement, as above, but all the other couplings will appear as normal. The splitting due to coupling from A to another spin, M, will appear in phase within the AX cross-peak group. Of course, in the cross-peak group joining A and M, then J_{AM} will be the active coupling.

As the coupling approaches zero the cross peak should vanish, so the net cross-peak intensity must be zero. However, adding a delay after the mixing pulse before the start of the acquisition will enhance cross peaks due to long-range coupling. This delay should be some fraction of the coupling,

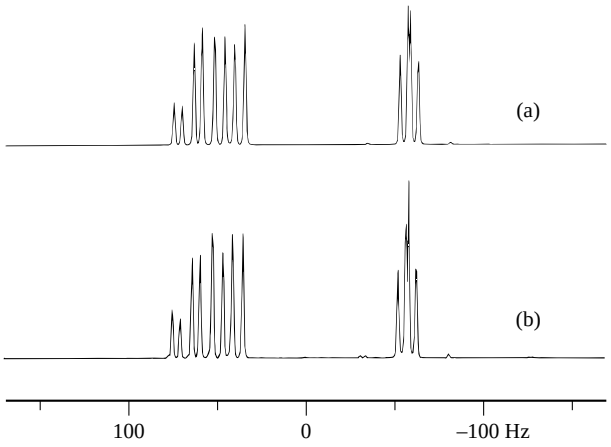

Figure 5 Plot of a row from the data matrix in Figure 4 (trace b) and a simulation of the same data (trace a). The row corresponds to the row of peaks at the bottom of the spectrum (highest frequency in f_1). The spectrum was simulated using the SIMPLTN program which provides an exact density matrix calculation

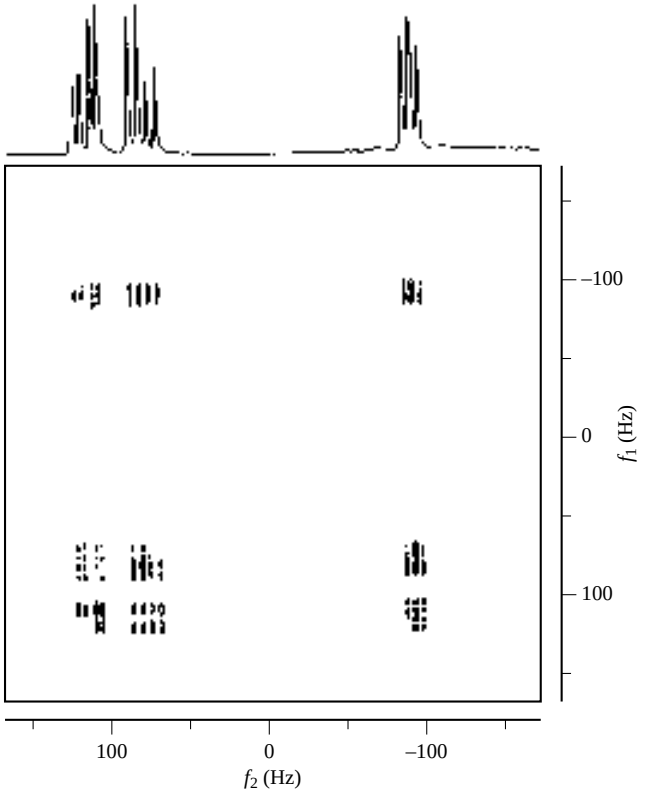

Figure 6 Magnitude calculation COSY on the same serine sample as in Figure 4, also with a mixing pulse of $\pi/2$ but at 500 MHz. The spectral width and the number of experiments is the same as in Figure 4

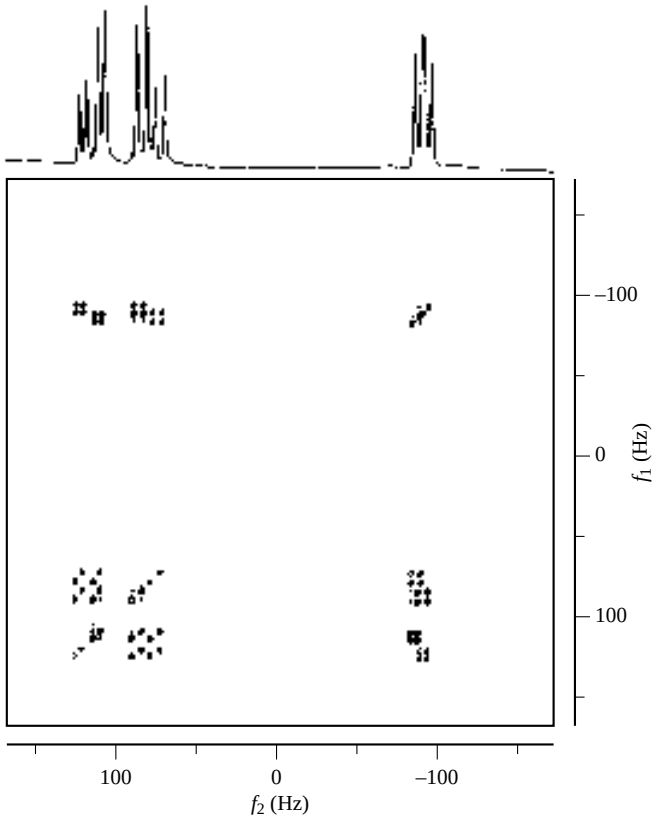

Figure 7 Magnitude calculation COSY on serine at 500 MHz, but with a mixing pulse of $\pi/4$. All other parameters are as in Figures 4 and 6

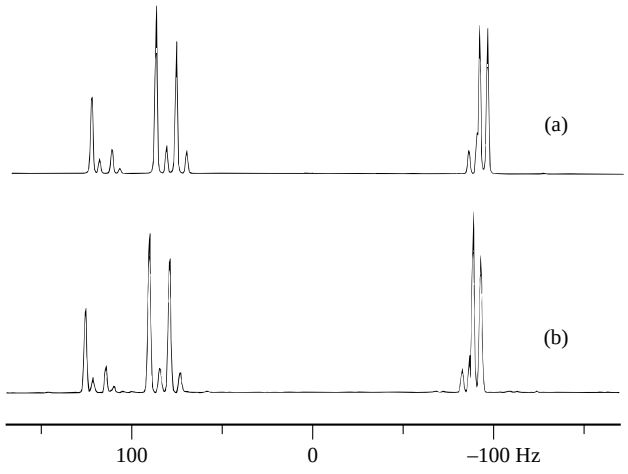

Figure 8 Plot of the row of peaks at the bottom (highest f_1 frequency) of the 2D spectrum in Figure 7[trace (b)]. Trace (a) represents a SIMPLTN simulation of the data

so that the peaks that are exactly out of phase after the mixing pulse have some time to approach being in phase. Similarly, a delay before the mixing pulse will allow multiplets time to get out of phase and enhance polarization transfer. If these delays are present, then the cross peak will acquire some net intensity and cross peaks due to quite small couplings will be evident in the 2D spectrum.[16]

Similarly, poor digitization should cause cross peaks to disappear. If the digitization is such that a single point in two dimensions represents an entire set of cross peaks due to two multiplets, that point should have zero intensity. Very good digitization should give accurate intensities. In between these extremes, however, the behavior is somewhat unusual. When the digitization (in Hz per point) approaches the value of the

coupling constant J (in Hz), simulations show that the apparent intensity of the cross peak rises rather than falls. The apparent intensity reaches a maximum at a ratio of J/digitization of approximately 1, and there is still significant intensity when the coupling is only 0.2 of the digitization.[17] This effect, combined with the possible use of fixed delays around the mixing pulse, permits us to use quite small data matrices and still see useful correlations.

Provided digital resolution is not a problem, the cross peak between an A spin and an X spin will be as follows. If it is the peak in f_1 which corresponds to the A frequency in f_2, then the rows will resemble the A spectrum and the columns the X spectrum, as shown in Figure 4. Similarly, the other cross peak will resemble the X spectrum along the f_2 rows and the A spectrum in f_1. The only difference will be that the splittings due to the A–X coupling will appear as an antiphase, 1: − 1, orientation, but all other couplings will be normal.

2.7 Flip Angle Effects

If we use the simple trigonometric identity given in equation (8), we can see from equation (3) that three of the lines in the simple two-spin COSY behave identically with respect to the flip angle of the mixing pulse. The odd line is the off-diagonal member of the diagonal group of peaks—the peak due to mixing of one line with the other line in the doublet. In Figure 2, we can observe that these are the only pairs of transitions that do not share at least one energy level. All other peaks in the 2D spectrum come from pairs of 'connected' transitions.

$$\sin^2\alpha = 2\sin^2\frac{\alpha}{2}(1+\cos\alpha) \tag{8}$$

Equation (3) predicts that this peak from 'unconnected' transitions will decrease in intensity relative to the others as the flip angle of the mixing pulse is decreased. For a flip angle of $\pi/4$, this peak is approximately 17% of the others. Judicious choice of a contour level in the plot of a 2D spectrum will make this peak disappear, so the diagonal region of the spectrum is much cleaner. This is shown by comparing Figures 6 and 7. As Figure 8 shows, the peaks do not disappear.

Another consequence of this shows up in the cross peaks of bigger spin systems. Here also there are peaks due to pairs of unconnected transitions. Depending on the relative signs of couplings, this gives a characteristic 'tilt' to the cross peak. This can be used to assign the relative signs of couplings. In an AMX spin system, the tilt of the cross peak between A and M will indicate the relative signs of J_{AX} versus J_{MX}. Figures 6 and 7 show this effect for serine. The cross peak between the two β protons at the high-frequency side of the spectrum tilts one way, since the couplings to the third (α) proton are both vicinal and of the same sign. However the α–β cross peaks tilt the other way because of the opposite signs of the vicinal and geminal couplings.

The use of a different flip angle for the mixing pulse will decrease the intensity of these peaks but it will not eliminate them, as shown in Figures 7 and 8. If the peaks are to be eliminated, then another variation of the simple experiment, ECOSY, should be used.[18] This is more complex to set up, but it will give more reliable and useful intensities. This will be useful, for example, in the automatic interpretation of COSY spectra.

2.8 Strong Coupling Effects

Most homonuclear spin systems show some signs of strong coupling. This is more evident in the intensities of the lines rather than in the line positions. This is because the intensities of the lines are determined by the xy magnetizations of the spin system, which are perturbed to first order by strong coupling. The line positions depend on the energy levels and z magnetizations, which are perturbed only to second order. The general rule that no new frequencies will appear in f_1 in COSY still holds. However, since the COSY experiment involves the mixing of xy magnetizations it is clear that intensities will be greatly affected by strong coupling.

As an example, let us consider a magnitude calculation COSY on a simple AB spin system. In such a system, we need only consider the negative frequency coherences, as in equation (2), and how much is transferred to the positives for detection, as in equation (5). For such a system, it is convenient to define the frequencies of the four lines in the spectrum in the following way. Let ν_0 be the average of the A and B Larmor frequencies, and let δ be the difference of the Larmor frequencies in Hz. If J is the scalar coupling constant between A and B, then we can define $C = (J^2 + \delta^2)^{1/2}$ and an angle, θ, by the relationship $\sin(2\theta) = J/C$. For simplicity of notation, let $c = \cos(\theta)$ and $s = \sin(\theta)$. For simplicity, let us number the frequencies as in equation (9).

$$\left.\begin{aligned}\nu_1 &= \nu_0 + C/2 + J/2\\ \nu_2 &= \nu_0 + C/2 - J/2\\ \nu_3 &= \nu_0 - C/2 + J/2\\ \nu_4 &= \nu_0 - C/2 - J/2\end{aligned}\right\} \tag{9}$$

With these definitions, we can calculate the evolution of the negative frequencies up to the mixing pulse, as in equation (2), to give equation (10).

$$\left.\begin{aligned}|-\nu_1) &= (c-s)\mathrm{e}^{-\mathrm{i}(\nu_0+C/2+J/2)t_1}\\ |-\nu_2) &= (c+s)\mathrm{e}^{-\mathrm{i}(\nu_0+C/2-J/2)t_1}\\ |-\nu_3) &= (c+s)\mathrm{e}^{-\mathrm{i}(\nu_0-C/2+J/2)t_1}\\ |-\nu_4) &= (c-s)\mathrm{e}^{-\mathrm{i}(\nu_0-C/2-J/2)t_1}\end{aligned}\right\} \tag{10}$$

Note that the coherences do not have equal intensity as was the case in the weakly coupled spin system.

Let us only consider the case of a flip angle of the mixing pulse of $\pi/2$, in order to simplify the calculation somewhat. Using published methods,[19,20] it is relatively easy to show that the effect of the mixing pulse on the coherences in equation (10) is given by the matrix in equation (11). This is the strong-coupling equivalent of equation (3) for a flip angle of $\pi/2$.

$$1/4\begin{bmatrix}(c-s)^2 & c^2-s^2 & c^2-s^2 & -(c+s)^2\\ c^2-s^2 & (c+s)^2 & -(c-s)^2 & c^2-s^2\\ c^2-s^2 & -(c-s)^2 & (c+s)^2 & c^2-s^2\\ -(c+s)^2 & c^2-s^2 & c^2-s^2 & (c-s)^2\end{bmatrix} \tag{11}$$

Finally, strong coupling also implies that not all lines are detected with equal intensity. This means that the final intensities are the result of multiplying the coherences in

equation (10) by the matrix in equation (11) and then multiplying by the detection efficiency, as in equation (12).

$$\left.\begin{aligned}
|\nu_1) = {} & \tfrac{1}{4}(c-s)[+(c-s)^2(c-s)\mathrm{e}^{-\mathrm{i}\nu_1 t_1} + (c^2-s^2)(c+s)\mathrm{e}^{-\mathrm{i}\nu_2 t_1} \\
& +(c^2-s^2)(c+s)\mathrm{e}^{-\mathrm{i}\nu_3 t_1} - (c+s)^2(c-s)\mathrm{e}^{-\mathrm{i}\nu_4 t_1}] \\
|\nu_2) = {} & \tfrac{1}{4}(c+s)[+(c^2-s^2)(c-s)\mathrm{e}^{-\mathrm{i}\nu_1 t_1} + (c+s)^2(c+s)\mathrm{e}^{-\mathrm{i}\nu_2 t_1} \\
& -(c-s)^2(c+s)\mathrm{e}^{-\mathrm{i}\nu_3 t_1} + (c^2-s^2)(c-s)\mathrm{e}^{-\mathrm{i}\nu_4 t_1}] \\
|\nu_3) = {} & \tfrac{1}{4}(c+s)[+(c^2-s^2)(c-s)\mathrm{e}^{-\mathrm{i}\nu_1 t_1} - (c-s)^2(c+s)\mathrm{e}^{-\mathrm{i}\nu_2 t_1} \\
& +(c+s)^2(c+s)\mathrm{e}^{-\mathrm{i}\nu_3 t_1} + (c^2-s^2)(c-s)\mathrm{e}^{-\mathrm{i}\nu_4 t_1}] \\
|\nu_4) = {} & \tfrac{1}{4}(c-s)[-(c+s)^2(c-s)\mathrm{e}^{-\mathrm{i}\nu_1 t_1} + (c^2-s^2)(c+s)\mathrm{e}^{-\mathrm{i}\nu_2 t_1} \\
& +(c^2-s^2)(c+s)\mathrm{e}^{-\mathrm{i}\nu_3 t_1} + (c-s)^2(c-s)\mathrm{e}^{-\mathrm{i}\nu_4 t_1}]
\end{aligned}\right\} \quad (12)$$

Equation (12) shows the intensities of all the lines in a COSY spectrum of an AB spin system. If we apply the trigonometric identities in equation (13), we can further simplify the expressions.

$$\left.\begin{aligned}
&\cos^2\theta - \sin^2\theta = \cos 2\theta \\
&(\cos\theta + \sin\theta)^2 = (1 + \sin 2\theta) \\
&(\cos\theta - \sin\theta)^2 = (1 - \sin 2\theta)
\end{aligned}\right\} \quad (13)$$

The final expressions for the COSY on an AB system are given in equation (14).

$$\left.\begin{aligned}
|\nu_1) = {} & \tfrac{1}{4}[+(1-\sin 2\theta)^2\mathrm{e}^{-\mathrm{i}\nu_1 t_1} + \cos^2 2\theta\mathrm{e}^{-\mathrm{i}\nu_2 t_1} \\
& +\cos^2 2\theta\mathrm{e}^{-\mathrm{i}\nu_3 t_1} - \cos^2 2\theta\mathrm{e}^{-\mathrm{i}\nu_4 t_1}] \\
|\nu_2) = {} & \tfrac{1}{4}[+\cos^2 2\theta\mathrm{e}^{-\mathrm{i}\nu_1 t_1} + (1+\sin 2\theta)^2\mathrm{e}^{-\mathrm{i}\nu_2 t_1} \\
& -\cos^2 2\theta\mathrm{e}^{-\mathrm{i}\nu_3 t_1} + \cos^2 2\theta\mathrm{e}^{-\mathrm{i}\nu_4 t_1}] \\
|\nu_3) = {} & \tfrac{1}{4}[+\cos^2 2\theta\mathrm{e}^{-\mathrm{i}\nu_1 t_1} - \cos^2 2\theta\mathrm{e}^{-\mathrm{i}\nu_2 t_1} \\
& +(1+\sin 2\theta)^2\mathrm{e}^{-\mathrm{i}\nu_3 t_1} + \cos^2 2\theta\mathrm{e}^{-\mathrm{i}\nu_4 t_1}] \\
|\nu_4) = {} & \tfrac{1}{4}[-\cos^2 2\theta\mathrm{e}^{-\mathrm{i}\nu_1 t_1} + \cos^2 2\theta\mathrm{e}^{-\mathrm{i}\nu_2 t_1} \\
& +\cos^2 2\theta\mathrm{e}^{-\mathrm{i}\nu_3 t_1} + (1-\sin 2\theta)^2\mathrm{e}^{-\mathrm{i}\nu_4 t_1}]
\end{aligned}\right\} \quad (14)$$

The true diagonal peaks show the expected behavior: the result of mixing a line with itself gives the square of the intensity in the 1D spectrum. However, all the other peaks show the same intensity, even as a result of mixing one low-intensity outer peak with the other outer peak. This is somewhat unexpected, but is shown experimentally in the spectra of serine in Figures 4 and 5.

3 LARGER SPIN SYSTEMS

Larger spin systems can be treated as simple combinations of two-spin systems in most cases. The cross peaks will reflect the structures of the f_1 and f_2 spectra as above, with the proviso about the active coupling being in antiphase. Provided the system is in equilibrium, there will be no new frequencies appearing in f_1. In strongly coupled systems, the intensities of some individual peaks may be such that they are missing from a contour plot, but a cross peak will still be visible. Some spin systems, such as the ABX system, can be analyzed algebraically, but the calculations can get quite complex even for a simple experiment like COSY. For these systems, computer simulations provide a very useful tool.[21–25] With modern computers, exact density matrix calculations can be done in a few minutes on systems of four or five strongly coupled spins. For example, the simulations for Figures 5 and 8 were undertaken in under 30 s on a 1992 model UNIX workstation. For systems with several spins, a combination of the basic rules for two spins and some simulations and experience will faithfully predict the quantitative nature of the COSY spectrum.

4 FAST PULSING ARTIFACTS

The statement that no new frequencies appear in a COSY rests on the assumption that the spins relax completely between pulse sequences, and this is almost never true in practice. Under normal circumstances, artifacts that are derived from the f_2 frequencies will appear in the spectrum. Usually these appear as peaks at $f_1 = 0$, small P-type peaks which have not been totally suppressed or peaks at multiples of the f_2 frequency. These are especially evident for strong singlets due to methyl groups, which often have long relaxation times. These artifact peaks can be minimized by doing dummy scans before the actual acquisition, in order to get the spin system into a steady state. Also, careful attention to the phase cycling sequence and how one experiment interacts with the next can be very helpful.[26,27] Also, the use of magnetic field gradients, rather than phase cycling, to select coherence pathways is very effective in reducing the artifacts due to incomplete relaxation.

5 CONCLUSIONS

The COSY experiment serves as the best example of two-dimensional NMR spectroscopy. In its many forms it is an extraordinarily useful experiment, and yet it is quite simple to analyze and understand. The two-spin systems described here illustrate almost all the important features of the experiment. A few pages suffice to describe these systems completely and quantitatively, so it is well within the reach of all NMR spectroscopists. This combination of simplicity and power makes the COSY experiment stand out.

6 RELATED ARTICLES

Analysis of High-Resolution Solution State Spectra; COSY Two-Dimensional Experiments; Phase Cycling; Radiofrequency Pulses: Response of Nuclear Spins; Two-Dimensional J-Resolved Spectroscopy

7 REFERENCES

1. W. P. Aue, E. Bartholdi, and R. R. Ernst, *J. Chem. Phys.*, 1976, **64**, 2229.
2. K. Nagayama, K. Wüthrich, and R. R. Ernst, *Biochem. Biophys. Res. Commun.*, 1979, **90**, 305.
3. A. D. Bain, R. A. Bell, J. R. Everett, and D. W. Hughes, *J. Chem. Soc., Chem. Commun.*, **1980**, 256.
4. O. W. Sørensen, G. W. Eich, M. H. Levitt, G. Bodenhausen, and R. R. Ernst, *Prog. Nucl. Magn. Reson. Spectrosc.*, 1983, **16**, 163.
5. A. D. Bain, *Prog. Nucl. Magn. Reson. Spectrosc.*, 1988, **20**, 295.
6. A. D. Bain, I. W. Burton, and W. F. Reynolds, *Prog. Nucl. Magn. Reson. Spectrosc.*, 1994, **26**, 59.

7. S. Boentges, B. U. Meier, C. Griesinger, and R. R. Ernst, *J. Magn. Reson.*, 1989, **85**, 337.
8. A. D. Bain, *J. Magn. Reson.*, 1988, **77**, 125.
9. A. D. Bain, *J. Magn. Reson.*, 1984, **56**, 418.
10. G. Bodenhausen, H. Kogler, and R. R. Ernst, *J. Magn. Reson.*, 1984, **58**, 370.
11. D. Marion and K. Wüthrich, *Biochem. Biophys. Res. Commun.*, 1983, **113**, 967.
12. D. J. States, R. A. Haberkorn, and D. J. Ruben, *J. Magn. Reson.*, 1982, **48**, 286.
13. J. Keeler and D. Neuhaus, *J. Magn. Reson.*, 1985, **63**, 454.
14. U. Piantini, O. W. Sørensen, and R. R. Ernst, *J. Am. Chem. Soc.*, 1982, **104**, 6800.
15. A. J. Shaka and R. Freeman, *J. Magn. Reson.*, 1983, **51**, 169.
16. A. Bax and R. Freeman, *J. Magn. Reson.*, 1981, **44**, 542.
17. T. Allman and A. D. Bain, *J. Magn. Reson.*, 1986, **68**, 533.
18. C. Griesinger, O. W. Sørensen, and R. R. Ernst, *J. Chem. Phys.*, 1986, **85**, 6837.
19. A. D. Bain, *Chem. Phys. Lett.*, 1978, **57**, 281.
20. L. E. Kay and R. E. D. McClung, *J. Magn. Reson.*, 1988, **77**, 258.
21. P. Meakin and J. P. Jesson, *J. Magn. Reson.*, 1975, **18**, 411.
22. B. K. John and R. E. D. McClung, *J. Magn. Reson.*, 1984, **58**, 47.
23. H. Widmer and K. Wüthrich, *J. Magn. Reson.*, 1986, **70**, 270.
24. W. Studer, *J. Magn. Reson.*, 1988, **77**, 424.
25. A. Majumdar and R. V. Hosur, *Prog. Nucl. Magn. Reson. Spectrosc.*, 1992, **24**, 109.
26. C. J. Turner and S. L. Patt, *J. Magn. Reson.*, 1989, **85**, 492.
27. C. J. Turner and W. C. Hutton, *J. Magn. Reson.*, 1992, **100**, 469.

Biographical Sketch

Alex D. Bain. *b* 1948. B.Sc., 1970, Toronto, M.Sc., 1972, U.B.C., Ph.D., 1975, Cambridge, (Ph.D. supervisor, Ruth Lynden-Bell, who introduced him to NMR). After postdoctoral work, was employed as Applications Spectroscopist by Bruker-Spectrospin Canada for six years. Since 1986 has been Professor of Chemistry, McMaster University. Approx. 50 publications. Research interests: spin dynamics, relaxation, chemical exchange.

Quantitative Measurements

James N. Shoolery
Varian Associates, Palo Alto, CA, USA

1	Introduction	1
2	Advantages and Disadvantages as an Analytical Tool	1
3	Theory	1
4	Accuracy of CW NMR Integral Measurements	2
5	Pulsed Fourier Transform NMR	3
6	Sources of Error in FT NMR Integral Measurements	3
7	Stability and Linearity of Spectrometer Hardware	4
8	Applications	4
9	Quantitation in ^{13}C NMR	5
10	Applications of ^{13}C NMR	7
11	Quantitation of Other Nuclei	8
12	Conclusions	9
13	References	10

1 INTRODUCTION

Quantitative analytical measurements have been dominated for many years by optical spectroscopy in the infrared, visible, and ultraviolet regions of the electromagnetic spectrum. Such instruments have become the basis for a large number of routine analytical procedures, especially in the chemical and pharmaceutical industries and in medicine. Stability problems, which plagued early instruments prior to the development of solid state electronics in the 1950s, have been largely overcome, and the relative small size, low cost, simplicity of operation, and reproducibility of results have led to widespread reliance on optical spectrometers in analytical and chemical laboratories.

Nuclear magnetic resonance spectroscopy has also been used as a quantitative analytical tool since the early 1950s, shortly after its discovery. However, it has not achieved the same degree of user confidence and widespread routine application as optical spectroscopy. Perceived as a large, expensive, complex, unfriendly, and marginally stable instrument, NMR has tended to be used as a last resort when other quantitative methods fail. However, continuous improvement of NMR instrumentation over the past 40 years has gradually narrowed the differences and even reversed some of those perceptions. NMR is now in a position to be considered seriously for a wide range of analytical and clinical applications, and even regarded as the method of choice for some analyses.

Above and beyond the role that quantitation of NMR measurements can play in the analytical laboratory is the application of such measurements to the assignment and interpretation of NMR spectra used for the determination of molecular structure. The complexity of such problems often requires that the NMR spectroscopist utilize all the information in the spectra, including the quantitative relationships that exist between the peaks and multiplets, arising from the various nuclei in the sample. Internuclear distance measurements, necessary for establishing molecular conformation, depend upon quantitative measurement of nuclear Overhauser enhancement (NOE). Because of the reputation of NMR as the most effective physical tool for structure determination, that aspect of quantitative NMR spectroscopy may well achieve more importance than the less glamorous analytical applications.

2 ADVANTAGES AND DISADVANTAGES AS AN ANALYTICAL TOOL

NMR spectroscopy excels in the measurement of relative amounts of the components of a mixture. One reason for this is that the absorption coefficient for the absorption of electromagnetic energy is essentially identical for all nuclei of the same species in a molecule or mixture of molecules. In contrast, the absorption coefficient in optical spectroscopy must be calibrated (by measurement) for each spectroscopic transition assigned to the various components of the mixture, because the coefficient is a complex function of transition probability, energy differences, and perturbations of the energy level system. Thus, while an analysis of the relative amounts of the components in a mixture can be carried out by NMR without ever separating the mixture into its components or having authentic samples of them, the absorption coefficients must either be known or measured before such an analysis can be performed in the optical region.

A second advantage for NMR spectroscopy in mixtures arises from the effective isolation of the nuclei from forces acting on the molecules, leading to linewidths many orders of magnitude less than those in the optical range. The effective resolution of NMR spectrometers, particularly since the widespread incorporation of high-field superconducting magnets, is far better than their optical counterparts, often resulting in little or no interference or overlap of the analytical peaks.

Whether a particular behavior of a system is viewed as an advantage or a disadvantage depends upon what one is trying to accomplish. A highly absorbing substance can confer superiority on the optical spectroscopic analysis for trace amounts of that substance, or make minor fluctuations in the amount of it a disastrous source of error in the measurement of something it overlaps. The uniformly low sensitivity of NMR spectroscopy relative to optical spectroscopy, which arises from the low frequency of NMR transitions compared with the electronic, vibrational, and rotational transitions in the optical range, has placed NMR at a significant disadvantage for analyses of trace amounts, which are easily overwhelmed by the signals from the major components of a mixture or may even be too weak to distinguish from the random background noise of the instrument.

The timescale of NMR events is in the range of seconds to milliseconds, and, occasionally, microseconds, while optical events occur in the nanosecond and picosecond range. That has a profound effect on the ability to measure transient species, which must have a much larger halflife to be measurable by NMR than by optical spectroscopic methods.

Both optical and NMR spectrometers can be used to good effect in the analytical laboratory. The task of the analyst is to pick a method that utilizes the strengths and minimizes the weaknesses of the type of instrument chosen to perform a given analysis.

3 THEORY

Until the 1970s, nearly all high-resolution NMR spectrometers operated in the field-swept mode, and small, low-cost, permanent magnet instruments of that type continue in production up to the present time. Adjustment of the phase-sensitive detector in such instruments permits selection of either the absorption (v) or dispersion (u) component of the NMR signals.

Owing to its sharpness and suitability for integration, the absorption component is generally selected for quantitative measurements. Assuming slow passage conditions, i.e., a sweep rate $\mathrm{d}B/\mathrm{d}t$ small enough to ensure that the time to traverse each of the NMR signals is much longer than the longitudinal and transverse relaxation times (T_1 and T_2), the integral of the absorption component given by the Bloch equations[1–3] is

$$\int v\,\mathrm{d}B = \frac{(\text{const})M_0B_1}{[1+(\gamma B_1)^2T_1T_2)]^{1/2}} \tag{1}$$

where M_0 is the net nuclear magnetic moment, B_1 is the exciting radiofrequency field strength, and γ is the magnetogyric ratio. Mathematically, the integral is evaluated from 0 to infinity, but in practice need only be measured over a range sufficient to include all the area under the peaks within the desired accuracy of the measurement.

Numerical integration of the peak intensities plotted as a function of magnetic field, i.e., the total area under the signals arising from the species to be measured, has been used, but such methods involving counting squares, cutting out and weighing, or using a planimeter, are extremely unwieldy and subject to large errors. It is much better to measure the integral as a function of time, using an electronic integrator to sum the output voltage of the detector over the time of passage through the signals. That integral is given by the expression

$$\int v\,\mathrm{d}t = \frac{(\text{const})M_0B_1}{(\mathrm{d}B/\mathrm{d}t)[1+(\gamma B_1)^2T_1T_2]^{1/2}} \tag{2}$$

where the sweep rate $\mathrm{d}B/\mathrm{d}t$ is the rate of change of the field strength per unit time.

Since M_0 depends upon the number of nuclei per unit volume, N, and upon the excess population in the lower Zeeman level, which at room temperature is inversely proportional to the absolute temperature T, the integral becomes

$$\int v\,\mathrm{d}t = \frac{(\text{const})B_1N}{T(\mathrm{d}B/\mathrm{d}t)[1+(\gamma B_1)^2T_1T_2]^{1/2}} \tag{3}$$

Under the slow passage conditions required for the validity of equation (3), if B_1, T, and $\mathrm{d}B/\mathrm{d}t$ are kept constant, the integrals will be reproducible, but will depend upon the relaxation times T_1 and T_2. If, however, $(\gamma B_1)^2T_1T_2 \ll 1$, the integrals become independent of relaxation, and are an accurate measure of the concentration. That requires making B_1 small, and, because the integral is proportional to B_1, the signal-to-noise ratio may limit the accuracy of the measurement before the slow passage condition can be met. That is generally the case except for very broad lines (small T_2) or strongly interactive nuclei (short T_1).

Another difficulty in meeting slow passage conditions arises from the requirement that $\mathrm{d}B/\mathrm{d}t$ be small if the lines are narrow, allowing magnetic field drift or other instabilities to become comparable to $\mathrm{d}B/\mathrm{d}t$ and become significant sources of error. The time consumed in a single scan through the full spectrum can also become inconveniently large, especially at high magnetic field strengths.

Such practical considerations dictate that chosen values of B_1 and $\mathrm{d}B/\mathrm{d}t$ often violate the slow passage condition. Jacobsohn and Wangsness[4] modified the Bloch equations to take into account the transient response of the nuclei at faster sweep rates. They found that an oscillatory decay term must be added. That results in *wiggles* following sharp lines in most field-swept high-resolution spectra, but the oscillatory term contributes no area unless it is truncated.

The term $[1+(\gamma B_1)^2T_1T_2]^{1/2}$ in equation (3) represents the effect called *saturation*, and is proportional to the decrease in the excess population of the lower Zeeman level over the time interval T_1 required for slow passage during which transitions occur with the probability $(\gamma B_1)^2T_2$. An approximation to the behavior for more rapid passage conditions is obtained by replacing T_1 by the actual time of passage, $\Delta B\ (\mathrm{dB}/\mathrm{d}t)^{-1}$. Because the linewidth ΔB is $1/\gamma T_2$, equation (3) is modified to

$$\int v\,\mathrm{d}t = \frac{(\text{const})B_1N}{T(\mathrm{d}B/\mathrm{d}t)[1+\gamma B_1^2(\mathrm{d}B/\mathrm{d}t)^{-1}]^{1/2}} \tag{4}$$

The expression $1/(1+x)^{\frac{1}{2}}$ can be expanded to $1-\frac{1}{2}x+\ldots$ for small x, where $x=\gamma {B_1}^2(\mathrm{dB}/\mathrm{d}t)^{-1}$, giving

$$\int v\,\mathrm{d}t = \frac{(\text{const})B_1N[1-\frac{1}{2}\gamma B_1^2(\mathrm{d}B/\mathrm{d}t)^{-1}+\cdots]}{T\,\mathrm{d}B/\mathrm{d}t} \tag{5}$$

and consequently

$$\int v\,\mathrm{d}t \to \frac{(\text{const})B_1N}{T\,\mathrm{d}B/\mathrm{d}t} \tag{6}$$

if $\gamma {B_1}^2/(\mathrm{dB}/\mathrm{d}t) \ll 1$. Equation (6) predicts that, even at high rf power levels, the integrals can be made essentially independent of relaxation times for sufficiently fast sweep rates.

It would appear that a signal-to-noise problem might arise, since, in order to keep $\gamma {B_1}^2/(\mathrm{dB}/\mathrm{d}t) \ll 1$, an n-fold increase in sweep rate can only be accompanied by a $\sqrt{n}$ -fold increase in B_1, resulting in an integral smaller by $\sqrt{n}$. However, an n-fold faster sweep permits obtaining n times as many observations per unit time, and statistical averaging of n observations restores the factor $\sqrt{n}$ in the reliability of the result. The smaller integrals need to be measured rapidly and to three decimal places, making a digital voltmeter the preferred method of reading the integrals if integration for analytical purposes (1.0% or better) is the object.

An additional benefit of obtaining a statistically significant number of independent measurements of the integral arises from the possibility of estimating the confidence limits (standard deviation) of the results. Thus, a determination of the precision of the measurement can be obtained along with the measurement.

4 ACCURACY OF CW NMR INTEGRAL MEASUREMENTS

Using a sweep rate of 5–10 Hz s^{-1} for integrating instead of the usual 0.5–2 Hz s^{-1} for recording the absorption-mode high-resolution spectrum reduces the errors from random drifts in the magnetic field correspondingly, and in modern thermally stabilized permanent magnet systems should permit integration accuracy better than 1.0%. To achieve this, however, another source of error must be eliminated. That error is due to variation in the dc output of the rf detector, arising from instabilities in probe balance, dc amplifier balance, and stray coupling in cables and leads. The problem is greatly reduced by the use of audiofrequency modulation of the magnetic field at a frequency of 1 or 2 kHz. Several authors[5–7] have discussed the effect of such modulation on the NMR signals. A set of audiofrequency sidebands are obtained along with an audiofrequency signal at the usual field strength. By suitable adjustment of modulation amplitude and phase, the sidebands can be rejected, essentially completely, by a phase-sensitive detector, while the centerband signal, now free from low-frequency drifts after traversing an *RC* coupling circuit, is converted back to dc, recorded, and integrated.

The author performed tests to verify the validity of equation (6) in application. A fairly stringent test involved the determination of the total percentage of hydrogen by weight for several samples (25 mg) of pure organic compounds, compared with a standard sample of naphthalene ($C_{10}H_8$). Measurements of three standard samples (A, B, and C), and three complex natural products of molecular formulas $C_{27}H_{44}O_3$, $C_{15}H_{18}O_6$, and $C_{15}H_{20}O_6$ were made, and are shown in Table 1. The three standards were assigned the theoretical value of 6.29% hydrogen in column 3, and the measured values, which average 6.29, are shown in column 4. The three test compounds were run under the same experimental conditions, and their theoretical and observed percentages of hydrogen by NMR are compared in columns 3 and 4.

Table 1 Total Hydrogen Analyses by NMR for Complex Organic Molecules

Sample	Weight (mg)	%H by weight	%H (NMR)[a]
$C_{10}H_8$ (A)	25.1	6.29	6.31 ± 0.03[b]
$C_{10}H_8$ (B)	25.3	6.29	6.28 ± 0.01
$C_{10}H_8$ (C)	25.3	6.29	6.28 ± 0.02
$C_{27}H_{44}O_3$	25.1	10.65	10.58 ± 0.05
$C_{15}H_{18}O_6$	25.2	6.26	6.27 ± 0.04
$C_{15}H_{20}O_6$	25.1	6.80	6.81 ± 0.03

[a]Based on average integral of naphthalene solutions.
[b]Standard deviation.

5 PULSED FOURIER TRANSFORM NMR

Beginning in the 1970s, the pulsed Fourier transform mode of operation began to supplant the CW mode of operation, especially for superconducting magnet systems operating at high magnetic field strengths. Owing to the great improvement in sensitivity arising from simultaneous wideband excitation of all nuclei in the sample, and the flexibility of time domain detection, which makes two-dimensional NMR spectroscopy possible, FT NMR has completely replaced CW NMR except as noted at the beginning of Section 3. Workers with modern equipment will therefore find the following treatment of quantitation more relevant to their needs than the preceding one.

Following a short pulse of rf magnetic field in a coil surrounding the sample, the nuclei, which resonate in a band of frequencies (arising from the chemical shift) around the pulse frequency, are found initially precessing in a state of phase coherence and with altered populations of the upper and lower energy states. The system can be described as a set of precessing magnetization vectors, tipped (or rotated) away from the magnetic field (z) axis by an amount determined by the field strength and duration of the pulse. Each vector consists of all of the nuclei that contribute to the corresponding spectral line in the frequency (or magnetic field) spectrum. The receiver is turned on, and the system is allowed to precess freely, inducing sinusoidal voltages in the receiver coil. The resulting free induction decay (FID) is the interferogram of all those sine waves, decreasing exponentially with time as phase coherence is lost at the relaxation rate ${T_2}^{-1}$. Digitization of the interferogram and storage in a computer memory allows the waveform to be subjected to Fourier transformation, which generates the slow passage NMR spectrum.[8]

During the data acquisition, the field strength is held constant, using the deuterium nuclei in the solvent as the source of an error signal to correct the infinitesimal drifts in the superconducting magnet field strength or shifts in the master-clock controlled frequency. Multiple acquisitions can then be added together digitally to improve the signal-to-noise ratio.

The Bloch equations applicable in CW NMR are derived for an equilibrium between the perturbing effect of the exciting rf field and the restoration of magnetization by relaxation processes. In pulsed FT NMR, there is no rf field present during data acquisition; consequently, the situation is greatly simplified. The transformed FID reproduces the static spectrum faithfully, and can simply be integrated numerically from the digital representation of the spectrum. The phase parameters should be adjusted to display the pure absorption, or v mode, and then the integral of the transformed spectrum from the FID following a single pulse is given by the expression

$$\int v \, dB = \frac{(\text{const})N}{T} \cos\theta \tag{7}$$

where θ is the tip angle through which the magnetization has been rotated by the rf pulse. A 90° tip angle is often chosen for quantitative work to maximize the integral.

Equation (7) appears deceptively simple, and may give the impression that integration of FT NMR spectra is inherently more accurate than integrals from CW NMR. It is best to reserve judgment on that point until consideration is given to the possible sources of error in FT NMR quantitation.

6 SOURCES OF ERROR IN FT NMR INTEGRAL MEASUREMENTS

Filter bandwidth response is a common source of error. The sampling rate or digitization rate during data acquisition determines the width of the band of frequencies centered on

the pulse frequency that can be identified from the digital samples by Fourier transformation. It is common to insert a filter in the circuit to reject all voltage fluctuations of higher frequency than this spectral width in order to avoid the folding-in of noise from regions immediately adjacent to both sides of the spectral window. Unfortunately, filters with a very steep cut-off characteristic cause troublesome phase shifts, and a compromise is made by choosing a more gradual roll-off, which begins to attenuate noise (and signals) near the ends of the range defined by the spectral width. Thus, NMR signals that are near either end of the spectrum may give a low result. It is normally possible to deactivate the filter or to choose a value for the filter bandwidth larger than the spectral width in such cases to avoid attenuating NMR signals, but at a sacrifice of about a factor of two in the signal-to-noise.

A more fundamental source of error can arise from the profile of excitation associated with a pulse of rf magnetic field. For a perfect pulse with a rectangular shape and instantaneous rise and fall times, the energy distribution over a range of frequencies is described by a Bessel function involving the reciprocal of the pulse length. Thus, very short pulses give a flat power distribution around the pulse frequency and fall off far from the pulse. For nuclei with a small range of chemical shifts, such as ^{1}H and ^{13}C, most modern commercial NMR instruments supply enough pulse power to achieve a 90° tip angle in a pulse of $10\,\mu s$ or less. That makes the energy distribution an insignificant source of error, since all nuclei within the spectral width experience essentially the same tip angle. In the case of ^{19}F and other nuclei with chemical shifts of several thousand ppm, it may be necessary to shorten the pulse length and accept the loss in sensitivity resulting from a smaller, but more constant, tip angle over the spectral range.

Another source of error is pulse breakthrough and acoustic ringing. The receiver is turned off for a few microseconds after the pulse to allow recovery of the tuned circuit from the induced current. Sometimes, when the receiver is first turned on, those currents have not died away completely or have excited acoustic modes in the probe structure that decay more slowly and result in distortion of the first several data points in the FID. Those points transform to a very broad roll in the baseline, which requires the operator to make some subjective judgments about the type of baseline correction routines to apply. The simplest baseline correction routine for that situation is a correction in which a linearly increasing or decreasing amount is subtracted from each successive data point, adjusted by the computer to set the endpoints to zero. That type of software correction often works well over a narrow spectral range, e.g., a few linewidths on either side of a sharp line, but over a wider range it is usually not adequate to deal with the complex shapes arising from transient distortions, particularly if the NMR signals are weak. These transform into 'rolling' baselines with hills and valleys that cannot be corrected with a simple linear function.

Commercial NMR instruments often include more elaborate baseline correction routines that allow the operator (or, better yet, the computer) to identify and specify regions representing baseline, alternating with regions containing NMR signals. All of the baseline regions can be set to zero and the signal-containing regions joined smoothly to them with a software command. In well-resolved spectra, integral accuracy can be greatly improved by that means.

If the tails of the signals overlap, or if the operator makes subjective errors in judging where the tails cease to contribute significantly to the integrals and thereby defines the baseline regions incorrectly, errors may be introduced. Integrating the spectrum many times with independent baseline corrections, or using several operators, allows statistical reduction of random baseline correction errors, but it does not eliminate systematic errors from operator bias.

A recent advance in dealing with such problems is the technique of *linear prediction*,[9] by which the FID waveform can be extended in either direction in time, based on the data obtained during the acquisition. The early data points can be discarded and replaced with data points reconstructed from the rest of the data, after which baseline correction requirements are minimal.

7 STABILITY AND LINEARITY OF SPECTROMETER HARDWARE

Phase and amplitude instabilities of the rf pulses were significant sources of error in early FT spectrometers, but major manufacturers have greatly improved amplifier performance in modern instruments and have reduced such errors to the point of insignificance. Since errors of that type tend to be random, they can be further decreased by making a series of independent measurements.

Modern instruments also have built-in safeguards against overflowing the digital memory channels of the computer, and are linear over a large dynamic range. Older instruments may require vigilance on the part of the operator to ensure that amplifier gains are set properly.

8 APPLICATIONS

The ability to integrate accurately leads to the solution of a variety of physical organic chemical problems and analytical problems. By the end of the 1960s, a number of examples were available.

8.1 Analysis of Rapidly Equilibrating Mixtures

A remeasurement of the ratio of keto to enol forms of the tautometric mixture of the two, first reported by Jarrett, Sadler, and Shoolery[10] in 1953, illustrates the excellent precision of the analysis using the CW methodology described in Sections 3 and 4. Figure 1 shows the spectrum and integral with typical digital voltmeter readings for the steps *a*, *b*, and *c*, corresponding to the olefinic proton of the enol form, the two methylene protons of the keto form, and the methyls in both forms. The percentages of keto and enol can be easily calculated, as shown in Figure 1.

A series of five repeated measurements allowed a statistical evaluation of the precision of the measurement, giving standard deviations of 0.4% for the keto and 0.7% for the enol content. Since the system remains in equilibrium during the measurement, a more accurate measurement of the equilibrium constant is possible than that obtained from bromine titration.

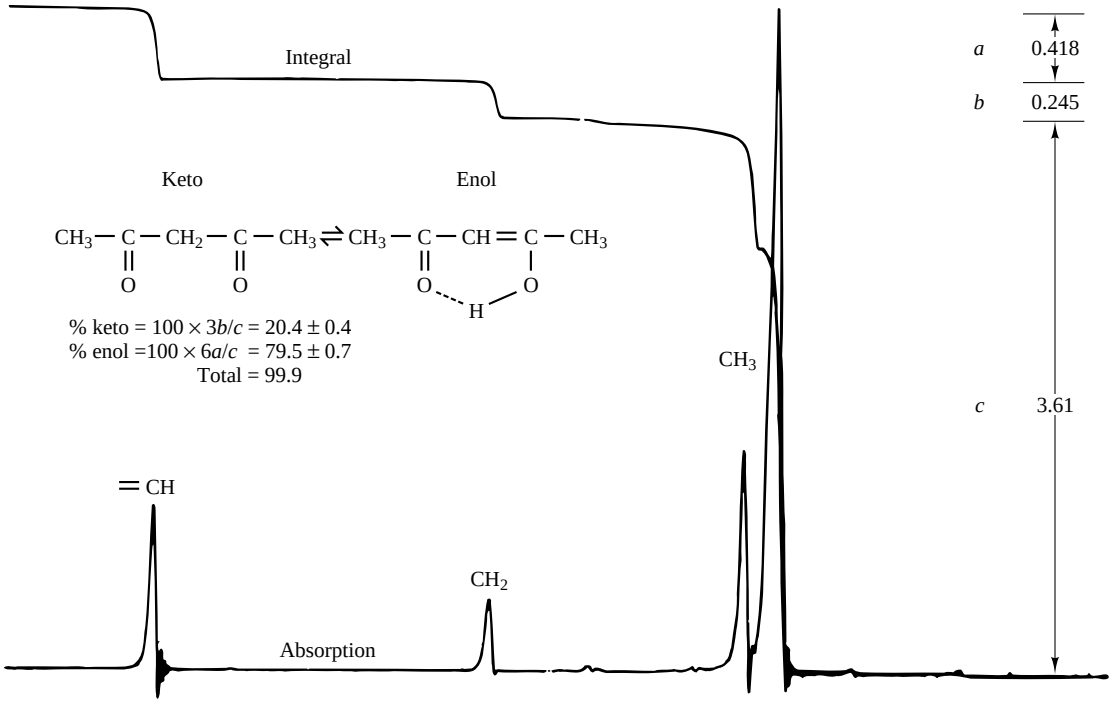

Figure 1 Analysis of a tautomeric mixture

8.2 Monitoring Purification and Separation Processes

Coenzyme Q_{10} has the structure shown in Figure 2, where the number of isoprene units in the side chain is $n = 10$. Separation of compounds with 9 or 11 units is difficult. The absence of such contaminants in the sample is confirmed by the ratio of the area arising from the six protons of the two methoxy groups to the area of the peak at 5.0 ppm that contains a proton from each repeated unit. The average number of units in the chain is found to be within 0.2% of the expected value of 10.

8.3 Iodine Value of Fats and Oils

Johnson and Shoolery[11] showed in 1962 that the number of protons attached to doubly bonded carbons could be determined from the proton spectrum of edible oils consisting of various triglyceride mixtures of mono-, di-, and tri-unsaturated C_{18} fatty acids. Each fat or oil molecule contains five protons attached to the three carbon atoms of the glyceryl chain. Four of these are the CH_2 protons in the 1,3 positions, which give a multiplet centered at 4.2 ppm, and the fifth (the proton on C-2) gives a multiplet at 5.3 ppm that is not resolved from the olefinic protons found between 5.2 and 5.3 ppm. In the 200 MHz spectrum of corn oil, shown in Figure 3, the integral over the region from 5.6 to 5.0 ppm between points 1 and 2 represents the olefinic protons plus the proton on C-2, while the integral of the 4.5–3.9 ppm region between points 2 and 3 represents four protons per molecule of oil. If these two integrals are designated A and B, respectively, it follows that the number of olefinic protons (and doubly bonded carbons), N, per molecule of oil is $4A/B - 1$.

The degree of unsaturation is routinely measured by titrating the oil with iodine. The uptake of iodine at the endpoint is expressed as the iodine value (IV), and is the number of grams of iodine consumed by 100 g of fat. There is an exact correspondence in the number of iodine atoms per molecule at the completion of the reaction and the number of olefinic protons in the original fat. This leads to the expression

$$\text{IV} = \frac{12\,691N}{\text{Mol. wt. of fat}} \tag{8}$$

and if the fat consists entirely of C_{18} fatty acid triglycerides, equation (8) becomes

$$\text{IV} = \frac{12\,691N}{890.88 - N} \tag{9}$$

This formula can be corrected for oils containing fatty acids with a variety of chain lengths if the total integral of the proton spectrum is also measured.

The modern 200 MHz superconducting FT NMR spectrometer used for this analysis was programmed by standard keyboard commands to execute a macro command when instructed by pressing a function key. After automatic locking and shimming, the spectrometer acquired the spectrum, processed the FID, and performed numerical integration of regions A and B. The integrals were stored, and the IV was calculated and printed on the chart and on a printer. Thus, rapid, nondestructive analysis of small samples (50–100 mg) of fats and oils by proton NMR, requiring no special operator skills or judgment, can be regarded as routine.

9 QUANTITATION IN ^{13}C NMR

Quantitative measurements in ^{13}C NMR are complicated by the fact that two techniques that are necessary to improve

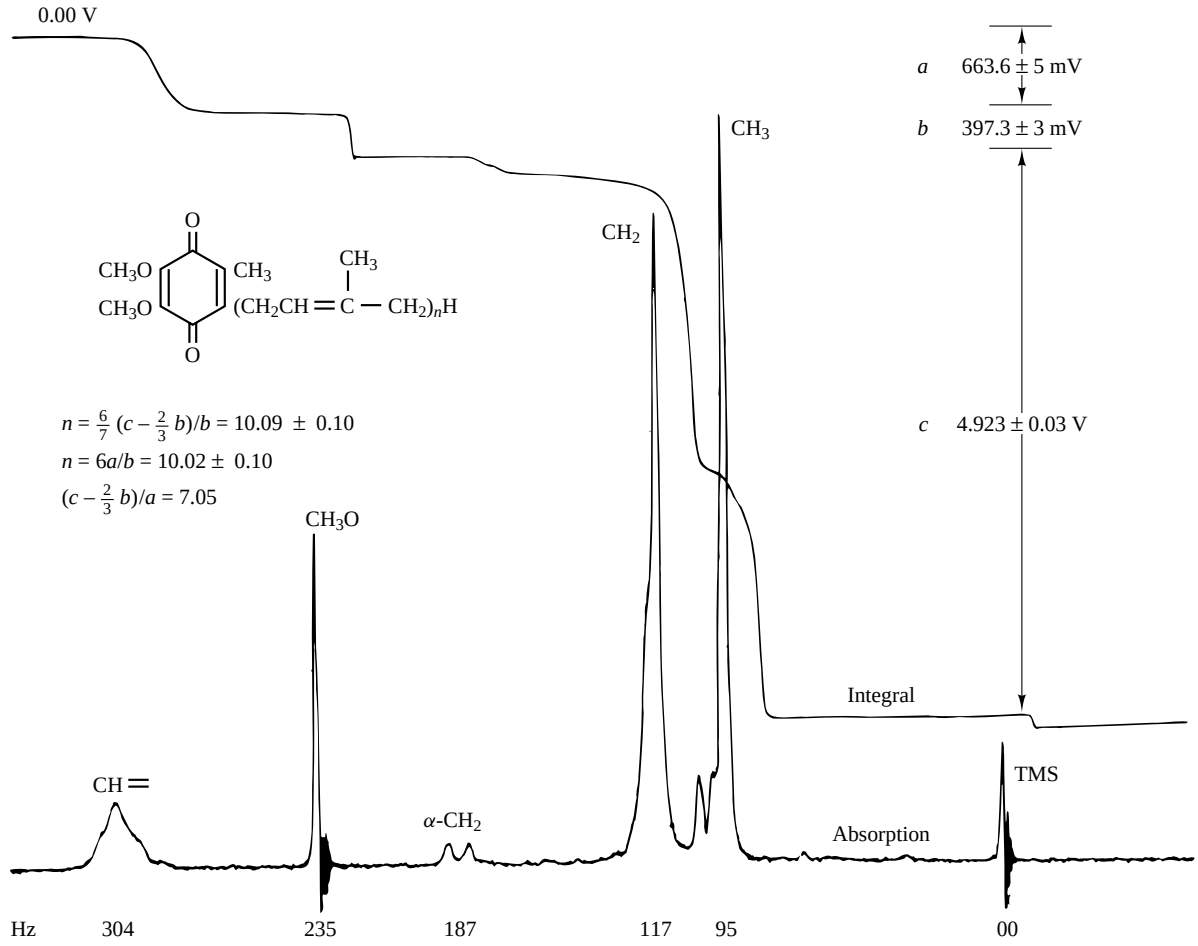

Figure 2 Determination of chain length of coenzyme Q_{10} (Molecular weight 862.7)

sensitivity and resolution can strongly perturb the populations of the ^{13}C nuclear energy levels. The integrated intensities of the NMR peaks will then depend on factors other than the number of nuclei giving rise to the peak. Fortunately, methods for restoring the equilibrium magnetization can be employed to circumvent this problem.[12,13]

9.1 Time Averaging of Multiple Data Acquisitions

This technique is used in all FT NMR spectrometers whenever the signal-to-noise ratio needs to be improved, or when phase cycling is required to suppress artifacts. If the magnetization is not allowed to recover fully after each pulse, the next acquisition will reflect the decreased magnetization. That process will continue until an equilibrium is reached, which depends upon the relative values of the spin–lattice relaxation time T_1 for each transition, the pulse tip angle, and the pulse repetition rate. The integrals no longer depend only upon the number of nuclei. The problem occurs in all time-averaged FT NMR spectra, regardless of the nucleus being studied, but is much more troublesome for ^{13}C NMR, because of the long T_1 values found for ^{13}C in a variety of chemical environments.

There are three ways to remedy this situation.

1. One can introduce a recovery delay between pulses long enough to result in complete repolarization of even the nuclei with the longest T_1. This may require several hundred seconds, and can therefore result in very long total accumulation times.
2. One can use a very short pulse, which perturbs the population of the spin states very little.
3. One can dissolve a paramagnetic material in the sample to make all T_1 values short compared with the pulse repetition rate.

9.2 Broadband Proton Decoupling

Broadband decoupling involves irradiating all protons in the sample with an intense rf magnetic field at their resonance frequency so that their spins are effectively decoupled from the ^{13}C nuclei and the latter consequently appear with all of their intensity in a single sharp line rather than a widely split multiplet of many weak lines. That technique has been a major factor in the successful application of ^{13}C to solving chemical problems. An auxiliary benefit has been a badly needed gain in sensitivity, as a result of nuclear Overhauser enhancement (NOE). Strong irradiation of the proton transitions in a coupled spin system perturbs the populations of the spin states involved in the carbon transitions, and results in an increase in the peak intensity to a value 2.988 times the Boltzmann value. Unfortunately, the excess population generated in this manner can leak off if the ^{13}C nuclei can exchange energy with their

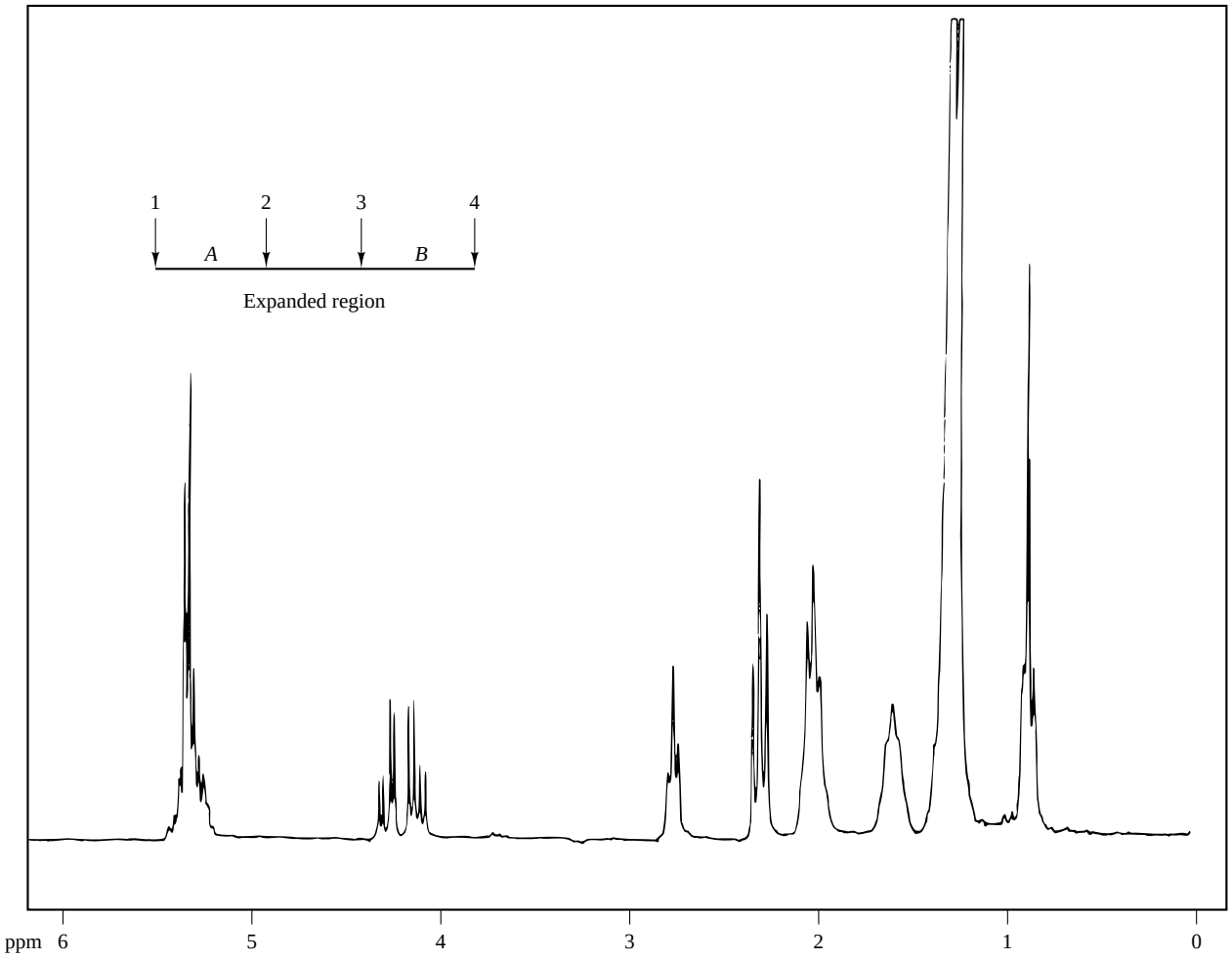

Figure 3 200 MHz proton spectrum of corn oil

surroundings in other ways. This can lead to a range of NOE values for carbons in the same molecule from 1.0 to 2.988, and invalidates quantitative comparison of integrals.

There are also three ways of dealing with the problem of variable NOE factors.

1. One can operate without proton broadband decoupling. This has the disadvantage that the reappearance of the rather large proton–carbon scalar couplings will cause severe overlap of the ^{13}C spectral regions of interest. Furthermore, the usual gain in sensitivity due to NOE will not be realized.
2. One can gate the decoupler on during the acquisition of data and off during the rather long delay necessary to avoid relaxation recovery effects. The build-up of excess ^{13}C population during acquisition will die away again during the delay period. Of course, the sensitivity will suffer because of the loss of the NOE, but the ^{13}C signals will be collapsed into sharp peaks, with all of the intensity for each carbon in a single line.
3. One can provide an alternative relaxation mechanism for all ^{13}C nuclei in the molecule. Except possibly for ^{13}C atoms deeply buried within a large rigid molecule, it appears that the addition of a paramagnetic species can quench the NOE for all of the carbon atoms without unduly broadening the lines.[14]

From the foregoing, two approaches emerge as possible ways to deal with the difficulties arising from unequal T_1 values and NOE values.

1. The decoupler can be gated on only during the acquisition time, and off during a repolarization time chosen long enough to be 4–5 times as long as the longest T_1.
2. One can add approximately 0.1 M chromium acetylacetonate [$Cr(AcAc)_3$] to the $CDCl_3$ solution of the sample, to shorten all T_1 values and quench all NOE effects. If the acquisition time is not 4–5 times longer than the shortened T_1 then a repolarization delay will also be needed.

10 APPLICATIONS OF ^{13}C NMR

Several examples of the utility of quantitative measurements of ^{13}C spectra in various branches of chemistry illustrate the wide range of applications.

10.1 Structure of an Unknown Hydrocarbon

A hydrocarbon found in a sample of cod liver oil was found to have ten ^{13}C peaks. Spectral editing showed two CH carbons, five CH_2 carbons, and three methyl carbons.

That leads to the unacceptable formula $C_{10}H_{21}$, which violates the bonding requirements and is impossible to reconcile with the proton spectrum. A quantitative experiment using a 30 s recovery delay and gated decoupling to eliminate NOE effects showed conclusively that one of the CH_2 carbon peaks exhibits exactly half the intensity of the other nine carbons. That means that the molecule is *symmetrical* and has two C_9 fragments attached to a unique CH_2 group. That leads to the acceptable formula $C_{19}H_{40}$, and the structure of the hydrocarbon pristane can easily be deduced from the chemical shifts. This compound may be produced by photochemical or thermal rearrangement in storage of cod liver oil, since it has the carbon skeleton (**1**)

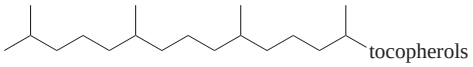

(1)

of the side chain in the tocopherols present in cod liver oil.

10.2 Aromaticity of Petroleum Mixtures

Crude oil varies greatly in the ratio of aliphatic (and alicyclic) carbon atoms to aromatic carbon atoms in various substituted and fused ring configurations. A quantitative measurement of this ratio is of considerable value in the industry to obtain the most useful products from a given crude. A sample of crude oil was run with a 200 s delay and gated decoupling, since it was known that carbons at aromatic fused ring junctions can be quite isolated and exhibit a long T_1. The value of 1.75 obtained for the aliphatic-to-aromatic carbon ratio was then compared with the value of 1.73 obtained by doping the chloroform solution of the oil with 0.1 M $Cr(AcAc)_3$ and running the spectrum under standard conditions. Both methods appear to have eliminated discrepancies from T_1 and NOE effects, but the $Cr(AcAc)_3$ doping enjoyed a time advantage of nearly a factor of 10, and is clearly the choice for repetitive routine analyses. Oils with olefin content would need to be corrected by proton NMR measurements, since the chemical shifts of olefinic and aromatic carbons fall in the same range.

10.3 Analysis of Edible Oils and Seeds

A hypothetical triglyceride composed of oleic acid (18 : 1) and linolenic acid (18 : 3) at the 1 and 3 positions of the glycerol molecule, and linoleic acid (18 : 2) at the 2 position, is shown in Figure 4, along with the ^{13}C spectrum of linseed oil, which contains all three acids along with stearic (18 : 0). The acids may be randomly distributed on the glyceride chains in linseed oil (although the biochemical synthesis in living organisms may be selective), but the ^{13}C spectra are not very sensitive to positional effects. Sixteen peaks or regions can be integrated, and have been assigned contributions from the various carbons in all 18 positions along the fatty acid chains of all four types of fatty acids. Some peaks measure a fatty acid component directly, e.g., B, E, and O represent the C_{16}, C_{15}, and C_{17} carbons, respectively, in 18 : 3, while L represents C_{11} and C_{14} in 18 : 2, overlapped by C_{11} of 18 : 1. All 16 integrals overdetermine the analysis of the four acids, and the best result is obtained by iterating to a least squares fitting of all the data by adjusting a starting composition to minimize the error. The starting set is estimated from the peaks that are most sensitive to the three unsaturated acids, peaks B, C, E, O, H, and I.

Oil samples were dissolved in $CDCl_3$ and doped with 0.04 M $Cr(AcAc)_3$. The T_1 values were all 1.0 s or less, allowing a 5 s recovery delay with gated decoupling. Table 2 shows the comparison of the ^{13}C NMR analysis with the GC analysis for five widely used vegetable oils. The excellent agreement gives confidence that the relaxation and NOE factors have been eliminated and that the baseline correction and numerical integration routines are obtaining accurate peak areas.

While ^{13}C NMR is not competitive with GC in the analysis of oils expressed from seeds, it is the only way that a noninvasive measurement of oil composition can be made in a viable seed. The oil in seeds is present as a liquid dispersed throughout the seed membranes in minute cavities. The spatial variations in magnetic susceptibility throughout the seed result in significant line broadening due to local dipolar fields, but these can be averaged out completely by spinning the seed about an axis inclined to the magnetic field at the magic angle used in studies of solids by NMR.

11 QUANTITATION OF OTHER NUCLEI

11.1 Nuclei with Spin $\frac{1}{2}$

Other nuclei with nuclear spin-$\frac{1}{2}$, such as ^{31}P and ^{19}F, pose essentially the same problems that have been covered for protons and ^{13}C. The larger range of chemical shifts may, in a few cases, require attention to the uniformity of excitation over the spectral width, and pulsewidths or power may have to be decreased. The strong magnetic moments and 100% abundance of both ^{31}P and ^{19}F make them strong candidates for stable isotope tracers in biological and biochemical studies. Furthermore, the ubiquitous occurrence of ^{31}P in living organisms and the increasing applications of in vivo ^{31}P spectroscopy in medicine will surely lead to greater and greater need for accurate quantitative assays based on the general procedures discussed in previous sections.

A study of organophosphorus insecticides in 1977 concluded that ^{31}P NMR provides a very rapid method of analyzing technical samples of these insecticides for both fenitrothion and its artifacts, some of which are present at levels below 0.1%.[15] While both GC and LC are unable to determine some of the possible phosphorus compounds present in technical fenitrothion samples, owing to lack of volatility or nonabsorbance in the UV, the ^{31}P NMR method analyzes for all the phosphorus artifacts. Although the initial cost of the NMR instrumentation is high, the speed of ^{31}P NMR analysis and its use with any organophosphorus insecticide may well be justified when the number of samples is high.

11.2 Nuclei with Spin Greater than $\frac{1}{2}$

Many isotopes of common elements have adequate magnetic moments for NMR detection, but possess other unfavorable nuclear properties that make them unsuitable for NMR studies.

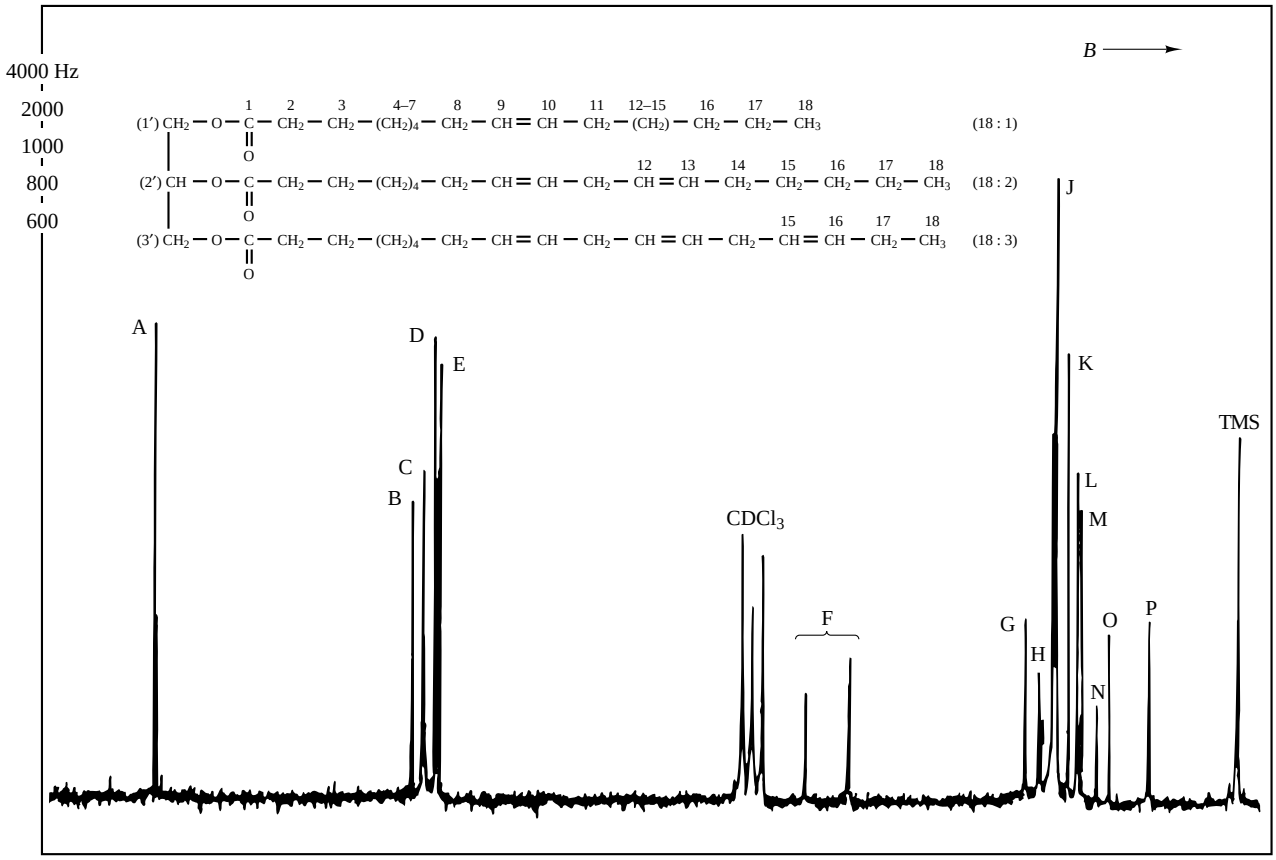

Figure 4 ^{13}C spectrum of linseed oil

Low abundance is often a problem, followed in nuclei with spin greater than $\frac{1}{2}$ by line broadening arising from very short spin–lattice relaxation times. If the nucleus has a spin greater than $\frac{1}{2}$, it possesses a nonspherical distribution of electric charge, manifested by an electric quadrupole moment, which can interact very strongly with fluctuating electric field gradients at the nucleus.

That relaxation mechanism can be a benefit in making quantitative measurements, acting, as it were, like a built-in relaxation agent. Nuclei such as ^{7}Li, ^{11}B, ^{17}O, ^{23}Na, and several others fall into that category. If, however, the quadrupole moment is too large, which is frequently the case in the heavier elements, or if the type of bonding typical of the element results in a strong ionic component to the bonds it forms, the relaxation times may be in the microsecond range, and the linewidths may be of the order of megahertz. The lifetime of the FID becomes so short that only a few data points can be obtained, and the NMR signals cannot readily be distinguished from artifacts due to pulse breakthrough and acoustic ringing of the probe structure. Future improvements in hardware may alleviate those problems to some degree, but the best advice for anyone seeking to study the NMR behavior of elements whose nuclei have spin greater than $\frac{1}{2}$ is to check the electric quadrupole moment and compare with ^{17}O. If it is 10–100 times larger then detecting the signals may be next to impossible, and accurate quantitation is out of the question.

12 CONCLUSIONS

While quantitation in NMR spectroscopy is more dependent on control of experimental conditions than is the case in optical spectroscopy, modern NMR spectrometers are sensitive, stable, and relatively user-friendly. The requirements for accurate quantitation in NMR are now well understood and can be met quite easily given the flexibility of the software

Table 2 Fatty Acid Composition of Oils by ^{13}C NMR[a]

Component	Rapeseed	Cottonseed	Peanut	Soybean	Safflower
18 : 3	6.7 (6.4)	0.0 (0.0)	0.0 (0.0)	4.5 (3.6)	0.0 (0.3)
18 : 2	11.0 (10.0)	54.9 (57.4)	32.0 (32.6)	34.8 (37.8)	74.2 (76.3)
18 : 1	76.0 (76.9)	20.4 (19.0)	49.5 (48.7)	46.5 (44.8)	14.1 (13.0)
18 : 0	6.3 (6.8)	24.7 (23.5)	18.4 (18.6)	14.0 (13.8)	10.7 (10.4)

[a]Values in parentheses are from GC analysis (% of total).

in commercially available instruments. The biggest barrier to widespread analytical use of NMR is the cost, which can make some analytical applications less cost-effective than other alternatives. In research applications, however, the ability to make accurate quantitative measurements adds one more dimension to the utility of an instrumental technique that has proved itself indispensable in every branch of organic chemistry and biochemistry.

13 REFERENCES

1. F. Bloch, *Phys. Rev.*, 1946, **70**, 460.
2. *Technical Information Bulletin*, Varian Associates, Palo Alto, CA, 1960, Vol. 3, No. 2.
3. *Proceedings of the 5th International Instruments and Measurements Conference, Stockholm*, Academic Press, New York, 1960.
4. B. A. Jacobsohn and R. K. Wangsness, *Phys. Rev.*, 1948, **73**, 942.
5. W. A. Anderson, *Phys. Rev.*, 1956, **102**, 151.
6. M. Karplus, *J. Chem. Phys.*, 1959, **30**, 11.
7. H. Primas, *Helv. Phys. Acta*, 1958, **31**, 17.
8. R. Ernst and W. A. Anderson, *Rev. Sci. Instrum.*, 1962, **37**, 85.
9. H. Barkhuijsen, R. de Beer, W. M. M. T. Boree, and D. Van Armondt, *J. Magn. Reson.*, 1985, **61**, 465.
10. H. S. Jarrett, M. S. Sadler, and J. N. Shoolery, *J. Chem. Phys.*, 1953, **21**, 2092.
11. L. F. Johnson and J. N. Shoolery, *Anal. Chem.*, 1962, **34**, 1136.
12. J. N. Shoolery and W. C. Jankowski, *Application Note NMR-73-4*, Varian Associates, Palo Alto, CA, 1973.
13. J. N. Shoolery, in *Progress in Nuclear Magnetic Resonance Spectroscopy*, ed. J. W. Emsley, J. Feeney and L. H. Sutcliffe, Pergamon Press, London, 1977, Vol. 11, Pt. 2, p. 79.
14. G. N. LaMar, *J. Am. Chem Soc.*, 1971, **93**, 1040.
15. R. Greenhalgh and J. N. Shoolery, *Proceedings of the Symposium on Fenitrothion, Ottawa*, National Research Council of Canada, Publication NRCC 16 073, 1977.

Biographical Sketch

James N. Shoolery. *b* 1925. B.S., 1948, University of California, Berkeley, Ph.D., 1952, California Institute of Technology, physical chemistry. Joined Varian Associates 1952, founded the NMR Applications Laboratory and served as its Manager until 1960. Marketing Manager for the Instrument Division of Varian, 1960–1965, Applications chemist 1965–retirement, 1990. NMR consultant 1990–present. Approx. 170 publications. Research specialties: application of NMR to organic structure elucidation, quantitation in high resolution NMR, microsample techniques.

Adsorbed Species: Spectroscopy and Dynamics

Ian D. Gay
Department of Chemistry, Simon Fraser University, Burnaby, B.C., Canada

1	Introduction	1
2	Early Results	2
3	Multinuclear Magnetic Resonance	2
4	High-Resolution Solid State Techniques	3
5	Adsorbates on Metals	3
6	Adsorption Probes of Surface Sites	3
7	Surface Hydroxyl Groups	4
8	Chemical Reaction in Adsorbed Layers	4
9	Structure of Adsorbed Species	4
10	Motion in Adsorbed Layers	4
11	Related Articles	5
12	References	5

1 INTRODUCTION

The term 'adsorbed' implies concentrated at an interface. This article deals with the NMR of small molecules adsorbed, i.e. bound, to solid sufaces. (For a general introduction to adsorption and the properties of surfaces, see Adamson[1] or Somorjai.[2]) In addition to being of intrinsic scientific interest, adsorbed layers are of great practical importance in the areas of heterogeneous catalysis, separation science, and chromatography.

Molecules may bind to surfaces by any type of interaction, ranging from chemical bonding to van der Waals interaction. The case of chemical bonding is often called 'chemisorption', while the term 'physisorption' is sometimes used for weaker interactions. An adsorbed layer one molecule thick is called a 'monolayer' and thicker adsorbed deposits are called 'multilayers'. Clearly temperature is a major factor in determining the extent of adsorption, and appreciable adsorption will only be found when the interaction energy is greater in magnitude than *kT*.

NMR is the least sensitive of the common spectroscopic techniques, and thus the observation of adsorbed monolayers is dependent upon having a large amount of surface area in the NMR sample. The surfaces of highest specific area are those of activated carbon, and refractory oxides such as SiO_2 and Al_2O_3. Because of their great importance as adsorbents, catalysts, and catalyst supports, the preparation of these has been much studied.[3,4] These substances are readily prepared with specific surface areas of the order of hundreds of square meters per gram ($m^2\ g^{-1}$). Their densities as powders are typically about $1\ g\ cm^{-3}$, so an NMR sample may contain hundreds of $m^2\ cm^{-3}$. A monolayer of moderate sized molecules might contain 5 μmol m^{-2}, so that the bulk concentration of an adsorbed monolayer can be of the order of 0.5 M. Such concentrations of sensitive high-abundance nuclei, e.g. ^1H, ^{19}F, and ^{31}P, can be observed in a single scan with modern instrumentation. Those familiar with liquid NMR will find the effective sensitivity for adsorbed species to be considerably less, due to the much broader lines which arise for reasons noted below. None the less, high sensitivity nuclei are easily observed on such solids, and more difficult nuclei such as natural abundance ^{13}C can typically be observed in thousands or tens of thousands of scans. Often spin–lattice relaxation times for adsorbed molecules are appreciably shorter than for the same molecules in the liquid phase. This can make the signal averaging of large numbers of scans more feasible than might have been expected.

Another family of high area solids is the zeolites,[5] crystals with internal pores of molecular size. The interior of these pores is equivalent to a high surface area, again typically of the order of hundreds of $m^2\ g^{-1}$. Whether guest molecules inhabiting these pores can be said to be adsorbed is a matter of semantic convention. In this article the NMR of such guest molecules will be only briefly touched upon.

A large number of substances can be prepared in the $10\ m^2\ g^{-1}$ range, and almost any solid can be prepared with $1\ m^2\ g^{-1}$. Whether a high area preparation is stable with respect to loss of area by sintering depends mainly on the temperature. Typically the temperature must be kept below about one-half of the melting point to prevent substantial loss of area. A system of great practical interest is the supported metal catalyst.[6] These catalysts consist of metal crystallites dispersed on a refractory oxide, such as silica or alumina. This technique permits a very high dispersion of the metal, with reduced tendency to sinter, and makes the most effective use of expensive platinum group metals. While the metal dispersion is extremely high, such catalysts typically contain a few per cent of metal by mass and have metal areas of 1 to $10\ m^2\ g^{-1}$ of catalyst. Monolayers of high sensitivity nuclei are straightforward even at $1\ m^2\ g^{-1}$; however, if one wishes to explore nuclei of low sensitivity, or small fractions of a monolayer, severe sensitivity problems eventually arise. One possible approach to this problem is to use the Curie law enhancement of NMR sensitivity at extremely low temperatures in the millikelvin range.[7]

In general, the preparation of high-area solids will result in an aggregate of randomly oriented crystallites. Some preparations, e.g. silica gels, will lack long-range order entirely. In a few favorable cases, high-area oriented samples can be prepared, e.g. in the case of lamellar clay particles by sedimentation.[8]

If one imagines a surface prepared by the sudden cleavage of a solid, it is evident that the surface may be viewed as a macroscopic radical with large numbers of 'dangling bonds', resulting from the disruption of the chemical bonds responsible for the integrity of the solid. Such a surface will be a very reactive entity and will be subject to structural rearrangement, which can lower its free energy, and to chemical reaction with its environment. Thus all metal surfaces (with the possible exception of Au) that have been in contact with the atmosphere will be covered by a layer of oxide. This layer may be a monolayer, or may be many layers thick. Similarly, oxide surfaces that have been exposed to the atmosphere normally have a monolayer of –OH groups, resulting from their reaction with H_2O. This surface OH may be regarded either as the result of chemisorption of H_2O or as a normal constituent of oxide surface.

A 'clean' surface is one whose properties approximate the idealized cleaved crystal, at least as regards chemical

composition. (Many clean surfaces undergo rearrangement of their atoms to positions different from the bulk crystal.[2]) Clean surfaces are of much interest in fundamental surface science studies. In general, really clean surfaces are achieved only under ultrahigh vacuum conditions on areas of the order of 1 cm^2; adsorption on such surfaces is inaccessible to conventional NMR study at the present time. A possible exception to this statement is scattering experiments involving polarized atomic beams,[9,10] which can yield nuclear relaxation data and possibly other NMR-like parameters. For the most part, however, present NMR studies involve surfaces that are at best partially clean. Thus, surface oxide can be removed from the noble metals by H_2 reduction, followed by thermal desorption of the resulting adsorbed H; surface OH can be largely removed from oxide surfaces by thermal treatment under vacuum. While not too attractive from the point of view of fundamental studies, the surfaces studied by NMR can easily be kept in a state similar to those used in practical applications for adsorption and catalysis, and NMR has substantial contributions to make to these fields.

The main features of the NMR of any sample will be determined by the mobility of the molecules studied. In this context, adsorbed layers are somewhat intermediate between liquid and solid samples. For many strongly chemisorbed samples, the adsorbed species are held in place by strong chemical bonds and are solids for NMR purposes. However, strong bonding to the surface does not necessarily imply localized bonding. For example, H atoms bind to most metal surfaces with an energy in excess of 200 kJ mol^{-1}, but in the case of the platinum group metals at room temperature they are mobile parallel to the surface on the NMR timescale, and are in some sense a two-dimensional fluid. Rotational motion of adsorbed molecules is also common, but the presence of the surface is likely to introduce greater anisotropy in this motion than would be observed in a liquid. Weakly bound physisorbed molecules are typically in rapid exchange with the gas phase, and average NMR properties will be observed. For high-area solids it will usually be the case that the adsorbed population is much larger than the gas-phase population, so that properties like chemical shifts will be dominated by those of the adsorbed phase, while the rapid exchange ensures that the motional properties of the layer appear liquid-like, both translationally and rotationally.

2 EARLY RESULTS

Not surprisingly, the first NMR studies of adsorbed species involved proton NMR[11,12]. Since these predated high resolution solid state techniques, the possible experiments were broadline studies of immobile species, 'high-resolution' studies of mobile adsorbates, relaxation/linewidth measurements, and diffusion measurements by field gradient techniques. Examples of most of these exist from before 1960. For example, O'Reilly et al.[13] observed that surface OH on silica and silica–alumina is chemically shifted with respect to liquid H_2O, and inferred from the temperature-independent Lorentzian lineshape that the OH forms a dilute randomly populated dipolar coupled system. Hickmott and Selwood[14] studied the relaxation of water and several organics on various oxides, and showed the importance of surface paramagnetic species as relaxation agents. Fuschillo and Renton[15] studied the linewidth of methane on TiO_2 at low temperatures, and demonstrated the now well-known result that submonolayer amounts of physisorbed species do not become immobile until the temperature is well below the bulk freezing point.

In spite of these early successes, surface NMR in succeeding years proved somewhat disappointing. In general, very few chemical shifts proved to be measurable because of the large linewidths found for proton resonances. The sources of these linewidths were eventually realized to be rapid relaxation, especially by surface paramagnetic species, exchange with surface protons, heterogeneity of surface with respect to adsorption energetics, and inhomogeneous broadening from the nonzero magnetic susceptibility of irregular adsorbent particles; no proton linewidths less than 1 ppm were observed and much larger linewidths were common. Given the limited range of proton shifts, little of interest was shown regarding the structure and bonding of adsorbed molecules. Furthermore, with some notable exceptions,[16] it turned out to be difficult to obtain information regarding molecular motion from relaxation studies. This was largely because of the difficulties of disentangling different relaxation processes, and the often dominant effect of paramagnetic surface species, in the presence of which correlation times may be determined more by electron relaxation than by adsorbate motions. The results of this early period are well summarized in the reviews by Packer[17] and Pfeifer.[18] Diffusion measurements, particularly in the context of guest molecules in zeolites, have recently been reviewed by Kärger et al.[19]

3 MULTINUCLEAR MAGNETIC RESONANCE

More possibilities were opened by the increasing availability of multinuclear and Fourier transform NMR equipment beginning in the 1970s. If, as it turns out, lines from adsorbed species will be at least a few ppm in width, chemical shifts should be observable for nuclei whose shift range is of the order of hundreds of ppm or more. An extreme example of this is the observation[20] of an 80 ppm shift for Tl^+ adsorbed from H_2O onto silica. In a more practical vein, the early 1970s saw the first natural abundance ^{13}C spectra of molecules in zeolites[21] and physisorbed on silica[22]. Linewidths were a few ppm and it was possible to observe chemical shifts due, for example, to the hydrogen-bonding interaction of adsorbed acetone with surface hydroxyls. These works also demonstrated the possibility of measuring relaxation times separately for chemically different groups within a molecule. This could lead to simpler analysis of relaxation experiments for rigid molecules and the study of internal motions for others. In the early 1980s spectra were obtained for ^{15}N in a variety of molecules in zeolites[23] and adsorbed on SiO_2,[24] showing the advantages of studying the NMR of the atom which is the site of interaction between adsorbate and adsorbent. Relaxation studies of ^{17}O in H_2O on montmorillonite and kaolinite were performed.[25] These showed the desirability of measuring adsorbate correlation times in a system where strong quadrupolar interaction dominates the relaxation, and yielded surprisingly short correlation times for water in these systems, on the order of 10^{-11} s. Results to 1985 on multinuclear spectroscopy and relaxation measurements on adsorbed mobile molecules are comprehensively reviewed by Nagy, Engelhardt, and Michel.[26]

4 HIGH-RESOLUTION SOLID STATE TECHNIQUES

The advent of high-resolution solid state NMR techniques in the 1960s and 1970s opened up new possibilities for the study of adsorbate systems. The most obvious of these is the identification of immobile chemisorbed species. The first use of these techniques by Kaplan et al.[27] was however a CP study of physisorbed benzene and toluene at low temperatures. Observation of an axially symmetric CSA powder pattern showed that benzene undergoes rapid rotation about the hexad axis, even at 77 K. Further experiments demonstrated that rapid cooling can trap molecules in a metastable isotropically rotating state at this temperature.

Magic angle spinning was first applied to surface problems by Stejskal et al.[28] in their study of CO_2 in zeolites. This showed that substantial line broadening which may arise from microscopic susceptibility variations in the adsorbate can be removed by MAS. Use of MAS in surface problems suffers from the conflicting requirements of atmospheric integrity, best achieved with sealed samples, and of excellent mechanical balance, which is likely to be degraded by the sealing process. This conflict was resolved in a semisatisfactory way in 1984.[29]

The first use of multiple pulse line narrowing in surface studies was by Schreiber and Vaughan.[30] This permitted the measurement of the shielding anisotropy of surface protons on SiO_2; strong dipolar coupling to ^{27}Al prevented similar measurements on Al_2O_3. The combination of multiple pulse narrowing with MAS (CRAMPS), together with the use of higher magnetic fields, has recently been leading to growing success in the proton spectroscopy of adsorbed species.

5 ADSORBATES ON METALS

The resonance of hydrogen chemisorbed on platinum was first observed by Ito et al.[31] Subsequently, the resonance of hydrogen has been observed on Cu, W, Ru, Rh, Pd, Os, Ir, and a few alloys, by these and other workers. (In the case of W, the cleanliness of the surface is questionable.) For all of the metals, large shifts are observed which cannot reasonably be chemical shifts and must therefore be Knight shifts. For Cu the shift is to high frequency, for the others to low frequency. With Ru–Cu bimetallic clusters[32] the Knight shift of H on Ru decreases steadily as the Cu content is increased.

Platinum has been the most studied of these metals and it has been established that there is little difference between metallic powders and supported Pt catalysts. It has also been found that Knight shifts are smaller when the Pt particles are very small and when the adsorbed H covers a large fraction of the metal surface. As yet these trends have not received a satisfactory quantitative explanation in terms of the bonding between H and the metal surface. For all of the above metals the linewidth of the H resonance indicates that the hydrogen is mobile at room temperature. For those which have been studied to lower temperatures, motion generally ceases before liquid nitrogen temperature is reached.

^{13}C NMR of CO chemisorbed on a metal was first studied by Duncan et al. on Rh.[33] Since then it has been studied on the remaining noble metals, and on bimetallic Pt–Rh particles. Much of this work is described in the reviews by Slichter[34] and Duncan.[35] On Ru and Rh an average shift is observed that corresponds to the known shifts of metal carbonyl complexes. In static samples a broad powder pattern is observed with an anisotropy of some 400 ppm, corresponding to a linear carbonyl. On Rh, bridging carbonyl has also been observed. At room temperature, with the highest CO loadings, a narrow line appears from CO that is rotating isotropically on the NMR timescale. Thus the NMR of CO on Rh and Ru can be interpreted in terms of chemical shifts which are completely analogous to those observed in diamagnetic metal carbonyl complexes.

On the other hand, CO on supported Pt and Pd shows large high-frequency Knight shifts. Knight shifts are not observed for CO on colloidal platinum,[36] but it is not clear whether this is due to loss of metallic properties in the smaller particles or to interactions with the reagents used to stabilize the colloid. Supported Os and Ir show smaller high-frequency shifts and it is hard to be certain whether these are chemical or Knight shifts. Observations on Pt–Rh clusters[37] show that the Knight shift disappears above about 50% Rh, even though SEDOR measurements clearly show the presence of Pt in the surface layer of the particles.

The above results indicate that one must proceed with caution in interpreting the observed line positions of chemisorbed species on metals. For example, the metal (Rh) giving the largest Knight shift for adsorbed H gives no Knight shift for adsorbed CO. Thus in the absence of a reliable and comprehensive theory for Knight shifts of adsorbed species, every adsorption system must be examined carefully on its own merits.

6 ADSORPTION PROBES OF SURFACE SITES

The nature and concentration of specific types of site on solid surfaces has long been an area of interest, especially from the point of view of catalytic activity. These features can be probed spectroscopically by observing changes in the spectrum of a small molecule upon its binding to the surface. The archetypal example is the study of acid sites on oxide surfaces by IR spectroscopy of adsorbed amines;[38] pyridine, for example, gives distinct lines when physisorbed, protonated by a surface Brønsted acid, or coordinated to a surface Lewis acid.

This type of probing can obviously be done by NMR, which has the advantage that quantitative accuracy is in principle better. With IR spectroscopy it is generally difficult to be confident regarding the extinction coefficient of chemisorbed species, and there are often considerable uncertainties regarding path length and adsorbate concentration. Surface acids have thus been probed by direct proton NMR and by ^{13}C, ^{15}N, and ^{31}P NMR of adsorbed amines and phosphines. Such attempts have been generally successful and are complementary to IR studies. Much of the work in this area has been reviewed by Freude.[39]

Proton NMR cannot of course detect Lewis acids directly. For quantitative assessment of differing types of acid, ^{31}P spectroscopy seems the most desirable. The high sensitivity of this nucleus permits spectra to be obtained in reasonable time periods by 90° pulse excitation, avoiding the need for cross polarization which may compromise quantitative accuracy. Most results have so far been obtained with trimethylphosphine as a probe; studies of a wider range of phosphorus bases seem likely in the future.

Solid surfaces may also contain basic sites; indeed, the same surface may simultaneously contain both strong acid and strong base sites. Probing these surfaces by NMR is less well developed, but a few results are available. For example, ^{13}C spectroscopy has been used to demonstrate, through the formation of surface bicarbonate from CO_2, the unsurprising result that surface OH on MgO is basic.

7 SURFACE HYDROXYL GROUPS

As mentioned above, all oxides are covered with a layer of –OH groups, which may in a formal sense be regarded as the result of water chemisorption on an ideal oxide surface. The surface chemistry of oxides in their normal state is largely determined by the properties of these hydroxyl groups. The properties of these hydroxyl groups vary from one oxide to another, and the same oxide may show differing types of –OH groups, reflecting different exposed crystal planes, or different structural arrangements. Many of the classic NMR investigations[13,30] have dealt with these groups, and the literature of studies by IR spectroscopy is particularly voluminous. Much of the IR literauture and some of the NMR investigations have been reviewed by Morrow.[40] A recent review by Mastikhin et al.[41] is devoted to NMR studies, particularly of recent results obtained through magic angle spinning.

8 CHEMICAL REACTION IN ADSORBED LAYERS

Adsorbed layers are the site of heterogeneous catalysis and hence reaction in these layers is a topic of immense scientific, technical, and economic interest. NMR studies of such reactions may proceed in two rather different ways. For reasonably rapid reactions of systems that are in equilibrium under NMR conditions, the familiar methods of shift, relaxation, and lineshape analysis may be employed, as in solution NMR. The possibilities for this type of study of adsorbed systems have been reviewed by Resing.[42] On the other hand, slow reactions may easily be studied by recording NMR spectra as a function of time. A sealed NMR tube is in many ways an ideal contamination-free reactor. Reaction studies have been greatly advanced by CP MAS techniques, which permit the potential observation of a wide range of reaction products and intermediates.

For species reacting at a convenient rate at room temperature, e.g. the reaction of trimethyl phosphite with the silica surface,[43] straightforward MAS spectroscopy as a function of time can provide kinetic data for the surface reaction processes. For systems that are only reactive above room temperature, a ‘quick and dirty’ technique is to heat samples for controlled periods of time at the reaction temperature, and then cool to room temperature for NMR observation.[44] While this method provides useful insights, it suffers from uncontrolled conditions during the heating and cooling phases, together with uncertainties about desorption.

Clearly this type of study awaits the development of reliable high-temperature sealable MAS equipment, and recent progress has been made in this direction by Haw and coworkers.[45] Unfortunately, sealed-sample MAS is always open to uncertainties arising from the possibility of desorption when the sample is heated above its preparation temperature. There seems no obvious way of combining the traditional catalytic flow reactor with MAS NMR. For the case of static samples, an NMR-compatible flow reactor has been designed by Reimer and co-workers.[46]

9 STRUCTURE OF ADSORBED SPECIES

NMR of solids has the possibility of yielding direct structural information through measurement of dipolar interactions. Since the structures of chemisorbed species are in general not readily determined, this is a powerful possibility. The fundamental problem is that the motional state of observed species is not known a priori, and it will be unclear whether an observed dipolar coupling should be corrected for motional averaging. Thus, early observations of Pake doublets from adsorbed water[8] (see also bibliography in Pfeifer[18]) generally gave splittings much too small to correspond to static H_2O molecules. These results were therefore not used to infer structural information, but were instead interpreted to give motional information based on the assumption of the known structure of isolated water molecules. In a system where significant structural changes have occurred due to chemical reaction, it seems necessary to demonstrate that observed dipole couplings are independent of temperature, or to give some other evidence for lack of motion, before inferring structural parameters.

Duncan and Vaughan[47] were among the first to use modern solid state methods to determine dipolar couplings in adsorbed layers. Their H–C dipolar modulation studies of adsorbed formic acid gave essentially the same coupling as observed in crystalline formates. A deviation from the expected bond length based on X-ray measurements of calcium formate was attributed to motion, even though the couplings in the adsorbed layer appeared temperature independent.

More recently, Slichter and co-workers[34] have applied spin echoes and SEDOR to measure homonuclear and heteronuclear dipole couplings in adsorbed layers, and to attempt to measure the bond length between adsorbate and surface. The latter endeavor is complicated by the possibility, with heavy nuclei such as ^{195}Pt, of indirect (‘scalar’) couplings of magnitudes comparable to the dipolar couplings.

In principle, dipolar couplings could be estimated from relaxation or NOE measurements. In practice, the often dominant effects of surface paramagnetic impurities, and the general anisotropy of motion in adsorbed layers, render this a complicated and unattractive prospect.

A less direct way of obtaining structural information from dipolar couplings is by the observation of multiple quantum coherence, from which the size of coupled spin aggregations may be inferred. This was first applied to surface problems by Slichter and co-workers,[48] and has recently been reviewed by Hwang and Gerstein.[49]

10 MOTION IN ADSORBED LAYERS

As mentioned in the previous section, structural and motional determinations are a coupled problem pair. In general

the study of motions is simpler, because for many adsorbed systems the assumption of known structures in the adsorbed layer will be chemically tenable.

As indicated above, interpretation of relaxation is difficult in adsorbed systems. More reliable motional information is likely to be obtained by the observation of approximately local molecular properties, such as chemical shift anisotropies, dipolar splittings, and quadrupolar couplings. Thus the first CP study[27] of an adsorbed layer revealed an axially symmetric CSA powder pattern for physisorbed benzene at 77 K. This indicated rapid rotation about the sixfold axis at a temperature well below that at which such rotation occurs in the solid.

Subsequently, Resing and co-workers used analysis of CSA powder patterns to determine the motions of various adsorbed species, such as anchored phenyl groups.[50] Sindorf and Maciel[51] used cross polarization rates as an indicator of average C–H dipolar coupling to study the dynamics of long alkyl chains bound to silica surfaces. Yannoni et al.[52] observed C–C dipolar splittings in doubly-labeled benzene to study its structure and motions on a $Pt–Al_2O_3$ catalyst. The use of deuterium quadrupolar powder patterns to study motions in adsorbed phases is exemplified by the elegant studies of Luz et al.[53] on methyl amines sorbed in zeolites.

11 RELATED ARTICLES

CRAMPS; Cross Polarization in Solids; Deuterium NMR in Solids; Diffusion in Porous Media; Knight Shift; Line Narrowing Methods in Solids; Magic Angle Spinning: Effects of Quadrupolar Nuclei on Spin-1/2 Spectra; Multiple Quantum NMR in Solids; Reactions in Zeolites; Silica Surfaces: Characterization; Supported Metal Catalysts.

12 REFERENCES

1. A. W. Adamson, *Physical Chemistry of Surfaces*, 5th edn., Wiley, New York, 1990.
2. G. A. Somorjai, *Chemistry in Two Dimensions: Surfaces*, Cornell University Press, Ithaca, N.Y., 1981.
3. *Physical and Chemical Aspects of Adsorbents and Catalysts*, ed. B. G. Linsen, Academic, London, 1970.
4. A. B. Stiles, *Catalyst Supports and Supported Catalysts*, Butterworths, Boston, 1987.
5. R. M. Barrer, *Zeolites and Clay Minerals as Sorbents and Molecular Sieves*, Academic, London, 1978.
6. J. R. Anderson, *Structure of Metallic Catalysts*, Academic, London, 1975.
7. Q. Geng, O. Gonen, P. Kuhns, C. Zuo, and J. Waugh, *Bull. Magn. Reson.*, 1989, **11**, 154.
8. D. E. Woessner, in *Mass Spectrometry and NMR Spectroscopy in Pesticide Chemistry*, eds. R. Haque and F. J. Biros, Plenum, New York, 1974, p. 279.
9. B. Horn, E. Koch, and D. Fick, *Phys. Rev. Lett.*, 1984, **53**, 364.
10. R. F. Haglund, Jr., *Chem. Rev.*, 1988, **88**, 697.
11. T. M. Shaw and R. H. Elsken, *J. Chem. Phys.*, 1953, **21**, 565.
12. N. Fuschillo and J. G. Aston, *J. Chem. Phys.*, 1956, **24**, 1277.
13. D. E. O'Reilly, H. P. Leftin, and W. K. Hall, *J. Chem. Phys.*, 1958, **29**, 970.
14. T. W. Hickmott and P. W. Selwood, *J. Phys. Chem.*, 1956, **60**, 452.
15. N. Fuschillo and C. A. Renton, *Nature (London)*, 1957, **180**, 1063.
16. D. Michel and H. Pfeifer, *Z. Naturforsch.*, 1968, **23a**, 339.
17. K. J. Packer, *Prog. Nucl. Magn. Reson. Spectrosc.*, 1967, **3**, 87.
18. H. Pfeifer, *NMR Basic Principles and Progress*, Springer, New York, 1972, Vol. 7, p. 53.
19. J. Caro, M. Bülow, H. Jobic, J. Käger, and B. Zibrowius, *Adv. Catal.*, 1993, **39**, 351.
20. V. V. Morariu, *Chem. Phys. Lett.*, 1978, **56**, 272.
21. D. Michel, *Z. Phys. Chem. (Leipzig)*, 1973, **252**, 263.
22. I. D. Gay, *J. Phys. Chem.*, 1974, **78**, 38.
23. D. Michel, A. Germanus, and H. Pfeifer, *J. Chem. Soc., Faraday Trans. 1*, 1982, **78**, 237.
24. T. Bernstein, L. Kitaev, D. Michel, H. Pfeifer, and P. Fink, *J. Chem. Soc., Faraday Trans. 1*, 1982, **78**, 761.
25. V. I. Kvlividze and A. V. Krasnushkin, *Dokl. Akad. Nauk SSSR, Ser. Khim.*, 1975, **222**, 388.
26. J. B. Nagy, G. Engelhardt, and D. Michel, *Adv. Colloid Interface Sci.*, 1985, **23**, 67.
27. S. Kaplan, H. A. Resing, and J. S. Waugh, *J. Chem. Phys.*, 1973, **59**, 5681.
28. E. O. Stejskal, J. Schaefer, J. M. S. Henis, and M. K. Tripodi, *J. Chem. Phys.*, 1974, **61**, 2351.
29. I. D. Gay, *J. Magn. Reson.*, 1984, **58**, 413.
30. L. B. Schreiber and R. W. Vaughan, *J. Catal.*, 1975, **40**, 226.
31. T. Ito, T. Kadowaki, and T. Toya, *Jpn. J. Appl. Phys. Suppl. 2*, **1974**, 257.
32. X. Wu, B. C. Gerstein, and T. S. King, *J. Catal.*, 1990, **121**, 271.
33. T. M. Duncan, J. T. Yates, Jr., and R. W. Vaughan, *J. Phys. Chem.*, 1979, **71**, 3129.
34. C. P. Slichter, *Annu. Rev. Phys. Chem.*, 1986, **37**, 25.
35. T. M. Duncan, *Colloid Surf.*, 1990, **45**, 11.
36. J. S. Bradley, J. M. Millar, E. W. Hill, and S. Behal, *J. Catal.*, 1991, **129**, 530.
37. Z. Wang, J.-P. Ansermet, and C. P. Slichter, *J. Chem. Soc., Faraday Trans. 1*, 1988, **84**, 3785.
38. A. Zecchina, S. Coluccia, and C. Morterra, *Appl. Spectrosc. Rev.*, 1985, **21**, 259.
39. D. Freude, *Adv. Colloid Interface Sci.*, 1985, **23**, 21.
40. B. A. Morrow, *Stud. Surf. Sci. Catal.*, 1990, **57A**, 161.
41. V. M. Mastikhin, I. L. Mudrakovsky, and A. V. Nosov, *Prog. Nucl. Magn. Reson. Spectrosc.*, 1991, **23**, 259.
42. H. A. Resing, in *Magnetic Resonance in Colloid and Interface Science, Int. Symp. Menton, 1979, Reidel, Dordrecht*, 1980, p. 219.
43. I. D. Gay, A. J. McFarlan, and B. A. Morrow, *J. Phys. Chem.*, 1991, **95**, 1360.
44. S. H. C. Liang and I. D. Gay, *J. Catal.*, 1986, **101**, 293.
45. F. G. Oliver, E. J. Munson, and J. F. Haw, *J. Phys. Chem.*, 1992, **96**, 8106.
46. G. W. Haddix, J. A. Reimer, and A. T. Bell, *J. Catal.*, 1987, **106**, 111.
47. T. M. Duncan and R. W. Vaughan, *J. Catal.*, 1981, **67**, 49.
48. P.-K. Wang, C. P. Slichter, and J. H. Sinfelt, *Phys. Rev. Lett.*, 1984, **53**, 82.
49. S.-J. Hwang and B. C. Gerstein, *Bull. Magn. Reson.*, 1993, **15**, 211.
50. D. Slotfeldt-Ellingsen and H. A. Resing, *J. Phys. Chem.*, 1980, **84**, 2204.

51. D. W. Sindorf and G. E. Maciel, *J. Am. Chem. Soc.*, 1983, **105**, 1848.
52. M. Engelsberg, C. S. Yannoni, M. A. Jacintha, and C. Dybowski, *J. Am. Chem. Soc.*, 1992, **114**, 8319.
53. I. Kustanovich, Z. Luz, S. Vega, and A. J. Vega, *J. Phys. Chem.*, 1990, **94**, 3138.

Biographical Sketches

Ian D. Gay, *b* 1939, B.Sc., 1959, M.Sc., 1960 Dalhousie; Ph.D., D.I.C., 1964, London. Member of Faculty, Simon Fraser University, 1966–present. Research specialties: application of NMR to surface chemical problems.

Brønsted Acidity of Solids

Claudine Dorémieux-Morin and Jaques Fraissard
Université P. et M. Curie (Paris 6), Paris, France

1	Introduction	1
2	Measuring the Chemical Shift	1
3	Results from the Simulation of Broadline Spectra Recorded under Rigid Lattice Conditions	2
4	Conclusions	5
5	Related Articles	5
6	References	5

1 INTRODUCTION

^{1}H NMR spectroscopy is a powerful tool for investigating acid sites on solids, especially Brønsted sites. The main advantage of ^{1}H NMR compared with other spectroscopies is quantitativity. High resolution ^{1}H NMR techniques are used to measure the chemical shift of Brønsted acid sites without interaction of a basic reagent. With adsorption of a base, this shift cannot be obtained directly because of fast exchange of the H atoms. However, this chemical exchange provides a means of measuring the acidic hydrogen chemical shift with conventional NMR techniques. Broadline NMR of ^{1}H in rigid lattice conditions is also used to study acidity by means of the interaction of acid sites with water, as detailed in the following discussion.

2 MEASURING THE CHEMICAL SHIFT

The ^{1}H chemical shift of the H atoms of SOH groups (S being the solid lattice) in solid Brønsted acids can be thought of as related to the deprotonation energy and therefore to the acidity of the O–H bonds. A quantum mechanical model of this concept has been formulated.[1]

The chemical shift is a second-rank tensor characterized by an anisotropy, an asymmetry, and an isotropic value (δ_{iso}). The anisotropy of the chemical shift of ^{1}H in strongly homonuclear dipolar coupled solids can be measured by using appropriate multipulse sequences. The isotropic value is obtained by MAS techniques; when there are large dipolar interactions CRAMPS or isotopic dilution is used.

As moisture can seriously perturb a proton spectrum, sealed glass tubes containing pretreated samples are often used.

2.1 Isotropic Chemical Shift

2.1.1 Effect of Hydrogen Bonding

The chemical shift of SOH group H atoms depends not only on their bond polarization but also on hydrogen bond formation. Harris and Jackson[2] confirmed the previously reported trends, especially in correlations between δ_{iso} and both the O ··· O and the H ··· O distances.

2.1.2 Dependence of δ_{iso} on Acid Strength

Pfeifer's group[3–10] has been the most active in the use of ^{1}H MAS NMR of samples in sealed tubes. Working on 'anhydrous' H-zeolites (this means without template, hydration water, ammonia or any adsorbed phase, but still containing hydroxyl groups), these authors assigned the different δ_{iso} values obtained.

For Hy,[3] they are (Figure 1): (a) 1.3–2.3 ppm: silanol groups, SiOH; (b) 3.8–4.4 ppm: bridging OH groups pointing towards the supercages; (c) ca. 5 ppm: bridging OH groups pointing towards the sodalite cavities; (d) 6.5–7 ppm: remaining ammonium ions; (e) 2.6–3.6 ppm: AlOH groups still bonded to the framework. They related the δ_{iso} value of signals a, b, and c to the IR frequencies of the corresponding stretching vibrations.[6] Brunner,[7] working at 500 MHz, showed that the proton concentrations corresponding to signals b and c are equal (Figure 1), in agreement with Freude et al.[8] Signals a and b are common to all H-zeolites. For zeolites of different families, δ_{iso} of b increases with the Si/Al ratio[5] for values lower than 10 and then remains approximately constant (Figure 2).

Sites with enhanced catalytic activity have been studied in mildly hydrothermally dealuminated HZSM-5 zeolite:[3] this enhanced activity does not correspond to a change of δ_{iso}. The authors proposed that some of these sites are acid-insoluble tetracoordinated extraframework Al atoms. The same team identified Lewis acid sites in zeolites from the 6.5 ppm ^{1}H signal of H atoms of water molecules bonded to these sites.[9]

Pfeifer's team used ^{1}H MAS NMR for the quantitative detection of OH groups at framework defects of ZSM-5 zeolites, created during the synthesis.[3] The SiOH signal, at ca. 2 ppm, represents a much greater concentration of these groups than the concentration calculated for terminal groups, in particular for ZSM-5 synthesized with TPA^+: this template leads to a damaged lattice with a high concentration of nonintact Si–O–Si bonds after calcination.

Various combined ^{1}H and ^{27}Al MAS NMR studies address the hydrothermal dealumination and the realumination process of the hydrogen form of zeolites.[3] Bridging OH group dehydroxylation is accompanied by the removal of the same number of aluminum atoms from the zeolite framework. After

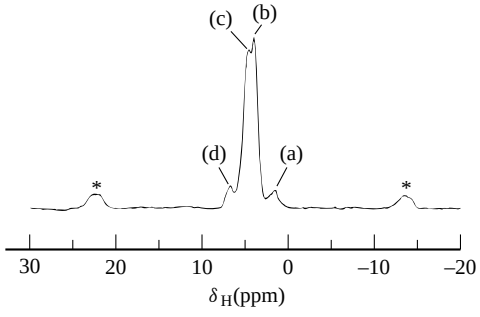

Figure 1 ^{1}H MAS NMR spectrum of a completely ammonium exchanged shallow-bed activated Hy zeolite under the following experimental conditions: resonance frequency, 500 MHz; sample spinning rate, 9 kHz, pulse width, 1.6 μs; delay time, 20 s. The asterisks denote spinning sidebands[7]

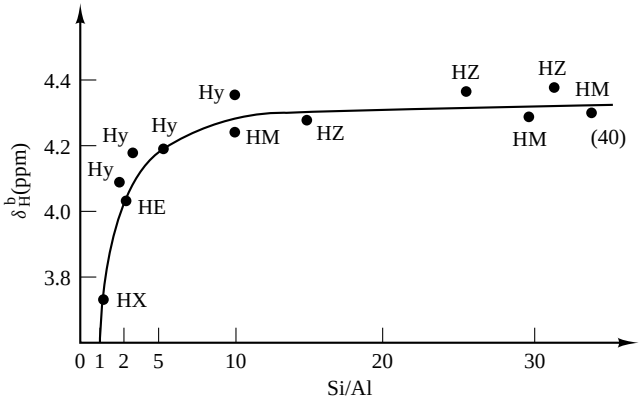

Figure 2 ^{1}H isotropic chemical shift of signal b of zeolites versus their Si/Al ratio. HE stands for erionite, HZ for ZSM-5, HM for mordenite[4], and Hy for faujasite structure

realumination, the total number of bridging OH groups is approximately equal to that of the parent sample. However, it must be noticed that after a hydrothermal dealumination process all the proton spectra contain a signal characteristic of AlOH groups at ca. 3 ppm.

After adsorption of water, MAS NMR spectra recorded at room temperature cannot be used to identify and quantify the oxyhydrogenated species formed because of the superposition of several effects,[4] in particular chemical exchange. Experiments at temperatures low enough to slow down the exchange are required for identification of individual sites.

Certain OH groups, formed by dissociation of water on divalent cations in zeolites which are known as cracking and alkylation catalysts, have also been studied.[3] The bridging OH groups in MgNa-Y behave as in CaNa-Y but the OH groups associated with the metal behave differently. A line at 0 ppm, observed for MgNa-Y, is partially accessible to pyridine and attributed to MgOH. For very small amounts of water in CaNa-Y, a signal at 0.5 ppm appears and for increasing water adsorption (1–2 H_2O per cavity) a new signal at 2.8 ppm is present, the corresponding site being inaccessible to pyridine. The signal at 0.5 ppm is attributed to CaOH groups pointing to the supercages and the 2.8 ppm one to CaOH groups pointing to sodalite cavities, hydrogen bonded to framework oxygen atoms.

Rosenberger et al.[10] applied the CRAMPS technique to silica gel with and without adsorption of benzene, acetone, or pyridine. Without adsorption these authors found that the OH group δ_{iso} value is spread over less than 0.5 ppm. However, adsorbed species cause δ_{iso} to change by 0–1.4, 4, or 7 ppm, respectively. Comparison of these values with those obtained with liquids suggests a pK_a value of 10.

Dorémieux-Morin et al.[11], working with ^{1}H MAS NMR on samples out of thermodynamic equilibrium, proposed the following process for the dehydration–rehydration of amorphous silica–aluminas in vacuum:

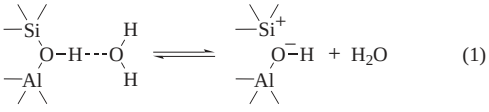

(1)

which differs from that for zeolites:

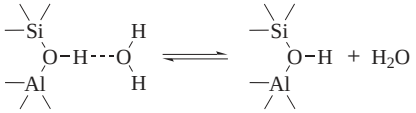

(2)

To conclude, the above examples demonstrate clearly the interest of ^{1}H MAS NMR on sealed samples for determining the processes implying their acid properties. Though there is no general linear dependence between δ_{iso} and the deprotonation energy ΔE_{DP},[1] the relationship:

$$d(\Delta E_{DP})/d(\delta_{iso}) = -84 \pm 12 \text{ kJ ppm}^{-1} \text{ mol}^{-1} \quad (3)$$

has been proposed for catalyst surface hydroxyl groups when these groups are all bonded to cations (B, Al, Si, or P) whose first coordination sphere consists solely of oxygen atoms.[1]

2.1.3 Line Narrowing by Fast Chemical Exchange

This technique can be used if MAS is not available. The interaction between SOH and a gaseous base, AH, mobilizes the OH group protons so that they give a sharp NMR signal, whereas when static they give a broad one. The heterogeneous equilibrium is:

$$SOH + AH \rightleftharpoons SO^- + AH_2^+ \quad (4)$$

When fast chemical exchange takes place between the protons of the different groups outlined in equation (4), the spectrum consists of a single line at $(\delta_H)_{obs}$, resulting from the coalescence of the lines associated with the groups AH, AH_2^+, and OH at δ_{AH}, δAH_2^+, and δ_{OH}, respectively. The line is then narrow enough for the chemical shift to be measured on a spectrometer appropriate for liquid state NMR:

$$(\delta_H)_{obs} = p_{OH}(\delta_H)_{OH} + p_{AH}(\delta_H)_{AH} + (p_{AH_2^+})(\delta_H)_{AH_2^+} \quad (5)$$

where p_i is the molecular fraction of group i. Due to the number of parameters in equation (5) the dissociation coefficient, α, of SO–H is needed before δ_{iso} can be determined. This is possible when the absorbed phase AH contains at least one nucleus other than ^{1}H which can be detected by NMR, for example ^{15}N or ^{17}O.

The case of ammonia adsorbed on silica xerogel pretreated at 10^{-2} Pa at different temperatures has been detailed.[12] Nitrogen-15 NMR gives:

$$(\delta_N)_{obs} = p_{NH_3}(\delta_N)_{NH_3} + (p_{NH_4^+})(\delta_N)_{NH_4^+} \quad (6)$$

from which $p_{NH_4^+}$ and α are determined. Bonardet et al. calculated δ_{iso} = 2 ppm for silica xerogel; they found 4–5 ppm for silica–alumina.[12] These values are in agreement with results obtained under conditions of MAS.

2.2 Anisotropic Chemical Shift

A chemical shift anisotropy of 5.5 ppm has been measured by Ernst[13] for silica OH groups. For zeolite bridging OH groups, the measured values are 19 ± 2 ppm; SAPO-5 exhibits a smaller value, 14.5 ± 2 ppm.[14]

3 RESULTS FROM THE SIMULATION OF BROADLINE SPECTRA RECORDED UNDER RIGID LATTICE CONDITIONS

There are two reasons why the proton is a convenient nucleus for investigating catalysts using broadline NMR: (a) its spin is $\frac{1}{2}$; (b) the range of its chemical shifts is small enough to be negligible compared with the main effect which is the dipolar interaction between spins. When this effect is studied two important points must be borne in mind: (i) the experimental temperature must be low enough to prevent diffusional and rotational motion of molecules or groups of atoms within the sample: this is the so-called 'rigid-lattice condition'; (ii) the interaction between two spins distance r apart is proportional to r^{-3};[15] consequently, closest neighbor spins will give the greatest effect.

The interaction of water (as a base) with Brønsted acidic sites is proposed as:

$$\mathrm{SOH} + \mathrm{H_2O} \rightleftharpoons \mathrm{SOH \cdots OH_2} \rightleftharpoons \mathrm{H_3O^+} + \mathrm{SO^-} \qquad (7)$$

From the standpoint of broadline NMR, each of the chemical species in equation (7) is a magnetic configuration of protons, characterized by their number and the geometry of this configuration. The interaction between neighboring protons belonging to distinct configurations is approximated by Gaussian broadening of the spectra of each configuration. The parameter of the Gaussian for each configuration is related to the shortest distances between protons of distinct configurations. The spectrum of each chemical species in powder samples is calculated by using the following magnetic configurations: (i) H_2O: the two-spin configuration calculated by Pake;[15] (ii) $H_2O \cdots$ HOS: the three-spin isosceles configuration revised by Dorémieux-Morin;[16] (iii) H_3O^+ the three-spin equilateral configuration revised by Richards and Smith,[17] or the three-spin isosceles configuration, if the ion is assumed to be deformed (all three spin configurations were first calculated by Andrew et al.); (iv) SOH: either a Gaussian and/or a Lorentzian curve for the SOH groups considered together, or a much broadened two-spin configuration.

The species H_2O and H_3O^+ (assumed to be undeformed) are characterized by a single intraconfiguration H H distance parameter (r); two are required to characterize $H_2O \cdots$ HO and distorted H_3O^+ (r and r', the value r in the base being the shorter). The concentrations of the oxygen-protonated species known from the weights of the corresponding contributions to the fitted spectrum are normalized to the total number of H atoms in the sample. Furthermore, since the number of independent parameters for each simulation is high, it is assumed that no initial SOH group can be condensed to water molecules and that no adsorbed water molecule gives SOH groups.

The spectra are generally recorded at 4 K as the derivative of the absorption relative to the static magnetic field, using a 'homemade' probe matched and tuned at the experimental temperature.

Studies of two catalysts are described. In the second, H zeolites, the result of a synergy between Brønsted and Lewis acid sites is shown. Together with these results on catalysts, those obtained on other solids allow a Brønsted scale of acidity to be proposed.

3.1 Study of the Superficial Constitutive Water of Titania

The spectra of the superficial constitutive water of large specific surface area titanium oxides (rutile,[18] anatase,[19] and an amorphous sample[20]) have been recorded at -130°C for dehydration in vacuum at various temperatures.

At each step of dehydration, simulation gives the nature and the relative concentration of the various species (SOH and $H_2O \cdots$ HOS in this case) and the approximate shortest H–H distances between these species.

For rutile and anatase, the numerical results are compared with the proton distribution which can compensate the electrostatic imbalance created by the lattice breaking, i.e. the existence of the surface. Considering the weight and distance parameters, the authors selected the high atomic density planes for which the change in the hydration remained compatible with the NMR spectra. They deduced that the most probable surface planes are (110) for rutile and (001) for anatase. In the most hydrated samples, OH groups cover the surface completely. Half the OH groups are hydrogen bonded to water molecules. Preexisting water molecules and some formed by condensation of OH groups are eliminated as soon as dehydration is performed at a temperature higher than 20°C.

In the most hydrated sample of the amorphous oxide each OH group is hydrogen bonded to a water molecule and, taken together, they cover the whole surface which means that water molecules probably form several hydrogen bonds to the surface.

3.2 Acidity of Zeolites

Batamack et al.[21,22] studied, in HY-zeolite, the equilibria described in equation (7). The 'anhydrous' samples were first obtained by shallow-bed treatment at 400°C. The concentrations of the oxygen-protonated species were measured for different amounts of readsorbed water which gains access to all acid sites. Comparison with results obtained by ^{1}H MAS NMR indicated that the samples were cooled to 4 K quickly enough for these concentrations to be equal to those at room temperature. A nondealuminated HY sample,[21] denoted ND, and a partially dealuminated HY sample obtained by $(NH_4)_2SiF_6$ exchange in aqueous solution,[22] denoted D, were studied.

The main results were the following:

(1) No interaction was found between silanol groups and water molecules, which is in agreement with results from ^{1}H MAS NMR.

(2) For ND HY:[21] (i) The first step of interaction between ZOH groups (ZOH denotes the bridging Brønsted sites) and water molecules may be described by equation (8) (where x and y are numerical values): the hydrogen-bonded species concentration is limited by the smallest of the initial concentrations of ZOH or H_2O,

$$x\mathrm{ZOH} + y\mathrm{H_2O} \rightarrow \inf(x, y)\mathrm{H_2O \cdots HOZ} + |x - y|\mathrm{ZOH \text{ or } H_2O} \qquad (8)$$

where inf(x,y) means the smallest value of x or y. (ii) An equilibrium is established between the hydrogen-bonded species and the ionized ones,

$$\mathrm{H_2O \cdots HOZ} \rightleftharpoons \mathrm{H_3O^+} + \mathrm{ZO^-} \qquad (9)$$

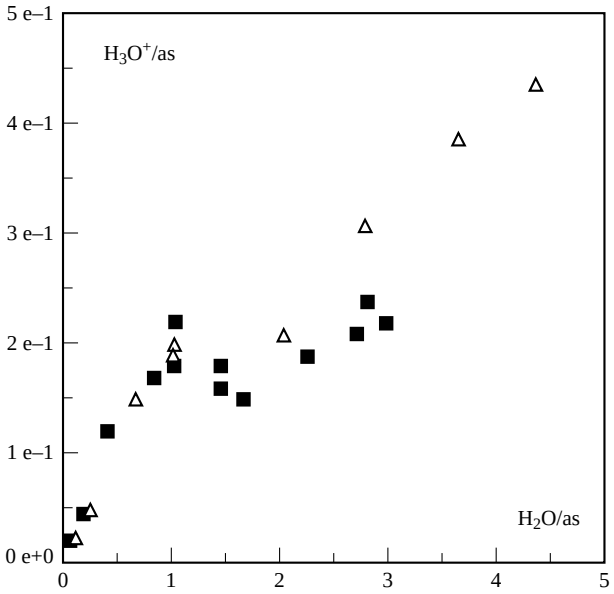

Figure 3 Plot of hydronium concentration in Y-zeolite per Brønsted acid site, H_3O^+/as, versus the adsorbed water molecule concentration per Brønsted acid site, H_2O/as; ■, ND HY;[21] Δ, D HY[22]

From Figure 3, the hydronium concentration per Brønsted acid site, H_3O^+/as, remains constant when the adsorbed water concentration, H_2O/as, is larger than 1, in agreement with the value calculated from equations (8) and (9).

(3) For D HY,[22] on the contrary, H_3O^+/as increases strongly when H_2O/as is larger than two. The authors proposed that a synergy between Brønsted and Lewis acid sites explains this difference (the Lewis sites are identified, using ^{1}H MAS NMR, by the molecular water that they bond).[23]

The conclusion is that broadline ^{1}H NMR provides a means of quantitatively determining the Brønsted acidity obtained by the interaction of water with the acid sites of the H-zeolites, whatever the nature of these sites. ^{1}H MAS NMR and other physicochemical techniques can help to identify these sites.

3.3 Scale of Brønsted Acidity in Solids

Using broadline ^{1}H NMR, Batamack et al.[24] compared for different solids the results obtained when the number of water molecules is equal to the number of OH groups being tested.

First, hydronium ion concentrations can be compared (Table 1). The ionization coefficient for ND HY-zeolite, H_3O^+/as, is 0.2 (see Section 3.2). For dihydrated antimonic acid, $H_2Sb_4O_{11}\cdot 2H_2O$, this coefficient attains a value of 0.4. In these cases simulations required two distinct magnetic configurations (Figure 4). For Nafion, the sensitivity is low but the ionization coefficient has been found to be about 1.

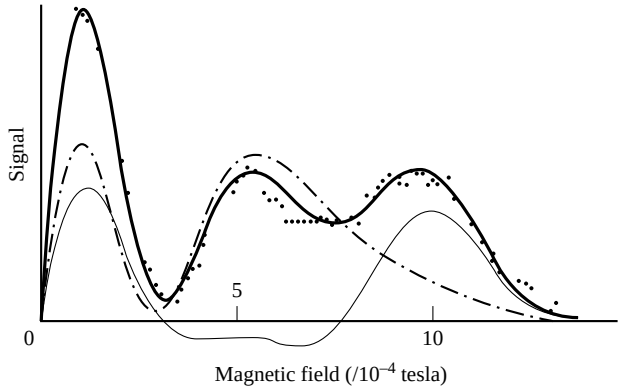

Figure 4 Half experimental absorption derivative curve for $H_2Sb_4O_{11}\cdot 2H_2O$, ... ; fitted spectrum, ——; weighted contribution of H_3O^+ ions, ——; weighted contribution of $H_2O\cdots$ HO groups, –·–·.

Since zeolite silanol OH groups are not observed to interact with water molecules, they are considered not to be acidic. No hydronium ions were found for amorphous titanium oxide nor for dihydrated dihydrogeno-aluminum tripolyphosphate. Hence, basing an acidity scale on the ionization coefficient gives only limited results: zeolite ($SiOH\cdot H_2O$) ≈ $TiOH\cdot H_2O$ ≈ $H_2AlP_3O_{10}\cdot 2H_2O$ < HY-zeolite $SiOH(Al)\cdot H_2O$ < $H_2Sb_4O_{11}\cdot 2H_2O$ < Nafion.

However, broadline ^{1}H NMR improves the classification of the samples relative to their acid strength by comparing the hydrogen-bonded complexes that their SOH groups form with water molecules. The values of r and r' allow a description of the hydrogen bond strength in terms of the O O distance, assuming C_{2v} symmetry for the $H_2O\cdots$ HOS group (Table 1).

For amorphous titanium oxide the O O distance is ca. 285 pm: the hydrogen bonds are weak. Only one three-spin magnetic configuration was required for a good simulation of $H_2AlP_3O_{10}\cdot 2H_2O$ (Figure 5), showing that the H atoms are really at the apices of an isosceles triangle. A very short O O distance, 242 pm was obtained: the hydrogen bonds are relatively strong. The O O distances are found to be about 259 pm and 247 pm in the zeolite and the antimonic acid, respectively. Ordering the samples versus the strength of the

Table 1 Acidity Scale Using Broadline ^{1}H NMR : The Condition is that Samples Contain One Water Molecule Per OH Group being Tested[24]

Order of increasing Brønsted acid strength	Sample	Number of H_3O^+ per initial OH: ionization coefficient	Number of $H_2O\cdots$HO per initial OH	O O distance (pm) in $H_2O\cdots$HO (assumed C_{2v}) from r and r'
1	Zeolite silanols	0	0	
2	Superficial OH groups on amorphous TiO_2	0	1	285
3	$H_2AlP_3O_{10}\cdot 2H_2O$	0	1	242
4	Zeolite SiO(H)Al	0.2	0.8	259
5	$H_2Sb_4O_{11}\cdot 2H_2O$	0.4	0.6	247
6	Nafion	1	0	

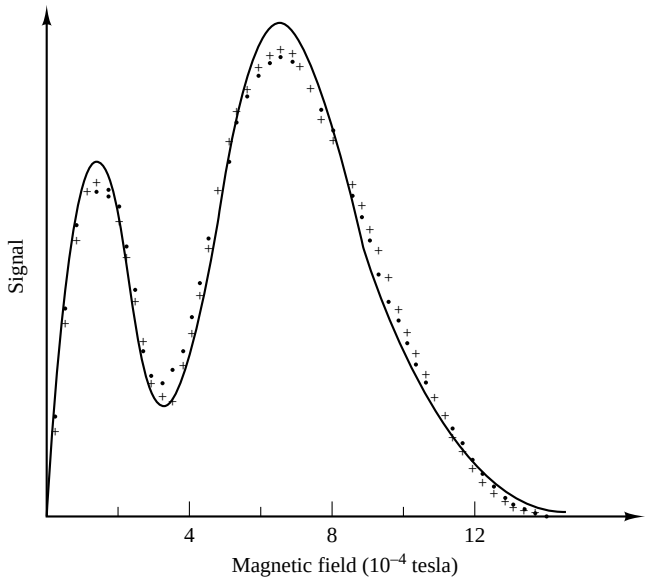

Figure 5 Half experimental absorption derivative curves for $H_2AlP_3O_{10}\cdot 2H_2O$, ... and ++++; fitted spectrum which is the weighted contribution of $H_2O \cdots HO$ groups, ——[24]

hydrogen bonds gives: zeolite $SiOH\cdot H_2O$ < $TiOH\cdot H_2O$ on amorphous titanium oxide < HY-zeolite $SiOH(Al)\cdot H_2O$ < $H_2Sb_4O_{11}\cdot 2H_2O \leq H_2AlP_3O_{10}\cdot 2H_2O$.

By analogy with the usual expression for acidity in aqueous media, the ionization coefficient is regarded as the principal criterion of acid strength. When the classification obtained differs from that based on the hydrogen bond length, the ionization coefficient order will be adopted. However, the strength of the hydrogen bonds can be used when no ionization occurs. The results are summarized in Table 1, the complete order of the samples being: zeolite $SiOH\cdot H_2O$ < $TiOH\cdot H_2O$ on amorphous titanium oxide < $H_2AlP_3O_{10}\cdot 2H_2O$ < HY-zeolite $SiOH(Al)\cdot H_2O$ < $H_2Sb_4O_{11}\cdot 2H_2O$ < Nafion.

4 CONCLUSIONS

The interest of ^1H MAS NMR for determining the properties of solid acids and the processes implying their acid characteristics is evident. However, using δ_{iso} of the SOH group as a measure of acidity is limited to samples where the first coordination sphere of the cation (B, Al, Si, or P) consists solely of oxygen atoms. When ^1H MAS NMR at low temperature becomes routine, it will be possible to measure the interaction between SOH groups and an external base of convenient strength and hardness, chemical exchange being then frozen. It must, however, be remembered that δ_{iso} can be measured under conditions of fast chemical exchange by applying conventional NMR techniques to two nuclei of the sample, ^1H and another.

When molecular water is the base, rigid lattice ^1H broadline NMR with simulation of the spectra is, at the moment, the only tool for analyzing the distribution of protons between the oxygen-protonated species formed, useful also in the case of synergy between Lewis and Brønsted acidity. Most of the spectra can be simulated with three kinds of magnetic configuration: (i) two spins, (ii) three spins at the corners of an equilateral triangle, and (iii) three spins at the corners of an isosceles triangle, plus Gaussian and/or Lorentzian curves.

A scale of Brønsted acidity of solids can be deduced from rigid lattice ^1H broadline NMR experiments performed when the number of water molecules is equal to the number of Brønsted sites. The ionization coefficient and the strength of the hydrogen-bonded species formed are used to set up this acidity scale.

5 RELATED ARTICLES

Chemical Exchange on Solid Metal Surfaces; CRAMPS; Line Narrowing Methods in Solids; Magic Angle Spinning; Microporous Materials and Xenon-129 NMR; Molecular Sieves: Crystalline Systems; Probe Design and Construction; Reactions in Zeolites; Rotating Solids

6 REFERENCES

1. U. Fleischer, W. Kutzelnigg, A. Bleiber, and J. Sauer, *J. Am. Chem. Soc.*, 1993, **115**, 7833.
2. R. K. Harris and P. Jackson, *J. Chem. Soc., Faraday Trans. 1*, 1988, **84**, 3649.
3. D. Freude, *Stud. Surf. Sci. Catal.*, 1989, **52**, 169, and references therein.
4. H. Pfeifer, D. Freude, and J. Kärger *Catalysis and Adsorption by Zeolites*, ed. G. Öhlmann et al., Elsevier Science, Amsterdam, 1991, p. 89, and references therein.
5. H. Pfeifer, *Colloids Surf.*, 1989, **36**, 169, and references therein.
6. H. Pfeifer, *J. Chem. Soc., Faraday Trans. 1*, 1988, **84**, 3777, and references therein.
7. E. Brunner, *Microporous Materials*, 1993, **1**, 431.
8. D. Freude, J. Klinowski, and H. Hamdan, *Chem. Phys. Lett.*, 1988, **149**, 355, and references therein.
9. M. Hunger, D. Freude, and H. Pfeifer, *J. Chem. Soc., Faraday Trans. 1*, 1991, **87**, 657.
10. H. Rosenberger, H. Ernst, G. Scheler, I. Jünger, and R. Sonnenberger, *Z. Phys. Chem. (Leipzig)*, 1982, **263**, 846.
11. C. Dorémieux-Morin, P. Batamack, C. Martin, J. M. Brégeault, and J. Fraissard, *Catal. Lett.*, 1991, **9**, 403.
12. J. L. Bonardet, J. Fraissard, and L. C. de Ménorval, *Proc. 6th Int. Cong. Catal. B6*, eds. G. Bond, P. Wells, and F. Tompkins, The Chemical Society, London, 1977, p. 633.
13. H. Ernst, *Z. Phys. Chem. (Leipzig)*, 1987, **268**, 405.
14. H. Pfeifer, *Proc. NATO ASI Acidity and Basicity of Solids: Theory, Assessment, Utility*, eds. J. Fraissard and L. Petrakis, Kluwer, Amsterdam, 1994, p. 255.
15. G. E. Pake, *J. Chem. Phys.*, 1948, **16**, 327.
16. C. Dorémieux-Morin, *J. Magn. Reson.*, 1976, **21**, 419, and references therein.
17. R. E. Richards, and J. A. S. Smith, *Trans. Faraday Soc.*, 1952, **48**, 675, and references therein.
18. M. A. Enriquez, C. Dorémieux-Morin, and J. Fraissard, *Appl. Surf. Sci.*, 1980, **5**, 180.
19. M. A. Enriquez, C. Dorémieux-Morin, and J. Fraissard, *J. Solid State Chem.*, 1981, **40**, 233.
20. M. A. Enriquez, C. Dorémieux-Morin, J. Sanz, and J. Fraissard, *J. Colloid Interface Sci.*, 1983, **95**, 502.
21. P. Batamack, C. Dorémieux-Morin, and J. Fraissard, *J. Chim. Phys.*, 1992, **89**, 423.

22. P. Batamack, C. Dorémieux-Morin, and J. Fraissard, *Catal. Lett.*, 1991, **11**, 119.
23. P. Batamack, C. Dorémieux-Morin, R. Vincent, and J. Fraissard, *Microporous Materials*, 1994, **2**, 515.
24. P. Batamack, C. Dorémieux-Morin, R. Vincent, and J. Fraissard, *J. Phys. Chem.*, 1993, **97**, 9779, and references therein.

Biographical Sketches

Claudine Dorémieux-Morin. *b* 1931. Maîtrise ès Sciences, 1954, Doctorat ès Sciences, 1960, Paris. Introduced to NMR by R. Freymann, Faculty of Science, University of Paris, 1962. Centre National de la Recherche Scientifique, 1954–present. Approx. 60 publications. Research specialties: application of solid state ^{1}H NMR to structural and catalytic chemistry of materials.

Jacques Fraissard. *b* 1934. Maîtrise ès Sciences, 1957, Doctorat ès Sciences, 1961, Paris. Introduced to NMR by I. Solomon. Centre National de la Recherche Scientifique 1960–63; University of Paris, 1963–present. Approx. 180 publications; five books including 'Thermodynamics and Kinetics' and, with R. Mahé, 'Chemical Equilibria in Aqueous Solutions'. Coeditor of four NATO ASI Series on Magnetic Resonance Applications: 'Colloid and Interface Science', 'Fossil Energy' and 'Acidity of Solids'. Research interests: applications of solid state NMR to problems of gas–solid interactions and catalysis.

Chemical Exchange on Solid Metal Surfaces

Frank Engelke
Ames Laboratory, Ames, IA, USA

1	Introduction	1
2	Theory of Magnetization Exchange	1
3	Advanced NMR Techniques to Monitor Exchange	2
4	Chemical Exchange of Adsorbed Species on Metal Surfaces: Examples	3
5	Related Articles	4
6	References	4

1 INTRODUCTION

Chemical exchange, i.e. the transfer of atoms, molecules or molecular groups between two or more different environments or regions, is a phenomenon encountered frequently in studies by NMR of a wide variety of chemical, physical and biological systems. Different environments are usually revealed in NMR experiments through distinct resonance frequencies, spin–spin coupling constants, or relaxation times characteristic of the regions between which chemical exchange takes place. The types of atomic or molecular motion most often investigated on metal surfaces include surface diffusion, adsorption and desorption, exchange between different surface sites or different types of adsorbed species, molecular reorientation, and reorientation of molecular groups.

Because NMR requires at least ca. 10^{18} spins at the surface to be able to detect a signal, single crystal surfaces cannot be studied (10^{15} spins). However, introducing the metal in the form of small particles with diameters in the order of nanometers into porous materials, provides a sufficiently high number of surface sites for adsorption to be studied by NMR. These support materials are mostly oxide compounds like silica, alumina, titania, or zeolites with high internal surfaces of several hundred square meters. At the same time, highly dispersed supported metals, e.g. group VIII elements like ruthenium, rhodium, palladium, osmium, iridium, and platinum, are very often of interest in basic and applied research in catalysis (see also ***Supported Metal Catalysts***, and ***Adsorbed Species: Spectroscopy and Dynamics***).

Several NMR techniques are available to study exchange phenomena of adsorbed species. Spin–lattice relaxation[1] measurements are useful if chemical exchange dominates as a source for relaxation, or can be separated from other relaxation mechanisms, e.g. relaxation via the conduction electrons of the metal, called Korringa relaxation (see ***Electron–Nuclear Hyperfine Interactions***). To be investigated by relaxation measurements, the characteristic time constants of exchange τ_{ex} have to be in the order of 10^{-9} s for spin–lattice relaxation in the laboratory frame to 10^{-5} s for spin–lattice relaxation in the rotating frame.[1] For a review of the relaxation method used to study the dynamics on surfaces we refer the reader to the literature.[2–4] The analysis of lineshapes or resonance shifts obtained by conventional NMR techniques are sensitive in the dynamic range of $10^{-6} \leq \tau_{ex} \leq 10^{-3}$ s. Spin labeling methods extend this range up to more than 10^{-1} s. Two-dimensional NMR techniques, applicable in approximately the same slow dynamic range, are most effective if the exchanging species exhibit separate NMR peaks or if well-defined lineshapes due to anisotropic interactions can be observed.[5]

In the present article the theoretical basis necessary to understand the evolution of nuclear spin magnetization influenced by chemical exchange is outlined briefly. The reader is introduced to spin-labeling and two-dimensional (2D) NMR techniques, which are frequently used to monitor exchange. Finally, experimental examples regarding chemical exchange on metal surfaces are discussed.

2 THEORY OF MAGNETIZATION EXCHANGE

In the following it is assumed that the spatial motion of molecules or atoms can be described classically. If all spin interactions are secular with respect to the Zeeman interaction, i.e., the corresponding interaction Hamiltonians commute with the Zeeman Hamiltonian, then each spin can be considered as being subjected to a local field arising from the environment, superimposed on the external static field. Chemical exchange has the effect of causing random fluctuations of the local field. For example, a nuclear spin situated in a molecule or atom, which jumps randomly between two regions on a surface, such that each region gives rise to a different isotropic resonance shift, experiences a random modulation of its resonance frequency. The influence of such frequency fluctuations upon the NMR lineshape was first treated by Hahn, Maxwell, Gutowsky, McCall, and Slichter.[6]

If the spin Hamiltonian contains nonsecular terms, arising, for example, from J couplings observed commonly in liquids, a quantum-mechanical treatment (spin density matrix formalism) is required.[7] Splittings due to J couplings are often difficult to detect in NMR studies of adsorbates on metal surfaces because of insufficient spectral resolution, caused by the heterogeneity of the system, leading to distributions of isotropic chemical or Knight shifts, and/or the presence of 'solid-like' spin interactions much stronger than J coupling, like chemical shift anisotropy (see ***Internal Spin Interactions and Rotations in Solids***) and paramagnetic shifts.

We confine ourselves here exclusively to the case of secular spin interactions, leading to a classical probabilistic model for the magnetization exchange originating from chemical exchange processes. The probabilistic model is commonly represented by a stationary Markov process,[8,9] allowing the derivation of equations of motion for the nuclear spin magnetization in the form of generalized Bloch equations.[9–11] The evolution of longitudinal and transversal magnetization components for all regions, between which exchange takes place, are given as a system of coupled differential equations with rate coefficients describing the magnetization exchange process. Solving these equations is a standard problem of analysis and matrix algebra (see Ernst et al.[11] and Jeener et al.[13]) and enables explicit calculation of NMR lineshapes.

Figure 1 illustrates the principal effects on the NMR lineshapes originating from magnetization exchange between two regions or sites. Regions A and B, populated by N_A and N_B spins, respectively, are characterized by distinct resonance

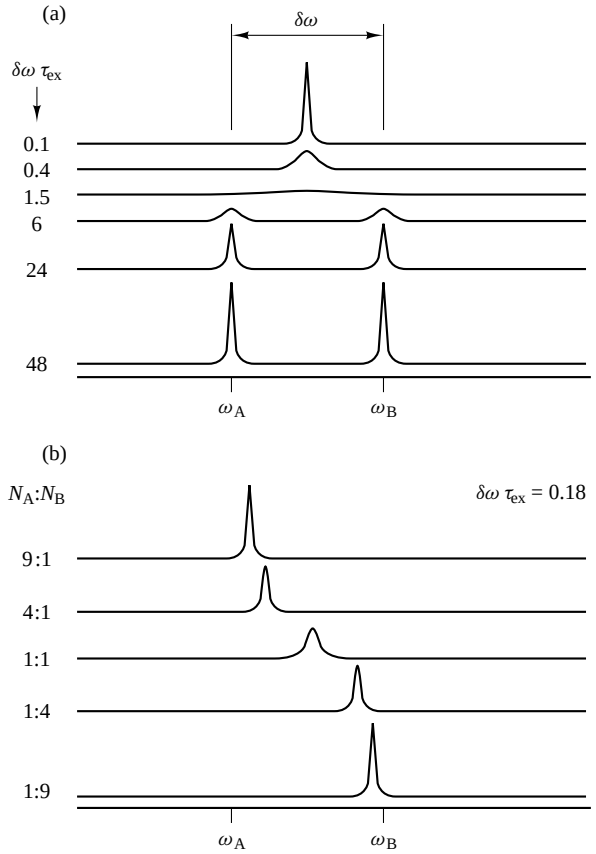

Figure 1 (a) NMR lineshape versus $\delta\omega\tau_{ex}$ for symmetric two-site exchange ($N_A = N_B$). (b) Variation of the resonance frequency in the fast exchange limit as a function of N_A:N_B

frequencies ω_A and ω_B, $\delta\omega = \omega_B - \omega_A$. This difference of resonance freqencies may be caused by different isotropic chemical or Knight shifts. In the slow exchange limit, $\delta\omega\tau_{ex} \gg 1$, where τ_{ex} is a characteristic time constant for the exchange process, two separate lines appear in the NMR spectrum [Figure 1(a)], which become broadened with decreasing $\delta\omega\tau_{ex}$, and coalesce to a single broad line at $\delta\omega\tau_{ex} \approx 1$. With $\delta\omega\tau_{ex}$ decreasing further, only one single 'exchange-averaged' narrow line is observed (fast exchange limit, $\delta\omega\tau_{ex} \ll 1$). The spectra in Figure 1(b) were calculated for the fast exchange limit varying the ratio N_A:N_B of spin numbers in regions A and B, leading to a variation in the resonance frequency of the exchange averaged resonance line as well as to a broadening for values of N_A:N_B near unity. The dependence of the resonance shift δ on N_A and N_B can be expressed for the fast exchange limit as the weighted average:

$$\delta = \frac{N_A}{N_A + N_B} + \delta_A \frac{N_B}{N_A + N_B}\delta_B \qquad (1)$$

of the individual resonance shifts δ_A and δ_B. The mathematical formalism to calculate the above lineshapes is still applicable if anisotropic interactions, to be described by interaction tensors, e.g. chemical shift anisotropy, are present. However, because of the random spatial orientations of the principal tensor axes in a powder sample, the resulting orientation dependence of the resonance frequencies has to be taken into account to obtain the lineshape.[10]

3 ADVANCED NMR TECHNIQUES TO MONITOR EXCHANGE

As shown above, no significant changes of the one-dimensional NMR lineshapes or frequencies occur in the slow exchange limit. More advanced NMR techniques are available to detect such slow exchange processes.

3.1 Spin Labeling by Selective Excitation

The idea of spin labeling is based on the fact that the actual chemical exchange process, being in thermal equilibrium, causes an exchange of spin magnetization.[12] The latter is initially prepared by irradiation of rf pulses to be in nonequilibrium. The irradiation of an rf pulse, or a sequence of rf pulses affects only spins resonating within the spectral excitation window defined by the Fourier transform of the pulse sequence [Figure 2(a) and (b)]. Although this Fourier picture is only an approximation when selective saturation or inversion is considered,[12] it is a useful qualitative description. Denoting the length of a single rf pulse or the total duration of a pulse sequence by τ_p, the excitation width in the frequency domain is proportional to $1/\tau_p$, with the rf carrier frequency in the center of the excitation window. The irradiation of either a long pulse of low rf power or a sequence of strong, but very short pulses, as indicated in Figure 2(a), allows selective excitation of spins. The pulse sequence can be adjusted to act in total like a 90° pulse (selective saturation) or a 180° pulse [selective inversion, illustrated in Figure 2(c)]. Therefore, spins within the spectral window can be labeled, for example, by inversion of their magnetization, while spins which resonate outside the window remain unaffected. If a pulse sequence is used, excitation sidebands also occur [Figure 2(b)]. During a subsequent time interval τ_m [Figure 2(a)] the spin system is allowed to undergo free time evolution. The NMR signal is detected finally by a short (nonselective) 90° pulse. Selective excitation (saturation or inversion) of a narrow frequency band within a broad NMR line, for example, caused by chemical shift anisotropy, is called 'spectral hole-burning'. If chemical exchange is present, the labeled spins may change their resonance frequencies resulting in a redistribution of spin

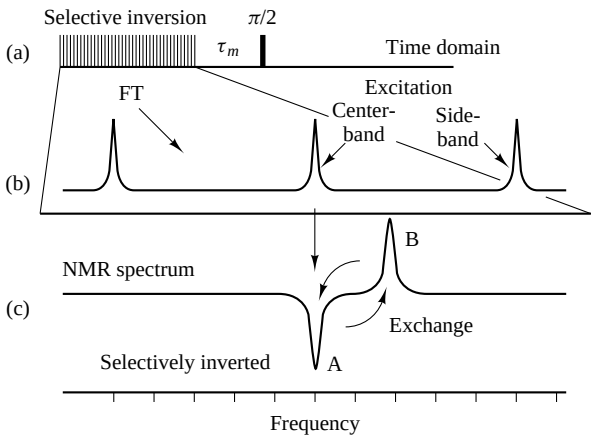

Figure 2 Spin labeling by selective excitation: (a) pulse sequence, (b) Fourier transformation of the train of equidistant pulses, and (c) NMR spectrum showing a selectively inverted line

magnetization toward spectral regions outside of the selected window. The recovery of the spectral hole, or of the intensity of an inverted single resonance line, can be measured as a function of the recovery time τ_m to reveal the kinetics of a chemical exchange process.

Magnetization recovery is also caused by spin–lattice relaxation of the spin magnetization. Only exchange processes with a characteristic time τ_{ex} shorter than the spin–lattice relaxation time T_1 can be observed. Spin-labeling becomes ineffective if the chemical exchange process is faster than the spin-labeling process itself (characteristic time constant τ_p). Thus accessible by spin-labeling techniques are exchange processes within a timescale $\tau_p < \tau_{ex} < T_1$.

3.2 Two-Dimensional Exchange NMR

Two-dimensional exchange NMR techniques[13] are based on the idea of measuring the frequency of spin magnetization components at two different times during the NMR experiment. After the initial preparation period, which consists of a waiting period to allow equilibration of the longitudinal magnetization and irradiating the first $\pi/2$ pulse, transversal magnetizations are present, oscillating with frequencies ω_A and ω_B during the time t_1 [evolution period, Figure 3(a)] corresponding to spins located in regions A and B. A second $\pi/2$ pulse converts the magnetization present at time t_1 into longitudinal magnetization. During the mixing time τ_m (usually much longer than the time t_1) slow chemical exchange leads to a random modulation of the precession frequencies of the two magnetization components M_{zA} and M_{zB}. Spins which were resonating at ω_A at the end of the period t_1 may resonate at either ω_A or ω_B at the end of the mixing period τ_m (and vice versa). The NMR signal is detected after the final $\pi/2$ pulse during the time period t_2. Repeating the experiment by incrementing the time t_1 in small steps, yields a two-dimensional time-domain interferogram which after 2D Fourier transformation[11] with respect to t_1 and t_2 gives the 2D NMR spectrum $S(\omega_1,\omega_2)$. If exchange occurs between A and B, cross peaks are observed, labeled A → B and B → A in Figure 3(b), in addition to main peaks A and B located along the principal diagonal.[14]

4 CHEMICAL EXCHANGE OF ADSORBED SPECIES ON METAL SURFACES: EXAMPLES

Chemical exchange phenomena at or near metal surfaces observed by NMR encompass a wide dynamical range extending from the fast exchange limit ($\tau_{ex} < 10^{-5}$ s) to extremely slow processes ($\tau_{ex} > 1$ s). The details of the chemical exchange processes might be quite different, originating, for example, from adsorption or desorption, exchange between different surface sites, exchange between different populations of adsorbed species or surface diffusion.[15]

4.1 Exchange Dynamics of CO Adsorbed on Metals

Carbon-13 spin labeling techniques have been applied by Duncan, et al.[16] to elucidate in detail surface diffusion of CO and slow exchange between different carbonyl species adsorbed on rhodium. Molitor and Apple[17] performed ^{13}C NMR powder lineshape calculations for reorientating dicarbonyl groups bonded to rhodium. Surface diffusion of CO chemisorbed on palladium has been investigated by means of ^{13}C relaxation measurements and lineshape analysis.[18]

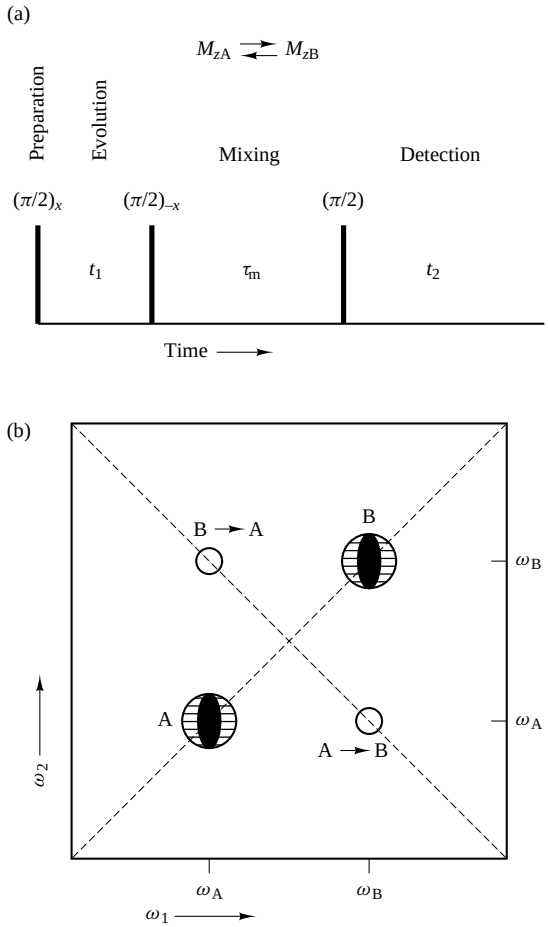

Figure 3 (a) Basic 2D NMR pulse sequence to monitor exchange. (b) Schematic representation of a 2D NMR spectrum for exchange between two sites A and B

4.2 Fast Exchange of Hydrogen on Metal Surfaces

Proton NMR peaks of hydrogen interacting with metal surfaces are commonly shifted to lower frequency (i.e. upfield) due to the Knight shift interaction and reveal relatively small linewidths, especially at elevated external H_2 pressures and temperatures above room temperature, indicating high intrinsic mobility. Variations of the resonance frequency of ^1H NMR peaks, attributed to hydrogen on the metal surface, versus pressure (i.e. changing the number of hydrogen atoms or molecules on the surface) may be caused by at least two different mechanisms: (i) fast exchange between surface environments with different Knight shifts [as illustrated in Figure 1(b)]; and (ii) by a variation of the Knight shift interaction itself, because the latter may be a function of the surface coverage. As pointed out above, fast exchange between two regions leads to an averaged NMR line representing hydrogen in both regions. Variation of the resonance shift

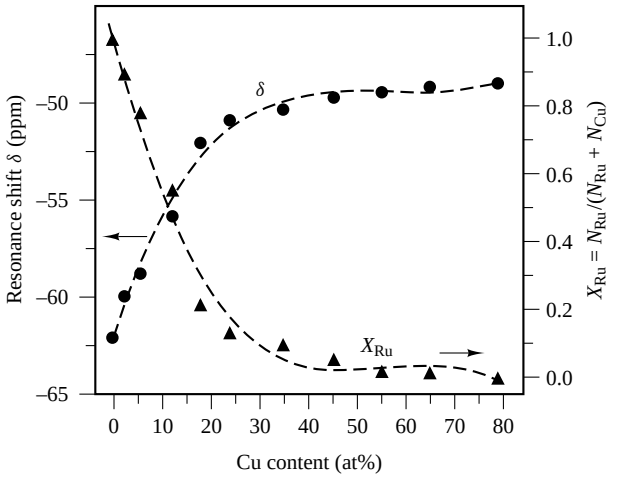

Figure 4 ^{1}NMR resonance shift δ for hydrogen adsorbed on ruthenium–copper bimetallic particles and fraction X_{Ru} of surface ruthenium as a function of the copper content

with pressure, or coverage, has been observed quite frequently by ^{1}H NMR[19] or ^{2}H NMR[20] for hydrogen adsorbed on various metals like platinum, rhodium, and ruthenium (see also refs. [18–20] and 23–24 given in Wu et al.[19]). The resonance shift variation of hydrogen due to fast exchange between different surfaced regions has been used to monitor the surface composition of bimetallic particles.[21] In this case hydrogen atoms are rapidly exchanging between sites on the bimetallic particle surface, composed of sites with different Knight shifts for adsorbed hydrogen. As shown in Figure 4, on particles consisting of pure ruthenium, hydrogen resonates at −62 ppm [to low frequency relative to tetramethylsilane (TMS)]. Increasing the total copper content of the sample leads to a systematic decrease of the ^{1}H resonance shift δ, approaching asymptotically the value of −49 ppm for a copper content near 80 at%. This shift value is regarded as the resonance shift for hydrogen adsorbed on copper sites of ruthenium–copper bimetallic particles. Applying equation (1) inserting $\delta_{Cu} = -49$ ppm and $\delta_{Ru} = -62$ ppm, the fraction $X_{Ru} = N_{Ru}/(N_{Ru} + N_{Cu})$ of ruthenium atoms exposed at the particle surface can be determined (see Figure 4). Therefore, in this example the ^{1}H NMR resonance shift provides a sensitive measure for the composition of the surface.

4.3 Slow Exchange Between Different Hydrogen Populations on the Metal Surface

Figure 5(a) shows an in situ ^{1}H NMR spectrum of silica supported ruthenium, obtained at T = 400 K and at an external H_2 pressure of 300 Torr.[22] Two distinct resonance lines (denoted as α and β) are observed, originating from two different hydrogen species, characterized by different heats of adsorption. The 2D exchange NMR spectrum [Figure 5(b)] was obtained by the pulse sequence illustrated in Figure 3(a). The cross peaks reveal a slow exchange process within the timescale of the experiment, given by the mixing time τ_{mix} = 2 ms, occurring between α and β hydrogen, but there is no exchange within this timescale between the α or β species and the hydrogen residing on the silica support. Spin

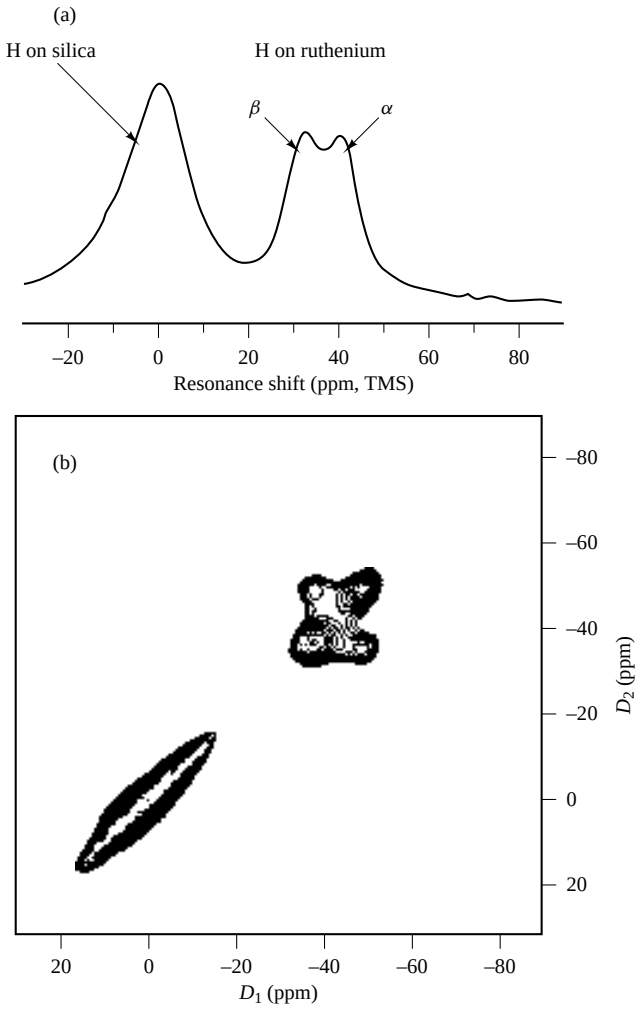

Figure 5 (a) Conventional ^{1}H NMR spectrum of silica supported ruthenium. (b) 2D exchange NMR spectrum at T = 400 K and external H_2 pressure p = 300 Torr

labeling of one of the two spin species, α or β, by selective excitation (Figure 2) allows the determination of the average time constant, τ_{ex} = 700 μs, for the magnetization exchange between α and β hydrogen.

5 RELATED ARTICLES

Adsorbed Species: Spectroscopy and Dynamics; Brønsted Acidity of Solids; Diffusion in Porous Media; Electron–Nuclear Hyperfine Interactions; Internal Spin Interactions and Rotations in Solids; Microporous Materials and Xenon-129 NMR; Silica Surfaces: Characterization; Spin Diffusion in Solids; Supported Metal Catalysts

6 REFERENCES

1. C. P. Slichter, *Principles of Magnetic Resonance*, 3rd edn., Springer, Berlin 1990, Chaps. 4–6.
2. H. Pfeifer, in *NMR Basic Principles and Progress*, eds. P. Diehl, E. Fluck, and R. Kosfeld, Springer, Berlin, 1972, Vol. 7, p. 53.

3. H. Winkler and D. Michel, *Adv. Colloid Interface Sci.*, 1985, **23**, 149.
4. C. P. Slichter, *Ann. Rev. Phys. Chem.*, 1986, **37**, 25.
5. H.-W. Spiess, *Chem. Rev.*, 1991, **91**, 1321.
6. E. L. Hahn and D. E. Maxwell, *Phys. Rev.*, 1952, **88**, 1070; H. S. Gutowsky, D. W. McCall, and C. P. Slichter, *J. Chem. Phys.*, 1953, **21**, 279.
7. J. I. Kaplan and G. Fraenkel, *NMR of Chemically Exchanging Systems*, Academic, New York, 1980.
8. A. Abragam, *The Principles of Nuclear Magnetism*, Clarendon, Oxford, 1961, Chap. X.
9. C. S. Johnson, Jr., in *Advances in Magnetic Resonance*, ed. J. S. Waugh, Academic, New York, 1965, Vol. 1, p. 33.
10. M. Mehring, *Principles of High Resolution NMR in Solids*, 2nd edn., Springer, Berlin, 1983, Chap. 28.
11. R. R. Ernst, G. Bodenhausen, and A. Wokaun, *Principles of Nuclear Magnetic Resonance in One and Two Dimensions*, Clarendon, Oxford, 1987, Chaps. 2.4, 4.6, 6.4 and 9.
12. G. A. Morris and R. Freeman, *J. Magn. Reson.*, 1978, **29**, 433; R. Freeman, *Chem. Rev.*, 1991, **91**, 1397.
13. J. Jeener, B. H. Meier, P. Bachmann, and R. R. Ernst, *J. Chem. Phys.*, 1979, **71**, 4546.
14. If direct dipolar spin–spin couplings are present, spin diffusion (a process to be distinguished from chemical exchange) may also lead to cross peaks (see Jeener et al.[13] and ***Spin Diffusion in Solids***).
15. Spin labeling is well suited to monitor surface diffusion. However, the theoretical treatment of surface diffusion is based on the diffusion equation, and not on Bloch-type equations to describe exchange as discrete jumps between distinct environments.
16. T. M. Duncan, A. M. Thayer, and T. W. Root, *Phys. Rev. Lett.*, 1989, **63**, 62. See also: T. M. Cuncan, *Colloids Surfaces*, 1990, **45**, 11, and references therein.
17. P. Molitor and T. Apple, *J. Phys. Chem.*, 1989, **93**, 7055.
18. S. E. Shore, J.-P. Ansermet, C. P. Slichter, and J. H. Sinfelt, *Phys. Rev. Lett.*, 1987, **58**, 953.
19. X. Wu, B. C. Gerstein, and T. S. King, *J. Catal.*, 1989, **118**, 238.
20. T. Chang, C. P. Cheng, and C. Yeh, *J. Phys. Chem.*, 1991, **95**, 5239.
21. X. Wu, B. C. Gerstein, and T. S. King, *J. Catal.*, 1990, **121**, 271.
22. F. Engelke, S. Bhatia, T. S. King, and M. Pruski, *Phys. Rev. B*, 1994, **49**, 2730; F. Engelke, R. Vincent, T. S. King, and M. Pruski, *J. Chem. Phys.*, 1994, **101**, 7262.

Biographical Sketch

Frank Engelke. *b* 1955. M.Sc. (physics), Ph.D. (supervisor Dieter Michel) 1985, habilitation, University of Leipzig, Germany. Postdoctoral work at Saarbruecken University, Germany (with Jörn Petersson), and since 1992–1994 at Ames Laboratory, USA (with Bernie Gerstein, Marek Pruski and Terry King). Since 1994 affiliated with Bruker Analytische Messtechnik. Approx. 20 publications. Current research specialties: solid state NMR in rotating solids, solid state NMR applications on metal surfaces, NMR probe development.

Cokes

Marek Pruski

Ames Laboratory and Iowa State University, Ames, IA, USA

1	Introduction	1
2	Relaxation Parameters of Hydrogen and Carbon in Cokes	1
3	Quantitation of Hydrogen and Carbon	2
4	NMR Lineshapes in Cokes	2
5	Structural Parameters of Cokes	4
6	Related Articles	5
7	References	5

1 INTRODUCTION

The advances in NMR over the last three decades have resulted in an increasingly important role that this technique has played in studies of various types of carbonaceous materials. Among these materials are fossil fuels which, due to their impact as a main world energy source, are of primary concern in scientific and engineering research. Of great interest are naturally occurring raw materials, such as coal, crude oil, and oil shales, as well as products of fossil fuel processing. The latter include 'coke', a term used to describe a solid by-product of the petroleum refining process, or a hard, often porous residue left after the destructive distillation (pyrolysis) or liquefaction of coal.

Fossil fuels are known to be enormously heterogeneous and complex materials and no single approach can provide adequate understanding of their structure and best way of utilization. Although the classical chemical methods and some modern analytical techniques (e.g. mass spectroscopy, liquid and gas chromatography, thermogravimetry) have proved useful in characterizing parent materials as well as liquid and gaseous products of coals and petroleum processing, determination of the chemical and physical structure of solid fossil fuels and solid products of fuels processing has not been possible by employing these methods. This need has stimulated application of other spectroscopic techniques including X-ray spectroscopies (X-ray atomic fluorescence and X-ray photoelectron spectroscopy), infrared spectroscopy, optical spectroscopies (laser spark spectroscopy, Raman spectroscopy), ESR spectroscopy, and NMR spectroscopy, which soon came to the forefront of this research. Earlier NMR studies utilized primarily relaxation studies, quantitative analysis of ^{1}H in solids using wideline NMR, and provided quantitative and structural analysis of fossil fuel derived liquids (mainly from coal and petroleum) via liquid state NMR. Since the implementation of high-resolution methods of ^{1}H decoupling, magic angle spinning and CRAMPS, and the methods of enhancing polarization of rare nuclear spins (cross polarization and dynamic nuclear polarization) it became possible to acquire high-resolution spectra of ^{1}H and ^{13}C in a short measuring time.[1]

In spite of different origins, petroleum and coal derived cokes consist primarily of carbon (typically ca. 90% by weight) and hydrogen (below 5%). While smaller concentrations of oxygen, sulfur, nitrogen and various metals (vanadium, nickel, iron) are also present in cokes, it is not surprising that NMR spectroscopy utilizes ^{1}H and ^{13}C nuclei to probe these materials. Below, an overview is given of the fundamental aspects of solid state NMR of ^{1}H and ^{13}C as applied to the studies of carbonaceous solids. The topics include relaxation studies, quantitation, high-resolution methods in ^{13}C and ^{1}H NMR, lineshape analysis, and the relationship between NMR derived data and the chemical structure. Although the utilization of solid state NMR techniques will be shown largely for petroleum derived cokes, most of the approaches described here are also pertinent to fossil fuels, semi-cokes, coal tar pitches, petroleum pitches and other 'bottom-of-the-barrel residues' (see also ***Coal Structure from Solid State NMR*** and ***Fossil Fuels***), as well as for characterization of carbonaceous residues (cokes) from catalyst-controlled reactions.

2 RELAXATION PARAMETERS OF HYDROGEN AND CARBON IN COKES

Measurements of nuclear spin relaxation in solid fossil fuels have been performed in order to provide gross information about local environments and molecular motions, long before modern high-resolution solid state NMR techniques were introduced as an analytical tool. Three relaxation times were commonly measured: (a) T_1, the longitudinal relaxation time characterizing attainment of equilibrium of spin magnetization along a static magnetic field, and generally associated with dipolar fields fluctuating at the Larmor frequency, generated by motion of other magnetically active nuclei and/or unpaired electron spins associated with free radicals; (b) $T_{1\rho}$, the longitudinal relaxation time in the rotating frame characterizing similar motions in the tens of kilohertz frequency range; and (c) T_2, the transverse relaxation time characterizing static spin interactions in solids.

Most of the spin–lattice relaxation studies reported for cokes employed ^{1}H NMR and showed that $T_1{}^{\mathrm{H}}$ and $T_{1\rho}{}^{\mathrm{H}}$ relaxation processes (typical values in the 50–200 ms and 0.3–5 ms range, respectively) depend upon interactions between protons and unpaired electrons (via spin diffusion), while dipolar interactions between protons have a lesser significance. To limit the number of parameters, only a biexponential function is usually used to fit the experimental data although no physical model that justifies such procedure has yet been established. Also, due to the presence of different relaxation mechanisms, and different types of paramagnetic species, a distribution of relaxation parameters is very likely. In such cases the relaxation parameters are the result of a complicated interplay between competing relaxation mechanisms, and spin diffusion may not be effective to identify structural inhomogeneities, even if they existed in cokes. For example, the detailed study of 15 petroleum cokes, produced from pure and mixed residues of various origins, showed that the $T_1{}^{\mathrm{H}}$ and $T_{1\rho}{}^{\mathrm{H}}$ relaxation parameters (including relative fractions of magnetization exhibiting fast and slow relaxation) could not be directly correlated with different structural parameters of cokes as determined by high-resolution methods.[2] In particular, these results did not reveal structural inhomogeneities in cokes in which

aliphatic and aromatic structures dominate. In spite of difficulties with the interpretation of spin lattice processes in cokes, the accurate analysis of $T_1{}^H$ and $T_{1\rho}{}^H$ is often required to characterize quantitatively the cokes via ^{13}C CP MAS experiments.

The proton T_2 relaxation time (or the NMR linewidth), determined under a single pulse excitation, reflects the strength of static $^1H-{}^1H$ dipolar interactions in cokes, and in the absence of molecular motion is a measure of the average internuclear distance in a sample. Unlike coals, which generally exhibit at least two exponential decays, the pyrolyzed cokes show typically a Gaussian decay of transverse magnetization with a single value of T_2 of roughly $20\,\mu$s, indicating homogeneously rigid character of the coke structure, where only hindered motions of functional groups (e.g. CH_3) take place.[2] When molecular motion characterized by correlation time $\tau_c < 10^{-5}$ s is present, e.g. in coals with mobile molecular fragments, solvent swollen coals, pitches above their softening point or during pyrolysis, the increased values of T_2 are a measure of molecular mobility. The measurements of T_2 versus temperature allowed the study, for example, of the glass transition temperature in materials resulting from pyrolysis of petroleum pitches and coal extracts through the mesophase stage to a coke.[3]

3 QUANTITATION OF HYDROGEN AND CARBON

One of the main reasons NMR has become a powerful analytical tool is because for spin-$\frac{1}{2}$ nuclei, such as are ^1H and ^{13}C, the NMR signal may generally be used for quantitative analysis. Using NMR for hydrogen (or carbon) spin counting in cokes implies that: (1) all spins are observed by NMR, (2) the initial (near $t = 0$) time dependence of the FID is known and can be compared with that of a standard, and (3) the physical meaning of all components of the FID is well understood. In single pulse experiments the first few microseconds of the FID are always obscured by the probe ringdown and receiver deadtime, which may result in considerable signal loss in samples with short T_2. This short time behavior of the NMR signal can be determined, and the lost intensity recovered, by using a solid echo excitation sequence, or by applying linear prediction techniques directly to the FID.[2]

Hydrogen is the most sensitive nucleus commonly detected by NMR, but it is also one of the least sensitive when analyzed by chemical methods. In general, NMR offers quick and most reliable measurements of hydrogen concentration in fossil fuel materials, which compare favorably with the results of combustion analysis, Karl–Fisher titration and other techniques. The main possible source of systematic loss of the NMR signal (typically below 10%) is the broadening of the NMR line from dipolar interactions with unpaired electrons present in organic free radicals in cokes. As already mentioned, the analysis of the FID also provides information about molecular mobility.

The quantitative analysis of carbon by single pulse NMR is time consuming due to long ^{13}C relaxation times $T_1{}^C$ and is considered less accurate than chemical analyses. It is mainly used to address the potential quantitation problems in the CP MAS spectra.

4 NMR LINESHAPES IN COKES

The dominant line broadening interactions that affect the NMR lineshapes are chemical shift anisotropy and $^1H-{}^1H$ and/or $^1H-{}^{13}C$ dipolar couplings. However, even if these interactions are eliminated, or reduced, by the high-resolution techniques, the observation of sharp resonances in ^1H and ^{13}C NMR is often precluded by the heterogeneous chemical nature of cokes. The results of high-resolution ^1H and ^{13}C NMR when combined with spin counting, elemental analysis, and other analytical methods, can be used to infer several structural parameters and the 'average' model of a coke.

4.1 ^1H CRAMPS NMR

With values of transverse relaxation times T_2 around $20\,\mu$s, proton linewidths in cokes are ca. 30 kHz, corresponding to 100 ppm at a resonance frequency of 300 MHz. This line broadening results from high abundance and large magnetic moment of ^1H spins, and exceeds the range of proton chemical shifts in hydrocarbons, which is about 15 ppm. Consequently, no information concerning chemical environment of hydrogen can be derived from the NMR spectrum, unless the $^1H-{}^1H$ dipolar interactions are overcome by a suitable NMR technique. However a combination of MAS and homonuclear dipolar decoupling via a multiple pulse sequence (WAHUHA, MREV or BR-24) allows the achievement of quantitative ^1H NMR spectra with linewidths of less than 0.3 ppm in favorable cases [Figure 1(a)]. This technique is referred to as CRAMPS (combined rotation and multiple pulse spectroscopy) (see ***CRAMPS***).[4]

In general, CRAMPS spectra of cokes are less resolved than the spectra of pure crystalline hydrocarbons and some coals; nevertheless, two absorption bands can usually be distinguished, centered at ca. 7 ppm and ca. 2 ppm, and associated with aromatic CH protons, and protons attached to sp^3 carbon atoms, respectively (Figure 1).[2,5] The linewidths corresponding to the two maxima are typically 3–5 ppm [full width at half maximum height (FWHM)], with the inhomogeneous broadening mainly attributed to distribution of chemical shifts. The use of the MREV-8 sequence seems satisfactory for CRAMPS spectroscopy of fossil fuels, as the application of more sophisticated pulse sequences like BR-24 does not lead to increased resolution in these materials. Due to substantial overlap of the aromatic and aliphatic peaks, the spectra are deconvoluted for quantitative analysis by using a superposition of Gaussian lines. The usefulness of the CRAMPS technique becomes apparent when differences in the spectra are viewed as a function of coking conditions, e.g. time or temperature of pyrolysis.[6]

4.2 ^{13}C NMR Techniques: CP MAS and Bloch Decay

^{13}C NMR spectra of cokes, coals and coal-derived products can be measured using conventional single pulse excitation (Bloch decay experiment), or by $^1H-{}^{13}C$ cross polarization, which, combined with high-power ^1H decoupling and MAS, yield spectra with well resolved aromatic and aliphatic carbon bands (Figure 2). Typically, the low-frequency (aliphatic) part of the spectrum consists of a peak located between 10 and

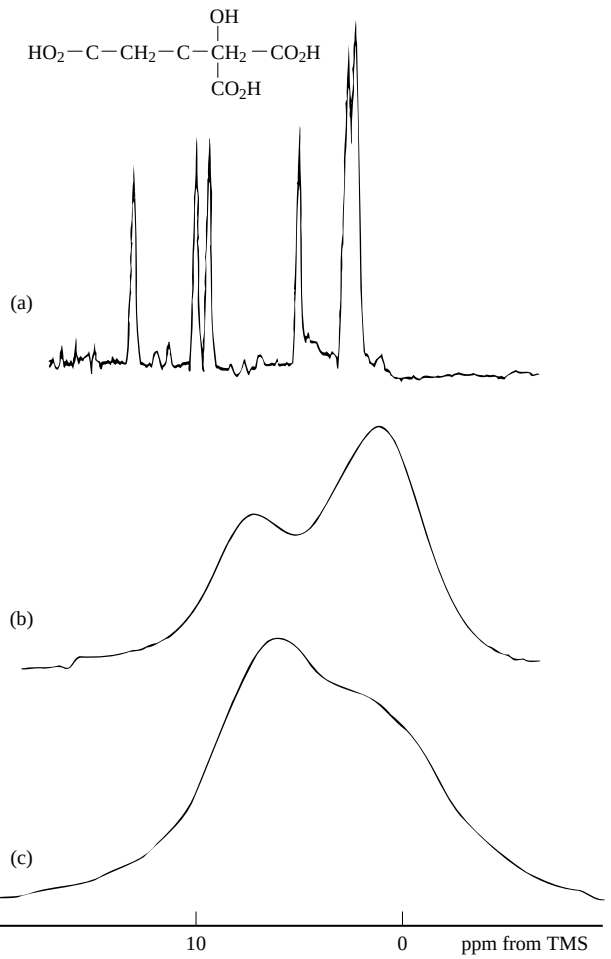

Figure 1 ^{1}H CRAMPS spectra of (a) citric acid, 187 MHz; (b) Pittsburgh No. 8 Argonne Premium Coal, 300 MHz; and (c) petroleum coke produced at Mobil from heavy crude oil, 300 MHz. [Spectrum (a) reproduced by permission of Academic Press from G. E. Maciel, C.E. Bronnimann, and B.L. Hawkins, in 'Advances in Magnetic Resonance: The Waugh Symposium', ed. W.S. Warren, 1990, Vol. 14, p. 125. Spectrum (c) reproduced by permission of Pergamon Press from M. Pruski, D. Michel, and B. C. Gerstein, *Carbon*, 1994, **32**, 31]

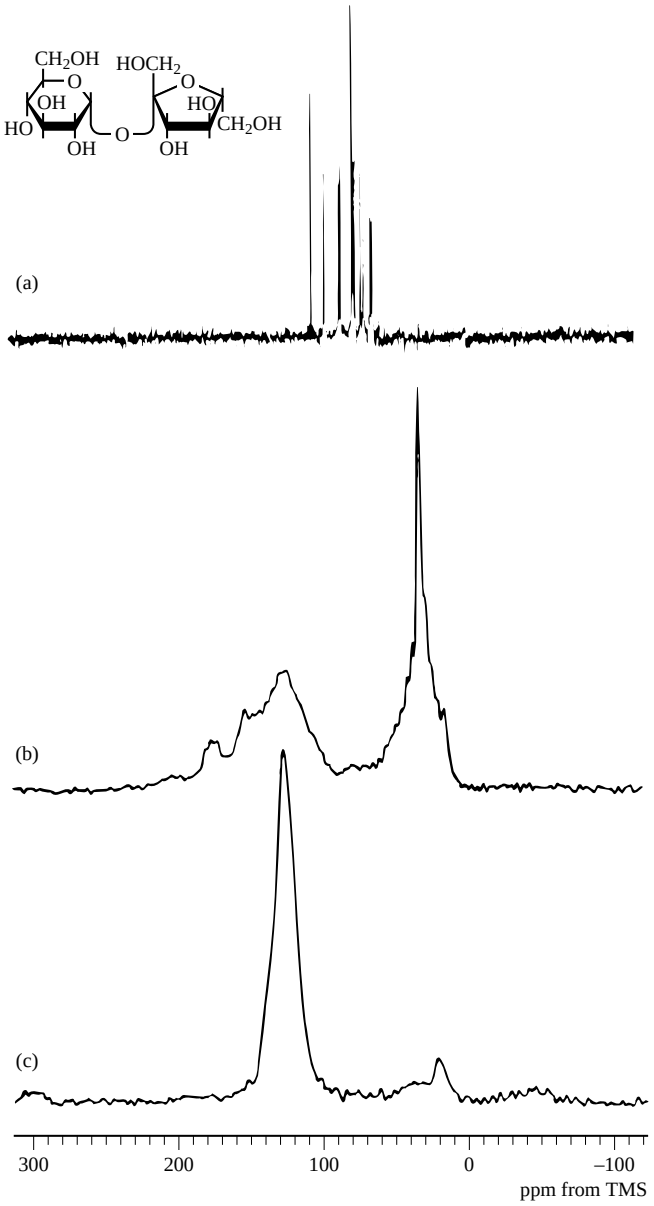

Figure 2 25 MHz ^{13}C CP MAS spectra of (a) sucrose, (b) German brown coal, and (c) petroleum coke produced from heavy crude oil (t_{cp} = 1 ms, spinning speed ν_r = 4.5 kHz)

50 ppm with features that can be assigned to methyl and methylene carbons. The aromatic peak, centered at ca. 130 ppm, is associated mainly with C–H perimeter and nonprotonated aromatic carbons. Although ^{1}H decoupling and MAS substantially reduce the large broadening due to ^{1}H–^{13}C dipolar interaction (ca. 20 kHz) and chemical shift anisotropy (ca. 200 ppm), the ^{13}C spectra of coals and cokes cannot match the liquid-like resolution achieved for many crystalline organic compounds (Figure 2). Again, NMR reflects the chemical complexity of these materials, because the resonances originating from a distribution of chemical environments are superimposed in the spectra.

A variety of sources can limit the accuracy of the intensities measured in these experiments which raised serious concern about the quantitative reliability of ^{13}C NMR methods in the analysis of carbonaceous solids.[7] Several factors that define resolution and quantitative information are general for ^{13}C NMR spectroscopy, e.g. interference of molecular motions with MAS and ^{1}H decoupling, incomplete recovery of carbon magnetization in Bloch decay experiments due to very long $T_1{}^{C}$ relaxation times, and signal loss due to broadening from paramagnetic centers (cokes contain typically ca. 10^{19} unpaired electrons per gram).

Additional difficulties arise when cross polarization is used to enhance the carbon signal.[7–10] The time evolution of carbon magnetization during the CP MAS experiment is a result of a complicated interplay between the spin–lattice relaxation processes in the rotating frame and the cross-polarization processes (described by relaxation time $T_{1\rho}{}^{H}$ and the time constant for cross-polarization process, T_{CH}), which, in turn, are further influenced by sample spinning and sample heterogeneity (see ***Cross Polarization in Rotating Solids: Spin-1/2 Nuclei***). In the simplest case, the time dependence of the ^{13}C magnetization $M_c(t_{CP})$ during the cross polarization contact is given by:

$$M(t_{CP}) = M_0\lambda^{-1}\left[1 - \exp\left(-\lambda\frac{t_{CP}}{T_{CH}}\right)\right] \times \exp\left(-\frac{t_{CP}}{T_{1\rho}^{H}}\right) \quad (1)$$

where M_0 is the carbon equilibrium magnetization, t_{CP} is the cross polarization contact time, and $\lambda = 1 - (T_{CH}/T_{1\rho}{}^{H})$.[11] For quantitative measurements it is required that the build-up of carbon magnetization, determined by T_{CH}, is completed before the loss of proton polarization occurs due to $T_{1\rho}{}^{H}$ relaxation (i.e. hydrogen having short $T_{1\rho}{}^{H}$ values are not contributing to cross polarization, leaving a substantial fraction of carbons 'undetected', unless $T_{CH} << T_{1\rho}{}^{H}$). In general, a wide distribution of T_{CH} times exists in cokes due to different $^{13}C-^{1}H$ distances and internal motion. MAS introduces additional time dependencies to homo- and heteronuclear dipolar Hamiltonians and further complicates the polarization transfer. Since, as described earlier, the $T_{1\rho}{}^{H}$ relaxation processes are also complex in cokes, with substantial fractions of spins having $T_{1\rho}{}^{H}$ values of 500 μs or less,[2] the condition $T_{CH} << T_{1\rho}{}^{H}$ may not be satisfied for those ^{13}C nuclei that are far from the nearest proton, e.g. those that are deeply incorporated in polycondensed aromatic rings.

In spite of the unfavorable cross-polarization dynamics, CP MAS experiments are being successfully applied in the studies of fossil fuels. Most researchers have conceded that, when carefully performed, CP MAS experiments provide quite accurate ^{13}C lineshapes, which in most cases agree well with those obtained from Bloch decay experiments. This assertion seems particularly pertinent for cokes, which by nature are more homogeneous than coals, and a too low carbon spin count in the CP MAS spectra does not necessarily imply an incorrect analysis of carbon functionality. In addition, several CP MAS-based spectral editing techniques have been proposed and applied to carbonaceous solids. The dipolar dephasing experiment has been traditionally used for discriminating between different carbons based on the strength of their dipolar interactions with protons.[12] In coals and cokes, this technique allowed discrimination between aromatic tertiary and aromatic quaternary ring carbons, as well as between aliphatic quaternary and CH_3 carbon atoms and combined CH and CH_2.[12,13] The recently proposed CP MAS sequences that combine depolarization and polarization inversion allow the generation of subspectra representing each of four CH_n (n = 0, 1, 2, 3) subsystems (see ***Spectral Editing Techniques: Hydrocarbon Solids***).[14]

The following experimental conditions and procedures are recommended for obtaining the most reliable CP MAS spectra of solid fossil fuels.[7,9,10]

1. The longitudinal relaxation times T_{1H} and $T_{1\rho}{}^{H}$ should be carefully measured using ^{1}H NMR.
2. Measuring of ^{13}C intensities with variable cross-polarization contact times in the 10 μs to 30 ms range, and fitting the data to equation (1) to obtain the total magnetization $M_c(0)$. Often two components of T_{CH} and $T_{1\rho}{}^{H}$ are necessary to produce a good fit.
3. The use of low MAS frequency (<5 kHz) is useful to avoid the interference of sample spinning with the cross-polarization process. Consequently, the measurements should be performed at low static magnetic fields (<2.5 T) to avoid the spinning sidebands in the spectra and the necessity of spinning sideband suppression. Since the dominant line broadening mechanisms in the CP MAS spectra are heterogeneous, resolution is almost independent on the magnetic field strength.
4. Accurate adjustment of the Hartmann–Hahn match, especially when MAS frequencies of >5 kHz are used.

Finally, the last few years have seen the development of a variety of CP MAS based experiments designed in order to enable efficient cross polarization and evade some of the quantitative distortions in ^{13}C NMR spectra. These techniques include stop-and-go spinning (STAG),[15] magic angle hopping[16] (see ***Magic Angle Turning and Hopping***) and amplitude-modulated cross polarization schemes (AMCP).[17]

While the CP MAS technique is applied in most studies, the Bloch decay experiment has recently become a feasible alternative. With the advent of large MAS rotors, spinning of several cubic centimeters of sample is now possible at 4 kHz, and a reasonable signal-to-noise (S/N) ratio can be achieved in ^{13}C MAS spectra of cokes within a few hours of measuring time, even if the recycle delay of several minutes is required between successive transients.[18] The Bloch decay spectra represent >90% of carbon in many cokes, with the only loss of signal attributed to paramagnetic broadening, and the method is preferable for quantitative studies. As the MAS capabilities continue to improve, Bloch decay may become increasingly used in the future research, leaving CP MAS measurements for quick qualitative surveys, comparative studies, measurements of C–H interactions and spectral editing.

4.3 Other NMR Techniques

The rotating frame dynamic nuclear polarization cross polarization experiment (rf DNP-CP)[19] is an alternative $^{1}H-^{13}C$ polarization scheme which allows nuclear polarization to be enhanced by irradiating the free electrons in a sample. The DNP technique is particularly well suited for solid fossil fuels and substantial carbon signal enhancements have been reported for coals.[19] The DNP experiment requires, however, a source of microwave power and some modifications of the NMR spectrometer (see ***Dynamic Nuclear Polarization and High-Resolution NMR of Solids***).

Variable angle sample spinning (VASS) is another method which partly averages the chemical shift anisotropy while allowing measurements of CSA lineshapes and CSA tensor values (see ***Variable Angle Sample Spinning***). The technique has proved useful in supplementing other types of NMR data to estimate the structure of polycondensed aromatic materials such as some coals and chars.[9]

Also, high temperature in situ NMR has recently embraced fossil fuels and related materials.[20] Several NMR studies were reported in which thermally induced changes in molecular dynamics and chemical shift information during pyrolytic decomposition and formation of solid carbonaceous residues, including coking processes, have been monitored at temperatures as high as 800 K. For these materials, which could be studied above their softening point (e.g. hard coal tar pitch and mesophase pitch prepared from decant oil), ^{1}H and ^{13}C NMR provided highly resolved signals (<1 ppm) that allowed for identification of various structural units.[21]

5 STRUCTURAL PARAMETERS OF COKES

The primary implication of solid state NMR studies of cokes is an enhanced understanding of their chemical

composition. Although the structural information obtained from solid state NMR studies is less detailed than that provided for the feedstocks using liquid state NMR techniques,[22] the parameters measured by ^{1}H and ^{13}C NMR can be used to estimate the 'average' models of these materials.[2,8] The parameters include: hydrogen and carbon concentrations (from quantitative NMR analysis); hydrogen and carbon aromaticities, as obtained from high-resolution NMR of ^{1}H and ^{13}C; fraction of aromatic carbon atoms with directly bonded protons (from ^{13}C NMR with dipolar dephasing); the total H/C mole ratio; and the mole fractions H/C (aromatic) and H/C (aliphatic). Due to their heterogeneity, the validity of 'average' models to describe coals has been questioned by some researchers. However, it is often useful to describe these materials in terms of average properties, as the identification of all individual constituents is very difficult, if not impossible, to accomplish. Also, NMR and elemental analysis show that cokes are more chemically homogeneous, and have low concentrations of heteroatoms, which facilitates structural determination. Two examples of basic structural types present in cokes produced from heavy crude oils by delayed coking at ca. 700 K are shown in Figure 3.[2] These materials may be viewed as high molecular weight conglomerates of polycyclic aromatic, hydrogen deficient structures, formed by covalent bonds or methylene bridges. The structures shown in Figure 3 are typical of cokes, although carbon aromaticities close to 100% were observed for materials produced under more severe coking conditions. Similar structural parameters were also measured for coal liquefaction residues, coal tar pitches, and residual carbons (coke) from thermal decomposition of oil shales.[23] In the last study, a CP MAS technique was used to monitor the decrease of aliphatic carbon peak intensity and formation of polycondensed quaternary carbon at higher temperatures.

For a variety of fossil fuels, solid state NMR spectra can be combined with characterization of feedstocks by liquid state NMR, MRI and high temperature in situ NMR to provide unique identification of structural changes during the entire coking, pyrolysis or liquefaction processes. Such studies allow monitoring of the loss of organic aliphatic matter, while cracking, polymerization and aromatization reactions progress during pyrolysis and the precursors of coke are formed. Following the progress of these reactions has notably improved the understanding of the chemistry of carbonization, and allowed optimization of the technology used in the coking process.

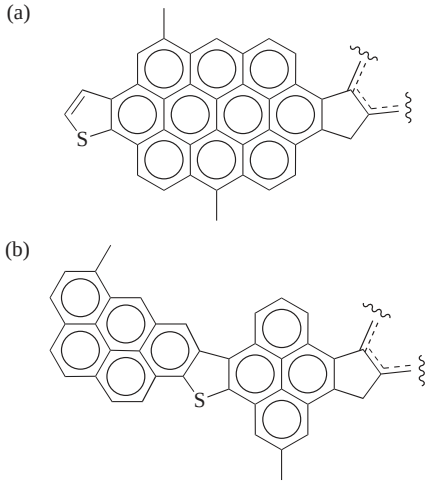

Figure 3 Typical structures of cokes based on structural parameters from solid state NMR of ^{1}H and ^{13}C and elemental analysis. (Reproduced by permission of Pergamon Press from M. Pruski, D. Michel, and B. C. Gerstein, *Carbon*, 1994, **32**, 31)

6 RELATED ARTICLES

Coal Structure from Solid State NMR; CRAMPS; Cross Polarization in Rotating Solids: Spin-1/2 Nuclei; Cross Polarization in Solids; Fossil Fuels; Internal Spin Interactions and Rotations in Solids; Line Narrowing Methods in Solids; Oil Reservoir Rocks Examined by MRI; Wood and Wood Chars.

7 REFERENCES

1. B. C. Gerstein and C. R. Dybowski, *Transient Techniques in NMR of Solids: An Introduction to Theory and Practice*, Academic, New York, 1985.
2. D. Michel, M. Pruski, and B. C. Gerstein, *Carbon*, 1994, **32**, 31; M. Pruski, D. Michel, and B. C. Gerstein, *Carbon*, 1994, **32**, 41.
3. J. S. Hayward, B. Ellis, and B. Rand, *Carbon*, 1988, **26**, 71.
4. B. C. Gerstein, C. Chou, R. G. Pembleton, and R. C. Wilson, *J. Phys. Chem.*, 1977, **81**, 565.
5. G. E. Maciel, C. E. Bronnimann, and B. L. Hawkins, in *Advances in Magnetic Resonance: The Waugh Symposium*, ed. W. S. Warren, Academic, San Diego, 1990, Vol. 14, p. 125.
6. B. C. Gerstein, M. Pruski, and D. Michel, in *Advances in Coal Spectroscopy*, ed. H. L. C. Meuzelaar, Plenum, New York, 1992, Chap. 9
7. R. A. Wind, G. E. Maciel, and R. E. Botto, in *Magnetic Resonance of Carbonaceous Solids* (*Advances in Chemistry Series, Vol. 229*), ed. R. E. Botto and Y. Sanada, American Chemical Society, Washington, 1993, Chap. 1
8. A. M. Orendt, M. S. Solum, N. K. Sethi, R. J. Pugmire, and D. M. Grant, in *Advances in Coal Spectroscopy*, ed. H. L. C. Meuzelaar, Plenum, New York, 1992, Chap. 10
9. C. E. Snape, D. E. Axelson, R. E. Botto, J. J. Delpuech, P. Tekely, B. C. Gerstein, M. Pruski, G. E. Maciel, and M. A. Wilson, *Fuel*, 1989, **68**, 547.
10. M. Pruski, L. dela Rosa, and B. C. Gerstein, *Energy Fuels*, 1990, **4**, 160.
11. M. Mehring, *Principles of High Resolution NMR in Solids*, 2nd edn., Springer, Berlin, 1983, Chap. 4
12. S. J. Opella and M. H. Frey, *J. Am. Chem. Soc.*, 1979, **101**, 5854.
13. P. DuBois Murphy, T. J. Cassady, and B. C. Gerstein, *Fuel*, 1982, **61**, 1233.
14. X. Wu, S. T. Burns, and K. W. Zilm, *J. Magn. Reson., Ser. A*, 1994, **111**, 29.
15. R. C. Zeigler, R. A. Wind, and G. E. Maciel, *J. Magn. Reson.*, 1988, **79**, 299.
16. A. Bax, N. M. Szeverenyi, and G. E. Maciel, *J. Magn. Reson.*, 1983, **52**, 147.
17. S. Hediger, B. H. Meier, and R. R. Ernst, *Chem. Phys. Lett.*, 1993, **213**, 627.
18. G. E. Maciel, C. E. Bronnimann, A. Jurkiewicz, R. A. Wind, and V. H. Pan, *Fuel*, 1991, **68**, 925.

19. R. A. Wind, in *Magnetic Resonance of Carbonaceous Solids* (*Advances in Chemistry Series, Vol. 229*), ed. R. E. Botto and Y. Sanada, American Chemical Society, Washington, 1993, Chap. 10
20. Y. Sanada and L. J. Lynch, in *Magnetic Resonance of Carbonaceous Solids Advances in Chemistry Series, Vol. 229*, ed. R. E. Botto and Y. Sanada, American Chemical Society, Washington, 1993, Chap. 7
21. T. Nishizawa and M. Sakata, *Fuel*, 1991, **70**, 124.
22. See, for example, C. E. Snape, *Fuel* 1983, **62**, 34.
23. J. A. MacPhee, B. N. Nandi, J. A. Ripmeester, and R. E. Hawkins in *Magnetic Resonance, Introduction, Advanced Topics and Applications to Fossil Energy*, ed. L. Petrakis and J. P. Fraissard, Riedel, Dordrecht, 1984, p. 575; F. P. Miknis and G. E. Maciel, *ibid.*, p. 545.

Biographical Sketch

Marek Pruski. *b* 1954. M.S., 1977, Ph.D., 1981, N. Copernicus University (supervisor T. Marszalek), Torun, Poland; Postdoctoral fellow, Ames Laboratory, Iowa State University (with B.C. Gerstein), 1985–88; scientist, Ames Laboratory, Iowa State University, 1988–present. Approx. 50 publications. Current research specialty: solid state NMR and its applications to surface and material sciences.

Diffusion in Porous Media

Jörg Kärger

Leipzig University, Germany

1 Introduction 1
2 Pieces of Information 1
3 Principles of PFG-NMR 2
4 Diffusion in Microporous Crystallites (Zeolites) 5
5 Related Articles 7
6 References 7

1 INTRODUCTION

Porous media are of considerable interest in a very diverse range of activities. Porous media comprise a wide variety of substances—plastics, ceramics, cements, clays, rocks, porous glasses, carbons, silica gels, and zeolites. Even biological tissues may share many features of porous media. Depending on the given nature, the pore diameters in these substances may range from the subnanometer region up to macroscopic dimensions. The efficiency of their technical use is intimately connected with their transport properties. Diffusion measurements in porous systems are therefore of direct practical relevance. Moreover, systematic diffusion studies in such systems may contribute to a better understanding of such fundamental questions as the interaction between molecules and solid surfaces,[1–3] and the behavior of molecular systems of reduced dimensionality.[4]

Among the methods of studying molecular diffusion in porous media, NMR spectroscopy is of particular relevance. As a noninvasive method, it allows the observation of molecular transportation without interfering with the internal processes. The technique may be applied under both equilibrium and nonequilibrium conditions. Using different NMR techniques, various aspects of molecular transport may be investigated, including the elementary processes of diffusion and the rate of molecular propagation over microscopic and macroscopic distances. A review of the principles of these techniques and examples of their application is given in Section 2. Probably the most powerful NMR method for studying molecular propagation is the pulsed field gradient method (PFG-NMR), and this is described in more detail in Section 3. The capability of PFG-NMR to trace indications of anomalous diffusion in porous media is discussed in Section 4. Finally, as an illustration of the versatility of PFG-NMR, Section 5 summarizes the information provided by this method about molecular diffusion in beds of microporous crystallites (zeolites).

2 PIECES OF INFORMATION

The most straightforward way of applying NMR to study diffusion in porous media is based on the fact that the intensity of an NMR signal is directly related to the number of the observed nuclei. Using this correlation it was possible to measure the rate of molecular exchange between zeolite crystallites of type ZSM-5[5] and NaX,[6] loaded with ordinary (i.e. hydrogen containing) benzene and the surrounding atmosphere of deuterated benzene. The intracrystalline diffusivities estimated on the basis of the measured exchange rates were in excellent agreement with the data determined directly by PFG-NMR in the identical sample and verified the equivalency of macroscopically and microscopically measured diffusivities.

The information provided by the NMR signal intensity is significantly enhanced when the measurements are performed under the influence of well defined inhomogeneities of the magnetic field. Under such conditions, the resonance frequency becomes space dependent, so that the NMR spectrum may be directly correlated with the distribution of the nuclei under consideration within the sample. This method has become popular under the names ‘NMR tomography’ or ‘NMR spin mapping’, due to its spectacular progress in application to anatomical imaging in medicine[7] (cf. articles on biomedical applications in this Encyclopedia). However, its application is certainly not confined to biomedicine; in particular, a wide variety of NMR imaging studies have been concerned with molecular propagation in porous media.[8,9] A summary of the most recent results may be found in the proceedings of the ‘International Meeting on Recent Advances in NMR Applications to Porous Media’, Bologna, 1990,[10] and Canterbury, 1993.[11]

An interesting possibility of tracing mass transfer in porous systems is provided by ^{129}Xe NMR.[12] For this purpose, the system under study is brought into contact with a xenon atmosphere. Since, besides the pore architecture and the chemical composition of the pore surface, the chemical shift of ^{129}Xe NMR also depends on the nature and the concentration of the molecules in the interior of the porous system, the ^{129}Xe NMR spectrum reflects the distribution function of molecular concentrations within the sample. If there are, for example, two regions of different concentration of the molecular species under study, the ^{129}Xe NMR spectrum should consist of two different lines. Obviously, the merging rate of the two lines is directly correlated with the rate of equilibration of the internal concentration, and provides direct information about the intrinsic diffusivities. This measuring principle has been used to study molecular transportation in both the micropores[13] and the macropores[14,15] in zeolitic adsorbate–adsorbent systems.

In the methods so far mentioned, we have exclusively considered samples that are not at equilibrium, either in the strict macroscopic sense, or at least with respect to the different isotopes involved. As soon as equilibrium is attained, these methods cannot provide any information about molecular diffusion. It is one of the great advantages of NMR spectroscopy to be able to follow even the molecules themselves on their individual diffusion paths. The information thus obtained may concern the elementary steps of diffusion as well as the rate of molecular propagation over much larger distances. Information about the elementary steps of diffusion of molecules under the influence of the internal system of porous media may be deduced from an analysis of the nuclear magnetic relaxation times and the NMR spectra.

Proton magnetic relaxation studies offer the advantage that most molecules of interest in diffusion studies of porous media

contain hydrogen atoms, and that, except for the non-naturally-occurring tritium, the magnetogyric ratio, and hence the signal-to-noise ratio, is largest for the hydrogen nucleus.[16] Proton magnetic relaxation of molecules in contact with solid surfaces is mainly determined by magnetic dipole interaction with protons of the same molecule (intramolecular proton–proton interaction), with protons of other molecules (intermolecular proton–proton interaction), and with paramagnetic ions. The different contributions may be separated by a 'relaxation analysis'.[17] Except for extremely pure substances, longitudinal relaxation is controlled by the magnetic dipole interaction with paramagnetic ions. If the longitudinal electron spin relaxation time of these paramagnetic ions is much greater than the mean residence time between subsequent diffusion jumps, then proton magnetic relaxation is affected by the translational motion of the molecules with respect to the ions, and the temperature dependence of the longitudinal relaxation time is found to pass a distinct minimum, which is characterized by the condition that at this temperature the mean residence time is of the order of the reciprocal of the resonance frequency.[17]

The problem of separating the various contributions to nuclear magnetic relaxation can be overcome to a certain degree by studying the deuteron magnetic resonance. This is due to the almost completely dominant interaction energy of the electric quadrupolar moment of the deuteron with the intramolecular electric field gradient at the nuclear site in comparison with the various magnetic coupling energies. Since the deuteron magnetic resonance frequency depends on the orientation of this electric field gradient with respect to the external magnetic field, molecular reorientations with time constants of the order of the reciprocal of the linewidths will lead to characteristic changes in the NMR spectra, including a narrowing of the total spectrum.[18,19] The thus-estimated reorientation times for several hydrocarbons in X-type zeolites were found to be in excellent agreement with the directly measured diffusivity, if one assumes that the molecular mean jump lengths are of the order of the distance between neighboring supercages.[20]

In an identical manner, molecular reorientation also leads to a narrowing of NMR lines in the case of chemical shift anisotropy. Measurements of this type have been carried out with various nuclei (^{13}C and ^{31}P), and numerical simulations have been developed to allow the measured spectra to be attributed to the corresponding reorientation times in the relevant geometry.[21,22]

Since the confinement of the molecules to the internal surface of porous media often leads to a preferential orientation of the molecules, the orientation correlation function will generally not decay to zero by mere local reorientation. Rather, the complete decay to zero necessitates molecular migration to positions with changed orientational preference. This process of 'reorientation mediated by translational displacements' (RMTD)[23] may be traced by measuring the longitudinal nuclear magnetic relaxation times in the range of low resonance frequencies (in particular by the field cycling technique[24]), corresponding to the large correlation times of this process. Tracing RMTD has been shown to be an informative tool for studying both molecular dynamics and structural properties in micrometer and submicrometer length scales of porous systems.[23,25]

In more open porous structures, overall nuclear magnetic relaxation is significantly influenced by the rate of exchange between the region of intense relaxation (the magnetization 'sinks') and the bulk phase. The theoretical analysis of this situation[26,27] shows that the relaxation pattern is controlled by the relationship between the mean diffusion time over a characteristic length scale of the individual pores (e.g. their radius) and the overall relaxation time to be expected under the condition of fast exchange. For diffusion times exceeding the (hypothetical) overall relaxation time, the observed relaxation behavior depends notably on the exchange conditions, yielding information about both the pore sizes and the intrinsic diffusivities.[26–28]

At the beginning of this section ^{129}Xe NMR was introduced as a tool for following the evolution of molecular concentration profiles within porous media. This technique clearly includes the observation of the distribution of the xenon atoms themselves. In microporous materials where the individual cavities are separated by narrow 'windows', the population distribution of the xenon atoms within the individual cavities may be determined.[29] In addition to this local structural information, by using a second time dimension in the NMR experiments (two-dimensional exchange NMR), one may even determine the rate of molecular exchange between cavities of different occupation numbers. This method has been successfully applied to the study of intracrystalline diffusion of xenon in NaA-type zeolites.[30]

Common to all the methods so far considered is the fact that the information about molecular self-diffusion is based on the applicability of certain models. There is, however, the possibility of monitoring directly the probability distribution of molecular propagation. This possibility is provided by transient NMR measurements in a magnetic field with well-defined inhomogeneities of large intensity. The most important representative of these techniques, PFG-NMR, is described in more detail in the rest of this article.

3 PRINCIPLES OF PFG-NMR

The principles of diffusion measurement by NMR may be easily visualized by using the classical concept of nuclear magnetism. According to this concept, any individual spin will carry out a precessional motion about the direction of the constant magnetic field with a precessional frequency given by the Larmor relationship:

$$\omega = -\gamma B \tag{1}$$

where γ is the magnetogyric ratio. In PFG-NMR, the constant magnetic field is superimposed over two short time intervals δ by an inhomogeneous field

$$B_{\mathrm{add}}(\boldsymbol{r}) = \boldsymbol{g} \cdot \boldsymbol{r} \tag{2}$$

the so-called 'field gradient pulses'. According to equation (1) these pulses have the effect that the positions of the individual spins at the instants of the field gradient pulses are recorded by the precessional phases

$$\phi(\boldsymbol{r}) = \int \omega \, \mathrm{d}t = -\gamma(B + \boldsymbol{g} \cdot \boldsymbol{r})\delta \tag{3}$$

accumulated during these time intervals. The two field gradient pulses are generally incorporated into the classical $\pi/2-\tau-\pi$ rf pulse sequence which gives rise to a transient NMR signal (the 'spin echo') at time 2τ after the initial $\pi/2$ pulse. Being proportional to the total magnetization, the intensity of the spin echo depends on the dephasing of the precessional phases of the individual spins at time 2τ. Since the dephasing effected by the first field gradient pulse according to equation (3) is inverted by the π pulse, for immobile spins it is exactly compensated by the second field gradient pulse which is applied after the π pulse. However, if the individual molecules (and with them the spins) have moved during the time interval between the field gradient pulses, the refocusing will be incomplete and the intensity of the transverse magnetization will not be fully restored to its original value. NMR signal attenuation must therefore be expected to increase with increasing displacements during the 'observation time' (i.e. the time interval between the two field gradient pulses), and with increasing width δ and amplitude g of the field gradient pulses.

For a quantitative analysis we consider a particular spin which has been at positions $\boldsymbol{r}_1$ and $\boldsymbol{r}_2$ during the first and second field gradient pulses, respectively. According to equation (3), the phase shift of such a spin in comparison with a spin fixed in space is equal to $\gamma\delta\boldsymbol{g}\cdot(\boldsymbol{r}_2-\boldsymbol{r}_1)$. The total magnetization is the vector sum of the dipolar moments of the individual spins. Thus, in complex notation, the vector sum of the transverse nuclear magnetic moments of all spins involved yields

$$\Psi = \int\int \exp[\mathrm{i}\gamma\delta\boldsymbol{g}\cdot(\boldsymbol{r}_2-\boldsymbol{r}_1)]\, p(\boldsymbol{r}_1) P(\boldsymbol{r}_2, \boldsymbol{r}_1, \Delta)\, \mathrm{d}\boldsymbol{r}_1\, \mathrm{d}\boldsymbol{r}_2 \tag{4}$$

where Ψ denotes the ratio between the NMR signal intensity observed with and without magnetic field gradient pulses, $p(\boldsymbol{r}_1)$ denotes the probability (density) of finding a spin at position $\boldsymbol{r}_1$ (i.e. during the first magnetic field gradient pulse), and $P_2(\boldsymbol{r}_2, \boldsymbol{r}_1, \Delta)$ denotes the probability (density) that a spin which has been at position $\boldsymbol{r}_1$ during the first field gradient pulse will have come to $\boldsymbol{r}_2$ after a time interval Δ(i.e. during the second field gradient pulse). As it contains the complete information about the process of molecular propagation, the function $P(\boldsymbol{r}_2,\boldsymbol{r}_1,\Delta)$ has been termed the 'propagator'. (This expression must clearly not be confused with the operator $\hat{U}(t)$ which is generally termed in the same way and describes the evolution of the ensemble of the magnetically resonant nuclei under study.) Integrating over all possible starting positions $\boldsymbol{r}_1$, one may introduce a mean propagator[31]

$$P(\boldsymbol{r}, \Delta) = \int p(\boldsymbol{r}_1) P(\boldsymbol{r}_1 + \boldsymbol{r}, \boldsymbol{r}_1, \Delta)\, \mathrm{d}\boldsymbol{r}_1 \tag{5}$$

which denotes the probability that during time Δ an arbitrarily selected molecule within the sample will be displaced over $\boldsymbol{r}$. With this notation, equation (4) becomes

$$\Psi = \int \exp\{\mathrm{i}\gamma\delta\boldsymbol{g}\cdot\boldsymbol{r}\} P(\boldsymbol{r}, \Delta)\, \mathrm{d}\boldsymbol{r} \tag{6}$$

Since equations (4) and (6) formally coincide with the expressions for the intermediate incoherent scattering function in neutron scattering, PFG-NMR has been repeatedly interpreted as a scattering experiment[32–35] with a generalized scattering vector

$$\boldsymbol{k} = \gamma\delta\boldsymbol{g} \tag{7}$$

The maximum value of this quantity is of the order of $10^7\ \mathrm{m}^{-1}$, yielding a lower limit of about 100 nm for the space scale covered in PFG-NMR experiments. The much larger scattering vectors in neutron scattering experiments confine diffusion measurements by this technique to maximum displacements of the order of only a few nanometers. Hence, for the observation of molecular transportation phenomena on the micrometer scale, PFG-NMR represents a unique method.

PFG-NMR has been successfully applied to the study of molecular diffusion in a wide spectrum of substances, including pure liquids and gases, polymers, liquid crystals, membranes, biological tissues, as well as the vast group of porous media. Detailed introductions to the experimental procedure with special emphasis on the various techniques which may be applied to enhance the sensitivity of this method and to circumvent the omnipresent pitfalls in experimental work may be found in the literature.[33–39] In most cases, molecular diffusion, as observed by PFG-NMR, is considered to follow the laws of ordinary diffusion. The validity of this assumption is considered in the next section.

4 ORDINARY VS ANOMALOUS DIFFUSION

The total molecular displacement of any molecule during the observation time Δ of a PFG-NMR experiment may be understood as the result of the displacements of this molecule during the different time intervals into which the observation time Δ may be subdivided. Under the assumption that subsequent displacements are independent of each other and are controlled by the same probability distribution then, according to the central limit theorem of statistics for a sufficiently large number of time intervals, the distribution of the sum of these displacements will be given by a Gaussian function with a mean square distribution being proportional to the number of time intervals considered and, hence, to the observation time. Since this probability distribution is in fact the propagator, in the case of three-dimensional diffusion, for example, we may thus write

$$P(\boldsymbol{r}, \Delta) = (4\pi D\Delta)^{-3/2} \exp(-r^2/4D\Delta) \tag{8}$$

where the self-diffusion coefficient D has been introduced via the required proportionality between the mean square displacement and the observation time:

$$\langle r^2(\Delta)\rangle = 6D\Delta \tag{9}$$

Molecular random walk following equation (8) [and hence equation (9)] is called 'ordinary diffusion'. It is completely described by the self-diffusion coefficient D. The definition of the self-diffusion coefficient by the Einstein relationship [equation (9)] is equivalent to that by Fick's first law:[40]

$$\boldsymbol{j}^* = -D\ \nabla\ c^* \tag{10}$$

where the self-diffusion coefficient is introduced as the factor of proportionality between the negative concentration gradient and the flux density of labeled molecules at macroscopic equilibrium. Inserting equation (8) into equation (6), one obtains for the signal attenuation in PFG-NMR for ordinary diffusion:

$$\Psi = \exp(-\gamma^2\delta^2 g^2 D\Delta) \tag{11}$$

With equation (9), signal attenuation may also be expressed as a function of the mean square displacement:

$$\Psi = \exp(-\gamma^2\delta^2 g^2 \langle r^2\rangle/6) \tag{12}$$

In deriving equation (4) [and hence equations (11) and (12)] it has implicitly been assumed that the molecular displacements during the field gradient pulses are much smaller than those in the interval between the two gradient pulses (narrow-pulse limit).[33] Only under this assumption can the NMR signal attenuation be related to the propagator in such a straightforward way. In the case of ordinary diffusion, the finite field gradient pulse width may be exactly taken into account by replacing Δ by an 'effective' observation time $\Delta - \delta/3$.

Any violation of the conditions for the applicability of the central limit theorem must be expected to lead to deviations from ordinary diffusion. Very often, in particular considering molecular diffusion in fractal networks, in the case of 'anomalous' diffusion the mean square displacement should obey a simple scaling law

$$\langle r^2(t)\rangle \propto t^{\kappa} \tag{13}$$

where now, in contrast to ordinary diffusion, the time exponent κ is smaller than 1. It may be shown[40] that the fractal dimension of the trajectory of a random walker obeying equation (13) is equal to $2/\kappa$. As a simple inversion of the central limit theorem, one may conclude that in the case of anomalous diffusion subsequent displacements must be correlated. Analytical expressions for this correlation may be deduced from equation (13).[41] By using these expressions it can be shown that in the narrow-pulse approximation for anomalous diffusion the PFG-NMR spin echo attenuation is also given by equation (12). For finite pulse widths δ, the expression for the spin echo attenuation is more complicated[41] and cannot be deduced from the narrow-pulse approximation by simply introducing an effective observation time.

The search for indications of anomalous diffusion is a current topic of PFG-NMR. Recent progress in the sensitivity towards smaller molecular displacements, in particular including the possibilities of the stray-field modification of the steady-gradient spin echo NMR method,[42] did in fact allow the observation of anomalous diffusion in polymer melts and solutions.[34,43,44] Scaling laws with time exponents κ differing in the range 0.25–0.5 could be confirmed, partially by varying the observation time over orders of magnitude. No similar breakthrough in detecting indications of anomalous diffusion in porous media has yet been achieved. As an example, Figure 1 shows the mean square displacement of *n*-hexadecane adsorbed on active carbon as a function of the observation time.[45] Over two orders of magnitude the observed time dependence is in complete agreement with that of ordinary diffusion,

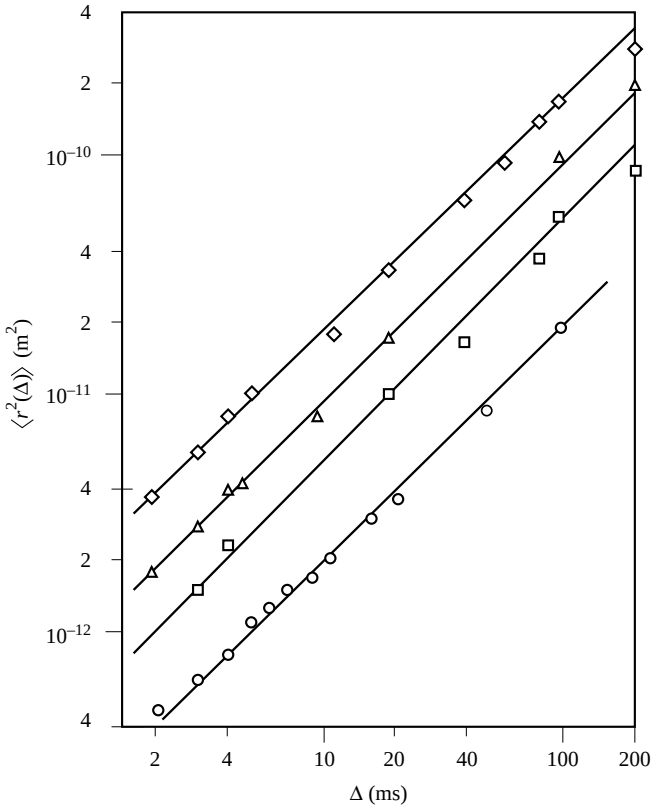

Figure 1 Mean square displacement of *n*-hexadecane adsorbed on active carbon at a pore filling factor of 0.43 versus observation time Δ at: (○) 291 K, (□) 323 K, (△) 363 K, and (◇) 413 K. The straight line indicates the dependence[45] $\langle r^2(\Delta)\rangle \propto \Delta$

although the internal pore system can be described by introducing fractal dimensions. One should note, however, that in the measurements there was only a very small overlap between the pore distribution function and the minimum displacements observable by PFG-NMR.

Molecular transportation in porous crystallites over distances sufficiently exceeding the dimensions of the elementary units clearly fulfils the conditions for the application of the central limit theorem. It is not surprising, therefore, that PFG-NMR measurement of intracrystalline diffusion in zeolites has not thus shown any deviation from ordinary diffusion. There is, however, an intriguing exceptional case, where even in zeolites molecular transportation must be expected to deviate from ordinary diffusion. Such a situation may occur when the zeolite pore system consists of parallel channels, as for example in zeolites ZSM-12 or $AlPO_4$-5. As soon as the channel diameters are so small that the molecules cannot pass each other, by theoretical considerations[46] the molecular mean square displacement may be shown to be proportional to the square root of the observation time rather than to the observation time itself. The experimental verification of this phenomenon of 'single-file' diffusion[47] is a task for PFG-NMR.

In the following final section, by reviewing selected PFG-NMR studies on zeolites, typical examples are given of the application of this NMR technique to diffusion measurements in porous systems. The variety of attainable information will demonstrate that the confinement to ordinary diffusion in these

substances in no way diminishes the attractiveness of such investigations.

5 DIFFUSION IN MICROPOROUS CRYSTALLITES (ZEOLITES)

According to the original definition, zeolites are microporous crystalline aluminosilicates. In the last few years, dramatic progress in zeolite synthesis has made possible the production of a large number of zeolite structure types with the aluminum and/or silicon atoms replaced by other components such as phosphorus, gallium, germanium, boron, and beryllium. Moreover, with these new structural components, a number of new structure types have been realized which have no equivalent among the aluminosilicates.[48] It has become common use, therefore, to apply the term 'zeolites' quite generally to microporous crystalline solids. The diameters of the zeolite crystallites are typically in the micrometer range. Therefore, molecular propagation within beds of zeolite crystallites proceeds both within the individual crystallites (in the 'micropores') and in the intercrystalline space (the macropores or transport pores). In the case of gas phase adsorption, which we shall consider exclusively in the following discussion, molecular concentration in the intercrystalline space is negligibly small in comparison with intracrystalline concentration.

A survey of the different features of molecular transportation as accessible by PFG-NMR under such conditions is provided by the propagator representation. As an example, Figure 2 shows the mean propagator of ethane in zeolite NaCaA[31] for two different crystallite sizes at three different temperatures, determined from the measured spin echo attenuations by using the inversion of equation (6). Depending on the crystallite size, the observation time and the temperature, the observed mean propagator may be exclusively determined by intracrystalline diffusion [e.g. in Figure 2(a) at 153 K] or by migration through the bed of crystallites ['long-range' diffusion, in Figure 2(b) at 293 K]. In the intermediate range between these two limiting cases, the propagator additionally depends on the rate of molecular exchange between the intra- and intercrystalline spaces. Under appropriate conditions, PFG-NMR is therefore able to provide three different dynamic quantities: the coefficients of intracrystalline and of long-range self-diffusion, and the intracrystalline mean lifetime.

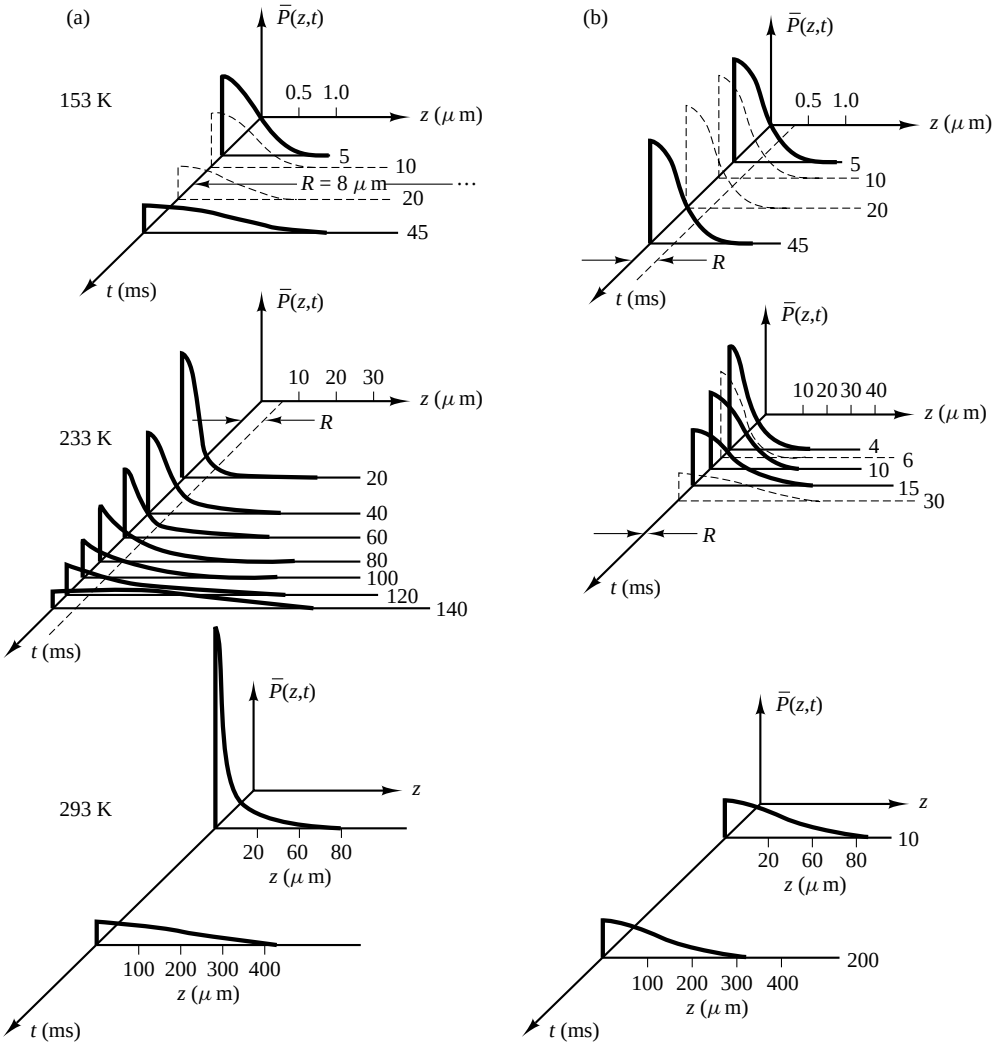

Figure 2 Propagator representation for the self-diffusion of ethane in NaCaA zeolites: (a) 40 mg g^{-1}, $R \approx 8$ μm; (b) 58 mg g^{-1}, $R \approx 0.4$ μm[31]

A detailed description of the procedure and examples of application may be found in the literature.[40,49]

At sufficiently low temperatures, the thermal energy of the adsorbate molecules is not high enough to allow them to overcome the step in the potential energy from the intracrystalline to the intercrystalline space. The molecules are confined, therefore, to the interior of the individual crystallites, and the situation is comparable to that within a pore with impenetrable walls,[50] where now the pore size corresponds to the size of the crystallites. Following the scattering analogy, the PFG-NMR spin echo attenuation due to diffusion between connected pores has been used to analyze the pore distribution and connectivity.[51,52] It is a challenge for PFG-NMR to adopt this concept to study molecular exchange between the different crystallites in the transition range between 'restricted' and long-range diffusion.

One of the most remarkable features of intracrystalline diffusion is the large variety of patterns of concentration dependence. So far, at least five different types of concentration dependence have been observed. Examples of adsorbate–adsorbent systems that follow these different patterns are presented in Figure 3.[40] It is an attractive task for molecular dynamics simulations to correlate the different patterns with possible microdynamic models.[53–55]

A large number of zeolite structure types are of noncubic symmetry, so that intracrystalline molecular migration must be described by a diffusion tensor rather than by a diffusion coefficient, i.e. a scalar quantity. As a consequence of the microscopic size of the crystallites, only recently have PFG-NMR measurements of diffusion anisotropy in zeolites become possible. The measurements have been carried out in two different ways: (i) by introducing the zeolite crystallites into an array of parallel capillaries with their longitudinal extension preferentially parallel to the capillary axes; and (ii) by analyzing the shape of the signal decay function.[56,57] In both cases, the measured diffusivities (methane and ethane in zeolite ZSM-5) were found to be in satisfactory agreement with the results of molecular dynamics simulations.[53,54]

As a noninvasive method, PFG-NMR represents an excellent tool for the in situ observation of molecular transportation under reaction conditions. As an example, Figure 4 represents the results of Fourier transform PFG-NMR measurements[56,58] of the time dependence of the diffusivities of the reactant and the product molecules during the conversion of cyclopropane to propene on zeolite NaX.[59] In addition, Figure 4 also shows the relative amount of both species as determined by analyzing the free induction decay. Comparing the intrinsic reactivities with the rather high intracrystalline mobilities, any essential influence of molecular transport on the rates of molecular conversion in flow reactors may be excluded. Using zeolite crystallites of different size, this prediction could in fact be confirmed by direct measurement in flow reactors.[59]

Since the first applications of PFG-NMR to study intracrystalline diffusion in zeolites, repeatedly dramatic differences between these data and the results of conventional sorption measurements have been stated.[17,40] This discrepancy led to a critical reexamination of the earlier sorption data, which revealed that in many cases the effects of external heat- and mass-transfer resistances in limiting the adsorption–desorption rates were far greater than originally assumed, and the discrepancy with the NMR data could be explained on this

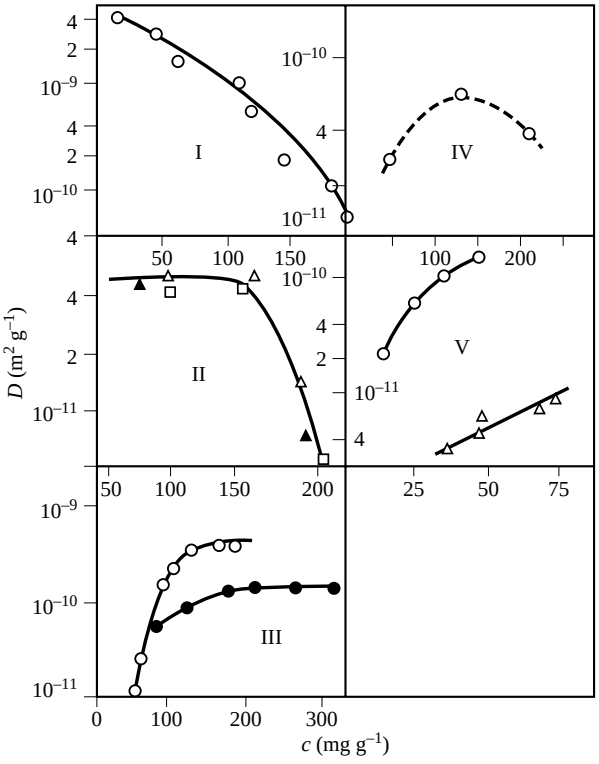

Figure 3 Patterns of the concentration dependence of intracrystalline diffusivities. I, *n*-Hexane in NaX at 358 K. II, (△) *ortho*-, (□) *meta*-, and (▲) *para*-xylenes in NaX at 393 K. III, Ammonia (○) and water (●) in NaX at 298 K. IV, Acetonitrile in NaX at 393 K. V, (○) Ethane at 173 K and (△) propane at 413 K in NaCaA[40]

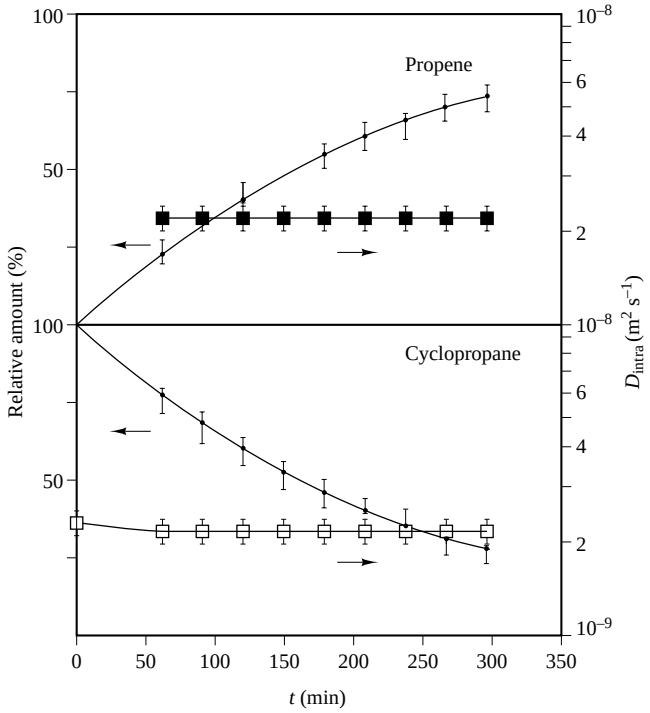

Figure 4 Time dependence of the relative amounts of cyclopropane and propene during the conversion of cyclopropane to propene in NaX and their self-diffusion coefficients at 473 K[59]

basis. Moreover, as the PFG-NMR data are in satisfactory agreement with the results of quasielastic neutron scattering experiments[60] and with molecular dynamics simulations,[53,54] there should be no doubt that PFG-NMR yields the correct values for the intracrystalline mobility under equilibrium conditions.

A comparison with the results of adsorption–desorption measurements is complicated by the fact that the latter experiments are carried out under nonequilibrium conditions, yielding transport- rather than self-diffusivities.[40] However, being based on the same elementary processes, i.e. the stochastic movement of the individual molecules, at least for small concentrations, agreement between the transport- and self-diffusivities should be expected. For A-type zeolites this agreement has in fact repeatedly been confirmed.[40,61,62] Remaining differences, mainly observed for zeolites NaX and ZSM-5, are difficult to explain. Following the adsorption process of *n*-hexane in beds of zeolites NaX by space- and time-resolved PFG-NMR, the molecular mobility of the *n*-hexane molecules immediately after adsorption was found to coincide with that at equilibrium.[63] Therefore, as a possible explanation of this discrepancy, it must also be excluded that the diffusivities as obtained by PFG-NMR with sealed samples are only attained after some period of relaxation within the adsorbate–adsorbent system. It is one of the current tasks of zeolite research to decide whether the remaining differences are real indications of different transport properties under equilibrium and nonequilibrium conditions, or whether they are mere consequences of not yet revealed shortcomings in the experimental procedure.

6 RELATED ARTICLES

Anisotropically Restricted Diffusion in MRI; Brownian Motion and Correlation Times; Complex Radiofrequency Pulses; Diffusion: Clinical Utility of MRI Studies; Diffusion and Flow in Fluids; Diffusion Measurements by Magnetic Field Gradient Methods; Diffusion and Perfusion in MRI; Diffusion in Rare Gas Solids; Imaging Techniques for Solids and Quasi-Solids; Intercalation Compounds; Microporous Materials and Xenon-129 NMR; Molecular Motions: T_1 Frequency Dispersion in Biological Systems; Molecular Sieves: Crystalline Systems; Oil Reservoir Rocks Examined by MRI; Reactions in Zeolites.

7 REFERENCES

1. H. Pfeifer, *NMR Basic Principles Prog.*, 1994, **31**, 31.
2. G. Ertl, *Langmuir*, 1987, **3**, 4.
3. H. Pfeifer and H. Ernst, *Ann. Rep. NMR Spectrosc.*, in press.
4. D. Avnir (ed.), *The Fractal Approach to Heterogeneous Chemistry*, Wiley, New York, 1989.
5. C. Förste, J. Kärger, H. Pfeifer, L. Riekert, M. Bülow, and A. Zikánová, *J. Chem. Soc., Faraday Trans.*, 1990, **86**, 881.
6. C. Förste, J. Kärger, and H. Pfeifer, *J. Am. Chem. Soc.*, 1990, **112**, 7.
7. P. Mansfield and P. G. Morris, *NMR Imaging in Biomedicine*, Academic, New York, 1982.
8. W. Heink, J. Kärger, and H. Pfeifer, *Chem. Eng. Sci.*, 1978, **33**, 1019.
9. G. Guillot, G. Kassab, J. P. Hulin, and P. Rigord, *J. Phys. D: Appl. Phys.*, 1991, **24**, 763.
10. G. C. Borcia, R. J. S. Brown, P. Fantazzini, J. Gore, P. Mansfield, B. Maraviglia, E. Mesini, and L. Sgubini (eds.), *Magn. Reson. Imaging*, 1991, 9(5).
11. G. C. Borgia, P. Fantazzini, J. C. Gore, M. E. Smith, and J. H. Strange (eds), *Magn. Reson. Imaging*, 1994, 12(2).
12. J. Fraissard and T. Ito, *Zeolites*, 1988, **8**, 350.
13. J. Kärger, H. Pfeifer, T. Wutscherk, S. Ernst, and J. Weitkamp, *J. Phys. Chem.*, 1992, **96**, 5059.
14. B. F. Chmelka, J. V. Gillis, E. E. Petersen, and C. J. Radke, *AIChE J.*, 1990, **36**, 1562.
15. N. Bansal and C. Dybowski, *J. Magn. Reson.*, 1990, **89**, 21.
16. H. Pfeifer, in *NATO ASI Ser. B*, 1991, **265**, 151.
17. H. Pfeifer, *Phys. Rep.*, 1976, **26**, 293.
18. H. W. Spiess, *NMR Basic Principles Prog.*, 1978, **15**, 55.
19. B. Zibrowius, J. Caro, and H. Pfeifer, *J. Chem. Soc., Faraday Trans. 1*, 1988, **84**, 2347.
20. B. Boddenberg and R. Burmeister, *Zeolites*, 1988, **8**, **480**, 488.
21. H. W. Spiess, *Chem. Phys.*, 1974, **6**, 217.
22. B. Zibrowius, M. Bülow, and H. Pfeifer, *Chem. Phys. Lett.*, 1985, **120**, 420.
23. R. Kimmich, W. Nusser, and T. Gneiting, *Colloid. Surf.*, 1990, **45**, 283.
24. F. Noack, *Prog. NMR Spectrosc.*, 1986, **18**, 17.
25. R. Kimmich, T. Gneiting, K. Kotitschke, and G. Schnur, *Biophys. J.*, 1990, **58**, 1183.
26. D. Michel and H. Pfeifer, *Z. Naturforsch., Teil a*, 1965, **20**, 220.
27. K. R. Brownstein and C. E. Tarr, *Phys. Rev. A*, 1979, **19**, 2446.
28. G. C. Borgia, R. J. S. Brown, P. Fantazzini, and E. Mesini, *Nuov. Cim. D*, 1993, **15**, 1025.
29. B. F. Chmelka, D. Raftery, A. V. McCormick, L. C. de Menorval, R. D. Levine, and A. Pines, *Phys. Rev. Lett.*, 1991, **66**, 580.
30. R. G. Larsen, J. Shore, K. Schmidt-Rohr, L. Emsley, H. Long, A. Pines, M. Janicke, and B. F. Chmelka, *Chem. Phys. Lett.*, 1993, **214**, 220.
31. J. Kärger and W. Heink, *J. Magn. Reson.*, 1983, **51**, 1.
32. D. G. Cory and A. N. Garroway, *Magn. Reson. Med.*, 1990, **14**, 435.
33. P. T. Callaghan, *Principles of Nuclear Magnetic Resonance Microscopy*, Clarendon, Oxford, 1991.
34. G. Fleischer and F. Fujara, *NMR Basic Principles Prog.*, 1994, **30**, 159.
35. R. M. Cotts, *Nature*, 1991, **351**, 443.
36. P. Stilbs, *Prog. NMR Spectrosc.*, 1986, **19**, 1.
37. J. Kärger, H. Pfeifer, and W. Heink, *Adv. Magn. Reson.*, 1988, **12**, 1.
38. J. Kärger, *Adv. Colloid Interface Sci.*, 1985, **23**, 129.
39. M. Silva-Crawford, B. C. Gerstein, A.-L. Kuo, and C. G. Wade, *J. Am. Chem. Soc.*, 1980, **102**, 3728.
40. J. Kärger and D. M. Ruthven, *Diffusion in Zeolites and Other Microporous Solids*, Wiley, New York, 1992.
41. J. Kärger, H. Pfeifer, and G. Vojta, *Phys. Rev. A*, 1988, **37**, 4514.
42. R. Kimmich, W. Unrath, G. Schnur, and E. Rommel, *J. Magn. Reson.*, 1991, **91**, 136.
43. P. T. Callaghan and A. Coy, *Phys. Rev. Lett.*, 1992, **68**, 3176.
44. M. Appel, G. Fleischer, J. Kärger, and F. Fujara, *Macromolecules*, 1994, **27**, 4274.
45. J. Kärger and H. Spindler, *J. Am. Chem. Soc.*, 1991, **113**, 7571.

46. J. Kärger, *Phys. Rev. A*, 1992, **45**, 4173; *Phys. Rev. E*, 1993, **47**, 1427.
47. J. Kärger, M. Petzold, H. Pfeifer, S. Ernst, and J. Weitkamp, *J. Catal.*, 1992, **136**, 283.
48. R. von Ballmoos, J. B. Higgins, and M. H. J. Treacy (eds.), *Proceedings of the 9th International Zeolite Conference, Montreal 1992*, Butterworth-Heinemann, Boston, MA, 1993.
49. J. Kärger and H. Pfeifer, in *NMR and Catalysis*, eds. A. Pines and A. Bell, Marcel Dekker, New York, 1994, p. 69.
50. S. Frey, J. Kärger, H. Pfeifer, and P. Walther, *J. Magn. Reson.*, 1988, **79**, 336.
51. P. T. Callaghan, A. Coy, D. MacGowan, K. J. Packer, and F. O. Zelaya, *Nature*, 1991, **351**, 467.
52. P. T. Callaghan, A. Coy, T. P. J. Halpin, D. MacGowan, K. J. Packer, and F. O. Zelaya, *J. Chem. Phys.*, 1992, **97**, 651.
53. P. L. June, A. T. Bell, and D. N. Theodorou, *J. Phys. Chem.*, 1990, **94**, **1508**, 8232.
54. S. D. Picket, A. K. Nowak, J. M. Thomas, B. K. Peterson, J. F. P. Swift, A. K. Cheetham, C. J. J. den Ouden, B. Smit, and M. F. M. Post, *J. Phys. Chem.*, 1990, **94**, 1233; 1992, **95**, 848.
55. S. Fritzsche, R. Haberlandt, J. Kärger, H. Pfeifer, and K. Heinzinger, *Chem. Phys.*, 1993, **174**, 229.
56. U. Hong, J. Kärger, R. Kramer, H. Pfeifer, G. Seiffert, U. Müller, K. K. Unger, H.-B. Lück, and T. Ito, *Zeolites*, 1991, **11**, 816.
57. D. Fenzke and J. Kärger, *Z. Phys. D. Atom. Mol. Cluster.*, 1993, **25**, 345.
58. U. Hong, J. Kärger, and H. Pfeifer, *J. Am. Chem. Soc.*, 1991, **113**, 4812.
59. U. Hong, J. Kärger, B. Hunger, N. N. Feoktistova, and S. P. Zhdanov, *J. Catal.*, 1992, **137**, 243.
60. H. Jobic, M. Bée, J. Kärger, H. Pfeifer, and J. Caro, *J. Chem. Soc., Chem. Commun.*, **1990**, 341.
61. D. M. Ruthven, *Zeolites*, 1993, **13**, 594.
62. F. Stallmach, J. Kärger, and H. Pfeifer, *J. Magn. Reson. A*, 1993, **102**, 270.
63. J. Kärger, G. Seiffert, and F. Stallmach, *J. Magn. Reson. A*, 1993, **102**, 327.

Acknowledgments

The development of PFG-NMR for the study of molecular diffusion in porous media, particularly in zeolites, has profited significantly from the continuous engagement of Harry Pfeifer, one of the pioneers of NMR in Central Europe (see ***Pfeifer, Harry: Leipzig, Summer 1951***). I have had the privilege of personal contact and many stimulating discussions with him over many years, and I would like to thank him for his continuous help and encouragement and for countless discussions

Biographical Sketch

Jörg Kärger. *b* 1943. Ph.D. (supervisor Harry Pfeifer), 1970; Habilitation, Leipzig University, 1978. Lecturer, 1982–89 Professor of Experimental Physics, 1989–present, Leipzig University. Approx. 200 publications, including *Diffusion in Zeolites and Other Microporous Solids* (with Douglas M. Ruthven). Research interests include various topics within the field of molecular dynamics at interfaces, in particular in adsorbate–adsorbent systems.

Microporous Materials and Xenon-129 NMR

Jacques Fraissard

Université Pierre et Marie Curie, Paris, France

1	Introduction	1
2	Chemical Shift of Xenon Adsorbed on a Zeolite	1
3	Influence of the Pore Structure on δ_s: Application to Porosity	1
4	Influence of Temperature	3
5	Effect of the Si/Al Ratio of Zeolites	3
6	Influence of Cations	4
7	Cation Exchange Between Different Zeolites	5
8	Distribution of the Adsorbed Phases	5
9	Effect of Extraframework Aluminum	5
10	Conclusions	6
11	Related Articles	6
12	References	6

1 INTRODUCTION

The central idea of the pioneers of this general research was to find a molecule[1] which was nonreactive and particularly sensitive to its environment, physical interactions with other chemical species, and the nature of adsorption sites, which could be used as a probe for determining in a new way solid properties that are difficult to detect by classical physicochemical techniques. In addition, the probe needed to be detectable by NMR spectroscopy, since this technique is particularly suitable for investigating electron perturbations in rapidly moving molecules.

Xenon is this ideal probe because it is an inert gas, is monoatomic, and has a large spherical electron cloud. From the NMR point of view, the ^{129}Xe isotope has a spin of $\frac{1}{2}$, its natural abundance in xenon is 26%, and its sensitivity of detection relative to the proton is about 10^{-2}. The recent development by Pines and co-workers of xenon optical polarization techniques offers increased sensitivity by a factor of 10^3 for the detection of adsorbed xenon.[2,3] The high polarizability of the xenon atom makes it very sensitive to its environment. Small variations in the physical interactions with the environment cause marked perturbations of the electron cloud; these are transmitted directly to the xenon nucleus and greatly affect the NMR chemical shift.

2 CHEMICAL SHIFT OF XENON ADSORBED ON A ZEOLITE

In pure xenon gas,[4] the ^{129}Xe chemical shift can be expressed by a virial expansion of the xenon density ρ:

$$\delta(T, \rho) = \delta_0 + \delta_{1,\mathrm{Xe}}(T) \cdot \rho_{\mathrm{Xe}} + \delta_{2,\mathrm{Xe}}(T) \cdot \rho_{\mathrm{Xe}}^2 + \delta_{3,\mathrm{Xe}}(T) \cdot \rho_{\mathrm{Xe}}^3 + \ldots \quad (1)$$

where $\delta(T,\rho)$ is the resonance shift at temperature T and density ρ. The term δ_0 is the value of the resonance shift extrapolated to an infinitely low density; $\delta_{i,\mathrm{Xe}}(T)$ are the virial coefficients of the shift in density.

For mixtures of xenon and another gas A, Jameson et al.[4] showed that, in the linear range,

$$\delta = \delta_0 + \delta_{1,\mathrm{Xe}}(T) \cdot \rho_{\mathrm{Xe}} + \delta_{1,\mathrm{A}}(T) \cdot \rho_{\mathrm{A}} \quad (2)$$

where ρ_{Xe} and ρ_{A} are the densities of xenon and 'solvent' molecules A, respectively; $\delta_{1,\mathrm{Xe}}$ and $\delta_{1,\mathrm{A}}$ characterize the Xe–Xe and Xe–A interactions, respectively.

As in the gas phase, most information has been obtained from analyzing the variation in the chemical shift with xenon concentration, generally at 26 °C. The amount of xenon adsorbed is expressed as the number of atoms N per gram of anhydrous zeolite or the number of atoms n_s per cage (zeolites Y, ZK-4, erionite, etc.).

Fraissard et al. have shown that the chemical shift of adsorbed xenon is the sum of several terms corresponding to the various perturbations that it experiences[1,5,6]

$$\delta = \delta_{\mathrm{ref}} + \delta_s + \delta_{\mathrm{Xe}} + \delta_{\mathrm{SAS}} + \delta_{\mathrm{E}} + \delta_{\mathrm{M}} \quad (3)$$

δ_{ref} is the reference (gaseous xenon at zero pressure). The term δ_s accounts for interactions between xenon and the surface of the zeolitic pores, assuming that the solid does not contain any electrical charge; thus it depends only on the dimensions of the cages or channels and on the ease of xenon diffusion. The term $\delta_{\mathrm{Xe}} = \delta_{\mathrm{Xe-Xe}} \cdot \rho_{\mathrm{Xe}}$ accounts for Xe–Xe interactions; it increases with increasing local density of adsorbed xenon and becomes predominant at high xenon pressure. When the Xe–Xe collisions are isotropically distributed (large spherical cage) the relationship $\delta = f(N)$ is a straight line (Figure 1, curve 1). The slope, $\mathrm{d}\delta/\mathrm{d}n$ is proportional to the local xenon density and, therefore, inversely proportional to the 'void volume'. If the Xe–Xe collisions are anisotropically distributed (narrow channels), $\mathrm{d}\delta/\mathrm{d}N$ increases with N (Figure 1, curve 2).

When there are strong adsorption sites (SASs) in the void space, these interact with xenon much more than do the cage or channel walls, and each xenon atom spends a relatively long time on the SAS, particularly at low xenon concentration. The corresponding chemical shift δ_{SAS} will be greater than in the case of a noncharged structure (Figure 1, curve 3). When N increases, δ must decrease if there is fast exchange of the atoms adsorbed on the SASs with those adsorbed on other sites. When N is high enough, the effect of Xe–Xe interactions again becomes the most important factor, and the dependence of δ on N is then similar to that shown by curve 1 in Figure 1. In this case, $\delta_{N\to 0}$, (the chemical shift extrapolated to zero concentration) depends on the nature and number of these SASs. Often, these SASs are charged, and sometimes they are paramagnetic cations. The theoretical curve (3 in Figure 1), is displaced to high frequency (Figure 1, curve 4). The difference between curves 1 and 3 shows the effect (δ_{E}) of the electrical field and, if present, the effect (δ_{M}) due to the magnetic field created by these cations.[1]

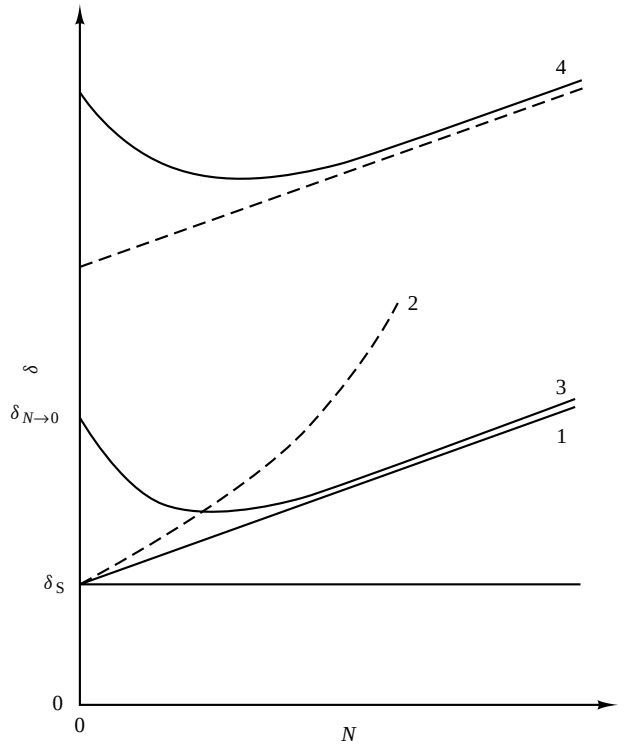

Figure 1 Variation in the chemical shift of xenon adsorbed on a porous solid. See text for details

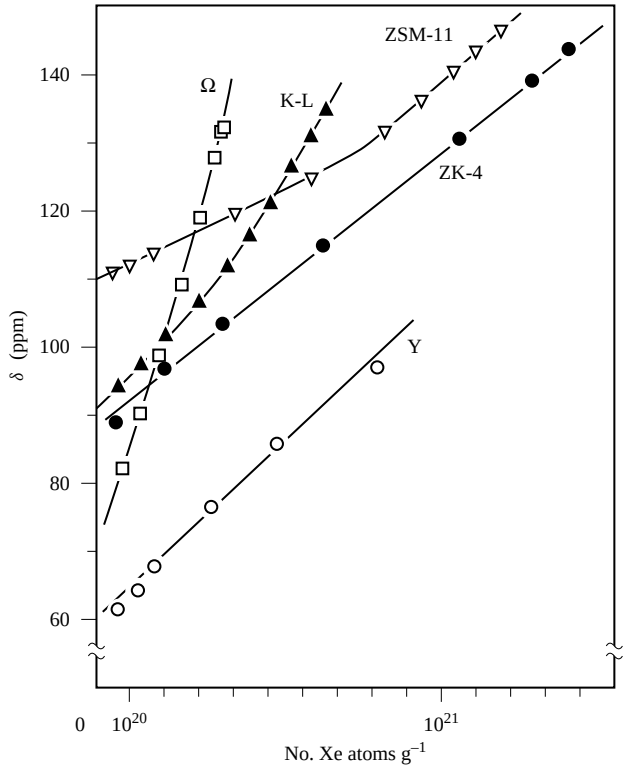

Figure 2 Chemical shift δ of adsorbed ^{129}Xe versus the number of xenon atoms per gram of solid

3 INFLUENCE OF THE PORE STRUCTURE ON Δ_s: APPLICATION TO POROSITY

The relationship $\delta = f(N)$ is characteristic of the zeolite structure when the Si/Al ratio is very high and when there are no strong adsorption sites accessible to xenon. Figure 2 illustrates the sensitivity of this technique to the pore structure. The slopes of the curves depend on the void volume of the pores; this is logical because for a given number of xenon atoms per gram, the local density and thus the Xe–Xe interactions depend on this volume. The chemical shift δ_s at zero concentration is related to the structure; the smaller the channels or cavities, or the more restricted the diffusion, and the greater δ_s becomes.

It is assumed that at 26 °C the experimental chemical shift is the average of the shift of xenon in rapid exchange between a position A on the pore surface (denoted by δ_a) and a position in the volume V of the cavity or channel (denoted by $\langle\delta_v\rangle$):

$$\delta = \frac{N_a\delta_a + N_v\langle\delta_v\rangle}{N_a + N_v} \tag{4}$$

where N_a and N_v are the number of xenon atoms in each state. This equation is valid for any xenon concentration, and thus for $N \to 0$, $\delta \to \delta_s$.

$\langle\delta_v\rangle$ is a function of δ_a and the distance traveled by the xenon atom between two successive collisions with the pore wall. In fact, $\delta_v = \delta_a$ when the xenon leaves the surface. δ_v then decreases during the journey between two collisions, and thus the need to determine the mean value $\langle\delta_v\rangle$.

In order to obtain by ^{129}Xe NMR precise data on the void space of a zeolite of unknown structure and the dimensions of structural defects, Springuel-Huet et al.[7] have calculated the 'mean free path' $\bar{l}$ of xenon imposed by the structure, and determined the dependence of δ_s on $\bar{l}$, both experimentally and by calculation (sphere, infinite cylinder):

$$\delta_s = \delta_a\frac{a}{a+\bar{l}} \tag{5}$$

where a is a constant. Equation (5) can be deduced from equation (4).[8] The large variation in δ_s with $\bar{l}$ (Figure 3) proves that ^{129}Xe NMR is very sensitive to pore dimensions.

Derouane and Nagy have been able to relate δ_a to the curvature of the adsorbing surface and, therefore, also to the pore diameter.[5] Finally, Ripmeester et al.[8] have continued this study by calculating the Lennard–Jones potential curves for a xenon atom and a spherical layer representing the atoms of a cage. They deduced that in small cages xenon is 'solid like' and in larger cages 'gas like', and that consequently it is difficult to imagine a single correlation between the xenon chemical shift and the dimensions of the adsorption zones.[8]

The symmetry of the adsorption site can sometimes be reflected by the form of the signal when the interactions to which the xenon atom is subjected are highly anisotropic. For example, Springuel-Huet and Fraissard have shown that the ellipsoid-shaped channels of SAPO-11 and $AlPO_4$-11 cause chemical shift anisotropy effects to be observed in the ^{129}Xe NMR spectra of adsorbed xenon,[3,5] due to the similarity between the small axis of the pore section (0.67 × 0.39 nm) and the diameter of the xenon atom (0.44 nm). Similar results have been obtained by Ripmeester et al. on Xe/clathrates systems.[3]

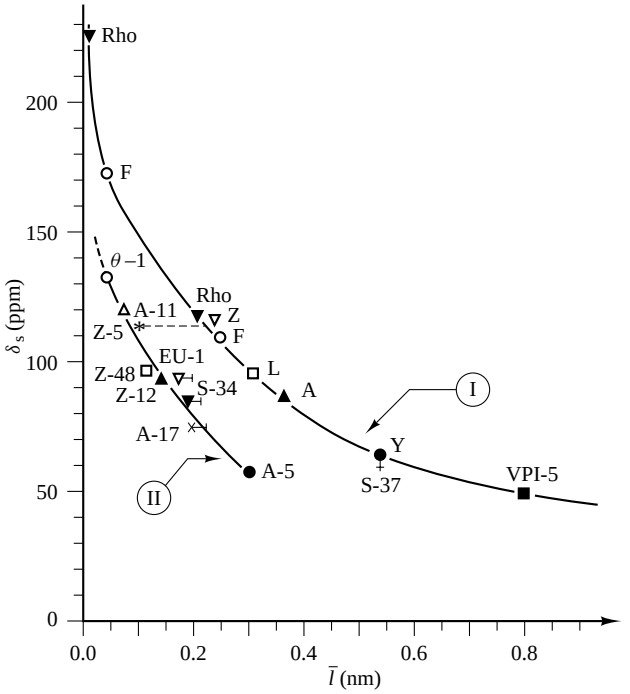

Figure 3 Variation in δ_s versus the mean free path l. F, ferrierite; Z-5, ZSM-5; Z-12, ZSM-12; Z-48, ZSM-48; A-5, $AlPO_4$-5; A-11, $AlPO_4$-11; A-17, $AlPO_4$-17; S-34, SAPO-34; S-37, SAPO-37

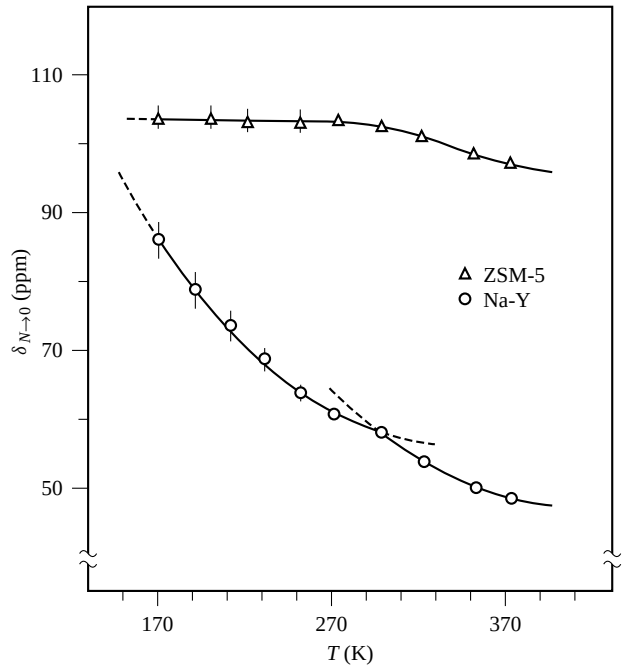

Figure 4 Variation in δ_s versus the temperature T of the experiment

When the zeolite structure includes several adsorption zones, the xenon spectrum must contain an equal number of components characteristic of these zones, provided that the diffusion of the xenon atoms is not too rapid on the NMR timescale.[1] Thus, the spectrum of sodium mordenite shows two signals at 26 °C, arising from xenon in the main channels and in the side pockets.[1,3,5] However, because of rapid exchange of xenon between these two regions there is only one signal for H^+-exchanged mordenite. The spectrum of ferrierite at 26 °C shows two signals characteristic of two types of channel.[3,5] In this case it was even possible to detect the presence of a mordenite intergrowth. Two signals have also been detected for the Xe/H-Rho system, but only at a temperature as low as − 50 °C so as to avoid rapid exchange of atoms located in the octagonal prisms and the large cavities. In Cs-Rho, only the signal corresponding to the large cavities is detected, since all the prisms are occupied by Cs^+.[5,6]

It is clear from these examples that this ^{129}Xe NMR can be used to identify all the different microporous adsorption zones, namely the structure defects in zeolites,[1] heteropolyanions, solid polymers,[3] clathrates,[3,6] etc.

4 INFLUENCE OF TEMPERATURE

The study of the temperature dependence is another way of checking the size of the pores in which the xenon is adsorbed.[9] The variation in temperature changes the relative residence times of xenon on the surface and in the free space, which in turn influence the xenon chemical shift. The variation in δ thus depends on $\langle\delta_v\rangle$. The variation is very small if $\langle\delta_v\rangle \simeq \delta_a$ (ZSM-5), and very large if $\langle\delta_v\rangle << \delta_a$ (Na-Y) (Figure 4).

From a quantitative point of view, Chen and Fraissard[9] have shown that

$$\mathrm{d}\left(\ln\frac{\delta_a-\delta_s}{\delta_s-\langle\delta_v\rangle}\right)\Big/\mathrm{d}T=-\frac{\Delta E}{RT^2} \qquad (6)$$

where ΔE is the energy difference between the xenon in the two states A and V. The fast exchange model is valid in the temperature range where the plot of $\ln[\delta_a - \delta_s/\delta_s - \langle\delta_v\rangle] = f(1/T)$ is a straight line.

5 EFFECT OF THE Si/Al RATIO OF ZEOLITES

The relationship between δ_s and the porous structure is strictly valid only for an electrically neutral surface. The chemical shift of xenon must therefore depend on the chemical composition of the zeolite, in particular on the number of charges, i.e. on the Si/Al ratio. This dependence is more pronounced when the temperature is low and the pore diameter is small (increased effect of δ_a with the contact time of xenon at the surface).

In the case of faujasite, either with Na^+ or decationized, the $\delta = f(N)$ relationships are almost parallel straight lines at 26 °C, and $\delta_{N\to0}$ decreases monotonically by 4 ppm when Si/Al increases from 1.28 to 54.[1] For ZSM-5 and ZSM-11 (narrow channels) the dependence of $\delta_{N\to0}$ on the aluminum concentration is greater than for faujasite (large cavities). In addition, this variation shows a break at about [Al] = 2 Al atoms per unit cell, which demonstrates that the xenon–wall interactions change at this concentration.[10] Thus aluminum is not randomly distributed in the lattice; rather, its distribution depends on the concentration. Finally, we mention the difference between the $\delta = f(N)$ relationships for ZSM-5 and ZSM-11 for [Al] ≥ 2 Al atoms per unit cell. Despite the similarity of the structures of these two zeolites, the sensitivity

of the ^{129}Xe NMR technique is sufficient to differentiate between them.

6 INFLUENCE OF CATIONS

It has been explained in Section 2 why the $\delta = f(N)$ curve goes through a minimum when there are strong adsorption sites in the zeolite. This has been shown for X and Y zeolites with divalent cations such as Mg^{2+}, Ca^{2+}, Zn^{2+}, Cd^{2+}, and Ni^{2+},[1,6,11] where xenon adsorption becomes saturated within the given pressure range.

Using a fast exchange model analogous to the one proposed by Springuel-Huet et al.,[7] but taking into account the possible presence of SASs, Cheung et al. were able to give an analytical expression of these curves in the form:[12]

$$\delta = \frac{\alpha}{\rho} + \delta_g \cdot \rho \qquad (7)$$

where ρ is the overall xenon density in the zeolite, δ_g is the $\delta_{1,Xe}$ coefficient [as in equation (1)], and α depends on the distribution of N_a and N_v [as defined in equation (4)]. The $1/\rho$ dependence results in an initial decrease in δ with increasing surface coverage, before the term linear in ρ begins to dominate. Let us consider, for example, Mg_λ-Y and Ca_λ-Y zeolites, dehydrated under vacuum at 500 °C, where λ denotes the degree of cation exchange with Na^+.[1] When Ca^{2+} cations are in the sodalite cage or the hexagonal prisms ($\lambda < 55\%$), δ is a linear function of the xenon concentration (as for Na-Y), regardless of the extent of dehydration of the sample. When some Ca^{2+} cations are situated within the supercages ($\lambda > 55$ %), for Ca_λ-Y one observes values of δ (compared with Na-Y) that are greatest when λ is high, especially at low xenon concentration. According to Ito et al., the experimental value of $\delta_{N\to 0}$ for $N = 0$ is roughly proportional to the square of the electric field at the nuclei of xenon atoms adsorbed on Ca^{2+} cations.[1]

According to Cheung et al., the high value of δ is not due solely to the high degree of polarization of xenon and the distortion of the xenon electron cloud by the strong electric fields created by the divalent cations. They suggest the formation of a partial bond between these two species formed by the donation of a xenon 5p electron to the empty s orbital of the divalent cation.[12] A similar model concerning electron transfer from xenon to platinum was proposed by Ito et al. to explain the large shift in δ for platinum supported on Na-Y.[1]

The effect of the dehydration and rehydration of zeolites on the influence of Ca^{2+} cations can also be studied by ^{129}Xe NMR.[1] For example, the chemical shift δ and the signal width $\Delta\omega$ of xenon adsorbed on Mg_{70}-Y increase with increasing dehydration of the solid. The values of δ and $\Delta\omega$ are greatest when dehydration is complete. Conversely, the spectra evolve with rehydration: for a given xenon pressure, line *a* due to xenon in the supercages containing only bare Mg^{2+} decreases in favor of line *b* corresponding to Mg^{2+} surrounded by water molecules. ^{129}Xe NMR therefore makes it possible to follow the diffusion of an adsorbate in a zeolite crystallite.

The problem is more difficult in the case of paramagnetic cations, especially when the extent of exchange is so high that the magnetic term [δ_M in equation (3)] becomes large. However, Scharf et al. have succeeded, using this technique, in following the reduction and reoxidation of the $Ni_{7.5}$-Na-Y zeolite desorbed under vacuum at 350 °C.[1,6] When the sample was reduced at lower temperatures (about 100 °C) two types of environment for the xenon atoms were evident: one corresponding to xenon in the nickel-exchanged material, and the other corresponding to xenon in contact with Na-Y or H-Y. Reduction at higher temperatures produced a low-frequency shift of the first resonance, indicating that this environment becomes more like the environment of xenon in the Na-Y zeolite. At the highest temperature (370 °C) studied, only the line corresponding to xenon in Na-Y was detected. These results prove that nickel ions are removed from the supercages upon reduction. Using this method, Scharf et al. showed that reoxidation under 80 kPa of oxygen at various temperatures does not reverse the process of reduction.

A particularly interesting case is that of faujasite-type zeolites containing Ag^+ or Cu^+ cations, the external electron structure of which is *n*d.[11] The ^{129}Xe NMR isotropic chemical shifts of xenon in Na-X and in the fully silver-exchanged zeolite Ag-X are shown in Figure 5. The shifts in dehydrated and oxidized Ag-X are distinctly lower than that for Na-X over the range of concentration studied. Most remarkably, the shifts decrease with concentration, down to negative values in the range -40 to -50 ppm at low xenon concentration. In contrast to these results, the samples reduced at 100 °C and 300 °C show high-frequency shifts with respect to Na-X. After reduction at 100 °C, δ increases steadily with the number of xenon atoms per supercage (n_s) from +100 ppm to about +170 ppm for about $0.3 < n_s < 4$, whereas after reduction at 300 °C the shift values are between +140 and +160 ppm for $0.1 < n_s < 1$, with a shallow minimum at about $n_s = 0.7$. In the latter case, the plot of $\delta = f(N)$ has the classical shape of zeolite-supported metals. The very unusual low-frequency shift in the case of the dehydrated and oxidized samples is due to a specific interaction of xenon with Ag^+ cations in the supercages. This shielding is due to $d_\pi - d_\pi$ back-donation from silver to xenon, involving the silver 4d and the xenon 5d orbitals.

Similar studies have confirmed that Cu^{2+} is autoreduced to Cu^+ during the dehydration of Cu-Y at 400 °C, and it has been

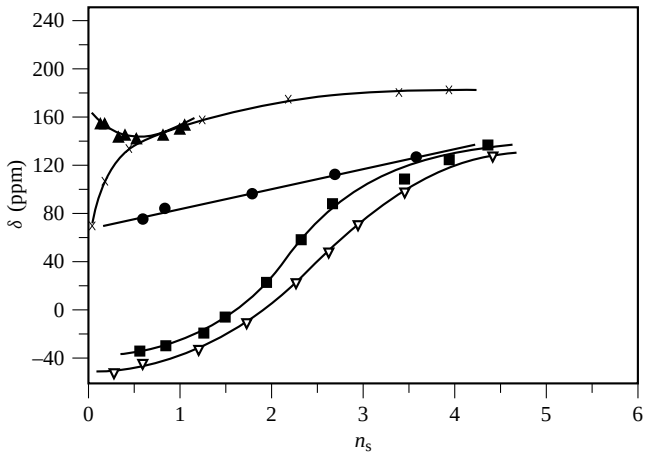

Figure 5 ^{129}Xe NMR chemical shift versus the number of xenon atoms per supercage (n_s) for the zeolites: Na-X (400 dehydrated, ●); Ag-X (400 dehydrated, ■) Ag-X (450 oxidized, ▽); Ag-X (100 reduced ×); Ag-X (300 reduced, ▲)

shown that there are only Cu^{+} ions in the supercages.[11] The Cu^{2+} cations are located in the sodalite cavities or the prisms.

7 CATION EXCHANGE BETWEEN DIFFERENT ZEOLITES

^{129}Xe NMR of adsorbed xenon can be used to follow the exchange of cation sites in the zones accessible to xenon in a given crystallite, and to visualize the exchange of cations between different zeolites. For example, the two peaks in Figure 6(a) at 144 and 89 ppm correspond to xenon adsorbed in dehydrated RbNa-X and Na-Y zeolites, respectively.[13] Upon mechanical mixing at 300 K [Figure 6(b)] the intensities of the two signals decrease and a third broad signal at about 141 ppm appears. After further treatment of the mixture at 673 K and 0.01 Pa [Figure 6(c)], there is a further larger decrease in the intensities of the RbNa-X and Na-Y signals, the peak at 141 ppm disappears and two additional broad signals are seen at 128 and 109 ppm.

The two xenon resonance signals corresponding to the two pure zeolites can be restored upon cooling the sample to 200 K, which proves that the third signal in Figure 6(b) is a coalescence of two signals. The mixture obtained directly in the tube by shaking is very inhomogeneous with regards to the distribution of the crystallites of the two zeolites. There are three types of zone: pure RbNa-X, pure Na-Y, and a RbNa-X–Na-Y mixture. Because of diffusion, the three corresponding lines can be distinguished at 300 K. Consequently, the information obtained by ^{129}Xe NMR at 300 K is characteristic of macroscopic zones, i.e. zones containing several crystallites. The extent of these zones depends on the mean lifetime of the xenon atom in the crystallites compared with the NMR timescale. These zones can be reduced by lowering the temperature of the NMR experiment in order to obtain more and more localized information. The rate of exchange of xenon atoms between one crystallite and another must also depend on the crystallite size and, above all, on the barrier to diffusion to the external surface; all other things being equal, this barrier is related to the size of the windows of the cavities and channels.

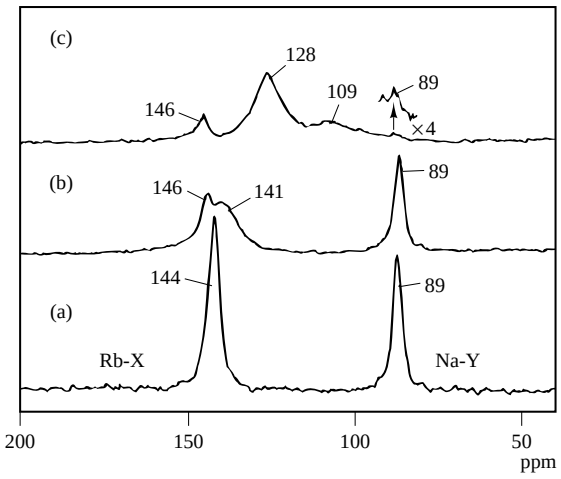

Figure 6 ^{129}Xe NMR spectra of xenon adsorbed at 300 K and 80 kPa on RbNa-X and Na-Y treated at 673 K under 0.01 Pa: (a) before mixing; (b) after mixing; (c) mixture retreated at 673 K under 0.01 Pa

The low-temperature ^{129}Xe NMR spectra of xenon adsorbed on the zeolite in Figure 6(b) show that [in contrast to the case of the zeolite in Figure 6(c)], down to 200 K there are still four well-resolved peaks, two of them corresponding to the original RbNa-X and Na-Y zeolites. The other two signals located between those of RbNa-X and Na-Y should correspond to the $Rb_{58-x}Na_{24+x}$-X and Rb_xNa_{56-x}-Y zeolites, that result from ion exchange between the two original solids.

8 DISTRIBUTION OF THE ADSORBED PHASES

Gedeon et al. showed that the values of the slope $d\delta/dN$ and $\delta_{N\to 0}$ of the $\delta = f(N)$ plots for each degree of Na-Y hydration can be used to distinguish the water located in zones accessible or inaccessible to xenon, and to measure the volume of water in the pores.[1] Conversely, during adsorption the spectrum of the xenon probe is characteristic of the concentration gradient of the adsorbate in the sample tube and even that within the zeolite crystallite.

Pines and co-workers[14] confirmed the interest in this technique by applying it to the study of the adsorption of various compounds (benzene, trimethylbenzene and hexane). Their results were confirmed by multiple quantum NMR spectroscopy.[14]

9 EFFECT OF EXTRAFRAMEWORK ALUMINUM

It is well known that extraframework aluminum Al_{NF} plays an important role in the catalytic properties of zeolites. The presence of these species is usually checked by ^{27}Al NMR spectroscopy of the dehydrated samples normally used in catalytic reactions, but the nature of these species is still unclear. Chen et al.[15] have recently studied the nature of the Al_{NF} in MFI type zeolite by ^{129}Xe and ^{27}Al NMR. ^{27}Al NMR showed that the reference sample (R) did not contain any extraframework aluminum (Table 1). Conversely, the samples prepared in fluoride medium always contained some Al_{NF}. The quantity of Al_{NF} in the samples depends on the synthesis conditions.

The four samples studied by ^{129}Xe NMR (Table 1) have different xenon chemical shift δ dependences on the xenon loading N (Figure 7). For sample R, δ increases monotonically with N. For the samples synthesized in fluoride medium, δ first decreases and then increases with N. This indicates the presence of some strong adsorption sites inside the channels of the samples. These sites can only be more or less charged Al_{NF} species. Comparison of the number of Al_{NF} and the $\delta_{N\to 0}$

Table 1 Aluminum Concentration per Unit Cell

Sample	Total aluminum	Framework aluminum	Nonframework aluminum
R[a]	4.0	4.0	0
A	8.0	4.0	4.0
B	3.4	2.9	0.5
C	2.2	1.6	0.6

[a]R, reference.

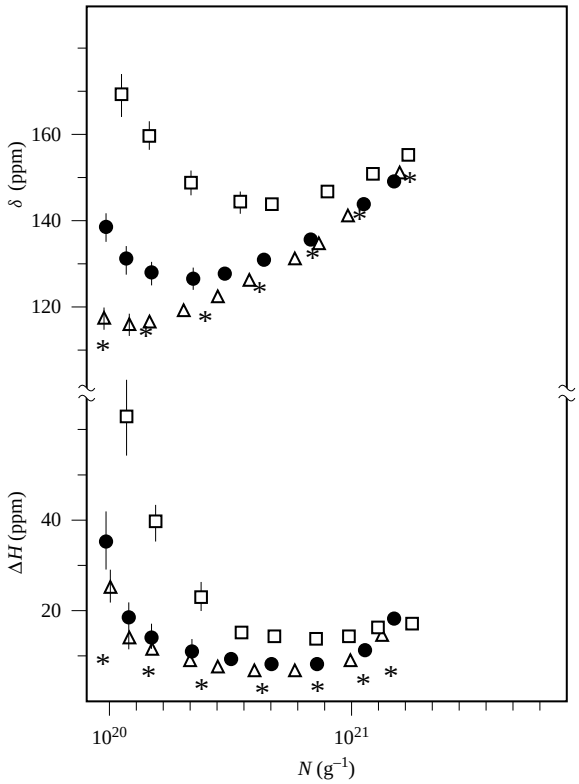

Figure 7 Variation in the chemical shift δ and the linewidth ΔH versus the number of xenon atoms (N) per gram of solids. △, A; •, B; □, C; * R. See Table 1

value shows that the charge on Al_{NF} increases in the order A < B < C. The average charge on each Al_{NF} atom depends on the amount of Al_{NF} and on the Al_{NF}/Al_F ratio inside the zeolite.

10 CONCLUSIONS

Using ^{129}Xe NMR spectroscopy with adsorbed xenon as a probe, it is possible:

1. To determine the dimensions and the forms of the internal free volumes of zeolites without knowing their structures:[16] (a) to reveal structure defects produced by, for example, dealumination, and to determine their characteristics; and (b) to calculate the short-range crystallinity, as opposed to that determined by X-ray crystallography.
2. To follow the mechanism of the synthesis and crystallization of zeolites during their preparation.[17]
3. To locate cations in the zeolite structure and to follow their migration or a change in their environment, depending on various factors.
4. To locate any 'encumbering' species, e.g. adsorbed molecules, extraframework species, coke formed during catalytic cracking reactions.[18]
5. To determine the dispersion of metals (particularly when the particles are too small to be detected by electron microscopy),[19] and the distribution of the molecules adsorbed on the particles (as opposed to the mean coverage).
6. To compare the diffusion of species as a function of the size of the zeolite 'windows'.[20]

The above list of applications is not exhaustive. Indeed this technique can also be applied to any microporous system (amorphous solid, polymer, clay, etc.), provided that one works at low temperature.

11 RELATED ARTICLES

Adsorbed Species: Spectroscopy and Dynamics; Chemical Exchange Effects on Spectra; Electric Field Effects on Shielding Constants; Gas Phase Studies of Chemical Exchange Processes; Gas Phase Studies of Intermolecular Interactions and Relaxation; Molecular Sieves: Crystalline Systems; Polarization of Noble Gas Nuclei with Optically Pumped Alkali Metal Vapors; Polymers: Regio-Irregular Structure; Reactions in Zeolites; Silica Surfaces: Characterization; Supported Metal Catalysts.

12 REFERENCES

1. J. Fraissard and T. Ito, *Zeolites*, 1988, **8**, 350, and references therein.
2. D. Raftery, L. Reven, H. Long, A. Pines, P. Tang, and J. A. Reimer, *J. Phys. Chem.*, 1993, **97**, 1649.
3. D. Raftery and B. Chmelka, in *NMR. Basic Principles and Progress*, ed. B. Blümich and R. Kosfeld, Springer, Berlin, 1994, Vol. 30, p. 111, and references therein.
4. C. J. Jameson, A. K. Jameson, and S. M. Cohen, *J. Chem. Phys.*, 1973, **59**, 4540, and references therein.
5. P.-J. Barrie and J. Klinowski, *Prog. NMR Spectrosc.*, 1992, **24**, 91, and references therein.
6. C. Dybowski, N. Bansal, and T. M. Duncan, *Ann. Rev. Phys. Chem.*, 1991, **42**, 433, and references therein.
7. M. A. Springuel-Huet, J. Demarquay, T. Ito, and J. Fraissard, *Studies Surf. Sci. Catal.*, 1988, **37**, 183.
8. J. A. Ripmeester, C. J. Ratcliffe, and J. S. Tse, *J. Chem. Soc., Faraday Trans. 1*, 1988, **84**, 3731.
9. Q. Chen and J. Fraissard, *J. Phys. Chem.*, 1992, **96**, 1809.
10. Q. Chen, M. A. Springuel-Huet, J. Fraissard, L. Matthew, L. Smith, D. Corbin, and C. Dubowski, *J. Phys. Chem.*, 1992, **96**, 10 914.
11. A. Gedeon and J. Fraissard, *Chem. Phys. Lett.*, 1992, **219**, 440 and references therein.
12. T. T. P. Cheung, C. M. Fu, and S. Wharry, *J. Phys. Chem.*, 1988, **92**, 5170.
13. Q. Chen and J. Fraissard, *Chem. Phys. Lett.*, 1990, **169**, 595.
14. B. F. Chmelka, J. G. Pearson, S. B. Liu, R. Ryoo, L. C. de Menorval, and A. Pines, *J. Phys. Chem.*, 1991, **95**, 303, and references therein.
15. Q. Chen, J. L. Guth, A. Seive, P. Caullet, and J. Fraissard, *Zeolites*, 1991, **11**, 799.
16. M. A. Springuel-Huet and J. Fraissard, *Zeolites*, 1992, **12**, 841.
17. T. Ito, J. Fraissard, Y. B'Nagy, N. Dewaele, Z. Gabelica, A. Nastro, and E. Derouane, *Studies Surf. Sci. Catal.*, 1989, **49**, 579.
18. J. L. Bonardet, M. C. Barrage, and J. Fraissard, *Studies Surf. Sci. Catal.*, 1993, **75**, 2577.
19. M. Boudart, M. G. Samant, and R. Ryoo, *Ultramicroscopy*, 1986, **20**, 125.
20. J. Karger, H. Pfeifer, T. Wutscherk, S. Ernst, J. Weitkamp, and J. Fraissard, *J. Phys. Chem.*, 1992, **96**, 5059.

Biographical Sketch

Jacques Fraissard. *b* 1934. Maîtrise ès Sciences, 1957, Doctorat ès Sciences, 1961, Paris. Introduced to NMR by I. Solomon. Centre National de la Recherche Scientifique, 1960–63; University of Paris, 1963–present. Approx. 210 publications; including research interests mainly in applications of solid state NMR to problems of gas–solid interactions and catalysis.

Molecular Sieves: Crystalline Systems

Jacek Klinowski
University of Cambridge, UK

1	Zeolites: Structure and Properties	1
2	Composition of Zeolitic Frameworks and the Nature of Extraframework Aluminum	2
3	Resolving Crystallographically Nonequivalent Tetrahedral Sites in Zeolites	4
4	Two-Dimensional NMR Spectra of Zeolitic Frameworks	6
5	Dealumination and Realumination of Zeolites	6
6	NMR Studies of the Structure of BrØnsted Acid Sites in Zeolites	7
7	Gallosilicate and Borosilicate Zeolites	8
8	Chemical Status of Guest Organics in Zeolites	8
9	In Situ Studies of Catalytic Reactions on Zeolites	8
10	Direct Observation of Shape Selectivity	8
11	Structure of Aluminophosphate Molecular Sieves	9
12	NMR Studies of $AlPO_4$-5, $AlPO_4$-11, and $AlPO_4$-21	10
13	VPI-5 and $AlPO_4$-8	12
14	SAPO Molecular Sieves	13
15	MeAPO Molecular Sieves	14
16	^{2}H NMR Studies of Motion in Molecular Sieves	14
17	Related Articles	16
18	References	16

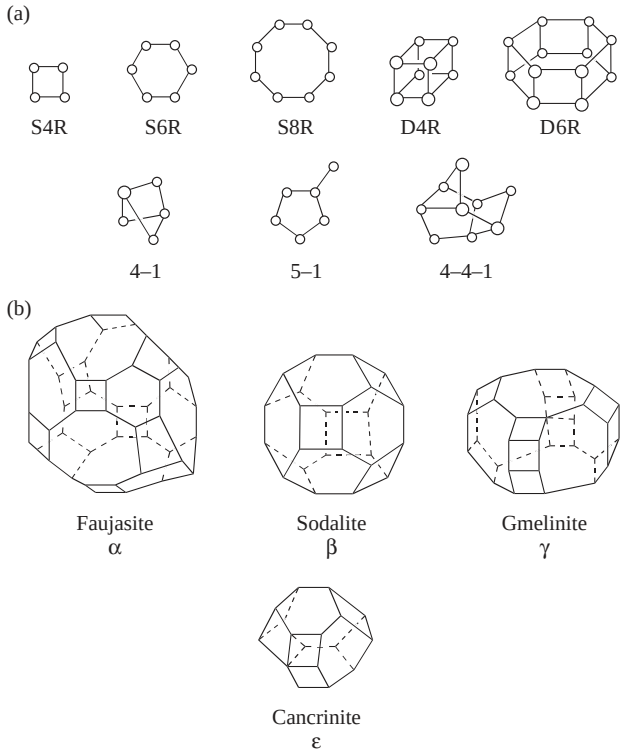

Figure 1 (a) Secondary building units in zeolite structures. (○) Positions of tetrahedral silicon and aluminum atoms; oxygen atoms (not shown) lie approximately halfway between them. (b) Some polyhedra found in zeolite frameworks: the 'α-cage' (26-hedron of type I); the sodalite cage; double eight-membered ring; double six-membered ring (hexagonal prism); the 18-hedron ('γ-cage'); the 11-hedron ('ε-cage' or 'cancrinite cage')

1 ZEOLITES: STRUCTURE AND PROPERTIES

Molecular sieves are a class of porous open-framework solids which includes aluminosilicates (zeolites), aluminophosphates, and related materials. Zeolites[1–3] are built from corner-sharing SiO_4 and AlO_4 tetrahedra linked by the apical oxygen atoms to form frameworks of high internal surface area with regular channels and cavities of molecular dimensions. The zeolitic channel systems, which may be one-, two- or three-dimensional, may occupy more than 50% of crystal volume. Their micorporous structure enables zeolites to be used as molecular sieves, as they can only adsorb molecules of certain size. The net negative charge of the framework, equal to the number of the constituent aluminum atoms, is balanced by exchangeable cations M^{n+} located in the channels which normally also contain water. The name 'zeolite' (from the Greek $\zeta\epsilon\omega$ = to boil and $\lambda\iota\theta\sigma$ = stone) was coined by Cronstedt[4] to describe the behavior of the mineral stilbite which rapidly loses water on heating and thus seems to boil.

The general oxide formula of a zeolite is $M_{x/n}$-$(AlO_2)_x(SiO_2)_y{\cdot}mH_2O$, with $y \geq x$. According to the Loewenstein rule,[5] which applies to all hydrothermally synthesized zeolites, aluminate tetrahedra cannot be neighbors in the framework, and so Al–O–Al linkages are forbidden. There are about 40 identified zeolite minerals (with $1 \leq y/x \leq 5$) and at least 140 synthetic species with a wide range of compositions. Figure 1 shows the secondary building units and some of the cages found in molecular sieves, and Figure 2 illustrates framework structures based on the sodalite cage.

Zeolites are prepared under mild (60–400 °C) hydrothermal conditions in strongly basic media. The type and concentration of the base are important structure-directing factors, and a variety of organic bases (usually secondary or tertiary amines or quaternary ammonium compounds) have been used. A preparative method utilizing low pH which relies on F^- anions to solubilize the reactants as complex fluorides has recently been developed. Other elements, such as Ga, Ge, B, Fe, and P can substitute for Si and Al in the framework.

The physical and chemical behavior of zeolites is the subject of various monographs.[6–10] The most important properties are the ability to adsorb organic and inorganic substances and to act as cation exchangers and catalysts. Depending on the pore diameter and the molecular dimensions, species such as gaseous elements, ammonia, alkali metal vapors, hydrocarbons, and many other organic and inorganic species may be accommodated in the intracrystalline space of dehydrated zeolites. This process, known as 'molecular sieving', is a powerful method for the resolution of mixtures. Commercial applications include the drying of organics, separation of hydrocarbons and of N_2 and O_2 in air, and the removal of NH_3 and CS_2 from industrial gases.

Cations neutralizing the electrical charge of the aluminosilicate framework can be exchanged for other cations from solution. Zeolites often possess selectivities for certain cations, and

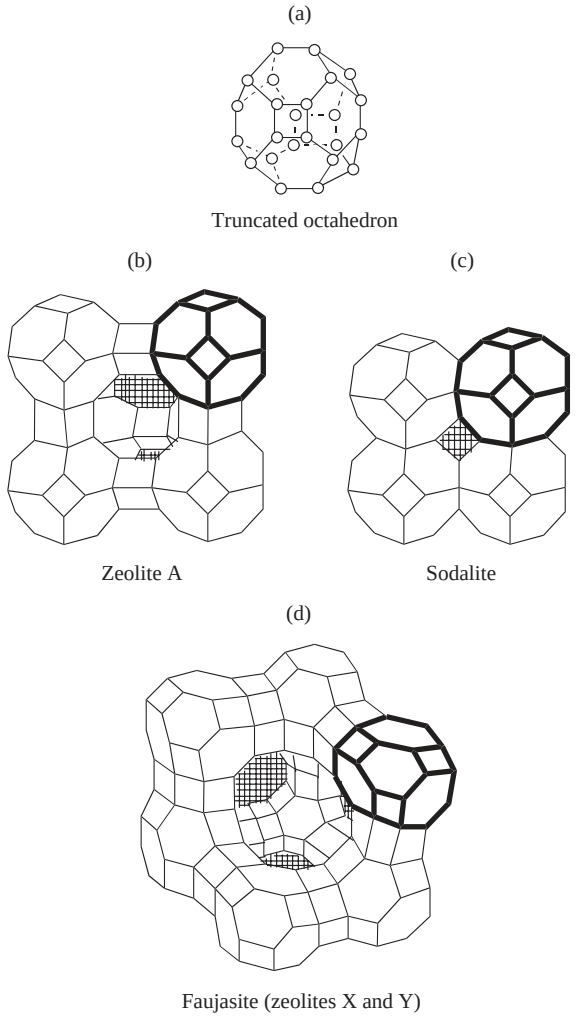

Figure 2 (a) The truncated octahedron, more correctly a tetrakaidodecahedron (also known as 'sodalite cage' or 'β-cage'). (b) The structure of zeolite A is formed by linking the sodalite cages through double four-membered rings. (c) The structure of sodalite is formed by direct face-sharing of four-membered rings in the neighboring sodalite cages. (d) The faujasite structure is formed by linking the sodalite cages through double six-membered rings. For clarity, exchangeable nonframework cations are not shown

this is used for their isolation and concentration. Applications include the removal of ammonia from sewage and agricultural effluents, collection of harmful products of nuclear fission (such as $^{137}Cs^{+}$ and $^{90}Sr^{2+}$), water softening, and the recovery of precious elements. Molecular sieving properties of zeolites are further modified by ion exchange. Thus zeolite Na-A sorbs both N_2 and O_2, while Ca-A sorbs nitrogen preferentially to oxygen.

However, the ability to catalyze a wide range of reactions, such as cracking, hydrocracking, oxidation, and isomerization of hydrocarbons, overshadows all other applications of zeolites. Rare-earth exchanged and hydrogen forms of some zeolites (such as zeolite Y) have a cracking activity which is orders of magnitude greater than that of conventional silica/aluminas.[11] The synthetic zeolite ZSM-5,[12] is a particularly powerful catalyst (Figure 3). Its high silica content (the Si/Al ratio is typically 30) gives it high thermal stability,

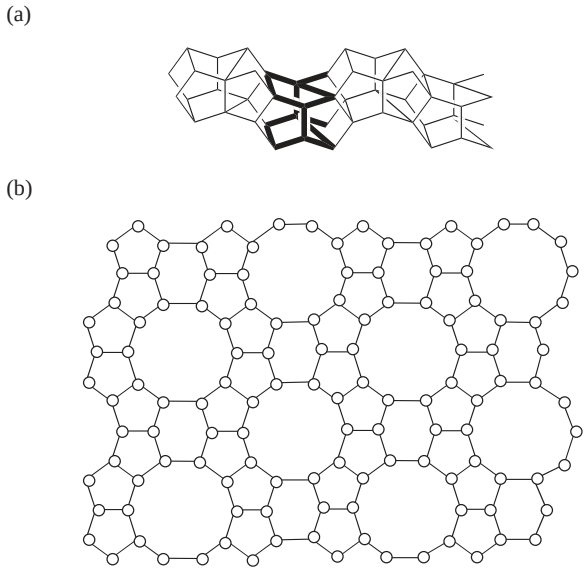

Figure 3 The structure of ZSM-5/silicalite

while the channel diameter is convenient for many applications. Catalytic properties of ZSM-5 include the ability to synthesize gasoline from methanol in a single step. Silicalite, a material which is isostructural with ZSM-5, but contains only small amounts of aluminum is, by contrast to other zeolites, hydrophobic and organophilic, and is used in the removal of dissolved organics from water. The annual industrial consumption of zeolites is about 550 000 ton, of which 135 000 ton are used in catalysis, 375 000 ton as ion exchangers in detergent powders, and 40 000 ton as sorbents.

Synthetic zeolites are usually microcrystalline and, furthermore, typically contain four 10-electron atomic species (Si^{4+}, Al^{3+}, O^{2-} and Na^{+}), which makes their structure difficult to study by conventional methods. High-resolution solid state NMR techniques, such as magic angle spinning (MAS), gave zeolite chemistry a powerful structural tool for monitoring all elemental components of such frameworks.

2 COMPOSITION OF ZEOLITIC FRAMEWORKS AND THE NATURE OF EXTRAFRAMEWORK ALUMINUM

Framework silicon in zeolites is 4-coordinate, and thus there are five different possible environments of a silicon atom: $Si(OAl)_4$, $Si(OAl)_3(OSi)$, $Si(OAl)_2(OSi)_2$, $Si(OAl)(OSi)_3$, and $Si(OSi)_4$. For simplicity, we denote these by Si(nAl) where n (≤ 4) is the number of aluminum atoms connected, via oxygen atoms, to a silicon. Each type of Si(nAl) building block corresponds to a definite range of ^{29}Si chemical shift (Figure 4).[13] When a ^{29}Si MAS NMR spectrum of a zeolite contains more than one peak and is correctly assigned in terms of Si(nAl) units, the Si/Al ratio in the zeolitic framework may be calculated from the spectrum alone. Because of the absence of Al–O–Al linkages, the environment of every aluminum atom is Al(4Si). Each Si–O–Al linkage in an Si(nAl) unit incorporates 0.25 aluminum atoms, and the whole unit contains $0.25n$ aluminum atoms. The Si/Al ratio may therefore be

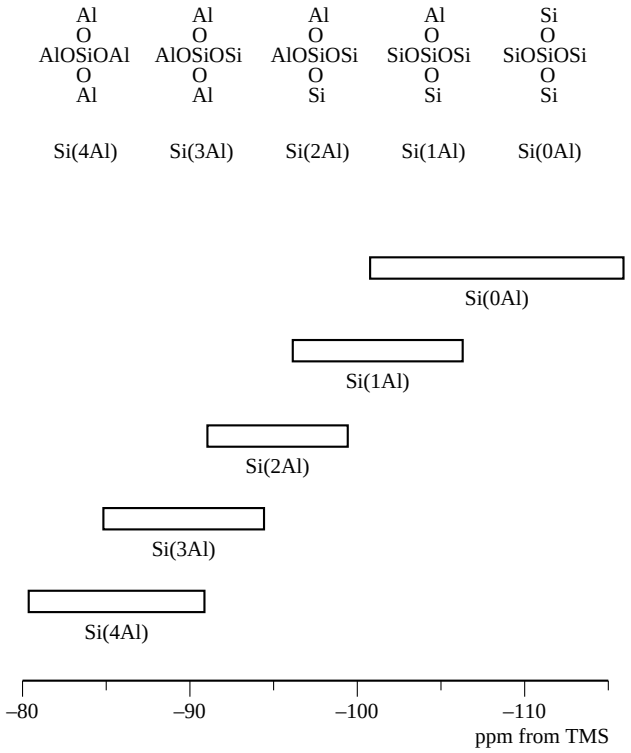

Figure 4 Ranges of ^{29}Si chemical shift for Si(nAl) building blocks in zeolites. The Si(4Al) range in some synthetic sodalites containing various enclathrated salts is exceptionally wide, from −76.5 to −97 ppm

calculated directly from the ^{29}Si MAS NMR spectrum using the formula[14]

$$(\mathrm{Si/Al})_{\mathrm{NMR}} = \frac{I_4 + I_3 + I_2 + I_1 + I_0}{I_4 + 0.75I_3 + 0.5I_2 + 0.25I_1} \qquad (1)$$

where I_n is the intensity (peak area) of the NMR peak corresponding to the Si(nAl) building unit. By comparing values of $(\mathrm{Si/Al})_{\mathrm{NMR}}$ with the results of chemical analysis, which gives bulk composition, the amount of extraframework aluminum in chemically modified zeolites can be calculated.

Equation (1) applies to all zeolites with framework Si/Al ratios less than about 10.[14–16] It can also serve as a test for the correctness of spectral assignment. Its validity has been confirmed in the case of zeolites X and Y, which can be synthesized in a range of compositions. The spectra can be deconvoluted using Gaussian peak shapes, and the areas of the individual deconvoluted peaks used in equation (1). However, equation (1) cannot be applied directly to spectra containing overlapping peaks from Si(nAl) units of crystallographically inequivalent silicon atoms, to zeolites containing framework defects (nests of hydroxyl groups), or to dealuminated zeolites in which vacancies created by the expulsion of framework aluminum have not subsequently been resubstituted by silicon. As aluminum is removed, the number of Si(0Al) (i.e. Si(4Si)) units is unchanged, while Si(3Al,1Si) units, for example, give rise not to Si(2Al,2Si) and Si(1Al,3Si) units, but to Si(2Al,1OH) and Si(1Al,2OH) groupings, the ^{29}Si NMR peaks from which overlap with those from Si(nAl) groupings. Although the intensities of ^{29}Si peaks corresponding to silicon atoms linked to one or more hydroxyl groups are enhanced by

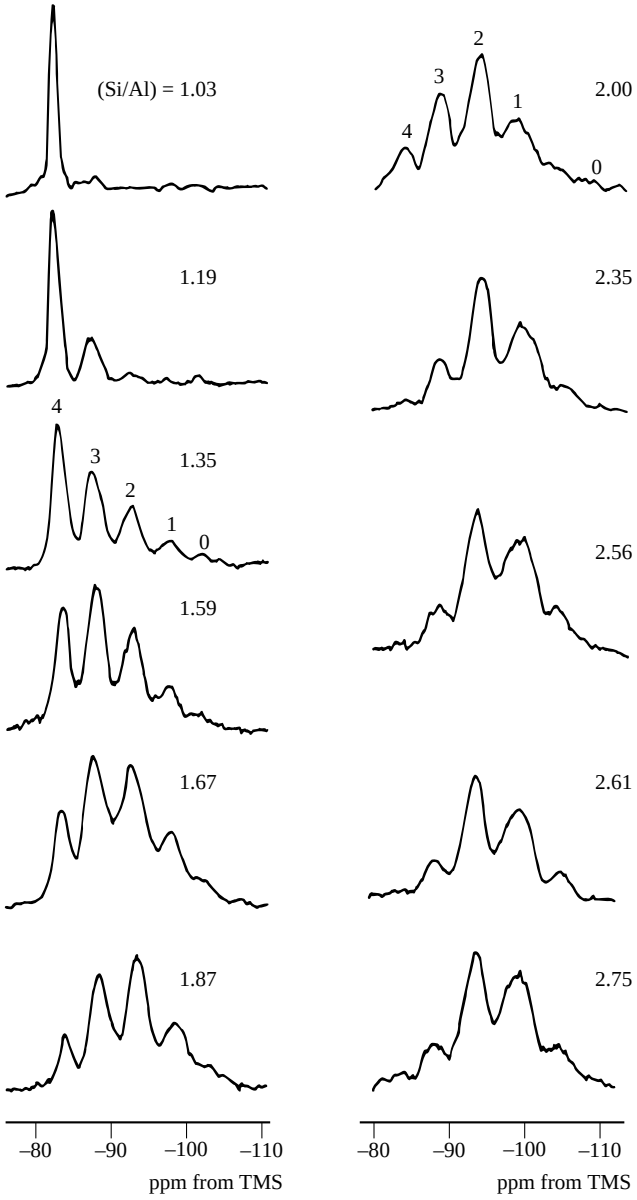

Figure 5 High-resolution ^{29}Si MAS NMR spectra of synthetic zeolites Na-X and Na-Y.[15] Si(nAl) peaks are identified by the n above the peaks

^{1}H–^{29}Si cross polarization, their individual intensities cannot be determined easily because the efficiency of the technique depends on the distance between the silicon and the hydrogen atoms.

^{29}Si MAS NMR can also be used to determine the ordering of silicon and aluminum in the framework. The areas under the peaks in the deconvoluted spectrum are proportional to the populations of the corresponding structural units in the sample. It is therefore possible to compare the experimental data (Figure 5) with the relative numbers of such units in models involving different silicon/aluminum ordering schemes. For most Si/Al ratios more than one ordering scheme is compatible with the Si(nAl) intensities determined by ^{29}Si MAS NMR. The choice between the various schemes is made on the basis of: (a) the degree of agreement between the spectral intensities and those required by the given model; (b) compliance with crystal symmetry requirements; and (c) minimum electrostatic

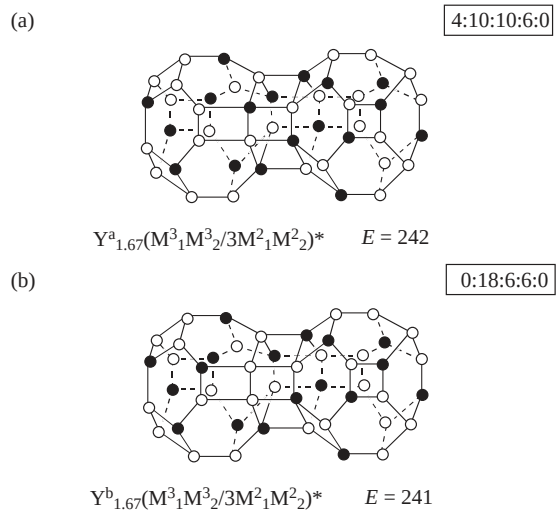

Figure 6 Two of the possible silicon/aluminum ordering schemes for zeolite Y with Si/Al = 1.67.[15] (○) Silicon atoms; (●) aluminum atoms. The ratio of intensities Si(4Al):Si(3Al):Si(2Al):Si(1Al):Si(0Al) corresponding to each scheme is given in the upper right-hand corner. E is the calculated electrostatic energy for the double cage in units of $(qe)^2/a$, where a is the T–O–T distance. The asterisk denotes the preferred scheme

repulsion within the framework. Figure 6 shows the preferred ordering schemes for Si/Al = 1.67.

Many ^{29}Si spectra of natural and synthetic zeolites have been measured by various workers since the pioneering papers by Lippmaa et al.[13] and Engelhardt et al.[14] appeared. The results for zeolites, the spectra of which can be directly assigned to Si(nAl) units, are listed in Table 1.

3 RESOLVING CRYSTALLOGRAPHICALLY NONEQUIVALENT TETRAHEDRAL SITES IN ZEOLITES

In naturally occurring zeolites, the Si/Al ratio is less than about 5, but materials with lower aluminum contents can be prepared synthetically. One might expect an uncomplicated spectrum for such materials, containing the Si(0Al) peak, sometimes with a smaller Si(1Al) resonance, depending on the Si/Al ratio. The discovery[17] that the spectrum of ZSM-5/silicalite, which has a very low aluminum content and the structure shown in Figure 3, has considerable fine structure was therefore a surprise. The fine spectral detail arises from crystallographically inequivalent tetrahedral environments of the Si(4Si) sites. Figure 7(a) shows a spectrum in which as many as 19 individual lines can be separately resolved, the linewidth of the narrowest line being only about 5 Hz.[18] The room temperature spectrum may be simulated by 24 Gaussian peaks, and the unit cell of ZSM-5/silicalite contains 24 inequivalent silicon sites.

X-ray diffraction (XRD) shows that silicalite can exist in the monoclinic and the orthorhombic forms. ^{29}Si MAS NMR detects minute temperature-induced variations in atomic positions[18–21] which do not necessarily involve symmetry changes detectable by XRD. The spectra are sensitive even to small temperature changes and reveal the corresponding

Table 1 Parameters of ^{29}Si MAS NMR Spectra of Zeolites for Which the Individual Spectral Signals can be Assigned Directly to Si(nAl) Structural Units

			^{29}Si chemical shift (ppm from TMS)				
Zeolite	Idealized unit cell composition	Si/Al	Si(4Al)	Si(3Al)	Si(2Al)	Si(1Al)	Si(0Al)
Na-A	$[Na_{12}Al_{12}Si_{12}O_{48}{\cdot}27H_2O]_8$	1.0	−88.9	–	–	–	–
Li-A(BW)	$Li_4Al_4Si_4O_{16} \cdot 4H_2O$	1.0	−80.1	–	–	–	–
Analcime	$Na_{16}Al_{16}Si_{32}O_{96} \cdot 16H_2O$	2.0	–	−92.0	−96.3[a]	−101.3	−108.0
Cancrinite	$Na_6Al_6Si_6O_{24} \cdot CaCO_3 \cdot 2H_2O$	1.0	−85.4	–	–	–	–
Chabazite	$Ca_5Al_{10}Si_{26}O_{72} \cdot 40H_2O$	2.6	–	−94.0	99.4[a]	−104.8	−110.0
Gismondine	$Ca_4Al_8Si_8O_{32} \cdot 16H_2O$	1.0	−89.9	–	–	–	–
Gmelinite	$Na_8Al_8Si_{16}O_{48} \cdot 24H_2O$	2.0	−86.8	−91.7	−97.1[a]	−102.7	−108.0
Laumontite	$Ca_4Al_8Si_{16}O_{48} \cdot 16H_2O$	2.0	–	–	−92.4	–	–
Leucite	$KAlSi_2O_6$	2.0	−81.0	−85.2	−91.6	−97.4	−101.0
Losod	$Na_{12}Al_{12}Si_{12}O_{48} \cdot 13H_2O$	1.0	−88.9	–	–	–	–
Mordenite	$Na_8Al_8Si_{40}O_{96} \cdot 24H_2O$	5.0	–	–	−100.0	−105.5	−111.6[a]
Natrolite	$Na_{16}Al_{16}Si_{24}O_{80} \cdot 16H_2O$	1.5	–	−87.7[a]	−95.4	–	–
RHO	$(Na,Cs)_{12}Al_{12}Si_{36}O_{96} \cdot 44H_2O$	3.0	–	−92.5	−97.2	−102.7[a]	−108.0
Scolecite	$Ca_8Al_{16}Si_{24}O_{80} \cdot 24H_2O$	1.5	–	−86.0 −88.6	−95.3	–	–
Sodalite	$Na_6Al_6Si_6O_{24} \cdot 2NaCl$	1.0	−84.8	–	–	–	–
Thomsonite	$Na_4Ca_8Al_{20}Si_{20}O_{80} \cdot 24H_2O$	1.0	−83.5	–	–	–	–
ZK-5	$Na_{30}Al_{30}Si_{66}O_{192} \cdot 98H_20$	2.2	−87.5	−92.0	−97.6[a]	−103.5	−108.6
Silicalite	$(SiO_2)_{96}$	–	–	–	–	–	−109.2; −111.2; −111.5; −112.1; −112.3; −112.7; −113.0; −113.3[a]; −113.5; −113.8; −114.1; −114.6; −115.2; −116.4
ZSM-5	$Na_3Al_3Si_{96}O_{192} \cdot xH_2O$	31.0	–	–	–	−101.8	−111.8[a]

[a]The largest peak.

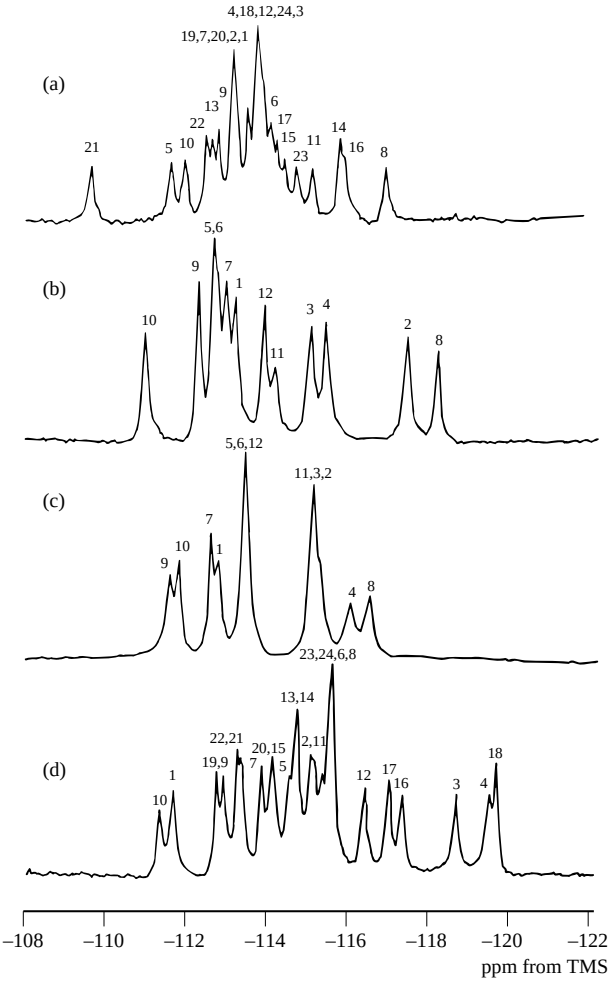

Figure 7 ^{29}Si MAS NMR spectra of ZSM-5/silicalite.[18] (a) At 300 K; (b) with two molecules of *p*-xylene per unit cell; (c) at 403 K; (d) ^{29}Si CP MAS NMR spectrum of ZSM-5 with eight molecules of *p*-xylene per unit cell

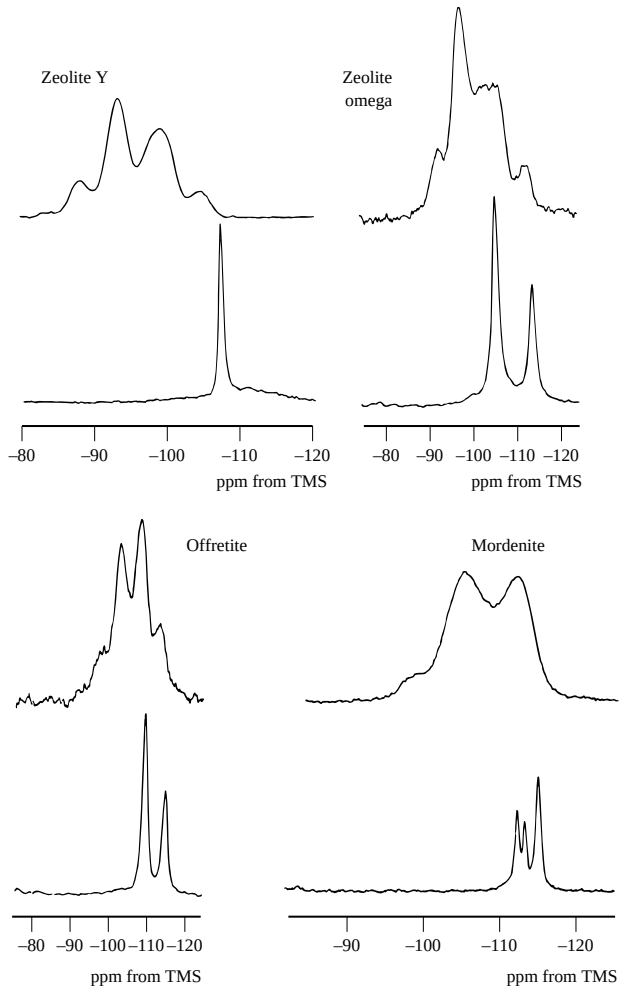

Figure 8 ^{29}Si MAS NMR spectra of (above) zeolites Y, omega, offretite and mordenite; and (below) their dealuminated forms[22]

structural transformations. Above 363 K silicalite contains only 12 inequivalent silicon sites, and the spectrum shown in Figure 7(c) can be simulated using Gaussian peaks of total intensity 12. Figure 7 also shows that the addition of small amounts of adsorbed organics to dehydrated silicalite induces similar changes in the spectra.

^{29}Si spectral peaks from most synthetic zeolites cannot easily be linked to specific silicon sites because the Si(*n*Al) manifolds from inequivalent sites overlap. However, when the ammonium form of a highly siliceous zeolite is heat treated in the presence of water vapor so that most framework aluminum is removed, the resolution of the ^{29}Si spectrum improves considerably.[22,23] Figure 8 shows the spectra of several zeolites before and after hydrothermal treatment. The intensities of the two peaks in the spectra of the siliceous zeolites omega and offretite are in a 2:1 ratio corresponding to the two inequivalent tetrahedral sites in the same population ratio. Mordenite, on the other hand, has four inequivalent sites in a 2:1:1:2 population ratio, so that the peak at −115 ppm in Figure 8 is a composite.

The fact that the ^{29}Si chemical shift is related to the T−O−T angles in zeolitic frameworks is useful for structural determination.[22,24] Chemical shifts in framework silicates have been correlated with the mean Si−O bond distances, and relationships have been developed which are in good agreement with the results of semiempirical calculations of chemical shift. A quantum mechanical rationalization of the correlation between the ^{29}Si chemical shift in framework silicates and the change in the s character of the oxygen orbitals in the Si−O−Si s bond has also been proposed (see Figure 9). The observed correlation between chemical shifts of Si(4Si) units and mean bond angles has been explained[25] in terms of a quantum mechanical model and confirmed by an extended set of experimental data consistent with relationships involving θ, $\cos\theta/(\cos\theta - 1)$, $\sin(\theta/2)$ and $\sec\theta$. These arguments have been extended to all five Si(*n*Al) units,[26] giving an approximately linear semiempirical relationship between the chemical shift of Si(*n*Al) peaks and the nonbonded Si$\cdots$T distance (T = Si or Al) calculated from the T−O−T angle.

^{29}Si MAS NMR peaks in the spectra of certain zeolites lead to incorrect values of $(Si/Al)_{NMR}$ when assigned to individual Si(*n*Al) units, as described above. When the difference in chemical shifts between peaks from inequivalent Si(*n*Al) units with the same value of *n* [8.4 ppm in the case of $Si_A(0Al)$ and $Si_B(0Al)$ in zeolite omega] is similar to the shift difference between Si(*n*Al) and Si[$(n \pm 1)$Al] units, the effects

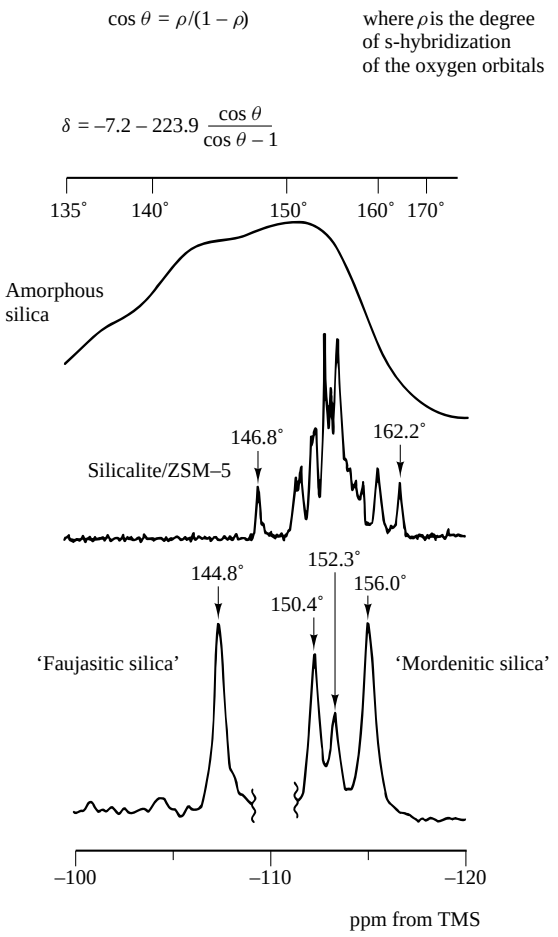

Figure 9 The mean T–O–T angle versus the isotropic ^{29}Si chemical shift for amorphous silica and several purely siliceous equivalents of zeolites

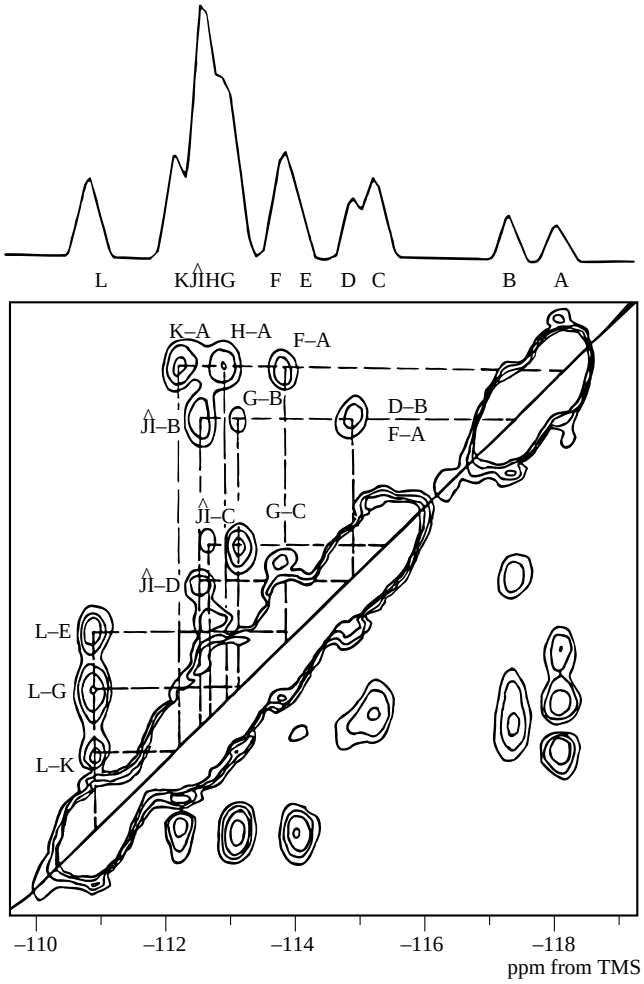

Figure 10 Two-dimensional ^{29}Si COSY-45 spectrum of the orthorhombic form of zeolite ZSM-5/silicalite with adsorbed *p*-xylene[18]

of aluminum substitution and crystallographic inequivalence overlap. The peaks are composites, and their intensities $I_{\mathrm{Si}(n\mathrm{Al})}$ cannot be read off the spectrum directly. In the case of 'as-prepared' zeolite omega, the spectrum (Figure 8) is the sum of two overlapping families of peaks. When this is taken into account, the entire spectrum can be correctly assigned and interpreted.

The chemical shift of ^{129}Xe NMR is very sensitive to the environment. When xenon is adsorbed inside a molecular sieve, its chemical shift is affected by the size and shape of the pores, by xenon–xenon collisions, by the presence of strong adsorption sites, paramagnetic species, adsorbed molecules, and phase transitions.[27] Most of the work in this area was done by Fraissard in Paris. While the initial hopes of predicting pore dimensions of unknown structures from ^{129}Xe NMR are still unfulfilled, the technique does provide valuable information, particularly where structural information is absent.

4 TWO-DIMENSIONAL NMR SPECTRA OF ZEOLITIC FRAMEWORKS

Two-dimensional solid state NMR techniques have been used to assign the individual NMR peaks to specific crystallographic sites. Figure 10 shows a ^{29}Si COSY-45 spectrum of the orthorhombic form of zeolite ZSM-5/silicalite with adsorbed *p*-xylene.[18] Of the expected 22 ^{29}Si–O–^{29}Si connectivities, 12 are present in the spectrum. The corresponding ^{29}Si 2D INADEQUATE spectrum (Figure 11) is superior, with as many as 21 connectivities being observed.[18] Excitation of a double quantum coherence has been used in double quantum filtered COSY, as in the experiment using a ^{29}Si-enriched sample of the highly siliceous zeolite ZSM-39[28] which contains three kinds of silicon site in a 1:4:12 population ratio. The most intense spectral peak is split into three components of equal intensity, which indicates loss of face centering of the *Fd*3*m* unit cell, resulting in the disappearance of the three-fold symmetry axis.

J-scaled COSY scales up the scalar splittings between the cross-peak components, thereby enhancing cross-peak intensities and consequently improving spectral resolution between adjacent diagonal and cross peaks. The ^{29}Si *J*-scaled COSY spectrum[29] measured with a scaling factor of 5 at natural isotopic abundance allows the resonances from highly siliceous mordenite to be assigned unambiguously, something which cannot be done by means of one-dimensional spectra or by conventional COSY.

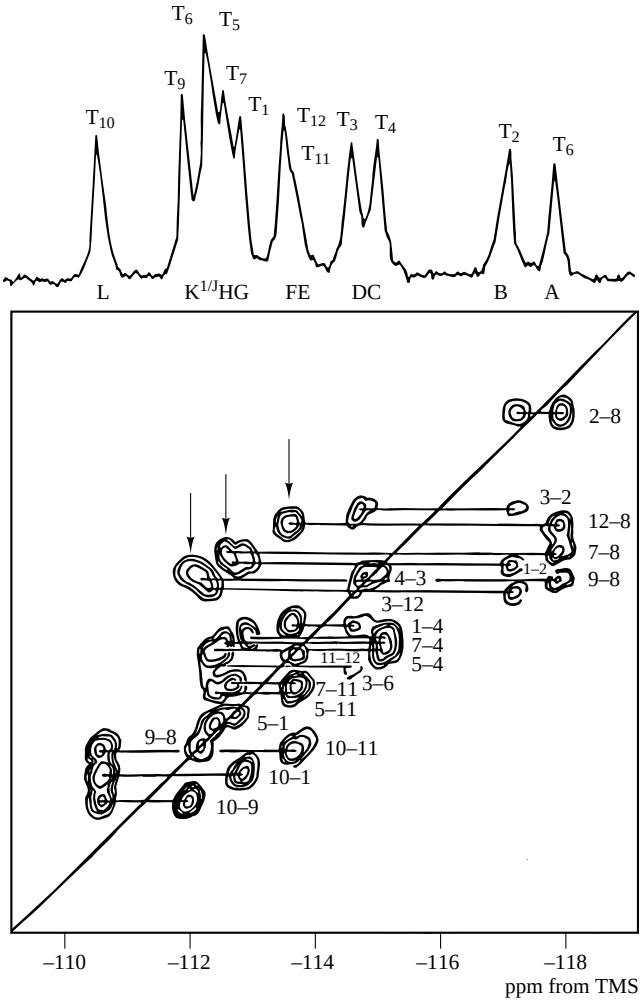

Figure 11 ^{29}Si two-dimensional INADEQUATE spectrum of the orthorhombic form of zeolite ZSM-5/silicalite with adsorbed *p*-xylene[18]

5 DEALUMINATION AND REALUMINATION OF ZEOLITES

Solid state ^{27}Al MAS NMR spectra of 'as-prepared' zeolites normally contain a single peak corresponding to four-coordinate aluminum. Its position as measured in a 9.4 T magnetic field ranges, for different materials, from about 51 to about 65 ppm from $Al(H_2O)_6^{3+}$. When the correction is made for the second-order quadrupole interaction, the chemical shift is found to be related to structural parameters in a similar manner to ^{29}Si chemical shifts. ^{27}Al MAS NMR spectra of 'as-prepared' zeolites are thus much simpler than their ^{29}Si counterparts. This is a direct consequence of the fact that while five types of Si(*n*Al) environments are possible for the silicon atom, only one possibility, Al(4Si), exists for the aluminum. However, while the coordination of silicon in zeolites is always four-fold, aluminum can be four-, five- or six-coordinate. The latter resonates at about 0 ppm from $Al(H_2O)_6^{3+}$ and is often subject to large quadrupole interactions. Quantitatively reliable ^{27}Al spectra are obtained with fast MAS at very high magnetic fields and using strong rf pulses with small flip angles.

Since Brønsted acid groups in zeolites are associated with framework aluminum, their catalytic activity depends on the

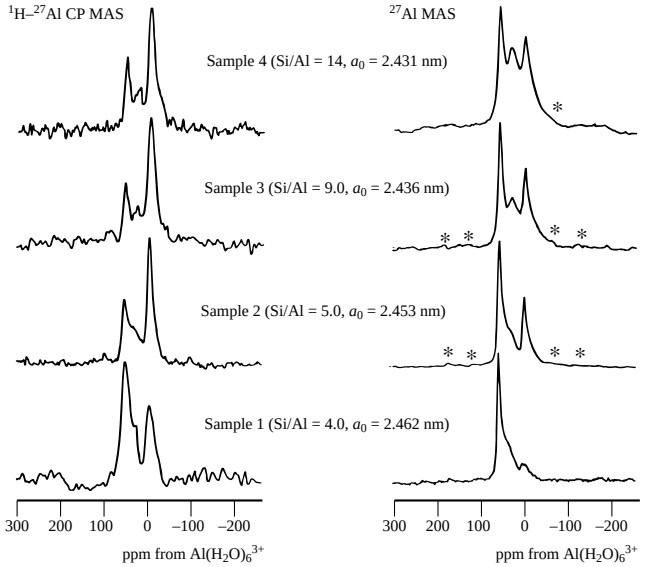

Figure 12 ^{27}Al (MAS at 12–13 kHz) and ^{1}H–^{27}Al CP MAS (MAS at 8–10 kHz) NMR spectra of increasingly dealuminated (from bottom to top) zeolite HY.[80] The Si/Al ratios calculated from ^{29}Si MAS NMR spectra and the cubic unit cell parameters a_0 are indicated. Asterisks denote spinning sidebands

concentration and location of aluminum in the structure. It is often desirable to reduce the aluminum content of the zeolitic framework. Upon hydrothermal treatment of zeolite NH_4-Y, the process known as 'ultrastabilization', part of the aluminum is ejected from the framework into the intracrystalline space, and the vacancies are reoccupied by silicon from other parts of the crystal. As a result, thermal stability of the zeolite is greatly increased. Ultrastable zeolite Y has been examined by ^{29}Si and ^{27}Al MAS NMR.[30–32] ^{29}Si spectra of ultrastable zeolite Y clearly show that aluminum is removed from the framework, and that the resulting vacancies are subsequently reoccupied by silicon. ^{27}Al MAS NMR shows how six-coordinate nonframework aluminum species (Al^{NF}) build up at the expense of the four-coordinate framework aluminum (Al^{F}) as the calcination temperature is increased, and ^{1}H–^{27}Al CP MAS NMR spectra of dealuminated samples help to elucidate the nature of Al^{NF}.[33] Figure 12 shows that the intensity of the peaks at 0 and 30 ppm increases relative to the peak at 60 ppm. This indicates that the 30 ppm peak is a separate ^{27}Al resonance from five-coordinate aluminum.

The process of ultrastabilization of zeolite Y can be reversed by a hydrothermal treatment with aqueous solutions of strong bases.[34] NMR indicates that aluminum atoms originally eliminated from the framework can be subsequently reinserted into the framework. ^{29}Si MAS spectra of dealuminated samples reflect the removal of framework aluminum from the parent sample. In the spectra of samples treated with KOH the intensities of the Si(0Al) peaks are greatly reduced, and the intensities of the Si(1Al), Si(2Al), Si(3Al), and Si(4Al) peaks are correspondingly increased, signifying that an aluminum has reentered the framework. The spectra of realuminated samples are very different from that of the parent material, despite the fact that their overall composition is similar. This demonstrates that the silicon/aluminum distribution among the tetrahedral sites is different. ^{27}Al quadrupole nutation NMR offers further insights into the dealumination–realumination process.[35,36]

6 NMR STUDIES OF THE STRUCTURE OF BRØNSTED ACID SITES IN ZEOLITES

The study of acidic surface sites capable of donating protons to adsorbed molecules is crucial to heterogeneous catalysis. It is vital to know the concentration, strength, and accessibility of the Brønsted and Lewis acid sites and the details of their interaction with the adsorbed organics. The Brønsted acidity of zeolites arises from the presence of accessible hydroxyl groups associated with framework aluminum ('structural hydroxyl groups'). Extensive ^{1}H MAS NMR measurements of zeolites have led to the assignment of the various proton resonances. ^{1}H NMR of static samples can probe the geometry of the Brønsted acid site and determine the Al–H distance, because the second moment of the broadline proton spectra, which is inversely proportional to the sixth power of the distance between the dipole-coupled nuclei, is dominated by the $^{1}H–^{27}Al$ interaction.

^{15}N NMR of molecules sorbed on zeolites is also useful for the study of zeolitic acidity, as the nitrogen atom in molecules such as ammonia and pyridine binds directly to the acid site. The ^{15}N chemical shift of ammonia adsorbed in ultrastable zeolite Y does not depend on the amount absorbed and is similar to that in liquid ammonia. Consideration of the equilibrium between the surface sites and the sorbate allows the resonance shifts for the surface complexes to be obtained. The formation of pyridinium ions in ultrastable zeolites has led to direct determination of the number of interacting hydroxyl groups. Acetonitrile has also been used to characterize the interactions with the acid sites.

When trimethylphosphine is used as a probe molecule in zeolite H-Y,[37] the ^{31}P MAS NMR spectrum contains resonances from at least two types of $(CH_3)_3PH^+$ complex: an immobilized complex coordinated to hydroxyl protons, and a highly mobile one which desorbs at 300 °C.

7 GALLOSILICATE AND BOROSILICATE ZEOLITES

Tetrahedral aluminum and silicon in the zeolitic framework can be substituted by several other elements. (Si,Ga)-, (Ge,Al)- and (Ge,Ga)-zeolites are structurally similar to their silicon/aluminum counterparts. ^{29}Si MAS NMR spectra of (Si,Ga)-sodalites and (Si,Ga)-faujasites[38,39] allow $(Si/Ga)_{NMR}$ ratios to be calculated from a formula similar to equation (1), which shows that no Ga–O–Ga linkages are present. The distribution of Si(nGa) peak intensities in gallosodalite is different from the Si(nAl) in aluminosilicate zeolites of similar Si/T ratio (T = Al or Ga), indicating that the distribution of silicon and gallium is different from the distribution of silicon and aluminum. The ^{29}Si chemical shifts in silicon/gallium zeolites span 25.1 ppm, a wider range than in the corresponding aluminosilicates (18.5 ppm).

Borosilicate ZSM-5 ('boralite') containing up to five boron atoms per unit cell has been prepared. ^{11}B spectra show that four-coordinate boron resonates at about −3.5 ppm from $BF_3{\cdot}OEt_2$.[40] On dehydrating boralite, the intensity of the line decreases reversibly and a second broad line appears. The width of that line, assigned to trigonal boron, is dependent on the magnetic field intensity, which indicates that the effect is quadrupolar in nature.[41]

8 CHEMICAL STATUS OF GUEST ORGANICS IN ZEOLITES

The declining oil reserves have stimulated efforts aimed at converting methanol (MeOH) into higher molecular weight organics over shape-selective catalysts, particularly zeolite H-ZSM-5 which is capable of converting MeOH to hydrocarbons up to C_{10}. The mechanism of the reaction is a subject of some controversy. ^{1}H NMR has been used[42] to monitor the chemistry of MeOH adsorbed on ZSM-5 inside sealed capsules which can be spun in the MAS probehead.

The ^{1}H MAS NMR spectrum of MeOH adsorbed on zeolite H-ZSM-5 contains peaks at 4.1 and 9.1 ppm, from methyl and hydroxyl protons, respectively. The large high-frequency (downfield) shift of the latter resonance is caused by very strong hydrogen bonding and/or direct protonation of the alcohol, and serves as a measure of the proton donating ability of the solid acid catalyst: in zeolites H-Y and H-L the shifts are considerably smaller than in ZSM-5.

9 IN SITU STUDIES OF CATALYTIC REACTIONS ON ZEOLITES

^{13}C MAS NMR can probe the kind and quantity of chemical species present inside the particle in the course of the conversion of MeOH to gasoline on zeolite ZSM-5. This information is usefully compared with the composition of the gaseous products.[43] These experiments have: (i) identified 29 different organic species in the adsorbed phase and monitored their fate during the course of the reaction; (ii) observed directly different kinds of shape selectivity in a zeolite; and (iii) unequivocally distinguished between mobile and attached species.

The spectrum of a sample with adsorbed MeOH and maintained at 20 °C, contains a single resonance at 50.8 ppm due to MeOH (Figure 13). After heating the sample to 150 °C the spectrum is composed of two peaks, at 50.5 and 60.5 ppm, corresponding to MeOH and dimethyl ether (DME), respectively. In a sample treated at 300 °C for 35 min, MeOH and DME have been completely converted to a mixture of aliphatics and aromatics.

Two-dimensional ^{13}C spectra can determine the connectivity of carbon atoms and the number of protons attached to each carbon atom in the various products, enabling firm assignments for many resonances to be made.[44] For example, the line at −10.7 ppm in Figure 14 is split into five components with a requisite intensity ratio, which confirms that it must be due to adsorbed methane. Spin diffusion ^{13}C NMR spectra further confirm the spectral assignments and provide new details on distribution of hydrocarbons in the intracrystalline space.

10 DIRECT OBSERVATION OF SHAPE SELECTIVITY

The distribution of adsorbed species in the sample of ZSM-5 with adsorbed methanol treated at 300 °C is different from the thermodynamic equilibrium distribution and from the distribution of the reaction products.[43] The main species found in the adsorbed phase are *o*- and *p*-xylene, 1,2,4,5-tetramethylbenzene, 1,2,4-trimethylbenzene,

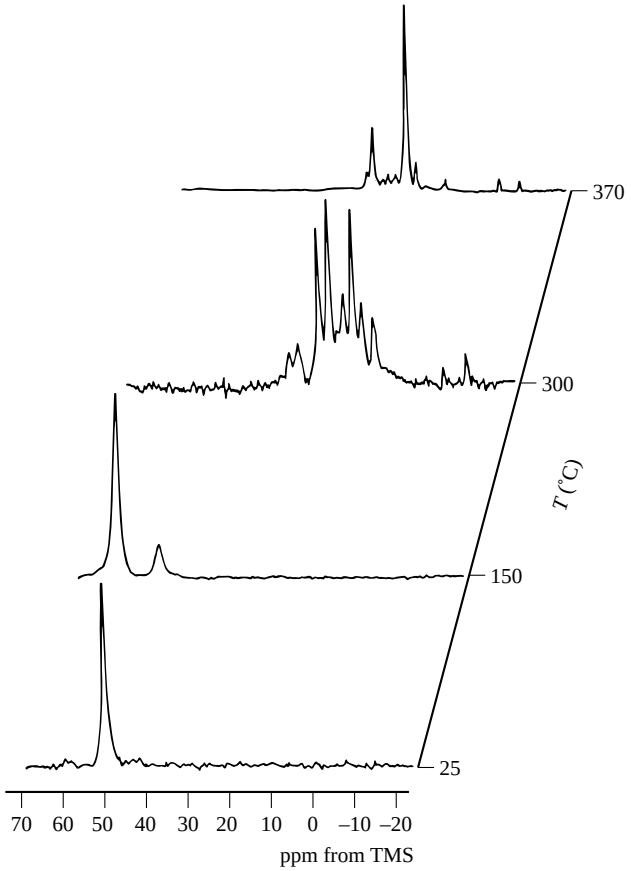

Figure 13 Solid state ^{13}C NMR spectra reveal the successive steps in the conversion of methanol to gasoline over zeolite ZSM-5. The methanol, resonating at 50 ppm, is first dehydrated to DME (60 ppm). Subsequent carbon–carbon bond formation leads to a host of aliphatic (−10 to 35 ppm) and aromatic (not shown) compounds[43]

and 1,2,3,5-tetramethylbenzene. The fact that 1,2,3- and 1,3,5-trimethylbenzenes are not found among the products, but are present in the adsorbed phase, while the smaller 1,2,4-trimethylbenzene is found in both, demonstrates the reality of the concept of product selectivity. The two larger isomers are unable to diffuse out of the crystal. The distribution of the tetramethylbenzenes in the intracrystalline space (none of which are found in the products of the reaction at 300 °C) is equally unexpected.

Table 2 $AlPO_4$ Structures Divided into Very Large Pore Materials (>12-Membered Rings), Large Pore (12-Membered Rings), Intermediate Pore (10-Membered Rings), Small Pore (8-Membered Rings), Very Small Pore (6-Membered Rings), and Other Structures (Layered Materials and Those which Transform on Template Removal)[53]

$AlPO_{4-n}$ structure	Related structure
Very large pore	
VPI-5[a]	Novel
$AlPO_4$-8	Novel
Large pore	
$AlPO_4$−5[b]	Novel
−31	Novel
−36	Novel
−37	Faujasite
−40	Novel
−46	Novel
−50	Novel
Intermediate pore	
$AlPO_4$−11	Novel
−41	Novel
Small pore	
$AlPO_4$−14	Novel
−17	Erionite
−18	Novel
−24	Analcime
−25	Novel
−26	Novel
−33	Novel
−34	Chabazite
−35	Levynite
−39	Novel
−42	Zeolite A
−43	Gismondine
−44	Chabazite
−47	Chabazite
−52	Novel
Very small pore	
$AlPO_4$−16	Novel
−20	Sodalite
−28	Novel
Other	
$AlPO_4$−12	Novel
−14A	Novel
−15	Novel
−21	Novel
−H3	

[a]Also known as $AlPO_4$−54.
[b]An all-silica analog of $AlPO_4$−5 (known as SSZ-24) has recently been synthesized.

11 STRUCTURE OF ALUMINOPHOSPHATE MOLECULAR SIEVES

The $AlPO_4$ molecular sieves, the porous crystalline equivalents of aluminum phosphate, are built from alternating AlO_4 and PO_4 tetrahedra.[45,46] Some of them have the framework topologies of known zeolites, but many are novel structures. The various $AlPO_4$ structure types are listed in Table 2, and the structures of $AlPO_4$-5 and $AlPO_4$-11 are shown in Figure 15. Synthesized from gels containing sources of aluminum, phosphorus, and at least one organic structure-directing template, $AlPO_4$ materials have electrically neutral frameworks and thus no exchangeable cations. Incorporation of a silicon source into the synthesis gel results in the formation of silicoaluminophosphates (SAPOs)[47] and the incorporation of a metal Me (such as Mg, Mn, Fe, Co or Zn), into $AlPO_4$ and SAPO gives the MeAPO and MeAPSO sieves, respectively.[48] SAPO and MeAPO have negatively charged frameworks, and thus potential uses as ion exchangers and catalysts. In SAPO the predominant substitution mechanism is of silicon onto phosphorus sites, though pairwise substitution of silicon onto both aluminum and phosphorus sites is also possible. In MeAPO the metal substitutes onto the aluminum sites of the equivalent $AlPO_4$ structure. Other elements (Li, Be, B, Ti, Ga, Ge and As) have been claimed to substitute into the aluminophosphate framework to give ElAPO materials.[49] By

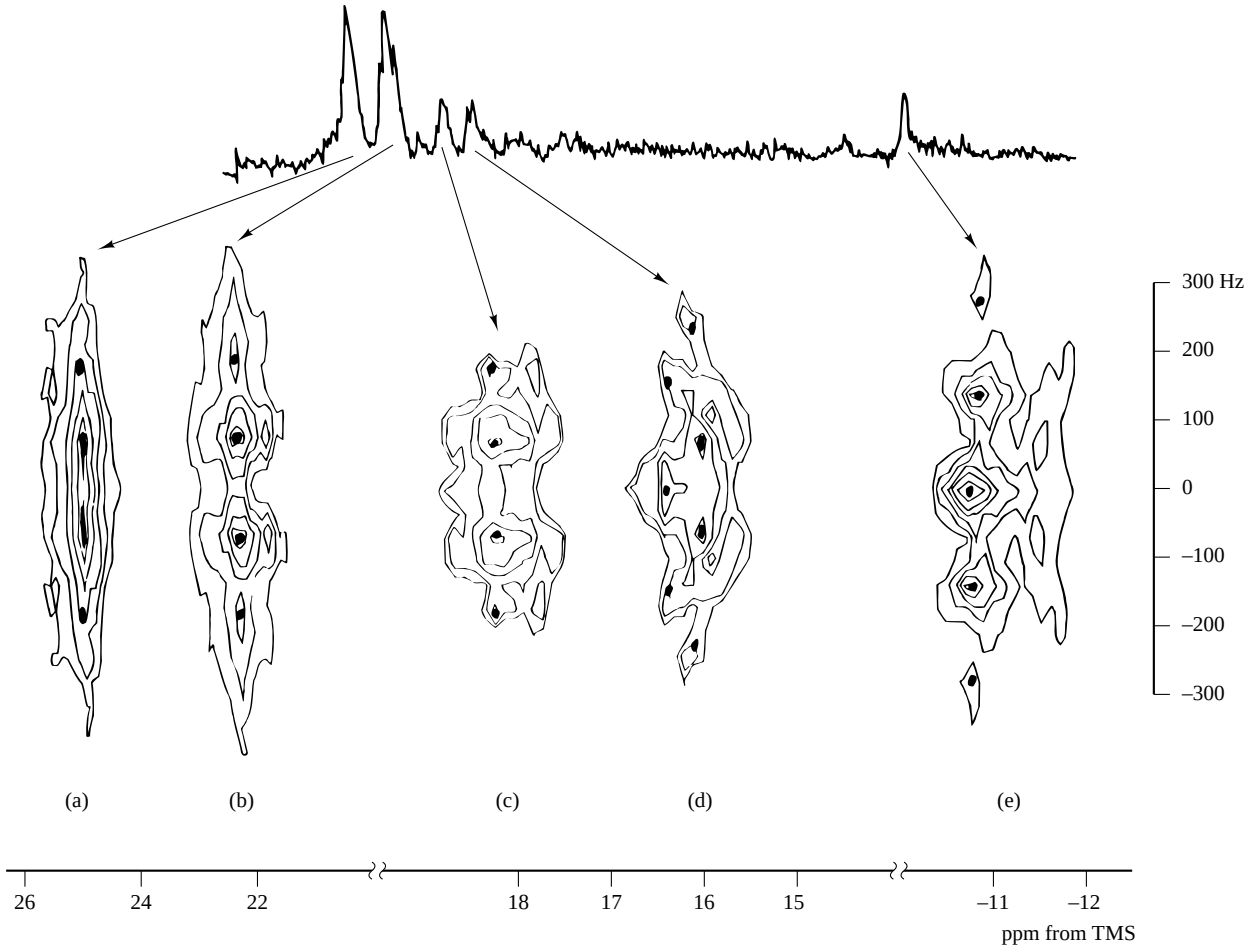

Figure 14 Heteronuclear two-dimensional J-resolved ^{13}C MAS NMR spectrum of zeolite H-ZSM-5 with adsorbed methanol treated at 300 °C for 30 min[44]

introducing more than one kind of heteroatom into the framework, or a metal and silicon simultaneously, MeAPSO and ElAPSO sieves were prepared.[50,51]

Remarkable $AlPO_4$ and related materials include VPI-5, the topology of which had been predicted in advance of its being synthesized, and cloverite, a gallophosphate molecular sieve with 20-membered rings, the most porous molecular sieve prepared so far.

12 NMR STUDIES OF $AlPO_4$-5, $AlPO_4$-11, AND $AlPO_4$-21

The $AlPO_4$ materials are a challenge to multinuclear solid state MR, given the wide variety of new crystal structures and the fact that they contain two different kinds of 100% abundant nuclei (^{31}P and ^{27}Al) in close proximity. Furthermore, framework aluminum in $AlPO_4$ can be linked to one or two oxygen species such as $-OH$ or $-OH_2$, so that some of the aluminum atoms may be five- or six-coordinate with respect to oxygen. Another challenge are the strong quadrupolar effects involving ^{27}Al as a result of which the quadrupole correction to chemical shifts is much larger than in zeolites. The aluminum and phosphorus atoms alternate in the frameworks of all $AlPO_4$, so that only even-numbered rings may be formed. However, the three allowed coordination numbers of aluminum make possible a wide range of new structures.

Table 3 summarizes the ^{31}P chemical shifts in $AlPO_4$ materials. Note that the precise value of the chemical shift often depends on the kind of organic template and on the water content of calcined samples. A similar table for ^{27}Al chemical shifts cannot be readily provided as the quadrupole coupling parameters, necessary if the quadrupole correction is to be made, are rarely known. Corrected ^{27}Al chemical shifts are between 37 and 48 ppm for $Al(OP)_4$ sites, about 15 ppm for $Al(OP)_4(OH)$, and between -9.5 and -12 ppm for $Al(OP)_4(OH_2)_2$ sites.[52] There is a recent review of $AlPO_4$-based molecular sieves.[53] A correlation between chemical shift and bond angle for $AlPO_4$ materials[65] relies on the comparison of mean Al–O–P bond angles with ^{27}Al chemical shifts corrected for the second-order quadrupole interaction. The imperfection of the correlation[66] is probably caused by the presence of five- and six-coordinate aluminum.

The spectra of $AlPO_4$-5, $AlPO_4$-11, $AlPO_4$-17, and $AlPO_4$-31 are consistent with known framework structures. ^{31}P and ^{27}Al MAS spectra of $AlPO_4$-5 each consist of a single peak.[54,55] The ^{31}P chemical shift (about -30 ppm) is characteristic of the $P(OAl)_4$ environment. The corrected chemical shift of the broad ^{27}Al peak is about 44 ppm, which is characteristic of four-coordinate $Al(OP)_4$ sites. This

Table 3 Summary of ^{31}P Chemical Shifts in $AlPO_4$ Structures[53]

Structure	Form	Chemical shift (ppm from 85% H_3PO_4)
$AlPO_4$-5	Tripropylamine	−30.6
	Tetraethylammonium	−28.6
	Hydrated calcined	−27.8
$AlPO_4$-8	Hydrated	−22.6, −25.7, −26.9, −31.1
	Dehydrated	−12.3, −30.1
$AlPO_4$-11	Dipropylamine	−31.8
	Hydrated calcined	−23.4, −29.6
$AlPO_4$-12	2-Imidazolidone	−6.6, −15.0
$AlPO_4$-14	Isopropylamine	−5.7, −20.3, −24.3
	Piperidine	−22.1, −28.0, −30.6
	Hydrated calcined	−22.4, −23.7, −25.3, −28.1
	Dehydrated calcined	−21.9, −27.1, −32.0
$AlPO_4$-14A	Isopropylamine	−19.4, −29.0
$AlPO_4$-17	Not specified	−24.2
	Hydrated calcined	−29.9
	Dehydrated calcined	−29.5, −35.0
$AlPO_4$-20	Tetramethylammonium	−35.2
$AlPO_4$-21	Pyrolidine	−13.3, −21.1, −30.3
	Not specified	−14.8, −21.4, −26.4
$AlPO_4$-25	Hydrated	−30.7
$AlPO_4$-31	Not specified	−30.2
	Hydrated calcined	−29.9
	Dehydrated calcined[a]	−30.5
$AlPO_4$-34	Tetraethylammonium + dipropylamine[a]	−28.5
	Hydrated calcined[a]	−27.4
$AlPO_4$-35	Not specified[a]	−27.4, −32.8
$AlPO_4$-37	Tetrapropylammonium + tetramethylammonium[a]	−26.4
$AlPO_4$-42	Tetramethylammonium[a]	−27.5
VPI-5	Hydrated	−23.3, −27.2, −33.1
	Dehydrated	−26.6, −32.5
$AlPO_4$-H3	Hydrated	−24.1, −25.9
$AlPO_4$-Q	(Quartz)	−24.8
		−25.6
$AlPO_4$-T	(Tridymite)	−29.5
$AlPO_4$-C	(Cristobalite)	−27.1

[a]Measured in an equivalent SAPO structure.

means that aluminum and phosphorus strictly alternate in the framework. The ^{31}P peak from the calcined and partially hydrated form is split as a result of the interaction between the framework and the intracrystalline water, presumably giving rise to $Al(OP)_4(OH_2)_2$ environments. Hydration produces significant amounts of six-coordinate framework aluminum which returns to four-coordination upon rehydration. Four- and six-coordinate aluminum resonate at 23−31 ppm and about −17 ppm, respectively.

$AlPO_4$-11 has an orthorhombic unit cell, but the symmetry of the hydrated calcined material is lower. Adsorbates such as cyclohexane stabilize the higher symmetry form which has three distinct crystallographic sites for both aluminum and phosphorus in the population ratio of 2:2:1. The lower symmetry form requires five sites in the population ratio of 1:1:1:1:1. Figure 16 shows that the ^{27}Al and ^{31}P NMR spectra of 'as-synthesized' $AlPO_4$-11 show single asymmetric peaks (suggesting that more than one environment is present). The relatively low intensity resonance at −5.5 ppm in the ^{31}P spectrum is probably due to terminal $P(OAl)_3OH$ sites at defects and the surface of the crystallites. The ^{31}P spectrum of the calcined and hydrated material (Figure 16) consists of two well-resolved resonances at −23.4 and −29.6 ppm in the intensity ratio of 1:4, which suggests that four of the five phosphorus sites have similar chemical shifts.

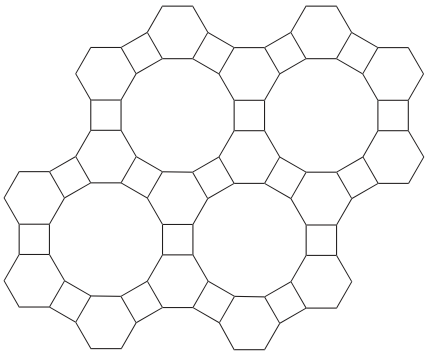

$AlPO_4$-5

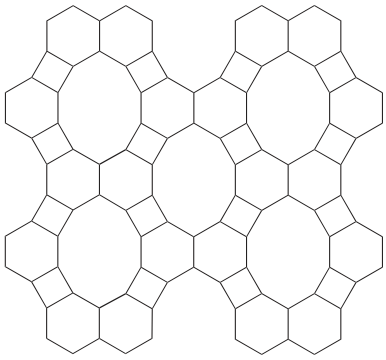

$AlPO_4$-11

Figure 15 The structures of $AlPO_4$-5 and $AlPO_4$-11 viewed down the (001) axis

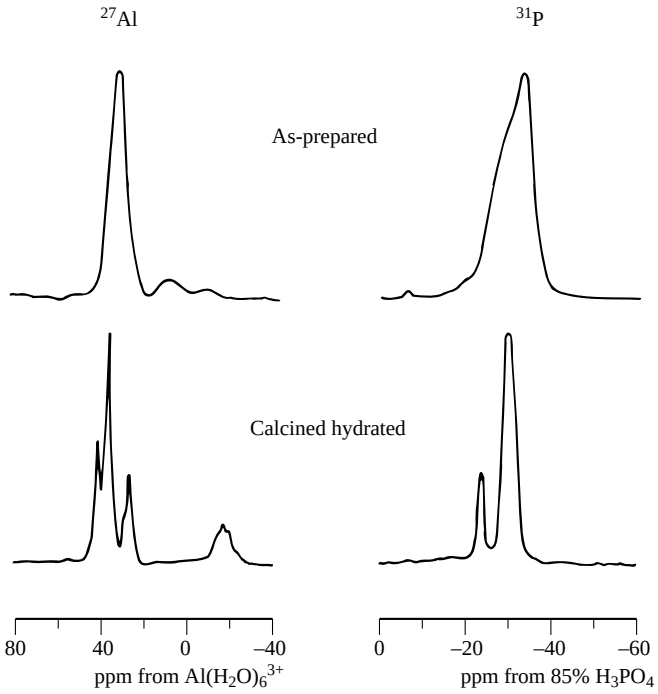

Figure 16 ^{27}Al and ^{31}P MAS NMR spectra of 'as-prepared' and hydrated calcined $AlPO_4$-11 obtained in a 9.4 T field[57]

The development of double rotation (DOR), in which the sample is rotated around two different axes simultaneously and dynamic angle spinning (DAS), in which the sample is rotated sequentially about two different axes, was a major advance in the study of solids. DAS and DOR remove not only chemical shift anisotropy, but also second-order quadrupolar interactions.[56] ^{27}Al DOR distinguishes the distorted five-coordinate aluminum sites in the molecular sieve precursor $AlPO_4$-21. Upon calcination, $AlPO_4$-21 transforms to $AlPO_4$-25, which has two four-coordinate aluminum sites with similar isotropic chemical shifts. These cannot be resolved in an 11.7 T field, but are resolved by DOR at 4.2 T because of their different quadrupole coupling constants.

^{27}Al DOR was used[57] to monitor the nature of the phase transition of $AlPO_4$-11 observed when water is adsorbed. The DOR spectrum of hydrated $AlPO_4$-11 shows that the line at 30 ppm is indeed due to a single environment. However, the broad DOR peak from six-coordinate aluminum indicates the presence of a range of sites, suggesting that all five crystallographic sites are hydrated to a similar extent. The DOR spectrum of the dehydrated calcined sample shows only a single peak in the 11.7 T field, despite the fact that three crystallographic sites are present. This indicates that the three sites have similar chemical shifts.

13 VPI-5 AND $AlPO_4$-8

VPI-5 is a crystalline aluminophosphate molecular sieve containing 18-membered rings of aluminum and phosphorus atoms (Figure 17). The large (about 1.2 nm) channel diameter gives VPI-5 considerable potential for the separation of large molecules, and for catalytic cracking of the heavy fractions of petroleum. The material has thus been studied extensively. The room-temperature ^{31}P MAS NMR spectrum of hydrated VPI-5 contains three peaks in an intensity ratio of 1:1:1 (Figure 18) and the ^{27}Al spectrum resonances from four- and six-coordinate aluminum. This is because 'as-prepared' VPI-5 is an aluminophosphate hydrate with three inequivalent sites for both phosphorus and aluminum: one of the aluminum sites is bonded to two chemisorbed water molecules, thus becoming six-coordinate. Variable temperature NMR[58,59] (Figure 18) shows that VPI-5 undergoes a reversible phase transition to a higher symmetry structure with two ^{31}P resonances in a 2:1 intensity ratio and two sites for both aluminum and phosphorus. The peaks at −23 ppm (1) and −27 ppm (2) were assigned to phosphorus atoms in 6−4 sites (P2 and P3), and the peak at −33 ppm (3) to P atoms in 4−4 sites (P1). ^{31}P–^{31}P spin diffusion spectra were used to establish how peaks 1 and 2 are to be assigned to particular P2 and P3 sites.[60] Each pair of ^{31}P resonances gives rise to cross peaks (Figure 19) and the efficiency of spin diffusion (cross-peak intensity) decreases with increasing spinning rates. An analysis of the plot of cross-peak intensity versus the spinning rate in the light of interatomic distances known from the XRD structure showed that peaks 1, 2, and 3 should be assigned to sites P2, P3, and P1, respectively.

^{27}Al DOR spectra[61] confirm that the peak from four-coordinate aluminum arises from two crystallographic sites, and the broad peak from six-coordinate aluminum from a single site. Although the two four-coordinate aluminum sites are not resolved by DOR at high fields because of their similar chemical shifts, they may be resolved at lower fields because the sites have different quadrupolar coupling constants.

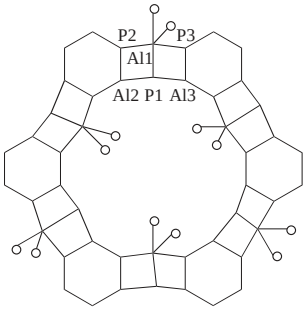

Figure 17 One layer of the framework structure of hydrated VPI-5 taken from the stereoscopic view along the [001] direction showing the deviation from $P6_3cm$ symmetry.[59] Aluminum and phosphorus atoms are located at the apices of the polygons. Sites located between two fused four-membered rings are known as 4–4 sites; those located between six-membered and four-membered rings are known as 6–4 sites. P2 and P3, and Al2 and Al3 sites are inequivalent as a result of the distortion. The Al1 site is six-coordinate as a result of bonding to four bridging oxygen atoms and two 'framework' water molecules

Heating hydrated VPI-5 results in a transformation to $AlPO_4$-8. ^{27}Al DOR shows[61] that in dehydrated VPI-5 there are also only two four-coordinate aluminum environments in the intensity ratio of 2:1. However, after a period during which the sample had been kept in a rotor which was not completely air-tight, many additional NMR resonances are found, corresponding to a partially rehydrated material (Figure 20).

Spin echo double resonance (SEDOR) allows the relative spatial disposition of spins to be deduced. By measuring the dipolar interaction between nuclei, which is inversely proportional to the cube of the internuclear distance, SEDOR probes only their immediate vicinity. ^{27}Al–^{31}P SEDOR can measure Al–P distances in $AlPO_4$ materials.[62] MAS NMR with dipolar dephasing has been used[63] for the study of mixed pairs of quadrupolar and spin-$\frac{1}{2}$ nuclei in VPI-5. Dipolar connectivities between ^{31}P and ^{27}Al were examined in both directions.

NMR spectra of $AlPO_4$-8 show single ^{31}P and ^{27}Al peaks and a small ^{31}P peak at -12.1 ppm.[64] In hydrated $AlPO_4$-8, about 34% of the aluminum is six-coordinate. The ^{31}P spectrum shows several environments, and at least five peaks are required for the simulation. The structure of dehydrated $AlPO_4$-8 calls five sites in the population ratio of 2:2:2:2:1.

14 SAPO MOLECULAR SIEVES

The general formula for a SAPO molecular sieve is $M_{(y-z)/n}[Si_xAl_yP_zO_2]\cdot wH_2O$, where $x + y + z = 1$, M is the charge-balancing cation, and the amount of silicon depends on the structure type. It is generally found that $y > z$, indicating that substitution of silicon into phosphorus sites is more frequent than substitution into aluminum sites. However, the aluminum content is often less than 50%, so that substitution of two silicon atoms for an Al + P pair must also occur. ^{29}Si NMR spectra of SAPO suffer from low signal-to-noise ratios due to the low concentration of silicon and the low natural abundance of ^{29}Si. The ^{29}Si chemical shift of SAPO-5 (isostructural with $AlPO_4$-5) is -92 ppm, which is slightly more negative than

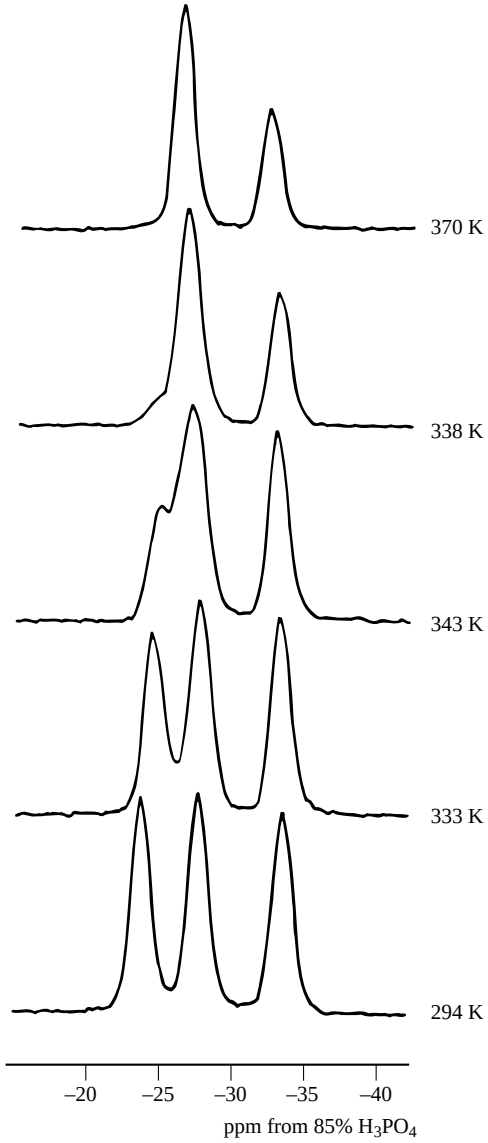

Figure 18 Variable temperature ^{31}P MAS NMR spectra of hydrated VPI-5 in a closed rotor system[59]

that for $Si(OAl)_4$ environments in zeolites, and it appears that the silicon is substituting exclusively onto the phosphorus sites of the framework. ^{27}Al, ^{31}P, and ^{29}Si NMR spectra[67] each contain single peaks, but some ^{29}Si spectra show peaks at -92, -102, and -108 ppm, indicating the presence of two or more silicon environments. The -102 ppm peak may originate from siliceous species on the surface of the crystallites. It also appears that, even allowing for the possible presence of amorphous silica, some regions are richer in silicon than are $Si(OAl)_4$ sites. Pairwise substitution of silicon onto aluminum and phosphorus sites seems to take place. The ^{31}P peak has the same chemical shift as in $AlPO_4$-5, which indicates that all phosphorus is in the $P(OAl)_4$ environment. Narrow ^{31}P NMR peaks from SAPO materials indicate that no Si–O–P bonds are present, and no case has yet been reported where all the silicon is present exclusively in $Si(OAl)_4$ environments.

The framework structure of SAPO-37 is that of the zeolite faujasite. There is a single ^{31}P peak at -26.4 ppm corresponding to $P(OAl)_4$ sites, and a single ^{29}Si peak at

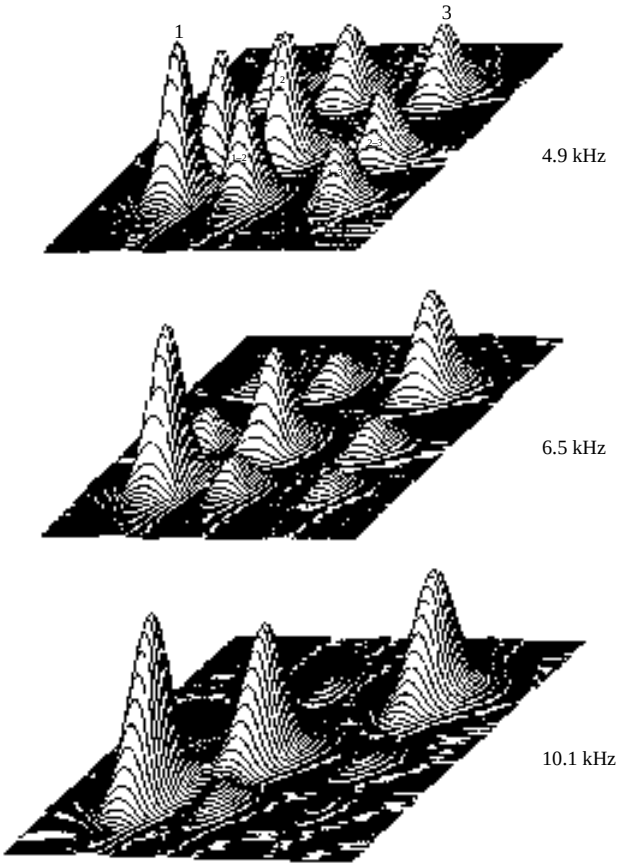

Figure 19 Two-dimensional ^{31}P NMR spin diffusion spectra of hydrated VPI-5 recorded with MAS at 4.9, 6.5, and 10.1 kHz.[60] The three spectra are not on the same intensity scale, and so only the relative intensities within each can be compared

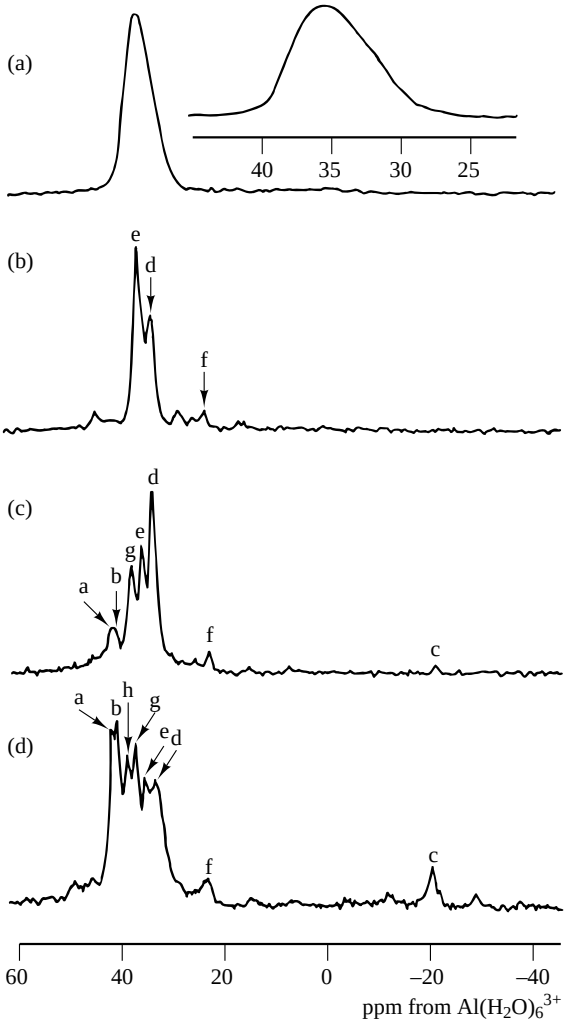

Figure 20 ^{27}Al NMR spectra of dehydrated and partially rehydrated VPI-5:[61] (a) ^{27}Al MAS and (b) ^{27}Al DOR spectrum of dehydrated VPI-5; (c) DOR spectrum after 2 days of rehydration; (d) DOR spectrum after 23 days of rehydration

−90.2 ppm corresponding to $Si(OAl)_4$ sites, indicating that the ideal silicon-for-phosphorus mechanism operates. Samples with high silicon content give more complicated ^{29}Si spectra, with features at −86, −90, −94, −98, −102, and −106 ppm.[68] The strongest of these, at −90 ppm, corresponds to the $Si(OAl)_4$ units in pure SAPO materials, while the others correspond to $Si(OAl)_x(OSi)_{4-x}$ units in zeolite Y. This suggests that SAPO-37 may contain inhomogeneous growths of silicoaluminophosphate and aluminosilicate regions.

The structure of SAPO-34 is that of the zeolite chabazite. The single NMR peak of ^{29}Si at −92 ppm[69,70] indicates that the exclusive substitution mechanism of silicon onto phosphorus sites applies, leading to the creation of Brønsted acid sites. ^{13}C MAS NMR spectra of SAPO-34 with adsorbed MeOH reveal hydrocarbon transformations upon heating the sample.[69] The major products are C_1 and C_2 organics; although formed, C_4 to C_6 hydrocarbons are too large to diffuse out through the eight-membered rings. The C_3 species are present in the product in a lower yield than expected, because the pore system is partially blocked by longer chain hydrocarbons.

15 MeAPO MOLECULAR SIEVES

The framework formula of a MeAPO sieve is $[Me_xAl_yP_zO_2]$, with $x + y + z = 1$, and $z = 0.5$, indicating that the metal substitutes exclusively onto the aluminum sites of the equivalent $AlPO_4$ structure. MeAPOs can therefore contain Brønsted acid sites. Deviations from $z = 0.5$ are attributed to extraframework metal ($z < 0.5$) or phosphorus ($z > 0.5$). $x > 0.125$ implies the presence of Me−O−P−O−Me bonds.

The ^{27}Al MAS NMR spectrum of MgAPO-20 containing 15% magnesium[71] (Figure 21) shows a single $Al(OP)_4$ environment, while the ^{31}P spectrum contains two major peaks at −21.1 and −28.0 ppm from P(2Al,2Mg) and P(3Al,1Mg) units in an intensity ratio of 1:2. The low intensity peaks come from P(1Al,3Mg) and P(4Al) units. Magnesium is therefore present exclusively on aluminum sites, which makes it possible to calculate the framework composition from the intensities of the NMR peaks and to distinguish between possible ordering schemes for phosphorus, aluminum, and magnesium.

^{11}B spectra of BAPO-5 show that boron is four-coordinate, but is not necessarily a part of the framework. Only one ^{31}P peak is found, even though $P(OAl)_3(OB)$ sites are expected to be present. Similarly, there is no direct evidence for the presence of framework lithium in LiAPO-5.

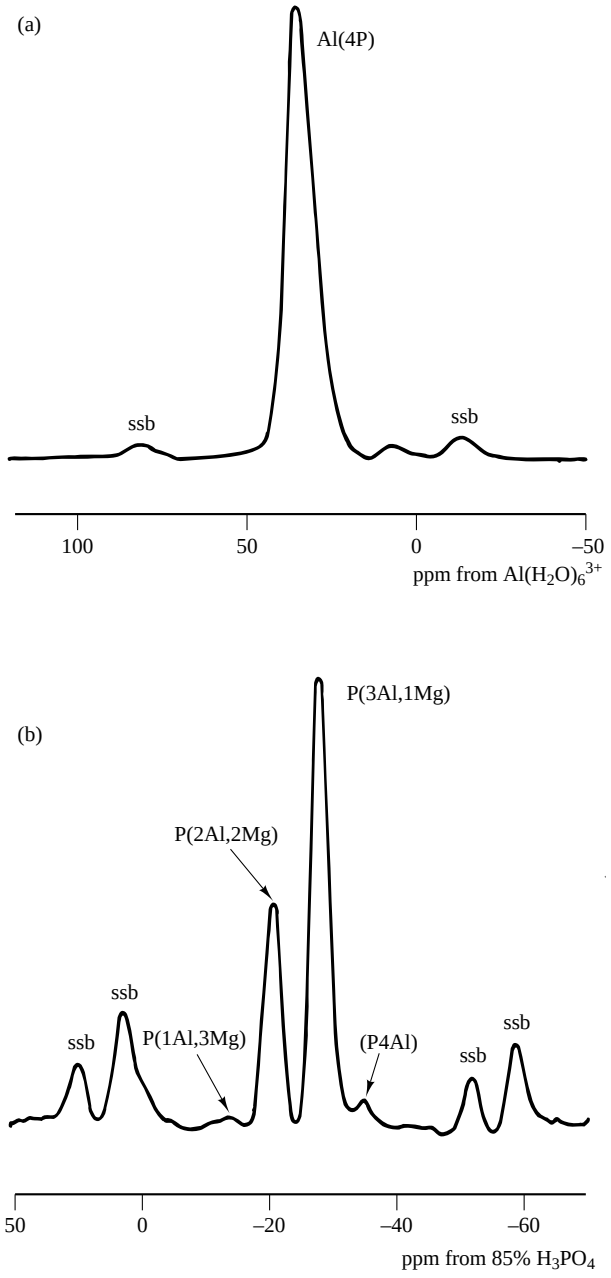

Figure 21 (a) ^{27}Al and (b) ^{31}P MAS NMR spectra of 'as-prepared' MgAPO-20[71]

16 ^{2}H NMR STUDIES OF MOTION IN MOLECULAR SIEVES

Since the quadrupolar interactions of ^{2}H are sensitive to molecular motion, the nucleus is useful for the study of molecular dynamics over a wide range of frequencies. Variable temperature studies of small organic molecules adsorbed on a series of zeolites[72] provide information on the filling of the intracrystalline space, the motion of the adsorbed species and site-selective adsorption. The ^{2}H spectra of deuterated *p*-xylenes $CH_3C_6D_4CH_3$ and $CD_3C_6H_4CD_3$ on zeolite Na-ZSM-5 in terms of possible dynamic states and sorption sites of the guest molecules identify five dynamic states, the relative populations varying with the level of loading and the temperature.[73] ^{2}H NMR results on *p*-xylene-d_6, toluene-d_3 and benzene-d_6 adsorbed on H-ZSM-5,[74] as well as on mono-, di-, and trimethylamine on zeolites ZK-5 and Y[75] yield a wealth of dynamic information.

Examination of the dynamic behavior of water in the channels of VPI-5 leads to a motional model which applies in the temperature range 225–348 K.[76,77] There are at least two sites for the intracrystalline water: one is bound to framework aluminum, and undergoes rotational motion about the $Al-OH_2$ bond, the other is a free site within the VPI-5 channels. The motion in this site is approximately isotropic, and the tumbling rate increases with temperature. The dynamic behavior of water in the temperature range 261–297 K is rather unexpected.

Multiple quantum (MQ) NMR, a 'spin counting' tool for homonuclear spin clusters,[78] is also suitable for the study of species adsorbed in molecular sieves.[79,80] Nuclear spins are forced to act collectively via their dipolar couplings, and the resulting multiple quantum coherences are detected after conversion into observable single quantum coherences. If the system constitutes a collection of isolated clusters, the multiple quantum count reaches a plateau corresponding to the number of spins in the cluster. Figure 22 shows the results of ^{1}H MQ NMR experiments for hexamethylbenzene, a molecule containing 18 hydrogen atoms, adsorbed on zeolite Na-Y.[79] At lower loadings the plateau corresponds to about

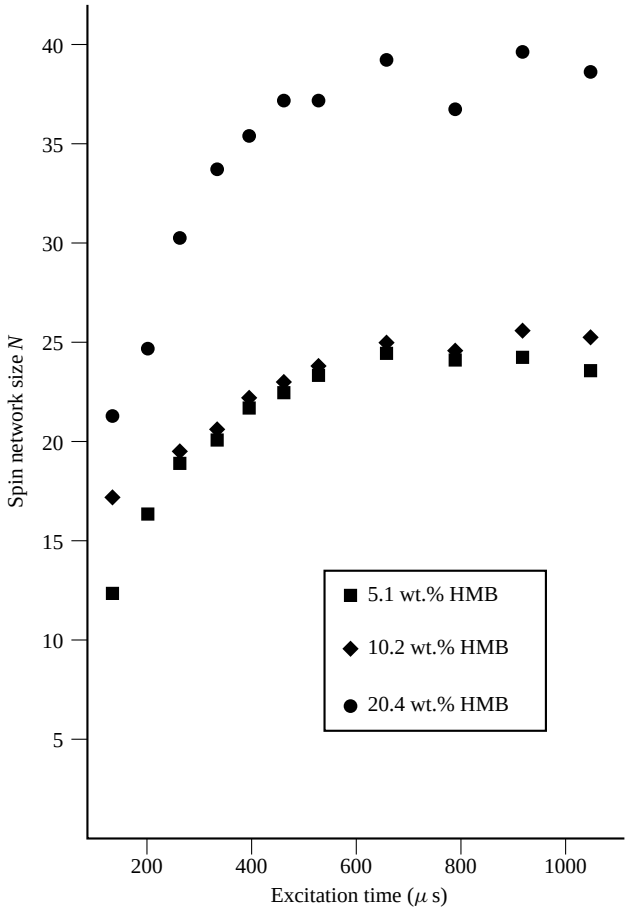

Figure 22 Results of ^{1}H MQ NMR experiments for hexamethylbenzene adsorbed at 573 K on dehydrated zeolite Na-Y[79]

one hexamethylbenzene molecule per supercage, and at higher loading to two molecules per supercage.

17 RELATED ARTICLES

Brønsted Acidity of Solids; Cross Polarization in Rotating Solids: Spin-1/2 Nuclei; Magic Angle Spinning; Nutation Spectroscopy of Quadrupolar Nuclei; Quadrupolar Nuclei in Solids; Reactions in Zeolites; Silicon-29 NMR of Solid Silicates.

18 REFERENCES

1. G. Engelhardt and D. Michel, *High-Resolution Solid-State NMR of Silicates and Zeolites*, Wiley, Chichester, 1987.
2. J. Klinowski, *Chem. Rev.*, 1991, **91**, 1459.
3. C. A. Fyfe, Y. Feng, H. Grondey, G. T. Kokotailo, and H. Gies, *Chem. Rev.*, 1991, **91**, 1525.
4. A. Fr. Cronstedt, *Kongl. Svenska Vetenskaps Acad. Handlingar*, 1756, **17**, 120.
5. W. Loewenstein, *Am. Mineral.*, 1954, **39**, 92.
6. W. M. Meier and D. H. Olson, *Atlas of Zeolite Structure Types*, Butterworth, Sevenoaks, 1992.
7. D. W. Breck, *Zeolite Molecular Sieves: Structure, Chemistry and Use*, Wiley, London, 1974.
8. R. M. Barrer, *Zeolites and Clay Minerals as Sorbents and Molecular Sieves*, Academic, London, 1978.
9. R. M. Barrer, *Hydrothermal Chemistry of Zeolites*, Academic, London, 1982.
10. R. Szostak, *Molecular Sieves: Principles of Synthesis and Identification*, Van Nostrand Reinhold, New York, 1989.
11. P. B. Weisz and V. J. Frilette, *J. Phys. Chem.*, 1960, **64**, 382.
12. R. J. Argauer and G. R. Landolt, US Patent 3 702 886 1972.
13. E. Lippmaa, M. Mägi, A. Samoson, G. Engelhardt, and A.-R. Grimmer, *J. Am. Chem. Soc.*, 1980, **102**, 4889.
14. G. Engelhardt, U. Lohse, E. Lippmaa, M. Tarmak, and M. Mägi, *Z. Anorg. Allg. Chem.*, 1981, **482**, 49.
15. J. Klinowski, S. Ramdas, J. M. Thomas, C. A. Fyfe, and J. S. Hartman, *J. Chem. Soc., Faraday Trans. II*, 1982, **78**, 1025.
16. M. T. Melchior, D. E. W. Vaughan, and A. J. Jacobson, *J. Am. Chem. Soc.*, 1982, **104**, 4859.
17. C. A. Fyfe, G. C. Gobbi, J. Klinowski, J. M. Thomas, and S. Ramdas, *Nature*, 1982, **296**, 530.
18. C. A. Fyfe, H. Grondey, Y. Feng, and G. T. Kokotailo, *J. Am. Chem. Soc.*, 1990, **112**, 8812; C. A. Fyfe, Y. Feng, H. Gies, H. Grondey, and G. T. Kokotailo, *Chem. Phys. Lett.*, 1990, **173**, 211; C. A. Fyfe, Y. Feng, H. Grondey, and G. T. Kokotailo, *J. Chem. Soc., Chem. Commun.*, 1990, 1224.
19. J. Klinowski, T. A. Carpenter, and L. F. Gladden, *Zeolites*, 1987, **7**, 73.
20. H. Strobl, C. A. Fyfe, G. T. Kokotailo, and C. T. Pasztor, *J. Am. Chem. Soc.*, 1987, **109**, 4733.
21. G. W. West, *Aust. J. Chem.*, 1984, **37**, 455.
22. J. M. Thomas, J. Klinowski, S. Ramdas, B. K. Hunter, and D. T. B. Tennakoon, *Chem. Phys. Lett.*, 1983, **102**, 158.
23. C. A. Fyfe, G. J. Kennedy, G. T. Kokotailo, and C. T. DeSchutter, *J. Chem. Soc., Chem. Commun.*, 1984, 1093.
24. J. V. Smith and C. S. Blackwell, *Nature*, 1983, **303**, 223.
25. R. Radeglia and G. Engelhardt, *Chem. Phys. Lett.*, 1985, **114**, 28.
26. S. Ramdas and J. Klinowski, *Nature*, 1984, **308**, 521.
27. P. J. Barrie and J. Klinowski, *Prog. NMR Spectrosc.*, 1992, **24**, 91.
28. C. A. Fyfe, H. Gies, and Y. Feng, *J. Am. Chem. Soc.*, 1989, **111**, 7702.
29. W. Kolodziejski, P. J. Barrie, H. He, and J. Klinowski, *J. Chem. Soc., Chem. Commun.*, 1991, 961.
30. J. Klinowski, J. M. Thomas, C. A. Fyfe, and G. C. Gobbi, *Nature*, 1982, **296**, 533.
31. I. E. Maxwell, W. A. van Erp, G. R. Hays, T. Couperus, R. Huis, and A. D. H. Clague, *J. Chem. Soc., Chem. Commun.*, 1982, 523.
32. G. Engelhardt, U. Lohse, A. Samoson, M. Mägi, M. Tarmak, and E. Lippmaa, *Zeolites*, 1982, **2**, 59.
33. L. Kellberg, M. Linsten, and H. J. Jakobsen, *Chem. Phys. Lett.*, 1991, **182**, 120.
34. H. Hamdan, B. Sulikowski, and J. Klinowski, *J. Phys. Chem.*, 1989, **93**, 350.
35. A. Samoson, E. Lippmaa, G. Engelhardt, U. Lohse, and H.-G. Jerschkewitz, *Chem. Phys. Lett.*, 1987, **134**, 589.
36. G. A. H. Tijink, R. Janssen, and W. S. Veeman, *J. Am. Chem. Soc.*, 1987, **109**, 7301.
37. J. H. Lunsford, W. P. Rothwell, and W. Shen, *J. Am. Chem. Soc.*, 1985, **107**, 1540.
38. J. M. Thomas, J. Klinowski, C. A. Fyfe, G. C. Gobbi, S. Ramdas, and M. W. Anderson, *ACS Symp. Ser.*, 1983, **218**, 159.
39. H. Kessler, J. M. Chézeau, J. L. Guth, H. Strub, and G. Coudurier, *Zeolites*, 1987, **7**, 360.
40. K. F. M. G. J. Scholle and W. S. Veeman, *Zeolites*, 1985, **5**, 118.
41. G. L. Turner, K. A. Smith, R. J. Kirkpatrick, and E. Oldfield, *J. Magn. Reson.*, 1986, **67**, 544.
42. M. W. Anderson, P. J. Barrie, and J. Klinowski, *J. Phys. Chem.*, 1991, **95**, 235.
43. M. W. Anderson and J. Klinowski, *Nature*, 1989, **339**, 200; *J. Am. Chem. Soc.*, 1990, **112**, 10.
44. M. W. Anderson and J. Klinowski, *Chem. Phys. Lett.*, 1990, **172**, 275.
45. S. T. Wilson, B. M. Lok, and E. M. Flanigen, US Patent 4 310 440 1982.
46. S. T. Wilson, B. M. Lok, C. A. Messina, T. R. Cannan, and E. M. Flanigen, *J. Am. Chem. Soc.*, 1982, **104**, 1146.
47. B. M. Lok, C. A. Messina, R. L. Patton, R. T. Gajek, T. R. Cannan, and E. M. Flanigen, US Patent 4 440 871, 1984.
48. S. T. Wilson and E. M. Flanigen, European Patent Application 0 132 708 1985.
49. E. M. Flanigen, B. M. Lok, R. L. Patton, and S. T. Wilson, *Pure Appl. Chem.*, 1986, **58**, 1351.
50. B. M. Lok, B. K. Marcus, L. D. Vail, E. M. Flanigen, R. L. Patton, and S. T. Wilson, European Patent Application 0 159 624, 1985.
51. B. M. Lok, B. K. Marcus, and E. M. Flanigen, European Patent Application 0 158 350, 1985.
52. R. Jelinek, B. F. Chmelka, Y. Wu, A. Pines, P. J. Grandinetti, P. J. Barrie, and J. Klinowski, *J. Am. Chem. Soc.*, 1991, **113**, 4097.
53. P. J. Barrie, *Adv. Spectrosc.*, 1993, **22**, 151.
54. C. S. Blackwell and R. L. Patton, *J. Phys. Chem.*, 1984, **88**, 6135.
55. D. Müeller, E. Jahn, B. Fahlke, G. Ladwig, and U. Haubenreisser, *Zeolites*, 1985, **5**, 53.
56. A. Samoson, E. Lippmaa, and A. Pines, *Mol. Phys.*, 1988, **65**, 1013.
57. P. J. Barrie, M. E. Smith, and J. Klinowski, *Chem. Phys. Lett.*, 1991, **180**, 6.

58. J. P. van Braam Houckgeest, B. Kraushaar-Czarnetzki, R. J. Dogterom, and A. de Groot, *J. Chem. Soc., Chem. Commun.*, **1991**, 666.
59. J. Rocha, W. Kolodziejski, H. He, and J. Klinowski, *J. Am. Chem. Soc.*, 1992, **114**, 4884.
60. W. Kolodziejski, H. He, and J. Klinowski, *Chem. Phys. Lett.*, 1992, **191**, 117.
61. Y. Wu, B. F. Chmelka, A. Pines, M. E. Davis, P. J. Grobet, and P. A. Jacobs, *Nature*, 1990, **346**, 550.
62. E. R. H. van Eck and W. S. Veeman, *Solid State NMR*, 1992, **1**, 1.
63. C. A. Fyfe, K. T. Mueller, H. Grondey, and K. C. Wong-Moon, *Chem. Phys. Lett.*, 1992, **199**, 198.
64. M. Stöcker, D. Akporiaye, and K.-P. Lillerud, *Appl. Catal.*, 1991, **69**, L7.
65. D. Müller, E. Jahn, G. Ladwig, and U. Haubenreisser, *Chem. Phys. Lett.*, 1984, **109**, 332.
66. G. Engelhardt, *Stud. Surf. Sci. Catal.*, 1989, **52**, 151.
67. I. P. Appleyard, R. K. Harris, and F. R. Fitch, *Chem. Lett.*, **1985**, 1747.
68. J. A. Martens, C. Janssens, P. J. Grobet, H. K. Beyer, and P. A. Jacobs, *Stud. Surf. Sci. Catal.*, 1989, **49**, 215.
69. M. W. Anderson, B. Sulikowski, P. J. Barrie, and J. Klinowski, *J. Phys. Chem.*, 1990, **94**, 2730.
70. B. Zibrowius, E. Löffler, and M. Hunger, *Zeolites*, 1992, **12**, 167.
71. P. J. Barrie and J. Klinowski, *J. Phys. Chem.*, 1989, **93**, 5972.
72. R. R. Eckman and A. J. Vega, *J. Phys. Chem.*, 1986, **90**, 4679.
73. I. Kustanovich, D. Fraenkel, Z. Luz, S. Vega, and H. Zimmermann, *J. Phys. Chem.*, 1988, **92**, 4134.
74. I. Kustanovich, H. M. Vieth, Z. Luz, and S. Vega, *J. Phys. Chem.*, 1989, **93**, 7427.
75. I. Kustanovich, Z. Luz, S. Vega, and A. L. Vega, *J. Phys. Chem.*, 1990, **94**, 3138.
76. D. Goldfarb, H.-X. Li, and M. E. Davis, *J. Am. Chem. Soc.*, 1992, **114**, 3690.
77. M. J. Duer, H. He, W. Kolodziejski, and J. Klinowski, *J. Phys. Chem.*, 1994, **98**, 1198.
78. R. Ryoo, S.-B. Liu, L. C. de Menorval, K. Takegoshi, B. Chmelka, M. Trecoske, and A. Pines, *J. Phys. Chem.*, 1987, **91**, 6575.
79. B. F. Chmelka, J. G. Pearson, S.-B. Liu, R. Ryoo, L. C. de Menorval, and A. Pines, *J. Phys. Chem.*, 1991, **95**, 303.
80. J. Rocha, S. W. Carr, and J. Klinowski, *Chem. Phys. Lett.*, 1991, **187**, 401.

Biographical Sketch

Jacek Klinowski. *b* 1943. M.Sc., 1965, Dr. Rer. Nat., 1968, Jagiellonian University, Kraków (Cracow), Poland, Ph.D., University of London, 1973, Diploma of Imperial College, 1973, M.A., University of Cambridge, 1988. Assistant Director of Research, University of Cambridge. Approx. 280 publications. Current research specialties: quadrupolar nuclei, two-dimensional NMR of novel materials.

Reactions in Zeolites

Tom M. Apple

Rensselaer Polytechnic Institute, Troy, NY, USA

1	Introduction	1
2	Reactions of Olefins	1
3	Reactions of Alcohols	3
4	Coking	6
5	Related Articles	6
6	References	6

1 INTRODUCTION

Zeolites are crystalline aluminosilicates composed of tetrahedra of oxygen anions which surround either a Si^{4+} or Al^{3+} cation. These tetrahedra are arranged such that each oxygen is shared by a neighboring aluminum or silicon atom. Due to an overall stoichiometry of two oxygen anions per tetrahedral center, a net charge of -1 accrues for each aluminum in the zeolite lattice. This negative charge is compensated for by a cation, most commonly a proton or a metal ion of Group IA or IIA. The nature of the cation influences the strength of the acid/base properties of the zeolite.

A great deal of the interest in zeolites stems from the strong Brønsted acidity of the hydrogen forms. Two very important processes are currently carried out over acidic zeolites, the cracking of petroleum and the conversion of methanol to gasolines (MTG process). Petroleum cracking is carried out over hydrogen forms of the faujasite zeolite Y, a medium-pore zeolite comprised of cages with a 1300 pm diameter. Access to these cages is provided by tetrahedrally arranged windows having diameters of 740 pm. Much of the NMR work dealing with the chemistry of olefins is, in part, motivated by the need for a better understanding of the mechanisms of petroleum cracking. The MTG process provides an alternative source of gasoline from methanol, which can be obtained from synthesis gas, itself a product of coal gasification. The MTG process is a relatively recent discovery.[1,2] It is carried out over the acidic form of the zeolite ZSM-5, a pentasil zeolite having two types of slightly elliptical intersecting channels, one straight and the other sinusoidal. The channel cross-sections are 530 pm by 560 pm and 510 pm by 550 pm respectively. Where the channels intersect a larger void region results.

While both of the above catalytic processes rely on the acidic nature of the zeolites involved, they are also facilitated by the molecular sieving properties of the zeolites. The size and shape of the channels and cages leads to several types of shape selectivity, reactant selectivity, product selectivity, and selectivity caused by restriction at the active site of catalysis.

Most NMR studies of reactions in zeolites have involved the reactions of olefins or alcohols. A prime concern has been the manner in which the acid (or base) properties of the zeolites affect the intermediates and products of these reactions. Shape-selective aspects of the catalysis, particularly those relating to the MTG process, have also been intensely studied by NMR. With time, olefin and alcohol reactions are accompanied by coking of the catalyst. The formation of coke deposits during reaction has been the focus of several NMR studies. This review will focus primarily on these areas. NMR studies dealing strictly with adsorption into zeolites will not be addressed in this article.

2 REACTIONS OF OLEFINS

While many techniques can be applied to study product distributions over catalysts, very few have the capability of probing the chemistry within a zeolite catalyst. Such internal monitoring provides direct evidence for shape selectivity as well as information on the nature of the adsorbed intermediates in a chemical process. NMR is becoming a very powerful tool for obtaining this type of information.

One of the earliest studies of olefin reactions in zeolites involved low-resolution ^{13}C NMR spectra of ethylene reacting over H–ZSM-5.[3] At room temperature immobile polymeric paraffins were evident. When water was added, and the sample heated to 573 K, lighter olefins and paraffins were observed as a product of cracking of the polymeric material.

Van den Berg et al.[4] applied ^{13}C NMR to the study of a number of adsorbed olefins on H–ZSM-5. These authors adsorbed ethylene, propene, isobutene, and 2-methyl-1-butene at room temperature. The ^{13}C NMR spectra revealed that at 300 K a majority of linear oligomers were formed over the catalyst for all of the adsorbates studied. The average chain length decreased in the series $C_2H_4 \gg C_3H_6 > i\text{-}C_4H_8 >$ 2-methyl-1-butene. Some small amounts of branched hydrocarbons were observed with ethylene and isobutene. When ethylene was adsorbed into H–ZSM-5 at 373 K a significant amount of branching occurred and the average chain length decreased. When this reaction was performed over H–mordenite the products were highly branched. The formation of primarily linear chains in H–ZSM-5 was attributed to restrictions due to the pore dimensions. The authors proposed that branched oligomers originally formed at channel intersections and were then linearized through isomerization reactions. The larger pores of the mordenite allowed for branched species.

Zardkoohi et al.[5] studied the reaction of propene labeled with ^{13}C at the 2-site over both normal and ultrastable (Si/Al = 4) H–Y zeolite. In this work it was assumed that carbons scrambled via a cyclopropane intermediate prior to oligomerization. Cross polarization with magic angle spinning (CP MAS) was used to acquire the spectra. A peak at 250 ppm was assigned to formation of a carbenium ion $CH_3C^+HCH_3$. Olah's work[6] with superacids had shown that stationary secondary carbocations should resonate between 300 and 330 ppm. The carbenium ion proposed in this work interacts with zeolitic oxygen, and, because of the typical 80 ppm shift to low frequency (upfield) of oxygenated species such as RC^+OH relative to RC^+R moieties, the shift of 250 ppm was deemed a reasonable one for such a species. The methyl groups associated with the isopropyl cation should resonate at 48 ppm, but this area was obscured by peaks due to oligomers. The authors proposed the following mechanism (Scheme 1):

A peak at 160 ppm was assigned to a dynamic equilibrium between carbons in an ethyl isopropyl carbenium ion and a methyl isobutyl carbenium ion. This resonance position is an

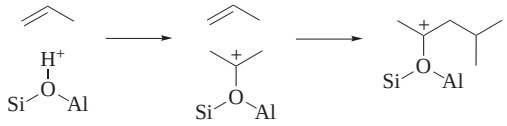

Scheme 1

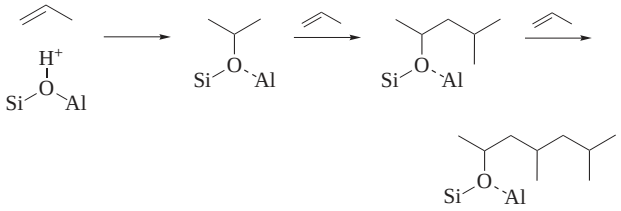

Scheme 2

average of a resonance at 330 ppm due to the carbenium ion and one at 60 ppm due to the methylene. The average value of 195 is consistent with the observed value of 160 ppm if one again considers the low-frequency shift induced by the framework oxygen. A peak also appeared at 70 ppm which was assigned to the carbon at the β position relative to the carbenium center.

Intense peaks at 40 ppm and 30 ppm were assigned to methylene and methyl groups respectively from oligomeric species and carbocations. The intensity of these peaks was higher in H–Y than in the ultrastable H–Y sample due to the blocking of pores by detrital aluminum species in the ultrastable H–Y.

In later work by this group[7] an apparatus called CAVERN (cryogenic adsorption vessel enabling rotor nestling) was employed for adsorption studies. Propene samples labeled at the 1-, 2-, and 3-positions gave different spectra on H–Y. As a result, label scrambling was not present as had been presumed in their previous study. When [2-^{13}C]propene was adsorbed, signals were observed at 250, 143, and 87 ppm. Both single pulse Bloch decays and CP MAS spectra were employed in this study. Signals in the aliphatic region and those of unreacted propene had T_1 values of approximately 80 ms, while the peak at 87 ppm had a T_1 of 2–3 s. The short T_1 values indicated mobile species while the longer T_1 was indicative of a more strongly bound species. In experiments of this type Bloch decays are more quantitative, since they do not depend upon efficiency of magnetization transfer between carbons and protons. In the Bloch decays the size of the signal at 87 ppm was greatly reduced, comprising only about 2% of the spectral intensity. Carbon-13 $T_{1\rho}$ values were equal to 5–10 ms for all species. The CAVERN was loaded and spectra were recorded at temperatures from 213 to 293 K. At 213 K very little propene had reacted. At 253 K the oligomer peak appeared. At 263 K about one-third of the propene had reacted and peaks at 87 and 140 ppm were now evident. At 273 K there was 70% conversion with increasing intensity at 87 and 140 ppm.

The peak at 87 ppm had been previously assigned to those carbons adjacent to the nonequilibrating carbenium ions, which resonated at 250 ppm. However, there was no peak observed at 250 ppm in this series of spectra; therefore, the assignment of the peak at 87 ppm to carbons adjacent to the cation had to be abandoned. A reasonable alternative explanation was to assign the resonance to an alkoxy (alkyl silyl ether) species bound to a zeolite lattice oxygen atom. The peak at 140 ppm was assigned to olefinic carbon atoms of oligomeric species. At room temperature there was complete conversion, and a peak at 250 ppm appeared, which was assigned to a carbocation. When 1-propene was used, two major changes were exhibited: no peak at 87 ppm was observed and, secondly, the aliphatic region extended further to low frequency (indicating a greater contribution of methyl groups). Thus, the carbon atoms in the 1-position ended up in more methyl groups than carbon atoms at the 2-position. No scrambling of label was observed. The authors proposed the following mechanism (Scheme 2) to explain these observations:

Upon adsorption, propene forms an alkoxy species. This is followed by Markovnikow addition of a second propene prior to cleavage of the alkoxy. A third propene adds, followed by cleavage, to form a disubstituted olefin. Probable rearrangement of the olefin to more stable olefins occurs in the acidic environment of the zeolite.

This mechanism relied heavily on the assignment of the peak at 87 ppm to the alkoxide. To support this assignment the authors noted that the intensity of this peak did not correlate at all with the peak at 250 ppm assigned to the carbocation. Also, upon exposure of the sample to moisture, there was a loss of intensity of the resonance at 87 ppm and formation of a peak at 67 ppm. A peak at 67 ppm is consistent with secondary ethers or alcohols having the hydroxyl group in the 2-position, but not from primary or tertiary alcohols. The expected product from the alkoxide would be an alcohol with the hydroxyl group in the 2-position. The peak at 67 ppm survived interrupted decoupling of 50 μs, while that at 87 ppm did not. This suggested that the species resonating at 87 ppm was an immobilized, protonated carbon. The peak at 87 ppm was never observed with 1- or 3-propene. This finding rules out a long-lived carbocation which would surely scramble. The shift of this peak was about 20 ppm to high frequency from that expected for an alkyl silyl ether. However the presence of a nearby Al atom and the incipient carbocation nature of the species may explain the high-frequency shift. Low-temperature experiments confirmed that propene itself was mobile in the zeolite at low temperatures and could diffuse to form alkoxy intermediates.

The assignment of the peak at 250 ppm to a nonequilibrating carbocation, is now believed to be incorrect. The interaction between the carbocation and the zeolitic oxygen atom is apparently so strong that an alkoxy is formed. For a long-lived carbocation to exist in the zeolite it cannot interact with an oxygen atom and must be stabilized in some way. The authors suggested that olefins are formed, and then undergo hydride abstraction and cyclization, as is observed in the conjunct polymerization of alkenes. In this process alkanes are formed at the expense of hydrogen from the olefins, which in turn are converted into alkyl cyclopentenyl cations. The proposed cations contain carbons that should resonate at 249 and 158 ppm.[8,9] If this assignment is correct there should be a correlation between intensity at 158 ppm and 250 ppm. Careful examination of their spectra show this to be the case. The peaks appear at a roughly 2:1 intensity ratio as expected. The same alkoxy intermediate was observed by Aronson et al.[10] (see below) upon adsorption of 2-methyl-2-propanol on HZSM-5.

Later work by the Haw group[11] involved studies of samples prepared at 298 K by adsorbing both 1- and 2-labeled propene. The samples were then heated in situ to 503 K. After heating, the low-frequency region showed many highly resolved resonances indicative of small mobile species. Resonance shifts and *J* couplings allowed the identification of isopentane, isobutane, 2,3-dimethylbutane, and propane. The high-temperature spectra of 1- and 2-labeled samples are identical, indicating scrambling of the labels. This is consistent with carbocation mechanisms proposed for high-temperature cracking reactions.[12] The hydrogen necessary for formation of the alkanes from the olefins comes about by coke formation. Coke is observed by CP MAS as a peak between 120 and 140 ppm.

The alkylation of isobutane with 1-butene in LaNaY zeolite was studied by ^{13}C CP MAS NMR.[13] During the initial feed, all of the butene was consumed and the products were comprised primarily of a mixture of isoalkanes. In the second stage the butene conversion dropped to about 40% and the product distribution changed drastically to isoalkenes, indicating that in the early portion of the reaction the isobutane was being alkylated by the olefin. In the latter stage, however, the olefin was oligomerizing. At higher temperatures the product distributions shifted to lower molecular weights as a result of more pronounced contributions from cracking reactions. Above 220 °C aromatics began to appear.

Butadiene reactions on H–Y and H–ZSM-5 were studied by ^{13}C MAS NMR.[14] Bloch decays were used to probe mobile species whereas CP MAS was used for immobile molecules. Butadiene oligomerizes by primarily 1,4-addition upon adsorption on H–ZSM-5. 1,4-Addition accounts for most of the oligomer in H–Y as well, although 1,2-addition was a minor contributor. As the reaction proceeded there was a loss of intensity in the olefinic region and a corresponding increase in the aliphatic region due to cyclization. These subsequent reactions were zeolite-dependent. In H–Y the linear product underwent cyclization to form fused rings, while isolated rings were formed in H–ZSM-5. Branching reactions and 1,2-enchainment resulted in oligomers with a large methyl group content in H–Y. The 1,4-addition reactions, followed by cyclization, result in pore blockage and catalyst deactivation. No reactive intermediates or carbenium ions were observed.

The Haw group[15] adsorbed acetylene on H–Y and HZSM-5 zeolite. At room temperature no reaction was observed. Upon heating to 473 K, however, two major resonances appeared under CP MAS conditions at 143 and 107 ppm, along with peaks from aliphatic and aromatic carbons (tar). The fact that these reactions were not occurring in the gas phase was confirmed by attempting the reaction over NaY. The authors suggested the species analogous to those observed by Chin and Ellis[16] on alumina (**1**). Reaction of this sample with water in

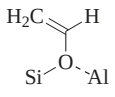

(1)

the atmosphere produced acetaldehyde. Further heating in atmosphere eventually resulted in acetic acid. Control experiments involving acetylene and water produced tars with a highly paraffinic nature. The hydrogen source for these tars appears to be water. In fact, the amount of tar formed could be correlated with the degree of hydration of the zeolite. Interrupted decoupling experiments at low and high temperature indicated that the adsorbed species probably undergoes rotation about its O–C bond at 298 K.

The reaction of ethylene over a series of cocation-exchanged Ru–Y zeolites was studied.[17] At room temperature ethylene was converted to ethane and butane on the timescale of days. 2-Butenes appear to be intermediates in the reaction. Coadsorption of hydrogen led to an increase in the initial rate, which was roughly first order with respect to hydrogen. The rate of reaction of ethylene was strongly dependent upon the cocation in the order Ru–H–Y > Ru–Ca–Y > Ru–NaY. At intermediate temperatures isomerization of butane to isobutane occurred presumably at acid sites. Above 623 K, carbon–carbon bond cleavage caused methane to be the only detectable product.

Methyl halides were found to convert to hydrocarbons over a large number of faujasite zeolites.[18] Upon adsorption of methyl iodide onto Cs–X a zeolite-bound methoxy species was formed. This species appears at 58 ppm. The assignment of this resonance was proven unequivocally by several NMR methods, including interrupted decoupling, slow MAS, and rotational resonance. Chemical verification was achieved by interacting the adsorbate with water to produce the corresponding alcohol. Ethyl iodide forms the corresponding framework-bound ethoxy species with resonances at 68 and 17 ppm. These peaks also passed all of the criteria for assignment to framework-bound species.

At higher temperatures, both the surface methoxy and the surface ethoxy groups were converted to ethylene, and subsequently to aliphatic moieties. Ethylene did not convert to aliphatic species in the absence of the alkyl iodides over these catalysts. Evidently this conversion of ethylene to aliphatics was catalyzed by HI which was released upon formation of the alkoxy from the alkyl halide.

Methyl chloride and methyl bromide also react in an analogous manner to methyl iodide; however, the concentration of methoxy groups and the reactivity to hydrocarbon synthesis was in the order $CH_3I > CH_3Br > CH_3Cl$. This order of reactivity is as expected for S_N2 reactions based upon the leaving group ability. One may consider the reaction of methyl halide with the zeolite as attack on the carbon by the nucleophilic oxygen atom of the zeolite lattice, resulting in displacement of the halogen. The basicity of a zeolite increases with the size of the cation. The activity of this reaction should, therefore, increase with increasing size of the cation.

The effect of cation nature on the reaction was investigated. Different cations affected both the activity and the selectivity of the catalysts. NaX was the most active, while K–X and Rb–X were less active than Cs–X. H–X was very unreactive, indicating that activity is not due to acidity. With the exception of NaX, the activities were in line with those predicted by consideration of zeolite basicity. Rb–X was unique in that it showed a high selectivity for olefin and aromatic products. Small shifts in the methyl resonance as a function of the cation were observed. These shifts correlated with activity of the catalyst: the higher the resonance frequency, the more active the catalyst. Cesium-133 NMR showed that the adsorbates interact with the cation sites and that this interaction may be significant in affecting catalyst activity. The framework also affected catalyst activity in the order Cs–X > Cs–Y > Cs–ZSM-5.

3 REACTIONS OF ALCOHOLS

NMR has been used extensively to investigate the mechanism of formation of the first carbon–carbon bond in the MTG process. Direct evidence for two types of shape selectivity have been revealed by NMR: product selectivity and active site selectivity.

A study of methanol and ethanol conversion over H–ZSM-5 was undertaken using ^{13}C NMR without MAS.[19] The NMR results were compared with those from gas chromatography. Below 250 °C there was nearly complete conversion of methanol to dimethyl ether. When the temperature was raised to 300 °C there was a loss of intensity in the ether range and an increase in $-CH_2-$ and $-CH_3$ resonances. With increasing temperature these peaks shifted to high frequency, indicative of formation of branched chains on aromatic residues. The aliphatic to aromatic ratio of the initially low-temperature adsorbed methanol was 5:1, while a fresh dose of methanol converted directly at 350 °C yielded a ratio of 2:1. It therefore appears that there is competition between aliphatic and aromatic product, rather than a sequential change from aliphatic to aromatic moieties.

Ethanol adsorption at 150 °C yielded diethyl ether. Between 150 and 250 °C an olefinic peak appeared and was assigned to ethylene. Above 250 °C the olefinic peak diminished and an aliphatic resonance formed between 14 and 23 ppm. No distinct aromatic peaks were visible. The authors proposed mechanisms involving carbenium ions.

Carbon-13 NMR studies of methanol on a germanic, near-faujasite zeolite[20] showed that methanol reversibly yielded dimethyl ether. Greater conversion occurred at higher temperatures. No other products were observed on the faujasite. Following prolonged heating at 300 °C, a broader resonance appeared underneath that for dimethyl ether (DME) near 60 ppm. This peak was attributed to surface methoxy formation. Peaks due to aldehydes were observed at 193 ppm during reaction of methanol on H–ZSM-5 in the presence of CO.[21] It was proposed that this signal derives from incorporation of CO via a carbenium ion mechanism.

Carbon-13 CP MAS NMR was used to study the carbonaceous residues formed in H–ZSM-5 and H–mordenite from methanol and ethylene.[22] Methanol on H–ZSM-5 yielded a broad distribution of aliphatics including propene, propane, *n*-butane, isobutane, and isopentane. In the aromatic region there was some evidence of benzene, toluene, and xylenes. Over mordenite a much narrower aliphatic product distribution was obtained: only propane, propene, and *n*-butane. The aromatic distribution was, however, broader and included fused aromatics. On both catalysts, surface methoxides were suggested as intermediates. Isoparaffins were more prevalent than linear ones on H–ZSM-5, while on mordenite isoparaffins and C_5-aliphatics were not seen. Instead, the larger pores of mordenite allowed conversion of C_4–C_6 olefins into aromatics by mechanisms similar to conjunct polymerization.

Ethylene formed linear chains on H–ZSM-5. The average chain length was 10–12 carbon atoms. Steam cracking of this sample resulted in a large number of C_5 and C_6 residues and some alkylation, as evidenced by the appearance of ethylbenzene. When an ethylene-loaded sample was heated to 573 K in the presence of water, products included the linear paraffins (propane and butane), branched paraffins (isobutane and isopentane), and aromatics (toluene, xylene, and ethylbenzene). Unlike in the steam-cracked catalyst, xylenes were quite abundant, indicating that they are formed by the conjunct polymerization of olefins.

Kotanigawa et al.[23] studied the adsorption and reaction of methanol on H–Y zeolite by ^{13}C NMR. At room temperature a signal from adsorbed methanol was observed at 48.9 ppm. When the sample was heated to 220 °C four peaks appeared, one of which was derived from the adsorbed methanol. A peak at 59.2 ppm was assigned to a surface methoxyl; however, later work by Anderson and Klinowski[24] suggests that this peak was probably due to DME. The two other resonances at 27.2 and 64.7 ppm were tentatively assigned to the methyl carbon of 2-propanol and carbons adjacent to oxygen (either the 2-carbon of 2-propanol or the carbon of a hydroxymethyl group) respectively. Higher temperatures produced surface alcohols as well as a resonance which these authors assigned to a surface epoxy based upon IR data. When 480 °C was reached, olefins were observed. Based upon these assignments the authors proposed that the formation of the first carbon–carbon bond involves a surface methoxyl reacting with a hydroxymethyl group via a carbenium ion intermediate.

Aronson et al.[10] studied the 1:1 adsorption complex of 2-methyl-2-propanol with a Brønsted site on H–ZSM-5. The 2-methylpropanol was labeled at the hydroxyl carbon. Under the conditions of the experiment the adsorbate was dehydrated and the water which was formed desorbed completely, as verified by temperature-programed description (TPD) and thermogravimetric analysis (TGA). Two broad features appeared in the Bloch decay ^{13}C spectra at 80 and 30 ppm in the ratio of 2:3. The peak at 30 ppm indicated that some additional reaction had occurred changing the hydroxyl carbon to an aliphatic one, probably through oligomerization. No peak in the area of 330 ppm was seen, thereby ruling out a carbenium ion resonating in the area reported by Olah.[6] Furthermore, no line shifts were evident with changes in temperature, thereby ruling out exchange. A small resonance at 123 ppm from carbon–carbon double bonds was observed. Heating of this sample to 373 K resulted in an increase in the intensity and complexity of the aliphatic region. There was a compensatory decrease in the intensity in the 80 ppm region associated with carbons attached to oxygen. Most of the oligomers were still attached to the zeolite in alkyl silyl ethers, since the intensity in the region above 100 ppm remained low. The peak near 80 ppm exhibited an axially symmetric powder pattern with $\sigma_{\parallel} = 93$ and $\sigma_{\perp} = 44$ ppm at 200 K. The isotropic shift was slightly to high frequency from that of the 72.6 ppm shift of the *tert*-butoxide group in bis[(2-ethylhexyl)oxy]di-*tert*-butoxysilane, but to low frequency from the *tert*-butoxide group attached to the more electropositive Ti atom in Ti(*t*-BuO)$_4$.[25] The authors presented a carbenium ion-mediated scheme for formation of some olefinic carbons as well as oligomers (Scheme 3).

The complexity of the spectra in the aliphatic region could not be explained by their scheme. In particular, the appearance of a well-resolved peak at 13 ppm indicates that the labeled carbon has been converted into methyl or methylene groups. This implies rearrangement of tertiary carbenium ions.

From a combination of their TPD–TGA, IR, and NMR work, a potential energy surface was constructed. Reaction proceeds by protonation of the alcohol to form the oxonium ion. This dehydrates to form the alkyl silyl ether via the

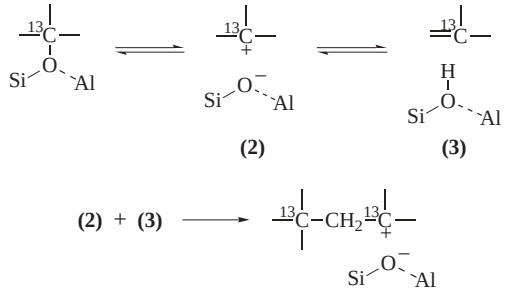

Scheme 3

carbenium ion intermediate. The reaction proceeds again through the carbenium ion to the olefin product.

Anderson and Klinowski[24,26] studied the adsorption and reaction of methanol in H−ZSM-5 zeolite. At room temperature a signal at 50 ppm was observed from adsorbed methanol. Higher pressures of methanol resulted in a second peak due to either vapor or methanol on the outer surfaces of the zeolite. Following heating at 150 °C for 5 or 20 min a resonance at 60 ppm attributable to dimethyl ether appeared. The authors showed via ^{1}H NMR that this occurs through interaction of the methanol with an acid site in the zeolite. The hydroxyl resonance was shifted to higher frequency by 7.9 ppm upon adsorption, due to formation of a methoxonium ion hydrogen bonded in the intracrystalline space. At larger coverages protonated clusters were formed.[27,28] The ratio of DME/MeOH was constant with time, indicating that an equilibrium was attained. After treatment of the methanol-loaded sample for longer than 20 min at 150 °C a new resonance appeared at 184 ppm which could be identified as CO. CO was also produced at 250 °C. The production of CO from DME by two different mechanisms has been reported.[29,30] Both mechanisms, however, involve formation of methane, which was not observed coincident with the formation of CO. CO is formed on ZSM-5 from methanol through a formaldehyde intermediate.[31]

After heating a methanol-treated sample at 250 °C for 54 min and then at 300 °C for 10 min, aliphatic resonances began to appear with a corresponding drop in the DME/MeOH ratio. It would seem that the higher hydrocarbons are either formed preferentially from DME and their formation occurs quicker than the reestablishment of equilibrium between DME and MeOH, or the equilibrium between DME and MeOH (which involves water) is affected by subsequent dehydration reactions. Further heating at this temperature caused complete conversion of methanol and DME to aliphatics and aromatics. Two narrow peaks due to mobile methane and cyclopropane were observed under Bloch decays, but not under CP. Despite spectral overlap, under MAS conditions a large number of products were readily identified, due to the multiplicity of resonances associated with most products. Because CO formed prior to hydrocarbon formation, and its resonant intensity decreased upon formation of hydrocarbon products, the authors suggested that CO was an intermediate in hydrocarbon formation. This was proposed to occur by hydrocarbonylation to ethanol at an iron impurity site, followed by dehydration of ethanol to ethylene. The authors were able to obtain ethylene as the primary olefinic product from an Fe^{3+}-exchanged catalyst in support of this suggestion. Haw's group[32] tested this hypothesis by carrying out the reaction of methanol over H−ZSM-5 in the presence of CO generated from formic acid. Carbon-13 from CO was not incorporated in the product hydrocarbon. CO also did not catalyze the reaction of methanol to hydrocarbon as had been suggested by Jackson and Bertsch.[33]

An examination of the aromatic region of the NMR spectrum following the 300 °C treatment revealed that the distribution of the adsorbed species during methanol conversion was very different from the product distribution. Product distribution data suggested that primarily *m*- and *p*-xylene, toluene and 1,2,4-trimethylbenzene would be found. The major species found by NMR in the adsorbed phase were, however, *o*- and *p*-xylene and 1,2,4,5-tetramethylbenzene, with smaller amounts of other species including some trimethylbenzenes. These trimethyl species were found in their equilibrium distribution[34] in the adsorbed phase, but the larger 1,2,3- and 1,3,5-forms were not found in the product distribution. This was a clearcut example of product selectivity. In ZSM-5 the channel dimensions are 560 × 530 pm; however, more space is available at channel intersections. The larger 1,2,3- and 1,2,5-forms must isomerize to the smaller 1,2,4-form in order to diffuse out of the zeolite. All four tetramethylbenzenes were observed in the catalyst, having been formed at channel intersections. They were not found in the product, again showing product selectivity. The tetramethylbenzenes were not formed in their equilibrium distributions, showing active site selectivity.

At 300 °C signals from the aliphatic region came predominantly from isobutane and propane. Large signals were also observed, however, from *n*-butane, *n*-hexane, *n*-heptane, isopentane, and methane. At 370 °C the number of straight-chain alkanes decreased and larger numbers of branched alkanes were evident. At higher temperatures many larger species were observed in the product distributions due to the larger channel dimensions which allowed diffusion out of the catalyst.

This group also studied methanol adsorption on SAPO-5 and H−ZSM-5 in order to determine the nature of the strong bonding of methanol to Brønsted sites in the zeolites and the conversion of methanol to DME.[35] On SAPO-5 at room temperature only mobile methanol was observed. Heating to 150 °C resulted in conversion of about one-third of the methanol to dimethyl ether which was still mobile. Further heating at 250 °C produced two species: methanol and another species exhibiting chemical shift anisotropy due to reduced mobility. The chemical shift suggested either a surface methoxyl or possibly immobile dimethyl ether.[36] Heating the sample above 300 °C produced mobile alkenes and aliphatic compounds. By contrast in H−ZSM-5 methanol adsorbed as methanol, but hydrogen bonded to a Brønsted site. The resonance shift remained at 50 ppm in the ^{13}C spectra, but the ^{1}H spectra revealed a hydroxyl resonance near 9.4 ppm. When one methanol was adsorbed per Brønsted site there was considerable line broadening indicating strong bonding. The shift indicated that methanol was still intact. Thus, in H−ZSM-5 methanol strongly adsorbs by hydrogen bonding prior to dehydration, while on SAPO-5 the dehydration precedes the strong binding to the surface. This strong bonding pursuant to dehydration is followed by formation of the C−C bond.

Two-dimensional (2D) *J*-resolved spectroscopy was used to unravel the product distribution of a sample of H−ZSM-5 reacted with methanol for 30 min at 300 °C.[37] From the 2D spectrum the authors were able to show that the resonance at 22 ppm had a contribution from the methyl resonance of

isopentane. In later work using 2D spin diffusion NMR[38] they showed that this resonance also contained intensity from carbon atoms adjacent to methyl groups in *n*-hexane and *n*-heptane. This work showed the power of 2D techniques in the solid to resolve the many lines in the aliphatic regions of a working MTG catalyst.

Methanol conversion was also studied over SAPO-34.[39] The authors discovered an interesting shape selectivity in the chabazite-like structure. At 300 °C treatments many aliphatics up to C_6 were in abundance on the catalyst. This included branched hydrocarbons. Only C_3 and smaller species were present in anything but trace amounts in the product stream, however. Due to the small 380 pm windows to the cages, two types of shape selectivity occur. C_1 and C_2 molecules have unrestricted diffusion. C_3 species are somewhat restricted by occluded hydrocarbons, and C_4 and larger species are diffusion-restricted.

The question of the formation of the first carbon–carbon bond in the MTG process has been a source of great interest. In order to test the hypothesis that the trimethoxonium ion (derived from dimethyl ether) may play a role, trimethyloxonium salts were cation-exchanged into ZSM-5 and the ^{13}C NMR spectrum was recorded under CP MAS conditions as a function of time.[40] The methyl groups of the trimethyloxonium ion resonated at 80 ppm. This signal gradually converted to two overlapping signals at 60 ppm which the authors attributed to surface methoxyl and dimethyl ether. Munson and Haw[41] adsorbed DME on H–ZSM-5. At 293 K a resonance appeared at 80 ppm which could be assigned to the trimethoxonium ion. This species was generated from two dimethyl ether molecules and formed in a 1:1 ratio with methanol. This species could not be seen in methanol adsorption studies due to the shift in the equilibrium toward DME. At high temperatures DME yielded similar products as adsorbed methanol. The observation of this species in H–ZSM-5, while not proving that it is a reaction intermediate, lends some credibility to the Chang mechanism involving deprotonation of the trimethoxonium ion to form the methylenedimethyloxonium ylide.[42]

A comparison of methanol conversion on straight channel offretites and increasingly tortuous erionite-like zeolites was undertaken.[43] The most fault-free (least tortuous) zeolite showed a proclivity for formation of long-chain polymeric hydrocarbons, which were highly branched. A chemical shift at 46 ppm due to tertiary carbons, and a peak at 58 ppm due to quaternary carbons were seen. Formation of these polymeric species was inhibited by the presence of only a few blockages in the channel structure. Channel tortuosity is, therefore, necessary to maintain selectivity to low olefins.

4 COKING

Richardson and Haw[44] coked samples with a single feed of butadiene at six different temperatures for 1 h. Carbon-13 NMR spectra generally showed two peaks, one due to aliphatics and one due to aromatic and olefinic resonances. The relative size of the aromatic peak increased drastically with treatment temperature. Over 90% of the NMR intensity observed from samples treated above 400 °C was attributed to aromatic species. A sample was heated under butadiene at 150 °C and then subjected to chemical extraction techniques. Virtually all of the coke was unrecoverable, indicating that the coke comprised large, insoluble, high molecular weight species. Interrupted decoupling experiments confirmed that few carbons were protonated. This result suggests that cross polarization may not be quantitative. Spin counting experiments confirmed that at 150 °C about 80% of the carbon was observable, but that at higher temperatures a significant fraction of the carbon in the coked samples was unobservable.

A number of rare-earth-exchanged zeolites were investigated by CP MAS NMR and relaxation analysis.[45] Cross polarization was not greatly affected by diamagnetic La^{3+} or those ions having short electron T_1 values, including Nd^{3+} and Pr^{3+}. For Gd^{3+}- and Dy^{3+}-exchanged zeolites the ^1H $T_{1\rho}$ was drastically decreased, allowing insufficient time for cross polarization. This prevents quantifying coking reactions in these zeolites by CP MAS NMR. The effect was localized. As a result, dilution of the ion concentration in the zeolite allowed spectra to be obtained.

5 RELATED ARTICLES

Adsorbed Species: Spectroscopy and Dynamics; Brønsted Acidity of Solids; Intercalation Compounds.

6 REFERENCES

1. S. Meisel, J. McCullough, C. Lechtaler, and P. Weisz, *Chem. Tech.*, 1976, **6**, 86.
2. W. Kaeding and S. Butter, *J. Catal.*, 1980, **61**, 155.
3. E. Derouane, J. Gilson, and J. Nagy, *J. Mol. Catal.*, 1981, **10**, 331.
4. J. van den Berg, J. Wolthuizen, A. Clague, G. Hays, R. Huis, and J. van Hooff, *J. Catal.*, 1983, **80**, 130.
5. M. Zardkoohi, J. Haw, and J. Lunsford, *J. Am. Chem. Soc.*, 1987, **109**, 5278.
6. G. Olah and D. Donovan, *J. Am. Chem. Soc.*, 1977, **99**, 5026.
7. J. Haw, B. Richardson, I. Oshiro, N. Lazo, and J. Speed, *J. Am. Chem. Soc.*, 1989, **111**, 2052.
8. N. Deno, H. Richey, J. Hodge, and M. Wisotsky, *J. Am. Chem. Soc.*, 1962, **84**, 1498.
9. G. Olah and G. Liang, *J. Am. Chem. Soc.*, 1972, **94**, 6434.
10. M. Aronson, R. Gorte, W. Farneth, and D. White, *J. Am. Chem. Soc.*, 1989, **111**, 840.
11. J. White, N. Lazo, B. Richardson, and J. Haw, *J. Catal.*, 1990, **125**, 260.
12. B. Gates, J. Katzer, and G. Schuit, in *Chemistry of Catalytic Processes*, McGraw-Hill, New York, 1979.
13. J. Weitkamp and S. Maixner, *Zeolites*, 1987, **7**, 6.
14. B. Richardson, N. Lazo, P. Schettler, J. White, and J. Haw, *J. Am. Chem. Soc.*, 1990, **112**, 2886.
15. N. Lazo, J. White, E. Munson, M. Lambregts, and J. Haw, *J. Am. Chem. Soc.*, 1990, **112**, 4050.
16. Y. Chin and P. Ellis, *J. Am. Chem. Soc.*, 1989, **111**, 7653.
17. Y. Kye, S. Wu, and T. Apple, *J. Phys. Chem.*, 1992, **96**, 2632.
18. D. Murray, J. Chang, and J. Haw, *J. Am. Chem. Soc.*, 1993, **115**, 4732.
19. E. Derouane, J. Nagy, P. Dejaifve, J. van Hooff, B. Spekman, J. Vedrine, and C. Naccache, *J. Catal.*, 1978, **53**, 40.
20. E. Derouane, P. Dejaifve, and J. Nagy, *J. Mol. Catal.*, 1977, **3**, 453.

21. J. Nagy, J.-P. Gilson, and E. Derouane, *J. Mol. Catal.*, 1979, **5**, 393.
22. E. Derouane, J.-P. Gilson, and J. Nagy, *Zeolites*, 1982, **2**, 42.
23. T. Kotanigawa, K. Shimokawa, and T. Yoshida, *J. Chem. Soc., Chem. Commun.*, 1982, 1185.
24. M. Anderson and J. Klinowski, *J. Am. Chem. Soc.*, 1990, **112**, 10.
25. Sadtler Indices of ^{13}C NMR Data, No. 2073, Sadtler, Philadelphia, PA, 1985.
26. M. Anderson and J. Klinowski, *Nature (London)*, 1989, **339**, 200.
27. G. Mirth, J. Lercher, M. Anderson, and J. Klinowski, *J. Chem. Soc., Faraday Trans. 1*, 1990, **86**, 3039.
28. M. Anderson, P. Barrie, and J. Klinowski, *J. Phys. Chem.*, 1991, **95**, 238.
29. C. Chu and C. Chang, *J. Catal.*, 1984, **86**, 297.
30. G. Olah, H. Doggweiler, J. Feldberg, S. Frohlich, M. Grdina, R. Karpeles, T. Keumi, S. Inaba, W. Ip, K. Lammertsma, G. Salem, and D. Tabor, *J. Am. Chem. Soc.*, 1984, **106**, 2143.
31. Y. Matsumara, K. Hashimoto, and S. Yoshida, *J. Catal.*, 1986, **100**, 392.
32. E. Munson, N. Lazo, M. Moellenhoff, and J. Haw, *J. Am. Chem. Soc.*, 1991, **113**, 2783.
33. J. Jackson and F. Bertsch, *J. Am. Chem. Soc.*, 1990, **112**, 9085.
34. S. Hastings and D. Nicholson, *J. Chem. Eng. Data*, 1961, **6**, 1.
35. M. Anderson and J. Klinowski, *J. Chem. Soc., Chem. Commun.*, 1990, 918.
36. J. Klinowski and M. Anderson, *Magn. Reson. Chem.*, 1990, **S28**, 68.
37. M. Anderson and J. Klinowski, *Chem. Phys. Lett.*, 1990, **172**, 275.
38. W. Kolodziejski and J. Klinowski, *Appl. Catal.*, 1992, **A81**, 133.
39. M. Anderson, B. Sulkowski, P. Barrie, and J. Klinowski, *J. Phys. Chem.*, 1990, **94**, 2730.
40. S. Hellring, K. Schmitt, and C. Chang, *J. Chem. Soc., Chem. Commun.*, 1987, 1320.
41. E. Munson and J. Haw, *J. Am. Chem. Soc.*, 1991, **113**, 6303.
42. C. Chang, *Catal. Rev.-Sci. Eng.*, 1983, **25**, 1.
43. M. Anderson, M. Occelli, and J. Klinowski, *J. Phys. Chem.*, 1992, **96**, 388.
44. B. Richardson and J. Haw, *Anal. Chem.*, 1989, **61**, 1821.
45. E. Munson and J. Haw, *Anal. Chem.*, 1990, **62**, 2532.

Biographical Sketch

Tom M. Apple. *b* 1954. B.S., 1976, Pennsylvania State University; Ph.D., 1981, University of Delaware. Introduced to NMR by C. R. Dybowski. Faculty in Chemistry, University of Nebraska, 1983–1991, Faculty in Chemistry, Rensselaer Polytechnic Inst., 1991–present. Approx. 40 publications. Research interests include applications of solid state NMR to catalysis and materials science.

Silica Surfaces: Characterization

Gary E. Maciel
Colorado State University, Fort Collins, CO, USA

1	Introduction	1
2	NMR Strategies for Silica Surface Selectivity	1
3	$^{1}H \rightarrow {}^{29}Si$ CP in Silicas	2
4	$^{1}H \rightarrow {}^{17}O$ Cross Polarization	5
5	Proton NMR Approaches	5
6	Correlating ^{1}H-based and ^{29}Si-based Information	11
7	Subsurface Silanols	14
8	Summary and Conclusions	14
9	Related Articles	15
10	References	15

1 INTRODUCTION

Silica (SiO_2) is one of the most abundant materials on Earth.[1] If the wide range of silicate minerals in which silica 'formally' occurs is included, one can account for more than 60% of the Earth's crust in terms of silica. From the industrial point of view, the number of applications of silica is enormous, and we make no attempt to represent them all here. These technological applications of silica include its use in separations (e.g. column chromatography), in composite materials, in consumer products (e.g. as thickening agents), in immobilized reagents (e.g. heterogeneous catalysts), and even in foods. Although a variety of high-surface-area forms of silica are important, including precipitated and fumed silicas, in this article we will focus mainly on samples originating as *silica gels*, i.e. silica samples precipitated from the products of reactions such as:

$$Si(OCH_2CH_3)_4(aq.) + 2H_2O(l) \rightarrow SiO_2(s) + 4CH_3CH_2OH(aq.) \qquad (1)$$

The materials prepared in this manner tend to have high surface areas and high porosities, although these properties depend substantially on details of the preparation conditions. Most of the technologically important properties of silica depend substantially on the characteristics of the silica *surface*, e.g. the numbers, types, distributions, and reactivities of silanols, i.e. ≡Si-OH groups, at the silica surface.

A priori, it would appear that the spin-$\frac{1}{2}$ nuclides ^{29}Si (4.7% natural abundance) and ^{1}H (∼100% natural abundance) should be useful for characterizing the silica surface, and possibly also the quadrupolar nuclides ^{17}O ($I = \frac{5}{2}$, 0.04% natural abundance) and ^{2}H (I = 1, 0.02% natural abundance). Clearly, for these quadrupolar nuclides to be useful, isotopic enrichment is required, but that has not been a major difficulty. Indeed, there has been a great deal of NMR work done on silicas and silica-based systems,[2–5] and it would be impossible to review it all comprehensively here, because of reasonable space limitations. Furthermore, because of restrictions on space, it will not be possible to list all of the worthwhile studies in this research area. For these reasons, the convenient approach of emphasizing studies from our own laboratory is adopted, with apologies to those who feel their work may have been neglected.

2 NMR STRATEGIES FOR SILICA SURFACE SELECTIVITY

2.1 The Need

With any NMR experiment on a solid, a technique that provides no major detection advantage to nuclei at the surface will generate spectra that are dominated by peaks due to nuclei that are in positions in the interior (bulk) of a particle, because the number of nuclei that constitute the bulk of a particle will typically be much larger than the number of corresponding nuclei in analogous structural sites at the surface (unless the surface area is very large, say, $\gg 100\,m^2\ g^{-1}$). This intensity dominance by peaks due to bulk sites can be overcome if (1) the nuclei being observed are located only (or largely) at the surface or (2) the method of generating the polarization to be observed discriminates strongly in favor of nuclei at the surface. The former situation often obtains for protons in a typical silica, because most of the protons in such systems exist at the surface as covalently attached −OH groups (vide infra), as physisorbed H_2O, or as covalently attached structures that result from derivatization processes.

Perhaps the most obvious strategy for preferentially or selectively polarizing surface nuclei in the presence of an overwhelmingly larger number of nuclei in analogous structural sites in the interior would be to use a relaxation reagent that can, at least briefly, interact with the surface and thereby relax the surface nuclei. Although surprisingly little effort seems to have been expended in this direction, one must note the elegant ultra-low-temperature (∼10 mK) NMR studies of Waugh and co-workers,[6] who have used the relaxation effects of ^{3}He impinging on a surface for the selective relaxation of nuclei at the surface. Other surface-selective (or preferential) relaxation mechanisms would seem possible via the dipolar mechanism of impinging species with large nuclear magnetic moments (say, ^{1}H or ^{19}F) or even the electron spin magnetic moments of paramagnetic relaxation agents. In the case of paramagnetic surface relaxants, the possibility of dynamic nuclear polarization (DNP)[7] of surface nuclei from adsorbed paramagnetic species seems attractive, possibly with the Overhauser mechanism operating if the adsorption is rapidly reversible, or the solid state mechanism if the adsorption/desorption process is very slow. Possibilities would also appear to exist for surface-selective relaxation mechanisms based on quadrupolar relaxation of a nuclide with $I > \frac{1}{2}$ (e.g. ^{2}H or ^{17}O) due to rapid, reversible adsorption/desorption causing a modulation of the local electric field gradient. Recent progress in the surface transfer of ^{129}Xe polarization that has been dramatically enhanced via electron → nuclear polarization transfer (e.g. from optically pumped rubidium) is promising for not only providing a surface-selective NMR strategy, but also for providing huge enhancements in the effective sensitivity of NMR detection at surfaces.[8]

2.2 Cross Polarization

To date, the most popular and generally successful surface-selective polarization strategies have been based on $^{1}H \rightarrow X$ cross polarization (CP),[9] where X is a nucleus present at the surface (and presumably also with the bulk).[10,11] These strategies are often based on the assumption that essentially all

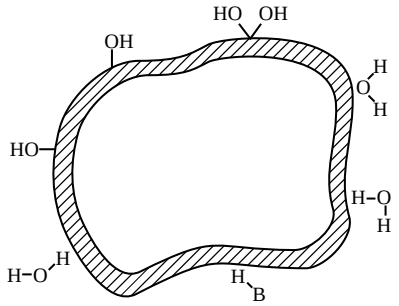

Figure 1 Cross polarization as a surface-selective strategy, showing only protons near the (hatched) surface region, as covalently attached hydroxyls, physisorbed water, or physisorbed acids (B–H) of some other type. (Taken from Maciel and Ellis[4])

(or, at least, most) of the protons in the system are present at the surface and on the fact that cross polarization depends upon a static component of the $^{1}H–X$ dipolar interaction, which has an inverse cube dependence on the $^{1}H–X$ internuclear distance (in many cases the cross polarization rate appears to have an essentially r^{-6} dependence). Cross polarization was developed during the early 1970s by Pines, Gibby, and Waugh.[9] Its early impact was primarily the dramatic increase in ^{13}C signal-to-noise ratio in NMR experiments on organic solids, which rendered such experiments especially attractive when carrried out with magic angle spinning (MAS), as demonstrated first by Schaefer and Stejskal.[12] From the point of view of surface applications, at least as important as the effective increase in sensitivity is the above-mentioned dependence of the cross-polarization rate on internuclear distances. Figure 1 displays the essence of a surface-selective CP strategy, in which only those X nuclei that are close enough to the surface (within, say, 5–6 Å, as represented by the 'cross-hatched' area) can be cross polarized by surface protons. The more remote X nuclei in the 'interior' or 'bulk' of the material are not cross polarized efficiently. Hence, the efficiency, or dynamics, of cross polarization can be used to discriminate in favor of the surface nuclei.

3 $^{1}H \rightarrow {}^{29}Si$ CP IN SILICAS

3.1 Silica Gels and Derivatized Silica Gels

In 1980, Sindorf and Maciel[10,11] published the first high-resolution example of the use of $^{1}H \rightarrow X$ cross polarization for surface-selective X detection in a demonstration of $^{1}H–{}^{29}Si$ CP in silica gel. Since that time $^{1}H \rightarrow {}^{29}Si$ CP has remained the most popular application of this strategy, although there has been significant success with applications to other types of systems. Figure 2 shows typical ^{29}Si spectra of silica gel and related samples obtained by CP MAS (cross polarization and magic angle spinning) and DP MAS (direct polarization, based on ^{29}Si spin–lattice relaxation, not CP). The DP MAS spectrum [Figure 2(a)] of an undried silica gel is dominated by the peak due to $(\equiv SiO)_4\mathbf{Si}(Q_4)$ sites, which represent the bulk (nonsurface regions) of silica particles. The ^{29}Si CP MAS spectrum of an undried silica gel [Figure 2(b)] selects primarily surface sites and shows the following three peaks: a peak at −89 ppm (relative to liquid TMS) due to

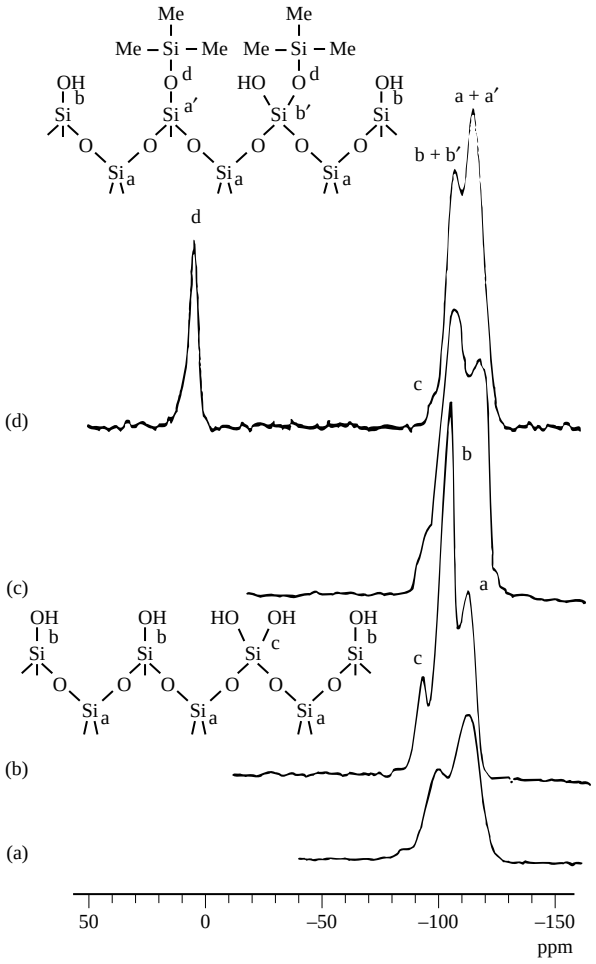

Figure 2 ^{29}Si MAS spectra of silica gel samples. (a) DP MAS spectrum of an undried sample. (b) CP MAS spectrum of the same sample as in (a). (c) CP MAS spectrum of a sample dehydrated under vacuum at 209 °C. (d) Sample derivatized with $(CH_3)_3SiCl$. (Taken from Maciel[5])

$(\equiv SiO)_2\mathbf{Si}(OH)_2$ (geminal, Q_2) sites; a peak at −99 ppm arising from $(\equiv SiO)_3\mathbf{Si}OH$ (single silanol, Q_3) sites; and a peak at −109 ppm from the Q_4 (siloxane) sites near the surface. These peak assignments can be made on the basis of the usual kinds of empirical chemical shift correlations with structure from liquid sample data on silicic acid solutions. However, the dynamics of the $^{1}H–{}^{29}Si$ CP process can also be used to make these assignments.

Figure 3 shows the results of a variable contact time CP experiment, in which the $^{1}H \rightarrow {}^{29}Si$ CP contact period (t_{cp}) is varied in order to elucidate the $^{1}H \rightarrow {}^{29}Si$ CP (relaxation) time constant (T_{HSi}) for each ^{29}Si peak. The early (small t_{cp}) part of such curves is typically dominated by the rate of CP transfer, as characterized by the rate constant $T_{HSi}{}^{-1}$, and the latter part of such curves is usually determined by the rate constant of the rotating frame spin–lattice relaxation of the protons responsible for polarization transfer to the observed silicons, as characterized by the time constant, $T_{1\rho}^{H}$ (assuming $T_{1\rho}^{H} \rangle T_{HSi}$). These curves can be analyzed mathematically in terms of equation (1),[13]

$$M(t_{cp})/M^{*} = \frac{1}{1 - T_{HSi}/T_{1\rho}^{H}}(e^{-t_{cp}/T_{1\rho}^{H}} - e^{-t_{cp}/T_{HSi}}) \qquad (2)$$

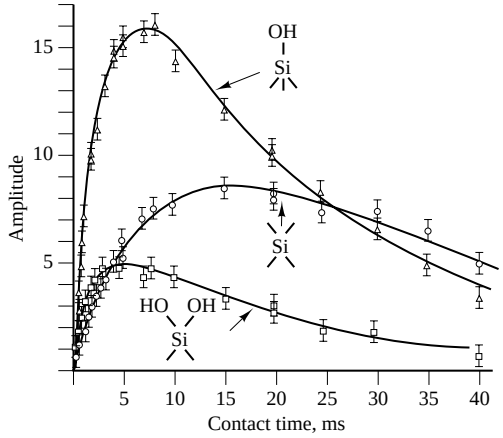

Figure 3 Variable contact time ^{29}Si CP MAS plots for silica. (Taken from Maciel and Sindorf[10])

where $M(t_{cp})$ is the ^{29}Si magnetization generated by ^{1}H–^{29}Si CP as a result of a CP contact period t_{cp}, and M^* is the 'ideal' maximum ^{29}Si magnetization that would be generated if $T_{1\rho}^{H}$ and $T_{HSi}{}^{-1}$ were both infinite. This analysis shows that $T_{HSi}{}^{-1}$ for the -89 ppm peak is roughly twice that of the -99 ppm peak, which in turn is an order of magnitude larger than the $T_{HSi}{}^{-1}$ value for the -109 ppm peak. In terms of the number and distances of nearby protons, the ^{29}Si chemical shift assignments given above in terms of Q_2, Q_3, and Q_4 sites are entirely consistent with these T_{HSi} determinations.

3.2 Dehydration of Silica

The ^{29}Si CP MAS spectra collected in Figure 2 also represent two important classes of chemical transformations of silica surfaces that were studied by ^{29}Si CP MAS spectra by Sindorf and Maciel.[10,11,14–18] Figure 2(c) shows a spectrum obtained on a silica gel sample that has been dehydrated under vacuum at 209 °C. One can see in this spectrum the subtle redistribution of peak intensity and the dramatic line broadening relative to the spectrum observed on an 'air hydrated' silica gel sample. These changes, especially the line broadening, are presumably due to a redistribution of hydrogen bonding patterns, and perhaps bond angles and bond lengths (and strains) introduced with the removal of the (predominantly physically) adsorbed water of the 'hydrated' and essentially 'annealed' silica surface represented in Figure 2(b). Such experiments carried out over a wide range of dehydration temperatures, and corresponding rehydration experiments, have revealed valuable information on the effects of dehydration and rehydration on the silica gel surface.

3.3 Silylation of Silica

The ^{29}Si CP MAS spectrum shown in Figure 2(d) represents a sample prepared by the silylation of a silica gel by $(CH_3)_3SiCl$. This silylation reaction is a member of an important class of derivatizations of the silica surface, represented by the following chemical equation:

(3)

where X represents a labile leaving group (e.g. Cl or OCH_2CH_3) and Si represents a silanol site on the reactant silica surface or a corresponding derivatized silica site in the reacted sample. Such reactions are important, or potentially important, technologically—for the preparation of stationary phases for chromatographic separations, as a means of immobilizing reactive chemical centers (e.g. catalytic sites), in coupling agents for composite materials, and for a wide range of other applications in which it is desired to anchor or 'immobilize' a chemically important moiety. Peak d in the spectrum of Figure 2(d), at ca. 10 ppm, is assigned to the trimethylsilyl group covalently attached to the silica surface. Clearly the silylation process has brought about a change of intensities of peaks a, b, and c in Figure 2(b), corresponding to the $(\equiv SiO)_2\mathbf{Si}(OH)_2$ or Q_2 sites, the $(\equiv SiO)_3\mathbf{Si}OH$ or Q_3 sites, and $(\equiv SiO)_4\mathbf{Si}$ or Q_4 sites, at the underivatized surface. At the relatively low level of structural detail represented by the Q_2, Q_3, Q_4 notation, the silylation process transforms Q_2 sites into Q_3 sites, and Q_3 sites into Q_4 sites, and these changes are seen by comparing the spectra in Figure 2(b) and (d). By examining such intensity changes systematically, it has been possible to elucidate important reactivity patterns in these systems.[10,11,14–18] Indeed, ^{29}Si CP MAS NMR, along with supporting data from ^{13}C CP MAS experiments, can serve as an analytical technique for monitoring chemical reactivity

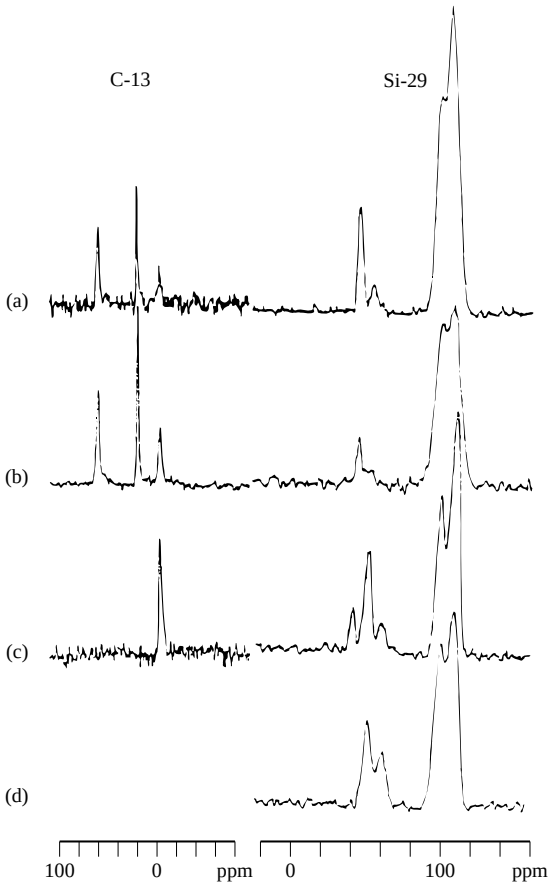

Figure 4 ^{29}Si (right) and ^{13}C (left) CP MAS spectra of silica gel derivatized with $(CH_3)_2Si(OCH_2CH_3)_2$. (a) Product of reaction with predried silica at 138 °C. (b) Product of reaction with predried silica at 240 °C. (c) Product of reaction with undried silica at 115 °C. (d) Sample (c) heated in air at 150 °C. (Taken from Sindorf and Maciel[17])

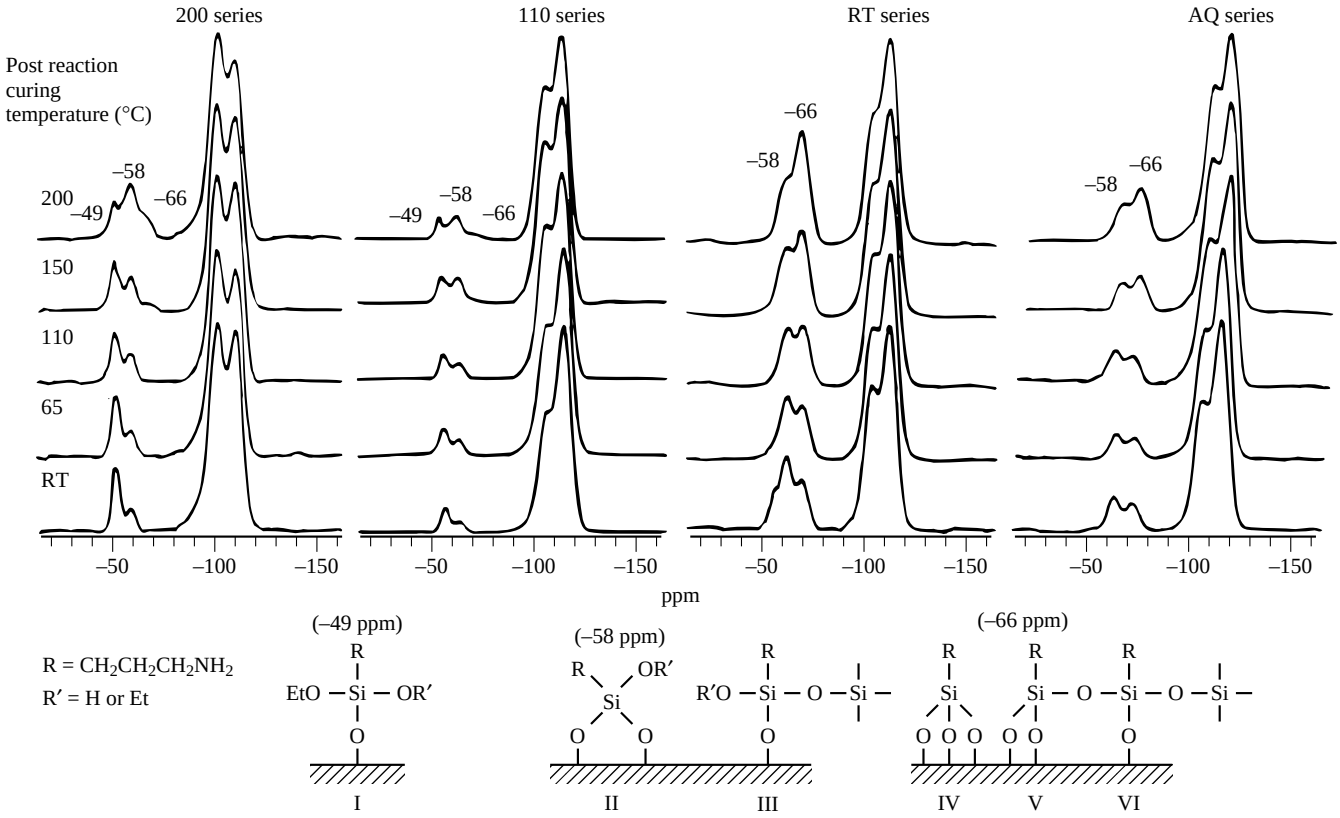

Figure 5 ^{29}Si CP MAS spectra of APTS-modified silica gels. Each column of spectra corresponds to the drying temperature of silica gel (°C; RT = room temperature) under vacuum prior to reaction in dry toluene, or aqueous reaction conditions (AQ). Postreaction treatment (curing) temperature shown on the left. Structural assignments given at the bottom. (Taken from Caravajal et al.[19])

patterns, e.g. the relative reactivities of the various types of silanols on a silica surface.

The complex chemistry that can occur on a silica surface after silylation by a reagent with more than one leaving group (X), e.g. $RR'SiX_2$ or $RSiX_3$, is also amenable to study by CP MAS NMR.[17] In the ^{29}Si CP MAS spectra shown in Figure 4 one sees that the product formed initially from the reaction of silica with $(CH_3)_2Si(OCH_2CH_3)_2$ depends on the reaction conditions and predrying of the silica, and can be converted by the moisture in air [Figure 4(c), (d)] to products in which ≻**Si**-OCH_2CH_3 moieties are replaced by ≻**Si**-OH and ultimately ≻**Si**-OSi- moieties. In this case, ^{13}C CP MAS spectra are also useful, because they detect the presence and amount of residual ≻Si-OCH_2CH_3 moieties.

The ^{29}Si CP MAS spectra shown in Figure 5 represent an even more complex derivatized silica system, a series of samples prepared by the silylation of silica with 3-aminopropyltriethoxysilane (APTS) under a variety of conditions (pretreatment temperature = 200 °C for 200 series, or 110 °C for 110 series, 25 °C for RT series, or with silylation carried out in an aqueous slurry, AQ series).[19] APTS-derivatization of the silica surface is of interest for such diverse applications as a variety of composite materials (in which APTS serves as a coupling agent between a silica-like component and, usually, an organic polymer) and for metal complexation agents. One sees from the spectra of Figure 5 that increasing the amount of water in the silylation process or increasing the postsilylation 'curing' temperature brings about changes in attached silane populations from species with one **Si**-OSi attachment (−49 ppm) to species with two such attachments (−58 ppm) to three such attachments (−66 ppm). Although ^{13}C spectra are primarily useful for monitoring the residual ≻Si-OCH_2CH_3 moieties in this system, a careful analysis of the ^{13}C CP MAS spectra of samples corresponding to those represented in Figure 5 reveals that the ^{13}C chemical shift of the central carbon of the pendant $-(CH_2)_3-$group originating from APTS is sensitive to protonation or hydrogen bonding of the amino group. ^{1}H CRAMP spectra (vide infra) and ^{15}N CP MAS spectra are also useful for studying this important issue.

3.4 Fumed Silica

Other types of silicas (and derivatized silicas), besides those based on silica gels, have also been studied by ^{29}Si CP MAS (and DP MAS) experiments, e.g. by Brinker and co-workers[20,21] and by Legrand and co-workers.[22,23] Figure 6 shows a comparison of ^{29}Si CP MAS spectra of a fumed silica (a Cab-O-Sil, formed by the vapor-phase combustion of $SiCl_4$) and a silica gel equilibrated to about the same H_2O vapor pressure.[24] The same peaks are present, but they are broader in the case of the fumed silica, and the percentage of surface silica sites that are single silanols is seen to be smaller for the fumed silica than for silica gel. The greater linewidth presumably relates to the greater dispersion of local surface geometries (and chemical shifts) in the Cab-O-Sil structure, which is formed at a higher temperature, and possibly to

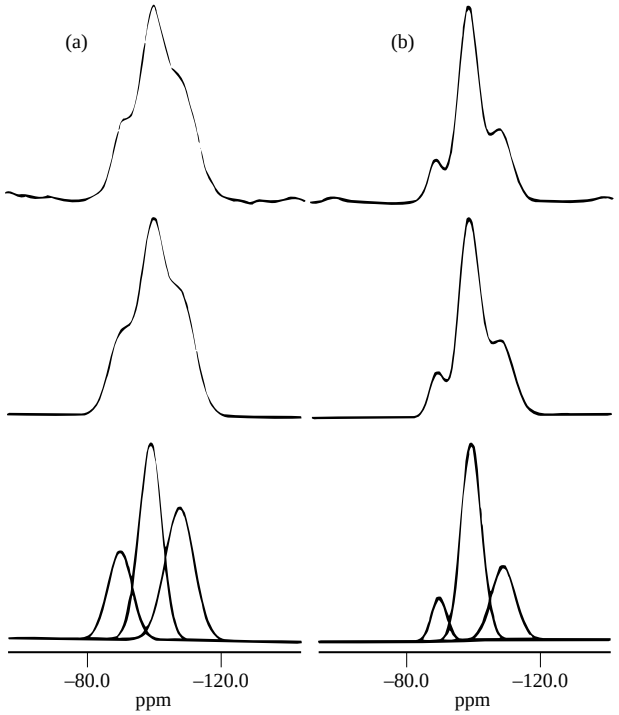

Figure 6 ^{29}Si CP MAS spectra of (a) Cab-O-Sil fumed silica and (b) silica gel. Top: experimental spectra. Bottom: individual Q_2, Q_3, and Q_4 peaks by deconvolution. Middle: computer sum of the contributions shown at the bottom. (Taken from Liu and Maciel[24])

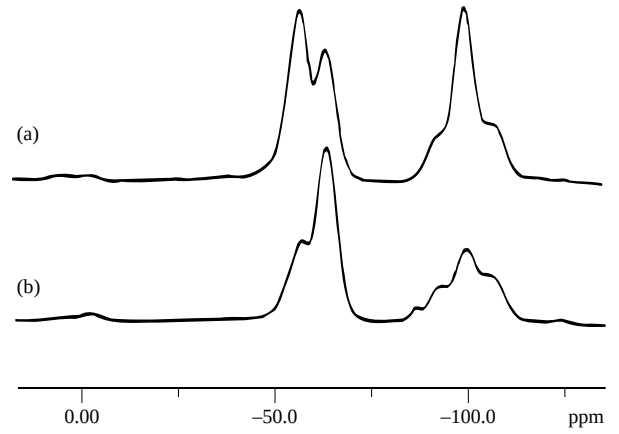

Figure 7 ^{29}Si CP MAS spectra of polysiloxane polymer prepared from $Si(OEt)_4$ and $(CH_3O)_3SiCH_2CH_2CH_2Cl$ with (a) $Bu_2Sn(OAc)_2$ or (b) 0.1 M HCl as catalyst. (Taken from Elnahhal et al.[26])

the potential effects of so-called 'interparticle sites' at the junctures of the primary particles that contribute to the overall topography of a fumed silica.[23] Detailed studies of ^{29}Si CP MAS spin dynamics of fumed silicas, especially when viewed in relationship to analogous silica gel results, appear promising for identifying the main similarities and differences between these two types of silica surfaces.[24]

3.5 Polysiloxane Systems

There has been a great deal of interest recently in a class of polysiloxane polymers prepared by the hydrolysis and gelation of mixtures of reagents of the types, $Si(OR')_4$ and $RSi(OR'')_3$, where R′ and R″ are typically methyl or ethyl and R is a 'pendant' group that contains some desired chemical moiety, e.g. a specific ligand.[25] By varying the nature of R and the ratios of the two types of starting reagents, a wide range of polysiloxane materials, with a broad variety of potentially useful properties, can be prepared. These polysiloxane materials bear a substantial similarity to derivatized (silylated) silicas, with a silica-like three-dimensional network to which the pendant (R) groups are attached. Hence, the NMR techniques that are useful for characterizing derivatized silicas are also useful for these polysiloxane systems.

Figure 7 shows ^{29}Si CP MAS spectra of polysiloxane systems with $-CH_2CH_2CH_2Cl$ as the pendant group, prepared by the reaction of $Si(OEt)_4$ with $(MeO)_3SiCH_2CH_2CH_2Cl$, using two different catalysts.[26] One notes substantially different intensity ratios for the Q_2, Q_3, and Q_4 peaks in the two spectra [and possibly a Q_1 peak at about −82 ppm in Figure 7(b)], and for the peaks due to the pendant groups (at about 60 and 65 ppm), as well as a dramatic difference in intensities between the 60 and 65 ppm peaks relative to the Q_2, Q_3, Q_4 peaks, for the products from the two catalyst systems employed.

4 ^{1}H → ^{17}O CROSS POLARIZATION

In addition to cross polarization to ^{29}Si in silica, or to ^{13}C (or ^{15}N, ^{31}P, etc.) in derivatized silicas, cross polarization to ^{17}O in isotopically-enriched silicas has also been illuminating. Oldfield and co-workers have during the past several years made significant progress in the application of solid state ^{17}O NMR techniques for the characterization of inorganic materials. Walter, Turner, and Oldfield[27] have demonstrated that ^{1}H → ^{17}O CP experiments are not only feasible, but they are also very informative from the point of view of *editing* ^{17}O spectra, by discriminating against ^{17}O signals from oxygen sites with no directly bonded hydrogen. Figure 8 shows ^{1}H → ^{17}O CP spectra of amorphous silica and a model SiOH system. From a comparison of the spectra obtained from static samples and by MAS, with and without CP, it was possible to assign the ^{17}O signal due to SiOH groups at the surface.

5 PROTON NMR APPROACHES

5.1 Dipole–Dipole Broadening

High-resolution ^{1}H NMR spectroscopy has proved to be highly useful in studying the surfaces of silicas and a variety of other solids. In order to obtain high-resolution ^{1}H NMR spectra of solids (including their surfaces), it is necessary to average not only the chemical shift anisotropy (easily done by MAS), but also ^{1}H–^{1}H dipolar interactions.[28,29] The latter can be very large (tens of kHz). Magnetic dipole–dipole interactions manifest an inverse cube dependence on internuclear distance. Therefore such interactions, and the ^{1}H–^{1}H spin–spin flip-flops that they can generate, are especially strong if the protons are situated in close proximity to each other, e.g. in a typical organic solid, but also perhaps in hydrogen-bonded clusters of hydroxy groups on a surface. Hence, a priori one can feel confident that moderate-speed MAS experiments (say, less

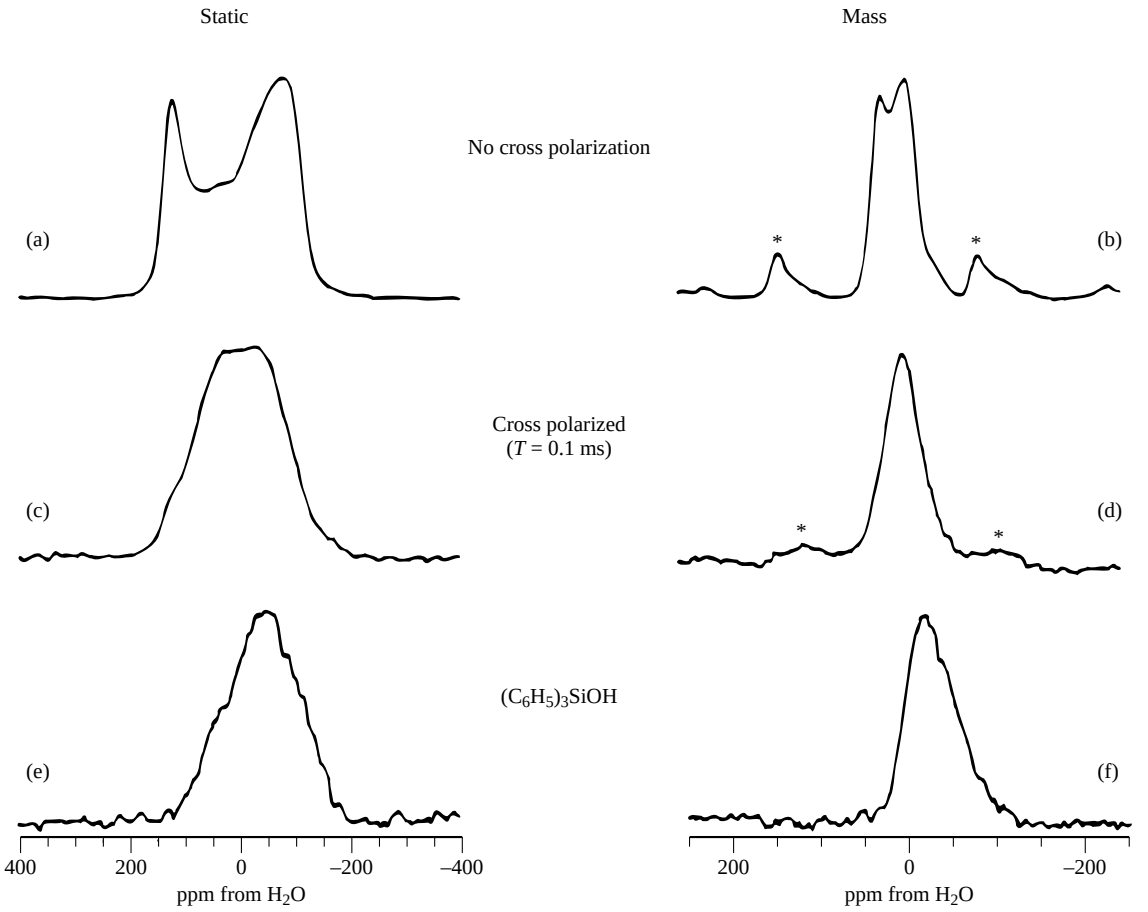

Figure 8 Static and MAS ^{17}O spectra of amorphous SiO_2 and polycrystalline $(C_6H_5)_3SiOH$ obtained at 67.8 MHz. (a) ^1H-decoupled static spectrum of SiO_2 without CP: 108 scans. (b) ^1H-decoupled MAS spectrum: 100 scans, 7.6 kHz spinning speed (*indicates spinning sidebands). (c) $^1H \rightarrow {}^{17}O$ static spectrum of SiO_2, 200 scans, 0.1 ms contact time. (d) $^1H \rightarrow {}^{17}O$ MAS spectrum of SiO_2, 200 scans, 0.1 ms contact time. (e) ^1H-decoupled static spectrum of $(C_6H_5)_3SiOH$ without CP: 500 scans. (f) ^1H-decoupled MAS spectrum of $(C_6H_5)_3SiOH$: 800 scans, 4.0 kHz spinning speed. All spectra were obtained using a 2 s recycle time. (Taken from Walter et al.[27])

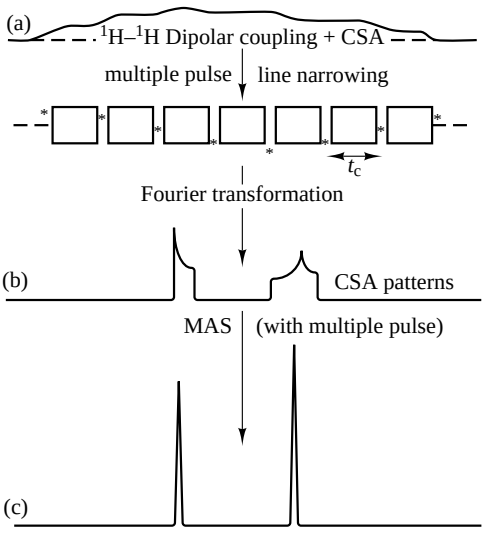

Figure 9 The multiple pulse line-narrowing strategy for averaging homonuclear dipolar interactions. Each rectangle [between (a) and (b)] represents one multiple pulse cycle (e.g. four pulses for WAHUHA, eight for MREV-8 or 24 for BR-24). There is one data acquisition point for each cycle (e.g. between each rectangle). (Taken from Maciel[5])

than 20 kHz) are adequate for studying silica surfaces only for substantially dehydrated samples. For nondehydrated or nondeuterated samples, in which the *local* surface density of protons can be substantial, multiple pulse techniques may be required for eliminating the line-broadening effects of ^1H–^1H dipolar interactions. Alternatively, a useful strategy employed by Vega and co-workers is to ensure that the ^1H concentration is small by exchanging protons at the surface with deuterons.[30]

5.2 Multiple Pulse Line Narrowing: CRAMPS

In 1968, Waugh and co-workers[31] introduced a *multiple pulse* approach for averaging strong homonuclear dipolar interactions. The strategy of this kind of approach is that, over the *entire* period of each individual multiple pulse cycle (four 90° pulses in the original work), the average Hamiltonian that governs the evolution of the spins over the entire cycle does not include the homonuclear dipolar interaction. A nonvanishing chemical shift effect, albeit scaled down, is present in the average Hamiltonian. Hence, if one acquires one data point stroboscopically between each adjacent pair of multiple pulse cycles in a long string of such cycles, the resulting time-dependent signal (analogous to a free induction decay) is

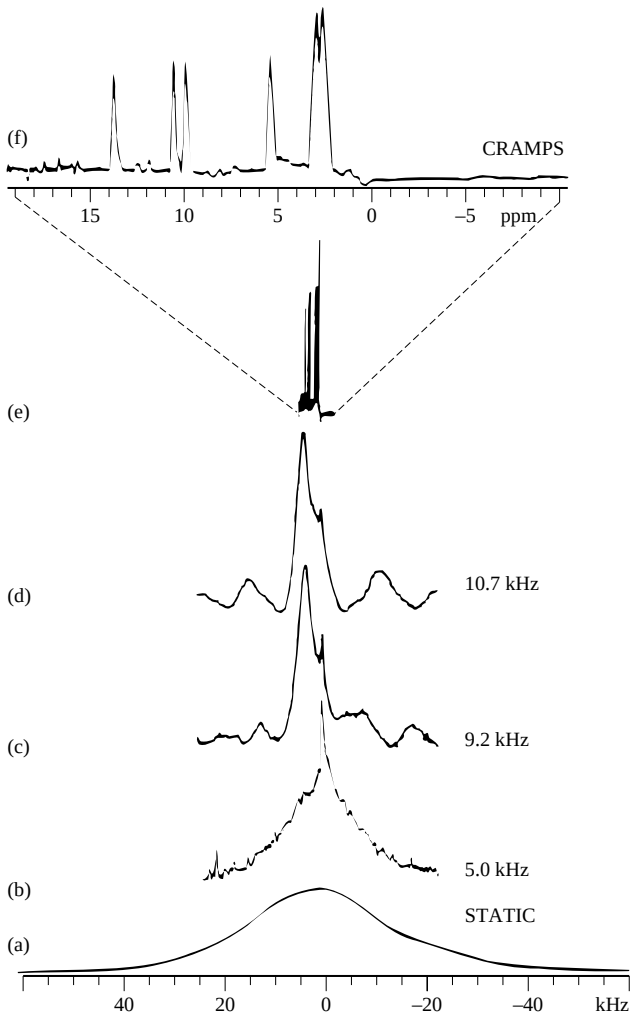

Figure 10 ^{1}H NMR spectra of citric acid. (a) Static sample, single pulse, (b),(c),(d) MAS-only with indicated MAS speed. (e) and (f) CRAMPS. (Taken from Dec et al.[35])

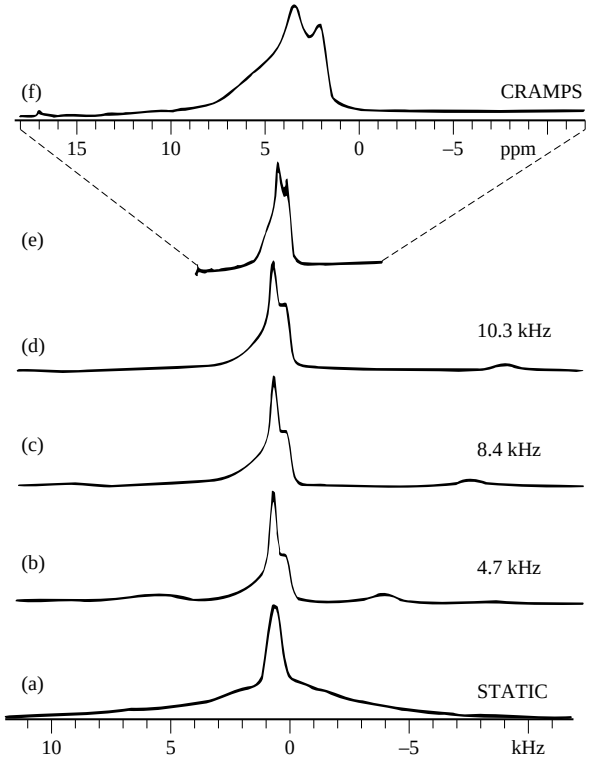

Figure 11 ^{1}H NMR spectra of untreated silica gel. (a) Static sample, single pulse. (b),(c),(d) MAS-only with indicated MAS speed. (e) CRAMPS. (f) CRAMPS on an expanded scale. (Taken from Dec et al.[35])

modulated by chemical shift effects, but not by homonuclear dipolar effects. The strategy is outlined in Figure 9 in which each rectangle represents a multiple pulse cycle and each asterisk represents a data acquisition point. The bandwidth of the experiment depends on $1/t_c$, the inverse of the multiple pulse cycle time.

The original homonuclear line-narrowing pulse sequence (WAHUHA)[31] was a four pulse sequence; later elaborations involve more pulses in the total cycle and offer compensation for pulse imperfections and/or higher order averaging of the homonuclear dipolar interaction.[32,33] In general, this class of experiments requires short ($<1.5\,\mu$s), powerful 90° pulses with precisely defined phases and until recently has been technically one of the most difficult experiments in the solid state NMR laboratory. Currently, the most popular multiple pulse sequences are the eight pulse MREV-8 sequence[32] and the 24 pulse BR-24 sequence.[33]

For powdered or amorphous samples, in order to avoid line broadening due to chemical shift anisotropy, magic angle spinning is employed (which also averages various heteronuclear dipolar couplings). Gerstein and co-workers[34] were the first to combine a multiple pulse homonuclear line-narrowing technique with magic angle spinning, and introduced the acronymn CRAMPS for Combined Rotation And Multiple-Pulse Spectroscopy.[28,29]

5.3 ^{1}H CRAMPS Studies of Silicas

Figures 10 and 11 show the difference in ^{1}H line-narrowing capabilities between CRAMPS and MAS-only (no multiple pulse sequence) with a modestly high MAS speed (10–11 kHz).[35] For powdered crystalline citric acid (Figure 10), one sees six distinctly resolved ^{1}H CRAMPS peaks, but essentially no resolution in the 10.7 kHz MAS-only ^{1}H spectrum. This difference reflects the high proton concentration (∼29 atom %) and molecular rigidity of crystalline citric acid. For the more proton-dilute (∼2.5 atom %) silica gel system (Figure 11), the ^{1}H NMR experiment yields a modestly narrowed ^{1}H spectrum even on a static sample, and 4.7 kHz MAS yields a spectrum that is superficially similar to that obtained by CRAMPS. However, close inspection reveals important details that differentiate the ^{1}H spectra obtained by these two techniques [Figure 11(d) and (e)]. All of the remaining ^{1}H spectra discussed in this article were obtained by the CRAMPS technique.

One should note that the CRAMPS technique is not necessarily a panacea for ^{1}H NMR studies on surfaces, or for any other type of sample. Dynamics associated with motion and/or chemical reactions with a time constant that is comparable to the cycle time (t_c) of the multiple pulse sequence interferes with the multiple pulse averaging of

$^1H-^1H$ dipolar interactions.[29,36] Of course, an analogous problem can also arise with magic angle spinning, for which the critical period is $\nu_{MAS}{}^{-1}$, where ν_{MAS} is the MAS frequency.[37] To quench this kind of dynamic interference with the line-narrowing efficiency of any cyclic technique, like MAS and/or a multiple pulse sequence, one can try to alter the dynamics, e.g. by changing (usually lowering) the sample temperature.

As an example of the application of the ^1H CRAMPS technique to the study of silica surfaces,[38] Figure 12 shows the ^1H CRAMPS spectra obtained on untreated [Figure 12(a), (a′), (a″)] and dried [Figure 12(b), (c), (d)] silica gel samples. Comparison of spectra (a) and (b) show that the relatively sharp peak at about 3 ppm in the spectrum of an untreated silica is removed by moderate dehydration; this peak is therefore identified as physisorbed water. The broad nonsymmetrical peak that is largely to the left of the sharp 1.9 ppm peak is unaffected by sample evacuation at 200 °C, but removed by evacuation at 500 °C; this behavior suggests that this peak can be identified tentatively with clustered (or hydrogen bonded) silanols, which are close enough together that suitable dehydration pathways are available. The sharp peak at 1.9 ppm remains after evacuation at 500 °C; this behavior implies that the silanol groups represented by this peak are sufficiently far from each other to make dehydration difficult, so it is assigned to isolated (non-hydrogen-bonded) silanols. These assignments are consistent with 35 years of literature results on liquid solution samples, which show that hydrogen bonding typically reduces proton shielding, and with the reasonable point of view that a wide range of hydrogen-bonding structures exist on a silica surface (chemical shift dispersion:broad peak). These assignments are also consistent with the results of proton dipolar-dephasing experiments, as shown in Figure 13.

5.4 CRAMPS-Based Time Domain Studies of Silicas

Figure 13(a) shows a ^1H CRAMPS version[38] of the popular 'dipolar-dephasing' experiment used routinely in ^{13}C CP MAS NMR. In this ^1H CRAMPS version, a 'dephasing period' 2τ is inserted between the initial $\pi/2$ pulse that generates transverse magnetization and the multiple pulse line-narrowing pulse train that detects the transverse magnetization. During the dephasing period, those proton magnetic moments that experience strong dipolar interactions undergo a corresponding degree of dephasing, and the resulting detected signal will be accordingly attenuated. Figure 13(b) and (c) show the results of applying the dipolar-dephasing CRAMPS experiment to untreated silica gel [Figure 13(b)] and to a silica gel sample evacuated at 200 °C [Figure 13(c)]; in both cases one sees that the broad (3.0 ppm) peak is attenuated by a dephasing period (2τ) of 160 μs, whereas the sharp (1.7 ppm) peak is largely unattenuated. From the relationship between hydrogen bonding and proximity (between atoms that participate in a hydrogen bond) and the r^{-3} dependence of dipolar interactions, this dipolar-dephasing behavior provides strong support for identifying the 1.7 ppm peak as arising from isolated (non-hydrogen-bonded) silanols and the broad 3.0 ppm peak as clustered (hydrogen bonded) silanols. This is the same conclusion regarding proximity (and hydrogen bonding) that one would reach from the dehydration behavior shown in Figure 12. It would be difficult to rationalize the elimination

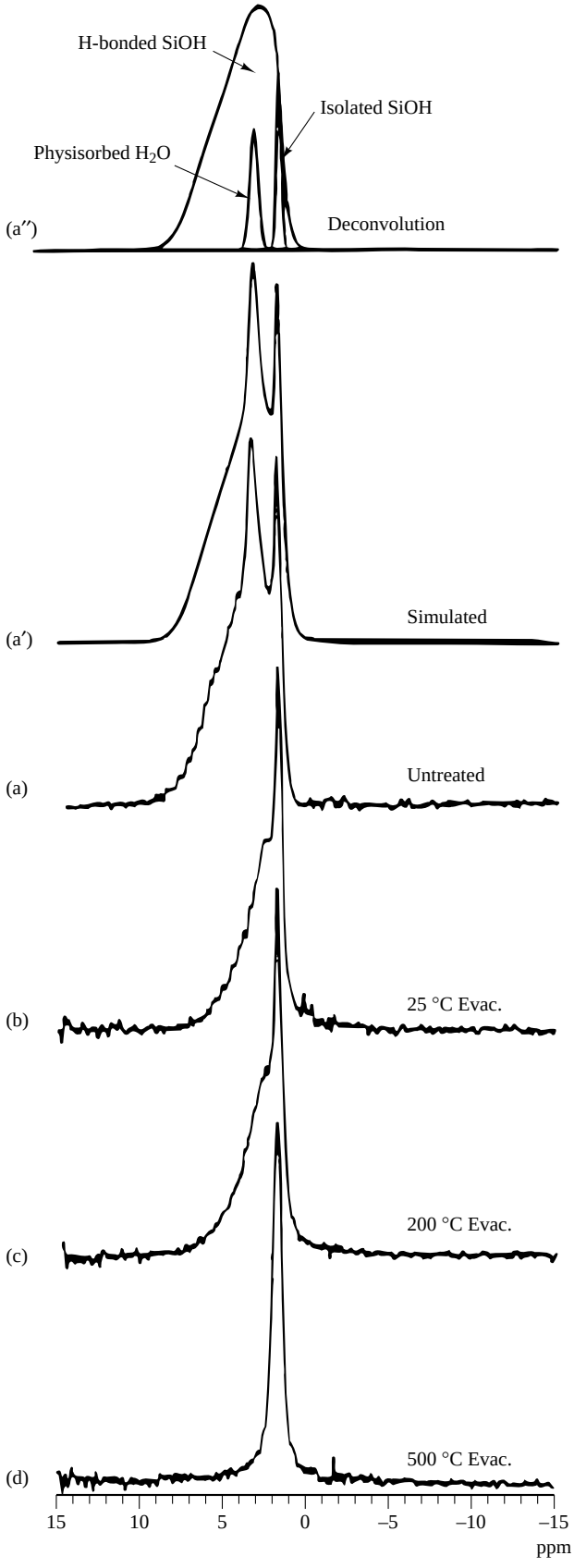

Figure 12 187-MHz ^1H CRAMPS spectra of Fisher S-679 silica gel. (a) untreated; (b) evacuated at 25 °C; (c) evacuated at 200 °C; (d) evacuated at 500 °C; (a″) deconvolution of spectrum (a); (a′) computer simulation based on (a″). (Taken from Bronnimann et al.[38])

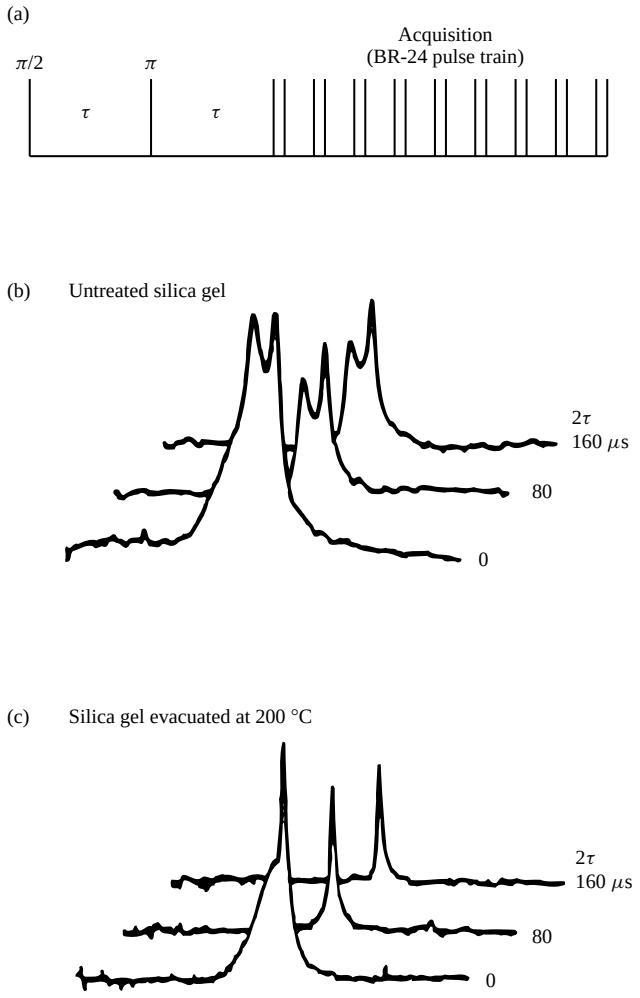

Figure 13 ^{1}H CRAMPS dipolar-dephasing experiment. (a) Pulse sequence. (b) results for untreated silica gel (showing τ values). (c) Results for sample evacuated at 200 °C (showing τ values). (Taken from Bronnimann et al.[38])

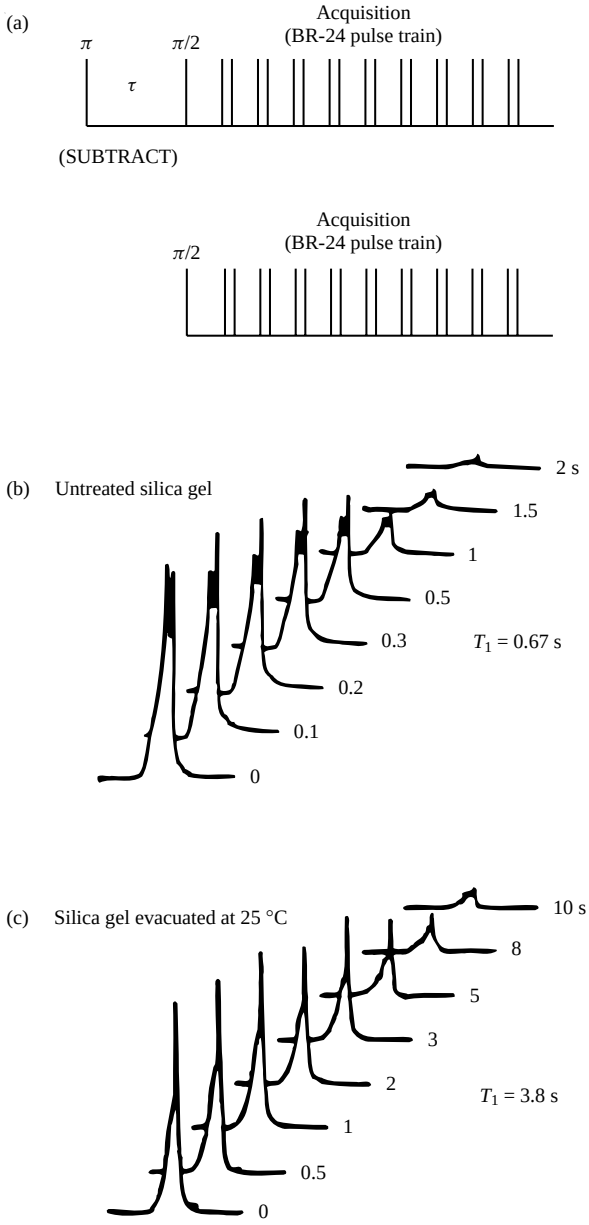

Figure 14 ^{1}H CRAMPS T_1 determination. (a) Pulse sequence, showing individual sequences employed in alternate scans (lower case subtracted from upper case in computer memory). (b) Results for untreated silica gel (showing τ values). (c) Results for sample evacuated at 25 °C. (Taken from Bronnimann et al.[38])

of water via the 'dehydration' of silanols that are *isolated* from each other. Since the physisorbed water peak (3.5 ppm) is only slightly attenuated by the 160 μs dephasing period [Figure 13(b)], one can conclude that water protons experience only weak resultant dipolar interactions, the result of efficient motional averaging.

Other CRAMPS-based ^{1}H time domain approaches have also been useful in studying silica surfaces. Figure 14 summarizes a CRAMPS-detected T_1^H determination on silica gel samples, based on an alternating, two-sequence scheme of the Freeman–Hill type.[39] One sees that for each of the two silica samples, untreated (b) and dried (c), all components of proton magnetization relax essentially homogeneously, which suggests that proton spin diffusion among the different spin isochromats is much more efficient that spin–lattice relaxation, which is characterized overall by T_1^H values of 0.7–4 s. Furthermore, the marked increase in T_1^H that results from sample drying indicates that the physisorbed water in the sample of Figure 14(b) provides an important relaxation source, and is presumably in a rapid state of motion at room temperature.[36] Having the ability to establish, via dipolar dephasing, different spin polarizations for hydrogen bonded and isolated silanols, one can explore spin exchange between these two spin sets by an experiment of the type shown in Figure 15(a).[38] One sees for the untreated silica [Figure 15(b)] that in a mixing time of a few ms after eliminating ^{1}H magnetization due to hydrogen-bonded silanols there is a substantial transfer of magnetization (spin exchange) from the isolated silanol reservoir to the hydrogen-bonded silanol protons. In any attempt to interpret or model the structure of the silica surface, the rate of this spin exchange places constraints on the spatial proximities of these two proton spin sets in terms of the dipole–dipole interactions that can be responsible for ^{1}H–^{1}H flip-flops, and/or chemical (H^+) exchange.

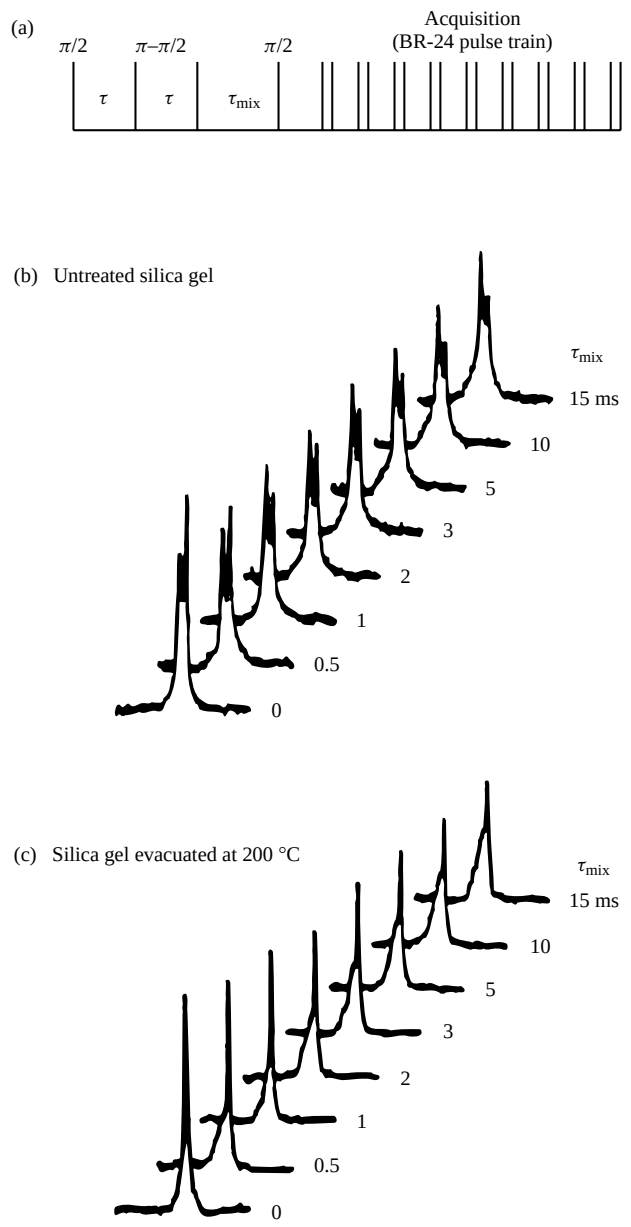

Figure 15 ^{1}H CRAMPS spin exchange experiment. (a) Pulse sequence. (b) Results for untreated silica gel (showing τ_{mix} values). (c) Results for sample evacuated at 200 °C (showing τ_{mix} values). (Taken from Bronnimann et al.[38])

A variety of CRAMPS-based ^{1}H NMR experiments of the types represented in Figures 12, 13, 14, and 15 have been carried out on silica samples in which there have been systematic variations of physisorbed water content or dehydration, and often temperature. Figure 16 shows ^{1}H CRAMPS dipolar-dephasing results obtained at room temperature on three different silica gels.[36] The behavior shown is consistent with the ideas described above. Figure 17 shows ^{1}H CRAMPS spectra of a hydrated (exposed to air) silica gel over a temperature range from 138 K to 298 K.[36] An effective freezing point depression of about 45 K can be noted from these kinds of measurements; this result is consistent with previous reports based on other types of experiments.[41]

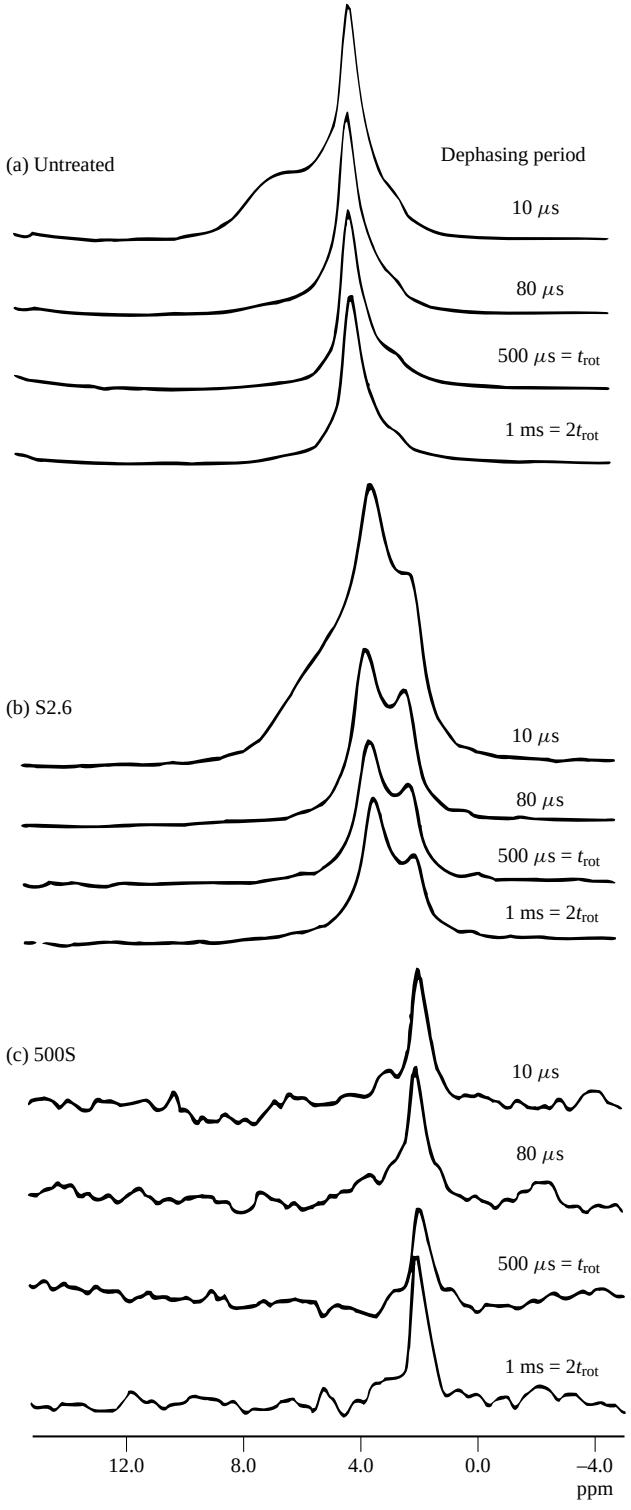

Figure 16 ^{1}H CRAMPS dipolar-dephasing spectra of three different silica gels. (a) Untreated. (b) Modestly dehydrated (2.6% weight loss). (c) Drastically dehydrated (at 500 °C)

5.5 Derivatized Silicas

Figures 18 and 19 show ^{1}H CRAMPS spectra of silica surfaces that have been derivatized with $(CH_3)_3SiCl$ and

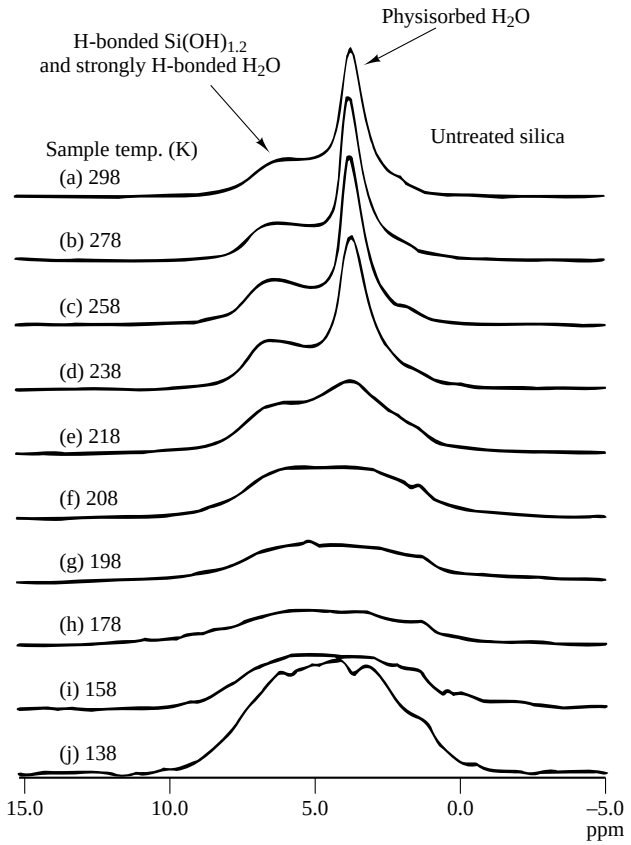

Figure 17 ^{1}H CRAMPS spectrum of an untreated silica gel as a function of temperature, as shown

$(CH_3CH_2O)_3SiCH_2CH_2CH_2NH_2$ (APTS), respectively. These spectra show that this technique can provide a rich level of structural detail on derivatized silica samples. The difference between the spectra of unprotonated and protonated APTS-derivatized samples (Figure 19) is the absence and presence, respectively, of a clearly distinct peak corresponding to the amino group of APTS.[29] This difference reflects, at least in part, the interference of ^{14}N quadrupole effects of the $-NH_2$ group with MAS averaging of $^{1}H-^{14}N$ dipolar interactions. Calculations on $=N-H$ groups show that, because of the small internuclear N–H distances for directly bonded pairs, very high NMR fields (>1000 MHz) would be required to reduce this broadening to an acceptable level by the 'brute force' approach of simply going to a higher field.[42]

6 CORRELATING ^{1}H-BASED AND ^{29}Si-BASED INFORMATION

6.1 Complementary Results

While one can distinguish between hydrogen bonded and isolated silanols by ^{1}H CRAMPS experiments and between single silanols and geminal silanols by ^{29}Si CP MAS experiments, it is important to correlate these two types of information. Ideally, one would base such a correlation on two-dimensional (2D) $^{1}H-^{29}Si$ heteronuclear chemical shift

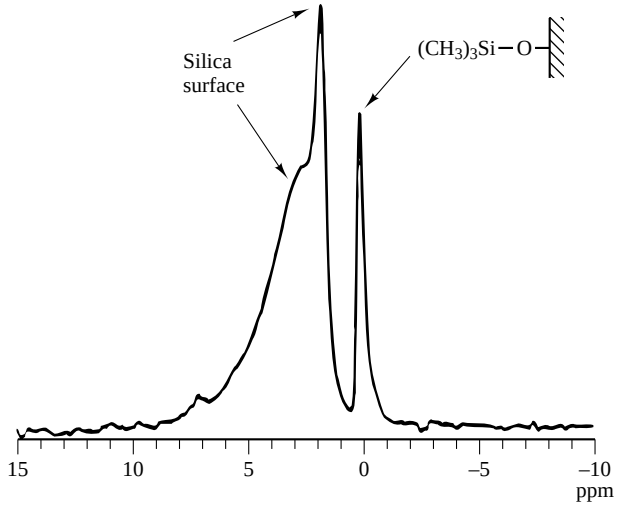

Figure 18 ^{1}H CRAMPS spectrum of trimethylsilyl-derivatized silica gel

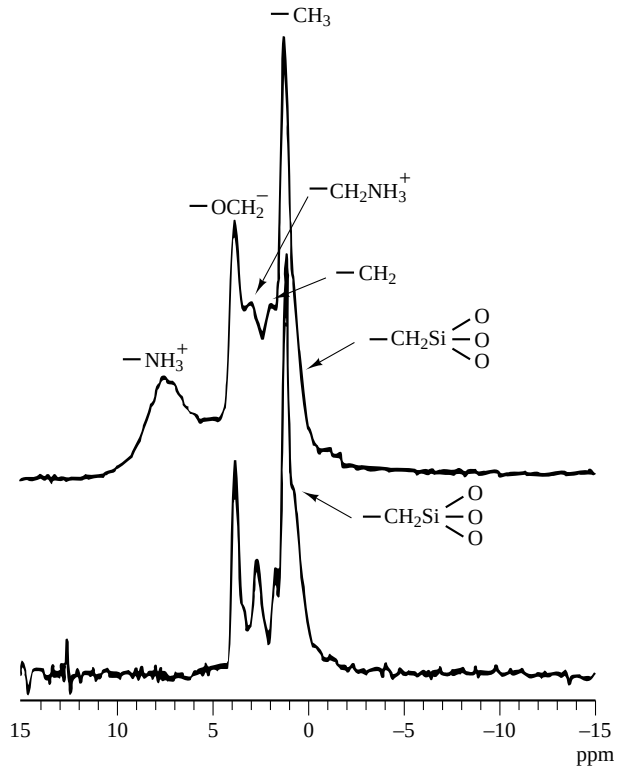

Figure 19 ^{1}H CRAMPS spectra of APTS-modified silica gel. Lower, untreated. Upper, treated with HCl. (Taken from Maciel et al.[29])

correlation (HETCOR) experiments of the general type that are employed routinely for $^{1}H-^{13}C$ correlation in liquids and more recently in solids.[43,44] Indeed, Vega has reported such experiments based on $^{1}H \rightarrow {}^{29}Si$ CP for the polarization transfer step.[45] However, as is seen below, rotating frame ^{1}H spin diffusion among the protons in a typical silica gel during the spin lock state in a $^{1}H \rightarrow {}^{29}Si$ CP experiment can substantially scramble what one would hope are discrete H $\leftrightarrow {}^{29}Si$ CP correlations in the time frame (>200 μs) required for relatively efficient CP transfer. Furthermore, the multiple

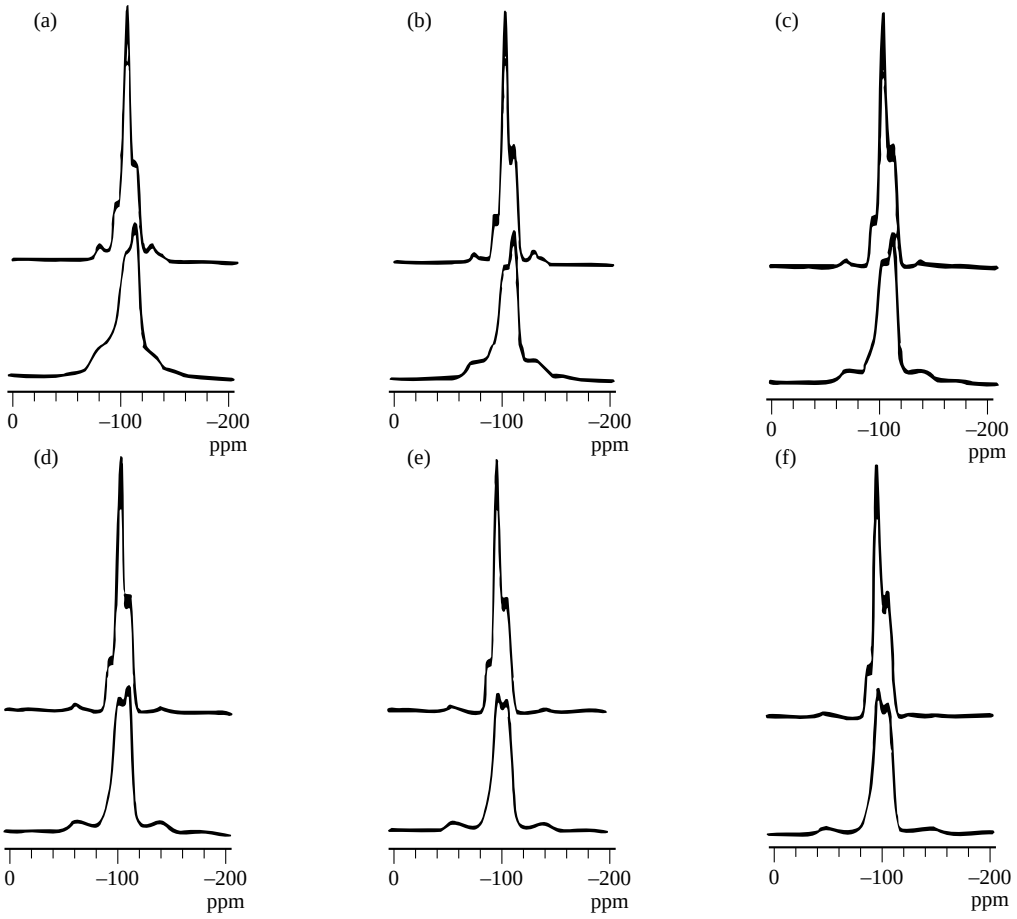

Figure 20 Proton-decoupled (top spectrum of each set) and proton-coupled (bottom spectrum of each set) 39.75 MHz ^{29}Si CP MAS NMR spectra of Fisher S-679 silica gel at six different magic angle spinning speeds. Cross polarization time, 5 ms. (a) 1.0 kHz, 1096 accumulations (b) 1.1 kHz, 3000 accumulations (c) 1.4 kHz, 720 accumulations (d) 1.6 kHz, 2000 accumulations (e) 1.8 kHz, 2000 accumulations (f) 2.0 kHz, 2000 accumulations. (Taken from Chuang et al.[47])

pulse approaches used in ^{1}H–^{13}C HETCOR experiments on solids are not very efficient in these ^{1}H–O–^{29}Si systems, although recently reported successes in ^{1}H–^{31}P 2D HETCOR experiments on P–O–H systems[46] indicate that ^{1}H–^{29}Si HETCOR in silica may be attractive. In any case, as an alternative to the 2D HETCOR approach, a variety of ^{29}Si-detected ^{1}H–^{29}Si CP experiments have been carried out, in which the behavior of protons is monitored by ^{29}Si, establishing the correlation.[47]

6.2 ^{29}Si Detection of Proton Spin Behavior

The simplest such experiment is a ^{29}Si CP MAS experiment in which ^{29}Si detection is carried out *without* proton decoupling. MAS should still average the ^{1}H–^{29}Si dipolar interaction during detection, yielding a corresponding sideband pattern to the extent that this interaction behaves inhomogeneously, i.e. to the extent that the ^{1}H–^{29}Si dipolar interaction is not altered (by chemical reaction, motion, or ^{1}H–^{1}H flip-flops) during a MAS rotor period.[47] Figure 20 shows a comparison of spectra obtained with and without ^{1}H decoupling; it is clear that the geminal silanol peak suffers most dramatically from the absence of high-power ^{1}H decoupling, implying that ^{1}H spin exchange is most efficient in the protons of geminal silanols.

Another ^{29}Si CP MAS experiment useful for correlating ^{1}H and ^{29}Si spin behaviors is the ^{1}H–^{29}Si analog of the common ^{1}H–^{13}C dipolar-dephasing experiment. In this technique, rotational and Hahn echo formation occur for a dephasing period (2τ) corresponding to two MAS rotor periods ($2\tau_{rot}$) for the isotropic ^{29}Si chemical shift, the ^{29}Si chemical shift anisotropy, and the ^{1}H–^{29}Si dipolar interaction (to the extent that it behaves inhomogenously).[47] Figure 21 shows results of the ^{1}H–^{29}Si dipolar-dephasing ^{29}Si CP MAS experiment with the dephasing period ranging over more than $4t_{rot}$. Focusing on the points at $2\tau = 0$, $2t_{rot}$ and $4t_{rot}$, one sees very little dephasing decay for the Q_4 (siloxane) signal, and more efficient decay for the Q_2 (geminal silanol) signal than for the Q_3 (single silanol) signal. This again suggests more efficient ^{1}H–^{1}H spin diffusion among the $=Si(OH)_2$ protons than among $\equiv$SiOH protons.

A very direct correlation of ^{1}H CRAMPS dipolar-dephasing behavior with ^{29}Si CP MAS signals is obtained in the experiment shown in Figure 22, in which there is a 2τ ^{1}H–^{1}H

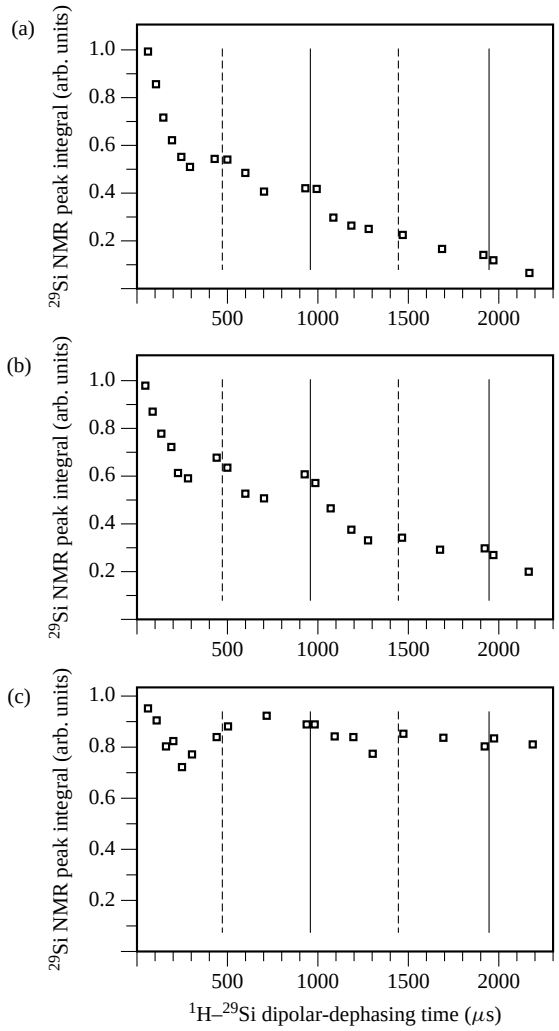

Figure 21 Plots of deconvoluted peak integrals of the 39.75-MHz ^{29}Si CP MAS NMR spectra of Fisher S-679 silica gel versus ^{1}H–^{29}Si dipolar-dephasing time up to four rotor periods. CP contact time, 5 ms; magic angle spinning speed, 2.0 kHz. Vertical dashed lines show odd numbers of rotor periods and vertical solid lines show even numbers of rotor periods. (a) −89 ppm peak (geminal silanols); (b) −99 ppm peak (single silanols); (c) −109 ppm peak (siloxane silicons). (Taken from Chuang et al.[47])

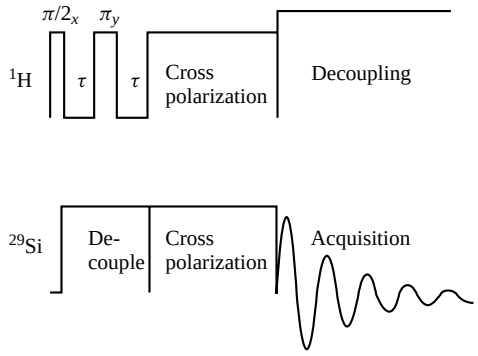

Figure 22 ^{29}Si CP MAS NMR experiment with ^{1}H–^{1}H dipolar-dephasing prior to ^{1}H → ^{29}Si cross polarization. (Taken from Chuang et al.[47])

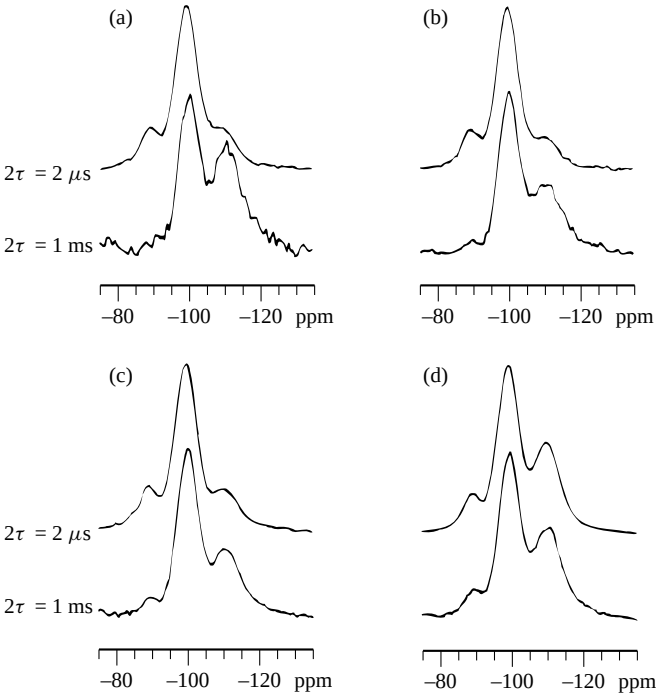

Figure 23 ^{29}Si CP MAS NMR spectra of Fisher S-679 silica gel obtained with 2 μs (top spectrum of each set) and two rotor periods (1.04 ms; bottom spectrum of each set) of ^{1}H–^{1}H dipolar-dephasing prior to four different ^{1}H–^{29}Si CP contact times. Magic angle spinning speed, 1.9 kHz. (a) t_{cp} = 100 μs (top spectrum, 7376 accumulations; bottom spectrum, 82 504 accumulations); (b) t_{cp} = 300 μs (top spectrum, 2400 accumulations; bottom spectrum, 46 200 accumulations); (c) t_{cp} = 1 ms (top spectrum, 432 accumulations; bottom spectrum, 21 232 accumulations); (d) t_{cp} = 5 ms (top spectrum, 600 accumulations; bottom spectrum, 8320 accumulations). (Taken from Chuang et al.[47])

dipolar-dephasing period *before* CP transfer to ^{29}Si.[47] Taking account of the rotational echo behavior of ^{1}H magnetization, for $2\tau = 2nt_{rot}$ essentially all relevant proton interactions refocus except the ^{1}H–^{1}H dipolar interaction. Hence, the magnetization of those protons involved in the strongest (shortest, least mobile) hydrogen bonds is most effectively dephased during $2\tau = 2nt_{rot}$ and unavailable for CP transfer to ^{29}Si. Figure 23 shows the results obtained on a silica gel sample. For a CP contact time (t_{cp}) that is small enough (100 μs) to avoid the rotating frame spin diffusion that scrambles the desired ^{1}H–^{29}Si correlation (vide supra), the geminal silanol peak at −89 ppm is the one that suffers most from ^{1}H–^{1}H dipolar dephasing for a $2t_{rot}$ period. The effect of rotating frame proton spin diffusion is also clear from the spectra in Figure 23: if a long CP contact period (e.g. 1–5 ms) is employed, essentially the same relative peak intensities are obtained whether or not the $2t_{rot}$ ^{1}H–^{1}H dipolar-dephasing period is included in the experimental sequence.

One overriding theme emerges from all the results embodied in Figures 20–23: the protons that are primarily responsible for cross polarization to geminal silanol silicons are much more extensively involved in hydrogen bonding than are the protons primarily responsible for cross polarization to single silanol silicons. This theme is consistent with structural models of the

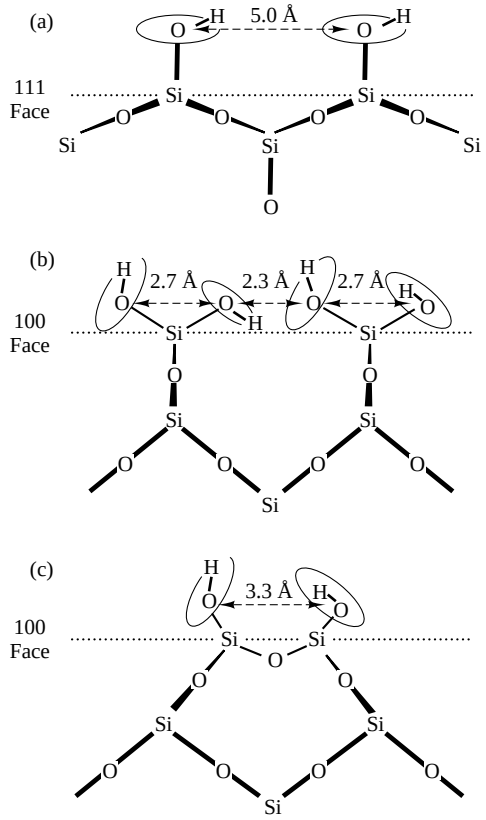

Figure 24 Side views of specific silicon planes (dashed line representing an edge of such a plane) of β-cristobalite. Drawing approximately to scale: (a) 111 face; (b) 100 face; (c) vicinal sites from dehydration of the 100 face. (Taken from Chuang et al.[47])

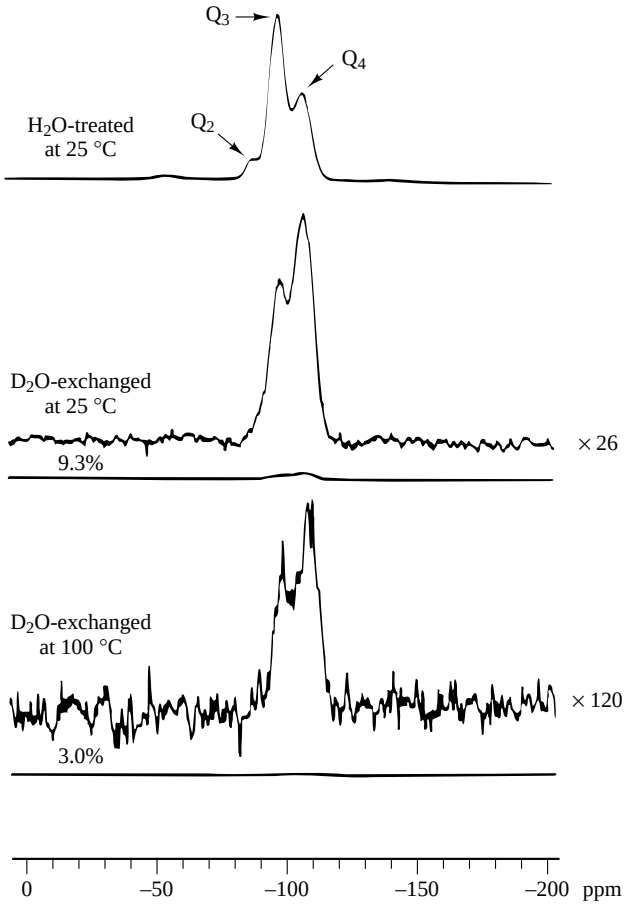

Figure 25 ^{29}Si CP MAS spectra of silica gels stirred in H_2O or D_2O at 25 °C or 100 °C, as indicated

silica surface (or, at least fragments of it) that correspond to specific faces of a β-cristobalite crystal.[47,48]

Figure 24 shows views looking 'into' the 111 and 100 faces, which contain single silanols (Q_3) and geminal silanols (Q_2), respectively. From the O–O distances between hydroxyl oxygens of these surfaces, we see that one should expect hydrogen bonding between adjacent geminal silanols, but not between adjacent single silanols; this is in agreement with the NMR results summarized above. Of course, the silica surface is not a homogeneous one, and may be describable as a composite of these two types of surfaces, with suitable interfaces. The geometrical relationship between silanols that are adjacent *across* these interfaces is important in the overall hydrogen-bonding patterns at silica surfaces. Furthermore, the presence of water on the surface dramatically changes the pattern of hydrogen bonding, including the establishment of hydrogen-bonding networks among the single silanols.

7 SUBSURFACE SILANOLS

An implicit assumption on which the use of ^{29}Si CP MAS as a kind of surface-selective technique is based is the following: essentially all (or at least most) of the protons of a sample like SiO_2 are at the surface. This assumption has been tested in a variety of ways, including ^{29}Si NMR. One NMR avenue for testing this assumption is to examine the ^{1}H and/or ^{29}Si NMR spectra of samples that have been subjected to repeated exchanges with D_2O. Figure 25 shows the ^{29}Si CP MAS spectra of silica gel samples that have been treated in this way.[40] From such studies, it has been determined that for a typical silica gel, 91–97% of the silanols are exchangeable with D_2O, the exact percentage depending on the time and temperature of the exchange. The geminal silanol signal is completely depleted by D_2O exchange, and Figure 26 shows that this signal is immediately restored to its equilibrium intensity shortly after a D_2O-exchanged silica is exposed to the moisture in air. Hence, none of the inaccessible or subsurface silanols are of the Q_2 type.

Extensive studies of spin dynamics in D_2O-exchanged samples have revealed a substantial amount of detail about the local environment and motional dynamics of 'internal' silanols in silica gel.[40] The T_{HSi} values indicate that the hydroxy groups of 'internal' silanols rotate freely about the Si–O axis in a manner similar to the rotation of non-hydrogen-bonded silanols on a dehydrated silica surface. Analogous studies have also been carried out on a fumed silica Cab-O-Sil.[24] While the D_2O-exchange behavior and various features of ^{1}H and ^{29}Si spin dynamics in Cab-O-Sil are qualitatively similar to what is discussed above for silica gel, some significant and possibly important differences are observed,[24] perhaps because of interparticle (particle bridging) silanols that have been suggested by some authors for fumed silicas.

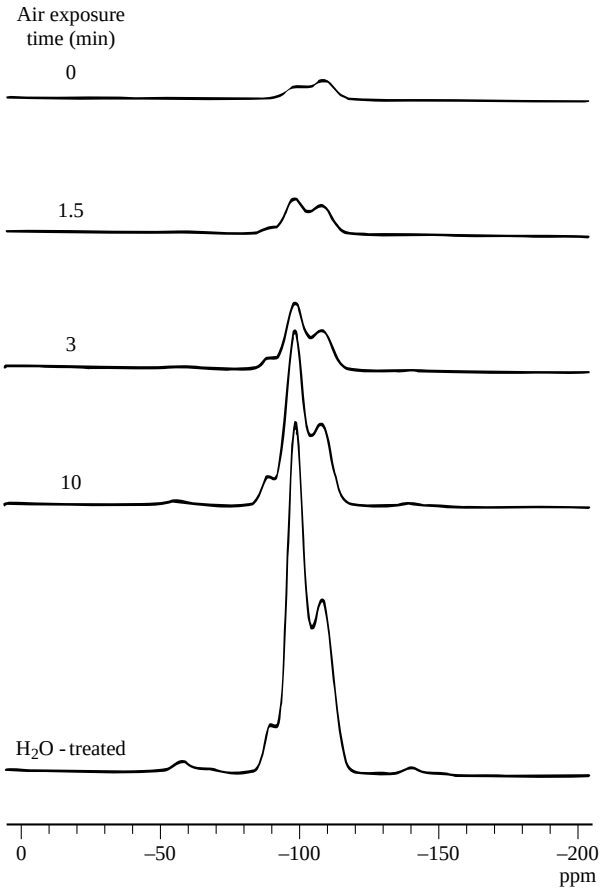

Figure 26 ^{29}Si CP MAS spectra of a D_2O-exchanged silica gel, after air exposure for the indicated times, or (bottom) stirred in H_2O

8 SUMMARY AND CONCLUSIONS

MAS NMR approaches based on ^{1}H and ^{29}Si are enormously useful in the characterization of silica surfaces, including derivatized silica surfaces. The CRAMPS technique, and especially dipolar-dephasing elaborations, provide a powerful way to distinguish between hydrogen bonding and isolated silanols. Silicon-29 CP MAS spectra clearly distinguish between Q_2, Q_3, and Q_4 sites at the surface. Via $^{1}H \rightarrow {}^{29}Si$ cross polarization, the ^{29}Si CP MAS technique provides avenues for projecting ^{1}H spin behavior onto a ^{29}Si NMR spectrum. D_2O-exchange approaches allow the use of ^{1}H and ^{29}Si NMR behavior to examine subsurface or trapped silanols.

9 RELATED ARTICLES

CRAMPS; Silicon-29 NMR of Solid Silicates.

10 REFERENCES

1. R. K. Iler, *The Chemistry of Silica. Solubility, Polymerization, Colloid and Surface Properties, and Biochemistry*, Wiley-Interscience, New York, 1979.
2. G. Engelhardt and D. Michel, *High Resolution Solid-State NMR of Silicates and Zeolites*, Wiley, New York, 1987.
3. G. E. Maciel, C. E. Bronnimann, R. C. Zeigler, I.-S. Chuang, D. R. Kinney, and E. A. Keiter, in *The Colloid Chemistry of Silica. Adv. Chem. Ser. No. 234*, ed. H. Bergna, Am. Chem. Soc., Washington, DC, 1994, p. 269.
4. G. E. Maciel and P. D. Ellis, in *NMR Techniques in Catalysis*, eds. A. T. Bell and A. Pines, Marcel Dekker, New York, 1994, pp. 231–310.
5. G. E. Maciel, in *Nuclear Magnetic Resonance in Modern Technology, NATO ASI Series C* ed. G. E. Maciel, Kluwer, Amsterdam, 1994, p. 225.
6. P. C. Hammel, P. L. Kuhns, O. Gonen, and J. S. Waugh, *Phys. Rev. B*, 1986, **34**, 6543.
7. R. A. Wind, M. J. Duijvestijn, C. Van Der Lugt, A. Manenschijn, and J. Vriend, *Prog. NMR Spectrosc.*, 1985, **17**, 33.
8. D. Raftery, H. Long, T. Meersmann, P. J. Grandinetti, L. Reven, and A. Pines, *Phys. Rev. Lett.*, 1991, **66**, 584.
9. A. Pines, W. G. Gibby, and J. S. Waugh, *J. Chem. Phys.*, 1973, **59**, 569.
10. G. E. Maciel and D. W. Sindorf, *J. Am. Chem. Soc.*, 1980, **102**, 7606.
11. D. W. Sindorf and G. E. Maciel, *J. Phys. Chem.*, 1982, **86**, 5208.
12. J. Schaefer and E. O. Stejskal, *J. Am. Chem. Soc.*, 1976, **98**, 1031.
13. M. Mehring, *High Resolution NMR in Solids*, Springer, Berlin, 1983, p. 135.
14. D. W. Sindorf and G. E. Maciel, *J. Am. Chem. Soc.*, 1983, **105**, 1487.
15. G. E. Maciel, D. W. Sindorf, and V. J. Bartuska, *J. Chromatogr.*, 1981, **205**, 438.
16. D. W. Sindorf and G. E. Maciel, *J. Am. Chem. Soc.*, 1981, **103**, 4263.
17. D. W. Sindorf and G. E. Maciel, *J. Am. Chem. Soc.*, 1983, **105**, 3767.
18. D. W. Sindorf and G. E. Maciel, *J. Phys. Chem.*, 1983, **87**, 5516.
19. G. S. Caravajal, D. E. Leyden, G. R. Quinting, and G. E. Maciel, *Anal. Chem.*, 1988, **60**, 1776.
20. C. J. Brinker, R. J. Kirkpatrick, D. R. Tallant, B. C. Bunker, and B. Montez, *J. Non-Cryst. Solids*, 1988, **99**, 418.
21. C. J. Brinker, R. K. Brow, D. R. Tallant, and R. J. Kirkpatrick, *J. Non-Cryst. Solids*, 1990, **120**, 26.
22. S. Léonardelli, L. Facchini, C. Fretigny, P. Tougne, and A. P. Legrand, *J. Am. Chem. Soc.*, 1992, **114**, 6412.
23. A. Tuel, H. Hommel, A. P. Legrand, Y. Chevallier, and J. C. Morawski, *Colloid Surf.*, 1990, **45**, 413.
24. C. Liu and G. E. Maciel, unpublished results.
25. L. L. Hench and J. K. West, *Chem. Rev.*, 1990, **90**, 33.
26. I. Elnahhal, J. Yang, I.-S. Chuang, S. F. Dec, and G. E. Maciel, *J. Non-Cryst. Solids*, submitted.
27. T. H. Walter, G. L. Turner, and E. Oldfield, *J. Magn. Reson.*, 1988, **76**, 106.
28. C. E. Bronnimann, B. L. Hawkins, M. Zhang, and G. E. Maciel, *Anal. Chem.*, 1988, **60**, 1743.
29. G. E. Maciel, C. E. Bronnimann, and B. L. Hawkins, in *Advances in Magnetic Resonance: The Waugh Symposium*, ed. W. S. Warren, Academic Press, San Diego, CA, 1990, Vol. 14, pp. 125–150.
30. Z. Luz and A. J. Vega, *J. Phys. Chem.*, 1987, **91**, 374.
31. J. S. Waugh, L. M. Huber, and V. Haeberlen, *Phys. Rev. Lett.*, 1968, **20**, 180.
32. W.-K. Rhim, D. D. Elleman, and R. W. Vaughan, *J. Chem. Phys.*, 1973, **58**, 1772.
33. D. P. Burum and W. K. Rhim, *J. Chem. Phys.*, 1979, **71**, 944.
34. B. C. Gerstein, R. G. Pembleton, R. C. Wilson, and L. M. Ryan, *J. Chem. Phys.*, 1977, **66**, 361.

35. S. F. Dec, C. E. Bronnimann, R. A. Wind, and G. E. Maciel, *J. Magn. Reson.*, 1989, **82**, 454.
36. D. R. Kinney, I.-S. Chuang, and G. E. Maciel, *J. Am. Chem. Soc.*, 1993, **115**, 6786.
37. D. Suwelack, W. P. Rothwell, and J. S. Waugh, *J. Chem. Phys.*, 1980, **73**, 2559.
38. C. E. Bronnimann, R. C. Zeigler, and G. E. Maciel, *J. Am. Chem. Soc.*, 1988, **110**, 2023.
39. R. Freeman and H. D. Hill, *J. Chem. Phys.*, 1971, **54**, 3367.
40. I.-S. Chuang, D. R. Kinney, and G. E. Maciel, *J. Am. Chem. Soc.*, 1993, **115**, 8695.
41. R. J. Wittebort, M. G. Usha, D. J. Ruben, D. E. Wemmer, and A. Pines, *J. Am. Chem. Soc.*, 1988, **110**, 5668.
42. R. A. Lewis, Ph.D. Dissertation, Colorado State University, 1994.
43. D. P. Burum and A. Bielecki, *J. Magn. Reson.*, 1991, **94**, 645.
44. C. E. Bronnimann, C. Ridenour, D. R. Kinney, and G. E. Maciel, *J. Magn. Reson.*, 1992, **97**, 522.
45. A. J. Vega, *J. Am. Chem. Soc.*, 1988, **110**, 1049.
46. R. A. Santos, R. A. Wind, and C. E. Bronnimann, *35th Exp. NMR Conf., Asilomar, CA, April 14, 1994*.
47. I.-S. Chuang, D. R. Kinney, C. E. Bronnimann, R. C. Zeigler, and G. E. Maciel, *J. Phys. Chem.*, 1992, **96**, 4027.
48. D. W. Sindorf, Ph.D. Dissertation, Colorado State University, 1982.

Acknowledgments

For that portion of the research described in this paper that was carried out at Colorado State University, the author gratefully acknowledges partial support by National Science Foundation grants during the past few years. He also acknowledges the invaluable assistance over many years of Dr. I.-Ssuer Chuang.

Biographical Sketch

Gary E. Maciel. *b* 1935. B.S., 1956, chemistry, University of California, Berkeley, Ph.D., 1960, Massachusetts Institute of Technology (MIT). Postdoctoral work at MIT (with John S. Waugh), 1960–61 which provided first hands-on experience with NMR. Assistant professor, associate professor, professor at the University of California, Davis, 1961–70. Professor of Chemistry, Colorado State University, 1971–present. Approx. 320 publications. Research specialties: development and application of NMR techniques, especially for solids and surfaces, and currently for environmental studies.

Supported Metal Catalysts

Marek Pruski

Iowa State University, Ames, IA, USA

1	Introduction	1
2	Samples	1
3	NMR of Metals	1
4	Proton NMR	3
5	Adsorption and Reaction of Simple Molecules on Supported Metals	7
6	Conclusion	12
7	Related Articles	12
8	References	12

1 INTRODUCTION

Catalysis is playing an increasingly important role in a variety of industries and has become a very significant contributor to the world economy. For example, the total value of fuels and chemicals derived through catalysis in the USA exceeds 20% of the US gross national product. Today, most of the applications of industrial significance use heterogeneous catalysis, the term being restricted to catalytic phenomena involving a solid catalyst and reactants in a gas or liquid phase. The first industrial heterogeneous catalytic reaction was introduced over 100 years ago and used platinum to oxidize SO_2 to SO_3; other important processes soon followed. Metal catalysts are of great significance in heterogeneous catalysis, particularly in processes involving hydrogen (e.g. hydrogenation, hydrogenolysis, and catalytic reforming) and in oxidation reactions. In most applications metals are used in the form of small particles (typically 1–10 nm) highly dispersed on thermally stable materials with large surface area, such as metal oxides, zeolites, and silica.

As the use of catalysis has continued to grow, so has the need for a basic understanding of catalytic processes. A realistic description of catalytic reactions requires both detailed information on catalytic surfaces and a fundamental knowledge of the nature and dynamics of the elementary phenomena involved. This knowledge, along with past experience and intuition, should make it possible to develop catalysts that are more active, selective, stable, and less expensive. Despite the enormous growth of surface science in the last two decades, the understanding of how catalysts work continues to be insufficient. Although most researchers still use traditional methods (e.g. volumetric, gravimetric, and reactor studies, calorimetry, and microscopy), spectroscopic studies are essential for gaining further insight into elementary processes on surfaces. Most of the spectroscopic methods used to investigate single crystal metal surfaces require ultrahigh vacuum, and cannot be applied to working catalysts; however, X-ray spectroscopies, infrared spectroscopy, and, lately, NMR have become the tools of particular value. Several review articles have been already published which summarize the early[1,2] and recent[3,4] NMR results.

The use of NMR begins with characterization of metal surfaces and then correlation of this information with catalytic performance. Such studies can be performed directly by using NMR of metals or by observing probe molecules adsorbed on the metal surface. NMR can be also used in its traditional role as a tool to study the structure of reactants and products and to perform quantitative investigations under conditions typical of catalytic reactions. In addition, NMR has the ability to probe the dynamics of all processes that are essential for catalysis, including diffusion, adsorption, and reaction. This article describes and discusses some of these significant applications.

2 SAMPLES

The metals most commonly used for catalysis involve elements from Group VIII of the Periodic Table (e.g. Co, Ni, Ru, Rh, Pd, and Pt), and Cu, used in pure or mixed (e.g. bimetallic) form. The supports include alumina (Al_2O_3), silica (SiO_2), titania (TiO_2), silica–alumina, and aluminosilicates (zeolites), usually synthesized in a highly porous form with characteristic surface area ranging from few to about 1000 m^2 g^{-1}. The metals are deposited on supports by impregnation or ion exchange, which is usually followed by drying, calcination, and reduction that result in the formation of metal particles. Loadings of 1–2 wt % or more are common in industrial catalysts but can be as high as 20 wt % in catalysts used for the laboratory studies. Only a small fraction of the support is covered with metal, and the average interparticle distances are usually several times larger than the particle size. Depending on the metal and the support used, and the preparation conditions, dispersions range between about 1.0 and < 0.05 which corresponds to particle sizes of about 1–50 nm and 10^{19}–10^{20} of metal surface sites per gram of catalyst. Particles bigger than 2 nm consist largely of low index plane facets, and their adsorption sites are similar to those on single crystals. However, in highly dispersed metals, the number of lower coordinated sites increases significantly. For example, a perfect cuboctahedral particle composed of 586 atoms has 272 atoms on the surface (and the corresponding dispersion of 272/586 = 0.345), 44% of which are less than nine-fold coordinated, e.g. occupying edge and corner sites. In a larger cuboctahedral particle composed of 37 766 atoms, the corresponding values are 4332, 0.13 and 27%, respectively. In real catalysts a distribution of particle sizes can exist with a variety of possible shapes and irregularities that further increase the number of low coordinated sites.

Prior to adsorption, the metal surfaces are cleaned and activated. The detailed descriptions of these procedures and the adsorption conditions can be found in the literature and are thus not given here. Only note that in the studies of catalytic processes, the results are strongly susceptible to small changes in the way that adsorbents and adsorbates are prepared and brought into contact as well as in the conditions of the measurements.

3 NMR OF METALS

The most 'NMR-friendly' metal nuclei that are of interest in catalysis include ^{63}Cu ($I = \frac{3}{2}$, natural abundance 69%, and

relative sensitivity versus ^{1}H of 9.3×10^{-2}), ^{109}Ag ($I = \frac{1}{2}$, 48%, about 10^{-4}), and ^{195}Pt ($I = \frac{1}{2}$, 34%, about 10^{-2}). The NMR properties of these nuclei in bulk metals are dominated by the Knight shift interaction between nuclear spins and the conduction electrons. A detailed review of the theory and experimental data can be found elsewhere[5] (see also ***Knight Shift***), and only a brief description of this phenomenon is given below. The hyperfine interaction between the electron and nuclear spin $\boldsymbol{I}$ can be written as:

$$\hat{\mathcal{H}}_{en} = -\gamma_n \hbar \hat{\boldsymbol{I}} \cdot \boldsymbol{B}_{\text{eff}} \tag{1}$$

where γ_n is the nuclear gyromagnetic ratio and $\boldsymbol{B}_{\text{eff}}$ is the effective magnetic field induced by an electron at the nuclear site. The position of the NMR line is determined by the time average value of $\hat{\mathcal{H}}_{en}$ due to all electrons in the metal. In para- and diamagnetic substances, this value is nonzero only in the presence of an external magnetic field $\boldsymbol{B}_0$, and the NMR frequency is usually proportional to that field:

$$\omega_0 = \gamma_n (1 + K) B_0 \tag{2}$$

where $(\gamma_n B_0)/2\pi$ describes the frequency of a reference, and K is the resonance shift which in metals includes the Knight shift and the generally smaller chemical shift. Three terms can contribute to $\hat{\mathcal{H}}_{en}$: the Fermi contact interaction, the dipolar interaction, and the interaction with electronic orbital moment. The dipolar term results in line broadening but does not change the resonance frequency. The orbital term is responsible for the chemical shift and is usually much smaller than the Knight shift. The Knight shift results from the contact interaction, described by the Hamiltonian:

$$\hat{\mathcal{H}}_c = \frac{8\pi}{3} \gamma_e \gamma_n \hbar^2 \hat{\boldsymbol{I}} \cdot \hat{\boldsymbol{S}} \delta(\boldsymbol{r}) \tag{3}$$

where γ_e is the electronic gyromagnetic ratio and $\boldsymbol{r}$ is the vector that has its origin at the nuclear site and describes the position of the electron spin $\boldsymbol{S}$. The main contribution to the Knight shift is from the s electrons because their wave function does not vanish at the nuclear site.

An extensive ^{195}Pt NMR study of small particles of platinum supported on alumina has been performed by Slichter and co-workers.[6–8] The samples consisted of about 10 wt % platinum with dispersions between 4% and 58%, as determined by hydrogen chemisorption. Due to large inhomogeneous broadening of the NMR lines (3–5 MHz at the frequency of 74 MHz), only a small fraction of the nuclei could be excited in a single experiment, and the spin echo mapping technique was used to measure the NMR lineshapes (see Figure 1). In this technique, the intensities produced by an add–subtract spin echo pulse sequence at different values of the static magnetic field $\boldsymbol{B}_0$ and at a fixed frequency were plotted, point by point, to produce the complete NMR spectrum.[6]

The spectra shown in Figure 1 exhibit a full distribution of Knight shifts in the samples with platinum particles of different dispersions and subjected to various types of treatment. The Knight shift in bulk platinum results from a direct contact interaction with the 6s electrons [high-frequency (downfield) shift] and a core polarization via the 5d electrons (low-frequency shift). The net effect of these two contributions results in a low-frequency shift of about 4% of the ^{195}Pt resonance in the bulk platinum relative to the nonmetallic compounds. In Figure 1 the bulk ^{195}Pt nuclei located in the interior of platinum particles are represented by a sharp

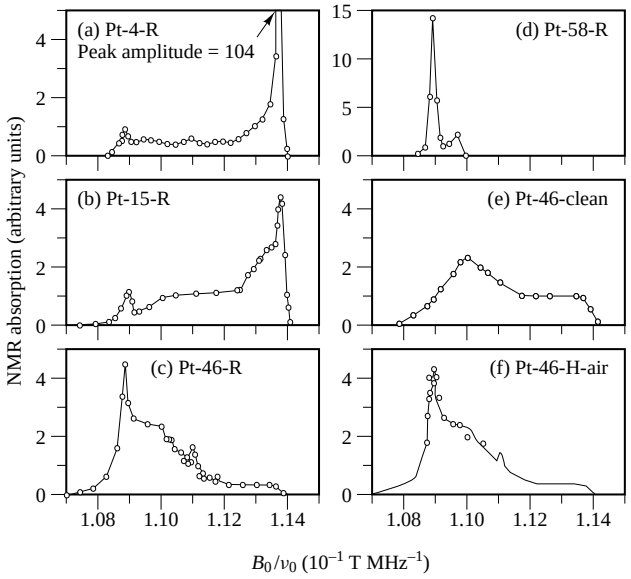

Figure 1 ^{195}Pt NMR lineshapes for several alumina-supported platinum catalysts: (a)–(d) Untreated catalysts (exposed to air) with dispersions of 0.04, 0.15, 0.46, and 0.58, respectively; (e) same as (c) but adsorbed molecules cleaned from the surface by alternate flow of O_2 and H_2, each followed by evacuation at 600 K; (f) same as (e) but again exposed to hydrogen and air for several weeks. All spectra were measured at 77 K using a spin echo mapping technique. (Reproduced by permission of The American Physical Society from H. E. Rhodes, P.-K. Wang, H. T. Stokes, C. P. Slichter, and J. H. Sinfelt, *Phys. Rev. B*, 1982, **26**, 3559)

feature in the low-frequency portion of the spectrum at $B_0/\nu_0 \approx 0.114$ T MHz^{-1}. Note that this feature is only observed in samples with less dispersed, large particles. The contributions from the contact interaction of the 6s electrons and 5d core polarization progressively cancel for nuclei located in a less bulk-like environment, i.e. closer to the particle surface. Almost complete cancellation occurs at the surfaces of particles when they are covered with adsorbed molecules. In this case, the surface platinum atoms are tied up in chemical bonds and lose their metallic character.[7] In the spectra shown in Figure 1, the surface platinum is represented by the high-frequency, narrow peak at $B_0/\nu_0 = 0.1089$ T MHz^{-1}. This assignment was verified by measuring the areas of this peak relative to the total intensity of the spectrum, which correlated well with the platinum dispersions obtained from hydrogen chemisorption. Furthermore, the use of SEDOR allows resolution of the NMR spectrum of the surface layer of platinum particles coated with ^{13}C enriched CO.[8] In this experiment, the magnetization of ^{13}C spins was flipped concurrently with the ^{195}Pt π pulse, which modified the ^{195}Pt spin echo amplitude for the spins located at the particle surface. By subtracting appropriately scaled signals measured with and without ^{13}C π pulses, the surface ^{195}Pt spins could be singled out in the NMR spectra (see Figure 2). The final width of the SEDOR line results from distribution of isotropic Knight shifts at different platinum sites, anisotropy of chemical shifts, and anisotropic hyperfine coupling.[8]

Significant changes in the ^{195}Pt lineshape were observed upon removal of the adsorbed species from the platinum surface [Figure 1(e)]. The narrow high-frequency peak disappeared and the intensity of the 'metallic' portion of the

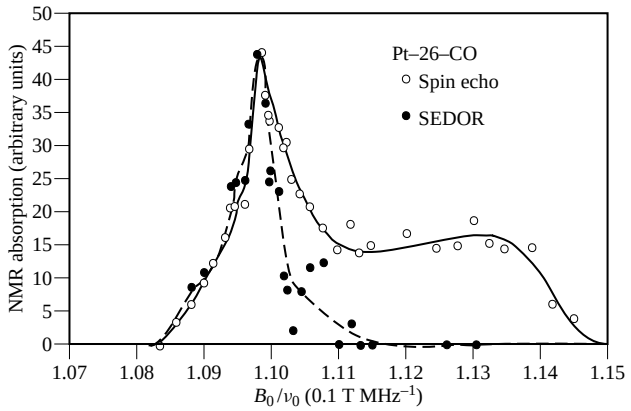

Figure 2 ^{195}Pt NMR lineshape at 77 K obtained with spin echo mapping and SEDOR for platinum particles (dispersion 0.26) adsorbed with CO. (Reproduced by permission of The American Physical Society from D. Makowka, C. P. Slichter, and J. H. Sinfelt, *Phys. Rev. B*, 1985, **31**, 5663)

spectrum increased, suggesting that for the platinum atoms on a clean surface the 5d–6s Knight shift cancellation is not complete (although still greater than in the bulk metal). The ^{195}Pt NMR lineshape in Figure 1(c) was restored upon exposure of the catalyst to air for several weeks [Figure 1(f)]. The spectra shown in Figures 1 and 2 were reproduced by lineshape calculations based on a phenomenological model of the spatial variation of the Knight shift in the platinum particles.[8] Similar ^{195}Pt NMR studies were performed on titania-supported platinum particles.[9]

The NMR of ^{109}Ag was applied to study silver particles supported on Al_2O_3 and SiO_2 by Mastikhin.[10] In the bulk metal the ^{109}Ag nuclei are located in a highly symmetrical environment of cubic, face-centered, metal crystals and exhibit a narrow [about 200 Hz full width at half maximum (FWHM)] resonance with a Knight shift of 5000 ppm (to high frequency relative to water solution of $AgNO_3$). The ^{109}Ag NMR of supported catalysts showed that the resonance from the bulk metal was only observed for samples containing particles larger than 40 nm. The 'nonmetallic' silver particles (<40 nm) could not be detected, presumably because of longer spin–lattice relaxation times, greater linewidth, or both. A similar effect was reported in a ^{63}Cu NMR study on a series of silica-supported copper catalysts by Gerstein and coworkers.[11] In this case, the electric field gradient asymmetries near the copper surface were too large to allow detection of the surface nuclei, and the reduced catalysts showed only one resonance characteristic of the Cu(0) bulk copper. However, the surface atoms could be observed after chloriding the surface of copper with HCl gas. The intensity of the ^{63}Cu NMR peak assigned to CuCl showed good agreement with the amount of surface copper determined by a reaction with nitrous oxide.[11]

4 PROTON NMR

Hydrogen is the simplest and most important of all adsorbates and plays a dual role in catalysis; it is not only a reactant or product in many catalytic reactions but also can be a powerful probe for investigating the surface of the catalyst. In addition, it is the most common of all NMR active nuclides, and with about 100% natural abundance and a large magnetic moment is relatively easy to detect on surfaces. The earliest ^{1}H NMR work involved hydrogen adsorbed on Al_2O_3- and SiO_2-supported platinum,[12] TiO_2-supported rhodium,[13–15] and all platinum metals (Ru, Rh, Pd, Os, Ir, and Pt) supported on SiO_2.[16] The samples used in these studies were sealed in glass tubes and measured at room temperature under single pulse excitation. Later work included more complicated catalytic systems, e.g. bimetallic catalysts[17] and promoted metals,[18] and involved more advanced NMR methods: selective excitation, two-dimensional NMR, and in situ NMR at variable pressures and temperatures.[19] In general, application of MAS and decoupling techniques did not lead to increased resolution in ^{1}H NMR on supported metals because of the heterogeneity of samples and the high intrinsic mobility of hydrogen.

A set of ^{1}H NMR spectra for supported rhodium, ruthenium, and copper is shown in Figure 3. Each spectrum shows a peak at about 0 ppm (from TMS), which represents diamagnetic hydrogen on the support, mainly in OH groups, and hydrogen that spilled over from the metal. Other resonance lines in the spectra represent hydrogen interacting with the metal and are usually observed outside of the chemical shift range for ^{1}H (0–15 ppm). The observed resonance frequency and lineshape depend on the type of metal, conditions under which the metal surface was prepared, particle size, temperature, and hydrogen pressure.[13,15–20] For hydrogen adsorbed on the Group VIII metals, low-frequency shifts of ^{1}H NMR lines are observed, ranging from less than −20 ppm for osmium to above −140 ppm for rhodium,[16] whereas hydrogen on copper has a high-frequency shift of about 90 ppm. Although

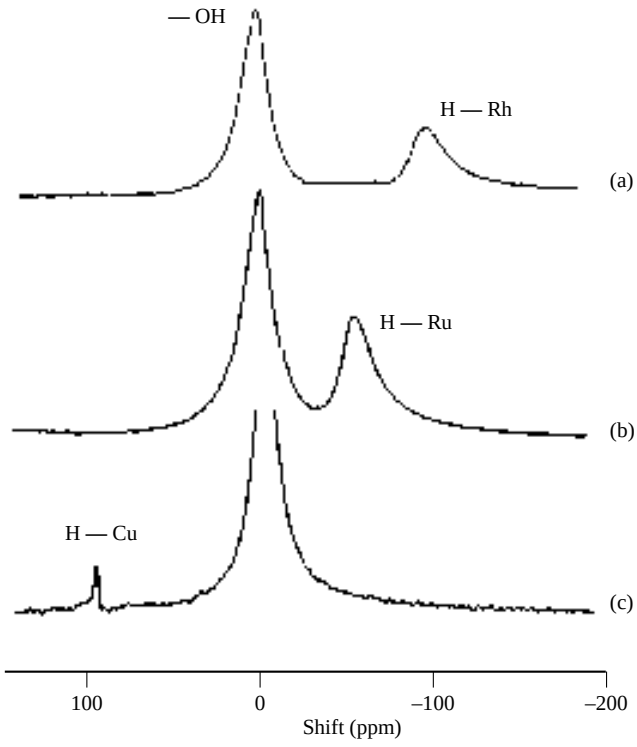

Figure 3 ^{1}H NMR spectra of hydrogen adsorbed at 4000 Pa on supported catalysts: (a) Rh/TiO_2; (b) Ru/SiO_2; (c) Cu/SiO_2

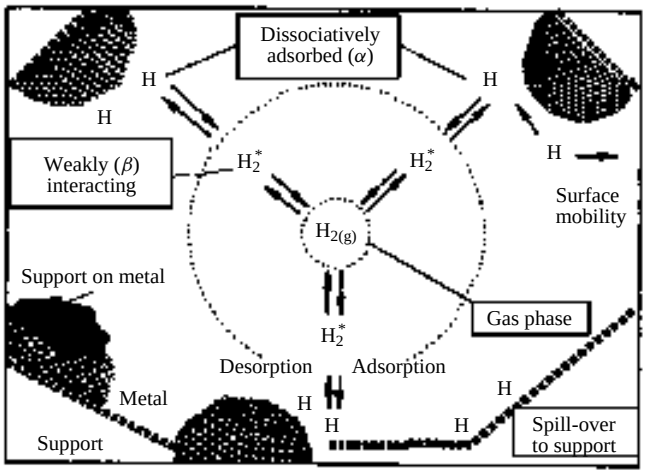

Figure 4 Model of a catalyst in the presence of hydrogen

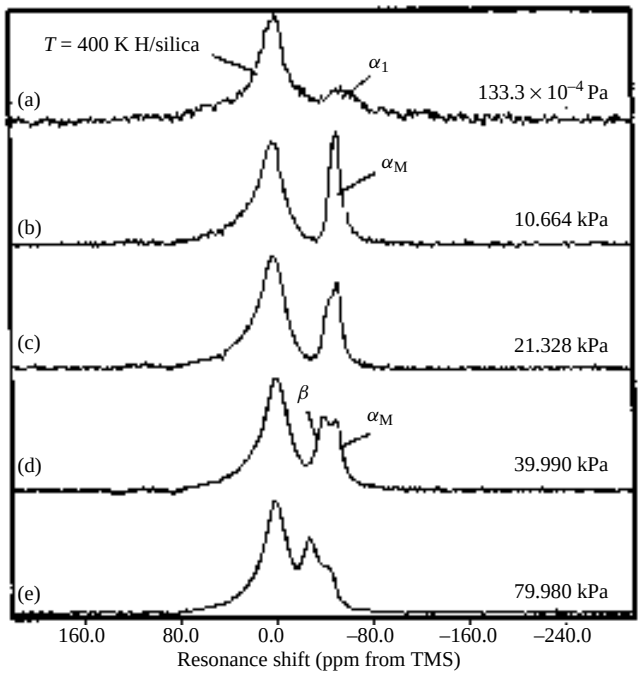

Figure 5 In situ ^{1}H NMR spectra of hydrogen at 400 K on an Ru/SiO_2 catalyst (dispersion 0.30, Ru loading 8 wt %) at various H_2 pressures. (Reproduced by permission of The American Physical Society from F. Engelke, S. Bhatia, T. S. King, and M. Pruski, *Phys. Rev. B.*, 1994, **49**, 2730)

in most studies only one resonance line is observed arising from hydrogen on metals, the presence of several types of adsorbed hydrogen species was inferred from the analysis of NMR data. The large shifts in the spectra shown in Figure 3 are associated with the Knight shift—the polarization of the adsorbed hydrogen species occurs because of the bonding overlap between the hydrogen 1s orbitals and the conduction s electrons or the d electrons of the underlying metal. In general, Knight shifts decrease with increasing coverages due to pairing of the electron spins in the metal by chemisorbed hydrogen. At high coverages the observed shift can be affected by exchange processes with other types of adsorbed species, H_2 gas, or both.

A scheme representing the supported catalyst surface in the presence of hydrogen is shown in Figure 4. Probing catalyst surfaces with ^{1}H NMR presents a variety of opportunities: (i) studies of the chemical composition and structure of the metal particles; (ii) studies of the interaction between the metal and the support; (iii) determination of concentrations of various hydrogen species on the metal and the support (intrinsic and spilt over); and (iv) measurements of the dynamics on surfaces, including transport phenomena, molecular or atomic mobility, exchange rates between various species, adsorption and desorption rates, and activation energies.

4.1 Studies of Metal Surfaces by ^{1}H NMR: the SMSI Effect

Determining the surface chemical composition, dispersion, and electronic properties and how these factors affect catalyst performance is crucial for understanding the mechanisms of catalytic reactions. The questions of primary importance are: What is the dispersion of the metal? Which atoms are present on the surface? How do these atoms interact with the underlying atomic layers?

The standard method for determining metal dispersion uses volumetric measurement of hydrogen uptake and is based on the assumed surface hydrogen-to-metal stoichiometry H/M = 1. This assumption is supported by investigations of single crystals using X-ray diffraction and transmission electron microscopy (TEM). However, the irreversible spill-over of hydrogen from the metal to the support may result in overestimating the H/M ratio when using the volumetric technique. Quantitative measurements of hydrogen uptake by NMR are obtained by comparing the intensity of the adsorbed hydrogen with that of a reference standard. Several studies on the supported Ru, Rh, Pt, Ru–Cu, Ru–Ag, Ru–Au, and other systems clearly showed the advantage of an NMR method for estimating dispersions because of NMR's ability to distinguish and measure the adsorption states on the support in addition to the metal.[15,17,18,21]

Figure 5 shows a series of ^{1}H NMR spectra of the Ru/SiO_2 catalyst adsorbed with varying amounts of hydrogen at room temperature. The spectra were acquired by using an in situ NMR probe attached to a volumetric adsorption apparatus. This technique allowed investigation of catalytic systems in steady-state equilibria at variable temperatures and pressures that could be easily and precisely controlled during the experiments.[19–21] Under low-pressure conditions (133×10^{-5}–133×10^{-1} Pa) a resonance α_1 at about −60 ppm was observed, which represented dissociatively adsorbed (chemisorbed) hydrogen on ruthenium that could not be removed from the surface by short evacuation at room temperature. The integrated intensity of this peak measured after 10 min evacuation is used as an estimate of metal dispersion. At elevated pressures the weakly adsorbed hydrogen species are observed. First, an increase of the peak at about −60 ppm occurs as the pressure rises from 133×10^{-1} to 133×10^{2} Pa (hydrogen α_M), whereas another hydrogen species (β) is detected at about −45 ppm upon further elevation of pressure to above 133×10^2 Pa.[19,20] The nature and dynamics of hydrogen at elevated pressures are described later.

In addition, NMR can be used to investigate the chemical composition of metallic particles. The particles composed of more than one metal (e.g. bimetallic) often exhibit surface composition much different from what the catalyst synthesis would suggest. Also, small particles of the catalyst precursor may react with the support, resulting in partial or complete encapsulation of the metal surface and thus lowering their catalytic activity. Characterization of SiO_2-supported Ru–Cu bimetallic catalysts by Wu et al.[17] is an excellent example of such a study. In this work the ^{1}H NMR spectra were measured for a series of Ru–Cu/SiO_2 catalysts prepared with various copper loadings (Figure 6). The bimetallic clusters were formed on silica by coimpregnation with copper atoms which blanketed the ruthenium in a manner similar to chemisorption. A resonance at about −60 ppm observed at 0 atom % copper shifted to high frequency with the increasing coverage of ruthenium by copper. For a copper loading >40 atom % a resonance characteristic of hydrogen on bulk copper appeared at 90 ppm, indicating the formation of larger copper islands on ruthenium or buildup of separate copper particles.

Two different hydrogen spill-over processes were found in this catalyst system: (i) the hydrogen-on-metal NMR intensities indicated a spill-over from ruthenium to copper, and (ii) a spill-over from the metal onto the support was measured by comparing the NMR spectra with the hydrogen uptake from volumetric studies. More importantly, the surface compositions of Ru–Cu particles could be obtained from the observed NMR shifts.[17] If one assumes a fast exchange between hydrogen on ruthenium and copper, the lineshift δ_{obs}, from Figure 6, can be expressed as the weighted average:

$$\delta_{obs} = X_{Ru}\delta_{Ru} + X_{Cu}\delta_{Cu} \quad (4)$$

where δ_{Ru} and δ_{Cu} are lineshifts for hydrogen on ruthenium and copper deposited on ruthenium, and X_{Ru} and X_{Cu} are surface fractions of ruthenium and copper, respectively. Since $X_{Ru} + X_{Cu} = 1$, the surface fraction of ruthenium can easily be obtained from the NMR data. Figure 7 shows the surface fraction of ruthenium plotted against copper content and compared with a theoretical curve for monolayer coverage. Clearly, copper preferentially segregates to the ruthenium surface and in so doing covers the ruthenium in a monolayer fashion before forming three-dimensional copper islands, pure copper particles, or both. The ^{1}H NMR experiments performed for the Ru–Ag and Ru–Au systems showed the formation of three-dimensional particles at much lower silver and gold contents (Figure 7).[22]

The so-called strong metal–support interaction (SMSI) effect, which leads to suppression of H_2 and CO adsorption after a high-temperature reduction of the metal–support system, is often observed in Group VIII metals supported on TiO_2. Possible explanations of this effect include: (a) migration of a reduced form of titania (TiO_x) onto the metal surface, resulting in a physical blockage of the metal sites; and (b) an electronic interaction, either via an electron transfer from the reduced, hydrogen-rich support to the metal, or from the metal to the nonreduced, hydrogen-free support. NMR proved instrumental in studying the SMSI effect. For the Rh/TiO_2 catalyst, the NMR studies indicated that, in addition to the formation of strongly bonded hydrogen on rhodium, a

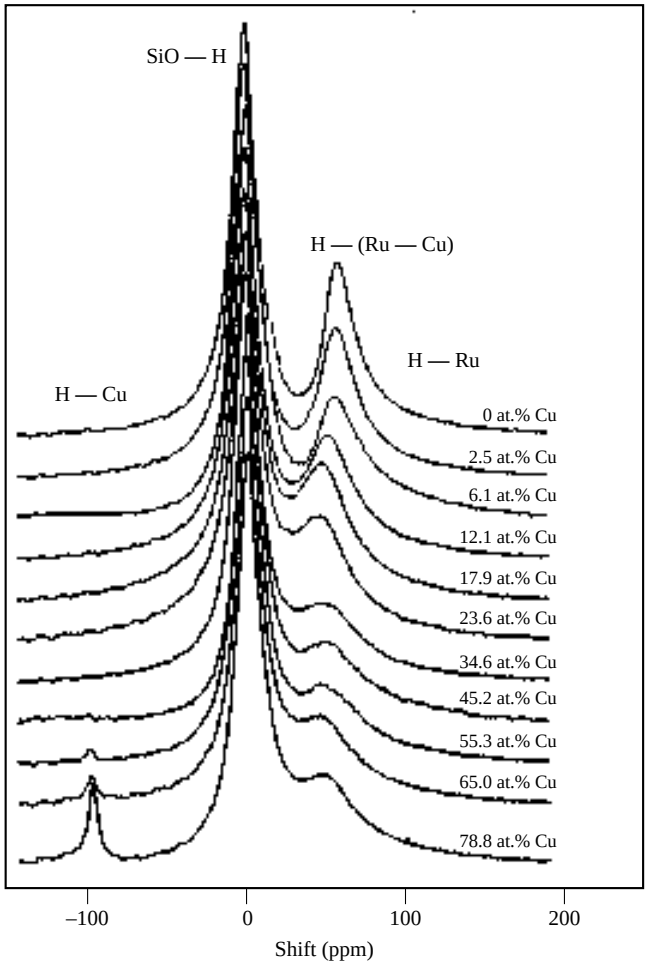

Figure 6 ^{1}H NMR spectra of hydrogen at 300 K on a series of Ru–Cu/SiO_2 catalysts under a hydrogen pressure of 8 kPa. The amount of copper in the bimetallic particles is expressed as atomic per cent. (Reproduced by permission of Academic Press from X. Wu, B. C. Gerstein, and T. S. King, *J. Catal.*, 1990, **121**, 271)

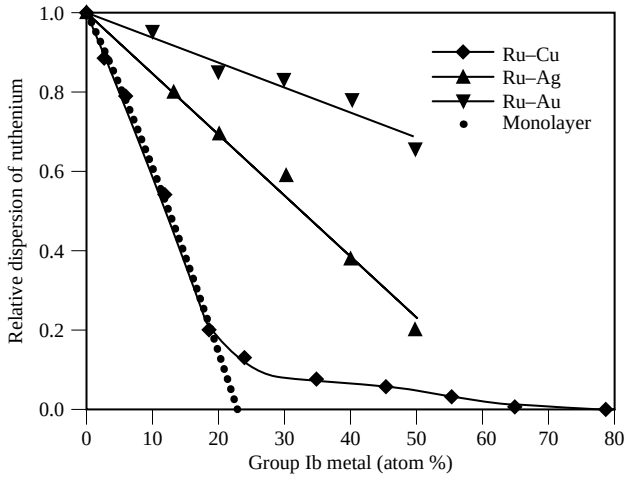

Figure 7 Plots of the surface fraction of ruthenium obtained from NMR as a function of Group Ib metal loading for Ru–Cu/SiO_2, Ru–Ag/SiO_2, and Ru–Au/SiO_2 catalysts. The dotted line represents the ruthenium surface fraction corresponding to a monolayer growth of a second metal on ruthenium. (Reproduced by permission of Academic Press from X. Wu, B. C. Gerstein, and T. S. King, *J. Catal.*, 1990, **123**, 43)

weakly adsorbed species exists. For this species a mechanism was proposed that implied dissociation at the metal–support interface followed by proton stabilization on the support, most likely at the Rh–TiO_2 borderline.[14] This hydrogen affects the surface electronic states of the metal, which is manifested by the decreasing Knight shift of the hydrogen atoms irreversibly bonded to rhodium. As a result of a fast chemical exchange between the two species, only one low-frequency resonance was observed with a shift that could be roughly approximated by the weighted average of strongly and weakly adsorbed species. Also proposed was a metal-to-support electron transfer mechanism that generates Ti^{3+} ions in the vicinity of metal particles, which may be followed by stabilization of H^- species at the surface of the oxide. This electron injection from the metal to the support was proposed to induce the SMSI effect as it reduced the density of states at the Fermi level of rhodium and thereby reduced its capacity to adsorb hydrogen. The hydride-type species on the support were shown to be reversibly generated, and the SMSI condition could be removed by evacuation at elevated temperatures. For that reason the SMSI effect was not explained by the encapsulation of rhodium with TiO_x species migrating from the support, although partial coverage of the rhodium surface or other morphological changes of the metal particles were not ruled out.[15]

Other studies proved quite unambiguously that at least partial encapsulation of metal particles by TiO_x occurs in Ru/TiO_2 catalysts upon high-temperature reduction or during catalyst preparation. Recently, a combination of in situ ^1H NMR, TEM, and H_2 chemisorption was used to determine the metal particle size, the fraction of metal surface available for H_2 chemisorption, and the H_2 adsorption capacity of the catalyst as a function of the reduction temperature.[21] The true particle size of dispersed ruthenium was determined from TEM micrographs, and the fraction of exposed ruthenium atoms was determined by in situ ^1H NMR. By combining these two techniques a quantitative estimate of the extent of ruthenium particle encapsulation was measured as the reduction temperature varied between 470 and 770 K. Since no change in particle size with a reduction temperature was observed by TEM, the decrease in the ratio of hydrogen irreversibly adsorbed on ruthenium to the total amount of ruthenium ($H_{i,Ru}/Ru_{total}$ in Figure 8) was attributed to the progressive coverage of ruthenium particles by TiO_x. The evidence of an amorphous overlayer of TiO_x on ruthenium was also shown in the TEM micrographs. In addition, the extent of hydrogen spillover onto the TiO_2 (H_{i,TiO_2} in Figure 8) was estimated by NMR. This study showed that while ^1H NMR provided an accurate measure of the exposed metal surface available for chemisorption, H_2 volumetric chemisorption could not be reliably used to determine dispersion of a Ru/TiO_2 catalyst, even after reduction at temperatures as low as 473 K, because irreversible hydrogen spill-over from the metal caused this method to overestimate the result. This conclusion implies that turnover frequencies based on volumetric hydrogen uptake cannot be accurate. ^1H NMR and TEM showed no encapsulation of ruthenium by silica in a Ru/SiO_2 catalyst.[21] These results are consistent with similar phenomena found on TiO_2^- and SiO_2^- supported platinum catalysts by using ^{195}Pt NMR.[9]

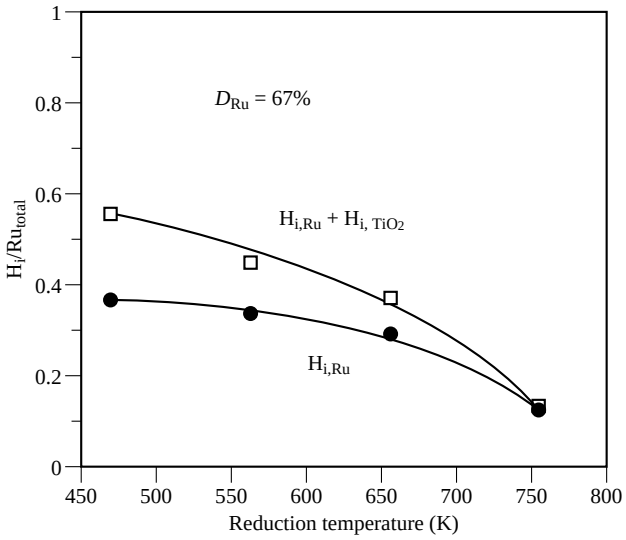

Figure 8 The amount of irreversibly adsorbed hydrogen on ruthenium and TiO_2 versus the catalyst reduction temperature. (Reproduced by permission of Academic Press from T. Komaya, A. T. Bell, Z. Weng-Sieh, R. Gronsky, F. Engelke, T. S. King, and M. Pruski, *J. Catal.*, in press)

4.2 Dynamics of Hydrogen on Surfaces

The NMR studies of dynamics of hydrogen adsorbed on catalysts (adsorption, desorption, diffusion, and exchange) are of great interest since these processes cannot be characterized by most surface spectroscopic techniques. The NMR methods used for these studies depend on the timescale of the dynamic process:

1. The measurements of the longitudinal (spin–lattice) relaxation time T_1 and the longitudinal relaxation time in the rotating frame $T_{1\rho}$ can be used to study relatively fast motions. The T_1 and $T_{1\rho}$ relaxation processes are generally associated with dipolar fields fluctuating at the frequencies $\omega_0 = \gamma B_0$ and $\omega_1 = \gamma B_1$ (where B_1 is the rf magnetic field), respectively. Such fields are generated by motions of other magnetically active nuclei or unpaired electron spins, with correlation times $\tau_c \approx (\omega_0)^{-1}$ for T_1 (nanosecond and microsecond range) and $\tau_c \approx (\omega_1)^{-1}$ for $T_{1\rho}$ (microsecond and millisecond range). The analysis of relaxation has been widely applied to study mobilities of molecules adsorbed on zeolites. On supported metals, however, other sources of relaxation (e.g. Knight shift interaction, collisions with molecules in the gas phase) may supplement the motional effect, rendering this technique less efficient.
2. The analysis of NMR lineshapes has been routinely used to detect slower motions associated with the static spin interactions in solids, characterized by $\tau_c \approx (\Delta\omega)^{-1}$, where $\Delta\omega$ is the NMR linewidth ($10^{-6}\,s < \tau_c < 10^{-2}\,s$). By applying spin labeling techniques (e.g. selective excitation by DANTE or by using a 'soft pulse'), two-dimensional NMR techniques, or field gradient methods, slower motions with $(\Delta\omega)^{-1} < \tau_c < T_1$ can be studied.
3. The isotope labeling method proved to be a powerful tool for probing the dynamic processes with $\tau_c > T_1$.

A recent review by Duncan[4] and several articles in this Encyclopedia (see ***Adsorbed Species: Spectroscopy and Dynamics*** and ***Chemical Exchange on Solid Metal Surfaces***)

discuss these methods in more detail. Demonstrated below is a study of several dynamic processes for hydrogen adsorbed on Ru/SiO_2. As outlined earlier, there are various types of hydrogen species present in this system: strongly and weakly adsorbed hydrogen on ruthenium, hydrogen that spilled over to the support, hydrogen in surface OH groups, and H_2 gas (Figure 4). These species undergo different types of motion, including exchange.

The line broadening of irreversibly adsorbed hydrogen α_I on ruthenium [about 10 kHz FWHM, see Figure 5(a)] is mainly inhomogeneous, due to distribution of Knight shifts and particle sizes and to heteronuclear ^1H-Ru dipolar coupling.[19] The two-dimensional NMR spectra, based on the pulse sequence $[(\pi/2)_x - t_1(\text{evolution}) - (\pi/2)_{-x} - \text{mixing} - (\pi/2) - t_2$ (acquisition)], revealed that the homogeneous linewidth of α_I is only about 2 kHz. This linewidth can be explained by assuming hydrogen located at the average distance of 0.5 nm, which is consistent with the estimated metal coverage H_{Ru}/Ru of about 0.5. However, a remarkable change occurs in the two-dimensional spectra as the H_{Ru}/Ru ratio increases to about 1.5 at a hydrogen pressure of 10.7 kPa.[19] A linewidth of about 3 kHz is now observed, which is approximately the same as in the one-dimensional NMR spectrum shown in Figure 5(b). Calculating the corresponding second moment due to $^1H-^1H$ dipolar interactions yields about 20 kHz for rigid spins, and about 10 kHz assuming two-dimensional diffusion. Clearly, at elevated pressures hydrogen α_M undergoes three-dimensional motion sufficient to average out the dipolar interaction, i.e. the correlation time for this process $\tau_c \ll (2\pi \times 20\,\text{kHz})^{-1} \approx 10\,\mu\text{s}$. This type of motion can be understood by assuming hydrogen whirling around the metal particles without desorbing from the surface. However, exchange between different particles via a quick desorption–interparticle diffusion–adsorption process was recently found to be a more likely scenario. Similarly, the β-hydrogen was shown to be highly mobile.[19]

One of the exchange processes in this system occurs between adsorbed hydrogen and the H_2 gas, with both species contributing to the β peak in Figure 5.[19] The H_2 gas resonates at about 0 ppm and on pure silica could be easily distinguished from the OH resonance by using a T_1 inversion–recovery experiment. The absence of this peak for the catalyst indicated the fast exchange between nonadsorbed and weakly adsorbed hydrogen with time $\tau_{ex} \ll (2\pi\Delta\nu)^{-1} \approx 10\,\mu\text{s}$, where $\Delta\nu \approx 14$ kHz is an approximated difference of resonance frequencies for the exchanging species. On the basis of this model, the pressure dependence of the β resonance shift (which moved to high frequency with increasing pressure) was explained, and the relative mole fractions of the exchanging species were calculated by using a formula analogous to equation (4).[19]

The presence of separate NMR lines for hydrogen α and β in the single pulse spectra shown in Figure 5 implies that these two species are not exchanging on the timescale of this experiment, meaning that the time constant for exchange is $\tau_{ex} > (2\pi\Delta\nu_{\alpha\beta})^{-1} \approx 50\,\mu\text{s}$. However, the slow exchange process between α and β could be detected in a two-dimensional exchange NMR spectrum, that revealed cross peaks after a mixing time of 2 ms. The time constant for this process (about 700 μs at 400 K) was measured by monitoring the evolution of magnetization of both resonance lines after one of them was selectively inverted with the DANTE-type pulse sequence (a similar experiment can be performed by using a two-dimensional exchange sequence with a fixed evolution time and various mixing periods).[19]

Finally, a very slow exchange process between hydrogen adsorbed on ruthenium and silanol protons was monitored by hydrogen–deuterium exchange.[18] The time constant τ_{ex} of about 12 h was measured for this process at room temperature for the catalyst dosed with 666 Pa of deuterium at the onset of the experiment. For the deuterium-dosed sample that was subsequently evacuated, no exchange was observed, which suggested that the exchange between the reversibly adsorbed hydrogen and silanol protons occurred via the spilt-over hydrogen that acted as an intermediate in this process.

5 ADSORPTION AND REACTION OF SIMPLE MOLECULES ON SUPPORTED METALS

Studies of adsorption and transformation of hydrocarbons on catalyst surfaces are the most important and challenging problems in catalytic chemistry. The detailed description of the structure and dynamics of adsorbed species and the changes induced upon variation of temperature and coverage can provide insight into the mechanisms of surface reactions. The main reason NMR spectroscopy became a highly esteemed tool in these studies is its ability to observe the nuclei of ^{13}C. The possibility of identifying various species via the isotropic shifts or by analysis of nuclear dipolar couplings is of primary importance. In addition, ^{13}C NMR has the ability to probe molecular dynamics by using many of the concepts and methods similar to those described previously for protons. Because of the low natural abundance of ^{13}C (1.1%) and its low relative sensitivity, most of these studies are performed by using ^{13}C-enriched molecules and require extensive data acquisition times.

5.1 Studies of CO on Metals

Carbon monoxide is one of the most studied adsorbates in surface science. It has received special attention as a model system and because of the technological importance of catalytic hydrogenation of CO. The chemisorption and reaction of CO on Group VIII metals was traditionally observed by using infrared (IR) spectroscopy; however, after the first report of the ^{13}C spectra of CO on rhodium and ruthenium by Duncan et al.,[23] these studies have extended to solid state NMR.[1–4]

Carbon monoxide occurs on supported metals in one of three basic structures—linear, bridging, or multicarbonyl—which (in the absence of the Knight shift) exhibit the isotropic chemical shifts of 185 (±15), 220 (±20), and 185 (±15) ppm, respectively. In general, the linear and bridging structures are formed on metal sites on extended surfaces, with the ratio between the two depending on the metal, surface geometry, coverage, and temperature; multicarbonyls, on the other hand, are mainly formed with isolated atoms. The static ^{13}C NMR spectra of adsorbed CO can be fitted by assuming typical CSA powder patterns for the three structures that are convoluted with appropriate broadening functions. Because of the low signal-to-noise ratio and the number of fitting parameters involved, additional information regarding particle

morphology and the amount of adsorbed CO is often needed to reduce the ambiguities. The dicarbonyl species may give rise to several lineshapes: (i) a full powder pattern characteristic of rigid species (which is indistinguishable from linear CO); (ii) a narrower (by a factor of 2) and reversed lineshape proposed for $Rh(CO)_2$ species undergoing a 180° flipping motion about the C_2 axis that bisects the C–Rh–C angle (as shown by Molitor and Apple using a Carr–Purcell–Meiboom–Gill multiple pulse sequence[24]); and (iii) a Lorentzian component that is motionally narrowed, e.g. via rotation about both the Si–O and O–Rh bonds. An example of a ^{13}C NMR spectrum for CO on highly dispersed Rh/SiO_2 is shown in Figure 9.[25] A four-component simulation was used to fit the data, as explained in the figure.

Although the static ^{13}C NMR spectra of CO bonded on metals are broadened due to CSA, clean CSA patterns are rarely observed because they are often overwhelmed by inhomogeneous broadening imposed by the distribution of adsorption sites, Knight shifts, and magnetic susceptibility. The susceptibility is of the order of $(4\pi/3)\chi$, where χ is the static magnetic susceptibility of the metal particle, and has an effect comparable to ^{13}C CSA.[2] The exact calculation of line broadenings associated with the Knight shift and susceptibility is difficult, since both depend on the particle size (in general, they decrease with increasing dispersion) and adsorbate. These factors can reduce the resolution of the NMR spectra to the extent that only one broad Gaussian peak is observed. For example, a lineshape of ^{13}CO measured by Slichter and coworkers on Pt/Al_2O_3 exhibits a >300 ppm broad Gaussian line shifted 200 ppm to high frequency from the CO gas.[26] The Knight shift was shown to arise from mixing of 5σ orbital of CO with the conduction electrons of the platinum particle (Knight shift). The T_1 relaxation of ^{13}C obeyed the Korringa relationship $T_1 \cdot \text{Temperature} = \text{Constant}$, and was independent of the magnetic field, which is consistent with the Knight interaction being operable in this system. Larger Knight shifts (resonance position at about 750 ppm) were found for CO on palladium but were negligibly small for CO on rhodium and ruthenium.[27]

MAS was first employed in the studies of CO by Gay, who introduced a system for the stable spinning of samples sealed in glass vials at speeds exceeding 3 kHz.[28] The MAS spectrum of ^{13}CO on Ru/SiO_2 revealed a 17 ppm wide peak located at 194 ppm and assigned to linear CO (Figure 10). The narrowing effect of MAS was significant in this case because the static spectrum was 400 ppm wide. Several other studies following this work achieved various degrees of success in terms of spectral resolution.[4,27,29,30] For example, Duncan et al.[29] reported high-resolution ^{13}C NMR spectra of CO on Ru/SiO_2 and Rh/SiO_2 that showed isotropic peaks consistent with linearly bonded CO and multicarbonyl CO on isolated metal atoms, but failed to detect bridged CO, whose presence was inferred from the analysis of the static spectra. In contrast, substantial amounts of bridging CO were observed in a study of a Rh/SiO_2 catalyst by Gay.[30] However, MAS appeared rather ineffective in narrowing the CO resonances on supported metals with relatively large magnetic susceptibilities, such as platinum and palladium. For example, Zilm et al. measured static and MAS ^{13}C spectra of CO adsorbed on a series of Pt/SiO_2, $Pt/\eta\text{-}Al_2O_3$, and $Pd/\gamma\text{-}Al_2O_3$ catalysts.[27] Both static and MAS spectra of ^{13}CO on platinum exhibited a >400 ppm wide, slightly asymmetric peak with a first

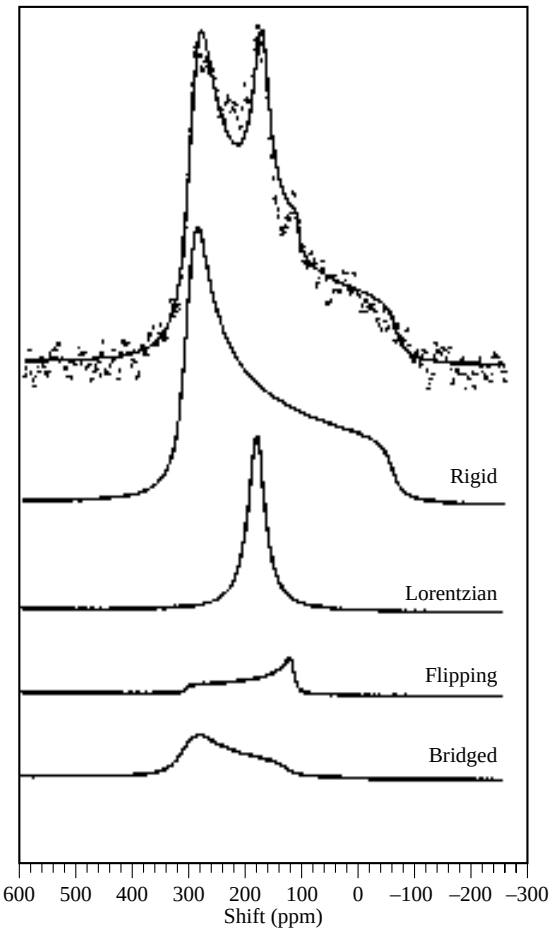

Figure 9 ^{13}C NMR spectrum of CO adsorbed on Rh/SiO_2 with a four-component least-squares fit. The rigid component represents linear CO on rhodium particles and immobile $Rh(CO)_2$ species; the Lorentzian and flipping components are interpreted as mobile and flipping $Rh(CO)_2$; and bridging represents Rh_2CO. (Reproduced by permission of the American Chemical Society from A. M. Thayer and T. M. Duncan, *J. Phys. Chem.*, 1989, **93**, 6763)

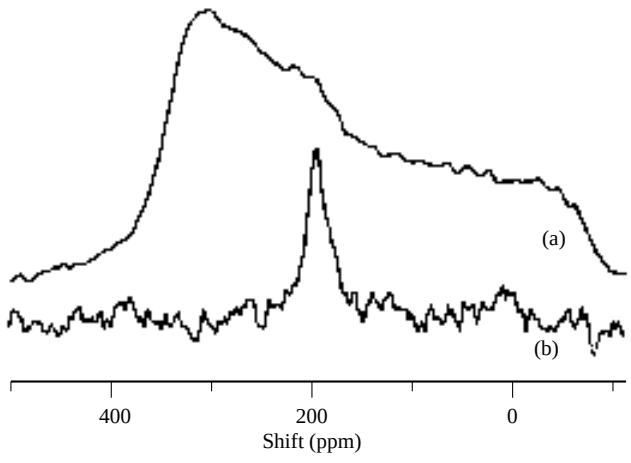

Figure 10 Static (a) and MAS (b) spectra of ^{13}CO on an Ru/SiO_2 catalyst. (Reproduced by permission of Academic Press from I. D. Gay, *J. Magn. Reson.*, 1984, **58**, 413)

moment M_1 of about 350 ppm from TMS. A motionally narrowed featureless peak found at 750 ppm on palladium also remained unaffected by MAS. The spin–spin couplings of any kind were insignificant relative to the broadening observed, and the inefficiency of MAS was not found to be the result of molecular motion. Clearly, large distributions of shift-like (linear in the magnetic field) interactions exist in these samples, resulting in different Knight shifts, chemical shifts, and magnetic susceptibilities experienced by ^{13}CO that depended on the adsorption site as well as the metal particle size and shape.[27] Even for systems in which it remains ineffective for line narrowing, however, MAS provides useful information about the variation of adsorption sites responsible for the inhomogeneous broadening and can also be used in the studies of molecular dynamics. (For more detail, see Section 5.2.)

The strong dependence of dipolar couplings between nuclei on the internuclear distance ($\hat{\mathcal{H}} \propto r^{-3}$) is often used to study the geometrical arrangements of interacting spins. On metal surfaces, the NMR lineshapes obtained by using single pulse excitation cannot be used to study dipolar couplings since the characteristic spectral features of dipolar broadened spectra are obscured by CSA, the Knight shift, and magnetic susceptibility. However, these inhomogeneous interactions can be refocused by suitable spin echo techniques and will then yield the NMR decays modulated only by the weaker dipolar coupling. For example, Slichter and co-workers[31] demonstrated that a simple spin echo sequence ($\pi/2-\tau-\pi-\tau-$observe) when applied to a system consisting of homonuclear pairs of coupled spins (e.g. ^{13}C–^{13}C), can produce oscillations (called 'slow beats') of the echo envelope versus τ. After the Fourier transformation, these oscillations give rise to a Pake doublet and provide an accurate measure of nearest-neighbor internuclear distances. The slow beat analysis was applied to study the distribution of chemisorbed CO molecules on supported platinum. By analyzing the echo envelopes for a series of platinum catalysts with various ^{13}CO coverages, the contribution to relaxation from dipolar interactions between ^{195}Pt and ^{13}C was separated from ^{13}C–^{13}C spin echo decays. When the measured decays were compared with theoretical predictions for various arrangements of CO on Pt(111) and Pt(100), the geometry of the CO layer was inferred and the formation of islands of CO on platinum particles was demonstrated at low coverages.

The heteronuclear dipolar couplings can be studied by using the previously described SEDOR technique. In the studies of CO, the ^{195}Pt–^{13}C SEDOR experiment was used to determine the Pt–C distance of CO bonded to platinum. Also, ^{13}C–^{17}O SEDOR allowed the determination of the C–O bond length of ^{13}C- and ^{17}O-enriched CO chemisorbed on palladium.[32] In the ^{17}O NMR experiment, the signal was enhanced by cooling the sample to 4 K and by using the Carr–Purcell method to acquire several echoes within each time interval T_1.

The CO motion on metals can be characterized by using the NMR methods similar to those described previously for hydrogen. An example of the relaxation analysis is the study of CO on platinum.[26] The results showed that a distribution of relaxation times T_1 existed at 77 K, whereas a single exponential decay was observed at 290 K. The averaging of relaxation at room temperature suggested the diffusion of CO over the platinum surface. This diffusion process could be studied in greater detail by monitoring the NMR linewidth as a function of temperature.[2,3] Using this technique gave an activation energy of E = 29 kJ mol^{-1} for the diffusion of CO on Pt. The ^{13}C resonance line narrowed from >400 ppm to about 50 ppm around room temperature, with the remaining broadening due to variation of isotropic shifts from particle to particle. Further motional narrowing was observed in this catalyst at about 560 K and was attributed to interparticle diffusion of CO with activation energy E = 100 kJ mol^{-1}.[2,3]

Slower motions of CO were studied by Duncan et al. on supported rhodium and ruthenium by using the spin population labeling technique.[4,33] For catalysts that exhibit well-defined CSA powder patterns and exhibit motions that are slower than the reciprocal linewidth, a selective inversion of a narrow portion of these spectra (hole burning) can be performed. This inversion results in labeling the CO molecules with a C–O bond orientation in the external magnetic field depending on the position of the 'hole' in the spectrum (Figure 11). The motional process can be studied by monitoring the nonequilibrium magnetization created by the labeling pulse as a function of recovery time. In addition, the mathematical

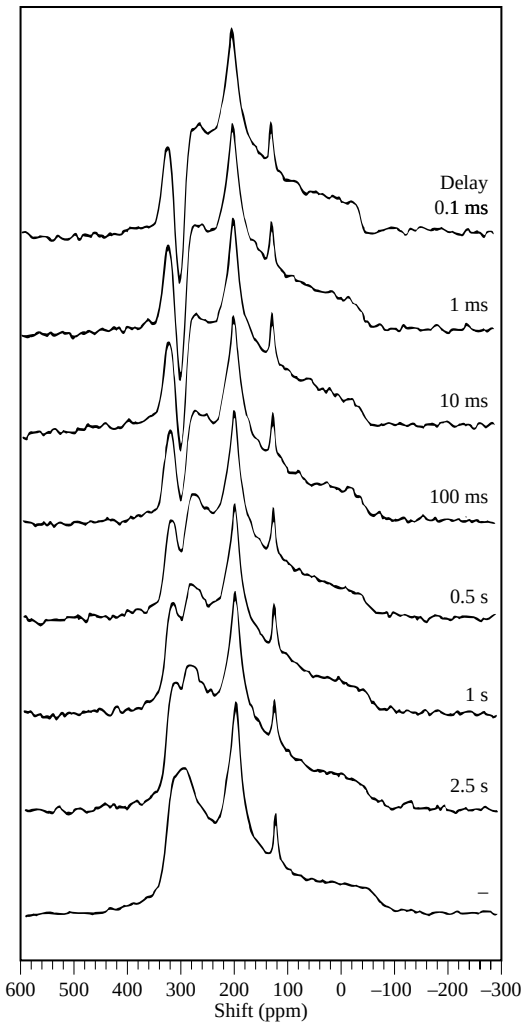

Figure 11 ^{13}C NMR spectra of CO chemisorbed on an Ru/SiO$_2$ catalyst as a function of recovery time after hole burning at 300 ppm. (Reproduced by permission of the American Institute of Physics from T. M. Duncan, A. M. Thayer, and T. W. Root, *J. Phys. Chem.*, 1990, **92**, 2663)

models which describe evolution of the hole profile for several models of CO dynamics (desorption, surface–gas exchange, and various types of surface diffusion) were developed. For CO adsorbed on ruthenium, the recovery of the hole resulted from surface diffusion on multifaceted particles, and its temperature dependence between 298 and 375 K indicated that the activation energy for this process was $E = 22.6\,\text{kJ mol}^{-1}$.[33]

5.2 Studies of Simple Hydrocarbon Molecules and their Reactions

Understanding the structure and dynamics of simple hydrocarbon molecules on metal surfaces is of great importance in catalysis. The studies of surface species formed upon initial adsorption and their reaction at various conditions require understanding chemistry well enough to allow tailoring catalyst–support systems for specific reaction pathways. Most of the NMR techniques used in these studies have already been described in previous sections. The identification of adsorbed species can be performed by using a variety of NMR techniques:

1. Studies of ^{13}C NMR shifts in the spectra acquired at variable temperatures via direct polarization of ^{13}C nuclei (Bloch decay) or by ^{1}H–^{13}C CP, with or without MAS and ^{1}H decoupling, are prevalent. The CP MAS technique is most useful when chemical shifts are good fingerprints of the adsorbed species. The additional advantage of the CP technique is that it can be used to discriminate between different carbon atoms on the basis of the strength of their dipolar interactions with protons. The dipolar dephasing experiment and the recently proposed spectral editing CP sequences allow distinguishing between various CH_n (n = 0, 1, 2, 3) carbon resonances (see ***Spectral Editing Techniques: Hydrocarbon Solids***). However, considerable uncertainties often exist regarding identification of surface-bound species based on the ^{13}C shifts because of the potential complication of Knight shift dominance and the previously discussed heterogeneous broadening of resonances. The easiest approach of assuming direct correspondence to ^{13}C shifts observed in organometallic species in solutions may be applicable for surface species on ruthenium and rhodium, that exhibit negligible Knight shift, but is highly questionable on platinum and palladium,[27] for example.
2. When the isotropic chemical shifts of ^{13}C (or ^{1}H) fail to provide diagnostic fingerprints of the structures of the species chemisorbed on metals, dipolar couplings are often used to obtain information that is quite distinct from chemical shift data. For instance, ^{13}C–^{13}C and ^{13}C–^{1}H dipolar couplings can be measured by using spin echo and SEDOR techniques, respectively. The spin echo (slow beat) technique allows determination of the ^{13}C–^{13}C bond length in hydrocarbon molecules as well as the fraction of ^{13}C nuclei that are not bound in pairs. The utility of the SEDOR technique, on the other hand, relies mainly on its ability to measure the fraction of ^{13}C nuclei which are bonded to hydrogen.
3. Multiple quantum (MQ) NMR provides another characteristic of a nuclear spin system that is supplied by dipolar coupling between spin-$\frac{1}{2}$ nuclei and that relates to the densities of protons on the catalyst surface. In short, MQ NMR allows measurement of the numbers of strongly coupled spins in solids (see also ***Multiple Quantum NMR in Solids***).
4. Deuterium NMR is increasingly used to probe the functional groups in surface species. The spectra of ^{2}H exhibit singularities that are characteristic of the configuration and motion of interacting spin systems and can be used to identify rigid C–D bonds, and rotating CD_3 groups, for example.

A considerable number of catalytic reactions have been studied over the last few years in several laboratories by using the above techniques. Since the results of these studies generally depend very strongly on the preparation of the catalyst (dispersion, reduction, and cleaning procedure) and the reaction conditions (adsorbate loading and temperature) it is not surprising that disparate results were reported for seemingly similar catalytic systems. In the following paragraphs I briefly review some representative studies, most of which involve the adsorption of ethene (C_2H_4). This process has been studied with particular interest because of the importance of the ethene-derived intermediates in cracking, hydrogenation, and hydrogenolysis reactions. ^{13}C techniques described in this section have also been used in the studies of CO hydrogenation on supported metal catalysts.[34]

The CP MAS technique was first used to investigate the adsorption and reaction of ^{13}C enriched acetylene (C_2H_2) on Ru/SiO_2 and C_2H_4 on SiO_2- and Al_2O_3-supported platinum catalysts.[28,35] Samples for these studies were reduced and dosed with adsorbates in NMR tubes attached to a vacuum line. After sealing, the catalysts were spun in a MAS system at 2.5 kHz. The CP MAS spectra required $1–8 \times 10^5$ cross polarizations and exhibited rather broad features that were assigned on the basis of the observed shifts and the results obtained using dipolar dephasing. The spectra for clean Pt/SiO_2 catalysts indicated that π-bonded C_2H_4 was the dominating surface species. In the presence of Cl^- or when Al_2O_3 was used as a support, the catalysts were more reactive, and the detected species included alkyl groups and σ-vinyl groups, or σ-diadsorbed species with a C=C bond. The presence of ethylidyne (CCH_3) on platinum was excluded in this study.

In another investigation of C_2H_4 on a Pt/Al_2O_3 catalyst, broadline NMR of ^{2}H and ^{13}C was used to monitor structural changes brought about by heating.[36] Following adsorption at 253 and 297 K, the deuterium spectra were measured using a quadrupolar echo sequence. Two types of quadrupolar powder pattern exist with widths between singularities of 130 and 41 kHz, which are characteristic of static C–D bonds and rapidly rotating CD_3 groups, respectively. The ^{13}C spectra, acquired by using CP and proton decoupling, consisted of superimposed broad Gaussian lines that were interpreted with the aid of dipolar dephasing and variable contact time CP measurements. The results of ^{2}H and ^{13}C NMR demonstrated that below room temperature π-bonded C_2H_4 was formed on platinum and was partly converted to ethylidene ($CHCH_3$) at about 300 K. Upon further heating, $CHCH_3$ decomposed into methane gas and surface carbon.[36] In a similar study, a conversion of vinylidene (CCH_2) and hydrogen to CCH_3 on Pt/Al_2O_3 catalysts was postulated and monitored via ^{2}H NMR.[37] The progress of the conversion reaction was monitored by measuring the intensities of methyl groups in ^{2}H NMR spectra (taken at 77 K) as a function of annealing

temperature. The data were then analyzed by means of a set of differential rate equations describing H–D exchange for CCH_2, conversion of CCH_2 to CCH_3, and H–D exchange for CCH_3, yielding the activation energy for conversion of 38.9 ($\pm$10.5) kJ mol^{-1}. This analysis also demonstrated that the hydroxyl groups of the support served as an additional source of hydrogen in this reaction.

A variety of transient techniques in the NMR of ^{13}C, including variable temperature CP MAS, were used in a study of decomposition and reaction of ^{13}C-enriched ethene on Ru/SiO_2 catalysts.[38,39] Figure 12 shows the CP MAS, ^1H-decoupled spectra taken 1, 7, and 30 days after the adsorption of C_2H_4 at room temperature. The narrow resonances in the spectra represent species of high mobility ($\tau_c < 10\,\mu s$) that are not rigidly attached to ruthenium or the support. These resonances broadened only slightly in the absence of MAS and decoupling and could be easily assigned on the basis of chemical shifts, *J* splittings, and relative peak intensities at various conditions. (In the absence of paramagnetic adsorption sites, the shift deviations from the values determined in the liquid state are primarily due to bulk susceptibility and van der Waals interactions, and in most cases are not expected to exceed 2 ppm.) The following reaction products were identified in the spectra shown in Figure 12: peak (1) is a superposition of the CH carbon atoms of *trans*- and *cis*-2-butene; peak (2) represents the CH_2 carbon atom of butane; peak (3) is a CH_3 group of *trans*-2-butene; peak (4) is a CH_3 group in butane and *cis*-2-butene; and peak (5) originates from ethane.[38] The underlying broad features in the spectra represent species chemically bound to the ruthenium that could not be removed through evacuation [see Figure 12(d)]. Although MAS and strong ^1H-decoupling led to a considerable reduction of their linewidth, a severe inhomogeneous line broadening remained. The high-frequency peak centered at about 85 ppm was assigned to acetylide (CCH), although a small contribution to that peak at about 130 ppm due to the vinyl group ($CHCH_2$) could not be excluded. These assignments were based on chemical shifts and the CP MAS experiments performed with dipolar dephasing and variable contact times, which indicated that a significant fraction of carbon atoms contributing to the high-frequency peak had no directly bonded hydrogen. The resonances at 0–40 ppm were assigned to various surface-attached alkyl groups. Although high mobility did not preclude cross polarization of weakly adsorbed species, direct excitation of ^{13}C nuclei was necessary for quantitative analysis of the observed resonances. The results of intensity measurements indicated that there was approximately one chemisorbed carbon atom per surface ruthenium atom in the sample. Furthermore, the spectra taken for a series of samples sequentially dosed with ^{13}C-labeled and unlabeled ethene showed that the strongly adsorbed species resonating at 85 ppm was not appreciably consumed in the formation of reaction products.[38] Similar ^{13}C NMR studies were extended to low (< 90 K) and high (up to 700 K) temperatures and provided a coherent picture of the chemistry of this relatively complex system.

The concepts involved in the production and detection of *n*-quantum coherences in NMR and their applications to the studies of protons on surfaces have been recently described by Gerstein et al.[40] In catalysis, the technique has been used to study the structure of C_2H_2 on platinum.[41] In this work, the SEDOR experiment was first performed and yielded

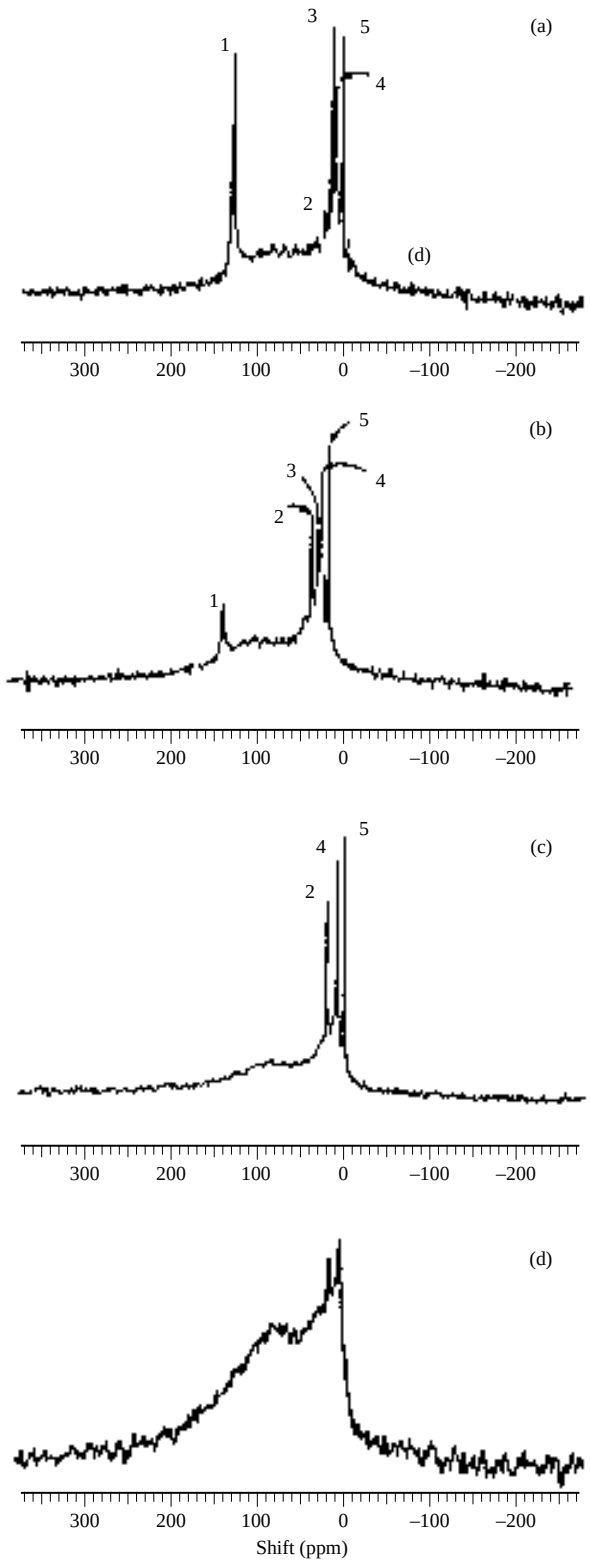

Figure 12 ^{13}C CP MAS spectra of surface species on an Ru/SiO_2 catalyst at 300 K taken 1 day (a), 7 days (b), and 30 days (c) after ethene adsorption at room temperature. Spectrum (d) represents a sample that had been exposed to 13.3 kPa of C_2H_4 at 300 K for 15 min and then evacuated for 10 min. Each spectrum is a result of 150 000 cross polarizations taken with a contact time of 2 ms. (Reproduced by permission of the American Chemical Society from M. Pruski, J. C. Kelzenberg, B. C. Gerstein, and T. S. King, *J. Am. Chem. Soc.*, 1990, **112**, 4232)

several possible models for the composition of the adsorbed species. The final determination of the adsorbed structures (77 ± 7% CCH_2 and 23 ± 7% HCCH) was made by measuring the amplitudes of 1-, 2-, and 3-quantum coherences as a function of C_2H_2 concentration. In another study, the use and limitations of MQ spin counting were tested by probing intermediates in the reaction of C_2H_4 on supported ruthenium.[42] The maximum MQ coherence of k_{max} = 5, corresponding to n_{max} = 6 coupled protons, was observed after the catalyst reacted with C_2H_4 at 300 K for 1 h, was evacuated to 26×10^{-6} Pa, and sealed. The possible strongly bound C_mH_n fragments postulated in this work involved the metallocyclic intermediate Ru−CH_2−CH=CH−CH_2−Ru. This result was consistent with the finding that butenes were among the observed products in this reaction.[38] The limitations of the MQ technique are imposed by the background from protons in the support (which can be partly eliminated by deuteration[41]), the difficulties in extracting information about the distribution of sizes of the proton clusters, and possible intermolecular interference in the development of *n*-quantum coherences.

The spin echo technique was used to measure the $^{13}C-^{13}C$ internuclear distance (carbon−carbon bond length) in a number of systems. For example, the $^{13}C-^{13}C$ bond length of C_2D_2 on osmium, iridium, and platinum was found to be 0.144 (±0.002) nm, whereas C_2H_4 on the same metals had a carbon−carbon bond length of 0.149 (±0.002) nm.[43] It is preferable to perform the bond length measurements in systems with a single type of intact $^{13}C-^{13}C$ pair, although the bond scission between carbon atoms can also be measured with the spin echo method. To obtain a more complete picture of the surface chemistry, the spin echo technique can be used in conjunction with $^{1}H-^{13}C$ SEDOR measurements. For example, after simultaneously observing $^{13}C-^{13}C$ bond scission and a fraction of ^{13}C nuclei with carbon−hydrogen bonds at various reaction temperatures, the proposal was made that dehydrogenation preceded the decomposition of C_2 surface species on platinum.[43]

6 CONCLUSION

This article has demonstrated the enormous potential of solid state NMR in the field of surface science. The choice of experimental methods for successful NMR studies of catalytic chemistry is critically important, but not always obvious. Undoubtedly, further collaboration between NMR spectroscopists, chemists, and chemical engineers will bring new and exciting advances in this fast evolving area of surface science.

7 RELATED ARTICLES

Adsorbed Species: Spectroscopy and Dynamics; Brønsted Acidity of Solids; Chemical Exchange on Solid Metal Surfaces; Internal Spin Interactions and Rotations in Solids; Line Narrowing Methods in Solids; Magic Angle Spinning; Molecular Sieves: Crystalline Systems; Multiple Quantum NMR in Solids; Reactions in Zeolites; Silica Surfaces: Characterization; Vanadium Catalysts: Solid State NMR.

8 REFERENCES

1. T. M. Duncan and C. Dybowski, *Surf. Sci. Rep.*, 1981, **1**, 157.
2. C. P. Slichter, *Annu. Rev. Phys. Chem.*, 1986, **37**, 25.
3. J.-Ph. Ansermet, C. P. Slichter, and J. H. Sinfelt, *Prog. NMR Spectrosc.*, 1990, **22**, 401.
4. T. M. Duncan, *Colloids Surf.*, 1990, **45**, 11.
5. C. P. Slichter, *Principles of Magnetic Resonance*, Springer, New York, 1989.
6. H. E. Rhodes, P.-K. Wang, H. T. Stokes, C. P. Slichter, and J. H. Sinfelt, *Phys. Rev. B*, 1982, **26**, 3559.
7. H. E. Rhodes, P.-K. Wang, C. D. Makowka, S. L. Rudaz, H. T. Stokes, C. P. Slichter, and J. H. Sinfelt, *Phys. Rev. B*, 1982, **26**, 3569
8. C. D. Makowka, C. P. Slichter, and J. H. Sinfelt, *Phys. Rev. B*, 1985, **31**, 5663.
9. J. P. Bucher, J. J. van der Klink, and M. Graetzel, *J. Phys. Chem.*, 1990, **94**, 1209.
10. V. M. Mastikhin, *Colloids Surf.*, 1993, **78**, 143.
11. T. S. King, W. J. Goretzke, and B. C. Gerstein, *J. Catal.*, 1987, **107**, 583.
12. L. C. De Menorval and J. P. Fraissard, *Chem. Phys. Lett.*, 1981, **77**, 309.
13. T. M. Apple, P. Gajardo, and C. Dybowski, *J. Catal.*, 1980, **68**, 103.
14. J. C. Conesa, P. Malet, G. Munuera, J. Sanz, and J. Soria, *J. Phys. Chem.*, 1984, **88**, 2986.
15. J. Sanz and J. M. Rojo, *J. Phys. Chem.*, 1985, **89**, 4974.
16. T.-C. Sheng and I. D. Gay, *J. Catal.*, 1982, **77**, 53.
17. X. Wu, B. C. Gerstein, and T. S. King, *J. Catal.*, 1990, **121**, 271.
18. X. Wu, B. C. Gerstein, and T. S. King, *J. Catal.*, 1989, **118**, 238.
19. F. Engelke, S. Bhatia, T. S. King, and M. Pruski, *Phys. Rev. B.*, 1994, **49**, 2730.
20. F. Engelke, R. Vincent, T. S. King, and M. Pruski, *J. Chem. Phys.*, 1994, **101**, 7262.
21. T. Komaya, A. T. Bell, Z. Weng-Sieh, R. Gronsky, F. Engelke, T. S. King, and M. Pruski, *J. Catal.*, 1994, **149**, 142.
22. X. Wu, B. C. Gerstein, and T. S. King, *J. Catal.*, 1990, **123**, 43.
23. T. M. Duncan, J. T. Yates, and R. W. Vaughan, *J. Chem. Phys.*, 1979, **71**, 3129.
24. P. Molitor and T. Apple, *Colloids Surf.*, 1990, **45**, 33.
25. A. M. Thayer and T. M. Duncan, *J. Phys. Chem.*, 1989, **93**, 6763.
26. S. L. Rudaz, J.-Ph. Ansermet, P.-K. Wang, and C. P. Slichter, *Phys. Rev. Lett.*, 1985, **54**, 71.
27. K. W. Zilm, L. Bonneviot, D. M. Hamilton, G. G. Webb, and G. L. Haller, *J. Phys. Chem.*, 1990, **94**, 1463.
28. I. D. Gay, *J. Magn. Reson.*, 1984, **58**, 413.
29. T. M. Duncan, K. W. Zilm, D. M. Hamilton, and T. W. Root, *J. Phys. Chem.*, 1989, **93**, 2583.
30. I. D. Gay, *J. Phys. Chem.*, 1990, **94**, 1207.
31. J.-Ph. Ansermet, C. P. Slichter, and J. H. Sinfelt, *J. Chem. Phys.*, 1988, **88**, 5963.
32. S. E. Shore, J.-Ph. Ansermet, C. P. Slichter, and J. H. Sinfelt, *Phys. Rev. Lett.*, 1987, **58**, 953.
33. T. M. Duncan, A. M. Thayer, and T. W. Root, *J. Phys. Chem.*, 1990, **92**, 2663.
34. T. M. Duncan, P. Winslow, and A. T. Bell, *J. Catal.*, 1985, **93**, 1, and references therein.

35. I. D. Gay, *J. Catal.*, 1987, **108**, 15.
36. J. M. Griffiths, A. T. Bell, and J. A. Reimer, *J. Phys. Chem.*, 1993, **97**, 9161.
37. C. A. Klug, C. P. Slichter, and J. H. Sinfelt, *J. Phys. Chem.*, 1991, **95**, 7033.
38. M. Pruski, J. C. Kelzenberg, B. C. Gerstein, and T. S. King, *J. Am. Chem. Soc.*, 1990, **112**, 4232.
39. M. Pruski, D. K. Sanders, T. S. King, and B. C. Gerstein, *J. Magn. Reson.*, 1992, **96**, 574.
40. B. C. Gerstein, M. Pruski, and S. J. Hwang, *Anal. Chim. Acta*, 1993, **283**, 1059.
41. P.-K. Wang, C. P. Slichter, and J. H. Sinfelt, *Phys. Rev. Lett.*, 1984, **53**, 82.
42. S. J. Hwang, T. S. King, and B. C. Gerstein, *Catal. Lett.*, 1991, **8**, 367.
43. P.-K. Wang, C. P. Slichter, and J. H. Sinfelt, *J. Phys. Chem.*, 1990, **94**, 1154.

Biographical Sketch

Marek Pruski. *b* 1954. M.S., 1977, Ph.D., 1981, N. Copernicus University (supervisor T. Marszalek), Torun, Poland. Postdoctoral fellow (with B. C. Gerstein), 1985–88, scientist, 1988–present, Ames Laboratory, Iowa State University. Approx. 50 publications. Current research specialty: solid state NMR and its applications to surface and material sciences.

Vanadium Catalysts: Solid State NMR

Vjatcheslav M. Mastikhin and Olga B. Lapina
Boreskov Institute of Catalysis, Siberian Branch of Russian Academy of Sciences, Novosibirsk, Russia

1 Introduction 1
2 Vanadium-51 NMR Spectra of Solids With a Well-Characterized Structure. Interrelation Between ^{51}V NMR Parameters and the Local Environment of V Nuclei 1
3 Study of Vanadium Catalysts 4
4 Related Articles 12
5 References 12

1 INTRODUCTION

Measurements of ^{51}V NMR spectra of solids (see ***Quadrupolar Nuclei in Glasses***; ***Quadrupolar Nuclei in Solids***) with the use of modern NMR spectrometers (see ***Spectrometers: A General Overview***) equipped with line-narrowing techniques for obtaining high-resolution spectra of solids (see ***Double Rotation***; ***High Speed MAS of Half-Integer Quadrupolar Nuclei in Solids***; ***Magic Angle Spinning***; ***Variable Angle Sample Spinning***) provide important information on the local environment of V nuclei.[1] The latter is known to be a key factor determining the activity and selectivity of heterogeneous catalysts. Due to this fact ^{51}V NMR solid state spectroscopy is successfully used for the studies of vanadia-based catalysts. The latter are used for the production of sulfuric acid, the selective oxidation of hydrocarbons, and also for reduction of atmospheric pollution.[2]

The results presented below show that ^{51}V NMR provides important information concerning the structure and reactivity of surface V sites. Herein will be discussed the main features of ^{51}V NMR in solids and its application for the studies of vanadium catalysts.

The vanadium-51 nucleus (natural abundance 99.76%) has a spin $I = \frac{7}{2}$, its electric quadrupole moment being $-4 \times 10^{-2} \times 10^{-24}\,\mathrm{cm}^2$; the relative intensity of ^{51}V NMR is 0.38 compared with an equal number of protons.

In general, three different types of interactions influence the ^{51}V NMR spectra of solid diamagnetic samples (see ***Internal Spin Interactions and Rotations in Solids***): (1) the dipole interaction (see ***Dipolar and Indirect Coupling Tensors in Solids***) of the magnetic moment of the ^{51}V nucleus with the magnetic moments of other nuclei that broadens the lines; (2) the quadrupole interaction (see ***Quadrupolar Interactions***) of the ^{51}V nucleus with the electric field gradient that splits the lines and contributes to the shift of the central ($m_I = \frac{1}{2} \leftrightarrow m_I = -\frac{1}{2}$) line; and (3) the chemical shielding interaction (see ***Chemical Shift Tensors***) that changes the position of the lines and makes them asymmetric.

In general, the lineshape might be rather complicated due to the simultaneous action of all types of interactions. For powdered samples (the case typically met in heterogeneous catalysts) only the central transition ($m_I = \frac{1}{2} \leftrightarrow m_I = -\frac{1}{2}$) can most commonly be observed, while other transitions are too broad to be recorded. The line from the central transition is typically anisotropic, i.e. it has a rather complicated shape. This complicated shape reflects the fact that the observed line is actually a superposition of individual lines from vanadium sites having various orientations with respect to the external magnetic field. When these individual lines are narrow enough, the positions of the so-called discontinuity points can be readily identified in the overall ^{51}V NMR spectrum. From the position of the discontinuity points one can easily obtain the quadrupole coupling constant, χ, the asymmetry parameter, η, and the shielding anisotropy parameters σ_{11}, σ_{22}, and σ_{33}.[3]

Unfortunately, in the ^{51}V NMR spectra of many solid catalysts the effects from the discontinuity points are often completely or partially obscured due to the large broadening of individual lines. In this case computer analysis of the spectra recorded at various frequencies becomes necessary if one wishes to obtain the above-mentioned values. Note, that interactions affecting ^{51}V NMR spectra exhibit different frequency dependences. Indeed, the dipole interaction and the first-order quadrupole interaction do not depend on the spectrometer frequency ν_0, while the second-order quadrupole effects are inversely proportional to ν_0. The effects of the shielding anisotropy are directly proportional to ν_0. Thus, at a sufficiently high ν_0, the second-order quadrupole effects are suppressed and can be neglected, while the effects of the chemical shielding anisotropy become more pronounced and can be measured more precisely (***Chemical Shift Tensor Measurement in Solids***). A comparison of ^{51}V NMR spectra recorded at various ν_0 with computer simulated spectra has been demonstrated to allow sufficiently precise measurements of the spectral parameters characterizing vanadium sites in the solid catalysts.[1]

Typical examples of computer simulated ^{51}V NMR spectra of V(V) sites in solid V_2O_5 are presented in Figure 1. Calculations were performed using the program for high magnetic fields ($B_0 > 7\,\mathrm{T}$) when the perturbation theory approach can be applied, i.e. the values of the quadrupole and nuclear shielding terms are small when compared with the nuclear Zeeman energy.[1,4]

Figure 1(a) and (b) show the influence of the first-order quadrupole effects on the calculated spectra of solid V_2O_5 at $\nu_0 = 105.15\,\mathrm{MHz}$. Figure 1(c) demonstrates the spectral broadening in powdered or polycrystalline samples due to the distribution of quadrupole coupling constant.

2 VANADIUM-51 NMR SPECTRA OF SOLIDS WITH A WELL-CHARACTERIZED STRUCTURE. INTERRELATION BETWEEN ^{51}V NMR PARAMETERS AND THE LOCAL ENVIRONMENT OF V NUCLEI

To analyze the spectra of real catalytic systems one needs information on the spectra of vanadium compounds that might be present in the catalysts, as well as data on the interrelation between ^{51}V NMR parameters and the characteristics of the local environment of the V nuclei.

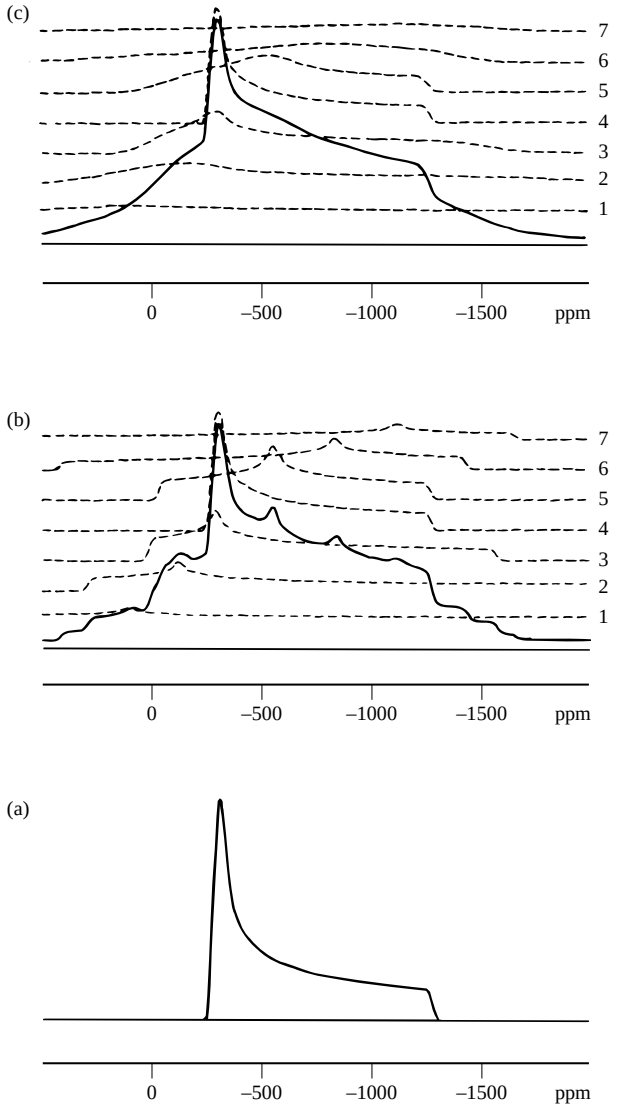

Figure 1 Computer simulated ^{51}V NMR spectra demonstrating the influence of the first-order quadrupole effects and line broadening on the spectra of solid V_2O_5 (at the frequency 105.15 MHz). The following parameters were used: χ = 0.805 MHz, η = 0.04;[5] σ_{11} = 310, σ_{22} = 1280, σ_{33} = 270 ppm. (a): The lineshape for the central transition ($\frac{1}{2}$, $-\frac{1}{2}$). (b) (Dotted lines): the lineshapes for all possible transitions: 1 ($-\frac{5}{2}$, $-\frac{7}{2}$), 2 ($-\frac{3}{2}$, $-\frac{5}{2}$), 3 ($-\frac{1}{2}$, $-\frac{3}{2}$), 4 ($\frac{1}{2}$, $-\frac{1}{2}$), the central transition, 5 ($\frac{3}{2}$, $\frac{1}{2}$), 6 ($\frac{5}{2}$, $\frac{3}{2}$), 7 ($\frac{7}{2}$, $\frac{5}{2}$). (b) (Solid line): the overall spectrum from all transitions. (c): Spectrum demonstrating the broadening of the lines from all transitions [dotted lines, numbered exactly as in (b)] and the overall spectrum from all transitions (solid line) due to the Gaussian distribution of quadrupole coupling constant χ. Dipolar linewidth *DF* = 1.5 kHz

The ^{51}V NMR spectra of various solid vanadium compounds[1,3,5–8] with well-characterized structures[9] and of the vanadates of alkali metals, which are often used for the preparation of catalysts, have been studied.

In Table 1 the ^{51}V NMR chemical shielding parameters[1,3,5,7,8] for vanadates are listed.

The ^{51}V NMR parameters of the large number of V compounds with a well-characterized crystal structure presented in Table 1 prove the high sensitivity of NMR spectra toward details of the local environment of V nuclei.

In most cases the shape of ^{51}V NMR spectra measured in high magnetic fields ($B_0 > 7$ T) depends on the anisotropy of the chemical shielding tensor. The influence of the second-order quadrupole effects is typically smaller and often is quite negligible.[10]

The following conclusions on V coordination (tetrahedral or octahedral, regular or distorted) and the extent of association of vanadium–oxygen polyhedra can be drawn based on the type and magnitude of the chemical shielding anisotropy.[1,7,10]

(a) For vanadium in regular tetrahedral sites (sites of the Q^0 type), the isotropic spectra with close values of the chemical shielding tensor components ($\sigma_{11} \approx \sigma_{22} \approx \sigma_{33}$) typically have $\Delta\sigma < 100$ ppm.

(b) For vanadium in slightly distorted tetrahedral sites with adjacent VO_4 tetrahedra sharing one common oxygen atom (sites of the Q^1 type), a fully anisotropic shielding tensor ($\sigma_{11} \neq \sigma_{22} \neq \sigma_{33}$) is typical, but with a larger $\Delta\sigma$ value ($\Delta\sigma$ = 70–300 ppm).

(c) For vanadium in strongly distorted tetrahedral sites with adjacent VO_4 tetrahedra sharing two common oxygen atoms (sites of the Q^2 type), a fully anisotropic shielding tensor ($\sigma_{11} \neq \sigma_{22} \neq \sigma_{33}$) is typical with $\Delta\sigma$ = 300–375 ppm).

(d) For vanadium in distorted octahedral sites (i.e. in a distorted octahedral environment of oxygen atoms), a nearly axial shielding anisotropy is typical with $\sigma_{11} \approx \sigma_{22} < \sigma_{33}$ ($\Delta\sigma$ = 450–900 ppm for structures 4 in Figure 2 and $\Delta\sigma$ = 900–1300 ppm for structures 5 in Figure 2).

Conclusions (a) to (d) are illustrated in Figure 2 for a family of Tl vanadates and V_2O_5.

Note, that ^{51}V NMR spectra with approximate axial symmetry of the σ tensor should also be expected for VO_4 tetrahedra with symmetry close to C_{3v}, i.e. when one V–O bond differs significantly from the other three (which have about the same length) (sites of the Q^1 type). In this case the direction of $\sigma_\parallel$ will coincide with the direction of the V–O bond which differs from the three others, with $|\sigma_\perp| < |\sigma_\parallel|$ if this bond is shorter than the three others and $|\sigma_\perp| > |\sigma_\parallel|$ if this bond is the longest one.

A comparison of the shielding anisotropy $\Delta\sigma = |\sigma_{33} - \frac{1}{2}(\sigma_{11} + \sigma_{22})|$ for metavanadates whose structural data are known shows a good correlation between $\Delta\sigma$, on the one hand, and the angle O_3–V–O_3' on the other hand [Figure 3(a)]. According to the structures of the metavanadates schematically presented in Figure 3(a) this angle characterizes the distortion of the tetrahedral environment of V. The larger the deviation of angle O_3–V–O_3' from that in the regular tetrahedron (109°28′), the larger is $\Delta\sigma$.

Distortion of the VO_4 tetrahedra also results in an increase in the electric field gradient on the V nucleus. It seems natural to expect a correlation between $\Delta\sigma$ and the quadrupole interaction parameters, χ and η. Indeed, such a correlation has been found for metavanadates [Figure 3(b)].

In contrast to ^{27}Al[11] and ^{29}Si[12] (see ***Aluminum-27 NMR of Solutions***; ***Molecular Sieves: Crystalline Systems***; ***Silicon-29 NMR***), the isotropic chemical shifts σ_{iso} for ^{51}V nuclei in vanadates are not too sensitive to V coordination (octahedral or tetrahedral). Compounds with rather different coordination may have very close σ_{iso} values. Thus, for vanadates, the anisotropy of the ^{51}V chemical shift is much more sensitive

Table 1 Components of ^{51}V Chemical Shieldings (Measured in ppm With Respect to $VOCl_3$ With An Accuracy of ±10 ppm) and Quadrupole Constants χ and η for Vanadates

Compound	Site	σ_{11}	σ_{22}	σ_{33}	σ_{iso}	$\Delta\sigma$	χ(MHz)	η
Virtually regular tetrahedra VO_4, Q^0 type								
Li_3VO_4[1]					544	50	1.52	
							1.51[3]	
Na_3VO_4[7]					545			
							1.05[3]	
K_3VO_4[1]					560	100		
Cs_3VO_4[1]		520	580	626	576	70		
Tl_3VO_4[1]					480	30		
$Mg_3(VO_4)_2$[1]					557	40		
$Ca_3(VO_4)_2$[1]					615	100		
							2.05[3]	
$Sr_3(VO_4)_2$[1]					610	20		
							0.53[3]	
$Ba_3(VO_4)_2$[1]					605	20		
							0.75[3]	
$Zn_3(VO_4)_2$[7]					522			
$Pb_3(VO_4)_2$[22]		521	508	467	486	48		0.41
$AlVO_4$[1]	V1	630	640	730	668	95		
	V2	605	745	800	747	55		
	V3	710	800	830	780	75		
$BiVO_4$[1]		355	405	500	420	120		
YVO_4[1]					664	30		
							4.75[3]	0.00[3]
$LaVO_4$[1]		555	616	657	609	72		
							5.21[3]	0.69[3]
$LuVO_4$[1]					663	30		
							4.23[3]	0.00[3]
Slightly distorted tetrahedra, Q^1 type								
$Na_4V_2O_7$[1]	V1				560			
	V2				575			
$K_4V_2O_7$[1]		500	582	642	578	100		
$Cs_4V_2O_7$[1]	V1				543			
	V2				567			
$Tl_4V_2O_7$[1]		443	512	556	504	89		
α-$Mg_2V_2O_7$[1]	V1	510	570	585	555	45		
	V2	570	580	700	617	125		
β-$Mg_2V_2O_7$[1]	V1	460	560	680	560	170		
	V2	590	660	700	650	75		
$Ca_2V_2O_7$[1]	V1	528	564	630	574	84		
	V2	530	564	640	578	93		
$Sr_2V_2O_7$[1]	V1	523	548	600	557	65		
	V2	480	620	650	582	155		
	V3	480	632	652	588	160		
	V4	480	638	658	592	168		
$Ba_2V_2O_7$[1]	V1	530	555	652	579	109		
	V2	575	574	615	588	140		
	V3	535	625	640	600	100		
$Zn_2V_2O_7$[7]		500	640	720	625	150		
$Cd_2V_2O_7$[7]		370	660	660	579	290		
$Pb_2V_2O_7$[7]		430	480	620	522	165		
ZrV_2O_7[1]		710	802	824	774	110		
Distorted tetrahedra, Q^2 type								
$LiVO_3$[8]		385	540	794	573	332	3.18	0.87
NH_4VO_3[1]		380	530	807	572	352		
		366[8]	534[8]	810[8]	570[8]	360[8]	2.95[8]	0.30[8]
							2.88[3]	0.30[3]
							2.95[3]	0.19[3]
							2.76[3]	0.37[3]
β-$AgVO_3$[22]		202	285	609	364	366		0.34
α-$NaVO_3$[1]		368	530	820	582	371		
		355[8]	531[8]	833[8]	573[8]	390[8]	3.80[8]	0.46[8]
							3.70[3]	0.52[3]

						3.65[3]	0.60[3]
						3.15[3]	0.64[3]
						3.94[3]	0.64[3]
$TlVO_3$[1]	300	490	793	528	398		
	296[8]	497[8]	794[8]	529[8]	398[8]	3.67[8]	0.71[8]
$CsVO_3$[1]	330	522	863	583	437		
						3.92[3]	0.62[3]
						3.84[3]	0.63[3]
$RbVO_3$[1]	313	508	863	570	453		
						4.33[3]	0.72[3]
KVO_3[1]	294	490	856	548	464		
	313[8]	501[8]	842[8]	552[8]	435[8]	4.20[8]	0.80[8]
						4.21[3]	0.65[3]
						4.35[3]	0.75[3]
						4.06[3]	0.76[3]
						4.34[3]	0.77[3]
Distorted octahedra							
$K_2V_6O_{16}$[1]	290	290	935	503	630		
$Rb_2V_6O_{16}$[1]	290	290	935	503	630		
$Cs_2V_6O_{16}$[1]	296	296	953	508	645		
$Tl_2V_6O_{16}$[1]	485	485	1165	700	680		
α-$Mg(VO_3)_2$[1]	310	470	950	576	560		
						6.79[3]	0.63[3]
$Ca(VO_3)_2$[1]	278	355	1080	575	764		
						3.30[3]	0.8[3]
						3.16[3]	0.60[3]
						2.81[3]	0.60[3]
$Sr(VO_3)_2$[22]	533	577	833	643	283		0.29
$Ba(VO_3)_2$[1]	540	614	950	660	373		
$Zn(VO_3)_2$[7]	270	410	920	517	580		
$Pb(VO_3)_2$[7]	310	320	1000	533	685		
$Cd(VO_3)_2$[1]	305	365	830	500	495		
V_2O_5[1]	310	310	1270	610	960		
						0.8[5]	0.04[5]
$VOAsO_4$[1]	218	255	1370	617	1134		
$VOPO_4$[1]	285	285	1547	734	1260		

to the character of the local arrangement of oxygen atoms around V than the isotropic chemical shift σ_{iso}. At the same time, for compounds with the same type of first coordination sphere, σ_{iso} depends notably on the type of atoms in the second coordination sphere of V, as also found for ^{27}Al and ^{29}Si atoms.[11,12]

3 STUDY OF VANADIUM CATALYSTS

Typically, other techniques and approaches are used for identification of individual surface V species, in addition to ^{51}V NMR. These include studies with magic angle spinning (MAS), NMR of nuclei of elements other than V and other spectroscopic methods, as well as chemical approaches. A combination of spectroscopic data with the measurements of catalytic activity allows one to identify the catalytically active sites.

3.1 V_2O_5/SiO_2 Catalysts

3.1.1 Prepared by Impregnation

Spectra of V_2O_5/SiO_2 samples prepared via impregnation of SiO_2 with NH_4VO_3 solution are presented in Figure 4. The spectrum of the sample dried at 120 °C indicates only a slight change in the vanadium surroundings in comparison to that in NH_4VO_3 (spectrum 1a) and can be ascribed to (VO_4) species adsorbed on the SiO_2 surface. Calcination in vacuum provides a species that may differ both in the number of bonds with the surface and with neighboring vanadium species (spectra 2, 3, and 4 in Figure 4). Thus, lines present in spectra 2, 3, and 4 (calcination at 200 °C, 500 °C, and 700 °C) may be assigned to V species bonded to the surface via one, two, or three V–O bonds, respectively, as well as to V species bonded to neighboring vanadium species via one or two bonds.

Spectra of samples with high V concentrations (spectra 5 and 6) suggest the formation of the amorphous (nonregular) precursor of V_2O_5, since no sidebands are observed in the MAS spectra of these samples. Increasing the treatment temperature up to 700 °C results in the appearance of a line with highly resolved sidebands, due to rearrangement of the amorphous V_2O_5 structure to the crystalline one.

3.1.2 Prepared by $VOCl_3$ Interaction With SiO_2

The spectrum of the sample after $VOCl_3$ deposition suggests the presence of physically adsorbed $VOCl_3$ (narrow line with $\delta = -6$ ppm) and of $VOCl_{3-n}(OSi)_n$ species bonded with the SiO_2 surface [a line with an axial anisotropy, Figure 4(b),

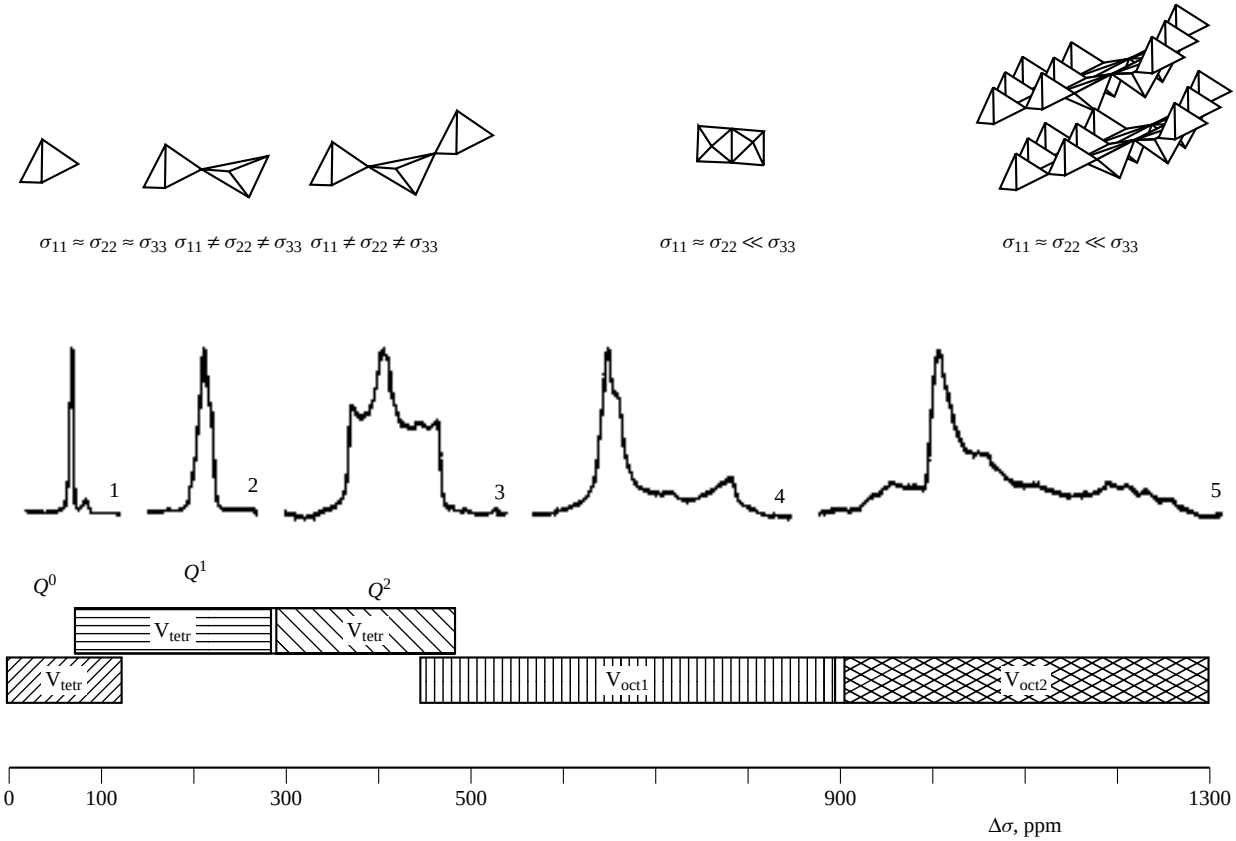

Figure 2 Relationship between the type of V coordination (tetrahedral or octahedral), the extent of polyhedra association (Q), and the shielding anisotropy $\Delta\sigma$. [As an example, the ^{51}V NMR spectra of Tl vanadates and V_2O_5 are presented: 1, Tl_3VO_4 (regular tetrahedra, Q^0); 2, $Tl_4V_2O_7$ (slightly distorted tetrahedra, Q^1); 3, $TlVO_3$ (strongly distorted tetrahedra, Q^2); 4, $Tl_2V_6O_{16}$ (distorted octahedra); 5, V_2O_5 (strongly distorted octahedron or square-pyramid)]

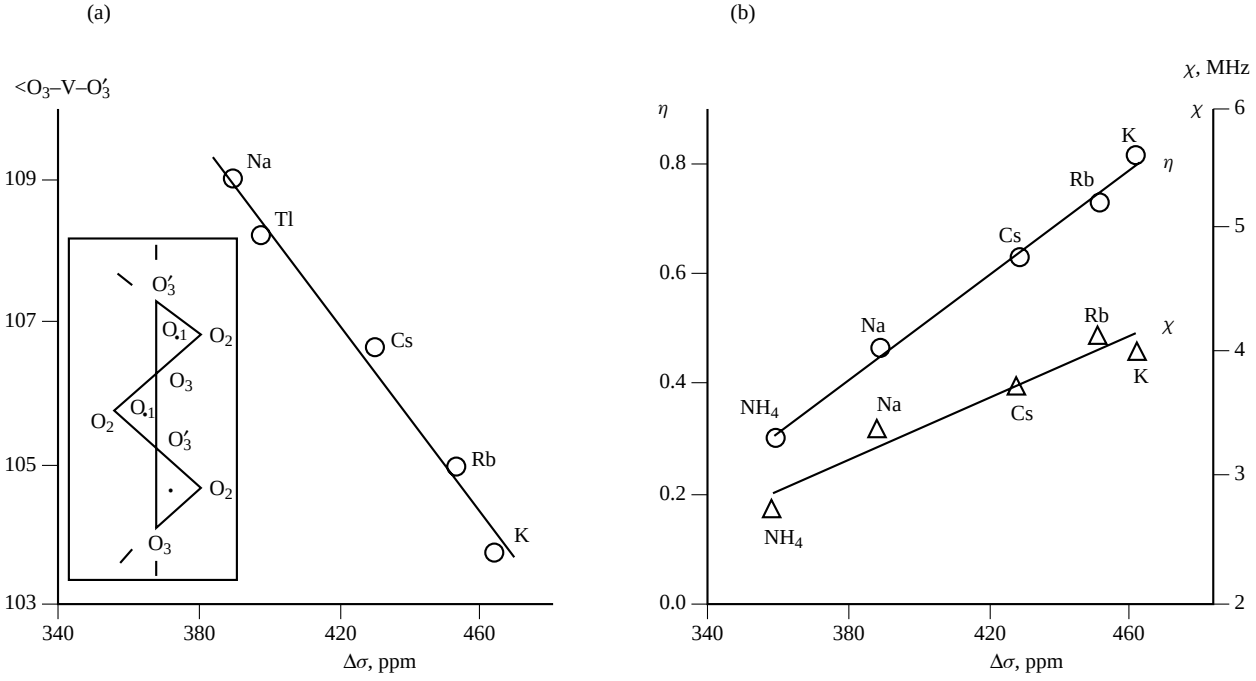

Figure 3 (a) Schematic representation of the structure of metavanadates of Na, Tl, Cs, Rb, and K and the dependence of the shielding anisotropy ($\Delta\sigma$) of their ^{51}V NMR spectra upon the $O_3–V–O_3'$ angle. This angle characterizes the distortion of the VO_4 tetrahedron from the regular form where $O_3–V–O_3' = 109°28'$. (b) Correlation between the shielding anisotropy $\Delta\sigma$ (data of Table 1) and the quadrupole coupling parameters χ and η (the latter taken from Pletnev et al.3 and Eckert and Wachs7) for metavanadates

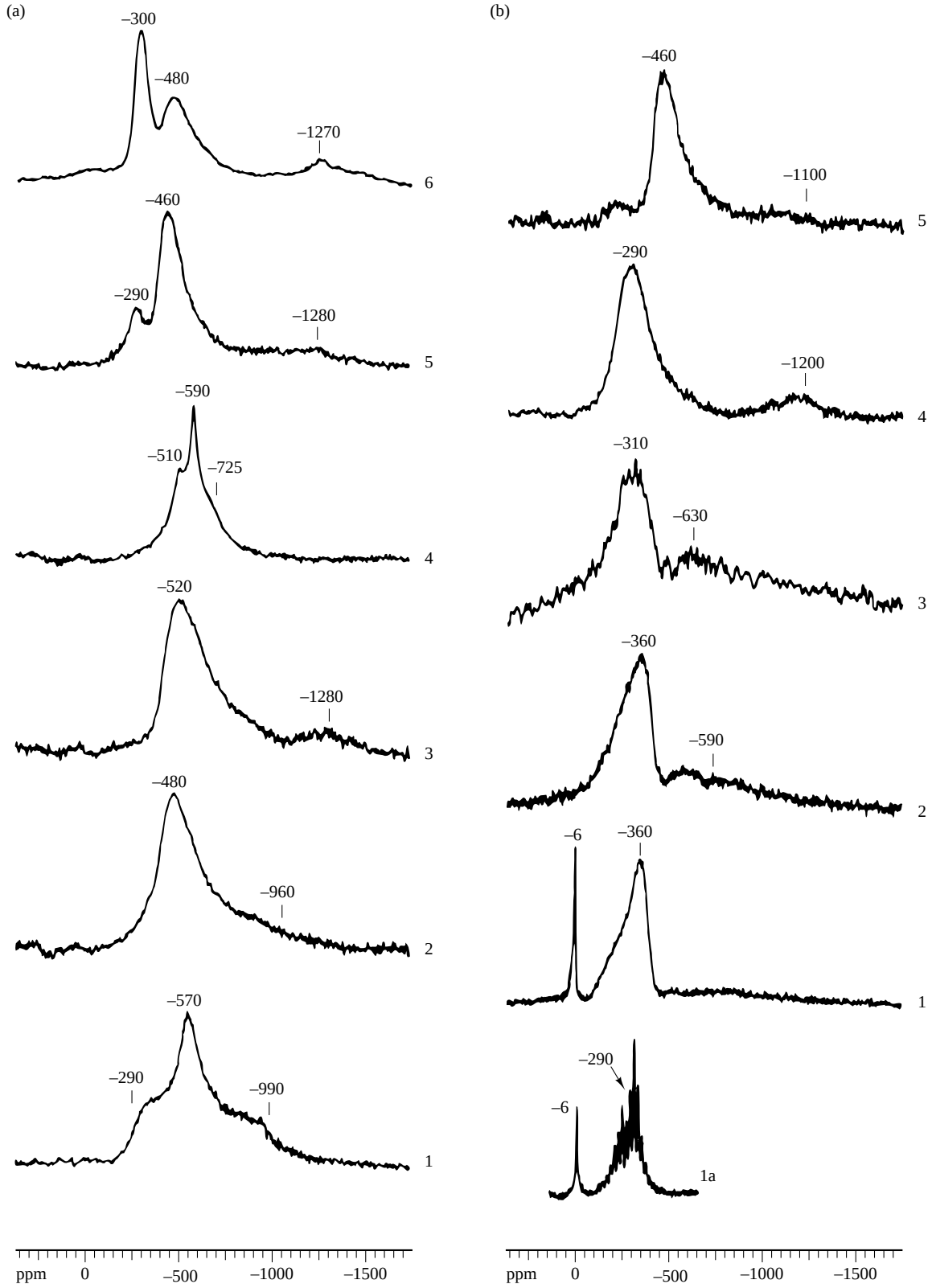

Figure 4 (a) ^{51}V NMR spectra of V_2O_5/SiO_2 samples prepared via impregnation of SiO_2 with NH_4VO_3 (pH 7, 2.6 wt.% V_2O_5) 1, after treatment in vacuum at 120 °C; 2, at 200 °C; 3, at 500 °C; 4, at 700 °C. Spectra 5 and 6 correspond to samples with a V content of 5.5 and 6.4 wt.% V_2O_5, respectively, calcined at 500 °C. (b) ^{51}V NMR spectra of $VOCl_3/SiO_2$ samples prepared by interaction of $VOCl_3$ from the gas phase with SiO_2: 1, after $VOCl_3$ deposition; 1a, MAS spectrum of the same sample [line at 6 ppm corresponds to physically adsorbed $VOCl_3$, anisotropic line with σ_{iso} = 290 ppm corresponds to $VOCl_2$(OSi) surface species]; 2, 3, 4, and 5, increase of H_2O content (replacement of Cl atoms to OH groups takes place during the first stage of hydration, then interaction of V species with the next H_2O molecules occurs); 6, spectrum 5 after evacuation at 100 °C. All the spectra here and in the remaining figures were recorded at 105.15 MHz, pulse duration = 0.5 μs, pulse repetition frequency = 1 Hz. Chemical shifts are presented with respect to $VOCl_3$ as external reference

spectrum 1]. Deposition of $VOCl_3$ at room temperature yields complexes with $n = 1$ (a line with $\sigma_{iso} = 290$ ppm, spectrum 1a). Increasing the deposition temperature to 400 °C leads to complexes with $n = 2$ or 3. The first additions of water cause the disappearance of physically adsorbed $VOCl_3$ [Figure 4(b), spectrum 2], then water interacts with the $VOCl_{3-n}(OSi)_n$ surface species producing partially hydrated $VO(OH)_y$-$Cl_{3-n-y}(OSi)_n$ ($y \leq n$, $n = 1$, 2, or 3) species (spectra 2 and 3) and fully hydrated $VO(OH)_{3-n} \cdot 2H_2O(OSi)_n$ species (for these species the sign of the anisotropy is opposite to that for species containing Cl in their coordination sphere, $\sigma_{\parallel} > \sigma_{\perp}$). Dehydration under mild conditions (100 °C) results in the removal of water from the first coordination sphere and in the formation of associated tetrahedral complexes (spectrum 5). The latter was ascribed to $VO(OSi)_3$ by Das et al.[13]

Application of magic angle spinning does not improve the resolution, unlike the situation when complexes contain Cl in the first coordination sphere. This indicates a nonregularity in the structure of the surface oxide complexes.

These data along with results presented by Lapina et al.[14] show that after calcination at 400–500 °C similar complexes are formed on the SiO_2 surface by the different deposition procedures.

3.2 V_2O_5/Al_2O_3 Catalysts

Vanadium-51 NMR spectra of V_2O_5/Al_2O_3 catalysts prepared by interaction of Al_2O_3 with $VOCl_3$, impregnation of Al_2O_3 with NH_4VO_3, and ultra-high-intensity grinding (UHIG) of V_2O_5-Al_2O_3 mixtures are shown in Figures 5 and 6.

3.2.1 Prepared by Impregnation

The various ^{51}V NMR spectra of these catalysts can be classified in terms of the five different types of lines contained[15,16] (Figure 5). Line A [spectrum (a)-1] observed for wet samples of low V content (1 wt.%) has been attributed to tetrahedral VO_4 species relatively loosely bound to the Al_2O_3 surface via one or two oxygen atoms. Line B, which was detected for calcined samples of low V content (1 wt.%) [spectrum (a)-2] was attributed to VO_4 tetrahedra bound more firmly to the Al_2O_3 surface via two or more oxygen atoms. Line C observed for samples with a large V content either dried or calcined [spectrum (a)-3] has been attributed to polynuclear V species of the decavanadate type on the Al_2O_3 surface. Line D is attributed to the $AlVO_4$ phase. It has been detected in calcined samples with a large V concentration [spectrum (a)-4]. From the MAS spectra, the σ_{iso} values for each of the three nonequivalent V sites in the structure of this compound were as follows: $\sigma_{iso1} = 668 \pm 5$; $\sigma_{iso2} = 747 \pm 5$; $\sigma_{iso3} = 780 \pm 5$ ppm. Line E ($\sigma_{\perp} = 310$ ppm, $\sigma_{\parallel} = 1270$ ppm) relates to V_2O_5 [spectrum (a)-5]. In the spectra of real catalysts, superposition of lines from different V sites occurs as shown in Figure 5(b).

3.2.2 Prepared by Interaction of Al_2O_3 With $VOCl_3$

Figure 6(a) shows that at least four types of particles are formed on the Al_2O_3 surface after $VOCl_3$ deposition: physically adsorbed $VOCl_3$ (narrow line with $\delta \approx 0$ ppm) and particles containing Cl atoms in the first coordination sphere, i.e. $VOCl_{3-n}(OAl)_n$, where $n = 1$, 2, or 3 (broad lines in the range from 0 to −1000 ppm, spectrum 1). The process of hydration occurs initially by hydration of the physically adsorbed $VOCl_3$ (disappearance of the signal at $\delta \approx 0$ ppm) and then exchange of Cl atoms in the first coordination sphere of V by OH groups takes place; after sample treatment at 500 °C, the formation of V sites typical for catalysts prepared by impregnation are also formed [cf. Figure 6(a), spectrum 5 and Figure 6(b), spectrum 3].

3.2.3 Prepared by UHIG Treatment

The ultra-high-intensity grinding (UHIG) of V_2O_5-Al_2O_3 mixtures was found to induce a heterogeneous chemical reaction between these oxides producing highly dispersed V species on the support surface.[17] The ^{51}V NMR spectrum of V_2O_5 after UHIG treatment demonstrates the broadening of the peaks from first-order quadrupole effects due to distortion of the local vanadium environment while the general crystal structure of V_2O_5 is retained [spectra 1 and 2 in Figure 6(c)]. Only a small part of the V_2O_5 reacts with Al_2O_3 when a V_2O_5-Al_2O_3 mixture is calcined for 14 h at 500 °C (peak at −570 ppm) (spectrum 3). A more complete interaction between V_2O_5 and Al_2O_3 takes place in the samples after UHIG treatment at room temperature (spectrum 4). As the concentration of V increases, the other tetrahedral V state (peak near −750 ppm) appears. Subsequent calcination at 500 °C produces V in octahedral coordination. In general, ^{51}V NMR spectra of the samples treated at 500 °C after UHIG treatment show the formation of surface structures that are similar to those for V_2O_5/Al_2O_3 catalysts prepared by the conventional impregnation/calcination method.

Thus, the types of surface V species on Al_2O_3 are the same for all three preparation procedures discussed above. Their relative amounts depend in a similar way on the total V concentration on the Al_2O_3 surface and on the treatment temperature. At low V concentration species A prevail, while at the increased V concentration species B and C appear on the catalyst surface. At still larger amounts of supported V (>10 wt.%), V_2O_5 and $AlVO_4$ also form.

3.3 V_2O_5/MgO Catalysts

Vanadium-51 NMR spectra of V_2O_5/MgO catalysts, recorded at various vanadium content, show four different V sites on the MgO surface (Figure 7).[18] Only one of them can be attributed to magnesium vanadate, $Mg_3(VO_4)_2$. Other V sites have been identified on the basis of correlations between the structure of the local environment of the V nuclei and the shielding anisotropy.

The narrow isotropic line with $\sigma_{iso} = 480$ ppm observed at low vanadium concentration (from 1.6–2.6 wt.% V) [spectra 1 and 2 in Figure 7(a)] has been attributed to isolated surface V atoms which have a virtually regular tetrahedral oxygen environment. Two broadened lines, i.e. an almost isotropic line with $\sigma_{iso} = 570$ ppm and a line with $\sigma_{\perp} = 510$ ppm, $\sigma = 720$ ppm have been assigned to surface clusters with V atoms in a tetrahedral environment (spectra 2, 3, and 4). At large V content, orthovanadate $Mg_3(VO_4)_2$ ($\sigma_{iso} = 560$ ppm) is formed in the catalysts (spectrum 4). The calculated shapes of the individual lines for various V sites in V_2O_5/MgO catalysts and

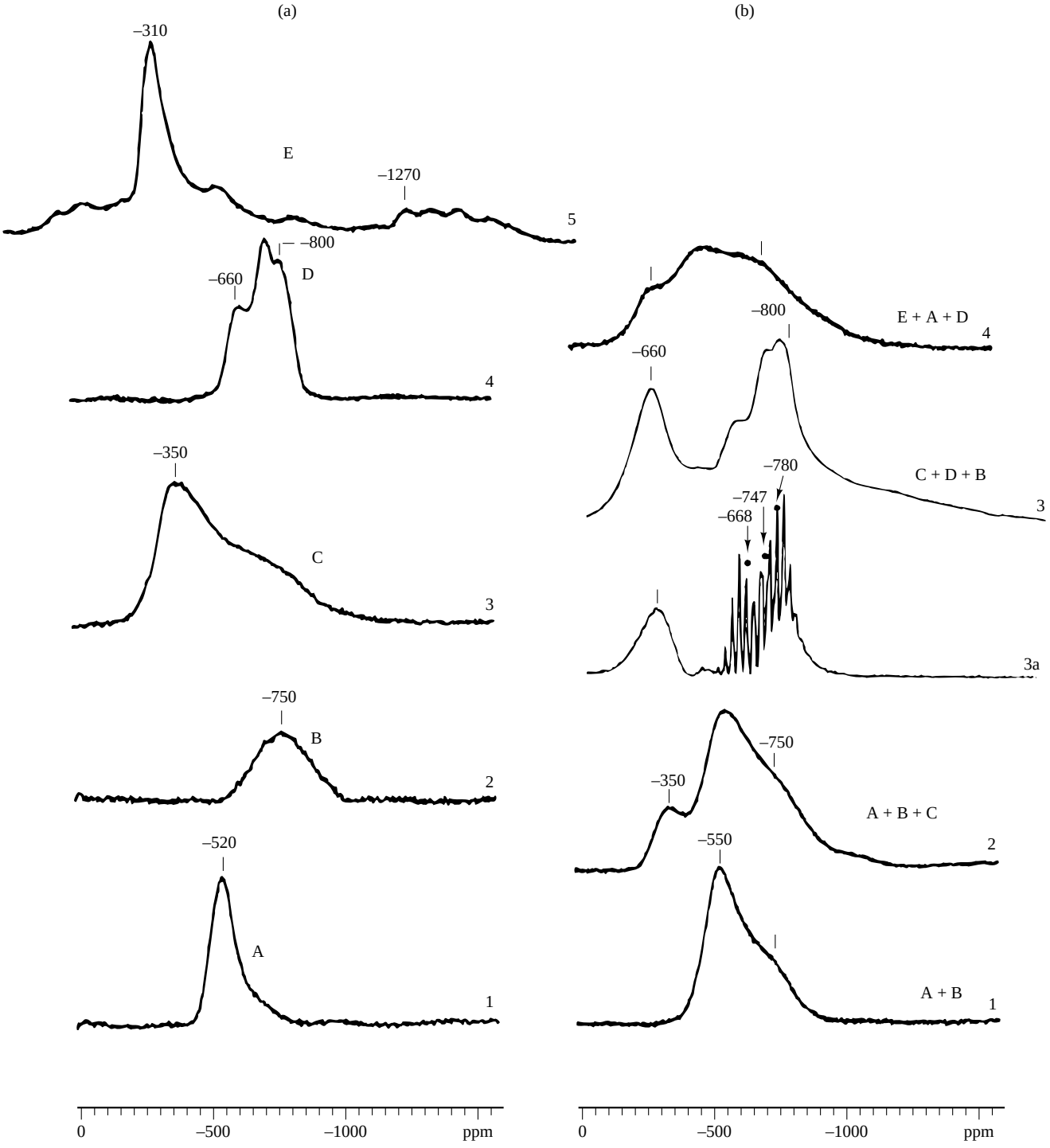

Figure 5 Classification of ^{51}V NMR lines observed in V_2O_5/Al_2O_3 catalysts prepared by Al_2O_3 impregnation with NH_4VO_3 solution. (a) Individual lines: 1, line A, σ_{iso} = 520–590 ppm, observed in wet samples at a V content from 1–2 wt.%; 2, line B, σ_{iso} = 750 ppm observed at a V content of 1 wt.% for samples calcined at 500 °C; 3, line C, $\sigma_{\perp}$ = 350 ppm observed for wet samples at high V content; 4, line D from polycrystalline $AlVO_4$; 5, line E from polycrystalline V_2O_5. (b) Spectra of various catalysts: 1, prepared by impregnation with NH_4VO_3 (pH 12, 2.2 wt.% V) dried at 110 °C, superposition of lines A and B; 2, the same sample calcined at 550 °C, superposition of lines A, B, and C; 3a, MAS spectrum of sample 3; 3, catalyst prepared via impregnation with VOC_2O_4 (pH 0.4, 14 wt.% V) calcined at 500 °C, superposition of lines B, C, and D (line D gives well-resolved sidebands with MAS); 4, catalyst prepared via impregnation with NH_4VO_3 (pH 7, 14.8 wt.% V), the superposition of lines A, D, and E

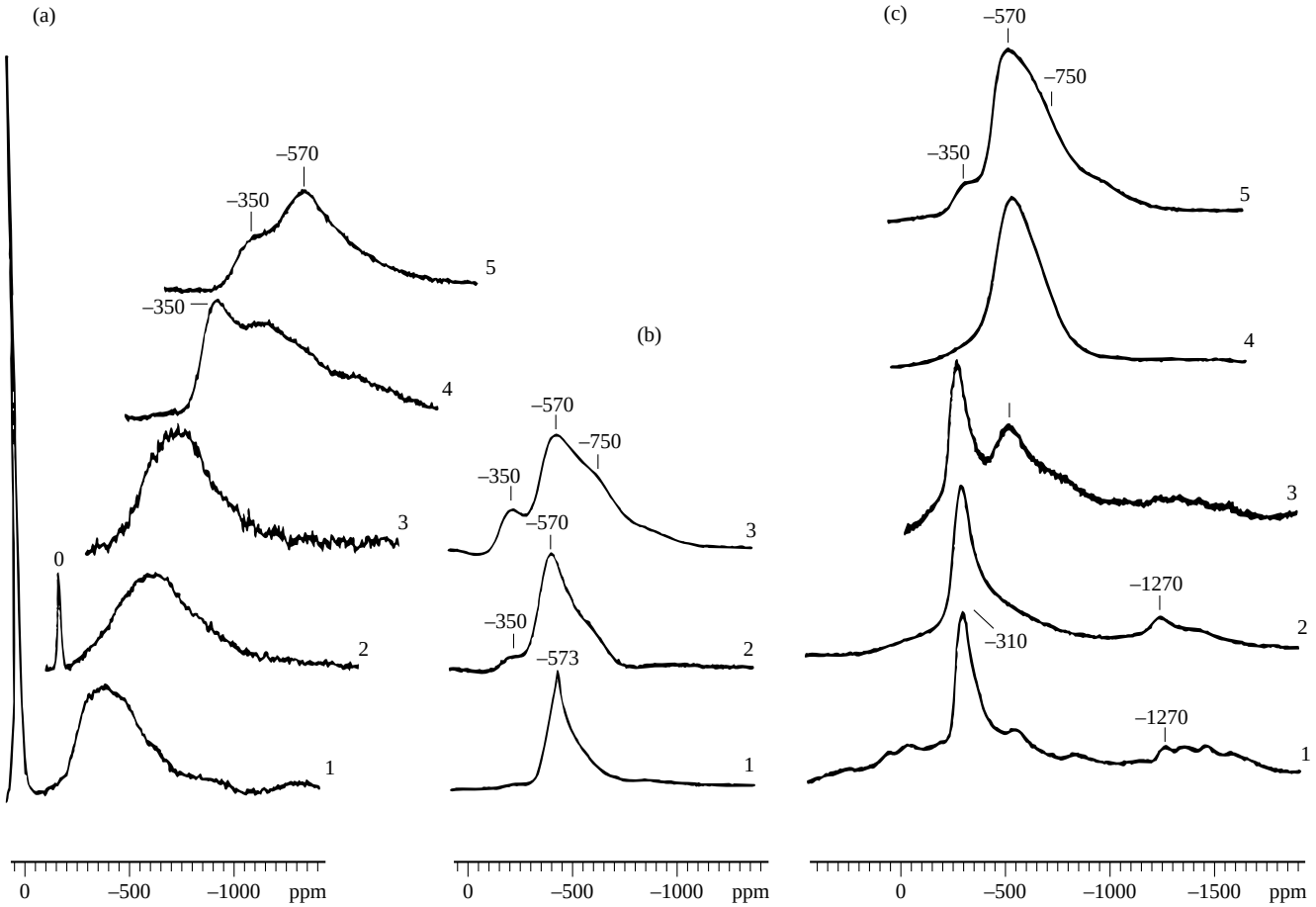

Figure 6 Vanadium-51 NMR spectra of V_2O_5/Al_2O_3 catalysts at different stages in their preparation: (a) Catalysts prepared by interaction with gaseous $VOCl_3$: 1, spectrum after $VOCl_3$ deposition; 2, 3, and 4, increase of H_2O content; 5, sample 4 after calcination at 500 °C. (b) Catalysts prepared by impregnation with NH_4VO_3 (pH 12, 3.8 wt.% V): 1, wet sample; 2, sample dried at 120 °C; 3, sample calcined at 500 °C. (c) Catalysts prepared by ultra-high-intensity grinding (UHIG): 1, V_2O_5; 2, V_2O_5 after UHIG; 3, V_2O_5-Al_2O_3 mixture (5 wt.% V_2O_5) calcined at 500 °C for 14 h; 4, after UHIG treatment at room temperature; 5, UHIG with subsequent calcination of the samples at 500 °C for 2 h

deconvolution of the experimental spectrum into individual lines are also shown in Figure 7(b) and (c). Figure 7(c) also presents the relative amounts of the various V species as measured by deconvolution of the experimental spectra.

Hence, the ^{51}V NMR spectra of V_2O_5/MgO catalysts allow one to form certain conclusions on the structure of surface V species and their concentration as a function of the total vanadium content.

3.4 V_2O_5/TiO_2 Catalysts

The influence of the admixtures on the structure of the supported species has been demonstrated for V_2O_5/TiO_2 supported catalysts[1,19] (Figure 8). Spectra of catalysts prepared via the gas-phase reaction of $VOCl_3$ with TiO_2 followed by subsequent hydration and H_2O removal at 350 °C are shown in Figure 8(a). The catalyst prepared from the most pure anatase (impurities less than 0.1 wt.%) contains two tetrahedral (peaks at $\delta = -440$ and -560 ppm) and one octahedral species (peak at $\delta = -320$ ppm) as follows from spectrum 1 in Figure 8(a). An admixture containing sulfate anions (3.9 wt.%) increases the content of the octahedral vanadium species (spectrum 2). The presence of 3 wt.% Si leads to tetrahedral vanadium complexes typical for V_2O_5/SiO_2 samples (peak at $\delta = -490$ ppm, spectrum 3) and with anatase containing Na (2.3 wt.%) the formation of Na_3VO_4 was observed (line with $\delta = -535$ ppm, spectrum 4). Similar surface species have also been identified for the same catalysts prepared by impregnation of the same anatase samples with a solution of vanadyl oxalate [cf. Figure 8(a) and (b)].

Thus, the type of surface V species on TiO_2 depends mainly on the presence of the impurities in anatase with the preparation procedure having a considerably smaller effect on the type of V sites on the catalyst surface.

Data analysis presented above and by Lapina et al.[1] shows that the structure of surface V species depends mainly on the type of support. The preparation procedure (impregnation, grafting, UHIG treatment) appears to have much less of an effect on the type of V sites on the catalyst surface provided that the concentration of vanadium and the treatment temperatures are the same.

At a V concentration less than 0.5 monolayer, surface tetrahedral species with different extents of distortion of the oxygen environment are formed, with the distortion depending on the type of the support used.

(a) For MgO and $AlPO_4$, the surface vanadium species has an almost regular tetrahedral environment with σ_{iso} depending

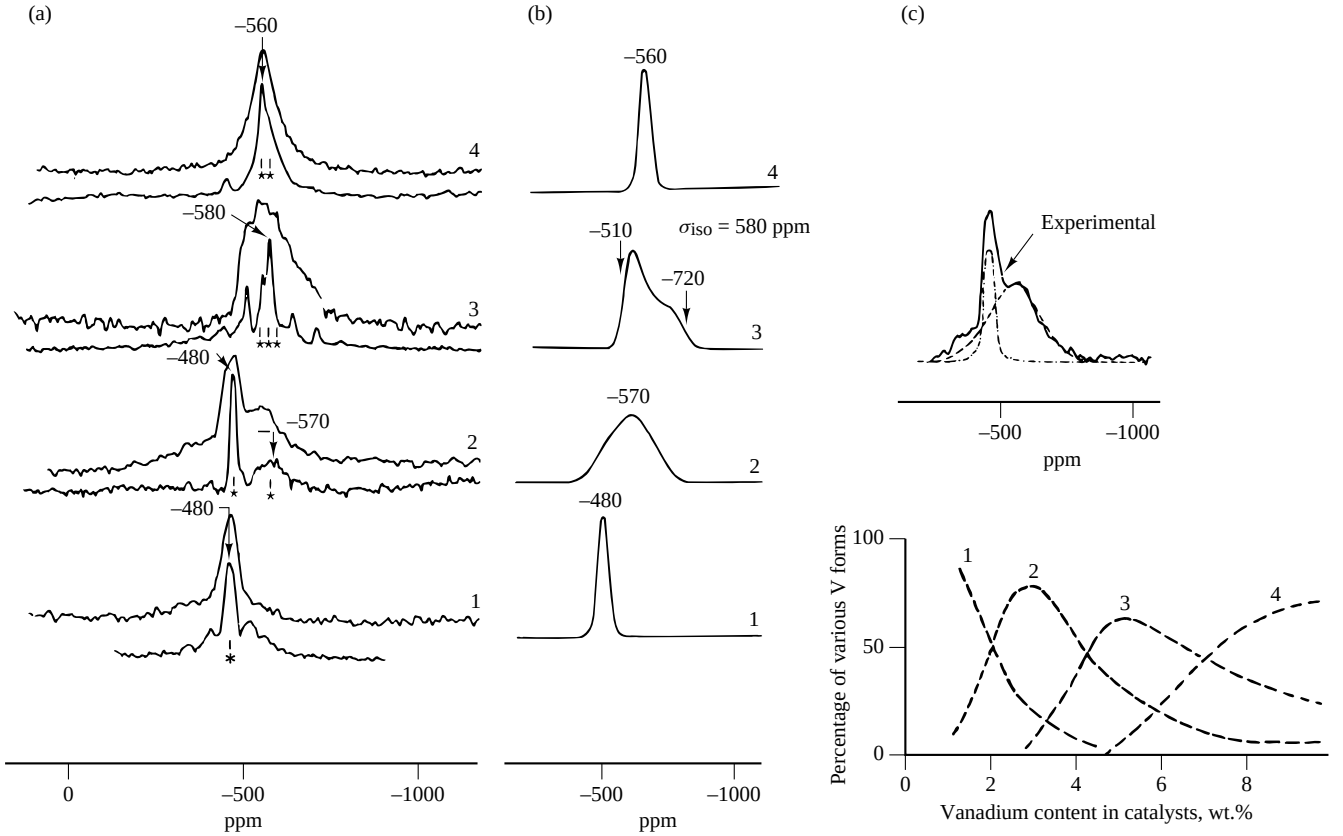

Figure 7 (a) ^{51}V NMR spectra of V_2O_5/MgO catalysts of various vanadium content: 1, 1.6 wt.%; 2, 2.6 wt.%; 3, 5.0 wt.%; 4, 9.6 wt.%. The upper spectra were recorded without MAS; the MAS spectra are shown below. The isotropic chemical shifts are indicated by asterisks (*). (b) The simulated lineshapes of ^{51}V NMR spectra for various V species found in V_2O_5/MgO catalysts: 1, isolated tetrahedral surface species; 2, tetrahedral surface clusters; 3, tetrahedral surface clusters of another type; 4, $Mg_3(VO_4)_2$. (c) Deconvolution of an experimental spectrum (2.6 wt.% V) into individual lines and the percentage of various V species on the MgO surface as a function of the total V content in V_2O_5/MgO catalysts: 1, isolated tetrahedral surface species; 2, tetrahedral surface clusters; 3, tetrahedral surface clusters of another type; 4, $Mg_3(VO_4)_2$

on the type of support employed (σ_{iso} = 480 and 880 ppm for MgO and $AlPO_4$, respectively) and $\Delta\sigma < 100$ ppm.

(b) For Al_2O_3, ZrO_2, ZrO_2/TiO_2, and SnO_2, slightly distorted tetrahedral V species exist with σ_{iso} values ranging from 500–600 ppm and $\Delta\sigma < 200$ ppm.

(c) For SiO_2 and TiO_2, distorted tetrahedral V species with one short V–O bond are formed. They exhibit axial anisotropy of chemical shielding with $\Delta\sigma < 600$ ppm.

An increase in V concentration (up to monolayer coverage) results in association of surface species. The following features associated with their ^{51}V NMR spectra can be noted.

(a) On MgO, $AlPO_4$ associated tetrahedral surface V species exhibit spectra with a fully anisotropic σ tensor, which points to a distortion of the VO_4 tetrahedra in these species (σ_{iso} = 560–570 ppm). The lines for such associated species are usually broader when compared with those for isolated species.

(b) For associated V species on Al_2O_3, ZrO_2, SnO_2, and TiO_2/ZrO_2, fully anisotropic lines from distorted VO_4 surface tetrahedra are also observed (σ = 700–800 ppm). The widths of the lines are close to those for isolated V species on this surface.

(c) For associated V species on Al_2O_3, ZrO_2, TiO_2/ZrO_2, and SnO_2 of another type, lines with an axial anisotropy of the shielding tensor arising from distorted octahedral V sites are observed ($\sigma_\perp$ = 320–330 ppm, $\Delta\sigma$ = 600 ppm).

(d) For associated V species on SiO_2 and TiO_2, lines with an axial anisotropy of the shielding tensor arising from distorted octahedral V sites are observed ($\sigma_\perp$ = 290–300 ppm, $\Delta\sigma > 900$ ppm).

A further increase of V concentration above monolayer coverage provides crystalline compounds [V_2O_5 on SiO_2, TiO_2, $AlPO_4$, TiO_2/ZrO_2, and SnO_2; $AlVO_4$ on Al_2O_3; and $Mg_3(VO_4)_2$ on MgO].

Water adsorption changes the V coordination from tetrahedral to octahedral on SiO_2 and TiO_2. In these cases, water molecules insert into the first coordination sphere of V. For V sites on ZrO_2, $AlPO_4$, TiO_2/ZrO_2, and SnO_2, water molecules adsorb in the second coordination sphere, providing slight shifts of the ^{51}V NMR lines upon adsorption.

Addition of promoters, such as rhodium, titania, or zirconia (or impurities), results in notable changes in both the structure of the surface V species and their redistribution on the surface.

3.5 Vanadium Catalysts for SO_2 Oxidation

The active component of vanadium catalysts for SO_2 oxidation is known to consist of vanadium oxide and sulfates or pyrosulfates of alkali metals (K, Na, Cs are most commonly

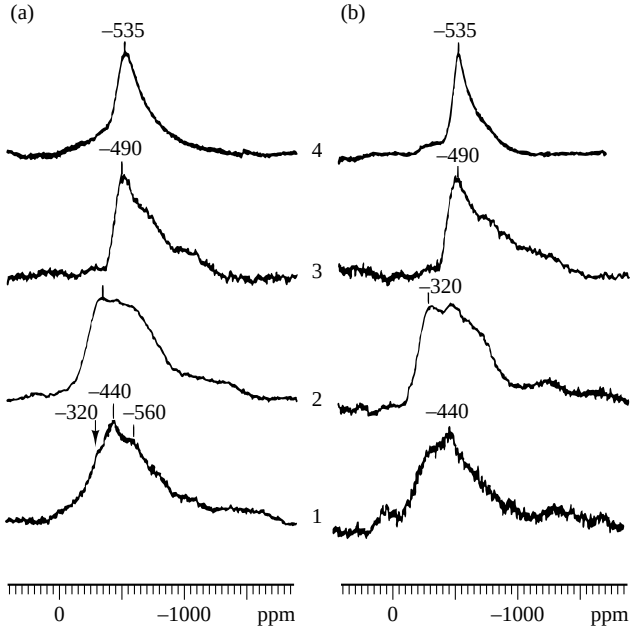

Figure 8 Vanadium-51 NMR spectra of V_2O_5/TiO_2 catalysts (a) prepared by gas phase reaction of $VOCl_3$ with TiO_2 followed by subsequent hydration and removal of H_2O with a stream of He at 350 °C and (b) prepared via impregnation with a solution of VOC_2O_4: 1, anatase (all impurities less 0.1 wt.%); 2, TiO_2 (3.9 wt.% SO_4); 3, TiO_2 (3 wt.% Si); 4, TiO_2 (2.3 wt.% Na)

used) supported on porous materials such as silica or silica alumina. At ambient temperature the active component forms a thin vitreous film dispersed over the support. Under the reaction conditions (400–500 °C), the active component exists as a melt forming a very thin liquid layer on the support surface.

We present here the results of ^{51}V NMR studies of oxosulfatovanadates(V), chemical compounds formed between V_2O_5 and alkali pyrosulfates that are assumed to be present in the active component of these catalysts, as well as of V_2O_5-$K_2S_2O_7$ alloys and of commercial catalysts. Combined with other spectroscopic methods and kinetic studies, these results have helped to reveal the active sites in SO_2 oxidation and the mechanism of this catalytic reaction.[1,20,21]

The spectra of oxosulfatovanadate(V) $K_3VO_2(SO_4)_2$, the alloy $V_2O_5 \cdot 3K_2S_2O_7$, and a commercial catalyst are presented in Figure 9. All oxosulfatovanadates(V) exhibit axial anisotropy of the chemical shielding tensor with parameters close to those for V_2O_5. Thus the local environment of the vanadium atom in oxosulfatovanadates(V) is similar to that in V_2O_5, where vanadium has a distorted octahedral (bipyramidal) oxygen atom environment with one V–O bond being considerably shorter than the others. Comparison of the spectrum of $V_2O_5 \cdot 3K_2S_2O_7$ alloy (Figure 9) with that for oxosulfatovanadate(V) $K_3VO_2(SO_4)_2$ shows that the former exhibits σ values close to those for oxosulfatovanadate(V). This indicates the same local environment for the V atoms in the glassy alloy and in crystalline oxosulfatovanadate(V).

The ^{51}V NMR spectra for various catalysts after treatment with a reaction gas mixture become quite similar and exhibit the same two lines, namely an almost isotropic line with σ_{iso} = 520–560 ppm and a line with axial anisotropy of the shielding tensor. Only the relative intensities of the

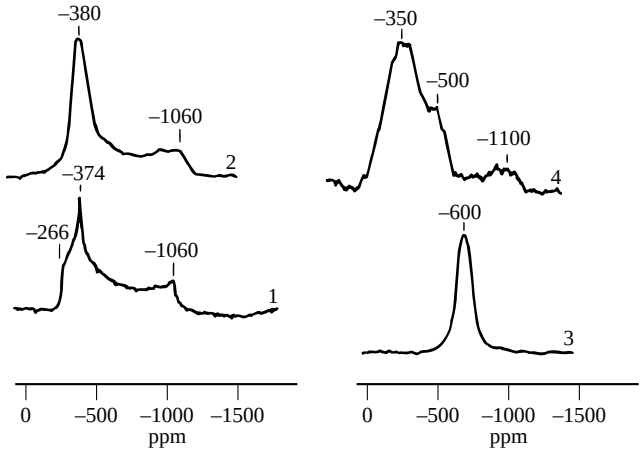

Figure 9 Vanadium-51 NMR spectra of (1) oxosulfatovanadate(V) $K_3VO_2(SO_4)_2$; (2) the solid alloy $V_2O_5 \cdot 3K_2S_2O_7$; (3) the industrial catalyst BAV before treatment under the reaction conditions; (4) the same after treatment

two lines but not their character vary from one catalyst to another. In particular, the average chemical shifts for both the isotropic and anisotropic lines ($\sigma_\perp$ = 320–350 ppm, $\sigma_\parallel$ = 1200–1300 ppm) are almost the same for all the catalysts studied. This indicates that the active component in these catalysts is the same and is actually formed during the course of catalytic reaction.[2] Initially, catalysts arising from different preparations contain a variety of V sites. However, on interaction with the components of the reaction media only the two sites mentioned above are formed. The nearly isotropic line belongs to V atoms in a slightly distorted tetrahedral environment and can be attributed to vanadium bonded to the support. This line exhibits an increase in relative intensity with a decrease in the overall V content of the sample. Thus, the isotropic line belongs to V complexes on the SiO_2 surface.

Measurement of the catalytic activity for a series of samples with different contents of surface tetrahedral V has showed the latter to be inactive in SO_2 oxidation.[20]

To elucidate the nature of the vanadium complexes which are active in SO_2 oxidation, ^{51}V, ^{17}O, ^{23}Na, ^{39}K, and ^{133}Cs NMR were combined with catalytic activity measurements of V_2O_5-$K_2S_2O_7$ melts and of catalysts with different amounts of the active component on SiO_2.[1,20,21]

Vanadium-51 NMR spectra of V_2O_5 and $V_2O_5 \cdot 3Cs_2S_2O_7$ alloy at temperatures below and above their melting points (Figure 10) demonstrate the spectrum of molten $V_2O_5 \cdot 3Cs_2S_2O_7$ (see ***Molten Salts***) to be substantially broader than that of V_2O_5. This means, that unlike V_2O_5, where melting leads to a separation of the vanadium–oxygen layers and breaks them into relatively short fragments, in molten $V_2O_5 \cdot 3Cs_2S_2O_7$ substantially larger particles are formed.

Oxygen-17 NMR (see ***Oxygen-17 NMR***) has also been used to characterize the melt of the active component in SO_2 oxidation at 500 °C in the presence of an SO_3 + SO_2 + O_2 mixture, i.e. under typical conditions for the catalytic process in industry.[1,20,21] Addition of V_2O_5 to $K_2S_2O_7$ leads to a shift and a broadening of the ^{17}O line, indicating V coordination with pyrosulfate anions. A more sophisticated analysis using a thermodynamic model of the ^{17}O linewidths has shown that at small vanadium concentrations approximately two to three pyrosulfate anions are coordinated to one V atom.

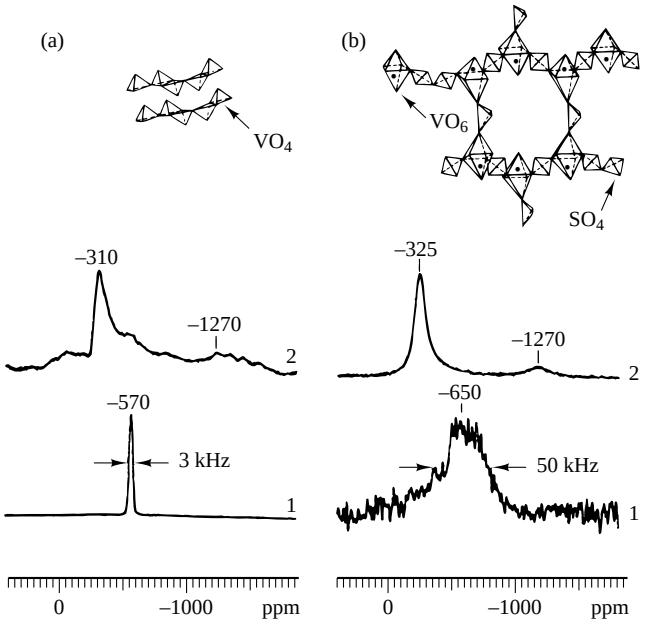

Figure 10 Vanadium-51 NMR spectra of (a) V_2O_5 and (b) of the alloy $V_2O_5 \cdot 3Cs_2S_2O_7$ (1) below the melting point (i.e. at 20 °C) and (2) above the melting point (670 °C and 370 °C for (a) and (b), respectively). Above: the structures formed in molten V_2O_5 and $V_2O_5 \cdot 3Cs_2S_2O_7$ alloy

Oxygen-17 NMR data also suggest a fast exchange between terminal and bridging oxygen atoms in the pyrosulfate anion which may occur via the reaction $S_2O_7^{2-} \rightleftarrows SO_4^{2-} + SO_3$. The characteristic time τ during which this equilibrium is established is less than 10^{-3} s. Oxygen-17 and ^{51}V NMR data show that on addition of V_2O_5 to $K_2S_2O_7$, complexes are formed according to the reaction: $V_2O_5 + 3K_2S_2O_7 \rightleftarrows 2K_3VO(SO_4)_3$. The increase in the ^{51}V and ^{17}O linewidths on increasing the V concentration suggests a further association of the V species leading to larger oligomers of the type shown in Figure 10. The large size of these oligomers makes their rotational diffusion very slow. Internal rotation of their fragments can also be hindered because of branching and linking of the oligomeric chains. Because of these factors, the ^{17}O and ^{51}V NMR lines of these species are too broad to be detected.

When supported on SiO_2, the dimeric or oligomeric vanadium species can be more stabilized on the surface due to their interaction with Si–OH groups. These results agree well with studies of the catalytic activity of thin films of active melts on Pyrex glass and on SiO_2, as well as with kinetic studies of SO_2 oxidation.[20]

4 RELATED ARTICLES

Aluminum-27 NMR of Solutions; Chemical Shift Tensor Measurement in Solids; Anisotropy of Shielding and Coupling in Liquid Crystalline Solutions; Chemical Shift Tensors; Dipolar and Indirect Coupling Tensors in Solids; Internal Spin Interactions and Rotations in Solids; High Speed MAS of Half-Integer Quadrupolar Nuclei in Solids; Internal Spin Interactions and Rotations in Solids; Magic Angle Spinning; Molecular Sieves: Crystalline Systems; Molten Salts; Oxygen-17 NMR; Quadrupolar Interactions; Quadrupolar Nuclei in Glasses; Quadrupolar Nuclei in Solids; Silicon-29 NMR; Variable Angle Sample Spinning.

5 REFERENCES

1. O. B. Lapina, V. M. Mastikhin, A. A. Shubin, V. N. Krasilnikov, and K. I. Zamaraev, *Prog. Nucl. Magn. Reson. Spectrosc.*, 1992, **24**, 457.
2. B. E. Leach (ed.), *Applied Industrial Catalysis*, Academic Press, New York, 1983.
3. R. N. Pletnev, V. A. Gubanov, and A. A. Fotiev, *NMR in Oxide Vanadium Compounds*, Nauka, Moscow, 1979 (in Russian); [*Chem Abs.*, 1980, **92**, 159 005x].
4. M. H. Cohen and F. Reif, *Solid State Phys.*, 1957, **5**, 321.
5. S. D. Gornostansky and G. V. Stager, *J. Chem. Phys.*, 1967, **46**, 4959.
6. D. Rehder, *Bull. Magn. Reson.*, 1982, **4**, 33.
7. H. Eckert and I. E. Wachs, *J. Phys. Chem.*, 1989, **93**, 6796.
8. J. Skibsted, N. C. Nielsen, H. Bildsoe, and H. J. Jakobsen, *J. Am. Chem. Soc.*, 1993, **115**, 7351.
9. A. A. Fotiev, B. V. Slobodin, and M. Ya. Hodos, *Vanadates, their Synthesis, Composition and Properties*, Nauka, Moscow, 1988 (in Russian); [*Chem. Abs.*, 1989, **110**, 68 625c].
10. V. M. Mastikhin, O. B. Lapina, V. N. Krasilnikov, and A. A. Ivakin, *React. Kinet. Catal. Lett.*, 1984, **24**, 119.
11. D. Muller, W. Gessner, and A. R. Grimmer, *Z. Chem.*, 1977, **B12**, 453.
12. J. Klinowsky, *Prog. Nucl. Magn. Reson. Spectrosc.*, 1984, **16**, 237.
13. N. Das, H. Eckert, H. Hu, I. E. Wachs, J. F. Walzer, and F. J. Feher, *J. Phys. Chem.*, 1993, **97**, 8240.
14. J. B. Lapina, V. M. Mastikhin, A. V. Nosov, T. Beutel, and H. Knozinger, *Catal. Lett.*, 1992, **13**, 203.
15. J. B. Lapina, V. M. Mastikhin, L. G. Simonova, and Yu. O. Bulgakova, *J. Mol. Catal.*, 1991, **69**, 61.
16. L. R. Le Costumer, B. Taouk, M. Le Meur, E. Payen, M. Guelton, and J. Grimblot, *J. Phys. Chem.*, 1988, **92**, 1230.
17. Z. Sobalik, O. B. Lapina, O. N. Novgorodova, and V. M. Mastikhin, *Appl. Catal.*, 1990, **63**, 191.
18. O. B. Lapina, A. V. Simakov, V. M. Mastikhin, S. A. Veniaminov, and A. A. Shubin, *J. Mol. Catal.*, 1989, **50**, 55.
19. H. Eckert, G. Deo, I. E. Wachs, and A. M. Hirt, *Colloids Surf.*, 1990, **45**, 347.
20. V. M. Mastikhin, O. B. Lapina, B. S. Balzhinimaev, L. G. Simonova, L. M. Karnatovskaya, and A. A. Ivanov, *J. Catal.*, 1987, **103**, 160.
21. B. S. Balzhinimaev, A. A. Ivanov, O. B. Lapina, V. M. Mastikhin, and K. I. Zamaraev, *Faraday Discuss. Chem. Soc.*, 1989, **87/88**, 133.
22. S. Hayakawa, T. Yoko, and S. Sakka, *J. Solid State Chem.*, 1994, **112**, 329.

Biographical Sketches

Vjatcheslav M. Mastikhin. *b* 1937. Graduated 1959, Kharkov University, Ph.D. 1969, Dr.S., 1986, Boreskov Institute of Catalysis. Leading Scientist, Boreskov Institute of Catalysis, Novosibirsk, 1986–1995.

Approx. 200 publications. Research interests: application of solid state NMR to problems of heterogeneous catalysis.

Olga B. Lapina. *b* 1953. Graduated 1976, from Novosibirsk University, Ph.D., 1984, Dr.S., 1995, Boreskov Institute of Catalysis. Senior Scientist, Boreskov Institute of Catalysis, Novosibirsk, 1990–present. Approx. 100 publications. Research interests: application of solid state NMR to problems of heterogeneous catalysis.

Chemical Exchange Effects on Spectra

Jerome I. Kaplan

Indiana University-Purdue University at Indianapolis, IN, USA

1	Derivation of the Exchange Operator	1
2	Short List of Common Exchange Events	3
3	Systems Undergoing more than One Exchange Process	4
4	Linearization of the Nonlinear Exchange Terms	4
5	Discussion for a Simple Spin System of Techniques for Obtaining the Exchange Time τ_e	4
6	The Exception when the Exchange Time τ_e is Equal to or Less than the Correlation Time τ_c	7
7	The Exception when the Exchange Relaxation is not Exponential	8
8	References	10

It will be assumed that the reader is familiar with the NMR density matrix equation [1] of a molecule given as

$$\dot{\hat{\rho}} = -\mathrm{i}[\hat{\mathcal{H}}^{\circ}_{\mathrm{spin}} + \hat{\mathcal{H}}_{\mathrm{rf}}, \hat{\rho}] + \hat{R}_{\mathrm{op}}\hat{\rho} \tag{1}$$

where the relaxation operator $\hat{R}_{\mathrm{op}}$ [2] couples the spin system to the external world—sometimes referred to as the 'bath'. We will show how equation (1) is modified to allow for chemical exchange.

1 DERIVATION OF THE EXCHANGE OPERATOR

The form of the exchange operator is derived using the 'usual' assumptions that: (a) exchange time τ_e is much longer than the correlation time τ_c used to obtain $\hat{R}_{\mathrm{op}}$; and (b) exchange relaxation time is exponential. Consider an equilibrium exchanging system where two species, AB and CD, mutually exchange two different fragments, B with C, in a bimolecular collision. For reasons which become apparent later it is convenient to describe the molecules in terms of the fragments which exchange

$$\mathrm{AB} + \mathrm{CD} \underset{k_r}{\overset{k_f}{\Leftrightarrow}} \mathrm{AC} + \mathrm{BD} \tag{2}$$

The fragments A, B, C, and D can be single protons or more complex moieties. Throughout this presentation it is important to be aware that we are always dealing with molecular components which are in equilibrium.

The mean lifetime between exchanges τ_{sp} of each species involved in the equilibrium process is defined as the ratio of its rate of formation R_{ex} (or disappearance, they are the same) to its concentration (sp):

$$1/\tau_{\mathrm{sp}} = R_{\mathrm{ex}}/(\mathrm{sp}) \tag{3}$$

Then the τ_e values for the different species are given by:

$$\left.\begin{array}{ll} 1/\tau_{\mathrm{AB}} = k_f(\mathrm{DC}), & 1/\tau_{\mathrm{CD}} = k_f(\mathrm{AB}), \\ 1/\tau_{\mathrm{AC}} = k_r(\mathrm{BD}), & 1/\tau_{\mathrm{BD}} = k_r(\mathrm{AC}) \\ k_f(\mathrm{AC})(\mathrm{BD}) = k_r(\mathrm{AC})(\mathrm{BD}) & \end{array}\right\} \tag{4}$$

We can pictorially rewrite the reaction in equation (2) as

$$\mathrm{AB} + \mathrm{CD} \Leftrightarrow \frac{\mathrm{AB}}{\mathrm{CD}} \Leftrightarrow \begin{matrix}\mathrm{A}\\ \mathrm{C}\end{matrix}\Big|\begin{matrix}\mathrm{B}\\ \mathrm{D}\end{matrix} \Leftrightarrow \mathrm{AC} + \mathrm{BD} \tag{5}$$

(**1**) (**2**)

to proceed via two intermediate bimolecular complexes, (**1**) before new bonds are formed, and (**2**) after rearrangement but before dissociation to products.

Let us concentrate on AB for the moment. The nuclear spin Hamiltonian of AB in the rotating coordinate system is

$$\hat{\bar{\mathcal{H}}}^{\mathrm{AB}} = \sum_s (\omega_{0s} - \omega)\hat{I}^z_s + \sum_{s\rangle t} J_{x,t}\hat{\boldsymbol{I}}_s \cdot \hat{\boldsymbol{I}}_t + \omega_1 \sum_s \hat{I}^x_s \tag{6}$$

where for the moment we do not need to specify which spins belong to A and B. (Exchange for weakly coupled systems where $\hat{\boldsymbol{I}}_s \cdot \hat{\boldsymbol{I}}_t$ is replaced by $\hat{I}^z_s\hat{I}^z_t$ was developed by Gutowsky et al.[3]) The density matrix equation for AB in the rotating frame between collisions is given as (denoted by $\sim$)

$$\dot{\hat{\tilde{\rho}}}^{\mathrm{AB}} = -\mathrm{i}[\hat{\bar{\mathcal{H}}}^{\mathrm{AB}}, \hat{\tilde{\rho}}^{\mathrm{AB}}] + \hat{R}^{\mathrm{AB}}\hat{\tilde{\rho}} \tag{7}$$

(Note that material in this article up to Section 5 has been taken from the book by Kaplan and Fraenkel.[4]) Now rewrite equation (7) as

$$\dot{\hat{\tilde{\rho}}}^{\mathrm{AB}} = -\mathrm{i}(\hat{\bar{\mathcal{L}}}^{\mathrm{AB}}_{\mathrm{S}} + \hat{\bar{\mathcal{L}}}^{\mathrm{AB}}_{\mathrm{R}})\hat{\tilde{\rho}}^{\mathrm{AB}} \tag{8}$$

where by comparison one sees that

$$\hat{\bar{\mathcal{L}}}^{\mathrm{AB}}_{\mathrm{S}}\hat{\tilde{\rho}}^{\mathrm{AB}} = [\hat{\bar{\mathcal{H}}}^{\mathrm{AB}}, \hat{\tilde{\rho}}^{\mathrm{AB}}] \tag{9}$$

$$\mathrm{i}\hat{\bar{\mathcal{L}}}^{\mathrm{AB}}_{\mathrm{R}}\hat{\tilde{\rho}}^{\mathrm{AB}} = \hat{R}^{\mathrm{AB}}\hat{\tilde{\rho}} \tag{10}$$

We do this in order to make equation (8) appear as a conventional first-order differential equation. Next, equation (8) is integrated, with the initial condition that

$$\hat{\tilde{\rho}}^{\mathrm{AB}}(t') = \hat{\tilde{\rho}}^{\mathrm{AB}}(\mathrm{col}, t') \tag{11}$$

where the right-hand side is the value of $\hat{\tilde{\rho}}^{\mathrm{AB}}$ at time t' immediately after a collision which has resulted in the formation of an AB molecule. Note that the collision time is taken to be instantaneous on the NMR timescale.

The result is that

$$\hat{\tilde{\rho}}^{\mathrm{AB}}_{(t)} = \exp[-\mathrm{i}(\hat{\bar{\mathcal{L}}}^{\mathrm{AB}}_{\mathrm{S}} + \hat{\bar{\mathcal{L}}}^{\mathrm{AB}}_{\mathrm{R}})(t - t')]\hat{\tilde{\rho}}^{\mathrm{AB}}(\mathrm{col}, t') \tag{12}$$

The probability that after a time $t - t'$, AB will not suffer an exchange collision is, for exponential exchange relaxation,

$$\frac{\exp[-(t-t')/\tau_{AB}]}{\tau_{AB}} \tag{13}$$

and, therefore, the ensemble average $\hat{\tilde{\rho}}^{AB}(t)$ is the weighted probability of all AB molecules created at t' which survive until time t:

$$\hat{\tilde{\rho}}^{AB}(t) = \int_{-\infty}^{t} \exp\{-[i(\hat{\tilde{\mathcal{L}}}_S^{AB} + \hat{\tilde{\mathcal{L}}}_B^{AB})(t-t')]\, \hat{\tilde{\rho}}^{AB}(\text{col}, t') \times \frac{\exp[-(t-t')/\tau_{AB}]}{\tau_{AB}}\, dt' \tag{14}$$

We next differentiate equation (14) to obtain the differential form of the $\hat{\tilde{\rho}}^{AB}$ equation. This is done using the result from calculus that for

$$y(t) = \int_A^t g(t,t')\, dt' \tag{15}$$

$$\frac{dy}{dt} = \int_A^t \frac{d}{dt}[g(t,t')]\, dt' + g(t,t) \tag{16}$$

Applying equation (16) to equation (14), we obtain the result

$$\dot{\hat{\tilde{\rho}}}^{AB} = -i(\hat{\tilde{\mathcal{L}}}_S^{AB} + \hat{\tilde{\mathcal{L}}}_R^{AB})\hat{\tilde{\rho}}^{AB} + \frac{1}{\tau_{AB}}[\hat{\tilde{\rho}}^{AB}(\text{col}) - \hat{\tilde{\rho}}^{AB}] \tag{17}$$

or going back to the definitions of $\hat{\tilde{\mathcal{L}}}_S^{AB}$ and $\hat{\tilde{\mathcal{L}}}_S^{AB}$ in equations (9) and (10), we have

$$\dot{\hat{\tilde{\rho}}}^{AB} = -i[\hat{\tilde{\mathcal{H}}}^{AB}, \hat{\tilde{\rho}}^{AB}] + \hat{R}^{AB}\hat{\tilde{\rho}} + (1/\tau_{AB})[\hat{\tilde{\rho}}^{AB}(\text{col}) - \hat{\tilde{\rho}}^{AB}] \tag{18}$$

To abbreviate the exchange contribution in the density matrix equation, we write

$$\hat{E}\hat{\tilde{\rho}}^{AB} = (1/\tau_{AB})[\hat{\tilde{\rho}}^{AB}(\text{col}) - \hat{\tilde{\rho}}^{AB}] \tag{19}$$

where $\hat{\tilde{\rho}}(\text{col})$ will be evaluated in the following section.

1.1 Permutation of Indices Method

What remains is to evaluate $\hat{\tilde{\rho}}^{AB}(\text{col})$. We can do this in two ways. First, we can think backward in time, starting with $\hat{\tilde{\rho}}^{AB}(t)$ just after formation of AB by collision and ask what are its antecedents (AC and BD).[4] Alternatively, one can think forward in time taking AC and BD before an exchange collision and take them through the chemical reaction. The latter was the first method suggested.[5] However, the former is calculationally, if not conceptually, the much simpler approach and the one we will use in this article. This 'backward' approach is simpler only if one works in the product representation.

The product representation is written as

$$\psi = \prod_{s=1}^{n} \phi_{ms} \tag{20}$$

where s labels the spins and ϕ_{ms} are eigenfunctions of $\hat{I}^z$:

$$\hat{I}_s^z \phi_{ms} = m_s \phi_{ms} \tag{21}$$

For $I = \frac{1}{2}$,

$$\phi_{1/2} = \alpha; \quad \phi_{-1/2} = \beta \tag{22}$$

and for a molecule made up of only half spins, a product wavefunction would have the form

$$\phi_{\text{molecule}} = \alpha_1\beta_2\alpha_3\beta_4\beta_5\alpha_6\cdots \tag{23}$$

The 'product representation' has a special utility because the exchange collision is assumed to happen so fast on the timescale of the nuclear spin Hamiltonian that the nuclear spin wavefunction is not changed by the collision. This is an example of the so-called 'sudden approximation' in quantum mechanics.[6] Thus, the product wavefunction before and after the collision will be the same.

Now let us see how we make use of these ideas. A particular product wavefunction of molecule AB can be written as

$$\phi_{ab}^{AB} = \phi_a^A \phi_b^B \tag{24}$$

where ϕ_a^A and ϕ_b^B are the individual product wavefunctions of fragments A and B, respectively. An arbitrary matrix element of $\hat{\tilde{\rho}}^{AB}$ in the product representation just after an exchange collision can be written as

$$\langle ab|\hat{\tilde{\rho}}^{AB}|a'b'\rangle \tag{25}$$

Multiplying equation (25) by 1 in the form of

$$1 = \text{Tr}\,\hat{\tilde{\rho}}^{CD} = \sum_{cd}\langle cd|\hat{\tilde{\rho}}^{CD}|cd\rangle \tag{26}$$

equation (25) takes the form

$$\langle ab|\hat{\tilde{\rho}}^{AB}|a'b'\rangle = \sum_{cd}\langle ab|\hat{\tilde{\rho}}^{AB}|a'b'\rangle\langle cd|\hat{\tilde{\rho}}^{CD}|cd\rangle \tag{27}$$

During an exchange collision, there is a mutual reorganization where B is replaced by C to form $\hat{\tilde{\rho}}^{AC}$ and $\hat{\tilde{\rho}}^{BD}$ and where the product wavefunctions ab and cd are rearranged respectively into ac and bd. Since the product wavefunction b (or b') belongs solely to the fragment B (this would not be true for an eigenfunction), the wavefunctions, a, b, c, and d follow along with the fragments A, B, C, and D, with which they are associated. In other words, the quantum mechanics follows the chemistry; thus equation (27) becomes, after reorganization

$$\langle ab|\hat{\tilde{\rho}}^{AB}(\text{col})|a'b'\rangle = \sum_{cd}\langle ac|\hat{\tilde{\rho}}^{AC}|a'c\rangle\langle bd|\hat{\tilde{\rho}}^{BD}|b'd\rangle \tag{28}$$

which gives $(\hat{E}\hat{\tilde{\rho}}^{\mathrm{AB}})_{ab,a'b'}$ as

$$(\hat{E}\hat{\tilde{\rho}}^{\mathrm{AB}})_{ab,a'b'} = \frac{1}{\tau_{\mathrm{AB}}}\left[\sum_{cd}\hat{\tilde{\rho}}^{\mathrm{AC}}_{ac,a'c}\hat{\tilde{\rho}}^{\mathrm{BD}}_{bd,b'd} - \hat{\tilde{\rho}}^{\mathrm{AB}}_{ab,a'b'}\right] \quad (29)$$

2 SHORT LIST OF COMMON EXCHANGE EVENTS

For a comprehensive list of exchange events, see Fraenkel.[7] For a 'hands-on' description of how to obtain τ_{e} lineshape analysis, see Nageswara Rao.[8]

2.1 Mutual Exchange of Fragments

$$i \text{ of } \phi_i \quad \underset{\substack{ab\\a'b'}}{\mathrm{AB}} + \underset{\substack{cd\\c'd'}}{\mathrm{CD}} \overset{k_1}{\underset{k_1}{\Leftrightarrow}} \underset{\substack{ac\\a'c'}}{\mathrm{AC}} + \underset{\substack{bd\\b'd'}}{\mathrm{BD}} \quad (30)$$

$$\hat{\tilde{\rho}}^{\mathrm{CD}}_{cd,c'd'}(\mathrm{col}) = \sum_{ab}\hat{\tilde{\rho}}^{\mathrm{AC}}_{ac,ac'}\hat{\tilde{\rho}}^{\mathrm{BD}}_{bd,bd'} \quad (31)$$

$$\hat{\tilde{\rho}}^{\mathrm{AC}}_{ac,a'c'}(\mathrm{col}) = \sum_{bd}\hat{\tilde{\rho}}^{\mathrm{AB}}_{ab,a'b}\hat{\tilde{\rho}}^{\mathrm{CD}}_{cd,c'd} \quad (32)$$

$$\hat{\tilde{\rho}}^{\mathrm{BD}}_{bd,b'd'}(\mathrm{col}) = \sum_{ac}\hat{\tilde{\rho}}^{\mathrm{AB}}_{ab,ab'}\hat{\tilde{\rho}}^{\mathrm{CD}}_{cd,cd'} \quad (33)$$

$$\hat{\tilde{\rho}}^{\mathrm{AB}}_{ab,a'b'}(\mathrm{col}) = \sum_{cd}\hat{\tilde{\rho}}^{\mathrm{AC}}_{ac,a'c}\hat{\tilde{\rho}}^{\mathrm{BD}}_{bd,b'd} \quad (34)$$

$$\underset{ab,a'b'}{\mathrm{AB}} + \underset{c,c'}{\mathrm{C}} \Leftrightarrow \underset{ac,a'c'}{\mathrm{AC}} + \underset{bb'}{\mathrm{B}} \quad (35)$$

$$\hat{\tilde{\rho}}^{\mathrm{AB}}_{ab,a'b'}(\mathrm{col}) = \sum_{c}\hat{\tilde{\rho}}^{\mathrm{AC}}_{ac,a'c}\hat{\tilde{\rho}}^{\mathrm{B}}_{b,b'} \quad (36)$$

$$\hat{\tilde{\rho}}^{\mathrm{C}}_{c,c'}(\mathrm{col}) = \sum_{ab}\hat{\tilde{\rho}}^{\mathrm{AC}}_{ac,ac'}\hat{\tilde{\rho}}^{\mathrm{B}}_{b,b} = \sum_{a}\hat{\tilde{\rho}}^{\mathrm{AC}}_{ac,ac'} \quad (37)$$

$$\hat{\tilde{\rho}}^{\mathrm{AC}}_{ac,a'c'}(\mathrm{col}) = \sum_{b}\hat{\tilde{\rho}}^{\mathrm{AB}}_{ab,a'b}\hat{\tilde{\rho}}^{\mathrm{C}}_{c,c'} \quad (38)$$

$$\hat{\tilde{\rho}}^{\mathrm{B}}_{b,b'}(\mathrm{col}) = \sum_{ac}\hat{\tilde{\rho}}^{\mathrm{AB}}_{ab,ab'}\hat{\tilde{\rho}}^{\mathrm{C}}_{c,c} = \sum_{a}\hat{\tilde{\rho}}^{\mathrm{AB}}_{ab,ab'} \quad (39)$$

2.2 Group Transfer

$$\underset{\substack{ab\\a'b'}}{\mathrm{AB}} + \underset{\substack{cd\\c'd'}}{\mathrm{CD}} \Leftrightarrow \underset{\substack{abc\\a'b'c'}}{\mathrm{ABC}} + \underset{\substack{d\\d'}}{\mathrm{D}} \quad (40)$$

$$\hat{\tilde{\rho}}^{\mathrm{AB}}_{ab,a'b'}(\mathrm{col}) = \sum_{cd}\hat{\tilde{\rho}}^{\mathrm{ABC}}_{abc,a'b'c}\hat{\tilde{\rho}}^{\mathrm{D}}_{d,d} = \sum_{c}\hat{\tilde{\rho}}^{\mathrm{ABC}}_{abc,a'b'c} \quad (41)$$

$$\hat{\tilde{\rho}}^{\mathrm{CD}}_{cd,c'd'}(\mathrm{col}) = \sum_{ab}\hat{\tilde{\rho}}^{\mathrm{ABC}}_{abc,abc'}\hat{\tilde{\rho}}^{\mathrm{D}}_{d,d'} \quad (42)$$

$$\hat{\tilde{\rho}}^{\mathrm{ABC}}_{abc,a'b'c'}(\mathrm{col}) = \sum_{d}\hat{\tilde{\rho}}^{\mathrm{AB}}_{ab,a'b'}\hat{\tilde{\rho}}^{\mathrm{CD}}_{cd,c'd} \quad (43)$$

$$\hat{\tilde{\rho}}^{\mathrm{D}}_{d,d'}(\mathrm{col}) = \sum_{abc}\hat{\tilde{\rho}}^{\mathrm{AB}}_{ab,ab}\hat{\tilde{\rho}}^{\mathrm{CD}}_{cd,cd'} = \sum_{c}\hat{\tilde{\rho}}^{\mathrm{CD}}_{cd,cd'} \quad (44)$$

2.3 Dissociation–Recombination

$$\underset{\substack{ab\\a'b'}}{\mathrm{AB}} \Leftrightarrow \underset{\substack{a\\a'}}{\mathrm{A}} + \underset{\substack{b\\b'}}{\mathrm{B}} \quad (45)$$

$$\hat{\tilde{\rho}}^{\mathrm{AB}}_{ab,a'b'}(\mathrm{col}) = \hat{\tilde{\rho}}^{\mathrm{A}}_{a,a'}\hat{\tilde{\rho}}^{\mathrm{B}}_{b,b'} \quad (46)$$

$$\hat{\tilde{\rho}}^{\mathrm{A}}_{a,a'}(\mathrm{col}) = \sum_{b}\hat{\tilde{\rho}}^{\mathrm{AB}}_{ab,a'b} \quad (47)$$

2.4 Unimolecular Rearrangements

These rearrangements include rotation, pseudorotation, and Berry rotation, where A is different from B:

$$\underset{\substack{a\\a'}}{\mathrm{A}} \Leftrightarrow \underset{\substack{a\\a'}}{\mathrm{B}} \quad (48)$$

$$\hat{\tilde{\rho}}^{\mathrm{A}}_{a,a'}(\mathrm{col}) = \hat{\tilde{\rho}}^{\mathrm{B}}_{a,a'} \quad (49)$$

$$\hat{\tilde{\rho}}^{\mathrm{B}}_{b,b'}(\mathrm{col}) = \hat{\tilde{\rho}}^{\mathrm{A}}_{a,a'} \quad (50)$$

2.5 Unimolecular Degenerate Rearrangements

$$\underset{\substack{abc\\a'b'c'}}{\mathrm{A}} \Leftrightarrow \underset{\substack{acb\\a'c'b'}}{\mathrm{A}} \tag{51}$$

This situation includes all rearrangements where the chemical identity of the species is preserved and the spins become scrambled. In this case the labels of spins are given by the order

$$\hat{\tilde{\rho}}^{\mathrm{A}}_{abc,a'b'c'}(\mathrm{col}) = \hat{\tilde{\rho}}^{\mathrm{A}}_{acb,a'c'b'} \tag{52}$$

3 SYSTEMS UNDERGOING MORE THAN ONE EXCHANGE PROCESS

The exchange processes considered in the previous section all involved one step, and the exchange contributions to the density matrix equations had the form

$$\hat{E}\hat{\tilde{\rho}}^{\mathrm{sp}} = (1/\tau_{\mathrm{sp}})[\hat{\tilde{\rho}}^{\mathrm{sp}}(\mathrm{col}) - \hat{\tilde{\rho}}^{\mathrm{sp}}] \tag{53}$$

Now, the question arises as to what is the form of $\tilde{\rho}(\mathrm{col})$ in a system undergoing several exchange processes at the same time.[4] The result must clearly be the weighted average

$$\hat{\tilde{\rho}}^{\mathrm{sp}}(\mathrm{col}) = \sum_{\mathrm{ex}} \frac{1/\tau_{\mathrm{spex}}}{1/\tau_{\mathrm{sp}}} \hat{\tilde{\rho}}(\mathrm{colex}) \tag{54}$$

where ex sums over all exchange processes, τ_{sp} is the mean lifetime of species sp given as

$$\frac{1}{\tau_{\mathrm{sp}}} = \sum_{\mathrm{ex}} \frac{1}{\tau_{\mathrm{spex}}} \tag{55}$$

and τ_{spex} is the survival time until sp undergoes a particular exchange step ex. Substituting equations (54) and (55) into equation (53) gives

$$\hat{E}\hat{\tilde{\rho}}^{\mathrm{sp}} = \sum_{\mathrm{ex}} (1/\tau_{\mathrm{spex}})[\hat{\tilde{\rho}}^{\mathrm{sp}}(\mathrm{colex}) - \hat{\tilde{\rho}}^{\mathrm{sp}}] \tag{56}$$

As an example, consider the following set of coupled exchange processes:

$$\mathrm{AB} \overset{k_{\mathrm{a}}}{\Leftrightarrow} \mathrm{A} + \mathrm{B} \tag{57}$$

$$\mathrm{AB} + \mathrm{C} \overset{k_{\mathrm{b}}}{\Leftrightarrow} \mathrm{AC} + \mathrm{D} \tag{58}$$

$$\mathrm{AB} + \mathrm{E} \overset{k_{\mathrm{c}}}{\Leftrightarrow} \mathrm{AE} + \mathrm{B} \tag{59}$$

with

$$1/\tau_{\mathrm{AB},a} = k_a \tag{60}$$

$$1/\tau_{\mathrm{AB},b} = k_b(\mathrm{C}) \tag{61}$$

$$1/\tau_{\mathrm{AB},c} = k_c(\mathrm{E}) \tag{62}$$

Then $\hat{E}\hat{\tilde{\rho}}^{\mathrm{AB}}$ is given by

$$\hat{E}\hat{\tilde{\rho}}^{\mathrm{AB}} = k_a[\hat{\tilde{\rho}}^{\mathrm{AB}}(\mathrm{col}, a) - \hat{\tilde{\rho}}^{\mathrm{AB}}] + k_b(\mathrm{C})[\hat{\tilde{\rho}}^{\mathrm{AB}}(\mathrm{col}, b) - \hat{\tilde{\rho}}^{\mathrm{AB}}] + k_c(\mathrm{E})[\hat{\tilde{\rho}}^{\mathrm{AB}}(\mathrm{col}, c) - \hat{\tilde{\rho}}^{\mathrm{AB}}] \tag{63}$$

and the different $\hat{\tilde{\rho}}^{\mathrm{AB}}(\mathrm{col})$ terms can be readily obtained by use of the catalog in Section 2.

4 LINEARIZATION OF THE NONLINEAR EXCHANGE TERMS

As can be seen by looking at the examples in Section 2, $\hat{\rho}(\mathrm{col})$ is often nonlinear. The nonlinear terms are made linear by noting that for low rf power:[4]

$$\hat{\rho}_{\mathrm{A}} \simeq \hat{\rho}_0 + \hat{\rho}_1 \tag{64}$$

where

$$\hat{\rho}_0 = \frac{\exp(-\hat{\mathcal{H}}^0_{\mathrm{A}}/kT)}{\mathrm{Tr}\exp(-\hat{\mathcal{H}}^0_{\mathrm{A}}/kT)} \simeq \frac{1 - \hat{\mathcal{H}}^0_{\mathrm{A}}/kT}{(2I+1)^{N_{\mathrm{A}}}} \tag{65}$$

$\hat{\rho}_1$ is linear in the rf field, and N_{A} is the number of spins in molecule A. A typical off-diagonal matrix element at resonance (its greatest value) is given approximately as

$$\langle\alpha|\hat{\rho}_1|\beta\rangle \simeq \frac{T_2\omega_1(\hbar\omega_0/kT)}{(2I+1)^{N_{\mathrm{A}}}} \tag{66}$$

Thus the ratio of a diagonal to an off-diagonal matrix element is given approximately as

$$\frac{\rho_{\mathrm{off-diagonal}}}{\rho_{\mathrm{diagonal}}} \simeq T_2\omega_1(\hbar\omega_0/kT) \tag{67}$$

which is very small for NMR operating conditions. Thus at low power one only need keep terms in $\hat{\rho}(\mathrm{col})$ which are linear in the off-diagonal elements. For high power, where one expresses

$$\hat{\rho}_{\mathrm{A}} \simeq \frac{1}{(2I+1)^{N_{\mathrm{A}}}} + \hat{\rho}_2 \tag{68}$$

a similar argument shows that one only need keep terms in $\hat{\rho}(\mathrm{col})$ which are either linear in $\hat{\rho}_{2\mathrm{off-diagonal}}$ or linear in $\hat{\rho}_{2\mathrm{diagonal}}$.

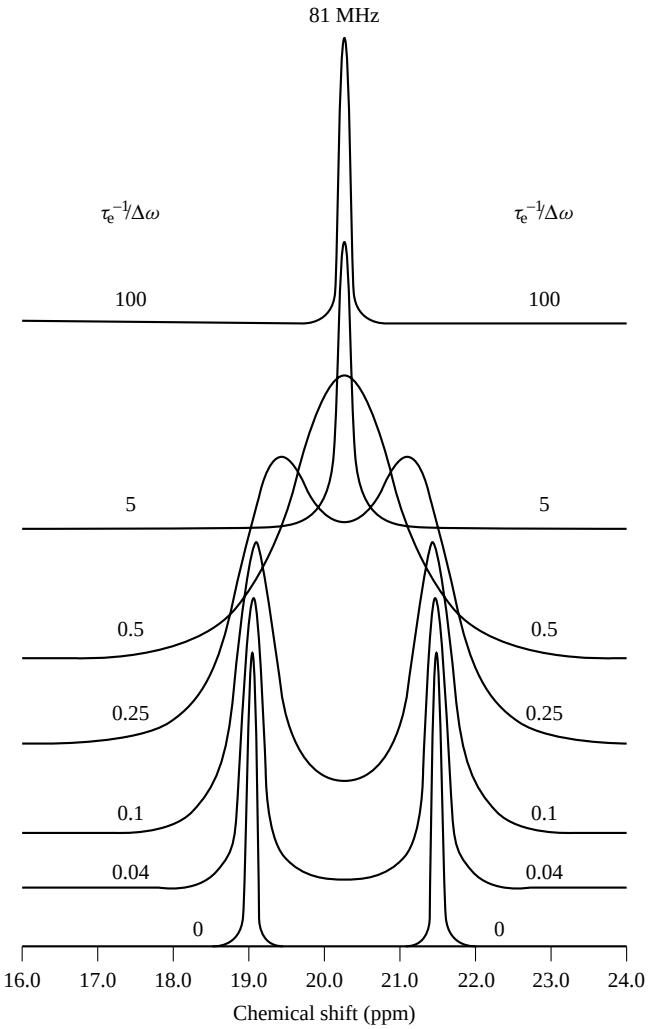

Figure 1 Computer plot of an exchange coupled doublet for slow to fast exchange

5 DISCUSSION FOR A SIMPLE SPIN SYSTEM OF TECHNIQUES FOR OBTAINING THE EXCHANGE TIME τ_e

Figure 1 shows the one-dimensional (or CW) chemical exchange spectra for two exchanging protons. It illustrates the effects of exchange when τ_e varies from $1/\tau_e \ll \Delta\omega$(see Figure 2), for which the doublet linewidth is approximately $1/T_2 + 1/\tau_e$, to the collapsed doublet, where for $1/\tau_e \gg \Delta\omega$ the linewidth is approximately $1/T_2 + \frac{1}{2}\Delta\omega^2\tau_e$.

5.1 Intermediate Exchange Rates

To obtain the exchange width in the intermediate range, i.e. for

$$\frac{1}{\tau_e} \rangle \frac{1}{10}\frac{1}{T_2} \tag{69}$$

$$\Delta\omega^2\tau_e \rangle \frac{1}{10}\frac{1}{T_2} \tag{70}$$

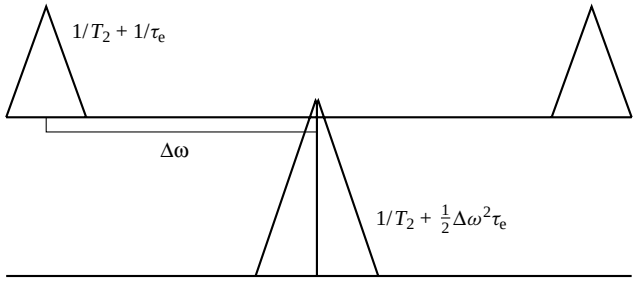

Figure 2 Schematic drawing of an exchange coupled doublet in the slow and fast exchange limits

one can use either CW lineshape or two-dimensional (2D) spectroscopy. We will first exhibit the CW lineshape for the doublet and then the two-dimensional mapping analog.

For the exchanging doublet AB where the doublet spins have the same $1/T_2$ and concentration and are separated by $2\Delta\omega$(see Figure 2), the CW absorption lineshape is given as the real part of

$$M = \frac{2}{x^- - x^+}\left(\frac{x^- - 1/T_2}{x - x^+} - \frac{x^+ - 1/T_2}{x - x^-}\right) \tag{71}$$

where

$$x = \mathrm{i}(\omega - \omega_0) \tag{72}$$

$$\omega_0 = \tfrac{1}{2}(\omega_{0A} + \omega_{0B}) \tag{73}$$

$$x^{\pm} = \left(\frac{1}{T_2} + \frac{1}{\tau_e}\right) \pm \mathrm{i}\left[\Delta\omega^2 - \left(\frac{1}{\tau_e}\right)^2\right]^{\frac{1}{2}} \tag{74}$$

For $1/\tau_e \ll \Delta\omega^2$, equation (71) is approximately given as

$$M \simeq \frac{1}{\mathrm{i}(\omega - \omega_0 - \Delta) - 1/T_2 - 1/\tau_e} + \frac{1}{\mathrm{i}(\omega - \omega_0 + \Delta) - 1/T_2 - 1/\tau_e} \tag{75}$$

with absorption at $\omega_0 \pm \Delta$ with widths $1/T_2 + 1/\tau_e$, and for $1/\tau_c \gg \Delta\omega$,

$$x^+ \simeq \left(\frac{1}{T_2} + \frac{1}{\tau_e}\right) - \left(\frac{1}{\tau_e} - \frac{1}{2}\Delta\omega^2\tau_e\right) \simeq \frac{1}{T_2} + \frac{1}{2}\Delta\omega^2\tau_e \tag{76}$$

$$x^- \simeq \left(\frac{1}{T_2} + \frac{1}{\tau_e}\right) + \left(\frac{1}{\tau_e} - \frac{1}{2}\Delta\omega\tau_e\right) \simeq \frac{2}{\tau_e} - \frac{1}{2}\Delta\omega^2\tau_e \tag{77}$$

$$M \simeq \frac{2}{2/\tau_e}\left[\frac{2/\tau_e}{i(\omega-\omega_0)-1/T_2-\frac{1}{2}\Delta\omega^2\tau_e} - \frac{\frac{1}{2}\Delta\omega^2\tau_e}{i(\omega-\omega_0)-2/\tau_e}\right] \quad (78)$$

Thus, effectively, for $2/\tau_e \gg \frac{1}{2}\Delta\omega^2\tau_e$ there is only one line centered at $\omega = \omega_0$ with a width $(1/T_2) + (1/2)\ \Delta\omega^2\tau_e$.

The 2D description is described in detail by Ernst et al.[9] One uses a series of three 90° pulses, as shown in Figure 3. (See ***Two-Dimensional Methods of Monitoring Exchange***.)

The period t_m is a chemical exchange mixing time which exchange mixes the components from time period 1 which are precessing at the frequencies ω_A and ω_B. The result is a 2D spectrum as shown in Figure 4. The great advantage of 2D spectroscopy is that it explicitly exhibits the exchange pathways for the entire spectra.

5.2 Slow Exchange

To obtain $1/\tau_e$ when

$$\frac{1}{\tau_e} < \frac{1}{10}\frac{1}{T_2} \quad (79)$$

one can use selective inversion, selective saturation, or amplitude modulated saturation.[10] The problem is most simply illustrated by using selective inversion. For the equal concentration two spin exchange coupled system the diagonal components can be expressed as the coupled Bloch equations:

$$\dot{M}_{ZA} = -\frac{1}{T_1}(M_{ZA} - M_{0A}) - \frac{1}{\tau_e}(M_{ZA} - M_{ZB}) \quad (80)$$

$$\dot{M}_{ZB} = -\frac{1}{T_1}(M_{ZB} - M_{0B}) - \frac{1}{\tau_e}(M_{ZB} - M_{ZA}) \quad (81)$$

Now, if $1/\tau_e < 1/T_1$ the effect of the $(1/\tau_e)\ (M_{ZA} - M_{ZB})$ term will be very small since $M_{ZA} \approx M_{ZB}$, but if we invert M_{ZB}, the exchange term in equation (81) will, in effect, be

$$-\frac{1}{\tau_e}(M_{ZA} + M_{ZB}) \quad (82)$$

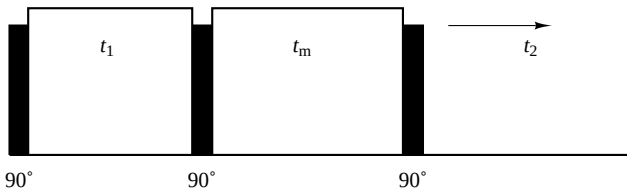

Figure 3 Two-dimensional spectra of fast and slow exchange. (Reproduced by permission of Clarendon Press from R. Ernst, G. Bodenhausen, and A. Wokaum, Principles of Nuclear Magnetic Resonance in One and Two Dimensions, Clarendon Press, Oxford, 1987, Chap. 9)

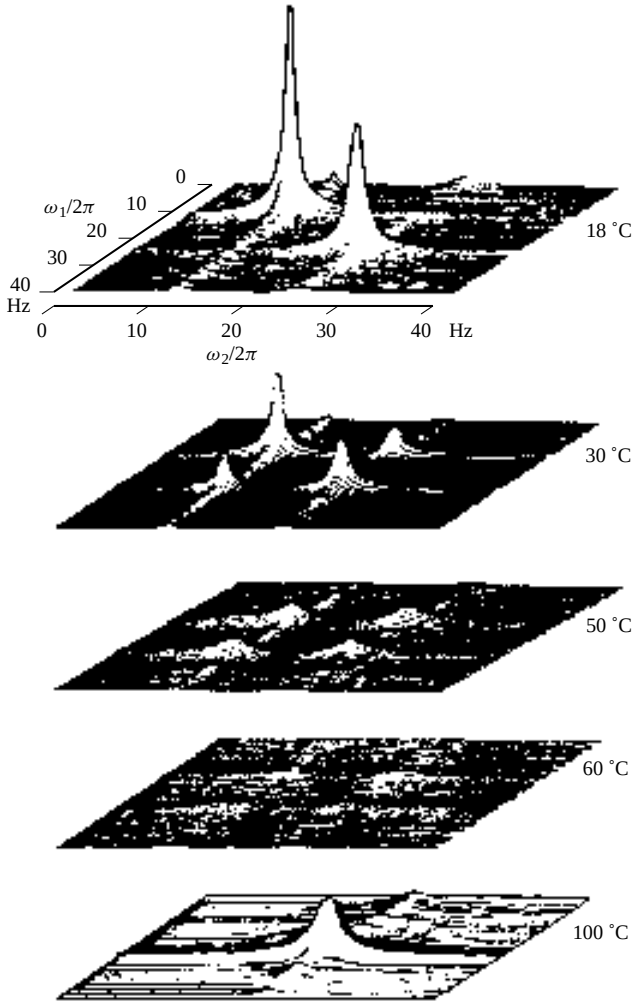

Figure 4 Two-dimensional exchange spectra showing the exchange of the two methyl groups in *N*,*N*-dimethylacetamide for five different temperatures, demonstrating the lineshape effects for rapid chemical exchange

which will amplify the exchange process. The solution for $M_{ZA}(t)$ after the inversion of M_{ZB} at $t = 0$ is given as

$$M_{ZA}(t) = M_0\left\{1 + \exp\left[-\left(\frac{1}{T_1} + \frac{2}{\tau_e}\right)t\right] - \exp\left(-\frac{t}{T_1}\right)\right\} \quad (83)$$

which is plotted in Figure 5 for

$$\tau_e = 10T_1 \simeq 100T_2 \quad (84)$$

We can further enhance the observed depolarization of M_{ZA} by again inverting M_{ZB} at $t = 2T_1$ to obtain the result given in Figure 6.

The various exchange pathways can be explored by selectively inverting spins. This can be done in one fell swoop using 2D spectroscopy, but slow exchange processes will be missed.[10]

We finally suggest an alternative procedure to obtain slow exchange. We saturate the B spin using an amplitude-modulated saturation. Again consider the exchange coupled

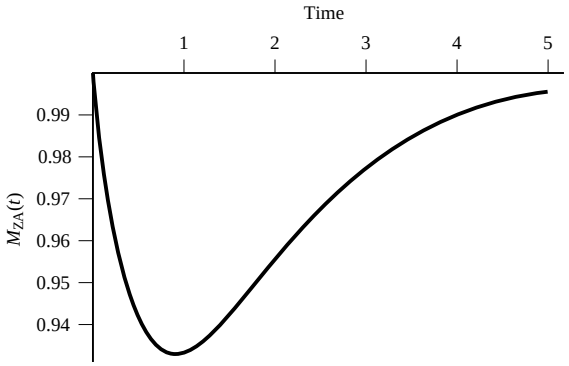

Figure 5 Plot of $M_{ZA}(t)$ as a function of time as given in equation (83) for M_{ZB} inverted at $t = 0$

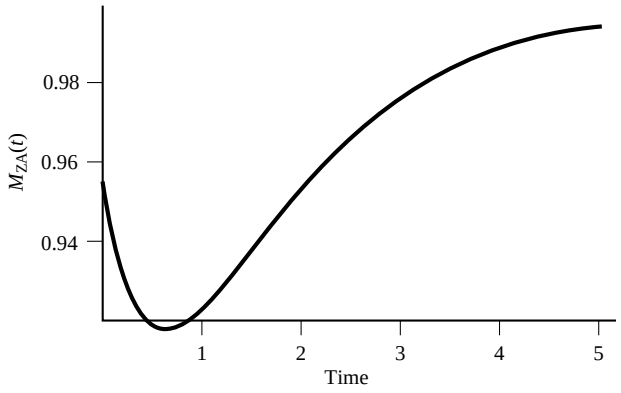

Figure 6 Plot of $M_{ZA}(t)$ as a function of time after M_{ZB} was inverted at $t = 0$ and $t = 2T_1$

Bloch equations, but now with a saturating rf field acting on the B sites:

$$\dot{M}_{ZA} = -\frac{1}{T_1}(M_{ZA} - M_{0A}) - \frac{1}{\tau_e}(M_{ZA} - M_{ZB}) \tag{85}$$

$$\dot{M}_{ZB} = -\frac{1}{T_1}(M_{ZB} - M_{0B}) - \frac{1}{\tau_e}(M_{ZB} - M_{ZA}) + \omega_1^2 T_2 M_{ZB} \tag{86}$$

Note that for $1/\tau_e = 0$, we obtain the standard saturated value for M_{ZB}:

$$M_{ZB} = \frac{M_{0B}}{1 + T_1 T_2 \omega_1^2} \tag{87}$$

We now choose the time-dependent rf field so that

$$\omega_1^2 = \omega_{10}^2(1 + \cos \alpha t) \tag{88}$$

The coupled equations are solved by writing

$$M_{ZA}(t) = M_{A0} + \sum_i M_{Aic} \cos(n_i \alpha t) + \sum M_{Aic} \sin(n_i \alpha t) \tag{89}$$

$$M_{2B}(t) = M_{B0} + \sum M_{Bic} \cos(n_i \alpha t) + \sum M_{Bic} \sin(n_i \alpha t)$$

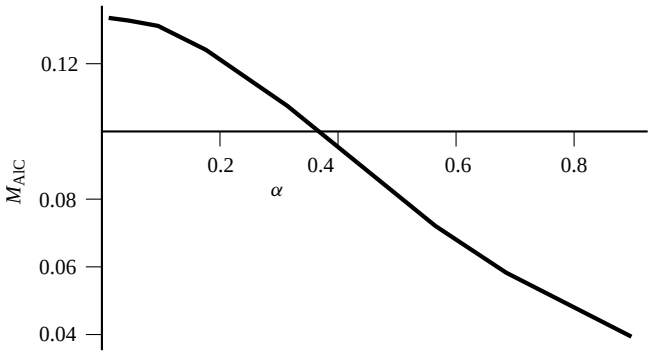

Figure 7 Plot of $M_{Aic}(t)$ as a function of α [see equation (89)]

If $\alpha < 1/\tau_e$, we expect the magnetization on the A site to follow the modulation, but if $\alpha > 1/\tau_e$, we expect the modulation to be too fast to follow and thus the response on the A site to be reduced. This intuitive argument is borne out by plotting M_{A1c} as a function of α (Figure 7). What is important in this procedure is that one can introduce an artificial time variation to obtain selectively very long τ_e values. Modification of this procedure may make it better suited for experimentally determining τ_e.

5.3 Fast Exchange

To obtain information on τ_e when

$$\frac{\Delta\omega^2 \tau_e}{2} \ll \frac{1}{T_2} \tag{90a}$$

we can look at the FID version of equation (71), which is

$$\text{FID}(t) \sim \exp\left[-\left(\frac{1}{T_2} + \frac{1}{2}\Delta\omega^2\tau_e\right)t\right] - \frac{1}{4}\Delta\omega^2\tau_e^2 \exp\left(-\frac{2t}{\tau_e}\right) \tag{90b}$$

If we could digitize FID(t) for times much less than τ_e, we could plot (d/dt)[FID(t)] and (d^2/dt^2)[FID(t)]. This is easy for a nonexperimentalist to say. The second derivative is then given as

$$\frac{d^2}{dt^2}\text{FID}(t) = \left(\frac{1}{T_2} + \frac{1}{2}\Delta\omega^2\tau_e\right)^2 \exp\left[-\left(\frac{1}{T_2} + \frac{1}{2}\Delta\omega^2\tau_e\right)t\right] - \left(\frac{2}{\tau_e}\right)^2 \frac{1}{4}\Delta\omega^2\tau_e^2 \exp\left(-\frac{2}{\tau_e}t\right) \tag{91}$$

$$\frac{d^2}{dt^2}\text{FID}(t) \simeq \frac{1}{T_2^2}\exp\left(-\frac{t}{T_2}\right) - \Delta\omega^2 \exp\left(-\frac{2}{\tau_e}t\right) \tag{92}$$

where now the fast decaying exponential has the largest amplitude.

6 THE EXCEPTION WHEN THE EXCHANGE TIME τ_e IS EQUAL TO OR LESS THAN THE CORRELATION TIME τ_c

The circumstance under which the exchange time τ_e approaches or is less than the correlation time τ_c could arise when a small molecule hops on and off a very large molecule. The large molecule could have a rotational correlation time longer than the hopping time τ_e.

This problem has been treated by a number of authors[11] with various degrees of approximation. In the standard approach ($\tau_c \ll \tau_e$) one obtains a time-independent relaxation operator $\hat{R}_A$. If the time for the exchange interaction approaches that of the relaxation interaction, the expression[2]

$$\hat{R}_A \hat{\rho}_A \simeq \int_{-\infty}^{+\infty} \ldots d\tau \tag{93}$$

is no longer valid and must be replaced by

$$\hat{R}_{A'} \hat{\rho}_A \approx \int_{-t}^{+t} \ldots d\tau \tag{94}$$

where t is the elapsed time after the last exchange collision. This line of reasoning leads to the result that the collapsed linewidth is given by

$$\frac{1}{T_2} + \frac{1}{2}\tau_e \Delta\omega^2 - \frac{1}{T_2}\frac{\tau_c}{\tau_e}, \text{ valid for } \frac{\tau_c}{\tau_e} < 1 \tag{95}$$

A more rigorous approach[12] starts with

$$\dot{\hat{\rho}}_A = -i[\hat{\mathcal{H}}_Z^A + \hat{\mathcal{H}}_{\text{dipolar}}^A, \hat{\rho}_A] - i[\hat{\mathcal{H}}_{\text{rf}}^A, \hat{\rho}_A] + D_A \nabla_A^2 \hat{\rho}_A - \hat{E}_{AB}\hat{\rho}_A \tag{96}$$

treating relaxation and exchange simultaneously. The result for $\Delta\omega \approx 0$ is that the linewidth is given (for equal spin concentration) as

$$\frac{1}{T_2} - \frac{1}{T_2}\left(\frac{\tau_c/\tau_e}{1 + \tau_c/\tau_e}\right) \tag{97}$$

which agrees with equation (95) in the limit $\tau_c/\tau_e < 1$.

7 THE EXCEPTION WHEN THE EXCHANGE RELAXATION IS NOT EXPONENTIAL

For nonexponential exchange,[13,14] we replace equation (14) with

$$\hat{\tilde{\rho}}^{AB} = \int_{-\infty}^{+t} dt' \exp[-(\hat{\tilde{\mathcal{L}}}_S^{AB} + \hat{\tilde{\mathcal{L}}}_R^{AB})]\psi(t - t')\hat{\rho}_{\cos}^{AB}(\text{col}, t')dt' \tag{98}$$

where for exponential relaxation[12]

$$\psi_{\exp}(t)\, dt = \lim\left[\exp\left(-\frac{t}{\tau_e}\right) - \exp\left(-i\frac{(t + dt)}{\tau_e}\right)\right] = \exp\left(-\frac{t}{\tau_e}\right)\frac{dt}{\tau_e} \tag{99}$$

For nonexponential relaxation,

$$\psi_{\text{non-exp}}^{(t)}(t)dt = \lim\,[\phi(t) - \phi(t + dt)] \tag{100}$$

If we represent

$$\phi(t) = \sum_j p_j \exp\left(-\frac{t}{\tau_j}\right) \tag{101}$$

then equation (99) becomes

$$\psi(t)\, dt = \sum_i \tau_j^{-1} p_j \exp\left(-\frac{t}{\tau_j}\right) dt \tag{102}$$

It follows that equation (98) modified for the nonexponential autocorrelation function becomes

$$\hat{\tilde{\rho}}^A(t) = \int_{-\infty}^{t} dt' \exp\,[(\hat{L}_A + \hat{R}_A)(t - t')] \times \sum_j \tau_j^{-1} p_j \exp\left(-\frac{t - t'}{\tau_j}\right)\hat{\tilde{\rho}}_{\text{col}}(t') \tag{103}$$

To express equation (103) in differentiated form, write

$$\hat{\tilde{\rho}}^{AB}(t) = \sum_j p_j \hat{\tilde{\rho}}_j^{AB}(t) \tag{104}$$

Substituting equation (104) in equation (103), one obtains the coupled equations for the jth component as

$$\hat{\tilde{\rho}}_j^{AB}(t) = \int_{-\infty}^{t} dt' \exp\,[(\hat{L}_A + \hat{R}_A)(t - t')]\tau_j^{-1} \times \exp\left(-\frac{t - t'}{\tau_j}\right)\hat{\tilde{\rho}}_{\text{col}}(t') \tag{105}$$

which, upon differentiation with respect to t, becomes

$$\dot{\hat{\tilde{\rho}}}_{Aj}(t) = -i[\hat{\mathcal{H}}_A, \hat{\tilde{\rho}}_{Aj}] + \hat{R}_A\hat{\tilde{\rho}}_{Aj} - \tau_j^{-1}(\hat{\tilde{\rho}}_{Aj} - \hat{\tilde{\rho}}_{\text{col}}) \tag{106}$$

To proceed further, we must choose a form for $\phi(t)$. A suggested form is the so-called stretched exponential:[15]

$$\exp\,[-(t/\tau_p)^\alpha] \tag{107}$$

The solution for the stretched exponential for $\alpha = 1$ and for $\alpha = 0.3$ is given in Kaplan and Garroway[13] and is

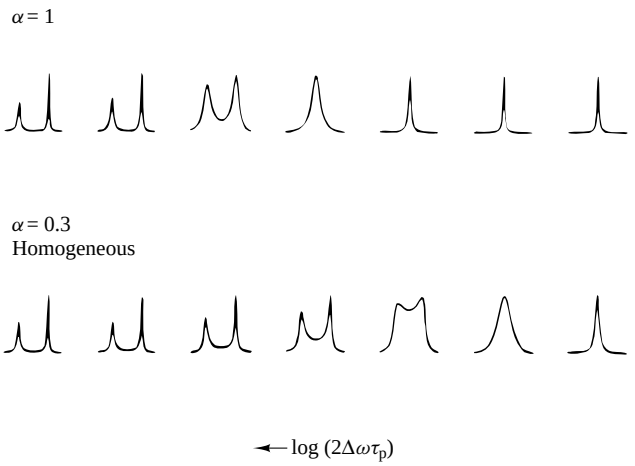

Figure 8 Chemical exchange lineshapes simulated for a distribution of correlation times described by the stretched exponential autocorrelation function $\exp[-(t/\tau_p)^{\alpha}]$. The situation corresponds to two-site exchange with equal populations and relaxation time $2\Delta\omega\tau_{2A} = 40$, $2\Delta\omega T_{2B} = 20$. Spectra are shown at decade intervals of τ_p. The $\alpha = 1$ limit recovers the single correlation time model. (Reproduced by permission from J. I. Kaplan and A. N. Garroway, *J. Magn. Reson.*, 1985, **64**, 32)

shown in Figure 8 for $2\Delta\omega T_{2A} = 40$ and $2\Delta\omega T_{2B} = 20$ as a function of log $(2\Delta\omega\tau_p)$. As can be seen, the lineshape between the fast and slow exchange rates is sensitive to α.

The origin of nonexponential relaxation arises from memory, i.e. the upcoming exchange event is functionally related to the preceding exchange event. A simple model for this is given in Kaplan.[14] The exchange event is a transformation of a molecule from one geometrical structure (I_{ABB}) to another (II_{BBA}). The transformation can only proceed when the molecule is in a normal mode whose motion mimics the motion necessary to make the geometrical rearrangement. The modes which make the rearrangement possible are called 'hopping modes' and all other modes are called 'nonhopping modes'.

The normal mode coupling of configurations I and II can be written in matrix form as

$$\begin{bmatrix} -\frac{1}{\tau_{h,nh}} - \frac{1}{\tau_h} & \frac{1}{\tau_{nh,h}} & & \frac{1}{\tau_h} \\ \frac{1}{\tau_{h,nh}} & -\frac{1}{\tau_{nh,h}} & & \\ & & -\frac{1}{\tau_{nh,h}} & \frac{1}{\tau_{h,nh}} \\ \frac{1}{\tau_h} & & \frac{1}{\tau_{nh,h}} & -\frac{1}{\tau_{h,nh}} - \frac{1}{\tau_h} \end{bmatrix} \begin{bmatrix} N_{h_{\mathbf{I}}} \\ N_{nh_{\mathbf{I}}} \\ N_{nh_{\mathbf{II}}} \\ N_{h_{\mathbf{II}}} \end{bmatrix} = \begin{bmatrix} \dot{N}_{h_{\mathbf{I}}} \\ \dot{N}_{nh_{\mathbf{I}}} \\ \dot{N}_{nh_{\mathbf{II}}} \\ \dot{N}_{h_{\mathbf{II}}} \end{bmatrix} \tag{108}$$

where N_h (N_{nh}) is the population of the hopping (nonhopping) modes, τ_h defines the hopping–hopping time, and $\tau_{h,nh}$ defines the hopping–nonhopping time within configuration I or II. $\tau_{h,nh}$ and $\tau_{nh,h}$ are related as

$$\frac{\tau_{h,nh}}{\tau_{nh,h}} = \frac{N_{h\text{equil.}}}{N_{nh\text{equil.}}} \tag{109}$$

The application of this model to NMR chemical exchange is expressed by the following density matrix equation:

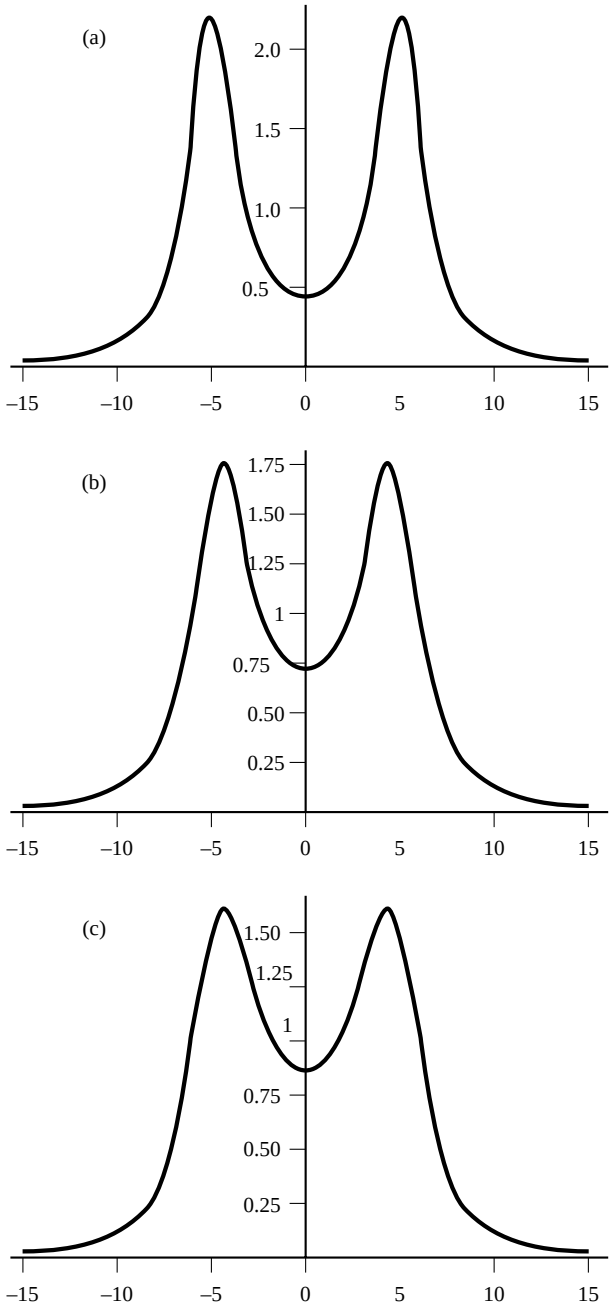

Figure 9 Plot of equation (106) with $\Delta\omega = 10$; $1/T_2 = 1$; $N_{nh}/N_h = 2$; $1/T_{h,nh} = 4$; $1/T_{nh,h} = 2$; and (a) $1/T_h = 2$, (b) $1/T_h = 6$, (c) $1/T_h = 10$. (Reproduced by permission from J. I. Kaplan, *J. Magn. Reson.*, 1991, **91**, 39)

$$\begin{bmatrix} \mathrm{i}(x+\Delta\omega/2) & & & \\ -\left(\frac{1}{T_2}+\frac{1}{\tau_{\mathrm{h}}}+\frac{1}{\tau_{h,nh}}\right) & \frac{1}{\tau_{nh,h}} & & \frac{1}{\tau_h} \\ & \mathrm{i}(x+\frac{1}{2}\Delta\omega) & & \\ \frac{1}{\tau_{nh,h}} & -\left(\frac{1}{T_2}+\frac{1}{\tau_{nh,h}}\right) & & \\ & & \mathrm{i}(x-\frac{1}{2}\Delta\omega) & \\ & & -\left(\frac{1}{T_2}+\frac{1}{\tau_{nh,h}}\right) & \frac{1}{\tau_{nh,h}} \\ & & & \mathrm{i}(x-\frac{1}{2}\Delta\omega) \\ \frac{1}{\tau_h} & & \frac{1}{\tau_{nh,h}} & -\left(\frac{1}{T_2}+\frac{1}{\tau_h}+\frac{1}{\tau_{h,nh}}\right) \end{bmatrix} \begin{bmatrix} \rho_{\mathbf{I}_h} \\ \rho_{\mathbf{I}_{nh}} \\ \rho_{\mathbf{II}_{nh}} \\ \\ \rho_{\mathbf{II}_h} \end{bmatrix} = \begin{bmatrix} C \\ C \\ C \\ \\ C \end{bmatrix} \tag{110}$$

Lineshapes arising from equation (110) are shown in Figure 9.

8 REFERENCES

1. A. Abragam, *The Principles of Magnetic Resonance*, Oxford University Press, London, 1961, Chap. VIII.
2. K. Wangsness and F. Bloch, *Phys. Rev.*, 1953, **89**, 728; P. Argyres and P. L. Kelley, *Phys. Rev.*, 1964, **134**, A98; A. G. Redfield, *IBM Res. Dev.*, 1957, **1**, 19; P. S. Hubbard, *Rev. Mod. Phys.*, 1961, **33**, 249.
3. H. S. Gutowsky, D. W. McCall, and C. P. Slichter, *J. Chem. Phys.*, 1953, **21**, 279.
4. J. I. Kaplan and G. Fraenkel, *NMR of Chemically Exchanging Systems*, Academic Press, London, 1980.
5. J. I. Kaplan, *J. Chem. Phys.*, 1958, **28**, 278.
6. L. Schiff, *Quantum Mechanics*, McGraw-Hill, New York, 1949, p. 211.
7. G. Fraenkel, in *Investigations of Rates and Mechanisms of Reactions. Part II: Investigation of Elementary Reaction Steps in Solution and Fast Reaction Techniques*, ed. C. F. Bernasconi, Wiley-Interscience, New York, 1986, Chap. 10
8. B. D. Nageswara Rao, *Methods Enzymol.*, 1989, **177**, 358.
9. R. R. Ernst, G. Bodenhausen, and A. Wokaum, *Principles of Nuclear Magnetic Resonance in One and Two Dimensions*, Clarendon Press, Oxford, 1987, Chap. 9, Section 9.1.
10. S. Forsen and R. A. Hoffman, *J. Chem. Phys.*, 1963, **39**, 2892; S. Forsen and R. A. Hoffman, *J. Chem. Phys.*, 1964, **40**, 1189; J. Hennig and H. H. Limbach, *J. Magn. Reson.*, 1982, **49**, 322; R. Poupko and Z. Luz, *J. Chem. Phys.*, 1981, **75**, 1675; C. Bracken and J. Baum, *J. Am. Chem. Soc.*, 1993, **115**, 6346. Modified two-dimensional procedure to obtain slow exchange rates.
11. H. G. Hertz, *Ber. Bunsenges Phys. Chem.*, 1967, **71**, 979; J. E. Anderson and P. A. Fryer, *J. Chem. Phys.*, 1968, **48**, 3493; H. J. Sillescu, *J. Chem. Phys.*, 1971, **54**, 2110; A. G. Marshall, *J. Chem. Phys.*, 1970, **52**, 2527; J. I. Kaplan, *Phys. Rev., Ser. A*, 1980, **22**, 1022. (There is a sign error introduced in equation (17) which propagates to equation (30), which should be $1/T_2 - (1/T_2)(\tau_c/\tau_e) + 1/2\tau_e\delta^2$.)
12. K. V. Vasavada and J. I. Kaplan, *J. Magn. Reson.*, 1985, **64**, 32.
13. J. I. Kaplan and A. N. Garroway, *J. Magn. Reson.*, 1982, **49**, 464.
14. J. I. Kaplan, *J. Magn. Reson.*, 1991, **91**, 39.
15. G. Williams and D. C. Watts, *Trans. Faraday Soc.*, 1970, **66**, 80.

Biographical Sketches

Jerome I. Kaplan. *b* 1926. B.S., University of Michigan, Ann Arbor, 1950; Ph.D., University of California, Berkeley, 1954. Research scientist, Naval Research Laboratories, Washington, DC 1954–58; Louis Lipsky Fellow, Weizman Institute, Israel, 1956–57; research associate, 1958–61 and then Assistant Professor of Physics, Brandeis University, 1961–62; Fulbright Lecturer, University College of Rhodesia and Nyasaland, 1962–63; Associate Professor of Research, Brown University, 1963–67; research scientist, Battelle Institute, Columbus, Ohio, 1967–73; staff scientist, Krannert Institute of Cardiology, Indianapolis, 1974–80; Center Fellow, Indianapolis Center for Advanced Research, 1974–83; currently Professor of Physics at Indiana University–Purdue University at Indianapolis. Research interests are in solid state physics, biophysics, and solar energy.

Chemical Exchange on Solid Metal Surfaces

Frank Engelke
Ames Laboratory, Ames, IA, USA

1	Introduction	1
2	Theory of Magnetization Exchange	1
3	Advanced NMR Techniques to Monitor Exchange	2
4	Chemical Exchange of Adsorbed Species on Metal Surfaces: Examples	3
5	Related Articles	4
6	References	4

1 INTRODUCTION

Chemical exchange, i.e. the transfer of atoms, molecules or molecular groups between two or more different environments or regions, is a phenomenon encountered frequently in studies by NMR of a wide variety of chemical, physical and biological systems. Different environments are usually revealed in NMR experiments through distinct resonance frequencies, spin–spin coupling constants, or relaxation times characteristic of the regions between which chemical exchange takes place. The types of atomic or molecular motion most often investigated on metal surfaces include surface diffusion, adsorption and desorption, exchange between different surface sites or different types of adsorbed species, molecular reorientation, and reorientation of molecular groups.

Because NMR requires at least ca. 10^{18} spins at the surface to be able to detect a signal, single crystal surfaces cannot be studied (10^{15} spins). However, introducing the metal in the form of small particles with diameters in the order of nanometers into porous materials, provides a sufficiently high number of surface sites for adsorption to be studied by NMR. These support materials are mostly oxide compounds like silica, alumina, titania, or zeolites with high internal surfaces of several hundred square meters. At the same time, highly dispersed supported metals, e.g. group VIII elements like ruthenium, rhodium, palladium, osmium, iridium, and platinum, are very often of interest in basic and applied research in catalysis (see also ***Supported Metal Catalysts***, and ***Adsorbed Species: Spectroscopy and Dynamics***).

Several NMR techniques are available to study exchange phenomena of adsorbed species. Spin–lattice relaxation[1] measurements are useful if chemical exchange dominates as a source for relaxation, or can be separated from other relaxation mechanisms, e.g. relaxation via the conduction electrons of the metal, called Korringa relaxation (see ***Electron–Nuclear Hyperfine Interactions***). To be investigated by relaxation measurements, the characteristic time constants of exchange τ_{ex} have to be in the order of 10^{-9} s for spin–lattice relaxation in the laboratory frame to 10^{-5} s for spin–lattice relaxation in the rotating frame.[1] For a review of the relaxation method used to study the dynamics on surfaces we refer the reader to the literature.[2–4] The analysis of lineshapes or resonance shifts obtained by conventional NMR techniques are sensitive in the dynamic range of $10^{-6} \leq \tau_{ex} \leq 10^{-3}$ s. Spin labeling methods extend this range up to more than 10^{-1} s. Two-dimensional NMR techniques, applicable in approximately the same slow dynamic range, are most effective if the exchanging species exhibit separate NMR peaks or if well-defined lineshapes due to anisotropic interactions can be observed.[5]

In the present article the theoretical basis necessary to understand the evolution of nuclear spin magnetization influenced by chemical exchange is outlined briefly. The reader is introduced to spin-labeling and two-dimensional (2D) NMR techniques, which are frequently used to monitor exchange. Finally, experimental examples regarding chemical exchange on metal surfaces are discussed.

2 THEORY OF MAGNETIZATION EXCHANGE

In the following it is assumed that the spatial motion of molecules or atoms can be described classically. If all spin interactions are secular with respect to the Zeeman interaction, i.e., the corresponding interaction Hamiltonians commute with the Zeeman Hamiltonian, then each spin can be considered as being subjected to a local field arising from the environment, superimposed on the external static field. Chemical exchange has the effect of causing random fluctuations of the local field. For example, a nuclear spin situated in a molecule or atom, which jumps randomly between two regions on a surface, such that each region gives rise to a different isotropic resonance shift, experiences a random modulation of its resonance frequency. The influence of such frequency fluctuations upon the NMR lineshape was first treated by Hahn, Maxwell, Gutowsky, McCall, and Slichter.[6]

If the spin Hamiltonian contains nonsecular terms, arising, for example, from J couplings observed commonly in liquids, a quantum-mechanical treatment (spin density matrix formalism) is required.[7] Splittings due to J couplings are often difficult to detect in NMR studies of adsorbates on metal surfaces because of insufficient spectral resolution, caused by the heterogeneity of the system, leading to distributions of isotropic chemical or Knight shifts, and/or the presence of 'solid-like' spin interactions much stronger than J coupling, like chemical shift anisotropy (see ***Internal Spin Interactions and Rotations in Solids***) and paramagnetic shifts.

We confine ourselves here exclusively to the case of secular spin interactions, leading to a classical probabilistic model for the magnetization exchange originating from chemical exchange processes. The probabilistic model is commonly represented by a stationary Markov process,[8,9] allowing the derivation of equations of motion for the nuclear spin magnetization in the form of generalized Bloch equations.[9–11] The evolution of longitudinal and transversal magnetization components for all regions, between which exchange takes place, are given as a system of coupled differential equations with rate coefficients describing the magnetization exchange process. Solving these equations is a standard problem of analysis and matrix algebra (see Ernst et al.[11] and Jeener et al.[13]) and enables explicit calculation of NMR lineshapes.

Figure 1 illustrates the principal effects on the NMR lineshapes originating from magnetization exchange between two regions or sites. Regions A and B, populated by N_A and N_B spins, respectively, are characterized by distinct resonance

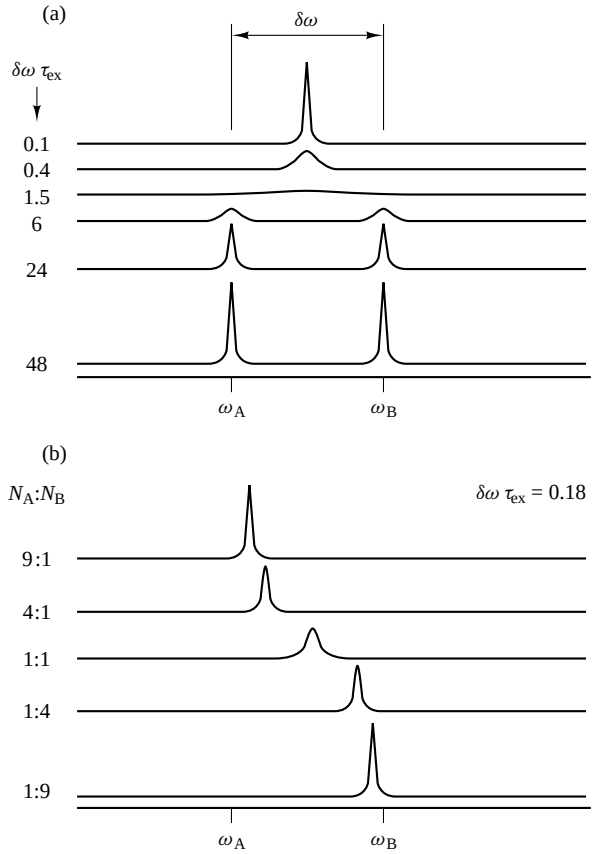

Figure 1 (a) NMR lineshape versus $\delta\omega\tau_{ex}$ for symmetric two-site exchange ($N_A = N_B$). (b) Variation of the resonance frequency in the fast exchange limit as a function of N_A:N_B

frequencies ω_A and ω_B, $\delta\omega = \omega_B - \omega_A$. This difference of resonance freqencies may be caused by different isotropic chemical or Knight shifts. In the slow exchange limit, $\delta\omega\tau_{ex} \gg 1$, where τ_{ex} is a characteristic time constant for the exchange process, two separate lines appear in the NMR spectrum [Figure 1(a)], which become broadened with decreasing $\delta\omega\tau_{ex}$, and coalesce to a single broad line at $\delta\omega\tau_{ex} \approx 1$. With $\delta\omega\tau_{ex}$ decreasing further, only one single 'exchange-averaged' narrow line is observed (fast exchange limit, $\delta\omega\tau_{ex} \ll 1$). The spectra in Figure 1(b) were calculated for the fast exchange limit varying the ratio N_A:N_B of spin numbers in regions A and B, leading to a variation in the resonance frequency of the exchange averaged resonance line as well as to a broadening for values of N_A:N_B near unity. The dependence of the resonance shift δ on N_A and N_B can be expressed for the fast exchange limit as the weighted average:

$$\delta = \frac{N_A}{N_A + N_B} + \delta_A \frac{N_B}{N_A + N_B}\delta_B \qquad (1)$$

of the individual resonance shifts δ_A and δ_B. The mathematical formalism to calculate the above lineshapes is still applicable if anisotropic interactions, to be described by interaction tensors, e.g. chemical shift anisotropy, are present. However, because of the random spatial orientations of the principal tensor axes in a powder sample, the resulting orientation dependence of the resonance frequencies has to be taken into account to obtain the lineshape.[10]

3 ADVANCED NMR TECHNIQUES TO MONITOR EXCHANGE

As shown above, no significant changes of the one-dimensional NMR lineshapes or frequencies occur in the slow exchange limit. More advanced NMR techniques are available to detect such slow exchange processes.

3.1 Spin Labeling by Selective Excitation

The idea of spin labeling is based on the fact that the actual chemical exchange process, being in thermal equilibrium, causes an exchange of spin magnetization.[12] The latter is initially prepared by irradiation of rf pulses to be in nonequilibrium. The irradiation of an rf pulse, or a sequence of rf pulses affects only spins resonating within the spectral excitation window defined by the Fourier transform of the pulse sequence [Figure 2(a) and (b)]. Although this Fourier picture is only an approximation when selective saturation or inversion is considered,[12] it is a useful qualitative description. Denoting the length of a single rf pulse or the total duration of a pulse sequence by τ_p, the excitation width in the frequency domain is proportional to $1/\tau_p$, with the rf carrier frequency in the center of the excitation window. The irradiation of either a long pulse of low rf power or a sequence of strong, but very short pulses, as indicated in Figure 2(a), allows selective excitation of spins. The pulse sequence can be adjusted to act in total like a 90° pulse (selective saturation) or a 180° pulse [selective inversion, illustrated in Figure 2(c)]. Therefore, spins within the spectral window can be labeled, for example, by inversion of their magnetization, while spins which resonate outside the window remain unaffected. If a pulse sequence is used, excitation sidebands also occur [Figure 2(b)]. During a subsequent time interval τ_m [Figure 2(a)] the spin system is allowed to undergo free time evolution. The NMR signal is detected finally by a short (nonselective) 90° pulse. Selective excitation (saturation or inversion) of a narrow frequency band within a broad NMR line, for example, caused by chemical shift anisotropy, is called 'spectral hole-burning'. If chemical exchange is present, the labeled spins may change their resonance frequencies resulting in a redistribution of spin

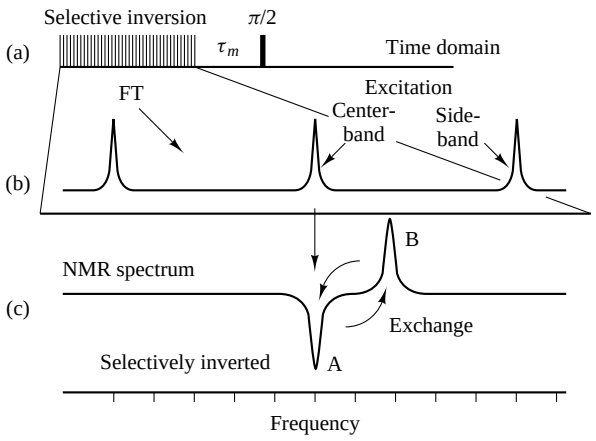

Figure 2 Spin labeling by selective excitation: (a) pulse sequence, (b) Fourier transformation of the train of equidistant pulses, and (c) NMR spectrum showing a selectively inverted line

magnetization toward spectral regions outside of the selected window. The recovery of the spectral hole, or of the intensity of an inverted single resonance line, can be measured as a function of the recovery time τ_m to reveal the kinetics of a chemical exchange process.

Magnetization recovery is also caused by spin–lattice relaxation of the spin magnetization. Only exchange processes with a characteristic time τ_{ex} shorter than the spin–lattice relaxation time T_1 can be observed. Spin-labeling becomes ineffective if the chemical exchange process is faster than the spin-labeling process itself (characteristic time constant τ_p). Thus accessible by spin-labeling techniques are exchange processes within a timescale $\tau_p < \tau_{ex} < T_1$.

3.2 Two-Dimensional Exchange NMR

Two-dimensional exchange NMR techniques[13] are based on the idea of measuring the frequency of spin magnetization components at two different times during the NMR experiment. After the initial preparation period, which consists of a waiting period to allow equilibration of the longitudinal magnetization and irradiating the first $\pi/2$ pulse, transversal magnetizations are present, oscillating with frequencies ω_A and ω_B during the time t_1 [evolution period, Figure 3(a)] corresponding to spins located in regions A and B. A second $\pi/2$ pulse converts the magnetization present at time t_1 into longitudinal magnetization. During the mixing time τ_m (usually much longer than the time t_1) slow chemical exchange leads to a random modulation of the precession frequencies of the two magnetization components M_{zA} and M_{zB}. Spins which were resonating at ω_A at the end of the period t_1 may resonate at either ω_A or ω_B at the end of the mixing period τ_m (and vice versa). The NMR signal is detected after the final $\pi/2$ pulse during the time period t_2. Repeating the experiment by incrementing the time t_1 in small steps, yields a two-dimensional time-domain interferogram which after 2D Fourier transformation[11] with respect to t_1 and t_2 gives the 2D NMR spectrum $S(\omega_1,\omega_2)$. If exchange occurs between A and B, cross peaks are observed, labeled A → B and B → A in Figure 3(b), in addition to main peaks A and B located along the principal diagonal.[14]

4 CHEMICAL EXCHANGE OF ADSORBED SPECIES ON METAL SURFACES: EXAMPLES

Chemical exchange phenomena at or near metal surfaces observed by NMR encompass a wide dynamical range extending from the fast exchange limit ($\tau_{ex} < 10^{-5}$ s) to extremely slow processes ($\tau_{ex} > 1$ s). The details of the chemical exchange processes might be quite different, originating, for example, from adsorption or desorption, exchange between different surface sites, exchange between different populations of adsorbed species or surface diffusion.[15]

4.1 Exchange Dynamics of CO Adsorbed on Metals

Carbon-13 spin labeling techniques have been applied by Duncan, et al.[16] to elucidate in detail surface diffusion of CO and slow exchange between different carbonyl species adsorbed on rhodium. Molitor and Apple[17] performed ^{13}C NMR powder lineshape calculations for reorientating dicarbonyl groups bonded to rhodium. Surface diffusion of CO chemisorbed on palladium has been investigated by means of ^{13}C relaxation measurements and lineshape analysis.[18]

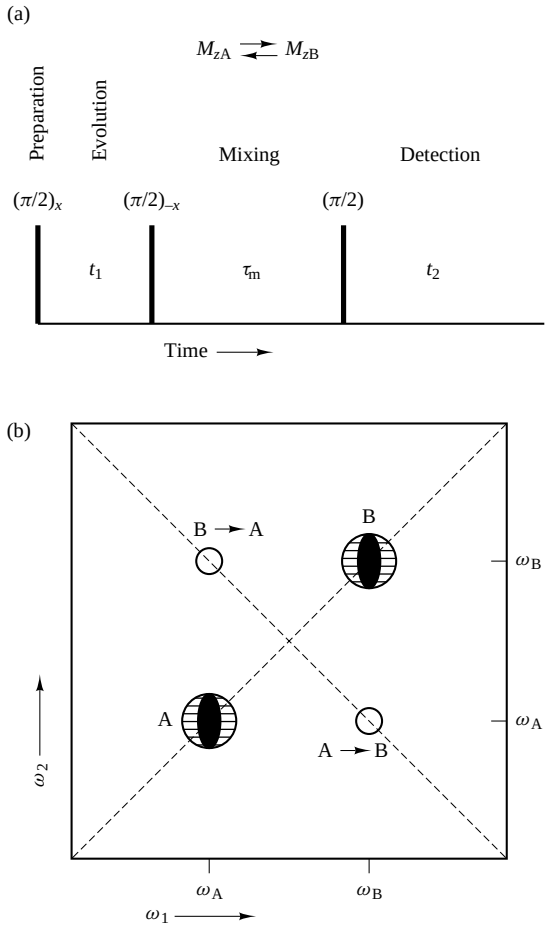

Figure 3 (a) Basic 2D NMR pulse sequence to monitor exchange. (b) Schematic representation of a 2D NMR spectrum for exchange between two sites A and B

4.2 Fast Exchange of Hydrogen on Metal Surfaces

Proton NMR peaks of hydrogen interacting with metal surfaces are commonly shifted to lower frequency (i.e. upfield) due to the Knight shift interaction and reveal relatively small linewidths, especially at elevated external H_2 pressures and temperatures above room temperature, indicating high intrinsic mobility. Variations of the resonance frequency of ^1H NMR peaks, attributed to hydrogen on the metal surface, versus pressure (i.e. changing the number of hydrogen atoms or molecules on the surface) may be caused by at least two different mechanisms: (i) fast exchange between surface environments with different Knight shifts [as illustrated in Figure 1(b)]; and (ii) by a variation of the Knight shift interaction itself, because the latter may be a function of the surface coverage. As pointed out above, fast exchange between two regions leads to an averaged NMR line representing hydrogen in both regions. Variation of the resonance shift

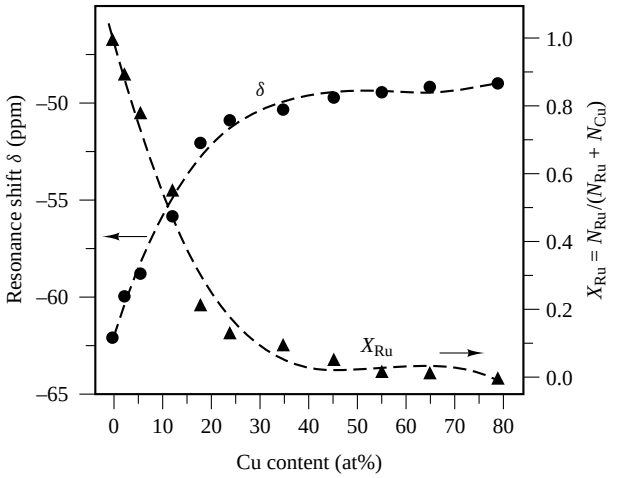

Figure 4 ^{1}NMR resonance shift δ for hydrogen adsorbed on ruthenium–copper bimetallic particles and fraction X_{Ru} of surface ruthenium as a function of the copper content

with pressure, or coverage, has been observed quite frequently by ^{1}H NMR[19] or ^{2}H NMR[20] for hydrogen adsorbed on various metals like platinum, rhodium, and ruthenium (see also refs. [18–20] and 23–24 given in Wu et al.[19]). The resonance shift variation of hydrogen due to fast exchange between different surfaced regions has been used to monitor the surface composition of bimetallic particles.[21] In this case hydrogen atoms are rapidly exchanging between sites on the bimetallic particle surface, composed of sites with different Knight shifts for adsorbed hydrogen. As shown in Figure 4, on particles consisting of pure ruthenium, hydrogen resonates at −62 ppm [to low frequency relative to tetramethylsilane (TMS)]. Increasing the total copper content of the sample leads to a systematic decrease of the ^{1}H resonance shift δ, approaching asymptotically the value of −49 ppm for a copper content near 80 at%. This shift value is regarded as the resonance shift for hydrogen adsorbed on copper sites of ruthenium–copper bimetallic particles. Applying equation (1) inserting $\delta_{Cu} = -49$ ppm and $\delta_{Ru} = -62$ ppm, the fraction $X_{Ru} = N_{Ru}/(N_{Ru} + N_{Cu})$ of ruthenium atoms exposed at the particle surface can be determined (see Figure 4). Therefore, in this example the ^{1}H NMR resonance shift provides a sensitive measure for the composition of the surface.

4.3 Slow Exchange Between Different Hydrogen Populations on the Metal Surface

Figure 5(a) shows an in situ ^{1}H NMR spectrum of silica supported ruthenium, obtained at T = 400 K and at an external H_2 pressure of 300 Torr.[22] Two distinct resonance lines (denoted as α and β) are observed, originating from two different hydrogen species, characterized by different heats of adsorption. The 2D exchange NMR spectrum [Figure 5(b)] was obtained by the pulse sequence illustrated in Figure 3(a). The cross peaks reveal a slow exchange process within the timescale of the experiment, given by the mixing time τ_{mix} = 2 ms, occurring between α and β hydrogen, but there is no exchange within this timescale between the α or β species and the hydrogen residing on the silica support. Spin

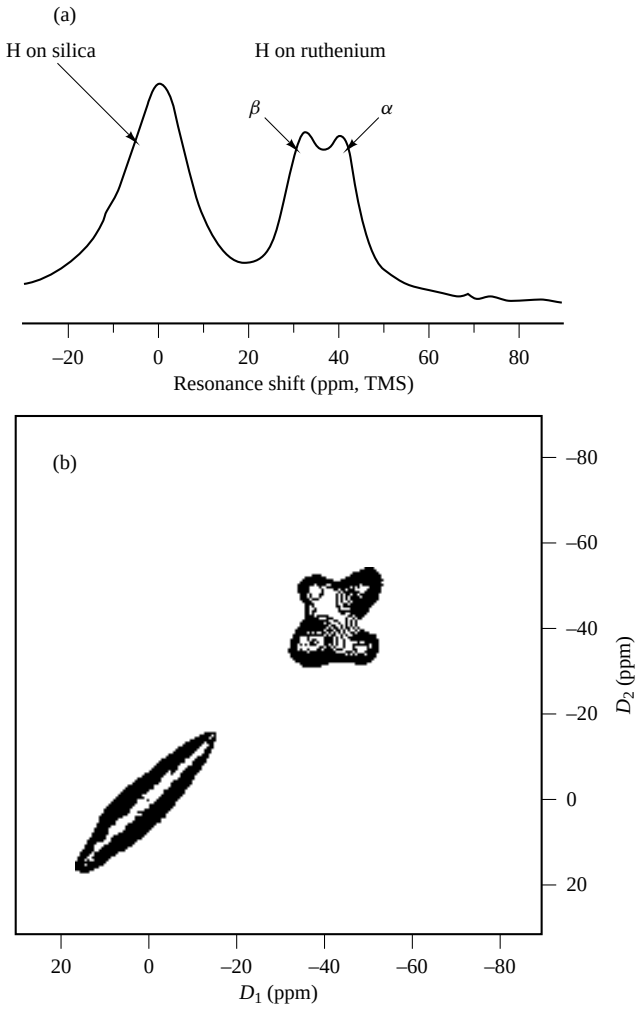

Figure 5 (a) Conventional ^{1}H NMR spectrum of silica supported ruthenium. (b) 2D exchange NMR spectrum at T = 400 K and external H_2 pressure p = 300 Torr

labeling of one of the two spin species, α or β, by selective excitation (Figure 2) allows the determination of the average time constant, τ_{ex} = 700 μs, for the magnetization exchange between α and β hydrogen.

5 RELATED ARTICLES

Adsorbed Species: Spectroscopy and Dynamics; Brønsted Acidity of Solids; Diffusion in Porous Media; Electron–Nuclear Hyperfine Interactions; Internal Spin Interactions and Rotations in Solids; Microporous Materials and Xenon-129 NMR; Silica Surfaces: Characterization; Spin Diffusion in Solids; Supported Metal Catalysts

6 REFERENCES

1. C. P. Slichter, *Principles of Magnetic Resonance*, 3rd edn., Springer, Berlin 1990, Chaps. 4–6.
2. H. Pfeifer, in *NMR Basic Principles and Progress*, eds. P. Diehl, E. Fluck, and R. Kosfeld, Springer, Berlin, 1972, Vol. 7, p. 53.

3. H. Winkler and D. Michel, *Adv. Colloid Interface Sci.*, 1985, **23**, 149.
4. C. P. Slichter, *Ann. Rev. Phys. Chem.*, 1986, **37**, 25.
5. H.-W. Spiess, *Chem. Rev.*, 1991, **91**, 1321.
6. E. L. Hahn and D. E. Maxwell, *Phys. Rev.*, 1952, **88**, 1070; H. S. Gutowsky, D. W. McCall, and C. P. Slichter, *J. Chem. Phys.*, 1953, **21**, 279.
7. J. I. Kaplan and G. Fraenkel, *NMR of Chemically Exchanging Systems*, Academic, New York, 1980.
8. A. Abragam, *The Principles of Nuclear Magnetism*, Clarendon, Oxford, 1961, Chap. X.
9. C. S. Johnson, Jr., in *Advances in Magnetic Resonance*, ed. J. S. Waugh, Academic, New York, 1965, Vol. 1, p. 33.
10. M. Mehring, *Principles of High Resolution NMR in Solids*, 2nd edn., Springer, Berlin, 1983, Chap. 28.
11. R. R. Ernst, G. Bodenhausen, and A. Wokaun, *Principles of Nuclear Magnetic Resonance in One and Two Dimensions*, Clarendon, Oxford, 1987, Chaps. 2.4, 4.6, 6.4 and 9.
12. G. A. Morris and R. Freeman, *J. Magn. Reson.*, 1978, **29**, 433; R. Freeman, *Chem. Rev.*, 1991, **91**, 1397.
13. J. Jeener, B. H. Meier, P. Bachmann, and R. R. Ernst, *J. Chem. Phys.*, 1979, **71**, 4546.
14. If direct dipolar spin–spin couplings are present, spin diffusion (a process to be distinguished from chemical exchange) may also lead to cross peaks (see Jeener et al.[13] and ***Spin Diffusion in Solids***).
15. Spin labeling is well suited to monitor surface diffusion. However, the theoretical treatment of surface diffusion is based on the diffusion equation, and not on Bloch-type equations to describe exchange as discrete jumps between distinct environments.
16. T. M. Duncan, A. M. Thayer, and T. W. Root, *Phys. Rev. Lett.*, 1989, **63**, 62. See also: T. M. Cuncan, *Colloids Surfaces*, 1990, **45**, 11, and references therein.
17. P. Molitor and T. Apple, *J. Phys. Chem.*, 1989, **93**, 7055.
18. S. E. Shore, J.-P. Ansermet, C. P. Slichter, and J. H. Sinfelt, *Phys. Rev. Lett.*, 1987, **58**, 953.
19. X. Wu, B. C. Gerstein, and T. S. King, *J. Catal.*, 1989, **118**, 238.
20. T. Chang, C. P. Cheng, and C. Yeh, *J. Phys. Chem.*, 1991, **95**, 5239.
21. X. Wu, B. C. Gerstein, and T. S. King, *J. Catal.*, 1990, **121**, 271.
22. F. Engelke, S. Bhatia, T. S. King, and M. Pruski, *Phys. Rev. B*, 1994, **49**, 2730; F. Engelke, R. Vincent, T. S. King, and M. Pruski, *J. Chem. Phys.*, 1994, **101**, 7262.

Biographical Sketch

Frank Engelke. *b* 1955. M.Sc. (physics), Ph.D. (supervisor Dieter Michel) 1985, habilitation, University of Leipzig, Germany. Postdoctoral work at Saarbruecken University, Germany (with Jörn Petersson), and since 1992–1994 at Ames Laboratory, USA (with Bernie Gerstein, Marek Pruski and Terry King). Since 1994 affiliated with Bruker Analytische Messtechnik. Approx. 20 publications. Current research specialties: solid state NMR in rotating solids, solid state NMR applications on metal surfaces, NMR probe development.

Dynamic NMR in Liquid Crystalline Solvents

Raphy Poupko and Zeev Luz

Weizmann Institute of Science, Rehovot, Israel

1	Introduction	1
2	Dynamic NMR LineShapes in Liquid Crystalline Solutions	1
3	Experimental Aspects	3
4	Applications to Spin $I = \frac{1}{2}$ Nuclei	3
5	Multiple Quantum Dynamic NMR for Spin $I = \frac{1}{2}$ Nuclei	6
6	Dynamic NMR for Spin $I = 1$ Nuclei	7
7	Two-Dimensional Exchange NMR Spectroscopy for Spin $I = 1$ Nuclei	9
8	Dynamic Echo Train Experiments	12
9	Related Articles	13
10	References	14

1 INTRODUCTION

The effect of dynamic processes on high-resolution NMR spectra in liquids was first observed[1] in 1953 soon after the discovery of the chemical shift[2] and spin–spin coupling phenomena.[1,3] Since then the effect has been extensively used to study a wide range of dynamic processes in liquids including protolysis, solvation, hindered rotation, bond shift tautomerism, and a variety of other isomerization reactions.[4,5] The effect of dynamic processes on the high-resolution spectra is manifested in line broadening, coalescence, and eventual line narrowing, yielding motionally averaged spectra with average magnetic parameters. The effect on the lineshape is most pronounced when the exchange rate is of the order of the magnetic interactions. For protons these range from several hertz to several kilohertz, while for ^{13}C the range is an order of magnitude larger. Quantitative studies can generally be made within the range where the lifetime broadening or the exchange-narrowed linewidth exceeds that of the natural width, i.e. $1–10^6$ s^{-1} for protons and one to two orders of magnitude faster for carbon-13.

Proton or carbon-13 high-resolution spectra of molecules dissolved in liquid crystalline solvents usually exhibit more complicated structures than in normal (isotropic) liquids and often span a wider frequency range.[6] This is so because in anisotropic solvents, in addition to the scalar spin–spin coupling and isotropic chemical shift, anisotropic interactions also affect the spectrum. These include intramolecular dipole–dipole interactions, anisotropic indirect spin–spin couplings, anisotropic chemical shifts, and, for $I > \frac{1}{2}$ nuclei, also quadrupolar interactions. The fast anisotropic motion of the molecules reduces these interactions, but unlike in isotropic liquids their averages are, in general, not zero and depend on the ordering characteristics of the molecules in the liquid crystals. If the number of magnetic nuclei in the molecule is not too large (say below 10) a well-resolved high-resolution spectrum can usually be observed, but for more nuclei the number of lines becomes exceedingly large and the spectrum unresolved. It should be emphasized that the fast translational diffusion completely averages out the intermolecular dipolar interactions. Otherwise a featureless spectrum as in solids would always be observed.

When the solute molecules dissolved in liquid crystals undergo dynamic processes, lineshape changes similar to those observed in isotropic liquids take place.[7] We refer to this phenomenon as 'dynamic NMR in liquid crystalline solvents' and in the present article we outline its basic theory and review some applications. Because of the more complex structure of the spectra in liquid crystalline solutions the interpretation is more complicated, but the basic principles are the same as in isotropic liquids. On the other hand, due to the larger interactions involved, the dynamic range over which kinetic parameters can be measured is much wider. Nuclei with spins $I > \frac{1}{2}$ usually exhibit splittings due to quadrupole interactions which are often much larger than the dipolar or chemical shift interactions. The structure of the spectrum is then predominantly determined by the quadrupole splittings with the other interactions often within the experimental linewidth.

We start the review by extending the theory of dynamic lineshape in isotropic liquids to the liquid crystalline case by adding anisotropic terms to the spin Hamiltonian (Section 2). After a short section (3) dealing with some experimental aspects, we review applications (Section 4) for spin $I = \frac{1}{2}$ nuclei (^{1}H and ^{13}C), including the use of multiple quantum spectroscopy (Section 5). In Sections 6 and 7 we discuss applications of one- and two-dimensional dynamic NMR to deuterium and in Section 8 we briefly describe a dynamic deuterium study using quadrupole echo pulse trains.

2 DYNAMIC NMR LINESHAPES IN LIQUID CRYSTALLINE SOLUTIONS

The theory of dynamic NMR lineshapes in anisotropic liquids is, in principle, identical to that for isotropic liquids.[1,5,8–12] However, since dipolar interactions involve essentially all magnetic nuclei in the molecule, and for homonuclei cases these interactions are usually larger than the chemical shifts, the NMR spectra always correspond to combination transitions. The simple Bloch–McConnell type treatment[8] is therefore not adequate for the analysis of the dynamic lineshapes and the more general density matrix formalism must be used.[9–13] We shall restrict ourselves to intramolecular rearrangement kinetics because higher order processes involving two or more molecules[10] have not been applied so far in liquid crystalline solutions. The equation of motion of the density matrix, $\hat{\rho}(t)$, during free induction decay, is then:

$$\frac{\mathrm{d}\hat{\rho}(t)}{\mathrm{d}t} = -\mathrm{i}[\hat{\mathcal{H}}, \hat{\rho}(t)] + k[\hat{R}\hat{\rho}(t)\hat{R}^{-1} - \hat{\rho}(t)] - \hat{\rho}_{\mathrm{od}}(t)/T_2 - [\hat{\rho}_0 - \hat{\rho}_{\mathrm{dg}}(t)]/T_1 \quad (1)$$

where $\hat{R}$ is an operator describing the exchange process, k the rate constant for the reaction, $\hat{\rho}_0$ the equilibrium density

matrix, and $\hat{\rho}_{\rm dg}(t)$ and $\hat{\rho}_{\rm od}(t)$ the diagonal and off-diagonal parts of $\hat{\rho}(t)$ which are assumed to relax by respectively single longitudinal and transverse modes. Limiting ourselves to the homonuclei case the Hamiltonian, $\hat{\mathcal{H}}$, in the rotating coordinate system includes both single and binuclear terms,

$$\hat{\mathcal{H}} = \hat{\mathcal{H}}_Z + \hat{\mathcal{H}}_Q + \hat{\mathcal{H}}_S \tag{2}$$

where

$$\hat{\mathcal{H}}_Z = -\sum_i \omega_0(1-\sigma_i)\hat{I}_{iz} = \sum_i \omega_i \hat{I}_{iz} \tag{3a}$$

$$\hat{\mathcal{H}}_Q = \sum_i \omega_{Qi}[(\hat{I}_{iz})^2 - \hat{I}_i(\hat{I}_i+1)/3] \tag{3b}$$

$$\hat{\mathcal{H}}_S = \sum_{i<j}\{2(D_{ij}+J^{\rm a}_{ij})[\hat{I}_{iz}\hat{I}_{jz} - (\hat{I}_{i+}\hat{I}_{j-}+\hat{I}_{i-}\hat{I}_{j+})/4] + J_{ij}[\hat{I}_{iz}\hat{I}_{jz} - (\hat{I}_{i+}\hat{I}_{j-}+\hat{I}_{i-}\hat{I}_{j+})/2]\} \tag{3c}$$

In these equations ω_0 and ω_i are the reference and resonance frequencies in the rotating frame, σ_i the motionally averaged chemical shift, ω_{Qi} the average quadrupole interaction, D_{ij} the average direct dipole–dipole interaction, and $J^{\rm a}_{ij}$ and J_{ij} are respectively the average anisotropic and scalar spin–spin couplings. The sum is over all magnetic nuclei in the molecule assumed to belong to the same isotope (homonuclei). The averaged anisotropic parameters, $T = \sigma_i$, ω_{Qi}, D_{ij}, $J^{\rm a}_{ij}$, are related to their static tensorial components, $T_{\alpha\beta}$, in the molecular-fixed frame $\alpha, \beta = x, y, z$ via the so-called motional constants, C^2_α.[14,15] The liquid crystal is assumed to have a nonpolar cylindrical symmetry defined by a director which aligns parallel to the magnetic field. The molecular orientation distribution function can then be expanded in even orders of the (real) spherical harmonic functions

$$P(\theta,\phi) = \frac{1}{4\pi} + C^2_{3z^2-r^2}D^2_{3z^2-r^2} + C^2_{x^2-y^2}D^2_{x^2-y^2} + C^2_{xz}D^2_{xz} + C^2_{yz}D^2_{yz} + C^2_{xy}D^2_{xy} + \mathrm{O}(D^4) \tag{4}$$

where the D^2_αs are normalized so that $\int_0^{2\pi}\int_0^{\pi} D^2_\alpha D^2_{\alpha'} \sin\theta \, \mathrm{d}\theta \, \mathrm{d}\phi = (1/4\pi)\delta_{\alpha\alpha'}$

$$\left.\begin{aligned} D^2_{3z^2-r^2} &= \left(\frac{\sqrt{5}}{4\pi}\right)\tfrac{1}{2}(3\cos^2\theta - 1) \\ D^2_{x^2-y^2} &= \left(\frac{\sqrt{15}}{4\pi}\right)\tfrac{1}{2}(\sin^2\theta\cos 2\phi) \\ D^2_{xy} &= \left(\frac{\sqrt{15}}{4\pi}\right)\tfrac{1}{2}(\sin^2\theta\sin 2\phi) \\ D^2_{xz} &= \left(\frac{\sqrt{15}}{4\pi}\right)(\sin\theta\cos\theta\cos\phi) \\ D^2_{yz} &= \left(\frac{\sqrt{15}}{4\pi}\right)(\sin\theta\cos\theta\sin\phi) \end{aligned}\right\} \tag{5}$$

and $C^2_\alpha = 4\pi \int_0^{2\pi}\int_0^{\pi} P(\theta,\phi) D^2_\alpha \sin\theta \, \mathrm{d}\theta \, \mathrm{d}\phi$. The averages of the anisotropic interactions are given by

$$T = \frac{1}{\sqrt{15}}\left\{C^2_{3z^2-r^2}\frac{2}{\sqrt{3}}[T_{zz} - \tfrac{1}{2}(T_{xx}+T_{yy})] + C^2_{x^2-y^2}(T_{xx}-T_{yy}) + C^2_{xz}(T_{xz}+T_{zx}) + C^2_{yz}(T_{yz}+T_{zy}) + C^2_{xy}(T_{xy}+T_{yx})\right\} \tag{6}$$

Molecular symmetry will reduce the number of nonzero motional constants by choosing the appropriate molecular coordinates x, y, and z.[15]

To calculate the time domain signal it is necessary to compute the expectation value of the transverse magnetization

$$M_+(t) = \mathrm{Tr}(\hat{\rho}(t)\hat{I}_+) = \sum_{k,\ell}\rho_{k\ell}(t)(I_+)_{\ell k} \tag{7}$$

which upon Fourier transformation yields the frequency spectrum

$$I(\omega) = \mathrm{Re}\int M_+(t)\exp(-\mathrm{i}\omega t)\,\mathrm{d}t \tag{8}$$

As $(I_+)_{lk} \propto \delta_{k,l-1}$ we only need off-diagonal elements of the density matrix of the type $\rho_{k,k+1}(t)$. Consequently, since the Hamiltonian is secular and the exchange operators only mix states of the same total azimuthal quantum number, m_l we extract from equation (1) those blocks of equations which couple between m_k and m_{k-1} states. For a spin system with N nuclei of spin $I = \frac{1}{2}$, there are N such blocks with dimensions

$$(N!)^2/[(N/2-m)!(N/2+m)!(N/2+1-m)!(N/2-1+m)!] \tag{9}$$

The largest blocks are the $0 \rightarrow \pm 1$ transitions for N even and the $-\frac{1}{2} \rightarrow +\frac{1}{2}$ transitions for N odd with dimensions

$$\frac{N}{N+2}\frac{(N!)^2}{[(N/2)!]^4} \quad \text{and} \quad \left(\frac{(N+1)}{2}\right)^2\frac{(N!)^2}{[((N+1)/2)!]^4} \tag{10}$$

respectively. The general equation for the $m_k \rightarrow m_l$ manifold becomes

$$\frac{\mathrm{d}}{\mathrm{d}t}\rho_{kl}(t) = \mathrm{i}\left[\sum_r \rho_{kr}(t)H_{rl} - \sum_i H_{ki}\rho_{il}(t)\right] + k\left[\sum R_{kn}\rho_{nm}(t)(R^{-1})_{ml} - \rho_{kl}(t)\right] - \frac{\rho_{kl}}{T_2}(t) \tag{11}$$

These equations can be cast into the following matrix form

$$\frac{\mathrm{d}}{\mathrm{d}t}\boldsymbol{\rho}(t) = \mathbf{L}\boldsymbol{\rho}(t) \tag{12}$$

where $\boldsymbol{\rho}(t)$ is the vector of the $\rho_{kl}(t)$ quantities. The formal solution of $\boldsymbol{\rho}(t)$ then becomes

$$\boldsymbol{\rho}(t) = \exp(\mathbf{L}t)\boldsymbol{\rho}(0) = \mathbf{T}\exp(\Lambda t)\mathbf{T}^{-1}\boldsymbol{\rho}(0) \qquad (13)$$

where Λ is the diagonal matrix of the eigenvalues of $\mathbf{L}$ and $\mathbf{T}$ the matrix of its eigenvectors. From equation (10), it follows that the dimensions of the blocks corresponding to the $m = 0$ to $m = \pm 1$ or $m = \frac{1}{2}$ to $m = -\frac{1}{2}$ transitions for $N = 6$, 7, and 8 become 300, 1225, and 3920, respectively, rendering the calculation of such spectra rather time-consuming and prone to roundoff errors even on large mainframe computers.

Symmetry considerations can often be helpful in factorizing the blocks.[16,17] To do so, the $\rho_{kl}(t)$ terms are calculated in bases of symmetry adapted linear combinations of spin product functions belonging to irreducible representations of the symmetry group of the static molecule.[18] This reduces the dimension of the blocks to just the number of allowed transitions which depending on the symmetry of the molecule can be considerably smaller than given by equation (10). Further factorization is provided by the fact that the exchange operator usually couples only between a limited number of representations, in fact only between those representations that induce the same irreducible representation of the symmetry group of the exchange-averaged Hamiltonian.[16] They can readily be determined by correlation diagrams relating the symmetries of the two groups. These symmetry considerations have in many cases very effectively reduced the size of the matrices that need be solved. For example, in the case of the bondshift reaction of cyclooctatetraene, the largest matrix that need be diagonalized in order to calculate the proton NMR spectrum in a liquid crystalline solution is 3920×3920, while when symmetry considerations are included it reduces to 224×224.

3 EXPERIMENTAL ASPECTS

3.1 Liquid Crystalline Solvents

So far only thermotropic nematic phases with positive anisotropic magnetic susceptibility, $\Delta\chi > 0$, i.e. which align with their director parallel to the magnetic field, have been used as solvents for dynamic NMR studies. The nematic phase is usually very fluid and consequently yields sharp-line spectra for dissolved solute molecules. The samples are contained in long cylindrical tubes as for high-resolution NMR of isotropic liquids. If a permanent magnet or an electromagnet with the magnetic field perpendicular to the tube axis is used, it is not allowed to spin the sample because the spinning smears out the director orientation and causes broadening of the spectrum. However, for superconducting magnets where the magnetic field is parallel to the sample axis, spinning usually sharpens the lines and increases the spectral resolution. The choice of solvent depends on the solubility of the solute, its degree of ordering, and the desired temperature range for the measurements. The solute concentrations range between 1–10 wt.%. Addition of solute usually reduces the clearing temperature but on the other hand it also often facilitates supercooling. Table 1 lists some common liquid crystals used in dynamic NMR studies with their nematic ranges.

For proton (and ^{13}C), NMR background signal may also be a consideration in the choice of solvent. For certain solutes, such as polar or hydroxylic compounds, lyotropic nematic phases may be the preferred choice as a solvent, but these have so far not been used for dynamic studies. Compounds exhibiting the uniaxial smectic A phase may also serve as adequate solvents. This phase, once aligned, for example, by cooling from a nematic or an isotropic phase within a magnetic field, will remain aligned in the sample holder even if rotated with respect to the field.[19] This allows reduction of the frequency range of the spectrum if a small sweep width is desired. Smectic phases are however usually more viscous than nematic and in the presence of solutes often undergo phase separation.

3.2 NMR Measurements

Most dynamic NMR studies in liquid crystalline solvents have been performed on protons, carbon-13, and deuterons.[20–38] The proton spectra are dominated by dipolar interactions and usually span several kHz. Carbon-13 dynamic studies have so far only been made[24,25] under proton decoupling so that the spectrum depends on the chemical shift anisotropy which is of the same order as that of the isotropic shift in normal liquids. For deuterium NMR the dominant effect on the spectrum is due to the quadrupole interaction, which depending on the motional constants of the solute may extend up to several tens of kHz.

When the frequency range does not exceed about 5–10 kHz, adequate spectra can be obtained by single pulse experiments. For wider frequency ranges, echo experiments are required. This is particularly true for deuterium NMR, where the method of choice is that of quadrupole echo.[39] In such experiments the observed lineshape will depend on the time intervals between the pulses in the sequence. This is taken into account[40] in the simulation by repeated application of equation (13) for the time intervals, where the magnetization evolves freely and performing proper transformations of the density operators representing the rf pulses.

Temperature stability and homogeneity are crucial for obtaining high-resolution spectra. Because of the sensitivity of the orientational order to temperature, small gradients may cause excessive line broadening and corresponding loss of resolution. Imperfect alignment may also be a source for loss of resolution. This is caused by the fact that different domains have slightly different orientations and accordingly slightly different splittings. The effect is often manifested by progressive line broadening for peaks which are further removed from the spectrum center.

4 APPLICATIONS TO SPIN I = $\frac{1}{2}$ NUCLEI

Several applications of high-resolution proton NMR in liquid crystalline solutions have been published and here we describe two such cases. Dynamic ^{13}C spectra recorded under proton decoupling will also be reviewed. The emphasis is on systems for which kinetic information was derived from a lineshape analysis, rather than on dynamic equilibria between species in the extreme fast regime.

Table 1 Nematic Liquid Crystals Used as Solvents for NMR Studies of Solute Molecules

Brand name or acronym	Chemical name and/or composition	Nematic range (°C)
DHAB	4,4′-dihexyloxyazoxybenzene	84–127
TBBA	terephthalaldehyde-bis(4-*n*-butylaniline)	199–233
S 1131 BCH	*trans*-4-pentyl-1-(4′-cyanobiphenylyl-4)-cyclohexane	96–222
10836	*p*-(*p*-ethoxyphenylazo)phenyl crotonate	109–194
Phase V	eutectic mixture of (two isomers each): *p*-ethoxy-*p*′-butyloxyazoxybenzene *p*-methoxy-*p*′-butyloxyazoxybenzene	5–75
ZLI 2452	mixture of derivatives of cyanophenylcyclohexane, cyanobiphenylcyclohexane, and unspecified esters	−40–110
ZLI 2142	—	−40–85
1565 TNC	mixture of derivatives of phenylcyclohexane and biphenylcyclohexane	−20–85
E8	mixture of derivatives of cyanobiphenyls	−12–72
Nematic mixture	several undisclosed mixtures by Kodak	5–105

4.1 Ring Inversion of *s*-Trioxan

The rate of the ring inversion of *s*-trioxan (Scheme 1) was studied by proton NMR in isotropic solutions.[41] The chemical shift difference between the axial and equatorial protons and their spin–spin coupling are quite small (0.093 ppm and 6.3 Hz, respectively), while the rate of the process at room temperature is rather high. It was therefore necessary to cool the solutions to below −50 °C to obtain dynamic spectra. When the compound is dissolved in a nematic solvent the spectrum is dominated by the dipolar interactions and its spectral width is considerably larger. Above about 70 °C it exhibits sharp peaks with splittings corresponding to the average dipolar interaction of the two conformations.[42] However on cooling to room temperature and below, the lines broaden because the exchange rate becomes of the order of the dipolar interactions.[22] Examples of spectra are shown in Figure 1. Note that the spectra were recorded in two different nematic solvents which give different background signals. The

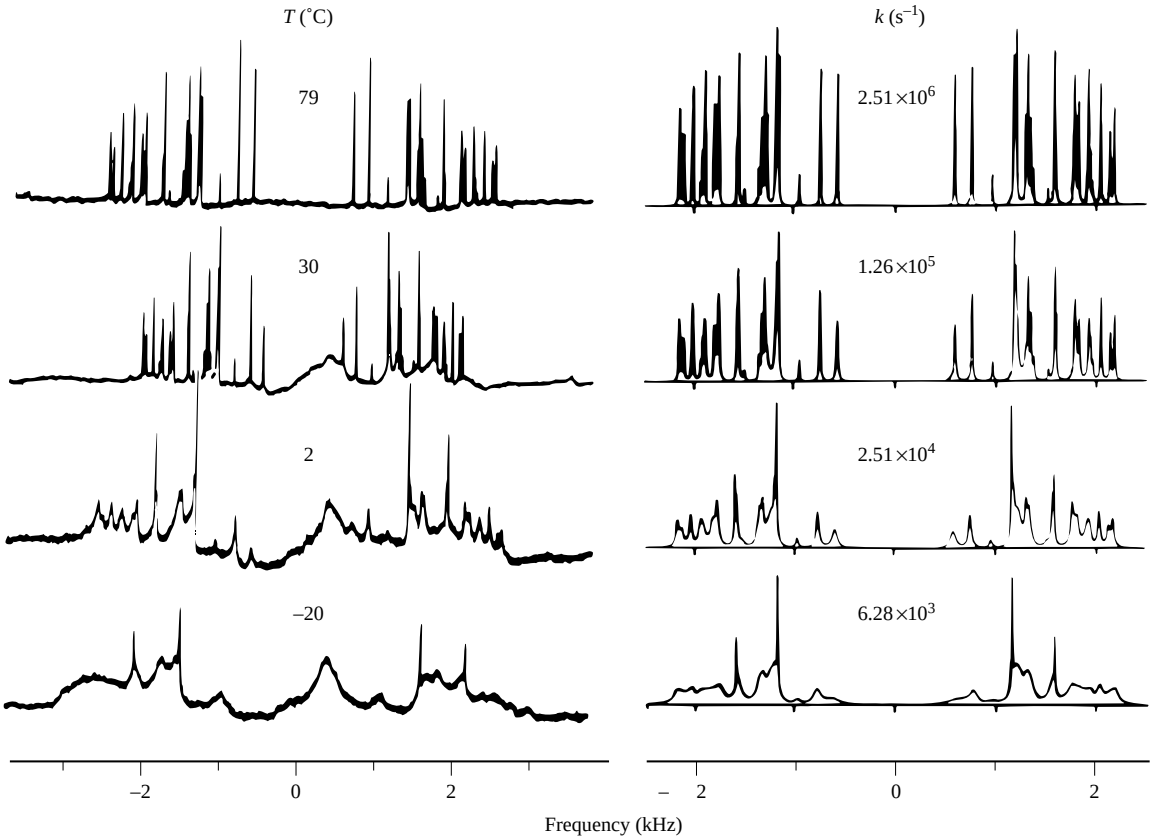

Figure 1 Left: Experimental proton NMR spectra of solutions of *s*-trioxan in liquid crystalline solvents at various temperatures. The solvent used was phase V (2.8 wt.%), except for the 79 °C spectrum which corresponds to a 2.0 wt.% solution in DHAB. Note the different background signals for the two liquid crystal solvents. Right: Corresponding simulated spectra, calculated using the indicated rate constants and the magnetic parameters given in Table 2 with a fixed motional constant $C^2_{3z^2-r^2} = -0.2$

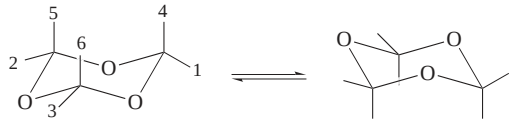

Scheme 1

Table 2 Parameters Used in the Simulation of the *s*-Trioxan Spectra in Figure 1

J_{14} = 6.3 Hz	$D_{12} = D_{13} = D_{23} = C^2_{3z^2-r^2}$ 3941.6 Hz
σ_{ae} = 0.093 ppm	$D_{14} = D_{25} = D_{36} = C^2_{3z^2-r^2}$ (−9651.26) Hz
	$D_{45} = D_{56} = D_{46} = C^2_{3z^2-r^2}$ 775.59 Hz
$D_{15} = D_{16} = D_{24} = D_{26} = D_{34} = D_{35} = C^2_{3z^2-r^2}$ 499.28 Hz	

spectra were simulated using equation (11) with magnetic and kinetic parameters as given in Table 2 and in Figure 1. For simplicity a fixed motional constant was used for displaying the calculated spectra. The dipole–dipole, indirect spin–spin, and chemical shift interactions were determined from low-temperature spectra in isotropic solutions and high-temperature spectra in liquid crystalline solvents. The anisotropic chemical shift and the anisotropic indirect spin–spin coupling were neglected. Since the molecule has threefold symmetry only one motional constant, $C^2_{3z^2-r^2}$, is required. Its value can be obtained from the line splittings, in particular from the so-called dynamically invariant lines, i.e. lines that remain sharp throughout the dynamic range. These lines correspond to transitions that are not modulated (or nearly not modulated) by the dynamic process. Such lines are the two $\pm 1 \rightarrow 0$ pairs of A_2 symmetry clearly seen in the low-temperature spectra of Figure 1. Inspection of the eigenfunctions[22] between which these transitions occur shows that the exchange-induced permutation of nuclei does not change the dipolar interactions of either the initial or final states. The chemical shift on the other hand is modulated by the exchange, but the effect is small and is averaged out already at much lower temperatures than those for which spectra are depicted in Figure 1.

The derived rate constants for the ring inversion reaction are plotted in Figure 2. The figure demonstrates one of the main advantages of the method, i.e. the large dynamic range over which measurements can be made. The lower bound of the dynamic range (10^4 s^{-1}) in this experiment was set by the lack (at the time) of suitable nematic liquids for high-resolution measurements below −20 °C. Also depicted in Figure 2 are the results obtained in an isotropic solvent. These correspond to rates which are orders of magnitude slower than those obtained in the nematic solvent and span a much smaller dynamic range. It may be seen however that both sets of data fit a single Arrhenius line. This indicates that within the accuracy of the experiment the kinetic parameters for the reaction are not very sensitive to the solvent, not even on going from an isotropic to a nematic solvent. This is not surprising for a ring-inversion process, since its rate is predominantly determined by the internal coordinates of the molecule. In other cases, where solute–solvent interactions play a role or for bimolecular reactions where ordering effects are important, the situation may be different.

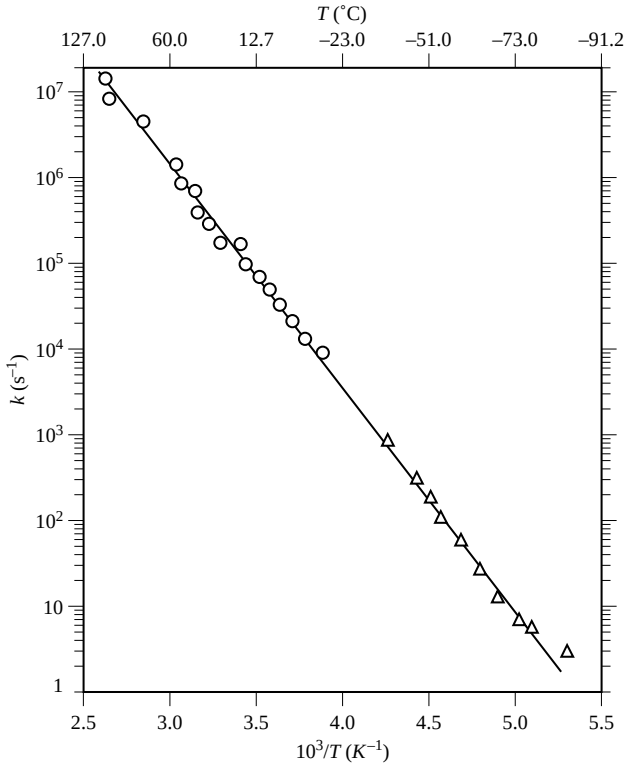

Figure 2 Arrhenius plot of the rate constant for the ring inversion of *s*-trioxan in liquid crystalline (circles) and isotropic (triangles) (Freon) solvents. The circles above 60 °C correspond to solvent DHAB while those below to phase V

4.2 Bond Shift in Cyclooctatetraene (COT)

As a second example we consider the bond shift process in COT (Scheme 2). This molecule has D_{2d} symmetry rendering all eight protons of the molecule equivalent. Consequently the proton NMR spectrum in an isotropic solvent consists of a single line and is not useful for dynamic measurements. The bond shift reaction could therefore only be studied in substituted molecules and in a qualitative manner from the ^{13}C spectrum.[43,44] The proton NMR spectrum of COT in a liquid crystalline solvent on the other hand is highly structured, reflecting the dipolar interactions between all protons in the molecule and exhibits dynamic effects as the temperature is raised from below −20 °C to well above 100 °C.[21] Examples of spectra are depicted in Figure 3. The 'static' spectrum at −25 °C could readily be interpreted with the parameters summarized in Table 3. On heating to above −25 °C line broadening sets in and at room temperature only a number of invariant (or almost invariant) lines are observed. Above 100 °C the spectrum coalesces yielding at 170 °C a pattern corresponding to the averaged dipolar interactions. Simulation of such dynamic spectra would require, without the use of

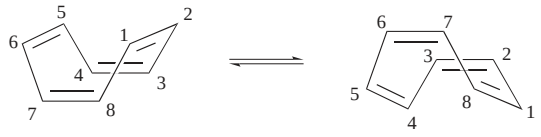

Scheme 2

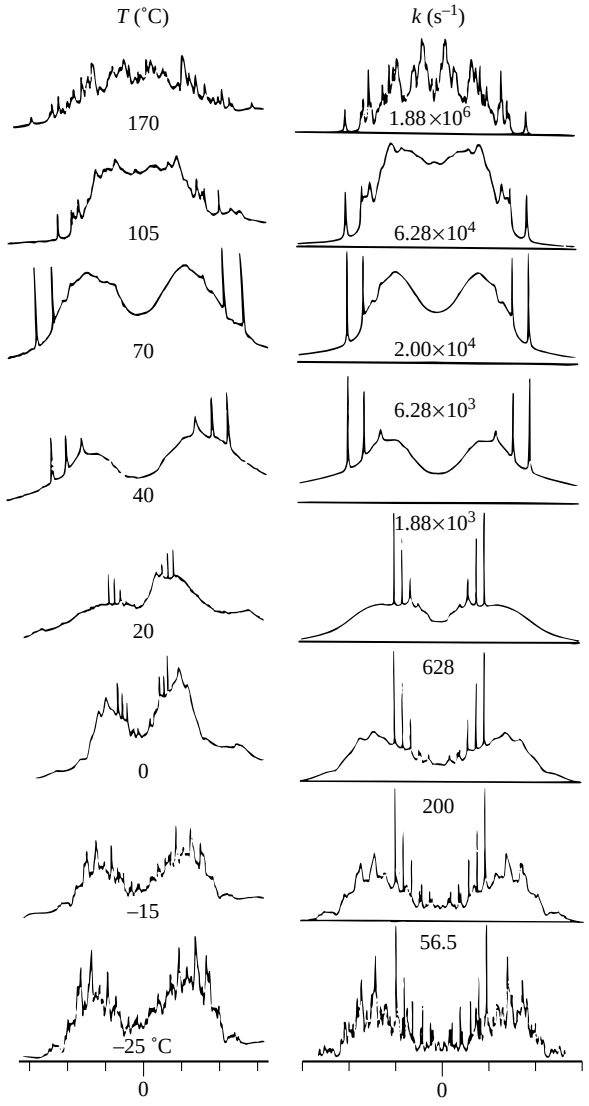

Figure 3 Left: Experimental proton NMR spectra of COT in liquid crystalline solvents at different temperatures. The solvents were: for −25 °C to 20 °C, phase V; for 40 °C, 'Nematic Mixture'; 70 °C and 105 °C, DHAB; and for 170 °C, TBBA. Right: Simulated spectra calculated with the indicated rate constants and the magnetic parameters given in Table 3. A fixed motional constant was used for all the simulated spectra. The spacings between the markers on the left are 500 Hz for the bottom four spectra, 250 Hz for the next three and 125 Hz for the topmost one. On the right, the spacings are 1000 Hz for the bottom four traces and 500 Hz for the four upper ones

symmetry, the diagonalization of matrices as large as 3920 × 3920. When symmetry considerations are included[16] and group theoretical methods are applied to factorize the matrices, the largest block becomes 224 × 224. This in fact made the problem solvable in practice,[23] as shown by the simulated spectra in the right column of Figure 3.

In the original work on the NMR spectrum of COT in liquid crystalline solutions[21] dynamic information was derived from proton spectra of almost but not completely deuterated COT. The isotopic mixture contained a relatively large fraction of $C_8D_6H_2$ isotopomers, each yielding at slow exchange a single doublet. From the initial broadening of the peaks and from the width of the lines in the fast exchange region, estimates

Table 3 Magnetic Parameters of COT used in the Simulation of the Dynamic Spectra Depicted in Figure 3

D_{12}	−1620.3
$D_{13} = D_{17}$	−103.8
D_{14}	−84.5
D_{15}	−147.5
D_{16}	−206.3
D_{18}	+960.9
J_{12}	11.8

of the rate parameters for the bond shift process were derived. The use of such incompletely deuterated samples to obtain simplified proton spectra was found helpful in many structural studies of solute molecules.[45–48] To eliminate broadening due to dipolar interactions with the deuterons, a special decoupling technique was designed involving saturation of the deuterium double quantum transition.[45,46] This requires much less rf power and eliminates sample heating problems.

4.3 Hindered Rotation Measurements

Dynamic NMR has also been applied to natural-abundant ^{13}C of solute molecules dissolved in liquid crystals as demonstrated by Fung et al.[24] Since such spectra are extremely weak and are often masked by the more intense solvent peaks, they were recorded under proton decoupling conditions. The spectra are then essentially identical to those in isotropic solutions except that the chemical shift is modified by the solute ordering. To reduce the interference effect of the solvent signals, special spin echo sequences were used to take advantage of the shorter T_1 values of the nematic solvent carbons, but even then special solvents with ^{13}C windows at the solute frequencies had to be used.

Further simplification may be achieved by using magic angle spinning.[25] For $\Delta\chi > 0$ solvents the director aligns along the spinning axis and the spectrum becomes identical to that in an isotropic solvent. Under these conditions, there is no advantage in using a liquid crystalline solvent, unless of course one wishes to study the effect of ordering on the dynamic process. The method was applied to several systems exhibiting hindered rotations; 4-(dimethylamino)pyrimidine and 6-(dialkylamino)fulvenes. The main conclusion of the work confirms that within the experimental accuracy the ordering by the nematic solvent does not affect the kinetic parameters of the process.

5 MULTIPLE QUANTUM DYNAMIC NMR FOR SPIN $I = \frac{1}{2}$ NUCLEI

The proton NMR spectra in liquid crystalline solvents for molecules with 10 or more hydrogens are so rich in lines that they become structureless with few features that can be used for quantitative analysis. The difficulty can partially be resolved by employing the method of multiple quantum spectroscopy. In such experiments one displays $\Delta m > 1$ spectra which involve less transitions than the corresponding ordinary $\Delta m = 1$ spectra, and are therefore better resolved and more convenient for comparison with calculations.[49] As for

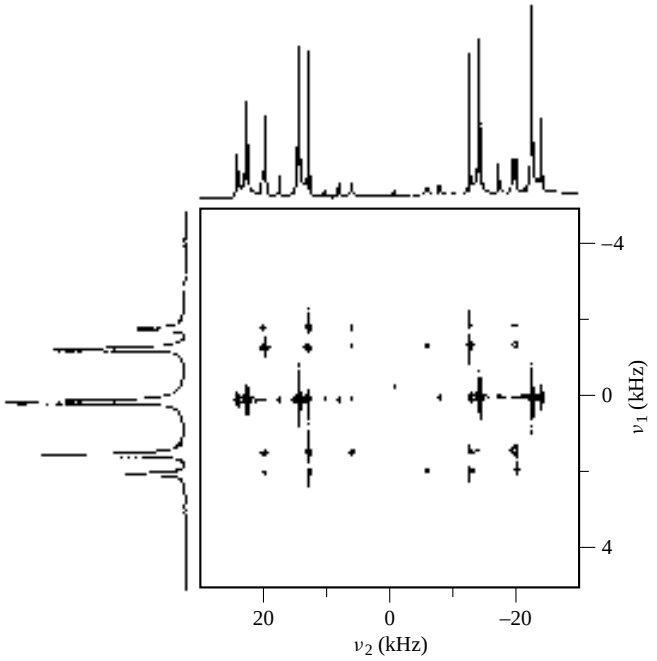

Figure 4 Experimental 2D fourth quantum order contour plot for a solution of *s*-trioxan (2.7 wt.%) in phase V at 17 °C using the SMQ experiment. The one-dimensional spectra along ν_1 and ν_2 are skyline projections and correspond respectively to fourth and single quantum order transitions

single quantum spectra these also exhibit line broadening and coalescence effects. They cannot be detected by ordinary pulse NMR, but can be obtained by several indirect ways which usually involve 2D methods. Two methods were considered for dynamic proton NMR in liquid crystalline solvents. The time proportional phase increment (TPPI) sequence[50] was employed for simulating[26] dynamic multiple quantum spectra and, subsequently, a simpler version[51] which allows recording a particular single multiple quantum (SMQ) spectrum was used.[27] We refer to the literature[26,27] for the theoretical background and confine ourselves here to briefly reviewing experimental results obtained in liquid crystalline solutions.

In Figure 4 a 2D plot of the proton SMQ spectrum of a solution of *s*-trioxan recorded at 17 °C is displayed[27] together with skyline projections along ν_1 (the evolution coordinate) and ν_2 (the detection coordinate). The latter is a $\Delta m = 1$ spectrum but the much simpler ν_1 projection corresponds to the fourth quantum order. Similar fourth quantum projection spectra recorded at different temperatures are presented in Figure 5. These are compared with simulated spectra which were computed by two methods; exact calculation employing the full density matrix formalism and approximate methods. The latter are the density matrix analogs for the slow (bottom trace) and fast (all other traces) exchange regimes. No adjustable parameters were used in the calculations (except for the order parameter), rather the known rate constants and magnetic parameters from earlier studies were adopted. As may be seen, the fit of the experimental and simulated spectra is quite satisfactory. It should be noted however that despite the simple appearance of the MQ spectra their simulations are as complicated as those for the single quantum spectra. This is so because for the calculations it is necessary to follow the evolution of a multitude of coherences. Fortunately, approximate methods exist[26] that are much simpler and as may be seen in Figure 5 they result in spectra very similar to those calculated by the exact method.

6 DYNAMIC NMR FOR SPIN I = 1 NUCLEI

Of the nuclei with spin I = 1, deuterium is the most important for dynamic NMR studies in nematic solvents. However due to its low natural abundance it is necessary to work with isotopically enriched samples. This might require special skills, but techniques are available that allow complete or selective deuteration of many compounds.[52] The method has several advantages; the spectrum is free of background signals and is usually very simple. The dipolar interactions between the deuterons or with other nuclei (protons) are usually within the linewidths, and the structure of the spectrum is predominantly due to the much larger quadrupole interaction. For spin I = 1 nuclei, this corresponds to a single doublet for each type of nucleus, and thus the deuteron spectrum of a deuterated solute in a nematic solvent consists of a number of doublets according to the number of inequivalent deuterons in the molecule. The simulation of dynamic spectra then requires only the solution of Bloch–McConnell type equations rather than the full density matrix equations. In the absence of chemical shift effects, the spectrum of the $m = -1$ to $m = 0$ manifold is the mirror image about the center frequency of the $m = 0$ to $m = +1$ manifold. A third advantage is the large dynamic range that can be studied by deuterium NMR. Since the splitting can be as high as several dozens of kHz, the upper limit of the dynamic range may be considerably higher than that for protons.

6.1 Ring Inversion in Cyclohexane and *p*-Dioxan

As a simple example where the advantages of dynamic deuterium NMR in nematic solvents are well demonstrated, consider the ring inversion process in cyclohexane-d_{12} (C_6D_{12}) (Scheme 3). Experimental spectra[28] are depicted in the left column in Figure 6. At low temperatures the spectrum consists of two doublets due to the axial (outer doublet) and equatorial (inner doublet) deuterons with a relative splitting of ~3. The quadrupole interaction for aliphatic deuterons are nearly constant at $\nu_Q^s \approx 125$ kHz (as compared to ~140 kHz for aromatic deuterons) with cylindrical symmetry about the C–D bond. Accordingly the average quadrupole splitting for a molecule with threefold symmetry, such as cyclohexane, will be proportional to $\nu_Q^s \frac{1}{2}(3\cos^2\beta - 1)$ where β is the angle between the C–D bond and the molecular symmetry axis. For the axial and equatorial deuterons in cyclohexane, this corresponds to $\langle\nu_Q{}^{ax}\rangle/\langle\nu_Q{}^{eq}\rangle \sim -3$ as observed experimentally. In the dynamic spectra the opposite signs of the $\langle\nu_Q\rangle$ quantities is reflected in the mixing of the high-frequency axial

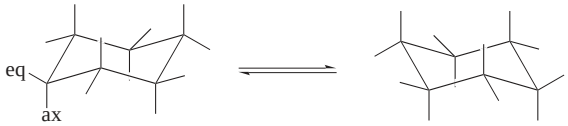

Scheme 3

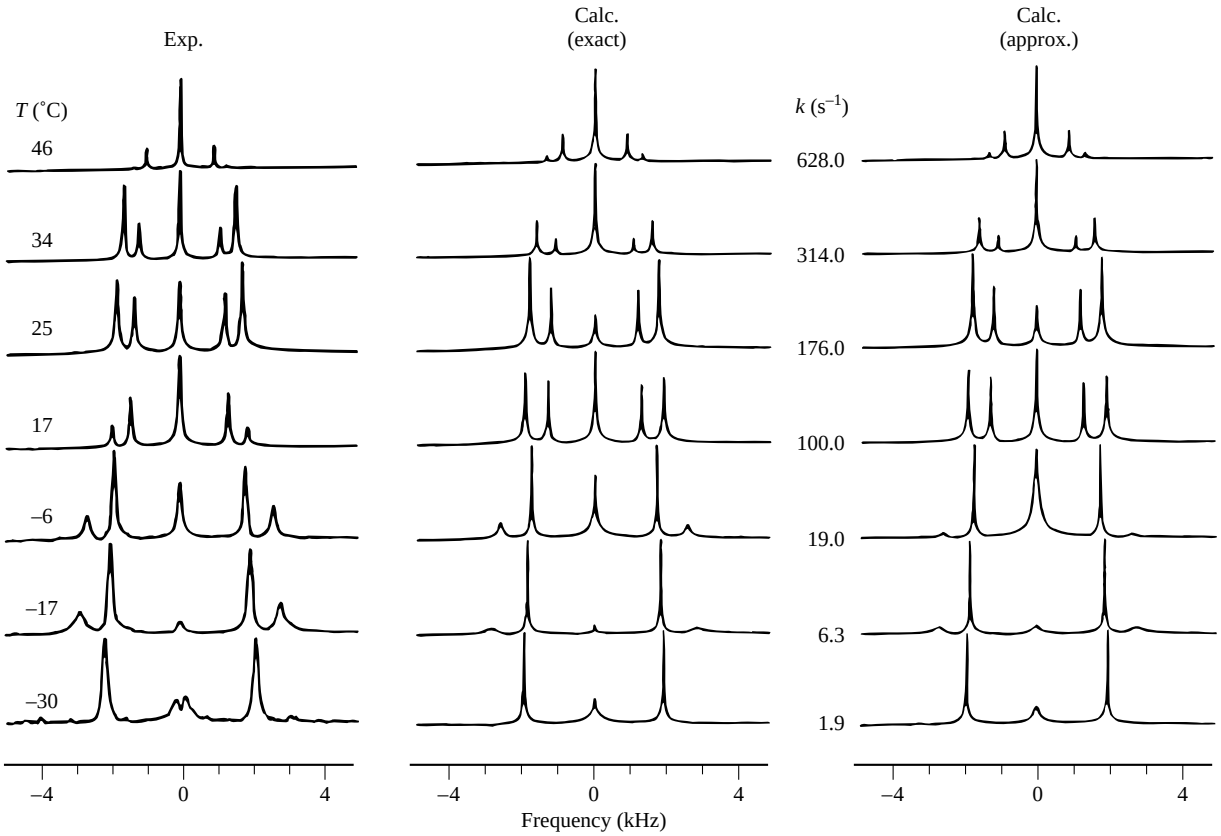

Figure 5 Experimental (left) and calculated (center and right) fourth order quantum spectra of *s*-trioxan solutions in phase V. The experimental spectra were obtained as in Figure 4, the spectra in the middle column were calculated by the exact density matrix formalism, those in the right column were calculated by approximate methods

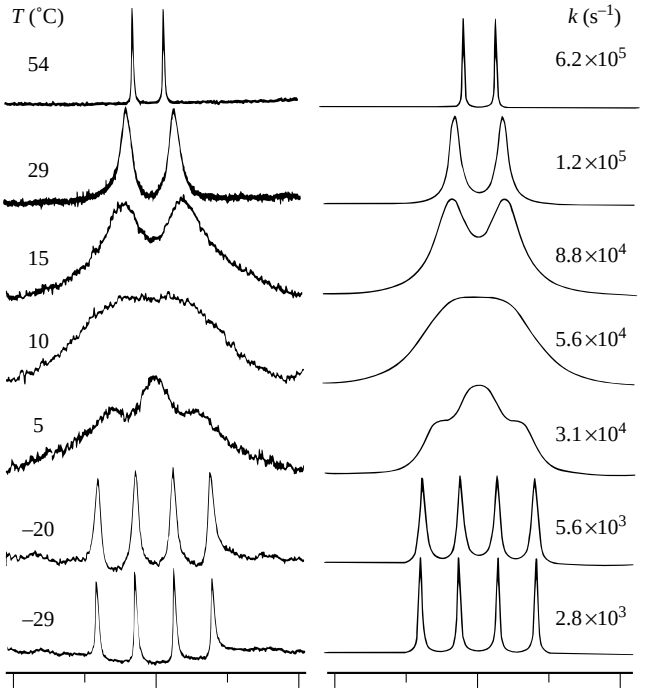

Figure 6 Experimental (left) and simulated (right) deuterium NMR spectra of cyclohexane-d_{12} (3.6 wt.%) in phase V. The overall frequency range corresponds to 83.3 kHz for the lowest three traces and 50.0 kHz for the upper four

peak with the low-frequency equatorial peak and vice versa. This is clearly observed in the experimental spectra depicted in Figure 6 and in the corresponding simulated traces. The spectra correspond to inversion rates ranging from $10^3\,s^{-1}$ to almost $10^6\ s^{-1}$, and when semilogarithmically plotted as a function of the inverse absolute temperature a straight Arrhenius line is obtained which extrapolates perfectly through the results obtained in isotropic liquids at much lower temperatures.[53] In the simulation of the spectra the order parameter, $C^2_{3z^2-r^2}$, must be known. In the low- and high-temperature regions, where sharp peaks are observed, this parameter can be calculated from the line splitting and by interpolation the values at the intermediate range can be derived.[28]

As a second example we consider the case of *p*-dioxan (Scheme 4). This molecule has C_{2h} symmetry and therefore three motional constants are required to describe its orientation in a liquid crystalline solvent. The average quadrupole splitting is given by

$$\langle \nu_Q^i \rangle = \nu_Q^s \sqrt{\frac{3}{5}} \left[\frac{1}{\sqrt{3}} C^2_{3z^2-r^2} \tfrac{1}{2} (3\cos^2\beta^i - 1) + C^2_{x^2-y^2} \tfrac{1}{2} \sin^2\beta^i \cos 2\alpha^i - C^2_{xy} \tfrac{1}{2} \sin^2\beta^i \sin 2\alpha^i \right] \quad (14)$$

where β^i and α^i are the polar and azimuthal angles of the C–D^i bond in the molecular coordinate system x, y, z with

Scheme 4

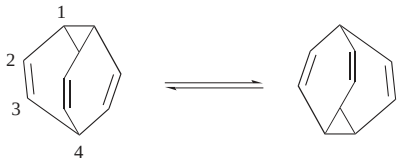

Scheme 5

z perpendicular to the symmetry plane of the molecule. The motional constants are independent and their ratios vary with temperature and from solvent to solvent. Therefore there is no a priori relation between the quadrupole splittings of the axial and equatorial deuterons as is in cyclohexane. In particular their relative sign can be both positive and negative.

The *p*-dioxan molecule undergoes ring inversion in a similar fashion to cyclohexane[53] and the reaction was studied by deuterium dynamic NMR in two nematic solvents, phase V and 1565 TNC.[29] Experimental spectra are shown in the left columns of Figure 7. As may be seen, their evolution with temperature is quite different and this has been interpreted as due to different relative signs of the axial and equatorial quadrupole interactions (same signs in phase V and opposite signs in 1565 TNC). When this effect is taken into account, satisfactory simulation of both sets of spectra are obtained as shown in the right columns of Figure 7. The derived rate constants for the ring-inversion process were found to be identical in both solvents.

The spectra shown above for C_6D_{12} and $C_4O_2D_8$ (Figures 6 and 7) were recorded by single pulses and are therefore distorted due to the dead-time effect. In subsequent works this problem was resolved by using the quadrupole echo method. The spectrum is then also a function of the time interval between the pulses and this must be included in the simulation.[55]

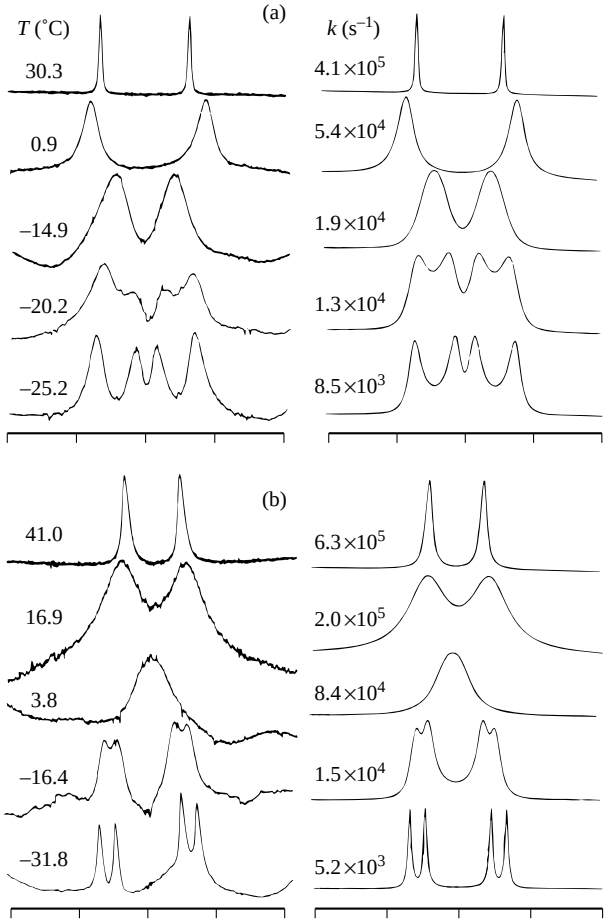

Figure 7 (a) Experimental and simulated deuterium NMR spectra of *p*-dioxan-d_8 dissolved in phase V. The overall frequency scale is 50 kHz for the bottom three spectra and 20 kHz for the top two. In the simulation identical signs of the quadrupole interactions were assumed for the axial and equatorial deuterons. (b) Same as in (a) but for a solution in 1565 TNC. The overall scale is 100 kHz for the bottom three traces and 20 kHz for the top two. In the simulation, opposite signs for the axial and equatorial deuterons were assumed

6.2 Cope Rearrangement in Bullvalene

Bullvalene undergoes fast Cope rearrangement (Scheme 5) and this process has been extensively studied by ^{1}H and ^{13}C NMR in isotropic solutions.[54] The reaction is highly degenerate and results in complete equivalence of all the carbons and all the hydrogens in the molecule. Proton spectra of bullvalene dissolved in a nematic solvent were also recorded[56] but only at high temperatures where they correspond to the fast exchange limit. More extensive studies involving liquid crystalline solutions were made by deuterium NMR.[30] At low temperatures the spectrum consists of four doublets with relative intensities 3:3:3:1 [see Figure 8(a)]. The identification of the outer peaks with deuteron number 4 is straightforward while the other peaks were identified from the known structure of the molecule. The spectrum shows a small asymmetry which is due to the fact that the olefinic deuterons have a slight high-frequency shift relative to the aliphatic ones. At high temperatures [upper trace in Figure 8(a)] the spectrum coalesces into a single doublet, reflecting the fact that all deuterons become equivalent. In the intermediate temperature range typical dynamic spectra are observed, Figure 8(b), that could readily be simulated as shown in Figure 8(c). The deuterium quadrupolar couplings, ν_Q^i, used for the simulation of the dynamic spectra are listed in Table 4 in units of the largest splitting, ν_Q^4. The good fit between the experimental and simulated spectra confirms the high degeneracy of the Cope rearrangement. A more direct confirmation of the kinetic pathway was obtained by the two-dimensional exchange method described in the next section.[33]

Table 4 Deuterium Quadrupolar Couplings, ν_Q^i, Used in the Simulation of the Dynamic Spectra of Bullvalene [Figure 8(b)], in Units of the Largest Splitting, ν_Q^4

i	1	2	3	4
ν_Q^i/ν_Q^4	0.727	−0.401	0.271	1.0

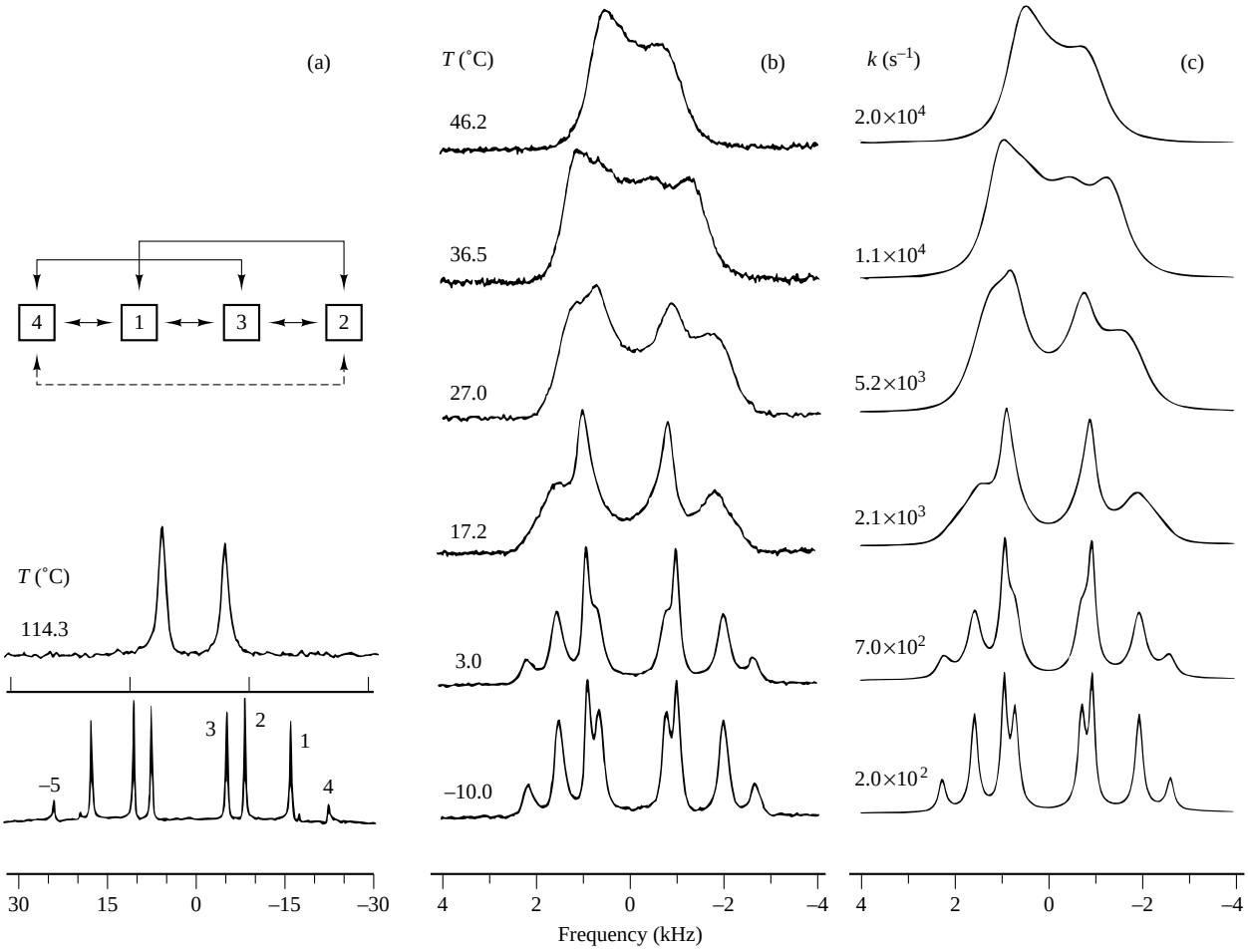

Figure 8 (a) Experimental deuterium NMR spectra of bullvalene-d_{10} dissolved in ZLI 2452 (3.8 wt.%) at $-5\,^{\circ}$C (lower trace) and in DHAB (4.7 wt.%) at 114.3 °C (upper trace). The diagram at the top indicates the different orders of exchange by the Cope rearrangement. Double arrow, full line, and dashed line correspond to first-, second-, and third-order exchanges. (b) Experimental dynamic NMR spectra of bullvalene-d_{10} in phase V (5.7 wt.%) at the indicated temperatures. (c) Simulated dynamic spectra calculated using the indicated rate constants and the relative quadrupole interactions given in Table 4. For each spectrum, a suitable motional constant was chosen[30]

7 TWO-DIMENSIONAL EXCHANGE NMR SPECTROSCOPY FOR SPIN I = 1 NUCLEI

Two-dimensional (2D) exchange NMR was introduced by Jeener et al. to study slow exchange processes for spin $I = \frac{1}{2}$ nuclei.[57] The method was subsequently extended to deuterons (I = 1) in solids and ordered systems in general by Spiess and collaborators.[58–60] It is most useful in the dynamic window for which $1/T_1 \lesssim k < 1/T_2$ and has also found interesting application in liquid crystalline solutions of deuterated solutes. Some of these will be described below.

The basic scheme of the experiment consists of three pulses (Scheme 6).[31] Following the first 90° pulse (P_1) which takes the magnetization to the transverse plane, the various nuclei precess according to their quadrupole interactions and are thus phase-encoded. A second θ pulse (P_2) then produces either Zeeman or quadrupole order depending on the relative phases ($\phi_1 - \phi_2$) of the two pulses. These longitudinal magnetizations are allowed to undergo exchange during a preset mixing time, τ_m, following which a third pulse (P_3) takes them back to the transverse plane and the signal is detected as a function of the detection period t_2. To obtain pure 2D exchange spectra, signals from Zeeman and quadrupole order experiments are combined with appropriate relative intensities, so as to eliminate nonexchange off-diagonal peaks. Two-dimensional Fourier transformation then produces a 2D map with peaks corresponding to the one-dimensional spectrum along the main diagonal and exchange cross peaks off the main diagonal. These cross peaks link between sites i, j which interchange by the exchange process. Their intensity is proportional to

$$I_{ij} = P_i[\exp(kK\tau_m)]_{ij}\ \exp(-\tau_m/T_1) \qquad (15)$$

where P_i is the equilibrium population of site i, and k and K are respectively the rate constant and the exchange matrix for the process. The experiment has several important advantages; measurements can be made in a dynamic range inaccessible by the lineshape method; the cross peaks directly identify the interchanging sites and thus the mechanistic pathway of the process; the cross peaks provide information on the relative signs of the quadrupole interactions of the interchanging sites, and from their evolution with τ_m kinetic parameters may be derived.

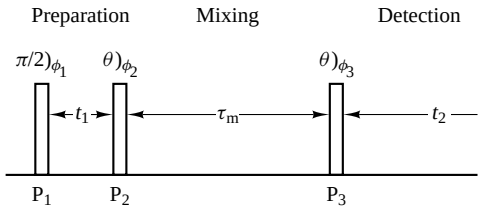

Scheme 6

7.1 Peak Assignment and Relative Signs of Quadrupole Interactions

An example where some of the points mentioned in the last paragraph are demonstrated is that of *p*-dioxan-d_8 already discussed[29] in Section 6.1. It was pointed out there that the signs of the quadrupole interactions of the axial and equatorial deuterons are the same when *p*-dioxan is dissolved in phase V and the opposite in 1565 TNC. This is clearly seen in the exchange 2D spectra[31] in Figure 9, where for phase V the cross peaks link separately the high-field and the low-field signals of the axial and equatorial deuterons, while in 1565 TNC a low-field axial peak is linked with a high-field equatorial peak and vice versa.

An application of the 2D exchange method which was essential for the peak assignment, is that of perdeuterated *cis*-decalin.[34] The molecule undergoes ring inversion (Scheme 7)[61] and in liquid crystalline solutions exhibits temperature dependent dynamic spectra as shown in the left column of Figure 10. To simulate the spectra it is necessary to identify the peaks with particular deuterons in the molecule, or at least to identify the interchanging pairs of peaks. This can readily be done for deuterons 1,1′ which are bonded to the tertiary carbons and remain invariant to the dynamic process. However for all other lines the assignment is not trivial. Since the molecule has C_2 symmetry, three motional constants are required to describe the ordering of the molecules [equation (14)] and the assignment cannot be made simply from a knowledge of the molecular structure. The problem was resolved by 2D exchange spectroscopy.[34] A 2D spectrum recorded at $-5\,^{\circ}C$ is shown in Figure 11 where cross peaks linking pairs of diagonal signals are clearly observed. Although this does not completely assign the peaks, it does identify the signals which interchange by the ring-inversion process. Using this information, dynamic spectra could be simulated which satisfactorily reproduce the experiments as shown in the right-hand column of Figure 10. Other examples where 2D exchange provided assignment and even identified hidden peaks masked by strong signals include 1,1- and 1,4-dimethylcyclohexane.[38]

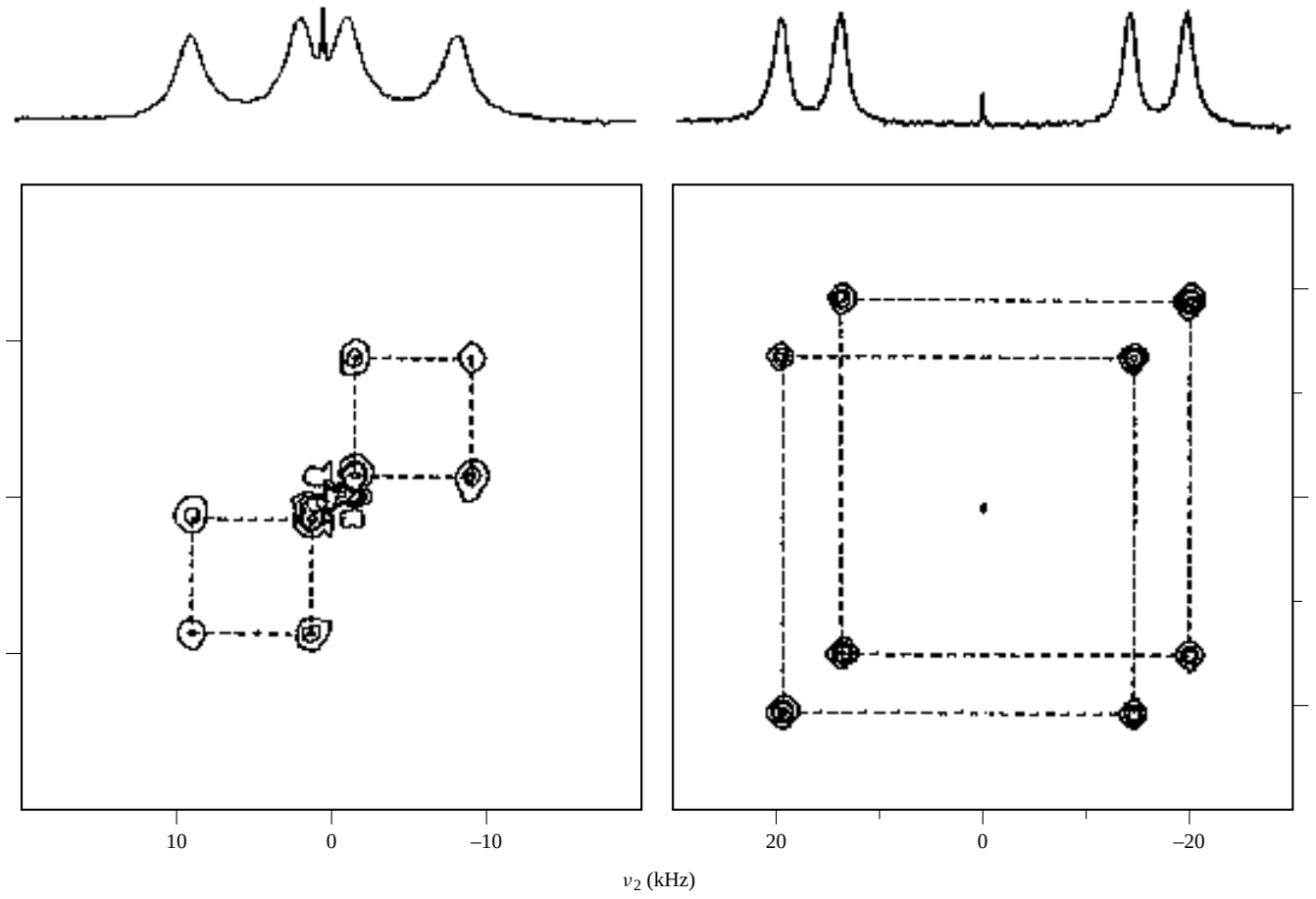

Figure 9 Two-dimensional deuterium exchange spectra on solutions of *p*-dioxan-d_8 dissolved in phase V (left) and 1565 TNC (right). The spectra were taken at $-43\,^{\circ}C$ with a mixing time τ_m = 1 ms. Note that the signs of the quadrupole interactions of the two exchanging deuterons is the same in phase V and the opposite in 1565 TNC

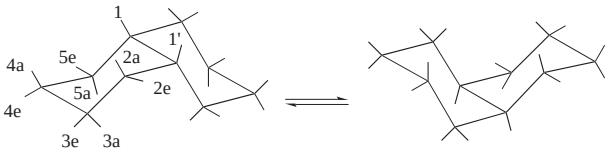

Scheme 7

7.2 Cope Rearrangement In Bullvalene: Higher Order Cross Peaks

Most examples of monomolecular exchange phenomena involve twofold degeneracy, i.e. interchange between two configurations. In the 2D exchange spectrum this is manifested by cross peaks linking separate pairs of lines. The bullvalene molecule provides an example of a high degree of degeneracy where a diagonal peak can be linked by the exchange to more than one other signal. Consequently at longer mixing times, when two or more exchange steps occur, higher order cross peaks between signals not directly connected by the exchange process may show up.

This is demonstrated[33] in the 2D exchange spectra of bullvalene depicted in Figure 12. For a mixing time of 2 ms only first-order cross peaks are observed [see diagram in Figure 8(a)], i.e. between peaks directly linked by a single Cope rearrangement. At 5 ms an additional second order cross peak appears $(1, \bar{2})$ which is linked by two successive rearrangement steps, while at 10 ms even a third-order cross peak (4, 2) may

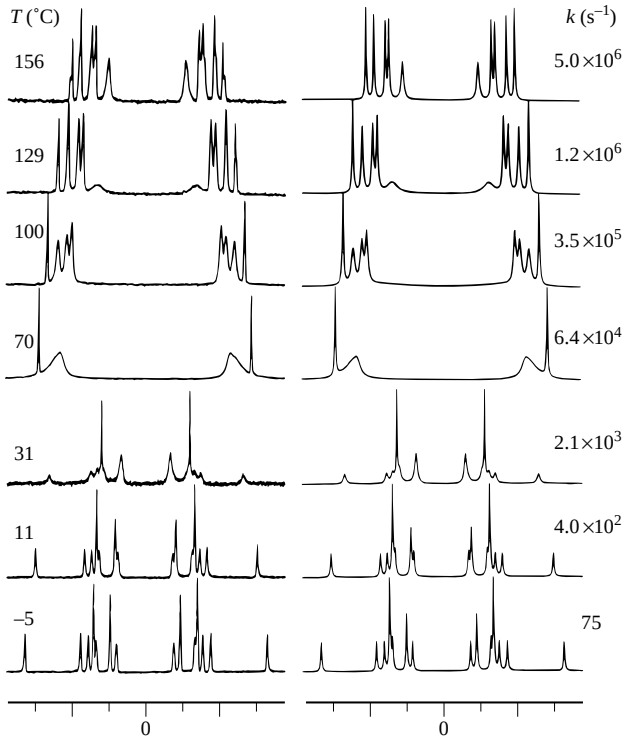

Figure 10 Experimental (left) and simulated (right) deuterium spectra of *cis*-decalin-d_{18} in liquid crystalline solvents. The bottom three traces correspond to the solvent ZLI 2452 while the upper four to S 1131 BCH. The separation between the frequency markers corresponds to 10 kHz for the bottom three traces and to 5 kHz for the top four

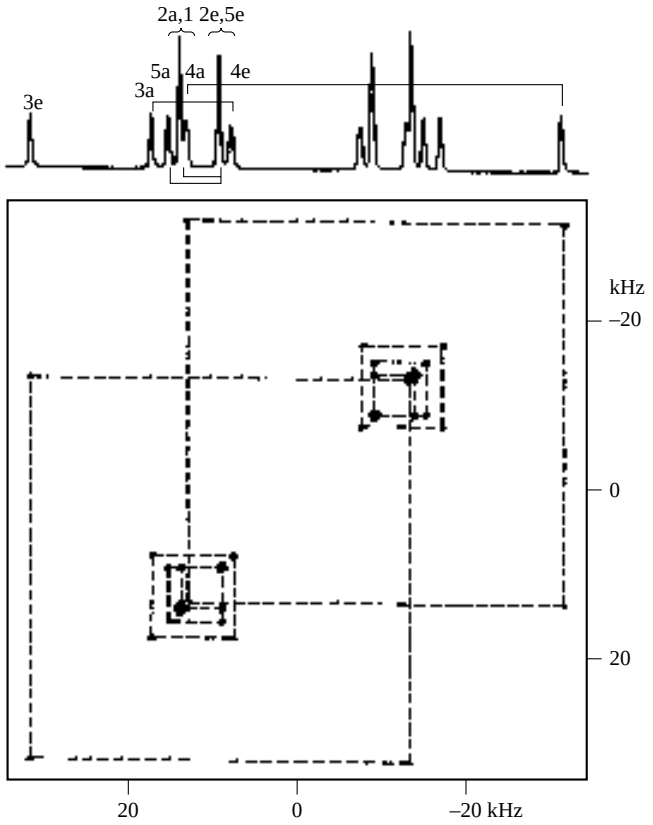

Figure 11 A two-dimensional deuterium-exchange spectrum of a solution of *cis*-decalin-d_{18} in ZLI 2452 at −5 °C. The dashed lines identify the interchanging peaks due to ring inversion. The assignment of the peaks based on the 2D spectra and other considerations are indicated on the 1D spectrum above

be identified. Expanding equation (15) in powers of τ_m gives

$$I_{ij} = P_i[\delta_{ij} + k\boldsymbol{K}\tau_m + \tfrac{1}{2}k^2\boldsymbol{K}^2\tau_m^2 + \tfrac{1}{6}k^3\boldsymbol{K}^3\tau^3 + \ldots]_{ij} \quad (16)$$

where for the case of bullvalene

$$\boldsymbol{K} = \begin{bmatrix} -1 & 0 & 2/3 & 1/3 \\ 0 & -1/3 & 1/3 & 0 \\ 2/3 & 1/3 & -1 & 0 \\ 1 & 0 & 0 & -1 \end{bmatrix} \quad (17)$$

Computation of $\boldsymbol{K}^2$ and $\boldsymbol{K}^3$ shows that indeed the element $\underline{1}, \bar{2}$ which is zero in $\boldsymbol{K}$ is nonzero in $\boldsymbol{K}^2$ while an entry at 4, 2 appears only at $\boldsymbol{K}^3$ and higher powers of K. In the short τ_m approximation, second- and third-order peaks should therefore increase as ${\tau_m}^2$ and ${\tau_m}^3$, while first-order cross peaks (and the diagonal peaks) should increase (decrease) linearly. This is indeed confirmed experimentally.

8 DYNAMIC ECHO TRAIN EXPERIMENTS

In some cases dynamic spectra can only be obtained in the fast exchange regime, e.g. when the rate is fast and the activation energy too low to reduce it effectively to the intermediate and slow-exchange limit by cooling. Kinetic data can then be obtained by transverse relaxation studies but the

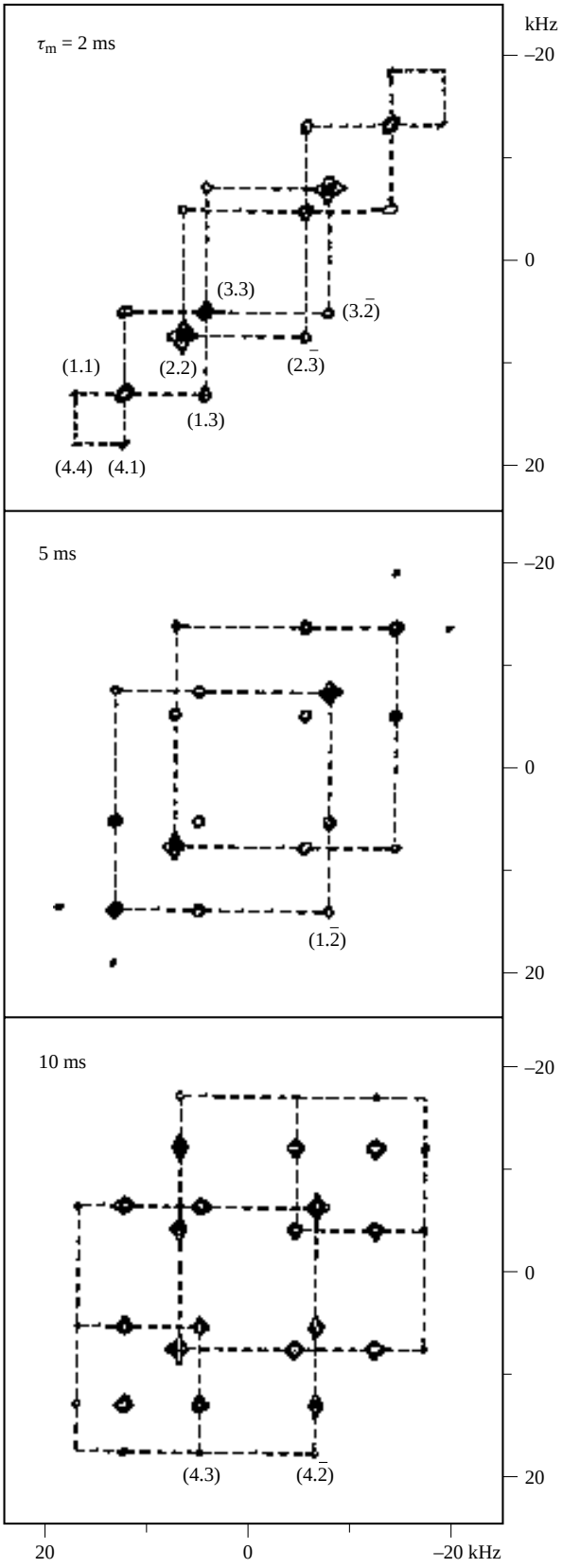

Figure 12 Two-dimensional deuterium exchange spectra of bullvalene-d_{10} dissolved in ZLI 2452 at 5 °C for several mixing times as indicated in the figure. The dashed lines connect first-, second-, and third-order cross peaks in respectively the upper, middle and bottom spectra

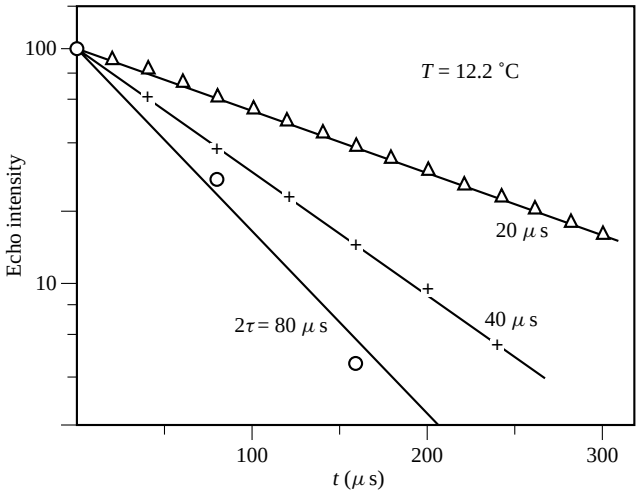

Figure 13 Semilog plots of the echo intensity versus time in quadrupole echo train experiments performed on a solution of C_6D_{12} in phase V (7 wt.%) at 12.2 °C for different pulse repetition rates as indicated

calculation requires knowledge of the magnetic interactions. When these are not known, ordinary relaxation data are not very useful. However when the transverse relaxation is measured by the Carr–Purcell sequence, or for spin $I = 1$ in liquid crystalline solvents by its quadrupole echo train analog, a determination of the rate constant can still be made if the time interval, τ, between the pulses is of the order of the mean lifetime between exchanges. In the fast-exchange regime, the transverse relaxation rate, as measured by the echo decay, is then also a function of the ratio of the exchange and pulse repetition rates.[62] For deuterons jumping between two sites of equal populations the contribution to the decay rate of the echoes in a quadrupole echo train experiment becomes[32,35]

$$\frac{1}{T_{2\epsilon}} = \frac{(\Delta\omega_Q)^2}{8k}\left[1 - \frac{\tanh(2k\tau)}{2k\tau}\right] \qquad (18)$$

where $\Delta\omega_Q = \omega_Q{}^A - \omega_Q{}^B$ is the difference between the quadrupole splittings of the nuclei at the two sites.

The method was demonstrated[32] for the case of ring inversion of C_6D_{12} in the nematic phase V between 0 °C and the clearing temperature. Experimental echo intensities at 12.2 °C for different time intervals between pulses are depicted in Figure 13 and the dependence of the decay rate, $1/T_{2\epsilon}$ on the pulse repetition rate, $1/\tau$, is plotted in Figure 14 for several temperatures. Analysis of these data in terms of equation (18) yields results for k that are in good agreement with those derived from the ordinary lineshape analysis.

The method was subsequently extended to the intermediate and slow-exchange regime[35] and although not very often used it has been successfully applied to study the self-diffusion in the plastic phase of succinonitrile.[63]

9 RELATED ARTICLES

Anisotropy of Shielding and Coupling in Liquid Crystalline Solutions; Deuteron Relaxation Rates in Liquid Crystalline Samples: Experimental Methods; Liouville Equation of

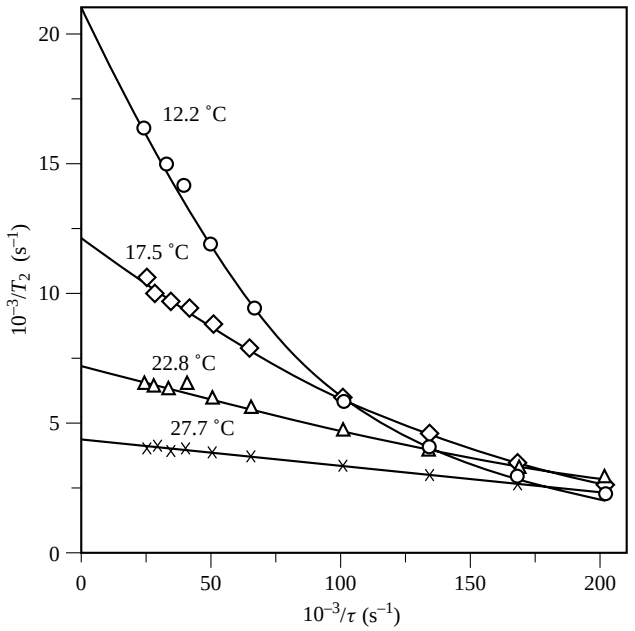

Figure 14 Plots of $1/T_{2\epsilon}$ as function of the pulse repetition rate obtained from the same solution as in Figure 13 for different temperatures. The lines are calculated using equation [18]

Motion; Liquid Crystalline Samples: Carbon-13 NMR; Liquid Crystalline Samples: Deuterium NMR; Liquid Crystalline Samples: Diffusion; Liquid Crystalline Samples: Relaxation Mechanisms; Liquid Crystalline Samples: Spectral Analysis; Liquid Crystalline Samples: Structure of Nonrigid Molecules; Liquid Crystals: General Considerations; Multiple Quantum Spectroscopy in Liquid Crystalline Solvents; Relaxation Effects of Chemical Exchange; Structure of Rigid Molecules Dissolved in Liquid Crystalline Solvents; Two-Dimensional NMR of Molecules Oriented in Liquid Crystalline Phases.

10 REFERENCES

1. H. S. Gutowsky, D. W. McCall, and C. P. Slichter, *J. Chem. Phys.*, 1953, **21**, 279.
2. W. G. Proctor and F. C. Yu, *Phys. Rev.*, 1950, **77**, 717; W. C. Dickenson, *Phys. Rev.*, 1950, **77**, 736.
3. E. L. Hahn and D. E. Maxwell, *Phys. Rev.*, 1952, **88**, 1070.
4. L. M. Jackman and F. A. Cotton (eds.), *Dynamic Nuclear Magnetic Resonance Spectroscopy*, Academic Press, New York, 1975.
5. C. S. Johnson, Jr., *Advances in Magnetic Resonance*, ed. J. S. Waugh, Academic Press, New York, 1965, Vol. 1, p. 33.
6. J. W. Emsley and J. C. Lindon, *NMR Spectroscopy Using Liquid Crystal Solvents*, Pergamon Press, Oxford, 1975.
7. Z. Luz, *Isr. J. Chem.*, 1983, **23**, 305.
8. H. M. McConnell, *J. Chem. Phys.*, 1958, **28**, 430.
9. S. Alexander, *J. Chem. Phys.*, 1962, **37**, 967.
10. S. Alexander, *J. Chem. Phys.*, 1962, **37**, 974.
11. J. I. Kaplan and G. Fraenkel, *NMR of Chemically Exchanging Systems*, Academic Press, New York, 1980.
12. G. Binsch, *J. Am. Chem. Soc.*, 1969, **91**, 1304.
13. J. Kaplan, *J. Chem. Phys.*, 1958, **28**, 278; ibid., 1958, **29**, 462.
14. A. Saupe, *Z. Naturforsch.*, 1964, **19a**, 161.
15. L. C. Snyder, *J. Chem. Phys.*, 1965, **43**, 4041.
16. Z. Luz and R. Naor, *Mol. Phys.*, 1982, **46**, 891.
17. D. Gamliel, Z. Luz, and S. Vega, *J. Chem. Phys.*, 1986, **85**, 2516.
18. P. L. Corio, *Structure of High Resolution NMR Spectra*, Academic Press, New York, 1966.
19. Z. Luz and S. Meiboom, *J. Chem. Phys.*, 1973, **59**, 275.
20. J. M. Anderson and A. C.-F. Lee, *J. Magn. Reson.*, 1970, **3**, 427.
21. Z. Luz and S. Meiboom, *J. Chem. Phys.*, 1973, **59**, 1077.
22. Z. Luz, R. Naor, and E. Meirovitch, *J. Chem. Phys.*, 1981, **74**, 6621.
23. R. Naor and Z. Luz, *J. Chem. Phys.*, 1982, **76**, 5662.
24. B. M. Fung, R. V. Sigh, and M. M. Alcock, *J. Am. Chem. Soc.*, 1984, **106**, 7301.
25. J. Afzal and B. M. Fung, *J. Chem. Phys.*, 1986, **84**, 6119.
26. D. Gamliel, Z. Luz, and S. Vega, *J. Chem. Phys.*, 1988, **88**, 25.
27. D. Gamliel, Z. Luz, A. Maliniak, R. Poupko, and A. J. Vega, *J. Chem. Phys.*, 1990, **93**, 5379.
28. R. Poupko and Z. Luz, *J. Chem. Phys.*, 1981, **75**, 1675.
29. M. E. Moseley, R. Poupko, and Z. Luz, *J. Magn. Reson.*, 1982, **48**, 354.
30. R. Poupko, H. Zimmermann, and Z. Luz, *J. Am. Chem. Soc.*, 1984, **106**, 5391.
31. C. Boeffel, Z. Luz, R. Poupko, and A. J. Vega, *Isr. J. Chem.*, 1988, **28**, 283.
32. A. J. Vega, R. Poupko, and Z. Luz, *J. Magn. Reson.*, 1989, **83**, 111.
33. C. Boeffel, Z. Luz, R. Poupko, and H. Zimmermann, *J. Magn. Reson.*, 1989, **85**, 329.
34. C. Boeffel, Z. Luz, R. Poupko, and H. Zimmermann, *J. Am. Chem. Soc.*, 1990, **112**, 7158.
35. K. Müller, R. Poupko, and Z. Luz, *J. Magn. Reson.*, 1990, **90**, 19.
36. E. Gelerinter, Z. Luz, R. Poupko, and H. Zimmermann, *J. Phys. Chem.*, 1990, **94**, 8845.
37. K. Müller, R. Poupko, and Z. Luz, *J. Magn. Reson.*, 1991, **93**, 291.
38. K. Müller, Z. Luz, R. Poupko, and H. Zimmermann, *Liq. Cryst.*, 1992, **11**, 547.
39. J. H. Davis, K. R. Jeffrey, M. Bloom, and M. I. Valic, *Chem. Phys. Lett.*, 1976, **42**, 390.
40. A. J. Vega and Z. Luz, *J. Chem. Phys.*, 1987, **86**, 1803.
41. B. Pedersen and J. Schaug, *Acta Chem. Scand.*, 1968, **22**, 1705.
42. M. Cocivera, *J. Chem. Phys.*, 1967, **47**, 3061.
43. F. A. L. Anet, A. J. R. Bourn, and Y. S. Lin, *J. Am. Chem. Soc.*, 1964, **86**, 3576.
44. F. A. L. Anet, *J. Am. Chem. Soc.*, 1962, **84**, 671.
45. R. C. Hewitt, S. Meiboom, and L. C. Snyder, *J. Chem. Phys.*, 1973, **58**, 5089.
46. L. C. Snyder and S. Meiboom, *J. Chem. Phys.*, 1973, **58**, 5096.
47. S. Meiboom, R. C. Hewitt, and Z. Luz, *J. Chem. Phys.*, 1977, **66**, 4041.
48. R. Poupko, Z. Luz, and H. Zimmermann, *J. Am. Chem. Soc.*, 1982, **104**, 5307.
49. W. S. Warren, D. P. Weitekamp, and A. Pines, *J. Chem. Phys.*, 1980, **73**, 2084.
50. G. Drobny, A. Pines, S. Sinton, D. P. Weitekamp, and D. Wemmer, *Faraday Symp. Chem. Soc.*, 1978, **13**, 49.
51. A. Wokaun and R. R. Ernst, *Chem. Phys. Lett.*, 1977, **52**, 407.
52. H. Zimmermann, *Liq. Cryst.*, 1989, **4**, 591.
53. Reference 4, Chap. 14.

54. J. F. M. Oth, K. Müllen, J.-M. Gilles, and G. Schröder, *Helv. Chim. Acta*, 1974, **57**, 1415.
55. R. Poupko, Z. Luz, A. J. Vega, and H. Zimmermann, *J. Chem. Phys.*, 1987, **86**, 5358.
56. C. S. Yannoni, *J. Am. Chem. Soc.*, 1970, **92**, 5237.
57. J. Jeener, B. H. Meier, P. Bachmann, and R. R. Ernst, *J. Chem. Phys.*, 1979, **71**, 4546.
58. C. Schmidt, S. Wefing, B. Blümich, and H. W. Spiess, *Chem. Phys. Lett.*, 1986, **130**, 84.
59. C. Schmidt, B. Blümich, and H. W. Spiess, *J. Magn. Reson.*, 1988, **79**, 269.
60. C. Schmidt, B. Blümich, S. Wefing, S. Kaufmann, and H. W. Spiess, *Ber. Bunsenges. Phys. Chem.*, 1987, **91**, 1141.
61. D. K. Dalling, D. M. Grant, and L. F. Johnson, *J. Am. Chem. Soc.*, 1971, **93**, 3678.
62. Z. Luz and S. Meiboom, *J. Chem. Phys.*, 1963, **39**, 366.
63. A. Golemme, S. Zamir, R. Poupko, H. Zimmermann, and Z. Luz, *Mol. Phys.*, 1994, **81**, 569.

Biographical Sketches

Raphy Poupko. *b* 1936. B.Sc., 1963, M.Sc., 1965, D.Sc. 1969, Technion—Israel Institute of Technology. Senior research fellow, Weizmann Institute of Science, 1970–present. Postdoctoral training at Southampton University (with G. Luckhurst), 1973–1974; UCSD, San-Diego, 1977–78; University of Paris, Orsay, 1987; M.P.I. für Medizinische Forschung, AG. Molekülkristalle, Heidelberg, 1993. Research activities: dynamic NMR, liquid crystals, solid state.

Zeev Luz. *b* 1932. M.Sc., 1957, Hebrew University, Jerusalem, Ph.D., 1961, The Weizmann Institute of Science, Rehovot. Postdoctoral training at Bell Telephone Laboratories (with Saul Meiboom), 1961–64. Since 1964, at The Weizmann Institute of Science. Successively scientist, senior scientist, associate, and full professor. Oxford University, 1966–67; Bell Laboratories, Murray Hill, 1971–72; University of California, Berkeley, 1976–77; DuPont, Wilmington, 1984–85; MPI f. Poly. Research, Mainz, 1990–91. Approx. 220 publications. Research specialties: dynamic NMR, liquid crystals, solid state.

Dynamics in Solid Organic Compounds: Intramolecular Motions

Frank G. Riddell

The University of St Andrews, St Andrews, UK

1 Introduction 1
2 Line Shape Methods 1
3 Spin Lattice Relaxation Time Methods 2
4 Maximum Dipolar Broadening 4
5 $T_{1\rho}$ Measurements 5
6 ^{2}H Quadrupolar Echo Methods 7
7 Measurement of Temperature in MAS Experiments 8
8 Related Articles in this Volume 8
9 Related Articles in Volumes 1–8 8
10 References 8

1 INTRODUCTION

Conventional crystallographic representations of molecules in solids give the impression that the molecules are held rigidly in place in the crystal as static motionless bodies. However, molecules and their component groups and atoms are certainly not motionless in solids. Molecules in solids are dynamic entities with a wide range of different molecular motion types.

Although most types of molecular motion are generally slower in solids than in liquids, they may have an important role in determining the macroscopic properties of solid materials. This applies to all solids irrespective of their degree of crystallinity. For example, the mechanical properties of important materials such as polymers are closely related to their microscopic structures and molecular motions. In addition, the conductivity of solid polymer electrolytes and the electrical properties of conducting polymers originate from motions at the molecular level. It becomes important, therefore, to gain an understanding of the nature of these motions in all types of solids and their relative rates and activation energies.

Several physical techniques can be employed to examine these molecular dynamics including the measurement and interpretation of anisotropic displacement parameters from diffraction techniques, Raman scattering, Brillouin scattering and dielectric relaxation. However, the most versatile technique is NMR spectroscopy. NMR is particularly powerful because by judicious choice of the nucleus to be observed and the NMR technique to be employed a wide range of time scales for molecular motions are available.[1] A general rule of thumb is that if the frequency, or time scale for a nuclear interaction is similar to that of the molecular process occurring, the molecular process will modulate the NMR interaction, which will give rise to an observable effect in most cases. Since many more NMR interactions are present in solids than in solution (where they are averaged to zero by rapid isotropic molecular tumbling) observation of molecular motions in solids is greatly facilitated. Moreover, both broad line (static samples) and high resolution (magic angle spinning) methods are available. Such processes have included, but are not restricted to, rotations or displacements of whole molecules; segmental motions in polymer chains; conformational dynamics in molecules such as bond rotations, ring inversions and pseudorotations; molecular rearrangements such as sigmatropic rearrangements and dynamic tautomerism; and hydrogen bond exchange processes.

An alternative way in which NMR can be used to measure the kinetics of molecular processes is to create a magnetic label at one site (chemical shift) and watch it being transferred to another. Such methods include inversion and saturation transfer and 2D EXSY spectroscopy. These measurements are made in real time and consequently their time scale is dependent on the nuclear relaxation times involved. This article reviews several diverse applications of solid-state NMR spectroscopy falling into the categories described above. Table 1 summarizes the major methods, their origins, and the typical rate ranges that they can be employed to study.

It is interesting to compare the kinetics of processes happening in the solid state with those observed in solution. In many cases involving conformational rate processes the rates in solids are considerably slower than those observed in solution. This is because of the additional constraints imposed upon such process by the neighboring molecules in the lattice. These constraints are not present in solution leading to lower energies of activation. This effect has been referred to as the principal of least distress.[3] On the other hand for intramolecular tautomerization processes in which hydrogen atoms travel short distances such effects are negligible.

2 LINE SHAPE METHODS

Line shape methods have been used extensively in high resolution solution state NMR for many years, and are also available in solids under conditions of magic angle spinning (MAS). In particular ^{13}C CP/MAS NMR has yielded much useful information. Line shape effects occur in the exchange region where the chemical shift difference between sites in a molecule is of the same order as the rate at which they are exchanging. The basic theory for these effects was given by McConnell,[2] and often the modified Bloch equations are used for line shape calculations. Many computer programs are available for line shape calculations.

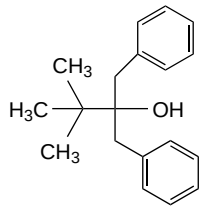

(1)

Table 1 Widely used methods for studying dynamic processes in solids

Method	Approximate rate range	Outcomes
T_1	Near Larmor frequency 10^6–10^9 Hz	Frequency of motion
$T_{1\rho}$	Near spin lock frequency 10^3–10^6 Hz	Frequency and often mode of motion
Line shape	Near chemical shift difference 10–10^4 Hz	Frequency of motion
2D EXSY	Near $1/T_1$ 10^{-2}–10 Hz	Frequency of motion
Magnetization transfer	Near $1/T_1$ 10^{-2}–10 Hz	Frequency of motion
^{2}H quadrupole echo spectra	Near quadrupole coupling constant 125– kHZ	Frequency and often mode of motion

Line shape changes due to dynamic effects in ^{13}C CP/MAS spectra are illustrated very simply in Figure 1.[3] The changes arise from the *t*-butyl group rotation in **(1)**. At low temperatures rotation of the *t*-butyl group is slow (i.e., rate of rotation is $\ll \delta\nu$(hz)) and three methyl resonances are seen. The coalescence of the three methyls into a single peak is observed at around 293 K ($\Delta G_c^{\neq} = $ ca 55 kJ mol^{-1}) The solution state coalescence takes place at approximately 183 K ($\Delta G_c^{\neq} = $ ca 38 kJ mol^{-1}). The lifting of the degeneracy of two of the methyl groups in solution is due to molecular dissymetry in the crystal lattice. The increase in the activation energy by around 17 kJ mol^{-1} is due to the additional constraints imposed upon the process in the solid by the neighboring molecules.

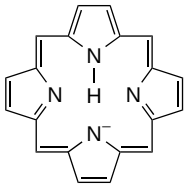

(2)

An alternative, both in the nucleus employed and the result obtained, is seen in Figure 2.[4] This shows the line shape changes in the ^{15}N CP/MAS spectra due to hydrogen exchange between the nitrogens in the porphyrin anion **(2)** encased in a solid matrix. In contrast to the example given above the degeneracy of the exchange seen in solution is not lifted in the solid state with only three ^{15}N resonances being observed. The rates of hydrogen transfer are very similar to those determined in solution. In this case there is no effect from neighboring molecules as the exchange is buried deep inside the molecule.

An example of six-membered ring inversion between two unequal sites is seen in Figure 3.[5] In this case the dynamic spectral effects arise from ring inversion of cyclohexanol encased in a thiourea inclusion compound and were obtained by a ^{13}C single pulse MAS technique not CP/MAS. The smaller set of peaks in the low temperature spectra arise from the axial conformation. The free energy of activation for the ring inversion process (51 kJ mol^{-1} (eq to ax)) and the free energy difference (ca. 2.5 kJ mol^{-1}) are close to those observed for the compound in non-hydrogen bonding solvents (50 kJ mol^{-1} (eq to ax)) and (ca. 2.1 kJ mol^{-1}). Interestingly for several other mono-substituted cyclohexanes in thiourea inclusion compounds very different conformational parameters are obtained from those of the molecules free in solution.

In the above examples there were no spinning side bands in the high resolution solid state ^{13}C spectra. Where there is a spinning sideband manifold, line shape analysis in principle requires consideration of the whole sideband pattern and not just the peaks at the isotropic chemical shifts. This is seen in a ^{13}C CP/MAS study of the sigmatropic Cope rearrangement of bullvalene in the solid state.[6,7] Because the crystal structure of bullvalene as determined by X-ray crystallography is very highly ordered it was originally thought that the Cope rearrangement was not taking place in the solid. However, NMR studies have shown that in the solid state the molecule of bullvalene undergoes a sigmatropic rearrangement followed by a reorientation to regain the original molecular orientation in the solid. This process is given the rate constant k_c. Accompanying this process is a 3-fold rotation of the molecules as a distinct process given the rate constant k_r. These processes are shown in Figure 4 and the observed CP/MAS spectra are shown in Figure 5.

If the rotation were the only process the resonance for C4 would remain unaffected. The fact that this line broadens less rapidly than the others as the temperature is increased indicates the existence of the two processes and the line shape patterns at varying temperatures can be fitted to a process involving the two rate constants k_c and k_r. It should be noted that the spinning sidebands are observed for the superimposed resonances of C2 and C3 and that these form part of the coalescence pattern. Extracted Arrhenius activation energies for the Cope rearrangement and the three-fold rotation are found to be 63 and 88 kJ mol^{-1} respectively.

3 SPIN LATTICE RELAXATION TIME METHODS

Spin lattice relaxation, designated by the relaxation time T_1, and relaxation in the rotating frame, designated by the relaxation time T_1 can form excellent probes for molecular motions in very different regions of molecular dynamics. The stimulation of NMR transitions at the heart of these relaxation processes occurs when the nucleus interacts with fluctuating fields inside the sample. There are two important fluctuating fields. The first is a fluctuating magnetic field that can interact with the nuclear magnetic moment. The second is a fluctuating electric field gradient (EFG) that can interact with the electric quadrupole moment of the nucleus (if it possesses one). Only quadrupolar nuclei ($I > 1/2$) have electric quadrupole moments. In all cases the frequency of the fluctuating field must be at or close to the field in which the nuclei are held. In addition, the exchange process to be studied must be the exclusive or principal cause of the nuclear relaxation.

For heteronuclei three cases can be identified: (i) static powders, (ii) powders being spun at the magic angle, and (iii) powders where longitudinal relaxation is isotropically

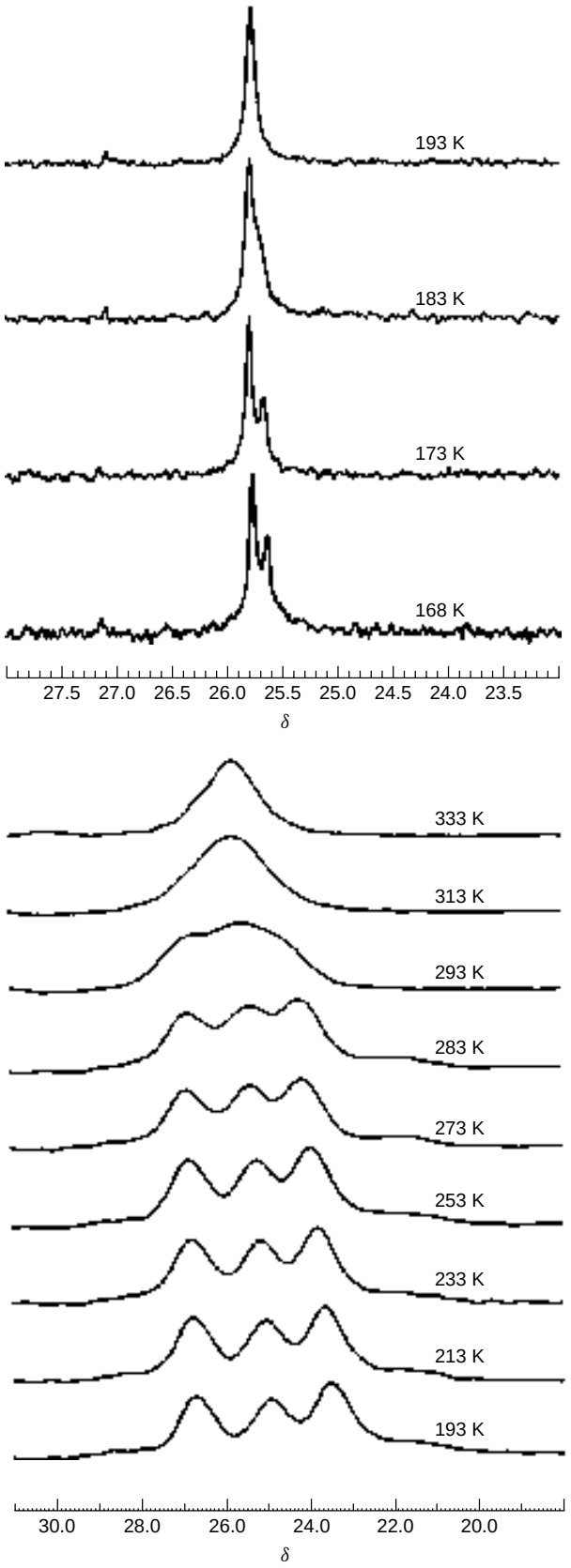

Figure 1 125.758 MHz ^{13}C line shape changes at variable temperature for **(1)** in the solid (CP/MAS) (lower set) and solution states. The changes are due rotation of the *tert*-butyl group. Reproduced with permission from Ref.[5]

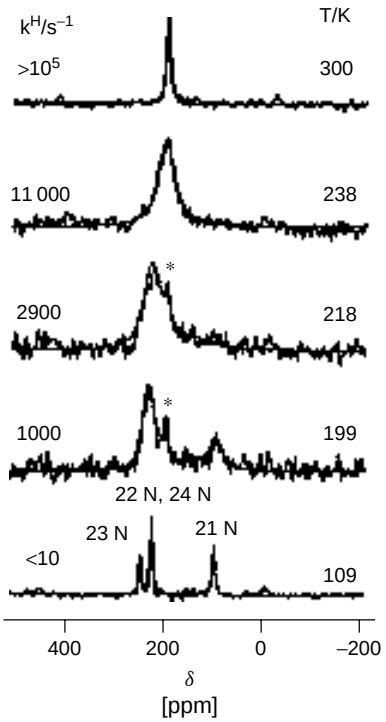

Figure 2 Line shape changes in the 9.12 MHz ^{15}N CP/MAS spectra of **(2)** at variable temperature. The changes are due to hydrogen exchange between the nitrogens in the porphyrin anion. Reproduced with permission from Figure 5 in Ref.[4]

averaged by magnetization transfer. In (i) relaxation is multiexponential and consequently difficult to evaluate. In (iii) relaxation is truly exponential with a single relaxation time T_1, which is related in a straightforward way to the dipolar interaction(s) and the equilibrium and rate constants, but this is experimentally very difficult to obtain. In contrast (ii) represents an ideal compromise – relaxation is quasi exponential and is governed to a good approximation by the dipolar interaction(s), rate and equilibrium constants. Rates of ultrafast exchanges can be measured by this technique. For example, this technique was employed by Hoelger et al.[8] to study the hydrogen exchange dynamics in ^{15}N labelled dimethyldibenzyltetraaza[14]annulene (see Figure 6).[8] The hydrogen transfer rates that were measured were in the range $10^6-10^8\ s^{-1}$.

Cross polarization is often used to generate the magnetization needed for T_1 measurements for ^{13}C or ^{15}N, for example. Under these circumstances the pulse sequence of Torchia is in widespread use.[9] In this sequence for ^{13}C the ^{13}C magnetization is generated in an enhanced form by a cross polarization sequence and then an inversion recovery type sequence is used to follow the recovery of the magnetization as a function of time. During the evolution period the ^{1}H nuclei are decoupled by continuous phase irradiation to avoid the possibility of their dephasing the ^{13}C magnetization. The FID is then collected accompanied by high power ^{1}H decoupling.

For ^{1}H in organic solids the spins are strongly coupled via a spin diffusion process and consequently all have the same T_1 value. Thus no information about specific sites can be obtained even if separate peaks for these sites can be seem by special spectral techniques, for example CRAMPS.

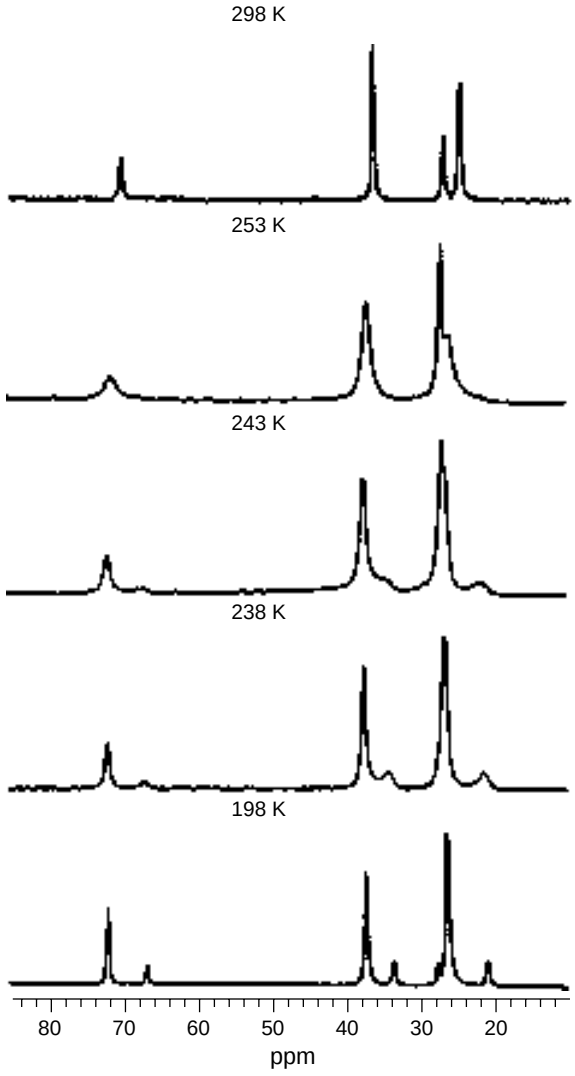

Figure 3 125.758 MHz ^{13}C line shape changes due to ring inversion of cyclohexanol in a thiourea inclusion complex (single pulse MAS spectra). Reproduced with permission from Figure 2 in Ref.[5]

This greatly decreases the utility of ^{1}H T_1 measurements for characterizing molecular motions. They have, however, been applied in simple cases in which all the protons are equivalent such as molecular rotation in benzene.

For ^{2}H T_1 is the most unambiguous relaxation time as it depends exclusively on molecular motion. The relaxation of quadrupolar nuclei such as ^{2}H depends upon the interaction between the quadrupole moment of the nucleus and the electric field gradient it experiences. Fluctuating electric field gradients produce spin lattice relaxation of the ^{2}H nucleus and the correlation time for molecular motion can be inferred if details of the quadrupole interaction are known. Modulation of the electric field gradient in molecular solids is usually produced by rotational or segmental motions. This technique has proved of particular value in chain-like structures, e.g., polymers or lipids where selective deuteriation along the chain can characterize the motion of different segments. Measurement of ^{2}H relaxation times for broad powder patterns can be troublesome and is often best achieved by a saturation recovery technique using the pulse sequence of Hirschinger et al.[10]

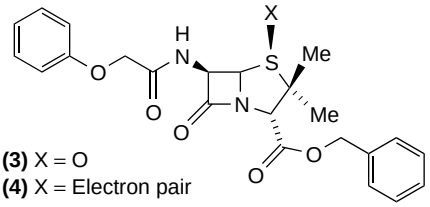

(3) X = O
(4) X = Electron pair

For powder samples, however, its interpretation is complicated by the anisotropy of T_1 because the relaxation time depends upon the orientation of the unique principal axis (C–D bond) with respect to the external magnetic field. This means that different parts of the sample relax with different rates. Fortunately, in general, this effect is small and the powder average T_1 often describes the relaxation process in the crystal satisfactorily.[11]

For the spin-lattice relaxation of ^{2}H the dependence of T_1 on the correlation time is given by

$$\frac{1}{T_1} = C\left\{\frac{\tau_c}{1+\omega_o^2\tau_c^2} + \frac{4\tau_c}{1+4\omega_o^2\tau_c^2}\right\} \tag{1}$$

Two regions occur depending on the magnitude of the correlation time. On the low temperature side of the T_1 minimum the rate of the molecular motion is slower than at the minimum, i.e., $\omega_o\tau_c \gg 1$. Combining equation (1) with the Arrhenius equation, it can be seen that the natural logarithm of the spin-lattice relaxation time depends on inverse temperature

$$\ln(T_1) = \frac{E_a}{RT} + \ln\left\{\frac{\omega_o^2 A}{2C}\right\} \tag{2}$$

On the high temperature side of the minimum the motion is faster than at the minimum, i.e., $\omega_o\tau_c \ll 1$

$$\ln(T_1) = \frac{E_a}{RT} - \ln(5CA) \tag{3}$$

Thus in both cases the Arrhenius activation energy (E_a) can be obtained from the slope of a plot of $\ln(T_1)$ vs $1/T$.

In certain cases, however, there is also a dependence of T_1 upon the amplitude of the motion. In these cases the parameter E_a is called the apparent activation energy.

4 MAXIMUM DIPOLAR BROADENING

In high resolution CP/MAS NMR, ^{1}H dipolar decoupling is extensively used to remove any remaining dipolar and J coupling from ^{1}H to heteronuclei. Invariably this is done by a single frequency placed near the centre of the ^{1}H resonance. Typical values for the dipolar decoupling field are in the region 50–100 kHz. If there is a molecular motion or exchange taking place at or near this frequency it can interfere with the efficiency of the decoupling and this causes an increase in the line widths of the affected resonances. This effect was first noted by Rothwell and Waugh.[12] In effect the frequency of the incoherent molecular motion is interfering with the coherent decoupling field reducing its efficiency and broadening the line. Maximum dipolar broadening is most often observed as an increase followed by a reduction in line width as the

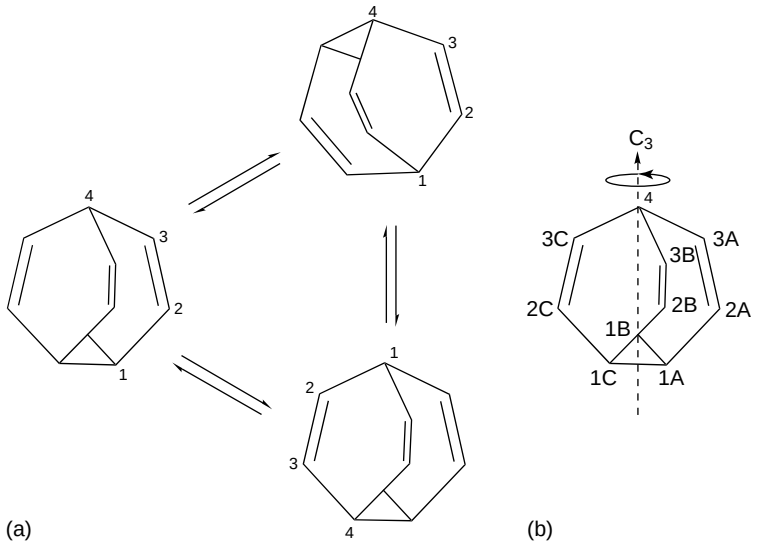

Figure 4 The sigmatropic rearrangement and rotational processes in solid bullvalene that give rise to the dynamic spectral changes seen in Figure 5. Reproduced with permission from Figure 1 in Ref.[6]

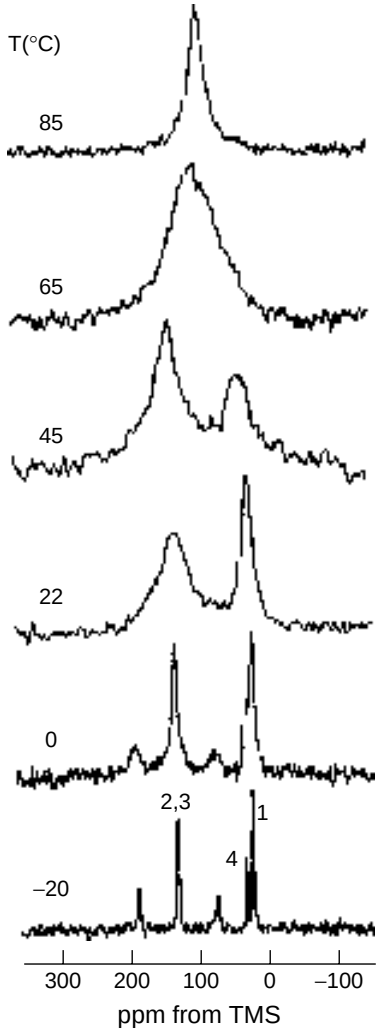

Figure 5 75.47 MHz ^{13}C CP/MAS spectra at variable temperature arising from the dynamic processes inside solid bullvalene illustrated in Figure 4. Reproduced with permission from Figure 2 in Ref.[6]

temperature is varied. A single rate constant at the temperature of maximum broadening may be extracted in the region $5-10 \times 10^4\ s^{-1}$.

An example of the use of maximum dynamic broadening may be found in work by Twyman and Dobson.[13] They showed that a combination of line shape analysis, maximum dipolar broadening and magnetization transfer could be used to study the phenyl rotation in the compounds **(3)** and **(4)** over a wide range of rates of rotation.

5 $T_{1\rho}$ MEASUREMENTS

Maximum dynamic broadening is, however, generally not the best way to study molecular motions in this frequency range in CP/MAS spectra. Measurements of $T_{1\rho}$ are generally superior.[14] In the $T_{1\rho}$ experiment the magnetization to be studied is flipped from equilibrium through 90° to take the magnetization into the x′y′ plane, where it is spin locked along a particular axis.[15] Thus a 90° +x′ pulse placing the magnetization onto the +y′ axis would be followed by a spin lock field (ω_1) (ca. 50–100 kHz) being applied along the y′ axis. The time course of the decay of the spin locked magnetization gives the relaxation rate in the rotating frame with time constant $T_{1\rho}$. In general the 90° pulse would be applied by a cross polarization sequence in which the ^{1}H and X nucleus fields are matched. The same fields would be used for spin locking (X) and for decoupling (^{1}H). This makes the $T_{1\rho}$ method sensitive in the same region as maximum dipolar broadening.

In principle the spin lock frequency can be varied to probe different rates of molecular motion. In practice dynamic information is more readily obtained by following the variation of $T_{1\rho}$ with temperature than by varying the spin lock field.

^{13}C $T_{1\rho}$ can be modulated both by molecular motions and by the ^{1}H spin diffusion process

$$\frac{1}{^{13}\mathrm{C}\,T_{1\rho}} = \frac{1}{^{13}\mathrm{C}\,T_{1\rho\,\mathrm{spin\ lattice}}} + \frac{1}{T_{\mathrm{CH}}(\mathrm{ADRF})} \qquad (4)$$

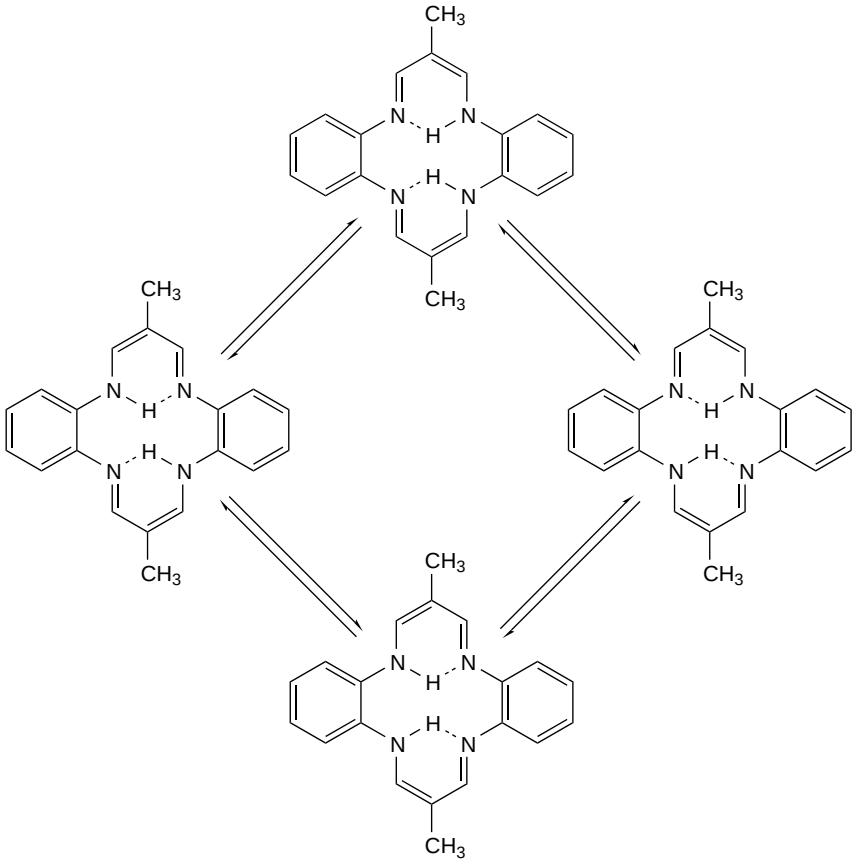

Figure 6 The ultrafast hydrogen bond exchanges in dimethyldibenzotetraaza[14]annulene studied by ^{15}N T_1 relaxation methods

^{13}C $T_{1\rho}$ spin lattice arises from modulation of the spin locking field by the molecular motion. T_{CH}(ADRF) comes from modulation of the dipolar interaction by the spontaneous rigid lattice proton fluctuations (spin diffusion). In practice the latter effects are generally found to be negligible with spin locking fields in excess of ca. 35 kHz. Also in practice $T_{1\rho}$ measurements in CP/MAS NMR are generally made with spin lock fields that are the same as those used for cross polarization and are 50 kHz or greater.

For a dipolar interaction between two unlike spins, e.g., ^{13}C and ^{1}H

$$\frac{1}{T_{1\rho}} = \frac{B^2\tau}{(1+\omega_1^2\tau^2)} \tag{5}$$

where ω_1 is the frequency of ^{13}C in the spin lock field, τ is the rotational correlation time for the molecular motion causing the relaxation (rotational correlation time), and B^2 is a measure of the ^{13}C–^{1}H dipolar interaction.[16] B^2 may be calculated for a particular model of motion and geometry from the equation given by Abragam.[17] The rate of the molecular motion will vary with temperature T and therefore $T_{1\rho}$ will have a temperature dependence. Equation (5) predicts that $T_{1\rho}$ will have a minimum at the temperature at which $\omega_1\tau = 1$.

Hence at the minimum value of $T_{1\rho}$, $\omega_1\tau = 1$ and B^2 conforms to

$$B^2 = \frac{2}{(T_{1\rho})_{\min}\tau} \tag{6}$$

Thus the minimum value of $T_{1\rho}$ allows an experimental determination of B^2. Two things follow from this. First the values of τ at each temperature may be extracted by solving the appropriate quadratic equation. Secondly the mode of motion may be checked by comparison of the calculated and experimental values of B^2.[18]

The use and validity of $T_{1\rho}$ methods is illustrated in a study of the rotation of both *tert*-butyl groups in **(5)**. Line shape analysis in the temperature range 202–233 K and $T_{1\rho}$ measurements in the temperature range 224–320 K were carried out.

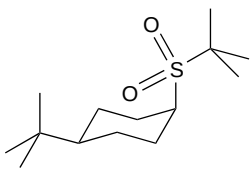

(5)

If the reductions in ^{13}C $T_{1\rho}$ in the *tert*-butyl groups arise from group rotations then four predictions can be made.

- Both the central and the methyl carbons in the same *tert*-butyl group should show $T_{1\rho}$ minima at the same temperature.
- For a constant geometry of *tert*-butyl groups the $T_{1\rho}$ minima should be the same for both groups.

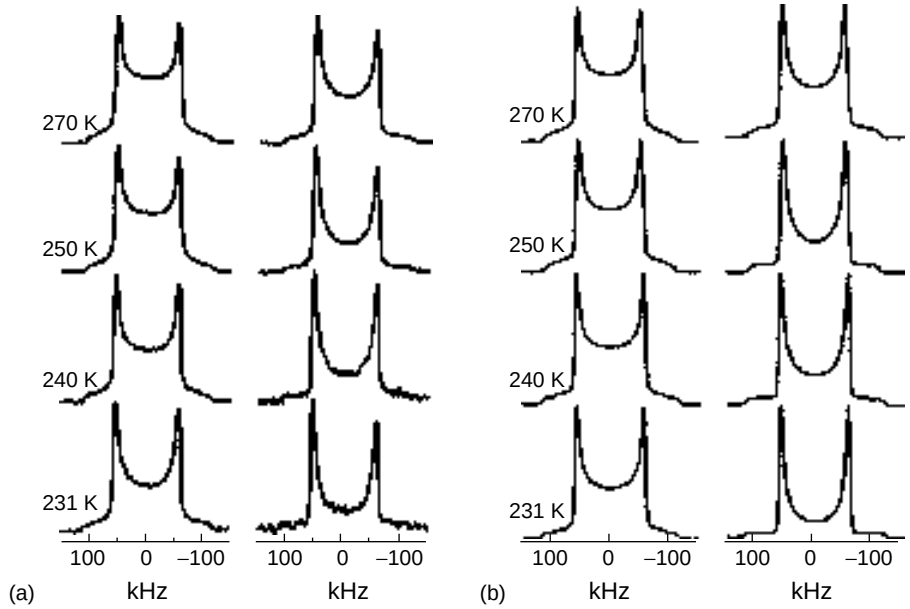

Figure 7 Observed (a) and calculated (b) 76.773 MHz ^{2}H quadrupole echo spectrum of 1,1,6,6-d_4-hexane-1,6-diyl bis(*p*-nitrobenzoate) at varying temperatures. The changes arise from librational motions of the CD_2 groups. Refocusing delays are 20 (a) and 120 μs (b). Reproduced with permission from Figure 6 in Ref.[20]

- Rate constants determined from the $T_{1\rho}$ data and the line shape analyses should fall on the same Eyring or Arrhenius plots.
- Experimentally determined B^2 values for the methyl and quaternary carbons should agree with those derived from calculation.

All four predictions are found to be correct.[16]

The same group went on to examine a wide variety of molecular motions in crystalline organic compounds including the related rotations of trimethylammonium and trimethylphosphonium groups. Interestingly and satisfyingly for the trimethylphosphonium group the data from the ^{13}C line shape changes, the ^{13}C $T_{1\rho}$ data and the ^{31}P $T_{1\rho}$ data all fitted the same activation plot.[19]

One further important point about $T_{1\rho}$ methods is that the measure of the dipolar interaction B^2 depends upon the geometry of the molecular motion.[17] In principle this allows differentiation between alternative models for the molecular motion. For example, in *trans*-1,2-cyclopentanediol this method allowed a differentiation to be made between a whole molecule rotation process and an internal ring pseudorotation process with the latter process being the more likely origin of the experimental measurements.[18]

6 ^{2}H QUADRUPOLAR ECHO METHODS

^{2}H quadrupolar echo line shape studies have been perhaps the widest used NMR technique for studying molecular motions in solids. Although ^{2}H incorporation in the molecule is required the technique has the compensation that information about both the frequency and geometry of the molecular motion can be obtained. Typically ^{2}H spectra of solids are a few hundred kilohertz wide. In the absence of molecular motions the spectrum is a Pake doublet with the horns of the pattern separated by the quadrupolar coupling constant. For a C–D bond this is ca. 125 kHz. As the frequencies of the molecular motions approach the value of the quadrupolar coupling constant the line shape changes. Figure 7 shows typical changes in the quadrupole echo spectra for 1,1,6,6-d_4-hexane-1,6-diyl bis(*p*-nitrobenzoate) **(6)**.[20] The line shape depends upon the motion of the C–D bond and can be calculated on the basis of frequency of the molecular motion and various possible geometric modes that are possible.[21] Conclusions can then be drawn.

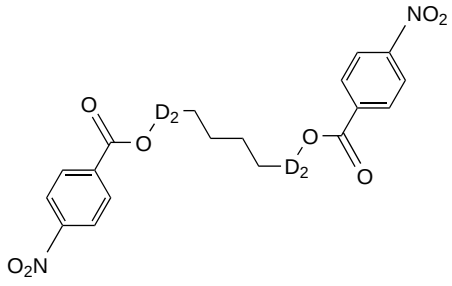

(6)

With line shapes of this width the free induction delays can be very short and some or all of the FID can be lost in the receiver dead time delay. This would lead to weak and distorted signals. To overcome this the quadrupole echo sequence is used in which a second $\pi/2$ pulse is applied in quadrature with the first at time τ. This results in refocussing of the magnetization and the formation of an echo at approximately 2τ after the first pulse.[22] By starting the FT at the echo maximum one does not need to worry about signal that has been lost during the receiver dead time and undistorted spectra may be obtained.

An additional complication is that artifacts can be caused by the finite length of the $\pi/2$ pulse width. This can lead to uneven excitation of the spectrum, to a feed through signal or to a virtual FID. Fortunately the program MXET1 that is most often used for the simulation of 2H quadrupolar echo spectra includes a correction factor for the $\pi/2$ pulse width meaning that correct spectra can be calculated.[23]

Finally, for a more certain assignment between different models of motion it is important that spectra are measured with different refocusing delays for comparison with simulated spectra. With longer delays more spectral intensity is lost and the measurement of quadrupole echo spectra in the intermediate exchange regime can become very time consuming for long refocusing delays since the echo intensity decays exponentially with the refocusing delay. In addition to the motional effects (T_2) in the intermediate exchange region the echo intensity is also decreased by dipolar couplings between deuterons and protons as the quadrupole echo sequence fails to refocus these couplings. Dipolar couplings also broaden the line shape and their effect can be taken into account by multiplying the free induction decay by a Gaussian broadening function that is a few kilohertz wide. Such a broadening has a fairly small effect on the line shape but the decrease in the echo intensity during the refocusing delay is considerable. For refocusing delays of 20 μs and 160 μs and an effective 2 kHz broadening it can be shown that the effect is an echo reduction of 0.67, and for an effective 3 kHz broadening the corresponding reduction would be 0.40. Thus, dipolar couplings reduce the echo intensity to about half its original intensity in addition to the T_2 effects in the intermediate exchange region. Thus for delays of 20 μs and 160 μs an echo reduction factor of ca. 0.5 is expected. If the echo reduction factor falls below this it is indicative of T_2 effects becoming important during the refocusing delay. If the echo reduction factor is greater than this it seems likely that the dipolar couplings between deuterons and protons are becoming less important. Either way an additional pointer is given to assist interpretation.[24] Figure 7 shows the effect of the echo reduction factor in the quadrupole echo spectra of 1,1,6,6-d_4-hexane-1,6-diyl bis(*p*-nitrobenzoate) **(6)**.

The angle of the C–D bond motion can be measured directly from a two-dimensional deuterium exchange experiment.[25] In the absence of molecular motion the 2D exchange spectrum consists of a Pake doublet along the diagonal. Molecular motions in the slow exchange regime where the correlation time is longer than a millisecond induce intensity off the diagonal. These off-diagonal ridges are very characteristic to motional modes and also in favourable cases allow direct measurements of the angle of the C–D bond motion to be made. Slowly moving deuterons, however, tend to relax very slowly and so in the absence of any additional relaxation modes these long relaxation times can make this technique very time-consuming.

7 MEASUREMENT OF TEMPERATURE IN MAS EXPERIMENTS

The establishment of temperatures in MAS NMR experiments is an important but difficult problem.[26] It is important because accurate temperatures are needed if activation parameters are to be determined for a particular process. It is difficult because it has been demonstrated by several groups that MAS causes the sample to heat. This heating is probably due to friction. It has been proposed and demonstrated that the heating varies with the square of the spinning speed.[26,27] Thus, at high spinning speeds careful temperature calibration becomes even more important. Several methods have been proposed for the measurement of sample temperatures. Probably the most reliable is to follow accurately known phase changes that show changes in the spectra through the transition.[26] Using this method it is possible to reliably calibrate a probe/temperature controller combination.

8 RELATED ARTICLES IN THIS VOLUME

Dynamics of Hydrogen Transfer in Liquids and Solids.

9 RELATED ARTICLES IN VOLUMES 1–8

Chemical Exchange Effects on Spectra, Volume 2; Cross Polarization in Rotating Solids: Spin-1/2 Nuclei, Volume 3; Deuterium NMR in Solids, Volume 3; Dynamic Nuclear Polarization & High-Resolution NMR of Solids, Volume 3; Magic Angle Spinning, Volume 5; Relaxation Effects of Chemical Exchange, Volume 6.

10 REFERENCES

1. K. D. M. Harris and A. E. Aliev, *Chem. Br.*, 1995, **31**, 132.
2. F. G. Riddell, S. Arumugam, and J. E. Anderson, *J. Chem. Soc., Chem. Commun.*, 1991, 1525–1527.
3. H. M. McConnell, *J. Chem. Phys.*, 1958, **28**, 430.
4. J. Braun, R. Schwesinger, P. G. Williams, H. Morimoto, D. E. Wemmer, and H. H. Limbach, *J. Am. Chem. Soc.*, 1996, **118**, 11 101–11 110.
5. A. E. Aliev and K. D. M. Harris, *J. Am. Chem. Soc.*, 1993, **115**, 6369.
6. J. J. Titman, Z. Luz, and H. W. Spiess, *J. Am. Chem. Soc.*, 1992, **114**, 3765.
7. Z. Luz, R. Poupko, and S. Alexander, *J. Chem. Phys.*, 1993, **99**, 7544.
8. C. G. Hoelger, B. Wehrle, H. Benedict, and H. H. Limbach, *J. Phys. Chem.*, 1994, **98**, 843–851.
9. D. A. Torchia, *J. Magn. Reson.*, 1978, **30**, 613–616.
10. J. Hirschinger, H. Miura, K. H. Gardner, and A. D. English, *Macromolecules*, 1990, **23**, 2153–2169.
11. D. A. Torchia and A. Szabo, *J. Magn. Reson.*, 1982, **49**, 107.
12. W. P. Rothwell and J. S. Waugh, *J. Chem. Phys.*, 1981, **74**, 2721.
13. J. M. Twyman and C. M. Dobson, *J. Chem. Soc., Chem. Commun.*, 1988, 786.
14. D. C. Ailon, in 'Encyclopedia of NMR', eds D. M. Grant and R. K. Harris, Wiley: Chichester, 1996, vol. 8, p. 4874.
15. A. J. Vega, *J. Magn. Reson.*, 1985, **65**, 252–267.
16. F. G. Riddell, S. Arumugam, K. D. M. Harris, M. Rogerson, and J. H. Strange, *J. Am. Chem. Soc.*, 1993, **115**, 1881.
17. A. Abragam, 'Principles of Nuclear Magnetism', Oxford University Press: Oxford, 1961.
18. F. G. Riddell, K. S. Cameron, S. A. Holmes, and J. H. Strange, *J. Am. Chem. Soc.*, 1997, **119**, 7555–7560.
19. F. G. Riddell, M. Rogerson, W. B. Turnbull, and F. Fülöp, *J. Chem. Soc. Perkin II*, 1997, 95.

20. J. K. Kujanpää and F. G. Riddell, *J. Chem. Soc. Perkin II*, 2000, 2225–2231.
21. A. K. Roy and P. T. Inglefield, *Prog. Nucl. Magn. Reson. Spectrosc.*, 1990, **22**, 569–603.
22. K. Müller, P. Meier, and G. Kothe, *Prog. Nucl. Magn. Reson. Spectrosc.*, 1985, **17**, 211–239.
23. M. S. Greenfield, A. D. Ronemus, R. L. Vold, R. R. Vold, P. D. Ellis, and T. E. Raidy, *J. Magn. Reson.*, 1987, **72**, 89–107.
24. For a more detailed description of the use of echo reduction factors see J. Kujanpää, PhD thesis, St Andrews, 1999.
25. H. W. Spiess, *Chem. Rev.*, 1991, **91**, 1321–1338.
26. F. G. Riddell, R. A. Spark, and G. V. Günther, *Magn. Reson. Chem.*, 1996, **34**, 824–828.
27. F. D. Doty and P. D. Ellis, *Rev. Sci. Instrum.*, 1981, **52**, 1868.

Biographical Sketch

Frank G. Riddell, *b* 1940. Studied chemistry at the University of Liverpool 1958–65, Ph.D., 1965, Liverpool, with M. J. T. Robinson. Ciba research fellow, Institut de Chimie, Université de Strasbourg, France with J. M. Lehn, 1965–67. Lecturer, Senior Lecturer and Reader, University of Stirling 1967–88. Reader, University of St Andrews since 1988. Approx. 150 publications nearly all involving the application of NMR spectroscopy to the solution of problems in organic and biological chemistry, particularly those related to molecular conformation, conformational dynamics and membrane transport.

Dynamics of Hydrogen Transfer in Liquids and Solids

Hans-Heinrich Limbach

Freie Universität Berlin, Berlin, Germany

1 Introduction 1
2 Single H/D/T Transfer Along Weak Hydrogen Bonds 1
3 Micro- and Nanosecond Hydrogen Transfer Processes in Hydrogen Bonds of Medium Strength 3
4 Conclusions 11
5 References 11

The use of NMR spectroscopy as a tool for the study of the dynamics of hydrogen and deuterium transfer in liquids and solids is demonstrated using a number of examples. (1) Single H Transfer dynamics in weak Hydrogen bonds. Example: Kinetic H/D/T isotope effects on the tautomerism of the porphyrin anion in the liquid and the solid state studied by NMR lineshape analysis. (2) Ultrafast Hydrogen Transfer in Hydrogen bonds of medium strength. Example: Solid tetraazaannzulene, studied using ^{15}N CPMAS NMR relaxometry. (3) Triple Proton Transfer in solid Dimethylpyrazole: An example of determination of multiple kinetic isotope effects by ^{15}N CMAS lineshape analysis and magnetization transfer experiments.

1 INTRODUCTION

Hydrogen Transfer and Bonding are important phenomena in biophysical chemistry.[1] Whereas theoretical and laser chemistry have allowed us a deep understanding of these phenomena in the case of isolated molecules and molecular systems our knowledge referring to the liquid state where the majority of chemical and biochemical reactions takes place is much less advanced. This is mainly because different hydrogen bonded species, different local environments and molecular conformations often lead to a lack of resolution in optical and vibrational spectroscopy. On the other hand, high resolution NMR spectroscopy as a 'slow' method sees a molecule in solution as a single entity, where the different environments are averaged out by fast molecular translational and rotational diffusion. Nevertheless, NMR has been always used as a tool for the study of hydrogen bond phenomena, in spite of its limitations. However, many NMR spectroscopists have not yet realized the progress of NMR made in this field in the past decades, which was induced by the general improvement of NMR such as high resolution and dipolar solid state NMR, solid state NMR-relaxation or low-temperature liquid state NMR techniques.

The purpose of this article is, therefore, to review these recent developments using simple introductory examples which are self-explanatory for the NMR-spectroscopists. These examples are taken from my work in the past years. Thus, no attempt is made to give a comprehensive description but rather to give an overall impression of the number of phenomena studied.

One general comment concerning the nomenclature. By NMR we observe either the moving nuclei, i.e., protons, deuterons, tritons which are generally called 'hydrons', or nuclei to which these particles are attached. In the nomenclature of chemistry, hydrons are, however, always bound to heavy atoms, i.e., they do not exist as isolated particles. Therefore, we will often use the term 'hydrogen transfer' instead of proton transfer, if we can not decide whether only a hydron changes place or whether also electrons are moving at the same time which compensate the charge of the proton. We will use the term 'proton transfer' mainly if it is clear that a proton is transferred with its positive charge.

We will start with single and multiple hydrogen transfer processes between nitrogen involving a barrier that will be gradually removed as the N–H- -N hydrogen bond strength is increased. The techniques of line shape analysis, magnetization transfer and longitudinal relaxation are used in order to follow the hydrogen transfer kinetics. Generally, we will exploit the modulation of isotropic chemical shifts associated with the hydrogen transfer, a stratagem which works in the case of liquids and solids, where high-resolution NMR spectroscopy under the conditions of magic angle spinning (MAS) and cross polarization (CP) can be employed.[2] In the case of liquids and hydrogen transfer from and to nitrogen, however, also the modulation of scalar ^{1}H–^{15}N coupling during hydrogen transfer is a very useful phenomenon to exploit.

2 SINGLE H/D/T TRANSFER ALONG WEAK HYDROGEN BONDS

2.1 Example: The Conjugate Porphyrin Anion

In this section we will discuss the elucidation of the kinetics of the tautomerism of the conjugate ^{15}N-labeled porphyrin anion (Por-H$^-$), a process reported by Braun et al.[3,4] which is depicted Figure 1. The anion was prepared by abstraction of a proton from the ^{15}N-labeled parent compound porphyrin (Por-H_2) by the phosphazene base P_4 (Figure 1). The rate constants of the proton transfer k^{H} in the conjugate porphyrin anion were determined by analysis of the variable temperature NMR signals of the inner proton of in Por-H$^-$ dissolved in THF-d_8 as depicted in Figure 1(a). The signals appear around -2.7 ppm which is typical for porphyrins; for comparison, the corresponding signals of the parent compound appear at -3.5 ppm.[5] At low temperatures, a doublet is observed arising from scalar coupling with the attached ^{15}N nucleus, indicating a slow exchange of the proton between the nitrogen sites. A differential line broadening of the ^{1}H–^{15}N doublet is observed at low temperature and arises from a reduced molecular mobility and an interference between the ^{1}H–^{15}N dipolar interaction and the chemical shift anisotropy.[6] As temperature is increased, rotational diffusion becomes faster and the asymmetry disappears.

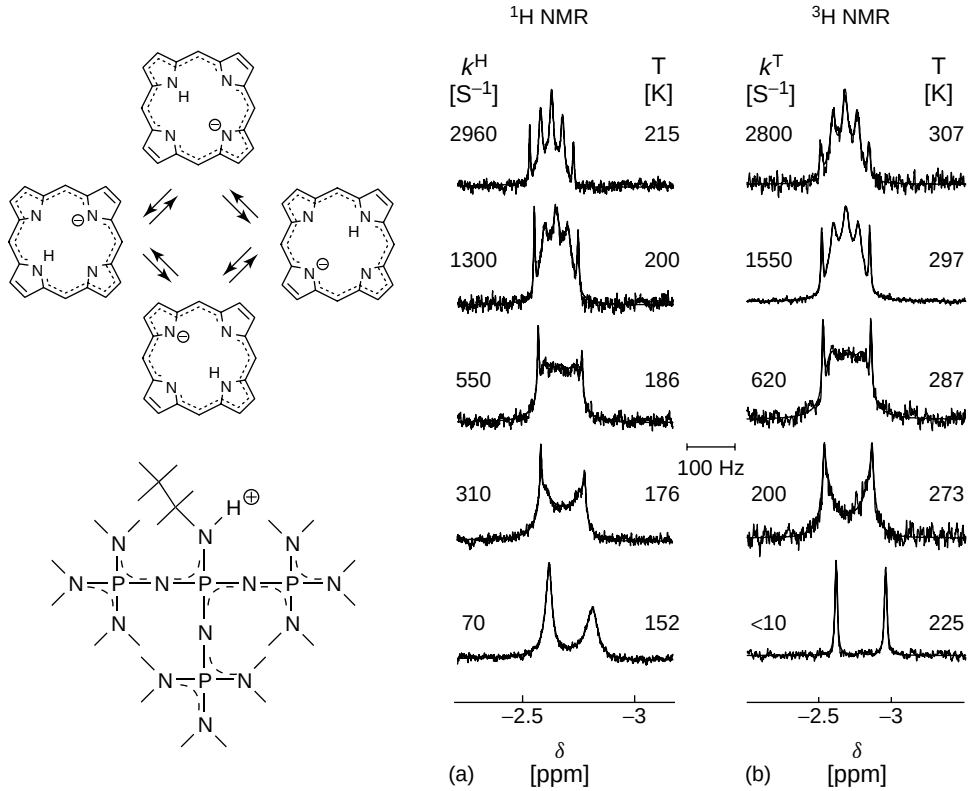

Figure 1 Superposed experimental and calculated variable temperature high field NMR signals of the inner hydrons of the ^{15}N-labeled conjugate porphyrin anion, with the protonated P4-phosphacene base as countercation. Adapted from Braun et al.[4] (a) ^{1}H NMR of a sample containing 65% Por-H$^-$ and 35% Por-D$^-$ dissolved in THF-d_8. Concentration app. 0.015 M; 500 MHz, 65° pulses, duration 6.5 μs, 9 KHz spectral width, 3.5 s repetition time, up to 600 scans. (b) ^{3}H NMR of a sample containing 10% Por-T$^-$ dissolved in THF-h_8; 320 MHz, 5 μs 60° pulses, 8 KHz spectral width, 3.6 s repetition time, number of scans between 200 and 1400 below 250 K and up to 10 000 above 290 K

At the same time, a doublet-pentet transition is observed at about 200 K arising from a fast intramolecular proton transfer between all four nitrogen atoms. The observation of the pentet is proof for an intramolecular reaction pathway of the tautomerism. The rate constants k^H determined by adapting the computed spectra to the experimental spectra corresponds to the inverse average life-time of the proton in a given nitrogen site until either a clockwise or counterclockwise jump to an adjacent nitrogen site occurs, characterized by equal probabilities. No evidence for direct jumps to opposite nitrogen sites were obtained by line-shape analysis as such a process would induce a change of the inner proton signal from a doublet at low to a triplet at a higher temperature. In order to obtain k^H by line-shape analysis the value of the line-width W_o in the absence of exchange is needed. This quantity can be derived at higher temperatures from the line-width of the outer signal components. At low temperatures, where only an exchange broadened doublet is observed, this procedure is not practicable. Here, the signals were simulated by simulating the carbon bound proton signals from which after partial deuteration, also the rate constants k^D are obtained.[4]

In a similar way, the NMR signals of the inner triton of (Por-T$^-$) were measured and analyzed by ^{3}H NMR, and the rate constants k^T of the triton transfer determined, as indicated in Figure 1(b). The doublet-pentet transition temperature is substantially higher for the triton as compared to the proton, indicating a large kinetic H/T isotope effect on the tautomerism.

In order to know the influence of possible cation-anion or other interactions on the tautomerism, variable temperature ^{15}N CPMAS NMR experiments at 9.12 MHz were performed on [Por-H]$^-$ embedded into the phosphacene fluoride depicted in Figure 2. Due to the small magnetic field applied, spinning speeds of between 1.9 KHz and 2.2 KHz were sufficient to suppress the rotational sidebands. At low temperatures, three singlets are observed. exhibiting a ratio of app. 1 : 2.1. The assignment is straightforward: the high-field line arises from the protonated nitrogen, the low-field line from the opposite nitrogen, and the remaining line from the two lateral chemically equivalent nitrogen atoms. As temperature is increased, all lines broaden and coalesce indicating a rapid tautomerism also in the solid state. Moreover, at high temperatures only one single line is observed indicating that the tautomerism renders all nitrogen atoms equivalent. In other words, the gas phase and liquid state degeneracy of the tautomerism is not lifted in the solid matrix. This result is not trivial; although it was also found for the parent compound porphyrin:[5] in most substituted porphyrins the symmetry is lifted by the crystal field.[7]

The line-shape analysis of Figure 2 was carried out in the usual way by setting up the appropriate line-shape equations of intramolecular exchange. The line-width in the absence of exchange were taken from the spectrum at 109 K and the chemical shifts kept constant within the whole temperature range.

The Arrhenius diagram obtained is depicted in Figure 3. Within the margin of error, the rate constants of the proton

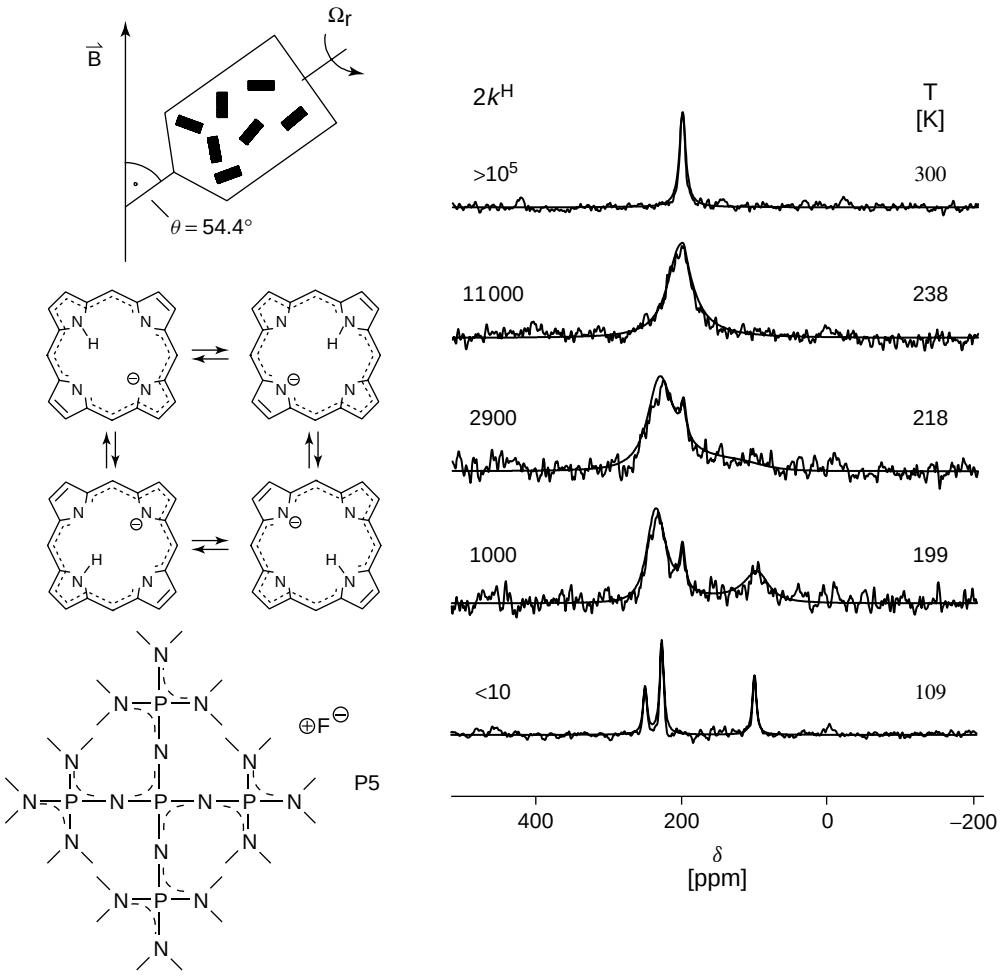

Figure 2 Superposed experimental and calculated variable temperature ^{15}N CPMAS NMR spectra of Por-H$^-$ embedded in solid $P_5{}^+F^-$. 9.12 MHz, 3 to 9 ms CP times, 7 KHz spectral width, 3.3 s repetition time, 1.9–2.2 KHz spinning speed. Flame-sealed glass insert in a 7 mm rotor. The peak labeled with an asterisk arises from an impurity formed during flame sealing. (Adapted from Braun et al.[4])

tautomerism are identical in the liquid and the solid. This means, that in first order the porphyrin skeleton shields the reaction center from the surroundings. The Arrhenius curves of the corresponding processes in the parent compound[5] are also included. We note that especially the proton tautomerism becomes much faster by removing one proton from porphyrin whereas the effect on the D- and the T-transfers are less pronounced. Moreover, the temperature dependence of the rate constants does not follow the Arrhenius law. Together with the large size of the kinetic H/D/T-isotope effects these results indicate a proton tunneling mechanism. This finding is reproduced in terms of a modified Bell[8] tunnel model for both systems.[4] For the parent porphyrin, the tautomerism is stepwise and the transfer of the first proton leads to a metastable intermediate (Figure 3). Proton tunneling cannot occur below the energy of this intermediate. By contrast, in the anion the single proton transfer is degenerate, and tunneling can occur at lower energies. As this phenomenon is very dependent on the mass, it follows that the H-transfer in the anion is especially accelerated as compared to the D- and the T-transfer.

Vangberg et al. have performed ab initio calculations on the tautomerism of the anion.[9] This surface was used by Brackhagen et al.[10] in order to formulate a quantum-mechanical description of the H/D/T-tautomerism. By adapting the calculated set of rate constants to the experimental one insight into the details of the tautomerism could be obtained. This example shows already how dynamic NMR can provide kinetic data which can be used in order to calibrate quantum-mechanical reaction models in polyatomic molecules in condensed phases.

3 MICRO- AND NANOSECOND HYDROGEN TRANSFER PROCESSES IN HYDROGEN BONDS OF MEDIUM STRENGTH

3.1 Example: Tetraazaannzulenes

Whereas in the previous section rate constants were obtained by line shape analysis in the millisecond time scale, the relaxation method allows us to obtain rate constants of proton transfer in solids in the micro- to nanosecond timescale. This method can be used for solids where normal rotational diffusion as a source of relaxation is suppressed. The reason is that the dipolar interactions between moving and nonmoving protons are modulated leading to an important source of relaxation in the solid state.[11,12] On the other hand, moving deuterons lead to a modulation of the quadrupole interaction

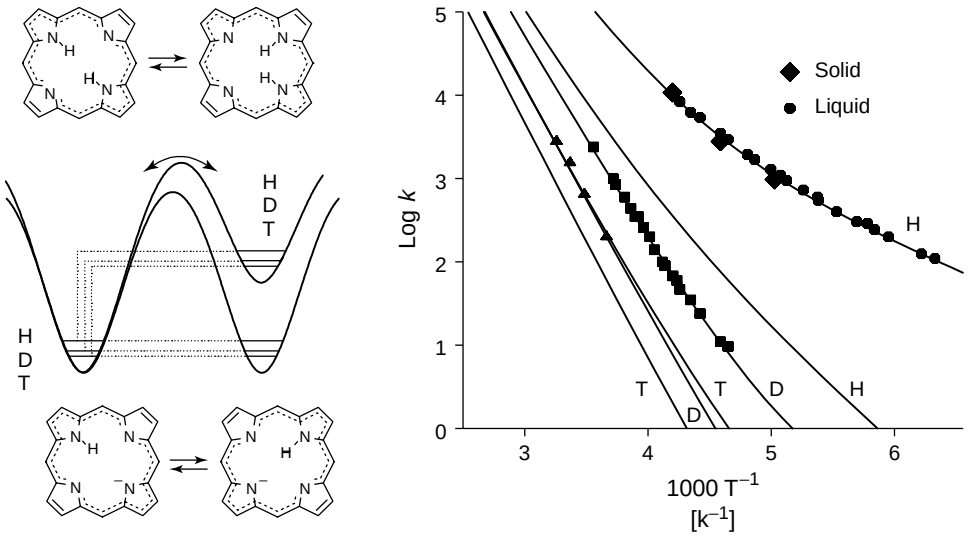

Figure 3 Arrhenius diagram of the H, D, and T transfer in the conjugate porphyrin anion evaluated by dynamic NMR. For comparison, the Arrhenius curves of the parent porphyrin Por-H_2 are included. (Adapted from Braun et al.[4])

and hence to quadrupole relaxation.[13] In order to obtain rate constants of the proton motion it is necessary to know the equilibrium constants. The latter can be obtained in the case of ^{2}H NMR studies but not easily by ^{1}H NMR. Also, the study of polycrystalline powders is difficult.

Finally, we note that the problem can also be overcome by ^{1}H relaxation as a function of the strength of the magnetic field, a method advanced by Horsewill et al.[12]

In the case of proton transfer from and to nitrogen, ^{15}N CPMAS can provide the equilibrium constants in a simple way. By combination with ^{15}N relaxation measurements under CPMAS conditions it is then possible to obtain also the rate constants.

3.2 Dimethyltetraaza[14]annulene (DTAA)

First we will treat the tautomerism of the tetraazaannulene derivative DTAA – discovered by Limbach et al.[14] Hoelger et al.[15] have used this molecule in order to establish the method of ^{15}N longitudinal relaxation under CPMAS conditions and to link it to the technique of line shape analysis, as shown in the following.

In Figure 4(a) are depicted the variable-temperature ^{15}N CPMAS spectra of ^{15}N labeled DTAA. At low temperatures two lines are observed, the high-field line for the protonated and the low-field line for the non-protonated nitrogen. As temperature is increased the lines broaden, but do not coalesce. This situation is typical for an asymmetric situation, where the equilibrium constant of the tautomerism $K = k_{12}/k_{21} = x_1/x_2 < 1$ in the whole temperature range, where k_{12} represents the forward reaction rate constant and x_1 the mole fraction of state **1**, with $x_1 + x_2 = 1$. This leads at high temperatures to two different nitrogen atoms **a** and **b**, where **a** experiences a higher average proton density as compared to **b**. Hence, the chemical shift of **a** at high temperatures is given by

$$\nu_a = x_1\nu_{a1} + x_2\nu_{a2} = \frac{\nu_{a1} + K\nu_{a2}}{1+K} \tag{1}$$

where ν_{a1} represents the chemical shift of nucleus a in tautomeric state **1**. A similar equation is valid for ν_b from which it follows, that the chemical shift difference at high temperature is given by

$$\delta\nu_{ab} = \nu_a - \nu_a = \Delta\nu_{ab}\frac{1-K}{1+K}, \Delta\nu = \nu_N - \nu_{NH} \tag{2}$$

From equation (2) it is easy to obtain the equilibrium constant at high temperatures by comparison of the high and the low-temperature line splittings $\delta\nu_{ab}$ and $\Delta\nu_{ab}$. Once K is obtained at different temperatures it can be extrapolated using the van't Hoff equation to lower temperatures. Then, by line shape analysis rate constants k_{12} can be obtained as indicated in Figure 4(a).

Because of the limited dynamic range the longitudinal ^{15}N relaxation times of ^{15}N labeled DTAA were measured under MAS conditions at 2.1 and 7 Tesla,[15] as indicated in Figure 4(b). For this purpose, the usual sequence of Torchia[16] in connection with CP was employed. A T_1 – minimum was observed around 350 K and 2.1 Tesla. Deuteration of the compound increased the T_1 values strongly, providing evidence that relaxation is caused by the proton jumps that modulate the heteronuclear ^{1}H–^{15}N dipolar coupling. Starting from the homonuclear ^{1}H relaxation theory in the presence of solid state proton transfer[11] equations for the heteronuclear case were derived. It was shown that both nitrogen atoms a and b of a N_a–H- -N_b exhibit the same relaxation times. The latter are normally strongly dependent in the case of a static sample on the orientation of the crystallite with respect to the magnetic field. However, MAS averages out these differences and the relaxation times measured under MAS conditions are almost identical with the isotropic values, which one would obtain for the case of an isotropic rotational diffusion when the latter is not active for relaxation. The final equation used for the data analysis of Figure 4(b) is given by

$$\frac{1}{T_1} = \frac{1}{40}\gamma_N^2\gamma_H^2\left(\frac{h}{2\pi}\right)^2\left(\frac{\mu_o}{4\pi}\right)^2 D\left[\frac{4K}{(1+K)^2}\right] \times \left[\frac{\tau_c}{1+(\omega_H-\omega_N)^2\tau_c^2} + \frac{3\tau_c}{1+\omega_N{}^2\tau_c^2} + \frac{6\tau_c}{1+(\omega_H+\omega_N)^2\tau_c^2}\right] \tag{3}$$

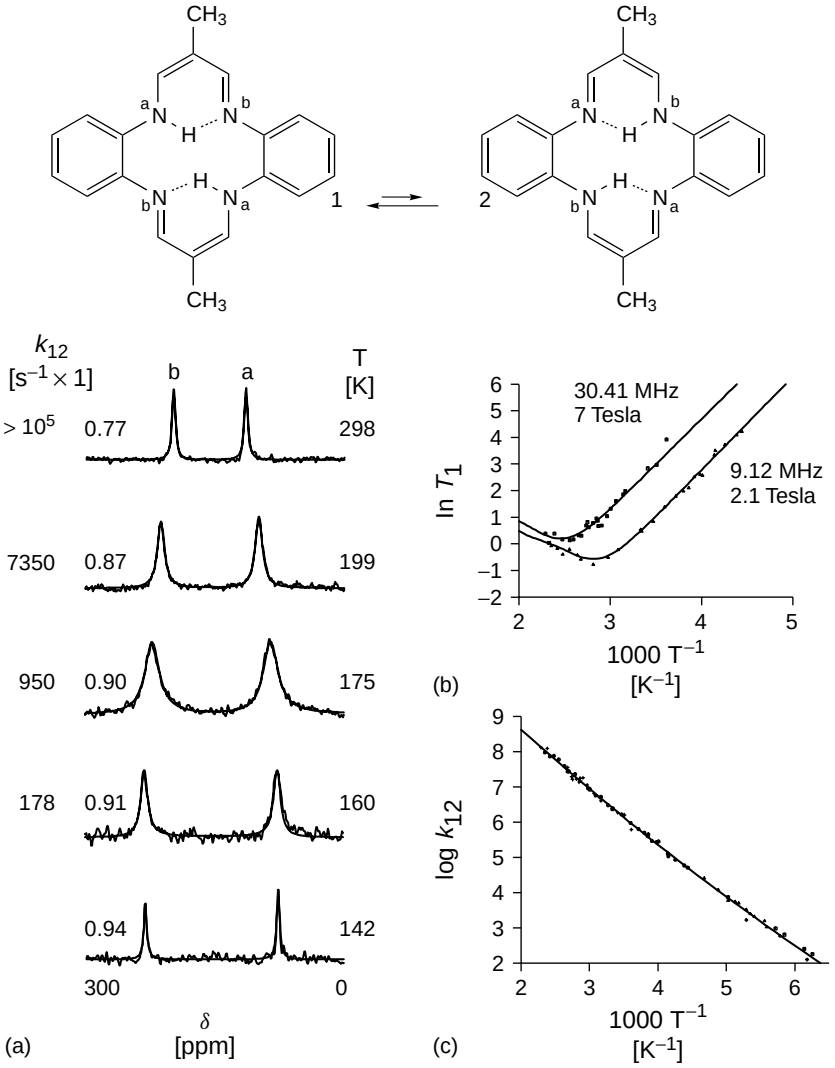

Figure 4 (a) Superposed experimental and theoretical ^{15}N CPMAS NMR spectra of crystalline DTAA. (b) ^{15}N–T_1 analysis. (c) Arrhenius diagram. (Adapted from Hoelger et al.[15])

τ_c is the correlation time of the proton motion whose temperature dependence may be expressed in a first approximation by the Arrhenius equation

$$\frac{1}{\tau_c} = k_{12} + k_{21}, k_{12} = A_{12} \exp\left(\frac{-E_{a12}}{RT}\right) \tag{4}$$

where E_{a12} is the energy of activation of the forward reaction and A_{12} the corresponding frequency factor. The factor D represents the change of the dipolar interaction during the proton jump

$$D = r_1^{-6} + r_2^{-6} + r_1^{-3} r_2^{-3} (1 - 3\cos^2 \theta^d) \tag{5}$$

r_1 represents – for a given nitrogen atom – the short NH distance before and r_2 the long N···H distance after the proton has jumped. θ^d represents the angle between the NH vectors before and after the proton transfer, ω represents a Larmor frequency and γ a gyromagnetic ratio.

Using equation (4), the solid lines in Figure 5(b) were calculated using a non-linear least-squares fitting routine, by adapting D – characterizing the T_1 value in the minimum, A_{12} and E_{a12} and assuming an Arrhenius law for the tautomerism. From the value of D it is possible to obtain an approximation of the cubic average short NH-distance $r_1 \equiv r_{NH} = 1.03$ Å which coincides within the margin of error with the value obtained by dipolar NMR for the deuterated compound.[17] Using the parameter set obtained, the relaxation data at 7 Tesla included in Figure 4(b) could be calculated. However, the calculated values were slightly longer than the experimental ones, indicating that at 7 Tesla relaxation via the modulation of the Chemical Shielding Anisotropy by the jumping protons is no longer negligible. Thus, this technique is preferentially performed at lower magnetic fields.

In a second stage of the analysis the assumption of an Arrhenius-law for the proton motion was dropped, and each ^{15}N T_1 value obtained at 2.1 Tesla separately converted into the rate constant k_{12} of the forward proton transfer. The values are plotted together with those obtained by line shape analysis in the Arrhenius diagram of Figure 4(c). The two methods are nearly overlapping, and provide in the overlapping range

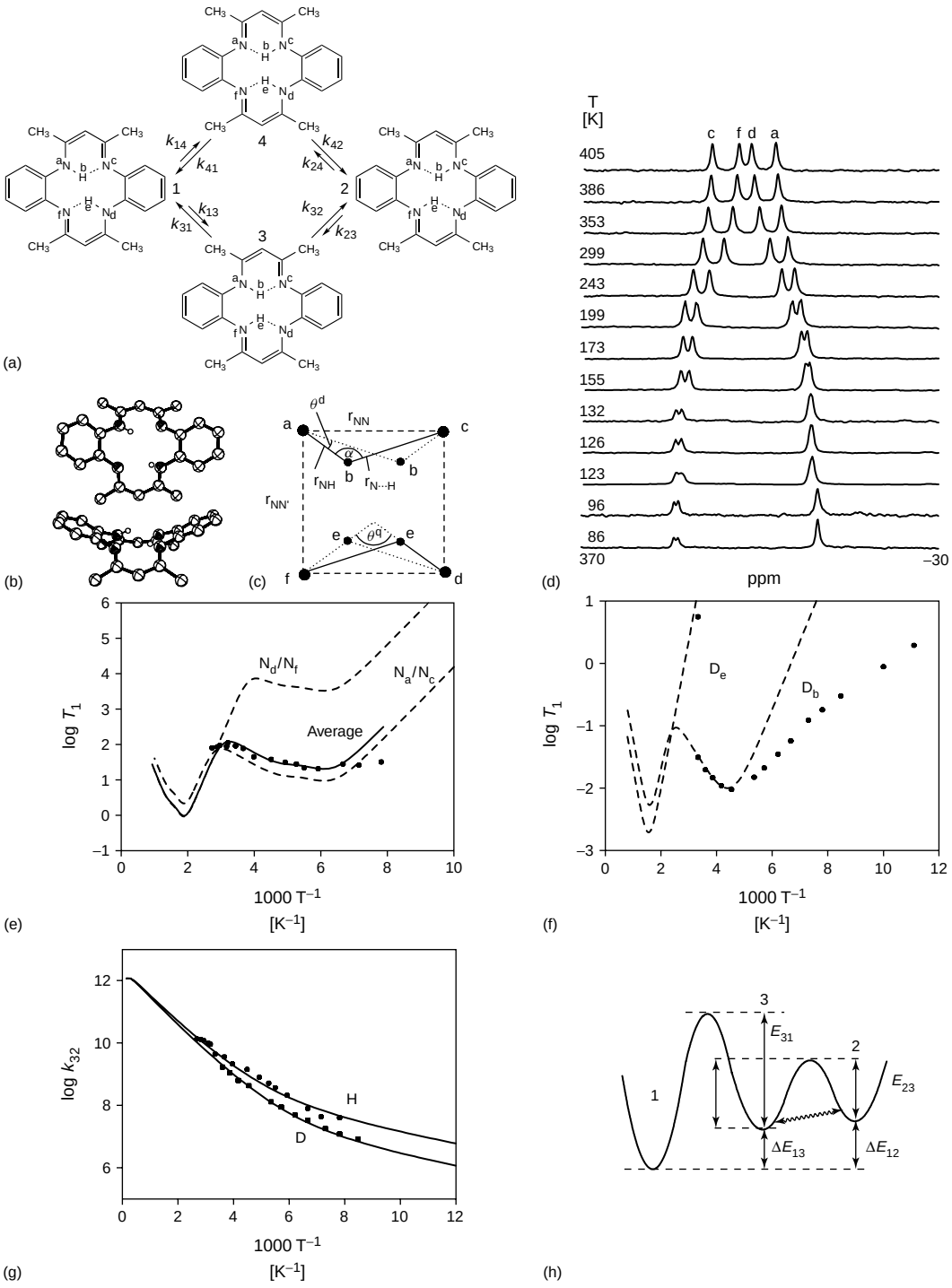

Figure 5 Results of the NMR-experiments on solid TTAA according to Langer et al.[21] (a) The solid state tautomerism of TTAA. (b) Crystal structure of TTAA according to Goedken et al.[19] (c) Geometries of the two intramolecular hydrogen bonds in TTAA, adapted from the crystal structure assuming a planar arrangement. The two positions of each proton are indicated, the angle θ^{d} is the jump angle of the dipolar ^{1}H–^{15}N interaction, and α the hydrogen bond angle. θ^{q} represents the corresponding jump angle of the quadrupole interaction. (d) 9.12 MHz ^{15}N CPMAS-NMR spectra of 95% ^{15}N enriched TTAA at 9.12 MHz as a function of temperature; 6–10 ms cross-polarization time, 7 KHz spectral width, 2.7 s repetition time, 100 scans on average, 2–2.8 KHz rotation frequency (adapted from Wehrle et al.[22]). (e) Temperature dependence of the spin diffusion averaged ^{15}N T_1 relaxation time of polycrystalline TTAA at 9.12 MHz. The solid line was calculated according to equation (3) using the fixed ratios $A_{31}/A_{13} = 1.31$ and $A_{32}/A_{23} = 1.66$ derived in equation (17) and parameter fit of $A_{13} = 1.6 \times 10^{12}\,s^{-1}$, $E_{23} = 14\,KJ\,mol^{-1}$, $E_{31} = 41\,KJ\,mol^{-1}$, and the NH-bond length 1.04 Å. The dashed lines correspond to the intrinsic relaxation times of the nitrogen pairs Na/Nb and Nc/Nd. The T_1 values of the two nitrogen atoms in each pair are identical. (e) T_1 values of deuterons b and e in TTAA plotted in a logarithmic scale as a function of the inverse temperature. (f) Arrhenius diagram of the relaxation active proton and deuteron transfer step **3** $\rightleftharpoons$ **2** of the solid state tautomerism of TTAA. The solid lines were calculated using a modified Bell tunneling model. (h) Energy profile for the double proton transfer in TTAA

similar rate constants which establishes the ^{15}N relaxation method as an important kinetic tool. Rate constants are obtained until the nanosecond time scale. A slight deviation from an Arrhenius behavior is observed, which is, however, less pronounced as in the case of porphyrin and its conjugated anion. This effect was explained again in terms of a stepwise proton motion, where the cis- intermediate exhibits, however, such a high energy that tunneling is not operative.

Finally, we note that the relaxation method discussed here has been recently used in order to obtain the rate constants of the proton motion in the solid porphyrin analog porphycene.[18]

3.3 Tetramethyltetraaza[14]annulene (TTAA)

As an example of the determination of kinetic H/D-isotope effects on the tautomerism we discuss in the following the related TTAA molecule (Figure 5a). Its crystallographic structure is shown in Figure 5(b),[19] and a simplified hydrogen bond structure needed for the interpretation of the relaxation experiments described below in Figure 5(c). The solid state tautomerism of this compound was discovered by Limbach et al.[20] The following results are taken from a recent paper of Langer et al.[21]

The ^{15}N CPMAS spectra of the polycrystalline powder obtained at 2.1 Tesla exhibit four sharp lines a, c, d, and f in the whole temperature range between 86 and 405 K, as depicted in Figure 5(d), with the line separations $\delta_{ac} = \delta_a - \delta_c$ and $\delta_{df} = \delta_d - \delta_f$. This result indicated four chemically inequivalent nitrogen atoms exhibiting different temperature-dependent proton densities. By performing so-called 'spin diffusion' experiments discussed in a later section it was shown that each molecule in the asymmetric unit contains all types of nitrogen atoms. This result is then only consistent with the presence of more than two tautomeric states, i.e., with a stepwise proton transfer mechanism. In other words, in contrast to DTAA, the energy of the cis-intermediate must be substantially lowered. Deuteration of the inner proton sites did not affect at all line positions. This means that there are no H/D-isotope effects on the proton transfer equilibria of solid TTAA. A careful analysis of the splittings δ_{ac} and δ_{df} in terms of the reaction network of Figure 5(a) showed that only states **1**, **2** and **3** are populated but not state **4**.[22] Furthermore, the energy differences between the states could be obtained.

In order to analyze the ^{15}N T_1 values obtained at 9.12 MHz of Figure 5(e) as a function of temperature – which exhibited only a very small and puzzling temperature dependence – we needed to extend the ^{15}N relaxation theory to the two-step proton transfer $\mathbf{1} \rightleftarrows \mathbf{3} \rightleftarrows \mathbf{2}$ and to have an idea of the exact hydrogen bond geometry which was obtained in approximation as follows as no neutron diffraction study of TTAA was available. Knowing the array of the nitrogen atoms from the crystal structure, we assumed that the hydrogen atoms are located in the plane of this array, and that the short NH distances r_{NH} and the long NH-distances $r_{H\cdots N}$ distances are the same for all hydrogen bonds in all tautomers. First we set $r_{NH} = 1.03$ Å which is within the margin of error identical with the value of 1.04 Å obtained by dipolar relaxometry and dipolar ND – coupling for the related DTAA molecule.[17] The slightly smaller value was later justified by a least squares fit of the relaxation data. Knowing the short N–H distance, we made use of the well-known correlation between r_{NH} and $r_{H\cdots N}$ of NHN–Hydrogen bonds established by neutron diffraction,[23] NMR and theoretical calculations,[24] from which we obtained a long N···H distance of 1.94 Å. Taking into account the crystallographic distance of $r_{NN} = 2.675$ Å between the two nitrogen atoms of a given hydrogen bond and of $r_{NN'} = 2.699$ Å between closest nitrogen neighbors in different hydrogen bonds,[19] we derived then the proton positions of Figure 5(c), exhibiting a hydrogen bond angle of $\alpha = 134°$, a dipolar proton jump angle of $\theta^d = 13.7°$, and a quadrupolar jump angle of $\theta^q = 104°$.

With this parameter set, the individual T_1 values of all nitrogen atoms could be calculated, and hence the value of all nitrogen atoms, averaged by spin diffusion. The energy profile for this motion is depicted in Figure 5(h). The agreement between the calculated and experimental values is very satisfactory. The theory predicts two minima, one at low temperatures for the fast process $\mathbf{3} \rightleftarrows \mathbf{2}$ and one at high temperatures, arising from the process $\mathbf{1} \rightleftarrows \mathbf{3}$. As in the fast process only H_b is jumping between N_a and N_c, only these two atoms should experience a short relaxation time at low temperatures, but not N_d and N_c. However, spin diffusion averages this difference.

Independent evidence for this interpretation could be obtained by ^2H NMR relaxation time measurements of the static deuterium labeled solid, where the results are depicted in Figure 5(f). Effectively, two deuterons were observed at room temperature exhibiting different relaxation times, a short one (31 ms) attributed to D_b and a very long one (5.6 s) attributed to D_e.

In the final step, the ^{15}N T_1 values could be converted to the rate constants k_{32}^H and the ^2H T_1 to k_{32}^D. The Arrhenius diagram is depicted in Figure 5(g). As compared to DTAA, the process is much faster which we attributed to the more symmetric profile of the reaction, in a similar way as in the porphyrin anion case. Tunneling is pronounced as the Arrhenius curves exhibit a strong curvature. The kinetic H/D isotope effects are much smaller than in the porphyrin anion. These results may provide again input data for computational studies of this reaction.

Finally, we note that TTAA is not only interesting from the standpoint of theory but also from a practical view, as it provides a very convenient chemical shift thermometer for ^{15}N CPMAS measurements.[22] Temperature control in MAS is very important as spinning can strongly increase temperature.[22] An example of its use will be reported in a subsequent section.

3.4 The Tautomerism of TTAA in a Glassy Polystyrene Matrix

The observation that intermolecular interactions perturb the symmetry of a proton transfer system can be rationalized in the scenario of Figure 6. When a bistable molecule exhibiting a symmetric double well for the proton motion in the gas phase is placed in a molecular crystalline environment, the crystal field will induce an energy difference ΔE between the tautomers (Figure 6b), whereas ΔE will be the same for all molecules in a crystal and ΔE will depend in a disordered system such as a glass on the local environment, leading to a distribution of ΔE-values (Figure 6c). At the glass point, some environments may become mobile leading to an average value of $\Delta E_{av} = 0$, whereas other environments still experience non-zero values.

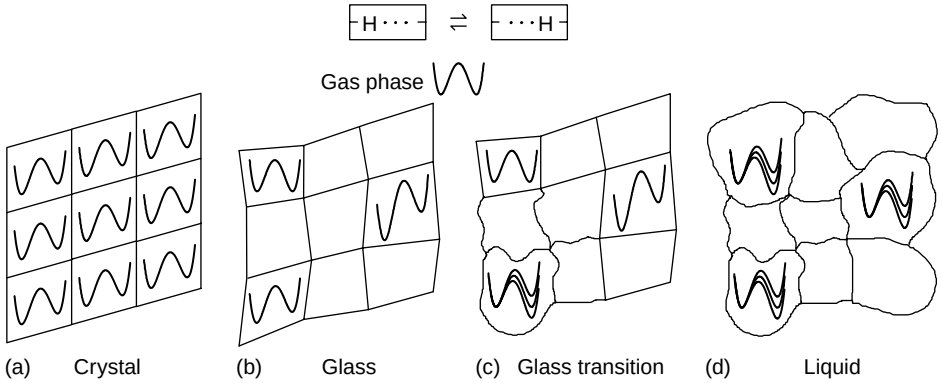

Figure 6 Model for the dependence of the proton transfer potential on the environment arising from experimental observations. (Adapted from Wehrle et al.[25])

Only well above the glass transition is a situation typical for the liquid reached where all molecules exhibit an average value $\Delta E_{av} = 0$ (Figure 6d).

In the case of N–H- -N proton transfer systems the ^{15}N CPMAS line shape for the sequence of Figure 5 has been described, and experimentally verified using the example of TTAA dissolved in solid polystyrene.[25]

3.5 Triple Proton Transfer in Solid Dimethylpyrazole: An Example of Determination of Multiple Kinetic Isotope Effects by ^{15}N CMAS Lineshape Analysis and Magnetization Transfer Experiments

In this section we will introduce three complications, i.e., the problem of the determination of kinetic isotope effects in multiple proton transfer reactions, the case of slow proton dynamics, and the use of the chemical shift thermometer TTAA. In previous liquid state NMR work, we have determined kinetic HH/HD/DD isotope effects of the double proton transfer between acetic acid and methanol already in 1984.[26] However, only in this year, has this process has been modeled a priori.[27] In addition, multiple kinetic isotope effects have been measured for diarylaamidines,[28] which represent the nitrogen analogs of carboxylic acids. The solid state tautomerism of this class of compounds has been reported recently.[29] These studies are still underway. Therefore, as an example, we will treat here the triple proton transfer in solid 3,5-dimethylpyrazole (DMP) (Figure 7a), a process described by Elguero et al.[30] The following results are taken from the paper of Aguilar et al.[31]

The X-ray crystal structure (Figure 7b) shows that this molecule forms a cyclic trimer in the solid state, with half protons close to each nitrogen atom. X-ray diffraction can, however, not distinguish between a 'dynamic disorder' where each molecule can form both tautomeric states to a comparable extent and a 'static disorder' with alternate fixed proton positions from one molecule to the other. The ^{15}N CPMAS spectra of DMP and of its deuterated analog obtained at 7 Tesla with fast speed spinning in order to avoid spinning sidebands are depicted in Figure 7(c) and (d). At low temperatures, two signals are observed for the amino-(–NH–, –ND–) and imino-(–N=) nitrogen atom sites. The cross polarization times used in the experiments were adjusted in such a way that the signals of the amino and imino nitrogen atoms sites were equal. As temperature is increased, the lines broaden and coalesce. As we know from the crystal structure that the molecule forms cyclic trimers, the dynamic process averaging the two isotropic ^{15}N chemical shifts can only correspond to a triple proton transfer. At high temperatures, only a single sharp line survives. This observation indicates that within the margin of error the transfer is degenerate. The coalescence temperature of the deuterated sample is much higher than for the protonated sample and is not reached at 7 Tesla within the temperature range where the compound is solid and indicates the presence of large primary isotope effect k^{HHH}/k^{DDD} on the tautomerism. To the sample of Figure 7(c) a small amount of TTAA was added whose four lines (see Figure 5d) give information about the sample temperature. Thus, line shape analysis of the DMP signals using the usual two-site theory and simulation of the TTAA line positions give both the rate constants as well as the sample temperature, which is increased substantially as compared to the temperature of incoming nitrogen gas by fast MAS. Some rate constants k^{HHD} and k^{HDD} of the other isotopic reactions were obtained by ^{15}N CPMAS NMR line shape analyses of spectra obtained for partially deuterated samples at 2.1 Tesla.

Since at low temperatures the reaction rates are too small to be determined accurately enough by lineshape analysis, one-dimensional ^{15}N CPMAS magnetization transfer experiments in the laboratory frame between the amino nitrogen magnetization S and the imino nitrogen magnetization frame were performed at low temperatures, using a pulse sequence described previously.[32] In these experiments S and X are created by cross polarization and stored by 90° pulses parallel to the magnetic field B_o. The time dependence during this period is monitored after application of a second 90° pulse. The dependence is given by

$$S + X = (S_o + X_o)\exp(-\rho t),\ S - X = (S_o - X_o)\exp\left(-\left(\frac{1}{T_1 + \sigma + 2k}\right)t\right) \qquad (6)$$

where σ represents the rate of spin diffusion between S and X, and k the rate constant of the degenerate triple proton transfer. Two experiments are performed by setting a time interval t_1 between the spin lock pulses and the 90° pulse either to 0 or to $1/2(\nu_S - \nu_X)$, where ν_S and ν_X represent the chemical shifts in Hz of the exchanging sites. In the 'parallel' experiment (i) S_o and X_o have the same sign and are almost equal. Therefore $S - X = 0$ and S and X each decay with the longitudinal

relaxation rate ρ. In the 'antiparallel' experiment (ii) S_o and X_o are antiparallel, i.e., $S_o \approx -X_o$, and each magnetization decays with $\rho + \sigma + 2k$ in time. As ρ is already known from experiment (i) the sum $\sigma + 2k$ is obtained in experiment (ii). Various stratagems have been proposed in order to obtain σ and k separately. Here we exploit the circumstance that σ is strongly dependent on the distance between the ^{15}N nuclei in contrast to k.

As the ^{15}N spin diffusion term σ in equation (6) depends on the internuclear ^{15}N distances, we minimized this term by performing experiments on singly ^{15}N labeled DMP, which reduced the decay constant $\sigma + 2k$ to $2k$ alone; a check by embedding singly ^{15}N labeled DMP into non-labeled DMP at 35% and 10% did not further reduce the observed decay rates.

In Figure 7(e) the results of a typical experiment at a deuterium fraction of $x_D = 0$ and 0.96, carried out at 30.41 MHz and 131 K and spinning speeds of about 8 to 9 KHz i.e., in the regime of suppressed sidebands are depicted. No variation of the magnetizations within the time period covered is observed indicating that $1/T_1$ is so small that it can be neglected. In experiment (ii) performed on the same sample under otherwise similar conditions the two magnetizations cancel each other in the same time period because of the triple proton transfer. For comparison, the results of experiment (ii) on a sample with $x_D \approx 1$ are shown for comparison: no change of the magnetization is observed as the DDD process is very slow. The data analysis (Figure 7e bottom) indicates a mono-exponential from which k^{HHH} is obtained.

In Figure 7(f) are depicted the results of experiment (ii) performed at 210 K on two singly ^{15}N labeled DMP samples with $x_D = 0.2$ and 0.8 are compared. Assuming a statistical isotopic distribution, the ratio for the former sample is given

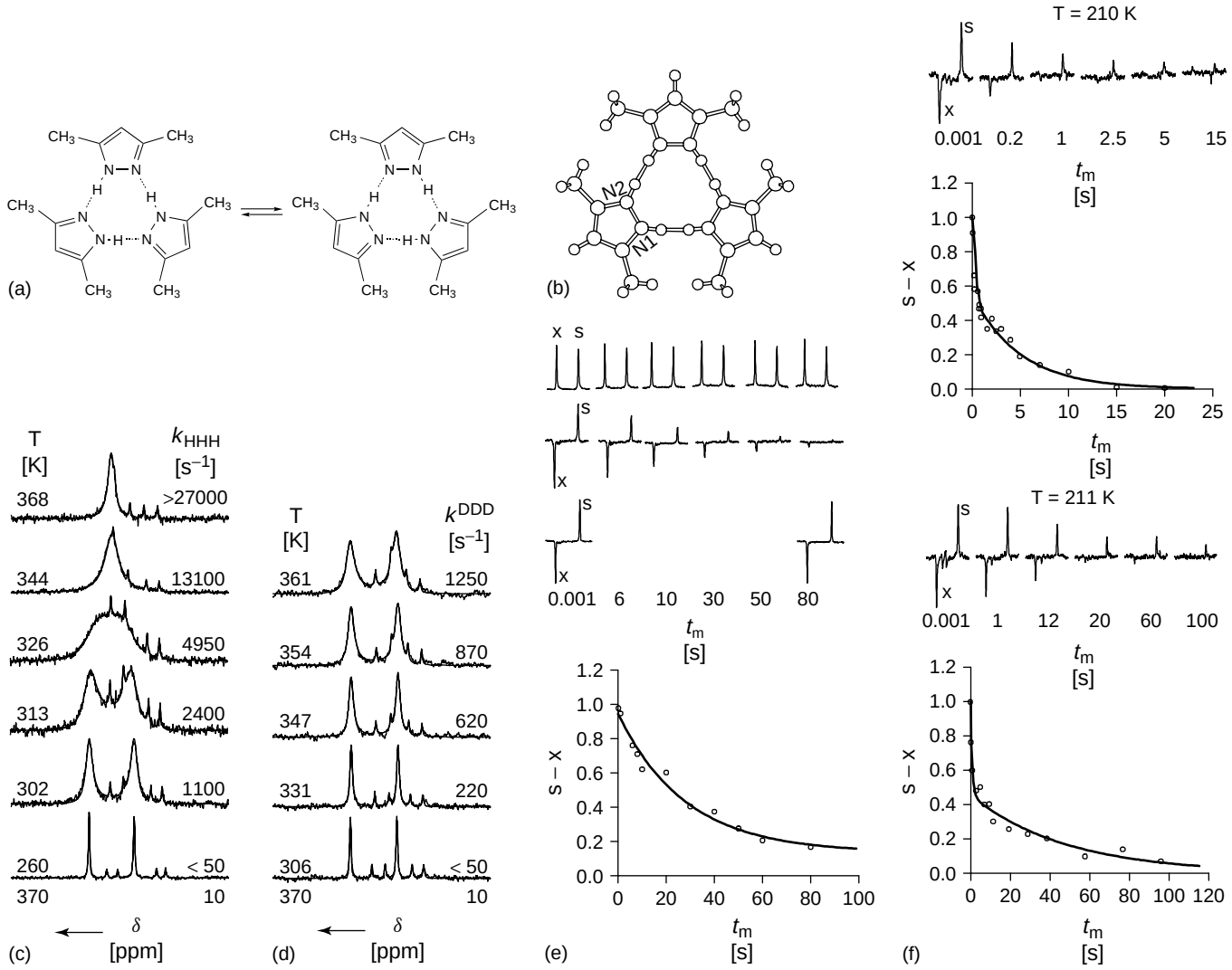

Figure 7 NMR results for the tautomerism of DMP according to Aguilar et al.[31] (a) Triple proton transfer process monitored. (b) X-ray crystal structure of DMP according to Baldy et al.[30a] (c) and (d) Superposed experimental and calculated 30.41 MHz (7 Tesla) ^{15}N CPMAS-NMR spectra of 95% ^{15}N enriched DMP at the deuterium fractions $x_D = 0$ (c) and $x_D = 1$ (d). Experimental conditions: 8–9 KHz sample spinning, 6–12 ms CP times, 4.3 s repetition time, 5 μs ^{1}H 90° pulses. k^{HHH} and k^{DDD} are the rate constant of the triple proton and deuteron transfer. The four sharp lines with temperature dependent line positions stem from a small quantity of the chemical shift thermometer TTAA, added in a separate capsule inside the rotor. (e) 30.41 MHz ^{15}N CPMAS magnetization transfer experiment in the laboratory frame performed on a sample of singly ^{15}N labeled DMP at 131 K. From top to bottom: longitudinal T_1 experiment and magnetization transfer experiment at $x_D = 0$, and MT at $x_D = 0.99$, data analysis for $x_D = 0$. (f) Related experiment at 210 K with $x_D = 0.2$ and $x_D = 0.8$. For further information see text

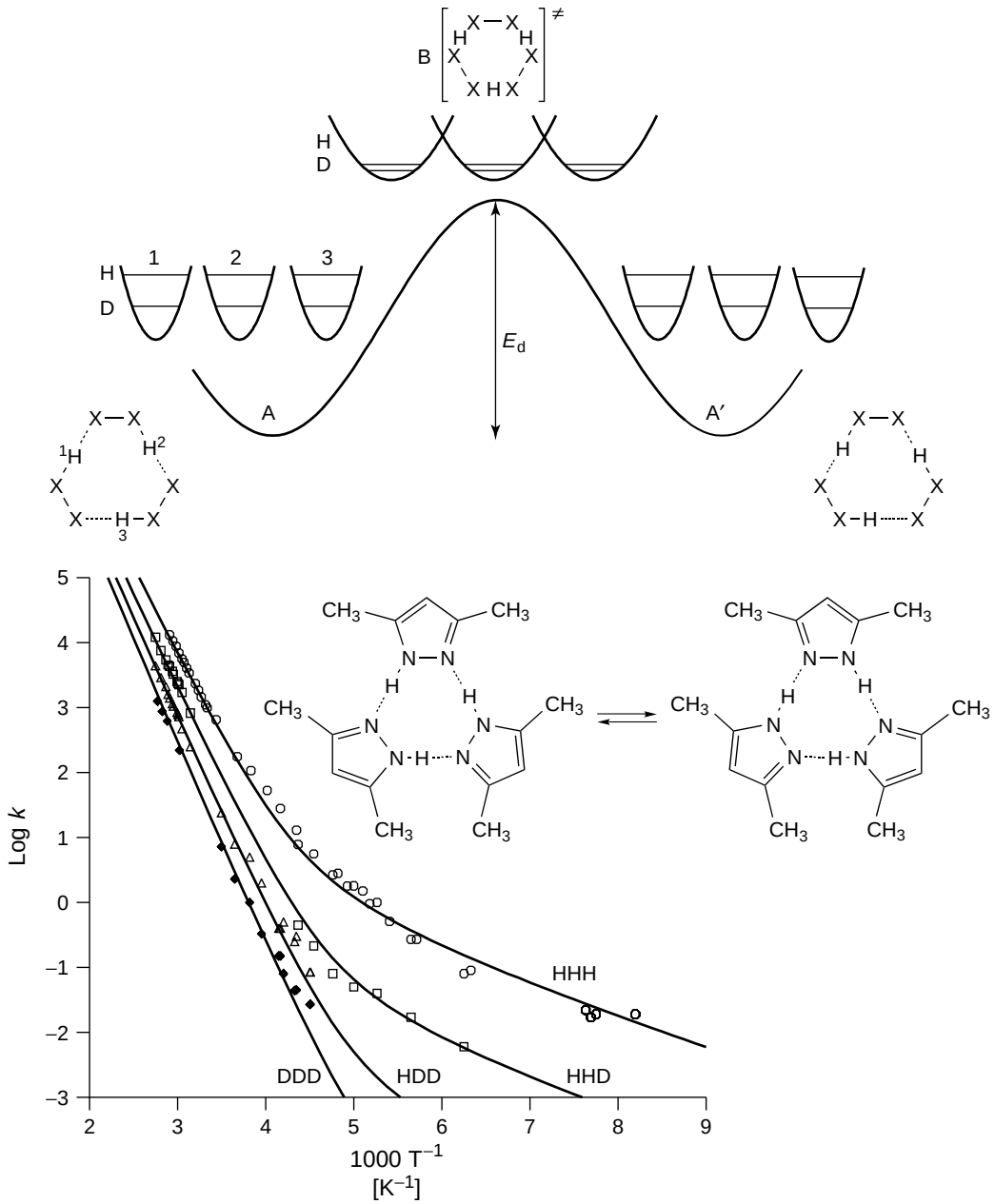

Figure 8 Arrhenius diagram for the triple proton and deuteron transfer in solid DMP according to Aguilar-Parrilla et al.[31]

by $x_{HHH} : x_{HHD} : x_{HDD} : x_{DDD} = 0.512 : 0.384 : 0.096 : 0.08$ and in the second by $x_{HHH} : x_{HHD} : x_{HDD} : x_{DDD} = 0.008 : 0.096, 0.384 : 0.512$. Thus, in the former mainly the HHH and the HHD, and in the latter the HDD and the DDD species dominate, leading to apparently bi-exponential decays in both cases; in the former case the fast and slow decay components are governed by $2k^{HHH}$ and $2k^{HHD}$, and in the second by $2k^{HDD}$ and $2k^{DDD}$. As a consequence the full kinetic HHH/HHD/HDD/DDD isotope effects of the triple proton transfer of DMP could be detected in a large temperature interval.

The Arrhenius diagram containing all the rate constant data for the proton and deuteron transfer in the different DMP species is depicted in Figure 8. Especially in the HHH and the HHD reaction, deviations from a classical Arrhenius behavior were found. The solid lines were calculated in terms of a modified Bell tunneling model as mentioned already in the porphyrin anion case. The interpretation of the data is illustrated at the top of Figure 8. The kinetic data at high temperature indicate that the rule of the geometric mean (RGM) is fulfilled. This rule assumes that all values $k^{HHH}/k^{HHD} \approx k^{HHD}/k^{HDD} \approx k^{HDD}/k^{DDD}$ are equal.[31] Such a case is expected for a concerted triple proton transfer mechanism where all protons loose zero-point energy in the transition state as illustrated in Figure 8. At lower temperatures deviations from the RGM indicate the presence of tunneling. Furthergoing experiments on pyrazole molecules exhibiting a variety of substituents of different size and electronic properties indicated that in the transition state the NHN–Hydrogen bonds are strongly compressed.[33]

4 CONCLUSIONS

In this review, we have demonstrated the use of dynamic liquid and solid state NMR for the study of fast proton and deuteron transfer processes in heterocyclic compounds. The data obtained all indicate the importance of tunneling. They are important for the development of quantum theories of proton transfer and kinetic isotope effects in condensed matter. Techniques have been devised which allow us to use NMR as a tool for the study of proton transfer not only in the second- and millisecond timescale but also in the micro- to nanosecond timescale, if other molecular motions are suppressed as in the solid state.

Naturally, a challenging field opens up when the barrier of proton transfer is further reduced. Then, the realm of H/D isotope effects on hydrogen bond geometries, chemical shifts and coupling constants is reached that provides further details into the phenomenon of hydrogen bonding. This challenging field uses dipolar NMR spectroscopy[24] and low-temperature liquid state NMR techniques.[34] In this realm scalar couplings across hydrogen bonds provide new insight into this phenomenon, if it is possible to reach the slow hydrogen bond exchange regime in the liquid. This is naturally achieved by low temperature NMR methods that also provide information about the influence of the dielectric properties of the solvent on the hydrogen bond geometries. In addition, the technique of isotopic fractionation provides insights into the zero-point energy of hydrogen bonds. This field will be covered in another review that will appear elsewhere. The same is true for the rapidly expanding field of rotational tunnel splittings of hydrogen pairs in transition metal hydrides that give rise to interesting quantum exchange and tunneling phenomena.[35]

5 REFERENCES

1. (a) H. H. Limbach, Dynamic NMR Spectroscopy in the Presence of Kinetic Hydrogen/Deuterium Isotope Effects, in 'NMR-Basic Principles and Progress', Vol. 23, p. 63–164, Springer: Heidelberg, 1991; (b) H. H. Limbach, G. Scherer, L. Meschede, F. Aguilar-Parrilla, B. Wehrle, J. Braun, C. Hoelger, H. Benedict, G. Buntkowsky, W. P. Fehlhammer, J. Elguero, J. A. S. Smith, and B. Chaudret, in 'Ultrafast Reaction Dynamics and Solvent Effects', eds Y. Gauduel and P. J. Rossky, American Institute of Physics, AIP Conference Proceedings 298, 1994, Part III. p. 225–239. NMR Studies of Elementary Steps of Hydrogen Transfer in Condensed Phases; (c) Special Issue 'Hydrogen Transfer; Experiment and Theory', eds H. H. Limbach and J. Manz, *Ber. Bunsenges. Phys. Chem.*, 1998, **102**, 289; (d) Special Issue on 'Proton-Transfer Reactions in Bioenergetics', ed P. Brzezinski, *Biochemica Biophysica Acta – Bioenergetics*, 2000, Vol. 1458.
2. J. Schaeffer and E. O. Stejskal, *J. Am. Chem. Soc.*, 1976, **98**, 1031.
3. J. Braun, C. Hasenfratz, R. Schwesinger, and H. H. Limbach, *Angew. Chem.*, 1994, **106**, 2302; *Angew. Chem. Int. Ed. Engl.*, 1994, **33**, 2215.
4. J. Braun, R. Schwesinger, P. G. Williams, H. Morimoto, D. E. Wemmer, and H. H. Limbach, *J. Am. Chem. Soc.*, 1996, **118**, 11 101.
5. (a) B. Wehrle, H. H. Limbach, M. Köcher, O. Ermer, and E. Vogel, *Angew. Chemie*, 1987, **99**, 914; *Angew. Chem. Int. Ed.*, 1987, **26**, 934; (b) J. Braun, M. Schlabach, B. Wehrle, M. Köcher, E. Vogel, and H. H. Limbach, *J. Am. Chem. Soc.*, 1994, **116**, 6593; (c) J. Braun, H. H. Limbach, P. Williams, H. Morimoto, and D. Wemmer, *J. Am. Chem. Soc.*, 1996, **118**, 7231.
6. (a) H. Shimizu, *J. Chem. Phys.*, 1964, **40**, 3357; (b) H. Rüterjans, E. Kaun, W. E. Hull, and H. H. Limbach, *Nucleic Acids Res.*, 1982, **10**, 7027; (c) R. H. Griffey, C. D. Poulter, Z. Aamaizumi, S. Nishimura, and R. E. Hurd, *J. Am. Chem. Soc.*, 1982, **104**, 5811; (d) M. Gueron, J. L. Leroy, R. H. Griffey, *J. Am. Chem. Soc.*, 1983, **105**, 7262.
7. (a) H. H. Limbach, J. Hennig, R. D. Kendrick, and C. S. Yannoni, *J. Am. Chem. Soc.*, 1984, **106**, 4059; (b) R. D. Kendrick, S. Friedrich, B. Wehrle, H. H. Limbach, and C. S. Yannoni, *J. Magn. Reson.*, 1985, **30**, 159; (c) H. H. Limbach, B. Wehrle, M. Schlabach, R. D. Kendrick, and C. S. Yannoni, *J. Magn. Reson.*, 1988, **77**, 84; (d) M. Schlabach, B. Wehrle, J. Braun, G. Scherer, and H. H. Limbach, *Ber. Bunsenges. Phys. Chem.*, 1992, **96**, 821.
8. (a) R. P. Bell, 'The Tunnel Effect', 2nd edn., Chapman and Hall: London, 1980.
9. T. Vangberg and A. Ghosh, *J. Phys. Chem. B*, 1997, **101**, 1496.
10. O. Brackhagen, Ch. Scheurer, R. Meyer, and H. H. Limbach, *Ber. Bunsenges. Phys. Chem.*, 1998, **102**, 303.
11. (a) A. Stöckli, B. H. Meier, R. Kreis, R. Meyer, and R. R. Ernst, *J. Chem. Phys.*, 1990, **93**, 1502 and references cited therein; (b) S. Takeda, A. Tsuzumitani, and C. A. Chatzidimitriou-Dreismann, *Chem. Phys. Lett.*, 1992, **198**, 316; (c) S. Takeda, T. Inabe, C. Benedict, U. Langer, and H. H. Limbach, *Ber. Bunsenges. Phys. Chem.*, 1998, **102**, 1358.
12. (a) A. J. Horsewill, P. J. McDonald, and D. Vijayaraghavan, *J. Chem. Phys.*, 1994, **100**, 1889; (b) D. F. Brougham, A. J. Horsewill, and R. I. Jenkinson, *Chem. Phys. Lett.*, 1997, **272**, 69; (c) A. J. Horsewill, *Prog. NMR Spectrosc.*, 1999, **35**, 359; (d) A. J. Horsewill, N. H. Jones, and R. Caciuffo, *Science*, 2001, **291**, 100.
13. A. Heuer and U. Haeberlen, *J. Chem. Phys.*, 1991, **95**, 4201; 1991, **187**, 471.
14. H. H. Limbach, B. Wehrle, H. Zimmermann, R. D. Kendrick, and C. S. Yannoni, *Angew. Chem.*, 1987, **99**, 241; *Angew. Chem. Int. Ed. Engl.*, 1987, **26**, 247.
15. C. G. Hoelger, B. Wehrle, H. Benedict, and H. H. Limbach, *J. Phys. Chem.*, 1994, **98**, 843.
16. D. Torchia, *J. Magn. Reson.*, 1978, **30**, 613.
17. C. G. Hoelger and H. H. Limbach, *J. Phys. Chem.*, 1994, **98**, 11 803.
18. U. Langer, Ch. Hoelger, B. Wehrle, L. Latanowicz, E. Vogel, and H. H. Limbach, *J. Phys. Org. Chem.*, 2000, **13**, 23.
19. V. L. Goedken, J. J. Pluth, S. M. Peng Shie-Ming, and B. Bursten, *J. Am. Chem. Soc.*, 1976, **98**, 8014.
20. (a) H. H. Limbach, B. Wehrle, H. Zimmermann, R. D. Kendrick, and C. S. Yannoni, *J. Am. Chem. Soc.*, 1987, **109**, 929.
21. U. Langer, L. Latanowicz, C. Hoelger, G. Buntkowsky, H. M. Vieth, and H. H. Limbach, *Phys. Chem. Chem. Phys.*, 2001, **3**, 1446.
22. (a) B. Wehrle, F. Aguilar-Parrilla, and H. H. Limbach, *J. Magn. Reson.*, 1990, **87**, 584; (b) F. Aguilar-Parrilla, B. Wehrle, H. Bräunling, and H. H. Limbach, *J. Magn. Reson.*, 1990, **87**, 592.
23. Th. Steiner, *J. Chem. Soc. Chem. Commun.*, 1995, 1331.
24. (a) H. Benedict, C. Hoelger, F. Aguilar-Parrilla, W. P. Fehlhammer, M. Wehlan, R. Janoschek, and H. H. Limbach, *J. Mol. Struct.*, 1996, **378**, 11; (b) H. Benedict, H. H. Limbach, M. Wehlan, W. P. Fehlhammer, N. S. Golubev, and R. Janoschek, *J. Am. Chem. Soc.*, 1998, **120**, 2939.
25. (a) B. Wehrle, H. H. Limbach, and H. Zimmermann, *Ber. Bunsenges. Phys. Chem.*, 1987, **91**, 941; (b) B. Wehrle, H. H. Zimmermann, and H. H. Limbach, *J. Am. Chem. Soc.*, 1988, **110**, 7014; (c) B. Wehrle and H. H. Limbach, *Chem. Phys.*, 1989, **136**, 223.
26. D. Gerritzen and H. H. Limbach, *J. Am. Chem. Soc.*, 1984, **106**, 869.

27. A. F. Ramos, Z. Zmedarchina, and J. Rodríguez-Otero, *J. Chem. Phys.*, 2001, **114**, 1567.
28. L. Meschede and H. H. Limbach, *J. Phys. Chem.*, 1991, **95**, 10 267.
29. R. Anulewicz, I. Wawer, T. M. Krygowski, F. Männle, and H.-H. Limbach, *J. Am. Chem. Soc.*, 1997, **119**, 12 223.
30. (a) A. Baldy, J. Elguero, R. Faure, M. Pierrot, and E. J. Vincent, *J. Am. Chem. Soc.*, 1985, **107**, 5290; (b) J. A. S. Smith, B. Wehrle, F. Aguilar-Parrilla, H. H. Limbach, M. C. Foces-Foces, F. H. Cano, J. Elguero, A. Baldy, M. Pierrot, M. M. T. Khurshid, and J. B. Larcombe-McDouall, *J. Am. Chem. Soc.*, 1989, **111**, 7304; (c) F. Aguilar-Parrilla, G. Scherer, H. H. Limbach, M. C. Foces-Foces, F. H. Cano, J. A. S. Smith, C. Toiron, and J. Elguero, *J. Am. Chem. Soc.*, 1992, **114**, 9657; (d) C. G. Hoelger, H. H. Limbach, F. Aguilar-Parrilla, J. Elguéro, O. Weintraub, and S. Vega, *J. Magn. Res.*, 1996, **A120**, 46; (e) O. Klein, M. M. Bonvehi, F. Aguilar-Parrilla, J. Elguero, and H. H. Limbach, *Isr. J. Chem.*, 1999, **34**, 291.
31. F. Aguilar-Parrilla, O. Klein, J. Elguero, and H. H. Limbach, *Ber. Bunsenges. Phys. Chem.*, 1997, **101**, 889.
32. (a) N. M. Szeverenyi, M. J. Sullivan, and G. E. Maciel, *J. Magn. Reson.*, 1982, **47**, 462; (b) H. H. Limbach, B. Wehrle, M. Schlabach, R. D. Kendrick, and C. S., Yannoni, *J. Magn. Reson.*, 1988, **77**, 84.
33. O. Klein, M. M. Bonvehi, F. Aguilar-Parrilla, J. Elguero, and H. H. Limbach, *Isr. J. Chem.*, 1999, **34**, 291.
34. (a) N. S. Golubev, S. N. Smirnov, V. A. Gindin, G. S. Denisov, H. Benedict, and H. H. Limbach, *J. Am. Chem. Soc.*, 1994, **116**, 12 055; (b) S. N. Smirnov, H. Benedict, N. S. Golubev, G. S. Denisov, M. M. Kreevoy, R. L. Schowen, and H. H. Limbach, *Can. J. Chem.*, 1999, **77**, 943. P. Schah-Mohammedi, I. G. Shenderovich, C. Detering, H. H. Limbach, P. M. Tolstoy, S. N. Smirnov, G. S. Denisov, and N. S. Golubev. *J. Am. Chem. Soc.*, 2000, **122**, 12 878. I. Shenderovich, S. Smirnov, G. S. Denisov, V. Gindin, N. S. Golubev, A. Dunger, R. Reibke, S. Kirpekar, O. L. Malkina, and H. H. Limbach, *Ber. Bunsenges. Phys. Chem.*, 1998, **102**, 422. H. Benedict, I. G. Shenderovich, O. L. Malkina, V. G. Malkin, G. S. Denisov, N. S. Golubev, and H. H. Limbach, *J. Am. Chem. Soc.*, 2000, **122**, 1979. N. S. Golubev, I. G. Shenderovich, S. N. Smirnov, G. S. Denisov, and H. H. Limbach, *Chem. Eur. J.*, 1999, **5**, 492.
35. N. S. Golubev, G. S. Denisov, S. N. Smirnov, D. N. Shchepkin, and H. H. Limbach, *Z. Phys. Chem.*, 1996, **196**, 73.
36. (a) H. H. Limbach, S. Ulrich, G. Buntkowsky, S. Gründemann, S. Sabo-Etienne, B. Chaudret, G. J. Kubas, and J. Eckert, *J. Am. Chem. Soc.*, 1998, **120**, 7929; (b) F. Wehrmann, T. P. Fong, R. H. Morris, and H. H. Limbach, Gerd Buntkowsky, *Phys. Chem. Chem. Phys.*, 1999, **1**, 4033.

Acknowledgements

I thank all colleagues that have been coauthors of the papers of our group for their impact on this work. Especially, I thank my coworkers Dr. Gerd Buntkowsky and Dr. Klaus Weisz, Prof. J. Elguero, CSIC, Madrid. This work has been supported by the following sponsors: Deutsche Forschungsgemeinschaft, Bonn-Bad Godesberg, Fonds der Chemischen Industrie, Frankfurt, European Community, Brussels.

Biographical Sketch

Hans-Heinrich Limbach, *b* 1943. Dr. Rer.Nat. 1973, Dr. Habil. 1980, (Physical Chemistry), Universität Freiburg, Germany. Guest scientist with C. S. Yannoni 1983, IBM Research Laboratory, San José, USA, with C. B. Moore, UC Berkeley, 1984. Since 1990 Full Professor of Chemistry, Freie Universität Berlin. Chair Gordon Research Conference Isotopes in the Biological and Chemical Sciences 2002. Editorial Board Magn. Reson. Chem., Spect. Lett., Chem. Phys. Approx 190 publications. Principal research interest: Hydrogen Bond NMR.

Fluxional Motion

Keith G. Orrell
University of Exeter, Devon, UK

1	Introduction	1
2	Fluxional Inorganic Compounds	2
3	Fluxional Organometallic Compounds	6
4	Related Articles	11
5	References	11

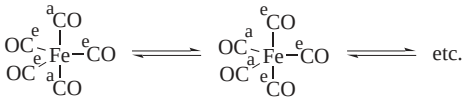

Scheme 1

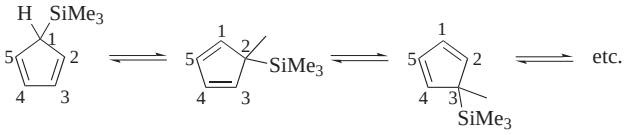

Scheme 2

1 INTRODUCTION

Most chemical species in solution do not possess a fixed structure but exist in some type of dynamic equilibrium. This may involve intramolecular exchange between identical or different configurations of the same compound or intermolecular exchange involving other chemical species. NMR spectroscopy is uniquely powerful for investigating both categories of dynamic process. This stems from the diversity of one- and two-dimensional NMR techniques and the wide magnitude range of their associated timescales.

1.1 Intramolecular Rearrangements

Molecules which undergo purely intramolecular rearrangements at rates which affect NMR lineshapes are described as stereochemically nonrigid. This terminology was proposed originally by Muetterties[1] and popularized by Cotton et al. from 1966 onwards. In 1968, Binsch[2] proposed that the study of the precise way in which NMR lineshapes are affected by chemical exchange be known as 'dynamic NMR' (DNMR) spectroscopy and he developed a general theoretical treatment for such lineshape changes in both first- and second-order spectra arising from single-site and multi-site exchanges.[3] Total bandshape analysis has been very widely exploited and is discussed in depth elsewhere in this Encyclopedia (see ***Chemical Exchange Effects on Spectra***). In 1975, an entire book[4] was devoted to DNMR, and this still provides a recommended starting point for interested readers. More recent treatments of the theory are the monographs by Kaplan and Fraenkel,[5] and Sandström.[6] The reader is also referred to a number of reviews.[7–10]

In cases where the intramolecular movement of atoms produces chemically distinguishable species the change is known as isomerization, but where the interconverting structures are chemically indistinguishable the term 'fluxionality' was proposed.[11,12] The difference between these two cases is often debated, especially where the changes are largely configurational in nature. Whatever the circumstances, fluxional molecules are clearly a subset of nonrigid molecules. In this article, 'fluxional motion' will be interpreted somewhat more widely than its original definition to avoid an unnatural restriction in the discussion of stereochemical nonrigidity. The variety of intramolecular dynamic processes in inorganic and organometallic molecules is considerable, but the processes can usefully be divided into those where atomic positions in a molecule are permuted without bond breaking and those which require the breaking and making of (different) bonds in the molecule.

These two different cases can be illustrated by the fluxionalities of pentacarbonyliron (Scheme 1) and η^1-cyclopentadienyltrimethylsilicon (Scheme 2). In $Fe(CO)_5$, interconversion between species involves only changes of C–Fe–C bond angles, but in the case of $Me_3Si(\eta^1\text{-}C_5H_5)$ there is a concerted breaking and making of Si–C bonds at each step. In less symmetrical examples of these rearrangements the interchanging species may not have totally indistinguishable structures, but the processes are still described as fluxional.

1.2 DNMR Methods and Timescales

The two fluxional organometallic species described above illustrate the strengths and weaknesses of DNMR spectroscopy. $[Fe(CO)_5]$ is known to possess a trigonal bipyramidal structure, yet its ^{13}C NMR spectra measured at all accessible temperatures (down to $-170\,^{\circ}C$) consist of a single line rather than two lines for the axial and equatorial CO environments, indicating that the fluxionality rapidly exchanges the ^{13}C shifts at rates too high to be measured at any temperature. In contrast, the breaking and making of Si–C bonds in $[Me_3Si(\eta^1\text{-}C_5H_5)]$ is slow on the ^1H NMR timescale at ambient temperatures and fast exchange is not achieved at the highest accessible temperatures before thermal decomposition sets in.[13] Standard bandshape methods based on chemical shift and scalar coupling modulation can be used to measure rate processes typically in the range $1–10^4\ s^{-1}$. However, this range can be extended in an upward direction, as required for compounds such as $[Fe(CO)_5]$ or PF_5, if other NMR parameters are used as probes of the rate processes. Such parameters are spin–lattice relaxation times either in the rotating frame ($T_{1\rho}$) or in the laboratory frame (T_1), the operative ranges of accessible rate constants now being $10^3–10^6\ s^{-1}$ and $10^6–10^{10}\ s^{-1}$, respectively. In contrast, the techniques of one-dimensional magnetization transfer[14,15] and two-dimensional exchange spectroscopy (EXSY) (see ***Two-Dimensional Methods of Monitoring Exchange***)[16] enable much slower rate processes, in the approximate range $10^2–10^{-2}\ s^{-1}$, to be measured with high accuracy. Thus, nowadays rate constants within a total range of $10^{-2}–10^{10}\ s^{-1}$ may be determined by NMR methods. This corresponds to timescales, or nuclear site lifetimes, in the range $10^2–10^{-10}$ s, i.e. between hundreds of

seconds and picoseconds. Fortunately for chemists, this range embraces a wide variety of intramolecular fluxional rearrangements.

Activation energies of these fluxional processes, based on temperature dependences of rate constants, generally fall in the range 15–100 kJ mol^{-1}. Rate processes are preferably described in terms of the thermodynamic activation parameters $\Delta G^{\ddagger}$, $\Delta H^{\ddagger}$, and $\Delta S^{\ddagger}$ arising from the Eyring rate theory. The Gibbs function changes $\Delta G^{\ddagger}$ are least prone to systematic error[6] and so this parameter, usually calculated for a temperature of 298.15 K, is chosen wherever possible for comparing energy barriers of different fluxional processes. The activation entropy $\Delta S^{\ddagger}$ is exceptionally difficult to measure with high precision. For purely intramolecular rearrangements of the type considered here, a value of around zero is expected unless there is a statistical contribution to the value arising from multiple pathways between exchanging structures.[6]

In this article a few seminal examples of fluxionality as studied by NMR techniques are used to illustrate the contribution of NMR to this area of structural chemistry. More detailed coverage may be found in more recent reviews.[17]

2 FLUXIONAL INORGANIC COMPOUNDS

The first report[18] of fluxionality in inorganic chemistry was in 1955 when high-resolution NMR was in its infancy. In aluminum tris(tetrahydroborate) [$Al(BH_4)_3$] the BH_4 groups are doubly bonded to the central aluminum atom and distinct bridging and terminal ^1H signals were expected. However, only one ^1H resonance was detected. ^{27}Al decoupling and observation of the ^{11}B spectrum proved that an intramolecular process equilibrated the hydrogen atom environments, but the same four hydrogen atoms remained attached to each boron atom.

2.1 Unidentate Ligands

2.1.1 Three Coordination

An atom bonded to three groups in a pyramidal geometry and possessing a lone pair of electrons may undergo a spontaneous inversion of configuration, generally via a planar transition state (Scheme 3). This process may be studied by DNMR, providing its rate matches the NMR timescale and it causes an exchange between different chemical environments. Thus pyramidal inversion of ML_3 groups cannot be studied, whereas species $ML_1L_2L_3$ where one of the ligands (L) is a diastereotopic group such as isopropyl or $C_6H_5CH_2$, may be investigated. Barriers to inversion vary widely according to the central atom.[19] For instance in Group V, barriers increase in the order N < P < As, and in Group VI the order is O < S < Se < Te. Nitrogen and sulfur atoms provide the greatest number of examples of NMR-detectable inversion.[17] Sulfur inversion rates are usually detectable only when the atom is coordinated to metals, whereas in many cases phosphorus atoms are stereochemically rigid at all accessible temperatures.

2.1.2 Four Coordination

The favored geometry here is the regular tetrahedron, but in certain cases the square planar form may have a similar energy

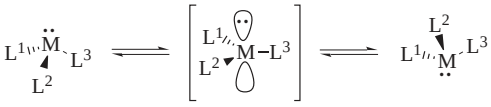

Scheme 3

and interconversion of these forms may occur, as in the case of bisphosphine complexes of nickel(II) halides, $(R_3P)_2NiX_2$.[20]

The other common geometry for four coordination is the trigonal bipyramid, where one equatorial position is occupied by a lone pair. This structure is adopted by SF_4 but is only evident at about −50 °C when its ^{19}F spectrum consists of two 1 : 2 : 1 triplets confirming the C_{2v} structure. At higher temperatures rapid exchange of axial and equatorial ^{19}F atoms occurs.[21] Related compounds and metal complexes of SF_4 are similarly fluxional.

2.1.3 Five Coordination

Stereochemical nonrigidity is a common and unifying feature of five-coordinate trigonal bipyramidal structures,[22] energy barriers being low (<40 kJ mol^{-1}) and sometimes too low for NMR detection. PF_5 is the classical example. Its trigonal bipyramidal structure has been established by electron diffraction, but its ^{19}F NMR spectrum at all temperatures above about −150 °C consists of a single chemically shifted signal (with $^{31}P-^{19}F$ splitting) indicative of a low-energy exchange process which permutes all fluorine positions. The favored mechanism is the Berry pseudorotation mechanism. This is shown in Scheme 4 for the case when F^3 acts as the pivot and exchanges axial (1,2) and equatorial (4,5) fluorine atoms. Direct evidence for this type of fluxion was obtained from the ^{19}F spectra of PF_3Cl_2 and PF_3Br_2.

While most ML_5 species undergo fluxionality which is too rapid for NMR detection, cationic transition metal complexes of the type $M[P(OR)_3]_5^{n+}$ (M = Co^{I}, Rh^{I}, Ir^{I}, Ni^{II}, Pd^{II}, or Pt^{II}) are a notable exception and detailed total bandshape studies have been carried out.[23] Complexes of type ML_4X are also stereochemically nonrigid, the rate of fluxionality being very dependent on whether the unique X ligand occupies an equatorial or axial site. In the hydride species ML_4H, the H ligand is in an axial position and energy barriers to fluxion are low, e.g. $Rh(PF_3)_4H$, 36 kJ mol^{-1}, and $Rh(POEt_3)_4H$, 30 kJ mol^{-1}.

In ML_3X_2 complexes with C_{2v} symmetry, the fluxionality depends on the electronic natures of X and L. Thus, PF_3Cl_2 and PF_3Br_2 are nonrigid, whereas PF_3Me_2 is rigid. Energy differences between trigonal bipyramidal and square pyramidal geometries may sometimes be very small, as illustrated by the complexes $Pd(PMe_3)_3X_2$. When X = Br or I trigonal bipyramidal structures occur, but when X = Cl a distorted

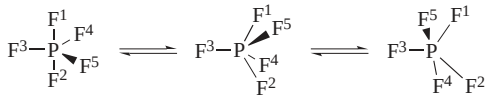

Scheme 4

square pyramidal geometry is adopted. The fluxional process in this case is an intermolecular double-replacement mechanism.

2.1.4 Six Coordination

The octahedral geometry of six coordination is exceptionally stable and stereochemical nonrigidity is here the exception rather than the rule. An example is the molecule $C_6H_5SF_5$, the ^{19}F spectrum of which consists of an AB_4 pattern at all accessible temperatures. Any fluxional rearrangement would have an associated barrier of $>120\,kJ\ mol^{-1}$. For this reason the regular octahedral structure of SF_6 is assumed to be rigid.[22] In this instance, NMR is *not* a useful kinetic probe because all ^{19}F environments are equivalent irrespective of whether the structure is static or dynamic.

Metal dihydride complexes of the type MH_2L_4 (M = Fe or Ru; L = phosphine) form an important example of nonrigid species. They adopt a *cis*-octahedral stereochemistry but with considerable distortions from regular octahedral geometry. The complex $FeH_2[P(OEt)_3]_4$ was the focal point of a classic DNMR study.[24] Variable temperature ^1H NMR spectra are shown in Figure 1. Certain lines remain sharp throughout and these are clearly due to spin transitions unaffected by the ligand permutations. A full analysis of the problem shows that the total of 48 permutations fall into four basic sets. NMR bandshapes based on all four sets, plus a fifth set for random exchange, were computed and compared with the experimental spectra. Only the set corresponding to a tetrahedral jump mechanism gave very close agreement. This mechanism involves FeH bending, which moves a single H

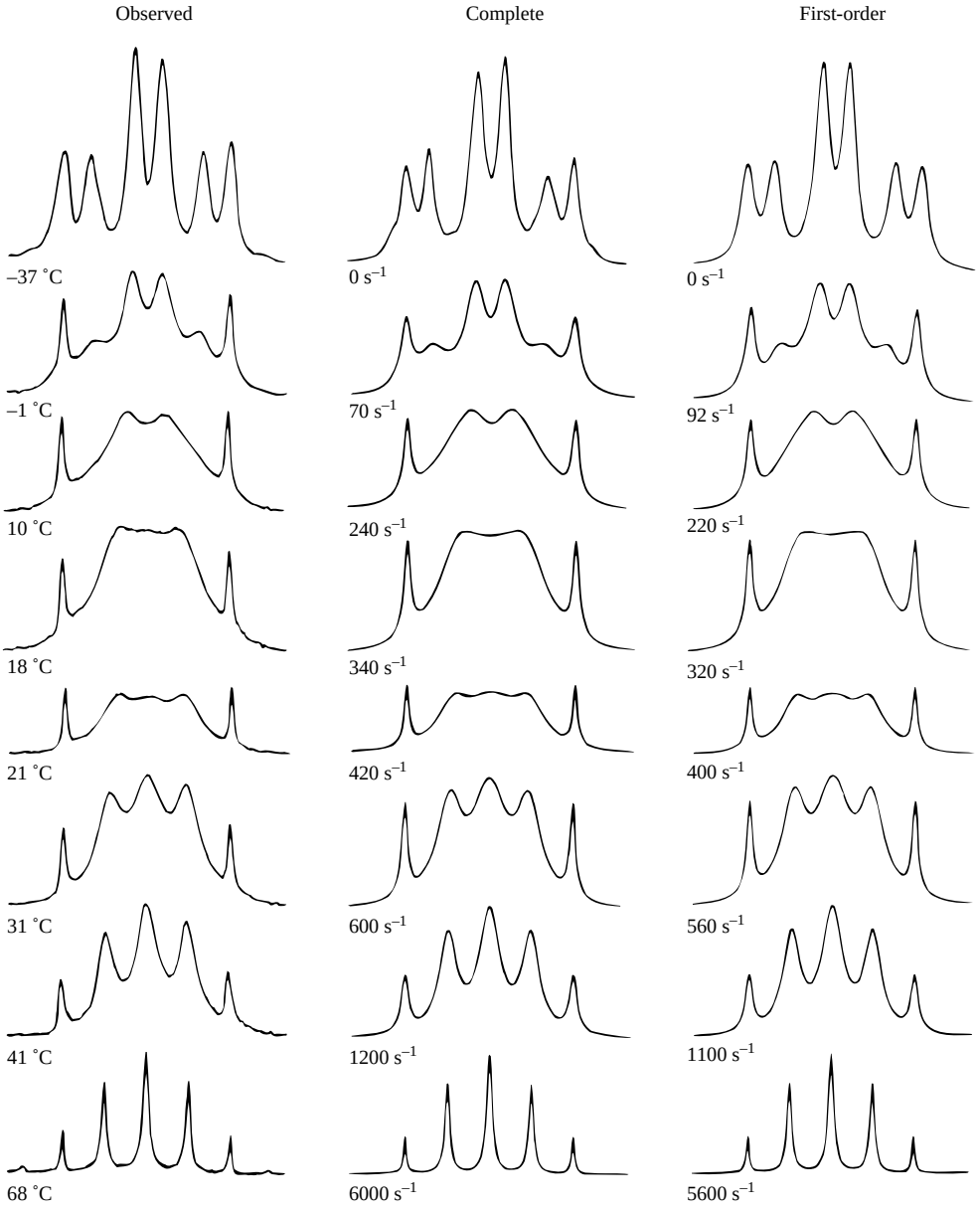

Figure 1 Observed and calculated 220 MHz ^1H NMR spectra (hydride region) of $FeH_2[P(OEt)_3]_4$ as a function of temperature. The results are shown for first order and complete calculations using the basic computational set IV. (Reproduced by permission of The American Chemical Society from J. P. Jesson and P. Meakin, *Acc. Chem. Res.*, 1973, **6**, 269)

ligand from a tetrahedral face to a tetrahedral edge with concomitant increase in the associated P–Fe–P angle. The results of the DNMR study gave the activation parameters, $\Delta G^{\ddagger}$ (289 K) = 57.3 kJ mol^{-1}, $\Delta H^{\ddagger}$ = 46.4 kJ mol^{-1} and $\Delta S^{\ddagger}$ = −36.8 J K^{-1} mol^{-1}.

An enormous variety of six-coordinate complexes with unidentate ligands exist. Some of these exhibit fluxionality involving ligand site exchange, but rather more involve ligand-based movements (inversions, rotations and isomerizations). ML_5L' complexes are widespread, particularly when M is a transition metal, L is carbonyl and L′ is a nitrogen or sulfur donor ligand, e.g. [M(CO)$_5$L′] (M = Cr, Mo, or W) complexes. Many such complexes are fluxional. For example, if L′ contains an azo or dithio linkage then 1,2-metallotropic shifts can occur [equations (1) and (2)],[25] and these are detectable by NMR by the exchange effects on the R protons. In general, energies of these metal commutations are quite high [$\Delta G^{\ddagger}$ (298 K) = 55–80 kJ mol^{-1}], and in some cases the two-dimensional EXSY method is preferable to one-dimensional bandshape analysis. 1,3-Metallotropic shifts are also a common fluxional type, typical examples being complexes of naphthyridine [equation (1)] and 2,4-dithiapentane [equation (4)].[25]

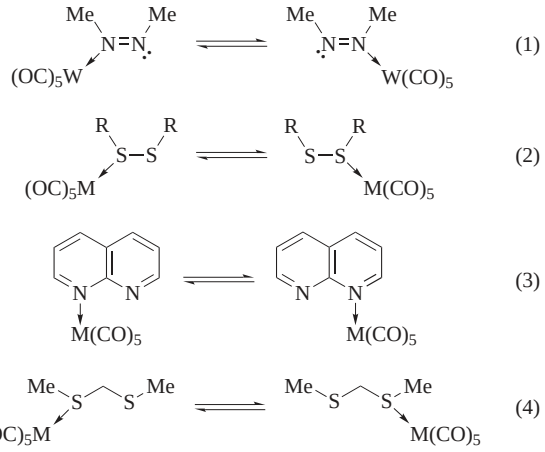

Complexes of type MX_3L_3 can exist in both meridional (*mer*) and facial (*fac*) forms, but *mer* ⇌ *fac* exchange is normally too slow for detection. Complexes of the type $MXL_3L'_2$ include platinum(IV) complexes [$PtXMe_3L'_2$] and isoelectronic rhenium(I) complexes [$ReX(CO)_3L'_2$], in both cases X being a halogen. Both series form *fac* complexes with nitrogen or sulfur as donor ligands. In bis(pyridazine) complexes, 1,2-M-N shifts occur on each ligand. In substituted pyridazine complexes, exchange between four linkage isomers has been measured by bandshape analysis and two-dimensional EXSY experiments (Scheme 5).[26]

2.1.5 Seven Coordination

Seven-coordinate complexes with unidentate ligands are normally highly nonrigid and NMR cannot always identify the static structure, usually a pentagonal bipyramid of D_{5h} symmetry (e.g. IF_7). Fluxional behavior in complexes of the types MH_3L_4 and MH_2L_5 has, however, been detected. The case of $CrH_2[P(OMe)_3]_5$ is illustrative.[27] The static spectrum (excluding OMe signals) comprises an $AB_2CC'XX'$

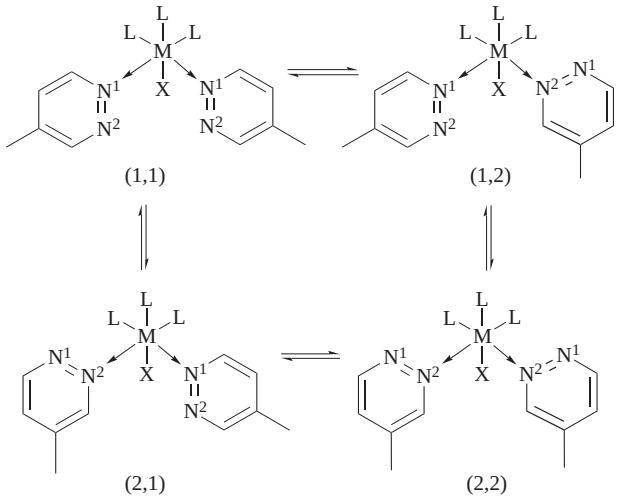

Scheme 5

spin system. From a full permutational analysis 16 basic sets of permutations of hydride and phosphine ligands were calculated. NMR bandshapes were calculated for all sets, but only two gave a reasonable matching with experimental spectra (Figure 2). The preferred mechanism involves simultaneous exchange of the two axial phosphines with two of the equatorial phosphines, the total fluxion corresponding to permutation of the CrP_5 framework related to the Berry pseudorotation process in five-coordinate complexes. The computation of the NMR bandshapes for this complex was far from trivial since the $^{31}P-\{^1H\}$ and ^1H spectra were five- and seven-spin problems, respectively. The work represents one of the most ambitious applications of DNMR total bandshape analysis.

Fluxional energy barriers decrease quite rapidly as the coordination number of the metal complexes increases beyond seven, and in most cases limiting slow exchange spectra are not accessible.

2.2 Bidentate Ligands

2.2.1 Four Coordination

The most common types are the bisbidentate complexes which possess either planar or tetrahedral structures. In the case of nickel(II) complexes, rapid interconversion between the two forms commonly occurs, namely planar (S = 0) ⇌ tetrahedral (S = 1). This equilibrium has been studied extensively for aminotroponeimine, salicylaldimine, and β-ketoamine complexes. The paramagnetism of the tetrahedral form causes large contact shifts of the ^1H or ^{13}C signals. The mechanism is thought to involve a *trans* planar intermediate via a diagonal twist process (Scheme 6). Bischelate complexes of the type $M(L-L')_2$ existing solely in the tetrahedral form may also display inversion of configuration ($\Delta \rightleftharpoons \Lambda$) which may be followed by NMR. For further details the reader is referred to the monograph by La Mar et al.[28]

2.2.2 Six Coordination

2.2.2.1 Monobidentate. Many fluxional complexes fall into this category. Some early studies concerned

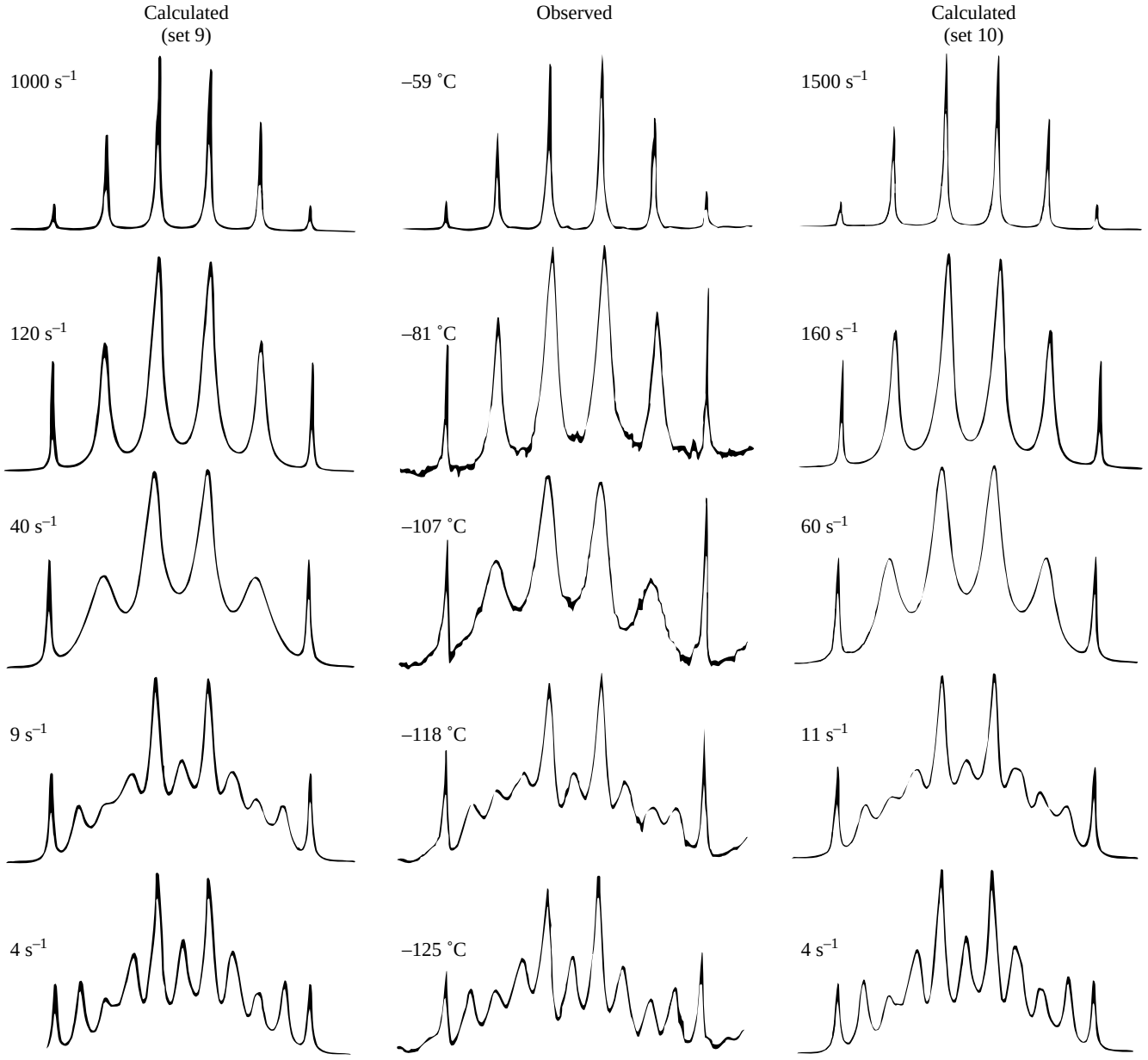

Figure 2 Experimental 90 MHz ^{1}H spectra (hydride region) of $CrH_2[P(OMe)_3]_5$ compared with theoretical spectra based on permutational sets 9 and 10. (Reproduced by permission of The American Chemical Society from F. A. Van-Catledge, S. D. Ittel, and J. P. Jesson, *Organometallics*, 1985, **4**, 18)

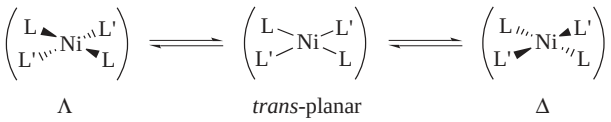

Scheme 6

titanium(IV) complexes of the type $RTiCl_3(L–L)$ where R = Me or OMe and the bidentate ligand (L–L) is of the type XCH_2CH_2Y with X, Y = OMe, SMe, or NMe_2.[29] These complexes can exist as *mer* or *fac* structures; the *mer* forms exchange as shown in equation (5). The mechanism is either via a five-coordinate dissociative intermediate or a ligand rotation via a seven-coordinate intermediate. The latter mechanism occurs in the complexes $[PtXMe_3(L–L)]$ and $[ReX(CO)_3(L–L)]$ (X = halogen; L–L = thioethers of the type $MeSCH_2CH_2SMe$, corresponding selenoethers and mixed thio/selenoethers). These complexes display multiple types of fluxionality, namely pyramidal inversions of the coordinated sulfur or selenium atoms, ligand 180° rotations, and, in the case of the platinum(IV) complexes, correlated $PtMe_3$ 120° rotations. These fluxions were separately measurable in the complexes $[PtXMe_3(MeSCH_2SCH_2SMe)]$, where all methylene ^{1}H signals become averaged at elevated temperatures. Pyramidal sulfur inversion leads to AB patterns for the diastereotopic methylene groups, but only a 180° ligand rotation process can lead to the additional A/B averaging [equation (6)].[25]

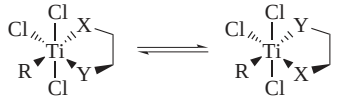

(5)

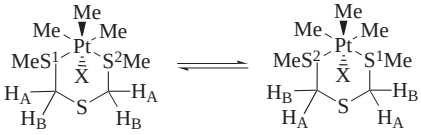

(6)

The use of ligands with redundant but potential donor atoms greatly increases the probability of fluxionality. This has been demonstrated for the complexes $[PtXMe_3\{(MeS)_2CHCH(SMe)_2\}]$, where the ligand possesses four sulfur donors but only two are involved in coordination at any time. However, a 1,3-Pt–S pivot fluxion occurs whereby all sulfur atoms become involved in the bonding.[10] Transition metal complexes of heterocyclic nitrogen donor ligands are widespread. Recently, a novel type of fluxionality has been shown to exist in bidentate chelate complexes where the ligand contains a third nitrogen donor. Such an example is 2,2′:6′,2″-terpyridine (terpy) when complexed with the metal moieties $PtXMe_3$ or $ReX(CO)_3$. These complexes are fluxional as a consequence of the ligand trying, but failing, to adopt its more usual terdentate binding mode.[17] Pyridylpyrazole ligand complexes are similarly fluxional and the complex $[ReBr(CO)_3(Me_2\text{-bppy})]$ [bppy = 2,6-bis(pyrazol-1-yl)pyridine] [equation (7)] has been studied in detail by means of both one-dimensional bandshape analysis and two-dimensional EXSY. In this case, the fluxion exchanges chemically distinct complexes by a process which involves a twist of the metal moiety through the N–Re–N angle via a seven-coordinate intermediate. The ^1H two-dimensional EXSY spectrum at $-10\,^\circ C$ shows exchange between pairs of ring hydrogen atoms with the exception of hydrogens J and S which are virtually isochronous (Figure 3)[30] Such 1,4-M–N shifts appear to be a common feature of complexes of aromatic nitrogen heterocycles with redundant nitrogen donors.

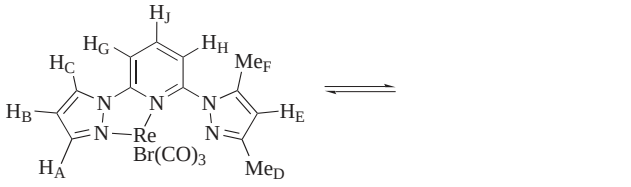

75%

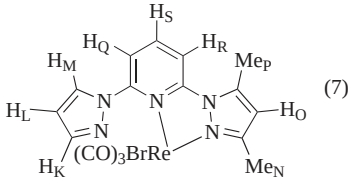

(7)

25%

2.2.2.2 Bisbidentate. Complexes of four main types fall into this category, namely $M(L–L)_2X_2$, $M(L–L')_2X_2$, $M(L–L)_2XY$, and $M(L–L')_2XY$, where X and Y denote unidentate ligands. Most studies have been performed on the complexes $M(L–L)_2X_2$, where (L–L) are β-diketonates and X are halides. Both *cis* and *trans* isomers can exist, the *cis* isomer usually being preferred. In contrast, the complexes $M(L–L')_2X_2$ can exist as five geometric isomers. The first such complex to be examined in detail was $[Ti(bzac)_2X_2]$ (X = F, Cl, or Br; bzac = benzoylacetonate), but no mechanistic information could be obtained from the DNMR bandshape changes.[31]

2.2.2.3 Trisbidentate. The study of the stereochemical nonrigidity of octahedral tris chelate complexes represents a major challenge to DNMR techniques. This is a large and complex subject and space does not allow other than a brief mention of its scope. The reader is referred to the article by Holm[31] for more detail on early work in this field.

The complexes of symmetrical chelates, $M(L–L)_3$ do not possess geometrical isomers and their only source of nonrigidity is inversion of configuration, $\Delta \rightleftharpoons \Lambda$. This may be followed by NMR, providing that the ring substituents contain a diastereotopic group. Complexes of the type $M(L–L')_3$ can exist as *cis* or *trans* isomers, each of which is enantiomeric. The isomers can undergo both inversion ($\Delta \rightleftharpoons \Lambda$) and isomerization (*cis* $\rightleftharpoons$ *trans*) by twist or bond-rupture mechanisms. In the case of β-diketonate complexes, isomerization generally occurs via a bond-rupture mechanism. The case of $[Al(pmhd)_3]$ (Hpmhd = 1-phenyl-5-methylhexane-2,4-dione) has been examined closely.[32] Variable temperature spectra of the methyl signals were compared with computer-simulated spectra based on a variety of fluxional mechanisms and signal assignments. Three mechanisms produced satisfactory fits between experimental and theoretical spectra. The DNMR problem involved a 16-site exchange matrix. The degree of complexity of the problem can be appreciated from the fact that there are 720 different ways of assigning the methyl signals in the slow exchange spectrum!

Other tris chelate ligand complexes which have been examined in detail by DNMR are complexes of substituted tropolonates and dithiocarbamates.

3 FLUXIONAL ORGANOMETALLIC COMPOUNDS

3.1 Rotations about Metal–Ligand and Metal–Metal Bonds

The diversity of bonding types in organometallic chemistry is reflected in the wide range of rotation rates of M–L and M–M bonds, where both steric and electronic factors appear to play distinctive roles.[33]

3.1.1 σ Metal–Carbon Bonds

The degree of double bond character of M–C bonds can vary enormously. In the case of carbene ligands this can cause the free energy of activation for rotation to rise to around 100 kJ mol^{-1}. However, there is no simple relationship between the degree of double bond character and the size of the rotational barrier, as exemplified by the complexes $[(\eta\text{-}C_5H_5)(CO)_2(Et_3P)\ M\text{-}CH_2]^+$: when M = W, the energy barrier is about 35 kJ mol^{-1}, whereas when M = Mo the barrier is too low for NMR estimation.[34]

3.1.2 Metal–Alkene and Metal–Alkyne Bonds

NMR techniques have been applied very extensively to these rotations. Two fundamentally different processes may

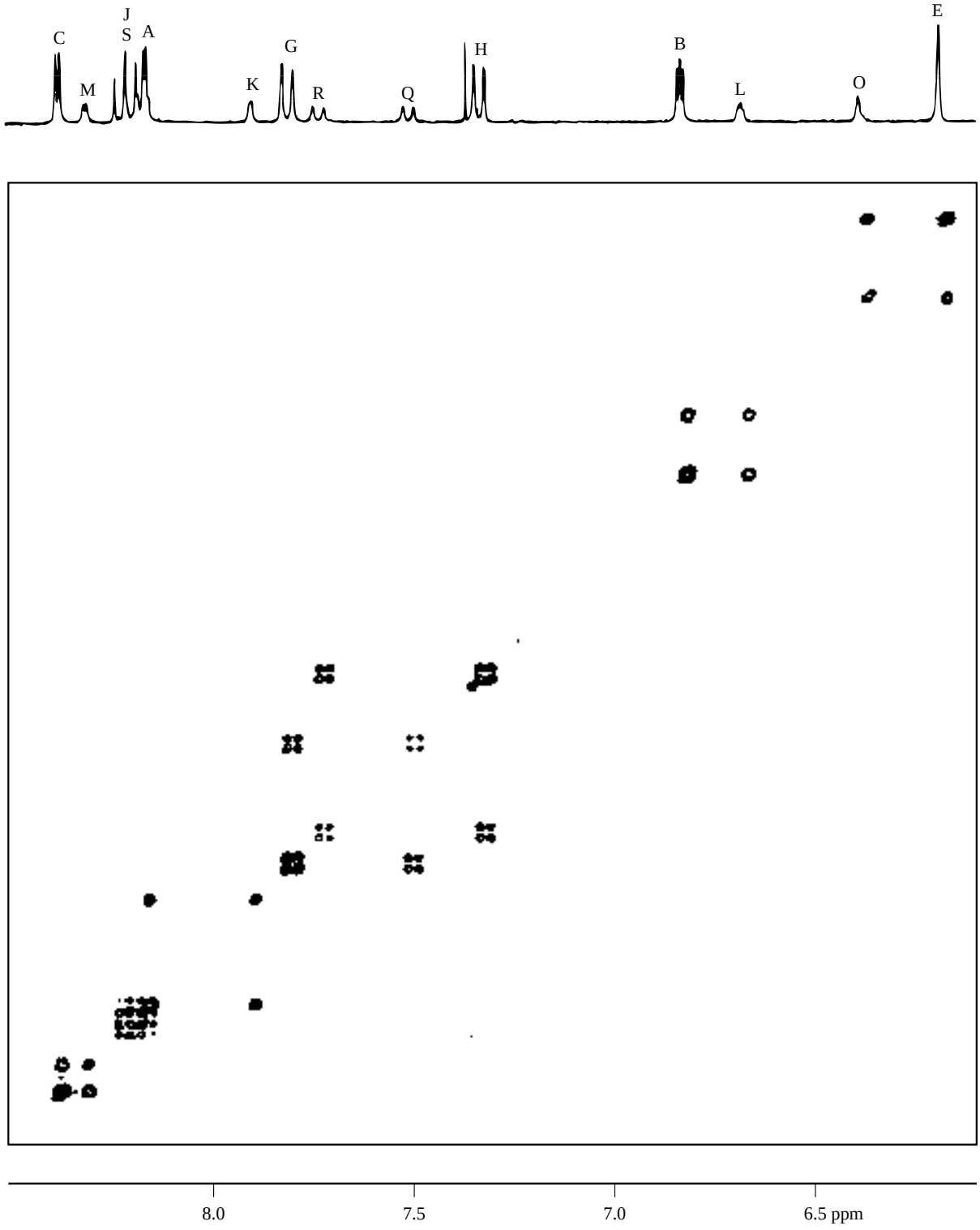

Figure 3 The ^{1}H two-dimensional EXSY spectrum of [$ReBr(CO)_3(Me_2$-bppy)] in CD_2Cl_2 at $-10\,^{\circ}C$ showing the effects of the 1,4-fluxional shift. The mixing time for the experiment was 0.5 s. (Reproduced by permission of The Chemical Society from E. W. Abel, K. A. Hylands, M. D. Olsen, K. G. Orrell, A. G. Osborne, V. Šik, and G. N. Ward, *J. Chem. Soc., Dalton Trans.*, 1994, 1079)

be envisaged (see Scheme 7). In (a) there is rotation about an axis between the metal and the center of the C=C bond, whereas in (b) the C−C bond itself acts as the rotation axis. In highly symmetrical molecules these two mechanisms are not distinguishable, but there is extensive evidence for pathway (a). Such a mechanism operates in the carbonyl nitrosyl complexes (**1**) and (**2**). In (**2**) each ethene hydrogen is in a unique environment which at low temperature results in an ABCD spectrum. The observation[35] of collapse to an AA′BB′ spectrum on warming is in accord with rotation about the

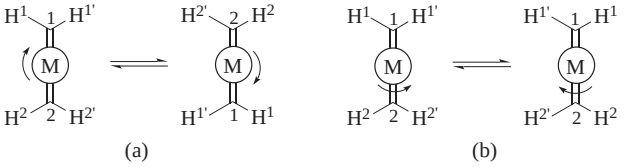

(a) (b)

Scheme 7

metal–alkene bond. Any additional rotation about the C=C axis would have produced further collapse to an A_4 spectrum.

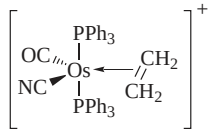

(1)

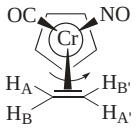

(2)

Alkene–metal rotations have free energies of activation ranging between about 30 and 80 kJ mol^{-1}. A similar range is associated with alkyne–metal rotations.

3.1.3 Metal–η-Enyl Bonds

The simplest η-enyl metal complexes are those containing η-allyl groups. A typical example is shown in equation (8).[36] Here the influence of the R group is surprisingly large: when R = H, E_a = 52 kJ mol^{-1}, whereas when R = Me, E_a = 70 kJ mol^{-1}. Numerous variable temperature NMR studies have demonstrated rotations in acyclic (e.g. pentadienyl) and cyclic (e.g. five-, seven-, and eight-membered) poly(enyl) metal complexes. Several of these have such low activation energies that they have been characterized by solid state CP MAS experiments. In the case of cyclopentadienyl (Cp) ligands, ring substitution can greatly hinder the ligand rotation, even in solution. For example, in 1,1′,2,2′,4,4′-hexakis(trimethylsilyl)ferrocene[37] the barrier to mutual rotation of the Cp rings can be measured by NMR ($\Delta G‡$ = 46 kJ mol^{-1}), in contrast to ferrocene itself where the barrier is too low for detection by solution NMR studies and is <10 kJ mol^{-1} in the solid state.

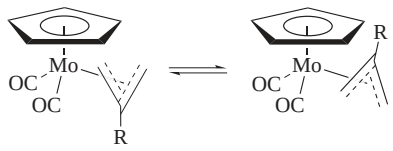

(8)

3.1.4 Metal Polyenes and Arenes

An example of rotation of the simplest polyene, butadiene, is in the complex (η-C_4H_6)Fe(CO)$_3$ (**3**). At room temperature only one carbonyl signal is observed in the ^{13}C spectrum, but, on cooling, the slow rotation region can be reached. The ^{1}H spectra show that the *syn* and *anti* terminal hydrogen atoms do not exchange, showing the molecules to be conformationally labile but configurationally stable. There have been numerous other studies of rotations of acyclic η^4-dienes, cyclic η^4-dienes, and cyclic η^6-trienes about metal atoms. In general, the rotations are quite facile with $\Delta G‡$ values usually falling in the range 30–50 kJ mol^{-1}.

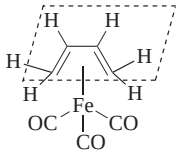

(3)

Rotations about metal–arene bonds are extremely facile, even in the solid state. For the compound Cr(η-C_6H_6)(CO)$_3$, lineshape measurements gave[38] an activation energy, E_a of 3.4 kJ mol^{-1}, whilst T_1 measurements (in good agreement) gave a value of 4.2 kJ mol^{-1}. Ring substitution predictably raises the energy barrier to rotation. Thus for [Cr(η-Et_6C_6)(CO)$_2$(CS)] in solution the barrier is about 35 kJ mol^{-1}, the ethyl groups needing to twist out of the path of the carbonyls so that the Cr(CO)$_2$(CS) moiety may rotate. In the complexes [M(η^6-C_6H_5Me)(CO)$_3$] (M = Cr or Mo), metal–arene rotations are too fast for detection in solution but are measurable by ^{13}C CP MAS spectroscopy in the solid. Here, however, the arene rings are locked in the lattice and the detectable rotations are due to the spinning of the M(CO)$_3$ groups.[39] The highly facile rotation of the metal–arene system is associated with the full delocalization of the aromatic ring. In cases where the ring has a localized hexatriene character, the barrier to rotation becomes accessible to solution NMR studies.

3.1.5 Metal–Metal Bonds

Many examples of rotations about metal–metal bonds have been observed and characterized by NMR spectroscopy, but their activation energies are difficult to rationalize, since values do not increase steadily with bond order. For instance, in the case of rotation about tungsten–tungsten bonds, in [W(η-C_5H_5)(CO)$_3$]$_2$ and [WMe(NEt$_2$)$_2$]$_2$ activation energies are 68 and 89 kJ mol^{-1}, this being a surprisingly small difference for rotations about formally single and triple metal–metal bonds, respectively. Many heteronuclear metal–metal bonds have also been investigated, one such case[40] being rotation about the W=As bond in (**4**) where ^{1}H spectra show coalescence of the two *t*-Bu signals on rotation, $\Delta G‡$ being estimated as 46 kJ mol^{-1}. Clearly, in all these metal–metal bond rotations the measured rates are a complex function of both electronic and steric factors.

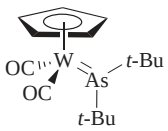

(4)

3.2 Metallotropic Shifts

The first observations of metallotropic shifts in the mid-1950s launched the whole field of fluxionality in organometallic compounds. It was in 1956 that the unexpected temperature

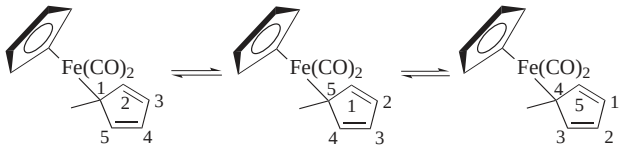

Scheme 8

dependence of the ^{13}C spectra of [Fe(σ-C_5H_5)(η-C_5H_5)$(CO)_2$] led to the radical proposal, for that time, that whilst the molecule was static at about −80 °C, at higher temperatures the [Fe(η-$C_5H_5(CO)_2$] moiety migrated around the σ-C_5H_5 ring by a series of [1,2]-shifts (Scheme 8). A similarly important observation was made in 1959 when the allyl Grignard reagent was shown to be fluxional [equation (9)] since its ^1H spectrum consisted of only two instead of the expected four signals. The mechanism here involves rapid [1,3]-shifts of the MgX group across the allyl group, with free rotation about the C−C single bond.

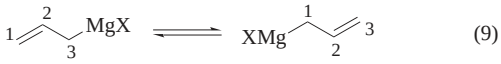

(9)

3.2.1 σ-Cyclopentadienyls

The sigmatropic shift of metals and metalloids around the cyclopentadienyl ring system, in addition to being the first organometallic fluxion to be detected by NMR spectroscopy, is also now one of the most common. The shift, illustrated in Scheme 2, has been observed for a remarkable range of metals and metalloids such as B, In, Si, Ge, Sn, As, Sb, Cu, Hg, Ti, Cr, Mo, Fe, Ru, Pd, and Pt. Distinction between [1,2]- and [1,3]-shifts around the ring is a subtle and challenging problem in DNMR spectroscopy, and has been the subject of much debate in recent years. The weight of evidence strongly favors [1,2]-shifts in most cases, and in some the evidence is definitive. Such an example is the silylcyclopentadiene (**5**). The chiral silicon atom produces anisochronicity among the C-2,5 and C-3,4 carbon pairs in the low-temperature ^{13}C spectra. At higher temperatures the C-2 and C-5 signals coalesce more rapidly with C-1 then do C-3 and C-4. A full bandshape analysis of this five-site exchange problem demonstrates that the [1,2]- and [1,3]-pathways are fully distinguishable and that only the [1,2]-shift case fits the observed ^{13}C spectra.[41]

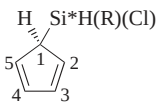

(5)

When there are multiple cyclopentadienyl rings attached to one metal it is conceptually easier to view the rings as rotating with respect to the metal. Thus, in (σ-$C_5H_5)_3As$ all three rings migrate by [1,2]-shifts on the arsenic atom. Such situations may be further complicated by ligand role exchange. Thus, in [Ti(η-$C_5H_5)_2$(σ-$C_5H_5)_2$] (Figure 4)[42] the lowest energy process is the [1,2]-shift of the σ-C_5H_5 rings, but there is evidence of [1,3]-shifts as a minor pathway. At higher temperature all ^1H signals collapse to a singlet, indicating the rapid interchange of roles of the σ- and η^5-bonded rings. This occurs readily in solution above about 333 K, but is substantially retarded in the solid state. In contrast, the σ-C_5H_5 migration occurs with similar facility in both solid and solution phases.

3.2.2 σ-Cycloheptatrienyls

Thermal sigmatropic shifts for metal cycloheptatrienyl complexes are predicted, by the Woodward–Hoffmann rules, to be of the [1,5]-type, and this has been confirmed by NMR in compounds such as Sn(σ-$C_7H_7)R_3$. At first sight such shifts appear to be less likely than the 'shortest distance' [1,2]-shift, but the folded conformation of the C_7H_7 ring allows the [1,5]-shift to be only a marginally more distant migration than the [1,2]-shift. For [Re$(CO)_5$(σ-C_7H_7)], however, the situation is reversed and elegant spin saturation experiments[43] have shown the migration to be of the [1,2]-type. There is clearly a delicate balance between 'shortest distance' and Woodward–Hoffmann criteria, and in some cases more than one pathway is followed. For example, in Rn(η-C_5H_5)(η^1-C_7H_7)$(CO)_2$ both [1,2]- and [1,5]-shifts occur at comparable rates.[44]

3.2.3 Noncyclic σ-Enyls

The σ-allyl complexes are the simplest example here and the overall fluxion is a [1,3]-shift as described for the Grignard complexes [equation (9)]. Similar migrations have been observed for other elements, notably B, Hg, Ti, and Pd.

[1,5]-Suprafacial shifts have been detected by spin saturation transfer and line-broadening studies of a hexadiene tin compound [equation (10)]. This symmetry-allowed shift has an activation energy of 81.5 kJ mol^{-1}.

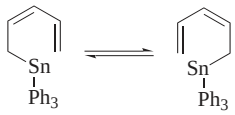

(10)

3.2.4 Metal Migrations on π Systems

When a metal is π-bonded to an organic moiety there is considerable potential for metal migrations and large numbers of π-bonded transition metal organometallics have been thus characterized by NMR. Illustrative examples of six-, seven-, and eight-membered ring complexes are given below.

A six-membered ring case is represented by the η^6-naphthalene $Cr(CO)_3$ complex where NMR spectra show the metal moiety to move between the two rings, as shown in equation (11).[45] A similar shift occurs between the six- and eight-membered rings in benzocyclooctatetraenetricarbonyl chromium.

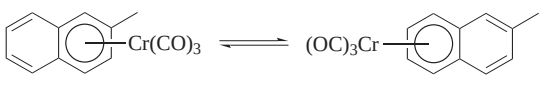

(11)

Seven-membered ring cycloheptatrienyl complexes may be η^3, η^4, or η^5 bonded, but all types have been shown to undergo [1,2]-shifts. The case of the η^4 complex [Fe$(CO)_3$(η^4-C_7H_8)]

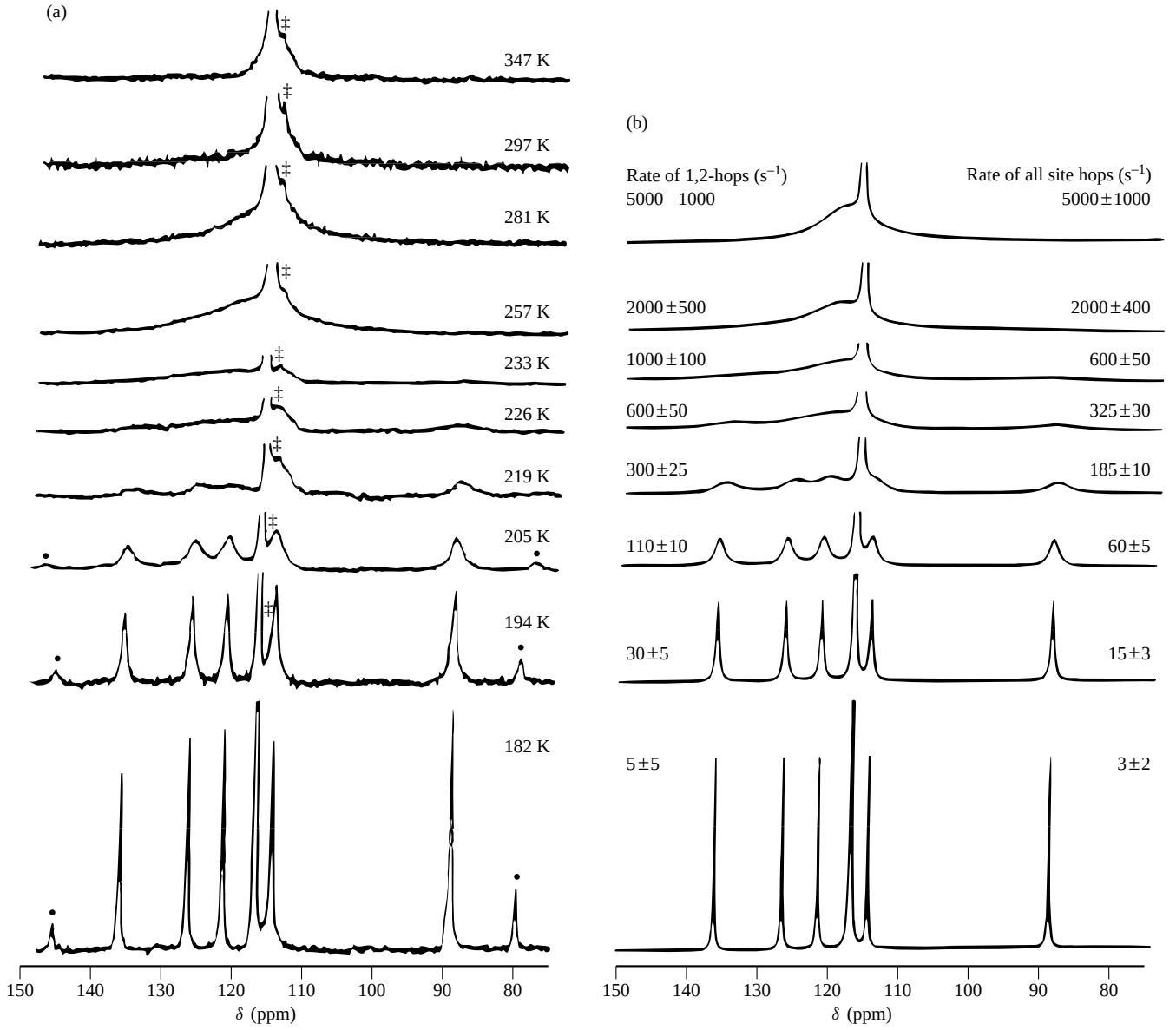

Figure 4 (a) ^{13}C CP MAS spectra of $Ti(C_5H_5)_4$ at various temperatures, showing the isotropic resonances. Signals (•) are spinning sidebands. (b) Simulation of the centerband spectrum using the program DNMR4. A simple five-site exchange model was used and exchange was modeled with [1,2] or random shifts. (Reproduced by permission of The American Chemical Society from S. J. Heyes and C. M. Dobson, *J. Am. Chem. Soc.*, 1991, **113**, 463)

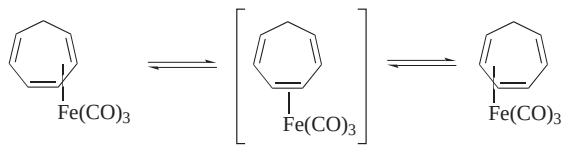

Scheme 9

is illustrated in Scheme 9, the mechanism invoking an η^2 16-electron intermediate.

Cyclooctatetraene (COT) is the main example of eight-membered π systems. When it is η^2 bonded to metals no metal migration is detectable, whereas all η^4-COT compounds are highly fluxional. In the compound $(\eta^4\text{-COT})Ru(CO)_3$, the ^{1}H spectrum at ambient temperatures is a singlet, but this changes to a complex AA′BB′CC′DD′ spectrum at about −150 °C, the different collapse rates for different proton pairs firmly establishing a [1,2]-shift mechanism.[46] The commutation of the $M(CO)_3$ moiety in $[(\eta^6\text{-COT})M(CO)_3]$ (M = Cr or W) has been studied extensively, originally by magnetization transfer experiments[47] and latterly by ^{1}H and ^{13}C two-dimensional EXSY experiments.[48] Even now the transition state for these migrations cannot be precisely defined, since both [1,2]- and [1,3]-shifts occur at comparable rates. When M = W both shifts are almost equally favored, whereas when M = Cr the [1,3]-pathway is slightly preferred.

Examples of interesting fluxional π-enyl metal complexes are structures (**6**)–(**8**). In (**6**) the static structure produces an A_2B_2X ^{1}H spectrum showing distinct *syn* and *anti* protons. On warming, these signals collapse to an A_4X spectrum, this

being attributed to a $\pi-\sigma-\pi$ mechanism whereby the metal effectively moves from one face of the allyl ligand to the other. An interesting extension to this shift occurs in η^3-benzyl complexes such as (**7**) where the benzene double bonds are frozen due to the allylic metal bond. On warming the complex the ^{1}H spectrum changes as a result of a ligand 'flip-over' analogous to that for allyl groups. The ^{1}H spectra of (**8**) change from three singlets (relative intensities 2:1:1) to one singlet on warming. This is attributed to the $Fe(CO)_4$ moiety moving between all four available alkene faces of the allene structure, presumably by the metal moving to either face of the adjacent double bond by a [1,2]-shift with a simultaneous 90° rotation about the allene axis, and then back again in a type of corkscrew shuttle motion.[49]

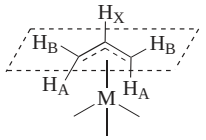

(6)

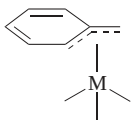

(7)

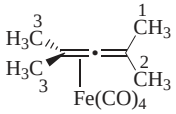

(8)

3.3 Miscellaneous Rearrangements

The diversity of fluxional processes in organometallic compounds, as revealed by NMR experiments, is enormous and the examples chosen above are simply representative of some of the major types. As the size of organometallic species increases so does the number of possible fluxional modes. In metal cluster compounds, for example, the many types of skeletal rearrangement and ligand migration (e.g. carbonyl exchanges) which can occur have been characterized primarily by NMR methods.

In many systems, stereochemical nonrigidity manifests itself in conformational changes within ligands (e.g. hindered internal rotations, site inversions, or ring reversals) rather than exchanges between ligands. Again, NMR has been invaluable in revealing and quantifying rates of such processes.

This article can only hint at the enormous contribution NMR has made to our understanding of stereochemical nonrigidity in molecules. Readers requiring more detailed literature coverage should see the regular reviews *Rearrangements, Intramolecular Exchanges and Isomerizations of Organometallic Compounds*,[50] and *Dynamic NMR Spectroscopy in Inorganic and Organometallic Chemistry*.[17]

4 RELATED ARTICLES

Chemical Exchange Effects on Spectra; Inorganic Chemistry Applications; Organometallic Compounds; Two-Dimensional Methods of Monitoring Exchange.

5 REFERENCES

1. E. L. Muetterties, *Inorg. Chem.*, 1965, **4**, 769; *Acc. Chem. Res.*, 1970, **3**, 266.
2. G. Binsch, *Topics Stereochem.*, 1968, **3**, 97.
3. G. Binsch, *J. Am. Chem. Soc.*, 1969, **91**, 1304.
4. L. M. Jackman and F. A. Cotton (eds), *Dynamic NMR Spectroscopy*, Academic, New York, 1975.
5. J. I. Kaplan and G. Fraenkel, *NMR of Chemically Exchanging Systems*, Academic, New York, 1980.
6. J. Sandström, *Dynamic NMR Spectroscopy*, Academic, London, 1982.
7. I. O. Sutherland, *Annu. Rep. NMR Spectrosc.*, 1971, **4**, 71.
8. P. D. Buckley, K. W. Jolly, and D. N. Pinder, *Prog. NMR Spectrosc.*, 1975, **10**, 1.
9. J. W. Faller, *Adv. Organomet. Chem.*, 1977, **16**, 211.
10. K. G. Orrell, V. Šik, and D. Stephenson, *Prog. NMR Spectrosc.*, 1990, **22**, 141.
11. W. von E. Doering and W. R. Roth, *Angew. Chem., Int. Ed. Engl.*, 1963, 2, 120.
12. F. A. Cotton, *Acc. Chem. Res.*, 1968, **1**, 257.
13. A. Davison and P. E. Rakita, *J. Am. Chem. Soc.*, 1968, **90**, 4479; *J. Organomet. Chem.*, 1970, **23**, 407.
14. S. Forsén and R. A. Hoffman, *J. Chem. Phys.*, 1963, **39**, 2892; 1964, **40**, 1189.
15. R. A. Hoffman and S. Forsén, *J. Chem. Phys.*, 1966, **45**, 2049.
16. J. Jeener, B. H. Meier, P. Bachmann, and R. R. Ernst, *J. Chem. Phys.*, 1979, **71**, 4546.
17. K. G. Orrell and V. Šik, *Annu. Rep. NMR Spectrosc.*, 1993, **27**, 103; 1987, **19**, 79.
18. R. A. Ogg and J. D. Ray, *Discuss. Faraday Soc.*, 1955, **19**, 239.
19. A. Rauk, L. C. Allen, and K. Mislow, *Angew. Chem., Int. Ed. Engl.*, 1970, **9**, 400.
20. L. H. Pignolet, W. D. Horrocks, Jr., and R. H. Holm, *J. Am. Chem. Soc.*, 1970, **92**, 1855.
21. F. A. Cotton, J. W. George, and J. S. Waugh, *J. Chem. Phys.*, 1958, **28**, 944.
22. J. P. Jesson and E.L Muetterties in *Dynamic NMR Spectroscopy*, ed. L. M. Jackman and F. A. Cotton, Academic, New York, 1975, p. 253.
23. P. Meakin and J. P. Jesson, *J. Am. Chem. Soc.*, 1973, **95**, 7272.
24. J. P. Jesson and P. Meakin, *Acc. Chem. Res.*, 1973, **6**, 269, and references therein.
25. E. W. Abel, S. K. Bhargava, and K. G. Orrell, *Prog. Inorg. Chem.*, 1984, **32**, 1.
26. E. W. Abel, E. S. Blackwall, P. J. Heard, K. G. Orrell, V. Šik, M. B. Hursthouse, M. A. Mazid, and K. M. A. Malik, *J. Chem. Soc., Dalton Trans.*, **1994**, 445.
27. F. A. Van-Catledge, S. D. Ittel, and J. P. Jesson, *Organometallics*, 1985, **4**, 18.
28. G. N. La Mar, W. D. Horrocks, and R. H. Holm, *NMR of Paramagnetic Molecules, Principles and Applications*, Academic, New York, 1973.
29. R. J. H. Clark and A. J. McAlees, *Inorg. Chem.*, 1972, **11**, 342.
30. E. W. Abel, K. A. Hylands, M. D. Olsen, K. G. Orrell, A. G. Osborne, V. Šik and G. N. Ward, *J. Chem. Soc., Dalton Trans.*, **1994**, 1079.
31. R. H. Holm, in *Dynamic NMR Spectroscopy*, ed. L. M. Jackman and F. A. Cotton, Academic, New York, 1975, p. 317.
32. J. R. Hutchinson, J. G. Gordon II, and R. H. Holm, *Inorg. Chem.*, 1971, **10**, 1004.
33. B. E. Mann, in *Comprehensive Organometallic Chemistry*, ed. G. Wilkinson, F. G. A. Stone, and E. W. Abel, Pergamon, Oxford, 1982, Vol. 3, Chap. 20
34. S. E. Kegley, M. Brookhart, and G. R. Husk, *Organometallics*, 1982, **1**, 760.

35. H. Alt, M. Herberhold, C. G. Kreiter, and H. Strock, *J. Organomet. Chem.*, 1974, **77**, 353.
36. J. W. Faller and M. J. Incorvia, *Inorg. Chem.*, 1968, **7**, 840.
37. J. Okuda and E. Herdtweck, *Chem. Ber.*, 1988, **121**, 1899.
38. P. Delise, G. Allegra, E. R. Mognaschi, and A. Chierico, *J. Chem. Soc., Faraday Trans. 2*, 1975, **71**, 207.
39. G. W. Wagner and B. E. Hansen, *Inorg. Chem.*, 1987, **26**, 2019.
40. M. Luksza, S. Himmel, and W. Malisch, *Angew. Chem., Int. Ed. Engl.*, 1983, **22**, 416.
41. A. Bonny, R. D. Holmes-Smith, G. Hunter, and S. R. Stobart, *J. Am. Chem. Soc.*, 1982, **104**, 1855.
42. S. J. Heyes and C. M. Dobson, *J. Am. Chem. Soc.*, 1991, **113**, 463.
43. D. M. Heinekey and W. A. G. Graham, *J. Am. Chem. Soc.*, 1979, **101**, 6115.
44. D. M. Heinekey and W. A. G. Graham, *J. Am. Chem. Soc.*, 1982, **104**, 915.
45. E. P. Kuendig, V. Desobry, C. Grivet, B. Rudolph, and S. Spichiger, *Organometallics*, 1987, **6**, 1173.
46. F. A. Cotton, in *Dynamic NMR Spectroscopy*, ed. L. M. Jackman and F. A. Cotton, Academic, New York, 1975, p. 401.
47. M. Grassi, B. E. Mann, B. T. Pickup, and C. M. Spencer, *J. Magn. Reson.*, 1986, **69**, 92.
48. E. W. Abel, K. G. Orrell, K. B. Qureshi, V. Šik, and D. Stephenson, *J. Organomet. Chem.*, 1988, **353**, 337.
49. R Ben-Shoshan and R. Pettit, *J. Am. Chem. Soc.*, 1967, **89**, 2231.
50. M. V. Twigg (ed.), *Mechanisms of Inorganic and Organometallic Reactions*, Plenum, New York, Vols 1–8, Chap. 13

Biographical Sketch

Keith G. Orrell. *b* 1940. B.Sc.Tech., 1960, Ph.D., 1964, D.Sc., 1989, University of Manchester, UK. Successively lecturer, senior lecturer and (currently) reader, University of Exeter, UK. Approx. 150 publications on dynamic NMR, NMR of paramagnetic species and studies in liquid crystalline phases. Current research specialties: NMR studies of intramolecular motions, particularly in inorganic and organometallic compounds.

Gas Phase Studies of Chemical Exchange Processes

Nancy S. True

University of California, Davis, CA, USA

1	Introduction	1
2	Equilibrium Constants of Chemical Exchange Processes	2
3	Gas Phase Kinetics of Chemical Exchange Processes	3
4	Related Articles	5
5	References	5

1 INTRODUCTION

NMR spectroscopy was applied to gas samples very early in its history. In 1946, Purcell, Pound, and Bloembergen reported the first gas phase NMR study.[1] They measured the nuclear spin–lattice relaxation rate constant, T_1, of H_2 gas at 10 atm and, based on the calculated correlation time, suggested that the rotationally inelastic collision cross section of H_2 is smaller than the hard sphere cross section. During the next 25 years, applications of NMR spectroscopy to gases were relatively uncommon. A review written by Govil discusses NMR applications to gases prior to 1972.[2] Because of sensitivity limitations, sample pressures above 1 atm were required, and most studies were concerned with density dependent chemical shifts and nuclear spin–lattice relaxation of diatomic and small polyatomic molecules. A few years after Govil's review, spectrometers employing superconducting magnets became available, making it possible to study gases below ambient pressure and to study spectra of many more nuclei in the gas phase. Now it is possible to observe spectra of samples at pressures of a few torr, and NMR spectroscopy can be used successfully to address a variety of chemical and physical properties and processes in the gas phase. Several reviews have recently appeared. Jameson reviewed recent gas phase NMR applications in 1991,[3] and Armstrong reviewed gas phase NMR relaxation studies in 1987.[4] True and Suarez reviewed gas phase NMR studies of conformational processes in 1994.[5] The present article focuses on selected chemical applications of gas phase NMR spectroscopy.

Gas phase equilibrium constants and rate constants of chemical exchange processes can, in some cases, be obtained from NMR studies, with an accuracy comparable with that obtained in the best liquid phase studies. Since intermolecular effects are minimal at the low pressures which can be studied with current NMR instrumentation, gas phase conformational equilibrium constants obtained from NMR experiments can be directly compared with theoretical calculations for isolated molecules. Comparisons with equilibrium constants obtained for condensed phase samples provide a critical test of theoretical methods of calculating solvent effects. NMR spectroscopy has been used to determine rate constants for chemical exchange processes in the gas phase as a function of pressure as well as temperature. At high pressures, unimolecular rate constants which can be compared with corresponding rate constants in solutions are obtained. At lower pressures, rate constants decrease with decreasing pressure and in many cases it has been possible to study the kinetics of chemical exchange processes in the low-pressure bimolecular region and to address questions about the microscopic dynamics of these processes.

Gases and liquids produce qualitatively similar NMR spectra. For typical molecules which undergo chemical exchange, gas phase spin–lattice relaxation at pressures above a few hundred torr do not contribute appreciably to observed linewidths for spin-$\frac{1}{2}$ nuclei and under slow exchange conditions scalar coupling is as well resolved as it is in liquids. Gas phase spectra are offset a few parts per million from corresponding solution phase spectra of the same molecule due to differences in the bulk susceptibility of the sample. The magnitude and direction of the offset depends on the spectrometer field, sample shape, and orientation in the field and the sample composition.[6] Gas phase coupling constants and relative resonance positions are similar but not identical in gases and liquids. In the gas phase, conformer chemical shifts have only small linear temperature and pressure dependences over the temperature and pressure ranges used in most conformational studies and so can facilitate analysis of exchange broadened lineshapes. In solutions, chemical shifts can have strong nonlinear temperature dependences which can complicate the analysis of exchange broadened lineshapes to yield reliable rate constants.

Gas and liquid phase nuclear spin–lattice relaxation rates and mechanisms are different. Most studies of T_1 for ^{1}H in the gas phase have concluded that this nucleus relaxes primarily through spin–rotation interactions.[3,4] In the gas phase, T_1 can vary considerably over the temperature and pressure range where conformational data are obtained. Spin–rotation coupling constants are larger for nuclei in small molecules resulting in faster relaxation. At 1 atm, the values of T_1 for ^{1}H in NH_3 and benzene are 70 ms and 8 s, respectively.[4–7] Carbon-13 spin–lattice relaxation in benzene gas below 1000 torr also occurs primarily through spin–rotation interactions.[7] The T_1 of ^{13}C in benzene at 1 atm is about 1000 times shorter than in the liquid phase, a factor which greatly facilitates spectral acquisition. Efficient spin–rotation relaxation in the gas phase, however, usually makes it impossible to employ techniques which require dipolar relaxation.

Short NMR tubes are usually used in gas phase NMR experiments for better temperature control and to eliminate contributions to observed linewidths and relaxation rate constants from bulk diffusion of magnetized molecules out of the active volume during the acquisition time. Most commonly, 10 and 12 mm tubes have been used for samples at pressures below 1 atm, and heavy walled (2.2 mm i.d., 4 mm o.d) tubes have been used in the range 5–40 atm. With few exceptions, most gas phase NMR studies of conformational processes have utilized samples containing the molecule of interest which is of necessity present at a low partial pressure and varying pressures of inert bath gases. Inert gases increase T_1 and also provide a critical experimental variable for kinetic studies. NMR spectra of dilute gases are routinely obtained using superconducting high-resolution NMR spectrometers.

Proton chemical shifts have been measured for samples with partial pressures of less than 1 torr, while a few torr are generally required to produce exchange broadened lineshapes suitable for rate constant analysis. To date, gas phase chemical exchange studies have utilized ^{1}H, ^{2}D, ^{19}F, ^{13}C, ^{10}B, and ^{11}B, and gas phase studies of many other nuclei are also feasible.[4] Some studies have utilized external lock materials or added several atmospheres pressure of a deuterated gas to provide a frequency lock. For studies where linewidths of 1 Hz are acceptable it is usually not necessary to use a frequency lock if total acquisition times are less than 1–2 hours. Longer acquisitions are feasible without sacrificing resolution if spectra are acquired in blocks and added manually or if the voltage in the Z_0 shim coil is ramped during the experiment to compensate for the small linear field drift encountered with most superconducting magnets.

2 EQUILIBRIUM CONSTANTS OF CHEMICAL EXCHANGE PROCESSES

NMR spectroscopy is especially well suited for studies of conformational equilibria in many cases. Spectroscopic absorption coefficients depend on transition dipole matrix elements as well as populations of absorbing species. Since dipole matrix elements for nuclear magnetic transitions are not significantly different for different conformers, relative intensities in NMR spectra are directly related to the relative populations of the absorbing species. Relative intensity temperature dependent NMR measurements can yield a complete set of thermodynamic parameters characterizing the equilibrium process. In contrast, values of electric dipole transition matrix elements for rotational, vibrational, and electronic transitions can be significantly different for different conformations of the same molecule, making it impossible to determine a conformational equilibrium constant from relative intensity measurements alone. Lifetimes must be long enough so that each species produces a distinct NMR spectrum, and this is a serious limitation which has been partially overcome by measuring fast exchange coupling constants and using these measurements to deduce the conformational equilibrium. Measurements of both relative intensities and coupling constants have been used to determine equilibrium constants in the gas phase.

Keto–enol tautomerism of β-diketones has been studied in the gas phase. Keto–enol conversion occurs via an intramolecular proton shift between the methylene carbon in the keto form and one of the carbonyl oxygens in the enol tautomer. The activation energy for this process in the gas phase is not known, but since equilibrium is established rapidly after temperature changes and since the system still produces slow exchange spectra at temperatures as high as 200 K, the barrier can be estimated to be between 100 and 175 kJ mol^{-1}. Harris demonstrated the feasibility of using gas phase NMR intensity measurements to determine keto $\rightleftharpoons$ enol equilibrium constants, K_{eq}, of acetylacetone and ethyl acetoacetate.[9] A later gas phase NMR study reported the thermodynamic parameters characterizing keto–enol equilibria of acetylacetone, methyl acetoacetate, and ethyl acetoacetate.[10] For all three molecules, gas phase keto $\rightleftharpoons$ enol K_{eq} values were obtained from integration of

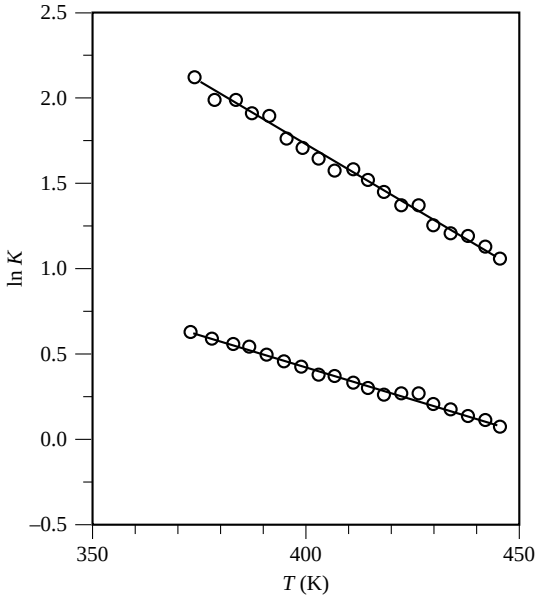

Figure 1 Gas and solution phase equilibrium constant, K_{eq} = [enol]/[keto], for the keto–enol tautomerism of acetylacetone as a function of temperature. Data on the upper line were obtained for a 200 torr gas sample and the data on the lower line were obtained for a neat liquid sample. (Reprinted by permission of the American Chemical Society from M. M. Folkendt, B. E. Weiss-Lopez, J. P. Chauvel, Jr., and N. S. True, *J. Phys. Chem.*, 1985, **89**, 3347)

^{1}H NMR spectra obtained between 373 and 445 K. Figure 1 shows equilibrium constants of acetylacetone gas and neat liquid as a function of temperature. For acetylacetone gas, ΔG^{0}_{298}(E–K) is -9.2 ± 1.9 kJ mol^{-1}, ΔH^{0}(E–K) is -19.5 ± 0.7 kJ mol^{-1}, and ΔS^{0}(E–K) is -34.6 ± 1.9 J mol^{-1} K^{-1}. The corresponding values in the neat liquid are -3.8 ± 1.2 kJ mol^{-1}, -11.8 ± 0.5 kJ mol^{-1}, and -26.7 ± 1.3 J mol^{-1} K^{-1}, respectively. A similar trend is observed for the keto $\rightleftharpoons$ enol equilibria of methyl acetoacetate and ethyl acetoacetate. The intramolecular hydrogen bond which is formed in the enol tautomer is primarily responsible for its lower energy. For all three molecules, in all phases the keto tautomer has the larger entropy, consistent with its lower torsional frequencies. ΔH^{0}(E–K) is smaller in the neat liquid, possibly indicating that solvent interactions lower the energy of the more polar keto tautomer.

The *syn* $\rightleftharpoons$ *anti* conformational equilibrium of gaseous methyl nitrite (O=NOCH$_3$) was studied using ^{1}H NMR spectroscopy. The first study reported thermodynamic parameters which were obtained from direct integration of resolved *syn* and *anti* methyl proton resonances.[11] The limitations of the low conformer interconversion barrier and sample volatility restricted the observation of slow exchange spectra to temperatures between 193 and 223 K. Thermodynamic parameters are ΔH^{0}(*anti*–*syn*) = 4.2 ± 0.2 kJ mol^{-1}, ΔG^{0}(*anti*–*syn*) = 2.2 ± 0.01 kJ mol^{-1}, and ΔS^{0}(*anti*–*syn*) = 9.75 ± 1.0 J mol^{-1} K^{-1}. The observed ΔS^{0}(*anti*–*syn*) value agrees with previously determined rotational and vibrational frequencies. The largest factor contributing to the calculated entropy difference is the methyl internal rotation barrier, which is 8.77 kJ mol^{-1} in *syn*-methyl nitrite and only 0.12 kJ mol^{-1} in the *anti* conformer. Cordell et al. reported ab initio molecular orbital calculations which show that a favorable interaction between

a C–H bond of the methyl group and the nitrogen lone pair when the CH and N groups are eclipsed stabilizes the *syn* conformer and also results in its higher methyl group internal rotation barrier.[12]

Chemical shifts of larger alkyl nitrites were measured in the slow exchange limit. Lower vapor pressures restricted measurements of slow exchange conformer relative intensities. Changes in the conformer equilibria of methyl nitrite with temperature produce large temperature dependent shifts in the fast exchange resonance position, and thermodynamic parameters obtained for methyl nitrite from direct signal integrations agree with those obtained from measurements of chemical shifts in the fast exchange limit. Therefore, fast exchange chemical shift measurements were used to obtain *syn* $\leftrightharpoons$ *anti* equilibrium constants of the larger nitrites.[13] In the gas phase, the *syn*–*anti* conformer energy difference is smaller for the larger nitrites and the *anti* conformers have larger entropies than the corresponding *syn* conformers with the exception of isopropyl nitrite. These trends are also observed in alkyl nitrite solutions but here the entropies of the *syn* and *anti* conformers are more similar.

For relatively large molecules, long-range coupling constants can be measured in the gas phase with the same accuracy as in solution. Figure 2 shows the ^{19}F NMR spectrum at 376 MHz of 1,2-difluoroethane in the gas phase at 353 K obtained by Hirano et al.[14] Nitrogen at a pressure of 1 atm was added to samples containing 507 torr of 1,2-difluoroethane, 47 torr of TMS, and 104 torr of $CFCl_3$ to increase T_1 and narrow the natural linewidth. The gas sample was contained in a 3 mm o.d. inner tube placed in a 5 mm o.d. outer tube containing [$^2H_6$]dimethyl sulfoxide as a lock solvent. ^3J coupling constants of 1,2-difluoroethane ranging from 2.78 to 25.69 Hz, with an estimated error of less than 0.002 Hz, were obtained by comparing simulated and observed spectra. They are consistent with a *trans*–*gauche* energy difference of 3.3 kJ mol^{-1}. Coupling constants have been obtained in the gas phase with similar accuracy for several other compounds. Analyzing long-range coupling constants to provide information about conformer populations and interconversion barriers is difficult. In addition to the difficulty of calculating coupling constants with current theory,[15] there is a small intrinsic temperature dependence of coupling constants of molecules which do not exist as conformational mixtures,[16,17] and it is not possible to separate the observed temperature dependence into intrinsic and conformationally dependent contributions. Despite these difficulties, large phase dependent differences in coupling constants are an indication of a phase dependent shift in the conformational equilibrium.

Hirano et al. also measured long-range coupling constants of gaseous 1,2-di[$^2H_3$]methoxypropane.[18,19] Analysis of the second-order spectrum produced by this $ABCX_3$ spin system yielded ^3J(AC) and ^3J(BC) of 4.89 and 6.38 Hz, respectively. Assuming that ^3J is 9.1 Hz for the antiperiplanar and 2.6 Hz for the synclinal form, based on results for 1-methoxypropan-2-ol, the observed coupling constants are consistent with G^+ and G^- conformers with relative energies 3.4 and −2.1 kJ mol^{-1} higher than the T conformer. Hirano et al. also determined that 1-methoxypropan-2-ol and 2-methoxyethanol are intramolecularly hydrogen bonded in the gas phase based on hydroxyl proton chemical shifts.[18,19]

Pachler and Wessels measured the temperature dependence of the vicinal coupling constants of 1-bromo-2-chloroethane

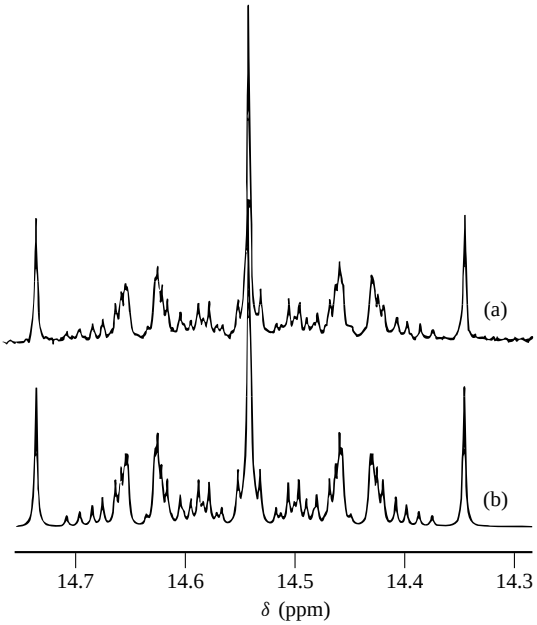

Figure 2 Fluorine-19 NMR spectra (376 MHz) of 1,2-difluoroethane in the gas phase at 353 K. (a) observed, (b) simulated. (Reprinted by permission of the Royal Society of Chemistry from T. Hirano, S. Nonoyama, T. Miyajima, Y. Kurita, and H. Sato, *J. Chem. Soc., Chem. Commun.*, 1986, 606)

in the gas phase between 375 and 478 K.[20] Since the internal rotation potential function in the gas phase was known, it was possible to evaluate the coupling constants for the *trans* and *gauche* isomers which were then used to analyze solution phase data. Inomata and Abe recently obtained gas phase values of ^3J(H,H) for 1,2-dimethoxyethane which ranged from 5.80 to 5.85 Hz between 398 and 443 K with an estimated error of less than 0.05 Hz.[21] The observed gas phase ^{1}H–^{1}H and ^{13}C–^{1}H vicinal coupling constants were compared with those in nonpolar solvents, and the authors concluded that the *gauche* oxygen effect in 1,2-dimethoxyethane is due to intramolecular factors rather than interactions with solvent molecules.

3 GAS PHASE KINETICS OF CHEMICAL EXCHANGE PROCESSES

In solutions, chemical exchange processes invariably exhibit unimolecular kinetics, and in most cases transition state (TS) theory has provided a convenient framework for reporting kinetic parameters for these processes.[8] In the gas phase, however, rate constants of chemical exchange processes are pressure dependent, and unimolecular kinetics are only observed at high pressures. The pressure dependence is due to competition between bimolecular deactivation,

$$A^* + M \underset{k_a}{\overset{k_d}{\rightleftharpoons}} A + M' \qquad (1)$$

and reaction of energized molecules (A*),

$$A^* \overset{k(E)}{\rightarrow} P \qquad (2)$$

where k_a, k_d, and $k(E)$ are the activating, deactivating, and internal energy dependent reaction rate constants. The macroscopic unimolecular reaction rate constant, k_{uni}, consistent with this mechanism is

$$k_{uni} = -\frac{1}{[A]}\frac{d[A]}{dt} = \int_{E^*=0}^{E} \frac{k(E)k_a/k_d}{1 + k(E)/k_d[M]} dE \qquad (3)$$

which reduces in the high-pressure limit to $k_{uni} = k(E)k_a/k_d$, and in the low pressure limit to $k_{uni} = k_a[M]$.[22] Accordingly, three pressure regions, unimolecular (high pressure), fall-off (intermediate), and bimolecular (low pressure), can, in principle, be observed for a gas phase chemical exchange process. Studies in each region provide different information about the process.

High-pressure unimolecular rate constants are most directly comparable to rate constants obtained in solutions. To a good first approximation, the temperature dependence of rate constants in the unimolecular region can be analyzed to provide Eyring parameters, i.e. $\Delta H^{\ddagger}$ $\Delta G^{\ddagger}$, and $\Delta S^{\ddagger}$, which can then be compared with those obtained for other molecules and with corresponding parameters in the liquid phase for the same molecule and also with theoretical calculations. Some precautions are needed in making these comparisons. First, it is not clear if transition state theory, which is the high-pressure limiting form of Rice–Ramsperger–Kassel–Marcus (RRKM) theory provides a valid description of all conformational processes under all conditions. Non-RRKM behavior can occur in either phase. Few conformational processes have been studied over the extensive pressure range in either the gas or solution phase required to provide a definitive test of RRKM theory. Also most solution phase studies of conformational processes have measured rate constants as a function of temperature at ambient pressure. These experiments do not allow the static and dynamic solvent effects to be separated. Solution phase studies under conditions of isoviscosity, obtained by applying pressure to the sample, show that isobaric and isoviscosity activation parameters can differ. Isoviscosity measurements are more directly comparable with gas phase results.[23]

Rate constants of many chemical exchange processes at or near the unimolecular limit have been determined using NMR spectroscopy and, despite the possible complication described above, several conclusions can be drawn. The earliest kinetic study of a conformational process using NMR spectroscopy was a study of the internal rotation in *N,N*-dimethylnitrosamine reported by Harris and Spragg.[24] The CW ^{1}H NMR spectrum of the gas at 100 MHz is at intermediate exchange at 160°C while that of the neat liquid is at slow exchange, consistent with a gas phase barrier about 8.4 kJ mol^{-1} lower than in the neat liquid. Additional studies have also demonstrated that gas and solution phase kinetic parameters can be significantly different. Internal rotation has been studied for several symmetrically substituted amides.[25–32] In each case, exchange broadened ^{1}H spectra were obtained for samples containing the amide at its vapor pressure and several atmospheres of an inert gas; measurements were made at several pressures to ensure that the rate constants were at the unimolecular limit. Feigel measured rate constants for internal rotation of *N,N*-dimethylacetamide at bath gas pressures ranging from 0.5 to 24.5 atm which were found to be independent of pressure.[29] Other amides

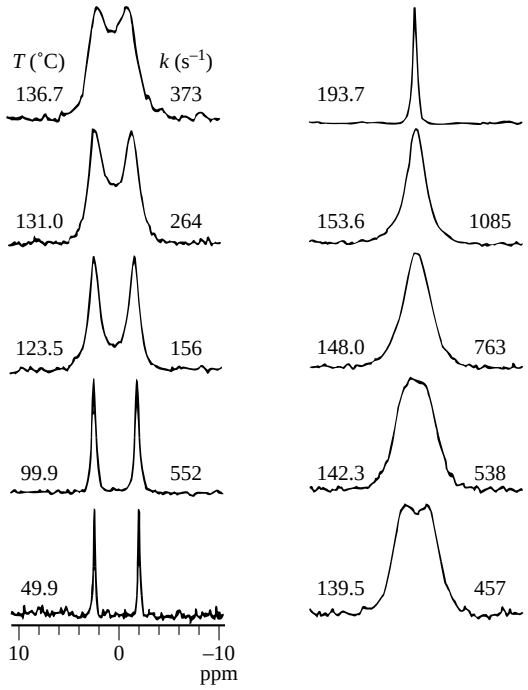

Figure 3 Carbon-13 NMR spectra of *N,N*-dimethylformamide. Spectra are Fourier transforms of the sum of about 2000 transients obtained at 50 MHz using a 99% ^{13}C enriched sample at its vapor pressure. (Reprinted by permission of the American Chemical Society from B. D. Ross and N. S. True, *J. Am. Chem. Soc.*, 1984, **106**, 2451)

were studied over a less extensive pressure range, typically from a few torr to 5 atm. For the simplest amide studied, *N,N*-dimethylformamide, the ^{1}H dimethylamino resonances are magnetically equivalent in the gas phase, and exchange broadened ^{13}C NMR spectra were used to obtain rate constants.[28] Figure 3 shows ^{13}C gas phase NMR spectra of *N,N*-dimethylformamide as a function of temperature. For all the amides studied, Gibbs activation energies, $\Delta G^{\ddagger}$ are 5–10 kJ mol^{-1} lower in the gas phase than in solutions for the same molecule. In solutions, the additional energy required to move solvent molecules when the dialkylamino group rotates partially explains the observations. Recent Monte Carlo simulations of solvent effects on the internal rotation barrier of *N,N*-dimethylacetamide, however, were not able to reproduce the observed phase dependent differences in activation parameters.[33]

For cyclohexane and seven other six-membered rings which have been studied in the unimolecular pressure region, much smaller differences between gas and solution phase activation parameters were observed.[34–41] NMR studies of cyclohexane demonstrated that gas phase rate constants are lower and activation parameters are higher than in the liquid phase. Early liquid phase studies at atmospheric pressure reported an activation energy of 42.7 ± 0.8 kJ mol^{-1}.[34] Recently, Jonas et al. have shown that measurements at constant sample viscosity produce a significantly higher activation energy, 47.2 ± 0.1 kJ mol^{-1}, which is much closer to the gas phase value, 52.5 ± 1.0 kJ mol^{-1}, obtained at 2500 torr.[23]

Pressure dependent rate constants of unimolecular processes provide a test of kinetic theories. Statistical kinetic theories such as RRKM theory assume that the rate constant for intramolecular energy redistribution (IVR), k_{ivr}, in critically

energized molecules is rapid compared with the energy dependent reaction rate constant, $k(E)$ and that IVR is ergodic. According to the Fermi golden rule, k_{ivr}, is directly proportional to the density of states $\rho(E)$. Since $k(E)$ is inversely proportional to $\rho(E)$, the condition $k_{ivr} \gg k(E)$ is most likely to be valid at high state densities, and statistical theories of chemical reactions are therefore most applicable to large molecules undergoing processes at high activation energies. At the low activation energies required for conformational processes, critically energized molecules have sparse state densities and the anharmonic coupling constants among vibrational states are small. Under these conditions, statistical kinetic theories may not provide an adequate description of these processes. A qualitative indication of the applicability of statistical kinetic theories to conformational processes can be obtained by comparing the general shape and location of the falloff curve calculated with RRKM theory with pressure dependent rate constants obtained from NMR experiments. Experimental studies so far have been limited to a rather narrow pressure range. Recent work has shown that fall-off curves over an extended pressure range obtained with as high a definition as possible can provide a more critical test of intramolecular dynamics.

Pressure dependent chemical exchange rate constants over limited pressure ranges typically between a few torr and 4–5 atm have been obtained for larger nitrites,[42–44] six-membered rings,[34–39] SF_4,[45] bullvalene,[46] and aziridine.[47] All these molecules, with the exception of aziridine, undergo processes with activation energies below 55 kJ mol^{-1}. For dialkyl amides which have activation energies above 70 kJ mol^{-1}, rate constants are independent of pressure at pressures between a few torr and several atmospheres, and the fall-off region, predicted to occur below a few torr, has not been observed experimentally.

Methyl nitrite was the first molecule for which pressure dependent gas phase NMR spectra were obtained.[42] Figure 4 shows recently obtained experimental and calculated rate constants for the *syn* ⇋ *anti* exchange process of methyl nitrite. The solid line represents rate constants calculated using RRKM theory and the data points were obtained by analyzing exchange broadened lineshapes. The location of the fall-off is sensitive to the cross section for deactivating collisions, and a value of 0.3 nm adequately reproduces the location of the fall-off. The shape of the experimental and calculated curves are different, and the values of the parameters used in the RRKM calculation cannot be adjusted reasonably to reproduce the experimentally determined curvature.

Less extensive pressure dependent data are available for larger alkyl nitrites,[42–44] six-membered rings,[34–39] SF_4,[45] bulvalene,[46] and aziridine.[47] Comparisons of the location and shape of the fall-off curves for these molecules with RRKM theory have been made. The location of the fall-off curve depends strongly on the cross section for deactivating collisions, a parameter which has not been determined independently for any of these processes. Because of this uncertainty and additional uncertainties in the model parameters used in these calculations, and the experimental uncertainties in the shapes of the fall-off curves which have been obtained to date, only qualitative conclusions can be drawn from these studies. Acceptable agreement of observed and calculated fall-off curves is obtained for the larger nitrites[43,44] and six-membered rings.[37–41] Molecules with lower state densities at the threshold energy such as SF_4,[45] aziridine,[47] and, possibly, methyl nitrite[42] and cyclohexane[34] show less satisfactory agreement.

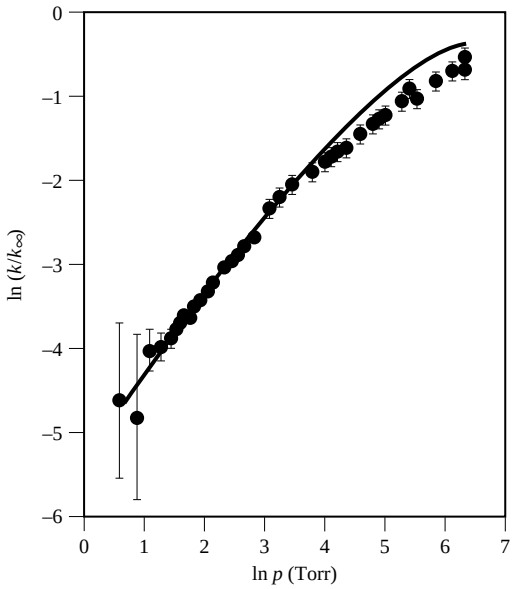

Figure 4 Pressure dependent rate constants (k/k_∞) for the *syn*–*anti* conformer exchange process of methyl nitrite gas. The solid line represents RRKM calculated rate constants

Rate constants in the low-pressure bimolecular region depend on the rate of activating collisions and are dependent on the nature of the collider. Bath gas relative collision efficiencies, β, for activating the methyl nitrite conformational conversion and the ring inversion of cyclohexane were determined by measuring rate constants as a function of bath gas pressure in the bimolecular region using ^{1}H NMR spectroscopy. For methyl nitrite *syn* ⇋ *anti* conformer exchange, β correlates strongly ($R > 0.9$) with polarizability, indicating that the attractive portion of the intermolecular potential is important in determining collision efficiency.[48] For ring inversion in nonpolar cyclohexane there is no correlation between β and polarizability for the five noble gases studied, while β correlates positively with polarizability for homonuclear diatomics. The observed β values of the larger polyatomic molecules correlate strongly with polarizability, showing a greater dependence than the diatomic molecules. These results suggest that for monatomic gases colliding with cyclohexane the attractive portion of the intermolecular potential is not the dominant factor in collisional energy transfer. As the molecular complexity of the bath gas increases, it appears to play a more important role.[49]

4 RELATED ARTICLES

Chemical Exchange Effects on Spectra; Kinetics at High Pressure; Relaxation Effects of Chemical Exchange; Spin–Rotation Relaxation Theory.

5 REFERENCES

1. E. M. Purcell, R. V. Pound, and N. Bloembergen, *Phys. Rev.*, 1946, **70**, 986.

2. G. Govil, *Appl. Spectrosc.*, 1973, **7**, 47.
3. C. J. Jameson, *Chem. Rev.*, 1991, **91**, 1375.
4. R. L. Armstrong, *Magn. Reson. Rev.*, 1987, **12**, 91.
5. N. S. True and C. Suarez, in Advances in Molecular Structure Research, ed. I. Hargittai and M. Hargittai, JAI Press, Greenwich, CT, Chap. 4, in press.
6. E. D. Becker, High Resolution NMR: Theory and Practice, 2nd edn., Academic Press, 1980, p. 44.
7. M. M. Folkendt, B. E. Weiss-Lopez, and N. S. True, *J. Phys. Chem.*, 1988, **92**, 1859.
8. L. M. Jackman and F. A. Cotton, eds., Dynamic Nuclear Magnetic Resonance Spectroscopy, Academic Press, New York, 1975.
9. R. K. Harris and R. C. Rao, *Org. Magn. Reson.*, 1983, **21**, 580.
10. M. M. Folkendt, B. E. Weiss-Lopez, J. P. Chauvel, Jr., and N. S. True, *J. Phys. Chem.*, 1985, **89**, 3347.
11. J. P. Chauvel, Jr.and N. S. True, *J. Phys. Chem.*, 1983, **87**, 1622.
12. F. R. Cordell, J. E. Boggs, and A. Skancke, *J. Mol. Struct.*, 1980, **64**, 57.
13. C. B. Conboy, J. P. Chauvel, Jr., P. O. Moreno, N. S. True, and C. M. Ott, *J. Phys. Chem.*, 1986, **90**, 4353.
14. T. Hirano, S. Nonoyama, T. Miyajima, Y. Kurita, and H. Sato, *J. Chem. Soc., Chem. Commun.*, 1986, 606.
15. L. B. Krivden and E. W. Della, *Progress in NMR*, 1991, **25**, 301.
16. A. K. Jameson and J. P. Reger, *J. Phys. Chem.*, 1971, **75**, 437.
17. I. Ando, T. Inoue, S. Watanabe, Y. Sakamoto, and G. A. Webb, *J. Mol. Liquids*, 1984, **27**, 179.
18. T. Hirano and T. Miyajima, *J. Mol. Struct.*, 1984, **125**, 97.
19. T. Hirano and T. Miyajima, *J. Mol. Struct.*, 1985, **126**, 141.
20. K. G. Pachler and P. L. Wessels, *J. Mol. Struct.*, 1980, **68**, 145.
21. K. Inomata and A. Abe, *J. Phys. Chem.*, 1992, **96**, 7934.
22. P. A. Robinson and K. D. Holbrook, Unimolecular Reactions, Wiley Interscience, 1972.
23. D. M. Campbell, M. Mackowiac, and J. Jonas, *J. Chem. Phys.*, 1992, **96**, 2717.
24. R. K. Harris and R. A. Spragg, *Chem. Commun.*, 1967, 362.
25. B. D. Ross, N. S. True, and D. L. Decker, *J. Phys. Chem.*, 1983, **87**, 89.
26. C. B. LeMaster and N. S. True, *J. Phys. Chem.*, 1989, **93**, 1307.
27. C. Suarez, C. B. LeMaster, C. L. LeMaster, M. Tafazzoli, and N. S. True, *J. Phys. Chem.*, 1990, **94**, 6679.
28. B. D. Ross and N. S. True, *J. Am. Chem. Soc.*, 1984, **106**, 2451.
29. M. Feigel, *J. Phys. Chem.*, 1983, **87**, 3054.
30. B. D. Ross, G. B. Matson, and N. S. True, *J. Phys. Chem.*, 1984, **88**, 2675.
31. K. A. Turner, C. L. LeMaster, and C. B. LeMaster, *J. Mol. Struct.*, 1992, **271**, 261.
32. B. D. Ross, L. T. Wong, and N. S. True, *J. Phys. Chem.*, 1985, **89**, 836.
33. E. M. Duffy, D. L. Severance, and W. L. Jorgensen, *J. Am. Chem. Soc.*, 1992, **114**, 7535.
34. B. D. Ross and N. S. True, *J. Am. Chem. Soc.*, 1983, **105**, 1382, 4871.
35. P. S. Chu and N. S. True, *J. Phys. Chem.*, 1985, **89**, 2625.
36. P. S. Chu and N. S. True, *J. Phys. Chem.*, 1985, **89**, 5613.
37. C. B. LeMaster, C. L. LeMaster, M. Tafazzoli, C. Suarez, and N. S. True, *J. Phys. Chem.*, 1988, **92**, 5933.
38. C. B. LeMaster, C. L. LeMaster, M. Tafazzoli, C. Suarez, and N. S. True, *J. Phys. Chem.*, 1990, **94**, 3461.
39. C. B. LeMaster, C. L. LeMaster, C. Suarez, M. Tafazzoli, and N. S. True, *J. Phys. Chem.*, 1989, **93**, 3993.
40. M. Tafazzoli, C. Suarez, N. S. True, C. B. LeMaster, and C. L. LeMaster, *J. Phys. Chem.*, 1992, **96**, 10 201.
41. M. Tafazzoli, C. Suarez, N. S. True, C. B. LeMaster, and C. L. LeMaster, *J. Mol. Struct.*, 1994, in press.
42. J. P. Chauvel, Jr., C. B. Conboy, W. M. Chew, G. B. Matson, C. A. Spring, B. D. Ross, and N. S. True, *J. Chem. Phys.*, 1984, **79**, 1469.
43. C. B. Conboy, J. P. Chauvel, Jr., and N. S. True, *J. Phys. Chem.*, 1986, **90**, 4388.
44. P. O. Moreno, C. B. LeMaster and N. S. True, *J. Phys. Chem.*, 1990, **94**, 8780.
45. C. A. Spring and N. S. True, *J. Am. Chem. Soc.*, 1983, **105**, 7231.
46. P. O. Moreno, C. Suarez, M. Tafazzoli, N. S. True, and C. B. LeMaster, *J. Phys. Chem.*, 1992, **96**, 10 206.
47. D. B. Borchard and S. H. Bauer, *J. Chem. Phys.*, 1986, **85**, 4980.
48. J. P. Chauvel, Jr., B. R. Friedman, H. Van, E. D. Winegar, and N. S. True, *J. Chem. Phys.*, 1985, **82**, 3996.
49. P. O. Moreno and N. S. True, *J. Chem. Phys.*, 1991, **95**, 57.

Biographical Sketch

Nancy S. True. *b* 1951. B.S., 1973, Ph.D., 1977, University of Connecticut. Introduced to spectroscopy by R. K. Bohn. Faculty in Chemistry, University of California, 1980–present. Approximately 90 publications. Research interests include applications of gas phase spectroscopic techniques, especially NMR and microwave spectroscopy, to problems in conformational equilibria and interconversion.

Kinetics at High Pressure

D. Hugh Powell and André E. Merbach
University of Lausanne, Lausanne, Switzerland

1	Introduction	1
2	High-Pressure NMR Instrumentation and Methodology	2
3	Examples of Variable Pressure Kinetic Studies	3
4	Fields of Application of High-Pressure NMR in Chemical Kinetics	5
5	Related Articles	8
6	References	8

1 INTRODUCTION

In order to elucidate the mechanisms of chemical reactions, the kineticist studies the dependence of the reaction rate on a number of parameters, both chemical (reactant concentrations, pH, ionic strength, and solvent composition) and physical (normally temperature). The empirical rate law, the electronic and steric effects induced by changing the reactants, the variable temperature activation parameters (activation enthalpy, $\Delta H^{\#}$ and activation entropy, $\Delta S^{\#}$), and any other experimental or theoretical information available on the system are then used to assign a reaction mechanism. Such information may, however, be insufficient to distinguish clearly between alternative reaction mechanisms. Temperature is, however, not the only physical variable that can be varied in kinetic studies. Pressure can also affect the rate of a substitution reaction in solution, and variable pressure measurements yield an activation volume, $\Delta V^{\#}$, which is now widely used as a supplementary (and often decisive) parameter for mechanistic assignment.[1] Although the first high pressure kinetic study in inorganic chemistry was made over 30 years ago, the rapid development of the field has occurred in the last 20 years, since the adaptation for variable pressure studies of most fast reaction techniques: stopped flow, temperature jump, pressure jump, and, especially, NMR. This is illustrated by the number of recent reviews in the field, of which the reader is referred to the most recent.[2–4]

The pressure dependence of the rate of a chemical reaction is usually described by transition state theory. The activation volume, the difference between the partial molar volumes of the transition state and the reactants, at a temperature T is defined by

$$(\partial \ln k/\partial P)_T = -\Delta V^{\#}/RT \qquad (1)$$

where k is the rate constant. The activation volume may itself depend on pressure, and it is useful to define the compressibility coefficient of activation, $\Delta\beta^{\#}$, as

$$\Delta\beta^{\#} = -(\partial \Delta V^{\#}/\partial P)_T \qquad (2)$$

It is usual to assume that $(\partial^2\ \Delta V^{\#}/\partial P^2)_T = 0$, so that ln k has the quadratic form

$$\ln k = \ln k_0 - P\Delta V_0^{\#}/RT + P^2\Delta\beta^{\#}/2RT \qquad (3)$$

where $\Delta V_0{}^{\#}$ is the activation volume at zero pressure. It should be stressed that there is no physical justification for such a quadratic form. On the other hand, ln k is often found empirically to be approximately linear in pressure, and a simplified form of equation (3) with $\Delta\beta^{\#} = 0$ may be preferred.

Variable pressure NMR has most often been applied to ligand substitutions on metal ions as shown in equation (4), where X is the leaving ligand, Y the entering ligand, and L the nonreacting ligands on a metal M. The measured activation volume for such reactions is usually considered to be the sum of an intrinsic contribution, $\Delta V_{\text{int}}{}^{\#}$, due to changes in internuclear distances within the reactants on formation of the transition state and a solvent electrostrictive contribution, $\Delta V_{\text{elec}}{}^{\#}$. For substitution reactions involving charged species, $\Delta V^{\#}$ may be dominated by $\Delta V_{\text{elec}}{}^{\#}$, so that the sign of $\Delta V^{\#}$ may be different from $\Delta V_{\text{int}}{}^{\#}$. The power of the activation volume as a mechanistic indicator is particularly well illustrated by solvent exchange reactions [X = Y in equation (4)], which are of fundamental importance to all substitution reactions in inorganic chemistry. In this case, one cannot easily vary the concentrations of the reactants so that the mechanistic assignment must often be made on the basis of activation parameters alone. For these reactions there is no significant charge or dipole formation on going to the transition state, so that $\Delta V_{\text{elec}}{}^{\#}$ may be neglected. The sign of $\Delta V^{\#} \approx \Delta V_{\text{int}}{}^{\#}$ is then an immediate diagnostic of the activation step: dominant bond breaking results in a positive $\Delta V^{\#}$ while dominant bond making gives a negative $\Delta V^{\#}$.

$$L_nMX + Y \rightarrow L_nMY + X \qquad (4)$$

The classification of substitution reaction mechanisms originally proposed by Langford and Gray,[5] and widely used in coordination chemistry, is based on operational criteria. If kinetic tests show the presence of an intermediate of increased coordination number, an associative mechanism, A, is assigned. Conversely, if an intermediate of reduced coordination number is detected, a dissociative, D, mechanism is assigned. When no intermediate can be found, a concerted interchange, I, mechanism is assigned. This last category may be subdivided further, depending whether evidence is found for important incoming group influences (I_a) or not (I_d). Swaddle[6] has argued that this operational definition is too restrictive, and may be extended to include activation parameters as operational criteria. This is especially true for solvent exchange reactions, where few kinetic tests are applicable. The activation volume is of primary importance in this context. Microscopic reversibility for solvent exchange reactions means that the forward reaction path must be symmetrical to the reverse one. For an interchange process, with no true minimum along the reaction coordinate, the bond lengths to the entering and leaving solvent molecules must be equivalent at the transition state. Thus, for an I_a mechanism, the incoming and outgoing solvent molecules will both have relatively strong bonds, whereas for an I_d mechanism they will have relatively weak bonds. The difference between the two mechanisms will be manifested as a contraction or expansion at the transition state. If the bond distances between the central ion and nonexchanging solvent molecules are unaltered, $\Delta V^{\#}$ will be a direct measure of the degree of associativity or dissociativity

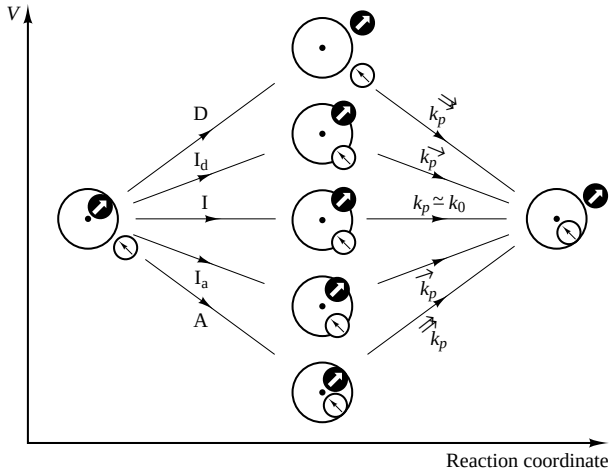

Figure 1 Volume profiles for solvent exchange mechanisms. (Reproduced by permission of Reidel from A. E. Merbach, in High Pressure Chemistry and Biochemistry, ed. R. van Eldik, 1987)

at the transition state. A continuous spectrum of transition states can thus be envisaged (Figure 1), ranging from limiting associative, A, with $\Delta V^{\#} = -|\Delta V_{\lim}{}^{\#}|$, via I_a and I_d to limiting dissociative, D, with $\Delta V^{\#} = +|\Delta V_{\lim}{}^{\#}|$. For interchange mechanisms characterized by $\Delta V^{\#} \approx 0$, the activation mode cannot be specified, and no subscript is assigned to the I mechanism.

We have established the primary importance of $\Delta V^{\#}$, and hence of variable pressure kinetic measurements, for the classification of reaction mechanisms. In Section 2 we will discuss the different approaches used to perform NMR measurements on liquids at high pressures. The rates of chemical reactions cover an enormous range of timescales: for example, water exchange rates at 298 K on metal cations vary from 10^{-8} s^{-1} for Rh^{3+} to almost 10^{10} s^{-1} for Cu^{2+}. A large battery of NMR techniques must be called on, therefore, to study these reactions. In Section 3 we draw on our work in Lausanne to illustrate some of the different techniques that are used and the importance of the activation volume in specific cases. Finally, in Section 4, we will give a brief review of the areas of chemical kinetics where high-pressure NMR has been applied, by our group and various others. In this section, we will give references only when the examples are drawn from recent research papers, otherwise the original references can be found in the aforementioned reviews.

2 HIGH-PRESSURE NMR INSTRUMENTATION AND METHODOLOGY

Two approaches have emerged for the measurement of NMR spectra at high pressure.[7,8] The simplest approach is to design a pressurizable thick-walled glass sample tube which can be placed directly in a standard spectrometer probe. Such systems work well, and sample spinning can be used, but there are certain disadvantages. If small pressure dependences (e.g. activation volumes) are to be measured with any precision, pressures of at least 1 kbar are required. This can be achieved with very thick-walled tubes where the sample is confined to a capillary, but the poor filling factor of these tubes results in low sensitivity. Furthermore, the temperature control of such tubes is not very good, and it cannot be emphasized too strongly that temperature has to be known as accurately as possible if the results of kinetic variable pressure measurements are to be meaningful.

The alternative approach is to manufacture a dedicated high-pressure probehead which will replace the ambient pressure commercial probehead. The probe is built around a high-pressure chamber provided with electrical lead-through contacts so that both the coil and sample are immersed in the high-pressure transmitting fluid. The coil can be wound on a support placed closely around the sample tube and so have a high filling factor. The pressure fluid is also a good heat transfer medium, and its heat capacity and that of the metallic bomb are such that temperature control can be more precise than is possible with the normal gas flow-type unit. The sample cannot be made to spin, or at least there are practical difficulties which preclude this, but using field lock and small diameter tubes (5 mm), good resolution can be obtained from the static sample. The signal-to-noise ratio does not suffer too much from this approach because of the good filling factor, and cryomagnets are capable of producing a remarkable magnetic field homogeneity over small volumes. In practice the static, specially built system has proved superior to the spinning pressure tube in all the factors outlined above, and especially for chemical kinetic studies.

For illustration we present a probe designed for a high-field spectrometer (Bruker AM-400).[9] Figure 2(a) is a schematic drawing of a probehead designed for a wide bore (87 mm diameter) superconducting magnet (9.4 T), which can be used up to 200 MPa and is made of a nonmagnetic beryllium–copper alloy. Three connectors are located at the bottom: one for the pressure transmitting liquid, and two for the inlet and outlet of the thermostating liquid. An upper aluminum support (not shown in Figure 3) contains the high-frequency cables, screwdrivers for the adjustment of the matching/tuning capacitors and the frequency adapter box. The adapter box contains a capacitive matching/tuning network that

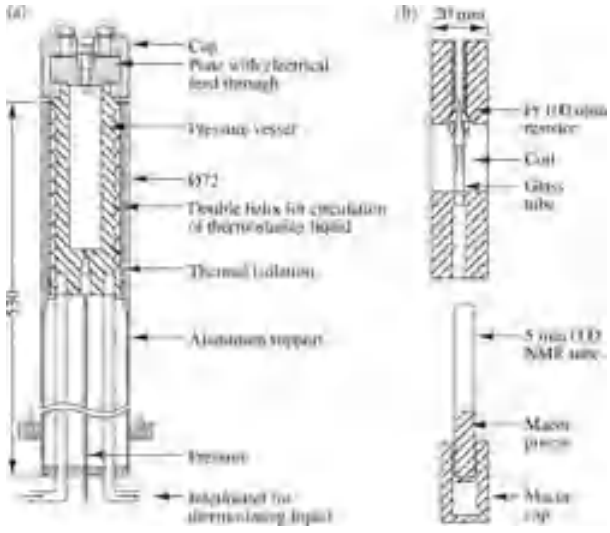

Figure 2 Schematic drawing of (a) a wide bore superconducting magnet multinuclear high-pressure bomb and (b) the internal component of the bomb made of Vespel (top) and the sample tube (bottom). (Reproduced by permission of Gordon and Breach from Frey et al.[9])

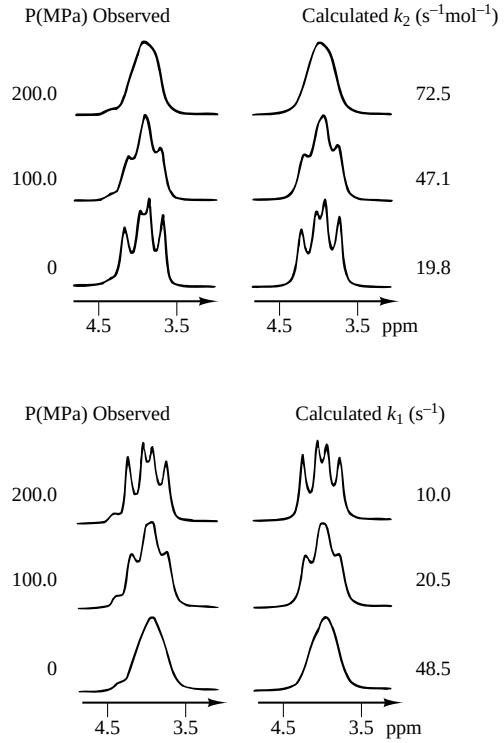

Figure 3 Observed and calculated 60 MHz ^{1}H NMR spectra of a solution of $M(TMPA)_6(ClO_4)_3$ dissolved in a mixture of TMPA and CD_3NO_2, recorded as a function of pressure. The top spectra are for M = In and the bottom spectra are for M = Al. (Reproduced by permission of Pergamon Press from Merbach[10])

is specific for a small frequency range and so must be changed in order to observe different nuclei. Provision is made for the use of a ^{2}H lock.

The internal components of the bomb and the sample tube are shown in Figure 2(b). The radiofrequency coil is wound in a saddle shaped form on 7 mm o.d. glass tubing to produce a radiofrequency field perpendicular to the vertical static magnetic field. The temperature is measured inside the bomb by a platinum resistor placed just above the sample tube. The temperature stability is better than ± 0.2 K and is not a limiting factor in the accuracy of measurements of activation volumes. The sample tube is a 5 mm o.d. NMR tube cut to the right length and closed with a movable seal, made of machinable glass, which allows pressure transmission to the sample. The sample tube was designed to minimize the volume (1 cm^3) to economize on expensive solvents such as ^{17}O enriched water. The surrounding pressure transmitting liquid is chosen so as not to contain the observed nucleus. The spectral resolution and magnetic field stability with this nonspinning high-pressure probe is better than 0.5 Hz at 400 MHz and routinely better than 1 Hz.

3 EXAMPLES OF VARIABLE PRESSURE KINETIC STUDIES

3.1 TMPA Exchange on Aluminum(III) and Indium(III)[10]

Here we describe the use of proton NMR to observe the way TMPA exchanges on two related metal ions, both of which form octahedral solvates with this ligand: $[M(TMPA)_6]^{3+}$, with M = Al and In. The ^{1}H spectrum of TMPA is a doublet due to spin–spin coupling to the phosphorus atom, and this doublet is maintained when the phosphate is complexed by a cation though it is shifted to high frequency. The spectrum of a solution of $[M(TMPA)_6]^{3+}$ with excess TMPA, using deuterated nitromethane (CD_3NO_2) as a diluent, is thus two doublets, provided exchange is sufficiently slow. Exchange between free and bound solvent will cause line broadening and eventual collapse of the doublets.

The use of an inert diluent gives reduced viscosity leading to better resolution and definition of the linewidths and also permits the free ligand concentration to be varied so that information can be obtained regarding the order of reaction. For TMPA exchange on Al^{3+} this is first order while for In^{3+} it is second order. The entropies of activation also have opposite signs so that the ambient pressure data indicate strongly that the activation mode for TMPA exchange is dissociative on Al^{3+} and associative on In^{3+}. The variable pressure kinetics (Figure 3) provide a very good visual proof that the mechanisms are indeed different. The ^{1}H NMR spectrum for the TMPA exchange on In^{3+} at ambient pressure shows a doublet at low frequency which is due to free TMPA and a doublet at high frequency due to the six TMPA molecules coordinated to In^{3+}. With increasing pressure, at constant temperature, one observes a coalescence of the signals. This means that the exchange rate is increasing and therefore the activation volume will be negative ($\Delta V^{\#} = -21.4\,cm^3\ mol^{-1}$). For $[Al(TMPA)_6]^{3+}$ the change in spectra with pressure is the contrary: the deceleration of the ligand exchange with pressure indicates a positive activation volume ($\Delta V^{\#} = +22.5\,cm^3\ mol^{-1}$). The difference in mechanistic behavior can be explained in terms of ionic radii. The large In^{3+} cation (r_i = 80 pm) can easily accommodate, at least partially, a seventh solvent molecule in forming the activated complex. The small Al^{3+} ion (r_i = 54 pm), on the other hand, is rather crowded, and has to expel a solvent molecule from the first coordination sphere at the transition state, before a new molecule can be accepted.

3.2 Water Exchange on the Lanthanide(III) Aqua Ions[11–14]

We now turn to aqueous solutions of the paramagnetic lanthanides, where the bound solvent signal is too broad to be observed and where the influence of the paramagnetic ion on the bulk solvent relaxation is given by the Swift and Connick equations (see ***Paramagnetic Relaxation in Solution***). Water exchange on the lanthanide(III) aqua ions is sufficiently rapid that the ^{17}O relaxation rates of aqueous lanthanide(III) perchlorate solutions are always in the fast exchange limit. In addition, for the paramagnetic lanthanide(III) ions Ce^{3+} to Yb^{3+} (except Gd^{3+}), the bound water relaxation is in the extreme narrowing limit, allowing one to use the approximate equation

$$\frac{1}{P_m}\left[\frac{1}{T_2} - \frac{1}{T_1}\right] = \frac{\Delta\omega_m^2}{k_{ex}} \qquad (5)$$

where P_m is the mole fraction of bound water. $\Delta\omega_m$, the difference in chemical shift between the bound water and the

bulk water (in the absence of paramagnetic interaction with the bulk water), can be determined from the chemical shift of the paramagnetic solution compared with a nonparamagnetic reference solution. Measurement of the longitudinal and transverse ^{17}O relaxation rates, $1/T_1$ and $1/T_2$, in the paramagnetic solution therefore allows the water exchange rate, k_{ex}, to be determined.

For the series Tb^{3+} to Yb^{3+} the relaxation rate difference, $1/T_2 - 1/T_1$, was observed at 4.7 T and 8.5 T to be proportional to the square of the magnetic field, confirming the approximations used in equation (5), and reliable parameters were obtained for this series. For the lighter lanthanides, Nd^{3+} and Eu^{3+}, the bound water chemical shift, $\Delta\omega_m$, was too small for the relaxation rate difference in equation (5) to be measurable. Variable pressure ^{17}O relaxation rate measurements were made in a high-pressure probe at 9.4 T.

As mentioned above, Gd^{3+} is a case apart. The relatively slow electronic relaxation rates lead to breakdown of the extreme narrowing approximation for bound water relaxation, and equation (5) cannot be used. In order to determine k_{ex} it is necessary to consider the microscopic origins of the relaxation of the bound water. The transverse ^{17}O relaxation rate in bound water, $1/T_{2m}$, is dominated by relaxation due to the scalar or contact interaction originating from the finite Gd^{3+} electron spin density at the ^{17}O nucleus and given in approximate form by

$$\frac{1}{T_{2m}} = \frac{1}{P_m}\left[\frac{1}{T_2} - \frac{1}{T_{2A}}\right] = \frac{S(S+1)}{3}\left(\frac{A}{\hbar}\right)^2\left[k_{ex} + \frac{1}{T_{1e}}\right]^{-1} \quad (6)$$

where $1/T_{2A}$ is the transverse relaxation rate in the nonparamagnetic reference, $S = \frac{7}{2}$ is the Gd^{3+} electron spin, and $1/T_{1e}$ is the longitudinal electronic relaxation rate. The scalar coupling constant, $A/\hbar$, is accessible from the chemical shift. Thus, ^{17}O NMR relaxation rate measurements allow one to determine k_{ex}, provided that $1/T_{1e}$ is known. It is therefore necessary to also make ESR measurements: the ESR linewidth is directly proportional to the transverse electronic relaxation rate, $1/T_{2e}$, which can be related to $1/T_{1e}$ using a theoretical model.

A combined ^{17}O NMR and EPR study of the Gd^{3+} aqua ion was first made in 1980, and has recently been improved by extension to a greater number of ESR and NMR magnetic fields. The calculated contribution of $1/T_{1e}$ to $1/T_{2m}$ decreases to less than 3% at 9.4 T, so that k_{ex} and the temperature and pressure activation parameters are determined well from these high-field measurements.

The water exchange parameters for the lanthanide(III) aqua ions Gd^{3+} to Yb^{3+} are shown in Figure 4. The water exchange rates decrease as one progresses along the series, as one might expect for a dissociative process (the energy required to remove a water molecule increasing with the lanthanide ion charge density). The negative $\Delta V^{\#}$, however, clearly indicate an associatively activated exchange mechanism. The coordination number of the lanthanide aqua ions is known from neutron diffraction experiments to change from nine for the larger aqua ions on the left of the series to eight for the smaller aqua ions on the right of the series. This coordination number change is manifested in the measured absolute partial molar volumes of the ions shown in Figure 4, which approach the calculated values for the ennea and octa aqua species for the lighter and heavier lanthanides respectively. The

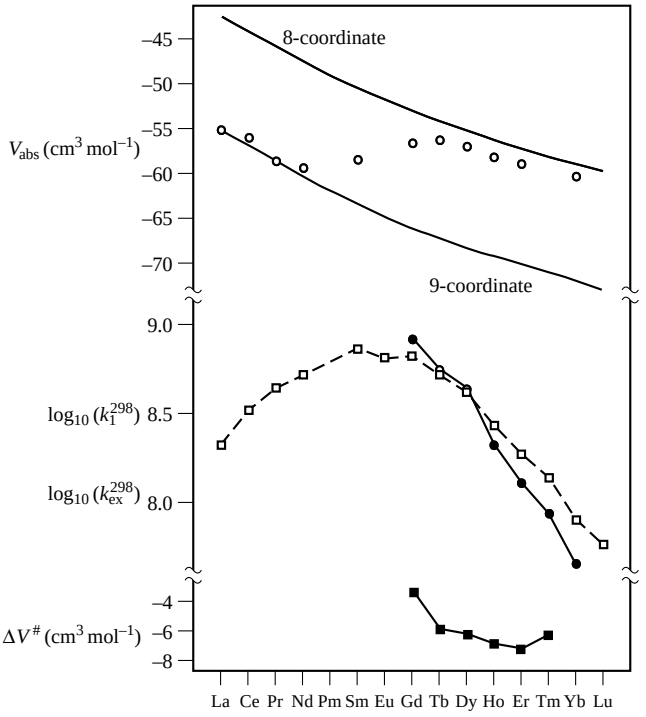

Figure 4 Absolute partial molar volumes, V_{abs}, of the Ln^{3+} aqua ions in $LnCl_3$ solutions, compared with calculated values for the octa and ennea aqua ions. □, interchange rate constants, k_I^{298} (s^{-1}), for complexation of the Ln^{3+} aqua ions with SO_4^{2-}; •, water exchange rates, k_{ex}^{298} (s^{-1}), and the corresponding activation volumes (■) for the Ln^{3+} aqua ions

water exchange mechanism on the lanthanide aqua ions can, therefore, be understood in terms of the reaction in equation (7). For the heavy lanthanides, the octa ion is the lowest energy species, and the ennea aqua ion is the intermediate (or transition state) in the associatively activated water exchange reaction. The activation volumes are, therefore, negative, and the water exchange rates increase toward the middle of the series, as less energy is required to reach the ennea aqua transition state. For the light lanthanides the ennea aqua ion is now the lowest energy species. One can expect, therefore, that the octa aqua ion will be the intermediate (or transition state) in the exchange process, which will proceed via a dissociative, D, or dissociative interchange, I_d, mechanism. For the mid-series lanthanides (Pm^{3+} to Eu^{3+} according to Figure 4), the octa and ennea aqua species are in equilibrium. The transition from one species to the other requires relatively little energy, so that these lanthanides should have the fastest water exchange rates for the series. This interpretation is supported by results from studies of complex formation on the lanthanide(III) aqua ions. The interchange rate, k_I^{298} (s^{-1}), of an inner sphere water molecule by a SO_4^{2-} ion already in an outer sphere complex is shown in Figure 4. The values are closely correlated with the rate of water exchange, and show a maximum in the middle of the series, which corresponds to the cross over in the absolute partial molar volumes of the aqua ions. If one could measure the water exchange rates on the light lanthanide ions, Ln^{3+} to Nd^{3+} (e.g. by using the very high NMR fields now available) one would, therefore, expect positive activation volumes for these aqua ions, and water exchange rates that decrease as one moves away from the middle of the series and more energy is

needed to reach the octa aqua transition state.

$$[\mathrm{Ln}\,(\mathrm{H_2O})_9]^{3+} \rightleftharpoons [\mathrm{Ln}\,(\mathrm{H_2O})_8]^{3+} + \mathrm{H_2O} \qquad (7)$$

3.3 TMPA Exchange on Tetrachlorobis(TMPA)zirconium(IV)[15]

The system discussed here involves a much more complex ligand exchange process. The two ligands, L, in $ZrCl_4 \cdot 2L$ can be either *cis* or *trans* with respect to one another so that there are three possible exchange reactions given by equations (8)–(10).

At 236 K, the ^{1}H NMR spectrum of a solution of $ZrCl_4 \cdot 2TMPA$ in chloroform with excess TMPA consists of three doublets due to the two forms of the complex and the free ligand, with $^3J(^{31}P,^1H)$ = 14.0 Hz for the latter and 11.7 and 11.8 Hz in the *cis* and *trans* complexes, respectively. As the temperature is raised, the doublets of the *cis* and *trans* isomers broaden and eventually coalesce, indicating that the *cis*/*trans* isomerization reaction occurs first. At a slightly higher temperature, the doublet of the free ligand also broadens and coalesces with the signal of the *cis*/*trans* isomers. The source of this second broadening could be due to a ligand exchange reaction between free ligand and the *cis* and/or *trans* isomer. In this case, NMR line-broadening simulation cannot easily be used to quantify the individual contribution of the three exchange reactions to the observed spectra.

$$cis\text{-}ZrCl_4 \cdot 2L + {}^*L \overset{k_c}{\rightleftharpoons} cis\text{-}ZrCl_4 \cdot L\,{}^*L + L \qquad (8)$$

$$trans\text{-}ZrCl_4 \cdot 2L + {}^*L \overset{k_t}{\rightleftharpoons} trans\text{-}ZrCl_4 \cdot L\,{}^*L + L \qquad (9)$$

$$cis\text{-}ZrCl_4 \cdot 2L \overset{k_i}{\rightleftharpoons} trans\text{-}ZrCl_4 \cdot 2L \qquad (10)$$

It has now been shown that this problem can be overcome by using the very powerful 2D NMR techniques. In the moderately slow exchange region where all the signals can be observed, a pulse sequence that is sensitive to exchange effects gives off-diagonal peaks where there is an exchange reaction. So, all the signals can be examined for exchange coupling and the individual exchange rate can be obtained. In addition, if a high-pressure probe is available for a suitable spectrometer, then it is possible to carry out a variable pressure 2D experiment without too much difficulty.

Proton (400 MHz) EXCSY spectra were recorded on a Bruker AM-400 spectrometer equipped with a home built high-pressure probe, using the pulse sequence $90^\circ(\Phi_1)-t_1-90^\circ(\Phi_2)-\tau_m-90^\circ(\Phi_3)-t_2$. A double Fourier transformation with respect to t_1 and t_2 gives a rectangular stacked spectrum plot (Figure 5) with the resonances of the normal spectrum displayed on a diagonal and any exchange is manifested by off-diagonal peaks at the intersection of the chemical shifts of the connected peaks in the two frequency directions. The relative intensities of the cross peaks is related to the relative rates of exchange and so these can be measured for all pathways and changes in both relative and absolute rates with pressure can be measured.

The length of the diagonal in Figure 5 is 0.50 ppm, and the doublet due to free ligand is at low frequency, to the right

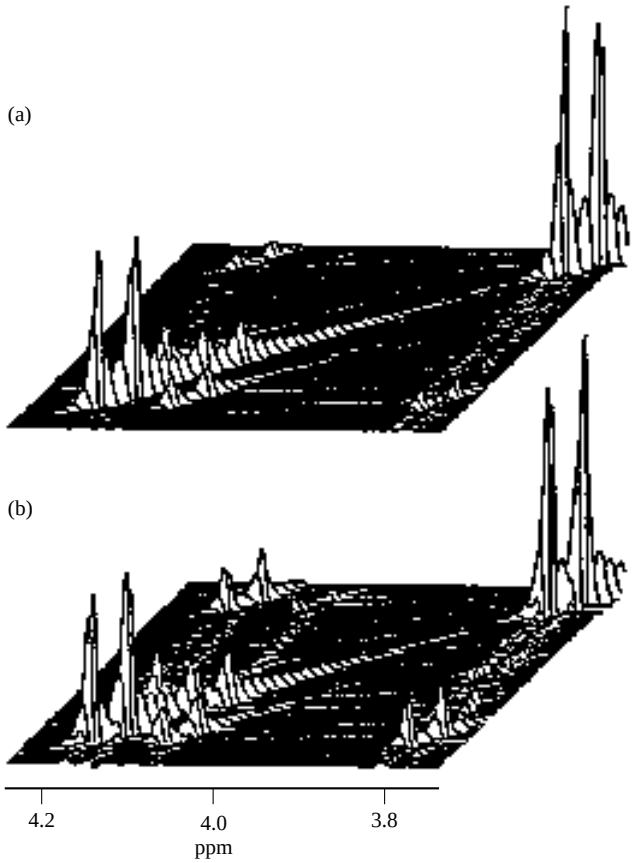

Figure 5 (400 MHz) 2D Proton EXCSY spectra of *cis*- and *trans*-$ZrCl_4 \cdot 2TMPA$ in the presence of excess TMPA, at two different pressures [(a) 0.1 MPa, (b) 198 MPa] demonstrating the effect of pressure on the intramolecular and intermolecular exchange pathways. (Reproduced by permission of Elsevier from Frey et al.[15])

of the plot. The doublet at the extreme opposite end of the diagonal is due to the *trans* isomer and the doublet of the *cis* isomer can be discerned a little to low frequency. At ambient pressure there are strong off-diagonal peaks connecting the resonances of the *cis* and *trans* isomers as would be expected (see above). Weaker off-diagonal peaks connect the free ligand with the *trans* isomer, and those connecting free ligand with the *cis* isomer are just discernible. An increase in the pressure produces a small increase in intensity of the off-diagonal peaks due to the *cis*/*trans* isomerisation reaction. This isomerization, with a small negative activation volume ($\Delta V_i^{\#} = -1.6 \pm 0.6\,\mathrm{cm^3\ mol^{-1}}$), is intramolecular and proceeds via a slightly contracted six-coordinate transition state. On the other hand, the intensities of the off-diagonal peaks due to the intermolecular ligand exchange on both *cis* and *trans* isomers increase strongly with pressure ($\Delta V_t^{\#} = -11.1 \pm 0.8\,\mathrm{cm^3\ mol^{-1}}$), showing that the ligand exchange reactions are both associative. This is in marked contrast to the similar reactions occurring with the analog with the smaller Ti^{4+} ion ($\Delta V^{\#}_c = +17.5\,\mathrm{cm^3\ mol^{-1}}$). Given that the reaction of the *trans* complex predominates, it is then possible to obtain activation parameters in the normal way and show, by changing the free ligand concentration, that the ligand exchange is second order, as required for an associative process.

4 FIELDS OF APPLICATION OF HIGH-PRESSURE NMR IN CHEMICAL KINETICS

4.1 Substitution Reactions and Solvent Exchange

The substitution reactions that have been most extensively studied by NMR are the solvent exchange reactions on divalent and trivalent first row transition metal ions. The measured activation volumes shown in Tables 1 and 2 clearly show a progressive change of activation mode from associative for the early elements to dissociative for the late elements. This change can be explained by the combined effect of the progressive filling of the d orbitals and the decrease in ionic radii across the series, both of which disfavor bonding processes. The only case where the mechanistic changeover is not clear cut is dimethylformamide (DMF) exchange on the divalent ions: the activation volumes are all positive, although very small for Mn^{2+}. This is presumably due to the relative bulkiness of DMF favoring a dissociative activation mode.

The effect of the size of the solvent molecules can be seen very clearly in studies of solvent exchange on tetravalently coordinated Be^{2+}. The measured activation volumes and assigned mechanisms are shown in Table 3. Solvent exchange takes place via associatively activated mechanisms (A or I_a) for H_2O, dimethyl sulfoxide (DMSO), and TMPA, but the greater bulk of the TMU and DMPU ligands prevents the incoming solvent molecule from entering the coordination sphere before the outgoing solvent molecule leaves, and the exchange mechanism is dissociative, D.

Another factor in determining solvent exchange mechanism is the effect of multidentate ligands on the exchange of remaining solvent molecules. This has been shown to be especially important for Gd^{3+} polyaminocarboxylates, where the rate of water exchange is important for their use as contrast agents in medical magnetic resonance imaging. Kinetic parameters for the Gd^{3+} octa aqua ion and the complexes with propylenediaminetetraacetate ($PDTA^{4-}$),[14] diethylenetriaminepentaacetate ($DTPA^{5-}$),[16] tetraazacyclododecanetetraacetate ($DOTA^{4-}$),[16] and diethylenetriaminepentaacetate bismethylamide ($DTPA\text{-}BMA^{3-}$)[17] are shown in Table 4. The exchange rates on the three contrast agents, $[Gd(DTPA)(H_2O)]^{2-}$, $[Gd(DOTA)(H_2O)]^{-}$, and $[Gd(DTPA\text{-}BMA)(H_2O)]$, are 200–2000 times lower than on the octa aqua ion. This rate decrease is accompanied by a change of sign of the activation volume, the large positive values for the three contrast agents indicating dissociatively, rather than associatively, activated water exchange. This is a consequence of the change of coordination number to nine for the contrast agents, which prevents the entry of a second water molecule into the coordination sphere. Without the participation of the incoming water molecule, more energy is required to break the bond between the outgoing water molecule and the highly charged Gd^{3+}, leading to the higher activation enthalpies and lower water exchange rates.

4.2 Redox Reactions

The effect of pressure on the classic outer sphere electron transfer reaction between the aqueous anions MnO_4^{2-} and MnO_4^{-} has been investigated by ^{55}Mn NMR line broadening. The reaction proceeds by two pathways: in one the cation facilitates the approach of the two anions whereas in the other the reaction is cation independent. The first pathway has a rather small activation volume, but for the second $\Delta V^{\#} \approx -21\,cm^3\ mol^{-1}$. This can be accommodated with current theory if it is assumed that the Mn–Mn distance in the

Table 1 Volumes of Activation ($cm^3\ mol^{-1}$) for Solvent S Exchange on MS_6^{2+} of the First Row Transition Metal Series by NMR[2]

M^{2+}	V	Mn	Fe	Co	Ni	Cu
r_i (pm)	79	83	78	74	69	(73)[a]
	t_{2g}^3	$t_{2g}^3e_g^2$	$t_{2g}^4e_g^2$	$t_{2g}^5e_g^2$	$t_{2g}^6e_g^2$	$t_{2g}^6e_g^3$
H_2O	−4.1	−5.4	+3.8	+6.1	+7.2	
MeOH		−5.0	+0.4	+8.9	+11.4	+8.3
MeCN		−7.0	+3.0	+8.1	+8.5	
DMF		+2.4	+8.5	+9.2	+9.1	
NH_3[b]					+5.9	

[a]Effective ionic radius.
[b]In 15 M aqueous NH_3.

Table 2 Volumes of Activation ($cm^3\ mol^{-1}$) for Solvent S Exchange on MS_6^{3+} of the First Row Transition Metal Series by NMR[a][2]

M^{3+}	Sc	Ti	V	Cr	Fe	Ga
r_i (pm)	75	67	64	61	64	62
	t_{2g}^0	t_{2g}^1	t_{2g}^2	t_{2g}^3	$t_{2g}^3e_g^2$	$t_{2g}^6e_g^4$
H_2O		−12.1	−8.9	−9.6	−5.4	+5.0
DMSO			−10.1	−11.3	−3.1	+13.1[b]
DMF				−6.3	−0.9	+7.9[b]
TMP	−21.3					+20.7[b]

[a]Except for Cr^{3+} by isotopic labeling.
[b]In CD_3NO_2 as the diluent.

Table 3 Activation Volumes and Assigned Mechanisms for Solvent S Exchange on BeS_4^{2+}[a]

	H_2O	DMSO	TMPA	TMU	DMPU
$\Delta V^{\#}$ (cm^3 mol^{-1})	−13.6	−2.5	−4.1	+10.5	+10.3
Mechanism	A	A, I[a]	A, I[a]	D	D

[a]In CD_3NO_2 as diluent by ^1H NMR, except for H_2O in neat water by ^{17}O NMR.
[b]TMU = tetramethylurea.
[c]DMPU = dimethylpropyleneurea.

Table 4 Water Exchange Kinetic Parameters Obtained for Different Gd^{3+} Complexes

	k_{ex}^{298} (s^{-1})	$\Delta H^{\#}$ (kJ mol^{-1})	$\Delta S^{\#}$ (J K^{-1} mol^{-1})	$\Delta V^{\#}$ (cm^3 mol^{-1})
$[Gd(H_2O)_8]^{3+}$	$(8.30 \pm 0.95) \times 10^8$	14.9 ± 1.3	−24.1 ± 4.1	−3.3 ± 0.2
$[Gd(PDTA)(H_2O)_2]^-$	$(1.02 \pm 0.10) \times 10^8$	11.0 ± 1.4	−54.6 ± 4.6	−1.5 ± 0.5
$[Gd(DTPA)H_2O]^{2-}$	$(4.1 \pm 0.3) \times 10^6$	52.0 ± 1.4	+56.2 ± 5	+12.5 ± 0.2
[Gd(DTPA-BMA)H_2O]	$(4.3 \pm 0.4) \times 10^5$	46.6 ± 1.3	+18.9 ± 4	+7.3 ± 0.2
$[Gd(DOTA)H_2O]^-$	$(4.8 \pm 0.4) \times 10^6$	48.8 ± 1.6	+46.6 ± 6	+10.5 ± 0.2

transition state ion pair is reduced as the pressure is increased, at a rate that allows the solvent cavity in which the ion pair is contained to compress to the same extent as the solvent. The outer sphere electron transfer between $[Mn(CNR)_6]^+$ and $[Mn(CNR)_6]^{2+}$ has also been studied using ^{55}Mn NMR with R = $CNBu^t$ and R = CNC_6H_{11} and in a series of solvents. The activation volumes range from −9 to −22 cm^3 mol^{-1}, and show evidence for ion pairing in the solvents of lower dielectric constant. The qualitative difference in the solvent dependence of the rate constant for R = $CNBu^t$ and R = CNC_6H_{11} is evidence for the significant influence of subtle differences in solvation on the molecular level that is not approximated by continuum models. Variable pressure NMR studies have also been made of electron transfer between the pairs Fe(II)/Fe(III), Cu(I)/Cu(II), and Ru(II)/Ru(III).

4.3 Spin Equilibria

Where Ni^{2+} is complexed by certain tetraaza macrocyclic ligands, an equilibrium exists between unsolvated planar diamagnetic and disolvated pseudooctahedral paramagnetic forms. The contact shift of the ligand protons can be used to measure the equilibrium between the forms, and a reaction volume for going from the planar to the pseudooctahedral form of -10.0 ± 0.1 cm^3 mol^{-1} was obtained in this way for the complex with the ligand 1,4,8,11-tetramethyl-1,4,8,11-tetraazacyclotetradecane in aqueous solution. This volume is much less than the molar volume of the two molecules that enter the first coordination sphere (36 cm^3 mol^{-1}). This is because the volume reduction is partially compensated by an expansion of the complex due to a change in the Ni−N distance on changing spin state.

4.4 Bioinorganic Chemistry

Variable pressure NMR has been used to study the kinetics of internal motions on proteins. For example, the reorientational motions of amino acid residues [phenylalanine (Phe45) and tyrosine (Tyr35)] buried in the interior of the basic pancreatic trypsin inhibitor were studied by ^1H NMR. The interior of this globular protein is quite compact, implying that internal fluctions of the protein backbone are necessary in order to permit reorientation within the residues. The motion of the aromatic rings had a similar activation volume for the two residues: 30 cm^3 mol^{-1} for Phe45 and 36 cm^3 mol^{-1} for Tyr35. These volumes correspond reasonably with the difference between the volume of a ring and the smallest volume that it can be regarded as sweeping out as it rotates. Alternatively, it was suggested that since the region around a ring contains a significant proportion of void space among the atoms hindering rotation, quite small adjustments to the positions of these atoms will provide free space to permit ring rotation.

4.5 Organometallic Chemistry and Catalysis

The study of organometallic catalytic processes under gas pressure is of great interest despite the hazards involved in using compressed gases. A striking recent example is the catalytic dimerisation of ethylene in aqueous Ru^{2+} solutions, which was studied by ^{17}O, ^{13}C, and ^1H NMR in pressurizable sapphire NMR tubes.[18] Three identical ^{17}O enriched aqueous solutions of $[Ru(H_2O)_6]^{2+}$ in 10 mm o.d. sapphire tubes were pressurized with ethylene at 6 MPa and mixed by shaking for different amounts of time. The NMR spectra showed the successive formation of $[Ru(CH_2{=}CH_2)(H_2O)_5]^{2+}$ and $[Ru(CH_2{=}CH_2)_2(H_2O)_4]^{2+}$. After shaking under ethylene pressure for 3 days, an organic phase formed above the solution. The ^{13}C spectra of this new organic phase, separated under pressure, show characteristic signals of butenes. This aqueous catalytic dimerization reaction is not stereoselective, and all the possible butenes are formed except 2-methylpropene. These results show the utility of NMR studies under gas pressure for the study of catalytic reactions in aqueous solution, which are increasingly attractive with respect to ecological considerations.

There is also interest in the measurement of activation volumes for reactions and internal processes in organometallic compounds. For instance, the ring inversion of cyclic thio ligands in *trans*-$PdBr_2(SCH_2CMe_2CH_2)_2$ was studied under pressure. The activation volume was essentially zero, indicating no association, dissociation, or solvent participation in the inversion process. The exchange processes in a mixture of dimeric $[Pd(2\text{-methylallyl})Cl]_2$ and monomeric Pd(2-methylallyl)Cl(PPh_3) was also studied by variable pressure ^1H NMR. The activation volume depends on temperature, indicating a change of mechanism. At 22 °C, $\Delta V^{\#}$ is essentially zero. The *syn*−*anti* exchange of the allyl hydrogen atoms occurs in the monomer, catalysed by association with

the dimer and the volume change due to this association is canceled by that due to cleavage of the dimer bridge. A 56 °C, $\Delta V^{\#} = +11 \pm 2\,\mathrm{cm^3\ mol^{-1}}$: methylallyl exchange now occurs by a process involving dimer cleavage followed by PPh_3 transfer, and it is the cleavage that produces the expansion.

4.6 Organic Chemistry

High-pressure NMR has been used to study a variety of reactions in organic chemistry. For instance, the volume profiles for the rearrangement of two norbornyl cations have been studied. For rearrangement of the 1,2-dimethoxy-2-norbornyl cation, $\Delta V^{\#} = +8.7 \pm 0.5\,\mathrm{cm^3\ mol^{-1}}$, expansion occurs because the transition state cation has a delocalized charge distribution that reduces interactions with the solvent. Rearrangement of the 7-methyl-7-norbornadienyl cation, on the other hand, takes place via an intermediate with increased charge localization, and one would expect a negative activation volume due to contraction around the transition state. In fact $\Delta V^{\#} \approx 0$, and this is explained by a cancellation of the contraction by an expansion due to bond rupture during the rearrangement.

In the thermolysis of acetyl benzoyl peroxide it was found that pressure retards the rate of peroxide cleavage and increases the ratio of cage product to escape product. The data yield the activation volume for the initiator decomposition ($4\,\mathrm{cm^3\ mol^{-1}}$) and the difference in activation volume for the formation of escape and cage products ($8\,\mathrm{cm^3\ mol^{-1}}$). The effect of pressure on the rates of sigmatropic shifts in 5-(trimethylsilyl)cyclopentadiene, 5-formylpentamethylcyclopentadiene, and bullavene has also been observed. The activation volumes for the silyl compound are negative and depend strongly on solvent, indicating that considerable charge separation occurs in the transition state in chloroform solution, but much less in benzene. The activation volume is much smaller for the formyl compound, indicating that no charge separation occurs, at least in benzene–Freon.

Two reactions that comprise equilibrium addition of a protic species to a carbonyl group have been studied. In the first case, the intramolecular hydroketone–hemiacetal interconversion, $\Delta V^{\#} = -3.2\,\mathrm{cm^3\ mol^{-1}}$, is interpreted as being the volume change necessary for bond formation in this necessarily associative process. The second reaction, the intramolecular addition of thiol to acetyl cyanide, has $\Delta V^{\#} = -13\,\mathrm{cm^3\ mol^{-1}}$. This much larger value is believed to comprise the volume change necessary for bond formation plus the larger volume contraction that occurs upon the simple association of two molecules.

4.7 Silicates

The initial stages of the sol–gel condensation process that occurs following hydrolysis of $Si(OMe)_4$ have been followed by variable pressure ^{29}Si NMR. Increased pressure increases markedly the rate of condensation without changing the mechanism, and it is possible that by carrying out such preparations at high pressure one can improve the properties of the glasses and ceramics that are the final objective of the process.

5 RELATED ARTICLES

Gadolinium Chelate Contrast Agents in MRI: Clinical Applications; Gadolinium Chelates: Chemistry, Safety and Behavior; High- Pressure NMR; Inorganic Chemistry Applications; Paramagnetic Relaxation in Solution; Probes for Special Purposes.

6 REFERENCES

1. R. van Eldik (ed.), *Inorganic High Pressure Chemistry: Kinetics and Mechanisms*, Elsevier, Amsterdam, 1986.
2. A. E. Merbach and J. W. Akitt, *NMR Basic Principles Progr.*, 1990, **24**, 189.
3. R. van Eldik and A. E. Merbach, *Comments Inorg. Chem.*, 1992, **12**, 341.
4. J. Jonas, *NMR Basic Principles Progr.*, 1990, **24**, 85.
5. C. H. Langford and H. B. Gray, *Ligand Substitution Processes*, Benjamin, New York, 1965.
6. T. W. Swaddle, *Adv. Inorg. Bioinorg. Mechanisms*, 1983, **2**, 95.
7. H. Vanni, W. L. Earl, and A. E. Merbach, *J. Magn. Reson.*, 1978, **29**, 11.
8. W. L. Earl, H. Vanni, and A. E. Merbach, *J. Magn. Reson.*, 1978, **30**, 571.
9. U. Frey, L. Helm, and A. E. Merbach, *High Press. Res.*, 1990, **2**, 237.
10. A. E. Merbach, *Pure Appl. Chem.*, 1982, **54**, 1479.
11. C. Cossy, L. Helm, and A. E. Merbach, *Inorg. Chem.*, 1988, **27**, 1973.
12. C. Cossy, L. Helm, and A. E. Merbach, *Inorg. Chem.*, 1989, **28**, 2699.
13. D. H. Powell, A. E. Merbach, G. González, E. Brücher, K. Micskei, M. F. Ottaviani, K. Köhler, A. von Zelewsky, O. Ya. Grinberg, and Ya. S. Lebedev, *Helv. Chim. Acta*, 1993, **76**, 2129.
14. K. Micskei, D. H. Powell, L. Helm, E. Brücher, and A. E. Merbach, *Magn. Res. Chem.*, 1993, **31**, 1011.
15. U. Frey, L. Helm, and A. E. Merbach, *Helv. Chim. Acta*, 1990, **73**, 199.
16. K. Micskei, L. Helm, E. Brücher, and A. E. Merbach, *Inorg. Chem.*, 1993, **32**, 3844.
17. G. González, D. H. Powell, V. Tissières, and A. E. Merbach, *J. Phys. Chem.*, 1994, **98**, 53.
18. G. Laurenczy and A. E. Merbach, *J. Chem. Soc., Chem. Commun.*, 1993, 187.

Acknowledgments

We wish to thank the large number of people who have contributed over the years to the work performed at Lausanne, as well as all those groups elsewhere with whom we have had fruitful collaborations. We also wish to thank the Swiss National Science Foundation for continued and generous support of our work.

Biographical Sketches

D. Hugh Powell. *b* 1965. B.Sc., 1986, Ph.D., 1989, Physics (supervisors G. W. Neilson and J. E. Enderby), University of Bristol, UK. Research Associate at the Institute of Inorganic and Analytical Chemistry of the University of Lausanne, Switzerland (with A. E. Merbach),

1989–1994, lecturer at the Dept. of Chemistry, University of Adelaide, 1995–present. Approx. 25 publications. Current research interests: multinuclear magnetic resonance, ESR and neutron diffraction studies of dynamics and structure in solution particularly of lanthanide based MRI contrast agents and related complexes.

André E. Merbach. *b* 1940. Diploma in Chemical Engineering, 1962 (EPUL), Ph.D., 1964, Chemistry, University of Lausanne, Switzerland. Postdoctoral work at the University of California at Berkeley, USA (with O. Redlich), 1964–65. Institute of Inorganic and Analytical Chemistry of the University of Lausanne, 1965–present. Full Professor of Chemistry, 1973–present. Approx. 200 publications. Research specialties: high pressure NMR, high-pressure kinetics, inorganic reaction mechanisms, metal ion solvation, MRI contrast agents, coordination chemistry.

Magnetic Equivalence

Thomas H. Siddall III

University of New Orleans, New Orleans, LA, USA

1	Introduction	1
2	A Hypothetical Molecule	1
3	Dimethylformamide: Internal Rotation	2
4	Biphenyl-Like Rotation in certain Anilides	2
5	Rotation of Methyl Groups as a Dynamic Symmetry Operation	3
6	Geared Isopropyl Groups	3
7	An Amine/Amine Hydrochloride Equilibrium with Amine Inversion	4
8	Exchange in an Iron Hydride	5
9	Change of Shape: Polyhedral Exchange	5
10	Interchange of Hydride Hydrogen with Molecular Hydrogen as Ligands	5
11	Inversion and Isomerization in Metal Tris(diketonates)	6
12	Slow Rotation and Possible Ring Inversion in a Lanthanum Compound	7
13	Ring Whizzing	8
14	Bridge/Terminal Exchange and Isomerism in a Bridged Iron Compound	9
15	Conclusions	9
16	General References	10
17	Related Articles	10
18	References	10

1 INTRODUCTION

Magnetic equivalence arises from symmetry. It is convenient to divide symmetry into two parts. The first is the point group symmetry of the molecule (or ion). The second is the symmetry that involves rapid intramolecular motions such as internal rotation of parts of the molecule against other parts, molecular inversion, or shifting of bonds between atoms in the molecule. As the temperature is lowered, these motions or rearrangements may slow down so much that nuclei (or sets of nuclei) that were equivalent at higher temperature become magnetically nonequivalent. (Magnetic equivalence that is achieved by interaction between molecules and/or intermolecular events is excluded from discussion in this article.)

Rapid processes are those by definition that occur with a frequency greater than the chemical shift difference between the NMR signals from the nuclei if they were nonequivalent. The spectrum that occurs at higher temperature when processes are rapid and the nuclei are equivalent is known as the *fast exchange spectrum*. The spectrum at lower temperature and when processes are slow is known as the *slow exchange spectrum*. The spectra at intermediate temperatures are said to be *intermediate exchange spectra*. Typically signals are broadened to become perhaps almost featureless humps for nuclei in the temperature region of intermediate exchange. Signal shape analysis of broadened signals can yield rate data and kinetic parameters. The kinetic window for signal shape analysis can vary substantially for different situations. However, typically rates of $10-1000\,s^{-1}$ can be determined by signal shape analysis. (The free energy of activation, $\Delta G^{\ddagger}$, as reported in the literature for various processes is quoted in this article. The temperature is always 298 K, unless otherwise noted.)

For convenience in discussion, point group symmetry will be referred to as *static symmetry*. The effect of internal motions will be referred to as *dynamic symmetry*. In fact, manifestation of dynamic symmetry is commonly called DNMR (dynamic NMR).

The operations of static symmetry and dynamic symmetry can be brought together to form a *permutation group* for the nuclei or groups of nuclei under discussion. This may seem strange since static symmetry depends only on geometry and does not actually move nuclei, while dynamic symmetry depends on actually moving nuclei. However, mathematically there is no qualitative distinction between the outcome of the two kinds of symmetry. In any event the nuclei are permuted (or in more common language they are exchanged). Permutation group theory is not discussed as such in this article, but it will be useful to use some of the ideas of permutation groups.

It is important to note that NMR of itself does not necessarily specify uniquely the dynamic physical process that permutes nuclei in any given case. It may, however, reveal which nuclei are exchanging with which nuclei. The detection of mutual exchange will be discussed in the main body of this article. But any analysis as to detailed mechanism requires additional information or theory outside the NMR experiment. However, a knowledge of mutual exchange may rule out certain mechanisms from a list of otherwise plausible mechanisms.

In spite of this caveat as to the limits of mechanistic information from NMR alone, the main article is organized to some extent around demonstrations of rotation around bonds, molecular inversion, and other specific internal motions, shifting of bonds, or combinations of such as these. The choice of interpretation of the nuclear exchange has always been assisted by outside considerations, even though these considerations may not be explicitly stated in the discussion that follows.

Individual studies have been selected for discussion in this article to represent principles. There is no attempt to give a review-like coverage of the very large literature that is continuing to emerge on the subject. Selection has not been made on the basis of clear superiority of one report over similar reports. The literature is too large and choice too subjective to guarantee that the selection has been made entirely on the basis of merit or of scientific importance.

Finally, a large share of the literature covered in this article was published in the approximate period from 1960 to 1975. The principles that were established in that period are now almost a matter of routine, but of course with newly interesting manifestations. Section 16, General References, refers to a variety of reviews and literature collections and should be consulted for a much wider coverage of magnetic equivalence and dynamic NMR than was possible to give in composing the present article. Also the bulk of the NMR studies have been undertaken by proton NMR methods. Unless otherwise specified or obvious, NMR stands for proton NMR in this article.

2 A HYPOTHETICAL MOLECULE

Some of the discussion in the Introduction can be illustrated with simple examples. The first example deals with a hypothetical molecule (**1**). So long as the R^1, R^2, and R^3 groups are all different, the carbon atom, C*, is asymmetric and the molecule has no symmetry plane. As a consequence, the hydrogen atoms, H_A and H_B, are nonequivalent since there is no static symmetry between them. Inversion of the asymmetric carbon atom would be a dynamic symmetry operation, but inversion of such a carbon atom is much too slow by many orders of magnitude to be an effective dynamic symmetry operation.

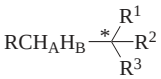

(1)

It might be supposed that rotation around the bond between the carbon atoms could constitute a dynamic symmetry operation, but this is not correct. Rapid rotation around that bond might tend to average out the environments of the hydrogen atoms, but the averaging could never be complete. It is suggested here that this last point is best demonstrated by experimenting with molecular models. On the other hand, if any two of the R^1, R^2, or R^3 groups were the same, there could be a symmetry plane between the hydrogen atoms. This static symmetry element would make the hydrogen atoms magnetically equivalent.

The usual twisting and turnings, rotations and vibrations of the rest of the molecule would ordinarily be much too rapid on the NMR timescale to destroy this equivalence. Variable temperature NMR studies are at the heart of much of the discussion of magnetic equivalence or the lack of it. If an internal rearrangement is so rapid that it cannot be 'frozen out' at the lowest experimentally attainable temperature, then it is just part of the background. It does not stand out as a dynamic symmetry operation, the effect of which is amenable to study by variable temperature NMR.

Given the asymmetric carbon atom, the hydrogen atoms are *diastereotopic*. This term will be used frequently in later discussions. In principle any geminal species can be diastereotopic. Isopropyl radicals are often included in molecules chosen for study. The methyl groups within an isopropyl group can be diastereotopic. Molecular inversion is the only dynamic operation that can render the methyl groups equivalent. If the methyl groups remain nonequivalent, then rapid inversion is not occurring. Of course other geminal pairs can serve the same purpose but their utility is usually lessened by the complex spectra that can occur, while methyl nonequivalence can lead to signal patterns that are easy to analyze, often at a glance.

3 DIMETHYLFORMAMIDE: INTERNAL ROTATION

The observation by Phillips[1] of the effect of temperature on the proton magnetic resonance spectrum of *N*,*N*-dimethylformamide and its explanation as internal rotation is one of the earliest records of intramolecular exchange in NMR. The core framework of amides is planar. There is partial double bond character in the carbonyl-to-nitrogen bond (the amide bond). Pauling[2] calculated the resonance energy to be 88 kJ mol^{-1}. For present purposes, resonance energy and the partial double bond character are manifest as the barrier to rotation around the amide bond.

Phillips observed that there is only one methyl signal at the fast exchange limit, but that this signal splits into two methyl signals at the slow exchange limit. He explained this behavior as being due to rapid rotation around the amide bond at higher temperature with the rotation slowing down as the slow exchange limit is reached at lower temperature.

Gutowsky and Holm[3] utilized the techniques of Gutowsky's earlier signal shape studies to determine the rate of rotation in dimethylformamide. They obtained a $\Delta G^{\ddagger}$ value of 92 kJ mol^{-1}. Since this pioneering work, there has been and continues to be a veritable torrent of applications to a large variety of intermolecular as well as intramolecular rate problems.

The symmetry considerations that are involved are straightforward. In the planar ground state, both methyl groups lie in the amide plane. Since there is no static symmetry element between the methyl groups, they are nonequivalent in the ground state. One methyl group is *cis* to the carbonyl oxygen and the other is *trans*. Rapid rotation around the amide bond is the dynamic symmetry operation that makes the methyl groups equivalent.

This set of symmetry considerations applies for amides in general and even more generally to rotation around the bond between trigonally bonded atoms in a variety of molecules that have a planar ground state. On the other hand, biphenyls, as examples, have the rotating parts in an out-of-plane ground state, and the barrier to rotation is substantially steric rather than electronic as it is in rotation around the amide bond.

4 BIPHENYL-LIKE ROTATION IN CERTAIN ANILIDES

Dynamic NMR of anilides with unsymmetrical substitution in the benzene ring demonstrates how a missing static symmetry operation can be replaced by a dynamic symmetry operation and magnetic equivalence is then achieved.

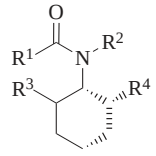

(2)

In ground state anilides of the general type (**2**) the benzene ring is perpendicular to the amide plane. If the ring is symmetrically substituted, the perpendicular plane through the ring is a symmetry plane (a static symmetry element). If both *ortho* substituents are not the same, this symmetry plane is lost, a chiral center is established, and the molecule becomes chiral. This situation was first reported by Adams and his students[4] well before the advent of NMR in chemistry.

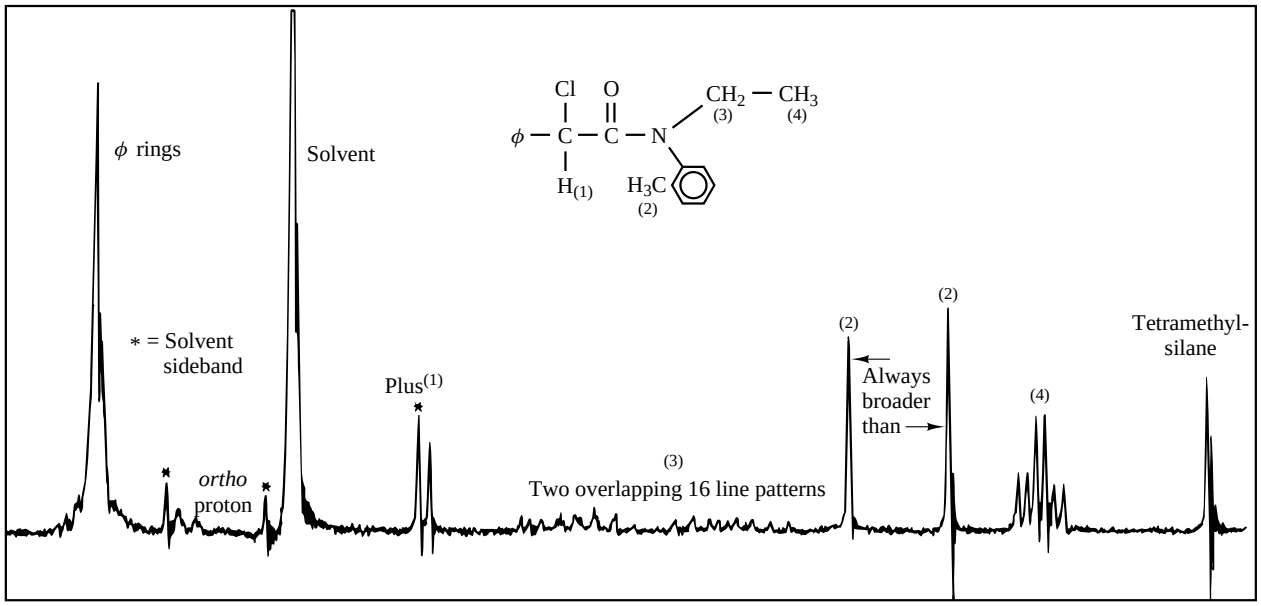

Figure 1 Double proton signals at 40 °C of an anilide dissolved in $CHCl_2CHCl_2$. [Reprinted with permission from Siddall and Stewart, *J. Phys. Chem.*, **73**, 40. Copyright (1969) American Chemical Society]

Rotation around the benzene-to-nitrogen bond is generally slow on the NMR timescale at room temperature, but becomes rapid at elevated temperature. Rapid rotation then becomes a dynamic symmetry operation and substitutes for the lost symmetry plane. (Generally, the *cis*/*trans* isomerism due to slow rotation around the carbonyl-to-nitrogen bond is not observed in anilides of this type except in formanilides. Probably this is due to the predominance of one geometric isomer over the other to the point of excluding the lesser isomer from observation.)

This situation is demonstrated in a striking manner if a second chiral center is introduced into the anilide molecule.[5] With two chiral centers the molecule exists as two diastereoisomers. In the slow exchange limit each of the two isomers exhibits its own set of NMR signals. This in effect doubles the signals in the NMR spectrum as can be seen in Figure 1.

However, raising the temperature increases the rate of rotation around the benzene-to-nitrogen bond and the doubled signal sets coalesce into a single set of signals. The single set is the average over the rapid equilibrium between the two isomers. Rapid rotation has substituted for the lost symmetry plane and leads to magnetic equivalence.

5 ROTATION OF METHYL GROUPS AS A DYNAMIC SYMMETRY OPERATION

The barrier to rotation of methyl groups is typically quite small, 12–13 kJ mol^{-1}. As a consequence, rotation of the methyl group is very rapid on the NMR timescale and is usually not explicitly considered as a dynamic symmetry operation in evaluating symmetry for NMR purposes. However, extreme crowding in 1-*t*-butyl-5,6,7,8-tetrachloro-1,4-dihydronaphthalene 1,4-endoxide (**3**) slows methyl group rotation down sufficiently to be detectable.[6]

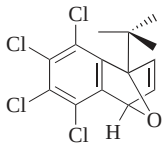

(3)

At room temperature, the *t*-butyl group gave a sharp singlet. At −60 °C, the methyl groups within the *t*-butyl group are nonequivalent and the orginal singlet becomes three sharp singlets. Rotation around the bond to the *t*-butyl group evidently has slowed down. As the temperature was lowered still further to − 121 °C and finally to − 133 °C, two of the three methyl signals broadened almost to the point of decoalescence, while the singlet from the third methyl group remained little changed. Apparently the temperature could not be lowered sufficiently to give the slow exchange spectrum. The authors examined possibilities other than slow methyl rotation as explanations for the broadening, but were able to dismiss these other possible explanations.

6 GEARED ISOPROPYL GROUPS

Rapid rotation of isopropyl groups is usually automatically taken for granted as part of a big background of rapid internal molecular motions that are not singled out as dynamic symmetry operations, since they are rapid on the NMR timescale at accessible temperatures. However, there is considerable evidence that isopropyl rotation can be slow, especially if isopropyl groups are in close enough proximity to each other to interact sterically. This steric interaction apparently can take the form of synchronous rotation. Such isopropyl rotations have been quite aptly labeled as geared rotation[7] or cogwheeling. Furthermore, the rotation of other groups that are adjacent to the geared isopropyl groups can

be slowed because of steric interactions with the isopropyl groups.

In the molecule described below, benzyl group rotation is slowed because of interaction with the isopropyl groups. (The NMR studies were made both with proton NMR and with carbon-13 NMR. The two spectroscopies substantiated each other in detail. This being the case and in the interest of economy in discussion, only the proton behavior is described below.)

The room temperature spectrum[7] of 1,3-dibenzyl-4,5-diisopropyl-2-thione (**4***a*, **4***b*) is just as would be expected. At highest frequency, the benzene ring protons give a multiplet; moving to low frequency, the methylene protons give a singlet, then there is the methine septet, and finally at lowest frequency there is the expected methyl doublet. The static symmetry is C_{2v}. The molecule lies in one plane. The plane perpendicular to the molecular plane makes the isopropyl groups equivalent as whole groups and also the benzyl groups equivalent as whole groups. The molecular symmetry plane makes the protons within a methylene group equivalent and the methyl groups within an isopropyl group equivalent.

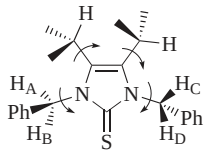

anti
(4*a*)

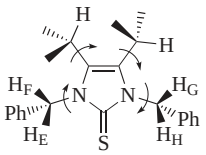

syn
(4*b*)

The spectrum at $-112\,^{\circ}$C is anything but routine. The C_{2v} symmetry is destroyed. There are no longer any symmetry planes nor a C_2 axis. Methylene protons give four separate AB patterns and are clearly diastereotopic. The methine signals have disappeared into baseline noise, but there are four methyl doublets. The increase to four AB patterns definitely shows that there are four different low temperature environments for the methylene groups and eight environments for the methylene protons.

The existence of only four methyl doublets from the isopropyl groups might be unexpected. If there are eight environments for the methylene protons, eight environments would be expected for the methyl groups. This could lead to eight doublets rather than just four. Precise signal overlap to give just four pairs of doublets could be an explanation, but does require an uncomfortable degree of coincidence. However, since no alternative explanation is readily forthcoming, the discussion will be continued, while ignoring this difficulty, which is what the authors of the paper did.

The spectra taken between $-20\,^{\circ}$C and $-90\,^{\circ}$C indicate that more than one rate process is taking place. The process that is observed below $-20\,^{\circ}$C is assigned to the synchronous rotation of the isopropyl groups. At lower temperature, the process of rotation around the bond of one of the benzyl groups is being slowed down. At still lower temperature, the rotation of the other benzyl group is slowing. The $\Delta G^{\ddagger}$ value was calculated to be 48 kJ mol^{-1} at 223.6 K for the isopropyl process, and 45 and 36 kJ mol^{-1} for the two different benzyl rotations.

The process shown below is central to rationalizing the spectral observations. The isopropyl groups, acting as gears, tend to lock into one or the other of two positions. The positions are mirror images of each other. The gears rotate rapidly on the NMR timescale at room temperature. The gears lock and unlock so quickly that the locked positions average out. At about $-20\,^{\circ}$C the lock–unlock rotation slows down to the slow exchange limit as far as the isopropyl rotations are concerned. Meanwhile, the rotamer lifetime of the benzyl groups is still very short, still at rapid exchange. Many benzyl rotations occur during the lifetime of one lock of the isopropyl gears.

As the temperature is lowered still further, first one of the benzyl rotations slows to the slow exchange limit. Finally, at still lower temperature, the other benzyl rotation slows to the slow exchange limit. Once all three of these rotations have slowed enough, the slow exchange NMR spectrum obtains.

In ground states a benzyl rotamer can have two positions. In one position the benzene ring is above the molecular ring plane. In the other position the benzene ring is below that plane. This leads to *syn*/*anti* isomerism, both benzene rings on one side of the ring plane or one benzene ring on one side of the plane and the other on the other side of the plane. In each of the *syn*/*anti* isomers the benzyl groups are in different environments and within each methylene group the protons are in a different environment. Since $2 \times 2 \times 2 = 8$, there are eight proton environments and four AB quartets.

As the temperature is raised from the overall slow exchange limit, each of these dynamic symmetry operations are involved to give finally the fast exchange spectrum, to result in C_{2v} molecular static symmetry, and to give magnetic equivalences consistent with that symmetry.

7 AN AMINE/AMINE HYDROCHLORIDE EQUILIBRIUM WITH AMINE INVERSION

This example[8] is interesting enough that it is included even though it may be a violation of the restriction to intramolecular events as stated in the Introduction. The discussion involves the static symmetry and also molecular inversion as a dynamic symmetry operation.

Nitrogen inversion in simple acyclic amines and with hydrocarbon substituents is usually too rapid to be observed directly by NMR. On the other hand, inversion of the hydrochloride of amines is very slow and magnetic equivalence is dictated by static symmetry alone. However, with an amine/amine hydrochloride equilibrium, nonequivalent protons in the hydrochloride can become equivalent in the amine. The amine in this example is dibenzylmethylamine.

The symmetry plane between the benzyl groups in the amine hydrochloride makes the benzyl radicals equivalent as entire radicals, but there is no static symmetry element that makes the protons of the methylene group magnetically equivalent within a benzyl radical. As a consequence the methylene protons with the methylene groups give an AB quartet. Inversion is much too slow within the hydrochloride to act as a dynamic symmetry operation.

On the other hand, inversion of the amine is rapid and acts as a dynamic symmetry operation to make the methylene protons equivalent. As the pH of the hydrochloride solution is raised, enough amine exists in the equilibrium mixture that the methylene AB quartet coalesces as the methylene protons become equivalent.

Since inversion occurs only during the amine lifetime, and the amine/amine salt equilibrium is fast, the exchange of methylene proton identities is given by k(exchange) = k(inversion) × (amine)/[(salt) + (amine)]. With a pH of 2.5, using the pK_a value of the amine as 7.5 and obtaining k(exchange) from signal shape analysis, the authors were able to calculate the inversion rate of the amine as 2×10^5 s^{-1}. In effect the salt sequestered enough of the amine to make the inversion rate measurable.

8 EXCHANGE IN AN IRON HYDRIDE

Inorganic compounds can be a very rich source for all sorts of NMR studies. The examination of the temperature-dependent proton spectra and ^{31}P spectra of $H_2Fe[P(OC_2H_5)_3]_4$ illustrates this richness.[9] (Of the proton spectra only the hydride part is relevant to the discussion. The spectra of ethyl protons are omitted.)

The compound exists as the *cis* isomer, (**5**), where the Ps represent ligand triethyl phosphite molecules and the Hs the ligand hydrogen atoms. The subscripted numbers will be used in the continued discussion. Because of space limitations, the discussion is drastically curtailed. Readers may wish to consult the original paper.

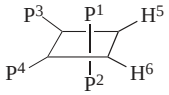

(5)

At 68 °C, the spectrum of the hydride hydrogens is a binomial quintet which indicates that the protons are magnetically equivalent as are the phosphorus atoms. The proton-decoupled phosphorus spectrum is just one singlet which also indicates that the phosphorus atoms are equivalent. It must be that some exchange processes are rapid enough at this temperature to be dynamic symmetry operations that lead to the patterns of magnetic equivalence.

At −50 °C, the magnetic equivalence of the phosphorus atoms has disappeared. The proton-decoupled phosphorus spectrum gives an A_2B_2 pattern which is just what would be expected from C_{2v} symmetry for the *cis* isomer.

The low temperature proton spectrum for the hydride hydrogens is a deceptively simple triplet of doublets which represents an $AA'XX'Y_2$ pattern (A for protons, X and Y for phosphorus). The authors found six different coupling constants which is consistent with such a pattern.

As the temperature is lowered from 68 °C, the three central peaks of the proton quintet broaden, as would be expected if the relevant exchanges were occurring. However, the wing peaks of the quintet remain sharp and unaffected by exchange. This shows that two of the phosphorus atoms remain equivalent as the temperature is lowered. The axial phosphorus atoms are magnetically equivalent and are the Y_2 part of the $AA'XX'Y_2$ spectrum. On the other hand, the equatorial phosphorus atoms are the XX' part of the spectrum and are not magnetically equivalent.

The phosphorus spectra at intermediate temperatures were compared with calculated spectra assuming various phosphorus atom exchange schemes. The only exchange scheme that fits the experimental spectra was to have P^1 exchange with P^3 or P^4 and to have P^2 exchange with P^3 or P^4. Or, in other words, there was axial–equatorial exchange, but no axial–axial or equatorial–equatorial exchange of phosphorus atoms. The observed exchanges are the fundamental dynamic symmetry operations, but without revealing the mechanistic detail as to how they occur.

The authors felt that the complexity of this molecule is appropriate to demonstrate this kind of permutational analysis. Less complex molecules would not exhibit interesting exchange patterns, while more complex molecules might present too much of a computational problem. It should be noted that the development of two-dimensional NMR techniques after this paper was published provides direct instrumental access to revealing which nuclei are exchanging with which nuclei.

9 CHANGE OF SHAPE: POLYHEDRAL EXCHANGE

Four-coordinate nickel compounds often exist in solution as an equilibrium of 'square planar' and 'tetrahedral' isomers. (Generally the square planar complexes are not strictly D_{4h} and the tetrahedral complexes are not strictly T_d, but this distinction in the isomers is common in the literature and is useful. The quotation marks will be dropped in the discussion below.) The square planar isomers are diamagnetic while the tetrahedral isomers are paramagnetic. The paramagnetism in the tetrahedral isomers leads to very large shifts of NMR signals from their normal positions in diamagnetic isomers (or molecules in general). These very large shifts facilitate signal assignment in the slow exchange limit where the signal sets of the two isomers can be seen as two separate sets. It may stretch the definition somewhat, but the conversion between isomers could be called a dynamic symmetry operation. There have been detailed mechanistic proposals as to how the conversion occurs but they will not be discussed here. The components of these mechanisms could be more properly labeled as dynamic symmetry operations rather than the overall conversion.

Unfortunately in most instances the slow exchange limit is evidently below attainable temperatures and the only spectra obtained are the spectra averaged between isomers. The molecule, $[MeP(Ph)_2]_2NiBr_2$, and related molecules, provide fortunate exceptions.[10] At −65 °C, the slow exchange spectrum demonstrates the very large chemical shifts that are induced by paramagnetism. For example, the signal from the *meta* protons in the tetrahedral isomer occurs at almost δ − 30 ppm, while the corresponding signal for the square planar isomer occurs at the normal position for aromatic proton signals.

As the temperature is raised the separate signals begin to coalesce. Finally at 40 °C, the averaged spectrum is obtained and with it, magnetic equivalence. The authors obtained 57 kJ mol^{-1} for $\Delta G^{\ddagger}$.

10 INTERCHANGE OF HYDRIDE HYDROGEN WITH MOLECULAR HYDROGEN AS LIGANDS

The dynamic symmetry operation here is the exchange back and forth, on the one hand, of two hydrogen atoms

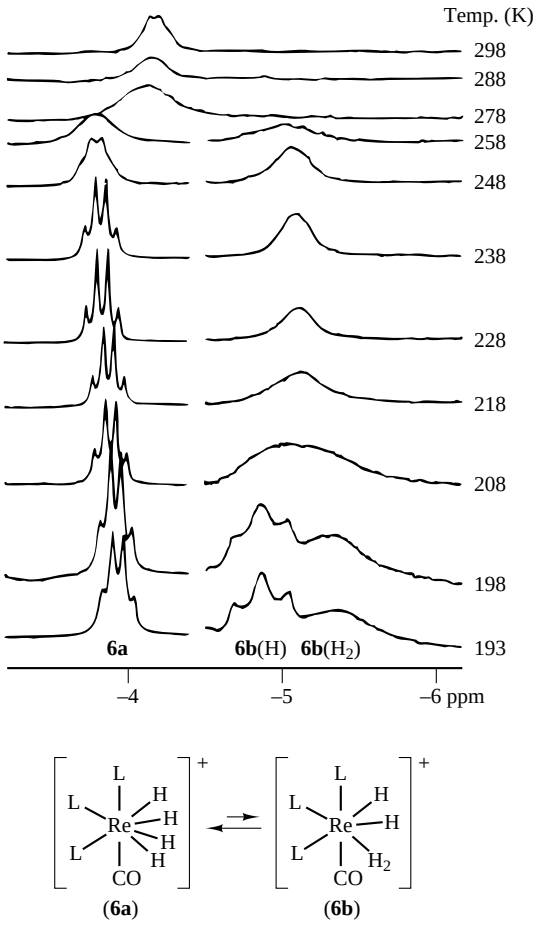

Figure 2 The hydrogen/hydride equilibrium and the hydride region of the 250 MHz spectrum of the ion $[ReH_4(CO)(PMe_2Ph)_3]^+$. (Reproduced with permission from Crabtree, *Acc. Chem. Res.*, 1990, **23**, 95)

as a hydrogen molecule bound as one ligand, with the two hydrogen atoms bound separately as two separate hydride ligands, on the other hand.

This change between molecule and hydride manifests itself in several features of the variable temperature NMR spectra[11] of the ion $[ReH_4(CO)(PMe_2Ph)_3]^+$. The hydride region of the spectra is shown in Figure 2.

At 298 K, the entire hydride spectrum is just one broadened quartet with coupling to the three phosphorus atoms. The fast exchange limit and magnetic equivalence are being approached. As the temperature is lowered, this signal decoalesces quickly to give an AB quartet at high frequency (low field) and to produce an unresolved hump at lower frequency. At the lowest temperature, the low-frequency hump has decoalesced into a somewhat broadened AB quartet and a smaller hump. There must be two rate processes at work.

The higher temperature coalescence depends on the slowing down of the isomer equilibrium. The value of $\Delta G^{\ddagger}$ for the isomerization was found to be 49 kJ mol^{-1} at 213 K. The sharp, high frequency quartet is assigned to isomer (**6a**). In (**6a**) all the hydrogen atoms are bound to the metal as hydride hydrogens and, as a consequence, there is no further change in the spectrum of that isomer as the temperature is lowered. The spectrum of isomer (**6b**) continues to change as the temperature is lowered, which indicates that some dynamic operation is coming into play. The final partial decoalescence of the spectrum of (**6b**) reflects the slowing down of the hydride/molecule interconversion within that isomer. The value of $\Delta G^{\ddagger}$ was found to be 41 kJ mol^{-1}. The interconversion has then played a role twice. This is one interesting example of the role of a dynamic process as occurring more than once in the same molecule. A number of examples have been published of multiple rotations, inversions, and combinations of these and other processes.

An interesting sidelight arises from the above experiment. Generally, 7- and 8-coordinate structures are *fluxional*. Interconversions between competing polyhedra are so rapid that the slow exchange spectrum is not attainable at the lowest temperatures that are available to NMR experiments. In the case discussed above, not only is the slow exchange spectrum of one such structure achieved, but also that of the other, competing polyhedron with a different coordination number. The 7-coordinate structure involves a molecule of hydrogen occupying only one coordination site. The 8-coordinate structure involves two hydrogen atoms, each occupying a coordination site.

11 INVERSION AND ISOMERIZATION IN METAL TRIS(DIKETONATES)

The octahedral complexes in which a metal is bonded to three β-diketone ligands provide instructive examples of the role of symmetry in NMR. ('Octahedral' is at best only approximately octahedral, but the term is used widely when discussing these complexes.) There is a very large amount of literature on this subject, but discussion here is focused on the complexes of (a) symmetrical diketones, $RC(O)CH_2C(O)R$, and (b) unsymmetrical diketones, $RC(O)CH_2^-C(O)R'$, and where a given complex has all three diketones as either (a) or (b).

The static symmetry of the symmetrical complexes (a) is D_3 (and not O_h). The three diketone chelate rings with the metal are all magnetically equivalent as entire rings. The complex is chiral and chirality will be apparent if diastereotopic nuclei or groups of nuclei are included. In practice it has been very useful for both R groups to be isopropyl. With this choice of ligand all the isopropyl groups are magnetically equivalent as entire groups, but the methyl groups within an isopropyl group are nonequivalent. In the slow exchange limit there will be two methyl doublets and the two will become one methyl doublet at the fast exchange limit. The dynamic symmetry operation is inversion of the complex.

The simplest visualization of the actual inversion mechanism is to assume a trigonal prism as the transition state. The transition state molecule could then either fall back into its original ground state geometry or into its enantiomer. While this mechanism has the virtue of simplicity, it is not generally accepted. Instead a dissociative mechanism is preferred. One end of one of the ligands breaks its bond to the metal such that the metal then becomes five-coordinate. The transition state geometry around the metal is supposed to be either a trigonal bipyramid or a square pyramid. The ligand that became unidentate in the transition state reattaches itself either to reform the original ground state or to form its enantiomer. These complexities admittedly stretch the concept of a single dynamic symmetry operation.

Complexes of type (b) can exist as *cis* or *trans* isomers. For the *cis* isomer there is one triangular face defined by three R groups. The vertices of the triangle opposite to this triangle are occupied by R′ groups. The *cis* isomer has C_3 symmetry with the C_3 axis through the centers of the triangles above. As a consequence the three chelate rings are equivalent as entire rings. With R being isopropyl, the methyl groups are diastereotopic. The fast exchange spectrum of the methyl groups in an isopropyl group would consist of one doublet. The slow exchange spectrum would consist of two methyl doublets. Qualitatively the isopropyl spectrum of the *cis* isomer of a type (b) complex would be the same as for a type (a) complex.

On the other hand, the *trans* isomer of a type (b) complex has no static symmetry. The chelate rings are magnetically nonequivalent. With R being isopropyl, there would be six methyl doublets, two from each ring, at the slow exchange limit. However, the fast exchange limit would exhibit only one methyl doublet.

The dynamic symmetry operation for both *cis* and *trans* isomers is inversion. However, *cis* and *trans* isomers do not stand alone, each by itself. A *cis*/*trans* interconversion can also occur at the same time and can be considered as a dynamic symmetry operation. The discrete separation into racemization and isomerization events is considered to be difficult-to-impossible to achieve experimentally. The dissociation mechanism followed by arrangement into a five-coordinate geometry and a return to six-coordinate geometry could accomplish one or the other or both at once.

This complex situation with the tris(chelates) reflects the caveat stated in the Introduction. Straightforward dynamic NMR may reveal permutation patterns but cannot of itself supply mechanistic details.

Two studies of temperature-dependent NMR spectra particularly exemplify the discussion above. In both cases the metal was aluminum. The first[12] involved Al(Isopr(CO)CH(CO)Isopr)$_3$ as type (a). The second[13] study was with Al(PhCH$_2$(CO)CH(CO)Isopr)$_3$ as a type (b) complex. (The formula for the isopropyl group is abbreviated as Isopr and that for the benzene ring as Ph.)

At 37 °C the symmetrical complex, type (a), gives a slow exchange methyl spectrum that consists of two equal intensity doublets. At 120 °C the two doublets coalesce and at 145 °C the fast exchange spectrum as just one doublet is reached. At the lowest temperature isopropyl groups are equivalent as entire groups, but the diastereotopic methyl groups exhibit their nonequivalence as two doublets.

At 93 °C the spectrum of the unsymmetrical complex shows 13 of the expected 16 methyl signals. At 139 °C these doublets coalesce into one broad doublet. Finally, at 156 °C, the one doublet sharpens. The fast exchange limit and magnetic equivalence obtain. There is no clear indication at intermediate temperatures that isomerization and inversion may be occurring as separate events in two well-defined temperature regions. The two dynamic symmetry operations must be very much entangled.

12 SLOW ROTATION AND POSSIBLE RING INVERSION IN A LANTHANUM COMPOUND

As a rule, complexes, molecules, and ions with central metal atoms with coordination number greater than six rearrange so rapidly that the slow exchange limit and spectrum are not attainable. (They are said to be fluxional or *stereochemically nonrigid*.) Analysis indicates that with higher coordination numbers there are a number of competing polyhedra with nearly the same free energy. As a consequence there are one or more low-lying excited states that are readily accessible even at very low temperatures. As a result, magnetic equivalence persists in the variable temperature spectra of such compounds. However, macrocyclic ligands can confer enough rigidity to the structure of the complex species that slow exchange spectra become accessible. An example[14a] is available with the lanthanum(III) complex ion (**7**) with 1,4,7,10-tetrakis(2-carbamoylethyl)-1,4,7,10-tetraazacyclododecane (**8**).

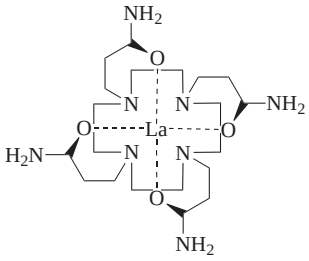

(7)

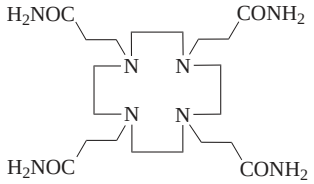

(8)

Ring inversion and rotation around the amide bonds are both dynamic symmetry operations for this complex ion. (The authors do not specifically label the first process as ring inversion, but this seems to be one likely explanation of what is observed. This label is used throughout the rest of the discussion below.) The lanthanum atom is eight-coordinate. It is bound to the octadentate ligand through the four ring nitrogens and the oxygen atoms of the four amide groups. The lanthanum ion lies above the approximate plane of the macrocycle ring. There is a C_4 axis through the lanthanum atom and the center of the ring. Rotation around this axis is the static symmetry operation and it renders the four chelate rings equivalent as entire rings and the four amide groups equivalent as entire groups. The C_4 axis is the only static symmetry element. There is no symmetry plane. Much of the detail of the slow exchange structure of the complex in solution is suggested by the solid state structure of the complex.

The slow exchange disposition of the ring ethylene moieties is very important in rationalizing the slow exchange spectrum. Carbon-13 NMR shows that the carbon atoms within an ethylene moiety are nonequivalent. One carbon atom is closer to the lanthanum atom than is the other. For convenience in discussion, the carbon atoms within each ring ethylene group are described below as head- and tail-ends of the group. Also, the attached hydrogen atoms can be either axial or equatorial. Therefore, there are four environments for the ring ethylene hydrogen atoms. Also the head-and-tail arrangement of the carbon atoms alternates in going around the macrocycle ring. Hence, each of the ring nitrogens is chiral. These nitrogens are bound to four different atoms: (1) the lanthanum atom; (2) a carbamoylethyl carbon atom; (3) a head carbon atom; and (4) a tail carbon atom. The hydrogen atoms are diastereotopic in both the methylene groups of the carbamoyl moieties. Also at the slow exchange limit, rotation around the amide bond in each amide group is slow.

The net result of all this is that the slow exchange spectrum for the protons should consist of two ABCD patterns, one

pattern for the ring hydrogens and one for the methylene hydrogens of the carbamoyl moiety, and finally an AB pattern for the amide nitrogen protons. Five different ^{13}C signals would be expected.

The experimental spectra in the slow exchange limit (0 °C) confirmed these expectations, except that the protons attached to the amide nitrogen atom have a very small or even zero coupling constant to each other. As a consequence, two separate singlets were obtained for these protons rather than the expected AB quartet. Also the spectra for the ring hydrogens and for the hydrogens of the methylene groups of the carbamoyl moiety are so complicated, and with considerable overlap, that it is not easily possible to discern clearly two ABCD patterns. However, the authors did assign parts of these signals to specific protons or groups of protons.

A complete proton spectrum in the fast exchange limit was not given. However, the two amide proton singlets collapsed into one singlet as these protons became magnetically equivalent at 92 °C. Signal shape analysis showed that the activation energy for rotation around the amide bond is 69 kJ mol^{-1}.

The ring carbon atoms coalesced in the ^{13}C spectrum at 29 °C and a barrier of 60 kJ mol^{-1} was obtained. The ring carbons become magnetically equivalent, the head-to-tail difference is lost, and with it the chirality of the ring nitrogens. It would be expected that the loss of the head-to-tail difference and the axial/equatorial distinction between ring protons would lead to a collapse into a singlet for those protons at the fast exchange limit. If on the other hand some dynamic operation other than ring inversion is occurring, and the axial/equatorial difference is preserved, a doublet or possibly an AB quartet would be observed. The loss of chirality should alter the low temperature ABCD pattern of the methylene protons of the carbamoyl moiety to an AA′ BB′ pattern since these protons would no longer be diastereotopic in the chemical shift sense.

NMR studies of the complexes with paramagnetic lanthanides would be interesting, since chemical shift differences would be enhanced and first-order NMR patterns could result with easy analysis of these patterns. The variable temperature spectra of the paramagnetic complexes of the related tetraacetate macrocycle have been reported.[14b] With this macrocycle the situation is further complicated by the coexistence of two isomers of the complexes. However, the expanded chemical shift scales that are obtained tend to compensate for this complication.

13 RING WHIZZING

Cyclopentadiene rings can be bonded to metals in either of two modes. In one mode, the bonding (pentahapto bonding symbolized as η^5 bonding) is to the ring as a whole. In this mode the metal is bonded to the ring as a whole rather than being bonded to one specific carbon atom in the ring (monohapto bonding or η^1). For the pentahapto situation, the protons of the ring are all magnetically equivalent as are the carbon atoms. The monohapto mode gives three sets of nuclei that are not equivalent between the sets. The proton attached to the bonded carbon atom is by itself one set (H_a, shown as A in Figure 3). The two protons in the once removed positions (H_b, shown as B) are the second set and are magnetically equivalent

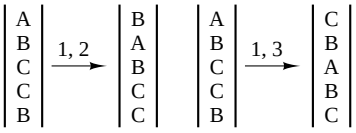

Figure 3 Exchange patterns in a cyclopentadiene ring

to each other. The remaining two protons (H_c, shown as C) form the third set and are equivalent to each other.

In effect, the static symmetry of the monohapto-bonded ring is a symmetry plane perpendicular to the ring, including the bonding site and passing between the carbon atoms of each of the pairs of carbon atoms. The dynamic symmetry operation is the changing of site of the bonded-to-metal carbon atom. This operation is commonly called *ring whizzing*.

From the pentahapto-bonded ring, the proton resonance should just be a sharp singlet at all temperatures. In the fast exchange limit for the protons of the monohapto-bonded ring, rapid change in the bonding site should also lead to a singlet. While in the slow exchange limit (slow change in the bonding site), the magnetically equivalent sets should give signals from each set. In practice the lone proton gives a singlet and the remaining four protons give an AA′BB′ pattern.

The ring complex (η^5-C_5H_5)(η^1-C_5H_5)$Fe(CO)_2$ has a ring of each kind in the molecule and demonstrates this behavior.[15] The results of a variable temperature study are shown in Figure 4.

At 30 °C the fast exchange limit is achieved. The whole proton spectrum consists of just two singlets. The signal at lower frequency is from the pentahapto-bonded ring and the one at higher frequency the signal averaged over all the protons of the monohapto-bonded ring.

The signals at the slow exchange limit are assigned as follows, going from high frequency to low frequency. The multiplet at highest frequency is assigned to the two H_b and the two H_c protons as the expected AA′BB′ pattern. The lower half of this pattern is assigned to the H_b protons and the other half to the H_c protons. This particular part of the overall assignment of proton signals is absolutely crucial to the rationalization of the variable temperature spectra as given below. The singlet at

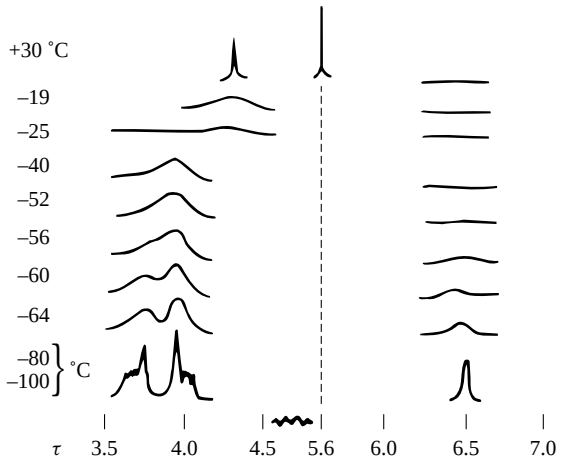

Figure 4 Ring whizzing and its effect on the proton spectrum of (η^5-C_5H_5)(η^1-C_5H_5)$Fe(CO)_2$. (Reproduced with permission from Cotton, *Acc. Chem. Res.*, 1968, **1**, 257)

about 5.6 ppm is from the pentahapto ring protons and remains unaltered throughout the temperature changes. The singlet at about 6.5 ppm is from the lone hydrogen that is attached to the bonding carbon atom.

As the temperature is raised all the signals from the bonded ring broaden, but the high frequency half of the AA′BB′ set broadens more rapidly than the lower frequency half. This shows that exchange of the H_b protons is occurring more rapidly than of the H_c protons. This, in turn, provides the decisive evidence as to how the bonding site shifts around the ring as ring whizzing (or, more elegantly, metal migration around the ring) takes place. The two plausible mechanisms are (1) a 1,2-shift or (2) a 1,3-shift. The exchange (or permutation) patterns that result are shown in Figure 3.

With the 1,2-shift, both H_bs are exchanged in each migration of the iron atom, but only one H_c. For one metal migration, the H_b exchange is twice as fast and the higher-frequency wing of the AA′ BB′ pattern would be expected to broaden twice as fast as the lower-frequency wing when the temperature is increased. On the other hand, with a 1,3-shift, the situation is reversed and the lower-frequency wing should broaden first.

This analysis, overall, is impressive and seems to demonstrate that not only in a general way is ring whizzing the dynamic symmetry operation, but in more detail that the 1,2-shift is the dynamic symmetry operation. A ^{13}C temperature study could make the analysis even more impressive.

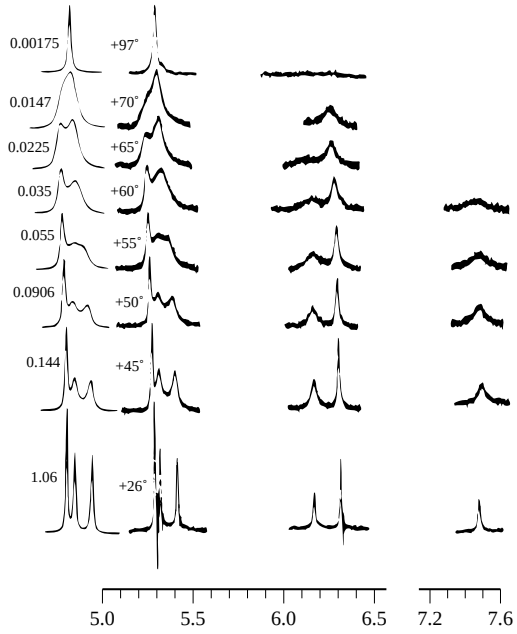

Figure 5 Variable temperature proton spectra of the compound (η^5-$C_5H_5)_2Fe_2(CO)_2(CNCH_3)_2$. [Reprinted with permission from Adams and Cotton, *J. Am. Chem. Soc.*, **95**, 6589. Copyright (1973) American Chemical Society]

14 BRIDGE/TERMINAL EXCHANGE AND ISOMERISM IN A BRIDGED IRON COMPOUND

The compound under discussion could exist as any one or several of the isomers shown below.

cis *trans*

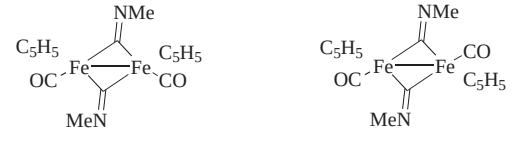

(9) **(10)**

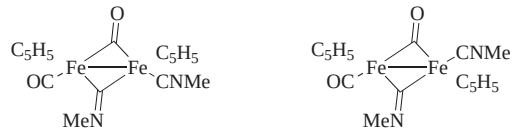

(11) **(12)**

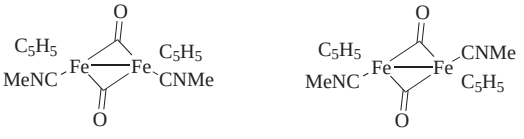

(13) **(14)**

By a combination of infrared and NMR spectroscopy and elegant reasoning, the authors[16] were able to eliminate all possibilities except isomers (**9**) and (**14**). Isomer (**9**) has C_{2v} static symmetry with one $CNCH_3$ group above the plane of the paper and the other below that plane. (The above-the-plane, below-the-plane detail is omitted from the structural formulas.) There is a C_2 axis through the nitrogen atoms. (The dispositions of the CH_3 groups is represented in an arbitrary fashion and does not affect the symmetry.) On the other hand, isomer (**12**) has no static symmetry.

The slow exchange proton spectrum at 26 °C (Figure 5) reflects these symmetry considerations. The static symmetry of isomer (**9**) renders the cyclopentadienyl groups magnetically equivalent within the pair of these groups and does the same for the methyl groups. The signals at 5.33 and 6.37 ppm and with relative intensity 5:3 are assigned to the cyclopentadienyl and methyl groups of isomer (**9**). The set of signals at 5.38, 5.47, 6.23, and 7.48 ppm with relative intensity within the set of 5:5:3:3 are assigned to one cyclopentadienyl group, to the other cyclopentadienyl group, to the bridging $CNCH_3$ group, and to the terminal $CNCH_3$ group, respectively, all for isomer (**12**).

The signals for isomer (**9**) remain relatively sharp as the temperature is raised at first. Meanwhile the signals from isomer (**12**) are noticeably broadened even at 45 °C. At about 60 °C and higher the isomer (**9**) signals also broaden. At 97 °C all the cyclopentadienyl signals coalesce into one sharp singlet and fast exchange is approached. The methyl signals have coalesced, but due to large chemical shift differences have not yet emerged from the baseline.

Two dynamic processes (or symmetry operations) must be taking place. The first, at lower temperature, is the exchange of bridge and terminal cyclopentadienyl and $CNCH_3$ groups within isomer (**12**). The second process, at higher temperature, must be that the isomerization process itself becomes rapid.

15 CONCLUSIONS

Two closely related aspects of NMR, magnetic equivalence and dynamic NMR, have been foci of investigations at least

since the Phillips paper[1] on dimethylformamide. Magnetic equivalence in the slow exchange limit can often be analyzed to reveal the static symmetry of a chemical species or at least to limit the choices of static symmetry. Structural details of species in solution (or even the gas phase) are deducible from static symmetry. Structural determination in whatever phase is always an important goal in chemistry. Structural determination by NMR is now in an advanced state of development.

1. Dynamic NMR can provide two sorts of information. Signal shape analysis can yield rate data in a range of rates that are much too fast to be accessible by classical rate experiments. Signal shape analysis is also now in an advanced state of development.
2. Dynamic NMR can provide information that bears on the mechanisms for various intramolecular motions and rearrangements. Mechanisms are always dear to the hearts of chemists. Mechanism elucidation, aided by dynamic NMR, has been successful in many cases. Nevertheless, this is a *relatively* undeveloped approach to the study of mechanisms.

It seems likely that continued development will depend heavily on an expanding combination of two endeavors. The first of these is the use of two-dimensional NMR (and perhaps, other NMR instrumental techniques) to identify mutually exchanging nuclei. The second is the application of the theory of permutation groups.

16 GENERAL REFERENCES

1. L. M. Jackson and F. A. Cotton (eds.), *Dynamic Nuclear Magnetic Resonance Spectroscopy*, Academic Press, New York, 1975. A major part of this volume bears directly on dynamic symmetry operations that contribute to achieving magnetic equivalence.
2. R. G. Jones, The Use of Symmetry in Nuclear Magnetic Resonance, in *NMR Principles and Progress*, Springer-Verlag, New York, 1969, Vol. 1.
3. J. D. Atwood, *Inorganic and Organometallic Reaction Mechanisms*, Brooks/Cole, Monterey, CA, 1985.
4. F. A. Cotton, *Chemical Applications of Group Theory*, 2nd edn., Wiley, New York, 1971. Generations of American chemists have been introduced to group theory via the editions of this work. The book is directed toward static symmetry (as defined in this article).
5. M. Hammermesh, *Group Theory and its Application to Physical Problems*, Addison-Wesley, Reading, MA, 1962. Chapter 7 provides an introduction to permutation groups. Other chapters introduce continuous groups such as the group of the sphere and also higher groups.
6. I. G. Kaplan, *Symmetry of Many Electron Systems*, English edition published by Academic Press, New York, 1975. Although this book is primarily devoted to electronic problems, Chap. II is an especially useful introduction to permutation groups. There are useful tables in the appendices.
7. K. Vrieze and P. W. N. M. Van Leeuwen, Studies of Dynamic Organometallic Compounds of The Transition Metals by means of Nuclear Magnetic Resonance, in *Prog. Inorg. Chem.*, 1971, **14**, 1.
8. J. W. Emsley, J. Feeney, and L. H. Sutcliffe, *The Effects of Chemical Equilibria and Molecular Conformational Motion on NMR Spectra*, Chap. 9 of 'High Resolution Nuclear Magnetic Resonance Spectroscopy', Pergamon Press, New York, 1965. This chapter provides an excellent review through 1964 of a variety of exchange processes. It is a good starting point for reading on dynamic processes and symmetry.
9. G. N. Lamar, W. DeW. Horrocks, Jr., and R. H. Holm (eds.), *NMR of Paramagnetic Molecules. Principles and Application*, (especially Chaps. 7 and 8), Academic Press, New York, 1973.
10. B. E. Mann, Dynamic NMR Spectroscopy in Inorganic and Organometallic Chemistry in *Annu. Rep. NMR Spectrosc.*, 1982, **12**, 12.
11. S. Szymanski and G. Binsch, Permutation Symmetry in NMR Relaxation and Exchange, in *Annu. Rep. NMR Spectrosc.*, 1991, **23**, 210.
12. Michinori Öki, *Applications of Dynamic NMR Spectroscopy to Organic Chemistry*, published as *Volume 4 of Methods in Stereochemical Analysis*, VCH Publishers, Inc., Deerfield Beach, FL, 1985. This valuable volume is an exhaustive review of the title material over the entire period, 1955–83. It contains over 1000 references. Chapter 1, entitled'General Considerations', is an excellent introduction to dynamic NMR. However, symmetry and group theoretical considerations are not emphasized.

17 RELATED ARTICLES

Aluminum-27 NMR of Solutions; Boron NMR; Chemical Exchange Effects on Spectra; COSY Spectra: Quantitative Analysis; COSY Two-Dimensional Experiments; Coupling Constants Determined by ECOSY; Fluxional Motion; Hydrogen–Metal Systems; Hydrogen Molecules; Inorganic Chemistry Applications; Organic Chemistry Applications; Organometallic Compounds; Phosphorus-31 NMR; Quantitative Measurements; Stereochemistry and Long Range Coupling Constants; Two-Dimensional J-Resolved Spectroscopy; Two-Dimensional Methods of Monitoring Exchange.

18 REFERENCES

1. W. D. Phillips, *J. Chem. Phys.*, 1955, **23**, 1363.
2. L. Pauling, *The Nature of the Chemical Bond*, Cornell University Press, Ithaca, NY, 1944.
3. H. S. Gutowsky and C. H. Holm, *J. Chem. Phys.*, 1956, **25**, 1228.
4. R. Adams, *Record Chem. Prog.*, 1949, **10**, 91.
5. T. H. Siddall, III and W. E. Stewart, *J. Phys. Chem.*, 1969, **73**, 40.
6. H. Nakanishi and O. Yamamoto, *Tetrahedron Lett.*, **1973**, 727.

7. U. Berg and C. Roussel, *J. Am. Chem. Soc.*, 1980, **102**, 7848.
8. M. Saunders and F. Yamada, *J. Am. Chem. Soc*., 1963, **85**, 1882.
9. P. Meakin et al., *J. Am. Chem. Soc.*, 1973, **95**, 75.
10. G. N. La Mar and E. O. Sherman, *J. Am. Chem. Soc.*, 1970, **92**, 2691.
11. R. H. Crabtree, *Acc. Chem. Res*., 1990, **23**, 95.
12. B. Jurado and C. S. Springer, *Chem. Commun.*, **1971**, 85.
13. J. R. Hutchison et al., *Inorg. Chem.*, 1971, **10**, 1004.
14. (a) J. R. Morrow et al., *Inorg. Chem.*, 1993, **32**, 4566; (b) S. Aime et al., *Inorg. Chem.*, 1992, **31**, 4291.
15. F. A. Cotton, *Acc. Chem. Res.*, 1968, **1**, 257.
16. R. D. Adams and F. A. Cotton, *J. Am. Chem. Soc.*, 1973, **95**, 6589.

Biographical Sketch

T. H. Siddall, III. *b* 1922. B.A., 1942, University of North Carolina, M.S., 1948, University of Chicago, Ph.D., 1951, Duke University. G. W. Wheland stimulated interest in molecular rearrangements and intramolecular motions. Atomic Energy Division of DuPont, 1950–69; Professor of Chemistry, University of New Orleans, 1969–89; Professor Emeritus, 1989–present. Approx. 95 publications. Research interests have included a variety of problems in NMR, chemistry, chemical engineering, and physics. Present research interest: application of group theory, especially higher groups, to NMR of higher spin nuclei.

Molten Salts

W. Robert Carper
Wichita State University, KS, USA

1	Introduction	1
2	Microdynamics	1
3	Chemical Shifts	2
4	Chemical Exchange	3
5	Diffusion Coefficients	3
6	Related Articles	4
7	References	4

1 INTRODUCTION

Molten salts represent an interesting class of liquids possessing unique ionic interactions. In this type of liquid, the usual ion–solvent forces are replaced by ion–ion interactions and possess Lewis acid–base properties. Molten salts may be classified according to either composition and/or temperature range: (1) high temperature molten salts which generally contain only inorganic salts, and (2) room temperature molten salts which contain both organic and inorganic components. There are numerous excellent books and reviews of molten salt chemistry, however only a few contain references to NMR studies of these highly ionic liquids.[1–5]

NMR studies of high-temperature molten salts often require special equipment (high-temperature probes, etc.), as described in a recent review article.[3] Room temperature molten salts need special treatment only in the preparation of the sample itself (usually in a drybox, followed by sealing with a torch immediately after removing the sample from the drybox). Both types of molten salt have been used as the subject of basic studies by NMR over a wide range of nuclei including ^{1}H, ^{2}H, ^{7}Li, ^{13}C, ^{17}O, ^{19}F, ^{23}Na, ^{27}Al, ^{39}K, ^{81}Br, ^{87}Rb, ^{127}I, and ^{205}Tl.

2 MICRODYNAMICS

2.1 Spin State Population

The distribution of nuclear spin states is affected by the application of low intensity radiation, resulting in a net absorption of energy and a redistribution of spin states. Removal of the source of radiation results in a return (relaxation) of the excited nuclei to ground state conditions. The rate of this relaxation process in the liquid state is controlled by rapidly fluctuating magnetic fields associated with rotational and translational motion. Theoretical models typically describe relaxation processes in terms of either rotational and/or translational correlation times. The correlation time τ_c typically represents the time taken by the involved nuclei to rotate, translate or be involved in such events as phase changes (see ***Brownian Motion and Correlation Times***).

2.2 Relaxation and Correlation Times

Relaxation times are designated as either spin–lattice (T_1) or spin–spin (T_2), depending upon the type of interaction and the method used to obtain them. Relaxation rates are simply the inversion of relaxation times ($R = 1/T$). Spin–lattice (longitudinal) relaxation times (T_1) are obtained by the inversion–recovery method and spin–spin (transverse) relaxation times are obtained from either linewidth ($T_2^* \approx T_2$) or spin echo (T_2) measurements (see ***Relaxation: An Introduction***). The theoretical equations that define relaxation times (rates) as a function of correlation time are relatively simple in the 'extreme narrowing region' where $\omega\tau_c \ll 1$ ($\omega = 2\pi\nu$). At low temperatures (approaching the solid or glassy state) where $\omega\tau_c \approx 1$, the equations become increasingly complex. In this region (T_1 minimum), one can still solve the correlation equations by assuming that $\omega\tau_c = 1$.

2.3 Relaxation Mechanisms

Relaxation studies of molten salts provide an excellent source of structural information which is difficult or impossible to obtain by other physical methods. Much useful information can be obtained from knowledge of spin–lattice (longitudinal) and/or spin–spin (transverse) relaxation times (see ***Relaxation Processes: Cross Correlation and Interference Terms***). The relaxation mechanisms that may be observed include dipolar, quadrupolar, spin–rotation, chemical shift anisotropy, scalar, and paramagnetic (see ***Relaxation Theory for Quadrupolar Nuclei*** and ***Carbon-13 Relaxation Measurements: Organic Chemistry Applications***). Of these mechanisms, paramagnetic relaxation is often the most effective. Consequently, one must be careful to exclude paramagnetic impurities from the melts under observation.

2.4 Relaxation Studies

The first significant papers on molten salt relaxation studies dealt with ^{1}H linewidth studies of potassium stearate.[6,7] These early investigations demonstrate the usefulness of this technique by correlating large changes in R_2 (= $1/T_2$) with phase transitions. A recent ^{1}H relaxation study[8] of the *N*-(1-butyl)pyridinium chloride–aluminum chloride system compares intramolecular rotational correlation times with melt viscosities. The data obtained in the acidic melt[8] region ($AlCl_3$ in excess) where $Al_2Cl_7^-$ is present, indicates that the extreme narrowing condition ($\omega\tau \ll 1$) is not met in these highly viscous melts. In the basic or neutral melts, where $AlCl_4^-$ is the primary anionic species, the extreme narrowing condition is apparently upheld.

In the initial studies of group I cations in high temperature molten salts[9,10] the spin–lattice relaxation times (T_1) of ^{23}Na and ^{7}Li in molten $NaNO_3$ and $LiNO_3/KNO_3$ mixtures are reported and the relationships between quadrupolar relaxation, diffusion and ionic radii carefully analyzed (see ***Relaxation Theory for Quadrupolar Nuclei***). The conclusion[10] that long-range order in the melt no longer exists as it does in the solid is supported by the fact that the largest part of the electric field gradient comes from only one neighboring anion and, therefore, models of ionic interactions in the melt should

involve only nearest neighbors. It should be pointed out, however, that the author[10] assumes that ^{7}Li relaxes by a purely quadrupolar relaxation mechanism, although it is likely that dipolar effects are also present as is often the case for ^{7}Li relaxation.

This type of high-temperature study is extended[11] to ^{23}Na and ^{87}Rb in molten $NaNO_3$ and $RbNO_3$. The authors[11] calculate field gradients around the cations using results from X-ray diffraction studies to test various models and conclude that relaxation processes from translational motion are more important than those from rotational motion. In a following report, they[12] study the relaxation of ^{81}Br and ^{127}I in molten LiBr and LiI. As is often the case, the NMR relaxation correlation times[12] differ by several orders of magnitude from those obtained from viscosity measurements of the same systems.

Chloroaluminate room temperature melts have been the focus of a number of relaxation studies (^{1}H, ^{13}C, ^{23}Na, and ^{27}Al).[8,13–16] Attempts by investigators[8,13] using viscosity to calculate correlation times from

$$\tau_c = \eta V/kT = 4\pi a^3 \eta/3kT \tag{1}$$

and to determine adequately molecular size from this equation have generally been unsuccessful. The correlation times determined from viscosity are typically two orders of magnitude larger than those determined from NMR.[8] Use of equation (1) to calculate ionic radii a from NMR correlation times also provides unrealistic values. The use of the Stokes–Einstein equation

$$D = kT/6\pi\eta a \tag{2}$$

with diffusion coefficients to obtain complex radii is more promising.[13]

Another use of relaxation measurements involves the dual spin probe (DSP) method.[14,15] The DSP method requires that neighboring nuclei form a chemical bond or complex, which implies that these nuclei undergo simultaneous rotation and therefore have the same correlation time (assuming that a rotational model is appropriate). In the case of ^{13}C and ^{27}Al, this leads to approximate equality between the ^{13}C dipolar correlation time τ_{eff} and the ^{27}Al quadrupolar correlation time τ_Q:

$$R_1^{\text{dipolar}}(^{13}\text{C}) = N_H(\hbar\gamma_C\gamma_H)^2 r_{CH}^{-6}\tau_{eff} \tag{3}$$

$$R_1^{Q} = [(3/10)\pi^2(2I+3)/I^2(2I-1)][1+(z^2/3)]\chi^2\tau_Q \tag{4}$$

$$\chi[e^2Qq/h] = \text{QCC} \tag{5}$$

The DSP assumptions include: (1) the asymmetry factor z is zero; (2) the intramolecular dipolar relaxation model (^{13}C) is adequate; and (3) the system is within the boundary of the extreme narrowing condition ($\omega\tau < 1$). If all these conditions are met, a plot of $R_1{}^{\text{dipolar}}(^{13}\text{C})$ versus $R_1{}^{Q}$ will be linear and pass through the origin.[14,15] An important result of this analysis is that it provides a method for determining quadrupolar coupling constants (QCCs) in the liquid state.[14,15]

An alternative method for determining QCC values is to lower the melt temperature until a T_1 minimum is observed. At this point, $\omega\tau_c \approx 1$ and the correlation equation can be solved exactly.[16] This same approach can be used in all melts for ^{13}C, ^{1}H, and other nuclei. Solution of the correlation equations is readily accomplished using a desktop computer system.

3 CHEMICAL SHIFTS

3.1 Physical Interpretation

Chemical shift studies[17,18] of a series of molten thallium salts are able to relate the ^{205}Tl chemical shift to the square of the overlap integral giving a measure of the degree of covalency. In these studies, ^{205}Tl chemical shifts in Tl(I) and Tl(III) salts are reported relative to $TlNO_3$ as a function of temperature. The observation that $TlCl_3$ has a large chemical shift relative to $TlNO_3$ and that it undergoes a very small change upon melting leads to the conclusion that the Tl(III) atoms are deshielded by the chlorine atoms within the molecule and yet are strongly shielded from neighboring molecules within the melt. The authors[17,18] also conclude that Coulombic forces predominate in molten halides while in covalent species ($AlCl_3$) intermediate forces such as ionic, covalent, dipolar, and van der Waals forces must play roles of varying importance.

3.2 Equilibrium Constants

Chemical shift values are often used to calculate equilibrium constants of molecular and ionic complexes. The basic assumption is that the observed chemical shift is the sum of the concentration-weighted chemical shifts of the free and complexed nuclei. One can usually solve these equations using either mole fraction or molar concentration terms. The resulting information is extremely useful and relatively easy to interpret compared with attempts to analyze chemical shifts of individual species which, by definition, contain a number of complex terms (see ***Shielding Calculations: LORG and SOLO Approaches***).[17,18] The following is a typical derivation[19] of the equations necessary for equilibrium analysis given the system, A + B $\rightleftharpoons$ C, where (a) B > A, (b) one assumes that A and C have characteristic chemical shifts δ_A and δ_C, and (c) the observed chemical shift δ_{obs} is the weighted arithmetic mean of δ_A and δ_C:

$$K = C/B_0(A_0 - C) \tag{6}$$

$$\delta_{obs} = [C/A_0]\delta_C + [(A_0 - C)/A_0]\delta_A \tag{7}$$

If we let $\Delta = \delta_{obs} - \delta_A$ and $\Delta_0 = \delta_C - \delta_A$, then

$$\Delta/B_0 = -K(\Delta - \Delta_0) \tag{8}$$

The major advantage of equation (8) is that a plot of Δ/B_0 versus Δ will give a straight line with a slope equal to $-K$ and an intercept of $K\Delta_0$. This avoids the inherent errors produced from a plot that gives the equilibrium constant as the reciprocal of the intercept (this often results in $1/K$ values close to the origin, producing a considerable error in the value of K). There still remains, however, the problem of determining δ_A.

In molten salts, it may be necessary to plot δ_A (observed) versus $1/A$ and extrapolate to the y intercept ($A = \infty$) by the use of a polynomial fit to obtain a value of δ_A(free). Interative methods can also be used to solve equations (6)–(8).

Examples of equilibrium constant determination include studies of tetrachloroaluminate melts[20–22] in which the cationic source is either 1-ethyl-3-methylimidazolium chloride[20,22] or *n*-butylpyridinium chloride.[21] The first of these studies[20] used ^{13}C NMR chemical shifts to establish which anionic species were present as a function of melt composition. The second study[21] identified and analyzed the equilibrium between $LiCl_2^-$ and the $LiCl_2^-$ dimer using ^{7}Li NMR. The last report[22] examined the equilibrium between HCl, Cl^-, and HCl_2^-

$$Cl^- + HCl \rightleftharpoons HCl_2^- \quad (9)$$

using ^{2}H NMR and provides an excellent example of the use of the iterative method.

3.3 Contaminant Species

A problem that always exists in molten salt studies is the possible presence of water (and similar contaminants) resulting in the formation of various oxides. The presence of these impurities have led to several honest misinterpretations of NMR spectra in the literature. An important ^{17}O NMR study of chloroaluminate melts containing water has analyzed this problem in careful detail.[23]

4 CHEMICAL EXCHANGE

4.1 Categories of Molecular Events Based on Rate of Occurrence

These categories include: (a) equilibrium species whose interconversion is slow relative to the NMR timescale, thus providing specific chemical shifts for each species; (b) species whose interconversion is extremely rapid relative to the NMR timescale, resulting in an average chemical shift which includes all equilibrium components commensurate with their relative concentration; and (c) species whose interconversion is intermediate on the NMR timescale. In the case of (c), one may observe a 'coalescence' of NMR signals which collapse into a single broad signal as the temperature is raised. The existence of such a 'coalescence' is necessary evidence that a dynamic chemical exchange process is actually occurring [species whose chemical shifts are similar undergo changes in T_2 (line broadening) as a function of temperature, producing spectra that give the false appearance of chemical exchange]. Furthermore, the analysis of such an exchange is best accomplished when the chemical shifts of the individual species are cleanly separated. Attempts to separate peaks that overlap severely can only result in significant errors (see ***Chemical Exchange Effects on Spectra***; ***Relaxation Effects of Chemical Exchange***).

4.2 Examples of Chemical Exchange

The most obvious examples of chemical exchange to be studied involve room temperature chloroaluminate melts and ^{27}Al NMR. The primary species expected to undergo exchange are included in the equilibrium

$$AlCl_3 + Al^*Cl_4^- \rightleftharpoons Al_2^*Cl_7^- \quad (10)$$

The ^{27}Al chemical shifts of the tetrachloro- and heptachloroaluminate anions given above are similar, creating a large error in any attempted mathematical analysis based on lineshapes alone. Unfortunately, studies of the chemical exchange (^{27}Al) of molten salts, where the authors have attempted to analyze equation (10), either deal with an impurity in the form of an oxide or else fail to provide examples of 'clean' reversible coalescence, as suggested earlier. The questionable use of preacquisition delay[5] is also present in a number of the aforementioned analyses. A comprehensive review[5] of ^{27}Al NMR is highly recommended, as it points out some of the many discrepancies in the few ^{27}Al chemical exchange papers in the literature.

5 DIFFUSION COEFFICIENTS

5.1 Introduction

The latest NMR method for determining self-diffusion coefficients involves the use of pulsed field gradients, as first demonstration by Stejskal and Tanner.[24] The recent availability of field gradient coils for all high-field NMR spectrometers guarantees that this technique[24] will replace various other methods (gravimetric, electrical, optical, radioactive, and stable tracers) that have been used to obtain diffusion data in molten salts (see ***Diffusion Measurements by Magnetic Field Gradient Methods***).

5.2 Experimental Description

The pulsed field gradient experiment[24] is based on the use of two identical magnetic field pulses of duration t_1 and strength g inserted into the basic $90^\circ-\tau-180^\circ$ spin echo sequence (see ***Diffusion Measurements by Magnetic Field Gradient Methods*** and ***Field Gradients and Their Application***). The first gradient pulse is applied between the 90° and 180° rf pulses, effectively 'labeling' the position of individual nuclei in the sample. The second field gradient pulse is applied between the 180° pulse and the echo after a time t_2. This second field gradient pulse monitors the movement (observation of the diffusion process) of any nuclear spins during t_2. The effect of diffusion on the spin echo appearing at time 2τ is to decrease the echo amplitude relative to that observed in absence of gradient pulses. The echo attenuation is a quantitative measure for the precession frequency changes of diffusing nuclei during t_2 and allows the evaluation of the self-diffusion coefficient for the observed nucleus. The spin echo amplitude $M(2\tau,g)$ is given by

$$M(2\tau, g) = M(2\tau, 0)\exp\{-\gamma^2 D g^2 t_1^2[t_2 - (t_1/3)]\} \quad (11)$$

5.3 Diffusion Coefficients

The spin echo method using pulsed field gradients was first used[25] successfully to determine a value of 2.30×10^{-9} m^2 s^{-1}

for the self-diffusion coefficient D of Na^+ in molten $NaNO_3$, which is in excellent agreement with values obtained using other methods.

6 RELATED ARTICLES

Chemical Shift Tensors; Carbon-13 Relaxation Measurements: Organic Chemistry Applications; Relaxation Processes: Cross Correlation and Interference Terms.

7 REFERENCES

1. S. V. Volkov, *Pure Appl. Chem.*, 1987, **59**, 1151.
2. J. S. Wilkes, *NATO ASI Ser.* C, 1987, 202, 217.
3. W. E. Warren, in *Magnetic Measurement Techniques in Molten Salt Techniques*, ed. R. J. Gale and D. G. Lovering, Plenum, New York, 1991, Vol. 4, p. 111.
4. J. F. Stebbins, *Chem. Revs.*, 1991, **91**, 1353.
5. J. W. Akitt, *Prog. NMR Spectrosc.*, 1989, **21**, 1.
6. R. F. Grant and B. A. Dunell, *Can. J. Chem.*, 1960, **38**, 1951.
7. R. F. Grant and B. A. Dunell, *Can. J. Chem.*, 1961, **39**, 359.
8. T. A. Zawodzinski, R. Kurland, and R. A. Osteryoung, *J. Phys. Chem.*, 1987, **91**, 962.
9. D. Harold-Smith, *J. Chem. Phys.*, 1973, **59**, 4771.
10. D. Harold-Smith, *J. Chem. Phys.*, 1974, **60**, 1405.
11. W. W. Filho, R. L. Havill, and J. M. Titman, *J. Magn. Reson.*, 1982, **49**, 296.
12. W. W. Filho, R. L. Havill, and J. M. Titman, *J. Phys. C.: Solid State Phys.*, 1982, **15**, 3617.
13. W. R. Carper, J. L. Pflug, A. M. Elias, and J. S. Wilkes, *J. Phys. Chem.*, 1992, **96**, 3828.
14. W. R. Carper, J. L. Pflug, and J. S. Wilkes, *Inorg. Chim. Acta*, 1992, **193**, 201.
15. W. R. Carper, J. L. Pflug, and J. S. Wilkes, *Inorg. Chim. Acta*, 1992, **202**, 89.
16. C. E. Keller and W. R. Carper, *Inorg. Chim. Acta*, 1993, **210**, 203.
17. S. Hafner and N. H. Nachtrieb, *J. Chem. Phys.*, 1964, **40**, 2891.
18. S. Hafner and N. H. Nachtrieb, *J. Chem. Phys.*, 1965, **42**, 631.
19. W. R. Carper, C. M. Buess, and G. R. Hipp, *J. Phys. Chem.*, 1970, **74**, 4229.
20. J. S. Wilkes, J. S. Frye, and G. F. Reynolds, *Inorg. Chem.*, 1983, **22**, 3870.
21. R. R. Rhinebarger, J. W. Rovang, and A. I. Popov, *Inorg. Chem.*, 1986, **25**, 4430.
22. P. C. Trulove, D. K. Sukumaran, and R. A. Osteryoung, *Inorg. Chem.*, 1993, **32**, 4396.
23. T. A. Zawodzinski and R. A. Osteryoung, *Inorg. Chem.*, 1990, **29**, 2842.
24. E. O. Stejskal and J. E. Tanner, *J. Chem. Phys.*, 1965, **42**, 288.
25. C. Herdlicka, J. Richter, and M. D. Zeidler, *Z. Naturforsch., Teil a*, 1988, **43**, 1075.

Biographical Sketch

W. Robert Carper. *b* 1935. B.S. SUNY at Albany, 1960; Ph.D., University of Mississippi, 1963. Introduced to NMR by M. Eisner. Faculty in Chemistry, Wichita State University, 1967–present. Approx. 90 publications. Research interests include the theory and application of NMR relaxation methods to molten salts, enzyme structure and function, metal ion–sugar complexes, and metal ion–humic acid complexes.

Relaxation Effects of Chemical Exchange

Donald E. Woessner
The University of Texas Southwestern Medical Center at Dallas, Department of Radiology, The Mary Nell and Ralph B. Rogers Magnetic Resonance Center, Dallas, TX, USA

1	Introduction	1
2	Relaxation Under Extremely Rapid Exchange Conditions	1
3	'Two-Site'Chemical Exchange	2
4	Relaxation for the Case of Equal Larmor Frequencies	3
5	Transverse Relaxation for the Case of Unequal Larmor Frequencies	4
6	'Multiple Site'Chemical Exchange and Transverse Relaxation	6
7	Preferential Orientation, Exchange, and Order in Aqueous Heterogeneous Systems	8
8	Effects of Diffusive Exchange in Heterogeneous Systems	10
9	Related Articles	10
10	References	10

1 INTRODUCTION

The NMR properties of atomic nuclei in atoms, molecules, and ions depend mainly on short-range effects. For example, the chemical shift of a nucleus in a molecule depends mainly on the molecular structure and only slightly on whether the molecule is in a gas, a liquid, or a solid. In a solid, the chemical shift is anisotropic, depending on the orientation of the molecule in the magnetic field. In a liquid, the molecular motions are very rapid, so that the chemical shift is the weighted average over the solid 'powder pattern'. The liquid molecule moves very rapidly, or exchanges, among all orientations and local molecular associations. In this general sense, exchange is ubiquitous, and the results are readily understood in terms of the appropriate average. Multicomponent NMR relaxation behavior can occur when the nuclei under study are constrained in different regions or at different sites that are characterized by different time-averaged environmental parameters that affect the relaxation times. These parameters include any that affect the nuclear spin energy levels and the mobility or time dependences of these parameters.

The NMR relaxation times are expressed[1] in terms of the Fourier intensities or spectral densities $J_h(\omega)$ of the time correlation function $\langle F_h(t)F_h{}^*(t+\tau)\rangle$ of nuclear spin interactions $F_h(t)$ at the angular frequency ω as given by

$$J_h(\omega) = \int_{-\infty}^{\infty} \langle F_h(t) F_h^*(t+\tau)\rangle \exp(\mathrm{i}\omega\tau)\,\mathrm{d}\tau \qquad (1)$$

The interaction function $F_h(t)$ is the product of a nuclear relaxation interaction strength (r^{-3} for magnetic dipolar relaxation) and a function of orientation (second-order spherical harmonic). (The average value $\langle F_h(t)\rangle$ is zero, unless there is preferential orientation such as that imposed by a stationary interface on a nonspherical molecule.) Let us consider the case when the correlation function of a site is

$$\langle F_h(t) F_h^*(t+\tau)\rangle = \langle F_h(t) F_h^*(t)\rangle \exp(-|\tau|/\tau_c) \qquad (2)$$

in which the correlation time τ_c depends on the rate of molecular motion (see ***Brownian Motion and Correlation Times***). Because equation (2) is an exponential function, the spectral densities $J_h(\omega)$ are given by the Lorentzian functions

$$J_h(\omega) = \langle F_h(t) F_h^*(t)\rangle \frac{2\tau_c}{1+\omega^2\tau_c^2} \qquad (3)$$

To illustrate the relationship between the spectral densities and the NMR relaxation times, consider the cases of magnetic dipolar interaction between two identical spin-$\frac{1}{2}$ nuclei and of nuclear quadrupolar interaction of a spin-1 nucleus. In both instances, the relaxation times are given by the equations[1]

$$\frac{1}{T_1} = H[J_1(\omega_0) + J_2(2\omega_0)] \qquad (4a)$$

$$\frac{1}{T_2} = \tfrac{1}{4}H[J_0(0) + 10J_1(\omega_0) + J_2(2\omega_0)] \qquad (4b)$$

where T_1 is the spin–lattice relaxation time, T_2 is the transverse relaxation time, and ω_0 is the angular Larmor frequency. The interaction strength $H = \frac{9}{8}\gamma^4\hbar^2 r^{-6}$ for magnetic dipolar relaxation and $\frac{9}{8}\pi^2\chi^2$ for nuclear quadrupolar interaction with zero asymmetry parameter. These equations apply (see ***Relaxation Theory: Density Matrix Formulation***) to the motionally narrowed limit in which $H^{1/2}\tau_c < 1$. When this limit does not apply, the $J_0(0)$ term is incorrect and the transverse relaxation must be calculated differently. We can do this by replacing the $J_0(0)$ term with the time dependence of the ensemble average of $M_+ = M_x + \mathrm{i}M_y$ obtained by introducing time dependence into the Larmor frequency. This is done in Sections 5–8 of this article for the transverse relaxation in many systems that involve chemical exchange of nuclei between sites with different Larmor frequencies.

In a more general approach that includes chemical exchange between different types of sites that are designated by j, we need to look closely at the evaluation of the correlation function $\langle F_h(t)F_h{}^*(t+\tau)\rangle$ in equation (2), which is an ensemble average (see ***Relaxation Theory: Density Matrix Formulation***) to calculate NMR relaxation phenomena properly.[2] Take any given nucleus at time t in site j, evaluate the interaction function at this time to obtain $F_{hj}(t)$, evaluate the autocorrelation function for this nucleus at later times $t+\tau$, and continue to do this as τ increases from zero to 'large' values. Finally, take the sum over all the j-type sites, weighting each site by its fractional population P_j. Note that the fraction of time that a nucleus occupies a j-type site is equal to P_j. The average time that nucleus occupies a j-type site is τ_j.

2 RELAXATION UNDER EXTREMELY RAPID EXCHANGE CONDITIONS

If chemical exchange of nuclei is merely rapid so that all the lifetimes τ_j are long compared with the correlation times τ_{cj}, the relaxation times of nuclei in the different j types of sites are independent of the exchange, and the preceding treatment for calculating the $J_h(\omega)$ for the relaxation times of a given site j is valid. However, when the exchange is extremely rapid so that the lifetimes in a site are shorter than the correlation times, this condition is not met and the effective correlation time depends on the average lifetime in a site. There are several different cases, depending on whether the strength of the nuclear relaxation interaction is the same in the different types of sites.[2]

When the strength of the relaxation interaction is the same in all sites and when there is complete randomization of the interaction direction upon chemical exchange, each τ_{cj} for equation (3) is replaced by an effective correlation time

$$\tau_{\text{eff},j} = \left(\frac{1}{\tau_{cj}} + \frac{1}{\tau_j}\right)^{-1} \tag{5}$$

If the direction of interaction is retained, instead of randomized, upon exchange, the exchange process can have several different effects on relaxation.[2] When the rotational correlation time is much longer in one site than in another, exchange involving this site can give a very large contribution to the rate of relaxation. As a nucleus in this slow site moves by chemical exchange to a site with much faster motion, the effective correlation time for the slow site is shortened. Another possible effect is that the strength of the relaxation interaction may be changed. When the exchange is much faster than the molecular rotational motions, there is a single effective correlation time

$$\tau_{\text{eff}} = \left\{\sum_i \frac{p_i}{\tau_{cj}}\right\}^{-1} \tag{6}$$

Also, the ensemble interaction average $\langle F_h(t)F_h{}^*(t)\rangle$ for a single type of site in equation (3) is replaced by the square of the weighted average of $F(t)$ at a given orientation, taken over all types j of sites, and then averaged over all orientations. This type of averaging, in the case of extremely rapid motions, is important for nonspherical molecules at the interface in many aqueous heterogeneous systems (see Section 7 of this article).

3 'TWO-SITE' CHEMICAL EXCHANGE

In all the cases described above, the nuclear relaxation is single component. However, when the nuclei are constrained in the sites, the observed NMR relaxation behavior is merely the weighted sum taken over the different sites that are characterized by specific relaxation times. When the nuclei migrate among these sites at rates that are small compared with molecular motions, the observed relaxation behavior is modified even when the relaxation time of each site is unaffected by this migration or exchange. Zimmerman and Brittin[3] have treated this situation with a stochastic theory, and McConnell[4] has presented a mathematically equivalent approach of adding exchange terms to the Bloch equations. These modified Bloch equations are particularly convenient for discussing the simplest case that illustrates the main features of the effects of chemical exchange on NMR relaxation: exchange between two different types of sites under the condition that the relaxation time of a nucleus in a given site is independent of the lifetime of the nucleus in that given site.

The Bloch equations are written for a rectangular coordinate system that rotates at angular frequency ω about its Z axis, which is parallel to the direction of $\boldsymbol{B}_0$, i.e., the rotating frame of reference. The modified Bloch equations that include chemical exchange[5] between states a and b are

$$\frac{dM_{xa}}{dt} = -(\omega_a - \omega)M_{ya} - \frac{M_{xa}}{T_{2a}} - \frac{M_{xa}}{\tau_a} + \frac{M_{xb}}{\tau_b} \tag{7a}$$

$$\frac{dM_{xb}}{dt} = -(\omega_b - \omega)M_{yb} - \frac{M_{xb}}{T_{2b}} - \frac{M_{xb}}{\tau_b} + \frac{M_{xa}}{\tau_a} \tag{7b}$$

$$\frac{dM_{ya}}{dt} = (\omega_a - \omega)M_{xa} - \frac{M_{ya}}{T_{2a}} - \frac{M_{ya}}{\tau_a} + \frac{M_{yb}}{\tau_b} - \omega_1 M_{za} \tag{7c}$$

$$\frac{dM_{yb}}{dt} = (\omega_b - \omega)M_{xb} - \frac{M_{yb}}{T_{2b}} - \frac{M_{yb}}{\tau_b} + \frac{M_{ya}}{\tau_a} - \omega_1 M_{zb} \tag{7d}$$

$$\frac{dM_{za}}{dt} = -\frac{M_{za} - M_{0a}}{T_{1a}} - \frac{M_{za}}{\tau_a} + \frac{M_{zb}}{\tau_b} + \omega_1 M_{ya} \tag{7e}$$

$$\frac{dM_{zb}}{dt} = -\frac{M_{zb} - M_{0b}}{T_{1b}} - \frac{M_{zb}}{\tau_b} + \frac{M_{za}}{\tau_a} + \omega_1 M_{yb} \tag{7f}$$

where ω is the angular rf frequency and $\omega_1 = \gamma B_1$, with γ the nuclear magnetogyric ratio. Also, P_a is the fraction of nuclei that are in state a, ω_a is the Larmor frequency, τ_a is the average lifetime of a given nucleus in state a before it leaves a and enters state b, T_{1a} and T_{2a} are the longitudinal and transverse relaxation times for nuclei while in state a, and M_{0a} is the equilibrium nuclear magnetization along $\boldsymbol{B}_0$. Similar definitions apply for state b. Since we are interested in relaxation, and relaxation times are defined in terms of the time-dependent behavior of the nuclear magnetization when $\boldsymbol{B}_1 = 0$, the coupled differential equations that describe the effects of chemical exchange can be written as

$$\frac{d(M_{0a} - M_{za})}{dt} = -\alpha_{1a}(M_{0a} - M_{za}) + \frac{M_{0b} - M_{zb}}{\tau_b} \tag{8a}$$

$$\frac{d(M_{0b} - M_{zb})}{dt} = -\alpha_{1b}(M_{0b} - M_{zb}) + \frac{M_{0a} - M_{za}}{\tau_a} \tag{8b}$$

for longitudinal relaxation. For transverse relaxation, it is convenient to combine the M_x and M_y magnetizations into the transverse magnetization:

$$\frac{dM_{+a}}{dt} = -\alpha_{2a}M_{+a} + \frac{M_{+b}}{\tau_b} \tag{9a}$$

$$\frac{dM_{+b}}{dt} = -\alpha_{2b}M_{+b} + \frac{M_{+a}}{\tau_a} \tag{9b}$$

In these equations, we use the definitions

$$M_{+a} = M_{xa} + \mathrm{i}M_{ya} \tag{10a}$$

$$\alpha_{1a} = \frac{1}{T_{1a}} + \frac{1}{\tau_a} \tag{10b}$$

$$\alpha_{2a} = \frac{1}{T_{2a}} + \frac{1}{\tau_a} - \mathrm{i}(\omega_a - \omega) \tag{10c}$$

for state a. Similar definitions apply for state b. The principle of detailed balance requires that $M_{0a}/\tau_a = M_{0b}/\tau_b$.

Equations (8a,b) and (9a,b) represent two sets of two simultaneous differential equations of the form

$$\frac{\mathrm{d}m}{\mathrm{d}t} = -\alpha m + bn \tag{11a}$$

$$\frac{\mathrm{d}n}{\mathrm{d}t} = -\beta n + am \tag{11b}$$

The solutions of each of these sets of equations are[5]

$$m(t) = A_+ \,\mathrm{e}^{-\phi_+ t} + A_- \,\mathrm{e}^{-\phi_- t} \tag{12a}$$

$$n(t) = B_+ \,\mathrm{e}^{-\phi_+ t} + B_- \,\mathrm{e}^{-\phi_- t} \tag{12b}$$

where

$$2\phi_\pm = (\alpha + \beta) \pm [(\alpha - \beta)^2 + 4ab]^{1/2} \tag{13}$$

and $A_\pm$ and $B_\pm$ are related by

$$B_\pm = -(\phi_\pm - \alpha)A_\pm/b \tag{14}$$

The net magnetizations are given by the sum $m(t) + n(t)$. The integration constants $A_\pm$ and $B_\pm$ are determined by the values of m and n at time $t = 0$, with the aid of equation (13). These initial values of m and n are determined by the rf pulse flip angles and the nuclear magnetizations that exist when the pulse is applied.

These solutions to equation (11) fail[5] mathematically when

$$(\alpha - \beta)^2 + 4ab = 0 \tag{15}$$

As shown later, this condition represents a point at which there is a change in behavior of the solutions when the Larmor frequencies are unequal. The appropriate solutions are

$$m(t) = \{A'[1 - \tfrac{1}{2}(\alpha - \beta)t] + bB't\}\,\mathrm{e}^{-(\alpha+\beta)t/2} \tag{16a}$$

$$n(t) = \{B'[1 + \tfrac{1}{2}(\alpha - \beta)t] + aA't\}\,\mathrm{e}^{-(\alpha+\beta)t/2} \tag{16b}$$

The integration constants A' and B' are also determined by the initial conditions.

4 RELAXATION FOR THE CASE OF EQUAL LARMOR FREQUENCIES

4.1 General Case

Here, we apply an rf pulse and examine the subsequent behavior of the longitudinal and transverse magnetization. We define the relaxation curve as the time dependence of the deviation of the particular nuclear magnetization from its equilibrium value. When there is no chemical exchange and $\omega_a = \omega_b$, the NMR signal is the sum of signals from the 'uncoupled' sites, and the T_1 and T_2 relaxation curves are each the sum of two exponential functions whose preexponential coefficients and decay time constants are the intrinsic state populations and relaxation times, respectively. When chemical exchange occurs, we see from equations (12a) and (12b) that the NMR signal is *still* the sum of two exponential functions. For convenience, we designate state a as that with the longer relaxation time. The mathematical form of the T_1 and T_2 curves is

$$F(t) = P_a' \exp\left(-\frac{t}{T_a'}\right) + P_b' \exp\left(-\frac{t}{T_b'}\right) \tag{17}$$

where T' and P' signify the apparent relaxation times and population fractions, respectively. These quantities are related to the intrinsic values by the equations

$$\frac{1}{T_a'} = C_1 - C_2 \tag{18a}$$

$$\frac{1}{T_b'} = C_1 + C_2 \tag{18b}$$

$$P_b' = \frac{1}{2} - \frac{1}{4}\left[(P_b - P_a)\left(\frac{1}{T_a} - \frac{1}{T_b}\right) + \frac{1}{\tau_a} + \frac{1}{\tau_b}\right] \Big/ C_2 \tag{19a}$$

$$P_a' = 1 - P_b' \tag{19b}$$

in which

$$C_1 = \frac{1}{2}\left(\frac{1}{T_a} + \frac{1}{T_b} + \frac{1}{\tau_a} + \frac{1}{\tau_b}\right) \tag{20a}$$

$$C_2 = \frac{1}{2}\left[\left(\frac{1}{T_b} - \frac{1}{T_a} + \frac{1}{\tau_b} - \frac{1}{\tau_a}\right)^2 + \frac{4}{\tau_a \tau_b}\right]^{1/2} \tag{20b}$$

Under all exchange conditions, the parameters in equation (17) obey the relationship

$$\frac{P_a'}{T_a'} + \frac{P_b'}{T_b'} = \frac{P_a}{T_a} + \frac{P_b}{T_b} = \frac{1}{T_\mathrm{m}} \tag{21}$$

where T_m is defined as an effective mean relaxation time. This means that the initial slope of $F(t)$ in equation (17) is independent of the exchange rate between the two states—a consequence of the assumption that the inherent relaxation times are unaffected by chemical exchange. Other relationships that are useful in deriving simplified, approximate relationships for limiting cases are

$$P_a' + P_b' = P_a + P_b = 1 \tag{22}$$

$$P_a/\tau_a = P_b/\tau_b \tag{23}$$

4.2 Limiting Cases

Let us examine the case where $P_a \approx P_b$ and $T_a \gg T_b$ when the exchange rate is increased from small values. Initially, P_a', P_b', and T_b' are nearly equal to the inherent values, and

T_a' is decreased from T_a. With increasing exchange rate, T_a' continues to decrease, and can be completely different from T_a. When τ_b becomes of the same order of magnitude as T_b, T_b' decreases, P_b' becomes smaller than P_b, and T_a' continues to decrease. Finally, when τ_b is small compared with T_b, P_b' is very small, and the relaxation decay curve is approximately a single exponential with a relaxation time given by equation (21). Thus, exchange can cause the observed, or apparent, relaxation decay curve parameters to be completely different from the values inherent to the different types of sites.

There are several pertinent limiting cases[6] that involve the relative values of the inherent relaxation times and the residence times.

When the exchange is very slow so that

$$\frac{1}{\tau_a} + \frac{1}{\tau_b} \ll \frac{1}{T_b} - \frac{1}{T_a} \tag{24}$$

the P_a' and P_b' values are very close to P_a and P_b; however, the apparent relaxation times are decreased:

$$\frac{1}{T_a'} = \frac{1}{T_a} + \frac{1}{\tau_a} \tag{25a}$$

$$\frac{1}{T_b'} = \frac{1}{T_b} + \frac{1}{\tau_b} \tag{25b}$$

As the exchange rate increases, the values of T_a' and T_b' decrease and the value of P_a' increases. In the special case where the intrinsic relaxation times are very different and the lifetimes are intermediate,

$$T_b \ll \tau_a,\ \tau_b \ll T_a \tag{26}$$

the results are $P_a' = P_a$, $P_b' = P_b$, and

$$T_a' = \tau_a \tag{27a}$$

$$T_b' = T_b \tag{27b}$$

Clearly, this is a favorable case for the determination of lifetimes.

Finally, when the chemical exchange is very fast so that

$$\frac{1}{\tau_a} + \frac{1}{\tau_b} \gg \frac{1}{T_b} - \frac{1}{T_a} \tag{28}$$

the rapid exchange limit is obeyed in which a single average relaxation time is observed:

$$P_a' = 1 \tag{29}$$

$$T_a' = T_{\mathrm{m}} \tag{30}$$

Another special case involves very different population fractions. When $T_b \ll T_a$ and $P_a \approx 1$ (which also means that $\tau_b \ll \tau_a$), the observable relaxation is approximately a single exponential with

$$\frac{1}{T_a'} = \frac{1}{T_a} + \frac{P_b}{P_a T_b + P_b \tau_a} \tag{31}$$

The observed relaxation time may bear no obvious relationship to that of type a sites. Even by changing the exchange rates by a large factor, such as by changing the temperature, the relaxation curve will not reveal that the system is two-site. The inherent relaxation times of the site types and the value of P_b might not be available from simple relaxation time measurements. This case applies, for example, to heterogeneous systems and biological materials that may have a small concentration of strongly relaxive sites, such as strong adsorption sites or paramagnetic centers. Note that if P_b is very small so that the b sites are widely spaced, τ_a may not be single valued, because the exchange will involve translational diffusion of the molecules of state a (see Section 8 of this article).

5 TRANSVERSE RELAXATION FOR THE CASE OF UNEQUAL LARMOR FREQUENCIES

5.1 General Case for the NMR Signal Following One Pulse

The effect of unequal Larmor frequencies is nonexistent for longitudinal relaxation, but transverse relaxation can be greatly increased. The following general solution[5] of the set of equations given by equations (9a) and (9b) following the application of a pulse to a spin system at equilibrium is relatively simple because there is no transverse nuclear magnetism at the time of application of the pulse:

$$F_2(t) = \frac{M_+(t)}{M_0 \sin\theta_1} = P_{2+}\,\mathrm{e}^{-(\phi_2 + c)t} + P_{2-}\,\mathrm{e}^{-(\phi_2 - c)t} \tag{32}$$

where

$$P_{2+} = -(f + \mathrm{i}g)\,\mathrm{e}^{-\mathrm{i}dt} \tag{33}$$

$$P_{2-} = [f - \mathrm{i}(1-g)]\,\mathrm{e}^{\mathrm{i}dt} \tag{34}$$

$$\phi_2 = \frac{1}{2}\left(\frac{1}{T_{2a}} + \frac{1}{T_{2b}} + \frac{1}{\tau_a} + \frac{1}{\tau_b}\right) \tag{35}$$

$$f = -\frac{1}{4}\left\{c(P_b - P_a)(\omega_a - \omega_b) + d\left[(P_b - P_a)\left(\frac{1}{T_{2a}} - \frac{1}{T_{2b}}\right) + \frac{1}{\tau_a} + \frac{1}{\tau_b}\right]\right\}(c^2 + d^2)^{-1} \tag{36}$$

$$g = \frac{1}{2} - \frac{1}{4}\left\{c\left[(P_b - P_a)\left(\frac{1}{T_{2a}} - \frac{1}{T_{2b}}\right) + \frac{1}{\tau_a} + \frac{1}{\tau_b}\right] - d(P_b - P_a)(\omega_a - \omega_b)\right\}(c^2 + d^2)^{-1} \tag{37}$$

$$|c| = [(X^2 + Y^2)^{1/2} + X]^{1/2}/\sqrt{8} \tag{38}$$

$$|d| = [(X^2 + Y^2)^{1/2} - X]^{1/2}/\sqrt{8} \tag{39}$$

with

$$X = \left(\frac{1}{T_{2a}} - \frac{1}{T_{2b}} + \frac{1}{\tau_a} - \frac{1}{\tau_b}\right)^2 - (\omega_a - \omega_b)^2 + \frac{4}{\tau_a \tau_b} \tag{40}$$

$$Y = -2(\omega_a - \omega_b)\left(\frac{1}{T_{2a}} - \frac{1}{T_{2b}} + \frac{1}{\tau_a} - \frac{1}{\tau_b}\right) \quad (41)$$

and θ_1 is the pulse flip angle. The algebraic sign of d is always positive; the sign of c is positive except for negative Y values. The value of ω is $\frac{1}{2}(\omega_a + \omega_b)$.

This function is even more complicated than the case of equal Larmor frequencies, and examination of limiting cases is necessary to show the effects of the Larmor frequency difference on transverse relaxation. When the exchange is slow so that the term $4/\tau_a\tau_b$ in equation (40) can be neglected, $d = \frac{1}{2}|\omega_a - \omega_b|$, $f \approx 0$, $g = P_b$, and $c = \pm\frac{1}{2}(1/T_{2b} - 1/T_{2a} + 1/\tau_b - 1/\tau_a)$. The upper algebraic sign applies when $\omega_a > \omega_b$, and the lower when $\omega_a < \omega_b$. Equation (32) then becomes

$$F_2(t) \approx -\mathrm{i}\left\{P_a \exp[\tfrac{1}{2}\,\mathrm{i}(\omega_a - \omega_b)t]\exp\left[-\left(\frac{1}{T_{2a}} + \frac{1}{\tau_a}\right)t\right] + P_b \exp[-\tfrac{1}{2}\mathrm{i}(\omega_a - \omega_b)t]\exp\left[-\left(\frac{1}{T_{2b}} + \frac{1}{\tau_b}\right)t\right]\right\} \quad (42)$$

Equation (42) is the sum of the two transverse magnetizations with separate frequencies, because d is not equal to zero. The decay rate of each signal increases (see ***Chemical Exchange Effects on Spectra***) with increasing exchange rate, as in equations (25a) and (25b) for equal Larmor frequencies, but it is insensitive to the difference between the Larmor frequencies. This may be expected, since a nucleus that enters a state from the other state has a random phase because it has existed in the former state for many periods of the frequency difference $\omega_a - \omega_b$. When the exchange rate increases, the amount of dephasing per transfer becomes dependent on the Larmor frequency difference.

The terms $\mathrm{e}^{-\mathrm{i}dt}$ and $\mathrm{e}^{\mathrm{i}dt}$ in equations (33) and (34) represent two different nuclear magnetizations rotating at frequencies that differ by $2d$. At very slow exchange rates, as shown above, the frequency difference is $\omega_a - \omega_b$. With increasing exchange rates, as examination of equation (39) reveals, the value of $2d$ decreases. The peaks in the NMR spectrum approach each other (see ***Chemical Exchange Effects on Spectra***). In general, the value of d never becomes zero, even at extremely high exchange rates such that $4/\tau_a\tau_b \gg (\omega_a - \omega_b)^2$. This means that, rigorously, there is *some* splitting in the NMR spectrum and that the NMR signal following a pulse *cannot* be a simple sum of two exponential decays when there is a difference in Larmor frequencies.

The above conclusion holds even in the specific case where $d = 0$. Examination of equations (38)–(41) shows that $d = 0$ when $1/T_{2a} - 1/T_{2b} + 1/\tau_a - 1/\tau_b = 0$. When the additional condition $(\omega_a - \omega_b)^2 = 4/\tau_a\tau_b$ holds, the special case in equation (15) holds, and the relatively simple solutions in equations (16a) and (16b) describe the NMR signal. This signal is

$$F_2(t) = -\tfrac{1}{2}(P_b - P_a)(\omega_a - \omega_b)t\,\mathrm{e}^{-\phi_2 t} - \mathrm{i}\left[1 + \frac{1}{2}(P_b - P_a) \times \left(\frac{1}{T_{2a}} - \frac{1}{T_{2b}}\right)t + \frac{1}{2}\left(\frac{1}{\tau_a} + \frac{1}{\tau_b}\right)t\right]\mathrm{e}^{-\phi_2 t} \quad (43)$$

Clearly, this is not a simple exponential decay.

When the exchange rate is very large so that the conditions $1/\tau_a,\ 1/\tau_b \gg 1/T_{2a},\ 1/T_{2b},\ |(\omega_a - \omega_b)|$ and $(\omega_a - \omega_b)^2 \gg (1/T_{2a} - 1/T_{2b})^2$ prevail, $F_2(t)$ is closely approximated by

$$F_2(t) = \sin(\omega_{\mathrm{av}}t)\,\mathrm{e}^{-t/T_2} \quad (44)$$

where

$$\omega_{\mathrm{av}} = P_a\omega_a + P_b\omega_b \quad (45)$$

$$\frac{1}{T_2} = \frac{1}{T_{\mathrm{m}}} + \frac{P_a P_b \tau_a \tau_b}{\tau_a + \tau_b}(\omega_a - \omega_b)^2 \quad (46)$$

This expression shows that the difference in Larmor frequencies enhances the transverse relaxation when the chemical exchange is fast. As the exchange rate increases to extremely large values, the observed T_2 value approaches T_{m}, the relaxation time when the Larmor frequencies are equal.

5.2 General Case for the NMR Signal Following Two Pulses

As usual, the NMR signal following the second pulse, applied at time $t = \tau$, is the sum[5] of three signals. The first signal results from the M_z component of magnetization that exists at the time of application of the second pulse. It is given by

$$\frac{M_+(t\rangle\tau)}{M_0 \sin\theta_2[1 - (1 - \cos\theta_1)]} = F(T_1, \tau)F_2(t\rangle\tau) \quad (47)$$

where $F(T_1, \tau)$ is equation (17) evaluated at time τ for T_1, and $F_2(t > \tau)$ is equation (32) evaluated as a function of the time after the second pulse, $t > \tau$.

The other two signals result from the transverse magnetization that exists at the time of application of the second pulse. The first is the reduced continuation of the signal following the first pulse as follows:

$$\frac{M_+(t)}{\frac{1}{2}M_0 \sin\theta_1(1 + \cos\theta_2)} = F_2(t) \quad (48)$$

where $F_2(t)$ is given by equation (32).

The other signal is the spin echo that can be found by using the complex conjugate of the one-pulse signal evaluated at time τ as the initial condition for the signal following the second (a 180°) pulse:

$$\begin{aligned} E(t) &= \frac{M_+(t)}{-\frac{1}{2}M_0 \sin\theta_1(1 - \cos\theta_2)} \\ &= P_{\mathrm{E}+}\,\mathrm{e}^{-(\phi_2 + c)t} + P_{\mathrm{E}-}\,\mathrm{e}^{-(\phi_2 - c)t} \\ &\quad +\{2[\,f\cos dt + (g + j)\sin dt]\sinh[c(t - 2\tau)] \\ &\quad +2\mathrm{i}[\,f\sin dt - (g + j)\cos dt]\cosh[c(t - 2\tau)]\} \\ &\quad \times\mathrm{e}^{-\phi_2 t} \end{aligned} \quad (49)$$

where

$$P_{\mathrm{E}+} = \mathrm{i}j\,\mathrm{e}^{-\mathrm{i}d(t - 2\tau)} \quad (50a)$$

$$P_{\mathrm{E}-} = \mathrm{i}(2g + j - 1)\,\mathrm{e}^{\mathrm{i}d(t - 2\tau)} \quad (50b)$$

with

$$j = \frac{1}{2} - g - \frac{1}{2}\frac{c^2 + \frac{1}{4}(\omega_a - \omega_b)^2}{c^2 + d^2} \tag{51}$$

The dependences of terms in equation (49) on the quantity $t - 2\tau$ clearly show the refocusing action of the second pulse on the attenuation of the signal following the first pulse that is caused by the difference in Larmor frequencies. When the exchange rates and the Larmor frequency differences are comparable, the use of equations (16a) and (16b) shows that the spin echo signal is

$$\begin{aligned} E(t) = {} & \tfrac{1}{2}(P_b - P_a)(\omega_a - \omega_b)(t - 2\tau)\,\mathrm{e}^{-\phi_2 t} \\ & + \mathrm{i}\left[1 + \frac{1}{2}(P_b - P_a)\left(\frac{1}{T_{2a}} - \frac{1}{T_{2b}}\right)t + \frac{1}{2}\left(\frac{1}{\tau_a} + \frac{1}{\tau_b}\right)t \right. \\ & \left. + \frac{1}{2}(\omega_a - \omega_b)^2\tau(t - \tau)\right]\mathrm{e}^{-\phi_2 t} \end{aligned} \tag{52}$$

When $P_a = P_b$, comparison of equation (52) with equation (43) shows that at the time of the peak of the spin echo, $t = 2\tau$, the spin echo signal is greater than the signal from a single pulse. This refocusing phenomenon is qualitatively similar to that for the spin echoes of molecules that diffuse into different values of B_0. Aside from a different statistical problem, the main difference here is that the precession frequency is restricted to two values; in molecular diffusion, a range of values is available to each nucleus.

Transverse relaxation is easily measured from the dependence of the spin echo amplitude at time $t = 2\tau$ determined as a function of 2τ. At very small chemical exchange rates, the Larmor frequency difference has a negligible effect on the transverse relaxation. With increasing exchange rates, the nucleus alternately experiences two different precession frequencies for random periods of time, causing a contribution to transverse relaxation by dephasing of the NMR signal. This dephasing passes through a maximum when the exchange rate and the Larmor frequency difference are comparable. Then, with increasing exchange rates, the transverse relaxation contribution from the frequency difference decreases, and is given by equation (46) when the exchange rates are large compared with the frequency difference. In the intermediate range, the spin echo time dependence is significantly modulated, and is not approximated by a sum of two exponential decays. We can readily see this from the sine and cosine terms in the time dependence of the spin echo amplitude by writing equation (49) at time $t = 2\tau$:

$$\begin{aligned} E(2\tau) = {} & \mathrm{i}[\, j\,\mathrm{e}^{-ct} + (2g + j - 1)\,\mathrm{e}^{ct} + 2f\sin dt \\ & - 2(g + j)\cos dt]\,\mathrm{e}^{-\phi_2 t} \end{aligned} \tag{53}$$

For zero exchange rate, $f = 0$ and $g + j = 0$; the magnitudes of these quantities increase with increasing exchange rate, become greatest when $\frac{1}{2}\pi(1/\tau_a + 1/\tau_b) \approx |\omega_a - \omega_b|$, decrease with further increase in exchange rate, and approach zero as the exchange rates approach infinity. Also, when the exchange rate is large compared with the Larmor frequency difference, the spin echo amplitude closely approximates an exponential decay with a T_2 value given by equation (46). Calculations[5] of the decay curves show that when T_{2a}, $T_{2b} \approx \infty$, the shapes are closely approximated by exponential decays under the condition $|\omega_a - \omega_b| \ll 1/\tau_a$, $1/\tau_b$. In the intermediate range of $1/\tau_a$ and $1/\tau_b$ values, the decay curves are not exponential, and are modulated. If we define T_{2E}* as the time required for the curve to decay from its initial value at $t = 0$ to 1/e of this value, T_{2E}* passes through a minimum when $\frac{1}{2}\pi(1/\tau_a + 1/\tau_b) \approx |\omega_a - \omega_b|$.

5.3 The Spin Echo Amplitudes in Carr–Purcell Pulse Sequences

The spin echo for the special mathematical case, equation (52), when evaluated at time $t = 2\tau$ and compared with the single pulse signal, includes the extra term $(\omega_a - \omega_b)^2\tau^2$; this suggests that the contribution of the Larmor frequency difference to the transverse relaxation can be eliminated by using the Carr–Purcell sequence with sufficiently small pulse separations. The effect of each 180° pulse in the sequence can be calculated by using the complex conjugate of the transverse magnetization at the time of the pulse as the initial condition for the solutions, equations (12a) and (12b), of equations (11a) and (11b) for the time after the pulse. We might expect that the plot of the peak spin echo amplitudes is a sum of two exponential decays or, one exponential when the exchange rates are rapid. Much theoretical work has been done for various cases to obtain exchange rates from Carr–Purcell sequences,[7–9] and complete solutions for the two-site case are available.[8,9] Generally, computer-assisted calculations are needed to analyze experimental data. From the complex preexponential coefficients, we may anticipate that alternations in echo amplitudes could occur along the pulse sequence, especially in cases where the exchange rates and the Larmor frequency differences are of the same order of magnitude. The early echoes observed in Carr–Purcell sequences frequently show amplitude alternations. This behavior may be related to the alternations in consecutive spin echo amplitudes for powder pattern distributions of Larmor frequencies, calculated in Section 6.2.1 of this article. These alternations die away with a time constant that is comparable to the reciprocal of the exchange rate. The shift of the peak of the first echo, and presumably other odd-numbered echoes, to 'short' times may also be related to this.

6 'MULTIPLE SITE' CHEMICAL EXCHANGE AND TRANSVERSE RELAXATION

6.1 Gaussian Frequency Distribution

The mathematical treatment of the general multiple-site case is extremely complicated. However, the case of a continuous Gaussian distribution[10] of Larmor frequencies ω_j is tractable mathematically and computationally. The results parallel those of the two-site case and are instructive. If the nucleus exchanges among the ω_j values so that the covariance function

$$\langle \Delta\omega(t)\Delta\omega(t + \tau)\rangle = \langle \Delta\omega(t)^2\rangle\,\mathrm{e}^{-\tau/\tau_\mathrm{e}} \tag{54}$$

is obeyed then the decay curve following a single pulse is

$$F_2(t) = \exp\left[-\sigma^2\tau_\mathrm{e}^2\left(\mathrm{e}^{-t/\tau_\mathrm{e}} + \frac{t}{\tau_\mathrm{e}} - 1\right)\right] \tag{55}$$

where σ is the rms value of $\Delta\omega = \omega_j - \omega_0$ and τ_e is an exchange time. The signal following the second pulse that is applied at time $t = \tau$ is

$$F_2(t\rangle\tau) = \exp\left[-\sigma^2\tau_e^2\left(\frac{t}{\tau_e} - 3 - e^{-t/\tau_e} + 2e^{-\tau/\tau_e} + 2e^{-(t-\tau)/\tau_e}\right)\right] \quad (56)$$

and the maximum value of this signal occurs at time

$$t_m = \tau_e[\ln(2e^{\tau/\tau_e} - 1)] \quad (57)$$

Equation (57) shows that $t_m < 2\tau$. For very slow exchange, t_m is nearly equal to 2τ. However, $t_m = 1.4899\tau$ when $\tau_e = \tau$; this is a large shift from the expected value, 2τ. The conventional spin echo amplitude curve is given by equation (56) evaluated at time $t = 2\tau$:

$$E(2\tau) = \exp\left[-\sigma^2\tau_e^2\left(\frac{2\tau}{\tau_e} - 3 - e^{-2\tau/\tau_e} + 4e^{-\tau/\tau_e}\right)\right] \quad (58)$$

We can examine the time dependences of these functions by defining T_2^* as the time required for equation (55) to decay from its initial value at $t = 0$ to 1/e of this value, and T_{2E}^* as the comparable quantity for equation (58). When the exchange rate is fast (i.e., $\sigma\tau_e \ll 1$), both of the above curves approximate exponential decays with decay rates

$$\frac{1}{T_2^*} \approx \frac{1}{T_{2E}^*} = \sigma^2\tau_e \quad (59)$$

This result agrees with equation (46) for the two-site case. Also, in qualitative agreement with the two-site case, with changing exchange rate, T_{2E}^* passes through a minimum at $\sigma\tau_e \approx 1$. With decreasing exchange rate, the decay curve $E(2\tau)$ becomes

$$E(2\tau) \approx \exp\left(-\frac{2}{3}\frac{\sigma^2\tau^3}{\tau_e}\right) \quad (60)$$

below the T_{2E}^* minimum. However, equation (60) shows that T_{2E}^* becomes equal to $(12\tau_e/\sigma^2)^{1/3}$ instead of the value τ_e that is found in the two-site case. This dependence of the attenuation of the spin echo amplitude on τ^3 is analogous to that of nuclei diffusing[11] in a gradient in $\boldsymbol{B}_0$ (see ***Diffusion Measurements by Magnetic Field Gradient Methods***). When a molecule diffuses, there is a Gaussian probability distribution of changes in Larmor frequency; the width of this distribution increases in time. Also, with decreasing exchange rate, T_2^* monotonically decreases and asymptotically approaches the constant value $\sigma^{-1}\sqrt{2}$.

6.2 Powder Pattern Frequency Distribution

6.2.1 'Rotational Diffusion' Site Exchange

A logical choice for ω_j values is that which appears in NMR magnetic dipolar splitting and nuclear quadrupolar splitting:

$$\omega_j = C(3\cos^2\theta_j - 1) \quad (61)$$

in which C is the splitting constant. For a 'powder' sample, the values of P_j are directly proportional to $\sin\theta_j$ and the number of different sites is very large. The resultant mean square value of ω_j is $\frac{4}{5}C^2$.

The rotational diffusion case[12] allows direct exchanges only between sites with adjacent θ values and thus between adjacent frequencies. The signal following one pulse can be computed[12] by solving the differential equation

$$\frac{\partial A}{\partial t} = (6\tau_e)^{-1}\cot\theta\frac{\partial A}{\partial\theta} + (6\tau_e)^{-1}\frac{\partial^2 A}{\partial\theta^2} + iC(3\cos^2\theta - 1) \quad (62)$$

as a function of time using the initial condition $A_j(0, \theta_j) = P_j$. The NMR signal following the second pulse is computed by using the complex conjugate $A_j^*(\tau, \theta_j)$ as the initial condition for equation (62). As in the Gaussian case, T_2^* is the time at which the signal following one pulse has 1/e times the value at time $t = 0$; T_{2E}^* is the value of 2τ at which the NMR signal following the second pulse has 1/e times the value at $2\tau = 0$. When the exchange is fast (i.e., $C\tau_e \ll 1$), both the T_2 and T_{2E} curves approximate exponential decays with decay rates

$$\frac{1}{T_2^*} \approx \frac{1}{T_{2E}^*} = \tfrac{4}{5}C^2\tau_e \quad (63)$$

in agreement with equation (46) for the two-site case and equation (59) for the Gaussian case. Also in agreement with these cases, with decreasing exchange rate, T_{2E}^* passes through a minimum at $(\frac{4}{5})^{1/2}C\tau_e \approx 1$. With further decreases in exchange rate, the spin echo amplitude asymptotically approaches

$$E(2\tau) \approx \exp\left(-\frac{8}{15}\frac{C^2\tau^3}{\tau_e}\right) \quad (64)$$

so that T_{2E}^* becomes equal to $(15\tau_e/C^2)^{1/3}$. Simultaneously, T_2^* decreases monotonically and approaches the constant value $T_2^* = 1.46/C$.

The computed NMR signals in multiple pulse sequences[12] show several interesting features. When pulses are applied at times $t = 0$, τ, 3τ, 5τ, etc., the amplitudes calculated at times 2τ, 4τ, 6τ, etc., increase when the number of pulses per unit time increases. The result is analogous to that for liquid molecules diffusing in a magnetic field gradient.[11] In addition, the odd-numbered spin echoes in a given multipulse sequence, calculated at the above times, are of smaller amplitude than the even-numbered echoes. This amplitude alternation decreases with succeeding spin echoes. The time constant for this decay appears to be equal to τ_e. An alternation of spin echo amplitudes in multiple pulse sequences is also predicted and observed[11] for liquid molecules flowing in a magnetic field gradient (see ***Diffusion and Flow in Fluids***).

Also, as calculation of the NMR signal shapes for three pulses shows, this formalism predicts that the peak of the first spin echo, as in the Gaussian case, is shifted to times shorter than 2τ. This shift appears to be given approximately by equation (57), which was derived for the Gaussian case.

However, the peak value of the calculated second spin echo appears at the expected time, $t = 4\tau$. This predicted shift of the first echo peak but not of the second is indeed observed experimentally[12,13] in aqueous heterogeneous systems.

6.2.2 Random Site Exchange

We can predict the NMR behavior of systems with other chemical exchange dynamics[14] by generalizing equations (11a) and (11b) to allow direct exchange among many types of sites that are characterized by different frequencies. To emphasize the contribution of the Larmor frequency distribution to transverse relaxation, we set the T_2 values in equation (10c) equal to infinity.

The total transverse magnetization of a system of N types of sites is

$$M_+(t) = \mathrm{i}M_0 \sum_{j=1}^{N} P_j A_j(t, \omega) \tag{65}$$

where P_j is the occupation probability of sites of type j normalized so that

$$\sum_{j=1}^{N} P_j = 1 \tag{66}$$

We express the time dependences of the A_j by the set of N coupled differential rate equations

$$\frac{\partial A_j}{\partial t} = \mathrm{i}\omega_j - \frac{A_j}{\tau_j} + \sum_{\substack{j=1 \\ k\neq j}}^{N} \frac{A_k}{\tau_{kj}}, \quad j = 1, 2, \ldots, N \tag{67}$$

where ω_j is the difference frequency (compared with the average frequency) for j-type sites, τ_j is the average lifetime of a nucleus in j-type sites, and $1/\tau_{kj}$ is the average rate at which nuclei in k-type sites move to j-type sites.

To solve the set of N equations in equation (67), we must specify the frequencies (ω_j values), occupation probabilities (P_j values), and exchange probabilities (τ_j and τ_{kj} values). We choose the powder pattern frequencies as described by equation (61) and P_j values that are directly proportional to $\sin\theta_j$. The exchange probabilities implicit in the preceding sections of this article represent one extreme case. The opposite extreme case is to allow direct exchanges between sites of all the different frequencies. This case more closely corresponds to the two-site case in that the individual exchange events can involve large changes in Larmor frequency. To set up the exchange probabilities, we use the principle of detailed balance, which requires that the total number of exchanges per second between sites j and k is directly proportional to the product P_jP_k. Then, if we define $1/\tau_e$ as the average rate for nuclei to leave the sites that they occupy, we obtain

$$\frac{1}{\tau_j} = V \sum_{\substack{j=1 \\ k\neq j}}^{N} P_k = V(1 - P_j) \tag{68}$$

$$\frac{1}{\tau_{kj}} = V P_j \tag{69}$$

where

$$V = \left[\tau_e\left(1 - \sum_{j=1}^{N} P_j^2\right)\right]^{-1} \tag{70}$$

When N is very large, $V = 1/\tau_e$.

The signal following one pulse[14] can be calculated by solving equation (67) as a function of time using the initial condition $A_j(0, \omega_j) = P_j$. The T_{2E} curves[13] can be computed by using the complex conjugate $A_j{*}(\tau, \omega_j)$ as the initial condition after the second pulse in evaluating the signal at time τ after the second pulse. When the exchange is fast (i.e., $C\tau_e \ll 1$), both the T_2 and T_{2E} curves approximate exponential decays with decay rates

$$\frac{1}{T_2^*} \approx \frac{1}{T_{2E}^*} = \tfrac{4}{5}C^2\tau_e \tag{71}$$

in agreement with equation (46) for the two-site case and with the Gaussian and rotational diffusion cases. Also in agreement with the two-site case, with decreasing exchange rate, $T_{2E}{*}$ passes through a minimum at $(\frac{4}{5})^{1/2}C\tau_e \approx 1$ and approaches τ_e when $C\tau_e \gg 1$. This result represents a much stronger dependence of the spin echo attenuation on exchange rate than in the Gaussian and rotational diffusion cases. Simultaneously, $T_2{*}$ decreases monotonically and approaches the constant value $T_2{*} = 1.46/C$.

In calculations of the NMR signals for the three-pulse case, the peak of the first spin echo is shifted to times smaller than 2τ, while the second echo peak remains at time 4τ. The shapes of the signals and the effects of changes in exchange rates differ between the present case and the preceding cases, and measurements of them allow us to determine which case better describes the sample under consideration.

7 PREFERENTIAL ORIENTATION, EXCHANGE, AND ORDER IN AQUEOUS HETEROGENEOUS SYSTEMS

In aqueous heterogeneous systems[14,15] such as biological tissue, biopolymer gels, polyelectrolyte solutions, clay–water gels, etc., the water molecule or a hydrated ion such as sodium can be located in the bulk liquid or at the solid/liquid interface. The nonspherical bonding and electric charge distribution (electric dipole and quadrupole moments) strongly affect the motions and arrangements of water molecules at the interface. When a water molecule is at the solid surface, its motion is slowed down, and some orientations with respect to the local surface plane are more probable than others. This preferential orientation due to the nonspherical interaction causes different rotational rates about different molecular axes. The structure of the interfacial water is different from that of bulk water because this water interacts differently with the relatively immobile solid material compared to other rapidly moving water molecules. At each allowed molecular orientation at the surface, there is a different magnetic dipolar interaction of the protons (H_2O) or nuclear quadrupolar interaction of the deuterons (D_2O). The water molecules not only occupy the various site environments at the interface, but they migrate

among them and also into the bulk liquid away from the interface. This rapid chemical exchange enables all of the water molecules to experience the interfacial environment. Consequently, the spectral densities $J_h(\omega)$ that determine NMR relaxation phenomena are influenced by the effects on the correlation functions caused by the motions and local structure of the interface and the exchange between the bulk and interfacial sites.

The correlation functions of the water in such a heterogeneous system can be written[14] as the sum over the different j environments:

$$\langle F_h(t)F_h^*(t+\tau)\rangle = \sum_j P_j \langle F_{hj}(t)F_{hj}^*(t+\tau)\rangle \qquad (72)$$

where the sum of the occupation probabilities P_j is unity. We now assume, with good evidence, that all local permitted molecular reorientations and all local chemical exchange rates are rapid compared with the Larmor frequency ω_0. Then, at times τ that are long compared with $1/\omega_0$, nuclei that were in a given j at time t are now distributed among all the different j sites in accordance with P_j, and $\langle F_{hj}{}^*(t+\infty)\rangle = \langle F_h{}^*(t)\rangle$. Also, for each of these nuclei, the value of $F_{hj}{}^*(t+\infty)$ is independent of the value of the original $F_{hj}(t)$, and equation (72) can be written as

$$\begin{aligned}\langle F_h(t)F_h^*(t+\infty)\rangle &= \langle F_h(t)\langle F_h^*(t+\infty)\rangle\rangle \\ &= \langle F_h(t)\rangle\langle F_h^*(t+\infty)\rangle \\ &= \langle F_h(t)\rangle\langle F_h^*(t)\rangle \end{aligned} \qquad (73)$$

In a bulk liquid, the values of $\langle F_h(t)\rangle$ and $\langle F_h{}^*(t+\infty)\rangle$ at such long times are zero. However, preferential molecular orientation at the interface can result in nonzero values.

Let us temporarily assume that the surface is an infinite plane, so that the interface is planar. The orientation of the interface in $\boldsymbol{B}_0$ is defined by the 'director', which is normal to the surface. For simplicity, let the molecular orientation distribution be axially symmetric about the director. If the orientation of the director in $\boldsymbol{B}_0$ is given by the polar and azimuthal angles θ' and ϕ', and the orientation of the nuclear spin interaction vector with respect to the director is given by the polar and azimuthal angles θ'' and ϕ'', then $\langle F_0(t)\rangle = \langle 3\cos^2\theta - 1\rangle$ is given by

$$\langle 3\cos^2\theta - 1\rangle = \tfrac{1}{2}(3\cos^2\theta' - 1)\langle 3\cos^2\theta'' - 1\rangle \qquad (74)$$

The last term on the right-hand side of equation (74) expresses the preferential orientation. The correlation function is then given by

$$\langle F_h(t)F_h^*(t+\tau)\rangle = \langle F_h(t)F_h^*(t)\rangle \times\left(P_p\,\mathrm{e}^{-\tau/\tau_{cp}} + \sum_{j=1}^{p-1} P_j\,\mathrm{e}^{-\tau/\tau_{cj}}\right) \qquad (75)$$

where

$$P_p + \sum_{j=1}^{p-1} P_j = 1 \qquad (76a)$$

$$P_p = \frac{\tfrac{1}{4}(3\cos^2\theta' - 1)^2\langle 3\cos^2\theta'' - 1\rangle_{av}^2}{\langle F_0(t)F_0^*(t)\rangle} \qquad (76b)$$

The τ_{cj} are short correlation times that result from the rapid molecular motions, including exchange. The correlation time associated with the preferential orientation, τ_{cp}, is infinite in the present case.

When τ_{cp} is extremely long, its contributions to $J_1(\omega_0)$ and $J_2(2\omega_0)$ in the relaxation times given in equations (4a) and (4b) are extremely small and can be neglected. However, the $J_0(0)$ term in equation (4b) is incorrect, and the contribution of the terms that involve τ_{cp} to transverse relaxation must be calculated differently. The term $3\cos^2\theta - 1$ in equation (74) is $F_0(t)$, and a nonzero average value causes a residual magnetic dipolar or nuclear quadrupolar splitting in the NMR spectrum due to the preferential orientation. From equation (61), this residual splitting is

$$\omega' = \tfrac{1}{2}C(3\cos^2\theta' - 1)\langle 3\cos^2\theta'' - 1\rangle \qquad (77)$$

where C is the splitting constant for a stationary molecule. At any instant of time, a certain number of water molecules are preferentially oriented by the interface, so that these molecules have a certain nonzero value of $\langle 3\cos^2\theta'' - 1\rangle$ and the remainder of the molecules has a zero value for this quantity. We assume that the value of $\langle 3\cos^2\theta'' - 1\rangle$ for the instantaneously preferentially oriented water molecules and the number of these molecules are independent of the number of other water molecules. When rapid exchange between these two environments occurs, all of the water experiences preferential orientation, as referred to the director, for a fraction F of the time. The value of F is the fraction of the water molecules at any instant that is preferentially oriented, and the value of ω' is

$$\omega' = C'(3\cos^2\theta' - 1) \qquad (78)$$

where

$$C' = \tfrac{1}{2}FC\langle 3\cos^2\theta'' - 1\rangle \qquad (79)$$

The effective splitting constant C' depends on the surface-to-volume ratio of the water.

In addition to the surface-to-volume ratio, the value of C' depends on the geometry of the surface. If the surface is that of the circumference of a cylinder and if rapid exchange occurs over all of the surface of the cylinder, the value of C' is one-half of that for the same surface on a plane, and the direction of the director is along the axis of the cylinder.

A system that contains many parallel planes or cylinders with uniform distribution of water will have a doublet NMR spectrum with a splitting that varies as $3\cos^2\theta' - 1$. This is observed in many ordered systems such as water distributed among parallel fibers, water among parallel smectite clay platelets (smectite clay minerals are comprised of 1 nm thick aluminosilicate sheets that are many micrometers or even millimeters in length and width), and lyotropic liquid crystals.

The doublet splitting constant depends on the degree of order in the system. If the system has a large number of cylinders that are not parallel and if rapid exchange occurs among all of them, the value of C' is reduced[16] by this disorder as described by the second-rank order parameter

$$S = \tfrac{1}{2}(3\langle\cos^2\theta_{C1C2}\rangle - 1) \qquad (80)$$

where θ_{C1C2} is the angle between the axes of a pair of cylinders C1 and C2. When all the cylinders are parallel, $S = 1$ and the splitting constant is maximum. However, if the cylinders are randomly oriented (i.e., a powder), $S = 0$ and there is no spectral splitting. A similar statement applies to a system of sheets.

The above illustration describes the extreme case of rapid exchange and local disorder. Another case is local order and global disorder as occurs with a powder made of crystallites. A crystallite may be a domain in which there is perfect order. If the molecules are constrained in individual domains, the NMR signal is the superposition of the signals of all the domains, i.e., a powder pattern. This signal will be changed if molecules are exchanged among the domains with different orientations in $\boldsymbol{B}_0$. This exchange will affect the transverse relaxation, and the methods described in Section 6 of this article can be used to calculate the NMR signals for various assumed models of order/disorder. In these calculations, the ω_j values are given by equations (78) and (79). If there is less than perfect order in the domains or if the degree of order is changed, the splitting constant must be reduced by the factor in equation (80). Also, if the water content is changed, the splitting constant is changed in accordance with equation (79). The exchange lifetime τ_e will depend on the size of a domain and on the diffusion coefficient of the water. Changes in the domain size or internal order caused by purely physical treatment of the sample, without any change in chemical composition, will cause changes in the transverse NMR relaxation behavior.

These phenomena are observed in deuteron NMR measurements on aqueous biopolymer gels[17] and clay–water systems.[13,14] Values of τ_e are obtained by using the methods of Section 6 to analyze the data, and the splitting constants and the domain sizes are found. Also, when a hydrated ion such as sodium is at an interface, the distortion of the hydration atmosphere causes a nuclear quadrupolar coupling that is described by a quadrupolar coupling constant and the orientation of the director. The transverse relaxation of sodium in linear polyelectrolyte solutions is quantitatively explained[16] by the scheme described above for the NMR signals of water.

8 EFFECTS OF DIFFUSIVE EXCHANGE IN HETEROGENEOUS SYSTEMS

In the preceding sections, chemical exchange has been modeled so that all nuclei in a given site environment have the same time-independent exchange or transition probability to move to different environments. However, this picture fails to describe completely the spatial aspects of the exchange process.[18–20] For example, consider the case of water in heterogeneous and biological systems. The probability per unit time that a given molecule in the interface leaves the interface may be the same for all the interfacial molecules. An interfacial molecule exchanges places with a neighboring bulk water molecule, and the interface is only a molecular layer or two in thickness. Therefore, when the bulk water is many molecular diameters in thickness, the lifetime in the bulk for a molecule that is next to the interface can be much shorter than that of a molecule that is many molecular diameters away from the interface. In order for the latter molecule to be able to exchange with the interface, it first must diffuse to the interface, taking some time and lowering its effective exchange rate. This is not a simple diffusion problem, because the mobility of water molecules in the interface is less than that in the bulk. Also, because of proximity, a molecule that has just left the interface is likely to reenter[18] the interface before a molecule away from the interface has a chance to enter the interface. The exchange rate of such molecules is thus enhanced. This can lead to some relaxation behavior that is qualitatively different from the simple exchange picture.[18] Also, the occupation probability for a diffusing molecule to occupy a given volume of space is a sum of exponential decays. However, the major term of this probability is generally a single exponential. Thus, the simple exchange view provides a convenient framework that is adequate, in most cases, to formulate the effects of molecular migration on NMR relaxation and interpret experimental results.

9 RELATED ARTICLES

Brownian Motion and Correlation Times; Chemical Exchange Effects on Spectra; Diffusion and Flow in Fluids; Diffusion Measurements by Magnetic Field Gradient Methods; Dynamics of Water in Biological Systems: Inferences from Relaxometry; Magnetization Transfer and Cross Relaxation in Tissue; Magnetization Transfer between Water and Macromolecules in Proton MRI; Molecular Motions: T_1 Frequency Dispersion in Biological Systems; Quadrupolar Nuclei in Liquid Samples; Relaxation Theory: Density Matrix Formulation; Relaxometry of Tissue; Sodium-23 NMR; Well Logging.

10 REFERENCES

1. A. Abragam, *The Principles of Nuclear Magnetism*, Clarendon Press, Oxford, 1961.
2. H. Wennerström, *Mol. Phys.*, 1972, **24**, 69.
3. J. R. Zimmerman and W. E. Brittin, *J. Phys. Chem.*, 1957, **61**, 1328.
4. H. M. McConnell, *J. Chem. Phys.*, 1958, **28**, 430.
5. D. E. Woessner, *J. Chem. Phys.*, 1961, **35**, 41.
6. H. Winkler and D. Michel, *Adv. Colloid Interface Sci.*, 1985, **23**, 149.
7. A. Allerhand and H. S. Gutowsky, *J. Chem. Phys.*, 1964, **41**, 2115.
8. J. P. Carver and R. E. Richards, *J. Magn. Reson.*, 1972, **6**, 89.
9. W. T. Sobol, *Magn. Reson. Med.*, 1991, **21**, 2.
10. J. R. Klauder and P. W. Anderson, *Phys. Rev.*, 1962, **125**, 912.
11. H. Y. Carr and E. M. Purcell, *Phys. Rev.*, 1954, **94**, 630.
12. D. E. Woessner, B. S. Snowden, Jr., and G. H. Meyer, *J. Chem. Phys.*, 1969, **51**, 2968.
13. D. E. Woessner, B. S. Snowden, Jr., and G. H. Meyer, *J. Colloid Interface Sci.*, 1970, **34**, 43.
14. D. E. Woessner, *Mol. Phys.*, 1977, **34**, 899.
15. K. J. Packer, *Phil. Trans. R. Soc. Lond. B*, 1977, **278**, 59.
16. B. Halle, H. Wennerström, and L. Piculell, *J. Phys. Chem.*, 1984, **88**, 2482.
17. D. E. Woessner and B. S. Snowden, Jr., *Ann. N. Y. Acad. Sci.*, 1973, **204**, 113.
18. B. Halle, *Mol. Phys.*, 1984, **53**, 1427.
19. P. S. Belton and B. P. Hills, *Mol. Phys.*, 1987, **61**, 999.
20. B. Halle and P.-O. Westlund, *Mol. Phys.*, 1988, **63**, 97.

Biographical Sketch

Donald E. Woessner. *b* 1930. A.B., 1952, Ph.D. (supervisor Herbert Gutowsky), 1957, Chemistry, University of Illinois, USA. Postdoctoral work at University of Illinois (with Herbert Gutowsky). Successively senior research chemist, research associate, senior research associate, Mobil Research and Development Corporation, Dallas, TX. Adjunct Assistant Professor of Radiology, The University of Texas Southwestern Medical Center at Dallas, 1992–present. Approx. 72 publications. Research specialties: NMR relaxation and molecular motions in liquids, and relationships of NMR relaxation of hydrogen and ionic nuclei to motions, structure and order in aqueous heterogeneous systems and biological tissue.

Reorientation in Crystalline Solids: Propeller-Like R_3M Species

Jörg Kümmerlen and Angelika Sebald
Universität Bayreuth, Bayreuth, Germany

1 Introduction 1
2 Some Illustrative Examples of R_3M Reorientation in the Solid State as Viewed by High-Resolution Solid State NMR Techniques 2
3 Some Concluding Remarks 5
4 Related Articles 6
5 References 6

1 INTRODUCTION

Ever since the pioneering investigations on the anisotropic reorientation of solid benzene by Andrew and Eades,[1] NMR spectroscopy has proved to be a valuable tool for the elucidation of various types of nonrigidities and fluxional behavior of molecules in both the solid and solution state: the following years have seen an ever-increasing importance of NMR methods for the detection and quantification of dynamic solid state processes. In line with the instrumental development of NMR from wideline methods to include high-resolution solid state techniques, a whole range of techniques, sensitive to a large range of correlation times τ_c, and each typical for the respective experimental approach, are available nowadays.

More traditional NMR methods for the investigation of solid state dynamics utilize spin–lattice relaxation[2,3] in either the laboratory frame (T_1) or in the rotating frame ($T_{1\rho}$), and the calculation of second moments.[4] These techniques have been extremely important and are still popular. Multiple pulse techniques[5] have further made the timescale of chemical shielding anisotropy available; examples for the application of such techniques are the molecular dynamics of solid C_6F_{12},[5] the reorientation of P_4,[3] and $Fe(CO)_5$.[6] Coherent averaging of anisotropic spin interactions by magic angle spinning (MAS) and high-power decoupling, in combination with cross-polarization (CP) techniques[7] in order to overcome inherent sensitivity problems for low-γ and/or low natural abundance nuclei, has also opened up new possibilities for the investigation of dynamic solid state processes by means of NMR: adaptation of solution state-type NMR experiments such as lineshape analysis of exchange-broadened spectra or one- and two-dimensional (1D, 2D) magnetization transfer experiments,[8] have become accessible for the solid state.

One prime target for the investigation of solid state dynamics has recently been the area of organic polymers[9–12] where 2D ^{13}C exchange spectroscopy (EXSY) and 1D and 2D ^2H NMR of selectively deuterated compounds are the methods of choice. The research field of organometallic chemistry has so far been fairly reluctant to use high-resolution solid state NMR techniques for the elucidation of molecular dynamics. Where activation parameters have been determined at all, this was mostly done by considering ^1H spin–lattice relaxation.[13] Anisotropic $2\pi/n$ reorientation of aromatic ligands (n denotes the n-fold axis of the idealized geometry of the ligand) π-bonded to transition metals and CO chemical exchange in carbonyl–transition metal complexes are fairly well documented,[13] while processes such as diene jumps[14] are much less common.

Activation energies E_a of the $2\pi/n$ jump reorientation of such aromatic ligands are generally fairly uniform and quite similar in solution and in the solid state. For instance, E_a for η^5-$C_5H_5TM(CO)_3$ (TM = transition metal) is in the range 7–10 kJ mol^{-1}, E_a for η^6-$C_6H_6TM(CO)_3$ is approximately 15–27 kJ mol^{-1}. The $2\pi/5$ and $2\pi/6$ reorientation of the analogous permethylated ligands C_5Me_5 and C_6Me_6 (Me = methyl), respectively, in such complexes do not show significantly higher activation energies. The $2\pi/n$ jump reorientation of such 'disk-like' aromatic ligands is sterically not very demanding, which explains the experimental finding of fairly uniform and low activation energies for such processes. In contrast, CO exchange in transition metal–carbonyl complexes is far more sterically demanding and much more dependent on the actual crystal structure, so that activation energies for CO exchange in solid transition metal complexes are far less uniform and, in general, exceed 50 kJ mol^{-1}.[13]

In contrast to the uniform dynamic behavior found for the $2\pi/n$ reorientation of π-bonded aromatic ligands in transition metal complexes, no such uniform dynamic behavior is to be expected for the $2\pi/3$ reorientation of R_3M species, simply because a great variety of such species in an even greater variety of chemical and structural environments exists. R_3M species such as CH_3, BH_3, or NH_3 groups will usually show very fast $2\pi/3$ reorientation, depending on the steric constraints of their molecular environment. At very low temperatures, $2\pi/3$ reorientation of such small R_3M moieties is a tunneling process,[15] and at still fairly low temperatures the onset of thermally activated $2\pi/3$ reorientation is observed.[16] Rates of reorientation of such small R_3M species do correlate with the steric and electronic requirements of their molecular environment and are generally strongly temperature-dependent: the activation characteristics of thermally activated $2\pi/3$ reorientation, e.g. the internal reorientation of Me groups, normally catapult into a very fast regime at or near room temperature.

Even for much bulkier species R_3M, such as CF_3,[2,5] CMe_3,[17] $SiMe_3$,[18] NMe_3,[19] and PMe_3,[20] an enormous spread of $2\pi/3$ jump rates and activation energies is to be expected for this thermally activated process owing to the great variety of molecular and crystal structures which can accommodate this process, in addition to the rich chemistry of compounds containing Me_3M groups. For M = C, Si, N, and P, M will usually be in a more or less distorted tetrahedral coordination. An even greater variation of $2\pi/3$ jump rates and activation energies can be predicted for species Me_3M where M denotes a metal such as Sn or Pb: for R_3M = Me_3Sn, Me_3Pb, both fourfold tetrahedral or fivefold trigonal-bipyramidal coordination of M = Sn, Pb are found in the solid state.

From the above it is obvious that $2\pi/3$ reorientation is a common solid state dynamic process, involving R_3M species all over the Periodic Table of the elements. Schematically we may describe this process as is shown in Scheme 1, regardless of whether $R_{A,B,C}$ are crystallographically equivalent or

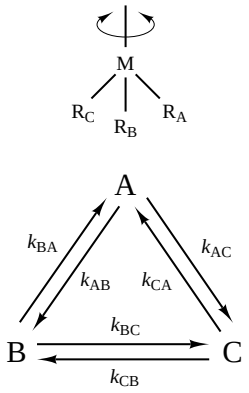

Scheme 1

not. Clearly, the dynamic properties of chemically different propellers R_3M will vary greatly and, thus, will challenge the unique potential of solid state NMR to provide the appropriate window of observation for an enormous range of correlation times.

We should also address the question why one should be interested to learn about $2\pi/3$ reorientation of R_3M species in crystalline solids. For small R_3M species such as CH_3, naturally, the quantum chemical low-temperature behavior and the gradual take-over by thermal activation are of major theoretical importance. For bulky species R_3M, with $R \neq H$, thermally activated R_3M reorientation is the focus of attention: the single crystal X-ray structures of many compounds containing R_3M fragments are known. However, X-ray crystallography cannot normally detect this random $2\pi/3$ jump process so that necessarily the static picture of such compounds obtained by diffraction methods is somewhat incomplete. The geometric, static picture from X-ray diffraction, in turn, provides important information about the potential barriers (van der Waals interactions) for the $2\pi/3$ reorientation monitored by NMR. We may, thus, expect to learn more about the subtle interplay of packing in the crystal versus the steric requirements of anisotropic R_3M reorientation. However, we cannot expect to be able to definitely separate cause and effect in this interplay.

The following practical examples are taken from a group of reorienting species Me_3M which are (i) at least, in part, fragments of molecules of known single crystal X-ray structure and (ii) accessible to high-resolution solid state NMR methods for the determination of their dynamic R_3M properties.

2 SOME ILLUSTRATIVE EXAMPLES OF R_3M REORIENTATION IN THE SOLID STATE AS VIEWED BY HIGH-RESOLUTION SOLID STATE NMR TECHNIQUES

Even if—with one exception—all the following examples have been borrowed from organotin and organolead chemistry (R_3M = Me_3Sn and Me_3Pb), we do not wish to highlight a particular branch of chemistry. The examples were chosen because the entire range of very slow to very fast reorientation is represented here by one group of reasonably closely related chemicals and, in particular, because depending on the ligands X in solid Me_3SnX or Me_3PbX, the three regimes of reorientation—fast, intermediate, slow—as discussed in Sections 2.1–2.3 are accessible at or near room temperature and, thus, can be investigated conveniently by using standard CP MAS equipment.

2.1 Fast R_3M Reorientation: Rates of the Order of 10^4 Hz

Let us consider particles CH_3 and/or Me_3M, and jump rates for the mutual exchange in these particles of the same order of magnitude as the applied B_1 field strength. Under these conditions destructive interference between coherent averaging of the $^1H-^{13}C$ dipolar interaction (high-power ^1H decoupling) and incoherent averaging due to the (random) jump processes occurs, resulting in enhanced transverse relaxation of the observed ^{13}C magnetization and, thus, temperature-dependent ^{13}C linewidths. Rothwell and Waugh[16] have theoretically and experimentally investigated this T_2 effect as a versatile tool to characterize motional processes in solids. Following Rothwell and Waugh,[16] the inverse T_2 relaxation time can be written as:

$$\frac{1}{T_2} = \frac{4\gamma_I^2\gamma_S^2\hbar^2}{15r^6} I(I+1)\left(\frac{\tau_c}{1+\omega_1^2\tau_c^2}\right) \qquad (1)$$

and three regimes can be distinguished: a so-called long correlation limit ($\omega_1\tau_c \gg 1$), where the S spin linewidth (here ^{13}C) is dependent on τ_c *and* ω_1, an intermediate regime ($\omega_1\tau_c \approx 1$) of maximum line-broadening, and a short correlation regime ($\omega_1\tau_c \ll 1$) where the S spin linewidth is independent of ω_1 but dependent on τ_c.

This type of line-broadening mechanism is illustrated in Figure 1, depicting the ^{13}C CP MAS spectra of hexamethylethane as a function of temperature.[16] In the temperature

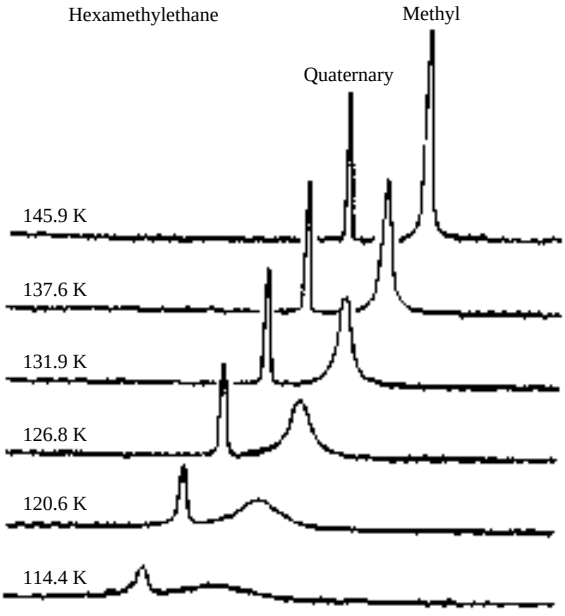

Figure 1 ^{13}C CP MAS spectra of solid hexamethylethane, Me_3C-CMe_3, illustrating the combined effect of internal methyl group plus Me_3C reorientation in the temperature range T = 114.4–145.9 K. (Reproduced with permission of the American Institute of Physics from Rothwell and Waugh[16])

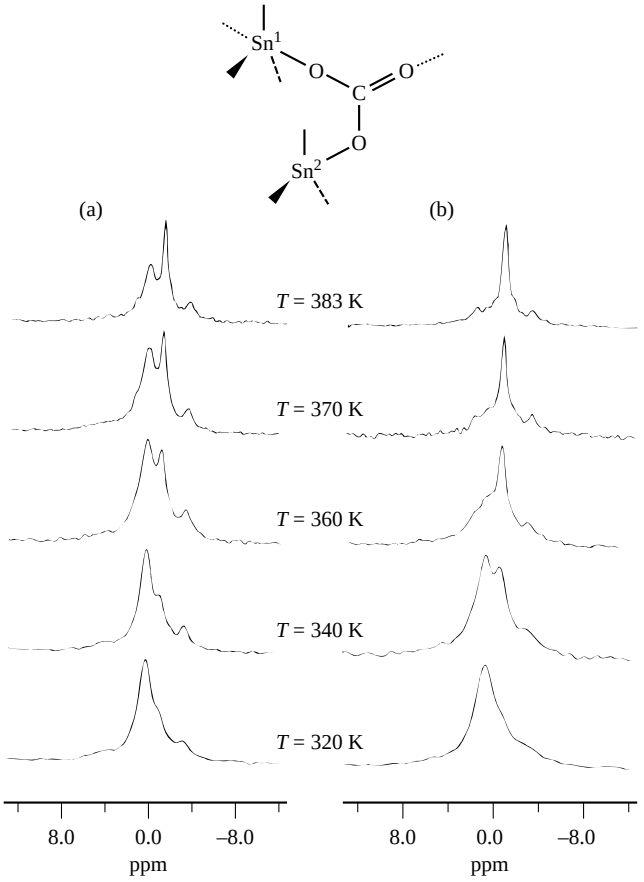

Figure 2 Methyl region of 75.5 MHz ^{13}C CP MAS spectra of polymeric crystalline $(Me_3Sn)_2CO_3$ in the temperature range T = 320–383 K for two different decoupling field strengths ω_1 (a) 4.5×10^5 and (b) 1.96×10^5 rad s^{-1}. Note that the faster reorienting trigonal-bipyramidal Me_3Sn^1 group ($\delta^{13}C \approx -1$ ppm) is in the short correlation limit over this T = 320–383 K range, while the tetrahedral Me_3Sn^2 group ($\delta^{13}C \approx 1$ ppm) is in the long correlation limit for this temperature range and, thus, shows a dependence of the ^{13}C linewidths on both T and ω_1. The linewidth of the ^{13}C resonance of the Me_3Sn^1 group depends on the temperature but is independent of ω_1. (Reproduced by permission of John Wiley & Sons, Ltd, from Kümmerlen and Sebald[21])

range 114.4–145.9 K, Me_3C-CMe_3 shows appropriate correlation times to allow simultaneous Me and Me_3C reorientation to be monitored by this T_2-related method.

A useful correlation time regime for the extraction of the kinetic parameters of R_3M reorientation by this method for the reorientation of R_3M = $SnMe_3$ in solid $(Me_3Sn)_2CO_3$ is reached at higher temperatures.[21] Figure 2 illustrates the ^{13}C CP MAS spectra of $(Me_3Sn)_2CO_3$ in the temperature range T = 320–383 K. Solid $(Me_3Sn)_2CO_3$ contains two different Me_3Sn moieties (one trigonal-bipyramidal Me_3Sn^1 unit, one tetrahedral Me_3Sn^2 group) per molecular unit; in this temperature range Me_3Sn^1 is in the short correlation limit while Me_3Sn^2 is in the long correlation limit.[21]

This method, as developed by Rothwell and Waugh,[16] is a truly versatile tool: it does not depend on the chemical inequivalence of exchanging sites (see below), it operates by using two easily adjustable experimental parameters (ω_1, T), it will be relevant for a great number of solid organic and organometallic compounds at or near room temperature, and is by no means restricted to the $I-S$ combination $^1H-^{13}C$. In our view, it should clearly contribute to the development of an attitude which no longer 'considers the prospect of broadening due to incomplete removal of the dipolar interaction an evil'.[16]

2.2 Intermediate R_3M Reorientation Rates: 1D Exchange broadening Regime

Intuitively, one may be tempted to assume that in solids at ambient temperatures somewhat slower reorientational R_3M processes (depending on the nature of R and M, $R_3M \neq CH_3$) with jump rates in the range approximately 10^1-10^3 Hz are as common as are the faster R_3M reorientation processes discussed in Section 2.1. If we wish to obtain kinetic data in this intermediate range 10^1-10^3 Hz, straightforward 1D variable temperature CP MAS spectroscopy, focused on the ligands R, in conjunction with lineshape analysis of the exchange broadened spectra often provides the appropriate NMR tool.

In order for this tool to be useful, the R_3M species under consideration must fulfill several conditions. The ligands R must be crystallographically inequivalent and give rise to separate isotropic resonances for the different sites involved in the exchange process at low temperatures. The accessible range of correlation times is then further defined by the external magnetic field strength B_0 (defining the separation of resonances on the chemical shift scale in Hz) plus the available CP MAS temperature range. Of course, a change of B_0 corresponds to a fictitious change in temperature and, thus, can be used to extend the range of accessible jump rates for this method. The accessible CP MAS temperature range must cover the entire range from 'rigid on the 1D chemical shift scale' through 'coalescence' to 'fast on the 1D chemical shift scale' to allow for lineshape simulations. If, furthermore, the condition is fulfilled that the ligands R give rise to isotropic resonances under suitable CP MAS conditions (the so-called fast spinning regime), then well-established methods[2,3] to simulate three-site exchange broadened spectra to obtain kinetic data can be absorbed directly from existing procedures[22–24] originally designed for solution state NMR purposes. Of course, lineshape simulation of variable temperature exchange-broadened CP MAS spectra is not a model-free procedure but depends on the components Π_{jk} of the matrix describing the exchange process:[2]

$$\frac{d}{dt}M_j(t) = i\omega_j M_j(t) - \frac{1}{T_{2j}}M_j(t) + \sum_k \Pi_{jk}M_k(t) \quad (2)$$

For solid state CP MAS purposes, lineshape simulations should only be used if sufficient independent evidence exists that no further causes but the R_3M three-site exchange can be responsible for lineshape changes as a function of temperature. For instance, single crystal X-ray crystallography and/or the variable temperature NMR properties of the remainder of the R_3M-containing molecule are helpful sources of information.

One type of reorienting R_3M species which often falls into the appropriate regime of reorientation rates near room temperature, allowing kinetic data to be obtained from variable temperature ^{13}C CP MAS plus lineshape analysis, are Me_3Sn groups in solid trimethyltin compounds.[25–28] Two such examples are illustrated in Figures 3 and 4.

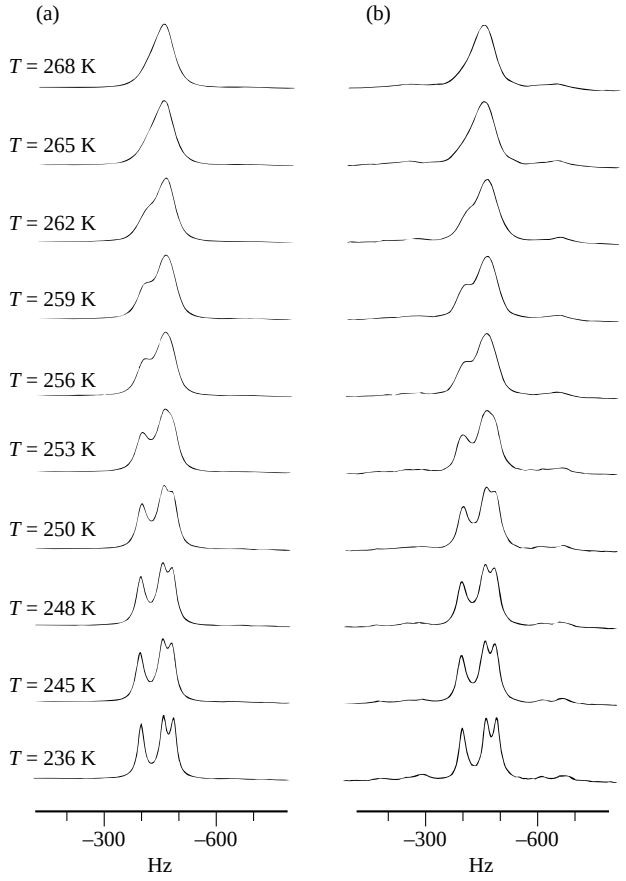

Figure 3 Methyl region of 75.5 MHz ^{13}C CP MAS spectra of $Me_3Sn{-}C{\equiv}C{-}SnMe_3$ in the temperature range T = 236–268 K; (a) simulation assuming three-site exchange due to Me_3Sn reorientation, (b) experimental spectra. (Reproduced with permission from Kümmerlen et al.,[27] copyright 1994 American Chemical Society)

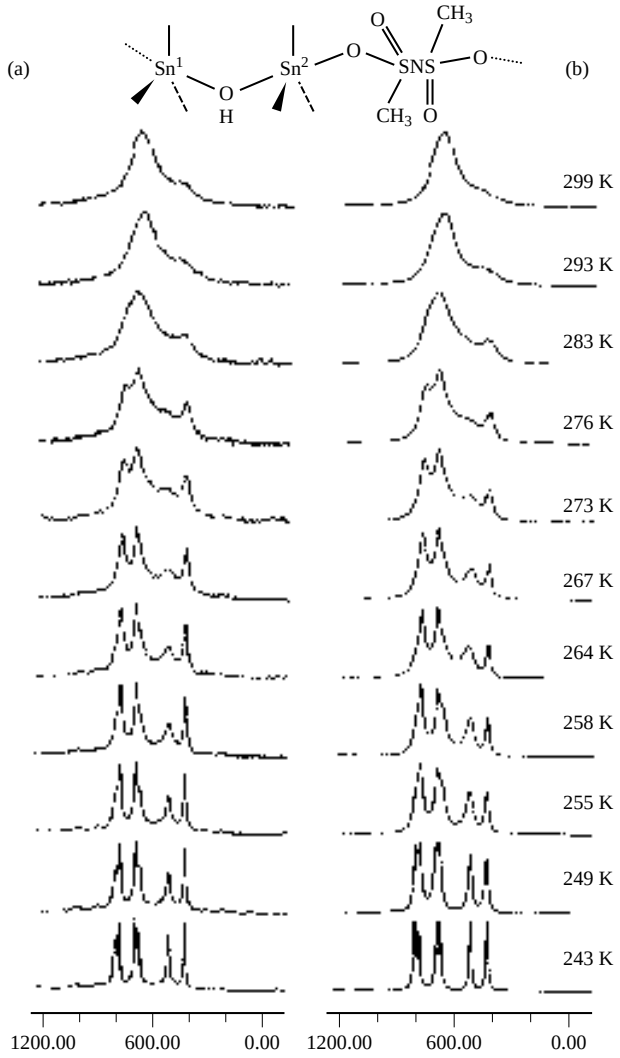

Figure 4 Me_3Sn methyl region of 75.5 MHz ^{13}C CP MAS spectra of polymeric crystalline $[Me_3SnN(SO_2Me)_2{\cdot}Me_3SnOH]$ in the temperature range T = 243–299 K; (a) experimental spectra, (b) simulation; scales for (a) and (b) are in Hz. This compound contains two different Me_3Sn propellers per molecular unit which display different jump rates and activation energies for this process over the entire temperature range investigated (T = 200–299 K). See also Figure 6 for comparison. (Reproduced with permission from Kümmerlen and Sebald,[25] copyright 1993 American Chemical Society)

The methyl region of the ^{13}C CP MAS spectra of $Me_3Sn{-}C{\equiv}C{-}SnMe_3$[27] in the temperature range T = 236–268 K and corresponding simulations are shown in Figure 3. Solid $Me_3Sn{-}C{\equiv}C{-}SnMe_3$ contains two symmetry-equivalent Me_3Sn groups which at room temperature are in their respective fast exchange regime of Me_3Sn reorientation on the 1D ^{13}C CP MAS scale. At T = 236 K and below, three ^{13}C resonances corresponding to three inequivalent methyl groups per Me_3Sn group are clearly resolved (see also Figure 5 on $Me_3Pb{-}C{\equiv}C{-}PbMe_3$ for comparison). An Arrhenius plot of Me_3Sn jump rates as a function of temperature yields an activation energy E_a = 45.8 ± 2.4 kJ mol^{-1} for Me_3Sn reorientation in solid $Me_3Sn{-}C{\equiv}C{-}SnMe_3$.[27]

Figure 4 illustrates a slightly more complicated case, Me_3Sn reorientation in solid $[Me_3SnN(SO_2Me)_2{\cdot}Me_3SnOH]$ as characterized by variable temperature ^{13}C CP MAS.[25,26] This compound is a crystalline polymer, containing two crystallographically inequivalent trigonal-bipyramidal Me_3SnO_2 groups per molecular unit. From inspection of Figure 4 it is clear that over the entire temperature range Me_3Sn^1 and Me_3Sn^2 show different jump rates. Accordingly, different activation energies are obtained as well, E_a = 38.6 and 44.8 kJ mol^{-1}.

The examples shown in Figures 3 and 4 represent R_3M propellers which are truly 'convenient' from an experimental CP MAS point of view: moderate temperatures suffice to obtain all necessary data points. The limits of thermal stability for slower reorienting Me_3M species, or the inaccessibility of sufficiently low temperatures under CP MAS conditions in the case of faster Me_3M reorientation, can severely handicap the practical usefulness of this 1D variable temperature ^{13}C CP MAS plus lineshape analysis approach.

2.3 Slow R_3M Reorientation: 2D Exchange Spectroscopy

Under conditions where the Me_3M rate of reorientation is/becomes significantly smaller than the chemical shift differences between the ^{13}C resonances of the inequivalent methyl groups, the lineshape of these ^{13}C methyl resonances

is unaffected by the reorientational process and kinetic information can no longer be obtained from 1D ^{13}C CP MAS. At this point 2D ^{13}C exchange spectroscopy (2D EXSY) steps in, as (long) mixing times τ_m in the pulse sequence CP-t_1-$\pi/2$-τ_m-$\pi/2$-t_2[22] can accommodate the situation of slow Me_3M reorientation fairly well; in principle, useful possible durations of τ_m are only limited by the eventual onset of T_1 relaxation. This 2D EXSY solid state experiment is analogous to solution state 2D EXSY—only the ^{13}C preparation pulse is replaced by the cross-polarisation sequence for solid state applications. Not only does 2D EXSY extend the range of accessible jump rates towards slow reorientation, but also in those cases where 1D ^{13}C CP MAS *is* informative because the exchange-broadened ^{13}C regime is accessible, additional 2D EXSY experiments usually help to obtain better, more extensive data sets to determine activation energies from jump rates.

In contrast to the analysis of exchange broadened 1D ^{13}C CP MAS spectra, where kinetic information can only be extracted from simulations based on an explicit kinetic model of the dynamic process, 2D EXSY spectra let us directly unravel the kinetic network, model-free, by simple integration of relative off-diagonal intensities as a function of temperature and τ_m. For rather simple systems such as reorienting Me_3M species, where either the number of simultaneously present different jump rates is small or the spread of jump rates is limited, mixing times τ_m can usually be chosen to be short enough so that quantification of the dynamic process can be carried out within the limits of the initial rate approximation.[22] ^{13}C 2D EXSY is particularly convenient for cases such as Me_3M reorientation owing to the fact that methyl ^{13}C resonances will usually be in the fast spinning regime, not giving rise to spinning sidebands even with fairly moderate spinning frequencies ν_{rot}.

Finally, we will consider two examples of Me_3M reorientation as seen by ^{13}C 2D EXSY. Our first example is Me_3Pb reorientation in $Me_3Pb{-}C{\equiv}C{-}PbMe_3$.[27] The room temperature ^{13}C 2D EXSY experiment depicted in Figure 5 shows that

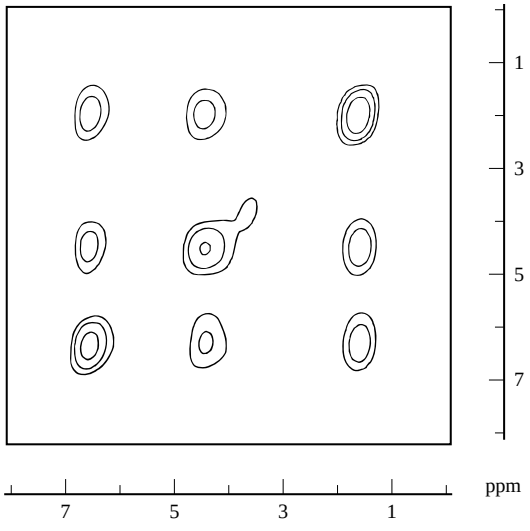

Figure 5 Methyl region of 75.5 MHz ^{13}C CP MAS EXSY of $Me_3Pb{-}C{\equiv}C{-}PbMe_3$ at T = 298 K, mixing time τ_m = 600 ms, ν_{rot} = 3.5 kHz; corresponding to an Me_3Pb reorientation rate κ = 0.3 Hz. (Reproduced with permission from Kümmerlen et al.,[27] copyright 1994 American Chemical Socieity)

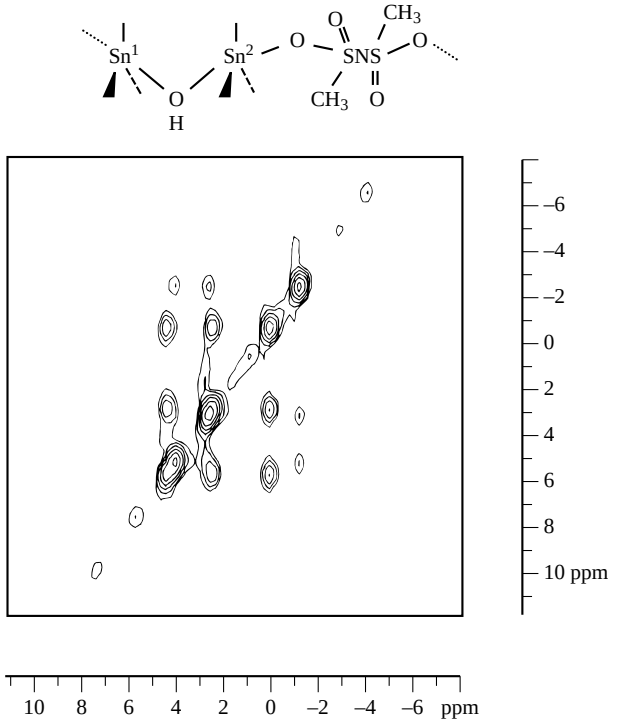

Figure 6 Me_3Sn methyl region of 75.5 MHz ^{13}C CP MAS EXSY of $[Me_3SnN(SO_2Me)_2{\cdot}Me_3SnOH]$ at T = 220 K, mixing time τ_m = 500 ms, ν_{rot} = 2.2 kHz. Note the differing off-diagonal intensities for the two different Me_3Sn propellers in this compound, due to differing rates of reorientation for Me_3Sn^1 and Me_3Sn^2. See also Figure 4 for comparison. (Reproduced with permission from Kümmerlen and Sebald,[25] copyright 1993 American Chemical Socieity)

$Me_3Pb{-}C{\equiv}C{-}PbMe_3$ is in a slow exchange regime on the 1D ^{13}C chemical shift scale at T = 298 K—in contrast to the analogous tin compound, $Me_3Sn{-}C{\equiv}C{-}SnMe_3$ (see Figure 3). In addition, ^{13}C 2D EXSY proves that the three methyl groups in this Me_3Pb unit *are* indeed inequivalent: exchange peaks between all diagonal resonances occur. Also the ^{13}C 2D EXSY experiment on $[Me_3SnN(SO_2Me)_2{\cdot}Me_3SnOH]$[25] in Figure 6 serves for assignment purposes: first of all, it is easily seen from the different off-diagonal intensities that Me_3Sn^1 and Me_3Sn^2 in this compound do show different rates of Me_3Sn reorientation as was also obvious from variable temperature 1D ^{13}C CP MAS (see Figure 4 for comparison). Second, 2D EXSY in this case also proves which methyl ^{13}C resonances belong together in Me_3Sn^1 and Me_3Sn^2, respectively.

3 SOME CONCLUDING REMARKS

We hope to have demonstrated that—beyond the specific dynamic properties of Me_3Sn or Me_3Pb groups in the solid state—high-resolution solid state NMR investigations concerned with the dynamic properties of solid organic and organometallic compounds have an important role to play for a deeper understanding of the principles governing the overall structure of a crystalline solid. The task of bulky reorienting R_3M groups is to act as a sensitive probe of their intra- and intermolecular environment and its influence on the dynamic properties of R_3M. From a practical point of view,

better quantitative knowledge of the solid state dynamics of organic and organometallic compounds should help to prevent frustration with routine ^{13}C CP MAS applications in this field of chemistry.

4 RELATED ARTICLES

Brownian Motion and Correlation Times; Chemical Exchange Effects on Spectra; Cross Polarization in Rotating Solids: Spin-1/2 Nuclei; NOESY; Polymer Dynamics and Order from Multidimensional Solid State NMR; Two-Dimensional Methods of Monitoring Exchange.

5 REFERENCES

1. (a) E. R. Andrew, *J. Chem. Phys.*, 1950, **18**, 607; (b) E. R. Andrew and R. G. Eades, *Proc. R. Soc. London, Ser. A*, 1953, **218**, 517.
2. M. Mehring, *Principles of High Resolution NMR in Solids*, Springer Verlag, Berlin, 1983.
3. H. W. Spiess, in *NMR—Basic Principles and Progress*, eds. P. Diehl, E. Fluck, and R. Kosfeld, Springer Verlag, Berlin, 1978, Vol. 15, p. 59.
4. C. P. Slichter, *Principles of Magnetic Resonance*, Springer Verlag, Berlin/Heidelberg/New York, 1978
5. U. Haeberlen, *Adv. Magn. Reson.*, 1976, Suppl. 1.
6. H. W. Spiess, R. Grosescu, and U. Haeberlen, *Chem. Phys.*, 1974, **6**, 226.
7. A. Pines, M. G. Gibby, and J. S. Waugh, *J. Chem. Phys.*, 1972, **56**, 1776.
8. J. Jeener, B. H. Meier, P. Bachmann, and R. R. Ernst, *J. Chem. Phys.*, 1979, **71**, 4546.
9. B. Blümich and H. W. Spiess, *Angew. Chem.*, 1988, **100**, 1716; *Angew. Chem., Int. Ed. Engl.*, 1988, **27**, 1655.
10. H. W. Spiess, *Chem. Rev.*, 1991, **91**, 1321.
11. A. Hagemeyer, K. Schmidt-Rohr, and H. W. Spiess, *Adv. Magn. Reson.*, 1989, **13**, 85.
12. C. Schmidt, B. Blümich, and H. W. Spiess, *J. Magn. Reson.*, 1988, **79**, 269.
13. D. Braga, *Chem. Rev.*, 1992, **92**, 633.
14. (a) R. Benn, H. Grondey, R. Nolte, and G. Erker, *Organometallics*, 1988, **7**, 777; (b) R. Benn, H. Grondey, G. Erker, R. Aul, and N. Reiner, *Organometallics*, 1990, **9**, 2493.
15. B. Black, G. Majer, and A. Pines, *Chem. Phys. Lett.*, 1993, **201**, 550 and references therein.
16. W. P. Rothwell and J. S. Waugh, *J. Chem. Phys.*, 1981, **74**, 2721.
17. F. G. Riddell, S. Arumugam, K. D. M. Harris, M. Rogerson, and J. H. Strange, *J. Am. Chem. Soc.*, 1993, **115**, 1881.
18. (a) A. E. Aliev, K. D. M. Harris, and D. C. Apperley, *J. Chem. Soc., Chem. Commun.*, 1993, 251; (b) G. H. Penner and J. M. Polson, *J. Chem. Soc., Dalton Trans.*, 1993, 803.
19. Y. N. Chihara, N. Nakamura, and H. Chihara, *Can. J. Chem.*, 1988, **66**, 1848.
20. S. J. Heyes, M. L. H. Green, and C. D. Dobson, *Inorg. Chem.*, 1991, **30**, 1930.
21. J. Kümmerlen and A. Sebald, *Magn. Reson. Chem.*, 1994, **32**, 173.
22. R. R. Ernst, G. Bodenhausen, and A. Wokaun, *Principles of Nuclear Magnetic Resonance in One and Two Dimensions*, Oxford Science Publishers, Oxford, UK, 1991.
23. J. Sandström, *Dynamic NMR Spectroscopy*, Academic Press, London/New York, 1982.
24. G. Binsch and H. Kessler, *Angew. Chem.*, 1980, **92**, 445.
25. J. Kümmerlen and A. Sebald, *J. Am. Chem. Soc.*, 1993, **115**, 1134.
26. J. Kümmerlen, I. Lange, W. Milius, A. Sebald, and A. Blaschette, *Organometallics*, 1993, **12**, 3541.
27. J. Kümmerlen, A. Sebald, and E. Sendermann, *Organometallics*, 1994, **13**, 802.
28. R. K. Harris, M. M. Sünnetcioglu, and R. D. Fischer, *Spectrochim. Acta*, 1994, **50A**, 2069.

Acknowledgments

Generous support of our work by the Deutsche Forschungsgemeinschaft and the Fonds der Chemischen Industrie is gratefully acknowledged.

Biographical Sketch

Angelika Sebald. *b* 1955. Dipl. Chem., 1979, Ph.D., 1983, Universität München. University of Durham, UK, 1985–87; Universität Bayreuth, 1987–present; Habilitation, 1990; since 1991 Heisenberg fellowship (DFG). Approx. 90 publications. Research interests: applications of solid state NMR techniques to problems in inorganic and organometallic chemistry.

Jörg Kümmerlen. *b* 1962. Dipl. Chem., 1990, Ph.D. 1993, Universität Bayreuth. ETH Zürich, 1993–94; University of Nijmegen, 1994–95; Universität Bayreuth, 1995–present. Approx. 20 publications. Research interests include: applications of solid state NMR techniques to dynamic processes in solids and biopolymers.

Structural and Dynamic Characterization of Soft Polymers by Solid State NMR and Field Gradient NMR

Isao Ando, Masatoshi Kobayashi, Chenhua Zhao, Yige Yin, and Shigeki Kuroki

International Research Center of Macromolecular Science, Tokyo Institute of Technology, Tokyo, Japan

1 Introduction 1
2 Microscopic Structure and Dynamics of Polymer Gels 1
3 References 18

1 INTRODUCTION

Most recently, the term '*soft* materials' is frequently used in the field of materials science. *Soft* polymers considered here are classified into soft materials, and contain polymer gels, polymer liquid crystals, vulcanized elastomers, etc., in which molecular motion is much higher compared with solid polymers. Most recently *soft* polymers have attracted attention as useful materials as detailed below.

Polymer gels consist of two components of network polymer chains and solvent. Further, a third component such as a low molecular-weight compound or polymer is often contained in the gels. Polymer gels have attracted considerable attention from the point-of-view of various physical and chemical properties.[1] For example, hydroelectrolyte gels show a dramatic change in volume in response to change in solvent composition, pH, ionic strength and temperature. They contract upon application of an electric field. Further, water-swollen polymer gels can convert chemical energy into mechanical energy. These properties lead to the vitality of polymer research and development of a diversity of interests in polymer gel systems. In order to develop new polymer materials, polymer gel design has been performed on the basis of advanced polymer science and technology. The properties of polymer gels are closely related to their structures and dynamics. From such situations, the establishment of methods for elucidating the structures and dynamics is important for making reliable polymer gel design and developing new advanced polymer gels. In polymer gels, although the mobility of network polymer chains is much higher than solids, it is much lower than solvent and the low-molecular weight molecules. Thus, by taking into account such a difference in molecular motion between the mobile and immobile regions, solid-state high-resolution NMR proves to be a useful tool to characterize such systems.

On the other hand, liquid crystalline polymers have both positional and orientational orders in the liquid crystalline phase.[2] The amount of order in a liquid crystal is quite small compared with a crystal. The polymer chain is rapidly rotating around the long axis and diffusing along and perpendicular to the long axis. Such anisotropic structures induce various characteristic properties to be used as materials.

From such a background, the structure and dynamics of polymer gels, liquid crystalline polymers and vulcanized elastomers by solid-state NMR, and the diffusion process of polymer gels by pulse-field-gradient spin-echo (PFGSE) NMR have been widely used in order to make reliable polymer gel and liquid crystalline polymer designs and to develop new advanced polymer gels and liquid crystalline polymers.[3–5] Details of this work will be described.

2 MICROSCOPIC STRUCTURE AND DYNAMICS OF POLYMER GELS

Polymer gels consist of mobile and immobile regions. For this, conventional solution NMR gives useful information about mobile regions, but sometimes not on the more rigid regions. To obtain structural information on relatively rigid regions, solid-state NMR is required. Then, in order to elucidate structure and dynamics of the immobile and mobile regions in polymer gels, we must use some appropriate NMR methods or must design special methods. In this section, some studies of microscopic structure of polymer gels by ^{1}H pulse NMR (including use of gradient-field) and high-resolution solid-state ^{13}C NMR will be introduced.

2.1 Approach by ^{1}H Pulse NMR Method

In the pulse NMR experiment, high power radio-frequency (rf) pulses are applied and the free induction decay (FID) of the T_2 component is detected as a time-dependent function that becomes a measure of the mobility.[53] The Fourier transform converts the FID into the corresponding frequency spectrum, in which the chemical shift gives information about chemical structures. On the other hand, the FID contains information about molecular dynamics, and so the experiment with some rf pulses gives T_1, T_2 and the diffusion coefficient (D).[6] T_1 and T_2 are closely related with the correlation-time for molecular motion by BPP (Bloembergen–Purcell–Pound) theory when they are governed by dipolar interactions, and D as obtained by pulse NMR under a field gradient provides information about the translational motion.[7] Therefore, pulse NMR is useful method for the elucidation of molecular dynamics in polymer systems.

2.1.1 Volume Transition of a Poly(N-Isopropylacrylamide) Gel

It is known that the volume of a poly(*N*-isopropylacrylamide) (PNIPAM) gel with water as solvent experiences a transition with temperature at about 33 °.[8] In order to elucidate molecular motion of water in the gel through the transition temperature (T_{vt}) by temperature variation, the ^{1}H T_2 has been measured as a function of temperature.[9]

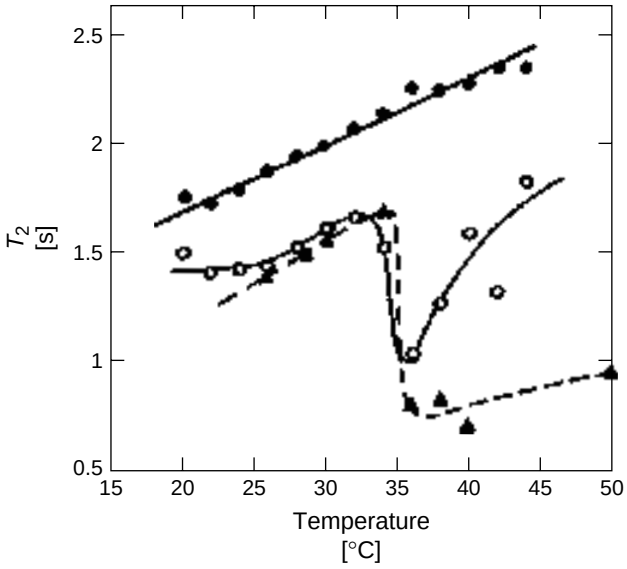

Figure 1 Plots of the ^{1}H T_2 values of H_2O in neat water (●) and in the PNIPAM gel (○) against temperature at atmospheric pressure

Figure 1 shows plots of the ^{1}H T_2 values of H_2O in neat water (●) and water in the PNIPAM gel (○), as a function of temperature at atmospheric pressure. The T_2 value of neat water increases as the temperature is linearly increased. This shows that the mobility of water is monotonically increased with increase in temperature in the measurement temperature range. The T_2 of HDO in the PNIPAM gel increases as the temperature increases up to 33 °C. At T_{vt} (33 °C), the T_2 value is transitionally decreased. As the temperature is further increased, the T_2 value is transitionally decreased. Such behavior is similar to that of water in aqueous PNIPAM solution as reported previously.[10] During the NMR measurements, the gel shrinks with an increase in temperature and exuded water is physically removed. The degree of swelling Q, which is defined by the ratio of the mass of swollen gel to the mass of dried gel and shows a measure of the size of the network. This implies that the mobility of water in the gel increases with an increase in temperature up to 33 °C in spite of much smaller change of the Q value, but decreases transitionally at 33 °C due to a large decrease in the Q value and increases again with a further increase in temperature during which the Q value does not change. Such a behavior can be understood by assuming that intermolecular interaction between the network polymer chains above the transition temperature occurs and so the mobility of water molecules is more restricted by the polymer networks than that below the transition temperature.

2.1.2 Gelation of Poly(N-isopropylacrylamide) Aqueous Solution

PNIPAM in water undergoes a phase transition from sol to gel at around 32 °C[11] ^{1}H pulse NMR experiments provide useful information about molecular motion of the polymer and solvent in the solution and gel state. The abrupt change in molecular motion for solvent in the gel is caused by the formation of the gel structure at the phase transition temperature and therefore, the change of relaxation times sensitively reflects the change of states.

The ^{1}H T_2 values for water in 1, 2.5, 5 and 10% w/v PNIPAM/water solutions and for neat water against temperature were measured as a function of temperature.[10] The ^{1}H T_2 value increases as the temperature is increased up to 30 °C, where an increase in T_2 means an increase in molecular motion according to BPP theory.[7] The ^{1}H T_2 value of neat water increases linearly with temperature up to 50 °C. At the gelation temperature (about 32 °C), the ^{1}H T_2 value in all of the polymer solutions transitionally decreases. As temperature is further increased, the T_2 value increases again. The mobility of water increases with increasing temperature up to 30 °C, then decreases transitionally at about 32 °C due to the gelation of the system and increases again with a further increase of temperature. This trend is very different from that of neat water. Furthermore, it is seen that the increase in the polymer concentration leads to a decrease in ^{1}H T_2 for water. The molecular motion of water is restricted by an increase in intermolecular interactions between the polymer chains and water. As the polymer concentration increases up to 5% at the gelation temperature, the magnitude of the decrease for ^{1}H T_2 value is larger. As the concentration increases further up to 10% w/v, the magnitude of the change in T_2 value for the transition becomes smaller.

The ^{1}H T_1 value of water molecules in 5% w/v PNIPAM/water solution was measured as a function of temperature. The ^{1}H T_1 value slowly increases as does the ^{1}H T_2 mentioned above as the temperature is increased. At the gelation temperature, the T_1 value transitionally decreases. As the temperature is further increased, the ^{1}H T_1 value slowly increases. This behavior is very similar to that for T_2. As seen from the observed ^{1}H T_1 and T_2 behaviors, the water molecules are in the fast motion region ($\omega\tau_c \ll 1$, where ω is the resonance frequency). At 1, 2.5 and 10% w/v solutions, similar results were obtained. Therefore, the ^{1}H T_1 and T_2 values for water in the PNIPAM/water system are very sensitive to the phase transition and provide dynamic information.

In PNIPAM/deuterated water solution, the ^{1}H T_2 signal is composed mainly of two components, a long T_2 component corresponding to the side chains and extremely short T_2 component corresponding to the main chain. The T_2 value for the main chain and side chains of PNIPAM in 10% w/v PNIPAM/deuterated water solution were determined as a function of temperature. For the main chain, at temperatures from 10 to 30 °C, the T_2 value is almost constant, but at the gelation temperature (32 °C) it decreases transitionally, and at temperatures of 40–50 °C it returns to being constant. This indicates that at the gelation temperature, the molecular motion of the main chain is greatly restricted. On the other hand, for the side chains, at temperatures from 10 to 30 °C the T_2 value remains almost constant, increases transitionally at the gelation temperature, and at temperatures from 40 to 50 °C it becomes a constant again. This is evidence that the molecular motion of the side chains increases transitionally at the gelation temperature.

By evaporating water slowly from PNIPAM aqueous solution, a PNIPAM gel is obtained. The ^{1}H T_2 behavior of water for this gel is very similar to that for PNIPAM aqueous solution. This shows that temperature changes of structure and dynamics for both of these systems up to 32 °C are very similar to each other.[10] Further insight into structural and dynamic changes by changing temperature has been studied by high-resolution solid-state ^{13}C NMR technique.

2.1.3 *Structure and Dynamics of Poly(vinyl alcohol) Gel*

Amorphous-poly(vinyl alcohol) (PVA) gel prepared by repeating freeze-thaw cycles from its aqueous solution is one of the physical gels.[12] A ^{1}H spin echo signal of PVA gel measured is composed of three components such as a long T_2 component corresponding to the mobile region (C), a short T_2 component corresponding to the immobile region (A) and an intermediate T_2 component corresponding to the interfacial region (B), which exists between the mobile and immobile regions.[13] It can be said that the mobile region (C) comes from the non-crosslinked region, the immobile region (A) comes from the crosslinked region and the interfacial region (B) comes from the vicinity of the crosslinked region in the gel. With an increase in the polymer concentration, ^{1}H T_2 of three regions are slowly decreased. This means that the molecular motion is restrained, as the polymer concentration is increased. The fractions of the corresponding three regions were determined as a function of polymer concentration. The fractions of the mobile and immobile regions are largely decreased and increased with an increase in the polymer concentration, respectively. The fraction of the intermediate region over a wide range of polymer concentrations is very small.

2.1.4 *Gelation of Poly(vinyl alcohol)/Water System Under High Pressure*

As mentioned above, PVA aqueous solution forms a gel by undergoing freeze-thaw cycles. The gelation is induced by network formation, and at the initial step of the gelation phase separation occurs by forming polymer-aggregation region and polymer-unaggregation regions. It has been suggested that the cause of the gel formation in PVA aqueous solution is due to the formation of intermolecular hydrogen bonds.[14,15]

The use of variable pressure is very effective in overcoming the limited interpretability of the results obtained at atmospheric pressure. Additionally, a change in pressure is expected to provide another dimension in the investigation of aqueous PVA solution and gel because volume changes by the application of pressure lead to reduction of intermolecular distance and to a major effect on molecular motion in the system compared with experiments conducted at atmospheric pressure. As viewed from high pressure NMR experiments, it can provide more useful information about intramolecular dynamics, structures of liquids, molecular conformations and intermolecular interactions through the observation of some NMR parameters such as chemical shift, T_1, T_2 and dipolar splitting.[13,16] From such a situation, it can be expected that more detailed information about the dynamical behavior of PVA/water system is obtained by the application of pressure. Therefore, the dynamical behavior of PVA aqueous solution and gel through the observation of ^{1}H T_2 values is elucidated as a function of pressure from 1 to 500 kg cm^{-2} by using high pressure ^{1}H pulse NMR.[17]

The degree of polymerization of amorphous PVA used in this experiment was 300. PVA was dissolved in D_2O at 90 °C to observe the ^{1}H signal from the polymer. To remove the ^{1}H signal from HDO, which came from chemical exchange between hydroxyl proton and deuteron in PVA and D_2O, the following procedure was performed. By adding PVA/D_2O solution into excess acetonitrile, PVA substituted hydroxyl proton by deuterium (*d*-PVA) was precipitated. The precipitated *d*-PVA was dried by a vacuum pump. The obtained *d*-PVA was dissolved in D_2O again. This procedure was repeated three times. Deuterated PVA samples were dissolved in D_2O at 90 °C. The concentration was 10% (w/w). The solution was cooled to 25 °C and kept for 10 days (sample I). PVA chains in aqueous solution aggregate slightly by such a cooling process. For this, the ^{1}H T_2 value for the PVA solution was measured as a function of the elapsed time during the cooling process. It is obvious that the change of the ^{1}H T_2 with the elapsed time is much smaller compared with that under pressure. PVA gel was prepared from PVA/D_2O solution by repeating freeze-thaw cycles 3 times (frozen and kept at −15 °C for 3 hours, and melted and kept at 25 °C for 2 hours) (sample II).

Pulse ^{1}H NMR measurements were carried out at 20 MHz. ^{1}H T_2 was determined by the CPMG (Carr–Purcell–Meiboom–Gill) method to obtain information about the molecular motion of PVA chain in the solution state, and was determined by the solid echo pulse sequence to obtain information about the molecular motion of the immobile component in the gel state. The T_2 decay for the PVA solution was analyzed as a sum of Lorentzian-type decays and for the PVA gel was analyzed as sum of Gaussian-type decays using the nonlinear least-squares method.

In high pressure experiments, the sample cell was made from a Pyrex glass capillary tube with an outside diameter of 5.0 mm and an inside diameter of 2.6 mm. The cracks on the surface of the outside and inside of the capillary tube were etched by aqueous HF solution. The capillary was glued to a nonmagnetic stainless steel tube using epoxy resin. The pressure can be changed from 1 to 500 kg cm^{-2} with no failure of the system.

From the ^{1}H CPMG experiments on PVA aqueous solution at room temperature, the T_2 signal is mainly composed of two components. The PVA chains in aqueous solution aggregate partly by the cooling process when the solution is prepared. From such a situation, the long T_2 component comes from the mobile region, which is assigned to non-aggregated PVA chains. The short T_2 component comes from the immobile region, which is assigned to aggregated PVA chains in the solution state. The ^{1}H FID signals of PVA/D_2O solution are shown as a function of pressure in Figure 2. The ^{1}H FID signals of PVA chains at pressures from 1 to 100 kg cm^{-2} slowly decay, and at pressures over 200 kg cm^{-2} the variation of decay increases. The ^{1}H T_2 values for PVA/D_2O solution were determined as a function of temperature. The ^{1}H T_2 value for the immobile region is almost a constant to be about 25 ms at pressures from 1 to 500 kg cm^{-2}. On the other hand, the ^{1}H T_2 value for the mobile region is changed by pressure. The ^{1}H T_2 value is lowered from ca. 650 to 600 ms in the pressure range from 1 to 100 kg cm^{-2}, and again decreases from ca. 600 to ca. 100 ms in the pressure range from 100 to 200 kg cm^{-2}. At pressures over 200 kg cm^{-2}, the ^{1}H T_2 values for the long T_2 component are constant at about 100 ms. These experimental results indicate that the molecular motion of PVA chains in the aggregated region is not changed by varying pressure up to 500 kg cm^{-2}, but the molecular motion in the non-aggregated region is affected by pressure in the pressure range over 200 kg cm^{-2}. The ^{1}H T_2 value for mobile component is about 320 ms and the ^{1}H T_2 value for mobile component at 1 kg cm^{-2} decreases by applying pressure. The long T_2 component disappears in the pressure range over 200 kg cm^{-2}

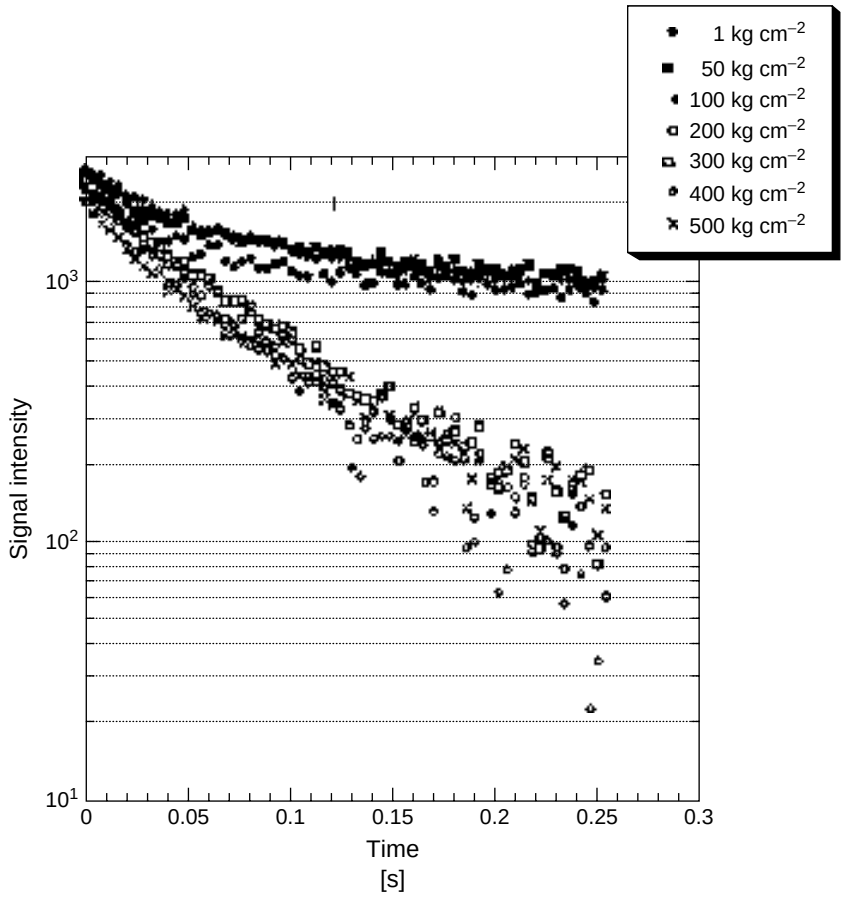

Figure 2 Pressure dependence of ^{1}H T_2 signal of PVA/D_2O solution obtained by the CPMG method

and the fraction of the short T_2 component increases up to 200 kg cm^{-2}. In the pressure range over 200 kg cm^{-2}, the short T_2 component occupies the whole fraction. From these results, it can be said that the molecular motion of PVA chains in non-aggregated region is restricted by applying pressure up to 500 kg cm^{-2}, and the process of gelation is induced. Finally, it can be said that high-pressure ^{1}H pulse NMR gives useful information about the dynamics of PVA chains in aqueous solution state and in gel state.

2.1.5 Structure and Dynamics of (Ethylene-Vinyl Alcohol) Copolymer Gels

Ethylene-vinyl alcohol (EVOH) copolymer gel can be prepared by repeating freeze-thaw cycles from its aqueous solution similarly to the preparation of the PVA gel. The ^{1}H T_2 signal of EVOH gel with a relatively high ethylene content of 32% as obtained by ^{1}H solid echo method was observed.[18] The ^{1}H T_2 value is determined from the slope of the plot of ln M against t^2, where M is the amplitude of the spin echo signal and the T_2 signal is assumed to be a Gaussian decay in the spectral analysis. According to the BPP theory for NMR relaxation, T_2 decreases continuously as the correlation time τ_c in molecular motion is increased.[7] This means that shorter T_2 corresponds to slower molecular motion. Thus, T_2 can give dynamic information about the gels through the BPP theory. The ^{1}H T_2 curve is composed of three kinds of the components; the short T_2 component corresponding to the immobile region (A), the intermediate T_2 component corresponding to the interfacial region (B), which exists between the mobile and immobile regions, and the long T_2 component corresponding to the mobile region (C). By aid of the computer-fitting, the ^{1}H T_2 value was obtained from the T_2 signal with experimental error of $\pm$5%. The result is the same as that of PVA gel.[13] It can be said that the short T_2 component corresponding to the immobile region comes from the crosslinked region in the EVOH gels, the long T_2 component corresponding to the mobile region comes from the non-crosslinked region, the intermediate T_2 component with the intermediate mobility comes from the vicinity of the crosslinked region.

The ^{1}H T_2 values determined for the individual regions were plotted against the ethylene content. It is found that the ^{1}H T_2 values for the immobile, mobile and intermediate regions are gradually decreased with an increase in ethylene content. The increase of the ethylene content in EVOH samples in the gel state leads to reduction in molecular motion for the individual regions.

The fraction of each of the immobile, mobile and intermediate regions with different molecular motion were determined as a function of ethylene content. In the range of ethylene content less than 55%, the fractions of three kinds of regions with different mobilities are almost independent of ethylene content. In the ethylene content range greater than 55%, the fractions of the mobile region are rapidly decreased with an increase in ethylene content. On the other hand, the fractions

of the intermediate and immobile regions are largely increased with an increase in ethylene content. Their fractions are similar in value. This means that the fraction of the crosslinked region as formed by an addition of hydrophobic interaction between the ethylene parts to hydrogen bonds between the vinyl alcohol units is increased with an increase in ethylene content. From such a situation, the molecular motion for all of the three regions are more restrained with an increase in ethylene content.

2.1.6 Structure and Dynamics of Swollen Polymer Networks

The structural and dynamic characterization of swollen polymer networks has been one of the important research programs in polymer science. Samulski, et al. have elucidated the effect of orientation on residual quadrupolar splitting of deuterated solvents in swollen strained polyisoprene by ^{2}H NMR.[57] The quadrupolar splitting depends linearly on $\lambda^2-\lambda^{-1}$ over a large range of the extension ratios (λ) and the degree of swellings. A phenomenological description based on a lattice model of the deformed, swollen network, which induces short-range nematic-like interactions successfully accounts for the observations. Also, the structural characterization of the other swollen networked polymers have been studied by ^{2}H NMR.[58–60]

2.2 Approach by High-Resolution Solid-State ^{13}C NMR

It is well known that ^{13}C CP/MAS (cross polarization/magic angle spinning) NMR method obtains high-resolution solid-state NMR spectra of solid polymers and enhances the peak intensity of carbons in the immobile region.[3,19–21] The CP efficiency is relatively high for carbons in rigid solid polymers. Polymer gels and polymers in the liquid crystalline state are relatively mobile. For this reason, care must be exercised to obtain ^{13}C CP/MAS NMR spectra because the ^{13}C signals of carbons in the mobile region may not appear due to the large reduction of the CP efficiency. It is often convenient to use MAS with strong ^{1}H decoupling, which leads to NOE (Nuclear Overhauser Effect), and without CP for obtaining the ^{13}C signals of carbons in the mobile state, for example, the PST (pulse saturation transfer)/MAS is often used, in which ^{1}H decoupling is carried out by using a number of pulses.[22] MAS removes effectively weak dipolar coupling of carbons in the mobile state. In the case of polymer gels there exist mobile and immobile regions. For this, ^{13}C CP/MAS and PST/MAS methods are often used to get useful information about both regions. This leads to reasonable structural characterization of polymer gels.

If a conventional NMR rotor is used under high speed rotation (about 4 kHz), polymer gels and polymer liquid crystals come out of a conventionally sealed NMR rotor due to high speed rotation. From such a situation, it is convenient to use an NMR rotor sealed with an O-ring rubber, the use of which prevents loss of samples.[14]

2.2.1 Structural Characterization of Poly(Vinyl Alcohol) Gel

As mentioned above, amorphous-PVA gel is prepared by repeating freeze-thaw cycles from its aqueous solution. At the beginning of the gelation of the PVA aqueous solution, phase separation into polymer-rich and polymer-poor regions occurs with a decrease in temperature. It is suggested that the gel formation is due to the formation of intermolecular hydrogen bonds.[14] The structure and the amount of hydrogen bonds may play an important role for properties of PVA gel, and high-resolution solid-state ^{13}C NMR gives useful information about them.[14,15] Figure 3 shows ^{13}C NMR spectra for PVA in the solution (a), gel (b–d) and solid (e) states as measured by solution and solid-state NMR. In conventional solution ^{13}C NMR spectrum for PVA gel shown in Figure 3(b), the ^{13}C signal for the CH carbon splits into three peaks assigned to mm, mr and rr triads. The signals for the CH and CH_2 carbons become broader as compared with those for PVA solution (Figure 3(a)). This is caused by the increase in dipole–dipole interactions due to a decrease in molecular motion. The ^{13}C PST/MAS NMR spectrum of the PVA gel shown in Figure 3(c) is similar to the solution NMR spectrum of Figure 3(b). However, the resolution of spectrum (c) is better than that of spectrum (b), because of a MAS and a high-power proton decoupling. NOE enhancement is used to obtain more intense ^{13}C signal using PST method.[22] The PST method effectively enhances peak intensity for the mobile regions in samples as compared with CP and vice versa. This means that the mobile region in the PVA gel is observed in both spectra (b) and (c). The ^{13}C signal for the CH carbon of the solid PVA has three-split broad peaks in the ^{13}C CP/MAS NMR spectrum

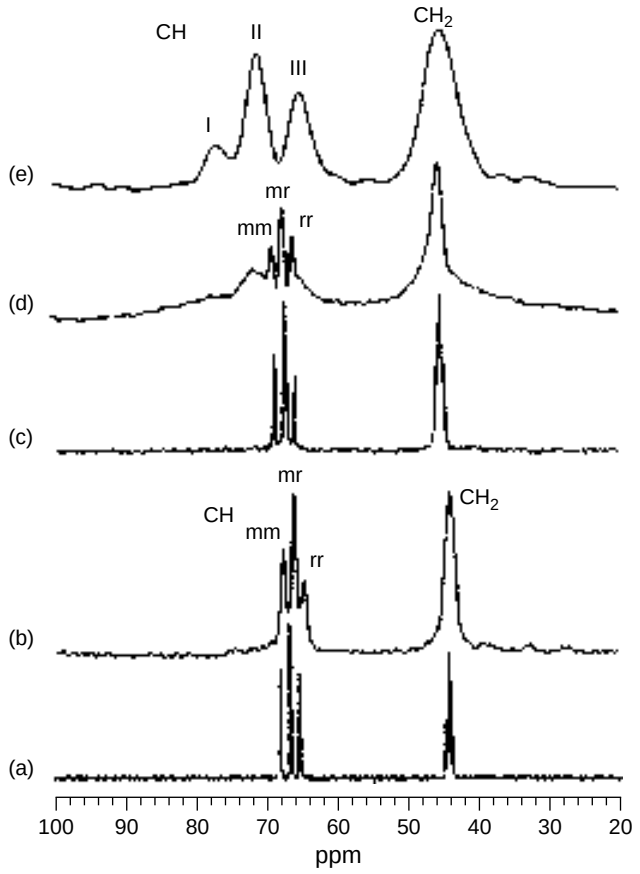

Figure 3 ^{13}C NMR spectra for the PVA in the solution, gel and solid states as measured by solution and solid-state NMR methods. For solution NMR method: PVA/D_2O solution (a) and PVA gel (b); for solid-state NMR method: PVA gel by PST/MAS (c) and CP/MAS (d), and solid PVA by CP/MAS (e)

as shown in Figure 3(e). Such a splitting is explained by the number of intramolecular hydrogen bonds formed among neighboring hydroxyl groups. Assuming that the ^{13}C chemical shift value for the CH carbon shifts to downfield by 6 ppm per one intermolecular or intramolecular hydrogen bond, the most deshielded peak (peak I) can be assigned to the CH carbon with two hydrogen bonds, the central peak (peak II) to the CH carbon with one hydrogen bond and the most shielded peak (peak III) to the CH carbon with no hydrogen bonds, respectively.[23] In the ^{13}C CP/MAS spectrum for the PVA gel as shown in Figure 3(d), the CH signal is composed of the three splitting peaks corresponding to the triad tacticity and the broad peaks as found in the solid PVA. This means that in this case both of the immobile and mobile regions of the PVA gel are observed by CP/MAS.

Figure 4 shows ^{13}C CP/MAS NMR spectra of the PVA gels with different polymer concentrations.[14] The polymer concentrations of samples (a), (b), (c) and (d) are 9.1, 11.8, 13.8 and 35.0% (w/w), respectively. The intensities of the three-split peaks due to stereochemical configurations decrease and those of peaks I, II and III increase with a decrease in water fraction in the gel. The three peaks due to stereochemical configurations completely disappear in sample (d). The schematic crosslinked structure of PVA gel formed by intermolecular and intramolecular hydrogen bonds can be inferred from these spectra. The increase in the fraction of the immobile region and the formation of hydrogen bonds are promoted by the increase in the polymer concentration of the gel.

In order to clarify the dynamics of PVA gel, ^{13}C T_1 measurements were carried out.[12] The ^{13}C T_1 values for the mobile region in a PVA gel were determined by the inversion-recovery method combined with the PST/MAS technique and the immobile region was also determined using CP/MAS combined with Torchia's pulse sequence.[54] The T_1 values for the triads are

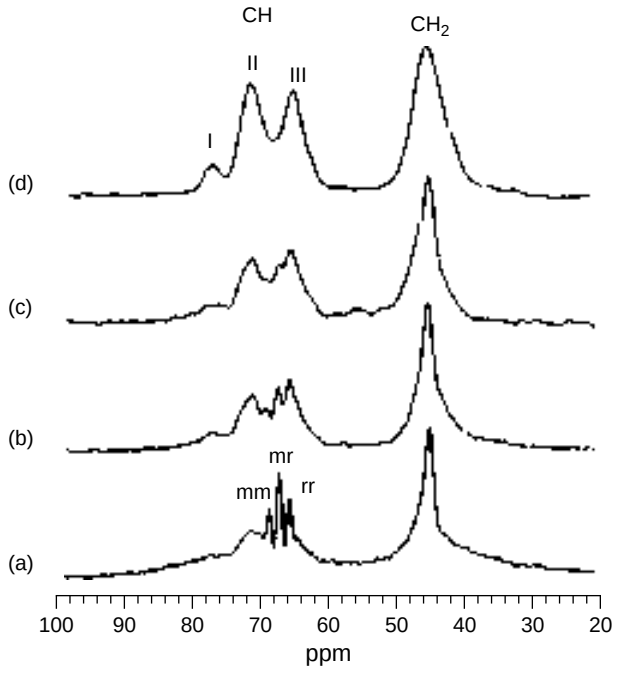

Figure 4 ^{13}C CP/MAS NMR spectra for PVA gels with different polymer concentrations. The polymer concentrations are (a) 9.1, (b) 11.8, (c) 13.8 and (d) 35.0% (w/w), respectively

smaller than those for peaks II and III. The immobile region corresponds to the CH carbons in the crosslinked regions formed by intermolecular and intramolecular hydrogen bonds in the gel, and the mobile ones to the regions away from the crosslinked regions that undergo fast molecular motion in the gel. The mobility of the network polymer in the PVA gel is restrained by hydrogen bonds and especially that of the crosslinked region is very low.

2.2.2 *Gelation Mechanism of Poly(Vinyl Alcohol) in Aqueous Solution*

PVA in aqueous solution forms a gel by undergoing freeze-thaw cycles. We have studied the structure and dynamics of PVA gels that were prepared using PVA samples with different microtacticity at some polymer concentrations under atmospheric pressure and high pressure by high-resolution solid-state ^{13}C NMR and ^{1}H pulse NMR.[14,15,17] From these studies, we have demonstrated that the crosslinked region is formed by the formation of intermolecular hydrogen bonds. From such a situation, in this work we aim to measure high-resolution solid-state ^{13}C NMR spectra during the freeze-thaw cycles, and to elucidate the mechanism of gelation process for PVA in aqueous solution.

The degree of polymerization and the degree of saponification of amorphous PVA were 1700 and 99.9%, respectively. The PVA sample was dissolved into water at 120 °C using an autoclave. The polymer concentration was 10% (g dl^{-1}). The obtained PVA aqueous solution was cooled to room temperature and was contained in a cylindrical rotor with a rubber O-ring to prevent loss of water during the NMR measurements. Prior to NMR measurement, it was kept at room temperature for one month to reach a stable state.

^{13}C CP/MAS NMR spectra of PVA/water system during the freeze-thaw cycles are shown in Figure 5.[24] There are no signals in the ^{13}C CP/MAS NMR spectrum of aqueous PVA solution at 40 °C, because in the solution state the PVA chains are undergoing much faster molecular motion compared with a frequency of ^{1}H decoupling to be ca. 60 kHz used in this experiment, and so the CP efficiency is quite reduced. In the ^{13}C CP/MAS NMR spectrum of the PVA/water system in the freezing state at −30 °C, three peaks I, II and III for the CH signal, which come from the formation of hydrogen bonds as reported previously appear clearly.[14] Peak I was assigned to carbons with two intermolecular or intramolecular hydrogen bonds, peak II to those with one intermolecular or intramolecular hydrogen bond, and peak III with no hydrogen bond. From this spectrum, it can be seen that some hydroxyl groups form hydrogen bonds at −30 °C as in the PVA gel. If the temperature is increased from −30 to 40 °C again, peak II at 71 ppm becomes broad and the three splitting peaks due to the triad configurations (mm, mr and rr) appear. This result shows that the molecular motion of PVA chains is decreased compared with that in the original solution state due to the formation of hydrogen bonds, and so the CP efficiency was enhanced. This means that the freeze-thaw process induces gel formation. In ^{13}C CP/MAS NMR spectrum of the PVA/water system in the 2nd frozen state, the three CH peaks are observed as clearly as the case in the 1st frozen state. The ^{13}C CP/MAS NMR spectra in the 3rd and 4th frozen states are almost identical. On the other hand, in the ^{13}C CP/MAS NMR spectrum of the PVA/water system in the thawing state

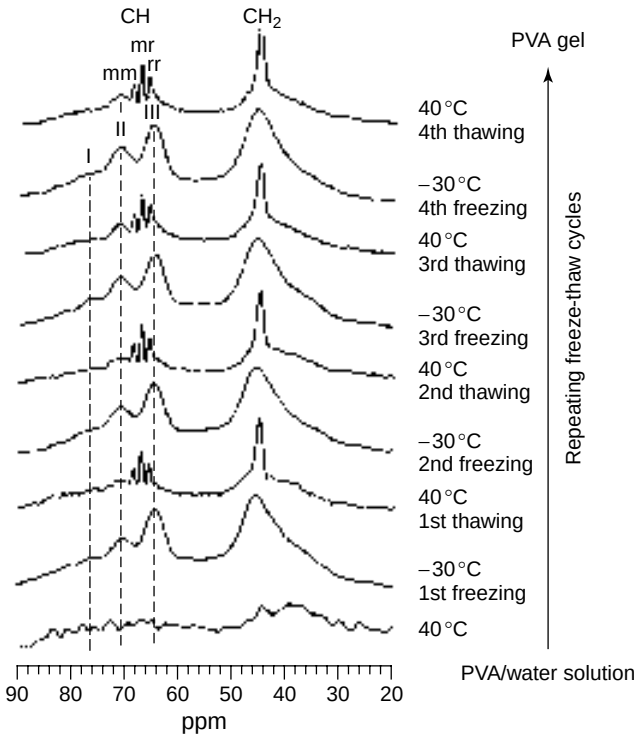

Figure 5 ^{13}C CP/MAS NMR spectra for PVA/water system under the freeze-thaw cycles

at 40 °C, the intensity of peak II is gradually increased with an increase in the number of freeze-thaw cycles. In the 4th thawing state, peak II clearly appeared. This shows that the amount of hydrogen bonds in the course of the formation of the PVA gel is increased by repeating the freeze-thaw cycles. These experimental results mean that the repeating of freeze-thaw cycles induces the gelation of the PVA/water system.

From these experiments, the mechanism of gelation for the PVA/water system was proposed as follows: in the solution state, there are no strong intermolecular hydrogen bonds and so the corresponding CH peak cannot be obtained using ^{13}C CP/MAS NMR method. In the frozen state, water is frozen and the PVA chains aggregate to form the polymer-rich domain. In the polymer-rich region, strong intermolecular hydrogen bonds may be formed and the corresponding CH peaks are clearly observed by ^{13}C CP/MAS NMR. By repeating the freeze-thaw cycles, the fraction of the polymer-rich regions is increased, and then the crosslinked region is formed, which consists of strong hydrogen bonds. Therefore, it can be said that the process of repeating the freeze-thaw cycles induce intermolecular hydrogen bonds and so is essential for the gelation of the PVA/water system.

2.2.3 *Structure and Dynamics of Poly(γ-Methyl L-Glutamate) Gel*

The properties of the polymer gels swollen in organic solvents are different from those of hydro-swollen gels. Crosslinked poly(γ-methyl L-glutamate) (PMLG) is prepared by the ester-amide exchange reaction using diaminododecane as a cross-linker and is swollen in trifluoroacetic acid (TFA) and $CHCl_3$. The PMLG gel was studied by using high-resolution solid-state ^{13}C NMR spectroscopy.[55] A typical ^{13}C PST/MAS NMR spectrum of PMLG gel swollen in $CHCl_3$ is shown in Figure 6. The amide and ester carbonyl carbons of PMLG appear at 176.2 and 173.5 ppm, respectively. The Cα, OCH_3, Cγ and Cβ carbons appear at 57.6, 52.3, 31.3, and 26.1 ppm, respectively. The peak intensities of the side chain carbons is more intense than that of the main chain carbons.

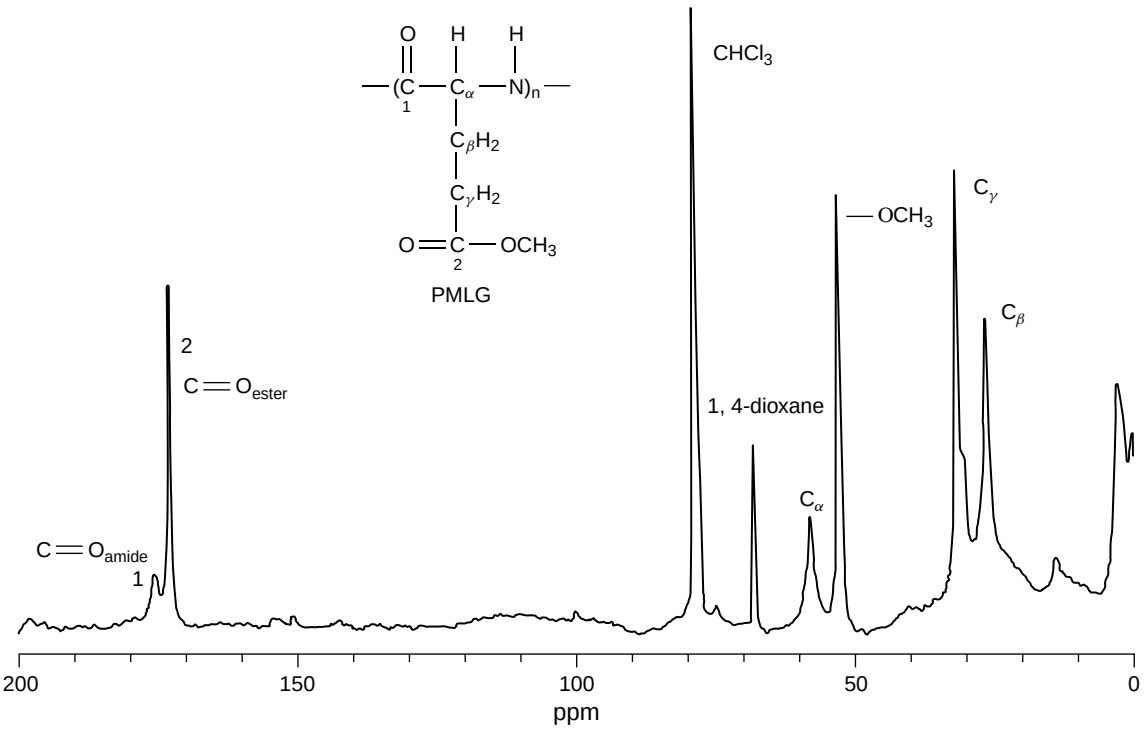

Figure 6 ^{13}C PST/MAS NMR spectrum of PMLG gel swollen in $CHCl_3$

This means that the side chains are undergoing faster molecular motion compared with the main chain.

The ^{13}C chemical shifts of the individual carbons of PMLG gel are changed as a function of the TFA content (f_{TFA}) in a mixture of $CHCl_3$ and TFA. In the PMLG gel with $CHCl_3$, the ^{13}C chemical shift values of the main chain amide C=O and Cα carbons are 176.2 and 57.6 ppm, respectively. The PMLG chain part of the crosslinked network takes the α-helix conformation as determined by reference data[25] of solid polypeptides at about 176 and 57 ppm. The amide C=O and Cα ^{13}C chemical shifts change transitionally from 176.5 and 57.6 ppm to 174.0 and 54.4 ppm, respectively, and so move upfield with an increase in TFA content. Such a transitional upfield shift shows that the main chain conformation of the PMLG network changes from the α-helix to the random coil form. The midpoint of the transition is at about $f_{TFA} = 0.15$. On the other hand, it is shown that in the side chain carbons the ester C=O carbon moves downfield at the transition point, but the chemical shifts of the other carbons do not change clearly. The chemical shift of the main chain arises from the conformational change due to the formation of intramolecular hydrogen bond between the C=O and N–H in the main chain. The main chain chemical shift is considered to be very sensitive to the helix-coil transition. The large shift difference of the ester carbonyl carbons is due to the interaction with TFA. The ^{13}C chemical shifts of the other side chain carbons also show small changes at $f_{TFA} = 0.15$.

The degree of swelling for the PMLG gel is a function of f_{TFA}. The degree of swelling is transitionally decreased at 0–0.05 f_{TFA}, is constant at 0.05–0.2 f_{TFA} and is gradually increased at $f_{TFA} > 0.2$. In the range 0.05–0.2, the fraction of the random coil form is increased gradually with an increase in f_{TFA} and the degree of swelling is constant. The TFA content dependence of the ^{13}C T_1 of amide C=O and ester C=O carbons was observed at 20 and 40 °C. As the temperature decreases from 40 to 20 °C, the ^{13}C T_1 for the amide C=O carbon increases and that of the ester C=O carbon decreases. The molecular motion of the amide C=O carbon is in the slow motion region ($\omega\tau_c \gg 1$, where ω is the resonance frequency) and that of the ester C=O carbon is in the fast motion region ($\omega\tau_c \ll 1$) according to the BPP theory. The decrease in ^{13}C T_1 of the ester C=O carbon in f_{TFA} from 0 to 0.05 shows that the decrease in molecular motion of side chain caused by a rapid shrinkage of the gel. In the range $f_{TFA} = 0.05–0.20$, ^{13}C T_1 of the amide C=O carbon decreases with an increase in TFA content. This means that the molecular motion of main chains is increased in going from the α-helix to the random coil in the constant degree of swelling. On the other hand, the molecular motion of the side chains is not so affected by the helix-coil transition.

2.2.4 Structural and Dynamic Characterization of EVOH Gels

In the CP method, enhancement of the ^{13}C magnetization is effective for the relatively immobile solid-like region, but is greatly reduced for the mobile region in gels. For this, it is expected that ^{13}C CP/MAS NMR gives us dynamic information about gels in an addition to structural information. ^{13}C CP/MAS NMR spectra of EVOH gel samples were measured over a wide range of ethylene contents from 5 to 74% at room temperature.[18] Only the intense background signal in the ^{13}C CP/MAS spectra of EVOH gels with low ethylene contents from 5 to 48% appears. This results from the following reasons. At the measurement temperature, the gels are very soft, so the mobility of EVOH network chains becomes high. This leads to a large reduction of the CP efficiency. Thus, the background signal that comes from the polymer materials used in an NMR probe appears intensely in the spectrum. This was recognized from the CP/MAS experiment using an NMR rotor containing no sample. The ^{13}C CP/MAS spectra of EVOH samples with high ethylene content of 55 and 74% were obtained with a reasonable signal-to-noise ratio. It is found that the spectral patterns for the CH carbon of the V units and for the CH_2 carbon of the E and V units are greatly changed by varying the ethylene content. In order to obtain the sufficient CP efficiency for the immobile component of EVOH gels with low ethylene content, ^{13}C CP/MAS NMR spectra of EVOH gel with the ethylene content of 5% were measured with repetition time of 5 s by changing of the contact time in the range from 100 to 2000 μs. At long contact time the noncrystalline region that is undergoing slow molecular motion can be often observed.

The ^{13}C PST/MAS NMR spectrum of EVOH gel with ethylene content of 5% was shown in Figure 7(b). This spectrum is similar to solution-state ^{13}C NMR spectrum of EVOH, like the case of PVA gel.[14,15] In the spectrum, the mm, mr and rr triad peaks for the CH carbon (in the 65–69 ppm region), and the m and r diad peaks for the CH_2 carbon (in the 45–48 ppm region) of V units in EVOH appear clearly. It can be said that the V units in the highly mobile region are observed by the PST/MAS NMR. On the other hand, ^{13}C CP/MAS NMR spectrum of its gel was measured under different conditions of the contact time of 1000 μs, the repetition time of 3 s and the accumulation number of 150 000 from the measurement condition used for the observed ^{13}C CP/MAS NMR spectra (see Figure 7(a)). In this spectrum, peaks I, II and III for the CH carbon of V units, which come from the immobile region, and the mr peak of the triad peaks (as appeared in the 65–69 ppm region) for the CH carbon, which comes from the mobile region appears clearly as shown in Figure 7(a). On the other hand, EVOH gel samples with higher ethylene-content become very hard, and thus ^{13}C CP/MAS NMR spectra of EVOH gels with the ethylene contents of 55 and 74% appear more clearly with a reasonable signal-to-noise ratio even at room temperature because the gels are solid-like, so their molecular motion is greatly restrained. This does not conflict with the pulse ^{1}H NMR results, in which the ^{1}H T_2 value of EVOH gels is decreased with ethylene content and the fractions of the mobile and intermediate regions (corresponding to the crosslinked and non-crosslinked regions, respectively) in EVOH gels with ethylene content larger than 55% are increased.

Next, we are concerned with temperature-variable ^{13}C CP/MAS NMR spectra of EVOH gels to obtain further dynamic information on the gels. ^{13}C CP/MAS NMR spectra of EVOH gels with ethylene content of 32% at 0 and 23 °C are shown in Figure 8. The ^{13}C CP/MAS NMR spectrum at 23 °C has very low signal-to-noise ratio and thus the intense background signal appears as a whole as shown in Figure 8(a). This means that the CP efficiency of the gels becomes insufficient by undergoing fast molecular motion at 23 °C, where these gel samples are very soft and thus mobility is high. As temperature is decreased, the individual peaks

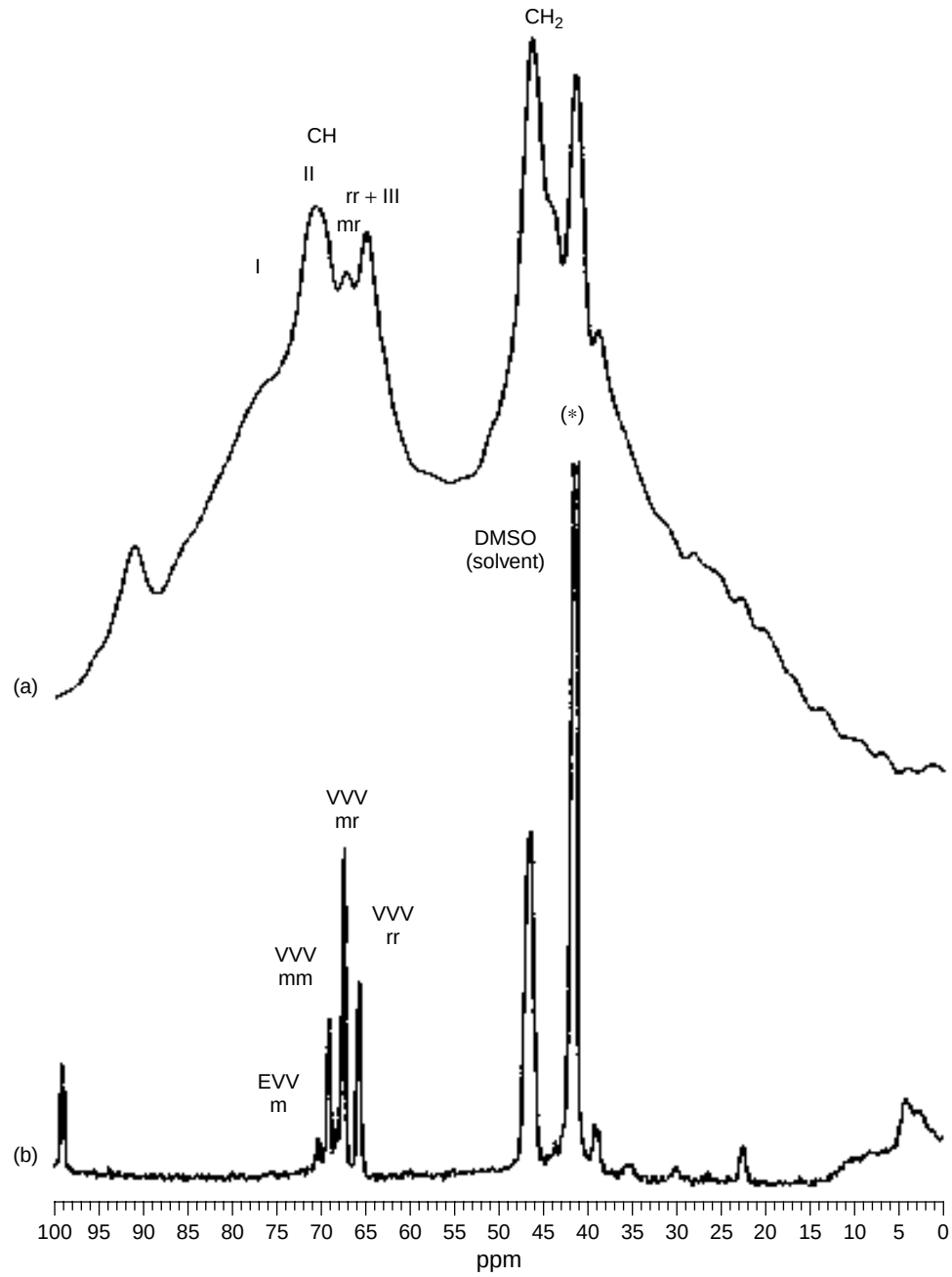

Figure 7 67.8 MHz ^{13}C NMR spectra of EVOH gel with ethylene content of 5% at room temperature. (a) CP/MAS NMR spectrum and (b) PST/MAS NMR spectrum

in the spectrum (a) at 0 °C appear more clearly compared with the spectrum (b) at 23 °C. This is due to an increase in the CP efficiency by reduction of molecular motion at low temperature. The three peaks I, II and III for the CH carbon of the V units appear like the ^{13}C CP/MAS NMR spectra of solid EVOH samples.[29] Further, the EVOH copolymer gel prepared by using a mixture of DMSO and water as solvent is relatively harder compared with one prepared by using DMSO as solvent. This is because the intermolecular affinity between EVOH and mixture solvent of DMSO and water becomes much lower compared with that between EVOH and DMSO solvent, and then the hydrophobic and/or hydrophilic interactions between polymer chains are enhanced. Thus, the EVOH copolymer with the ethylene content of 32% as prepared by using a mixture of DMSO and water as solvent becomes relatively solid-like. This leads to the ^{13}C CP/MAS NMR spectrum of the EVOH gel being well resolved with a reasonable signal-to-noise ratio, similar to solid EVOH.[26–29] All peaks in these spectra can be assigned in the same way as already assigned in PVA gel[14] and solid EVOH[29] as below.[14,29]

Next, we are concerned with the spectral analysis. The spectral assignment was made according to the previous assignments on solid EVOH samples.[29] First, the assignment of the ^{13}C peaks of the CH carbon was made. The assignment of three peaks I, II and III of the CH carbon in EVOH gel with low ethylene content, which appeared at about 77, 71 and

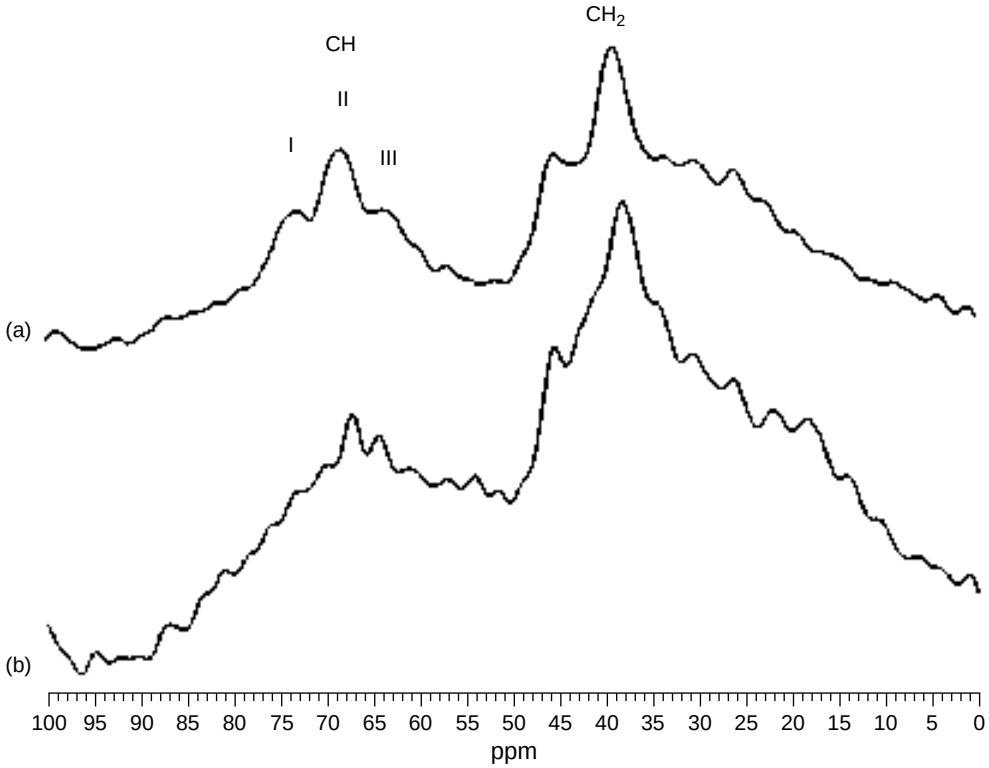

Figure 8 67.8 MHz ^{13}C CP/MAS NMR spectra of EVOH gel with ethylene content of 32% at 0 °C (a) and 23 °C (b)

65 ppm, respectively, can be made according to the assignment of the CH peaks in PVA gel.[14] Peak I comes from the formation of two intramolecular or intermolecular hydrogen-bonds, peak II from the formation of one intramolecular or intermolecular hydrogen-bond, and peak III from no hydrogen bond. On the other hand, in EVOH gel samples with high ethylene content, the ^{13}C chemical shift positions of peaks I and II are different from those in EVOH gel samples with low ethylene content. This is due to appearance of new configurational arrangements by the large amount of the ethylene units in the copolymers. From such a situation, according to the previous assignment we assign peak I to CH carbon of the V unit in EVE sequence as the major contribution in addition to two intramolecular or intermolecular hydrogen-bonded CH carbon of the V units as the minor contribution, and peak II from one intramolecular or intermolecular hydrogen bonded CH carbon of the central V unit in VVV sequences as the minor contribution.[29] Further, by analyzing the partially-relaxed spectra of EVOH gel (with the ethylene content of 5%) by using the Torchia method, it was found that each of three CH peaks I, II and III in EVOH gel remains even at longer delay time (=15 000 ms). This arises from the fact that peaks I, II and III in EVOH gel are frozen in molecular motion on the NMR timescale, because these three peaks comes from the crosslinking region in the gel. From the present results and the previous results in the sample of low ethylene content, it is concluded that the formation of hydrogen bonds between vinyl alcohol parts of EVOH contributes to gel formation.[16,17]

Further, we are concerned with the peak assignment of the CH_2 carbon in EVOH gel with high ethylene content. The CH_2 peaks at 30 and 33 ppm come from the asterisked central CH_2 carbons in both of the $–CH_2–CH_2–CH_2*–CH_2–CH_2–$ unit and $–CH_2–CH_2–CH_2*–CH_2–CH_2–$ unit with and without fast exchange between the *trans* and *gauche* conformations, respectively. The CH_2 peak at 30 ppm decays more rapidly than the CH_2 peak at 33 ppm. This arises from the fact that the CH_2 carbons of the ethylene units with the *trans* zigzag conformation in the crystalline region, which appear at 33 ppm, are frozen on the NMR timescale. On the other hand, the CH_2 carbons in the non-crystalline region, which appear at 30 ppm, are undergoing fast exchange between the *trans* and *gauche* conformations at room temperature.[30,31] In this case, in EVOH samples with high ethylene content, the gel may be formed in the crystalline region by hydrophobic interactions between the ethylene units of EVOH.

2.2.5 *Structural Characterization of Poly(Methacrylic Acid) Gel*

The structural and dynamic characterization of poly(methacrylic acid) gel with water as a function of degree of crosslinking was carried out through the observation of high-resolution solid-state ^{13}C NMR spectra by using ^{13}C PST/MAS NMR.[41] ^{13}C PST/MAS NMR spectra of PMAA gels with $Q = 3.4, 21.7$ and 105.8 are shown in Figure 9.[56] It is seen that high-resolution spectra are obtained. This indicates that the efficiency of MAS to obtain high resolution spectrum is very high for polymer gel systems. The peaks of the PMAA gel can be assigned to the C=O, CH_2, quaternary C, and CH_3 carbons from downfield. Each of the C=O and CH_3 carbon signals is split into three peaks due to the triad configurations of PMAA. These peaks are designated by the C=O (rr:182.5 ppm), C=O (mr:181.5 ppm), C=O (mm:180.8 ppm), CH_3 (mm:22.3 ppm), CH_3 (mr:19.8 ppm)

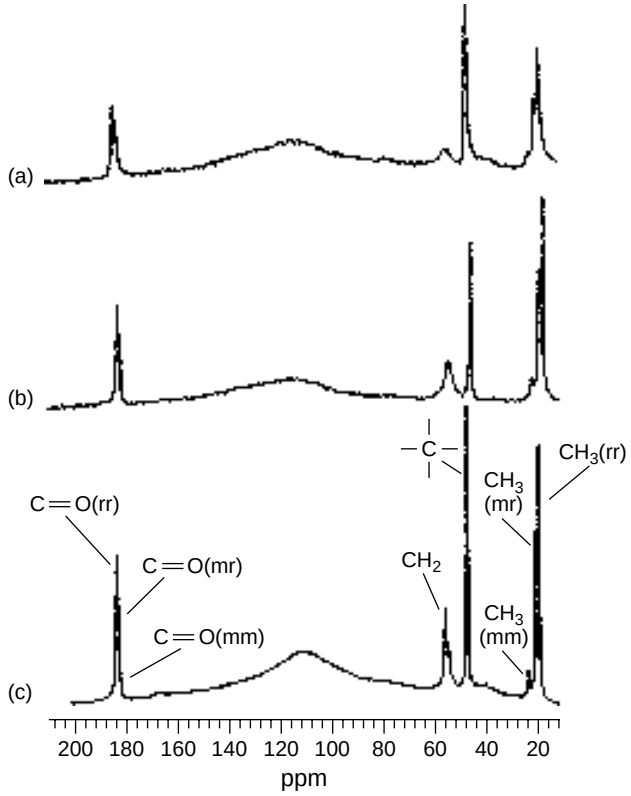

Figure 9 ^{13}C PST/MAS spectra of PMAA gels with $Q = 105.8$ (a), 21.7 (b) and 3.4 (c) at 300 K

and CH_3 (mm:18.2 ppm). The peak intensity ratio of these triad signals corresponds to the triad fraction. From the CH_3 signals, the triad fraction is evaluated as rr : mr : mm = 67.4 : 27.1 : 5.5%. The ^{13}C chemical shift values for the PMAA gels are independent of Q. This means that there is no specific effect on the ^{13}C chemical shift by changing Q.

From the ^{13}C T_1 measurements, it was found that molecular motion of the side chain carbons is in the extremely narrowing region in the BPP theory and that of the main chain carbons is in the slow motion region, and an increase in the degree of crosslinking in the PMAA gel leads to restraint in the segmental motion of the network polymer.

2.2.6 Structural and Dynamic Characterization of Poly(L-Glutamates) with N-Alkyl Side Chains in the Thermotropic Liquid Crystalline State

It is known that in a series of α-helical poly(L-glutamates) with n-alkyl side chains of various lengths, n-alkyl side chains longer than $n = 10$ form a crystalline phase composed of paraffin-like crystallites together with an α-helical main chain packing into a characteristic layer structure. The polymers form thermotropic liquid crystals by the melting of the side chain crystallites. The structural and dynamic behavior of the polymers over a wide range of temperatures in going from the solid state to the thermotropic liquid crystalline state has been elucidated by variable temperature ^{13}C CP/MAS NMR.[33,34] It has been demonstrated that the ^{13}C chemical shifts of the main chain amide carbonyl and Cα carbons in polypeptides are conformation-dependent and thus the main chain conformation can be determined by the ^{13}C chemical shift position of the main chain carbons.[25] Also, like polypeptides the conformation of long n-alkyl side chains can be determined by the ^{13}C chemical shift position.[46]

In Figure 10 the ^{13}C CP/MAS NMR spectra of poly(γ-n-octadecyl L-glutamate) (POLG) with long n-alkyl[$-(CH_2)_{17}CH_3$] side chains are shown over a wide range of temperatures from −40 to 230 °C. Assignments for peaks are straightforward as indicated in the spectra. The ^{13}C chemical shift values of the amide carbonyl and Cα carbons are 176.2 and 57.4 ppm, respectively. These values are characteristic of the right-handed α-helix conformation of the main chain of POLG. On the other hand, the assignment for peaks of n-alkyl side chains of POLG is performed by the using reference data on n-alkanes. At temperatures from −40 to 40 °C, the ^{13}C chemical shift values of the inner CH_2 carbons of the side chains are 33 ppm. This means that the inner CH_2 carbons of the side chains take an all-*trans* zigzag conformation in the orthorhombic form. At temperatures above 50 °C, the ^{13}C chemical shift value moves transitionally upfield by ca. 3 ppm. This means that n-alkyl side chains melt like liquid n-alkanes and then the fast exchange between the *trans* and *gauche* conformations occurs. Such an upfield shift occurs according to equation (1)

$$\delta_{obs} = \delta_o - 2\gamma f_g \quad (1)$$

where δ_{obs} and δ_o are the observed ^{13}C chemical shift and the ^{13}C chemical shift for the *trans* conformation, f_g is the fraction of the *gauche* conformation, and γ is attributed to the chemical shift difference (ca. 5.3 ppm) between the *trans* and *gauche* conformations.[30] At temperatures above 50 °C, this polymer forms a thermotropic liquid crystalline state.

In Figure 10 it is shown that the broadening phenomenon for peaks of the main chain carbons can be explained on the basis of the consideration that when the orientation rate of the main chain in the liquid crystalline state is close to a frequency corresponding to the amplitude of the proton decoupling field (about 60 kHz for this experiment), the efficiency of the proton decoupling is considerably reduced and the line width becomes the maximum. Thus, it can be said that the main chain is undergoing reorientation at a frequency of ca. 60 kHz in the temperature range from 50 to 90 °C.

In poly(L-glutamate) with long oleyl [$-(CH_2)_8CH{=}CH(CH_2)_7CH_3$] side chains which contain a double bond (POLLG), the melting of the side chain crystallites is at a much lower temperature than that of POLG. This polymer forms thermotropic liquid crystals from lower temperature.[45] The spectral behavior is very similar to POLG.[34]

2.3 Approach by Pulse Field-Gradient Spin-Echo ^{1}H NMR

2.3.1 Pulse Field-Gradient Spin-Echo ^{1}H NMR Measurements

In order to determine the diffusion coefficient of solvent and probe molecules in a gel, pulse field-gradient spin-echo (PFGSE) NMR is used. This method is very powerful.[5,35,36] However, if one wants to determine relatively small diffusion coefficients with high accuracy, a strong strength of the field gradient must be used. We have designed two kinds of PFGSE NMR probe systems of generating the strength of the field

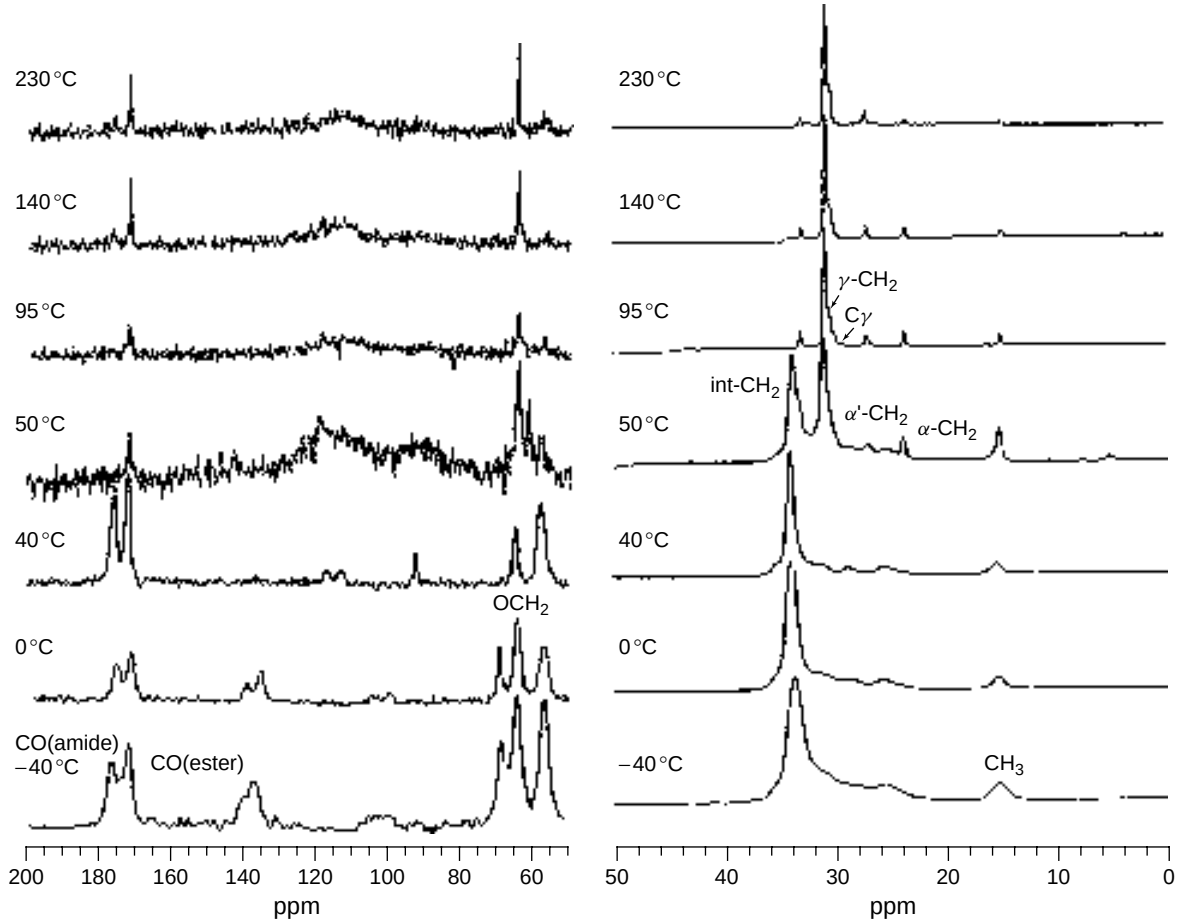

Figure 10 ^{13}C CP/MAS NMR spectra of poly(γ-octadecyl L-glutamate) over a wide range of temperatures

gradient pulse of $7.8\,\mathrm{T\,m^{-1}}$ and $22.8\,\mathrm{T\,m^{-1}}$.[3] This leads to a determination of the diffusion coefficient on the order of $10^{-14}\,\mathrm{m^2\,s^{-1}}$. As the PFGSE pulse sequence, two field gradient pulses are added to the ($\pi/2$ pulse $-\tau-\pi$ pulse) sequence, in which the first field gradient pulse is added at the mid position between the $\pi/2$ and π pulses (that is, at the position of τ^* after the $\pi/2$ pulse), and the second at the position of τ^* after the π pulse.[37]

The relationship between the echo signal intensity and pulse field gradient parameters is given by equation (2)

$$\mathrm{A}(\delta)/\mathrm{A}(0) = \exp[-\gamma^2 G^2 D\delta^2(D-\delta/3)] \qquad (2)$$

where A(δ) and A(0) are echo signal intensities at $t = 2\tau$ with and without the magnetic field gradient pulse, respectively, whose length is δ. τ is the pulse interval, γ the gyromagnetic ratio of the proton ($\gamma = 2.675 \times 10^8$ rad $T^{-1}\,\mathrm{s^{-1}}$), G the field gradient strength, D the self-diffusion coefficient, and Δ the gradient pulse interval. The echo signal intensity was measured as a function of δ. The plot of ln[A(δ)/A(0)] against $\gamma^2G^2\delta^2$ $(\Delta-\delta/3)$ gives a straight line with a slope of $-D$. Therefore, D can be determined from the slope. The τ, Δ and δ values employed in these experiments were 10, 10 and 0.001–0.12 ms, respectively. The D value of $2.5 \times 10^{-9}\,\mathrm{m^2\,s^{-1}}$ for water at 303 K was used as the calibration of the field gradient strength.[3] The experimental error for the D value is estimated to be less than ca. 5%.

2.3.2 *Diffusional Behavior of Synthetic Polymer Gels*

2.3.2.1 *Diffusional Behavior of Water in Poly(methacrylic acid) Gels*

In order to investigate changes in the translational motion of water contained in the poly(methacrylic acid) (PMAA) gel by a change in the degree of crosslinking, the diffusion coefficient of water molecules ($D_{\mathrm{H_2O}}$) in PMAA gels with the degree of swelling $Q = 3.4$–105.8 was determined by PFGSE ^{1}H NMR method at 300 K.[38] As seen from this table, $D_{\mathrm{H_2O}}$ increases as Q is increased. This means that an increase in Q leads to an increase in mobility of water molecules. If the $D_{\mathrm{H_2O}}$ increases are plotted against $Q^{1/3}$, it is seen from Figure 11 that $D_{\mathrm{H_2O}}$ increases linearly from 1.37×10^{-9} to $2.19 \times 10^{-9}\,\mathrm{m^2\,s^{-1}}$ with increasing $Q^{1/3}$.[39] This shows that the translational molecular motion of water molecules in the PMAA gel increases with an increase in the degree of swelling. The $D_{\mathrm{H_2O}}$ value of neat water at 300 K is $2.5 \times 10^{-9}\,\mathrm{m^2\,s^{-1}}$. Therefore, it can be said that the translational molecular motion of water molecules in the gel is more restrained compared with that of neat water by the intermolecular interactions with the polymer network.

We are concerned with the reason why there exists a linear relationship between the $D_{\mathrm{H_2O}}$ and $Q^{1/3}$. The volume for the gel that contains network polymer and water may be associated with $Q^{1/3}$. Assuming that the volume for the gel is a cube with the length of an edge being r, the degree of swelling for the

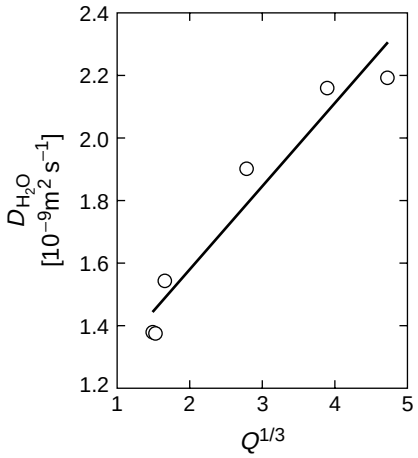

Figure 11 Plots of diffusion coefficient of water (D_{H_2O}) in PMAA gel against $Q^{1/3}$ at 300 K

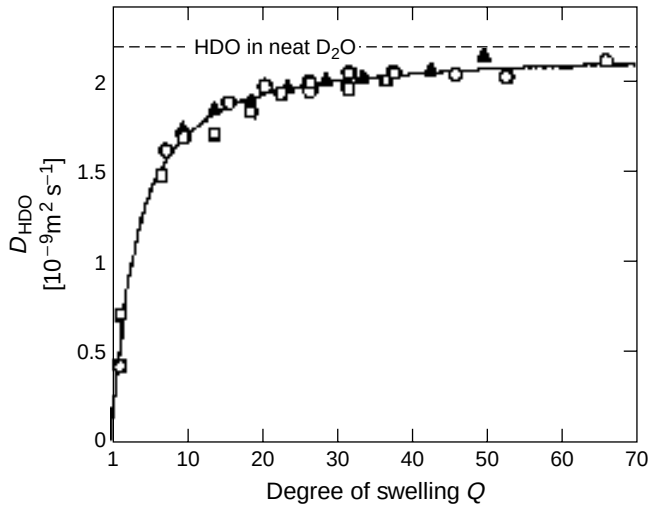

Figure 12 Dependence of the diffusion coefficient of water molecules (D_{HDO}) on the degree of swelling (Q) in a PDMAA gel containing PEG with $M_w = 4250$ (□), 10 890 (▲) and 20 000 (○) at 303 K

gel is rearranged as equation (3)

$$Q = M_{swollen}/M_{dry} = (\rho_{swollen} \cdot V_{swollen})/M_{dry} = (\rho_{swollen}/M_{dry})r^3 \quad (3)$$

where $\rho_{swollen}$ is the density of swollen polymer gel and $V_{swollen}$ the volume of swollen polymer gel. M_{dry} is a constant. By rearranging equation (3), we obtain equation (4)

$$r = (M_{dry}/\rho_{swollen})^{1/3} Q^{1/3} \quad (4)$$

If Q is changed as a function of the degree of crosslinking of the gel, $\rho_{swollen}$ does not change greatly (at 300 K $\rho_{swollen} = 1.001\,g\,cm^{-3}$ at $Q = 3.4$ and $\rho_{swollen} = 0.997 \times 10^3\,Kg\,m^{-3}$ at $Q = 106$). Therefore, it can be said that the length of an edge of the volume of the gel (r) is proportional to $Q^{1/3}$. This means that r of the volume containing a constant amount of network polymer increases with an increase in $Q^{1/3}$ and so the size of the polymer network in the gel expands the intermolecular distance between water molecules increases. For this, the molecular motion of molecules increases with an increase in $Q^{1/3}$. From the linear relationship between the D_{H_2O} and $Q^{1/3}$, it can be said that the molecular motion of water depends on intermolecular distance.

2.3.2.2 *Diffusional of Water and Poly(Ethylene Glycol) in Poly(Dimethylacrylamide) Gels*

The diffusion coefficients of HDO(D_{HDO}) and poly(ethylene glycol) (PEG) contained in poly(dimethylacrylamide) (PDMAA) gel were determined by the PFGSE ^{1}H NMR method as described above at 303 K varying Q and molecular weight (M_w) of PEG.[40] The D_{HDO} values obtained were plotted against Q as shown in Figure 12. As seen from this figure, D_{HDO} increases as Q is increased, and is almost independent of M_w of PEG contained in the gel. The change of D_{HDO} in the small Q region is much larger than that in the large Q region. The D_{HDO} value in the large Q region asymptotically approaches that for HDO in neat D_2O ($2.22 \times 10^{-9}\,m^2\,s^{-1}$). Therefore, it can be said that the intermolecular interaction between water and polymer network, of which the strength depends on the size of a network, restrains translational motion of the water. There is almost no effect on the molecular motion of HDO by the change of M_w of PEG, indicating that the diffusion of HDO is independent of M_w of PEG.

We can understand these results by using the modified free volume theory proposed by Fujita.[41] The diffusion coefficient is related to the friction ζ by the equation $D = kT/\zeta$, where k is the Boltzmann constant and T the absolute temperature. The dependence of ζ on solvent concentration is expressed as an exponential function of the fractional free volume f. Thus, we have equation (5)

$$D_{HDO} = D^0_{HDO} \exp[Q^{-1}/(Q^{-1} f_{solv} - f^2_{solv}/\beta)] \quad (5)$$

The dynamic behavior of a probe polymer in a gel can be analyzed by the ratio of the screening length of polymer network to the dimensional size of PEG. It is shown that the diffusion of a particle in semi-dilute polymer solution and in a polymer gel is obeyed by the relation shown in equation (6)

$$D/D^0 = \exp(-\kappa R) \quad (6)$$

where D^0 is the diffusion coefficient of an isolated particle, R the radius of a particle and κ^{-1} the dynamical screening length of the polymer chain. When $D/D^0 = \kappa^{-1}$, κ^{-1} is equivalent to R. This relation has also been employed for elucidating the self-diffusion of random-coil polymers in solution and gel, in which the values of κ^{-1} are large enough for probe polymers to have the same motion as for a hard sphere. In these cases, the interchain hydrodynamic interactions more significantly contribute to the diffusion process compared with the topological constraints. For this, the hydrodynamic radius of a probe polymer can be replaced by R. When the topological constrains cannot be neglected compared with the interchain hydrodynamic interactions, Ds becomes larger than the value expected from equation (6). When the diffusion coefficient of an isolated PEG (D^0_{PEG}) is determined from the diffusion coefficient of PEG in aqueous dilute solution (D^{soln}_{PEG}), it is necessary to take into account the change of local friction of polymer, which is estimated by the change for the

diffusion coefficient of the solvent. Then, D^0_{PEG} is given by equation (7)

$$D^0_{PEG} = D^{soln}_{PEG}/(D^{neat}_{HDO}/D_{HDO}) \quad (7)$$

where D^{neat}_{HDO} is the diffusion coefficient of HDO in D_2O. In this work, the diffusion of water and PEG in a PDMAA gel has been analyzed by the above mentioned equations (6) and (7).

2.3.2.3 *Diffusion Coefficient of HDO in a PDMAA Gel*

We can more clearly understand the dynamic behavior of water in the gel system using equation (5) obtained from modified free volume theory.[31,41] The solid curve obtained from a least-squares fitting to the experimental data using equation (5) is shown in Figure 12. The theoretical curve agrees well with the experimental data. From this result, the diffusion coefficient for HDO in infinite swollen gel ($Q \rightarrow \infty$) is obtained to be $D^0_{PEG} = 2.16 \times 10^{-9}\,m^2\,s^{-1}$, which is lower than HDO in neat D_2O ($2.22 \times 10^{-9}\,m^2\,s^{-1}$). This means that the diffusion coefficient for HDO in neat D_2O is different from the Q-extrapolated value to infinity given by the modified free volume theory for the diffusion concentration dependence. The diffusion coefficient for an isolated HDO molecule in bulk PDMAA ($Q \rightarrow 1$) obtained from Figure 12 was $2.5 \times 10^{-11}\,m^2\,s^{-1}$. It is seen that the translational motion of isolated water in bulk polymer is more strongly restrained compared to that in the gel. Further, it can be said that the rapid decrease of D_{HDO} in the small Q region can be explained by the decrease in free volume.

2.3.2.4 *Diffusion Coefficient of PEG in a PDMAA Gel*

In order to investigate the translational motion of PEG contained in PDMAA gel as a probe polymer, the diffusion coefficient of PEG (D_{PEG}) was determined by PGSE ^1H NMR at 303 K varying Q and M_w of PEG contained in the gel. It was found that D_{PEG} increases as Q is increased and also depends on M_w of PEG. The D_{PEG} value in the gel is smaller than that at 1% wt aqueous PEG solution (D^{soln}_{PEG}) at 303 K. Therefore, it can be said that the translational motion of PEG in the gel is more restrained by large intermolecular interaction with polymer network as compared with PEG in aqueous solution and that PEG with higher M_w is more strongly restrained.

Next, we are concerned with the relationship between the degree of restraint in molecular motion of PEG in the gel and the ratio of the screening length of polymer network to the size of PEG.[40] The dynamic behavior of PEG in the gel can be analyzed by using equation (6). The relationship between the dynamic screening length (κ^{-1}) and the concentration of network polymer (c) or the degree of swelling (Q) is expressed by equation (8)

$$\kappa^{-1} = c^u = Q^{-u} \quad (8)$$

where u may be a constant in the range from -0.5 to -1.0, but depends largely on the polymer species. Substitution of equations (6) and (7) into equation (8) gives equation (9)

$$D_{PEG}\,D^{neat}_{HDO}/D^{soln}_{PEG}\,D_{HDO} = \exp(-Q^u R). \quad (9)$$

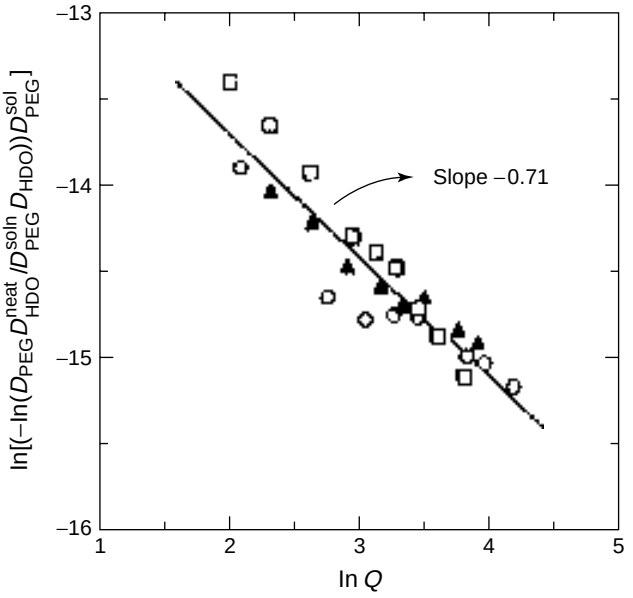

Figure 13 Plots of $\ln(-\ln(D_{PEG}D^{neat}_{HDO}/D^{soln}_{PEG}D_{HDO}))$ against $\ln Q$ at 303 K. M_ws of PEGs used are 4250 (□), 10 890 (▲) and 20 000 (○)

It is convenient to rewrite it in the form shown in equation (10)

$$\ln\left(-\ln\frac{D_{PEG}D^{neat}_{HDO}}{D^{soln}_{PEG}D_{HDO}}\right) = u\ln Q + \ln R. \quad (10)$$

In Figure 13, the $\ln[(-\ln(D_{PEG}D^{neat}_{HDO}/D^{soln}_{PEG}D_{HDO}))D^{soln}_{PEG}]$ value calculated using the experimental data is plotted against $\ln Q$. A straight line with a slope of – 0.71 is obtained and so $u = -0.71$. Therefore, we have $\kappa^{-1} \sim Q^{0.71} = c^{-0.71}$. Depending on the nature of network and solvent, there are a variety of theoretical calculations for the concentration dependence of the dynamical screening length. de Gennes proposed that for flexible polymer chains in a gel with good solvent the relationship $\kappa^{-1} \sim c^{-0.71}$ is obtained.[54] This prediction is in agreement with the above experimental results.

2.3.2.5 *Diffusion Behavior and Intermolecular Hydrogen-Bond Between Probe Polymer and Network Polymer in (N,N-Dimethylacrylamide–Acrylic Acid) Copolymer Gels*

Molecular dynamics of a probe polymer is strongly affected in polymer gel systems with various kinds of intermolecular interactions between the probe polymer and the network polymer, such as hydrogen-bonding interactions, hydrophobic interactions, Coulomb interactions, etc. For example, by adding aqueous PEG solution to aqueous poly(acrylic acid) (PAA) solution the complex between PEG and PAA is formed by the formation of hydrogen bonds between the oxygen atoms of PEG and the carboxyl groups of PAA. Also, in PMAA hydrogel the complex between PEG and PMAA is formed by the same interaction. The justification for the formation of such complexes has been carried out by macroscopic methods such as viscosity measurements for solutions and mass measurements for gels. Nevertheless, in order to clarify more clearly such intermolecular interactions between probe polymer and network polymer in the gel systems, systematic studies by microscopic methods such as NMR spectroscopy are needed.[43]

2.3.2.6 *Diffusion Coefficient of HDO in (DMAA-AA) Copolymer Gels*

The diffusion coefficients of HDO (D_{HDO}) contained in PDMAA gels, PAA gels and (DMAA-AA) copolymer gels with PEG were determined by PGSE ^{1}H NMR at 303 K varying Q and f_{AA}.[44] The D_{HDO} values obtained were plotted against Q. From this plot, it was found that the D_{HDO} increases as Q is increased. The molecular motion of HDO is not affected by a change of f_{AA} in the region of $f_{AA} < 0.9$. This means that the translational motion of the HDO molecule increases as the size of the network becomes larger. The dynamic behavior of solvent in a gel can be analyzed by the modified free volume theory. As described above D_{HDO} in a PDMAA gel can be expressed by equation (9). From a least-squares fit to the experimental data for PDMAA gels using equation (9), we can determine D^0_{HDO}, f_{solv} and β to be $2.16 \times 10^{-9}\,m^2\,s^{-1}$, 0.178 and 0.079, respectively. The calculation by using equation (6) and parameters obtained for PDMAA gels, agrees well with the experimental data obtained for (DMAA-AA) copolymer gels with f_{AA} value less than 0.9. This indicates that the diffusion of HDO is independent of the concentration of carboxylic acid group in this region. D_{HDO}s in PAA gels are larger than those in (DMAA-AA) copolymer gels. This may be because the concentration of H^+ ions dissociated from carboxylic acid groups in PAA gels, which diffuse faster than HDO, is higher than that in (DMAA-AA) copolymer gel.

2.3.2.7 *Diffusion Coefficient of PEG in (DMAA-AA) Copolymer Gels*

In order to investigate the translational motion of PEG contained in PDMAA gels and PAA gels as probe polymer, the diffusion coefficient of PEG (D_{PEG}) was determined by PGSE ^{1}H NMR at 303 K varying Q of the gel.[44] The D_{PEG} value in PDMAA gel is smaller than that in aqueous 1% wt PEG solution (dashed line), and increases as Q is increased. From the plot of $\ln(-\ln(D/D_0))$ against $\ln Q$, it was shown that this behavior is followed by $D/D_0 = \exp(-Q^{\alpha}R)$, and is similar to that mentioned above. Therefore, it can be said that the translational motion of PEG in PDMAA gel is restrained by hydrodynamic interaction with polymer network. This means that polymer network is working as only a spatial obstruction for the displacement of PEG. The D_{PEG} value in PAA gels is much smaller than that in PDMAA gel. This suggests that the loose complex of PEG and PAA network is formed by intermolecular hydrogen-bond interactions between the oxygen atoms of PEG and the carboxyl groups of PAA.[49] By addition of a small amount of HCl into the solution for the gel to be 0.15 mM in concentration, the gel shrinks and D_{PEG} is decreased. The complexation arises from intermolecular hydrogen-bond interaction between oxygen atoms of PEG and the carboxylic groups of AA units in the undissociated state as shown below. Therefore, it can be said that the addition of HCl leads to an increase in the amount of undissociated carboxylic groups and so enhances the formation of the complex and induces the shrinkage of the gel. This leads to slow diffusion of PEG. The addition of amine decreases the amount of dissociated carboxylic group and so inhibits the formation of the complex. This leads to fast diffusion of PEG and the swelling of the gel.

2.4 Diffusion Behavior of Polypeptide Gels

NMR methods involving pulsed magnetic field gradients provide one of the most attractive techniques for studies of molecular dynamics in polypeptide solution and gel systems. In particular, PFGSE NMR has been an invaluable tool in determining the anisotropic structures of polypeptide lyotropic liquid crystalline phase. Almost two decades ago, the first lateral diffusion coefficient of an amphiphile in a lamellar liquid crystalline phase was measured directly using PFGSE NMR. In recent years, the range of applications of NMR diffusion techniques has been growing rapidly, due to the great improvements in the NMR equipment for the diffusion microscopy. The diffusion behavior of solvent molecule in polypeptide gel system with α-helix-random coil transition, and on the diffusion behavior of solvent and probe n-alkanes molecules in polypeptide gel system with highly-oriented structures is introduced.

2.4.1 *Diffusion Behavior of Solvents in Unoriented Polypeptide Gels*

In high-resolution solid-state ^{13}C NMR experiments on cross-linked poly(γ-methyl L-glutamate) (PMLG) gel, we have found that the conformation of cross-linked PMLG with a mixture of chloroform ($CHCl_3$) and trifluoroacetic acid (TFA) largely depends on the solvent composition. The increase of volume fraction of TFA (f_{TFA}) in a mixture of $CHCl_3$ and TFA induces the α-helix-random coil transition of the main chain of cross-linked PMLG. $CHCl_3$ and TFA are sometimes so-called 'helix' and 'coil' solvents, respectively. It is important for gel science in polypeptide gel systems to elucidate how the translational motion of these solvents is affected when the main-chain of PMLG changes from the α-helix form to the random coil form. In such systems, the diffusion of solvent molecules contained in the polypeptide gel system strongly depends on the dynamics of polypeptide chains. As demonstrated above, PFGSE NMR gives useful information about the diffusion process of polymer gel system. From such a background, the dynamics of solvents in cross-linked PMLG gel with a mixture of $CHCl_3$ and TFA on going from the α-helix form to the random coil form through the diffusion coefficients were determined by PFGSE ^{1}H NMR.[45]

2.4.2 *Diffusion Behavior of Solvent and Probe-Molecules in Highly-Oriented Polypeptide Gels*

As is well known, poly(γ-benzyl L-glutamate) (PBLG) forms the lyotropic liquid crystalline state in good solvents such as dichloromethane, dioxane, chloroform, etc. and when the PBLG liquid crystalline solution is placed in a strong magnetic field, the main chain can be oriented in the direction of the magnetic field. The molecular motion of solvent and PBLG in the liquid crystalline solution is considerably influenced by intermolecular interactions. By reacting highly-oriented PBLG chains with a cross-linker in a strong magnetic field, cross-linked PBLG gel with the highly-oriented α-helical chains is assumed to be formed.[46] We are interested in the problem of the diffusion process of solvent and n-alkanes with relatively extended conformation in the gel with anisotropic structure. The interest lies in the fact that n-alkanes are basic

molecules for understanding structure and dynamics of linear polymer chains.

According to the work on the orientation of *n*-alkanes in PBLG liquid crystalline solution by ^{1}H NMR, in which PBLG chains are highly oriented, *n*-alkanes being guest molecules are highly oriented to the magnetic field of an NMR magnet with the relatively extended conformation along the α-helical PBLG chains.[47] Also, as elucidated by NMR *n*-alkanes in the rotator phase take an extended conformation, which are rotating rapidly around the long axis. Thus, the diffusion coefficients for the directions parallel and perpendicular to the long axis differ.[36,37]

With this as a background, cross-linked PBLG gels with highly-oriented α-helical chains are prepared. The diffusion coefficient of the solvent and *n*-alkanes in the gel for the directions parallel and perpendicular to the α-helical PBLG axis by using the PFGSE ^{1}H NMR method with strong field-gradient strength has been studied. In the liquid crystalline and gel states, the orientation of the PBLG chains can be determined by using high-resolution solid-state ^{13}C NMR.

2.4.3 Diffusional Process of Water in Starch Gels

The diffusional phenomena of compartmentalized water such as water in biological cells reflect the size and shape of the microstructure of the compartments and permeability of the barriers. The diffusion coefficients of water in corn starch gels, various wheat starch pastes and potato starch gels were measured.[48–50] The diffusion coefficient (D_0) of water, the permeability of the barriers and the size of microstructure in potato starch gels have been determined by using the equation of restricted diffusional motion. The D_0 value is gradually decreased with an increase in the starch concentration and approaches a constant value of about $1.0 \times 10^{-9}\,\mathrm{m^2\,s^{-1}}$. If the diffusion comes from restricted diffusion by a structural barrier (a), the interbarrier diffusion coefficient may be equal to the diffusion coefficient of pure water. These results show that the diffusion coefficient is affected by obstruction and hydration effects by polymers that are dispersed in the water compartments. The compartmentalized water experiences higher viscosity and/or a longer lifetime in the hydration sphere of starch chains. The permeability is gradually decreased with an increase in the starch concentration and is reached a constant value at more than 30% concentration. This shows that the polymer network of barriers is more dense in the gels at higher concentration. This does not conflict with general experimental results that the higher is the starch concentration, the stiffer is corresponding gel. The value of the distance between the neighboring barriers is independent of the starch concentration for fresh gels. The increase in polymer concentration causes an increase in the density of barriers until the latter reaches its limiting value. The density of barriers reaches the limit value (at a concentration between 33.3 and 37.9%), further increase in the concentration causes a decrease in the a value. From these experimental results, the fresh starch gel structure may be pictured that some of the polymers aggregate to make the starch network of the gel and the remaining polymers, and/or parts of polymer chain, are free from the starch network and function as a solute in water compartmentalized by the network.

2.5 Diffusion in Poly(γ-*n*-octadecyl L-glutamate) and Poly(γ-oleyl L-glutamate) (POLLG) in the Thermotropic Liquid Crystalline State

In order to elucidate more deeply dynamics of the polypeptides in the thermotropic liquid crystalline state, it is important to have some knowledge of the magnitude of the diffusion coefficient and the anisotropy of the diffusion for the directions parallel and perpendicular to the α-helical chain axis. For measurements of the diffusion coefficients, it has been demonstrated that PFGSE ^{1}H NMR can provide useful information to elucidate the diffusion process of solvents for polypeptides in the liquid crystalline state, in addition to polymer gel systems and *n*-alkanes in the rotator phase like the liquid crystalline state.[51]

To this end, the isotropic and anisotropic diffusion coefficients of the POLG chain in an highly-oriented sample prepared in the magnetic field produced by 500 MHz NMR equipment and the isotropic diffusion coefficients of the POLLG chain in the thermotropic liquid crystalline state were measured over a wide range of temperatures.[52] Further, T_2 of the side chain protons of POLG and POLLG were measured over a wide range of temperatures, and then the dynamics of the side chains were elucidated.

The highly-oriented POLG sample was prepared by the following procedure:

1. POLG was dissolved in 1,2-dichloroethane in an NMR glass tube to form the lyotropic liquid crystalline state.
2. the sample was placed in an NMR glass tube with a diameter of 5 mm and thence into the magnetic field of a 500 MHz NMR magnet for 60 hours until the POLG chains were aligned parallel to the magnetic field. The direction of the magnetic field was along the long axis of the NMR tube. After the full orientation of the polypeptide chains, solvent was vaporized from the NMR tube and then the highly-oriented film was obtained on the wall of the NMR tube. The complete orientation of the POLG chains in the film was confirmed by cross-polarized microscopy.

2.5.1 Diffusional Behavior and Dynamics of POLG and POLLG

In the spin-echo ^{1}H NMR spectra of POLG in the liquid crystalline state at 80 °C, an asymmetric relatively sharp signal appears, which has a chemical shift position (0.9 ppm) at the peak. This peak can be straightforwardly assigned to the methyl protons in the side chains. The upper shoulder peaks may be assigned to the methylene protons in the side chains. The peaks that come from the main chain protons such as α-CH proton and amide proton do not appear within the measurement temperature range. This is due to dipolar-broadened signal because of anisotropic molecular motion slow compared to the dipolar frequency, $\omega_0/2\gamma$. However, the spin-echo ^{1}H NMR spectra of POLLG are similar to those of POLG. Thus, the peak assignment can be made by comparison.

The plots of $\ln[\mathrm{A}(\delta)/\mathrm{A}(0)]$ against $\gamma^2G^2\delta^2\,(\Delta - \delta/3)$ for the above-mentioned peak (at ca. 0.9 ppm) in the PFGSE ^{1}H NMR spectra of POLG and POLLG, become straight lines (not shown here). This shows that the diffusion of POLG and POLLG consists of a single component during the observation time. Hence, the diffusion coefficients for POLG and POLLG

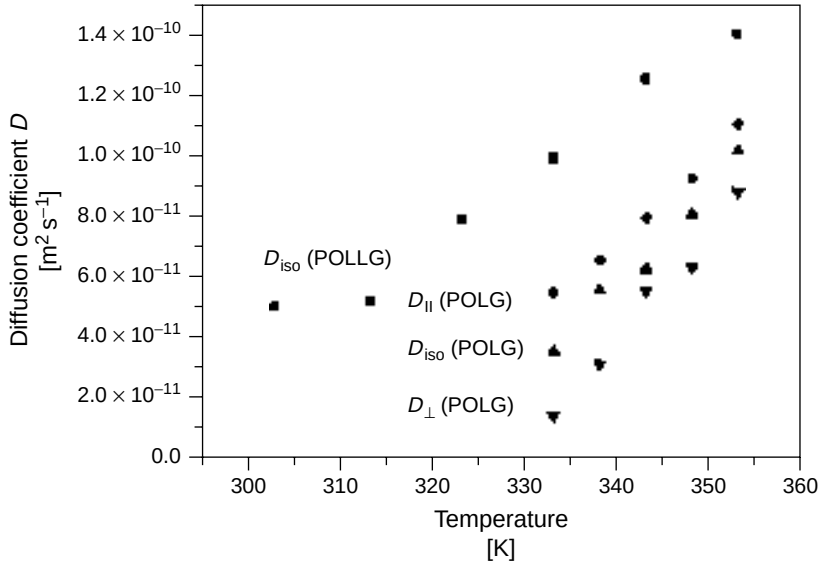

Figure 14 Temperature dependence of the diffusion coefficients of POLG chains in the direction parallel and perpendicular to the α-helical axis magnetic field and the isotropic diffusion coefficients (D_{iso} ($= D_{\parallel} + 2D_{\perp})/3$), and the isotropic diffusion coefficients of POLLG within the temperature range from 30 to 80 °C

considered here were determined from the slope of the straight line as seen from equation (1).[52]

The diffusion coefficients of the rod-like polypeptide chains for the directions parallel ($D_{\parallel}$) and perpendicular ($D_{\perp}$) to the α-helical chain axis were determined, and the isotropic diffusion coefficient (D_{iso}) was estimated by an average of the determined $D_{\parallel}$ and $D_{\perp}$ values as $(D_{\parallel} + 2D_{\perp})/3$ (Figure 14). As the temperature is increased from 60 to 80 °C, the $D_{\parallel}$ values of POLG in the liquid crystal state increase monotonically from 5.48×10^{-11} to $1.11 \times 10^{-10}\,m^2\,s^{-1}$ and, the $D_{\perp}$ values increase monotonically from 1.41×10^{-11} to $8.87 \times 10^{-11}\,m^2\,s^{-1}$. The determined $D_{\parallel}$ and $D_{\perp}$ values at 60 °C are 5.48×10^{-11} and $1.41 \times 10^{-11}\,m^2\,s^{-1}$, respectively, and those at 80 °C are 1.11×10^{-10} and $8.87 \times 10^{-11}\,m^2\,s^{-1}$, respectively. The diffusion of POLG in the thermotropic liquid crystalline state is anisotropic. The diffusion of the polypeptide along the long α-helical chain axis at 60 °C is roughly four times faster than that perpendicular to the long α-helical chain axis. At 80 °C, their diffusion coefficients are close to each other. As reported previously, the determined $D_{\parallel}$ and $D_{\perp}$ values of *n*-alkane, *n*-$C_{24}H_{50}$, in the rotator phase like the liquid crystalline state, which takes the all-*trans* zigzag conformation, are 1.64×10^{-10} and $2.70 \times 10^{-10}\,m^2\,s^{-1}$, respectively. The diffusion of the *n*-alkane in the rotator phase along the long chain axis is slower by roughly two times than that perpendicular to the long chain axis. This is opposite to the results of POLG. From the number of amino acid residues of POLG (ca. 780) considered here, the α-helical chain length is roughly estimated to be ca. 117 nm by using the pitch of an α-helix chain per one amino acid residue to be 0.15 nm. However, the chain length of *n*-$C_{24}H_{50}$ with the all-*trans* zigzag conformation is roughly estimated to be ca. 1.8 nm. From these simple estimations, it is seen that the corresponding rod-like POLG is much longer than *n*-$C_{24}H_{50}$. This leads to the experimental finding that the diffusion of the POLG along the long α-helical chain axis is much faster than that perpendicular to the long α-helical chain axis.

As for POLLG, only the isotropic diffusion coefficients were determined for an interval of 10 °C in the temperature range from 30 to 80 °C (Figure 14). The diffusion coefficients of POLLG in the liquid crystalline state were determined as a function of temperature similarly to POLG. It is shown that with an increase in temperature from 30 to 80 °C, the D value increases gradually from 4.9×10^{-11} to $1.4 \times 10^{-10}\,m^2\,s^{-1}$. Let us compare these D_{iso} values with those of POLG calculated from the determined $D_{\parallel}$ and $D_{\perp}$ values. As the temperature is increased from 60 to 80 °C, the D_{iso} values of POLG increase gradually from 3.53×10^{-11} to $1.02 \times 10^{-10}\,m^2\,s^{-1}$ and those of POLLG increase from 4.9×10^{-11} to $1.40 \times 10^{-10}\,m^2\,s^{-1}$. At 60 °C, POLLG in the thermotropic liquid crystalline state diffuses faster by ca. 2.8 times than POLG irrespective of the same α-helical chain length and at 80 °C their diffusion rates are close to each other. At 60 °C such a large difference in D_{iso} between POLG and POLLG may come from large differences in their side-chain conformation and molecular motion (as seen from the T_2 experiments below). The melting temperature of side chain crystallites in POLG is ca. 60 °C and that of POLLG is below −40 °C as DSC measurements as reported previously.[34] This means that at 60 °C the side chains of POLLG are undergoing much faster *trans-gauche* exchange around the C–C bond compared with those of POLG, and the expansion of the side chains from the main chain in the former is much smaller than that of the latter. At a higher temperature (80 °C) their mobilities are close to each other. This leads to the difference in D_{iso} between POLG and POLLG.

In order to understand the diffusion process of the polypeptide in the thermotropic liquid crystalline state more thoroughly, the activation energy $E^{\ddagger}$ for diffusion process can be determined. $E^{\ddagger}$ can be obtained from the plots of $\ln D$ against $1/T$ within the temperature range from 60 to 80 °C. As for POLG, the measured values of $E^{\ddagger}$ are 33.4, 77.4 and 49.8 kJ mol^{-1} for $D_{\parallel}$, $D_{\perp}$, and D_{iso}, respectively. However, the activation energy for D_{iso} of POLLG is determined to be 20.6 kJ mol^{-1}. From these experimental results, it can be said

that the activation energy for the diffusion process for POLLG in the thermotropic liquid crystalline state is much lower than that of POLG. In the case of POLG, the activation energy for the diffusion along the α-helical chain axis is much lower than that in the direction perpendicular to the α-helical chain axis.

3 REFERENCES

1. (a) Y. Osada and K. Kajiwara, 'Polymer Gels Handbook', Academic Press: New York, 2000; (b) D. DeRossi, K. Kajiwara, Y. Osada, and A. Yamauchi, 'Polymer Gels – Fundamentals and Biomedical Applications', Plenum Press: New York, 1991; (c) Y. Osada, *Adv. Polym. Sci.*, 1987, **82**, 1.
2. (a) P. J. Collings and M. Hird, 'Introduction to Liquid Crystals', Taylor and Francis: London, 1998; (b) V. P. Shibaeb and Lui Lan, 'Liquid Crystalline and Mesomorphic Polymers', Springer-Verlag: Berlin, 1993.
3. (a) I. Ando and T. Asakura, 'Solid State NMR of Polymers', Elsevier Science: Amsterdam, 1998; (b) I. Ando, M. Kobayashi, M. Kanekiyo, S. Kuroki, S. Ando, S. Matsukawa, H. Kurosu, H. Yasunaga, and S. Amiya, 'Experimental Methods in Polymer Science', John Wiley: New York, 1999, Chapter 4, pp 261–483.
4. M. Mori and J. L. Koenig, *Annu. Rept. NMR Spectrosc.*, 1997, **34**, 231.
5. (a) S. Matsukawa, H. Yasunaga, C. Zhao, S. Kuroki, H. Kurosu, and I. Ando, *Prog. Polymer Sci.*, 1999, **24**, 995; (b) I. Ando, H. Kurosu, S. Matsukawa, A. Yamazaki, Y. Hotta, and N. Tanaka, 'The Wiley Polymer Networks Review Series', Vol. 1, eds K. te Nijenhuis and W. J. Mijs, Wiley: New York, 1998, pp 331–346.
6. P. T. Callaghan, 'Principles of Nuclear Magnetic Resonance Microscopy', Claredon Press: Oxford, 1991.
7. N. Bleombergen, E. M. Purcell, and R. V. Pound, *Phys. Rev.*, 1948, **73**, 679.
8. T. Tanaka, *Phys. Rev. Lett.*, 1978, **244**, 110.
9. N. Tanaka, S. Matsukawa, H. Kurosu, and I. Ando, *Polymer*, 1998, **39**, 4703.
10. H. Ohta, I. Ando, S. Fujishige, and K. Kubota, *J. Polymer Sci.*, 1991, **B29**, 963.
11. M. Heskins and J. E. Guillet, *Macromol. Sci. Chem.*, 1986, **A2**, 1441.
12. A. Takahashi and S. Hiramitsu, *Polymer J.*, 1974, **6**, 103.
13. M. Kanekiyo, M. Kobayashi, I. Ando, H. Kurosu, T. Ishii, and S. Amiya, *J. Mol. Struct.*, 1998, **447**, 49.
14. M. Kobayashi, I. Ando, T. Ishii, and S. Amiya, *Macromolecules*, 1995, **28**, 6677.
15. M. Kobayashi, I. Ando, T. Ishii, and S. Amiya, *J. Mol. Struct.*, 1998, **440**, 155.
16. J. Jonas and A. Jonas, *Annu. Rev. Biophys. Biomol. Struct.*, 1994, **23**, 287.
17. M. Kobayashi, M. Kanekiyo, and I. Ando, *Polymer Gels Networks*, 1998, **6**, 347.
18. M. Kanekiyo, M. Kobayashi, I. Ando, H. Kurosu, and S. Amiya, *Macromolecules*, 2000, **33**, 7971.
19. J. Schaefer and E. O. Stejskal, *J. Am. Chem. Soc.*, 1976, **98**, 1031.
20. J. Schaefer and E. O. Stejskal, *Macromolecules*, 1977, **10**, 384.
21. B. C. Gerstein and C. R. Dybowski, 'Transient Techniques in NMR of Solids', Academic Press: New York, 1985.
22. T. Fujito, K. Deguchi, M. Ouchi, M. Imanari, and M. J. Albright, 'The Twentieth Meeting in NMR', Tokyo, 1981, p 68.
23. T. Terao, S. Maeda, and A. Saika, *Macromolecules*, 1983, **16**, 1535.
24. M. Kobayashi, M. Kanekiyo, I. Ando, and S. Amiya, *Polymer Gels Networks*, 1998, **6**, 425.
25. H. Saito and I. Ando, *Annu. Rept. NMR Spectrosc.*, 1989, **21**, 210.
26. H. Ketels, J. Buelen, and G. Velden, *Macromolecules*, 1988, **21**, 2032.
27. H. Ketels, J. de. Haan, A. Aerdts, and G. Velden, *Polymer*, 1990, **31**, 1419.
28. D. L. VandeHart, S. Simmons, and J. W. Gilman, *Polymer*, 1995, **36**, 4223.
29. M. Kanekiyo, M. Kobayashi, I. Ando, H. Kurosu, and S. Amiya, *Polymer*, 2000, **41**, 2391.
30. (a) A. E. Tonelli, *Accts. Chem. Res.*, 1981, **14**, 233; (b) A. E. Tonelli, *Annu. Rept. NMR Spectrosc.*, 1997, **34**, 185.
31. W. L. Earl and D. L. VanderHart, *Macromolecules*, 1979, **12**, 769.
32. H. Yasunaga and I. Ando, *J. Mol. Struct.*, 1993, **301**, 129.
33. T. Yamanobe, M. Tsukahara, T. Komoto, J. Watanabe, I. Ando, I. Uematsu, K. Deguchi, T. Fujito, and M. Imanari, *Macromolecules*, 1998, **21**, 48.
34. B. Mohanty, T. Komoto, J. Watanabe, I. Ando, and T. Shiibashi, *Macromolecules*, 1989, **22**, 4451.
35. W. S. Price, *Annu. Rept. NMR Spectrosc.*, 1996, **32**, 51.
36. A. K. Whittaker, *Annu. Rept. NMR Spectrosc.*, 1997, **34**, 105.
37. J. E. Tanner and E. O. Stejskal, *J. Chem. Phys.*, 1968, **49**, 1768.
38. H. Yasunaga and I. Ando, *Polymer Gels Networks*, 1993, **1**, 267.
39. H. Yasunaga and I. Ando, *Polymer Gels Networks*, 1993, **1**, 81.
40. S. Matsukawa and I. Ando, *Macromolecules*, 1996, **29**, 7136.
41. H. Fujita, *Advance Polymer Sci.*, 1961, **3**, 1.
42. P. G. de Gennes, *Macromolecules*, 1976, **9**, 594.
43. S. Matsukawa and I. Ando, *Macromolecules*, 1997, **30**, 8310.
44. S. Matsukawa and I. Ando, *Macromolecules*, 1999, **31**, 1865.
45. C. Zhao, S. Matsukawa, H. Kurosu, and I. Ando, *Macromolecules*, 1998, **31**, 3139.
46. C. Zhao, H. Zhang, T. Yamanobe, S. Kuroki, and I. Ando, *Macromolecules*, 1999, **32**, 3389.
47. C. Zhao, S. Kuroki, and I. Ando, *Macromolecules*, 2000, **33**, 4486.
48. W. von Basler and H. Lechert, *Staeke*, 1974, **2**, 39.
49. P. T. Callaghan, K. W. Levievre, and R. K. B. King, *J. Coll. Interface Sci.*, 1983, **92**, 332.
50. A. Ohtsuka and T. Watanabe, *Carbohydr. Polymers*, 1996, **30**, 135.
51. H. Yamakawa, S. Matsukawa, H. Kurosu, S. Kuroki, and I. Ando, *J. Chem. Phys.*, 1999, **111**, 7110.
52. Y. Yige, C. Zhao, S. Kuroki, and I. Ando, *J. Chem. Phys.*, 2000, **113**, 9606.
53. T. C. Farra and E. D. Becker, 'Pulse and Fourier Transform NMR', Academic Press: New York, 1971.
54. D. A. Torchia, *J. Magn. Reson.*, 1978, **30**, 613.
55. C. Zhao, S. Matsukawa, M. Kobayashi, and I. Ando, *J. Mol. Struct.*, 1998, **442**, 235.
56. H. Ohta, I. Ando, S. Fujishige, and K. Kubota, *J. Mol. Struct.*, 1991, **245**, 391.
57. B. Beloche and E. T. Samulski, *Macromolecules*, 1981, **14**, 575.
58. W. Gronski, R. Stadler, and M. M. Jacobi, *Macromolecules*, 1984, **17**, 741.
59. H. E. Gottlieb and Z. Luz, *Macromolecules*, 1984, **17**, 1959.
60. M. I. Lifshits, *Polymer*, 1987, **28**, 454.
61. W. Gronski, F. Foster, W. Pyckhout-Hintzen, and T. Springer, *Macromol. Chem., Macromol. Symp.*, 1990, **40**, 121.
62. D. Yang, F. Li, and Z. Qiu, *J. Macromol. Sci., Chem.*, 1990, **A27**, 149.

Two-Dimensional Methods of Monitoring Exchange

Keith G. Orrell
University of Exeter, Exeter, UK

1	Introduction	1
2	Theory and Methodology of 2D Exchange Spectroscopy	1
3	Applications of EXSY	5
4	Related Articles	7
5	References	7

1 INTRODUCTION

The suitability of NMR spectroscopy for monitoring exchange processes of molecules has been realized since the earliest days of the technique. In those formative years, rate processes were studied primarily by their effects on internal resonance frequencies of nuclei (bandshape analysis)[1] or on signal intensities (magnetization transfer experiments).[2,3] The first method relies on exchange processes occurring at frequencies comparable to differences in nuclear resonance frequencies $\Delta\nu_i$ (see ***Chemical Exchange Effects on Spectra***), whereas the second approach requires exchange rates to be comparable to spin–lattice relaxation rates R_{1i}. The consequences of such criteria are that bandshape analysis methods are applicable to rather faster rate processes, with pseudo-first-order rate constants k in the range $1–10^4$ s^{-1}, than magnetization transfer methods, where typically k values are in the range $10^{-2}–10^2$ s^{-1}. Such ranges, however, are very imprecise, and depend on the nucleus chosen to monitor the process and the nature of the chemical species itself—for example, whether it is diamagnetic or paramagnetic.

In magnetization transfer experiments, based on the classic work of Forsén and Hoffman,[2,3] nuclei in one of the exchanging sites are labeled by disturbing their energy population distribution, either by selective decoupling, which equalizes their populations (saturation), or by applying a selective 180° pulse, which inverts their populations (inversion). Chemical exchange causes these nuclei to move to one or more different sites, thus introducing a further disturbance to the populations in that site. This leads to a time dependence of populations of exchanging sites, which is reflected in the changing intensities of signals following the perturbing pulse. Measurements of this intensity variation can provide accurate exchange rate data. The method can be made very reliable for two-site exchange,[4] and has been very widely applied. The method can also be generalized for multisite exchange, where it has been shown that for a system of N exchanging sites $\frac{1}{2}N(N-1)$ exchange rates and N spin–lattice relaxation rates need to be evaluated.[5] However, this requires many experiments, and this type of problem is far more efficiently handled by two-dimensional experiments[6–8] (see ***Multidimensional Spectroscopy: Concepts***), which is the subject of this article.

Rate processes that cause exchange of magnetization between nuclear sites are many and varied. They range from examples of intermolecular exchange (e.g., ligand or solvent exchange processes) to subtle intramolecular rearrangements between chemically identical species (e.g., fluxional processes) (see ***Fluxional Motion***). This article presents the basic theory of two-dimensional exchange spectroscopy (EXSY), illustrates the scope and limitations of the technique, and provides examples of its application, employing a variety of different sensor nuclei, to different areas of chemistry.

The focus will be on chemical exchange arising from structural rearrangements of molecules, but the reader is reminded that essentially the same technique is used for studying motional processes as revealed by cross relaxation rather than chemical exchange effects. In this context, the technique is known as two-dimensional NOE spectroscopy, and has been widely exploited[9] (see ***NOESY***).

2 THEORY AND METHODOLOGY OF 2D EXCHANGE SPECTROSCOPY

The application of 2D NMR for chemical exchange studies was first described by Jeener, Meier, Bachmann, and Ernst.[10] Its theoretical basis was elaborated by Macura and Ernst,[11] and has been the subject of a number of reviews.[12–15]

2.1 Basic EXSY Experiment

The fundamental principle of the EXSY experiment is the frequency labeling of the spin–lattice (longitudinal) magnetization of various sites before exchange occurs, in order that, after exchange, the pathways of magnetization can be traced back to their origins.

The basic pulse sequence is shown in Figure 1. A two-spin system of spins A and B, mutually interacting purely through chemical exchange with no cross relaxation, will be considered. Equal concentrations of spins (i.e., $k_{AB} = k_{BA} = k$), equal spin–lattice relaxation rates ($R_1^A = R_1^B = R_1$), and equal transverse relaxation times ($T_2^A = T_2^B = T_2$) will be assumed. After the first $90°_x$ pulse, the magnetization vectors will evolve in the (x', y') plane in the usual manner of free induction decay

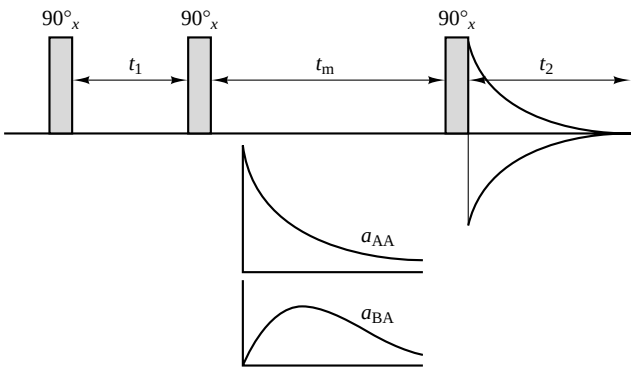

Figure 1 Basic EXSY pulse sequence, showing typical variations in the mixing coefficients for diagonal and cross peaks during the mixing time t_m

(FID) for a period t_1 (evolution time). The total magnetization M^+ is given by

$$M^+ = M_y(t) + \mathrm{i}M_x(t) \tag{1}$$

If exchange is slow, the effect of lineshape may be neglected, and the two magnetization components are given by

$$M_\mathrm{A}^+(t_1) = M_\mathrm{A0}\exp(\mathrm{i}\omega_\mathrm{A}t_1 - t_1/T_2) \tag{2}$$

$$M_\mathrm{B}^+(t_1) = M_\mathrm{B0}\exp(\mathrm{i}\omega_\mathrm{B}t_1 - t_1/T_2) \tag{3}$$

where $\omega_\mathrm{A,B}$ are the effective precession frequences in the rotating frame. When a second 90°_x pulse, the mixing pulse, is applied, the magnetization vectors are tipped into the $-z$ direction, the real components of the transverse magnetization being converted into longitudinal magnetization:

$$M_\mathrm{AZ}(t_\mathrm{m} = 0) = -M_\mathrm{A0}\cos\omega_\mathrm{A}t_1\exp(-t_1/T_2) \tag{4}$$

$$M_\mathrm{BZ}(t_\mathrm{m} = 0) = -M_\mathrm{B0}\cos\omega_\mathrm{B}t_1\exp(-t_1/T_2) \tag{5}$$

The imaginary x components are unaffected by this pulse, and may be destroyed by a field gradient pulse during the mixing time t_m. The t_1-modulated longitudinal components in equations (4) and (5) migrate from one site to another by chemical exchange, with a rate constant k, while the spin–lattice relaxation attenuates the memory of the initial labeling:

$$\begin{aligned} M_\mathrm{AZ} = {} & M_\mathrm{AZ}(t_\mathrm{m} = 0)\tfrac{1}{2}[1 + \exp(-2kt_\mathrm{m})]\exp(-t_\mathrm{m}R_1) \\ & + M_\mathrm{BZ}(t_\mathrm{m} = 0)\tfrac{1}{2}[1 - \exp(-2kt_\mathrm{m})]\exp(-t_\mathrm{m}R_1) \end{aligned} \tag{6}$$

$$\begin{aligned} M_\mathrm{BZ} = {} & M_\mathrm{AZ}(t_\mathrm{m} = 0)\tfrac{1}{2}[1 - \exp(-2kt_\mathrm{m})]\exp(-t_\mathrm{m}R_1) \\ & + M_\mathrm{BZ}(t_\mathrm{m} = 0)\tfrac{1}{2}[1 + \exp(-2kt_\mathrm{m})]\exp(-t_\mathrm{m}R_1) \end{aligned} \tag{7}$$

The final 90°_x pulse converts these longitudinal components into observable magnetization. Double Fourier transformation will produce signals at (ω_1, ω_2) = (ω_A, ω_A) and (ω_B, ω_B) for nuclei that have not exchanged during the time t_m. Nuclei that have exchanged sites will produce signals at (ω_A, ω_B) and (ω_B, ω_A). The amplitudes $I_{kl}(t_\mathrm{m})$ of the diagonal and off-diagonal signals depend on the equilibrium magnetizations M_{l0} and on mixing coefficients $a_{kl}(t_\mathrm{m})$, which correspond to the factors in equations (6) and (7):

$$a_\mathrm{AA} = a_\mathrm{BB} = \tfrac{1}{2}[1 + \exp(-2kt_\mathrm{m})]\exp(-t_\mathrm{m}R_1) \tag{8}$$

$$a_\mathrm{AB} = a_\mathrm{BA} = \tfrac{1}{2}[1 - \exp(-2kt_\mathrm{m})]\exp(-t_\mathrm{m}R_1) \tag{9}$$

In this simple two-site exchange system, the equilibrium magnetizations M_A0 and M_B0 are equal, and the exchange rate can be determined from the ratio of diagonal and off-diagonal (cross peak) intensities:

$$\frac{I_\mathrm{AA}}{I_\mathrm{AB}} = \frac{a_\mathrm{AA}}{a_\mathrm{AB}} = \frac{1 + \exp(-2kt_\mathrm{m})}{1 - \exp(-2kt_\mathrm{m})} \approx \frac{1 - kt_\mathrm{m}}{kt_\mathrm{m}} \tag{10}$$

This intensity ratio is a sensitive function of the mixing time t_m, and care must be taken in the length chosen in order to obtain optimum accuracy of the rate constant. The amplitudes of the diagonal signals decay in the biexponential manner

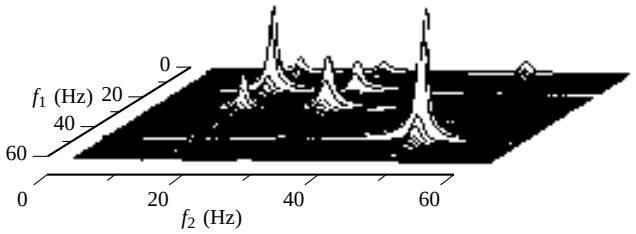

Figure 2 Hydrogen-1 EXSY spectrum of *N*,*N*-dimethylacetamide, showing the *N*-methyl exchange cross peaks. Experimental conditions: 128 equidistant t_1 values from 0 to 1016 ms, each FID represented by 256 samples, and a mixing time t_m = 0.5 s. Note that diagonal signals go from top left to bottom right

with increasing mixing time, whereas the off-diagonal signals first increase owing to exchange and then decrease because of spin–lattice relaxation (see Figure 1). The optimal value of t_m corresponds to the region on the graph where the intensity of the cross peak is almost linearly proportional to t_m and well before it reaches a level where its intensity is more dependent on T_1 than on t_m. It has been shown theoretically[13] that an approximate expression for the optimal value of t_m for an equally populated two-site exchange system is

$$t_\mathrm{m}(\mathrm{opt}) \approx (R_1 + 2k)^{-1} \tag{11}$$

One of the first reported EXSY spectra is shown in Figure 2.[10] It depicts the diagonal and cross-peak signals of the *N*-methyl hydrogens of *N*,*N*-dimethylacetamide, which exhibit exchange due to the slow rotation about the C–N bond in the molecule.

This theory can be extended to general *N*-site exchange when $N \geq 3$ using a matrix formulation. This has been described fully elsewhere,[12–15] and here space permits only a summary. For nuclei in site j, the initial 90°_x pulse causes their magnetization to evolve according to

$$M_j = M_{j0}\exp(\mathrm{i}\omega_j t_1 - t_1/T_{2j}) \tag{12}$$

The second 90°_x pulse, plus a gradient pulse, converts this transverse magnetization to z magnetization according to

$$M_{jz}(t_\mathrm{m} = 0) = -M_{j0}\exp(\mathrm{i}\omega_j t_1 - t_1/T_{2j}) \tag{13}$$

During the mixing period, chemical exchange and longitudinal relaxation affect this magnetization. We define m_j to be the deviation of M_{jz} from its equilibrium value by

$$m_j = M_{jz} - M_{j0} \tag{14}$$

The time dependences of these deviations are given by equations of the type

$$\frac{\mathrm{d}m_1}{\mathrm{d}t} = -\left(R_{11} + \sum_l k_{1l}\right)m_1 + k_{21}m_2 + \cdots + k_{N1}m_N \tag{15}$$

$$\frac{\mathrm{d}m_2}{\mathrm{d}t} = k_{12}m_1 - \left(R_{12} + \sum_l k_{2l}\right)m_2 + \cdots + k_{N2}m_N \tag{16}$$

$$\vdots$$

$$\frac{\mathrm{d}m_N}{\mathrm{d}t} = k_{1N}m_N + k_{2N}m_2 + \cdots - \left(R_{1N} + \sum_l k_{N1}\right)m_N \tag{17}$$

where k_{ij} are the rate constants for exchange from site i to site j, and R_{1i} are the spin–lattice relaxation rates of nuclei in site i. These equations may be written in matrix form as

$$\dot{\mathbf{m}} = -\mathbf{L}\mathbf{m} \tag{18}$$

where $\mathbf{m}$ is a column matrix whose components are m_1, m_2, ..., m_N, $\dot{\mathbf{m}}$ is the time derivative of $\mathbf{m}$, and $\mathbf{L}$ is a square $N \times N$ matrix whose off-diagonal elements are $L_{ij} = -k_{ji}$ and whose diagonal elements are $L_{ii} = \sum_l k_{il} + R_{1i}$. This matrix $\mathbf{L}$ contains all site-to-site rate constants, and the problem is to relate the elements of $\mathbf{L}$ to the signal intensities in an EXSY spectrum. The formal solution is given by

$$\mathbf{m}(t_\mathrm{m}) = \exp(-\mathbf{L}t_\mathrm{m})\mathbf{m}(0) \tag{19}$$

where $\mathbf{m}(0)$ is the column matrix of the deviations $m_j(0)$ at the start of the mixing period.

The explicit expression for the intensity of any EXSY signal (diagonal or off-diagonal) at ω_i along the frequency coordinate ω_2 and at ω_j along ω_1 is given by[13]

$$\begin{aligned} I_{ij}(t_\mathrm{m}) &= M_{j0}\exp(-\mathbf{L}t_\mathrm{m})_{ij} \\ &= \left(\delta_{ij} - t_\mathrm{m}L_{ij} + \tfrac{1}{2}t_\mathrm{m}^2\sum_k L_{ik}L_{kj} - \cdots\right)M_{j0} \end{aligned} \tag{20}$$

where $\delta_{ij} = 1$ $(i = j)$ or 0 $(i \neq j)$. Equation (20) shows that an EXSY spectrum represents a graphical display of the exchange pathways, with cross peaks corresponding to nuclei that exchange sites. Intensities of signals correspond to the exponential of the matrix $\mathbf{L}$, allowance being made for the fact that the mathematical convention of a matrix is with the diagonal running from top left to bottom right whereas an EXSY spectral map consists of a diagonal running from bottom left to top right.

2.2 Extraction of Rate Data from EXSY Spectra

The complexity of equation (20) arises because cross peaks for exchange between sites i and j can arise from both direct exchange $i \rightleftharpoons j$ and indirect exchange, $i \rightleftharpoons k \rightleftharpoons j$. For very short t_m values, the indirect cross peaks vanish, and equation (20) simplifies. However, short t_m values cause all cross-peak intensities to be low, so this approach is of limited applicability. Three strategies have been employed to extract reliable rate data from EXSY spectra.

2.2.1 Initial Rate Approximation

This involves measuring cross-peak intensities as a function of small values of t_m.[16] Rate constants k_{ij} are determined from the slope of the graph of $I_{ij}(t_\mathrm{m})$ versus $M_{j0}(t_\mathrm{m})$, but the method involves repeating the experiment for a range of mixing times and extrapolating to $t_\mathrm{m} = 0$, which is a time-consuming approach.

2.2.2 Iterative Analysis

In this method,[17] trial values of k_{ij} and R_{1i} are chosen, and a total magnetization transfer matrix $\mathbf{L}$ is constructed. Diagonalization of this yields a signal intensity matrix, which is compared with the experimental intensity array. An iterative fitting is then performed by varying exchange and relaxation rates until a 'best fit' is obtained.

2.2.3 Direct Matrix Transformation

Unlike the previous method, this approach does not require any prior knowledge of k_{ij} and R_{1i} values, and uses a matrix method for inverting equation (20) first presented by Perrin and Gipe.[18] It is based on expressing an EXSY spectrum as an intensity matrix $\mathbf{I}$ with elements

$$I_{ij} = p_i\sum_{k=1}^{N} A_{ijk}\exp(\lambda_k t_\mathrm{m}) \tag{21}$$

where p_i is the relative population of site i, and A_{ijk} and λ_k are constants depending on the experimental conditions. In matrix form,

$$\mathbf{I} = \mathbf{P}\mathbf{J} \tag{22}$$

where $\mathbf{P}$ is a column matrix of site populations and $\mathbf{J}$ is a matrix with elements $\exp(\lambda_k t_\mathrm{m})$. The kinetic matrix $\mathbf{K}$ consisting purely of rate constants k_{ij} can be related to the EXSY spectral intensity matrix $\mathbf{I}$ by

$$\mathbf{I} = \mathbf{P}\exp(\mathbf{K}t_\mathrm{m}) \tag{23}$$

Now, $\mathbf{J} = \mathbf{I}\mathbf{P}^{-1}$, and diagonalization of $\mathbf{J}$ will generate the array $\exp(\mathbf{\Lambda}t_\mathrm{m})$:

$$\mathbf{J} = \mathbf{X}\exp(\Lambda t_\mathrm{m})\mathbf{X}^{-1} \tag{24}$$

Taking the natural logarithm of the eigenvalues and dividing by t_m, i.e.,

$$\frac{\ln \mathbf{J}}{t_\mathrm{m}} = \frac{\mathbf{X}\ln\exp(\Lambda t_\mathrm{m})\mathbf{X}^{-1}}{t_\mathrm{m}} \tag{25}$$

generates the matrix $\mathbf{\Lambda}$.

Finally, matrix multiplication

$$\mathbf{X}\Lambda\mathbf{X}^{-1} = \mathbf{K} \tag{26}$$

yields the kinetic matrix $\mathbf{K}$, consisting of all rate constants for the multisite process. It should be noted that in this formulation,[19] all off-diagonal elements are positive and diagonal elements negative, in contrast to the kinetic part of the $\mathbf{L}$ matrix defined earlier [equation (18)].

It is also necessary to include spin–lattice relaxation of nuclei. This can take the form of a relaxation matrix $\mathbf{R}$, which when added to $\mathbf{K}$ gives the total magnetization transfer matrix $\mathbf{L}$:

$$\mathbf{L} = \mathbf{K} + \mathbf{R} \tag{27}$$

The matrix $\mathbf{R}$ consists of diagonal elements $-R_{1i}$ and off-diagonal elements $-\sigma_{ij} = -R_{ij}$, where these refer to cross-relaxation rates.

In cases where cross relaxation between nuclei can be neglected, the above procedures have been incorporated into a general computer program.[19] Its input consists of the number of exchanging sites (2–8), the relative populations of each site, spin–lattice relaxation rates, and experimental signal intensities, the latter being measured by integration of appropriate rows of the 2D spectral map, or, preferably, by volume integration. The accuracy of the final rate data depends on the choice of mixing time and on the accuracy of measured signal intensities. Pure absorption mode spectra

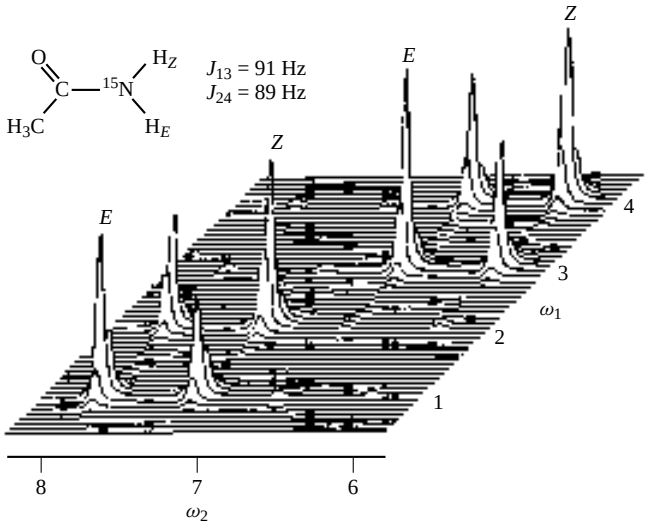

Figure 3 Partial phase-sensitive ^{1}H EXSY spectrum of ^{15}N-enriched-acetamide obtained with the TPPI method for t_m = 400 ms. A 1 K data block and spectral width in ω_2 of 614 Hz were used. A total of 256 t_1 values was used and zero filled to 1 K, resulting in a digital resolution of 1.2 Hz point^{-1} in both frequency domains

provide better resolution of closely separated signals than magnitude mode spectra. This can be achieved using time proportional phase incrementation (TPPI), and so this is the recommended procedure for accurate quantitative EXSY studies. The ^{1}H EXSY spectrum of [^{15}N]acetamide using this procedure is shown in Figure 3.[20] Both NH signals are doublets [^1J(NH) $\approx$ 90 Hz], and exhibit cross peaks due to slow C–N bond rotation. Intensity measurements of all eight signals provided accurate rate and R_1 values for the NH hydrogens. The much weaker cross peaks are due to ^{15}N spin–lattice relaxation occurring during the mixing period.

The assessment of errors in EXSY-based rate constants is an important matter which has received careful consideration.[19,21,22] The choice of mixing time has already been shown to be crucial. In multisite exchanges, it is usually impossible to find a single value of t_m that is optimal for all exchange pathways. Additional cross peaks due to indirect exchanges [equation (20)] may then arise if the mixing time is considerably greater than optimal, and so qualitative interpretations of exchange pathways from EXSY spectra must be made with caution.

2.3 Separation of Chemical Exchange and Cross-Relaxation Effects

The theoretical treatment above has neglected cross relaxation between nuclei; i.e., off-diagonal elements of the matrix **R** have been assumed to be negligibly small. This is generally valid for intermolecular exchanges and studies of intramolecular exchange using low-abundance sensor nuclei (e.g., ^{13}C). Also, it is often valid for studies of abundant nuclei (e.g., ^{1}H, ^{19}F, and ^{31}P) in small molecules, which can undergo rapid tumbling in solution. For large, slowly tumbling molecules, however, separation of chemical exchange and cross-relaxation rates is essential.

Cross-relaxation rates are given by

$$\sigma_{ij} = \frac{\gamma^4 \hbar^2 \tau_c}{10 r_{ij}^6} \left(\frac{6}{1 + 4\omega^2 \tau_c^2} - 1 \right) \tag{28}$$

where r_{ij} is the distance between nuclei i and j, and τ_c is the rotational correlation time of the molecule. The r^{-6} dependence provides proximity information, which has been widely exploited in conformational studies of complex molecules.[9] For small molecules, where τ_c is short, cross-relaxation cross peaks are of opposite sign to diagonal signals, whereas for macromolecules with relatively large τ_c values, cross-relaxation signals are of the same sign as the diagonals. Pure absorption mode (TPPI) spectra, therefore, can in theory distinguish the two cases, but in either case cross-peak intensities may not reflect chemical exchange alone.

Separation of cross relaxation and chemical exchange is most easily achieved by temperature dependence studies, since k_{ij} values increase greatly with temperature whereas σ_{ij} values do not. More recently, new pulse sequences have been suggested for achieving this separation. These include zz-EXSY,[23] an interlayed NOESY/ROESY method,[24] and gradient-enhanced exchange spectroscopy (GEXSY).[25]

2.4 One-Dimensional Variants of EXSY

The time required to obtain kinetic data from EXSY experiments can often be considerable, especially if long relaxation delays, long mixing times, and high digital resolution in both dimensions are required. Much time is incurred scanning through the whole range of incremental evolution periods, t_1, yet the majority of rows in the final spectrum do not contain useful information. However, certain t_1 values cannot simply be omitted, since each value contributes to all frequencies through the FID. One method for shortening the experimental time would be to dispense with the t_1 period completely and rely on selective excitation (see ***Selective Pulses***). The feasibility of this approach has been demonstrated for COSY experiments and is known as pseudo-COSY (ψ-COSY).[26] A similar technique has recently been proposed for exchange spectroscopy. It is described as multiplet-selective excitation or MUSEX,[27] and is based on selective excitation of only one nucleus of a coupled system using a typical DANTE pulse[28] (see ***Double Resonance***).

Another variant uses the normal nonselective pulse sequence and difference spectroscopy.[29] For N-site exchange, data for N evolution times must be collected, measuring each at zero and nonzero mixing times. Difference spectra obtained by subtracting the equilibrium spectrum from spectra recorded both without and with mixing yields exchange information. For a system of three spins A, B, and C, six one-dimensional spectra are measured for three t_1 periods, each without and with mixing. It follows that

$$\begin{bmatrix} A(t_m) - A_0 \\ B(t_m) - B_0 \\ C(t_m) - C_0 \end{bmatrix} = \exp(-\mathbf{L}t_m) \begin{bmatrix} A(t_m = 0) - A_0 \\ B(t_m = 0) - B_0 \\ C(t_m = 0) - C_0 \end{bmatrix} \tag{29}$$

The matrix **L** can then be computed by a version of the back transformation method (Section 2.2.3). Greater accuracy can be achieved if the experiment is performed for more t_1 values than are strictly necessary.[30]

2.5 Other Variants of EXSY

In 1989, Jeener, one of the pioneers of 2D NMR and its application to chemical kinetics, returned to this subject by examining the theoretical basis of the bandshapes of EXSY signals.[31] He has shown that the shapes, particularly of off-diagonal signals, provide a clear signature of the chemical exchange process even for a single temperature. Superoperator theory was applied to one- and two-spin exchanging signals. Computation, however, is not trivial, and no obvious advantages of this approach over conventional 1D bandshape analysis or 2D EXSY experiments are apparent at this stage.

In its most general form, the EXSY or NOESY pulse sequence involves three time variables, t_1, t_m, and t_2, Fourier transformation of all of which would lead to three-dimensional spectra. In practice, however, the mixing time t_m is not taken as a time variable, and 2D spectra based on a very limited range of t_m values are usually obtained. An alternative approach is to make t_m proportional to t_1 (i.e., $t_m = \kappa t_1$). The resulting 'accordion' technique[32] leads to EXSY-type spectra in which the signals are distorted from their usual shapes, and rate constants need to be extracted from signal widths rather than intensities. This restricts the versatility of the method.

Three-dimensional NMR experiments are now rapidly gaining ground[33] (see ***Multidimensional Spectroscopy: Concepts***). In 3D exchange spectroscopy, two successive exchange processes may be mapped. These may be chemical exchange (EXSY) or cross relaxation in either the laboratory frame (NOESY) or in the rotating frame (ROESY), resulting in such experiments as EXSY–EXSY and NOESY–ROESY. In the context of this article, it should be mentioned that a 3D EXSY–EXSY spectrum of heptamethylbenzenonium sulfate (in sulfuric acid) has been obtained,[33] showing the 1,2-commutation of the methyl group round the ring. It is too early to predict whether such experiments will provide more insight into dynamic processes than can be achieved by 1D and 2D experiments. Dynamic studies of highly complex molecules would appear to be most likely to gain by the extra frequency dimension.

3 APPLICATIONS OF EXSY

A few representative examples of EXSY experiments using different sensor nuclei will now be given.

3.1 Carbon-13 and Hydrogen-1

In Section 2.3, the separation of chemical exchange and cross-relaxation contributions to cross peak intensities was discussed. This problem does not arise in EXSY spectra of low-abundance nuclei (e.g., ^{13}C), where cross-relaxation effects are negligible, but is a potential problem with abundant nuclei such as ^1H. A specific case has been described where the effects of $^1H–^1H$ cross relaxation have been quantified.[34] In the trinuclear rhenium complex $[Re_3(\mu\text{-}H)_4(CO)_{10}]$, carbonyl scrambling occurs by a concerted mechanism (see NO315-***Organometallic Compounds***), the kinetics of which can be measured accurately by ^{13}C EXSY. Lower accuracy would be attached to ^1H-EXSY-based rates, since one-dimensional selective perturbation data showed that the cross-relaxation rate of a pair of bridging hydrogens was 0.04 s^{-1}, a small but not negligible rate. On the other hand, a combined ^{13}C and ^1H EXSY study of the metal migration in the cyclooctatetraene (COT) complexes $[M(CO)_3(\eta^6\text{-COT})]$ (M = Cr or W) produced kinetic data in excellent agreement with each other, indicating that $^1H–^1H$ cross relaxation in this case was negligible.[35]

3.2 Lithium-7

The first ^7Li EXSY spectra have recently been produced in connection with a kinetic study of the complex [lithium monobenzo-15-crown-5]$^+$ in nitromethane.[36] Mixing times varied between 5 and 100 ms, nine experiments being performed, each requiring 1 h of spectrometer time. Rate data were in close agreement with those measured by bandshape analysis, showing that the EXSY method can be applied with confidence to systems such as cryptands, where exchange is too slow for bandshape treatment.

3.3 Boron-11

The well-known redistribution reactions of boron trihalide mixtures have been examined by ^{11}B EXSY.[37] The particular mixture studied was a nearly 1:1 M mixture of BCl_3 and BBr_3 at 400 K. The spectrum for a mixing time of 50 ms is shown in Figure 4. Rate data were calculated by the three methods described in Section 2.2, with the direct matrix diagonalization method being preferred.

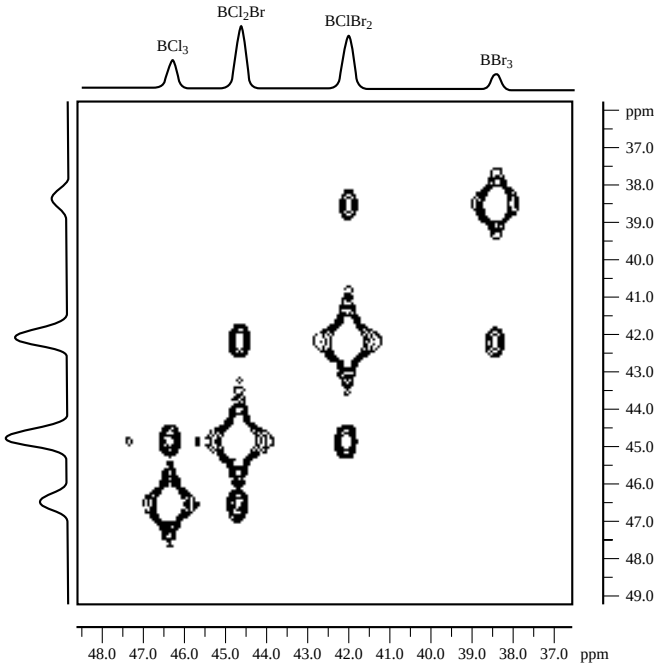

Figure 4 Boron-11 EXSY spectrum of a 1.05:1.0 M mixture of BCl_3 and BBr_3 at 400 K. The mixing time was 50 ms. The F_1 dimension contained 128 points, zero filled to 256 points. The F_2 dimension contained 512 real plus complex points. The number of scans per FID was 96

3.4 Silicon-29

Much insight into the silicate anion exchange pathways in ^{29}Si-enriched potassium silicate solutions has been gained by ^{29}Si EXSY.[38] Four intermolecular exchanges were discovered, involving monomeric anion, dimer, linear trimer, linear tetramer, and substituted cyclic trimer species, plus two intramolecular exchanges. Although this was only a qualitative study, it demonstrates the power of 2D EXSY over its 1D counterpart.

3.5 Phosphorus-31

This nucleus is well suited to EXSY studies in view of its high receptivity, wide chemical shift range, and common absence of ^{31}P–^{31}P cross relaxation. Numerous studies have been reported, one example being the octahedral organochromium(0) complexes $[Cr(CO)_2(CX)\{(MeO)_3P\}_3]$ (X = S, Se).[39] These stereochemically nonrigid complexes undergo rearrangements via trigonal-prismatic (Bailar) intermediates. The ^{31}P EXSY experiments were of the 'accordion' type[32] (Section 2.5), with the factor κ having a magnitude of 30.

3.6 Vanadium-51

Quantitative kinetic data on oligomerization reactions of vanadate in aqueous solutions has been provided by ^{51}V EXSY.[40] At pH 8.6, the EXSY spectrum shows all major oligomers, namely monomer, dimer, tetramer, and pentamer, exchanging with each other. Rates of several exchange pathways were identified. Mixing times were chosen in the range 8–10 ms.

3.7 Tin-119

The first example of ^{119}Sn EXSY was in connection with the dynamic stereochemistry of a ditin compound $CH_2[PhSn(SCH_2CH_2)_2NMe]_2$.[41] The spectrum, with a short mixing time of 5 ms, showed pairwise exchange of three isomers associated with uncorrelated isomerization of each tin centre. The same research group has also investigated $[MeSn(CH_2CH_2CH_2)_2NMe]_2$, which in solution exists as at least three isomers, two of which interconvert at rates measurable by ^{119}Sn EXSY.[42]

3.8 Tellurium-125

Platinum(IV) complexes of the type $[PtXMe_3\{MeE(CH_2)_n$-$EMe\}]$ (E = S, Se, Te; X = Cl, Br, I; n = 2, 3) undergo a variety of internal rearrangements, the most facile being pyramidal inversion of the coordinated chalcogen atoms. When the chalcogen, E, is Se or Te, the inversion process can in theory be followed by ^{1}H, ^{13}C, ^{77}Se, ^{125}Te, and ^{195}Pt spectra. To avoid any complications from cross-relaxation effects, the rare nuclei are the preferred probes. The inversion process causes exchange between four isomers according to Scheme 1.

For the complex $[PtIMe_3\{MeTe(CH_2)_3TeMe\}]$, the Te inversion rates were measured by ^{125}Te EXSY.[43] Cross peaks were detected between the DL and *meso* signals only, indicating that rates of synchronous inversion of both Te atoms are negligible.

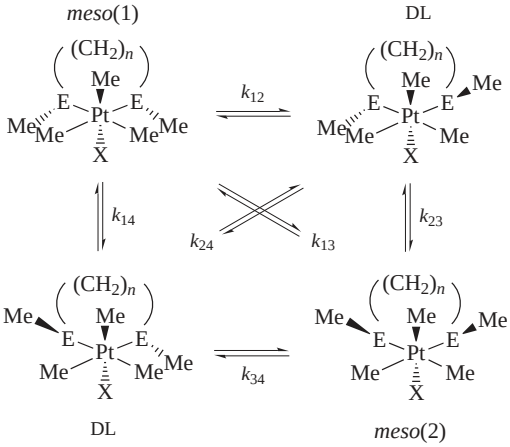

Scheme 1

3.9 Platinum-195

^{195}Pt EXSY experiments are particularly powerful in monitoring exchange rates in the above Pt(IV) complexes. The EXSY spectrum of $[PtIMe_3(MeSCH_2CH_2SMe)]$ is illustrated in Figure 5. The three isomers are identified as shown, the signals due to DL and *meso*(1) also possessing ^{13}C satellites. For the chosen mixing time of 0.3 s, cross peaks were detected between all three species. The inversion process is strictly represented by a four-site exchange problem (Scheme 1), but, when monitored by ^{195}Pt nuclei, it reduces to a three-site exchange since the DL pair are indistinguishable. Signal

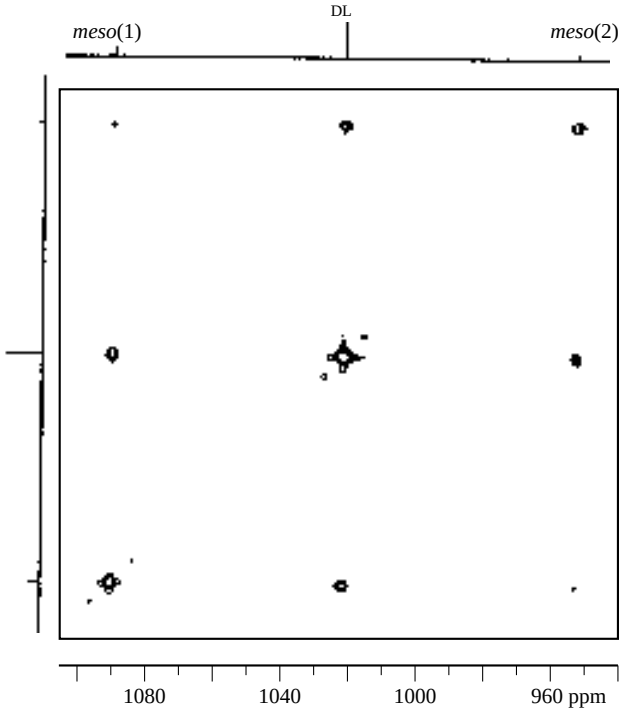

Figure 5 Platinum-195 EXSY spectrum of $[PtIMe_3(MeSCH_2CH_2SMe)]$ at 253 K. The mixing time was 300 ms. The F_1 dimension contained 256 points, zero filled to 512 points. The F_2 dimension contained 1024 points

intensity data from the spectra were used to set up the intensity matrix **I** as defined earlier,[19] and the relative populations of the isomers enabled the matrix **P** to be constructed. The matrix conversion program[19] then generated the kinetic-plus-relaxation matrix **L**, the off-diagonal elements of which provided rate constant magnitudes, namely, $k_{12} = 0.52 \pm 0.03$ s^{-1}, $k_{23} = 0.50 \pm 0.03$ s^{-1}, and $k_{13} = 0.004 \pm 0.04$ s^{-1}. This latter rate constant for synchronous double inversion of both sulfur atoms is clearly zero within experimental uncertainty, despite the appearance of weak cross peaks I_{13} and I_{31}. This illustrates the point made earlier (Section 2.2) that the existence of a cross peak does not necessarily imply direct exchange between the two sites in question, and so qualitative interpretations of EXSY spectra must be made with considerable caution. The same research group has studied the sulfur inversion dynamics of $[PtIMe_3(MeSCH_2CH_2SEt)]$.[44] This constitutes a four-site exchange problem, a case too complex to be analyzed by total bandshape analysis. In contrast, the ^{195}Pt EXSY spectrum provided definitive rate data for the six distinct inversion pathways.

4 RELATED ARTICLES

Chemical Exchange Effects on Spectra; Fluxional Motion; Homonuclear Three-Dimensional NMR of Biomolecules; Inorganic Chemistry Applications; Multidimensional Spectroscopy: Concepts; NOESY; Relaxation Processes: Cross Correlation and Interference Terms.

5 REFERENCES

1. H. S. Gutowsky and C. H. Holm, *J. Chem. Phys.*, 1956, **25**, 1228.
2. S. Forsén and R. A. Hoffman, *J. Chem. Phys.*, 1963, **39**, 2892; *J. Chem. Phys.*, 1964, **40**, 1189.
3. R. A. Hoffman and S. Forsén, *J. Chem. Phys.*, 1966, **45**, 2049.
4. J. J. Led and H. Gesmar, *J. Magn. Reson.*, 1982, **49**, 444.
5. H. Gesmar and J. J. Led, *J. Magn. Reson.*, 1986, **68**, 95.
6. R. Benn and H. Gunther, *Angew. Chem., Int. Ed. Engl.*, 1983, **22**, 350.
7. H. Kessler, M. Gehrke, and C. Griesinger, *Angew. Chem., Int. Ed. Engl.*, 1988, **27**, 490.
8. R. R. Ernst, G. Bodenhausen, and A. Wokaun, *Principles of Nuclear Magnetic Resonance in One and Two Dimensions*, Clarendon Press, Oxford, 1987, Chaps. 6–9.
9. D. Neuhaus and M. Williamson, *The Nuclear Overhauser Effect in Structural and Conformational Analysis*, VCH, New York, 1989.
10. J. Jeener, B. H. Meier, P. Bachmann, and R. R. Ernst, *J. Chem. Phys.*, 1979, **71**, 4546.
11. S. Macura and R. R. Ernst, *Mol. Phys.*, 1980, **41**, 95.
12. R. Willem, in *Progress in Nuclear Magnetic Resonance Spectroscopy*, ed. J. W. Emsley, J. Feeney, and L. H. Sutcliffe, Pergamon Press, Oxford, 1987, Vol. 20, p. 1.
13. C. L. Perrin and T. J. Dwyer, *Chem. Rev.*, 1990, **90**, 935.
14. K. G. Orrell, V. Šik, and D. Stephenson, in *Progress in Nuclear Magnetic Resonance Spectroscopy*, ed. J. W. Emsley, J. Feeney, and L. H. Sutcliffe, Pergamon Press, Oxford, 1990, Vol. 22, p. 141.
15. K. G. Orrell and V. Šik, in *Annual Reports on NMR Spectroscopy*, ed. G. A. Webb, Academic Press, London, 1993, Vol. 27, p. 103.
16. A. Kumar, G. Wagner, R. R. Ernst, and K. Wüthrich, *J. Am. Chem. Soc.*, 1981, **103**, 3654.
17. G. E. Hawkes, L. Y. Lian, E. W. Randall, K. D. Sales, and S. Aime, *J. Magn. Reson.*, 1985, **65**, 173.
18. C. L. Perrin and R. K. Gipe, *J. Am. Chem. Soc.*, 1984, **106**, 4036.
19. E. W. Abel, T. P. J. Coston, K. G. Orrell, V. Šik, and D. Stephenson, *J. Magn. Reson.*, 1986, **70**, 34.
20. E. R. Johnston, M. J. Dellwo, and J. Hendrix, *J. Magn. Reson.*, 1986, **66**, 399.
21. P. W. Kuchel, B. T. Bulliman, B. E. Chapman and G. L. Mendz, *J. Magn. Reson.*, 1988, **76**, 136.
22. C. L. Perrin and R. E. Engler, *J. Magn. Reson.*, 1990, **90**, 363.
23. G. Wagner, G. Bodenhausen, N. Muller, M. Rance, O. W. Sorensen, R. R. Ernst, and K. Wuthrich, *J. Am. Chem. Soc.*, 1985, **107**, 6440.
24. J. Fejzo, W. M. Westler, S. Macura, and J. L. Markley, *J. Magn. Reson.*, 1991, **92**, 20.
25. C. T. W. Moonen, P. Van Gelderen, G. W. Vuister, and P. C. M. Van Zijl, *J. Magn. Reson.*, 1992, **97**, 419.
26. S. Davies, J. Friedrich, and R. Freeman, *J. Magn. Reson.*, 1987, **75**, 540.
27. Yu E. Chernysh, G. S. Borodkin, E. V. Sukholenko, and L. E. Nivorozhkin, *J. Magn. Reson.*, 1992, **96**, 131.
28. G. A. Morris and R. A. Freeman, *J. Magn. Reson.*, 1978, **29**, 433.
29. R. E. Engler, E. R. Johnston, and C. G. Wade, *J. Magn. Reson.*, 1988, **77**, 377.
30. B. T. Bulliman, P. W. Kuchel, and B. E. Chapman, *J. Magn. Reson.*, 1989, **82**, 131.
31. J. Jeener, *J. Chem. Phys.*, 1989, **90**, 2959.
32. G. Bodenhausen and R. R. Ernst, *J. Am. Chem. Soc.*, 1982, **104**, 1304.
33. C. Griesinger, O. W. Sorensen, and R. R. Ernst, *J. Magn. Reson.*, 1989, **84**, 14.
34. T. Beringhelli, G. D'Alfonso, H. Molinari, G. E. Hawkes, and K. D. Sales, *J. Magn. Reson.*, 1988, **80**, 45.
35. E. W. Abel, K. G. Orrell, K. B. Qureshi, V. Šik, and D. Stephenson, *J. Organomet. Chem.*, 1988, **353**, 337.
36. K. M. Briere, H. D. Dettman, and C. Detellier, *J. Magn. Reson.*, 1991, **94**, 600.
37. E. F. Derose, J. Castillo, D. Saulys, and J. Morrison, *J. Magn. Reson.*, 1991, **93**, 347.
38. C. T. G. Knight, R. J. Kirkpatrick, and E. Oldfield, *J. Magn. Reson.*, 1988, **78**, 31.
39. A. A. Ismail, F. Sauriol, and I. S. Butler, *Inorg. Chem.*, 1989, **28**, 1007.
40. D. C. Crans, C. D. Rithner, and L. A. Theisen, *J. Am. Chem. Soc.*, 1990, **112**, 2901.
41. C. Wynants, G. Van Binst, C. Muegge, K. Jurkschat, A. Tzschach, H. Pepermans, M. Gielen, and R. Willem, *Organometallics*, 1985, **4**, 1906.
42. K. Jurkschat, A. Tzschach, C. Muegge, J. Piret-Meunier, M. Van Meerssche, G. Van Binst, C. Wynants, M. Gielen, and R. Willem, *Organometallics*, 1988, **7**, 593.
43. E. W. Abel, K. G. Orrell, S. P. Scanlon, D. Stephenson, T. Kemmitt, and W. Levason, *J. Chem. Soc., Dalton Trans.*, 1991, 591.
44. E. W. Abel, I. Moss, K. G. Orrell, V. Šik, and D. Stephenson, *J. Chem. Soc., Dalton Trans.*, 1987, 2695.

Biographical Sketch

Keith G. Orrell. *b* 1940. B.Sc.Tech., 1960, Ph.D., 1964, D.Sc., 1989, University of Manchester, UK. Successively lecturer, senior lecturer and (currently) reader, University of Exeter, UK. Approx. 150 publications on dynamic NMR, NMR of paramagnetic species and studies in liquid crystalline phases. Current research specialties: NMR studies of intramolecular motions, particularly in inorganic and organometallic compounds.

Electrolytes

Manfred Holz

Universität Karlsruhe, Karlsruhe, Germany

1	Introduction	1
2	Structural Studies of Simple Electrolyte Solutions	1
3	Dynamics in Electrolyte Solutions	5
4	Related Articles	7
5	References	7

1 INTRODUCTION

A simple electrolyte solution consists of at least three different constituents, namely the solvent molecules, cations and anions. Many systems, e.g. those of biological, geological or industrial interest, consist of mixed solvents and/or mixed electrolytes and have correspondingly higher numbers of constituents. Hence, electrolyte solutions are typical multicomponent systems and therefore not easily accessible to many investigational methods, including a number of spectroscopic techniques, where signal contributions from different constituents can overlap. However, NMR spectroscopy represents an exception among the spectroscopic techniques since it offers important advantages with respect to liquid multicomponent solutions, and electrolyte solutions are particularly well suited to investigation by NMR techniques.

The main advantages of NMR are: (i) the generally narrow resonance lines in liquid electrolytes, enabling the detection of small chemical shift differences or small line broadening effects; and (ii) the selectivity of NMR allows an overlap-free observation of distinct constituents, even in a complex mixture. This selectivity, the most important advantage, comes from normally well resolved NMR lines due to the chemical shift differences, e.g. in ^{1}H or ^{13}C spectra of electrolyte solutions of simple ions, allowing the distinction of solvent molecules and ionic species by NMR of the same nuclide. Even more important for the selectivity of NMR is the huge number of different nuclides from the whole Periodic Table which can be utilized, in particular when ionic species or their nearest neighborhood can be observed. A third advantage of NMR, especially for equilibrium studies, arises from the fact that the NMR experiment at the extremely low energies in the rf region does not disturb the thermal equilibrium of the system under observation.

The aim of NMR studies of electrolyte solutions is to gain information about the structure and dynamics of liquid systems on a microscopic level. Thus, in contrast to the well-known applications of NMR to the study of molecular structures, we are dealing here with structural and dynamical effects, which are caused by intermolecular interactions. These intermolecular interactions are often relatively weak and compared with chemical bonds less sensitive to distance and orientation, and therefore the 'structure' of a liquid solution is less sharply defined.[1] The best way to describe the structure of liquids and solutions is the use of pair correlation functions (or radial distribution functions) $g_{ij}(r)$, which are defined by statistical mechanics and which represent a measure of the probability of finding a molecule (or atom) i at a distance r from molecule (or atom) j. Unfortunately, NMR techniques do not yield $g_{ij}(r)$ directly, but certain nuclear magnetic relaxation rates $1/T_1$ are related to an integral over a pair correlation function. We will see that in NMR studies of electrolytes changes in the dynamics of the solvent molecules and of the ionic species are also often interpreted as a consequence of structural changes, and therefore sometimes a mixture of a structural and a dynamical description is used.[2]

The observation and detection of intermolecular interactions requires the measurement of quantities which are sensitive to intermolecular processes. This is the reason why in NMR studies on electrolyte solutions the measurement of nuclear magnetic relaxation times T_1 and T_2 (***Relaxation: An Introduction***) predominates by far over the measurement of chemical shifts and J couplings, the latter playing an almost negligible role.

The most characteristic property of electrolyte solutions is the electrical conductivity, that is the charge transport by migration of ionic species in an electric field. Therefore it is clear that an understanding of the translational motions in electrolytes is of outstanding importance. Here also NMR offers appropriate and unique measuring techniques for the study of translational displacements of selected species, namely the pulsed magnetic field gradient (PFG) spin echo techniques. These allow the selective measurement of translational diffusion coefficients (see ***Diffusion and Flow in Fluids*** and ***Diffusion Measurements by Magnetic Field Gradient Methods***) of solvent molecules as well as of many ionic species, and also allow mobility measurements[3] of charged particles (see ***Electrophoretic NMR***).

Taking all these special advantages of NMR into consideration, it is not surprising that in the very early years of NMR, after the introduction of the Bloembergen, Purcell and Pound theory[4] for T_1 relaxation in liquids, NMR studies on electrolyte solutions were already being performed, and since then an enormous amount of work has been published. Without any doubt, during the last 40 years NMR has developed into the most successful tool for investigating the microscopic properties of electrolyte solutions. Consequently, during the last 30 years a large number of reviews and book articles have appeared where the reader can find detailed descriptions of methods and applications.

The first really comprehensive review of the field of interest was given by Deverell in 1969.[5] This article was followed in 1986 by a second extensive review by the present author in the same review series.[6] A further comprehensive article, which gives a good introduction to the theoretical background of the different NMR methods used in the study of electrolyte solutions has been given by Hertz.[7] Most of the other accounts are devoted to selected methods and fields of application, and the most important of these will be used as references in the corresponding sections of the present contribution. The scope of the present article is confined to simple electrolyte solutions, excluding solutions of ionized macromolecules as polyelectrolytes or of complex organic ions. Thus the main emphasis lies on diamagnetic solutions of small (mostly inorganic) ions. More information on paramagnetic solutions may be found in another article in this Encyclopedia (see ***Paramagnetic Relaxation in Solution***).

2 STRUCTURAL STUDIES OF SIMPLE ELECTROLYTE SOLUTIONS

In this section it will be shown what information can be obtained from NMR techniques when 'microstructural' details of an electrolyte solution are required. It has already been mentioned that pair correlation functions $g_{ij}(r)$ cannot be derived directly from NMR measurement; however, in certain cases we can obtain a relatively well defined integral of $g_{ij}(r)$ over the first coordination sphere, delivering 'coordination numbers' n_c. We can also observe changes in this integral, which can reflect changes in $g_{ij}(r)$, when ion concentrations or generally the composition of the electrolyte solution are altered. We can further derive 'closest distances of approach', e.g. between ions and solvent molecules, and information can be gained about the orientation of solvent molecules near an ion. For example, the tendency to ion pair formation or to clustering of ions can be detected by NMR, equilibria studies are possible, and even the structural details of the ion pair configurations can be elucidated. All the microstructural properties of an electrolyte solution mentioned reflect the different interactions of relevance in such an electrolyte, namely the ion–solvent, the ion–ion, and the solvent–solvent interactions. Therefore this section is subdivided according to these interactions, and in the following discussion the most important NMR methods used under each topic are sketched and examples of typical applications are mentioned. Due to the unique importance of water on Earth, a great part of the NMR work on electrolytes has been devoted to the understanding of aqueous solutions. Furthermore, it is typical that for the investigation of a given electrolyte system the NMR of several nuclides, residing in solvent and solute species, is often utilized.

2.1 Solvation of Ions: Ion–Solvent Interactions

There are essentially four NMR measuring quantities which are used for structural solvation studies: the chemical shifts of the solute and solvent nuclei (e.g. ^{1}H and ^{17}O), the *inter*molecular dipole–dipole (DD) relaxation rate $(1/T_1)^{DD}_{inter}$ (e.g. of ^{1}H and ^{19}F), and the *inter*molecular quadrupole (QF) relaxation rate of nuclei (with $I > \frac{1}{2}$) residing in monatomic ions (e.g. ^{23}Na, ^{27}Al, ^{35}Cl, ^{39}K, ^{81}Br, ^{87}Rb, and ^{133}Cs) (see ***Aluminum-27 NMR of Solutions***, ***Quadrupolar Nuclei in Liquid Samples***, ***Quadrupolar Transition Metal and Lanthanide Nuclei*** and ***Sodium-23 NMR***).

2.1.1 Determination of Coordination Numbers

The introduction of ions into a solvent gives rise to changes of the chemical shift in the solvent molecules which are closest to the ion. The chemical shift difference between the bulk solvent and molecules in the solvation sphere Δ_m might be of the order of 10–1000 Hz. (Δ_m is especially large for paramagnetic ions.) In liquid electrolytes the solvent molecules exchange between the bulk liquid and the ionic solvation sphere, and the residence time (or lifetime) τ_m in the solvation sphere can vary strongly since it is dependent upon the strength of the ion–solvent interaction. If $\tau_m \gg 1/\Delta_m$ (strong interaction and slow exchange) is valid, we have the very favorable case that the solvent NMR signals (e.g. of ^{1}H or ^{17}O) from the bulk and solvation sphere can be observed separately, as shown in Figure 1. For example, this is the case for Be^{2+}, Mg^{2+}, Co^{2+}, Al^{3+}, Ga^{3+}, Ru^{2+}, Rh^{3+}, and Cr^{3+} (see also Figure 7). In this case the determination of the solvation numbers (primary coordination numbers) n_c of these cations by peak area integration is straightforward:

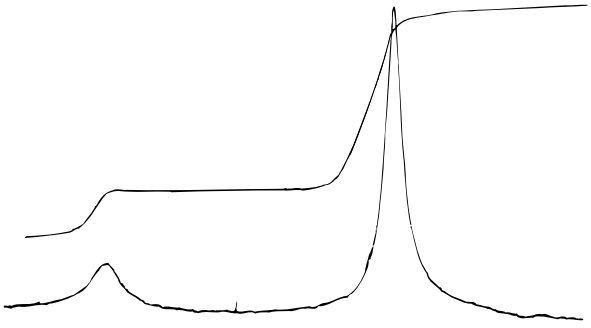

Figure 1 80 MHz ^{1}H NMR spectrum of an aqueous solution of 2.1 M $Al(ClO_4)_3$ $T = -46\,^\circ$C. Left resonance line: water in the Al^{3+} hydration shell. Right resonance line: bulk water. The peak area integration (upper line) allows the exact determination of the coordination number using equation **1** ($n_c = 6$ is found)

$$n_c = \frac{c^*_{solv}}{c^*_{ion}} \frac{I_B}{I_A + I_B} \tag{1}$$

where c^*_{ion} and c^*_{solv} are the ion and solvent concentrations on the molality scale, and I_A and I_B are the integrals of the signals of the free and bound solvent molecules, respectively.

It can be stated that the method described, which is due to Henry Taube (in 1960), is the most reliable source of information about the number of solvent molecules in the first solvation shell in liquid solutions. Results for n_c in aqueous solution are given in Hunt and Friedman[8] and are indicated in Figure 7; the coordination numbers of nonaqueous solvents are given by Lincoln.[9]

However, many ions which are of interest in biological or chemical processes, for example the alkali and halide ions, interact relatively weakly with the solvent and therefore there is fast solvent exchange ($\tau_m \ll 1/\Delta_m$) and only one common resonance line is observed. The position of this averaged line of course depends on the coordination numbers of the ions (cations and anions), and several attempts have been undertaken to derive ^{1}H chemical shifts for individual ions in a given solvent,[5,10,11] since these are required for the determination of coordination numbers. One can state that, in general, the results for n_c obtained in the fast exchange limit are less reliable than those for the slow exchange case.[6,7]

2.1.2 The Intermolecular Dipole–Dipole Relaxation

The intermolecular DD relaxation (***Relaxation: An Introduction***) is an extremely helpful tool for structural research in liquid systems. The dipolar interaction between nuclei with large γ values (e.g. ^{1}H and ^{19}F) is so strong that it can be detected even over intermolecular distances. The magnetic field produced fluctuates due to the relative translational motion of the particles which carry the interacting spins, and it induces transitions between spin states and thus relaxation occurs.[6,7] (It should be emphasized that essentially the same

is valid for intermolecular electron–nucleus DD interaction, see ***Paramagnetic Relaxation in Solution***.)

Generally a relaxation rate $1/T_1$ can be written as:

$$\frac{1}{T_1} = C \cdot \frac{E_i^2}{h^2} \cdot f(\tau_c) \tag{2}$$

where C is a constant, h is the Planck constant, E_i is the interaction energy of the underlying relaxation process, and $f(\tau_c)$ is a function of the correlation time τ_c. When $\omega_0\tau_c \ll 1$ is valid, $f(\tau_c)$ can be replaced by τ_c and we can recognize from equation (2) that the relaxation rate is essentially a product of a quantity which is determined by structural properties ($E_i{}^2$) and a quantity which is controlled by the dynamics of the system (τ_c). Therefore relaxation rates can deliver information on both structure and dynamics. In a first approximation the correlation time for intermolecular processes τ_c^{trans} is proportional to $1/D = 1/[2(D_1 + D_2)]$, where D_1 and D_2 are the translational diffusion coefficients of particles 1 and 2 carrying the DD interacting spins. Thus, if we measure D separately (e.g. by spin echo techniques) we obtain the structural information from $(\frac{1}{T_1})_{\text{inter}}$. One can write:[6,12]

$$\left(\frac{1}{T_1}\right)_{\text{inter}}^{\text{DD}} = A_{ij} \cdot \frac{c}{D} \tag{3a}$$

with:

$$A_{ij} = \frac{k}{a^4} \int_a^\infty \left(\frac{a}{r}\right)^6 g_{ij}(r) r^2 \, \mathrm{d}r \tag{3b}$$

where k is a constant, a is the closest distance of approach between the interacting spins, and c is the concentration of the interacting spins in (spins cm^{-3}). A_{ij} is called the 'A parameter' (association parameter) which contains information about the distances between two species in the solution. It should be pointed out that here intermolecular distances are probed by a microscopic magnetic field, which has the advantage that it is not disturbed in diamagnetic matter.

2.1.3 Aqueous Solutions

Other NMR techniques for the study of the solvation sphere are now described, in close connection with their application to special systems, and we begin with aqueous solutions.

Solvent isotope effects on reactions are of interest, e.g. for an understanding of acid and base catalyzed reactions. Therefore it is important to measure the deuterium/protium ratio in the solvation sphere of an ion, given by the so-called 'fractionation factor' ϕ_i. This factor can easily be determined by accurate water proton chemical shift measurements as a function of the variable H_2O/D_2O ratio of the solvent water.[6]

In favorable cases the orientation of solvent molecules in the first coordination sphere of an ion can be determined from $(\frac{1}{T_1})_{\text{inter}}^{\text{DD}}$. In order to determine an ion–molecule configuration, one needs information about more than one ion–atom pair distribution function.[7] However, isotopic substitution, e.g. replacing the nuclide ^{16}O by ^{17}O, or ^{1}H by ^{2}H, allows us to 'switch on and off' intermolecular DD interactions, and yields DD relaxation rates between the ionic nucleus and nuclei at different positions of the solvent molecule.[6,7] In this way, for example, the water orientation at the F^- and Li^+ ions has been investigated[6] (see also Figure 2).

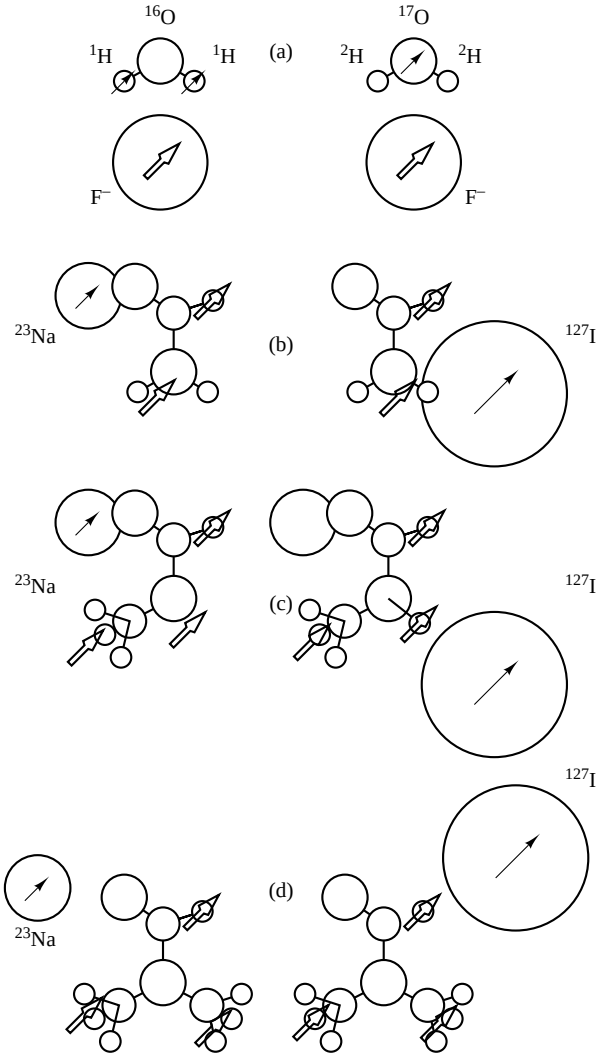

Figure 2 Ion–solvent configurations in the first solvation sphere as determined by intermolecular DD relaxation. The broad arrows indicate the relaxed spin under observation. The other arrows represent the DD interaction partners. (a) Hydration of F^-; (b–d) Na^+ and I^- solvation by (b) formamide, (c) *N*-methylformamide, and (d) *N*,*N*-dimethylformamide. (Reproduced by permission of Elsevier Science Publishers from H. G. Hertz, in 'The Chemical Physics of Solvation, Part B Spectroscopy of Solvation', ed. R. R. Dogonadze, E. Kálmán, A. A. Kornyshev, and J. Ulstrup, Amsterdam, 1986, Chap. 7)

Intermolecular quadrupole relaxation of nuclides in monatomic ions, as mentioned at the beginning of this section, can also reveal certain structural details of the solvation sphere. This relaxation mechanism is caused by the interaction of the nuclear electric quadrupole moment with fluctuating electric field gradients[6] (see ***Quadrupolar Nuclei in Liquid Samples*** and ***Quadrupolar Transition Metal and Lanthanide Nuclei***). According to the Hertz theory,[6,13] in electrolyte solutions the acting electric field gradient tensor arises from the electric fields of all electric mono- or multipoles in the closest neighborhood of the ion. In very dilute solutions

they arise solely from electric solvent dipoles in the first coordination sphere. Therefore, if the arrangement of solvent dipoles around an ion, for example Mg^{2+} in water, is of say, cubic symmetry the resulting electric field gradient at the center of the ion is quenched and we have comparatively long relaxation times T_1 and narrow resonance lines of the quadrupolar nucleus. Therefore, from linewidths and/or T_1 measurements of ionic nuclei we can learn something about the symmetry of the solvation shell. In water it turns out that Mg^{2+} has an extremely highly symmetric shell, and the field gradient is quenched by 99% of its maximum possible value, whereas for Na^+ the symmetry quenching is only about 50%,[6] indicating a symmetry distortion in this latter case.

2.1.4 Non-Aqueous Solutions and Ions in Mixed Solvents

Under certain assumptions with respect to the shape of the pair correlation function[7] it is possible to derive quite reliable values of a, the closest distance of approach [equation (3)] between the center of an anion and a distinct hydrogen atom of the solvent molecule in the electrolyte solution. These a values for a number of ions and solvents such as methanol, formamide, *N*-methylformamide (NMF) and formic acid are listed in the literature.[7] Information from QF relaxation of ionic nuclei about the symmetry of solvation shells for various solvents and ions has also been obtained and can be found in the original literature.[14] The orientation of highest probability of nonaqueous solvents in the first coordination sphere of ions has been investigated in the same manner as described above for water[2,7] and results are shown in Figure 2 for the Na^+ and I^- ions in three amides.

Specific interactions or comparatively strong unspecific interactions between a given ion and a solvent can often be easily detected by using binary mixed solvents. If the local mole fraction $x_{\text{local},1}$ of a solvent 1 in the solvation sphere of an ion is higher than x_1 its macroscopic mole fraction in the mixture, solvent 1 has a stronger interaction with the ion than does solvent 2, and there is preferential solvation of the ion by component 1. NMR chemical shift or relaxation measurements of ionic nuclei (or sometimes of solvent nuclei) can provide a very valuable insight into the actual composition of the solvation shell and thus into preferential solvation or selective solvation (the latter corresponds to the special case $x_{\text{local},1} = 1$, $x_{\text{local},2} = 0$). A huge number of preferential solvation studies exist,[6,15,16] allowing the determination of $\Delta G^{\ddagger}_{\text{ps}}$, the free energy of preferential solvation.[15] Figure 3 shows the results of such a study, where $x_{\text{local},1}$ and $x_{\text{local},2}$ could be determined separately. Since $x_{\text{local},1} + x_{\text{local},2} = 1$ must be valid, the reliability of the result can easily be checked.[17]

An interesting phenomenon, which has been detected for the first time by different NMR methods, occurs in aqueous electrolyte solutions containing nonpolar (hydrophobic) solutes. This is the attraction of anions to the nonpolar groups, which are hydrophobically hydrated,[13,18] a phenomenon which might be of general importance in various fields of pure and applied chemistry and life sciences.

2.2 Ion–Ion Interaction Effects

An extremely important aspect in the understanding of electrolyte solutions is the detection and elucidation of ion–ion interactions. For this problem the chemical shifts and relaxation data of nuclei residing in ions are utilized almost exclusively, and many examples from the NMR of metal nuclides are given by Dechter.[16] In particular, in nonaqueous solvents there is often a strong tendency to ion pair formation or to complexation. If there are long-living complexes, different cation–anion–solvent complexes can be identified by their separate resonance lines, in, for example, metal nuclide NMR. A very informative example of such a case is given in Figure 4.

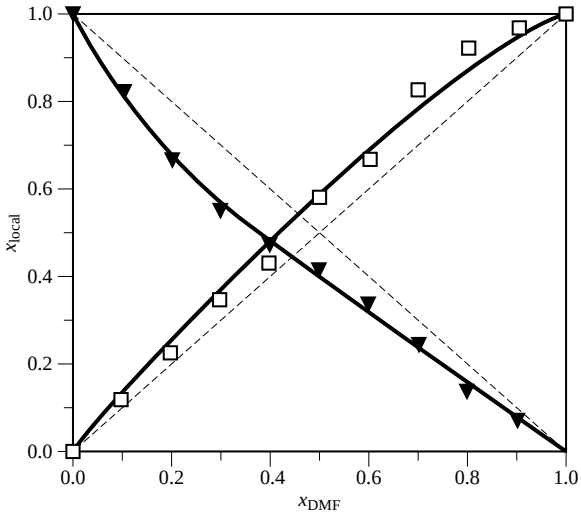

Figure 3 Preferential solvation study of Na^+ in *N*,*N*-dimethylformamide (DMF)–methanol by $^{23}Na^+$ QF relaxation;[17] x_{local}, the mole fraction of methanol (▼) and DMF (□) in the first solvation sphere of Na^+, is given as a function of x_{DMF}, the macroscopic mole fraction of DMF in the mixed solvent system. (- - - -) Nonpreferential solvation. T = 25 °C

In dilute solutions of strong electrolytes the behavior of the Debye–Hückel ion–ion pair distribution function is clearly reflected in a $\sqrt{c}$ dependence of the relaxation rate $1/T_1$ of monatomic ionic nuclei such as $^7Li^+$, $^{23}Na^+$, $^{87}Rb^+$, and $^{35}Cl^-$ [6] (Figure 5). From intermolecular QF relaxation of ionic nuclei[19] and intermolecular DD relaxation of ^1H or ^{19}F,[20] the sharpening of the cation–anion pair correlation function with decreasing ionic strength can be observed by the determination of the quantity $(1/T_1)_{\text{inter}} \cdot (\bar{D}/c)$ [see equation 3, 43] as a function of concentration c.

The DD interaction of the electron spin on the paramagnetic Ni^{2+} ion with nuclei of other ions, such as Li^+ or Al^{3+}, is an excellent tool for probing the effective forces between ions in solution by comparing the NMR relaxation results with model potentials.[21] The $^7Li^+$ and $^{27}Al^{3+}$ relaxation data revealed a surprisingly close distance of approach between Ni^{2+} and these cations in aqueous solution.[6] Cation–anion mean force potentials have recently been very carefully investigated by ^1H and ^{31}P relaxation of $(CH_3)_4P^+$ in the presence of a paramagnetic anion by Fries and co-workers.[22] These authors applied a refined theory of intermolecular DD relaxation.[6,22]

Electric field gradients acting at quadrupolar ionic nuclei can also arise from neighboring ions, giving the so-called 'ion–ion contribution' to the QF relaxation of nuclei in monatomic ions.[6] Despite the fact that this intermolecular (or interatomic) relaxation is of a complicated nature, attempts have been

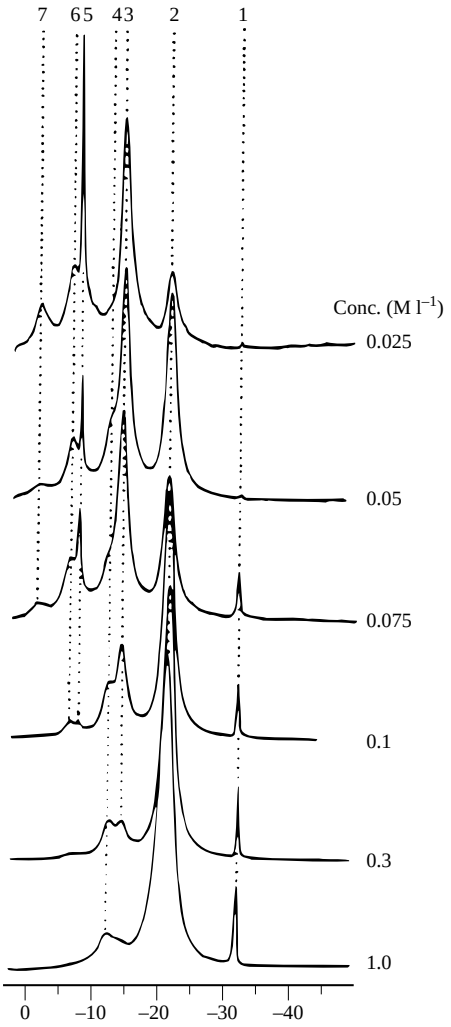

Figure 4 78.2 MHz ^{27}Al NMR studies of $AlCl_3$ in acetonitrile (AN) at different salt concentrations. Seven different hexacoordinated complexes were detected: (1) $Al(AN)_6^{3+}$; (2) $[AlCl(AN)_5]^{2+}$; (3) *cis*-$[AlCl_2(AN)_4]^+$; (4) *trans*-$[AlCl_2(AN)_4]^+$; (5) *cis*-$AlCl_3(AN)_3$; (6) *trans*-$AlCl_3(AN)_3$; (7) *cis/trans*-$[AlCl_4(AN)_2]^-$. (Reproduced by permission of Academic Press from F. W. Wehrli and S. Wehrli, *J. Magn. Reson.*, 1981, **44**, 197)

undertaken to derive from ion–ion relaxation rates models of clusters consisting of up to four ions.[6]

Studies of chemical equilibria for ion pair formation, for acid–base reactions or complexation reactions is an important practical field of NMR applications to electrolyte solutions, as shown in a recent review.[23] In these studies NMR parameters such as peak areas, chemical shifts and relaxation times are, in principle, used for the contactless and disturbance-free measurement of equilibrium concentrations which are needed for the determination of equilibrium constants. It should be emphasized once again that these NMR experiments can be performed under thermal equilibrium conditions.

2.3 Solvent–Solvent Interaction Effects in Electrolyte Solutions

The addition of salts to a pure or mixed solvent can alter the solvent–solvent interaction or the interaction of a

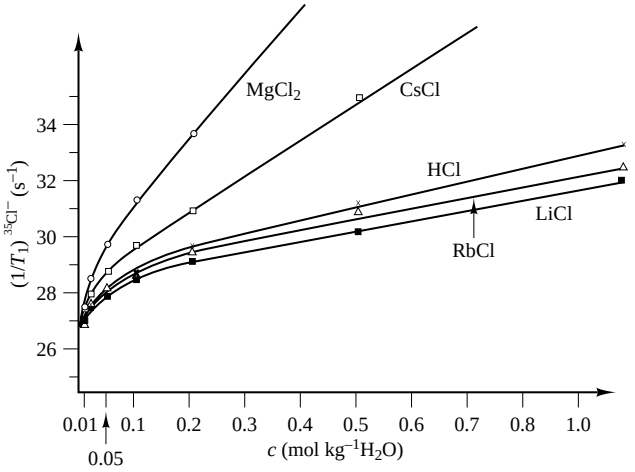

Figure 5 $^{35}Cl^-$ relaxation rates in aqueous solutions as a function of salt concentration c for different salts (T = 25 °C). At low concentrations the $\sqrt{c}$ dependence of $1/T_1$ can be clearly observed. (M. Holz and Xi-An Mao, unpublished data)

nonelectrolyte cosolute in the electrolyte solution. These often subtle effects can be investigated by '*A* parameter' [equation (3)] studies where an increase of A_{ij}, e.g. as a function of salt concentration, indicates a sharpening of the solvent–solvent pair distribution function. Such a behavior has been found in water, when 'structure-breaking' salts such as RbBr and RbI are added.[6] Another interesting example is the association behavior of nonpolar solutes or solutes with nonpolar groups in water when salts are added and where hydrophobic association can occur as an early stage of a salting-out effect. In a recent NMR study,[24] A_{22} for small hydrophobic solutes was determined with and without the presence of salts in water. It was shown that the salt influence follows the well-known empirical 'Hofmeister' (or 'lyotropic') series for the salting out of biomolecules, thus opening up the possibility of model studies by this NMR technique.

3 DYNAMICS IN ELECTROLYTE SOLUTIONS

Structural peculiarities caused by short-range interactions in electrolyte solutions are in most cases closely connected with changes in the microdynamics of the solution. Owing to this fact and to the general importance of dynamic processes, there is an enormous interest in NMR studies of the dynamics of electrolyte solutions.[7,25] Information about the rotational motion of solvent molecules in solvation complexes comes from solvent relaxation data; translational motions of solvent and ions are observable by PFG spin echo studies.

3.1 Rotational and Translational Motion of Solvent Molecules

When we dissolve a salt in a solvent the relaxation rate of solvent nuclei (e.g. ^{1}H, ^{2}H, ^{14}N, ^{13}C, and ^{17}O) is changed as a function of the salt concentration. This change is because a part of the solvent molecules now resides in the solvation spheres of the ions, where the rotational (and translational)

behavior is different from that in the bulk liquid. According to Hertz,[6,7] one can define coefficients B' and B_D by the following relationships (which correspond to the Jones–Dole equation for the concentration dependence of the viscosity):

$$\frac{(T_1)^0}{T_1(c^*)} = 1 + B'c^* + \cdots \tag{4a}$$

and

$$\frac{D^0}{D(c^*)} = 1 + B_D c^* + \cdots \tag{4b}$$

where $(T_1)^0$ and D^0 are the relaxation time and diffusion coefficient in the salt-free solvent, and c^* is the salt concentration on the molality scale. B' and B_D are obtained from the slope of the concentration dependence at $c^* \rightarrow 0$. Positive and negative B coefficients correspond to 'structure-forming' and 'structure-breaking' salts, respectively. With the convention $B'^+(K^+) = B'^-(Cl^-)$ it is possible to derive single ion $B'^{\pm}$ coefficients and to determine the rotational correlation times $\tau_c^{\pm}$ of the solvent molecule in the ionic solvation sphere:

$$\tau_c^{\pm}/\tau_c^0 = B'^{\pm} \cdot \frac{55.5}{n_c^{\pm}} + 1 \tag{5}$$

when c^* is given in the aquamolality scale. ($D^{\pm}/D^0$ can be obtained in a completely analogous way.) Example data for a number of ions in various solvents are given in Table 1.[7]

For most inorganic ions in water $B'^{\pm} \approx B_D^{\pm}$, showing the same influence of the ion on the rotational and translational motion in its surroundings. However, it seems that this is not true for hydrophobic ions, such as $(alkyl)_4N^+$ ions. The B' coefficients in aqueous solutions of strong acids (HCl, HBr, $HClO_4$, and HNO_3) have recently been measured, revealing a structure-breaking property of the H^+ ion at low temperatures.[26]

The translational diffusion of water in aqueous electrolyte solutions as a function of salt concentration has been very carefully investigated by the NMR spin echo technique, as shown in Figure 6.[7] In can be seen that the structure-breaking salts with their large ions increase the translational mobility of water, and there is a strong decrease in the water mobility when, for example, divalent cations are dissolved.

In very concentrated salt solutions (***Concentrated Solution Effects*** such as aqueous $ZnCl_2$ or $Ca(NO_3)_2$ solutions, NMR self-diffusion and relaxation measurements revealed that with increasing salt concentration the correlation time ratio $\tau_c^{trans}/\tau_c^{rot}$ of translational and rotational motion increases strongly up to a factor of about 7 compared with pure water.[6] This shows that in hydrous salt melts the degree of freedom for rotational motion of water is about one order of magnitude higher than that for the translational motion.[27] The molecular motions of the solvent water in undercooled electrolyte solution has also been extensively investigated,[28] as has the pressure dependence of diffusion and solvent reorientation times.[29]

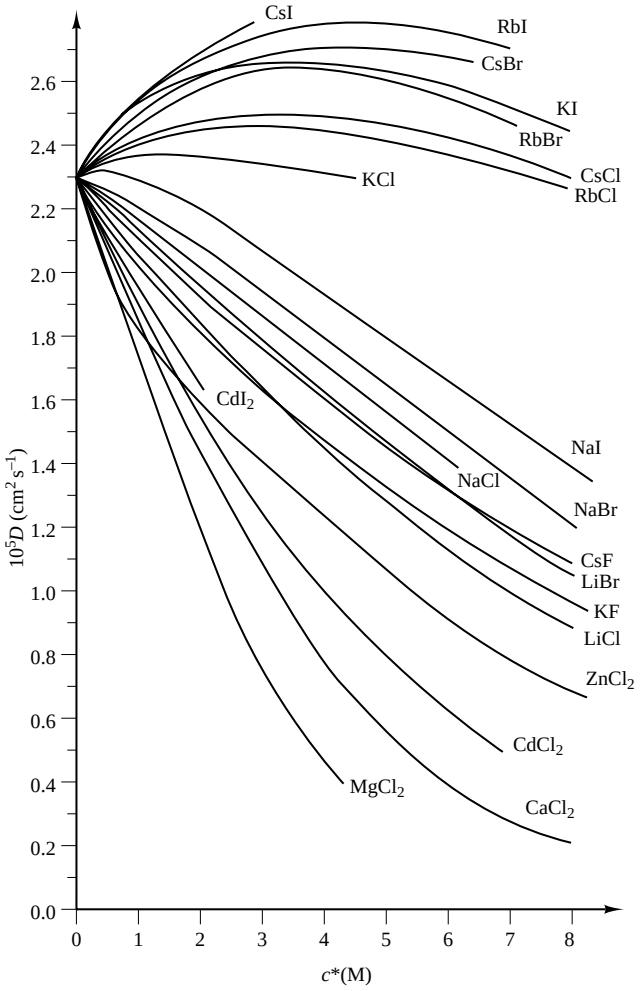

Figure 6 Self-diffusion coefficients of solvent water (H_2O) molecules in a number of electrolyte solutions as a function of the salt concentration c^* on the molality scale (T = 25 °C). (Reproduced by permission of Elsevier Science Publishers from H. G. Hertz, in 'The Chemical Physics of Solvation, Part B Spectroscopy of Solvation', ed. R. R. Dogonadze, E. Kálmán, A. A. Kornyshev, and J. Ulstrup, Elsevier, Amsterdam, 1986, Chap. 7)

3.2 Motion of Ions and Complexes

The reorientational motion of ions can serve as a probe of ion–ion and ion–solvent interactions.[7,25] In polyatomic ions such as ClO_4^- and SO_4^{2-}, the ^{17}O intramolecular QF relaxation can be used.[30] In particular, the study of rotational correlation times of solvation complexes of paramagnetic ions has a long tradition in NMR[5,7,30,31] (see ***Paramagnetic Relaxation in Solution*** and ***Relaxometry of Tissue***). Measurements of the self-diffusion coefficients $D^{\pm}$ of ions and mobility of ions have become of increasing interest in recent years,[3,7] and, at least for ionic diffusion in electrolytes, a large amount of data has been collected.[32] A relatively young field of NMR is the investigation of electrolytes in the nonequilibrium state, that is in the electrically conducting state, by the DCNMR (NMR in presence of a direct current) technique.[3,6] This allows measurement of electrophoretic mobilities (see ***Electrophoretic NMR***) and transference numbers of distinct ions in complex electrolyte systems.[3] Relaxation measurements of ionic quadrupolar nuclei moving in an electric field might yield information

Table 1 The Ratio $\tau_c^{\pm}/\tau_c^0$ of Rotational Correlation Times of Solvent Molecules in the Solvation Sphere of Ions ($\tau_c^{\pm}$) and in the Pure Liquid (τ_c^0)[7] (T = 25 °C, n_c = 6 was Assumed in All Cases)

Ion	H_2O	Methanol	Formamide	*N*-Methylformamide	Glycol	Glycerol
Li^+	2.3	3.1	–	2.0	–	–
Na^+	1.6	2.0	2.4	1.7	2.0	1.6
K^+	0.9	1.7	1.7	1.6	1.2	1.1
Cs^+	0.5	–	1.5	1.4	0.9	0.9
Mg^{2+}	5.2	–	–	–	–	–
Ca^{2+}	3.5	–	–	–	–	–
Cl^-	0.9	1.7	1.5	1.7	1.2	1.1
Br^-	0.6	1.5	1.4	1.6	1.0	0.9
I^-	0.3	1.3	1.1	1.5	0.9	0.8

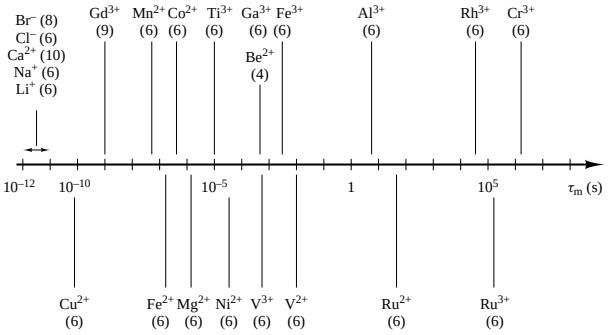

Figure 7 Lifetimes τ_m of water in the inner shell of various hydration complexes at 25 °C.[33] The coordination number n_c is given in brackets; τ_m for monovalent ions lies in the range 2 ps $< \tau_m <$ 10 ps

about changes in the solvation shell and in the ion–ion distribution function connected with the migration of the ion.[3]

3.3 Exchange Studies

Exchange studies where the lifetime τ_m of a solvent molecule (or a hydrogen atom) in the solvation complex is the quantity of interest, have an extraordinary importance for the understanding of electrolyte solutions (see ***Relaxation Effects of Chemical Exchange***). In particular, the aquo complexes have been studied extensively using ^1H and ^{17}O linewidth measurements,[6,8] but also many data exist for nonaqueous solvents.[6] The range of lifetimes τ_m is enormous, a lower limit of about 2 ps can be assumed. A sketch of the lifetimes in aquo complexes is given in Figure 7.[33] The water proton exchange rates in solutions of strong electrolytes have been studied as a function of the pH.[34] The mechanism of solvent exchange can be elucidated by pressure dependent ^1H and ^{17}O NMR linewidth studies[6,35] (see ***Kinetics at High Pressure***) and these investigations have contributed enormously to our present knowledge of ligand substitution reactions in electrolyte solutions.

4 RELATED ARTICLES

Aluminum-27 NMR of Solutions; Brownian Motion and Correlation Times; Concentrated Solution Effects; Diffusion and Flow in Fluids; Diffusion Measurements by Magnetic Field Gradient Methods; Electrophoretic NMR; Kinetics at High Pressure; Paramagnetic Relaxation in Solution; Quadrupolar Nuclei in Liquid Samples; Relaxation: An Introduction; Relaxation Effects of Chemical Exchange; Relaxometry of Tissue; Sodium-23 NMR.

5 REFERENCES

1. H. L. Friedman, *J. Electrochem. Soc.*, 1977, **124**, 421C.
2. H. G. Hertz, *Pure Appl. Chem.*, 1982, **54**, 2297.
3. M. Holz, *Chem. Soc. Rev.*, 1994, **23**, 165.
4. N. Bloembergen, E. M. Purcell, and R. V. Pound, *Phys. Rev.*, 1948, **73**, 679.
5. C. Deverell, *Prog. NMR Spectrosc.*, 1969, **4**, 235.
6. M. Holz, *Prog. NMR Spectrosc.*, 1986, **18**, 327.
7. H. G. Hertz, in *The Chemical Physics of Solvation, Part B Spectroscopy of Solvation*, ed. R. R. Dogonadze, E. Kálmán, A. A. Kornyshev, and J. Ulstrup, Elsevier, Amsterdam, 1986, Chap. 7
8. J. P. Hunt and H. L. Friedman, in *Prog. Inorg. Chem.*, 1983, **30** 359.
9. S. F. Lincoln, *Coord. Chem. Rev.*, 1971, **6**, 309.
10. M. C. R. Symons, *Pure Appl. Chem.*, 1979, **51**, 1671.
11. J. Burgess, *Metal Ions in Solution*, Wiley, London, 1979, Chap. 2
12. K. J. Müller and H. G. Hertz, *Chem. Scr.*, 1989, **29**, 277.
13. B. Lindman and S. Forsén, *Chlorine, Bromine and Iodine NMR* (*NMR Basic Principles and Progress, Vol. 12*), ed. P. Diehl, E. Fluck, and R. Kosfeld, Springer, Berlin, 1976.
14. H. Weingärtner and H. G. Hertz, *Ber. Bunsenges. Phys. Chem.*, 1977, **81**, 1204.
15. K. Covington and K. E. Newman, *Pure Appl. Chem.*, 1979, **51**, 2041.
16. J. J. Dechter, *Prog. Inorg. Chem.*, 1982, **29**, 285.
17. A. Sacco, M. C. Piccini, and M. Holz, *J. Solution Chem.*, 1992, **21**, 109.
18. M. Holz and M. Sörensen, *Ber. Bunsenges. Phys. Chem.*, 1992, **96**, 1441.
19. H. G. Hertz, M. Holz, and A. Sacco, *Chem. Scr.*, 1989, **29**, 291.
20. K. J. Müller and H. G. Hertz, *Chem. Scr.*, 1989, **29**, 277.
21. H. L. Friedman, in *Thermodynamics of Aqueous Systems with Industrial Applications* (*ACS Symposium Series No. 133*), ed. S. A. Newman, American Chemical Society, Washington, DC, 1980, p. 547.
22. M. Jeannin, E. Belorizky, P. H. Fries, and W. Gorecki, *J. Phys. II, France*, 1993, **3**, 1511.
23. A. I. Popov, in *Modern NMR Techniques and Their Application in Chemistry* (*Practical Spectroscopy Series, Vol. 11*), ed. A. I. Popov and K. Hallenga, Marcel Dekker, New York, 1991, Chap. 8

24. M. Holz, R. Grunder, A. Sacco, and A. Meleleo, *J. Chem. Soc., Faraday Trans.*, 1993, **89**, 1215.
25. Y. Masuda and M. Yamatera, in *Studies in Physical and Theoretical Chemistry*, ed. H. Ohtaki and M. Yamatera, Elsevier, Amsterdam, 1992, Vol 79, Chap. 4
26. H. G. Hertz, R. Maurer, and S. Killie, *Z. Phys. Chem., NF*, 1991, **172**, 157.
27. A. J. Dianoux, in *The Physics and Chemistry of Aqueous Ionic Solutions* (*NATO ASI Series*), ed. M. C. Belissant-Funel and G. W. Neilson, D. Reidel, Dordrecht, 1987, p. 147.
28. E. W. Lang, W. Fink and H. Radkowitsch, in *Hydrogen-Bonded Liquids* (*NATO ASI Series C, Vol. 329*), ed. J. Dore and J. Teixeira, Kluwer, Dordrecht, 1991, p. 393.
29. E. W. Lang and M.-D. Lüdemann, *Prog. NMR Spectrosc.*, 1993, **25**, 507.
30. H. G. Hertz, in *Water, a Comprehensive Treatise*, ed. F. Franks, Plenum, New York, 1973, Vol. 3, Chap. 7
31. L. Banci, I. Bertini, and C. Luchinat, *Nuclear and Electron Relaxation*, VCH, Weinheim, 1991.
32. R. Mills and V. M. M. Lobo, *Self-diffusion in Electrolyte Solutions*, Elsevier, Amsterdam, 1989.
33. H. L. Friedman, *Chem. Scr.*, 1985, **25**, 42.
34. J. Diratsaoglu, S. Hauber, H. G. Hertz, and K. J. Müller, *Z. Phys. Chem., NF*, 1990, **168**, 13.
35. A. E. Merbach, *Pure Appl. Chem.*, 1982, **54**, 1479.

Biographical Sketch

Manfred Holz. *b* 1938. Diplom (supervisor G. Laukien), 1966, Dr. rer. nat. (supervisor H. G. Hertz), 1973, physics, University of Karlsruhe, Germany. Member of the team which developed the first commercial pulsed NMR spectrometers, Bruker, 1966–70. Doctoral work, 1970–73. Research assistant, lecturer, 'Akademischer Direktor', Institute of Physical Chemistry, University of Karlsruhe, 1973–present. Approx. 80 publications, including contributions to the series *NMR, Specialist Periodical Reports*. Research interests: multinuclear magnetic resonance for the study of microstructure and dynamics of liquid systems, intermolecular quadrupole relaxation, NMR diffusion and flow studies, electrophoretic NMR.

Electrophoretic NMR

Charles S. Johnson Jr

University of North Carolina, Chapel Hill, NC, USA

1	Introduction	1
2	Principles of ENMR	1
3	Practical Considerations	4
4	Data Analysis	6
5	Illustrations of ENMR Spectra	8
6	Literature Sources	9
7	Related Articles	9
8	References	9

1 INTRODUCTION

Electrophoretic NMR (ENMR) combines pulsed field gradient NMR (PFG NMR) flow measurements with in situ electrophoresis. This arrangement permits the direct measurement of the drift velocities of NMR active ions in electric fields. Furthermore, the selectivity of high-resolution NMR is retained; and, in principle, all the components of a mixture can be detected simultaneously. Therefore, ions can be identified by their NMR spectra and, conversely, NMR spectra of mixtures can be edited on the basis of electrophoretic mobilities. The timescale of a single ENMR experiment, i.e. the ionic drift time, ranges from a few milliseconds to a few seconds. This provides some sensitivity to reaction rates and the ability to determine at least whether exchange reactions occur during the drift time. The disadvantage is that the drift time must be less than T_1 or T_2, depending on the particular experiment. It is this restricted drift time that limits resolution of drift velocities in ENMR to much lower values than found in classical electrophoresis, e.g. capillary zone electrophoresis (CZE).

In this brief article we present the theory of ENMR at the phenomenological level. The experimental aspects are treated in some detail because the methods and the instrumentation are unfamiliar to most NMR spectroscopists. We also discuss data analysis and display a few examples to illustrate the capabilities and limitations of the method.

2 PRINCIPLES OF ENMR

2.1 Electrophoresis

'Electrophoresis' refers to the transport of charged particles in electric fields. In a constant electric field $\boldsymbol{E}_{\mathrm{dc}}$ ions of a particular species attain the steady state or terminal velocity $\boldsymbol{v}_{\mathrm{e}} = \mu \boldsymbol{E}_{\mathrm{dc}}$, where μ is the electrophoretic mobility. This is of considerable interest in chemistry because the mobility is characteristic of the ionic species in a particular environment. The separation of ions according to mobilities is the basis of analytical electrophoresis. However, general theories relating μ to molecular properties are complicated and often difficult to use.

Consider a particle of radius a and charge Ze in medium with the dielectric constant ϵ_{r} and viscosity η. The counterions in the electrolyte, treated as a continuous distribution of charge (ionic atmosphere), effectively screen the charge of the particle so that the effective potential quickly drops to zero with distance. The range of the potential is determined by the inverse Debye screening length:[1]

$$\kappa = \left(\frac{2\rho F^2}{\epsilon_0 \epsilon_{\mathrm{r}} RT} \right)^{1/2} I_{\mathrm{c}}^{1/2} \tag{1}$$

where ρ is the density of the solvent, ϵ_0 is the permittivity of vacuum, F is the Faraday constant, R is the gas constant, T is the absolute temperature, and I_{c} is the ionic strength. It is assumed that κ^{-1} is approximately equal to the thickness of the electrical double layer. With the additional assumption that the applied electric field does not distort the ionic atmosphere, Henry was able to show that the electrophoretic mobility is given by:[2]

$$\mu = \frac{Ze}{6\pi\eta a} \frac{X_1(\kappa a)}{(1+\kappa a)} \tag{2}$$

where $X_1(\kappa a)$ is a monotonically increasing function that ranges from 1.0 for $\kappa a \ll 1$ to 1.5 for $\kappa a \gg 1$.

In the 'small particle' limit where $\kappa a \ll 1$, equation (2) gives $\mu = Ze/f$, where $f = 6\pi\eta a$ is the Stokes' law friction factor for a sphere. This result simply expresses the balance of electrostatic and frictional forces at steady state, i.e. $ZeE_{\mathrm{dc}} = fv_{\mathrm{e}}$. At the 'large particle' limit where $\kappa a \gg 1$, equation (2) is equivalent to $\mu = \sigma/\eta\kappa$, where $\sigma = Ze/4\pi a^2$ is the surface charge density. Also, in this limit Smoluchowski showed that $\mu = \epsilon_0\epsilon_{\mathrm{r}}\zeta/\eta$, where ζ is the potential at the plane of shear (between the stationary and moving solvent layers).[2] Thus, in principle, for $\kappa a \gg 1$ a measurement of the mobility provides a direct determination of σ and the ζ potential. It is interesting that in this limit there is no dependence of μ on particle size or even particle shape, but most macroions fall short of this limit and their mobilities show some size dependence.

In fact, applied electric fields can distort the ionic atmosphere, and Henry's equation is often a crude approximation. However, numerical solutions of the exact equations for flow and ion densities around a sphere, displayed as graphs of mobility versus the ζ potential, confirm that Henry's formula is accurate for sufficiently small values of the ζ potential.[3] Rigorous electrokinetic theories tend to be quite complicated. Modern analytical treatments of this problem have been reviewed by Hunter.[4,5] A major difficulty with all the theories is that the results are expressed in terms of ζ potentials. The ζ potential cannot be measured, and only in the Smoluchowski limit is it related to measurable quantities. The basic problem is that counterions inside the plane of shear move with the particle and affect the apparent surface charge density. This effect is clearly illustrated by 'fuzzy' polymer coatings, e.g. methylcellulose, which displace the plane of shear away from a surface into a region where the ζ potential vanishes. Experimental studies can only hope to relate electrophoretic mobilities to measurable quantities such as diffusion coefficients and, perhaps, estimated surface charge densities.

Analytical applications of ENMR depend on the fact that electrophoretic mobilities of molecular ions and charged molecular aggregates almost always lie in the range from 0 to ± 5 (μm s^{-1})(cm V^{-1}). The applied electric fields are typically 0–100 V cm^{-1}, and the maximum particle displacements in a typical drift time of one second are approximately 500 μm. This is conveniently larger than any particles of interest, but much less than the length of the active volume.

2.2 PFG NMR and the Measurement of Drift Velocities

The measurement of directed flow by means of PFG NMR was first reported by Stejskal.[6] In this experiment a magnetic field gradient is superposed on the applied magnetic field $\boldsymbol{B}_0$, here assumed to be in the z direction. For a gradient of magnitude g in the z direction, the local magnetic field is given by $B = B_0 + zg$, where the origin defines the center of the sample. The simplest description is obtained in a reference frame that rotates at the frequency $\omega_0 = -\gamma B_0$ about the z axis. The pulse sequence in Figure 1(a) shows the 90°_x and 180°_y rf pulses and the gradient pulses of amplitude γg and duration δ. A hard 90°_x rf pulse at $t = 0$ rotates the nuclear magnetization into the y direction. Then under the influence of the first gradient pulse the isochromats precess so that the isochromat associated with the volume element between z and z + dz rotates through the angle $\phi = \gamma g z \delta$ relative to the yz plane in the rotating frame. The net magnetization of the sample in the y direction vanishes and the nuclear spin positions are phase encoded. This is illustrated on the left-hand side of Figure 1(b), where the isochromats, represented by parallel lines after the 90°_x pulse, are wound into a helix of pitch $\Lambda = 2\pi/\gamma g \delta$ by the gradient.[7] In order to obtain a spin echo, the helix must be unwound. This is usually accomplished by means of a 180°_y pulse, reverses the signs of the x components of the isochromats or, equivalently, sets the phase back by $-2\gamma g z \delta$. Continued precession of the isochromats leads to a refocusing of the phase dispersion resulting from both the applied gradient and the inevitable weak background gradient. The unwinding and echo formation are illustrated on the right-hand side of Figure 1(b).

The first gradient pulse in the Stejskal–Tanner sequence sensitizes the transverse magnetization to translational motion of the spins.[8] The effect of diffusion is to smear out the helical pattern, i.e. to reduce its amplitude, while flow in the z direction displaces the helix so that an isochromat with $\phi \neq 0$ moves into the plane at $z = 0$. The important point is that the phase of the echo, as shown in Figure 1(b), is $\phi = qvt_1$. A complete description of these effects on the basis of modified Bloch equations gives an expression for the complex magnetization $M_+ = M_x + iM_y$ at the echo maximum ($t = 2\tau$). The phase detected signal can be written as:[6]

$$S(2\tau) = M_0 \exp(-2\tau/T_2) \exp[-Dq^2(t_1 + 2\delta/3)] \exp(iqvt_1) \quad (3)$$

where M_0 is the initial amplitude of the FID, $q = \gamma g \delta$, v is the component of velocity in the z direction (assumed to be nonzero only between the gradient pulses), and D is the tracer diffusion coefficient. Typically, $\delta \ll \Delta$, t_1 and the corrections for δ are unimportant.

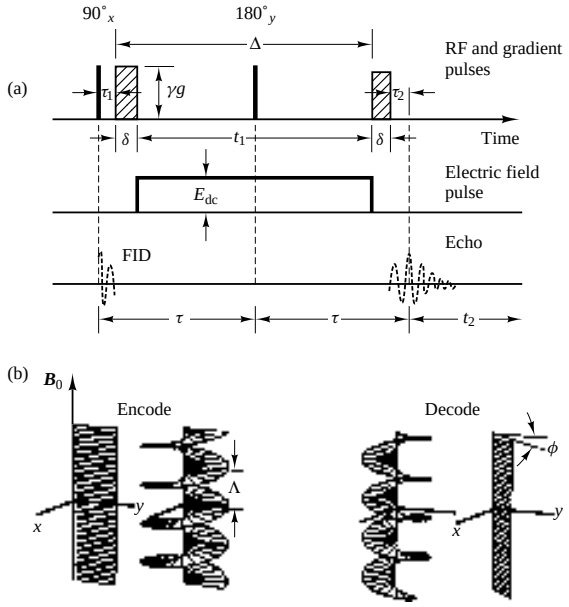

Figure 1 (a) The PFG NMR experiment for the measurement of drift velocities, and (b) pictorial representation of phase encoding through the formation of magnetization helices

2.3 One-Dimensional ENMR Experiments

In the simplest ENMR experiment the electric field is applied in the z direction during the time interval between the two gradient pulses in a Tanner–Stejskal spin echo experiment [Figure 1(a)]. If the drift velocity for an ionic species is v_e, the associated magnetization helix is translated through $\Delta z = v_e t_1$ and the phase of the echo is $\phi = qv_e t_1$. Therefore, the measurement of mobility amounts to a determination of the phase shift. If the experiment involves a counterflow of ions as in a U-tube electrophoretic cell or if only the y component of the magnetization is measured, information about the sign of the phase angle is lost and the phase factor must be replaced with $\cos(qv_e t_1)$.[9] In this case the magnitude of the phase angle can be determined by fitting the echo amplitude to a cosine function with q or E_{dc} as the independent variable. It is sometimes convenient to control E_{dc} by controlling the current I through the sample and making use of the relationship.

$$E_{dc} = \frac{I}{\kappa_e A} \quad (4)$$

where κ_e is the conductivity and A is the cross-sectional area of the cell. Therefore, the attenuation factor associated with electrophoretic drift can also be written as $\cos(q\mu I t_1/\kappa_e A)$.

The attenuation method was first used in the determination of the electrophoretic mobility of $(C_2H_5)_4NCl$ in D_2O stabilized by a 1 wt % agar gel.[10] The velocities were obtained from graphs of echo attenuation versus gradient duration δ for different potential differences across the electrophoretic cell (giving currents up to 250 mA) as shown in Figure 2. This experiment was performed on ^1H at 28 MHz without resolution of chemical shifts. The salt concentrations ranged up to 0.392 M and typical experimental parameters were:

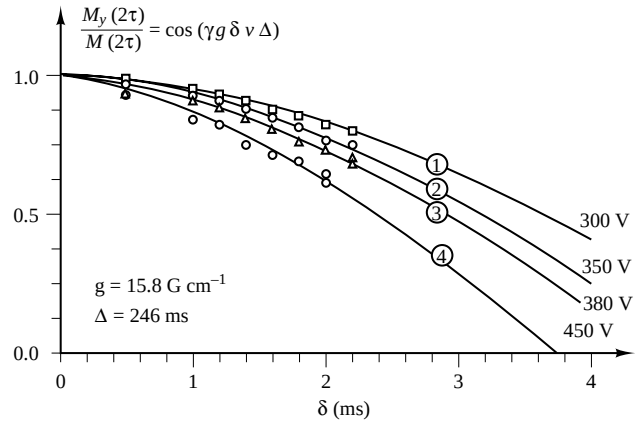

Figure 2 Signal attenuation versus δ for $(C_2H_5)_4NCl$ in D_2O stabilized by a 1 wt % agar gel

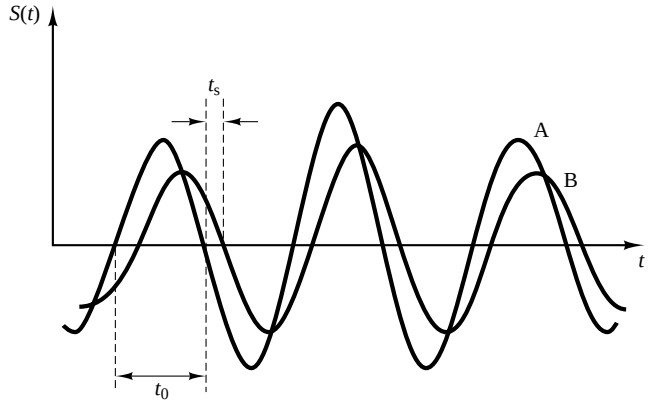

Figure 3 Two off-resonance echo signals in the presence of flow. (a) Spin echo detected when the gradient was switched off. (b) Spin echo detected when the gradient was switched on

$\Delta = 246$ ms, $g = 15.8$ G cm^{-1}, $T = 16\,^{\circ}$C, with currents up to 250 mA. The calculated mobilities were a few per cent lower than literature values for free D_2O solutions as expected from the gel obstruction effect.[11]

The echo attenuation method is not very accurate for the measurement of small phase angles that are often encountered when (a) the mobility is small, (b) the magnetogyric ratio is small, or (c) the range of useful q values is limited. A more accurate method for determining small phase changes is to measure the shift in the off-resonance echo signal 'wiggles' that results from the drift velocity.[12] When the resonance offset $\Delta\omega_{or}$ is small, i.e. $B_1 \gg \gamma\Delta\omega_{or}$ and $\Delta\omega_{or} \gg 2/T_2$*, the echo signal in the vicinity of 2τ is given by:

$$S(t) \propto \cos(\Delta\omega_{or}t + \Delta\phi) \tag{5}$$

Here $\Delta\phi$ is zero in the absence of the gradient pulses and becomes $q\nu_e t_1$ when the gradient pulses are present. Figure 3 illustrates the shift t_s of the zero points when the gradients are applied and inspection shows that $\Delta\omega_{or} = \pi/t_0$ and that $\Delta\phi = \pi t_s/t_0$. This method provides an accurate determination of the drift velocity when a single resonance line is present, and it has some advantages when extensive signal averaging is required.[13] However, it provides no information about the distribution of velocities.

Another scheme for measuring the phase of the echo begins with the Fourier transformation (FT) of the echo. A resulting spectral line is 'phased' and the parameters are recorded. The procedure is repeated in the presence of the electric field, and the phasing parameters are again determined. The difference between the phasing parameters with and without the drift velocity permits the velocity related phase angle to be estimated. This scheme also permits some frequency resolution since individual well resolved spectral lines can be phased independently.[14,15]

FT ENMR experiments give full frequency resolution and permit simultaneous measurement of mobilities for all components of a mixture.[7,16] This is accomplished by Fourier transforming the last half of the echo with respect to t_2 to obtain a set of high-resolution spectra associated with different values of either the duration t_1 or the amplitude E_{dc} of the electric field pulse. In FT ENMR a stack plot of one-dimensional NMR spectra is generated in which, for example, the current is incremented from spectrum to spectrum. In this display of spectra versus current, a peak associated with the ith ionic species is modulated by the factor $\cos(q\mu_i I t_1/\kappa_e A)$ and the mobility μ_i is obtained from the period of the oscillation (see Section 5, Figure 9).

2.4 Two-Dimensional ENMR Experiments

The FT ENMR experiment generates a two-dimensional data set with intensity versus chemical shift in one dimension and intensity versus either t_1 or the amplitude E_{dc} (or I) in the other. The dependence of the intensity of an NMR line (without spin coupling) on t_1 and E_{dc} is illustrated in Figure 4. This suggests two types of two-dimensional experiment based on the pulse sequence shown in Figure 1(a). The ν_2 (chemical shift) dimension is always obtained by Fourier transformation with respect to t_2, but the ν_1 dimension can be computed by transformation with respect to either t_1 or E_{dc}, depending on the way in which the experiment is performed.

First, consider an experiment in which τ_1, τ_2, and δ are constant and the pulse duration t_1 is stepped through a series of values up to the point where the echo intensity is severely attenuated. Throughout most of this range $t_1 \gg \tau_1$, τ_2, δ, and

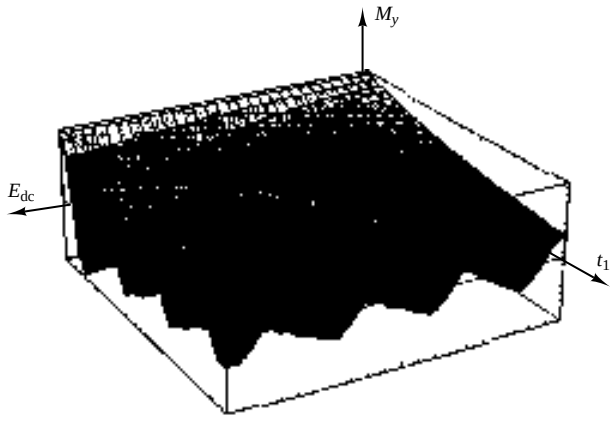

Figure 4 Signal intensity in ENMR versus t_1 and E_{dc}

$t_1 \approx 2\tau$. The attenuation of a spectral line with respect to t_1 for different values of E_{dc} is shown in Figure 4. Fourier transformation with respect to t_1 for every point in the NMR spectrum produces the ν_1 or velocity dimension. For the ith ionic species the velocity peaks appears at:

$$\nu_1^{(i)} = \pm q v_i/(2\pi) \tag{6}$$

and their full widths at halfheight are approximately given by:

$$\Delta\nu_1^{(i)} = [D_i q^2 + 1/T_2^{(i)}]/\pi \tag{7}$$

Diffusion makes the dominant contribution to the linewidth except when T_2 values are very short. However, polydisperse species may exhibit a range of electrophoretic mobilities at the same chemical shift and therefore contribute to the linewidth. The major disadvantages of this type of experiment are (a) loss of resolution and sensitivity resulting from diffusion and transverse spin relaxation, and (b) interference from J modulation.

In the second type of two-dimensional ENMR experiment all the timing parameters [Figure 1(a)] are held constant. A set of ν_2 spectra are obtained as described above, except that E_{dc} (or I) rather than t_1 is incremented. This leads to an important difference. As shown in Figure 4, the intensities oscillate as E_{dc} is increased, but there is no damping. This, of course, implies zero linewidths in the velocity dimension. In simple cases the mobility can be calculated with the equation $\mu = 2\pi/(qt_1\Delta E)$, where ΔE is the increase in electric field associated with one period of oscillation. However, the transformation of the data set with respect to $\boldsymbol{E}_{dc}$ to generate velocity spectra in the ν_1 dimension is not straightforward since the intensity curves are truncated, sometimes severely. This truncation results from the limited range of currents that can be used if heating effects are to be avoided. An exception occurs with some polydisperse samples where intensity versus E_{dc} curves are strongly damped because of a broad distribution of mobilities for ions contributing to the same NMR line (see Section 4.2, Figure 8).

Since Fourier transformation of the undamped but truncated curves yields unacceptable truncation broadening, another kind of transformation is needed. One possibility is the linear prediction (LP) method. On the other hand, damped curves for polydisperse samples can be Fourier transformed without difficulty to obtain the distribution of mobilities. However, the apparent mobility distribution may be distorted because of size dependent damping factors for diffusion and nuclear relaxation. A discussion of data analysis is given in Section 4.

3 PRACTICAL CONSIDERATIONS

The most serious problems associated with NMR in the presence of electrical currents are resistive (Joule) heating and the magnetic field gradients associated with ionic currents. The heating effects are well understood and can be avoided or controlled (see Section 3.1); and, fortunately, the current induced gradients are easy to handle. Holz and Müller[17] have pointed out that current parallel to the main field $\boldsymbol{B}_0$ makes no contribution to the z component of the magnetic field. This is, of course, the natural configuration for probes in superconducting magnets. In the event that currents perpendicular to $\boldsymbol{B}_0$ are present, external compensation of the resulting gradients is possible.[11]

3.1 The ENMR Spectrometer System

ENMR experiments can be performed with commercial NMR spectrometers equipped with custom built 'gradient' probes.[16] External computer controlled gradient drivers and electric field generators (electrophoresis drivers) are also available. The gradient driver employed in a number of ENMR experiments provided 0–10 A current pulses for 0–13 ms with pulse areas reproducible to 10 ppm.[18] Active feedback was incorporated to ensure constant gradients through continuous current control. A more recent driver provides bipolar pulse capability, pulse programmability on the millisecond timescale, and control of operating parameters by means of a standard MS-DOS compatible personal computer.[19]

Gradient amplitudes up to 300 G cm^{-1} have been used in ENMR. Even at this modest gradient level, eddy currents are induced in metal structures of the magnet and probe; and the resulting slowly decaying magnetic fields can distort NMR signals. It is, therefore, advisable to minimize the eddy currents through careful probe design and the use of actively shielded gradient coils.[20,21] If these precautions are inadequate, specially designed pulse sequences can be employed to delay data collection until the eddy currents have decayed (see Section 3.4).[22] Gradient drivers and probes with shielded gradient coils are now available from a number of vendors.

Homebuilt and commercial power supplies[10] have been used to provide the electrophoresis current. For example a convenient electric field generator has been reported that controls currents from 0 to 10 mA with 2.5 μA resolution and provides up to 1000 V.[18] This generator is used in connection with electrophoresis cells of the types illustrated in Figure 5(a) and (b), that are designed to fit inside a standard 10 mm NMR probe and to vent bubbles from the electrodes. The U-tube gives a counterflow of ions so that information about the signs of the mobilities is lost. Also, the filling factor is small and shimming can be a problem. The cylindrical design avoids these problems, but is less convenient because of the required gel plug. An alternative cylindrical cell design with a better filling factor but no provision for venting bubbles is shown in Figure 5(c).[15] The glass sieving was added to reduce electroosmotic flow (see Section 3.3). Platinum, blackened platinum, and Ag/AgCl electrodes have been used by various groups. The latter two types decrease gassing of the electrode.

3.2 Joule Heating and Convection

The heating of samples by electrical currents is a major problem in free solution electrophoresis. Temperature gradients give rise to convection currents associated with Rayleigh–Benard instabilities,[23] and this is especially serious in ENMR where displacements of less than 1 μm can be detected. The goal is to achieve the highest possible electric field E_{dc} without causing convection currents or otherwise perturbing the system. The power dissipation in the sample

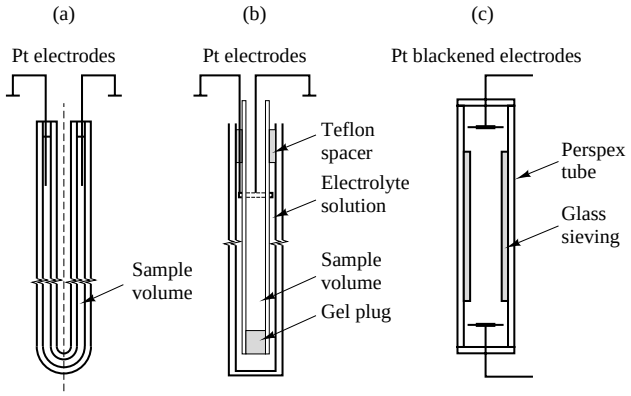

Figure 5 Electrophoretic cells for high-resolution ENMR

resulting from the current I is just I^2R, where R is the resistance, and it is easy to show that the cell develops heat (per unit volume) at the rate:[16,24]

$$H = \frac{I^2}{A^2\kappa_e} \tag{8}$$

Equations (4) and (8) can be combined to obtain $E_{dc} = (H/\kappa_e)^{\frac{1}{2}}$. Therefore, once the maximum acceptable heating rate has been established, the only way to increase the electric field is to reduce the conductivity. However, experience shows that convection is less of a problem in small bore tubes.

High-resolution ^{1}H ENMR in free solution is usually performed with currents less than 1 mA in order to avoid heating effects. Therefore, one must often work in the millimolar concentration range to obtain sufficient electric fields. The situation can be improved somewhat by stabilizing samples against convection through the use of dilute gels. In this way, currents up to about 4 mA can be tolerated with only small obstruction effects for small ions.[11,25]

ENMR studies involving nuclei with small magnetogyric ratios, e.g. $^7Li^+$ and $^{133}Cs^+$, present special problems because of low sensitivity and small values of q. Larger sample volumes and higher currents are essential for these experiments to succeed. Holz and co-workers[10,11,13] have reported various probe and electrophoresis cell designs for low sensitivity nuclei. For example, a probehead insert for an 89 mm superconducting magnet that permits the use of currents to 170 mA for a few seconds is shown in Figure 6.[13] Temperature gradients are minimized through liquid cooling with Fluorinert FC77 (3M Corp.), and convection is eliminated by the use of gel stabilized samples.

3.3 Electro-osmosis

Consider an electrolyte solution in contact with a charged planar surface fixed in space. Under the influence of an electric field E_{dc} parallel to the surface, the mobile diffuse layer moves and carries the solvent with it. This effect, known as electro-osmosis (EO), provides the pump for capillary zone electrophoresis (CZE),[26] but is usually a nuisance for other types of electrophoresis experiment. It can be shown that the steady state velocity of the diffuse layer is given by:[4,16,27]

$$v_{eo} = \epsilon_r\epsilon_0\zeta E_{dc}/\eta \tag{9}$$

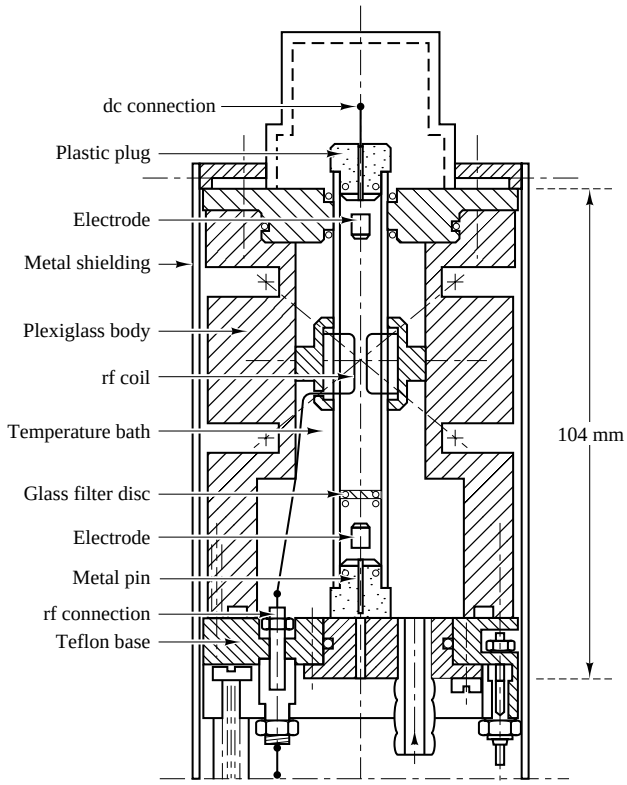

Figure 6 Probehead for liquid cooled electrophoresis

For a horizontal capillary tube between reservoirs the flow profile may approximate plug flow; but, in a vertical electrophoresis cell, flow along the walls must be compensated by backflow in the center. In fact, it is expected that the velocity profile for ions in a cylindrical tube is parabolic and can be described by:[15]

$$v(r) = v_e + v_{eo}\left(\frac{2r^2}{a^2} - 1\right) \tag{10}$$

where a is the radius of the tube, r is the distance from the center, v_e is the electrophoretic drift velocity, and v_{eo} is the EO velocity close to the wall.

Integration of equation (10) over the cross-sectional area confirms that the average contribution of EO to the ionic drift velocity is zero. Similarly, the contribution to the average phase angle for the spin echo is zero. Therefore, a measurement of the phase angle by a phase sensitive technique in the small angle limit should permit v_e to be measured without interference from EO. The problem is the EO gives a distribution of velocities and may produce severe damping of intensity versus current curves. In the presence of EO, the nuclei between r and $r + dr$ in the sample tube acquire the phase angle $qv(r)t_1$ at the time of the echo and the phase factor in equation (3) must be replaced by:

$$\frac{1}{\pi a^2}\int_0^a e^{iqv(r)t_1}2\pi r\,dr = e^{iqv_et_1}\left[\frac{\sin(qv_{eo}t_1)}{qv_{eo}t_1}\right] \tag{11}$$

Both v_e and v_{eo} are proportional to E_{dc} and they may have similar magnitudes. Therefore, the consequence of EO, described by equation (10), is damping of the intensity versus

current curves in ENMR and loss of resolution in the velocity spectra.

It is best to avoid complications associated with EO. EO always presents a problem with free solution electrophoresis since all surfaces in contact with electrolyte solutions acquire charges. Fortunately, gel stabilized samples are immune to EO since the flow of solvent at the wall is quenched. The standard procedure for reducing or eliminating EO in free solutions is to coat the surfaces with methylcellulose (MW = 110 000) that (a) increases the effective viscosity close to the wall and (b) moves the plane of shear into the region where the ζ potential vanishes.[16,28] The effectiveness of the coating should be apparent from the amplitude of the solvent (HOD) peak at the highest currents. In the presence of surfactant solutions, the coatings tend to deteriorate with time thus limiting the duration of experiments.

3.4 Dealing with Short T_2 Values and J Modulation

A wide range of T_2 values is found for mixtures containing molecules of different sizes and molecular aggregates. According to equation (3), the amplitude of each line in the ENMR spectra of such mixtures will be attenuated by transverse spin relaxation. For example, in microemulsion solutions the surfactant molecules at the interfaces have short T_2 values, while molecules in the interior of the droplets have long T_2 values. This leads to extremely distorted intensity distributions.[29] Also, for protein molecules with molecular weights over a few thousand, the T_2 values for protons are short and approach the rigid lattice limit.[16]

Coupled homonuclear spin systems also present problems because of both short T_2 values and J modulation.[30,31] J modulation arises because the hard rf pulses exchange the spin states of nuclei that are coupled to the nuclei being investigated. This causes the precession frequencies to change so that refocusing of the echo depends on the magnitude of the spin coupling constant J. As a consequence, signals in an FT ENMR experiment may be modulated as τ is increased and may have small or even negative amplitudes.[16]

An obvious solution for the problem of short T_2 values is to replace the spin echo (SE) pulse sequence with a stimulated echo (STE) sequence.[32–34] This causes an immediate loss of a factor of 2 in the signal if $T_1 = T_2$, but large gains can be achieved when $T_1 \gg T_2$. A modified version of the STE sequence is shown in Figure 7, where the first three 90° rf pulses and the fourth and fifth gradient pulses constitute the standard STE diffusion and flow experiment. The first rf pulse rotates magnetization into the xy plane, the gradient pulse phase encodes spatial positions, and the second rf pulse stores the magnetization in the z direction. The transverse components remaining during the interval T after the second rf pulse are eliminated by phase cycling, while the magnetization pattern created in the z direction relaxes by T_1 rather than T_2 processes. The third rf pulse returns magnetization to the xy plane, the following gradient pulse decodes spatial positions, and the STE forms at time $T + 2\tau$ relative to the first rf pulse.

It is advantageous to minimize the time intervals τ in the pulse sequence so that neither the short T_2 values nor the J modulation will affect the amplitude of the STE. The problem is that the gradient pulses induce eddy currents in metal components close to the gradient coils, and in turn the slowly

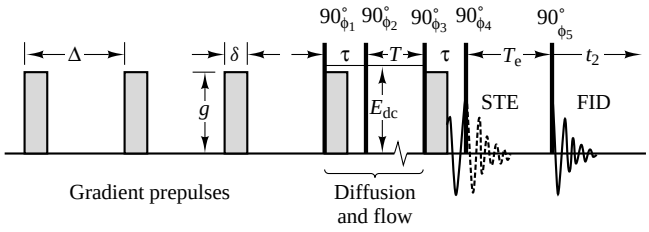

Figure 7 The LED pulse sequence for ENMR. Phase cycling (ϕ_i values) and homospoil pulses are not shown

decaying eddy currents produce magnetic field gradients that distort NMR signals. The longitudinal eddy current delay (LED) sequence shown in Figure 7 provides a partial solution by storing the STE in the z direction by means of the fourth rf pulse and then recalling the magnetization with the fifth rf pulse after an eddy current settling period.[22] The signal is then acquired as a FID. A train of at least three equally spaced gradient prepulses is introduced to insure a steady state response so that the effects of the fourth and fifth gradient pulses will be equal.

The complex data set obtained from either the echo in an STE experiment or the FID in a LED experiment is described by:

$$M_{xy} = \sum_{j=1}^{k} \exp[\mathrm{i}\phi_j(I)] f_j(\tau, T, T_\mathrm{e}) \tag{12}$$

where

$$\phi_j(I) = q\mu_j \Delta I/(\kappa_\mathrm{e} A) \tag{13}$$

and

$$f_j(\tau, T, T_\mathrm{e}) = \frac{M_0^j}{2} \exp\left[-\frac{2\tau}{T_2^j} - \frac{(T + T_\mathrm{e})}{T_1^j}\right] \times \exp\left[-D_j q^2 \left(\Delta - \frac{\delta}{3}\right)\right] \tag{14}$$

With STE the complex signal is acquired from a single half-echo by quadrature detection, while with LED the real and imaginary parts must be acquired in separate experiments in which the fourth rf pulse is phase shifted by 90°. In equation (12) k is the number of species in solution and $\Delta = T + \tau$ is the diffusion or electrophoretic drift time. For the jth species D_j is the tracer diffusion coefficient, μ_j is the electrophoretic mobility, and $T_1{}^j$ and $T_2{}^j$ are the spin–lattice and spin–spin relaxation times, respectively. Typically, δ is 1–2 ms and $\tau - \delta$ can be as small as 500 μs. Therefore, T_2 attenuation and J modulation are usually negligible, and the main concern becomes the relative magnitudes of $T + T_\mathrm{e}$ and T_1.

4 DATA ANALYSIS

Here we are concerned with transformations of intensity versus current data sets to obtain velocity spectra. In the following we assume that the data sets are acquired with

STE or LED pulse sequences. First we note that data sets described by equation (12) contain information about the signs of the mobilities. The signs can be determined for all lines in the ENMR spectrum by means of the reverse precession method.[35] With the alternating polarity of the STE experiment this requires the collection of two FIDs (half-echoes), one with positive and one with negative polarity of the electric field. After Fourier transformation with respect to t_2, the signals with positive and negative polarities can be represented by:

$$S_{\pm}(\omega_2, I) = S_0 \exp[\pm \mathrm{i}\phi(I)] f(\tau, \Delta, T_\mathrm{e})[a(\omega_2) + \mathrm{i}d(\omega_2)] \quad (15)$$

where $a(\omega_2)$ and $d(\omega_2)$ are Lorentzian absorption and dispersion components.[36] The combinations $\mathrm{Im}(S_+ - S_-)$ and $\mathrm{Re}(S_+ + S_-)$ give absorption mode spectra that are modulated by $\sin(q\mu\Delta I/\kappa_\mathrm{e}A)$ and $\cos(q\mu\Delta I/\kappa_\mathrm{e}A)$, respectively. These combinations can be transformed with respect to the current to obtain two-dimensional ENMR spectra that show both positive and negative mobilities.[36] The sign of the mobilities can also be obtained from LED data since the phase of the fourth rf pulse can be adjusted to store either the real or the imaginary part of the magnetization.

4.1 Data Inversion for Discrete Samples

The transformation required to convert intensity versus current data sets into velocity spectra depends on the nature of the sample. A discrete mixture, i.e. one that contains a small number of monodisperse components, gives a data set that can be described by equation (12). As discussed in Section 2.4 and illustrated in Figure 4, the data set at each chemical shift (ν_1) is described by a truncated cosine function or perhaps a sum of truncated cosine functions. In this situation the linear prediction (LP) method is an attractive alternative to the FT.[37,38] LP extends truncated data sets and can generate frequency spectra from incomplete sets. The LP procedure assumes that the data set y_n can be represented by a finite sum of damped sinusoids of the form:

$$y_n = \sum_{j=1}^{k} I_j \exp(-\gamma_j n\tau) \exp(-\mathrm{i}\omega_j n\tau + \mathrm{i}\phi_j) \quad (16)$$

where I_j, γ_j, ω_j, and ϕ_j are the intensity, damping factor, frequency and phase, respectively, of the jth component, and τ is the time step. The determination of the best values of these parameters makes use of two least squares procedures and one polynomial rooting, thus avoiding the slow iterative nature of other curve fitting techniques. When the best set of intensities, frequencies, damping factors, and phases has been determined, a frequency (velocity) spectrum can be synthesized from these parameters.[25,39] Various versions of LP have been implemented for spectroscopic applications, but the only one used in ENMR to data is LPZOOM, that was developed by Tang and Norris.[40] The LPZOOM program permits the user to specify a range of frequencies and thus to perform localized analysis with a reduction in computational time.

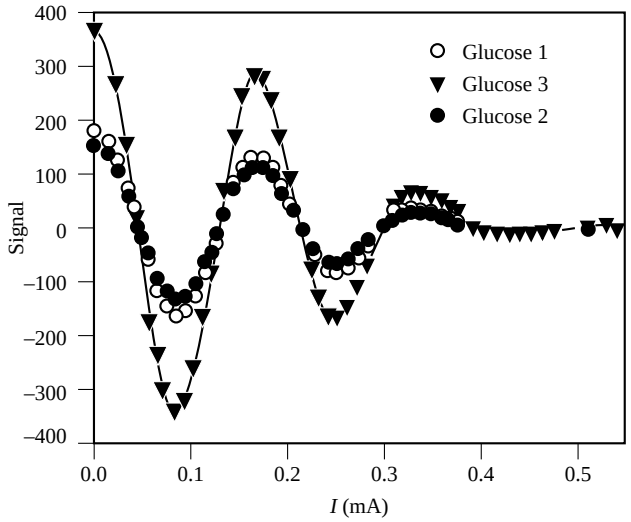

Figure 8 Signals versus current for three groups of protons on glucose molecules entrapped in vesicles

4.2 Data Inversion for Polydisperse Ions

Micelles, vesicles, and biological cells exhibit continuous distributions of electrophoretic mobilities. Often the chemical shifts for certain groups, e.g. phospholipid headgroups in vesicles, are relatively independent of the size of the aggregate, and peaks are found in the FT NMR spectrum that have contributions from a wide range of mobilities. In such cases the signal versus current curves show considerable damping. An example is shown in Figure 8 for glucose entrapped in charged phospholipid vesicles.[41] The sample was prepared with 30 mM total lipid and the mole ratio of L-α-lecithin (egg) (EPC) to L-α-dioleoylphosphatidylglycerol (DOPG) sodium salt was 4 : 1. At pH 7, where the EPC headgroup is neutral and the DOPG headgroup is negative, the vesicles are charged. The data were acquired in an STE experiment and the parameters were: τ = 20 ms, Δ = 420 ms, $q = 1.870 \times 10^3\ \mathrm{cm}^{-1}$, κ_e = 0.049 mS cm^{-1}, and $A = 0.0909\ \mathrm{cm}^2$.

For the description of damped interferograms the discrete summation in equation (12) must be replaced with an integral over the distribution of mobilities. Thus:

$$S(I, \nu_2) = S_0(\nu_2) \int_{-\infty}^{\infty} g(\mu, \nu_2) f(\tau, T, T_\mathrm{e}) \times \exp[\mathrm{i}(q\Delta) I\mu/\kappa_\mathrm{e}A]\mathrm{d}\mu \quad (17)$$

where $S_0(\nu_2)$ is the intensity in the absence of the current, $g(\mu,\nu_2)$ is the normalized distribution function for the mobility, and the relaxation factor $f(\tau,T,T_\mathrm{e})$ is defined in equation (14). We note that the signal amplitude is just the cosine FT of the distribution product $G(\mu,\nu_2) = g(\mu,\nu_2)f(\tau,T,T_\mathrm{e})$ and, therefore, that this product can be obtained by the inverse Fourier transform (IFT) of $S(I,\nu_2)$ with respect to the current. In the special case that the relaxation factor $f(\tau,T,T_\mathrm{e})$ is approximately constant over the range of integration, the IFT yields the distribution function $g(\mu,\nu_2)$ directly. This condition may be satisfied for solute molecules entrapped in the aqueous cavity of large vesicles ($a > 0.2\ \mu$m) when $q^2\Delta < 3 \times 10^6$ s cm^{-2} and the nuclear relaxation times are also relatively insensitive to changes in size. However,

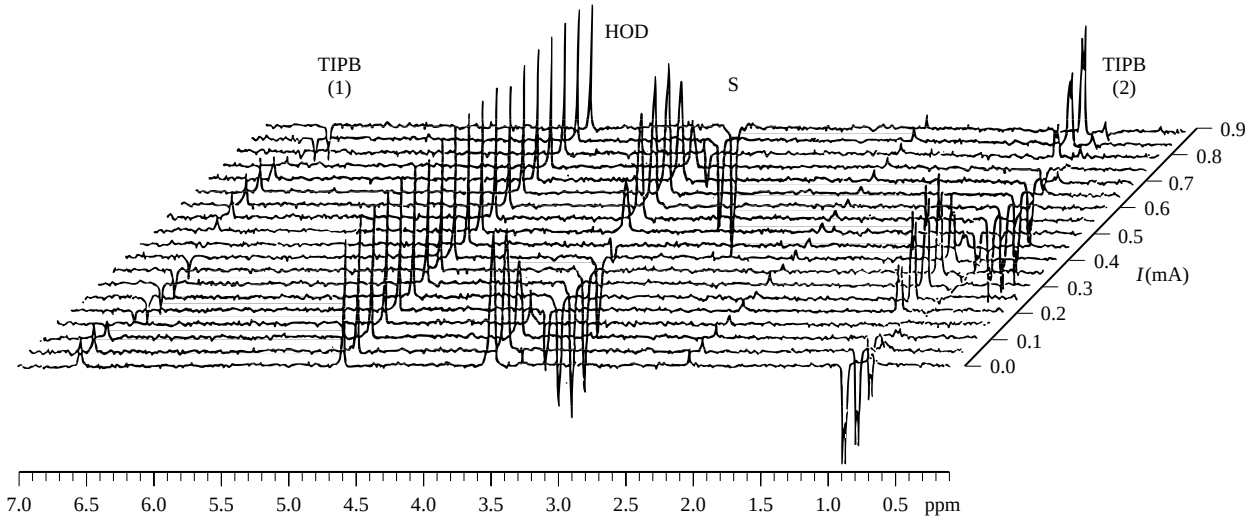

Figure 9 FT ENMR spectra of a mixture containing surfactants and TIPB in D_2O

in general, the apparent distribution function is weighted by the relaxation factor. This opens the possibility of relating mobilities to particle sizes by obtaining $G(\mu,\nu_2)$ with different values of q. In principle a plot of $\ln[G(\mu,\nu_2)]$ versus q^2 should give the diffusion coefficient associated with μ, but it must be kept in mind that the resolution of mobilities is determined by the range of current values, i.e. the duration of the interferogram $S(I,\nu_2)$.

5 ILLUSTRATIONS OF ENMR SPECTRA

High-resolution ENMR experiments have typically been performed with low ionic strengths and small diameter electrophoresis cells in order to obtain high electric fields with low currents. An example is provided by a microemulsion sample with microdroplets of oil in water (o/w). Surfactant molecules form the surface of the droplets with their hydrophobic tails extending into the oil. Both T_1 and T_2 are long for hydrocarbon (oil) protons in the droplets, but the surfactant protons exhibit a range of T_2 values. The spectra in Figure 9 were obtained by means of the simple SE experiment (Figure 1) for a sample prepared with 0.15 mL triisopropylbenzene (TIPB), 0.165 mL $CH_3(CH_2)_{11}(OCH_2CH_2)_4OH$ (Brij 30), 0.075 g sodium dodecyl sulfate (SDS), and 20 ml D_2O.[16] The sample was equilibrated, and then the translucent o/w microemulsion layer was separated and diluted by a factor of 6 with D_2O. The measured conductivity was κ_e = 0.106 mS cm^{-1} at 25 °C, and the experimental parameters were q = 686 cm^{-1}, t_1 = 0.41 s, and 2τ = 0.42 s; and the current ranged from 0 to 0.9 mA.

The peak height versus current plots shown in Figure 10 can be fitted to cosine functions to obtain the mobilities. This procedure yields $\mu = 3.4 \times 10^{-4}$ cm^2 V^{-1} s^{-1} for both the TIPB and the surfactant peaks, indicating that these components move together in the microemulsion droplets. This experiment illustrates T_2 attenuation since a major signal from the hydrophobic end of Brij 30 has completely relaxed to zero. J modulation is also illustrated by the inverted TIPB(2) signal, and the partial attenuation of the HOD signal at 0.9 mA shows the onset of electro-osmosis.

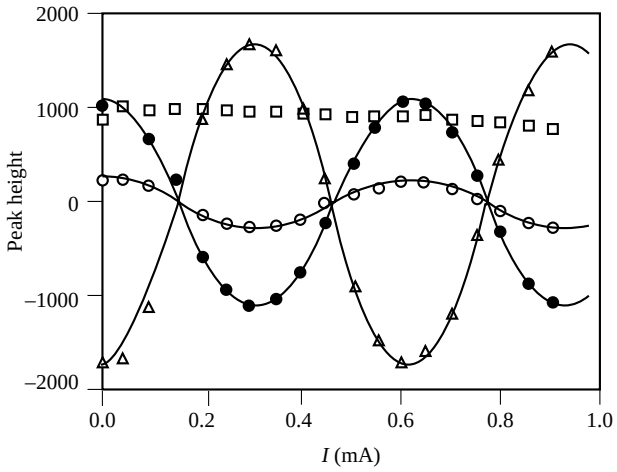

Figure 10 Peak heights versus current for the spectra in Figure 9: (□) HOD, (△) CH_3 in TIPB, (○) ϕH in TIPB, (●) S

The spectrum in Figure 11 illustrates mobility ordered two-dimensional NMR (MOSY) for a sample containing tetramethylammonium ion (TMA) (2.00 mM) with mixed micelles [1.50 mM SDS and 4.00 mM octaethylene glycol dodecyl ether ($C_{12}E_8$, with E = C_2H_4O)].[25,39] In its present form this method provides resolution of about one part per hundred in mobilities and permits the signs of the mobilities to be determined. The STE pulse sequence was used in this experiment, and the experimental parameters were: q = 722 cm^{-1}, Δ = 0.400 s, A = 0.0986 cm^2, and κ_e = 0.273 mS cm^{-2}. The current was limited to 0.75 mA to avoid heating effects, and the severely truncated data sets were transformed by means of LPZOOM, as discussed in Section 4.1. The mobilities indicated by the peak maxima are 2.75×10^{-4} and -1.55×10^{-4} cm^2 V^{-1} s^{-1} for protons in TMA and micelles, respectively. Note that the peak at 3.51 ppm is associated with $C_{12}E_8$ and its position on the mobility axis shows that this neutral compound migrates with the micelle. This ability to identify molecular species and to detect their interactions in solution is a major strength of MOSY. In this example the different ionic species have different chemical shifts. When

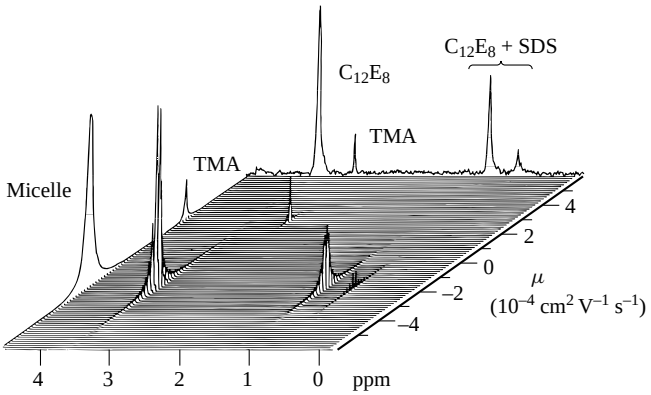

Figure 11 Mobility ordered two-dimensional NMR spectrum of tetramethylammonium ions and mixed micelles

there is overlap, the LPZOOM program has limited ability to separate components on the basis of their mobilities if the mobilities are quite different and the truncation is not too severe.[25]

6 LITERATURE SOURCES

Electrophoretic NMR up to 1989 has been reviewed by Johnson and He[16] and more recently two-dimensional ENMR has been reviewed by Johnson.[42] ENMR has also been reviewed by Holtz.[43] NMR methods for the measurement of diffusion and flow have recently been covered by Callaghan in a monograph on NMR microscopy.[44] Also, NMR flow measurements have been reviewed by Caprihan and Fukushima.[45]

An introduction to electrophoresis and electrokinetic effects can be found in the textbook on macromolecules by Tanford[2] and in the biophysical chemistry text by Cantor and Schimmel.[46] A more complete treatment of electrokinetic effects can be found in the monographs by Hunter.[4,5] Also, an accessible discussion of electro-osmosis and other surface phenomena is available in Adamson's textbook on the physical chemistry of surfaces.[27]

Reviews of electrophoretic light scattering (ELS) are also relevant since similar experimental problems are encountered in that field. In particular we note a somewhat dated review of ELS by Ware[47] and a recent monograph by Schmitz[48] which treats electrokinetic effects as well as experimental techniques. Holographic relaxation spectroscopy (HRS) combined with electrophoresis also has features in common in ENMR.[49,50]

7 RELATED ARTICLES

Diffusion and Flow in Fluids; Diffusion Measurements by Magnetic Field Gradient Methods; Electrolytes; Field Gradients and Their Application; Flow NMR; Micellar Solutions and Microemulsions; Spin Echo Spectroscopy of Liquid Samples.

8 REFERENCES

1. P. W. Atkins, *Physical Chemistry*, W. H. Freeman, New York, 1990.
2. C. Tanford, *Physical Chemistry of Macromolecules*, Wiley, New York, 1961.
3. R. W. O'Brien and L. R. White, *J. Chem. Soc., Faraday Trans. 2*, 1978, **74**, 1607.
4. R. J. Hunter, *Foundations of Colloid Science*, Oxford University Press, Oxford, 1987, Vol. I.
5. R. J. Hunter, *Foundations of Colloid Science*, Oxford University Press, Oxford, 1989, Vol. II.
6. E. O. Stejskal, *J. Chem. Phys.*, 1965, **43**, 3597.
7. T. R. Saarinen and C. S. Johnson, Jr, *J. Am. Chem. Soc.*, 1988, **110**, 3332.
8. E. O. Stejskal and J. E. Tanner, *J. Chem. Phys.*, 1965, **42**, 288.
9. K. J. Packer, C. Rees, and D. J. Tomlinson, *Adv. Mol. Relaxation Processes*, 1972, **3**, 119.
10. M. Holz and C. Müller, *Ber. Bunsenges. Phys. Chem.*, 1982, **86**, 141.
11. M. Holz, O. Lucas, and C. Müller, *J. Magn. Reson.*, 1984, **58**, 294.
12. M. Holz, C. Müller, and A. M. Wachter, *J. Magn. Reson.*, 1986, **69**, 108.
13. M. Holz, D. Seiferling, and X. A. Mao, *J. Magn. Reson., Ser. A*, 1993, **105**, 90.
14. F. M. Coveney, J. H. Strange, A. L. Smith, and E. G. Smith, *Colloids Surf.*, 1989, **36**, 193.
15. F. M. Coveney, J. H. Strange, and E. G. Smith, *Mol. Phys.*, 1992, **75**, 127.
16. C. S. Johnson, Jr, and Q. He, in *Adv. Magn. Reson.*, 1989, **13**, 131.
17. M. Holz and C. Mueller, *J. Magn. Reson.*, 1980, **40**, 595.
18. T. R. Saarinen and W. S. Woodward, *Rev. Sci. Instrum.*, 1988, **59**, 761.
19. R. M. Boerner and W. S. Woodward, *J. Magn. Reson., Ser. A*, 1994, **106**, 195.
20. P. Mansfield and B. Chapman, *J. Magn. Reson.*, 1986, **66**, 573.
21. S. J. Gibbs, K. F. Morris, and C. S. Johnson, Jr, *J. Magn. Reson.*, 1991, **94**, 165.
22. S. J. Gibbs and C. S. Johnson, Jr, *J. Magn. Reson.*, 1991, **93**, 395.
23. W. J. Goux, L. A. Verkruyse, and S. J. Salter, *J. Magn. Reson.*, 1990, **88**, 609.
24. R. A. Alberty, *J. Chem. Educ.*, 1948, **Aug.**, 426.
25. K. F. Morris and C. S. Johnson, Jr, *J. Magn. Reson., Ser. A*, 1993, **101**, 67.
26. J. W. Jorgenson and K. D. Lukacs, *Science*, 1983, **222**, 266.
27. A. W. Adamson, *Physical Chemistry of Surfaces*, Wiley, New York, 1982.
28. B. J. Herren, S. G. Shafer, J. V. Alstein, J. M. Harris, and R. S. Synder, *J. Colloid Interface Sci.*, 1987, **115**, 46.
29. Q. He and C. S. Johnson, Jr, *J. Magn. Reson.*, 1989, **81**, 435.
30. R. L. Vold and R. R. Vold, *J. Am. Chem. Soc.*, 1974, **96**, 4043.
31. R. L. Vold and R. R. Vold, *Prog. Nucl. Magn. Reson. Spectrosc.*, 1978, **12**, 79.
32. E. L. Hahn, *Phys. Rev.*, 1950, **80**, 580.
33. J. E. Tanner, *J. Chem. Phys.*, 1970, **52**, 2523.
34. Q. H. He and C. S. Johnson, Jr, *J. Magn. Reson.*, 1989, **85**, 181.
35. P. Bachmann, W. P. Aue, L. Mueller, and R. R. Ernst, *J. Magn. Reson.*, 1977, **28**, 29.
36. R. R. Ernst, G. Bodenhauen, and A. Wokaun, *Principles of Nuclear Magnetic Resonance in One and Two Dimensions*, Oxford University Press, Oxford, 1987.

37. J. Tang, C. P. Lin, M. K. Bowman, and J. R. Norris, *J. Magn. Reson.*, 1985, **62**, 167.
38. J. Tang, and J. R. Norris, *Chem. Phys. Lett.*, 1986, **131**, 252.
39. K. F. Morris and C. S. Johnson, Jr, *J. Am. Chem. Soc.*, 1992, **114**, 776.
40. J. Tang and J. R. Norris, *J. Magn. Reson.*, 1988, **79**, 190.
41. Q. He, D. P. Hinton, and C. S. Johnson, Jr, *J. Magn. Reson.*, 1991, **91**, 654.
42. C. S. Johnson, Jr, in *NMR Probes of Molecular Dynamics*, ed. R. Tycko, Kluwer, Dordrecht, 1994 Chap. 10, p. 455.
43. M. Holtz, *Chem. Soc. Rev.*, 1994, **23**, 165.
44. P. T. Callaghan, *Principles of Nuclear Magnetic Resonance Microscopy*, Oxford University Press, Oxford, 1991.
45. A. Caprihan and E. Fukushima, *Phys. Rep.*, 1990, **198**, 195.
46. C. R. Cantor and P. R. Schimmel, *Biophysical Chemistry, Part II: Techniques for the Study of Biological Structure and Function*, W. H. Freeman, San Francisco, 1980.
47. B. R. Ware, *Adv. Colloid Interface Sci.*, 1974, **4**, 1.
48. K. S. Schmitz, *An Introduction to Dynamic Light Scattering by Macromolecules*, Academic, Boston, 1990.
49. K. W. Rhee, J. Shibata, A. Barish, D. A. Gabriel, and C. S. Johnson, Jr, *J. Phys. Chem.*, 1984, **88**, 3944.
50. A. O. Barish, D. A. Gabriel, and C. S. Johnson, Jr, *J. Chem. Phys.*, 1987, **87**, 3594.

Biographical Sketch

Charles S. Johnson, Jr. *b* 1936. B.S., 1958, Georgia Institute of Technology, Ph.D., 1961, Massachusetts Institute of Technology, (supervisor John Waugh). NAS-NRS Postdoctoral fellow and instructor at Illinois (with Herb Gutowsky). Faculty member Yale University 1962–67, University of North Carolina, Chapel Hill, 1967–present. Research interests includedynamic light scattering (DLS), electrophoretic NMR, diffusion-ordered 2D NMR, and applications of DLS and NMR to complex liquid mixtures.

Agriculture and Soils

Roger H. Newman

Industrial Research Limited, Lower Hutt, New Zealand

1	Introduction	1
2	Sample Preparation	1
3	Signal Assignments for ^{13}C	1
4	Signal Assignments for Other Nuclei	2
5	Reliability of NMR Results	3
6	Applications	3
7	Separating Overlapping Signals	4
8	References	4

1 INTRODUCTION

Soils are heterogeneous mixtures of organic substances, minerals and organomineral complexes. The organic substances include macromolecules lacking well-defined structures or repeating units. The minerals include poorly ordered or amorphous matter. These difficulties have hindered scientific studies of soil, leaving fundamental questions of structural chemistry open to debate until recent years. NMR spectroscopic studies have provided some convincing answers that broaden our understanding of the origins of soil characteristics, the influences of land management on soil fertility, and the fate of agrochemicals.

Soil organic substances were extracted, methylated, and dissolved in deuterated solvents for the earliest ^{1}H and ^{13}C NMR studies of soil chemistry.[1–3] These studies provided little worthwhile information. Much more detail emerged from a 1976 paper describing ^{13}C NMR spectra of soil organic substances in alkaline aqueous solution.[4] The first ^{13}C CP MAS NMR spectrum of whole soil was published in 1981.[5] The publication rate has now risen to an average of about one paper per month describing ^{13}C CP MAS NMR studies of humic substances. Solution ^{13}C NMR spectroscopy is used on occasions, and several other nuclei provide useful spectra.

This article is not intended as a comprehensive review. More complete references to relatively early work can be found in two books published in 1987.[6,7]

2 SAMPLE PREPARATION

Soil organic substances are commonly separated into three fractions defined in terms of solubility. 'Humic acids' are not soluble in water under acid conditions, but are soluble under alkaline conditions. 'Fulvic acids' are soluble under all pH conditions. 'Humins' are not soluble under any pH conditions.

Humic acids generally account for the major part of soil organic matter. They have been characterized by CP MAS NMR or dissolved in aqueous alkali for solution NMR, the two procedures yielding similar patterns of signal intensities.[8,9] Fulvic acids are hygroscopic and yield poor CP MAS NMR spectra unless they are carefully dried.[10]

Differences between ^{13}C CP MAS NMR spectra of humic acids and the corresponding humins are not as pronounced as might be expected for separation based on differences in chemical properties.[11,12] It appears that differences in solubility are rather caused by differences in physical accessibility of the organic matter.[11] The NMR spectra of fulvic acids are usually distinctly different from the corresponding humic acids or humins,[11,12] so humic acids are not representative of the organic matter in the complete soil.

Soil extracts can be used for NMR studies without fractionation into humic and fulvic acids. This procedure is particularly advisable in preparing samples for ^{31}P NMR,[13] since phosphate esters could be hydrolyzed under the acidic conditions required for precipitation of the humic acid fraction. Sequential extraction procedures have been developed to remove over 80% of organic phosphorus from soils for solution NMR characterization.[14]

Removal of paramagnetic species such as Fe^{3+} can improve ^{13}C CP MAS NMR spectra of solid soils and humins.[15–17] As a general rule, the ratio C:Fe;>>1 is required for a good spectrum.[15] Pretreatment by a mixture of HCl and HF has the added advantage of removing inorganic substances and therefore concentrating the organic matter.[17]

3 SIGNAL ASSIGNMENTS FOR ^{13}C

A typical CP MAS NMR spectrum of whole soil (Figure 1) shows overlapping signals that are grouped in four chemical shift ranges for discussion here.

Signals in the range δ = 10–50 are assigned to alkyl carbon, including side chains in amino acids, structures derived from higher-plant polymers such as cutins and suberins, and structures formed by cross-linking between polyunsaturated

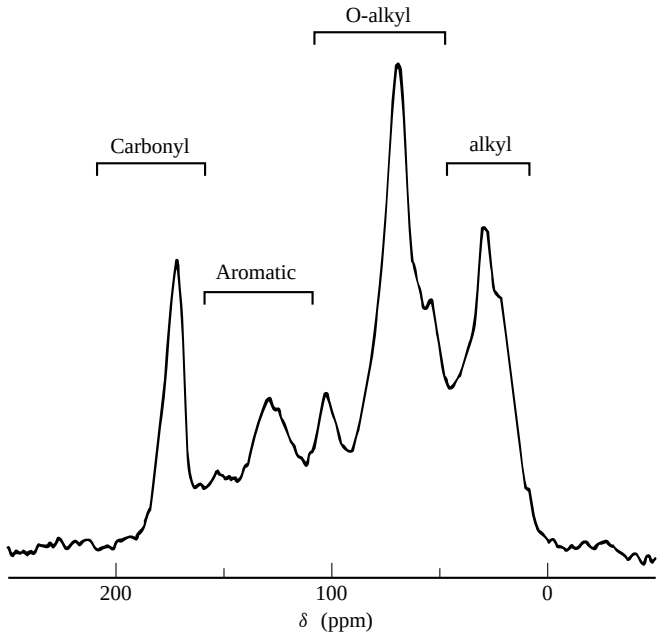

Figure 1 Carbon-13 CP MAS NMR spectrum (50.3 MHz) of Taupo Soil, A horizon: 7 mm diameter cylindrical rotor spun at 5.0 kHz, 1 ms contact time, 15 ms data acquisition time, 300 ms pulse delay, 10.6 h of data accumulation

microbial lipids.[18] Input from microbial activity has been demonstrated by incubating soil with ^{13}C-labeled glucose.[19] A signal near δ = 31 is sometimes relatively strong in spectra of soil fractions sieved to select particles with dimensions less than 2 μm.[20–22] This signal has been assigned to polymethylene chains, including organo-clay complexes.[20]

Signals in the range δ = 50–110 are assigned primarily to *O*-alkyl carbon, i.e. oxygen-substituted carbon in alcohols and ethers, including plant carbohydrates and their degradation products. These substances are relatively abundant in fractions sieved to select coarse particle sizes,[22] and are particularly well preserved in cold climates.[23] This chemical shift range includes signals between δ = 50 and 60 assigned to *N*-substituted carbon in amino acids.[4]

Signals in the range δ = 110–160 are assigned primarily to aromatic carbon. The question of whether aromatic substances form a major or minor component of soil organic matter has been debated as recently as 1985.[24,25] Perhaps the best answer is that considerable variation has been observed. A band centered on δ = 130 is particularly prominent in NMR spectra of organic matter found in soils that have been affected by fire.[26,27] Signals in the range δ = 150–160 have been assigned to oxygen-substituted aromatic carbon. The degree of oxygen substitution shows a strong negative correlation with soil development, perhaps as a result of selective degradation of the more highly substituted structures.[28]

Signals in the range δ = 160–210 are assigned to carbonyl carbon.[29] This region is usually dominated by a peak in the region δ = 170–180, assigned primarily to carboxylic acids. Secondary amides can also contribute to the peak.[30] The signal strength is usually stronger than would be expected from chemical analyses for carboxylic functional groups, and nitrogen contents fail to account for the discrepancies. Schnitzer and Preston concluded that 'it is possible that chemical methods do not react stoichiometrically with materials of high molecular weight, such as humic substances, because of steric factors.'[29]

4 SIGNAL ASSIGNMENTS FOR OTHER NUCLEI

Poor signal dispersion has discouraged widespread use of ^{1}H NMR in soil science. Bands of partly resolved signals have been observed in the ranges δ = 0.8–2.5 (alkyl), 3.3–3.8 (*O*-alkyl), and 6–8 (aromatic).[31] Features within these bands have been assigned to more specific chemical structures.[32] Aromatic protons can exchange with deuterons in solvent, resulting in underestimation of aromaticity.[33]

After ^{13}C, ^{31}P is the nucleus most commonly used in NMR studies of soil. Some generalized signal assignments are shown in Figure 2. The sample was chosen for the diversity of chemical species. The orthophosphate monoesters include choline phosphate (δ = 3.5) and inositol hexaphosphate (four signals).[13] Orthophosphate diesters include phospholipids. Phosphonates are clearly distinguished by the chemical shift range characteristic of a direct carbon–phosphorus bond. This category includes phosphonolipids (δ = 20) and their degradation products (δ = 18).[13] Many ^{31}P NMR spectra of pasture soil extracts show only a dominant signal near δ = 5, assigned to inorganic orthophosphate, with a weaker band across the range δ = 3–5, assigned to orthophosphate monoesters.[34] Some spectra of soil extracts include a signal near δ = – 21, assigned to polyphosphate chain units.[13]

The natural abundance of ^{15}N is so low that isotopic enrichment is necessary. Soil organic matter matures over periods of centuries, so only the first steps of humification can be studied by monitoring the fate of ^{15}N-enriched additives. At least three different chemical shift scales have been used in studies relevant to agriculture. The chemical shifts mentioned here are expressed in parts per million to high frequency from ammonia. Typical values are δ = 30–70 for amine nitrogen, 90–120 for amide nitrogen, and δ > 120 for heterocyclic nitrogen.[35] Chemical shifts have been reported for a number of specific substances considered relevant to the chemistry of humic substances.[35] When a soil humic acid was incubated with ^{15}N-enriched $NaNO_3$, the ^{15}N CP MAS NMR spectrum of the product was dominated by a broad band at δ = 119, assigned to secondary amides, e.g. in proteins.[36] The ^{15}N CP MAS NMR spectra of composts prepared with ^{15}N-enriched plant material are dominated by a peak assigned to proteins, with weaker signals at 83 and 71 ppm assigned to nucleic acids.[37]

NMR is not normally the technique of choice for studies of inorganic matter in soil, but there have been exceptions.

Most soil silicates contribute ^{29}Si NMR signals in a broad band across the region δ = – 80 to –115.[38] Fractionation of a soil into particle size ranges has been used to demonstrate the predominance of quartz (δ = – 113) in a coarse fraction, and layered aluminosilicates (δ = – 92) in a fine fraction.[39] One of the hydrated aluminosilicates, imogolite, contributes a relatively narrow peak at a distinctive chemical shift of δ = – 78.[38] Therefore, ^{29}Si NMR can be used to estimate the imogolite content of soil.

Solution NMR methods have been used to characterize aqueous ^{27}Al in plugs of soil.[40] Most of the signal strength was

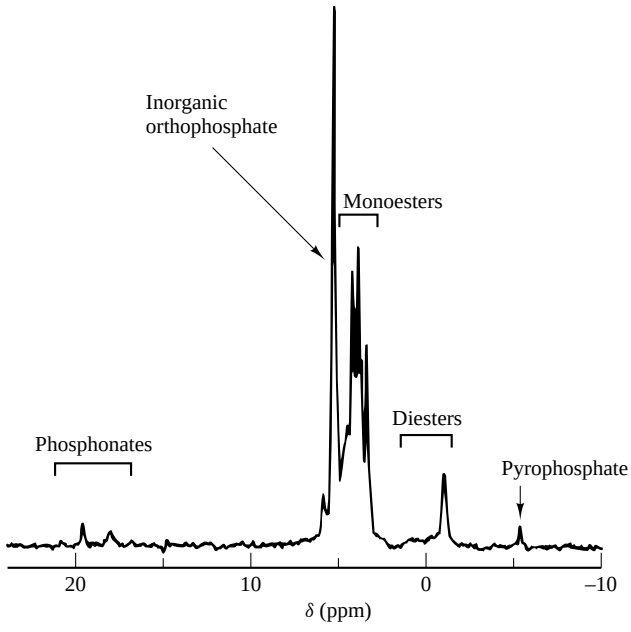

Figure 2 Phosphorus-31 NMR spectrum (32.2 MHz) of an aqueous NaOH extract from Carrick tussock-grassland soil. Sample mixed with D_2O in a 10 mm tube; 12 μs pulse width, 0.8 s data acquisition time with proton decoupling, 5.0 s pulse delay without proton decoupling, 79 h of data accumulation. The soil properties are described elsewhere[43]

found in a band from $\delta = -9$ to 12. This band was assigned to species with octahedral coordination, including complexes with humic substances. A relatively sharp peak at $\delta = 63.5$ was assigned to a polynuclear cation, believed to be more toxic to plants than the mononuclear cation.[40]

5 RELIABILITY OF NMR RESULTS

Patterns of relative signal areas have been compared for ^{13}C NMR spectra of extracted humic substances run as solids and as solutions.[8,9,41] The overall similarities have been encouraging, but sources of errors have been identified in both techniques.

In the case of solution NMR spectroscopy, it is necessary to choose a pulse delay that is adequate for both T_1 relaxation and suppression of NOEs. Preston and Blackwell drew attention to the need to consider magnetic field strength in selecting a suitable pulse spacing.[8] Values of $T_1 < 0.2$ s have been reported for protonated carbon in solutions of humic substances run at a field strength of 1.87 T,[42] but values in the range 0.2–0.8 s have been reported for experiments at 5.6 T.[8] These observations are consistent with molecular motion including components with correlation times longer than required for the T_1 minimum. Values of NOEs are particularly low and values of T_1 are particularly long for carboxyl carbon, so the content of this chemical functional group can be underestimated unless the decoupler output is gated off during the pulse delay.[8,42] A dramatic improvement in the strength of these signals has been reported for pulse delays increased from 0.5 to 5.0 s.[41] A pulse delay of 2 s has been suggested for solution ^{13}C NMR at 63 MHz.[8] Pulse delays as long as 20 s have been found necessary in ^{31}P NMR of soil extracts.[43]

The choice of magnetic field strength should be considered in ^{13}C CP MAS NMR also. Fründ and Lüdemann reported T_1(H) values in the range 3–6 ms for humic matter run at 2.35 T, rising to the range 10–20 ms for the same sample run at 7.05 T.[41] These values are fortunately all so short that the pulse spacing is more likely to be determined by the duty cycle of the spectrometer. It is important that the contact time should be long enough for adequate cross polarization, yet short enough to avoid the effects of variations in $T_{1\rho}$(H) between chemical functional groups. These two criteria conflict for most humic substances. On one hand, contact times as long as 1 ms are needed to achieve maximum signal strength for nonprotonated carbon, e.g. carboxylic carbon.[8] On the other hand, values of $T_{1\rho}$(H) can vary between chemical functional groups, because of the heterogeneous nature of soil organic matter. This was particularly evident in a clay fraction, where values of $T_{1\rho}$(H) ranged from 2.0 ms for *O*-alkyl carbon to 6.2 ms for *O*-substituted aromatic carbon.[44] Variations in $T_{1\rho}$(H) can arise, e.g. from selective binding of metal ions to specific chemical structures.[45] A contact time of 1 ms seems to provide a reasonable compromise.[45]

Paramagnetic ions such as Fe^{3+} can shorten values of $T_{1\rho}$(H) until organic matter in the immediate vicinity of each ion no longer responds to CP MAS NMR.[46] Interference from organic free radicals is not as important, as shown by a 'spin counting' experiment in which 97% of carbon in a solid ash-free fulvic acid responded to CP MAS NMR, despite the presence of organic free radicals.[46]

6 APPLICATIONS

Soils are often classified according to their color, so studies of the origin of color can provide a fundamental basis for classification schemes. NMR experiments have shown that the more intensely colored humic and fulvic acids contain relatively high proportions of aromatic carbon.[26,47] Humic substances in general display strong absorbance in the UV, tailing off across the visible region. Absorptivity at 272 nm has been found to be highly correlated ($r = 0.94$) with the strength of ^{13}C NMR signals assigned to aromatic carbon in humic acids.[48] Weaker correlations have been reported for fulvic acids.[49]

CP MAS NMR has been used to demonstrate a correlation ($r = 0.997$) between the aromatic carbon content of humic acids and the partition coefficient for binding of pyrene.[50] This suggests that the chemical structure of humic material should be considered in any attempts to model the transport or fate of organic pollutants. Carbon-13 NMR has been used to demonstrate formation of covalent bonds between ^{13}C-labeled 2,4-dichlorophenol and humic acid.[51] Decreased herbicide activity in tilled soil has been attributed to the organic matter being in a more reactive state than in soil that was not tilled.[52] The ^{13}C NMR spectrum of humic acid from the tilled soil showed a relatively strong band assigned to aromatic carbon, but the authors advised caution in the interpretation of the results, in view of the small magnitude of the observed differences and the small number of samples tested.[52]

A combination of ^{1}H, ^{13}C, and ^{31}P NMR has been used to monitor degradation of a herbicide, glyphosate (*N*-phosphonomethylglycine), in soil.[53]

Fecal fibre is rich in carbohydrates, particularly crystalline cellulose, contributing relatively sharp ^{13}C NMR signals across the region assigned to *O*-alkyl carbon.[54] These signals become weaker when feces are composted. In the case of composts formed from cattle manure, the relative signal area of the O-alkyl band dropped from 59% to 33% over a period of 147 days of composting.[55] CP MAS NMR has been described as the 'most quantitative procedure' of those tested for use in characterizing compost maturity.[56]

Intensive land management practices are known to cause long-term decreases in soil organic matter. Carbon-13 NMR has been used in attempts at characterizing the residual organic matter. Divergent results indicate a complex dependence on the nature of the initial material and details of the management regime. Oades et al. found relatively high aromaticity in a red–brown earth cultivated for 60 years, compared with undisturbed soil.[57] On the other hand, Schulten et al. found relatively low aromaticity in soils cultivated for periods up to 35 years.[58] Schulten et al. found lowest concentrations of residual organic matter in soils treated with high doses of mineral fertilizers. It is possible that their results reflect the influence of fertilizers rather than the influence of crops. Preston et al. observed a decrease in the area of the O-alkyl band and a corresponding increase in the area of the alkyl band in CP MAS NMR spectra of peat cultivated for periods up to 15 years.[59] These changes may reflect the influence of plowing, exposing organic matter to biological oxidation. Skjemstad et al. studied soils cultivated for periods up to 45 years.[60] They found no detectable changes in relative signal areas across CP MAS NMR spectra, but the signals became broadened in the spectra of soils with the lowest concentrations of residual

organic matter. They suggested that a major mechanism for the relative stability of persistent soil organic matter may be a physical association with the inorganic component. The effects of cultivation are also evident in ^{31}P NMR spectra of soil extracts, the diversity of chemical species being greater in uncultivated soils than in corresponding samples of cultivated soils.[61]

Several authors have studied the influence of climate and vegetation on soil properties. A negative correlation ($r = -0.998$) has been found between rainfall and the strength of ^{13}C signals assigned to aromatic carbon in humic acids.[62] The ^{31}P NMR spectra of soil extracts show a particularly wide diversity of chemical species for sites with high annual precipitation.[43] No correlations were found in a study of vegetation and its influence on the chemical structure of soil.[63]

7 SEPARATING OVERLAPPING SIGNALS

The applications sketched above have been hindered by problems with overlapping signals, particularly in solid state ^{13}C NMR. Most authors describe soil organic matter in very general terms, e.g. distinguishing 'aromatic' or 'aliphatic' carbon. Some spectra show hints of variations in details within one or more of the bands. Several strategies have been suggested for separating these overlapping signals.

Dipolar dephasing suppresses CP MAS NMR signals from most CH and CH_2 groups, leaving signals assigned to nonprotonated carbon or protonated carbon in functional groups with some freedom for internal motion. This technique has been used to demonstrate differences between the degrees of aromatic substitution in different humic acids.[64]

Proton spin relaxation editing exploits the heterogeneous nature of soil.[65] A proton inversion–recovery pulse sequence is combined with ^{13}C CP MAS NMR. Linear combinations of partly relaxed and fully relaxed spectra are generated to separate subspectra assigned to distinctly different forms of organic matter with distinctly different values of T_1(H). This procedure has been used to separate subspectra from the CP MAS NMR spectrum of a humic acid, suggesting that material extracted from clays may differ from material extracted from other soil fractions.[28] Variations in $T_{1\rho}$(H), mentioned above, could also be used for separation of subspectra.

2D NMR techniques show some promise for separation of overlapping signals. A ^{1}H–^{13}C heteronuclear chemical shift correlation experiment has been used to construct a 2D NMR plot for a sample of fulvic acid, with the ^{1}H CRAMP spectrum on one axis and the ^{13}C CP MAS spectrum on the other.[66] This showed that a broad band in the CRAMP spectrum could be assigned to a mixture of contributions from alkyl and *O*-alkyl structures, with the latter offset to slightly higher chemical shifts.

Despite this progress, the problem of separating overlapping signals remains one of the greatest challenges in NMR studies of agricultural and soil samples.

8 REFERENCES

1. D. H. R. Barton and M. Schnitzer, *Nature*, 1963, **198**, 217.
2. H.-D. Lüdemann and H. Nimz, *Biochem. Biophys. Res. Commun*., 1973, **52**, 1162.
3. J. A. Neyroud and M. Schnitzer, *Can. J. Chem.*, 1974, **52**, 4123.
4. F. J. Gonzalez Vila, H. Lentz, and H.-D. Lüdemann, *Biochem. Biophys. Res. Commun.*, 1976, **72**, 1063.
5. P. F. Barron and M. A. Wilson, *Nature*, 1981, **289**, 275.
6. R. L. Wershaw and M. A. Mikita (eds.), *NMR of Humic Substances and Coal*, Lewis, Chelsea, MI, 1987.
7. M. A. Wilson, *NMR Techniques and Applications in Geochemistry and Soil Chemistry*, Pergamon Press, Oxford, 1987.
8. C. M. Preston and B. A. Blackwell, *Soil Sci.*, 1985, **139**, 88.
9. R. Fründ and H.-D. Lüdemann, *Sci. Total Environ.*, 1989, **81/82**, 157.
10. P. G. Hatcher and M. A. Wilson, *Org. Geochem*., 1991, **17**, 293.
11. R. Fründ and H.-D. Lüdemann, *Z. Naturforsch*., 1991, **46c**, 982.
12. C. Saiz-Jimenez, B. L. Hawkins, and G. E. Maciel, *Org. Geochem*., 1986, **9**, 277.
13. R. H. Newman and K. R. Tate, *Commun. Soil Sci. Plant Anal*., 1980, **11**, 835.
14. L. M. Condron, K. M. Goh, and R. H. Newman, *J. Soil Sci*., 1985, **36**, 199.
15. M. A. Arshad, J. A. Ripmeester, and M. Schnitzer, *Can. J. Soil Sci*., 1988, **68**, 593.
16. M. Oades, A. M. Vassallo, A. G. Waters, and M. A. Wilson, *Aust. J. Soil Res*., 1987, **25**, 71.
17. C. M. Preston, M. Schnitzer, and J. A. Ripmeester, *Soil Sci. Soc. Am. J.*, 1989, **53**, 1442.
18. G. Almendros, J. Sanz, F. J. González-Vila, and F. Martín, *Naturwissenschaften*, 1991, **78**, 359.
19. J. A. Baldock, J. M. Oades, A. M. Vassallo, and M. A. Wilson, *Environ. Sci. Technol*., 1990, **24**, 527.
20. B. K. G. Theng, G. J. Churchman, and R. H. Newman, *Soil Sci*., 1986, **142**, 262.
21. J. A. Baldock, J. M. Oades, A. G. Waters, X. Peng, A. M. Vassallo, and M. A. Wilson, *Biogeochem*., 1992, **16**, 1.
22. G. Catroux and M. Schnitzer, *Soil Sci. Soc. Am. J*, 1987, **51**, 1200.
23. M. A. Wilson, K. M. Goh, P. J. Collin, and L. G. Greenfield, *Org. Geochem.*, 1986, **9**, 225.
24. M. Ghosal and E. S. K. Chian, *Soil Sci. Soc. Am. J*., 1985, **49**, 616.
25. V. C. Farmer and D. L. Pisaniello, *Nature*, 1985, **313**, 474.
26. K. R. Tate, K. Yamamoto, G. J. Churchman, R. Meinhold, and R. H. Newman, *Soil Sci. Plant Nutr*., 1990, **36**, 611.
27. G. Almendros, F.-J. González-Villa, F. Martín, R. Fründ, and H.-D. Lüdemann, *Sci. Total Environ.*, 1992, **117/118**, 63.
28. R. H. Newman and K. R. Tate, *J. Soil Sci*., 1991, **42**, 39.
29. M. Schnitzer and C. M. Preston, *Soil Sci. Soc. Am. J.*, 1986, **50**, 326.
30. R. H. Newman, B. K. G. Theng, and Z. Filip, *Sci. Total Environ*, 1987, **65**, 69.
31. M. A. Wilson, A. J. Jones, and B. Williamson, *Nature*, 1978, **276**, 487.
32. M. A. Wilson, *J. Soil Sci*., 1981, **32**, 167.
33. P. Ruggiero, F. S. Interesse, and O. Sciacovelli, *Soil Biol. Biochem*., 1980, **12**, 297.
34. G. E. Hawkes, D. S. Powlson, E. W. Randall, and K. R. Tate, *J. Soil Sci*., 1984, **35**, 35.
35. K. A. Thorn and M. A. Mikita, *Sci. Total Environ*., 1992, **113**, 67.
36. L. Benzing-Purdie, J. A. Ripmeester, and C. M. Preston, *J. Agric. Food Chem*., 1983, **31**, 913.
37. G. Almendros, R. Fründ, F. J. Gonzalez-Vila, K. M. Haider, and

H.-D. Lüdemann, *FEBS Lett.*, 1991, **282**, 119.

38. P. F. Barron, M. A. Wilson, A. S. Campbell, and R. L. Frost, *Nature*, 1982, **299**, 616.
39. M. A. Wilson, in *Soil Analysis: Modern Instrumental Techniques*, ed. K. A. Smith, Dekker, New York, 1991, Chap. 14, p. 601.
40. D. Hunter and D. S. Ross, *Science*, 1991, **251**, 1056.
41. R. Fründ, F. J. Gonzalez-Vila, H.-D. Lüdemann, and F. Martin, *Z. Naturforsch*., 1987, **42c**, 205.
42. R. H. Newman and K. R. Tate, *J. Soil Sci*., 1984, **35**, 47.
43. K. R. Tate and R. H. Newman, *Soil Biol. Biochem*., 1982, **14**, 191.
44. J. A. Baldock, J. M. Oades, A. M. Vassallo, and M. A. Wilson, *Aust. J. Soil Res*., 1990, **28**, 193.
45. C. M. Preston, R. L. Dudley, C. A. Fyfe, and S. P. Mathur, *Geoderma*, 1984, **33**, 245.
46. A. M. Vassallo, M. A. Wilson, P. J. Collin, J. Malcolm Oades, A. G. Waters, and R. L. Malcolm, *Anal. Chem*., 1987, **59**, 558.
47. S. Dou, E. Chen, X. Xu, S. Tan, S. Hua, and T. Zhu, *Turang Tongbao*, 1989, **20**, 263 (*Chem. Abstr*., 1990, **112**, 177 449k).
48. S. J. Traina, J. Novak, and N. E. Smeck, *J. Environ. Qual*., 1990, **19**, 151.
49. J. M. Novak, G. L. Mills, and P. M. Bertsch, *J. Environ. Qual*., 1992, **21**, 144.
50. T. D. Gauthier, W. R Seitz, and C. L. Grant, *Environ. Sci. Technol*., 1987, **21**, 243.
51. P. G. Hatcher, J. M. Bortiatynski, R. D. Minard, J. Dec, and J. M. Bollag, *Environ. Sci. Technol*., 1993, **27**, 2098.
52. G. K. Stearman, R. J. Lewis, L. J. Tortorelli, and D. D. Tyler, *Soil Sci. Soc. Am. J.*, 1989, **53**, 1690.
53. M. L. Rueppel, B. B. Brightwell, J. Schaefer, and J. T. Marvel, *J. Agric. Food Chem.*, 1977, **25**, 517.
54. R. M. Elofson, J. A. Ripmeester, N. Cyr, L. P. Milligan, and G. Mathison, *Can. J. Anim. Sci.*, 1984, **64**, 93.
55. Y. Inbar, Y. Chen, and Y. Hadar, *Soil Sci. Soc. Am. J.*, 1989, **53**, 1695.
56. Y. Inbar, Y. Chen, Y. Hadar, and H. A. J. Hoitink, *BioCycle*, 1990, **31**, 64.
57. J. M. Oades, A. G. Waters, A. M. Vassallo, M. A. Wilson, and G. P. Jones, *Aust. J. Soil Res.*, 1988, **26**, 289.
58. H.-R. Schulten, R. Hempfling, K. Haider, F. F. Gröblinghoff, H.-D. Lüdemann, and R. Fründ, *Z. Pflanzenernähr. Bodenk.*, 1990, **153**, 97.
59. C. M. Preston, S.-E. Shipitalo, R. L. Dudley, C. A. Fyfe, S. P. Mathur, and M. Levesque, *Can. J. Soil Sci.*, 1987, **67**, 187.
60. J. O. Skjemstad, R. C. Dalal, and P. F. Barron, *Soil Sci. Soc. Am. J.*, 1986, **50**, 354.
61. L. M. Condron, E. Frossard, H. Tiessen, R. H. Newman, and J. W. B. Stewart, *J. Soil Sci.*, 1990, **41**, 41.
62. M. A. Arshad, and M. Schnitzer, *Z. Pflanzenernähr. Bodenk.*, 1989, **152**, 11.
63. M. Krosshavn, J. O. Bjørgum, J. Krane, and E. Steinnes, *J. Soil Sci.*, 1990, **41**, 371.
64. P. G. Hatcher, M. Schnitzer, A. M. Vassallo, and M. A. Wilson, *Geochim. Cosmochim. Acta*, 1989, **53**, 125.
65. C. M. Preston and R. H. Newman, *Can. J. Soil Sci*, 1992, **72**, 13.
66. C. E. Bronnimann, C. F. Ridenour, D. R. Kinney, and G. E. Maciel, *J. Magn. Reson.*, 1992, **97**, 522.

Biographical Sketch

Roger H. Newman. *b* 1949. B.Sc.(Hons.), 1970, University of Canterbury, NZ. Ph.D. (supervisor Robin Harris), 1976, University of East Anglia, UK. NMR spectroscopist for the New Zealand DSIR, 1970–73 and 1976–92, and for Industrial Research Limited, 1992–present. Approx. 70 publications. Research specialty: applying solid state NMR to characterize heterogeneous organic solids.

Coal Structure from Solid State NMR

Ronald J. Pugmire
University of Utah, Salt Lake City, UT, USA

1	Introduction	1
2	Experimental Techniques	1
3	Description and Constituents	4
4	Applications to Coal Science	5
5	Note	9
6	References	9

1 INTRODUCTION

Coal has been used as an important source of fuel for thousands of years, but it is a complex, heterogeneous fuel which is difficult to burn or process without serious environmental implications. Coals can vary significantly among different geographic areas in important properties such as rank, ash, sulfur and nitrogen content, mineral impurities, and maceral constituents. Substantial worldwide attention is being focused on more efficient and cleaner methods for utilization of this important energy resource.

The wide heterogeneity of coal has made it difficult to characterize and to correlate its structure. Evidence exists that differences in geological histories and maceral constituents affect coal chemistry and technological applications of coals, since coals of the same apparent rank but of different geological history can exhibit a variety of physical and chemical properties. Coal structure varies with recognizable geological and geochemical features which affect its reactivity. The variations in the geochemical history and the complexities of the macromolecular structure of coal further confound a clear understanding of the complex nature and interrelationships among coals.[1]

Our understanding of the details of coal structure has improved markedly over the last decade. Coal is now believed to be a heterogeneous mixture composed of a macromolecular network of varying degrees of cross-linking within the macromolecular phase with a smaller molecular phase imbibed or associated with this network. A major portion of the credit for the present state of knowledge of the general characteristics of coal structure can be traced to studies that employed NMR spectroscopy. It is interesting to observe that NMR was first applied to the study of coals in 1955,[2] only nine years following the discovery of the NMR phenomenon in bulk matter. These first NMR observations employed broadline ^{1}H techniques which, in the absence of means to reduce the large proton dipole–dipole interactions, produced very broad bands in fossil fuel related materials. In 1968 Haeberlen and Waugh[3] demonstrated that the hydrogen dipole–dipole interaction could be significantly reduced by averaging in spin space via a multiple pulse approach[4] rather than attempting to spin the sample mechanically at very high MAS rates in order to achieve the same results. In the mid-1970s Schnable[5] and Gerstein et al.[6,7] demonstrated that if the sample is spun simultaneously about the magic angle then the chemical shift anisotropy (CSA) as well as the inhomogeneous heteronuclear dipolar interactions are simultaneously averaged. Hence, much narrower peaks are obtained with this experiment which Gerstein named CRAMPS. The proton CRAMPS experiment was first applied to coals by Gerstein in 1981.[8] The CRAMPS experiments have been especially useful as a probe to study the 'mobile phase' present in coal structure wherein solvents such as perdeuterated pyridine are imbibed into the parent coal.[9–13] The reduction in proton NMR linewidths is attributed to motional narrowing and to reduction of bulk and molecular susceptibility anisotropies by partial mobilization of certain structural moieties in coal caused by disruption of hydrogen bonds and other noncovalently bonded structural units.

As early as 1966 the first ^{13}C NMR spectra appeared of materials derived from coal.[14] Broadline ^{13}C NMR spectroscopy was first applied to whole coals in 1971 to confirm the high aromaticity of anthracite.[15] Significant improvements in resolution began to emerge five years later[16] with the application of the cross polarization technique followed by applications of magic angle spinning to coal.[17] In 1979 Opella and Frey[18] introduced the concept of the dipolar dephasing experiment which discriminates between nonprotonated and protonated carbons by means of the effective C–H dipole–dipole interaction. Alemany et al. studied the characteristics of the dipolar dephasing experiment on model compounds[19] and then demonstrated the utility of this experiment in a careful study of an Illinois No. 6 coal.[20] Work by Wilson,[21] Murphy,[22] and Gerstein[23] and their co-workers has verified the value of dipolar dephasing experiments in the study of coal. The data derived from the techniques described, together with others to be described in subsequent sections, have been extremely valuable in probing the general structural features of coals and have greatly enhanced the usable knowledge base for improved coal utilization.

2 EXPERIMENTAL TECHNIQUES

Since the organic constituents of coal are composed primarily of hydrogen and carbon with smaller amounts of oxygen, nitrogen, and sulfur (typical elemental compositions of a lignite, high volatile bituminous, and anthracite coal are $C_{100}H_{78.9}N_{1.4}S_{0.4}O_{22.7}$, $C_{100}H_{76.2}N_{1.7}S_{0.4}O_{6.1}$, and $C_{100}H_{17.5}N_{0.7}S_{0.2}O_{1.5}$, for the Beulah-Zap, Pittsburgh No. 8, and Buck Mountain, respectively) (see Section 5), NMR experiments have focused primarily on ^{1}H and ^{13}C applications. While ^{1}H NMR experiments (particularly the CRAMPS applications) have added valuable insight for coal structural studies, the major area of interest has been in the elucidation of the carbon skeletal structure since many of the questions regarding the physical and chemical properties can be addressed from a clear understanding of the details of the carbon backbone and associated functional groups. Carbon-13 NMR spectroscopy has become one of the premier tools in organic structure analysis due to the relationship between the local electronic environment of the carbon nucleus and the ^{13}C chemical shift and, hence, the use of ^{13}C NMR techniques has become essential for the study of solid carbonaceous materials such as coal chars, pitches, and geochemical materials in general.

2.1 CP MAS and Isotropic Shifts

The combination of cross polarization and magic angle spinning has been used to obtain high-resolution NMR spectra from solids for many years. Magic angle sample spinning at a rate greater than the chemical shielding anisotropy (CSA) of the carbon nuclei will average the principal values of the chemical shift tensor (δ_{11}, δ_{22}, δ_{33}) to the isotropic chemical shift value. Linewidths obtained by CP MAS experiments are typically of the order of 1–2 ppm in simple organic compounds but relaxation effects (T_2), anisotropy in bulk susceptibility, crystallinity, and solid state effects can considerably broaden the individual spectral lines. In some cases one may observe multiple lines due to lattice structures that contain multiple structures per unit cell or crystal lattice effects that impose a preferred conformation which breaks the local symmetry. In general, the solid state isotropic chemical shifts are similar to those in solution and the appropriate chemical shift/structure relationships developed in solution studies may be used to interpret solid state CP MAS spectra.

The Utah group[24,25] illustrated the relationship between isotropic chemical shifts and the CP MAS spectra of coals. While coal spectra are characterized by banded structures in the aliphatic and aromatic regions, it is evident from the bandshapes and shoulders on these bands that structural information is available beyond that obtained from aromaticity considerations only. Gerstein demonstrated that isotropic chemical shifts could be used to look .. 'beyond just aromaticity; chemical functionality'.[26] An example of the diversity of the ^{13}C NMR spectra of coals is presented in Figure 1 for a series of coals of ranks ranging from lignite through anthracite.

Solum et al.[27,28] have used a rather detailed isotropic chemical shift distribution together with dipolar dephasing data to obtain 12 structural parameters for the coals contained in the Argonne Premium Coal Sample Bank. Wilson et al.[29] and Hatcher et al.[30] have used isotropic ^{13}C NMR data to propose chemical transformation pathways for coal precursors, while Hatcher et al.[31] have used such data to construct a three-dimensional computer simulation of coal formation from components of plant precursors. Hence, CP MAS chemical shift data have had a major impact in geochemical applications in general and fossil fuels in particular.

2.2 Shielding Tensors and 2D Methods

The CSA is a reflection of the interaction of the electronic environment of the nuclei with the external magnetic field. Depending on the orientation of a given molecule in the field, a different value of the chemical shift is observed. If the sample simultaneously exists in all possible orientations (as in the case of a powder sample), a superposition of all the possible shift values for the nuclei in the molecule is observed. The frequencies obtained from the breakpoints or discontinuities of this powder pattern are the principal values of the chemical shift tensor. For a ^{13}C nucleus in an anisotropic environment, three distinct values are observed, and these values correspond to the three elements (δ_{11}, δ_{22}, δ_{33}) found as the diagonal elements of the chemical shift tensor. From the study of single crystals, both the principal values of the shift tensor and their orientation in the molecular framework can be determined.

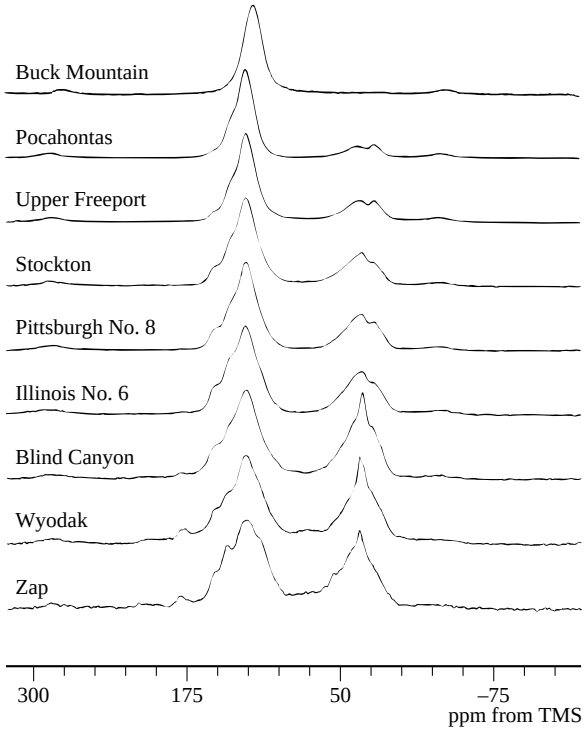

Figure 1 CP MAS spectra of the Argonne Premium Coals plus the Buck Mountain anthracite (PSOC-1468). The data were acquired as described by Solum et al.[27,28] Coal rank increases from bottom to top in the figure

Single crystal studies of aromatic compounds show that δ_{33} is always perpendicular to the plane of the aromatic ring[32] and its value in the aliphatic region reflects its independence of the π system. The other two tensor components, δ_{11} and δ_{22}, are oriented in the plane of the aromatic system. Theoretical studies have placed δ_{11} nearly perpendicular to the C–C bond with the largest π-bond order in all of the polycondensed aromatic hydrocarbons studied.[32]

Orendt et al.[33] have provided a brief description of experimental methods for studying chemical shift tensors in model compounds and coals. Extracting principal values from powders is extremely difficult due to the inherent low resolution of the experiment. Hence, principal values can normally be obtained only for very simple compounds or compounds of high symmetry containing only two to three tensors. The variable angle sample spinning (VASS) technique improves the resolving capacity to only three to four tensors.[34] Yet the information provided by CSA data is very valuable in the study of small molecules and even relatively large systems such as naphthalene, pyrene, hexahydropyrene, pyracene, and coals.[33,35] The data obtained on such systems have demonstrated that the shape of the tensor patterns can be used to distinguish different types of carbons in an environment where spectral overlap might preclude identification based on isotropic chemical shift information. This is particularly advantageous for coal due to spectral overlap in both the aromatic and aliphatic regions. Due to the large range in the principal values of the chemical shift tensors in aromatic carbons, an effort to obtain such data on coals is most fruitful since the carbon backbone of coals is dominated by aromatic species.

Table 1 Average Chemical Shift Tensor Values for Aromatic Carbons[a]

Carbon type	δ_{11}	δ_{22}	δ_{33}	δ_{av}
Protonated (75)	207 ± 22	146 ± 19	18 ± 12	124 ± 11
Substituted (21)	226 ± 11	165 ± 15	23 ± 14	138 ± 8
Phenolic (16)	227 ± 16	163 ± 9	72 ± 3	154 ± 6
Condensed (7)	205 ± 2	195 ± 2	−72 ± 5	133 ± 2

[a]The numbers in parentheses following the carbon type are the number of measurements considered in the analysis. Errors represent standard deviations of available data. All values are given in parts per million. The first three lines of data are from T.M. Duncan, 'A Compilation of Chemical Shift Anisotropies', Farragut Press, Chicago, IL, 1990, p. C-5. The data on condensed carbons come from data obtained at the University of Utah.

For convenience, the aromatic carbons in coal can be grouped into four categories: protonated, substituted (having an alkyl group substituent), phenolic (having a hydroxy or ether substituent), and bridgehead or condensed. Presently available chemical shift tensor data on these types of carbons are summarized in Table 1 while Figure 2 portrays the ideal lineshapes for the four types of carbon of interest. These ideal lineshapes were obtained by tabulating literature values for the shift tensor components for aromatic carbons in simple organic compounds measured by a variety of methods.[32–37] These data have been used to study the aromatic structure in a fusinite maceral, two anthracite, and three bituminous coals.[33,35]

A detailed description of methods for obtaining chemical shift tensors is contained elsewhere (see ***Chemical Shift Tensors***.). Hughes et al.[33] have used a static chemical shift–chemical shift correlation spectroscopy experiment (referred to as the 2D flipper experiment) to examine the chemical shift tensor patterns in a medium volatile and a low volatile bituminous coal. In a conventional 1D static solid state spectrum of coal, a large degree of overlap between aromatic and aliphatic signals occurs, whereas the 2D chemical shift–chemical shift correlation spectrum clearly separates the two spectral regions and exhibits the presence of multiple overlapping chemical shift tensors in both the aromatic and aliphatic regions of both samples. Furthermore, this separation of spectral regions allows for the determination of the aromaticity from a non-MAS spectrum. The aromaticity values (f_a) are 0.78 for the Upper Freeport and 0.87 for the Pocahontas No. 3 coals compared with values of 0.81 and 0.86 determined by CP MAS experiments.[27,28]

In an effort to address the problem of spectral overlap many 2D techniques have been developed to obtain a spectrum with an isotropic shift along one axis and a stationary or slow-spinning sideband powder pattern along the other. One such technique, the triple echo magic angle turning (triple echo MAT) experiment (see ***Magic Angle Turning and Hopping***), has proven to be especially effective for studying model compounds and has been used to examine a number of coals, including those in the Argonne Premium Coal Sample Bank,[38] a naphthalene-derived pitch, a semi-anthracite, and an anthracite coal.[39] The chemical shift tensor patterns taken at various isotropic shift values in coals clearly exhibit the presence of the characteristic shapes of the chemical shift tensors of protonated, substituted, phenolic, or bridgehead carbons and, hence, one is able to distinguish different types of carbons in broad spectral regions where it is impossible to distinguish individual lines. An example of the deconvolution of overlapping lines is given in Figure 3, where the slice taken at an isotropic chemical shift value of 124 ppm is shown for Pocahontas No. 3 low volatile bituminous coal.[40]

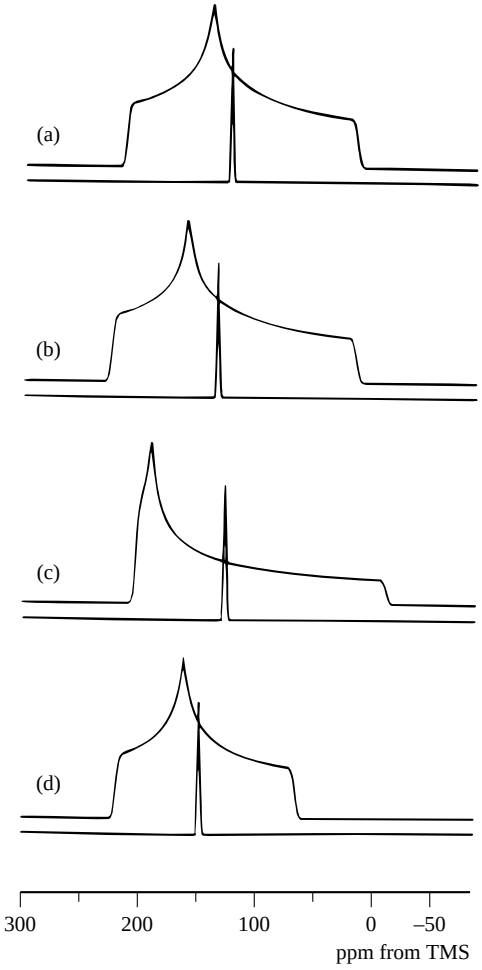

Figure 2 Ideal tensor patterns and average isotropic shifts for the four types of aromatic carbons in coal: (a) protonated, (b) alkyl substituted, (c) condensed or bridgehead, and (d) phenolic

The simulation of the individual powder patterns for an axially symmetric aromatic tensor and an overlapping protonated tensor are compared with the experimental data in Figure 3. A modified version of the triple echo MAT experiment called PHORMAT (see ***Magic Angle Turning and Hopping***), which incorporates rotor pulse synchronization, has been used in a blind comparison of the tensor principal values obtained from single crystal data in methyl α-D-glucopyranoside.[41] The principal values for the six carbons in this model compound have an rms average distance of 0.57 ppm from the tensors determined from the single crystal data, while the estimated variation in the principal values of the tensors studied with the triple echo MAT experiment vary by approximately 2 ppm.[40] Hence, the principal values reported by the Utah group have been shown to represent faithfully the single crystal data within 2 ppm when the triple echo MAT experiment is used, and an error of 0.5–1 ppm is expected if the more precise rotor pulse synchronized PHORMAT experiment is used. A remarkably good correlation is also obtained between the carbon aromaticities (ratio of

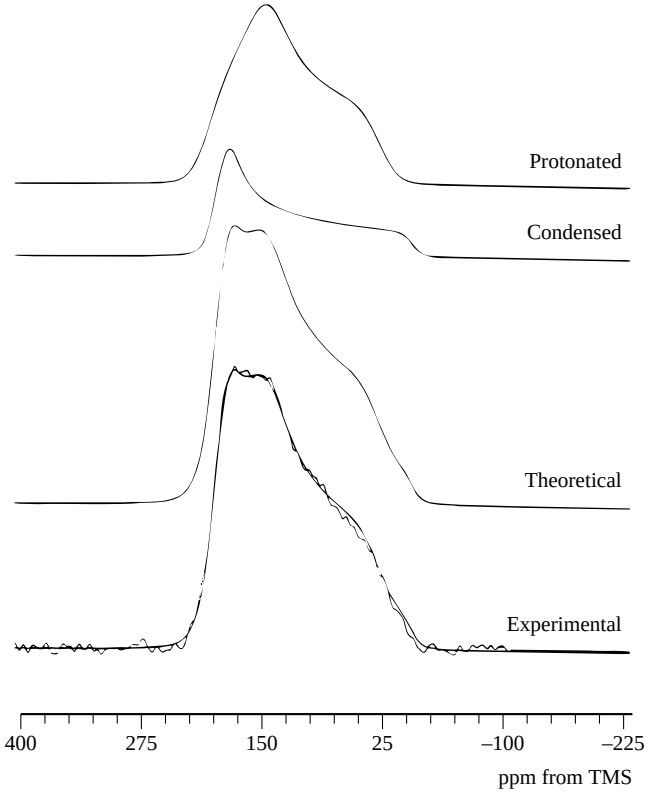

Figure 3 Spectral slice taken at an isotropic chemical shift of 124.5 ppm from the triple echo MAT experiment on Pocahontas No. 3 coal obtained from the Argonne Premium Coal Sample Bank. The experimental data were simulated as the superposition of protonated and condensed (bridgehead) aromatic carbon tensor patterns, labeled theoretical, which is overlaid on the experimental trace

aromatic to aromatic plus aliphatic carbons) determined from variable contact time CP MAS data and the triple echo MAT experiment. This relationship is shown in Figure 4 for the coals in the Argonne Premium Coal Sample Bank, two anthracites and a methylnapthalene-derived pitch (correlation coefficient $R^2 = 0.991$), demonstrating that the slow spinning triple echo MAT experiment does not lead to any apparent distortions of the structural components in coals.

3 DESCRIPTION AND CONSTITUENTS

3.1 General Nature of Coals and NMR Parameters

Coal is a complex sedimentary rock derived from plant remains. During the coalification process the accumulated plant material underwent differing degrees of chemical decomposition and depolymerization. These degradation processes formed peat which was subsequently transformed into coal of different ranks and properties based on sedimentary input, local environment, depth of burial, and local geological history. These various local conditions combined to produce a material that can be quite variable in terms of elemental composition and the nature of the inorganic materials incorporated into the coal material either as mineral inclusions or as chemically bound species. The elemental composition (particularly

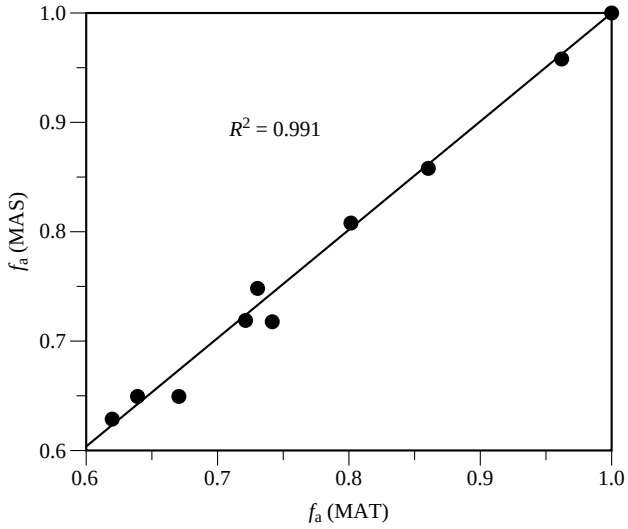

Figure 4 Comparison of aromaticity values for the Argonne Premium Coals, two anthracite coals (PSOC-867 and PSOC-628), and a methylnaphthalene-derived pitch. The CP MAS data were obtained as described by Solum et al.[27,28] while the MAT values were obtained from the triple echo MAT experiment (see ***Magic Angle Turning & Hopping***)

hydrogen, oxygen, and carbon) of the organic material can be used in a general classification scheme for describing the rank of a coal which, in increasing order, is given as peat, lignite, subbituminous, high volatile bituminous, medium volatile bituminous, low volatile bituminous, semianthracite, anthracite, and meta-anthracite. This rank progression exhibits a general order where the atomic ratios H/C and O/C decrease with increasing rank.

The most uniform microscopic constituents of coal, whose morphologically preserved or repolymerized materials retain distinct characteristics, are known as macerals. A large number of macerals have been identified and named. All macerals, however, can be conveniently grouped into three major subdivisions; liptinite, vitrinite, and inertinite. The vitrinite group of macerals are thought to be derived from plant cell wall material and make up the majority (50–90%) of most North American coals. The liptinite group of macerals is derived from algae and/or the resinous and waxy parts of plants such as resin, spores, pollen, and cuticules. These materials make up 5–15% of most North American coals but can be considerably higher in other coals and in coals derived from unique depositional environments. These macerals are the most aliphatic and hydrogen-rich of all the maceral groups. The inertinite group of macerals is derived from degraded woody tissue, making up 5–40% of most North American coals, but in western Canada and all southern hemisphere coals the percentage can be considerably higher.

The carbon aromaticity, f_a, is an important parameter in the study of coal and coal-derived materials and is the most widely used NMR parameter for coal studies. The first serious applications of ^{13}C NMR experiments to coal were directed at determining the carbon aromaticity. While several investigators studied a wide range of coals, Maciel et al.[42] and Gerstein et al.[23a] were the first investigators to investigate systematically the aromaticity/rank relationship. Gerstein et al. compared ^{13}C NMR-derived aromaticities with those obtained

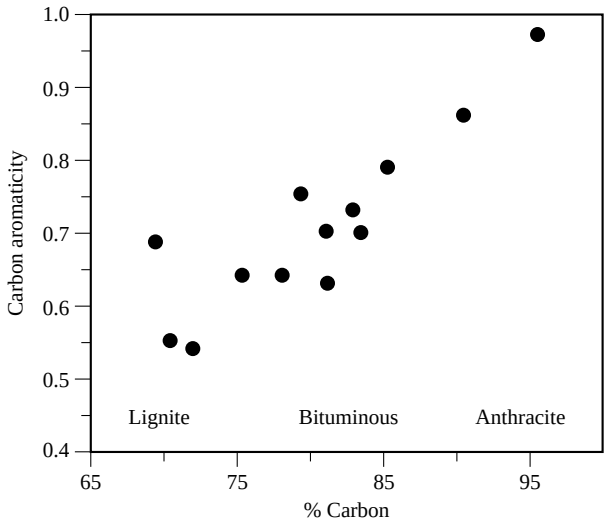

Figure 5 Carbon aromaticity, f_a, as a function of carbon content on a dry, ash-free basis

indirectly from graphical densities. The relationship between carbon aromaticity and rank (as derived from % carbon) is given in Figure 5. In NMR studies of macerals, the general trend in f_a values is liptinite < vitrinite < inertinite. Early studies by Maciel et al.[43] and Zilm et al.[44] helped to define the variations in aromaticity in the different maceral groups as well as the apparent differences is chemical functionality arising from differences noted in the isotropic shift/intensity distributions. More detailed NMR studies of maceral groups helped to refine the range of variations in aromaticities and chemical functionality.[25,45,46]

The quantitative accuracy of the f_a values derived from CP MAS experiments has been questioned and this controversy is addressed by Botto et al.[47] (see ***Fossil Fuels***). Orendt and co-workers have demonstrated that quantitative accuracy is obtainable if the CP MAS data are taken carefully with a variable contact time experiment and the data fitted to the proper model.[28]

3.2 Structural Components

The description of coal as a macromolecular network is credited to van Krevelen[48] who proposed a gel/sol model. The tools of polymer chemistry have been applied to study coal and advanced characterization techniques such as ^{13}C NMR have assisted in defining the parameters of the macromolecular structure of coals. The current model for coal structure consists of clusters of aromatic and hydroaromatic ring systems that are cross-linked such that domains exist which can, in some cases, undergo rapid reorientational motion. The argument that supports a cross-linked macromolecular network, other than the fact that the bulk of coals are not soluble in common solvents, is that coals swell by as much as 250% when brought into contact with appropriate solvents. The degree of reversibility is also consistent with a covalently cross-linked structure and rules out entanglements as the only associative force. Coals also display viscoelastic properties which are consistent with a macromolecular structure.

The type and characteristic of the second phase or component of coal is not as well defined as the macromolecular network, and has been the subject of extensive debate.[49] The 'mobile components' observed in proton NMR experiments have been shown to be complex and their relationship to a trapped molecular phase is yet to be completely resolved. Two views have been taken regarding the 'mobile protons' observed in ^{1}H NMR experiments. The first is that these protons can be attributed to molecules that are free to rotate in cages of the macromolecular network, and the second is that the mobile protons are associated with fragments of the macromolecular network capable of rotation due to single C–C or C–O bonds linking such fragments to the network. Jurkiewicz et al.[12,50] have used proton CRAMPS techniques to examine carefully the nature of the mobile protons in coal by comparing the native Argonne Premium Coals with those imbibed with pyridine-d_5. In pyridine-saturated coals the aliphatic and aromatic protons are better resolved and more structural details are evident. In addition, imbibing the samples with pyridine dramatically changes the structural or dynamic characteristics of a coal. The CRAMPS data provide a rough correlation between proton mobilities and the extractable components of coal. Employing a careful pyridine extraction study, Fletcher et al.[51] have studied the ^{13}C NMR structural components of the extracts and residues from the Argonne Premium Coals and contrasted the subtle differences between the extractable and residual components in terms of cross-linking between aromatic clusters.

An excellent review of the molecular structure, chemistry, and existing structural models of coal (up to 1986) is given by Davidson.[52] The early coal structure models proposed by Given and Weiser[53] and further refined by Shinn and Solomon[53] were based, in part, on available NMR data. From these models investigators attempted to construct an average or representative macromolecular structure of coal. In general, the information used for assembling a coal structure is molecular weight, aromatic cluster size, linkages between aromatic units, carbon aromaticity, elemental composition, as well as experimental results from chemical and thermal reactions. In order to explain the physical properties of coal and the thermal and chemical behavior of coal, network models have recently emerged[54–57] and solid state NMR data have become indispensable in constructing models that describe coal behavior.[51,54–57]

4 APPLICATIONS TO COAL SCIENCE

4.1 Refinements in Structural Detail

Gerstein suggested that ^{13}C NMR spectroscopy could provide more information on coal structure than just aromaticity and demonstrated that one could use dipolar dephasing techniques to examine functional groups and estimate aromatic cluster size.[22] Alemany et al.[19–21] refined the functionality studies employing painstakingly acquired dipolar dephasing data. Solum et al.[27,28] carefully employed a variety of experiments (i.e. dipolar dephasing, variable contact time experiments, and integrations of the ^{13}C spectra over selected chemical shift ranges) to derive 12 structural parameters for the eight

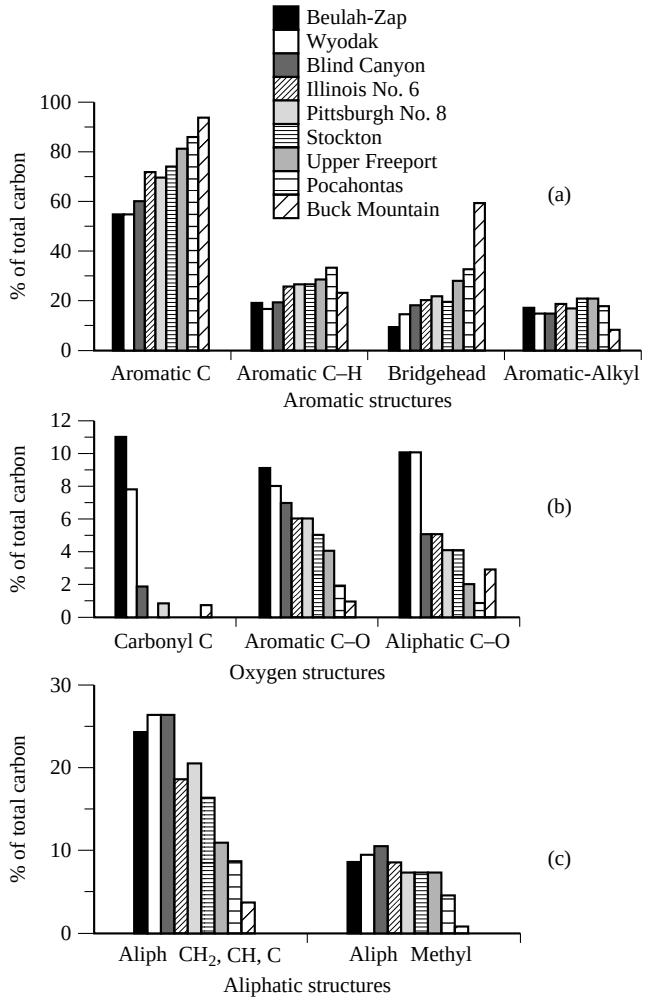

Figure 6 (a) Aromatic carbon structure distribution of the Argonne Premium Coals; (b) structural distribution of carbons associated with oxygen in the Argonne Premium Coals; and (c) carbon distribution of the aliphatic region of the Argonne Premium Coals

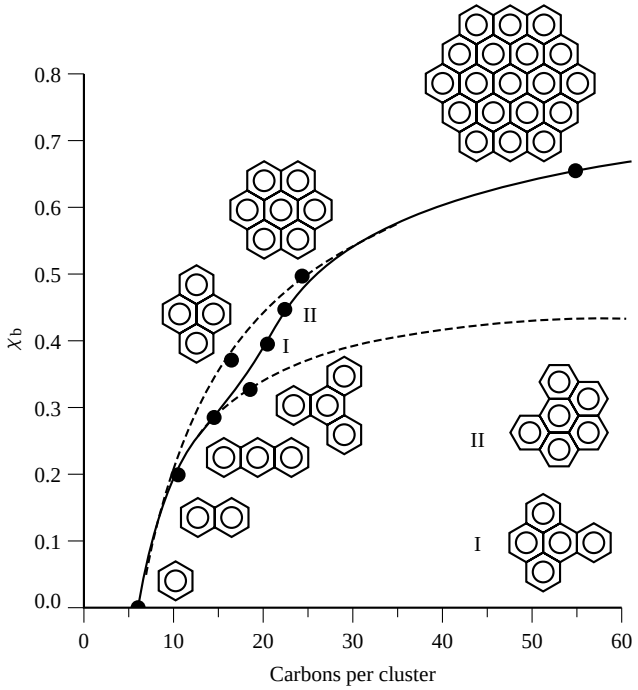

Figure 7 Plot of the mole fraction of bridgehead carbons, χ_b, versus C where C is the number of carbon atoms per aromatic cluster. The solid curve is for the combined model, the upper dashed curve is for the circular catenation model, and the lower dashed curve is for the primary catenation mode. (See Solum et al.[27] for details)

Argonne Premium Coals as well as a large variety of other coals and coal-derived chars.[51,56,57] The traditionally defined carbon aromaticity, f_a, is a sum of the contributions of all sp^2 carbons to an NMR spectrum. In coal samples it is assumed that ethylene groups are not present in any significant quantity. Hence, the f_a values are assumed to consist of aromatic plus carbonyl groups and these parameters have been redefined as f_a' and f_a^C, respectively. Employing lengthy dipolar dephasing experiments, the relative contributions of protonated and nonprotonated aromatic carbons can be estimated as f_a^H and f_a^N, respectively. The nonprotonated aromatic carbons, f_a^N, consist of contributions from alkyl-substituted, oxygen-substituted (phenols and phenolic ethers), and bridgehead carbons, defined as f_a^S, f_a^P, and f_a^B, respectively. The aliphatic groups have been segregated by chemical shift ranges which can be used to approximate the contributions from methyl groups, f_{al}*, oxygen-substituted alkyl carbons, f_{al}^O, and f_{al}^H, which is defined as the sum of all CH, CH_2, and nonprotonated aliphatic carbons. While these parameters are derived from chemical shift ranges that are known to contain some overlap with other functional groups, these approximations are reasonable and can be used to develop approximate model structures that are consistent with other analytical data. The major structural parameters derived from the coals in the Argonne Premium Coal Sample Bank plus Buck Mountain anthracite are given in Figure 6. From a knowledge of the relative number of peripheral and bridgehead carbons, it is possible to estimate the average aromatic cluster size of coal samples.[27] The average cluster size model for coal is shown in Figure 7 and the range of average number of aromatic carbons per cluster (AC/Cl) is given in Figure 8. This parameter has proven extremely useful in analyzing changes that occur during conversion and combustion processes.

If one defines the total number of ring attachments as the number of alkyl and oxygen substituents on the average aromatic cluster, it is possible to estimate the number of attachments per cluster. This number is between three and six for all coals studied but small variations in this parameter, defined as the cluster coordination number (σ + 1), are very important in explaining phenomena associated with coal structure, physical properties, and combustion behavior. The cluster coordination numbers for the coals previously described are given in Table 2.

4.2 Applications to Combustion and Pyrolysis Modeling

As previously discussed, the present model for coal structure is based on a network consisting of aromatic clusters of varying size connected by various types of bridging groups, and a simple schematic of the major types of structural elements that can by derived from NMR data is shown in Figure 9.

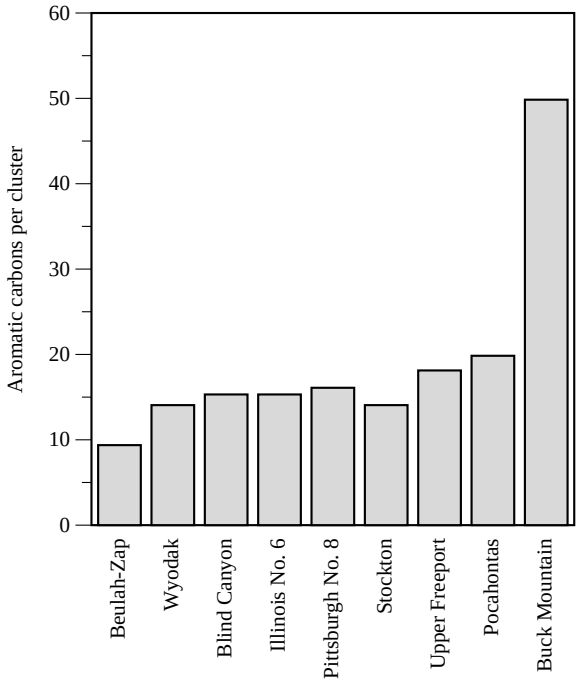

Figure 8 Aromatic cluster size of the Argonne Premium Coals and Buck Mountain anthracite, PSOC-1468

Table 2 Average Cluster Descriptions for ACERC Coals[a]

Coal	AC/Cl	(σ + 1)	P_o	*BL*	*MW*	m_δ
Beulah-Zap[b]	9	4.1	0.64	2.6	269	40
Wyodak	14	5.6	0.55	3.1	408	42
Blind Canyon	15	5.1	0.49	2.5	366	36
Illinois No. 6	15	5.0	0.63	3.2	322	27
Pittsburgh No. 8[b]	16	4.7	0.64	3.0	330	24
Stockton	14	4.8	0.69	3.3	272	20
Upper Freeport	18	5.3	0.67	3.6	312	17
Pocahontas No. 3	20	4.4	0.74	3.3	307	14
PSOC-1443	10	4.8	0.59	2.8	297	36
PSOC-1488	11	4.7	0.54	2.5	310	37
PSOC-1468	50	4.7	0.89	4.2	656	12

[a]The Advanced Combustion Engineering Research Center (ACERC) selected a set of standard coals for characterization and combustion testing and modeling. The 11 coals consist of the eight coals contained in the Argonne Premium Coal Sample Bank and three additional coals obtained from the Penn State Coal Sample Bank. Column headings are defined in the text.
[b]Averaged over two or more sample vials.

A number of investigators have applied statistical methods to predict how such a network would behave when subjected to thermally induced bridge-breaking cross-linking and mass transport processes. The geometry of a network is described by its degree of branching. An unbranched linear network will have one bridge per ring cluster attaching it to the next cluster. Thus, each cluster has two attachments and is said to have a coordination number (σ + 1) of two. A highly branched network would have several bridges attached to it and a higher coordination number. When coal is heated, the connecting bridges can break and new bridges can form. The objectives of network models of coals are, given the geometry

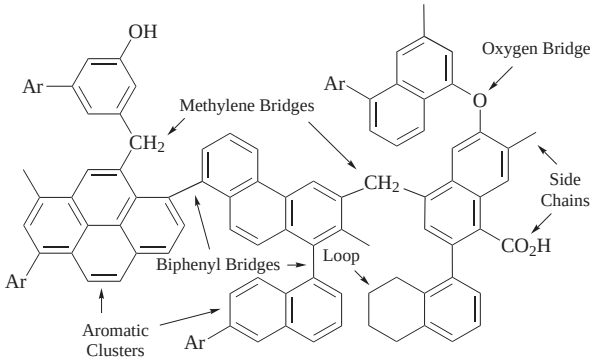

Figure 9 Representative chemical structural units identified in ^{13}C NMR analysis of coal and coal chars

of the macromolecular network, to predict the concentrations of individual aromatic ring clusters (monomers) and linked clusters (oligomers of *n* clusters, '*n*-mers') that are completely detached from the totally linked network, as a function of the number of unbroken bridges. By assigning an average or distribution of molecular weights to the ring clusters, the amounts of tar, extractables, liquids, or char can then be defined from the distribution of oligomer sizes. The application of network models appears to unify many observations of coal pyrolysis, including tar formation, extract formation, metaplast formation, fluidity, and solvent swelling behavior.[54]

A major challenge to all network models is the acquisition of analytical data that describe the network with sufficient detail that the investigator is not required to make guesses or fit the experimental data in order to derive critical network parameters. Grant et al.[55] have demonstrated that the coal macromolecular structure can be modeled as a Bethe lattice and that this lattice structure can explain the nonlinear behavior associated with devolatilization processes of coals. The coordination number of the Bethe lattice, σ + 1, is a key element in predicting the lattice behavior, and this parameter is determined directly from NMR data as the average number of substituents on an average aromatic cluster. Four other essential parameters, P_o, *BL*, *MW*, and m_δ, can be derived from the NMR data of coals.

The fraction of intact bridges between clusters, P_o is calculated with the assumption that all nonbridging cluster substituents are terminated by a methyl group and can be estimated as

$$P_o = [(\text{attachments}/100\text{C}) - f_{al}^*]/(\text{attachments}/100\text{C}) \quad (1)$$

While it is recognized that aryl–aryl bridges and phenolic groups are present in relatively small amounts in most coals, these structural units cannot be easily derived from NMR data and, hence, this approximation neglects hydroxy and aryl groups as possible chain terminators. The remaining cluster attachments must be either aliphatic or ether bridges between different clusters or aliphatic loops between two adjacent carbons in the same aromatic cluster, i.e. a hydroaromatic structure such as exists in tetralin. The number of bridges and loops, *BL*, on a cluster is defined as

$$BL = P_o \times (\sigma + 1) \quad (2)$$

The mechanical properties of the network will be related to this parameter because *BL* is related to the cross-link density of the macromolecular structure. The average cluster molecular weight (*MW*), and the total mass of the attachments to the aromatic cluster (m_δ) are

$$MW = (\text{aromatic carbons/cluster} \times 12.011)/(f_{a'} \times \%C) \quad (3)$$

$$m_\delta = (MW - C_{\text{clust}} \times 12.011)/(\sigma + 1) \quad (4)$$

where C_{clust} is the average number of carbons per cluster. While these parameters fall within certain ranges (see Table 2), each coal is unique and must be modeled separately.

During coal devolatilization, both tar (defined as volatiles, other than water, that condense at room temperature) and gas (CH_4, CO, CO_2, H_2O, light hydrocarbons, etc.) are released and a residual char remains. Employing the NMR-derived parameters needed to model the macromolecular network of each coal, it is possible to predict the tar and total mass loss (tar plus gas) of a set of coals with reasonable accuracy, as seen in Figure 10, without the necessity of invoking fitting parameters.

The mass of attachments to the aromatic ring is directly related to the amount of gas liberated during coal devolatilization through thermal cracking of the side chains.[57] During the pyrolysis process the physical and chemical properties of the residual char are continually changing. Solum et al.[56] were able to follow the details of the release of tar and gas together with the evolution of char structure from a lignite (Beulah-Zap) and a high volatile bituminous (Illinois No. 6) coal during devolatilization. The NMR data were used to track the lattice parameters associated with average cluster size and cross-linking reactions. Under rapid heating conditions (10^4 K s^{-1}), the data demonstrate that Zap coal undergoes early cross-linking behavior due to the loss of carboxy groups whereas Illinois No. 6 exhibits a slower overall rate of cross-linking. It was further noted from the NMR data that the number of cluster attachments remained constant during mass release during rapid pyrolysis at a temperature of 1250 K. However, near the end of the mass release the number of bridges and loops increased, suggesting that the coal lattice had begun to cross-link as tar release was terminated but as gas release continued. Under rapid heating but short resident time conditions in the reactor employed, the data exhibited little evidence of cluster size growth in the macromolecular structure. These data suggest that near the end of the devolatilization process cross-linking occurs at the same time as aliphatic carbons are released and the graphitization process does not occur under the conditions of the experiments performed. In the Illinois No. 6 coal, most of the mass loss occurred before the onset of significant changes in aromaticity. For the Zap coal, the changes in aromaticity occurred much earlier than for Illinois No. 6. The carbon skeletal structure of the final chars are similar for these two coals and Fletcher et al.[57] have reported similar results on a number of other chars even though the structure of the initial coals are quite different.

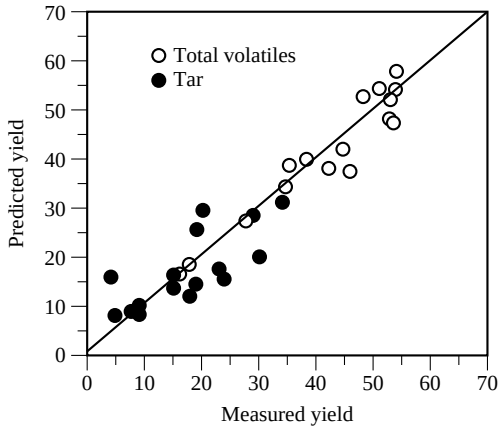

Figure 10 Comparison of predicted and measured tar and total volatiles yields for a wide range of coals. Data are for coals from the Argonne Premium Coal Sample Bank and from the Penn State Sample Bank for which NMR and pyrolysis data are available. (See Solum et al.[56] for details)

The physical properties of the macromolecular structure are related to the extent of cross-linking present. The NMR-derived bridges and loops parameter can be used estimate the degree of cross-linking that exists in coals and chars. An NMR cross-link index can be defined as

$$\text{NMR index} = (M_\infty - M_T)/(M_\infty - M_o) \quad (5)$$

where M_T is the number of bridges and loops per cluster at temperature T and the o and ∞ subscripts refer to the parent coal and the fully pyrolyzed char respectively.

Figure 11 compares the cross-link density obtained from the ^{13}C NMR data with that obtained from solvent swelling experiments.[57] These data clearly demonstrate that the functional form of the NMR cross-linking index is consistent with the normalized volumetric swelling index commonly used to study the cross-link structure in polymers. In the Beulah-Zap lignite, the number of bridges and loops increase with temperature, indicating that initial cross-linking has occurred at a relatively low temperature ($\sim$ 500 K) and progressive cross-linking occurs as the temperature increases. In the case of the Pittsburgh No. 8 coal, the NMR data suggest that the initial solvent swelling behavior is due to the breaking of labile bridges at moderate temperatures (500–600 K), which permits increased flexibility of the macromolecular network. At higher temperatures (>700 K), the number of bridges begins to increase as the swelling of the coal decreases. Such behavior would be expected as a more rigidly cross-linked network developed. The NMR data confirm that low-temperature cross-linking occurs in low-rank coals and that cross-linking at moderate temperatures is observed in both bituminous and low-rank coals.

The preceding examples demonstrate that NMR spectroscopy provides a great deal of information on coal structure and is perhaps the premier analytical tool in coal studies despite the inherent difficulties in carrying out experiments and interpreting the quantitative nature of the data. Even so, data carefully taken can be used to assess differences that occur in coals and follow many processes associated with coal utilization. Ambiguity exists in extracting information from overlapping spectral bands in both the aromatic and aliphatic regions. However, promising new experiments, such as the triple echo MAT and PHORMAT, that take advantage of the information contained in the chemical shift tensors, will probably resolve

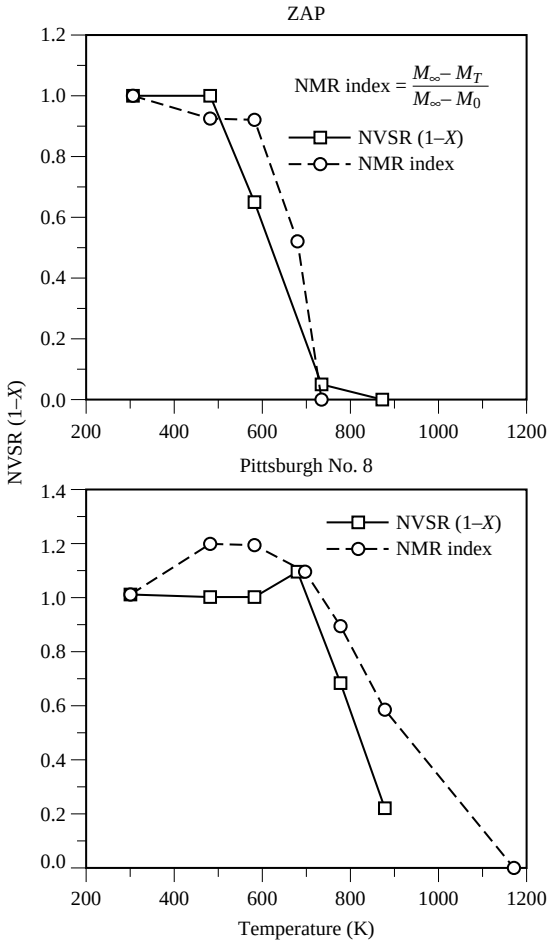

Figure 11 Comparison of the normalized volumetric swelling ratio (NVSR) for Beulah-Zap lignite and Pittsburgh No. 8 with the ^{13}C NMR index derived from the number of bridges and loops present in the parent coals and the pyrolysis chars. (See Solomon et al.[54] for details)

some of these ambiguities, particularly those associated with the aromatic region of the spectra.

5 NOTE

Beulah-Zap and Pittsburgh No. 8 are from the Argonne Premium Coal Sample Bank, while the Buck Mountain anthracite is available from the Penn State Sample Bank as PSOC-1468.

6 REFERENCES

1. K. L. Smith, L. D. Smoot, T. H. Fletcher, and R. J. Pugmire, *The Structure and Reaction Processes of Coal*, Plenum Press, New York, 1994, pp. 1–2.
2. P. C. Newman, L. Pratt, and R. E. Richards, *Nature (London)*, 1955, **175**, 645.
3. U. Haeberlen and J. S. Waugh, *Phys. Rev.*, 1968, **175**, 453.
4. J. S. Waugh, L. M. Huber, and U. Haeberlen, *Phys. Rev. Lett.*, 1968, **20**, 180.
5. B. Schnabel, U. Haubenreisser, G. Scheler, and R. Muller, *Proc. 19th Congr. AMPERE (Heidelberg), 1976*, 441.
6. B. C. Gerstein, R. G. Pembleton, R. D. Wison, and L. J. Ryan, *J. Chem. Phys.*, 1977, **66**, 361.
7. B. C. Gerstein, C. Chou, R. G. Pembleton, and R. C. Wilson, *J. Phys. Chem.*, 1977, **81**, 565.
8. B. C. Gerstein, *Philos. Trans. R. Soc. London*, 1981, **A299**, 521.
9. G. E. Maciel, D. E. Bronninmann, and C. F. Ridenour, in *Magnetic Resonance of Carbonaceous Solids*, eds. R. E. Botto and Y. Sanada, *Adv. Chem. Ser. No. 229*, Am. Chem. Soc., Washington, DC, 1993, Chap. 2
10. C. E. Bronnimann and G. E. Maciel, *Org. Geochem.*, 1989, **14**, 189.
11. M. F. Davis, G. R. Quinting, C. E. Bronnimann, and G. E. Maciel, *Fuel*, 1989, **68**, 763.
12. A. Jurkiewicz, C. E. Bronnimann, and G. E. Maciel, *Fuel*, 1989, **68**, 872.
13. A. Jurkiewicz, C. E. Bonnimann, and G. E. Maciel, *Fuel*, 1990, **69**, 804.
14. R. A. Friedel and H. L. Retcofsky, *Chem. Ind. (London)*, 1966, 455.
15. H. L. Retcofsky and R. A. Friedel, *Anal. Chem.*, 1971, **43**, 485.
16. D. L. VanderHart and H. L. Retcofsky, *Fuel*, 1976, **55**, 202.
17. V. J. Bartuska, G. E. Maciel, J. Schaefer, and E. O. Stejskal, *Fuel*, 1977, **56**, 354.
18. S. J. Opella and M. H. Frey, *J. Am. Chem. Soc.*, 1979, **101**, 5854.
19. L. B. Alemany, D. M. Grant, T. D. Alger, and R. J. Pugmire, *J. Am. Chem. Soc.*, 1983, **105**, 6697.
20. L. B. Alemany, D. M. Grant, R. J. Pugmire, and L. M. Stock, *Fuel*, 1984, **63**, 513.
21. M. A. Wilson, A. M. Vassalo, P. J. Connin, and H. Rottendorf, *Anal. Chem.*, 1984, **56**, 433; M. A. Wilson, R. J. Pugmire, J. Karas, L. B. Alemany, W. R. Woolfenden, P. H. Given, and D. M. Grant, *Anal. Chem.*, 1984, **56**, 933.
22. P. D. Murphy, T.J. Cassady, and B. C. Gerstein, *Fuel*, 1982, **61**, 1233; P. D. Murphy, B. C. Gerstein, V. L. Weinberg, and T. L. Yen, *Anal. Chem.*, 1982, **54**, 522.
23. (a) B. C. Gerstein, P. D. Murphy, and L. M. Ryan, in *Coal Structure*, Ed. R. A. Meyers, Academic Press, New York, 1982, Chap. 4; (b) P. DuBois, T. J. Cassady, and B. C. Gerstein, 1982, *Fuel*, **61**, 1233.
24. K. W. Zilm, R. J. Pugmire, D. M. Grant, R. E. Wood, and W. H. Weiser, *Fuel*, 1979, **58**, 11.
25. R. J. Pugmire, K. W. Zilm, D. M. Grant, S. R. Larter, J. Allen, J. T. Senftle, A. Davis, and W. Spackman, in *New Approaches in Coal Chemistry*, eds. B. D. Blaustein, B. C. Bockrath, and S. Friedman, *ACS Symp. Ser. No. 169*, Am. Chem. Soc., Washington, DC, 1981.
26. B. C. Gerstein, P. D. Murphy, and L. M. Ryan, in *Coal Structure*, ed. R. A. Meyers, Academic Press, New York, 1982, p. 120.
27. M. S. Solum, R. J. Pugmire, and D. M. Grant, *Energy Fuels*, 1989, **3**, 187.
28. A. M. Orendt, M. S. Solum, N. K. Sethi, R. J. Pugmire, and D. M. Grant, in *Advances in Coal Spectroscopy*, ed. H. L. C. Meuzelaar, Plenum Press, New York, 1992.
29. M. A. Wilson, J. V. Hanna, P. A. Cole-Clark, P. F. Greenwood, and G. D. Willett, *Fuel*, 1992, **71**, 1097; M. A. Wilson, J. V. Hanna, P. A. Cole-Clark, G. D. Willett, and P. F. Greenwood, *Org. Geochem.*, 1992, **18**, 555.
30. P. G. Hatcher, *Org. Geochem.*, 1990, **16**, 959; P. G. Hatcher, K. A. Wenzel, and J.-L. Faulon, *Am. Chem. Soc., Div. Fuel Chem., Prepr.*, 1993, **38**, 1270.

31. D. J. Clifford, J. P. Mathews, J.-L. Faulon, and P.G. Hatcher, *Am. Chem. Soc., Div. Fuel Chem., Prepr.*, 1994, **39**, 198.
32. J. C. Facelli, D. G. Grant, and J. Michl, *Acc. Chem. Res.*, 1987, **20**, 152; J. C. Facelli and D. M. Grant, *Theor. Chim. Acta*, 1987, **71**, 277; A. M. Orendt, N. K. Sethi, J. C. Facelli, W. J. Horton, R. J. Pugmire, and D. M. Grant, *J. Am. Chem. Soc.*, 1992, **114**, 2832.
33. A. M. Orendt, M. S. Solum, N. K. Sethi, C. D. Hughes, R. J. Pugmire, and D. M. Grant, in *Magnetic Resonance of Carbonaceous Solids*, eds. R. E. Botto and Y. Sanada, *Adv. Chem. Ser. No. 229*, Am. Chem. Soc., Washington, DC, 1993, Chap. 22
34. N. K. Sethi, D. M. Grant, and R. J. Pugmire, *J. Magn. Reson.*, 1987, **71**, 476.
35. N. K. Sethi, R. J. Pugmire, J. C. Facelli, and D. M. Grant, *Anal. Chem.*, 1988, **60**, 1574; A. M. Orendt, N. K. Sethi, J. C. Facelli, W. J. Horton, R. J. Pugmire, and D. M. Grant, *J. Am. Chem. Soc.*, 1992, **114**, 2832.
36. M. H. Sherwood, J. C. Facelli, D. W. Alderman, and D. M. Grant, *J. Am. Chem. Soc.*, 1991, **113**, 750; C. M. Carter, D. W. Alderman, J. C. Facelli, and D. M. Grant, *J. Am. Chem. Soc.*, 1987, **109**, 2639.
37. J. Z. Hu, A.M. Orendt, D. W. Alderman, C. Ye, R. J. Pugmire, and D. M. Grant, *Solid State Nucl. Magn. Reson.*, 1993, **2**, 235.
38. R. J. Pugmire, J. Z. Hu, D. W. Alderman, A. M. Orendt, C. Ye, and D. M. Grant, *Int. Conf. Coal Sci., Banff, Canada, September 12–17, 1993*, p. 485.
39. J. Z. Hu, M. S. Solum, D. W. Alderman, R. J. Pugmire, C. Ye, and D. M. Grant, *Energy Fuels*, 1995, **9**, 717.
40. J. Z. Hu, A. M. Orendt, D. W. Alderman, R. J. Pugmire, C. Ye, and D. M. Grant, *Solid State Nucl. Magn. Reson.*, 1994, **3**.
41. J. Z. Hu, W. Wang, F. Liu, M. S. Solum, D. W. Alderman, R. J. Pugmire, and D. M. Grant, *J. Magn. Reson.*, 1995, **A113**, 210.
42. F. P. Miknis, M. Sullivan, V. J. Bartuska, and G. E. Maciel, *Org. Geochem.*, 1981, **3**, 19.
43. G. E. Maciel, V. J. Bartuska, L. Petrakis, and D. W. Grandy, *Fuel*, 1982, **61**, 411.
44. K. W. Zilm, R. J. Pugmire, S. R. Larter, J. Allen, and D. M. Grant, *Fuel*, 1981, **60**, 717.
45. R. J. Pugmire, W. R. Woolfenden, C. L. Mayne, J. Karas, and D. M. Grant, in *Chemistry and Characterization of Coal Macerals*, eds. R. E. Winans and J. C. Crelling, *ACS Symp. Ser. No. 252*, Am. Chem. Soc., Washington, DC, 1984, Chap. 6
46. M. A. Wilson, R. J. Pugmire, J. Karas, L. B. Alemany, W. R. Woolfenden, P. H. Given, and D. M. Grant, *Anal. Chem.*, 1984, **56**, 933.
47. R. A. Wind, G. E. Maciel, and R. E. Botto, in *Magnetic Resonance of Carbonaceous Solids*, eds. R. E. Botto and Y. Sanada, *Adv. Chem. Ser. No. 229*, Am. Chem. Soc., Washington, DC, 1993, Chap. 1
48. D. W. van Krevelen, *Coal Science and Technology 3: Coal*, Elsevier, New York, 1981.
49. F. Derbyshire, A. Marzec, H-R. Schulten, M.A. Wilson, A. Davis, P. Tekely, J-J. Delpuech, A. Jurkiewicz, C. E. Bronnimann, R. A. Wind, G. E. Maciel, R. Narayan, K. Bartle, and C. Snape, *Fuel*, 1989, **68**, 1091.
50. A. Jurkiewicz, C. E. Bronnimann, and G. E. Maciel, in *Magnetic Resonance of Carbonaceous Solids*, eds. R.E. Botto and Y. Sanada, *Adv. Chem. Ser. No. 229*, Am. Chem. Soc., Washington, DC, 1993, Chap. 21
51. T.H. Fletcher, S. Bai, R. J. Pugmire, M. S. Solum, S. Wood, and D. M. Grant, *Energy Fuels*, 1993, **7**, 734.
52. R. M. Davidson, in *Coal Science*, eds. M. L. Gorbaty, J. W. Larsen, and I. Wender, Academic Press, New York, 1982, Vol. 1, p. 83; R. M. Davidson, Nuclear Magnetic Resonance Studies of Coal, Rep. No. ICTIS/TR32, January 1986, IEA Coal Research, London.
53. K. L. Smith, L. D. Smoot, T. H. Fletcher, and R. J. Pugmire, *The Structure and Reaction Processes of Coal*, Plenum Press, New York, 1994, Chap. 3
54. P. R. Solomon, T. H. Fletcher, and R. J. Pugmire, *Fuel*, 1993, **72**, 587.
55. (a) D. M. Grant, R. J. Pugmire, T. H. Fletcher, and A. R. Kerstein, *Energy Fuels*, 1989, **3**, 175; (b) T. H. Fletcher, A. R. Kerstein, R. J. Pugmire, and D. M. Grant, *Energy Fuels*, 1990, **4**, 54; (c) T. H. Fletcher, A. R. Kerstein, R. J. Pugmire, and D. M. Grant, *Energy Fuels*, 1992, **6**, 414.
56. R.J. Pugmire, M. S. Solum, D. M. Grant, S. Critchfield, and T. H. Fletcher, *Fuel*, 1991, **70**, 414.
57. T. H. Fletcher, M. S. Solum, D. M. Grant, and R. J. Pugmire, *Energy Fuels*, 1992, **6**, 643.

Biographical Sketch

R. J. Pugmire. *b* 1937. B.S., 1959, Idaho State College, Ph.D., 1966, Chemistry, University of Utah, USA, where he was introduced to NMR by David M. Grant. Postdoctoral research, University of Utah, 1966–68. Faculty in Chemical and Fuels Engineering, and Associate Vice President for Research, University of Utah, 1968–present. Approx. 140 publications. Research specialties: carbon-13 NMR, chemical shielding in liquids and solids, coal chemistry and applications of NMR spectroscopy to coal science.

Fossil Fuels

Robert E. Botto

Argonne National Laboratory, Argonne, IL , USA

1	Introduction	1
2	Applications to Coal Science	1
3	Applications to Shale Oil Research	12
4	Other Fuels	14
5	Related Articles	15
6	References	15

1 INTRODUCTION

Energy[1] is an important commodity because it affects our lives in many ways. In the past, a direct relationship had been drawn between energy consumption and economic growth. Advancement in economic growth was shown to have a favorable impact on the quality of life in economically advanced societies by fostering better health and educational services, a robust industrial base with which to sustain future development, and various forms of labor-saving devices for common use. Often concerns about the negative impacts from economic growth, such as pollution, overpopulation, and crime have been neglected by nations striving to improve their economic status.

In the rapidly changing world of the last 20 years, however, there have been escalating demands placed on global energy resources. An ever-increasing number of developing countries have competed for the existing energy supply. Environmental issues have become the highest priority in guiding the utilization of global resources. While traditional 'old-world' fuels such as wood, agricultural products, and animal dung are still in use around the globe, they remain effective sources of energy only for less developed societies. Alternative energy resources in the form of geothermal and hydroelectric power are limited throughout the world, while renewable resources such as solar, wind, and tidal have been slow to develop on a large commercial scale. Development of nuclear energy, once heralded as the answer to meet the future global energy demands into the next millennium, has been severely curtailed because of apprehension about radioactive release into the environment and problems in storage of high level radioactive wastes. Consequently, a greater burden of world energy demands over the past 20 years has centered on fossil fuels. With increasing demands on supplies worldwide, fuel quality has diminished significantly. In addition, utilization of fossil fuels as a carbon source for the production of bulk and specialty chemicals, and of high technology polymer blends and composites may be almost as important economically as their use as an energy source.

Fossil fuel energy resources include coal, peat, petroleum, oil shale, tar sands, and natural gas. Total world resources of coal are 15.1×10^{12} ton; total world production is estimated to be 3.0×10^{9} ton per year. The importance of coal as a resource is that, despite having greater problems with production, transportation and utilization compared with oil and gas, it represents a vast resource to meet energy demands well into the future (for more than 1000 years). World resources of peat, being far less utilized than the other fuels, is estimated to be only 0.2×10^{12} ton. Estimates of the reserves and resources of petroleum, having received considerable attention because of concern over their eminent depletion globally, are on the order of 0.3×10^{12} ton, of which about 0.1×10^{12} ton are proven reserves. Worldwide oil production is about 4×10^{9} ton per year. Enhanced oil recovery strategies have added approximately an additional 0.1×10^{12} ton to the estimate of total recoverable resources of petroleum. Tar sands are fairly localized throughout the world, with estimated reserves of only 0.03×10^{12} ton. On the other hand, oil shale deposits are widely distributed geographically and represent a potentially enormous resource, with estimates ranging between 100×10^{12} and 500×10^{12} ton of potential oil. Limitations for the commercialization of this vast energy resource are the large-scale operations required for production and hence prohibitive investment costs, and the severe environmental problems that would be created by the massive excavation of natural lands and subsequent disposal of enormous quantities of solid waste. Natural gas, with proven reserves similar in energy equivalence to those of petroleum, has the advantage of being the cleanest of the fossil fuels; however, transportation costs of this commodity between continents are high unless supplies can be reached economically via pipeline.

Applications of NMR spectroscopy to the study of fossil fuels have experienced extraordinary growth since the inception of the technique in 1946.[2,3] Early experiments focused on the application of broadline ^{1}H NMR spectroscopy to petroleum, oil shale, and coal research. High-resolution liquid state ^{1}H NMR proved to be an extremely useful structure elucidation tool for fuel extracts and solubilized conversion products in subsequent years. However, NMR did not flourish as a celebrated technique for fossil fuel characterization until the 1970s. The growth of the technique was brought about by several factors: (1) integration of computers with instrumentation in the late 1960s enhanced data acquisition capabilities considerably; (2) introduction of Fourier transform methods paved the way for the development of pulsed NMR spectroscopy, which made detection of less sensitive nuclei more routine, and spawned a wide variety of pulsed techniques for sensitivity enhancement, relaxation measurements and multidimensional NMR studies; and (3) the oil embargo of 1973–74 and the Organization of Petroleum Exporting Countries (OPEC) incident in 1979 catalyzed abrupt increases in the price of petroleum, reversing the trend of cheap and abundant energy supplies that had lasted over the past 100 years. This incident prompted general concern over the availability of energy resources in the future and, as a consequence, stimulated growth of basic and applied research in the area of fossil fuels to seek alternate forms of energy. Nearly two decades of intensive research in NMR characterization of fossil fuels ensued.

2 APPLICATIONS TO COAL SCIENCE

Coal[4] is considered to be a heterogeneous organic rock and is typically black in color, although geologically younger deposits can range in color from brown to brownish red. It is formed by the accumulation of plant debris which has been

altered over geological time by the action of biological, chemical, and physical (heat and pressure) degradation processes. The relative quantities of remaining plant parts, and the degree of their thermal maturation and degradation result in coals with varied properties. Coals may be classified as banded (humic coals) or nonbanded (cannel or boghead coals), are hard or soft, or can vary in rank from brown coal, through lignite, subbituminous, bituminous to anthracite. The degree of thermal maturation of plant matter, or coalification, is referred to as *rank*.

The evolution of coal, the enormous variation found in its composition, its microheterogeneity, and its differentiation toward chemical reactions suggest that coal is a complex mixture of compounds. While this is true, however, there is some order to its inherent, overall structure. There are microscopically discrete, optically homogeneous aggregates of organic materials derived from various plant parts that constitute coal. These individual domains are referred to as *macerals*.[5,6] There are three major maceral groups, each having their own distinct set of properties and selective chemistries. The most abundant of the macerals found in US coals is *vitrinite*, which is derived from woody tissue of plants and is a largely lignin based polymer. The group of macerals called *liptinite* may be derived either from waxy leaf cutin, parts of spores and pollen, or algal bodies. This group of macerals tend to be composed of highly aliphatic material. The last maceral group, *inertinite*, named for its relative unreactivity in most chemical reactions, is thought to be derived from material that has undergone extensive oxidation or that is a form of fossilized charcoal derived from primordial forest fires. The inertinite macerals have a high degree of aromatic character.

Apart from the organic components, there may be substantial quantities of water and mineral matter present in coal. The minerals can be varied and also rather complex in composition; hydrated aluminosilicates, clay minerals, quartz, sulfides, sulfates, pyrite and carbonates have been identified, to name a few. The main elemental constituents of coals, therefore, are carbon, hydrogen and oxygen, with varying amounts of nitrogen and sulfur, and lesser amounts of silicon, calcium, aluminum, iron, magnesium, sodium, and other trace elements. Given this diversity of chemistry and elemental composition, coals have been a rich source for study by NMR techniques.

2.1 Structure Characterization

2.1.1 Liquid State NMR

The first published account of high-resolution ^{1}H NMR of a coal liquid, or soluble reaction product, appeared in 1959.[7] This first ^{1}H spectrum (Figure 1) of a coal asphaltene recorded in carbon disulfide at 125 °C demonstrated that the technique could readily distinguish three magnetically inequivalent types of proton nuclei in the sample, and confirmed that few polynuclear aromatic structures were present. This was the first definitive structural information obtained on a fossil fuel material. Two years later, the first liquid state ^{1}H NMR spectrum of a coal extract was reported. Since that time, numerous workers have reported on similar studies involving

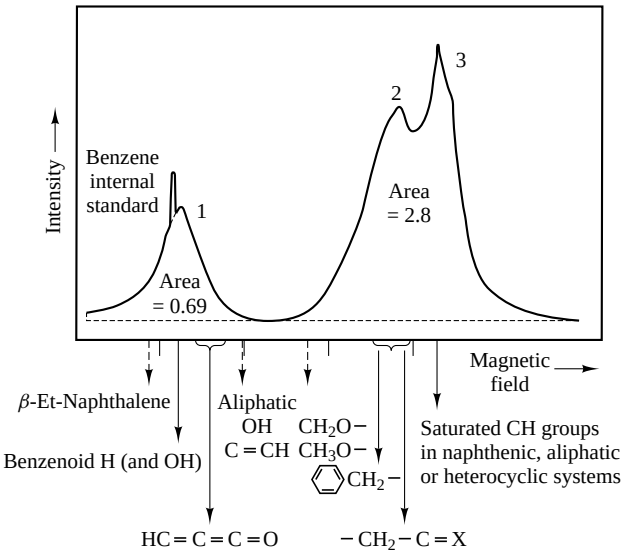

Figure 1 The first proton NMR spectrum of an asphaltene in carbon disulfide at 125 °C. Recorded by J. N. Shoolery, H. E. Weaver, and R. C. Jones at Varian Associates

coal extracts and have demonstrated the utility of the technique for analyzing the hydrogen distributions in these materials.[8]

In 1960, Brown and Ladner[9] were the first to demonstrate that the hydrogen distribution in carbonaceous fuels determined by ^{1}H NMR could be used to infer information about the carbon skeleton. Initial experiments were performed on a series of vacuum carbonization products from coals. The method used information from the ^{1}H NMR spectrum and carbon and hydrogen elemental analysis to determine several important structural parameters, including the fraction of aromatic carbon (f_a) of the sample. The fraction of carbon aromaticity was defined as that fraction of the total number of carbon atoms which are aromatic, $f_a = C_{ar}/C_{tot}$. The normalized intensities of the types of hydrogen were determined from integration of the proton spectrum to calculate the carbon aromaticity using the equation:

$$f_a = \left[(C/H) - (H_\alpha/x) - \frac{(H_\gamma + H_\beta)}{y} \right] \Big/ (C/H) \qquad (1)$$

where C/H is the atomic ratio of carbon to hydrogen from elemental analysis data; x and y are the average number of hydrogen atoms per α-alkyl group to an aromatic ring and the remaining alkyl groups, respectively; and H_α and $(H_\gamma + H_\beta)$ represent the normalized integrated intensities of the α-alkyl hydrogen atoms and other hydrogen atoms, respectively. From this basic equation can be deduced other key structural parameters, such as the degree of aromatic ring substitution, i.e. that fraction of peripheral aromatic carbon atoms bearing substituent groups, and the atomic H/C ratio for the hypothetical aromatic ring system, which provides an estimate of the average size of the polycondensed aromatic rings.

In subsequent years, numerous researchers applied the Brown–Ladner equation to a wide variety of coal-derived liquids, including coal extracts, autoclave asphaltenes, carbonization oils, solvent-refined coals, coal tar pitches, and coal liquefaction products. However, there were several assumptions which had to be made in the application of the

Brown–Ladner equation, and the results obtained often depended on assumed values for x and y. For most fossil fuels, x and y were assumed to be 2, which was the same as suggesting that the average aliphatic carbon structure in these materials represented a methylene group. There was also the problem with accurate integration of the H_α and (H_γ + H_β) protons because of severe overlap of the resonance lines. Derivation of the remaining parameters from the Brown–Ladner approach necessitated accurate deconvolution of the phenolic protons from aromatic protons, which was not always possible because of solvent-induced shifts of the hydroxyl resonances. Nevertheless, the approach was used to estimate the chemical structure parameters for many fossil fuels prior to the advent of high-resolution ^{13}C NMR.

The first high-resolution ^{13}C NMR spectrum of liquid products was published as early as 1966 using computer-assisted techniques. However, it was not until the mid-1970s, after the development of Fourier transform methods, that ^{13}C NMR of liquid and soluble materials from coal became routine.[9] The first studies focused on comparing aromaticity data obtained directly by ^{13}C NMR with those estimated from the Brown–Ladner treatment of the corresponding ^{1}H NMR spectra. Several laboratories reported generally good agreement; for example, one correlation of ^{1}H and ^{13}C NMR data for five coals of different rank, coal tar pitches, coal carbonization oils, coal-derived asphaltenes, and products from five different liquefaction processes is presented in Figure 2.[10] For the case of low boiling coal-derived oils, poor agreement was found because these materials tended to have shorter aliphatic chains, and hence the estimate for the ratio of aliphatic hydrogen to carbon (y in the Brown–Ladner equation) should have been greater than 2. Similar arguments were made for highly aromatic pyrolyzate products, in which there were high amounts of methyl substituents.

Later work focused on the assignment of chemical shift values to ^{13}C spectra of coal liquids. Efforts were made not only to assign chemical shifts to various carbon functional groups in samples, but also to estimate the relative abundances of these groups. Inference was made for a relationship between ^{1}H and ^{13}C NMR data on the same sample, leading to the idea that complementary information from both techniques could lead to detailed structural characterization of complex, multicomponent fractions of coal liquids. Thereafter, numerous separation methods and other spectroscopic techniques were combined with characterization by ^{1}H and ^{13}C NMR to provide detailed structural profiles of individual components in complex coal mixtures.

One of the cornerstones of structural analysis methods has been the information provided by NMR, and there have been many practices of presenting the data. Three approaches that have frequently been used are: characterization by the formulation of structural parameters; characterization by the construction of average, or representative, molecular structures; and characterization by functional group analysis.[11] The first approach is considered by many to be limited because estimation of numerous parameters often relies on assumptions about molecular structure, and the average parameters calculated are not guaranteed to represent actual structures in fuel liquids. The use of an average structure, or model, to represent the system is flawed by the latter drawback. The advantage of the functional group analysis approach is that, by definition, it is chemical functionalities that govern the overall chemical and physical behavior of these complex molecular systems.

Functional group analysis has been applied in several laboratories to describe coal extracts and soluble reaction products.[11] The initial step in the process was to propose a set of functional groups that described the structure of the complex mixture. The concentrations of this selected set of functional groups were subsequently related to experimental data through a sequence of equations, where the effects of known stoichiometry are taken into account. In general, a set of equations can be written:

$$\sum_{j=1}^{n} A_{ij}|y_j| = b_i \ (i = 1, \ldots, m) \qquad (2)$$

where y_j (j = 1, ... , n) represents the unknown functional group concentrations, b_i (i = 1, ... , m) represents quantities from experimental data, and A_{ij} represents the stoichiometric coefficients. The summation defined a range of possible solutions and a best fit was selected computationally through a minimization procedure by assuming that the distribution of atomic species among the functional groups is equally probable.

These methods have been tested on known mixtures and were subsequently used to characterize complex coal liquids. Utilizing data from NMR and elemental analysis gave fair estimates of molecular composition; incorporating data from mass spectrometry improved the results considerably. Characterization of separated fractions of coal asphaltenes derived from solvent-refined coal heavy distillate and supercritical gas extracts from two different coals provided information on the hydroaromatic content, distribution of heteroatomic functional groups, and nature of the polycondensed aromatic rings structures. In addition, these same methods have been used to reliably predict the thermophysical properties of liquid fuels,

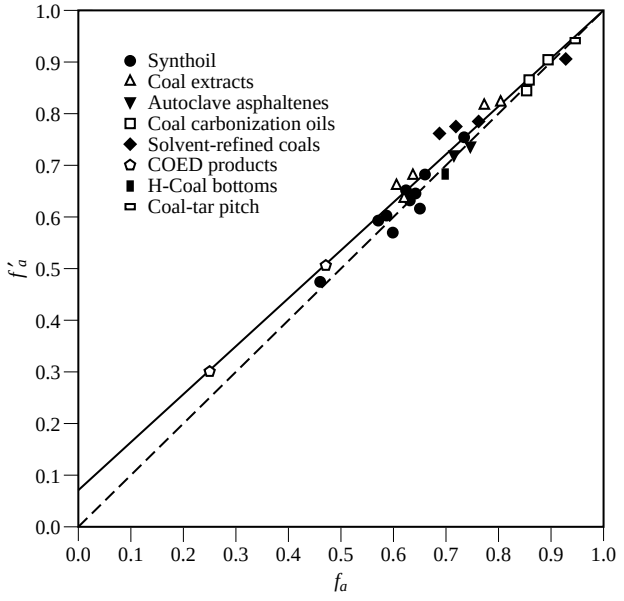

Figure 2 Comparison of proton (f'_a) and carbon (f_a) aromaticities for materials derived from coal; H-coal, solvent-refined coals, COED, and Synthoil are liquefaction processes

by utilizing group additivity principles and the idea of continuous thermodynamics.

Numerous studies have centered on the use of conventional solution state NMR techniques to study the heteroatomic functional groups in coal-derived liquids, principally those containing oxygen, nitrogen and sulfur.[12] Regions within the ^{13}C NMR spectra of coal asphaltenes and coal-derived oils were examined and assigned to carbonyl groups, aromatic ethers and phenols, aliphatic ether groups, and nitrogen groups. Other investigations have employed derivatization methods to specifically 'tag' functional groups in combination with NMR analysis. Several approaches have been attempted. These include: either acetylation or reductive alkylation followed by ^{13}C NMR; trimethylsilylation with analysis by ^{1}H, ^{13}C and ^{29}Si NMR (see Figure 3); hexafluoroacetone adduction which can be analyzed by ^{19}F NMR; and phosphorylation followed by ^{31}P NMR. Direct analysis by ^{17}O NMR has facilitated examination of some fractions of coal liquids, leading to the identification of oxygen functional groups on the basis of their chemical shifts: for instance, alcohols, phenols and ethers; furans and carboxylic acids; esters; and ketones and aldehydes.

Given the complicated nature of the ^{13}C spectra of coal-derived liquids, several multipulse techniques based on the spin echo method were developed which allowed the selective examination of different carbon types.[11,12] The gated spin echo (GASPE) or partially coupled spin echo (PCSE) pulse sequences were used to differentiate between aliphatic quaternary C and CH_2, as one phase-related spin group, and CH and CH_3 as the other. The same techniques were also applied to obtain edited aromatic carbon spectra, for which the distinction between quaternary and tertiary aromatic carbon atoms could readily be made. The spin echo broadband off-resonance decoupling (SEBBORD) technique was used to differentiate further between quaternary and CH resonances on the basis of broadening of the CH resonances. Later, with the development of polarization transfer pulse methods, the use of either INEPT or DEPT sequences allowed separation of the entire carbon spectrum, into quaternary C, CH, CH_2 and CH_3 resonances. Utilization of two-dimensional *J*-resolved and ^{1}H-^{13}C COSY experiments on coal liquids, however, has met with limited success.

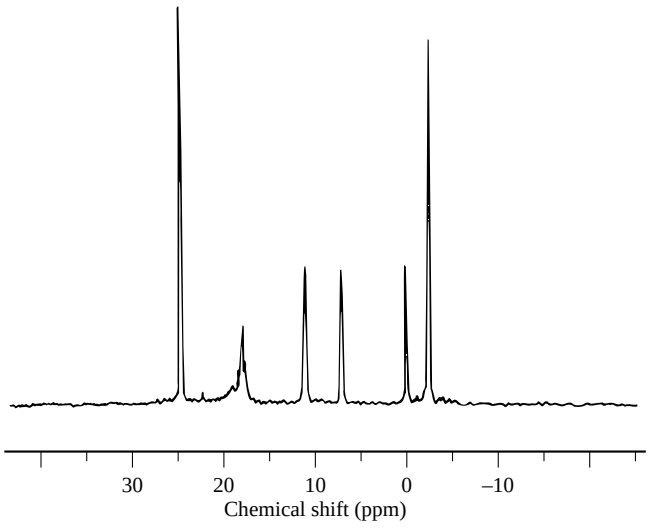

Figure 3 A typical ^{29}Si NMR spectrum of a coal liquid derivatized with trimethylsilyl chloride

2.1.2 Solid State NMR

The earliest report on the use of broadline ^{1}H NMR in coal research was published in 1955 by Newman et al.[13] However, apart from demonstrating that the NMR experiment was feasible on such materials, little chemical information was gleaned from this original work. It was more than 20 years later, in 1976, when the first solid state ^{13}C NMR spectra appeared in the literature,[14] utilizing then recently developed CP methods for sensitivity enhancement together with strong proton decoupling.[15] These initial ^{13}C spectra, recorded for four coal samples of different rank, are shown in Figure 4. It was the first time that coal structure was determined by a direct method for whole coals in their native state. Less than a year later, MAS with respect to the static magnetic field was used in combination with CP and proton decoupling to produce the first high-resolution solid ^{13}C CP MAS spectra of coal.[16] This constituted a major breakthrough in the field; removing broadening effects arising from both CSA and $^{1}H-^{13}C$ dipolar interactions produced isotropic resonance lines and facilitated the analysis of different carbon functional groups in coals. Also during 1977, MAS was combined with multiple pulse methods to produce the first high-resolution ^{1}H CRAMP spectra of whole coal samples.[17] The technique facilitated analysis of aromatic and aliphatic proton distributions of coals in their native state.

Applications of solid ^{13}C CP MAS and ^{1}H CRAMP spectroscopy in coal structure determination have been reviewed extensively.[12,18–22] Early ^{13}C CP spectra of coals (see Figure 4) exhibited two broad, overlapping resonance bands

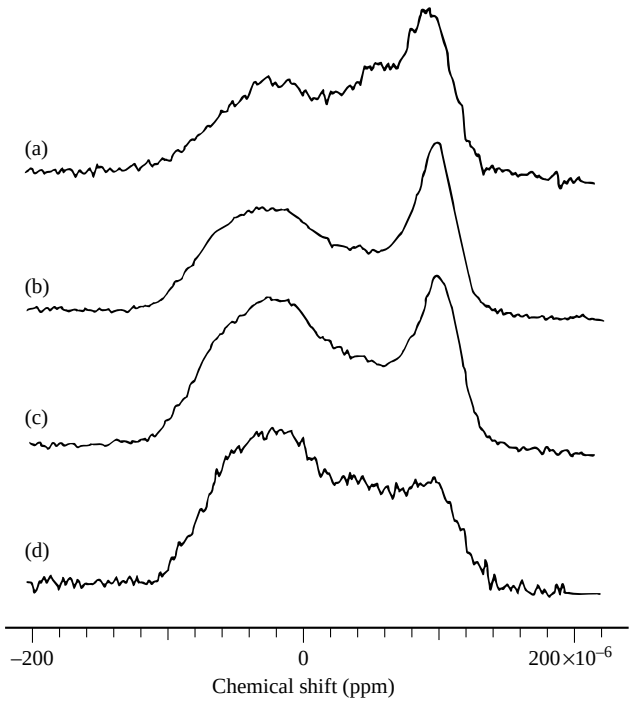

Figure 4 CP ^{13}C NMR spectra of coals of increasing rank

that could be assigned to regions of aliphatic (0–60 ppm) and aromatic (30–250 ppm) carbon atoms. From these spectra, the fractional carbon aromaticities (f_a) were estimated by employing peak deconvolution methods. The results supported the classical view that coals were highly aromatic materials and that the aromaticity of coals increased with increasing rank as calculated on the basis of their carbon content. Comparing ^{13}C CSA lineshapes of coals and model compounds allowed identification of regions of polycondensed aromatic ring structures, simple aromatic systems, aliphatic structures, and also aliphatic ether linkages. However, it was difficult to obtain estimates of these different functionalities with any degree of reliability because of lack of resolution in the spectra.

This situation changed dramatically with the introduction of MAS in the experiment to remove CSA. Narrowing of the resonances to their isotropic chemical shift values facilitated the assignment of a host of carbon functional groups, including aromatic and alkenic carbons, carboxylic acids and other carbonyl groups, phenolic and furanyl carbon atoms, carbon-substituted aromatic carbon atoms, oxygen-substituted carbon atoms (including methoxyl groups), as well as methylene and methyl carbon atoms. Assignments for a typical high-resolution solid ^{13}C spectrum of a whole coal is shown in Figure 5. First and second moments of the aromatic carbon resonance band were shown to vary as a function of the carbon content of coals ranging in rank from lignite to anthracite. The first moments were found to increase with increasing rank, which was in accord with estimates derived from models for the increase in the aromatic ring condensation index. The second moments decreased with rank, implying that the dispersion of chemical shifts in the aromatic region was decreasing, or becoming more homogeneous with increasing carbon content of the coal.

Structural parameters were derived from solid ^{13}C and ^{1}H NMR data of whole coals and maceral concentrates during subsequent years, leading to a greater understanding of coal structure. Carbon and proton aromaticities were found to increase with increasing rank of the coal; and for macerals, in the order liptinite < vitrinite < inertinite. Carbon and hydrogen aromaticities were used to estimate the aromatic and aliphatic hydrogen-to-carbon mole ratios, and given the weight per cent of carbon and hydrogen derived from elemental analysis, it was possible to approximate the average size of the polycondensed aromatic clusters in coals as a function of rank. Estimates of the aromatic cluster size ranged from 1 to 2 rings for low-rank coals, 2 to 6 rings for bituminous coals, and approached 30 rings for anthracite.

As the state of the art progressed, greater emphasis was placed on obtaining specific, detailed information on the chemical functionality of coals and coal macerals. Several approaches were implemented to enhance the resolution of ^{13}C CP MAS spectra so that greater structural information could be obtained.[12,17,18]

The first, and still most utilized, spectral editing technique developed for spectral simplification of coal spectra was the interrupted decoupling (or dipolar dephasing) experiment[23] which was originally proposed by Alla and Lippmaa.[24] The basic approach distinguished between carbon atoms on the basis of dissimilarities in transverse relaxation times between protonated and nonprotonated carbon atoms, owing to differences in the magnitudes of their $^{1}H-^{13}C$ dipolar couplings. In the absence of a strong proton decoupling field, which is turned off during a finite period of time during the course of the experiment, the protonated carbon magnetization decays at a significantly faster rate than that of nonprotonated carbons. Methyl carbon atoms exhibit intermediate decay rates due to fast molecular motion. In principle, this allowed signals from these four types of carbon to be separated quantitatively, provided that the appropriate mathematical solutions had been performed to calculate initial signal intensities (at $\tau = 0$) from experimental decay rates in a series of variable interrupted decoupling time experiments.

The interrupted decoupling experiment has been applied to the study of whole coals, isolated macerals, coal-derived asphaltenes, and coal oxidation products and pyrolysis chars. From the results of these experiments, it has been possible to

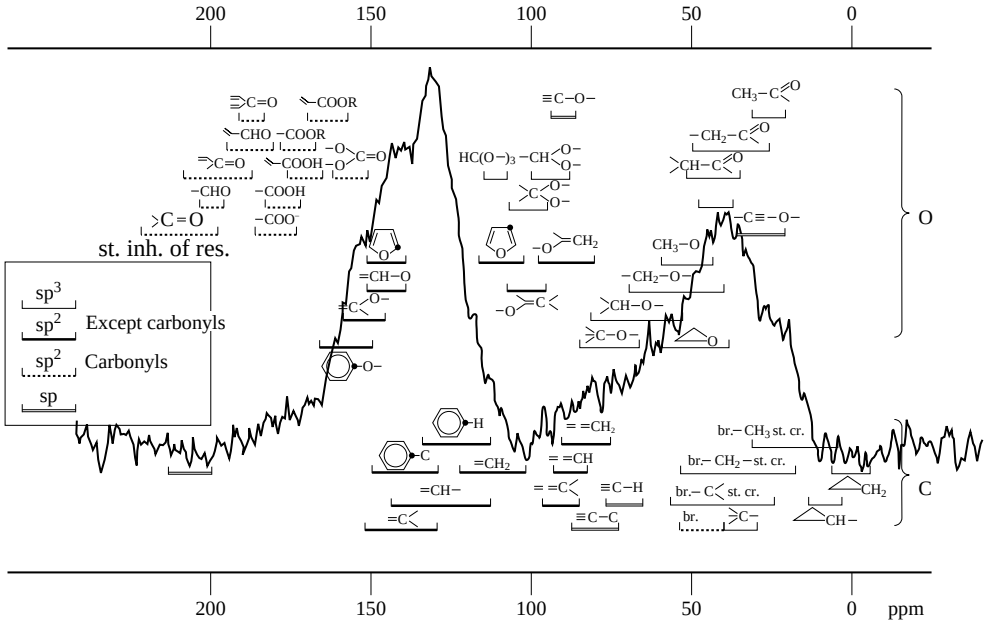

Figure 5 CP MAS spectrum of a whole coal with the NMR chemical shift correlation chart

estimate the fraction of substituted and bridgehead aromatic carbon atoms (f_{s+b}), and the number of quaternary aliphatic carbon atoms in these systems. Attempts to estimate the average cluster size of the aromatic rings from these data has had the caveat that it has been impossible to assign aromatic substituted and bridgehead carbon atoms with confidence because of severe overlap of the resonances. Nevertheless, interrupted decoupling solid state NMR has provided valuable insight into the nature of coal as a macromolecular material, and the technique has been used to explain some of the chemistry occurring upon its treatment under a variety of conditions.

Interrupted decoupling has also been employed with detection by CRAMPS to enhance the resolution of solid state proton spectra of carbonaceous materials.[22] Analogous to the carbon version of the experiment in CP MAS spectroscopy, a dephasing period is inserted between the initial $\pi/2$ pulse that places the proton magnetization in the transverse plane and initiation of the multipulse decoupling sequence used for detection. The technique has been used on pyridine-sorbed coals and has provided selectivity of protons on the basis of molecular mobility.[22]

Mathematical manipulation has been employed to enhance the resolution of solid NMR coal spectra.[18] The several methods that have been implemented include: (1) convolution difference spectroscopy, which uses a filtering function composed of two exponentials and an adjustable weighting constant; (2) Gaussian multiplication, which has been used to improve resolution on the basis of lineshape modification; and (3) a variety of curve and Fourier deconvolution methods, for which the usual practice has been to fit mathematically a broad band of unresolved resonances to a series of peaks that are varied according to frequency position, lineshape, linewidth, and intensity.

Resolution enhancement in these systems has also been achieved based on carbon and proton relaxation time differences in CP MAS experiments.[12] Differentiation of carbon atoms in coals has been accomplished on the basis of differences in $^{1}H-^{13}C$ polarization transfer rates R_{CH}, proton rotating frame spin–lattice relaxation rates $R_{1\rho}{}^{H}$, and carbon spin–lattice relaxation rates $R_1{}^{C}$.

Chemical derivatization techniques in conjunction with solid state ^{13}C NMR have been used to highlight the reactive oxygen functional groups, such as phenols, aliphatic alcohols and carboxylic acids. Acetylation[12] was employed to target specifically hydroxyl groups in coals and could be monitored by the introduction of additional carbonyl and methyl resonances in the solid reaction products. Comparing integrated signal intensities of the introduced acetyl resonances with those of native C–O gave estimates on the amounts of hydroxyl versus ether groups. The combined use of selective alkylation with ^{13}C-enriched methyl iodide and solid state ^{13}C NMR has also facilitated the assignment of methyl carboxylates, unhindered aryl methyl ethers, and hindered aryl methyl ethers in coals[25,26] and isolated coal macerals.[27]

Solid state NMR spectroscopy has seen limited applications to the study of mineral phases in coals. The first application focused on the use of ^{29}Si and ^{27}Al NMR to characterize mineral concentrates obtained by low temperature ashing of coals in order to obtain information on their mineralogy.[28] Silicon spectra allowed the identification of silicate resonances from quartz and clays, while aluminum spectra provided information on the tetrahedral and octahedral coordination sites which allowed discrimination between kaolinite and illite clays that were present in the concentrates. A subsequent study[29] on mineral residues obtained from coal flash pyrolysis indicated that ^{29}Si and ^{27}Al spectra were broad because of the presence of paramagnetic species; however, the spectra were sufficiently resolved to detect the thermal transformation of kaolinite to quartz and mullite with increasing pyrolysis temperature. Characterization of the layer silicate minerals in the suite of Argonne Premium coals was carried out by using sink-float techniques to isolate mineral concentrates in combination with ^{29}Si and ^{27}Al NMR.[30] CP MAS and VAS techniques were employed to distinguish between the various clay minerals; quartz, kaolinite and smectite clays could readily be identified. Tetrahedral/octahedral aluminum ratios were determined for the coals, and the observation of increasing tetrahedral aluminum content with coal rank indicated there was a parallel between the diagenesis of the organic and inorganic matter in the coals.

2.1.3 Determination of Physical Structure

Solid state NMR spectroscopy has been applied extensively to the study of complex molecular dynamics in synthetic polymers. However, such investigations of coals have been limited. Work in this area has been hampered by the complex nature of coal. Interpretation of nuclear relaxation, which underlies the study of molecular motion, is complicated by the existence of discrete heterogeneous domains in coals and by relatively large quantities of paramagnetic centers which are present either in the form of paramagnetic inorganic ions or as organic free radicals.

To date, an overwhelming majority of papers dealing with relaxation measurements on coals has focused on the study of ^{1}H NMR spin–lattice relaxation times both in laboratory (T_1) and rotating ($T_{1\rho}$) reference frames. Early ^{1}H NMR measurements[31–34] indicated that proton T_1 times in coals can either display single exponential or nonexponential relaxation behavior. The observation by Yokono et al.[33] that $T_1{}^{H}$ varied linearly with the square root of resonance frequency for several bituminous coals was consistent with diffusion-limited relaxation to paramagnetic centers. Several laboratories[34–37] later demonstrated similar behavior for a wide variety of evacuated coal samples. The work indicated that spin–lattice relaxation may be a fundamental property of coals themselves, and be independent of either their oxygen or moisture content. In two specific papers,[37,38] the authors independently proposed that proton relaxation in bituminous coals was influenced by differences in molecular mobilities rather than by the relative concentrations of paramagnetic species.

A difficulty with the interpretation of spin–lattice relaxation of abundant proton spins in coals rests with the development of an experimental strategy to separate contributions from molecular mobility from spin diffusion of the magnetization to paramagnetic centers within different phase (maceral) boundaries. Three thorough investigations of ^{1}H NMR spin–lattice relaxation in coals[39–41] have attempted to address this issue. The authors independently concluded that simple correlations of proton relaxation with other coal parameters was not easily realized. The presence of residual amounts of molecular oxygen in evacuated samples and the effects of different concentrations of unpaired electrons within different domains in

coals were thought to have a profound, yet undeterminable, influence on the relaxation times. Others[42] have reported proton relaxation data for eight Argonne Premium coals and three oxidized coals and have shown that oxidized samples have shorter $T_1{}^H$ values. Finally, in careful $T_1{}^H$ and ESR studies of Argonne coals, various chemical treatments established that the important proton relaxation mechanism in lignite and subbituminous coals was due to the presence of paramagnetic mineral ions, whereas that in the higher rank coals is due to organic free radicals.[43]

The problems were not confined to measurements of $T_1{}^H$. An early paper[44] reported proton $T_{1\rho}$ values for a pitch and three Canadian coals and had emphasized the effects of paramagnetic species, including oxygen, on the experimental results. Other studies indicated a general trend, but lack of any definitive correlation, between $T_{1\rho}{}^H$ values and radical concentrations for a series of 'more homogeneous' maceral concentrates.[45] It was concluded that the $T_{1\rho}{}^H$ values for macerals are clearly complicated by having two competing mechanisms for relaxation, i.e. molecular motion and heterogeneous spin diffusion to paramagnetic centers. Without knowledge of the relative contributions of each to the overall relaxation times in the individual samples, any meaningful interpretation of the data was impossible. In the case of a homogeneous resinite sample doped with increasing amounts of a stable organic radical, however, an excellent correlation of $T_{1\rho}{}^H$ with radical concentration could be established.

In contrast with proton relaxation, relatively little work has been done on the measurement of ^{13}C relaxation times in coals. Carbon-13 spin–lattice relaxation measurements have been carried out on a bituminous coal from the Powhatan No. 5 mine.[46,47] It was established that aromatic resonances in this sample decayed with a single time constant, while the aliphatic resonances could be separated into two distinct regions having markedly different time constants for decay. Differences observed in the $T_1{}^C$ values for different spectral regions were interpreted in terms of molecular motion, although the contribution of free radicals to spin relaxation were acknowledged as being important as well. Other researchers[48] investigated the effect of static field strength on the $T_1{}^C$ relaxation parameters of five Argonne Premium coals and five Canadian coals, and correlated the relaxation times with various coal properties.

In a recent study,[49] eight Argonne Premium coals and three weathered Argonne coal samples were investigated and the proton and carbon spin–lattice relaxation times were reported for aromatic and aliphatic carbon atoms. In general, the proton and carbon spin–lattice relaxation data could be evaluated as the sum of two exponential decays. The longer components of carbon relaxation times in the laboratory and rotating reference frames were found to vary in a systematic way with coal rank, and the trends were explained in terms of motional properties of the coals and the presence of paramagnetic species. Marked increases in the carbon $T_{1\rho}$ values observed between pristine and weathered coals were interpreted to indicate a decrease in molecular mobility resulting from increased cross-linking as a result of oxidation.

2.1.4 Advanced Characterization Techniques

Several NMR methods have appeared in the recent literature on coal which deserve particular attention. They often incorporate special pulse sequences for solids aimed at sensitivity enhancement, spectral simplification or resolution enhancement, and multidimensional NMR spectroscopy and imaging.

The first two-dimensional $^1H-^{13}C$ COSY experiment on a coal was demonstrated in the mid-1980s.[50] By dispersing the carbon and proton spectral information over two dimensions (see Figure 6), the proton resonances became separated such that the aromatic, methylene and methyl protons could be resolved and their abundances estimated. Similar methods were applied to the analysis of the proton content of macerals.[51] Overlapping carbon functional groups have been estimated from two-dimensional dipolar shift (DIPSHIFT) techniques.[52] In the latter experiment, isotropic chemical shifts were plotted on a frequency axis facing dipolar shift sideband spectra on a second axis. Multiplicity of individual sideband patterns in the aliphatic region were then used to assign resonances in the isotropic spectrum on the basis of the number of protons attached to each carbon atom.

Dynamic nuclear polarization has been used with some success for the analysis of a wide range of coals of varying rank.[53] By polarizing carbon spins via the electron spins directly, or by CP techniques through the protons, large signal enhancements have been possible.[54] The technique has allowed the analysis of coals in short measuring times; however, because polarization is transferred from electron spins that reside predominantly within aromatic structures, the technique has generally overestimated the carbon aromaticity values in these systems.

Determination of the principal values of carbon CSA in anthracite coals and fusinite macerals through lineshape analysis has led to the quantitative analysis of the different carbon bonding types in these systems.[55] Using powder pattern lineshapes, three different bands due to aromatic condensed bridgehead and inner carbon atoms, and substituted carbon atoms were readily distinguished. The mole fractions of the condensed aromatic carbon atoms were then used to estimate the average cluster size of the polycondensed aromatic hydrocarbons in the coals. Later, VAS experiments were

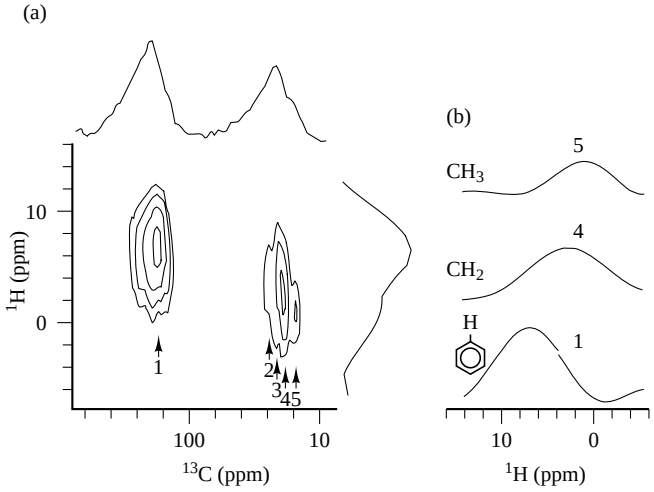

Figure 6 (a) The heteronuclear shift correlation spectra of Illinois No. 6 coal with three fully resolved contours (1, 4, and 5) and two partially resolved contours (2 and 3) observed. (b) Proton spectra from slices at 1, 4, and 5

carried out in conjunction with powder pattern analysis in order to unscramble overlapping shielding tensors in coals and macerals.[56] A review of possible methods for obtaining carbon shielding tensor information on coals has recently appeared;[57] methods for separating individual CSA patterns in complex spectra include VAS, slow MAS, chemical shift correlation spectroscopy, magic angle hopping (MAH), stop-and-go (STAG) methods, DAS, and MAS with synchronized pulsing.

The first direct magnetic resonance imaging (MRI) experiment on solid coal and maceral specimens appeared in 1989.[58] These initial studies (see Figure 7) demonstrated the potential of MRI spatially to map proton distributions in whole coals. Individual macerals within the coals were readily distinguished by image contrast based on differences in proton density or spin–lattice relaxation. A subsequent MRI investigation focused on elucidating changes in the physical structure and on determining solvent accessibility parameters in solvent swollen coals.[59] Other researchers have utilized MRI to determine the distribution of water in coalified woods and low-rank coals.[60] Correlation of proton spin distributions determined by MRI with the void spaces from other techniques allowed analysis of porosity and permeability in the specimens. Transient MRI studies of solvent penetration into solid coal and polymer specimens has led to a detailed understanding of transport phenomena for systems in which the glass transition is induced by solvent; the data have led to the development of a new model for anomalous transport behavior in coals and other glassy polymer systems.[61]

2.2 Conversion Processes

The combined use of ^{1}H and ^{13}C NMR has been employed to examine the chemical behavior of coal, in reactions such as oxidation which may be undesirable, in thermolysis and pyrolysis reactions, and in upgrading reactions for its conversion into clean, high quality liquid fuels, and chemical feedstocks.[62] Studies in the liquid state have provided information on the liquefied products, while solid state NMR has been used to characterize the original coal material as well as the chars and cokes produced in these reactions.

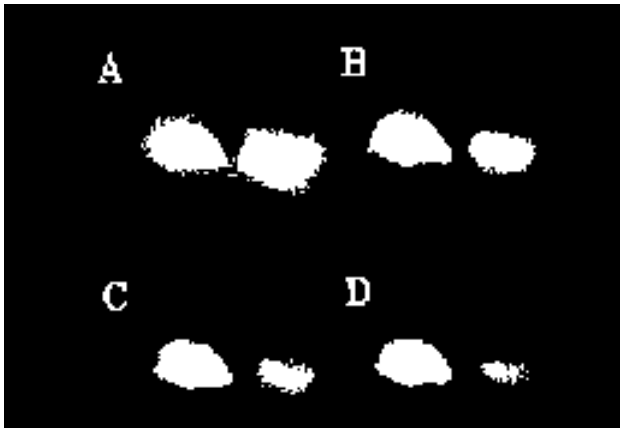

Figure 7 Two-dimensional *xy* images of resinite (left) and vitrinite (right) macerals using rotational gradients and MREV-8 back-projection reconstruction protocol with 90 projections about 180°, and 512 averages per projection. The recycle delays used in A–D were 235, 585, 1085, and 1585 ms, respectively

Several researchers have focused their efforts on characterization of coal oxidation. Early proton relaxation time measurements have been used to explore oxidation of cokes in air at elevated temperatures. The data were compared with changes in the optical texture of the coke, and a correlation between the appearance of an isotropic phase and the T_1 minimum was found. T_2 experiments indicated that the mobile phase becomes more rigid, which was interpreted to reflect an increase in the degree of cross-linking. Structural studies carried out with ^{13}C CP MAS showed that a decrease in aromaticity accompanied oxidation of coals in air at elevated temperatures. Independent studies indicated that oxidation caused a loss of specific functional groups in the aliphatic region; an increase in carbon aromaticity was observed, contradicting previous results. Conflicting evidence was also reported in the literature concerning either the appearance or disappearance of certain aromatic structures, with specific reference to phenolic structures.

Other researchers have focused on elucidating structural changes after low-temperature oxidation, or weathering, of coals of different rank. Little change in the aromatic carbon content was noticed; however, the amount of the aliphatic CH_2 was found to decrease significantly after weathering. Dipolar dephasing studies were also in conflict with earlier elevated temperature experiments. Consequently, the entire body of evidence in the NMR literature has been inconclusive regarding specific structural changes that accompany oxidation. Investigations[49,63] involving oxidation or prolonged weathering of Argonne Premium coals later established that changes in free radical content significantly affect pertinent relaxation times in CP MAS and dipolar dephasing experiments. These relaxation effects may in fact account for the discrepancies found in previous comparisons of NMR data between native and oxidized coal samples, ultimately leading to conflicting results on different coals.

The use of NMR for characterizing coal liquids derived from liquefaction processes began as early as 1975.[64] Proton NMR, and in several instances ^{13}C NMR methods, including CP and CP MAS, have been applied to study coal liquefaction under different conditions to produce solvent refined coals, H-coals and Synthoil products.[10–12,65,66] NMR has played an important role in coal liquefaction research because it has been the only method able to characterize the complement of materials involved in the process, including the original coal feedstocks, liquid products, solid residues and products, catalyst materials, and solvent systems. The functional group analysis approach has been widely used to examine the structural changes in coal liquefaction and has led to the following general conclusions concerning the overall process in tetralin: (1) hydroaromatic structures are partially or completely dehydrogenated, while others are cleaved during the reactions; (2) alkyl groups in the products result from cleavage of the hydroaromatic ring structures; and (3) aromatic structures are formed via dehydrogenation reactions.

With the advent of ^{13}C CP MAS spectroscopy, not only liquid products but also the solid residues from liquefaction became amenable to analysis by NMR. The chars formed after prolonged reaction times at higher temperatures tended to have extremely high aromatic carbon content, (f_a up to 0.96). In general, it was found that the aliphatic content of

the chars decreased with increasing hydrogenation time while the composition of the liquid products remained relatively constant. Also observed was a marked decrease in the number of polar functional groups. The general conclusions drawn from the NMR results suggested a mechanism involving the decomposition of hydroaromatic structures, whereby under higher temperature reaction conditions an increasing proportion of aliphatic structures was converted into aromatic material and/or gaseous products. Furthermore, the increase in the polycyclic aromatic content meant that hydroaromatic systems were decomposing via retrogressive condensation reactions. Most recently, coal liquefaction residues were characterized by solid state CP MAS techniques.[67]

Other researchers[62] have focused on the use of CP MAS to study coking deposition on coal liquefaction catalysts, which was thought to be one of the principal causes of catalyst deactivation. Several studies[62] have compared liquefaction behavior in the presence of different catalysts or with no catalyst at all, and have compiled results on the reaction yields and quality of liquid products. Both ^{13}C and ^{1}H NMR have been used to monitor the hydrogen donor solvent employed in liquefaction. The results demonstrated that loss of hydrogen in the solvent occurs primarily via aromatization of hydroaromatic structures. By estimating the concentration of donatable hydrogen of the liquefaction solvent through chemical shift assignments, hydrogen donor values of various solvents were independently derived.

Labeling studies employing deuterated tetralin have been used with great success to study hydrogen transfer processes during liquefaction and to follow the incorporation of deuterium into liquid products.[62] A combination of ^{1}H, ^{2}H, and ^{13}C NMR and separation methods such as gel permeation chromatography was employed to study the evolution of coal liquefaction products in d_4-tetralin.[68] Later on GASPE, INEPT, and two-dimensional J-resolved NMR were used to obtain more detailed structural information on exchange mechanisms of hydrogen and deuterium.[11,69,70] The majority of studies on a wide variety of coals and catalyst systems led to a common conclusion: the distribution of deuterium in liquefaction products was found to be reasonably representative of the fate of hydrogen incorporation into coal tars. While there was some total scrambling of hydrogen, for the most part hydrogen was incorporated into aromatic residues and at α- and β-carbon atoms preferentially attached to aromatic structures.

The ability of NMR methods to provide reasonably quantitative information on the distribution of hydrogen in both the starting coals, liquid and solid reaction products, and solvents has made it possible to account for the total hydrogen consumption in liquefaction.[62] A mass balance equation for the total consumption of hydrogen in liquefaction has been derived:

$$\Delta H = \Delta f_a + \Delta(C - C) + \Delta NOS \qquad (3)$$

where ΔH is the net change in hydrogen between the original coal and all liquefaction products, Δf_a is the corresponding change in total aromaticity, $\Delta(C-C)$ is the total number of carbon–carbon bonds ruptured via hydrogenolysis, and ΔNOS is the composite loss of nitrogen, oxygen, and sulfur atoms. The NMR data combined with information from elemental analysis were used to estimate the fate of total hydrogen utilized in hydrogenation processes leading to reduction, carbon–carbon bond-breaking reactions which generate either light gases or liquid products, and for removal of heteroatoms. The NMR approach of using the concept of total aromaticity as a means to assess the mass balance of consumed hydrogen has been an important step in evaluating the performance of liquefaction processes and has offered some of the best insights into coal liquefaction chemistry to date.

Numerous investigations have also been concerned with developing an understanding of the fundamental chemical processes involved during coal pyrolysis and carbonization.[62] NMR has been used to study the response of coals to heating, by comparing data on solid and liquid products with the data obtained on the original solid coals. Researchers have developed comprehensive models based on the changes in functional groups during pyrolysis. Specific information on changes in aromaticity, degree of substitution on aromatic structures, types of aliphatic functional groups, and aromatic ring condensation have been compiled by both ^{13}C NMR, and ^{1}H NMR using the approach of Brown and Ladner, together with compiled data on the yields of aromatic hydrogen and carbon as a function of temperature during pyrolysis. General conclusions have been summarized on the basis of the results: (1) only the weakest coal bonds fragmented at temperatures below 600 °C; (2) maximum yields were obtained at temperatures of 600–700 °C with little change observed in the aromatic structures and marked changes in the aliphatic components, suggesting that significant decomposition in the aliphatic substituents had occurred; and (3) at temperatures above 700 °C the less condensed aromatic structures began to decompose into gaseous products.

The nature of flash pyrolysis tars produced from a wide variety of coals throughout the world has been investigated by NMR techniques in several laboratories.[62] In general, it was found that larger polycyclic aromatic ring structures were produced at higher pyrolysis temperatures. However, results compiled from a survey of many pyrolysis experiments suggest that the nature of the coal and the method of pyrolysis rather than the final pyrolysis temperature were most important in determining tar structure. Alkenes in the tars were correlated with the decomposition of polymethylene chains, while ^{13}C NMR suggested that a large proportion of the alkyl carbon atoms were part of long-chain alkyl groups. NMR analysis of chars produced in variable temperature flash pyrolysis experiments showed that the aliphatic peak decreased with increasing pyrolysis temperature, while the aromatic band remained unchanged, suggesting that the aromatic content in the char was relatively constant. Furthermore, NMR studies demonstrated that the carbon aromaticity of the original coal, (f_a), or the amount of methylene structures present in the tars were linearly correlated with tar yields in coals ranging from bituminous to semianthracite; lignite tar yields, however, did not correlate well. Based on these results, it was concluded that aliphatic carbon atoms in coals, in particular the methylene groups, were essential to the production of pyrolysis tars. Later studies employing NMR considered correlating pyrolysis yields with the loss of specific regions of chemical shift within the aliphatic and aromatic resonance bands. The production of gases was consistent with decreases in the CH_2 resonance at 30 ppm. On the other hand, high tar yields correlated well with the loss of the remaining aliphatic groups in the region 13–47 ppm, i.e. consistent with the loss of hydroaromatic

structures in the coals. In addition, coal aromaticities correlated well with char production.

In general, the majority of coal processing technologies involve heating, and it is in this area that NMR has played a unique role in understanding the physical behavior of coal at the elevated temperatures typically employed in hydroliquefaction and other catalytic upgrading processes. Wideline ^{1}H NMR has been used to study changes in the molecular mobility or viscosity of coals during heating to temperatures as high as 875 K.[62,71,72] Early studies measured changes in $\Delta H_{\frac{1}{2}}$. However, later on the use of second moment (M_2) analysis of the solid echo signal led to a more accurate representation of average molecular mobility. Variations in M_2 with temperature were consistent with a depolymerization of the coal structure followed by recondensation. The concurrence of temperatures for M_2 minima and bulk fluidity from Giesler plastometry suggested that there was a significant molecular basis to the thermoplasticity of coal. In general, a strong correlation was found between hydrogen content, and perhaps high sulfur content, with coal fusibility.

2.3 The Quest for Quantitation

^{1}H and ^{13}C NMR spectroscopy have been applied with great utility to the analysis of hydrogen and carbon functional group distributions in a wide variety of liquid and solid fuels and their reaction products. The increasingly important role over the past three decades of NMR as a characterization tool for fuels has led to a significant advance in our understanding of their structure, origin, and evolution. The enormous impact that NMR has made in the area of fuel research has been a direct consequence of its utility as a quantitative tool. In principle, NMR of spin-$\frac{1}{2}$ nuclei is unique as a spectroscopic method in that the transition probabilities of each and every isochromat in the absorption spectrum is the same, or unity. Notwithstanding this unique capability, from the outset concerns about the quantitative reliability of ^{13}C NMR spectroscopy has placed the general utility of the method in question. Carbon-13 NMR in liquids was perceived in this way until the mid-1970s, when its usefulness as an analytical technique was demonstrated by the judicious implementation of the proper pulse techniques and recycle delay times, sometimes with the aid of relaxation reagents to shorten spin–lattice relaxation times and to suppress the nuclear Overhauser effect. For ^{13}C analysis of solid coal samples, the issues regarding quantitation were not resolved until the late 1980s because of the enormous complexities involved.

With the advent of ^{1}H decoupling,[15] CP[15] and MAS,[73] which have made it possible to obtain high-resolution ^{13}C NMR spectra in solids in a relatively short measuring time, CP MAS techniques have been applied extensively in coal research.[12,14,18,42,74–78] In fact, ^{13}C CP MAS NMR has become one of the most widely used methods for investigating coal. However, there has been growing concern during the past decade about the quantitative reliability of CP MAS spectroscopy for coal analyses. In the very first ^{13}C CP NMR study of coal,[14] it was estimated that only about 50% of the total carbon spins could be detected via this technique. Since then the issue of quantitation in NMR analyses of coal and related materials has been a topic of much debate.[14,44,45,47,75,79–85] Although the quantity of observable carbon atoms for coals and their macerals have been shown to vary widely, the general consensus was that, for reasons which can be related to both specific coal properties and the applied NMR techniques, a substantial fraction of the carbon atoms was not observed.

It was known that coal is one of the most complex carbonaceous materials known. It was by nature an extremely heterogeneous solid composed of a number of distinct organic phases termed macerals, and to a lesser extent, of an inorganic mineral phase. Each maceral and mineral phase exhibited a unique set of physical and chemical properties that contributed to the overall behavior of coal. The macerals typically ranged in size from micrometers upwards, and pure bands were commonly found in coal seams up to meters in thickness. Consequently, maceral dimensions were sufficiently large to expect that nuclear spin diffusion across maceral boundaries would be incomplete on the NMR timescale, typically on the order of 1000–2000 pm and 10^4 to 2×10^4 pm in the limits of proton relaxation in the rotating frame and laboratory frame, respectively. This meant that nuclei within different maceral phases acted as isolated spin reservoirs with very different magnetic properties.

There were additional factors to consider as well. Individual macerals were in many instances intimately associated with inorganic minerals, some of which may contain paramagnetic ions. Moreover, the macerals contained different concentrations of organic free radicals, causing relaxation time differences that would ultimately govern the evolution of magnetization within these isolated domains. The presence of paramagnetic centers raised the possibility that significant portions of the carbons were sufficiently broadened or shifted outside the spectral range to render them invisible in the NMR experiment. Moreover, variations in free-radical content among these isolated phases was shown to lead to serious distortions in the carbon signal measured for the entire coal sample.

Thus, complexities in the organic, inorganic, and physical structures of coal limited the quantitative reliability of solid ^{13}C NMR measurements. The inherent limitations associated with measuring a complex solid such as coal were unavoidable. However, a fundamental understanding of these complexities was necessary in order to establish confidence limits for the measurements so that meaningful parameters could be obtained from the data.

A comprehensive review on the subject of quantitation in solid NMR analysis of coals has recently appeared.[86] In that review, several factors limiting quantitation in both single pulse and cross polarization experiments were discussed along with possible remedies. Important aspects to the problem of quantitation included in that discussion were: the nature of the unpaired electron spin interactions; interference between molecular motions and the proton decoupling field; insufficient MAS rotation; interference between molecular motions and MAS; consequences of long spin–lattice relaxation times; dependence of the Hartmann–Hahn matching condition; modulation of C–H coupling due to MAS; and complexities involving CP spin dynamics.

Finally, resolution of the issues concerning the quantitative reliability of solid ^{13}C measurements was made possible by the establishment of a standard, homogeneous suite of coal samples. As in other disciplines of fuel science, the complex nature of carbonaceous fuels together with the diversity of

samples chosen for study has made comparisons between published results difficult. With the inception of the Argonne Premium Coal Sample Program,[87] NMR results on a common suite of pristine coal samples spanning a diverse rank range could be compared.[88] Thus, valid comparisons between data measured using different experimental techniques and under a variety of different experimental conditions had become feasible for the first time.

A comparison has been made of data obtained from experiments which were carried out at static field strengths ranging from 1.4 to 9.4 T (corresponding to carbon resonant frequencies of 15–100 MHz) and using a variety of methods, including CP MAS, single pulse excitation (SPE) with MAS, MAS with TOSS, and DNP CP without MAS. Carbon aromaticities were determined from CP experiments employing contact times generally between 1–2 ms and, in certain instances, by mathematically fitting signal intensities derived from variable contact-time experiments. Proton decoupling field strengths employed were typically 40–82 kHz; MAS frequencies varied from 3 to 13 kHz. Recycle delay times ranged from 1–3 s in CP experiments to 60 s in SPE experiments.

For bituminous coals, mean carbon aromaticity values that were determined for three data sets (CP MAS, CP MAS at 2.3 T, and SPE) were found to be the same within the limits of the standard deviations. The results indicated that the variability in carbon aromaticities reported by different laboratories for the coals was greater than the differences observed between experimental techniques, i.e. CP and SPE experiments. However, the mean values from SPE experiments always tended to be on the high end of the range of CP values.

Differences in mean carbon aromaticity values for CP and SPE experiments were found to be significant for the two low-rank sub-bituminous and lignite coals samples. Their mean SPE carbon aromaticities were clearly higher by approximately 10% and 20%, respectively. The differences were accounted for by complications arising from paramagnetic transition metal ions intimately associated with the coal organic phase. The presence of paramagnetic metal ions in these coals was shown adversely to affect their spin–lattice relaxation properties,[48] and these factors were invoked to explain lower derived CP MAS aromaticity values resulting from reduced CP efficiencies.

Comparing mean CP and SPE aromaticity values for Argonne coals with aromaticities obtained by other pulse techniques showed the expected trends. While carbon aromaticities obtained using the TOSS pulse sequence in one laboratory were in reasonable agreement with the mean, those reported by other laboratories turned out to be significantly lower than mean CP or SPE aromaticity values. The disparity of the TOSS results illustrated the severe demands that are placed on proper implementation of the TOSS pulse sequence for quantitative analysis. On the other hand, aromaticity values obtained from DNP CP experiments tended to be high, which was entirely consistent with signal enhancement via electron–nuclear polarization from free radical centers that reside within aromatic coal structures.

The principal conclusion gleaned from the interlaboratory study was that SPE methods generally gave the most reliable results. Proper sample handling techniques to prevent oxidation or weathering of samples was also thought to be an important factor in the analysis of coals.

2.4 Origin of Coal and its Evolution

From the beginning of its deposition at the surface of the Earth and throughout its burial, sedimentary organic plant debris underwent progressive changes in composition and structure; when the process involved has related specifically to the metamorphosis of coal, it has been generally referred to as 'coalification'.[89] The nature of metamorphic processes of coal has changed significantly at different stages of its evolution. At the earliest stages, coalification was dominated by microbial reactions and physical processes such as maceration and compaction. Later stages of coalification were governed predominantly by abiogenic chemical reactions such as dehydration, dehydrogenation, and aromatization, as well as polymerization and depolymerization reactions. The final stages involved graphitization processes, leading eventually to the formation of anthracite.

During the past three decades, there have been numerous investigations concerned with elucidating the important chemical processes responsible for the transformation of plant biopolymers into the specific organic macerals that compose coals.[89] During the 1980s, numerous studies employing NMR techniques sought to uncover the chemistry involved in the transformation of woody tissue, obtained from both natural and synthetic sources, into the maceral vitrinite. Often, NMR studies were carried out in parallel with analysis by mass spectrometry. The structural evolution of vitrinite was studied through detailed characterization of naturally occurring coalified log specimens which spanned the entire coalification range.[90–94] In independent studies, laboratory simulated coalification experiments were carried out on lignin samples isolated from modern wood, in the presence of clay catalysts at relatively low temperatures (150 °C).[95] Subsequent simulated coalification investigations[96,97] focused on solid state ^{13}C and ^{1}H NMR analyses of synthetically prepared ^{13}C-labeled lignins[98] and model compounds to monitor abiogenic evolution pathways. The remarkable parallels found between solid state ^{13}C spectra of artificial coals and naturally occurring coalified specimens of similar maturation level laid the framework which revolutionized modern thinking on the process of coalification.

Previous views of coalification held that in early stages of diagenesis plant biopolymers (predominantly lignin) were degraded and depolymerized through microbial transformation into low molecular weight humic substances, and these materials subsequently repolymerized to form the macromolecular building blocks that became coals. The bulk of recent results from studies by NMR has not validated this paradigm of coalification. Rather, evidence has mounted indicating that coalification of woody tissue proceeded primarily by selective preservation of lignin structures, as biochemical processes removed carbohydrates preferentially, followed by a subtle thermal alteration of lignin directly into the macromolecules found in coal. There was little evidence to suggest that any major disruption in lignin structure had taken place; consequently, humic acids were no longer considered major intermediates in the formation of coal.

From investigations of coalification of both natural and synthesized precursors, evolutionary changes in the chemical structure of vitrinite were clearly delineated throughout the principal stages of coalification, and detailed mechanisms leading to its transformation could be sketched. It was shown that

initial biochemical stages of coalification involved the complete loss of hemicellulose structures, as well as a significant loss in cellulose from woody tissue, with minimal alteration of lignin. Later diagenetic stages leading to the formation of lignite coals resulted in complete loss of all the carbohydrates and some modification of lignin structure. The changes observed were predominantly rearrangement reactions of the aryl–ether bonds that formed linkages between the 3-methoxyphenol subunits; concomitant with these processes was demethylation of methoxyl groups followed by concerted methylation of the aromatic rings to produce methylcatechol structures. The final stages involving transformation into bituminous coals were characterized by reactions that resulted in complete demethylation of the aromatic methoxyl groups and subsequent reductive elimination of the 3-hydroxyl groups to form predominantly phenol-like building blocks. Progression to the higher rank bituminous coals was distinguished by the continued loss of oxygen functionalities along with ring condensation reactions leading to the formation of increased amounts of polycyclic aromatic structures.

3 APPLICATIONS TO SHALE OIL RESEARCH

Oil shales[99] are fine-grained sedimentary rocks that contain complex organic polymers ranging in molecular weight. There are two fractions of organic matter present: bitumen constitutes the fraction that is soluble in common organic solvents and kerogen constitutes the major portion of organic matter that is insoluble in organic solvents. The organic kerogen fraction is thought to be a cross-linked, three-dimensional macromolecular network of high molecular weight. Oil shale deposits were formed throughout geological time by the slow deposition of organic and inorganic residues in ancient lakes and inland seas. As the bodies of water stagnated and evaporated to dryness, the organic and inorganic matter compacted into sedimentary rock. The structure and composition of the inorganic and organic kerogen components of oil shale vary significantly with the location and the history of the sedimentary basin. If the organic portion originated from a land-based plant source, the kerogen fractions are similar in composition to coal, tend to be highly aromatic materials with hydrogen contents of about 5 wt%, and yield little oil on pyrolysis. On the other hand, kerogen fractions derived from marine aquatic sources tend to have high hydrogen contents ranging from 10 to 12 wt% and are good sources of oil.

Because oil shale kerogen was completely insoluble in common solvents, direct structural and compositional data were difficult to obtain without first performing time-consuming isolation and preparation procedures to produce kerogen concentrates that would be amenable to analysis. As was the case for coal, solid state NMR techniques fostered a resurgence of research devoted to characterization of oil shale in its native state. With the application of high-resolution proton CRAMP and carbon CP MAS spectroscopy, a great deal of fundamental information was obtained about the carbon and proton structure of these materials, about which there was little direct structural information known previously.

3.1 Structure Studies

The first application of NMR to the study of oil shales was reported in 1971, and this initial investigation was focused on the use of broadline ^{1}H NMR as a quantitative approach to predict oil yields that was less time consuming than Fischer assay methods.[100] Three years later, a more comprehensive study was reported in which pulsed ^{1}H NMR techniques were employed for oil shale characterization.[101]

Analyses of oil shale components by high-resolution ^{1}H and ^{13}C NMR have been carried out on samples from the Green River formation that were thermally fractionated into naphtha, light distillate, heavy distillate and residue fractions.[102] Resonances in the spectra were assigned to normal alkanes, and to methyl- and dimethyl-branched alkanes, and the compositions of the various fractions were reported. Relaxation time experiments were correlated to the intermolecular segmental motion of the carbon chains in separate fractions. Solution NMR studies that followed have focused on applications of NMR to oil shale processing.[103,104] Two-dimensional NMR techniques have been applied to the characterization of shale oils.[105] Carbon and hydrogen functional group distributions for oils, obtained from eastern and western oil shales within the USA, were determined using DEPT and quaternary-only (QUAT) pulse methods for editing carbon spectra.[106]

The first solid state ^{13}C NMR spectra using CP enhancement techniques on native oil shales were reported in 1976;[107] however, the authors mentioned that the spectra were quite disappointing because of the lack of resolution between a broad aliphatic resonance band and a weak, partially resolved aromatic band. Later studies extended the CP measurements to include wide variety of oil shales.[108] Resing et al.[109] were the first to report CP MAS measurements on the aromaticity of a Colorado oil shale, the value of which was in basic agreement with that obtained by chemical degradation methods. In subsequent investigations, several laboratories performed CP MAS measurements in order to classify oil shale kerogens of varied origins and depositional environments throughout the globe.[110–113]

Early studies were also concerned with interference from mineral matter, particularly carbonate minerals, with the signals arising from the organic carbon in shales.[109,114] The general consensus reached was that spectra exhibited little interference from carbonates because of the long spin–lattice relaxation times of the minerals. For detailed investigations of the carbon structure of the organic fraction, NMR analyses were carried out on the kerogen concentrates that were prepared by removing the mineral matter by acid treatment (HCl or HF). Spectra of the kerogen concentrates were always found to be better resolved than those obtained from the raw shales, and even simple washing with HCl improved the quality of the spectra.[111,115] The question remained, however, whether the preparation of concentrates by acid treatment had altered the chemical structure of the kerogen in the raw oil shale. A detailed study was carried out to address this issue, employing CP MAS techniques to characterize the organic carbon distributions in six oil shales and their isolated kerogen concentrates.[116] It was determined that the raw shales and their corresponding kerogen concentrates had similar gross compositional features, e.g. carbon aromaticities, indicating that acid extraction did not significantly alter the chemical structure of the organic kerogen material. However,

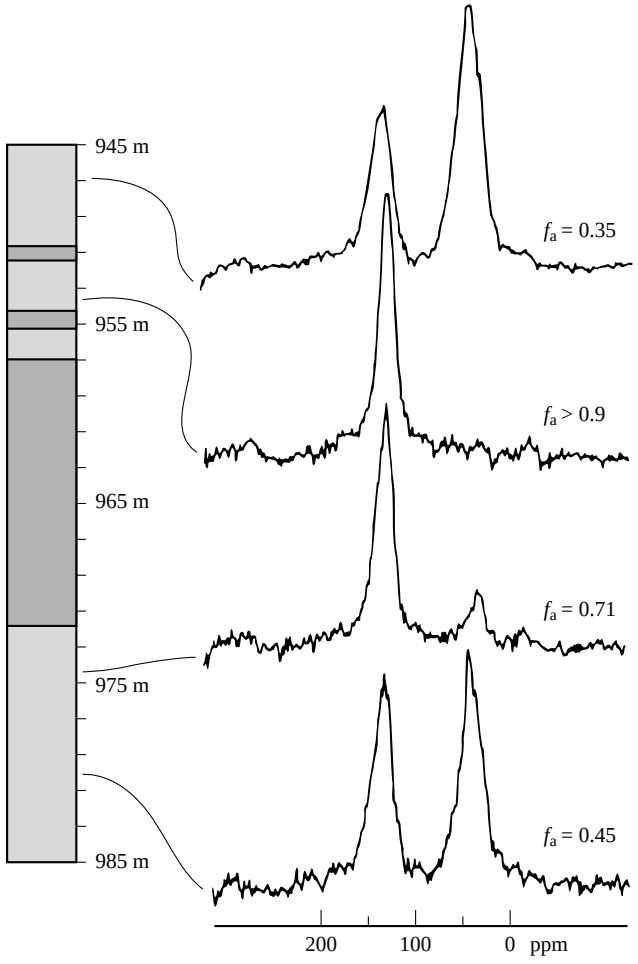

Figure 8 CP MAS ^{13}C NMR spectra and f_a values of oil shale samples at various depths in the vicinity of a basaltic intrusion. Dark areas indicate regions of intrusion

carbohydrate structures if present in the original oil shales, were removed during acid extraction.

The utility of CP MAS NMR as a chemical elucidation method was demonstrated on a series of samples from a section of core taken from the Atlantic ocean, where a basaltic intrusion of magma had permeated the sediment during the Miocene period (see Figure 8).[117] The thermal effects on the organic fraction were clearly visible in the spectra; samples closest to the basaltic intrusion zone clearly showed higher aromaticity values as a result of thermal cracking and subsequent loss of their long-chain aliphatic structures. Aromaticities derived from NMR were compared with results from more traditional vitrinite reflectance measurements, and it was concluded that NMR aromaticities were more sensitive and more quantitative to thermal changes in the kerogen structure.

NMR spectral editing using dipolar dephasing techniques has been applied to derive structural parameters for three oil shales from Colorado, Tennessee and Kentucky;[118] measurements were obtained on the native shales. Differences in carbon structure between the three shales were provided by the DD data, including the distribution of primary through quaternary aliphatic structures, protonated and nonprotonated aromatic groups, the number of methyl groups per aromatic ring, the number of substituted or bridgehead carbon atoms per aromatic ring, and the minimum aliphatic chain length. A later investigation employed curve fitting procedures in conjunction with DD techniques to determine the distribution of carbon bonding types in a kerogen from the Green River Formation.[119] Fourteen representative carbon functional groups were analyzed and these were used to derive an average structure for the kerogen. Analysis of the data indicated that the kerogen was composed of long-chain aliphatic residues as well as alicyclic ring structures, although relative proportions of each were not totally quantifiable on the basis of NMR results.

3.2 Resource Evaluation

The quality of the organic matter in oil shale has traditionally been used as the standard for its potential for bearing oil on heating. Conventional pulsed ^1H NMR has been employed as a rapid method of analysis for oil shale evaluation.[108,120–122] The method relies on the measurement of the amplitude of the free induction decay to assess the overall hydrogen content of the shale. In actuality, the measurement was simply a measure of the quantity of kerogen in the sample. To date, ^1H CRAMPS has not been employed for the analysis of oil shales.

With the development of ^{13}C CP MAS spectroscopy, a new method was introduced which has played a significant role in oil shale resource evaluation because it provides a direct means of analyzing aliphatic/aromatic carbon distributions in these systems, and thereby manifests an immediate relationship to yields of saturated oil products. Aliphatic structures tend to be hydrogen rich; thus oil shales having greater aliphatic carbon content were known to produce higher fractions of liquids than those more aromatic in nature.

The first CP MAS studies to establish a correlation between the aliphatic carbon content of oil shales and oil yields determined by traditional Fischer assay methods were performed by Maciel et al.[123,124] Several additional CP MAS studies followed on a wide range of kerogens and oil shales.[125–128] The correlation between aliphatic carbon and oil yields was determined to be linear for samples spanning a diverse range of geological time periods, geographic locations and depositional environments. The excellent correlation between genetic potential, or the amount of oil and gas that an oil shale kerogen is able to generate, and fraction of aliphatic carbon has since been documented in several laboratories.[129–133] Conversely, the aromatic carbon content has been shown to correlate with the carbon residue remaining after pyrolysis.[115,132–134] Solid state ^{13}C NMR has since been considered the paradigm for resource evaluation in the field, because the method relies on structure parameters that are closely identified with fuel yields. Moreover, the information is independent of the total kerogen content in the oil shale, which is often a misleading parameter for oil generation.

3.3 Oil Shale Conversion

Solid and liquid state NMR, in combination with elemental analysis and mass spectrometry, have provided valuable insight into the chemistry of oil shale conversion throughout the last two decades. From the perspective of processing, NMR has been attractive because it is capable of measuring directly

the changes associated with the carbon bonding distributions that occur as a function of temperature and other retorting parameters. Early studies involved liquid-state ^{1}H and ^{13}C NMR on oils produced from pyrolysis and hydropyrolysis of shales from eastern and western USA; a comprehensive set of average molecular structure parameters were derived for the hydrocarbon mixtures.[135] Research performed in several laboratories[115,136–141] has combined CP MAS NMR measurements with data from elemental analysis to determine the degree of aromatization during oil shale pyrolysis.

Hershkowitz et al.[136] were the first to quantify the increase in aromatic carbon formed in pyrolysis of Colorado oil shale. Their experiments were carried out at a slow heating rate up to a temperature of 600 °C under high pressure (2600 kPa) N_2 or H_2. The net increase in total aromatic carbon for the oil and residue products over that of the starting shale oil was determined by solution state and CP MAS ^{13}C NMR. The increase was rationalized in terms of aromatization of the aliphatic carbon functional groups and the associated evolution of light gases and oils that were composed of hydrogen-rich aliphatic species. Similar trends were observed in the pyrolysis studies of Green River and Kentucky oil shales,[137,138] where increases in aromatic carbon content of 29% and 17% were reported, respectively. Consequently, it had been shown that aromatization of aliphatic structures in oil shales was indeed a facile thermal reaction, and that only by carefully controlling the pyrolysis temperature was it possible to minimize aromatization reactions responsible for oil loss.

4 OTHER FUELS

4.1 Petroleum

The earliest high-resolution ^{1}H NMR spectra of petroleum fractions, obtained at a frequency of 30 MHz, were reported in 1957.[142–144] Two practical uses of the application of ^{1}H NMR in the petroleum industry appeared 2 years later, in 1959. A paper[145] was published which described NMR as a technique to evaluate the elemental hydrogen content of petroleum, and a patent[146] was issued in the same year concerning NMR as a method for process control for determining fuel quality on the basis of the degree of branching of alkylated aromatic hydrocarbons.

Although high-resolution ^{1}H NMR had proved to be valuable in the characterization of petroleum and petroleum fractions, the introduction of ^{13}C NMR in 1967 as a quantitative tool using time-averaged slow passage techniques[147] provided a prelude of what was soon to become a powerful analytical method. Nine years later, the first detailed ^{13}C NMR investigation of crude oils and petroleum fractions appeared using FT methods.[148] Replacement of continuous wave techniques by FT made the ^{13}C NMR characterization of crude oils and petroleum products more or less routine. Several conference proceedings and reviews have appeared in the literature which summarize much of the information that has been derived from NMR about the chemistry and structure of heavy crude oils and petroleum, including the use of NMR in petroleum exploration and as an oil logging tool.[149–151]

Several fundamental advances have been realized in the elucidation of heavy oils by NMR. In 1981, Gillet et al.[152] presented and discussed numerous criteria necessary for obtaining quantitatively reliable structural parameters from NMR experiments. One year later, NMR was used to provide a 'fingerprint' of various crude oils.[153] SEBBORD pulse methods were used for spectral editing of carbon spectra of petroleum fractions, facilitating the discrimination of the different bonding schemes of aliphatic carbon structures, i.e. between CH, CH_2, and CH_3 groups.[154,155] The analysis provided sufficient information such that average structural parameters could be derived for these complex mixtures. Carbon chemical shifts and spin–lattice relaxation times were later used to characterize oil products.[156] Nitrogen compounds in crude oils have also been examined and identified with ^{13}C NMR.[157]

The use of ^{33}S NMR as a tool for the characterization of petroleum oils[158] and an oxidized petroleum asphaltene[159] have been reported. The technique has met with limited success because of the considerable quadrupolar linewidths of sulfur combined with the large number of sulfur species present in these complex mixtures.

4.2 Peat

Humic substances have been described as the predominant fraction of the organic matter found in peat. Peat was formed in depositional environments where water had flowed near the surface of the peat profile, slowly but continually inundating the peat subsurface, and where anerobic conditions prevailed within the subsurface layers. These conditions led to the preservation, from oxidative and microbial processes, of the organic matter in peat which has always been thought to be derived from lignin from vascular plants.

An excellent treatise[160] on the use of ^{13}C CP MAS NMR as a structural tool for the investigation of sedimentary humic substances has appeared. The review covers the relevant literature concerning early liquid state and solid state NMR studies of aquatic and terrestrial sediments, and describes in detail recent CP MAS experiments on peat fractions from various geographical locations.

Early studies[161] on humic acids and humins from holocene sediments were the first to suggest that CP MAS NMR can be used to distinguish between humic acids from terrestrial and aquatic environments on the basis of their carbon aromaticities. Source materials for the two sediments were entirely different: terrestrial sediments were based on lignin-derived material that was highly aromatic, whereas aquatic sediments were formed from primarily algal or microbial remains. In a subsequent paper,[162] the same authors attributed the presence of aliphatic structures in marine humic acids to an algal source, and in terrestrial humic acids to lipid material. These initial observations provided the basis for understanding later NMR investigations on humic acids derived from peats.

In those subsequent studies,[160] CP MAS measurements were performed on isolated fractions of fulvic acid, humic acid, and humin from peats obtained from Minnesota, Okefenokee, and the Everglades. Absolute quantities of the aromatic and paraffinic structures, carboxyl, carbonyl and ether functional groups, and carbohydrates were determined and compared for individual fractions from the different peat samples. The data were used to determine the chemical composition of the varied structural components within peat samples from different

depositional environments, and the information was used to develop a model for the transformation of plant residues into humic substances. An investigation[163] published one year later focused on the use of ^{13}C CP MAS spectroscopy, among other techniques, to identify structural changes that occur in humic acids during coalification through the stages of peat, lignite, and sub-bituminous coal.

4.3 Tar Sands

Tar sands are composed of complex mixtures of minerals containing aliphatic, heteroaromatic, and polycyclic aromatic compounds. Because of the strong intermolecular associations between molecules, organic matter in tar sands is often considerably viscous. Bitumen and heavy oil fractions of tar sands from different geographical locations differ widely in chemical composition and physical properties.

To date, there have been few published reports on the use of NMR for characterizing tar sands. Two early studies have attempted to characterize organic–inorganic interactions directly in heavy oil/bitumen-derived solids using ^{13}C CP MAS NMR.[164,165] A subsequent investigation[166] used ^{1}H CRAMPS to provide information on the types of hydrogen functionality that were present at the surface of tar sand residues. The data indicated that hydroaromatic structures were bound more strongly to the mineral surfaces, and that residues of tar sands after pyrolysis became highly aromatic in nature. Relaxation time (T_1) measurements[167] were used to determine the rates of intermolecular association of a tar sand bitumen after its thermally induced dissociation. Separate studies were carried out whereby viscosities of tar sand bitumens could be calculated from T_2 relaxation time measurements performed at room temperature.[168] Viscosities of bitumens from three US tar sands were correlated to weighted T_2 relaxation rates for semiliquid, mobile solid-like and rigid phases.

5 RELATED ARTICLES

Chemical Shift Tensors; Coal Structure from Solid State NMR; Cokes; CRAMPS; Cross Polarization in Rotating Solids: Spin-1/2 Nuclei; Cross Polarization in Solids; Dynamic Nuclear Polarization and High-Resolution NMR of Solids; Geological Applications; Heteronuclear Assignment Techniques; Magnetic Resonance Imaging: A Historical Overview; Magic Angle Spinning; Magic Angle Turning and Hopping; Paramagnetic Relaxation in Solution; Polymers: Regio-Irregular Structure; Rotating Solids; Selective Excitation in MRI and MR Spectroscopy; Variable Angle Sample Spinning; Well Logging; Wood and Wood Chars.

6 REFERENCES

1. H. Perry, in *Kirk–Othmer Encyclopedia of Chemical Technology*, 3rd edn, Wiley, New York, 1978, Vol. 11.
2. E. M. Purcell, H. C. Torrey, and R. V. Pound, *Phys. Rev.*, 1946, **69**, 37.
3. F. Bloch, W. W. Hansen, and M. Packard, *Phys. Rev.*, 1946, **69**, 127.
4. K. S. Vorres, in *Kirk–Othmer Encyclopedia of Chemical Technology*, 4th edn, Wiley, New York, 1993, Vol. 6.
5. E. Stach and co-workers, *Stach's Textbook of Coal Petrology*, 3rd edn, Gebruder Bornstraeger, Berlin, 1982.
6. R. E. Winans and J. C. Crelling, *Chemistry and Characterization of Coal Macerals*, *American Chemical Society Symposium Series No. 252*, ACS, Washington, DC, 1984.
7. R. A. Friedel, *J. Chem. Phys.*, 1959, **31**, 280.
8. H. L. Retcofsky and R. A. Freidel, in *Spectrometry of Fuels*, Plenum, New York, 1970, Chap. 6
9. H. L. Retcofsky and R. A. Friedel, in *Spectrometry of Fuels*, Plenum, New York, 1970, Chap. 8
10. H. L. Retcofsky and T. A. Link, in *Analytical Methods for Coal and Coal Products*, Academic, San Diego, 1978, Vol. II, Chap. 24
11. L. Petrakis and D. Allen, *NMR of Liquid Fossil Fuels*, Elsevier, Amsterdam, 1987, Analytical Spectroscopy Library, Vol. 1.
12. R. M. Davidson, Nuclear Magnetic Resonance Studies of Coal, IEA Coal Research Report No. ICTIS/TR32, IEA Coal Research, London, 1986.
13. P. C. Newman, L. Pratt, and R. E. Richards, *Nature (London)*, 1955, **125**, 645.
14. D. L. Vanderhart and H. L. Retcofsky, *Fuel*, 1976, **55**, 202.
15. A. Pines, M. G. Gibby, and J. S. Waugh, *J. Chem. Phys.*, 1972, **15**, 1776; 1973, **59**, 596.
16. V. J. Bartuska, G. E. Maciel, J. Schaefer, and E. O. Stejskal, *Fuel*, 1977, **56**, 354.
17. B. C. Gerstein, C. Chow, R. G. Pembleton, and R. C. Wilson, *J. Phys. Chem.*, 1977, **81**, 565.
18. D. E. Axelson, Solid State Nuclear Magnetic Resonance of Fossil Fuels, Multiscience, 1985.
19. B. C. Gerstein, P. D. Murphy, and L. M. Ryan, in *Coal Structure*, ed. R. A. Meyers, Academic, New York, 1982, Chap. 4
20. H. Schmiers, *Konstitutionaufklarung von Kohlen und verwandten Produkten*, Freiberger Forshungshefte, VEB Deutscher Verlag fur Grundstoffindustrie, 1986.
21. H Rosenberger and K.-H. Rentrop, Strukturuntersuchungen an Kohlen und kohlestammigen Verbindungen mittels hochflosender ^{1}H- und ^{13}C-NMR in Festkorpern, Vortrag auf der Arbeitstagung *Moderne Methoden und Ergebnisse der Festkorper-NMR-Spektroskopie* ed. H. Rosenberger, Eisenach-Wartburg, Freiberg, 1982.
22. G. E. Maciel, C. E. Bronnomiann, and C. F. Ridenour, in *Magnetic Resonance of Carbonaceous Solids*, ed. R. E. Botto and Y. Sanada, *American Chemical Society Advances in Chemistry Series No. 229*, ACS, Washington, DC, 1992, Chap. 2
23. P. D. Murphy, B. C. Gerstein, V. L. Weinberg, and T. F. Yen, *Anal. Chem.*, 1982, **54**, 522.
24. M. Alla and E. Lippmaa, *Chem. Phys. Lett.*, 1976, **37**, 260.
25. R. Liotta, and G. J. Brons, *J. Am. Chem. Soc.*, 1981, **103**, 1735.
26. R. R. Chambers, Jr., E. W. Hagaman, M. C. Woody, K. E. Smith, and D. R. McKamey, *Fuel*, 1982, **61**, 53.
27. C.-Y. Choi, J. V. Muntean, A. R. Thompson, and R. E. Botto, *Energy Fuel.*, 1989, **3**, 528.
28. J. R. Barnes, A. D. H. Clague, N. J. Claydent, C. M. Dobson, and R. B. Jones, *Fuel*, 1986, **65**, 437.
29. M. A. Wilson, B. C. Young, and K. M. Scott, *Fuel*, 1986, **65**, 1584.
30. A. R. Thompson and R. E. Botto, *Preprint, ACS Division Fuel Chem.*, 1987, **32**, 280.
31. H. L. Retcofsky and R. A. Friedel, *Fuel*, 1968, **47**, 391.
32. B. C. Gerstein, C. Chow, R. G. Pembleton, and R. C. Wilson, *J. Phys. Chem.*, 1977, **81**, 565.

33. T. Yokono, K. Miyazawa, Y. Sanada, and H. Marsh, *Fuel*, 1979, **58**, 896.
34. L. J. Lynch and D. S. Webster, *J. Magn. Reson.*, 1980, **40**, 259.
35. D. S. Webster and L. J. Lynch, *Fuel*, 1981, **60**, 549.
36. J. A. Ripmeester, C Couture, J. A. MacPhee, and J. A. Nandi, *Fuel*, 1984, **63**, 522.
37. R. A. Wind, M. J. Duijvestijn, C. van der Lugt, J. Smidt, and H. Vriend, *Fuel*, 1987, **66**, 876.
38. M. J. Sullivan, N. M. Szeverenyi, G. E. Maciel, L. Petrakis, and D. W. Grandy, in *Magnetic Resonance: Introduction, Advanced Topics and Applications to Fossil Energy*, ed. L. Petrakis, J. P. Fraissard, *NATO ASI Series C124*, Reidel, Dordrecht, 1984, p. 607.
39. W. A. Barton and L. J. Lynch, *Energy Fuel.*, 1989, **3**, 402.
40. R. A. Wind, A. Jurkiewicz, and G. E. Maciel, *Fuel*, 1989, **68**, 1189.
41. L. dela Rosa, M. Pruski, D. Lang, B. Gerstein, and P. Solomon, *Energy Fuel.*, 1992, **6**, 460.
42. M. S. Solum, R. J. Pugmire, and D. M. Grant, *Energy Fuel.*, 1989, **3**, 187.
43. K. Hayamizu, S. Hayashi, K. Kamiya, and M. Kawamura, in *Magnetic Resonance of Carbonaceous Solids*, ed. R. E. Botto and Y. Sanada, *American Chemical Society Advances in Chemistry Series No. 229*, ACS, Washington, DC, 1992, Chap. 15
44. R. L. Dudley and C. A. Fyfe, *Fuel*, 1982, **61**, 651.
45. R. E. Botto, R. Wilson, and R. E. Winans, *Energy Fuel.*, 1987, **7**, 173.
46. C. E. Snape, D. E. Axelson, R. E. Botto, J. J. Delpuech, P. Tekely, B. C. Gerstein, M. Pruski, G. E. Maciel, and M. E. Wilson, *Fuel*, 1989, **68**, 547.
47. M. J. Sullivan and G. E. Maciel, *Anal. Chem.*, 1982, **54**, 1606, 1615.
48. R. E. Botto and D. E. Axelson, *Preprint, ACS Division Fuel Chem.*, 1988, **33**, 50.
49. C. Tsiao and R. E. Botto, in *Magnetic Resonance of Carbonaceous Solids*, ed. R. E. Botto and Y. Sanada, *American Chemical Society Advances in Chemistry Series No. 229*, ACS, Washington, DC, 1992, Chap. 18
50. K. W. Zilm and G. G. Webb, *Fuel*, 1986, **65**, 721.
51. M. Wilson, J. Hanna, K. B. Anderson, and R. E. Botto, *Org. Geochem.*, 1993, **20**, 985.
52. K. W. Zilm and G. G. Webb, *Preprints, ACS Division Fuel Chem.*, 1986, **31**, 230.
53. R. A. Wind, M. J. Duijvestijn, C. van der Lugt, J. Smidt, and H. Vriend, *Fuel*, 1987, **66**, 876.
54. R. A. Wind, R. Lewis, H. Lock, and G. E. Maciel, in *Magnetic Resonance of Carbonaceous Solids*, ed. R. E. Botto and Y. Sanada, *American Chemical Society Advances in Chemistry Series No. 229*, ACS, Washington, DC, 1992, Chap. 3
55. N. K. Sethi, R. J. Pugmire, J. C. Facelli, and D. M. Grant, *Anal. Chem.*, 1988, **60**, 1574.
56. N. K. Sethi, R. J. Pugmire, and D. M. Grant, in *1987 International Conference on Coal Science*, ed. J. A. Moulijn, and H. A. Chermin, Elsevier, Amsterdam, 1987, p. 41.
57. A. M. Orendt, M. S. Solum, N. K. Sethi, C. D. Hughes, R. J. Pugmire, and D. M. Grant, in *Magnetic Resonance of Carbonaceous Solids*, ed. R. E. Botto and Y. Sanada, *American Chemical Society Advances in Chemistry Series No. 229*, ACS, Washington, DC, 1992, Chap. 22
58. S. L. Dieckman, N. Gopalsami, and R. E. Botto, *Energy Fuel.*, 1990, **4**, 417.
59. D. C. French, S. L. Dieckman, and R. E. Botto, *Energy Fuel.*, 1993, **7**, 90.
60. L. Hou, G. D. Cody, P. G. Hatcher, S. Gravina, and M. A. Mattingly, *Fuel*, 1994, **73**, 199.
61. G. D. Cody and R. E. Botto, *Energy Fuel.*, 1993, **7**, 561.
62. R. M. Davidson, Nuclear Magnetic Resonance Studies of Coal, IEA Coal Research Report No. ICTIS/TR32, IEA Coal Research, London, 1986, Chap. 10
63. J. A. McPhee, H. Kawashima, Y. Yamashita, and Y. Yamada, in *Magnetic Resonance of Carbonaceous Solids*, ed. R. E. Botto and Y. Sanada, *American Chemical Society Advances in Chemistry Series No. 229*, ACS, Washington, DC, 1992, Chap. 17
64. H. Z. Sternberg, R. Raymond, and F. K. Schweighardt, *Science*, 1975, Apr., 49.
65. R. J. Pugmire, D. M. Grant, K. W. Zilm, L. L. Anderson, A. G. Oblad, and R. E. Wood, *Fuel*, 1977, **56**, 295.
66. J. W. Stadelhofer, K. D. Bartle, and R. S. Matthews, *Erdol Kohle-Erdgas-Petrochem. vereinigt Brennstoff-Chem.*, 1981, **34**, 71.
67. N. Cyr and N. O. Egiebor, in *Magnetic Resonance of Carbonaceous Solids*, ed. R. E. Botto and Y. Sanada, *American Chemical Society Advances in Chemistry Series No. 229*, ACS, Washington, DC, 1992, Chap. 14
68. J. Franz, *Fuel*, 1979, **58**, 405.
69. D. K. Dalling, G. Haider, R. J. Pugmire, J. Shabtai, and W. E. Hull, *Fuel*, 1983, **62**, 587.
70. P. J. Collin and M. A. Wilson, *Fuel*, 1983, **62**, 1243.
71. R. Sakurovs, L. J. Lynch, and W. A. Barton, in *Magnetic Resonance of Carbonaceous Solids*, ed. R. E. Botto and Y. Sanada, *American Chemical Society Advances in Chemistry Series No. 229*, ACS, Washington, DC, 1992, Chap. 11
72. Y. Sanada and L. J. Lynch, in *Magnetic Resonance of Carbonaceous Solids*, ed. R. E. Botto and Y. Sanada, *American Chemical Society Advances in Chemistry Series No. 229*, ACS, Washington, DC, 1992, Chap. 7
73. E. O. Stejskal, J. Schaefer, and R. A. McKay, *J. Magn. Reson.*, 1977, **25**, 569.
74. G. E. Maciel, V. J. Bartuska, and F. P. Miknis, *Fuel*, 1979, **58**, 391.
75. F. P Miknis, M. J. Sullivan, V. J. Bartuska, and G. E. Maciel, *Org. Geochim.*, 1981, **3**, 19.
76. K. W. Zilm, R. J. Pugmire, D. M. Grant, S. R. Larter, and J. Allen, *Fuel.*, 1981, **60**, 717.
77. R. E. Botto and R. E. Winans, *Fuel*, 1983, **62**, 271.
78. R. A. Wind, M. J. Duijvestijn, C. van der Lugt, J. Smidt, and J. Vriend, *Fuel*, 1987, **66**, 876.
79. M. S. Solum, R. J. Pugmire, and D. M. Grant, *Energy Fuel.*, 1989, **3**, 187.
80. D. E. Wemmer, A. Pines, and D. D. Whitehurst, *Phil. Trans. R. Soc. London, Ser. A*, 1981, **300**, 15.
81. E. W. Hagaman and M. C. Woody, *Proceedings of the International Conference on Coal Science*, Glueckauf, Essen, 1981, 807.
82. P. D. Murphy, T. J. Cassady, and B. C. Gerstein, *Fuel*, 1981, **61**, 1233.
83. M. A. Wilson, R. J. Pugmire, J. Karas, L. B. Alemany, W. R. Woolfenden, D. M. Grant, and P. H. Given, *Anal. Chem.*, 1984, **56**, 933.
84. J. M. Dereppe, in *Magnetic Resonance: Introduction, Advanced Topics and Applications to Fossil Energy*, ed. L. Petrakis and J. P. Fraissard, Reidel, Dordecht, 1984, p. 585.
85. C. E. Snape, D. E. Axelson, R. E. Botto, J. J. Delpuech, P. Tekely, B. C. Gerstein, M. Pruski, G. E. Maciel, and M. A. Wilson, *Fuel*, 1989, **68**, 547.

86. R. A. Wind, G. E. Maciel, and R. E. Botto, in *Magnetic Resonance of Carbonaceous Solids*, ed. R. E. Botto and Y. Sanada, *American Chemical Society Advances in Chemistry Series No. 229*, ACS, Washington, DC, 1992, Chap. 14
87. K. S. Vorres, *Energy Fuel.*, 1990, **4**, 420.
88. B. G. Silbernagel and R. E. Botto, in *Magnetic Resonance of Carbonaceous Solids*, ed. R. E. Botto and Y. Sanada, *American Chemical Society Advances in Chemistry Series No. 229*, ACS, Washington, DC, 1992, Chap. 33
89. J. R. Levine, in *Hydrocarbons from Coal*, ed. B. E. Rice and D. D. Law, *American Association of Petroleum Geologists Studies in Geology Series No. 38*, AAPG, 1993, Chap. 3
90. P. G. Hatcher, I. A. Breger, and W. L. Earl, *Org. Geochem.*, 1981, **3**, 49.
91. P. G. Hatcher, I. A. Breger, N. Szeverenyi, and G. E. Maciel, *Int. J. Coal Geol.*, 1989, **13**, 99.
92. P. G. Hatcher, M. A. Wilson, and A. M. Vassalo, *Int. J. Coal Geol.*, 1989, **13**, 99.
93. P. G. Hatcher, H. E. Lerch, and T. V. Verheyen, *Int. J. Coal Geol.*, 1989, **13**, 65.
94. P. G. Hatcher, *Org. Geochem.*, 1990, **16**, 959.
95. R. Hayatsu, R. L. McBeth, R. G. Scott, R. E. Botto, and R. E. Winans, *Org. Geochem.*, 1984, **6**, 463.
96. R. E. Botto, *Energy Fuel.*, 1987, **1**, 228.
97. R. E. Botto, R. Hayatsu, K. A. Carrado, and R. E. Winans, *'Proceedings of the International Conference on Coal Science', Tokyo, Japan, 23–27 October 1989*, New Energy and Industrial Technology Development Organisation, p. 1.
98. R. E. Botto, *Macromolecules*, 1988, **21**, 1246.
99. T. F. Yen and G. V. Chilingarian (eds), *Oil Shale*, Elsevier, New York, 1976.
100. A. W. Decora, F. McDonald, and G. Cook, United States Bureau of Mines Report of Investigation 7523, USBMR, 1971.
101. F. Miknis, A. Decora, and G. Cook, United States Bureau of Mines Report of Investigation 7984, USBMR, 1974.
102. D. A. Netzel, D. R. McKay, R. A. Heppner, F. D. Guffey, S. D. Cooke, D. L. Varie, and D. E. Linn, *Fuel*, 1981, **60**, 307.
103. F. P. Miknis, *Proc. Intersoc. Convers. Eng. Conf.*, 1982, **17**, 935.
104. D. E. Lambert and M. A. Wilson, *Preprint, ACS Division Fuel Chem.*, 1985, **30**, 256.
105. W. T. Sobol, L. J. Schreiner, L. Miljkovic, M. E. Marcondes-Helene, L. W. Reeves, and M. M. Pintar, *Fuel*, 1985, **64**, 583.
106. A. D. Netzel, *Anal. Chem.*, 1987, **59**, 1775.
107. F. P. Miknis and D. A. Netzel, in *Magnetic Resonance in Colloid and Interface Science*, ed. H. A. Resing and C. G. Wade, *American Chemical Society Symposium Series No. 34*, ACS, Washington, DC, 1976, Chap. 16
108. D. Vitorovic, D. Vucelic, M. J. Gasic, N. Juranic, and S. Macura, *Org. Geochem.*, 1978, **1**, 89.
109. H. A. Resing, A. N. Garroway, and R. N. Hazlett, *Fuel*, 1978, **57**, 450.
110. D. Vucelic, N. Juranic, and D. Vitorovic, *Fuel*, 1979, **58**, 759.
111. F. P. Miknis, G. E. Maciel, and V. J. Bartuska, *Org. Geochem.*, 1979, **1**, 169.
112. F. P. Miknis, A. W. Lindner, A. J. Gannon, M. F. Davis, and G. E. Maciel, *Org. Geochem.*, 1984, **7**, 239.
113. F. P. Miknis and J. W. Smith, *Org. Geochem.*, 1984, **5**, 193.
114. F. P. Miknis, J. Jhou, D. B. MacGowan, and R. C. Surdam, *Org. Geochem.*, 1993, **20**, 339.
115. F. P. Miknis, *Fuel*, 1993, **71**, 731.
116. G. E. Maciel and L. W. Dennis, *Org. Geochem.*, 1982, **3**, 105.
117. L. W. Dennis, G. E. Maciel, P. G. Hatcher, and B. R. T. Simoneit, *Geochim. Cosmochim. Acta*, 1982, **46**, 901.
118. K. D. Schmitt and E. W. Sheppard, *Fuel*, 1984, **63**, 1241.
119. M. J. Trewhella, I. J. F. Poplet, and A. Grint, *Fuel*, 1986, **65**, 541.
120. F. P. Miknis, A. W. Decora, and G. L. Cook, United States Bureau of Mines Report of Investigation 7984, USBMR, 1974.
121. F. P. Miknis, A. W. Decora, and G. L. Cook, in *Science and Technology of Oil Shale* ed. T. F. Yen, Ann Arbor Science, Ann Arbor, MI, 1976.
122. R. D. Sydansk, *Fuel*, 1978, **57**, 66.
123. G. E. Maciel, V. J. Bartuska, and F. P. Miknis, *Fuel*, 1978, **57**, 505.
124. G. E. Maciel, V. J. Bartuska, and F. P. Miknis, *Fuel*, 1979, **58**, 155.
125. F. P. Miknis and G. E. Maciel, in *Nuclear Magnetic Resonance*, ed. R. H. Filby, B. S. Carpenter, and R. C. Ragaini, Plenum, New York, 1982.
126. F. P. Miknis, D. A. Netzel, J. W. Smith, M. A. Mast, and G. E. Maciel, *Geochim. Cosmochim. Acta*, 1982, **46**, 977.
127. F. P. Miknis and G. E. Maciel, in *Magnetic Resonance. Introduction, Advanced Topics and Applications to Fossil Energy*, ed. L. Petrakis and J. P. Fraissard, Reidel, Dordrecht, 1984.
128. F. P. Miknis, J. W. Smith, E. K. Maughan, and G. E. Maciel, *Am. Assoc. Petrol. Geol. Bull.*, 1982, **66**, 1396.
129. G. E. Maciel, V. J. Bartuska, and F. P. Miknis, *Fuel*, 1978, **57**, 505.
130. E. W. Hagaman, F. M. Schell, and D. C. Cronauer, *Fuel*, 1984, **63**, 915.
131. E. Evans, B. Batts, and N. Cant, *Fuel*, 1987, **66**, 326.
132. F. P. Miknis and P. J. Conn, *Fuel*, 1986, **65**, 248.
133. S. Sato, M. Enomoto, and S. Takahashi, *Fuel Proc. Technol.*, 1988, **18**, 305.
134. K. Qin, D. Chen, and Z. Li, *Org. Geochem.*, 1991, **17**, 856.
135. D. A. Netzel and F. P. Miknis, *Fuel*, 1982, **61**, 1101.
136. F. Hershkowitz, W. N. Olmstead, R. P. Rhodes, and K. D. Rose, in *Geochemistry and Chemistry of Oil Shales*, ed. F. P. Miknis and J. F. McKay, *American Chemical Society Symposium Series No. 230*, ACS, Washington, DC, 1983, Chap. 15
137. A. K. Burnham, and J. A. Happe, *Fuel*, 1984, **63**, 1353.
138. F. P. Miknis and P. J. Conn, *Fuel*, 1986, **65**, 248.
139. F. P. Miknis, N. M. Szeverenyi, and G. E. Maciel, *Fuel*, 1982, **61**, 341.
140. G. E. Maciel, V. J. Bantuska, and F. P. Miknis, *Fuel*, 1978, **57**, 505.
141. F. P. Miknis, T. F. Turner, L. W. Ennen, and D. A. Netzel, *Fuel*, 1988, **67**, 1568.
142. R. B. Williams, ASTM Special Technical Publication No. 224, American Society for Testing Materials Philadelphia, 1957, p. 168.
143. J. R. Zimmerman and J. A. Lasater, ASTM Special Technical Publication No. 224, American Society for Testing Materials, Philadelphia, 1957, p. 195.
144. S. H. Hastings, B. H. Johnson, H. E. Lumpkin, and R. B. Williams, ASTM Special Technical Publication No. 224, American Society for Testing Materials, Philadelphia, 1957, p. 250.
145. R. B. Williams, *Spectrochim. Acta*, 1959, **14**, 24.
146. R. B. Williams, US Patent No. 2 871 443, January 1959.
147. S. A. Knight, *Chem. Ind.*, 1967, 1920.
148. J. N. Shoolery and W. L. Budde, *Anal. Chem.*, 1976, **48**, 1458.

149. H. L. Retcofsky and K. D. Rose, *Preprint, ACS Division Petrol. Chem.*, 1985, **30**, 232.
150. L. Petrakis and E. Edelheit, *Appl. Spectros. Rev.*, 1979, **15**, 195.
151. J. Speight, *Liquid Fuel. Technol.*, 1984, **2**, 211.
152. S. Gillet, P. Rubini, J. J. Delpuech, J. C. Encalier, and P. Valentin, *Fuel*, 1981, **60**, 221.
153. M. Bouquet and A. Bailleul, *Proc. Inst. Pet., London, 1982*, 2, 394.
154. D. F. Cookson and B. E. Smith, *Fuel*, 1983, **62**, 34.
155. D. F. Cookson and B. E. Smith, *Fuel*, 1983, **62**, 39.
156. T. A. Holak, D. W. Aksnes, and M. Stocker, *Anal. Chem.*, 1984, **56**, 725.
157. I. A. Khan, Z. A. K. Al-Asadi, F. S. Muttawalli, and A. H. Tameesh, *J. Petr. Res.*, 1982, **1**, 58.
158. M. B. Ngassoum, R. Faure, J. M. Ruiz, L. Lena, E. J. Vincent, and B. Neff, *Fuel*, 1986, **65**, 142.
159. D. D. McIntyre and O. P. Strausz, *Magn. Reson. Chem.*, 1987, **25**, 36.
160. P. G. Hatcher, I. A. Breger, L. W. Dennis, and G. E. Maciel, in *Aquatic and Terrestrial Humic Materials*, ed. R. F. Christman and E. T. Gjessing, Ann Arbor Science, Ann Arbor, MI, Chap. 3, 1983.
161. P. G. Hatcher, D. L. VanderHart, and W. L. Earl, *Org. Geochem.*, 1980, **2**, 87.
162. P. G. Hatcher, G. E. Maciel, and L. W. Dennis, *Org. Geochem.*, 1981, **3**, 43.
163. J. V. Ibarra and R. Juan, *Fuel*, 1985, **64**, 650.
164. A. Majid, J. A. Ripmeester, and D. W. Davidson, NRC Report No. C1095-825, Ottawa, Ontario, 1982.
165. D. E. Axelson, *Fuel*, 1987, **66**, 40.
166. D. A. Netzel, P. T. Coover, and C. E. Bronnimann, *Fuel*, 1990, **69**, 429.
167. D. A. Netzel and P. T. Coover, *Energy Fuel.*, 1989, **3**, 259.
168. D. A. Netzel and T. F. Turner, *Fuel Sci. Technol. Int.*, 1990, **8**, 379.

Biographical Sketch

Robert E. Botto. *b* 1946. A.B., Rutgers College, New Brunswick, 1968; M.S., Michigan State University, 1970; US Army Science and Engineering Corps, 1970–72; Ph.D. (supervisor Donald G. Farnum), Michigan State University, 1975. Postdoctoral work at California Institute of Technology (with John D. Roberts). Successively, visiting professor at University of Southern California; NRC fellow at National Bureau of Standards; chemist at Argonne National Laboratory. Approx. 90 publications. Research specialties: solid state NMR spectroscopy and imaging of fossil fuels, polymers, catalysts, and advanced materials.

Aluminum-27 NMR of Solutions

Lars-Olof Öhman and Ulf Edlund
University of Umeå, Sweden

1	Introduction	1
2	Properties and Operational Considerations	1
3	Aluminum-27 NMR Parameters	2
4	The Aqueous Solution Chemistry of Aluminum(III)	4
5	The Anhydrous Solution Chemistry of Aluminium(III)	6
6	Related Articles	8
7	References	8

1 INTRODUCTION

The dramatically increased use of acidifying fossil fuels has, during the last decades, caused a significant pH-drop of rain and surface waters in large parts of the industrialized world. In areas situated on noncalcareous aluminosilicate bedrocks, the solid phases have thereby responded by mobilizing aluminum. As a result, it has been found that this element, which was previously thought to be quite harmless, can cause severe damage to water-living plants and animals, and also to man. In fact, some researchers claim that the main ecological danger with surface water acidification is not the increased proton concentration per se, but rather the increased aluminum concentration it causes.[1]

What has made this area particularly interesting from an ^{27}Al NMR point of view is that it has been shown unambiguously that different chemical forms of aquatic aluminum exert highly different bioavailabilities and toxicities.[2] Thus, with regard to water-living organisms, Al bound to organic compounds seems practically nontoxic while, at the same time, the most efficient route to uptake in man is obtained by reacting the aluminum ion with certain organic compounds (e.g. citric acid or maltol). These findings underline the need for increased knowledge about the chemical speciation of Al(III) under different conditions, a subject for which solution ^{27}Al NMR has proved to be a highly valuable tool.

It should also be pointed out that there are numerous other applications in which solution ^{27}Al NMR can provide a better understanding for the chemistry of that application. Thus, hydrolyzed aqueous Al(III) solutions are used for raw and wastewater clarification, as retention agents in the paper industry, and as the active agent in antiperspirants. Aluminum compounds in nonaqueous media are excellent Lewis acid catalysts and are used in many catalytic reactions for the stereospecific polymerization of α-alkenes (Ziegler–Natta) and for Friedel–Crafts alkylation or acylation.

Several reviews[3–6] on the subject of aluminum-27 NMR have been published, the most recent and comprehensive by Akitt.[6] In this article most of the original papers reviewed by Akitt will not be separately referenced when referred to, and the reader is recommended to consult the article by Akitt. Also, with regard to tabulations of registered chemical shifts and linewidths of different chemical species, Delpuech[4] or Akitt[6] should be consulted.

2 PROPERTIES AND OPERATIONAL CONSIDERATIONS

From the strict aspect of NMR receptivity, the ^{27}Al nucleus is one of the 10 most sensitive nuclei of the Periodic Table. Its receptivity is 1170 times that of ^{13}C and 0.206 times that of ^{1}H. This implies that, under favorable conditions, good signal/noise ratios can also be obtained from highly dilute (<0.0001 M) solutions.[7] In contrast to these two nuclei, however, ^{27}Al is a quadrupolar nucleus (I = 5/2; Q = 0.149 $\times$ 10^{-28} m^2) which, on the one hand, implies that problems with long relaxation times and, accordingly, low pulse repetition rates rarely occur. On the other hand, the linewidths of the appearing signals are strongly dependent on the symmetry (electric field gradient) of the species causing the signal. The reported linewidths range from a few Hz for highly symmetric octahedral or tetrahedral complexes up to linewidths so high that they easily pass the limit of detection.

In many cases, the ^{27}Al NMR spectrum of a given solution contains a mixture of broad and narrow resonances. This can either result from the simultaneous occurrence of several coexisting species or from the presence of a polynuclear species containing Al in several coordination environments. An often cited example of this latter situation is the spectrum from $AlO_4Al_{12}(OH)_{24}(H_2O)_{12}^{7+}$, cf. spectrum (a) of Figure 1 which at room temperature contains one signal from the central tetrahedral Al ion 25 Hz wide and one signal from the 12 octahedral ions 8000 Hz wide. Unless the presence of this latter signal is expected, it may then easily be missed.

An implicit problem with wide and/or undetected signals is that the integrated areas of detected signals do not correspond to the total Al concentration in the sample. This is an obvious fact for undetected signals, while for broad but detected signals it results from a partial relaxation during the dwell time between excitation pulse and data acquisition.

Akitt[6] states, as a rough guide, that to obtain better than 90% quantitative information from such resonances, the total spectral width covered must be at least six times the width of the observed signal. Other prerequisites for a successful quantification of the spectrum are to suppress the occurrence of baseline roll and to identify correctly the baseline position, tasks, which are by no means trivial when dealing with spectra containing overlapping broad and narrow resonances.

Due to these difficulties, one should always relate the ^{27}Al spectrum of an unknown sample to that of an external standard of known concentration and containing all Al in a single species with a narrow resonance line. By comparing the integrated area from this signal with the sum of the integrated area from the sample, conclusions with regard to 'missing Al' can be drawn. Furthermore, the absolute concentration of each resolved resonance can be evaluated and this is crucially important when the identity of the species causing the resonances is to be interpreted.

Overlapping resonances also pose a difficult problem which, to some extent, can be solved by using spectral deconvolution techniques. The major problem is, however, that the number of

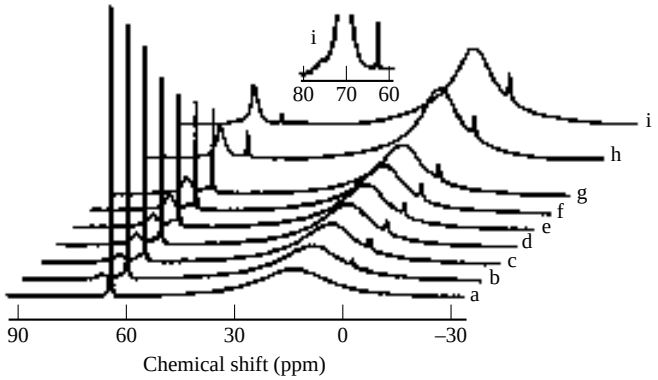

Figure 1 ^{27}Al NMR spectra showing the thermal evolution of a 0.035 M solution of $AlO_4Al_{12}(OH)_{24}(H_2O)_{12}^{7+}$ (Al_{tot} = 0.45 M) at 85°C. Spectra were recorded in situ at 130.3 MHz as a function of aging time: (a) 0; (b) 6; (c) 12; (d) 18; (e) 24; (f) 30; (g) 38; (h) 80; (i) 130 h. Inset shows expansion in the tetrahedral region. (Reproduced by permission of the American Chemical Society from G. Fu, L. F. Nazar, and A. D. Bain, Chem. Mater., 1991, **3**, 602)

species which together result in a broad ill-resolved spectrum cannot be determined, and thus the basic requirement for spectral deconvolution cannot be fulfilled. However, one resonance that is always discernible is the signal from free Al^{3+} and it can therefore be stated that ^{27}Al NMR, even in the worst case, always functions as an unique 'ion-selective electrode' for Al^{3+}.[8,9]

The best choice for the external standard is probably an acidic aqueous solution of aluminum perchlorate [e.g. 0.1 M $Al(ClO_4)_3$ in 0.1 M $HClO_4$] [linewidth 2 Hz for $Al(H_2O)_6^{3+}$], which might then also serve as a chemical shift standard (see Section 3.1). Another standard in use is an alkaline aluminate solution, but for this standard the resonance is broader [linewidth 10 Hz for $Al(OH)_4^-$]; the excess alkali present in this standard slowly dissolves Si from glass with the risk of aluminosilicate complex formation (cf. Section 4.2) and the standard must also be protected from atmospheric CO_2 to avoid $Al(OH)_3$(s) precipitation.

There are, in principle, two ways in which the external standard can be applied. Either the time domain of the FID is employed by calibrating the area of the reference FID for a given number of transients and spectral width (i.e. running the spectrometer in the absolute intensity mode), or the frequency domain is employed by arranging the standard in a capillary in the center of the sample tube. The relative ratio between the two compartments can, in this second case, be determined by measuring the $Al^{3+}/Al(OH)_4^-$ integral ratio when the compartments are filled with the two standards described above and containing equal Al(III) concentrations.

An obvious drawback, when using the concentric sample tube technique with Al^{3+} as the reference standard, is that the signal from the reference will coincide with the signal from the Al^{3+} in the sample. As shown by Koch,[7] this problem can be avoided if the reference also contains a suitable amount of Eu^{3+}, a lanthanide shift reagent moving the reference Al signal to a position where no interference with sample signals occurs.

As a final operational warning, it should be pointed out that many of the modern NMR spectrometers have probes manufactured of an aluminum-containing ceramic material and that these solid state Al(III) ions give rise to a broad high-frequency resonance. When working with samples containing broad signals, this resonance must be subtracted by running a blank sample or erroneous conclusions will be drawn.

3 ALUMINUM-27 NMR PARAMETERS

The most commonly used parameters of aluminum-27 are chemical shift, spin–spin coupling, and nuclear spin relaxation, and they will be discussed separately in that order.

3.1 Chemical Shifts

The acidic perchlorate solution is, as mentioned, the best reference (δ = 0) for external use, since the uncorrected shift value is very close to that obtained after susceptibility correction. It could be convenient to prepare the reference sample in deuterium oxide since this sample can then act as both standard and lock. However, a small low-frequency isotope shift of 0.25 ppm for the hexaaqua cation must be corrected for if high precision measurements are required.

Aluminum(III) interacts with other molecules in solution to an extent that is determined by the donor ability of the species present. Broadly speaking, aluminum-27 chemical shifts in diamagnetic solutions cover roughly a range of 300 ppm and this range can be subdivided grossly into three shift regions: (i) alkylaluminum compounds with resonances at 100 ppm or more to high frequency of the hexaaqua reference; (ii) tetrahedrally coordinated aluminum compounds with shifts between 140 and 40 ppm; and (iii) octahedrally coordinated aluminum between 40 and − 46 ppm. The observed chemical shift is thus broadly diagnostic of the actual coordination state, although there are significant overlaps between the regions mentioned. The complex ion AlI_4^-, for instance, has an absorption at − 26.7 ppm, i.e. to significantly lower frequency than the general expectation, and the hexamethylphosphoric triamide (HMPA) aluminum complex [$Al(HMPA)_4^{3+}$] has a shift value of 34.1 ppm. For aluminum salts in mixed dimethyl sulfoxide (DMSO)/dimethylformamide (DMF), seven signals appear around 0 ppm indicative of seven pure and mixed solvates, which provides evidence of six coordination.

One may ask whether the observed low-frequency shifts in aluminum species are due to increased hybridization of atomic orbitals or only to increased overall electron density at aluminum as the number of donating ligands increases. The existence of additivity in structurally related series of compounds seems to support the electron donation hypothesis. Thus, the order of successive signals in AlX_nY_{4-n} or AlX_nY_{6-n} is strictly monotonic, and in most cases with a constant frequency interval between two consecutive signals. However, the obtained shifts of mixed halide anions do not vary linearly with the number n of ligands, but Malinowski[10] has shown that a pairwise additivity model can account for the observed shifts in such series.

3.2 Spin–Spin Coupling Constants

Although well-resolved coupling patterns are of a fundamental interest to structural chemists, such information

rarely occurs in aluminum-27 NMR spectroscopy due to the quadrupolar properties of that nucleus. Scalar coupling between two spins will only appear if the spin–lattice relaxation time, T_1, of both nuclei are sufficiently long to fulfill the relationship $2\pi JT_1 \gg 1$. If $2\pi JT_1$ for one nucleus, like aluminum, is small enough, then no splitting will be noticed for the signal of the other nucleus. A partly collapsed pattern will be observed in borderline cases when this term is close to unity. The expected sextet splitting pattern due to coupling to a spin-$\frac{5}{2}$ nucleus will only appear in highly symmetrical complexes, i.e. where the electric field gradient (EFG) at aluminum is small.

Most of the reported scalar couplings refer to observations of aluminum bound to ^{1}H, ^{2}D, ^{31}P, or ^{14}N nuclei. The existence of 12 coupled equivalent protons in aluminum borohydride was proven by two-bond coupling, giving a 13-line multiplet in amine adducts. Conclusive structural information was also obtained for alkali tetrahydroaluminates in dimethoxyethane, where a quintuplet was seen. ^{27}Al–^{31}P coupling has been reported for phosphine adducts of $AlC1_3$ and $AlBr_3$, octahedral and tetrahedral solvates of the Al^{3+} ion, and mixed solvation complexes. Surprisingly sharp ^{27}Al–^{14}N coupling patterns are obtained with anions such as $AlCl_3(SCN)^-$ and $AlCl_2(SCN)_2^-$, whose structures are thus clearly verified. The observation of multiplets in the spectra of both quadrupolar nuclei provides interesting support to the claim that EFGs are generated near the nuclei. If the symmetry of the whole molecule determined the low EFG point, then only one such point could exist, but if the local symmetry is the important factor then there could be several such points.

Values of scalar couplings can also be obtained from lineshape analysis of partially averaged out multiplets. The existence of contact ion pairs of $LiAlMe_4$ and $NaAlMe_4$ in ether and tetrahydrofuran has been shown by such calculations. Analysis of the carbon spectrum of the terminal and bridging methyls in Al_2Me_6 is one of the rare examples where a spin-1/2 nucleus is coupled to two equivalent spins $\frac{5}{2}$. The exceptionally small ^{1}J(Al,C) coupling of 19 Hz found for the bridging methyl indicates the formation of a rather strong Al–Al bond, mainly s in character, and a consequent reduction in the s-electron contribution in the bridge bond.

Splittings between ^{27}Al and ^{31}P are typically in the range of 250–290 Hz for one-bond couplings and 12–30 Hz for two bonds. The two-bond coupling increases from 19.9 to 30 Hz on going from a hexacoordinate solvate, e.g. $Al(TMPA)_6^{3+}$, to the tetracoordinate complex $Al(HMPA)_4^{3+}$. This is in accord with the classic dependence of J on the proportion of s character in the aluminum orbitals, e.g. $\frac{1}{6}$ and $\frac{1}{4}$ for the d^2sp^3 and sp^3 hybridizations, respectively. The magnitudes of ^{27}Al–^{13}C in $AlMe_4^-$ being ca. 70 Hz illustrate the predominant contribution of Fermi contact interaction on the basis of the correlations proposed in the literature for such couplings.

3.3 Nuclear Spin Relaxation Processes

Aluminum-27 relaxation is dominated by quadrupolar interactions, as expected from its relatively high quadrupolar moment. If certain requirements are fulfilled such as: (i) time-independent coordination to the aluminum nucleus; (ii) extreme narrowing conditions; and (iii) isotropic chelate reorientation described by a single correlation time, then the quadrupolar relaxation rate can be described by the classical equation [equation (1)] by Abragam:

$$1/T_{1Q} = 1/T_{2Q} = 3\pi^2/10((2I+3)/I^2(2I-1))(1+\eta^2/3)(e^2qQ/h)^2\tau_c \quad (1)$$

where e^2qQ/h is the quadrupolar coupling constant, of which eq is the main component of the electric field tensor, and η is the asymmetry parameter.

Species with high symmetry, like certain tetrahedral or octahedral complexes, in which $q = 0$, have relaxation rates as small as a few Hz. In many of these cases, other relaxation mechanisms come into play, such as scalar relaxation for aluminum halides and dipolar relaxation for alkylaluminum compounds. Mixed scalar and quadrupolar relaxation can be noticed in symmetrical species and the scalar part can be used to determine coupling constants between Al and other quadrupolar nuclei. If the extreme narrowing condition is not fulfilled, i.e. where the rate of molecular reorientation is lower than the spectrometer frequency, then the above equation is not applicable. For instance, if the aluminum nucleus is situated in a colloidal particle, then $\omega\tau_c \gg 1$ and $T_1 = T_2$. The relaxation behavior becomes much more complex now with a multiexponential relaxation consisting of, in ideal cases, three superimposed exponential decays and a super-Lorenzian lineshape. However, lines are normally too broad to be detected due to long correlation times. However, if chemical exchange between bound and free aluminum is fast enough, then the nonexponential behavior in the bound state will be detected in the narrow resonance of the free aluminum cation.

3.4 Chemical Exchange Processes

In the slow exchange limit, where two separate signals are detected, the exchange broadening is given by equation (2):

$$1/T_2 = 1/T_{2Q} + 1/\tau_e \quad (2)$$

where T_2 is the apparent relaxation time of one of the exchanging species, T_{2Q} is the relaxation time of that species in the absence of exchange, and τ_e is the lifetime of the nucleus in the part of the population that gives rise to the signal.

When two or more species are undergoing fast exchange on the NMR timescale, then the resulting linewidth will be the weighted mean over exchanging sites. This situation is equivalent to considering an averaged EFG tensor $q = p_Aq_A + p_Bq_B + \cdots$, where p_A and p_B, etc. are mole fractions of those species involved in the dynamic process. This process is of no major interest for spin-1/2 nuclei since such conditions will only afford a single narrow line. In the case of quadrupolar nuclei, however, the linewidths of the species involved can vary by orders of magnitude and significant changes in linewidths will be noticed as the relative proportions of the species vary. Hence, the linewidth of ^{27}Al in aqueous solutions will vary with both pH and temperature, since these conditions influence the degree of hydrolysis yielding $Al(H_2O)_5(OH)^{2+}$ (cf. Section 4.1).

Further complications will be seen in cases where the rate of exchange is fast enough to cause coalescence, but still not too

different to the rate needed to cause coalescence of chemically shifted lines. In such cases, where exchange rates are within the NMR timescale window, the magnitude of the chemical shifts must be taken into account. In variable temperature studies, such conditions can cause a line to narrow in the same sense as the natural quadrupolar relaxation.

4 THE AQUEOUS SOLUTION CHEMISTRY OF ALUMINUM(III)

An investigation of an aquatic chemical system can aim at several different levels of complexity. The first level, which also constitutes an absolute prerequisite for all subsequent levels, is that the compositions, i.e. stoichiometries, of the appearing species are determined. The second level then is to determine the interrelation between the analytical composition of the solution and the amount of different species formed in it. These two levels have traditionally been investigated by means of potentiometric and spectrophotometric measurements, with data being analyzed under the presumed condition of chemical equilibrium.

A third level in the investigation of an aquatic system is to determine the three-dimensional structures of the appearing species, and a fourth level is to determine the interconversion rates between the species and to relate these back to their chemical structures.

As will be shown in the following, ^{27}Al NMR provides a valuable tool, when carefully used, at all these four levels. Ideally, however, it should not be viewed as a self-contained analytical technique but should be supplemented with traditional solution chemistry methods mentioned above and, whenever possible, with measurements of other nuclei in the sample. Furthermore, to fulfill the requirement of level two above, the law of mass action is probably invaluable. This implies that constraints with regard to basic solution thermodynamics, such as high-precision concentration control, temperature control, activity factor control, and so on have to be obeyed.

4.1 The Hydration and Hydrolysis of Al^{3+}

The aluminum ion is one of the most typical examples of a hard acid and, as such, prefers coordination to hard bases such as oxygen and fluorine. This implies that water molecules form relatively strong bonds to the Al^{3+} ion and it has been found that few other solvents are able to replace water from its first coordination sphere. It has also been found that practically invariant chemical shift values are obtained for acidic aluminum perchlorate, chloride, bromide, iodide, and nitrate solutions, thereby implying that the presence of contact ion pairs with these anions is negligible.

The number of water molecules in this coordination sphere can be determined via ^{27}Al NMR measurements of solutions containing mixtures of water and organophosphates, R_3PO. In these mixtures, and depending on the H_2O/R_3PO ratio, seven different resonances can be recorded, corresponding to the formation of $Al(H_2O)_{6-n}(OPR_3)_n^{3+}$; $0 \leq n \leq 6$. Thus, six water molecules surround the Al^{3+} ion and, from the narrow appearance of the signal, it can be concluded that these are coordinated in a highly regular, octahedral manner.

This species has also been studied by ^{17}O and ^{1}H NMR, through which it has been shown that while the rate of whole water molecule exchange is relatively slow, $k = 1.3\ s^{-1}$, the rate of proton exchange is much faster, $k = 10^5\ s^{-1}$.

When a strong base (i.e. OH^-) is gradually added to a moderately concentrated ($\leq$0.1 M) $Al(H_2O)_6^{3+}$ solution, a number of consecutive changes in its ^{27}Al spectrum can be observed. The linewidth for the resonance corresponding to Al^{3+}, δ = 0 ppm, increases and its integrated area decreases. A new signal appears at δ = 4.0 ppm with a linewidth of $\sim$500 Hz. The intensity of this resonance passes a maximum at around 1–1.5 OH^- added per Al^{3+} and is gradually replaced by a narrow resonance ($\sim$25 Hz) at δ = 62.5 ppm together with a very wide (8000 Hz) resonance at 12 ppm. At 2.2–2.5 added OH^- per Al^{3+}, the solution gradually turns milky due to the formation of $Al(OH)_3$(s) so that, at 3 OH^- added per Al^{3+}, no signal intensity is obtained. Finally, at >3 added OH^- per Al^{3+}, a new resonance appears at 80 ppm (10 Hz wide). Its intensity increases until all $Al(OH)_3$(s) has dissolved and then stays invariant up to very high pH values.

These are all effects from the hydrolysis of Al^{3+} and it has been shown that the broadening of the Al^{3+} signal is caused by a fast exchange with the species $Al(OH)(H_2O)_5^{2+}$. By assuming a chemical shift of 0 ppm and a linewidth of 620 Hz for this species, Akitt and Elders[11] found that the experimental line broadening at low Al concentration ($\leq$ 0.005 M) corresponds to a pK_a for $Al(H_2O)^{3+}{}_6$ of 4.93, a value in good agreement with available thermodynamic data. The variation of activity coefficients with concentration was, however, neglected and the numerical value of the equilibrium constant was therefore found to vary with aluminum concentration.

The decrease in area with increasing base additions is balanced by the area found for the signal at 4.0 ppm. This implies that a new species, exchanging slowly on the NMR timescale, is being formed. Until recently, and because of its appearance as a solid phase, this resonance has generally been assigned to the species $Al_2(\mu\text{-}OH)_2(H_2O)_8^{4+}$. This was questioned by Akitt et al.[12] who, based on ^{1}H measurements of dried samples transferred to acetone, suggested instead the formation of a species $Al_3O_2(OH)_4(H_2O)_8^{+}$. The OH^-/Al^{3+} ratio assigned to this species must however be questioned, since it is higher than in the species known to succeed it with increasing OH^-/Al^{3+} ratio, the $AlO_4Al_{12}(OH)_{24}(H_2O)_{12}^{7+}$ ion.

As already mentioned, this species consists of a central symmetric AlO_4 tetrahedron resonating at 62.5 ppm and 12 surrounding distorted AlO_6 octahedra, giving rise to the very wide signal at 12 ppm. The formation of this species depends critically on a supersaturation with respect to crystalline $Al(OH)_3$(s), gibbsite. This means that its very existence depends on kinetic restraints with regard to $Al(OH)_3$(s) precipitation. It has therefore been widely questioned whether this species is ever formed under natural water conditions.

To answer this, Furrer et al.[13] recently simulated a natural neutralization process by flowing a highly dilute Al^{3+} solution over granulated marble and found, by ^{27}Al NMR, that indeed considerable amounts of $AlO_4Al_{12}(OH)_{24}(H_2O)_{12}^{7+}$ were formed.

The resonance finally appearing at 80 ppm in alkaline solutions can, without doubt, be assigned to the aluminate, $Al(OH)_4^-$, ion. It has been shown,[14] that up to NaOH concentrations of $\sim$5 M, this ion is the sole hydrolysis product.

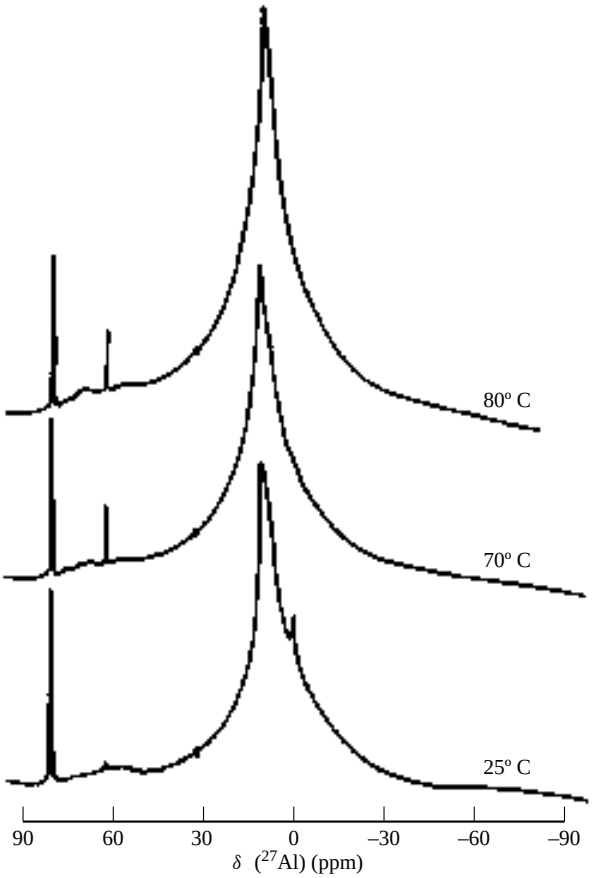

Figure 2 ^{27}Al NMR spectra at 104.2 MHz of a concentrated (Al_{tot} = 6.0 M) sample with 2.5 OH^- per Al^{3+} as a function of temperature. The line at 80 ppm is due to the standard capillary. The amounts of aluminum visible in the spectra are 14% at 25°C, 30% at 70°C, and 39% at 80°C. (Reproduced by permission of The Royal Society of Chemistry from J. W. Akitt, J. M. Elders, X. L. R. Fontaine, and A. K. Kundu, J. Chem. Soc., Dalton Trans., 1989, 1889)

Above this limit, a certain loss in integrated area is observed, possibly pointing to the formation of other species.

At high aluminum concentrations, and strongly depending on preparation variables such as total concentration, neutralizing agent, base injection velocity, reaction temperature, and aging time, the significance of $AlO_4Al_{12}(OH)_{24}(H_2O)_{12}^{7+}$ diminishes. The complex(es) replacing it result in very ill-resolved ^{27}Al spectra[12,15] (cf. Figures 1 and 2) and, based on very complex ^{1}H spectra, it was concluded that a wide range of products is formed.[12] These are all of high molecular weight, coordinate approximately 2.5 OH^- per Al^{3+}, and may contain tridecamer-like subunits in their structures.

4.2 Complexes with Inorganic Ligands

A basic requirement for a ligand to form an inner sphere complex with Al^{3+} in water is that it must be able to compete with and replace water molecules of $Al(H_2O)_6^{3+}$. This restricts the number of possible ligands to the fluoride ion and to ligands coordinating via oxygen ions, i.e. sulfate, carbonate, phosphate, and silicate, but also tungstate, molybdate and gallate. Since the water exchange rate of $Al(H_2O)_6^{3+}$ is slow on the NMR timescale, so generally is the ligand exchange rate. Hence, appearing complexes normally form separate resonances in the ^{27}Al spectrum at low temperatures which, due to the dominating quadrupolar relaxation mechanism for ^{27}Al, regularly become narrower on heating. Also, the ligand exchange rates can be suitably studied by variable temperature measurements. These measurements are, however, sometimes obscured by strongly temperature dependent equilibrium constants, and even the formation of 'new' complexes at high temperatures.

With F^-, it is well known that the Al^{3+} ion reacts with the formation of $AlF_n{}^{3-}$n ($0 \leq n \leq 6$). Of these species, only the first two and the last have been characterized by ^{27}Al NMR. The resonances for AlF^{2+} and AlF_2^+ are both wide (620 and 890 Hz, respectively), while that for $AlF3_6^-$ is a septet [J(Al,F) = 19 Hz] which when decoupled results in a line 17 Hz wide. The chemical shift values are all close to zero (0.7, 1.3, and − 1.2 ppm), strongly indicating that the whole series should be written as $Al(H_2O)_{6-n}F_n^{3-n}$ ($0 \leq n \leq 6$). The profound effect of asymmetry is very clear and this system is much more conveniently studied with ^{19}F NMR spectroscopy.[16]

With SO_4^{2-}, two well-resolved resonances can be observed at −3.3 ppm and −6.7 ppm. These probably originate from the formation of $Al(H_2O)_5SO_4^+$ and $Al(H_2O)_4(SO_4)_2^-$, respectively. The almost additive effect of substituting one or two water molecules with ligands is a regular, but not general, feature of ^{27}Al spectroscopy. When evaluating the formation constant for $AlSO_4{}^+$ from the signal at −3.3 ppm, the value obtained is approximately three orders of magnitude lower than the value obtained from potentiometric measurements. The conclusion has therefore emerged that $SO_4{}^{2-}$ mainly interacts with Al^{3+} via the formation of an outer sphere complex, $Al(H_2O)_6{\cdot}SO$+/4. Indirect support for this view is provided by the fact that the resonance for Al^{3+} in sulfate solutions is situated 0.2 ppm to higher frequency than in perchlorate solutions.

It has long been known that strong complexes are formed between Al^{3+} and orthophosphate. Their characterization has proved notoriously difficult, however, partly because of their formation at very low pH and partly because of the onset of precipitation of $AlPO_4$(s) at pH ≥ 3. The NMR technique is more or less ideally suited for characterizing this system since not only ^{27}Al but also ^{31}P can be employed with high sensitivity. Such measurements have shown that the system is also highly complex with regard to the number of species that can form. On the basis of only seven strategically selected samples, Wilson et al.[17] were able to identify five different Al environments and at least 11 different PO_4 environments. Based on an assumed proportionality between the partial charge on the P atom and its chemical shift, Mortlock et al.[18] have attempted to assign the resonances appearing at very high concentrations. From unpublished work by the author, the most acidic complexes at much lower concentrations, $\sim 10^{-2}$ M, seem to be $Al(H_2PO_4)^{2+}$ (δ_{Al} = − 3.3 ppm; δ_P = − 7.5 ppm vs. 85% H_3PO_4) and $Al(H_2PO_4)_2^+$ (δ_{Al} = −7.3 ppm; δ_P = −6.9 ppm). Much work, however, remains to be carried out until this system is fully characterized. This is probably also true with respect to interactions between Al^{3+} and multidentate phosphates.

The main products formed by the interaction between Al^{3+} and silicates in acid solution are different solids. Only a few reports describing soluble complexes have appeared and no

solution NMR data have been reported. In mildly alkaline solutions, $9 \leq \text{pH} \leq 12$, the silicate ion polymerizes with the formation of a large number of chain, ring, cage, and network silicates. Aluminum, in the form of $Al(OH)_4^-$, can be incorporated into these structures and its chemical surrounding can thereby be described in the form of $Al(OH)_{4-n}(OSi)_n$ units. For $0 \leq n \leq 4$, the effect of this substitution is almost linear with n, each exchange resulting in an upfield shift of 5 ppm.[19] More detailed information about the structures of these complexes is obtained from ^{29}Si NMR spectroscopy.[20]

Vanadate, molybdate, and tungstate are three anions known to form polymeric anions in acidic solution. They are also known to incorporate suitably sized foreign ions into what are called heteropolyanions. Due to their difference in size, their interactions with Al^{3+} are quite divergent. Thus, with the smallest vanadate ion, no interactions can be recorded. With the molybdate ion, a single complex with octahedral Al symmetry, $Al(OH)_6Mo_6O_{18}^{3-}$, is formed, while with the large tungstate ion, aluminum can be incorporated both in tetrahedral and octahedral form. The formation of $Al(OH)_6Mo_6O_{18}^{3-}$ has been fully characterized through the use of quantitative ^{27}Al NMR in combination with potentiometric methods.[21]

As described in Section 4.1, $AlO_4Al_{12}(OH)_{24}(H_2O)_{12}^{7+}$ is a major hydrolysis product of Al^{3+}. By exchanging the central AlO_4 tetrahedron of this species for a GaO_4 tetrahedron, a ternary complex of even higher stability results.[22] The reason for this is that the size of GaO_4 is more ideal, thereby resulting in a less strained structure. This is directly reflected in the linewidth of the resonance for Al_{12}, which decreases by almost 50%

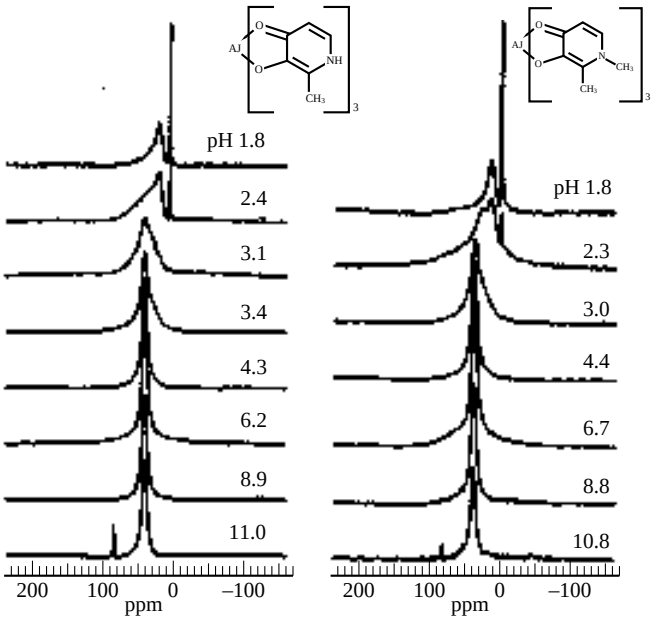

Figure 3 Variable pH ^{27}Al NMR spectra of $Al(mpp)_3$ (left; 0.02 M) and of $Al(dpp)_3$ (right; 0.03 M). (Reproduced by permission of the American Chemical Society from W. O. Nelson, T. B. Karpishin, S. J. Rettig, and C. Orvig, Inorg. Chem., 1988, **27**, 1045)

4.3 Complexes with Organic Ligands

In aqueous solution, the aluminum ion forms complexes of great stability, preferentially with ligands containing strongly basic O atoms (aliphatic and aromatic hydroxylate, carboxylate, phosphate and phosphonate groups). Because of the chelate effect, complexes of higher stabilities are formed by bidentate and polydentate ligands, in which appropriately situated N atoms (amines) and carbonyls can also act as coordinating groups. A characteristic feature for this complexation is that it occurs in competition with ligand protonation and that, therefore, the speciation is strongly pH and Al/ligand ratio dependent. Many of the ligands also form bridging polynuclear complexes with Al^{3+}, especially at low ligand excess and near neutral pH, where the formation of mixed hydroxo ligand complexes is considerable.

Aluminum-27 NMR has been widely applied to the study of these systems but, with few exceptions, the resonances are broad and the resulting spectra are complex and ill-resolved. Assignments and interpretations based on such data alone should be regarded as highly tentative. By also extending the measurements to the ligand nuclei, i.e. ^{1}H, ^{13}C, and ^{17}O, the reliability of species identification can be highly improved.[23] Unfortunately, however, these measurements must be performed at very high concentrations, and the data generated cannot be used for a proper thermodynamic characterization of the complexes.

There are, in principle, two different situations in which the complexation behavior of Al^{3+} is greatly simplified. One situation is when it is exposed to a more than threefold excess of a strong bidentate ligand devoid of bridging properties, such as dicarboxylic acids, catecholates, 3-hydroxy-4-pyrones, and 3-hydroxy-4-pyridinones. The gradual increase in pH of such solutions results in the consecutive formation of three complexes, $Al(H_2O)_{6-2n}L_n$ ($0 \leq n \leq 3$). The resonances from these complexes are often resolved[24] (cf. Figure 3) and an additive effect of ligand substitution is regularly encountered.

The other situation is when an excess of an aminopolycarboxylic acid, such as NTA or EDTA, is applied. The predominating complex is then $Al(H_2O)_nL$ ($n \leq 2$) and the hydrolysis of the remaining water molecules[25] can be recorded in the ^{27}Al NMR spectra as a function of pH.

Much of the work performed on Al complexation during the past decade has been motivated by the involvement of Al in a number of toxic biological processes. In these investigations, low molecular weight substances of relevance for the uptake of Al have been studied. Recently, the ^{27}Al NMR technique has also been used to study high molecular weight protein complexation. With albumin,[26] a broad resonance at ~ -7 ppm was recorded and from the maximum intensity of the signal it was concluded that each albumin molecule can coordinate approximately three Al^{3+} ions. A considerable excess of Al is however needed to reach saturation, and it can therefore be concluded that the complexation strength of albumin is relatively low.

The coordination of Al^{3+} to ovotransferrin and its half-molecules was studied in the presence of the synergistic anions carbonate and oxalate.[27] Surprisingly narrow resonances ($\sim$200–400 Hz) in the octahedral range were obtained and, supported by ^{13}C data, an assignment with regard to N- and C-terminal site complexation was made. Based on several ^{27}Al NMR arguments, it was concluded that the molecular motion of this protein is well outside extreme narrowing.

5 THE ANHYDROUS SOLUTION CHEMISTRY OF ALUMINIUM(III)

Because of the marked solvent dependence of the aluminum nucleus, NMR chemical shifts for solvated aluminum ions have long been used as a direct probe of cationic solvation. It is thus possible to construct a solvent classification scheme for Al(III), according to the behavior of salts like halides or perchlorates when dissolved in a given choice of solvents. Preferential solvation has also been studied in mixed solvents, normally a mixture of two strongly donating solvents.

Solvents of common use span from inert or very weak donicity solvents like hydrocarbons, via weakly donating ones like chlorinated hydrocarbons, ethers, and acetonitrile, and finally to strong aprotic donors like DMSO, DMF, HMPA, or protic donors like alcohols. Studies in very weak donicity solvents have normally been restricted to aggregation studies, like monomer–dimer equilibrium studies of trialkylaluminums.[28] Aluminum chloride remains more or less totally as a dichloro-bridged dimer in such solvents. ^{29}Si NMR of species such as silyl 'cations' are better NMR probes for the classification of these very weakly donating solvents.[29]

Ion-pairing effects are of course of major concern if organic solvents, are used. However, for a large sphere cation like Al(III), only first coordination sphere effects will normally be noticeable, and changes in charge polarization on going from inner to outer sphere complexation of the ligand nuclei will also be largely suppressed for such a large positive cation sphere.

5.1 Complexes with High Donicity Aprotic Solvents

The possibility of observing resolved signals will increase in the case of highly charged small cations dissolved in solvents which are strong Lewis bases, such as DMF, DMSO, or organic phosphates. Hence, for aluminum cations, a large number of studies have been performed where complexation to such high donicity solvents has been investigated in detail. Most studies have been conducted using the perchlorate salt, since its hexasolvate is relatively easily prepared. In neat DMSO solution, separate ^{13}C NMR signals are observed for both bulk and bound solvent (i.e. the hexa-DMSO solvate) at temperatures up to 40°C, where the signals broaden. This system has been carefully analyzed by stopped-flow proton spectroscopy, where changes in signal intensities have been monitored as solvent exchange occurs between bound and bulk states in nitromethane diluent. It has been reported that the rate of exchange is independent of DMSO concentration, as expected for a dissociative mechanism.

The complexation to DMF has been studied in a similar fashion to give proton signals from both bulk and bound solvent at temperatures as high as 95°C. The coordination number is always six, whatever salt is used, and the large chemical shift change observed for the formyl protons indicates, as expected, that DMF is coordinated via oxygen. If aluminum chloride is dissolved in nitromethane and titrated with small amounts of DMF, then a variety of octahedral and tetrahedral complexes will be formed, for example $AlCl(DMF)_5^{2+}$ which has a chemical shift of 5 ppm to high frequency of the hexasolvate.

Since ligand exchange rate is slow in both DMSO and DMF, then if a perchlorate salt is dissolved in a binary mixed solvent system one would be able to detect all seven possible solvates by aluminum spectroscopy. Such a study has indeed produced seven rather narrow lines, and the relative intensities could be used to derive the stepwise equilibrium constants which were then compared with the results from the Covington model of preferential solvation.[30] Without any added diluent, the overall equilibrium constant, $K^{1/6}$, is equal to 4.5, indicating preferential solvation by DMSO over DMF, which is consistent with the higher donicity number for DMSO (29.8) versus that of DMF (26.6). Addition of an inert solvent such as nitromethane or acetonitrile shows two profound effects on the NMR spectrum. First, there is a clear change in the distribution of peak intensities upon dilution, in which the preferential solvation by DMSO is decreased, i.e. $K^{1/6}$ approaches unity. Secondly, a line narrowing is observed for all lines, irrespective of the actual symmetry. This is another indication that the interaction occurs through the same type of bonding (namely oxygen) for both ligands and that they are roughly indistinguishable to the aluminum core as far as EFG is concerned. The chemical shift parameter is by far a more sensitive probe in this respect.

Aluminum perchlorate has also been studied recently in aqueous mixtures of DMF and urea and it was found that Al(III) is hexacoordinated in both aqueous mixtures over the concentration ranges studied.[31] Although both organic ligands displace water from the first coordination sphere, there is a marked difference between their complexation ability, although they both show monodentate binding to the oxygen atom. The preferential solvation of Al(III) by DMF is particularly evident at the lower concentrations of this ligand, where most of the DMF is complexed at the expense of water.[32] This preferred solvation persists up to 1:1 mole ratios of DMF to water, where water then becomes the ligand of choice. In fact, even at DMF concentrations as high as 5:1, water still makes a substantial contribution to the metal coordination shell. This strongly implies that steric interactions play an important role in the binding of these ligands, hindering the formation of higher DMF complexes.

These steric effects are not so obvious for the urea ligands. Hence, urea essentially selectively solvates Al(III) in aqueous mixtures, almost to the complete exclusion of water. The preferential solvation tendency of urea is increased if the bulk solvent contains increasing amounts of the relatively inert solvent acetone. In 50:1 acetone–water, a bound water signal could not be detected at a mole ratio of 6:1 urea to Al(III).

As far as organic phosphates and related compounds are concerned, this group of solvents form well-defined stable solvates via the P=O oxygen atom. They are of a particular interest to NMR spectroscopists since they provide examples of structurally useful spin–spin coupling to aluminum.

In DMMP [$Me(MeO)_2PO$], TMPA [$(MeO)_3PO$], and similar phosphates, octahedral complexes are formed, as shown by a well-defined septet aluminum resonance from the spin–spin coupling to six phosphorus atoms. The exchange data are generally consistent with a dissociative mechanism and the perchlorate salt of the DMMP hexasolvate exhibits much faster exchange than TMPA (at 25°C, k = 5.1 s^{-1} and k = 0.4 s^{-1} respectively).

HMPA, on the other hand, shows a different behavior. Although being one of the best donating (and, unfortunately,

most carcinogenic) solvents, it only forms a tetracoordinated complex, presumably due to steric reasons. The ^{27}Al resonance is consequently only a quintet. The coupling constant increases, as consistent with an increase in the s character in the bonding. The exchange rate also becomes faster and is proportional to the concentration of free HMPA. The enthalpy of activation is reduced and the entropy of activation is negative, all consistent with an associative mechanism of exchange for this HMPA complex.

5.2 Aluminum(III) Complexation in Alcohols

Alcohols are relatively strong donors to Al(III), but are more easily displaced by water molecules than the solvents mentioned in the preceding section. If completely anhydrous, alcohols do not displace chloride from $AlCl_3$ entirely, a tendency which seems to be more apparent with increasing length of the alkyl chain.

The current understanding of solutions of $AlCl_3$ or $Al(ClO_4)_3$ in carefully dried methanol is based on high-field ^{27}Al NMR experiments, and these studies show, in the case of $AlCl_3$, three resonances at 13.15, 9.55, and 3.45 ppm. The major peak at 9.55 is suggested to be $AlCl_2(MeOH)_4^+$, and this peak decreases if the perchlorate is used. The peak at 3.45 ppm then dominates. The broad low-frequency peak, close in shift to the hexahydrate, is argued to be due to exchange between the MeOH pentasolvate and the hexasolvate. Finally, the high-frequency resonance is then assigned to $AlCl_3 \cdot 3MeOH$. If higher alcohols are used, the signals will become broader, although ethanol seems to behave differently. At high dilution in $CDCl_3$, there is ample evidence of a hexasolvate complex appearing as a weak narrow peak at 3 ppm. A recent MAS study of anhydrous ethanolic solutions yielded similar complexes and shifts to those reported for methanol solutions using high-resolution NMR.[33]

5.3 Hydridoaluminates in Organic Solvents

Reducing agents such as various hydridoaluminates have been studied frequently in a variety of organic solvents in an attempt to understand ion-pairing effects, hydride exchange, etc. The scalar coupling between aluminum and hydrogen is sufficiently large (ca. 174 Hz for AlH_4^-) for it to be observed for a wide range of aluminum relaxation times. In THF, the linewidths change only slightly with concentration or temperature. In monoglyme, the coupling pattern is only seen at concentrations below l M, while in diglyme the opposite effect is noticed. In the latter case, the linewidths are quite narrow at high concentrations, but increase upon dilution.

Alkoxyaluminates, formed by the reaction between $LiAlH_4$ and alcohols, are also important species since they can serve as useful selective reducing agents. Many attempts have been made to design chiral complex metal hydrides, such as complexes with $LiAlH_4$ and chiral alcohols, for asymmetric reduction of prochiral carbonyl compounds. However, disproportionation equilibria take place with many primary, secondary, and tertiary alcohols, which of course is a limiting factor for the success of asymmetric reduction.[34] Addition of various chiral amino alcohols to $LiAlH_4$ in THF or diglyme has been studied by aluminum NMR, and disproportionation reactions have been found to vary with the structure of the amino alcohol. The small and flexible (−)-*N*-methylephedrine causes disproportionation to a significant degree, the bulkier and more rigid (−)-quinine less so.[35] The tridentate alcohol (−)-(*S*)-4-anilino-3-methylaminobutan-1-ol forms a bicyclic complex with the reagent without production of any measurable amount of free $LiAlH_4$. These results are consistent with the order of effectiveness of these reagents as asymmetric reducing agents, confirming that disproportionation equilibria have to be taken into account when designing useful asymmetric reduction experiments. Contrary to Li^+ and Na^+, tetrabutylammonium alkoxyhydridoaluminates are selective reducing agents in which the catalysis of the ligand exchange and consequent disproportionation are strongly suppressed.[36] It was shown that very high stereoselectivity, proportional to the steric strain, could be obtained for bulky alkoxy ligands, high temperatures, and polar solvents. Under these conditions, disproportionation is practically absent during the reduction process.

6 RELATED ARTICLES

Electrolytes; Geological Applications; High Speed MAS of Half-Integer Quadrupolar Nuclei in Solids; Inorganic Chemistry Applications; Phosphorus-31 NMR; Quadrupolar Interactions; Quadrupolar Nuclei in Liquid Samples; Relaxation Effects of Chemical Exchange; Transferrins.

7 REFERENCES

1. *The Surface Waters Acidification Programme*, ed. B. J. Mason, Cambridge University Press, Cambridge, 1990.
2. *Metal Ions in Biological Systems*, eds. H. Sigel and A. Sigel, Dekker, New York, 1988, Vol. 24.
3. J. F. Hinton and R. W. Briggs, in *NMR and the Periodic Table*, eds. R. K. Harris and B. E. Mann, Academic, New York, 1978, Chap. 9A.
4. J. J. Delpuech, in *NMR of Newly Accessible Nuclei* ed. P. Laszlo, Academic, New York, 1983, Vol. 2, Chap. 6
5. J. W. Akitt, in *Multinuclear NMR*, ed. J. Mason, Plenum, London, 1987, Chap. 9
6. J. W. Akitt, *Prog. NMR Spectrosc.*, 1989, **21**, 1.
7. K. R. Koch, *Analyst (London)*, 1990, **115**, 823.
8. L.-O. Öhman and A. Nordin, *Acta Chem. Scand.*, 1992, **46**, 515.
9. J.-P. Laussac, P. Lefrancier, M. Dardenne, J.-F. Bach, M. Marraud, and M.-T. Cung, *Inorg. Chem.*, 1988, **27**, 4094.
10. E. R. Malinowski, *J. Am. Chem. Soc.*, 1969, **91**, 4701.
11. J. W. Akitt and J. M. Elders, *J. Chem. Soc., Faraday Trans. 1*, 1985, **81**, 1923.
12. J. W. Akitt, J. M. Elders, X. L. R. Fontaine, and A. K. Kundu, *J. Chem. Soc., Dalton Trans.*, **1989**, 1889.
13. G. Furrer, B. Trusch, and C. Muller, *Geochim. Cosmochim. Acta*, 1992, **56**, 3831.
14. J. W. Akitt, W. Gessner, and M. Weinberger, *Magn. Reson. Chem.*, 1988, **26**, 1047.
15. G. Fu, L. F. Nazar, and A. D. Bain, *Chem. Mater.*, 1991, **3**, 602.
16. D. J. Nelson and R. B. Martin, *J. Inorg. Biochem.*, 1991, **43**, 37.
17. M. A. Wilson, P. J. Collin, and J. W. Akitt, *Anal. Chem.*, 1989, **61**, 1253.
18. R. F. Mortlock, A. T. Bell, and C. J. Radke, *J. Phys. Chem.*, 1993, **97**, 767, 775.

19. S. D. Kinrade and T. W. Swaddle, *Inorg. Chem.*, 1989, **28**, 1952.
20. R. F. Mortlock, A. T. Bell, A. K. Chakraborty, and C. J. Radke, *J. Phys. Chem.*, 1991, **95**, 4501.
21. L.-O. Öhman, *Inorg. Chem.*, 1989, **28**, 3629.
22. S. M. Bradley, R. A. Kydd, and R. Yamdagni, *Magn. Reson. Chem.*, 1990, **28**, 746.
23. F. R. Venema, Thesis, Delft University of Technology, The Netherlands, 1992.
24. W. O. Nelson, T. B. Karpishin, S. J. Rettig, and C. Orvig, *Inorg. Chem.*, 1988, **27**, 1045.
25. R. K. Iyer, S. B. Karweer, and V. K. Jain, *Magn. Reson. Chem.*, 1989, **27**, 328.
26. S. J. A. Fatemi, D. J. Williamson, and G. R. Moore, *J. Inorg. Biochem.*, 1992, **46**, 35.
27. J. M. Aramini and H. J. Vogel, *J. Am. Chem. Soc.*, 1993, **115**, 245.
28. Z. Cerny, J. Fusek, O. Kriz, S. Hermanek, M. Solc, and B. Casensky, *J. Organomet. Chem.*, 1990, **386**, 157.
29. C. A. Reed, Z. Xie, R. Bau, and A. Benesi, *Science*, 1993, **262**, 402.
30. J. B. Sloan, S. A. Cannon, E. C. Delionback, and J. J. Dechter, *Inorg. Chem.*, 1985, **24**, 883.
31. A. Fratiello, V. Kubo-Anderson, S. Azimi, C. Fowler, E. Marinez, R. Perrigan, S. Shayegan, and B. Yao, *Magn. Reson. Chem.*, 1992, **30**, 280.
32. H.-H. Emons, M. Siedler, B. Thomas, and A. Porzel, *Z. Anorg. Allg. Chem.*, 1988, **558**, 231.
33. H.-H. Emons, M. Siedler, B. Thomas, and E. Hallas, *Z. Anorg. Allg. Chem.*, 1988, **566**, 165.
34. A.-C. Malmvik, U. Obenius, and U. Henriksson, *J. Chem. Soc., Perkin Trans. 2*, **1986**, 1905.
35. A.-C. Malmvik, U. Obenius, and U. Henriksson, *J. Chem. Soc., Perkin. Trans. 2*, **1986**, 1899.
36. S. Hermanek, O. Kriz, J. Fusek, Z. Cerny, and B. Casensky, *J. Chem. Soc., Perkin Trans. 2*, **1989**, 987.

Biographical Sketches

Lars-Olof Öhman, *b* 1951. B.S., 1974, M.S., 1975, Ph.D. (supervisor N. Ingri), 1983, Chemistry, University of Umeå, Sweden. Introduced to NMR by U. Edlund. Currently Associate Professor of Inorganic Chemistry, University of Umeå, Sweden. Approx. 50 publications. Research specialty: complexation and precipitation of aluminum in systems of bio- and geochemical relevance.

Ulf Edlund, *b* 1945. B.S., 1969, Ph.D. (supervisor G. Bergson), 1974, Chemistry, University of Umeå, Sweden. Introduced to NMR by G. C. Levy. Presently Professor in Organic Chemistry, University of Umeå, Sweden. Approx. 100 publications. Research specialties: solution and solid state NMR characterization of reactive organometallic intermediates containing Group 4 elements, electronic structure, ion-pairing and dynamics of delocalized organolithium compounds.

Boron NMR

David Reed

Edinburgh University, Edinburgh, Scotland, UK

1	Introduction	1
2	NMR of Boron Compounds, Except Polyhedral Boranes	1
3	NMR of Polyhedral Boranes	3
4	Future Possibilities	12
5	Related Articles	13
6	References	13

1 INTRODUCTION

Boron NMR is a term that is often used to encompass a range of techniques which use the properties of boron nuclei to assist in the elucidation of structures and/or dynamics of solutions of boron-containing molecules. When such species are studied it is common practice to obtain NMR spectra of other nuclei in addition to boron, with the results being combined to give a more complete picture of the system under investigation. The main properties of the boron nuclei (namely ^{10}B and ^{11}B) are presented in Table 1, with those of some other nuclei for comparison.

The data in Table 1 indicate why ^{11}B is often preferred to ^{10}B as a nucleus of study, with the main reasons being: (i) boron-11 is considerably more sensitive than boron-10, due to both its greater natural abundance and its greater magnetogyric ratio, γ; (ii) boron-11 has a greater dispersion, in terms of Hz/ppm, than boron-10; and (iii) coupling constants to ^{11}B are three times greater than to ^{10}B, i.e., $^{n}J(^{11}\mathrm{B,X}) = 3 \times {}^{n}J(^{10}\mathrm{B,X})$. Both ^{11}B and ^{10}B are quadrupolar nuclei ($I = \frac{3}{2}$ and 3, respectively) and the quadrupolar relaxation mechanism is often the dominant one of these nuclei. Consequently, T_1 values for the boron nuclei are often quite short, typically in the range 10^{-2} s to 10^{-3} s for ^{11}B, though if the boron is in a particularly symmetrical environment (e.g. in $[BH_4^-]$, where the boron is tetrahedrally coordinated by four equivalent ligands), then the T_1 value can be of the order of seconds.

This article will try to show how boron NMR, predominantly ^{11}B and ^{1}H, can be used to assist in the study of boron chemistry. It will not be a list of data, but will try to show how NMR techniques have been applied in this area and will be confined to the use of boron NMR in the solution state.

2 NMR OF BORON COMPOUNDS, EXCEPT POLYHEDRAL BORANES

Boron chemistry covers a wide subject area, incorporating such diverse topics as, for example, boron oxides, boron halides, organoboron compounds, and polyhedral boranes.[1] The use of boron NMR in some of these areas is limited. Thus, boron oxides often produce very broad and ill-defined ^{11}B NMR signals with few, if any, additional NMR experiments possible to assist in the analysis of such systems.

The chemistries of the organoboron compounds, boron halides, and mixed systems containing organo-, halo-, and/or other heteroatom groups often involve a single boron atom surrounded by three or four ligands, trigonally or tetrahedrally, respectively. Table 2 shows some ^{11}B NMR chemical shift data for a selection of compounds of this type.[2] Throughout this article, $\delta(^{11}\mathrm{B})$ values will be quoted relative to that of $[BF_3{\cdot}OEt_2] = 0$.

The table highlights a number of points, the most important of these being: (i) boron-11 chemical shifts vary significantly with the coordination number of the boron (3 or 4); and (ii) the shifts vary significantly with the nature of the ligands.

A semiintuitive rationale for such behavior is provided by considering the nuclear screening constant, σ, which is thought of as being made up of a number of components, i.e. $\sigma = \sigma_d + \sigma_p +$ others, where σ_d is the so-called 'diamagnetic' component and σ_p the 'paramagnetic' component of the screening constant. The others are, for example, neighboring anisotropy effects, ring current effects, electric field effects, etc.

The value of σ_d for nuclei arises as a result of the effects of the external magnetic field on the motion of electrons associated with the nucleus, which causes a secondary magnetic field about the nucleus opposed to the external field. Consequently, the nucleus is shielded from the external field. Hence, any reduction in the electron density about the nucleus will result in the deshielding of the nucleus (for example, as a result of nearby electronegative atoms).

The paramagnetic term, σ_p, can be thought of as arising from a hindrance to the motion of electrons about a nucleus as a result of other electrons and nuclei in the molecule. In the case of the simple boron compounds, σ_p depends on both $1/r^3$ for the valence electrons and their orbital angular momentum. It is of opposite sign to the diamagnetic term and is of greater magnitude.

For tetrahedrally coordinated boron, the significance of the above is that there are limitations on how the paramagnetic contribution to the shielding term can arise. Four-coordinate boron must be sp^3 hybridized, meaning that there are no orbitals available for the acceptance of π electrons from potential π-donor ligands. Also, there are only likely to be minor variations in the orbital angular momentum contributions, as deviations from tetrahedral symmetry will not be significant. Consequently, the major contribution to the nuclear screening constant in the four-coordinate boron systems is the degree of covalency between the ligand and boron.

The situation is rather different for trigonally coordinate boron systems (BR_3, BX_3, etc.) in which the boron can be regarded as sp^2 hybridized, with a p orbital available for interaction with π-donor ligands. This leads to a significant variation in orbital angular momentum at three-coordinate boron arising from using ligands of differing π-donor strength, and hence a generally greater range of chemical shifts.

The above points may be most easily understood by considering some examples. Thus, comparing like-for-like trigonal and tetrahedral coordinate boron systems [e.g. BF_3 vs. $[BF_4^-]$, BCl_3, vs. $[BCl_4^-]$, BR_3 vs. $[BR_4^-]$ (R = alkyl), etc.], it is clear that $\delta(^{11}\mathrm{B}$, trigonal) is to high frequency of

Table 1 Comparison of Some Physical Properties of Boron Nuclei with Other Common Nuclei

Isotope	Natural Abundance (%)	Nuclear spin, I	Magnetogyric ratio, γ	Resonance frequency (MHz) at 2.35 T	Relative sensitivity (^{1}H = 1.00)
^{10}B	19.58	3	2.875	9.3	3.9×10^{-3}
^{11}B	80.42	$\frac{3}{2}$	8.584	32.1	1.33×10^{-1}
^{13}C	1.108	$\frac{1}{2}$	6.728	25.2	1.76×10^{-1}
^{31}P	100	$\frac{1}{2}$	10.841	40.5	0.66×10^{-1}
^{19}F	100	$\frac{1}{2}$	25.181	94.1	0.83
^{1}H	99.98	$\frac{1}{2}$	26.752	100.0	1.00

$\delta(^{11}\text{B}$, tetrahedral), with the trigonal systems showing a greater range of $\delta(^{11}\text{B})$ values.

Comparison of the effects of different ligands on the $\delta(^{11}\text{B})$ values of trigonal boron systems, for example $B(CH_3)_3$, $B(OCH_3)_3$, $B(NR_2)_3$, and BF_3, reveals that the B–C system is at the highest frequency, followed by the B–N, B–O, and B–F systems respectively. This is consistent with the π-donor capability of the ligating atoms. Thus, $B(CH_3)_3$ has sp^3 hybridized carbon bound to the boron and this does not have any π-donor capability to provide any additional shielding to the boron, whereas F will have considerable $p-\pi$ overlap with the boron in BF_3, resulting in a more shielded ^{11}B environment.

Heavier ligating atoms introduce additional difficulties. For example, examination of the series BF_3, BCl_3, BBr_3, and BI_3 shows that $\delta(^{11}\text{B})$ goes to increasing frequency with the series F < Cl < Br. In contrast, BI_3 has the lowest frequency $\delta(^{11}\text{B})$ value of any trigonal boron compound. The results of the F, Cl, Br series can be explained by the decreasing overlap between the ligand p orbitals and the p orbital on the boron, as a result of the increased size of the ligand p orbital with increasing atomic number. The iodo compound is less readily explained, though if a series of mixed organohalo boron chemical shifts are charted (Figure 1), then it becomes clear that the unusual iodo chemical shifts only occur beyond monosubstitution.

The effects of different ligands on chemical shifts of tetrahedrally coordinated boron, with the exception of the iodo derivatives, are much smaller than those observed for trigonally coordinated compounds, in keeping with the reduced σ_p component to the nuclear shielding constant.

2.1 The Use of Other Nuclei

In addition to ^{11}B NMR data, in many cases it is also possible to look at NMR spectra from other nuclei to assist in establishing the nature of the compounds. Thus in the case of organoboron systems, standard ^{1}H and ^{13}C NMR experiments could be used to establish the nature of the organic ligands. Clearly, the data thus obtained may not be free of the influence of the boron, as can be seen in the ^{1}H and ^{13}C NMR spectra of the anion $[BPh_4^-]$, shown in Figures 2 and 3. The figure captions indicate where the areas of interest lie. The spectra shown here have very clearly defined couplings because of the very symmetrical nature of the molecule, though a tetrahedrally coordinate species which did not have four equivalent ligands around the boron would be unlikely to show such clearly defined couplings as the ^{11}B relaxation would be

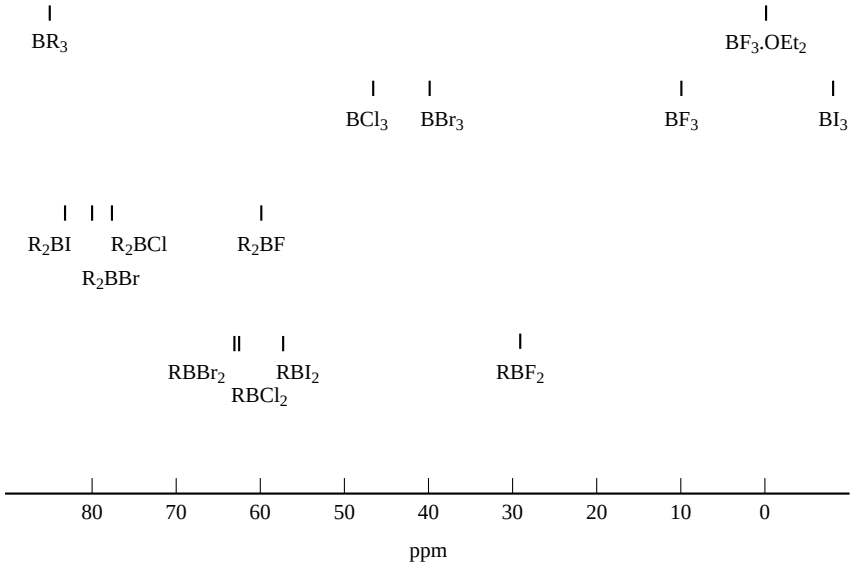

Figure 1 Chemical shift chart for some organo-, halo-, and mixed organohaloboron compounds

Table 2 Chemical Shift Data for a Series of Trigonally and Tetrahedrally Coordinated Boron Compounds

Trigonal		Tetrahedral	
Compound	δ (ppm)	Compound	δ (ppm)
BR_3	80–90	$[BR_4^-]$	−16 to −20
$R_2B{-}C{\equiv}C{-}R^1$	71.5–73.5	$[BPh_4^-]$	−6
$B(CH{=}CH_2)_3$	57.4	$[B(OR)_4^-]$	3
$RB(NR_2)_2$	ca. 34	$[(OPh)_4^-]$	2
$RB(OR)(NR_2)$	ca. 32	$[BF_4^-]$	−2.2
$RB(OR)_2$	ca. 30	$[BCl_4^-]$	6.6
$B(NR_2)_3$	ca. 27	$[BBr_4^-]$	−24
$B(OR)_3$	ca. 18	$[BI_4^-]$	−128
BF_3	10	$[BF_3{\cdot}OEt_2]$	0
BCl_3	47	$[BCl_3{\cdot}OMe_2]$	11.3
BBr_3	40	$[BBr_3{\cdot}OMe_2]$	−3.5
BI_3	−8	$[BCl_3{\cdot}Ph_3]$	1.7
BPh_3	ca. 60	$[BBr_3{\cdot}PPh_3]$	−22.7
RBF_2	29	$[BI_3{\cdot}PPh_3]$	−90.3
R_2BF	60		
$RBCl_2$	63		
R_2BCl	77		
$RBBr_2$	64		
R_2BBr	80		
RBI_2	53		
R_2BI	83		

more efficient. In the case of the haloboranes, only ^{19}F is of any significance, with chlorine, bromine, and iodine nuclei all being quadrupolar and exhibiting such rapid relaxation that they are effectively not observable, either directly or indirectly (via J coupling).

3 NMR OF POLYHEDRAL BORANES

It is in the study of polyhedral boranes and related compounds that the most extensive use of boron NMR has been made, with particular emphasis in establishing B–B and B–H connectivities. The problems implicit in carrying out NMR analyses on borane systems lie in the quadrupolar nature of the boron nucleus ^{11}B. This results in many potentially useful parameters being difficult, or impossible, to measure directly. For example, with the exception of $^1J(^{11}B, ^1H)$, coupling constants are usually totally obscured within the linewidth of an ^{11}B NMR signal. This arises because coupling constants are often quite small [e.g. $^1J(^{11}B, ^{11}B)$ values are usually in the range 10–60 Hz, and ^1J values between ^{11}B and bridging ^1H nuclei are often of the order of 40 Hz], the natural linewidth of the signal may be quite large ($\geq$10 Hz) and there may be several couplings associated to any given ^{11}B signal. The situation obtained in ^1H NMR spectra of such compounds is not any clearer.

To illustrate these points, let us consider the ^{11}B, $^{11}B\{^1H\}$, ^1H, and $^1H\{^{11}B\}$ NMR spectra of a 'typical' borane, the anion $[B_{10}H_{11}Se^-]$**3** (Figures 4 and 5). The ^{11}B and $^{11}B\{^1H\}$ data in this case give some indication of the degree of symmetry of the anion, though such interpretations have to be treated with caution as ^{11}B signal overlap is not uncommon. Furthermore, it is clear that these spectra only permit $\delta(^{11}B)$ and $^1J(^{11}B,^1H)$ data to be extracted [though occasionally other parameters may be measured directly, e.g. $^1J(^{11}B,^{11}B)$]. The fully coupled ^1H NMR spectra of boranes are very complex [Figure 5(a)] due to the following:

1. The $\delta(^1H)$ range is often quite small, from δ 0.0–4.0 ppm for resonances arising from *exo*-polyhedral terminal ^1H nuclei.
2. Each resonance will have at least four lines of equal intensity arising from coupling to ^{11}B ($I = \frac{3}{2}$), with $^1J(^{11}B,^1H)$ being typically in the range 120–160 Hz.
3. The lines are often very broad ($\geq$10 Hz is not uncommon).

These factors result in ^1H spectra which are comprised of many overlapping 1:1:1:1 multiplets over a relatively narrow δ range. Signals arising from bridging protons (either B–H–B or B–H–M) are found at much lower δ values, normally several ppm to low frequency of TMS. In these cases $^1J(^{11}B,^1H)$

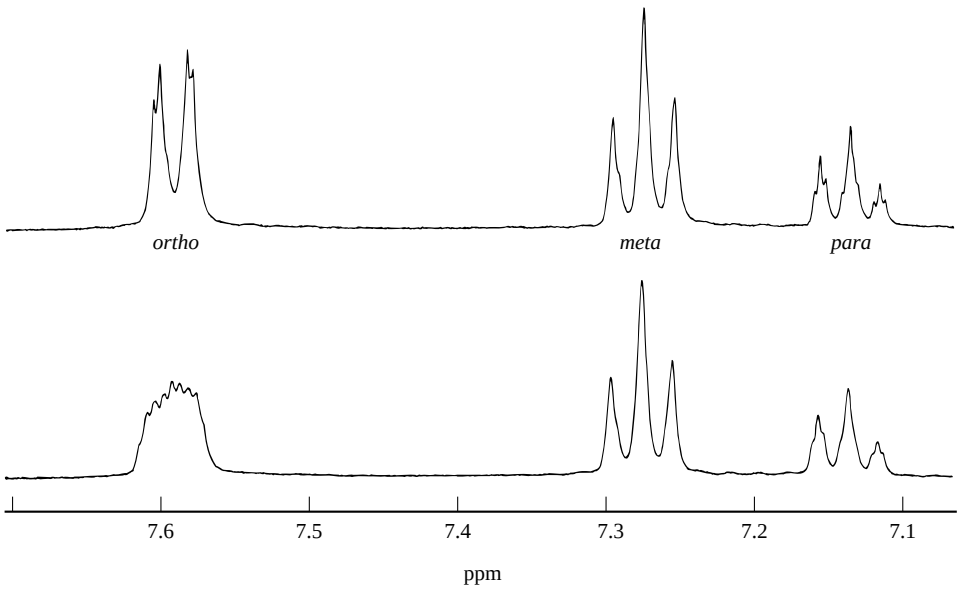

Figure 2 The 360.13 MHz ^1H (bottom) and $^1H\{^{11}B\}$ (top) NMR spectra of the $[BPh_4^-]$ anion. Note only the signals arising from the protons *ortho* to the boron show any significant coupling to ^{11}B

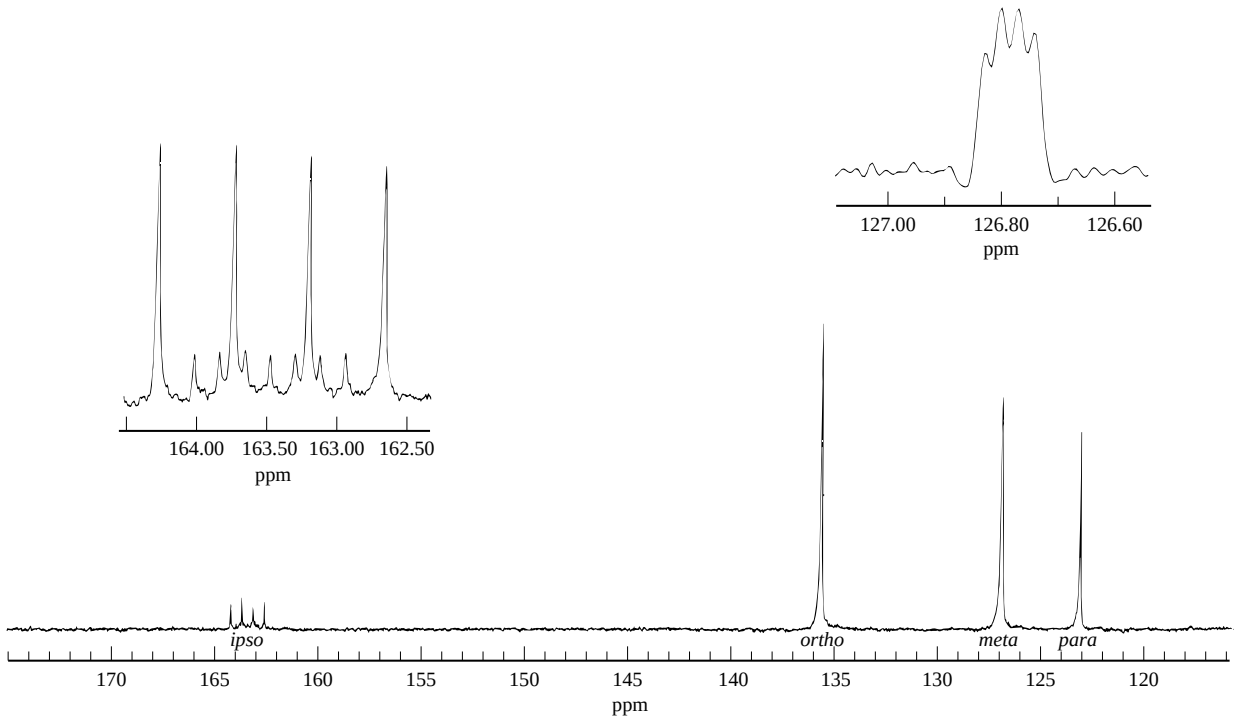

Figure 3 The 90.56 MHz $^{13}C\{^1H\}$ NMR spectrum of $[BPh_4^-]$. Insets show the effects of coupling to boron on the *ipso* carbon, and on the carbon *meta* to boron. The signal due to the *ipso* carbon (δ = 163.4 ppm) shows four lines of equal intensity, due to a $^1J(^{11}B,^{13}C)$ = 49.8 Hz. Seven smaller lines are also observed, due to $^1J(^{10}B,^{13}C)$ = 16.6 Hz. By use of resolution enhancement, the $^3J(^{11}B,^{13}C)$ coupling between the boron and the *meta* carbons is measured at 2.3 Hz

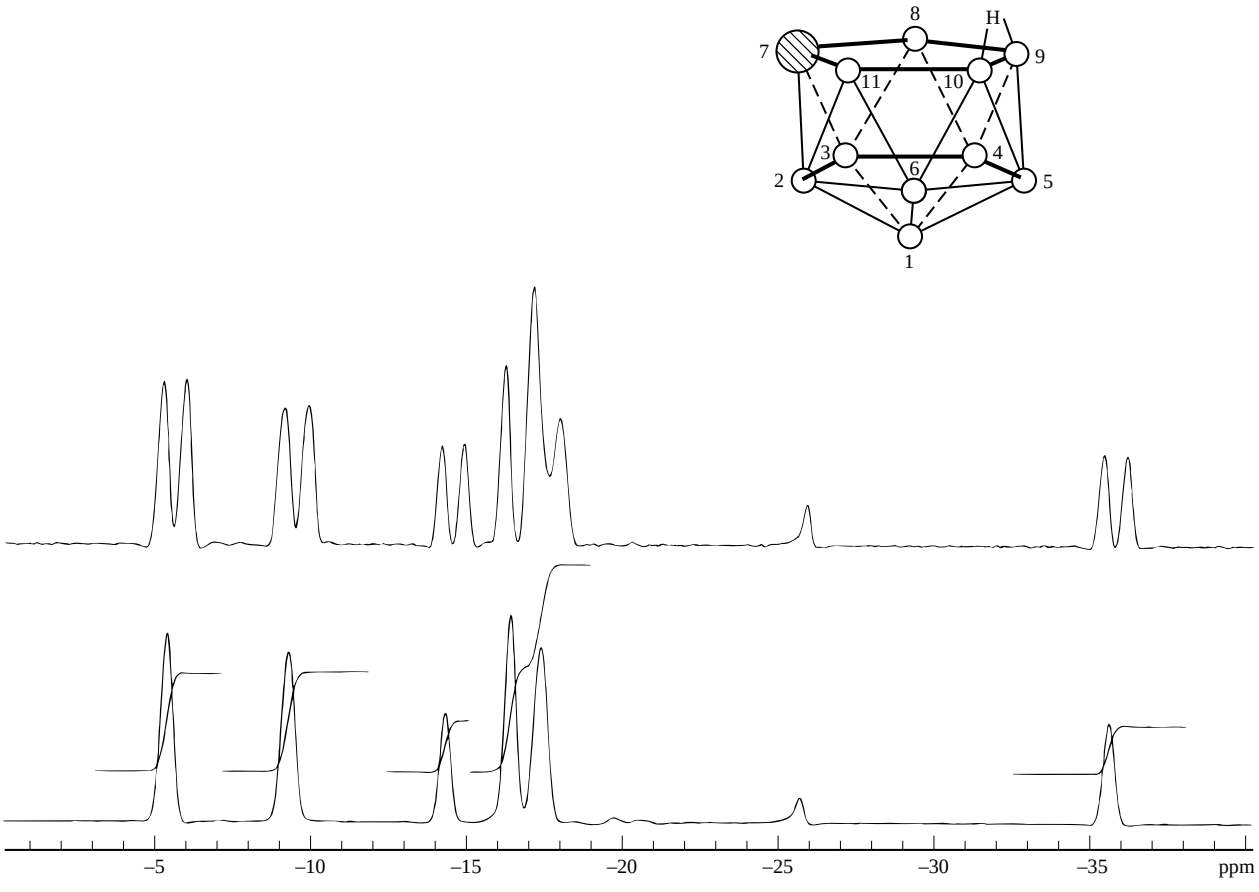

Figure 4 The 192.5 MHz ^{11}B and $^{11}B\{^1H\}$ NMR spectra of the $[B_{10}H_{11}Se^-]$ anion, whose structure is shown as an inset

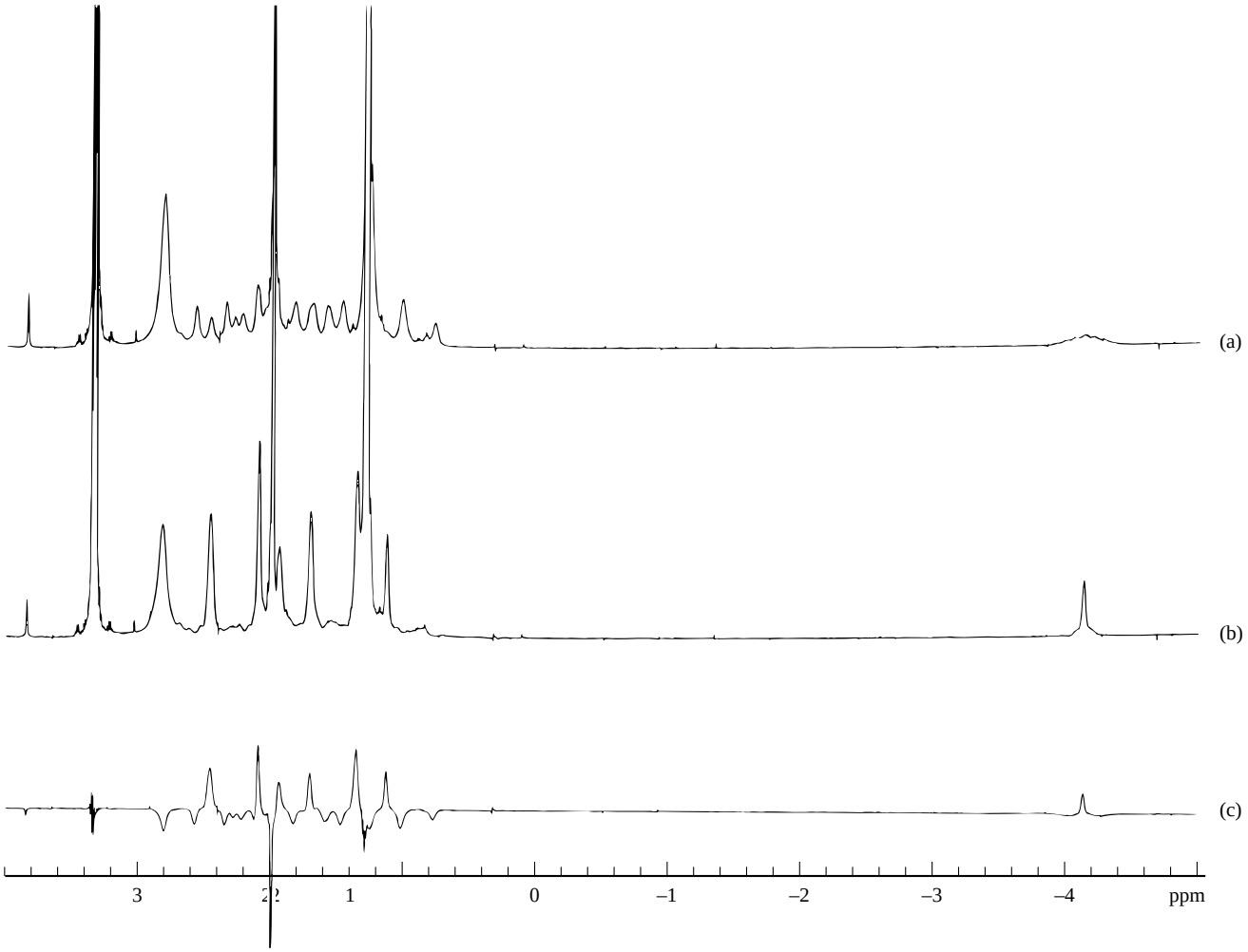

Figure 5 The 600 MHz ^{1}H (a), $^{1}H\{^{11}B\}$ (b) and difference spectrum (c) of $[B_{10}H_{11}Se^{-}]$

values are smaller than those observed for terminal *exo*-polyhedral sites, often being in the range 30–50 Hz, with the ^{1}H displaying coupling to two ^{11}B nuclei to give a 1:2:3:4:3:2:1 multiplet.

The ^{1}H spectra can be greatly simplified by broadband ^{11}B decoupling, with the results of this type of experiment being shown in Figure 5(b) for $[B_{10}H_{11}Se^{-}]$. This, while being much simpler than the fully coupled spectrum, is still a little unclear because of the large signals due to protons in the counterion $[NEt_3H^{+}]$. This type of complication is often overcome by presenting the data as a difference spectrum [see Figure 5(c)].

As mentioned earlier, for both ^{11}B and ^{1}H spectra of borane derivatives, signal overlap is a common problem, and as a result NMR studies of such materials often benefit from the use of higher magnetic fields. The compound $[B_9H_9Se_2]$ provides an example of an $^{11}B\{^{1}H\}$ spectrum with considerable overlapping of signals, and Figure 6 shows how this spectrum varies with increasing field strength.

3.1 Experimental Techniques

The previous section showed how only limited information can be extracted from ^{11}B, $^{11}B\{^{1}H\}$, ^{1}H, and $^{1}H\{^{11}B\}$ spectra of 'unknown' borane derivatives. To try to establish required information, it is most common to use methods of homonuclear ($^{11}B/^{11}B$ and $^{1}H/^{1}H$) and heteronuclear ($^{11}B/^{1}H$) correlation, as appropriate.

Heteronuclear $^{11}B/^{1}H$ correlation can be carried out either two-dimensionally, using the so-called HETCOR sequence,[4] or one-dimensionally by carrying out a series of selective $^{1}H\{^{11}B\}$ experiments. Historically, the first demonstration of the application of two-dimensional (2D) NMR to boron chemistry was shown using the HETCOR sequence, and was applied to the carbaborane $C_2B_5H_7$,[5] followed by two papers showing $^{11}B/^{1}H$ correlation spectra of decaborane(14), $B_{10}H_{14}$.[6,7] The standard HETCOR sequence (Figure 7) uses delays, indicated in the figure, which are responsible for the transfer of magnetization between ^{1}H and ^{11}B, and are equal to $0.5/^{1}J(^{11}B,^{1}H)$.

This leads to problems where the values of the coupling constants are quite different, e.g. between *exo*-polyhedral B–H terminal environments and B–H–B bridging sites (typical coupling are ca. 140 Hz and 40 Hz, respectively). In these cases it may be necessary to perform two experiments using delays derived from the different J values.

An alternative, and often more popular, way of achieving effective $^{11}B/^{1}H$ correlation is by ^{1}H observation with selective, low power, ^{11}B decoupling. Such data are usually

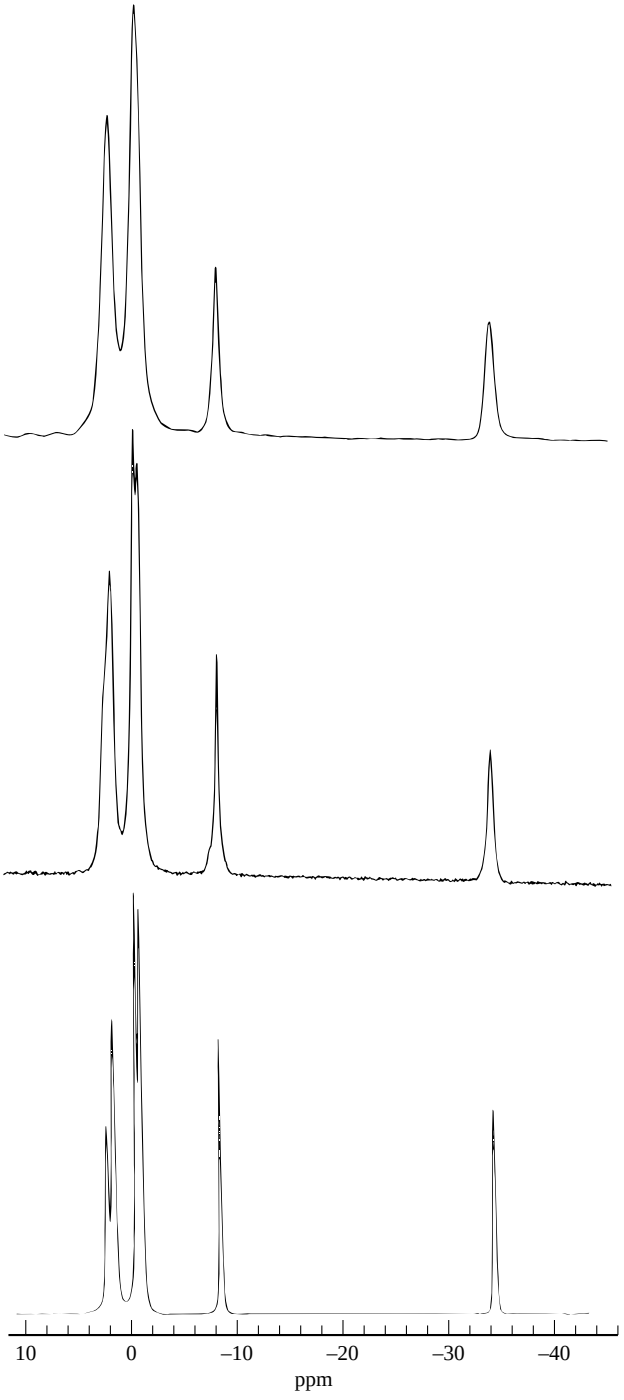

Figure 6 The effect of increasing field strength illustrated by the $^{11}B\{^1H\}$ NMR spectra of $[B_9H_9Se_2]$ obtained at 64.2 MHz (top), 115.5 MHz (center), and 192.5 MHz (bottom)

presented as a series of decoupling difference spectra. This type of experiment is performed by acquiring ^1H spectra whilst simultaneously irradiating at the resonance frequency of each individual ^{11}B site in turn. A spectrum obtained by applying decoupler power at an ^{11}B off-resonance position is also obtained. By subtracting the off-resonance decoupled spectrum from the selectively irradiated spectra in turn, a series of difference spectra are produced.

Homonuclear $^{11}B/^{11}B$ correlation experiments are performed using the simplest of the various 2D COSY sequences (Figure 8). The first demonstrations of the use of this type of experiment to boron chemistry were published in 1982.[8] Subsequent work widened the range of borane derivatives studied and from these experiments conclusions have been drawn as to the applicability of COSY to such clusters, along with some limitations,[9,10] these being: (i) no cross peaks have been observed between nonadjacent ^{11}B nuclei; (ii) boron nuclei linked by bridging hydrogen atoms are less likely to show cross peaks, though such peaks can be found in some cases. (iii) boron-11 relaxation can be very efficient, and where $1/T_1 \leq 2\pi J$, i.e. for very broad signals, useful data may be impossible to obtain; (iv) where signal overlap occurs, interpretation may be a problem; and (v) expected cross peaks do not always show up.

Very often a combination of $^{11}B/^{11}B$ and $^{11}B/^1H$ correlation experiments proves to be enough to resolve the structure of a cluster. However, sometimes additional information is needed, and may be provided by homonuclear $^1H/^1H$ correlation experiments. As with the $^{11}B/^{11}B$ experiments, the simplest of the COSY sequences is used. Although ^1H COSY has been widely used for organic molecules since the introduction of 2D NMR in 1976,[11,12] it was not until 1986 that its application to borane clusters was first shown,[13] presumably partly as a result of the difficulties in achieving effective ^{11}B decoupling.

Because of the relatively rapid ^1H relaxation, it is $^3J(^1H,^1H)$ couplings that are the most likely to be observed this way. Thus it should be possible to observe cross peaks between ^1H nuclei on adjacent cluster positions. This is potentially useful for the following reasons: (a) if an expected cross peak between adjacent boron nuclei is not observed, it may be that the $^1H/^1H$ cross peaks could establish the connectivity; and (b) in carbaboranes, if a CH moiety is adjacent to BH moieties in the cluster, then B–C connectivities can be established.

3.2 Case Studies

To establish the effectiveness of the techniques described in the previous section, three case studies will be outlined to illustrate them.

3.2.1 Case Study 1

The objective was the complete assignment of the ^{11}B and ^1H spectra of the anion $[B_{10}H_{11}Se^-]$, these being shown earlier in Figures 4 and 5. This was achieved by a combination of selective $^1H\{^{11}B\}$ experiments and an ^{11}B COSY experiment.

The structure of the anion (see Figure 4), which had been determined X-ray crystallographically, showed a plane of symmetry through positions 1, 5, and 7 in the cluster. This meant that the ^{11}B and $^{11}B\{^1H\}$ spectra should show six distinct boron environments, four of area 2 and two of area 1 (as shown in Figure 4). Equally, the $^1H\{^{11}B\}$ spectrum should show six signals arising from *exo*-terminal hydrogens, and a signal due to a bridging hydrogen, these being clearly shown in Figure 5(c).

A series of selective $^1H\{^{11}B\}$ results are presented in Figure 9 as difference spectra, along with an $^{11}B\{^1H\}$ spectrum showing the irradiation sites labeled A–F. Each ^{11}B signal is correlated with a signal deriving from a terminal *exo*-hydrogen,

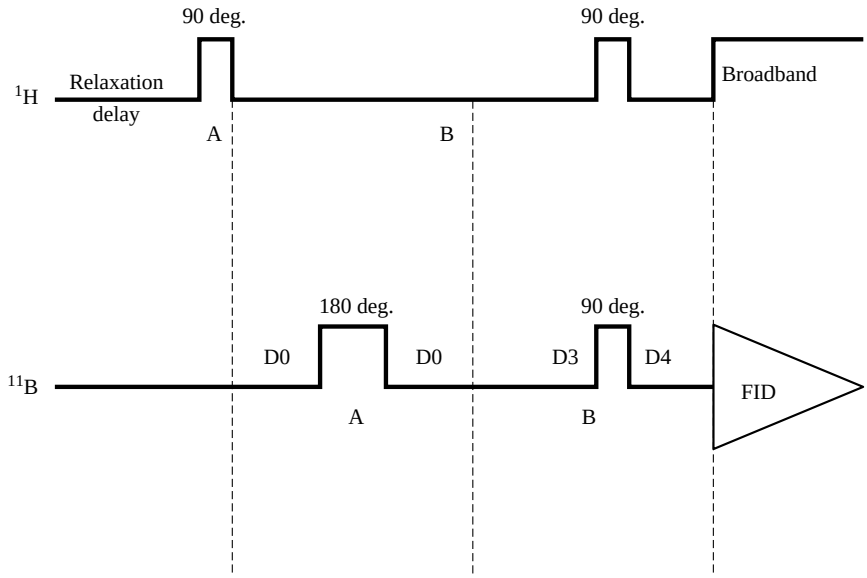

Phase cycling:

^{1}H(A) : (x) ^{11}B(A) : $(x)_8\ (y)_8\ (-x)_8\ (-y)_8$

^{1}H(B) : $(x)\ (-x)\ (y)\ (-y)$ ^{11}B(B) : $(x)_4\ (-x)_4$

Receiver phases : $(x)\ (-x)\ (y)\ (-y)\ (x)\ (-x)\ (y)\ (-y)\ (y)\ (-y)\ (-x)\ (x)\ (y)\ (-y)\ (-x)\ (x)$
$(-x)\ (x)\ (-y)\ (y)\ (-x)\ (x)\ (-y)\ (y)\ (-y)\ (y)\ (x)\ (-x)\ (-y)\ (y)\ (x)\ (-x)$

Figure 7 The HETCOR sequence as often used in ^{11}B–^{1}H correlation experiments. The delay periods D3 and D4 are set by taking D3 = 0.5/J(^{11}B, ^{1}H) and either D4 = D3 or D4 = 0.25/J(^{11}B, ^{1}H). Relaxation delays of 1.0 s to 2.0 s are not uncommon

with ^{11}B signal E also correlating with the bridging hydrogen signal. Hence signal E derives from B (9,10).

The ^{11}B COSY experiment (Figure 10) permits full assignment, with two major starting points.

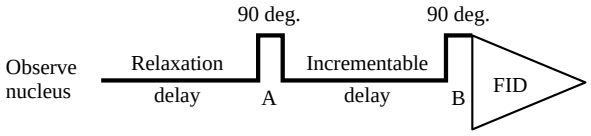

Phase cycles

Pulse A : $(x)_4\ (y)_4\ (-x)_4\ (-y)_4$

Pulse B : $(x)\ (-x)\ (y)\ (-y)\ (y)\ (-y)\ (-x)\ (x)$
$(y)\ (-y)\ (-x)\ (x)\ (-x)\ (x)\ (-y)\ (y)$

Receiver : $(x)\ (x)\ (-x)\ (-x)\ (y)\ (y)\ (-y)\ (-y)$

Figure 8 The COSY sequence as used in both homonuclear ^{11}B and ^{1}H correlation experiments. Note that the ^{1}H decoupling used in ^{11}B COSY experiments can be applied as indicated or throughout the entire experiment. For ^{1}H COSY experiments, the ^{11}B decoupling is usually applied as indicated to minimize sample heating

1. B(9,10) give signal E. This shares a cross peak with C which has relative area 1, hence C must arise from B(5) and F (also area 1) must derive from B(1).
2. Signal A couples to all the others and must be due to B (4,6).

This leaves only signals B and D unassigned. Signal B shares a cross peak with E, and must be due to B(8,11), leaving signal D as B(2,3). It is notable that an expected cross peak between B and D is missing. Table 3 summarizes these results.

3.2.2 Case Study 2

This involved distinguishing between two possible structures for $[B_9H_9Se_2]$,[14] these being shown in Figure 11 along with its ^{11}B and ^{11}B{^{1}H} spectra. Both of the proposed structures possess a plane of symmetry through cluster positions 1, 3, and 10, and hence would be expected to give six resonance

Table 3 Assignments of ^{11}B and ^{1}H Spectra of $[B_{10}H_{11}Se^-]$

B–H site	δ(^{11}B)	δ(^{1}H)
8, 11	−9.2	2.05
2, 3	−16.3	1.67
9, 10	−17.6	1.26
		(also μ-H, −4.11)
4, 6	−5.6	2.37
1	−35.6	1.05
5	−14.6	1.83

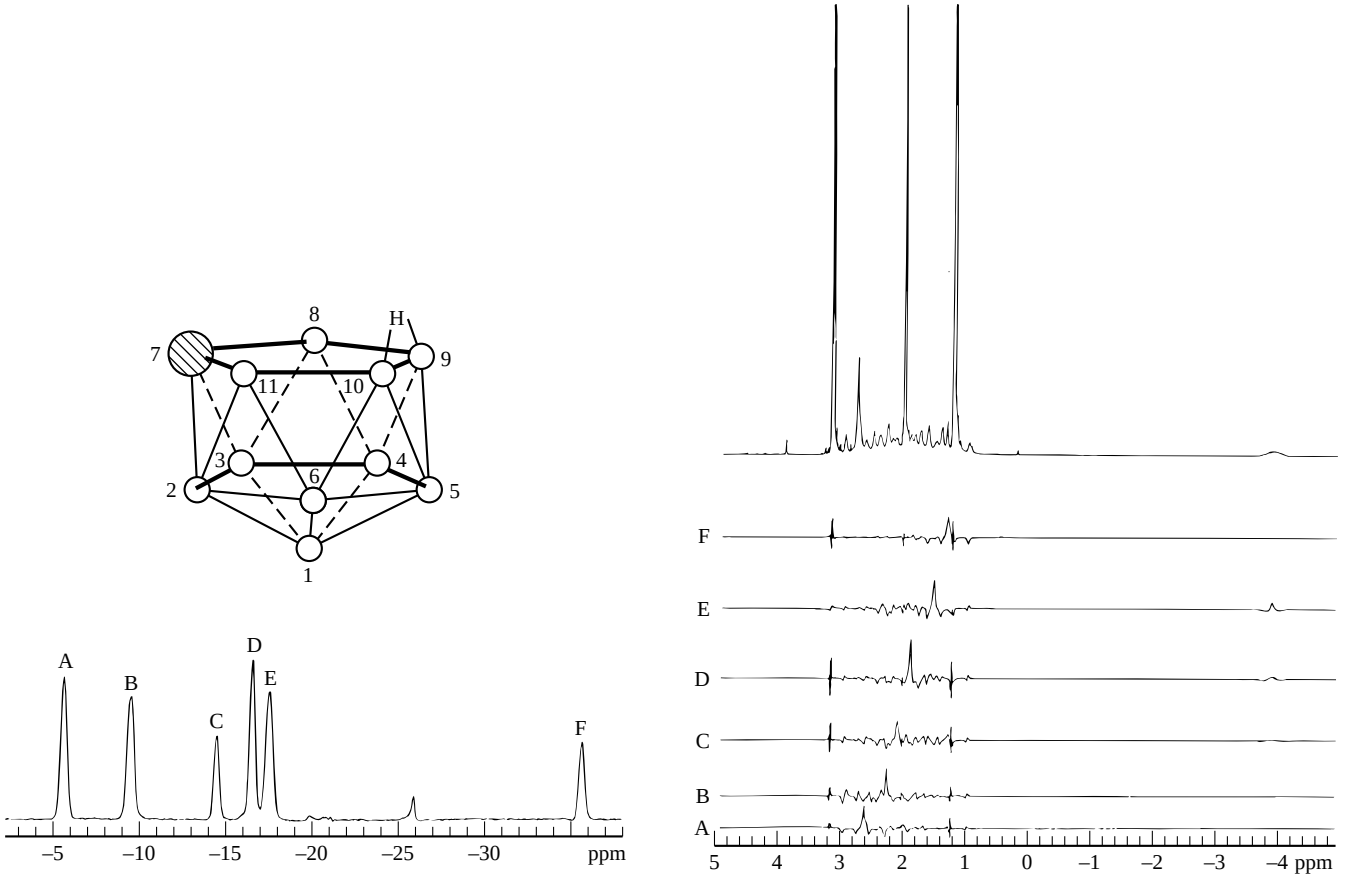

Figure 9 A series of 600 MHz selective $^{1}H\{^{11}B\}$ NMR difference spectra of $[B_{10}H_{11}Se^{-}]$, with an $^{11}B\{^{1}H\}$ spectrum indicating the irradiation positions

positions in the ^{11}B and $^{11}B\{^{1}H\}$ spectra, three of area 2 and three of area 1. As we saw earlier, (Figure 6) only the highest field spectra can show this unambiguously.

The solution to this problem is obtained from the ^{11}B COSY experiment (Figure 12), using the premise that only adjacent ^{11}B nuclei give rise to 2D cross peaks.

If the correct structure were structure I, then B(1), B(3) and B(10) should display three, three, and one cross peak, respectively. If the structure were II, with adjacent selenium atoms, then B(1), B(3), and B(10) would show three, two and two cross peaks, respectively. The COSY plot shows signals A and F have three cross peaks each, with E having one cross peak. Hence I is the correct structure.

It is also possible to complete a full assignment of the ^{11}B spectrum by noting that E must derive from B(10), and couples to D which must be due to B(5,6). Signal D also couples with F but not A, so F arises from B(1) and A from B(3). There is an F/B cross peak but not an F/C one, so B derives from B(2,4) and C from B(7,8).

Again there were cross peaks missing which were expected, namely B/C and B/D.

3.2.3 Case Study 3

Here, as in case study 1, the question was one of assignment, this being for the molecule [1-Ph-1,2-$C_2B_{10}H_{11}$], the structure of which is shown in Figure 13, along with its ^{11}B and $^{11}B\{^{1}H\}$ NMR spectra.[15]

The spectra are consistent with the structure, comprising six signals (labeled A–F) of relative intensities 1:1:2:2:2:2, respectively. The $^{1}H\{^{11}B\}$ spectrum [Figure 14(a)] showed six peaks of relative intensities 1:2:2:1:3:2, labeled I–VI respectively, arising from cage hydrogen atoms, with signals due to phenyl protons showing in the range δ 7.0–8.0 ppm. Comparison with the ^{1}H spectrum [Figure 14(b)] confirmed signal I as the CH cage proton.

Heteronuclear $^{11}B/^{1}H$ correlations showed the following B/H matches: A/IV, B/V, C/V, D/III, E/II, and F/VI. The homonuclear ^{11}B COSY experiment (Figure 15) showed all the potentially expected cross peaks, but even when combined with the heteronuclear data, unambiguous assignment is not possible. The exception is that ^{11}B signal C must derive from B(8,10), as this signal displays cross peaks to all the others. Complete and unambiguous assignment was obtained with the help of a ^{1}H COSY experiment (Figure 16).

From this it is clear that signal I couples to signals II and VI, each of which must be either H(3,6) or H(7,11), because these are the H positions most likely to couple to the cage CH. The $^{11}B/^{1}H$ correlation data link II to ^{11}B signal E, and VI to ^{11}B signal F. The ^{11}B COSY shows F couples to B, but E does not couple to any ^{11}B signal of relative area 1. Hence F arises from B(7,11) and E from B(3,6). This means signal B is due to B(12), meaning A derives from B(9). Signal C was

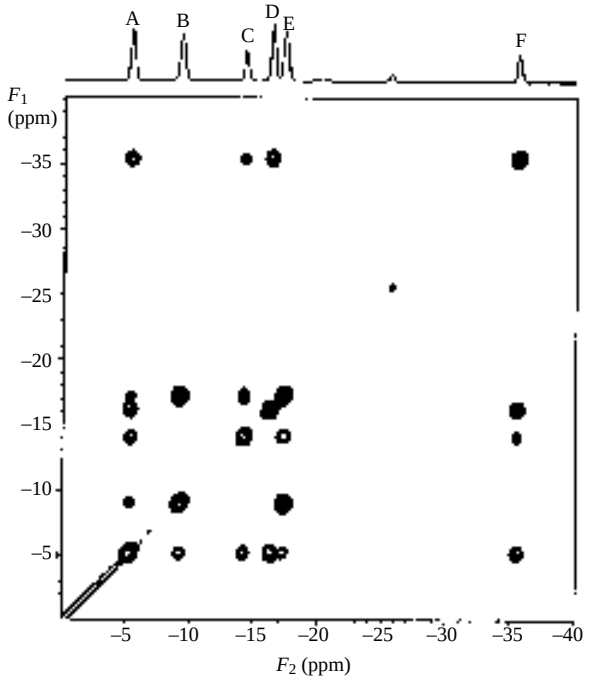

Figure 10 A 192.5 MHz ^{11}B COSY experiment on $[B_{10}H_{11}Se^-]$

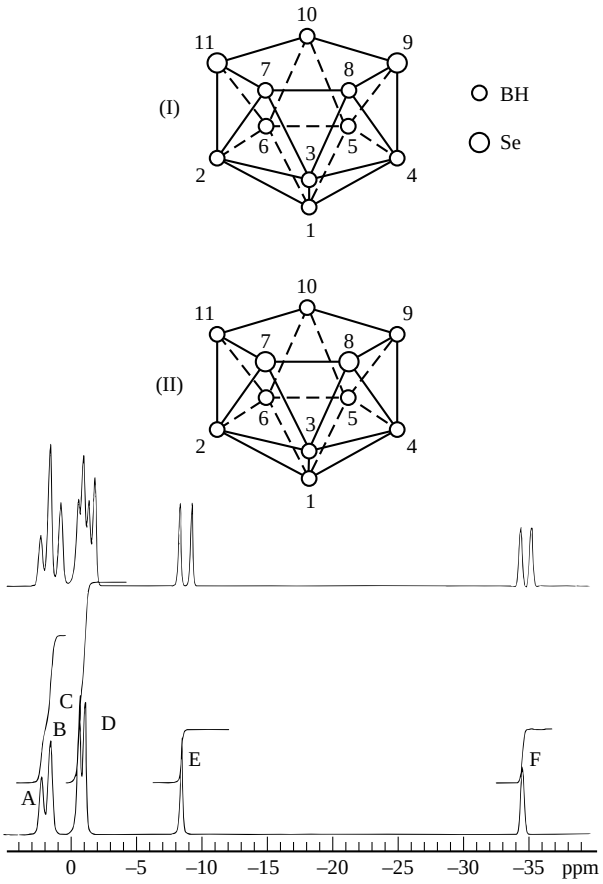

Figure 11 The ^{11}B and ^{11}B{^{1}H} NMR spectra of $[B_9H_9Se_2]$ obtained at 192.5 MHz, and its structure

already shown to be B(8,10), leaving D as B(4,5). From this, the ^{1}H assignments can also be made.

3.3 Chemical Shifts

Considerable effort has been invested into devising a rationale for $\delta(^{11}B)$ values in polyhedral borane derivatives over the years, with major advances being made in the understanding of ^{11}B shifts of boranes and main group heteroboranes in particular.[16] In Section [2], a qualitative introduction to the ideas of ^{11}B chemical shift theory was outlined, and these ideas will now be developed to incorporate polyhedral systems.

To appreciate fully the factors involved in the chemical shifts of these systems, it is useful to consider the bonding in them.[1] Boranes are made up of a series of (usually) sp_3 hybridized boron atoms, with one of the orbitals involved in bonding to an *exo*-polyhedral atom (usually H), with the remaining lobes involved in bonding to the cluster. As boron has three valence electrons, and one of these is taken up in the *exo*-polyhedral bond, it means that each boron vertex contributes two electrons to the cluster, giving rise to the so-called electron deficient nature of these systems. In fact, the clusters are considered to be made up of B-H units linked by a series of two- and three-center bonds (i.e. B–B, B–H and BBB, BHB, respectively). This is illustrated in Figure 17, with the bonding situation for B_6H_{10}, hexaborane(10).

Thus we see that whilst each B vertex of the cluster is sp^3 hybridized, it may have more than four nearest neighbors, creating strain on the nominal tetrahedral geometries associated with the boron atoms, and this would affect the shielding about the nuclei and hence influence their chemical shifts. In addition to this, the electron delocalization about such clusters would produce ring current effects (analogous to those found

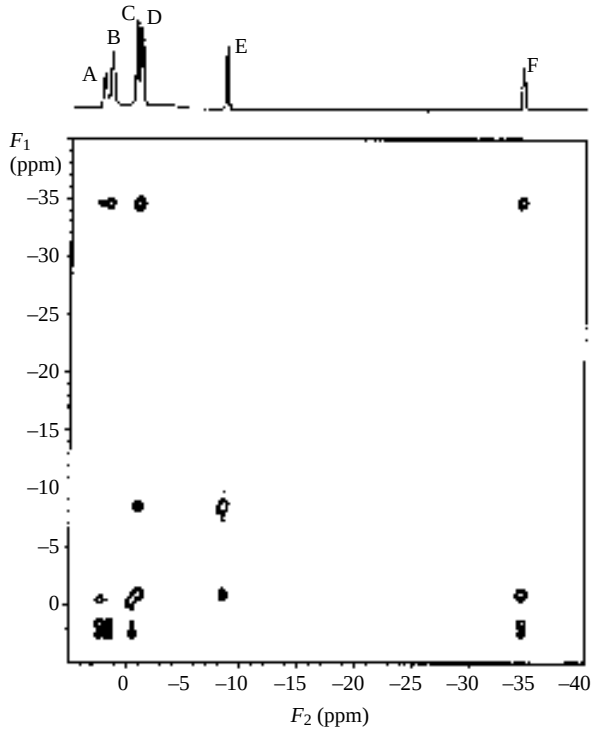

Figure 12 The results of a 192.5 MHz ^{11}B COSY experiment performed on $[B_9H_9Se_2]$

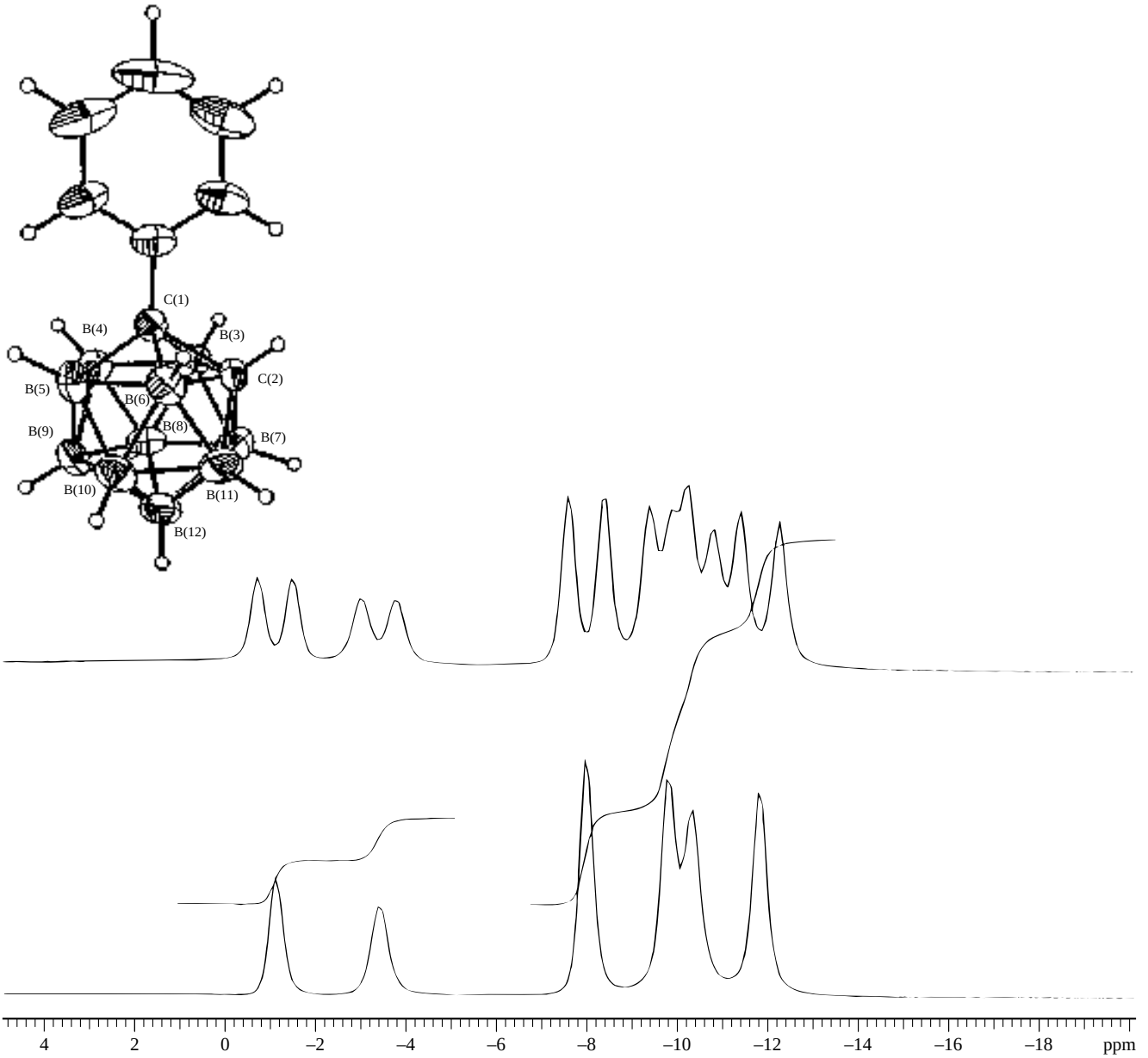

Figure 13 The 192.5 MHz ^{11}B and $^{11}B\{^1H\}$ NMR spectra of the closo-carbaborane [1-Ph-1,2-$C_2B_{10}H_{11}$], and an ORTEP diagram of its structure. Note there is a plane of symmetry through C-1, C-2, B(9), and B(12)

in aromatic organic compounds) which would have effects on nuclei nearby. Further potentially significant factors are the presence of other nuclei as cluster vertices (see the case studies for examples of these heteroboranes), and the presence and nature of *exo*-polyhedral atoms other than hydrogen. In particular, not only can substituents influence the boron chemical shift of the atom they are bonded to, but they can also have significant effects on the shifts of certain remote boron nuclei, the TRANS and ANTIPODAL effects.[10]

Recently, with the increasing amounts of ^{11}B chemical shift data that are accruing, techniques for calculating chemical shifts are being developed, most notably the IGLO method (Individual Gauge for Localized Orbitals).[17] Good levels of success have been attained on a range of smaller boranes, borane ions and some *closo* carba- and heteroboranes.[18] These calculations do require precise atomic coordinates, which may be experimentally measured (X-ray crystallography) or calculated (ab initio methods).

3.4 Dynamic Systems

Boron hydrides and their metallo derivatives are often found to exhibit various types of fluxional behavior. In the case of metallo derivatives, this often involves ligands other than the borane moiety, e.g. phosphine rotation, and this type of fluxionality will not be dealt with here. The most common type of fluxional process which is inherent to boranes is bridge

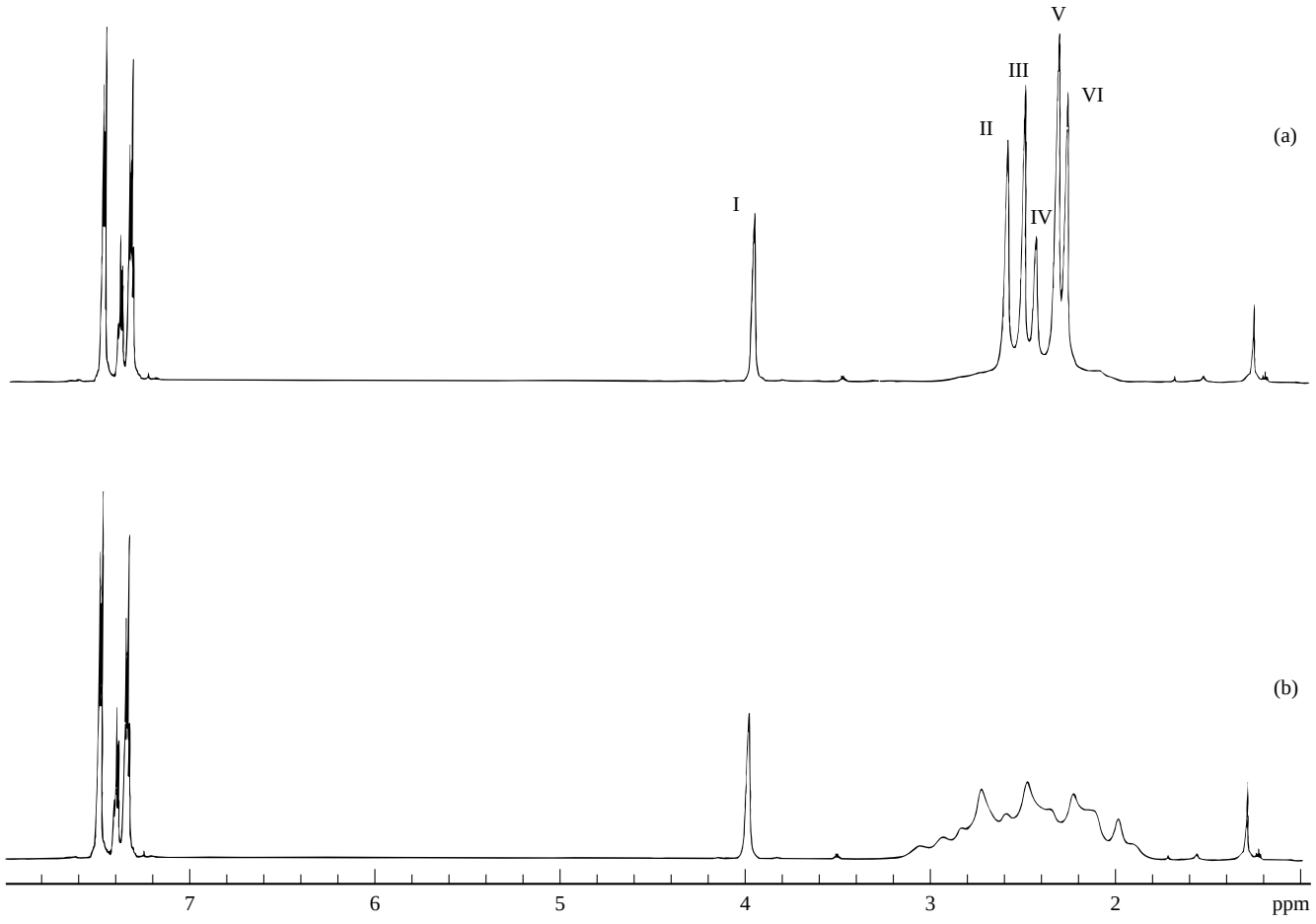

Figure 14 The 600 MHz $^{1}H\{^{11}B\}$ (top) and ^{1}H (bottom) NMR spectra of [1-Ph-1,2-$C_2B_{10}H_{11}$]

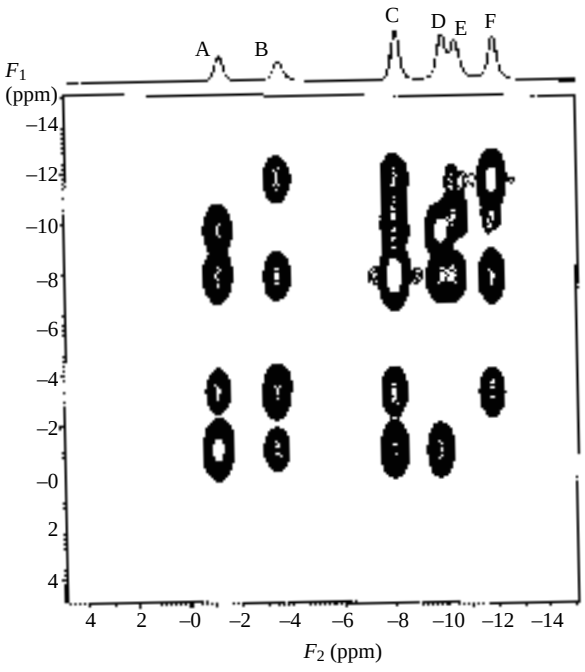

Figure 15 The 192.5 MHz ^{11}B COSY spectrum of [1-Ph-1,2-$C_2B_{10}H_{11}$]

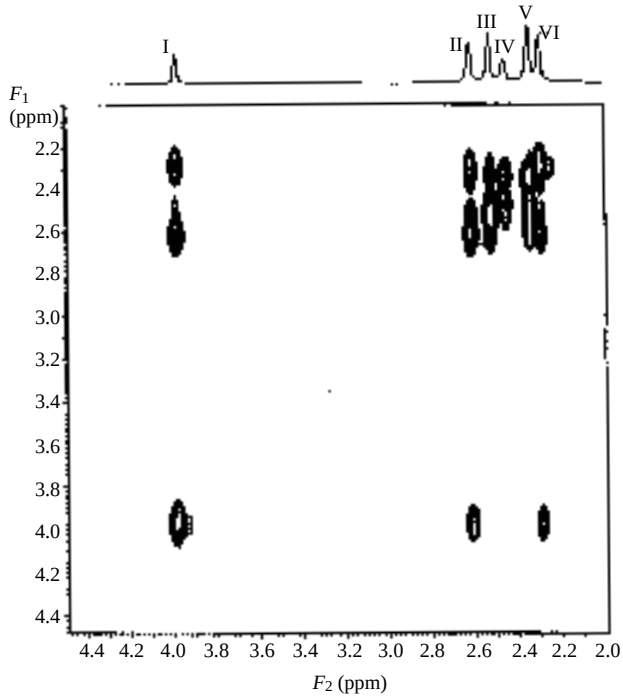

Figure 16 The 600 MHz ^{1}H COSY spectrum of [1-Ph-1,2-$C_2B_{10}H_{11}$]

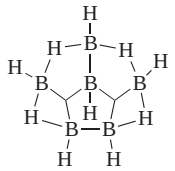

Figure 17 The bonding in *nido*-hexaborane(10), $[B_6H_{10}]$

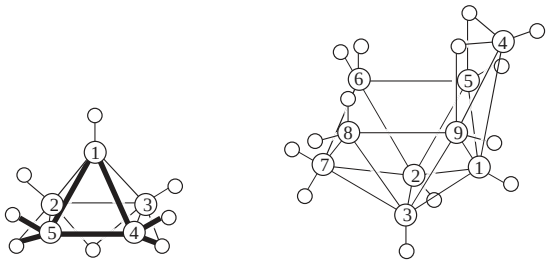

Figure 18 The structures of anions (a) $[B_5H_8^-]$ and (b) $[B_9H_{14}^-]$

hydrogen fluxionality. In some cases, particularly some simple borane anions, the energy barrier to this can be demonstrated to be very low; for example, the ^{11}B NMR data for the anions $[B_5H_8^-]$ and $[B_9H_{14}^-]$ [Figure 18(a) and (b)] are much simpler than might be expected from the structures.[19,20]

The ^{11}B spectra of $[B_5H_8^-]$ show only two signals of relative intensities 1:4, indicating fluxionality of the bridging hydrogens (μ-H atoms) about the square base. Perhaps even more surprising is the fact that the ^{11}B data on $[B_9H_{14}^-]$ only show three resonances of relative areas 1:1:1. These have been shown to be due to B(4,6,8), B(5,7,9), and B(1,2,3). This has been rationalized as the creation of an effective C_{3v} symmetry arising from fluxionality between the two μ-H atoms and the three *endo* hydrogens nominally located at B(6), B(7), and B(8). For both of these anions, even cooling the system to very low temperature failed to slow down the fluxional process enough to detect the solid state asymmetry with NMR.

The derivatization of $[B_9H_{14}^-]$ to form $[B_9H_{13}L]$ (Figure 19), where L can be one of a large range of neutral or anionic ligands (e.g. Me_2S, NCS^-, etc.), has shown that a considerable reduction in the rate of fluxionality can be effected, though the larger ligand (L instead of H^-) has also affected the solid state structure.[21,22] A comparison of the fully coupled ^{11}B NMR spectra of $[B_9H_{13}SEt_2]$ and $[B_9H_{13}NCS^-]$ (Figure 20) shows that the nature of L can have a marked effect on the fluxional behavior, with the H on B(4) exhibiting rapid

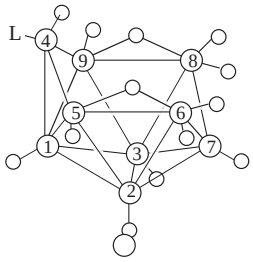

Figure 19 The structure of $[B_9H_{13}L]$, where L can be one of a range of neutral or anionic ligands (e.g. R_2S, MeCN, NCS^-, etc.)

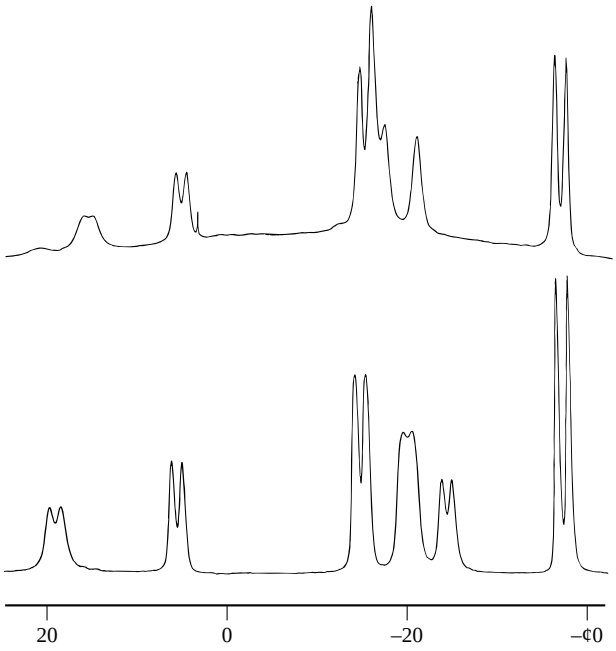

Figure 20 The 115.5 MHz ^{11}B NMR spectra of $[B_9H_{13}SEt_2]$ and $[B_9H_{13}NCS^-]$

exchange with the μ-H atoms and the *endo*-H-6 and H-8 atoms in the anionic case [hence no coupling between H-4 and B(4)] but an effectively static structure being observed for the neutral molecule where the B(4) signal appears as a doublet due to coupling to H-4.

4 FUTURE POSSIBILITIES

Thus far, we have seen that a range of 1D and 2D NMR experiments can greatly assist in the characterization of a variety of different boron compounds. To a large extent the experiments available are limited by the nature of the boron nuclei, in particular their efficient relaxation properties. These problems are mostly found in metallo derivatives, particularly for boron nuclei close to the metals. For 2D experiments (in particular ^{11}B COSY), this means that information resulting from the first pulse (the preparation pulse) vanishes more quickly than for many other (usually spin-$\frac{1}{2}$) nuclei. This can, to some extent, be overcome by either: (i) warming the sample, thereby decreasing the efficiency of the quadrupolar relaxation (this is not always an option as many samples are thermally unstable); or (ii) reducing the value of the incrementation in the variable delay periods in 2D spectra. This has the effect of decreasing the digital resolution because it is accomplished by increasing the spectrum width. For broad lines this is not necessarily a major problem. However if T_1 is too short, effective decoupling will occur between nuclei and cross peaks will not be found.

These factors aside, other 2D experiments will undoubtedly continue to be investigated. Homonuclear TOCSY spectra,[23] which show cross peaks between all nuclei in a given spin system, have recently been obtained on borane clusters (Figure 21) thereby providing a possible means by which multicluster systems can be studied.[24]

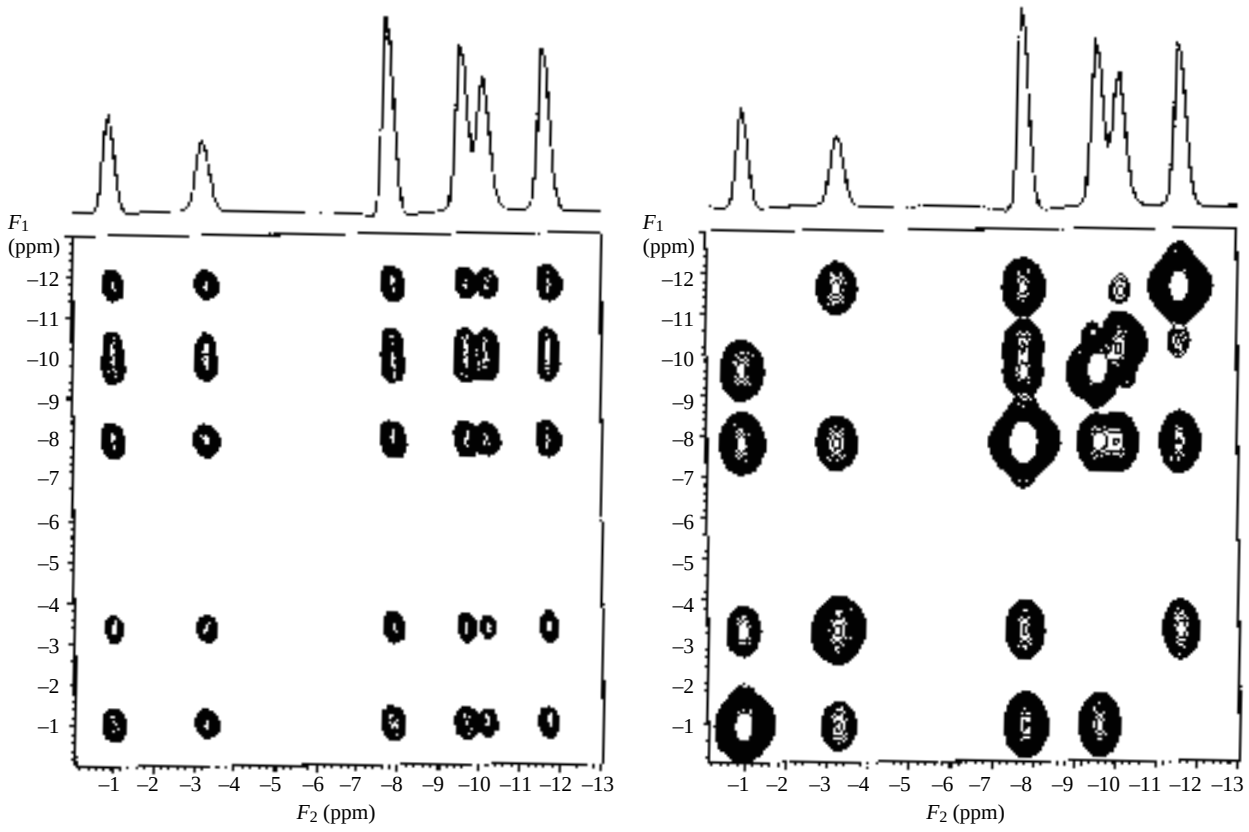

Figure 21 A comparison of a 192.5 MHz ^{11}B TOCSY experiment on [1-Ph-1,2-$C_2B_{10}H_{11}$] with a COSY experiment performed under similar conditions

An additional benefit of the TOCSY experiment is the relative narrowness of the diagonal and cross peaks relative to a COSY spectrum of the same material. This arises because COSY experiments are carried out in the absolute value mode and TOCSY experiments in the phase-sensitive mode.

It is difficult to see how 3D NMR[25] could be applied to more than a few isolated cases in boron chemistry because of the extended nature of the 3D pulse sequences and the problems that rapid boron relaxation would introduce as a result.

Finally, it may be that ^{10}B will be utilized more often as a result of increased magnetic field strengths giving both greater signal sensitivity and dispersion. In addition there has been a great deal of investment in the development of boron neutron-capture compounds[26] with a view to their eventual use in cancer treatment, and it is ^{10}B that is the active isotope in such studies.

The potential for the application of 2D techniques to ^{10}B is likely to be even more limited than to ^{11}B, because T_1 values of ^{10}B nuclei are similar to equivalently located ^{11}B nuclei but $^nJ(^{10}B,X)$ values are much smaller. Hence the transmission of information from ^{10}B nuclei to other nuclei is not going to be as effective as that from equivalent ^{11}B nuclei.

5 RELATED ARTICLES

COSY Two-Dimensional Experiments; Heteronuclear Shift Correlation Spectroscopy; Inorganic Chemistry Applications; Organometallic Compounds; Quadrupolar Nuclei in Liquid Samples; ORelaxation of Quadrupolar Nuclei Measured via Multiple Quantum Filtration; Shielding Calculations: IGLO Method

6 REFERENCES

1. A straightforward introduction to boron chemistry is given in N. N. Greenwood and A. Earnshaw, *Chemistry of the Elements*, Pergamon, Oxford 1990, Chap. 6
2. Data have been abstracted from: *NMR and the Periodic Table*, R. K. Harris and B. E. Mann, eds. Academic Press, London, 1978; R. Garth Kidd, in *NMR of Newly Accessible Nuclei*, ed. P. Laszlo, Academic Press, London, 1983, Vol. 2, Chap. 3, p. 49; L. J. Todd and A. R. Siedle, *Prog. NMR Spectrosc.*, 1979, **13**, 87.
3. D. Reed, G. Ferguson, B. L. Ruhl, O. Ni. Dhubhghail, and T. R. Spalding, *Polyhedron*, 1988, **7**, 17.
4. Various two-dimensional NMR techniques including HETCOR are well summarized in G. E. Martin and A. S. Zetkzer, *Two-Dimensional NMR Methods for Establishing Molecular Connectivity*, VCH Publishers, New York, 1988.
5. D. C. Finster, W. C. Hutton, and R. N. Grimes, *J. Am. Chem. Soc.*, 1980, **102**, 400.
6. I. Colquhoun and W. McFarlane, *J. Chem. Soc., Dalton Trans.*, **1981**, 2014.
7. D. P. Burum, *J. Magn. Reson.*, 1984, **59**, 430.

8. T. L. Venable, W. C. Hutton, and R. N. Grimes, *J. Am. Chem. Soc.*, 1982, **104**, 4716.
9. T. L. Venable, W. C. Hutton, and R. N. Grimes, *J. Am. Chem. Soc.*, 1984, **106**, 29.
10. D. Reed, *J. Chem. Res. (S)*, **1984**, 198.
11. W. P. Aue, E. Bartholdi, and R. R. Ernst, *J. Chem. Phys.*, 1976, **64**, 2229.
12. COSY techniques are well described in Ref. 4, Chap. 2
13. X. L. R. Fontaine and J. D. Kennedy, *J. Chem. Soc., Chem. Commun.*, **1986**, 779.
14. O. Ni Dhubhghaill, T. R. Spalding, and D. Reed, *Polyhedron*, 1993, **12**, 1977.
15. D. Reed, unpublished results.
16. S. Hermanek, *Chem. Rev.*, 1992, **92**, 325.
17. M. Schindler and W. Kutzelnigg, *J. Chem. Phys.*, 1982, **76**, 1919.
18. M. Buhl and P. v. R. Schleyer, in *Electron Deficient Boron and Carbon Clusters*, eds. G. A. Olah, R. E. Williams, and K. Wade, Wiley, New York, 1991, Chap. 4, p. 113.
19. H. D. Johnson, R. A. Geanangel, and S. G. Shore, *Inorg. Chem.*, 1970, **9**, 908.
20. P. C. Keller, *Inorg. Chem.*, 1970, **9**, 75.
21. F. E Wang, P. G Simpson, and W. N. Lipscomb, *J. Chem. Phys.*, 1961, **35**, 1335.
22. G. B. Jacobson, J. H. Morris, and D. Reed, *J. Chem. Soc., Dalton Trans.*, **1984**, 415.
23. L. Braunschweiler and R. R. Ernst, *J. Magn. Reson.*, 1983, **53**, 521.
24. D. Donohoe, D. Reed, and A. J. Welch, *Polyhedron*, 1995, **14**, 961.
25. A good review of three-dimensional NMR is found in G. M. Clore and A. M. Gronenborn, *Prog. NMR Spectrosc.*, 1991, **23**, 43.
26. An introductory review is given by J. H. Morris, *Chem. Br.*, 1991, **27**, 331.

Biographical Sketches

David Reed. *b* 1954. B.Sc. (Hons.), 1975, Ph.D., 1978, University of Leeds. Specialized in NMR at Edinburgh, 1981. Approximately 60 publications. Research interests include the applications of NMR to main group and transition metal cluster compounds, and to small organic molecules.

Ceramics

Raymond Dupree

University of Warwick, Coventry, UK

1	Introduction	1
2	Ceramics of SiC and Si_3N_4	1
3	Oxynitride Ceramics	1
4	Zirconia Ceramics	3
5	Related Articles	4
6	References	4

1 INTRODUCTION

Whilst most people have some idea of what constitutes a metal or a polymer, 'ceramic' is a less certain term. Dictionaries define ceramics in terms of pottery and earthenware; however, a more scientific definition is 'nonmetallic, inorganic materials that are made or used at high temperatures'. The range of ceramics is very broad and covers both very old and very new materials. This article will be mostly concerned with what might be termed advanced structural ceramics, since it is for these materials that NMR has been most useful in characterization and in providing structural information. (The ceramic superconductors are covered in ***High Temperature Superconductors***, and will not be discussed here.) These engineering ceramics are typically based on oxides or low-density covalently bonded materials such as silicon nitride or carbide. They are often compositionally complex and, in addition, many ceramics contain atoms of similar X-ray scattering factors such as silicon and aluminum, oxygen and nitrogen, or carbon and nitrogen, so that X-ray scattering techniques are of limited value for obtaining structural information. NMR is a particularly valuable investigative tool for ceramics because it is element- and site-specific. The chemical shift, which is the most often used NMR parameter to obtain structural information in these systems, is most sensitive to the local environment around the atom under investigation, i.e. the nature, number, and position of nearest-neighbor atoms with some sensitivity to the next neighbor shell but very little sensitivity to the structure beyond the fourth coordination sphere. Hence, NMR can be used to characterize poorly crystallized or glassy (see ***Amorphous Materials***) samples and to study the formation of the crystalline phase from the amorphous precursor. Many practical ceramics are solid solutions of different compounds and thus, at least in principle, compositionally disordered (i.e. a particular site can be occupied by, say, either a silicon or an aluminum atom); the distinct shifts observed for each 'local' configuration are very useful in determining this local order.

2 CERAMICS OF SIC AND SI_3N_4

The sensitivity of NMR to small structural changes in these systems is illustrated by the ^{29}Si, ^{13}C, and ^{15}N shifts of two important ceramic materials, Si_3N_4 (using ^{15}N-enriched samples for Si_3N_4) and SiC, given in Table 1. The different polymorphs of Si_3N_4 and polytypes of SiC all have readily distinguishable shifts (except the 6H and 15R polytypes, which differ only slightly in the stacking order). It can be seen that ^{15}N is a particularly sensitive probe: each nitrogen is bonded to three silicon atoms, [NSi_3], yet the different sites have shifts which cover ∼20 ppm in both Si_3N_4 polymorphs compared with only 2.1 ppm for the two silicon sites in α-Si_3N_4.[1–6]

Table 1 The ^{29}Si, ^{13}C, and ^{15}N Shifts of the Different Polytypes of SiC and Polymorphs of Si_3N_4[10]

β-SiC	4H SiC	6H SiC	15R SiC	α-Si_3N_4	β-Si_3N_4
δSi/ppm					
−17.2	−19.7	−14.3	−14.6	−49.0	−48.5
	−22.5	−20.4	−20.5	−47.1	
		−24.9	−24.9		
δC/ppm					
23.7	14.7	15.2	16.0		
	21.5	20.2	20.7		
		22.7	22.7		
δN/ppm				51.6	50.9
				53.4	68.4
				64	
				74.6	

Because of the differences in spectra of the different polymorphs and polytypes, the phase purity of a particular material (often very important in determining the final product of a reaction) can be readily determined. Figure 1 shows, as an example, the ^{29}Si resonance of two samples of Si_3N_4 which differed only slightly in preparation conditions. Whilst both spectra show two lines indicative of the presence of α-Si_3N_4, in the upper spectrum the lines are of unequal intensity, and careful inspection shows that the right-hand line is slightly shifted from the value expected for pure α-Si_3N_4, indicating that some β-Si_3N_4 is present. The amount can be estimated by subtraction to an accuracy of order 1%, which is difficult to achieve using other techniques. However, one problem with NMR investigations of spin $I = \frac{1}{2}$ nuclei in ceramic materials is their very long spin−lattice relaxation times, T_1, which can make experiments fairly time-consuming or difficult. Typically, in pure samples, T_1 of ^{29}Si, ^{13}C, and ^{15}N can all be >1000 s, and in fact in one experiment on SiC[4] no signal was observed even after allowing the sample to polarize in the magnet field for 96 h! For samples with more than one site it is therefore important for quantitative results to make sure that possible differences in T_1 of the different sites have been investigated.

3 OXYNITRIDE CERAMICS

A number of oxynitride ceramics, particularly the 'sialons', have practical applications as high-temperature engineering components. The simplest (in the compositional sense) of these 'sialons' are those based upon the β-Si_3N_4 structure into which alumina has been substituted. These β'-sialons have the general formula $Si_{3-x}Al_xO_xN_{4-x}$ ($0 \leq x \leq 2$). The ^{29}Si spectrum changes very little with alumina substitution even for $x = 2$, which seems to indicate that silicon is always surrounded by nitrogen.[1] If this is the case, then aluminum will have a range of tetrahedral AlO_yN_{1-y} ($y = 0, \ldots, 4$)

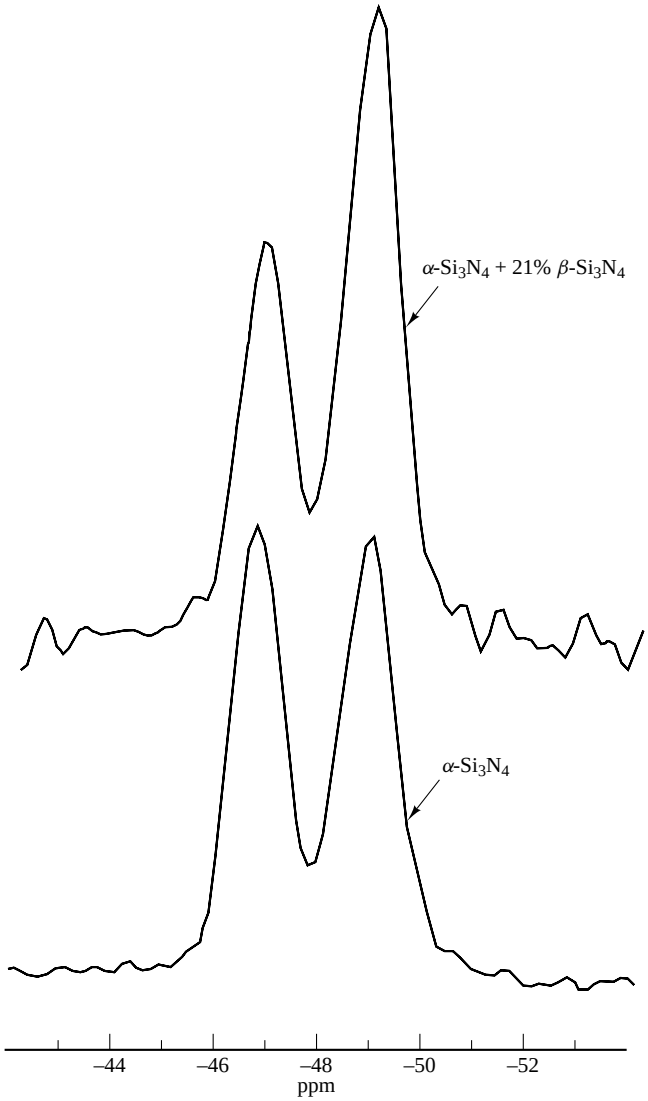

Figure 1 The ^{29}Si spectrum of two samples of Si_3N_4. The lower spectrum is pure α-Si_3N_4, while the upper is from a sample with 79% α-Si_3N_4 and 21% β-Si_3N_4

environments. In the case of mixed AlON tetrahedra, one can expect there to be a very large electric field gradient (EFG) at the aluminum site; furthermore, because of the different possibilities for the arrangement of the oxygen and nitrogen around the aluminum, there will be several different EFGs associated with each possibility. Thus, very broad ^{27}Al lines are to be expected. In fact in early experiments at 8.45 T it was found that because of the extreme breadth of the line only a small fraction of the ^{27}Al was being observed, the fraction increasing with oxygen content because more AlO_4 tetrahedra which have relatively smaller EFGs are formed.[7] Later work at 11.7 T using a probe with a short ($\sim$2 μs) dead time and fast (16 kHz) spinning was able to observe more of the aluminum present. A broad line from AlO_4 tetrahedra at 68 ppm for $x = 2$ ($SiAl_2O_2N_2$) shifts to $\sim$75 ppm, and further broadens as x decreases. The peak at $\sim$75 ppm was assigned to AlO_3N.[8] A small shoulder at 89 ppm, probably from AlO_2N_2, is also visible for all samples. It should be noted that if the aluminum and silicon were randomly distributed, then AlO_4

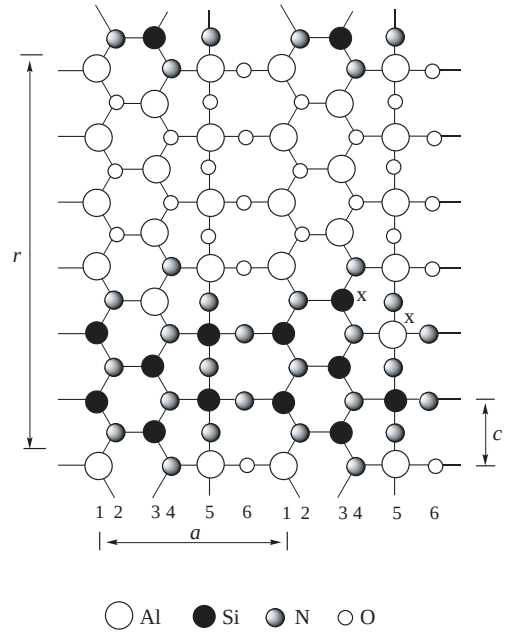

Figure 2 Schematic representation of the local structure of β'-sialon with $x = 2$ (i.e. Si_{3-x} $AI_xO_xN_{4-x}$ or $SiAl_2O_2N_2$). The atoms in columns 1, 4, and 6 are above the plane of the paper, those in column 3 below, with columns 2 and 5 in the plane. The repeat unit along c is between the lines r. x are defects within the layers. (Adapted from Dupree et al.[7])

would not be dominant even at $x = 2$, and mixed tetrahedra for ^{29}Si would be expected. When combined with the ^{29}Si data the ^{27}Al results strongly indicate a 'microdomain' type of structure in this material. A schematic diagram of this is shown in Figure 2. For small x the thickness of the AlO_4 'block' is reduced, leading to a rapidly increasing amount of mixed AlON tetrahedra.

Many practical oxynitride ceramics require sintering aids in their manufacture, and these react with the SiO_2 found on the surface of the Si_3N_4 grains, forming glassy intergranular phases. Study of these phases and their crystallization products is important in achieving an understanding of the limiting factors which determine the high-temperature properties of these ceramics. One popular aid in sintering is Y_2O_3, and a number of compounds formed in the Y–Si–Al–O–N have been studied by NMR, as has the crystallization behavior of the glasses formed in this system. Initial measurements on ^{29}Si in this and related systems have determined the shifts of the various compounds, such as Y_2SiAlO_5N, $YSiO_2N$, etc., which are formed and helped to delineate the shift ranges of the SiO_xN_{1-x} ($0 \leq x \leq 2$) tetrahedra shown in Figure 3.[9,10] Note that, as with SiO_4 tetrahedra where there are different numbers of bridging oxygens, there is considerable overlap in the shift range of each local structural unit so that the number of oxygen and nitrogen neighbors cannot be unambiguously determined by the shift position alone. For a proper understanding of the local structure, full multinuclear studies are needed, and ^{15}N on enriched samples has been quite helpful in clarifying several issues. In general, it is found that when nitrogen is coordinated to three silicon atoms, [NSi_3], the shifts are typically 40–80 ppm, whereas when coordinated to two silicon atoms, [NSi_2], it resonates in the range 90–160 ppm.[5] When a glass of the composition

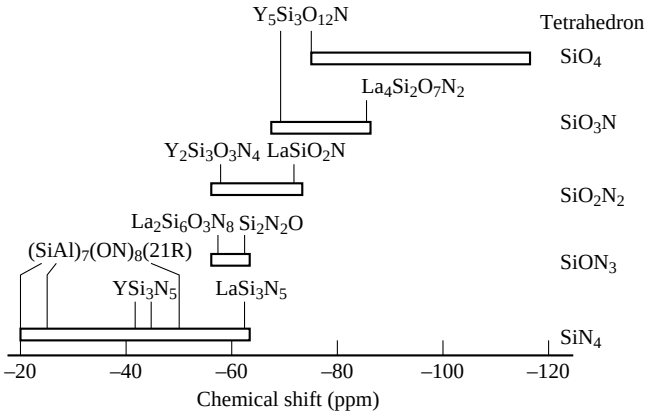

Figure 3 Silicon-29 shift ranges in oxynitrides showing the effect of differing numbers of oxygen neighbors. (Adapted from Dupree et al.[10])

$Y_{1.04}Si_{1.27}Al_{1.27}O_{4.8}N_{0.8}$ was crystallized at 1100°C the ^{29}Si spectrum showed that six different compounds containing silicon were present including β'-sialon and Si_2N_2O, both of which are also evident in the ^{15}N spectrum. The ^{15}N spectrum also showed a broad peak at ∼148 ppm and a sharp peak at 285 ppm. The former was shown to be from metastable Y_2SiAlO_5N, where nitrogen coordination would be either $[NSi_2]$ or [NSiAl], by annealing at 1250°C when both the ^{29}Si signal from this phase and the ^{15}N line at 148 ppm were markedly reduced. The peak at 285 ppm was identified as nitrogen substituted into yttrium aluminum garnet, $Y_3Al_5O_{12}$ (YAG), which is a major phase present. Analysis with TEM-EDAX showed that in the crystalline YAG approximately 14% of the aluminum was replaced by silicon, and it is likely that nitrogen will concurrently substitute for oxygen to maintain charge balance. The shift of this peak is much larger than for $[NSi_2]$ sites, so the most likely local environment is a nitrogen coordinated to a single silicon atom at the tetrahedral site in YAG and a vacancy at the octahedral aluminum site, i.e. [NSi*].

4 ZIRCONIA CERAMICS

Zirconia (ZrO_2) is an important high-toughness engineering ceramic which in its practical form is usually a mixture of several different crystallographic phases and/or is stabilized by some substituent such as yttrium or magnesium. Neither ^{91}Zr nor ^{17}O (unless enriched) can be regarded as ideal NMR probes, both have spin $I = \frac{5}{2}$, and whilst the natural abundance of ^{91}Zr at 11.2% is enough for NMR experiments (the sensitivity is 2.9 times ^{29}Si) the quadrupole moment is quite large such that in noncubic environments the linewidth is much too great for narrowing techniques such as MAS or DOR to be effective. Oxygen-17 has a much smaller (10^{-2}) quadrupole moment than ^{91}Zr, such that in an ionic environment such as ZrO_2 the EFG is quite small, the quadrupole coupling constant χ ($= e^2qQ/h$) being less than 3 MHz. In this case, despite the natural abundance of ^{17}O being only 0.037%, it is possible (with considerable averaging) to obtain spectra from unenriched materials that clearly distinguish between the tetragonal phase with one oxygen site ($\delta \approx 380$ ppm), the monoclinic phase with two sites ($\delta \approx 325$ and 401 ppm), and the cubic phase with a broad line at ∼375 ppm from the disorder due to vacancies in the structure.[11] Natural abundance ^{17}O experiments are time-consuming, however, and of limited practicality for day-to-day examination of these materials.

The phases of ZrO_2 zirconium have either seven (orthorhombic and monoclinic) or eight (cubic and tetragonal) oxygen neighbors, and thus the ^{91}Zr chemical shift difference between these phases is likely to be small. However, because of differences in local symmetry the ^{91}Zr EFG and the asymmetry parameter, η, are likely to be very different, and thus the phases can be distinguished by their quadrupolar lineshapes. The very large linewidth (∼500 kHz in a 9.4 T field) means that the spectrum is best acquired on a static sample point by point. An advantage of a static NMR experiment is that the sample does not have to be powdered, which on this type of material may change the relative phase content via the phase transformation (tetragonal → monoclinic, tetragonal → orthorhombic). The spectra of cubic, monoclinic, and a fired, partially stabilized zirconia (PSZ), acquired at 25 kHz intervals using a spin echo sequence, are shown in Figure 4.[12] In the cubic phase (which contains ∼13.5 mol% MgO for stabilization) the presence of

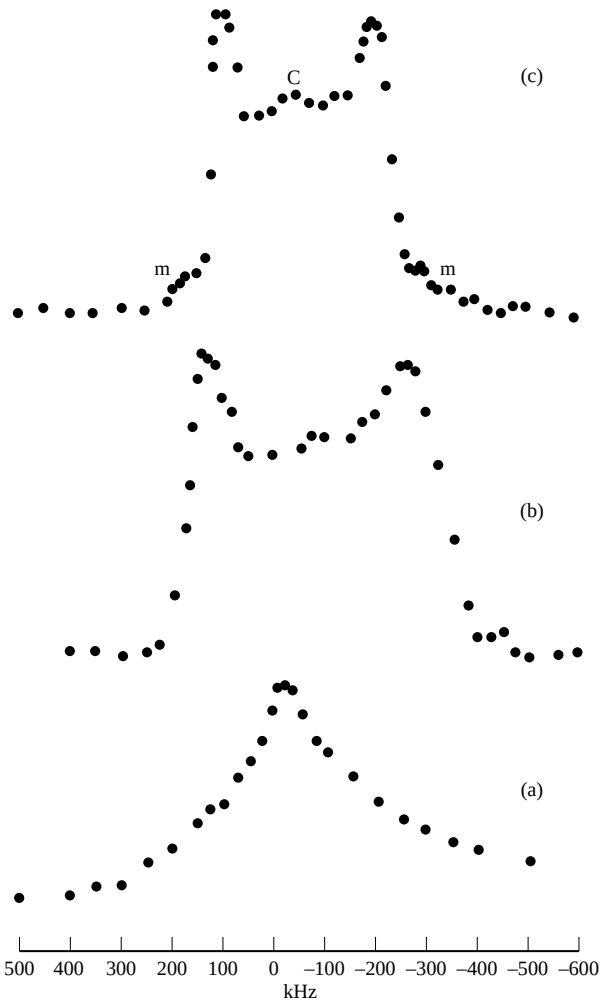

Figure 4 The ^{91}Zr spectra of several forms of ZrO_2. (a) Magnesia-stabilized cubic zirconia (13.5 mol% MgO), (b) monoclinic ZrO_2, and (c) tetragonal ZrO_2 (MS grade MgPSZ). The minor peaks are from residual monoclinic (m) and cubic (c) phases. (Adopted from Bastow et al.[12])

oxygen vacancies, needed for charge balance, means that there will be a distribution of quadrupolar coupling constants; thus, a broad featureless line is observed and any structure is lost. The monoclinic phase is well fitted by a line with χ = 23.1 MHz and η = 0.1, whilst the spectrum of MS grade PSZ is narrower (χ = 19.1 MHz, η = 0), showing that it is mostly tetragonal with some monoclinic and cubic phase material present.

5 RELATED ARTICLES

Amorphous Materials; Inorganic Solids.

6 REFERENCES

1. R. Dupree, M. H. Lewis, G. Leng-Ward, and D. S. Williams, *J. Mater. Sci. Lett.*, 1985, **4**, 393.
2. G. R. Finlay, J. S. Hartmann, M. F. Richardson, and B. L. Williams, *J. Chem. Soc. Chem. Commun.*, 1985, 159.
3. J. R. Guth and W. T. Petuskey, *J. Phys. Chem.*, 1987, **91**, 5361.
4. J. S. Hartman, M. F. Richardson, B. L. Sherriff, and B. G. Winsbarrow, *J. Am. Chem. Soc.*, 1987, **109**, 6059.
5. R. K. Harris, M. J. Leach and D. P. Thompson, *Chem. Mater.*, 1990, **2**, 320.
6. D. Kruppa, R. Dupree, and M. H. Lewis, *Mater. Letts.*, 1991, **11**, 195.
7. R. Dupree, M. H. Lewis, and M. E. Smith, *J. Appl. Cryst.*, 1988, **21**, 109.
8. M. E. Smith, *J. Phys. Chem.*, 1992, **96**, 1444.
9. R. Dupree, M. H. Lewis, and M. E. Smith, *J. Am. Chem. Soc.*, 1988, **110**, 1083.
10. R. Dupree, S. C. Kohn, C. M. B. Henderson, and A. M. T. Bell, *NATO ASI Ser.*, 1992, **386**, 421.
11. T. J. Bastow, M. E. Smith, and S. N. Stuart, *Chem. Phys. Lett.*, 1992, **191**, 125.
12. T. J. Bastow and M. E. Smith, *Solid State NMR*, 1992, **1**, 165.

Biographical Sketch

Raymond Dupree. *b* 1937. B.Sc., Ph.D., University of Exeter, UK. Assistant lecturer, University of Exeter, 1963–66, lecturer and currently Professor, University of Warwick, UK, 1966–present. Sabbaticals at AT&T Bell Laboratories, USA, Oregon State University, USA, University of California at Berkeley, USA, and University of California at Santa Barbara, USA. Approx. 140 publications. Current research specialties: the application of NMR to structurally and compositionally disordered materials, including glasses, ceramics, and minerals, NMR in oxide superconductors.

Chiral Discrimination Using Chiral Ordering Agents

Jacques Courtieu, Philippe Lesot, Abdelkrim Meddour, Denis Merlet, and Christie Aroulanda

Université Paris-Sud, Orsay, France

1 Introduction 1
2 History 1
3 Chiral Discrimination Using Polypeptidic Lyotropic Liquid Crystals 3
4 Chiral Differentiation Using Quadrupolar Splitting 4
5 Chiral Differentiation Using Chemical Shift Anisotropy 4
6 Chiral Differentiation Using Dipolar Coupling 6
7 Visualizing Isotopic Chirality 6
8 Using Achiral Derivatizing Agents 7
9 Using Natural Abundance Deuterium 8
10 Summary 8
11 References 8

1 INTRODUCTION

The NMR spectra of enantiomers are fundamentally identical. This is because the projection of magnetic properties along the magnetic field axis is independent of the "handedness" of the molecules. An other way to tell this is to recall that enantiotopic nuclei are isochronous and consequently two objects that are mirror images cannot be differentiated. On the contrary, diastereomers may be distinguished because diastereotopic nuclei are non equivalent. The determination of enantiomeric purity using NMR therefore requires the use of a chiral auxiliary that, in one way or another, converts the mixture of enantiomers into a mixture of diastereomers. Whenever the induced chemical shift inequivalence is large enough to produce well resolved lines, then integration gives a direct measure of the diastereomeric composition which can be easily related to the enantiomeric composition of the original mixture.

Since the late sixties, three types of chiral auxiliaries have been commonly in use in classical NMR in the liquid state. Chiral Lanthanide Shift Reagents[1] and Chiral Solvating Agents[2] form diastereomeric complexes with substrate enantiomers and may be use directly. Chiral Derivatizing Agents[3] require the synthesis of discrete diastereomers prior to NMR analysis. These techniques and their limitations have been nicely reviewed recently by David Parker.[4]

In this contribution we describe a more recent technique which proceeds through the use of chiral liquid crystals as the NMR solvent. Here the chiral discrimination originates in a difference of the enantiomer ordering when dissolved in such a medium. Consequently, all order sensitive NMR interactions are different, namely chemical shift anisotropies, dipolar coupling and quadrupolar splitting. The major advantage of this later method is that it works with all types of chiral molecules, independently of any functional group, as in alkanes for instance. Furthermore, this method has been shown to work amazingly well for molecules whose chirality arises by virtue of isotopic substitution. Finally, this technique has been shown to give interesting results in the study of diastereomers with remote asymmetric centres.

2 HISTORY

The idea of using chiral liquid crystal solvents to distinguish enantiomers emerged in the sixties, shortly after the discovery by Saupe and Englert of the usefulness of nematic liquid crystals as anisotropic NMR solvents.[5] The response of a cholesteric phase to an external homogeneous magnetic field has been studied by McColl et al.[6] It depends on the sign of the anisotropic magnetic susceptibility, $\Delta\chi$. When the molecular $\Delta\chi$ is positive the helix axis tends to align perpendicular to the magnetic field, B_0. In this situation the director is distributed in a plane that contains B_0. Very broad NMR spectra are then expected as there is not a homogeneous orientation of the director toward the magnetic field. However, if the field is larger than some critical field,[7] particular to each liquid crystal system, the field unwinds the supramolecular cholesteric helix, thus giving rise to a chiral nematic phase where high resolution NMR may be achieved. The situation is more interesting when the molecular $\Delta\chi$ is negative. Then the supramolecular helix axis orientates parallel to B_0 and consequently the director is distributed in a plane perpendicular to the magnetic field. The director orientation is then expected to be homogeneous and at 90° to B_0. Unfortunately, it has been shown[8,9] that in this situation the director generally does not orientate homogeneously enough to provide high-resolution spectra. This has been attributed to existing textural defects due to visco-elastic forces that the magnetic field cannot overcome. This is an unfavorable effect that prevented development of NMR in such chiral-oriented solvents, even if they were expected to act differently on enantiomers.

In 1968, Snyder et al. performed a clever experiment.[10] Realizing that the supramolecular helicity of the cholesteric phase was the origin of the low quality of the orientation, they made up a chiral nematic solvent from a compensated mixture of two different cholesteric compounds of opposite helicity. By using racemic 3,3,3-trichloropropylene oxide as a guest molecule, they announced that they obtained separate spectra for each enantiomer (Figure 1). Unfortunately, the linewidth were still rather large and the solvent used, a mixture of cholesterol derivatives, prevented any development of this technique.

In 1975, Tracey and Dieh[11] reported a small ^{1}H NMR separation observed for *D-L* alanin when dissolved in a lyotropic liquid crystal made of sodium n-decylsulfate doped with chiral sodium decyl-2-sulfate (Figure 2). This experiment, which may be seen as the first chiral discrimination using a cholesteric liquid crystal as solvent, has been reproduced several times by Tracey and Radley using lyotropic liquid crystals made of chiral polar head amphiphiles.[12–15] In these

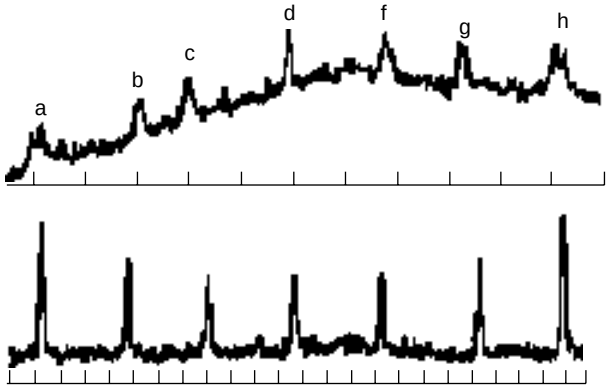

Figure 1 60 MHz proton spectrum of racemic 3,3,3-trichloropropylene oxide in a liquid crystal solvent. The lower trace solvent was a classical nematic. The upper trace solvent was made of a mixture of 0.53 g of cholesteryl chloride and 0.28 g of cholesteryl myristate. Note the apparent doubling of the external lines when using this compensated nematic mixture of cholesterics. (Reproduced by permission of the American Chemical Society from Sackmann et al.[10])

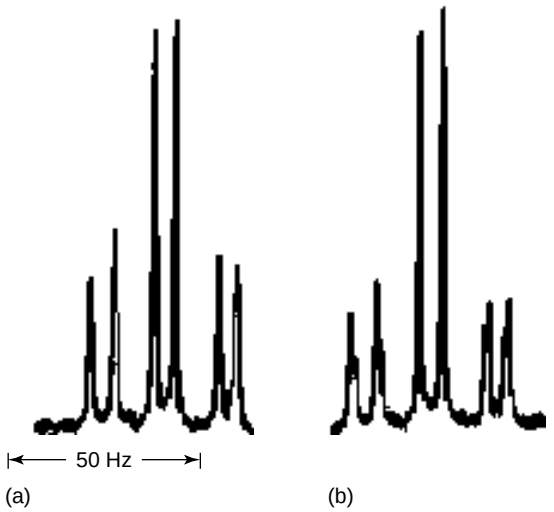

Figure 2 (a) The methyl proton resonance at 100 MHz from *D*-alanine in the chiral lyotropic phase described in the text. (b) The methyl resonance of a non-racemic mixture of *D*- and *L*-alanine. Clearly there are two superimposed spectra corresponding to the enantiomers. (Reproduced by permission of North-Holland Publishing Company, Amsterdam, from Tracey et al.[11])

experiments, the spectroscopic separation between the alanin enantiomers were correlated to the cholesteric pitch to inquire about the origin of the micelle to micelle twist. No practical applications to measuring enantiomeric excess developed, mainly because these liquid crystals are difficult to orient homogeneously in the magnetic field and also because proton NMR was used, and consequently only the study of very small molecules was possible.

Independently, in the 1960s, considerable attention was devoted to the cholesteric liquid crystal properties of organic solutions of some synthetic homo-polypeptides such as poly-γ-benzyl L-glutamate (PBLG).[16–19] In 1967 three sets of workers, Samulski and Tobolski,[20] Sobajima[21] and Panar and Philips,[22] independently found that the ^{1}H NMR spectrum of CH_2Cl_2 is split into a doublet in the liquid crystalline phase PBLG/CH_2Cl_2. This result indicates clearly that, in a strong magnetic field, the supramolecular pitch is unwounded due to the bulk anisotropy of the diamagnetic susceptibility, thus producing a cholesteric to chiral-nematic transition. This medium thus furnishes a very interesting oriented solvent for high resolution NMR.[22]

Most of the work done between 1965 and 1990 was essentially dedicated to the study of the rather unusual liquid crystal properties of these polymeric solutions.[23] Nevertheless, in 1981, Czarniecka and Samulski[24] noticed that the enantiotopic deuterons in benzyl alcohol-d_7 give each a quadrupolar doublet when dissolved in PBLG liquid crystal solution. This means that in such a chiral anisotropic medium enantiotopic nuclei are not equivalent, as they are in non-chiral liquid crystalline solvents. We will see later that this finding has important consequences regarding isotopic chirality.

In 1989, our group presented a new chiral liquid crystal solvent made of a mixture of cholesteryl propionate (60%) and ZLI-2806 (40%), the latter being a commercially available nematic eutectic mixture of different cyano-bicyclohexyl derivatives.[25] This cholesteric $\Delta\chi < 0$ mixture has the unique property to orient homogeneously with the helicity axis parallel to the NMR magnetic field. In this situation, the director being entirely perpendicular to Bo, good high-resolution dipolar spectra were obtained for dissolved molecules. The next step was to study the high-resolution spectrum of a simple chiral molecule using the above solvent. The first ^{1}H spectrum obtained using racemic 3,3,3-trichloropropylene oxide is shown in Figure 3. Due to the size of the dipolar couplings an ABC pattern was expected for the three spin system and two superimposed ABC patterns are easily visible, one spectrum for each enantiomer.

An analysis of the sub-spectra attributed to each enantiomers has been realized, and lead to the following results:

(a) In each sub-spectra the chemical shifts and the scalar couplings are the same within experimental error.
(b) The only difference between the spectra originates from a difference in the inter proton dipolar couplings.

The importance of this last point is seen when looking at the parameters involved in the dipolar coupling:

$$D_{ij} = -\left(\frac{\mu_o}{4\pi}\right)\frac{h\gamma_i\gamma_j}{4\pi^2 r_{ij}^3}\cdot\frac{1}{2}\langle 3\cos^2\theta_{ij}^z - 1\rangle$$

It is clear that the observed difference in the dipolar couplings cannot come from the magnetogyric ratios γ_i and γ_j because the same nuclei are involved in the enantiomers. The difference also cannot come from the internuclear distance r_{ij} since symmetry through a plane keeps distances constant. So it must be concluded that the dipolar coupling difference between the enantiomers originate from a difference in the so-called order parameters, $S_{ij} = \langle 3\cos^2\theta - 1\rangle/2$, of the internuclear vector, θ being the angle between the ij direction and the magnetic field and the brackets meaning an ensemble average over the anisotropic molecular motion.

The fundamental conclusion is that two enantiomers are not ordered in the same way when dissolved in a cholesteric liquid crystal, $S_s \neq S_r$, and consequently all the order sensitive NMR parameters are in principle different: the dipolar coupling as

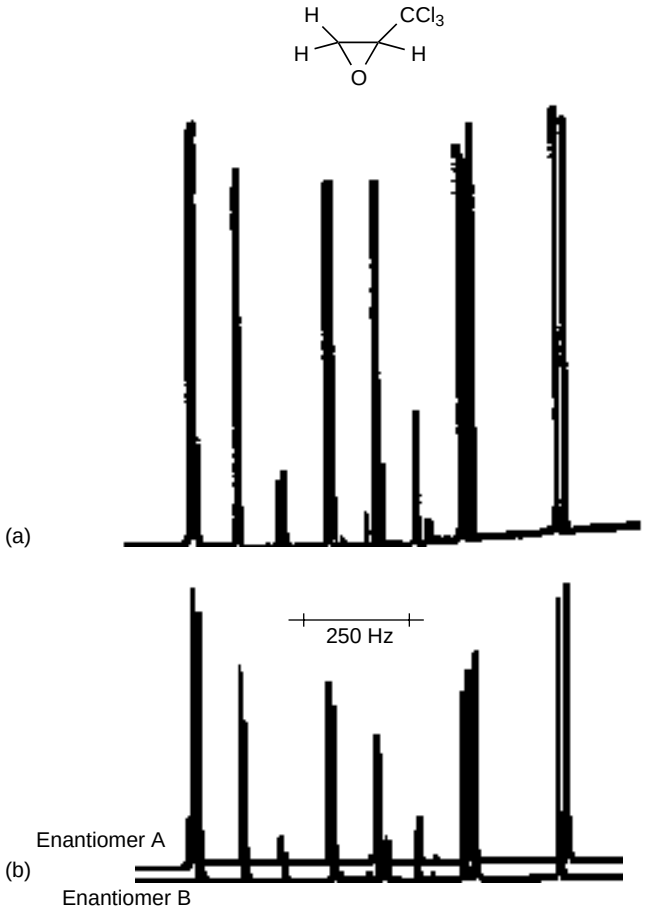

Figure 3 250 MHz proton spectrum of racemic 3,3,3-trichloropropylene oxide obtained in the cholesteric liquid crystal described in the text, together with the simulated ABC sub-spectra associated with each enantiomer

we have shown, but also the chemical shift anisotropy and the quadrupolar coupling for a spin larger than one half.

Unfortunately, no efficient applications can be made using spectra dominated by dipolar couplings except for very simple molecules. This is because of the tremendous complexity of second order dipolar spectra, which is due to the large values of the dipolar couplings compared to chemical shift differences. Actually, it is possible to overcome this problem using proton-decoupled deuterium NMR.[26] Now the spectra are dominated by the deuterium quadrupolar couplings. It is well known that quadrupolar interaction is purely anisotropic and a nucleus with $I = 1$ depends on the ordering through the following relationship:

$$\Delta\nu_Q = \frac{3e^2qQ}{2h} \cdot S_{CD}^Z$$

where $3e^2qQ/2h$ is the quadrupolar coupling constant for the deuterium and $S_{CD}^Z = \langle 3\cos^2\theta_{CD}^Z - 1\rangle/2$ is the order parameter of the C–D vector, with θ_{CD}^Z being the angle the C–D direction makes with B_0. Here it is assumed that the electric field gradient is symmetric along the CD bond. Let us then assume a monodeuterated chiral molecule D–C*($R_1R_2R_3$). The proton decoupled deuterium NMR of such a compound in an isotropic solvent will result in a single line centred at the isotropic chemical shift. Using a non-chiral liquid crystal as the solvent we will observe a doublet with spacing $\Delta\nu_Q$ due to the quadrupolar splitting. Now, in a chiral liquid crystal, whenever the enantiomers are not ordered the same, we should observe two quadrupolar doublets, one for each enantiomer, as depicted in Figure 4(c).

This is exactly what was observed as may be seen in the example shown in Figure 5. It is clear that integration allows an eventual enantiomeric excess to be measured very easily using this very simple 1D NMR experiment.

3 CHIRAL DISCRIMINATION USING POLYPEPTIDIC LYOTROPIC LIQUID CRYSTALS

Working for a while with the above thermotropic cholesteric mixture[27] lead to two conclusions. The first one is positive as essentially this technique works with almost everything contrary to conventional methods. It does not require a specific strong interaction between the chiral solute and solvent molecules. Here the discrimination between enantiomers arises from a difference in molecular orientational order, or in other words how the *R* and *S* molecules install themselves in the most "comfortable situation" among the chiral liquid crystal molecules. The second one is negative: the cholesteric mixture used so far is based on cholesterol esters, and it must appear evident that this steroidic compound is anything but a good solvent! Consequently we started to search for other chiral liquid crystals that could both exhibit this differential ordering effect of enantiomers and be good solvents and easier to use than thermotropic cholesterics. It was during a visit of Loewenstein as an invited professor in Orsay that we began to use polypeptidic lyotropic liquid crystals[28] and this has been very rewarding. The main advantages of these chiral lyotropic mesophases are listed below.

(a) The samples are easy to prepare: the polymer is dissolved in an organic solvent such as chloroform, methylene chloride, dimethyl formamide or many other helicogenic solvents. The resulting mixture is a good solvent for many organic compounds to be studied.
(b) The order parameters of molecules dissolved in such chiral liquid crystal are small, generally one to two orders of magnitude smaller than in thermotropics ($S \cong 10^{-3} - 10^{-4}$). This is useful because the sense that second order effects are limited compares to thermotropics.
(c) The chiral differentiation power of these media is absolutely fantastic. It works with almost everything, alcohols, amines, ethers, ketones, acids,[29] aminoacids,[30] organometallic complexes, alkynes, alkenes and even with alkanes.[31]

The three NMR anisotropic interactions may be used to differentiate enantiomers, the quadrupolar splitting for nuclei with $I > 1/2$, essentially deuterium, the chemical shift anisotropy or the dipolar spin-spin coupling. Examples for each case are described below.

Many homopolypeptides may be used. The most common are poly-γ-benzyl L-glutamate (PBLG) and poly-ε-carbobenzoxy L-lysine (PCBLL). Furthermore, it is often interesting to make spectra using a racemic mixture of PBLG and PBDG, its enantiomer synthetized from D-glutamic acid. In

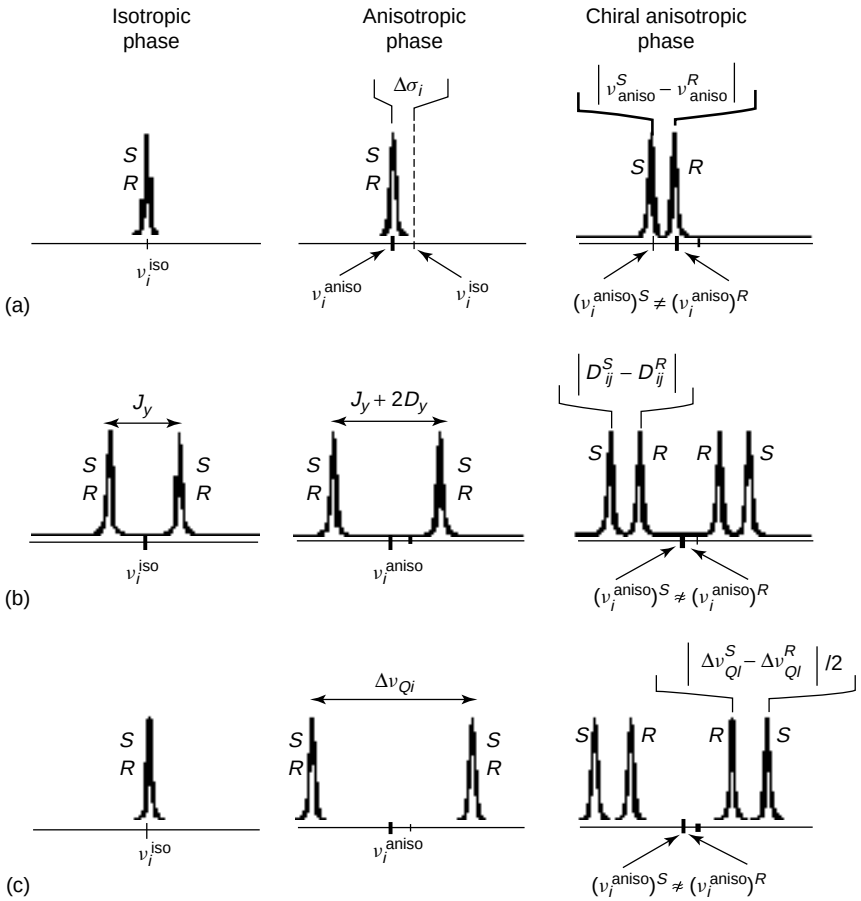

Figure 4 Schematic representation of the effect of a difference in the ordering of enantiomers on the NMR spectra when observing the following interactions (a) chemical shift anisotropy (b) dipolar coupling (c) quadrupolar splitting. (Reproduced by permission of the Royal Society of Chemistry from Sarfati et al.[41])

such a solvent all the effects coming from the chirality of the solvent disappear.

4 CHIRAL DIFFERENTIATION USING QUADRUPOLAR SPLITTING

The principles have been described above. If two deuterated enantiomers are not ordered the same in the polypeptide lyotropic liquid crystal then a quadrupolar doublet will be observed, one for each enantiomer.[29] In Figure 6 is an example on an allenic compound.

Clearly, the quadrupolar splitting is without contest the most sensitive to order differences as, in a diamagnetic molecules, it is the strongest NMR interaction. The main disadvantage is of course that it is necessary to deuterate selectively the molecules because natural abundance deuterium content, 0.015%, is too small to be of routine use at the moment (see Section 9 for the perspectives).

Beside deuterium other quadrupolar nuclei may be used, in the extent where the quadrupolar relaxation is long enough to provide high-resolution spectra. Some interesting applications have been discussed by Hosseini et al. involving ^{133}Cs, ^{11}B or ^{14}N NMR on different ions inserted in chiral cages.[32]

5 CHIRAL DIFFERENTIATION USING CHEMICAL SHIFT ANISOTROPY

It is possible to obtain a chiral discrimination via a difference in the anisotropy of the chemical shift, $\Delta\sigma$, which is also sensitive to order parameters through:

$$\Delta\sigma = \frac{2}{3}\sum \sigma_{\alpha\beta} S_{\alpha\beta}$$

where $S_{\alpha\beta}$ are the elements of the order matrix and $\sigma_{\alpha\beta}$ are the elements of the electronic screening tensor expressed in the same frame. To illustrate the expected effect consider a ^{13}C nucleus in a chiral molecule. Following Figure 4(a), the proton-decoupled spectrum obtainable in classical isotropic NMR is a single line centred on the isotropic shift, ν^{iso}. Using a non chiral nematic solvent the resonance frequency will be different as the chemical shift anisotropy is not averaged to zero anymore, $\nu^{aniso} = \nu^{iso} + \Delta\nu$, where $\Delta\nu = \gamma B_o \Delta\sigma/2\pi$. Here again, $\Delta\nu$ depends on the order parameters and consequently if two enantiomers are not ordered the same we can have $\Delta\nu_R$ different to $\Delta\nu_S$. This will split the signal in two lines, one for each enantiomer. This is exactly what is observed in Figure 7 for most of the aromatic carbons of an enriched mixture of 1,1′-bi-2-naphthols.

Nevertheless, to be efficient this method needs nuclei with a large chemical shift anisotropy. It has been rather successful

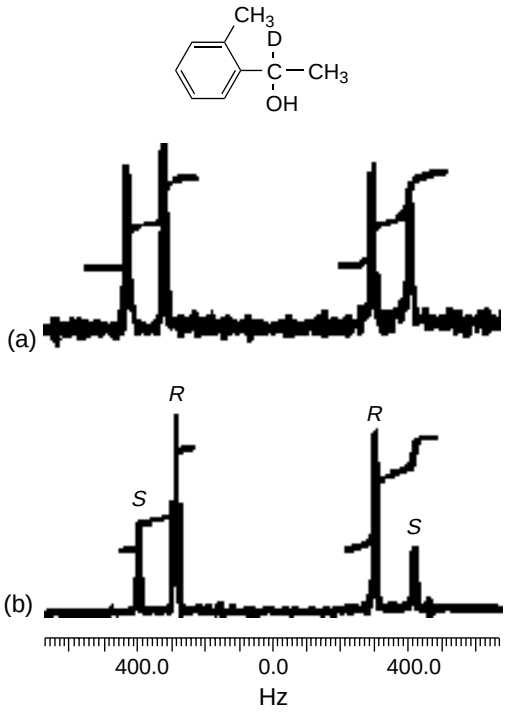

Figure 5 250 MHz proton decoupled deuterium spectrum of a chiral alcohol dissolved in the cholesteric liquid crystal described in the text. Note that we see two quadrupolar doublets, one for each enantiomer. (Reproduced by permission of Taylor and Francis Ltd from Courtieu et al.[26])

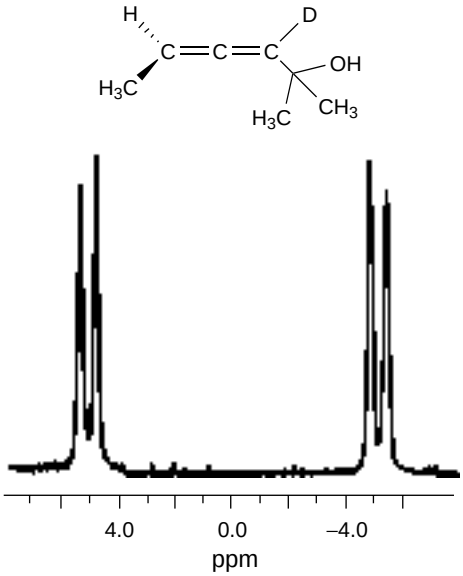

Figure 6 61.4 MHz proton-decoupled deuterium spectrum of a racemic mixture of an allenic alcohol dissolved in the PBLG-CH_2Cl_2 chiral liquid crystal system. Note again a quadrupolar splitting for each enantiomer

using sp and sp^2 ^{13}C, ^{19}F in –N–CO–CF_3 group,[35] ^{77}Se NMR. But the chemical shift anisotropy is generally too small to give measurable effects using NMR on the following nuclei ^{1}H, ^{2}H, sp^3 hybridized ^{13}C, ^{19}F in fluorocarbons, ^{31}P in phospine

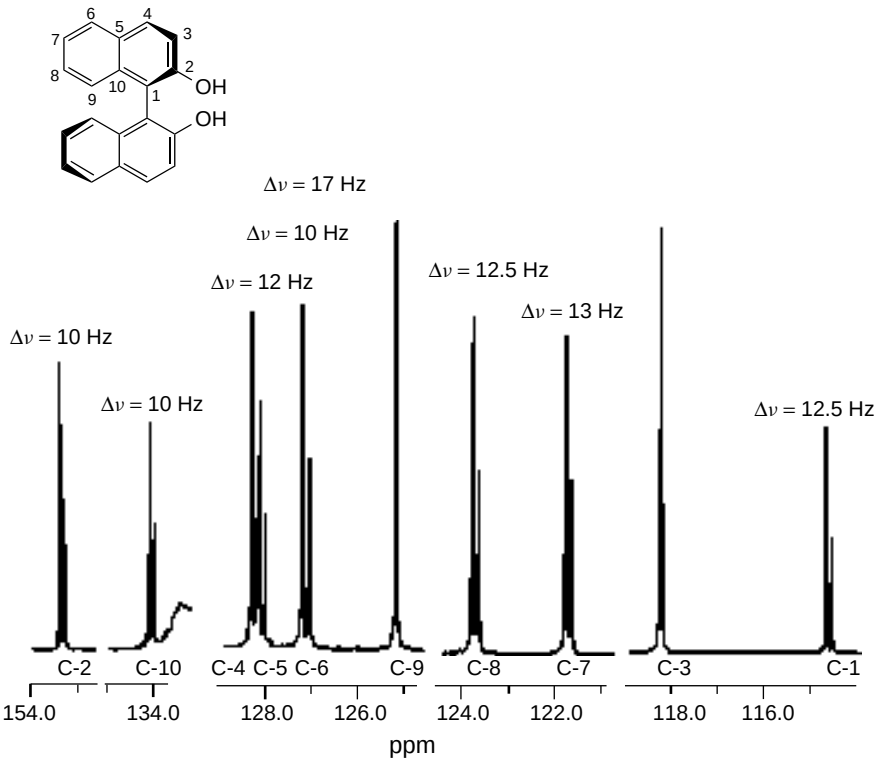

Figure 7 100.1 MHz proton-decoupled carbon-13 spectrum of a non-racemic mixture of the enantiomers of binaphthol dissolved in the PBLG-DMF-d_7 chiral liquid crystal. Note the chiral separation due to the chemical shift anisotropy on many of the ^{13}C transitions. (Reproduced by permission of the American Chemical Society from Meddour et al.[34])

oxides. So using chemical shift anisotropy is far from general and less efficient than the deuterium quadrupolar splitting. However, whenever it works no chemistry is involved to discriminate enantiomers and the use of higher fields will make it more efficient.

6 CHIRAL DIFFERENTIATION USING DIPOLAR COUPLING

Dipolar spin-spin couplings are also sensitive to ordering and may be used to differentiate enantiomers.[34] As already described, inter proton dipolar coupling will generally not be measurable using ^{1}H NMR. Indeed, the large number of couplings, even if they are small with this liquid crystal solvent, usually makes proton NMR lines not resolved. But the rather large dipolar ^{13}C–^{1}H coupling may often be used. To see the effect consider an isolated ^{13}C–^{1}H in a chiral molecule. Using isotropic proton coupled ^{13}C NMR we will observe a doublet due to the isotropic part of the scalar coupling, J_{CH}, as shown in Figure 4(b). In a non-chiral nematic solvent the same experiment will also furnish a doublet but with a different line spacing. This is due to the ^{13}C–^{1}H dipolar coupling that adds to the scalar: $\Delta\nu = J_{CH} + 2D_{CH}$. As D_{CH} is sensitive to order, using a chiral liquid crystal will yield two doublets, one for each enantiomer, when the dipolar couplings are different enough for the *R* and *S* enantiomers. Such an experiment is shown in Figure 8 for different enantiomeric mixtures of (±)-β-(trichloromethyl)-β-propiolactone.

The method is rather general, though less efficient than deuterium NMR. The main limitation here arises when numerous long distance dipolar and scalar couplings make the ^{13}C linewidth large and unresolved. But it works very nicely as soon as there is an isolated group like –COO–CH_3 for instance. Again the advantage here is that no chemistry is involved. It may be noted also that the method works rather well using ^{19}F–^{19}F dipolar coupling in poly-fluorinated compounds.[35]

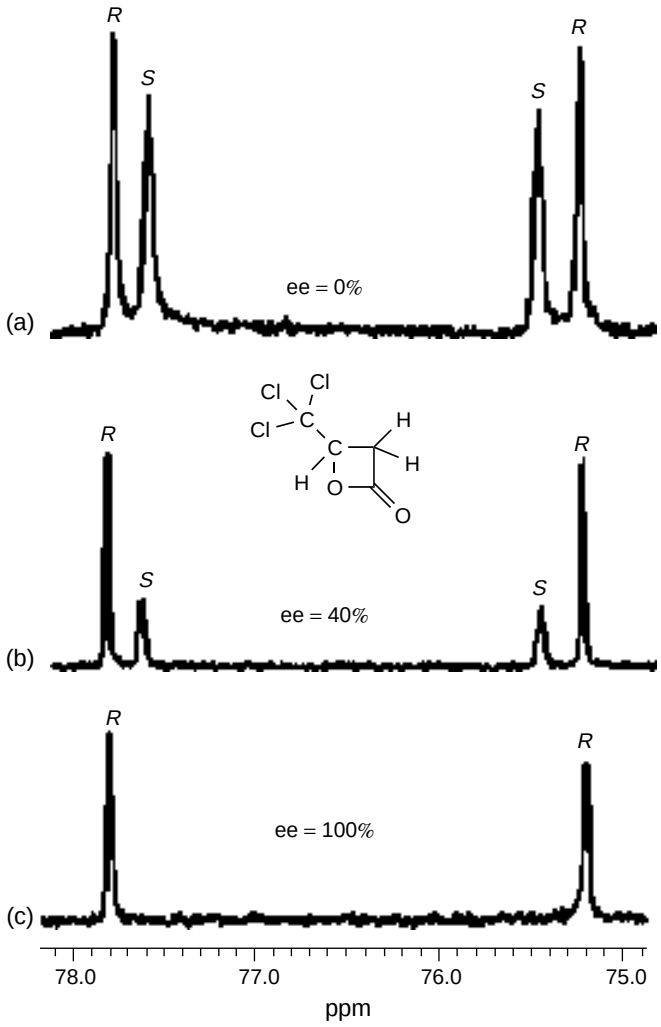

Figure 8 101.1 MHz proton-coupled carbon-13 spectra of the methine group of (±)-β-(trichloromethyl)-β-propiolactone in PBLG-CD_2Cl_2 chiral liquid crystal solvent. (a) Racemic mixture. (b) *R*(+) enriched mixture, 40% *ee*. (c) pure *R*(+) enantiomer. (Reproduced by permission of the Royal Chemical Society from Lesot et al.[33])

7 VISUALIZING ISOTOPIC CHIRALITY

One of the most remarkable properties of these polypeptide liquid crystals is their ability to distinguish perfectly well enantiomers of chiral molecules by virtue of isotopic substitution.[42] An example is shown in Figure 9 of the monodeutero-propionic acid.

In this case the differentiation does not come from a difference in the ordering of the enantiomers. Intuitively, the small difference in geometry between a proton and a deuterium could not produce a differential ordering effect as large as that in Figure 9. Here the discrimination comes from the symmetry properties of the orientational distribution function, which may be lower than the molecular point group symmetry.[44] For instance, for a molecule having a plane of symmetry, C_S, the orientational distribution function in a chiral liquid crystal has no symmetry, C_1, due to the orientational

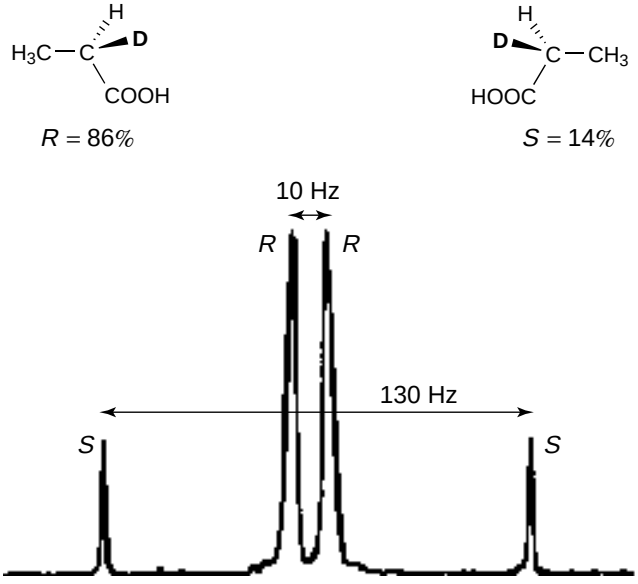

Figure 9 38.4 MHz proton-decoupled deuterium spectrum of *R*-enriched mixture of CH_3–CHD–COOH enantiomers (*ee* 72%) dissolved in PBLG-CD_2Cl_2 chiral liquid crystal. (Reproduced by permission of the American Chemical Society from Meddour et al.[42])

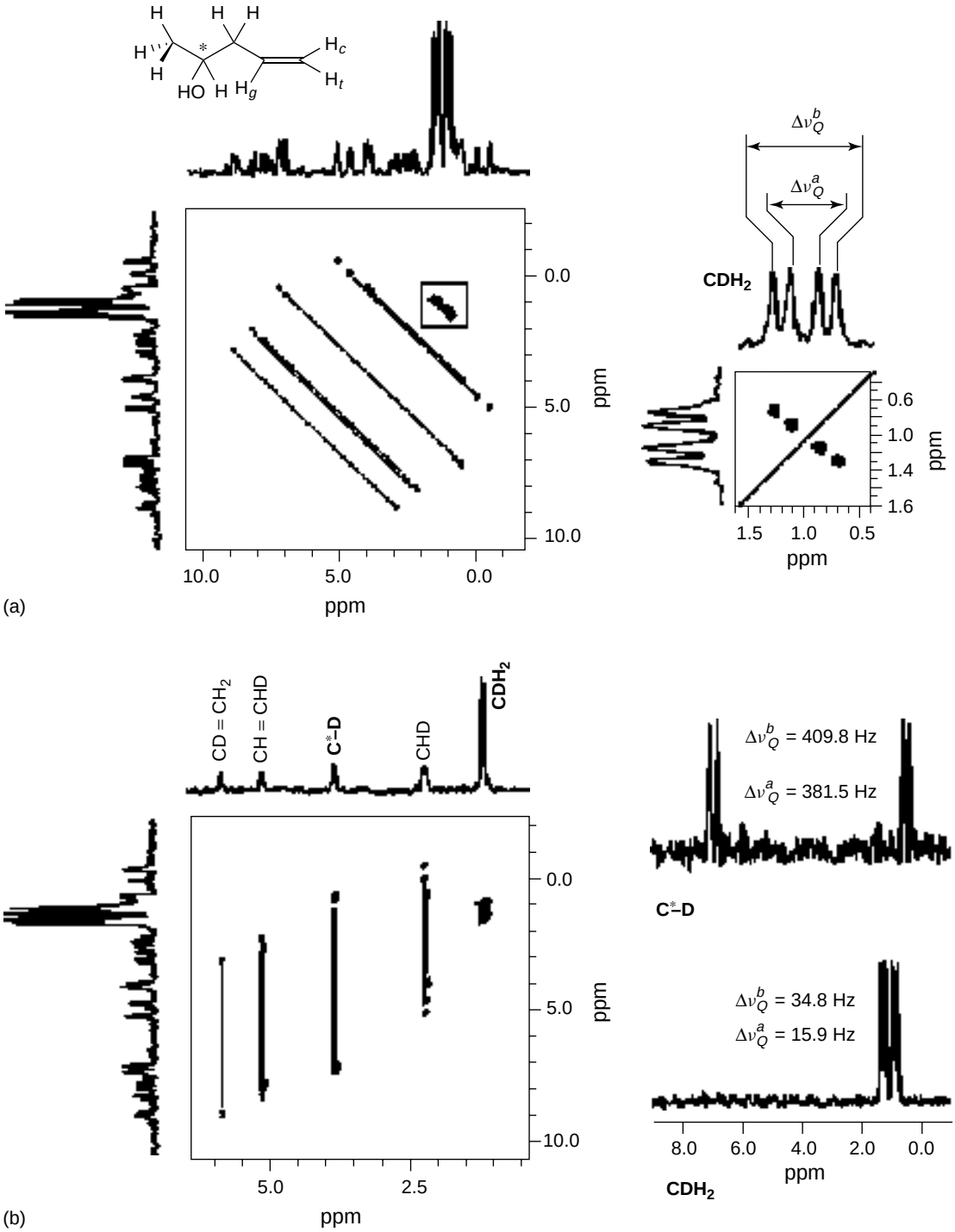

Figure 10 (a) 61.4 MHz natural abundance Q-COSY 2D deuterium spectrum with proton decoupling of a racemic mixture of 4-penten-2-ol. Note that chemical shifts appear along the main diagonal and that quadrupolar doublets lie perpendicular to the diagonal. (b) Same spectrum after a 45° tilt of the 2D matrix. Note that a quadrupolar decoupled spectrum appears in dimension one and that a column extracted at a given chemical shift furnishes a very simple spectrum: a quadrupolar doublet for each enantiomer. Two such columns are shown on the right of the figure. (Reproduced by permission of The Owner Societies from Merlet et al.[43])

chiral field. This means that enantiotopic deuterons in such a C_S molecule are not equivalent as is the case in non-chiral solvents. Consequently one observes a quadrupolar doublet for the pro-*S* and an other one for the pro-*R* deuterons. The chiral discrimination of isotopic enantiomers appears then as a simple consequence of the inequivalence of enantiotopic nuclei.

8 USING ACHIRAL DERIVATIZING AGENTS

When deuteration is not possible and when neither the CSA nor the dipolar coupling give good results there may be the opportunity to use derivatizing agents. Contrary to the classical method in isotropic solvents one does not

need chiral agents when using a chiral solvent, but we do need deuterium nuclei in the agent.[36–40] These achiral, but deuterated, derivatizing agents have the advantage when compared to their chiral equivalent because they react at the same rate with enantiomers and consequently no care has to be taken about the completeness of the reaction.

9 USING NATURAL ABUNDANCE DEUTERIUM

Clearly the deuterium quadrupolar splitting is the most useful way of detecting differences in orientational order. But it generally needs the synthesis of labelled compounds, which may be difficult. Is it possible to work at natural abundance level? Two problems have to be resolved to do so. First, the spectra are going to be quite crowded because we are expecting two quadrupolar doublets for all the possible isotopomers. Second, we will have a severe sensitivity problem as deuterium is only 0.015% abundant. This very low natural abundance results in one of the less sensitive nuclei in the periodic table, 1.45 10^{-6}, relative to proton.

The spectrum-crowding problem has been solved using a specific 2D experiment.[43] The sequence $90° - t_1 - 180° - t_2$ produces a total single quantum coherence transfer between the quadrupolar doublets, resulting in a very simple 2D pattern where the chemical shifts appear along the diagonal and the quadrupolar splitting perpendicular to the diagonal. This technique, called Q-COSY, allows a very straightforward assignment of auto-correlated quadrupolar doublets. An example is shown in Figure 10(a)where two quadrupolar doublets may be observed for each isotopomer of (±)-4-penten-2-ol. In Figure 10(b) the same spectrum is shown following a simple 45° tilt of the original spectrum resulting in a quadrupolar decoupled deuterium spectrum in dimension one. Extracting out a column of the 2D matrix gives a simple 1D spectrum with a doublet for each enantiomer that allows an eventual enantiomeric excess (*ee*) to be measured.

The 2D proton-decoupled deuterium spectra in Figure 10 were obtained at natural abundance levels using a solution containing 100 mg of the molecule and 17 hours acquisition time on a Bruker 400 MHz instrument equipped with a 5 mm o.d. BBI probe. Clearly the sensitivity has to be increased to get a precise *ee* measurement. But we think that higher magnetic fields joined with the use of a specific deuterium cryoprobe could solve the sensitivity problem. Then this technique would become some kind of a panacea for enantiomeric measurements.

10 SUMMARY

When dissolved in polypeptidic lyotropic liquid crystals enantiomers are not ordered the same and consequently all the anisotropic NMR observables are different. This technique, which allows measurements of enantiomeric excesses, is still in its infancy. Many other stereochemical problems need to be addressed. Among them are the differentiation of enantiotopic nuclei[42] and the visualization of diastereoisomers with remote stereogenic centres.[45]

One challenging question remains open: are we going to be able to predict the absolute configurations non-ambiguously? This is an old dream of the NMR spectroscopist, but there is still a lot to do to succeed on this point.

11 REFERENCES

1. G. M. Whitesides and D. W. Lewis, *J. Am. Chem. Soc.*, 1970, **92**, 6979.
2. T. G. Burlingame and W. H. Pirkle, *Tetrahedron Lett.*, 1967, 4039.
3. M. Raban and K. Mislow, *Tetrahedron Lett.*, 1965, 4249.
4. D. Parker, *Chem. Rev.*, 1991, **91**, 1441.
5. A. Saupe and G. Englert, *Phys. Rev. Lett.*, 1963, **11**, 462.
6. P. J. Collings, S. I. Goss, and J. R. McColl, *Phys. Rev. A.*, 1975, **11**, 684.
7. P. G. de Gennes, in 'The Physics of Liquid Crystals', Clarendon Press: Oxford, 1976, p. 238.
8. Z. Luz, R. Poupko, and E. T. Samulski, *J. Chem. Phys.*, 1981, **74**, 5825.
9. J. P. Bayle, E. Lafontaine, and J. Courtieu, *J. Chem. Phys.*, 1988, **85**, 985.
10. E. Sackmann, S. Meiboom, and L. C. Snyder, *J. Am. Chem. Soc.*, 1968, **90**, 2183.
11. A. S. Tracey and P. Diehl, *FEBS Lett.*, 1975, **59**, 131.
12. K. Radley and A. Saupe, *Mol. Phys.*, 1978, **35**, 1405.
13. A. S. Tracey and K. Radley, *J. Phys. Chem.*, 1984, **88**, 6044.
14. K. Radley and A. S. Tracey, *Can. J. Chem.*, 1985, **63**, 95.
15. A. S. Tracey and K. Radley, *Langmuir*, 1990, **6**, 1221.
16. A. Elliott and E. J. Ambrose, *Faraday Soc. Discuss.*, 1950, **9**, 246.
17. C. Robinson, *Trans. Faraday Soc.*, 1955, **52**, 571.
18. C. Robinson, *Mol. Crystals*, 1966, **1**, 467.
19. C. Robinson, *Tetrahedron*, 1961, **13**, 219.
20. E. T. Samulski and A. V. Tobolski, *Macromolecules*, 1968, **1**, 555.
21. S. Sobajima, *J. Phys. Soc. Jpn.*, 1967, **23**, 1070.
22. M. Panar and W. D. Phillips, *J. Am. Chem. Soc.*, 1968, **90**, 3880.
23. E. T. Samulski, in 'Liquid Crystalline Order in Polymers', Academic Press: Oxford, 1978, p. 166.
24. K. Czarniecka and E. T. Samulski, *Mol. Cryst. Liq. Cryst.*, 1981, **63**, 205.
25. J. Courtieu, J. P. Bayle, and E. Lafontaine, *J. Am. Chem. Soc.*, 1989, **111**, 8294.
26. J. Courtieu, E. Lafontaine, J. M. Pechine, and C. L. Mayne, *Liquid Crystals*, 1990, **7**, 293.
27. I. Canet, J. Løvschall, and J. Courtieu, *Liquid Crystals*, 1994, **16**, 405.
28. J. P. Bayle, J. Courtieu, E. Gabetty, A. Loewenstein, and J. M. Pechine, *N. J. Chem.*, 1992, **16**, 837.
29. I. Canet, J. Courtieu, A. Loewenstein, A. Meddour, and J. M. Pechine, *J. Am. Chem. Soc.*, 1995, **117**, 6520.
30. I. Canet, A. Meddour, J. Courtieu, J. L. Canet, and J. Salaun, *J. Am. Chem. Soc.*, 1994, **116**, 2155.
31. M. Sarfati, J. Courtieu, and P. Lesot, *Chem. Commun.*, 2000, 1113.
32. E. Graf, R. Graff, M. W. Hosseini, C. Huguenard, and F. Taulelle, *Chem. Commun.*, 1997, 1459.
33. P. Lesot, D. Merlet, A. Meddour, J. Courtieu, and A. Loewenstein, *J. Chem. Soc. Faraday Trans. II*, 1995, **91**, 1371.
34. A. Meddour, P. Berdague, A. Hedhli, J. Courtieu, and P. Lesot, *J. Am. Chem. Soc.*, 1997, **119**, 4502.
35. M. Jakubcova, A. Meddour, A. Baklouti, J. M. Pechine, and J. Courtieu, J. *Fluorine Chem.*, 1997, **86**, 149.
36. I. Canet, J. L. Canet, J. Courtieu, S. da Silva, J. Gelas, and Y. Troin, *J. Org. Chem.*, 1996, **61**, 9035.
37. A. Meddour, A. Loewenstein, J. M. Pechine, and J. Courtieu, *Tetrahedron Asym.*, 1997, **8**, 485.
38. A. Meddour and J. Courtieu, *Tetrahedron Asym.*, 2000, **11**, 3635.

39. P. Lesot, D. Merlet, J. Courtieu, and J. W. Emsley, *Liquid Crystals*, 1996, **21**, 427.
40. D. Merlet, B. Ancian, J. Courtieu, and P. Lesot, *J. Am. Chem. Soc.*, 1999, **121**, 5249.
41. M. Sarfati, P. Lesot, D. Merlet, and J. Courtieu, *Chem. Commun.*, 2000.
42. A. Meddour, I. Canet, A. Loewenstein, J. M. Pechine, and J. Courtieu, *J. Am. Chem. Soc.*, 1994, **116**, 9652.
43. D. Merlet, M. Sarfati, B. Ancian, J. Courtieu, and P. Lesot, *Phys. Chem. Chem. Phys.*, 2000, **2**, 2283.
44. D. Merlet, J. W. Emsley, P. Lesot, and J. Courtieu, *J. Chem. Phys*, 1999, **111**, 6890.
45. A. Meddour, C. Canlet, L. Blanco, and J. Courtieu, *Angew. Chem. Int. Edn.*, 1999, **38**, 2391.

Biographical Sketches

Jacques Courtieu, *b* 1944. Ph.D. 1974, Chemistry, University of Paris-Sud-Orsay, France. Research associate, University of Utah with D. M. Grant, 1976–78. Lecturer University of Paris-Sud, 1968–83; Professor at University of Paris-sud since 1983. Director, Institute for Molecular Chemistry, Orsay since 1998. Approx. 150 publications. Current research interest: NMR in chiral liquid crystals and its applications in stereochemistry.

Philippe Lesot, *b* 1967. Ph.D. 1995, Chemistry, University of Paris-Sud-Orsay, France. Research associate, University of Southampton with J. W. Emsley, 1995–96. Lecturer, University of Paris-Sud-Orsay 1997–98. Scientific Researcher at the CNRS, Institute for Molecular Chemistry, Orsay since 1998. Approx. 30 publications. Current research interest: NMR methodology in liquid crystal solvents.

Abdelkrim Meddour, *b* 1968. Ph.D. 1996, Chemistry, University of Paris-Sud-Orsay, France. Research associate, Wrije Universteit with R. Willem, 1966–97. Lecturer, University of Paris-Sud-Orsay since 1997. Approx. 20 publications. Current research interest: NMR in oriented systems and stereochemistry.

Denis Merlet, *b* 1970. Ph.D. 1998, Physical-Chemistry, University Paris VII, France. Research associate, University of Southampton with J. W. Emsley, 1998–99. Lecturer, University of Paris-Sud since 1999. Approx. 15 publications. Current research interest: NMR in oriented media.

Christie Aroulanda, *b* 1974. Ph.D. student, Physical Chemistry, University of Paris-Sud-Orsay, France. 4 Publications. Current research interest: NMR in oriented media.

Diamond Thin Films

Karen K. Gleason

Massachusetts Institute of Technology, Cambridge, MA, USA

1	Introduction	1
2	Carbon-13	1
3	Proton NMR	4
4	Fluorine-19 NMR	5
5	Spin–Lattice Relaxation	5
6	Related Articles	6
7	References	6

1 INTRODUCTION

The unique properties of diamond, such as its high thermal conductivity, mechanical characteristics, optical transparency, and semiconductor characteristics, make it an attractive material for many applications.[1] Synthetic diamond powders and single crystals were first made in high-pressure/high-temperature (HPHT) processes in the 1950s. More recently, diamond films have been grown at technologically significant rates using a variety of subatmospheric chemical vapor deposition (CVD) processes. The primary distinction between these CVD techniques is the method by which energy is introduced in order to dissociate and excite the gas phase reactants.[2] Activation of the gas phase diamond precursors has been achieved by direct current (DC) plasmas, microwave (MW) plasmas, hot filaments, and combustion flames. Although significant variations in growth rates exist between these methods, all seem capable of producing highly faceted polycrystalline films with little evidence of nondiamond carbon and with low hydrogen concentrations ($<$0.5 at.%). Thus, diamond films are distinctly different from diamond-like carbon (DLC) films, which are amorphous, can have a significant fraction of sp^2-bonded carbon, and can have $>$30 at.% hydrogen.[3]

The deposition of diamond at low pressures, where it is metastable, appears to involve a kinetic competition between the growth and etching of various forms of carbon ranging from diamond (tetrahedral sp^3 bonded), through amorphous sp^3 and sp^2 configurations, to graphic carbon (sp^2). The range of successful reactant compositions is surprisingly similar for the various types of CVD processes.[3] Diamond films are most commonly deposited from a dilute mixture of hydrocarbons (0.5–2.0%), such as methane or acetylene, in hydrogen. However, studies of carbon sources containing oxygen (e.g. acetone, ethanol, and carbon monoxide) and halogens (fluorine and chlorine) have also shown promising results. The energy introduced into the gas phase produces molecular fragments and excited species which react on the surface of the substrate which is generally maintained at 800–1000 °C.

The hydrogen which is often predominant in the gas phase has been proposed both to stabilize the growing diamond surface and to etch graphitic carbon.[1–3] The electrical resistivity of diamond has been proposed to depend on hydrogen incorporation.[4] Also, increased hydrogen contents correlate with decreased transparency in the 8–10 μm wavelength region, degrading the performance of diamond as an infrared window.[5,6] Thus, the location and distribution of hydrogen can provide insight into diamond deposition chemistry and structure–property relationships in these films.

The commercial exploitation of CVD diamond requires consistent high-quality production, and defect-free films and coatings. While many techniques have been used to evaluate diamond film quality, most provide only qualitative information on which to evaluate differences in deposition conditions. Hydrogen is particularly difficult to measure in solid thin films.[7] The primary advantage of NMR measurements is their quantitative nature. In addition, the low-energy radiofrequency irradiation used in NMR is unlikely to result in chemical alteration of the diamond samples, unlike some higher-energy spectroscopic techniques. To date, diamond has been studied by ^{1}H,[5–10] ^{13}C,[11–22] and ^{19}F[23] NMR, often providing information which is unattainable by other techniques.

For static NMR measurements, one or more sections of a free-standing diamond film, generally $>10\,\mu$m thick, may be inserted directly into the NMR sample coil.[5] By not using a conventional NMR tube or rotor, a potential source of background signal is eliminated.[7] This is a particularly important consideration when studying thin films, since sample sizes are generally limited and the concentration of NMR active nuclei is often low. In addition, the macroscopic integrity of the film is maintained. Similarly, laser-cut disks of free-standing diamond can be stacked into MAS rotors if examination of intact films is desired.[22] Alternatively, powder, formed by crushing a film or removing a very thin film from its substrate, can be packed into an NMR tube or rotor.

In some instances, NMR spectra of films can also be acquired without removing their growth substrates.[17] For such experiments, the substrate must be nonmagnetic, have a low conductivity, have a similar magnetic susceptibility to the diamond film, and must contribute little background signal for the nuclei to be observed. These conditions can be met by using high-resistivity silicon wafers manufactured by the float zone process. The use of thin wafers ($\leq$75 mm in thickness) maximizes the number of film sections which can be inserted into the NMR coil.

2 CARBON-13

The isotropic chemical shift can resolve sp^2- from sp^3-bonded carbon. Bulk diamond is characterized by a single resonance at 36 ± 2 ppm[11] relative to tetramethylsilane (Figure 1).[13] The sp^2 carbon peak generally appears between 120 and 200 ppm, with the lower values observed for amorphous carbon films,[4] while soot gives a peak centered at 189 ppm.[18] The ratio of sp^2/sp^3 bonded carbon is quantitatively determined from the ratio of the integrated area under the peaks corresponding to these respective environments and has been experimentally demonstrated for diamond powder and soot mixture of known weight fraction.[18]

The linewidth of the sp^3 peak of natural diamond in the static ^{13}C spectra is dominated by homonuclear dipole

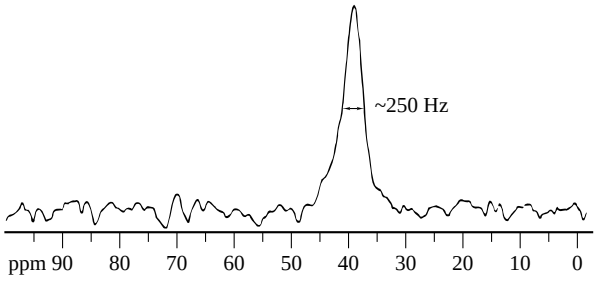

Figure 1 Static direct polarization (DP) ^{13}C NMR at 67.9 MHz of 3 carats of gemstone natural diamonds. The $\Delta\nu_{\frac{1}{2}}$ of 250 Hz includes 50 Hz added Lorentzian broadening. (Adapted from Henrichs et al.)[13]

broadening. The second moment of this interaction can be calculated via the Van Vleck equation:[12,25]

$$M_2 = \tfrac{3}{4}\gamma^4\hbar^2 I(I+1) f \sum_k \frac{(1-3\cos^2\theta_{jk})^2}{r_{jk}^6} \qquad (1)$$

where r_{jk} is the distance between two sites, and f is the fraction of these sites randomly occupied by the NMR-active nuclei of interest. The dependence on θ_{jk}, the angle the intersite vector makes with the external magnetic field, causes M_2 for a powdered sample to differ from that of a single crystal having an identical chemical structure. When active nuclear spins are dilute ($f < 0.01$), a truncated Lorentzian lineshape results, with a full width given by

$$\Delta\nu_{1/2} = \frac{\pi}{\sqrt{3}}\left(\frac{M_2^2}{M_4}\right)^{1/2}(M_2)^{1/2} \qquad (2)$$

Note that the point chosen for truncation influences the ratio $M_2{}^2/M_4$. For higher spin densities, a Gaussian lineshape is observed, with a linewidth of

$$\Delta\nu_{1/2} = 2.35(M_2)^{1/2} \qquad (3)$$

These linewidths are independent of the applied magnetic field; hence, chemical shift resolution can be improved at higher fields.

Using equation (1) for a diamond lattice with a natural abundance of ^{13}C (f = 0.011) yields M_2 = 0.037 kHz^2 for a single crystal oriented with its (014) axis parallel to the external magnetic field, which compares favorably with the measured value of M_2 = 0.041 kHz^2, confirming that homonuclear dipolar interactions are the dominant source of broadening in this environment.[12] The corresponding observed lineshape is a truncated Lorentzian with $\Delta\nu_{\frac{1}{2}}$ = 200 Hz,[12] similar to that shown in Figure 1.[13]

In materials with high hydrogen concentrations, like polymers and DLC films,[24] CP can be used to enhance the ^{13}C spectrum. However, variations in CP dynamics can cause the quantitative character of the NMR experiment to be lost. The low hydrogen concentrations found in polycrystalline diamond films make CP difficult, although achievable.[14] In the vicinity of hydrogen, where CP is most efficient, only sp^3-bonded carbon nuclei were detected. Also, because ^{1}H–^{13}C heteronuclear dipole couplings are generally negligible in diamond films, proton decoupling is often not required. Direct polarization (DP) ^{13}C NMR, while requiring larger samples, is a means of obtaining quantitative sp^2/sp^3 ratios. Typically, $>5 \times 10^{18}$ ^{13}C nuclei are required,[18] corresponding to ~10 mg of a natural abundance diamond, which is equivalent to a 10 μm thick film over an area of 2.8 cm^2.

In samples which are free of paramagnetic defects, DP NMR experiments are quantitative in that each ^{13}C nucleus gives rise to the same integrated signal intensity, regardless of its bonding environment. In samples containing paramagnetic impurities, a small fraction of nuclei in close proximity to such defects will remain undetected as a result of extreme line broadening due to interaction with the unpaired electron of the paramagnetic impurity.[12,13] However, only a small fraction of nuclei should be affected by the paramagnetic densities (10^{17}–10^{18} g^{-1}) in diamond films.[20,21] This assumption can be verified by comparing the experimental signal intensity to the expected intensity based on mass and ^{13}C enrichment in the sample and response of the spectrometer to standards of known ^{13}C content. Fortunately, these experiments show that the effects of broadening by paramagnetic centers are often below the NMR detection limit.[18] For quantitative measurements, it is also important to insure that a sufficient delay ($\geq 5T_1$) is used between signal acquisitions.

Isotopic enrichment can be used to decrease sample size requirements.[17–19,21] The spin–lattice relaxation rate will also increase as a result of enhanced spin diffusion in the ^{13}C-enriched samples. Both factors lead to increased sensitivity and/or decreased acquisition times. The concentration of ^{13}C in the solid film can be determined via the second moment of the homonuclear dipole couplings [see equation (1)]. The degree of enrichment determined in this manner is in excellent agreement with measurements of the isotopic shift of the diamond one-phonon absorption in the Raman spectra.[19] However, enrichments >25% will limit spectral resolution of sp^2 versus sp^3 carbon due to homonuclear dipolar line broadening [see equation (1)]. Resolution may be restored by MAS at speeds greater than the ^{13}C–^{13}C homonuclear dipole broadening in hertz, i.e. spinning frequencies of more than 4 kHz.

Selective isotopic labeling can be used to gain insight into the chemistry of diamond formation when more than one chemically distinct carbon is present in the gas phase reactant mixture.[17–19] For instance, films have been grown using acetone, selectively ^{13}C labeled at either the methyl or carbonyl site, as the reactive carbon source. Measuring the resulting ^{13}C concentration in a pair of otherwise identical films determines the relative efficiency at which the methyl and carbonyl sites from the selectively labeled acetone are incorporated into diamond. When such experiments are carried out in a hot filament reactor, both labels are incorporated equally when a tantalum filament is used.[17,18] In contrast, diamond deposits preferentially from the methyl site when a rhenium filament is employed.[19] However, some growth from the carbonyl site is still observed when rhenium is used. Such experiments demonstrate the importance of heterogeneous chemistry at the filament in this type of CVD reactor.

In polycrystalline CVD films, the diamond peak is nearly symmetric, revealing little CSA, as expected for a tetrahedrally symmetric bonding environment. For static spectra, the $\Delta\nu_{\frac{1}{2}}$ ranges from 310 to 500 Hz in unenriched films,[18,21] indicating broadening in addition to homonuclear dipole interactions. MAS at sufficient speeds can average broadening due

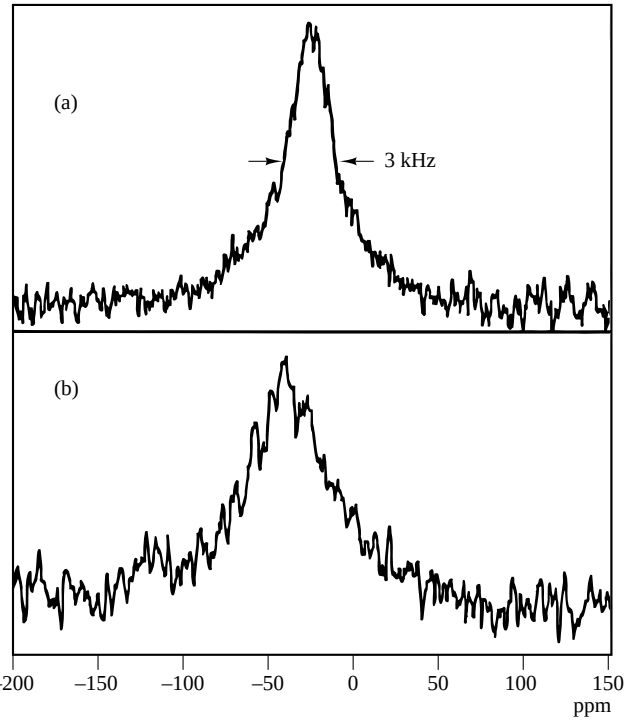

Figure 2 Static DP ^{13}C NMR at 75 MHz of two CVD diamond films, enriched to 22% ^{13}C. (a) The highly faceted film shows only the 36 ppm resonance characteristic of sp^3 bonding environments. (b) A broader sp^3 peak and a second peak at ~120 ppm due to sp^2 carbon are seen in the second film, which also has much poorer morphology. (Adapted from McNamara et al.)[18]

to dipolar interactions, CSA, and variations in magnetic susceptibility. Thus, any remaining broadening can be attributed to a wider distribution of bond angles and lengths in the film. A highly faceted hot filament film on its substrate, with 22% ^{13}C enrichment, produces a symmetric Gaussian lineshape with $\Delta\nu_{\frac{1}{2}} \sim 3$ kHz [Figure 2(a)],[17] in reasonable agreement with equations (1) and (3). Upon crushing this sample and performing MAS, the $\Delta\nu_{\frac{1}{2}}$ was reduced to 150 Hz. Variations in MAS $\Delta\nu_{\frac{1}{2}}$ from 6 to 55 Hz in natural abundance samples have been linearly correlated to increases in Raman one-phonon linewidth, which is also associated with increasing disorder of the diamond phase.[21]

Asymmetry in the sp^2 peak is expected as a result of CSA and/or bond angle disorder. Unfortunately, sp^2-bonded carbon in visibly faceted films produced via hot filament, DC arc jet, or MW plasma CVD is generally below the ^{13}C NMR detection limit.[18] An sp^2 resonance has been observed in a film of poor morphology and no detectable diamond one-phonon Raman absorption.[17] This film was prepared under identical conditions to the highly faceted hot filament film discussed above [Figure 2(a)], with the sole exception that the C/H ratio in gas feed was increased, resulting in poorer film quality. The static NMR spectra of this 22% enriched film, intact on its substrate, resolves both broad sp^2 and sp^3 peaks at ~120 and ~38 ppm, respectively [Figure 2(b)]. The ratio of the areas of these two peaks gives a quantitative sp^2/sp^3 ratio of 0.11 ± 0.2, indicating that ~10% of the carbon in this film is bonded in an sp^2 configuration. The MAS linewidth of the sp^3 peak narrows to only $\Delta\nu_{\frac{1}{2}} = 690$ Hz, indicating some disorder in the sp^3 environment, while the lineshape of the sp^2 peak remains relatively unaltered, indicating a high degree of disorder in this phase.

Quantitative sp^2/sp^3 ratios measured by solid state ^{13}C NMR have been compared with qualitative results of Raman spectroscopy,[18] one of the most widely used techniques for characterizing diamond thin films. Raman is sensitive to both the sp^2 and sp^3 bonding environments but is difficult to quantify since the scattering efficiency of sp^2-bonded carbon differs from sp^3-bonded material, and each may vary from film to film. In addition, the sp^2- and sp^3-bonded carbons may have different absorptivities, which can lead to nonuniform sampling as a function of depth in the film.

As expected, Raman spectroscopy is extremely sensitive to sp^2-bonded carbon, identifying small amounts below the detection limit of the NMR spectrometer. Comparison of the two techniques, however, indicates that Raman spectroscopy may be so sensitive to sp^2-bonded carbon that sp^3-bonded carbon in films containing as much as 90% sp^3-bonded material may remain undetected. This is undesirable when new deposition conditions are being explored, since conditions which yield a majority of sp^3-bonded sites can be overlooked by the Raman analysis.

These two techniques also differ in that NMR spectroscopy is sensitive to short-range order, while Raman spectroscopy probes order over a longer range. NMR provides only information averaged over the entire sample volume and requires relatively large samples and long acquisition times. Raman spectroscopy has the advantage of giving fast, spatially resolved information. A combination of the two techniques is desirable for obtaining reliable information for all types of diamond.

Another method for enhancing the sensitivity of NMR for characterizing diamond films is DNP.[20,21] The work on diamond films builds upon earlier DNP investigations of natural and HPHT diamond.[15,16] Polarization from paramagnetic defects is transferred to the nuclear spin reservoir by simultaneous irradiation at the electron spin and ^{13}C Larmor frequencies. The ^{13}C nuclei close to paramagnetic sites polarize most quickly. Thus, the local composition can be investigated as a function of distance from the paramagnetic sites using variable contact time experiments. Often DNP is combined with MAS in order to suppress spin diffusion.[16] When DNP is combined with CP from ^{1}H nuclei, hydrogenated regions can be selectively probed.[20,21]

The 1.4 T ^{13}C DNP MAS spectra of CVD diamond have been published for an 83 mg natural abundance sample (Figure 3) and for two ~14% enriched samples of 20 and 29 mg, respectively. Although acquisition time is reduced by using DNP, this advantage is somewhat offset by the use of high magnetic fields by the more commonly available conventional NMR spectrometers.[20] The ^{13}C DP MAS spectra of the enriched samples was also acquired on a conventional NMR spectrometer, using a 14 T magnet.[21] In addition, the static DP spectra of the same three samples had previously been reported using a 7 T NMR spectrometer.[18]

The main feature of the three DNP MAS spectra is a characteristic line at 36 ppm (Figure 3), which is also observed for bulk diamond. In some cases, a small, broad shoulder on this peak at ~45 ppm has been identified as hydrogenated sp^3-bonded carbon through its response to both $^{1}H-^{13}C$ variable CP contact times and dipolar dephasing experiments.[21] This

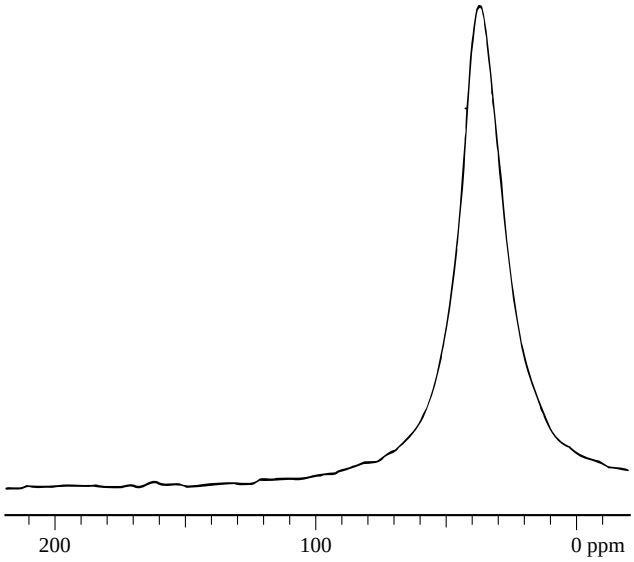

Figure 3 Static DP–DNP ^{13}C NMR at 15 MHz of natural isotopic abundance CVD diamond film, showing only the characteristic peak for diamond. (Adapted from Lock and Maciel[20])

position falls in the calculated chemical shift range of 25–54 ppm for saturated hydrocarbons with an underlying diamond skeleton. These calculations start with adamantane and progress through fully hydrogen-terminated diamond surfaces, and are compared to experimental measurements where possible.[21] A sharp peak centered at 28 ppm, observed only in DP MAS experiments may indicate freely rotating methyl groups. Only when intermediate $^{1}H-^{13}C$ CP contact times were employed with the DNP MAS experiments was a broad, weak resonance observed at ~140 ppm in one of the enriched films. This peak was not observed using DNP MAS in the absence of CP, suggesting this sp^2-bonded carbon is localized near hydrogenated sites. Unfortunately, the sp^2/sp^3 ratio could not be quantified because the polarization dynamics from both the paramagnetic defects and the proton reservoir are not well known in these samples.

3 PROTON NMR

Figure 4 shows representative ^{1}H NMR spectra, taken at a Larmor frequency of 270 MHz.[5–10] Approximately 1500 signal transients were acquired at a repetition rate of 5 s, in accordance with typical proton T_1s of less than 1 s in these samples, which contained $>10^{17}$ total proton spins. By not using an NMR sample tube and purging the NMR probe with dry nitrogen, the need for background subtraction was eliminated. Integrating such spectra yields concentrations ranging from <0.017 to ~0.5 at.% hydrogen, depending upon the exact film growth conditions used. The concentrations of hydrogen determined by NMR were used to quantify the CH_x stretching absorption in the infrared spectra of the same films. The infrared spectra reveal that the hydrogen is bonded covalently to the diamond lattice primarily as CH, CH_2, and CH_3 groups,[5,6] with some $-OCH_3$ and $-NCH_3$ moieties also possible.[10]

The ^{1}H spectra in Figure 4 are well represented by two components, a narrow Lorentzian and a broad Gaussian,[5] as shown

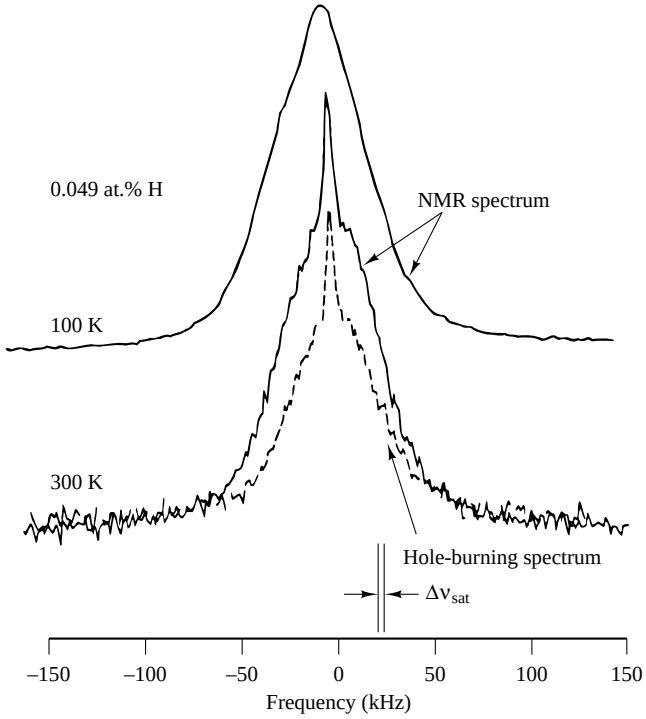

Figure 4 Static ^{1}H NMR spectra at 270 MHz of a free-standing diamond film (solid lines). Two components are resolved at 300 K (middle), but the sharp Lorentzian is broadened when the temperature is decreased to 100 K (top). A 300 K 'hole-burning' experiment (bottom, dashed line) shows uniform attenuation of both components after selective irradiation of the small band, $\Delta\nu_{sat}$, indicating dipolar communication among the two resolved proton environments

by the solid line representing a least squares fit to the data, indicating at least two different bonding configurations for hydrogen in polycrystalline diamond. Similar two-component proton lineshapes, with different narrow to broad ratios, have been observed from films deposited by a variety of CVD processes.[9,10] However, in CVD diamond with relatively high hydrogen concentrations, often only the broad feature can be resolved.[21]

A 'hole-burning' NMR experiment shows that these two resolved hydrogen environments are in close proximity.[5] When a 1 kHz-wide region, 20 kHz from the center of the lineshape, was selectively saturated, uniform attenuation of both components is observed after a 2 ms delay (Figure 4). This indicates that rapid dipolar communication occurs between protons in the two environments, requiring internuclear distances of less than 50 nm. Figure 4 also shows that at 100 K the Lorentzian component is broadened, while the Gaussian component is not significantly affected.[5] Thus, at room temperature, the narrow Lorentzian lineshape results from motional averaging, while the broad Gaussian line indicates rigidly held hydrogen. The CRAMPS ^{1}H spectra show an unresolved peak centered at ~2 ppm.[20]

The homonuclear broadening resulting from static distributions of hydrogen bonded in a rigid polycrystalline lattice can be calculated by the van Vleck equation [see equation (1)]. For polycrystalline diamond samples, if all the hydrogen in the Gaussian component were randomly distributed as CH, the resulting $\Delta\nu_{\frac{1}{2}}$ range would be more than

two orders of magnitude smaller than typically observed values of ∼60 kHz. Randomly dispersed CH_2 groups also provide too little homonuclear broadening. These discrepancies indicate locally high hydrogen concentrations, requiring significant segregation of hydrogen in polycrystalline diamond.[5,6] However, this analysis cannot distinguish between isolated small clusters and larger groupings of spins.

Possible locations for segregation are hydrogen-decorated defects and voids within the crystal, a heavily hydrogenated phase stable at the deposition temperature or at the grain boundaries in polycrystalline diamond.[5] If hydrogen was uniformly distributed on a surface, a density of 3×10^{15} H cm^{-2} would be required to give the observed $\Delta\nu_{\frac{1}{2}} = 60$ kHz. This compares favorably with areal densities of 3.1×10^{15}, 2.2×10^{15}, and 1.8×10^{15} H cm^{-2} for fully hydrogen passivated, unreconstructed ⟨100⟩, ⟨110⟩, and ⟨111⟩ diamond surfaces, respectively. In order to account for the NMR-observed bulk hydrogen incorporation of 0.01–0.22 at.%, monolayer hydrogen coverage of films composed of 0.5–150 μm cubes is required, dimensions which compare favorably to observed crystallite sizes in CVD films.[6] The structure of hydrogenated surfaces present during growth may resemble those preserved at grain boundaries, which would allow these ^{1}H NMR measurements to act as a potential test of surface chemistry models of diamond growth.

The assumption of a surface distribution of hydrogen in polycrystalline diamond films is also supported by multiple quantum (MQ) NMR studies.[8] Figure 5 shows the rate at which groups of protons are effectively correlated with increasing dimensionless MQ excitation time, $M_2^{\frac{1}{2}}\tau$, for two hot filament diamond films (CVD-1 and CVD-2) and one DC arc jet film (CVD-3). Initially, the data for the films are coincident with a known surface distribution of protons, hydrogenated diamond powder, and slower than that of known bulk hydrogen distributions, such as exist in CaH_2. Up to 20 spins were correlated in the films despite the very low (<0.1 at.%) bulk concentrations, confirming the large-scale clustering of hydrogen, most likely in a two-dimensional distribution. The morphology of hydrogen incorporated into these films, as determined by MQ NMR, depends only weakly on the manufacturing process, suggesting that similar surface chemistry has occurred in both types of reactors.

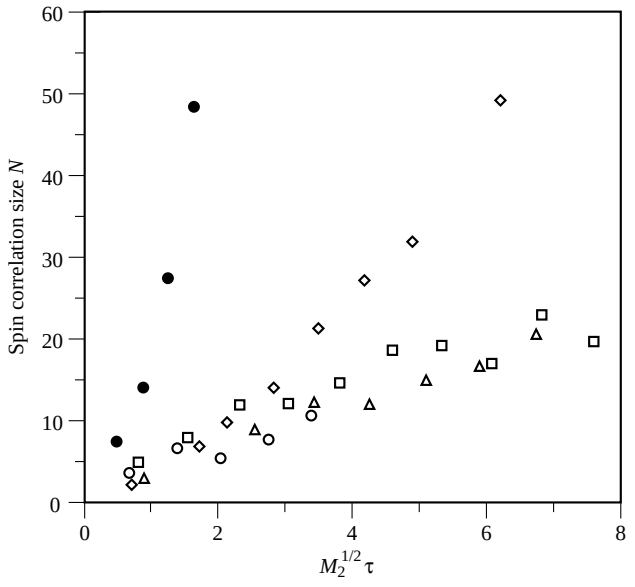

Figure 5 The number of effectively correlated protons (N) versus the dimensionless MQ excitation time, $M_2{}^{1/2}\tau$. The CaH_2 data (•) fall on the universal curve for MQ growth of three-dimensional proton distributions. This growth is faster than for two-dimensional systems, represented by the hydrogenated diamond powder data (◊). The MQ growth of the three different CVD samples (□, CVD-1; △, CVD-2; ○, CVD-3) is similar to that of the hydrogenated diamond powder at early excitation times. Nearly 20 protons are correlated in these films which have <0.5 at.% hydrogen, confirming the presence of large-scale hydrogen segregation. (Adapted from Levy and Gleason[8])

4 FLUORINE-19 NMR

The lower substrate temperatures which have been achieved using fluorine-containing CVD reactants[26] opens the possibility of depositing diamond onto materials of low thermal stability, such as organic polymers. In addition, fluorination has been proposed to enhance the chemical inertness and lower the coefficient of friction of diamond surfaces.[27] Thus, knowledge of surface passivation of diamond by fluorine is desirable.

Solid state ^{19}F NMR has been used to characterize the surfaces of diamond powder after 100% CF_4 and 98% CF_4/2% O_2 radiofrequency plasma treatments.[23] The pure CF_4 plasma results in 7.1×10^{14} F cm^{-2}, a coverage equivalent to approximately half of the available surface bond density. With the addition of 2% O_2, the equivalent coverage is reduced by roughly an order of magnitude, to 7.4×10^{13} F cm^{-2}. MQ NMR reveals that ^{19}F is not distributed uniformly on either surface.

High-speed MAS was used to average the effects of chemical shift anisotropy (Figure 6). On both surfaces, only CF_x (x = 1–3) functionalities were observed, with the predominant species being carbon monofluoride. Only 5–10% of the fluorine was bonded as CF_3. The isotropic chemical shifts were resolved and assigned relative to $CFCl_3$ as follows: CF = 148 ± 1 ppm; CF_2 = 106 ± 2 and 123 ppm; CF_3 = 78 ± 1 ppm. The peak at 123 ppm was only observed in the CF_4/O_2 plasma-treated sample, and is speculated to be the result of atomic fluorine etching of diamond.

5 SPIN–LATTICE RELAXATION

Paramagnetic defects facilitate spin–lattice relaxation in both natural and synthetic diamond.[12,13] At a fixed degree of enrichment, an increase in the ^{13}C T_1 qualitatively indicates a lower relaxation center density, hence an increase in crystal quality. The T_1s of commercial natural diamond powder are on the order of tens of seconds, while significantly longer time constants, on the order of a few hours, can be observed for large, gem-quality natural diamonds. An increase in T_1 has also been observed within a series of CVD diamond films as the morphology, observed by scanning electron microscopy, improved.[17] However, detailed quantitative studies of T_1 behavior, analogous to those on single crystal diamond,[12] are often hindered by the higher complexity of defect distributions in the polycrystalline films.

Paramagnetic defects in diamond result from either unsatisfied bonding arrangements, so-called dangling bonds, present

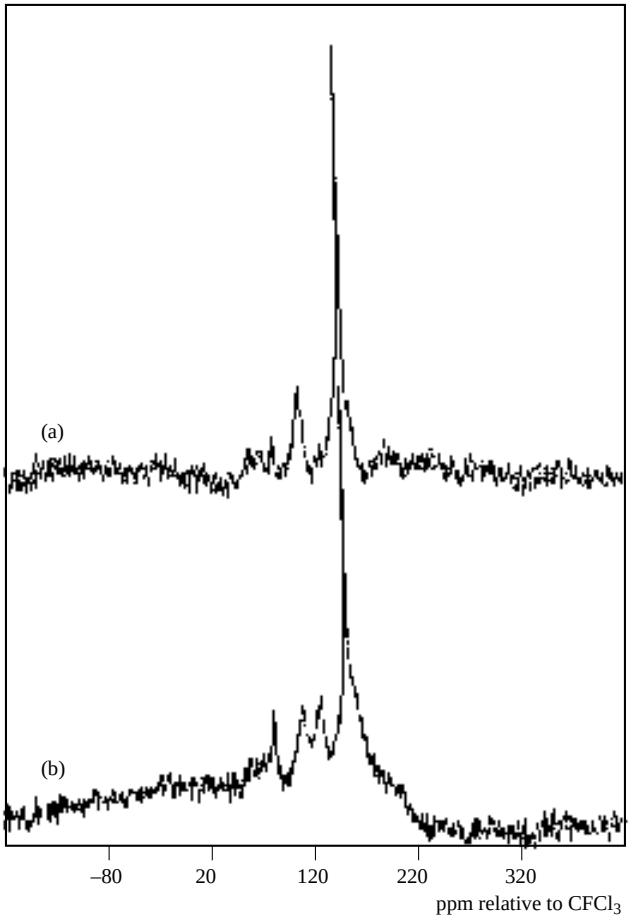

Figure 6 Room-temperature, high-speed (15 kHz) MAS ^{19}F NMR spectra at 376.5 MHz of diamond powder surfaces, fluorinated by two different methods. (Adapted from Scruggs and Gleason[23])

either internally or at the surface of a crystal or from impurity incorporation. Nitrogen is a common impurity that gives rise to a variety of ESR-active centers.[28] Often these sites act as color centers, providing a visible manifestation of their presence. Boron incorporation imparts a blue color, and is sometimes intentionally used to produce p-type semiconducting diamond (type IIb).[12] However, most impurities are unintentionally introduced. For example, ferromagnetic impurities originating from the catalyst are common in HPHT synthetic diamond, and metallic impurities from the hot filament used are common in this variety of CVD film.

The ^{13}C spin–lattice relaxation of diamond can be described by[21]

$$M(t) = M_0\{1 - \exp[-(t/T_1)^x]\} \quad (4)$$

where x is constrained by the limits, $0.5 \leq x \leq 1.0$, and M_0 is the equilibrium magnetization. For the upper bound, x = 1.0, equation (4) represents simple exponential relaxation, as predicted from the Bloch equations. In this case, every ^{13}C site has the same relaxation rate. In diamond, this limit occurs if spin diffusion among the ^{13}C nuclei is fast compared with the rate at which an individual ^{13}C nucleus relaxes as a result of a neighboring paramagnetic site. If the situation is reversed, poor communication among the ^{13}C nuclei requires that each relaxes directly with a neighboring paramagnetic site. Since there is a distribution of ^{13}C to paramagnetic site distances, a dispersion of spin–lattice relaxation rates results. Fortunately, integration over all possible rates, with appropriate assumptions, simplifies to equation (4) with x = 0.5.[13]

An excellent consideration of influence of direct ^{13}C relaxation to paramagnetic defects in comparison to spin diffusion rates in diamond is provided by Hoch et al.[12] Unfortunately, both limits as well as mixed behavior are possible. Spin diffusion is slowed when no ^{13}C enrichment is employed and MAS is used. Thus, behavior approaching the x = 0.5 limit has been observed for MAS spectra of samples having natural abundance or a 14% ^{13}C enrichment.[20,21] In contrast, pure exponential behavior (x = 1.0) is observed in static spectra of more highly enriched (22%) samples.[16] Analysis of spin diffusion rates as a function of enrichment suggests that paramagnetic centers are distributed uniformly in polycrystalline CVD diamond films, rather than being localized at grain boundaries.[14]

Short spin–lattice relaxation time constants have been reported for of both ^{1}H and ^{19}F bonded to diamond. These fast rates suggest paramagnetic centers contribute to spin–lattice relaxation and are further enhanced by rapid spin diffusion among these clustered, high-gyromagnetic ratio nuclei. For ^{1}H, room temperature T_1 values are in the range of 5 ms to 1 s.[8,9,21] These values increase after annealing CVD diamond at 500–750 °C suggesting passivation of paramagnetic centers.[9] The relaxation appears nonexponential, but exact determination of x [see equation (4)], involves a large degree of uncertainty due to the low signal levels available.[9,21,23] Also, caution must be applied in directly interpreting x, since multicomponent relaxation, motion, and, in the case of ^{19}F, CSA can also lead to nonexponential relaxation. For ^{19}F, nonexponential spin–lattice relaxation with a time constant of ~0.5 s has been observed for two samples at room temperature.[23] The ^{19}F T_1 increases as the temperature is lowered to 150 K, but remains fixed upon further decreasing the temperature to 100 K. This behavior is consistent with changes in the static ^{19}F lineshape, indicating motion is occurring at room temperature.

6 RELATED ARTICLES

Amorphous Silicon Alloys; Chemical Shift Tensors; Coal Structure from Solid State NMR; Cokes; Cross Polarization in Solids; Dynamic Nuclear Polarization and High-Resolution NMR of Solids; Fluorine-19 NMR; Fossil Fuels; Magic Angle Spinning; Multiple Quantum NMR in Solids; Silica Surfaces: Characterization; Spectral Editing Techniques: Hydrocarbon Solids.

7 REFERENCES

1. (a) R. C. DeVries, *Am. Rev. Mater. Sci.*, 1987, **17**, 161. (b) F. G. Celii and J. E. Butler, *Ann. Rev. Phys. Chem.*, 1991, **42**, 64.
2. P. K. Bachmann, D. Leers, and H. Lydtin, *Diamond Rel. Mater.*, 1991, **1**, 1.
3. M. I. Landstrass and K. V. Ravi, *Appl. Phys. Lett.*, 1989, **55**, 1391.

4. M. A. Petrich, *Mater. Sci. Forum*, 1989, **52–53**, 387.
5. K. M. McNamara, D. H. Levy, K. K. Gleason, and C. J. Robinson, *Appl. Phys. Letts.*, 1992, **60**, 580.
6. K. M. McNamara, K. K. Gleason, and C. J. Robinson, *J. Vac. Sci. Technol. A.*, 1992, **10**, 3143.
7. D. H. Levy and K. K. Gleason, *J. Vac. Sci. Technol. A.*, 1993, **11**, 195.
8. D. H. Levy and K. K. Gleason, *J. Phys. Chem.*, 1992, **31**, 8125.
9. S. Mitra and K. K. Gleason, *Diamond Rel. Mater.*, 1993, **2**, 1145.
10. K. M. McNamara and K. K. Gleason, *Chem. Mater.*, 1994, **6**, 39.
11. (a) H. L. Retcofsky and R. A. Friedel, *J. Phys. Chem.*, 1973, **77**, 68. (b) C. A. Wilkie, T. C. Ehlert, and D. T. Haworth, *J. Inorg. Nucl. Chem.*, 1978, **40**, 1983.
12. M. J. R. Hoch and E. C. Reynhardt, *Phys. Rev. B*, 1988, **37**, 9222.
13. P. M. Henrichs, M. L. Cofield, R. H. Young, and J. M. Hewitt, *J. Magn. Reson.*, 1984, **58**, 85.
14. M. Pruski, D. P. Lang, S-J. Hwang, H. Jia, and J. Shinar, *Phys. Rev. B*, 1994, **49**, 10635.
15. M. J. Duijvestijn, C. van der Lugt, J. Smidt, R. A. Wind, K. W. Zilm, and D. C. Staplen, *Chem. Phys. Lett.*, 1983, **102**, 25.
16. R. A. Wind, M. J. Duijvestijn, C. van der Lugt, A. Manenschijn, and J. Vriend, *Prog. NMR Spectrosc.*, 1985, **17**, 33.
17. K. M. McNamara and K. K. Gleason, *J. Appl. Phys.*, 1992, **71**, 2884.
18. K. M. McNamara, K. K. Gleason, D. J. Vestyck and J. Butler, *Diamond Rel. Mater.*, 1992, **1**, 1145.
19. K. M. McNamara and K. K. Gleason, *J. Electrochem. Soc.*, 1993, **140**, L22.
20. H. Lock and G. E. Maciel, *J. Mater. Res.*, 1992, **7**, 1291.
21. H. Lock, R. A. Wind, G. E. Maciel, and C. E. Johnson, *J. Chem. Phys.*, 1993, **99**, 3363.
22. L. H. Merwin, C. E. Johnson, and W. A. Weimer, *J. Mater. Res.*, 1994, **9**, 631.
23. B. E. Scruggs and K. K. Gleason, *J. Phys. Chem.*, 1993, **97**, 9187.
24. S. Kaplan, F. Jansen, and M. Machonkin, *Appl. Phys. Lett.*, 1985, **47**, 750.
25. A. Abragam, *Principles of Nuclear Magnetism*, Oxford University Press, Oxford, 1961, pp. 112–126.
26. D. E. Patterson, B. J. Bai, C. J. Chu, R. H. Hauge, and J. L. Margrave, *Proceedings of the Second International Conference on New Diamond Science and Technology, Materials Research Society, Pittsburgh, 1990*, p. 433.
27. R. A. Rudder, G. C. Hudson, J. B. Posthill, R. E. Thomas, and R. Markunas, *J. Appl. Phys. Lett.*, 1991, **59**, 791.
28. J. H. N. Loubser and J. A. van Wyk, *Rep. Prog. Phys.*, 1978, **41**, 1201.

Biographical Sketch

Karen K. Gleason. *b*. 1960 B.S., 1982, M.S., 1982, Massachusetts Institute of Technology, USA. Ph.D., University of California Berkeley, USA, 1987. Introduced to NMR by J. A. Reimer. Faculty in Chemical Engineering, Massachusetts Institute of Technology, 1987–present. Approx. 50 publications. Research interests include applying NMR to thin films and interfaces, particularly for detecting low concentrations of hydrogen, and development of multiple quantum NMR spectroscopy.

Diffusion in Solids

Robert M. Cotts
Cornell University, Ithaca, NY, USA

1	Introduction	1
2	Spin Relaxation and Diffusion	2
3	Direct Measurement of Diffusion Coefficients Using Magnetic Field Gradients	9
4	Applications of NMR to Diffusion in Solids	11
5	Further Reading	14
6	Related Articles	14
7	References	14

1 INTRODUCTION

Soon after the first observations[1,2] of nuclear magnetic resonance (NMR) in condensed matter it became clear that this new experiment had promising potential for the measurement and study of atomic transport. Two of the early questions asked about nuclear spin systems were: 'How does a spin system reach the temperature of the surrounding "lattice" ', and 'How long does it take to reach this thermal equilibrium?'. Here, the term 'lattice' is used to represent all the other degrees of freedom of the material, be it a solid or liquid, containing the spin system. In his phenomenological equations describing the interaction between the nuclear spins and applied static and time-dependent magnetic fields, Bloch[3] identified the spin–lattice, or longitudinal, relaxation time T_1, and the spin–spin, or transverse, relaxation time T_2. In the presence of a large constant magnetic field, the difference between the instantaneous nuclear spin system's magnetization and its equilibrium magnetization decays exponentially with the time contant T_1, while T_2 is the time constant for exponential decay of the magnitude of the coherent component of the magnetization transverse to the large field.

Only 2 years after the publications of discovery of NMR, the first comprehensive description of the relationship between the nuclear spin relaxation rates and atomic motion came in the definitive paper of Bloembergen, Purcell, and Pound,[4] which identified the relationship between the relaxation rates ${T_1}^{-1}$ and ${T_2}^{-1}$ and the modulation of the nuclear dipolar interactions caused by diffusive motion. They showed that each rate could be expressed by a linear combination of spectral density functions evaluated, for like nuclei, at the Larmor frequency and at twice that frequency. Each such function was expressed as the Fourier transform of pair correlation functions for interacting nuclear dipole moments. There are two distinct classifications of NMR experiments used to measure fundamental parameters of translational diffusion of atoms or molecules in solids; both are associated with spin system relaxation times.

The first technique is the measurement of the dependence of relaxation times upon temperature and the Larmor precession frequency. These measurements may be analyzed to yield the temperature dependence of the mean residence time τ_d of the diffusing entity on a lattice site. The second is the measurement at one temperature of the attenuation of the spin echo in the presence of applied magnetic field gradients, from which the tracer diffusion coefficient D is deduced. The first method relies on having good theoretical understanding of the relationship between the mean residence time, the Larmor frequency and the measured relaxation time. The second technique is simpler theoretically, since it relies only on the assumption that the solution to the diffusion equation holds for the spin system, and it yields the diffusion coefficient directly. A disadvantage of the second technique is that it is more difficult and limited experimentally. It also requires higher diffusivity than does the measurement of some relaxation times.

This use of NMR to measure D directly was suggested by Hahn.[5] Some kind of atomic or molecular label is needed to measure the diffusion coefficient. In Hahn's proposal, the atom's position along a particular direction was effectively labeled by making its Larmor frequency linearly dependent upon position through application of a uniform gradient of the magnitude of the applied magnetic field. With a very small gradient, the precession frequency of each spin is essentially constant. This constancy makes the spin echo[5,6] experiments possible with echo attenuation limited only by the decay due to T_2. When diffusion occurs in a sufficiently strong gradient, diffusive motion of each spin makes its precession frequency unpredictably time dependent, so that at the time of echo formation the accumulated disorder in the phases of spins in the transverse plane causes a spin echo attenuation given by[6]

$$S(t)/S(0) = \exp(-t/T_2 - \tfrac{1}{12}\gamma^2 G^2 t^3 D) \qquad (1)$$

where γ is the nuclear magnetogyric ratio, G is the magnitude of the applied magnetic field gradient, τ is the time between the first and second rf pulses, and $t = 2\tau$. Echo attenuation may be measured as a function of G, and the resulting data are analyzed to determine D. The measured D is the tracer diffusion coefficient because the effect of the applied magnetic field gradient is to produce a nearly zero gradient in the chemical potential of the atoms in the system. As noted by Carr and Purcell,[6] 'A more innocuous label would be difficult to imagine'.

In terms of the tracer correlation factor f_t ($0 < f_t \leq 1$) and the step length l, D for a crystalline solid is given by

$$D = f_t l^2/6\tau_d \qquad (2)$$

From independent determinations of τ_d (from relaxation times) and D, the product, $f_t l^2$, can be determined and used to test models for diffusion paths in the solid. For such detailed study, accurate theory for the relationships between relaxation rates and mean residence times are needed and have been calculated for common crystal structures. With these tools at hand, step lengths have been determined, and mixed monovacancy and divacancy diffusion mechanisms and effects of interactions between diffusing atoms have been identified; these topics are discussed below. Sophisticated pulsed gradient techniques have greatly extended the possibilities for measuring D in solids, and some of their applications are presented.

This review is presented in three parts, with the use of relaxation rates in Section 2, measurements of D in Section 3, and applications of these two in Section 4.

2 SPIN RELAXATION AND DIFFUSION

2.1 Introduction

Bloembergen, Purcell, and Pound[4] (BPP) identified the nuclear dipolar coupling as a strong interaction for inducing spin relaxation. The interaction between two nuclear moments having spins I and S,

$$\hat{\mathcal{H}}_{\mathrm{D}} = \frac{\hbar^2 \gamma_I \gamma_S}{r_{IS}^3}\left[\hat{\boldsymbol{I}}\cdot\hat{\boldsymbol{S}} - \frac{3(\hat{\boldsymbol{I}}\cdot\boldsymbol{r}_{IS})(\hat{\boldsymbol{S}}\cdot\boldsymbol{r}_{IS})}{r_{IS}^2}\right] \tag{3}$$

varies in time as the internuclear vector $\boldsymbol{r}_{\mathrm{IS}}$ changes because of the diffusive motion of one or both atoms. BPP described how that motion produced Fourier components of fluctuating dipolar fields at the precession frequencies and their sum and difference frequencies needed to induce spin transitions of one or both spins. Transitions in which both spins flip or one spin flips are driven by the raising and lowering operators $\hat{I}^+$, $\hat{I}^-$, S^+, or S^-, implicitly contained in equation (3). Therefore, Fourier components which drive spin lattice relaxation of the I spin system are ω_{0I}, $2\omega_{0I}$, $(\omega_{0I} + \omega_{0S})$, and $(\omega_{0I} - \omega_{0S})$, where ω_{0I} and ω_{0S} are the resonant frequencies of the I and S spin systems, respectively. General theory of spin system relaxation is available.[7,8]

For nuclei with $I > \frac{1}{2}$, the nuclear electric quadrupole interaction may, for the same reasons, be an effective relaxation mechanism. Here, atomic motion modulates the electric field gradient,[9] and in some circumstances, the quadrupolar mechanism is stronger than magnetic dipolar relaxation. However, for measuring parameters of diffusion, utilization of the dipolar mechanism is, when possible, usually preferred because of high uncertainties in the knowledge of electric field gradients in the solid of interest.

As noted above, for accurate analysis of relaxation data, what is needed are accurate calculations, specific to each crystal structure, that relate relaxation rates to a characteristic diffusion parameter, i.e. the mean residence time of the diffusing atom on a crystal site. Relaxation rate theories are calculated in the weak or the strong collision regime. In the strong collision regime, the dipolar correlation time τ_{d} is greater than the thermal mixing time τ_{m} for the spin system. τ_{m} is the characteristic time needed for the Zeeman spin reservoir to come to a common spin temperature with the dipole spin reservoir.[10] This process requires that the Zeeman field be smaller than characteristic dipolar fields, which is a relevant issue in the rotating coordinate system. The book by Goldman[11] treats the spin temperature concept in detail. Comments on strong collision experiments are reserved here until after the presentation of weak collision theory.

Weak collision theory applies when the Zeeman field is much larger than the characteristic dipolar field. In this regime $\tau_{\mathrm{d}} \ll \tau_{\mathrm{m}}$. This theory applies to many spin systems and temperatures where (depending upon the magnitude of γ) $\tau_{\mathrm{d}} < 10^{-5}$ s, but strong collision theory extends to slower motion where 10^{-5} s $< \tau_{\mathrm{d}} < 10^{-1}$ s.

2.2 Weak Collision Theory

The spectral density functions are defined by[7,8]

$$J^{(q)}(\omega) = 2\int_0^\infty G^{(q)}(t)\cos(\omega t)\,\mathrm{d}t \tag{4}$$

where $\boldsymbol{G}^{(\mathrm{q})}(t)$ is an ensemble average correlation function for the spatial coordinates of the dipolar interaction, and

$$G^{(q)}(t) = \sum_j \overline{F_{ij}^{(q)}(0)F_{ij}^{(q)*}(t)} \tag{5}$$

where the bar indicates the ensemble average. The functions $F_{ij}^{(q)}(t) = d_q Y_{2q}(\Omega_{ij})/r_{ij}^3$ are the dipolar interactions between spins i and j separated by $(r,\Omega)_{ij}$ at time t, and where $Y_{2q}(\Omega)$ are the normalized spherical harmonics having the z axis along the applied magnetic field, $\boldsymbol{B}_0$. The d factors are: ${d_0}^2 = (16\pi/5)$, $d_1^2 = (8\pi/15)$, and $d_2^2 = (32\pi/15)$. The spin operators have been incorporated in the expressions for the relaxation rates,[7,12,13] given here for identical (like) spins:

$$\frac{1}{T_1} = R_1 = \tfrac{3}{2}\gamma^4\hbar^2 I(I+1)[J^{(1)}(\omega_0) + J^{(2)}(2\omega_0)] \tag{6}$$

$$\frac{1}{T_{1\rho}} = R_{1\rho} = \tfrac{3}{8}\gamma^4\hbar^2 I(I+1) \times[J^{(0)}(2\omega_1) + 10J^{(1)}(\omega_0) + J^{(2)}(2\omega_0)] \tag{7}$$

$$\frac{1}{T_2} = R_2 = \tfrac{3}{8}\gamma^4\hbar^2 I(I+1) \times[J^{(0)}(0) + 10J^{(1)}(\omega_0) + J^{(2)}(2\omega_0)] \tag{8}$$

where $T_{1\rho}$ is the spin–lattice relaxation time in the rotating frame[12] and ω_1 is the precession frequency in the rotating field $\boldsymbol{B}_1$. The correlation functions are given by:[14]

$$G^{(q)}(t) = d_q^2 \sum_{\alpha,\beta} \frac{Y_{2q}^*(\Omega_\alpha)^*}{r_\alpha^3}\frac{Y_{2q}(\Omega_\beta)}{r_\beta^3}P(\boldsymbol{r}_\alpha, \boldsymbol{r}_\beta, t) \tag{9}$$

where $P(\boldsymbol{r}_\alpha, \boldsymbol{r}_\beta, t)$ is the probability of a pair of spins being separated by $\boldsymbol{r}_\beta$ at a time t given that they were separated by $\boldsymbol{r}_\alpha$ at time zero, and $P(\boldsymbol{r}_\alpha, \boldsymbol{r}_\beta, t)$ is determined by the diffusive motion in the solid. The correlation function decays with a characteristic time τ_{c}, which for translational diffusion should be approximately the mean residence time. The above expressions apply directly to a single crystal, but can also be averaged over all orientation angles for polycrystalline samples.

It is convenient to express the spherically averaged rates in terms of a single dimensionless spectral function $F(\omega\tau_{\mathrm{c}})$, which applies to any spin transition (parameter q). Equations (6)–(8) then become (for like spins only):

$$\frac{1}{T_1} = R_1 = \tfrac{2}{3}M_{II}^2\tau_{\mathrm{c}}[F(\omega_0\tau_{\mathrm{c}}) + 4F(2\omega_0\tau_{\mathrm{c}})] \tag{10}$$

$$\frac{1}{T_{1\rho}} = R_{1\rho} = \tfrac{1}{3}M_{II}^2\tau_c[3F(\omega_1\tau_c) + 5F(\omega_0\tau_c) + 2F(2\omega_0\tau_c)] \quad (11)$$

$$\frac{1}{T_2} = R_2 = \tfrac{1}{3}M_{II}^2\tau_c[3F(0) + 5F(\omega_0\tau_c) + 2F(2\omega_0\tau_c)] \quad (12)$$

where

$$M_{II}^2 = (\mu_0/4\pi)^2\tfrac{3}{5}\gamma^4\hbar^2 I(I+1)\sum_i r_i^{-6} \quad (13)$$

is, here, the dipole second moment for like spin interactions only.

2.2.1 The BPP Model

A simple assumption of an exponential decay was made by BPP for $\boldsymbol{G}^{(q)}(t)$:

$$G^{(q)}(t) = G^{(q)}(0)\exp\left(-\frac{t}{\tau_c}\right) \quad (14)$$

It follows that the spectral density has the form

$$J^{(q)}(\omega) = \frac{G^{(q)}(0)2\tau_c}{[1+(\omega\tau_c)^2]} \quad (15)$$

Torrey[15] pointed out that, for like spins, the *relative* motion of spins contributes to the decay of $G^{(q)}(t)$, and therefore $\tau_c = \tau_d/2$. The relatively simple BPP form of $J^{(q)}(\omega)$ has made it a very useful, though approximate, model for analysis of data. In the low frequency, or short correlation time, regime ($\omega\tau_d \ll 1$), $J^{(q)}(\omega)$ is essentially independent of frequency, and for like spins $J^{(q)}(\omega) \approx G^{(q)}(0)\tau_d[1-(\omega\tau_d/2)^2]$. At high frequencies, or long correlation times $\omega\tau_d \gg 1$, and again for like spins, $J^{(q)} \approx 4G^{(q)}(0)/(\omega^2\tau_d)$.

The low-frequency behavior of the BPP model is inconsistent with the solution to the diffusion equation when applied to calculation of $J^{(q)}(\omega)$, which for solids[16] or liquids[17] is

$$J^{(q)}(\omega) \approx J^{(q)}(0)[1 - c_1\omega^{1/2}] \quad (16)$$

where $J^{(q)}(0) \propto \tau_d$ and c_1 is a constant, different for solids than for liquids. In fact, c_1 specifically depends on D, so that in principle D could be determined from the frequency dependence of $J^{(q)}(\omega)$ in the short correlation time regime.[16] [For two-dimensional diffusion[16] there is a much stronger frequency dependence at $\omega\tau_d \ll 1$. Here, $J^{(q)}(\omega) \approx c_2\tau_d \ln(\omega)^{-1}$, where c_2 is dependent upon D and the structure of the solid.] In the very low and high frequency limits, accurate calculations show that $J^{(q)}(\omega)$ is proportional to τ_d and to $(\omega^2\tau_d)^{-1}$, respectively, as in the BPP model, but the constants of proportionality in the BPP model can be in error[16,18] by up to a factor of 3. For thermally activated diffusion $\tau_d = \tau_0 \exp(E_a/RT)$, where E_a is the activation energy (per mole) for diffusion. It is usually convenient experimentally to hold the NMR frequency constant and vary the temperature. In such an experiment a graph of the relaxation rate, R_1 versus $(1/T)$, would have slope $+(E_a/R)$ at very high temperatures and $-(E_a/R)$ at low temperatures. On such a graph the maximum of R_1 in the BPP model occurs for a system of like spins, at $(\omega\tau_d) = 1.23$. Although the BPP model is an approximation and not specific to any crystal lattice, it is highly regarded for its ease in applicability and its utility. It is seen in the next section that the errors noted above may be significantly reduced if it is assumed that for like spins $\tau_c = \tau_d$. The dependences of R_1, $R_{1\rho}$, and R_2, upon $\omega\tau_d$ in the BPP model are shown in Figure 1. On the low-temperature side of the peak in R_1, the transverse rate, $R_2 \propto \tau_d$. Using this relationship, Hultsch and Barnes[19] measured the pressure dependence of T_2 of ^{7}Li and ^{23}Na in solid lithium and sodium, respectively, and determined the activation volumes for self-diffusion in these solids.

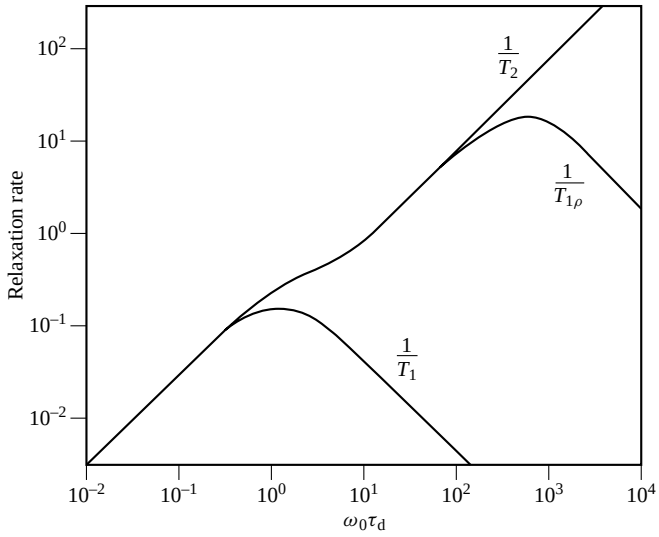

Figure 1 Relaxation rate (in arbitrary units) as a function of $\omega_0\tau_d$ for R_1, $R_{1\rho}$ and R_2 in the BPP model with $\omega_0 = 500\ \omega_1$

2.2.2 Lattice-Specific Models

In many solids, translational diffusion is enabled by vacancies, (empty lattice sites) in the solid. Only atoms next to a site vacancy can move. For most solids, vacancies must be thermally activated. Typically, vacancy concentrations are very small, increase strongly with temperature, but reach fractional concentrations of only about 10^{-4} to 10^{-3} near the melting point. When a vacancy encounters an atom the atom can move, but its motion during the encounter is not random in that it has a significant probability of jumping back to take the place of a vacancy immediately after it has exchanged sites with it. The effect of this correlated motion[20] on the NMR spectral density is distinguishable from an uncorrelated random walk process that would occur with low atom concentration on an otherwise empty lattice. The interstitialcy mechanism has also been considered in lattice-specific calculations.

High vacancy concentrations are characteristic of a number of systems, such as hydrogen in metals and fast ionic conductors. For example, in the α' phase of the VH_x, NbH_x, and TaH_x systems, hydrogen atoms occupy the tetrahedral interstitial sites and the solubility of hydrogen atoms in this phase ranges from $x = 0$ to about 0.7, depending on the host metal. Therefore, there is interest in knowing $J^{(q)}(\omega, \tau_d)$ for the full range of atomic concentration, c. Figure 2 shows a plot

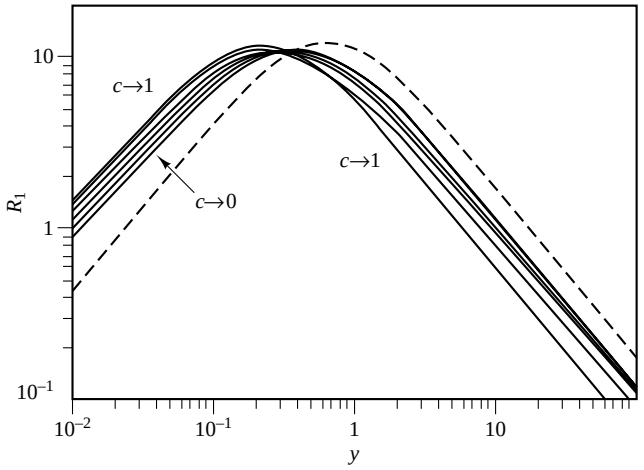

Figure 2 Angular average of the spin–lattice relaxation rate (in arbitrary units), divided by c, as a function of $y = \omega_0\tau_d/2$ for like spins on the simple cubic lattice. (- - - -) The BPP model. (——) Lattice-specific models for atom concentrations, from left to right: $c \rightarrow 1$, 0.99, 0.90, 0.70, 0.50, and $c \rightarrow 0$, respectively. (Reproduced by permission of IOP Publishing Ltd from C. A. Scholl, *J. Phys. C: Solid State Phys.*, 1988, **21**, 319)

of R_1 versus $(\omega\tau_d/2)$ calculated from lattice-specific models[14] for the simple cubic lattice. It can be seen in Figure 2 that letting $\tau_c = \tau_d$ in the BPP model moves the BPP curve a factor of 2 to the left and into better agreement with the others. Many calculations of $J^{(q)}(\omega, \tau_d)$ must be done numerically.

The relationships between relaxation rates and the mean residence time, τ_d have been calculated specifically for the more common crystal structures, for example: simple cubic (s.c.); body-centered cubic (b.c.c.); and face-centered cubic (f.c.c.). These relationships do indeed differ perceptibly from one lattice to another. It is known that the dependence of R_1 upon τ_d for a given lattice changes with the microscopic diffusion mechanism, but that these differences are small. Measurements of high precision on spin systems with very well understood relaxation mechanisms are needed before one can hope to use experimental data to rule out a contending microscopic mechanism.

The first lattice-specific relaxation rate theoretical calculations for R_1 and R_2 were made by Torrey[15] and Resing and Torrey.[21] In these calculations, nuclear dipoles were assumed to move by an uncorrelated random walk by nearest neighbor jumps through the lattice. The average of relaxation rates over all crystalline directions were approximated by the use of an isotropic diffusion model. Relaxation rates were calculated numerically for like spins only; their most accurate results are presented in Resing and Torrey[21] in tabular form for the b.c.c. and f.c.c. lattices. At fixed frequency, R_1 reaches a maximum at $\omega\tau_d = 1.06$ and 1.04 for the f.c.c. and b.c.c. lattices, respectively. Because of the assumption of uncorrelated motion, these results would be expected to be applicable at low concentrations of atoms on a crystal lattice, or sublattice.

Before it appeared in print, the Torrey model was applied to analyze data in the first comprehensive set of pulsed NMR experiments[22] measuring effects of diffusion on NMR relaxation rates in alkali metals. Holcomb and Norberg[22] convincingly demonstrated the applicability of NMR to the study of diffusion in solids. Their most extensive data were

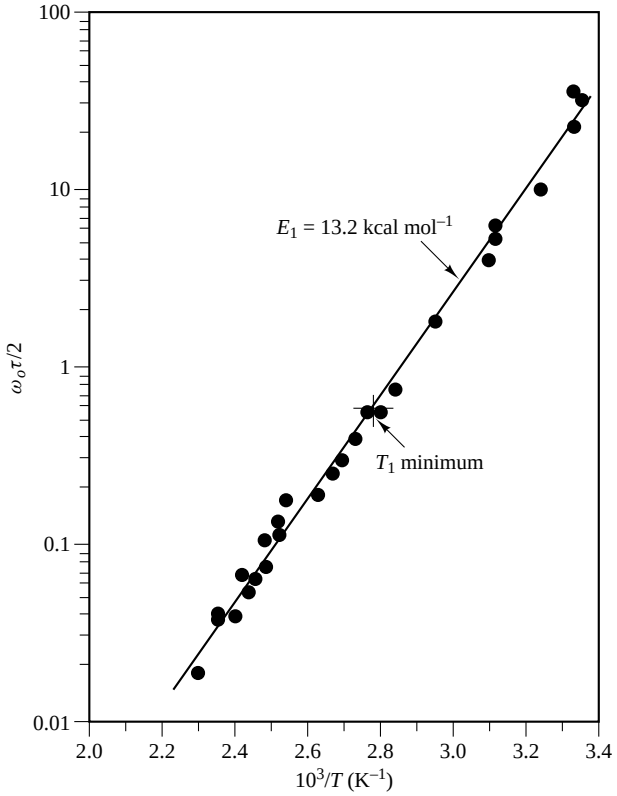

Figure 3 Plot of $\omega_0\tau/2$, where $\tau = \tau_d$, against $10^3/T$ for ^{7}Li in solid lithium. Values of τ were obtained from analysis of R_1 data at 3 MHz using the Torrey theory. The slope is 13.2 kcal mol^{-1} = 55.2 kJ mol^{-1}. (Reproduced by permission of The American Physical Society from D. F. Holcomb and R. E. Norberg, *Phys. Rev.*, 1955, **98**, 1074)

from ^{7}Li with temperature dependence of T_1 measured at 3, 6, 9, and 15 MHz. ^{7}Li data at 3 MHz were analyzed by trying both the BPP and the Torrey theory. The better fit to the data, shown in Figure 3 came from Torrey theory for the b.c.c. lattice, and from it they found that $E_a = 55.2 \pm 2$ kJ mol^{-1}.

Sholl[23,24] and Wolf[25] addressed the random walk problem without the approximation of isotropic diffusion. Both took the discrete nature of the lattice into account for both single and polycrystalline materials. The papers of Barton and Sholl,[26] provide good perspective on the random walk model and include tables that conveniently allow calculation of R_1, $R_{1\rho}$, or R_2, for any product of $\omega\tau_d$ in s.c., b.c.c., or f.c.c. lattices. These improved calculations have, for like spins in a polycrystalline sample, the maximum in R_1 occurring at $\omega\tau_d = 1.04$, 0.99, and 0.92 for f.c.c., b.c.c., and s.c. lattices, respectively.

While few real systems were expected to have atoms diffusing by random walk, these lattice-specific calculations were still important in the development of the theory. The shape of the R_1 versus τ_d curve for random walk fit the data better than the shape of the BPP curve did. A second improvement to the random walk came with the mean field model[27] which accounted for the effects of site blocking. That is, it excluded the possibility of having two atoms on the same site. The mean field theory is exact where a single jump for a pair of spins is relevant, in the low-temperature (high-frequency) limit, except where the fractional atom concentration is $c \rightarrow 1$. It is also exact in the dilute

limit as $c \rightarrow 0$, and the model was expected to be a good approximation for most concentrations except[26] as $c \rightarrow 1$. In the mean field model, for like spins in a polycrystalline sample, the maximum in R_1 occurs at $\omega\tau_d = 0.95$, 0.89, and 0.77 for f.c.c., b.c.c., and s.c. lattices, respectively.

2.2.3 Monovacancy Diffusion

Diffusion enabled by vacancies at extremely low concentration is known as 'monovacancy diffusion'. Wolf[28] provided the first relaxation rate theory applicable to this mechanism. At their characteristically low concentration, vacancies move with random walk and atoms are displaced only through encounters with vacancies. Eisenstadt and Redfield[29] identified the encounter model and its role in NMR relaxation in their study of diffusion in ionic crystals.

Wolf[30] calculated relaxation rates in the encounter model for both the weak and strong collision regimes, and he identified characteristic features of temperature-dependent experimental data that could, in principle, be applied to identify microscopic diffusion mechanisms. He emphasized the valuable information contained in the anisotropy of relaxation rates,[28,30,32] especially $R_{1\rho}$, for single crystal samples. For polycrystalline or single crystal samples, Wolf et al.[32] defined measures of the width and asymmetry of the relaxation peak that were dependent upon the mechanism of diffusion.

A comprehensive series of experiments were performed by Figueroa and Strange and reported with Wolf[32,33] on the NMR of ^{19}F in pure BaF_2 and crystals doped with K^+ to control F^- vacancy concentrations, or with La^+ to control number of interstitial F^-. This element of control made it possible to determine the activation energies for migration of F^- by vacancies (E_{mv} = 59 kJ mol^{-1}) and by interstitials (E_{mi} = 74 kJ mol^{-1}). From the pure BaF_2 data (Figure 4), the energy of formation of Frenkel anion pairs (E_f = 174 kJ mol^{-1}) was determined. Comparison with conductivity data[34] showed satisfactory agreement with diffusion parameters obtained by the two techniques. In their analysis of the NMR data, there was clear agreement with the encounter model but not the random walk model. Even though the data appear to have little scatter, especially considering the very high temperatures at which much of it was recorded, the difference between the interstitialcy and monovacancy mechanisms could not be distinguished.

Building upon previous calculations on relaxation rate theory,[16,35] MacGillivray and Sholl[36] improved the accuracy of the encounter model in the monovacancy limit to better than 4% and 1% in the low- and high-frequency regimes, respectively. Their paper contains numerical tables from which spectral densities $J^{(q)}(\omega, \tau_d)$ can conveniently be calculated for s.c., b.c.c., and f.c.c. lattices. From these, more accurate predictions of the width and asymmetry of relaxation rate peaks can be made. In the monovacancy limit, the peaks in the spin–lattice relaxation rate R_1 for like spins occur at[35] $\omega\tau_d = 0.57$, 0.51, and 0.42 for the f.c.c., b.c.c., and s.c. lattices, respectively. All these peaks in R_1 occur at significantly lower values of $\omega\tau_d$ than in the random walk or the mean field models. This means that if NMR data for R_1 or $R_{1\rho}$ from a solid having monovacancy diffusion were analyzed with the random walk, mean field, or the BPP models, the deduced τ_d at temperatures near maximum relaxation rates would be too large by at least 67% for the first two, and by more than 100% for the BPP model. But the error in the activation energy would probably be very small for the first two models because they give essentially the same shape for the relaxation peaks. However, since the peak is narrower in the BPP model, the activation energy derived from its use could be systematically too small by an amount that depends upon the range of temperature over which data were available (see Section 2.2.5).

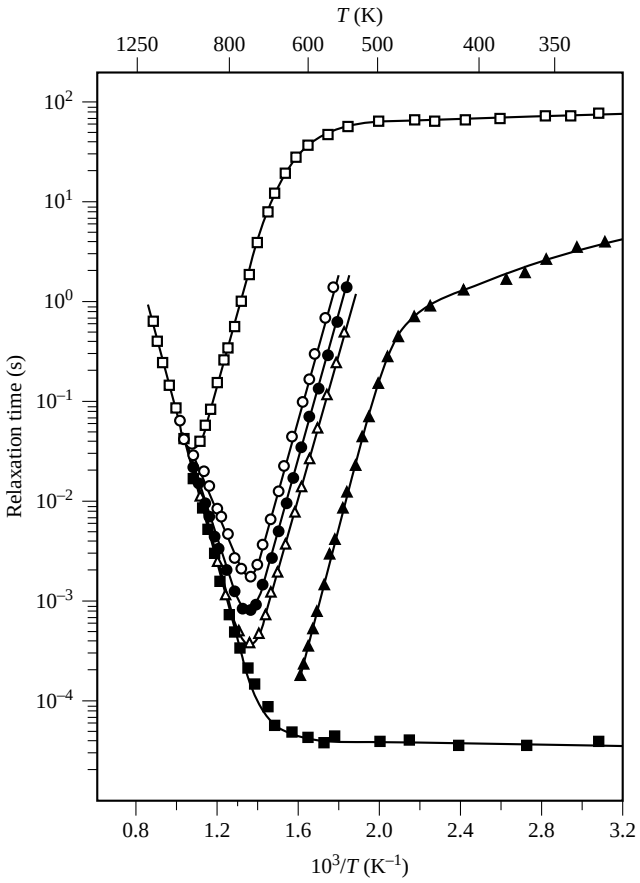

Figure 4 Relaxation times plotted against $10^3/T$ for ^{19}F in a pure BaF_2 single crystal. (□) T_1 taken at 10 MHz; (○, ●, △) $T_1\rho$, B_1 = 1.2×10^{-3} T, for three different crystal orientations; (▲) $T_{1\,Dipolar}$; (■) T_2. Details on crystal orientations may be found in Figreroa et al.[33] (Reproduced by permission of The American Physical Society from D. R. Figueroa, J. H. Strange, and D. Wolf, *Phys. Rev. B*, 1979, **19**, 148)

2.2.4 Models for Arbitrary Concentrations

In 1978, Fedders and Sankey[18] published their multiple scattering theory for the s.c. lattice using a reciprocal space formalism that can be applied to any concentration from c = 0 to nearly the monovacancy limit. They published their numerical results for the spectral densities in the low- and high-frequency limits for $c = 0$ to $c \rightarrow 1$ in steps of $\Delta c = 0.2$. While they gave no numerical tables for the spectral densities at arbitrary $\omega\tau_d$, they offered to supply tables of T_1 versus $\omega\tau_d$ upon request. It is pointed out that the lattice-specific relaxation function (Figure 5) approaches its high- and low-temperature limits more gradually than the BPP model does. Results for the f.c.c. lattice were reported in a later paper.[37] An interesting product of their formalism is a simple analytic

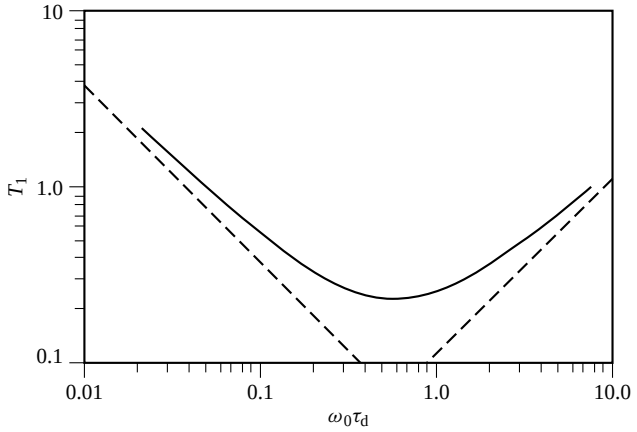

Figure 5 Angular average of spin–lattice relaxation time (in arbitrary units) for like spins on the s.c. lattice as a function of $\omega_0\tau_d$ calculated for the multiple scattering theory with atomic concentration c = 0.85. (- - - -) Asymptotic limits for $\omega_0\tau_d$ sufficiently large and small; they show how gradually the curve approaches each line. (Reproduced by permission of The American Physical Society from P. A. Fedders and O. F. Sankey, *Phys. Rev. B*, 1978, **18**, 5938)

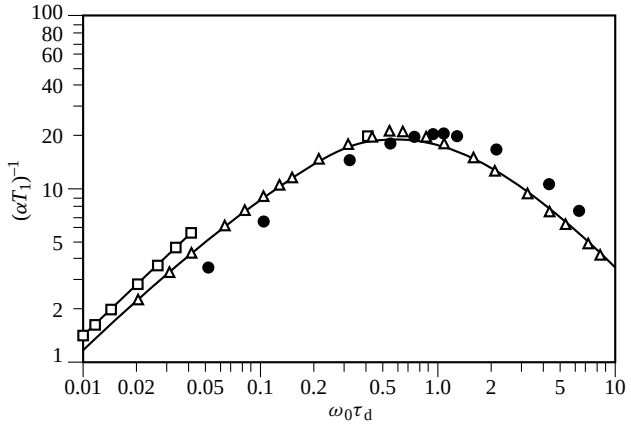

Figure 6 Angular average of spin–lattice relaxation rates as a function of $\omega_0\tau_d$, as calculated for like spins from simple cubic lattice theories. (□) Monovacancy encounter model;[10] (•) random walk model;[26] (△) vacancy concentration, c_v = 0.15.[18] (——) Monte Carlo for c_v = 0.15. (Reproduced by permission of The American Physical Society from L. D. Bustard, *Phys. Rev. B*, 1980, **22**, 1))

expression (accurate to about 1%) for the tracer correlation factor for atoms at concentration c in a simple cubic lattice:

$$f_t = 0.7882[1 + 0.1059(6c - 4)/(2 - c)] \qquad (17)$$

Fedders[38] also considered the effect that interactions between mobile atoms would have on the dipolar relaxation mechanism. These interactions are more likely to be important in systems having intermediate concentrations of diffusing atoms (with number of vacancies exceeding 10% of the number of lattice sites), as in metal hydrides. At short distances, the H–H interaction is repulsive, and in some metals, (for example, the group V transition metals) it is sufficiently strong to prevent simultaneous occupation of nearest neighbor interstitial sites. In the BPP model, one would be tempted to compensate for this interaction by simply removing nearest neighbor terms from the lattice sums contained in calculating the second moment of the hydrogen spin system. Doing this underestimates the dipolar interaction strength in the low-frequency (high-temperature) regime because here the motions of atoms further from each other than the nearest neighbor positions are the most effective in inducing spin transitions. For this motion short-range repulsive reactions are irrelevant.[38] On the high-frequency (low-temperature) side of the relaxation rate peak, single steps of atoms account for the decay of the pair correlation function and the reduction of the second moment is a good approximation[38] to the effects of the above repulsive interaction.

2.2.5 Monte Carlo Simulations

For any crystal structure, the pair correlation functions $G^{(q)}(t, \tau_d)$ can be computed numerically by simulating motion with the Monte Carlo technique. Bustard[39] established an s.c. lattice having 8000 sites (20 lattice constants on each side) and assumed periodic boundary conditions. Using the Monte Carlo technique he calculated numerically T_1^{-1} versus $\omega\tau_d$ for like spins on this s.c. lattice with vacancy concentrations, c_v = 3.75 × 10^{-4}, 0.15, 0.225, and 0.90, and published the appropriate tables for these concentrations. The Monte Carlo results are in substantial agreement with multiple scattering theory[18] for c_v = 0.15 (Figure 6) and with mean field theory[26] for c_v = 0.90. A difficulty in the Monte Carlo calculations is their inaccuracy in the low-frequency regime. Bustard[39] dealt with this by making a least-squares fit to $G^{(q)}(t, \tau_d)$ with a sum of decaying exponentials. This substitution facilitated making the Fourier transform to $J^{(q)}(\omega, \tau_d)$ but, since the long time tails of the exponential decay curves decay faster than the actual[16] $t^{-3/2}$ form of the tail of $\boldsymbol{G}^{(q)}(t, \tau_d)$, Bustard's Monte Carlo magnitudes of R_1 and $R_{1\rho}$ were too small where $\omega\tau_d \ll 1$. Nevertheless, the calculations were accurate enough for R_1 data to be analyzed at two NMR frequencies in order to obtain the temperature dependences of τ_d for ^{1}H in $TiH_{1.55}$ and $TiH_{1.70}$, where c_v = 0.225 and 0.15 on the interstitial s.c. lattice, respectively. These results for τ_d were combined with direct NMR measurements[40] of the diffusion coefficient D using the pulsed field gradient technique in the stimulated echo experiment, so that the mean squared jump length l^2 could be determined from $D = f_t l^2/(6\tau_d)$. It was found that hydrogen atoms jump to their nearest neighbor sites and not to their third nearest neighbor sites as had been found theoretically to be feasible.[41] Similar sets of experiments have recently been done for the isomorphic system ZrH_x,[42] analyzing R_1 data with more recent Monte Carlo calculations[43] for τ_d, and reaching the same conclusion.

Faux et al.[43] made Monte Carlo calculations for like spins moving according to the simple hopping model on f.c.c., b.c.c. and s.c. lattices. They fitted their numerical calculations of $J^{(q)}(\omega, \tau_d)$ in the low- and high-frequency limiting cases to the corresponding expected frequency dependences calculated earlier by Sholl.[16] This fitting also checked the accuracy of their Monte Carlo numerical procedures.[43] Numerical tables provide spectral densities and R_1 at many selected values of $\omega\tau_d$ for concentrations c approaching 0, 0.5, 0.7, 0.9, and 0.99. For $c \leq 0.4$, application of mean field theory might be an

acceptable and convenient approximation, since its difference from the Monte Carlo results is quite small.[43]

Because use of numerical tables is not as convenient as an analytic expression (such as that for the BPP model) in fitting experimental data, analytic approximations to the numerical tables given by Faux et al.[43] for intermediate concentrations, by Barton and Sholl[26] for mean field theory, and by MacGillivray and Sholl[36] for monovacancy diffusion have been developed by Sholl.[14] Faux et al.[43] and Sholl[14] provide an overview of the dependences of the relaxation rates upon atom concentration on the f.c.c., b.c.c., and s.c. lattices from $c \rightarrow 0$ to $c \rightarrow 1$. Figure 2 shows R_1 versus $\omega\tau_d/2$ for the full range of concentration on a simple cubic lattice plotted from the analytic expressions given by Sholl[14] and, for comparison, the BPP model. It is seen here, and is apparent for all cubic lattices, that the relaxation peak is narrower in the BPP model than for any concentration of the lattice-specific models. There is little concentration or model dependence in the maximum relaxation rates shown in Figure 2. For all the lattice-specific relaxation rate curves, their peaks are located at significantly lower values of $\omega\tau_d$ than for the BPP model (using $\tau_c = \tau_d/2$). It can be seen in Figure 7 that

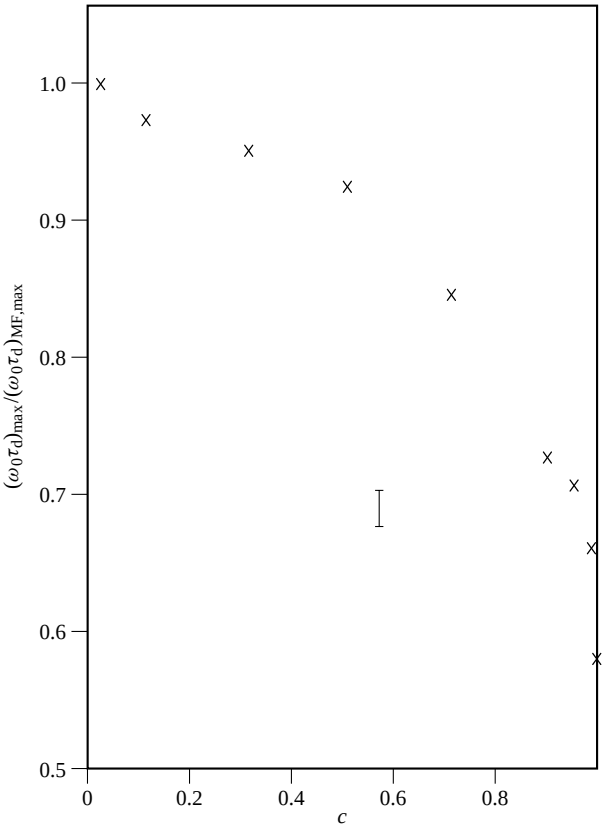

Figure 7 The value of $(\omega_0\tau_d)_{max}$ at the maximum of the R_1 versus $\omega_0\tau_d$ curve, plotted against atom concentration c for a polycrystalline b.c.c. lattice. The $(\omega_0\tau_d)_{max}$ values are normalized to the mean field theory value of 0.89. The point at $c = 1$ is for the monovacancy limit. The bar is the estimated error of the Monte Carlo results. The points for the f.c.c. and s.c. lattices lie above and below these points, respectively. On this graph, the points for the BPP model would be at 1.38, independent of c. (Reproduced by permission of IOP Publishing Ltd from D. A. Faux, D. K. Ross, and C. A. Sholl, *J. Phys. C: Solid State Phys.*, 1986, **19**, 4115)

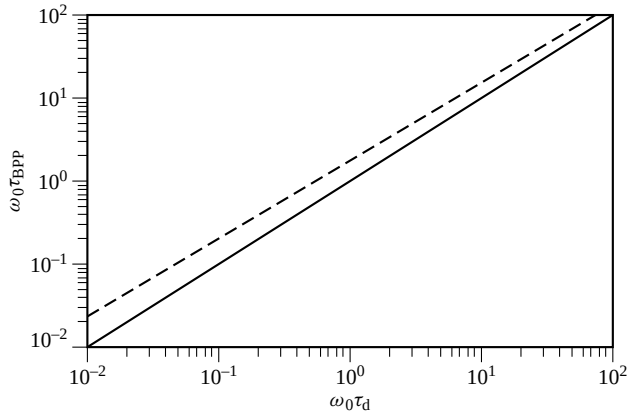

Figure 8 (- - - -) $\tau_d = \tau_{BPP}$, obtained by analyzing the R_1 relaxation results of the mean field theory using the BPP model. The horizontal axis shows τ_d in the mean field theory, and $(\omega_0\tau_d)_{max}$ is approximately centered. The solid line has the 'correct' slope. In the limits of large and small τ_d, the two lines are parallel, but over the region shown, the average slope of the dashed line is seen to be the smaller one. (Reproduced by permission of Sci-Tech Publications from C. A. Scholl, *Diffus. Defect Data, Solid State Data A, Defect Diffus. Forum*, 1993, **95–98**, 91)

the value of $\omega\tau_d$ at the peak decreases monotonically from the $c = 0$ limit to the $c = 1$ limit, with most of the change coming between $c = 0.5$ and $c = 1.0$. Because the value of $\omega\tau_d$ at the peak may be used to set the absolute values of the determinations of τ_d from experimental R_1 data, Figure 2 is useful for estimating the relative error resulting from application of an inappropriate model. The activation energies determined by application of the BPP model should be accurate if there are experimental data extending far into the wings of the relaxation peak. However, often the data are most accurate or only available near the peak where there is relatively less competition from other relaxation mechanisms. In this regime, the narrowness of the peak in the BPP model means that if it were used to analyze data obtained with a lattice-specific model, the resulting values of τ_d (shown as τ_{BPP} in Figure 8) might be interpreted in terms of an activation energy that would be too small. The resulting systematic error in E_a could exceed 10%.[44]

2.2.6 Quadrupolar Relaxation Mechanisms

As noted earlier, nuclear electric quadrupolar interactions may be an effective mechanism for spin relaxation where the interaction is modulated by atomic motion. Its utilization for the study of diffusion is more complicated than the dipolar mechanism because: (1) the electric field gradient (EFG) might be unknown; and (2) the spin system's recovery might be multiexponential. Lack of knowledge of the magnitude of the EFG might be acceptable, since it mainly affects the magnitude of spin–lattice relaxation rates, but it might have a temperature dependence strong enough to complicate data interpretation. The recovery through spin–lattice relaxation will be a single exponential[7] if the spin $I = 1$, if the motion is so fast that $\omega_0\tau_d \ll 1$, or if the dipolar interaction can maintain a spin temperature in the spin system.[10] Otherwise, the recovery is the sum of exponentials the number of which depends upon I.[45] If the spin system has a static quadrupole interaction,

establishment of a spin temperature is unlikely outside of thermal equilibrium with the lattice.

Without a static quadrupole interaction, it is likely that the dipolar interactions within the spin system can maintain a spin temperature during recovery. If so, the recovery occurs with the relaxation rate[7,10]

$$\frac{1}{T_{1Q}} = R_{1Q} = C_Q[J_Q^{(1)}(\omega_0) + J_Q^{(2)}(2\omega_0)] \tag{18}$$

where

$$C_Q = (9/160)(eQ/\hbar I)^2(2I+3)/(2I-1) \tag{19}$$

and the dynamic EFG is contained in the spectral densities, $J_Q{}^{(i)}(\omega_0)$. If the dynamic EFG is due to point charges, as in ionic compounds, the spectral densities will depend upon normalized spherical harmonics as do those for dipolar interactions. But the quadrupolar spectral densities may differ from the dipolar because of the potential importance of three particle correlation functions in many solids.[46] A difference in principle is that the $J_Q^{(2)}(2\omega_0)$ term in quadrupolar relaxation corresponds to $\Delta m = \pm 2$ of one spin, but in dipolar relaxation it means Δm = nbsp;±1 for a *pair* of spins If a spin temperature is not maintained during recovery, the recovery is a combination of I exponentials for integral spins and $(I + \frac{1}{2})$ exponentials for half-integral spins.[45] For a system with a static quadrupole interaction, the mix of exponentials is expected to be similar to that with no static interaction except that the spectral density functions would have arguments different from ω_0 and $2\omega_0$. The mix would depend upon the initial conditions of the spin system at the start of the recovery as established by the rf pulse sequence used and the energy levels to which it was applied. Gordon and Hoch[45] present results for excitation of the central transition only.

Because of the uncertainties of the magnitude of the dynamic quadrupole interactions, and because static interactions often occur in the less common crystal structures and in disordered solids, very few lattice-specific calculations are available for data analysis. The BPP model is often applied to obtain numerical values of diffusion parameters from these experiments.

2.2.7 Disordered Solids

In disordered solids, such as alloys or glasses, it would be expected that each atom of a given type would have different probabilities for jumping in each of its likely jump directions because of different barrier heights and vibration frequencies. Also, there would be a distribution of site binding energies, and, ignoring other possible effects of the disorder, it is still not obvious how these variations would affect the temperature and frequency dependences of NMR relaxation rates.

It is commonly found experimentally that at fixed frequency, when the relaxation rate due to translational diffusion has been plotted against T^{-1}, the characteristic peak in the rate has a lower magnitude slope on the low-temperature side than on the high-temperature side. In systems where, for example, the mean squared dipolar interaction is known through independent measurement of the second moment of the NMR line, the maximum relaxation rate may be reduced from the rate estimated from the known second moment. These characteristics may be emulated in the calculation of a mean relaxation rate for a distribution of activation energies where the dependence of R_1 upon E_a follows from its dependence upon τ_d and the Arrhenius relationship:

$$\tau_d = \tau_0 \exp(E_a/RT) \tag{20}$$

Assuming a distribution of activation energies, $g(E_a)$, the mean relaxation rate is

$$\left\langle \frac{1}{T_1} \right\rangle = \int g(E_a) R_1(E_a)\, d(E_a) \tag{21}$$

There are other models for NMR relaxation in disordered systems. Beckmann[47] has reviewed many and presented them in a format readily applied to NMR. The question for each is: what is the physical significance of the parameters that would be derived from a fit to NMR relaxation data? McDowell[48] has applied Monte Carlo techniques to solids disordered with distributions of site energies and, separately, with distributions of barrier height energies. He has found that in the Monte Carlo simulations the observed asymmetry of the relaxation peak occurs with the barrier height distribution but not with the site energy distribution.

The Kohlrausch–Williams–Watts (KWW) model[47] has seen considerable application. It produces the characteristic asymmetric shape of the relaxation peak and is known as the 'stretched exponential' for the form of its correlation function, which is proportional to $\exp[-(t/\tau^*)^{1-n}]$, where $n < 1$. Ngai and Martin[49] argue that at long times, decay of the correlation function is slowed down due to dynamic correlations among the atoms that arise from their mutual interactions.

Elliot's diffusion controlled relaxation (DCR) model[50] has recently been applied to NMR in ionic conducting glasses.[51] The transport mechanism involves the motion of interstitialcies followed by ionic relaxation in the vicinity of a recently arrived interstitial atom. The form of the correlation function can be viewed as a stretched exponential, but the power β to which the time t is raised would be itself time dependent.

No one model is expected to be applicable to all disordered systems, and more than one model might fit the data of one system. What remains to be seen is which models can be convincingly identified with the structure and dynamic processes in glasses. A good test of the applicability of a spin relaxation model is to compare its predictions of the diffusion coefficient of the mobile atom, based on relaxation rate measurements, to an independent set of measurements of D obtained from, for example, NMR pulsed field gradient measurements, or from electric conductivities, preferably in the same temperature range, although this cannot always be realized because of the limitations in measuring low values of D.

2.3 Strong Collision Theory and Experiments

The strong collision regime, defined by Slichter and Ailion,[52] is characterized by fast thermal mixing between the dipolar and Zeeman energy reservoirs that meets the condition $\tau_m \ll \tau_c$, where τ_m is the mixing time, and $\tau_c = (\tau_d/2)$ for a system of like spins in the solid. This energy exchange cannot occur if $B_1 > B_{D\rho}$, where $B_{D\rho}$ is the measure of the

nuclear dipolar field in the rotating frame. At sufficiently low temperatures, $\tau_m^{-1} \approx \gamma B_{D\rho}$, so that the inequality, $\tau_m \ll \tau_c$ requires that the lattice temperature be below the motional narrowing temperature of the solid.[8] Under these conditions, Slichter and Ailion find

$$R_{1\rho} = \frac{2(1-p)}{\tau_d} \frac{B_{D\rho}^2}{B_1^2 + B_{D\rho}^2} \tag{22}$$

where p is a parameter which represents the fact that the local field is not completely random after a single atom jump. The important concept in the strong collision regime is that the correlation time is essentially determined by single jumps. In the rotating frame experiment, the relatively high degree of order in the spin polarization, originally along the large applied field in the laboratory frame, becomes transferred to dipolar and Zeeman order in the rotating frame. This order is locally disrupted when an atom jumps to a neighboring site and may be gradually eroded by some other spin–lattice relaxation mechanism. The latter limits $T_{1\rho}$, which puts an upper limit on τ_d that is measurable. In the Slichter and Ailion experiment[53] on ^{7}Li in lithium metal, relaxation by conduction electrons limited observation to temperatures above about 190 K where $\tau_d \leq 1$ s, a very long time in translational diffusion. The values of τ_d obtained in this regime were found to be consistent with those found from T_1 measurements by Holcomb and Norberg.[22]

The strong collision theory is lattice specific in that the parameter p must be carefully calculated for each lattice. In their experimental paper,[53] Slichter and Ailion derived p for the b.c.c. lattice and found $p = 0.2663$. Of course, $B_{D\rho}$ is also lattice dependent (see ***Ultraslow Motions in Solids***).

3 DIRECT MEASUREMENT OF DIFFUSION COEFFICIENTS USING MAGNETIC FIELD GRADIENTS

3.1 Introduction

Analysis of measurements of the temperature and frequency dependence of nuclear spin relaxation rates yields the temperature dependence of the mean residence time of atoms in the solid. For a known structure of the solid, and from an assumed or known mechanism of diffusion and its tracer correlation factor, D can be calculated using equation (2). But it is not necessary to rely upon theory to obtain D, because it is directly measurable with NMR from echo attenuation caused by application of uniform magnetic field gradients in a selected spin echo experiment. As noted in Section 1, the field gradient provides the label needed in the measurement of the tracer D. At a coordinate, $\boldsymbol{r}$, the precession frequency is given by $\omega(\boldsymbol{r}) = \gamma B_0 + \gamma \boldsymbol{G}\cdot\boldsymbol{r}$, where $\boldsymbol{B}_0$ is the applied magnetic field, $\boldsymbol{G}$ is the applied gradient, and $\boldsymbol{G} = \nabla B_z$. Usually only the z component of ∇B_z is applied in measuring D, although the others might be used to measure diffusivity in directions normal to $\boldsymbol{B}_0$. (Unless otherwise stated, D is assumed to be isotropic.) In addition to the applied gradient, there is usually a background gradient $\boldsymbol{G}_0$, which includes the inhomogeneity of $\boldsymbol{B}_0$ and constant gradients in the sample due to the sample material susceptibility and its shape.

3.2 Application of a Constant Field Gradient

Although it is possible through extraordinary measures to remove the dipolar interaction in solids with multiple pulse techniques, most diffusion measurements are made at temperatures where the dipolar interactions are motionally narrowed. For the Hahn spin echo, the echo attenuation for gradients constant in time, is given by[6]

$$S(t) = 2\tau/S(0) = \exp[-(2\tau/T_2) - \tfrac{2}{3}\gamma^2 D\tau^3(\boldsymbol{G} + \boldsymbol{G}_0)^2] \tag{23}$$

where τ is the time between the $\pi/2$ and the π rf pulses. At a fixed echo time, the numerical value of D may be obtained from dependence of the echo attenuation upon the magnitude of $\boldsymbol{G}$. This method is relatively easy to implement especially in application to fluid samples where D is large. For example, for ^{1}H in water where $D \approx 2 \times 10^{-9}$ m^2 s^{-1}, and $\tau = 30$ ms, $G \geq 2 \times 10^{-2}$ T m^{-1} to attenuate the echo by a factor 1/e, and it has been assumed that $G \gg G_0$. In solids, where D may be much smaller, considerably larger field gradients would be needed for acceptable echo attenuations.

The need for larger constant gradients presents two experimental problems, beyond the nontrivial ones of gradient coil design and coil cooling, which are: (1) the need for high rf power to provide the larger tipping field in the rotating coordinate system; and (2) the need for broader bandwidth, $\Delta\omega_{rec}$ for the rf receiver in the NMR spectrometer to accompany the broader spectrum of the spin system being observed. The NMR linewidth will be broadened by the gradient field by approximately $\Delta B \approx GR$, where R is the radius of the sample. Therefore, the tipping field B_1 must be increased as G is increased, and the rf power must increase as G^2 is increased. To avoid having the observed echo shape distorted, $\Delta\omega_{rec}$ must exceed the spectral width of the spin system observed. An increased $\Delta\omega_{rec}$ increases the noise observed with the echo and, therefore, reduces the signal-to-noise ratio and increases the accumulation time needed for an acceptable signal-to-noise ratio. These experimental problems are so severe that the constant gradient has not seen much use for solids.

3.3 Application of Pulsed Field Gradients

3.3.1 The Spin Echo Pulsed Field Gradient Experiment

The solution to these problems, turning off the field gradient during rf pulses and during signal accumulation, was proposed by Stejskal and Tanner in their definitive paper[54] describing the use of pulsed field gradients (PFGs) for the measurement of D. The timing of the gradient pulses in the spin echo experiment is shown in Figure 9 where a gradient pulse of amplitude $\boldsymbol{G}$ is applied at a time t_1 after the $\pi/2$ pulse and again after the π pulse at a time Δ after the start of the first gradient pulse. The width of each gradient pulse is δ. Using the calculation method of Torrey[55] and Abragam,[7] Stejskal and Tanner derived the expression for echo attenuation for their two-pulse PFG:

$$\begin{aligned} F(t = 2\tau) = \exp\{-(t/T_2) - \gamma^2 D[&\delta^2(\Delta - \tfrac{1}{3}\delta)G^2 + \tfrac{2}{3}\tau^3 G_0^2 \\ &-\delta\left(t_1^2 + t_2^2 + \delta(t_1 + t_2)\right. \\ &\left.+\tfrac{2}{3}\delta^2 - 2\tau^2\right)\boldsymbol{G}\cdot\boldsymbol{G}_0]\} \end{aligned} \tag{24}$$

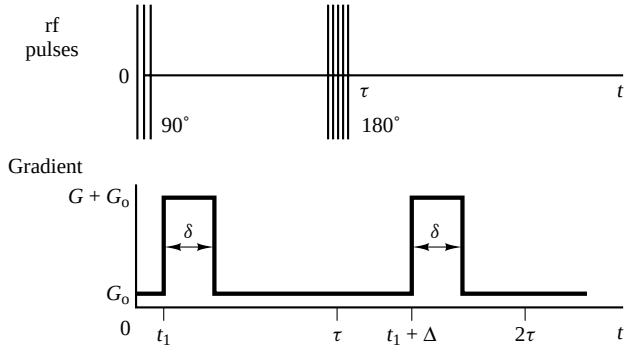

Figure 9 Timing of rf and magnetic field gradient pulses in the PFG spin echo experiment. G is the applied gradient, G_0 is the background gradient, and the spin echo (not shown) occurs at $t = 2\tau$

where $t_2 = 2\tau - (t_1 + \delta + \Delta)$. Other parameters are defined in Figure 9. The G_0^2 term is the usual one for a constant gradient. The $\boldsymbol{G}\cdot\boldsymbol{G}_0$ (cross) term arises in the Stejskal and Tanner derivation of $F(t = 2\tau)$. To ignore the $\boldsymbol{G}_0$ terms, it is necessary that $\delta G \gg \tau G_0$. Under these conditions the cross term is larger than the ${G_0}^2$ term, and if G_0 were essentially uniform across the sample, the cross term would make a plot of $\ln F(t = 2\tau)$ versus G^2 nonlinear.

There are stringent requirements for generating the pulsed currents that create the field gradients. The coils and sample must be firmly supported in order to minimize mechanical vibration caused by the large magnetic forces that act on the gradient coils. Since the first pulse defocuses the spins and the second refocuses them, their areas, $G\delta$ must match each other to high precision. For example, at a maximum gradient strength of 0.1 T m^{-1} with a 0.2 cm diameter sample and pulse widths of the order of 10 ms, one pulse gives ^{1}H spins an angular displacement of more than 10^4 rad. Therefore the matching precision must be better than 10 ppm for reproducible echo amplitudes. Callaghan[56] recently proposed a sequence to improve this pulse matching.

3.3.2 Background Gradients

The G_0 associated with a very homogeneous applied field B_0 is usually negligible. But in samples that are heterogenous on a small length scale, background gradients can be large. The apparently anomalous rapid transverse decay of the ^{7}Li spin envelope of liquid lithium was attributed by Zamir et al.[57] to diffusion in the distribution of background gradients in closely, but randomly, packed spherical lithium particles in oil. Similar effects were observed[58] in the NMR of ^{1}H in small granules of $NbH_{0.7}$. The importance of particle size is evident in their estimate of the typical $G_0 \approx 3\chi_0 B_0/R$, where χ_0 is the magnetic susceptibility of lithium and R is a typical particle radius. In lithium, for $B_0 = 1.0$ T, G_0 exceeds 0.1 T m^{-1} (10 G cm^{-1}) for particle radii of about 10^{-5} m. If the distribution of values of G_0 is symmetric about zero, the effect of the cross term would vanish for $\delta G \gg \tau G_0$. The effect of the cross term in second order is to reduce the *apparent* value of D deduced from the data.[59] G_0 can be reduced by reducing B_0 or by using larger particles. For metals, small particles are needed for penetration of the rf field and a good coil filling factor. This and a loss of signal-to-noise ratio at lower fields work against reduction of G_0. Pulse techniques for reducing or eliminating the cross term are listed in Section 3.3.4

3.3.3 Restricted Diffusion

In the derivations of the echo attenuation, it is assumed that the sample has infinite extent. For the PFG experiment, this means that $(2D\Delta)^{1/2} \ll d$, where d is the spacing between sample boundaries in the direction of the gradient. If this condition is not well met, the apparent value of D will be less than the true value. For some high diffusivity solids such as metal hydrides and fast ion conductors, diffusion might be restricted in the time of PFG measurements. A practical expression for echo attenuation in the PFG experiment on samples with spherical boundaries has been calculated by Murday and Cotts[59] who adapted the 'constant gradient' model of Newman.[60] Tanner and Stejskal[61] have calculated expressions for PFG echo attenuation for planar, cylindrical and spherical boundaries in the approximation that $\delta \ll \Delta$. Kärger, Pfeifer, and Heink[62] have reviewed the principles and applications of diffusion measurements by NMR.

3.3.4 Other Pulse Sequences

In the PFG spin echo experiment, the minimum measurable diffusion coefficient is inversely proportional to the diffusion time Δ, and Δ is limited by T_2 of the spin system. In systems where $T_1 \gg T_2$, the stimulated spin echo experiment can provide a greater diffusion time, since the time between the defocusing and refocusing intervals is limited by T_1. Tanner[63] proposed the stimulated echo sequence shown in Figure 10. In this sequence δ is still limited by T_2, but the diffusion time is limited by T_1. The cost of gaining an increase in Δ is an intrinsic reduction in the echo amplitude by a factor of $\frac{1}{2}$ created by the 'storage' of the spin magnetization along the z axis between second and third rf pulses. Tanner calculated the echo attenuation for the stimulated spin echo PFG experiment to be

$$F[t = (\tau_1 + \tau_2)] = -\gamma^2 D\{\delta^2(\Delta - \tfrac{1}{3}\delta)G^2 + \tau_1^2(\tau_2 - \tfrac{1}{3}\tau_1)G_0^2 - \delta[t_1^2 + t_2^2 + \delta(t_1 + t_2) + \tfrac{2}{3}\delta^2 - 2\tau_1\tau_2]\boldsymbol{G}\cdot\boldsymbol{G}_0\} \quad (25)$$

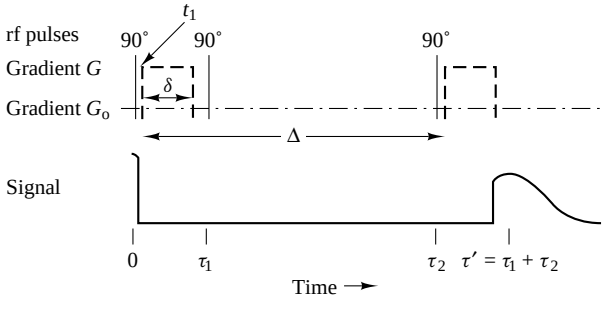

Figure 10 Timing of rf and magnetic field gradient pulses for the PFG stimulated echo experiment. The applied gradient is G, and G_0 is the background gradient. The stimulated echo is shown peaking at $t = (\tau_1 + \tau_2)$. (Reproduced by permission of The American Institute of Physics from J. E. Tanner, *J. Chem. Phys.*, 1970, **52**, 2523)

where $t_2 = \tau' - (t_1 + \delta + \Delta)$. The times in equation (21) are defined in Figure 10. The diffusion time Δ is approximately $(\tau_2 - \tau_1)$.

A number of techniques have been developed to reduce or eliminate effects of the cross term in equations (20 and 21). Karlicek and Lowe[64] invented a very effective pulse sequence that *eliminates* the cross term and substantially reduces the effect of the G_0^2 term relative to the G^2 term. It requires bipolar (or alternating) gradient pulses, and utilizes the Carr–Purcell[6] spin echo train with one gradient pulse inserted between each pair of π pulses; that is, δ is limited by 2τ instead of τ. In this scheme, the minimum usable Carr–Purcell sequence has five π pulses, and it can be extended by units of four such pulses at a time. The technical requirement of bipolar current pulses is not insignificant.

The Karlicek–Lowe concept has been extended to the stimulated echo experiment,[65] with three different sequences that eliminate the cross term in the expression for echo attenuation. All these sequences use bipolar gradient pulses. One simple unipolar sequence reduces the ratio of the cross term to the G^2 term by a factor of about τ/Δ, which is less than the factor of about unity in the Tanner stimulated echo PFG experiment. In summary, the systematic errors due to background gradients can be nearly eliminated in diffusion coefficient measurements (see ***Diffusion Measurements by Magnetic Field Gradient Methods***).

4 APPLICATIONS OF NMR TO DIFFUSION IN SOLIDS

4.1 Solids with Low Vacancy Concentrations

4.1.1 Lithium

Solid lithium is a good example of a simple elemental low-vacancy solid which has been investigated by relaxation rate and PFG diffusion coefficient measurements. Lithium has the b.c.c. structure from about 77 K to its melting point at 454 K. The ^{7}Li relaxation times have been measured over this full temperature range, covering both the strong and weak collision regimes, and they have been analyzed over eight decades of lithium jump rates from about $3\,s^{-1}$ to $3 \times 10^8\ s^{-1}$ between 200 K and the melting point.[66] (Messer and Noack[66] give references to earlier works.) Direct PFG measurements of D in the solid have been made by Mali et al.[67] at temperatures above about 350 K where $D > 10^{-13}\,m^2\ s^{-1}$ for both ^{6}Li and ^{7}Li in nearly isotopically pure and mixed samples. There is consistency between these D measurements and lithium atomic jump rates analyzed from relaxation data using lattice specific encounter models. These results demonstrate the importance of assembling relaxation data over a wide range of NMR frequencies as well as temperature. An exemplary data set[68] for R_1 and $R_{1\rho}$ is shown in Figure 11.

Messer and Noack[66] combined the R_1 data of Figure 11 with $R_{1\rho}$ data[69] at one ω_1 and strong collision data.[53] These data were analyzed with the monovacancy encounter theory of Wolf[28] and the encounter model with divacancies,[70] for the self-diffusion coefficient with the following expected temperature dependence:

$$D_{SD} = D_{10} \exp(-E_1/RT)[1 + D_{12} \exp(-E_{12}/RT)] \quad (26)$$

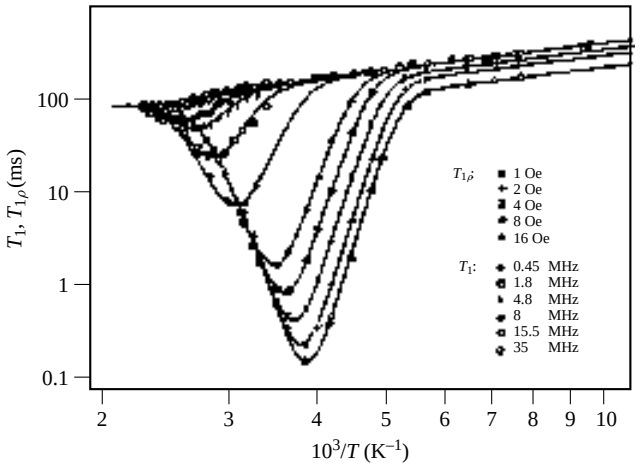

Figure 11 Temperature dependences of T_1 and $T_{1\rho}$ of ^{7}Li in solid lithium. The T_1 curves are labeled with the NMR frequency, and the $T_{1\rho}$ curves list the rotating frame magnetic field in oersteds (1 Oe $\equiv 1 \times 10^{-4}$ T). The upper limits on values of relaxation times is set by the conduction electron relaxation mechanism. (From Messer[68])

D_{SD} simply expresses the mean jump rate τ_d^{-1} of lithium atoms in that, by definition,[66] $D_{SD} = l^2/(6\tau_d)$, where l is the nearest neighbor distance in the b.c.c. lattice. Results of the analysis are plotted in Figure 12. The evident deviation from the Arrhenius relationship in equation (22) at high temperatures is attributed to divacancies and is offered as the explanation of the form of the curve in Figure 12. They obtained $E_1 = 50.2\,kJ\ mol^{-1}$, $E_{12} = 16.7\,kJ\ mol^{-1}$, $D_1 = 3.8 \times 10^{-6}\,m^2\ s^{-1}$, and $D_{12} = 2.5 \times 10^{-2}\,m^2\ s^{-1}$. Using the set of data in Figure 11 with a modified formula for the strong collision regime, Messer[68] obtained values of D_{SD} a factor of about 1.5 greater than those he reported previously.[66] A similar analysis has been done in solid sodium,[71] but without the availability of R_1 data which were masked because of the stronger conduction relaxation rate in sodium.

PFG measurements[67] of D are given in Figure 13 for three lithium samples having different isotopic composition. These data occur in the high temperature range where the divacancy term in equation (22) appears to be in evidence. The PFG measurements[67] of D have been compared with the two sets of D_{SD} from Messer and Noack[66] and Messer.[68] Theoretically, for the b.c.c. lattice with monovacancies only, $(D/D_{SD}) = f_t = 0.727$. Mali et al.[67] found values of this ratio to be between about 0.33 and 0.60, depending on temperature for the data analysis used by Messer and Noack.[66]

4.1.2 Fluorides

As noted in Section 2.2.3, the work[32–34] on pure and doped BaF_2 represents a very successful application of NMR to a low-vacancy system. The comparison made by Figueroa et al.[34] between values of D calculated by analysis of relaxation rate data and values of D deduced from electrical conductivity is shown in Figure 14 (from the review by Chadwick).[72] Experimentalists who have ever taken NMR data from samples at temperatures within a few hundred degrees of these high temperatures (up to about 1200 K) will especially appreciate Figure 14. The same research group settled many questions regarding the interpretation of relaxation rates in PbF_2 at high

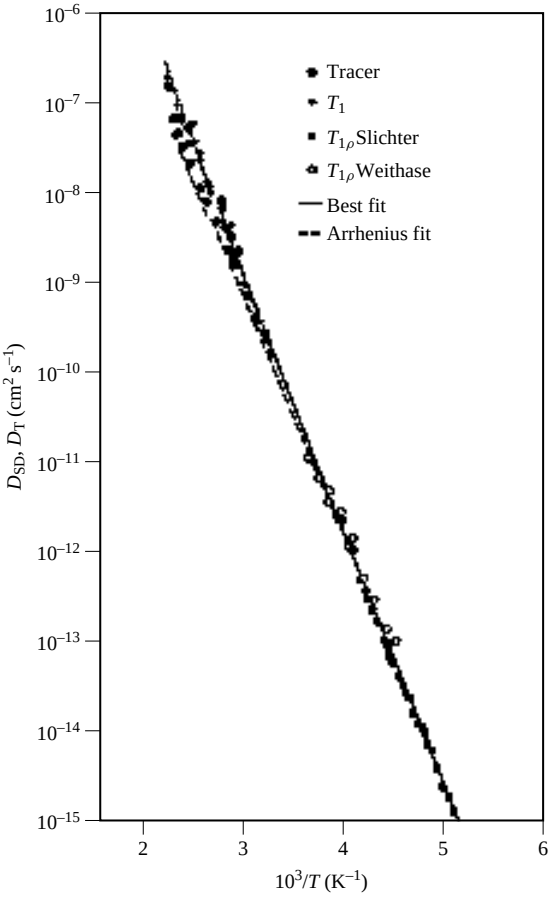

Figure 12 Temperature dependence of the self-diffusion coefficient D_{SD} based on ^{7}Li relaxation times measured in solid lithium. (+) T_1 from Messer and Noack;[66] (■) $T_{1\rho}$ from Ailion and Slichter;[53] (○) $T_{1\rho}$ from Weithase and Noack;[69] (●) mass spectroscopy tracer diffusion coefficients; (—) D_{SD} fit to equation [22]; (- - -) Arrhenius fit. (Reproduced by permission of Springer-Verlag from R. Messer and F. Noack, *Appl. Phys.*, 1975, **6**, 79)

temperatures by making direct PFG diffusion measurements of fluoride ions and showing their agreement with D deduced from conductivity measurements.[73]

4.1.3 Plastic Crystals

Some molecular crystals with approximately spherical molecules, e.g. adamantane, have a plastic phase just below the melting point in which the molecules are in a state of rapid reorientation combined with translational diffusion. Many of these solids have low melting points, and so the transition to the plastic phase limits the temperature range for their study. The rapid reorientation effectively averages out the intramolecular dipole interaction and provides the fluctuating fields needed for spin relaxation. The understanding of the rotational motion has relied on analysis of NMR relaxation rate measurements. Analyses of the several spin relaxation rates have identified translational jumping rates of the rotators in the plastic phase, but the jump rates are usually so low near the melting point that PFG measurements of D have not been practical. Typically, the plastic crystal has f.c.c. or b.c.c. structure, considering the equilibrium sites of the rotators, and

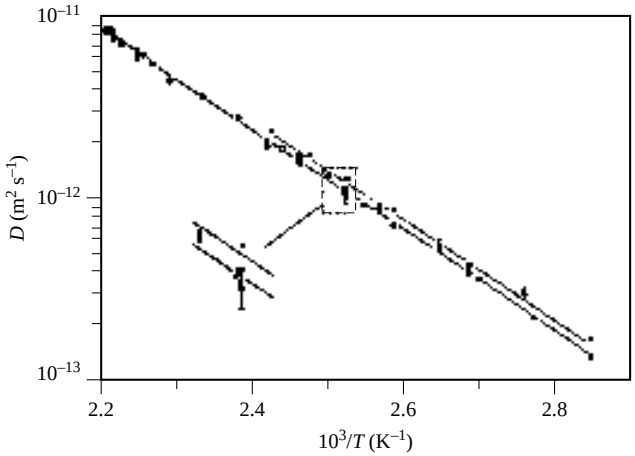

Figure 13 Temperature dependence of ^{7}Li diffusion coefficients in solid lithium measured with the PFG spin echo technique. (○, ●) Natural lithium (92.6%^{7}Li, 7.4%^{6}Li); (▲) sample with 99.97%^{7}Li; (×) sample with 95.5%^{6}Li, 4.5%^{7}Li. (○) Magnetic field $\boldsymbol{B}_0$ = 2.11 T; for all other symbols, $\boldsymbol{B}_0$ = 5.17 T. The data near 400 K are shown enlarged in order better to display the error bars. (Reproduced by permission of IOP Publishing Ltd from M. Mali, J. Roos, M. Sonderegger, D. Brinkmann, and P. Heithjans, *J. Phys. F: Met. Phys.*, 1988, **18**, 403)

monovacancy diffusion obtains in these systems. Observations of R_2 and the peak(s) in $R_{1\rho}$ at one or more values of ω_1 have been most useful in exposing diffusion because τ_d is usually too long to allow observation of the peak in R_1 at the selected NMR operating frequencies. Figure 15 shows relaxation time data for the ordered and the b.c.c. plastic phase

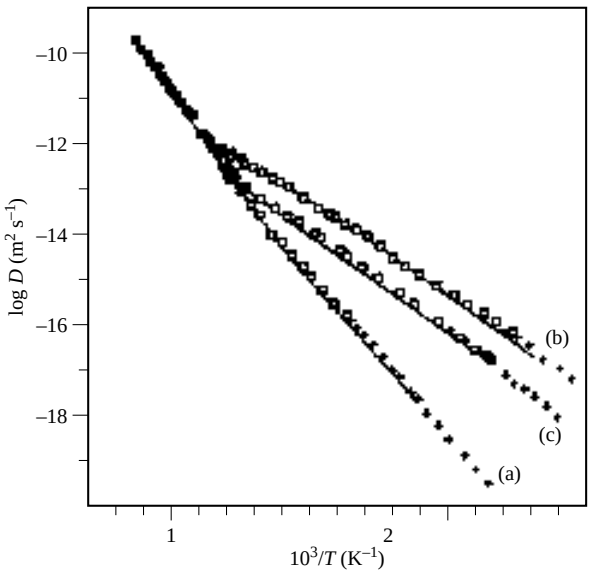

Figure 14 Temperature dependence of ^{19}F diffusion coefficients in BaF_2 single crystals: (a) pure; (b) doped with 0.04 mol% KF; (c) doped with 0.05 mol% LaF_3. Diffusion coefficients were calculated from relaxation time measurements using the monovacancy encounter model. (■) From T_1; (□) from $T_{1\rho}$; (+) from $T_{1\text{Dipolar}}$; (—) calculated from the ionic conductivity. The changes in slope occur between the extrinsic and intrinsic regions.34, 72 (Reproduced by permission of the Royal Society of Chemistry from A. V. Chadwick, *J. Chem. Soc. Faraday Trans.*, 1990, **86**, 1157)

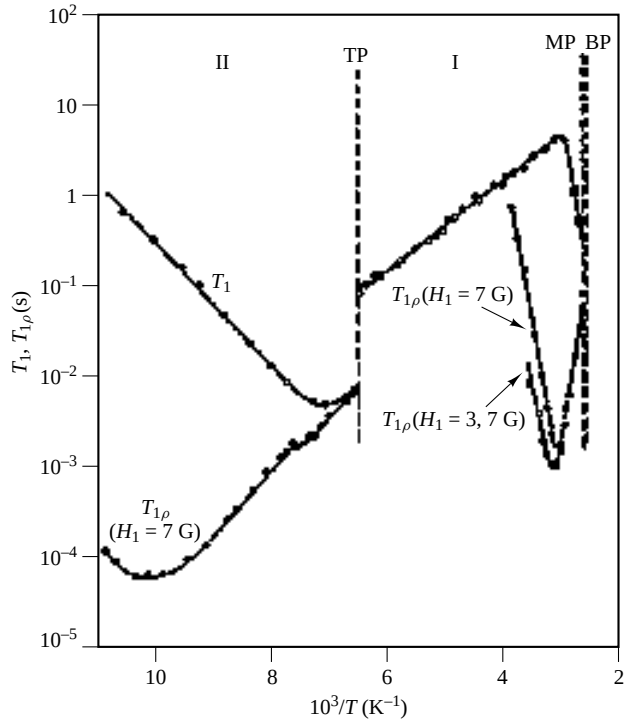

Figure 15 Temperature dependences of T_1 and $T_{1\rho}$ for ^{1}H in hexamethylethane. Region I is the plastic crystal phase, and region II is the ordered phase. The NMR frequency is 14.3 MHz. The temperature increases from left to right. (Reproduced by permission of Taylor & Francis Ltd. from J. M. Chezeau, J. Dufourcq, and J. H. Strange, *Mol. Phys.*, 1971, **20**, 305)

of hexamethylethane (HME).[74] The reorientational motion in the low-temperature phase produces the minimum in T_1 and in $T_{1\rho}$, and the effects of the translational motion in the plastic phase is similarly evident. In the plastic phase, second moment measurements indicated isotropic molecular reorientation.

From the encounter model for monovacancies,[25,28] estimates of D deduced from NMR relaxation times for three compounds have been compared with D obtained from radiotracer results, with acceptable agreement.[75] In HME, $D \approx 1 \times 10^{-12}$ m^2 s^{-1} at the melting point (374 K). Boden has prepared a review of NMR in plastic crystals.[76]

4.2 High-Vacancy Solids

4.2.1 Metal Hydrides

Nearly half of the transition metals, the rare earth metals, and many intermetallic compounds and alloys can absorb large amounts of hydrogen, which for some systems can exceed three hydrogen atoms for each metal (M) atom. Usually the hydrogen resides as atoms in one set of interstitial sites of the metal host lattice, though not necessarily the lattice of the pure, unhydrided metal. Norberg[77] explored the application of NMR early to metal hydrides by conducting pulsed and continuous wave experiments on PdH_x and identifying motional narrowing, susceptibility shifts, and testing for the conduction electron relaxation mechanism.

High diffusivities of the hydrogen atoms (i.e. those exceeding 10^{-9} m^2 s^{-1}) can occur in these metal–hydrogen (M–H) systems. Wide ranges of hydrogen solubility exist wherein hydrogen atoms reside nearly randomly (subject to site-blocking effects) on one set of sites. Vacancy concentrations can be large. Fractional concentrations exceeding 0.2 are not unusual, but 'monovacancy' levels are rare. This means that there are opportunities in M–H systems to use mean field,[26] multiple scattering,[18] or Monte Carlo[39]emrstm0123-bib-0043 models in relaxation rate analyses. Because of its low atomic number, hydrogen has a weak conduction electron relaxation mechanism[78] to compete with relaxation due to diffusion. T_1 and T_2 are sufficiently long to allow use of the PFG methods for measuring D.

Most M–H systems are good metals. As noted earlier, systematic errors in PFG measurements are reduced if metal particles are made as large as possible. This consideration favors lower laboratory frame NMR frequencies, so that 7 MHz was selected[40] for the determination of the step length of hydrogen in the subdihydrides of TiH_x. In the first PFG measurement[79] of D for hydrogen in the metal hydride, $NbH_{0.6}$, a cylindrical single crystal was used partly to avoid the concerns over small particles. This experiment[79] also combined R_1 and D measurements to determine the step length. In a series of measurements on b.c.c. hydrides, summarized by Sevilla and Cotts,[80] two special PFG sequences[64,81] were used to eliminate the $\boldsymbol{G}\cdot\boldsymbol{G}_0$ cross term. Hydrogen is found to be more mobile in the b.c.c. host metals than in those with more closely packed metal atoms.[80]

The combining of measurements of D and R_1 to learn about step lengths has been done impressively by a collaboration between the Stuttgart Max Planck Institute and Iowa State University groups. Majer et al.[42,82] have measured D for ^{1}H using the PFG stimulated echo[63] for five concentrations of hydrogen in the subdihydride ZrH_x at temperatures from 600 to 950 K using applied gradients up to 25 T m^{-1}. Their results are shown in Figure 16. Using lattice specific R_1 theories,[14,18,43] combined with R_1 measurements by Han et al.[83] on the same samples, it was demonstrated that hydrogen atoms jump between nearest neighbor tetrahedral interstitial sites.

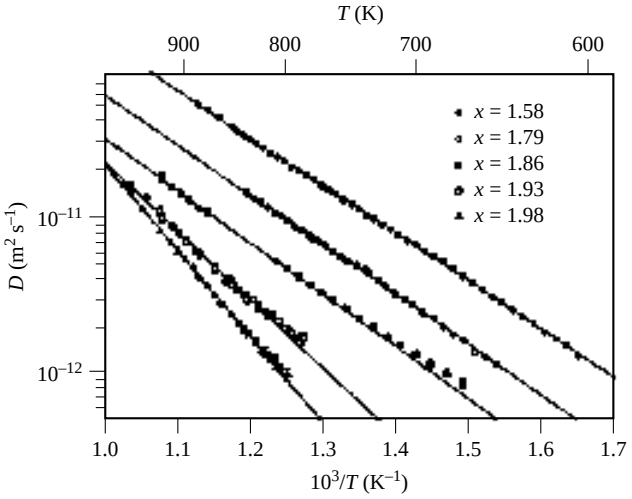

Figure 16 Temperature dependences of diffusion coefficient of hydrogen in five samples of ZrH_x measured by the ^{1}H PFG stimulated echo. (——) Fits to the data with the Arrhenius equation. (Reproduced by permission of IOP Publishing, Ltd from G. Majer, W. Renz, and R. G. Barnes, *J. Phys. Condens. Matter*, 1994, **6**, 2935)

Non-Arrhenius plots at high temperatures for high concentration samples have been attributed to having a small fraction of hydrogen atoms located on a second, but as yet unidentified, site. References cited by Han et al.[83] offer a good introduction to the literature on applications of NMR in metal hydrides (see ***Hydrogen–Metal Systems***).

4.2.2 Fast Ion Conductors

In the more than 20 years that there has been a high level of interest in understanding ionic conductivity in solids, NMR has been an important tool for the study of structure and ionic motion in what are regularly known as 'solid electrolytes' or 'superionic conductors'. The work on the fluorides which has already been mentioned[32–34,74,75] is representative of the application of NMR in this field. The search for high ionic conductivity has identified a wide variety of solids that meet the necessary criterion. These include crystals, glasses and polymer electrolytes. The recent report by Brinkmann[84] provides an informative and comprehensive review of NMR in this field.

Interesting examples of combining R_1 measurements with the PFG technique for D are found in the work by the University of Zürich group on ^{109}Ag ($I = \frac{1}{2}$) in fast ion conductors. Because nuclear moments of both silver isotopes are less than one-twentieth of that of ^{1}H, it is necessary to have access to high magnetic fields to get the NMR frequency into a workable range (above 10 MHz). However, even in this frequency range signals will be low because of the low magnetogyric ratio of ^{109}Ag. Compared to working with large γ spins such as those of ^{1}H, ^{7}Li, ^{19}F, or ^{23}Na, doing the PFG experiment on silver at first appears daunting because of the γ dependence of the important exponent in the echo attenuation expression in equation (20): $[\gamma^2 D\delta^2(\Delta - \frac{1}{3}\delta)G^2]$. This term should equal or exceed unity in order effectively to attenuate the echo. However, because γ of ^{109}Ag is small, its relaxation rates are also reduced, so the difference can be made up by increasing the times δ and Δ in the sequence. Nevertheless, the long relaxation times and the lower NMR signal amplitudes mean longer signal accumulation times for an acceptable signal-to-noise ratio and good data.

Looser et al.[85] used the PFG spin echo technique to measure D in the two isostructural crystals $RbAg_4I_5$ and KAg_4I_5 from 150 to 300 K covering the α and β phases of these crystals. They found little difference in D between these crystals except in the $\alpha-\beta$ phase transition temperatures, which are visible in Figure 17. From comparison between D measured by the PFG and D_σ deduced from conductivity data, they concluded that there was increased correlation of the silver motion in the β phase.

In their work on β-Ag_3SBr, Huber et al.[86] brought together experimental data on the temperature, pressure, and NMR frequency dependence of the silver R_1 and PFG D measurements. Having the diffusion data allowed them to identify a model for silver motion that includes local hopping between the four silver sites within one face of the cubic unit cell and diffusional jumps between neighboring faces.

5 FURTHER READING

Review papers provide special perspectives on their selected applications of NMR and references to other works of interest.

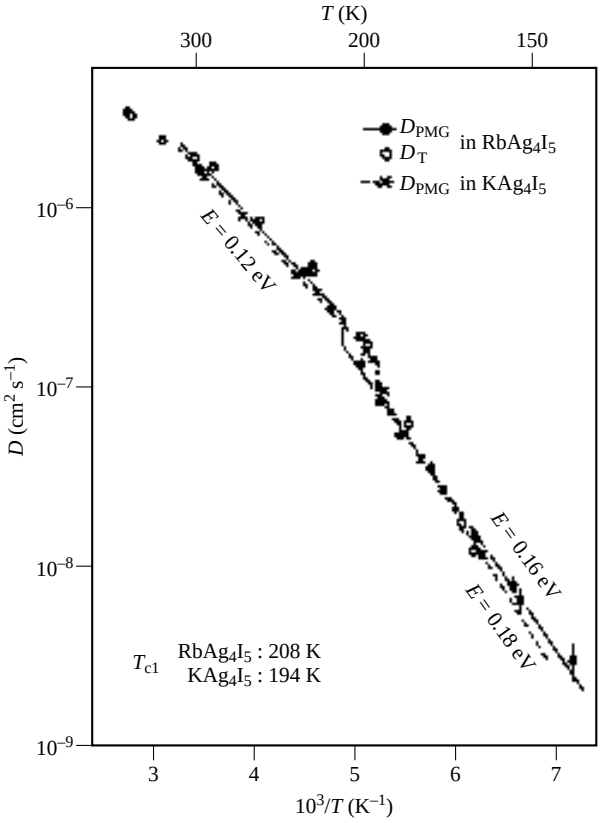

Figure 17 Temperature dependences of diffusion coefficients of silver in fast ion conductors, $RbAg_4I_5$ and KAg_4I_5. ^{109}Ag PFG spin echo measurements: (•) $RbAg_4I_5$; (×) KAg_4I_5; (○) radioactive tracer data. The positions of the $\alpha-\beta$ phase transitions are visible. (Reproduced by permission of Elsevier Science Publishers B.V. From Looser et al.[85])

Polymer systems have been reviewed by von Meerwall.[87] Boden et al.[88] have discussed model polymer electrolytes. Both polymer electrolytes and glasses have been discussed by Brinkmann.[84] Seymour[89] and Barnes[90] have reviewed metal hydrides, and Strange[91] has summarized work on ionic transport. Chadwick's paper[72] is broader in its coverage of mass transport in a number of solids.

6 RELATED ARTICLES

Diffusion Measurements by Magnetic Field Gradient Methods; Diffusion in Rare Gas Solids; Fast Ion Conductors; Field Gradients and Their Application; Hydrogen–Metal Systems; Liquid Crystalline Samples: Diffusion; Polymer Dynamics and Order from Multidimensional Solid State NMR; Radiofrequency Gradient Pulses; Relaxation Theory: Density Matrix Formulation; Spin Diffusion in Solids; Ultraslow Motions in Solids.

7 REFERENCES

1. E. M. Purcell, H. C. Torrey, and R. V. Pound, *Phys. Rev.*, 1946, **69**, 37.
2. F. Bloch, W. W. Hansen, and M. Packard, *Phys. Rev.*, 1946, **69**, 127.

3. F. Bloch, *Phys. Rev.*, 1946, **70**, 460.
4. N. Bloembergen, E. M. Purcell, and R. V. Pound, *Phys. Rev.*, 1948, **73**, 679.
5. E. L. Hahn, *Phys. Rev.*, 1950, **80**, 580.
6. H. Y. Carr and E. M. Purcell, *Phys. Rev.*, 1954, **94**, 630.
7. A. Abragam, *The Principles of Nuclear Magnetism*, Clarendon, Oxford, 1961.
8. C. P. Slichter, *Principles of Magnetic Resonance*, 3rd edn, Springer, Berlin, 1990.
9. S. W. Kelly and C. A. Sholl, *J. Phys.: Condens. Matter*, 1992, **4**, 3317, and references therein.
10. D. Wolf, *Spin-temperature and Nuclear-spin Relaxation in Matter*, Clarendon, Oxford, 1979.
11. M. Goldman, *Spin Temperature and Nuclear Magnetic Resonance*, Oxford, London, 1970.
12. D. C. Look and I. J. Lowe, *J. Chem. Phys.*, 1966, **44**, 2995.
13. R. Kubo and K. Tomita, *J. Phys. Soc. Jpn*, 1954, **9**, 888.
14. C. A. Sholl, *J. Phys. C: Solid State Phys.*, 1988, **21**, 319.
15. H. C. Torrey, *Phys. Rev.*, 1953, **92**, 962.
16. C. A. Sholl, *J. Phys. C: Solid State Phys.*, 1981, **14**, 447.
17. J. F. Harrmon and B. H. Muller, *Phys. Rev*, 1969, **182**, 400.
18. P. A. Fedders and O. F. Sankey, *Phys. Rev. B*, 1978, **18**, 5938.
19. R. A. Hultsch and R. G. Barnes, *Phys. Rev.*, 1962, **125**, 1832.
20. K. Compaan and Y. Haven, *Trans. Faraday Soc.*, 1956, **52**, 786.
21. H. A. Resing and H. C. Torrey, *Phys. Rev.*, 1963, **131**, 1102.
22. D. F. Holcomb and R. E. Norberg, *Phys. Rev.*, 1955, **98**, 1074.
23. C. A. Sholl, *J. Phys. C: Solid State Phys.*, 1974, **7**, 3378.
24. C. A. Sholl, *J. Phys. C: Solid State Phys.*, 1975, **8**, 1737.
25. D. Wolf, *J. Magn. Reson.*, 1975, **17**, 1.
26. W. A. Barton and C. A. Sholl, *J. Phys. C: Solid State Phys.*, 1976, **9**, 4315; 1978, **11**, 4405.
27. W. A. Barton and C. A. Sholl, *J. Phys. C: Solid State Phys.*, 1980, **13**, 2579.
28. D. Wolf, *Z. Naturforsch., Teil a*, 1971, **26**, 1816; *Phys. Rev. B*, 1974, **10**, 2710.
29. M. Eisenstadt and A. G. Redfield, *Phys. Rev.*, 1963, **132**, 635.
30. D. Wolf, *Phys. Rev. B.*, 1974, **10**, 2724.
31. D. C. Ailion and P. P. Ho, *Phys. Rev.*, 1968, **168**, 662.
32. D. Wolf, D. R. Figueroa, and J. H. Strange, *Phys. Rev. B*, 1977, **15**, 2545.
33. D. R. Figueroa, J. H. Strange, and D. Wolf, *Phys. Rev. B*, 1979, **19**, 148.
34. D. R. Figueroa, A. V. Chadwick, and J. H. Strange, *J. Phys. C: Solid State Phys.*, 1978, **11**, 55.
35. C. A. Sholl, *J. Phys. C: Solid State Phys.*, 1982, **15**, 1177.
36. I. R. MacGillivray and C. A. Sholl, *J. Phys. C: Solid State Phys.*, 1986, **19**, 4771.
37. O. F. Sankey and P. A. Fedders, *Phys. Rev. B.*, 1979, **20**, 39.
38. P. A. Fedders, *Phys. Rev. B*, 1982, **25**, 78.
39. L. D. Bustard, *Phys. Rev. B.*, 1980, **22**, 1.
40. L. D. Bustard, R. M. Cotts, and E. F. W. Seymour, *Phys. Rev. B.*, 1980, **22**, 12.
41. C. L. Bisson and W. D. Wilson, in *Effect of Hydrogen on the Behavior of Matter.*, ed. A. W. Thompson and I. M. Bernstein, AIME, New York, 1976, p. 416.
42. G. Majer, W. Renz, A. Seeger, and R. G. Barnes, *Z. Phys. Chem.*, 1993, **181**, 187.
43. D. A. Faux, D. K. Ross, and C. A Sholl, *J. Phys. C: Solid State Phys.*, 1986, **19**, 4115.
44. C. A. Sholl, *Diffus. Defect Data, Solid State Data A, Defect Diffus. Forum*, 1993, **95–98**, 91.
45. E. R. Andrew and D. P. Tunstall, *Proc. R. Soc.*, 1961, **78**, 1; M. I. Gordon and M. J. R. Hoch, *J. Phys. C: Solid State Phys.*, 1978, **11**, 783; P. S. Hubbard, *J. Chem. Phys.*, 1970, **33**, 985; and S. W. Kelly and C. A. Sholl, *J. Phys. Condens. Matter*, 1992, **4**, 3317.
46. W. A. Barton, *J. Phys. C: Solid State Phys.*, 1982, **15**, 5123.
47. P. A. Beckmann, *Phys. Rep.*, 1988, **171**, 85.
48. A. F. McDowell, Ph.D. Thesis, Cornell University, 1993 (unpublished).
49. K. L. Ngai and S. W. Martin, *Phys. Rev. B*, 1989, **40**, 10 550.
50. S. R. Elliot, *Solid State Ionics*, 1988, **27**, 131.
51. S. R. Elliot and A. P. Owens, *Phys. Rev. B*, 1991, **44**, 47.
52. C. P. Slichter and D. Ailion, *Phys. Rev. A*, 1964, **135**, 1099.
53. D. Ailion and C. P. Slichter, *Phys. Rev. A*, 1965, **137**, 235.
54. E. O. Stejskal and J. E. Tanner, *J. Chem. Phys.*, 1965, **42**, 288.
55. H. C. Torrey, *Phys. Rev.*, 1956, **104**, 563.
56. P. T. Callaghan, *J. Magn. Reson.*, 1990, **88**, 493.
57. D. Zamir, R. C. Wayne, and R. M. Cotts, *Phys. Rev. Lett.*, 1964, **12**, 327.
58. D. Zamir and R. M. Cotts, *Phys. Rev.*, 1964, **134**, A666.
59. J. S. Murday and R. M. Cotts, *Z. Naturforsch., Teil a*, 1971, **26**, 85; *J. Chem, Phys.*, 1968, **48**, 4938.
60. C. H. Newman, *J. Chem. Phys.*, 1974, **60**, 4508.
61. J. E. Tanner and E. O. Stejskal, *J. Chem. Phys.*, 1968, **49**, 1768; J. E. Tanner, Ph.D. Thesis, University of Wisconsin, 1966.
62. J. Kärger, H. Pfeifer, and W. Heink, *Adv. Magn Reson.*, 1988, **12**, 1.
63. J. E. Tanner, *J. Chem. Phys.*, 1970, **52**, 2523.
64. R. F. Karlicek, Jr and I. J. Lowe, *J. Magn. Reson.*, 1980, **37**, 75.
65. R. M. Cotts, M. J. R. Hoch, T. Sun, and J. T. Markert, *J. Magn. Reson.*, 1989, **83**, 252.
66. R. Messer and F. Noack, *Appl. Phys.*, 1975, **6**, 79.
67. M. Mali, J. Roos, M. Sonderegger, D. Brinkmann, and P. Heithjans, *J. Phys. F: Met. Phys.*, 1988, **18**, 403.
68. R. Messer, *1976 Magnetic Resonance and Related Phenomena, Proceedings of the 19th Congress Ampère, Heidelberg*, ed. H. Brunner et al. Groupment Ampère, Heidelberg, p. 269.
69. M. Weithase and F. Noack, *Phys. Stat. Sol. (b)*, 1973, **57**, K111.
70. E. Cavelius, *Phys. Stat. Sol. (b)*, 1974, **65**, 181.
71. G. Brünger, O. Kanert, and D. Wolf, *Phys. Rev. B*, 1980, **22**, 4247.
72. A. V. Chadwick, *J. Chem. Soc. Faraday Trans.*, 1990, **86**, 1157.
73. R. E. Gordon and J. H. Strange, *Faraday Symp. Chem. Soc.*, 1978, **13**, 154; *J. Phys. C: Solid State Phys.*, 1978, **11**, 3213.
74. J. M. Chezeau, J. Dufourcq, and J. H. Strange, *Mol. Phys.*, 1971, **20**, 305.
75. A. R. Britcher and J. H. Strange, *Mol. Phys.*, 1979, **37**, 181.
76. N. Boden, *The Plastically Crystalline State*, ed. J. N. Sherwood, Wiley, New York 1979, p. 147.
77. R. E. Norberg, *Phys. Rev.*, 1952, **86**, 745.
78. C. Korn and D. Zamir, *J. Phys. Chem. Sol.*, 1970, **31**, 489.
79. O. J. Zogal and R. M. Cotts, *Phys. Rev. B*, 1975, **11**, 2443.
80. E. H. Sevilla and R. M. Cotts, *J. Less-Common Metals*, 1987, **129**, 223.
81. W. D. Williams, E. F. W. Seymour, and R. M. Cotts, *J. Magn. Reson.*, 1978, **31**, 271.
82. G. Majer, W. Renz, and R. G. Barnes, *J. Phys. Condens. Matter*, 1994, **6**, 2935.

83. J.-W. Han, D. R. Torgeson, R. G. Barnes, and D. T. Peterson, *Phys. Rev. B*, 1991, **44**, 12 353.
84. D. Brinkmann, *Prog. NMR Spectrosc.*, 1992, **24**, 527.
85. H. Looser, M. Mali, J. Roos, and D. Brinkmann, *Solid State Ionics*, 1983, **9/10**, 1237.
86. H. Huber, M. Mali, J. Roos, and D. Brinkmann, *Phys. Rev. B*, 1988, **37**, 1441; *Solid State Ionics*, 1986, **18/19**, 1188.
87. E. D. von Meerwall, *J. Non-Cryst. Solids*, 1991, **131–133**, 735.
88. N. Boden, S. A. Leng, and I. M. Ward, *Solid State Ionics*, 1991, **45**, 261.
89. E. F. W. Seymour, *J. Less-Common Met.*, 1982, **88**, 323.
90. R. G. Barnes, in *Hydrogen in Metals*, ed. H. Wipf, Springer, Berlin, Vol. 3, in press.
91. J. H. Strange, *Crystal Lattice Defects Amorph. Mater.*, 1987, **14**, 183.

Biographical Sketch

Robert M. Cotts. *b* 1927. B.S., Wisconsin, Madison, 1950; Ph.D., California, Berkeley, 1954. Introduced to NMR by Walter D. Knight. Instructor–research associate (with Felix Bloch), Stanford University, 1954–57; Faculty, Cornell University, 1957–present. Approx. 55 publications. Research interests: the physics of condensed matter, including applications of NMR and NQR; translational diffusion in solids and liquids; and motion and siting of hydrogen in transition and rare earth metals.

Fluorine-19 NMR

Wallace S. Brey and Mary Louise Brey
University of Florida, Gainesville, FL, USA

1	Introduction	1
2	Chemical Shifts	1
3	Indirect Spin–Spin Coupling	3
4	Relaxation; Nuclear Overhauser Effects	5
5	Applications to Biochemical Problems	6
6	Applications of Special Techniques	7
7	Related Articles	8
8	References	8

1 INTRODUCTION

1.1 Properties of Fluorine-19

Aside from carbon and hydrogen, fluorine-19 is possibly the most-studied nucleus. The reasons for this include both the properties of the nucleus and the practical importance of molecules containing this element. The nucleus ^{19}F has the advantage of 100% natural abundance and a high magnetogyric ratio, about 0.94 times that of ^{1}H. The chemical shift range is 20 or more times that of hydrogen, so that resonances of different fluorine nuclei are usually well separated. Furthermore, spectral positions are sensitive to the environments of fluorine atoms. The nuclear spin quantum number is $\frac{1}{2}$, and thus relaxation times are sufficiently long that spin–spin splittings may be resolved. Long-range spin–spin coupling constants have substantial magnitude; this has the advantage of providing extensive connectivity information but, for highly fluorinated molecules, it tends to create large spin systems and make resonances very complex and non-first-order.

Fluorinated molecules have achieved industrial prominence in the production of polymers, as surface active and lubricating materials, as refrigerants, and as anesthetics and drugs. Fluorine is particularly useful as a tracer in biological systems, as there is essentially no natural background, and it is often possible to substitute a single fluorine atom for a hydrogen atom without materially changing the properties of a molecule such as a protein.

Observation of ^{19}F in high-field spectrometers may present some problems, and care is required in selecting appropriate instrumentation. At a field of 11.75 T, corresponding to 500 MHz frequency for protons, the full spectral range for ^{19}F approaches 0.5 MHz. This requires appropriate high speeds for the analog-to-digital converter and wide bandwidths for the amplifiers, as well as large data arrays to afford good spectral resolution for narrow lines. Furthermore, uniform excitation over the whole spectrum requires quite short pulses from the transmitter.

1.2 Reviews and Compilations of Data

A small paperback volume by E. F. Mooney presents an introduction to ^{19}F NMR spectroscopy.[1] It includes a variety of typical spectra, as well as some representative NMR parameters for organic molecules, and it gives the reader an excellent feel for the field. Two full volumes have been devoted to compilations of chemical shifts,[2,3] one is devoted almost entirely to discussions and tables of spin–spin coupling constants,[4] and a database for C_xF_y compounds has been described.[5] A number of reviews covering publications on ^{19}F NMR over specific periods of 1 or 2 years have been included in the *Annual Reports on NMR Spectroscopy*.[6–12]

2 CHEMICAL SHIFTS

The shielding of fluorine nuclei varies quite widely, as illustrated in Table 1 for the range from XeF_6 at low fields to CH_3F at high fields. Several specific structure types will be discussed later. Compared with the situation for hydrogen, the effects of anisotropic magnetic fields, such as those generated by ring currents, are relatively much less important for fluorine, and the nature of the bonding of the atom has a much greater influence. The presence of unshared electron pairs leads to the existence of excited molecular states at relatively low energies, and these are mixed into the ground state as the result of a perturbation by the magnetic field of a spectrometer, producing an unshielding or 'paramagnetic' effect.

Table 1 Representative ^{19}F Chemical Shifts (in ppm to High Frequency of $CFCl_3$)

XeF_6	550	$CFBr_3$	7
F_2	430	CF_2Cl_2	−8
ReF_7	345	CF_3CH_3	−62
$ClF_{5,eq.}$	412	SiF_6^{2-}	−127
$ClF_{5,ax.}$	247	BF_3	−131
WF_6	166	$CF_2{=}CF_2$	−135
$C_6H_5SO_2F$	66	CH_3F	−272

2.1 References for Chemical Shift Measurements

Many early reports of ^{19}F shifts were based on the use of trifluoroacetic acid as an external reference. Because this is a hazardous and reactive material and because values based upon any external reference suffer from errors related to the magnetic susceptibility and geometry of the sample, it has been replaced by the internal reference fluorotrichloromethane, assigned a shift of zero. Under poor spectrometer resolution, the spectrum of this material has only a single peak, but in an instrument with good resolution this is resolved into four lines, corresponding in order, from low frequency to high frequency, to the presence of three, two, one, or no ^{37}Cl nuclei in the molecule. Thus a different result is obtained if the position of one of the individual lines is taken as reference rather than the center of gravity of the overall pattern. However, effects of medium and temperature on shifts are so large for fluorine that they are likely to lead to greater uncertainties than does the small isotope effect in the reference material.

Table 2 Chemical Shifts of Reference Compounds (in ppm to High Frequency of $CFCl_3$)

$CFCl_3$	0
$CFCl_2CF_2Cl$	−68.05
$CFCl_2CF_2Cl$	−72.2
CF_3CO_2H	−76.6
C_4F_8	−135.2
C_6F_6	−163

Since the resonance of $CFCl_3$ is well removed from those of most fluoroorganic molecules, and since many of these molecules require $CF_2ClCFCl_2$ in order to dissolve, it is often convenient to use one of the multiplets of this material as a reference for the sample peaks. The shift values for these two resonances compared with $CFCl_3$, along with the shifts of a few other materials which have sometimes been used as references, are given in Table 2.

By general agreement, the direction of the chemical shift is taken as positive in the direction of higher *resonance frequency* or lower magnetic field. This requires that the great majority of shift values for ^{19}F be negative with respect to $CFCl_3$. It is appropriate in discussing factors affecting *nuclear shielding* to follow the opposite convention: the greater the degree of shielding, the further to high field or *lower frequency* is the resonance.

2.2 Shifts of Fluorines Attached to Carbon

Some generalizations may be made about the ranges of shifts to be found in various environments in highly fluorinated organic molecules. First, we consider the effects of halogens or oxygen, along with other fluorine atoms in aliphatic molecules. In specifying the group in which the fluorine is found, the letter X will be used to represent either another fluorine atom, or an atom of chlorine, bromine, or oxygen. Thus $-CFX_2$ might be $-CF_3$, $-CF_2Br$, $-CFCl_2$, $-CF_2O-$, and so on, and $-CFX-$might be $-CFCl-$or $-CFBr-$.

The fluorine resonance in CF_3 in a saturated molecule appears at −75 to −82 ppm with respect to $CFCl_3$ and in other $-CFX_2$ units at −65 to −80 ppm. If the shift in $-CF_2Cl$ is compared with that in $-CF_3$, it is found that this chlorine substitution produces a high-frequency (*downfield*) shift or unshielding of about 10 ppm. However, the second substitution of a chlorine for a fluorine atom, giving $-CFCl_2$, has the opposite effect, so that the resonance is now more shielded than, and about 5 ppm upfield from, that of $-CF_2Cl$. The shifts of CF_3 attached to oxygen or to an alkenic carbon are in the region of −50 to −60 ppm.

The shifts of the fluorine in a −CFX group in a saturated molecule are observed at about −120 to −130 ppm, and here, in contrast to the $-CFX_2$ case, substitution of one fluorine by a chlorine, forming a CFCl group, causes an increased shielding of about 6–8 ppm. In a straight-chain fluorocarbon unit, the CF_2 group next to the terminating CF_3 can be identified because it is at −127 ppm, rather than at the −122 ppm characteristic of CF_2 fluorines flanked by other CF_2 groups.

The effect on nearby fluorine atoms of substitution of a chlorine for a fluorine atom in a highly fluorinated straight chain is an unshielding of about 6 ppm if the chlorine is on the adjoining carbon, and about 3 ppm if the chlorine is on a carbon atom one removed from the fluorine being observed. Calculations have been made to predict and correlate shifts in a wide variety of highly halogenated molecules.[13,14]

Shifts to lower field or to higher frequency, as for chlorine substitution, are produced by substitution of bromine on a vicinal carbon. The effect of chlorine or bromine has been attributed to a van der Waals interaction between the halogen and fluorine and termed ‘repulsive unshielding’. Similar unshielding is caused by crowding of a fluorine atom by a methyl group.[15]

Substitution of hydrogen for fluorine in either $-CF_2$ or $-CF_2X$ increases the shielding of the remaining fluorine. A tertiary fluorine atom is usually found at a relatively high field (about −160 to −180 ppm).

A carbonyl group in a perfluorinated chain typically causes unshielding of 2–5 ppm for fluorine atoms attached to the α carbon atoms, and an amine nitrogen in the chain produces an unshielding effect for α fluorine atoms of 5–10 ppm. A fluorine atom attached directly to a carbonyl carbon, in an acid fluoride unit, resonates at +30 to +50 ppm.

Fluorine atoms attached to an alkenic carbon atom appear anywhere in the range −50 to −220 ppm. In aromatic molecules, a fluorine substituent resonates anywhere from −100 to −180 ppm. The chemical shift difference produced by a second substituent in the *meta* or *para* position on a benzene ring correlates well with Hammett substituent parameters. If the substituent is *ortho* to the fluorine atom, substantial deviations appear, caused either by van der Waals forces or by electric field effects, and are experienced at the relatively short distances between the fluorine and the *ortho* substituent.

2.3 Shifts of Fluorine Atoms Attached to Other Nonmetals

Many fluorine atoms attached to nitrogen, oxygen, or sulfur resonate to low field or high frequency of $CFCl_3$ and thus are assigned positive shift values. In F–O–C units, the shift is often in the range 144–155 ppm,[16] but may vary as much as ±100 ppm from this region. In an NF_2 group, the shift is 15–20 ppm if the group is attached to CF_2, 20–30 ppm if attached to saturated −CF–, 50–60 ppm if attached to CH_2 in an aliphatic chain, and 30–45 ppm if attached to CH in an aliphatic chain. In an −NF–group the shifts are −80 to −120. In =NF, there is a very wide variation with the attached structure, from +55 to −67 ppm.[17]

Several compounds illustrate these shifts as well as shifts of fluorine attached to sulfur. In SF_5SO_3F, the fluorine atom attached to oxygen is at 46 ppm, the equatorial and axial fluorine atoms on sulfur are at 73 and 57 ppm, respectively. In FSO_3F, the OF is at 249 ppm and the SF is at 37 ppm.[18] In OF_2, the shift is 250 ppm, also far downfield. In SF_5NF_2, the NF_2 fluorine atoms are at 78 ppm, the equatorial fluorine atoms on sulfur are at 38 ppm, and the axial fluorine atom is at 50 ppm; with nitrogen attached to the sulfur, the equatorial–axial order is reversed from that when the octahedral sulfur atom is attached to another sulfur or to oxygen.

2.4 Isotope Effects on Shifts

Because fluorine is relatively sensitive to its environment, it exhibits considerable changes in chemical shift when

a nearby atom is replaced by an isotope. As mentioned above, the differential effect of ^{35}Cl versus ^{37}Cl attached to the carbon bearing the ^{19}F is readily resolved, and three-bond effects are also measurable. Studies of isotope shifts in several molecules show that they increase substantially with decreasing temperature, a behavior consistent with an explanation relating them to populations of vibrational energy levels.[19]

Replacement of ^{12}C by ^{13}C, either for the atom to which the fluorine is attached or for the carbon one removed, gives a quite measurable shift, usually to lower frequency. A consequence of the isotope effect is that ^{13}C satellites in a fluorine spectrum are not symmetrical about the $^{12}C-F$ resonance. Table 3 lists some carbon isotope effects on fluorine.

Table 3 Shifts of ^{19}F Resonance (in Hz to Lower Frequency in a Spectrometer at 94.1 MHz) on Substitution of ^{13}C for ^{12}C

Molecule	One-bond shift (Hz)	Two-bond shift (Hz)
$CF_2{=}CCl_2$	9.20	2.50
$CFCl{=}CCl_2$	10.28	2.61
$CF_3CCl{=}CCl_2$	12.31	0.95
CF_3CCl_3	11.70	1.20
CF_2ClCF_2Cl	13.05	1.46
$C\underline{F}_3CF_2CF_2CCl{=}O$	11.96	1.56
1,1,2,2-Tetrafluoro-3,3-dichlorocyclopropane	10.74	

Isotope shifts also result from the replacement of a nearby hydrogen atom by deuterium or by tritium.[20,21] Increased shielding of the fluorine in fluorobenzene is produced by substitution of ^{2}H at any ring position or by substitution for the three hydrogen atoms in a *para*-methyl group. If one is dealing with a nonrigid molecule, there is always the possibility that a change in chemical shift may arise in part from the effect of the isotope on a conformational equilibrium, as well as on an 'intrinsic' property of a specific geometrical structure. This seems to be the situation for trifluoromethylcyclohexane and may also be true for vicinal deuteration in monofluorocyclohexane.[22]

3 INDIRECT SPIN–SPIN COUPLING

Spin–spin coupling, usually represented by the symbol J, is an interaction transmitted from one nucleus which has a spin, through the electron cloud in a molecule, and then from the electrons to a second nucleus. The magnitude and sign of J is often characteristic of structural or geometrical relationships between the two nuclei involved, as well as of the nature of bonding of the nuclei. A number of attempts have been made to develop Karplus-type relationships for the angular dependence of coupling of ^{19}F to other nuclei, particularly ^{1}H or ^{13}C, but the difficulty of treating the effects of substituents, including that of fluorine itself, has led to only modest success for these relationships.

The value of J may be used as a test for the conformation of a fluorinated molecule which may exist in two structures. If the conformations are equilibrating rapidly, the observed J is a weighted average of the values in the two forms. The question then arises whether a change in conditions of temperature or solvent that affects the conformational equilibrium might also affect the values of J in the individual conformers. Experience indicates that the intrinsic values of J for interactions involving fluorine are more sensitive to conditions than are those for hydrogen, which are almost independent of circumstances.

In fluoropropenes, in which one would not expect conformational changes to occur, the J values in the vinyl moiety change by 1–2 Hz with a temperature change of 150 °C and by a few tenths of a hertz with a change in medium. In $CF_2{=}CFCF{=}O$, for which the two-bond constants are 4.0 and <1 Hz in the two conformational isomers frozen out at low temperature, the value at room temperature is 6.0 Hz, well outside the possible range for a weighted average.[23] Solvent and temperature effects have been shown to be appreciable for several types of coupling constant in fluorobenzene and 1,2-difluorobenzene.[24]

3.1 Trends in Homonuclear Coupling Constants

Coupling constants between fluorine atoms are usually relatively large compared with the homonuclear couplings of hydrogen atoms, and they extend over much longer distances than do those of hydrogen. Some ranges of values are given in Table 4, and J values for several perfluorinated molecules are shown in Figure 1.

Three-bond F–F couplings in substituted ethanes have been found to depend upon the sum of the electronegativities of the other four atoms or groups attached to the two carbon atoms. The higher the sum of the electronegativities, the smaller the magnitude, until for the highest possible value of the sum, corresponding to four fluorine atoms in hexafluoroethane, the value of J has gone through zero and changed sign. Calculations indicate that this behavior is the result of offsetting contributions of opposite sign from various pathways for transmission of spin information. The value of ^{3}J(F,F) for hexafluoroethane may be measured by observing the carbon-13 satellites for those molecules containing one carbon-13 atom, in which the fluorine atoms attached to that carbon atom are no longer equivalent to those attached to ^{12}C.

In the trifluorovinyl group, the values of $^{3}J_{trans}$ are surprisingly invariant, ranging only from about 106 to 130 Hz for a wide range of substituents. The values of $^{3}J_{cis}$, in

Table 4 Typical Values of Homonuclear Fluorine–Fluorine Coupling Constants

Structure	J (Hz)
Two-bond, F–C–F, aliphatic, noncyclic	170–220
Two-bond, three-carbon ring	150–180
Two-bond, four-carbon ring	190–230
Two-bond, epoxide ring	13–44
Two-bond, oxetane ring, on carbon next to oxygen	84–95
Two-bond, F–C–F, trifluorovinyl	5–100
Three-bond, F–C–C–F, aliphatic	0–30
Three-bond, alkene, *trans*	−106 to −127
Three-bond, alkene, *cis*	−24 to −65
Three-bond, aromatic	18–35
Four-bond, aromatic	0–15
Five-bond, aromatic	4–16

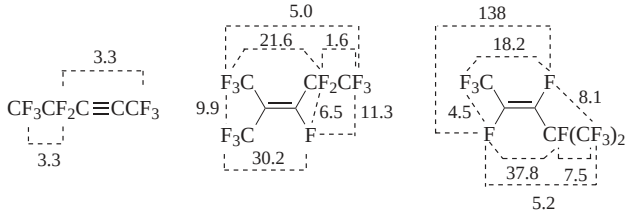

(1) **(2)** **(3)**

Figure 1 Homonuclear $^{19}F-^{19}F$ spin–spin coupling constants in three typical unsaturated fluorocarbon molecules. Values of J are given in hertz, adjoining the lines which link the two interacting nuclear types

contrast, vary from 24 to 65 Hz. The largest values are those where a halogen or an oxygen atom is bonded directly to the vinyl group, suggesting that it is the availability of lone-pair electrons that is significant.[25]

In contrast with proton–proton coupling across an ether oxygen atom, which is usually unresolvable, fluorine–fluorine coupling may be easily observed in a similar situation. Table 5 includes some values for J(F,F) in several simple ethers containing fluorine.

Table 5 Coupling Constants in Fluoroethers

Compound	^4J(F,F) (Hz)	^2J(F,H) (Hz)
CF_3OCF_3	8.2	
$CF_3OCF_2CF_3$	8.5	
CF_3OCHF_2	4.0	69
$CHF_2OCHFCl$	5	58, 70
CHF_2OCFCl_2	4	69
$CHFClOCF_2Cl$	4.5	59
$CF_3OCFClCHCl_2$	11	

3.2 Heteronuclear Coupling

3.2.1 Coupling to Hydrogen

Two-bond couplings through carbon are typically 40–60 Hz and are very characteristic in both ^{19}F and ^1H spectra for $-CF_2H$, $-CFH_2$, or $-CFH-$ groups. Table 5 illustrates the larger values, up to 80 Hz, found when the carbon is attached to an ether oxygen atom. Three-, four-, or five-bond coupling constants in aromatic compounds are about the same as the analogous H–H coupling constants. Three-bond (vicinal) couplings in aliphatic compounds range from very small values up to 15 Hz.

3.2.2 Coupling to Carbon-13

Multiplets produced by ^{19}F coupling in the ^{13}C spectrum of an organic molecule also containing many hydrogen atoms are easily resolved with the aid of proton broadband decoupling.

Values of ^1J(F,C) vary from 160 to 400 Hz in magnitude and are negative in sign, an exception to the general rule that one-bond couplings are positive. On comparison of the values in halo-substituted methanes with that in CF_4, it can be seen from Table 6 that substitution of other halogens for fluorine increases the value of the coupling constant substantially, whereas substitution of a hydrogen, except for the first one, reduces the value.

Table 6 Values (in Hz) of $^1J(^{19}F, ^{13}C)$ in Fluoromethanes

			CF_4	-259			
CHF_3	-274	CF_3Cl	-301	CF_3Br	-323	CF_3I	-344
CH_2F_2	-235	CF_2Cl_2	-325	CF_2Br_2	-352		
CH_3F	-158	$CFCl_3$	-337	$CFBr_3$	-372		

In alkenes, the values of ^1J(F,C) are about -300 Hz (our work); in the $=CF_2$ unit of an alkene which is unsymmetrically substituted, the values of the two coupling constants differ from one another. When a fluorine atom is attached to a carbonyl carbon, the value increases to about -370 Hz. In fluorinated aromatics, values lie between -260 for C_6F_6 and -245 for C_6H_5F when there is no other substituent; electron-withdrawing substituents on the ring increase J, while electron-releasing substituents decrease J. It is tempting to say that the former increase the π-electron donation of the fluorine atom to the ring system, whereas the electron-releasing substituents compete with the tendency for this donation.

The sign of ^2J(F,C) is positive, and values are typically 20–45 Hz. The value is about 20 Hz for a single fluorine atom in an aliphatic compound. The magnitude increases with substitution of electronegative groups. The value in alkenes depends upon the substitution pattern and is especially large when an electronegative substituent is *trans* to the fluorine. In benzenoid aromatics, the value is 15–25 Hz, except when the carbon bears a substituent, which is thus *ortho* to the fluorine. In cyclopropane rings, the values are small, between 5 and 15 Hz. An especially large value has been found for the two-bond coupling in the molecule CFBr=CFBr. Similarly, J between the fluorine attached to the carbonyl and the α carbon atom in (**4**) is 91 Hz, although ^2J between the carbonyl carbon and the α fluorine atom in (**4**) is only 31 Hz. Some other related molecules with very large values of ^2J are listed in Table 7.

Table 7 Molecules with Large Values of $^2J(^{19}F, ^{13}C)$

Compound	^2J between α-C and CFO (Hz)	^1J in CFO group (Hz)
$CF_3CF_2CF_2CF{=}O$	78	374
$(CF_3)_2CFCF{=}O$	66	369
$CF_2ICF_2OCF_2CF{=}O$	93	374
$O{=}CFCF_2OCF_2CF{=}O$	94	372
$(CF_3)_2C{=}CClCF{=}O$	85	355
$CF_3ClC{=}CClCF{=}O$	84	352

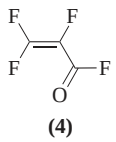

(4)

3.2.3 Coupling to Phosphorus and Nitrogen

The one-bond coupling constant to ^{31}P is negative and large. For units such as five-coordinate PF_4- or $XYPF_3$ or six-coordinate CH_3PF_5-, values range from about 700 to 1100 Hz.

Often the fluorine nuclei undergo a pseudorotation process which averages out values for the axial and equatorial positions, but if this process is sufficiently slow, a distinction can be made between the coupling constants for the two fluorine positions and the axial value is smaller, for some molecules by as much as 100–150 Hz, than the equatorial value. In five-coordinate compounds in which one ligand is a CF_3 group, ^2J(P,F) is 24–88 Hz for the axial position and 107–190 Hz for the equatorial position, providing sterochemical information about the complexes. The barrier to fluxional behavior in a number of complexes has been obtained from analysis of the NMR lineshapes.

The values for one-bond coupling to ^{15}N are usually between 110 and 160 Hz. In *cis*-N_2F_2, J is 203 Hz, in *trans*-N_2F_2 it is 190 Hz, but in the azide N_3F it is only 58 Hz.[26] There is an unusually large value of 53 Hz for ^2J(F,N) in 2-fluoropyridine, perhaps attributable to transmission via unshared electrons. No large couplings are found for adjacent substituents in benzene: in 2-fluoronitrobenzene, ^3J(F,N) is 2.66 Hz; and in 2-fluoroaniline, it is about 0.5 Hz. In 2-CF_3-aniline, ^4J(F,N) is 1.68 Hz. In 5-fluorouracil, the two values of ^3J are 1.12 and 1.66 Hz.

3.2.4 Coupling to Metals

Fluorine forms bonds to a wide variety of metals. In several binary compounds with nuclei having spin $\frac{1}{2}$ or small quadrupole moments, splittings can be resolved and values of J can be measured. Examples are TiF_6^{2-}, J = 34 Hz, and NbF_6^-, J = 335 Hz. Mercury compounds show positive two-bond couplings with magnitudes up to more than 2000 Hz and three-bond couplings as large as several hundred hertz. Some other examples are given in Table 8.

In TeF_6, $^1J(^{125}Te, ^{19}F)$ is 3746 Hz and in TeF_7^- it is 2876 Hz.[27] The smaller value in the latter has been attributed to weaker, more polar bonds. That there is only a single value of J and only a single shift for all six fluorine atoms indicates rapid exchange between axial and equatorial positions. It is interesting that the number of naturally occurring isotopes of tellurium leads to multiple, slightly shifted, fluorine resonances.

3.3 Long-Range Coupling

It has been proposed that many of the examples of coupling between two fluorine nuclei which are separated by a number of bonds (four, five, six or more) may result from overlap of electronic orbitals occupied by electrons which are unshared and therefore not involved in normal covalent bonding. The term applied to this effect, 'through space', is somewhat misleading, since only the anisotropic dipole–dipole interaction is effective through 'empty' space. All isotropic coupling is transmitted in some way by electrons, either in bonds or in unshared pairs.

Table 8 Fluorine–Metal Coupling Constants

Species	Solvent	Coupling Constant (magnitude) (Hz)
VOF_3	THF	110
VOF_4^-	CH_3CN	86
$VO(CF_3CO)_3F^-$	CH_3CN	80
VO_2ClF^-	CH_3CN	207
$VO_2F_2^-$	CH_3CN	272
$NbOF_4^-$	CH_3CN	410
$(CF_3)_2Hg$	CH_2Cl_2	1263

The idea of transmission of the indirect coupling through electrons not involved in bonds was proposed by Petrakis and Sederholm.[28] It has since been extended to systems involving nuclei other than fluorine.

Coupling via nonbonding electrons may be invoked to explain the temperature dependence of ^4J(F,F) in $CF_2ClCFClCFCl_2$ (**5**). As the temperature is lowered from room temperature to −100 °C, the value of the coupling between the fluorine atom in $CFCl_2$ and one of the fluorine atoms in the CF_2Cl unit increases from 17 to 28 Hz, whereas the other ^4J decreases from about 13 to 12 Hz. The large coupling at low temperature can be assigned to two fluorine atoms forced to be closer together by the increasing effects of steric repulsions with decreasing temperature, as represented in the diagram for (**5**).

(5)

Another example which can be explained by the 'through-space' mechanism involves coupling of the fluorine atoms in an oxetane ring with the *ortho* fluorine atoms in a pentaphenyl group substituted in the ring. The molecule (**6**) exists in two isomeric forms, differing in whether the pentafluorophenyl group and the chlorine atom are on the same side or on opposite sides of the ring. In one isomer, $J(F_A, F_D)$ is 1.3, $J(F_B, F_D)$ is 10.7, and $J(F_C, F_D)$ is 11.4 Hz. In the other isomer, $J(F_A, F_D)$ is 7.5, $J(F_B, F_D)$ is 1.4, and $J(F_C, F_D)$ is 0.9 Hz.

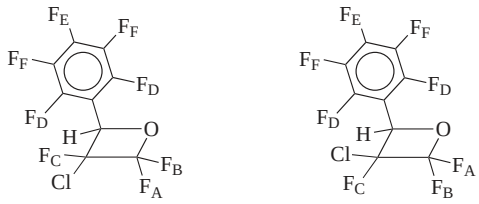

(6)

There are other examples of long-range coupling which cannot be explained by direct orbital overlap, but are probably associated with electron delocalization in π orbitals. Thus the stereochemistry of fluorinated alkenes and dienes is related to ^3J(F,C) in a way not fully explained by nuclear proximity.[29]

Outstanding among the interactions transmitted by π orbitals are those across aromatic ring systems. A number of these have been related to studies of molecular conformation. In 3,5-dichlorobenzyl fluoride, as an example, ^6J(F,H) is related to the rotational orientation of the $-CH_2F$ group with respect to the ring.[30] Long-range C–F coupling in derivatives of benzoic acid and benzoyl fluoride are related experimentally and theoretically to the dihedral twist angles of the substituent-to-ring C–C bond.[31] A study of fluorinated methyl phenyl sulfoxides showed that ^5J(F,H), ^4J(F,C), ^5J(F,C), and ^6J(F,C) are dependent upon the conformation about the sulfur atom.[32]

4 RELAXATION; NUCLEAR OVERHAUSER EFFECTS

Fluorine-19 nuclei may undergo spin–lattice relaxation by the direct dipolar mechanism, in much the same way as do protons. However, because of the presence of unshared electrons, spin–rotation (SR) and chemical shift anisotropy (CSA) mechanisms also contribute to the relaxation of ^{19}F. Because of the additional relaxation pathways, T_1 values are often substantially smaller than for protons in a similar environment.

Early workers reported that the CSA contribution is negligible and that spin rotation predominates. This is true for molecules such as CF_4 or SF_6, which are small and freely rotating, and for measurements at 2.4 T or lower magnetic field strength. Since the spin–rotation relaxation time decreases with increasing temperature, whereas the dipole–dipole relaxation time increases with increasing temperature, a maximum may be observed for T_1 as a function of temperature, as has been found, for example, for *o*-fluoroiodobenzene at about 110 °C.

Spin–rotation interaction constants can be calculated from the paramagnetic term of the NMR shielding constant.[33] They can also be measured by molecular beam methods, and the values for HF, F_2, SiF_5, CF_4, and CHF_3 show good agreement by the two methods. It should also be possible to calculate the spin–rotation constants from measured spin–lattice relaxation times, but this requires knowledge of the correlation time, and reasonable guesses for the latter give values of the constant too large by a factor of 2 to 3.

Rapid spin–spin relaxation is associated with broadening of spectral lines, such as is caused by inhibition of motion, as occurs with macromolecules. The extent of broadening is related to the anisotropy of the chemical shift, which is often large for ^{19}F. Since the CSA contribution increases with field, the broadening is greater at higher fields, often offsetting the improvement in sensitivity and resolution expected, such as by going to a frequency of 470 MHz. Since macromolecules do rotate more slowly, the SR contribution for the ^{19}F relaxation in them is small, except possibly for freely rotating CF_3 groups.

The nuclear Overhauser effect (NOE) of fluorine nuclei is much like that of protons. Most applications of the NOE to fluorine have been heteronuclear, where the close approach of one or more particular hydrogens atoms to a fluorine atom is monitored. In macromolecules, dipolar interactions are often the predominant T_1 relaxation mechanism, and saturation of protons should fully invert the normal ^{19}F intensities. Under circumstances where the T_1 of the ^{19}F nucleus is shorter than that of the ^1H, it is preferable in a one-dimensional NOE experiment to use the ^{19}F as the source of the Overhauser transfer so that irradiation maintains the nonequilibrium population.

Indirect Overhauser enhancements through ^{19}F from ^1H to ^1H or from ^1H to ^{13}C have been obtained for several cyclic compounds.[34] In NOE difference spectra, antiphase doublets were observed for protons undergoing simultaneous scalar coupling and dipolar relaxation with ^{19}F. The geometrical factors inherent in the three-spin NOE were utilized in conformational analysis. NOE measurements have also been used to confirm the proximity of hydrogen nuclei to fluorine nuclei in some tetrahydroindazole derivatives where long-range coupling between these nuclei was suspected of being the result of a 'through-space' interaction.[35]

It is interesting that pioneering work in the analysis of the NOE was the application by Solomon and Bloembergen[36] to the HF system. Because of the very large value of $^1J(F,H)$ in this molecule (more than 600 Hz), there is relaxation by interrupted scalar coupling, which produces a negative enhancement instead of the positive intensity change expected for the dipole–dipole mechanism.

5 APPLICATIONS TO BIOCHEMICAL PROBLEMS

By virtue of the circumstances that there is almost never any fluorine background in living systems and that fluorine shifts are quite sensitive to the environment, applications of ^{19}F NMR to biochemical problems have been extensive. Several reviews have appeared.[37,38]

Fluorine NMR has been applied in the investigations of several types of system, perhaps most extensively to proteins. Pioneer work in this field was that of Sykes and Hull,[39] who applied ^{19}F relaxation measurements to the study of motions of groups in proteins. Alkaline phosphatase was labeled with fluorotyrosine residues. Both overall rotation of the protein and internal rotation of the aromatic ring contribute to ^{19}F relaxation, which includes a substantial CSA component. Two of the tyrosine rings relax by chemical exchange, indicating that they are free to rotate, and one of the tyrosines relaxes faster in ^1H_2O than in ^2H_2O, indicating that it is exposed to the solvent.

In other systems, the nature of binding of small molecules to proteins has been studied. On binding of an inhibitor such as cytidine manophosphate (CMP) to ribonuclease S trifluoroacetylated at lysines-1 and -7, the fluorine resonance assigned to lysine-7 splits and becomes pH dependent.[40] This change could, of course, come either directly from contact of the inhibitor with the lysine or indirectly as a result of a conformational change of the protein caused by the inhibitor. A summary of the considerations involved in using fluorine as a tool in the investigation of ligand binding has been provided by Gerig.[41]

Several efforts have been made recently to provide a theoretical analysis of the effects of the environment on fluorine nuclei, and to explain the chemical shift effects of up to 20 ppm observed when a protein folds about the fluorine indicators.[42,43] The conclusion has been that the principal influence is via electrostatic interactions, and that this influence is effective in proportion to the magnitude of the paramagnetic term in the nuclear shielding expression.

Fluorine shifts and coupling constants are valuable in the conformational analysis of carbohydrates. Pioneering work in this area was that of Hall.[44] The spectrum of 6-deoxy-6-fluoro-D-glucose has been carefully analyzed in terms of the conformer population in various solvents; this analysis illustrates the very important point that, although the resonance frequency of ^{19}F is very far removed from that of ^1H, it may represent the X part of a non-first-order system, such as the ABCX system in this molecule, and a first-order interpretation is misleading.[45]

Fluorine-19 has been used as an indicator of the presence of various free ions in living systems. 5-Fluoro derivatives of

the molecule APTRA (*o*-aminophenol-*N*,*N*,*O*-triacetic acid) give separate resonances for free and magnesium-bound forms of the indicator, and knowledge of the equilibrium constants involved and the ratios of the two peaks permits evaluation of the free magnesium concentration. The 4-fluoro derivative of APTRA as well as fluorocitrate are in fast exchange with Mg^{2+}, giving a resonance which is at the weighted-average position of the free and magnesium-bound indicator resonances.[46] Chelators have also been employed to assess calcium concentrations. One, known as 5F RBAPTA, a 1,2-diphenoxyethane derivative, provides slow exchange with Ca^{2+}, and is designed to give rapid spin–lattice relaxation because it contains a *t*-butyl group adjacent to the fluorine.[47]

6 APPLICATIONS OF SPECIAL TECHNIQUES

Two- or three-dimensional ^{19}F correlation spectroscopy provides an attractive means of structure studies, especially for highly fluorinated materials. By firmly establishing coupling connections in a molecule which typically has a very complex spectrum, often with overlapping and non-first-order patterns, these techniques facilitate the relationship of resonances to structural features. COSY has been applied to the assignment of resonances and the study of microstructure of fluorinated polymers.[48]

Figure 2 shows an illustrative COSY spectrum of a mixture of three chlorofluorocarbon isomers. From the one-dimensional ^{19}F spectrum, it was not possible to assign the various multiplets unambiguously or even to be certain that the mixture did not contain some six-carbon as well as four-carbon components. Based on inspection of the off-diagonal correlations in the COSY spectrum, combined with consideration of the multiplets in the one-dimensional spectrum and the symmetries of possible components, definitive assignments of structure could be made.

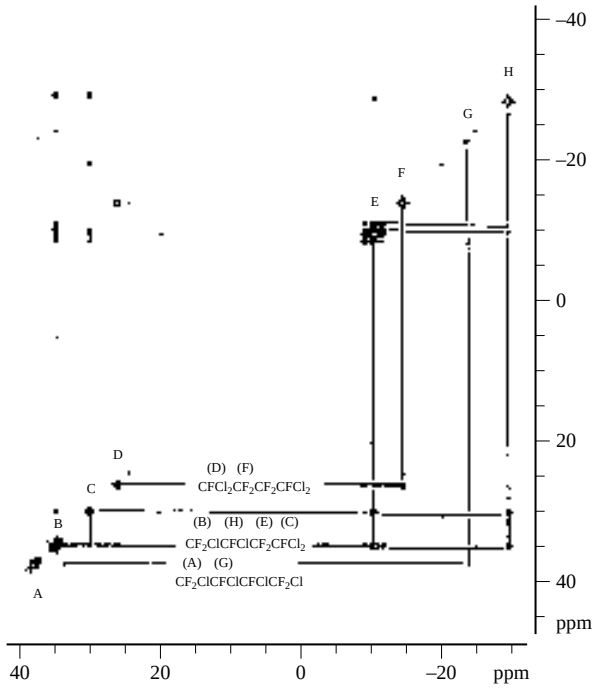

Figure 2 Homonuclear $^{19}F-^{19}F$ COSY (correlation spectroscopy) spectrum of a mixture of three isomers. Formulas of the three components of the mixture are shown and assignments of the resonances are indicated by letters. The spectrometer frequency was 282 MHz. The axes are labeled with arbitary scales based on the carrier frequency of the spectrometer

Because of the difficulties of chromatographic resolution of mixtures of isomers of compounds of this type, it is thus very helpful to be able to sort out the resonances belonging to each of the components in a mixture. Hartmann–Hahn-based experiments (HOHAHA or TOCSY) are difficult to apply to a typical fluorinated molecule, especially at the fields now in use, because of the difficulty of maintaining a spin lock over the very wide frequency range required, and a COSY or relayed COSY sequence may be more appropriate.[49] Even here, however, problems may arise from the spectral widths often encountered, because of the many data points in each dimension required to ensure adequate resolution. Thus selective excitation or selective polarization transfer, such as is possible with the pulse-shaping capabilities of modern instruments, is helpful in reducing the large size of the data arrays required.

By use of appropriate correlation experiments optimized for coupling constants of various magnitudes, it is also possible to determine the relative signs of coupling constants from the sense of the skew in the off-diagonal peaks.[50]

Two-dimensional heteronuclear NOE spectroscopy can be applied to structural studies of ^{19}F-labeled oligodeoxyribonucleotides. In macromolecules, chemical shift anisotropy dominates the spin–spin relaxation of ^{19}F, although T_1 relaxation is primarily dipolar in nature. As a result, the fluorine lines are broad, and small spin–spin couplings to hydrogen cannot be resolved. Since the Overhauser enhancement ratio for $^{19}F-\{^1H\}$ in a large molecule is -1, this technique affords a means of determining spatial adjacencies.[51]

In fluorine-labeled molecules such as steroids, there may be many proton spin–spin interactions with the label atom, and it is experimentally difficult to unravel the splittings in the fluorine spectrum by selective decoupling of protons. Two-dimensional heteronuclear correlation experiments, analogous to homonuclear COSY, can be used to establish long-range couplings, from which conformational information can be obtained.[52] In a number of steroids, small splittings caused by protons remained unresolved in the proton spectrum because of their number and the widths of the lines. In COSY, all interactions down to the limit imposed by the intrinsic linewidth can be resolved, and long-range couplings of 0.5 Hz or less are observable. Combining the information from the coupling constants with known effects on chemical shifts made it possible to assign the NMR spectra completely and to derive complete steroid structures.

As another means to establish connectivities, one might examine the proton spectrum with the fluorine decoupled; in the absence of a fluorine decoupler, this has been done by using the proton decoupler as the source of the observe signal and pulsing the fluorine signal from the transmitter between the acquisition intervals in the FID. Both COSY and one-dimensional experiments have been performed in this way.[53]

Finally, an alternative approach to unraveling complex fluorine–proton interactions involves the use of fluorine decoupling achieved by a spin-flip technique. The output of two channels of a dual-channel spectrometer is combined and

applied to the high-frequency coil in a probe. During the period of acquisition of the proton signals, pulses from the fluorine channel, applied in the empty time slots, are phase cycled according to an XY-4 or XY-32 scheme, spreading the irradiation frequency over the needed wide bandwidth.[54]

7 RELATED ARTICLES

Bilayer Membranes: Proton and Fluorine-19 NMR; Coupling Through Space in Organic Chemistry; Isotope Effects on Chemical Shifts and Coupling Constants; Nuclear Overhauser Effect.

8 REFERENCES

The data cited in this article come from so many sources, including the laboratory of the authors, that it is impracticable to list the sources individually. References for recent work are provided, and access to earlier results is usually possible through some of the reviews which are mentioned.

1. E. F. Mooney, *An Introduction to ^{19}F NMR Spectroscopy*, Heyden, London, 1970.
2. C. H. Dungan and J. R. Van Wazer, *Compilation of Reported F-19 NMR Chemical Shifts*, Wiley Interscience, New York, 1970.
3. J. W. Emsley and L. Phillips, *Prog. NMR Spectrosc.*, 1971, **7**, 1.
4. J. W. Emsley, L. Phillips, and V. Wray, *Prog. NMR Spectrosc.*, 1976, **10**, 83.
5. F. J. Weigert and K. J. Karel, *J. Fluorine Chem.*, 1987, **37**, 125.
6. E. F. Mooney and P. H. Winson, *Annu. Rev. NMR Spectrosc.*, 1968, **1**, 243.
7. K. Jones and E. F. Mooney, *Annu. Rep. NMR Spectrosc.*, 1970, **3**, 261.
8. K. Jones and E. F. Mooney, *Annu. Rep. NMR Spectrosc.*, 1971, **4**, 391.
9. R. Fields, *Annu. Rep. NMR Spectrosc.*, 1972, **5A**, 99.
10. L. Cavalli, *Annu. Rep. NMR Spectrosc.*, 1975, **6B**, 43.
11. R. Fields, *Annu. Rep. NMR Spectrosc.*, 1977, **7**, 1.
12. V. Wray, *Annu. Rep. NMR Spectrosc.*, 1983, **14**, 1.
13. A. Battais, G. Bauduin, B. Boutevin, and Y. Pietrasanta, *J. Fluorine Chem.*, 1986, **31**, 197.
14. T. Tanuma, K. Ohnishi, H. Okamoto, T. Miyajima, and S. Morikawa, *J. Fluorine Chem.*, 1992, **57**, 259.
15. G. W. Gribble, D. J. Keavy, E. R. Olson, I. D. Rae, A. Staffa, T. E. Herr, M. B. Ferraro, and R. H. Contreras, *Magn. Reson. Chem.*, 1991, **29**, 422.
16. C. J. Hoffman, *Fluorine Chem. Rev.*, 1968, **2**, 161.
17. W. S. Brey and J. B. Hynes, *Fluorine Chem. Rev.*, 1968, **2**, 111.
18. H. Willner, F. Mistry, and F. Aubke, *J. Fluorine Chem.*, 1992, **59**, 333.
19. W. S. Brey, K. H. Ladner, R. E. Block, and W. A. Tallon, *J. Magn. Reson.*, 1972, **8**, 406.
20. G. Angelini, G. Lilla, C. Sparapani, O. Ursini, E. Rossi, A. L. Segre, M. A. McAllister, and T. T. Tidwell, *Can. J. Chem.*, 1992, **70**, 1221.
21. S. Berger, in *NMR Basic Principles and Progress*, ed. P. Diehl, E. Fluck, H. Günther, R. Kosfeld, and J. Seelig, Springer, Berlin, 1990, Vol. 22, pp. 1–29.
22. J. B. Lambert and L. G. Greifenstein, *J. Am. Chem. Soc.*, 1974, **96**, 5120.
23. K. C. Ramey and W. S. Brey, *J. Chem. Phys.*, 1964, **40**, 2349.
24. S. Suntioinen, U. Weber, and R. Laatikainen, *Magn. Reson. Chem.*, 1993, **31**, 406.
25. C. G. Moreland and W. S. Brey, *J. Chem. Phys.*, 1966, **45**, 803.
26. G. Schatte, H. Willner, and M. Willert-Porada, *Magn. Reson. Chem.*, 1992, **30**, 118.
27. K. O. Christe, D. A. Dixon, J. C. P. Sanders, G. J. Schrobilgen, and W. W. Wilson, *J. Am. Chem. Soc.*, 1993, **115**, 9461.
28. L. Petrakis and C. H. Sederholm, *J. Chem. Phys.*, 1961, **35**, 1243.
29. M. P. Bosch, F. Camps, G. Fabrias, and A. Guerrero, *Magn. Reson. Chem.*, 1987, **25**, 347.
30. T. Schaefer, J. R. Mansfield, F. E. Hruska, and R. Sebastian, *Can. J. Chem.*, 1992, **70**, 1750.
31. P. E. Hansen, A. Berg, and K. Schaumburg, *Magn. Reson. Chem.*, 1987, **25**, 508.
32. R. Benassi, U. Folli, D. Iarossi, A. Mucci, L. Schenetti, and F. Taddei, *Magn. Reson. Chem.*, 1990, **28**, 702.
33. C. Deverell, *Mol. Phys.*, 1970, **18**, 319.
34. F. Sanchez-Ferrando and J. K. M. Sanders, *Magn. Reson. Chem.*, 1987, **25**, 539.
35. J. W. Lyga, R. N. Henrie, II, G. A. Meier, R. W. Creekmore, and R. M. Patera, *Magn. Reson. Chem.*, 1993, **31**, 323.
36. I. Solomon and N. Bloembergen, *J. Chem. Phys.*, 1956, **25**, 261.
37. J. T. Gerig, in *Biological Magnetic Resonance*, ed. L. J. Berliner and J. Reuben, Plenum, New York, 1978, Vol. 1, pp. 139–203.
38. B. D. Sykes and J. H. Weiner, in *Magnetic Resonance in Biology*, ed. J. S. Cohen, Wiley, New York, 1980, Vol. 1, pp. 171–196.
39. B. D. Sykes and W. E. Hull, *Methods Enzymol.*, 1978, **49**, 270.
40. W. H. Huestis and M. A. Raftery, *Biochemistry*, 1971, **10**, 1181.
41. J. T. Gerig, *Methods Enzymol.*, 1989, **177**, 3.
42. J. D. Augspurger and C. E. Dykstra, *J. Am. Chem. Soc.*, 1993, **115**, 12016.
43. J. G. Pearson, E. Oldfield, F. S. Lee, and A. Warshel, *J. Am. Chem. Soc.*, 1993, **115**, 6851.
44. L. D. Hall and J. F. Manville, *Can. J. Chem.*, 1969, **47**, 361.
45. R. J. Abraham, E. J. Chambers, and W. A. Thomas, *Magn. Reson. Chem.*, 1992, **30**, S60.
46. J. C. Veniero and R. K. Gupta, *Annu. Rep. NMR Spectrosc.*, 1992, **24**, 219.
47. L. A. Levy, E. Murphy, B. Raju, and R. E. London, *Magn. Reson. Chem.*, 1992, **30**, 723.
48. D. W. Ovenall and R. C. Ferguson, in *Pulse Methods in 1D and 2D Liquid-phase NMR*, ed. W. S. Brey, Academic, San Diego, 1988, pp. 489–505.
49. W. I. Bailey, A. L. Kotz, P. L. McDaniel, D. M. Parees, F. K. Schweighardt, H. J. Yue, and C. Anklin, *Anal. Chem.*, 1993, **65**, 752.
50. A. A. Ribeiro and M. J. Glen, *J. Magn. Reson. A*, 1994, **107**, 158.
51. W. J. Metzler, P. Leighton, and P. Lu, *J. Magn. Reson.*, 1988, **76**, 534.
52. D. W. Hughes, A. D. Bain, and V. J. Robinson, *Magn. Reson. Chem.*, 1991, **29**, 387.
53. S. H. Grode and R. W. Gillis, *J. Magn. Reson.*, 1989, **82**, 122.
54. J. J. Kotyk, *J. Magn. Reson.*, 1991, **95**, 632.

Biographical Sketches

Wallace S. Brey. *b* 1922. B.S., Ursinus, 1942, M.S., Pennsylvania, 1946, Ph.D., 1948. Faculty at DePauw Univ., 1948–49, St. Joseph's University, 1949–52; University of Florida, 1952 to date. Approximately

85 publications. Author of three textbooks in physical chemistry; Editor of the volume 'Pulse Methods in 1D and 2D Liquid-Phase NMR', 1987; Editor, Journal of Magnetic Resonance, 1969–present. Research specialties heterogeneous catalysis and adsorption, structure and interactions of proteins, ^{19}F, ^{27}Al, ^{29}Si, and ^{31}P NMR in liquids and solids.

Mary Louise Brey. *b* 1926. B.S., Florida Southern College, 1948, M.S., Florida, 1952, Ph.D., 1956. University of Florida, 1952–1955, 1957–1959. Research: synthesis of organic fluorine compounds and determination of their structure by IR and NMR spectroscopy, rates of oxidation of Zr–Nb alloys.

Germanium, Tin, and Lead NMR

Bernd Wrackmeyer

Universität Bayreuth, Bayreuth, Germany

1	Introduction	1
2	Chemical Shifts δ^{73}Ge, δ^{119}Sn, and δ^{207}Pb	1
3	Indirect Nuclear Spin–Spin Coupling Constants	3
4	Nuclear Spin Relaxation Parameters	7
5	Related Articles	8
6	References	8

1 INTRODUCTION

The NMR properties of germanium, tin and lead are listed in Table 1. Except for ^{73}Ge ($I = \frac{9}{2}$), all NMR-active nuclides in Group 14 possess spin $I = \frac{1}{2}$. As a consequence of a medium quadrupolar moment, $Q(^{73}\text{Ge})$, ^{73}Ge NMR signals become rather broad if the charge distribution around the germanium atom is nonspherical. Therefore, chemical shifts δ^{73}Ge have been determined just for a few classes of compounds. Only a limited number of coupling constants involving ^{73}Ge is accessible, and many important NMR techniques for elucidating structure and bonding cannot be applied in the case of ^{73}Ge NMR. In contrast, tin and lead NMR are ideal tools for studying the chemistry of these elements. Whereas there is only one lead isotope (^{207}Pb) with $I = \frac{1}{2}$, there are three spin-$\frac{1}{2}$ isotopes of tin (^{115}Sn, ^{117}Sn, ^{119}Sn) of which two (^{117}Sn, ^{119}Sn) have an appreciable natural abundance. Owing to its slightly greater magnetic moment ^{119}Sn NMR is usually preferred for NMR measurements.

In principle it should be easy to measure ^{73}Ge NMR in the pulse Fourier transform (PFT) mode by the application of single $\pi/2$ pulses, using a very short delay between consecutive experiments, as the quadrupolar relaxation rate of the ^{73}Ge nuclides is fast in almost all cases. However, ^{73}Ge NMR suffers from the combined effects of broadened resonance signals and of the low ^{73}Ge resonance frequency. The latter is responsible for low NMR sensitivity hampering CW experiments and, in the PFT mode, acoustic ringing induces severe distortion of the baseline[1] ('rolling baseline') which makes the assignment of broad NMR signals very difficult. A number of pulse sequences have been developed to eliminate the influence of acoustic ringing,[2] most of which, however, introduce other limitations. The most efficient experiments include the application of composite pulses[3] and this enables the use of larger spectral windows for the observation of broad lines.[4,5] There are still many problems in measuring ^{73}Ge NMR, and the broadest lines observed possess linewidths in the order of 600 Hz.

The negative sign of $\gamma(^{119}\text{Sn})$ causes a negative NOE (see ***Nuclear Overhauser Effect***) which may cancel or severely reduce the intensity of ^{119}Sn NMR signals if dipolar interactions play an important role in ^{119}Sn nuclear relaxation. In this case it is advisable to use inverse gated ^{1}H decoupling. Otherwise, polarization transfer techniques (INEPT,[6] DEPT[7]) can be applied to circumvent this problem. Before PFT NMR became available, ^{119}Sn NMR was measured in the CW mode, most frequently by ^{1}H{^{119}Sn} heteronuclear double resonance experiments (INDOR) if ^{119}Sn–^{1}H scalar couplings were present.[8] Nowadays, modern PFT spectrometers can be used for 2D ^{1}H-detected (inverse) ^{1}H–^{119}Sn correlated spectroscopy in order to record ^{119}Sn NMR signals of dilute solutions and/or of broad ^{119}Sn resonances.[9] All multidimensional NMR techniques, originally developed for ^{13}C NMR, can also be applied to ^{119}Sn NMR. The presence of ^{119}Sn and ^{117}Sn in molecules containing two or more tin atoms allows the measurement of coupling constants ^{n}J(Sn,Sn) even for tin atoms which are chemically equivalent.[10,11] ^{119}Sn NMR is also an attractive method for studying solids, either of static samples, or by MAS or CP MAS methods because of the appreciable ^{119}Sn NMR sensitivity.

With modern instruments ^{207}Pb NMR spectra from solutions are readily measured[10,12] and the same techniques can be applied as outlined for ^{119}Sn NMR. In solid state ^{207}Pb NMR, the huge anisotropy of the ^{207}Pb nuclear shielding may pose a problem. This can be overcome by using faster spinning speeds in MAS experiments (which however may reduce the CP efficiency) or by measuring the spectra at lower field strength $\boldsymbol{B}_0$.

2 CHEMICAL SHIFTS δ^{73}Ge, δ^{119}Sn, AND δ^{207}Pb

2.1 General Remarks

The most extensive data set is available for δ^{119}Sn[10,11,13] (range: ≈+3000 to −2500), followed by δ^{207}Pb[10,12,13] (range: ≈+10 000 to −6000) and a small data set of δ^{73}Ge[14] has been collected. For all three nuclides the tetramethyl derivatives, Me_4M (M = ^{73}Ge, ^{119}Sn, ^{207}Pb), or better the corresponding frequencies Ξ(M) (see Table 1), serve as an external reference. The temperature dependence of δ_M can be significant in the case of M = ^{119}Sn and, in particular, for M = ^{207}Pb according to the greater range of chemical shifts. The same is true for solvent effects which may become rather large if there is a direct chemical interaction between the solvent and the compounds under investigation. In general, we find a dependence of nuclear shielding on the coordination number (*CN*): an increase in the value of *CN* causes increased nuclear shielding. This is exactly the same trend that has been observed for ^{29}Si nuclear shielding, amplified by the factor governed by the change in the radial term $\langle r^{-3}\rangle_{np}$ where r is the expected radius for an electron in the np orbital. In the case of ^{207}Pb nuclear shielding, relativistic effects may complicate this otherwise rather consistent pattern.

There are close to linear relationships between δM values (M = ^{29}Si, ^{73}Ge, ^{119}Sn, ^{207}Pb) of isostructural compounds [see equation (1),[15] equation (2),[15] and equation (3)[13]].

$$\delta^{73}\text{Ge} = 3.32 \times \delta^{29}\text{Si} + 39.9 \ (29; r = 0.967) \qquad (1)$$

$$\delta^{119}\text{Sn} = 1.56 \times \delta^{73}\text{Ge} - 87.4 \ (26; r = 0.991) \qquad (2)$$

$$\delta^{207}\text{Pb} = 2.43 \times \delta^{119}\text{Sn} + 34 \ (40; r = 0.996) \qquad (3)$$

Table 1 NMR Properties of Group 14 Elements

	Spin I	N. A.[a] (%)	Q (10^{-28} m^2)	γ (10^7 rad s^{-1} T^{-1})	Ξ (MHz)	Reference compound
^{13}C	$\frac{1}{2}$	1.108	–	6.7283	25.145 004	Me_4Si
^{29}Si	$\frac{1}{2}$	4.70	–	−5.3190	19.867 184	Me_4Si
^{73}Ge	$\frac{9}{2}$	7.76	−0.17	−0.9360	3.488 415	Me_4Ge
^{115}Sn	$\frac{1}{2}$	0.35	–	−8.8014	32.718 780	Me_4Sn
^{117}Sn	$\frac{1}{2}$	7.61	–	−9.589	35.632 295	Me_4Sn
^{119}Sn	$\frac{1}{2}$	8.58	–	−10.0318	37.290 665	Me_4Sn
^{207}Pb	$\frac{1}{2}$	22.6	–	5.6264	20.920 597	Me_4Pb

[a]Natural abundance

The comparison of δ^{119}Sn and δ^{207}Pb values of tin(II) and lead(II) derivatives shows a different type of correlation [equation (4)[13]] which, in the case of stannocenes and plumbocenes, merges with the relationship between δM of tin(IV) and lead(IV) compounds [equation (3)]. The greater slope and the large intercept in equation (4) as compared with equation (3) point towards relativistic effects,[16,17] connected with the nature of the lone pair of electrons.

$$\delta^{207}\text{Pb} = 3.30 \times \delta^{119}\text{Sn} + 2336 \ (20; r = 0.998) \qquad (4)$$

In the case of CN = 4, substituent effects can be used in an empirical way for the prediction of δM. Similarly, the concept of pairwise additive parameters[18] can be applied. The normal halogen dependence of δM is found (highest M nuclear shielding in MI_4). There is no direct relationship between δM and the substituent electronegativity if the substituent is linked directly to M. However, electronegative substituents other than fluorine which are removed from M by more than one bond may cause deshielding. Differing bond angles at M are expected to affect nuclear shielding. The comparison between δM values, if M is part of a five- or six-membered ring, indicates that significant deshielding of M (Δ^{73}Ge ≈ 50 ppm;[14,19] Δ^{119}Sn ≈ 100 ppm;[20] Δ^{207}Pb ≈ 200–250 ppm[21]) always occurs in the five-membered ring.

2.2 Application of δ^{73}Ge

Since the successful detection of ^{73}Ge NMR signals depends heavily on the quadrupolar relaxation rate, δ^{73}Ge values are not likely to be determined in routine experiments. Although mixtures (e.g., of germanium tetrahalides[15,22] or isomeric germacyclohexanes[23]) have been analyzed by ^{73}Ge NMR, and CN(Ge) > 4 has been proved by increased ^{73}Ge nuclear shielding[24] (Figure 1), the expected (vide supra) limitations because of the unfavorable NMR properties are obvious.

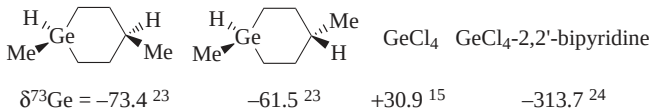

Figure 1 Chemical shift data, δ^{73}Ge, for isomeric germacyclohexanes, and CN(Ge) = 7 and 6

2.3 Application of δ^{119}Sn

Chemical shifts δ^{119}Sn serve in numerous ways in tin chemistry. All reactions of tin compounds can be monitored by ^{119}Sn NMR under realistic conditions, in rather dilute solutions and in nondeuterated solvents. Intermediates and products are characterized by typical δ^{119}Sn data, taking advantage of the large data set available.[10,11] Examples are shown in Figures 2 and 3. A typical application of δ^{119}Sn values concerns the study of exchange reactions[25] which may lead to numerous compounds which cannot be isolated but can readily be identified on the basis of their δ^{119}Sn values (see Figure 4).

Extreme ^{119}Sn nuclear deshielding is found in monomeric dialkylstannylenes as a result of low energy $\sigma-\pi^*$ and $n-\pi^*$ transitions (Figure 5). In analogous bis(amino)stannylenes the ^{119}Sn nuclides are better shielded because of the influence of the electronegative nitrogen atoms on these transitions. Dimerization via the Sn–Sn bond or via coordinate N–Sn bonds leads to a significant increase in ^{119}Sn nuclear shielding (e. g. in $[(Me_3Si)_2CH]_2Sn{=}Sn[CH(SiMe_3)_2]_2$ with δ^{119}Sn = +740 and +725[27] for the two conformers, and in $[Me_2Si(N^iPr)_2Sn]_2$ with δ^{119}Sn = +202[28]). This shows that any type of association of tin compounds can be studied most conveniently by ^{119}Sn NMR.

The electronic structure of Zintl anions (another class of compounds in which tin is formally in a low oxidation state) of the type $[Sn_4]^{2-}$ (δ^{119}Sn = −1895[29]), $[Sn_9]^{4-}$ (δ^{119}Sn = −1230[30]) $[Sn_8Tl]^{5-}$ (δ^{119}Sn = −1167[29]) or $[Sn_{9-n}Pb_n]^{4-}$ (n = 1–8; δ^{119}Sn = −1270 to −1600[30]) is reflected by the fairly high ^{119}Sn nuclear shielding in these highly fluxional cluster anions.

As shown in Figure 6, extreme ^{119}Sn nuclear shielding is typical of stannocenes,[11] both for a parallel[31] and bent arrangement[32,33] of the cyclopentadienyl rings. The high ^{119}Sn nuclear shielding also prevails in heterostannocenes.[34]

With few exceptions [e.g., δ^{119}Sn of $Sn(C{\equiv}CR)_4$, −350 to −380] δ^{119}Sn values of tin(IV) compounds with CN(Sn) = 4 are found in the range between +200 and −200.[11] A marked deshielding influence can be exerted if transition metals are linked to the tin atom, and, in particular, if multicenter bonding has to be taken into account, e.g. in $Sn[Fe(CO)_4]_4$ with δ^{119}Sn = +1532.[35]

Solid state ^{119}Sn NMR spectra of a great variety of tin compounds have been studied which reveal important information on structural changes as compared with solutions, in particular if direct structural information from X-ray analysis is available. Representative examples are organotin

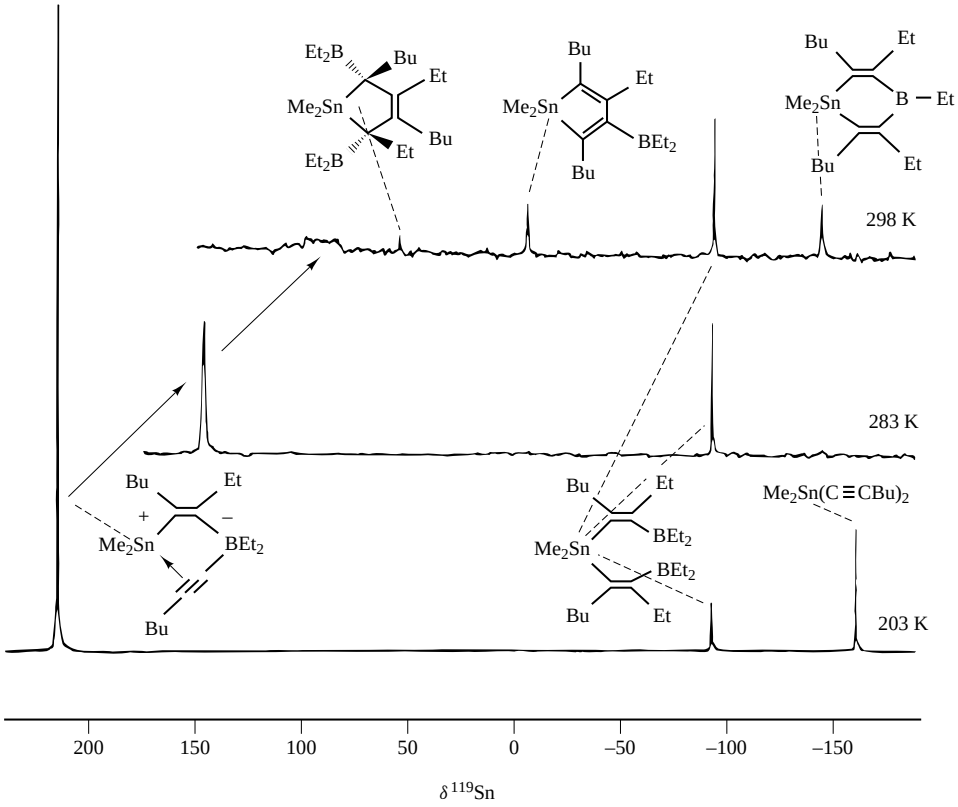

Figure 2 The 1,1-organoboration of $Me_2Sn(C{\equiv}CBu)_2$ with Et_3B (ratio 1:1.4):[73] 33.3 MHz ^{119}Sn NMR (^1H inverse gated decoupled) at 203 K, 283 K, and 298 K. At 203 K, the ^{119}Sn NMR signal of the starting material, $Me_2Sn(C{\equiv}CBu)_2$, can still be detected together with a signal for a bis(alkenyl)tin compound, and a strong signal appears for a zwitterionic intermediate. No starting material is left at 283 K, and at 298 K the zwitterionic intermediate has partially rearranged into a stannole derivative and a 1-stanna-4-bora-2,5-cyclohexadiene (see Figure 3 for further changes). Note the extreme temperature sensitivity of the ^{119}Sn NMR signal of the zwitterionic intermediate, indicating a dynamic equilibrium in which the bridging alkynyl group migrates between boron and tin

halides,[36] organotin chalcogenides,[37,38] stannocenes,[31–33] and various other cyclic and noncyclic organotin compounds.[39–41]

2.4 Application of δ^{207}Pb

In principle, applications of δ^{207}Pb values are similar to those of δ^{119}Sn. As a result of the greater range of δ^{207}Pb values,[12,13] these data are extremely sensitive to small changes in the surrounding of the lead atom. Extreme ^{207}Pb nuclear deshielding is observed for the monomeric plumbylene $[(Me_3Si)_2CH]_2Pb$ (δ^{207}Pb = +9110[42]) which apparently, in contrast to the analogous tin compound, is not in equilibrium with its dimer. The δ^{207}Pb values of monomeric bis(amino)plumbylenes are close to +5000 (e.g., $[(Me_3Si)_2N]_2Pb$ with δ^{207}Pb = +4916). The increased ^{207}Pb nuclear shielding in Zintl anions $[Pb_{9-n}Sn]^{4-}$ (n = 1–8; δ^{207}Pb = −3932 to −2667[30]) also corresponds to the δ^{119}Sn data. Similarly, high ^{207}Pb nuclear shielding is found for plumbocenes (e.g., $(\eta^5\text{-}Me_5C_5)_2Pb$ with δ^{207}Pb = −4390[32] or $(\eta^5\text{-}Ph_5C_5)_2Pb$ with δ^{207}Pb = −6150[31]).

The majority of δ^{207}Pb values for lead (IV) compounds with CN(Pb) = 4 is found in the range between +500 and −800 ppm. This includes compounds of the type $Pb(C{\equiv}CR)_4$ (e.g., R = Me in $CDCl_3$, δ^{207}Pb = −687.0[43]) and $Pb(CF_3)_4$ (δ^{207}Pb = −562.2[44]). Any kind of association is readily reflected by δ^{207}Pb data as shown for example in the case of the self-association of Me_3PbOMe, depending on concentration, and in the solid state with CN(Pb) = 5[45] (Figure 7).

The different ^{207}Pb nuclear shielding in solid Me_3PbOMe as compared with solutions indicates important applications of solid state ^{207}Pb NMR. There are also many applications to inorganic solids.[12]

3 INDIRECT NUCLEAR SPIN–SPIN COUPLING CONSTANTS

3.1 General Remarks

The signs of numerous coupling constants ^nJ(M,X) have been determined, mainly by application of heteronuclear double resonance techniques in 1D and 2D NMR experiments. Examples are given in Table 2. For the comparison of coupling constants involving different nuclides it is advisable to use the reduced coupling constants ^nK [equation (5)] instead of ^nJ in order to eliminate the individual magnetic properties of the nuclides.

$$^nK(\mathrm{M,X}) = 4\pi^2 \cdot {}^nJ(\mathrm{M,X}) \cdot (h\gamma_\mathrm{M}\gamma_\mathrm{X})^{-1} \qquad (5)$$

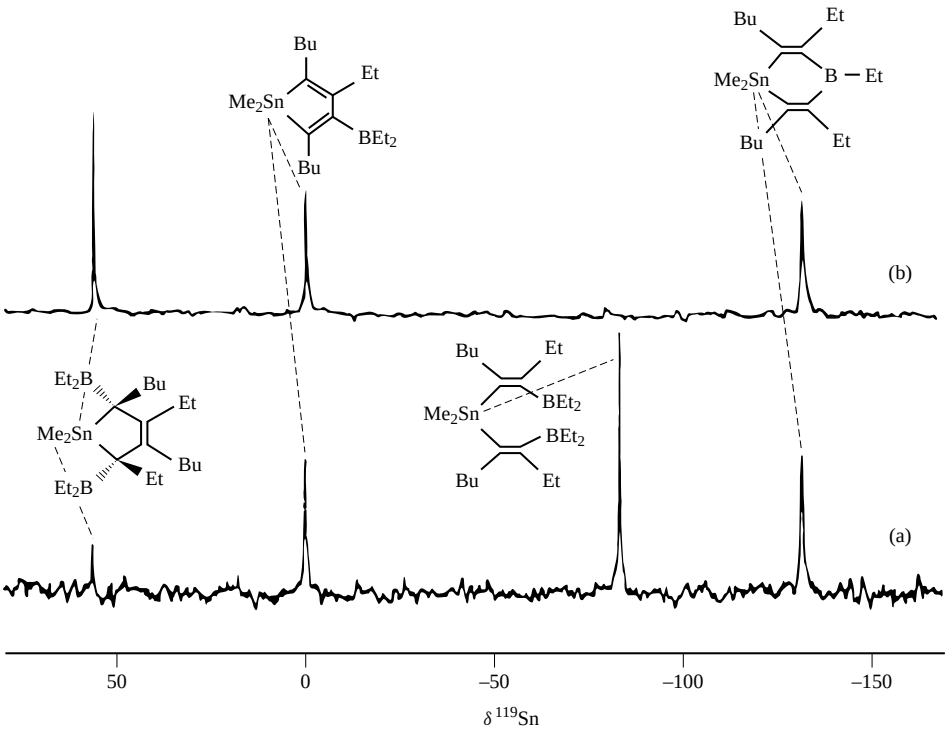

Figure 3 The 1,1-organoboration of $Me_2Sn(C{\equiv}CBu)_2$ with Et_3B (ratio 1:1.4):[73] (a) 33.3 MHz ^{119}Sn NMR (^1H inverse gated decoupled) of the reaction mixture which is formed immediately after warming to 298 K. (b) The same mixture after 24 h at 298 K. Note the significant change in intensity of two ^{119}Sn NMR signals: a stannolene derivative is formed at the expense of the noncyclic bis(alkenyl)tin compound

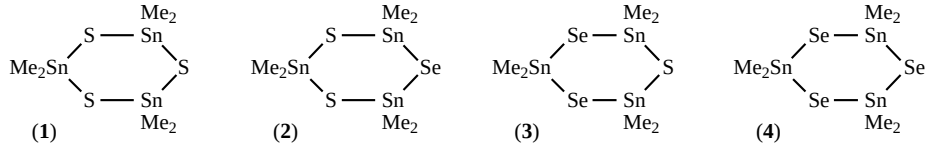

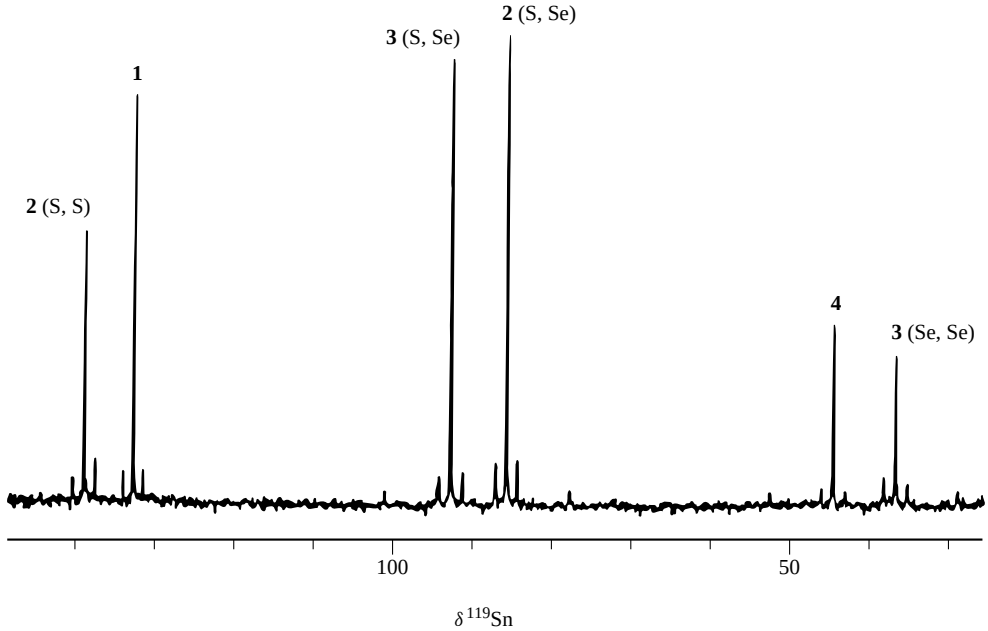

Figure 4 74.6 MHz ^{119}Sn NMR spectrum (^1H inverse gated decoupled) of an equilibrated mixture of $(Me_2SnS)_3$ (**1**) and $(Me_2SnSe)_3$ (**4**) in $CHCl_3$. The formation of the 'mixed' six-membered rings (**2**) and (**3**) is shown.[11] The weak signals are $^{117/119}Sn$ satellites (close to the parent signals) and ^{77}Se satellites (some are hidden in the range of the central lines)

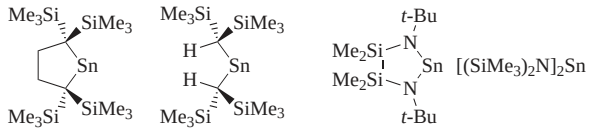

δ^{119}Sn = =2323[26] +2315 (+102 °C)[27] +759[13] +776[13]

Figure 5 Chemical shift data, δ^{119}Sn, for monomeric dialkylstannylenes and bis(amino)stannylenes

$(\eta^5\text{-}R_5C_5)_2$ Sn

R	H[33]	Me[32]	Bz[31]	Ph[31]
δ^{119}Sn	–2199	–2129	–2188	–2215

$(\eta^5\text{-}2,5\text{-}^tBu_2C_4N)_2$Sn –1889[34]

Figure 6 Chemical shift data δ^{119}Sn, for stannocenes and a 1,1′-diazastannocene

When the signs of $^nK(^{29}\text{Si,X})$ and $^nK(^{119}\text{Sn,X})$ have been determined to be the same, it can be safely assumed that $^nK(^{73}\text{Ge,X})$ has the same sign. In contrast, the sign of $^nK(^{207}\text{Pb,X})$ may change more readily, and it has to be determined, in particular if an unusual trend of the values $^nK(^{207}\text{Pb,X})$ becomes apparent.

It appears that the Fermi contact term is the dominating mechanism for electron mediated nuclear spin–spin coupling.[46] Accordingly, the sign and magnitude of one-bond coupling constants ^1J(M,X) (M = ^{73}Ge, ^{119}Sn, ^{207}Pb) depend on the valence s electron densities, $S(0)_M{}^2$ and $S(0)_X{}^2$, and on the mutual polarizability term, Π_{MX}, which involves the energies of the ground and excited electronic states and the s overlap integral of the bond between the two nuclides. At least in the case of ^{207}Pb, relativistic effects may become important because of spin–orbit splitting of non-s shells and because of the contraction of s and p shells.[16]

$Me_3Pb-OMe$				
Concentration (mol l^{-1}), 27 °C, in $CDCl_3$	0.16	0.40	1.18	Solid state
δ^{207}Pb (ppm)	+391.2	+379.9	+307.5	+103.8

Figure 7 Dependence of δ^{207}Pb values on the degree of self-association in trimethyllead methoxide

Table 2 Some Coupling Constants ^1J(M,X) (Hz) and Reduced Coupling Constants ^1K(M,X) (10^{20} N A^{-2} m^{-3}) (M = ^{29}Si,[49] ^{119}Sn,[11] ^{207}Pb[12])

Compound	X	$^1J(^{29}\text{Si,X})$	$^1K(^{29}\text{Si,X})$	$^1J(^{119}\text{Sn,X})$	$^1K(^{119}\text{Sn,X})$	$^1J(^{207}\text{Sb,X})$	$^1K(^{207}\text{Pb,X})$
Me_3M-H	^{1}H	−184.0	+7.7	−1744	+39.0	+2295	+92.3
Me_3M-BH_3	^{11}B	−74.0	+9.7	−554	+38.6	+460	+57.6
$Me_3M-B[NR_2]_2$	^{11}B	-97.0_a	+12.7	−930	+64.4	+1330	+166.6
Me_3M-CH_3	^{13}C	−50.3	+8.4	−340.0	+30.2	+250.0	+39.6
$Me_3M-C{=}CHMe$	^{13}C	-64.7_b	+10.8	−446.6	+39.7	+268.0	+56.8
$Me_3M-C{\equiv}CMe$	^{13}C	-79.4_c	+13.2	−502.9	+44.4	−59.0	−9.3
$[Me_2M-CH_3]^-$	^{13}C	–	–	+155.0	−13.7	−775.0	−122.0
$[Ph_2M-C_6H_5]^-$	^{13}C	±10	±1.66	+260.0	−23.1	−1030.0	−218.3
$M[CH(SiMe_3)_2]_2$	^{13}C	–	–	+414.0	−36.6	−734.0	−115.6
$Me_3M-SiMe_3$	^{29}Si	$+96.0_d$	+20.2	+656.0	+73.3	−764.2	+152.2
$Me_3M-SnMe_3$	^{119}Sn	+656.0	+73.3	+4460.0	+267.3	−3570.0	+381.2
$Me_3M-PbMe_3$	^{207}Pb	−764.2	+152.2	−3570.0	+381.2	+290.0	+55.3
$Me_3M-N(Me)Ph$	^{15}N	$+15.7_e$	+6.5	+2.2	+0.5	+261.0	−102.8
$M[N(SiMe_3)_2]_2$	^{15}N	–	–	−366.0	−80.2	+564.0	−233.7
Me_3M-PPh_2	^{31}P	$+20.3_f$	−2.1	+596.0	−32.9	−1335.0	−131.3
$Me_3M-SeMe$	^{77}Se	$+110.6_g$	−24.2	+1015.0	−118.9	−1170.0	−244.2
MF_4	^{19}F	+178.6	−7.9	–	–	–	–
$[MF_6]^{2-}$	^{19}F	+108.1	−4.8	+1550.0	−36.6	–	–
$Me_3M-W(CO)_3Cp$	^{183}W	–	–	−150.0	+80.5	+170.0	+159.5
$Me_3M-Fe(CO)_2Cp$	^{57}Fe	$(-)12.1_h$	(+)15.6	(+)42.7	(+)29.2	(+)89.1	(+)108.6
cis-$[Pt(MPh_3)Ph(PPh_3)_2]$	^{195}Pt	-1600.0_i	+307.0	−12 686.0	+1318.0	+18 380.0	+3403.0
$(Me_3Si)_2Hg$	^{199}Hg	−981.0	+226.8	-6157.0_j	+771.3	–	–

$_a$$NR_2$ = $N(Me)CH_2CH_2(Me)N$.
$_b$$Me_3Si-CH{=}CH_2$.
$_c$$Me_3Si-C{\equiv}CH$.
$_d$$(Me_3Si-SiMe_2)_2NH$.
$_e$$Me_3Si-NHPh$.
$_f$$Me_3Si-PMe_2$.
$_g$$(H_3Si)_2Se$.
$_h$$Me_{11}Si_6-Fe(Cp)(CO)_2$.
$_i$*trans*-$[PtCl(SiH_2Cl)(PEt_3)_2]$.
$_j$$[(Me_3SiCH_2)_3Sn]_2Hg$.

Table 3 Some Examples of Coupling Constants $J(^{73}Ge,X)$ (Hz), and Reduced Coupling Constants $^1K(^{73}Ge,X)$ (10^{20} N A^{-2} m^{-3})[14,15,22]

Compound	X	$^1J(^{73}Ge,X)$	$^1K(^{73}Ge,X)$	n	$^nJ(^{73}Ge,^1H)$
GeH_4	^1H	−97.6	+23.2		–
$MeGeH_3$	^1H	−94.5	+22.5	2	3.5
Me_2GeH_2	^1H	−92.3	+22.0	2	3.4
Me_3GeH	^1H	−93 ± 2	+22.1	2	n.o.[a]
Ge_2H_6	^1H	−95.5	+22.7	2	n.o.
H_3SiGeH_3	^1H	−91.5	+21.8	2	2.7
$GeMe_4$	^{13}C	−18.7	+17.7	2	3.0
$Ge(OMe)_4$	–	–	–	3	−1.9
$Ge(SMe)_4$	–	–	–	3	−2.5
GeF_4	^{19}F	+178.5	−45.1	–	
$[NH_4]_2[GeF_6]$	^{19}F	+98.0	−24.8	–	

[a]n.o. = not observed.

As for other geminal reduced coupling constants $^2K(A,X)$, a fairly large range is observed for $^2K(M,X)$ [e.g., $|^2J(^{119}Sn, ^{119}Sn)| \approx 0$ to 35 000 Hz], and both positive and negative signs have been determined.[10,11] The magnitude and sign of $^2K(M,X)$ depends in the usual way on the nature of the intervening atom E, the bond angle M–E–X, and on effects exerted by substituents linked to M, E, and X.[46] In the case of the vicinal reduced coupling constants $^3K(M,X)$ across E–E′ bonds (e.g. E = E′ = C), there is a dependence on the dihedral angle Φ (M–E–E′–X) [a positive sign of $^3K(M,X)$ with a minimum of $^3K(M,X)$ for Φ = 90° and maxima for Φ = 0 and 180°] which appears to be generally valid.[46] The influence of substituents on $^3K(M,X)$ corresponds to that found for many other values $^3K(A,X)$.

As a result of the increase in $S(0)^2_M$, as compared to lighter nuclides, many long-range coupling constants $^nJ(M,X)$ ($n > 3$; M = ^{119}Sn, ^{207}Pb) have been measured. At present, systematic trends have been observed only for a few classes of compounds such as alkynes (n = 4)[47] or allenes (n = 4, 5).[48]

3.2 Coupling Constants Involving ^{73}Ge

As a result of efficient ^{73}Ge quadrupolar relaxation, ^{73}Ge–X spin–spin coupling can be observed only in the case of symmetrical charge distribution around ^{73}Ge. So far examples are limited to X = ^1H, ^{13}C and ^{19}F (see Table 3 for representative examples).

3.3 Coupling Constants Involving ^{119}Sn

The magnitude of the coupling constants $^1J(^{119}Sn,^1H)$ in SnH_4 (−1930 Hz[50]) and in organotin hydrides $R_{3-n}SnH_n$ ranges from ≈−1500 to ≈−1900 Hz [$^1K(^{119}Sn,^1H) > 0$!], increasing in absolute magnitude with increasing number n, and depending on the group electronegativity of R, is completely in accord with the model of rehybridization[51] at the tin atom. There is also a wealth of data for $^2J(^{119}Sn,^1H)$ and $^3J(^{119}Sn,^1H)$, many of which are useful in structural assignments.

Except for tin(II) compounds (R_2Sn)[13] and triorganotin anions ($[R_3Sn]^-$),[52] it holds that all $^1J(^{119}Sn,^{13}C) < 0$ [$^1K(^{119}Sn,^{13}C) > 0$!]. The ‘s character’ of the Sn–C hybrid orbitals can be used to explain changes in $|^1J(^{119}Sn,^{13}C)|$, at least in the case of tetraalkyltin compounds. However, the data for alkynyltin compounds indicate that the situation may be much more complex, since in $R_3Sn–C{\equiv}C–R^1$ (e.g., R = alkyl, R^1 = alkyl, aryl, $SiMe_3$, SnR_3), in spite of the sp-hybridized carbon atom, the magnitude of $|^1J(^{119}Sn,^{13}C{\equiv})|$ is frequently smaller than $|^1J(^{119}Sn,^{13}C_{R'})|$. This shows that the electropositive tin atom is readily polarized by an electronegative ligand, and such polar Sn–C≡ bonds give rise to negative contributions to the Fermi contact term. The polarizability of the tin atom is reduced in the presence of more electronegative groups. Therefore, as shown in Figure 8, the magnitude of $|^1J(^{119}Sn,^{13}C{\equiv})|$ becomes ‘normal’ in di-, tri-, and tetra-1-alkynyltin compounds.[53]

$Me_{4-n}Sn(C{\equiv}C{-}SiMe_3)_n$		n = 0	1	2	3	4
$\lvert^1J(^{119}Sn,\ ^{13}CMe)\rvert$	(Hz)	340.0	402.6	489.1	603.7	–
$\lvert^1J(^{119}Sn,\ ^{13}C{\equiv}\ )\rvert$	(Hz)	–	398.0	552.5	760.0	1036.0

Figure 8 Comparison of the coupling constants between ^{119}Sn and sp^3- and sp-hybridized ^{13}C nuclides

Because of the readily polarizable tin atoms, the magnitude of $^1J(^{119}Sn,^{119}Sn)$ ranges from negative values in anions to rather large and presumably positive values in distannanes with $CN(Sn) = 5$. Examples are depicted in Figure 9. A large data set exists for $^2J(Sn,Sn)$. These data are particularly useful in the characterization of transition metal complexes with more than one $SnCl_3$ ligand.[11] The detection of ^{117}Sn satellites in ^{119}Sn NMR spectra proves that intermolecular exchange must be slow compared with the NMR timescale, and the intensities of the ^{117}Sn satellite signals enable the determination of the number of $SnCl_3$ groups present.

The sign of $^1J(^{119}Sn,^{15}N)$ changes, in most cases, from negative to positive in the series of $Me_{4-n}Sn(NR_2)_n$ for $n > 1$. For n = 1, Hahn echo extended (HEED) pulse sequences[58] (e.g., INEPT-HEED or DEPT-HEED) are most convenient for the determination of $^1J(^{119}Sn,^{15}N)$ and the isotope-induced chemical shifts $^1\Delta^{15/14}N(^{119}Sn)$. In cases with fairly large scalar coupling $^2J(^{119}Sn, ^{14}N)$, this technique can also be applied, as shown for 2-(trimethylstannyl)pyridine in Figure 10.

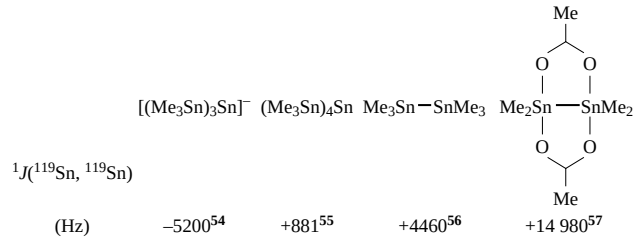

Figure 9 Change of sign for coupling constants $^{1}J(^{119}Sn,^{119}Sn)$

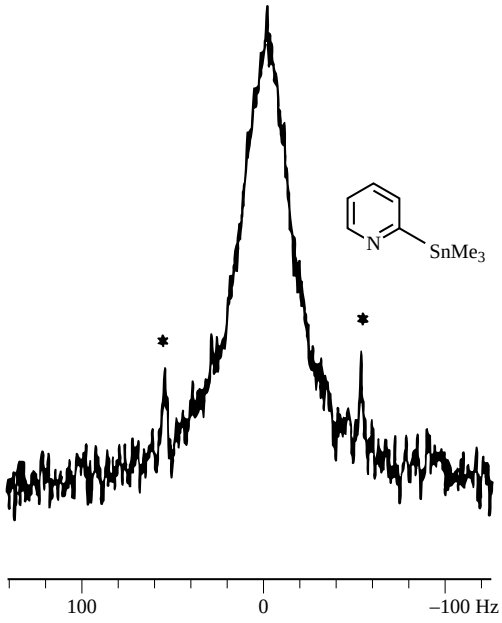

Figure 10 186.5 MHz ^{119}Sn NMR spectrum of 2-(trimethylstannyl)pyridine[74] (5 mm tube; ≈ 20% v/v in C_6D_6; 25°C; 64 scans; pulse repetition delay 5 s) recorded by using the refocused INEPTHEED pulse sequence[58] with a Hahn echo delay of 10 ms. The broad parent ^{119}Sn NMR signal represents the ^{119}Sn–^{14}N isotopomer, broadened by partially relaxed ^{119}Sn–^{14}N scalar coupling. The ^{15}N satellites [$^{1}J(^{119}Sn,^{15}N)$ = 108.2 Hz] are marked by asterisks

A positive sign of $^{1}J(^{119}Sn,^{31}P)$ [$^{1}K(^{119}Sn,^{31}P) < 0$!] has been found in stannylphosphanes, whereas $^{1}J(^{119}Sn,^{31}P)$ is large and negative in phosphane–$SnCl_4$ adducts[59] [e.g., $(Bu_3P)_2SnCl_4$ with $^{1}J(^{119}Sn,^{31}P)$ = 2550 Hz]. In transition metal complexes (Figure 11) the magnitude of $^{1}J(^{119}Sn,^{31}P)$ is also reduced [$^{1}K(^{119}Sn,^{31}P)$ becomes less negative], since the lone pair of electrons at the phosphorus atom is engaged in M–P bonding.[60]

In transition metal complexes with metal–tin bonds, rather large values for ^{119}Sn–metal coupling constants (e.g., metal = ^{183}W, ^{103}Rh, ^{195}Pt) are observed. In particular, in metal–$SnCl_2$[61] and metal–$SnCl_3$ complexes,[62,63] these data are indicative of the kinetic stability of the Sn–metal bond.

Interestingly, coupling constants between tin and quadrupolar nuclei can be frequently observed more easily in solid state ^{119}Sn NMR spectra as compared to NMR in solution. Typical examples include $^{1}J(^{119}Sn,^{11}B)$,[9] $^{1}J(^{119}Sn,^{35}Cl)$,[36] and even $^{1}J(^{119}Sn,^{39}K)$.[64]

$^{1}J(^{119}Sn,\ ^{31}P)$ (Hz)			
$(Me_3Sn)_3P$	+832.5	$(Me_3Sn)_3P—W(CO)_5$	+375.5
Me_3SnPPh_2	+586.0	$Me_3SnPPh_2—W(CO)_5$	+50.0

Figure 11 Comparison between coupling constants $^{1}J(^{119}Sn,^{31}P)$ in stannylphosphanes and their pentacarbonyl tungsten complexes

3.4 Coupling Constants Involving ^{207}Pb

The general trend of all ^{207}Pb–element coupling constants follows that observed for ^{119}Sn, although the sign of $^{1}J(^{207}Pb,X)$ changes much more readily than that of $^{1}J(^{119}Sn,X)$. This is shown by the correlation between $^{1}J(^{207}Pb,\ ^{13}C)$ and $^{1}J(^{119}Sn,^{13}C)$ of methyllead and methyltin compounds in equation (6).

$$^{1}J(^{207}Pb,\ ^{13}C_{Me}) = -2.26\ ^{1}J(^{119}Sn,^{13}\ C_{Me}) - 556.6\ (r = 0.985) \qquad (6)$$

Sign inversion of $^{1}J(^{207}Pb,^{13}C)$ has been observed in alkynyllead compounds,[43,65] in trimethylplumbyl methane derivatives,[66] and also in the series of trifluoromethyl derivatives $(CF_3)_{4-n}PbR_n$ (n = 0–3; R = Me, Et).[44] There is even one example with a positive and a negative sign for $^{1}J(^{207}Pb,\ ^{13}C_{Me})$ in the same molecule[65] (Figure 12). Negative contributions to the Fermi contact term arise because of the large polarizability of the lead atom and, in addition, relativistic effects are likely to become important. This is obvious by comparing the reduced coupling constants $^{1}K(^{207}Pb,M)$ (M = ^{119}Sn, ^{207}Pb) in $Me_3Pb–MMe_3$ (see Table 2). A number of hexaaryldiplumbanes has been studied with respect to $^{1}J(^{207}Pb,^{207}Pb)$,[67] and in some cases $^{1}J(^{207}Pb,^{207}Pb)$ can be determined from solid state ^{207}Pb CP MAS NMR spectra.[68] Large negative values of $^{1}K(^{207}Pb,^{15}N)$ and $^{1}K(^{207}Pb,^{31}P)$ are common (see Table 2).

4 NUCLEAR SPIN RELAXATION PARAMETERS

4.1 ^{73}Ge Nuclear Spin Relaxation in Solution[14,15,22]

The spin–lattice relaxation time $T_1{}^{73Ge}$ is dominated by quadrupolar relaxation, even in the case of the species GeR_4 (R = organyl) or GeX_4 (X = halogen) with tetrahedral surrounding of the germanium atom. This is the result of the interaction

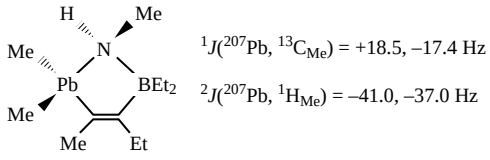

Figure 12 The signs of the coupling constants $^{1}J(^{207}Pb,^{13}C_{Me})$ are different, although the methyl groups are linked to the same lead atom. Note the small difference between the geminal coupling constants $^{2}J(^{207}Pb,^{1}H_{Me})$

between the quadrupole moment (eQ) and the electric field gradient (eq) which is modulated by molecular motion. In general it holds that $T_1{}^{73Ge} \geq T_2{}^{73Ge}$. The transverse relaxation time $T_2{}^{73Ge}$ may be further shortened by scalar interactions such as scalar coupling with other quadrupolar nuclides [e.g., $^1J(^{73}Ge,^{35/37}Cl)$**69**]. The longest $T_1{}^{73Ge}$ values are in the order of $\leq$0.5 s (e.g. in $GeMe_4$ and in $GeCl_4$ depending in the usual way on concentration, solvent, and temperature). In other compounds GeR_4, with larger groups R, the $T_1{}^{73Ge}$ values become shorter, as expected for longer rotational correlation times τ_c.

4.2 ^{119}Sn and ^{207}Pb Nuclear Spin Relaxation in Solution

As for other spin-$\frac{1}{2}$ nuclides, various relaxation mechanisms are expected to compete in ^{119}Sn**10**,**11**,**13**,**70** or ^{207}Pb nuclear relaxation.**10**,**12**,**13**,**71** Dipole–dipole (DD) interactions between ^{119}Sn and ^1H have to be taken into account (negative NOE in ^1H broadband decoupled spectra!) even in the case of medium-size molecules (MW < 1000) and, in particular, for measurements at low temperature. The other important relaxation mechanism are spin–rotation (SR) and scalar interactions (SC), the latter being significant for $T_2{}^{119Sn}$ or $T_2{}^{207Pb}$ (increase in the linewidths of ^{119Sn} or ^{207Pb}NMR signals)—a result of partially relaxed scalar coupling with quadrupolar nuclides [e.g., ^{11}B (see Figure 13), ^{14}N (see Figure 10), ^{35}Cl, ^{37}Cl, ^{79}Br, ^{81}Br, etc.]. In many cases of fairly small molecules, e.g. in MR_4 (M = Sn, Pb), the SR mechanism is of major importance. If the symmetry about M is reduced, the relaxation mechanism based on chemical shift anisotropy (CSA) has to be considered. Since the efficiency of this mechanism increases with $B_0{}^2$, it is frequently found with modern high-field NMR spectrometers ($\boldsymbol{B}_0 \geq 4.7$ T) that the CSA mechanism is dominant for ^{207}Pb nuclear spin relaxation if the local symmetry at the lead atom is reduced.

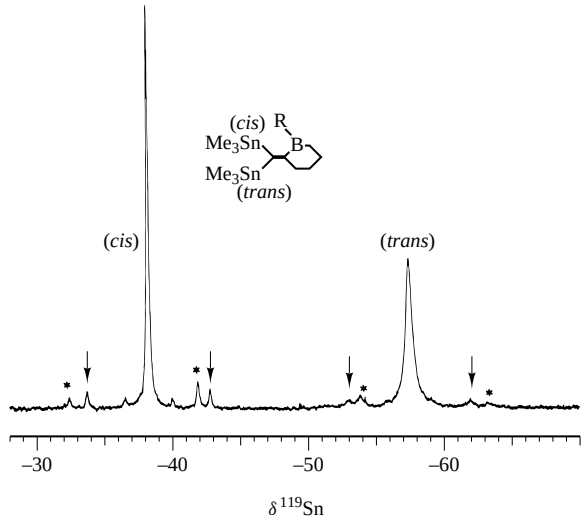

Figure 13 93.3 MHz ^{119}Sn NMR spectrum (^1H inverse gated decoupled) of a 1,1-bis(trimethylstannyl)alkenyltin compound (R = *N*-pyrrolyl) showing ^{119}Sn and ^{117}Sn satellites [marked by asterisks and arrows, respectively; $^2J(^{119}Sn,^{119}Sn)$ = 885.5 Hz] and rather different linewidths owing to partially relaxed vicinal ^{119}Sn–^{11}B scalar coupling: —$^3J(^{119}Sn,^{11}B)$—*trans* (≈73 Hz) > —$^3J(^{119}Sn,^{11}B)$—*cis* (≈41 Hz)**75**

The competition between various relaxation mechanisms has been demonstrated in the case of some monomeric tin(II) and lead(II) compounds.**13**,**72**

5 RELATED ARTICLES

Carbon-13 Spectral Simulation; Chemical Shift Tensors; Indirect Coupling: Theory and Applications in Organic Chemistry; Quadrupolar Nuclei in Glasses; Relaxation of Quadrupolar Nuclei Measured via Multiple Quantum Filtration; Shielding: Overview of Theoretical Methods; Silicon-29 NMR; Spin Echo Spectroscopy of Liquid Samples.

6 REFERENCES

1. E. Fukushima and S. B. W. Roeder, *J. Magn. Reson.*, 1979, **33**, 199.
2. I. P. Gerothanassis, *Magn. Reson. Chem.*, 1986, **24**, 428.
3. M. H. Levitt and R. Freeman, *J. Magn. Reson.*, 1981, **43**, 65.
4. A. J. Bensei and P. D. Ellis, *J. Magn. Reson.*, 1988, **78**, 511.
5. A. L. Wilkins, R. A. Thomson, and K. M. Mackay, *Main Group Met. Chem.*, 1990, **13**, 219.
6. G. A. Morris and R. Freeman, *J. Am. Chem. Soc.*, 1979, **101**, 760.
7. D. T. Pegg, D. M. Doddrell, and M. R. Bendall, *J. Chem. Phys.*, 1982, **77**, 2745.
8. W. McFarlane, *Annu. Rep. NMR Spectrosc.*, 1972, **5**, 353.
9. B. Wrackmeyer, Ē. Kupče, and J. Kümmerlen, *Magn. Reson. Chem.*, 1992, **30**, 403.
10. J. D. Kennedy and W. McFarlane, in *Multinuclear NMR*, ed. J. Mason, Plenum Press, New York, 1987, pp. 305–333.
11. B. Wrackmeyer, *Annu. Rep. NMR Spectrosc.*, 1985, **16**, 73.
12. B. Wrackmeyer and K. Horchler, *Annu. Rep. NMR Spectrosc.*, 1989, **22**, 249.
13. B. Wrackmeyer, in *Unkonventionelle Wechselwirkungen in der Chemie metallischer Elemente*, ed. B. Krebs, VCH, Weinheim 1992, pp. 111–124.
14. E. Liepins, I. Zicmane, and E. Lukevics, *J. Organomet. Chem.*, 1988, **341**, 315.
15. K. M. Mackay and R. A. Thomson, *Main Group Met. Chem.*, 1987, **10**, 83.
16. P. Pyykkö, *Chem. Phys.*, 1977, **22**, 289.
17. U. Edlund, T. Lejon, P. Pyykkö, T. Venktchalam, and E. Buncel, *J. Am. Chem. Soc.*, 1987, **109**, 5982.
18. T. Vladimiroff and E. R. Malinowski, *J. Chem. Phys.*, 1967, **46**, 1830.
19. Y. Takeuchi, K. Tanaka, and T. Harazono, *Bull. Chem. Soc. Jpn.*, 1991, **64**, 91.
20. J. D. Kennedy, W. McFarlane, and G. S. Pyne, *Bull. Soc. Chim. Belg.*, 1975, **84**, 289.
21. J. D. Kennedy, W. McFarlane, and G. S. Pyne, *J. Chem. Soc., Dalton Trans.*, **1977**, 2332.
22. A. L. Wilkins, P. Watkinson, and K. M. Mackay, *J. Chem. Soc., Dalton Trans.*, **1987**, 2365
23. Y. Takeuchi, M. Shimoda, and S. Tomoda, *Magn. Reson. Chem.*, 1985, **23**, 580.
24. E. Kupce, I. M. Ignatovich, and E. Lukevics, *J. Organomet. Chem.*, 1989, **372**, 189.

25. D. Dakternieks, K. Jurkschat, H. Wu, and E. R. T. Tiekink, *Organometallics*, 1993, **12**, 2788.
26. M. Kira, R. Yauchibara, R. Hiramo, C. Kabuto, and H. Sakurai, *J. Am. Chem. Soc.*, 1991, **113**, 7785.
27. K. W. Zilm, G. A. Lawless, R. M. Merrill, J. M. Millar, and G. G. Webb, *J. Am. Chem. Soc.*, 1987, **109**, 7236.
28. B. Wrackmeyer, K. Horchler, H. Zhou, and M. Veith, *Z. Naturforsch., Teil B*, 1989, **44**, 288.
29. R. W. Rudolph, W. L. Wilson, and R. C. Taylor, *J. Am. Chem. Soc.*, 1981, **103**, 2480.
30. W. L. Wilson, R. W. Rudolph, L. L. Lohr, R. C. Taylor, and P. Pyykkö, *Inorg. Chem.*, 1986, **25**, 1535.
31. C. Janiak, H. Schumann, C. Stader, B. Wrackmeyer, and J. J. Zuckerman, *Chem. Ber.*, 1988, **121**, 1745.
32. B. Wrackmeyer, A. Sebald, and L. H. Merwin, *Magn. Reson. Chem.*, 1991, **29**, 260.
33. B. Wrackmeyer, E. Kupce, G. Kehr, and A. Sebald, *Magn. Reson. Chem.*, 1992, **30**, 964.
34. N. Kuhn, G. Henkel, and S. Stubenrauch, *J. Chem. Soc., Chem. Commun.*, **1992**, 760.
35. B. Wrackmeyer, B. Distler, and M. Herberhold, *Z. Naturforsch., Teil B*, 1992, **47**, 1749.
36. R. K. Harris, A. Sebald, D. Furlani, and G. Tagliavini, *Organometallics*, 1988, **7**, 388.
37. I. D. Gay, C. H. W. Jones, and R. D. Sharma, *J. Magn. Reson.*, 1991, **91**, 186.
38. R. K. Harris and A. Sebald, *Magn. Reson. Chem.*, 1989, **27**, 81.
39. B. Wrackmeyer, K. Wagner, A. Sebald, L. H. Merwin, and R. Boese, *Magn. Reson. Chem.*, 1991, **29**, S3.
40. T. P. Lockhart, H. Puff, W. Schuh, H. Reuter, and T. N. Mitchell, *J. Organomet. Chem.*, 1989, **366**, 61.
41. T. B. Grindley, R. E. Wasylishen, R. Thangarasa, W. P. Power, and R. D. Curtis, *Can. J. Chem.*, 1992, **70**, 205.
42. B. Wrackmeyer, K. Horchler, and H. Zhou, *Spectrochim. Acta*, 1990, **46A**, 809.
43. B. Wrackmeyer, *J. Magn. Reson.*, 1981, **42**, 287.
44. R. Eujen and A. Patorra, *J. Organomet. Chem.*, 1992, **438**, 57 and C1.
45. B. Wrackmeyer, K. Horchler, A. Sebald, and L. H. Merwin, *Magn. Reson. Chem.*, 1990, **28**, 465.
46. C. J. Jameson, in *Multinuclear NMR*, ed. J. Mason, Plenum Press, New York, 1987, pp. 89–131.
47. B. Wrackmeyer, K. Horchler von Locquenghien, E. Kupce, and A. Sebald, *Magn. Reson. Chem.*, 1993, **31**, 45.
48. B. Wrackmeyer, *J. Organomet. Chem.*, 1980, **205**, 1.
49. E. Kupce and E. Lukevics, in *Isotopes in the Physical and Biomedical Sciences*, eds. E. Buncel and J. R. Jones, Elsevier, Amsterdam, 1991, Vol. 2, pp. 213–295.
50. C. Schumann and H. Dreeskamp, *J. Magn. Reson.*, 1970, **3**, 204.
51. H. A. Bent, *Chem. Rev.*, 1961, **61**, 275.
52. J. D. Kennedy and W. McFarlane, *J. Chem. Soc., Chem. Commun.*, 1974, 983.
53. B. Wrackmeyer and K. Horchler, *Prog. NMR Spectrosc.*, 1990, **22**, 209.
54. J. D. Kennedy and W. McFarlane, *J. Chem. Soc., Dalton Trans.*, 1976, 1219.
55. W. Biffar, T. Gasparis-Ebeling, H. Nöth, W. Storch, and B. Wrackmeyer, *J. Magn. Reson.*, 1981, **44**, 54.
56. W. McFarlane, *J. Chem. Soc. A*, 1968, 1630.
57. B. Mathiasch and T. N. Mitchell, *J. Organomet. Chem.*, 1980, **185**, 351.
58. E̅. Kupče and B. Wrackmeyer, *J. Magn. Reson.*, 1992, **97**, 568.
59. W. McFarlane and N. H. Rees, *Polyhedron*, 1989, **8**, 2047.
60. W. McFarlane and D. S. Rycroft, *J. Chem. Soc., Dalton Trans.*, 1974, 1977.
61. W. W. du Mont and H. J. Kroth, *Z. Naturforsch., Teil B*, 1980, **35**, 700.
62. M. Kretschmer, P. S. Pregosin, and H. Rüegger, *J. Organomet. Chem.*, 1983, **241**, 87.
63. K. H. A. Ostoja-Starzewski, P. S. Pregosin, and H. Rüegger, *Helv. Chim. Acta*, 1982, **65**, 785.
64. P. B. Hitchcock, M. F. Lappert, G. A. Lawless, and B. Royo, *J. Chem. Soc., Chem. Commun.*, 1993, 554.
65. B. Wrackmeyer and K. Horchler, *Magn. Reson. Chem.*, 1990, **28**, 56.
66. B. Wrackmeyer and H. Zhou, *Spectrochim. Acta*, 1991, **47A**, 849.
67. P. Granger, C. Brevard, and M. Devaud, *J. Magn. Reson.*, 1988, **76**, 232.
68. A. Sebald and R. K. Harris, *Organometallics*, 1990, **9**, 2096.
69. T. Harazono, K. Tanaka, Y. Takeuchi, and H. Fukutomi, *Inorg. Chem.*, 1987, **26**, 3851.
70. S. Chapelle and P. Granger, *J. Magn. Reson.*, 1988, **76**, 1.
71. G. R. Hays, D. G. Gillies, L. P. Blaauw, and A. D. H. Clague, *J. Magn. Reson.*, 1981, **45**, 102.
72. B. Wrackmeyer, C. Stader, K. Horchler, and H. Zhou, *Inorg. Chim. Acta*, 1990, **176**, 205.
73. B. Wrackmeyer, S. Kundler, and R. Boese, *Chem. Ber.*, 1993, **126**, 1361.
74. B. Wrackmeyer, H. E. Maisel, and H. Zhou, *Main Group Met. Chem.*, 1993, **16**, 461.
75. B. Wrackmeyer, *Polyhedron*, 1986, **5**, 1709.

Biographical Sketch

B. Wrackmeyer. *b* 1947. Diploma, 1971, Dr. rer.nat., 1973, Habilitation, 1979, University of Munich. Introduced to NMR by H. Nöth and W. McFarlane. Institute of Inorganic Chemistry, University of Munich, 1979–86; Laboratory of Inorganic Chemistry, University of Bayreuth, 1986–present. Approx. 320 publications. Research interests include developments of NMR techniques in solution, application of multinuclear MR to problems in inorganic and organometallic chemistry.

Hydrogen Molecules

Mark S. Conradi

Washington University, St. Louis, MO, USA

1	Introduction	1
2	Properties of Hydrogen Molecules	1
3	Solid H_2	2
4	H_2 Gas	3
5	Dilute H_2 in Inert Solid Matrices	4
6	H_2 as a Relaxation Center	5
7	Multiple Echoes	6
8	Physisorbed Hydrogen	7
9	Related Articles	8
10	References	8

1 INTRODUCTION

By any measure, H_2 is one of the simplest molecules. Hence, it is remarkable how many surprises and unusual phenomena appear in the NMR of the hydrogens. This article will describe the surprises.

At the outset, it should be noted that hydrogen NMR signals from the liquid and solid phases are particularly strong. The density of protons in liquid H_2 is only 20% less than that in water; near the freezing point of 14 K, the Boltzmann factor is 20 times larger for H_2 than for room temperature H_2O. Partly because of the large signals, H_2 was studied early in the history of NMR.[1,2] With such a large spin magnetization come the so-called radiation damping (or radiation reaction) effects[3] (see ***Concentrated Solution Effects***).

One of the unique features of hydrogen NMR is that a quantum description of the molecular orientation and rotation is required. Furthermore, H_2 remains 'lively' (molecular reorientations still rapid) at low temperatures, where most other systems are completely frozen, except for small-amplitude vibrations. The existence of the several isotopic forms H_2, HD, and D_2 (and radioactive HT, DT, and T_2) is also unusual; the large mass ratios can cause large isotope effects.

Part of this article is concerned with hydrogen molecules in inert matrices or physically adsorbed on a substrate. But first the subject will be placed in proper perspective by describing the behavior of solid H_2 (in particular, the lineshape) and gaseous H_2 (in particular, the relaxation mechanism), after a short discussion of the molecular properties.

2 PROPERTIES OF HYDROGEN MOLECULES

A clear, thorough overview of the physical properties of liquid and solid hydrogen, starting with molecular characteristics, has been presented by Silvera.[4]

The rotational energy levels of H_2 are given by $E_J = J(J + 1)(\hbar^2/2I)$. Here J is the angular momentum quantum number (0, 1, 2, . . .) and $\hbar^2/2I$ is the rotational constant. The moment of inertia I is $I = ML^2/4$ from classical mechanics, with L the bond length and M the molecular mass. Because the mass of H_2 is so small (the lightest molecule, in fact) and L is so short ($\sim$0.075 nm, the shortest chemical bond) the inertia I is unusually small. Thus the rotational constant $\hbar^2/2I$ is 86 K (multiply by k_B for energy units), unusually large. As shown in Figure 1, the energy levels of the first few states are 0 for $J = 0$, 172 K for $J = 1$, 516 K for $J = 2$, and 1032 K for $J = 3$. Thus, even at room temperature the quantum nature of molecular rotation must be considered. At low temperatures, where the splittings exceed k_BT, this is especially important.

Because H_2 has two identical fermions (protons, $I = \frac{1}{2}$), the overall wavefunction ψ must be antisymmetric with respect to proton interchange. The wavefunction is a product of spin (χ) and spatial (ϕ) (i.e. rotational) parts: $\psi = \chi\phi$. The desired antisymmetry under proton interchange can be obtained in two ways (Figure 1). The spin function χ may be symmetric (i.e. total nuclear spin $I = 1$, the parallel arrangement of the proton spins) with the rotational function ϕ antisymmetric (i.e. odd values of quantum number J). This case is *ortho*-H_2. The second possibility is *para*-H_2, which has antiparallel proton spins ($I = 0$) and J restricted to even values.

The distinction between *ortho*-H_2 and *para*-H_2 has profound effects. Most importantly for NMR, only *ortho*-H_2 molecules yield proton NMR signals, since *para*-H_2 has $I = 0$. The specific heats of *ortho*-H_2 and *para*-H_2 in the gas phase are different so they have different thermal conductivities. A simple resistance bridge thermal conductivity analyzer can be used to determine the fraction of *ortho*-H_2 in a mixture.

The equilibrium concentration c of *ortho*-H_2 is 0.75 at and above room temperature. This reflects the multiplicities of the nuclear spin states: $2I + 1$ is 3 for $I = 1$ (*ortho*) and 1 for $I = 0$ (*para*). At lower temperatures the equilibrium concentration falls to 0 at low temperatures, since $J = 0$, is the rotational ground state. At 77 K, for example, the equilibrium $c \simeq 0.50$.

Thus, if H_2 could attain thermal equilibrium at low temperatures, all of the H_2 would be *para*-H_2, $I = 0$, and there would be no NMR signals! However, conversion between *ortho*-H_2 and *para*-H_2 is a very slow process, requiring

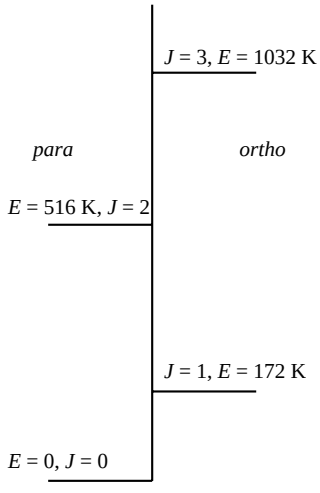

Figure 1 Energy level diagram of the H_2 molecule. The rotational energy is $E_J = J(J + 1)\hbar^2/2I$, with $\hbar^2/2I = 86$ K. States are divided into *para*-H_2 (even J, total nuclear spin $I = 0$) and *ortho*-H_2 (odd J, $I = 1$)

days or weeks, depending on the material phase. *Ortho–para* conversion is slow because it requires a magnetic field gradient to provide a different field at the two protons, to cause a relative precession of the two spins. Furthermore, the magnetic field gradient must oscillate (or have spectral components) at the frequency corresponding to the 172 K splitting between $J = 1$ and $J = 0$. Thus, static field gradients are ineffective. Paramagnetic materials of high surface area can serve as catalysts to speed the process.

D_2 has two spin-1 deuterons, which are bosons. Thus, the overall wavefunction must be symmetric under interchange of the deuterons. *Para*-D_2 has total nuclear spin $I = 1$ and odd values of J. *Ortho*-D_2 has $I = 0$ or $I = 2$ coupled with even J values. Thus, both *ortho*-D_2 and *para*-D_2 generate deuterium NMR signals. The rotational ground state is $J = 0$; therefore, at low temperatures D_2 becomes increasingly *ortho*-D_2. The rotational constant $\hbar^2/2I$ is 43 K for D_2. The high-temperature equilibrium composition is 33.3% *para*-D_2, as dictated by the spin multiplicities: $2I + 1 = 3$ for *para*-D_2. For *ortho*-D_2, there are five states of $I = 2$ and one state of $I = 0$, a total of six spin states. A more sensible naming convention has been suggested: 'even-J' and 'odd-J' are accurate names that self-explain.[5]

For HD, the two nuclei are not identical. There are no interchange symmetry requirements, so no *ortho–para* distinction. At low temperatures, HD readily falls into its $J = 0$ ground state. We remark that $J = 0$ HD is a spherically symmetric molecule (!), so the intramolecular dipole interaction between H and D is averaged to zero.

It should be remarked that other molecules (e.g. H_2O, N_2, and $^{15}N_2$) have *ortho* and *para* species. As their rotational constants ($\hbar^2/2I$) are much smaller, one cannot make the gas cold enough for the equilibrium concentration to deviate substantially from the high-temperature limit. At lower temperatures they solidify and the rotational motion is hindered (librations). The splitting between the lowest librational states of the *ortho* and *para* species is very small in such cases. Thus, the effects of the *ortho–para* distinction are by far most prominent with H_2 and D_2.

Molecular beam measurements[6] of the molecular energy levels in H_2, HD, and D_2 have been reported. Thus, the parameters of the nuclear spin Hamiltonian are known to high accuracy. As discussed thoroughly by Abragam,[3] there are four terms in the spin Hamiltonian of *ortho*-H_2. The nuclear Zeeman interaction is the splitting between spin states that results in NMR. There is a molecular Zeeman interaction; this term is relatively unimportant in bulk phases. Even in H_2 gas, collisions occur so frequently that magnetic resonance associated with the molecular Zeeman term is unobservable. The third term is spin–rotation coupling; rotation of the molecule generates a magnetic field at the nuclei. The fourth term is dipole–dipole interaction between the spins. In HD and D_2, there is an additional, quadrupole interaction between the deuteron(s) and the electric field gradient from the charges in the molecule (see ***Quadrupolar Interactions***).

3 SOLID H_2

The contours of constant electronic density of the H_2 molecule are nearly spherical, particularly for the contours at distances of van der Waals contact.[4] Thus, the angular momentum quantum number J 'is a good quantum number' even in liquid and solid H_2. Although the rotation state is generally an admixture of many eigenstates of different J values, the rotational states in liquid and solid H_2 are nearly pure eigenstates of a single J value. The existence of free-rotor states in the solid does not occur for other systems.

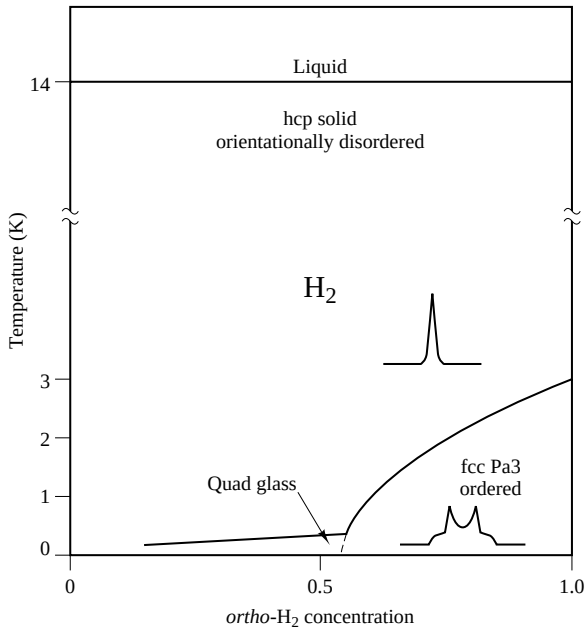

Figure 2 Phase diagram of solid H_2 at ambient pressure. The *ortho*-H_2 concentration can be controlled by waiting for the sample to *ortho–para* convert partially. Proton NMR lineshapes in the hcp disordered and Pa3 ordered phases are sketched

Solid H_2 forms from the liquid at temperatures below 14 K, independent of the *ortho* concentration c, as shown in Figure 2. In the high-temperature, hexagonal close packed (hcp) phase, the proton NMR line (of the *ortho*-H_2) is comparatively narrow.[7] At temperatures from 14 K down to ≈ 3 K the linewidth is determined primarily by intermolecular dipole interactions. The linewidth is more or less independent of temperature below 10 K; above 10 K the line narrows due to diffusion. The intramolecular interactions (dipole–dipole and spin–rotation) are averaged nearly to zero by rapid transitions among the three m_J sublevels of the $J = 1$ manifold of rotational states. Higher J states are not occupied at such low temperatures (see Figure 1). The rapid Δm_J transitions are analogous to (and are more or less equivalent to) the rapid tumbling of a classical molecule in a fluid. Thus, the hcp phase is 'orientationally disordered'.

Below the phase transition (Figure 2), an orientationally ordered H_2 structure appears, as studied in the classic paper of Reif and Purcell.[2] The center of mass lattice is face-centered cubic (fcc), and there are four interpenetrating sublattices (Pa3 crystal symmetry). The *ortho*-H_2 molecules are 'no longer rotating', to put it classically. In quantum terms, the energy of one of the three sublevels is lower than the others; this sublevel may be regarded as $J = 1$, $m = 0$ or, equivalently, the p_z function of orientation. In this state the expectation value of the intramolecular dipole–dipole interaction does not vanish, so the proton NMR line appears as a wide Pake powder doublet, as also discussed by Abragam.[3]

The dipole splitting in the ordered phase Pa3 is unusually wide, 172 kHz cusp-to-cusp. It is so large because of the very short distance between the protons in H_2. Yet it is interesting to note that the splitting is only $\frac{2}{5}$ the value one would expect from classical formulae for the dipole interaction of fixed protons. The $\frac{2}{5}$ factor is the expectation value of the dipolar $(3\cos^2\theta - 1)/2$ term for the p_z wavefunction. That is, in the p_z state, many orientations are present; p_z is not a delta function of orientation. The spin–rotation interaction does not contribute to the linewidth in the ordered phase, because the wavefunction is real and the angular momentum components are quenched: $\langle J_i \rangle = 0$.

It should be noted that Reif and Purcell even measured the dipole interaction strength by zero field NMR, a remarkable feat for the time (see ***Zero Field NMR***).

The orientationally disordered phase of H_2 is similar to the rotor (or plastic) crystal phases[8] of many classical molecules, especially solid N_2 and CO. The high-temperature structures, β-N_2 and β-CO, are rotor solids with the hcp lattice. The low-temperature forms, α-N_2 and α-CO, have the Pa3 crystal structure.[9] The transition temperatures, 35.6 K for N_2 and 61.5 K for CO, are much higher than for H_2. The parallelism between these systems is intriguing, in light of the quantum mechanical description required for rotation in H_2, while N_2 and CO are well described classically. The only analog to dilution of the *ortho*-H_2 by *para*-H_2 is to form N_2/Ar or N_2/CO/Ar alloys, with argon serving to dilute the molecules.

The orientational ordering of solid H_2 is driven by the electrostatic quadrupole–quadrupole (EQQ) interaction between *ortho*-H_2 molecules. *Para*-H_2 molecules, being $J = 0$ and thus spherical, do not participate in the orientational ordering (they have no orientation). At such temperatures, the *ortho*-H_2 molecules are all $J = 1$ and the *para*-H_2 molecules are $J = 0$. Thus, it is convenient to consider the *ortho*-H_2 as 'molecular spins-1'; the EQQ coupling is then a molecular spin–molecular spin coupling which induces flip-flops (spin exchanges) between the molecular spins. Thus, spin A may go from $m_J = 1$ to 0 while spin B makes a transition from $m_J = 0$ to 1. In this way, the *ortho*-H_2 molecular spins behave analogously to nuclear spins coupled by magnetic dipole interactions in a solid.

In the high-temperature phase, the nuclear spin T_1 can be calculated using the Bloembergen–Purcell–Pound (BPP) relaxation theory, where the correlation time τ_c describing the intramolecular interactions is the mean time between molecular spin flip-flops: $T_1 \propto \omega_c = {\tau_c}^{-1}$, because $\omega_0\tau_c \ll 1$. The rate ω_c of flip-flops, as in the nuclear spin analogy, is independent of temperature and increases with increasing concentration (c) of the *ortho*-H_2 molecular spins. Indeed, this is observed.[10] For $1 > c > \frac{1}{2}$, T_1 varies approximately as $c^{1/2}$; this results from a nearly Gaussian correlation function of the molecular spin quantities (recall that lineshapes in concentrated dipolar solids are nearly Gaussian). For $c \leq 0.3$, T_1 varies nearly as $c^{5/3}$; this result can be rationalized from the (distance)$^{-5}$ variation of the EQQ, imagining dilution to occur on a regular sublattice. The statistical theory of dilute-spin lineshapes gives the same results.

When the temperature is decreased to a value roughly equal to the EQQ interaction strength, a first-order transition to the ordered structure occurs. The mean interaction strength involves the pair interaction (about 0.85 K) and the number of nearest *ortho*-H_2 neighbors. Thus, dilution with *para*-H_2 reduces the transition temperature, as in Figure 2. For $c \leq 0.56$, no long range ordered structure appears; this high value of the critical concentration is believed to result from a high degree of frustration of the EQQ interaction. For $c \leq 0.56$ and at low temperatures, a quadrupole glass phase[11] appears (see ***Ortho–Para Hydrogen at Low Temperature*** for a thorough discussion of the quadrupole glass).

Another analog of spin flip-flops is resonant *ortho–para* interchange. In this process, written as $po \rightarrow op$, an *ortho* and a *para* hydrogen interchange. This is not a physical interchange where one molecule moves past the other, but an interchange of the *ortho* and *para* label only. This slow process is driven by a weak term in the intermolecular nuclear spin dipole–dipole interaction between the $I = 1$ *ortho* and the $I = 0$ *para* (the $I = 0$ molecule still has an intermolecular dipole interaction, because the antiparallel proton spins are spatially separated).[12] The effect of the interchanges is to allow *ortho*-H_2 in a dilute sample to cluster together at $T \leq 1$ K. By clustering and properly orienting themselves, they can reduce their energy (by virtue of the EQQ interaction). Horst Meyer, who has contributed so much to the understanding of solid H_2, has reviewed this topic.[13]

Ortho–para conversion is a process which destroys *ortho*-H_2 molecules at low temperatures. In the ordered state (high concentration c of odd-J species at low temperatures), the molecules are all $J = 1$, $m_J = 0$. Because the conversion rate depends on the nuclear spin state m_I, the spin state populations will be driven away from their thermal equilibrium values. For $c \sim 1$ (nearly pure *para*-D_2), a remarkably enhanced deuterium spin signal was observed (by as much as $\times$ 50, with some features negative, 'in emission').[14] This phenomenon is closely related to the CIDNP effect (see ***Chemically Induced Dynamic Nuclear Polarization***). The nuclear spin populations can only be driven away from equilibrium by *ortho–para* conversion in the ordered phase, where T_1 is sufficiently long.

4 H_2 GAS

The nuclear magnetic relaxation of H_2 gas is discussed briefly in the venerable paper[1] of BPP. At ~10 atm, it was correctly deduced that H_2 gas was in the limit $\omega_0\tau_c \ll 1$, explaining why T_1 increased with increasing pressure. It should be remarked that a general familiarity with the 'pressure broadening' of infrared absorption lines would lead one to expect the opposite result.

Hardy published the classic study of spin relaxation in H_2 gas at 77 K.[15] The measurements employed extensive signal averaging to improve the signal to noise ratio, long before the digital revolution in signal processing. The work is a beautiful application of the BPP relaxation theory. The correlation time τ_c of the intramolecular spin–spin and spin–rotation interactions is the time between collisions that change the rotational state J, m_J. At 77 K all of the *ortho*-H_2 molecules are confined to $J = 1$, so τ_c refers to the time for m_J to change. Thus, the language of gas phase relaxation is that of molecular scattering. Here, one is interested in scattering events (collisions) that change m_J of one or both molecules. The rate of collisions and hence τ_c are experimentally controlled by varying the density (or pressure) of the gas.

Hardy was able to pass through the T_1 minimum ($\omega_0\tau_c \approx 1$) by going to sufficiently low densities. In the BPP

theory, the value of the minimum T_1 depends primarily on the strength of the spin–spin and spin–rotation interactions (see ***Spin–Rotation Relaxation Theory***), which are known accurately for H_2 from molecular beam studies. The minimum T_1 also depends on the shape of the autocorrelation function (exponential here) and the ratio of correlation times for terms of different multipolar operators. Remarkable agreement between the experimental data and the results of relaxation theory were obtained.

It should be noted that the intramolecular spin interactions in H_2 are unusually large. For example, for relaxation through the dipole–dipole interaction, the relaxation rate T_1^{-1} varies as the square of the interaction strength, R^{-6}. As H_2 has the shortest bond length, it has an unusually rapid spin relaxation rate (Hardy's minimum T_1 at 29 MHz is 200 μs!).

The reader is referred to other articles on NMR in gases (***Gas Phase Studies of Intermolecular Interactions and Relaxation*** and ***Gases at High Pressure***).

5 DILUTE H_2 IN INERT SOLID MATRICES

H_2 has been studied at low concentrations in liquified[16] and solidified[17] rare gas solids (neon, argon, and krypton). For the solids, the H_2 concentrations ranged from 30 to 2000 ppm (0.2%). The solid solutions were prepared, for example, by bubbling H_2 gas through liquid argon, in a recirculating scheme. The solution was frozen rapidly (several minutes) and the expelled H_2 was then evacuated. Once in solid solution, the H_2 was stable at all temperatures below $\sim 0.8\ T_{\mathrm{MELT}}$. The proton NMR data ($T_1$ and T_2) were independent of the H_2 concentration, suggesting the H_2 molecules were well dispersed. The absence of *ortho–para* conversion confirms that the H_2 molecules were not clustered. The H_2 concentration was determined from the proton NMR signal amplitude, in comparison with H_2 gas. With such small concentrations, the 20 MHz proton signals were extensively averaged (up to 100 000 averages); the relatively small value of T_1 (0.5–10 ms) allowed the averaging to be accomplished within a reasonable time.

As a function of temperature, the data for T_1 and T_2 of H_2 in solid neon, argon, and krypton display classic BPP behavior. In argon, for example, there is a T_1 minimum at 13.5 K, with T_2 nearly equal to T_1 above this temperature. Below 13 K, T_2 is much shorter than T_1. The temperature dependence of T_1 and T_2 is due to a temperature-dependent rate ω_c of Δm_J transitions. Because the data are independent of concentration, the transitions are not driven by the EQQ coupling between the molecular spins (as in solid H_2, see above). Instead, the transitions are due to phonon–rotation coupling, 'T_1' processes of the molecular spins. Such a coupling has also been observed in pure H_2 (dilute in *ortho*-H_2), as well.[18]

The minimum value of T_1 in the BPP relaxation theory is determined by the spin interaction strengths and the resonance frequency ω_0. Thus, it was surprising that the T_1 minimum values in neon, argon, and krypton were nearly equal (0.56 ms), but about four times longer than the minimum T_1 of Hardy's 77 K gas measurements (corrected for the different ω_0 values). In a remarkable paper, Fedders adapted the BPP relaxation theory to the quantum mechanical description of rotational states in *ortho*-H_2.[19] He postulated a crystal field acting on the H_2 that lifts the degeneracy of the three sublevels. His calculation makes specific predictions for the minimum T_1 in the case of crystal fields of cubic symmetry (three levels degenerate), axial symmetry (two levels degenerate), and no symmetry (no degeneracies). In brief, various terms in the relaxation Hamiltonian are shifted in frequency by the frequencies separating the $J = 1$ sublevels. Provided the crystal fields are sufficiently strong, the frequency-shifted terms are no longer effective in relaxation. Thus, for splittings much larger than ω_0, the minimum T_1 values depend only on the symmetry of the crystal fields, and not their strength. In the original paper,[19] the values for the case of no symmetry depend weakly on a parameter R. A technical correction to the angular averaging shows that R is unimportant; the correct values are the ones listed for $R = 0$.[17]

Fedders's calculated value for no symmetry agrees to within 10% of the minimum T_1 in neon and argon, and to within 25% for krypton. The crystal field may arise from strains produced from other H_2 impurities. Also, dislocation lines are inevitable in rare gas solids and result in quadrupolar broadening in pure solid krypton (^{83}Kr) and xenon (^{131}Xe), despite their fcc structure (see ***Diffusion in Rare Gas Solids***). The dislocations may also produce the crystal fields acting on the H_2.

Dilute *ortho*-H_2 was also studied in solid *para*-H_2.[17] The inside of the sample vessel was coated with ferric hydroxide gel, an *ortho–para* conversion catalyst. The sample was held in the liquid phase to promote conversion. When the desired concentration of *ortho*-H_2 remained, the sample was frozen; the greatly reduced mobility halted the catalytic conversion. *Para*-H_2 remains in the hcp structure (Figure 2), so an axially symmetric crystal field is expected. A T_1 minimum is observed to occur at the melting point of 14 K; the minimum value (0.30 ms) is in close agreement with Fedders's value for the case of axial symmetry. It is not known why the crystal fields from dislocations and neighboring impurities do not lower the symmetry further, as in the cubic rare gas solids.

Using Fedders's calculations, the observed values of T_1 and T_2 were used to determine the rate ω_c of Δm_J transitions. The behavior of ω_c generally follows a power law, $\omega_c \propto T^n$, with n varying between 2 (high temperature) and ~ 7 (lowest temperatures). This demonstrates that a two-phonon Raman process drives the molecular reorientation. The theory[20] of relaxation of quadrupolar nuclei by phonons (two phonons, Raman) can be adapted here, where the 'molecular spin' is being relaxed. It was found in all solids (neon, argon, krypton, and *para*-H_2) that an unusually low value of 40 K of the characteristic temperature θ_c of the phonon spectrum (essentially the Debye temperature) was required to fit ω_c as a function of temperature. The origin of the apparently low-frequency modes is not known.

More recently, the behavior of HD in solid argon has been examined with deuteron NMR.[21] HD has a singlet rotational ground state, $J = 0$, so at low temperatures its T_1 will be relatively long. Above 10 K, the observed relaxation will be due to the few molecules in the first excited states, $J = 1$. At low temperatures, this fraction f is $3e^{-128/T}$, where 128 K is the energy of the three $J = 1$ states. The observed relaxation rate can be divided by this fraction to yield the T_1^{-1} of molecules characterized by $J = 1$. For HD in argon, it appears that transitions among the $J = 1$ sublevels, Δm_J transitions, are responsible for the relaxation, not ΔJ transitions. Using the formalism of Fedders, the T_1^{-1} of $J = 1$ molecules yields the rate ω_c (Γ_2 in the original article)[19] of the Δm_J transitions.

The transition rates ω_c for *ortho*-H_2 and *para*-D_2 at the same temperature in argon differ only by a factor of two, as expected from the masses. But ω_c for HD in argon is larger by a factor of 100! This effect is attributed to the off-center rotation of HD. The electronic cloud of HD, like H_2 and D_2, is nearly spherical and centered on the point ('force center') halfway between the nuclei. But this is not the center of mass, which is closer to the deuteron, away from the proton. For free rotation (about the center of mass), the force center sweeps out a circle of 0.025 nm diameter. In light of this, rotation of HD should generate larger forces and displacements of its neighbors. This is the origin of the enhanced phonon–rotation coupling of HD in argon.

6 H_2 AS A RELAXATION CENTER

The term 'relaxation center' has its origins in paramagnetic species (bearing electronic spins and magnetic moments) which serve to relax the nuclear spins in their vicinity (see ***Paramagnetic Relaxation in Solution***).[3] But *ortho*-H_2, because of its short bond length, can have a relatively small value of its proton T_1. By spin diffusion (see ***Spin Diffusion in Solids***), the magnetization is propagated to other proton spins in the sample. Thus, *ortho*-H_2 may function as a relaxation center.

6.1 H_2 Relaxation Centers in Solid HD

At temperatures below 4.2 K, HD molecules are confined by the Boltzmann factor to the $J = 0$ state ($J = 1$ is 128 K higher in energy). Since $J = 0$ is a singlet state, no fluctuation or transition between sublevels is possible (compare to $J = 1$ *ortho*-H_2, which has three sublevels). Thus T_1 of pure HD would be expected to be relatively large.

But all HD samples bear some H_2 (and D_2) impurities. For relaxation of the protons in HD, the *ortho*-H_2 content is particularly important. Either through EQQ interaction between $J = 1$ molecules or through coupling of the $J = 1$ 'molecular spins' to phonons, the *ortho*-H_2 will have a mechanism for longitudinal relaxation. Because spin diffusion here is rapid, the overall relaxation rate is then given by spin thermodynamics reasoning as follows:

$$(T_1^{-1})_{\text{overall}} = (T_1^{-1})_{H_2} \frac{2[ortho\text{-}H_2]}{2[ortho\text{-}H_2] + \frac{3}{4}[HD]} \qquad (1)$$

In equation (1), the factors of 2 and $\frac{3}{4}$ are the values of $I(I + 1)$ for $I = 1$ (*ortho*-H_2) and $I = \frac{1}{2}$ (proton in HD). The square brackets represent number concentrations. Thus, for a known concentration of *ortho*-H_2, the T_1^{-1} of the *ortho*-H_2 molecules themselves may be extracted from the measured, overall T_1^{-1}.

Hardy and Gaines studied the proton T_1 of HD with varying amounts x of H_2 impurity.[22] At 4.2 K and $x = 2\%$ they find a broad T_1 minimum as a function of x. This indicates that the correlation time τ_c describing the *ortho*-H_2 rotational states varies with H_2 concentration and passes through the condition $\omega_0\tau_c \sim 1$. At sufficiently low concentrations, $x \leq 10^{-3}$, the observed $T_{1_{\text{overall}}} \propto x^{-8/3}$, yielding $(T_1)_{H_2} \propto x^{-5/3}$. This last result is just that expected for EQQ interactions among the *ortho*-H_2, given the variation of EQQ as r^{-5}.

The above explanation is not the entire story. For example, there is a temperature dependence of T_1 and a field dependence as well. The result varying as $x^{-8/3}$ only obtains near 4 K, perhaps serendipitously. No complete explanation has appeared for these effects, which have been studied further by others.

Nevertheless, the overall T_1 observed by Hardy and Gaines varied from 0.04 to 10^3 s with H_2 contents from 2×10^{-2} to 10^{-4}. That T_1 is still changing at $x = 10^{-4}$ is a clear demonstration of the role of *ortho*-H_2 molecules as relaxation centers for the HD protons in this solid.

6.2 H_2 Relaxation Centers in Amorphous Silicon

Amorphous silicon (see ***Amorphous Silicon Alloys***) is commonly formed from a plasma or glow discharge containing silicon and hydrogen atoms (from SiH_4 with added H_2). The solid that forms has hydrogen atoms covalently bonded to silicon, with the silicons forming a covalent, noncrystalline network. The hydrogen atoms are crucial for this semiconductor, tying up dangling bonds that result for non-fourfold-coordinated silicon atoms. Typical material has $\sim$ 10 at% hydrogen. The hydrogen atoms are dipolar coupled to each other, with separate broad (more clustered) and narrow (less clustered) components in the proton NMR line.

A pronounced T_1 minimum was observed as a function of temperature near 30 K for the protons in amorphous silicon. Given the covalent nature of the structure, atomic motions at $\sim 10^8$ s^{-1} are completely unexpected at such low temperatures. Two-level tunneling systems were suspected. However, a small fraction of the protons being involved in fairly small atomic displacements (the usual picture of the tunneling systems) is incompatible with the rapid relaxation observed ($T_1 \sim 0.25$ s near 30 K).

It was proposed that a small fraction of the hydrogen atoms form H_2 molecules which serve as relaxation centers.[23] The model assumed (see below) that the H_2 were dilute, as in the study of H_2 in inert solids (above). The correlation rate ω_c of the *ortho*-H_2 molecules was assumed to arise from phonons (being dilute, EQQ interactions should be negligible). Thus, the model predicted a temperature-dependent relaxation rate T_1^{-1} of the *ortho*-H_2. The overall relaxation rate in the limit of rapid spin diffusion would be given by an equation similar to equation (1), with the protons covalently bonded to silicon in place of the HD protons. To account for finite spin diffusion, the above estimate must be modified:

$$(T_1)_{\text{overall}} = T_{\text{spin diffusion}} + (T_1)_{H_2} \frac{2[ortho\text{-}H_2] + \frac{3}{4}[H]}{2[ortho\text{-}H_2]} \qquad (2)$$

In equation (2), the right-hand term is the reciprocal of the overall T_1^{-1} from equation (1) (that is, $T_{1\text{overall}}$); the two terms are added as times because they are sequential processes, as shown in Figure 3.

With approximately 1% of the hydrogen atoms present as H_2 molecules, the model accurately describes the data. The value of $T_{\text{spindiffusion}}$ in equation (2) is in reasonable accord with calculations based on the assumed concentration of H_2. In fact, the spin diffusion bottleneck is crucial, because it explains

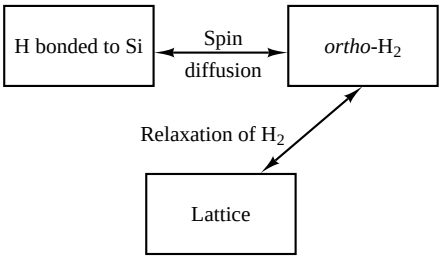

Figure 3 Relaxation of hydrogen atoms covalently bonded to silicon proceeds through two sequential steps. First, spin diffusion transports magnetization to and from the *ortho*-H_2 relaxation centers. Second, the *ortho*-H_2 relax to the lattice through phonon-induced transitions among the three sublevels of $J = 1$

the absence of a strong ($\sim \omega_0$) frequency dependence of the minimum value of T_1. Instead, the minimum T_1 is controlled by spin diffusion.

The ultimate test of the above model was performed by Carlos and Taylor.[24] Over a period of 3 months, an amorphous silicon sample was held at 4.2 K. Occasionally the sample was removed and its proton T_1 measured at temperatures near 30 K. The T_1 minimum remained at 30 K, but the minimum value of T_1 increased from 0.25 to 3.5 s as the H_2 relaxation centers *ortho–para* converted. Both terms in equation (2) are expected to increase as the *ortho*-H_2 becomes dilute through conversion. The minimum value of T_1 decreased rapidly during a 300 K 'anneal', showing reconversion of *para*-H_2 to *ortho*-H_2.

The observation of an *ortho–para* conversion rate in reasonable agreement with that in bulk solid H_2 suggests that the H_2 molecules are clustered. However, the dipole coupling between a covalently bonded hydrogen atom and an H_2 molecule would also result in *ortho–para* conversion, in the case of dispersed H_2. There is additional evidence of clustering from later work. If the H_2 molecules are in fact clustered, why is their τ_c determined by phonon-induced transitions instead of EQQ-driven flip-flops? If clustered, the EQQ-driven flip-flops must be quenched by different and strong crystal fields at neighboring molecules (similar to the quenching of nuclear spin diffusion near a paramagnetic impurity).

The observation of the effects of *ortho–para* conversion and reconversion on the proton T_1 is conclusive evidence of the role of H_2 as a relaxation center in amorphous silicon. At the time, there was no other evidence of H_2 in this material, nor was there acceptance of the notion.

6.3 H_2 Relaxation Centers from Metal Hydrides

Many metals are capable of absorbing large amounts of hydrogen (see ***Hydrogen–Metal Systems***). The hydrogen dissociates and occurs as individual protons at interstitial sites in the metal lattice. The principal mechanisms of proton spin relaxation are through hydrogen diffusion and the Korringa mechanism.[25] But in many metal hydrides there is an additional and strong relaxation mechanism that appears at high temperatures (typically above 1273 K). The identity of the anomalous relaxation has been a lively issue.

In one hydrogen–metal system, $Nb_{0.5}V_{0.5}H_{0.36}$, it has been demonstrated that the anomalous relaxation is due to the diffusion of hydrogen to the surface of the small metal particles (necessarily small to allow penetration of the rf fields), surface recombination to yield H_2 gas, and rapid relaxation of H_2 in the gas.[26] This seems remarkable because the density of protons in the gas phase is only $\sim$ 1% of that in the metal host. At typical temperatures, the H_2 vapor pressure is a few atmospheres.

The most conclusive experiments on the anomalous relaxation were conducted with argon gas overpressures applied to the metal hydride. Argon pressures of only $\sim$ 30 atm served to reduce the anomalous relaxation rate by a factor of 4; such a large effect could not possibly arise from the minuscule compression of the metal hydride solid itself. Instead, the increase in T_1 is due to the increased rate of scattering of *ortho*-H_2 molecules upon addition of argon to the gas phase surrounding the particles. A simple model yields a good fit to the variation of T_1 with argon overpressure, the change in proton T_1 upon 90% deuterium substitution, and the temperature dependence of the anomalous relaxation.

Because of its large spin interactions, the H_2 molecule functions as a relaxation center in the gas phase. At these high temperatures, physical diffusion and surface exchange rapidly transport the magnetization through the solid.

7 MULTIPLE ECHOES

The deuteron spin in HD has an electric quadrupole interaction with the charges in the molecule and a magnetic dipole interaction with the proton spin. These interactions have the same angular dependence. An important result is that any molecular motion will have the same averaging effect on the two interactions, so their ratio will be unchanged.

The quadrupole interaction splits the Zeeman lines, resulting in a symmetric spectrum with lines at $\omega_0 \pm \omega_Q$. The dipole interaction with the proton (assumed to be up) shifts these lines by ω_D, resulting in a two-line spectrum at $\omega_0 \pm \omega_Q + \omega_D$. A different HD molecule with its proton down generates two lines at $\omega_0 \pm \omega_Q - \omega_D$. So, a sample of HD (at least partially oriented so ω_Q and ω_D are not averaged to zero) contains four lines—a double doublet. The overall spectrum is symmetric about ω_0, though this is not so for the spectra of individual molecules. In a powder, the spectrum will be a pair of Pake doublets; the ratio of their splittings will be $(\omega_Q + \omega_D)/(\omega_Q - \omega_D)$, outer doublet to inner doublet. For HD, where the interactions are know accurately from molecular beam work, this ratio is 1.72.

Consider the response of a deuteron in HD (with proton up) to a two-pulse sequence (Figure 4). A component of the spin coherence will dephase after the first pulse by running at the lower transition frequency $(\omega_0 - \omega_Q + \omega_D)$; we will consider the portion at the upper frequency later. The second pulse has two effects. Part of the coherence is phase inverted and continues to run at the lower frequency, forming an echo at 2τ. Part of the coherence is moved to the higher-frequency transition $(\omega_0 + \omega_Q + \omega_D)$, so that it rephases faster $(\omega_Q + \omega_D)$ than it dephased $(|-\omega_Q + \omega_D| = \omega_Q - \omega_D$, as $\omega_D < \omega_Q$ here). This part of the coherence is refocused at a time t^* after the second pulse: $t^* = \tau(\omega_Q - \omega_D)/(\omega_Q + \omega_D)$. That is, this echo is early! Similar consideration of the coherence starting at $\omega_0 + \omega_Q + \omega_D$ and ending at $\omega_0 - \omega_Q + \omega_D$ (rephases slower than it dephased) leads to a late echo, at $t^* = \tau(\omega_Q + \omega_D)/(\omega_Q - \omega_D)$.[27] Similar treatment of the case with proton down yields the same times of echo formation. The above reasoning can easily be framed in terms of the density matrix; these echoes

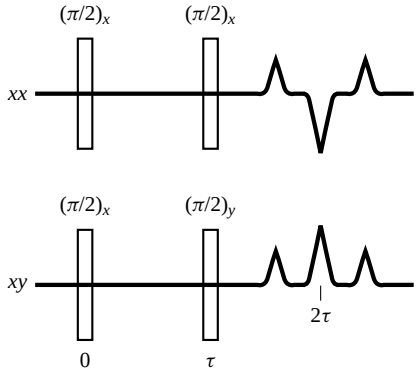

Figure 4 Sketch of deuteron multiple echoes from HD molecules, in response to a pair of rf pulses. The cases *xx* and *xy* refer to the rf phases of the pulses

are similar to the multiple echoes observed by Solomon[28] in a purely quadrupolar case.

Thus, echoes are expected as shown in Figure 4 at the usual times 2τ, 1.58τ, and 2.72τ (here 0.58 = 1/1.72). The echoes are observed in an amorphous silicon sample[27] with HD and for HD adsorbed on MgO[29] at 1.56τ, τ, and 2.78τ, in good agreement. Presumably, the molecular parameters leading to ω_Q and ω_D are slightly perturbed in the solid state.

In *para*-D_2 with total nuclear spin $I = 1$, only the 2τ echo is predicted and observed. But *ortho*-D_2 (even J and $I = 0$ and 2) yields three echoes, just like HD. The correct treatment of the problem requires the energies of the six spin states and the transition frequencies to be calculated. There are two states of $m_I = 0$, which are linear combinations of $I = 0$ and $I = 2$, $m_I = 0$. In other words, I is not a good quantum number in *ortho*-D_2. Multiple echoes are predicted at the times 1.86τ, 2τ, and 2.17τ, in good agreement with observations in deuterated amorphous silicon[27] and with D_2 absorbed on MgO (see below).[29] The early and late echoes are closer to the 2τ echo, because the dipole interaction is smaller in D_2 than in HD.

The behavior of the echoes with respect to the phases of the rf pulses is sketched in Figure 4 and agrees with a calculation invoking the density matrix. By adding or subtracting the echoes from *xx* and *xy* pulse sequences, one can obtain just the early and late echoes or just the 2τ echo.

The explanation of the multiple echoes is so natural that one may wonder why multiple echoes are not commonly observed in other systems. Quadrupole and dipole interactions are required, with identical angular dependences. Furthermore, neither interaction can be overwhelmingly larger than the other, because this will lead to the three echoes all occurring very near 2τ. A likely candidate is a deuteron bonded to a ^{13}C in an organic molecule. Still, the dipole interaction will be much smaller than in HD or even D_2, so the extra echoes will occur quite near the 2τ echo.

8 PHYSISORBED HYDROGEN

Here, two-dimensional (2D) H_2 films are discussed. The H_2 (or HD or D_2) has been adsorbed (see ***Adsorbed Species: Spectroscopy and Dynamics***) by van der Waals forces onto a smooth, clean, uniform substrate. In order to obtain observable signal intensities, the substrate cannot be a cleaved single crystal, but is a high-area powder which, nevertheless, has surfaces that are smooth on the atomic scale. The emphasis of the work discussed is on 2D phases and phase transitions. This is in contrast to work which emphasizes molecular orientation on the substrate and is aimed at understanding surface chemistry (see ***Supported Metal Catalysts***).

8.1 H_2 and D_2 Adsorbed on Graphite

The goal of this work was to study the orientational ordering phase transition (see Figure 2) in 2D. At the coverages employed by Kubik, Hardy, and Glattli,[30] the H_2 forms a commensurate (registered, epitaxial) monolayer above the graphite basal plane. Because the critical concentration for long-range orientational ordering is large even in 3D (see Figure 2), H_2 and D_2 enriched in the $J = 1$ species were used. That is, the $J = 1$ concentration was increased to nearly 100%, much larger than the 75 and 33% high-temperature limiting values for H_2 and D_2 in thermal equilibrium, respectively.

There are two important anisotropic interactions acting on the H_2 molecules. First, the crystal field from the substrate may tend to align the molecular axis perpendicular or parallel to the surface. For the symmetry of a graphite surface and at the registered sites, the crystal field is expected to be axially symmetric. This will split one of the degeneracies of the three $J = 1$ sublevels, leaving two states degenerate. The other important interaction is the coupling from one molecule to the next, which should be predominantly EQQ. The molecular orientations result from the interplay of the two interactions. This can be understood by regarding H_2 as a classical rotor characterized by $J = 1$. For example, if the crystal field is large and establishes an orientation of the H_2 perpendicular relative to the surface, there is no degeneracy for the EQQ interactions to lift, and no ordering phase transition. For a large crystal field preferring the H_2 molecules to lie in the substrate plane, the coupling between the molecules will split the degenerate (planar) orientations, with a phase transition to the herringbone structure.

NMR experiments on such samples are carried out in a continuous wave mode to avoid heating of the somewhat conductive Grafoil substrate. Because the samples *ortho–para* convert and because the enriched $J = 1$ samples are difficult to make, the experiments are quite difficult.

Near 0.6 K, H_2 with $c = 0.9$ undergoes a sharp phase transition. The orientations of the molecules on the substrate were determined by using oriented stacks of Grafoil, thus avoiding a powder average. With the magnetic field perpendicular to the Grafoil planes, there are peaks in the proton NMR corresponding to molecules perpendicular to the field (i.e. in the plane) and molecules parallel to the field (normal to the plane). The relative intensities agree with the pinwheel structure. Surprisingly, D_2 with high $J = 1$ concentration did not display an orientational ordering transition. It is not understood why the isotopes should behave so differently.

8.2 HD Adsorbed on MgO

MgO can be prepared from magnesium ribbon to yield cubes of $\sim$ 40 nm per side with atomic smoothness. This substrate

is preferable to graphite/Grafoil for NMR, because it is not magnetic and because it is not conductive. MgO can have almost as large a specific area as Grafoil ($\sim 25\,m^2\ g^{-1}$).

For coverages $x \leq 0.85$ ($x = 1$ is a compressed monolayer) and $T \approx 5\,K$, the deuteron resonance of HD on MgO[29] displays a pair of Pake doublets—a double doublet. This is due to the combination of the deuteron quadrupole interaction and the proton–deuteron intramolecular dipole coupling (see above); the ratio of the splittings is 1.78, as expected. At these two temperatures, HD is in its rotational ground state ($E = 128\,K$ for $J = 1$). If this were a pure $J = 0$ (spherical) state, the quadrupole and dipole couplings would be zero. The existence of the doublets then demonstrates that the rotational ground state has a substantial admixture of higher J states, resulting from the strong crystal field of the ionic substrate. By comparison, the crystal fields acting on $J = 1$ H_2 and D_2 on graphite are only $\sim$2 K.[30]

The splitting value indicates that $\bar{P}_2 = < \frac{3}{2}\cos^2\theta - \frac{1}{2} \rangle = 0.15$ for HD on MgO. This may be compared with $P_2 = 0$ for $J = 0$ and $P_2 = 0.4$ for $J = 1$, $m = 0$. Thus, there are large numbers of higher J states for HD on MgO, implying strong crystal fields ($\sim$50 K). Importantly, the crystal field will be different at different sites, as will the splitting.

For $x \leq 0.60$ and $T \simeq 5\,K$, the splittings are essentially constant, with a single set of double doublets. This demonstrates that all molecules occupy equivalent substrate sites (commensurate structure) in an island growth regime. The structure is $c(2 \times 2)$, and the area per molecule agrees with the limiting coverage of 0.60. Motional averaging is ruled out by the unchanged spectrum down to 1.8 K at $x = 0.48$.

For $0.60 < x \leq 0.85$, the spectrum is still a single set of double doublets, but with splittings that decrease $\sim$ 20% from $x = 0.60$ to $x = 0.85$. Together, these imply motional averaging over inequivalent sites. This is remarkable at the temperatures (4–6 K) of the observations. The decrease in splitting with increasing coverage reflects an increasing fraction of sites with smaller crystal fields. This explanation (motional averaging) is confirmed by broadening of the lines at reduced temperatures. For example, at $x = 0.73$, broadening is evident already by 4.2 K. For $0.9 \leq x \leq 1.0$, the deuteron NMR line is broad and featureless. Evidently, a broad distribution of sites results in a distribution of splittings. Whatever avenue of motion and motional averaging is available for lower coverages is blocked at these higher densities. The analogy of a filled parking garage may be relevant.

Coverages greater than $x = 1$ yield multilayers. For example, $x = 1.5$ corresponds to a full monolayer, with half of it covered by a second layer. The deuteron NMR spectrum of the first layer is broad and featureless, as found for $0.9 \leq x \leq 1.0$. The signal of the second layer, however, is a sharp, single line. Second layer HD molecules are far from the MgO and feel a much weaker crystal field, so their rotational state is nearly pure $J = 0$; a sharp NMR line is the result. Thus, deuteron NMR allows an unambiguous separation of first-layer and second-layer molecules.

A sample of $x = 0.5$ HD plus $x = 1.0$ H_2 was mixed, adsorbed, annealed at 40 K, and recooled. The deuteron NMR (only from HD) consisted only of a broad line. This proves that all of the HD was in the first layer, with the H_2 in both layers. A sample of $x = 0.4$ HD plus $x = 1.1$ D_2 was similarly prepared. The deuteron NMR signal here comes from both species, so they are harder to distinguish. But multiple echoes (see above) are observed only from first-layer molecules, because of the long T^*_2 of the second layer. For this mixture, the multiple echoes occurred only at the times appropriate for *ortho*-D_2, and not for the times appropriate for HD. Thus, all of the first-layer molecules are D_2.

These remarkably complete isotope separations are believed to result from zero-point motion effects. The binding of a hydrogen molecule to a substrate will decrease in the order D_2, HD, H_2, the order of increasing vibrational frequency above the substrate and increasing zero-point motion. Thus, the more massive molecules will be found in the first layer and the less massive in the second layer, to the extent permitted by the starting composition.

9 RELATED ARTICLES

Gas Phase Studies of Intermolecular Interactions and Relaxation; Gases at High Pressure; Hydrogen–Metal Systems; Ortho–Para Hydrogen at Low Temperature.

10 REFERENCES

1. N. Bloembergen, E. M. Purcell, and R. V. Pound, *Phys. Rev.*, 1948, **73**, 679.
2. F. Reif and E. M. Purcell, *Phys. Rev.*, 1953, **91**, 631.
3. A. Abragam, *The Principles of Nuclear Magnetism*, Oxford University Press, London, 1961.
4. I. F. Silvera, *Revs. Mod. Phys.*, 1980, **52**, 393.
5. P. C. Souers, *Hydrogen Properties for Fusion Energy*, University of California Press, Berkeley, CA, 1986.
6. N. F. Ramsey, *Molecular Beams*, Oxford University Press, London, 1956.
7. L. I. Amstutz, H. Meyers, S. M. Myers, and D. C. Rorer, *Phys. Rev.*, 1969, **181**, 589.
8. N. Boden, *The Plastically Crystalline State*, ed. J. N. Sherwood, Wiley, New York, 1979, Chap. 5
9. T. A. Scott, *Phys. Rep.*, 1976, **27**, 89.
10. F. Weinhaus and H. Meyer, *Phys. Rev. D*, 1973, **7**, 2974.
11. N. S. Sullivan, *Can. J. Chem.*, 1988, **66**, 908.
12. J. Van Kranendonk, *Solid Hydrogen*, Plenum Press, New York, 1983.
13. H. Meyer, *Can. J. Phys.*, 1987, **65**, 1453.
14. W. N. Hardy and A. J. Berlinsky, *Phys. Rev. B*, 1973, **8**, 4996.
15. W. N. Hardy, *Can. J. Phys.*, 1966, **44**, 265.
16. M. S. Conradi, K. Luszczynski, and R. E. Norberg, *Phys. Rev. B*, 1979, **19**, 20.
17. M. S. Conradi, K. Luszczynski, and R. E. Norberg, *Phys. Rev. B*, 1979, **20**, 2594.
18. R. F. Buzerak, M. Chan, and H. Meyer, *J. Low Temp. Phys.*, 1977, **28**, 415.
19. P. A. Fedders, *Phys. Rev. B*, 1979, **20**, 2588.
20. J. Van Kranendonk and M. B. Walker, *Can. J. Phys.*, 1968, **46**, 2441.
21. J. Ganem, P. A. Fedders, and R. E. Norberg, *Phys. Rev. B*, 1993, **47**, 2581.
22. W. N. Hardy and J. R. Gaines, *Phys. Rev. Lett.*, 1966, **17**, 1278.
23. M. S. Conradi and R. E. Norberg, *Phys. Rev. B*, 1981, **24**, 2285.
24. W. E. Carlos and P. C. Taylor, *Phys. Rev. B*, 1982, **25**, 1435.

25. C. P. Slichter, *Principles of Magnetic Resonance*, Springer-Verlag, New York, 1990.
26. D. B. Baker, M. S. Conradi, R. E. Norberg, R. G. Barnes, and D. R. Torgeson, *Phys. Rev. B*, 1994, **49**, 11 773.
27. M. P. Volz, P. Santos-Filho, M. S. Conradi, P. A. Fedders, R. E. Norberg, W. Turner, and W. Paul, *Phys. Rev. Lett.*, 1989, **63**, 2582.
28. I. Solomon, *Phys. Rev.*, 1958, **110**, 61.
29. E.-K. Jeong, B. Ouyang, R. E. Norberg, P. A. Fedders, and M. S. Conradi, *Phys. Rev. Lett.*, 1992, **69**, 2983.
30. P. R. Kubik, W. N. Hardy, and H. Glattli, *Can. J. Phys.*, 1985, **63**, 605.

Acknowledgments

The author gratefully acknowledges crucial collaborations with R. E. Norberg and P. A. Fedders. Some of the work described was performed by several dedicated students, now colleagues. The support of NSF grant DMR 90-24502 is appreciated.

Biographical Sketch

Mark S. Conradi. *b* 1952. B.S., 1973, Ph.D., 1977, Washington University, USA. Postdoctoral work at Oak Ridge National Laboratory, USA (with Ralph Livingston), studying free radicals by ESR. Assistant and associate professor at College of William and Mary, USA. Currently professor at Washington University. Approx. 80 publications. Research interests: orientational glasses, metal hydrides, high-pressure NMR, and new techniques for NMR.

Hydrogen–Metal Systems

David R. Torgeson
Iowa State University, Ames, IA, USA

1	Introduction to NMR of Hydrogen–Metal Systems	1
2	Hydrogen Motion in Metals Detected by NMR	2
3	Dynamic Studies of Hydrogen Motion in a Metal	2
4	Deuteron Lineshape for Combined Electric Quadrupole and Knight Shifts	5
5	Low Temperature Local Hydrogen Motion and Hydrogen Tunneling in HMSs	7
6	Spin–Lattice Relaxation in Amorphous Hydrogen–Metal Systems	8
7	Related Articles	9
8	References	9

1 INTRODUCTION TO NMR OF HYDROGEN–METAL SYSTEMS

The exposure of hydrogen to metals often produces significant changes in the physical properties of those metals. The absorption of hydrogen into interstitial lattice sites between metal atoms causes metallic materials to expand their volume, changes the crystal structure, and may change the electronic structure or electrical character of the material. Unable to withstand the strain, some metals fracture into powder, sometimes a useful method of producing powder of ductile metals, but at other times a possibly disastrous result as in the case of hydrogen embrittlement of steels. All the materials included in hydrogen–metal systems (HMSs) are occasionally incorrectly referred to as metal hydrides. As we will see below, metal hydrides do make up the majority of materials in HMSs. Metal hydrides can be either covalent, ionic, or metallic[1] in nature. We will confine our attention to metallic hydride materials.

One of the earliest NMR studies of hydrogen in metals was done some 40 years ago by R. E. Norberg,[2] who applied hydrogen to the palladium metal wires which made up the rf coil of his NMR probe. Linewidth, Knight shift, and relaxation times of the hydrogen in the rf skin depth of the palladium wires were studied by continuous wave and spin echo techniques.

Some of the most basic NMR studies of HMSs have been the investigation of the underlying physical principles governing hydrogen location and motion at the atomic or 'microscopic' level. Long-range hopping or diffusion of hydrogen is currently understood in terms of thermally activated, over the barrier hopping between interstitial lattice sites, which will be discussed, in part, below. Pulse magnetic field gradient NMR to measure hydrogen (and other atomic) diffusivities is discussed elsewhere (see ***Diffusion in Solids***). Attempts to characterize tunneling of hydrogen at low temperatures between interstitial vacancies in metals at low temperatures by NMR will be discussed briefly here.

Although NMR is a powerful tool for observing hydrogen interactions in HMSs, interpretation of NMR data cannot be done properly without other knowledge of the materials. Crystal structure and phase diagram results from X-ray, neutron diffraction,[3] and detailed magnetic information from susceptibility measurements are often crucial to the interpretation of NMR results of HMS.

Many of the applied NMR studies of hydrogen, deuterium, and tritium in HMSs have been undertaken to determine the location and motions of hydrogen within the metallic materials in efforts to characterize and improve the hydrogen–metal materials for applications such as purification of hydrogen, hydrogen isotope separation, and hydrogen storage for fuel or energy storage (batteries); or closed cycle, metal hydride refrigerators for remote or applications to vehicles in space.[4]

HMSs include elemental metals, MH_x, with small concentrations of hydrogen, e.g. $x < 0.01$, dissolved in the host material with hydrogen located in interstitial vacancies without significant change in the crystal structure of the metal host, M. These materials are referred to as hydrogen (metal) solid solution (α) phases. The solubility of hydrogen in metal solid solutions often diminishes rapidly with decreasing temperature, forming metal hydride precipitates at lower temperatures. High hydrogen concentrations, x = H/M, often extend to x = 3 or 4 for metal hydrides, e.g. LaH_3, SnH_4, and PbH_4, where the crystal structure of the hydride (β or γ) phase, e.g. face centered cubic (fcc) (or CaF_2 structure) for YH_2, is usually quite different from the parent metal, e.g. hexagonal close packed (hcp) for Y, and the density of the metal hydride typically is less than the parent metal density. Intermediate hydrogen concentration samples may be mixed hydrogen–metal solid solution α and metal hydride β phases. The observed NMR spectra and nuclear spin–lattice, R_1, and spin–spin, R_2, relaxation rates as functions of temperature may give evidence of the mixed phases (see ***Phase Transitions and Critical Phenomena in Solids***).

HMSs include hydrogen solid solutions of elemental metals, binary metal alloys, and intermetallic compounds, and also hydrides of metals, alloys, and intermetallic compounds. In addition, metallic halide compounds[5] and metal sulfides[6] adsorb hydrogen to significant degrees and should be included in HMSs. Some alloys and intermetallic compounds do not survive the hydriding process, but will disproportionate into hydrides of one or more of the metals and other compounds. In these cases, the hydride of the constituent metal is more stable than the hydride of the parent material.

Most NMR hydrogen–metal studies are made with samples sealed in quartz tubes to prevent loss of hydrogen upon heating the samples and to prevent oxidation or other contamination. Generally, the metallic nature of the materials requires powdered samples (particle size $\leq 100\,\mu$m) to permit the $\boldsymbol{B}_1$ rf magnetic field to penetrate the metallic particle's 'rf skin depth' uniformly. The spaces between powder particles contain hydrogen gas molecules which represent a characteristic hydrogen over pressure of the particles typical for that material, nominal hydrogen concentration, and sample temperature. The hydrogen gas molecules between particles are in constant exchange with the hydrogen atoms or ions within the metallic particles. The hydrogen exchange rate is often quite low for room temperature, but may be many orders of magnitude greater for $T > 700$ K.

The density of the hydrogen inside some hydrogen storage materials, e.g. $LaNi_5H_6$, is greater than the hydrogen density in liquid hydrogen by a factor of two or three. Generally, the

hydrogen density in the metallic powders is many orders of magnitude greater than the density of gas molecules between powder particles. Thus, the observed hydrogen spectrum is typically the spectrum of the hydrogen in the metal only. Recently, anomalously high proton spin–lattice relaxation rates, R_1, observed for $T > 700\,\mathrm{K}$ within the metal particles[7] have been understood in terms of exchange between bulk hydrogen atoms in the metallic powder and the much faster relaxing hydrogen gas molecules between the metallic powder particles[8] (see ***Hydrogen Molecules***).

2 HYDROGEN MOTION IN METALS DETECTED BY NMR

The early measurements of Norberg[2] demonstrated the motion of hydrogen in palladium. HMSs have been studied by NMR beginning with wideline CW methods measuring rigid lattice or low temperature linewidths and lineshapes. The low temperature or rigid lattice hydrogen linewidth originates from the magnetic interactions of the nuclear dipoles in the solid HMSs. Narrowing of the spectral lines with increasing temperatures gave clear evidence of hydrogen motion or hopping into interstitial vacancies within the solid.[9] This rapid hopping of hydrogen results in a simple averaging of the local magnetic field $\boldsymbol{B}_\mathrm{L}$ or the distribution of magnetic fields 'seen' by the hopping proton magnetic dipole moment. These motional narrowing studies yielded activation E_a energies of diffusion and moderately precise estimates of hydrogen jump frequencies, $\nu_\mathrm{j}(T)$, or alternately, of hydrogen 'dwell times' or mean residence time, $\tau_\mathrm{D}(T) = 1/\nu_\mathrm{j}(T)$, and hydrogen correlation times, $\tau_\mathrm{c}(T)$. With increasing T, when the average hydrogen jump frequencies exceeded the rigid lattice linewidth, the observed spectral lines narrowed. The temperature range for line-narrowing measurements was generally less than 100 K; Figure 1 from Schreiber and Cotts[10] shows multiple line-narrowing graphs of LaH_{2+x} against temperature. Lanthanum hydride shows the unusual ability to absorb hydrogen between compositions LaH_2 and LaH_3, maintains an fcc structure, and with each additional hydrogen, every hydrogen atom jumps more rapidly. In most HMSs, with increasing temperature, the average hydrogen jump frequency can easily exceed the proton resonance frequency.

The proton linewidths versus temperature[11] in zirconium chloride hemihydride ($ZrClH_{0.5}$) and zirconium chloride monohydride (ZrClH) are shown in Figure 2. This transition metal halide structure consists of two zirconium metal layers sandwiched between two chlorine layers. Hydrogen is known to reside in interstitial tetrahedral sites between the two zirconium metal layers. In addition, the crystal structures for the hemi- and monohydrides are know to be slightly different, due to the presence of the hydrogen in the material.[12]

Indirect evidence of hydrogen (deuterium) hopping was also observed on studying the ^{93}Nb electric quadrupole perturbed, NMR satellite line narrowing in $NbH_{0.73}$ and $NbD_{0.82}$ with increasing temperature.[13] Figure 3 shows the narrowing of the inhomogeneously broadened ^{93}Nb NMR satellite linewidth. This narrowing can be understood in terms of reducing the randomness (inhomogeneity) of the average value at the niobium ion sites due to the increased rapidity of the hopping motion of the hydrogen (deuterium) ions with temperature and their associated electrical charges in the vicinity of the niobium ion sites. The reduced average EFG at the ^{93}Nb site yielded a narrower NMR satellite linewidth. Thus, the stationary niobium NMR showed evidence of the mobile hydrogen (deuteron) ions hopping.

3 DYNAMIC STUDIES OF HYDROGEN MOTION IN A METAL

The magnetic dipole interactions of hydrogen with other hydrogen magnetic moments, with the host metal nuclear

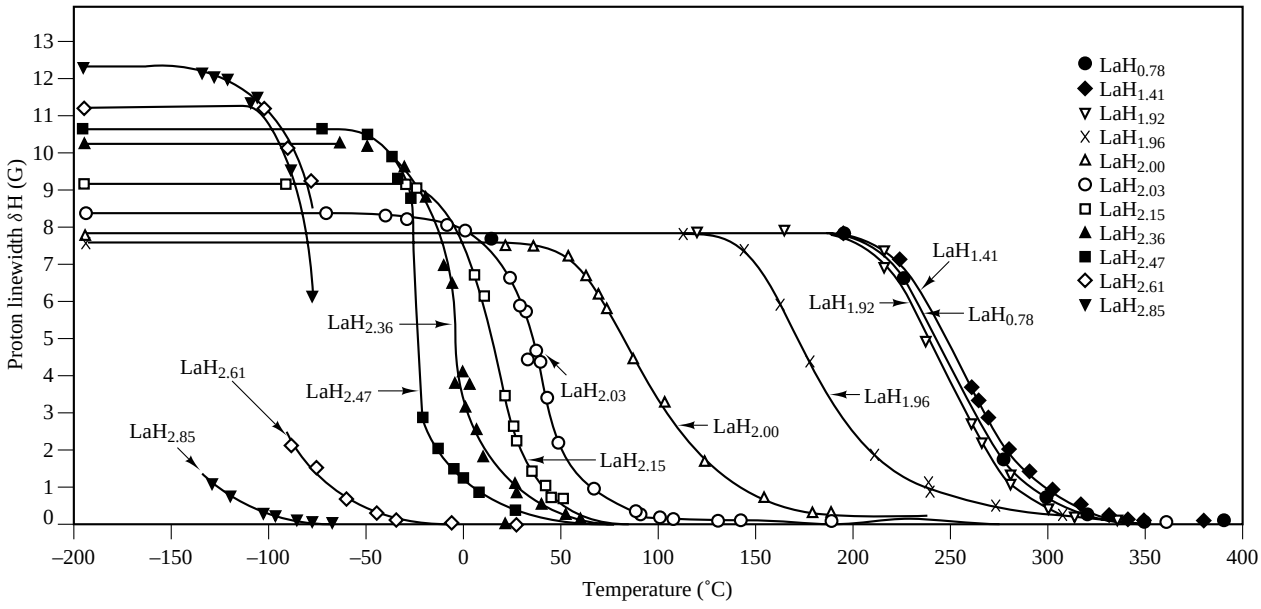

Figure 1 Proton linewidths (1G = 10^{-4} T) plotted against T for different x values. (Reproduced by permission of the American Physical Society from Schreiber and Cotts[10])

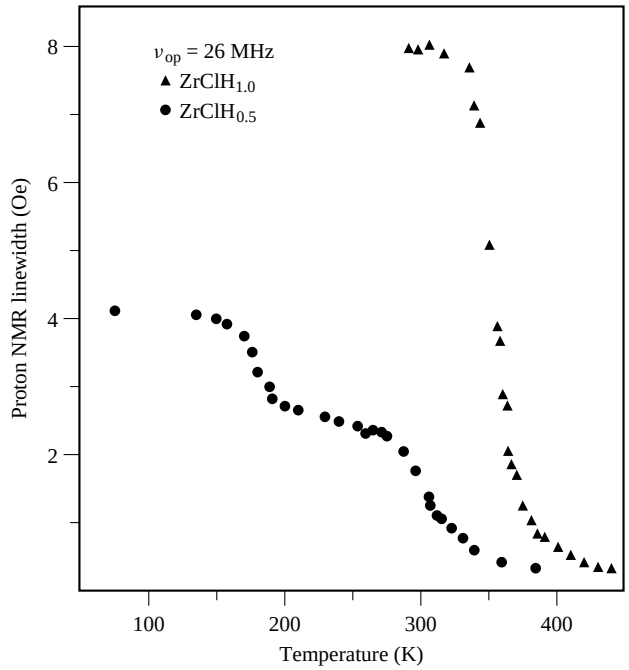

Figure 2 Temperature dependence of the proton linewidth in the two hydride phases of ZrCl, measured at nominal resonance frequency of 26 MHz. (Reproduced by permission of Elsevier Science Publishers B.V. from Hwang et al.[11])

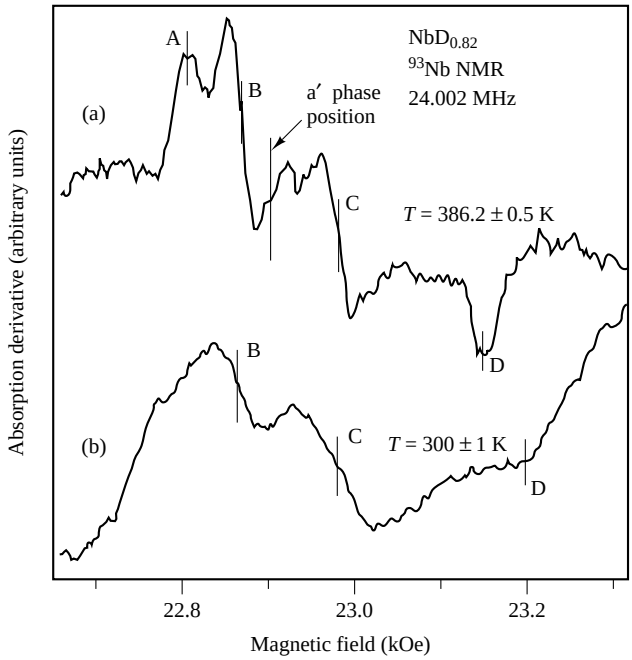

Figure 3 Wide line absorption derivative spectra of ^{93}Nb for 300 and 386 K. At 386 K hydrogen jumping rates are sufficiently fast to produce a spatial average of the electric field gradient at the Nb metal sites which narrows the spectra. (Reproduced by permission of Elsevier Science, Inc., from Hwang et al.[13])

moments, paramagnetic impurity moments, and with conduction electron magnetic moments generally govern the flow of spin energy within HMSs. Cross relaxation of protons and host metal nuclei having large nuclear electric quadrupole interactions has been observed. Also, as shown below, the hopping deuteron can be relaxed by interactions of its electric quadrupole moment with fluctuating EFGs within the material.

The observed hydrogen spin–lattice relaxation rate $R_1(\omega, T)$ varies greatly with temperature in HMSs, and is often the sum of several independent $R_1(T)$ rates, each due to separate physical relaxation mechanisms active in the material. Fortunately, these several R_1 rates have different resonance frequency and/or temperature dependences. With this fact in mind, we shall see how one can separate these spin–lattice relaxation mechanisms and thereby begin to characterize the materials.

The observed hydrogen spin–lattice relaxation rate (HSLR) R_1, in general, may be the sum of several of the following rates:[14]

$$R_1 = R_{1d} + R_{1e} + R_{1p} + R_{1CR} \tag{1}$$

where R_{1d} is the magnetic dipole–dipole relaxation of the hydrogen due to other hopping hydrogen. Bloembergen, Purcell and Pound[15] (BPP) were first to suggest the form of relaxation

$$R_{1d} = \frac{1}{T_{1d}} = M_2(T)J(\omega_0, T) \tag{2}$$

where M_2 is a mean-square fluctuating field most commonly thought to be related to the magnetic dipole–dipole interaction of the hydrogen with other magnetic moments. However, in the case of the deuteron, this formalism can also be expressed in terms of the fluctuations of the EFG about the deuteron electric quadrupole moment.[16] In this case, R_{1d} is then written R_{1q} (q denoting quadrupolar relaxation). ω_0 is the spin precession frequency in angular frequency units. $J(\omega_0)$ is the power spectrum or spectral density function of the fluctuation magnetic fields (or fluctuating EFGs) within the sample. The simplest form of $J(\omega)$ is the Lorentzian

$$J(\omega) = \frac{\tau_c}{1 + \omega^2\tau_c^2} \tag{3}$$

where τ_c is the correlation time and is strongly temperature dependent. Often τ_c varies exponentially with temperature, where $\tau_c = \tau_0 \exp(-E_a/kT)$ and where $1/\tau_0$ is thought to be the attempt frequency of hydrogen jumping or the high temperature 'rattling' frequency of hydrogen within the interstitial site.

Equation (2) is often written with an additional Lorentzian term, including dipolar interaction terms at 2ω, as

$$R_{1d} = M_2(T)\left(\frac{\tau_c}{1 + \omega^2\tau_c^2} + \frac{4\tau_c}{1 + (4\omega^2\tau_c^2)}\right) \tag{4}$$

This simple description includes no details of the hydrogen interactions with metal nuclear moments or structure considerations of the HMS. It also ignores any orientation dependence of the crystal (sample) with the magnetic field $\boldsymbol{B}_0$ direction. Nonetheless, this BPP description is quite a good characterization of the hydrogen relaxation in many simple HMSs.

In a detailed description of hydrogen relaxation anisotropy in single crystal HMSs, Hoke et al.[17] gave the relaxation rate

of protons in an hcp single crystal of $ScH_{0.25}$ as

$$R_1 = \left(\frac{\mu_0}{4\pi}\right)^2 \gamma_H^2 \gamma_S^2 \left(\frac{h}{2\pi}\right)^2 S(S+1)\left(\tfrac{1}{12}J^{(0)}(\omega_H - \omega_S) + \tfrac{3}{2}J^{(1)}(\omega_H) + \tfrac{3}{4}J^{(2)}(\omega_H + \omega_S)\right) \quad (5)$$

following Abragam[18] where γ_H and γ_S are the gyromagnetic ratios of the hydrogen and metal, S is the spin (in this case, ^{45}Sc $S = \frac{7}{2}$), and $J^{(q)}(\omega)$ are spectral density functions which depend on the diffusion model chosen and on the orientation of the crystal in the magnetic field. Within the three spectral density functions $J^{(0)}$, $J^{(1)}$, and $J^{(2)}$ the frequencies $\omega_H - \omega_S$, ω_H, and $\omega_H + \omega_S$ are the difference between hydrogen and metal frequencies, the hydrogen frequency, and the sum of hydrogen and metal frequencies, respectively.

Interestingly, the anisotropy in R_1 originates in the anisotropy of $J^{(q)}(\omega)$, written by Sholl[19] as

$$J_{qq'} = \sum_{\alpha,\beta} \frac{Y_{2q}(\Omega_\alpha)}{r_\beta^3} \frac{Y_{2q'}(\Omega_\beta)}{r_\beta^3} P(r_\alpha, r_\beta, \omega) \quad (6)$$

where Y_{2q} are spherical harmonics, r_α is the distance between the proton and metal spin at time zero, and r_β is the distance between the proton and metal spin at time t. $P(r_\alpha, r_\beta)$ is the Fourier transform of the probability function for the diffusion model chosen.[17]

The conduction electron moments in the HMS relax the hydrogen moment through a contact hyperfine interaction the same as is associated with the Knight shift.[18,20] The relaxation rate R_{1e} is proportional to the temperature and the square of the Knight shift (see Section 4 for a simple description of the Knight shift) and the square of the density of unpaired electronic (moment) states at the Fermi energy $N(E_F)$. Generally, the better the conductivity of the metallic material the greater the electronic relaxation rate R_{1e}:

$$R_{1e} = \frac{1}{T_{1e}} \propto N^2(E_F)T \quad (7)$$

For a simple metallic material, combining the Knight shift with relaxation rate,

$$T_{1e}TK^2 = \frac{T}{R_{1e}}K^2 = \frac{h/2\pi}{4\pi k}\frac{\gamma_e^2}{\gamma_n^2} \quad (8)$$

where γ_e and γ_n are the electron and nuclear (hydrogen) gyromagnetic ratios. This equation is known as the Korringa or Heitler–Teller–Korringa (HTK) relation,[21] where the Knight shift and R_{1e}/T are theoretically constant in temperature and R_{1e}/T or $1/T_{1e}T$ is often used to characterize the electronic relaxation in HMSs.

Unwanted paramagnetic ion concentrations, ignored in several NMR studies of HMSs, have shown unusual, anomalous relaxation rates and 'extra features' in the measured HSLR which have been attributed to a fictitious complex or additional diffusion mechanism. Phua et al.[22] showed that many such unusual or extra relaxation mechanisms were most likely due to the existence of residual paramagnetic impurities (dirt) in the host metals present at the time of the formation of the HMS. That study showed, generally, that the extra spin–lattice relaxation rates, R_{1p}, were linearly proportional to the concentration of paramagnetic impurities present. In addition, extra minima in $\log(T_1)$ versus $1/T$ were a direct result of the impurity relaxation; see Figure 4 for evidence of the suppression of $\log(T_1)$ versus $1/T$ and 'extra minima'. The paramagnetic moments produce a relaxation rate R_{1p} in HMS and can relax hydrogen by spin diffusion at low temperature in the low hydrogen diffusion regime. At higher temperatures, in the fast diffusion regime, hydrogens approach the stationary paramagnetic ions by rapid hopping within the sample and are relaxed via direct dipolar interactions with the paramagnetic impurity ions.

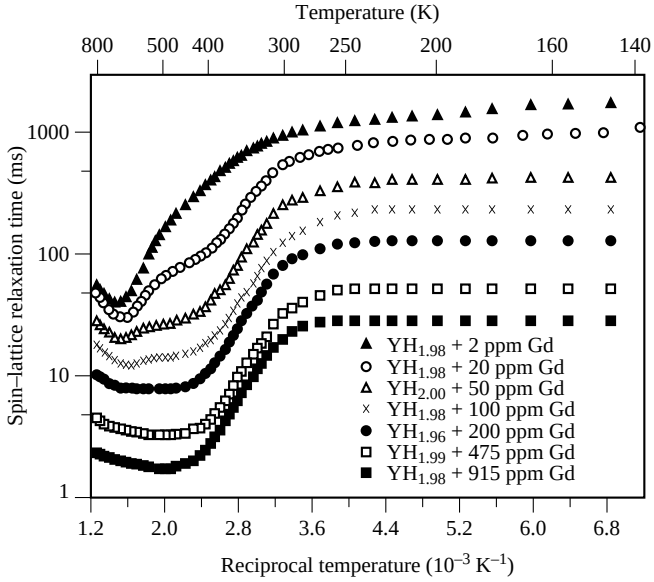

Figure 4 Proton spin–lattice relaxation time T_1 vs. $1000/T$ in YH_2 vs. Gd impurity concentration. (Reproduced by permission of American Physical Society from Phua et al.[22])

The cross relaxation of the proton, R_{1cr}, with certain host metal nuclei which have large electric quadrupole moments and subsequently large quadrupole interactions was recognized for protons in HMS at low temperatures (see Figure 5) where hydrogen hopping rates are slow. The strong nuclear electric quadrupole interactions of the metal nuclei, e.g. ^{175}Lu in $LuH_{0.20}$[23] and ^{181}Ta in Ta_2H[24] are many tens of megahertz in extent (width) and are only perturbed by the static magnetic field $\boldsymbol{B}_0$ required for proton resonance. Although the ^{93}Nb quadrupole moment and interaction in $V_xNb_{1-x}H_y$, for example, is weaker than ^{181}Ta in Ta_2H and ^{175}Lu in $LuH_{0.20}$, for frequencies $f_{max} < 24$ MHz, protons also cross relax to ^{93}Nb. When the proton resonance frequency matches one of the many spectral features of the metal NQR, spin polarization energy is transferred from the proton to the metal nucleus. The spin polarization energy is taken from the metal nucleus by the conduction electron interaction to the lattice because the contact hyperfine interaction is much stronger and thus faster (or higher rate) for the metal nucleus than for the proton. Figure 6 shows the proton cross relaxation to ^{181}Ta in $TaH_{0.32}$ as a function of proton resonance frequencies[24] (for a series of magnetic field values) while at $T = 130$ K. The calculation of the cross relaxation as a function of proton frequencies is described by Lichty et al.[24]

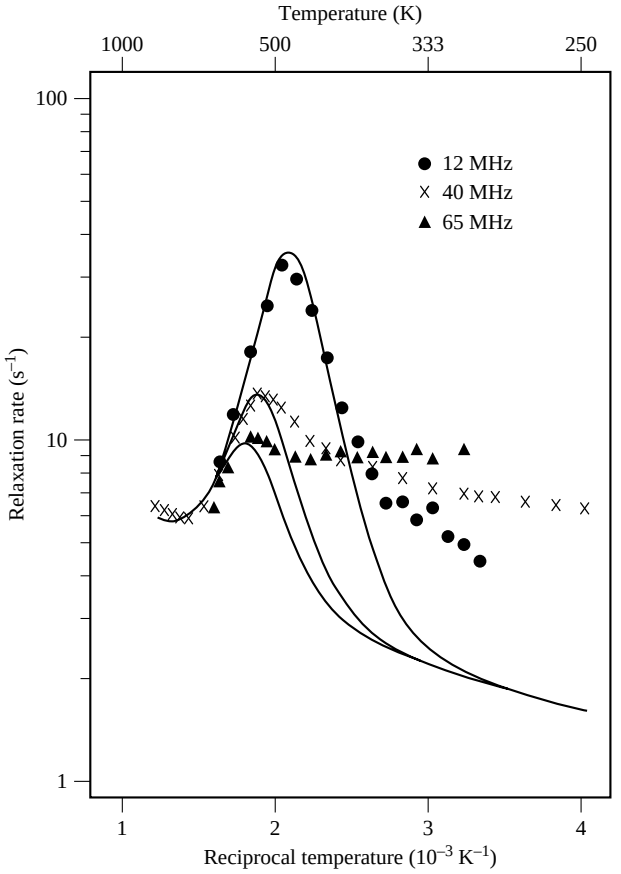

Figure 5 Proton spin–lattice relaxation rates R_1 vs. $1000/T$ in LuH_x at 12, 40 and 65 MHz. Cross relaxation between the protons and the ^{175}Lu nuclear electric quadrupole broadened NMR lines can be seen at low temperatures in the loss of temperature dependence for $T \leq 400$ K. (Reproduced by permission of R. Oldenbourg Verlag from Torgeson et al.[23])

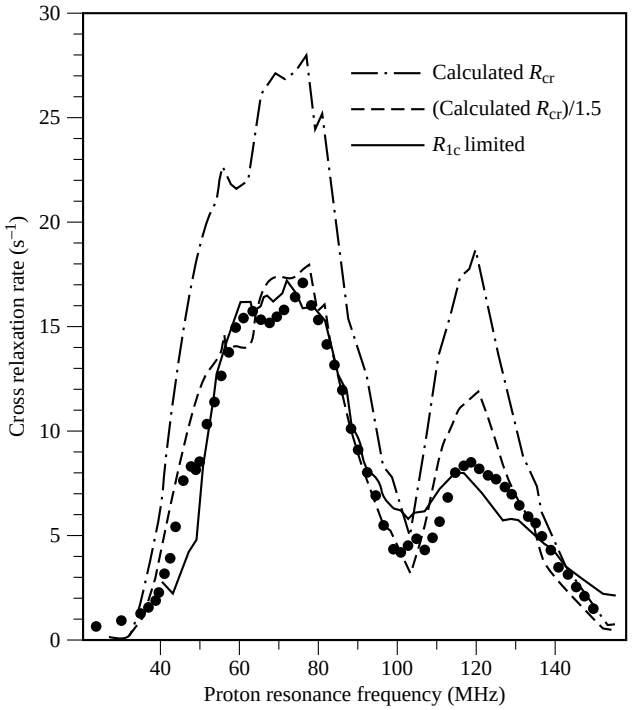

Figure 6 Proton cross-relaxation data (•) to ^{181}Ta nuclear electric quadrupole broadened NMR lines in Ta $H_{0.32}$ as a function of a series of proton resonance frequencies at 130 K. See Lichty et al.[24] for details of the theoretical calculations and the three curves presented. The analysis yielded a ^{181}Ta nuclear electric quadrupole frequency γ_Q = 43 MHz and electric field gradient asymmetry parameter η = 0.35. (Reproduced by permission of American Physical Society)

Figure 7 shows the total spin–lattice relaxation rate versus reciprocal temperature in schematic form, typical of many HMSs with the several component relaxation rates identified.

4 DEUTERON LINESHAPE FOR COMBINED ELECTRIC QUADRUPOLE AND KNIGHT SHIFTS

The Knight shift of hydrogen results from a small magnetic field at the hydrogen nucleus in an HMS from the conduction electron wave function $|\psi(0)|^2 \neq 0$ for the s electron character of the conduction electrons. This is often called the 'contact hyperfine interaction' or Fermi contact term. The application of the $\boldsymbol{B}_0$ field causes a small paramagnetic polarization of the conduction electrons, called the Pauli paramagnetism, where $M_s = \chi_s B_0$ and χ_s is the Pauli spin susceptibility. χ_s can be related to the density $N(E_F)$ of unpaired conduction electron states at the top of the conduction electron distribution or at the Fermi energy via the Pauli susceptibility $\chi_s = \frac{1}{2}(\gamma_e h)^2 N(E_F)$. The Knight shift can be written simply as $K \approx \chi_s |\psi(0)|^2/N$. The Knight shift causes a fractional change in the proton (deuteron) gyromagnetic ratio, that is, a small shift in position of the hydrogen resonance ΔH for fixed frequency or $\Delta\nu$ for fixed field measurements

$$K = \frac{\Delta H}{H} = \frac{H_R - H_M}{H_R} = \frac{\Delta\nu}{\nu} = \frac{\nu_M - \nu_R}{\nu_R} \qquad (9)$$

where subscript M refers to the metal field or frequency and R refers to the reference (solution or free ion) field or frequency. These fractional shifts are generally independent of the field or frequency.

Knight shifts of hydrogen in HMSs are generally quite small in magnitude compared with Knight shift values of metals, and often smaller in field shift magnitude ΔH than the dipolar broadened width or the $\boldsymbol{B}_L$ local magnetic field in the solid. However, the magnetic moment of the deuteron is smaller than the proton by a factor of 3.3, and effects of local magnetic fields are correspondingly smaller than for the proton. Figure 8 shows the combined effects of ^{2}D nuclear electric quadrupole interaction and Knight shifts[25] in a sample of $NbD_{0.76}$. The general subject of combined nuclear electric quadrupole interactions and Knight shift interactions in metals was first presented by Jones et al.[26] Since the ^{2}D spin I = 1, there are $2I$ + 1 or 3 levels and two transitions and no 'central line'. These two transitions for spin I = 1 are commonly referred to as the Pake doublet,[27] following the terminology established by George Pake in 1948 for the interaction of two coupled protons of combined spin I = 1 in the water of hydration in gypsum.

$NbD_{0.76}$ is orthorhombic in structure and thus the EFG and the Knight shifts must be described by tensors. The principal

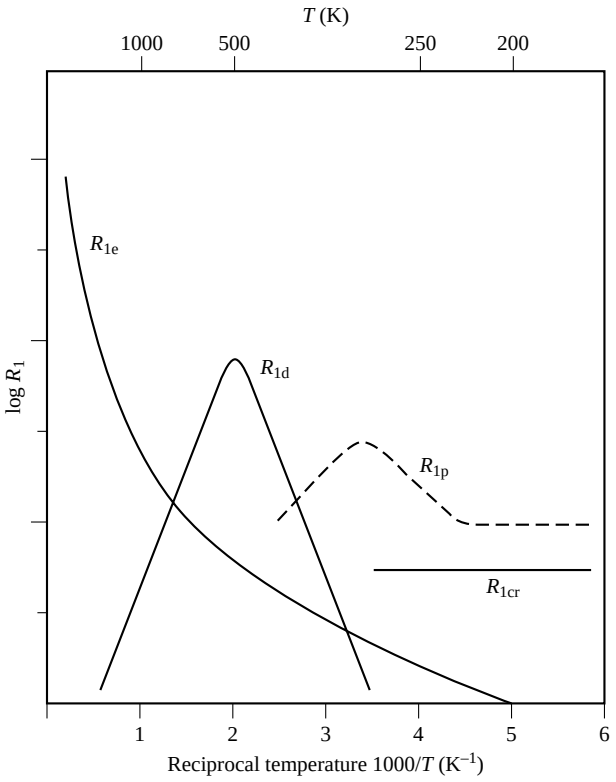

Figure 7 Generalized proton spin–lattice relaxation rate R_1 contributions vs 1000/T. These relaxation rates are: conduction electron, R_{1e}; long range diffusion/dipole–dipole, R_{1d}; paramagnetic impurity ion, R_{1p}; and cross-relaxation to quadrupole (metal) nucleus, R_{1cr}. The relative weighting of these mechanisms depends on the purity and physical details of the HMS sample studied

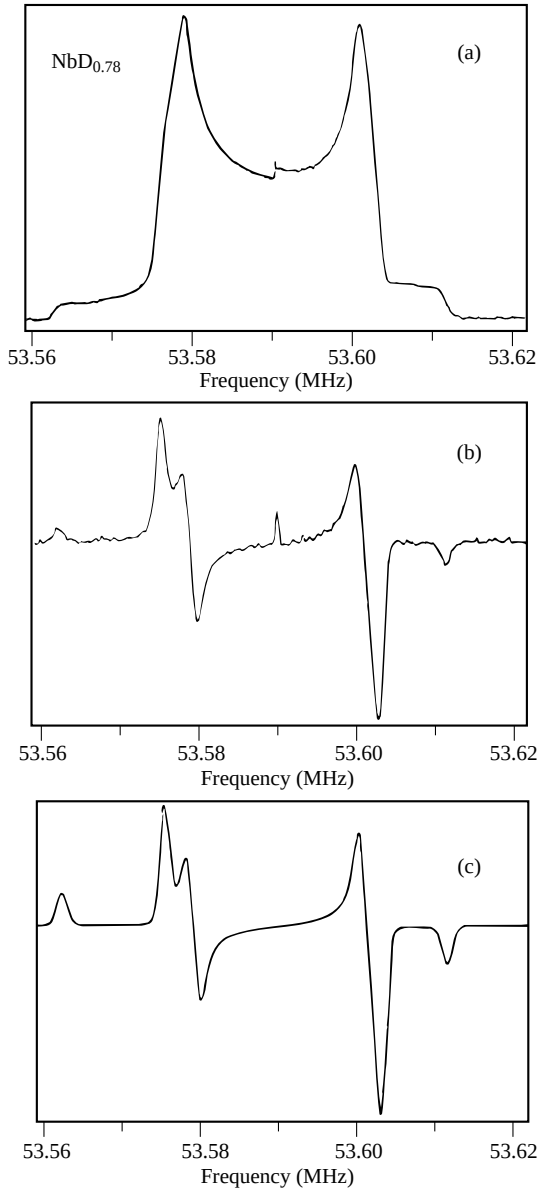

Figure 8 (a) Deuteron absorption curve vs. frequency for $NbD_{0.56}$, (b) derivative of observed deuteron absorption curve, and (c) calculated deuteron absorption derivative curve lineshape. (Reproduced by permission of Academic Press from Torgeson et al.[25])

axis system of the EFG has three separate components V_{xx}, V_{yy}, and V_{zz}, the second derivatives of the crystalline potential with respect to the coordinates x, y, and z. Note that $\nabla^2 V = V_{xx} + V_{yy} + V_{zz} = 0$ is Laplace's (electrical) equation. In the principal axis system, $|V_{xx}| < |V_{yy}| < |V_{zz}|$. The EFG asymmetry parameter for $NbD_{0.76}$ is $\eta = (V_{xx} - V_{yy})/V_{zz} = 0.11$. If η were equal to 0, then $V_{xx} = V_{yy}$ would require axial symmetry, i.e. at least three-fold rotational symmetry about the z axis. $\eta \neq 0$ implies the $\Delta m = \pm 1$ transitions $-1 \leftrightarrow 0$ and $0 \leftrightarrow +1$ in combination with the K_x, K_y, and K_z Knight shift components will produce different frequency dependences for the two transitions or ^{2}D 'powder' lineshapes.[25] The width of the pattern essentially measures the strength of the deuteron electric quadrupole interaction described by the lowest pure quadrupole frequency $\nu_Q = 3eQV_{zz}/2h = 49.3$ kHz, where eQ is the deuteron quadrupole moment, V_{zz} is the principal component of the EFG tensor and h is Planck's constant. Incidentally, $\nu_Q = 3eQV_{zz}/[2I(2I-1)h]$ is the best measure of the strength of the quadrupole interaction relative to the strength of the NMR interaction characterized by ν_0, the Larmor frequency.[28]

For powdered metal hydrides with less than cubic crystal symmetry, the single grain particles' major symmetry axes will simply point in random directions in space. However, with an applied magnetic field switched on, the majority of particles' major symmetry axes will be nearly perpendicular to the field direction and a small minority of crystal symmetry directions will point along the field direction. This produces the well known sin θ dependence of the distribution of powder particle orientations with respect to the magnetic field direction. As pointed out by Jones et al.[26] the major peaks of the absorption spectrum are due to 'singularities' at the perpendicular ($\theta = 90^\circ$) powder grains, and the smaller 'steps' at the extremes of the spectrum are due to those particle crystallites nearly parallel ($\theta = 0^\circ$) to the magnetic field.

The deuteron Knight shift, as for all hydrogen Knight shifts, originates from the contact hyperfine interaction of the conduction electrons at the deuteron (hydrogen) nucleus. In the HMS, the conduction electrons are attracted or 'cored' to the hydrogens in the same way conduction electrons are attracted to the metal nuclei. This, of course, makes the conduction electron wave functions more complex than in the pure metal, alloy, or intermetallic compound. The presence of

the hydrogen may actually change the electronic character of the HMS by changing the conduction electron wave functions and by the hydrogen donating an electron to the conduction band when hydrogen is absorbed, which may greatly modify the electronic band structure of the HMS.

The effect of the Knight shifts on the observed lineshape is simply a small displacement of the resonance position due to an additional magnetic field at the nucleus from the contact hyperfine interaction. For a non-cubic metal or HMS, the magnitude of the shift of the resonance is dependent upon orientation of the crystalline axes of the grain with respect to the field direction. Figure 8 (a) shows the observed absorption curve, (b) a derivative of the observed absorption and (c) a calculated absorption derivative with appropriate Knight shift and EFG components included. Absorption derivative lineshapes actually show more subtle lineshape features than do the absorption curves. Absorption derivatives lineshapes were commonly recorded in field or frequency scanned CW wideline studies in past years because of the use of lock-in amplifiers and small amplitude magnetic field or frequency modulation to record spectra.

5 LOW TEMPERATURE LOCAL HYDROGEN MOTION AND HYDROGEN TUNNELING IN HMSs

Scandium, yttrium, and lutetium plus other rare earth hcp metals provide a nearly unique opportunity to observe hydrogen dissolved in metals and measure hydrogen motions in metals at temperatures below 150 K. Unlike many transition metals, scandium, yttrium, and lutetium can maintain up to 30 at% hydrogen in solution without precipitating any of the hydride phase[29] down to 4 K or without transforming to another crystal structure.

Lichty et al.[30] measured proton R_1s in $ScH_{0.27}$ ($H_{0.18}$) and found both an electronic relaxation R_{1e} and a weak low temperature motional relaxation peak R_{1L} near 60 K (105 K). That peak moved with the proton resonance frequency in a manner similar to the movement of R_{1d}, the over the barrier hopping, long range diffusion relaxation rate peak at much higher temperatures. In Figure 9 we see these low temperature data for two proton frequencies. The R_{1L} motional relaxation peak is superimposed on the R_{1e} electronic relaxation, which is linear in temperature T ($R_{1L} = R_1 - R_{1e}$; R_{1L} will be discussed below).

The location of hydrogen (deuterons) in the scandium hcp lattice was studied by neutron scattering.[29] Deuterons were found to prefer to form pairs with a scandium atom between. From these neutron scattering studies, models of hydrogen ordering in chains of paired hydrogens in scandium were proposed.

The pairing of hydrogen with a scandium metal between is an interesting and unusual ordering. However, not all hydrogens are paired with a metal between. Some of the hydrogens are unpaired and thus occupy vacant tetrahedral (T) sites in a random or inhomogeneous manner. The random occupation of hydrogen in metal–solid solutions has been referred to by Barnes[14] as a proton glass. The result of an inhomogeneous hydrogen occupation can be seen in the proton spin–lattice relaxation rate data and will be explained below.

The scandium hcp lattice has two adjacent, closely spaced interstitial T sites along the c axis where hydrogen is known[29]

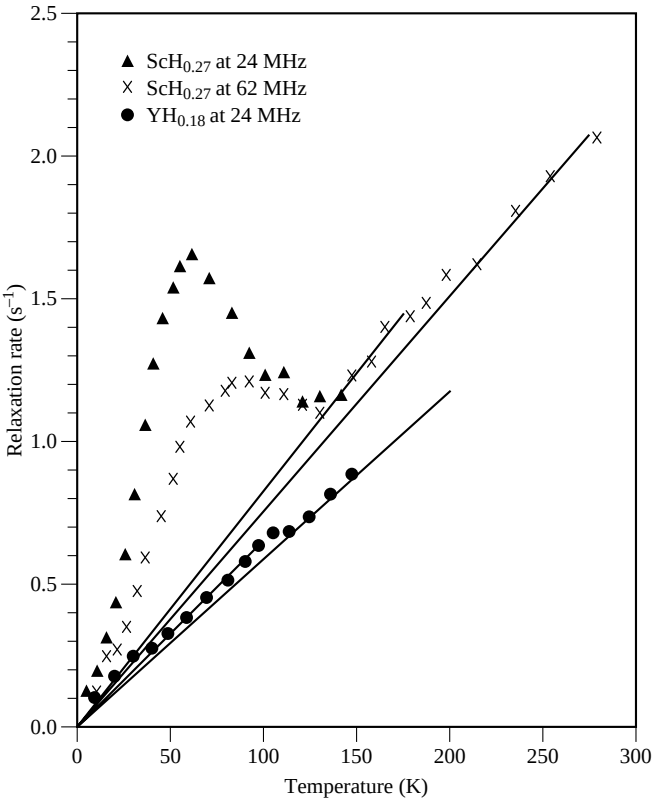

Figure 9 Proton spin–lattice relaxation rate (R_1) in $ScH_{0.27}$ as a function of temperature at 24 and 62 MHz. Proton R_1 in $YH_{0.18}$ at 24 MHz (●) shows a weak peak at ~105 K. The peak heights are due to the relaxation of the proton's tunneling motion and proton dipole 'collisions' with fixed (^{45}Sc or ^{89}Y) metal nuclear magnetic moments. Note the ^{89}Y moment is <1/20 of the ^{45}Sc moment. (Reproduced by permission of the American Physical Society from Lichty et al.[30])

to sit in one of the sites. These two sites are too closely spaced to permit two hydrogens to occupy both sites simultaneously.[31] The local motion is understood to be one hydrogen moving between these two closely spaced T sites. Activation energies derived from a 'local over a small barrier' hopping model were found to be $E_a \approx 50$ meV, much smaller than the nominal 500 meV activation energies typical of long-range hopping over a barrier found for activation energies in higher temperature hydrogen diffusion. Lichty et al.[30] were able to fit the proton spin–lattice relaxation rates versus 1000/T with two separate and quite different models for hydrogen hopping over an energy barrier. As can be seen from Figure 10, the data are not symmetrical about the peaks of the three relaxation curves. The slope of the three curves on the high temperature (low 1/T values) side of the peak is much greater than the low temperature (higher 1/T values) slopes. Symmetrical log R_1 versus 1/T curves in HMSs is a signature of hydrogen hopping where there is one unique activation energy typifying a simple hopping process and/or a simple and often cubic solid. Symmetrical log R_1 or log T_1 vs 1/T curves are often referred to as BPP type behavior. The relaxation rate curves in Figure 10 show the signature of hydrogen motion in a disordered solid with a distribution of activation energies. This subject will be discussed at length below. Lichty et al.[30] were able to fit the data with two hopping models, one assuming a distribution of activation energies and a second model with a correlation

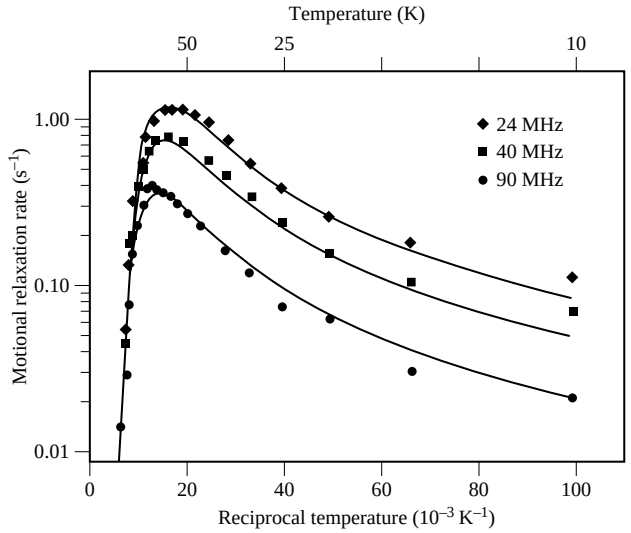

Figure 10 Proton spin–lattice relaxation rate in $ScH_{0.27}$ vs. 1000/T for proton resonance frequencies 12, 40, and 90 MHz fitted with a thermally activated over the barrier hopping model and a distribution of activation energies. (Reproduced by permission of the American Physical Society from Lichty et al.[30])

function having a stretched exponential character. Localized hydrogen motion has also been found by Skripov et al.[32] in TaV_2H_x in the temperature range 10–100 K.

Tunneling of hydrogen from one tetrahedral interstitial site to an adjacent empty T site at low temperature is an alternate mechanism rather than hydrogen thermally activated hopping over a low energy barrier. Svare et al.[33] suggested that the same proton spin–lattice relaxation data of Lichty et al.[30] in $ScH_{0.27}$ could also be described by hydrogen tunneling between adjacent T sites in the Sc hexagonal close packed lattice. The potential wells for the two sites were thought to have sinusoidal curvature near the bottoms. The two wells of the adjacent T sites were also thought to have different minimum energies, that is, the wells were asymmetric. In fact, Svare et al.[33] suggested the asymmetry, A, for the hydrogen–scandium metal solid solution would have a distribution of minimum energy difference values typical of an inhomogeneous hydrogen solid solution or proton glass. With increasing temperature, the tunneling model must include a tunneling mechanism not appropriate (or yet thermally switched on) at lower temperature. Figure 11 shows the proton spin–lattice relaxation data of Lichty et al.[30] fit with this tunneling model. The data fit adequately this tunneling theory and support the proposition that hydrogen tunneling exists in scandium at low temperatures. Hydrogen tunneling in scandium was also found by Leisure et al.[34] in a resonant ultrasound spectroscopy (not an NMR technique) study of $ScH_{0.25}$ and $ScD_{0.18}$ employing small scandium single crystals.

6 SPIN–LATTICE RELAXATION IN AMORPHOUS HYDROGEN–METAL SYSTEMS

An amorphous metal alloy may be formed by extremely rapid cooling of the molten metal alloy. Such materials are often referred to as metallic glasses. An amorphous alloy is a

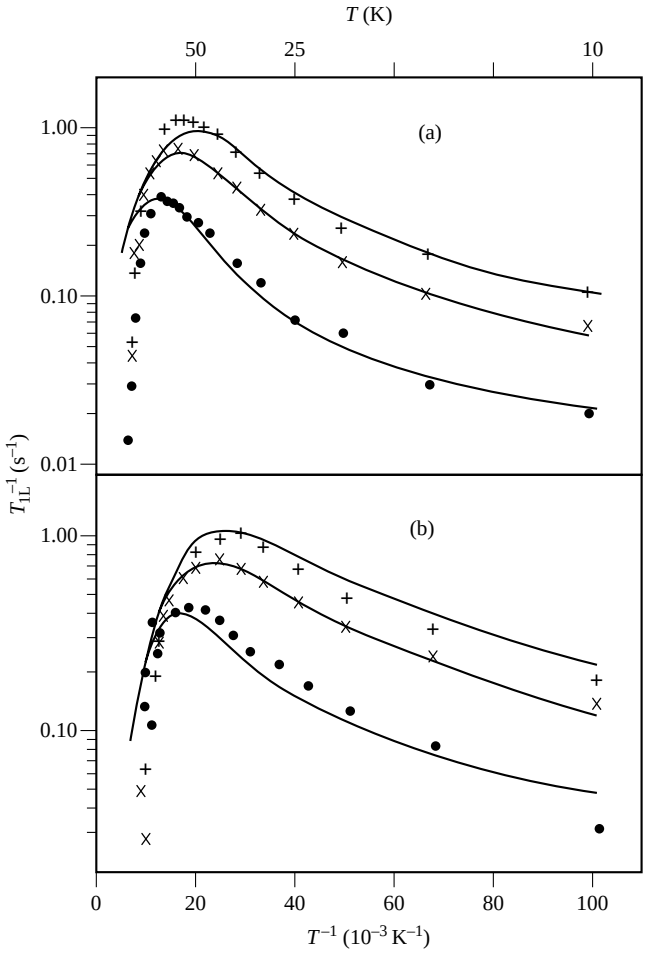

Figure 11 Low temperature proton spin-lattice relaxation rates $R_{1L} \equiv T_{1L}^{-1}$ versus reciprocal temperature in two hcp scandium–hydrogen solid solution compositions. (a) $ScH_{0.27}$ and (b) $ScH_{0.11}$ at 24 MHz (+), 40 MHz (×), and 90 MHz (•), respectively. The curves represent the fits of the tunneling model with a distribution of asymmetric energy well minima for hydrogen tunneling between adjacent tetrahedrally coordinated interstitial (T) sites. Data are from Lichty et al.[30] and tunneling model can be found in Svare et al.[33]

disordered metal and is without long range topological order. There may be short range or compositional order in amorphous alloys. These amorphous materials are then hydrided by more or less conventional means, but care must be taken not to heat the material high enough to 'recrystallize' the amorphous sample. This may be somewhat difficult as the absorption of hydrogen by metals is generally an exothermic reaction.

Bowman[35] points out that metallic alloy glasses must contain one of certain metals, i.e. titanium, zirconium, hafnium, palladium, or a rare earth metal, for the glass to be able to hold hydrogen, H/M > 0.1, where M is the total metal content. Even with one of these metals in the alloy, an alloy glass may not be formed upon quenching.

Hydrides of metallic glasses generally have quite different hydrogen motions, with lower hydrogen diffusion activation energies and spin–lattice relaxation rates than do hydrides of the crystalline HMSs of similar composition as we shall see below. In the case of crystalline and amorphous Zr_2PdH_x, Bowman et al.[36] point out the log T_1 versus 1000/T plots for $Zr_2PdH_{2.90}$ and amorphous a-$Zr_2PdH_{2.90}$ are noticeably

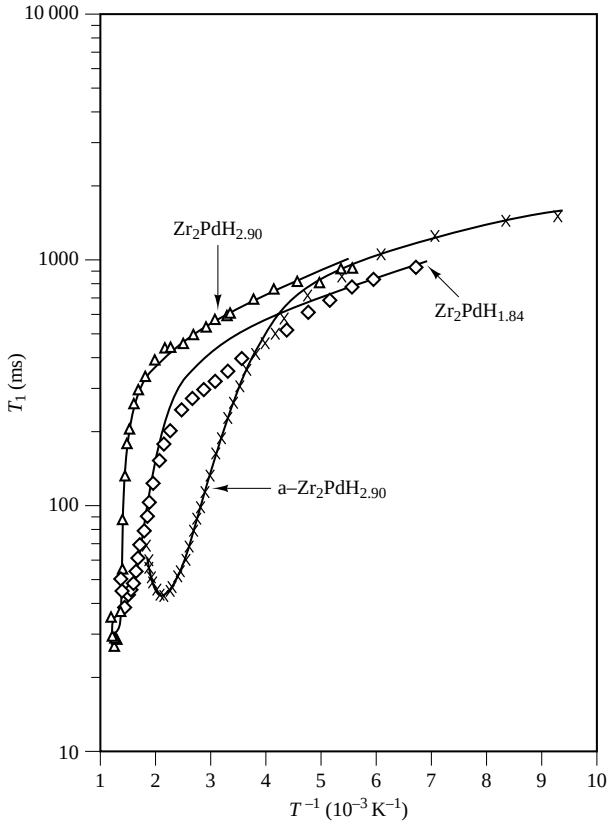

Figure 12 Proton spin–lattice relaxation times vs. 1000/T for crystalline $Zr_2PdH_{1.84}$ and $Zr_2PdH_{2.90}$ at 40 MHz and amorphous $Zr_2PdH_{2.90}$ at 34.5 MHz, and proton relaxation times for crystalline and amorphous $Zr_2PdH_{2.90}$ vs 1000/T. The latter curve shows hydrogen diffusion at lower temperatures and with lower activation energy (slope of T_1 vs. 1000/T curve) than the crystalline $Zr_2PdH_{2.90}$. (Reproduced by permission of R. Oldenbourg Verlag from Bowman et al.[36])

different. The crystalline and amorphous curves have minima at different temperatures and have different slopes or diffusion activation energies. Generally, the amorphous samples display more rapid hydrogen diffusion at lower temperatures and have lower activation energies for diffusion than do the crystalline equivalents. This can be seen in Figure 12. A simplistic explanation of this effect may relate in part to the fact that the glassy HMSs have a somewhat lower density and have more 'open' paths for hydrogen to hop through than the crystalline equivalents. A more complete description of hydrogen motion must also include the differences in electronic character known to exist between the glassy and crystalline HMSs.

7 RELATED ARTICLES

Amorphous Materials; Deuterium NMR in Solids; Diffusion in Solids; Electron–Nuclear Hyperfine Interactions; Knight Shift; Spin Diffusion in Solids.

8 REFERENCES

1. W. H. Mueller, J. P. Blackledge, and G. C. Libowitz. *Metal Hydrides*, Academic Press, New York, 1968.
2. R. E. Norberg, *Phys. Rev.*, 1952, **86**, 745.
3. D. Khatamin, W. A. Karmatakahara, R. G. Barnes, and D. T. Peterson, *Phys. Rev. B*, 1980, **21**, 2622.
4. R. C. Bowman, Jr., B. D. Freeman, and J. R. Phillips, *Cryogenics*, 1992, **32**, 127.
5. A. Struss and J. D. Corbett, *Inorg. Chem.*, 1977, **38**, 612.
6. Y. S. Hwang, D. R. Torgeson, A. S. Khan, and R. G. Barnes, *Phys. Rev. B*, 1977, **15**, 4564.
7. R. G. Barnes, M. Jerosch-Herold, J. Shinar, F. Borsa, D. R. Torgeson, D. T. Peterson, A. J. Lucas, G. A. Styles, and E. F. W. Seymour, *Phys. Rev. B*, 1987, **35**, 890.
8. D. B. Baker, N. Adolphi, M. S. Conradi, P. A. Fedders, R. E. Norberg, R. G. Barnes, and D. R. Torgeson, *Phys. Rev. B*, 1992, **46**, 184.
9. E. F. W. Seymour, *J. Less-Common Met.*, 1982, **88**, 323.
10. D. S. Schreiber and R. M. Cotts, *Phys. Rev.*, 1963, **131**, 1118.
11. T. Y. Hwang, D. R. Torgeson, and R. G. Barnes, *Phys. Lett.*, 1978, **66A**, 137.
12. H. S. Marek, J. D. Corbett, and R. L. Daake, *J. Less-Common Met.*, 1983, **89**, 249.
13. Y. S. Hwang, D. R. Torgeson, and R. G. Barnes, *Solid State Commun.* 1977, **24**, 773.
14. R. Barnes, *J. Less-Common Met.*, 1991, **172–174**, 509.
15. N. Bloembergen, E. M. Purcell, and R. V. Pound, *Phys. Rev.*, 1948, **73**, 679.
16. F. Borsa, R. G. Barnes, B. J. Beaudry and D. R. Torgeson, *Phys. Rev. B*, 1982, **26**, 1471.
17. H. C. Hoke, H. E. Schone, C. A. Sholl, S. P. Usher, R. G. Barnes, D. R. Torgeson, R. Hempelmann, and G. A. Styles, *J. Less-Common Met.*, 1991, **172–174**, 603.
18. A. Abragam, *The Principles of Nuclear Magnetism*, Oxford Press, 1961.
19. C. A. Sholl, *J. Phys. C: Solid State Phys.*, 1986, **19**, 2547.
20. C. P. Slichter, *Principles of Magnetic Resonance*, Springer-Verlag, 3rd ed, 1990.
21. W. Heitler and E. Teller, *Proc. R. Soc. London*, 1936, **A155**, 637; and J. Korringa, *Physica*, 1950, **88**, 323.
22. T.-T. Phua, B. J. Beaudry, D. T. Peterson, D. R. Torgeson, R. G. Barnes, M. Belhoul, G. A. Styles, and E. F. W. Seymour, *Phys. Rev. B*, 1983, **28**, 6227.
23. D. R. Torgeson, J.-W. Han, P.C-T. Chang, L. R. Lichty, R. G. Barnes, E. F. W. Seymour, and G. W. West, *Z. Phys. Chem. NF*, 1989, **164**, 853.
24. L. R. Lichty, J.-W. Han, D. R. Torgeson, R. G. Barnes, and E. W. F. Seymour, *Phys. Rev. B*, 1990, **42**, 7734.
25. D. R. Torgeson, R. J. Schoenberger, and R. G. Barnes, *J. Mag. Reson.*, 1986, **68**, 85.
26. W. H. Jones, Jr., T. P. Graham, and R. G. Barnes, *Phys. Rev.*, 1963, **132**, 1898.
27. G. Pake, *J. Chem. Phys.*, 1948, **16**, 327.
28. D. R. Torgeson and R. G. Barnes, *Phys. Rev. Lett.*, 1962, **9**, 255.
29. O. Blaschko, G. Krexner, J. N. Daou, and P. Vajda, *Phys. Rev. Lett.*, 1985, **55**, 2876.
30. L. R. Lichty, J.-W. Han, R. Ibanez-Meier, D. R. Torgeson, R. G. Barnes, E. F. W. Seymour, and C. A. Sholl, *Phys. Rev. B*, 1989, **39**, 2012.
31. L. R. Lichty, R. J. Schoenberger, D. R. Torgeson, and R. G. Barnes, *J. Less-Common Met.*, 1987, **129**, 31.
32. A. V. Skripov, M. Yu Belyaev, S. V. Rychkova, and A. P. Stepanov, *J. Phys. Condens. Matter*, 1989, **1**, 2121.
33. I. Svare, D. R. Torgeson, and F. Borsa, *Phys. Rev. B*, 1991, **43**, 7448.

34. R. G. Leisure, R. B. Schwarz, A. Migliori, D. R. Torgeson, and I. Svare, *Phys. Rev. B*, 1993, **48**, 893.
35. R. C. Bowman, Jr., *Mater. Sci. Forum*, 1988, **31**, 197.
36. R. C. Bowman, Jr., D. R. Torgeson, R. G. Barnes, A. J. Maeland, and J. J. Rush, *Z. Phys. Chem., NF*, 1989, **163**, 425.

Biographical Sketch

David R. Torgeson. *b* 1936. B.A., 1958, Luther College. M.S., 1960, Iowa State University. Introduced to NMR by R. G. Barnes. Basic physics research utilizing nuclear and electron resonance techniques, Ames Laboratory, Iowa State University, 1960–present. Assistant Professor of Physics, Luther College, 1967–68, and ISU, 1972. Physicist, Ames Laboratory, 1982–present. Adjunct Assistant Research Professor of Physics, Iowa State University, 1993–present. Approx. 120 publications. Research interests include: application of NMR for materials characterization of hydrogen–metal systems, fast ion conductors, high temperature superconductors, and quasicrystals; and instrumentation for solid state NMR.

Inorganic Chemistry Applications

Bernd Wrackmeyer

Universität Bayreuth, Bayreuth, Germany

1	Introduction	1
2	Application of Chemical Shifts δX	1
3	Application of Indirect Nuclear Spin–Spin Coupling Constants ^nJ(A,X)	7
4	Application of Nuclear Spin Relaxation Parameters	9
5	Related Articles	10
6	References	10

1 INTRODUCTION

Inorganic chemistry is a vast discipline dealing with more than 100 elements, many of which have at least one magnetically active isotope that is suitable for recording its high-resolution NMR spectra in solution and in the solid state. Therefore, application of NMR (today one strives for an approach using multinuclear magnetic resonance)[1,2] has contributed considerably to the development of inorganic chemistry and also to the present vigorous research activity. This article cannot cover all aspects involved. Therefore examples of important applications in various fields of inorganic chemistry will be given. These examples are confined to diamagnetic samples such as liquids or solids, although there are numerous inorganic chemistry applications of NMR to paramagnetic samples. The NMR techniques employed and the physical background of the NMR parameters are dealt with elsewhere in the Encyclopedia as indicated by the cross references at the end of the article.

The nuclides of particular interest for inorganic chemistry applications range from ^{1}H, with the greatest magnetic moment of all naturally occurring nuclides, to heavy metal nuclides like ^{207}Pb, including those with both a small magnetic moment and low natural abundance (e.g. ^{57}Fe or ^{187}Os). For many applications the different relaxation behavior of spin-$\frac{1}{2}$ and quadrupolar nuclides (spin $I \geq 1$) must be considered.

Chemical shifts (δX), indirect nuclear spin–spin coupling or scalar coupling [^nJ(A,X)], and the nuclear relaxation properties (represented by the relaxation rate constants $T_1{}^X$, $T_2{}^X$) are the prominent NMR parameters. For both liquid and solid samples these data can be related to the structure and to various types of dynamic processes such as motion in solids, inter- or intramolecular exchange and molecular dynamics in solution. Structural changes and in general all types of chemical processes are reflected by characteristic changes in the NMR parameters.

The δX value (Section 2) as a measure of nuclear magnetic shielding characterizes the chemical neighborhood of the nucleus X if a sufficiently large δX data set is available for comparison. Thus, for a new compound with unknown structure the parameter δX indicates the nature of groups linked to X and, frequently, it is possible to evaluate the coordination number of X (CN_X). This means of course that important structural information can be gained by comparing solid- and liquid-state δX values. The dependence of δX values on particular properties of the electronic structure implies that changes in δX are related to changes in other spectroscopic properties, e.g. to the λ values for magnetic-dipole-allowed electronic transitions in UV spectra. From solid state NMR spectra one can obtain more detailed information on nuclear magnetic shielding by analysis of the anisotropic contributions.

The magnitude and sign of coupling constants measured for NMR-active nuclides, ^nJ(A,X) (Section 3; heteronuclear or homonuclear spin–spin coupling), depend on the structural relationship between the nuclides since this interaction is electron mediated. In order to compare J values for various nuclides A and X it is advisable to use the reduced coupling constants K instead. These K values are independent of the individual nuclear magnetic properties of the respective nuclides: $K(\mathrm{A,X}) = 4\pi^2 \cdot J(\mathrm{A,X}) \cdot (h \cdot \gamma_\mathrm{A} \cdot \gamma_\mathrm{X})^{-1}$. The splitting pattern in the A or the X NMR spectrum indicates the number of X or A, respectively, and can be analyzed as a first or higher order spectrum according to the spin system. Furthermore, in solution, the parameters ^nJ(A,X) enable us to carry out a great variety of NMR experiments (e.g. based on spin polarization transfer) for tracing the connectivity of NMR-active nuclides within the same molecule.

Relaxation rate constants T_1^X (longitudinal or spin–lattice relaxation time), T_2^X (transverse or spin–spin relaxation time), and $T_{1\rho}^X$ (spin–lattice relaxation time in the frame of reference rotating with $\boldsymbol{B}_1$) reveal a wealth of information on solution- and solid state properties (Section 4) if the contributions according to the respective relaxation mechanism can be determined. Thus, NOE measurements or dipolar spin–spin coupling constants enable us to assess internuclear distances, e.g. $d_{\mathrm{X}\text{-}^1\mathrm{H}}$ or $d_{\mathrm{X-X}}$. Other important information concerns the thermodynamic parameters and the mechanism of exchange processes, quadrupolar interactions in solution and in solids, anisotropic motion in solution, and all types of motion in solids.

2 APPLICATION OF CHEMICAL SHIFTS δX

2.1 Chemical Shifts δ^1H and δ^{13}C

Although less dominant compared with organic chemistry applications, ^{1}H NMR studies play a major role in inorganic chemistry. Looking at inorganic compounds, we find that the range of δ^1H values [internal reference $(CH_3)_4Si$] known for most organic compounds (δ^1H 0 to +10) is increased at both ends. Important examples are the ^{1}H resonance signals shifted toward high frequency (δ^1H +10 to +20) if hydrogen atoms are involved in so-called strong hydrogen bonding[3] (e.g. $[FHF]^-$ or $[H(NO_3)_2]^-$) and the ^{1}H NMR signals of transition metal hydrides which can be found at rather low frequency[4], e.g. in the range of δ^1H 0 to −50. This range is not fixed since there are also some examples of ^{1}H NMR signals of transition metal hydrides at higher frequencies, e.g. in the case of some clusters containing interstitially bonded hydrogen atoms. The pH dependence of δ^1H values as the result of hydrogen bridging enables us to determine pK_a values if other methods are not straightforward.

Thus the pK_a values of *cis*-$[PtCl(H_2O)(NH_3)_2]^+$ (5.37) and *cis*-$[Pt(H_2O)_2(NH_3)_2]^{2+}$ (7.21), the hydrolysis products of 'cisplatin', *cis*-$[PtCl_2(NH_3)_2]$, have been determined by using ^{15}N-edited ^{1}H NMR.[5]

Most ^{1}H NMR applications deal with liquids. Of course, solid state ^{1}H NMR studies are also very attractive, but strong dipolar interactions between protons cannot be removed solely by MAS. Even by using advanced techniques like CRAMPS, the necessary resolution of separate ^{1}H NMR signals is difficult to achieve because of broadened signals and the rather small range of ^{1}H chemical shifts. If the hydrogen content of solids is low, e.g. in zeolites, narrow ^{1}H NMR signals can be expected.[6] A value of δ^1H $\approx$ 7 has been assigned to catalytically active acidic hydroxyl groups.

Application of δ^2H (^{2}H: I = 1) plays a minor role in inorganic chemistry. The δ^1H and δ^2H values can be regarded as identical.

Values of δ^{13}C [reference $Si(CH_3)_4$] of the carbonyl ligand in metal–carbonyl complexes[7] are characteristic of the respective metal and of the nature of metal–carbon bonding, e.g. for a terminal or a bridging carbonyl group (μ-CO), the ^{13}C nuclide of the latter being significantly deshielded, as shown for δ^{13}C ranges of Fe-, Ru-, Co-, and Rh-carbonyl compounds (Figure 1). In particular for transition metal carbonyl clusters, ^{13}C-enriched material ($\approx$ 10–20%) is commonly used. The high-frequency ^{13}C NMR signals typical of carbene and carbyne–metal complexes (δ^{13}C 200–400) are noteworthy since they are mostly far outside the δ^{13}C range for organic compounds (0–220). Similar to organic chemistry applications, there is a wealth of δ^{13}C data for all types of organic ligands attached to metals.[7]

Carbon-13 nuclear shielding in solids is increasingly used in inorganic chemistry. Examples of applications are carbonates which have only a small range (3.6 ppm) of δ^{13}C values[8] and carbides with a large range (>100 ppm) of δ^{13}C values.[9]

2.2 Chemical Shifts of Some Other Spin-$\frac{1}{2}$ Nuclides

2.2.1 ^{29}*Si*

Chemical shifts δ^{29}Si [external reference $Si(CH_3)_4$] cover a range of $\approx$600 ppm.[1,2,10] These data are extremely useful for determining structural principles of silicates in solution[11] and in the solid state.[12] Major applications concern zeolites where the different sites of silicon atoms according to the structure of the zeolite can be determined and also the number of Si–O–Al bridges for a particular silicon atom. The latter is evident from ^{29}Si nuclear deshielding with an increasing number of Si–O–Al bridges (Figure 2). In silicone polymers, separate

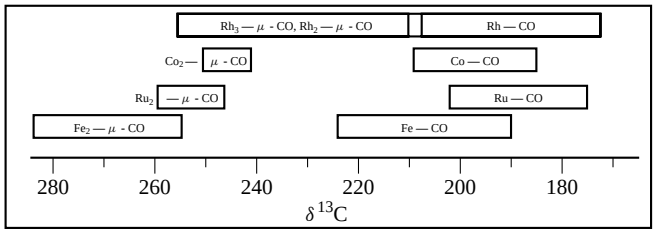

Figure 1 Carbon-13 chemical shift ranges of Fe-, Ru-, Co-, and Rh-carbonyl compounds

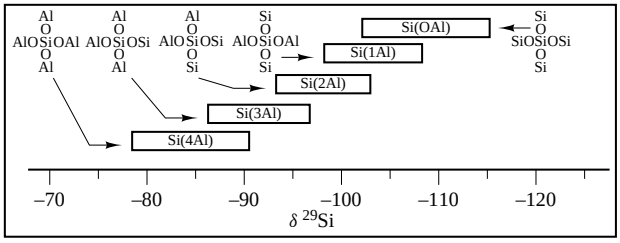

Figure 2 Silicon-29 chemical shift ranges of zeolites with different surroundings of the silicon in tetrahedral SiO_4 moieties

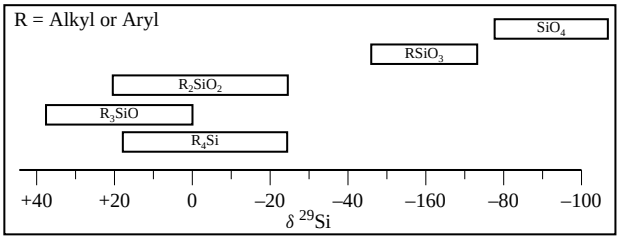

Figure 3 Silicon-29 chemical shift ranges in silanes with Si–O and Si–C bonds

^{29}Si NMR signals are found for the basic structural units, such as $Me_3Si–O–$, $Me_2Si(O–)_2$, $MeSi(O–)_3$ and $Si(O–)_4$ (Figure 3).

In the case of three-coordinate silicon atoms, e.g. in Si–element double bonds, ^{29}Si NMR signals are shifted to higher frequencies, similar to the situation for δ^{13}C in alkenes or ketones. If CN_{Si} > 4, the ^{29}Si nuclear shielding increases significantly. For solutions of decamethylsilicocene $[(\eta^5\text{-}C_5Me_5)_2Si]$, a single ^{29}Si NMR signal is found at very low frequency (δ^{29}Si = –398.0). In the solid state, there are two ^{29}Si NMR signals,[13] one for the bent structure (δ^{29}Si = –403.2) and the other one (δ^{29}Si = –423.4) for the silicon atom with a parallel arrangement of the C_5Me_5 rings in a ratio of 2:1, in agreement with the results of X-ray analysis.

2.2.2 ^{119}*Sn*, ^{207}*Pb*

Values of δ^{119}Sn [external reference $Sn(CH_3)_4$] cover a range of $\approx$5000 ppm,[1,2,14] compared with a range of $\approx$17 000 ppm for δ^{207}Pb,[1,2,15] with tin(II) or lead(II) compounds at both ends (Table 1): The lowest ^{119}Sn, ^{207}Pb nuclear shielding is observed for monomeric stannylenes or plumbylenes, SnR_2, PbR_2 [R = bulky organyl group, e.g. $(Me_3Si)_2CH$], whereas high ^{119}Sn, ^{207}Pb nuclear shielding is typical of stannocenes and plumbocenes.[13]

As for other heavy nuclides, both ^{119}Sn and ^{207}Pb nuclear shieldings are very sensitive toward small structural changes and, therefore, readily reflect strong or weak coordination in Lewis acid/Lewis base interactions. Thus, the temperature-, solvent-, and concentration-dependence of δ^{119}Sn and δ^{207}Pb

Table 1 Extreme Values for ^{119}Sn and ^{207}Pb Chemical Shifts

	$[(Me_3Si)_2CH]_2M$	$[(Me_3Si)_2N]_2M$	$(\eta^5\text{-}C_5Me_5)_2M$
δ^{119}Sn	+2320	+776	–2129
δ^{207}Pb	+9110	+4916	–4390

data is of interest, and the comparison of δ^{119}Sn and δ^{207}Pb data in the solid and liquid state is particularly attractive.

2.2.3 ^{15}N

In spite of its low natural abundance (0.37%) and its unfavorable nuclear magnetic properties (low and negative γ^{15}N), ^{15}N NMR measurements of both nonlabeled and ^{15}N-labeled (bioinorganic applications) nitrogen compounds are becoming increasingly attractive.[16] The application of δ^{15}N values has a potential similar to that of δ^{13}C. Values of δ^{15}N (identical with δ^{14}N; external reference neat CH_3NO_2) cover a range of ≈ 1300 ppm, and the trends in changes of N atom nuclear shielding are similar to those of ^{13}C in corresponding carbon compounds (e.g. the linear relationship of δ^{15}N/δ^{13}C data of linear compounds such as **N**≡**N**/[**C**≡N]$^-$, C_4H_9−C≡**N**/[C_4H_9−C≡**C**]$^-$, [H−C≡**N**−H]$^+$/H−**C**≡**C**−H, [**N**O]$^+$/**C**O, NO_2^+/**C**O_2, N=**N**=O/[N=**C**=O]$^-$, [C_6H_5−N≡**N**]$^+$/C_6H_5−N≡**C**, [C_6H_5−**N**≡N]$^+$/C_6H_5−**C**≡N: δ^{13}C = 0.536, δ^{15}N = +196.5). Extreme shielding [e.g. in $N(SiH_3)_3$: δ^{15}N −417.7] and deshielding [e.g. in $(CH_3)_3Si$−N=N−$Si(CH_3)_3$: δ^{15}N +618] of nitrogen nuclides is observed for inorganic nitrogen compounds. An example for the high sensitivity of N atom nuclear shielding to changes in the electronic structure is given by comparing δ^{15}N values of bent and linear M−NO arrangements [the NO group functions as one-electron (bent) or three-electron donor (linear)]. In all cases studied, confirmed by the results of X-ray analyses and solid state ^{15}N NMR measurements, the bent structure causes considerable deshielding of the ^{15}N nucleus. The same is true for the azenido ligand in complexes with a linear or a bent MNR arrangement.[17]

2.2.4 ^{31}P

The ^{31}P nucleus is one of the 'traditional' nuclides since it was relatively easy to measure ^{31}P NMR spectra, even in the early days of NMR. Today, ^{31}P NMR is of prime importance in phosphorus chemistry,[18,19] and chemical shifts δ^{31}P serve as convenient parameters for identifying reaction products or monitoring the progress of reactions. In this context the huge range of δ^{31}P values (external reference H_3PO_4, 85% aq) of almost 2000 ppm is very helpful, although there is no decided dependence on CN_P or on the formal oxidation state of phosphorus (see, e.g., Tables 2 and 3). The extreme bonding situation in inorganic phosphorus compounds is reflected by examples with very high ^{31}P nuclear shielding (e.g. P_4: δ^{31}P −488) or deshielding [e.g. $(CH_3)_3C$−P[Cr$(CO)_5]_2$ δ^{31}P +1362].[20] Major applications of δ^{31}P values can be found in the chemistry of polyphosphanes,[21] in the investigation of low-coordinated phosphorus compounds, with or without phosphorus−element multiple bonds (e.g. element = C, Si, Ge, Sn, N, P), and in the transition metal chemistry involving the countless number of metal−phosphane complexes.

Like solid state ^{29}Si NMR in silicates, solid state ^{31}P NMR of all kinds of phosphates[22] is extensively studied. Even very small changes in the crystal structure of phosphates are reflected by changes in the isotropic chemical shifts δ^{31}P.

2.2.5 ^{77}Se, ^{125}Te

Chemical shifts δ^{77}Se [external reference $(CH_3)_2Se$; range ≈ +2000 to −800] and δ^{125}Te [external reference $(CH_3)_2Te$; range ≈ +3300 to −1200] are related by a factor of ≈ 1.6−1.8 for analogous compounds.[23] Important inorganic chemistry applications deal with the studies of cluster cations, e.g. $[Se_nTe_m]^{2+}$ (Table 4) for which the δ^{77}Se and δ^{125}Te values cover ranges of ≈ 1400 and ≈ 3000 ppm, respectively.[24]

Table 2 Some δ^{31}P Values of Simple Phosphorus Compounds.

	δ^{31}P
PH_3	–241
$[PH_4]^+$	–105.3
$NaPH_2$	–303.4
P_2H_4	–204
PMe_3	–63.3
PPh_3	–5.6
$P(SiH_3)_3$	–378.0
	+211
	–49.2
	+76.6
P≡C−H	–32

Table 3 Some δ^{31}P Values of Selected Transition Metal Complexes with Different Types of Metal–Phosphorus Bonding: P (Interstitial), P_4, η^5-P_5 (Compare LiP_5: δ^{31}P = +468.2), P_6, and η^6-P_6.

	δ^{31}P	
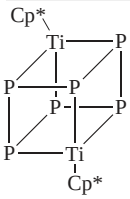	+386.7	
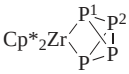	–104.4[1], –211.5[2]	$J(^{31}P,^{31}P)$ = 201 Hz
Cp*Fe(η^5-P_5)	+153	
	M = V, +165 M = Mo, –316 M = W, –339	
$[Rh_9P(CO)_{21}]^{2-}$	+282.3	J (^{103}Rh,^{31}P) at –80 °C = 34.0, 46.0 J (^{103}Rh,^{31}P) at +25 °C = 38.4

Table 4 Selenium-77 and ^{125}Te NMR Data of the Cation $[Se_6Te_2]^{2+}$.

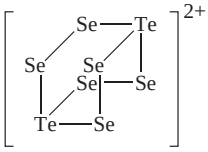

δ^{77}Se	δ^{125}Te	$^1J(^{125}Te,^{77}Se)$	$^2J(^{125}Te,^{77}Se)$	$^3J(^{125}Te,^{77}Se)$
+584	+1613	355 Hz	31 Hz	120 Hz

of ^{19}F nuclear shielding.[25] Like ^{1}H NMR of organic or organometallic compounds, ^{19}F NMR is extremely useful in the analysis of mixtures of fluorine compounds, e.g. equilibrium mixtures of element–halides such as WF_6 and WCl_6, BF_3, BCl_3 and BBr_3 (Figure 4), or anionic species such as $[BF_4]^-$ and $[BCl_4]^-$.

Many inorganic fluorides are insoluble solids, some of which have been studied by various solid state NMR techniques.[26] Thus, changes in δ^{19}F values of solid alkali-metal fluorides appear to be a function of the cation electronegativity. In principle, high-resolution solid state ^{19}F NMR spectra would be of great interest. However, this field is not very well developed so far, since it suffers to some extent from similar physical and instrumental problems as high-resolution solid state ^{1}H NMR spectra.

2.2.7 ^{129}Xe

Chemical shifts δ^{129}Xe (external reference $XeOF_4$) cover a range of $\approx$ 7000 ppm,[27] including gaseous xenon (δ^{129}Xe ≈ -5300, depending on solvent, temperature, or if xenon is a guest atom, e.g. in clathrates or zeolites). With few exceptions, the ^{129}Xe nuclides become more deshielded with the higher the oxidation state of Xe. The most deshielded example is found in an aqueous solution of Na_2XeO_6 (δ^{129}Xe = +2077). Clearly, ^{129}Xe NMR is a major tool in xenon chemistry in the well-established field of xenon–fluorine and xenon–oxygen compounds as well as in the new and exciting field of xenon–carbon compounds.

2.2.8 Some Transition Metal Spin-$\frac{1}{2}$ Nuclides (^{57}Fe, ^{103}Rh, ^{109}Ag, ^{113}Cd, ^{199}Hg, ^{183}W, ^{195}Pt)[1,2,28]

Although iron chemistry is a very important field, δ^{57}Fe values have found only limited applications. This is mainly due

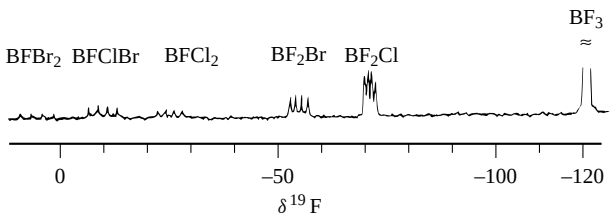

Figure 4 Fluorine-19 NMR spectrum at 75.3 MHz of an equilibrated mixture of BF_3, BCl_3 and BBr_3: the boron halides $BFBr_2$, BFClBr, BF_2Br and BF_2Cl cannot be isolated in the pure state. Note the splitting of the ^{19}F NMR signals due to $^1J(^{19}F,^{11}B)$

to the low NMR sensitivity of ^{57}Fe. In principle, δ^{57}Fe values [external reference $Fe(CO)_5$] are sensitive to small changes in the iron–ligand sphere and cover a large range, considering, e.g., diene $Fe^{(0)}$ complexes (δ^{57}Fe ≈ -600 to $\approx +1700$) or ferrocene (Cp_2Fe) derivatives and other cyclopentadienyl iron compounds (δ^{57}Fe $\approx +1000$ to $\approx +5100$). An increase in ^{57}Fe nuclear shielding in α-ferrocenyl carbocations indicates the fulvenoid character and the presence of an Fe–C-α bond, whereas ^{57}Fe deshielding points toward a nonfulvenoid structure together with the influence of an electron deficient substituent (Table 5). Extreme deshielding of ^{57}Fe is observed in myoglobin derivatives with δ^{57}Fe $\approx +7200$ to +8200.

With modern NMR instruments ^{103}Rh NMR spectra can easily be measured and many δ^{103}Rh data {the absolute frequency Ξ^{103}Rh = 3.16 MHz [Ξ^1H(Me_4Si) = 100.00 MHz] serves as reference} are known, covering a large range (δ^{103}Rh $\approx +10\,000$ to -2000). The extreme examples are the cation $[Rh(H_2O)_6]^{3+}$ (δ^{103}Rh = +9992), $[Rh(acac)_3]$ (δ^{103}Rh = +8358) and the rhodium(I) sandwich complex [(η^5-C_5H_5)Rh(η^4-C_4H_4)] (δ^{103}Rh = −2057). There is no correlation between δ^{103}Rh and the formal oxidation state of rhodium. The cluster chemistry of rhodium is well developed, also with respect to the structure and dynamic properties in solution. This has been achieved by measurement of δ^{103}Rh values either directly by using ^{103}Rh NMR or indirectly via heteronuclear double resonance experiments, e.g. ^{13}C{^{103}Rh} in rhodium clusters bearing ^{13}C-labeled carbonyl ligands (Figure 5).[29]

The major applications of δ^{109}Ag values (identical with δ^{107}Ag; external reference Ag^+ at infinite dilution in H_2O or the absolute frequency Ξ^{109}Ag = 4.653 623 MHz) concern the complexation behavior of Ag^+ cations in various solvents and in the presence of various ligands. The δ^{109}Ag values thus obtained cover a range of $\approx$ 1500 ppm to high frequency of the reference.

Chemical shifts δ^{113}Cd [identical with δ^{111}Cd; external reference $Cd(ClO_4)_2$(aq) 0.1 M; or neat $(CH_3)_2$Cd (Ξ^{113}Cd = 22.193 173 MHz) with δ^{113}Cd = +641.0] cover a range of $\approx$ 1000 ppm to high frequency of the reference. The δ^{113}Cd values have been used to establish the equilibria involved between halide anions and Cd^{2+} ions in various solvents or of species such as $[CdX_4]^{2-}$ with X = Cl, Br, I or SCN. Numerous chemical shifts δ^{113}Cd have been measured for solid cadmium compounds. In some of these the ^{113}Cd nuclear shielding is

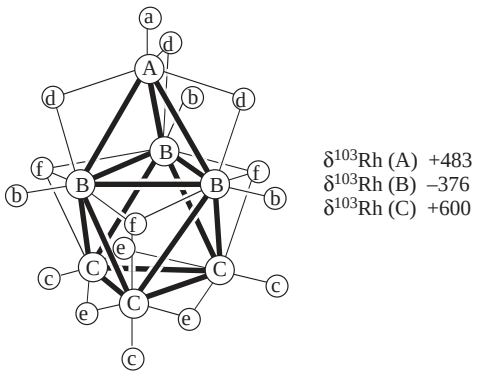

Figure 5 An anionic ^{13}C-labeled carbonyl rhodium cluster and its δ^{103}Rh values determined by ^{13}C{^{103}Rh} heteronuclear double resonance

Table 5 Iron-57 Chemical Shifts of Some α-Ferrocenyl Carbocations

	Cp_2Fe	$[CpFeC_5H_4CH_2]^+$	$[CpFeC_5H_4CHMe]^+$	$[CpFeC_5H_4CMe_2]^+$	$[(CpFeC_5H_4)_2CH]^+$
δ^{57}Fe	+1532.4	+1008.8	+1313.1	+1821.1	+2231.4

Table 6 Some Examples of ^{183}W Deshielding in Tungsten Complexes with WC and WW Multiple Bonds

	$[(CH_3)_3CCH_2]_3W{\equiv}C(CH_3)_3$	$[(CH_3)_3CO]_3W{=}W[OC(CH_3)_3]_3$	$(CF_3CO_2)_2W{\equiv}W(O_2CCF_3)_2$
δ^{183}W	+2867	+4489	+6760

increased with respect to the reference owing to the nature of the ligand and CN_{Cd} = 6 (e.g. in solid CdI_2: δ^{113}Cd = −677) or CN_{Cd} = 8 (e.g. in solid $Cd(NO_3)_2 \cdot 4H_2O$: δ^{113}Cd −100 or in solid CdF_2: δ^{113}Cd = −288).

Chemical shifts δ^{199}Hg [external reference $Hg(ClO_4)_2$ (0.1 M in 0.1 M $HClO_4$), corresponding to Ξ^{199}Hg = 17.870 535 MHz or neat $(CH_3)_2$Hg (δ^{199}Hg = +2255) with Ξ^{199}Hg = 19.910 841 MHz] have been reported for all types of mercury compounds with a range from ≈ −1200 (HgI_2 in tetrahydrofuran) to ≈ +3070 {neat $[(C_2H_5)_3Si]_2Hg$}.[30] Attempts have been made to characterize the poorly defined nature of mercury salts in aqueous and other solutions by the change in ^{199}Hg nuclear shielding. Similarly, δ^{199}Hg values can be used to determine the binding site (e.g. to O, N or S) of $[MeHg]^+$ cations. In the case of organomercury compounds, it is possible to measure δ^{199}Hg values even from very dilute solutions (e.g. aqueous solutions of ethylmercury phosphates and their interaction with amino acids) by taking advantage of indirect (^{1}H-detected) methods, based on scalar ^{199}Hg−^{1}H spin−spin coupling. High-resolution solid state ^{199}Hg NMR measurements are feasible in the case of tetrahedral mercury complexes, e.g. $[Hg(SR)_4]^{2-}$, otherwise the huge anisotropy of ^{199}Hg nuclear shielding causes problems.

Major applications of δ^{183}W values (referred to a ≈ 1 M solution of Na_2WO_4 in D_2O with pD = 9; or WF_6: δ^{183}W = −1121 with Ξ^{183}W = 4.161 733 MHz) concern the structural characterization of polytungstates and heteropolytungstates in solution.[31] Other tungsten compounds studied are mostly those with a W−F, W−P, or W−H bond, using indirect detection of the ^{183}W resonances or polarization transfer, taking advantage of scalar ^{183}W−^{19}F, ^{183}W−^{31}P or ^{183}W−^{1}H spin−spin coupling. Further examples of the application of δ^{183}W comprise carbyne complexes and dinuclear complexes with WW double and quadruple bonds (Table 6).

The favorable nuclear magnetic properties of ^{195}Pt and the well-developed platinum chemistry guarantee numerous applications of δ^{195}Pt values {external reference is the absolute frequency Ξ^{195}Pt = 21.4 MHz [Ξ^1H (Me_4Si) = 100.00 MHz] or the $Na_2[PtCl_6]$ in D_2O with Ξ^{195}Pt = 21.496 770 MHz corresponding to δ^{195}Pt = +4522}. The range of δ^{195}Pt values covers ≈ 15 000 ppm {$[PtF_6]^{2-}$: δ^{195}Pt ≈ +11 840; many Pt(0) and Pt(II) complexes have δ^{195}Pt values up to −3000}. There is no clear dependence of δ^{195}Pt values on the formal oxidation state of the metal. The analysis of mixtures of platinum compounds is readily achieved since the dispersion of δ^{195}Pt values is much larger than that of δ^{13}C or δ^1H for the respective ligands. This is helpful for monitoring reactions and for assigning the structures of the final products, e.g. to distinguish between diastereomers. High-resolution solid state ^{195}Pt NMR spectra are relatively simple for octahedrally surrounded platinum and become complex and much more difficult to measure in the case of square-planar platinum complexes because of the large anisotropy of ^{195}Pt nuclear shielding.

2.3 Chemical Shifts of Some Quadrupolar Nuclides

2.3.1 ^{6}*Li*, ^{7}*Li*, ^{23}*Na*, ^{39}*K*, ^{87}*Rb*, ^{133}*Cs*[1,2]

The range of chemical shifts δLi [external reference Li^+(aq)] is small (≈ 15 ppm). However, in accord with the usual trend, the range of δ values for the heavier nuclides [external references: M^+(aq)] of this group increases with the mass of the nuclides and, therefore, it is possible to study the influence of the counterion, and of solvent effects, including the function of cryptands and concentration effects on the nuclear shielding of the cations, in great detail. Furthermore, the formation of the metal anions $[Na]^-$, $[K]^-$, $[Rb]^-$, and $[Cs]^-$ (alkalides) is readily proved (Table 7) by the extreme shifts of the NMR signals to low frequency[32] as a consequence of the ns^2 electron configuration.

2.3.2 ^{9}*Be*,[1,2] ^{25}*Mg*[33]

Limited applications have been found for δ^9Be and δ^{25}Mg [external references: Be^{2+}(aq) and Mg^{2+}(aq)], with respect to both changes in coordination number and in CpBe and CpMg derivatives.

2.3.3 ^{11}*B*

The nuclear shielding of ^{11}B has received considerable attention. A large data set of chemical shifts δ^{11}B (external reference $Et_2O{-}BF_3$) is available for all types of boron compounds in solution.[34,35] Low nuclear shielding of boron (δ^{11}B ≈ +10 to +130) is observed for three-coordinate boron (Table 8), depending on the electronic structure of the boranes. An interstitial boron atom in the anion $[Ru_6(H)_2(CO)_{18}B]^-$ represents the most deshielded ^{11}B nucleus (δ^{11}B +205.9).[36] For a large number of trigonal boranes an empirical, crudely linear relationship is observed between boron nuclear shielding and the calculated π-electron densities at the boron atoms.

In compounds containing two-coordinate boron, we find rather high ^{11}B nuclear shielding in the iminoboranes, R−B≡N−R′ (δ^{11}B ≈ 0 to +20) and deshielded ^{11}B nuclides if

Table 7 Nuclear Shielding of Alkalide Anions

	$[Na]^-$	$[K]^-$	$[Rb]^-$	$[Cs]^-$
δM	−62	−105	−185	−280

Table 8 Boron-11 Chemical Shifts of Selected Simple Boranes (Compare Me_3B: $\delta^{11}B$ = +86)

	$\delta^{11}B$		$\delta^{11}B$		$\delta^{11}B$		$\delta^{11}B$		$\delta^{11}B$
BF_3	10.0	BCl_3	46.5	$B(OMe)_3$	18.3	$B(SMe)_3$	61.0	$B(NMe_2)_3$	27.3
$MeBF_2$	28.2	$MeBCl_2$	62.3	$MeB(OMe)_2$	29.5	$MeB(SMe)_2$	66.3	$MeB(NMe_2)_2$	33.5
Me_2BF	60.1	Me_2BCl	75.5	Me_2BOMe	53.0	Me_2BSMe	74.0	Me_2BNMe_2	44.6

the symmetry is reduced, e.g. in $[R-B{=}NR'R'']^+$ ($\delta^{11}B \approx +36$ to +60). As for other pairs of isostructural and isoelectronic boron and carbon compounds, this situation is similar to the greatly different $\delta^{13}C$ values of alkyne derivatives and vinyl cations, if one substitutes the BN by the CC moiety. Many trigonal boranes are used as π ligands in transition metal complexes. The resulting metal–boron interaction, even if it is weak, is in general reflected by the increase in boron nuclear shielding (Table 9).

Table 9 Boron-11 Chemical Shifts of Selected Boranes in π Complexes with Transition Metals. Note the Increased ^{11}B Nuclear Shielding in the Bridging Ligand.

	$\delta^{11}B$
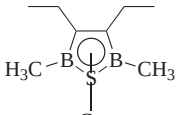	+30.0
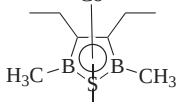	+14.0
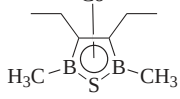	+30.0
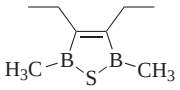	+66.0
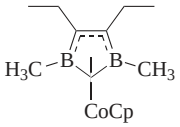	+27.3
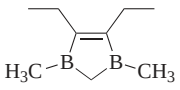	+69.0

The ^{11}B resonance signals of borane adducts and borates are also found at low frequencies with respect to boranes, in accord with the increase in CN_B. Clearly, chemical shifts $\delta^{11}B$ have been very useful in the elucidation of the complex structures of polyboranes, carboranes, and the enormous number of other heteropolyboranes.[35]

2.3.4 ^{27}Al[1,2]

Chemical shifts $\delta^{27}Al$ [external reference $Al^{3+}(aq)$] reflect the CN_{Al} by ^{27}Al NMR signals at highest frequency for CN_{Al} = 3, at lower frequency for CN_{Al} = 4, overlapping with the range for CN_{Al} = 5, and at lowest frequencies for CN_{Al} = 6. There are few exceptions to this general trend. Since the AlO_4 tetrahedron is an important building block in zeolites, solid state ^{27}Al chemical shifts serve, together with ^{29}Si chemical shifts,[12] for monitoring changes in the structure of zeolites.[37] Since MAS cannot remove the anisotropic or line broadening part of the second-order quadrupolar interaction, double rotation NMR has been developed to improve high-resolution solid state NMR spectra of nuclides with half-integer spin such as $^{27}Al(I = \frac{5}{2})$.

2.3.5 ^{14}N[1,2]

Chemical shift values $\delta^{14}N$ are identical to those of $\delta^{15}N$. As a consequence of the high natural abundance of ^{14}N (99.63%), the solution state $\delta^{14}N$ values are much more readily determined than $\delta^{15}N$ values. However, owing to efficient quadrupolar relaxation, the ^{14}N NMR signals may be rather broad and, in the case of different ^{14}N NMR signals, the resolution may be insufficient for accurate determination of $\delta^{14}N$ data.

2.3.6 ^{17}O, ^{33}S[1,2,27]

In spite of its low natural abundance (0.037%) numerous applications of $\delta^{17}O$ values [external reference H_2O or neat acetone at 301 K ($\delta^{17}O$ = +569, with the absolute frequency $\Xi^{17}O$ = 13.564 269 MHz)] are reported. In solution, most classes of inorganic oxygen compounds have been studied and a range of $\delta^{17}O \approx 1650$ has been found, with ^{17}O resonance signals for two-coordinate oxygen in gaseous H_2O ($\delta^{17}O$ −36.1) or Me_2O ($\delta^{17}O$ −53) at low frequency and for $[MnO_4]^-$ ($\delta^{17}O$ = +1230) or for the terminal and central oxygen atoms in ozone [$\delta^{17}O$ = +1032 (terminal) and +1598 (central)] at very high frequencies. The solution structure of the transition metal carbonyl cluster is revealed by the different $\delta^{17}O$ values of terminal ($\delta^{17}O \approx +350$ to +440) and bridging ($\delta^{17}O \approx +500$) carbonyl groups. Another field of application of $\delta^{17}O$ values concerns polyoxometalates, where the ^{17}O nuclear shielding in general increases with the number of metal atoms in the neighborhood. Thus, a terminal oxygen atom is characterized by low shielding with $\delta^{17}O$ values in the range $\approx +800$ to $\approx +1250$, depending on the metal, although the ^{17}O NMR signals are mostly at higher frequencies compared with those of tetrahedral $[MO_4]^{n-}$ (n = 0–3) (Table 10).

The comparison with $\delta^{17}O$ values of corresponding tetrahedral main group oxo anions (Table 11) indicates that the electronic structures of the transition metals have a major influence on ^{17}O nuclear shielding.

Solid state ^{17}O MAS NMR spectra of ^{17}O-enriched materials are readily measured, in particular if the oxygen atoms occupy sites of cubic or close-to-cubic symmetry.

Table 10 Oxygen-17 Chemical Shifts in Tetrahedral Oxometalate Anions

	RuO_4	OsO_4	$[MnO_4]^-$	$[TcO_4]^-$	$[ReO_4]^-$	$[CrO_4]^{2-}$	$[MoO_4]^{2-}$	$[WO_4]^{2-}$	$[VO_4]^{3-}$
$\delta^{17}O$	+1106	+796	+1230	+749	+569	+835	+530	+420	+568

Table 11 Oxygen-17 Chemical Shifts of Oxo Anions of Main Group Elements

	$[ClO_4]^-$	$[SO_4]^{2-}$	$[SeO_4]^{2-}$	$[PO_4]^{3-}$
$\delta^{17}O$	+290	+167	+204	+113

In alkaline earth metal oxides the $\delta^{17}O$ values range from +22 (BeO) to +640 (BaO), following the changes in cation electronegativity and in the cation radius.

Values of $\delta^{33}S$ [external reference Cs_2SO_4(aq) 2 M with the absolute frequency $\Xi^{33}S$ = 7.670 123 MHz] have found only limited application as a result of rather broad lines in most cases [exceptions are SF_6, $SO_4{}^{2-}$, metal thiocarbonyl complexes and thiooxo metal anions such as $MoS_{4-n}O_n{}^{2-}$ or $WS_{4-n}O_n{}^{2-}$ (n = 0–3)] owing to the efficient quadrupolar relaxation. A range of ≈ 1000 ppm has been found with COS ($\delta^{33}S$ = −594) and alkali metal sulfides at lowest frequency and SO_2 ($\delta^{33}S$ = +375) at highest frequency. In general, the $\delta^{33}S$ values follow the trend set by $\delta^{17}O$ values. Hence, changes of solid state $\delta^{33}S$ values of alkaline earth metal sulfides are similar to those of the corresponding $\delta^{17}O$ values.

2.3.7 Some Transition Metal Quadrupolar Nuclides (^{51}V, ^{59}Co, ^{95}Mo)[1,2,28]

Vanadium-51 NMR has been extensively used for all soluble vanadium compounds. Owing to the high NMR sensitivity of the ^{51}V nucleus, very dilute reaction solutions can be studied. There are large and characteristic ranges of $\delta^{51}V$ values (external reference neat $VOCl_3$) for various types of vanadium compounds {whole range of $\delta^{51}V \approx -2000$, $[Ph_3SnV(\eta^5\text{-}C_5H_5)(CO)_3]^-$ $\delta^{51}V = -2052$ to ≈ +4000 (solid Cu_3VTe_4 $\delta^{51}V$ = +3950)}. Important applications concern polyvanadates and heteropolyvanadates and all areas of organometallic vanadium chemistry.

Cobalt-59 NMR signals have provided very early (back to 1951) examples of the chemical shift of metal nuclides. Values of $\delta^{59}Co$ (external reference $K_3[Co(CN)_6]$ in D_2O 0.1 M with the absolute frequency $\Xi^{59}Co$ = 23.727 118 MHz) cover a large range between $\delta^{59}Co \approx +14\,000$ to ≈ -4000.[1,2,28,39] Although it is always pointed out that a crude relationship between the formal oxidation state of cobalt and $\delta^{59}Co$ exists [increase in ^{59}Co nuclear shielding with decrease in the formal oxidation number from Co(III) to Co(−1)], it is important to remember that $\delta^{59}Co$ values for Co(III) complexes are found in the range between $\delta^{59}Co \approx +14\,000$ and 0. In the case of octahedral Co(III) complexes, we find instructive examples of linear correlations between electronic transition wavelengths (as a measure of the average excitation energy, ΔE) and ^{59}Co nuclear shielding: a decrease in ΔE causes a decrease in ^{59}Co nuclear shielding.[40]

Values of $\delta^{95}Mo$ [external reference Na_2MoO_4(aq) at pH 11] cover a range of ≈ 6000 ppm with greatest deshielding in compounds with MoMo multiple bonds of the type $R_4Mo{=}MoR_4$ (e.g. R = ^{t}BuC(O)O with $\delta^{95}Mo$ = +3667) or $R_3Mo{\equiv}MoR_3$ (e.g. R = CH_2SiMe_3 with $\delta^{95}Mo$ = +3624), and with high ^{95}Mo nuclear shielding in $Mo(CO)_6$ ($\delta^{95}Mo$ = −1856), $Na[(\eta^5\text{-}C_5H_5)Mo(CO)_3]$ ($\delta^{95}Mo$ = −2123), or $[Mo(\eta^5\text{-}C_5H_5)_2H_3]Cl$ ($\delta^{95}Mo$ = −2953).[41] In spite of fairly broad lines, the ^{95}Mo shift differences are sufficiently large to distinguish between diastereomers with molybdenum as the chiral center. Molybdenum-95 chemical shift data of polyoxomolybdates and heteropolyoxomolybdates are useful for structural characterization in solution and in the solid state.

3 APPLICATION OF INDIRECT NUCLEAR SPIN–SPIN COUPLING CONSTANTS ^NJ(A,X)

3.1 One-Bond Coupling Constants ^1J(A,X)

All reduced coupling constants $^1K(X,^1H)$ have a positive sign. Scalar spin–spin coupling across one bond between ^1H and other nuclides (including ^1H) has been extensively studied. Thus, $^1J(^1H,^1H)$ [measured as $^1J(^2H,^1H)$ in partially deuterated compounds, converted to $^1J(^1H,^1H)$ values by multiplication with γ^1H/γ^2H = 6.514] in η^2-H_2 transition metal complexes [$^1J(^1H,^1H) \approx 144$ to ≈ 208 Hz][42,43] is considerably smaller (Table 12) than in free H_2 [$^1J(^1H,^1H)$ = 278 Hz], indicating the weakening of the strong H–H bond as a result of interaction with the metal. In the absence of a lone pair of electrons at atom X, the magnitude of $^1J(X,^1H)$ reflects in a qualitative way the so-called 's character' of the X–H hybrid bond orbital and changes in $^1J(X,^1H)$ fit the model of rehybridization at atom X. Coupling constants $^1J(^{11}B,^1H)$ in diborane, B_2H_6, demonstrate the dependence of $^1J(^{11}B,^1H)$ on the s electron density available for the terminal B–H bond [$^1J(^{11}B,^1H_t)$ = 133.5 Hz] and in the two-electron BHB three-center bond [$^1J(^{11}B,^1H_b)$ = 46.3 Hz]. In the case of a closed s shell configuration at atom X (e.g. X = ^{31}P in phosphines PH_3, RPH_2 or R_2PH, or ^{77}Se in H_2Se, RSeH), changes in the magnitude of $^1J(X,^1H)$ are much less predictable.

There are numerous applications of ^1J(A,X) values for any suitable combination of A and X (A,X ≠ ^1H). The reduced coupling constants ^1K(A,X) can be of either sign, and there are numerically very small or very large values. So far the largest coupling constant has been measured in the cationic mercury species $[Hg{-}Hg{-}Hg]^+$ with $^1J(^{199}Hg,^{199}Hg) \approx 139\,700$ Hz.[44] If A and X are spin-$\frac{1}{2}$ nuclides ^1J(A,X) data are readily obtained from either the A or the X NMR spectra. If one or both nuclides, A or X, are quadrupolar nuclides, the quadrupolar relaxation rate determines whether the measurement of ^1J(A,X) is straightforward (see Section 4). In general, similar to $^1J(X,^1H)$, the magnitude of ^1J(A,X) can be related to the nature of bonding between these two nuclides, and it provides information on the influence of other substituents at A or X or of the whole molecular structure on the bonding situation. The structural elucidation of polyphosphane and polyborane derivatives by using two-dimensional (2D) homonuclear $^{31}P/^{31}P$ and $^{11}B/^{11}B$ COSY experiments (Figure 6) respectively, serve as examples. Both

Table 12 Transition Metal Complexes with η^2-H_2 and Hydride Ligands

$\{MH(\eta^2\text{-}H_2)[PhP(OEt)_2]_4\}^+$	$^1J(^1H,^1H)$ (Hz)	T_1 ^1H: η^2-H_2–M (10^{-3}s)	H–M (10^{-3}s)
M = Fe	–	4	65
Ru	208.5	5	90
Os	–	8	44

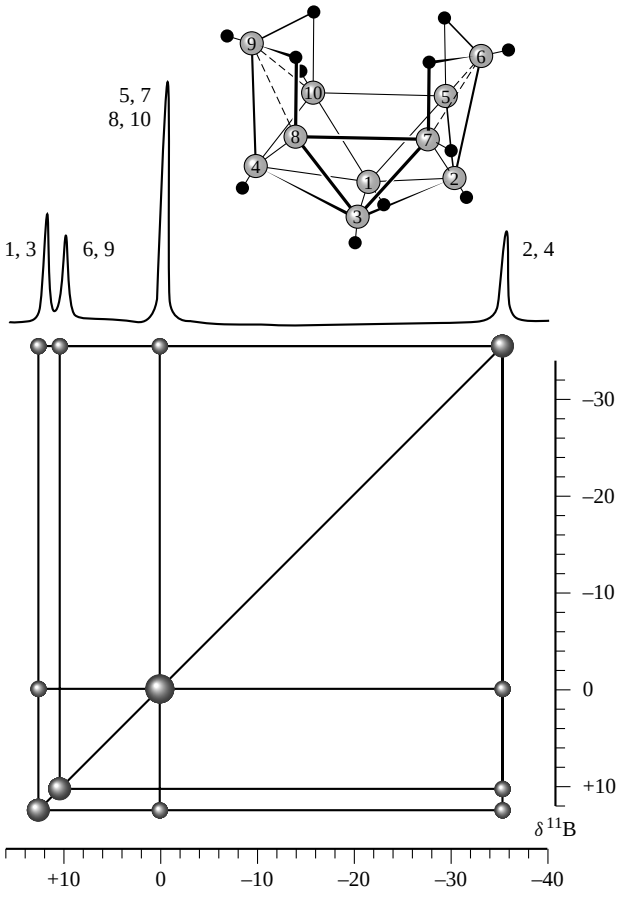

Figure 6 Contour plot of the two-dimensional $^{11}B/^{11}B$ COSY spectrum at 64.2 MHz of decaborane(14), $B_{10}H_{14}$, showing off-diagonal peaks for ^{11}B nuclides linked together via BBB three-center bonds

experiments are based on scalar one-bond spin–spin coupling. In the case of ^{31}P ($I = \frac{1}{2}$), the splittings due to $^1J(^{31}P,^{31}P)$ are resolved in the one-dimensional (1D) spectra which, however, may be complex and difficult to analyze with respect to the connectivity of the molecular backbone consisting of many phosphorus atoms. Owing to quadrupolar relaxation of the ^{11}B nuclides ($I = \frac{3}{2}$) most couplings $^1J(^{11}B,^{11}B)$ are not well resolved in 1D ^{11}B NMR spectra. Nevertheless, the cross peaks observed in the 2D $^{11}B/^{11}B$ COSY experiments are indicative of the connectivity of those boron atoms engaged in BBB three-center bonds, whereas cross peaks for ^{11}B nuclides forming BHB three-center bonds are rather weak and, in most cases, cannot be detected.

The determination of the composition of fluxional cluster compounds in solution can be achieved if coupling is observed (i.e. exchange processes occur intramolecularly). Thus, in Zintl anions of the type $[Sn_{9-n}Pb_n]^{4-}$ (n = 0–9) the nature of the anion and its composition follows conclusively from the relative intensities of ^{117}Sn (Figure 7) or ^{207}Pb satellites [due to $J(^{119}Sn,^{117}Sn)$ or $J(^{207}Pb,^{117/119}Sn)$] in ^{119}Sn or ^{207}Pb NMR spectra.[45]

3.2 Two-Bond (Geminal) Coupling Constants ^2J(A,X)

In many organyl derivatives of various elements X, e.g. X = Si, Sn, Pb, P, Se, Te, or Hg, the coupling constants $^2J(X,^1H)$ are routinely measured. Such couplings help to improve the NMR sensitivity of spin-$\frac{1}{2}$ X nuclei by using polarization transfer experiments [INEPT or DEPT, based on coupling constants $^2J(X,^1H)$] for direct or inverse detection of the X resonances.

In transition metal chemistry, *cis* and *trans* arrangements of ligands in complexes with square planar, trigonal bipyramidal or octahedral geometry provide a wide field of application of $^2J(A,X)$ values. Although the greatest number of examples involves A and/or X = ^1H and ^{31}P, there are also important examples for A and/or X = ^{13}C, ^{19}F, $^{119/117}Sn$, ^{199}Hg,

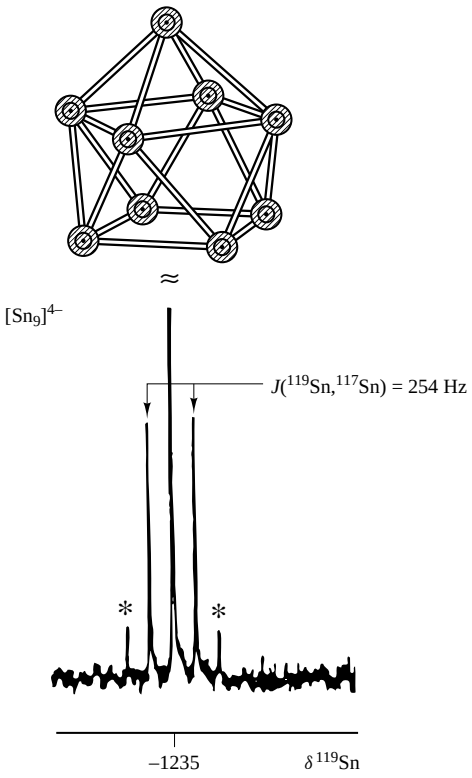

Figure 7 Tin-119 NMR spectrum at 74.6 MHz of the highly fluxional Zintl anion $[Sn_9]^{4-}$ in ethylenediamine. The parent signal due to $[Sn_8{}^{119}Sn]^{4-}$ is cut off and the satellites are due to the species $[Sn_7{}^{119}Sn^{117}Sn]^{4-}$ and $[Sn_6{}^{119}Sn^{117}Sn_2]^{4-}$ (the outer lines of the corresponding triplet are marked by asterisks)

or ^{207}Pb. In general, it is observed that the *cis* coupling pathway leads to fairly small ^2K(A,X) values which can be of either sign, whereas the *trans* position of A and X gives much larger couplings, usually with $^2K(A,X) > 0$. Geminal coupling constants in polytungstates and in heteropolytungstates, in particular if one of the heterotoms is phosphorus, are important for structural assignment in solution. The values $^2J(^{183}W,^{183}W)$ across the oxygen atom indicate the nature of W–O–W bridging[46] and also reflect distortions of WO_6 octahedral units.[47] Furthermore, it allows us to perform 2D INADEQUATE experiments that enable us to trace the connectivity of tungsten atoms.[48] The coupling constants $^2J(^{183}W, ^{31}P)$ across the oxygen atom reveal the environment of the PO_4 tetrahedron in the framework.

3.3 Three-Bond (Vicinal) Coupling Constants ^3J(A,X)

As described for ^2J(X,H), coupling constants ^3J(X,H) are measured routinely and serve for various polarization transfer experiments in the measurement of X NMR spectra. Most other applications of vicinal coupling constants deal with the geometric relationship between the nuclides as has been found empirically for ^3J(H,H) and as expressed in the Karplus equation[49]

$$^3K = C\ \cos 2\Phi + B\ \cos\ \Phi + A$$

in which Φ is the dihedral angle and A, B, and C are constants depending on the coupled nuclides, on the electronegativity of substituents, and on the nature of the intervening atoms.

4 APPLICATION OF NUCLEAR SPIN RELAXATION PARAMETERS

4.1 Structural Information

Although dipolar interactions between magnetically active nuclides in liquids are averaged, these interactions can still be responsible for relaxation (T_1^{DD}, T_2^{DD}, depending on r_{AX}^6), which can be proved by 1D or 2D NOE measurements (NOESY, etc.). These are of prime importance in biochemistry applications, in particular for homonuclear NOE between protons, but it is certainly also a useful approach in inorganic chemistry. In some cases decisive structural information can already be gained by measuring T_1 values as shown for complexes containing the η^2-H_2–M group and the corresponding hydrides with M–H bonds. The persistent H–H bond in the former is identified by much shorter T_1^{1H} values compared with the η^1-hydrides[50] (Table 12).

With few exceptions (e.g. ^{2}H, ^{6}Li, ^{7}Li, ^{9}Be) the nuclear spin relaxation of quadrupolar nuclides ($I > \frac{1}{2}$) in liquids is dominated by electric quadrupole interactions. Consequently, large quadrupolar coupling constants reflecting an asymmetric distribution of charge around the nucleus, are related to broad resonance signals or short relaxation times T_Q [$W_{1/2} = (\pi T_Q)^{-1}$]. This can be used for studying the coordination sphere of cations (e.g. Na^+, Cs^+, Mg^{2+}, etc.) or anions (e.g. Cl^-, Br^-, ClO_4^-, SO_4^{2-}, etc.) in solution. Similarly, different linewidths as a result of quadrupolar relaxation support the structural assignment in mixtures of octahedral complexes [e.g. of Co(III) or of Al(III)]. If the local symmetry at the quadrupolar nucleus does not change, but the molecular size increases, this will cause an increase in the linewidth of the NMR signal. Hence equilibria involving intermolecular association are readily shown.

If a paramagnetic material is added to a diamagnetic sample, the relaxation processes are significantly perturbed owing to the very large magnetogyric ratio of the electron. This has been used to shorten T_1 values (relaxation agent) or to simplify complex ^{1}H NMR spectra (shift agent). In the latter case, it is also possible to obtain structural information if the shift in the ^{1}H NMR spectra results from interactions between a polar group in the diamagnetic species with the paramagnetic metal center (usually a lanthanoid metal).

4.2 Chemical Exchange

There are many labile bonding situations in inorganic chemistry, leading eventually to chemical exchange, either intra- or intermolecularly. These processes are reflected by temperature-dependent changes of the linewidth $W_{1/2}$ of the relevant NMR signals and/or by the appearance of a typical splitting pattern due to spin–spin coupling [e.g. $[B_3H_8]^-$ (Figure 8), ClF_3, SF_4, or pseudorotation in fluorophosphoranes] if the rate of the exchange processes fits the NMR timescale defined by chemical shifts and coupling constants (see Figure 8). However, this timescale can be readily expanded for monitoring very fast or rather slow processes by making use of nuclear spin relaxation behavior.

Slow processes may be simply revealed by time-dependent signal intensities, a very basic approach to the study of kinetics. If the rate of chemical exchange corresponds to the spin–lattice relaxation time T_1 of the nuclides involved, various 1D and 2D techniques (based on magnetization- and spin-saturation transfer) are available to monitor such exchange processes. The nature of the Wilkinson catalyst in solution in the presence of an excess of triphenylphosphine (Figure 9) is an instructive example.[51]

Fast exchange processes can be characterized by determining the difference between spin–spin and spin–lattice relaxation times. The exchange contribution to T_2, $(T_{2,ex})^{-1}$ is dependent on $B_0{}^2$, which means that high-field NMR spectrometers open up the access to fast exchange rate constants (up to 10^7 to $10^8\,s^{-1}$).

4.3 Motion in Liquids and Solids

Most major relaxation mechanisms both in solution and in the solid state arise from some sort of motion. There are too

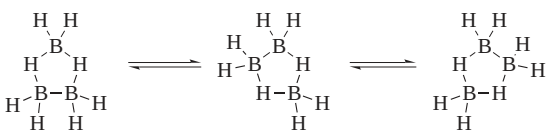

Figure 8 Fast intramolecular exchange between, and bridging hydrogen atoms in, the anion $[B_3H_8]^-$, leading to an averaged coupling $J(^{11}B,^1H) = 33$ Hz (the ^{11}B NMR spectrum at 64.2 MHz shows seven of the expected nine lines with the correct ratio)

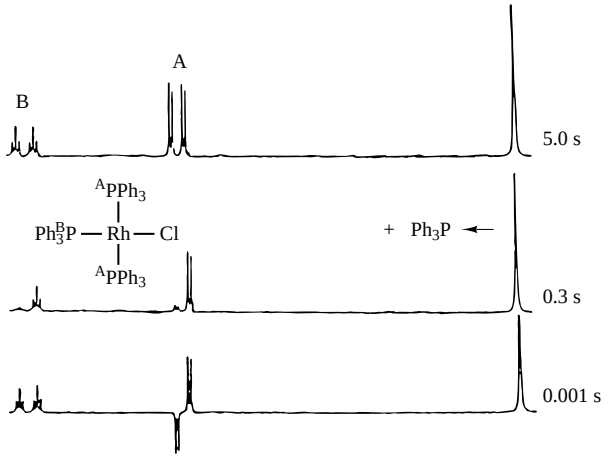

Figure 9 Spin saturation transfer experiment (based on DANTE) showing that intramolecular exchange between sites A and B is much faster (see the experiment with 0.3 s delay) than intermolecular exchange with free Ph_3P. The splitting of the signals A and B arises from $^{1}J(^{103}Rh,^{31}P)$ and $^{2}J(^{31}P,^{31}P)$. The ^{31}P spectra were recorded at 81.0 MHz

many different roots and applications, which are clearly not related just to inorganic chemistry, in order to discuss this topic in detail. The rotational correlation times in solution can be determined, e.g., by NOE measurements of spin-$\frac{1}{2}$ nuclides, by measurement of T_Q of quadrupolar nuclides (if the quadrupolar coupling constant is known), or by using information on the anisotropy of nuclear shielding. MAS in the solid state has opened the way to study the dynamic behavior of solids more accurately and more conveniently as shown in the case of the mobility of π bonded aromatic ligands or carbonyl groups in organometallic compounds.[52]

5 RELATED ARTICLES

Aluminum-27 NMR of Solutions; Boron NMR; Brownian Motion and Correlation Times; Chemical Exchange Effects on Spectra; Chemical Shift Tensors; Fluorine-19 NMR; Germanium, Tin, and Lead NMR; Heteronuclear Shift Correlation Spectroscopy; Hydrogen Bonding; Hydrogen–Metal Systems; INADEQUATE Experiment; Indirect Coupling: Semiempirical Calculations; Inorganic Nuclei: Low Sensitivity Transition Metals; Inorganic Solids; Lithium NMR; Nitrogen NMR; Noble Gas Elements; Nuclear Overhauser Effect; Nuclear Spin Properties and Notation; Organic Chemistry Applications; Organometallic Compounds; Oxygen-17 NMR; Phosphorus-31 NMR; Polarization Transfer Experiments via Scalar Coupling in Liquids; Recording One-Dimensional High Resolution Spectra; Relaxation: An Introduction; Shielding: Overview of Theoretical Methods; Silicon-29 NMR; Silicon-29 NMR of Solid Silicates; Spin Echo Spectroscopy of Liquid Samples; Sulfur, Selenium, and Tellurium NMR; Thallium NMR; Two-Dimensional Carbon–Heteroelement Correlation.

6 REFERENCES

1. eds. R. K. Harris and B. E. Mann, *NMR and the Periodic Table*, Academic Press, London, 1978.
2. ed. J. Mason, *Multinuclear NMR*, Plenum, New York, 1987.
3. J. Emsley, *Chem. Soc. Rev.*, 1980, **9**, 91.
4. G. L. Geoffroy and J. R. Lehman, *Adv. Inorg. Radiochem.*, 1977, **20**, 189.
5. S. J. Berners-Price, T. A. Frenkiel, U. Frey, J. D. Ranford, and P. J. Sadler, *J. Chem. Soc., Chem. Commun.*, **1992**, 789.
6. D. Freude, M. Hunger, and H. Pfeifer, *Chem. Phys. Lett.*, 1982, **91**, 307.
7. B. E. Mann and B. F. Taylor, *^{13}C NMR Data for Organometallic Compounds*, Academic Press, London, 1981.
8. H. W. Papenguth, R. J. Kirkpatrick, B. Montez, and P. A. Sandberg, *Am. Mineral.*, 1989, **74**, 1152.
9. B. Wrackmeyer, K. Horchler, A. Sebald, L. H. Merwin, and C. Ross II, *Angew. Chem., Int. Ed. Engl.*, 1990, **29**, 807.
10. E. Kupće and E. Lukevics, in *Isotopes in the Physical and Biomedical Sciences* eds. E. Buncel and J. R. Jones, Elsevier, Amsterdam, 1991, p. 213.
11. R. K. Harris, C. T. G. Knight, and W. E. Hull, *J. Am. Chem. Soc.* 1981, **103**, 1577.
12. C. A. Fyfe, Y. Feng, H. Grondey, G. T. Kokotailo, and H. Gies, *Chem. Rev.*, 1991, **91**, 1525.
13. B. Wrackmeyer, A. Sebald, and L. H. Merwin, *Magn. Reson. Chem.*, 1991, **29**, 260.
14. B. Wrackmeyer, *Annu. Rep. NMR Spectrosc.*, 1985, **16**, 73.
15. B. Wrackmeyer and K. Horchler, *Annu. Rep. NMR Spectrosc.*, 1990, **22**, 249.
16. S. Berger, S. Braun, and H.-O. Kalinowski, *NMR-Spektroskopie von Nicht-Metallen*, Thieme, Stuttgart, 1992, Vol. 2
17. D. C. Bradley, S. R. Hodge, J. D. Runnacles, M. Hughes, J. Mason, and R. L. Richards, *J. Chem. Soc., Dalton Trans.*, **1992**, 1663.
18. S. Berger, S. Braun, and H.-O. Kalinowski, *NMR-Spektroskopie von Nicht-metallen*, Thieme, Stuttgart, 1993, Vol. 3
19. E. Fluck and G. Heckmann, in *Phosphorus-31 NMR Spectroscopy in Stereochemical Analysis*, eds. J. G. Verkade and L. D. Quin, VCH, Weinheim, 1987, pp. 61–113.
20. G. Huttner, *J. Organomet. Chem.*, 1986, **308**, C11.
21. J. Hahn, in *Phosphorus-31 NMR Spectroscopy in Stereochemical Analysis*, eds. J. G. Verkade and L. D. Quin, VCH, Weinheim, 1987, pp. 331–364.
22. A. K. Cheetham, N. J. Clayden, C. M. Dobson, and R. J. B. Jakeman, *J. Chem. Soc., Chem. Commun.*, **1986**, 195.
23. H. C. E. McFarlane and W. McFarlane, *J. Chem. Soc., Dalton Trans.*, **1973**, 2416.
24. M. J. Collins and R. J. Gillespie, *Inorg. Chem.* 1984, **23**, 1975.
25. J. W. Emsley and L. Phillips, *Prog. NMR Spectrosc.*, 1971, **7**, 1–515.
26. R. K. Harris and P. Jackson, *Chem. Rev.*, 1991, **91**, 1427.
27. S. Berger, S. Braun, and H.-O. Kalinowski, *NMR-Spektroskopie von Nicht-metallen*, Thieme, Stuttgart, 1992, Vol. 1
28. ed. P. S. Pregosin, *Transition Metal Nuclear Magnetic Resonance*, Elsevier, Amsterdam, 1991.
29. B. T. Heaton, R. D. Pergola, L. Strona, D. O. Smith, and A. Fumagalli, *J. Chem. Soc., Dalton Trans.*, 1982, 2553.
30. B. Wrackmeyer and R. Contreras, *Annu. Rep. NMR Spectrosc.*, 1992, **24**, 267.
31. R. Acerete, C. F. Hammer, and L. C. W. Baker, *J. Am. Chem. Soc.*, 1982, **104**, 5384.
32. D. M. Holton, P. P. Edwards, D. C. Johnson, C. J. Page, W. McFarlane, and B. Wood, *J. Chem. Soc., Chem. Commun.*, **1984**, 740.
33. R. Benn, H. Lehmkuhl, K. Mehler, and A. Rufinska, *Angew. Chem., Int. Ed. Engl.*, 1984, **23**, 534.

34. B. Wrackmeyer, *Annu. Rep. NMR Spectrosc.*, 1988, **20**, 61.
35. A. R. Siedle, *Annu. Rep. NMR Spectrosc.*, 1988, **20**, 204.
36. C. E. Housecroft, D. M. Matthews, A. L. Rheingold, and X. Song, *J. Chem. Soc., Chem. Commun.*, **1992**, 842.
37. J. Klinowski, *Chem. Rev.*, 1991, **91**, 1459.
38. E. Oldfield and R. J. Kirkpatrick, *Science*, 1985, **227**, 1537.
39. A. Yamasaki, *J. Coord. Chem.*, 1991, **24**, 211.
40. J. Mason, *Chem. Rev.*, 1987, **87**, 1299.
41. R. A. Grieves and J. Mason, *Polyhedron*, 1986, **5**, 415.
42. M. S. Chinn and D. M. Heinekey, *J. Am. Chem. Soc.*, 1987, **109**, 5865.
43. P. Amendola, S. Antoniutti, G. Albertin, and E. Bordignon, *Inorg. Chem.*, 1990, **29**, 318.
44. R. J. Gillespie, P. Granger, K. R. Morgan, and G. J. Schrobilgen, *Inorg. Chem.*, 1984, **23**, 887.
45. W. L. Wilson, R. W. Rudolph, L. L. Lohr, R. C. Taylor, and P. Pyykkö, *Inorg. Chem.*, 1986, **25**, 1535.
46. J. Lefebvre, F. Chauveau, P. Doppelt, and C. Brevard, *J. Am. Chem. Soc.*, 1981, **103**, 4589.
47. R. Thouvenot, A. Tézé, R. Contant, and G. Hervé, *Inorg. Chem.*, 1988, **27**, 524.
48. R. G. Finke, M. W. Droege, and P. J. Domaille, *Inorg. Chem.*, 1987, **26**, 3886.
49. M. Karplus, *J. Chem. Phys.*, 1959, **30**, 11.
50. R. H. Crabtree, *Acc. Chem. Res.*, 1990, **23**, 95.
51. J. M. Brown, P. L. Evans, and A. R. Lucy, *J. Chem. Soc., Perkin Trans. 2*, **1987**, 1589.
52. D. Braga, *Chem. Rev.*, 1992, **92**, 633.

Biographical Sketch

Bernd Wrackmeyer. *b* 1947. Diploma, 1971, Dr. rer.nat., 1973, Habilitation, 1979, University of Munich. Introduced to NMR by H. Nöth and W. McFarlane. Institute of Inorganic Chemistry, University of Munich, 1979–86; Laboratory of Inorganic Chemistry, University of Bayreuth, 1986–present. Approx. 320 publications. Research interests include developments of NMR techniques in solution, application of multinuclear MR to problems in inorganic and organometallic chemistry.

Inorganic Nuclei: Low Sensitivity Transition Metals

Paul S. Pregosin
ETH Zentrum, Zürich, Switzerland

1	Introduction	1
2	Methodology	1
3	Relaxation Times	3
4	Chemical Shifts	3
5	Coupling Constants	5
6	Applications	7
7	References	8
8	Appendix	9

1 INTRODUCTION

The reactions and physical properties of transition metal complexes are determined, naturally enough, by the nature of the metal. Historically, for metal complexes, classical methods of investigation relied heavily on ultraviolet/visible and infrared methods; however, these were often not capable of providing enough detail, especially for the relatively pale or colorless complexes of the third transition series. It was recognized early on[1] that direct observation of the NMR signal from a transition metal center would be advantageous since the metal chemical shift was determined to be very sensitive to its chemical environment. Nevertheless, progress in measuring metal NMR spectra was slow since most of the $I = \frac{1}{2}$ metal nuclei possess small magnetic moments and/or are not found in high natural abundance. Table 1 shows relative sensitivities and natural abundances for the transition metal isotopes, ^{57}Fe, ^{89}Y, ^{103}Rh, ^{107,109}Ag, ^{111,113}Cd ^{183}W, ^{187}Os, ^{195}Pt, and ^{199}Hg, the subjects of this article. Not all of these are low sensitivity nuclei, e.g. ^{113}Cd, ^{195}Pt, and ^{199}Hg are comparable to, or even easier to measure than, ^{13}C; nevertheless, it is reasonable to consider these together with the other, less sensitive nuclei. Where two isotopes with $I = \frac{1}{2}$ are present, e.g. silver and cadmium, it is usually the product of the relative sensitivity and the natural abundance which determines the selection, so that measurements on the isotopes ^{109}Ag and ^{113}Cd are usually preferred. There are a number of useful review articles which discuss aspects of the NMR spectroscopy for these nuclei in detail.[2]

2 METHODOLOGY

The earliest continuous wave,[3] and later INDOR, spectra were often obtained from relatively concentrated solutions but were nevertheless often unsatisfactory from a signal-to-noise viewpoint. In the early 1970s the introduction of pulsed NMR methods together with accumulation and ^{1}H decoupling procedures combined to improve matters by several orders of magnitude.[4]

These pulsed NMR experiments were carried out using comparatively low field instruments, so that the relatively long spin–lattice relaxation times (T_1) for some metal nuclei proved a problem. It was normal to overhear colleagues discussing the difficulties associated with obtaining a particular ^{57}Fe or ^{103}Rh signal, and the source of the problem was not always certain. We know today that T_1 relaxation processes for these relatively insensitive metal spins are often dominated by the shielding anisotropy relaxation mechanism. Indeed, it is no longer uncommon to find published T_1 values on the order of milliseconds for measurements made at 9.39 or 11.74 T.

In the 1980s the increasing commercial availability of spectrometers with both pulse programmers and higher magnetic fields ushered in a new era of interest in measuring spin $I = \frac{1}{2}$ nuclei. Although the increased signal-to-noise ratio was, in some cases, offset by an increase in the metal resonance linewidth, i.e. shorter T_2 values,[2a,b] it was much easier to implement new advantageous pulse sequences. The first major step forward came with the use of polarization transfer methods such as INEPT,[5] in that the metal signal can be enhanced by a factor of γ_H/γ_M, where γ_M is the magnetogyric ratio of the metal nucleus M (and is directly proportional to its magnetic moment). In the INEPT procedure, spin (I) polarization (which usually means ^{1}H, but can be ^{19}F or ^{31}P) is transferred to the spin = $\frac{1}{2}$ metal (S) via pulse sequence (a) shown below:

$$\begin{array}{l} I \text{ spin:} \text{----} \quad 90^\circ_x \text{--} \tau \text{--} 180^\circ \text{---} \tau \text{---} 90^\circ_y \\ \\ S \text{ spin:} \text{----------} 180^\circ_x \text{--} \tau \text{---} 90^\circ_y \text{- acquire} \end{array} \qquad \text{(a)}$$

If decoupling is required, the scheme should be extended as shown in pulse sequence (b):

$$\begin{array}{l} I \text{ spin:} \text{---} \quad 90^\circ_x \text{--} \tau_1 \text{--} 180^\circ \text{--} \tau_1 \text{--} 90^\circ_y \text{--} \tau_2 \text{--} 180^\circ \text{--} \tau_2 \text{--} \text{decouple} \\ \\ S \text{ spin:} \text{---} \text{----------} 180^\circ \text{------} 90^\circ \text{-------} 180^\circ \text{-----acquire} \end{array} \qquad \text{(b)}$$

Examples of this methodology are shown in Figures 1 and 2. Mann[2b] gives the optimum delay, τ_1, for differing numbers of I spins coupled to the metal center.

The major limitation with INEPT arises from the necessity of having a spin–spin coupling between the metal and a suitable proton in the complex. Unfortunately, this condition is frequently either not fulfilled [e.g. $Fe(CO)_5$, $RhCl_3$, $Cd(ClO_4)_2$, K_2PtCl_6, etc.] or one is not aware that a suitable interaction is present. An interesting example of this latter variant will be shown in connection with ^{183}W, in Figure 3. INEPT spectra can appear somewhat strange in that the multiplets reveal both positive and negative phases (typically a +1:−1 doublet or a +1:0:−1 triplet, and occasionally a +1:+1:−1:−1 quartet).

The most sensitive, and now routinely used, approach to obtaining spin $I = \frac{1}{2}$ metal NMR signals involves double polarization transfer[6] ($I \rightarrow S \rightarrow I$) and uses one of the following two-dimensional sequences, with optional pulses shown in braces:

Table 1 Transition Metals with $I = \frac{1}{2}$

Metal	Natural abundance	Sensitivity relative to ^{1}H	Sensitivity[a]	NMR frequency at 11.744 T[b]	Reference
^{57}Fe	2.19	3.37×10^{-5}	7.38×10^{-7}	16.156	$Fe(CO)_5$
^{89}Y	100%	1.18×10^{-4}	1.18×10^{-4}	24.496	YCl_3
^{103}Rh	100%	3.11×10^{-5}	3.11×10^{-5}	15.737	A frequency reference is recommended (=3 160 000)
^{107}Ag	51.82	6.62×10^{-5}	3.43×10^{-5}	20.233	
^{109}Ag	48.18	1.01×10^{-4}	4.86×10^{-5}	23.260	$Ag(NO_3)$
^{111}Cd	12.75	9.54×10^{-3}	1.21×10^{-3}	106.027	
^{113}Cd	12.26	1.09×10^{-2}	1.33×10^{-3}	110.914	$Cd(ClO_4)_2$
^{183}W	14.4	7.2×10^{-4}	1.03×10^{-5}	20.805	Na_2WO_4, WF_6
^{187}Os	1.64	1.22×10^{-5}	2.00×10^{-7}	11.515	OsO_4
^{195}Pt	33.7	9.94×10^{-3}	3.36×10^{-3}	107.495	(Na_2) or K_2PtCl_6
^{199}Hg	16.84	5.67×10^{-3}	9.54×10^{-4}	89.136	$HgMe_2$

[a]Product of natural abundance and relative sensitivity.
[b]500 MHz for protons.

Heteronuclear multiple quantum coherence (HMQC)

I spin: $-90^\circ_x - \tau_{1/2} - \{180^\circ\} - \tau_{1/2} -$

S spin: $-\{180^\circ\}-$

$\{90^\circ_x\} - t_{1/2} - \{180^\circ\} - t_{1/2} - \{-\tau_{1/2} - 180^\circ - \tau_{1/2}\}$ - acquire

90° $90^\circ\{-180^\circ-\}$ {decouple}

(c)

Heteronuclear single quantum coherence (HSQC)

I spin: $-90^\circ_x - \tau_{1/2} - 180^\circ - \tau_{1/2} -$

S spin: $-180^\circ-$

(d)

$90^\circ_y - t_{1/2} - 180^\circ - t_{1/2} - 90^\circ - \tau_{1/2} - 180^\circ - \tau_{1/2}$ - acquire

90° 90° 180° {decouple}

with the I spins again assumed to be a high receptivity nucleus, most often ^{1}H, but occasionally ^{31}P. The time τ is set to $\leq 1/2\ J(S, I)$, and the time t_1 represents the time variable for the second dimension. These sequences provide a theoretical

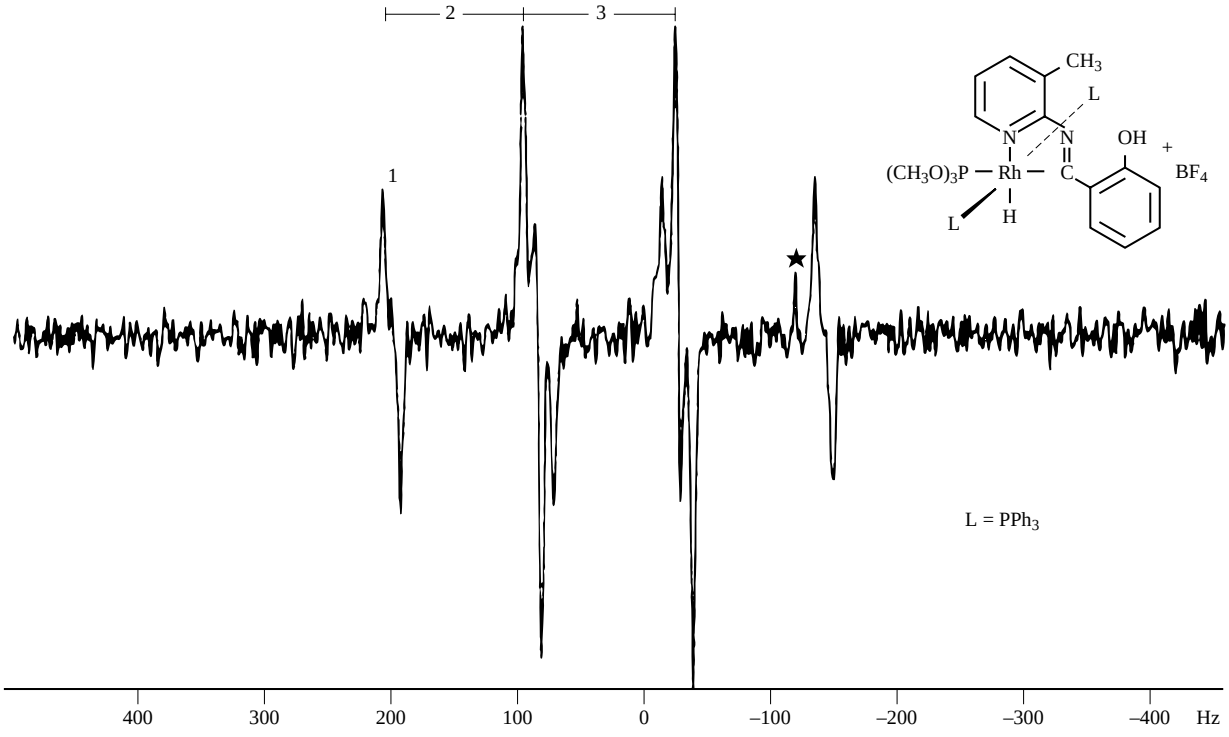

Figure 1 ^{103}Rh{^{1}H} INEPT spectrum, recorded with pulse sequence (a), of the complex shown, L = PPh_3. The fine structure arises from the small splitting due to the hydride proton (1), the two PPh_3 ^{31}P spins (2), and one $P(OMe)_3$ ^{31}P spin (3). (Reproduced by permission of Wiley from Blumer et al.[37])

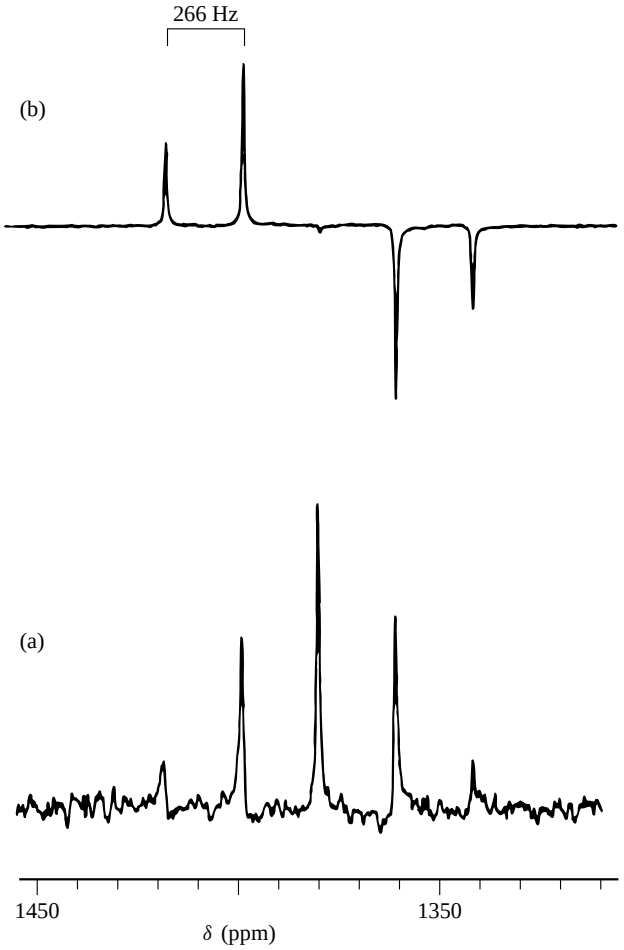

Figure 2 Conventional and $^{109}Ag\{^{31}P\}$ INEPT spectra, recorded with pulse sequence (a), of 0.6 M $[Ag(dppe)_2]NO_3$, dppe = bisdiphenylphosphinoethane, at 300 K. (a) Normal acquisition (12 111 pulses), 2 s delay 50° pulse; (b) $^{109}Ag\{^{31}P\}$ INEPT, 2048 repetitions, τ = 93 ms. (Reproduced by permission of the American Chemical Society from S. J. Berners-Price, C. Brevard, A. Pagelot, and P. J. Sadler, *Inorg. Chem.*, 1985, **24**, 4278)

enhancement of $(\gamma_I/\gamma_S)^{5/2}$. For nuclei such as ^{57}Fe and ^{103}Rh this means factors of 5328 and 5689, respectively, and 'only' 2831 for ^{183}W. The metal data are detected using the proton signals, and the spectra are usually presented as contour plots, as shown in Figures 3–5. For a complex of molecular weight 500–1000, one can obtain good quality ^{183}W data from about 25 mg in approximately 30 minutes.[7]

Once again, the success of this technique depends upon the presence of a spin–spin interaction between the metal and a suitable I spin (usually a proton in a ligand). For the pulse sequences (a) through (d) it is common to introduce a relaxation delay before repeating the sequences. It is interesting to note that, in Figure 3, there are cross peaks which arise due to spin–spin interactions from the ^{183}W to both the *ortho* and *para* protons of the aryl moiety.[7] These previously unknown coupling constants are < 1 Hz and could only be recognized using this type of inverse detection. One finds, increasingly, that inverse methodology is the best way of determining small, not readily measured spin–spin interactions with the transition metal center.

Since the ease with which one can readily detect an ^nJ(M, H) interaction in a one-dimensional experiment is proportional to the size of the magnetic moment of M (small J values are lost in the linewidth when the natural abundance of M is <100%), there is little known with respect to two- and three-bond coupling constants for ^{57}Fe, ^{103}Rh ^{109}Ag, ^{183}W, and ^{187}Os, but quite a lot for ^{195}Pt and ^{199}Hg. However, for metal complexes containing phosphorus ligands in which the ^{31}P is directly bound to the metal center, one always has a relatively large ^1J(M, P) value of the order of 10^2–10^3 Hz.[8] For instruments equipped with a suitable probehead, one can obtain inverse two-dimensional ^{57}Fe–^{31}P and ^{109}Ag–^{31}P spectra such as shown in Figures 6 and 7. The ratio $(\gamma^{31}P/\gamma_M)$, and thus the polarization transfer, is not so favorable as for ^1H; nevertheless, theoretical enhancements of 593 and 295 are possible for ^{103}Rh and ^{183}W, respectively.

3 RELAXATION TIMES

In contrast to a nucleus such as ^{13}C, the relaxation of a spin = $\frac{1}{2}$ metal is not generally controlled by the dipole–dipole relaxation mechanism and there is little or no proton induced NOE. However, ^1H NOE to ^{113}Cd has been observed,[9] and dipole–dipole relaxation has also been found for ^{113}Cd in the protein calbindin D_{9k}.[10] The two most frequently observed T_1 relaxation mechanisms derive from (a) the metal shielding anisotropy (SA),

$$1/T_{1,\mathrm{SA}} = \tfrac{2}{15}\gamma_{\mathrm{metal}}^2 B_0^2 \Delta\sigma^2 \tau_c \qquad (1)$$

where γ is the magnetogyric moment, B_0 is the magnetic field strength, σ represents the shielding anisotropy, and τ a molecular reorientation correlation time, and (b) spin rotation (SR),

$$1/T_{1,\mathrm{SR}} = IkTC^2\tau_{\mathrm{SR}} \qquad (2)$$

where I is the moment of inertia, C the spin–rotation coupling constant, and τ_{SR} the correlation time for spin–rotation.

In recent studies[2a,2b] it has been recognized that the SA relaxation is generally (but not always) the more important of the two, and especially so if the T_1 values are determined using relatively high field magnets. Solid state measurements on spin = $\frac{1}{2}$ metals have shown that the SA can be thousands of parts per million.[2a,11] Indeed, it is not always possible to rotate the solid sample fast enough to avoid finding useful, but none the less complicated sideband patterns.[11] There is no simple rule allowing one to estimate T_1 for the metal in a complex; however, the literature[2a,2b] shows that most values lie between 10^{-1} and 10^2 seconds. For complexes with large SA values, the T_1 values can be of the order of milliseconds[12,13] as noted above. Specifically, in the two-coordinate complex $Hg(CH_2Ph)_2$,[13] the T_1 values are 73.7 ms at 5.8 T and 35.6 ms at 9.4 T, whereas for the platinum(0) complex $Pt(PPr^i_3)_2$ one finds T_1 = 25 ms at 9.4 T and 97 ms at 4.7 T.[12] The last two T_1 values clearly show the dependence of the ^{195}Pt T_1 on B_0^2. For smaller SA values, i.e. more symmetrical complexes, T_1 can be much longer, e.g. 240 s for ^{89}Y in $Y(NO_3)_3$.[14]

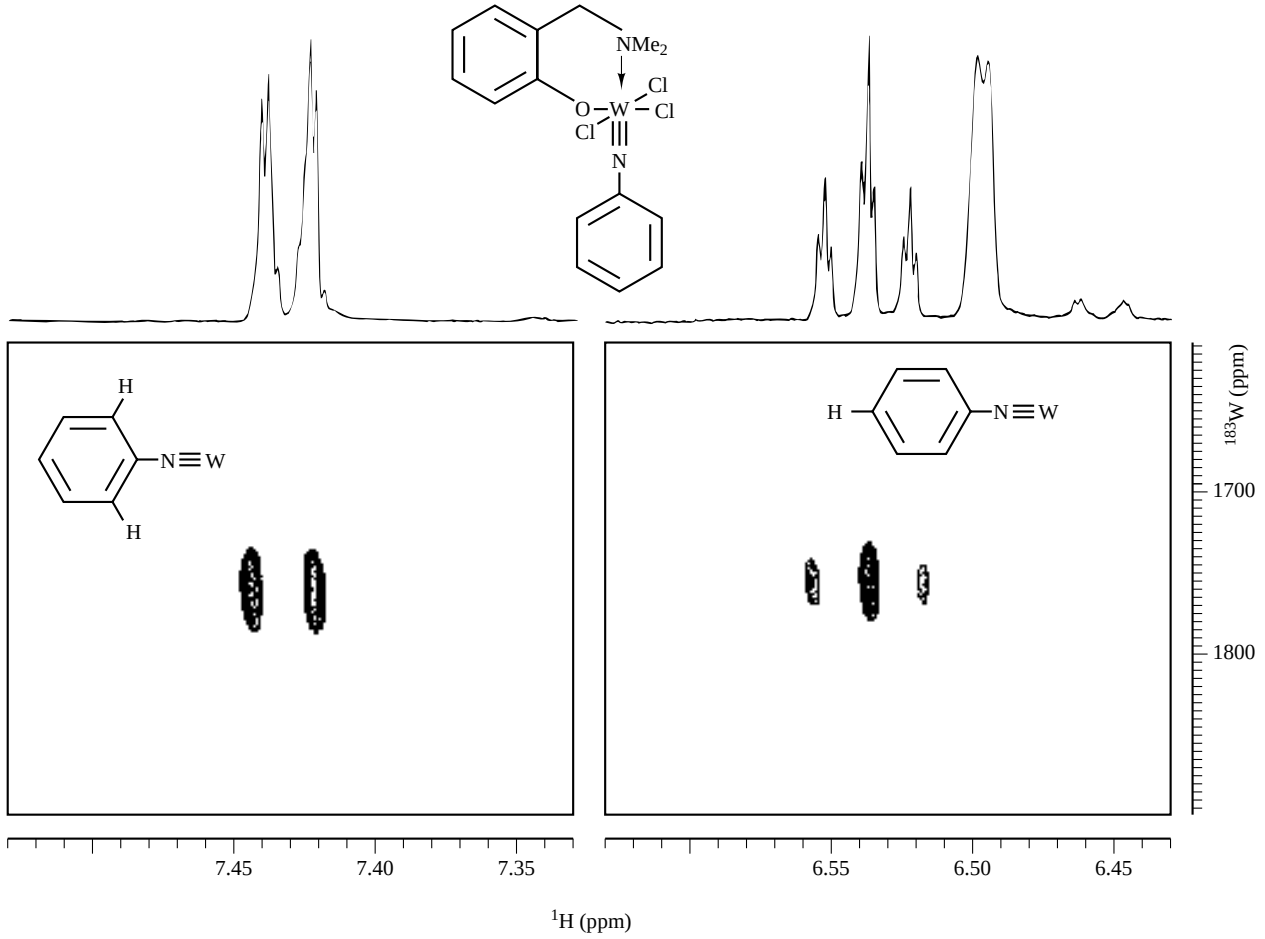

Figure 3 Sections of the 11.7 T $^{183}W-^{1}H$ HMQC shift correlation for the complex shown. Note that there are cross peaks for both the *ortho* and *para* protons of the imidophenyl group (C_6D_6). (Reproduced by permission of Wiley from Macchioni et al.[7])

4 CHEMICAL SHIFTS

It is now widely accepted that chemical shifts of heavy nuclei depend upon the paramagnetic contribution to the total screening, σ_p.[15] For a transition metal nucleus this means an expression related to

$$\sigma_p \propto \langle r^{-3} \rangle \sum_{j}^{occ} \sum_{k}^{unocc} (E_k - E_j)^{-1} S \qquad (3)$$

where r is a distance term, E_k and E_j are molecular orbital energies for unoccupied and occupied levels, and S is a sum involving the d orbital coefficients of the atomic orbitals used in making up the molecular orbitals.

As it is frequently not simple to obtain a clear molecular orbital picture for the metal center in low symmetry complexes with several different ligands, the analysis of metal chemical shifts remains, with some few exceptions,[16] on an empirical basis. The range of transition metal chemical shifts is of the order of thousands of parts per million and, for a given nucleus, e.g. ^{57}Fe, ^{103}Rh or ^{195}Pt, frequently in excess of 10 000 ppm. For the nuclei $^{107,109}Ag$, $^{111,113}Cd$, and ^{199}Hg, which often have the d^{10} electronic configuration, the range of chemical shifts is somewhat smaller than for those metal centers with less than 10 d electrons. Not surprisingly, the metal chemical shift is very sensitive to changes in—and close to—the coordination sphere. Solvent effects are routinely tens of parts per million.[2] Changes in temperature during a measurement result in large enough shifts (often in the range 0.1–0.5 ppm per degree) such that fine structure on the resonance is easily 'blurred',[2b] and isotope effects, e.g. ^{35}Cl vs. ^{37}Cl,[2b] ^{16}O vs. ^{18}O,[17] or ^{1}H vs. ^{2}H,[18] are sufficiently large such that the different chemical shifts from the individual isotopomers are often well resolved (see Figure 5).

The subject of referencing for metal chemical shifts is not clearly settled. There are several schools of thought: (a) referencing to a readily (usually commercially available) compound, (b) referencing to the metal, and (c) referencing to a frequency based on the ^{1}H frequency of tetramethylsilane at 100 000 000 MHz. Table 1 offers some commonly used references for the spin $I = \frac{1}{2}$ metals under discussion here. Where metal chemical shifts are concerned it is common to find both positive and negative signs with the latter denoting lower frequency than the reference.

Typical examples of the sensitivity of the chemical shift, δ, to the presence of different ligands are given in Figures 8 and 9. In the former, the metal signals were detected using the protons, and there are (a) cross peaks which arise from the coordinated ethylene molecule of the anion and (b) cross peaks arising from the protons of the chiral tridentate ligand

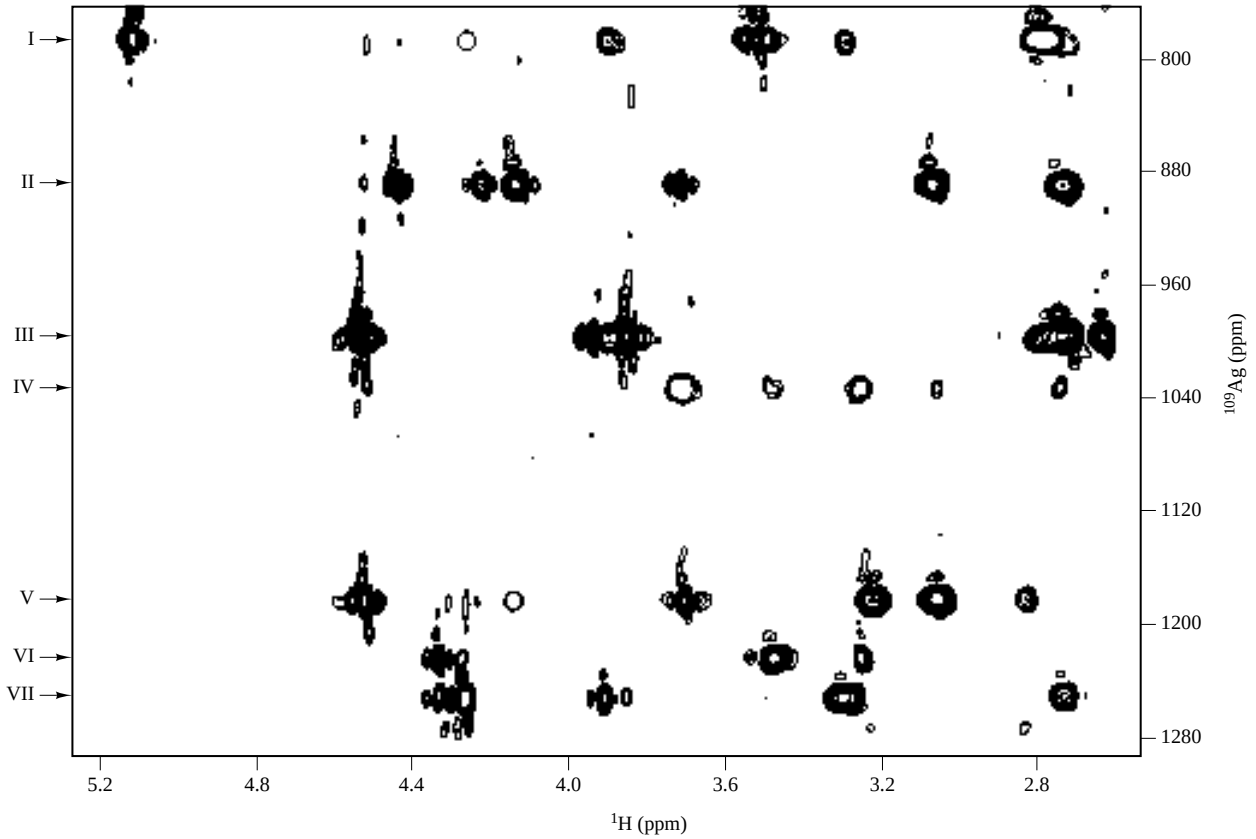

Figure 4 ^{109}Ag–^{1}H HMQC of a silver substituted yeast metallothionine, with an additional 90° pulse applied just after the refocusing interval to transfer magnetization from the NH to the H-α protons. The seven resonances are marked by roman numerals according to their increasing chemical shifts. The blank circles indicate the position of observed cross peaks in a similar experiment acquired with a preparation period of 45 ms (J = 11.1 Hz). (Reproduced by permission of the American Chemical Society from S. S. Narula, R. K. Mehra, D. R. Winge, and I. M. Armitage, *J. Am. Chem. Soc.*, 1991, **113**, 9354)

of the formally cationic platinum.[19] Figure 9 shows a one-dimensional solid state ^{113}Cd spectrum in which there are two different metal environments. One cadmium has two PPh_3 ligands coordinated and appears at high frequency as a triplet, whereas the phosphine free $CdCl_2$ absorption appears at lower frequency.[20]

There are not many general empirical chemical shift correlations which are valid for all of the spin $I = \frac{1}{2}$ metal centers. The higher metal oxidation states [Fe(II) vs. Fe(0), Rh(III) vs. Rh(I), or Pt(IV) vs. Pt(II)] are often found at higher frequency. For the metal centers with <10 d electrons, analogous halogen complexes often show algebraically smaller δ values (lower frequencies) when one moves down the column, i.e. Cl > Br > I. This latter trend is demonstrated by the selected examples in Table 2.

In some complexes there may be a correlation of the metal chemical shift with an empirical characteristic of the ligand(s), e.g. hardness or softness; however, these are not general effects for all of the metals,[16] and many exceptions are known [e.g. what is hard and what is soft may change with the oxidation state; or signals from the higher oxidation state platinum(II) can appear at lower frequency[2] than for some signals arising from platinum(0)]. It is important to remember that σ_p in equation (7) contains no expression related to any of these metal or ligand chemical characteristics. In any given complex either the $\langle r^{-3} \rangle$ or the $(E_k - E_j)^{-1}$ term may prove to be dominant, so that there is no reason to expect generality for all, or even many, of the metal centers. This point is valid for both spin $I = \frac{1}{2}$ and quadrupolar transition metal chemical shifts. Naturally, the nature of the specific chemistry will affect both the distance and energy parameters.

5 COUPLING CONSTANTS

The theory for spin–spin interactions between a spin $I = \frac{1}{2}$ metal and an appropriate ligand atom follows directly from the description developed by Pople and Santry.[24] A modified form of the expression is

$$^{1}J(\mathrm{M,L}) \propto (\gamma_\mathrm{M})(\gamma_\mathrm{L})|\psi_{\mathrm{s(M)}}(0)|^2|\psi_{\mathrm{s(L)}}(0)|^2 \times \sum_{j}^{\mathrm{occ}} \sum_{k}^{\mathrm{unocc}} (E_k - E_j)^{-1} C(\mathrm{M})^{\mathrm{s}}_k C(\mathrm{L})^{\mathrm{s}}_k C(\mathrm{M})^{\mathrm{s}}_j C(\mathrm{L})^{\mathrm{s}}_j \quad (4)$$

which reveals that the one-bond interaction depends on the metal and ligand atom magnetogyric ratios γ, the s expectation values ψ, the molecular orbital energies, and the s coefficients of the atomic orbitals used in making up the molecular orbitals.

Given that the γ and s expectation values ψ depend markedly on the individual metal and ligand atoms under

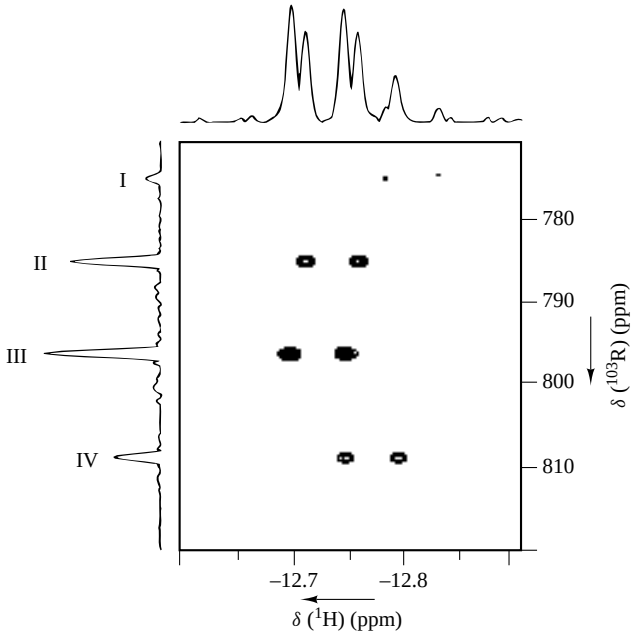

Figure 5 (^{1}H, ^{103}Rh)–{^{2}H} HMQC correlation spectrum for $RhY_2(Y_2)\{HB(3,5\text{-}Me_2pz)_3\}$ (Y = ^{1}H or ^{2}H; pz = pyrazolyl). The hydride ligands exchange rapidly on the NMR timescale with the hydrogen atoms of the coordinated H_2 molecule, so that four different isotopomers arise. (Reproduced by permission of Wiley from D. Nanz, W. von Philipsborn, U. E. Bucher, and L. M. Venanzi, *Magn. Reson. Chem.*, 1991, **29**, S38)

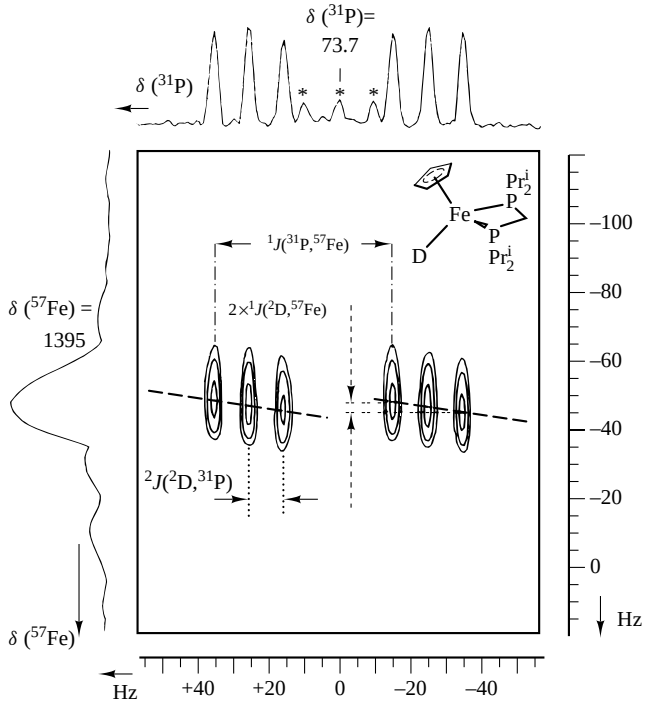

Figure 6 Inverse two-dimensional ^{57}Fe–^{31}P spectrum of the complex shown, at 161.2 MHz. The scalar couplings of both ^{31}P and ^{57}Fe with deuterium can be extracted from the contour plot. The asterisks denote the incompletely suppressed lines of the parent signal with magnetically inactive iron. (Reproduced by permission of the American Chemical Society from Benn et al.[6b])

consideration, it is not surprising that the signs and magnitudes of these spin–spin interactions vary enormously.

For hydride as the ligand, the magnitude of ^1J(M, ^{1}H) can be as small as a few hertz for M = W,[25] or in excess of 1000 Hz for M = Pt,[2a,26] with the largest value, of ^1J(^{195}Pt, ^{1}H), at about 1606 Hz.[27] One-bond ^1J(^{109}Ag, ^{1}H)[28], ^1J(^{103}Rh, ^{1}H),[29] and ^1J(^{187}Os, ^{1}H)[2a] values are much smaller than ^1J(^{195}Pt, ^{1}H), and frequently are of the order of 10–100 Hz. As the s coefficients C are important, one finds that, for L = ^{13}C, the hybridization of the carbon affects the magnitude of ^1J(M, ^{13}C) such that sp carbons (with a higher percentage of s character) afford larger values than for analogous complexes with an sp^3 carbon ligand. For the complexes *cis*-$Pt(CH_3)_2(PMe_2Ph)_2$, *cis*-$Pt(C_6H_5)_2(PEt_3)_2$, and $Pt(CN)_4^{2-}$, with sp^3, sp^2, and sp coordinated carbon ligands one observes values[30] of ^1J(^{195}Pt, ^{13}C) at 594, 817, and 1036 Hz, respectively, reflecting these differing coefficients. The hybridization at carbon is clearly not the only factor involved and this explains why the ^1J(^{195}Pt, ^{13}C) values are not exactly in the ratio 1.0:1.3:2.0.

There is an extensive literature on ^1J(M, ^{31}P)[2a] for complexes with directly bound phosphorus ligands.[8] Since both the γ and s expectation values, $|\psi_s(0)(L)|^2$, for ^{31}P are relatively large, one finds spin–spin interactions of the order of 10^2–10^4 Hz, depending upon the metal and the nature of the phosphorus ligand. ^1J(M, ^{31}P) has become an important analytical tool in the determination of molecular structure of phosphine complexes. The development of cisplatin [*cis*-$PtCl_2(NH_3)_2$] and related cancer drugs has been accompanied by a renewed interest in ^1J(^{195}Pt, ^{15}N).[26,31,32] This parameter varies between 88 and 821 Hz. For the specific complexes containing the fragment '*cis*-$Pt(NH_3)_2$' the values are often between 200 and 400 Hz. An extensive list of ^1J(^{195}Pt, ^{15}N) coupling constants can be found in the literature.[26] Spin–spin interactions between the metals themselves vary between a few hertz, as in the case for two rhodium atoms,[33] up to many thousands of hertz for the metal nuclei with larger γ values.

There are several useful empiricisms involving coupling constants of spin $I = \frac{1}{2}$ metal centers: (a) for ^1J(M, L) the magnitude depends on the *trans* influence[2a,8] of the ligand situated opposite to L, with stronger donors resulting in markedly reduced values, and (b) there can be the usual

Table 2 δ Values for Halogen Complexes of Metals with <10 d Electrons

Complex	X				Reference
	F	Cl	Br	I	
$[Fe(\eta^3\text{-}C_3H_5)X(CO)_3]$ BF_4 δ ^{57}(Fe)		1708.0	1528.0	1235.7	21
$RhX(CO)(PPh_3)_2$ δ (^{103}Rh)	−148	−369	−421	−532	2a
$[PtX_3(SMe_2)]^-$ δ (^{195}Pt)		−2757	−3415	−4973	22
$IrX_2(HgX)(CO)(PPh_3)_2$ δ (^{199}Hg)		−2645	−2814	−3093	23

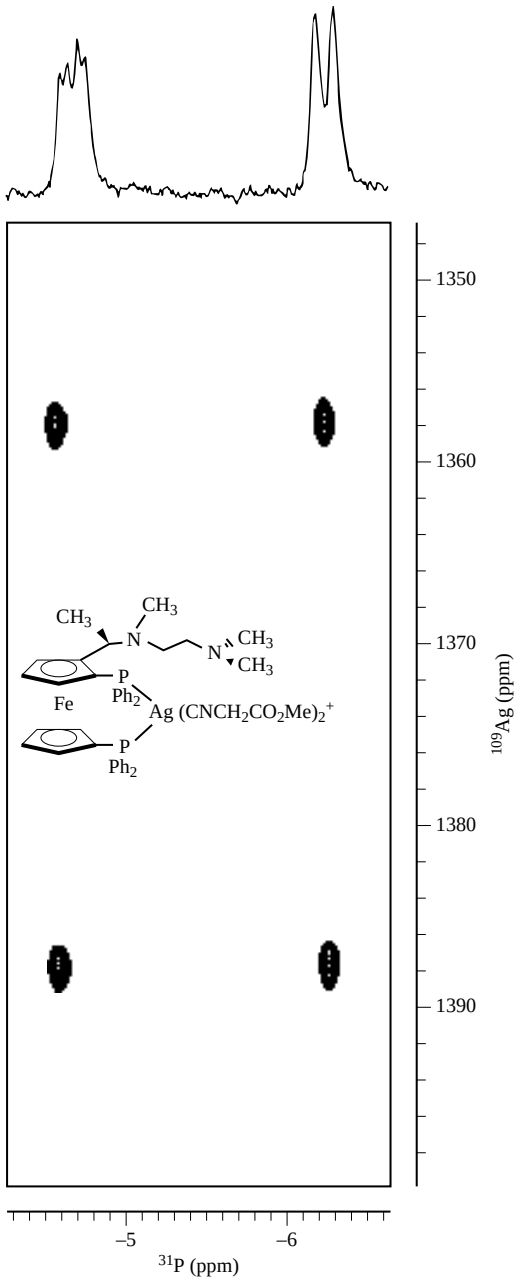

Figure 7 ^{109}Ag–^{31}P HSQC spectrum of the bis-isonitrile complex shown. There is only one ^{109}Ag resonance whose splitting in the metal direction represents the sum of the two $^{1}J(^{109}\text{Ag}, ^{31}\text{P})$ values. The two different ^{31}P signals overlap. (Reproduced by permission of the American Chemical Society from F. Lianza, A. Macchioni, P. S. Pregosin, and H. Rüegger, *Inorg. Chem.*, 1994, **33**, 4999)

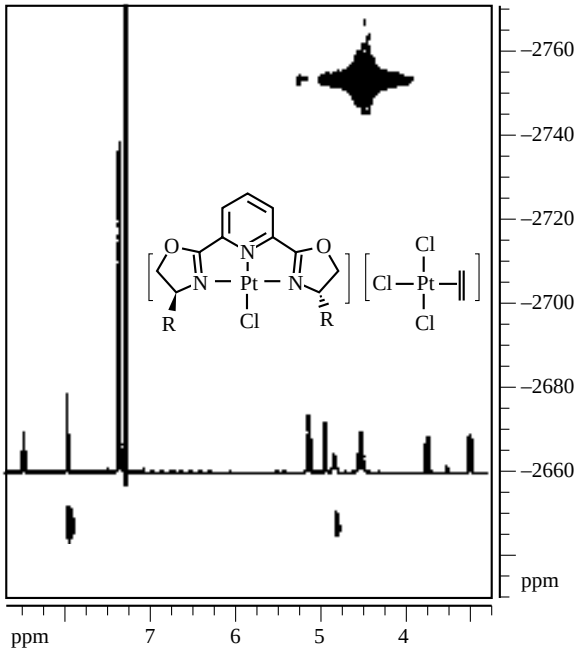

Figure 8 ^{195}Pt–^{1}H spectrum of the complex shown. There is a complex cation (relatively weak cross peaks from both the *meta* pyridine proton and the heterocyclic ring methine proton) and a complex anion (relatively strong cross peak from the coordinated ethylene) and the metal direction reveals the considerable difference in their chemical shifts. It is not obvious from the ^{1}H spectrum that two different metal centers are present. (P. S. Pregosin, K. Puntener, and H. Rüegger, unpublished results)

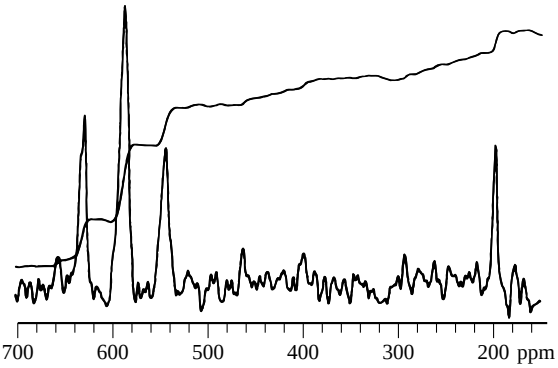

Figure 9 CP–MAS ^{113}Cd{^{1}H} NMR spectrum at 33.30 MHz of the solid isolated from the reaction of PPh_3 with $CdCl_2$ in a 1:1 ratio. The singlet at 200 ppm is due to $CdCl_2$, and the triplet at 590 ppm is due to $CdCl_2(PPh_3)_2$. (Reproduced by permission of Wiley from Kessler et al.[20])

Karplus type relationship associated with $^{3}J(\text{M}, ^{1}\text{H})$ or $^{3}J(\text{M}, ^{13}\text{C})$, although this is not always as well developed as for $^{3}J(^{1}\text{H}, ^{1}\text{H})$.

6 APPLICATIONS

There are certainly many instances in which the metal chemical shift was recorded primarily to learn where it could be found. This was often the case in the early years since—given the sensitivity of δ—it was not always certain that the resonance could be immediately located. Indeed, one still finds worthwhile studies involving compilations of chemical shifts, and there is no doubt that this body of empirical data is appreciated by many chemists. The Appendix provides a few examples of how and why these metal nuclei are currently being measured.

The more chemical reasons for measuring a spin $I = \frac{1}{2}$ metal spectrum are usually associated with:

1. the desire to prove the presence and specific number of one or more coordinated ligands;
2. an interest in learning about the ground state physical properties of a particular ligand, e.g. the *trans* influence;
3. the need for a unique probe with which to follow the kinetics of a reaction;[16]
4. the intention to correlate one or more NMR parameters with physical data from other methods,[34] e.g. ultraviolet, visible or infrared energies, or perhaps reduction–oxidation data; and
5. an inherent interest in the NMR properties for their own sake, e.g. signs of coupling constants in which transition metals are involved.[35,36]

The first of these is, statistically, the most abundant application. A particular chemical shift may be indicative of the presence of some ligand and/or coordination number.[37] The observation of a signal at very high or low frequency may be more consistent with one oxidation state than another. Often one finds that the multiplicity of the metal signal[37–41] or the relative intensities of weak satellite lines[41] provide keys to a particular structural puzzle. Does the metal spectrum appear as a doublet or a triplet? How many ^{29}Si or ^{119}Sn or ^{195}Pt spins (all of which are <100% abundant) are within the coordination sphere? These decisions cannot always be made using ^{1}H, ^{13}C, or some other NMR form, and this is especially true for homogeneous catalysts based on metal complexes since the organic reagents are present in a 100-fold or more excess.

The magnitudes of ^{1}J(M, L) or ^{n}J(M, L) can be employed as structural tools in that one knows that these parameters can be theoretically and empirically related to the geometry of square-planar or octahedral complexes.[8,30] This has led to many useful NMR empiricisms (the largest database involves ^{195}Pt) relating the ability of a coordinated ligand to weaken the ligand *trans* to it in the equilibrium state.[26,42] There are literally dozens of interesting coupling constants; however, two mercury examples stand out: for the Hg_3^{2+} ion,[43] $^{1}J(^{199}\mathrm{Hg}, ^{199}\mathrm{Hg})$ = 139 700 Hz and in $IrCl(SnCl_3)(HgCl)(CO)(PPh_3)_2$, $^{2}J(^{199}\mathrm{Hg}, ^{119}\mathrm{Sn})$ = 41 479 Hz.[23] The former is unique in that it represents the largest reported spin–spin coupling, and there is only the one example. The two-bond interaction is also amongst the largest of its kind, but is not unique in that several derivatives have been prepared and a 39 294–42 688 Hz range observed. Despite the existing richness, there is still much more to come from both spin $I = \frac{1}{2}$ and spin $I > \frac{1}{2}$ transition metal NMR.

7 REFERENCES

1. W. G. Proctor and F. C. Yu, *Phys. Rev.*, 1951, **81**, 20.
2. (a) P. S. Pregosin (ed.), *Transition Metal NMR Spectroscopy*, Elsevier, Amsterdam, 1991; (b) B. E. Mann, *Annu. Rep. NMR Spectrosc.*, 1991, **23**; (c) J. Mason, *Multinuclear N.M.R.*, Plenum Press, New York, 1987; (d) R. Benn and A. Rufinska, *Angew. Chem., Int. Ed. Engl.*, 1986, **25**, 861; (e) D. Rehder, *Magn. Reson. Rev.*, 1984, **9**, 125; (f) P. Laszlo, *N.M.R. of Newly Accessible Nuclei*, Academic Press, London, 1983.
3. A. von Zelewski, *Helv. Chim. Acta*, 1968, **51**, 803; A. Pidcock, R. E. Richards, and L. M. Venanzi, *J. Chem. Soc. (A)*, 1968, 1970.
4. R. K. Harris and B. E. Mann (ed.) *NMR and the Periodic Table*, Academic Press, London, 1978.
5. G. A. Morris and R. Freeman, *J. Am. Chem. Soc.*, 1979, **101**, 760; C. Brevard and R. Schimpf, *J. Magn. Reson.*, 1982, **47**, 528.
6. (a) R. Benn and A. Rufinska, *Magn. Reson. Chem.*, 1988, **26**, 895; (b) R. Benn and C. Brevard, *J. Am. Chem. Soc.*, 1986, **108**, 5622; (c) D. Nanz and W. von Philipsborn, *J. Magn. Reson.*, 1991, **92**, 560.
7. A. Macchioni, P. S. Pregosin, H. Rüegger, G. van Koten, P. A. van der Schaaf, and R. A. T. M. Abbenhuis, *Magn. Reson. Chem.*, 1994, **32**, 235.
8. P. S. Pregosin and R. W. Kunz, *NMR Basic Principles and Progress*, Springer-Verlag, Heidelberg, 1979; P. S. Pregosin, in *Methods in Stereochemical Analysis*, ed. J. G. Verkade and L. D. Quin, VCH, New York, 1987, Vol. 8, p. 465.
9. X. Yan, J. Fan, X. Xu, D. Wang, G. Nie, and B. Qian, *Magn. Reson. Chem.*, 1991, **29**, 1092.
10. J. Kördel, C. Johansson, and T. Drakenberg, *J. Magn. Reson.*, 1992, **100**, 581.
11. R. K. Harris, I. J. McNaught, R. Reams, and K. J. Packer, *Magn. Reson. Chem.*, 1991, **29**, S60; R. K. Harris, P. Reams, and K. J. Packer, *J. Chem. Soc., Dalton Trans.*, 1986, 1015; R. K. Harris and K. Sebald, *Magn. Reson. Chem.*, 1987, **25**, 1058; S. W. Sparks and P. D. Ellis, *J. Am. Chem. Soc.*, 1986, **108**, 3215; R. Wasylishen and J. F. Britten, *Magn. Reson. Chem.*, 1988, **26**, 1075.
12. R. Benn, H. M. Buch, and R. D. Reinhardt, *Magn. Reson. Chem.*, 1985, **23**, 559.
13. R. E. Wasylishen, R. E. Lenkinski, and C. Rodger, *Can. J. Chem.*, 1982, **60**, 2113; R. Wasylishen and J. F. Britten, *Magn. Reson. Chem.*, 1988, **26**, 1075.
14. G. C. Levy, P. L. Rinaldi, and J. T. Bailey, *J. Magn. Reson.*, 1980, **40**, 167.
15. G. A. Webb, in *NMR and the Periodic Table* ed. R. K. Harris and B. E. Mann, Academic Press, London, 1978, Chap. 3 and 8.
16. N. Juranic, *J. Chem. Soc., Dalton Trans.*, 1984, 1537; N. Juranic, *J. Magn. Reson.*, 1987, **71**, 144.
17. O. Gröning and L. I. Elding, *Inorg. Chem.* 1989, **28**, 3366; O. Groning, T. Drakenberg and L. I. Elding, *Inorg. Chem.* 1982, **21**, 1820.
18. S. M. Baxter, G. S. Ferguson, and P. T. Wolczanski, *J. Am. Chem. Soc.*, 1988, **110**, 4231.
19. P. S. Pregosin, K. Puntener, and H. Rüegger, unpublished results.
20. J. M. Kessler, J. Reeder, R. Vac. C. Yeung, J. H. Nelson, J. S. Frye, and N. W. Alcock, *Magn. Reson. Chem.*, 1991, **29**, S94.
21. W. von Philipsborn, *Pure Appl. Chem.*, 1986, **58**, 513.
22. P. L. Goggin, R. J. Goodfellow, S. R. Haddock, B. F. Taylor, and R. H. Marshall, *J. Chem. Soc., Dalton Trans.*, 1976, 459.
23. M. Kretschmer, P. S. Pregosin, P. Favre, and C. W. Schläpfer, *J. Organomet. Chem.*, 1983, **253**, 17.
24. J. A. Pople and D. P. Santry, *Mol. Phys.*, 1964, **8**, 1; J. A. Pople and D. P. Santry, *Mol. Phys.*, 1965, **9**, 311.
25. (a) J. L. Templeton, C. C. Philipp, P. S. Pregosin, and H. Rüegger, *Magn. Reson. Chem.*, 1993, **31**, 58; (b) A. A. H. van der Zeijden, C. Sontag, H. W. Bosch, V. Shklover, H. Berke, D. Nanz, and W. von Philipsborn, *Helv. Chim Acta*, 1991, **74**, 1194.
26. P. S. Pregosin, *Annu. Rep. NMR Spectrosc.*, 1986, **17**.
27. G. Minghetti, M. A. Cinellu, S. Stoccoro, G. Chelucci, and A. Zucca, *Inorg. Chem.*, 1990, **29**, 5138.
28. A. Albinati, S. Chaloupka, F. Demartin, T. F. Koetzle, H. Rüegger, L. M. Venanzi, and M. K. Wolfer, *J. Am. Chem. Soc.*, 1993, **115**, 169.
29. B. E. Mann, *NMR of Newly Accessible Nuclei*, Academic Press, London, 1983, Vol. 2, p. 301.

30. B. E. Mann and B. F. Taylor, *^{13}C NMR Data for Organometallic Compounds*, Academic Press, London, 1981.
31. T. G. Appleton, K. G. Barnham, J. R. Hall, and M. T. Mathieson, *Inorg. Chem.*, 1991, **30**, 2751; T. G. Appleton, A. J. Bailey, K. J. Barnham, and J. R. Hall, *Inorg. Chem.*, 1992, **31**, 3077.
32. Y. Qu, N. Farrell, M. Valsecchi, L. de Greco, and S. Spinelli, *Magn. Reson. Chem.*, 1993, **31**, 920.
33. A. L. Davis and R. J. Goodfellow, *J. Chem. Soc., Dalton Trans.*, 1993, 2273; B. E. Mann, N. J. Meanwell, C. M. Spencer, B. F. Taylor, and P. M. Maitlis, *J. Chem. Soc., Dalton Trans.*, 1985, 1555; A. Salzer, T. Egolf, and W. von Philipsborn, *Helv. Chim. Acta*, 1982, **65**, 1145.
34. M. Koller and W. von Philipsborn, *Organometallics*, 1992, **11**, 467.
35. W. McFarlane and N. H. Rees, *J. Chem. Soc., Dalton Trans.*, 1990, 3211.
36. B. Wrackmeyer, K. Horchler von Locquenghien, E. Kupce, and A. Sebald, *Magn. Reson. Chem.*, 1993, **31**, 45.
37. R. E. Blumer, F. Lianza, P. S. Pregosin, H. Ruegger, and A. Togni, *Inorg. Chem.*, 1993, **32**, 2663.
38. C. Arz, P. S. Pregosin, and C. Anklin, *Magn. Reson. Chem.*, 1987, **25**, 158.
39. W. Caseri and P. S. Pregosin, *J. Organomet. Chem.*, 1988, **356**, 259.
40. W. Caseri and P. S. Pregosin, *Organometallics*, 1988, **7**, 1373.
41. C. Ammann, P. S. Pregosin, H. Rüegger, M. Grassi, and A. Musco, *Magn. Reson. Chem.*, 1989, **27**, 355.
42. T. G. Appleton, H. C. Clark, and L. E. Manzer, *Coord. Chem. Rev.*, 1973, **10**, 335.
43. R. J. Gillespie, P. Granger, K. R. Morgan, and G. J. Schrobilgen, *Inorg. Chem.*, 1984, **23**, 887.

8 APPENDIX

To attain some feeling for how and to what purpose spin $I = \frac{1}{2}$ metal NMR spectroscopy is currently being used, the reader will find below several relatively recent references for each of these nuclei.

Iron-57

L. Baltzer and M. Landergren, *J. Am. Chem. Soc.*, 1990, **112**, 2804.
M. Landergren and L. Baltzer, *Inorg. Chem.*, 1990, **29**, 556.
C. M. Adams, G. Cerioni, A. Hafner, H. Kalchhauser, W. von Philipsborn, R. Prewo and A. Schwenk, *Helv. Chim. Acta*, 1988, **71**, 1116.
R. Benn, H. Brenneke, A. Frings, H. Lehmkuhl, G. Mehler, A. Rufinska, and T. Wildt, *J. Am. Chem. Soc.*, 1988, **110**, 5661.

Yttrium-89

C. Page, S. K. Sur, M. C. Lonergan, and G. K. Parashar, *Magn. Reson. Chem.*, 1991, **29**, 1191.
L. H. Merwin and A. Sebald, *J. Magn. Reson.*, 1990, **88**, 167.

Rhodium-103

B. R. Bender, M. Koller, D. Nanz, and W. von Philipsborn, *J. Am. Chem. Soc.*, 1993, **115**, 5889.
M. C. Read, J. Glaser, M. Sandström, and I. Toth, *Inorg. Chem.*, 1992, **31**, 4155.
M. C. Read, J. Glaser, and M. Sandström, *J. Chem. Soc., Dalton Trans.*, 1992, 233.
J. M. Ernsting, C. J. Elsevier, W. G. J. de Lange, and K. Timmer, *Magn. Reson. Chem.*, 1991, **29**, S118.
D. Imhof, H. Rüegger, L. M. Venanzi, and T. R. Ward, *Magn. Reson. Chem.*, 1991, **29**, S73.
P. B. Graham, M. D. Rausch, K. Täschler, and W. von Philipsborn, *Organometallics*, 1991, **10**, 3049.

Silver-109

L. H. Merwin and A. Sebald, *J. Magn. Reson.*, 1992, **97**, 628.
S. J. Berners-Price, P. J. Sadler, and C. Brevard, *Magn. Reson. Chem.*, 1990, **28**, 145.
S. S. D. Brown, I. D. Salter, V. Sik, I. J. Colquhoun, W. McFarlane, P. A. Bates, M. B. Hursthouse, and M. Murray, *J. Chem. Soc., Dalton Trans.*, 1988, 2177, 2787.

Cadmium-113

P. A. W. Dean, N. C. Payne, J. J. Vittal, and Y. Y. Yu, *Inorg. Chem.*, 1993, **32**, 4632.
J. J. Vittal and P. A. W. Dean, *Inorg. Chem.*, 1993, **32**, 791.
J. Kördel, C. Johansson and T. Drakenberg, *J. Magn. Reson.*, 1992, **100**, 581.
S. Nishikiori, C. I. Ratcliffe, and J. A. Ripmeester, *J. Am. Chem. Soc.*, 1992, **114**, 8590.
S. Nishikiori, C. I. Ratcliffe, and J. A. Ripmeester, *J. Chem. Soc., Chem. Commun.*, 1991, 735.

Tungsten-183

Y. Lin, T. J. R. Weakley, B. Rapko, and R. G. Finke, *Inorg. Chem.*, 1993, **32**, 5095.
W. Clegg, R. J. Errington, P. Kraxner, and C. Redshaw, *J. Chem. Soc., Dalton Trans.*, 1992, 1431.
S. Chapelle and J. Verchère, *Inorg. Chem.*, 1992, **31**, 648.
G. S. Kim, K. S. Hagen, and C. L. Hill, *Inorg. Chem.*, 1992, **31**, 5316.
Y. N. Ma, P. Demou, and J. W. Faller, *Inorg. Chem.*, 1991, **30**, 62.
R. Benn, H. Brenneke, J. Heck, and A. Rufinska, *Inorg. Chem.*, 1987, **26**, 2826.

Osmium-187

R. Benn, H. Brenneke, E. Joussen, H. Lehmkuhl, and F. L. Ortiz, *Organometallics*, 1990, **9**, 756.
R. Benn, E. Joussen, H. Lehmkuhl F. L. Ortiz, and A. Rufinska, *J. Am. Chem. Soc.*, 1989, **111**, 8754.
J. A. Cabeza, B. E. Mann, P. M. Maitlis, and C. Brevard, *J. Chem. Soc., Dalton Trans.*, 1988, 629.
J. A. Cabeza, A. Nutton, B. E. Mann, P. M. Maitlis, and C. Brevard, *Inorg. Chim. Acta*, 1986, **115**, L47.

Platinium-195

D. Imhof, U. Burckhardt, K. H. Dahmen, H. Rüegger, T. Gerfin, and V. Gramlich, *Inorg. Chem.*, 1993, **32**, 5206.
S. O. Dunham, R. D. Larsen, and E. H. Abbott, *Inorg. Chem.*, 1993, **32**, 2049.
F. D. Rochon, M. Doyon, and I. S. Butler, *Inorg. Chem.*, 1993, **32**, 2717.
S. Hintermann, P. S. Pregosin, H. Rüegger, and H. C. Clark, *J. Organomet. Chem.*, 1992, **435**, 225.
L. D. Boardman and R. A. Newmark, *Magn. Reson. Chem.*, 1992, **30**, 481.

S. Hayashi and K. Hayamizu, *Magn. Reson. Chem.*, 1992, **30**, 658.
F. D. Rochon, R. Melanson, and A. Morneau, *Magn. Reson. Chem.*, 1992, **30**, 697.
S. O. Dunham, R. D. Larsen, and E. H. Abbott, *Inorg. Chem.*, 1991, **30**, 4328.
H. Rüegger and D. Moskau, *Magn. Reson. Chem.*, 1991, **29**, S11.
S. G. Bott, A. D. Burrows. O. J. Ezomo, M. F. Hallam, J. G. Jeffrey, and D. M. P. Mingos, *J. Chem. Soc., Dalton Trans.*, 1990, 3335.
D. P. Bancroft, C. A. Lepre, and S. J. Lippard, *J. Am. Chem. Soc.*, 1990, **112**, 6860.
H. C. Clark and A. M. de P. Nicholas, *Magn. Reson. Chem.*, 1990, **28**, 99.
P. Salvadori, G. Uccello-Barretta, R. Lazzaroni, and A. M. Caporusso, *J. Chem. Soc., Chem. Commun.*, 1990, 1121.
L. G. Marzilli, Y. Hayden, and M. D. Reily, *Inorg. Chem.*, 1986, **25**, 974.

Mercury-199
R. E. Blumer, F. Lianza, P. S. Pregosin, H. Ruegger, and A. Togni, *Inorg. Chem.*, 1993, **32**, 2663.
V. Neirinck, D. Robert, and R. Nardin, *Magn. Reson. Chem.*, 1993, **31**, 815.
G. Klose, F. Volke, G. Peinel, and G. Knobloch, *Magn. Reson. Chem.*, 1993, **31**, 548.
G. Wu and R. E. Wasylishen, *Magn. Reson. Chem.*, 1993, **31**, 537.
C. J. Groombridge, *Magn. Reson. Chem.*, 1993, **31**, 380.
H. Adachi, N. Ueyama, and A. Nakamura, *Inorg. Chim. Acta*, 1992, **200**, 805.
J. M. Robert and D. L. Rabenstein, *Anal. Chem.*, 1991, **63**, 2674.

Biographical Sketch

Paul S. Pregosin. *b* 1943. B.S., Ph.D., 1970, The City University of New York, Postdoctoral studies at the University of London, 1970–71, the University of Delaware, 1972–73, and the ETH, Zürich, 1973–present. Approx. 150 publications. Research interests include applications of NMR spectroscopy to problems in coordination and organometallic chemistry, and homogeneous catalysis with transition metal complexes.

Inorganic Solids

Leslie G. Butler

Louisiana State University, Baton Rouge, LA, USA

1	Introduction	1
2	Fluxional Organometallic Compounds	1
3	Quadrupolar and Chemical Shift Interactions and Chemical Bonding	4
4	A Few Examples of Solid State NMR and Inorganic Solids	9
5	Related Articles	10
6	References	11

1 INTRODUCTION

In the 1930s, the first NMR test samples were inorganic solids such as lithium chloride and potassium fluoride.[1] Unfortunately, NMR spectra could not be obtained from these particular samples because of long spin–lattice relaxation times (the samples were of high purity), and so began the field of NMR of inorganic solids. Fortunately, there have been many successes in the past 50 years. This article is designed to introduce a number of issues pertinent to NMR and inorganic chemistry. It is expected that the section on fluxional organometallic compounds will build on the reader's existing knowledge of NMR. Then, we turn to chemical bonding and NMR, followed by a brief section illustrating the range of applications of NMR to inorganic chemistry.

2 FLUXIONAL ORGANOMETALLIC COMPOUNDS

One of the many interesting aspects of transition metal chemistry is the property of fluxionality. A fluxional transition metal complex can interchange the arrangement of ligands about the metal through an intramolecular mechanism. In some cases, fluxionality will interconnect stereochemical isomers such as trisubstituted amines and also many five-coordinate metal complexes, especially complexes with a trigonal-bipyramidal structure. For commonly observed fluxional processes, the activation barriers range from 10 to 100 kJ mol^{-1}. Measurement of the mode of motion and the activation energy of a fluxional process can give insight into bond formation and bond scission processes that are so critical in catalysis and synthesis. For this reason, the study of fluxional processes has been of great interest, and NMR is the spectroscopic tool most often applied, usually in conjunction with X ray crystallography. The combination of a static structural model and the dynamic information from solution state and solid state NMR is usually enough to define the fluxional process.

2.1 Cyclooctatetraene

It is interesting to consider the motion of a large ligand such as cyclooctatetraene, C_8H_8 (COT), bound to a single metal atom or a multinuclear metal complex. On one hand, the four double bonds of the COT ligand lead to a large ligand cluster binding energy. On the other hand, delocalization of the double bonds can render each carbon site in the COT ligand electronically equivalent. These two conditions lead to a ligand that exhibits fluxionality over a wide temperature range; the low activation barrier allows motion at low temperatures, and the high binding energy prevents decomposition until high temperatures are reached.

The chemistry of COT with iron and ruthenium carbonyls is extensive, and monometallic and multinuclear complexes can be made. From an NMR viewpoint, COT iron carbonyl complexes are interesting since the hydrogen nuclei in the COT ligand comprise the only significant NMR spin system. There is strong dipolar coupling in the proton spin system leading to a homogeneously broadened lineshape. The linewidth and spin–lattice relaxation rate are a function of COT reorientation, thus making solid state proton NMR spectroscopy a useful probe of COT fluxionality.

In 1976, Fyfe and co-workers reported ^{1}H T_1 and $T_1\rho$ studies for several complexes: (COT)$Fe(CO)_3$, (COT)$[Fe(CO)_3]_2$, (μ-COT)(μ-CO)$[Fe(CO)_2]_2$, and (μ-COT)$_2[Ru_3(CO)_4]$.[2] In this work, spin–lattice relaxation rates, both in the laboratory frame and in the rotating frame, are dominated by proton dipolar interactions, and the modulation of these interactions by molecular motions; the motions are described by a correlation time, τ_c. With these conditions, T_1 is given by

$$\frac{1}{T_1} = C\left[\frac{\tau_c}{1+\omega_0^2\tau_c^2} + \frac{4\tau_c}{1+4\omega_0^2\tau_c^2}\right] \quad (1)$$

The correlation time is assigned to a thermally activated process and is modeled by an Arrhenius equation:

$$\tau = \tau\ \exp(E_a/RT) \quad (2)$$

The parameter ω_0 is the resonant frequency of the ^{1}H NMR experiment in units of radians per second, and C is an empirically determined constant. A plot of $\log(T_1)$ versus $1/T$ yields a V shaped curve; the minimum occurs at $\omega_0\tau_c$ = 0.62, as shown in Figure 1. Two different strategies were used to change the resonant frequency so that widely different correlation times could be measured. In some cases, the ^{1}H T_1 was measured at two different applied field strengths corresponding to Larmor frequencies of 5.3 and 14 MHz; and also the ^{1}H $T_{1\rho}$ was measured with a spin lock pulse sequence.

The complex with the lowest activation barrier is (μ-COT)(μ-CO)$[Fe(CO)_2]_2$. The molecular structure and experimental results are shown in Figure 1. The fit of the T_1 data to equation (1) and $T_{1\rho}$ to a similar relationship yields an activation barrier of only 9 kJ mol^{-1} for the fluxional process. While the ^{1}H T_1 NMR experiment does not yield any definitive information about the mode of motion, the solution ^{1}H NMR spectra have been interpreted as due to a series of 1,2-shifts of a metal atom around the cyclooctatetraene ring. In summary, solid state ^{1}H NMR is shown here to be an effective probe of molecular motion over a wide range of correlation

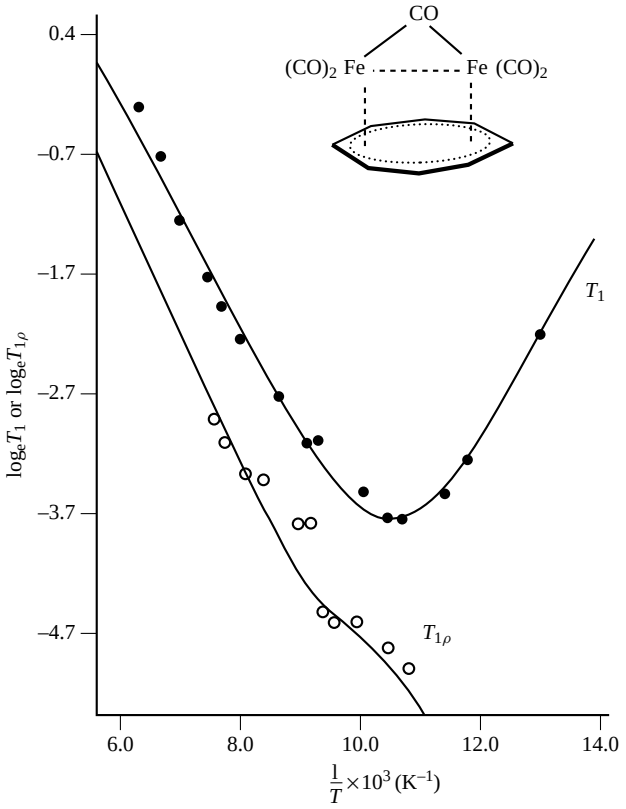

Figure 1 A plot of ^{1}H T_1 and $T_{1\rho}$ for (μ-COT)(μ-CO)[Fe(CO)$_2$]$_2$ as a function of inverse temperature. The ^{1}H T_1 data were collected at a Larmor frequency of 14 MHz. The ^{1}H T_1 data were fitted to equation (1), and the $T_{1\rho}$ data to a similar equation, yielding an activation energy of 9 kJ mol^{-1}. (Reproduced by permission of the American Chemical Society from Campbell et al.[2])

times. It is curious that the activation barrier to rotation can be as small as 9 kJ mol^{-1}. One can conclude that the metal–ligand bonding has little angular dependence and that few lattice interactions have the necessary symmetry to create a significant steric effect. In addition to ^{1}H NMR, relaxation data for other $S = \frac{1}{2}$ nuclei such as ^{19}F in xenon tetrafluoride have been used to study molecular motion.[3]

Even though the ^{1}H T_1 NMR experiment is quite informative, there are some unresolved issues. As mentioned above, the mode of motion is not revealed, be it exclusively 1,2-shifts or a combination of 1,2 and higher order shifts. Also, molecular motion may be occurring elsewhere in the molecule, for example bridging-terminal carbonyl exchange. To address these issues, other NMR experiments may be employed.

2.2 Arene/Ethene

The triosmium arene/ethene complex Os$_3$(CO)$_8$(η^2-CH$_2$CH$_2$)(μ_3:η^2:η^2:η^2-C$_6$H$_6$) has been studied by solid state ^{13}C CP MAS NMR.[4] Previous solution NMR experiments showed an incredible five independent fluxional processes, as summarized in Figure 2: (a) alkene rotation, (b) arene rotation, (c) turnstile rotation of the Os(CO)$_3$ moieties [the Os(CO)$_3$ moieties that are *cis* and *trans* with respect to the Os(μ-CH$_2$CH$_2$)(CO)$_3$ moiety have slightly different coalescence temperatures], and

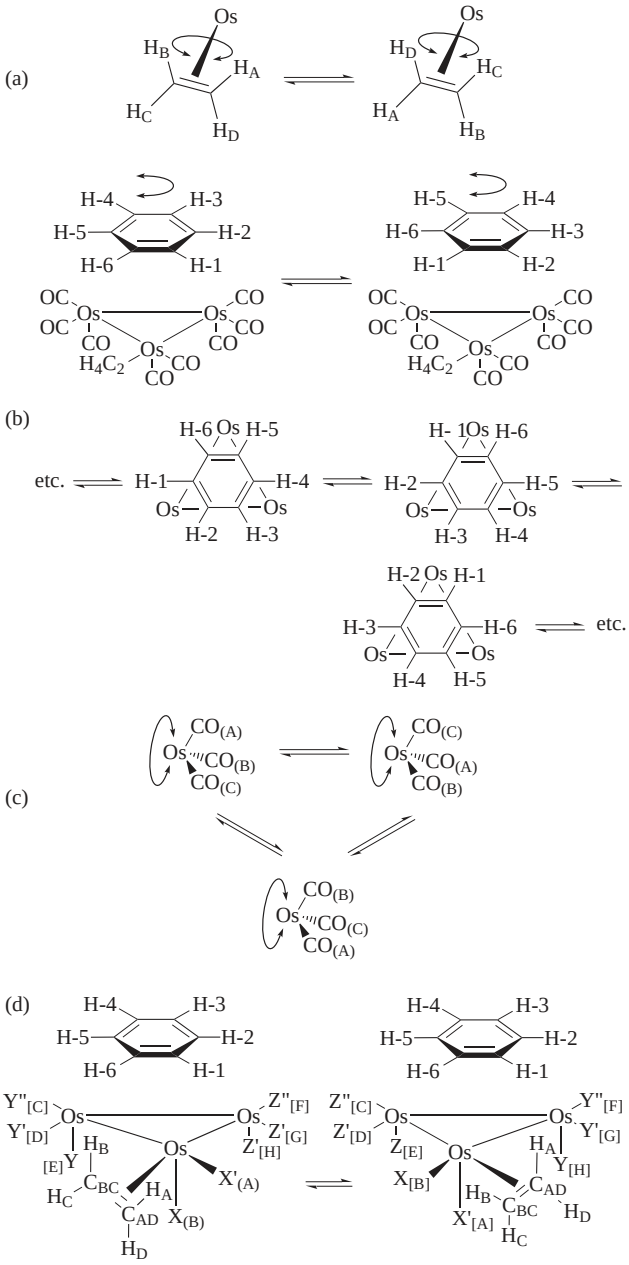

Figure 2 Fluxional processes deduced from solution state NMR of Os$_3$(CO)$_8$(η^2-CH$_2$CH$_2$)(μ_3:η^2:η^2:η^2-C$_6$H$_6$). (Reproduced by permission of the American Chemical Society from Heyes et al.[4])

(d) a trigonal-twist process for the Os(μ-CH$_2$CH$_2$)(CO)$_3$ moiety. To study fluxional processes in the solid state, the ^{13}C CP MAS NMR spectra were acquired with significant variations of experimental parameters. For the aromatic and ethene resonances, the spectra were acquired as a function of the ^{1}H decoupling field strength, as a secondary test of ligand motion; broader resonances were observed when the Larmor frequency of the ^{1}H decoupling field matched the rate of ligand motion. Also, the ^{13}C CP MAS spectra were acquired at two different spin rates to yield high-resolution spectra and spectra with extensive spinning sideband patterns. The high-resolution spectra were modeled with a lineshape analysis program to extract exchange rates between sites with different chemical shifts. The spinning sideband patterns of the low-temperature

spectra, especially the carbonyl resonances, were used to verify that indeed a low-temperature limit had been reached; the patterns were analyzed and compared with known chemical shift tensors of static carbonyl systems.

Over the temperature range of 219–335 K, five fluxional processes were observed, and four of these matched the previous solution state processes. Not observed in the solid state was the trigonal-twist process of the $Os(\mu\text{-}CH_2CH_2)(CO)_3$ moiety [see process (d) in Figure 2]. The activation barriers for benzene and ethene ligand reorientation in the solid state are very similar to the solution state values. Evidently, the trigonal-twist process is sterically demanding in the solid state.

2.3 Bent Nitrosyl Ligand

The spinning sideband patterns in an MAS NMR experiment can provide information about a fluxional process that is inaccessible in solution state NMR. The ^{15}N CP MAS spectrum of a bent nitrosyl ligand clearly demonstrates fluxionality that most probably exists in the solution state, but is practically impossible to study except in the solid state.[5] The square-pyramidal complex *meso*-tetraphenylporphinato(nitrosyl) cobalt(III), [Co(NO)(TPP)], has a nitrosyl ligand in the apical position, as shown in Figure 3. From the X-ray crystallographic work, and with the assumption of fourfold disorder, the ∠CoNO is 128.5° (in addition to the fourfold disorder, there is also twofold disorder across the basal plane). The fourfold disorder gives the average structure C_{4h} symmetry, and the potential fluxional process, interchange of the nitrosyl ligand among the four sites, is difficult to study by most spectroscopic techniques. However, the ^{15}N chemical shift anisotropy provides a clever route for solid state NMR techniques.

Slow speed ^{15}N CP MAS spectra acquired at 200 K of a ^{15}N-enriched sample of [Co(NO)(TPP)] show a spinning sideband pattern which, based on a Herzfeld–Berger analysis, is due to ^{15}N chemical shift elements characteristic of a static nitrosyl ligand. In particular, the nitrosyl chemical shift tensor in [Co(NO)(TPP)] does not have axial symmetry, and the tensor elements correspond to that of model nitrosyl compounds believed to have nonfluxional nitrosyl ligands. On warming [Co(NO)(TPP)] to 260 K, the slow speed ^{15}N CP MAS spectrum changes markedly, yielding a spinning sideband pattern characteristic of an apparently axially symmetric chemical shift tensor. The change is attributed to motional averaging of the chemical shift tensor. A simple model for the motionally averaged chemical shift tensor yields an estimate for ∠CoNO of 127°, in very good agreement with the X ray crystallographic result. Unfortunately, the model for the ^{15}N spinning sideband pattern does not yield a measure for the rate of motion of the nitrosyl ligand among the four sites.

2.4 Copper Chemical Vapor Deposition

In the fluxional processes discussed thus far, the site populations are determined by statistics since there is no significant change in the free energy of the system among the different conformers. If, however, the fluxional process leads to conformers with differing free energies, the site populations are determined by the equilibrium constant(s), and the analysis

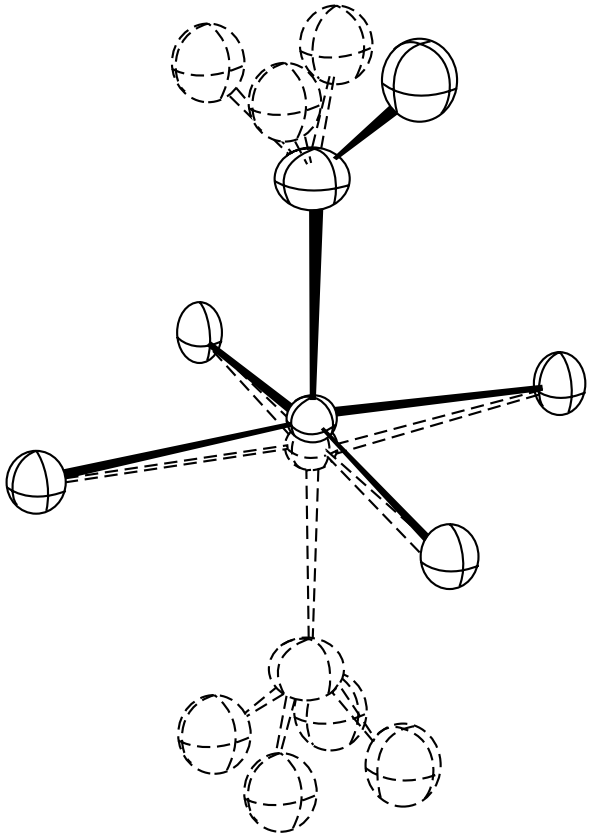

Figure 3 A partial representation of the molecular structure of [Co(NO)(TPP)] showing the disorder of the nitrosyl ligand. (Reproduced by permission of the American Chemical Society from W. R. Scheidt and J. L. Hoard, *J. Am. Chem. Soc.*, 1973, **95**, 8281)

becomes more difficult. A successful analysis leads to a rather detailed understanding of the potential energy surface governing the fluxional process. Since potential energies of bond formation and dissociation are important in many fields, the study of complex fluxional processes can generate results with applications to seemingly unrelated subjects, for example chemical vapor deposition.

From an inorganic chemist's perspective, chemical vapor deposition (CVD) requires a metal complex with fluxional ligands—in fact, the ultimate in fluxionality.[6] Copper(I) complexes have been considered for CVD under two conditions, with and without added hydrogen:

$$2(\text{hfac})\text{Cu}(\text{COD})(\text{g}) + \text{H}_2(\text{g}) \rightarrow 2\text{Cu}(\text{s}) + 2\text{hfacH}(\text{g}) + 2\text{COD}(\text{g}) \quad (3)$$

$$2(\text{hfac})\text{Cu}(\text{COD})(\text{g}) \rightarrow \text{Cu}(\text{s}) + \text{Cu}(\text{hfac})_2(\text{g}) + \text{COD}(\text{g}) \quad (4)$$

where hfac is 1,1,1,5,5,5-hexafluoro-2,4-pentadionate, and COD is 1,5-cyclooctadiene. The added hydrogen increases the rate of CVD, but the single reactant process is, at this writing, easier to control. For both reactions, the first step is believed to be loss of COD from the copper(I) complex, so it becomes useful to measure the Cu–COD bond dissociation energy. It is already known that the activation energy, based on copper film growth rate, for CVD with (hfac)Cu(COD) as

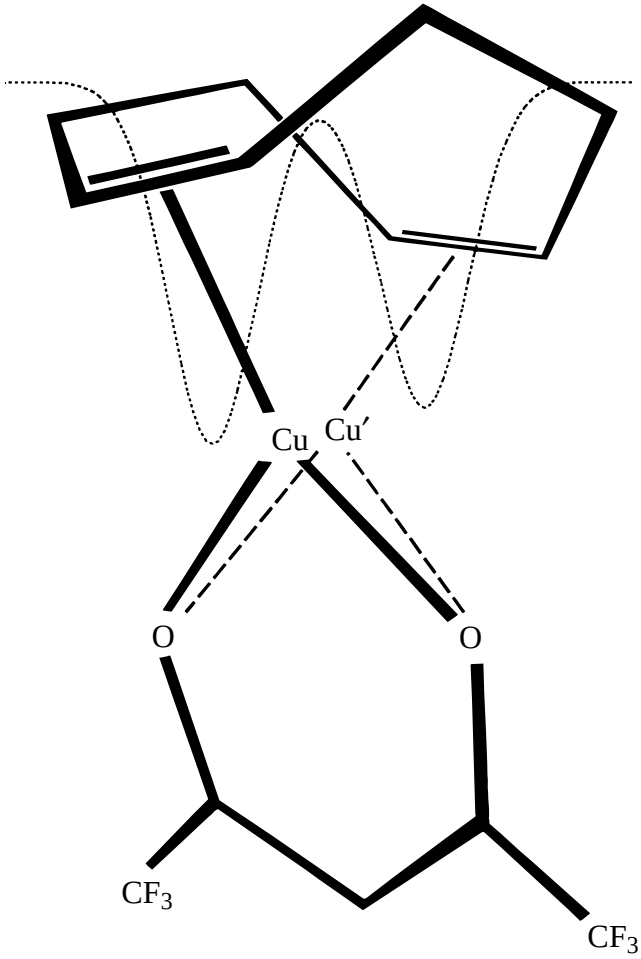

Figure 4 Representation of the structure of (hfac)Cu(COD) and the two-site disorder of the copper atom. (Reproduced by permission of the American Chemical Society from Kumar et al.[6])

the precursor ranges from 109 to 125 kJ mol^{-1}. Admittedly, one would not normally employ a solid state technique such as NMR to study a process like CVD. In fact, early NMR interest was drawn to the molecule because of unusual aspects of its molecular structure as determined by variable temperature X-ray crystallography. The solid state structure showed two-site disorder of the copper atoms, as illustrated in Figure 4. The variable temperature ^{13}C CP MAS of (hfac)Cu(COD) shows two resonances for the alkenic carbons at 190 K that coalesce to a single resonance by 340 K. The two resonances were assigned to alkenic carbons bound and not bound to the copper atom. Motion of the copper atom between the two sites, labeled η^2 and $\eta^{2\prime}$, interchanges the sites involved in copper–oxygen bonding. For this fluxional process, the NMR results could not be used to measure the relative populations of the copper sites, even though the rate of interchange was measured. The X-ray crystallographic data yields the copper site population, and the combination of the two techniques leads to the proposed double-minimum potential energy surface. The minima of the two potential energy wells are about 0.06 nm apart and differ in energy by 3–5 kJ mol^{-1}. The barrier connecting the two conformers is about 60 kJ mol^{-1}. This value is less than the activation energy for Cu CVD but is similar to that reported from temperature-programmed-desorption work for (hfac)Cu(COD) absorbed on Cu(100) where the activation energy is 59 kJ mol^{-1}.

2.5 Cyclopentadienyl Rotation

Recently, solid state ^{2}H NMR has been used to monitor fluxional processes. Briefly, ^{2}H NMR offers several advantages: a much wider range of rate constants can be measured than is possible from NMR of $S = \frac{1}{2}$ nuclei; the mode of motion is revealed in the solid state ^{2}H NMR lineshape; and selective labeling of sites with deuterium offers great practical advantages.

The motion of the cyclopentadienyl ligand (Cp) in $(\mu\text{-CO})_2[\text{FeCp(CO)}]_2$ has been studied by solid state ^{2}H NMR over the temperature range of 100–300 K.[7] Over this range, the ^{2}H NMR lineshape is constant, always in the fast exchange limit. The good ^{2}H NMR signal-to-noise ratio for the ~70% deuterated Cp ring permits inversion–recovery experiments, and the ^{2}H T_1 was also measured from 100 to 300 K. The ^{2}H T_1 is anisotropic; somewhat different values were measured for the parallel and perpendicular singularities in the spectrum. Also, the anisotropy is evident in both the experimental inversion–recovery spectra and the corresponding lineshape simulations; the rate constant for Cp ring rotation was determined via the lineshape simulations. The mode of motion in the simulations was assigned as jumps among nearest neighbor sites, C_5 jumps. A test of this mode of motion was done by observing the ^{2}H T_2 anisotropy in a series of spectra acquired with different quadrupole echo refocusing times; the simulations for C_5 jumps agreed much better than did simulations for $C_5{}^2$ jumps, jumps to next-nearest neighbor sites. The activation energy for the C_5 jumps is only 12.5(3) kJ mol^{-1}.

2.6 Cyclopentadienyl Motion

In the case of an organometallic salt, ferrocenium hexaflurophosphate, $[Cp_2Fe][PF_6]$, the ^{2}H T_1 could not be used to determine Cp ring motion because of the fast paramagnetic relaxation from the iron center.[8] Nevertheless, the ^{2}H NMR lineshape was quite informative because of a dramatic change occurring at a first-order phase transition at 347 K. X-ray crystallography of $[Cp_2Fe][PF_6]$ in the low-temperature phase shows disorder, presumably static, among the ferrocenium cations, and the disorder increases in the high-temperature phase. The ^{2}H NMR spectra, combined with calorimetry, indicate that the transition at 347 K is from a low-temperature static disorder to a high-temperature dynamic disorder. The ^{2}H NMR lineshape changes remarkably (Figure 5), indicating extensive motion in the high-temperature phase. However, the motion of the ions in the crystal lattice is somewhat restricted since the entropy gain indicates not all possible mutual orientations of Cp_2Fe^+ and PF_6^- are accessible, probably due to steric interactions.

3 QUADRUPOLAR AND CHEMICAL SHIFT INTERACTIONS AND CHEMICAL BONDING

Chemical bonding in organometallic and inorganic chemistry is highly variable. Bonds can be as seemingly weak as a

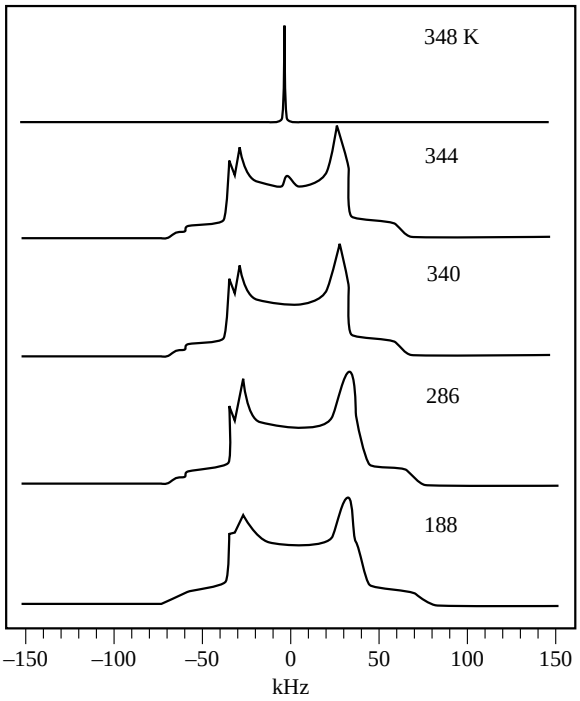

Figure 5 Variable temperature solid state ^{2}H NMR spectra of $[Cp_2Fe][PF_6]$. At 344 K and below, there is rapid Cp ring rotation but no fast reorientation of the Cp_2Fe^+ complex. (Reproduced by permission of the American Chemical Society from Webb et al.[8])

metal to η^2-dihydrogen, to bonds as complex as the quadruple bond in octachlorodirhenate, $Re_2Cl_8^{2-}$. Given this wide range of bonds, many spectroscopic and other characterization techniques are used by inorganic chemists. Of course, X-ray crystallography is probably the premier technique, but NMR and NQR spectroscopy have also played a role in bonding characterizations. In this discussion, the quadrupolar interaction will be emphasized, followed by brief coverage of the chemical shift interaction.

3.1 Quadrupolar Interaction

Deuterium, because it lacks occupied orbitals with angular momentum (p, d, f), is the easiest spin system with which to begin our study of the quadrupolar interaction. The jargon of deuterium NMR and NQR spectroscopy includes the following terms: electric field gradient tensors, nuclear electric quadrupole moments, quadrupole coupling constants, and asymmetry parameters. If we first examine a collection of experimental values of the quadrupole coupling constant for deuterium bound to another atom, for example, atoms of the first and second row, we note a regular pattern, as shown in Figure 6.[9]

3.2 Progression of Electrostatic Interactions

For the purpose of understanding the properties of electric field gradients and electric quadrupole moments, it is helpful to place these terms in a linear progression used to describe any arbitrary electric charge distribution. Let us start with the

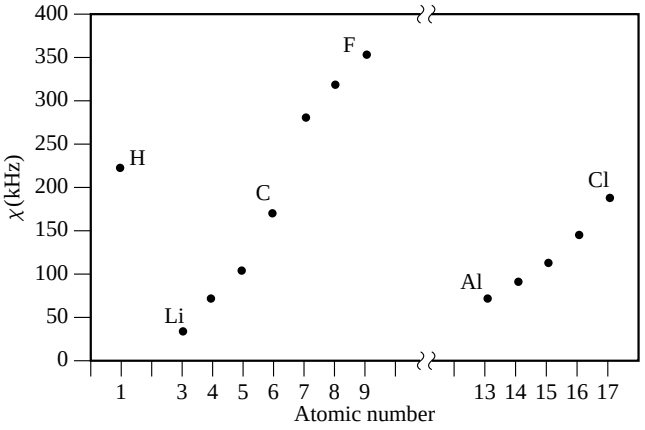

Figure 6 Deuterium quadrupole coupling constants for a deuteron bound to another atom; the HD molecule, the LiD molecule, etc. All data shown are for terminal X–D bonds; a deuteron in a bridging bond will have a considerably different value of the quadrupole coupling constant. (Reproduced by permission of Gordon and Breach from Butler and Keiter[9])

electric quadrupole moment and its place in a progression used to model the charge distribution, $\rho(\boldsymbol{r})$, of a nucleus:

$$\rho(\boldsymbol{r}) = Z + \boldsymbol{\mu} \cdot \boldsymbol{r} + Qr^2 + \ldots \tag{5}$$

For atomic nuclei, one is already familiar with the concept of a nuclear charge, Z, while the notion of an atomic electric dipole moment, $\boldsymbol{\mu}$, is distinctly unfamiliar. Of course, molecular electric dipole moments are often encountered in spectroscopy and molecular modeling; important for this discussion is the fact that the electrostatics are the same for both atomic and molecular dipole moments. That brings us to the nuclear electric quadrupole moment, Q, which can be nonzero if the nuclear spin angular momentum is greater than $\frac{1}{2}$. Similarly, electric charges surrounding the nucleus create electric fields that can be described by the following progression: electric potential, electric field, electric field gradient, and higher order terms. The electric potential and field are mathematically described by a scalar and a vector, respectively; the electric field gradient is expressed as a tensor.

There are some specific aspects of the electrostatic interactions that are pertinent for nuclei in atoms and molecules. First, a nucleus, even though surrounded by many electric charges, is always situated in space such that the electric field at the nucleus is zero. If the electric field happens to be nonzero, the nucleus experiences a force that pushes it to a region of zero electric field. Second, the nuclear electric dipole moment is required to be zero based upon the symmetry of the nuclear wave function; a nonzero dipole moment violates time reversal symmetry arguments. Third, the trace of the electric field gradient tensor at a nucleus is zero; additional details about the trace will be given below. Fourth, accurate values of Q are known for some nuclei but not others; a variety of measurement techniques are employed depending upon nuclear spin and atomic electron configuration. Pyykkö has recently summarized values of Q for the first 20 elements.[10] For deuterium, $Q = 2.86 \times 10^{-31}\,\mathrm{m}^2$.

3.3 The Electric Field Gradient Tensor

A tensor is a 3 × 3 matrix that is useful for describing an interaction that has a directional dependence.[11] For deuterium in a C–D bond, we find that the electric field gradient along the C–D bond is larger than for a direction perpendicular to the C–D bond.[12,13] Tensor orientations are expressed relative to an axis system, and there are several axis systems of note. The molecular axis system is preferred for analyzing the results of molecular orbital calculations, while the laboratory axis system has its place in the NMR experiment for defining the orientation of static and rf magnetic fields. However, we will start with yet another axis system called the principal axis system. One feature of the principal axis system is that the 3 × 3 matrix is diagonal; all off-diagonal elements are zero. The electric field gradient tensor in the principal axis system is

$$\boldsymbol{V}^{\mathrm{PA}} = \begin{bmatrix} q_{xx} & 0 & 0 \\ 0 & q_{yy} & 0 \\ 0 & 0 & q_{zz} \end{bmatrix} \tag{6}$$

where q is an electric field gradient component. A second feature of the principal axis system is a convention for ordering the diagonal elements of the electric field gradient tensor. By convention, the largest element (magnitude) is defined as the component along the z axis of the principal axis system, and the second largest element as the component along the y axis; thus

$$|q_{zz}| \geq |q_{yy}| \geq |q_{xx}| \tag{7}$$

We noted above that the trace of the electric field gradient tensor is zero, therefore the following relationship holds:

$$q_{xx} + q_{yy} + q_{zz} = 0 \tag{8}$$

Since the trace is zero, only two parameters are needed to describe the electric field gradient tensor in the principal axis system. Based on the NMR Hamiltonians, 'size' and 'shape' are expressed, respectively, by the quadrupole coupling constant, $e^2 q_{zz} Q/h$, and the asymmetry parameter, η,

$$\eta = \frac{q_{xx} - q_{yy}}{q_{zz}} \tag{9}$$

The term $e^2 q_{zz} Q/h$ is somewhat lengthy, so it is often represented by either C_Q or χ; the latter will be used herein. For the convention given in equation (7), the value of the asymmetry parameter ranges from 0 to 1. For η = 0, the two minor elements q_{xx} and q_{yy} are equal, and have a value of $-\frac{1}{2}q_{zz}$. NMR and NQR experiments yield values for the quadrupole coupling constant and the asymmetry parameter. A few experiments, single crystal NMR and microwave spectroscopy, also yield the orientation of the electric field gradient tensor with respect to the molecular axis system.

At this point, we can use symmetry arguments to predict values, zero or nonzero, for the quadrupole coupling constant χ, and the asymmetry parameter η. First, consider a deuterium nucleus surrounded by six electric charges in an octahedral array, as shown in Figure 7(a). In this high symmetry example, we expect $q_{xx} = q_{yy} = q_{zz}$. If this is so, and since equation (8) requires the sum of the three elements to be zero, then it follows that all elements must be equal to zero. Hence, χ = 0 and η = 0 for the deuteron in Figure 7(a). Likewise, a deuteron at a site with T_d symmetry will have zero values for χ and η. (One may wish to consult a text on group theory and note the similarity between T_d and O_h point groups insofar as the transformation of the x, y, and z axes.) Interestingly, χ and η are zero for the gas phase species, D^+, $D^{\cdot}$, and D^-; the quadrupolar interaction does not directly depend upon charge at deuterium when the charge resides in the deuterium centered, spherically symmetric s orbital.

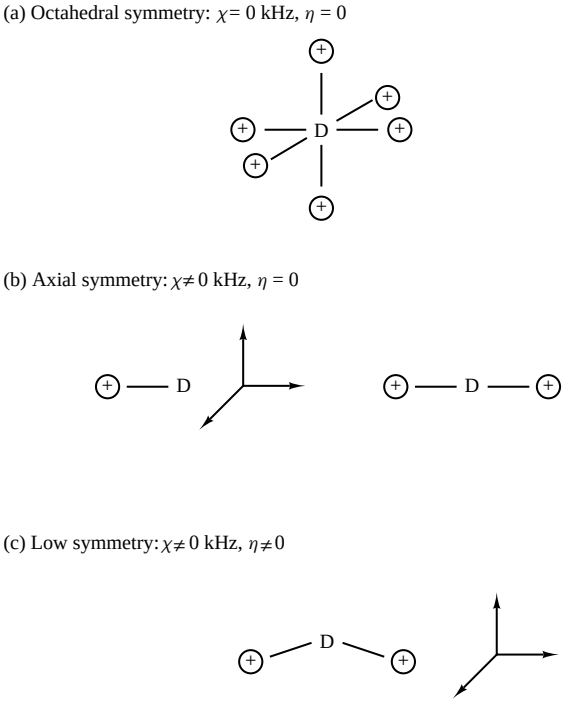

Figure 7 Some special electric field gradient tensors for common deuterium sites in molecules and solids. The values of the quadrupole coupling constant and the asymmetry parameter are obtained by symmetry and from equations (7) and (8). (Reproduced by permission of Gordon and Breach from Butler and Keiter[9])

As we move to metal hydride complexes, symmetry arguments also require that η is zero in M–D and linear M–D–M systems [Figure 7(b)]. In these cases, the axial symmetry requires that the two elements perpendicular to the M–D–M axis are equal. If the third element has a different value, and it usually does, then it must be labeled as q_{zz} to satisfy equations (7) and (8). In fact, η will be zero if there is C_3 or higher symmetry at the deuteron. For nonlinear M–D–M bonds [Figure 7(c)], the values of χ and η can be nonzero.

For the purpose of assessing the importance of nuclear charge, we can calculate the nuclear contribution to the electric field gradient at deuterium in an axially symmetric C–D bond of length 0.1095 nm (2.0693 au). Because of the symmetry [Figure 7(b)], η is zero and we need only calculate the field gradient along the z axis (principal axis system; z aligned with the C–D bond, Z_n = +6 au):

$$q_{zz}^{\mathrm{nuclear}} = +\sum_n Z_n \frac{3z_n^2 - r_n^2}{r_n^5} = 1.3544\,\mathrm{au} \tag{10}$$

Based on equations (7) and (8), the other elements of the electric field gradient in the principal axis system are

$$q_{xx} = q_{yy} = -\tfrac{1}{2}q_{zz} \tag{11}$$

again making use of $\eta = 0$.

The conversion of electric field gradient values into frequency units allows for comparison with experimental data. Of course, the conversion factor requires an accurate value for the nuclear electric quadrupole moment:

$$\chi[\text{Hz}] = e^2 q_{zz} Q/h[\text{Hz}] = q_{zz}[\text{au}] \times \frac{e^2 Q}{4\pi\epsilon_0 a_0^3 h} \tag{12}$$

where the field gradient, q_{zz}, is in atomic units, e is the electric charge in coulombs, ϵ_0 is the vacuum permittivity, a_0 is the Bohr radius in meters, and h is Planck's constant. The value of the conversion factor, based on the currently accepted value of Q for the deuteron, is 672 kHz au^{-1}.

In frequency units, the quadrupole coupling constant (nuclear contribution only) for a deuteron in a C–D bond is +910 kHz. This is considerably larger than the experimentally measured value of the deuterium quadrupole coupling constant of +175 kHz for a typical C–D bond. The conclusion is that the electronic contribution is both negative and slightly smaller in magnitude than the nuclear contribution. At first glance, one might have expected the electronic contribution to have exactly the same magnitude as the nuclear term based on the absence of an overall electric charge. However, the r^{-3} averaging tends to emphasize the charges close to the deuteron (the carbon nucleus) and rapidly reduces the contribution from electron density distant from the deuteron site, e.g. electron density in the other covalent bonds to carbon. For the HD molecule, a similar calculation shows that the nuclear contribution is 404 kHz (r = 0.079 nm); χ for the HD molecule is 225 kHz.[14] Again, the nuclear contribution is larger than the electronic contribution.

3.4 C–D Bonds

In principle, the value of χ for a deuteron in an X–D bond should be sensitive to the presence of excess electric charge on X. This principle was applied to a study of charge on carbon in the bridging methylene unit in *cis*-(μ-CD_2)(μ-CO)$[FeCpCO]_2$.[15] Earlier, a photoelectron study found an abnormally small C_{1s} binding energy; the low binding energy was interpreted by assigning a charge of −0.5 e on carbon relative to a model CH_2 unit.[16] A relative charge, Δq, of −0.5 e should reduce the value of χ as the shielding of the nuclear charge by the additional valence charge is larger. The problem is deducing the proportionality constant between charge and $\Delta\chi$. One estimate for the value of $\Delta\chi/\Delta q$ comes from a point charge model identical to the calculation, leading to the nuclear contribution to χ for carbon. For a C–D bond length of 0.1095 nm, the six protons of the carbon nucleus generate a field gradient at deuterium corresponding to χ^{nuclear} = +910 kHz. Since χ^{nuclear} depends linearly upon charge, $\Delta\chi/\Delta q$ = 152 kHz e^{-1}, indicating that deuterium NMR should be a very sensitive measure of charge on carbon in the bridging methylene unit. (Actually, a more realistic model for the spatial distribution of the excess charge is used based upon a carbon 2p atomic orbital; the diffuse charge reduces $\Delta\chi/\Delta q$ to 61.2 kHz e^{-1}.[15]) However, χ for the bridging methylene site in *cis*-(μ-CD_2)(μ-CO)$[FeCpCO]_2$ was not shifted to a lower value, thus indicating a normal charge on carbon relative to the aliphatic model. Interestingly, χ values for other bridging methylene sites do indicate a small negative charge on carbon; perhaps there is a *trans* effect from the bridging carbonyl that operates across the Fe–Fe bond.

3.5 M–D Bonds

For deuterium sites bound to metals, quadrupole coupling constants range from near zero to nearly that of the HD molecule. This wide range of χ values is, in the context of Figure 6, related to the metal nuclear charge, to the shielding by core and valence electrons, and to the wide range of M–D bond lengths. In addition, unusually symmetric environments can also reduce χ. In stoichiometric PdD, the deuterium sites have local octahedral symmetry, thus χ is near zero.[17] A few systems with terminal M–D bonds have been studied: LiD, 33 kHz;[18] Cp_2MoD_2, 52 kHz;[19] Cp_2WD_2, 54 kHz;[19] $DMn(CO)_5$, 68 kHz;[20]; and $[Cp_2ZrD_2]_x$, 46.7 kHz.[21] The relatively small values found in terminal M–D bonds are probably due both to a large electronic contribution and to the length of an M–D bond; the χ values are consistent with Salem's correlation between χ and the vibrational force constant.[21,22] Of all of these values, only that for LiD is known to be positive; χ is likely to be positive for all sites, but there are as yet no experimental data for the other metal hydrides.

Bridging metal hydride bonds have η values that depend upon ∠MDM. The bridging metal hydrides, $[DCr_2(CO)_{10}]^-$ and $[DW_2(CO)_{10}]^-$, have structures that vary as a function of counterion; asymmetry parameters range from near zero to 0.31.[23] The values of χ and η have been analyzed with a simple point charge model with the assumption that the sign of χ is positive.

Preliminary data and results from molecular orbital calculations of a model system show that χ and η vary in a predictable manner for the η^2 coordination of dihydrogen to a metal site. The model system indicates that χ and η slowly evolve until scission of the dihydrogen bond yields a *cis*-dihydride.[24] The limiting χ values are 225 kHz for the D_2 molecule and of the order of 50–80 kHz for the *cis*-dihydride. Kubas et al.[25] reported χ = 124 kHz for $W(CO)_3(PPr^i_3)_2(\eta^2\text{-}D_2)$, which is in good agreement with both the simple model described herein and the molecular orbital calculations.

3.6 Sign of the Deuterium Quadrupole Coupling Constant

In Figure 6, the sign of χ is positive, and all interpretative models to date are based on a positive value. However, there is some reason to suspect that the sign may be negative for some bridging metal hydride bonds; if so, the model must be improved, particularly for surface science studies. Experimentally, there are few methods for measuring the sign: gas phase microwave spectroscopy[26] and NMR spectra, showing both quadrupolar and dipolar interactions,[27] are two. Neither of these methods is generally useful in organometallic chemistry. However, at very high magnetic fields and very low temperatures, the Boltzmann distribution of spin state

populations is such that the solid state deuterium NMR lineshape is skewed. The direction of skew, either to low frequency or high frequency, uniquely determines the sign of the deuterium quadrupole coupling constant. Kuhns and Waugh[28] recently measured the sign of the ^{7}Li quadrupole coupling constant[29] in $LiNO_3$ at 5.9 T, and the sign of χ for ^{165}Ho in ferromagnetic gadolinium was reported by Shaw et al.[30] Signs of quadrupole coupling constants for some nuclei can be measured in Mössbauer spectroscopy, as has been done for dioxidized biferrocenylene.[31] The sign of χ for dioxidized biferrocenylene is negative, while for ferrocene it is positive.

3.7 Nitrogen

For nuclei other than hydrogen, the electric field gradient at the nucleus is often a function of the relative population of p orbitals centered on that nucleus. Thus, if the nucleus has an electric quadrupole moment, then NQR spectroscopy can be used to infer information about chemical bonding. A good illustration of this approach is a ^{14}N NQR study by Rubenacker and Brown of pyridine complexes with a range of Lewis acids.[32] In the pyridinium complexes, the relative populations of the donor nitrogen p orbital change with Lewis acid; for example, Li^+ accepts practically no charge from nitrogen whereas $CH_3{}^+$ accepts more than 0.5 e from the nitrogen lone pair.

A model for atomic orbital populations and NQR spectroscopy was developed in the 1950s, and is known as the Townes–Dailey model. The model, as adapted for pyridine, starts with expressions for the three components of the diagonalized electric field gradient tensor:

$$q_{xx} = [\mathrm{Np}_x - \tfrac{1}{2}(\mathrm{Np}_y + \mathrm{Np}_z)]q_0 \quad (13)$$

$$q_{yy} = [\mathrm{Np}_y - \tfrac{1}{2}(\mathrm{Np}_x + \mathrm{Np}_z)]q_0 \quad (14)$$

$$q_{zz} = [\mathrm{Np}_z - \tfrac{1}{2}(\mathrm{Np}_x + \mathrm{Np}_y)]q_0 \quad (15)$$

where q_0 is the electric field gradient that would be produced by only one electron in a nitrogen 2p orbital. The nitrogen atomic orbital populations are given by Np_x, Np_y, and Np_z. The local site symmetry for the pyridinium complexes is C_{2v}, leading to four hybrid atomic orbitals, written here in terms of 2s and 2p atomic orbital occupancies:

$$a = \mathrm{Np}_y \quad (16)$$

$$b = \tfrac{1}{2}[\cot^2(\tfrac{\alpha}{2})]\mathrm{Np}_z + \tfrac{1}{2}[1 - \cot^2(\tfrac{\alpha}{2})]\mathrm{Ns} + \tfrac{1}{2}\mathrm{Np}_x \quad (17)$$

$$\sigma = [1 - \cot^2(\tfrac{\alpha}{2})]\mathrm{Np}_z + [\cot^2(\tfrac{\alpha}{2})]\mathrm{Ns} \quad (18)$$

The hybrid orbitals are schematically illustrated in Figure 8, and are defined as follows: parameter a is the population of the nitrogen pπ orbital, parameter b is the population of nitrogen orbitals in each of the carbon–nitrogen σ bonds, parameter σ is the population of the nitrogen orbital in the σ bond of the Lewis acid–base complex, and α is the $\angle$CNC. The model development then continues with parameterization for the free pyridine base in which parameter σ is assigned the value of 2.

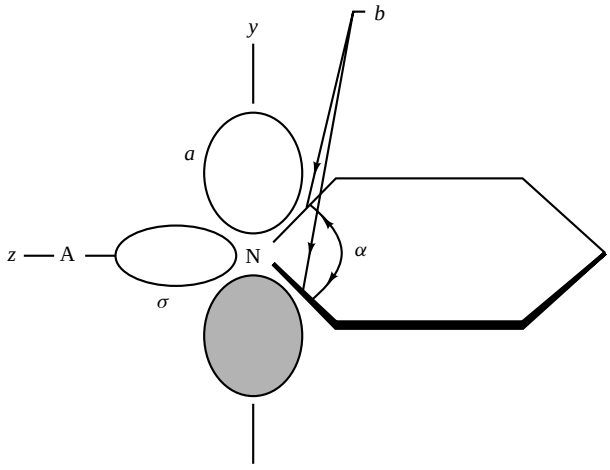

Figure 8 Coordinate system and nitrogen atomic orbital population parameters for the electric field gradient model of coordinated pyridine. (Reproduced by permission of the American Chemical Society from Rubenacker and Brown[32])

From the experimental quadrupole coupling constant and the asymmetry parameter, the values of $e^2q_{xx}Q/h$, $e^2q_{yy}Q/h$, and $e^2q_{zz}Q/h$ are calculated. One should note, however, that the principal axis system is not necessarily as depicted in Figure 8, thus a search is made for the best fit from among the 12 possible principal axis systems. The value of σ, the donor orbital occupancy, is obtained from the fit. For a poor Lewis acid such as Li^+, σ = 1.947, and for a strong Lewis acid such as BCl_3, σ = 1.537. One of the more extreme values, σ = 1.283, is found for pyridine *N*-oxide, where some π bonding is expected in addition to the σ charge donation described in the model. A similar extended Townes–Dailey model was applied to ^{14}N NQR data of divalent metal complexes with anthranilic acid (2-aminobenzoic acid).[33] This work showed that ^{14}N electric field gradients responded more strongly to the metal atom than did the nitrogen 1s binding energy, making NQR a more sensitive probe of metal–ligand bonding.

The interpretation of NQR data for transition metals is more complicated than for ^{14}N, and some of the models are similar to those used in Mössbauer spectroscopy. It has proved relatively easy to acquire ^{59}Co NQR spectra on several series of cobalt complexes, including the six-coordinate bis(dimethylglyoximato)cobalt(III) complexes.[34] The two dimethyl-glyoximato ligands form a planar array of nitrogens, leaving the remaining two axial sites accessible to ligands such as methyl, chloro, and triphenylphosphine. As the axial ligands are varied, the NQR parameters change considerably, and, based on the model, the principal axis system undergoes several reorientations. The model is based on partial field gradients and has parameters that represent the electric field gradient induced at the cobalt nucleus by each of the ligating atoms. The model fits the spectroscopic data for 27 cobalt complexes and shows that the amount of charge donation by the dimethylglyoximato ligand is not constant but is affected by the nature of the axial ligands.

3.8 Oxygen

The reversible binding of dioxygen to a metal center, as for hemoglobin and myoglobin, is an area where the study of

^{17}O sites could be useful. However, it is exceedingly difficult to acquire an ^{17}O NQR spectrum in these systems. Lumpkin and co-workers built a fast field cycling spectrometer and successfully acquired the ^{17}O NQR spectrum of dioxygen bound to Vaska's complex, $IrO_2Cl(CO)[P(C_6H_5)_3]_2$, by operating at 4.2 K.[35] Two oxygen sites were resolved, both with quadrupole coupling constants near 16 MHz. Unfortunately, the parameters were not further developed into a model of dioxygen bonding, even though later experimental work yielded spectra for oxyhemoglobin.

3.9 Rhenium

There have been relatively few NQR reports for metals such as rhenium in the third row of the transition metal series. Even so, the available data show that surprising results may be found. The complex dirhenium decacarbonyl $Re_2(CO)_{10}$ has approximate D_{4d} molecular symmetry in the crystalline phase, and so one might expect an asymmetry parameter near zero. Interestingly, NQR spectroscopy at room temperature and 77 K yields η = 0.63(3) and η = 0.88(3), respectively.[36] One explanation that has been offered starts with the equatorial carbonyls and the extreme sensitivity of the rhenium site to small distortions. In fact, more recent X-ray crystallographic work shows that Re–C bond lengths vary from 0.1973(6) to 0.2007(6) nm.[37] Furthermore, the radial distribution function for the rhenium 5 d wave function is so diffuse that even variations in the C–O bond length may be transmitted to the electric field gradient at the rhenium nucleus.

3.10 Chemical Shifts and Bonding

The chemical and physical properties of bridging methylene metal dimers are fascinating.[38] With a hydride acceptor, (μ-CH_2)(μ-CO)[FeCp(CO)]$_2$ can be converted to a bridging methine metal cation; treatment with a noncoordinating acid yields an agostic methyl bridged cation. In a molecular orbital picture of the bonding between a CH_2 unit and the metal dimer, the salient features are carbon based σ donating a_1 and π accepting b_1 valence orbitals interacting with metal based orbitals. With the presence of low lying metal–carbon antibonding orbitals, one can anticipate an unusual ^{13}C NMR chemical shielding interaction. The isotropic chemical shift is 145.6 ppm, showing substantially more paramagnetic shift than most organic methylene units with isotropic chemical shifts of 20–30 ppm.

An analysis of the paramagnetic contribution to the carbon chemical shift in the bridging methylene unit is quite interesting on several counts. First, the local C_{2v} site symmetry simplifies the molecular orbital picture as the carbon atomic p orbitals correspond to separate and easily identifiable molecular orbitals. Second, the bonding about the carbon site varies widely. The C–H bonds are expected to be strong, with a bond dissociation energy of the order of 430 kJ mol^{-1}. However, the C–Fe bonds should be much weaker, of the order of 200 kJ mol^{-1}. These two factors yield closely spaced occupied and empty molecular orbitals involving two, and only two, of the carbon atomic p orbitals. And, based on the angular momentum operators for the paramagnetic chemical shift interaction, a large shift is expected perpendicular to the plane defined by the Fe_2C metallocyclopropane unit. The results of the ^{13}C CP MAS and ^{13}C nonspinning NMR experiments yield a chemical shift tensor with two relatively normal tensor elements, 82 and −18 ppm (TMS), and one extraordinarily large element of 372 ppm that is perpendicular to the Fe_2C plane. In summary, the distinctive feature of the bridging methylene unit in a metal dimer or cluster is the remarkable range of chemical bonds to the carbon site, which is then reflected in the chemical shift tensor.

A similar analysis of the chemical shift tensor was attempted for the square-planar tetracyanometalates (M = Ni, Pd, Pt).[39] Surprisingly, there are only small differences in the tensor elements on going from nickel to platinum, and all of the chemical shift tensors are rather similar to that of acetonitrile. Since other information suggests that the metal–cyanide bond strength increases from nickel to platinum, the constancy of the chemical shift tensor is unexpected. Bonding and electronic conduction properties were the motivating factors in a study by Vaughan and co-workers of the one-dimensional conductor $K_2P(CN)_4Br_{0.3} \cdot 3H_2O$, a Krogmann salt.[40] The room temperature ^{13}C NMR spectrum shows some asymmetry about the C–N bond in accord with conduction along the stacking axis; the chemical shift along the conduction axis is 187 ppm (TMS), while perpendicular to the stacking axis the shift is 225 ppm. One might expect the metal center to be more affected by conduction. Indeed, the ^{195}Pt T_1 and T_2 show evidence of charge density waves below the metal–insulator transition.[41] The orientation of a chemical shift tensor is also of importance in ^{31}P NMR where a series of cyclic bidentate phosphine complexes have been studied.[42] In the model developed for the four- to seven-membered chelates, the ^{31}P chemical shift tensor orientation rotates smoothly and is correlated with ∠MPC.

4 A FEW EXAMPLES OF SOLID STATE NMR AND INORGANIC SOLIDS

Presented here are examples that build upon the principles and concepts given earlier. As a convenience to the reader, the examples are arranged by atomic number, though admittedly there are many other possible arrangements.

4.1 Hydrogen-2

The ability to follow motional processes even in paramagnetic solids is highly useful. In the business of environmental management, hazardous wastes such as phenol are mixed with Portland cement for the purpose of solidification/stabilization. While the material appears solid, and other evidence indicates complete deprotonation of the phenol and formation of calcium salts, it is the technique of solid state ^2H NMR that allows one to monitor the phenol over the cement cure time.[43] Unfortunately for solidification/stabilization, after 1 year cure, only 55% of the phenol is actually bound to the cement matrix (as measured by the fraction executing 180° ring flips). The remaining phenol fraction is freely mobile.

4.2 Carbon-13

Transition metal complexes of carbon suboxide (O=C=C=C=O) are highly reactive and difficult to characterize. Hillhouse and co-workers prepared $(PPh_3)_2Ni(C,C':\eta^2\text{-}C_3O_2)$ from selectively isotopically enriched carbon suboxide and obtained ^{13}C CP MAS NMR spectra.[44] The chemical shifts of the carbon suboxide ligand are distinctive and shift on coordination to nickel; also, the ^{13}C resonance *trans* to a phosphine shows J coupling, enabling identification of the mode of coordination of carbon suboxide.

Silica-supported $Os_3(CO)_{12}$ represents a large range of catalysts used in petroleum refining. In an extensive project by Shapley, Oldfield, and their co-workers, ^{13}C MAS NMR spectroscopy was used to study physisorbed $Os_3(CO)_{12}$ as well as to characterize reaction products such as chemisorbed $HOs_3(CO)_{10}(OSi\equiv)$.[45]

Fullerene-C_{60} (C_{60}) provides an interesting application of non-sample-spinning ^{13}C NMR spectroscopy. At 295 K, a single narrow resonance at 143 ppm is observed for solid C_{60}.[46] On cooling to 77 K, a chemical shift powder pattern is seen with components at 220, 186, and 40 ppm, consistent with the aromatic sites in C_{60} and facile rotation of the molecule in the solid state.

4.3 Fluorine-19

The intercalation of small molecules into layered structures[47] such as graphite, montmorillonite, and zirconium hydrogen phosphate is a field in which NMR is used extensively. The process of AsF_5 intercalation into graphite was monitored as a function of time by one-dimensional ^{19}F NMR imaging; the single narrow ^{19}F resonance simplifies the imaging experiment nicely.[48]

4.4 Sodium-23

Sodium is an important charge balancing cation in zeolites, and, thus, should be intimately involved when other charge species are introduced into the zeolite structure. Molybdenum and tungsten hexacarbonyls can be sorbed by sodium zeolite Y, then photo-oxidized with dioxygen. The ^{23}Na double rotation NMR (DOR) spectrum shows sufficient resolution, based on isotropic chemical shifts, that changes can be seen as the metal carbonyl is oxidized.[49]

4.5 Aluminum-27

Portland cement is a complex material and has been difficult to study well by NMR. Recently, Skibsted et al. made remarkable progress with high speed ^{27}Al MAS NMR and computer simulations of the ^{27}Al spinning sideband pattern.[50] The different phases are resolved based on chemical shift, quadrupole coupling constant, and asymmetry parameter. The relative concentration of several calcium aluminate and aluminate hydrates were measured as a function of cement cure.

Recently, magnetic field swept ^{27}Al NMR has been used to study $\alpha\text{-}Al_2O_3$ and hydrogen faujasites (FAU) zeolites.[51,52] The advantage of field swept NMR is that it easily allows operation at very low temperatures. The objective is to reduce ion motion and achieve a static limit in the NMR spectrum of the quadrupolar nuclei.

4.6 Silicon-29

The ZSM-5 zeolite has a complex structure, and this structure is also affected by temperature and the presence of sorbed *p*-xylene.[53] Because of the similarity of all the ^{29}Si sites, the 2D COSY and INADEQUATE experiments yield informative, yet still ambiguous results. Fortunately, a unique spectral assignment is possible with the additional symmetry information provided by X-ray powder diffraction.

4.7 Phosphorus-31

Nonlinear optical materials[54] can be made from solid solutions of $BaLiPO_4$ and $PbLiPO_4$. The greatest efficiency for the second harmonic generation of 1064 nm radiation occurs for a solid solution with the composition $Ba_{0.55}Pb_{0.45}LiPO_4$.[55] This composition lies near a structure phase transition, and the ^{31}P chemical shift is also sensitive to the phase transition. The combination of ^{31}P NMR and the Kurtz method for estimating second harmonic generation worked well in the search for the optimum composition.

Two-dimensional NMR techniques are not yet commonly used for inorganic systems, the ^{29}Si COSY and INADEQUATE experiments on zeolites by Fyfe being one of the few examples.[53] Wu and Wasylishen have tested and optimized SECSY, COSY, and homonuclear J resolved ^{31}P CP MAS NMR techniques for simple metal phosphine complexes.[56] Given the ubiquity of phosphines in transition metal catalysis, this is a timely contribution.

4.8 Yttrium-89

Yttrium organometallic chemistry ranges from the tetrahydrofuran adduct of Cp_3Y to alkoxide complexes such as $Y_3[CO(CH_3)_3]_7Br_2(THF)_2$. The NMR of a low gyromagnetic ratio nuclei such as ^{89}Y is somewhat difficult. However, cross polarization from the proton spin system has proven to be effective, and, therefore, ^{89}Y CP MAS NMR is becoming popular for these complexes.[57]

4.9 Niobium-93 and Tantalum-181

This article started with a negative result, and will end with another sad story. A series of M_2X_{10} complexes (M = Nb, Ta; X = Cl, Br) were studied by NQR in 1973 by McCarley and co-workers.[58] At the time, single crystal X-ray crystallography was not the routine experiment that it is today, and alternative structural characterization methods were examined. Unfortunately, while numerous transitions were observed, the NQR method did not prove to be a simple or straightforward structural identification method and this branch of chemistry appears to have been discontinued.

5 RELATED ARTICLES

Amorphous Materials; Ceramics; Coal Structure from Solid State NMR; Deuterium NMR in Solids; Field Gradients and Their Application; Geological Applications; Inter-

calation Compounds; Microporous Materials and Xenon-129 NMR; Molecular Sieves: Crystalline Systems; Organometallic Compounds; Quadrupolar Interactions; Quadrupolar Nuclei in Glasses; Quadrupolar Nuclei in Solids; Silica Surfaces: Characterization; Silicon-29 NMR of Solid Silicates; Supported Metal Catalysts; Vanadium Catalysts: Solid State NMR.

6 REFERENCES

1. C. J. Gorter and L. J. F. Broer, *Physica*, 1942, **9**, 591.
2. A. J. Campbell, C. E. Cottrell, C. A. Fyfe, and K. R. Jeffrey, *Inorg. Chem.*, 1976, **15**, 1321.
3. C. G. Wade and J. S. Waugh, *J. Chem. Phys.*, 1964, **40**, 2063.
4. S. J. Heyes, M. A. Gallop, B. F. G. Johnson, J. Lewis, and C. M. Dobson, *Inorg. Chem.*, 1991, **30**, 3850.
5. C. J. Groombridge, L. F. Larkworthy, and J. Mason, *Inorg. Chem.*, 1993, **32**, 379.
6. R. Kumar, F. R. Fronczek, A. W. Maverick, A. J. Kim, and L. G. Butler, *Chem. Mater.*, 1994, in press.
7. M. I. Altbach, Y. Hiyama, R. J. Wittebort, and L. G. Butler, *Inorg. Chem.*, 1990, **29**, 741.
8. R. J. Webb, M. D. Lowery, Y. Shiomi, M. Sorai, R. J. Wittebort, and D. N. Hendrickson, *Inorg. Chem.*, 1992, **31**, 5211.
9. L. G. Butler and E. A. Keiter, *J. Coord. Chem.*, 1994, in press.
10. P. Pyykkö, *Z. Naturforsch.*, 1992, **47a**, 189.
11. C. P. Poole and H. A. Farach, *Theory of Magnetic Resonance*, Wiley-Interscience, New York, 1987.
12. L. C. Snyder and H. Basch, *Molecular Wave Functions and Properties*, Wiley, New York, 1972.
13. L. C. Snyder, *J. Chem. Phys.*, 1978, **68**, 291.
14. N. F. Ramsey, *Molecular Beams*, Oxford University Press, New York, 1956, p. 238.
15. M. I. Altbach, Y. Hiyama, D. J. Gerson, and L. G. Butler, *J. Am. Chem. Soc.*, 1987, **109**, 5529.
16. S. F. Xiang, H. W. Chen, C. J. Eyermann, W. L. Jolly, S. P. Smit, K. H. Theopold, R. G. Bergman, W. A. Herrmann, and R. Pettit, *Organometallics*, 1982, **1**, 1200.
17. C. L. Wiley and F. Y. Fradin, *Phys. Rev. B*, 1978, **17**, 3462.
18. L. Wharton, L. P. Gold, and W. Klemperer, *J. Chem. Phys.*, 1962, **37**, 2149.
19. I. Y. Wei and B. M. Fung, *J. Chem. Phys.*, 1971, **55**, 1486.
20. P. S. Ireland, L. W. Olson, and T. L. Brown, *J. Am. Chem. Soc.*, 1975, **97**, 3548.
21. W. L. Jarrett, R. D. Farlee, and L. G. Butler, *Inorg. Chem.*, 1987, **26**, 1381.
22. L. Salem, *J. Chem. Phys.*, 1963, **38**, 1227.
23. A. J. Kim, F. R. Fronczek, L. G. Butler, S. Chen, and E. A. Keiter, *J. Am. Chem. Soc.*, 1991, **113**, 9090.
24. K. Guo, W. L. Jarrett, and L. G. Butler, *Inorg. Chem.*, 1987, **26**, 3001.
25. G. J. Kubas, C. J. Unkefer, B. I. Swanson, and E. Fukushima, *J. Am. Chem. Soc.*, 1986, **108**, 7000.
26. P. Thaddeus, L. C. Krisher, and J. H. N. Loubser, *J. Chem. Phys.*, 1964, **40**, 257.
27. S. D. Swanson, S. Ganapathy, and R. G. Bryant, *J. Magn. Reson.*, 1987, **73**, 239.
28. P. L. Kuhns and J. S. Waugh, *J. Chem. Phys.*, 1992, **97**, 2166.
29. X. Wu, F. R. Fronczek, and L. G. Butler, *Inorg. Chem.*, 1994, in press.
30. K. I. Shaw, I. S. MacKenzie, and M. A. H. McCausland, *J. Phys. F: Met. Phys.*, 1983, **13**, 1735.
31. W. H. Morrison, Jr.and D. N. Hendrickson, *Inorg. Chem.*, 1974, **13**, 2279.
32. G. V. Rubenacker and T. L. Brown, *Inorg. Chem.*, 1980, **19**, 392.
33. D. A. d'Avignon and T. L. Brown, *Inorg. Chem.*, 1982, **21**, 3041.
34. T. L. Brown, *Acc. Chem. Res.*, 1974, **7**, 408.
35. O. Lumpkin, W. T. Dixon, and J. Poser, *Inorg. Chem.*, 1979, **18**, 982.
36. C. B. Harris, *Inorg. Chem.*, 1968, **7**, 1691.
37. M. R. Churchill, K. N. Amoh, and H. J. Wasserman, *Inorg. Chem.*, 1981, **20**, 1609.
38. A. J. Kim, M. I. Altbach, and L. G. Butler, *J. Am. Chem. Soc.*, 1991, **113**, 4831.
39. A. J. Kim and L. G. Butler, *Inorg. Chem.*, 1993, **32**, 178.
40. M. E. Stoll, R. W. Vaughan, R. B. Saillant, and T. Cole, *J. Chem. Phys.*, 1974, **61**, 2896.
41. M. Mali, O. Kanert, M. Mehring, and D. Brinkmann, *Phys. Rev. B: Condens. Matter*, 1979, **20**, 4442.
42. E. Lindner, R. Fawzi, H. A. Mayer, K. Eichele, and W. Hiller, *Organometallics*, 1992, **11**, 1033.
43. M. A. Janusa, X. Wu, F. K. Cartledge, and L. G. Butler, *Environ. Sci. Technol.*, 1993, **27**, 1426.
44. A. K. List, M. R. Smith III, and G. L. Hillhouse, *Organometallics*, 1991, **10**, 361.
45. T. H. Walter, G. R. Frauenhoff, J. R. Shapley, and E. Oldfield, *Inorg. Chem.*, 1991, **30**, 4732.
46. C. S. Yannoni, R. D. Johnson, G. Meijer, D. S. Bethune, and J. R. Salem, *J. Phys. Chem.*, 1991, **95**, 9.
47. D. O'Hare, in *Inorganic Materials*, ed. D. W. Bruce, and D. O'Hare, Wiley, New York, 1992, p. 165.
48. G. C. Chingas, J. Milliken, H. A. Resing, and T. Tsang, *Synth. Metals*, 1985, **12**, 131.
49. R. Jelinek, S. Özkar, and G. A. Ozin, *J. Phys. Chem.*, 1992, **96**, 5949.
50. J. Skibsted, E. Henderson, and H. J. Jakobsen, *Inorg. Chem.*, 1993, **32**, 1013.
51. X. Wu, E. A. Juban, and L. G. Butler, *Chem. Phys. Lett.*, 1994, in press.
52. X. Wu and L. G. Butler, *Microporous Mater.*, 1994, submitted.
53. C. A. Fyfe, H. Grondey, Y. Feng, and G. T. Kokotailo, *J. Am. Chem. Soc.*, 1990, **112**, 8812.
54. S. R. Marder, in *Inorganic Materials*, ed. D. W. Bruce, and D. O'Hare, Wiley, New York, 1992, p. 116.
55. C. S. Liang, H. Eckert, T. E. Gier, and G. D. Stucky, *Chem. Mater.*, 1993, **5**, 597.
56. G. Wu and R. E. Wasylishen, *Organometallics*, 1992, **11**, 3242.
57. J. Wu, T. J. Boyle, J. L. Shreeve, J. W. Ziller, and W. J. Evans, *Inorg. Chem.*, 1993, **32**, 1130.
58. P. A. Edwards and R. E. McCarley, *Inorg. Chem.*, 1973, **12**, 900.

Biographical Sketch

Leslie G. Butler. *b* 1955. B.S., 1977, Arkansas. Ph.D., 1981, Illinois (supervisor Theodore L. Brown). Postdoctoral work at California Institute of Technology (with Harry B. Gray). Faculty in Chemistry at Louisiana State University, 1983–present. Research interests include applications of NMR, especially quadrupolar nuclei, to inorganic chemistry and environmental science.

Intercalation Compounds

Werner Müller-Warmuth
Institut für Physikalische Chemie der Westfälischen Wilhelms-Universität, Münster, Germany

1 Introduction 1
2 Typical NMR Experiments with Intercalation Compounds 1
3 Structure and Motions of Hydrated Layered Chalcogenides 5
4 Structure and Dynamics of Guest Phases in Molybdenum Cluster Chalcogenides 7
5 Related Articles 9
6 References 9

1 INTRODUCTION

Intercalation compounds are formed by the reversible insertion of guest species into solid matrices which retain their structure except for certain lattice expansions. They may be considered as a subclass of inclusion compounds, a term that has been used for a larger group of materials consisting of host and guest species. For intercalation reactions an increasing number of host lattices with different structural dimensionality is nowadays available ranging from insulators such as layered silicates to semiconductors and metallic conductors, e.g. graphite, transition metal dichalcogenides, or molybdenum cluster compounds. The guest species include small atomic ions as well as solvated systems and larger molecular units. As far as the aspects of the materials, the preparation of the compounds, and other chemical and physical properties are concerned, we have to refer to review articles and monographs which cover a broader horizon and some specific aspects of the subject.[1] Applications of intercalation compounds comprise battery systems, electrochromic displays, catalysis, and sensors, as well as the employment as model systems for low-dimensional solids.

Solid state NMR studies have contributed substantially to the understanding of the structure and dynamics of intercalation compounds. The location of guest molecules, their orientation and bonding characteristics, guest–host interactions, the donation of electrons to the host, and motions of the intercalated species are some of the problems that have been addressed using NMR. Chemical shift, nuclear quadrupole, and dipole–dipole interactions, and relaxation rates have been utilized to obtain data on the structure and dynamics of intercalation compounds. High-resolution techniques such as MAS or multiple pulse methods were only applied in exceptional cases, since the information on the anisotropy is of major importance. Broadline spectra of compounds with reduced dimensionality are often distinguished by much better resolved structures than those of three-dimensional solids.

Among the materials that have been investigated using NMR techniques, characteristic differences exist between intercalation compounds with insulator host lattices and those which exhibit electronic conductivity. The most important groups of the first class of compounds are zeolites, pyrochlores, sheet silicates, and β-alumina, which are generally discussed in another context. We will concentrate on host lattices with electronic conductivity, which have attracted increased interest in recent years because of the large diversity of compounds. The intercalation in these materials can be described by the concept of reversible topotactic redox reactions, and is connected with the transfer of electrons entering or leaving the conduction band of the host matrix.

The most important classes of such systems are two-dimensional layered intercalation compounds with cationic or solvated ionic guest species or with intercalated molecules, and three-dimensional framework structures containing channels or cavities for the uptake of small guest species. Among the materials known for a long time, the graphite intercalation compounds belong to the layered systems, and hydrogen bronzes may be formed in both three- and two-dimensional structures.

Within this article it is of course not possible to present a survey of all the NMR results which contributed to the understanding of the structure of intercalation compounds or of the motions of guest species. For this the reader is referred to the literature, and especially to a recent, comprehensive review.[2] Here it is attempted to illustrate the potential of NMR for the examination of intercalation compounds by means of typical examples. To this aim, in the next section some example techniques and experiments using multinuclear magnetic resonance will be discussed as an introduction to the methods. Section 3 contains more recent NMR studies of some special layered chalcogenide systems, while Section 4 is devoted to molybdenum cluster sulfides, the class of intercalation compounds with a framework structure which was recently investigated in most detail.

2 TYPICAL NMR EXPERIMENTS WITH INTERCALATION COMPOUNDS

2.1 Powder Patterns or Oriented Samples

Optimum information is of course obtained if—in exceptional cases—single crystals are available. Figure 1 shows, as an example, the ^{1}H NMR spectrum of the metal–ammonia intercalation compound $Na_x(NH_3)_y[MoS_2]$ for the two limiting orientations, where the angle Θ between the crystalline c axis and the external field is either 0 or 90°. The angular dependence follows a $(3\cos^2\Theta - 1)$ law. The following information was obtained: (i) the large triplet splitting belongs to the dipolar proton–proton interaction in a rotating three-spin system; (ii) each component is split once more by the interaction with the nitrogen nucleus; (iii) the C_3 axes of NH_3 are oriented parallel to the layer planes; and (iv) there is an additional reorientational motion of the NH_3 molecules about an axis parallel to the hexagonal c axis and perpendicular to the direction of the C_3 axis; this motion becomes frozen at temperatures below about 100 K.

Most investigations refer to powder samples consisting of small crystallites of the material. In conducting layered compounds, as a consequence of the Pauli paramagnetic anisotropy, there is a tendency of the crystallites in sufficiently high magnetic fields to become aligned. Figure 2 shows as an example the ^{1}H NMR spectra of the hydrated system Na_x

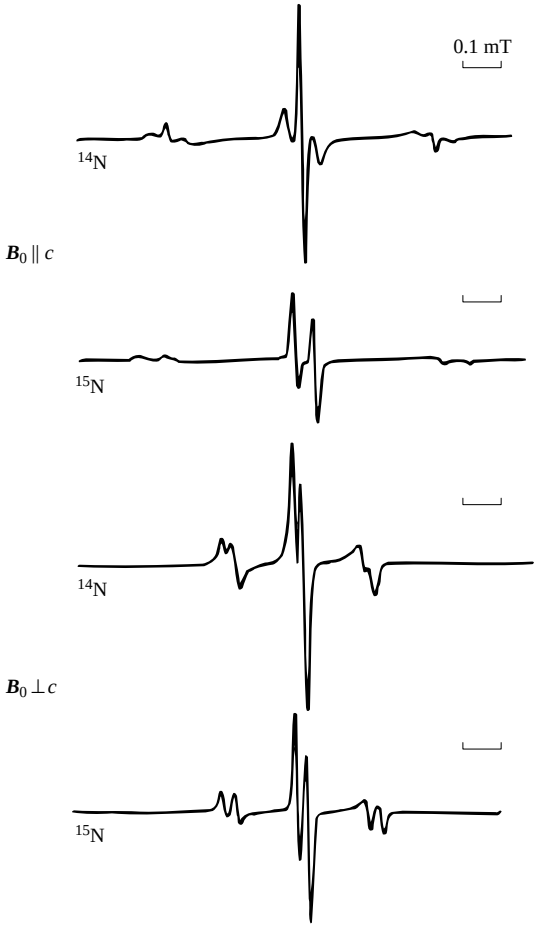

Figure 1 Proton NMR derivative spectra of an $Na_x(NH_3)_y[MoS_2]$ single crystal at 300 K for two orientations of the hexagonal *c* axis in a magnetic field of 0.19 T. Measurements were made for both intercalated $^{14}NH_3$ and $^{15}NH_3$. (Reproduced by permission of Oldenbourg Verlag from E. Wein, W. Müller-Warmuth, and R. Schöllhorn, *Z. Phys. Chem. (NF)*, 1987, **151**, 113)

$(H_2O)_y[NbS_2]$ for a loosely packed sample [Figure 2(a)], for a more compact sample [Figure 2(b)], and a sample where the small crystallites were embedded in Teflon powder and pressed into the ampule [Figure 2(c)]. The limiting spectra [Figure 2(a) and (c)] correspond to a normal powder pattern (Pake doublet with anisotropic chemical shift) and a situation where all the crystallites are completely oriented with their hexagonal *c* axes parallel to the external field.

The magnetic field induced orientation phenomena observed in many solid state NMR experiments of layered compounds can be explained in terms of the magnetic properties and depend on the density of states at the Fermi level of the transition metal chalcogenides or graphites.[3] Orientation or partial orientation may lead to misinterpretations of the spectra if not recognized, or we may profit from it by conducting experiments which are otherwise not possible. An example is given in Figure 3. The powder pattern of the ^{93}Nb NMR in the host lattice NbS_2 is broad and can be simulated by chemical shift and quadrupole interactions (δ_{iso} = 1350 ppm referred to niobium pentachloride, $\Delta\sigma$ = 4200 ppm, $\chi = e^2qQ/h$ = 61 MHz, $\eta_{CS} = \eta_Q = 0$). In a loosely packed sample, by contrast, only one narrow, central transition (CT) can be observed in the covered range. However, it is possible to detect

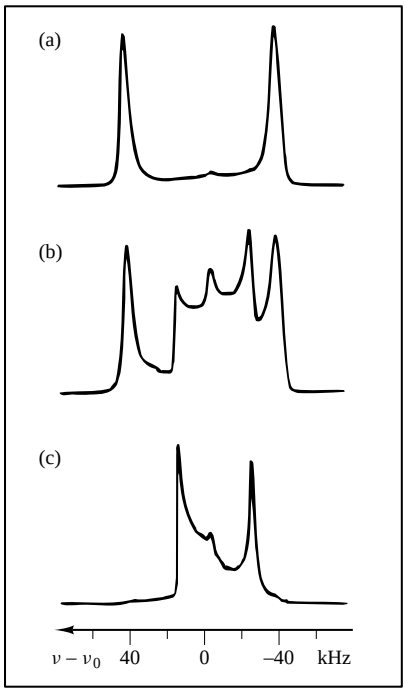

Figure 2 Proton NMR spectra of polycrystalline $Na_x(H_2O)_y[NbS_2]$ observed in a magnetic field of 7 T, whereby the density of the package of the sample was increased from top to bottom

all the eight satellite transitions (ST) of the spin-$\frac{9}{2}$ nucleus as well if the detection range is greatly expanded. The positions of these lines can be reproduced by spectrum simulation with first- and second-order quadrupole interactions, resulting in a very precise determination of the coupling constant.

Intercalation of copper produces a satellite spectrum of 18 lines [Figure 3(c)], which was explained by the superposition of two complete spectra with quadrupole coupling constants of 39.12 and 36.05 MHz instead of 60.02 MHz for the empty host. They belong to two distinct niobium environments in the host lattice with an occurrence ratio 1:1 caused by a well ordered arrangement of copper atoms in tetrahedral sites of the van der Waals gap.

Application of the magnetic field induced orientation effect is in many cases the only way at all to detect and to analyze NMR spectra in layered intercalation compounds. It is often possible to maintain the orientation in a sample by dispersing the crystallites in a resin, and curing the resin after a strong magnetic field had been applied to induce orientation. Angle-dependent measurements are then possible, as shown in Figure 4 for the ^{63}Cu NMR of $Cu_{0.5}[NbS_2]$.

2.2 Anisotropic Dynamics of an Intercalated Heteronuclear Four-Spin System

An instructive example from the NMR point of view is difluoromethane. In the presence of larger alkali cations it is possible to intercalate molecules with low solvating power such as CH_2F_2. Well structured ^{1}H and ^{19}F NMR spectra were observed (Figure 5) and could be simulated on the basis of a proper model.[4] They were calculated from the numerical solution of the eigenvalue problem of a Hamiltonian which

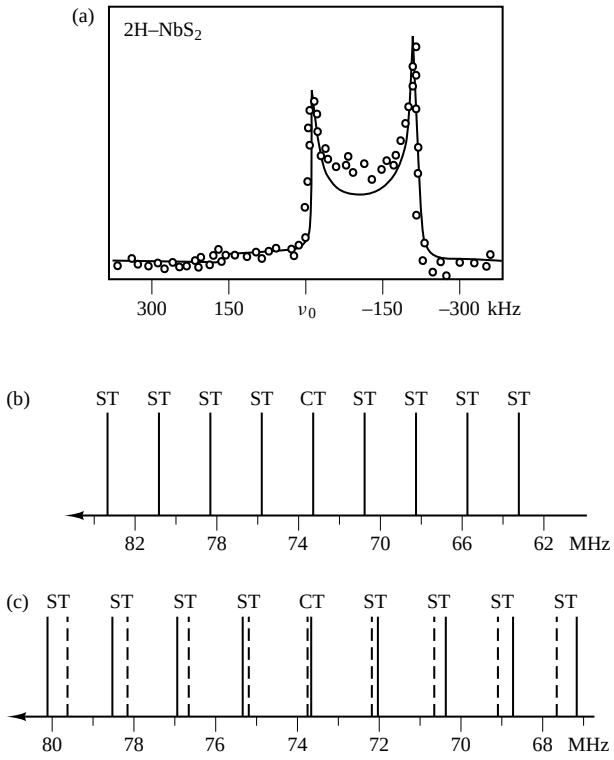

Figure 3 Niobium-93 NMR spectra of layered 2H−NbS_2 in a magnetic field of 7 T and 200 K. (a) The powder pattern (sample pressed in Teflon powder) was recorded at ν_0 = 73.41 MHz and superimposed of successively excited contributions (solid echo sequences with pulse lengths below 6 μs and delay times 15–40 μs). (b) For the loosely packed sample, where the crystallites appeared to be completely oriented in the external field, a central transition (CT) at 73.56 MHz and eight satellites (ST) were observed. (c) Upon intercalation, for $Cu_{0.5}[NbS_2]$ a spectrum of 18 lines was recorded (bottom). (Reproduced by permission of Elsevier Science Publishers from Janssen et al.[3])

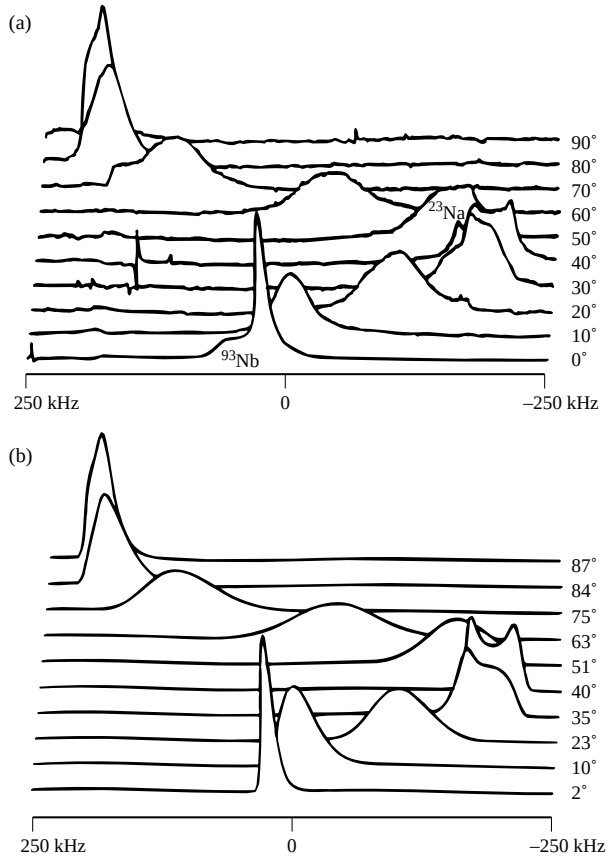

Figure 4 (a) Copper-63 NMR spectrum of $Cu_{0.5}[NbS_2]$ at 79.556 MHz and 210 K detected by the utilization of the field induced orientation of crystallites (solid echo sequences with pulse lengths 5 μs, delay 20 μs, repetition 0.1 s). The angles on the right-hand side indicate the angle between the c axis and $\boldsymbol{B}_0$. The satellites are not shown. (b) By computer simulation the following parameters were determined: δ_{iso} = 730 ppm (relative to CuCl), $\Delta\sigma = -600$ ppm, $\eta_{CS} = 0$, χ = 14.93 MHz, η_Q = 0.11; the principal axes of the CS and QF tensors coincide. Additional NMR signals arising from the ^{93}Nb nuclei and from ^{23}Na probe background are marked in the figure. (Reproduced by permission of Elsevier Science Publishers from Janssen et al.[3])

considers, in addition to the two Zeeman terms, 10 further interaction terms: the chemical shift of the four hydrogen and fluorine atoms [where the respective principal axis systems (PASs) are defined by the direction of the C−H and C−F bonds], the two homonuclear dipole−dipole interactions (PASs in the H−H and F−F directions), and the four heteronuclear dipole−dipole interactions (with the PASs given by the various H−F separation vectors).

In order to describe the orientation of a particular CH_2F_2 molecule with respect to the laboratory frame ($z \parallel \boldsymbol{B}_0$), a molecular fixed coordinate system was defined with its x' axis parallel to the F−F vector and the z' axis in the direction of the H−H vector of the tetrahedral molecule. In the further treatment, the transformation from the PASs of the various interactions to the laboratory frame was then replaced by the two successive transformations from the PASs to the molecular frame (Eulerian angles obtained from the geometry) and from the molecular to the laboratory frame (two Eulerian angles α' and β' appear in the result). Powder patterns result from spatially weighted sums over all possible orientations (α',β') of the CH_2F_2 molecules.

Theoretical NMR spectra were calculated for various chemical shift anisotropies and possible thermally activated reorientations about various axes. The obtained ^{1}H and ^{19}F NMR lineshapes were then compared with the experimental spectra such as those shown in Figure 5. In conclusion, intercalated difluoromethane appears to be oriented with its z' axis (H−H direction) perpendicular to the layer planes, and at 300 K it reorients rapidly about this axis. Another orientation of the intercalated molecules or another type of motion would result in quite different ^{1}H and ^{19}F NMR spectra.

2.3 NMR Spectra in the Presence of Various Interactions where the Principal Axes do not Coincide

Interpretation of solid state NMR spectra in the presence of dipole−dipole (DD), chemical shift (CS) and quadrupole (QF) interactions is straightforward if the principal axes of the CS and QF tensors coincide. Appropriate procedures and suitable computer programs have been developed. In two-dimensional intercalation compounds such a requirement is generally met (at least for the guest species), and the axis parallel to the layer planes is in most cases the principal axis for both the CS and QF tensors. The interpretation of the spectra shown in

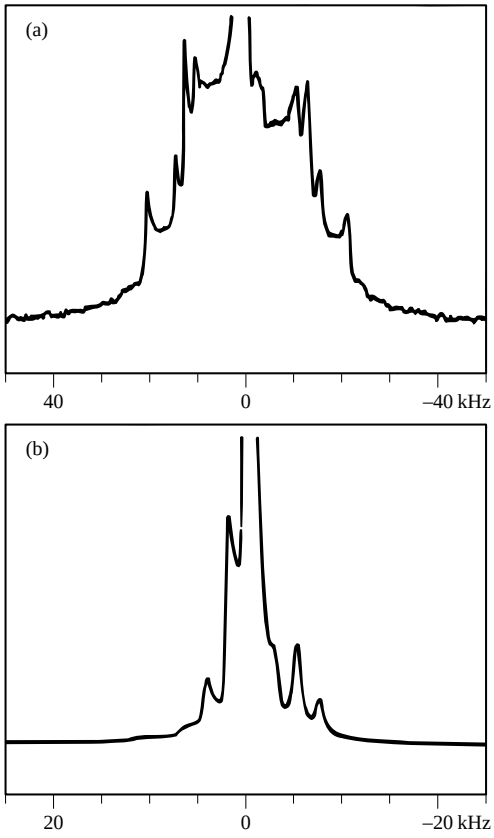

Figure 5 (a) Proton and (b) fluorine-19 NMR spectra of $Cs_x(CH_2F_2)_y[NbS_2]$ measured at 30 MHz and 295 K. The magnetic field was sufficiently low to rule out orientation effects of the crystallites. The intense central resonances belong to unreacted difluoromethane molecules in the sample. (Reproduced by permission of Academic Press from Möller et al.[4])

Figures 3 and 4 were examples of this behavior. Particularly in three-dimensional intercalation compounds, however, it may well be the case that the directions of the PASs do not coincide. An example is the broad and asymmetric ^{7}Li NMR spectra of the molybdenum cluster chalcogenides $Li_3Mo_6X_8$ (X = S, Se) shown in Figure 6.[5]

The lineshape was simulated by the following expression for the transition frequency from a state m to a state, $m-1$:

$$\begin{aligned}\omega = {} & \omega_0(1+\sigma_{\mathrm{iso}}) + \tfrac{1}{6}\omega_0\Delta\sigma \\ & \times\{3\sin^2\beta\sin^2\vartheta\cos 2\varphi - 3\sin 2\beta\sin 2\vartheta\cos\varphi \\ & +(3\cos^2\beta-1)(3\cos^2\vartheta-1) \\ & -\eta_{\mathrm{cs}}[\tfrac{1}{2}(1+\cos\beta)^2\sin^2\vartheta\cos 2(\varphi+\gamma) \\ & +\tfrac{1}{2}(1-\cos\beta)^2\sin^2\vartheta\cos 2(\varphi-\gamma) \\ & +(1+\cos\beta)\sin\beta\sin 2\vartheta\cos(\varphi+2\gamma) \\ & -(1-\cos\beta)\sin\beta\sin 2\vartheta\cos(\varphi-2\gamma) \\ & +\sin^2\beta\cos 2\gamma(3\cos^2\vartheta-1)]\} \\ & +\frac{3e^2qQ}{4I(2I-1)\hbar}(\tfrac{1}{2}-m)[3\cos^2\vartheta-1 \\ & -\eta_{\mathrm{Q}}\sin^2\vartheta\cos 2\varphi] \end{aligned} \quad (1)$$

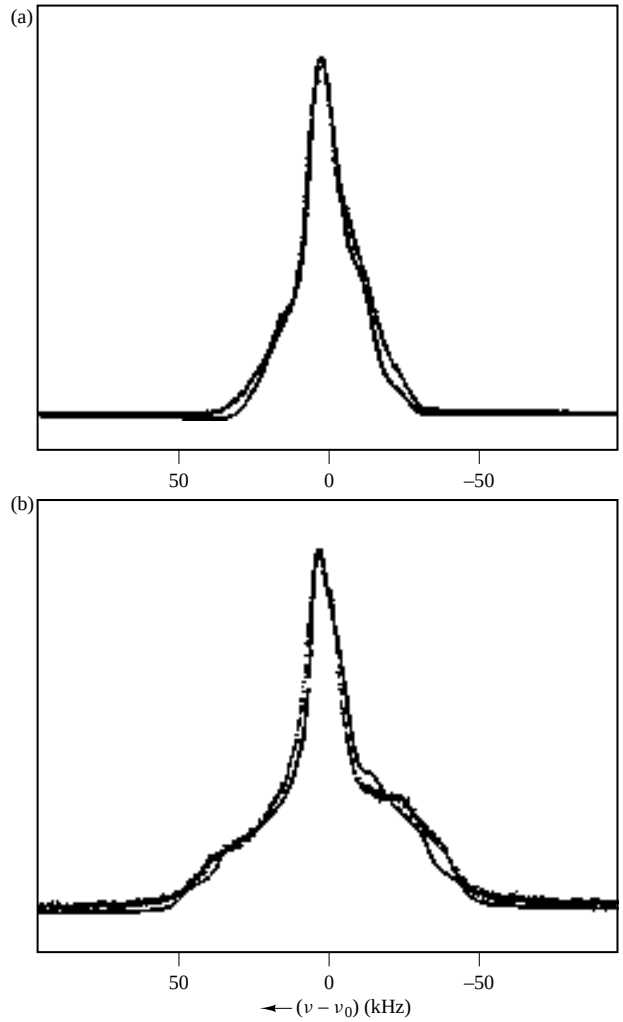

Figure 6 Lithium-7 NMR spectra of the molybdenum cluster chalcogenides (a) $Li_3Mo_6S_8$ and (b) $Li_3Mo_6Se_8$ obtained at 116.64 MHz and 100 K, and their simulations. (Reproduced by permission of the American Chemical Society from Prigge et al.[5])

The powder spectrum is obtained from a weighted integration over the angles ϑ and φ in equation (1) which describe the orientation of the PAS of the nuclear quadrupole interaction (QF) tensor with respect to the laboratory frame (determined by $\boldsymbol{B}_0$). The Eulerian angles β and γ can be determined from the experimental spectra by simulation using equation (1). β is the angle between the z axes of the QF and CS tensors. The projection of the z axis of the QF tensor on the azimuthal plane of the PAS of the CS tensor with the x axis of the latter makes the angle γ. For $\beta = \gamma = 0$, equation (1) changes into the well known formula for the transition frequencies if the PASs coincide. The other symbols have their usual meanings. Instead of the (negative) shielding constant σ_{iso}, the isotropic chemical shift δ = 94 (111) ppm relative to LiCl is given for $Li_3Mo_6S_8$ (in parentheses for $Li_3Mo_6Se_8$). The chemical shift anisotropy is $\Delta\sigma = -113$ (-90) ppm and the asymmetry factor $\eta_{\mathrm{cs}} = 0$. The quadrupole data thus obtained from the spectra are χ = 75 (95) kHz and η_{Q} = 0.25 (0.50). The angles turned out to be $\beta = 55^\circ$ and $\gamma = 90^\circ$ for both compounds. The DD interaction was taken into account by a Gaussian broadening with (full) width at halfheight of 8.2 (4.2) kHz. The results, and in

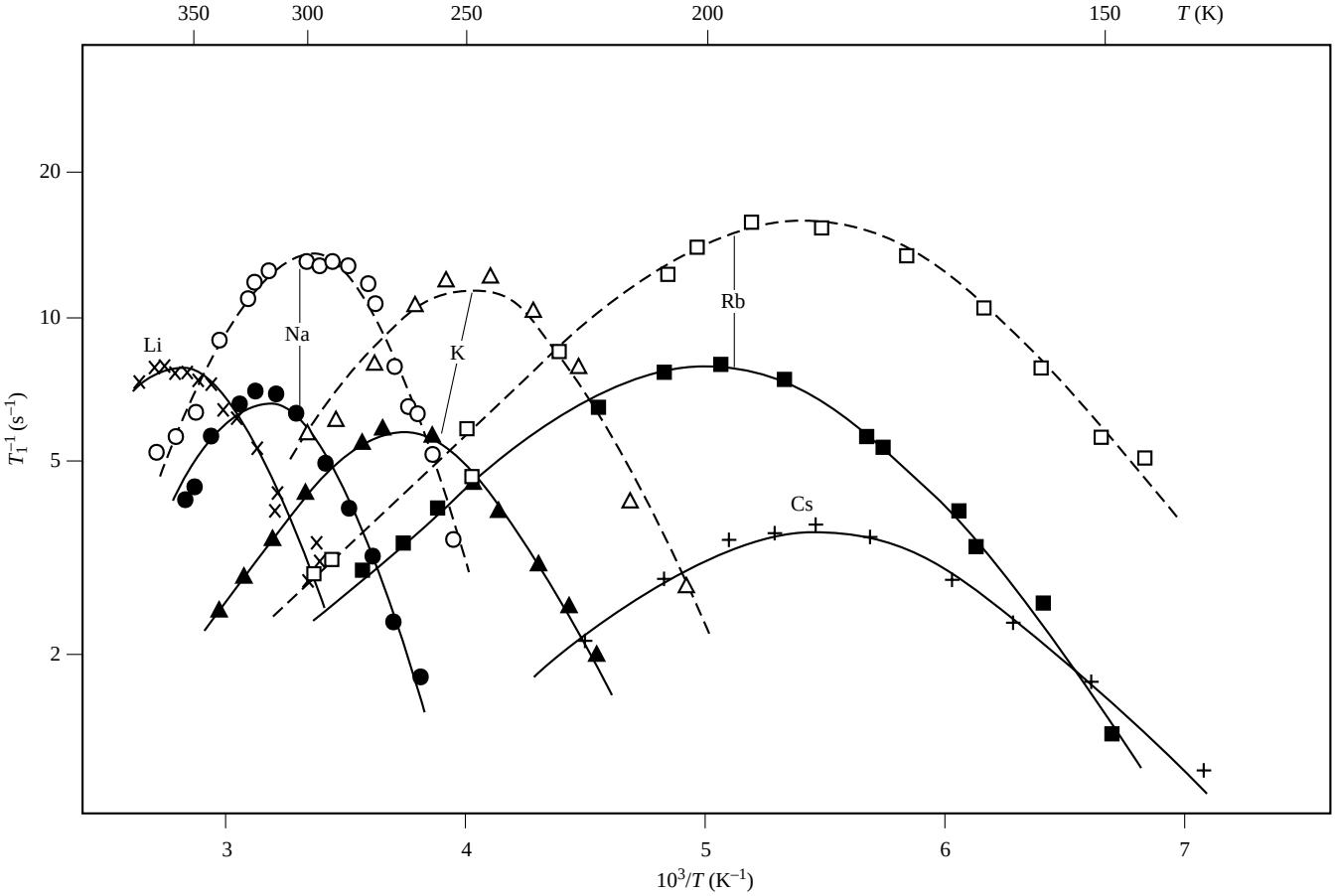

Figure 7 Dependence of the proton ^{1}H NMR spin–lattice relaxation rate upon reciprocal temperature for various hydrated chalcogenides $A_x(H_2O)_y[MS_2]$ with A = Li, Na, K, Rb, or Cs, and M = Nb or Ta, measured at 15 MHz (dotted lines) and 30 MHz (solid lines). (Reproduced by permission of the American Institute of Physics from Röder et al.[6])

particular the orientation of the PASs, can be well related to the structure, as will be shown in Section 4.

2.4 Molecular Motions

Molecular motions, the most important of which are those of the guest species, may either be studied from their influence on the spectra or by examining the relaxation behavior. An illustration of the first type of experiments was the example discussed in Section 2.2. If an intercalated molecule rotates, for instance, the Eulerian angles describing the orientation of the PAS (of the respective interaction) to $\boldsymbol{B}_0$ become time dependent and the spectra modified by partial averaging. In such cases it is useful to investigate the variation of the spectra with temperature.

Spin–lattice relaxation rates have been frequently used to explain details of the motional behavior. Two examples will be presented. Figure 7 shows $1/T_1$ versus reciprocal temperatures for hydrated transition metal disulfides with various alkali cations. The data depend strongly on the hydration enthalpy of the cations, and contain elements of low dimensionality. The fits were made on the basis of a model which included a logarithmic dependence on frequency, i.e. two-dimensional motions.[6] The second example refers to a material which will be discussed in a later section.

The relaxation rates of ^{7}Li in $Li_3Mo_6S_8$ (Figure 8) can be explained by the superposition of a BPP term due to diffusion and a term which is proportional to the temperature. The latter arises from the interaction of the lithium nuclei with conduction electrons.

Slow motions have also been investigated in intercalation compounds using standard techniques. An example is the proton exchange rate, i.e. the mean lifetimes τ_e in hydrated transition metal disulfides obtained via creation of spin alignment by the 'Jeener–Broekaert' pulse sequence. τ_e values between about 1 and 100 ms were thus determined (Figure 9). They display an Arrhenius behavior which could be extrapolated to lower temperatures (and shorter lifetimes) by lineshape analysis.

3 STRUCTURE AND MOTIONS OF HYDRATED LAYERED CHALCOGENIDES

A class of intercalation compounds that was studied in some detail by NMR and where NMR contributed substantially to the understanding of the structure and dynamics comprises the hydrated transition metal chalcogenides of the alkali and alkaline earth elements with the formula $A_x(H_2O)_y[MX_2]$, where M = Ti, V, Zr, Nb, Mo, Ta, or W and X = S or Se. These

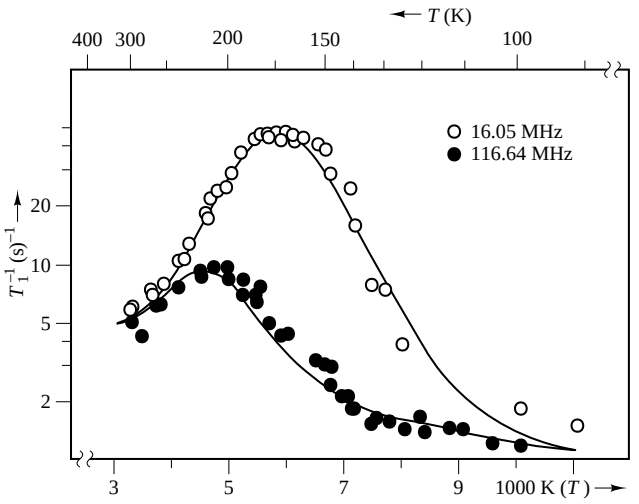

Figure 8 Lithium-7 NMR spin–lattice relaxation rate versus reciprocal temperature for the molybdenum cluster sulfide $Li_3Mo_6S_8$. The solid curve corresponds to the theoretical model description. (Reproduced by permission of the American Chemical Society from Prigge et al.[5])

compounds can be regarded as polyelectrolytes consisting of two-dimensional $[MX_2]^{x-}$ macroanions (host lattice) with monolayers of mobile hydrated cations in the van der Waals gap between the sheets (guest species). We shall present here only an outline of the most important NMR experiments to investigate the structure and dynamics.

3.1 Proton NMR Spectra

The ^{1}H NMR spectra of the guest species (Figures 2 and 10) display the influence of intra- and intermolecular dipole–dipole couplings as well as CSA interactions. Separation is possible either by studying the magnetic field dependence or by application of a multiple pulse sequence (cf. Figure 10). In a sufficiently low magnetic field, at ambient temperature a nearly perfect Pake doublet of isolated H_2O can be observed, since the intermolecular interactions are averaged out by hopping motions of the water molecules. However, there is an additional central signal which increases at elevated temperatures and which was explained by proton exchange in these two-dimensional hydrated systems. The fast motion process was further investigated by NMR T_1 measurements (cf. Figure 7), and the slower proton exchange by spin alignment techniques (cf. Figure 9).

As a final result of several ^{1}H NMR studies including the examination of single crystals and oriented crystallites, all the water molecules in the van der Waals gap appear to be aligned with their C_2 axes lying in the *a,b* planes defined by the chalcogenide layers and their H–H vectors parallel to the *c* axis (Figure 11). The proton–proton separations amount to 165 pm; they are not significantly different from those in water of crystallization (158 pm). Two-dimensional diffusion and/or reorientation about the *c* direction leaves the orientation of the water molecules unchanged. The activation energy for this motion varies from 9 kJ mol^{-1} (Cs^+) to 50 kJ mol^{-1} (Li^+) depending on the central cation which interacts immediately with the negatively polarized dipole ends of the H_2O molecules.

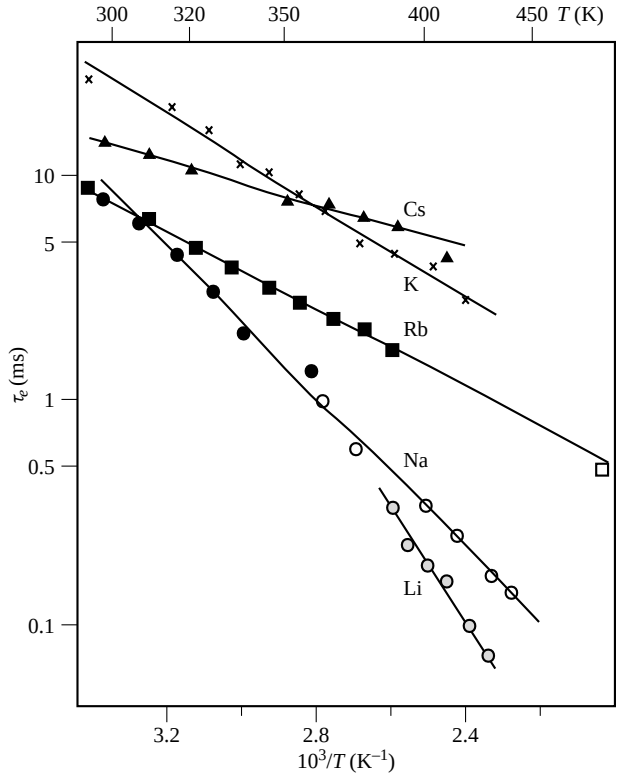

Figure 9 Proton mean lifetime versus reciprocal temperature for water in the chalcogenides $A_x(H_2O)_y[NbS_2]$ with A = Li, Na, K, Rb, or Cs derived from spin alignment measurements (solid symbols) and linewidth analysis (open symbols). (Reproduced by permission of VCH from E. Wein, W. Müller-Warmuth, and R. Schöllhorn, *Ber. Bunsenges. Phys. Chem.*, 1986, **90**, 158)

The diffusional motion of the water molecules explains also the axial symmetry of the chemical shift tensor derived from the spectra of Figure 10 (top). The PASs for the CS and DD interactions coincide. At lower temperature, the symmetry of the chemical shift disappears, and the intermolecular dipole interactions become important for broadening of the spectra (Figure 10) (bottom). The chemical shift anisotropy itself was found to depend greatly on the transition metal M. Going from W via Ta(1 T), Mo, Ta(2H), Ti, Nb to V, $\Delta\sigma$ increases from −11 to +69 ppm for fully intercalated compounds (x = 0.33). Upon increasing the degree of reduction x between 0.08 and 0.33, $\Delta\sigma$ increases from 8 to 17 ppm for M = Ti; it decreases, however, from 60 to 33 ppm for M = Nb.

The large range of chemical shift anisotropies cannot be interpreted in terms of the electronic proton shielding within the guest phase. This should lead to a contribution of only about −10 ppm, a value which was observed as a limit in two of the compounds. In all other cases the significant positive contribution from the host lattice has to be taken into account in addition. The effect was found to depend on the particular conduction band of the dichalcogenide material and its filling with electrons. In NbS_2 the lowest-lying energy level is the d_{z^2} band, which is half occupied and becomes further filled up during the course of intercalation. The density of states at the Fermi level $D(E_F)$ has its maximum, therefore, in the absence of any intercalant, and decreases as a function of x, if guest species are intercalated and s electrons donated. $\Delta\sigma$ appears to be proportional to $D(E_F)$.

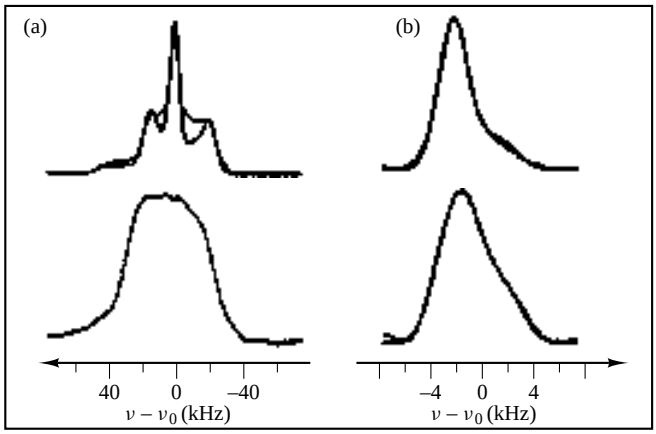

Figure 10 Proton NMR powder patterns of the hydrated layered compound $K_{0.25}(H_2O)_{0.75}[NbS_2]$ at two different temperatures (295 K, top and 150 K, bottom) measured in a magnetic field of 7 T. (a) Normal spectra. (b) Dipolar-decoupled spectra by MREV 8 multiple pulse sequences. The solid lines are computer simulations. (Reproduced by permission of VCH from M. Lobert, W. Müller-Warmuth, H. Katzke, and R. Schöllhorn, *Ber. Bunsenges. Phys. Chem.*, 1992, **96**, 1564)

This behavior was confirmed by the results for the compound $K_x(H_2O)_y[TiS_2]$. TiS_2 with the Group 4 element titanium has an empty d_{z^2} band, and, here, filling by progressive intercalation enhances both $D(E_F)$ and $\Delta\sigma$. Using the experimental data, the qualitative structure of the d_{z^2} band could be obtained for both compounds. The NMR results may be considered as a confirmation of the 'rigid band model', in which the only change to the electronic structure of the host is the increased d band filling. The proportionality between $\Delta\sigma$ and $D(E_F)$ was explained by the anisotropic Pauli paramagnetism; the magnetic susceptibility is also proportional to the density of states at the Fermi level.

3.2 Niobium-93 NMR Studies of the Intercalation

The process of intercalation from $x = 0$ to 0.33 could be studied in $K_x(H_2O)_y[NbS_2]$ and $K_x(H_2O)_y[NbSe_2]$ by observing the influence of the guest species on the ^{93}Nb NMR of the host lattice. The empty host lattices displayed spectra resembling those of Figures 3(a) and (b); the quadrupole coupling constants were determined with high accuracy, viz. 60.02 ± 0.02 MHz (60.05 ± 0.02 MHz) for 2H–NbS_2 (and 2H–$NbSe_2$). Intercalation of $K_x(H_2O)_y$ changes the mean local environment of niobium and reduces the coupling constant for a certain fraction of the ^{93}Nb NMR nuclei. For $x = 0.08$, 14% (11%) of the ^{93}Nb nuclei still have a coupling constant of 60 MHz, but 82% (89%) already one of 53 MHz, and 4% even one of 46 MHz. Upon increasing x further, the fractions with 60 MHz disappear in favor of the other two contributions. For $x = 0.33$ a coupling constant of 46 MHz (48 MHz) finally holds for 100% (41%) of the niobium sites in the NbS_2 ($NbSe_2$) host lattice. In $K_x(H_2O)_y[NbSe_2]$ the remaining 59% of ^{93}Nb nuclei experience the medium value of 53 MHz.

It is important to realize that there is no continuous variation of the NMR parameters with progressive intercalation, but there are three phases whose fractions change as a function of x. Structural variations are therefore responsible rather than electronic effects of the host. The three observed structures were attributed to local staging. For $x = 0$, the relatively large quadrupole coupling belongs to niobium atoms, which all 'see' on one side of the two-dimensional arrangement the empty van der Waals gap. Upon increasing x, two new environments occur, one with intercalated species on both sides (local ranges of first-stage character), the other one with intercalated species on one side only (second-stage character). The smaller coupling constant of the final compound ($x = 0.33$) was attributed to a homogenous occupation of the van der Waals gap ('first-stage compound').

3.3 Further NMR Studies of Layered Compounds

Among the materials that were studied in some detail by NMR and which cannot be discussed within the scope of this short article are metal–ammonia compounds with certain similarities to hydrated systems. Intercalated atoms or ions in dichalcogenides, such as hydrogen, lithium and copper, were examined as well as intercalated molecules, e.g. ammonia, amines, derivatives of methane, pyridine, and even larger intercalants. Layered compounds also include graphite intercalation compounds, where, in particular, ^{1}H, ^{7}Li and ^{13}C NMR was applied on a large scale by various authors. Some layered oxides were investigated as well. Further details can be found in the literature.[2]

4 STRUCTURE AND DYNAMICS OF GUEST PHASES IN MOLYBDENUM CLUSTER CHALCOGENIDES

Binary and ternary molybdenum cluster chalcogenides (Chevrel phases) with the compositions Mo_6X_8 and $A_xMo_6X_8$ (A = main group metal; X = S or Se) have attracted considerable interest because of their unusual structure (Figure 11) and remarkable physical properties. Using NMR, compounds with intercalated lithium, sodium and copper were investigated. The behavior of lithium as the intercalant was examined in particular, with the result that four distinct phases with $x = 1$, 3, 3.8, and 4 could be identified from the different isotropic chemical shifts, as shown in Figure 12 (at room temperature, narrow singlet lines or first-order quadrupole spectra were observed). From the δ_{iso} values it was concluded that lithium appears to be ionic in $Li_1Mo_6X_8$ and $Li_4Mo_6X_8$ whereas lithium clusters with partial metallic character are formed in $Li_3Mo_6X_8$ and $Li_{3.8}Mo_6X_8$. More details were obtained from broadline spectra at low temperatures and from relaxation measurements.[5,7]

In both $Li_1Mo_6X_8$ compounds the ^{7}Li NMR spectra display in addition to DD and CA interactions ($\Delta\sigma = -11$ ppm at 100 K for X = S, and -15 ppm for X = Se) well resolved quadrupole structures of first order ($\chi = 107$ kHz and 79 kHz, respectively). The chemical shift tensor is axially symmetric ($\eta_{cs} = 0$), but the quadrupole asymmetry factor η_Q varies from 0.24 (0.10 for X = Se) at 100 K to zero at 300 K upon increasing the temperature. Spectra simulations led to the conclusion that the intercalated Li^+ ions reside in one of the six equivalent inner tetrahedral sites Li_1 of Figure 11(b) (bottom). Hopping motions between these positions are thermally activated; the correlation times are of the order of 10^{-7}–10^{-3} s and follow an Arrhenius-type law (11 and 7 kJ mol^{-1}, respectively). In contrast to the other lithiated

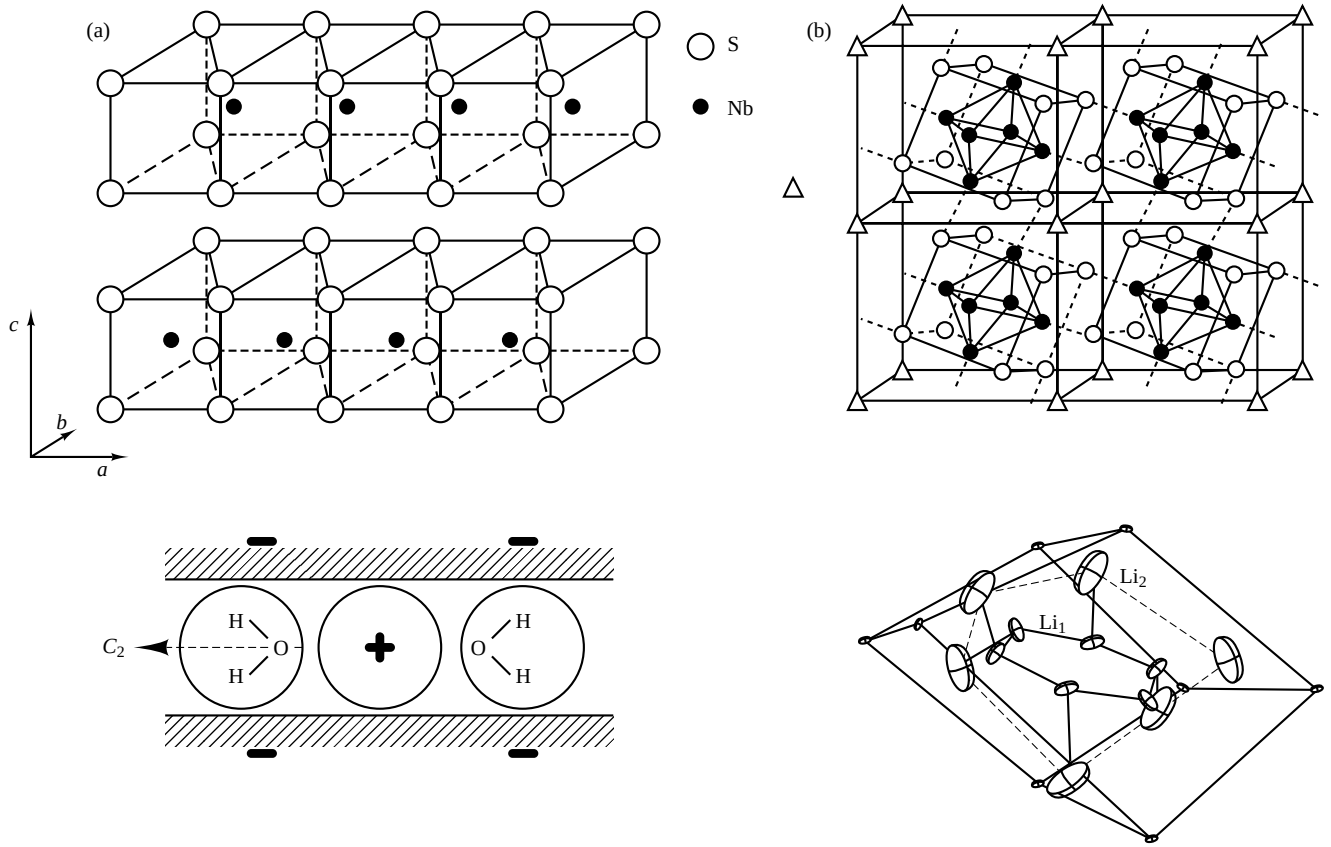

Figure 11 Schematic representation of the structure of the compounds discussed in Sections [3] and [4]. (a) Hydrated layered chalcogenides with the NbS_2 host lattice (top) and the arrangement of the H_2O molecules with the central cation (bottom). (b) Mo_6S_8 (● Mo, ○ S) structure with vacant channel positions (△) (top) and 2 × 6 potential lattice sites Li_1 (inner concentric ring) and Li_2 (outer ring) around the unit cell origin (bottom). The cavity is formed by sulfur atoms which belong to eight different Mo_6S_8 units

molybdenum cluster chalcogenides, at room temperature only this local motion is important; long range diffusion from cavity to cavity does not play a major role.

The extremely large δ_{iso} values of the $Li_3Mo_6X_8$ system were interpreted in terms of a Knight shift; the transfer of 2s electrons to the host lattice is incomplete, so that Li_3^{z+} clusters with $z < 3$ are formed. More detailed information was obtained from the ^{7}Li NMR spectra at low temperatures, which are governed by DD, CS, and QF interactions. The chemical shift tensor appears to be axially symmetric, with $\Delta\sigma$ being relatively large and negative (−113 and −90 ppm for the compounds containing S or Se, respectively). This was interpreted in terms of a symmetric arrangement of three lithium atoms on the potential sites of Figure 11(b) (bottom). The z principal axis of the CS tensor may thus be identified with the symmetry axis perpendicular to the plane of the two concentric rings of possible lithium positions; the residual 2s electron density at the intercalated lithium provides stronger screening in the plane.

The principal axes of the CS and QF tensors do not coincide as shown in Figure 6 and equation (1). The PAS of the QF (EFG) tensor seems to agree with the rhombohedral reference system of the structure [Figure 11(b) (top)]. Then the angles β and γ describing the relative positions of the noncoincident PASs of the CS and QF tensors should become 54.54 and 90°, respectively, as observed experimentally. The quadrupole coupling data are χ = 75 kHz, η_Q = 0.25 (X = S), and χ = 95 kHz, η_Q = 0.50 (Se).

The formation of lithium triclusters with short Li–Li distances and metal-like behavior is supported by spin–lattice relaxation measurements as in Figure 8. These contain in addition to a contribution from the lithium diffusion a term which is due to the interaction with conduction (2s) electrons and which fulfills the Korringa relation over a large range of temperatures. The diffusion of lithium species with activation energies of 13 and 19 kJ mol^{-1} corresponds to a high mobility of the translational motion from cavity to cavity. In contrast to $Li_1Mo_6X_8$, but in agreement with recent neutron diffraction studies,[8] for $Li_3Mo_6X_8$ the inner ring of lithium sites is enlarged and provides, together with the outer ring, a framework of symmetrically arranged potential sites. The distances between these sites are short and comparable, and are well suited as a diffusion pathway. Application of the van Vleck formula for the DD interaction leads to an estimate of 210 pm (370 pm) for the Li–Li separation in the triclusters of $Li_3Mo_6X_8$ ($Li_3Mo_6Se_8$).

In contrast to stoichiometries with $3 < x < 3.8$ where two ^{7}Li NMR signals appear, $Li_{3.8}Mo_6S_8$ is distinguished only by one NMR line, indicating a single-phase system. The chemical shift parameters (δ_{iso} = 39 ppm, $\Delta\sigma$ = −45 ppm)—though smaller than those of $Li_3Mo_6S_8$—and the other results, including relaxation, reveal that the lithium guest species possess metal-like properties as well. The Li–Li distances

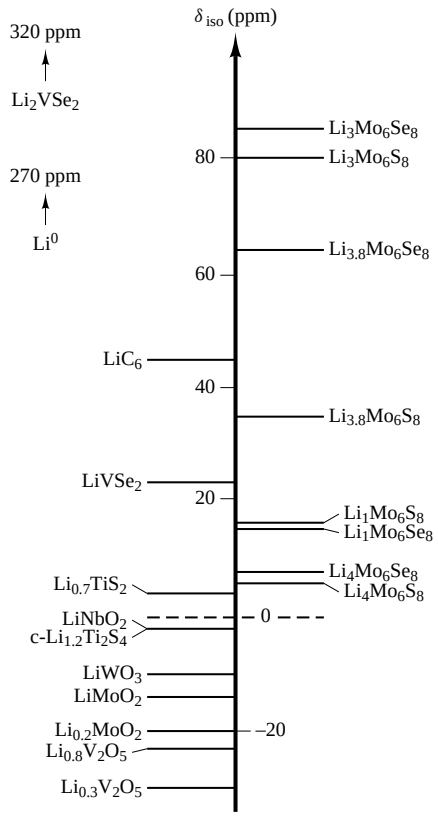

Figure 12 Lithium-7 NMR isotropic chemical shift values (related to LiCl in aqueous solution) for $Li_xMo_6X_8$ compounds (right). For the purpose of comparison, δ_{iso} values for various other lithium intercalation compounds and lithium metal are given (left)

are less and of the order of 330 pm, showing that the outer ring participates greatly in providing positions for the lithium atoms. The lithium mobility is again very high.

For the fully intercalated phases $Li_4Mo_6X_8$ there is no longer any Knight shift, and the chemical shift anisotropy is very small as well. Only the quadrupolar and dipolar data are of comparable orders of magnitude, but here the EFG values are somewhat distributed. The lithium mobility is much less as compared with the Li_3 and $Li_{3.8}$ compounds. The dramatic transition from Li_3 to Li_4, as observed by NMR and manifested by the macroscopic properties of the material, can be related to the electronic structure and to the arrangement of potential lithium sites. The inner ring is no longer enlarged, and there is a large separation between the Li1 and Li2 positions comparable to that in $Li_1Mo_6X_8$.

5 RELATED ARTICLES

Inorganic Solids; Lithium NMR; Magnetic Field Induced Alignment of Molecules; Quadrupolar Nuclei in Solids; Wide Lines for Nonquadrupolar Nuclei.

6 REFERENCES

1. R. Schöllhorn, in *Progress in Intercalation Research*, ed. W. Müller-Warmuth and R. Schöllhorn, Kluwer, Dordrecht 1994.
2. W. Müller-Warmuth, in *Progress in Intercalation Research*, ed. W. Müller-Warmuth and R. Schöllhorn, Kluwer, Dordrecht, 1994.
3. J. Janssen, M. Lobert, W. Müller-Warmuth, and W. Nonte, *Solid State NMR*, 1993, **2**, 201.
4. H. Möller, W. Müller-Warmuth, E. Wein, Z. T. Lalowicz, and R. Schöllhorn, *J. Magn. Reson.*, 1989, **83**, 1.
5. C. Prigge, W. Müller-Warmuth, E. Gocke, and R. Schöllhorn, *Chem. Mater.*, 1993, **5**, 1493.
6. U. Röder, W. Müller-Warmuth, H. W. Spiess, and R. Schöllhorn, *J. Chem. Phys.*, 1982, **77**, 4627.
7. C. Prigge, W. Müller-Warmuth, E. Gocke, and R. Schöllhorn, *Solid State Ionics*, 1993, **62**, 143.
8. C. Ritter, E. Gocke, E. Fischer, and R. Schöllhorn, *Mater. Res. Bull.*, 1992, **27**, 1217.

Biographical Sketch

Werner Müller-Warmuth. *b* 1929. Dr.phil.nat., 1955, Universität Frankfurt. Habilitation, 1961, Universität Mainz. Science collaborator Max Planck-Institut für Chemie, Mainz, 1955–65. Chief of Department, European Research Centre, Ispra (Italy), 1965–73. Professor of Physical Chemistry, Münster, 1973–present. Rector (president), Westfälische Wilhelms-Universität, 1978–82. Approx. 200 publications. Research interests include applications of solid state NMR (and other spectroscopic methods) to various classes of solid materials.

Lithium NMR

Harald Günther

University of Siegen, D-57068 Siegen, Germany

1	Introduction	1
2	The NMR Parameters of ^{6,7}Li	2
3	Experimental Methods	12
4	Related Articles	19
5	References	19

1 INTRODUCTION

1.1 General Aspects

The element lithium (from the Greek *lithos* = stone), discovered in 1817 by Arfvedson in the Swedish mineral *petalit*, has two stable isotopes, lithium-6 (^{6}Li) and lithium-7 (^{7}Li) in 7.42 and 92.58% natural abundance, respectively, which are both NMR active. Their position within the group of quadrupolar metal nuclei with respect to natural abundance and receptivity for the NMR experiment is shown in Table 1.

Historically it is of interest that an early, albeit unsuccessful, attempt to detect NMR in bulk matter was performed with powdered lithium chloride.[3] Only later did it become clear that under the experimental conditions used the ^{7}Li resonance was probably saturated. The first ^{7}Li NMR signal was recorded in 1946,[4] while ^{6}Li was measured a few years later.[5] High-resolution spectra for ^{7}Li were then reported in 1962[6] and for ^{6}Li in 1976.[7] For completeness, we mention that nuclear properties of the short-lived nuclides ^{8}Li (I = 2, half-life 0.88 s)[8] and ^{9}Li ($I = \frac{3}{2}$, half-life 178 ms)[9] have been studied in order to test nuclear models. Another unstable lithium nuclide is ^{11}Li (half-life 8.7 ms), with a spin of $I = \frac{3}{2}$. In the following discussion we use the notation ^{6,7}Li when discussing aspects relevant to both nuclei, and ^{6}Li or ^{7}Li otherwise. As in similar cases where different nuclides of the same element are reviewed, the chemical shifts (in ppm) are identical, scalar spin–spin coupling constants are related by the factor $\gamma(^7\text{Li})/\gamma(^6\text{Li})$, and relaxation mechanisms differ.

The properties of the stable lithium nuclides which are important for the NMR experiment are collected in Table 2, where data for the widely used nuclei ^{1}H and ^{13}C are included for comparison. Both ^{6}Li and ^{7}Li possess a quadrupole moment Q, but that of ^{6}Li is the smallest known for any nucleus. NMR of ^{6}Li is, therefore, not dominated by its quadrupole moment, and ^{6}Li has been termed an 'honorary spin-$\frac{1}{2}$ nucleus'.[10] The most pronounced advantage of ^{6}Li over ^{7}Li is the smaller NMR linewidth attainable in high-resolution measurements of liquids. The halfwidth $w_{1/2}$ of an NMR signal from a quadrupolar nucleus depends on molecular motion, characterized by the correlation time τ_c, its spin quantum number I, its electric quadrupole moment Q, the electric field gradient at the nucleus q_{zz}, and η, the asymmetry parameter of q, according to[13]

$$w_{1/2} = \tfrac{3}{10}\pi Q^2 \cdot \frac{(2I+3)}{I^2(2I-1)} \cdot \frac{e^4}{h^2} q_{zz}^2 (1 + \tfrac{1}{3}\eta^2)\tau_c \qquad (1)$$

For the linewidth factor WF of a certain nuclide we then have, for constant electric field gradients,

$$\text{WF} = Q^2 \frac{(2I+3)}{I^2(2I-1)} \qquad (2)$$

and with the data for the various parameters given in Table 2 we find that the smaller quadrupole moment of ^{6}Li renders WF(^{6}Li) smaller than WF(^{7}Li) by three orders of magnitude. Similarly, in solid state MAS experiments, ^{6}Li produces fewer sidebands than the heavier nuclide ^{7}Li.[14] In general, however, both ^{6}Li and ^{7}Li are less subject to quadrupolar effects than the heavier alkali metal nuclei because the Sternheimer antishielding factor, which is a measure of the effective field gradient produced at a nucleus as a result of the polarization effect induced for the atomic electron cloud by an external field gradient, is one to two orders of magnitude smaller for lithium than for the other alkaline metals (Table 2).

^{6}Li and ^{7}Li NMR spectra of liquids are conveniently measured with broadband probeheads in the FT mode employing the standard deuterium lock system. For organolithium compounds, spectra are usually run with ^{1}H decoupling in order to remove line broadening due to ^{6,7}Li–^{1}H spin–spin coupling (see Section 2.4). In addition, a considerable intensity increase may result for ^{6}Li measurements due to $\{^1\text{H}\}^6$Li NOEs (see Sections 2.6 and 3.2.1). Therefore, many NMR spectroscopists nowadays prefer to measure ^{6}Li instead of ^{7}Li, despite its lower receptivity. In order to eliminate the disadvantage of lower natural abundance, isotopic ^{6}Li labeling is widely used and lithium-6 metal is commercially available for this purpose. Due to ^{6}Li depletion of lithium metal in connection with its use in the atomic energy industry, the isotopic composition of lithium in commercially available compounds may vary. If necessary, the lithium isotopic abundance of a sample can be conveniently determined by comparing the NMR signal intensities of an unknown sample with that of a sample with known isotopic composition.

Long relaxation times (see Section 2.1) may sometimes cause difficulties for ^{6}Li NMR measurements. This has to be taken into account by choosing a sufficiently long relaxation delay between individual transients if data accumulation is used. It is of interest to note that the ^{2}H NMR frequency is close to that of ^{6}Li [61.40 versus 58.87 MHz on a 400 MHz (^{1}H) instrument]. For many probeheads, the ^{2}H coil can thus be tuned to the ^{6}Li frequency if this is desirable for certain experiments, for example ^{6}Li decoupling during ^{13}C observation. Determination of the 90° pulse is usually performed by standard techniques (180°, 360° search) with an aqueous or tetrahydrofuran solution of a lithium salt. If long relaxation times are anticipated, steady state pulse calibration[15] can be used to advantage. Selective excitation of ^{6}Li signals has been achieved using the DANTE sequence[16] in the case of overlapping ^{6}Li multiplets which resulted from ^{6}Li, ^{13}C coupling in a ^{13}C labeled organolithium compound.[17]

An important aspect of ^{6,7}Li NMR measurements is the dynamic behavior of the systems which contain the ^{6,7}Li nuclei to be studied. In salt solutions and in solutions of organometallic compounds, exchange processes operate and

Table 1 Classification of Quadrupolar Metal Nuclei According to NMR Sensitivity and Natural Abundance[a]

	Natural abundance (%)		
Magnetic moment	>90	10–90	<10
Strong	**^{7}Li**		
Medium	^{9}Be, ^{23}Na, ^{27}Al, ^{45}Sc, ^{51}V, ^{55}Mn, ^{59}Co, ^{75}As, ^{93}Nb, ^{115}In, ^{133}Cs, ^{181}Ta, ^{209}Bi	^{11}B, ^{63}Cu, ^{71}Ga, ^{87}Rb, ^{121}Sb, ^{137}Ba, ^{187}Re	**^{6}Li**
Weak	^{39}K, (^{197}Au)[b]	^{25}Mg, ^{91}Zr, ^{95}Mo, ^{101}Ru, ^{105}Pd, (^{177}Hf)[b], ^{193}Ir, ^{189}Os	^{43}Ca, ^{49}Ti, ^{53}Cr, ^{61}Ni, ^{67}Zn, ^{73}Ge, ^{87}Sr

[a]Adapted from Dechter[1] and Benn and Rufinska.[2]
[b]Not yet observed.

Table 2 Nuclear Properties of ^{6}Li and ^{7}Li, including Data for ^{1}H and ^{13}C for Comparison[a]

	Natural abundance N (%)	Spin I	Magnetic moment μ (μ_N)	Magnetogyric ratio γ (10^7 rad T^{-1} s^{-1})	Quadrupole moment Q (10^{-28} m^2)	Receptivity[b] relative to ^{13}C R^C	Resonance frequency, ν (MHz) 2.3488 T	9.3952 T	Linewidth factor, WF
^{6}Li	7.42	1	1.1624	3.9371	-6.4×10^{-4}	3.58	14.717	58.868	2.0×10^{-3}
^{7}Li	92.58	$\frac{3}{2}$	4.2035	10.3976	-3.7×10^{-2}	1.54×10^{3}	38.866	155.464	1.8
^{1}H	99.985	$\frac{1}{2}$	4.8371	26.7522	–	5.67×10^{3}	100.000	400.000	–
^{13}C	1.108	$\frac{1}{2}$	1.2162	6.7283	–	1.0	25.145	100.580	–

[a]Sternheimer antishielding factors for alkaline metals: Li, 0.7; Na, 5.1; K, 18.3; Rb, 48.2: Cs, 111.
[b]Adapted from Mason[11] and Harris.[12]
[c]Defined in Harris.[12]

the spectral properties measured may be average values for various species. This is certainly true for room temperature measurements of most organolithium compounds and must be kept in mind when ^{6,7}Li NMR parameters are discussed. It is only in the slow exchange limit, usually well below $-50\,^{\circ}$C, where ^{6,7}Li resonances of individual aggregates such as monomers, dimers, or tetramers (Figure 1) can be detected. If only one particular specimen is present, exchange does not affect spin–lattice relaxation times and chemical shifts, but it averages or completely eliminates line splittings due to scalar spin–spin coupling to neighboring nuclei.

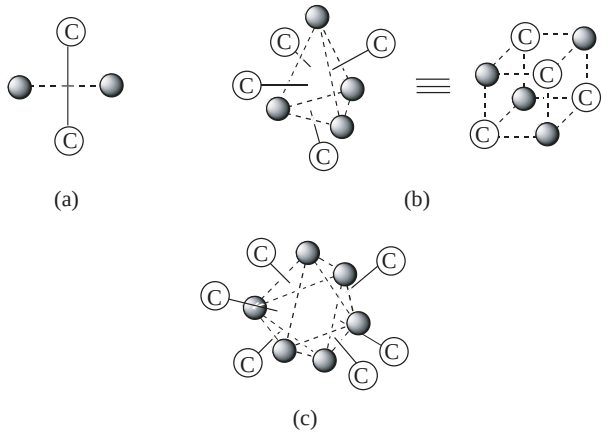

Figure 1 Schematic representation of organolithium aggregates: (a) dimer; (b) tetramer; (c) hexamer. Shaded circles represent lithium atoms, circled carbon atoms represent organic ligands

1.2 Applications of ^{6,7}Li NMR

High-resolution ^{6,7}Li NMR measurements are applied primarily in two different areas: measurements on ionic lithium in aqueous or nonaqueous solutions, on the one hand, and on lithium covalently bound mainly to carbon, nitrogen, or phosphorus in organometallic compounds on the other. The first encompasses research in inorganic chemistry and on the structure and dynamics of ion solvation. The second area is largely a domain of structural research in organometallic chemistry. In addition, due to the physiological effects of lithium ions, ^{6,7}Li NMR also extends to biochemistry as well as physiological and medical chemistry, an area not covered in this article.

1.3 Literature Review

There are a number of extensive reviews on alkaline metal NMR where data for ^{6}Li and ^{7}Li are reported. The earlier articles by Lindman and Forsén (1978),[18] Wehrli (1979),[19] Laszlo (1983),[10] Detellier (1983),[20] and Akitt (1987)[21] concentrate on NMR studies of ions in aqueous and nonaqueous solutions. Work on simple electrolyte solutions was treated by Holz (1986).[22] NMR of metal nuclei in organometallic compounds in general has been reviewed by Dechter (1982)[1] and Benn and Rufinska (1985)[2] and NMR of organolithium compounds is the subject of the more recent articles by Günther et al. (1987),[23] Thomas (1991),[24] Jackman,[25] Bauer and Schleyer (1992),[26] Collum (1993),[27] and Bauer (1994, 1995).[28] The pioneering work in this field has been summarized by Brown,29, 30 McKeever,[31] and Fraenkel.[32]

2 THE NMR PARAMETERS OF ^{6,7}Li

2.1 Longitudinal Relaxation

2.1.1 Electrolyte Solutions

Longitudinal relaxation measurements for ^{6,7}Li have been performed on the ions in aqueous and nonaqueous solutions as well as in mixed solvents and on organolithium compounds in organic solvents. Aside from an inherent interest in the relaxation mechanisms, such studies were undertaken in order to investigate solvation and coordination effects, ion–ion and ion–solvent interactions, ion and molecular dynamics as well as molecular structure.

For aqueous solutions of inorganic salts, the relaxation of the free ions is characterized by quite small longitudinal relaxation rates R_1. As compared with the familiar spin-$\frac{1}{2}$ nuclei, an interesting aspect of ^{6,7}Li relaxation is the role played by the quadrupolar mechanism. As it turns out, both $^6Li^+$ and $^7Li^+$ have been found to be relaxed by dipolar mechanisms in aqueous solution involving hydrate protons, while quadrupolar relaxation dominates for the heavier alkaline metals. Studies of several lithium salts have shown that the longitudinal relaxation of $^7Li^+$ is governed by a mixture of dipolar and quadrupolar contributions of comparable weight. For lithium halides in H_2O at 25 °C, R_1 ranges between 0.05 and 0.5 s^{-1}, depending on concentration, with dipole–dipole contributions of about 0.03 s^{-1}.[33] Due to its relatively long relaxation times, ^{7}Li is also of interest for measurements of ion velocities in connection with direct current or electrophoretic NMR.[34]

A mechanistic study on $^6Li^+$ in aqueous lithium chloride[7] showed that 84% of the relaxation is dipolar, 8% is spin rotation, while quadrupolar relaxation accounts for less than 0.1% and is thus negligible. The separation of the dipolar portion was accomplished on the basis of NOE experiments (see Section 2.6). Since the measurements were performed with lithium of natural isotopic distribution, a possible contribution of ^{7}Li–^{6}Li dipole interaction was also evaluated, but was found to be insignificant; 7% of the experimental relaxation rate has not been assigned and has been attributed to the presence of a small concentration of paramagnetic impurities. While in H_2O the relaxation rate (at 30 °C) is as small as 0.0059 s^{-1}, it is even smaller in D_2O (0.0012 s^{-1}). At 80 °C, T_1 was found to be 1040 ± 50 s^{-1} which is probably the longest T_1 observed so far in the liquid phase. Because of the smaller magnetic moment of the deuteron the ^{6}Li–^{2}H dipolar interaction is only about 7.5% of that in H_2O.

Several models have been developed for the mechanism of ion quadrupolar relaxation which are, according to the facts discussed above, more important for the heavier alkaline ions than for ^{6,7}Li, and will therefore be mentioned only briefly. The *electrostatic model* has been worked out by Valiev[35] and Hertz.[36] A detailed treatment distinguishes between three states of solvation: (1) a fully random distribution (FRD) model assumes both a random distribution and random orientation of the solvent molecules; (2) a model with nonoriented solvation, i.e. with a distinct first solvation sphere, but with random orientation of the solvent dipoles; and (3) a fully oriented solvation (FOS) model which is characterized by a distinct first solvation sphere with radial orientation of the solvent dipoles. In each case, relaxation is caused by the electric field gradients arising from the dipole moments of the solvent molecules, which are modulated by rotational and translational motion. The *electronic distortion model*, developed by Deverell,[37] assumes on the other hand that distortions of the spherical symmetry of the electron cloud are the origin of the field gradients causing relaxation. Such a mechanism also affects the paramagnetic term of the shielding constant. While the electrostatic model has found widespread application, the complexity of the physical problem involved has initiated further investigations[38] and studies on quadrupolar relaxation in general continue.[39]

2.1.2 Organometallic Compounds

^{7}Li and ^{6}Li spin–lattice relaxation times have been determined for organolithium compounds in solution.[40,24] The T_1 values vary from 0.01 to 10 s, and it was concluded that for ^{7}Li the quadrupolar relaxation mechanism dominates. Recent findings of $\{^1H\}^7$Li NOE effects, however, show that in symmetric surroundings considerable dipolar contributions to ^{7}Li relaxation can exist.[41,42] ^{6}Li T_1 values in organolithium compounds are typically of the order of seconds or even tens of seconds. Measurements for methyl-, *n*-butyl-, and phenyllithium in diethyl ether and hydrocarbon solvents[43] yielded T_1 values of 9 to 72 s, while the ^{7}Li T_1 values for the same compounds determined from identical samples are one to two orders of magnitude smaller. As again evidenced by the NOE effect, the ^{6}Li–^{1}H dipolar contribution to the overall relaxation rate was found to be 20, 35, and 17%, respectively. Assuming that ^{7}Li relaxes entirely by the quadrupolar mechanism, quadrupolar contributions of 5, 24, and 27%, respectively, can be calculated for ^{6}Li relaxation in the three species.[44] A possible ^{7}Li–^{6}Li dipolar contribution was estimated to be 6%. A much larger contribution (30–60%) from this source was found by Thomas,[24] who compared T_1 data from ^{6}Li enriched organolithium compounds with those from compounds with natural ^{6,7}Li distribution. A strong solvent effect on these parameters was also noted, while variable temperature studies showed a decrease in T_1 with decreasing temperature, as expected.[24]

The different contributions of ^{6}Li and ^{7}Li to the spin–lattice relaxation of neighboring nuclei provide, in suitable cases, a means for the determination of Li–C and Li–H distances in aggregates of solute organolithium compounds through the use of the isotopic substitution method,[45] as has been shown for phenyllithium by Jackman.[46] If one replaces a nucleus ^{n}X (spin quantum number I) with strong dipole–dipole interaction by its isotope ^{m}X (spin quantum number S) with weak dipole–dipole interaction, the difference in the spin–lattice relaxation rate R_1 of the neighboring ^{13}C nucleus is given by

$$R_1^{\exp}(^n\mathrm{X}) - R_1^{\exp}(^m\mathrm{X}) = R_1^{\mathrm{DD}}(^n\mathrm{X}) \left[1 - \frac{\gamma_{m_x}^2 S(S+1)}{\gamma_{n_x}^2 I(I+1)} \right] \quad (3)$$

If the correlation time τ_c is known, the distance r_{C-X} can be determined according to

$$r_{C-X} = \sqrt[6]{\hbar^2 \gamma_{^{13}C}^2 \gamma_{n_X}^2 \tau_c / R_1^{\mathrm{DD}}(^n\mathrm{X})} \quad (4)$$

τ_c is obtained from the dipolar relaxation rate R_1^{DD} of another ^{13}C nucleus in the same molecule, measured under identical conditions, and its respective C–H distance.

Finally, we mention that ^{7}Li $T_{1\rho}$ measurements have been used to study the rate of interconversion between tight and loose ion pairs of lithium fluorenide.[47] The quadrupolar relaxation contribution was derived from ^{6}Li and ^{7}Li T_1 data, and a change in the ^{7}Li quadrupole splitting constant (QSC), obtained via ^{7}Li quadrupolar and ^{13}C dipolar relaxation rates, with ion pair structure was indicated.

2.2 Transverse Relaxation

For quadrupolar nuclei with dominant quadrupolar relaxation, the relaxation rates for longitudinal and transverse magnetization (R_{1q} and R_{2q}) are identical in the motional narrowing limit. This situation is met in many cases for ^{7}Li, while for ^{6}Li the relation $R_2 > R_1$ will generally be found. For both nuclei, however, chemical exchange processes are quite common and the strongest contribution to R_2 will then originate from this source. This topic is discussed in Section 3.2.2.

2.3 Chemical Shifts

2.3.1 Reference Methods

Since chemical shifts are measured relative to the signal of a reference compound, the problem of referencing is an experimental detail of practical importance. For ^{6,7}Li measurements internal standards are not feasible in either inorganic or organometallic applications due to exchange reactions involving Li^+. Furthermore, in the study of organometallic compounds the high sensitivity of these systems towards acids as well as their general reactivity prevent the use of internal references. ^{6,7}Li chemical shifts have, therefore, been recorded relative to various external standards, as for example 1.0 or 0.1 molar solutions of lithium salts (LiCl, LiBr, or $LiClO_4$) in H_2O or organic solvents like tetrahydrofuran (THF) and the data are generally reported without bulk susceptibilty corrections. As Thomas has pointed out,[24] due to the different correction terms this may lead to chemical shift differences of several tenths of a ppm if data from iron magnets are compared with data from superconducting magnets.

An alternative method for referencing ^{6,7}Li shifts in organolithium compounds has recently been proposed by Jackman.[48] This method takes advantage of the multiple frequency probes and rf systems of modern spectrometers and is independent of volume susceptibility differences and the nature of the lock substance. The spectrometer has to be calibrated with, for example, a 0.3 M solution of LiCl in methanol-*d* containing 5% TMS. The methanol ^{13}C signal (secondary ^{13}C reference) is than referenced to the primary ^{13}C standard [tetramethylsilane (TMS)] which yields

$$\nu_{\mathrm{ref}}(^{13}\mathrm{C}) = \nu_{\mathrm{tr}}(^{13}\mathrm{C}) + \Delta\nu_{\mathrm{off}}(^{13}\mathrm{C}) - \Delta\nu_{\mathrm{shift}} \qquad (5)$$

where ν_{tr} is the transmitter frequency, $\Delta\nu_{\mathrm{off}}$ the offset between the secondary standard and the transmitter, and $\Delta\nu_{\mathrm{shift}}$ is the methanol–TMS frequency difference (all quantities in hertz).

In the next step, $\nu_{\mathrm{ref}}(^{6,7}\mathrm{Li}) = \nu_{\mathrm{tr}}(^{6,7}\mathrm{Li}) - \Delta\nu_{\mathrm{off}}(^{6,7}\mathrm{Li})$ is determined for the standard sample. A ^{13}C resonance of the sample of interest is than measured to yield $\nu_{\mathrm{ref}}'(^{13}\mathrm{C}) - \nu_{\mathrm{ref}}(^{13}\mathrm{C})$ and a new absolute ^{6,7}Li reference frequency $\nu_{\mathrm{ref}}'(^{6,7}\mathrm{Li})$ is obtained from the relationship

$$\frac{\nu_{\mathrm{ref}'}(^{6,7}\mathrm{Li}) - \nu_{\mathrm{ref}}(^{6,7}\mathrm{Li})}{\nu_{\mathrm{ref}'}(^{13}\mathrm{C}) - \nu_{\mathrm{ref}}(^{13}\mathrm{C})} = \frac{\gamma(^{6,7}\mathrm{Li})}{\gamma(^{13}\mathrm{C})} \qquad (6)$$

or

$$\nu_{\mathrm{ref}'}(^{6,7}\mathrm{Li}) = \nu_{\mathrm{ref}}(^{6,7}\mathrm{Li}) + [\nu_{\mathrm{ref}'}(^{13}\mathrm{C}) - \nu_{\mathrm{ref}}(^{13}\mathrm{C})]\gamma(^{6,7}\mathrm{Li})/\gamma(^{13}\mathrm{C}) \qquad (7)$$

The difference $\nu_{\mathrm{ref}}'(^{6,7}\mathrm{Li}) - \nu_{\mathrm{tr}}(^{6,7}\mathrm{Li})$ gives the offset (in hertz) required to reference the unknown lithium sample.

2.3.2 Structural Effects

As compared with other metal nuclei, the ^{6,7}Li chemical shift scale is rather small and the NMR signals of ^{6,7}Li encompass not more than about 6 ppm for salt solutions and about 12 ppm for organolithium compounds. This can be attributed to the relatively small paramagnetic contribution to the shielding constant of ^{6,7}Li, which leads to a near-cancellation of the diamagnetic term.[49] Due to the larger gyromagnetic ratio, spectral dispersion is better for ^{7}Li than for ^{6}Li, but the larger ^{7}Li linewidth (see above) may jeopardize this advantage. In addition, ^{6,7}Li shifts are sensitive to solvent effects, viscosity, temperature and concentration and these effects are of the same order as the structural effects. For solvent effects alone, a range of nearly 6 ppm was found for $\delta(^7\mathrm{Li})$ (Table 3).[50,51] Therefore, a comparison of $\delta(^{6,7}\mathrm{Li})$ values is difficult and, because of these uncertainties, ^{6,7}Li chemical shift arguments have been used in structural research to a much lesser extent than in the case of other nuclei. Furthermore, in the absence of spin–spin coupling, an unequivocal assignment of ^{6,7}Li resonances is not always possible.

The chemical shift of lithium ions has been investigated in connection with studies on ion pairing, solvation, and complexation, where sudden shifts are typically observed upon formation of complexes with defined stoichiometry. In the solvent effect studies, no correlation of $\delta(^7\mathrm{Li})$ with solvent properties was found, contrary to the situation with other alkaline metal ions and the influence of counterions on $\delta(^7\mathrm{Li})$ is solvent dependent.[51] These studies, which include ^{7}Li measurements of the complexation of crown ethers and cryptands, as well as naturally occurring ionophores, have been reviewed by Wehrli,[19] Dechter,[1] Detellier,[20] and most recently by Bartsch et al.[166] A graphical overview on ^{7}Li chemical shifts, presented by Akitt,[21] is given in Figure 2.

The ^{6,7}Li resonances of organolithium compounds were measured in different solvents, and representative results are shown in Figure 3[52] and Table 3. Some of the observed trends can be correlated with the structure of the ligands or the chemical bonding situation. There is a remarkable shielding effect, generally classified as a *ring current effect* on the ^{6,7}Li resonance in polyhapto lithium compounds of organic π systems,[53–56] where lithium is situated above the plane of the π system (Table 4). Low-frequency and high-frequency shifts indicate diatropic and paratropic properties, respectively. The shielding effect is most pronounced for situations where Li^+ is sandwiched between two π systems,[55,57–59] but smaller than expected in dianions of condensed benzenoid aromatics. Similarly, the study of ^{7}Li chemical shifts for a variety of alkyllithium compounds[52] (Figure 3) revealed that

Table 3 Chemical Shifts of ^{6,7}Li Magnetic Resonances in Lithium Salts and Organolithium Compounds[a]

Compound	$\delta(^{6,7}\text{Li})$ (ppm)	Solvent[b]
$^{7}Li^{+}$ in various salts at infinite dilution versus external 4.0 M aqueous $LiClO_4$, corrected for bulk magnetic susceptibility effects	−2.80	Acetonitrile
	−1.01	DMSO
	−0.61	Propylene carbonate
	−0.60	THF
	−0.54	Methanol
	−0.36	Nitromethane
	−0.03	Acetic acid
	0.45	DMF
	0.63	Tetramethylguanidine
	1.34	Acetone
	2.54	Pyridine
Organolithium Compounds[c]		
CH_3Li	1.32	Diethyl ether
C_2H_5Li	1.71	Cyclopentane
	1.00	Benzene
	0.6	Diethyl ether
	1.38	Triethylamine
	1.21 (−80 °C)	Triethylamine
n-C_4H_9Li	1.85	Cyclopentane
$(CH_3)_2CHLi$	1.17	Cyclopentane
	0.91	Triethylamine
$(CH_3)_3SiCH_2Li$	1.36	Toluene
	1.96	Cyclopentane
	1.74	Hexane
	2.26	Triethylamine
	2.64 (−80 °C)	Triethylamine
$(CH_3)_3CLi$	0.40	Toluene
	0.89	Cyclopentane
	0.89	Triethylamine
C_6H_5Li	1.2	Diethyl ether
$C_6H_5CH_2Li$	−0.54	Toluene–benzene
	0.20	Diethyl ether
C_6H_5Li:		
Dimer	1.52[d]	Diethyl ether (−102 °C)
Tetramer	2.26	
C_6H_5Li/TMEDA:		
Monomer	2.07[d]	Diethyl ether (−111 °C)
Dimer	2.32	
1-Lithio-*trans*-2,3-dimethylcyclopropane:		
Monomer	2.02[d]	Diethyl ether (−86 °C)
Dimer	2.08	
Tetramer	2.22	
CH_3Li/LiBr[e]	1.72 [R,R,R][f]	Diethyl ether (−90 °C)
	1.04 [R,R,Br]	
	0.44 [R,Br,Br]	
CH_3Li/LiI[e]	1.84 [R,R,R][d]	Diethyl ether (−95 °C)
	1.11 [R,R,I]	
	0.40 [R,I,I]	

[a]Data from Brown,[29] Cahen et al.,[51] Ladd and Parker,[60] and Eppers and Günther.[61] Note that the δ values in Brown[29] and Cahen et al.[51] are given using the now obsolete sign convention.
[b]DMF, *N*,*N*-dimethylformamide; DMSO, dimethyl sulfoxide; THF, tetrahydrofuran.
[c]At 25 °C relative to external 3 M aqueous LiBr; uncorrected for bulk magnetic susceptibility effects, unless otherwise stated.
[d]Relative to external 0.1 M LiBr in THF.
[e]The local environment is given in brackets.
[f]Relative to internal LiBr.

$\delta(^{7}\text{Li})$ is strongly influenced by the diamagnetic anisotropy of the organic ligands. A distinct low-frequency shift was observed in the majority of cases by changing the solvent from hydrocarbons to diethyl ether. For aryllithium compounds systematic substituent effects were found with high-frequency shifts for donor substituents in positions *meta* and *para* to the metallated carbon.[60] Low-temperature studies, which allow the measurements of ^{6,7}Li shifts for different aggregates of a particular system, showed that in a number of cases ^{6,7}Li is less shielded in the higher aggregates

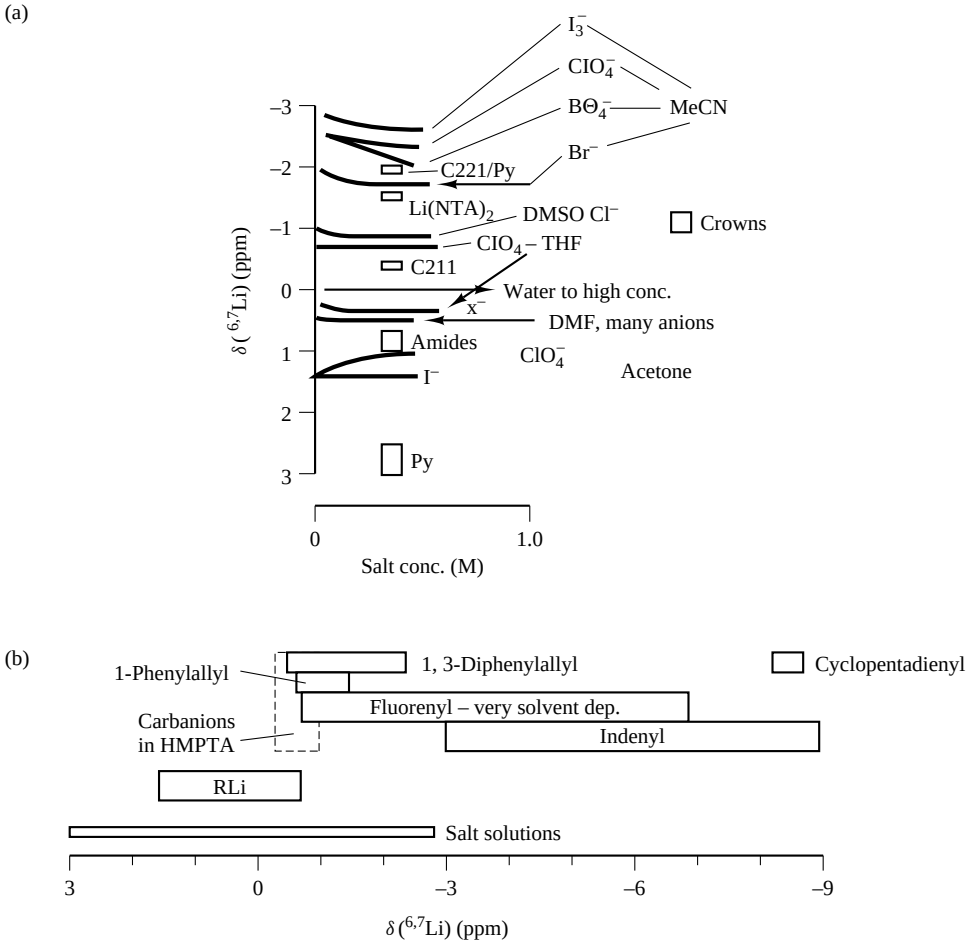

Figure 2 Graphical summary of ^{6,7}Li chemical shifts in (a) salt solutions, and (b) organolithium compounds. (Reproduced by permission of Plenum Press from J. W. Akitt, in 'Multinuclear NMR', ed. Joan Mason, New York, 1987, Chap. 7)

(Table 3).[61,62] This cannot be regarded as a general rule, however, because the reverse order has also been observed.[63,64] For mixed aggregates between simple alkyl lithium compounds and lithium salts, a type of *heavy atom effect* is documented by the shielding observed with increasing incorporation of halide ions (Table 3).[61,65] ^{6,7}Li chemical shifts (in particular the shielding effects of π systems) have been used as probes for ion pairing.[66–68] *IGLO calculations*[69] reproduce the effect of π systems well. In general, rather little variation of the shielding constant σ with chemical structure was found, in agreement with experimental observations (see above). Nevertheless, the results of such calculations for ^{6,7}Li chemical shifts have been shown to provide important insights into the structure–chemical shift relationship.[57]

2.3.3 *Deuterium-Induced Isotope Effects on ^{6}Li Chemical Shifts*

Theoretical calculations on LiH and LiD predicted a deuterium-induced high-frequency (downfield) ^{6}Li shift,[70] but early measurements on ^{6,7}Li salt solution in deuterated and nondeuterated solvents failed to demonstrate isotope shifts.[71] The first observation of deuterium-induced shifts for the ^{6}Li resonance was reported for deuterated methyllithium, where an isotope shift $\Delta\delta$ of 16 ppb was found.[65] Based on this observation, the *isotopic fingerprint method* was developed as a tool for structural investigations in the field of organolithium compounds.[65] With this method, typical ^{6}Li multiplets, which are characteristic of the aggregation state, can be expected for 1:1 mixtures of deuterated and nondeuterated RLi compounds in the region of slow inter- and intra-aggregate exchange. The principle of this technique, which is closely related to the SIMPLE NMR method for the assignment of ^{13}C NMR spectra of polyalcohols,[72,73] is best explained by using an example.

Given a dimeric structure of type (**1**), like that of phenyllithium (R = C_6H_5) in the presence of tetramethylethylene diamine (TMEDA),[74] and a 1:1 mixture of deuterated and nondeuterated ligands R (d and h, respectively), the ^{6}Li environments (**2**)–(**4**) exist.

According to a straightforward statistical consideration, a ^{6}Li triplet with an intensity distribution of 1:2:1 should then result in the case of slow inter-aggregate exchange, if a ^{2}H/^{1}H isotope effect for δ(^{6}Li) exists. Each line of this multiplet is characteristic for a different ^{6}Li environment. In turn, for a monomer we should find a doublet and for a tetramer with three direct neighbors (see Figure 1), a quadruplet with an intensity distribution of 1:3:3:1 is expected. Thus, clusters of different size are characterized by isotopic fingerprints, where the intensity ratio follows Pascal's triangle (Figure 4). An attractive feature of this method as compared to the

Table 4 Ring Current Effects on ^{6,7}Li Chemical Shifts in Lithium Salts of Cyclic π Systems

Compound[a]	Number of π electrons	$\Delta\delta(^{6,7}\text{Li})$ (ppm)[b]	Reference
$[Li(THF)_4][Li(OEP)]$:			
In C_6D_6/TMEDA	18	−16.5[c]	Arnold[58]
In DMSO		−11.55[c]	Arnold[58]
ICP−Li^+−ICP−Li^+	6 + 6	−12.78 (inner Li)[d] −1.10 (outer Li)[d]	Paquette et al.[56]
Cyclooctatetraene dianion	10	−8.55	Cox et al.[53]
Cyclopentadienide	6	−8.37	Cox et al.[53]
Indenide	10	−6.17	Cox et al.[53]
Biphenylene dianion	14	−6.10	Cox et al.[53]
Acenaphthylene dianion	14	−4.13	Cox et al.[53]
Azulene dianion	12	+2.05	Cox et al.[53]
15,16-Dimethyldihydropyrene dianion	16	+3.15	Cox et al.[53]
1,2,4,5-Tetrakis(trimethylsilyl)benzenide	8	+10.7	Sekiguchi et al.[59]

[a]DMSO, dimethyl sulfoxide; ICP, isodicyclopentadienyl; OEP, octaethylporphyrine; TMEDA, tetramethylethylenediamine.
[b]Relative to external aqueous 1 M LiCl, unless otherwise stated.
[c]Relative to external 0.3 M LiCl in MeOH.
[d]Relative to external 1 M LiBr in tetrahydrofuran (THF).

determination of the aggregation number from scalar ^{13}C−^{6}Li or ^{13}C−^{7}Li spin−spin coupling constants (see later) is its sensitivity which is achieved by twofold isotopic enrichment (^{2}H and ^{6}Li).

If only the inter-aggregate exchange is slow and the intra-aggregate exchange is still fast on the NMR timescale, the situation changes for clusters with aggregation numbers >2. The ^{6}Li nucleus then interacts with all ligands of the particular clusters, including the remote ones. Consequently, for a dynamic tetramer a 1:4:6:4:1 ^{6}Li quintuplet is then expected. Now, each line of the multiplet corresponds to a different aggregate (Figure 4). The isotopic fingerprint method has been applied to study the aggregation of alkyl- and aryllithium compounds,[61,65,75] of lithium disopropylamide[75] and of mixed aggregates between methyllithium and LiI[65] as well as LiBr.[61] These studies also revealed the existence of isotope shifts transmitted over more than two bonds. In all cases high-frequency shifts for the ^{6}Li resonance were observed.

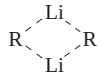

(1) [h,h] (2) [h,d] (3) [d,d] (4)

2.4 Scalar Spin−Spin Coupling

2.4.1 General Aspects

Homo- and heteronuclear scalar spin−spin coupling of ^{6,7}Li is a domain of organolithium compounds. It is of great importance for structural investigations and yields information about chemical bonding between lithium and other elements like carbon, nitrogen, or phosphorus. In particular, coupling between ^{6}Li and ^{13}C has led to a wealth of structural information on organolithium aggregates in solution. Due to the higher gyromagnetic ratio of ^{7}Li, ^{7}Li−X coupling constants are larger by a factor of $\gamma(^{7}\text{Li})/\gamma(^{6}\text{Li}) = 2.64$ than ^{6}Li−X coupling constants. As in the case of chemical shifts, this advantage is, however, very often annihilated by ^{7}Li quadrupolar effects, which lead to line broadening and partial decoupling. This is demonstrated by the ^{13}C NMR signal shown in Figure 5.

An important aspect with respect to the experimental observation of spin−spin coupling is the fact that lithiated carbon, nitrogen, silicon, and phosphorus compounds exist in the solid as well as in solution as aggregates or clusters (see Figure 1). Extensive X-ray work has revealed a large variety of solid state structures[76] which are, primarily according to the results of NMR investigations, also retained if the compounds are dissolved in hydrocarbon or ethereal solvents. However, in solution different, coexisting aggregates are formed in many cases and these systems become dynamic. Thus, intra- as well as inter-aggregate exchange operates and the observation of line splittings due to scalar coupling therefore crucially depends on the NMR timescale. Only in the slow exchange limit can couplings be detected, and thus measurements have to be performed almost exclusively at low temperatures ($T < -50\,^{\circ}$C). Starting in the high-temperature, fast exchange regime, one gradually slows down the inter- and the intra-aggregate exchange by low-temperature measurements until exchange is slow enough for individual species to be observed. Only rarely can these different stages be 'frozen out' stepwise,[77−79] and in general two situations are met. (1) If the energy barriers of the two fluxional processes are very similar, low-temperature measurements may lead directly to *static aggregates* where spin−spin coupling to ^{6,7}Li originates in the case of the heavier nuclei from nearest neighbors ('local environment approximation'[80]). (2) The barrier to intra-aggregate exchange may be low and only the inter-aggregate exchange can be slowed down. In these fluxional aggregates the observed line splittings result from an average of the spin−spin interactions between ^{6,7}Li and directly bonded and remote X nuclei. Since coupling to remote nuclei is smaller than the coupling to the direct neighbors or may even be zero, smaller line splittings are observed in these cases as compared with the situation met with static

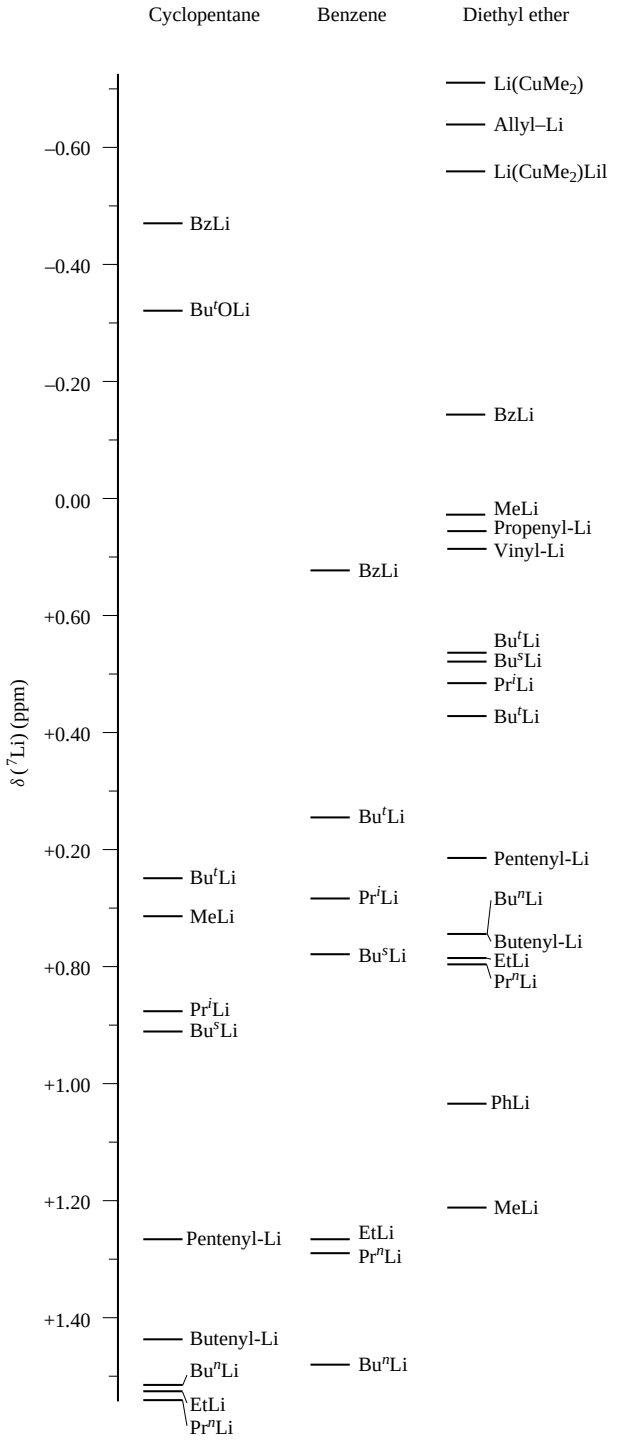

Figure 3 ^{7}Li chemical shifts for alkyl and alkenyl lithium compounds in different solvents relative to 0.1 M LiBr as external reference. (Reproduced with permission from P. A. Scherr, R. J. Hogan, and J. P. Oliver, *J. Am. Chem. Soc.*, 1974, **96**, 6055)

aggregates, but the multiplicity of the observed resonances is higher than in the static case.

2.4.2 Homonuclear Coupling

Homonuclear spin–spin coupling between nonequivalent lithium atoms in organolithium compounds is weak (J < 0.5 Hz). It was first detected indirectly by cross peaks in homonuclear ^{6}Li–^{6}Li COSY spectra.[81] Only recently, such a coupling (magnitude 0.16 Hz) could be resolved for the dimer of (*E*)-2-lithio-1-phenyl-1-(*o*-lithiophenyl)pent-1-ene[82] (for the structure of this compound see Figure 10). The coupling is best detected by the INADEQUATE experiment,[83] where the resulting antiphase magnetization facilitates the observation of line splittings which are otherwise barely resolved (see later). Indirect detection of ^{7}Li–^{7}Li couplings was recently achieved by means of ^{7}Li–^{7}Li COSY and ^{7}Li–^{7}Li INADEQUATE experiments.[84]

2.4.3 Heteronuclear Coupling

2.4.3.1 General Aspects. Due to the more favorable NMR properties and the possibility of 100% isotopic enrichment, scalar couplings to lithium are measured more easily in the majority of cases for ^{6}Li. Only where the larger magnitude of ^{7}Li couplings promises an advantage is the use of ^{7}Li preferable. For ^{6}Li$_n$–X$_m$ spin pairs, scalar coupling can be observed in the ^{6}Li as well as in the X spectrum if high natural abundance exists (^{6}Li enrichment, X = ^{1}H or ^{31}P). In case of X nuclei with low natural abundance (^{13}C or ^{29}Si), coupling is best measured in the X spectrum, since in the ^{6,7}Li spectra only X satellites are observed (Figure 6).[78,85] For the detection of ^{15}N–^{6}Li coupling, ^{15}N enrichment is required because of the low natural abundance of ^{15}N (0.37%) and the low substrate concentrations usually attainable as a consequence of low solubility.

If ^{6,7}Li–X couplings are well resolved, as is the case for X = ^{13}C, ^{15}N, or ^{31}P, spin multiplets are observed which are determined by the relevant spin quantum numbers. For first-order spectra, the multiplicity M of the resonances then follow the well-known rules with $M = 2nI + 1$, where n is the number of adjacent nuclei. For the ^{6,7}Li resonances of lithium coupled to spin-$\frac{1}{2}$ nuclei, $M = n + 1$; while for X nuclei coupled to ^{6}Li, $M = 2n + 1$; and for those coupled to ^{7}Li, $M = 3n + 1$. The intensity distribution of the ^{6,7}Li resonances is given by the binomial coefficients, and those of the X resonances are summarized in Figure 7. In recent years, investigations of polylithium compounds have revealed spin systems that are more complicated than first order (see below).

2.4.3.2 ^{6,7}Li–^{1}H Coupling. Scalar spin–spin coupling between protons and ^{6,7}Li is again rather small (<1 Hz), except in hydrido complexes where large ^{7}Li–^{1}H interactions have been reported in two cases [(**5**), J = 8.4 Hz;[86] (**6**) J = 10.5 Hz[87]]. In organolithium compounds ^{6,7}Li–^{1}H coupling has been recognized from ^{1}H lineshape changes observed by comparing ^{7}Li and ^{6}Li labeled compounds[88] and by lineshape simulations of ^{6}Li NMR spectra.[65] More recently, larger ^{6,7}Li–^{1}H coupling constants (up to 1 Hz) have been reported for the dilithio compound (**7**),[41] the dimer and tetramer of vinyllithium (**8**),[79] and the dilithio compound (**9**).[89] For vinyllithium, even the relative signs of these coupling constants could be determined from a two-dimensional experiment,[79] and it was concluded that geminal and vicinal ^{6}Li–^{1}H interactions are positive. In the case of (**9**), the assignment of the nonequivalent lithium resonances in the dimer structure was based on the observed ^{6}Li–^{1}H coupling,[89] where $^{3}J(^{6}\text{Li},^{1}\text{H})$ obeys the Karplus equation (Figure 8).

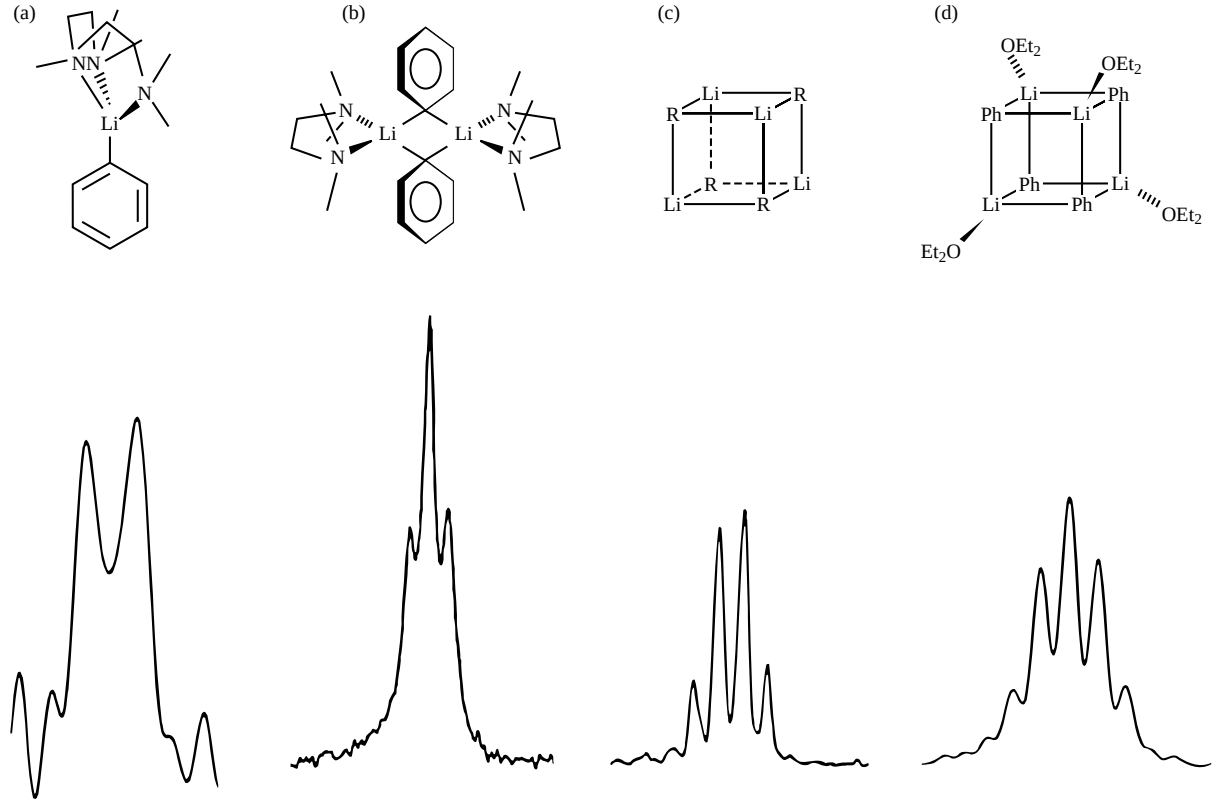

Figure 4 Isotopic fingerprints in ^{6}Li NMR spectra: (a) phenyllithium monomer (THF/PMTDA, −122°); (b) phenyllithium dimer (Et_2O/TMEDA, −111°); (c) methyllithium tetramer (R = CH_3) (Et_2O, −92°); (d) fluxional phenyllithium tetramer (Et_2O, −102°). The measured $^{2}H/^{1}H$ isotope shifts for $\delta(^{6}Li)$ are 19.2, 10.4, 15.6, and 7.0 ppb, respectively. All systems were ^{6}Li labeled and 50% of the organic ligands were perdeuterated; $\nu_0(^{6}Li)$ = 58.88 MHz

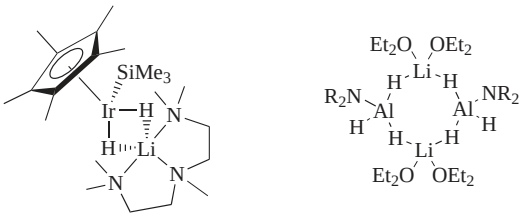

(5)

(6) R = $SiMe_3$

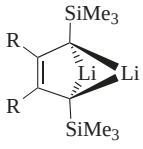

(7)

(8)

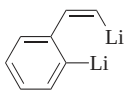

(9)

2.4.3.3 $^{7}Li–^{6}Li$ *Coupling.* A special case of heteronuclear interactions is the coupling between ^{6}Li and ^{7}Li, which has so far not been reported, despite earlier attempts to detect such couplings from partially labeled compounds.[90] Such interactions are of interest because they should be observed also for chemically equivalent lithium nuclei which are isochronous in the homonuclear case. From the known magnitude of a $^{6}Li–^{6}Li$ coupling (see above), one estimates values of about 0.4 Hz.

2.4.3.4 $^{13}C–^{6,7}Li$ *Coupling.* Scalar spin–spin interactions between ^{6,7}Li and ^{13}C lead to coupling constants of sizeable magnitude (3–17 Hz for ^{6}Li, and larger by a factor of 2.64 for ^{7}Li) and these interactions have been introduced as valuable parameters for structural determinations of organolithium compounds. After the first detection of such couplings in ^{13}C enriched methyllithium,[91] their potential was soon recognized and initiated (for reasons of improved detectibility) the use of ^{6}Li labeling, introduced by Fraenkel[92] and Seebach.[93,94] A large variety of these parameters has been collected over the years for ^{6}Li labeled systems, where the line splitting due to $^{13}C–^{6}Li$ coupling is measured in the region of slow exchange, usually below −50 °C, in the ^{1}H decoupled ^{13}C NMR spectra (Figure 9). Representative data are shown in Table 5; more extensive collections are given by Thomas[24] and Bauer and Schleyer.[26] While the magnitude of the coupling is usually easy to establish, the characterization of the multiplets with respect to the number of lines and their intensity distribution is often difficult, because the smaller lines in the wings are hard to detect if the signal-to-noise ratio is low. Even a careful line simulation will not allow distinction between a septuplet and a nonuplet in all cases. Only recently, a positive sign was established for $^{1}J(^{13}C,^{6}Li)$ in vinyllithium.[79] It is important to note that $^{13}C–^{6,7}Li$ coupling is not observed for organolithium

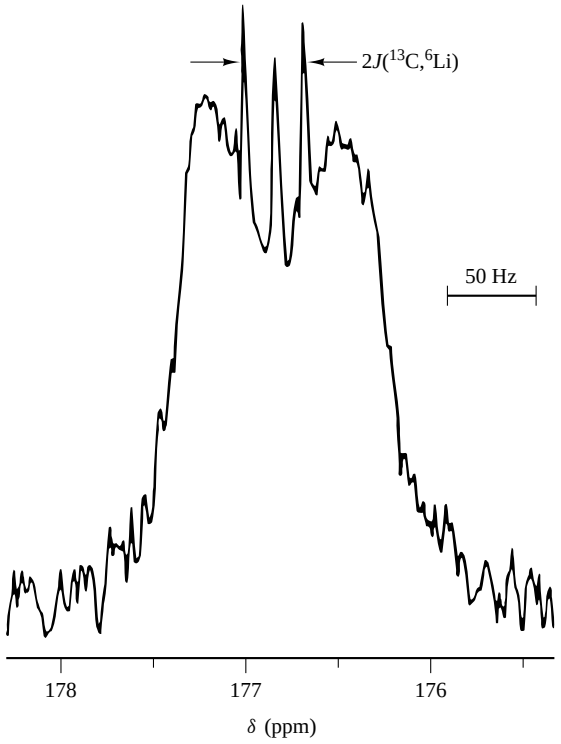

Figure 5 ^{13}C NMR signal of the lithiated carbon of 1-lithio-2,4,6-tri-*t*-butylbenzene with natural isotopic $^{6,7}Li$ distribution (THF-d_8/TMEDA 1:1, −79°). The quadruplet expected for ^{13}C, ^{7}Li coupling is not resolved (Reproduced with permission from W. Bauer, W. R. Winchester, and P. v. R. Schleyer, *Organometallics*, 1987, **6**, 2371)

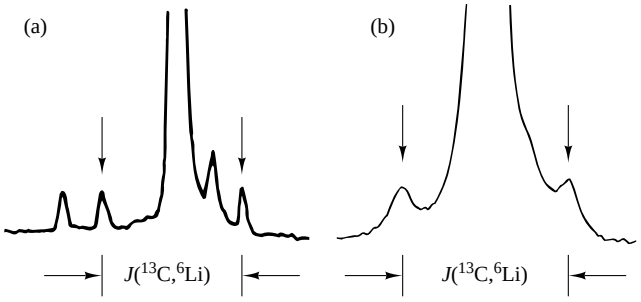

Figure 6 ^{13}C satellites (arrows) in the ^{6}Li NMR spectrum of: (a) [^{6}Li]*t*-butyllithium (1 M in cyclopentane, −40°); (b) [^{6}Li]phenyllithium (0.5 M in dimethoxymethane, −73°). The coupling constants are 5.4 and 8.0 Hz, respectively. (Reproduced, in part, with permission from R. D. Thomas, M. T. Clarke, R. M. Jensen, and T. C. Young, *Organometallics*, 1986, **5**, 1851)

compounds with π-bound lithium (benzyllithium, dilithionaphthalene, etc.).

Static aggregates are characterized by coupling to nearest neighbors, while in *fluxional aggregates* remote nuclei are also involved. An empirical rule[23,63,96] for the coupling (in hertz) is

$$J(^{13}C,^{6}Li)_{obs} \approx 17/n; \quad J(^{13}C,^{7}Li)_{obs} \approx 45/n \qquad (8)$$

where n is the number of equivalently coupled ^{6}Li nuclei. This leads to values of about 17 Hz for monomers, 8.5 Hz for dimers, and 5.7 Hz for tetramers and hexamers (see Figure 1). For fluxional tetramers and hexamers these numbers drop to 4.3 and 2.8 Hz, respectively. An important point is that only coupling over one formal $^{13}C–^{6,7}Li$ bond has so far been observed. In recent years a number of dilithio compounds have been synthesized which give rise to more complicated spin systems of the AA′XX′ and ABXY types.[85,99] Here the simple rule derived for the $(RLi)_n$ type systems breaks down.

2.4.3.5 $^{15}N–^{6}Li$ Coupling. Coupling between ^{6}Li and ^{15}N[100–102] is of similar importance in the field of lithiated amides and nitrogen compounds, as is $^{13}C–^{6}Li$ coupling in the field of carbon compounds. Due to the low natural abundance of ^{15}N (0.37%) and the concentration limits met when low temperature spectra have to be investigated, measurements have been made exclusively on doubly labeled (^{6}Li and ^{15}N) systems. Selected examples are shown in Table 5. Again, only one-bond coupling has been observed. The magnitude of these couplings is roughly only half that of the analogous $^{13}C–^{6}Li$ coupling constants. An empirical rule analogous to equation (8) can be formulated:[26]

$$J(^{15}N,^{6}Li)_{obs} = 7/n \qquad (9)$$

2.4.3.6 $^{6,7}Li$ Coupling to ^{29}Si, ^{31}P, ^{77}Se, ^{119}Sn, and ^{195}Pt. Finally, $^{6,7}Li$ coupling to ^{29}Si,[103] ^{31}P,[104–110] ^{77}Se,[111] ^{119}Sn[112,113] (^{7}Li, J = 6.2 and 412 Hz), and ^{195}Pt[114] (^{7}Li, J = 48 Hz) has been observed and examples are given in Table 5. The discovery of a ^{2}J coupling between the phosphorus atom of hexamethylphosphoric triamide (HMPTA) and coordinated ^{7}Li[109,110] has been used in an interesting NMR technique for the characterization of lithium ion pair structures.[68]

2.4.4 Scalar Spin–Spin Coupling and Lithium Bonding

Since scalar spin–spin interactions are generally transmitted via chemical bonds, the observation of scalar spin–spin coupling is often taken as experimental proof for the existence of covalent bonding between the nuclei of interest. Streitwieser, however, has pointed out[115] that coupling between $^{6,7}Li$ and, for example, ^{13}C may also be based on electron polarization through space, a mechanism met quite often for coupling of ^{19}F.[116] The observation of various $^{6,7}Li–X$ coupling constants is thus also compatible with a high ionic character of the respective Li–X bond.

As far as $^{6,7}Li–^{13}C$ coupling constants are concerned, two facts merit attention: (1) such couplings are observed only to carbon directly bonded to lithium; and (2) they seem to be independent of the s character of the carbon–lithium bond, which is a unique finding for one-bond couplings. As Bauer and Griesinger[79] have noted, the first observation may be rationalized if one remembers the hierarchy of $^{13}C–^{1}H$ coupling constants ($^{1}J \gg {}^{2}J, {}^{3}J$). A possible explanation for the second observation comes from results of ab initio calculations[117] which showed that the product of s character and the carbon–lithium covalent bond order is approximately constant for C–Li bonds in methyllithium, lithioethene, and lithioacetylene. If this product dominates the coupling, constant J values should result.

2.5 Quadrupolar Coupling Constants

The quadrupole splitting constant (QSC), of ^{7}Li has been used by Jackman[118] as an empirical parameter to obtain

n	^{6}Li
1	1 : 1 : 1
2	1 : 2 : 3 : 2 : 1
3	1 : 3 : 6 : 7 : 6 : 3 : 1
4	1 : 4 : 10 : 16 : 19 : 16 : 10 : 4 : 1
5	1 : 5 : 15 : 30 : 45 : 51 : 45 : 30 : 15 : 5 : 1
6	1 : 6 : 21 : 50 : 90 : 126 : 141 : 126 : 90 : 50 : 21 : 6 : 1

n	^{7}Li
1	1 : 1 : 1 : 1
2	1 : 2 : 3 : 4 :3 : 2 : 1
3	1 : 3 : 6 : 10 : 12 : 12 : 10 : 6 : 3 : 1
4	1 : 4 : 10 : 20 : 31 : 40 : 44 : 40 : 31 : 20 : 10 : 4 : 1
5	1 : 5 : 15 : 35 : 65 : 101 : 135 : 155 : 155 : 135 : 101 : 65 : 35 : 15 : 5 : 1
6	1 : 6 : 21 : 56 : 120 : 216 : 336 : 456 : 546 : 580 : 546 : 456 : 336 : 216 : 120 : 56 : 21 : 6 : 1

Figure 7 Intensity distribution of X resonances coupled to up to six ^{6}Li or ^{7}Li nuclei

Table 5 Examples of ^{6}Li,X Coupling (X = ^{13}C, ^{15}N, ^{29}Si, or ^{31}P) in Organolithium Compounds

Compound	Solvent[a]	Temp. (°C)	X mult.	m[b]	n[c]	J (Hz)	Reference
X = ^{13}C							
$LiCHCl_2$	THF	−100	3	1	1	16.3	Seebach et al.[93]
$LiCCl_3$	THF	−100	3	1	1	17.0	Seebach et al.[93]
n-BuLi	THF	−100	5	2	2	7.8	Seebach et al.[94]
			7	3	4	5.5	Seebach et al.[94]
t-BuLi	Cyclopentane	26	9	4	4[d]	4.1	Thomas et al.[77]
		−88	7	3	4	5.4	Thomas et al.[77]
	Cyclopentane/Et_2O	−80	5	2	2	7.8	Bates et al.[95]
	THF-d_8	−90	3	1	1	11.9	Bauer et al.[96]
n-PrLi	Cyclopentane	−56	13	6	6[d]	3.3	Fraenkel et al.[63]
			17	8	8[d]	2.5	Fraenkel et al.[63]
			19	9	9[d]	2.2	Fraenkel et al.[63]
i-PrLi	Cyclopentane	−15	7	3	4	6.1	Thomas et al.[78]
			13	6	6[d]	3.3	Thomas et al.[78]
Vinyllithium	THF-d_8	−90	5	2	2	8.3	Bauer and Griesinger[79]
			7	3	4	5.9	Bauer and Griesinger[79]
C_6H_5Li	THF-d_8	−118	5	2	2	8	Seebach et al.[94]
	THF/PMDTA	−103	3	1	1	15.6	Bauer et al.[96]
	TMEDA/Et_2O	−75	5	2	2	8	Fraenkel et al.[32]
t-BuC≡CLi	THF	−100	7	3	4	5.7	Fraenkel and Pramanik[97]
			5	2	2	8.3	Fraenkel and Pramanik[97]
C_6H_5C≡CLi	THF	−95	5	2	2	8.2	Hässig and Seebach[98]
X = ^{15}N							
$(C_6H)_2NLi$	Toluene/THF	−90	5	2	2	3.3	DePue and Collum[101]
C_6H_5(i-Pr)NLi	THF	−80	3	1	1	7.5	Jackman et al.[100]
(*i*-Pr)$_2$NLi	THF	−90	5	2	2	5.1	Galiano-Roth and Collum[102]
X = ^{29}Si and X = ^{31}P							
$(C_6H_5)_3SiLi$	THF	−100	3	1	1	15	Edlund et al.[103]
$(C_6H_5)_2PLi$	Et_2O	−73	7	2	2	45[e]	Colquhoun et al.[104]
(C_6H_5)(*i*-Pr)PLi	$N(Et)_3$	−83	10	3	4	33[e]	Zschunke and Riemer[105]
$((CH_3Si)_2CH)_2PLi$	Et_2O	25	7	2	2	80[e]	Hitchcock et al.[106]
	Et_2O/TMEDA	25	4	1	1	122[e]	Hitchcock et al.[106]

[a]THF, tetrahydrofuran; TMEDA, tetramethylethylenediamine; PMDTA, pentamethyldiethylenetriamine.
[b]Number of coupled lithium nuclei.
[c]Aggregation state.
[d]Fluxional aggregate.
[e]Coupling to ^{7}Li.

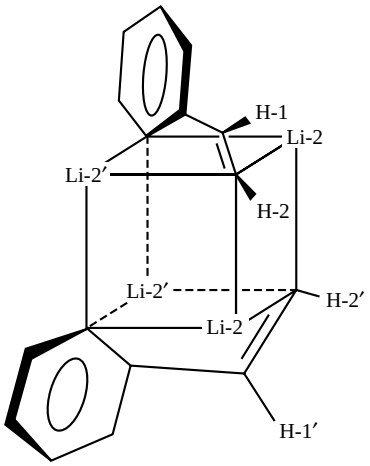

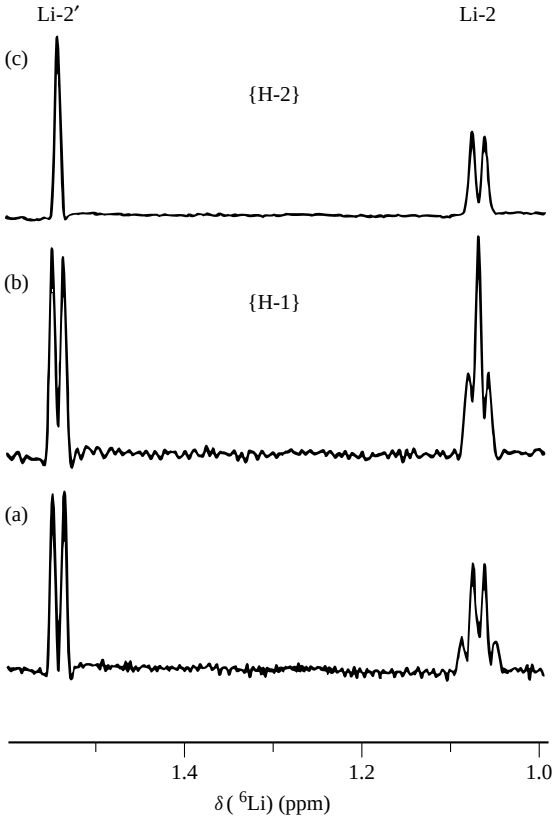

Figure 8 ^{6}Li NMR spectra of the dimer of (*Z*)-2-lithio-1-(*o*-lithiophenyl)ethene (**9**) with selective ^{1}H decoupling; due to the dihedral angles involved, H-1 only couples to Li-2 (c). (Reproduced with permission from H.-E. Mons, H. Günther, and A. Maercker, *Chem. Ber.*, 1993, **126**, 2747)

structural information on lithium enolates in solution. The QSC is given by

$$\mathrm{QSC} = (1 + \eta^2/3)^{1/2}(e^2 Q q_{zz}/h) \qquad (10)$$

where $\eta = (q_{xx} - q_{yy})/q_{zz}$ is the asymmetry parameter, and the q_{ii} are the diagonal elements of the electric field gradient

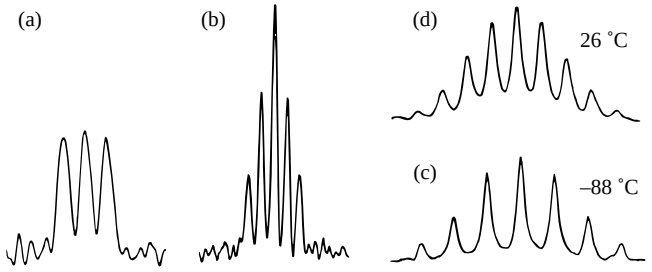

Figure 9 ^{6}Li coupled ^{13}C multiplets for various aggregates of organolithium compounds: (a) phenyllithium monomer; (b) *n*-butyllithium dimer; and (c) static and (d) fluxional *t*-butyllithium tetramer. The coupling constants are 14.8, 7.9, 5.4, and 4.1 Hz, respectively. (Reproduced, in part, with permission from R. D. Thomas, M. T. Clarke, R. M. Jensen, and T. C. Young, *Organometallics*, 1986, **5**, 1851)

tensor for the ^{7}Li nucleus. The other constants are from Table 2. The value of q_{zz} would be of most interest, but cannot be obtained separately. The QSC can thus be treated only as an empirical parameter related to the electrical environment of the ^{7}Li nucleus, and its experimental determination is possible via relaxation time measurements. If a dominance of quadrupolar relaxation is assumed for ^{7}Li in molecules in solution, then

$$1/T_1^{\mathrm{Q}} = (2\pi^2/5)(\mathrm{QSC})^2\tau_{\mathrm{c}} \qquad (11)$$

If τ_{c} can be determined from the dipolar longitudinal relaxation of a ^{13}C nucleus in the same molecule, which has its ^{13}C–^{1}H internuclear distance vector collinear or parallel to the assumed direction of q_{zz}, the relationship

$$\mathrm{QSC\,(kHz)} = 70.0[T_1(^{13}\mathrm{C})/T_1(^{7}\mathrm{Li})]^{1/2} \qquad (12)$$

can be used to determine the QSC. A further requirement for the applicability of equation (12) is that the ^{13}C–^{1}H bond does not reorient independently of q_{zz} by a rate comparable to or greater than the rotational diffusion of the whole molecule, for example by internal molecular motion.

2.6 The {^{1}H}^{6}Li Nuclear Overhauser Effect

An important result of the relaxation studies on ^{6}Li executed by Wehrli[7,43] was the finding that an appreciable {^{1}H}^{6}Li NOE exists, being η = 2.61 and 1.19 for ^{6}Li in aqueous LiCl and in *n*-butyllithium in *n*-hexane, respectively. The theoretical value is $\eta = \gamma(^{1}\mathrm{H})/2\gamma(^{6}\mathrm{Li}) = 3.40$ (Table 2). Due to the inefficient quadrupolar relaxation, the ^{6}Li nucleus shows considerable dipolar interactions with neighboring protons, and these can yield valuable structural information (see Section 3.2.1). Similar effects for ^{7}Li are uncommon because of the stronger dominance of quadrupolar relaxation for this nucleus, but appreciable {^{1}H}^{7}Li NOEs have been found for systems such as (**7**).[41] Finally, for ^{13}C enriched systems, NOEs between ^{13}C and ^{6}Li have been observed[119] which are of interest for polyhapto bound lithium where scalar coupling to ^{13}C is absent.

3 EXPERIMENTAL METHODS

The introduction of new one- and two-dimensional experimental techniques and the existence of scalar coupling to ^{6,7}Li as well as the $\{^1H\}^6$Li NOE have paved the way for new methods of structural elucidation and the study of bonding and dynamics, mainly in the field of organolithium compounds and related systems such as lithiated amides and phosphorus compounds. For ^{6}Li, appropriate product operator treatments for various pulse sequences are available which are based on density operators for spin-1 nuclei.[120,121] With respect to the applicability of the techniques, the natural abundance of the nuclei involved has to be considered in order to decide on the experimental strategy to be used. Experiments which involve rare nuclei such as ^{13}C or ^{15}N are, therefore, not always feasible for compounds which contain these nuclides in natural abundance, and require appropriate labeling.

3.1 Methods Based on Coherent Magnetization Transfer by Scalar Spin–Spin Coupling

3.1.1 Experiments Based on Homonuclear Spin–Spin Coupling

3.1.1.1 ^{6}Li–^{6}Li and ^{7}Li–^{7}Li COSY Experiments. An attractive feature of the two-dimensional Jeener experiment[122] is its sensitivity for small scalar interactions which give rise to cross peaks even if line splittings in the corresponding one-dimensional spectra are not resolved. This was first demonstrated for the ^{1}H NMR spectrum of a paramagnetic nickel complex[123] and for quadrupolar nuclei in the case of ^{11}B.[124] The first successful ^{6}Li–^{6}Li COSY-90 experiment was reported in 1986.[81] It yielded direct evidence for the existence of homonuclear ^{6}Li–^{6}Li couplings. Since the magnitude of these interactions is small (see above), improvements are possible if, instead of the COSY-90, the COSY-LR sequence[125] developed for the detection of long range couplings is used. In addition, a 45° pulse[125] serves as a mixing pulse in order to reduce the intensity of the diagonal signals:

$$90^\circ - t_1 -,\ \Delta,\ 45^\circ,\ \Delta,\ \mathrm{FID}(t_2) \qquad (13)$$

The importance of this experiment for structural research must be seen in the possibility of distinguishing ^{6}Li signals which belong to nonequivalent lithium sites in one particular cluster from those ^{6}Li signals which arise from lithium atoms in different clusters (Figure 10).

A similar experiment for ^{7}Li yields less unambigous results, because for small chemical shifts signal overlap may lead to the detection of artificial cross peaks.[126] This was later shown by the application of a ^{7}Li–^{7}Li COSY-DQF experiment, where the double quantum filter (DQF) eliminates the artifacts.[127] Recently, a genuine ^{7}Li–^{7}Li COSY experiment was successfully performed for the nonequivalent ^{7}Li nuclei in the dimer of (*Z*)-2-lithio-1-(*o*-lithiophenyl)ethene (**9**),[84] where the chemical shift between the nonequivalent lithium sites is sufficiently large to avoid line overlap.

Experimentally, modern software allows ^{6,7}Li–^{6,7}Li COSY spectra to be recorded in the phase-sensitive mode. Nevertheless, the fine structure in the cross peaks and diagonal peaks, which was calculated by the product operator formalism,[120] has been resolved only once[84] because of the small magnitude of the homonuclear coupling constants involved.

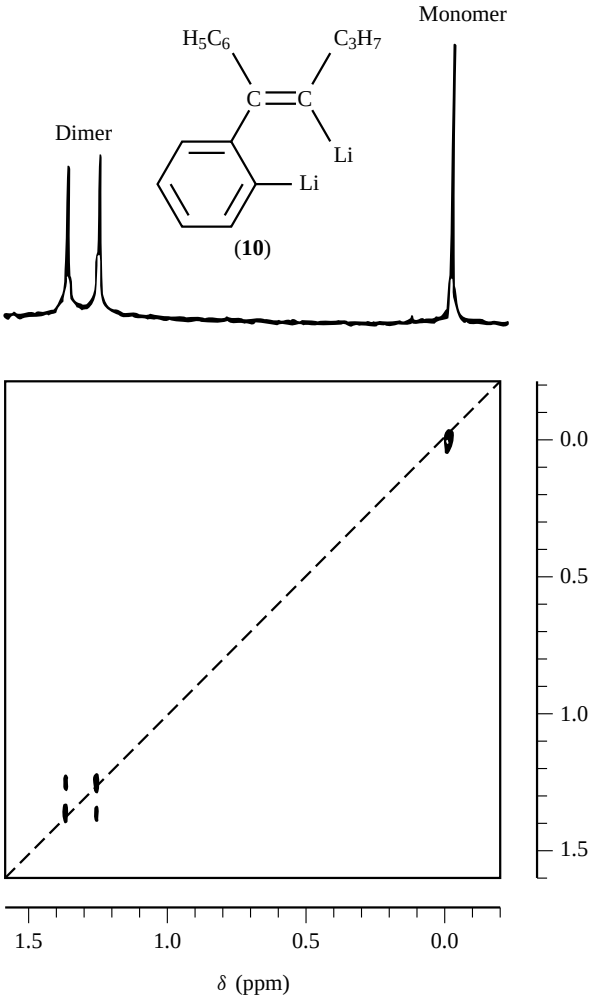

Figure 10 ^{6}Li–^{6}Li COSY spectrum for the mixture of monomer and dimer of (*E*)-2-lithio-1-phenyl-1-(*o*-lithiophenyl)pent-1-ene (**10**) recorded with the pulse sequence of equation (13)

3.1.1.2 ^{6}Li–^{6}Li and ^{7}Li–^{7}Li INADEQUATE Experiments. The direct detection of a homonuclear ^{6}Li–^{6}Li coupling in the case of (*E*)-2-lithio-1-phenyl-1-(*o*-lithiophenyl)pent-1-ene[82] [(**10**), see Figure 10] initiated the experimental realization of one- as well as two-dimensional ^{6}Li–^{6}Li INADEQUATE experiments.[83] Both experiments were performed with the standard pulse sequences available[129,130] and yielded an unequivocal assignment of the respective ^{6}Li–^{6}Li spin systems, which are of the AA′XX′ type in the compounds studied. The antiphase character of the detected magnetization proves to be advantageous for the observation of the small ^{6}Li–^{6}Li interactions, where single quantum magnetization does not interfere because of isotopic ^{6}Li enrichment. In addition, the chemical shift difference is a less critical parameter than in the COSY experiment. Due to the relatively short experimental time necessary, the one-dimensional INADEQUATE experiment is by far the most attractive choice for the detection of coupled, nonequivalent lithium nuclei in organolithium aggregates. An example is shown in Figure 11. In an analogous way,

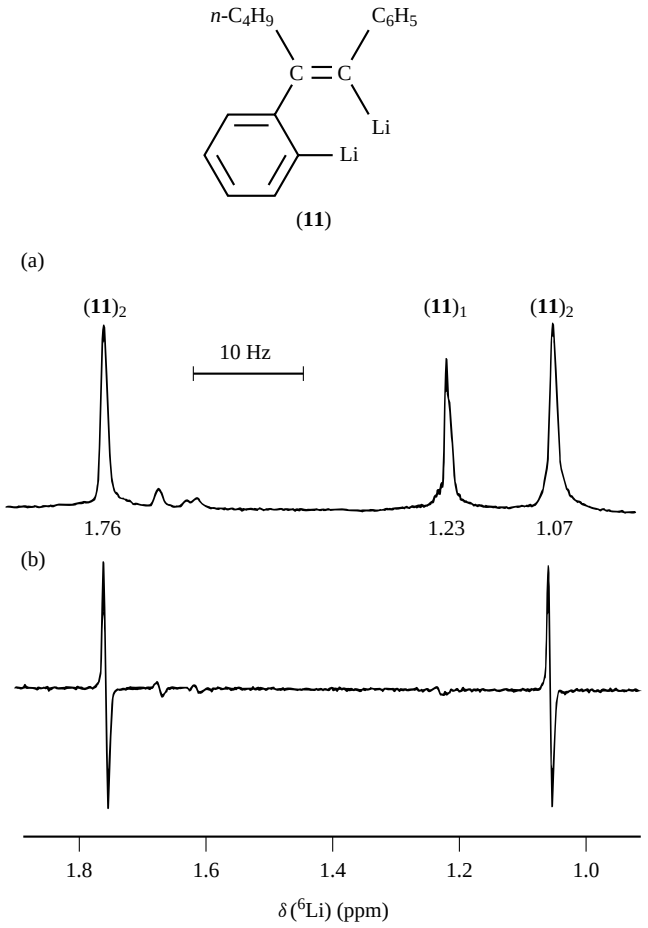

Figure 11 One-dimensional $^{6}Li-^{6}Li$ INADEQUATE spectrum of a mixture of the dimer and monomer of (*E*)-1-lithio-2-(2-lithiophenyl)-1-phenylhex-1-ene (**11**) which identifies the signals that belong to the $^{6}Li-^{6}Li$ AA′XX′ system of the dimer. (Reproduced with permission from O. Eppers, T. Fox, and H. Günther, *Helv. Chim. Acta*, 1992, **75**, 883)

successful one- and two-dimensional $^{7}Li-^{7}Li$ INADEQUATE experiments have been performed with compound (**9**).[84]

An interesting feature of two-dimensional INADEQUATE experiments with spin-1 nuclei is the observation of signals which arise from one-spin double quantum coherences in addition to those which originate from two-spin double quantum coherences.[131,132] Such signals have the coordinates $\omega_1 = 2\omega_i$, $\omega_2 = \omega_i$ and do not yield correlation information. They have been observed in $^{2}H-^{2}H$[131,132] as well as $^{6}Li-^{6}Li$ two-dimensional INADEQUATE experiments.[133]

3.1.2 *Experiments Based on Heteronuclear Spin–Spin Coupling*

3.1.2.1 One-Dimensional Spin Echo Experiments. The gated decoupler technique has been used in the manner similar to the well-documented experiments for ^{2}H-substituted carbon atoms[134] in order to edit signals of $^{13}C-^{6}Li$ spin systems with different multiplicity for the ^{13}C signals.[135] Phase selection for ^{13}C signals is then achieved with gated ^{6}Li decoupling, where the intensity of the detected ^{13}C signal from $^{13}C-^{6}Li_n$ systems for an evolution period of $\tau = 1/2J(^{13}C,^{6}Li)$ is governed by the equation

$$I = I_0(-1/3)^n \tag{14}$$

Practical applications are limited by the fact that for $n = 3$ the ^{13}C signal intensity is already rather weak and the signal virtually disappears for $n > 3$. The low natural ^{13}C abundance further complicates the situation. An interesting variation of the experiment, however, which works well for alkyllithium systems with relatively long ^{13}C relaxation times T_1 and T_2 is the observation of the totally refocused ^{13}C magnetization after the evolution delay $\tau = 1/J_{obs}$ with, according to equation (8), $\tau = k/17$ for monomers ($k = 1$), dimers ($k = 2$), and tetramers ($k = 3$).[136] As shown in Figure 12, this allows the selection of ^{6}Li signals of individual aggregates.

3.1.2.2 Two-Dimensional J-Resolved $^{13}C-^{6}Li$ and $^{31}P-^{7}Li$ Spectroscopy. Introducing a variable evolution time τ, a series of experiments with gated ^{6}Li decoupling leads to *J*-resolved ^{13}C spectra where the $^{13}C-^{6}Li$ multiplets appear parallel to the F_1 axis.[23] A similar experiment has been applied to $^{31}P-^{7}Li$ spin systems to separate the $^{31}P-^{7}Li$ coupling constants from the homonuclear $^{31}P-^{31}P$ interactions in lithiated organophosphorus compounds.[104]

3.1.2.3 Two-Dimensional Shift Correlations. Two-dimensional shift correlations certainly belong to the most important experimental techniques available for structure

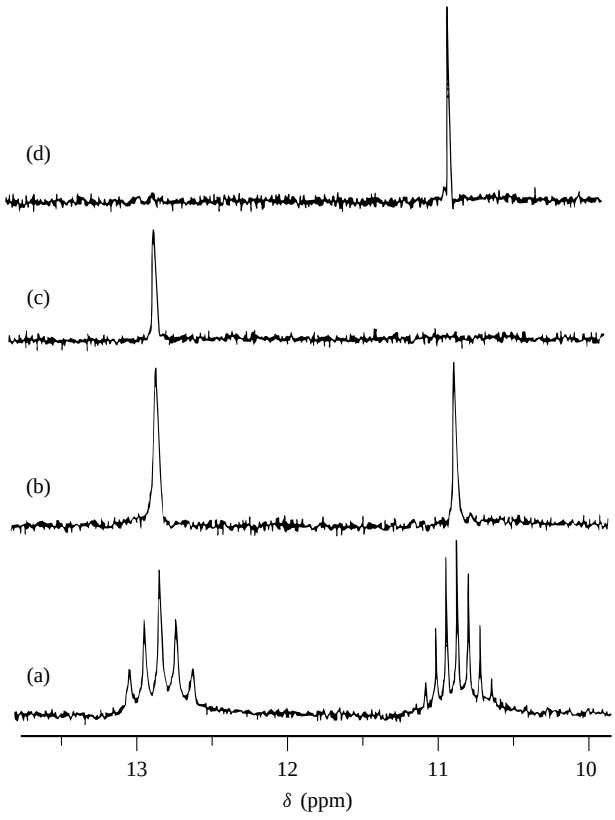

Figure 12 $J(^{13}C,^{6}Li)$-modulated ^{13}C spin echo spectra of ^{13}C-1 signals for oligomers of [^{6}Li]*t*-butyllithium (cyclopentane/ether, −60°): (a) multiplets for dimer and tetramer (see Table 5); (b) ^{6}Li decoupled spectrum; (c) selection of the dimer signal with $\tau = 128$ ms ($J = 7.8$ Hz); (d) selection of the tetramer signal with $\tau = 184$ ms ($J = 5.4$ Hz). (Reproduced with permission from R. D. Thomas and D. H. Ellington, *Magn. Reson. Chem.*, 1989, **27**, 628)

elucidation. This is also true for organometallic compounds and related systems, where quite a number of ^{6,7}Li–X correlation experiments have been performed. As is well known from ^{13}C–^{1}H experiments, there are two alternative methods for two-dimensional shift correlations: the standard heteronuclear correlation experiment based on polarization transfer[137] (HETCOR),

$$I \quad 90^\circ_x\text{------}t_1\text{------}|\text{------}\Delta_1\text{------}90^\circ_y, \text{BB} \qquad (15a)$$

$$S \quad \text{--------}180^\circ_x\text{----}|\text{----------}90^\circ_x, \text{FID}(t_2) \qquad (15b)$$

and the heteronuclear multiple quantum experiment[138] (HMQC)

$$I \quad 90^\circ_x\text{------}\Delta_1\text{------}|\text{------}180^\circ_x\text{------}\text{FID}(t_2) \qquad (16a)$$

$$S \quad \text{----------}90^\circ_x\text{------}t_1\text{-------}90^\circ_\phi \qquad (16b)$$

where $\Delta_1 = 1/2J$. For spin-1 nuclei, appropriate product operator treatments of these experiments have been given.[17,128,139,140] Both sequences can be performed with ^{6,7}Li as the I or S spin. This choice is determined by the relative magnitude of the γ factors as well as by the isotopic abundance of the two spins.

While the power of these two-dimensional experiments is unquestioned, it should be pointed out that in a number of cases single frequency X decoupling with ^{6,7}Li observation or the corresponding inverse experiments (X observation with selective ^{6,7}Li decoupling) may give the desired information equally well in a relatively straightforward way, especially if only a few, well-resolved ^{6,7}Li resonances exist.

Since ^{6}Li–^{1}H spin–spin coupling constants are seldom resolved and their existence is often only apparent from line-broadening effects, ^{6}Li–^{1}H shift correlation experiments have been performed only recently on compounds which show relatively large (of the order of 0.5 Hz) ^{6}Li–^{1}H coupling constants. Using the simple pulse sequence[137b]

$$90^\circ(I) - t_1 - \phi(I),\ 90^\circ(S),\ \text{FID}(S)(t_2) \qquad (17)$$

with ^{6}Li detection, which yields fully coupled two-dimensional ^{6}Li–^{1}H shift correlations, Bauer and Griesinger[79] were able to determine the magnitude and sign of all ^{6}Li–^{1}H coupling constants in the dimer and tetramer of vinyllithium by applying pulses with angles $\theta < 90^\circ$. For compound (**9**), ^{6}Li–^{1}H, shift correlation experiments were successful with the standard polarization transfer experiment [HETCOR, equations (15a) and (15b)] as well as with the inverse techniques based on multiple quantum coherences [HMQC, equations (16a) and (16b)].[89] The latter experiment also yielded splittings in the F_2 dimension which are due to homonuclear ^{6}Li–^{6}Li couplings.

^{13}C–^{6}Li shift correlation experiments are of vital importance for the assignment of ^{13}C and ^{6}Li resonances in organolithium clusters. They are based exclusively on one-bond ^{13}C–^{6}Li couplings (see above) and can be performed in their simplest version as selective ^{13}C–^{6}Li decoupling experiments. One way is to employ selective ^{6}Li decoupling to locate the corresponding ^{13}C neighbor. The alternative experiment, selective ^{13}C decoupling, is generally only feasible for ^{13}C-enriched materials, because otherwise the ^{13}C satellites in the ^{6}Li spectrum have to be observed.

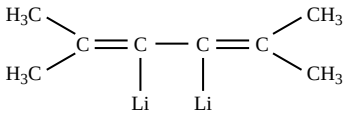

(**12**)

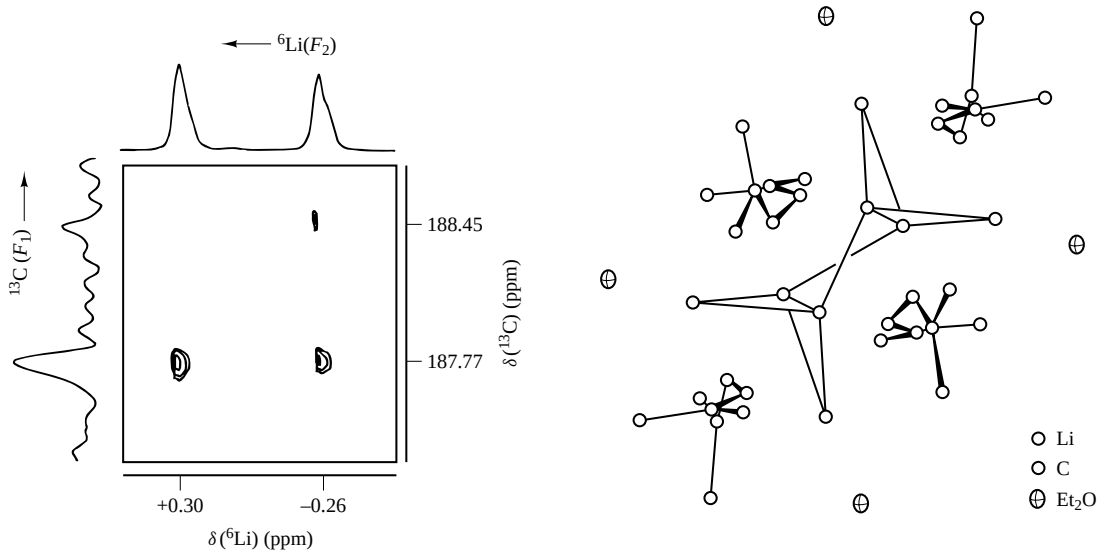

Figure 13 Two-dimensional ^{13}C–^{6}Li HMQC NMR shift correlation for 3,4-dilithio-2,5-dimethylhexa-2,4-diene (**12**) and X-ray structure. The cross peaks show that the carbon atoms of the 'inner' ligands couple exclusively to the 'inner' ^{6}Li sites, while the carbon atoms of the 'outer' ligands couple to both the 'inner' and the 'outer' ^{6}Li nuclei. (Reproduced with permission from D. Moskau, F. Brauers, H. Günther, and A. Maercker, *J. Am. Chem. Soc.*, 1987, **109**, 5532)

For the more elegant two-dimensional $^{13}C-^{6}Li$ shift correlations, which are indispensable in cases of low signal resolution, both pulse sequences shown above [equations (15a) and (15b) and equations (16a) and (16b)] were successfully employed with compounds that contained ^{13}C in natural abundance.[24,141] Since the γ factors for ^{6}Li and ^{13}C are not very different, the choice of the nucleus to be detected is not very critical. If ^{6}Li is decoupled, however, as in the HETCOR sequence with $I = {}^{6}Li$ and $S = {}^{13}C$, a relaxation delay is necessary for the recovery of I spin magnetization due to the longer ^{6}Li relaxation times. The HMQC experiment is especially easy to perform with a triple resonance probehead which has, apart from the ^{1}H and the ^{2}H lock channel, a fixed frequency for ^{13}C detection and a variable X frequency. An example of the experiment is shown in Figure 13. It is of interest to note that $^{13}C-^{6}Li$ cross peaks can also be observed in cases where the corresponding $^{13}C-^{6}Li$ coupling is not resolved in the one-dimensional spectrum.[24] A similar situation was met for homonuclear $^{6,7}Li-^{6,7}Li$ couplings with the COSY experiment (see above).

The $^{15}N-^{6}Li$ HMQC experiment was introduced by Collum for ^{6}Li and ^{15}N labeled samples of lithiated amines.[140] An example, which highlights the power of the two-dimensional method with respect to single frequency one-dimensional decoupling experiments is given in Figure 14.

An ingenious application of the HMQC experiment for $^{15}N-^{6}Li$ doubly labeled organonitrogen compounds in the form proposed by Müller[138a] and Bodenhausen and Ruben[142] has been introduced by Gilchrist and Collum,[143] who showed that the method allows—on the basis of homonuclear ^{15}N zero-quantum coherence selection—discrimination between symmetric cyclic dimers and higher oligomers of lithiated

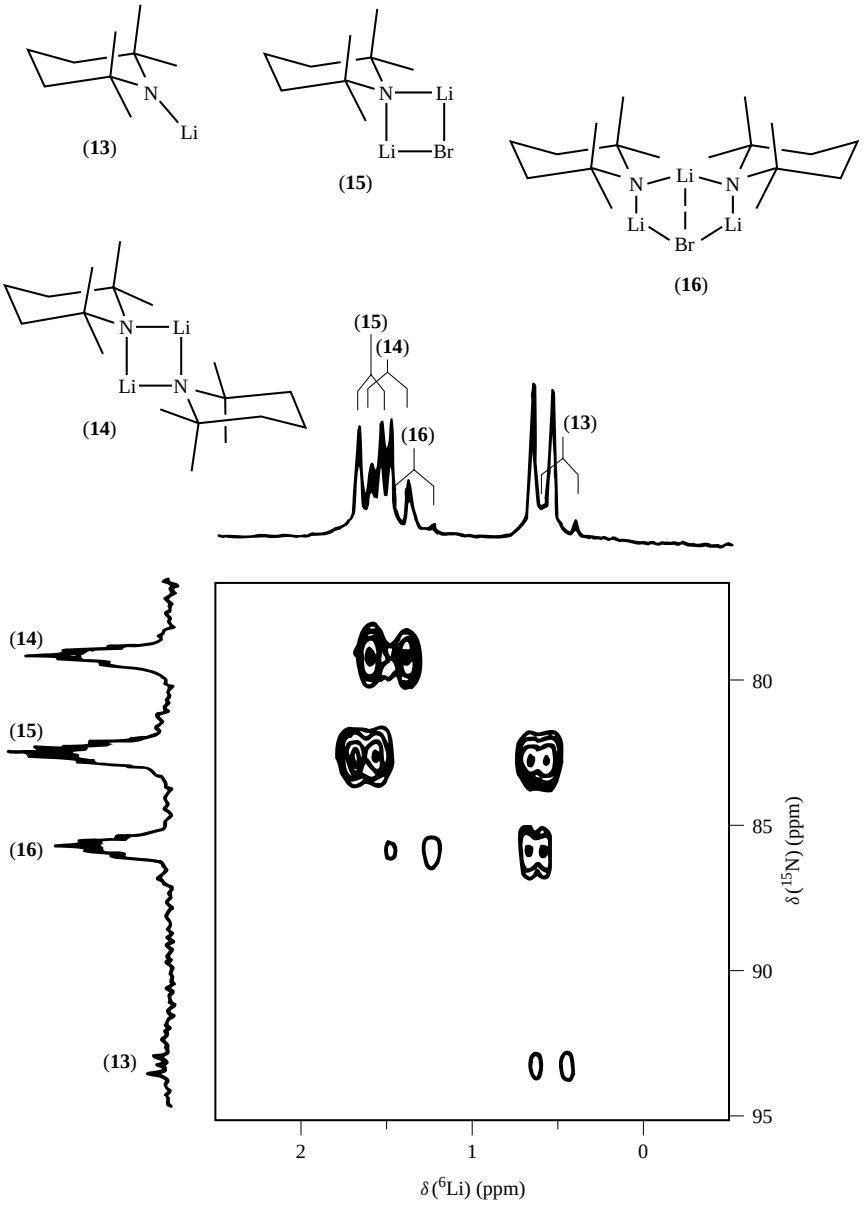

Figure 14 $^{15}N-^{6}Li$ HMQC spectrum of a sample of [^{6}Li,^{15}N]lithium tretramethylpiperidine (0.1 M in 3:1 THF/pentane, −120°) with one equivalent of added $^{6}LiBr$ showing cross peaks for the monomer (**13**), the dimer (**14**), and the mixed aggregates (**15**) and (**16**). (Reproduced with permission from J. H. Gilchrist, A. T. Harrison, D. J. Fuller, and D. B. Collum, *Magn. Reson. Chem.*, 1992, **30**, 855)

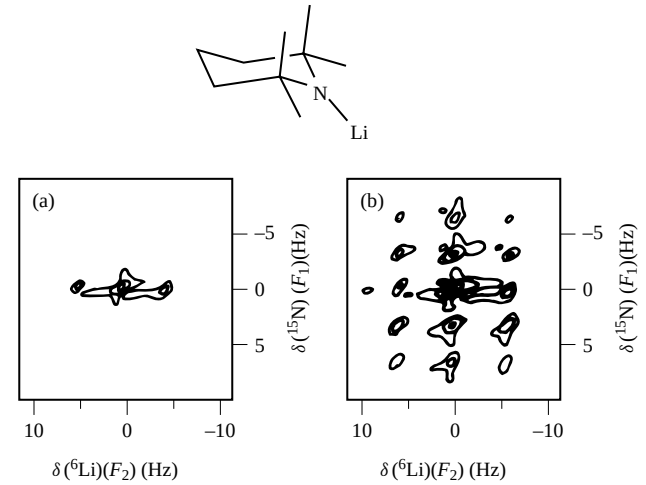

Figure 15 ^{6}Li-detected ^{15}N zero quantum NMR spectra of: (a) [^{6}Li,^{15}N]lithium tetramethylpiperidine (0.1 M in 3:1 THF/pentane, −115°); (b) the same compound dissolved in benzene (0.25 M, 30°). In (b), the 1:2:3:2:1 splitting pattern along F_1 is consistent with a higher oligomer of type (**18**) rather than the dimer. (Reproduced with permission from J. H. Gilchrist and D. B. Collum, *J. Am. Chem. Soc.*, 1992, **114**, 795)

amines.[143] This results from the fact that in the dimer (**17**), which gives rise to an A_2X_2 spin system, both ^{6}Li spins are coupled to both ^{15}N spins and the sum of the effective ^{15}N–^{6}Li coupling is zero,[120] while in a cyclic trimer or a higher cyclic oligomer (**18**) not all ^{6}Li spins couple to a certain ^{15}N spin, the spin system being of the AA′A″XX′ type with J(A′,X′) = J(A″,X) = 0. The nonequivalence of the neighboring ^{6}Li nuclei then leads to a 1:2:3:2:1 line splitting in the F_1 dimension (Figure 15).

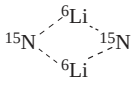

(17)

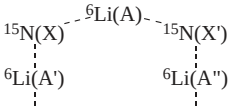

(18)

The utility of the HMQC experiment for structure determinations in organometallic compounds has been extended by the introduction of the ^{31}P–^{6}Li shift correlation experiment,[144] which is based on scalar coupling between lithium and the phosphorus in HMPTA. Here, detection of the sensitive ^{31}P nucleus, having short relaxation times, is of advantage.

The development of rotating frame experiments for the liquid phase[145] has produced a number of interesting homo- and heteronuclear pulse sequences with great potential for practical applications which are generally known as homo- and heteronuclear TOCSY experiments. Among these, TOCSY (total correlation spectroscopy)[145] has found widespread use. Homonuclear one- and two-dimensional TOCSY experiments with spin-1 nuclei have been performed for deuterium[146,147] and the heteronuclear ^{6,7}Li–X TOCSY experiment

$$I \quad 90^\circ\text{--------}\, t_1 \,\text{--------}, \text{MLEV16} \qquad (18a)$$

$$S\text{----------}180^\circ\text{-------}, \text{MLEV16, FID}(t_2) \qquad (18b)$$

has been tested for ^{7}Li–^{1}H as well as ^{6}Li–^{1}H shift correlations.[84,148] The MLEV16 decoupling sequence[149] was used for magnetization transfer and ^{6,7}Li as well as ^{1}H detection was successful. A ^{6}Li–^{1}H TOCSY experiment for phenyllithium, where magnetization transfer is detected up to the *meta* protons, is shown in Figure 16. An advantage of these experiments as compared with correlation experiments based on the sequences shown in equations (15a) and (15b) and equations (16a) and (16b) must be seen in the fact that pure absorption spectra are produced. Signal elimination as a consequence of small coupling constants, as observed for antiphase cross peaks, is thus prevented.

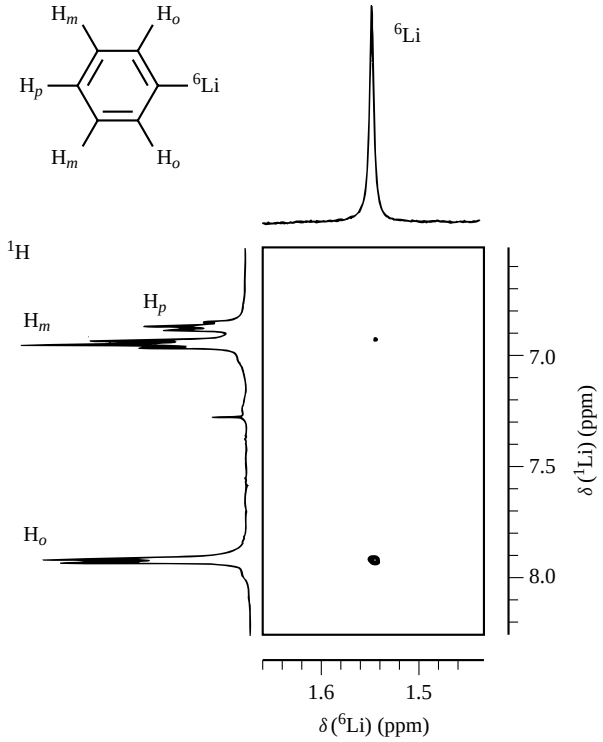

Figure 16 ^{6}Li–^{1}H HETERO TOCSY experiment for the phenyllithium dimer (0.3 M in THF, −70°), showing cross peaks for the *ortho* and *meta* protons

3.2 Methods Based on Incoherent Magnetization Transfer

3.2.1 {^{1}H}^{6}Li Nuclear Overhauser Spectroscopy

The great potential of the {^{1}H}^{6}Li NOE, discovered by Wehrli,[7,43] for structural research was recognized in 1986 independently by two groups. Avent et al.[150] reported one-dimensional NOE difference experiments for hydrido[tris(trimethylsilyl)methyl]metalates, while Bauer et al.[151] introduced the {^{1}H}^{6}Li HOESY (heteronuclear Overhauser) experiment. The pulse sequence for these types of experiment,

$$I \quad 90^\circ\text{------}t_1\text{------}90^\circ\text{------}t_M\text{------}|\text{---BB---} \qquad (19a)$$

$$S \quad \text{--------}180^\circ\text{-----}|\text{----------}90^\circ, \text{FID}(t_2) \qquad (19b)$$

was proposed in 1983 independently by Rinaldi[152] and Yu and Levy[153] for ^{13}C–^{1}H and ^{31}P–^{1}H spin pairs, but had not found widespread use. In particular, in the ensuing years Bauer et al. developed ^{1}Li–^{1}H HOESY measurement into a valuable

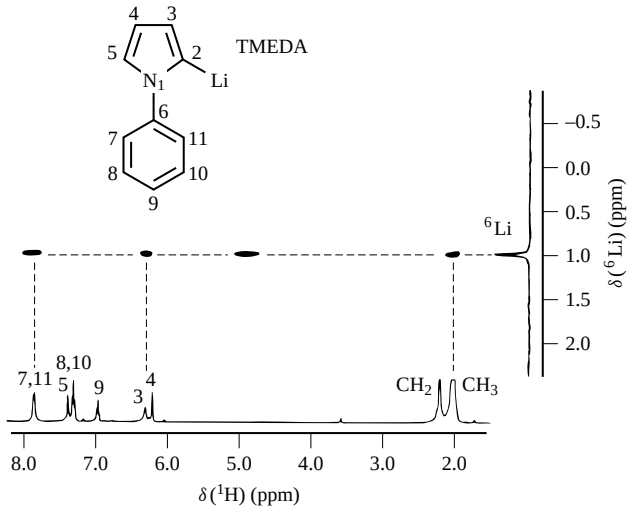

Figure 17 Two-dimensional $\{^1H\}^6Li$ HOESY spectrum of 2-lithio-1-phenylpyrrole/TMEDA (THF, −70°). Short $^6Li–^1H$ distances are indicated by cross peaks for H-3, H-7, H-11, and the CH_3 protons of the TMEDA ligand. (Reproduced with permission from W. Bauer, G. Müller, R. Pi, and P. v. R. Schleyer, *Angew. Chem.*, 1986, **98**, 1130)

tool for the detection of small $^6Li–^1H$ distances.[26,28,154,155] The advantage of the two-dimensional experiment is obvious if several $^6Li–^1H$ contacts exist (Figure 17), while the higher sensitivity and resolution attainable in one-dimensional NOE difference experiments often is of practical importance.[156]

$\{^1H\}^6Li$ NOE effects are also observed for the protons of TMEDA ligands (Figure 17) and those of solvent molecules, and can thus give interesting information about solvation phenomena. In addition, $\{^1H\}^6Li$ HOESY spectroscopy is a valuable tool for the study of ion pairs.[157] Even $\{^1H\}^7Li$ HOESY experiments are feasible in special cases where molecular symmetry around the ^7Li nucleus reduces its quadrupolar relaxation rate.[42] Qualitative and quantitative information on $^{6,7}Li–^1H$ distances have been obtained from cross-peak buildup rates,[42,150,158] where the scaling was derived from a bond length determined by X-ray diffraction of the solid. It is noteworthy that $\{^1H\}^6Li$ HOESY spectra can be successfully recorded for compounds with natural ^6Li abundance. Finally, a $^{13}C–^6Li$ HOESY experiment has been performed for benzyllithium compounds,[119] but it requires ^{13}C labeling and can thus be applied only in selected cases.

3.2.2 *Dynamic $^{6,7}Li$ NMR Spectroscopy and $^{6,7}Li–^{6,7}Li$ Two-Dimensional Exchange (EXSY) Spectroscopy*

The dynamic nature of most organolithium compounds in solution forms the basis for broad applications of dynamic NMR (DNMR) in this field. Lineshape changes are observed for all relevant nuclei (^1H, $^{6,7}Li$, ^{13}C, and ^{31}P) and can potentially be used for qualitative and quantitative analysis of the dynamic processes involved.[32,77,78,159,160] $^{6,7}Li$ spectra are favorable because line splittings due to scalar coupling are absent and the number of signals is usually low. The standard techniques available for DNMR investigations[161] are today supplemented by two-dimensional methods, where the two-dimensional EXSY experiment[162,163]

$$90^\circ - t_1 - 90^\circ - t_M - 90^\circ,\ \mathrm{FID}(t_2) \qquad (20)$$

can be applied to systems which are in slow exchange. $^{6,7}Li$ EXSY spectra[23,57,85] yield important information about the dynamic process responsible for the lineshape changes and the exchange mechanisms involved (Figure 18). Using the appropriate equations,[162–164] rate constants can be obtained from the relative intensities of the cross peaks and diagonal peaks.

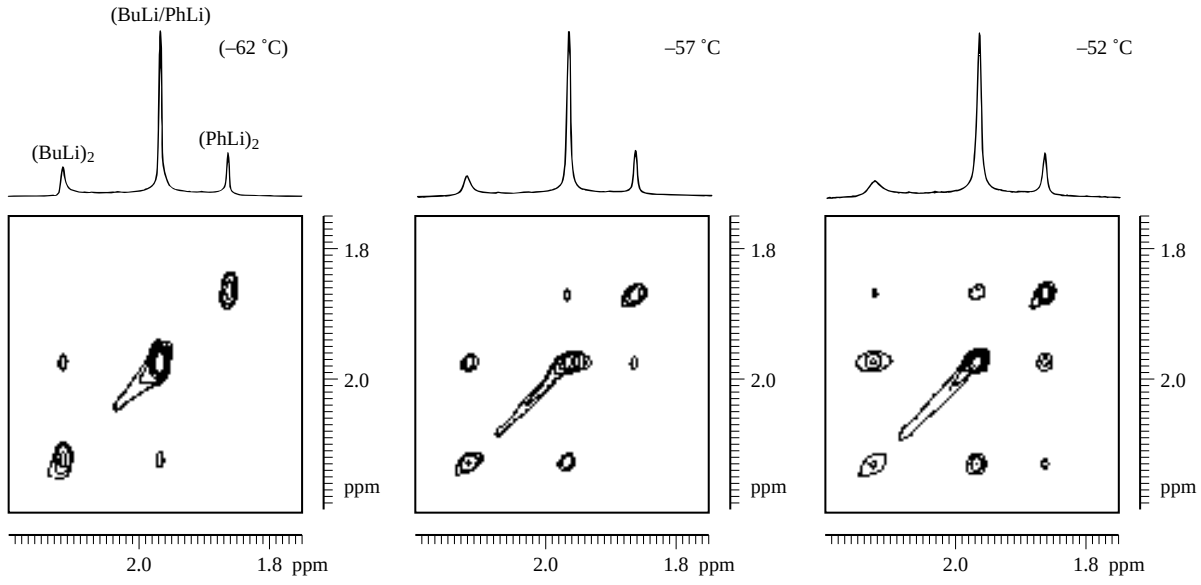

Figure 18 Two-dimensional EXSY ^6Li NMR spectra of a mixture of *n*-butyl- and phenyllithium (BuLi and PhLi) in the presence of TMEDA, which documents ^6Li exchange between dimers of BuLi and PhLi and the mixed aggregate BuLi/PhLi, and additional ^6Li exchange between $(BuLi)_2$ and $(PhLi)_2$[165]

4 RELATED ARTICLES

Chemical Exchange Effects on Spectra; COSY Two-Dimensional Experiments; Heteronuclear Shift Correlation Spectroscopy; INADEQUATE Experiment; Inorganic Chemistry Applications; Isotope Effects on Chemical Shifts and Coupling Constants; Nuclear Overhauser Effect; Organometallic Compounds; Quadrupolar Nuclei in Liquid Samples; Relaxation Theory for Quadrupolar Nuclei; Shielding Calculations: IGLO Method; Sodium-23 NMR; Two-Dimensional Carbon–Heteroelement Correlation; Two-Dimensional Methods of Monitoring Exchange.

5 REFERENCES

1. J. J. Dechter, *Prog. Inorg. Chem.*, 1982, **29**, 285.
2. R. Benn and A. Rufinska, *Angew. Chem.*, 1986, **98**, 851; *Angew. Chem., Int. Ed. Engl.*, 1986, **25**, 861.
3. C. J. Gorter and L. J. F. Broer, *Physica*, 1942, **9**, 591.
4. A. Bolle, G. Puppi, and G. Zantonelli, *Nuov. Cim.*, 1946, **3**, 412.
5. N. A. Schuster and G. E. Pake, *Phys. Rev.*, 1951, **81**, 157.
6. T. L. Brown, D. W. Dickerhoof, and D. A. Bafur, *J. Am. Chem. Soc.*, 1962, **84**, 1371.
7. F. W. Wehrli, *J. Magn. Reson.*, 1976, **23**, 527.
8. H. J. Jänsch, M. Detje, H. D. Ebinger, W. Preyss, H. Reich, R. Veith, W. Widdra, D. Fick, M. Rockelein, and H.-G. Völk, *Nucl. Phys. A*, 1994, **568**, 544.
9. E. Arnold, J. Bonn, W. Neu, R. Neugart, E. W. Otten, and the ISOLDE Collaboration, *Z. Phys. A, Atom. Nucl.*, 1988, **331**, 295.
10. P. Laszlo, in *The Multinuclear Approach to NMR Spectroscopy*, ed. J. B. Lambert and F. G. Riddell, Reidel, Dordrecht, 1983, Chap. 12
11. J. Mason (ed.), *Multinuclear NMR*, Plenum, New York 1987, p. 623 ff.
12. R. K. Harris, in *NMR and the Periodic Table*, ed. R. K. Harris and B. E. Mann, Academic, London, 1978, Chap. 1
13. A. Abragam, *The Principles of Nuclear Magnetism*, University Press, Oxford, 1961, p. 314.
14. J. E. Espidel, R. K. Harris, and K. Wade, *Magn. Reson. Chem.*, 1994, **32**, 166.
15. R. Wesener and H. Günther, *J. Magn. Reson.*, 1985, **62**, 158.
16. O. G. A. Morris and R. Freeman, *J. Magn. Reson.*, 1978, **29**, 433.
17. D. Moskau and H. Günther, unpublished.
18. B. Lindmann and S. Forsén, in *NMR and the Periodic Table*, ed. R. K. Harris and B. E. Mann, Academic, London, 1978, Chap. 6
19. F. Wehrli, *Ann. Rep. NMR Spectrosc.*, 1979, **9**, 126.
20. C. Detellier, in *NMR of Newly Accessible Nuclei*, ed. P. Laszlo, Academic, New York 1983, Vol. 2, Chap. 5
21. J. W. Akitt, in *Multinuclear NMR*, ed. J. Mason, Plenum, New York, 1987, Chap. 7
22. M. Holz, *Prog. NMR Spectrosc.*, 1986, **18**, 327.
23. H. Günther, D. Moskau, P. Bast, and D. Schmalz, *Angew. Chem.*, 1987, **99**, 1242; *Angew. Chem., Int. Ed. Engl.*, 1987, **26**, 1212.
24. R. D. Thomas, in *Isotopes in the Physical and Biomedical Sciences*, ed. E. Buncel and J. R. Jones, Elsevier, Amsterdam, 1991, Chap. 7
25. L. M. Jackman and J. Bortiatynski, in *Advances in Carbanion Chemistry*, ed. V. Snieckus, Jai, Greenwich, CT, 1992, p. 45.
26. W. Bauer and P. v. R. Schleyer, in *Advances in Carbanion Chemistry*, ed. V. Snieckus, Jai, Greenwich, CT, 1992, p. 89.
27. D. B. Collum, *Acc. Chem. Res.*, 1993, **26**, 227.
28. (a) W. Bauer, Habilitationsschrift, University of Erlangen, Germany, 1994; (b) W. Bauer, in *Lithium Chemistry—A theoretical and Experimental Overview*, eds. A.-M. Sapse and P. V. R. Schleyer, Wiley, Chichester, 1995, p. 125.
29. T. L. Brown, *Acc. Chem. Res.*, 1968, **1**, 23.
30. T. L. Brown, *Pure Appl. Chem.*, 1970, **23**, 447.
31. L. D. McKeever, in *Ions and Ion Pairs in Organic Reactions*, ed. M. Szwarc, Interscience, New York, 1972.
32. G. Fraenkel, H. Hsu, and B. M. Su, in *Lithium, Current Applications in Science, Medicine, and Technology*, ed. R. O. Bach, Wiley, New York, 1985, Chap. 19
33. H. G. Hertz, R. Tutsch, and H. Versmold, *Ber. Bunsenges. Phys. Chem.*, 1971, **75**, 1177.
34. M. Holz, D. Seiferling, and Xi-an Mao, *J. Magn. Reson. Ser. A*, 1993, **105**, 90; M. Holz, *Chem. Soc. Rev.*, 1994, 165.
35. K. A. Valiev and M. M. Zaripov, *J. Struct. Chem.*, 1966, **7**, 47; *Z. Strukt. Chim.*, 1966, **7**, 494.
36. H. G. Hertz, *Ber. Bunsenges. Phys. Chem.*, 1973, **77**, 531.
37. C. Deverell, *Prog. NMR. Spectrosc.*, 1969, **4**, 235.
38. H. Versmold, *Mol. Phys.*, 1986, **57**, 201.
39. M. Luhmer, D. van Belle, J. Reisse, M. Odelius, J. Kowalewski, and A. Laaksonen, *J. Chem. Phys.*, 1993, **98**, 1566.
40. G. E. Hartwell and A. Allerhand, *J. Am. Chem. Soc.*, 1971, **93**, 4415.
41. L. D. Field, M. G. Gardiner, C. H. L. Kennard, B. A. Messerle, and C. L. Raston, *Organometallics*, 1991, **10**, 3167.
42. L. D. Field, M. G. Gardiner, B. A. Messerle, and C. Raston, *Organometallics*, 1992, **11**, 3566.
43. F. W. Wehrli, *Org. Magn. Reson.*, 1978, **11**, 106.
44. The quadrupole moments given in Table 2 were used to calculate these data.
45. L. M. Jackman and J. C. Trewella, *J. Am. Chem. Soc.*, 1976, **98**, 5712.
46. L. M. Jackman and L. M. Scarmoutzos, *J. Am. Chem. Soc.*, 1984, **106**, 4627.
47. I. Sethson, B. Eliasson, and U. Edlund, *Magn. Reson. Chem.*, 1991, **29**, 1012.
48. L. M. Jackman, E. F. Rakiewicz, and A. J. Benesi, *J. Am. Chem. Soc.*, 1991, **113**, 4101.
49. C. J. Jameson and H. S. Gutowsky, *J. Chem. Phys.*, 1964, **40**, 1714.
50. G. E. Maciel, J. K. Hancock, L. F. Lafferty, P. A. Mueller, and W. K. Musker, *Inorg. Chem.*, 1966, **5**, 554.
51. Y. M. Cahen, P. R. Handy, E. T. Roach, and A. I. Popov, *J. Phys. Chem.*, 1975, **79**, 80.
52. P. A. Scherr, R. J. Hogan, and J. P. Oliver, *J. Am. Chem. Soc.*, 1974, **96**, 6055.
53. R. H. Cox, H. W. Terry, Jr., and L. W. Harrison, *Tetrahedron Lett.*, 1971, 4815; R. H. Cox, H. W. Terry, Jr., and L. W. Harrison, *J. Am. Chem. Soc.*, 1971, **93**, 3297.
54. R. H. Cox and H. W. Terry, Jr., *J. Magn. Reson.*, 1974, **14**, 317.
55. M. M. Exner, R. Waack, and E. C. Steiner, *J. Am. Chem. Soc.*, 1973, **95**, 7009.
56. L. A. Paquette, W. Bauer, M. R. Sivik, M. Bühl, M. Feigel, and P. v. R. Schleyer, *J. Am. Chem. Soc.*, 1990, **112**, 8776.

57. W. Bauer, G. A. O'Doherty, P. v. R. Schleyer, and L. A. Paquette, *J. Am. Chem. Soc.*, 1991, **113**, 7093; W. Bauer, M. R. Sivik, D. Friedrich, P. v. R. Schleyer, and L. A. Paquette, *Organometallics*, 1992, **11**, 4178.
58. J. Arnold, *J. Chem. Soc., Chem. Commun.*, 1990, 976.
59. A. Sekiguchi, K. Ebata, C. Kabuto, and H. Sakurai, *J. Am. Chem. Soc.*, 1991, **113**, 7081.
60. J. A. Ladd and J. Parker, *J. Chem. Soc., Dalton Trans.*, 1972, 930.
61. O. Eppers and H. Günther, *Helv. Chim. Acta*, 1992, **75**, 2553; Th. Fox and H. Günther, unpublished.
62. G. Fraenkel, A. Chow, and W. R. Winchester, *J. Am. Chem. Soc.*, 1990, **112**, 6190.
63. G. Fraenkel, M. Henrichs, J. M. Hewitt, B. M. Su, and M. J. Geckle, *J. Am. Chem. Soc.*, 1980, **102**, 3345.
64. G. Fraenkel, M. Henrichs, J. M. Hewitt, and B. M. Su, *J. Am. Chem. Soc.*, 1984, **106**, 255.
65. O. Eppers and H. Günther, *Helv. Chim. Acta*, 1990, **73**, 2071.
66. G. Fraenkel and M. P. Hallden-Abberton, *J. Am. Chem. Soc.*, 1981, **103**, 5657.
67. U. Edlund, T. Lejon, P. Pyykkö, T. K. Venkatachalam, and E. Buncel, *J. Am. Chem. Soc.*, 1987, **109**, 5982.
68. H. J. Reich, J. P. Borst, R. J. Dykstra, and D. P. Green, *J. Am. Chem. Soc.*, 1993, **115**, 8728.
69. W. Kutzelnigg, U. Fleischer, M. Schindler in *NMR Basic Principles and Progress*, ed. P. Diehl, E. Fluck, H. Günther, R. Kosfeld, and J. Seelig, Springer, Berlin, 1991, Vol. 23.
70. R. Ditchfield, *Chem. Phys.*, 1981, **63**, 185.
71. A. Loewenstein, M. Shporer, P. C. Lauterbur, and J. E. Ramirez, *J. Chem. Soc., Chem. Commun.*, 1968, 214.
72. J. Reuben, *J. Am. Chem. Soc.*, 1983, **105**, 3711.
73. J. C. Christofides and D. B. Davies, *J. Am. Chem. Soc.*, 1983, **105**, 5099.
74. D. Thoennes and E. Weiss, *Chem. Ber.*, 1978, **111**, 3157.
75. K. Bergander, R. X. He, N. Chandrakumar, O. Eppers, and H. Günther, *Tetrahedron*, 1994, **50**, 5861.
76. For reviews see: E. Weiss, *Angew. Chem.*, 1993, **105**, 1565; *Angew. Chem., Int. Ed. Engl.*, 1993, **32**, 1501; W. N. Setzer and P. v. R. Schleyer, *Adv. Organomet. Chem.*, 1985, **24**, 353; K. Gregory, P. v. R. Schleyer, and R. Snaith, *Adv. Inorg. Chem.*, 1991, **37**, 47.
77. R. D. Thomas, M. T. Clarke, R. M. Jensen, and T. C. Young, *Organometallics*, 1986, **5**, 1851.
78. R. D. Thomas, R. M. Jensen, and T. C. Young, *Organometallics*, 1987, **6**, 565.
79. W. Bauer and C. Griesinger, *J. Am. Chem. Soc.*, 1993, **115**, 10871.
80. L. M. Seitz and T. L. Brown, *J. Am. Chem. Soc.*, 1966, **88**, 2174.
81. H. Günther, D. Moskau, R. Dujardin, and A. Maercker, *Tetrahedron Lett.*, 1986, **27**, 2251.
82. O. Eppers, H. Günther, K.-D. Klein, and A. Maercker, *Magn. Reson. Chem.*, 1991, **29**, 1065.
83. O. Eppers, T. Fox, and H. Günther, *Helv. Chim. Acta*, 1992, **75**, 883.
84. H. Günther and H.-E. Mons, unpublished; D. Moskau, W. Frankmölle, O. Eppers, H.-E. Mons, and H. Günther, *Proc. Indian Acad. Sci. (Chem. Sci.)*, 1994, **106**, 1471.
85. W. Bauer, M. Feigel, G. Müller, and P. v. R. Schleyer, *J. Am. Chem. Soc.*, 1988, **110**, 6033.
86. T. M. Gilbert and R. G. Bergmann, *J. Am. Chem. Soc.*, 1985, **107**, 6391.
87. A. Heine and D. Stalke, *Angew. Chem.*, 1992, **104**, 941; *Angew. Chem., Int. Ed. Engl.*, 1992, **31**, 854.
88. T. L. Brown and J. A. Ladd, *J. Organomet. Chem.*, 1964, **2**, 373.
89. H.-E. Mons, H. Günther, and A. Maercker, *Chem. Ber.*, 1993, **126**, 2747.
90. T. L. Brown, L. M. Seitz, and B. Y. Kimura, *J. Am. Chem. Soc.*, 1968, **90**, 3245.
91. L. D. McKeever, R. Waack, M. A. Doran, and E. B. Baker, *J. Am. Chem. Soc.*, 1968, **90**, 3244.
92. G. Fraenkel, A. M. Fraenkel, M. J. Geckle, and F. Schloss *J. Am. Chem. Soc.*, 1979, **101**, 4745.
93. D. Seebach, H. Siegel, J. Gabriel, and R. Hässig, *Helv. Chim. Acta*, 1980, **63**, 2046.
94. D. Seebach, R. Hässig, and J. Gabriel, *Helv. Chim. Acta*, 1983, **66**, 308.
95. T. F. Bates, M. T. Clarke, and R. D. Thomas, *J. Am. Chem. Soc.*, 1988, **110**, 5109.
96. W. Bauer, W. R. Winchester, and P. v. R. Schleyer, *Organometallics*, 1987, **6**, 2371.
97. G. Fraenkel and P. Pramanik, *J. Chem. Soc., Chem. Commun.*, 1983, 1527.
98. R. Hässig and D. Seebach, *Helv. Chim. Acta*, 1983, **66**, 2269.
99. H.-J. Gais, J. Vollhardt, H. Günther, D. Moskau, H. J. Lindner, and S. Braun, *J. Am. Chem. Soc.*, 1988, **110**, 978.
100. L. M. Jackman, L. M. Scarmoutzos, and W. Porter, *J. Am. Chem. Soc.*, 1987, **109**, 6524.
101. J. S. DePue and J. B. Collum, *J. Am. Chem. Soc.*, 1988, **110**, 5518.
102. A. S. Galiano-Roth and D. B. Collum, *J. Am. Chem. Soc.*, 1989, **111**, 6772.
103. U. Edlund, T. Lejon, T. K. Venkatachalam, and E. Buncel, *J. Am. Chem. Soc.*, 1985, **107**, 6408.
104. I. J. Colquhoun, H. C. E. McFarlane, and W. McFarlane, *Phosphorus Sulfur*, 1983, **18**, 61.
105. A. Zschunke and M. Riemer, *Z. Chem.*, 1984, **24**, 380.
106. P. B. Hitchcock, M. F. Lappert, P. P. Power, and S. J. Smith, *J. Chem. Soc., Chem. Commun.*, 1984, 1669.
107. D. M. Anderson, P. B. Hitchcock, M. F. Lappert, W.-P. Leung, and J. A. Zora, *J. Organomet. Chem.*, 1987, **333**, C13.
108. A. Zschunke, *Z. Chem.*, 1989, **29**, 434.
109. D. Barr, W. Clegg, R. E. Mulvey, and R. J. Snaith, *J. Chem. Soc., Chem. Commun.*, 1984, 79.
110. H. J. Reich, D. P. Green, and N. H. Phillips, *J. Am. Chem. Soc.*, 1989, **111**, 3444.
111. R. R. Dykstra and H. J. Reich, unpublished (cited in Paquette et al.[56]).
112. N. Hertkorn and F. H. Köhler, *Z. Naturforsch., Teil B*, 1990, **45**, 848.
113. D. Reed, D. Stalke, and D. S. Wright, *Angew. Chem.*, 1991, **103**, 1539; *Angew. Chem., Int. Ed. Engl.*, 1991, **30**, 1459.
114. A. Sebald, B. Wrackmeyer, C. R. Theocharis, and W. Jones, *J. Chem. Soc., Dalton Trans.*, 1984, 747.
115. A. Streitwieser, Jr., J. E. Williams, S. Alexandratos, and J. M. McKelvey, *J. Am. Chem. Soc.*, 1976, **98**, 4778.
116. J. Hilton and L. H. Sutcliffe, *Prog. NMR Spectrosc.*, 1975, **10**, 27.
117. N. J. R. van Eikema Hommes, and P. v. R. Schleyer, unpublished (cited in Bauer and Griesinger[79]).
118. L. M. Jackman, L. M. Scarmoutzos, and C. W. DeBrosse, *J. Am. Chem. Soc.*, 1987, **109**, 5355.

119. S. Berger and S. Müller, *Chem. Ber.*, 1995, **128**, 799.
120. O. W. Sørensen, G. W. Eich, M. H. Levitt, G. Bodenhausen, and R. R. Ernst, *Prog. NMR Spectrosc.* 1983, **16**, 163.
121. N. Chandrakumar and S. Subramanian, *Modern Techniques in High-resolution FT NMR*, Springer, New York, 1987, p. 32.
122. J. Jeener, Ampère Int. Summer School, Basko Polje, 1971; W. P. Aue, E. Bartholdi, and R. R. Ernst, *J. Chem. Phys.* 1976, **64**, 2229.
123. W. Peters, M. Fuchs, H. Sicius, and W. Kuchen, *Angew. Chem.* 1985, **97**, 217; *Angew. Chem., Int. Ed. Engl.*, 1985, **97**, 231.
124. T. L. Venable, W. C. Hutton, and R. N. Grimes, *J. Am. Chem. Soc.*, 1984, **106**, 29.
125. A. Bax and R. Freeman, *J. Magn. Reson.*, 1981, **44**, 542.
126. D. Barr, W. Clegg, S. M. Hodgson, R. E. Mulvey, D. Reed, R. Snaith, and D. S. Wright, *J. Chem. Soc., Chem. Commun.*, 1988, 367.
127. R. Snaith, personal communication.
128. W. Frankmölle, Ph.D. thesis, University of Siegen, Germany, 1990.
129. A. Bax, R. Freeman, and P. S. Kempsell, *J. Am. Chem. Soc.*, 1980, **102**, 4849.
130. A. Bax, R. Freeman, and T. A. Frenkiel, *J. Am. Chem. Soc.*, 1981, **103**, 2102.
131. N. Chandrakumar, *J. Am. Chem. Soc.*, 1993, **115**, 3780.
132. H.-E. Mons, K. Bergander, and H. Günther, *Helv. Chim. Acta*, 1993, **76**, 1216.
133. Th. Fox, personal communication.
134. J. R. Wesener, P. Schmitt, and H. Günther, *J. Am. Chem. Soc.*, 1984, **106**, 10.
135. O. Eppers and H. Günther, *Tetrahedron Lett.*, 1989, **30**, 6155.
136. R. D. Thomas and D. H. Ellington, *Magn. Reson. Chem.*, 1989, **27**, 628.
137. (a) A. A. Maudsley, L. Müller, and R. R. Ernst, *J. Magn. Reson.*, 1977, **28**, 463; (b) G. Bodenhausen and R. Freeman, *J. Magn. Reson.*, 1977, **28**, 471.
138. (a) L. Müller, *J. Am. Chem. Soc.*, 1979, **101**, 4481; (b) A. Bax, R. H. Griffey, and B. L. Hawkins, *J. Magn. Reson.*, 1983, **55**, 301.
139. D. Nanz and W. v. Philipsborn, *J. Magn. Reson.*, 1992, **100**, 243.
140. J. H. Gilchrist, A. T. Harrison, D. J. Fuller, and D. B. Collum, *Magn. Reson. Chem.*, 1992, **30**, 855.
141. D. Moskau, F. Brauers, H. Günther, and A. Maercker, *J. Am. Chem. Soc.*, 1987, **109**, 5532.
142. G. Bodenhausen and D. J. Ruben, *Chem. Phys. Lett.*, 1980, **69**, 185.
143. J. H. Gilchrist and D. B. Collum, *J. Am. Chem. Soc.*, 1992, **114**, 794.
144. F. E. Romesberg, M. P. Bernstein, J. H. Gilchrist, A. T. Harrison, D. J. Fuller, and D. B. Collum, *J. Am. Chem. Soc.*, 1993, **115**, 3475.
145. L. Müller and R. R. Ernst, *Mol. Phys.*, 1979, **38**, 963.
146. H.-E. Mons, K. Bergander, and H. Günther, *Magn. Reson. Chem.*, 1993, **31**, 509.
147. N. Chandrakumar and A. Ramamoorthy, *J. Am. Chem. Soc.*, 1992, **114**, 1123.
148. K. Bergander and H. Günther, unpublished.
149. M. H. Levitt, *Prog. NMR Spectrosc.*, 1986, **18**, 61.
150. A. G. Avent, C. Eaborn, M. N. A. El-Kheli, M. E. Molla, J. D. Smith, and A. C. Sullivan, *J. Am. Chem. Soc.*, 1986, **108**, 3854.
151. W. Bauer, G. Müller, R. Pi, and P. v. R. Schleyer, *Angew. Chem.*, 1986, **98**, 1130; *Angew. Chem., Int. Ed. Engl.*, 1986, **25**, 1103.
152. P. L. Rinaldi, *J. Am. Chem. Soc.*, 1983, **105**, 5167.
153. C. Yu and G. C. Levy, *J. Am. Chem. Soc.*, 1983, **105**, 6994.
154. W. Bauer, T. Clark, and P. v. R. Schleyer, *J. Am. Chem. Soc.*, 1987, **109**, 970.
155. W. Bauer and P. v. R. Schleyer, *Magn. Reson. Chem.*, 1988, **26**, 827.
156. H.-J. Gais, G. Hellmann, H. Günther, F. López, H. J. Lindner, and S. Braun, *Angew. Chem.*, 1989, **101**, 1061; *Angew. Chem., Int. Ed. Engl.*, 1989, **28**, 1025.
157. D. Hoffmann, W. Bauer, and P. v. R. Schleyer, *J. Chem. Soc., Chem. Commun.*, 1990, 208.
158. W. Bauer and F. Hampel, *J. Chem. Soc., Chem. Commun.*, 1992, 903.
159. J. Heinzer, J. F. M. Oth, and D. Seebach, *Helv. Chim. Acta*, 1985, **68**, 1848.
160. G. Fraenkel, A. Chow, and W. R. Winchester, *J. Am. Chem. Soc.*, 1990, **112**, 6190.
161. J. Sandström, *Dynamic NMR Spectroscopy*, Academic, London, 1982.
162. J. Jeener, B. H. Meier, P. Bachmann, and R. R. Ernst, *J. Chem. Phys.*, 1979, **71**, 4546; R. R. Ernst, G. Bodenhausen, and A. Wokaun, *Principles of Nuclear Magnetic Resonance in One and Two Dimensions*, Clarendon, Oxford, 1987, p. 492.
163. For reviews see: R. Willem, *Prog. NMR Spectrosc.*, 1987, **20**, 1; C. L. Perrin and T. J. Dwyer, *Chem. Rev.*, 1990, **90**, 935.
164. M. Tomaselli, B. H. Meier, P. Robyr, U. W. Suter, and R. R. Ernst, *Chem. Phys. Lett.*, 1993, **205**, 145.
165. B. Böhler and H. Günther, unpublished.
166. R. A. Bartsch, V. Ramesh, R. O. Bach, T. Shono, and K. Kimura, in *Lithium Chemistry—A Theoretical and Experimental Overview*, eds. A.-M. Saspe and P. v. R. Schleyer, Wiley, New York, 1995, p. 393.

Acknowledgments

I am indebted to Dr M. Holz, Karlsruhe, for valuable information and to Drs H. Hausmann and Th. Fox, Siegen, for technical assistance in preparing this review. Cited work from our laboratory was supported by the Deutsche Forschungsgemeinschaft and the Fonds der Chemischen Industrie, which is gratefully acknowledged.

Biographical Sketch

Harald Günther. *b* 1935. Studied chemistry at the Universities of Stuttgart and Heidelberg, Ph.D., 1961, Heidelberg with G. Wittig. Research fellow at Mellon-Institute, Pittsburgh 1961–63; introduced to NMR by A. A. Bothner-By. 1963–77 Staff member at the Institute of Organic Chemistry, University of Cologne; Habilitation 1968 with E. Vogel; Associate Professor 1970; since 1977 Full Professor at the University of Siegen. 1973 Chemistry Award of the Academy of Sciences, Göttingen; 1973 Award of the Fonds der Chemischen Industrie, Frankfurt. Approx. 200 publications; author of NMR textbook (German, English, Russian, Polish, French editions). Editor-in-Chief of *Magnetic Resonance in Chemistry* since 1992. Research interests include applications of high-resolution and solid state NMR in organic and organometallic chemistry.

Metallodrugs

Hongzhe Sun

Department of Chemistry and Open Laboratory of Chemical Biology of the Institute of Molecular Technology for Drug Discovery and Synthesis, The University of Hong Kong, Hong Kong, P. R. China

1 Introduction 1
2 Platinum (and Other Metallo) Anticancer Drugs 1
3 Gold Anti-Arthritic Drugs 9
4 Lithium for Manic Depression 10
5 Bismuth Antiulcer (and Antimony Antileishmania) Agents 11
6 Summary 12
7 Related Articles in Volumes 1–8 12
8 References 12

1 INTRODUCTION

The use of metal containing compounds in medicine and health applications has been practiced for several thousand years.[1] The Egyptians used copper to sterilize water in 3000 BC and the Chinese were using gold in a variety of medicines 3500 years ago. In fact, the first modern chemotherapeutic agent was an organoarsenic compound (Erlich's arsphenamine), although modern pharmaceuticals are dominated by organic compounds. The success of cisplatin as an anticancer drug has largely stimulated the modern use of metal compounds for therapy and diagnosis. Beside platinum, clinically useful metal compounds include gold in antiarthritic agents, lithium for manic depression, antimony in antileishmaniasis, bismuth in antiulcer drugs, gadolinium (Gd^{3+}) as a magnetic resonance imaging contrast agent and technetium (^{99m}Tc) as radio-diagnostic agents (Table 1).[1–4] Not only do inorganic compounds extend the range of drugs available, but they are also successful in treating some diseases where organic compounds are not.

Both the metal and the bound ligands determine the biological activity of metallodrugs, not just the metal. The active species may not be that which is administered or tested in vitro, and it may be biotransformed by ligand substitution and/or redox reactions before it reaches the target sites. It is important to investigate both kinetic (ligand-exchange dynamics, mechanism and pathway) and thermodynamic aspects of the reactivity of a metal compound since biological systems are rarely at thermodynamic equilibrium. Modern multinuclear and multidimensional NMR spectroscopy is a very powerful method for investigation of the speciation of metal complexes in solution, and to a lesser extent in the solid-state, and is applicable for studies of the interaction of metal compounds with biomolecules under physiologically relevant conditions.

Although almost all of the available NMR techniques have been used for studying metallodrugs, ^{1}H NMR spectroscopy continues to be the most widely used method for monitoring the behavior of ligands and biomolecules. Other spin 1/2 nuclei such as ^{13}C, ^{15}N, ^{31}P and ^{195}Pt, and weak quadrupolar nuclei (e.g., ^{6}Li, ^{7}Li, ^{27}Al and ^{51}V, Table 2) have also quite often been used and ^{7}Li will be discussed in a later section. Most medicinally relevant metals are quadrupolar nuclei. Antimony, bismuth and gold have a limited number of useful NMR isotopes. This situation may improve at very high fields (e.g., 14.1 T and over), which are expected to dramatically sharpen the central transition ($m = 1/2$ to $-1/2$) of half-integer quadrupolar nuclei such as ^{27}Al ($I = 5/2$), ^{45}Sc ($I = 7/2$) and ^{71}Ga ($I = 3/2$), Table 2.[5] Other candidates include biologically important elements, e.g., ^{25}Mg, ^{43}Ca and ^{67}Zn. In the limit of slow isotopic molecular motion (e.g., macromolecules, $\omega\tau_c \gg 1$), the linewidth ($\Delta\nu_{1/2}$) of the central transition ($m = 1/2$ to $-1/2$) decreases with increasing magnetic field:

$$\Delta\nu_{1/2} = k\left[\frac{\chi^2}{\tau_c\nu_o^2}\right] \tag{1}$$

where χ is the quadrupolar coupling constant ($\chi = e^2qQ/h$), τ_c is the correlation time for fluctuations in the electric field gradient at the nucleus and ν_o is the resonance frequency which is proportional to the magnetic field. Decreasing temperature and increasing viscosity also give rise to a decrease in linewidths.[6] In these quadrupolar systems, the apparent shift is field-dependent, in contrast to $I = 1/2$ nuclei. The second-order dynamic frequency shift is given by:[7,8]

$$\Delta\delta_d = \delta_{obs} - \delta_{iso}\left(m = \frac{1}{2} \text{ to } \frac{-1}{2}\right) = k\left(\frac{\chi^2}{\nu_o^2}\right) \tag{2}$$

The chemical shift of ^{71}Ga in ovotransferrin, for example, is -103 ppm at 11.7 T but -57 ppm at 17.6 T.[5b]

This article provides examples of the application of NMR spectroscopy to the speciation of metallopharmaceuticals in solution and in the solid-state including biofluids and cells, and complexation to biomolecules (nucleic acids, peptides and proteins). Since the topic is vast, we focus on platinum anticancer, gold antiarthritic, lithium and bismuth antiulcer drugs. The reader is referred to related papers in this encyclopedia and elsewhere.[9]

2 PLATINUM (AND OTHER METALLO) ANTICANCER DRUGS

The accidental observation of the inhibition of bacterial division by *cis*-diamminedichloroplatinum(II) (cisplatin, *cis*-$Pt(NH_3)_2Cl_2$ or *cis*-DDP) in 1965 by Rosenberg led to the antiproliferative effects of this compound being applied to therapy of human tumours.[10–12] Today cisplatin is among the most active and widely used anticancer drugs, together with the second-generation drug carboplatin $Pt(NH_3)_2(CBDCA{-}O,O')$, where CBDCA is cyclobutane-1,1-dicarboxylate). Two new platinum compounds nedaplatin and oxaliplatin have recently been approved for clinical use in Japan and France, respectively (Scheme 1). Ru^{3+} compounds and the organometallic complex titanocene dichloride also have promising anticancer activities.

Table 1 Some metallodrugs and diagnostic agents

Compounds	Product	Use	Transformation events	Biological targets
Li_2CO_3	Camcolit	Manic depression	Widely distributed in body	Enzymes in inositol phosphate pathways
$Na_2[Fe^{II}(NO)(CN)_5]$	Nipride	Hypotensive crisis (vasodilator)	Release of CN^-, reaction with thiols	Release of NO to guanylate cyclase
Zn^{II} pyrithione	Omadine	Antimicrobial (antidandruff)		Skin
$^{67}Ga^{III}$ citrate	Neoscan	Diagnostic radio-imaging	Transferrin	Tumors and inflammatory lesions
$^{99m}Tc^{V}$-D,L-HM-PAO[a]	Ceretec	Diagnostic radio-imaging	Ligand exchange?	Brain
$^{99m}Tc^{I}[(C{\equiv}N{-}R)_6]^{+}$ [b]	Cardiolite	Diagnostic radio-imaging	Potassium channel?	Myocytes (heart)
Ag^{I} sulfadiazine	Flamazine	Antibacterial (burn wounds)	Protein binding	Enzymes (e.g., phosphomannose isomerase), cell walls?
$Na[Sb^{V}$ stibogluconate]	Pentostam	Antileishmanial	Unknown	Parasites in liver
$BaSO_4$	Baridol	X-ray contrast agent	None (insoluble in water)	Passage through GI tract
$[Gd^{III}(DTPA)](meglumine)_2$	Magnevist	MRI contrast agent	None	Extracellular water
$[Gd^{III}(DOTA)]^-$	Dotarem	MRI contrast agent	None	Extracellular water
cis-$[Pt^{II}Cl_2(NH_3)_2]$	Cisplatin	Anticancer	Hydrolysis, L-Met adducts and GSH	DNA
$Pt^{II}[(CBDCA)(NH_3)_2]$ [c]	Carboplatin	Anticancer	L-Met adducts, ring open and release of CBDCA, and GSH	DNA
Au^{I} thiomalate	Myocrisin	Antiarthritic drug	Thiol exchange, MT, albumin (Cys^{34}), oxidation to Au^{III}?	Lysosomes (aurosomes), thiol group of proteins
Et_3P Au^{I}(acetylthioglucose)	Auranofin	Oral antiarthritic drug	Phosphine oxidation, Au^{I} to Au^{III}?	Lysosomes (aurosomes), thiol group of proteins
Colloidal Bi^{III} citrate	De-Nol	Antiulcer and antimicrobial	GSH, MT and transferrin?	Block Fe^{III} uptake? enzymes in *Helicobacter pylori*?
Ranitidine Bi^{III} citrate	Pylorid	Antiulcer and antimicrobial	GSH, MT and transferrin?	Block Fe^{III} uptake? enzymes in *Helicobacter pylori*?

[a]HM-PAO is hexamethyl propyleneamine oxime.
[b]C≡N–R represents 2-methoxyisobutylisocyanide.
[c]CBDCA is 1,1-dicarboxycyclobutane.

Table 2 Useful NMR properties of selected elements

Nucleus	Spin	Natural abundance (%)	Quadrupole moment (10^{-28} m)	Receptivity/^{13}C	NMR Frequency (100 MHz ^{1}H)
^{6}Li	1	7.42	-6.4×10^{-4}	3.58	14.717
^{7}Li	3/2	92.58	-3.7×10^{-2}	1.54×10^3	38.864
^{13}C	1/2	1.108		1	25.145
^{14}N	1	99.63	1.6×10^{-2}	5.7	7.224
^{15}N	1/2	0.37		2.2×10^{-2}	10.136
^{25}Mg	5/2	10.00	0.1999	1.54	6.126
^{27}Al	5/2	100	0.140	1.17×10^3	26.077
^{31}P	1/2	100		3.77×10^2	40.480
^{51}V	7/2	99.76	-5.2×10^{-2}	2.16×10^3	26.350
^{67}Zn	5/2	4.11	0.150	0.665	6.252
^{69}Ga	3/2	60.40	0.168	2.38×10^2	24.040
^{71}Ga	3/2	39.60	0.106	3.19×10^2	30.495
^{109}Ag	1/2	48.18		0.276	4.653
^{195}Pt	1/2	33.8		19.1	21.414

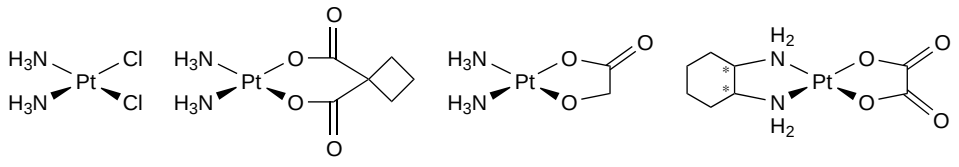

Scheme 1 Structures of clinically used platinum compounds. The carbons marked with asterisks are chiral carbons (Oxaliplatin contains *R*,*R*-1,2-diaminocyclohexane)

2.1 ^{195}Pt, ^{15}N NMR and Inverse [^{1}H, ^{15}N] NMR Spectroscopy

In addition to ^{1}H NMR, the use of ^{15}N and ^{195}Pt NMR spectroscopy has made an important impact, along with other biophysical techniques, in the understanding of the mode of action of platinum anticancer drugs. This includes the detection of intermediates arising during the hydrolysis process and in reactions with either DNA or amino acids (peptides and proteins), and metabolites in body fluids.[9] ^{195}Pt ($I = 1/2$) is a reasonably sensitive nucleus for NMR detection with natural abundance of 33.8% (Table 2) and a receptivity relative to ^{1}H of 3.4×10^{-3}. The spin-relaxation time for ^{195}Pt is usually in the range of 0.014–8.3 s, with most values less than 2 s.[13] The short relaxation times (T_1) are attributed to efficient relaxation via the chemical shift anisotropy (CSA) and spin-rotation (SR) contributions. The advantage of the increased sensitivity achievable at high magnetic field for ^{195}Pt is offset by the increase in linewidths due to CSA relaxation ($\propto B_0^2 \tau_c$). Similarly, ^{195}Pt satellites in either ^{1}H or ^{15}N spectra of Pt^{2+} complexes are often broadened beyond detection at high fields, again due to CSA relaxation of ^{195}Pt, which excludes the use of [^{1}H, ^{195}Pt] inverse detection to enhance the sensitivity of detection. The low detection limit (ca. 10 mM) precludes detection of natural abundance ^{195}Pt signals under biologically relevant conditions (e.g., in body fluids), but can be enhanced by isotopic enrichment of ^{195}Pt to >95%. A previous report has shown that DNA platination at millimolar concentrations can readily be studied with ^{195}Pt enrichment and both mono- and bi-functional guanine adducts were detected (Scheme 2 and Figure 1).[14] The rate-determining step for initial binding of cisplatin was found to be hydrolysis of the first chloride and similarly the rate-determining step for closure of the monofunctional species to form bifunctional adducts was found to be hydrolysis of the second chloride.

The chemical shift range of ^{195}Pt is very large (15 000 ppm and usually in the range from −6000 to 9000 ppm). Ready differentiation between Pt^{2+} and Pt^{4+} is usually possible. The former (Pt^{2+}) tends to have chemical shifts at the higher field while the latter resonates in the low-field end of the range. The ^{195}Pt chemical shift in monomeric compounds is usually highly sensitive to the nature of bound donor atoms and can

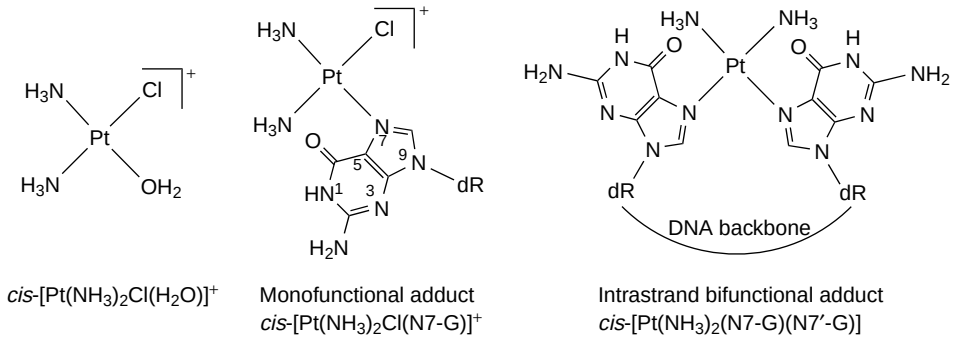

Scheme 2 Structures of cisplatin aqua-chloro intermediate, mono- and bi-functional DNA adducts

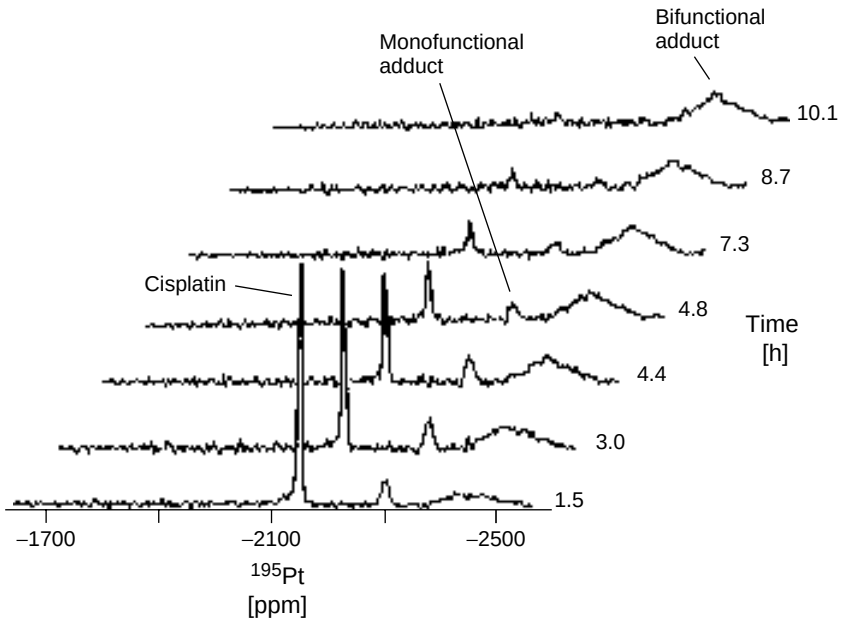

Figure 1 Time-dependent ^{195}Pt NMR spectra of the reaction between cisplatin and chicken erythrocyte DNA at 37 °C in 3 mM NaCl, 1 mM NaH_2PO_4. (Adapted with permission from Ref.[14])

Table 3 ^{195}Pt chemical shifts of *cis*-Pt complexes with different donor atoms

Cis-Pt complexes	$\delta(^{195}Pt)$ range[a]	References
cis-$[Pt(NH_3)_2Cl_2]$	−2048 to −2168[b]	**14,15**
cis-$[Pt(NH_3)_2Cl(O)]$	−1806 to −1841	**16**
cis-$[Pt(NH_3)_2Cl(N)]$	−2295 to −2369	**14,18,19**
cis-$[Pt(NH_3)_2(O)_2]$	−1570 to −1730	**15–17**
cis-$[Pt(NH_3)_2(N)_2]$	−2440 to −2661	**14,16,17**
cis-$[Pt(NH_3)_2(N)(O)]$	−2058 to −2147	**16,17**
cis-$[Pt(NH_3)_2(N)(S)]$	−2800 to −3218	**20,21**
cis-$[Pt(NH_3)_2(O)(S)]$	−2618 to −2800	**20,21**
cis-$[Pt(NH_3)_2(S)_2]$	−3200 to −3685	**20,21**

[a]Reference to Na_2PtCl_6.
[b]Slightly varies in different solvents, $\delta(^{195}Pt) = -2048$ (DMF), −2097 (DMSO) and −2149 (water).

be used as a diagnostic tool to distinguish various types of ligand binding to platinum (Table 3).[15–21] Moreover, the ^{195}Pt chemical shifts are very sensitive to complex geometry, e.g., geometrical isomers and diastereomers, and can be utilized in the detection of different intermediates formed during the reaction of platinum complexes with biomolecules. ^{195}Pt NMR shifts for conformers of bis-guanine derivatives differing only by rotation about the Pt–N7 bond can vary by as much as 13 ppm (see Scheme 2).[22] Sometimes even isotopomers are distinguishable: the ^{195}Pt isotope shift difference for Pt–^{35}Cl and Pt–^{37}Cl is 0.17 ppm and that for Pt–^{79}Br and Pt–^{81}Br is 0.03 ppm.[23] Therefore in principle it is possible to count the number of Cl and Br ligands bonded directly to Pt via the isotope-splitting pattern. But in practice it is difficult to resolve such multiple patterns because of line broadening, which is due to either relaxation mechanism or temperature drift. The latter is a problem since the chemical shift of ^{195}Pt is strongly temperature-dependent (up to 1 ppm/K).

^{14}N NMR spectroscopy can be useful for ammine ($-NH_3$) and amine ($-NH_2$,–NH) groups which coordinate to Pt. Since ^{14}N is a quadrupolar nucleus (Table 2), and quadrupolar relaxation is dominant when the environment of ^{14}N has a low symmetry. This leads to broad resonances and subsequently reduces the sensitivity. However, the quadrupolar nature of ^{14}N has the beneficial effect of shortening the relaxation rate and allowing rapid pulsing so that a large number of transients can be acquired. It is still possible to follow reactions of cisplatin in blood plasma and cell-culture media at millimolar drug concentrations and to monitor ammine release.[24]

^{15}N NMR is particularly useful in the study of the aqueous chemistry of cisplatin and other platinum ammine/amine compounds since ^{15}N-labeled compounds can readily be prepared. More importantly, both the ^{15}N NMR chemical shift (Figure 2) and the $^1J(^{15}N-^{195}Pt)$ coupling constant are sensitive to the nature of the *trans*-ligand in Pt–NH_3 (or Pt–NH_2) complexes which provide useful information for identifying the ligands in the coordination spheres of Pt^{2+} (and Pt^{4+}) (Figure 2). This technique has been used to characterize the reaction products of ^{15}N-labeled cisplatin.[25]

The low receptivity of ^{15}N (3.85×10^{-6} relative to ^{1}H) limits its usefulness for directly detected ^{15}N-NMR studies of cisplatin and related platinum ammine/amine complexes in biofluids. The sensitivity of detection can be improved to some extent by ^{15}N isotopic enrichment and further enhanced

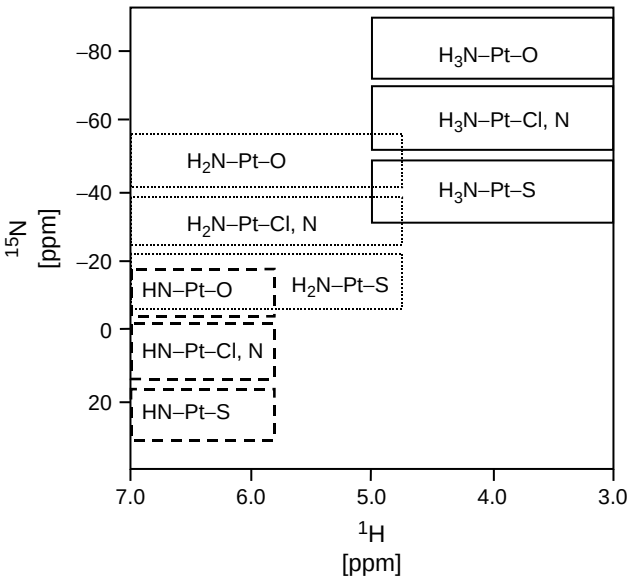

Figure 2 Variation of ^{1}H and ^{15}N chemical shifts with the *trans*-ligand in Pt^{II}–NH, Pt^{II}–NH_2 and Pt^{II}–NH_3 complexes. (Adapted with permission from Ref.[9b])

by polarization transfer from ^{1}H via for example, DEPT and INEPT experiments. But in practice, this enhancement of ^{15}N signal will be affected by the rate (k_{ex}) of exchange of protons between an ammine (and amine) and a solvent (e.g., water), and is hampered by rapid chemical exchange ($k_{ex} > J$). The maximum enhancement in ^{15}N signal via polarization transfer is only 9.8 (i.e., γ_{1H}/γ_{15N}). The repetition time of the pulse sequence is governed by the ^{1}H rather than the longer ^{15}N spin-lattice relaxation (T_1) which allows more rapid pulsing. ^{15}N{^{1}H} DEPT NMR techniques have been allowed the detection of rapidly changing intermediates in the reaction of ^{15}N labeled cisplatin with glutathione and also of ammine release following interaction of cisplatin with intracellular components of intact red blood cells at concentrations as low as 1 mM.[26] This method can be of values in situation where ^{1}H NMR resonances are very broad.

However, inverse ^{15}N methods (^{1}H{^{15}N}) are often preferred due to the greatly improved sensitivity for detection, by a theoretical maximum of 306 ($\{|\gamma_{1H}|/|\gamma_{15N}|\}^{5/2}$) with respect to directly detected ^{15}N. This technique is based on the large one-bond $^1J(^{15}N-^1H)$ coupling constant (ca. 70 Hz for $^{15}NH_3$) and it is necessary to work in H_2O (90% H_2O) since the NH protons normally exchange with deuterium rapidly in D_2O. The exchange of NH with solvent is much faster for Pt^{4+} than for Pt^{2+} complexes at neutral pH. Besides the high sensitivity, inverse detection also brings a simplification of complicated spectra since it selectively detects those protons directly attached to the labeled ^{15}N in the sample (e.g., Pt–NH_3), by use of the heteronuclear single (or multiple) quantum coherence transfer (HSQC or HMQC) pulse sequence. Each distinct type of Pt–NH resonance appears as a singlet, sometimes together with broadened ^{195}Pt satellites if ^{15}N decoupling is employed during the acquisition period (e.g., GARP method[27]). Water suppression can be achieved by the use of pulse sequences incorporating pulsed field gradient (which can be employed for both coherence selection and suppression of water signal).[28]

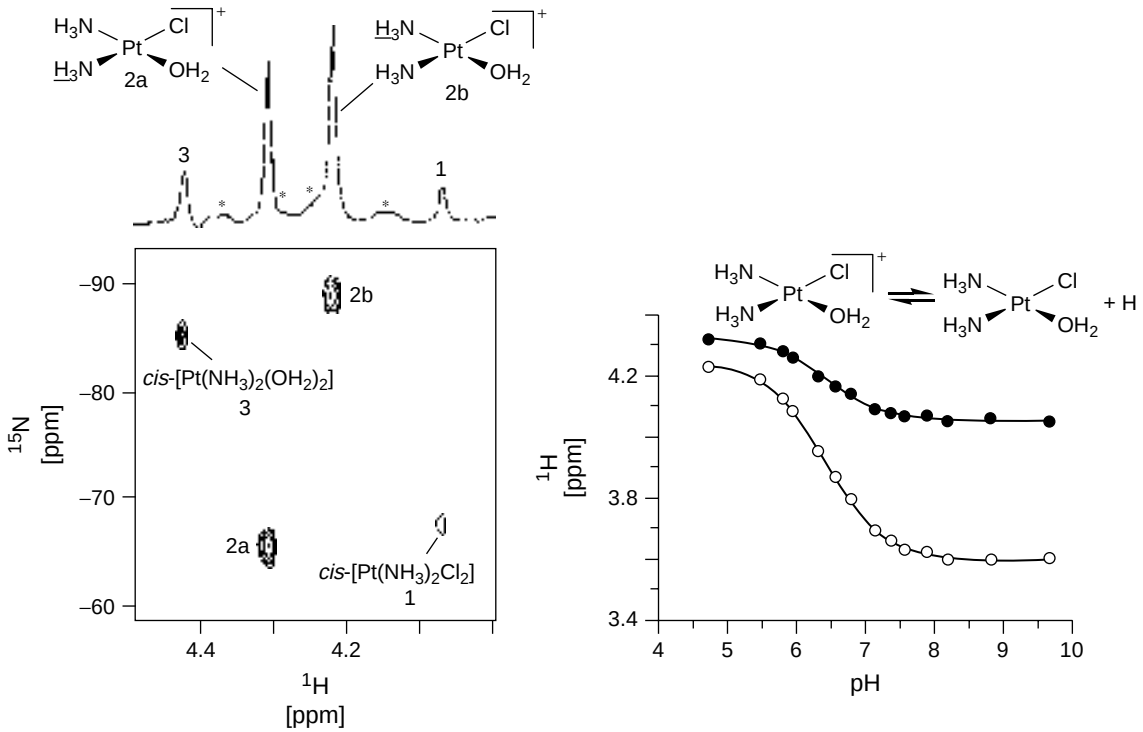

Figure 3 [^{1}H, ^{15}N] spectrum (left) of a 5 mM solution containing ^{15}N-cisplatin and its hydrolysis products in 95 : 5 = H_2O/D_2O at pH 4.72, 300 K. ^{195}Pt satellites are marked on the 1D ^{1}H spectrum with an asterisk. Plots of the ^{1}H shifts of Pt–NH_3 vs. pH allow direct determination of the pK_a values (right). (Adapted with permission from Ref.[29])

A one-dimensional ^{1}H spectrum (the first increment in a 2D experiment) contains only protons which are directly attached to the labeled ^{15}N in the sample (Pt–^{15}N<u>H</u>) and all others are eliminated. The combined detection of ^{1}H and ^{15}N in a reverse experiment, '2D [^{1}H, ^{15}N] HSQC NMR', is extremely powerful since the ^{15}N chemical shift range is large and diagnostic of the *trans*-ligand (Figure 2). The ^{195}Pt satellites in a 2D [^{1}H, ^{15}N] spectrum sometimes appears as diagonal peaks which correspond to the $^2J(^1\text{H}-^{195}\text{Pt})$ and $^1J(^{15}\text{N}-^{195}\text{Pt})$ coupling constants (again diagnostic) in the ^{1}H and ^{15}N dimensions, respectively (Figure 3) if they are not broadened beyond detection. The 2D [^{1}H, ^{15}N] method with ^{15}N-labeled platinum anticancer agents is particularly useful in studies of body fluids or cell culture media since thousands of overlapping ^{1}H resonances from other substances are filtered out. It takes just a few minutes to acquire a 2D [^{1}H, ^{15}N] spectrum at millimolar concentration and it is possible to detect ^{15}N-labeled species at concentrations as low as 20 μM.

2.2 Activation of Platinum Anticancer Drugs and Their Interaction with Nucleotides and DNA

It is widely accepted that the ultimate target for platinum anticancer drug is DNA and Pt–OH_2 bonds are much more reactive toward DNA and other biomolecules than Pt–Cl or Pt–OH bonds. The mechanism of action of cisplatin is believed to involve activation via hydrolysis inside cells where the concentration of chloride (Cl^-) (ca. 4 mM) is much lower than outside cells (ca. 104 mM). Therefore it is important to determinate the rates of hydrolysis and pK_a values of the hydrolysis products. By the use of 2D [^{1}H, ^{15}N] HMQC spectroscopy, the pK_a values can be rapidly measured at low concentration (Figure 3). By fitting the shift changes of ^{1}H NMR and ^{15}N-NMR as a function of pH, the pK_a values of the monoaqua *cis*-$[Pt(NH_3)_2Cl(H_2O)]^+$ (6.41) and diaqua adducts *cis*-$[Pt(NH_3)_2(H_2O)_2]^{2+}$ (5.37 and 7.21) were determined.[29] The equilibrium constant for the first stage of cisplatin hydrolysis was also determined to be 2.72 based on the resonance integration of reacted cisplatin, and the mono- and di-aqua adducts. Since all hydrolysis products can be readily distinguished in the spectrum, the problems associated with other methods are overcome. The pK_a values of aqua ligands of related platinum anticancer complexes such as *cis*- and *trans*-$[Pt(NH_3)(cyclohexamine)Cl_2]$, and *cis*-$[Pt(NH_3)(2\text{-Pic})Cl_2]$ (2-Pic is 2-methyl-pyridine), have also been determined by this [^{1}H, ^{15}N] NMR method.[30,31] The rate of hydrolysis for each chloride (Cl^-) ligand of *cis*-$[Pt(NH_3)(2\text{-Pic})Cl_2]$ was determined by the time-dependence of the [^{1}H, ^{15}N] NMR spectra for a period of over 20 h and was found to be slower than cisplatin.[31]

The reactions between ^{15}N-labeled cisplatin and guanosine-5′-monophosphate (5′-GMP) have also been investigated in aqueous solution by NMR spectroscopy.[32] The short-lived reactive species *cis*-$[Pt(NH_3)_2Cl(H_2O)]^+$ was detected during the early stages, followed by the formation of the mono- and bis-GMP adducts (Scheme 2). Hydrogen-bonding interactions were suggested to occur between N–H protons in Pt–NH_3 and deprotonated 5′-phosphate of GMP. Similar behavior was also observed between the N–H protons in ^{15}N-labeled ethylenediamine platinum complex $\{Pt(en)\}^{2+}$ with GMP and adenosine monophosphate (AMP).[33]

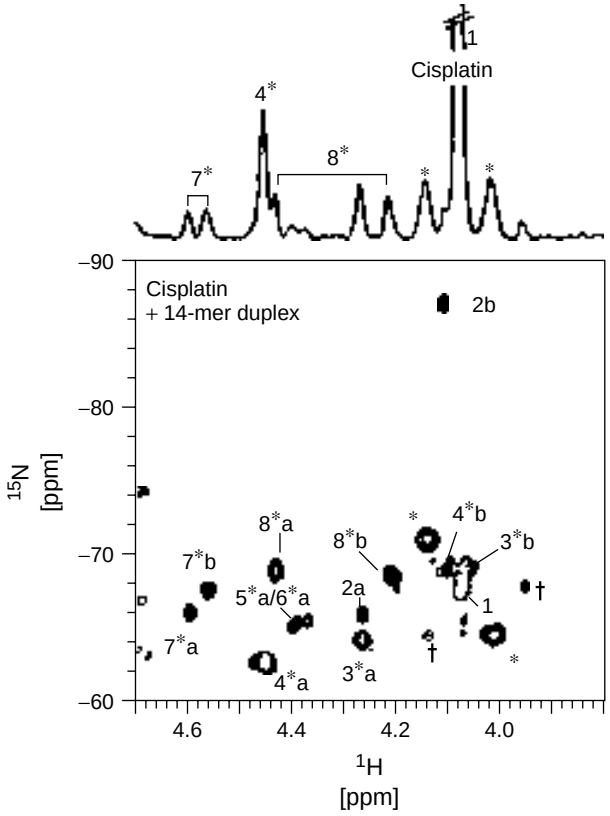

Figure 4 2D [^{1}H, ^{15}N] HSQC-NMR spectrum of 14-mer duplex d(ATACATG*G*TACATA)·d(TATGTACCATGTAT) after reaction with ^{15}N-cisplatin for 8 h. Labels: *, ^{195}Pt satellines; ‡, artefact. Peaks are assigned: **1**, cisplatin; **2**, *cis*-[Pt(NH$_3$)$_2$Cl(H$_2$O)]$^+$; **3**, *cis*-[Pt(NH$_3$)$_2$Cl(N(7)-G(7))]$^+$; **4**, *cis*-[Pt(NH$_3$)$_2$Cl(N(7)-G(8))]$^+$; **5/6**, *cis*-[Pt(NH$_3$)$_2$Cl(N(7)-G(18/25))]$^+$; **7,8**, *cis*-[Pt(NH$_3$)$_2$(N(7)-G(7))(N(7)-G(8))]$^+$ (distorted and kinked forms). (Adapted with permission from Ref.[35])

The detailed kinetics for the interaction of cisplatin with 10- and 14-mer oligonucleotides have been investigated. The major species in the pathways of platination of mono- and bi-functional adducts (both single- and double-strand GG adducts) can be simultaneously detected in a single [^{1}H, ^{15}N] NMR experiment (Figure 4).[34,35] The aqua-chloro intermediate which was usually present at micromolar concentrations, is readily monitored in these experiments and its lifetime was determined (ca. 8 min at 310 K) directly for the first time. Kinetic data obtained by [^{1}H, ^{15}N] NMR techniques are in close agreement with those determined by ^{195}Pt NMR spectroscopy (with enriched ^{195}Pt).[14] However, no aqua-chloro intermediate was detected previously by ^{195}Pt NMR during the course of the reaction with DNA. As expected, the reactions of cisplatin proceed via an aqua-chloro intermediate, and lead to two monofunctional adducts on the duplex and two on the GG-containing single strand. One of the GG residues is platinated three-fold faster than the other, which is in line with the results obtained by HPLC,[36] and ring closure to form a GG chelate on the duplex (3′-G) occurs also faster by about an order of magnitude for one monofunctional adduct than the other. Surprisingly, the 5′-G monofunctional adduct on the duplex has a very long lifetime (over 5 days at 298 K).[35,37] CD, ^{1}H and [^{1}H, ^{15}N] NMR data have shown that the 14-base GG-platinated DNA duplex d(ATACATG*G*TACATA)·d(TATGTACCATGTAT) where G*G* is platinated guanine (at N7) by the *cis*-[Pt(NH$_3$)$_2$]$^{2+}$, undergoes a reversible pH-induced structural transition (pK_a 4.8) between kinked-duplex and distorted forms. Binding of platinated duplex to the high-mobility-group protein 1 (HMG1) box A is at the concave face of the protein, and the kinked duplex may be converted to a different distorted form.[38] It is known that platinum forms bifunctional DNA adducts with the following order of sequence preference: –GG– > –AG– ≫ –GA– and that DNA platination is kinetically controlled. There is a clear preference for the formation of monofunctional adduct of cisplatin with –AG– over the –GA– sequence as judged from [^{1}H, ^{15}N] a HSQC NMR study. Closure to form the bifunctional adduct is more rapid in the former case than in the latter.[39] This could explain, at least in part, why –AG– bifunctional adducts are preferentially formed and few platinated –GA– adducts are observed.

2.3 Structures of Platinated Oligonucleotides

The anticancer activity of cisplatin and related complexes is believed to result from strong bonding of platinum to DNA affording mainly intrastrand –GG– and –AG– cross-links, the local structure of which are subsequently modified in such a way that apotosis is induced.[40] The presence of these DNA cross-links in cisplatin-treated cancer patients correlates with positive responses to treatment with the drug.[41] Such lesions have deleterious effects on DNA replication and transcription and cause mutations.[42,43] Previous studies have shown that platinated-DNA was recognized by proteins containing one or more high-mobility-group (HMG) domains[44–46] and structure-specific recognition protein 1.[47] The shielding of excision-repair caused by the binding of HMG proteins to DNA has been confirmed by both in vitro and in vivo experiments.[48,49] Elucidation of the structural distortion of the cisplatin (and related complexes) DNA adduct at the molecular level is definitely an important step toward understanding the activity of platinum anticancer drugs.

Various techniques especially those of X-ray crystallography and NMR spectroscopy, can be utilized to study the structure of platinated DNA adducts, but NMR spectroscopy is the focus of this paper. ^{1}H NMR is particularly useful for studying DNA and almost all of the modern NMR techniques can be used. Additional information can be obtained from studies with other nuclei such as ^{13}C, ^{15}N, ^{31}P and ^{195}Pt. Platinated DNA structures were determined based on observed 1D and 2D NMR data (e.g., NOE) with the aid of molecular mechanics and dynamics calculations, and have been reviewed previously.[50]

The structures of a number of platinated DNA adducts at either d(G*pG*) or d(A*pG*) sites have been solved and are listed in Table 3.[51–60] Platinum cross-link induced structural distortion seems to be a common feature. The solution structure of the platinated octameric duplex d(CCTG*G*TCC)·d(GGACCAGG) shows that it is unwound by ∼21°, and kinked by ∼58° toward the major groove at the d(G*pG*) site (Figure 5A).The minor groove is significantly widened and flattened at the platination site.[51] The overall features are similar to those observed for the crystal structure of the platinated dodecameric duplex.[61] The platinated duplex d(GCCG*G*ATCGC)·d(GCGATCCGGC) is also kinked by

Table 4 Lists of NMR structures of platinated DNA

Pt^{2+} complex	Sequence	Comments	References
cis-$[Pt(NH_3)_2]^{2+}$	d(CCTG*G*TCC)·d(GGACCAGG)	1,2-intrastrand cross-link d(G*pG*)	**51**
cis-$[Pt(NH_3)_2]^{2+}$	d(GCCG*G*ATCGC)·d(GCGATCCGGC)		**52**
cis-$[Pt(NH_3)$(4-amino-TEMPO)$]^{2+}$	d(CTCTCG*G*TCTC)·d(GAGACCGAGAG)		**56**
cis-$[Pt(NH_3)_2]^{2+}$	d(CCTCTG*G*TCTCC)·d(GGAGACCAGAGG)		**53**
cis-$[Pt(NH_3)_2]^{2+}$	d(ATACATG*G*TACATA)·d(TATGTACCATGTAT)		**54**
cis-$[Pt(NH_3)$(2-Pic)$]^{2+}$	d(ATACATG*G*TACATA)·d(TATGTACCATGTAT)		**55**
cis-$[Pt(NH_3)_2]^{2+}$	d(CTCA*G*CCTC)·d(GAGGCTGAG)	1,2-intrastrand cross-link d(A*pG*)	**57**
cis-$[Pt(NH_3)_2]^{2+}$	$d(CATAG*CTATG)_2$	1,2-interstrand cross-link	**58**
cis-$[Pt(NH_3)_2]^{2+}$	d(CCTCG*CTCTC)·d(GGAGCG*AGAG)	d(G*pG*)	**59**
cis-$[Pt(NH_3)_2]^{2+}$	d(CTCTAG*TG*CTCAC)·d(GTGAGCACTAGAG)	1,3-intrastrand cross-link d(G*pXpG*)	**60**

~60° toward the major groove at the Pt^{2+} coordination site and unwound by 12–19°.[52] The solution structure of the platinated dodecamer duplex was reported recently. The *cis*-$[Pt(NH_3)_2]^{2+}$–d(G*pG*) lesion causes the two adjacent –G*G*–bases to roll toward one another by 49°, leading to an overall helix kink by 78°.[53] The helix deformation in solution is greater than that in crystal, and the structural differences may be attributable to crystal packing interactions. The structure of a AT-rich DNA 14-mer d(ATACATG*G*TACATA)·d(TATGTACCATGTAT) was determined and it was suggested that the bend of DNA induced by cisplatin is sequence dependent.[54] Platination causes the overall DNA duplex to bend by ~52° toward the 3-end [with respect to the d(G*pG*) strand], in contrast to those GC-rich structures which bend toward the 5-end. The minor groove opposite the platination site is again widened and flattened. The solution structure of the d(G*pG*) platinated adduct of the nitroxide spin-labeled complex *cis*-$[Pt(NH_3)$(4-amino-TEMPO)$]^{2+}$ (TEMPO = 2, 2, 6, 6-tetramethylpiperidinyloxy) with the undecamer duplex has been determined by using conventional NMR methods (e.g., NOE studies) and long-range (10–20 Å) proton–electron distance constraints.[56] The use of long-range distance constraints did not affect the local geometry of the adduct only the global structure, but allows a better definition of the global structures of the duplexes. The platinated DNA duplex d(CTCA*G*CCTC)·d(GAGGCTGAG) cross-linked at the d(A*pG*) sequence by *cis*-$[Pt(NH_3)_2]^{2+}$ also bends to the double helix towards the major groove in a way similar to that observed for the d(G*pG*) crosslink.[52,57] Molecular modeling based on published NMR and X-ray data suggested that all duplexes in the three-base-pair d(XpG*pG*) and d(XpA*pG*) region are very similar and protein binding does not greatly change the structure of this region.[62]

Interstrand d(G*pG*) crosslinks formed by cisplatin with oligomers have also been studied.[58,59] They occur predominantly between two guanines on opposite strands, which requires a distance of ca. 2.8 Å between the two N7 atoms. As for the intrastrand crosslink, the interstrand crosslink also causes a kink in the DNA helix. However, unlike the intrastrand crosslink, the kink and unwound is toward the minor groove. The deoxyribose of the platinated deoxyguanosine (G) is inverted so that O4′ is pointing in the opposite direction to that of the remaining nucleotides. In addition, the complementary deoxycytidines (C), which were originally

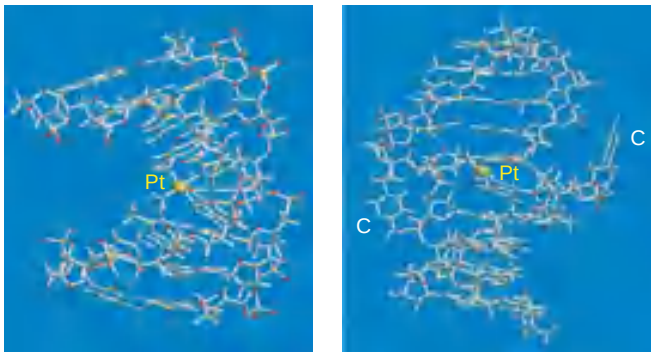

(A) (B)

Figure 5 NMR refined structures cisplatin-induced intrastrand (A) and interstrand cross-linked DNA duplex (B). The DNA is significantly altered from the B-form to accommodate cisplatin in (A), and the deoxycytosine residues originally base-paired to the platinated guanine have become extrahelical (B). Color code: C, green; H, metallic white; N, blue; O, red; P, orange; Pt, yellow. (Adapted with permission from Refs.[51,58])

base-paired to the platinated G are extruded and become extrahelical (Figure 5B).[58] The localized change from B-DNA to a left-handed Z-DNA structure around the platination site was also observed. *Cis*-$[Pt(NH_3)_2]^{2+}$ is also located in the minor groove of d(CCTCG*CTCTC)·d(GGAGCG*AGAG). The stacking of the two cross-linked guanines with the neighboring bases induces a kink of 40° toward the minor groove.

The 1,3-intrastrand d(G*XG*) (where X is C or T) cross-link minor adduct does not distort the global helical structure to the extent observed in the 1,2-intrastrand cross-link discussed above, but significantly disrupts local base-pairing and stacking at the 5′-end. The helix is bent by 24° and unwound by 19°. The platinum lesion causes a severe roll of 5′-G6 towards the major groove.[60]

2.4 Interaction with Amino Acids, Peptides and Proteins, and Their Metabolites in Biofluids

Increasing evidence has shown that platinum–peptide (amino acid and protein) interactions and particularly platinum–thioether interactions, play an important role in the mechanism of action of platinum drugs. The use of NMR

spectroscopy for studying these interactions has been summarized previously,[9] and Pt–methionine complexes with various isomers have been characterized by ^{13}C, ^{15}N, and ^{195}Pt NMR. In fact, it has been shown that platinum species can initially bind to thioether groups and then migrate to N7 of guanine.[63,64] ^{1}H and [^{1}H, ^{15}N] NMR spectroscopy has shown that L-methionine (Met) increases the rate of reaction of cisplatin with guanosine 5′-monophosphate (5′-GMP) at pH 7.[65] Therefore, methionines in peptides and proteins could play a role in the transfer of platinum onto DNA. Activation of carboplatin by reaction with L-Met derivatives could also provide an important pathway since carboplatin hydrolyses and interacts with chloride too slowly to account for its biological activity. Reaction with L-Met leads to a surprisingly stable ring-open intermediate with a half-life time 28 h at 310 K. By use of the 2D [^{1}H, ^{15}N] HSQC NMR method, a species with ^{1}H and ^{15}N shifts very similar to this intermediate was detected as a major metabolite in the urine samples from mice treated with ^{15}N-carboplatin.[66] This suggests that the ring-open intermediate is probably present in urine after carboplatin administration.

The thiolate-containing peptide glutathione (γ-L-Glu-L-Cys-Gly, GSH) is present in cells at mM concentrations. Various transient intermediates formed between the platinum complex and GSH during the reaction as judged by multinuclear NMR,[9b,67] and a novel dinuclear platinum GSH complex was also isolated and its structure was proposed based on ESI-MS and various advanced 2D NMR techniques.[68] In contrast to thioethers, the binding of Pt^{2+} to thiolate tends to be irreversible and ammine/amine ligands will finally be released from initial complex. Reactions between cisplatin and intracellular thiols such as GSH may therefore inactivate the drug and moreover the Pt–GSH complex can be pumped out of the cisplatin-resistant cells.

There are conflicting reports on the role of Pt–protein adducts in the mechanism of action. On the one hand, it has been postulated that the binding of cisplatin to protein is probably the cause of many of the drug's side-effects, while on the other hand several reports suggest that Pt^{2+}-albumin adducts may be anticancer active. One day after intravenous infusion of cisplatin, 65–98% of the platinum in blood plasma is protein bound.[69,70] Human serum albumin (66 kDa) is thought to be the major binding sites for cisplatin in human blood plasma. In contrast to previous reports, 1D and 2D [^{1}H, ^{15}N] NMR data suggest that ^{15}N-cisplatin mainly reacts with the methionine residues of albumin forming Met-S,N-macrocheltes together with minor monodentates Met-S adduct and Cys34, the only free thiol of the protein.[71] The iron binding protein transferrin (ca. 80 kDa) could deliver platinum to tumor cells, which are known to overexpress transferrin receptors. Diferric transferrin is taken up by cells via the known process of 'receptor-mediated endocytosis'. A combination of 2D [^{1}H, ^{13}C] and [^{1}H, ^{15}N] NMR spectroscopic studies using labeled transferrin (ε-[^{13}C]Met labeled protein) and ^{15}N-cisplatin has shown that preferred Pt^{2+} binding site appears to be Met256 with an additional site at the surface-exposed methionine.[72]

2.5 Other Metallo-anticancer Agents

Besides platinum, other metal complexes also have promising anticancer activity.[2,3] Gallium nitrate is known to exhibit anticancer activity and is now being used clinically for the treatment of cancer-induced hypercalcemia. The octahedral Ru^{3+} complexes (low spin d^5) are more active against metastases than primary tumors, and may be prodrugs which are bioreduced to Ru^{2+} species inside cells. Paramagnetically shifted ^{1}H NMR resonances are readily detected in ^{1}H spectra of Ru^{3+}

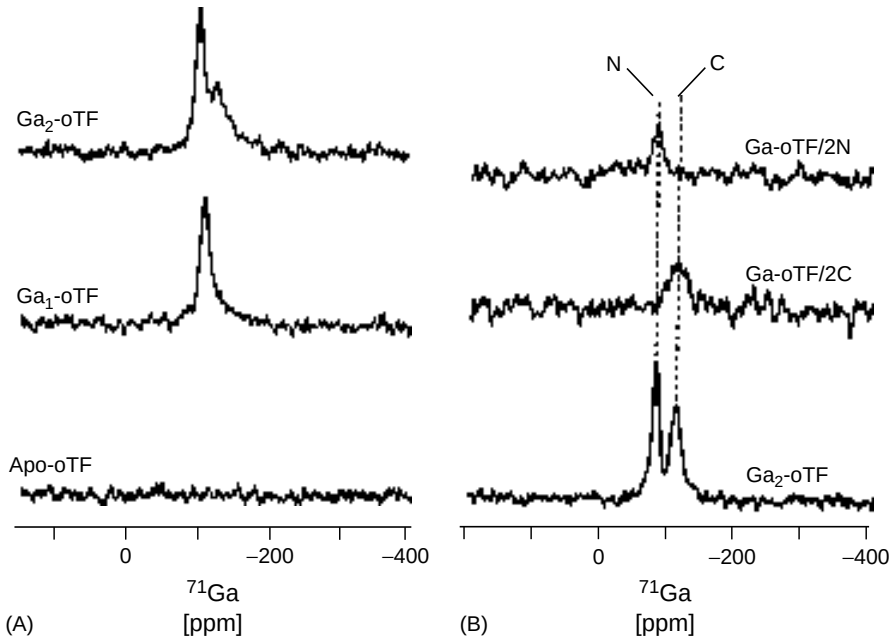

Figure 6 ^{71}Ga NMR spectra of ovotransferrin (1.3 mM, pH 7.6). (A) Before (bottom) and after addition of one (middle) and two mol equiv (top) of Ga^{3+} in the presence of 20 mM $NaHCO_3$. (B) ^{71}Ga NMR spectra of Ga_2-ovotransferrin (bottom), C-lobe of ovotransferrin (oTF/2C, 0.35 mM, 1.0 mol equiv of Ga^{3+}), and N-lobe of ovotransferrin (oTF/2N, 0.35 mM, 1.0 mol equiv. Of Ga^{3+}) in the presence of $Na_2C_2O_4$. (Adapted with permission from Ref.[75])

complexes and were used to determined the rate of hydrolysis of the anticancer agent *trans*-$[RuCl_4(Im)_2]^-$ where Im is imidazole.[73] Interestingly, both Ru^{3+} and Ga^{3+} are thought to be delivered by human transferrin (hTF).[2–4,74] It is known that many solid tumors express more transferrin receptor than normal cells. The binding properties of Ga^{3+} to ovotransferrin were investigated by ^{13}C and ^{71}Ga NMR. The latter technique is extremely useful at very high field once gallium has bound to large biomolecules.[5] Ga^{3+} interacts preferentially with the N-lobe of the protein when carbonate is present as the synergistic anion, but enters equally both the N- and C-lobes of the protein when oxalate is the anion (Figure 6).[75] The binding of Ru^{3+} complexes to lactoferrin is at the imidazole of His253, one of the iron ligands in the iron binding cleft of the N-lobe, and is reversible with Ru release at pH 4–5 or in the presence of a large excess of citrate or adenosine triphosphate (ATP).

The organometallic titanocene and another Ti^{4+} complex have entered phase II and I clinical trials for anticancer, respectively. We have demonstrated by UV and various NMR spectroscopies that the Ti^{4+} complex binds strongly to human serum transferrin at the specific iron (Fe^{3+}) site.[76] 2D [^1H, ^{13}C] studies of ε-[^{13}C]Met-hTF have shown that Ti^{4+} loads the C-lobe first followed by the N-lobe. Titanium (Ti^{4+}) bound transferrin effectively blocked cell uptakes of ^{59}Fe–hTF into BeWo cells,[77] which indicated that titanium transferrin could be recognized by transferrin receptor and be taken up into cells.

3 GOLD ANTI-ARTHRITIC DRUGS

Several injectable Au^+ thiolate drugs such as aurothiomalate and the oral drug auranofin are widely used for the treatment of difficult cases of rheumatoid arthritis and reviews on the medical use of gold have been published.[78–80] The injectable Au^+ complexes are polymers with thiolate sulfurs bridging to linear Au^+, in chain or cyclic structures. The crystal structure of aurothiomalate has shown that linear S–Au–S units are arranged into polymeric double-helical structures.[81] The structures of these polymers were found to be very sensitive to the ionic strength and pH of the solutions. Most of gold thiolate drugs often contain a small mol excess (10–15%) of thiol over gold.

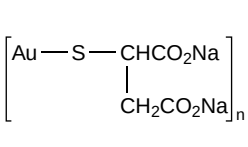

Aurothiomalate

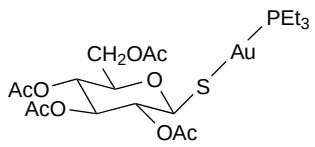

Auranofin

One feature of these linear Au^+ drugs is that they undergo facile thiolate exchange reactions and ^{13}C NMR studies have shown that thiols with lowest pK_a values bind most strongly to Au^+.[82] The administered drugs are probably not the active species. Gold(I) is a soft metal and therefore has a very high affinity for soft ligands such as thiolate sulfurs, but binds only weakly to nitrogen and hardly at all to oxygen. Consequently proteins (and enzymes) containing thiolate groups (Cys residues) particularly those with low pK_a values are targets for Au^+. In blood, a major site for gold transport is Cys34 of serum albumin which has a low pK_a (∼5). For the oral gold drug, ^{31}P NMR has been extensively used to probe speciations in proteins, bio-fluids and cells.[83–86] The ^{31}P chemical shift of bound phosphine (Au–PEt_3, where Et is ethyl) is sensitive to the nature of the coordinated ligands (X) and release of PEt_3 can readily be detected. The PEt_3 (and thiomalate) ligands of auranofin (and aurothiomalate, AuStm) are initially retained on binding of gold to albumin:

$$\text{Alb–Cys34–SH} + \text{auranofin}(\delta_{31P} = 37.0) \longrightarrow \text{Alb–Cys34–S–Au–PEt}_3(\delta_{31P} = 38.8)$$

Moreover, the ^{31}P chemical shift of bound phosphine in RS–Au–PR_3 was found to correlate with the pK_a of thiolates (SR),[82,86] ^1H and ^{31}P NMR studies have shown that the rate of binding of gold drugs to albumin appears to be determined by the rate of opening of the cleft in which Cys34 is situated.[87,88] Surprisingly, binding of auranofin and related gold compounds to Cys34 of albumin induces a structural transition, the effect of which can readily be observed by imidazole εCH^1H NMR resonances of His3 of the protein (Figure 7).[88,89] Such communication between His3 and Cys34 may be explained by small changes in the arrangement of intervening helices 1 and 2 of domain I of the protein. This may be mediated by a *cis-trans* isomerization of Pro35, changing the environment of Cys34 from a buried to an exposed form. The structural change can also be induced by blocking Cys34 as a disulfide, e.g., cystine. Such a structural transition of albumin induced by gold drugs has even been detected in intact blood plasma by ^1H NMR spectroscopy.[90] The exposed position of bound gold may have important implications for the transport and bioavailability of gold–drug metabolites.

Cyanide appears to play an important role in the metabolism of gold drugs. It can readily replace the thiomalate ligand from aurothiomalate in vitro and $Au(CN)_2^-$ has been shown to be a metabolite of gold drugs in vivo.[91,92] The enhanced uptake of gold into red blood cells of smokers is due to the formation of this species after inhalation of HCN in cigarette smoke. Interaction of aurothiomalate and cyanide (^{13}C-enriched CN^-) was followed by ^1H and ^{13}C NMR spectroscopy.[92] The mixed-ligand complex $[(Stm)Au(CN)]^-$ (Stm=S-bound thiomalate) readily forms as an intermediate when $[CN^-]/[\text{aurothiomalate}] < 2$, and $Au(CN)_2^-$ is the major species at higher ratio. Mixed-ligand complex of aurocyanide with other thiolates molecules such as glutathione, cysteine and captopril have also been reported.[92–95] Thiols and cyanide both bind to Au^+, although as expected, cyanide (CN^-) binds more strongly. Under biological conditions where [thiols] ≫ [HCN], substantial displacement of cyanide may take place. This may facilitate the accumulation of gold by red cells where the intracellular glutathione concentration is high (mM). An aurocyanide complex of albumin was recently studied by ^{13}C NMR spectroscopy and other techniques. There are two distinct binding mechanisms: the dominant mechanism is reversible association (non-specific binding) of intact $Au(CN)_2^-$ (δ_{13C} = 156.4) to albumin to form Alb·$[Au(CN)_2^-]_n$ (δ_{13C} = 154.7, broad signal).[96] The second binding mechanism is at Cys34 to form Alb-Cys34Au(CN) via a ligand exchange reaction which accounts for only a minor fraction of the bound-gold (ca. 11%).

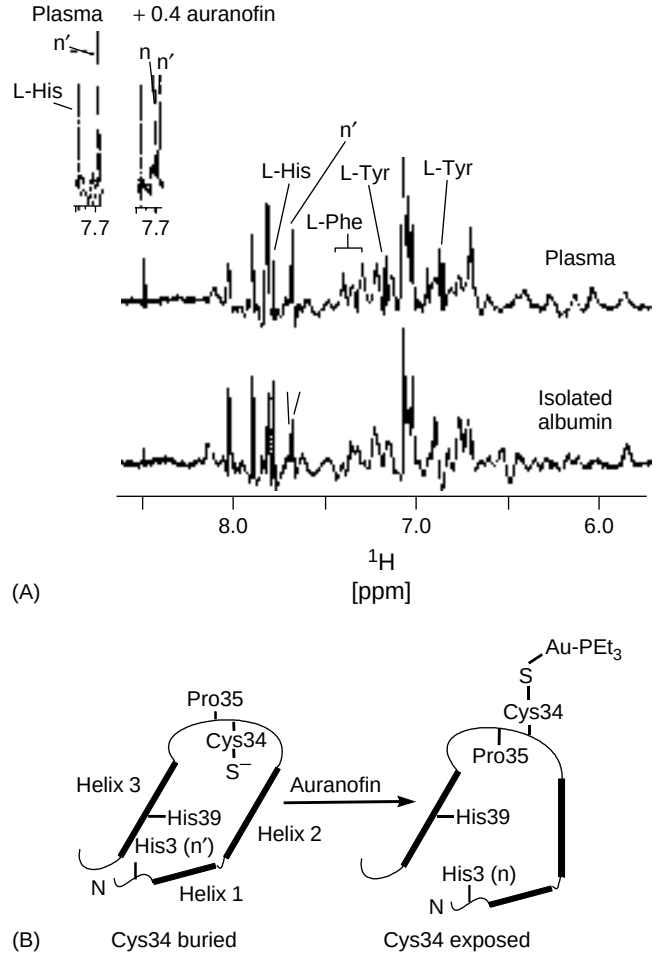

Figure 7 600 MHz ^{1}H spectrum of the aromatic region of a commercial sample of human albumin and fresh human blood plasma (A). The insert is Hε1 of His3 region of human blood plasma showing the n′ to n switch after addition of gold drug. (B) is the model for structural changes induced by gold in domain I of albumin. (Adapted with permission from Ref.[90])

4 LITHIUM FOR MANIC DEPRESSION

Lithium is an element discovered over 177 years ago (1817), but it was not until the seminal work of the Australian scientist, John Cade 50 years ago,[97] and subsequent clinical studies by Mogens Schou, that lithium was seen by modern psychiatry as an effective treatment for manic depression. Both lithium carbonate and citrate compounds are widely used as a prophylactic treatment for bipolar disorders.[98] Doses are normally gram quantities and the therapeutic level of lithium in serum is about 0.4–1.2 mM, and clinical efficacy usually takes 1–2 weeks to become established. Previous studies have shown that lithium was widely distributed in the body following oral administration due to its high lability and its weakness towards complexation.

Despite intensive research, the biochemical basis for lithium's therapeutic effects still remains to be fully elucidated. Lithium ions are small but highly hydrated and could interfere with Mg^{2+} biochemistry due to their comparably high charge densities, the so-called 'diagonal relationship' between Li^+ and Mg^{2+}. However, the favored mode of action of lithium is probably by interference with Ca^{2+} metabolism via inhibition of the inositol phosphate pathway.[99–101] Lithium also stimulates glutamate release and protects neurons by inhibiting N-methyl-D-asparate receptor-mediated calcium influx.[102,103] Determination of lithium is normally made by spectroscopic methods, e.g., atomic absorption and nuclear magnetic resonance. The former involves the disruption of samples (e.g., cells) and ensuing tedious separation. In addition, the atomic absorption measurements are not specific to the intracellular compartments. By contrast, NMR provides a non-invasive and direct way to investigate lithium in cells and tissues.[104]

Naturally occurring lithium consists of two isotopes ^{6}Li and ^{7}Li, with natural abundance 7.42 and 92.58%, respectively (Table 2). Both isotopes are weakly quadrupolar and the quadrupole moment of ^{6}Li is the smallest known while that of ^{7}Li is amongst the smallest, and they both give narrow resonance lines and have long spin-lattice relaxation times (T_1).[105] However, ^{7}Li is the choice for most biological studies because of its high sensitivity, higher natural abundance and more favorable relaxation as compared with ^{6}Li. The chemical shift range of ^{7}Li is small (ca. 15 ppm) due to its simple electronic structure and aqueous chemistry. The NMR spectrum of ^{7}Li generally contains a single peak corresponding to the overlapping signals from different environments, e.g., intra- and extra-cellular. It is possible to differentiate ^{7}Li signals from different compartments, for example, ions within the cells and those that are free in the extracellular bathing fluid, based either on their different relaxation properties or with the aid of shift reagent (e.g., dysprosium tripolyphosate), Figure 8.[106] Shift reagents, which are negatively charged lanthanide complexes and are insoluble in hydrophobic cell membrane, are repelled by the negatively charged head groups of phospholipids at the surface of cell membranes. In contrast to other alkali metals, ^{7}Li ($I = 2/3$) actually resembles a spin 1/2 nucleus and relaxation tends to be dominated by the dipolar mechanism.

The application of ^{7}Li and NMR of other alkali-metals to study the interaction of these metal ions with metalloproteins have been reviewed.[107] The chemical shifts of ^{6}Li, ^{7}Li and other alkali metal ions except Cs^+, are normally insensitive to either solvation or complexation by biomolecules. Li binds to myo-inositol monophosphatase, an enzyme that is inhibited by lithium and is thought to be the primary target for lithium therapy, and induces a downfield shift by <0.1 ppm and broadening of the ^{7}Li NMR signal. The binding constant at a single site was calculated to have a K_d of 1 mM, and lithium was found to compete with group II metal ions such as Mg^{2+} at that site.[108] NMR investigation of Li^+ binding to phospholipids and cell membrane have also been reported.

In order to get into the brain where the site of action of lithium is, Li^+ must be absorbed through the gastrointestinal tract into blood and pass the blood brain barrier. Clearly the membrane transport of lithium is a critical feature and several different NMR techniques have been used depending on the time-scale of the lithium transport process. The best model available for the study of Li^+ transport in human cells is the erythrocyte, which is also believed to be a good model for the blood brain barrier. Numerous NMR studies of Li^+ transport and environment in erythrocytes have been reported.[109,110] Depressed patients with a high $[Li]_i/[Li]_e$ ratio, where 'i' and 'e' represent intra- and extra-cellular concentration of lithium, were found to have a better therapeutic response that

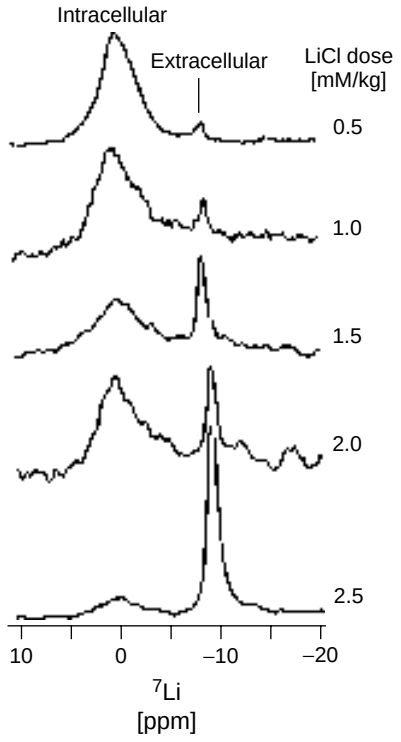

Figure 8 ^{7}Li NMR spectra of rat blood samples with added shift reagents (dysprosium tripolyphosphate, $Dy(ppp_i)_2^{7-}$). The peaks at 0 and ca. −10 ppm correspond to intracellular and extracellular ^{7}Li, respectively. The various doses of LiCl administered to the rats are indicated next to each spectrum. (Adapted with permission from Ref.[110b])

those patients with a lower ratio.[109] It was suggested that erythrocyte Li concentration could serve as a useful indicator of clinical response. However, subsequent studies were unable to substantiate the initial findings, and it is now generally accepted that this parameter is not clinically useful partly due to large interindividual variations in ionic transport process. It is known that a considerable amount of Li^+ enters the erythrocytes with the $[Li]_i/[Li]_e$ ratio typically at 0.3–0.6 which indicated that Li is actively extruded from the cells. Higher ratios have been reported recently in the low dose range in rats (Figure 8) and the coadministerated drug, thioridazine, has no effect on erythrocytes and plasma lithium levels.[110b,c]

In spite of extensive investigations of erythrocytes, little is known about the transport behavior of Li^+ in other cells and major differences are expected between erythrocytes and the excitable, nucleated cells of the central nervous system such as neurons and glia. Li^+ transport processes and intracellular concentrations in the brain have been approached by using human nerve 1321 N1 astrocytoma. ^{7}Li NMR spectroscopy showed that the uptake of Li^+ was approximately ten times faster than that into human erythrocytes and the steady-state was reached within 60 min. The low intracellular Li^+ concentration ($[Li]_i/[Li]_e \sim 0.3$) suggested the presence of an efflux mechanism in astrocytomas. Similar results have been obtained very recently for cultured human neuroblastoma SH-SY5Y cells.[112,113] Intra- and extra-cellular ^{7}Li resonances could be resolved in the presence of the shift reagent and relaxation measurements showed that Li^+ is immobilized more in human SH-SY5Y cells than in human erythrocytes. Significant increases in the first-order rate constants for Li^+ influx and efflux in the presence of veratridine (0.05 mM) suggested the Li^+ transport was mediated via Na^+ channels, a pathway not present in erythrocytes.[113] The studies of cultured central-nerve-system cells will also provide important information for in vivo study.

Direct investigation of Li^+ in the brain may be a better measure of efficacy or neurotoxicity than that in the serum. The spatial distribution of Li in the brain may also shed light on the still unknown mechanism of action of Li. Due to its relatively high sensitivity, the sufficiently high enough concentration of Li in tissues and most importantly the development of NMR spectroscopy in vivo, ^{7}Li NMR has successfully been used in recent years as a new tool to measure brain tissue lithium concentration.[104,114–117] Renshaw and coworkers' pioneering work demonstrated the feasibility of in vivo tissue measurements of lithium in animal and in human subjects.[118,119] In animals, efforts have been made to develop methods for measuring the pharmacokinetics of uptake in brain. It was found that the time constant for the uptake of a single dose of Li in rat brain was 48–98 min with signals that were uncontaminated by those from surrounding tissues.[120] Because of the high dose and long acquisition times used, the distribution of Li in the rat brain could be determined by ^{7}Li NMR imaging although the resolution of these imaging is overall quite poor.[121,122]

Most recent ^{7}Li work in vivo has focused on humans. Initial unlocalized studies measured the kinetics of uptake and elimination of ^{7}Li and compared serum and brain concentrations. Several studies have confirmed that the concentration of Li in brain is typically 0.1–0.6 mM and indicated brain/serum ratios of 0.4–0.7. Preliminary studies have attempted to examine a possible relationship between brain Li levels and therapeutic response, suggesting that Li brain levels may be of clinical relevance.[123–125] However, this question has yet to be properly addressed in patient samples large enough to provide a more clear answer. The potential for ^{7}Li in vivo NMR as an important tool for investigation of Li^+ refractoriness and predication of treatment outcome in bipolar disorder patients is currently being investigated.[116,126]

5 BISMUTH ANTIULCER (AND ANTIMONY ANTILEISHMANIA) AGENTS

Arsenic, antimony and bismuth have long been associated with medicine. Currently antimony compounds are used clinically for the treatment of leishmaniasis and bismuth compounds are widely used as antiulcer drugs (Table 1). Recently clinical studies in China demonstrated that the classical inorganic compound, arsenic trioxide (As_2O_3) can induce remission in patients with acute promyelocytic leukemia (APL, a rare blood cancer).[127,128] The induction of apoptosis and partial differentiation may be responsible for the activity of this metal.[129] Progress in the understanding the mode of action and design of drugs based on these elements are being greatly held up through lack of a suitable probe for the metal itself. NMR studies of these complexes have therefore relied on the observation of ligand nuclei such as ^{1}H and ^{13}C. The binding of citrate to Bi^{3+} in antiulcer complexes has been studied by ^{1}H, ^{13}C and [^{1}H, ^{13}C] NMR spectroscopy.[130–132] Citrate is a good bridging ligand and polymeric species are

formed in solution. The structures of bismuth citrate complexes are complicated, being dependent on pH, concentration, [Bi : citrate] ratio and the counter cations present. Different bismuth citrate species are in fast exchange on the NMR time-scale at pH < 6.2; the exchange rate decreases at pH > 6.2, and different species can be observed.[130,131] By means of diffusion-ordered 2D [^{1}H, ^{13}C] HSQC NMR spectroscopy together with isotope-labelling of citrate (^{13}C2/^{13}C4), a wide range of different types of bound citrate can readily be detected at low Bi concentrations (5 mM) in aqueous solutions of ranitidine bismuth citrate at pH* 7.4. There appears to be an equilibrium between free citrate, dinuclear species $[Bi(citrate)_2Bi]^{2-}$ and multinuclear bismuth citrate clusters at physiological pH values. The solid-state structure of the antiulcer drug, ranitidine bismuth citrate may be closely related to that of $Na_2[Bi_2(citrate)_2]\cdot 7H_2O$ in view of the similarity in their chemical compositions (Bi : citrate = 1 : 1), crystallization conditions (ca. pH 4), and solid-state ^{13}C NMR spectra.[133] Second coordination sphere interactions between coordinated citrate and ranitidine have been detected by ^{1}H NMR.[130]

Both antimony and bismuth form stable complexes with the tripeptide glutathione (GSH) with a stoichiometry $[Bi(GS)_3]$ or $[Sb(GS)_3]$. The rate of uptake of these metals into red blood cells and complexation with intracellular glutathione as determined by spin-echo ^{1}H NMR, is rapid for Sb^{3+} (minutes) and relatively slow for Bi^{3+} (hours).[134,135] Strong binding of Sb^{3+} to trypanothione $[T(SH)_2]$ was chemically characterized for the first time by ESI–MS spectrometry and NMR spectroscopy. In contrast to the glutathione complex, each Sb^{3+} coordinates to only one $T(SH)_2$ with two sulfurs being provided from Cys residues and probably an oxygen from water.[136]

Binding of bismuth to human transferrin was unexpectedly strong.[137,138] The uptake of Bi^{3+} by apo-transferrin from bismuth citrate complexes is very slow (hours at 310 K) and occurs in at least two steps, whereas transfer from bismuth nitrilotriacetate is rapid (min). ^{13}C NMR suggests that bismuth binds to transferrin along with carbonate (CO_3^{2-}) as the synergistic anion, which is similar to Fe^{3+}. Binding of Bi^{3+} occurs preferentially to the C-lobe of transferrin. This order of lobe-loading has been confirmed by 2D [^{1}H, ^{13}C] heteronuclear multiple-quantum coherence (HMQC) NMR studies using recombinant ε-[^{13}C]Met-hTF (ca. 0.3 mM) in which all Met residues are enriched with ^{13}C at the $-SCH_3$ group. The changes in shift of the ^{1}H and ^{13}C NMR resonances of Met can be used not only as a probe for determining the order of lobe-loading of transferrin with metal ions, but also as fingerprints of conformational changes induced by Bi^{3+} and other metal ions. Bi^{3+}, Fe^{3+}, Ga^{3+} and Al^{3+} probably induce similar conformational changes in hTF, since the changes in shifts of SCH_3 resonances (Met) are almost identical.[139] Due to the ^{13}C labeling of Met and the sensitivity enhancement obtainable by inverse detection, the possible metal binding (e.g., Bi^{3+}) to transferrin (ε-[^{13}C]Met-hTF) can readily detected in the presence of large excess of other proteins and even in blood plasma by 1D and 2D [^{1}H, ^{13}C] NMR spectroscopy.[140] Transferrin was found to be a potential mediator for Bi^{3+} transport in blood plasma, which may have implications for the mechanism of neurotoxicity of Bi^{3+} drugs.

6 SUMMARY

NMR spectroscopy is one of the most powerful techniques for the study of interactions of metallodrugs with molecules of biological importance. The chemical shifts of some nuclei such as ^{195}Pt are sensitive to either the oxidation state or to coordination sphere and provide information on the binding site of the metallodrug–biomolecule complex. With the development of NMR techniques and currently available high-fields (e.g., >17 T), more information is expected to be obtained from NMR experiments. The recent success of ^{67}Zn NMR in the study of a metalloprotein may shed light on other biologically relevant quadrupolar nuclei.[141] The use of inverse detection of ^{13}C or ^{15}N (e.g., 2D HSQC, HSQC-TOCSY, HSQC-NOESY) together with isotopically-labeled metallodrugs or biomolecules, allows studies to be conducted at physiologically relevant concentrations. The structures and dynamics of metallodrug-biomolecule complexes which have been investigated by 1D and 2D homo- and hetero-nuclear NMR techniques will continue to be an important field of study. Theoretically, drug discovery of inorganic compounds can also be screened based on structure-and-activity relationship NMR (SAR-NMR)[142] and we have demonstrated that metallodrug binding to the 80 kDa protein (transferrin) can readily be followed.[139,140] Screening the binding of inorganic compounds to larger proteins and enzymes should now be possible by the transverse relaxation-optimized spectroscopy (TROSY) experiment.[143] The combination of NMR techniques with chromatography (LC-NMR and HPLC-NMR) should be a powerful method for the identification of novel metallodrug metabolites.[144]

7 RELATED ARTICLES IN VOLUMES 1–8

Body Fluids, Volume 2, Contrast Agents in Whole Body Magnetic Resonance: An Overview, Volume 3, Lithium NMR, Volume 5, Nucleic Acids: Spectra, Structures, & Dynamics, Volume 5, Transferrins, Volume 8.

8 REFERENCES

1. (a) P. J. Sadler, *Adv. Inorg. Chem.*, 1991, **36**, 1; (b) *Metallopharmaceuticals (Top. Biol. Inorg. Chem.*, Vols. 1 and 2), Springer: Heidelberg, 1999; (c) N. P. Farrell, 'Uses of Inorganic Chemistry in Medicine', Royal Society of Chemistry: Cambridge, 1999.
2. (a) Z. Guo and P. J. Sadler, *Angew. Chem. Int. Edn.*, 1999, **38**, 1512; (b) Z. Guo and P. J. Sadler, *Adv. Inorg. Chem.*, 2000, **49**, 183.
3. Medicinal Inorganic Chemistry special issue of *Chem. Rev.*, 1999, **99**, 2201.
4. (a) M. J. Abrams and B. A. Murrer, *Science*, 1993, **261**, 725; (b) J. Reedijk, *Curr. Opin. Chem. Biol.*, 1999, **3**, 236.
5. (a) J. M. Aramini and H. J. Vogel, *Biochem. Cell. Biol.*, 1998, **76**, 210; (b) M. W. Germann, J. M. Aramini, and H. J. Vogel, *J. Am. Chem. Soc.*, 1994, **116**, 6971.
6. J. M. Aramini and H. J. Vogel, *J. Magn. Reson. Ser B*, 1996, **110**, 182.
7. P. O. Weslund and H. Wennerstrom, *J. Magn. Reson.*, 1982, **50**, 451.

8. (a) L. G. Werbelow, *J. Chem. Phys.*, 1979, **70**, 5381; (b) L. G. Werbelow and G. Pouzard, *J. Phys. Chem.*, 1981, **85**, 3887.
9. (a) S. J. Berners-Price and P. J. Sadler, *Coord. Chem. Rev.*, 1996, **151**, 1; (b) Y. Chen, Z. J. Guo, and P. J. Sadler, in 'Cisplatin – Chemistry and Biochemistry of a Leading Anticancer Drug', ed B. Lippert, Wiley-VCH: Weinheim, 1999; (c) S. O. Ana, Z. Kuklenyik, and L. G. Marzilli, *ibid.*
10. B. Rosenberg, L. van Camp, and T. Krigas, *Nature*, 1965, **205**, 698.
11. B. Rosenberg, L. van Camp, J. E. Trosko, and V. H. Mansour, *Nature*, 1969, **222**, 385.
12. (a) H. M. Pinto and J. H. Schornagel, 'Platinum and Other Coordination Compounds in Cancer Chemotherapy', Plenum: New York, 1996; (b) B. Lippert, 'Cisplatin – Chemistry and Biochemistry of a Leading Anticancer Drug', ed B. Lippert, Wiley-VCH: Weinheim, 1999.
13. P. S. Pregosin, *Annu. Rep. NMR Spectrosc.*, 1986, **17**, 285.
14. D. P. Bancroft, C. A. Lepre, and S. J. Lippard, *J. Am. Chem. Soc.*, 1990, **112**, 6860.
15. I. M. Ismail and P. J. Sadler, *ACS Symp. Ser.*, 1983, **209**, 171.
16. T. G. Appleton, J. R. Hall, and S. F. Ralph, *Aust. J. Chem.*, 1986, **39**, 1347.
17. T. G. Appleton, J. R. Hall, and S. F. Ralph, *Inorg. Chem.*, 1985, **24**, 673.
18. G. M. Clore and A. M. Gronenborn, *J. Am. Chem. Soc.*, 1982, **104**, 1369.
19. S. K. Miller and L. G. Marzilli, *Inorg. Chem.*, 1985, **24**, 2421.
20. T. G. Appleton, J. R. Hall, and S. F. Ralph, *Inorg. Chem.*, 1985, **24**, 4685.
21. T. G. Appleton, J. W. Connor, and J. R. Hall, *Inorg. Chem.*, 1988, **27**, 130.
22. S. T. Sullivan, A. Ciccarese, F. P. Fanizzi, and L. G. Marzilli, *Inorg. Chem.*, 2001, **40**, 455.
23. I. M. Ismail, S. J. S. Kerrison, and P. J. Sadler, *J. Chem. Soc. Chem. Commun.*, 1980, 1261.
24. R. E. Norman and P. J. Sadler, *Inorg. Chem.*, 1988, **27**, 3583.
25. T. G. Appleton, R. D. Berry, C. A. Davis, J. R. Hall, and H. A. Kimlin, *Inorg. Chem.*, 1984, **23**, 3514.
26. S. J. Berners-Price and P. W. Kuchel, *J. Inorg. Biochem.*, 1990, **38**, 327.
27. A. J. Shaka, P. B. Barker, and R. Freeman, *J. Magn. Reson.*, 1985, **64**, 547.
28. J. Stonehouse, G. L. Shaw, J. Keeler, and E. D. Laue, *J. Magn. Reson. Ser. A*, 1994, **107**, 174.
29. S. J. Berners-Price, T. A. Frenkiel, U. Frey, J. D. Ranford, and P. J. Sadler, *J. Chem. Soc. Chem. Commun.*, 1992, 789.
30. S. J. Barton, K. J. Barnham, A. Habtemariam, R. E. Sue, and P. J. Sadler, *Inorg. Chim. Acta*, 1998, **273**, 8.
31. Y. Chen, Z. Guo, S. Parsons, and P. J. Sadler, *Chem. Eur. J.*, 1998, **4**, 672.
32. S. J. Berners-Price, T. A. Frenkiel, J. D. Ranford, and P. J. Sadler, *J. Chem. Soc. Dalton. Trans.*, 1992, 2137.
33. S. J. Berners-Price, U. Frey, J. D. Ranford, and P. J. Sadler, *J. Am. Chem. Soc.*, 1993, **115**, 8649.
34. K. J. Barnham, S. J. Berners-Price, T. A. Frenkiel, U. Frey, and P. J. Sadler, *Angew. Chem. Int. Edn. Engl.*, 1995, **34**, 1874.
35. S. J. Berners-Price, K. J. Barnham, U. Frey, and P. J. Sadler, *Chem. Eur. J.*, 1996, **2**, 1283.
36. F. Gonnet, J. Kozelka, and J.-C. Chottard, *Angew. Chem. Int. Edn. Engl.*, 1992, **31**, 1483.
37. F. Reeder, Z. Guo, P. del S. Murdoch, A. Corazza, T. W. Hambley, S. J. Berners-Price, J.-C. Chottard, and P. J. Sadler, *Eur. J. Biochem.*, 1997, **249**, 370.
38. S. J. Berners-Price, A. Corazza, Z. Guo, K. J. Barnham, P. J. Sadler, Y. Ohyama, M. Leng, and D. Locker, *Eur. J. Biochem.*, 1997, **243**, 782.
39. M. S. Davies, S. J. Berners-Price, and W. Hambley, *J. Am. Chem. Soc.*, 1998, **120**, 11 380.
40. E. R. Jamieson and Lippard, *Chem. Rev.*, 1999, **99**, 2467.
41. E. Reed, R. F. Ozols, R. Tarone, S. H. Yuspa, and M. C. Poirier, *Proc. Natl. Acad. Sci. USA*, 1987, **84**, 5024.
42. Y. Corda, M. F. Anin, M. Leng, and D. Job, *Biochemistry*, 1992, **31**, 1904.
43. L. J. N. Bradley, K. J. Yarema, S. J. Lippard, and J. M. Essigmann, *Biochemistry*, 1993, **32**, 982.
44. C. S. Chow, C. M. Barnes, and S. J. Lippard, *Biochemistry*, 1995, **34**, 2956.
45. U. M. Ohndorf, J. P. Whitehead, N. L. Raju, and S. J. Lippard, *Biochemistry*, 1997, **36**, 14 807.
46. E. E. Trimmer, D. B. Zamble, S. J. Lippard, and J. M. Essigmann, *Biochemistry*, 1998, **37**, 352.
47. P. M. Pil and S. J. Lippard, *Science*, 1992, **256**, 234.
48. D. B. Zamble, D. Mu, J. T. Reardon, A. Sancar, and S. J. Lippard, *Biochemistry*, 1996, **35**, 10 004.
49. J.-C. Huang, D. B. Zamble, J. T. Reardon, S. J. Lippard, and A. Sancar, *Proc. Natl. Acad. Sci. USA*, 1994, **91**, 10 394.
50. S. O. Ano, Z. Kuklenyok, L. G. Marzilli, in 'Cisplatin – Chemistry and Biochemistry of a Leading Anticancer Drug', ed B. Lippert, Wiley-VCH: Weinheim, 1999.
51. D. Yang, S. S. G. E. van Boom, J. Reedijk, J. H. van Boom, and A. H.-J. Wang, *Biochemistry*, 1995, **34**, 12 912.
52. F. Herman, J. Kozelka, V. Stoven, E. Guittet, J.-P. Pirault, T. Huynh-Dinh, J. Igolen, J.-Y. Lallemand, and J.-C. Chottard, *Eur. J. Biochem.*, 1990, **194**, 119.
53. A. Gelasco and S. J. Lippard, *Biochemistry*, 1998, **37**, 9230.
54. J. A. Parkinson, Y. Chen, P. del S. Murdoch, Z. Guo, S. J. Berners-Price, T. Brown, and P. J. Sadler, *Chem. Eur. J.*, 2000, **6**, 3636.
55. Y. Chen, J. A. Parkinson, Z. Guo, T. Brown, and P. J. Sadler, *Angew. Chem. Int. Edn.*, 1999, **38**, 2060.
56. S. U. Dunham, S. U. Dunham, C. J. Turner, and S. J. Lippard, *J. Am. Chem. Soc.*, 1998, **120**, 5395.
57. M.-H. Fouchet, E. Guittet, J. A. H. Cognet, J. Kozelka, C. Gauthier, M. L. Bret, K. Zimmermann, and J.-C. Chottard, *J. Biol. Inorg. Chem.*, 1997, **2**, 83.
58. H. Huang, L. Zhu, B. R. Reid, G. P. Drobny, and P. B. Hopkins, *Science*, 1995, **270**, 1842.
59. F. Paquet, C. Pérez, M. Leng, G. Lancelot, and J.-M. Malinge, *J. Biomol. Struct. Dyn.*, 1996, **14**, 67.
60. C. J. van Garderen and L. P. A. van Houte, *Eur. J. Biochem.*, 1994, **225**, 1169.
61. P. M. Takahara, C. A. Frederick, and S. J. Lippard, *Nature*, 1995, **377**, 649.
62. L. G. Marzilli, J. S. Saad, Z. Kuklenyik, K. A. Keating, and Y. Xu, *J. Am. Chem. Soc.*, 2001, **123**, 2764.
63. J. M. Teuben, S. S. G. E. van Boom, and J. Reedijk, *J. Chem. Soc. Dalton Trans.*, 1997, 3979.
64. Z. Guo, T. W. Hambley, P. del S. Murdoch, and P. J. Sadler, *J. Chem. Soc. Dalton Trans.*, 1997, 469.
65. K. J. Barnham, M. I. Djuran, P. del S. Murdoch, J. D. Ranford, and P. J. Sadler, *J. Chem. Soc. Dalton Trans.*, 1997, 3721.
66. K. J. Barnham, U. Frey, P. del S. Murdoch, J. D. Ranford, and P. J. Sadler, *J. Am. Chem. Soc.*, 1994, **116**, 11 175.
67. T. G. Appleton, J. W. Connor, J. R. Hall, and P. D. Prenzler, *Inorg. Chem.*, 1989, **28**, 2030.
68. P. del S. Murdoch, N. A. Kratochwil, J. A. Parkinson, M. Patriarca, and P. J. Sadler, *Angew. Chem. Int. Edn.*, 1999, **38**, 2949.
69. J. J. Gullo, C. L. Litterst, P. J. Maguire, B. J. Sikis, D. F. Holth, and P. V. Woodley, *Cancer Chemother. Pharmacol.*, 1980, **5**, 21.
70. F. Kratz, in 'Metal Complexes in Cancer Chemotherapy', ed B. K. Keppler, VCH: Weinheim, Germany, 1993.
71. A. I. Ivanov, J. Christodoulou, J. A. Parkinson, K. J. Barnham, A. Tucker, J. Woodrow, and P. J. Sadler, *J. Biol. Chem.*, 1998, **273**, 14 721.

72. M. C. Cox, K. J. Barnham, T. A. Frenkiel, J. D. Hoeschele, A. B. Mason, Q.-Y. He, R. C. Woodworth, and P. J. Sadler, *J. Biol. Inorg. Chem.*, 1999, **4**, 621.
73. O. M. Ni Dhubhghaill, W. R. Hagen, B. K. Keppler, K.-G. Lipponer, and P. J. Sadler, *J. Chem. Soc. Dalton Trans.*, 1994, 3305.
74. F. Kratz, M. Hartmann, B. K. Keppler, and L. Messori, *J. Biol. Chem.*, 1994, **269**, 2581.
75. J. M. Aramini, D. D. McIntyre, and H. J. Vogel, *J. Am. Chem. Soc.*, 1994, **116**, 11 506.
76. H. Sun, H., H. Li, R. Weir, and P. J. Sadler, *Angew. Chem. Int. Edn.*, 1998, **37**, 1577.
77. M. Guo, H. Sun, H. J. McArdle, L. Gambling, and P. J. Sadler, *Biochemistry*, 2000, **39**, 10 023.
78. C. F. Shaw III, *Comments Inorg. Chem.*, 1989, **8**, 233.
79. (a) S. P. Fricker, *Gold Bull.*, 1996, **29**, 53; (b) S. L. Best and P. J. Sadler, *Gold Bull.*, 1996, **29**, 87; (c) P. J. Sadler, *Struct. Bonding*, 1984, **29**, 171.
80. C. F. Shaw III, *Chem. Rev.*, 1999, **99**, 2589.
81. R. Bau, *J. Am. Chem. Soc.*, 1998, **120**, 9380.
82. A. A. Isab and P. J. Sadler, *J. Chem. Soc. Dalton Trans.*, 1982, 135.
83. M. T. Razi, G. Otiko, and P. J. Sadler, *ACS Symp. Ser.*, 1983, **209**, 371.
84. J. R. Roberts, J. Xiao, B. Schliesman, D. J. Parsons, and C. F. Shaw III, *Inorg. Chem.*, 1996, **35**, 424.
85. P. J. Sadler and R. E. Sue, *Met. Based Drugs*, 1994, **1**, 107.
86. C. F. Shaw III, M. T. Coffer, J. Klingbeil, and C. K. Mirabelli, *J. Am. Chem. Soc.*, 1988, **110**, 729.
87. C. F. Shaw III, A. A. Isab, J. D. Hoeschele, M. Starich, J. Locke, P. Schulteis, and J. Xiao, *J. Am. Chem. Soc.*, 1994, **116**, 2254.
88. O. M. Ni Dhubhghaill, P. J. Sadler, and A. Tucker, *J. Am. Chem. Soc.*, 1992, **114**, 1118.
89. J. Christodoulou, P. J. Sadler, and A. Tucker, *Eur. J. Biochem.*, 1994, **225**, 363.
90. J. Christodoulou, P. J. Sadler, and A. Tucker, *FEBS Lett.*, 1995, **376**, 1.
91. R. C. Elder, Z. Zhao, Y. Zhang, J. G. Dorsey, E. V. Hess, and K. Tepperman, *J. Rheumatol.*, 1993, **20**, 268.
92. G. G. Graham, J. R. Bales, M. C. Grootveld, and P. J. Sadler, *J. Inorg. Biochem.*, 1985, **25**, 163.
93. G. Lewis and C. F. Shaw III, *Inorg. Chem.*, 1986, **25**, 58.
94. M. N. Akhtar, I. H. Gazi, A. A. Isab, A. R. Al-Arfaj, M. I. N. Wazeer, and M. S. Hussain, *J. Coord. Chem.*, 1995, **36**, 149.
95. A. A. Isab, I. H. Gazi, and A. R. Al-Arfaj, *J. Chem. Soc. Dalton Trans.*, 1993, 841.
96. A. J. Canumalla, S. Schraa, A. A. Isab, C. F. Shaw III, E. Gleichmann, L. Dunemann, and M. Turfeld, *J. Biol. Inorg. Chem.*, 1998, **3**, 9.
97. J. F. Cade, *Med. J. Aust.*, 1949, **36**, 349.
98. (a) L. H. Price and G. R. Heninger, *N. Engl. J. Med.*, 1994, **331**, 591; (b) N. J. Birch, 'Lithium: Inorganic Pharmacology and Psychiatric Use', IRL Press: Oxford, 1988.
99. J. R. Atack, H. B. Broughton, and S. J. Pollack, *Trends Neurosci.*, 1995, **18**, 343.
100. J. R. Atack, *Med. Res. Rev.*, 1997, **17**, 215.
101. G. Emilien, J. M. Maloteaux, A. Seghers, and G. Charles, *Arch. Int. Pharmacodyn.*, 1995, **330**, 251.
102. J. F. Dixon, G. V. Los, and L. E. Hokin, *Proc. Natl. Acad. Sci. USA*, 1994, **91**, 8358.
103. S. Nonaka, C. J. Hough, and D.-M. Chuang, *Proc. Natl. Acad. Sci. USA*, 1998, **95**, 2642.
104. (a) R. A. Komoroski, *Magn. Reson. Imaging*, 2000, **18**, 103; (b) F. G. Riddell, in 'Lithium: 50 years of Psychopharmacology. New Perspectives in Biomedical and Clinical Research', eds N. J. Birch, V. S. Gallicchio, and R. W. Becker, Weidner Publishing Group: Cheshire, CT, 2000; (c) F. G. Riddell, *J. Trace Microprobe. Technol.*, 1998, **16**, 99.
105. (a) C. Brevard and P. Granger, 'Handbook of High Resolution Multinuclear NMR', Wiley-Interscience Publication: New York, 1981; (b) J. E. Mason, 'Multinuclear NMR', 2nd edn, Plenum Press: London, 1989.
106. F. G. Riddell, in 'Lithium and the Cell: Pharmacology and Biochemistry', ed N. J. Birch, Academic Press: London, 1991, p. 85.
107. D. Mota de Freitas, *Methods Enzymol.*, 1993, **227**, 78.
108. V. Saudek, P. Vincendon, Q.-T. Do, R. A. Atkinson, V. Sklenár, P. D. Pelton, F. Piriou, and A. J. Ganzhorn, *Eur. J. Biochem.*, 1996, **240**, 288.
109. J. Mendels and A. Frazer, *J. Psychiat. Res.*, 1973, **10**, 9.
110. For example, (a) Q. Rong, M. Espanol, D. Mota de Freitas, and C. F. G. C. Geraldes, *Biochemistry*, 1993, **32**, 13 490; (b) S. Ramaprasad and V. W. Robbins, *Magn. Reson. Imaging*, 1998, **16**, 213; (c) S. Ramaprasad and V. W. Robbins, *Magn. Reson. Imaging*, 1998, **16**, 219.
111. J. Bramham, A. N. Carter, and F. G. Riddell, *J. Inorg. Biochem.*, 1996, **61**, 273.
112. J. Nikolakopoulos, C. Zacharich, D. Mota de Freitas, and C. F. G. C. Geraldes, *Inorg. Chim. Acta*, 1996, **251**, 201.
113. J. Nikolakopoulos, C. Zacharich, D. Mota de Freitas, E. B. Stubbs, R. Ramasamy, G. M. C. A. Castro, and C. F. G. C. Geraldes, *J. Neurochem.*, 1998, **71**, 1676.
114. T. Kato, S. Takahashi, and T. Inubushi, *Lithium*, 1994, **5**, 75.
115. P. F. Renshaw, G. S. Sachs, and R. G. Gonzalez, in 'NMR Spectroscopy in Psychiatric Brain Disorders', eds H. A. Nasrallah and J. W. Pettegrew, American Psychiatric Press: Washington, 1995.
116. J. C. Soares, F. Boada, and M. S. Keshavan, *Eur. Neuropsychopharmacol.*, 2000, **10**, 151.
117. (a) R. A. Komoroski, *Curr. Sci.*, 1999, **76**, 789; (b) R. A. Komoroski, *Anal. Chem.*, 1994, **66**, 1024A.
118. P. F. Renshaw, J. C. Haselgrove, J. S. Leigh, and B. Chance, *Magn. Reson. Med.*, 1985, **2**, 512.
119. P. F. Renshaw and S. Wicklund, *Biol. Psychiatry*, 1988, **23**, 465.
120. S. Ramaprasad, J. E. O. Newton, D. Cardwell, A. H. Fowler, and R. A. Komoroski, *Magn. Reson. Imaging*, 1992, **25**, 308.
121. R. A. Komoroski, J. M. Pearce, and J. E. O. Newton, *Magn. Reson. Med.*, 1997, **38**, 275.
122. R. A. Komoroski, J. M. Pearce, and J. E. O. Newton, *J. Magn. Reson.*, 1998, **133**, 98.
123. T. Kato, T. Inubushi, and S. Takahashi, *J. Clin. Psychopharmacol.*, 1994, **14**, 330.
124. T. Kato, K. Fujii, T. Shioiri, T. Inubushi, and S. Takahashi, *Prog. Neuropsychopharmacol. Biol. Psychiatry*, 1996, **20**, 87.
125. G. S. Sachs, P. F. Renshaw, B. Lafer, A. L. Stoll, A. R. Guimaraes, J. F. Rosenbaum, and R. G. Gonzalez, *Biol. Psychiatry*, 1995, **38**, 422.
126. J. C. Soares, F. Boada, S. Spencer, A. G. Mallinger, C. S. Dippold, K. F. Wells, E. Frank, M. S. Keshavan, S. Gershon, and D. J. Kupfer, *Biol. Psychiatry*, 2001, **49**, 437.
127. G. Q. Chen, X. G. Shi, W. Tang, S. M. Xiong, J. Zhu, X. Cai, Z. G. Han, J. H. Ni, G. Y. Shi, P. M. Jia, M. M. Liu, K. L. He, C. Niu, J. Ma, P. Zhang, T. D. Zhang, P. Paul, T. Naoe, K. Kitamura, W. Miller, S. Waxman, Z. Y. Wang, H. de The, S. J. Chen, and Z. Chen, *Blood*, 1997, **89**, 3345.
128. Z. X. Shen, G. Q. Chen, J. H. Ni, X. S. Li, S. M. Xiong, Q. Y. Qiu, J. Zhu, W. Tang, G. L. Sun, K. Q. Yang, Y. Chen, L. Zhou, Z. W. Fang, Y. T. Wang, J. Ma, P. Zhang, T. D. Zhang, S. J. Chen, Z. Chen, and Z. Y. Wang, *Blood*, 1997, **89**, 3354.
129. S. J. Soignet, P. Maslak, Z. G. Wang, S. Jhanwar, E. Calleja, L. J. Dardashti, D. Corso, A. De Blasio, J. Gabrilove, D. A. Scheinberg, P. P. Pandolfi, and R. P. Warrell, *N. Engl. J. Med.*, 1998, **339**, 1341.
130. P. J. Sadler and H. Sun, *J. Chem. Soc. Dalton Trans.*, 1995, 1395.

131. E. Asato, K. Katsura, M. Mikuriya, T. Fujii, and J. Reedijk, *Inorg. Chem.*, 1993, **32**, 5322.
132. J. A. Parkinson, H. Sun, and P. J. Sadler, *J. Chem. Soc. Chem. Commun.*, 1998, 881.
133. P. J. Barrie, M. I. Djuran, M. A. Mazid, M. McPartlin, P. J. Sadler, I. J. Scowen, and H. Sun, *J. Chem. Soc. Dalton Trans.*, 1996, 2417.
134. P. J. Sadler, H. Sun, and H. Li, *Chem. Eur. J.*, 1996, **2**, 701.
135. H. Sun, S.-C. Yan, and W.-S. Cheng, *Eur. J. Biochem.*, 2000, **267**, 5450.
136. S.-C. Yan, K. Ding, L. Zhang, and H. Sun, *Angew. Chem. Int. Edn.*, 2000, **39**, 4260.
137. H. Li, P. J. Sadler, and H. Sun, *J. Biol. Chem.*, 1996, **271**, 9483.
138. H. Sun, H. Li, A. B. Mason, R. C. Woodworth, and P. J. Sadler, *Biochem. J.*, 1999, **337**, 105.
139. H. Sun, M. C. Cox, H. Li, A. B. Mason, R. C. Woodworth, and P. J. Sadler, *FEBS Lett.*, 1998, **422**, 315.
140. H. Sun, H. Li, A. B. Mason, R. C. Woodworth, and P. J. Sadler, *J. Biol. Chem.*, 2001, **276**, 8829.
141. A. S. Lipton, G. W. Buchko, J. A. Sears, M. A. Kennedy, and P. D. Ellis, *J. Am. Chem. Soc.*, 2001, **123**, 992.
142. S. B. Shuker, P. J. Hajduk, R. P. Meadows, and S. W. Fesik, *Science*, 1996, **274**, 1531.
143. K. Pervushin, R. Riek, G. Wider, and K. Wüthrich, *Proc. Natl. Acads. Sci., USA*, 1997, **94**, 12 366.
144. J. C. Lindon, J. K. Nicholson, and I. D. Wilson, *J. Chromatogr. B*, 2000, **748**, 233.

Acknowledgements

We thank the University of Hong Kong (CRCG and UGC) Livzon Pharmaceutical Group and Area of Excellence Scheme of University Grants Committee (Hong Kong) for their support, and Dr. Geoffrey D. Brown for critical comments.

Biographical Sketch

Hongzhe Sun, *b* 1964. B.Sc. 1985, M.Sc. 1990, Ph.D., 1996, Postgraduate study (M.Sc.) at Wuhan Institute of Physics, the Chinese Academy of Sciences. Spent three years as a research associate and a lecturer at Nanjing University before undertaking Ph.D. research under the guidance of Peter J. Sadler at the University of London, Great Britain. Research fellow at the University of Edinburgh, 1996–1998. Assistant professor of chemistry, the University of Hong Kong, P. R. China, 1998–present. Over 30 publications. Current research interests: biological inorganic chemistry, structures and functions of metalloproteins.

Microporous Materials and Xenon-129 NMR

Jacques Fraissard

Université Pierre et Marie Curie, Paris, France

1	Introduction	1
2	Chemical Shift of Xenon Adsorbed on a Zeolite	1
3	Influence of the Pore Structure on δ_s: Application to Porosity	1
4	Influence of Temperature	3
5	Effect of the Si/Al Ratio of Zeolites	3
6	Influence of Cations	4
7	Cation Exchange Between Different Zeolites	5
8	Distribution of the Adsorbed Phases	5
9	Effect of Extraframework Aluminum	5
10	Conclusions	6
11	Related Articles	6
12	References	6

1 INTRODUCTION

The central idea of the pioneers of this general research was to find a molecule[1] which was nonreactive and particularly sensitive to its environment, physical interactions with other chemical species, and the nature of adsorption sites, which could be used as a probe for determining in a new way solid properties that are difficult to detect by classical physicochemical techniques. In addition, the probe needed to be detectable by NMR spectroscopy, since this technique is particularly suitable for investigating electron perturbations in rapidly moving molecules.

Xenon is this ideal probe because it is an inert gas, is monoatomic, and has a large spherical electron cloud. From the NMR point of view, the ^{129}Xe isotope has a spin of $\frac{1}{2}$, its natural abundance in xenon is 26%, and its sensitivity of detection relative to the proton is about 10^{-2}. The recent development by Pines and co-workers of xenon optical polarization techniques offers increased sensitivity by a factor of 10^3 for the detection of adsorbed xenon.[2,3] The high polarizability of the xenon atom makes it very sensitive to its environment. Small variations in the physical interactions with the environment cause marked perturbations of the electron cloud; these are transmitted directly to the xenon nucleus and greatly affect the NMR chemical shift.

2 CHEMICAL SHIFT OF XENON ADSORBED ON A ZEOLITE

In pure xenon gas,[4] the ^{129}Xe chemical shift can be expressed by a virial expansion of the xenon density ρ:

$$\delta(T, \rho) = \delta_0 + \delta_{1,\mathrm{Xe}}(T) \cdot \rho_{\mathrm{Xe}} + \delta_{2,\mathrm{Xe}}(T) \cdot \rho_{\mathrm{Xe}}^2 + \delta_{3,\mathrm{Xe}}(T) \cdot \rho_{\mathrm{Xe}}^3 + \ldots \quad (1)$$

where $\delta(T,\rho)$ is the resonance shift at temperature T and density ρ. The term δ_0 is the value of the resonance shift extrapolated to an infinitely low density; $\delta_{i,\mathrm{Xe}}(T)$ are the virial coefficients of the shift in density.

For mixtures of xenon and another gas A, Jameson et al.[4] showed that, in the linear range,

$$\delta = \delta_0 + \delta_{1,\mathrm{Xe}}(T) \cdot \rho_{\mathrm{Xe}} + \delta_{1,\mathrm{A}}(T) \cdot \rho_{\mathrm{A}} \quad (2)$$

where ρ_{Xe} and ρ_{A} are the densities of xenon and 'solvent' molecules A, respectively; $\delta_{1,\mathrm{Xe}}$ and $\delta_{1,\mathrm{A}}$ characterize the Xe–Xe and Xe–A interactions, respectively.

As in the gas phase, most information has been obtained from analyzing the variation in the chemical shift with xenon concentration, generally at 26 °C. The amount of xenon adsorbed is expressed as the number of atoms N per gram of anhydrous zeolite or the number of atoms n_s per cage (zeolites Y, ZK-4, erionite, etc.).

Fraissard et al. have shown that the chemical shift of adsorbed xenon is the sum of several terms corresponding to the various perturbations that it experiences[1,5,6]

$$\delta = \delta_{\mathrm{ref}} + \delta_s + \delta_{\mathrm{Xe}} + \delta_{\mathrm{SAS}} + \delta_{\mathrm{E}} + \delta_{\mathrm{M}} \quad (3)$$

δ_{ref} is the reference (gaseous xenon at zero pressure). The term δ_s accounts for interactions between xenon and the surface of the zeolitic pores, assuming that the solid does not contain any electrical charge; thus it depends only on the dimensions of the cages or channels and on the ease of xenon diffusion. The term $\delta_{\mathrm{Xe}} = \delta_{\mathrm{Xe-Xe}} \cdot \rho_{\mathrm{Xe}}$ accounts for Xe–Xe interactions; it increases with increasing local density of adsorbed xenon and becomes predominant at high xenon pressure. When the Xe–Xe collisions are isotropically distributed (large spherical cage) the relationship $\delta = f(N)$ is a straight line (Figure 1, curve 1). The slope, $\mathrm{d}\delta/\mathrm{d}n$ is proportional to the local xenon density and, therefore, inversely proportional to the 'void volume'. If the Xe–Xe collisions are anisotropically distributed (narrow channels), $\mathrm{d}\delta/\mathrm{d}N$ increases with N (Figure 1, curve 2).

When there are strong adsorption sites (SASs) in the void space, these interact with xenon much more than do the cage or channel walls, and each xenon atom spends a relatively long time on the SAS, particularly at low xenon concentration. The corresponding chemical shift δ_{SAS} will be greater than in the case of a noncharged structure (Figure 1, curve 3). When N increases, δ must decrease if there is fast exchange of the atoms adsorbed on the SASs with those adsorbed on other sites. When N is high enough, the effect of Xe–Xe interactions again becomes the most important factor, and the dependence of δ on N is then similar to that shown by curve 1 in Figure 1. In this case, $\delta_{N\to 0}$, (the chemical shift extrapolated to zero concentration) depends on the nature and number of these SASs. Often, these SASs are charged, and sometimes they are paramagnetic cations. The theoretical curve (3 in Figure 1), is displaced to high frequency (Figure 1, curve 4). The difference between curves 1 and 3 shows the effect (δ_{E}) of the electrical field and, if present, the effect (δ_{M}) due to the magnetic field created by these cations.[1]

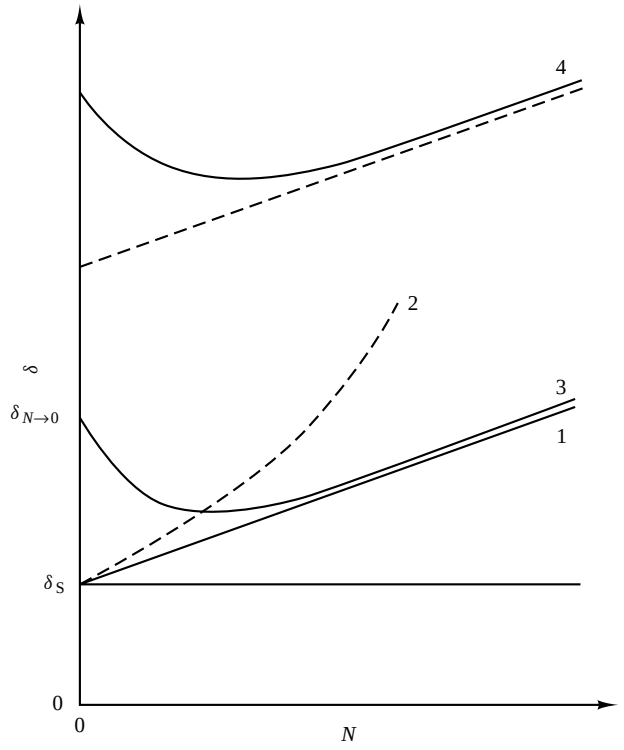

Figure 1 Variation in the chemical shift of xenon adsorbed on a porous solid. See text for details

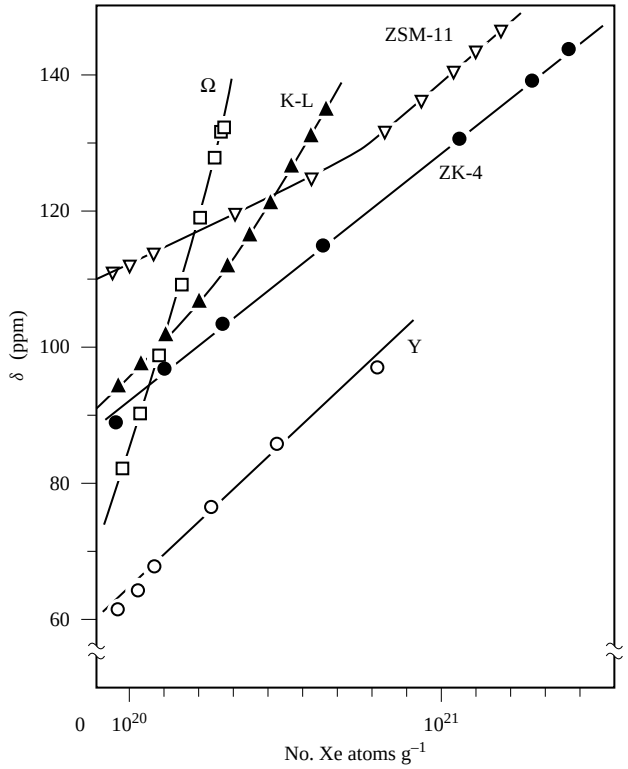

Figure 2 Chemical shift δ of adsorbed ^{129}Xe versus the number of xenon atoms per gram of solid

3 INFLUENCE OF THE PORE STRUCTURE ON Δ_s: APPLICATION TO POROSITY

The relationship $\delta = f(N)$ is characteristic of the zeolite structure when the Si/Al ratio is very high and when there are no strong adsorption sites accessible to xenon. Figure 2 illustrates the sensitivity of this technique to the pore structure. The slopes of the curves depend on the void volume of the pores; this is logical because for a given number of xenon atoms per gram, the local density and thus the Xe–Xe interactions depend on this volume. The chemical shift δ_s at zero concentration is related to the structure; the smaller the channels or cavities, or the more restricted the diffusion, and the greater δ_s becomes.

It is assumed that at 26 °C the experimental chemical shift is the average of the shift of xenon in rapid exchange between a position A on the pore surface (denoted by δ_a) and a position in the volume V of the cavity or channel (denoted by $\langle\delta_v\rangle$):

$$\delta = \frac{N_a\delta_a + N_v\langle\delta_v\rangle}{N_a + N_v} \tag{4}$$

where N_a and N_v are the number of xenon atoms in each state. This equation is valid for any xenon concentration, and thus for $N \to 0$, $\delta \to \delta_s$.

$\langle\delta_v\rangle$ is a function of δ_a and the distance traveled by the xenon atom between two successive collisions with the pore wall. In fact, $\delta_v = \delta_a$ when the xenon leaves the surface. δ_v then decreases during the journey between two collisions, and thus the need to determine the mean value $\langle\delta_v\rangle$.

In order to obtain by ^{129}Xe NMR precise data on the void space of a zeolite of unknown structure and the dimensions of structural defects, Springuel-Huet et al.[7] have calculated the 'mean free path' $\bar{l}$ of xenon imposed by the structure, and determined the dependence of δ_s on $\bar{l}$, both experimentally and by calculation (sphere, infinite cylinder):

$$\delta_s = \delta_a\frac{a}{a+\bar{l}} \tag{5}$$

where a is a constant. Equation (5) can be deduced from equation (4).[8] The large variation in δ_s with $\bar{l}$ (Figure 3) proves that ^{129}Xe NMR is very sensitive to pore dimensions.

Derouane and Nagy have been able to relate δ_a to the curvature of the adsorbing surface and, therefore, also to the pore diameter.[5] Finally, Ripmeester et al.[8] have continued this study by calculating the Lennard–Jones potential curves for a xenon atom and a spherical layer representing the atoms of a cage. They deduced that in small cages xenon is 'solid like' and in larger cages 'gas like', and that consequently it is difficult to imagine a single correlation between the xenon chemical shift and the dimensions of the adsorption zones.[8]

The symmetry of the adsorption site can sometimes be reflected by the form of the signal when the interactions to which the xenon atom is subjected are highly anisotropic. For example, Springuel-Huet and Fraissard have shown that the ellipsoid-shaped channels of SAPO-11 and $AlPO_4$-11 cause chemical shift anisotropy effects to be observed in the ^{129}Xe NMR spectra of adsorbed xenon,[3,5] due to the similarity between the small axis of the pore section (0.67 × 0.39 nm) and the diameter of the xenon atom (0.44 nm). Similar results have been obtained by Ripmeester et al. on Xe/clathrates systems.[3]

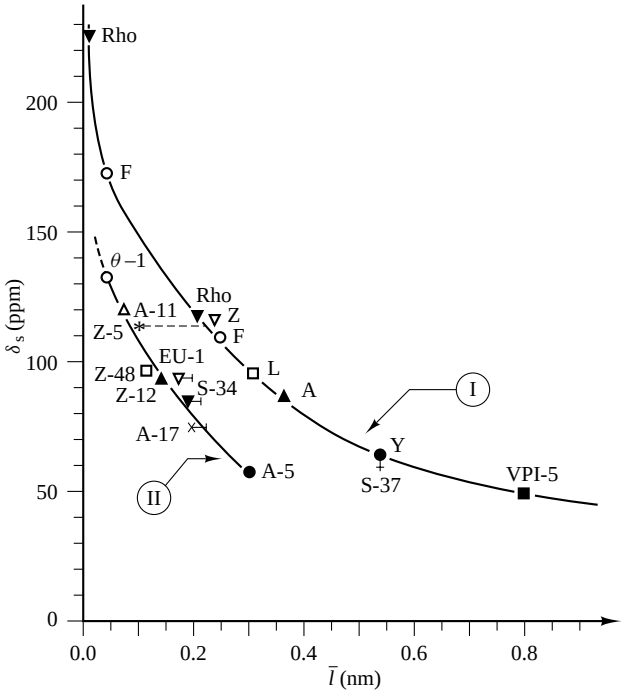

Figure 3 Variation in δ_s versus the mean free path l. F, ferrierite; Z-5, ZSM-5; Z-12, ZSM-12; Z-48, ZSM-48; A-5, $AlPO_4$-5; A-11, $AlPO_4$-11; A-17, $AlPO_4$-17; S-34, SAPO-34; S-37, SAPO-37

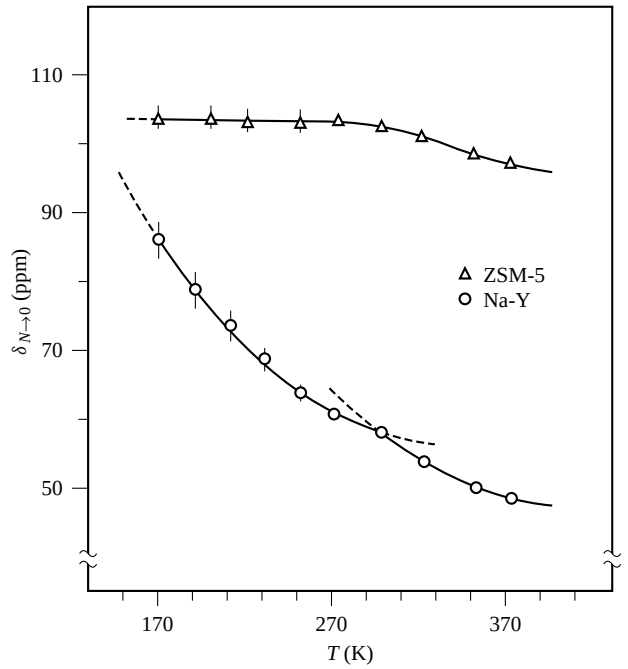

Figure 4 Variation in δ_s versus the temperature T of the experiment

When the zeolite structure includes several adsorption zones, the xenon spectrum must contain an equal number of components characteristic of these zones, provided that the diffusion of the xenon atoms is not too rapid on the NMR timescale.[1] Thus, the spectrum of sodium mordenite shows two signals at 26 °C, arising from xenon in the main channels and in the side pockets.[1,3,5] However, because of rapid exchange of xenon between these two regions there is only one signal for H^+-exchanged mordenite. The spectrum of ferrierite at 26 °C shows two signals characteristic of two types of channel.[3,5] In this case it was even possible to detect the presence of a mordenite intergrowth. Two signals have also been detected for the Xe/H-Rho system, but only at a temperature as low as − 50 °C so as to avoid rapid exchange of atoms located in the octagonal prisms and the large cavities. In Cs-Rho, only the signal corresponding to the large cavities is detected, since all the prisms are occupied by Cs^+.[5,6]

It is clear from these examples that this ^{129}Xe NMR can be used to identify all the different microporous adsorption zones, namely the structure defects in zeolites,[1] heteropolyanions, solid polymers,[3] clathrates,[3,6] etc.

4 INFLUENCE OF TEMPERATURE

The study of the temperature dependence is another way of checking the size of the pores in which the xenon is adsorbed.[9] The variation in temperature changes the relative residence times of xenon on the surface and in the free space, which in turn influence the xenon chemical shift. The variation in δ thus depends on $\langle\delta_v\rangle$. The variation is very small if $\langle\delta_v\rangle \simeq \delta_a$ (ZSM-5), and very large if $\langle\delta_v\rangle << \delta_a$ (Na-Y) (Figure 4).

From a quantitative point of view, Chen and Fraissard[9] have shown that

$$\mathrm{d}\left(\ln\frac{\delta_a-\delta_s}{\delta_s-\langle\delta_v\rangle}\right)\Big/\mathrm{d}T=-\frac{\Delta E}{RT^2} \qquad (6)$$

where ΔE is the energy difference between the xenon in the two states A and V. The fast exchange model is valid in the temperature range where the plot of $\ln[\delta_a - \delta_s/\delta_s - \langle\delta_v\rangle] = f(1/T)$ is a straight line.

5 EFFECT OF THE Si/Al RATIO OF ZEOLITES

The relationship between δ_s and the porous structure is strictly valid only for an electrically neutral surface. The chemical shift of xenon must therefore depend on the chemical composition of the zeolite, in particular on the number of charges, i.e. on the Si/Al ratio. This dependence is more pronounced when the temperature is low and the pore diameter is small (increased effect of δ_a with the contact time of xenon at the surface).

In the case of faujasite, either with Na^+ or decationized, the $\delta = f(N)$ relationships are almost parallel straight lines at 26 °C, and $\delta_{N\to0}$ decreases monotonically by 4 ppm when Si/Al increases from 1.28 to 54.[1] For ZSM-5 and ZSM-11 (narrow channels) the dependence of $\delta_{N\to0}$ on the aluminum concentration is greater than for faujasite (large cavities). In addition, this variation shows a break at about [Al] = 2 Al atoms per unit cell, which demonstrates that the xenon–wall interactions change at this concentration.[10] Thus aluminum is not randomly distributed in the lattice; rather, its distribution depends on the concentration. Finally, we mention the difference between the $\delta = f(N)$ relationships for ZSM-5 and ZSM-11 for [Al] ≥ 2 Al atoms per unit cell. Despite the similarity of the structures of these two zeolites, the sensitivity

of the ^{129}Xe NMR technique is sufficient to differentiate between them.

6 INFLUENCE OF CATIONS

It has been explained in Section 2 why the $\delta = f(N)$ curve goes through a minimum when there are strong adsorption sites in the zeolite. This has been shown for X and Y zeolites with divalent cations such as Mg^{2+}, Ca^{2+}, Zn^{2+}, Cd^{2+}, and Ni^{2+},[1,6,11] where xenon adsorption becomes saturated within the given pressure range.

Using a fast exchange model analogous to the one proposed by Springuel-Huet et al.,[7] but taking into account the possible presence of SASs, Cheung et al. were able to give an analytical expression of these curves in the form:[12]

$$\delta = \frac{\alpha}{\rho} + \delta_g \cdot \rho \qquad (7)$$

where ρ is the overall xenon density in the zeolite, δ_g is the $\delta_{1,Xe}$ coefficient [as in equation (1)], and α depends on the distribution of N_a and N_v [as defined in equation (4)]. The $1/\rho$ dependence results in an initial decrease in δ with increasing surface coverage, before the term linear in ρ begins to dominate. Let us consider, for example, Mg_λ-Y and Ca_λ-Y zeolites, dehydrated under vacuum at 500 °C, where λ denotes the degree of cation exchange with Na^+.[1] When Ca^{2+} cations are in the sodalite cage or the hexagonal prisms ($\lambda < 55\%$), δ is a linear function of the xenon concentration (as for Na-Y), regardless of the extent of dehydration of the sample. When some Ca^{2+} cations are situated within the supercages ($\lambda > 55$ %), for Ca_λ-Y one observes values of δ (compared with Na-Y) that are greatest when λ is high, especially at low xenon concentration. According to Ito et al., the experimental value of $\delta_{N\to 0}$ for $N = 0$ is roughly proportional to the square of the electric field at the nuclei of xenon atoms adsorbed on Ca^{2+} cations.[1]

According to Cheung et al., the high value of δ is not due solely to the high degree of polarization of xenon and the distortion of the xenon electron cloud by the strong electric fields created by the divalent cations. They suggest the formation of a partial bond between these two species formed by the donation of a xenon 5p electron to the empty s orbital of the divalent cation.[12] A similar model concerning electron transfer from xenon to platinum was proposed by Ito et al. to explain the large shift in δ for platinum supported on Na-Y.[1]

The effect of the dehydration and rehydration of zeolites on the influence of Ca^{2+} cations can also be studied by ^{129}Xe NMR.[1] For example, the chemical shift δ and the signal width $\Delta\omega$ of xenon adsorbed on Mg_{70}-Y increase with increasing dehydration of the solid. The values of δ and $\Delta\omega$ are greatest when dehydration is complete. Conversely, the spectra evolve with rehydration: for a given xenon pressure, line *a* due to xenon in the supercages containing only bare Mg^{2+} decreases in favor of line *b* corresponding to Mg^{2+} surrounded by water molecules. ^{129}Xe NMR therefore makes it possible to follow the diffusion of an adsorbate in a zeolite crystallite.

The problem is more difficult in the case of paramagnetic cations, especially when the extent of exchange is so high that the magnetic term [δ_M in equation (3)] becomes large. However, Scharf et al. have succeeded, using this technique, in following the reduction and reoxidation of the $Ni_{7.5}$-Na-Y zeolite desorbed under vacuum at 350 °C.[1,6] When the sample was reduced at lower temperatures (about 100 °C) two types of environment for the xenon atoms were evident: one corresponding to xenon in the nickel-exchanged material, and the other corresponding to xenon in contact with Na-Y or H-Y. Reduction at higher temperatures produced a low-frequency shift of the first resonance, indicating that this environment becomes more like the environment of xenon in the Na-Y zeolite. At the highest temperature (370 °C) studied, only the line corresponding to xenon in Na-Y was detected. These results prove that nickel ions are removed from the supercages upon reduction. Using this method, Scharf et al. showed that reoxidation under 80 kPa of oxygen at various temperatures does not reverse the process of reduction.

A particularly interesting case is that of faujasite-type zeolites containing Ag^+ or Cu^+ cations, the external electron structure of which is *n*d.[11] The ^{129}Xe NMR isotropic chemical shifts of xenon in Na-X and in the fully silver-exchanged zeolite Ag-X are shown in Figure 5. The shifts in dehydrated and oxidized Ag-X are distinctly lower than that for Na-X over the range of concentration studied. Most remarkably, the shifts decrease with concentration, down to negative values in the range -40 to -50 ppm at low xenon concentration. In contrast to these results, the samples reduced at 100 °C and 300 °C show high-frequency shifts with respect to Na-X. After reduction at 100 °C, δ increases steadily with the number of xenon atoms per supercage (n_s) from +100 ppm to about +170 ppm for about $0.3 < n_s < 4$, whereas after reduction at 300 °C the shift values are between +140 and +160 ppm for $0.1 < n_s < 1$, with a shallow minimum at about $n_s = 0.7$. In the latter case, the plot of $\delta = f(N)$ has the classical shape of zeolite-supported metals. The very unusual low-frequency shift in the case of the dehydrated and oxidized samples is due to a specific interaction of xenon with Ag^+ cations in the supercages. This shielding is due to $d_\pi - d_\pi$ back-donation from silver to xenon, involving the silver 4d and the xenon 5d orbitals.

Similar studies have confirmed that Cu^{2+} is autoreduced to Cu^+ during the dehydration of Cu-Y at 400 °C, and it has been

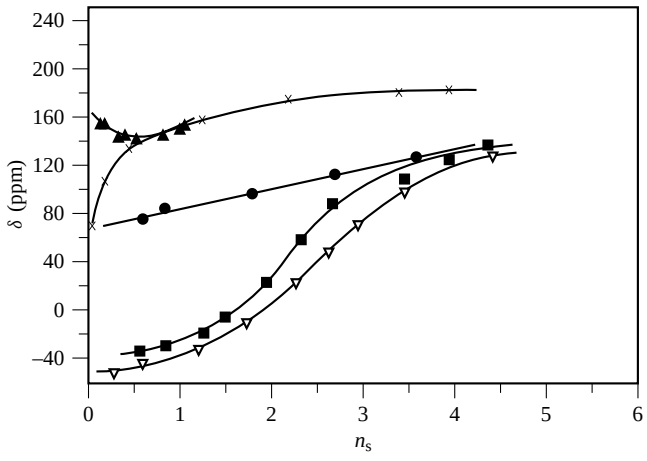

Figure 5 ^{129}Xe NMR chemical shift versus the number of xenon atoms per supercage (n_s) for the zeolites: Na-X (400 dehydrated, ●); Ag-X (400 dehydrated, ■) Ag-X (450 oxidized, ▽); Ag-X (100 reduced ×); Ag-X (300 reduced, ▲)

shown that there are only Cu^{+} ions in the supercages.[11] The Cu^{2+} cations are located in the sodalite cavities or the prisms.

7 CATION EXCHANGE BETWEEN DIFFERENT ZEOLITES

^{129}Xe NMR of adsorbed xenon can be used to follow the exchange of cation sites in the zones accessible to xenon in a given crystallite, and to visualize the exchange of cations between different zeolites. For example, the two peaks in Figure 6(a) at 144 and 89 ppm correspond to xenon adsorbed in dehydrated RbNa-X and Na-Y zeolites, respectively.[13] Upon mechanical mixing at 300 K [Figure 6(b)] the intensities of the two signals decrease and a third broad signal at about 141 ppm appears. After further treatment of the mixture at 673 K and 0.01 Pa [Figure 6(c)], there is a further larger decrease in the intensities of the RbNa-X and Na-Y signals, the peak at 141 ppm disappears and two additional broad signals are seen at 128 and 109 ppm.

The two xenon resonance signals corresponding to the two pure zeolites can be restored upon cooling the sample to 200 K, which proves that the third signal in Figure 6(b) is a coalescence of two signals. The mixture obtained directly in the tube by shaking is very inhomogeneous with regards to the distribution of the crystallites of the two zeolites. There are three types of zone: pure RbNa-X, pure Na-Y, and a RbNa-X–Na-Y mixture. Because of diffusion, the three corresponding lines can be distinguished at 300 K. Consequently, the information obtained by ^{129}Xe NMR at 300 K is characteristic of macroscopic zones, i.e. zones containing several crystallites. The extent of these zones depends on the mean lifetime of the xenon atom in the crystallites compared with the NMR timescale. These zones can be reduced by lowering the temperature of the NMR experiment in order to obtain more and more localized information. The rate of exchange of xenon atoms between one crystallite and another must also depend on the crystallite size and, above all, on the barrier to diffusion to the external surface; all other things being equal, this barrier is related to the size of the windows of the cavities and channels.

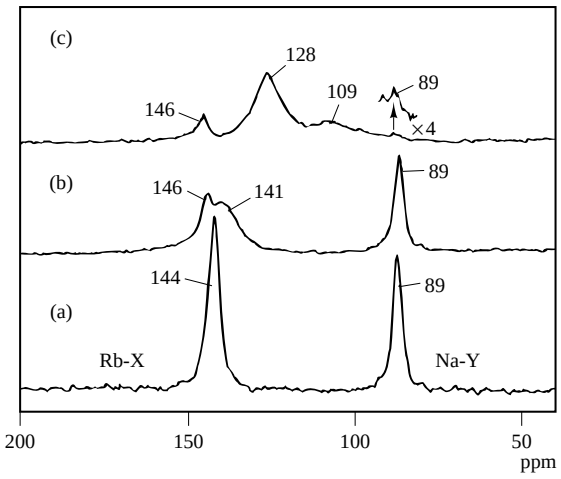

Figure 6 ^{129}Xe NMR spectra of xenon adsorbed at 300 K and 80 kPa on RbNa-X and Na-Y treated at 673 K under 0.01 Pa: (a) before mixing; (b) after mixing; (c) mixture retreated at 673 K under 0.01 Pa

The low-temperature ^{129}Xe NMR spectra of xenon adsorbed on the zeolite in Figure 6(b) show that [in contrast to the case of the zeolite in Figure 6(c)], down to 200 K there are still four well-resolved peaks, two of them corresponding to the original RbNa-X and Na-Y zeolites. The other two signals located between those of RbNa-X and Na-Y should correspond to the $Rb_{58-x}Na_{24+x}$-X and Rb_xNa_{56-x}-Y zeolites, that result from ion exchange between the two original solids.

8 DISTRIBUTION OF THE ADSORBED PHASES

Gedeon et al. showed that the values of the slope $d\delta/dN$ and $\delta_{N\to 0}$ of the $\delta = f(N)$ plots for each degree of Na-Y hydration can be used to distinguish the water located in zones accessible or inaccessible to xenon, and to measure the volume of water in the pores.[1] Conversely, during adsorption the spectrum of the xenon probe is characteristic of the concentration gradient of the adsorbate in the sample tube and even that within the zeolite crystallite.

Pines and co-workers[14] confirmed the interest in this technique by applying it to the study of the adsorption of various compounds (benzene, trimethylbenzene and hexane). Their results were confirmed by multiple quantum NMR spectroscopy.[14]

9 EFFECT OF EXTRAFRAMEWORK ALUMINUM

It is well known that extraframework aluminum Al_{NF} plays an important role in the catalytic properties of zeolites. The presence of these species is usually checked by ^{27}Al NMR spectroscopy of the dehydrated samples normally used in catalytic reactions, but the nature of these species is still unclear. Chen et al.[15] have recently studied the nature of the Al_{NF} in MFI type zeolite by ^{129}Xe and ^{27}Al NMR. ^{27}Al NMR showed that the reference sample (R) did not contain any extraframework aluminum (Table 1). Conversely, the samples prepared in fluoride medium always contained some Al_{NF}. The quantity of Al_{NF} in the samples depends on the synthesis conditions.

The four samples studied by ^{129}Xe NMR (Table 1) have different xenon chemical shift δ dependences on the xenon loading N (Figure 7). For sample R, δ increases monotonically with N. For the samples synthesized in fluoride medium, δ first decreases and then increases with N. This indicates the presence of some strong adsorption sites inside the channels of the samples. These sites can only be more or less charged Al_{NF} species. Comparison of the number of Al_{NF} and the $\delta_{N\to 0}$

Table 1 Aluminum Concentration per Unit Cell

Sample	Total aluminum	Framework aluminum	Nonframework aluminum
R[a]	4.0	4.0	0
A	8.0	4.0	4.0
B	3.4	2.9	0.5
C	2.2	1.6	0.6

[a]R, reference.

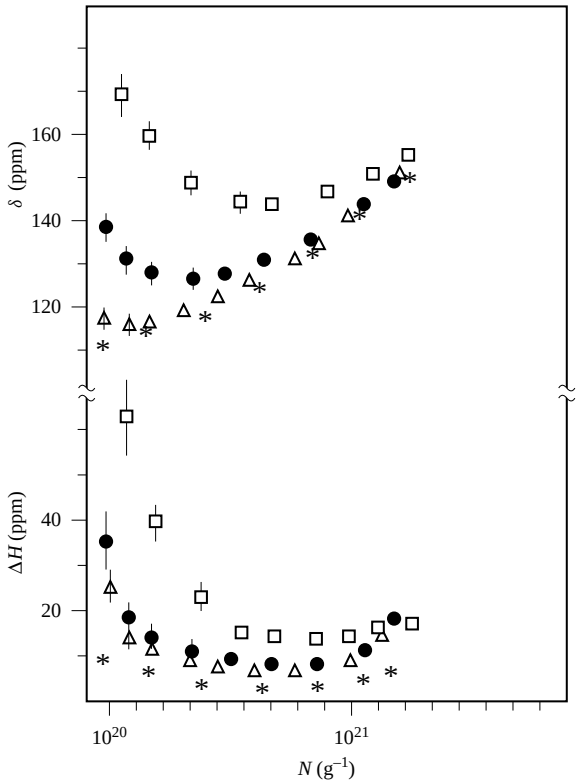

Figure 7 Variation in the chemical shift δ and the linewidth ΔH versus the number of xenon atoms (N) per gram of solids. △, A; •, B; □, C; * R. See Table 1

value shows that the charge on Al_{NF} increases in the order A < B < C. The average charge on each Al_{NF} atom depends on the amount of Al_{NF} and on the Al_{NF}/Al_F ratio inside the zeolite.

10 CONCLUSIONS

Using ^{129}Xe NMR spectroscopy with adsorbed xenon as a probe, it is possible:

1. To determine the dimensions and the forms of the internal free volumes of zeolites without knowing their structures:[16] (a) to reveal structure defects produced by, for example, dealumination, and to determine their characteristics; and (b) to calculate the short-range crystallinity, as opposed to that determined by X-ray crystallography.
2. To follow the mechanism of the synthesis and crystallization of zeolites during their preparation.[17]
3. To locate cations in the zeolite structure and to follow their migration or a change in their environment, depending on various factors.
4. To locate any 'encumbering' species, e.g. adsorbed molecules, extraframework species, coke formed during catalytic cracking reactions.[18]
5. To determine the dispersion of metals (particularly when the particles are too small to be detected by electron microscopy),[19] and the distribution of the molecules adsorbed on the particles (as opposed to the mean coverage).
6. To compare the diffusion of species as a function of the size of the zeolite 'windows'.[20]

The above list of applications is not exhaustive. Indeed this technique can also be applied to any microporous system (amorphous solid, polymer, clay, etc.), provided that one works at low temperature.

11 RELATED ARTICLES

Adsorbed Species: Spectroscopy and Dynamics; Chemical Exchange Effects on Spectra; Electric Field Effects on Shielding Constants; Gas Phase Studies of Chemical Exchange Processes; Gas Phase Studies of Intermolecular Interactions and Relaxation; Molecular Sieves: Crystalline Systems; Polarization of Noble Gas Nuclei with Optically Pumped Alkali Metal Vapors; Polymers: Regio-Irregular Structure; Reactions in Zeolites; Silica Surfaces: Characterization; Supported Metal Catalysts.

12 REFERENCES

1. J. Fraissard and T. Ito, *Zeolites*, 1988, **8**, 350, and references therein.
2. D. Raftery, L. Reven, H. Long, A. Pines, P. Tang, and J. A. Reimer, *J. Phys. Chem.*, 1993, **97**, 1649.
3. D. Raftery and B. Chmelka, in *NMR. Basic Principles and Progress*, ed. B. Blümich and R. Kosfeld, Springer, Berlin, 1994, Vol. 30, p. 111, and references therein.
4. C. J. Jameson, A. K. Jameson, and S. M. Cohen, *J. Chem. Phys.*, 1973, **59**, 4540, and references therein.
5. P.-J. Barrie and J. Klinowski, *Prog. NMR Spectrosc.*, 1992, **24**, 91, and references therein.
6. C. Dybowski, N. Bansal, and T. M. Duncan, *Ann. Rev. Phys. Chem.*, 1991, **42**, 433, and references therein.
7. M. A. Springuel-Huet, J. Demarquay, T. Ito, and J. Fraissard, *Studies Surf. Sci. Catal.*, 1988, **37**, 183.
8. J. A. Ripmeester, C. J. Ratcliffe, and J. S. Tse, *J. Chem. Soc., Faraday Trans. 1*, 1988, **84**, 3731.
9. Q. Chen and J. Fraissard, *J. Phys. Chem.*, 1992, **96**, 1809.
10. Q. Chen, M. A. Springuel-Huet, J. Fraissard, L. Matthew, L. Smith, D. Corbin, and C. Dubowski, *J. Phys. Chem.*, 1992, **96**, 10 914.
11. A. Gedeon and J. Fraissard, *Chem. Phys. Lett.*, 1992, **219**, 440 and references therein.
12. T. T. P. Cheung, C. M. Fu, and S. Wharry, *J. Phys. Chem.*, 1988, **92**, 5170.
13. Q. Chen and J. Fraissard, *Chem. Phys. Lett.*, 1990, **169**, 595.
14. B. F. Chmelka, J. G. Pearson, S. B. Liu, R. Ryoo, L. C. de Menorval, and A. Pines, *J. Phys. Chem.*, 1991, **95**, 303, and references therein.
15. Q. Chen, J. L. Guth, A. Seive, P. Caullet, and J. Fraissard, *Zeolites*, 1991, **11**, 799.
16. M. A. Springuel-Huet and J. Fraissard, *Zeolites*, 1992, **12**, 841.
17. T. Ito, J. Fraissard, Y. B'Nagy, N. Dewaele, Z. Gabelica, A. Nastro, and E. Derouane, *Studies Surf. Sci. Catal.*, 1989, **49**, 579.
18. J. L. Bonardet, M. C. Barrage, and J. Fraissard, *Studies Surf. Sci. Catal.*, 1993, **75**, 2577.
19. M. Boudart, M. G. Samant, and R. Ryoo, *Ultramicroscopy*, 1986, **20**, 125.
20. J. Karger, H. Pfeifer, T. Wutscherk, S. Ernst, J. Weitkamp, and J. Fraissard, *J. Phys. Chem.*, 1992, **96**, 5059.

Biographical Sketch

Jacques Fraissard. *b* 1934. Maîtrise ès Sciences, 1957, Doctorat ès Sciences, 1961, Paris. Introduced to NMR by I. Solomon. Centre National de la Recherche Scientifique, 1960–63; University of Paris, 1963–present. Approx. 210 publications; including research interests mainly in applications of solid state NMR to problems of gas–solid interactions and catalysis.

Molecular Sieves: Crystalline Systems

Jacek Klinowski
University of Cambridge, UK

1	Zeolites: Structure and Properties	1
2	Composition of Zeolitic Frameworks and the Nature of Extraframework Aluminum	2
3	Resolving Crystallographically Nonequivalent Tetrahedral Sites in Zeolites	4
4	Two-Dimensional NMR Spectra of Zeolitic Frameworks	6
5	Dealumination and Realumination of Zeolites	6
6	NMR Studies of the Structure of BrØnsted Acid Sites in Zeolites	7
7	Gallosilicate and Borosilicate Zeolites	8
8	Chemical Status of Guest Organics in Zeolites	8
9	In Situ Studies of Catalytic Reactions on Zeolites	8
10	Direct Observation of Shape Selectivity	8
11	Structure of Aluminophosphate Molecular Sieves	9
12	NMR Studies of $AlPO_4$-5, $AlPO_4$-11, and $AlPO_4$-21	10
13	VPI-5 and $AlPO_4$-8	12
14	SAPO Molecular Sieves	13
15	MeAPO Molecular Sieves	14
16	^{2}H NMR Studies of Motion in Molecular Sieves	14
17	Related Articles	16
18	References	16

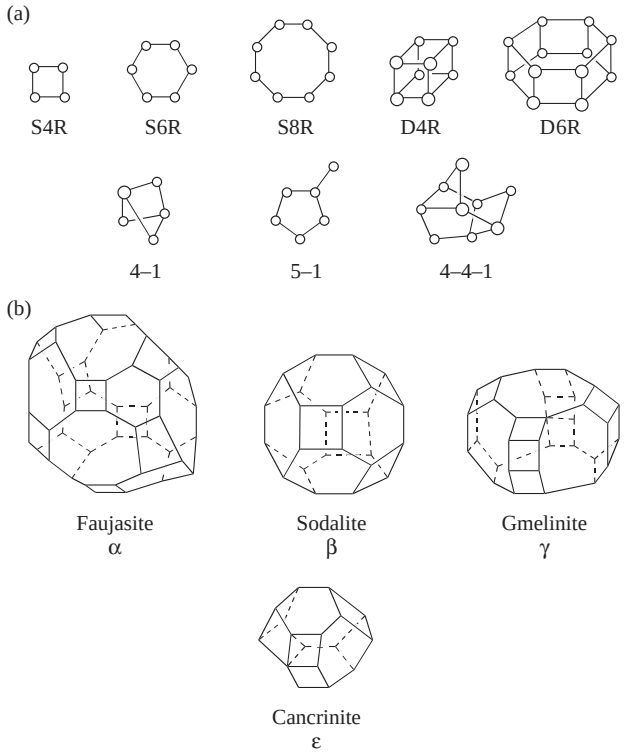

Figure 1 (a) Secondary building units in zeolite structures. (○) Positions of tetrahedral silicon and aluminum atoms; oxygen atoms (not shown) lie approximately halfway between them. (b) Some polyhedra found in zeolite frameworks: the 'α-cage' (26-hedron of type I); the sodalite cage; double eight-membered ring; double six-membered ring (hexagonal prism); the 18-hedron ('γ-cage'); the 11-hedron ('ε-cage' or 'cancrinite cage')

1 ZEOLITES: STRUCTURE AND PROPERTIES

Molecular sieves are a class of porous open-framework solids which includes aluminosilicates (zeolites), aluminophosphates, and related materials. Zeolites[1–3] are built from corner-sharing SiO_4 and AlO_4 tetrahedra linked by the apical oxygen atoms to form frameworks of high internal surface area with regular channels and cavities of molecular dimensions. The zeolitic channel systems, which may be one-, two- or three-dimensional, may occupy more than 50% of crystal volume. Their micorporous structure enables zeolites to be used as molecular sieves, as they can only adsorb molecules of certain size. The net negative charge of the framework, equal to the number of the constituent aluminum atoms, is balanced by exchangeable cations M^{n+} located in the channels which normally also contain water. The name 'zeolite' (from the Greek $\zeta\epsilon\omega$ = to boil and $\lambda\iota\theta\sigma$ = stone) was coined by Cronstedt[4] to describe the behavior of the mineral stilbite which rapidly loses water on heating and thus seems to boil.

The general oxide formula of a zeolite is $M_{x/n}$-$(AlO_2)_x(SiO_2)_y{\cdot}mH_2O$, with $y \geq x$. According to the Loewenstein rule,[5] which applies to all hydrothermally synthesized zeolites, aluminate tetrahedra cannot be neighbors in the framework, and so Al–O–Al linkages are forbidden. There are about 40 identified zeolite minerals (with $1 \leq y/x \leq 5$) and at least 140 synthetic species with a wide range of compositions. Figure 1 shows the secondary building units and some of the cages found in molecular sieves, and Figure 2 illustrates framework structures based on the sodalite cage.

Zeolites are prepared under mild (60–400 °C) hydrothermal conditions in strongly basic media. The type and concentration of the base are important structure-directing factors, and a variety of organic bases (usually secondary or tertiary amines or quaternary ammonium compounds) have been used. A preparative method utilizing low pH which relies on F^- anions to solubilize the reactants as complex fluorides has recently been developed. Other elements, such as Ga, Ge, B, Fe, and P can substitute for Si and Al in the framework.

The physical and chemical behavior of zeolites is the subject of various monographs.[6–10] The most important properties are the ability to adsorb organic and inorganic substances and to act as cation exchangers and catalysts. Depending on the pore diameter and the molecular dimensions, species such as gaseous elements, ammonia, alkali metal vapors, hydrocarbons, and many other organic and inorganic species may be accommodated in the intracrystalline space of dehydrated zeolites. This process, known as 'molecular sieving', is a powerful method for the resolution of mixtures. Commercial applications include the drying of organics, separation of hydrocarbons and of N_2 and O_2 in air, and the removal of NH_3 and CS_2 from industrial gases.

Cations neutralizing the electrical charge of the aluminosilicate framework can be exchanged for other cations from solution. Zeolites often possess selectivities for certain cations, and

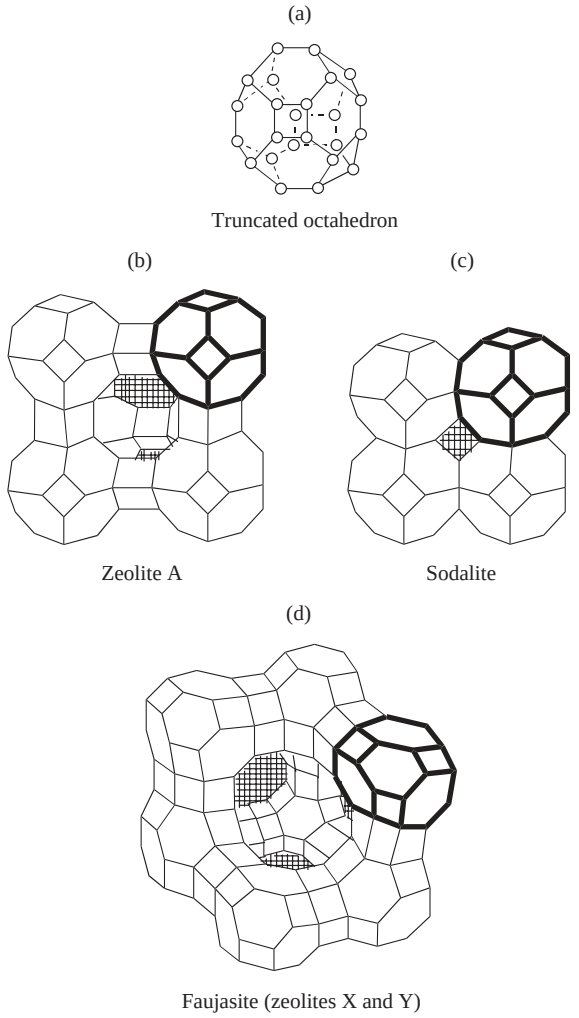

Figure 2 (a) The truncated octahedron, more correctly a tetrakaidodecahedron (also known as 'sodalite cage' or 'β-cage'). (b) The structure of zeolite A is formed by linking the sodalite cages through double four-membered rings. (c) The structure of sodalite is formed by direct face-sharing of four-membered rings in the neighboring sodalite cages. (d) The faujasite structure is formed by linking the sodalite cages through double six-membered rings. For clarity, exchangeable nonframework cations are not shown

this is used for their isolation and concentration. Applications include the removal of ammonia from sewage and agricultural effluents, collection of harmful products of nuclear fission (such as $^{137}Cs^{+}$ and $^{90}Sr^{2+}$), water softening, and the recovery of precious elements. Molecular sieving properties of zeolites are further modified by ion exchange. Thus zeolite Na-A sorbs both N_2 and O_2, while Ca-A sorbs nitrogen preferentially to oxygen.

However, the ability to catalyze a wide range of reactions, such as cracking, hydrocracking, oxidation, and isomerization of hydrocarbons, overshadows all other applications of zeolites. Rare-earth exchanged and hydrogen forms of some zeolites (such as zeolite Y) have a cracking activity which is orders of magnitude greater than that of conventional silica/aluminas.[11] The synthetic zeolite ZSM-5,[12] is a particularly powerful catalyst (Figure 3). Its high silica content (the Si/Al ratio is typically 30) gives it high thermal stability,

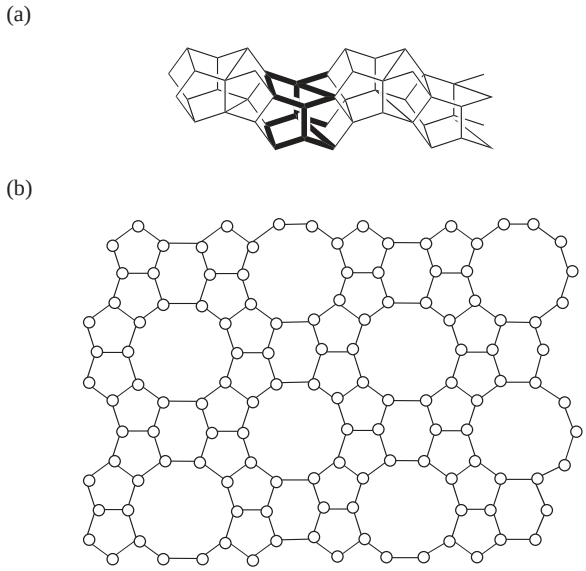

Figure 3 The structure of ZSM-5/silicalite

while the channel diameter is convenient for many applications. Catalytic properties of ZSM-5 include the ability to synthesize gasoline from methanol in a single step. Silicalite, a material which is isostructural with ZSM-5, but contains only small amounts of aluminum is, by contrast to other zeolites, hydrophobic and organophilic, and is used in the removal of dissolved organics from water. The annual industrial consumption of zeolites is about 550 000 ton, of which 135 000 ton are used in catalysis, 375 000 ton as ion exchangers in detergent powders, and 40 000 ton as sorbents.

Synthetic zeolites are usually microcrystalline and, furthermore, typically contain four 10-electron atomic species (Si^{4+}, Al^{3+}, O^{2-} and Na^{+}), which makes their structure difficult to study by conventional methods. High-resolution solid state NMR techniques, such as magic angle spinning (MAS), gave zeolite chemistry a powerful structural tool for monitoring all elemental components of such frameworks.

2 COMPOSITION OF ZEOLITIC FRAMEWORKS AND THE NATURE OF EXTRAFRAMEWORK ALUMINUM

Framework silicon in zeolites is 4-coordinate, and thus there are five different possible environments of a silicon atom: $Si(OAl)_4$, $Si(OAl)_3(OSi)$, $Si(OAl)_2(OSi)_2$, $Si(OAl)(OSi)_3$, and $Si(OSi)_4$. For simplicity, we denote these by Si(nAl) where n (≤ 4) is the number of aluminum atoms connected, via oxygen atoms, to a silicon. Each type of Si(nAl) building block corresponds to a definite range of ^{29}Si chemical shift (Figure 4).[13] When a ^{29}Si MAS NMR spectrum of a zeolite contains more than one peak and is correctly assigned in terms of Si(nAl) units, the Si/Al ratio in the zeolitic framework may be calculated from the spectrum alone. Because of the absence of Al–O–Al linkages, the environment of every aluminum atom is Al(4Si). Each Si–O–Al linkage in an Si(nAl) unit incorporates 0.25 aluminum atoms, and the whole unit contains $0.25n$ aluminum atoms. The Si/Al ratio may therefore be

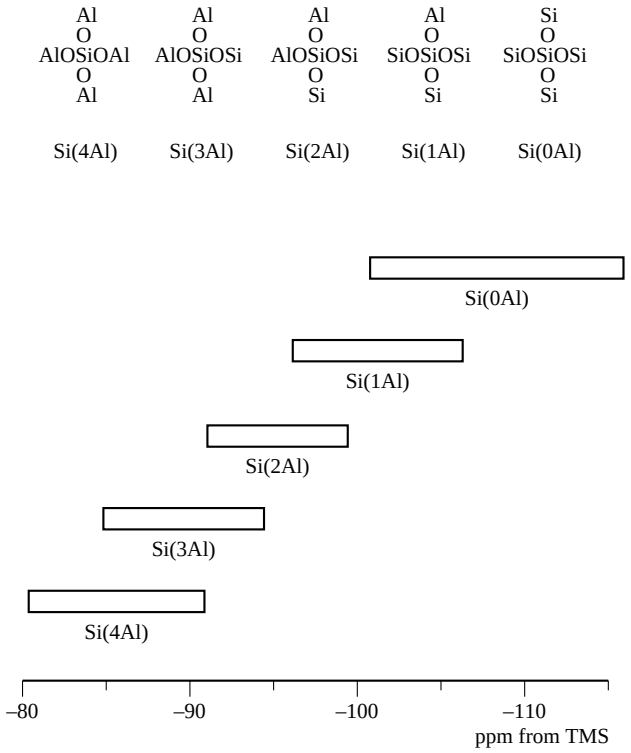

Figure 4 Ranges of ^{29}Si chemical shift for Si(nAl) building blocks in zeolites. The Si(4Al) range in some synthetic sodalites containing various enclathrated salts is exceptionally wide, from −76.5 to −97 ppm

calculated directly from the ^{29}Si MAS NMR spectrum using the formula[14]

$$(\mathrm{Si/Al})_{\mathrm{NMR}} = \frac{I_4 + I_3 + I_2 + I_1 + I_0}{I_4 + 0.75I_3 + 0.5I_2 + 0.25I_1} \qquad (1)$$

where I_n is the intensity (peak area) of the NMR peak corresponding to the Si(nAl) building unit. By comparing values of $(\mathrm{Si/Al})_{\mathrm{NMR}}$ with the results of chemical analysis, which gives bulk composition, the amount of extraframework aluminum in chemically modified zeolites can be calculated.

Equation (1) applies to all zeolites with framework Si/Al ratios less than about 10.[14–16] It can also serve as a test for the correctness of spectral assignment. Its validity has been confirmed in the case of zeolites X and Y, which can be synthesized in a range of compositions. The spectra can be deconvoluted using Gaussian peak shapes, and the areas of the individual deconvoluted peaks used in equation (1). However, equation (1) cannot be applied directly to spectra containing overlapping peaks from Si(nAl) units of crystallographically inequivalent silicon atoms, to zeolites containing framework defects (nests of hydroxyl groups), or to dealuminated zeolites in which vacancies created by the expulsion of framework aluminum have not subsequently been resubstituted by silicon. As aluminum is removed, the number of Si(0Al) (i.e. Si(4Si)) units is unchanged, while Si(3Al,1Si) units, for example, give rise not to Si(2Al,2Si) and Si(1Al,3Si) units, but to Si(2Al,1OH) and Si(1Al,2OH) groupings, the ^{29}Si NMR peaks from which overlap with those from Si(nAl) groupings. Although the intensities of ^{29}Si peaks corresponding to silicon atoms linked to one or more hydroxyl groups are enhanced by

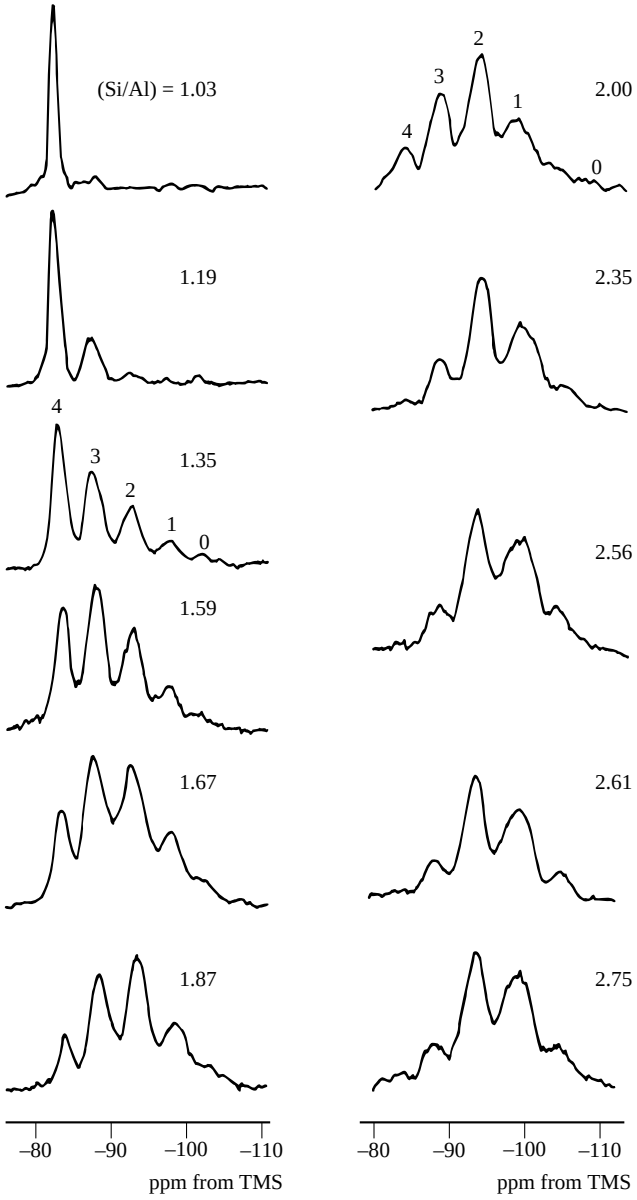

Figure 5 High-resolution ^{29}Si MAS NMR spectra of synthetic zeolites Na-X and Na-Y.[15] Si(nAl) peaks are identified by the n above the peaks

^{1}H–^{29}Si cross polarization, their individual intensities cannot be determined easily because the efficiency of the technique depends on the distance between the silicon and the hydrogen atoms.

^{29}Si MAS NMR can also be used to determine the ordering of silicon and aluminum in the framework. The areas under the peaks in the deconvoluted spectrum are proportional to the populations of the corresponding structural units in the sample. It is therefore possible to compare the experimental data (Figure 5) with the relative numbers of such units in models involving different silicon/aluminum ordering schemes. For most Si/Al ratios more than one ordering scheme is compatible with the Si(nAl) intensities determined by ^{29}Si MAS NMR. The choice between the various schemes is made on the basis of: (a) the degree of agreement between the spectral intensities and those required by the given model; (b) compliance with crystal symmetry requirements; and (c) minimum electrostatic

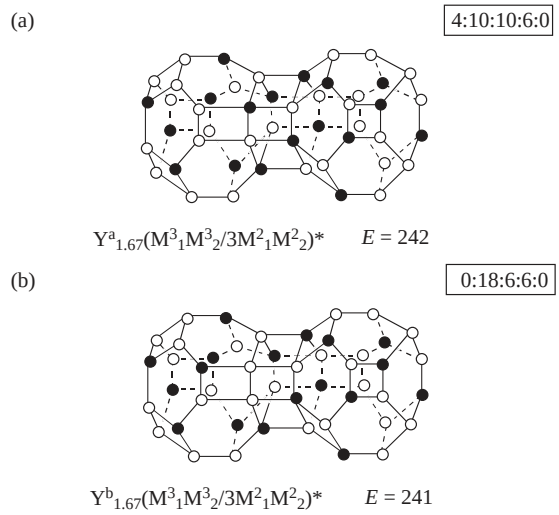

Figure 6 Two of the possible silicon/aluminum ordering schemes for zeolite Y with Si/Al = 1.67.[15] (○) Silicon atoms; (●) aluminum atoms. The ratio of intensities Si(4Al):Si(3Al):Si(2Al):Si(1Al):Si(0Al) corresponding to each scheme is given in the upper right-hand corner. E is the calculated electrostatic energy for the double cage in units of $(qe)^2/a$, where a is the T–O–T distance. The asterisk denotes the preferred scheme

repulsion within the framework. Figure 6 shows the preferred ordering schemes for Si/Al = 1.67.

Many ^{29}Si spectra of natural and synthetic zeolites have been measured by various workers since the pioneering papers by Lippmaa et al.[13] and Engelhardt et al.[14] appeared. The results for zeolites, the spectra of which can be directly assigned to Si(nAl) units, are listed in Table 1.

3 RESOLVING CRYSTALLOGRAPHICALLY NONEQUIVALENT TETRAHEDRAL SITES IN ZEOLITES

In naturally occurring zeolites, the Si/Al ratio is less than about 5, but materials with lower aluminum contents can be prepared synthetically. One might expect an uncomplicated spectrum for such materials, containing the Si(0Al) peak, sometimes with a smaller Si(1Al) resonance, depending on the Si/Al ratio. The discovery[17] that the spectrum of ZSM-5/silicalite, which has a very low aluminum content and the structure shown in Figure 3, has considerable fine structure was therefore a surprise. The fine spectral detail arises from crystallographically inequivalent tetrahedral environments of the Si(4Si) sites. Figure 7(a) shows a spectrum in which as many as 19 individual lines can be separately resolved, the linewidth of the narrowest line being only about 5 Hz.[18] The room temperature spectrum may be simulated by 24 Gaussian peaks, and the unit cell of ZSM-5/silicalite contains 24 inequivalent silicon sites.

X-ray diffraction (XRD) shows that silicalite can exist in the monoclinic and the orthorhombic forms. ^{29}Si MAS NMR detects minute temperature-induced variations in atomic positions[18–21] which do not necessarily involve symmetry changes detectable by XRD. The spectra are sensitive even to small temperature changes and reveal the corresponding

Table 1 Parameters of ^{29}Si MAS NMR Spectra of Zeolites for Which the Individual Spectral Signals can be Assigned Directly to Si(nAl) Structural Units

			^{29}Si chemical shift (ppm from TMS)				
Zeolite	Idealized unit cell composition	Si/Al	Si(4Al)	Si(3Al)	Si(2Al)	Si(1Al)	Si(0Al)
Na-A	$[Na_{12}Al_{12}Si_{12}O_{48}{\cdot}27H_2O]_8$	1.0	−88.9	–	–	–	–
Li-A(BW)	$Li_4Al_4Si_4O_{16} \cdot 4H_2O$	1.0	−80.1	–	–	–	–
Analcime	$Na_{16}Al_{16}Si_{32}O_{96} \cdot 16H_2O$	2.0	–	−92.0	−96.3[a]	−101.3	−108.0
Cancrinite	$Na_6Al_6Si_6O_{24} \cdot CaCO_3 \cdot 2H_2O$	1.0	−85.4	–	–	–	–
Chabazite	$Ca_5Al_{10}Si_{26}O_{72} \cdot 40H_2O$	2.6	–	−94.0	99.4[a]	−104.8	−110.0
Gismondine	$Ca_4Al_8Si_8O_{32} \cdot 16H_2O$	1.0	−89.9	–	–	–	–
Gmelinite	$Na_8Al_8Si_{16}O_{48} \cdot 24H_2O$	2.0	−86.8	−91.7	−97.1[a]	−102.7	−108.0
Laumontite	$Ca_4Al_8Si_{16}O_{48} \cdot 16H_2O$	2.0	–	–	−92.4	–	–
Leucite	$KAlSi_2O_6$	2.0	−81.0	−85.2	−91.6	−97.4	−101.0
Losod	$Na_{12}Al_{12}Si_{12}O_{48} \cdot 13H_2O$	1.0	−88.9	–	–	–	–
Mordenite	$Na_8Al_8Si_{40}O_{96} \cdot 24H_2O$	5.0	–	–	−100.0	−105.5	−111.6[a]
Natrolite	$Na_{16}Al_{16}Si_{24}O_{80} \cdot 16H_2O$	1.5	–	−87.7[a]	−95.4	–	–
RHO	$(Na,Cs)_{12}Al_{12}Si_{36}O_{96} \cdot 44H_2O$	3.0	–	−92.5	−97.2	−102.7[a]	−108.0
Scolecite	$Ca_8Al_{16}Si_{24}O_{80} \cdot 24H_2O$	1.5	–	−86.0 −88.6	−95.3	–	–
Sodalite	$Na_6Al_6Si_6O_{24} \cdot 2NaCl$	1.0	−84.8	–	–	–	–
Thomsonite	$Na_4Ca_8Al_{20}Si_{20}O_{80} \cdot 24H_2O$	1.0	−83.5	–	–	–	–
ZK-5	$Na_{30}Al_{30}Si_{66}O_{192} \cdot 98H_20$	2.2	−87.5	−92.0	−97.6[a]	−103.5	−108.6
Silicalite	$(SiO_2)_{96}$	–	–	–	–	–	−109.2; −111.2; −111.5; −112.1; −112.3; −112.7; −113.0; −113.3[a]; −113.5; −113.8; −114.1; −114.6; −115.2; −116.4
ZSM-5	$Na_3Al_3Si_{96}O_{192} \cdot xH_2O$	31.0	–	–	–	−101.8	−111.8[a]

[a]The largest peak.

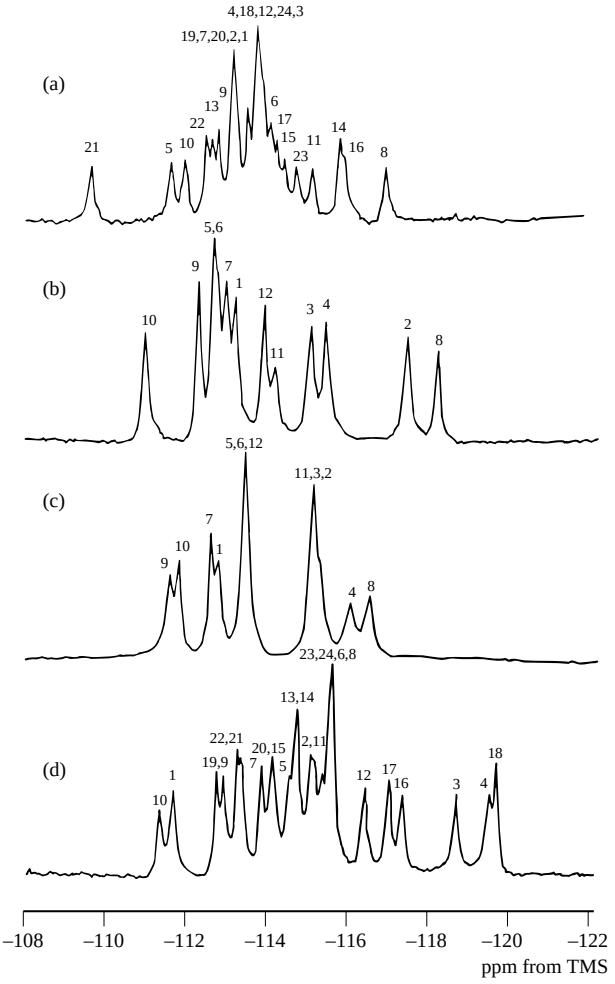

Figure 7 ^{29}Si MAS NMR spectra of ZSM-5/silicalite.[18] (a) At 300 K; (b) with two molecules of *p*-xylene per unit cell; (c) at 403 K; (d) ^{29}Si CP MAS NMR spectrum of ZSM-5 with eight molecules of *p*-xylene per unit cell

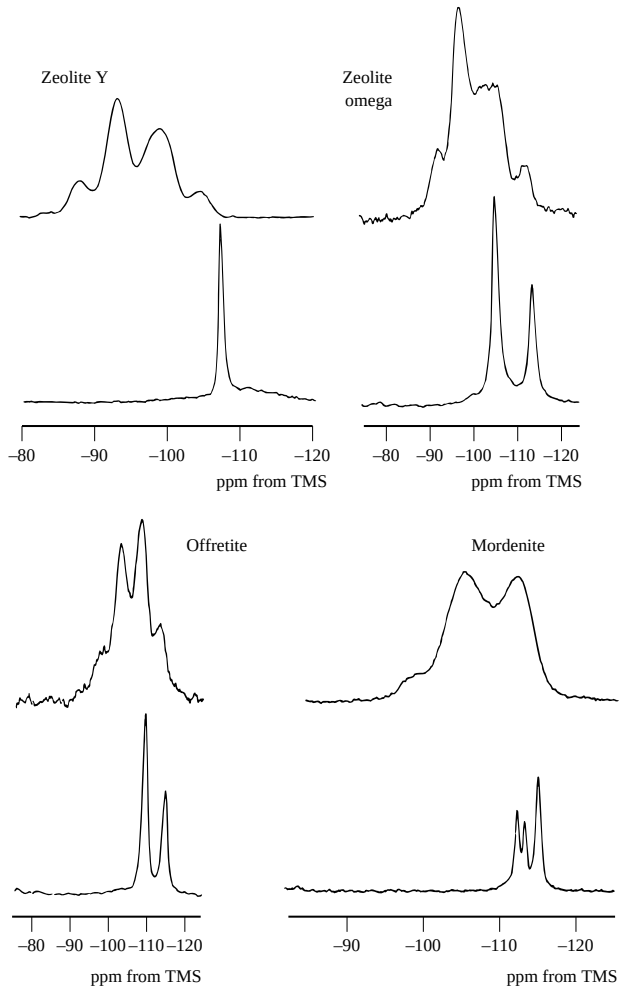

Figure 8 ^{29}Si MAS NMR spectra of (above) zeolites Y, omega, offretite and mordenite; and (below) their dealuminated forms[22]

structural transformations. Above 363 K silicalite contains only 12 inequivalent silicon sites, and the spectrum shown in Figure 7(c) can be simulated using Gaussian peaks of total intensity 12. Figure 7 also shows that the addition of small amounts of adsorbed organics to dehydrated silicalite induces similar changes in the spectra.

^{29}Si spectral peaks from most synthetic zeolites cannot easily be linked to specific silicon sites because the Si(*n*Al) manifolds from inequivalent sites overlap. However, when the ammonium form of a highly siliceous zeolite is heat treated in the presence of water vapor so that most framework aluminum is removed, the resolution of the ^{29}Si spectrum improves considerably.[22,23] Figure 8 shows the spectra of several zeolites before and after hydrothermal treatment. The intensities of the two peaks in the spectra of the siliceous zeolites omega and offretite are in a 2:1 ratio corresponding to the two inequivalent tetrahedral sites in the same population ratio. Mordenite, on the other hand, has four inequivalent sites in a 2:1:1:2 population ratio, so that the peak at −115 ppm in Figure 8 is a composite.

The fact that the ^{29}Si chemical shift is related to the T−O−T angles in zeolitic frameworks is useful for structural determination.[22,24] Chemical shifts in framework silicates have been correlated with the mean Si−O bond distances, and relationships have been developed which are in good agreement with the results of semiempirical calculations of chemical shift. A quantum mechanical rationalization of the correlation between the ^{29}Si chemical shift in framework silicates and the change in the s character of the oxygen orbitals in the Si−O−Si s bond has also been proposed (see Figure 9). The observed correlation between chemical shifts of Si(4Si) units and mean bond angles has been explained[25] in terms of a quantum mechanical model and confirmed by an extended set of experimental data consistent with relationships involving θ, $\cos\theta/(\cos\theta - 1)$, $\sin(\theta/2)$ and $\sec\theta$. These arguments have been extended to all five Si(*n*Al) units,[26] giving an approximately linear semiempirical relationship between the chemical shift of Si(*n*Al) peaks and the nonbonded Si$\cdots$T distance (T = Si or Al) calculated from the T−O−T angle.

^{29}Si MAS NMR peaks in the spectra of certain zeolites lead to incorrect values of $(Si/Al)_{NMR}$ when assigned to individual Si(*n*Al) units, as described above. When the difference in chemical shifts between peaks from inequivalent Si(*n*Al) units with the same value of *n* [8.4 ppm in the case of $Si_A(0Al)$ and $Si_B(0Al)$ in zeolite omega] is similar to the shift difference between Si(*n*Al) and Si[$(n \pm 1)$Al] units, the effects

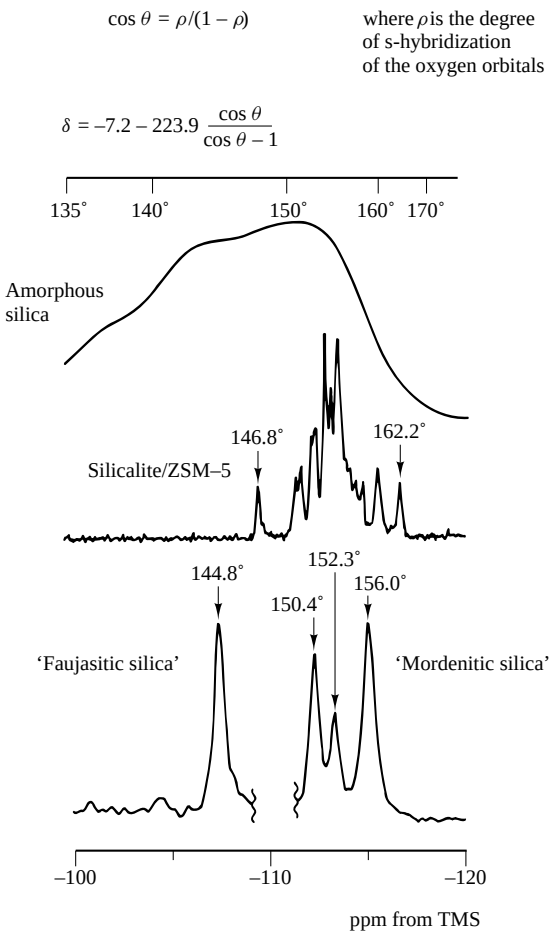

Figure 9 The mean T–O–T angle versus the isotropic ^{29}Si chemical shift for amorphous silica and several purely siliceous equivalents of zeolites

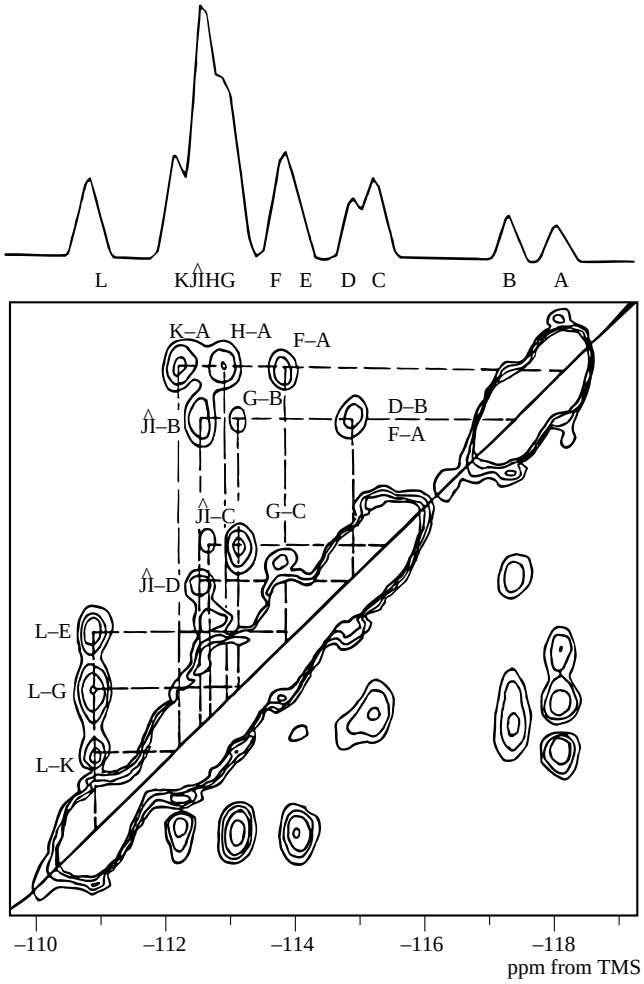

Figure 10 Two-dimensional ^{29}Si COSY-45 spectrum of the orthorhombic form of zeolite ZSM-5/silicalite with adsorbed *p*-xylene[18]

of aluminum substitution and crystallographic inequivalence overlap. The peaks are composites, and their intensities $I_{\mathrm{Si}(n\mathrm{Al})}$ cannot be read off the spectrum directly. In the case of 'as-prepared' zeolite omega, the spectrum (Figure 8) is the sum of two overlapping families of peaks. When this is taken into account, the entire spectrum can be correctly assigned and interpreted.

The chemical shift of ^{129}Xe NMR is very sensitive to the environment. When xenon is adsorbed inside a molecular sieve, its chemical shift is affected by the size and shape of the pores, by xenon–xenon collisions, by the presence of strong adsorption sites, paramagnetic species, adsorbed molecules, and phase transitions.[27] Most of the work in this area was done by Fraissard in Paris. While the initial hopes of predicting pore dimensions of unknown structures from ^{129}Xe NMR are still unfulfilled, the technique does provide valuable information, particularly where structural information is absent.

4 TWO-DIMENSIONAL NMR SPECTRA OF ZEOLITIC FRAMEWORKS

Two-dimensional solid state NMR techniques have been used to assign the individual NMR peaks to specific crystallographic sites. Figure 10 shows a ^{29}Si COSY-45 spectrum of the orthorhombic form of zeolite ZSM-5/silicalite with adsorbed *p*-xylene.[18] Of the expected 22 ^{29}Si–O–^{29}Si connectivities, 12 are present in the spectrum. The corresponding ^{29}Si 2D INADEQUATE spectrum (Figure 11) is superior, with as many as 21 connectivities being observed.[18] Excitation of a double quantum coherence has been used in double quantum filtered COSY, as in the experiment using a ^{29}Si-enriched sample of the highly siliceous zeolite ZSM-39[28] which contains three kinds of silicon site in a 1:4:12 population ratio. The most intense spectral peak is split into three components of equal intensity, which indicates loss of face centering of the *Fd*3*m* unit cell, resulting in the disappearance of the three-fold symmetry axis.

J-scaled COSY scales up the scalar splittings between the cross-peak components, thereby enhancing cross-peak intensities and consequently improving spectral resolution between adjacent diagonal and cross peaks. The ^{29}Si *J*-scaled COSY spectrum[29] measured with a scaling factor of 5 at natural isotopic abundance allows the resonances from highly siliceous mordenite to be assigned unambiguously, something which cannot be done by means of one-dimensional spectra or by conventional COSY.

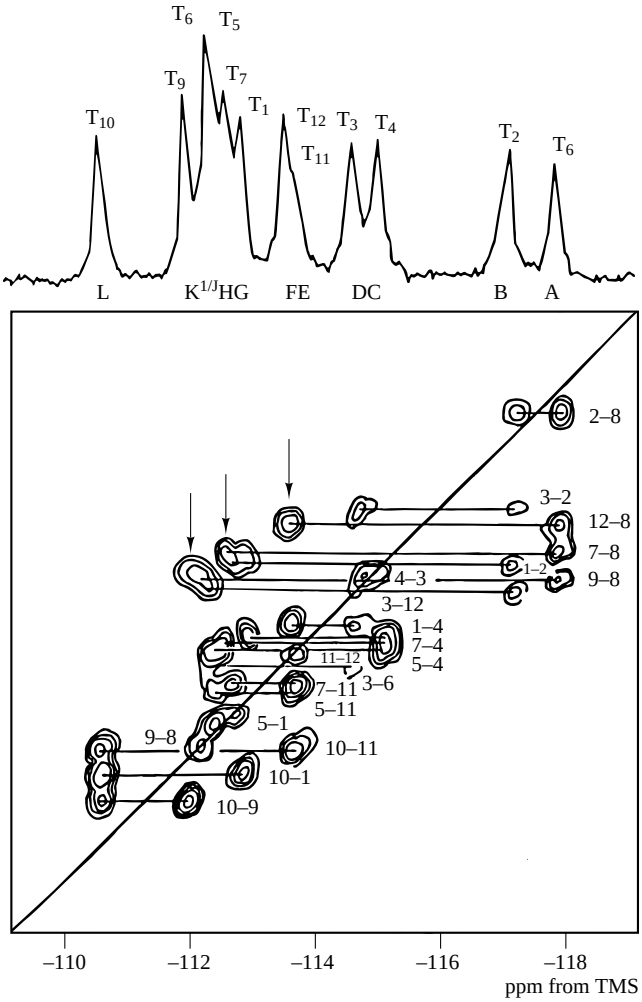

Figure 11 ^{29}Si two-dimensional INADEQUATE spectrum of the orthorhombic form of zeolite ZSM-5/silicalite with adsorbed *p*-xylene[18]

5 DEALUMINATION AND REALUMINATION OF ZEOLITES

Solid state ^{27}Al MAS NMR spectra of 'as-prepared' zeolites normally contain a single peak corresponding to four-coordinate aluminum. Its position as measured in a 9.4 T magnetic field ranges, for different materials, from about 51 to about 65 ppm from $Al(H_2O)_6^{3+}$. When the correction is made for the second-order quadrupole interaction, the chemical shift is found to be related to structural parameters in a similar manner to ^{29}Si chemical shifts. ^{27}Al MAS NMR spectra of 'as-prepared' zeolites are thus much simpler than their ^{29}Si counterparts. This is a direct consequence of the fact that while five types of Si(*n*Al) environments are possible for the silicon atom, only one possibility, Al(4Si), exists for the aluminum. However, while the coordination of silicon in zeolites is always four-fold, aluminum can be four-, five- or six-coordinate. The latter resonates at about 0 ppm from $Al(H_2O)_6^{3+}$ and is often subject to large quadrupole interactions. Quantitatively reliable ^{27}Al spectra are obtained with fast MAS at very high magnetic fields and using strong rf pulses with small flip angles.

Since Brønsted acid groups in zeolites are associated with framework aluminum, their catalytic activity depends on the

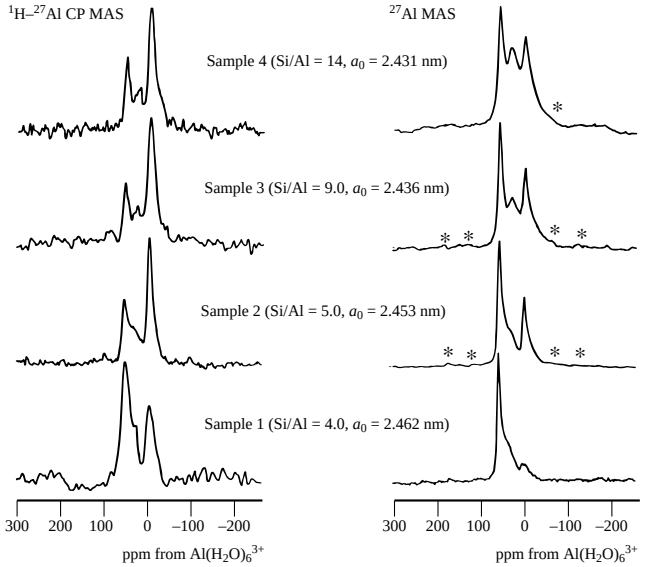

Figure 12 ^{27}Al (MAS at 12–13 kHz) and ^{1}H–^{27}Al CP MAS (MAS at 8–10 kHz) NMR spectra of increasingly dealuminated (from bottom to top) zeolite HY.[80] The Si/Al ratios calculated from ^{29}Si MAS NMR spectra and the cubic unit cell parameters a_0 are indicated. Asterisks denote spinning sidebands

concentration and location of aluminum in the structure. It is often desirable to reduce the aluminum content of the zeolitic framework. Upon hydrothermal treatment of zeolite NH_4-Y, the process known as 'ultrastabilization', part of the aluminum is ejected from the framework into the intracrystalline space, and the vacancies are reoccupied by silicon from other parts of the crystal. As a result, thermal stability of the zeolite is greatly increased. Ultrastable zeolite Y has been examined by ^{29}Si and ^{27}Al MAS NMR.[30–32] ^{29}Si spectra of ultrastable zeolite Y clearly show that aluminum is removed from the framework, and that the resulting vacancies are subsequently reoccupied by silicon. ^{27}Al MAS NMR shows how six-coordinate nonframework aluminum species (Al^{NF}) build up at the expense of the four-coordinate framework aluminum (Al^{F}) as the calcination temperature is increased, and ^{1}H–^{27}Al CP MAS NMR spectra of dealuminated samples help to elucidate the nature of Al^{NF}.[33] Figure 12 shows that the intensity of the peaks at 0 and 30 ppm increases relative to the peak at 60 ppm. This indicates that the 30 ppm peak is a separate ^{27}Al resonance from five-coordinate aluminum.

The process of ultrastabilization of zeolite Y can be reversed by a hydrothermal treatment with aqueous solutions of strong bases.[34] NMR indicates that aluminum atoms originally eliminated from the framework can be subsequently reinserted into the framework. ^{29}Si MAS spectra of dealuminated samples reflect the removal of framework aluminum from the parent sample. In the spectra of samples treated with KOH the intensities of the Si(0Al) peaks are greatly reduced, and the intensities of the Si(1Al), Si(2Al), Si(3Al), and Si(4Al) peaks are correspondingly increased, signifying that an aluminum has reentered the framework. The spectra of realuminated samples are very different from that of the parent material, despite the fact that their overall composition is similar. This demonstrates that the silicon/aluminum distribution among the tetrahedral sites is different. ^{27}Al quadrupole nutation NMR offers further insights into the dealumination–realumination process.[35,36]

6 NMR STUDIES OF THE STRUCTURE OF BRØNSTED ACID SITES IN ZEOLITES

The study of acidic surface sites capable of donating protons to adsorbed molecules is crucial to heterogeneous catalysis. It is vital to know the concentration, strength, and accessibility of the Brønsted and Lewis acid sites and the details of their interaction with the adsorbed organics. The Brønsted acidity of zeolites arises from the presence of accessible hydroxyl groups associated with framework aluminum ('structural hydroxyl groups'). Extensive ^{1}H MAS NMR measurements of zeolites have led to the assignment of the various proton resonances. ^{1}H NMR of static samples can probe the geometry of the Brønsted acid site and determine the Al–H distance, because the second moment of the broadline proton spectra, which is inversely proportional to the sixth power of the distance between the dipole-coupled nuclei, is dominated by the $^{1}H–^{27}Al$ interaction.

^{15}N NMR of molecules sorbed on zeolites is also useful for the study of zeolitic acidity, as the nitrogen atom in molecules such as ammonia and pyridine binds directly to the acid site. The ^{15}N chemical shift of ammonia adsorbed in ultrastable zeolite Y does not depend on the amount absorbed and is similar to that in liquid ammonia. Consideration of the equilibrium between the surface sites and the sorbate allows the resonance shifts for the surface complexes to be obtained. The formation of pyridinium ions in ultrastable zeolites has led to direct determination of the number of interacting hydroxyl groups. Acetonitrile has also been used to characterize the interactions with the acid sites.

When trimethylphosphine is used as a probe molecule in zeolite H-Y,[37] the ^{31}P MAS NMR spectrum contains resonances from at least two types of $(CH_3)_3PH^+$ complex: an immobilized complex coordinated to hydroxyl protons, and a highly mobile one which desorbs at 300 °C.

7 GALLOSILICATE AND BOROSILICATE ZEOLITES

Tetrahedral aluminum and silicon in the zeolitic framework can be substituted by several other elements. (Si,Ga)-, (Ge,Al)- and (Ge,Ga)-zeolites are structurally similar to their silicon/aluminum counterparts. ^{29}Si MAS NMR spectra of (Si,Ga)-sodalites and (Si,Ga)-faujasites[38,39] allow $(Si/Ga)_{NMR}$ ratios to be calculated from a formula similar to equation (1), which shows that no Ga–O–Ga linkages are present. The distribution of Si(nGa) peak intensities in gallosodalite is different from the Si(nAl) in aluminosilicate zeolites of similar Si/T ratio (T = Al or Ga), indicating that the distribution of silicon and gallium is different from the distribution of silicon and aluminum. The ^{29}Si chemical shifts in silicon/gallium zeolites span 25.1 ppm, a wider range than in the corresponding aluminosilicates (18.5 ppm).

Borosilicate ZSM-5 ('boralite') containing up to five boron atoms per unit cell has been prepared. ^{11}B spectra show that four-coordinate boron resonates at about −3.5 ppm from $BF_3{\cdot}OEt_2$.[40] On dehydrating boralite, the intensity of the line decreases reversibly and a second broad line appears. The width of that line, assigned to trigonal boron, is dependent on the magnetic field intensity, which indicates that the effect is quadrupolar in nature.[41]

8 CHEMICAL STATUS OF GUEST ORGANICS IN ZEOLITES

The declining oil reserves have stimulated efforts aimed at converting methanol (MeOH) into higher molecular weight organics over shape-selective catalysts, particularly zeolite H-ZSM-5 which is capable of converting MeOH to hydrocarbons up to C_{10}. The mechanism of the reaction is a subject of some controversy. ^{1}H NMR has been used[42] to monitor the chemistry of MeOH adsorbed on ZSM-5 inside sealed capsules which can be spun in the MAS probehead.

The ^{1}H MAS NMR spectrum of MeOH adsorbed on zeolite H-ZSM-5 contains peaks at 4.1 and 9.1 ppm, from methyl and hydroxyl protons, respectively. The large high-frequency (downfield) shift of the latter resonance is caused by very strong hydrogen bonding and/or direct protonation of the alcohol, and serves as a measure of the proton donating ability of the solid acid catalyst: in zeolites H-Y and H-L the shifts are considerably smaller than in ZSM-5.

9 IN SITU STUDIES OF CATALYTIC REACTIONS ON ZEOLITES

^{13}C MAS NMR can probe the kind and quantity of chemical species present inside the particle in the course of the conversion of MeOH to gasoline on zeolite ZSM-5. This information is usefully compared with the composition of the gaseous products.[43] These experiments have: (i) identified 29 different organic species in the adsorbed phase and monitored their fate during the course of the reaction; (ii) observed directly different kinds of shape selectivity in a zeolite; and (iii) unequivocally distinguished between mobile and attached species.

The spectrum of a sample with adsorbed MeOH and maintained at 20 °C, contains a single resonance at 50.8 ppm due to MeOH (Figure 13). After heating the sample to 150 °C the spectrum is composed of two peaks, at 50.5 and 60.5 ppm, corresponding to MeOH and dimethyl ether (DME), respectively. In a sample treated at 300 °C for 35 min, MeOH and DME have been completely converted to a mixture of aliphatics and aromatics.

Two-dimensional ^{13}C spectra can determine the connectivity of carbon atoms and the number of protons attached to each carbon atom in the various products, enabling firm assignments for many resonances to be made.[44] For example, the line at −10.7 ppm in Figure 14 is split into five components with a requisite intensity ratio, which confirms that it must be due to adsorbed methane. Spin diffusion ^{13}C NMR spectra further confirm the spectral assignments and provide new details on distribution of hydrocarbons in the intracrystalline space.

10 DIRECT OBSERVATION OF SHAPE SELECTIVITY

The distribution of adsorbed species in the sample of ZSM-5 with adsorbed methanol treated at 300 °C is different from the thermodynamic equilibrium distribution and from the distribution of the reaction products.[43] The main species found in the adsorbed phase are *o*- and *p*-xylene, 1,2,4,5-tetramethylbenzene, 1,2,4-trimethylbenzene,

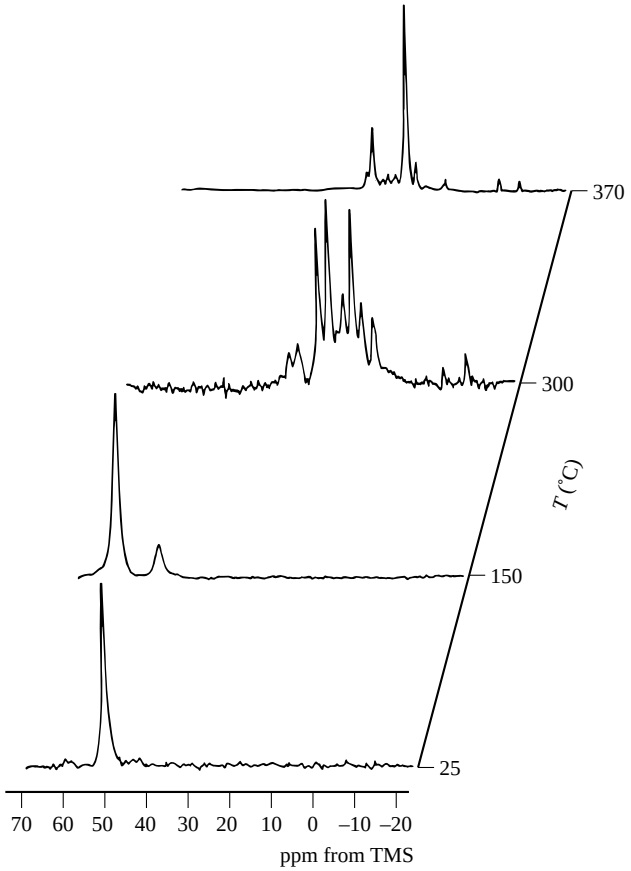

Figure 13 Solid state ^{13}C NMR spectra reveal the successive steps in the conversion of methanol to gasoline over zeolite ZSM-5. The methanol, resonating at 50 ppm, is first dehydrated to DME (60 ppm). Subsequent carbon–carbon bond formation leads to a host of aliphatic (−10 to 35 ppm) and aromatic (not shown) compounds[43]

and 1,2,3,5-tetramethylbenzene. The fact that 1,2,3- and 1,3,5-trimethylbenzenes are not found among the products, but are present in the adsorbed phase, while the smaller 1,2,4-trimethylbenzene is found in both, demonstrates the reality of the concept of product selectivity. The two larger isomers are unable to diffuse out of the crystal. The distribution of the tetramethylbenzenes in the intracrystalline space (none of which are found in the products of the reaction at 300 °C) is equally unexpected.

Table 2 $AlPO_4$ Structures Divided into Very Large Pore Materials (>12-Membered Rings), Large Pore (12-Membered Rings), Intermediate Pore (10-Membered Rings), Small Pore (8-Membered Rings), Very Small Pore (6-Membered Rings), and Other Structures (Layered Materials and Those which Transform on Template Removal)[53]

$AlPO_{4-n}$ structure	Related structure
Very large pore	
VPI-5[a]	Novel
$AlPO_4$-8	Novel
Large pore	
$AlPO_4$−5[b]	Novel
−31	Novel
−36	Novel
−37	Faujasite
−40	Novel
−46	Novel
−50	Novel
Intermediate pore	
$AlPO_4$−11	Novel
−41	Novel
Small pore	
$AlPO_4$−14	Novel
−17	Erionite
−18	Novel
−24	Analcime
−25	Novel
−26	Novel
−33	Novel
−34	Chabazite
−35	Levynite
−39	Novel
−42	Zeolite A
−43	Gismondine
−44	Chabazite
−47	Chabazite
−52	Novel
Very small pore	
$AlPO_4$−16	Novel
−20	Sodalite
−28	Novel
Other	
$AlPO_4$−12	Novel
−14A	Novel
−15	Novel
−21	Novel
−H3	

[a]Also known as $AlPO_4$−54.
[b]An all-silica analog of $AlPO_4$−5 (known as SSZ-24) has recently been synthesized.

11 STRUCTURE OF ALUMINOPHOSPHATE MOLECULAR SIEVES

The $AlPO_4$ molecular sieves, the porous crystalline equivalents of aluminum phosphate, are built from alternating AlO_4 and PO_4 tetrahedra.[45,46] Some of them have the framework topologies of known zeolites, but many are novel structures. The various $AlPO_4$ structure types are listed in Table 2, and the structures of $AlPO_4$-5 and $AlPO_4$-11 are shown in Figure 15. Synthesized from gels containing sources of aluminum, phosphorus, and at least one organic structure-directing template, $AlPO_4$ materials have electrically neutral frameworks and thus no exchangeable cations. Incorporation of a silicon source into the synthesis gel results in the formation of silicoaluminophosphates (SAPOs)[47] and the incorporation of a metal Me (such as Mg, Mn, Fe, Co or Zn), into $AlPO_4$ and SAPO gives the MeAPO and MeAPSO sieves, respectively.[48] SAPO and MeAPO have negatively charged frameworks, and thus potential uses as ion exchangers and catalysts. In SAPO the predominant substitution mechanism is of silicon onto phosphorus sites, though pairwise substitution of silicon onto both aluminum and phosphorus sites is also possible. In MeAPO the metal substitutes onto the aluminum sites of the equivalent $AlPO_4$ structure. Other elements (Li, Be, B, Ti, Ga, Ge and As) have been claimed to substitute into the aluminophosphate framework to give ElAPO materials.[49] By

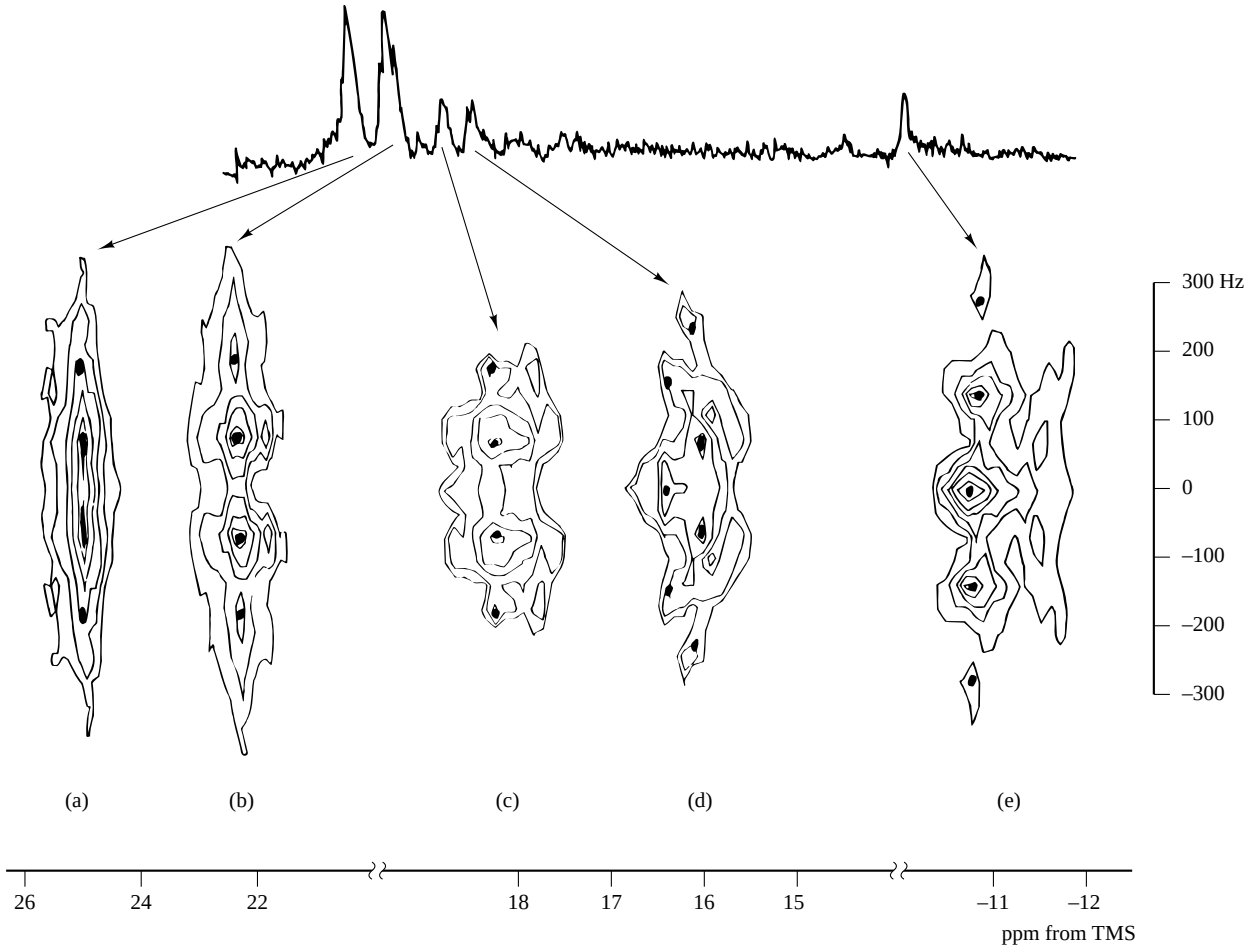

Figure 14 Heteronuclear two-dimensional J-resolved ^{13}C MAS NMR spectrum of zeolite H-ZSM-5 with adsorbed methanol treated at 300 °C for 30 min[44]

introducing more than one kind of heteroatom into the framework, or a metal and silicon simultaneously, MeAPSO and ElAPSO sieves were prepared.[50,51]

Remarkable $AlPO_4$ and related materials include VPI-5, the topology of which had been predicted in advance of its being synthesized, and cloverite, a gallophosphate molecular sieve with 20-membered rings, the most porous molecular sieve prepared so far.

12 NMR STUDIES OF $AlPO_4$-5, $AlPO_4$-11, AND $AlPO_4$-21

The $AlPO_4$ materials are a challenge to multinuclear solid state MR, given the wide variety of new crystal structures and the fact that they contain two different kinds of 100% abundant nuclei (^{31}P and ^{27}Al) in close proximity. Furthermore, framework aluminum in $AlPO_4$ can be linked to one or two oxygen species such as $-OH$ or $-OH_2$, so that some of the aluminum atoms may be five- or six-coordinate with respect to oxygen. Another challenge are the strong quadrupolar effects involving ^{27}Al as a result of which the quadrupole correction to chemical shifts is much larger than in zeolites. The aluminum and phosphorus atoms alternate in the frameworks of all $AlPO_4$, so that only even-numbered rings may be formed. However, the three allowed coordination numbers of aluminum make possible a wide range of new structures.

Table 3 summarizes the ^{31}P chemical shifts in $AlPO_4$ materials. Note that the precise value of the chemical shift often depends on the kind of organic template and on the water content of calcined samples. A similar table for ^{27}Al chemical shifts cannot be readily provided as the quadrupole coupling parameters, necessary if the quadrupole correction is to be made, are rarely known. Corrected ^{27}Al chemical shifts are between 37 and 48 ppm for $Al(OP)_4$ sites, about 15 ppm for $Al(OP)_4(OH)$, and between -9.5 and -12 ppm for $Al(OP)_4(OH_2)_2$ sites.[52] There is a recent review of $AlPO_4$-based molecular sieves.[53] A correlation between chemical shift and bond angle for $AlPO_4$ materials[65] relies on the comparison of mean Al–O–P bond angles with ^{27}Al chemical shifts corrected for the second-order quadrupole interaction. The imperfection of the correlation[66] is probably caused by the presence of five- and six-coordinate aluminum.

The spectra of $AlPO_4$-5, $AlPO_4$-11, $AlPO_4$-17, and $AlPO_4$-31 are consistent with known framework structures. ^{31}P and ^{27}Al MAS spectra of $AlPO_4$-5 each consist of a single peak.[54,55] The ^{31}P chemical shift (about -30 ppm) is characteristic of the $P(OAl)_4$ environment. The corrected chemical shift of the broad ^{27}Al peak is about 44 ppm, which is characteristic of four-coordinate $Al(OP)_4$ sites. This

Table 3 Summary of ^{31}P Chemical Shifts in $AlPO_4$ Structures[53]

Structure	Form	Chemical shift (ppm from 85% H_3PO_4)
$AlPO_4$-5	Tripropylamine	−30.6
	Tetraethylammonium	−28.6
	Hydrated calcined	−27.8
$AlPO_4$-8	Hydrated	−22.6, −25.7, −26.9, −31.1
	Dehydrated	−12.3, −30.1
$AlPO_4$-11	Dipropylamine	−31.8
	Hydrated calcined	−23.4, −29.6
$AlPO_4$-12	2-Imidazolidone	−6.6, −15.0
$AlPO_4$-14	Isopropylamine	−5.7, −20.3, −24.3
	Piperidine	−22.1, −28.0, −30.6
	Hydrated calcined	−22.4, −23.7, −25.3, −28.1
	Dehydrated calcined	−21.9, −27.1, −32.0
$AlPO_4$-14A	Isopropylamine	−19.4, −29.0
$AlPO_4$-17	Not specified	−24.2
	Hydrated calcined	−29.9
	Dehydrated calcined	−29.5, −35.0
$AlPO_4$-20	Tetramethylammonium	−35.2
$AlPO_4$-21	Pyrolidine	−13.3, −21.1, −30.3
	Not specified	−14.8, −21.4, −26.4
$AlPO_4$-25	Hydrated	−30.7
$AlPO_4$-31	Not specified	−30.2
	Hydrated calcined	−29.9
	Dehydrated calcined[a]	−30.5
$AlPO_4$-34	Tetraethylammonium + dipropylamine[a]	−28.5
	Hydrated calcined[a]	−27.4
$AlPO_4$-35	Not specified[a]	−27.4, −32.8
$AlPO_4$-37	Tetrapropylammonium + tetramethylammonium[a]	−26.4
$AlPO_4$-42	Tetramethylammonium[a]	−27.5
VPI-5	Hydrated	−23.3, −27.2, −33.1
	Dehydrated	−26.6, −32.5
$AlPO_4$-H3	Hydrated	−24.1, −25.9
$AlPO_4$-Q	(Quartz)	−24.8
		−25.6
$AlPO_4$-T	(Tridymite)	−29.5
$AlPO_4$-C	(Cristobalite)	−27.1

[a]Measured in an equivalent SAPO structure.

means that aluminum and phosphorus strictly alternate in the framework. The ^{31}P peak from the calcined and partially hydrated form is split as a result of the interaction between the framework and the intracrystalline water, presumably giving rise to $Al(OP)_4(OH_2)_2$ environments. Hydration produces significant amounts of six-coordinate framework aluminum which returns to four-coordination upon rehydration. Four- and six-coordinate aluminum resonate at 23−31 ppm and about −17 ppm, respectively.

$AlPO_4$-11 has an orthorhombic unit cell, but the symmetry of the hydrated calcined material is lower. Adsorbates such as cyclohexane stabilize the higher symmetry form which has three distinct crystallographic sites for both aluminum and phosphorus in the population ratio of 2:2:1. The lower symmetry form requires five sites in the population ratio of 1:1:1:1:1. Figure 16 shows that the ^{27}Al and ^{31}P NMR spectra of 'as-synthesized' $AlPO_4$-11 show single asymmetric peaks (suggesting that more than one environment is present). The relatively low intensity resonance at −5.5 ppm in the ^{31}P spectrum is probably due to terminal $P(OAl)_3OH$ sites at defects and the surface of the crystallites. The ^{31}P spectrum of the calcined and hydrated material (Figure 16) consists of two well-resolved resonances at −23.4 and −29.6 ppm in the intensity ratio of 1:4, which suggests that four of the five phosphorus sites have similar chemical shifts.

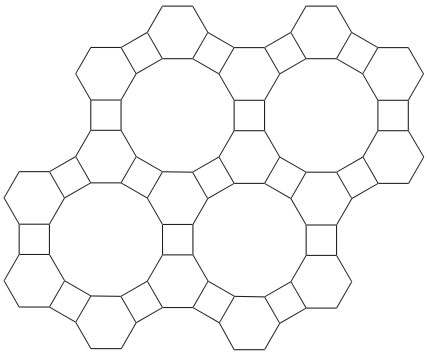

$AlPO_4$-5

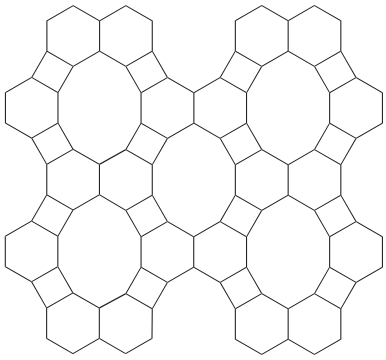

$AlPO_4$-11

Figure 15 The structures of $AlPO_4$-5 and $AlPO_4$-11 viewed down the (001) axis

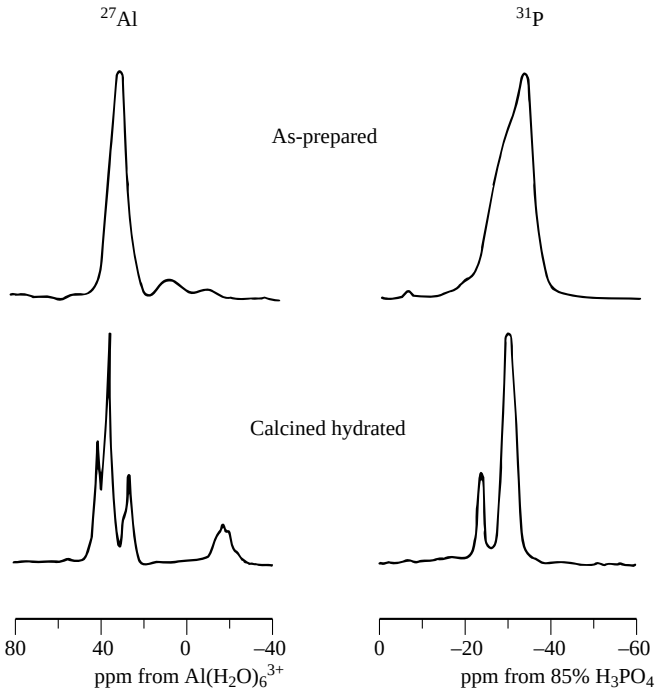

Figure 16 ^{27}Al and ^{31}P MAS NMR spectra of 'as-prepared' and hydrated calcined $AlPO_4$-11 obtained in a 9.4 T field[57]

The development of double rotation (DOR), in which the sample is rotated around two different axes simultaneously and dynamic angle spinning (DAS), in which the sample is rotated sequentially about two different axes, was a major advance in the study of solids. DAS and DOR remove not only chemical shift anisotropy, but also second-order quadrupolar interactions.[56] ^{27}Al DOR distinguishes the distorted five-coordinate aluminum sites in the molecular sieve precursor $AlPO_4$-21. Upon calcination, $AlPO_4$-21 transforms to $AlPO_4$-25, which has two four-coordinate aluminum sites with similar isotropic chemical shifts. These cannot be resolved in an 11.7 T field, but are resolved by DOR at 4.2 T because of their different quadrupole coupling constants.

^{27}Al DOR was used[57] to monitor the nature of the phase transition of $AlPO_4$-11 observed when water is adsorbed. The DOR spectrum of hydrated $AlPO_4$-11 shows that the line at 30 ppm is indeed due to a single environment. However, the broad DOR peak from six-coordinate aluminum indicates the presence of a range of sites, suggesting that all five crystallographic sites are hydrated to a similar extent. The DOR spectrum of the dehydrated calcined sample shows only a single peak in the 11.7 T field, despite the fact that three crystallographic sites are present. This indicates that the three sites have similar chemical shifts.

13 VPI-5 AND $AlPO_4$-8

VPI-5 is a crystalline aluminophosphate molecular sieve containing 18-membered rings of aluminum and phosphorus atoms (Figure 17). The large (about 1.2 nm) channel diameter gives VPI-5 considerable potential for the separation of large molecules, and for catalytic cracking of the heavy fractions of petroleum. The material has thus been studied extensively. The room-temperature ^{31}P MAS NMR spectrum of hydrated VPI-5 contains three peaks in an intensity ratio of 1:1:1 (Figure 18) and the ^{27}Al spectrum resonances from four- and six-coordinate aluminum. This is because 'as-prepared' VPI-5 is an aluminophosphate hydrate with three inequivalent sites for both phosphorus and aluminum: one of the aluminum sites is bonded to two chemisorbed water molecules, thus becoming six-coordinate. Variable temperature NMR[58,59] (Figure 18) shows that VPI-5 undergoes a reversible phase transition to a higher symmetry structure with two ^{31}P resonances in a 2:1 intensity ratio and two sites for both aluminum and phosphorus. The peaks at −23 ppm (1) and −27 ppm (2) were assigned to phosphorus atoms in 6−4 sites (P2 and P3), and the peak at −33 ppm (3) to P atoms in 4−4 sites (P1). ^{31}P–^{31}P spin diffusion spectra were used to establish how peaks 1 and 2 are to be assigned to particular P2 and P3 sites.[60] Each pair of ^{31}P resonances gives rise to cross peaks (Figure 19) and the efficiency of spin diffusion (cross-peak intensity) decreases with increasing spinning rates. An analysis of the plot of cross-peak intensity versus the spinning rate in the light of interatomic distances known from the XRD structure showed that peaks 1, 2, and 3 should be assigned to sites P2, P3, and P1, respectively.

^{27}Al DOR spectra[61] confirm that the peak from four-coordinate aluminum arises from two crystallographic sites, and the broad peak from six-coordinate aluminum from a single site. Although the two four-coordinate aluminum sites are not resolved by DOR at high fields because of their similar chemical shifts, they may be resolved at lower fields because the sites have different quadrupolar coupling constants.

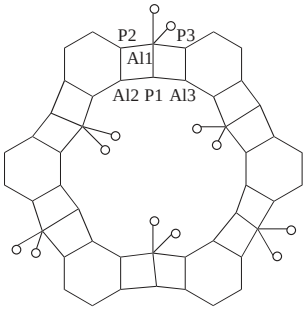

Figure 17 One layer of the framework structure of hydrated VPI-5 taken from the stereoscopic view along the [001] direction showing the deviation from $P6_3cm$ symmetry.[59] Aluminum and phosphorus atoms are located at the apices of the polygons. Sites located between two fused four-membered rings are known as 4–4 sites; those located between six-membered and four-membered rings are known as 6–4 sites. P2 and P3, and Al2 and Al3 sites are inequivalent as a result of the distortion. The Al1 site is six-coordinate as a result of bonding to four bridging oxygen atoms and two 'framework' water molecules

Heating hydrated VPI-5 results in a transformation to $AlPO_4$-8. ^{27}Al DOR shows[61] that in dehydrated VPI-5 there are also only two four-coordinate aluminum environments in the intensity ratio of 2:1. However, after a period during which the sample had been kept in a rotor which was not completely air-tight, many additional NMR resonances are found, corresponding to a partially rehydrated material (Figure 20).

Spin echo double resonance (SEDOR) allows the relative spatial disposition of spins to be deduced. By measuring the dipolar interaction between nuclei, which is inversely proportional to the cube of the internuclear distance, SEDOR probes only their immediate vicinity. ^{27}Al–^{31}P SEDOR can measure Al–P distances in $AlPO_4$ materials.[62] MAS NMR with dipolar dephasing has been used[63] for the study of mixed pairs of quadrupolar and spin-$\frac{1}{2}$ nuclei in VPI-5. Dipolar connectivities between ^{31}P and ^{27}Al were examined in both directions.

NMR spectra of $AlPO_4$-8 show single ^{31}P and ^{27}Al peaks and a small ^{31}P peak at -12.1 ppm.[64] In hydrated $AlPO_4$-8, about 34% of the aluminum is six-coordinate. The ^{31}P spectrum shows several environments, and at least five peaks are required for the simulation. The structure of dehydrated $AlPO_4$-8 calls five sites in the population ratio of 2:2:2:2:1.

14 SAPO MOLECULAR SIEVES

The general formula for a SAPO molecular sieve is $M_{(y-z)/n}[Si_xAl_yP_zO_2]\cdot wH_2O$, where $x + y + z = 1$, M is the charge-balancing cation, and the amount of silicon depends on the structure type. It is generally found that $y > z$, indicating that substitution of silicon into phosphorus sites is more frequent than substitution into aluminum sites. However, the aluminum content is often less than 50%, so that substitution of two silicon atoms for an Al + P pair must also occur. ^{29}Si NMR spectra of SAPO suffer from low signal-to-noise ratios due to the low concentration of silicon and the low natural abundance of ^{29}Si. The ^{29}Si chemical shift of SAPO-5 (isostructural with $AlPO_4$-5) is -92 ppm, which is slightly more negative than

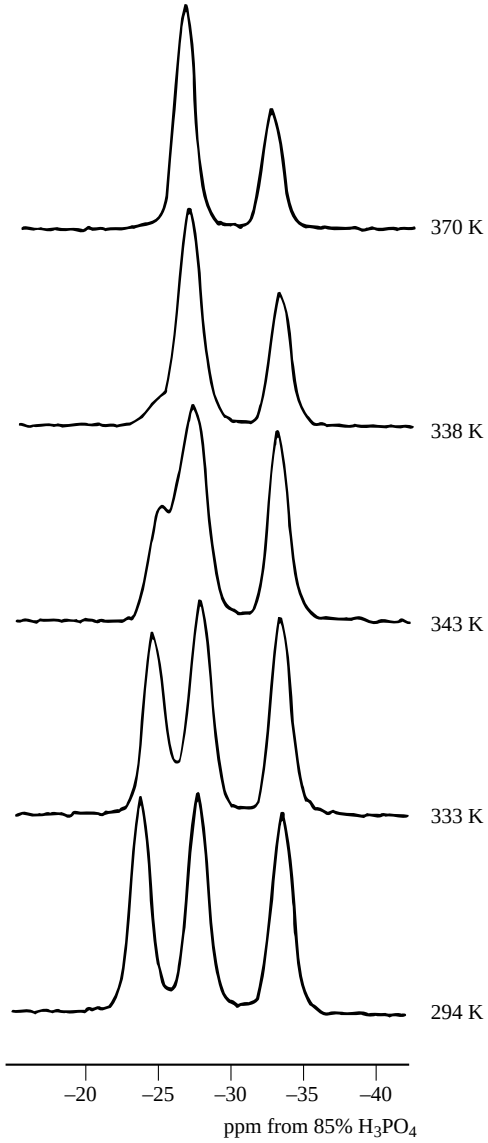

Figure 18 Variable temperature ^{31}P MAS NMR spectra of hydrated VPI-5 in a closed rotor system[59]

that for $Si(OAl)_4$ environments in zeolites, and it appears that the silicon is substituting exclusively onto the phosphorus sites of the framework. ^{27}Al, ^{31}P, and ^{29}Si NMR spectra[67] each contain single peaks, but some ^{29}Si spectra show peaks at -92, -102, and -108 ppm, indicating the presence of two or more silicon environments. The -102 ppm peak may originate from siliceous species on the surface of the crystallites. It also appears that, even allowing for the possible presence of amorphous silica, some regions are richer in silicon than are $Si(OAl)_4$ sites. Pairwise substitution of silicon onto aluminum and phosphorus sites seems to take place. The ^{31}P peak has the same chemical shift as in $AlPO_4$-5, which indicates that all phosphorus is in the $P(OAl)_4$ environment. Narrow ^{31}P NMR peaks from SAPO materials indicate that no Si–O–P bonds are present, and no case has yet been reported where all the silicon is present exclusively in $Si(OAl)_4$ environments.

The framework structure of SAPO-37 is that of the zeolite faujasite. There is a single ^{31}P peak at -26.4 ppm corresponding to $P(OAl)_4$ sites, and a single ^{29}Si peak at

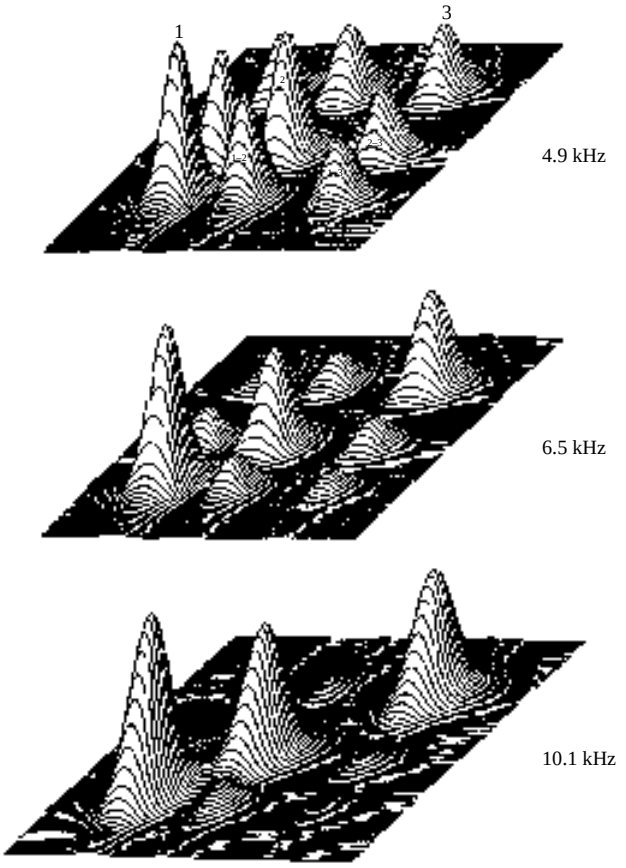

Figure 19 Two-dimensional ^{31}P NMR spin diffusion spectra of hydrated VPI-5 recorded with MAS at 4.9, 6.5, and 10.1 kHz.[60] The three spectra are not on the same intensity scale, and so only the relative intensities within each can be compared

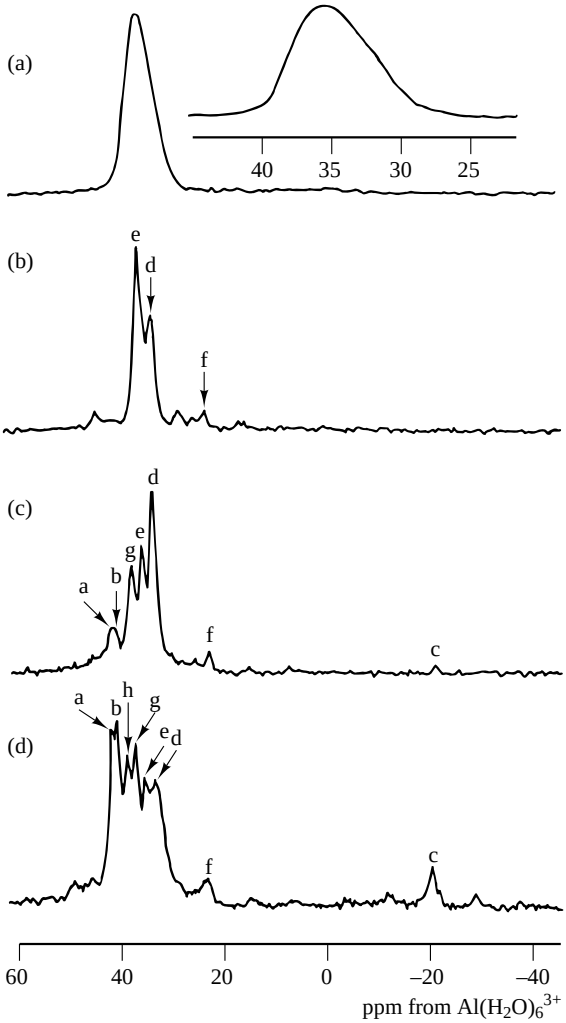

Figure 20 ^{27}Al NMR spectra of dehydrated and partially rehydrated VPI-5:[61] (a) ^{27}Al MAS and (b) ^{27}Al DOR spectrum of dehydrated VPI-5; (c) DOR spectrum after 2 days of rehydration; (d) DOR spectrum after 23 days of rehydration

−90.2 ppm corresponding to $Si(OAl)_4$ sites, indicating that the ideal silicon-for-phosphorus mechanism operates. Samples with high silicon content give more complicated ^{29}Si spectra, with features at −86, −90, −94, −98, −102, and −106 ppm.[68] The strongest of these, at −90 ppm, corresponds to the $Si(OAl)_4$ units in pure SAPO materials, while the others correspond to $Si(OAl)_x(OSi)_{4-x}$ units in zeolite Y. This suggests that SAPO-37 may contain inhomogeneous growths of silicoaluminophosphate and aluminosilicate regions.

The structure of SAPO-34 is that of the zeolite chabazite. The single NMR peak of ^{29}Si at −92 ppm[69,70] indicates that the exclusive substitution mechanism of silicon onto phosphorus sites applies, leading to the creation of Brønsted acid sites. ^{13}C MAS NMR spectra of SAPO-34 with adsorbed MeOH reveal hydrocarbon transformations upon heating the sample.[69] The major products are C_1 and C_2 organics; although formed, C_4 to C_6 hydrocarbons are too large to diffuse out through the eight-membered rings. The C_3 species are present in the product in a lower yield than expected, because the pore system is partially blocked by longer chain hydrocarbons.

15 MeAPO MOLECULAR SIEVES

The framework formula of a MeAPO sieve is $[Me_xAl_yP_zO_2]$, with $x + y + z = 1$, and $z = 0.5$, indicating that the metal substitutes exclusively onto the aluminum sites of the equivalent $AlPO_4$ structure. MeAPOs can therefore contain Brønsted acid sites. Deviations from $z = 0.5$ are attributed to extraframework metal ($z < 0.5$) or phosphorus ($z > 0.5$). $x > 0.125$ implies the presence of Me−O−P−O−Me bonds.

The ^{27}Al MAS NMR spectrum of MgAPO-20 containing 15% magnesium[71] (Figure 21) shows a single $Al(OP)_4$ environment, while the ^{31}P spectrum contains two major peaks at −21.1 and −28.0 ppm from P(2Al,2Mg) and P(3Al,1Mg) units in an intensity ratio of 1:2. The low intensity peaks come from P(1Al,3Mg) and P(4Al) units. Magnesium is therefore present exclusively on aluminum sites, which makes it possible to calculate the framework composition from the intensities of the NMR peaks and to distinguish between possible ordering schemes for phosphorus, aluminum, and magnesium.

^{11}B spectra of BAPO-5 show that boron is four-coordinate, but is not necessarily a part of the framework. Only one ^{31}P peak is found, even though $P(OAl)_3(OB)$ sites are expected to be present. Similarly, there is no direct evidence for the presence of framework lithium in LiAPO-5.

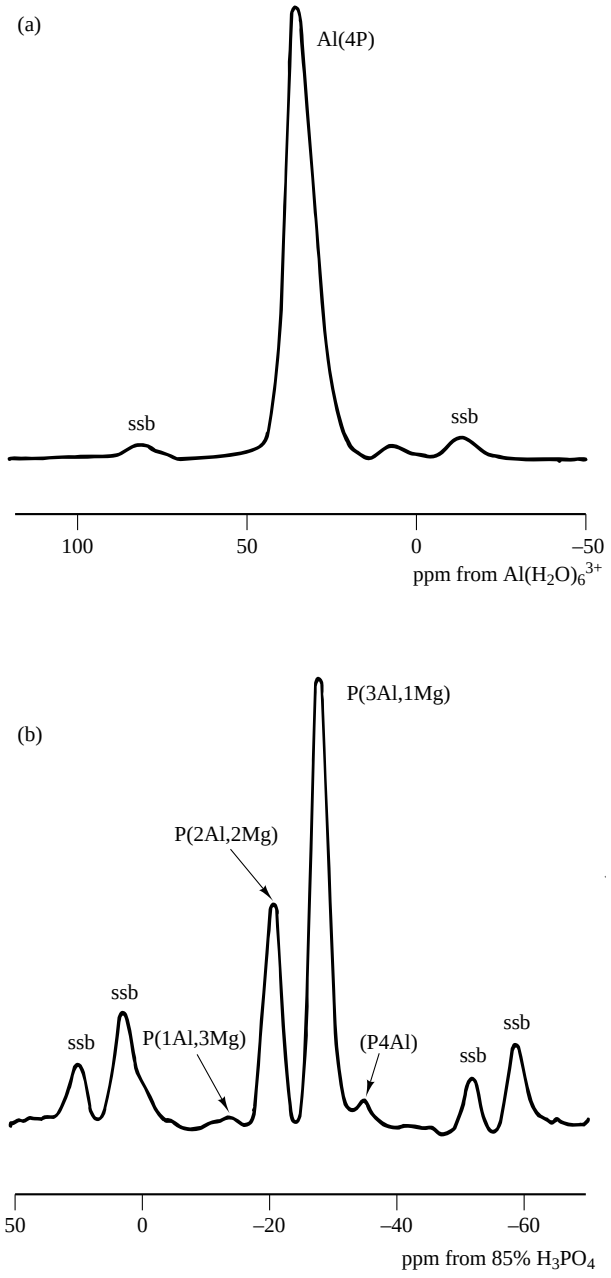

Figure 21 (a) ^{27}Al and (b) ^{31}P MAS NMR spectra of 'as-prepared' MgAPO-20[71]

16 ^{2}H NMR STUDIES OF MOTION IN MOLECULAR SIEVES

Since the quadrupolar interactions of ^{2}H are sensitive to molecular motion, the nucleus is useful for the study of molecular dynamics over a wide range of frequencies. Variable temperature studies of small organic molecules adsorbed on a series of zeolites[72] provide information on the filling of the intracrystalline space, the motion of the adsorbed species and site-selective adsorption. The ^{2}H spectra of deuterated *p*-xylenes $CH_3C_6D_4CH_3$ and $CD_3C_6H_4CD_3$ on zeolite Na-ZSM-5 in terms of possible dynamic states and sorption sites of the guest molecules identify five dynamic states, the relative populations varying with the level of loading and the temperature.[73] ^{2}H NMR results on *p*-xylene-d_6, toluene-d_3 and benzene-d_6 adsorbed on H-ZSM-5,[74] as well as on mono-, di-, and trimethylamine on zeolites ZK-5 and Y[75] yield a wealth of dynamic information.

Examination of the dynamic behavior of water in the channels of VPI-5 leads to a motional model which applies in the temperature range 225–348 K.[76,77] There are at least two sites for the intracrystalline water: one is bound to framework aluminum, and undergoes rotational motion about the $Al-OH_2$ bond, the other is a free site within the VPI-5 channels. The motion in this site is approximately isotropic, and the tumbling rate increases with temperature. The dynamic behavior of water in the temperature range 261–297 K is rather unexpected.

Multiple quantum (MQ) NMR, a 'spin counting' tool for homonuclear spin clusters,[78] is also suitable for the study of species adsorbed in molecular sieves.[79,80] Nuclear spins are forced to act collectively via their dipolar couplings, and the resulting multiple quantum coherences are detected after conversion into observable single quantum coherences. If the system constitutes a collection of isolated clusters, the multiple quantum count reaches a plateau corresponding to the number of spins in the cluster. Figure 22 shows the results of ^{1}H MQ NMR experiments for hexamethylbenzene, a molecule containing 18 hydrogen atoms, adsorbed on zeolite Na-Y.[79] At lower loadings the plateau corresponds to about

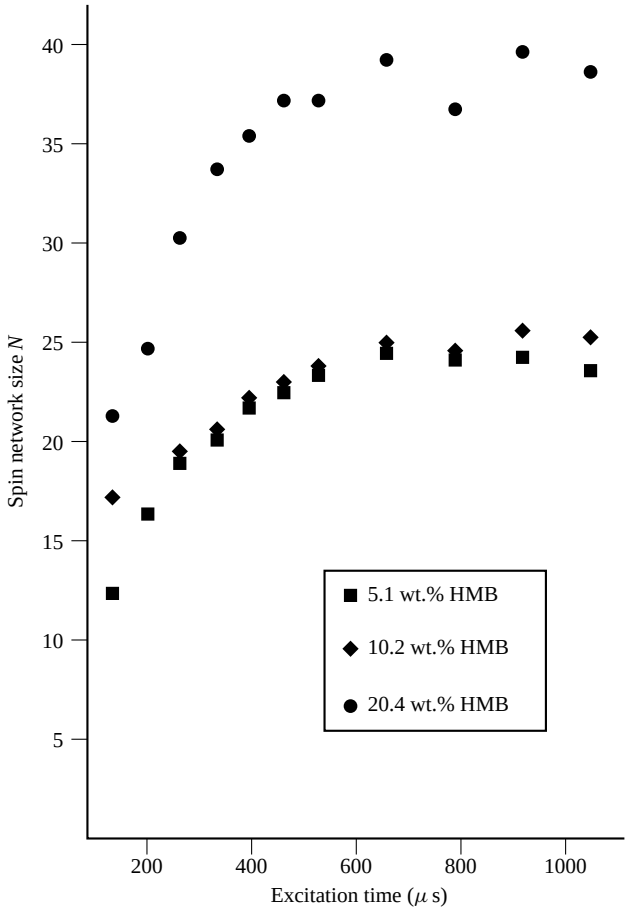

Figure 22 Results of ^{1}H MQ NMR experiments for hexamethylbenzene adsorbed at 573 K on dehydrated zeolite Na-Y[79]

one hexamethylbenzene molecule per supercage, and at higher loading to two molecules per supercage.

17 RELATED ARTICLES

Brønsted Acidity of Solids; Cross Polarization in Rotating Solids: Spin-1/2 Nuclei; Magic Angle Spinning; Nutation Spectroscopy of Quadrupolar Nuclei; Quadrupolar Nuclei in Solids; Reactions in Zeolites; Silicon-29 NMR of Solid Silicates.

18 REFERENCES

1. G. Engelhardt and D. Michel, *High-Resolution Solid-State NMR of Silicates and Zeolites*, Wiley, Chichester, 1987.
2. J. Klinowski, *Chem. Rev.*, 1991, **91**, 1459.
3. C. A. Fyfe, Y. Feng, H. Grondey, G. T. Kokotailo, and H. Gies, *Chem. Rev.*, 1991, **91**, 1525.
4. A. Fr. Cronstedt, *Kongl. Svenska Vetenskaps Acad. Handlingar*, 1756, **17**, 120.
5. W. Loewenstein, *Am. Mineral.*, 1954, **39**, 92.
6. W. M. Meier and D. H. Olson, *Atlas of Zeolite Structure Types*, Butterworth, Sevenoaks, 1992.
7. D. W. Breck, *Zeolite Molecular Sieves: Structure, Chemistry and Use*, Wiley, London, 1974.
8. R. M. Barrer, *Zeolites and Clay Minerals as Sorbents and Molecular Sieves*, Academic, London, 1978.
9. R. M. Barrer, *Hydrothermal Chemistry of Zeolites*, Academic, London, 1982.
10. R. Szostak, *Molecular Sieves: Principles of Synthesis and Identification*, Van Nostrand Reinhold, New York, 1989.
11. P. B. Weisz and V. J. Frilette, *J. Phys. Chem.*, 1960, **64**, 382.
12. R. J. Argauer and G. R. Landolt, US Patent 3 702 886 1972.
13. E. Lippmaa, M. Mägi, A. Samoson, G. Engelhardt, and A.-R. Grimmer, *J. Am. Chem. Soc.*, 1980, **102**, 4889.
14. G. Engelhardt, U. Lohse, E. Lippmaa, M. Tarmak, and M. Mägi, *Z. Anorg. Allg. Chem.*, 1981, **482**, 49.
15. J. Klinowski, S. Ramdas, J. M. Thomas, C. A. Fyfe, and J. S. Hartman, *J. Chem. Soc., Faraday Trans. II*, 1982, **78**, 1025.
16. M. T. Melchior, D. E. W. Vaughan, and A. J. Jacobson, *J. Am. Chem. Soc.*, 1982, **104**, 4859.
17. C. A. Fyfe, G. C. Gobbi, J. Klinowski, J. M. Thomas, and S. Ramdas, *Nature*, 1982, **296**, 530.
18. C. A. Fyfe, H. Grondey, Y. Feng, and G. T. Kokotailo, *J. Am. Chem. Soc.*, 1990, **112**, 8812; C. A. Fyfe, Y. Feng, H. Gies, H. Grondey, and G. T. Kokotailo, *Chem. Phys. Lett.*, 1990, **173**, 211; C. A. Fyfe, Y. Feng, H. Grondey, and G. T. Kokotailo, *J. Chem. Soc., Chem. Commun.*, 1990, 1224.
19. J. Klinowski, T. A. Carpenter, and L. F. Gladden, *Zeolites*, 1987, **7**, 73.
20. H. Strobl, C. A. Fyfe, G. T. Kokotailo, and C. T. Pasztor, *J. Am. Chem. Soc.*, 1987, **109**, 4733.
21. G. W. West, *Aust. J. Chem.*, 1984, **37**, 455.
22. J. M. Thomas, J. Klinowski, S. Ramdas, B. K. Hunter, and D. T. B. Tennakoon, *Chem. Phys. Lett.*, 1983, **102**, 158.
23. C. A. Fyfe, G. J. Kennedy, G. T. Kokotailo, and C. T. DeSchutter, *J. Chem. Soc., Chem. Commun.*, 1984, 1093.
24. J. V. Smith and C. S. Blackwell, *Nature*, 1983, **303**, 223.
25. R. Radeglia and G. Engelhardt, *Chem. Phys. Lett.*, 1985, **114**, 28.
26. S. Ramdas and J. Klinowski, *Nature*, 1984, **308**, 521.
27. P. J. Barrie and J. Klinowski, *Prog. NMR Spectrosc.*, 1992, **24**, 91.
28. C. A. Fyfe, H. Gies, and Y. Feng, *J. Am. Chem. Soc.*, 1989, **111**, 7702.
29. W. Kolodziejski, P. J. Barrie, H. He, and J. Klinowski, *J. Chem. Soc., Chem. Commun.*, 1991, 961.
30. J. Klinowski, J. M. Thomas, C. A. Fyfe, and G. C. Gobbi, *Nature*, 1982, **296**, 533.
31. I. E. Maxwell, W. A. van Erp, G. R. Hays, T. Couperus, R. Huis, and A. D. H. Clague, *J. Chem. Soc., Chem. Commun.*, 1982, 523.
32. G. Engelhardt, U. Lohse, A. Samoson, M. Mägi, M. Tarmak, and E. Lippmaa, *Zeolites*, 1982, **2**, 59.
33. L. Kellberg, M. Linsten, and H. J. Jakobsen, *Chem. Phys. Lett.*, 1991, **182**, 120.
34. H. Hamdan, B. Sulikowski, and J. Klinowski, *J. Phys. Chem.*, 1989, **93**, 350.
35. A. Samoson, E. Lippmaa, G. Engelhardt, U. Lohse, and H.-G. Jerschkewitz, *Chem. Phys. Lett.*, 1987, **134**, 589.
36. G. A. H. Tijink, R. Janssen, and W. S. Veeman, *J. Am. Chem. Soc.*, 1987, **109**, 7301.
37. J. H. Lunsford, W. P. Rothwell, and W. Shen, *J. Am. Chem. Soc.*, 1985, **107**, 1540.
38. J. M. Thomas, J. Klinowski, C. A. Fyfe, G. C. Gobbi, S. Ramdas, and M. W. Anderson, *ACS Symp. Ser.*, 1983, **218**, 159.
39. H. Kessler, J. M. Chézeau, J. L. Guth, H. Strub, and G. Coudurier, *Zeolites*, 1987, **7**, 360.
40. K. F. M. G. J. Scholle and W. S. Veeman, *Zeolites*, 1985, **5**, 118.
41. G. L. Turner, K. A. Smith, R. J. Kirkpatrick, and E. Oldfield, *J. Magn. Reson.*, 1986, **67**, 544.
42. M. W. Anderson, P. J. Barrie, and J. Klinowski, *J. Phys. Chem.*, 1991, **95**, 235.
43. M. W. Anderson and J. Klinowski, *Nature*, 1989, **339**, 200; *J. Am. Chem. Soc.*, 1990, **112**, 10.
44. M. W. Anderson and J. Klinowski, *Chem. Phys. Lett.*, 1990, **172**, 275.
45. S. T. Wilson, B. M. Lok, and E. M. Flanigen, US Patent 4 310 440 1982.
46. S. T. Wilson, B. M. Lok, C. A. Messina, T. R. Cannan, and E. M. Flanigen, *J. Am. Chem. Soc.*, 1982, **104**, 1146.
47. B. M. Lok, C. A. Messina, R. L. Patton, R. T. Gajek, T. R. Cannan, and E. M. Flanigen, US Patent 4 440 871, 1984.
48. S. T. Wilson and E. M. Flanigen, European Patent Application 0 132 708 1985.
49. E. M. Flanigen, B. M. Lok, R. L. Patton, and S. T. Wilson, *Pure Appl. Chem.*, 1986, **58**, 1351.
50. B. M. Lok, B. K. Marcus, L. D. Vail, E. M. Flanigen, R. L. Patton, and S. T. Wilson, European Patent Application 0 159 624, 1985.
51. B. M. Lok, B. K. Marcus, and E. M. Flanigen, European Patent Application 0 158 350, 1985.
52. R. Jelinek, B. F. Chmelka, Y. Wu, A. Pines, P. J. Grandinetti, P. J. Barrie, and J. Klinowski, *J. Am. Chem. Soc.*, 1991, **113**, 4097.
53. P. J. Barrie, *Adv. Spectrosc.*, 1993, **22**, 151.
54. C. S. Blackwell and R. L. Patton, *J. Phys. Chem.*, 1984, **88**, 6135.
55. D. Müeller, E. Jahn, B. Fahlke, G. Ladwig, and U. Haubenreisser, *Zeolites*, 1985, **5**, 53.
56. A. Samoson, E. Lippmaa, and A. Pines, *Mol. Phys.*, 1988, **65**, 1013.
57. P. J. Barrie, M. E. Smith, and J. Klinowski, *Chem. Phys. Lett.*, 1991, **180**, 6.

58. J. P. van Braam Houckgeest, B. Kraushaar-Czarnetzki, R. J. Dogterom, and A. de Groot, *J. Chem. Soc., Chem. Commun.*, **1991**, 666.
59. J. Rocha, W. Kolodziejski, H. He, and J. Klinowski, *J. Am. Chem. Soc.*, 1992, **114**, 4884.
60. W. Kolodziejski, H. He, and J. Klinowski, *Chem. Phys. Lett.*, 1992, **191**, 117.
61. Y. Wu, B. F. Chmelka, A. Pines, M. E. Davis, P. J. Grobet, and P. A. Jacobs, *Nature*, 1990, **346**, 550.
62. E. R. H. van Eck and W. S. Veeman, *Solid State NMR*, 1992, **1**, 1.
63. C. A. Fyfe, K. T. Mueller, H. Grondey, and K. C. Wong-Moon, *Chem. Phys. Lett.*, 1992, **199**, 198.
64. M. Stöcker, D. Akporiaye, and K.-P. Lillerud, *Appl. Catal.*, 1991, **69**, L7.
65. D. Müller, E. Jahn, G. Ladwig, and U. Haubenreisser, *Chem. Phys. Lett.*, 1984, **109**, 332.
66. G. Engelhardt, *Stud. Surf. Sci. Catal.*, 1989, **52**, 151.
67. I. P. Appleyard, R. K. Harris, and F. R. Fitch, *Chem. Lett.*, **1985**, 1747.
68. J. A. Martens, C. Janssens, P. J. Grobet, H. K. Beyer, and P. A. Jacobs, *Stud. Surf. Sci. Catal.*, 1989, **49**, 215.
69. M. W. Anderson, B. Sulikowski, P. J. Barrie, and J. Klinowski, *J. Phys. Chem.*, 1990, **94**, 2730.
70. B. Zibrowius, E. Löffler, and M. Hunger, *Zeolites*, 1992, **12**, 167.
71. P. J. Barrie and J. Klinowski, *J. Phys. Chem.*, 1989, **93**, 5972.
72. R. R. Eckman and A. J. Vega, *J. Phys. Chem.*, 1986, **90**, 4679.
73. I. Kustanovich, D. Fraenkel, Z. Luz, S. Vega, and H. Zimmermann, *J. Phys. Chem.*, 1988, **92**, 4134.
74. I. Kustanovich, H. M. Vieth, Z. Luz, and S. Vega, *J. Phys. Chem.*, 1989, **93**, 7427.
75. I. Kustanovich, Z. Luz, S. Vega, and A. L. Vega, *J. Phys. Chem.*, 1990, **94**, 3138.
76. D. Goldfarb, H.-X. Li, and M. E. Davis, *J. Am. Chem. Soc.*, 1992, **114**, 3690.
77. M. J. Duer, H. He, W. Kolodziejski, and J. Klinowski, *J. Phys. Chem.*, 1994, **98**, 1198.
78. R. Ryoo, S.-B. Liu, L. C. de Menorval, K. Takegoshi, B. Chmelka, M. Trecoske, and A. Pines, *J. Phys. Chem.*, 1987, **91**, 6575.
79. B. F. Chmelka, J. G. Pearson, S.-B. Liu, R. Ryoo, L. C. de Menorval, and A. Pines, *J. Phys. Chem.*, 1991, **95**, 303.
80. J. Rocha, S. W. Carr, and J. Klinowski, *Chem. Phys. Lett.*, 1991, **187**, 401.

Biographical Sketch

Jacek Klinowski. *b* 1943. M.Sc., 1965, Dr. Rer. Nat., 1968, Jagiellonian University, Kraków (Cracow), Poland, Ph.D., University of London, 1973, Diploma of Imperial College, 1973, M.A., University of Cambridge, 1988. Assistant Director of Research, University of Cambridge. Approx. 280 publications. Current research specialties: quadrupolar nuclei, two-dimensional NMR of novel materials.

Nitrogen NMR

Joan Mason

The Open University, Milton Keynes, UK

1	Introduction	1
2	Nitrogen-15 NMR Spectroscopy	3
3	Nitrogen-14 NMR Spectroscopy	6
4	Patterns of Nitrogen Shifts	9
5	Nitrogen Shielding Tensors	14
6	Patterns of Nitrogen Spin–Spin Couplings	19
7	Solid State Studies	23
8	Dynamics	24
9	Biomolecules	24
10	Related Articles	25
11	References	25

1 INTRODUCTION

Nitrogen has two useful nuclei for NMR spectroscopy, ^{14}N and ^{15}N, each with advantages and disadvantages. The drawbacks of these nuclei restricted the use of nitrogen NMR in the early decades of NMR spectroscopy, but Fourier transform spectroscopy, higher field magnets, larger samples, clever pulse techniques, and multidimensional spectroscopy have greatly expanded the use of nitrogen NMR.

The NMR properties of ^{14}N and ^{15}N are given in Table 1. Both nuclei have rather low magnetogyric ratios γ, so their sensitivity to NMR detection is rather low, relaxation processes are rather slow, coupling constants J(N,X) are small and J(N,N) values very small. Working at higher field (B_0) increases the accessibility, the signal intensity increasing as $\gamma^3 B_0^{\frac{3}{2}}$.

The spin-$\frac{1}{2}$ nucleus ^{15}N is now much used in high-resolution work, but its natural abundance is low, 0.36%. Another disadvantage is that $\gamma(^{15}\text{N})$ is negative, so NOE factors are negative, ^{15}N signals becoming more negative with proton decoupling. The maximal proton-induced NOE factor for ^{15}N is -4.93. A disadvantageous NOE can be removed by the use of paramagnetic additives such as [Cr(acac)$_3$].

Much work uses enrichment of ^{15}N, which may not be expensive if nitric acid, ammonium salts, or nitrites can be used as starting materials. With enrichment to 99% the NMR receptivity is six times that of ^{13}C in natural abundance. Sensitivity enhancement by polarization transfer, by INEPT or related methods, is helpful, particularly if there are protons directly attached to the ^{15}N. The gain compared with ^{13}C is now the greater, since $\gamma(^{15}\text{N})$ is smaller than $\gamma(^{13}\text{C})$.

The highly abundant nucleus ^{14}N (99.64%) has nearly six times the receptivity of ^{13}C in natural abundance (1%). Nitrogen-14, however, is quadrupolar (I = 1), so that ^{14}N NMR spectroscopy commonly suffers from line broadening and loss of spin–spin coupling due to too-fast relaxation. The ^{14}N quadrupole moment is relatively small, however, and if the local symmetry is high or the sample viscosity low ^{14}N work can be done in high resolution. This possibility is often overlooked nowadays, although the phenomenon of the chemical shift was uncovered very early on in ^{14}N resonance in an aqueous solution of ammonium nitrate NH_4NO_3, which gave two sharp lines.[1]

Quantitative work in ^{14}N or ^{15}N resonance is difficult because of the multiplicity of factors affecting the signal intensities, and in ^{14}N spectroscopy, the linewidth.

There is now a large volume of work in nitrogen resonance and only key or indicative references can be given. There have been two useful books on ^{15}N NMR spectroscopy.[2,3] The review literature includes the useful compendia of nitrogen NMR work published at intervals by Witanowski, Stefaniak, and Webb,[4–6] annual updates in appropriate chapters of the *Specialist Periodical Reports on Nuclear Magnetic Resonance*,[7] and several articles.[8–14] Experimental techniques are described in some detail in by Levy and Lichter,[2] Martin et al.,[3] and von Philipsborn and Müller,[13] and updates in Volumes 1–23 of *Specialist Periodical Reports on Nuclear Magnetic Resonance*.[7]

Nitrogen NMR spectroscopy affords a variety of information, with the choice of a spin $\frac{1}{2}$ or a quadrupolar nucleus, and an unusual variety of bond types, giving a range of 1350 ppm in chemical shift. Nitrogen forms bonds with all elements except those that are completely inert. Nitrogen can be found in nine stable oxidation states, with bond orders up to three, and coordination numbers up to six, the highest being in metal clusters. Moreover the shifts, coupling constants, and ^{14}N linewidths can be interpreted in terms of bond type, because of the characteristic influences of lone pair and π electrons associated with the observed nucleus, electrons which are of great importance to chemical structure and reactivity.

1.1 Nitrogen Referencing

Nitrogen NMR spectroscopy has suffered from a multiplicity of reference standards,[15] but consensus now favors the use of neat liquid nitromethane as external reference. Table 2 gives standards in the literature. Arguments in favor of nitromethane are that its ^{15}N signal is little affected by proton decoupling, the ^{14}N signal is sufficiently sharp, the neat liquid is accurately reproducible, and it can be obtained enriched with ^{15}N or ^{2}D with negligible effect on the chemical shift.

Nitrogen referencing should be by substitution. Internal referencing is unsatisfactory because of the magnitude and variety of medium effects for nitrogen (see Section 1.3 below). These are very large when nitrogen carries a lone pair, and can be quite large in the absence of lone-pair electrons if the nitrogen carries π electrons, as in nitromethane, as shown in Table 2. If [Cr(acac)$_3$] is used as a relaxation agent, a susceptibility correction, proportional to the concentration of the paramagnetic reagent, is necessary for precise work. The susceptibility shift in an electromagnet in which the field is perpendicular to the NMR tube is half the magnitude and opposite in sign to that in a superconducting magnet.

Ammonia is unsuitable as a reference substance since the nitrogen shift and the magnetic susceptibility are both highly sensitive to hydrogen bonding, and therefore to temperature, pressure, and to the presence of other substances. Ammonia is included in Table 2 as a 'theoretical' reference standard, since the spin–rotation determination of the nitrogen shielding (σ) in the isolated NH_3 molecule[16] forms the basis of an absolute scale for calculated values of σ.[17] Values of the shielding for

Table 1 NMR Properties of the Nitrogen Nuclei[a]

	^{14}N	^{15}N
Spin I	1	$\frac{1}{2}$
Natural abundance (%)	99.635	0.365
Magnetic moment μ (μ_N)	0.57099	−0.4903
Magnetogyric ratio γ (10^7 rad T^{-1} s^{-1})	1.9338	−2.712
Receptivity relative to that of ^{13}C	5.69	2.19×10^{-2}
Nuclear quadrupole moment Q (10^{-28} m^2)	1.99×10^{-2}	0
Linewidth factor l (10^{-59} m^4)[b]	2×10^{-3}	–
Reference standard	neat liquid CH_3NO_2/CD_3NO_2	
NMR frequency Ξ (MHz)	7.226329	10.136783

[a]I. Mills, T. Cvitas, K. Homann, N. Kally, and K. Kuchitsu, 'Quantities, Units and Symbols in Physical Chemistry', Blackwell (for IUPAC), Oxford, 1993, pp. 98–104.
[b]$l = Q^2(2I + 3)/I^2(2I - 1)$.

Table 2 Nitrogen Reference Standards

Substance	Concentration (M)	δ(N) (ppm)
Fluids[a]		
NH_3(equil. vap.), 302 K		−399.3[b]
NH_3(liq.), 300 K		−380.4[b]
NH_3(liq.), 223 K		−376.4[b]
NH_4NO_3(satd. aq.)	12.3	−359.6
NH_4Cl(satd. aq.)	5.64	−352.9
Me_4NCl(aq.)	0.30	−337.7
Me_4NCl(satd. aq.)	6.03	−336.7
CH_3CN(liq.)		−135.8
HNO_3(aq.)	10	−18.2
HNO_3(aq.)	7	−12.6
HNO_3(aq.)	1	−4.4
NH_4NO_3(in 2 M aq. HNO_3)	5	−4.6
NH_4NO_3(satd. aq.)	12.3	−4.0
$NaNO_3$(satd. aq.)	7.93	−3.7
$NaNO_3$ or KNO_3(aq.)	0.30	−3.5
CH_3NO_2 in CCl_4	0.30	−7.1
In $CHCl_3$	0.30	−3.8
Neat liquid	18.4	0.0
In D_2O	0.30	2.0
In DMSO	0.30	2.0
Solids[c]		
NH_4NO_3		−358.4
$(NH_4)_2SO_4$		−355.7
NH_4Cl		−341.0
NH_4NO_3		−5.0

[a]Shifts refer to 303 ± 2 K unless a temperature is specified, and are taken from Witanowski et al.[15] unless another source is given.
[b]Jameson et al.[17]
[c]Ratcliffe et al.[18]

other molecules are then obtained from the chemical shift (δ) by use of equation (1).

$$\sigma = -\delta - 135.8 \quad (1)$$

The use of ammonia or ammonium salts as reference material has been favored by those wishing to avoid negative shifts, as achieved by the use of TMS for ^1H, ^{13}C, or ^{29}Si. But ammonium salts are subject to medium effects, again because of hydrogen bonding. Table 2 shows that there is a difference of nearly 7 ppm from the nitrate to the chloride in saturated solutions. The use of Me_4NCl or Et_4NCl, which are less subject to medium effects, has not found favor. Nitrate ion, also, is susceptible to medium effects, which may be large in acidic solution because of equilibria involving nitric acid $HONO_2$.

Table 2 includes reference standards for solid state work. Ammonium chloride is commonly used for this, and should be the standard of choice.[18] There is a large variation in the NH_4^+ shift with different anions, particularly oxyanions, because of hydrogen bonding: Table 2 shows a difference of 17 ppm from the nitrate to the chloride.

The publications of Witanowski, Webb, and co-workers,[5,6] which use the nitromethane standard, give nitrogen shieldings (low frequency positive) rather than shifts (δ), maintaining consistency with their earlier reports when δ and σ had the same sign, before the IUPAC sign convention for δ was adopted in 1972.

1.2 Isotope Effects and Labeling

Nitrogen-14 and ^{15}N measurements are interchangeable, since primary isotope effects on nitrogen shifts are negligible. Bloch–Siegert shifts, arising from the negative magnetogyric ratio of ^{15}N, are detectable in double resonance experiments, and corrections may be needed in the determination of accurate values of chemical shifts by homonuclear decoupling experiments.[19]

Nearest-neighbor isotope effects are not uncommon. Normally a heavier isotopic substituent increases the nitrogen shielding, with some additivity for multiple substitution. Deuteration increases the nitrogen shielding by about 0.65 ppm per hydrogen replaced in NH_3, cf. 0.5–0.7 ppm in pyridinium ion, amines, or amides. The effects are smaller in NH_4^+, about 0.3 ppm per hydrogen.[20] Equilibrium isotope effects on the nitrogen shift have been reported, arising from the perturbation of tautomeric or hydrogen-bonding equilibria by deuteration.[21]

Neighbor effects of replacement of ^{16}O by ^{18}O are small, about 0.15 ppm per oxygen in nitrite ion, or 0.06 ppm in nitrate, but can be useful in mechanistic studies. In the oxidation of ammonia to nitrite by *Nitrosomonas europae*, or of nitrite to nitrate by *Nitrobacter vinogradsky*, the movement of the ^{18}O label has been monitored by ^{15}N NMR.[22]

Nitrogen-15 labeling for high-resolution NMR, particularly in biomolecules, has the added advantage that the isotope can

be used as a biological tracer. The most stable radioisotope, ^{13}N, has a half-life of only 10 min.

Equilibrium isotope effects can arise unexpectedly in studies of compounds partially enriched with ^{15}N. A doubling of the nitrogen line was observed for the five-coordinate dinitrosyl complex $[RuCl(NO)_2(PPh_3)_2]^+$, with 50% enrichment. This complex has one linear and one bent nitrosyl in the solid,[23] and shows bent linear fluxionality in solution.[24] ^{15}NO is slightly favored in the linear geometry in the $(^{14}NO)(^{15}NO)$ molecule, giving a slightly higher averaged shielding than the $(^{15}NO)_2$ molecule. Zero-point energies are generally small for nuclei as heavy as nitrogen. This isotope effect is observable because of large differences in stretching frequency and nitrogen shift in linear and bent nitrosyls, arising from the effects of the lone pair on the bent nitrogen.

1.3 Medium Effects

The NMR properties of nitrogen carrying a lone pair are very sensitive to changes of solvent, concentration, counterion, or pH. Nitrogen NMR spectroscopy is thus a useful probe of inter- and intramolecular influences and equilibria. Medium effects on the shielding may be pronounced if hydrogen bonding or acid–base interactions occur, as Table 2 indicates. The shifts are in the same direction as protonation shifts (Section 4.1), though smaller. Hydrogen bonding to a lone pair on nitrogen commonly decreases the nitrogen shielding in saturated groups such as ammonia and alkylamines,[25] with sizeable deshielding from gaseous to liquid NH_3, as from NH_3 to NH_4^+.[26] Nitrogen shielding is increased, however, by hydrogen bonding through hydrogen covalently bonded to nitrogen. The nitrogen shielding in NH_4^+ increases with an increase in the strength of the hydrogen bonding to the anion,[27] and is particularly high in anhydrous HF.[28] Corresponding results are observed for protonated amines.[26] Hydrogen-bonded systems, therefore, show complex behavior, including proton exchange.

For nitrogen in a π-bonded system, as in nitriles RCN, or aromatic azines such as pyridine, hydrogen bonding to a lone pair on nitrogen increases the nitrogen shielding. Again, the shifts are in the same direction as protonation shifts, but smaller in magnitude. Medium effects when the nitrogen carries π but not lone-pair electrons are illustrated by the 9 ppm range shown in Table 2 for the nitrogen shift in nitromethane in different solvents. Four-coordinate nitrogen not bonded directly to hydrogen is relatively insensitive to medium effects, as expected.

Medium effects are observable also in spin–spin couplings to nitrogen because of their sensitivity to the presence of lone pairs.

Nitrogen-14 Knight shifts have been used to study solutions of alkali metals in ammonia[29] or methylamine[30] which contain solvated electrons.

2 NITROGEN-15 NMR SPECTROSCOPY

Relaxation processes are important to the design of ^{15}N NMR experiments, because of the low natural abundance, one-third of that of ^{13}C, and low NMR sensitivity, one-fifteenth of that of ^{13}C, and because ^{15}N NOE factors are negative.

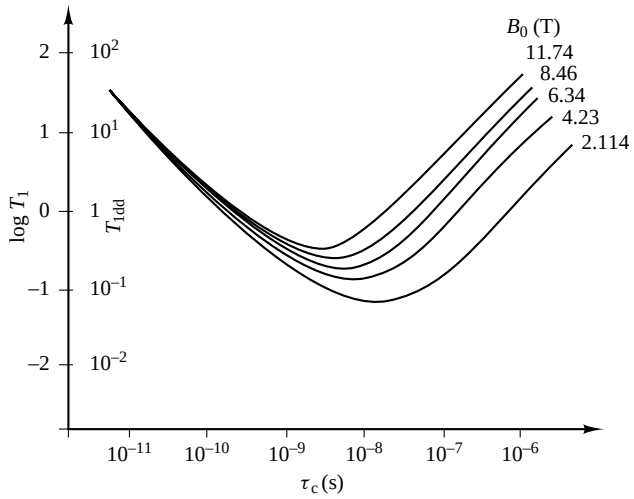

Figure 1 Dipolar spin–lattice relaxation times T_{1dd} as a function of the effective molecular correlation time τ_c for different field strengths B_0 (T). A field strength of 11.74 T for ^{15}N corresponds to 500 MHz for protons. Values of τ are given in Tables 3 and 4

2.1 Nitrogen-15 Relaxation[2–7,31,32]

Nitrogen-15 relaxation processes are qualitatively similar to those of ^{13}C in analogous environments, as in $>NH_2$ and $>CH_2$. The relative contributions of the possible mechanisms are usually different, because dipolar relaxation by protons is less efficient for ^{15}N than for ^{13}C, since $|\gamma(^{15}N)|$ is only 40% of $\gamma(^{13}C)$. This means that other relaxation mechanisms compete with the dipolar mechanism for ^{15}N. Representative values of relaxation times and NOE factors are given in Table 3, together with examples of particular relaxation mechanisms.

The dipole–dipole (dd) relaxation rate for nitrogen bonded to n_H hydrogens is given by equation (2). The relaxation time T_{1dd} depends on the changes in local fields as the molecule tumbles, and is proportional to $(1 + \omega^2\tau_c^2)$, where ω is the resonance frequency and τ_c is the 'correlation time'. This is the time the molecule takes to reorient itself in rotational motion, and may take an effective value in view of the complexity of tumbling motions in many molecules or groups, τ_c. Equation (2) assumes sufficient mobility that normal conditions of 'extreme narrowing' apply, with $\omega^2\tau_c \ll 1$.

$$1/T_{1dd} \approx \left(\frac{\mu_0}{4\pi}\right)^2 n_H(\gamma_N)^2(\gamma_H)^2 \left(\frac{\hbar^2}{r_{NH}^6}\right)\tau_c \qquad (2)$$

The contribution to the relaxation rate $(T_{1dd})^{-1}$ per hydrogen at a distance of 10 pm is then $5 \times 10^9\tau_c$. This corresponds to T_{1dd} values of 15–80 s for nitrogen with one attached hydrogen, in small-to-medium-sized molecules in common solvents. Liquid pyrrole has T_1 = 40 s[33] and aqueous acetamide T_1 = 14 s.[34]

As molecular tumbling slows down beyond the 'extreme narrowing' region, it reaches the Larmor precession frequency below which spin–lattice relaxation is less effective as τ_c increases.[35] The value of T_{1dd} falls to a minimum near $\omega\tau_c$ = 1 and then increases depending on the field strength B_0, as shown in Figure 1. There are concomitant changes in the NOE.

Such a decrease in T_{1dd} for longer correlation times is advantageous to the study of biomolecules such as lysozyme, a globular protein of molecular mass 14 600 Da, for which a

Table 3 Nitrogen-15 Spin–Lattice Relaxation Times (T_1), NOE Factors (η_{obs}), Correlation Times (τ_c), and Relaxation Mechanisms

Compound[a]	T_1(s)	B_0(T)	η_{obs}	τ_c (ps)[b]	Mechanism[c]
Gases					
NH_3(g)	0.3	6.35	0		sr
$^{14}N^{15}N$(g, 294 K)	0.8 (=T_2)	8.46	0		sc
Liquids					
$PhNO_2$(l)	450	1.41	−1.8	(τ_q = 10)	sr, dd
	170	7.42	−0.6	4	sa, sr
PhCN(l)	420	1.41	−1.6	(τ_q = 7.5)	dd, sr, e
NH_4NO_3(1:1 w/w in H_2O)	140	1.41	−0.9		sr
CH_3CN(l)	90	6.34			
CH_3CN(l) with 5×10^{-4} M [$Gd(pd)_3$]	53	6.34			e
Pyridine(l)	85	6.34	−0.4		sa, dd, sr
Pyridine(l) with 5×10^{-2} M [$Cr(pd)_3$]	3.7				e
n-$BuNH_2$	70	6.34	−3.9		dd
Pyrrolidine(l) (>NH)	58	6.34	−4.6	4	dd
trans-PhN=NPh (2.7 M in $CDCl_3$)	56	2.11			sr, dd, sa
Pyrrole(l) (aromatic >NH)	40	6.34	−4.3	5	dd
NH_4NO_3(1:1 w/w in H_2O)	37	1.41	−4.93		dd
n-BuONO(l)	24	2.11			sr(int)
$NaNO_2$ (0.7:1 w/w in H_2O)	23	1.41	−0.4		sr,sa
$NaNO_2$ (1.1 M in D_2O)	19.0	4.7			
	17.5	9.4			
KCN (1 M in 1:1 H_2O/D_2O, pH 12.5)	21	1.41	0		sa, sr
	14.5	4.23	0		sa, sr
CH_3CONH_2 (5.3 M in H_2O)	14.2	1.41	−5.1	7.5	dd
N_2(l, 77 K)	15	0.70		(τ_{sr} = 0.2)	sr
N_2(l, 126 K)	1.5	1.02		(τ_{sr} = 1)	sr
$TPPH_2^{2+}$	1.9	4.23	−4.93		dd
ZnTPP[d] (6×10^{-3} M in $CHCl_3$)	56	4.23	0		e, etc
Lysozyme (9.4×10^{-3} M in 0.1 M citrate, pH 5)		4.23			
(−C(O)−NH−)	0.16		−0.5	5000	dd
$>NH_2^+$	0.33		−3.5	3500	dd
Solids					
NH_4Cl		4	4.70	14	dd
TPP[d] (180 K) aromatic >NH	0.67	1.41	0.7		dd, pe
aromatic −N=	0.05	1.41	0.1		sa, dd, pe

[a]Measurements were made at ambient temperatures (300 ± 3 K) if no other temperature is given.
[b]Values of τ_c are in ps (10^{-12}s).
[c]Relaxation mechanisms are given in decreasing order of their contribution: dd = dipole–dipole (intra- or intermolecular), sr = spin–rotation, (int) = internal, sa = shielding anisotropy, e = electron–nuclear, sc = scalar coupling, pe = proton exchange.
[d]TPP is *meso*-tetraphenylporphin.

correlation time of 8.5×10^{-9} s was measured in aqueous solution. Lysozyme, hemoglobin, vitamin B_{12}, or transfer-ribonucleic acids could be studied in natural abundance of ^{15}N at 18.25 MHz (180 MHz for protons).[36] Internal motions, such as segmental rocking or spinning of a pendant group such as $-NH_3^+$, reduce the effective τ_c for the nitrogens concerned.

Working at higher fields is thus detrimental for biomolecules, since the T_{1dd} minima shift to smaller values of τ_c with an increase in B_0 (Figure 1).

Unlike T_1, the transverse (spin–spin) relaxation time T_2 decreases steadily with an increase in τ_c to a limiting value in the solid state determined by dipolar interactions. Uncertainty broadening may be a hazard, since T_{2dd} has an additional τ_c-dependence which is independent of ω. Deuteration was used to improve ^{15}N resolution in hemoglobin studies through the γ^2-dependence of the dipolar relaxation rate.[37]

The microviscosity η' is important, since the correlation time is proportional to η'/kT. In work with smaller molecules the relaxation rate may be doubled by the use of more viscous solvents such as dioxan or ethanol, rather than chloroform or acetone. Dipolar relaxation has been speeded up by the use of viscous additives, such as glycerol in aqueous solution, or polystyrene in toluene for organic-soluble molecules.[38] Higher macroviscosities are unlikely to broaden the lines by an increase in the transverse relaxation time T_2 since this depends on the microviscosity, which is smaller than the macroviscosity by a factor of six to seven.[33] Cooling is particularly effective as it increases the viscosity (depending exponentially on the temperature) and the sensitivity and the correlation time.

Relaxation times may be quite long in the absence of nearby hydrogen or of alternative mechanisms of relaxation. Neat liquid nitrobenzene and benzonitrile have T_1 values in excess of 400 s, compared with 140 s for aqueous nitrate (Table 3).[39] 'Exposed' nitrogen, as in a cyano group or in aromatic azines such as pyridine, experiences intermolecular dipolar relaxation

in which T_{1dd} is directly proportional to the distance of closest approach of the hydrogen.

Electron–nuclear relaxation, however, is likely to be present. This is promoted very efficiently by paramagnetic impurities, of iron or nickel for example, to which basic nitrogen is very sensitive. Rigorous purification is necessary for measurements of nitrogen relaxation times,[34] although the effects of dissolved oxygen are small.

Paramagnetic additives may be useful for quantitative studies, to quench dipolar relaxation and the NOE.[34] Susceptibility corrections may then be necessary for accurate shift measurement (Section 1.1). With [Cr(acac)$_3$] there is some hydrogen bonding between hydrogen attached to nitrogen and carbonyl groups in the ligand. Gadolinium complexes such as [Gd(acac)$_3$] interact quite strongly with basic nitrogen, and can be used for spin-labeling.

The spin–rotation (sr) mechanism is effective in the relaxation of ^{15}N in small molecules or ions, such as gaseous NH_3,[40] aqueous nitrate or nitrite ion,[40] or liquid dinitrogen; also in freely rotating substituents, nitro[40] or nitrite[41] for example (Table 3). The sr mechanism becomes more efficient at higher temperatures, the rate being proportional to kT.

Shielding anisotropy (sa) relaxation is important for linear groups such as $-C{\equiv}N$, as the aqueous ion CN^-,[42] in nitriles,[40] or as a ligand; the same applies to dinitrogen[43] (precise work with metal complexes is difficult because of the difficulty in excluding paramagnetic ions). This mechanism is efficient also in planar groups, such as nitro or nitrate, and azine nitrogen as in pyridine (Table 3). The rate is very sensitive to the shielding anisotropy $\Delta\sigma$, being proportional to $(\Delta\sigma)^2$; values of $\Delta\sigma$ are discussed in Section 5. This mechanism is very effective at higher fields, the rate being proportional to ${B_0}^2$. Table 3 shows the increase in relaxation rate with an increase in the applied field for the cyanide ion and nitrobenzene.[44]

In some molecules all three mechanisms (sa, dd, and sr) are operative, as for pyridine and *trans*-azobenzene. Another mechanism of importance for ^{15}N is afforded by proton exchange (pe) in hydrogen-bonded systems, magnetization being transferred by the migrating proton. Table 3 includes an example of the fast relaxation of ^{15}N by scalar coupling to fast-relaxing ^{14}N in $^{14}N^{15}N$ gas.[45]

In the solid state, the dipolar relaxation of ^{15}N is fast in NH_4Cl.[46] Relaxation is faster still in *meso*-tetraphenylporphin (TPP), in which two hydrogens exchange between the central four nitrogens, a process long known in solution. Studies of T_1 and NOE show that the unprotonated nitrogen relaxes by the sa mechanism, by dipolar interaction with the protons on the other nitrogens, and through proton exchange.[47]

2.2 Nitrogen-15 NOE Factors[48]

If ^{15}N is wholly relaxed by $^{15}N/^{1}H$ dipolar interactions, the NOE factor (η), with broadband proton decoupling, is given by equation (3):

$$\eta_{max} = \gamma(^1H)/2\gamma(^{15}N) = -4.93 \quad (3)$$

The negative sign corresponds to inversion of the signal. (Note the use of the symbol η for the NOE factor and also for the viscosity.) The net enhancement is then -3.93, better than the ^{13}C value of 2.99. There is a further gain in signal height from the collapse of multiplets.

The NOE factor observed depends on the proportion of the relaxation that takes place by $^{15}N/^{1}H$ dipolar interactions:

$$\eta_{obs} = (I - I_0)/I_0 = -4.93(T_1)_{obs}/T_{1dd} \quad (4)$$

If this proportion is small the signal intensity (I) is diminished and the signal vanishes if the proportion is 20% ($I = 0$, $\eta_{obs} = -1$).

Five mechanisms have been identified by which ^{15}N signals can be lost on proton decoupling.[49] The dipolar process diminishes when more efficient modes of relaxation are possible, as in the presence of paramagnetic compounds, or averaging by fast chemical exchange. Table 3 shows many molecules for which the full NOE factor -4.93 is not achieved under the conditions of the experiment.

The diminution in T_{1dd} as correlation times τ_c increase beyond the 'extreme narrowing' limit, illustrated in Figure 1, also diminishes the NOE, the more so at higher resonance frequencies ω. With large or highly associated molecules, the NOE may be unfavorable,[50] and working at higher fields disadvantageous. The maximal NOE factor shrinks from -4.93 to -0.12, and the signal is annulled for a correlation time of 1 ns at 11.7 T (500 MHz for protons). The NOE may be removed by gated decoupling or by paramagnetic additives, promoting electron–nuclear relaxation.

The NOE has various uses, i.e. as a measure of molecular mobility or dynamics, in spectral assignment, and to locate spin labels. A disadvantage is the difficulty in using signal intensities in quantitative work.

2.3 Nitrogen-15 Sensitivity Enhancement

Nitrogen-15 sensitivity is enhanced by the use of larger samples, higher fields, lower temperatures, and proton decoupling and the NOE, if favorable. Valuable enhancements are obtained by the use of special pulse sequences transferring polarization (magnetization) from a more sensitive nucleus, usually the proton, to which the ^{15}N nucleus is coupled. A 10-fold enhancement is given by the $\gamma(^1H)/\gamma(^{15}N)$ ratio, and the sign of γ is now immaterial. Further amplification may be gained by faster pulsing, allowed by the faster proton relaxation.

In the liquid phase magnetization can be transferred via spin–spin coupling to protons, if this is resolvable. Such methods have the advantage over NOE enhancement of not requiring the relaxation mechanism to be dipolar. They include J cross polarization (JCP), selective polarization transfer (SPT), 'insensitive nuclei enhanced by polarization transfer' (INEPT), 'distortionless enhancement by PT' (DEPT), and developments of these.[2,3,7,51] In >NH systems, as in bilirubins for example,[52] measurements may be made in this way in natural abundance of ^{15}N. Longer-range couplings also may be used in azaaromatic or peptide systems. The methods are used to determine coupling constants and their signs, to establish connectivities, to distinguish nitrogens bearing different numbers of hydrogens, to correlate signals of different nuclei, to investigate relaxation processes, and to measure relaxation times.

Multiple quantum methods involving a double transfer of magnetization, $^1H \rightarrow {}^{15}N \rightarrow {}^1H$, provide substantial improvements in ^{15}N sensitivity because of the detection in proton spectra. They are increasingly used to correlate ^{1}H and ^{15}N shifts in two-dimensional (2D) spectra through spin–spin

coupling pathways.[53] Polarization transfer from ^{15}N to ^{1}H decreases ^{1}H sensitivity, but has been used in 2D spectroscopy to assign all the ^{15}N signals of a labeled tRNA by heteronuclear decoupling difference spectroscopy.[54]

A variety of 2D, 3D, and even 4D experiments in correlation spectroscopy (COSY) are now being used to correlate ^{15}N, ^{13}C, and ^{1}H resonances.[55] A 3D experiment may correlate ^{15}N resonances with those of differently connected protons, as in $^{15}N^{1}H-C^{1}H$ groups in biological systems. 4D techniques are being used in protein research, as in the correlation of ^{1}H, ^{13}C, ^{15}N, and ^{13}CO resonances in calmodulin.[56]

Comparable experiments have been performed in which magnetization is transferred from ^{2}D, ^{19}F, or ^{31}P to ^{15}N. The faster relaxation of the deuteron, by the quadrupolar mechanism, compared with the proton, may outweigh the disadvantage of the relatively small magnetogyric ratio of ^{2}D. In the solid state, cross polarization (CP) is used to transfer magnetization via dipolar couplings. (See ***Organic Chemistry Applications***.)

3 NITROGEN-14 NMR SPECTROSCOPY

The ^{14}N quadrupole moment is relatively small ($Q = 0.0199 \times 10^{-28}\,m^2$) and a large volume of NMR work has been done in ^{14}N resonance, particularly when ^{15}N spectroscopy was less accessible. In some respects, ^{14}N work is coming into its own again as modern techniques turn the ^{14}N nuclear quadrupole interaction to advantage, to spread nitrogen spectra over a large range, more than compensating for quadrupolar line broadening.[57,58]

Nitrogen-14 linewidths vary quite widely, depending on the local electronic symmetry of the ^{14}N nucleus and its mobility. High-resolution spectroscopy is possible if the local electronic symmetry and the mobility are both high. Sharper lines may be obtained if the sample viscosity can be reduced by the use of higher temperatures or more mobile solvents (Section 3.2). Fast relaxation may be advantageous in allowing rapid pulsing. The variability of ^{14}N linewidths must be taken into account in quantitative work.[59]

^{14}N NMR is a useful probe of molecular dynamics, because of the sensitivity of the linewidth to local motions. Nitrogen-14 induced relaxation of protons in peptide ($-^{14}NH-CO-$) groups in protein backbones which exchange with water protons is of importance to proton NMR tomography.[60]

3.1 Nitrogen-14 Quadrupolar Relaxation[61]

The ^{14}N linewidth $W_{1/2}$, the width at halfheight of the (Lorentzian) line or component of a multiplet, is proportional to the relaxation rate and to the square of the nuclear quadrupole coupling constant (NQCC) χ [equation (5)]. The quadrupolar relaxation time T_q is equal to $T_1 = T_2$ in the extreme narrowing regime ($\omega^2\tau_c \ll 1$), i.e. for mobile species.

$$\pi W_{1/2} = 1/T_q = \tfrac{3}{8}\chi^2(1 + \eta^2/3)\tau_q \qquad (5)$$

where

$$\chi = e^2qQ/\hbar \text{ (in radians)} \qquad (6)$$

In equation (6), eq (or more precisely eq_z, where $|q_z| \geq |q_x| \geq |q_y|$) is the electric field gradient (efg) at the nucleus. The quantity η is now the asymmetry parameter, equal to $(q_x - q_y)/q_z$. Linewidths are very sensitive to χ but less sensitive to η, since $\eta \leq 1$ by definition. The quantity $\tau_q = \tau_c$ is the effective correlation or reorientation time of the ^{14}N quadrupole. NQCC values are obtained from the NQR spectroscopy of solids, from the microwave spectroscopy of gases, and by NMR methods.[62] Values of χ are usually similar in the liquid or solid phase of a particular species, and are about 15% greater in the gas phase.

The ^{14}N electric field gradient is largely determined by the disposition of the valence p electrons. In highly symmetric environments, in which there is no static efg, quadrupolar relaxation is mediated by collisional and vibrational distortion of molecules or ions.[63,64] Although the ^{14}N quadrupole moment is relatively small, relaxation of ^{14}N is almost invariably by the quadrupolar mechanism because of the χ^2-dependence of the rate. Even in the highly symmetric location in solid NH_4Cl, the dipolar relaxation mechanism is observed only below 220 K.[65] Above 220 K, rotation of the ammonium ion in the lattice switches the efg at the ^{14}N nucleus, so relaxing the nuclear electric quadrupole and the nuclear spin. In aqueous solution, ^{14}N in NH_4^+ shows zero NOE because of transient efgs arising from the buffeting by solvent dipoles.[66] In paramagnetic cyano complexes $K_3[M(CN)_6]$, where M = Cr, Mn, Fe, the ^{14}N relaxation was found to be wholly quadrupolar, even though the nitrogen shifts were determined by the contact interaction.[67]

3.2 Nitrogen-14 Linewidths

Table 4 lists the ^{14}N linewidths, relaxation times, NQCC values χ, and correlation times for a range of compound types, grouped by the coordination number of the nitrogen and in approximate order of increase in linewidth. Nitrogen-14 lines may be quite sharp, with χ values of 1 MHz or less, if the nitrogen is in a highly symmetrical location, as in NH_4^+,[61] NF_4^+ (tetrafluorammonium),[28] or tetraalkylammonium (R_4N^+) species.[68] Nitrogen-14 spectra were obtained in the first measurement of interstitial nitrogen, in the trigonal prismatic clusters of cobalt and rhodium[69] $[M_6N(CO)_{15}]^-$, before the ^{15}N lines were obtained with 97% enrichment. For the rhodium cluster there was some resolution of three lines of the septet, with $^{1}J(Rh,^{14}N) \approx 4$ Hz. The ^{14}N and ^{15}N lines were similar in width for the cobalt cluster because of line broadening by the ^{59}Co quadrupole and unresolved coupling.

Nitrogen-14 lines are sharp also if the nitrogen is centrally placed in linear groups such as the nitronium ion (NO_2^+)[6]a or azide ion (N_3^-),[70] or in trigonal planar groups such as nitrate ion,[71] all highly mobile in solution.

Linewidths may be small if the substituents on nitrogen do not differ greatly in electronegativity, as in the linear molecules NNO[72] and isonitriles RNC.[73,74] Compared with the nitrate ion, broader lines are observed for ethyl nitrate, nitromethane,[75,76] or NOF_2^+,[28] broader still for pyridine *N*-oxide,[77] $PhNO_2$,[78] or dimethylamide,[79] more bulky molecules. The line is very broad for the oxygenated nitrogen in azoxybenzene, which carries a π bond, a single bond, and a double bond.[80] The fluorammonium ion, NH_3F^+, with substituents of very different electronegativity, gives a broad

Table 4 Examples of ^{14}N Linewidths ($W_{1/2}$), Relaxation Times (T_q), Nuclear Quadrupole Coupling Constants (χ), and Correlation Times (τ_q)

Sample[a]	$W_{1/2}$[b] (Hz)	T_q (ms)	χ (MHz)	η[c] (cP)	τ_q[d] (ps)
Four-coordinate nitrogen					
Me_4NBr (1 M aq., 316 K)	0.1	10^4			
n-Bu_4NI (0.07 M aq., 316 K)	0.18	1800	0.04	0.45	20
n-Bu_4NI (0.07 M in benzene, 335 K)	3.7	85	0.23	0.39	15
NF_4AsF_6(HF)	3				
NH_4Cl (1 M aq., 316 K)		1600		1.08	5.9
NH_4Cl (1 M in D_2O, 316 K)		1200			7.2
NH_4Cl, ND_4Cl(s, 295 K)		700–800	0.016		20
n-HexylNMe_3Br (0.55 M in D_2O)		260	0.083		20
n-$C_{12}H_{25}NMe_3Cl$ (C_{12}TAC) (49% w/w in D_2O)		T_1 = 24	0.083		370 fast
		T_2 = 3.7			5×10^4 slow
n-$C_{16}H_{33}NMe_3Br$ (C_{16}TAB) (0.4 M aq.)		T_1 = 10	0.083		560 fast
		T_2 = 1			2×10^5 slow
Na[Co(*N*H_3)$_2$(NO_2)$_4$](aq.)	170		2.09		
(NH_3F)(CF_3SO_3)(HF) at 283 K	300				
at 233 K	550				
[Co(NH_3)$_6$]Cl_3(aq.)	370		3.62		10.3
[Co(NH_3)$_6$](ClO_4)$_3$ (0.24–0.5 M in DMSO-d_6)		0.29	3.3		20
[Co(en)$_3$]Cl_3(aq.)	600				22.1
Choline Me_3N headgroup of sphingomyelin (aq., 320 K)		T_1 = 37	0.135		
		T_2 = 2.0			
Six-coordinate nitrogen (see text)					
[Rh_6(μ_6-N)(CO)$_{15}$]$^-$(acetone-d_6)	20				
[Co_6(μ_6-N)(CO)$_{15}$]$^-$(acetone-d_6)	40				
Linear two-coordinate nitrogen					
N_2O (15 atm in hexane) (N*N*O)	0.45	2960	0.238		20
MeNC(*l*)	0.26	1220	0.27	0.35	30
t-BuNC(*l*)	1.6	180			
NO_2AsF_6(HF)	5				
PdCNBu^t complexes ($CDCl_3$)	4–12	30–80			
NaN_3 (1 M aq.) (N*N*N$^-$)		29.3	1.03		
[η^5-C_5H_5)Mo(CO)$_2$(NO)](CH_3CN)	30				
[Mo(NO)(S_2CNMe_2)$_3$](CH_2Cl_2)	40				
[Mo(NS)(S_2CNMe_2)$_3$](CH_2Cl_2)	150				
[Os(*N*Bu^t)O_3](CD_2Cl_2)	30				
[Ta(NHBu^t)$_2$(*N*$SiMe_3$)$_2${N($SiMe_3$)$_2$}] (CD_2Cl_2)	52				
[W(NBu^t)$_2$(OBu^t)$_2$](CD_2Cl_2)	185				
Terminal (one-coordinate) nitrogen					
N_2O (15 atm in hexane) (*N*NO)		280	0.792		
N_2(*l*, 126 K)		18.5	5.39		0.15
N_2 (*l*, 77 K)		1.7		0.074	0.2
$^{14}N^{15}N$(g, 294 K)		15.3			
NaN_3 (1 M aq.) (*N*NN$^-$)		7.4	1.79		
ClCN(*l*)		6	3.219		
MeCN (1% v/v in hexane)	53.5		3.74	0.29	0.82
MeCN(*l*)	78			0.34	0.67
$NO^+AsF_6^-$(HF)	95				
MeSCN(*l*)		2.0	3.75	0.72	2.4
HC–C≡C–CN (5 M in tol.-d_8)	189	1.7	4.14	0.45	2.36
NC–C≡C–CN (inf. diln. in hexane)	244		4.14	0.30	4.75
NC–C≡C–CN(*l*)	394			0.60	
CCl_3CN < *l*)		1.5	4.1	0.75	2.7
K_4[Fe(CN)$_6$] (0.2–0.8 M aq.)	550–650				
K_3[Co(CN)$_6$](aq.)	570		3.62		16.0
K_3[Fe(CN)$_6$] (0.2–1.0 M aq.)	780–1040				

Table 4 *Continued*

Sample[a]	$W_{1/2}$[b] (Hz)	T_q (ms)	χ (MHz)	η[c] (cP)	τ_q[d] (ps)
Planar three-coordinate nitrogen					
$NaNO_3$(s)		10^5	0.745		
$NaNO_3$ (1 M aq. 295 K)		85			$\tau_\perp$ = 1.43
$EtONO_2(l)$		45	0.9		2
$MeNO_2(l)$		22	1.7	0.6	1.03
$(NOF_2)AsF_6$(HF)	18				
Pyridine *N*-oxide (0.2 M in CCl_4)	28.3	11.2	1.1		3.4, 11.9, 2.9
$PhNO_2$ (1:1 v/v in hexane)		6.2	1.426	1.83	3.6, 11, 4.4
$PhNO_2(l)$		3.2		7.0, 21 6.3	
Pyrrole (17 mol% in pyridine)		4	2.12	1.2	12
Pyrrole(l)		2.0	2.06		8
$Me_2NCHO(l)$		2.0	3.6		
PhN = *N*(O)Ph(l, 284 K)	700		1.4		10
Pyramidal nitrogen					
$MeNH_2(l)$	30		3.98	0.18	0.55
$Me_3N(l)$	100		5.2	0.16	0.8
$Me_2NH(l)$	125		5.05	0.17	1.0
$(CH_2)_6N_4$ (0.1 M in hexane)	122	2.6	4.19	0.29	1.48
$(CH_2)_6N_4$ (0.1 M in CCl_4)	294		4.17	0.82	3.3
$(CH_2)_6N_4$ (0.1 M in $CDCl_3$)	1052		4.31	0.5	11.1
NF_3(l, 108 K)	318	1	7.07		1.35
$CH(CH_2CH_2)_3N$ (0.5 M in $CHCl_3$, 278 K)			5.4	0.51	$\tau_\parallel$ = 0.8, $\tau_\perp$ = 6.7
$N(CH_2CH_2)_3N$(s) at 415 K	484	T_2 = 0.658	4.925		4.23
$N(CH_2CH_2)_3N$(s) at 354 K	2100	T_2 = 0.152			18.4
Bent two-coordinate nitrogen					
$HNCO(C_6H_{12})$	20				
$MeNCO(l)$	35				
$EtONO(l)$		5.2	3.8		0.9
Pyridine(l)		1.65	4.58	0.89	1.95
i-C_5H_9 $ONO(l)$		1.6			3.0
$Na[Co(NH_3)_2(ONO)_4]$(aq.)	700		4.25		14.25

[a]Measurements were made at ambient temperatures (300 ± 3 K) if no other temperature is given.
[b]Observed linewidths may contain unresolved couplings.
[c]Viscosity.
[d]Values of τ_q are in ps (10^{-12} s); compare the values measured in ^{15}N resonance (Table 3). Where three values are given, these correspond to $\tau_{x,y,z}$, where the x direction is that of the axial bond to nitrogen and the y direction is in the molecular plane.

line[28] with some broadening being due to the hydrogen bonding in the HF solvent.

Long-chain tetraammonium species give very broad lines. The ^{14}N relaxation properties of Me_3N groups have been used to study reorientational motion. In the surfactants C_nTAC and C_nTAB, the two motions reported in Table 4 are rotation within a micelle and a slower diffusional motion.[81,82] In biomolecules, the choline Me_3N headgroup is a useful probe of orientation, as in studies demonstrating a phase transition in the phospholipid sphingomyelin, from bovine brain membrane,[83] or changes in phosphatidylcholine in the presence of anaesthetics.[84]

The efg and the linewidth are greatly increased by the presence of a lone pair on the nitrogen. This electronic charge is close to the nucleus, even closer if the substituents on the nitrogen are highly electronegative as in NF_3, in which the ^{14}N NQCC is very large.[28] Linewidths are sizeable generally for pyramidal nitrogen, as in amines,[85–88] and for bent (two-coordinate) nitrogen, as in organic isocyanates,[89] nitrites,[75] and pyridine.[90]

The lone pair on terminal (one-coordinate) nitrogen is less effective in line broadening because of the axial symmetry. Again, linewidths increase with an increase in electronegativity of the nearest neighbor, from dinitrogen[42,47] to nitrile species RCN[91–95] and to the nitrosyl ion NO^+.[28] In dinitrogen oxide, N_2O, the ratio of the linewidths for the two nitrogens in solution is as expected from the NQCCs determined by microwave spectroscopy in the gas phase.[73]

Similarly, protonation or coordination reduces NQCC values. They are reduced also by delocalization of a lone pair in conjugated systems, as in pyrrole,[96] and delocalization which flattens a pyramidal group, or increases the bond angle for two-coordinate nitrogen. The effects of bond-angle distortion are evident for nitrogen in three- to seven-membered rings.[69] Hydrogen bonding to a lone pair on nitrogen slightly reduces the NQCC, while hydrogen bonding of a lone pair on nitrogen has the opposite effect, as shown by pyrrole in pyridine.[96]

Certain ligands in metal complexes are usefully studied by ^{14}N NMR study, so long as the molecules are not too bulky or associated. Linear ligands may give sharp lines because of the axial symmetry at nitrogen. Sharp lines were observed for the imido (nitrene) ligand (=NR) in *trans*-$[WF_4(NMe)L]$ complexes,[97] and shifts were measurable for

the imido complexes of Ta, W, and Os, even with quite bulky R groups such as $SiMe_3$, helped by internal mobility.[98] Despite the ^{95}Mo quadrupole, ^{14}N lines were readily resolved in dialkyldithiocarbamato complexes of molybdenum with NO or NS coligands,[99] and ^{95}Mo–^{14}N couplings were resolved for η^5-cyclopentadienyl complexes with NO and CO ligands.[100] Quite sharp lines were observed in PdCN^{t}Bu complexes.[101] The kinetics of electron transfer reactions between ferricyanide and ferrocyanide ions in aqueous solution were studied by ^{14}N linewidth measurements.[102]

Otherwise, ^{14}N lines are usually broad for ligating nitrogen, whether with bulky (e.g. phosphine) coligands, of the difference in electronegativity of the nearest neighbors: examples in Table 4 are the ammine and ethylene diamine complexes of cobalt.[103,104]

There is a direct dependence of ^{14}N linewidth on the sample viscosity for a wide range of molecules. Linewidths may be halved by the use of diethyl ether solvent instead of chloroform, or acetone instead of water. Fluoronitrogen compounds are readily studied by ^{14}N NMR because of their high mobility.[28] Resolution of J couplings to quadrupolar nuclei has been achieved for super- or near-critical fluids in standard thick-walled tubes, including ^{14}N^{14}N and ^{14}N^{17}O couplings in liquid N_2O.[105]

Warming a sample is particularly helpful, the viscosity decreasing exponentially with increase in temperature. The rotational correlation time for a spherical molecule is given by the Stokes–Einstein–Debye theory as

$$\tau_c = V\eta/kT \tag{7}$$

where η is the viscosity and V is the molecular volume, equal to $4\pi r^3/3$.[33] equation (7) gives a correlation time of 1 ps for a molecule of radius 1 Å at 300 K for η = 1 cP. Observed rotational motions are faster by a factor of about 6, and a microviscosity η' that is one-sixth of the bulk viscosity is envisaged.

Direct dependence on viscosity breaks down for molecules that are small, linear, or flat, rotating or librating between neighboring molecules. Molecules rotating relatively freely in the liquid phase have a reduced temperature dependence of τ_c, according to equation (8), where I is a moment of inertia:

$$\tau_c = \tfrac{1}{2}(\pi I/3kT)^{1/2} \tag{8}$$

Quadrupolar relaxation in ionic solutions[67] is mediated by the rotations of ions and solvent dipoles, by collisions, and by molecular vibrations. In mobile solutions, with $\omega^2\tau_c \ll 1$, the relaxation rate is given approximately by equation (9):

$$\pi W_{1/2} = 1/T_q = 8\pi(\beta eqQ/\hbar)^2\left[\mu_s^2 c_s r_0^{-5}\tau_s + \sum_i z_i(3a_i^3)^{-1}c_i\tau_i\right] \tag{9}$$

Terms with the subscript s give the effects of solvent dipoles, and with the subscript i, the effects of ionic charges. The c terms are concentrations, r_0 and a_i are distances of closest approach, μ_s is the dipole moment, z_i are ionic charges, and τ_s, τ_i are the respective correlation times. Further terms are needed for hydrogen bonding or exchange processes. If D_2O replaces H_2O, the motions are slowed by the higher mass and stronger hydrogen bonds.

The electric field gradient is now amplified by a factor given by equation (10), as

$$\beta = P(1 - \gamma_\infty) \tag{10}$$

where $P = (2\epsilon + 3)/5\epsilon$ is the polarizability of the solvent, with dielectric constant ϵ. The quantity $(1 - \gamma_\infty)$ is the Sternheimer antishielding factor which represents the distortion of the inner electron shells by electric field gradients in the valence shell. Experimental determinations are rare: values of 9 and 22–26 have been determined for $(1 - \gamma_\infty)$ in solid NH_4Cl, compared with a calculated (ab initio) value of 6.8.[106]

4 PATTERNS OF NITROGEN SHIFTS

The large literature of nitrogen shifts is reviewed regularly.[6,7] Nitrogen shifts in diamagnetic compounds cover a range of 1350 ppm, over three times the carbon range. The comparison with carbon is helpful since carbon shielding patterns are well known. The greater range for nitrogen arises from its greater electronegativity, and its ability to carry lone-pair electrons with s character, which carbon does very rarely.

The major determinants of nuclear magnetic shielding are demonstrated by expressions such as equation (11) for the paramagnetic term σ_p, which dominates the nitrogen shift in diamagnetic compounds. The negative sign of σ_p (ppm) represents deshielding, so the shift δ increases with the absolute magnitude of σ_p.

$$\sigma_p \approx -\frac{\mu_0}{4\pi}\,\frac{e^2}{2m_e^2}\langle r^{-3}\rangle_{2p}\,\frac{\langle 0|\boldsymbol{L}^2|0\rangle}{\Delta E} \tag{11}$$

Equation (11) embodies an 'atom-in-a-molecule' approximation[107,108] in a simplified form. It does not give accurate results, but is useful in showing the three factors of importance to the shielding. The first is the radial term $\langle r^{-3}\rangle_{2p}$, where r represents the radius of the 2p electron on the observed atom. The value of the radial term for the free atom, which can be viewed as a scaling factor for the shifts of a particular nucleus, is twice as large for nitrogen (2.46 a.u.) as for carbon (1.23 a.u.);[109] the more electronegative atom holds its valence p electrons closer to the nucleus, giving a larger paramagnetic shift.

The second factor is the term in $\boldsymbol{L}^2$ representing the angular momentum which allows the electronic charge to circulate in a magnetic field, so as to reinforce the field. This paramagnetic circulation opposes the free diamagnetic circulation, which is fully realized only in the free atom or round the axis of a linear molecule. The paramagnetic circulation requires an asymmetry of charge in the valence shell of the observed atom, i.e. in the p orbitals of a second-row element such as carbon or nitrogen. The angular momentum term in equation (11) is analogous to the $\boldsymbol{Q}$ terms in the theory of Karplus and Pople, expressing imbalance of charge, or the $\boldsymbol{P}_u$ term in the theory of Jameson and Gutowsky.[109] Electronic asymmetries which potentiate the paramagnetic circulation are small in highly symmetric environments, as in CH_4 or NH_4^+, but may be large for two-coordinate nitrogen carrying a lone pair.

The third factor, ΔE, is an effective excitation energy for the paramagnetic circulation. This can be considered to arise from virtual excitations of p → p type, which may be $\pi \leftrightarrow \sigma$

(i.e., $\pi \rightarrow \sigma^*$ or $\sigma \rightarrow \pi^*$), $n \rightarrow \pi^*$, or $\sigma \rightarrow \sigma^*$ from one bond to another, as the magnetic field mixes into the ground state those excited states which allow circulation of charge. Excitation energies vary more widely for nitrogen than for carbon, since lone pair (n_N, or nonbonding) electrons afford a high lying HOMO, and LUMOs involving nitrogen are low lying because of the electronegativity of nitrogen. The frontier orbitals in question are those appropriate to charge rotation (e.g. $n_N \rightarrow \pi^*$, but not $\pi \rightarrow \pi^*$), and the terms HOMO and LUMO may represent more than one High lying Occupied MO, or Low lying Unoccupied MO, when more than one excitation contributes significantly to the deshielding. These magnetic-dipole-allowed excitations are normally forbidden in the electronic spectrum. They are weakly allowed in $n_N \rightarrow \pi^*$ excitations in which there is a component of the s $\rightarrow$ p type, giving the well-known long wavelength bands of the azo chromophore, for example. More precise formulations of equation (11) embody a summation over the magnetically active excitations.

Equation (11) shows that the deshielding (δ) is the greater the closer the paramagnetic circulation to the nucleus (the more electronegative the substituents), the smaller the energy ΔE of the virtual excitation (the HOMO–LUMO or frontier orbital gap for charge circulation), and the greater the imbalance of charge in the valence shell. All three factors are important when extremes of high or low shielding are observed.

In isoelectronic (isostructural) locations, the shieldings of nitrogen and carbon, indeed the shielding tensors, show similar shielding patterns, with scaling according to the radial factors. Similar patterns are evident in Figure 2, which compares nitrogen and carbon shift ranges for some standard bond types. Figure 3 gives nitrogen shift ranges for compounds formed with main group elements, and Figure 4 is a comparable chart for ligands in transition metal complexes.

4.1 Nitrogen Compared with Carbon

In Figure 2 the nitrogen and carbon charts are scaled by the 2:1 ratio of the radial terms $\langle r^{-3} \rangle_{2p}$ for the free atoms, to make the shifts readily comparable. A major difference between the nitrogen and carbon charts is the extension of the nitrogen range to lower shielding for π-bonded nitrogen carrying a lone pair of electrons, as in azo (diazene) groups RN=NR or nitroso compounds RNO.

High carbon or nitrogen shielding is observed in CH_4 or NH_4^+ because of the electropositive substituent hydrogen ($\langle r^{-3} \rangle_{2p}$ is small), the high electronic symmetry in the valence shell (the angular momentum term is small), and the high energy of the $\sigma \rightarrow \sigma^*$ excitations (ΔE is large).[110] The energy of the $n \rightarrow \sigma^*$ excitation is also high in ammonia, and the lower nitrogen shielding in NH_4^+ compared with NH_3 is largely attributable to the positive charge on the nitrogen, increasing the radial term and excitation energies. Nitrogen shifts are found to correlate with the atomic charges estimated for nitrogen in amines, nitro compounds, isonitriles, and azines.[111]

Nitrogen is strongly *de*shielded as an interstitial atom in the metal cluster carbonyls such as $[Rh_6N(CO)_{15}]^-$, a trigonal prism, and $[Ru_6N(CO)_{16}]^-$, which is octahedral.[70] The interstitial carbon in the corresponding clusters is even more strongly deshielded, as shown in Figure 2. The deshielding is unexpected in view of the high symmetry and the electropositive and heavy neighbors. Carbon in the corresponding clusters is even more strongly deshielded. Indeed, the deshielding increases with compression of the interstitial atom in the cluster, as observed in some other kinds of cages.[112]

The nitrogen shifts in alkylamines and hydrochlorides can be expressed by additive substituent parameters,[113] as for carbon in alkanes. For nitrogen shifts, as for carbon shifts, the increments for each C_α or C_β substituent arise from inductive effects, while the increments for C_γ substituents arise from steric and conformational effects. Substituent parameters have been developed for other compound types,[2,3] including peptides, but correlation spectroscopy is now used to assign nitrogen resonances.

Lower shielding is generally observed in multiply bonded compared with singly bonded compounds, because of the lower electronic symmetry of the observed atom when π and σ bonds are present and the lower energies of $\pi \leftrightarrow \sigma$ in comparison with $\sigma \rightarrow \sigma^*$ excitations. Figures 2–4 show that quite high shielding is observed for nitrogen as the central atom in a linear group, as in MeNC, N*N*O, or NO_2^+, or carbon in MeCN, NCO^-, or CO_2. The shielding is relatively high because of the free diamagnetic circulation about the axial direction, as in the noble gas compounds $RC{\equiv}N{-}XeF^+$, measured in ^{14}N resonance,[114] and $HC{\equiv}N{-}KrF$.[115]

The nitrogen shielding in comparable groups decreases with increasing electronegativity of the neighbor, or with an

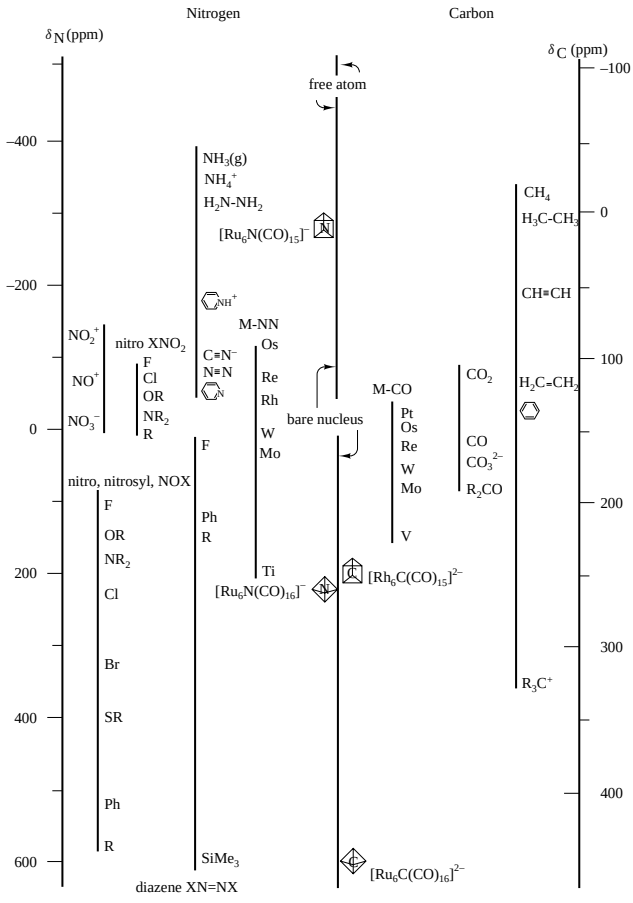

Figure 2 Comparison of nitrogen and carbon shifts

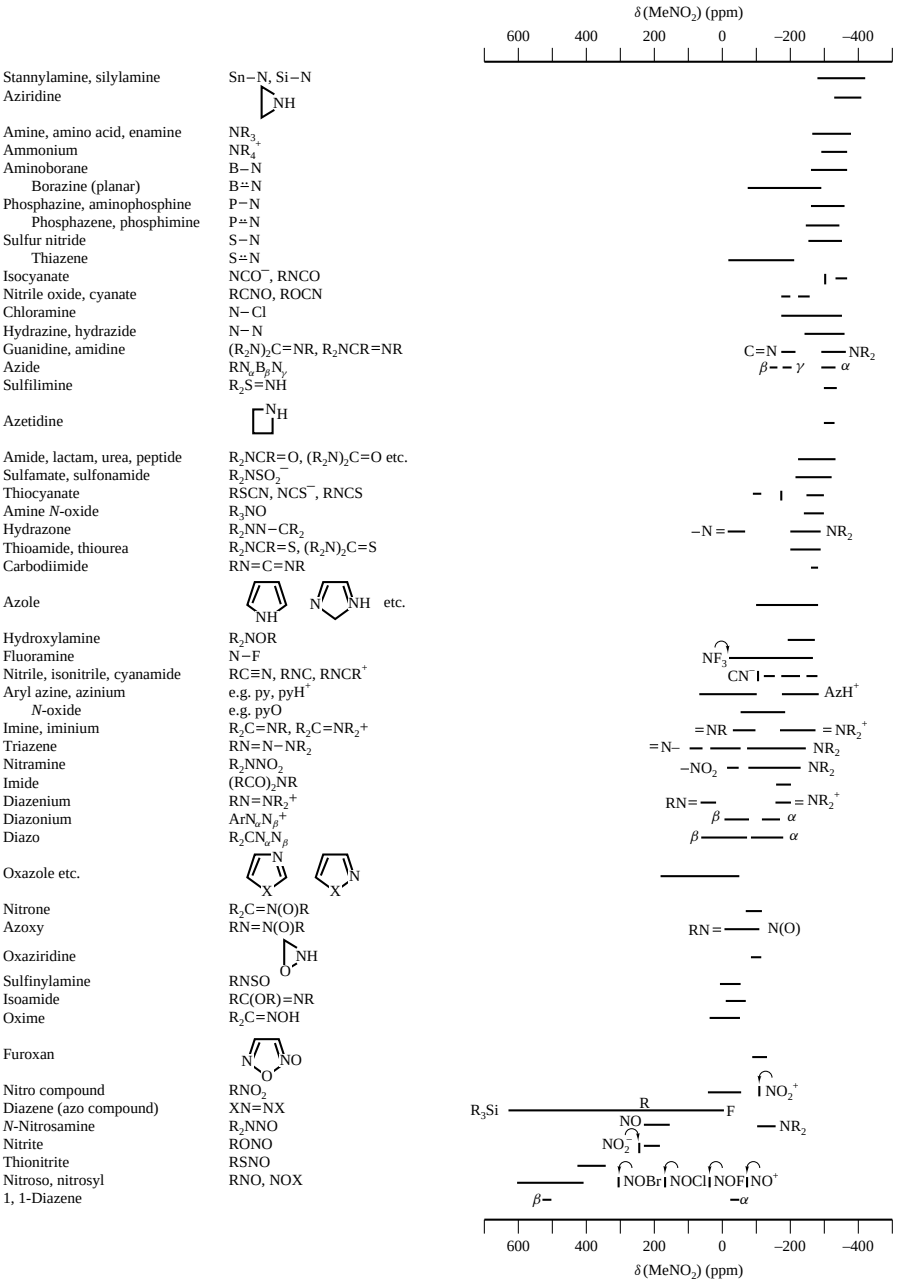

Figure 3 Ranges of nitrogen shifts in compounds with main group elements

increase in the positive charge on the ion. Lower shielding may be observed for terminal atoms in linear groups, as in MeCN > N_2 > NO^+, or MeNC > CN^- > CO.

Figure 2 shows the comparability of the carbon and the nitrogen shielding in isoelectronic pairs such as CH_4 and NH_4^+, CO (or CN^-) and NO^+, or CO_3^{2-} and NO_3^-, even for pairs which are not isostructural such as C_2H_6 and N_2H_4 since the lone-pair excitation energies in hydrazine are rather high. The shielding in comparable compounds decreases from single (e.g. $H_2N–NH_2$) to triple (N≡N) to double bonds (RN=NR) in nitrogen as in carbon resonance. This is the sequence of decrease in symmetry of the local electronic charge (and increase in the NQCC, as illustrated in Table 4) and of decreasing excitation energies.[116]

In the n → π* excitation, charge circulates from the p component of the lone pair into the π* orbital. The n → π* excitation energies are low for diazenes RN=NR, particularly in extended conjugated systems as in azo dyes.[117] The n → π* excitation energies and nitrogen shieldings are particularly low for nitroso compounds RNO and nitrosyls NOX. All three factors in equation (11) are operative: the bent nitrogen carrying a lone pair is highly anisotropic, $\langle r^{-3}\rangle_{2p}$ is large because of the electronegativity of oxygen, ΔE is very low since the π* LUMO is low (because of the electronegativity of oxygen), and the nitrogen lone pair HOMO is raised by the presence of lone-pair electrons on the oxygen.

When excitation energies are small, linear δ/λ correlations may be observed between the chemical shifts δ and the wavelength λ of the low-energy absorption band in the electronic

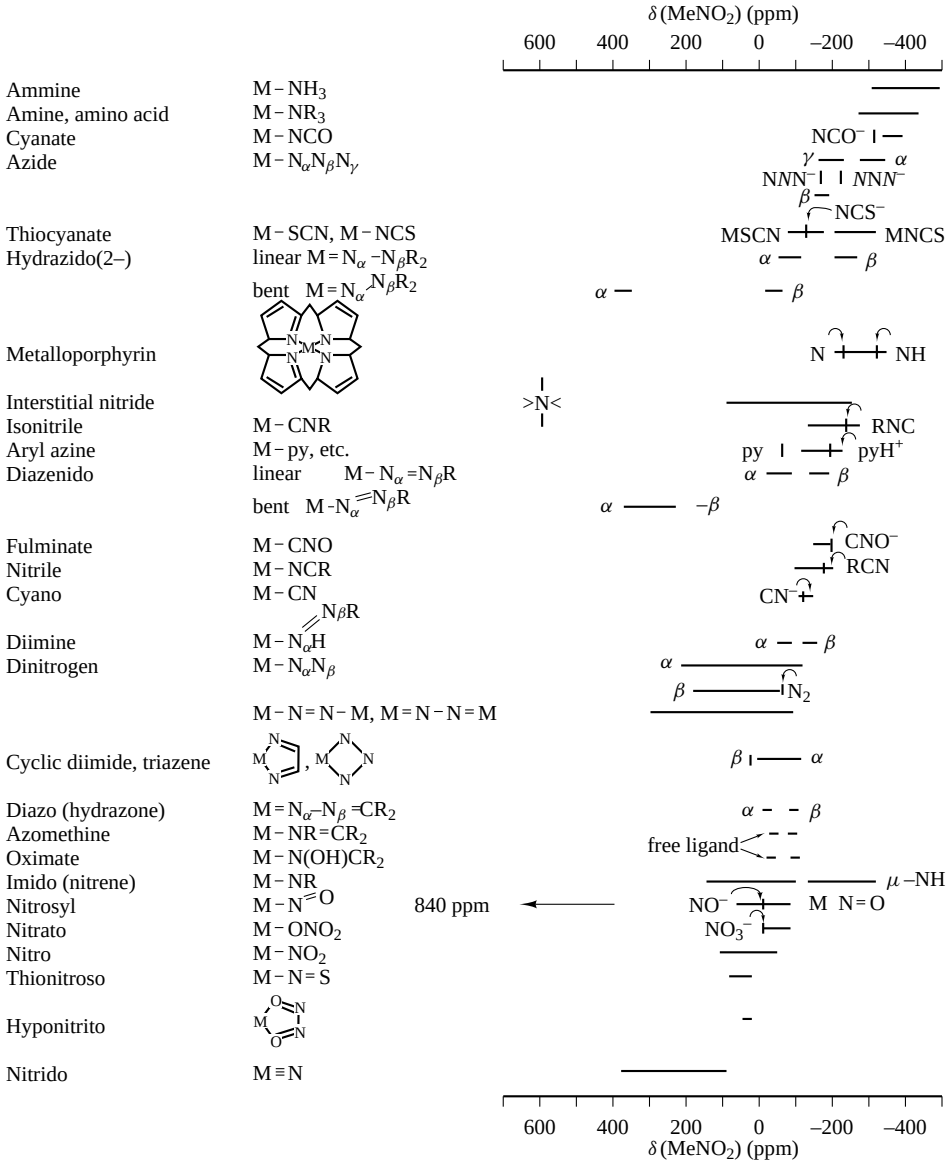

Figure 4 Ranges of nitrogen shifts in metal complexes

spectrum. Such correlations are well known for organic and inorganic compounds with $n_N \rightarrow \pi^*$ absorption: for carbonyl compounds RCHO or RCOR′ in carbon resonance, and in nitrogen resonance, for nitrosyl compounds NOX and RNO,[118] azo (diazene) compounds XN=NX and RN=NR,[119] diazo compounds YNN,[120] etc. The nitrogen shielding decreases as the $n_N \rightarrow \pi^*$ band moves to longer wavelengths, from the colorless oxo/fluoro compounds NOF, FNNF, etc., to the compounds with less electronegative substituents, such as PhNO, *t*-BuNO, or $Me_3SiN{=}NSiMe_3$ which are blue, and the 1,1-diazenes R_2NN which are purple.[121] In $n_N \rightarrow \pi^*$ chromophores, the nitrogen shift δ and $\lambda(n_N \rightarrow \pi^*)$ both increase in the sequence N=C < N=N < N=O of increase in the electronegativity of the partner in the double bond, lowering the π^* relative to the n_N orbital and increasing $\langle r^{-3} \rangle_{2p}$ for the nitrogen.

4.2 Protonation Shifts

Protonation of the singly bonded nitrogen in ammonia or amines deshields the nitrogen by up to 20 ppm. The deshielding is largest in ammonia in which the charge is strongly localized. Because of the relatively small protonation shifts in amines, there are similar shift relationships for amine nitrogen and alkane carbon in corresponding environments, depending on connectivity, although the groups are not isostructural. Amines which are branched at the α-carbon show small *in*creases in nitrogen shielding on protonation.

Since nitrogen is strongly deshielding by $n \rightarrow \pi^*$ circulations, the effects of protonation of nitrogen in a π-bonded system may be large. Protonation of pyridine increases the nitrogen shielding by about 100 ppm, as the lone-pair electrons on nitrogen are strongly stabilized by the formation of a bond to hydrogen. The radial term $\langle r^{-3} \rangle_{2p}$ is not greatly increased by the positive charge, which is delocalized. Large effects may be observed in metal complexes. Protonation of

dinitrogen attached to tungsten to form the (linear) diazenido ligand, and then the hydrazido(2-) ligand, increases the shielding of the β-nitrogen by 135 and then 55 ppm:[122] $W-N\equiv N \rightarrow W-N=NH \rightarrow W=N-NH_2$. Protonation shifts of 200 ppm are observed for the doubly bent diazenido group Pt(II)−N=NPh to give a hydrazido(1-) ligand, Pt−NH=NPh.[123]

An exception which proves the rule is the *de*shielding of nitrogen by ca. 100 ppm on protonation of the cyclic anion formed by deprotonation of 2,4,6-trimethylpyridine.[124]

4.3 Nitrogen NMR Criteria of Structure

The relationships illustrated in Figures 2–4 allow some generalizations on the structural determinants of nitrogen shieldings, in advance of more rigorous discussion of the shielding tensor.

1. In groups which may be bent or linear at nitrogen, the nitrogen is deshielded as the bond angle decreases. The deshielding on bending is the greater, the greater the deshielding in the linear group: thus, bent nitrogen in azides is still quite highly shielded.[125] Deshieldings are greater in aromatic azines and azoles, and may be greater still in triazenes, as in the $(Ts-NNN-Ts)^-$ ion (Ts = tosyl), in which the central nitrogen is deshielded by 286 ppm compared with the central nitrogen in azide ion, $N\mathit{N}N^-$.[126]
   The difference in nitrogen shift is small for linear and bent imido ligands M=NR,[127] but large in diazenido ligands M−N=NR which are bent at the ligating nitrogen.[124]
   The nitrosyl group shows large deshieldings. The bent nitrogen in the *N*-nitrosamine Me_2NNO is deshielded by 300 ppm compared with the central nitrogen in nitrous oxide, $N\mathit{N}O$, and the nitrogen is deshielded further if the group is distorted from planarity.[128] Deshieldings up to 800 ppm are reported for metal nitrosyls in the bent compared with the linear ligand,[129] with smaller shieldings for smaller MNO angles.[130]
   Reactions which involve the shift of a d-electron pair onto ligating nitrogen, allowing the metal to accept an incoming ligand and the nitrogen to coordinate a Lewis acid, are readily monitored by nitrogen NMR.]
2. In groups which may be pyramidal at nitrogen carrying a lone pair, or flat, with π delocalization of the lone-pair electrons, the nitrogen is deshielded the flatter the group, as noted early on in substituted anilines.[2,3] Planarity allows $\pi \leftrightarrow \sigma$ paramagnetic circulations of lower energy than $n_N \rightarrow \sigma^*$ circulations in the pyramidal group. In the planar hydrazido(2-) ligand $M=N-NH_2$, the nitrogen shift (ca. −230 ppm[131]) shows significant deshielding compared with hydrazines (ca. −320 ppm), being comparable with amide shifts (cf. −265 ppm for formamide).
3. Protonation and deprotonation shifts have considerable diagnostic value in structural studies. Hydrogen bonding to a lone pair on nitrogen leads to smaller shifts in the same sense. Hydrogen bonding of attached hydrogen gives nitrogen shifts in the opposite sense. Tautomeric and other acid–base systems involving nitrogen are thus well studied by nitrogen NMR methods, with the information from the shifts, ^{14}N linewidths, ^{15}N NOE, and couplings.
4. Coordination shifts may be comparable to protonation shifts. Thus, coordination of BH_3 or BMe_3 to ammonia or alkylamines deshields the nitrogen by a small amount, and coordination to π-bonded nitrogen increases the shielding markedly, as by 74 ppm when pyridine forms py · BH_3. Coordination to transition metals is a more complex question (Section 4.5).

4.4 Nitrogen Bonded to Heteroelements

Figures 3 and 4 show high shielding for carbon or nitrogen singly bonded to boron,[132] silicon, phosphorus,[133] etc., or to transition metals in ammine complexes. These elements are less electronegative than nitrogen. Nitrogen is strongly deshielded in singly-bonded compounds with fluoronitrogen compounds by 370 ppm for liquid NF_3 compared with NH_3, or 290 ppm for NF_4^+ compared with NH_4^+.[28] Because of the extreme electronegativity of fluorine, its effects as a substituent often have diagnostic value, and have been called (per)fluoro effects in photoelectron and electronic spectroscopy.

In a comparison of similar N–X compounds, the nitrogen shift ranges show periodic trends reflecting the inductive effects of the heteroelement. The nitrogen shielding decreases across the row of the heteroelement, e.g. from B–N to N–O and from Si–N to N–Cl, with an increase in the electronegativity of X; and increases down the group of the neighbor, with a decrease in the electronegativity of X, an increase in polarizability and relativistic effects, and with heavy atom neighbors.

Fluoro effects provide extreme examples, as in the σ-fluoro effects already described. These, and π-fluoro effects, are used in photoelectron and electronic spectroscopy for assignments to σ or π orbitals. Fluorination strongly stabilizes the σ-orbital manifold, of which the lone-pair orbital forms part. The stabilization is less for the π-orbital manifold, in part due to repulsion of π electrons by lone-pair electrons on fluorine. Although nitrogen is strongly deshielded in NF_3 and NF_4^+ compared with NH_3 and NH_4^+, nitrogen shielding is significantly increased on fluorination of azabenzenes and other planar species (cf. NOF, NO_2F, and N_2F_2).[134] π-Chloro effects are similar, and smaller.

4.5 Coordination Shifts in Metal Complexes

Coordination shifts from the free ligand to the complex are illustrated by a comparison of Figures 3 and 4, and in Figure 4 itself, since the shift for the free ligand is indicated.

Coordination shifts are usually small in the higher shielding ranges, and smaller for p-block than for d-block metals. On coordination to a transition metal, the nonbonding electrons on nitrogen are stabilized by bond formation, this tending to increase the nitrogen shielding, but low-lying orbitals may then become available to the paramagnetic circulation on ligating nitrogen.

Nitrogen NMR is a criterion of the mode of coordination of ambidentate ligands. Nitrogen is more shielded in M–NCS than in MSCN or in the free NCS^- ion.[135] Similarly, in the covalent azides $XN_\alpha N_\beta N_\gamma$, N_α is the most highly shielded nitrogen with N_β being buffered from the effects of coordination.[136]

Relatively low shielding is observed for ligating nitrogen in doubly bonded groups such as hydrazide(2−), $M=N-NH_2$, and for π-acceptor ligands such as NCMe, N_2, NO, NS, etc.

The importance of the ligand field splitting to the nitrogen shift is shown by the periodic dependence on the transition metal and by *trans* effects.[137] These influences are magnified if nitrogen is close to the metal, as in nitrido complexes,[133] and for bent or bridging nitrido or nitrosyl ligands.

Trans influences may parallel substituent effects in arenes, such as the increase in nitrogen shielding in anilines, pyridines, and benzonitriles with *para*-substituents which are π donors (and the deshielding if nitrogen with π acceptors). In linear nitrosyl or diazenido complexes, the shielding of ligating nitrogen is increased by *trans*-donors such as OH, and decreased by *trans*-acceptors such as CN or NCMe. The strength of binding of the *trans*-ligand is also significant, since the dσ-orbital splitting is larger with softer ligands for metals in low oxidation states. Such correlations include other physical properties such as IR stretching frequencies, reflecting back-bonding to acceptor ligands such as N_2, or redox potentials.

Interest in nitrogen fixation processes has stimulated the study of the dinitrogen ligand in complexes of molybdenum and related metals, and of ligands on the reduction pathway, diazenido, hydrazido, hydrazinium, imido, etc. Nitrogen NMR spectroscopy can usefully distinguish terminal and bridging, or linear and bent ligands, and monitor protonation reactions.

5 NITROGEN SHIELDING TENSORS

More rigorous consideration of the factors determining nitrogen NMR shifts requires a knowledge of the shielding tensor, preferably in conjunction with theoretical calculations. Shielding tensor components have been measured for a number of nitrogen bond types, including ligands in metal complexes. There has been much interest in groups of biological importance, in peptide or imino links for example, in which nitrogen shielding tensors give useful information on the effects of protonation and hydrogen bonding. Other articles discussing nitrogen shielding tensors in biomolecules are given at the end of this section.

Nitrogen tensors resemble those for carbon or phosphorus in isoelectronic and isostructural locations, with scaling by the respective radial factors $\langle r^{-3}\rangle_{np}$ which are in a 2:1 ratio for nitrogen and carbon, as discussed in Section 4.[109,110] Nitrogen shielding patterns are more closely related to those of phosphorus than of carbon, since the nitrogen and phosphorus valencies are closer, as are the scaling factors, since the ratio of $\langle r^{-3}\rangle_{2p}$(N) to $\langle r^{-3}\rangle_{3p}$(P) is 1:0.7.

A major factor for many nitrogen tensors is the presence of lone pair (n_N) electrons on the nitrogen which are strongly directional. The lone-pair axial direction then determines the principal axis system, and major deshieldings are observed for axes which mix n_N and π^* orbitals, following the arguments given in Section 4. Similarly, the nitrogen shielding tensor is a criterion for the bending of two-coordinate nitrogen and the flattening of three-coordinate nitrogen. Tensor measurements, combined with theoretical studies, can frequently throw light on the nature of the bonding.

5.1 Experimental Techniques

The spin–rotation interaction, measured as fine structure in the microwave spectra of gases, has given ^{14}N tensor information for NH_3,[16] N_2O,[142] HCN,[143] and PN[144] (Tables 5 and 6). Tensor measurements have been made on oriented single crystals of glycylglycine · HCl · H_2O[145,146] and L-histidine · HCl · H_2O in ^{15}N resonance, and some nitrates in ^{14}N resonance (Table 7). Most measurements, however, are made on powdered material by ^{15}N MAS or CP MAS techniques, and/or powder lineshape analysis on a static sample. Some anisotropies have been measured in liquid crystals (MeNC, MeCN, N_2O) and some by relaxation methods ($PhNO_2$, pyridine).

For some molecules or groups, the orientation of the shielding tensor in the molecular frame is obvious from the chemical structure, and for some it has been established by single crystal measurements. For some others, the orientation has been determined by concurrent measurement of dipolar interaction between ^{14}N or ^{15}N with ^{1}H, ^{2}H, ^{13}C, ^{31}P, or other nuclei.[140,145,147] Theoretical calculations, also, may help in the assignment of the axial directions.

Tables 5–7 give the principal components as absolute shieldings σ, with $\sigma_{33} > \sigma_{22} > \sigma_{11}$, and $\sigma_{iso} = \sigma_{tr} = (\sigma_{11} + \sigma_{22} + \sigma_{33})/3$. The shieldings are obtained from the chemical shift, δ, with neat liquid nitromethane as standard, according to equation (1), using the absolute scale[19] based on the spin–rotation measurement for NH_3, according to which nitrogen in neat liquid nitromethane has shielding $\sigma = -135.8$:

$$\sigma = -135.8 - \delta(MeNO_2) \qquad (12)$$

Some authors use a liquid ammonia standard, for which the nitrogen shieldings are 244.6 ppm at ambient temperatures and 240.6 at −50°C.[17] Some others use solid NH_4Cl as the reference material, with σ(N) = 202.5.

The tensor properties given in Tables 5–7 are the span $\Omega = \sigma_{33} - \sigma_{11}$ and the skew $\kappa = 3(\sigma_{22} - \sigma_{iso})/\Omega$.[148,149] For axial tensors, $\Omega = \sigma_{\parallel} \sim \sigma_{\perp}$ and $\kappa = \pm 1$. The parameters Ω and κ avoid ambiguities that have arisen with the traditional parameters,[150] the shielding anisotropy $\Delta\sigma$ and asymmetry η. For these, the ordering of the σ_{11}, σ_{22}, and σ_{33} axes depends on the ordering of the absolute values of the differences of the tensor elements from σ_{iso}. Some authors have followed the 'traditional' order σ_{33}, σ_{11}, and σ_{22},[145] while some use the numerical order σ_{33}, σ_{22}, and σ_{11}. In any case, the σ_{33} and σ_{11} axes have to be interchanged for those members of an extended series of compounds which have $\sigma_{22} < \sigma_{iso}$, as compared with those with $\sigma_{22} > \sigma_{iso}$. Such series include metal nitrosyls in nitrogen resonance, as described in Section 5.5, or organic carbonyl compounds in carbon resonance.[151]

Several authors[152] have used the relative magnitudes of the principal components to define the axes as here, rather than relative magnitudes of the absolute values of the differences from σ_{iso} as in the 'traditional' definition. The use of the skew parameter κ rather than the asymmetry parameter η preserves sign information, since on the traditional definition $0 \leq \eta \leq 1$ and $\eta = 0$ for axial symmetry whether $\sigma_{\parallel}$ is greater or less than $\sigma_{\perp}$. The skew κ, however, is +1 for $\sigma_{\parallel} > \sigma_{\perp}$ and −1 for $\sigma_{\parallel} < \sigma_{\perp}$.

5.2 Singly Bonded Nitrogen

Shielding tensors are given in Table 5 for nitrogen in ammonia and some derivatives. Although distortion of an oxyanion such as nitrate by hydrogen bonding to the

Table 5 Principal Components of Nitrogen Shielding Tensors in Ammonia, Ammines, and Ammonium

Compound	δ_{iso}	σ_{iso}	σ_{11}	σ_{22}	σ_{33}	Ω	κ	Reference
NH_3(g)	−400.3	263.5	237.7	278.0	278.0	40.3	1	Kukolich[16]
cis-[Pt($^{15}NH_3$)$_2$(SCN)$_2$]	−399.0	263.2	219.9	249.3	320.5	100.6	−0.41	Santos et al.[155]
(two crystal sites)	−386.0	250.2	212.5	244.1	294.1	81.6	−0.22	
$^{15}NH_4^+$ halides:								Ratcliffe et al.[153]
Cl^-	−338.1	202.3						
Br^-	−336.0	200.2						
I^-	−321.6	185.8						
$^{15}NH_4NCS$	−344.3	−171.9						Dickson et al.[154]

Table 6 Principal Components of Nitrogen Shielding Tensors in Linear and Near-Linear Groups

Compound	δ_{iso}	σ_{iso}	σ_{11}	σ_{22}	σ_{33}	Ω	κ	Reference
2,4,6-*t*Bu$_3$C$_6$H$_2$^{15}N≡P$^+$AlCl$_4^-$	−132	−3	−155	−121	266	421	−0.834	Curtis et al.[160]
4-MeC$_6$H$_4$C≡^{15}N	−126	−10	−151	−122	244	395	−0.851	Sardashti and Maciel[161]
MeN≡C	−266	130	10	10	370	360	−1	Yannoni[164]
*N*NO(g)	−240	105	−18	−18	349	367	−1	Casleton and Kukolish[142]
NH$_4$SC^{15}N	−169	34	−104	−104	311	415	−1	Dickson et al.[154]
MeC≡N	−157	21	−142	−142	346	488	−1	Kaplan et al.[159]
N*N*O(g)	−141	5	−174	−174	364	538	−1	Casleton and Kukolish[142]
HC≡N(g)	−109	−27	−215	−215	348	563	−1	Garvey and De Lucia[143]
N≡N(g)	−74	−62	−263	−263	340	603	−1	Ishol and Scott[162]
[Mo(dppe)$_2$(^{15}N$_2$)$_2$] N$_\beta$	−43.4	−92.2	−283	−283	289	572	−1	Groombridge et al.[165]
N$_\alpha$	−42.0	−93.6	−304	−304	327	631	−1	
P≡N(g)	213	−349	−698	−698	350	1048	−1	Raymonda and Klemperer[144]

Table 7 Principal Components of Nitrogen Shielding Tensors in Planar Groups

Compound	δ_{iso}	σ_{iso}	σ_{11}	σ_{22}	σ_{33}	Ω	κ	References
RC(O)^{15}NH$_2$·H$_2$O (asparagine)	−276.8	141.0	64.5	107.9	250.6	186	−0.53	Herzfeld et al.[166]
Nylon-6 (−CO^{15}NH−)	−268	132	34	154	209	175	0.37	Powell and Mathias[167]
Glycyl(^{13}C^{15}N)glycineHCl·H$_2$O	−267.4[a]	135.6	30.6	180.8	183.3	153	0.97	Hartzell et al.,[145] Harbison et al.[146]
L-Alanyl(^{13}C^{15}N)L-alanine	−256.8	121.0	25.1	162.5	175.3	150	0.83	Hartzell et al.[145]
Alanyl(^{13}C^{15}N)proline	−256	120	22	118	219	197	−0.030	Schweitzer and Spiess[172]
RCO^{15}NHR′ (peptides)	ca. −260	100–145	10–35	120–180	175–220			
L-Tryptophan·HCl		127.8	66.9	121.5	195	128	−0.15	Roberts et al.[157]
Tryptophan-26		126	70	116	185	115	−0.26	Cross and Opella[171]
L-Histidine·HCl·H$_2$O (π-^{15}N)		66.9	−19.8	35.6	184.9	205	−0.46	Roberts et al.[157]
Pyridine-^{15}N	−83	−53	−387	−168	395	782	−0.44	Schweitzer and Spiess[172]
Ph^{15}N(O)^{15}N(O)Ph		−66	−220	−43	65	285	0.24	Wasylishen[179]
PhCH=^{15}NPh	−48	−87	−365	−76	180	545	0.06	Curtis et al.[173]
PhCMe=^{15}NOH	−31.4	−104	−315	−83	85	400	0.16	Wasylishen et al.[174]
trans-RB (−CH=^{15}NH−)	−37.6	−97.8	−406.5	−92.5	205.6	612	0.026	de Groot et al.[180]
RBH$^+$Cl$^-$	−181.2	44.6	−79.2	22.5	189.8	269	−0.25	
RBH$^+$Br$^-$	−186.8	51.6	−69.5	33.8	190.4	260	−0.205	
RBH$^+$I$^-$	−198.5	62.5	−56.7	53.3	190.8	247	−0.11	
bR$_{568}$ (all-*trans*)	−209.3	73.6	−42.9	60.1	203.1	246	−0.165	
bR$_{548}$ (13-*cis*)	−202.3	66.5	−42.9	39.1	204.1	247	−0.33	
PhNO$_2$(soln.)	−2	−134	−399	−32	30	429	0.71	Friedrich and Wasylishen;[45] Stark et al.[78]
Nitrates:								
NH$_4$NO$_3$	−3.6	−132	−220	−189	11	231	−0.74	Delmotte et al.[226]
NaNO$_3$	−3	−133	−206	−206	16	222	−1	Barrie et al.[178]
KNO$_3$	−3	−133	−209	−207	17	226	−0.98	Bastow and Stuart[176]
AgNO$_3$		−142	−212	−206	−7	205	−0.94	Santos et al.[177]
Pb(NO$_3$)$_2$		−146	−220	−220	2	218	−1.02	Santos et al.[177]
Ba(NO$_3$)$_2$		−151	−227	−227	−0.5	226	−1.01	Santos et al.[177]
trans-Ph^{15}N=^{15}NPh	130	−267	−789	−146	136	925	0.39	Wasylishen et al.[175]
Na^{15}NO$_2$	245	−381	−915	−263	36	951	0.37	Wasylishen et al.,[140] Barrie et al.[178]
p-Me$_2$NC$_6$H$_4$^{15}NO	445	−581	−1457	−309	22	1479	0.55	Schweitzer and Spiess[172]

[a]Assumes glycine zwitterion reference has δ(N) −350 ppm.

ammonium ion has been observed in the nitrogen shielding tensor, the ammonium cation gives a symmetric tensor, as for near-tetrahedral symmetry and reorientational motion such as the switching in NH_4Cl (Section 3).

The shielding tensor for ammonia is unusual in having $\sigma_{\parallel} < \sigma_{\perp}$ ($\kappa = 1$) and a small span, 40.3 ppm.[16] Ammonia is unusual also in the substantial *decrease* in the nitrogen shielding on protonation, as discussed in Section 4. In ammonium salts, the NH_4^+ nitrogen shielding decreases with a decrease in strength of the hydrogen bond to the counteranion (i.e., with a decrease in the electronegativity of the anion), increasing the positive charge on nitrogen.[153,154] The deshielding is related to contraction of the 2p N orbitals from NH_3 to $NH_3 \cdots H^+$, with a strongly hydrogen-bonding anion, and then to NH_4^+, as the counterion hydrogen bonds more weakly.

Much smaller deshieldings are observed on the protonation of amines, in which cationic charge is less localized on the nitrogen. $R-NH_3^+$ tensors, of which a number have been measured in biomolecules such as histidine or glycine, have a very small span, about 10 ppm.

There is little change in the NH_3 isotropic shift on formation of ammine ligands in *cis*-[Pt($^{15}NH_3$)$_2$(SCN)$_2$], with weak bonding to the metal. There is some increase in span of the NH_3 tensor, but a considerable decrease in the skew, in this planar complex. The σ_{33} component is sensitive to a change in location in the crystal.[155]

Combined shielding tensor and dipolar shift measurements have been used to characterize NH protons and measure the bond distances in polycrystalline and amorphous solids of biological importance, in ^{14}N[156] and in ^{15}N[157] resonance. Protonated imine nitrogen is discussed under the heading of the parent compound.

5.3 Nitrogen in Linear Groups

The principal components of nitrogen shielding tensors for linear systems are given in Table 6. Maximal shielding is observed for the C_∞ axis with its largely diamagnetic circulation. Most values of the parallel shielding $\sigma_{\parallel}$ are in the range 300–370 ppm, resembling the (diamagnetic) shielding of atomic nitrogen, 325 ppm.[158]

The parallel shielding, 350 ppm in MeCN,[159] decreases by 80–100 ppm when the π electrons can delocalize into an aromatic ring, as in the iminophosphenium cation[160] and benzonitriles.[161] Interesting σ-inductive and π-conjugative effects of a 4-substituent in the benzene ring on the cyano-nitrogen shielding tensor have been monitored for benzonitriles 4-Y–C_6H_4–C≡^{15}N with Y = OMe, NMe_2, NO_2, CN, Cl, Br, F, Me, CMe_3, and NMe_3^+. Some of the largest changes in tensor components relative to Y = Me are produced by a positively charged substituent NMe_3^+, which decreases σ_{33} in the C≡N by 11 ppm (and σ_{11} and σ_{22} by 7 and 16 ppm, respectively). Similarly the parallel shieldings in dinitrogen N≡N[162] are reduced by 51 and 13 ppm on coordination to molybdenum.

The perpendicular tensor components arise from $\sigma \leftrightarrow \pi$ (i.e., $\sigma \rightarrow \pi^*$ and $\pi \rightarrow \sigma^*$) circulations, and for terminal nitrogen from $n_N \rightarrow \pi^*$ circulations also. The separation of the σ_{11} and σ_{22} components by around 30 ppm in the benzonitriles and iminophosphenium ion reflects conjugation with the aromatic ring. In the benzonitriles the separation is largest (41 ppm) with the π-donor Me_2N as the 4-substituent.

For terminal nitrogen in the linear groups the perpendicular shielding ($\sigma_{\perp}$) is highest in *N*NO and lowest for PN: the latter has the longest bond (so orbital splittings are smaller) and phosphorus is the least electronegative partner. For N_2O, ab initio calculations using the LORG method[163] show comparable (major) contributions to σ_p for the terminal nitrogen from its lone pair and the NN bond, and for the central nitrogen from the NN and NO bonds.

For two-coordinate nitrogen, the perpendicular shielding decreases from MeNC[164] to $ArNP^+$ and to [Mo(dppe)$_2$($^{15}N_2$)$_2$],[165] as the orbital splittings decrease.

5.4 Nitrogen in Planar Systems

Principal values for nitrogen tensors in planar systems are given in Table 7. The highest shielding and a small span are observed for three-coordinate nitrogen bound only to carbon and hydrogen, in amides or peptides, azinium nitrogen in the five-membered rings in tryptophan, and L-histidine · HCl · H_2O and iminium groups.

5.4.1 Peptides and Amides

Table 7 shows the similarities of the components in an amide, asparagine,[166] in which the σ_{33} axis bisects the NH_2 group, in Nylon-6,[167] and in peptides.[139–168] Concurrent observations of $^{13}C^{15}N$ and $^{15}N^{1}H$ dipolar interactions in L-(1-^{13}C)alanyl-L-(^{15}N)alanine confirmed earlier conclusions on the orientation of the nitrogen tensor.[142] The axis of lowest shielding σ_{11} is in the amide plane perpendicular to the CN bond, allowing relatively low-energy CN $\sigma \leftrightarrow \pi$ circulations. Unusually (in contrast to carbon tensors in peptides, and to carbon and nitrogen tensors in aromatic and other delocalized systems), the high-shielding axis σ_{33} is in-plane in the CN bond direction; the intermediate axis σ_{22} is perpendicular to the plane. These directions are approximate, varying somewhat in different peptides. In glycylglycine and related peptide links, there is, accidentally, near-axial symmetry, with $\kappa \approx +1$, and the σ_{11} axis is at 99° to the CN bond.

The σ_{11} component is the least variable because of constancy of the CN bond, although sensitive to the geometry of the hydrogen bonding, the σ_{11} axis being nearest to the N–H···O direction. The σ_{11} axis is smaller in an α-helix than in a β-sheet, and is sensitive also to the handedness of the helix. The out-of-plane component σ_{22} reflects the conformation and secondary structure, being larger in a β-sheet than in an α-helix.[169] The σ_{22} component is unusually low and σ_{33} unusually high ($\kappa = -0.3$) in the link to proline, in which the nitrogen is in a saturated five-membered ring, although the alanylalanine isotropic shift is maintained in alanylproline.[170] The importance of lattice effects is shown by differences of isotropic shifts in solution.

5.4.2 Azines, Azinium

Despite the chemical importance of aromatic azines, few of their nitrogen tensors have been studied to date. Table 7 includes ranges of principal components observed for protonated nitrogen in five-membered rings of biological interest, in tryptophan[159,171] and in histidine.[159] These components are comparable to the values for pyridine.[172] In delocalized ($p\pi$)

systems, the out-of-plane axis shows the highest shielding (σ_{33}) in carbon resonance, depending on the relatively high-energy $\sigma \rightarrow \sigma^*$ excitations in the plane. This is borne out in nitrogen resonance, as in the protonated imidazole ring in histidine hydrochloride: the σ_{33} axis is almost perpendicular to the ring and the σ_{11} axis almost along the NH bond. Similar components are observed for tryptophan, studied as the hydrochloride, and in vivo in a bacteriophage that orients in the magnetic field.

Comparison with pyridine shows the major increases in σ_{11} and σ_{22} on protonation. In pyridine, the σ_{11} axis is tangential to the ring, mixing n_N and π^* orbitals, and the σ_{22} axis radial, this shielding being mediated by $\sigma \leftrightarrow \pi$ circulations. The value of σ_{22} for pyridine resembles that of $\sigma_\perp$ in MeCN, rather than MeNC (Table 6).

5.4.3 Planar Systems with CN, NN, NP, and NO Bonds

The cyano and phosphenium groups in ArCN and ArN^+P can be described as planar, since conjugation with the aromatic system removes the axial symmetry of the CN and PN groups, although these bonds are triple and form the σ_{33} axis.

In the compounds with bent two-coordinate nitrogen, benzylideneaniline,[173] (*E*)-acetophenone oxime,[174] *trans*-azobenzene,[175] and 4-dimethylaminonitrosobenzene,[172] dipolar chemical shift measurements support the σ_{22} direction as bisecting the angle at nitrogen (effectively along the lone-pair axis). The σ_{11} axis is that of the $n_N \rightarrow \pi^*$ circulation. The nitrogen tensors show that the σ_{11} component in the planar groups becomes more strongly negative as the π^* LUMOs come down in energy relative to the n_N orbital, with increasing electronegativity of the partner in the double bond from C=N to N=N and to N=O. Very low shieldings are $\sigma_{11} = -789$ ppm for azobenzene (which is red–orange, with $n_N \rightarrow \pi^*$ absorption at 448 nm) and -1457 ppm for 1,4-dimethylaminonitrosobenzene[174] which is green.

In *trans*-azobenzene there are two molecular sites, differing in the span (925 and 880 ppm) and skew (0.392 and 0.325), while the isotropic shift is maintained. The azo group (CNNC) is effectively planar and centrosymmetric in both sites with the same N=N bond length, but the torsion angles NNCC are significantly different, 17° and <10°. (The low barrier to twisting of the phenyl group is shown by the torsion angle of 30° observed in the gas phase by electron diffraction.)

The nitrate ion is characterized by a small span.[176,177] The σ_{22} component is less negative in nitrobenzene because of the smaller paramagnetic contribution of the CN bond, and more negative when there is a lone pair on nitrogen in the plane as in the bent nitroso group in $Me_2NC_6H_4NO$. The nitrite ion is intermediate as expected.[178]

A sizeable (σ_{11}) deshielding is associated with the $n_N \rightarrow \pi^*$ circulation in bent nitrosyl groups, and to a lesser extent in NO_2^- for which LORG calculations[176] show that the contribution to $\sigma_{P_{iso}}$ of the n_N electrons on the symmetry axis exceeds that of the NO bonds. In contrast is the high shielding in the nitroso dimer PhN(O)N(O)Ph, which is a diazene bis-*N*-oxide: the σ_{11} and σ_{22} values match those in nitrobenzene, and σ_{33} matches $\sigma_\perp$ in the nitrate ion.[179]

The effects of protonation of π-bonded nitrogen, and of variations in the strength of hydrogen bonding to a counterion, have been studied in the Schiff base (aldimine) retinylidene-Bu^n-(^{15}N)imine, RB. This models the light-harvesting membrane protein bacteriorhodopsin (bR) which was measured with selective ^{15}N,^{13}C-enrichment. Protonation of bR with a strong acid (HCl) increases σ_{11} by 327 ppm and σ_{22} by 115 ppm (Table 7). From HCl to HBr to HI and to weak organic acids (carboxylic acids or phenols), σ_{11} and σ_{22} show small increases with strengthening of the $N-H^+$ bond (σ_{11} and σ_{22} being linearly related) while σ_{33} is little changed. The values for dark-adapted bR resemble those of RBH^+ when very weakly hydrogen bonded.[180]

The ^{15}N and ^{13}C studies demonstrate the major contribution of the counterion to the opsin shift in the photocycle. Color changes in the protein with pH correlate with changes in the ^{15}N shielding, which increases as the neutral purple membrane (568 nm) becomes the acid blue membrane (600 nm), reverting with the change to the acid purple membrane (565 nm); the weak hydrogen bond in the protein weakens in the blue form. The opsin-induced red shift, therefore, arises from interaction of an electronegative group in the protein with the Schiff base end of the chromophore, *cis–trans* isomerization being excluded by the comparison with the 13-*cis*,15-*syn*-bR_{548} tensor.

5.5 Linear and Bent Nitrosyls in Metal Complexes

The nitrogen shielding tensor is a useful criterion for the bending of the nitrosyl ligand, and many of the nitrosyls studied are unstable in solution. In five-coordinate $\{MNO\}^8$ complexes (i.e., with eight (d + n) electrons), the metal may have a trigonal pyramidal coordination sphere (d^8) with the nitrosyl linear (NO^+), or else a square-pyramidal coordination sphere (d^6) with bent apical nitrosyl (NO^-), and similarly for the diazenido ligand ($N{=}NR^+$ and $N{=}NR^-$). The first measurement of a nitrogen tensor in a metal complex was of $[RuCl(^{15}NO)_2(PPh_3)_2][BF_4]$,[23] which has one linear and one bent nitrosyl in the solid state and shows fast bent–linear fluxionality in solution.[24]

Table 8 lists the nitrogen tensor components for linear nitrosyl ligands, which may be compared with those of N*N*O and the bent nitrosyl in $[RuCl(^{15}NO)_2(PPh_3)_2]^+$ in Table 9. In the linear ligand, as in $[Fe(CO)_3(^{15}NO)]^-$,[181] the $\sigma_\parallel$ values are significantly more negative than is expected for the free ligand NO^+. This reflects greater back-bonding to the nitrosyl compared with the carbonyl ligand, which is a useful model with many ^{13}C tensors having been measured.[138] The perpendicular components in the nitrosyls are somewhat more negative than in N*N*O, and more negative in a bis-nitrosyl than in a mononitrosyl, for the same metal. Bis-nitrosyls are usually *cis* and the neighboring nitrosyls interact, to bend slightly. $[Fe(NO)_2$ (cystine)] is an example of a compound for which the nitrogen shielding tensor has given the structure: the solid is amorphous and insoluble, but the nitrogen tensors clearly show the nitrosyls to be linear and probably *cis*.[182]

The ruthenium complex with one bent and one linear nitrosyl shows that bending of the nitrosyl makes a large paramagnetic contribution to σ_{11} and a significant contribution also to σ_{33}. These effects can be seen to some degree in the bis-nitrosyls in Table 8, the adjacent linear ligands interacting to produce a small degree of bending.

Table 9 gives the tensor properties of bent nitrosyl ligands, and Figure 5 shows the structures of the complexes.[182–184] In some complexes the planarity of the basal ligand is maintained by chemical bonding or strong hydrogen bonding. In the

Table 8 Principal Components of ^{15}N Shielding Tensors in the Linear Nitrosyl Ligand[a]

Complex	δ_{iso}	σ_{iso}	$\sigma_{\perp}$	$\sigma_{\parallel}$	Ω	References
$[Fe(CO)_3(^{15}NO)]^-$	18	−154	−295	127	422	Laska and Root[181]
$[RuCl(^{15}NO)_2(PPh_3)_2][BF_4]$	26	−162	−309	133	442	Mason et al.[23]
$[Ru(^{15}NO)_2(PPh_3)_2]$	37	−173	−284	48	332	Mason et al.[23]
	40	−176	−281	35	316	
$[Fe(^{15}NO)_2$(cystine)]	40	−176	−337	145	482	Barrie et al.[182]

[a]All have $\kappa = -1$.

Table 9 Principal Components of ^{15}N Shielding Tensors in Bent Nitrosyl Ligands

Complex	<MNO (°)	δ_{iso}	σ_{iso}	σ_{11}	σ_{22}	σ_{33}	Ω	κ	$\delta_{soln.}$	Reference
$[RuCl(^{15}NO)_2(PPh_3)_2]^+$	136.0	303	−439	−994	−229	−94	900	0.700	flux.	Mason et al.[23]
$[CoCl_2(^{15}NO)(PPh_3)_2]$		531	−667	−1149	−550	−301	848	0.414	flux.	Barrie et al.[182]
$[Co(^{15}NO)(LL')_2]$:										
$LL' = (S_2CNMe_2)_2$	135.1	499	−535	−877	−672	−357	520	−0.790	501	Barrie et al.[182]
= (salen)	127	698	−835	−2050	−302	−151	1884	−0.85	725.4	Barrie et al.[182]
= (naphthen)		709	−875	−1819	−478	−226	1593	−0.898	n.o.	Barrie et al.[182]
= (benacen)	123	721	−857	−1536	−707	−327	1209	0.372	723.0	Barrie et al.[182]
= (amben)		721	−857	−1681	−576	−315	1366	0.617	734.3	Barrie et al.[182]
= (acacen)	122	723	−859	−1402	−850	−326	1076	0.025	714.3	Barrie et al.[182]
$= (phsal)_2$		720	−856	−1348	−740	−480	868	0.401	n.o.	Groombridge et al.[183]
$= (bzsal)_2$		722	−858	−2058	−427	−89	1969	0.657	530.2	Groombridge et al.[183]
$= (bsal)_2$		728	−864	−1398	−805	−390	1008	0.176	740.5	Groombridge et al.[183]
$= (msal)_2$		735	−871	−1273	−826	−510	763	0.177	n.o.	Groombridge et al.[183]
$= (esal)_2$	129	742	−878	−2095	−376	−162	1933	0.779	739.7	Groombridge et al.[183]
$= (ketox)_2$	126.3	781	−917	−1260	−1007	−484	776	−0.348	740.3	Groombridge et al.[183]
= (TPP) at 298 K	127	765	−901	−1062	−820	−820	242	1.0	770.7	Groombridge et al.[184]
at 220 K		758	−893	−1072	−804	−804	268	1.0		
at 200 K		757	−893	−1853	−626	−198	1655	0.484		
cf. $[Ru_3(CO)_{10}(\mu$-$^{15}NO)]^{-a}$		424	−560	−1160	−408	−112	1048	0.435	434	Laska and Root[181]

[a]Bridging NO.

others, the nitrogen tensor components are a useful proof of structure since all have the pyramidal structure, but not all the bis-chelate compounds are constrained to coplanarity. An example is the $[Co(NO)(rsal)_2]$ series, of which the parent complexes $[Co(rsal)_2]$ have tetrahedral coordination. For $[CoCl_2(^{15}NO)(PPh_3)_2]$, which is fluxional in solution, the tensor properties show the nitrosyl to be bent in the solid.

All three tensor components for bent nitrosyls show significant deshielding compared with those in linear nitrosyls. The σ_{11} values are strongly negative and very variable. The bridging nitrosyl in $[Ru_3(CO)_{16}(\mu_2$-NO)]$^-$ shows a relatively high σ_{11} shielding as the nitrogen is now three-coordinate, Ru_2NO; the σ_{33} shielding is unexpectedly high.

The apical nitrosyls show a remarkable variation in the span and skew, while the isotropic shift δ is maintained at 680−780 ppm, except for higher shielding with S_4 ligation of cobalt. All components reflect significant mixing of the nitrogen and the cobalt paramagnetic circulations (more precisely, the out-of-plane components of the ligand field circulations deshielding cobalt), as observed in solution studies showing some correlation of ^{15}N and ^{59}Co shifts.[129]

Because of the large effects of relatively small changes in small excitation energies, sensitivity may be expected to the internal MNO geometry and to the conformation of the nitrosyl relative to the ligators in the basal plane. The ligand field is also sensitive to the location of cobalt (usually above the plane), to the ligation, and to the bite of the chelate ligands. The nitrosyl oxygen may lie over a gap between two chelate ligands as in $[Co(NO)(ketox)_2]$ and $[Co(NO)(esal)_2]$, or over an electron acceptor such as a phosphine. It lies over the ethylene bridge in [Co(NO)(7-mesalen)] and [Co(NO)(salen)], over a linear nitrosyl in $[RuCl(^{15}NO)_2(PPh_3)_2]^+$, over sulfur in $[Co(NO)(S_2CNMe_2)_2]$, over oxygen in [Co(NO)(acacen)], and over nitrogen in [Co(NO)(benacen)].

The remarkable variation of the tensor components in Table 9 may involve the effects of the conformation of the nitrosyl relative to the ligand field of the coligands in the plane, and the small barrier to rotation of the nitrosyl which is disordered in many of the crystal structures. Torsional variation could account for compensatory effects in the tensor components, with σ_{22} and σ_{33} decreasing as σ_{11} increases, decreasing the span while maintaining the isotropic shift.

A low torsional barrier and the sensitivity of the projecting nitrosyl to intermolecular forces are shown by the unusual nitrogen tensors observed for $[Co(^{15}NO)(TPP)]$ at ambient temperatures, which demonstrate swinging or spinning of the nitrosyl in the solid state.[184] The isotropic shift is that of a bent nitrosyl, but from room temperature down to 220 K the tensor shows axial symmetry ($\kappa = 1$) and a small span, 242 ppm. The full span of 1655 ppm and nonaxial symmetry appeared when

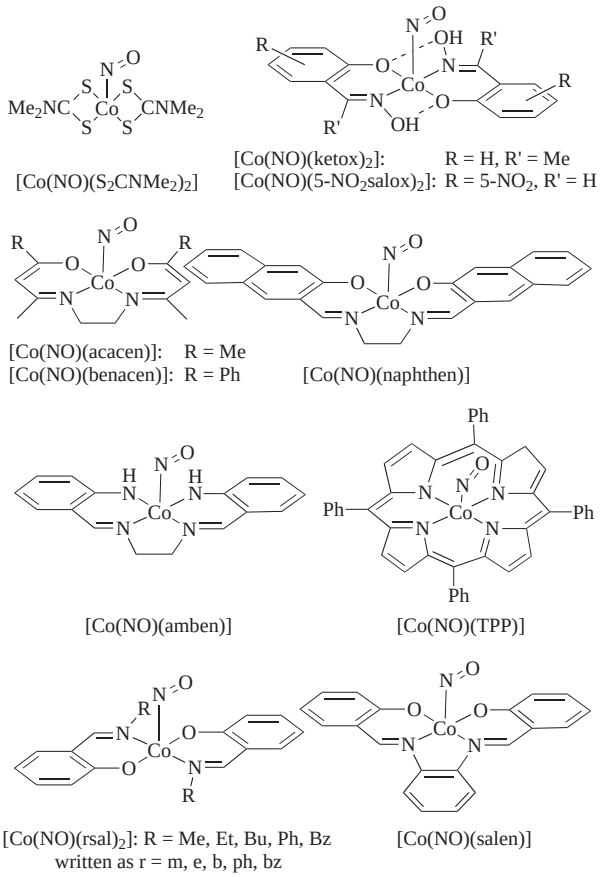

Figure 5 Structures of complexes with a bent apical nitrosyl ligand

the sample was cooled to 200 K, with little change in isotropic shift.

No intermediate rate behavior was observed and differential scanning calorimetry showed a phase transition in the solid at 206.7 K with ΔH = 649 J mol^{-1}. The lattice presumably relaxes at this temperature, allowing the nitrosyl to revolve about the C_4 axis at higher temperatures. A CoNO angle of 127° calculated from the tensor measurements agrees with the value of ≤128.5° estimated from the X-ray diffraction study at ambient temperatures.[185] This showed a fourfold disorder of the nitrosyl depicted in a many-headed 'hydra' diagram, the oxygen lying in the gap between two porphin nitrogens. This picture, therefore, is that of a swinging nitrosyl.

5.6 Theoretical Calculations of Nitrogen Shielding Tensors

Several ab initio methods are now being used with some success for the calculation of shielding tensors,[149] including the local-origin methods IGLO[186] and LORG.[187] Agreement with experiment is good for singly bonded molecules with high electronic excitation energies. It is less good when excitation energies are low, and for species with multiple bonds and lone pairs on the nucleus in question. This presents hazards in nitrogen studies, particularly in groups containing oxygen.

IGLO calculations[188] of nitrogen shieldings for a range of compounds have been analyzed in terms of the contributions from bonding electrons and lone pairs. The calculations show very small deshielding in NH_3, and greater deshielding on substitution of H by Me, then NH_2, OH, or F, with strong effects on the lone-pair contribution. The Cl and Ph groups behave as weakly electronegative substituents. Strong deshielding is found when the nitrogen is doubly bonded, with some exaggeration of the paramagnetic effect in the calculation. In aromatic azines, the calculations reflect the deshielding observed from pyrrole (with no n → π^* state) to pyridine and to pyridazine (with two adjacent nitrogens).

In molecules with low excitation energies the inclusion of electron correlation to second order, as in the SOLO (second-order LORG) method,[189] produces considerable improvement, as in a study of nitrite and nitrate ions.[178] There is further improvement with the inclusion of six surrounding cations for nitrite ion. The decrease in shielding with lengthening of the NO bonds, or, for nitrite, with an increase in the bond angle, shows that vibrational corrections are also significant.

6 PATTERNS OF NITROGEN SPIN–SPIN COUPLINGS

Figures 6–8 give ranges of one-bond J couplings between ^{15}N, ^{1}H, and ^{13}C in functional groups. Couplings to nitrogen are more commonly measured in ^{15}N than in ^{14}N resonance because of ^{14}N line broadening by quadrupolar relaxation. A large number of ^{14}N couplings have been measured, however, under favorable conditions of high local electronic symmetry and short correlation times (Section 3.2). All four ^{14}N couplings could be measured with accuracy in the linear cation RC≡NXeF$^+$.[114] More measurements of ^{14}N and other quadrupolar nuclei, such as the two ^{14}N^{17}O couplings measured in N_2O, are expected with the growing use of supercritical fluids.[105]

Values of $J(^{14}\text{N,X})$ are 30% smaller than $J(^{15}\text{N,X})$ values and opposite in sign, following the respective values of the magnetogyric ratios γ for ^{14}N and ^{15}N, as shown in equation (13):

$$-{}^{n}J(^{15}\text{N,X}) = 1.403\,{}^{n}J(^{14}\text{N,X}) = {}^{n}K(\text{N,X}) \times h\gamma_{\text{N}}\gamma_{\text{X}}/4\pi^2 \qquad (13)$$

Here K is the reduced coupling constant, which is independent of the nucleus, and n is the number of bonds through which the nuclei are coupled. The quantity J is in Hz and K is in N A^{-2} m^{-3}. Couplings to nitrogen are relatively small since the γ values are rather small. Couplings producing a 1:1 doublet in ^{15}N resonance produce a 1:1:1 triplet in ^{14}N resonance because of the three combinations of orientations for a nucleus with I = 1.

Figure 6 shows that ^{1}J(N,H) values are negative, becoming more negative with increasing s character in the N–H bonding orbital, from sp^3 hybridization of the nitrogen as in NH_4^+ or amines, to sp^2 as in the pyridinium ion pyH$^+$, and to sp as in the nitrilium ion RC≡NH$^+$. Linear equations have been given which relate the coupling to the percentage s character in the nitrogen orbital.[197–199] These equations, and a corresponding equation relating ^{1}K(C,N) to the product of the percentage s character in the nitrogen and carbon orbitals,[197] fail when there are lone pairs with s character on one or both of the coupled nuclei, and may fail in the presence of multiple bonding.

Values of ^{1}J(N,H) are reduced significantly in absolute magnitude by the presence of (s-type) lone pair electron density on nitrogen. The smallest couplings involve bent nitrogen in ketimines $R_2C{=}NH$ or diazenides M–N=NH,

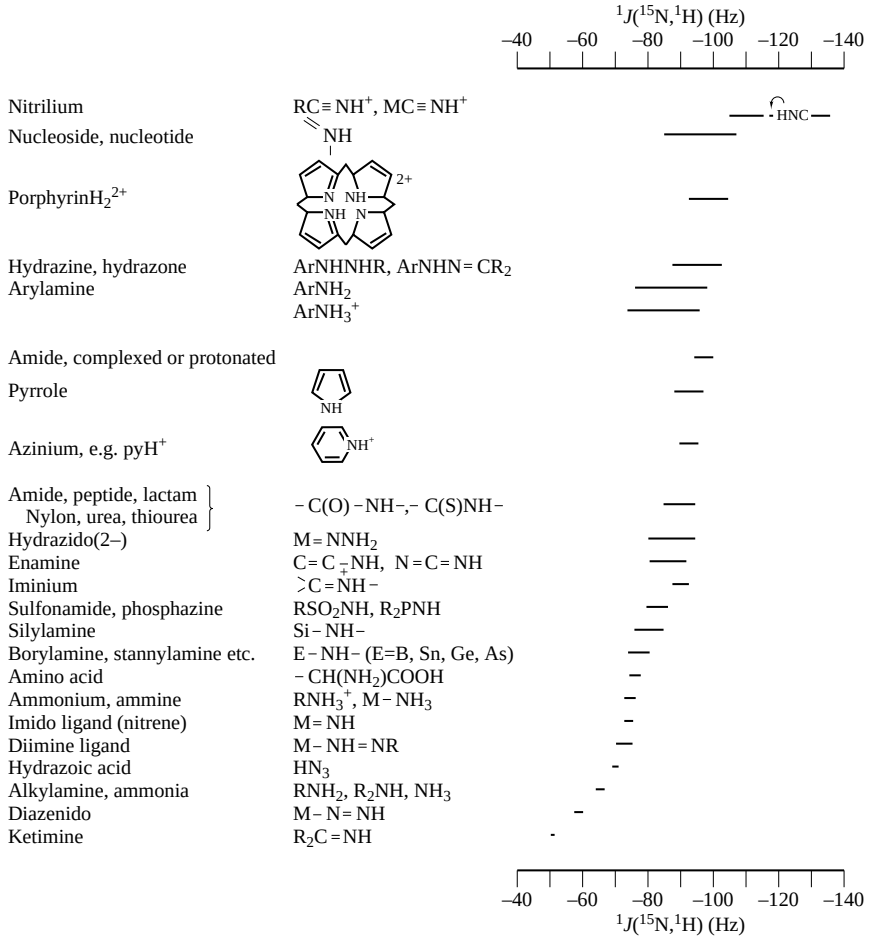

Figure 6 Ranges of $^1J(^{15}N,^1H)$ values

and those for amines or ammonia are small. Similarly, ^1J(N,H) values increase significantly in magnitude with the loss of lone pair electron density on nitrogen by coordination, delocalization (as in aniline), or protonation. They also increase with hydrogen bonding of the nitrogen, and may be solvent dependent. NH couplings may be lost through chemical exchange, and rigorous purification may be needed in order to observe them.

Couplings are increased in magnitude regardless of sign by the presence of more electronegative substituents on a coupled nucleus. Values of ^1J(N,H) are quite large in the –C(O)NH– link, present in peptides, amides, lactams, ureas, and Nylons. The values are larger if the proton is *trans* to oxygen but decrease with a departure from planarity at the nitrogen, with the development of a lone pair.

Signs reported for $^1J(^{15}N,^{13}C)$ are also normally negative, with some exceptional small positive values which change sign and increase in absolute magnitude on protonation. In pyridine $^1J(^{15}N,^{13}C)$ is +0.6 Hz, changing to −11.7 Hz on protonation and to −15.2 Hz in pyridine *N*-oxide.[200] Figure 7 shows that $^1J(^{15}N,^{13}C)$ values become more negative from azomethines $R_2{}^{13}C{=}{}^{15}NR$, with a lone pair on the nitrogen, to amines, and to ynamines $RC{\equiv}{}^{13}C{-}{}^{15}NR'_2$, in which there is no lone pair on the nitrogen. Such changes may thus be stereochemically diagnostic. In oximes $R_2C{=}NOH$, in which the nitrogen is pyramidal, the *Z* form is flatter than the *E* form thus reducing *cis* repulsions and, as expected, $^1J(^{15}N,C)$ is more negative for the *Z* than for the *E* form. Values of $^1J(^{15}N,C)$ are quite large in magnitude for pyrroles, in which the nitrogen 'lone pair' is of the p type.

Signs reported for $^1J(^{15}N,^{15}N)$ couplings are negative, but many are still unknown so the values in Figure 8 have been plotted regardless of sign. Values of $^1J(^{15}N,^{15}N)$ are generally small in magnitude when terminal nitrogen is involved, as in diazo compounds R_2N_2, N_2O, or dinitrogen ligands. Similarly in azides $RN_\alpha N_\beta N_\gamma$, which are bent at N_α, $^1J(^{15}N,^{15}N)$ couplings are much smaller for $N_\beta N_\gamma$ than for $N_\alpha N_\beta$. The couplings are very small, around 1 Hz, in arene-diazonium compounds $ArNN^+$. Many of these values are the result of complex effects of lone pairs and multiple bonds. Somewhat larger values are observed when the nitrogen is bonded to oxygen.[201]

Geminal couplings $^2J(^{15}N,H)$ and $^2J(^{15}N,C)$ are usually negative and relatively small. They become more negative if the nitrogen carries a *cis* or proximate lone pair, the more so if this lies in the NXH or NXC plane. Thus $^2J(^{15}N,H)$ is −3 Hz in pyH^+ but −11 Hz in pyridine. Such values are diagnostic of the geometry, and of protonation or coordination of the nitrogen. Couplings of the type $^2J(^{15}N,^{15}N)$, as observed in nucleotides for example, show similar lone-pair effects. Values of $^3J(^{15}N,H)$ also are increased in magnitude by a *cis* or proximate lone pair on the nitrogen as in oximes, and the magnitude increases with protonation of the nitrogen as

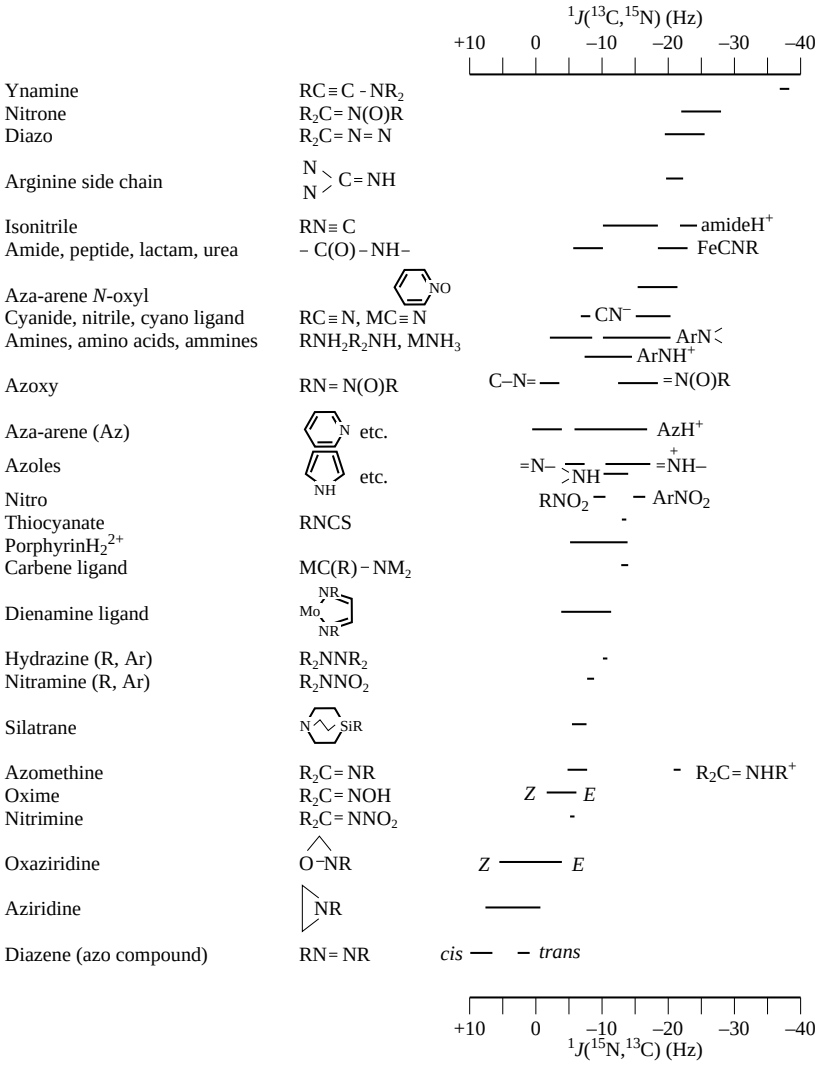

Figure 7 Ranges of $^1J(^{13}C,^{15}N)$ values

in pyridine. Values of $^3J(^{15}N,C,C,H)$ often show a Karplus-type dependence on the dihedral angles, and are of use in conformational studies of peptides in which the ^3J values may be larger than ^2J values of similar type.[202]

6.1 Contact, Orbital, and Spin–Dipolar Contributions to the Coupling[190,194,203–206]

Nitrogen couplings are sensitive to the s,p character of the bonding and to the presence and orientation of a lone pair with s character on the nitrogen, because the Fermi contact interaction of s electrons with the nucleus is usually the most important contribution to the coupling. The coupling patterns are usefully interpreted by means of the Dirac vector model[207] of the contact interaction (even though this model is incomplete, and sometimes misleading). Electrons in a bonding pair with antiparallel spins $\alpha\beta$ correlate their motions so that if the α spin is near one nucleus the β spin is near the other. For a nucleus with positive γ, the electron–nuclear configuration is more stable when the spins are antiparallel since $\gamma\epsilon$ is negative. The values of $^1J(X,Y)$, therefore, are normally positive, the difference hJ between the energy states with antiparallel and parallel spins being positive by definition. Corresponding values for $^1J(^{15}N,Y)$ are negative since $\gamma(^{15}N)$ is negative. The coupling increases in absolute magnitude with an increase in s character in the orbitals forming the bond between the coupled nuclei. Similarly, couplings are increased by the presence of more electronegative substituents on a coupled nucleus, since these demand greater p character, leaving more s character in the bond which is the coupling pathway.

Lone pair electron density on either or both of the coupled nuclei alters this picture. Figure 8 shows that if one of the coupled nuclei carries a lone pair, $^1J(N,C)$ diminishes in absolute magnitude by an amount that increases with the s character of the lone pair, e.g. from RNH_2, sp^3, to pyridine, sp^2 (though not to nitriles RCN, sp). As demonstrated in calculations of C–N and N–N couplings, the contribution to the Fermi contact term J^{fc} from the lone pair electrons is opposite in sign to that of the bonding electrons, since the nonbonding MO is antibonding with respect to the coupling pathway. Furthermore, the lone-pair contribution may be quite large, since the energy denominator is small for nonbonding

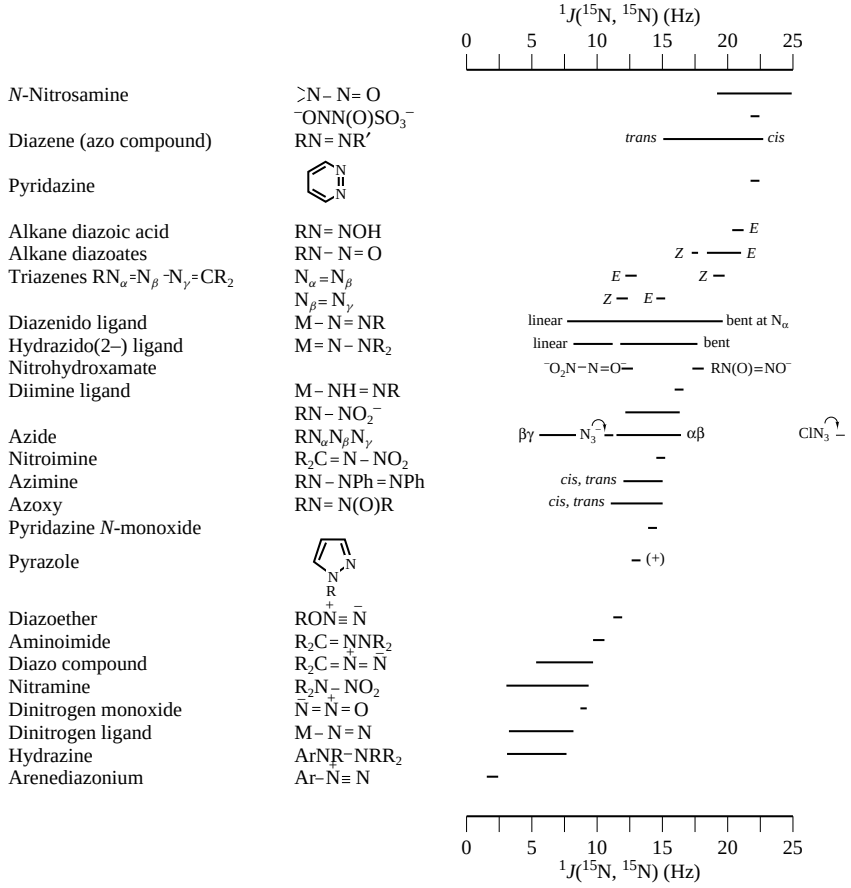

Figure 8 Ranges of $^1J(^{15}N,^{15}N)$ values

electrons. The most important energy term is that of the lowest singlet–triplet excitation, unpairing the electrons.

The changes in sign of $^1J(^{15}N,C)$ in Figure 8 can be understood in these terms. Thus, $^1J(^{15}N,C)$, which is commonly negative, becomes less negative and may become positive when the nitrogen carries a lone pair as in pyridine or *cis*-diazenes R–N=N–R. The value of $^1J(^{15}N,C)$ becomes negative again if the nitrogen is protonated.

Values of $J(^{15}N,^{15}N)$ may vary in a complex fashion if there is a lone pair on each of the nuclei. The coupling constant is very sensitive to the dihedral angle ϕ between the lone-pair orbitals, since they interact to give bonding and antibonding (HOMO) combinations. Calculations on hydrazine, N_2H_4, in which ϕ is near 90° show that $^1J(^{15}N,^{15}N)$ is negative and quite large for an N_2H_4 molecule with $\phi \approx 0°$, falling to zero for the geometry with ϕ = 115° and increasing to a large positive value for $\phi \approx 180°$.[207] Similarly, for planar systems such as diazenes as in azo compounds (RN=NR) or diazenido complexes (M–N=NR), $^1J(N,N)$ values are large and negative for *cis* compounds with $\phi \sim 0°$, but large and positive for *trans* compounds, with $\phi \approx 180°$. In longer range couplings, 'through-space' orbital overlap provides an additional route for the transmission of coupling information.

The contributions to the spin–spin coupling that are mediated by p,d,.. electrons are normally smaller than the contact contribution J^{fc}, and are very small for hydrogen, but may be sizeable if π bonding is present. The orbital term J^{o}(A,B) arising from the magnetic effect on nucleus B of the orbital motion of an electron on nucleus A, and the spin–dipolar term J^{sd}(A,B) arising from direct interaction of the spin of an electron on nucleus A with the spin (magnetic dipole) of nucleus B, increase in magnitude with the bond order. In the dinitrogen molecule N≡N with $^1J(^{15}N,^{15}N)$ = 2.5 Hz,[45] a theoretical study[208] found that the contact term made the smallest contribution, 0.82 Hz, compared with a dipolar contribution of −1.57 Hz and an orbital contribution of 3.35 Hz. Orbital and spin–dipolar contributions are large in the triply bonded molecules HCN, nitriles, and isonitriles.

The noncontact contributions, also, increase in magnitude when there are electronegative substituents on the coupled nuclei, because of a dependence on the radial term $\langle r^{-3}\rangle_{2p}$. Contact and noncontact contributions are all large in the benzonitrile *N*-oxide 2,4,6-$C_6Me_3H_2CNO$, giving an unusual overall value $^1J(^{15}N,^{13}C)$ = (−)77 Hz.[204]

6.2 Couplings to Other Nuclei

Nitrogen couplings to other nuclei are normally dominated by the contact interaction. They are sensitive to s character in the relevant bonding orbitals and to the presence of lone-pair electrons. Discussion of the signs is most usefully in terms of the reduced coupling constant K since $\gamma(^{15}N)$ is negative: thus, nitrogen couplings to fluorine are commonly measured in ^{14}N resonance as they are relatively large and the fluoro systems usually have low viscosity.

The periodic trends can be rationalized in terms of stabilization of bonding σ MOs and destabilization of nonbonding (lone pair) MOs with an increase in atomic number down the group or across the row of the Periodic Table. Amine–borane or aminoborane couplings ^1K are positive (and relatively small). Values of ^1K(C,N) and ^1K(Si,N) are normally positive, but ^1K(Sn,N) values may be of either sign and ^1K(Pb,N) values are negative. Couplings to transition metals are normally positive.

Couplings of the type ^1K(P,N) involving P(III) are negative as for ^1K(N,N), while couplings to P(V) may be of either sign. Couplings of the type ^2K(P,N) are usually small, but may be quite large for *trans* interactions in metal complexes.

Values of $^1K(^{19}F,N)$ are expected to be negative because of the lone-pair contribution. The largest value is $^1J(^{19}F,^{14}N)$ = 339 Hz in $FN{\equiv}NF^+$, corresponding to the maximal $^1J(^{15}N,H)$ = 135 Hz in the nitrilium ion $HC{\equiv}CNH^+$. The value of $^1J(^{19}F,^{14}N)$ is 231 Hz in $NF_4{}^+$ compared with 158 Hz in NF_3, another lone-pair effect.[28]

Ligating nitrogen is relatively low in the empirical series of *trans* influence, though above halides or alkoxy ligands. The *trans* influence measures the tendency of a ligand by forming a strong bond to the metal to weaken the *trans* bond in a metal complex, so reducing the magnitude of coupling constants involving the *trans* bond.

6.3 Couplings as Criteria of Structure

Nitrogen couplings may be diagnostic of *cis–trans* or *syn–anti* stereochemistry, conformation, hydrogen bonding, and related medium effects. The couplings are enhanced by protonation, alkylation, or coordination of the nitrogen, and so may be diagnostic of chelation or proton migration. The largest magnitudes of couplings are observed in linear systems. In ligands which may be bent or linear in their attachment to a metal, such as nitroso (–N=O), diazenido (–N=N–R), or hydrazido(2–) (=N–NR_2) ligands, M–N_α coupling constants are reduced on bending; the protonation of the bent α-nitrogen in $[PtCl(N{=}NPh)(PEt_3)_2]$ increases the $^1J(^{195}Pt,^{15}N)$ value from 157 to 510 Hz.[125] Couplings are also enhanced by flattening of a pyramidal group, delocalizing the s-type lone-pair electron density. Thus ^1J(N,H) values in the hydrazido(2–) ligand –N–NH_2 resemble those in amides rather than hydrazines, since the hydrazido(2–) ligand is flat.

Such relationships allow coupling constants to be estimated as required to optimize the experimental parameters. Equations relating ^1J values to percentage s character in the bond[197–199] can be used in this way if exceptional bond types are avoided.

7 SOLID STATE STUDIES[6,7,13,14]

The fast growth of nitrogen NMR studies in the solid state is documented in the annual reports of work on solid state techniques, macromolecules, natural and synthetic, and shielding tensors (Section 5).[7] Solid state NMR spectroscopy is increasingly being used in materials technology and for biological materials. Because of the volume of this work, reference can only be selective and directed towards new techniques or reviews.[209,210]

Molecular biology has seen a great increase in nitrogen NMR.[168,211,212] Peptide and protein backbones, planes, and side-chains can be studied with improved methods of orienting samples mechanically or magnetically. Ordered systems such as nucleoproteins or membrane–protein complexes[213] which are insufficiently soluble or mobile for solution studies, or insufficiently ordered for X-ray diffraction techniques, are becoming accessible to NMR study. Solid state NMR can provide spatial information which is lost by tumbling motions in solution, and can also monitor motions which are frozen or blurred in X-ray crystallographic studies.

For many systems, a combination of physical methods is needed; NMR to probe short-range interactions and X-ray crystallography methods showing long-range order.[214] Solid state NMR provides a useful link between X-ray crystallographic analysis and NMR solution studies, particularly as conformations may vary from solid to more fluid phases. Nitrogen spectra of biological material may be easier to interpret than carbon or proton spectra because of the relatively small number of nitrogens, characteristic shifts, and sizeable shielding range.

Nitrogen-14 properties measured in the solid state include electric field gradient (efg) tensors, quadrupole couplings, dipolar couplings, and spin diffusion[215] in studies of molecular structure and reorientation. Orientations of the ^{14}N efg tensors and carbonyl ^{13}C shielding tensors provide structural information in amino acids and peptides.[216] N–H bond lengths have been determined with high accuracy from dipolar interactions of ^{14}N or ^{15}N with ^1H.[217] Static ^{14}N powder spectra were used to study electric field gradients and reorientation in NH_4NCS.[218] Information on ^{14}N dipolar and quadrupolar couplings is also obtained by lineshape analysis of resonances of a bonded neighbor, whether ^{13}C,[219] ^{29}Si in nitrogen-containing ceramics,[220] ^{195}Pt in $K_2[Pt(CN)_4 \cdot 3H_2O]$,[221] etc.

Advantage can be taken of the high natural abundance of ^{14}N by using the ^{14}N nuclear quadrupole interaction to spread nitrogen spectra over a large range, more than compensating for quadrupolar line broadening. This method was used in ^{14}N and ^{13}C measurements of the CCN geometry and ^{14}N quadrupole coupling tensor in glycine single crystals.[57] The quadrupole interaction shifts the middle of the three ^{14}N energy levels (I = 1) relative to the other two, and produces a doublet splitting which is determined by the angular dependence of the first order quadrupole interaction. The second order quadrupole interaction, arising from the closeness of the Larmor and the quadrupole coupling frequencies, shifts the doublet somewhat and makes the overtone transition partially allowed. Information is thus available from the combination of the ^{14}N quadrupole splittings, second order ^{14}N quadrupole shifts, ^{14}N overtone frequencies, $^{14}N–^1H$ and $^{14}N–^{13}C$ dipolar splittings, and ^{13}C shielding tensor for determining orientations in a peptide plane in oriented samples. Cross polarization is very effective for ^{14}N spectra in amino acids, peptides, and proteins, because of strong NH coupling in the amido/peptide group. Peptide backbone conformations have been studied in this way by two-dimensional $^1H/^{14}N$ spectra and crystalline amino acids by $^{13}C/^{14}N$ spectra, with use also of $^1H/^{13}C/^{14}N$ triple resonance.[58,222]

Most nitrogen work in the solid state is done in ^{15}N resonance, using the techniques developed for ^{13}C of static powder patterns or CP MAS methods with high-power

proton dipolar decoupling. The principal components of the shielding tensors (Section 5) are obtained from powder pattern lineshapes, or from the intensities of spinning side-bands at slower spinning rates. The orientation of the principal axis system in the molecular frame is found by the use of oriented specimens or by the observation of dipolar interactions.[145,147]

Some solid state work has been done in natural abundance of ^{15}N, for example polymer studies of the α-helix and β-sheet components of homopolypeptides[223] and Nylons,[224] and of polyimines and the conducting polymers which they yield on oxidation.[225] Adsorption studies may be possible in natural abundance of ^{15}N, the occlusion of NPr_4^+ cations in zeolites[226] for example. Enrichment is usually necessary, however, and bioenrichment is particularly useful.

In a historic determination in 1972, the principal elements were reported for the nitrogen shielding tensor in the nitrate ion in ammonium nitrate, distorted by hydrogen bonding.[227] Recently, the principal values of the nitrate shielding tensors in five solid phases of NH_4NO_3, the phase transitions, crystal packing deformations, motional averaging at higher temperatures, and magnetic nonequivalence at low temperatures, have been examined by MAS and static NMR.[228] Section 5 discusses shielding tensors reported for nitrogen in ammonia and ammines, linear groups (iminophosphenium $RN{\equiv}P^+$, nitrile, isonitrile, N_2O, thiocyanate, N_2, the dinitrogen ligand, $P{\equiv}N$, linear NO), planar groups (amide, peptide, heterocycle, aldimine, ketimine, oxime, nitroso dimer, nitrobenzene, nitrates, nitrite ion, nitroso compounds, azo or diazene, nitrogen oxides), and metal nitrosyls, linear and bent.

The nitrogen tensor has been used as a criterion of bending of the nitrosyl ligand (Section 5),[183] and to investigate nitrosyl swinging in solid [Co(NO)TPP)],[184] and the bent–linear fluxionality of the five-coordinate complex $[RuCl(NO)_2(PPh_3)_2]BF_4$ in solution.[24]

Catalytic processes are usefully investigated by ^{15}N CP MAS NMR. Acid sites of the Brønsted or of Lewis type may be distinguished by nitrogen compounds of differing basicity, as in studies of γ-alumina and mordenites by the sorption of pyridine or ammonia,[229,230] and of zeolites by the sorption of ammonia[231] or trimethylamine,[232] cf. the interaction of pyridine with coals.[233] Some adsorption work can be done by conventional NMR techniques, as in the study of acetonitrile on zeolites.[234]

Double cross polarization in doubly labeled $^{13}C-^{15}N$ bonds, usually from ^1H to ^{13}C to ^{15}N, was developed to follow the progress of these bonds in vivo, in peptide and other linkages, an early application being to protein turnover in soybean leaves.[235]

The transferred echo double resonance (TEDOR) technique has been used to select a ^{13}C label by its dipolar coupling to ^{15}N, giving internuclear distances and geometries, in conjunction with the rotational echo double resonance (REDOR) technique measuring a dipolar coupling of the ^{13}C.[236]

Biological NMR studies using solid state techniques are discussed further in Section 9.

8 DYNAMICS[2–7,237,238]

Dynamic processes with a range of timescales have been monitored by nitrogen NMR. Fast motions such as the switching of the ammonium ion in the $^{14}NH_4Cl$ lattice are monitored by relaxation times (Section 3.1). Measurements of T_1 and NOE of the dipolar relaxation of ^{15}N by neighboring protons have been used to probe a variety of molecular motions, from segmental motions of large molecules to migrations of protons between nitrogens (Section 2). HH migrations between the nearby nitrogens, as in porphin or phthalocyanine molecules, were mentioned in Section 2.1, and a range of comparable systems has now been studied,[239] most recently, double, triple, and quadruple proton transfers in pyrazoles.[240]

Hindered motions about N–X bonds are studied by lineshape analysis, 2D spectroscopy, multicoalescence experiments, saturation transfer, or equilibration methods, or by methods involving longitudinal or transverse relaxation times. A large number of isomerization processes involving N–X bonds have been reviewed as to methods of investigation, dynamics, thermodynamics, and theoretical interpretation in terms of quantum mechanical treatments or empirical correlations.[241]

Examples of dynamic studies are fewer in inorganic chemistry. $^{14,15}N$ NMR spectroscopy has demonstrated kicking motions, as in the bent–linear fluxionality of the imido ligand M=NH in concert with a second imido or an alkoxy ligand in solution.[139] A corresponding fluxionality of nitrosyls in solution was observed for the five-coordinate complex $[RuCl(^{15}NO)_2(PPh_3)_2]^+$,[24] the averaged shift, the temperature dependence, and the equilibrium isotope effect with semienrichment suggesting that the trigonal bipyramidal form with two linear nitrosyls is present in dynamic equilibrium with the square-pyramidal form with one bent and one linear nitrosyl.[24] Swinging and spinning of the bent apical nitrosyl in solid $[Co(^{15}NO)(TPP)]$ was detected through changes in the nitrogen shielding tensor[184] (Section 5.5).

CIDNP enhancing absorption or emission in the NMR experiment, has been used in ^{15}N resonance to study a number of reactions in which radical pairs may be involved. The method is highly sensitive and species that give large signals may not be major intermediates. The contribution of radical pair mechanisms to the nitration of arenes by nitric and sulfuric acid mixtures is now thought to be small.[242] ^{15}N CIDNP has also been applied to the study of migrations of nitro groups,[243] azo coupling,[244] and the loss of dinitrogen from arene-diazonium salts.[245] Stable nitroxide radicals, also, are accessible to NMR spectroscopic study.[246]

9 BIOMOLECULES[2–7,9,13]

Biological applications of nitrogen NMR have increased in step with the development of NMR technology and have stimulated this development. Many examples of ^{14}N and ^{15}N NMR properties in biological materials have been given above together with the kinds of information now obtainable. Multidimensional correlation spectroscopy increasingly uses nitrogen as well as ^{13}C and ^1H.[6d,7] Other articles describing the use of nitrogen NMR in biomolecular and biological systems are listed at the end of this section.

Unique information can be obtained from nitrogen NMR on in vivo metabolism and cellular dynamics, as well as on protein (polypeptide) backbones, functional groups in enzymes, and DNA and RNA bases. Nitrogen-14 resonance may be used for material in which there is sufficient mobility for motional

averaging[247,248] and with solid state techniques making use of the quadrupolar interaction (Section 7). Bioenrichment of ^{15}N allows this to be used as a biological tracer in the absence of a stable radioisotope of nitrogen (^{13}N, the most stable, has a halflife of only 10 min). Highly selective bioenrichment can be obtained by supplying the organism with a ^{15}N-labeled nutrient, such as an amino acid. For ^{15}N work in the liquid phase, the dependence of the relaxation time T_{1dd} and the NOE on the molecular size has been discussed (Section 2.1).

Techniques and applications to biological systems have been described in a number of reviews[249] dealing with nucleic acids and nucleotides, enzyme systems, and intact cells,[250] amino sugars,[251] intermolecular interactions,[252] solid state peptide studies,[168] and work of pharmacological interest.[253,254] Nitrogen-15 spectra can resolve differences between diastereotopomers, as of 8-benzyl-5,6,7,8-tetrahydroquinoline in solutions of optically active carboxylic acids.[255]

In living cells, molecules that are sufficiently mobile can be studied by solution state techniques and bioenrichment of ^{15}N has been used to advantage. The first in vivo study was of a fungus *Ustilago sphaerogena* grow with ^{15}N-ammonium acetate as a nitrogen source, the resonances of small peptides being observed.[256] The mobilities of components of bacterial cell walls were estimated quite early on from ^{15}N NOE values, the observable resonances being those of mobile cross-linking groups.[257] The biosynthesis of amino acids from ^{15}N-ammonium salts and their intracellular environment was followed in the fungus *Neurospora crassa*[258] and in *Brevibacterium lactofermentum*.[259]

Nitrogen NMR is being used increasingly in metabolic studies using solid state techniques. In DNA from *E. coli* grown with $^{15}NH_4Cl$ as the source of nitrogen, 13 of the 14 nitrogens in the bases were distinguished by their dipolar coupling to protons.[260] This allowed the NH bond lengths to be measured, complementing the information available from X-ray and neutron diffraction.[261] DNA and protein spectra were obtained from the filamentous bacteriophage fd infecting the *E. coli*, and 2D spectra from oriented molecules of the virus.[262]

Solid state techniques have been developed for the study of nitrogen metabolism in growing plants using double cross polarization (DCP MAS) NMR (Section 8). This required double enrichment in vivo with $^{15}NH_4{}^{15}NO_3$ and pulsed $^{13}CO_2$ labeling, to form $^{13}C-^{15}N$ bonds, examined in intact or lyophilized material. Such DCP MAS NMR has been used to follow the metabolism of methionine[263] in soybean cotyledons, and also of allantoin[264] and alanine[265] in *Aerococcus viridans*.

Double labeling can establish biosynthetic pathways, such as cyclization to form the N–C(5) bond in isopenicillin N observed as a $^1J(^{15}N,^{13}C)$ coupling.[266]

With a variety of techniques, therefore, in vivo observation of components of appropriate mobility is now replacing the use of lyophilized (freeze-dried) tissue. Indeed, ^{15}N-labeled glycine has been detected by a probe implanted between the liver lobes, fixed to the abdominal wall, of a live rat.[267]

10 RELATED ARTICLES

Amino Acids, Peptides and Proteins: Chemical Shifts; Bacteriorhodopsin and Rhodopsin; Biosynthesis and Metabolic Pathways: Carbon-13 and Nitrogen-15 NMR; Carbon and Nitrogen Chemical Shifts of Solid State Enzymes; Shielding Calculations: LORG and SOLO Approaches; Chemical Shift Tensor Measurement in Solids; Chemical Shift Tensors; Chemical Shifts in Biochemical Systems; Chemically Induced Dynamic Nuclear Polarization; Coupling Through Space in Organic Chemistry; Dipolar and Indirect Coupling Tensors in Solids; Indirect Coupling: Semiempirical Calculations; Membrane Proteins; Nucleic Acid Structures in Solution: Sequence Dependence; Nucleic Acids: Chemical Shifts; Nucleic Acids: Spectra, Structures, and Dynamics; Organic Chemistry Applications; Overtone Spectroscopy of Quadrupolar Nuclei; Peptides and Polypeptides; Protein Dynamics from NMR Relaxation; Protein Dynamics from Solid State NMR; Protein Structures: Relaxation Matrix Refinement; Quadrupolar Nuclei in Glasses; Quadrupolar Nuclei in Solids; Ruby NMR Laser; Shielding Calculations: IGLO Method; Shielding: Overview of Theoretical Methods; Shielding in Small Molecules; Shielding Tensor Calculations; Shielding Theory: GIAO Method; Sideband Analysis in Magic Angle Spinning NMR of Solids; Solid Biopolymers; Solid Polymers: Shielding and Electronic States; Spin Diffusion in Solids; Structures of Larger Proteins, Protein-Ligand, and Protein-DNA Complexes by Multi-Dimensional Heteronuclear NMR; Synthetic Peptides.

11 REFERENCES

1. W. G. Proctor and F. C. Yu, *Phys. Rev.*, 1950, **77**, 717; W. G. Proctor and F. C. Yu, *Phys. Rev.*, 1951, **81**, 20.
2. G. C. Levy and R. L. Lichter, *^{15}N NMR Spectroscopy*, Wiley-Interscience, New York, 1979, pp. 1–221.
3. G. J. Martin, M. L. Martin, and J.-P. Gouesnard, *NMR Basic Principles Prog.*, 1981, **18**, 341.
4. M. Witanowski and G. A. Webb, *Annu. Rep. NMR Spectrosc.*, 1972, **5**, 395.
5. M. Witanowski and G. A. Webb (eds.), *Nitrogen NMR*, Plenum Press, London, 1973, pp. 1–403.
6. M. Witanowski, L. Stefaniak, and G. A. Webb, *Annu. Rep. NMR Spectrosc.*, 1977, **7**, 117; M. Witanowski, L. Stefaniak, and G. A. Webb, *Annu. Rep. NMR Spectrosc.*, 1981, **11B**, 1; M. Witanowski, L. Stefaniak, and G. A. Webb, *Annu. Rep. NMR Spectrosc.*, 1986, **18**, 1; M. Witanowski, L. Stefaniak, and G. A. Webb, *Annu. Rep. NMR Spectrosc.*, 1993, **25**, 1.
7. *Specialist Periodical Reports on Nuclear Magnetic Resonance*, Royal Society of Chemistry, London, UK, 1972–94, Vols. 1–23, et seq.
8. E. W. Randall and D. G. Gillies, *Prog. NMR Spectrosc.*, 1970, **6**, 119.
9. J. D. Roberts, in *Bloch Festschrift*, Rice University Press, Houston, TX, USA, 1980.
10. J. Mason, *Chem. Rev.*, 1981, **81**, 205.
11. R. L. Lichter, in *The Multinuclear Approach to NMR Spectroscopy*, eds. J. B. Lambert and F. G. Riddell, Reidel, Dordrecht, 1983, Chap. 10, pp. 207–244.
12. J. Mason, *Chem. Br.*, 1983, 654.
13. W. von Philipsborn and R. Müller, *Angew. Chem., Int. Ed. Engl.*, 1986, **25**, 383.
14. J. Mason, in *Multinuclear NMR*, ed. J. Mason, Plenum Press, New York, 1987, Chap. 12, pp. 335–367.
15. M. Witanowski, L. Stefaniak, S. Szymanski, and H. Januszewski, *J. Magn. Reson.*, 1977, **28**, 217 [compares reference standards; also see Witanowski et al.[6]a].

16. S. G. Kukolich, *J. Am. Chem. Soc.*, 1975, **97**, 5704.
17. A. K. Jameson, C. J. Jameson, D. Opposunggu, S. Wille, P. M. Burrell, and J. Mason, *J. Chem. Phys.*, 1981, **74**, 81; C. J. Jameson, A. K. Jameson, S. M. Cohen, H. Parker, D. Opposunggu, P. M. Burrell, and W. Wille, *J. Chem. Phys.*, 1981, **74**, 1608, give a value for (NH_3, liq.) at 223 K.
18. C. I. Ratcliffe, J. A. Ripmeester, and J. S. Tse, *Chem. Phys. Lett.*, 1983, **99**, 177; V. A. Pestunovich, B. Z. Shterenberg, E. T. Lippmaa, M. J. Miagi, M. A. Alla, S. N. Tandura, V. P. Baryshok, L. P. Petukhov, and M. G. Voronkov, *Dokl. Akad. Nauk SSSR*, 1981, **258**, 1410.
19. R. Freeman, *A Handbook of Nuclear Magnetic Resonance*, Longman, Harlow, 1987, pp. 14–16.
20. R. E. Wasylishen and J. O. Friedrich, *J. Chem. Phys.*, 1984, **80**, 585.
21. A. Lycka and P. E. Hansen, *Magn. Reson. Chem.*, 1985, **23**, 973.
22. J. M. Risley and L. van Etten, *Methods Enzymol.*, 1990, **117**, 376.
23. J. Mason, D. M. P. Mingos, J. Schaefer, D. Sherman, and E. O. Stejskal, *J. Chem. Soc., Chem. Commun.*, 1985, 444.
24. J. Mason, D. M. P. Mingos, D. Sherman, and R. W. M. Wardle, *J. Chem. Soc., Chem. Commun.*, 1984, 1223.
25. R. O. Duthaler and J. D. Roberts, *J. Magn. Reson.*, 1979, **34**, 129.
26. M. Alei, A. E. Florin, and W. M. Litchman, *J. Am. Chem. Soc.*, 1970, **92**, 4828, and refs. therein.
27. J. M. Briggs and E. W. Randall, *Mol. Phys.*, 1973, **26**, 699.
28. J. Mason and K. O. Christe, *Inorg. Chem.*, 1983, **22**, 1849.
29. M. Niibe and Y. Nakamura, *J. Phys. Chem.*, 1984, **88**, 5608.
30. D. M. Holton, P. P. Edwards, W. McFarlane, and B. Wood, *J. Am. Chem. Soc.*, 1983, **105**, 2104.
31. J. Kowalewski, *Annu. Rep. NMR Spectrosc.*, 1990, **22**, 307.
32. R. T. Boeré and R. G. Kidd, *Annu. Rep. NMR Spectrosc.*, 1982, **13**, 319.
33. G. C. Levy, J. J. Dechter, and J. Kowalewski, *J. Am. Chem. Soc.*, 1978, **100**, 2308.
34. D. D. Giannini, I. M. Armitage, H. Pearson, D. M. Grant, and J. D. Roberts, *J. Am. Chem. Soc.*, 1975, **97**, 3416.
35. N. Bloembergen, E. M. Purcell, and R. V. Pound, *Phys. Rev.*, 1948, **73**, 679.
36. D. Gust, R. B. Moon, and J. D. Roberts, *Proc. Natl. Acad. Sci. USA*, 1975, **72**, 4696; S. B. Dubin, N. A. Clark, and G. B. Benedek, *J. Chem. Phys.*, 1971, **54**, 5158.
37. A. Lapidot and C. S. Irving, *J. Am. Chem. Soc.*, 1977, **99**, 5488.
38. B. P. Bammel and R. F. Evilia, *Anal. Chem.*, 1982, **54**, 1318.
39. E. Lippmaa, T. Saluvere, and S. Laisaar, *Chem. Phys. Lett.*, 1971, **11**, 120.
40. A. D. H. Clague and J. P. C. M. van Dongen, personal communication.
41. J. B. Lambert and D. A. Netzel, *J. Magn. Reson.*, 1977, **25**, 531.
42. P. Loftus, W. H. Bearden, and J. D. Roberts, *Nouv. J. Chim.*, 1977, **1**, 283.
43. S. Donovan-Mtunzi, G. E. Hawkes, C. J. MacDonald, J. Mason, and R. L. Richards, *J. Chem. Soc., Dalton Trans.*, 1985, 2473.
44. D. Schweitzer and H. W. Spiess, *J. Magn. Reson.*, 1974, **16**, 243.
45. J. O. Friedrich and R. E. Wasylishen, *J. Chem. Phys.*, 1985, **83**, 3707.
46. B. K. Hunter and R. J. C. Brown, *J. Magn. Reson.*, 1982, **46**, 227.
47. J. Hennig and H.-H. Limbach, *J. Am. Chem. Soc.*, 1984, **106**, 292; H.-H. Limbach, J. Hennig, R. Kendrick, and C. S. Yannoni, *J. Am. Chem. Soc.*, 1984, **106**, 4059; H.-H. Limbach, D. Gerritzen, H. Rumpel, B. Wehrle, G. Otting, H. Zimmermann, R. Kendrick, and C. S. Yannoni, in *Photoreaktive Festkörper*, Karlsruhe, 1985.
48. J. H. Noggle and R. E. Schirmer, *The Nuclear Overhauser Effect*, Academic Press, New York, 1971; D. Neuhaus and M. Williamson, *The Nuclear Overhauser Effect in Structural and Conformational Analysis*, VCH Verlag, Berlin, 1989.
49. G. E. Hawkes, W. M. Litchman, and E. W. Randall, *J. Magn. Reson.*, 1975, **19**, 255.
50. C. S. Irving and A. Lapidot, *Biochim. Biophys. Acta*, 1977, **470**, 251.
51. R. Freeman, *A Handbook of Nuclear Magnetic Resonance*, Longman, Harlow, UK, 1987, pp. 157–163.
52. Y. Hiltunen, J. Jokisaari, J. Lounila, and A. Pulkkinen, *J. Am. Chem. Soc.*, 1989, **111**, 3217, and refs. therein.
53. A. Bax, R. H. Griffey, and B. L. Hawkins, *J. Magn. Reson.*, 1983, **55**, 301; L. Mueller, R. A. Schniksnis, and S. J. Opella, *J. Magn. Reson.*, 1986, **66**, 379.
54. S. Roy, M. Z. Papastavros, V. Sanchez, and A. G. Redfield, *Biochemistry*, 1984, **23**, 4395.
55. See, for example, Section 4.1 of Witanowski et al.[6]d
56. L. E. Kay, M. Ikura, G. Zhu, and A. Bax, *J. Magn. Reson.*, 1991, **91**, 422; M. Ikura, L. E. Kay, M. Krinks, and A. Bax, *Biochemistry*, 1991, **30**, 5498.
57. R. A. Haberkorn, R. E. Stark, H. van Willigen, and R. G. Griffin, *J. Am. Chem. Soc.*, 1981, **103**, 2534.
58. K. V. Ramanathan and S. J. Opella, *Trans. Am. Crystallogr. Assoc.*, 1988, **24**, 145; *J. Magn. Reson.*, 1990, **86**, 227, and refs. therein.
59. See, for example, Y. Seo and M. Murakami, *Proc. R. Soc. London, Ser. B*, 1991, **244**, 191.
60. S. H. Koenig, *Biophys. J.*, 1988, **53**, 91; S. H. Koenig, C. F. Beaulieu, R. D. Brown, III, and M. Spiller, *Biophys. J.*, 1990, **57**, 461.
61. J.-M. Lehn and J.-P. Kitzinger, *NMR Basic Principles Progr.*, 1981, **18**, 80.
62. E. A. C. Lucken, *Nuclear Quadrupole Coupling Constants*, Academic Press, London, 1969; J. A. S. Smith, *Chem. Soc. Rev.*, 1986, **15**, 225.
63. H. G. Hertz, *Ber. Bunsenges. Ges.*, 1973, **77**, 531, and refs. therein.
64. K. A. Valiyev, *Sov. Phys. JETP*, 1960, **10**, 77.
65. B. K. Hunter and R. J. C. Brown, *J. Magn. Reson.*, 1982, **46**, 227; D. F. Cooke and K. R. Jeffrey, *J. Magn. Reson.*, 1975, **18**, 455.
66. C. Deverell, *Prog. NMR Spectrosc.*, 1969, **4**, 235.
67. M. Shporer, G. Ron, and G. Navon, *Inorg. Chem.*, 1965, **4**, 358.
68. J.-P. Kintzinger and J.-M. Lehn, *Helv. Chim. Acta*, 1975, **58**, 905.
69. S. Martinengo, G. Ciani, A. Sironi, B. T. Heaton, and J. Mason, *J. Am. Chem. Soc.*, 1979, **101**, 7095.
70. A. Loewenstein, *J. Magn. Reson.*, 1982, **49**, 332.
71. M. Gourdji and L. Guibé, *C.R. Acad. Sci. Paris*, 1965, **260**, 1131; M. Gourdji, L. Guibé, and A. Peneau, *J. Phys.*, 1974, **35**, 497; A. M. de P. Nicholas and R. E. Wasylishen, *J. Phys. Chem.*, 1985, **89**, 5446.
72. A. Loewenstein and M. Brenman, *J. Magn. Reson.*, 1979, **34**, 193.
73. W. B. Moniz and C. F. Poranski, *J. Phys. Chem.*, 1969, **73**, 4145.

74. Y. Yamamoto and J. Uzawa, *Chem. Lett.*, 1978, 1213.
75. W. B. Moniz and H. S. Gutowsky, *J. Chem. Phys.*, 1963, **38**, 1155.
76. W. Suchanski and P. C. Canepa, *J. Magn. Reson.*, 1979, **33**, 389.
77. E. J. Pedersen, R. L. Vold, and R. R. Vold, *Mol. Phys.*, 1980, **41**, 811.
78. R. E. Stark, R. L. Vold, and R. R. Vold, *Chem. Phys.*, 1977, **20**, 337.
79. D. Wallach and W. T. Huntress, *J. Chem. Phys.*, 1969, **50**, 1219.
80. E. Lippmaa, T. Saluvere, and S. Laisaar, *Chem. Phys. Lett.*, 1971, **11**, 120.
81. P. O. Eriksson, A. Khan, and G. Lindblom, *J. Phys. Chem.*, 1982, **86**, 387.
82. U. Henriksson, L. Odberg, J. C. Eriksson, and L. Westman, *J. Phys. Chem.*, 1977, **81**, 76.
83. D. J. Siminovitch and K. R. Jeffrey, *Biochim. Biophys. Acta*, 1981, **645**, 270.
84. D. J. Siminovitch, M. F. Brown, and K. R. Jeffrey, *Biochemistry*, 1984, **23**, 2412.
85. A. Loewenstein and R. Waiman, *Mol. Phys.*, 1973, **25**, 49.
86. A. Maliniak, J. Kowalewski, and I. Panas, *J. Phys. Chem.*, 1984, **88**, 5628.
87. B. Ancian and B. Tiffon, *J. Chem. Soc., Faraday Trans. 2*, 1984, **80**, 1067.
88. R. E. Wasylishen, B. A. Pettit, and R. Y. Dong, *J. Chem. Soc., Faraday Trans. 2*, 1980, **76**, 571.
89. K. F. Chew, W. Derbyshire, N. Logan, A. H. Norbury, and A. I. P. Sinha, *J. Chem. Soc., Chem. Commun.*, 1970, 1708.
90. J.-M. Lehn and J.-P. Kintzinger, *Mol. Phys.*, 1971, **22**, 273.
91. N. M. Szeverenyi, R. R. Vold, and R. L. Vold, *Chem. Phys.*, 1976, **18**, **23**, 31.
92. K. T. Gillen and J. H. Noggle, *J. Chem. Phys.*, 1970, **52**, 4905.
93. B. Tiffon and B. Ancian, *J. Chem. Phys.*, 1982, **76**, 1212.
94. B. Lindman and S. Forsén, *NMR Basic Principles Prog.*, 1976, **12**.
95. R. R. Vold, R. L. Vold, and N. M. Szeverenyi, *J. Chem. Phys.*, 1979, **70**, 5213.
96. H. M. Ratajczak, J. A. Ladd, W. J. Orville-Thomas, and H. Ratajczak, *Mol. Phys.*, 1977, **34**, 1019.
97. O. R. Chambers, M. E. Harman, D. S. Rycroft, D. W. A. Sharp, and J. M. Winfield, *J. Chem. Res. (S)*, 1977, 150; *J. Chem. Res. (M)*, 1977, 1849.
98. D. C. Bradley, S. R. Hodge, J. D. Runnacles, M. Hughes, J. Mason, and R. L. Richards, *J. Chem. Soc., Dalton Trans.*, 1992, 1663.
99. M. Minelli, C. G. Young, and J. H. Enemark, *Inorg. Chem.*, 1985, **24**, 1111.
100. M. Minelli, J. L. Hubbard, K. A. Christensen, and J. H. Enemark, *Inorg. Chem.*, 1983, **22**, 2652.
101. Y. Yamamoto and J. Uzawa, *Chem. Lett.*, 1978, 1213.
102. M. Shporer, G. Ron, A. Loewenstein, and G. Navon, *Inorg. Chem.*, 1965, **4**, 361.
103. H. Hartmann and H. Sillescu, *Theor. Chim. Acta*, 1964, **2**, 371.
104. R. B. Jordan, *J. Magn. Reson.*, 1980, **30**, 287.
105. J. M. Robert and R. F. Evilia, *J. Am. Chem. Soc.*, 1985, **107**, 3733.
106. P. W. Fowler, H. M. Kelly, and R. J. C. Brown, *Chem. Phys. Lett.*, 1993, **216**, 200, and refs. therein.
107. C. J. Jameson and J. Mason, in *Multinuclear NMR*, ed. J. Mason, Plenum Press, New York, 1987, Chap. 3, p. 51.
108. J. Mason, *Adv. Inorg. Chem. Radiochem.*, 1979, **22**, 199; J. Mason, *Adv. Inorg. Chem. Radiochem.*, 1976, **18**, 197.
109. R. G. Barnes and W. V. Smith, *Phys. Rev.*, 1954, **93**, 95; T. A. Carlson, C. C. Lu, T. S. Tucker, W. W. Nestor, and F. B. Malik, *Eigenvalues, Radial Expectation Values, and Potentials for Free Atoms from Z = 2 to 126*, Oak Ridge National Laboratory, TN, USA, 1970.
110. M. B. Robin, *Higher Exited States of Polyatomic Molecules*, Academic Press, New York, Vol. I, 1974; Vol. II, 1975; and Vol. III, 1985.
111. M. Comeau, M. T. Béraldin, E. C. Vauthier, and S. Fliszar, *Can. J. Chem.*, 1985, **63**, 3226.
112. J. Mason, *J. Am. Chem. Soc.*, 1991, **113**, 6056.
113. R. O. Duthaler and J. D. Roberts, *J. Am. Chem. Soc.*, 1978, **100**, 3889; *J. Magn. Reson.*, 1979, **34**, 129.
114. A. A. A. Emara and G. J. Schrobilgen, *J. Chem. Soc., Chem. Commun.*, 1987, 1644.
115. G. J. Schrobilgen, *J. Chem. Soc., Chem. Commun.*, 1988, 863.
116. W. L. Jorgensen and L. Salem, *The Organic Chemist's Book of Orbitals*, Academic Press, New York, 1973.
117. A. Lyčka, *Ann. Rep. NMR Spectrosc.*, 1993, **24**, 247.
118. L.-O. Andersson, J. Mason, and W. van Bronswijk, *J. Chem. Soc. A*, 1970, 296.
119. J. Kroner, W. Schneid, N. Wiberg, B. Wrackmeyer, and G. Ziegleder, *J. Chem. Soc., Faraday Trans. 2*, 1978, **74**, 1909.
120. D. G. Morris and A. M. Murray, *J. Chem. Soc., Perkin Trans. 2*, 1976, 1579.
121. P. B. Dervan, M. E. Squillacote, P. M. Lahti, A. P. Sylwester, and J. D. Roberts, *J. Am. Chem. Soc.*, 1981, **103**, 1120.
122. A. Galindo, A. Hills, D. L. Hughes, M. Hughes, J. Mason, and R. L. Richards, *J. Chem. Soc., Dalton Trans.*, 1990, 283, and refs. therein.
123. B. L. Haymore, M. Hughes, J. Mason, and R. L. Richards, *J. Chem. Soc., Dalton Trans.*, 1988, 2935.
124. K. Konishi, A. Yoshino, M. Katoh, H. Matsumoto, K. Takahashi, and H. Iwamura, *Chem. Lett.*, 1982, 169.
125. R. D. Müller, J. D. Wallis, and W. von Philipsborn, *Angew. Chem. Int. Ed. Engl.*, 1985, **24**, 513.
126. C. Casewit and J. D. Roberts, *J. Am. Chem. Soc.*, 1980, **102**, 2364.
127. D. C. Bradley, S. R. Hodge, J. D. Runnacles, M. Hughes, J. Mason, and R. L. Richards, *J. Chem. Soc., Dalton Trans.*, 1992, 1663.
128. J. P. Gouesnard and G. Martin, *Org. Magn. Reson.*, 1979, **12**, 263.
129. P. A. Duffin, L. F. Larkworthy, J. Mason, A. N. Stephens, and R. M. Thompson, *Inorg. Chem.*, 1987, **26**, 2034.
130. D. H. Evans, D. M. P. Mingos, J. Mason, and A. Richards, *J. Organomet. Chem.*, 1983, **249**, 293.
131. S. Donovan-Mtunzi, J. Mason, and R. L. Richards, *J. Chem. Soc., Dalton Trans.*, 1984, 1329.
132. B. Wrackmeyer, *Annu. Rep. NMR Spectrosc.*, 1988, **20**, 175.
133. J. P. Gouesnard, J. Dorie, and G. J. Martin, *Can. J. Chem.*, 1980, **58**, 1295.
134. J. Mason, *J. Chem. Soc., Faraday Trans. 2*, 1982, **78**, 1539.
135. T. Yamaguchi, K. Yamamoto, and H. Ohtaki, *Bull. Chem. Soc. Jpn.*, 1985, **58**, 3235.
136. D. M. Kanjia, J. Mason, R. E. Banks, I. A. Stenhouse, and N. D. Venayak, *J. Chem. Soc., Perkin Trans. 2*, 1981, 975.
137. S. Donovan-Mtunzi, J. Mason, and R. L. Richards, *J. Chem. Soc., Dalton Trans.*, 1984, 469.

138. J. Mason, in *Nuclear Magnetic Shielding and Molecular Structure*, ed. J. A. Tossell, *NATO AST Series*, Kluwer, Dordrecht, 1993, p. 449.
139. T. M. Duncan, *A Compilation of Chemical Shift Anisotropies*, Farragut Press, 1990, Chicago, IL, USA, N1–9.
140. R. E. Wasylishen, R. D. Curtis, K. Eichele, M. D. Lumsden, G. H. Penner, W. P. Power, and G. Wu, in *Nuclear Magnetic Shielding and Molecular Structure*, ed. J. A. Tossell, *NATO AST Series*, Kluwer, Dordrecht, 1993, p. 297.
141. W. P. Power and R. E. Wasylishen, *Annu. Rep. NMR Spectrosc.*, 1991, **23**, 1.
142. K. H. Casleton and S. G. Kukolich, *J. Chem. Phys.*, 1975, **62**, 2696; P. K. Bhattacharyya and B. P. Dailey, *J. Chem. Phys.*, 1973, **59**, 5820.
143. R. M. Garvey and F. C. De Lucia, *J. Mol. Spectrosc.*, 1974, **50**, 38.
144. J. Raymonda and W. Klemperer, *J. Chem. Phys.*, 1971, **55**, 232.
145. T. G. Oas, C. J. Hartzell, T. J. McMahon, G. P. Drobny, and F. W. Dahlquist, *J. Am. Chem. Soc.*, 1987, **109**, 5956; C. J. Hartzell, T. K. Pratum, and G. Drobny, *J. Chem. Phys.*, 1987, **87**, 4324.
146. G. S. Harbison, L. W. Jelinski, R. E. Stark, D. A. Torchia, J. Herzfeld, and R. G. Griffin, *J. Magn. Reson.*, 1984, **60**, 79.
147. W. P. Power and R. E. Wasylishen, *Annu. Rep. NMR Spectrosc.*, 1991, **23**, 1.
148. J. Mason, *Solid State NMR*, 1993, **2**, 285 [proposals developed with A. E. Hansen, J. Herzfeld, and C. J. Jameson following discussions at the 1992 Workshop, see Tossell[149]].
149. J. A. Tossell (ed.), *Nuclear Magnetic Shielding and Molecular Structure*, *NATO ASI Series*, Kluwer, Dordrecht, 1993.
150. A. Abragam, *The Principles of Nuclear Magnetism*, Clarendon Press, Oxford, UK, 1961, et seq.; U. Haeberlen, *High Resolution NMR in Solids Supplement 1*, Academic Press, New York, 1976, p. 9.
151. R. G. Griffin, *Anal. Chem.*, 1977, **49**, 951A.
152. B. R. Appleman and B. P. Dailey, *Adv. Magn. Reson.*, 1974, **7**, 231; C. Fyfe, *Solid State NMR for Chemists*, CFC Press, Guelph, Ontario, Canada, 1983; B. C. Gerstein and C. R. Dybowski, *Transient Techniques in NMR of Solids*, Academic Press, Orlando, FL, USA, 1985.
153. C. I. Ratcliffe, J. A. Ripmeester, and J. S. Tse, *Chem. Phys. Lett.*, 1983, **99**, 177.
154. R. M. Dickson, M. S. McKinnon, J. F. Britten, and R. E. Wasylishen, *Can. J. Chem.*, 1987, **65**, 941.
155. R. A. Santos, W. J. Chien, and G. S. Harbison, *J. Magn. Reson.*, 1989, **84**, 357.
156. R. G. Griffin, G. Bodenhausen, R. A. Haberkorn, T. H. Huang, M. Munowitz, R. Osredkar, D. J. Ruben, R. E. Stark, and H. van Willigen, *Philos. Trans. R. Soc. London, Ser. A*, 1981, **299**, 547.
157. J. E. Roberts, G. S. Harbison, M. G. Munowitz, J. Herzfeld, and R. G. Griffin, *J. Am. Chem. Soc.*, 1987, **109**, 4163.
158. G. Malli and C. Froese, *Int. J. Quantum Chem.*, 1967, **1s**, 95.
159. S. Kaplan, A. Pines, R. G. Griffin, and J. S. Waugh, *Chem. Phys. Lett.*, 1974, **25**, 78; J. D. Kennedy and W. McFarlane, *Mol. Phys.*, 1975, **29**, 593.
160. R. D. Curtis, M. J. Schriver, and R. E. Wasylishen, *J. Am. Chem. Soc.*, 1991, **113**, 1493.
161. M. Sardashti and G. E. Maciel, *J. Phys. Chem.*, 1988, **92**, 4620.
162. L. M. Ishol and T. A. Scott, *J. Magn. Reson.*, 1977, **27**, 23.
163. E. A. Moore, in preparation.
164. C. S. Yannoni, *J. Chem. Phys.*, 1970, **52**, 2005.
165. C. J. Groombridge, J. Mason, and R. L. Richards, unpublished work.
166. J. Herzfeld, J. E. Roberts, and R. G. Griffin, *J. Chem. Phys.*, 1987, **86**, 597.
167. D. G. Powell and L. J. Mathias, *J. Am. Chem. Soc.*, 1990, **112**, 669.
168. A. Shoji, S. Ando, S. Kuroki, I. Ando, and G. A. Webb, *Annu. Rep. NMR Spectrosc.*, 1993, **25**, 55.
169. See, for example, A. Shoji, T. Ozaki, T. Fujito, K. Deguchi, S. Ando, and I. Ando, *J. Am. Chem. Soc.* 1990, **112**, 4693.
170. K. G. Valentine, A. L. Rockwell, M. Gierasch, and S. J. Opella, *J. Magn. Reson.*, 1987, **73**, 519.
171. T. A. Cross and S. J. Opella, *J. Am. Chem. Soc.*, 1983, **105**, 306.
172. D. Schweitzer and H. W. Spiess, *J. Magn. Reson.*, 1974, **15**, 529.
173. R. D. Curtis, G. H. Penner, W. P. Power, and R. E. Wasylishen, *J. Phys. Chem.* 1990, **94**, 4000.
174. R. E. Wasylishen, G. H. Penner, W. P. Power, and R. D. Curtis, *J. Am. Chem. Soc.*, 1989, **111**, 6082.
175. R. E. Wasylishen, W. P. Power, G. H. Penner, and R. D. Curtis, *Can. J. Chem.*, 1989, **67**, 1219.
176. T. J. Bastow and S. N. Stuart, *Chem. Phys. Lett.*, 1991, **180**, 305.
177. R. A. Santos, P. Tang, W.-J. Chien, S. Kwan, and G. S. Harbison, *J. Phys. Chem.*, 1990, **94**, 2717.
178. P. J. Barrie, C. J. Groombridge, J. Mason, and E. A. Moore, *Chem. Phys. Lett.*, 1994, **219**, 491.
179. R. E. Wasylishen, communication quoted in R. G. Griffin, *Anal. Chem.*, 1977, **49**, 951A.
180. H. J. M. de Groot, S. O. Smith, J. Courtin, E. van den Berg, C. Winkel, J. Lugtenburg, R. G. Griffin, and J. Herzfeld, *Biochemistry*, 1990, **29**, 6873, and refs. therein.
181. T. E. Laska and T. W. Root (1989), quoted in *Nuclear Magnetic Shielding and Molecular Structure*, ed. J. A. Tossell, *NATO ASI Series*, Kluwer, Dordrecht, 1993, p. N-4.
182. P. J. Barrie, C. J. Groombridge, L. F. Larkworthy, and J. Mason, in preparation.
183. C. J. Groombridge, L. F. Larkworthy, A. Marécaux, J. Mason, D. C. Povey, and G. W. Smith, *J. Chem. Soc., Dalton Trans.*, 1992, 3125.
184. C. J. Groombridge, L. F. Larkworthy, and J. Mason, *Inorg. Chem.*, 1993, **32**, 379.
185. W. R. Scheidt and J. L. Hoard, *J. Am. Chem. Soc.*, 1973, **95**, 8281.
186. W. Kutzelnigg, U. Fleischer, and M. Schindler, *NMR Basic Principles Prog.*, 1990, **23**, 165, and refs. therein.
187. Aa. E. Hansen and T. D. Bouman, *J. Chem. Phys.*, 1985, **82**, 5035.
188. M. Schindler, *J. Am. Chem. Soc.*, 1987, **109**, 5950; *Magn. Reson. Chem.*, 1988, **26**, 394; *J. Am. Chem. Soc.*, 1988, **110**, 6623.
189. T. D. Bouman and Aa. E. Hansen, *Chem. Phys. Lett.*, 1990, **175**, 292.
190. J. Kowalewski, *Annu. Rep. NMR. Spectrosc.*, 1982, **12**, 82; *Prog. NMR Spectrosc.*, 1977, **11**, 1.
191. W. Freyer, *Z. Chem.*, 1981, **21**, 47.
192. R. E. Wasylishen, in *NMR Spectroscopy of Nuclei Other than Protons*, eds. T. Axenrod and G. A. Webb, Wiley, New York, 1974, p. 105.
193. T. Axenrod, in *Nitrogen NMR*, ed. M. Witanowski and G. A. Webb, Plenum Press, London, 1973, p. 261.
194. R. E. Wasylishen, *Annu. Rep. NMR. Spectrosc.*, 1977, **7**, 262.
195. C. J. Jameson, in *Multinuclear NMR*, ed. J. Mason, Plenum, New York, 1987, Chap. 4, p. 89.
196. W. McFarlane, *Q. Rev. Chem. Soc.*, 1969, **23**, 187.
197. G. Binsch, J. B. Lambert, B. W. Roberts, and J. D. Roberts, *J. Am. Chem. Soc.*, 1964, **86**, 5564.

198. A. J. R. Bourn and E. W. Randall, *Mol. Phys.*, 1964, **8**, 567.
199. R. E. Wasylishen and T. Schaefer, *Can. J. Chem.*, 1971, **49**, 3627.
200. T. Bundgaard, H. J. Jakobsen, and E. J. Rahkamaa, *J. Magn. Reson.*, 1975, **19**, 345.
201. H. Schultheiss and E. Flück, *Z. Naturforsch.*, 1977, **32B**, 257.
202. S. Karplus and M. Karplus, *Proc. Natl. Acad. Sci. USA*, 1972, **69**, 3204.
203. J. M. Schulman and T. J. Venanzi, *J. Am. Chem. Soc.*, 1976, **98**, 4701.
204. J. M. Schulman and T. J. Venanzi, *J. Am. Chem. Soc.*, 1976, **98**, 6739; W. S. Lee and J. M. Schulman, *J. Am. Chem. Soc.*, 1979, **101**, 3182.
205. J. M. Schulman, J. Ruggio, and T. J. Venanzi, *J. Am. Chem. Soc.*, 1977, **99**, 2045.
206. J. Hilton and L. H. Sutcliffe, *Prog. NMR Spectrosc.*, 1975, **10**, 27; V. M. S. Gil and W. von Philipsborn, *Magn. Reson. Chem.*, 1989, **27**, 409; R. H. Contreras, M. A. Natiello, and G. E. Scuseria, *Magn. Reson. Rev.*, 1985, **9**, 239.
207. R. M. Lynden-Bell and R. K. Harris, *Nuclear Magnetic Resonance Spectroscopy*, Nelson, London, UK, 1969, p. 102.
208. J. Geertsen, J. Oddershede, and G. E. Scuseria, *J. Chem. Phys.*, 1987, **87**, 2138.
209. N. J. Clayden, *Annu. Rep. NMR Spectrosc.*, 1992, **24**, 1.
210. C. J. Groombridge, *Nucl. Magn. Reson.*, 1992, **21**, 201.
211. K. Wüthrich, *NMR of Proteins and Nucleic Acids*, Wiley, New York, 1986.
212. S. J. Opella, *Annu. Rev. Phys. Chem.*, 1982, **33**, 533; *Methods Enzymol.*, 1985, **17**, 327; S. J. Opella, P. L. Stewart, and K. G. Valentine, *Q. Rev. Biophys.*, 1987, **19**, 7.
213. K. J. Shon and S. J. Opella, *Biomed. Appl. Biotechnol.*, 1993, **1**, 87.
214. M. C. Etter (ed.), *NMR and X-ray Crystallography: Interfaces and Challenges*, Am. Crystallogr. Assoc, Washington, DC, 1988, Vol. 24.
215. D. Suter and R. R. Ernst, *Phys. Rev. B*, 1985, **32**, 5608.
216. Q. Teng, M. Iqbal, and T. A. Cross, *J. Am. Chem. Soc.*, 1992, **114**, 5312.
217. J. E. Roberts, G. S. Harbison, M. G. Munowitz, J. Herzfeld, and R. G. Griffin, *J. Am. Chem. Soc.*, 1987, **109**, 4163.
218. R. Blinc, J. Seliger, V. Zagar, T. Apih, J. Dolinsek, H. Warhanek, A. Fuith, and W. Schranz, *Phys. Rev. B*, 1990, **42**, 8125.
219. A. Naito, P. B. Barker, and C. A. McDowell, *J. Chem. Phys.*, 1984, **81**, 1583, and refs. therein.
220. A. C. Olivieri, *Z. Naturforsch.*, 1992, **47A**, 39.
221. A. J. Kim and L. G. Butler, *Concepts Magn. Reson.*, 1992, **4**, 205.
222. C. P. Grey and W. S. Veeman, *Chem. Phys. Lett.*, 1992, **192**, 379.
223. A. Shoji, T. Ozaki, T. Fujito, K. Deguchi, and I. Ando, *Macromolecules*, 1987, **20**, 2441.
224. L. J. Mathias and C. G. Johnson, *Macromolecules*, 1991, **24**, 6114, and refs. therein.
225. B. Chaloner-Gill, W. B. Euler, P. D. Mumbauer, and J. E. Roberts, *J. Am. Chem. Soc.*, 1991, **113**, 6831.
226. L. Delmotte, M. Soulard, and H. Kessler, *Chem. Lett.*, 1990, 1215.
227. M. G. Gibby, R. G. Griffin, A. Pines, and J. S. Waugh, *Chem. Phys. Lett.*, 1972, **17**, 80.
228. K. L. Anderson-Altmann and D. M. Grant, *J. Phys. Chem.*, 1993, **97**, 11 096; cf. S. Hayashi and K. Hayamizu, *Bull. Chem. Soc. Jpn.*, 1991, **64**, 688.
229. J. A. Ripmeester, *J. Am. Chem. Soc.*, 1983, **105**, 2925.
230. P. D. Majors and P. D. Ellis, *J. Am. Chem. Soc.*, 1987, **109**, 1648, and refs. therein.
231. D. Michel, A. Germanus, D. Scheller, and B. Thomas, *Z. Phys. Chem. (Leipzig)*, 1981, **262**, 113; D. Michel, A. Germanus, and H. Pfeifer, *J. Chem. Soc., Faraday Trans. 1*, 1982, **78**, 237.
232. W. L. Earl, P. O. Fritz, A. A. V. Gibson, and J. H. Lunsford, *J. Phys. Chem.*, 1987, **91**, 2091.
233. J. A. Ripmeester, R. E. Hawkins, J. A. MacPhee, and B. N. Nandi, *Fuel*, 1986, **65**, 740.
234. W. Meiler and T. Wutscherk, *Isotopenpraxis*, 1989, **25**, 41.
235. J. Schaefer, E. O. Stejskal, M. D. Sefcik, and R. A. McKay, *Philos. Trans. R. Soc. London, Ser. A*, 1981, **299**, 593; J. Schaefer, E. O. Stejskal, and R. A. McKay, *ACS Symp. Ser.*, 1982, **191**, 187; J. Schaefer, E. O. Stejskal, J. R. Garbow, and R. A. McKay, *J. Magn. Reson.*, 1984, **59**, 150.
236. S. M. Holl, G. R. Marshall, D. D. Beusen, K. Kociolek, A. S. Redlinski, M. T. Leplawy, R. A. McKay, S. Vega, and J. Schaefer, *J. Am. Chem. Soc.*, 1992, **114**, 4830.
237. M. L. Martin, G. J. Martin, and J.-J. Delpuech, *Practical NMR Spectroscopy*, Heyden, London, UK, 1980.
238. L. M. Jackman and F. A. Cotton (eds.), *Dynamic NMR Spectroscopy*, Academic Press, New York, 1975.
239. H. H. Limbach, *Intermol. Forces*, 1991, 281.
240. F. Aguilar-Parrilla, G. Scherer, H. H. Limbach, M. D. C. Foces-Foces, F. Hernandez Cano, J. A. S. Smith, C. Toiron, and J. Elguero, *J. Am. Chem. Soc.*, 1992, **114**, 9657.
241. M. L. Martin, X. Y. Sun, and G. J. Martin, *Annu. Rep. NMR Spectrosc.*, 1985, **16**, 188.
242. J. F. Johnston, J. H. Ridd, and J. P. B. Sandell, *J. Chem. Soc., Perkin Trans. 2*, 1991, 623, and refs. therein.
243. J. H. Ridd, S. Trevellick, and J. P. B. Sandall, *J. Chem. Soc., Perkin Trans. 2*, 1992, 1535.
244. N. N. Bubnov, K. A. Bilevitch, L. A. Poljakova, and O. Yu. Okhlobystin, *J. Chem. Soc., Chem. Commun.*, 1972, 1058.
245. E. L. Dreher, P. Niederer, A. Rieker, W. Schwarz, and H. Zollinger, *Helv. Chim. Acta*, 1981, **64**, 488.
246. I. A. Grigorev, L. B. Volodarsky, A. Z. Gogolev, and R. Z. Sagdeev, *Chem. Phys. Lett.*, 1985, **122**, 46.
247. D. J. Siminovitch, M. Rance, and K. R. Jeffrey, *FEBS Lett.*, 1980, **112**, 79.
248. T. M. Rothgeb and E. Oldfield, *J. Biol. Chem.*, 1981, **256**, 6004.
249. F. Blomberg and H. Rueterjans, *Biol. Magn. Reson.*, 1983, **5**, 21.
250. K. Kanamori and J. D. Roberts, *Acc. Chem. Res.*, 1983, **16**, 35.
251. B. Coxon, *Pure Appl. Chem.*, 1977, **49**, 1151.
252. Y. Kyogoku, *Appl. Spectrosc. Rev.*, 1982, **17**, 279.
253. E. Breitmaier, *Pharm. Unserer Zeit*, 1983, **12**, 161.
254. G. J. Martin, *Pharm. Weekbl.*, 1984, **119**, 5.
255. R. Dyllick-Brenzinger and J. D. Roberts, *J. Am. Chem. Soc.*, 1980, **102**, 1166.
256. M. Llinas, K. Wüthrich, W. Schwotzer, and W. von Philipsborn, *Nature (London)*, 1975, **257**, 817.
257. A. Lapidot and C. S. Irving, *Biochemistry*, 1979, **18**, 704, 1788.
258. K. Kanamori, T. L. Legerton, R. L. Weiss, and J. D. Roberts, *J. Biol. Chem.*, 1982, **257**, 4168, and refs. therein.
259. N. Haran, Z. E. Kahana, and A. Lapidot, *J. Biol. Chem.*, 1983, **258**, 2929.
260. T. A. Cross, J. A. Diverdi, and S. J. Opella, *J. Am. Chem. Soc.*, 1982, **104**, 1759.
261. J. A. DiVerdi and S. J. Opella, *J. Am. Chem. Soc.*, 1982, **104**, 1761.

262. T. A. Cross, P. Tsang, and S. J. Opella, *Biochemistry*, 1983, **22**, 721.
263. G. T. Coker, III, J. R. Garbow, and J. Schaefer, *Plant Physiol.*, 1987, **83**, 698.
264. G. T. Coker, III and J. Schaefer, *Plant Physiol.*, 1985, **77**, 129.
265. G. S. Jacob, J. Schaefer, and G. E. Wilson, Jr., *J. Biol. Chem.*, 1985, **260**, 2777.
266. R. L. Baxter, C. J. McGregor, G. A. Thomson, and A. I. Scott, *J. Chem. Soc., Perkin Trans. 1*, 1985, 369.
267. W. Gründer, P. Krumbiegel, K. Buchali, and H. J. Blesin, *Phys. Med. Biol.*, 1989, **34**, 457.

Biographical Sketch

Joan Mason. *b* 1923. B.A., 1944, M.A., 1947, Ph.D., 1950, Sc.D., 1982, Cambridge University. Introduced to fluorine and perfluoroalkyl chemistry by H. J. Emeléus at Cambridge, to boron chemistry by A. B. Burg at the University of Southern California, and to NO_x chemistry and bonding theory by C. K. Ingold at University College, London. Lecturer, senior lecturer, and Reader in Chemistry, the Open University, 1970–88. Research interests: nitrogen chemistry, nitrogen NMR, metal complexes, transition metal NMR.

Noble Gas Elements

Gary J. Schrobilgen

McMaster University, Hamilton, Ontario, Canada

1	Introduction	1
2	NMR Studies of Structure and Bonding in Noble Gas Compounds	1
3	Intermolecular Interactions with Noble Gas Nuclei	8
4	References	9

1 INTRODUCTION

With the exception of argon, all of the noble gases have at least one naturally abundant nuclide which is amenable to NMR investigation, i.e., ^{3}He, ^{21}Ne, ^{83}Kr, ^{129}Xe, and ^{131}Xe. Xenon is the most favorable noble gas from an NMR standpoint as it possesses a spin-$\frac{1}{2}$ nuclide having a high natural abundance, viz. ^{129}Xe (N = 26.44%). There is also a quadrupolar xenon nuclide, ^{131}Xe ($I = \frac{3}{2}$, N = 21.18%), but this has not been used for studies of chemical structure. Helium also has a very low abundance spin-$\frac{1}{2}$ nuclide, ^{3}He ($N = 1.3 \times 10^{-4}$%), and is of interest to physicists in their studies of solid and superfluid states of helium. Helium-3 NMR spectroscopy has recently found chemical applications in the study of the endohedral fullerenes, He@C_{60} and He@C_{70}.[1,2] Argon has no stable nuclide of nonzero spin, a rare occurrence in the Periodic Table. Both neon and krypton possess quadrupolar nuclei (^{21}Ne, $I = \frac{3}{2}$, N = 0.26% and ^{83}Kr, $I = \frac{9}{2}$, N = 11.55%), but NMR work has largely been confined to physics. The only noble gases known to form isolable compounds are krypton, xenon, and the metalloid noble gas radon. No information is available concerning the nuclear spins of naturally produced radon isotopes. Moreover, the inherent radiation hazard that accompanies the intense radioactivity of radon and the required tracer level experimentation would likely preclude any attempt at NMR characterization of radon compounds even if a suitable spin-active nuclide was available. Only ^{129}Xe NMR spectra have been observed in chemical environments other than the pure element. Although Kr compounds have been characterized by ^{19}F NMR spectroscopy, none of the known Kr compounds have been studied by ^{83}Kr NMR spectroscopy.[3–6]

Comprehensive reviews of this subject are available in 'NMR and the Periodic Table' in the chapter by Schrobilgen[7] and in 'Multinuclear NMR' in the chapter by Jameson,[8] up to the years 1978 and 1987, respectively. Developments in noble gas chemistry have been reviewed by many authors[9–17] and include crystallographic and spectroscopic evidence, in which ^{129}Xe and ^{19}F NMR studies of xenon compounds and krypton compounds are included. Xenon fluorides, $XeOF_4$, and their complexes are the only thermodynamically stable xenon compounds. The majority of xenon and krypton compounds are kinetically unstable at temperatures approaching ambient and all are potent oxidizers; in fact, KrF^+ salts are the most potent chemical oxidants known.[3,18] Compound properties dictate that the majority of their NMR spectra be obtained at temperatures well below ambient and that NMR samples be prepared in oxidatively resistant and rigorously anhydrous solvents. The chemistry of krypton is far less extensive than that of xenon. Consequently, a high proportion of the second part of this article concerns ^{129}Xe NMR spectroscopy. The favorable ^{129}Xe relaxation times (T_1) in various species in solution (285 780 ms)[19,20] which allow reasonable pulse repetition rates and the high receptivity of the nuclide (31.8 relative to that of ^{13}C) make ^{129}Xe NMR spectra relatively easy to acquire using modern Fourier transform spectrometers. The third part of this article briefly surveys NMR studies of intermolecular interactions with ^{3}He, ^{21}Ne, ^{83}Kr, ^{129}Xe, and ^{131}Xe.

2 NMR STUDIES OF STRUCTURE AND BONDING IN NOBLE GAS COMPOUNDS

Since the discovery of noble gas reactivity,[21] xenon compounds, including halides, oxides, oxofluorides, oxo salts, and numerous covalent derivatives with a number of compounds covalently bonded to other polyatomic ligands have been prepared.[9–17] Additionally, the fluorides and oxofluorides of xenon form a variety of fluoro and oxofluoro cations and anions in their reactions with strong Lewis acid acceptors and fluoride ion donors, respectively.[14] Examples of xenon covalently bonded to fluorine, oxygen, nitrogen, carbon, and to xenon itself are now known. An early report of a xenon–boron bond has never been substantiated.[22] Xenon has by far the most extensive chemistry of the noble gas elements and the ^{129}Xe nuclide is ideal for the thorough investigation of a heavy nucleus since it can be obtained in a variety of compounds in a wide range of oxidation states and geometries (Tables 1 and 2). Covalent compounds containing Xe–F, Xe–O, Xe=O, Xe–N, Xe–C, and fluorine bridge bonds, denoted Xe···F, have been characterized spectroscopically and by X-ray crystallography. The known xenon oxidation states and geometries categorized according to the terminology of the VSEPR model of molecular geometry[56] are represented by the following examples: +2 in xenon species having AX_2E_3 [XeF_2, $Xe(OTeF_5)_2$, $FXeN{\equiv}CH^+$] and AXE_3 [XeF^+, $XeN(SO_2F)_2{}^+$] types; +4 in AX_5E_2 ($XeF_5{}^-$), AX_4E_2 [XeF_4, $Xe(OTeF_5)_4$], and AX_3E_2 ($XeF_3{}^+$, $XeOF_2$) types; +6 in AX_8E ($XeF_8{}^{2-}$), AX_7E ($XeF_7{}^-$), AX_6E (XeF_6, $XeOF_5{}^-$), AX_5E [$XeF_5{}^+$, $XeOF_4$, $OXe(OTeF_5)_4$], AX_4E ($XeOF_3{}^+$, XeO_2F_2), and AX_3E (XeO_3, XeO_2F^+) types; and +8 in AX_6 ($XeO_6{}^{4-}$, XeO_2F_4), AX_5 (XeO_3F_2), and AX_4 (XeO_4) types, where A denotes the central xenon atom, X a bond domain, and E an electron lone pair domain. In addition, the $+\frac{1}{2}$ oxidation state is represented by the emerald green paramagnetic cation $Xe_2{}^+$, which has been stabilized in solution.[57] The majority of xenon species synthesized to date have been characterized by ^{129}Xe NMR spectroscopy. Because ^{129}Xe NMR spectroscopy is not limited by the need to isolate a species in the solid state, low-temperature ^{129}Xe NMR spectroscopy has proven invaluable for the characterization of unstable xenon species in the reactive solvent media in which they are frequently generated. The chemistry of krypton is far less extensive than that of xenon. Krypton compounds are limited to only a single oxidation state, namely +2, and to AX_2E_3 [KrF_2, $Kr(OTeF_5)_2$, $FKrN{\equiv}CH^+$] and AXE_3 (KrF^+) geometrical

Table 1 ^{129}Xe Chemical Shifts and $^{1}J(^{129}\text{Xe}, ^{19}\text{F})$ Values

$\delta(^{129}\text{Xe})$ (ppm)[a,b]	Molecule	$^{1}J(^{129}\text{Xe}, ^{19}\text{F})$ (Hz)[c,d]
Xe(0)		
ca. −5460[8]	Xe atom	
−5331[19]	Xe in *n*-C_6F_{14}, 25 °C	
Xe(II)		
−2903[16,23]	$F_5Te-N(H)-Xe^+$	
−2886[16,23]	$F_5S-N(H)-Xe^+$	
−2672[16,23]	$F_4S{=}N-Xe^+$	
[−2348.5[e]/−1975.1[f]]24	1-Xe^+-1,4-C_6F_7	
[−2294.6[e]/−1914.0[f]]24	1-Xe^+-C_6F_9	
[−1993.4[g]/−2012[h]]25	$C_6F_5Xe^+$	
[−1950[i]/−1980[j]][26,27,29]	$C_6F_5Xe^+$	
[−2380.4[k]/−2010.1[f]]24	$C_6F_5Xe^+$	
−3769.3[31]	$C_6F_5Xe^+$	
[−2073[l]][28,30]	2,4,6-$F_3C_6H_2Xe^+$	
[−2115[l]][28]	2,6-$F_2C_6H_3Xe^+$	
[−2073[l]][28]	$C_6H_2F_3Xe^+$	
[−1857.0[g]/−1883.7[h]][25,31]	*m*-$CF_3C_6H_4Xe^+$	
−3636.4[31]	*m*-$CF_3C_6H_4Xe^+$	
[−1857.1[g]]25	*p*-$CF_3C_6H_4Xe^+$	
[−2039[l]][25,28]	2-$FC_6H_4Xe^+$	
[−1874.6[g]]25	*m*-$FC_6H_4Xe^+$	
[−1914.6[g]/−1896[l]][25,28]	4-$FC_6H_4Xe^+$	
−2327/−2447.4[20,32]	$Xe(OTeF_5)_2$	
−2289[20]	$Xe(OTeF_5)(OSeF_5)$	
−2200[20]	$Xe(OSeF_5)_2$	
−2051/−2067[20,32]	$FXeOTeF_5$	5670/5743[20,32]
−1952[20]	$FXeOSeF_5$	5630[20]
−2235.7/−2105.8[33]	*cis,cis*-$Xe(OIOF_4)_2$	
−2120.0/−1987.0[33]	*cis,trans*-$Xe(OIOF_4)_2$	76.3/79.2[33]
−1860.7/−1994.6[33]	*trans,trans*-$Xe(OIOF_4)_2$	76.9[33]
−1962.0/−1823.5[33]	*cis*-$FXeOIOF_4$	5803/5870[33]
−1720.5/−1853.6[33]	*trans*-$FXeOIOF_4$	5880/5913[33]
−1943[34]	$XeN(SO_2F)_2^+$	
−2101/−2257[35]	$Xe[N(SO_2F)_2]_2$	
−1997.3/−2053[35–37]	$FXeN(SO_2F)_2$	5572/5624[35–37]
−1933[35]	$[(FSO_2)_2NXe]_2^+$	
−1956.4[33]	*cis*-$OF_4IOXeOSO_2F$	
−1834.2[33]	*trans*-$OF_4IOXeOSO_2F$	
−2246[16]	$C_5F_5N-XeOTeF_5^+$	
−2061[16]	$CH_3C{\equiv}N-XeOTeF_5^+$	
−2192[16]	*s*-$C_3F_3N_2N-XeOTeF_5^+$	
−1979[16,23]	$F_3S{\equiv}N-XeOSeF_5^+$	
−1592/−2009[19,20,30,31,35–37]	XeF_2	5550/5665[19,20,30,31,35–37]
−1871.9/−1922.5[40]	$C_5F_5N-XeF^+$	5926/5936[40]
−1807.9/−1862.4[41]	*s*-$C_3F_3N_2N-XeF^+$	5909/5932[41]
−1802.6/−1853.4[40]	4-$CF_3C_5F_4N-XeF^+$	5963/5977[40]
[−1818[m]]42	*t*-Bu−C≡C−Xe^+	
−1661[16,23]	$F_3S{\equiv}N-XeF^+$	6248[16,23]
−1552/−1570[43,44]	$HC{\equiv}N-XeF^+$	6150/6181[43,44]
−1708[43]	$CH_3C{\equiv}N-XeF^+$	6020[43]
−1541[43]	$CH_2FC{\equiv}N-XeF^+$	6163[43]
−1717[43]	$C_2H_5C{\equiv}N-XeF^+$	6107[43]
−1426[43]	$C_6F_5C{\equiv}N-XeF^+$	6610[43]
−1337[41]	$CF_3C{\equiv}N-XeF^+$	6397[41]
−1294[41]	$C_2F_5C{\equiv}N-XeF^+$	6437[41]
−1294[41]	$C_3F_7C{\equiv}N-XeF^+$	6430[41]
−1320/−1613[37]	$Xe(OSO_2F)_2$	
−1407/−1725[33,37–39]	$FXeOSO_2F$	5830/6051[33,37–39]
−1472/−1608[45,46]	$XeOTeF_5^+$	
−1278/−1306[45]	$XeOSO_2F^+$	
−1342[37,38]	$FXeOSOFOMoOF_4$	5853/5971[37,38]
−1335[37,38]	$FXeOSOFOWOF_4$	5992/6131[37,38]
−1258[47]	$[(FXeO)_2SOF]^+$	6428[47]
−1359[45]	$FXeFBrOF_2^+$	5680(av.)[45]
−1381/−1441[37,38]	$FXeF-MoOF_4$	6018/6140(term)[37,38] 5000/5117(br)
−1315/−1331[37,38]	$FXeF-WOF_4$	6058/6196(term)[37,38]

Continued

		5000/5051(br)
−1338[37,38]	$FXeF-MoOF_4(MoOF_4)$	6159(term)[37,38]
		5036/5110(br)
−1321[37,38]	$FXeF-MoOF_4(MoOF_4)_2$	6156(term)[37,38]
		5029(br)
−1189[37,38]	$FXeF-WOF_4(WOF_4)$	6260/6268(term)[37,38]
		4964/5000(br)
−1170[37,38]	$FXeF-WOF_4(WOF_4)_2$	6304(term)[37,38]
		4996(br)
−1146,−1633(Xe′)[32,45]	$FXeFXe'OTeF_5$	5747(av.)[32,45]
−1051/−1059[32,37,45,47]	$(FXe)_2F^+$	6662/6740(term)[32,37,45,47]
		4828/4865(br)
−955[37,38]	$FXeO-WF_5(WOF_4)$	6315/6373[37,38]
−906[37,38]	$FXeO-WF_5(WOF_4)_2$	6330/6373[37,38]
−574/−991[32,37,47]	XeF^+	6703/7594[32,37,47]
Xe(IV)		
−637/−662.8[32,48,49]	$Xe(OTeF_5)_4$	
−527.0[50]	XeF_5^-	3400[50]
−436[49]	$FXe(OTeF_5)_3$	3506[49]
−243[49]	*cis*-$F_2Xe(OTeF_5)_2$	3714[49]
−216[49]	*trans*-$F_2Xe(OTeF_5)_2$	3503[49]
−26[49]	$F'F_2Xe(OTeF_5)$	3552,3733[49]
+166.1/+316.9[19,32,37,49,50]	XeF_4	3801/3900[19,32,37,49,50]
−341.9[46]	$Xe(OTeF_5)_3^+$	
−178.4[46]	$FXe(OTeF_5)_2^+$	2900[46]
+22.4[46]	$F_2XeOTeF_5^+$	2893[46]
+595[37]	$XeF_2F'^+$	2384,2609(F′)[37]
Xe(VI)		
−169.3[51]	XeF_7^{-n}	2724[51]
−357.9[52]	$XeOF_5^{-o}$	
−170.3/−211.8[32,46,48,49]	$OXe(OTeF_5)_4$	
−133/−157[48,49]	$OXeF(OTeF_5)_3$	1056/1082[48,49]
−92/−106[48,49]	*trans*-$OXeF_2(OTeF_5)_2$	984/990[48,49]
−81/−118[48,49]	*cis*-$OXeF_2(OTeF_5)_2$	1074/1231[48,49]
−40/−66[48,49]	$OXeF_3(OTeF_5)$	1127/1148 and 945[48,49]
0[32,37,48,49]	$XeOF_4$	1115/1131[19,32,37,48,49]
−1.9[46]	$OXe(OTeF_5)_3^+$	
+60.6[46]	$OXeF(OTeF_5)_2^+$	1089[46]
+121.3[46]	$OXeF_2OTeF_5^+$	796[46]
−35/−60.8[19,37,53]	$(XeF_6)_4$[k]	330/331.7[19,37,53]
−23.9/+131.8[37]	$XeF_4F'^+$	1377/1400[37]
		165/159(F′)
+131[49]	$O_2Xe(OTeF_5)_2$	
+154[49]	$O_2XeF(OTeF_5)$	1046[49]
+171/+173.2[37,49]	XeO_2F_2	1213/1217[37,49]
+200.4/+242.8[37,46,54]	$OXeF_2F'^+$	1012/1021,464/434(F′)[37,47,54]
+543.0[46]	$O_2XeOTeF_5^+$	
+600/704.3[37,46]	XeO_2F^+	95[37,46]
+217[19,37]	XeO_3	
Xe(VIII)		
+2077[37]	XeO_6^{4-}	

[a]Unless indicated otherwise, the reference standard used is the accepted standard for ^{129}Xe NMR spectroscopy, neat liquid $XeOF_4$ at room temperature; Ξ = 27.810184 MHz at 24 °C.[49] Square brackets, [ ], denote chemical shifts not referenced to $XeOF_4$; unfortunately, a number of workers in the area of organoxenon chemistry have chosen not to reference the ^{129}Xe chemical shifts of their compounds to $XeOF_4$, but have used XeF_2 as a reference under a variety of solvent and temperature conditions without providing conversions to the $XeOF_4$ reference scale.
[b]Ranges of values are indicated by extremes of range separated by a slash.
[c]Bridging fluorine denoted 'br', terminal fluorine denoted by 'term'.
[d]Referenced to XeF_2 in CH_3CN at room temperature.
[e]Referenced to XeF_2 in HF at −30 °C.
[f]Referenced to XeF_2 in CD_3CN at −30 °C.
[g]Referenced to XeF_2 in CH_3CN/CH_3CH_2CN (1:3) at −80 °C.
[h]Referenced to XeF_2 in CH_3CN at −44 °C.
[i]Referenced to XeF_2 in CH_3CN at −30 °C.
[j]Referenced to XeF_2 in CD_3CN at room temperature
[k]Referenced to XeF_2 in HF at −10 °C
[l]Referenced to XeF_2 in CH_3CN at room temperature
[m]Referenced to XeF_2 in $CDCl_3$ at −40 °C.
[n]Fluxionality on the NMR timescale averages fluorine environments.
[o]The $^1J(^{129}Xe, ^{19}F)$ coupling is not observed owing to intermolecular fluorine exchange.

Table 2 Other Coupling Constants Involving ^{129}Xe

	Hz	Molecule
$^{1}J[^{129}Xe(II), ^{17}O]$	692/704	$XeOF_4$[37,49,55]
	521	XeO_2F_2[37,49]
	566	$XeOF_5^-$[52]
$^{1}J[^{129}Xe(II), ^{14}N]$	332/334	$HC{\equiv}NXeF^+$[43,44]
	333	$CH_2FC{\equiv}NXeF^+$[43]
	313	$CH_3C{\equiv}N{-}XeF^+$[43]
	311	$C_2H_5C{\equiv}N{-}XeF^+$[43]
	236	$C_5F_5N{-}XeF^+$[40]
	238	4-$CF_3C_5F_4N{-}XeF^+$[40]
	245	*s*-$C_3F_3N_2N{-}XeF^+$[41]
$^{1}J[^{129}Xe(II), ^{15}N]$	307.4	$FXeN(SO_2F)_2$[36,37]
	259	$Xe[N(SO_2F)_2]_2$[35]
	91.7	$XeN(SO_2F)_2^+$[34]
	471/483	$HC{\equiv}NXeF^+$[44]
$^{1}J[^{129}Xe(II), ^{13}C]$	119	$C_6F_5Xe^+$[27,28]
	103.6/104	2,4,6-$F_3C_6H_2Xe^+$[28,30]
	99	2,6-$F_2C_6H_3Xe^+$[28]
	104	4-$FC_6H_4Xe^+$[28]
	78	2-$FC_6H_4Xe^+$[28]
	113.9	1-$Xe^+{-}C_6F_9$[24]
	120	*t*-Bu−C≡C−Xe^+[42]
$^{2}J[^{129}Xe(II), ^{13}C]$	79	*t*-Bu−C≡C−Xe^+[42]
	84	$HC{\equiv}NXeF^+$[43,44]
	79	$CH_3C{\equiv}N{-}XeF^+$[43]
$^{2}J[^{129}Xe(II), ^{77}Se]$	130	$Xe(OSeF_5)_2$[20]
$^{2}J[^{129}Xe(II), ^{125}Te]$	470	$Xe(OTeF_5)_2$[20]
	540	$FXeOTeF_5$[20]
	480	$Xe(OTeF_5)(OSeF_5)$[20]
$^{2}J[^{129}Xe(IV), ^{125}Te]$	988/1107	$Xe(OTeF_5)_4$[32,48]
	1032(eq),1292(ax)	$FXe(OTeF_5)_3$[49]
	1166	*trans*-$F_2Xe(OTeF_5)_2$[49]
	1059	*cis*-$F_2Xe(OTeF_5)_2$[49]
	1192	$F_2Xe(OTeF_5)$[49]
$^{2}J[^{129}Xe(VI), ^{125}Te]$	1245	$OXe(OTeF_5)_3^+$[46]
	1281/1618	$OXe(OTeF_5)_4$[32,46,48,49]
	1535	$OXeF_2(OTeF_5)_2$[49]
	1364	$OXeF_3(OTeF_5)$[49]
	1684	$O_2Xe(OTeF_5)_2$[49]
	1856	$O_2XeF(OTeF_5)$[49]
$^{3}J[^{129}Xe(II), ^{1}H]$	24.7/26.8	$HC{\equiv}NXeF^+$[43,44]
$^{3}J[^{129}Xe(II), ^{19}F]$	60.4/69(*o*)	$C_6F_5Xe^+$[24–29]
	54	2,4,6-$F_3C_6H_2Xe^+$[28]
	52	2,6-$F_2C_6H_3Xe^+$[28]
	48	2-$FC_6H_4Xe^+$[28]
	68.5/82.1(*m*)	1-Xe^+-1,4-C_6F_7[24]
	69.7/84.5(*p*)	1-$Xe^+{-}C_6F_9$[24]
	19	*cis*,*trans*-$Xe(OIOF_4)_2$[33]
	38	*trans*,*trans*-$Xe(OIOF_4)_2$[33]
	42/43	*trans*-$Xe(OIOF_4)_2$[33]
	18.5(eq)	$XeOTeF_5^+$[45]
	30(eq)	$FXeOTeF_5$[20]
	31(eq)	$Xe(OTeF_5)_2$[20]
	37	$FXeOSeF_5$,$Xe(OSeF_5)_2$[20]
	18/18.7	$FXeN(SO_2F)_2$[35,36]
	129(ax),202(ax)	$F_4S{=}N{-}Xe^+$[16,23]
	≈0(eq)	$F_4S{=}N{-}Xe^+$[16,23]
$^{3}J[^{129}Xe(IV), ^{19}F]$	63/67.7(eq)	$Xe(OTeF_5)_4$[32,48]
$^{3}J[^{129}Xe(VI), ^{19}F]$	54/55.4(eq),4(ax)	$OXe(OTeF_5)_4$[32,46,48]
	52(eq)	$OXeF(OTeF_5)_3$[48]
	53(eq)	*trans*-$OXeF_2(OTeF_5)_2$[48]
	51(eq)	*cis*-$OXeF_2(OTeF_5)_2$[48]
	50(eq)	$OXeF_3(OTeF_5)$[48]
$^{4}J[^{129}Xe(II), ^{19}F]$	17.3/19.5(*m*)	$C_6F_5Xe^+$[25–27,29]
$^{5}J[^{129}Xe(II), ^{19}F]$	3.8/4.2(*p*)	$C_6F_5Xe^+$[25,29]

types. Like xenon(II) compounds, krypton(II) compounds have been characterized by ^{19}F NMR spectroscopy, but no $^{83}Kr-^{19}F$ couplings have been observed.[3–6]

2.1 ^{129}Xe Chemical Shifts

Theoretical approximations have been developed which make it easier to interpret the chemical shifts of ^{129}Xe and other heavy nuclei in chemical terms. One such approximation represents the shielding of a nucleus like ^{129}Xe by the local terms σ^{d}_{Xe} and σ^{p}_{Xe}, which are calculated by Ramsey's theory[58] applied to the electrons on Xe only.[59] Because ^{129}Xe exhibits a large dynamic range of ^{129}Xe chemical shifts (−5460 to +2077 ppm, Table 1), σ^{d}_{Xe} is assumed to differ little from the free-atom value so that chemical shift trends are largely ascribable to variations in the dominant σ^{p}_{Xe} term. Jameson and Gutowsky[60] used this approach in an early theoretical study to show that ^{129}Xe chemical shifts can be calculated with considerable accuracy in the limited number of cases then known by application of equation (1). These calculations show that a localized description of the bonding employing d hybridization provides a more satisfactory description than a delocalized description without d hybridization. Moreover, the approach shows that ΔE, $\langle r^{-3}\rangle_{5p}$ and $\langle r^{-3}\rangle_{5d}$ can be regarded as essentially constant over the entire range of $\delta(^{129}Xe)$ so that P_i and D_i determine variations in $\delta(^{129}Xe)$.

$$\sigma^{p} \simeq (-\mu_0/4\pi)(4\mu_B^2/\Delta E)[\langle r^{-3}\rangle_{np} P_i + \langle r^{-3}\rangle_{nd} D_i] \quad (1)$$

The large dynamic chemical shift range exhibited for ^{129}Xe is anticipated from trends among other nuclei. Existing experimental data show that chemical shift ranges tend to increase with atomic number Z across a given row of the Periodic Table and down a given group, and may be correlated with the variation of the radial term $\langle r^{-3}\rangle_{np}$ for the valence p electrons of the free atom.[61] Since the paramagnetic shielding term σ^{p}_{Xe} has this radial dependence, this places xenon (Z = 54) in a category among nuclei having one of the larger dynamic chemical shift ranges. Relativistic effects, which vary with Z^2, also make a significant contribution to the chemical shift range for ^{129}Xe as exemplified by the diamagnetic shielding term σ^{d}_{Xe} of atomic xenon, which has a relativistic value of 7040 ppm[62] compared with a nonrelativistic value of 5642 ppm.[63]

While absolute shielding components have not been measured for xenon in its various oxidation states, theoretical arguments predict rather large anisotropies: $(\sigma_{\parallel} - \sigma_{\perp})$ = +5125 to +7185 ppm for XeF_2; +725 to +3940 ppm for XeF_4, and +365 to +1500 ppm for $XeOF_4$.[60] Xenon quadrupole coupling constants, $|e^2qQ|$, obtained from Mössbauer experiments, yield values of the electric field gradient at the xenon nucleus, which, in turn, are a measure of the anisotropy of the σ^{p}_{Xe} term.[8]

There have been no recent calculations of Xe nuclear shielding or spin–spin coupling constants, so that the approach to the discussion of ^{129}Xe chemical shifts must remain an essentially empirical one. Of particular interest is the great sensitivity of the ^{129}Xe chemical shift to (1) the formal oxidation state, (2) the ionic character of the Xe–L bond, where L is F, O, or a polyatomic ligand which is bonded to Xe through O, N, or C, (3) the formal charge on the xenon atom, (4) isotropic effects, and (5) medium and temperature effects.

It is apparent from Table 1 that the paramagnetic shielding contribution to $\delta(^{129}Xe)$ mainly depends upon the formal oxidation number of xenon and is essentially in the order $\sigma(^{129}Xe)$: Xe(0) > Xe(II) > Xe(IV) > Xe(VI) > Xe(VIII), i.e., $\delta(^{129}Xe)$ = −5460 to −5331 ppm for Xe(0), −3769.3 to −574 ppm for Xe(II), −662.8 to +595 ppm for Xe(IV), −211.8 to +704.3 ppm for Xe(VI), and +2077 ppm for Xe(VIII), with considerable overlap in chemical shift ranges for Xe(IV) and Xe(VI). The lower shieldings for xenon in XeF_4 [$\delta(^{129}Xe)$ = 166.1–316.9 ppm] and XeF_3^+ [$\delta(^{129}Xe)$ = 595 ppm] relative to the Xe(VI) species are in marked contrast to the corresponding $\sigma(^{19}F)$ chemical trends, which vary monotonically with oxidation state, i.e., Xe(VI) < Xe(IV) < Xe(II).[64] The observed $\sigma(^{129}Xe)$ trend is, however, in agreement with the trend calculated by Jameson and Gutowsky[60] for XeF_4 < $XeOF_4$ < XeF_6 < XeF_2. Within a given oxidation state several trends are also apparent.

A monotonic deshielding of the central xenon atom for the two series $(XeF_6)_4$, $XeOF_4$, XeO_2F_2, XeO_3, and XeF_5^+, $XeOF_3^+$, XeO_2F^+ (additive for the latter series) is observed with increasing oxygen substitution (Table 1), and may be attributed to contributions of the sort Xe=O ↔ Xe^+–O^-, which serve to increase P_i and D_i, decreasing the σ^{p}_{Xe} term. The opposite effect is observed upon increasing oxygen substitution in the homologous series of mixed F/$OTeF_5$ derivatives of Xe(II), Xe(IV), and Xe(VI). Within each of the neutral series $XeF_{2-n}(OTeF_5)_n$, $XeF_{4-n}(OTeF_5)_n$, O=$XeF_{4-n}(OTeF_5)_n$, and $O_2XeF_{2-n}(OTeF_5)_n$ and the cation series XeF^+/$XeOTeF_5^+$, O_2XeF^+/$O_2XeOTeF_5^+$, $XeF_{3-n}(OTeF_5)_n^+$, and O=XeF_{3-n} $(OTeF_5)_n^+$, the ^{129}Xe chemical shifts are found to be additive (Table 1), exhibiting increased shielding with increasing number of $OTeF_5$ groups. These trends reflect the lower effective electronegativity of the $OTeF_5$ group compared with that of fluorine. This behavior is typified by the equations:

$$\delta(^{129}XeOL_4) = -43.9n - 26.1 \quad (2)$$

and

$$\delta(^{129}XeOL_3^+) = -91.1n + 232.7 \quad (3)$$

where n = number of $OTeF_5$ groups.[46,49]

For all oxidation states, the Xe nucleus of the cation having one less F or $OTeF_5$ group is less shielded: $\sigma(^{129}Xe)$: $XeL_n > XeL^+_{n-1}$ and $(O{=})_mXeL_n > (O{=})_mXeF^+_{n-1}$. This is illustrated by the chemical shifts of XeF_n and XeF_{n-1}^+ where n = 2: $\delta(^{129}Xe)$ = −2009 to −1592 ppm, −991 to −574 ppm; n = 4: $\delta(^{129}Xe)$ = +166.1 to +316.9, +595 ppm; n = 6: $\delta(^{129}Xe)$ = −35 to −60.8, −23.9 to +131.8 ppm, and by the chemical shifts of $(O{=})_mXe(OTeF_5)_n$ and $(O{=})_mXe(OTeF_5)_{n-1}^+$, where n = 2, m = 0; $\delta(^{129}Xe)$ = −2447.4 to −2327 ppm, −1608 to −1472 ppm, n = 4, m = 0; $\delta(^{129}Xe)$ = −662.8 to −637 ppm, −341.9 ppm, n = 4, m = 1; $\delta(^{129}Xe)$ = −211.8 to −170.3 ppm, −1.9 ppm, n = 2, m = 2; and $\delta(^{129}Xe)$ = 131 ppm, 543.0 ppm.

Xenon-129 NMR spectra have been recorded for only three xenon anions, XeF_5^-, XeF_7^-, and $XeOF_5^-$. The ^{129}Xe nucleus of the anion is, as anticipated, significantly more shielded than that of the neutral fluoride, i.e. XeF_4 and XeF_5^-: $\delta(^{129}Xe)$ = 166.1 to 316.9 ppm, −527.0 ppm; XeF_6 and XeF_7^-: $\delta(^{129}Xe)$ = −35 to −60.8 ppm, −169.3 ppm; and $XeOF_4$ and $XeOF_5^-$:

$\delta(^{129}Xe)$ = 0 ppm, −357.9 ppm (spectra of anions obtained in CH_3CN solvent).

The majority of known xenon compounds contain xenon in the +2 oxidation state and have been extensively studied by ^{129}Xe NMR spectroscopy. The xenon shielding in Xe(II) species follows the trend $\sigma(^{129}Xe)$: $XeL_2 > FXeL > (LXe)_2F^+ > XeL^+$, where L = F, $OTeF_5$, OSO_2F, and $N(SO_2F)_2$, and is found to hold without exception. NMR studies of xenon(II) derivatives containing XeF groups have established trends among ^{19}F and ^{129}Xe chemical shifts and $^1J(^{129}Xe, ^{19}F)$ couplings (vide infra) that are of importance in assessing the relative covalent characters of Xe–L and terminal Xe–F bonds in compounds of the type F–Xe–L and F–Xe–L^+, where L is a terminal fluorine, bridging fluorine or a ligand bonded to Xe(II) through oxygen or nitrogen.[7,8,16,37] In general, as the ionic character of the Xe–L bond increases, the covalent character of the terminal Xe–F bond increases, increasing the formal charge on xenon and deshielding the xenon nucleus, and vice versa.[16] This trend is also paralleled by increasing values of $^1J(^{129}Xe, ^{19}F)$ and decreasing values of $\delta(^{19}F)$ for the terminal XeF group (vide infra). The pattern observed in the ^{19}F and ^{129}Xe NMR spectra is corroborated by measurements of Xe–F stretching frequencies provided by Raman spectroscopy and, in a number of cases, by Xe–F bond lengths. Bonding models for XeF_2 indicate a high degree of Xe–F ionic character. The charge distribution represented as $F^{-\frac{1}{2}}Xe^+F^{-\frac{1}{2}}$ has been predicted by theoretical treatments[65] and is arrived at using either a three-center–two-electron bonding model or a valence bond description. A simple valence bond description also satisfactorily accounts for qualitative trends in xenon shieldings, $^1J(^{129}Xe(II), ^{19}F)$ couplings (vide infra), bond lengths, and vibrational frequencies in Xe(II) species.[16] The bonding in XeL_2, XeL^+, and the adduct cations $LXeF^+$ (L = fluorine, nitrogen- or oxygen-bonded ligand, carbon-bonded ligand only in LXe^+ types) may be represented by valence bond structures I–VI, where structures I and IV are the least important contributing structures.

$$\underset{\text{(I)}}{L^-Xe^{2+}F^-} \longleftrightarrow \underset{\text{(II)}}{L^-Xe^+F^-} \longleftrightarrow \underset{\text{(III)}}{L^-\ Xe^-F^+}$$

$$\underset{\text{(IV)}}{L\ Xe^{2+}F^-} \longleftrightarrow \underset{\text{(V)}}{L^-Xe^{2+}F^-} \longleftrightarrow \underset{\text{(VI)}}{L\ Xe^-F^+}$$

Accordingly, structures II and III apply to formally neutral species so that the XeF_2 molecule has a formal Xe–F bond order of $\frac{1}{2}$ whereas for LXeF the Xe–F bond order is $\geq\frac{1}{2}$ and <1, approaching 1 in the most weakly coordinated cases of XeF^+ and $XeOTeF_5^+$ in SbF_5 solvent. Due to the low fluoride ion basicities of the polymeric $Sb_nF_{5n+1}^-$ anions, which exist in solutions of XeF^+ and $XeOTeF_5^+$ in SbF_5, these solutions provide the closest approximations to free XeF^+ and $XeOTeF_5^+$ cations in solution, providing Xe–F and Xe–O formal bond orders that approach unity and Xe shieldings that are dramatically decreased relative to those of the parent molecules, i.e., XeF^+ (574 ppm, SbF_5 solvent) and XeF_2 (−1592 to −2009 ppm); $XeOTeF_5^+$ (−1472 ppm, SbF_5 solvent), $FXeOTeF_5$ (−2051 to −2067 ppm), and $Xe(OTeF_5)_2$ (−2327 to −2447.4 ppm). The chemical shift of XeF^+ in SbF_5 represents the most deshielded ^{129}Xe resonance observed for an Xe(II) species. As the base strength of L increases (group electronegativity decreases), the Xe–L bond becomes progressively more covalent, the shielding of the xenon nucleus increases as illustrated above by XeL_2 and XeL^+, where L = F, and/or $OTeF_5$. In cases where both fluorines are replaced by ligands that provide Xe–L bonds of greater covalent character than Xe–F bonds, the ^{129}Xe shieldings increase relative to that of XeF_2 and FXeL (Table 1). The opposite effect is observed for the ^{19}F shieldings of L–Xe–F (and L–Xe–F^+) species. Plots of the ^{129}Xe chemical shift versus the ^{19}F chemical shift of the terminal fluorine on xenon result in separate linear relationships, one for XeF groups bonded to oxygen and another for XeF groups bonded to bridging fluorines; the lines intersect, as expected, in the vicinity of the weakly fluorine-bridged XeF^+ cation in SbF_5 solvent.[37] The reader is cautioned that, where possible, such comparisons need to be made under the same solvent and temperature conditions (see Section 2.4 below).

Nitrogen bases such as nitriles, HC≡N, perfluoropyridines, and *s*-trifluorotriazine that are resistant to oxidation by the strongly oxidizing XeF^+, $XeOSeF_5^+$, and $XeOTeF_5^+$ cations form Lewis acid–base adducts with all three cations.[16,23,43,44] The ^{129}Xe shieldings indicate a significant measure of XeL^+ character and have been used to assess the nature of the Xe–N donor–acceptor bond. With corroboration from the vibrational spectra of L–Xe–F^+ cations, the nature of the Xe–N donor–acceptor bond can be rationalized in terms of structures V and VI. For the L–Xe–F^+ cations, resonance structure VI is dominant relative to structure V as a result of the high charge localization. Thus, the Xe–N bonds of L–Xe–F^+ cations are best described as essentially ionic interactions of the ligand L and XeF^+, and exhibit deshielded xenon nuclei that are consistent with weakly coordinated XeF^+ cations (Table 1). In general, this class of Xe(II) species exhibits trends similar to those of the neutral L–Xe–F species as the electron donor properties of L are varied, i.e., greater s contribution to the hybridization of the ligand donor atom lowers the effective electronegativity of the nitrogen donor atom, resulting in a more ionic Xe–L bond (greater contribution from structure V), producing greater XeF^+ character and a more shielded xenon nucleus.[66] This is illustrated in Table 1 by a series of cations containing formally sp-hybridized nitrogen (e.g., $F_3S{\equiv}N{-}XeF^+$, $RC{\equiv}N{-}XeF^+$) in which the xenon nuclei are consistently more deshielded (more ionic Xe–N bonds) than the xenon nuclei in cations containing formally sp^2-hybridized nitrogen (e.g., 4-$CF_3C_5F_4N{-}XeF^+$, $C_5F_5N{-}XeF^+$, *s*-$C_3F_3N_2N{-}XeF^+$).

In the extreme case of a formally neutral L–Xe–F species where L is strongly electron donating, structure II dominates to the extent that the Xe–F bond is completely ionized. Such XeL^+ cations are known in which xenon is bonded through strongly electron donating carbon and nitrogen ligand groups and are typified by $C_6F_5Xe^+$ (−3769.3 ppm), $F_5TeN(H)Xe^+$ (−2903 ppm), $F_5SN(H)Xe^+$ (−2886 ppm), and $F_4S{=}NXe^+$ (−2672 ppm) and are classified, on the basis of their ^{129}Xe shieldings, as the most highly covalent bonds formed by Xe(II). With the exception of the free Xe atom, the strong electron donating properties of Xe(II) result in the most shielded xenon environments known.

2.2 Isotopic Effects in Krypton and Xenon Compounds

The secondary effects of krypton isotopes on the nuclear shielding of ^{19}F have been reported for three krypton compounds: $^1\Delta\ ^{19}F(^{m'/m}Kr) = -0.0102$ ppm u^{-1} for KrF_2,[66] -0.0138 ppm u^{-1} for $FKrN{\equiv}CH^+$,[5] and -0.0105 ppm u^{-1} for $FKrN{\equiv}CF_3^+$.[6] The ^{19}F resonances arising from $^{83}KrF_2$ and $^{131}XeF_2$ are not detectable owing to line broadening from the quadrupolar ^{131}Xe ($I = \frac{3}{2}$) and ^{83}Kr ($I = \frac{9}{2}$) nuclei.[67] The only secondary effects of xenon isotopes on the nuclear shielding of ^{19}F have been reported for XeF_2: $^1\Delta\ ^{19}F(^{m'/m}Xe) = -0.00118$ ppm u^{-1}.[67] The only secondary isotopic effects on the nuclear shielding of ^{129}Xe that are known arise from oxygen isotopes: $^1\Delta\ ^{129}Xe(^{m'/m}O) = -0.29$ ppm u^{-1} for $XeOF_4$,[49] -0.26 ppm u^{-1} for XeO_2F_2,[49] and -0.345 ppm u^{-1} for $XeOF_3^+$.[54] All ^{19}F and ^{129}Xe chemical shifts of the various isotopomers of these molecules exhibit strict proportionality to the mass factor, $(m' - m)/m'$. No isotopic dependence of a spin–spin coupling to ^{129}Xe has been reported.

2.3 Spin–Spin Coupling to ^{129}Xe

One-bond $^{129}Xe-^{19}F$ scalar couplings are summarized in Table 1 and those involving ^{129}Xe coupled to other nuclei are listed in Table 2. Other than an early study of $^1J(^{129}Xe, ^{19}F)$ couplings, there have been no theoretical treatments of spin–spin coupling with xenon beyond the average energy approximation used in the theory of xenon and fluorine chemical shifts of XeF_2, XeF_4, XeF_6, and $XeOF_4$.[60] It is generally accepted that the Fermi contact mechanism is the dominant term in the spin–spin coupling constants involving xenon.[61] Owing to the high atomic number of xenon, the spin–spin coupling constants, as well as xenon nuclear shieldings, experience significant relativistic effects. Because the s-electron density at the nucleus, $|\Psi_s(0)|^2$, appears in the Fermi contact term of the spin–spin coupling, this term should be evaluated relativistically. Such a relativistic correction is estimated to increase $|\Psi_s(0)|^2$ by a factor of 1.484.[68,69]

The moduli of one-bond coupling constants, $^1J(^{129}Xe, ^{19}F)$, associated with the different oxidation states of xenon can be used as a diagnostic tool to confirm the formal oxidation number of a xenon species by virtue of their nonoverlapping ranges, $^1J(^{129}Xe, ^{19}F)$: Xe(VI) < Xe(IV) < Xe(II), and correspond to the ranges ^{129}Xe(II)–terminal ^{19}F: 5583–7594 Hz, ^{129}Xe(II)–bridging ^{19}F: 4828–5117 Hz, ^{129}Xe(IV)–^{19}F: 2384–3823 Hz, ^{129}Xe(VI)–^{19}F: 95–1400 Hz. The variation with oxidation number is in agreement with trends generally noted for the dependence of one-bond scalar couplings on oxidation number.[61]

Empirical correlations between ^{19}F chemical shifts and one-bond $^{129}Xe-^{19}F$ coupling constants exist in the literature. There is a smooth curve correlating the modulus of $^1J(^{129}Xe, ^{19}F)$ with $\delta(^{19}F)$ for all oxidation states of xenon.[64] The correlation provides a rationale for the small $^1J(^{129}Xe, ^{19}F)$ couplings observed for XeO_2F^+, $(XeF_6)_4$, and the equatorial fluorines of XeF_5^+, if it is assumed that a change in the signs of the coupling constants occurs over the series in the vicinity of these species, and implies that the signs of the axial and equatorial couplings of $XeOF_3^+$ and the axial coupling of XeF_5^+ are likely to be opposite in sign with respect to the remaining species. No absolute sign determinations have been made for any of the couplings to ^{129}Xe. However, the signs of the reduced couplings, $^1K(Xe, F)$, may be inferred by considering the isoelectronic series of Sn(IV)–I(VII) hexafluoro species.[64,70] A near-linear relationship is obtained when $K(X-F)^{\frac{1}{2}}$ is plotted versus Z and no change of sign is assumed along the series.[71] Since the signs of ^1K[Sn(IV), F] and ^1K[Te(VI), F] couplings have been determined to be negative, and the modulus of $^1K(X, F)$ increases along the series $SnF_6^{2-} < SbF_6^- < TeF_6 < IF_6^+$, the hypothetical Xe(VIII) cation, XeF_6^{2+}, would possess the most negative value for the reduced one-bond coupling. The signs of $K(Xe, F)$ for Xe(VIII) and Xe(VI) species excepting $XeOF_4$, XeO_2F_2, and possibly XeF_6 and XeO_2F^+, are taken as positive. Confirmation of the aforementioned ^{19}F chemical shift and $^{129}Xe-^{19}F$ coupling constant correlation and sign change awaits ^{19}F and ^{129}Xe NMR data on known Xe(VIII) compounds such as XeO_3F_2 and XeO_2F_4.

The $^1J(^{129}Xe, ^{19}F)$ coupling is sensitive to the charge on the xenon. In the case of Xe(II), it varies with the degree of XeF^+ character in L–Xe–F and L–Xe–F^+ species with the largest values observed for essentially 'free' XeF^+ in SbF_5 (7210 Hz) and $(FXe)_2F^+$ (6662–6740 Hz). Accordingly, $^1J[^{129}Xe(II), ^{19}F]$ trends may be rationalized in terms of valence bond structures I–VI and described in terms similar to those used to rationalize trends in ^{129}Xe(II) chemical shifts (vide supra). Thus, smaller $^1J[^{129}Xe(II), ^{19}F]$ values are observed for F–Xe–L and F–Xe–L^+ species having the more covalent Xe–L bonds as illustrated by $FXeN(SO_2F)_2$ (5572–5624 Hz) and *cis*- and *trans*-$FXeOIOF_4$ (5803–5913 Hz). Consequently, smooth correlations are observed not only where $^1J[^{129}Xe(II), ^{19}F]$ increases with increasing $\delta(^{129}Xe)$, but $^1J[^{129}Xe(II), ^{19}F]$ is also noted to increase with decreasing $\delta(^{19}F)$, increasing the Xe(II)–F stretching frequency and decreasing the Xe(II)–F bond length.[7,16]

Although the trend of increasing $^1J(^{129}Xe, ^{19}F)$ with increasing covalent character (decreasing Xe–F bond length) is clear for Xe(II), bond length data available for comparison with $^1J(^{129}Xe, ^{19}F)$ values of higher oxidation state species are sparse. The trend of increasing $^1J(^{129}Xe, ^{19}F)$ with decreasing bond length is apparent in the three cases for which two bond lengths and couplings can be compared in the same species, viz: XeF_3^+ {$^1J[^{129}Xe(IV), ^{19}F_{ax}]$ = 2384 Hz; Xe–F_{ax} distance = 191 pm and $^1J[^{129}Xe(IV), ^{19}F_{eq}]$ = 2609 Hz; Xe–F_{eq} distance = 184 pm}, XeF_5^+ {$^1J[^{129}Xe(VI), ^{19}F_{ax}]$ = 1400 Hz; Xe–F_{ax} distance = 177 pm and $^1J[^{129}Xe(VI), ^{19}F_{eq}]$ = 159 Hz; Xe–F_{eq} distance = 190 pm}, and $XeOF_3^+$ {$^1J[^{129}Xe(VI), ^{19}F_{ax}]$ = 464 Hz; Xe–F_{ax} distance = 188 pm and $^1J[^{129}Xe(VI), ^{19}F_{eq}]$ = 1012 Hz; Xe–F_{eq} distance = 182 pm}.

The only $^{129}Xe-^{17}O$ couplings reported are those for $XeOF_5^-$ (566 Hz), $XeOF_4$ (692–704 Hz), $XeOF_3^+$ (619 Hz), and XeO_2F_2 (521 Hz). For isoelectronic and structurally related species, a comparison of the reduced coupling constants $^1K(Xe, F)$ and $^1K(Xe, O)$ for axial Xe–F and Xe=O bonds in $XeOF_4$ (152.5–155.1) and XeF_5^+ (42.80–48.00) and for the equatorial Xe–F and Xe=O bonds in XeO_2F_2 (114.8) and $XeOF_3^+$ (13.78–14.73), all in units of 10^{20} N A^{-2} m^{-3}, is consistent with the formal bond orders of Xe–F and Xe=O bonds in these species. The $^{129}Xe-^{17}O$ coupling of $XeOF_5^-$ (566 Hz) is significantly smaller than the $^1J(^{17}O, ^{129}Xe)$ coupling in $XeOF_4$ and $XeOF_3^+$ (viz., 692–704 Hz

and 619 Hz, respectively) which may be a consequence of the more polar bonds in the anion.

Other one-bond coupling constants which have been reported include $^1J[^{129}Xe(II), ^{15}N]$, $^1J[^{129}Xe(II), ^{14}N]$, and $^1J[^{129}Xe(II), ^{13}C]$. Their reduced coupling constant ranges, expressed in units of 10^{20} N A^{-2} m^{-3}, are ^1K[Xe(II), N] = 27.0 to 142 and ^1K[Xe(II), C] = 9.3–14.3, and are substantially smaller than ^1K[Xe(II), F] values, which range from 176.2–228.9.

Two-bond couplings, $^2J(^{129}Xe, ^{13}C)$, have been observed for the Xe(II) cations, $FXeN{\equiv}CH^+$ and $FXeN{\equiv}CCH_3^+$. Pentafluorooxotellurate derivatives of xenon in its +2, +4, and +6 oxidation states exhibit $^2J(^{129}Xe, ^{125}Te)$ couplings and have nonoverlapping ranges which depend on the oxidation state of xenon, but which are in the opposite direction to those observed for $^1J(^{129}Xe, ^{19}F)$;$^2J(^{129}Xe, ^{125}Te)$: Xe(VI) > Xe(IV) > Xe(II), with $^2J(^{129}Xe, ^{125}Te)$ = 470–540 Hz for Xe(II), 988–1192 Hz for Xe(IV), and 1281–1856 Hz for Xe(VI). The reduced two-bond xenon–chalcogen coupling in $FXeOSeF_5$ is ^2K(Xe, Se) = 20.52 is significantly less than the equivalent coupling in $FXeOTeF_5$, ^2K(Xe, Te) = 44.8–51.4, both in units of 10^{20} N A^{-2} m^{-3}. Inclusion of relativistic corrections[69] gives values of 17.77 and 31.1–35.7; the difference may be a reflection of the anticipated higher electronegativity of the $OSeF_5$ group relative to that of the $OTeF_5$ group implied from the ordering of the Xe(II) chemical shifts for $FXeOSeF_5$ and $FXeOTeF_5$ and for $Xe(OSeF_5)_2$ and $Xe(OTeF_5)_2$ (Table 1).

A number of three-bond $^{129}Xe–^{19}F$ couplings have been observed for xenon and are associated with the Xe–C-bonded perfluorinated alkenyl and aryl cations of Xe(II) and the $OSeF_5$ and $OTeF_5$ derivatives of xenon in its +2, +4, and +6 oxidation states. While $^3J[^{129}Xe(II), ^{19}F]$ couplings in $OTeF_5$ and $OSeF_5$ derivatives are uniformly smaller than in Xe(IV)- and Xe(VI)$OTeF_5$ derivatives, there is less consistency among three-bond couplings than among one-bond and two-bond couplings with xenon. The relative magnitudes of three-bond couplings in the $XeN{=}SF_4^+$ cation and $OTeF_5$ and $OSeF_5$ derivatives differ considerably because the coupling paths differ. This is illustrated by xenon coupling to the equatorial fluorines of the $OTeF_5$ groups in the series $O{=}XeF_{4-n}(OTeF_5)_n$ (50–55 Hz) and to the two axial fluorines environments in the $XeN{=}SF_4^+$ cation (129 and 202 Hz) which have coupling paths with dihedral angles of 0° or 180°, whereas the paths to the axial fluorines in $OTeF_5$ groups (0–4 Hz) and to the equatorial fluorines in the $XeN{=}SF_4^+$ cation (∼0 Hz) involve a dihedral angle of 90°. The only reported xenon–proton spin–spin coupling is $^3J(^{129}Xe, ^1H)$ in the $FXeN{\equiv}CH^+$ cation.

Examples of a four-bond and a five-bond coupling have been observed between Xe(II) and the *meta*- and *para*-fluorines of the aromatic ring in the $C_6F_5Xe^+$ cation.

2.4 Solvation and Temperature Effects

Large temperature and solvent effects are observed for ^{129}Xe chemical shifts and $^{129}Xe–^{19}F$ spin–spin couplings. Solvation effects probably result from coordination of the solvent in the xenon valence shell and show an overall decrease with decreasing number of electron lone pairs (increasing number of substituents).[7] Thus, Xe(II) species exhibit the greatest sensitivity to medium and temperature effects among the xenon oxidation states. The sensitivity of the ^{129}Xe(II) chemical shift to the effects of temperature and solvent is exemplified by XeF_2, which shifts over a 400 ppm range, and by $Xe(OTeF_5)_2$, which shifts over a range of 200 ppm depending on the solvent, temperature, and concentration. In CH_3CN, XeF_2 exhibits a linear dependence with temperature and a slope $\Delta\delta(^{129}Xe)/\Delta T = -0.4718$ ppm K^{-1} compared with a considerably smaller and opposite trend for the ^{19}F chemical shift, $\Delta\delta(^{19}F)/\Delta T = 0.0042$ ppm K^{-1}, over the same temperature range (240–320 K).[67] The chemical shift range of Xe(0) is in excess of 300 ppm in the pure gaseous, liquid, and solid phases, and in organic solvents and clathrates. The chemical shift of XeF^+ has been shown to be particularly sensitive to solvent composition. For $XeF^+Sb_2F_{11}^-$ dissolved in HSO_3F/SbF_5 solvent mixtures of variable composition, the shifts range from −574 ppm in pure SbF_5 to −911 ppm in pure HSO_3F solvents.[37] The interaction is presumed to arise by formation of a labile Lewis acid–base complex with a solvent oxygen or fluorine electron pair, which may be described in terms of structures II and III, and is understood in terms of the rationale described earlier (see Section 2.1).

There are also large solvent and temperature effects on spin–spin couplings involving xenon. For example, in XeF^+, values of $^1J[^{129}Xe(II), ^{19}F]$ range from 6703 Hz in pure HSO_3F (−70 °C) to 7210 Hz in pure SbF_5 (25 °C).[45] For $FXeOSO_2F$ in HSO_3F solvent, values of $^1J[^{129}Xe(II), ^{19}F]$ range from 6051 Hz (−100 °C) to 5975 Hz (−84 °C), and in BrF_5 solvent from 5530 Hz (−77 °C) to 5848 Hz (−40 °C). The couplings of the axial and equatorial fluorines to xenon in the XeF_5^+ cation show large temperature and solvent dependences; $^1J[^{129}Xe(VI), ^{19}F_{ax}]$ = 1512 Hz and $^1J[^{129}Xe(VI), ^{19}F_{eq}]$ = 143.1 Hz in SbF_5 (35 °C) solvent compared with $^1J[^{129}Xe(VI), ^{19}F_{ax}]$ = 1357 Hz and $^1J[^{129}Xe(VI), ^{19}F_{eq}]$ = 175.0 Hz in HSO_3F (−90 °C) solvent.[64] The temperature variation of $^1J[^{129}Xe(VI), ^{19}F_{eq}]$ for XeF_5^+ has been studied in detail for XeF_5^+ in HSO_3F solvent and is found to range from 193.8 Hz at −80 °C to 149.9 Hz at 60 °C.[64]

When making comparisons of xenon couplings and chemical shifts, care must be taken to compare values that have been obtained under the same temperature and solvent conditions. Thus careful measurements of the ^{129}Xe chemical shifts of XeF^+ and $XeOTeF_5^+$ in SbF_5 solvent at 26 °C and those of XeF_4 and $Xe(OTeF_5)_4$ in $CFCl_3$ at 24 °C yield $\delta(XeF^+) - \delta(XeOTeF_5^+)$ = 898 ppm and $\delta(XeF_4) - \delta[Xe(OTeF_5)_4]$ = 828.9 ppm, confirming that, although the $OTeF_5$ group possesses a very high effective group electronegativity, it is less than that of fluorine.[32]

3 INTERMOLECULAR INTERACTIONS WITH NOBLE GAS NUCLEI

Intermolecular interactions among noble gas atoms ranging from the dilute gas, liquid to the solid phases have been studied by ^3He, ^{21}Ne, ^{83}Kr, ^{129}Xe, and ^{131}Xe NMR spectroscopy, and are manifested in the relaxation times and chemical shifts of these nuclides. The very large chemical shifts of ^{129}Xe and its sensitivity to intermolecular interactions allow it to be used as a van der Waals probe in other gases,[66,73–76] organic solvents,[77,78] liquid crystals,[79–82] clathrates,[83,84] and

zeolites.[85–90] In addition, there have been ^{3}He NMR studies of intermolecular interactions of entrapped helium within fullerenes.[2]

3.1 Medium Shifts

The only noble gases to exhibit medium-induced chemical shifts are xenon and helium. Shifts in the resonance of enriched ^{21}Ne (51% enrichment) in liquid and solid neon between 23 K and 34 K are less than 1 ppm and could not be observed.[91] Chemical shifts of krypton and xenon have been observed in the gas and condensed phases. The chemical shifts of ^{83}Kr, ^{129}Xe, and ^{131}Xe in the gas, liquid, and solid, as well as the deshielding effects of a second gas on the xenon chemical shift, are density proportional and have been reviewed and summarized by Schrobilgen,[7] Jameson,[8] and Cowgill and Norberg.[92] The deshielding effects of infinitely dilute xenon in organic solvents have also been studied and range from -148 ppm in CH_3OH to -335 ppm in CH_2I_2, and are found to be proportional to the refractive index of the organic solvent.[77,78]

NMR spectra have been observed for the entrapped noble gas nuclides ^{3}He and ^{129}Xe. Helium-3 has been used as a probe for the magnetic shielding environment inside fullerene cavities for the endohedral compounds ^{3}He@C_{60} and ^{3}He@C_{70}, providing the only example thus far of the application of ^{3}He NMR spectroscopy to a chemical problem.[1,2] The ^{3}He nucleus is shielded by 6.4 and 28.8 ppm, respectively, relative to dissolved ^{3}He in 1-methylnaphthalene solvent. These shieldings are large, indicating significant diamagnetic ring currents in C_{60} and even larger ones in C_{70}. Altering the π-bonding structure of the fullerene through reaction produces substantial changes in the shieldings of entrapped ^{3}He.[2] Azomethine ylide additions of *N*-methylglycine to the double bonds of ^{3}He@C_{60} and ^{3}He@C_{70} result in *N*-methylpyrrolidine adducts and in significant changes in ^{3}He shieldings upon addition to one or two fullerene double bonds. The ^{3}He nuclei of the ^{3}He@C_{60} adducts are more shielded and occur at -9.4 ppm and at -10.9 and -12.3 ppm relative to dissolved ^{3}He for the mono-adduct and bis-adducts, respectively. In contrast, mono-adducts of ^{3}He@C_{70} are deshielded with respect to ^{3}He@C_{70} and are assigned to resonances at -23.8 and -27.9 ppm.

The very large chemical shift range of ^{129}Xe and its sensitivity to intermolecular interactions in the gas phase[66,73–76] and in solution[77,78] have made ^{129}Xe NMR spectroscopy an extensively used probe for the characterization of zeolites, polymers, and other microporous solids. A large number of studies have resulted in which the ^{129}Xe chemical shift is found to vary with zeolite pore size, loading, temperature, and channel dimensions, with cation and coadsorbed molecule distributions, with dispersed metal atoms, and water content.[85–90] The estimation of zeolite pore sizes and the study of guest molecule distributions in zeolites by ^{129}Xe NMR spectroscopy are of major importance. Using ^{39}Ar as a model for intermolecular shielding, ab initio calculations indicate that the ^{129}Xe chemical shifts of individual Xe_n clusters and their temperature dependencies are largely due to Xe–Xe interactions, and the average chemical shifts observed for the xenon clusters arise from averaging of the ^{129}Xe shielding over the various cluster configurations.[89,93,94] Using Grand Canonical Monte Carlo methods for the simulation of the distribution and ^{129}Xe chemical shifts of individual Xe_n clusters in zeolite cages, the chemical shifts are quantitatively reproduced by making use of pairwise additive ab initio intermolecular shielding functions[95,96] based on suitable scalings of ^{39}Ar functions.[93,94]

3.2 Relaxation Times

Nuclear relaxation mechanisms among the noble gases are purely intermolecular and differ from noble gases that are chemically bound, which are dominated by intramolecular mechanisms. The spin–lattice relaxation times, T_1, of the noble gases decrease with increasing gas density.

Spin–lattice relaxation times have been determined in the pure gaseous, liquid, and solid phases of ^{3}He,[97–99] ^{21}Ne (no gas phase measurements),[91] ^{83}Kr,[92,100] ^{129}Xe,[101,102] and ^{131}Xe.[103] In the cases of the spin-$\frac{1}{2}$ nuclides, the relaxation of ^{129}Xe appears to be dominated by the spin–rotation mechanism in the transient Xe_2 molecule whereas ^{3}He relaxation is dominated by dipolar interactions. Relaxation of quadrupolar nuclides occurs by interaction of the nuclear quadrupole moment with electric field gradients arising from collisional deformations of the spherical atoms.[104,105] The observed relaxation times vary by nearly a factor of 10^3 among the three quadrupolar nuclides, ^{21}Ne, ^{83}Kr, and ^{131}Xe; T_1 = 23.5, 0.608, and 0.041 s for the liquid and T_1 = 150, 3.3, and 0.190 s for the solid, respectively. Spin–spin relaxation times (T_2) have also been measured for liquid and solid ^{129}Xe.[106]

4 REFERENCES

1. M. Saunders, H. A. Jiménez-Vázquez, R. J. Cross, S. Mroczkowski, D. I. Freedberg, and F. A. L. Anet, *Nature (London)*, 1994, **367**, 256.
2. M. Saunders, H. A. Jiménez-Vázquez, B. W. Bangerter, R. J. Cross, S. Mroczkowski, D. I. Freedberg, and F. A. L. Anet, *J. Am. Chem. Soc.*, 1994, **116**, 3621.
3. R. J. Gillespie and G. J. Schrobilgen, *Inorg. Chem.*, 1976, **15**, 22.
4. J. H. Holloway and G. J. Schrobilgen, *Inorg. Chem.*, 1981, **20**, 3363.
5. G. J. Schrobilgen, *J. Chem. Soc., Chem. Commun.*, **1988**, 863.
6. G. J. Schrobilgen, *J. Chem. Soc., Chem. Commun.*, **1988**, 1506.
7. G. J. Schrobilgen, in *NMR and the Periodic Table*, eds. R. K. Harris and B. E. Mann, Academic Press, London, 1978, Chap. 14, pp. 439–454.
8. C. J. Jameson, in *Multinuclear NMR*, ed. J. Mason, Plenum Press, New York, 1987, Chap. 18, pp. 463–477.
9. H. H. Hyman (ed.), *Noble Gas Compounds*, University of Chicago Press, Chicago, 1963.
10. N. Bartlett and F. O. Sladky, in *Comprehensive Inorganic Chemistry*, eds. J. C. Bailar, Jr., H. J. Emeléus, R. Nyholm, and A. F. Trotman-Dickenson, Pergamon Press, New York, 1973, Vol. 1, pp. 213–330.
11. D. T. Hawkins, W. E. Falconer, and N. Bartlett, *Noble Gas Compounds. A Bibliography, 1962–76*, Plenum Press, New York, 1978.
12. K. Seppelt, *Acc. Chem. Res.*, 1979, **12**, 211.
13. K. Seppelt and D. Lentz, in *Progress in Inorganic Chemistry*, ed. S. J. Lippard, John Wiley, New York, 1982, pp. 167–202.

14. H. Selig and J. H. Holloway, in *Topics in Current Chemistry*, ed. F. L. Boschke, Springer-Verlag, Berlin, 1984, Vol. 124, pp. 33–90.
15. B. Žemva, *Croat. Chem. Acta*, 1988, **61**, 163.
16. G. J. Schrobilgen, in *Synthetic Fluorine Chemistry*, eds. G. A. Olah, G. K. S. Prakash, and R. D. Chambers, John Wiley, New York, 1992, Chap. 1, pp. 1–30.
17. G. J. Schrobilgen and J. M. Whalen, in *Kirk–Othmer Encyclopedia of Chemical Technology*, 4th edn, John Wiley, New York, 1994, Chap. 13, p. 38.
18. K. O. Christe and D. A. Dixon, *J. Am. Chem. Soc.*, 1992, **114**, 2978.
19. K. Seppelt and H. H. Rupp, *Z. Anorg. Allg. Chem.*, 1974, **409**, 331.
20. K. Seppelt and H. H. Rupp, *Z. Anorg. Allg. Chem.*, 1974, **409**, 338.
21. N. Bartlett, *Proc. Chem. Soc.*, 1962, 218.
22. C. T. Goetschel and K. R. Loos, *J. Am. Chem. Soc.*, 1972, **94**, 3018.
23. G. J. Schrobilgen, Final Technical Report No. PL-TR-91-3108, Feb. 1992, Contract F49620-87-C-0049, Phillips Laboratory, Propulsion Directorate, USAF Systems Command, Edwards Air Force Base, CA, Vol. 2, pp. 23–103.
24. H. J. Frohn and V. V. Bardin, *J. Chem. Soc., Chem. Commun.*, 1993, 1072.
25. H. J. Frohn and C. Rossbach, *Z. Anorg. Allg. Chem.*, 1993, **619**, 1672.
26. H. J. Frohn and S. Jakobs, *J. Chem. Soc., Chem. Commun.*, 1989, 625.
27. H. J. Frohn, S. Jakobs, and G. Henkel, *Angew. Chem., Int. Ed. Engl.*, 1989, **28**, 1506.
28. D. Naumann, H. Butler, R. Grann, and W. Tyrra, *Inorg. Chem.*, 1993, **32**, 861.
29. D. Naumann and W. Tyrra, *J. Chem. Soc., Chem. Commun.*, 1989, 47.
30. H. Butler, D. Naumann, and W. Tyrra, *Eur. J. Solid State Inorg. Chem.*, 1992, **29**, 739.
31. H. J. Frohn, S. Jakobs, and C. Rossbach, *Eur. J. Solid State Inorg. Chem.*, 1992, **29**, 729.
32. T. Birchall, R. D. Myers, H. DeWaard, and G. J. Schrobilgen, *Inorg. Chem.*, 1982, **21**, 1068.
33. R. G. Syvret and G. J. Schrobilgen, *Inorg. Chem.*, 1989, **28**, 1564.
34. R. Faggiani, D. K. Kennepohl, C. J. L. Lock, and G. J. Schrobilgen, *Inorg. Chem.*, 1986, **25**, 563.
35. D. D. Desmarteau, R. D. LeBlond, S. F. Hossain, and D. Nothe, *J. Am. Chem. Soc.*, 1981, **103**, 7734.
36. J. F. Sawyer, G. J. Schrobilgen, and S. J. Sutherland, *Inorg. Chem.*, 1982, **21**, 4064.
37. G. J. Schrobilgen, J. H. Holloway, P. Granger, and C. Brevard, *Inorg. Chem.*, 1978, **17**, 980.
38. J. H. Holloway and G. J. Schrobilgen, *Inorg. Chem.*, 1980, **19**, 2632.
39. R. J. Gillespie, A. Netzer, and G. J. Schrobilgen, *Inorg. Chem.*, 1974, **13**, 1455.
40. A. A. A. Emara and G. J. Schrobilgen, *J. Chem. Soc., Chem. Commun.*, 1988, 257.
41. G. J. Schrobilgen, *J. Chem. Soc., Chem. Commun.*, 1988, 1506.
42. V. V. Zhdankin, P. J. Stang, and N. S. Zefirov, *J. Chem. Soc., Chem. Commun.*, 1992, 578.
43. A. A. A. Emara and G. J. Schrobilgen, *J. Chem. Soc., Chem. Commun.*, 1987, 1644.
44. A. A. A. Emara and G. J. Schrobilgen, *Inorg. Chem.*, 1992, **31**, 1323.
45. N. Keller and G. J. Schrobilgen, *Inorg. Chem.*, 1981, **20**, 2118.
46. R. G. Syvret, K. M. Mitchell, J. C. P. Sanders, and G. J. Schrobilgen, *Inorg. Chem.*, 1992, **31**, 3381.
47. R. J. Gillespie and G. J. Schrobilgen, *Inorg. Chem.*, 1974, **13**, 1694.
48. E. Jacob, D. Lentz, K. Seppelt, and A. Simon, *Z. Anorg. Allg. Chem.*, 1981, **472**, 7.
49. G. A. Schumacher and G. J. Schrobilgen, *Inorg. Chem.*, 1984, **23**, 2923.
50. K. O. Christe, E. C. Curtis, D. A. Dixon, H. P. Mercier, J. C. P. Sanders, and G. J. Schrobilgen, *J. Am. Chem. Soc.*, 1991, **113**, 3351.
51. J. C. P. Sanders and G. J. Schrobilgen, unpublished work.
52. K. O. Christe, D. A. Dixon, J. C. P. Sanders, G. J. Schrobilgen, and W. W. Wilson, *Inorg. Chem.*, 1995, **34**, 1868.
53. H. H. Rupp and K. Seppelt, *Angew. Chem., Int. Ed. Engl.*, 1974, **13**, 612.
54. H. P. A. Mercier, J. C. P. Sanders, G. J. Schrobilgen, and S. S. Tsai, *Inorg. Chem.*, 1993, **32**, 386.
55. J. Shamir, H. Selig, D. Samuel, and J. Reuben, *J. Am. Chem. Soc.*, 1965, **87**, 2359.
56. R. J. Gillespie and I. Hargittai, *The VSEPR Model of Molecular Geometry*, Allyn and Bacon, Boston, MA, 1991.
57. D. R. Brown, M. J. Clegg, A. J. Downs, R. C. Fowler, A. R. Minihan, J. R. Norris, and L. Stein, *Inorg. Chem.*, 1992, **31**, 5041.
58. N. F. Ramsey, *Phys. Rev.*, 1950, **77**, 567; N. F. Ramsey, *Phys. Rev.*, 1950, **78**, 699; N. F. Ramsey, *Phys. Rev.*, 1951, **83**, 540; N. F. Ramsey, *Phys. Rev.*, 1952, **86**, 243.
59. C. J. Jameson and H. S. Gutowsky, *J. Chem. Phys.*, 1964, **40**, 1714.
60. C. J. Jameson and H. S. Gutowsky, *J. Chem. Phys.*, 1964, **40**, 2285.
61. C. J. Jameson and J. Mason, in *Multinuclear NMR*, ed. J. Mason, Plenum Press, New York, 1987, Chap. 3, pp. 51–88.
62. G. Malli and C. Froese, *Int. J. Quantum Chem., Suppl.*, 1967, **1**, 95.
63. D. Kolb, W. R. Johnson, and P. Shorer, *Phys. Rev. A*, 1982, **26**, 19.
64. R. J. Gillespie and G. J. Schrobilgen, *Inorg. Chem.*, 1974, **13**, 765.
65. Ref. 10, pp. 223–228.
66. J. P. Jokisaari, L. P. Ingman, G. J. Schrobilgen, and J. C. P. Sanders, *Magn. Reson. Chem.*, 1994, **32**, 242.
67. C. J. Jameson, in *Multinuclear NMR*, ed. J. Mason, Plenum Press, New York, 1987, Chap. 4, pp. 89–131.
68. P. Pyykkö and L. Wiesenfeld, *Mol. Phys.*, 1981, **43**, 557.
69. R. C. Burns, L. A. Devereux, P. Granger, and G. J. Schrobilgen, *Inorg. Chem.*, 1985, **24**, 2615; M. Björgvinsson, H. P. A. Mercier, K. M. Mitchell, G. J. Schrobilgen, and G. Strohe, *Inorg. Chem.*, 1993, **32**, 6046.
70. R. J. Gillespie and G. J. Schrobilgen, *Inorg. Chem.*, 1974, **13**, 1230.
71. J. Feeney, R. Haque, L. W. Reeves, and C. P. Yue, *Can. J. Chem.*, 1968, **46**, 1389.
72. A. K. Jameson, C. J. Jameson, and H. S. Gutowsky, *J. Chem. Phys.*, 1970, **53**, 2310.
73. C. J. Jameson, A. K. Jameson, and S. M. Cohen, *J. Chem. Phys.*, 1975, **62**, 4224.

74. C. J. Jameson, A. K. Jameson, and S. M. Cohen, *J. Chem. Phys.*, 1976, **65**, 3401.
75. C. J. Jameson, A. K. Jameson, and S. M. Cohen, *J. Chem. Phys.*, 1977, **66**, 5226.
76. C. J. Jameson, A. K. Jameson, and H. Parker, *J. Chem. Phys.*, 1978, **68**, 3943.
77. T. R. Stengle, N. V. Reo, and K. L. Williamson, *J. Phys. Chem.*, 1981, **85**, 3772.
78. K. W. Miller, N. V. Reo, A. J. M. S. Uiterkamp, D. P. Stengle, T. R. Stengle, and K. L. Williamson, *Proc. Natl. Acad. Sci. USA*, 1981, **78**, 4946.
79. A. Loewenstein and M. Brenman, *Chem. Phys. Lett.*, 1978, **58**, 435.
80. J. Jokisaari and P. Diehl, *Liq. Cryst.*, 1990, **7**, 739.
81. P. Diehl and J. Jokisaari, *Chem. Phys. Lett.*, 1990, **165**, 389.
82. J. Jokisaari, P. Diehl, and O. Muenster, *Mol. Cryst. Liq. Cryst.*, 1990, **188**, 189.
83. J. A. Ripmeester and D. W. Davidson, *J. Mol. Struct.*, 1981, **75**, 67.
84. J. A. Ripmeester, *J. Am. Chem. Soc.*, 1982, **104**, 289.
85. T. Ito and J. Fraissard, *J. Chem. Phys.*, 1982, **76**, 5225.
86. L.-C. DeMenorval, J. Fraissard, T. Ito, and M. Primet, *J. Chem. Soc., Faraday Trans. 1*, 1985, **81**, 2855.
87. M. Primet, L.-C. DeMenorval, J. Fraissard, and T. Ito, *J. Chem. Soc., Faraday Trans. 1*, 1985, **81**, 2867.
88. E. W. Scharpf, R. W. Crecely, B. C. Gates, and C. Dybowski, *J. Phys. Chem.*, 1986, **90**, 9.
89. C. J. Jameson, A. K. Jameson, R. Gerald, and A. C. de Dios, *J. Chem. Phys.*, 1992, **96**, 1676.
90. C. J. Jameson, A. K. Jameson, R. Gerald, and A. C. de Dios, *J. Chem. Phys.*, 1992, **96**, 1690.
91. R. Henry and R. E. Norberg, *Phys. Rev. B*, 1972, **6**, 1645.
92. D. F. Cowgill and R. E. Norberg, *Phys. Rev. B*, 1973, **8**, 4966.
93. C. J. Jameson and A. C. de Dios, *J. Chem. Phys.*, 1992, **97**, 417.
94. C. J. Jameson and A. C. de Dios, *J. Chem. Phys.*, 1993, **98**, 2208.
95. C. J. Jameson, K. A. Jameson, B. I. Baello, and H.-M. Lim, *J. Chem. Phys.*, 1994, **100**, 5965.
96. C. J. Jameson, K. A. Jameson, H.-M. Lim, and B. I. Baello *J. Chem. Phys.*, 1994, **100**, 5977.
97. D. Vollhardt and P. Wölfle, *Physica B + C (Amsterdam)*, 1981, **108**, 1055.
98. L. J. Friedman, P. Millet, and R. C. Richardson, *Physica B + C (Amsterdam)*, 1981, **108**, 837.
99. G. Deville, M. Bernier, and J. M. Delrieux, *Phys. Rev. B*, 1979, **19**, 5666.
100. D. Brinkmann and D. Kuhn, *Phys. Rev. A*, 1980, **21**, 163.
101. R. L. Streever and H. Y. Carr, *Phys. Rev.*, 1961, **121**, 20.
102. E. R. Hunt and H. Y. Carr, *Phys. Rev.*, 1963, **130**, 2302.
103. W. W. Warren, Jr. and R. E. Norberg, *Phys. Rev.*, 1966, **148**, 402.
104. H. C. Torrey, *Phys. Rev.*, 1963, **130**, 2306.
105. B. Shizgal, *Can. J. Phys.*, 1976, **54**, 164.
106. W. M. Yen and R. E. Norberg, *Phys. Rev.*, 1963, **131**, 269.

Biographical Sketch

Gary J. Schrobilgen. *b* 1945. B.S., 1967, Loras College, IA; M.Sc., 1971, Brock University, St. Catharines, Ontario; Ph.D., 1974, McMaster University, Hamilton, Ontario. Postdoctoral fellow, University of Leicester, UK, 1974–76. Faculty in chemistry, State University of New York, Stony Brook, NY, 1976–77, and Guelph University, Ontario, 1977–78. Research associate in chemistry, McMaster University, 1978–80. University research fellow and faculty, McMaster University, 1980–90. Professor of Inorganic Chemistry, McMaster University, 1986–present. Approx. 130 publications. Research interests: synthetic and structural main group inorganic chemistry, fluorine chemistry including the chemistry of the noble gases and the polyatomic anions of main group elements.

Oxygen-17 NMR

Ioannis P. Gerothanassis
University of Ioannina, Greece

1	Introduction	1
2	Experimental Aspects	1
3	Characteristic Parameters	2
4	Selected Applications	6
5	Related Articles	9
6	References	9

1 INTRODUCTION

The structure and dynamics of oxygen-containing compounds is a subject of widespread significance. Compared with ^{1}H, ^{13}C, ^{31}P, and ^{19}F NMR, however, ^{17}O NMR has received little attention.[1–8] This neglect is not surprising since, of the naturally occurring oxygen isotopes, only ^{17}O possesses a nuclear spin ($I = \frac{5}{2}$). Due to its electric quadrupole moment ($Q_e = -2.6 \times 10^{-30}$ e m^2), its low natural abundance (0.037%), and the extremely low absolute sensitivity compared with that of ^{1}H (about 1.1×10^{-5}), the ^{17}O isotope is one of the more difficult nuclei to observe by NMR spectroscopy. It is, however, of great interest to use a nucleus such as oxygen that is located at strategic molecular sites and is directly involved in inter- and intramolecular interactions. The ^{17}O NMR parameters, i.e. isotropic shielding, principal elements of the ^{17}O shielding and electric field gradient tensors, and the transverse and longitudinal relaxation times, can be considered as excellent means of probing the structure, bonding, and dynamics of oxygen-containing compounds. Furthermore, recent advances in instrumentation, the extremely large chemical shift scale (which aids in the resolution of quadrupole broadened resonances), and the availability of ^{17}O enriched compounds have alleviated these difficulties; thus, an increased use of the ^{17}O NMR technique can be envisaged.[9–11]

2 EXPERIMENTAL ASPECTS

2.1 The Case of ^{17}O Enrichment

The stringent requirements in studies of compounds at natural abundance are the high concentrations (>0.1 M) and extensive signal averaging needed.[12] Recording of spectra can be greatly facilitated by the use of ^{17}O enriched samples (Figure 1). When using FT high field instruments and ^{17}O labeled compounds (^{17}O enrichment 10–40 atom %), concentrations of greater than 1 mM are desirable, depending on the linewidths. Synthesis involving oxygen isotopes tends to involve rather straightforward organic reactions. However, one caveat that should be kept in mind when contemplating the synthesis of an ^{17}O labeled compound is the expense of the starting reagents. Simple modifications of existing reactions are required. For example, $^{17}O_2$, C^{17}O, or C$^{17}O_2$, is added to evacuated systems, as opposed to more traditional procedures which involve bubbling through the reaction mixture. Recently, a comprehensive overview of ^{17}O enriched methods has been published.[14]

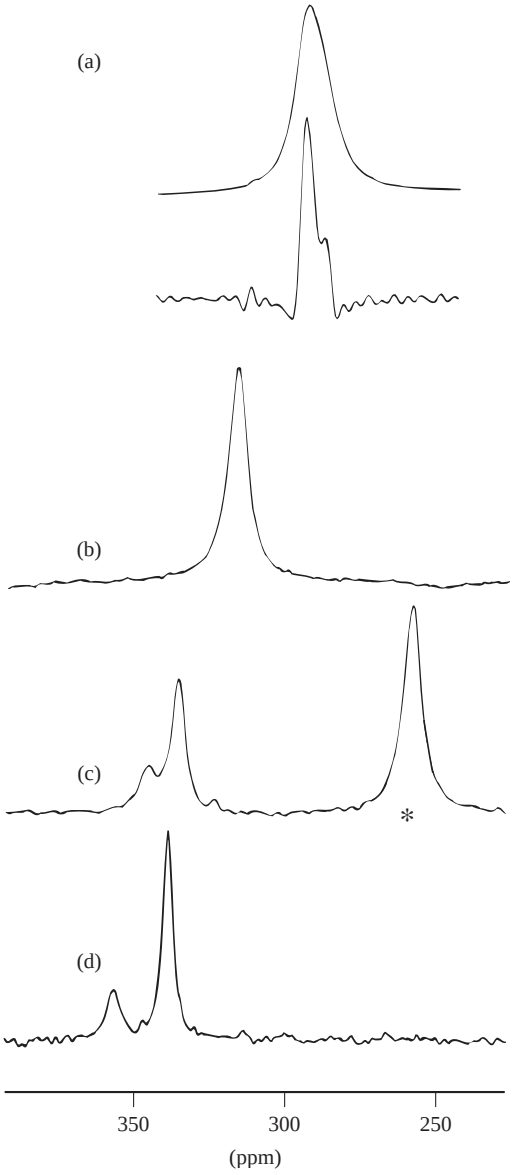

Figure 1 ^{17}O NMR spectra (48.8 MHz; 40 °C) of *N*-[^{17}O]acetyl-L-proline.[13] (a) 10% enrichment, 0.1 M in aqueous solution containing 1 M NaCl and 5×10^{-5} M EDTA; T_{acq} = 12 ms, NS = 300 000, total experimental time = 1 h: (upper trace) normal spectrum; (lower trace) after a Gaussian-exponential resolution enhancement. (b) 1% enrichment, 0.1 M in methanol, T_{acq} = 10 ms, NS = 200 000, total experimental time = 32 min, line broadening (LB) = 50 Hz. (c) 0.4 M natural abundance in acetone (the asterisk marks the carboxyl oxygen resonance); T_{acq} = 5 ms, number of scans (NS) = 1 900 000, total experimental time ≃10 h, LB = 50 Hz; (d) 1% enrichment, 0.1 M in acetone; T_{acq} = 10 ms, NS = 1 350 000, total experimental time ≃8 h, LB = 50 Hz. (Adapted by permission of The American Chemical Society from R. N. Hunston, I. P. Gerothanassis, and J. Lauterwein, *J. Am. Chem. Soc.*, 1985, **107**, 2654)

2.2 Referencing Techniques

As with many heteronuclei, a variety of reference compounds and referencing procedures (both internal and external) have been suggested for ^{17}O NMR. For diamagnetic solutions, an external standard in a combined use of two cylindrical cells has been recommended.[15] Using this technique, doubly distilled water or 1,4-dioxane can be used as external reference. Both compounds have chemical shifts which are indistinguishable at 30–40 °C and their magnetic susceptibility correction is small (<0.6 ppm) relative to common organic solvents. However, H_2O has the disadvantage that its chemical shift varies with temperature (−3 ppm between 27 and 90 °C) due to cleavage of intermolecular hydrogen bonds (the same applies for D_2O in addition to an isotopic effect of −3 ppm).

2.3 Solvent (H_2O) Suppression

Perhaps the most straightforward approach to solvent suppression is the use of ^{17}O depleted water, provided of course that rapid ^{17}O exchange does not occur between solvent and solute.[16] Further suppression can be achieved by exploiting the special relaxation properties of the solvent, by postexperiment data processing and by selectively exciting the whole spectrum apart from that of the solvent.[17] A critical note on the usefulness of the selective excitation pulse sequences in ^{17}O NMR has recently been published.[18]

2.4 Acoustic Ringing

Observation of very broad resonances in NMR is a potential problem due to baseline distortions. The most severe of the baseline artifacts is that due to the transient response of the NMR probe, often referred to as 'acoustic ringing', caused by the generation of ultrasonic waves from the action of the rf pulse. In the last decade, several pulse sequences designed for the suppression of acoustic ringing have been reported, and the reader should consult a relevant review article for details.[19] For experiments in solution, the extended spin echo sequence was found to be particularly useful, since it utilizes minimum pulse and preacquisition delay times. A closely related pulse sequence for experiments in the solid phase has also been suggested.[20]

3 CHARACTERISTIC PARAMETERS

3.1 Chemical Shifts

3.1.1 Experimental Shielding Ranges: Empirical Correlations

A general pattern of ^{17}O shielding is shown in Figure 2. For compounds containing oxygen bonded only to carbon and/or hydrogen there is a clear correlation between the C–O π bond order and a high frequency shift.[21] This type of correlation arises from the multiple bond term $\Sigma_{B\neq A}Q_{AB}$ in the Karplus–Pople equation.[22] For bridging oxygen atoms, a strong deshielding is observed when the substituents R are replaced by π-accepting acyl substituents which introduce π character into the C–O bond of the bridging oxygen. Thus, bridging oxygen resonances in carbonates and esters appear at high frequency relative to the corresponding resonances in alcohols, ethers, and acetals. An even greater high frequency shift is observed for anhydrides, where bridging oxygen atoms are bonded to two π acceptors. If chemical shifts are assumed to depend linearly on π bond order, the chemical shift of about 600 ppm for aliphatic aldehydes (π bond order of about 1) relative to water (π bond of 0) implies a chemical shift of about 200 ppm for CO_3^{2-} (π bond order of $\frac{1}{3}$). The observed shift of CO_3^{2-} (192 ppm) is in agreement with this crude prediction, further supporting the general correlation between π bond order and shielding discussed above.[2]

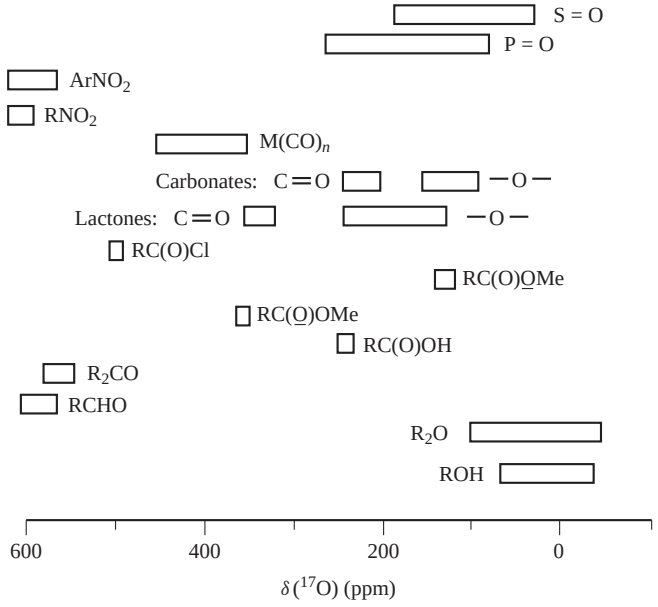

Figure 2 ^{17}O chemical shift ranges for different X–O bonds. (Adapted by permission of Plenum Press from W. McFarlane and H. C. E. McFarlane, in 'Multinuclear NMR', ed. J. Mason, 1987, Chap. 14)

In nitrogen-containing compounds, as in carbon compounds, chemical shift values are determined largely by π bonding effects.[23–25] Bridging oxygen resonances are observed at even higher frequency in nitrates, where π bonding is appreciable. A lesser, but nonetheless significant, effect is observed for bridging oxygen atoms in nitrates. The most striking feature of the ^{17}O shifts observed for P–O bonds is the small chemical shift range (20–260 ppm) which cannot be related to P–O bond order in a straightforward fashion. However, ^{17}O resonances for nonequivalent oxygen atoms in phosphates and polyphosphates can be resolved and have been used in stereochemical and binding site studies.[26–28] For S–O bonding, similar trends to those displayed by P–O bonds are observed. Modification of the π bond order in an X=O group due to substituents on X results in a decrease (or increase) in the net charge on X as the charge on oxygen increases (or decreases). The chemical shift variations experienced by the nuclei X and O are then opposite and roughly proportional to the ratio $\langle r^{-3}\rangle_{2p_X}/\langle r^{-3}\rangle_{2p_O}$.[24] For a series of oxyanions and a series of C=O and N=O compounds a linear correlation has been found between $\delta(^{17}O)$ and the variation in ΔE^{-1}.[29] A linear correlation exists between acetone chemical shifts and the first maximum of the $n \rightarrow \pi^*$ transition for acetone/water

solutions[30] and for acetone in different solvents.[31] Similar trends have also been observed in a variety of substituted acetophenones;[32] however, it was suggested that such trends may be fortuitous, since the transition energy depends upon the balance of several effects associated with both π donation and σ withdrawal.[33] From a study on a series of aliphatic ethers, a correlation between $\delta(^{17}O)$ and the first ionization potential has been suggested.[34]

Compounds containing oxygen–oxygen bonds and oxygen–fluorine bonds display large high-frequency shifts.[35–37] The ability, therefore, of ^{17}O NMR to distinguish unambiguously between nonequivalent oxygen atoms has found application in several structural and mechanistic studies. The same applies to oxygen bonded to transition metals (see below). Empirical correlations were extended to diamagnetic transition metal anions of the general formula MO_4^{n-}, and theoretical calculations were carried out to show that the absolute magnitude was reasonable.[29]

3.1.2 Theory of ^{17}O Chemical Shifts (see **Shielding: Overview of Theoretical Methods**)

3.1.2.1 Isolated Molecules. Ab initio calculations[38,39] of ^{17}O nuclear shielding tensors have been reported for a variety of simple molecules such as H_2O, CH_3OH, $(CH_3)_2O$, H_2CO, CH_3CHO, $HCONH_2$, and CO. The results are gauge dependent and in many cases vary considerably depending on the basis set used. Gauge independent ab initio results for H_2O and H_2CO indicate a ^{17}O shielding of 757.6, 860.3, or 858.8 ppm for H_2CO, with respect to H_2O, compared with the experimental result of 580–600 ppm. The calculated data represent a choice of three basis sets. Semiempirical INDO (intermediate neglect of differential overlap) calculations are numerically smaller than the experimental results, whereas the CNDO/S (complete neglect of differential overlap/S) calculations produce better overall agreement.[40–43] This probably reflects an insensitivity of the INDO orbital energies to changes in the environment of the oxygen. By omitting those molecules and ions which have nitrogen directly bonded to oxygen the CNDO/S results gave a standard deviation of 30.6 ppm and a correlation coefficient of 0.98 compared with the experimental values. Analysis of the CNDO/S results demonstrates that the ^{17}O shielding differences of some carbonyl compounds are dominated by the lowest energy $n \rightarrow \pi^*$ transition. For the linear species CO, CO_2, and NO_2^+, the largest contribution to the paramagnetic part σ_p of the ^{17}O shieldings arises from the lowest energy $\sigma \rightarrow \pi^*$ transition. Similarly, for the bent ion NO_2^- the lowest energy $\sigma \rightarrow \pi^*$ transitions are dominant for the in-plane components of the shielding tensor, while the out-of-plane contribution is controlled by $\sigma \rightarrow \sigma^*$ transitions. In general, these ^{17}O shieldings are in reasonable agreement with the available experimental data, and in some cases are an improvement upon ab initio results. Analogous calculations employing a basis set of gauge dependent atomic orbitals within the CNDO/2 framework have been reported for ^{17}O shieldings in electrolyte solutions.[44] For ozone,[45] the use of localized molecular orbitals within the IGLO method (see ***Shielding Calculations: IGLO Method***) allows the contributions to the total shielding to be partitioned into orbital contributions, so that the specific role played by the lone pairs on the atom in question and orbitals centered on neighboring atoms can be discerned.[46] The calculated shieldings for O_3 were found to be extremely large, highly anisotropic, and to differ from the experimental values by a factor of 2–3. The authors also noted that the paramagnetic contributions are mainly due to the lone pairs on the respective oxygen atoms, unlike the triatomic molecules CO_2 and FNO in which the paramagnetic contributions are mainly due to the bonds interacting with the antibonding π^* electrons and only to a limited extent to the lone pairs.

3.1.2.2 Solvent and medium effects. Recently, the effect of electrical polarization on the chemical shielding of carbon monoxide has been considered in detail.[47,48] In addition, the relationship between the vibrational frequency and the shieldings for three different types of electrical environments—a uniform field, a field gradient, and an axial point-charge dipole—together with experimental ^{13}C and ^{17}O isotropic shieldings and vibrational frequencies for a range of carbon monoxide derivatives of heme proteins has been described. For each type of environment, the shieldings vary linearly with the vibrational frequency for a relatively wide range of frequency shifts.[48] This shows, in agreement with experiment,[49] that there is a linear relationship that is opposite for ^{13}C and ^{17}O.[50]

The effects of solvents on the ^{17}O nuclear shielding of solute molecules may be categorized into hydrogen-bonding interactions and influences that arise from electronic interactions between the dipole moments of the solute and solvent molecules. Precise mathematical expressions are not available for many nonbonded interactions. Consequently, continuum models tend to be more popular for investigating solvent effects on NMR parameters. The most widely used of these, to date, is the solvaton model.[51] By means of this model the solute–solvent interaction can be included in the paramagnetic screening contribution, and the solvent induced shift is proportional to $(\epsilon - 1)/2\epsilon$, where ϵ is the dielectric constant of the medium. Some sum-over-states (SOS) and finite perturbation theory (FPT) calculations of oxygen nuclear shieldings of several organic functional groups, as obtained using the solvaton model, predict increases in shielding as ϵ increases.[50,52] An analysis of the various factors contributing to the paramagnetic term reveals that the increase in shielding arises from a concomitant decrease in $\langle r^{-3} \rangle_{2p}$ and an increase in the weighted average of the energies of the various transitions contributing to the paramagnetic term. The observed decrease in $\langle r^{-3} \rangle_{2p}$ is consistent with an increase in the average separation between the nucleus and its 2p electrons as the charge q increases. The increase in the weighted averaged of the transition energies is largely controlled by the increase in energy of the lowest $n \rightarrow \pi^*$ transition as the extent of solvation increases.

The shielding of the ^{17}O nuclei of several functional groups are quite sensitive to hydrogen-bonding interactions. From a theoretical standpoint the shielding may be considered by using the supermolecule approach. A good example is provided by formamide.[53] Ab initio calculations using GIAOs (gauge invariant atomic orbitals) within the FPT framework have been reported for formamide (FMA) in the presence of its first hydration shell. The ^{17}O shielding values reported for the complexes $FMA–(H_2O)_2$ show that the shift observed when the oxygen atom is directly involved in the hydrogen bond is much larger than the one occurring when the water molecules are bound to the NH group. The variation was calculated to be to low frequency in both cases. This is in agreement with

^{17}O NMR experimental data on FMA and several amides in different solvents.

3.2 Indirect Spin Coupling Constants

Because of the breadth of ^{17}O resonances, only relatively large coupling constants can be measured, and hence the majority of those recorded refer to couplings from directly bonded nuclei. ^{1}J(O,H) in water and alcohols has values close to 80 Hz.[54–56] The ^{1}J(P,O) couplings involving P=O groups cover a fairly wide range (145–210 Hz) and for a series of compounds of type OPX_3 (X = F or O in OMe, X = N in NMe_2, and X = C in Me) there is a consistent drop in coupling with decreasing electronegativity of X. This may be qualitatively attributed to the electronegative substituents removing electrons in outer orbitals from the phosphorus atom, leading to a greater effective atomic charge and hence stronger contact interaction between the phosphorus nucleus and the s orbitals. A finite perturbation theoretical treatment within the CNDO/2 formalism has reproduced the observed trends, but not the absolute values.[57] The oxygen atoms in P–OMe groups within phosphates give rise to a consistently smaller coupling constant, compared with P=O, of between 90 and 100 Hz; there is an indication of a considerably larger value for phosphites. The reduced coupling constants decrease with increasing atomic number of the central atoms along the isoelectronic sequence VO_4^{3-}, CrO_4^{2-}, and MnO_4^{-}.[58] The values of ^{17}O spin–spin couplings have been used to investigate H_3O^+ species.[59] The ^{17}O NMR spectrum revealed a perfect quartet with J(O,H) = 107 Hz. Furthermore, the effect of H/D substitution is evident in the ^{17}O NMR spectra of H_2O–D_2O in CH_2Cl_2. Thus, the species H_2O, HDO, and D_2O could be identified from coupling constants, without reference to chemical shift data.[60] ^{2}J couplings are normally about an order of magnitude smaller than the corresponding directly bonded couplings.[61] However, there seems to be a particularly favored coupling pathway from hydrogen to the 'ether' oxygen atom in HCOOR systems, which is probably associated with π bonding across the planar framework.

In some cases coupled resonances cannot be resolved into fine structure but exhibit a partially collapsed structure, depending on the rate of proton transfer. In such cases decoupling of the other nuclei can lead to reduced linewidths and information about coupling constants.

When a spin-$\frac{1}{2}$ nucleus is bonded directly to ^{17}O, the X nucleus will also be relaxed by virtue of its spin–spin coupling with ^{17}O. This has been termed 'scalar relaxation of the second kind'. Such a line-broadening effect for ^{17}O in ^{31}P NMR has been used to locate the position of the ^{17}O label and to calculate the percentage enrichment of ^{17}O. In addition, it has made possible analysis of the configuration of (^{16}O, ^{17}O, and ^{18}O) phosphate monoesters and (^{16}O, ^{17}O, and ^{18}O) thiophosphates by ^{31}P NMR.[62–64]

3.3 Nuclear Quadrupole Coupling Constants

The electrostatic interaction between the nuclear quadrupole electric moment Qe and the electric field gradient tensor eq_{ij} is the quadrupolar interaction. An appropriate reference axis system can be chosen to reduce this interaction to two values:[4] the main component

$$\chi = e^2 q_{zz} Q/h \tag{1}$$

and the asymmetry parameter (dimensionless)

$$\eta = (e^2 q_{xx} Q - e^2 q_{yy} Q)/e^2 q_{zz} Q \tag{2}$$

where $|e^2 q_{zz} Q| > |e^2 q_{yy} Q| > |e^2 q_{xx} Q|$.

The χ values for ^{17}O may be calculated by computing the field gradient from molecular wavefunctions and using the nuclear quadrupole moment Qe. Only relatively small molecules have been studied. Thus the calculated χ value for CO using the GAUSSIAN 88 program at the 6-31G* level[49] (3.1 MHz) was found to deviate from the experimental value (~4.4 MHz) (the value of 3.9 MHz obtained from ab initio calculations[47] is in better agreement with the experimental value). Furthermore, it was shown that hydrogen bonding to HF results in a significant decrease in χ of about 0.7 MHz for the linear species CO···HF.

Semiempirical methods of various degrees of sophistication have been used to compute electric field gradients. Within the framework of the Townes–Dailey theory, the three components of the field gradient can be related to the electronic populations in the orbitals describing the oxygen bonding and to eq, the field gradient created by an electron in a 2p atomic orbital (the contribution from the valence s electrons is neglected because of the spherical symmetry). More elaborate models incorporate hybridization of atomic orbitals into valence bonding and lone pair orbitals. Such studies include the determination of σ and π orbital populations for X–O bonds (X = C, N, P, or S).[65,66]

The majority of experimentally determined χ and η values have been obtained in the solid state by the use of NQR spectroscopy; however, some have been determined by NMR measurements on powders or single crystals, where χ is small with respect to the NMR frequency. Quadrupole coupling constants have also been derived from the splittings in the ^{17}O spectra of molecules partially oriented in an electric field[67] or dissolved in a nematic liquid crystal.[68,69] Detailed studies of polynuclear osmium carbonyl dynamics have been undertaken and together with ^{13}C measurements have provided estimates of the ^{17}O quadrupole coupling constants.[70] In molybdenum hexacarbonyl, the ^{95}Mo and ^{97}Mo linewidths gave the reorientational correlation time, which in turn made it possible to determine the χ values from the ^{17}O linewidth.[71]

Experimental χ values cover the range −8 to 17 MHz. The sign of χ is irrelevant to the NMR experiment, but from a theoretical point of view it gives information about the orientation of the field gradient. The experimental χ values for a series of compounds in the solid state that contain C=O, –O–, P–O, N–O, or S–O bonds show the following trends:[6]

1. For substituted nitrophenols, hydroxybenzaldehydes, and nitrobenzaldehydes, the χ values are nearly invariant with the electronic properties of the substituent, but are reduced by hydrogen bonding.
2. Strong hydrogen bonding reduces the χ values by as much as 2.6 MHz.

In summary, the following scale of χ values has been suggested:

O − O >	N − O >	NO_2 >	C = O >	P − OR ≃ S = O
16 − 17	16	13	11 − 9	9.5 − 9

ROH >	SO_2 >	P = O ≃ C = O >	XO_n^{m-}
9 − 8	6.7	4	1

The ^{17}O χ values for the terminal CO groups in metallocarbonyls were found to be 1–3 MHz, although values below 0.1 MHz have also been observed. It was suggested that increased dπ–pπ back-bonding from the metal will increase electron density perpendicular to the C–O axis and so reduce the χ values.[72]

3.4 Relaxation Properties (see *Relaxation Theory for Quadrupolar Nuclei*)

3.4.1 Relaxation in the Extreme Narrowing Condition

In isotropic systems and in the absence of chemical exchange, the T_1 and T_2 relaxation times are equal and are given by

$$1/T_1 = 1/T_2 = 3/125(1 + \eta^2/3)\chi^2 f(\omega,\ D) \qquad (3)$$

where χ is the nuclear quadrupole coupling constant. The asymmetry parameter η varies from 0 to 1 and describes the deviation of the electric field gradient from axial symmetry. $f(\omega,D)$ is the correlation function, which depends on the rotational diffusion constant D and its relative orientation with respect to the principal axes of the field gradient tensor. When isotropic reorientation is assumed, $f(\omega,D)$ reduces to the single correlation time τ_c. If the resonance absorption is a Lorentzian lineshape, the linewidth at halfheight $\Delta\nu_{\frac{1}{2}}$ is a direct measure of the relaxation time, provided that unresolved indirect spin coupling is not present and that chemical exchange phenomena do not take place. From equation (3) it is clear that the product $\chi^2(1 + \eta^2/3)$ can be obtained from ^{17}O relaxation times if the correlation time governing the relaxation is known. The Debye formula allows only the determination of the correct order of magnitude of τ_c. More precise values of τ_c could be obtained from the relaxation of other nuclei, such as ^{13}C or other quadrupolar nuclei; however, one should be aware of possible anisotropic reorientations due to molecular tumbling.[4]

3.4.2 Relaxation Outside the Extreme Narrowing Condition

In this case, the decay of the longitudinal (M_1) and transverse (M_2) magnetizations is no longer exponential but may be written as a weighted sum of $I + \frac{1}{2}$ exponentials:[73]

$$M_1(t) = M_1(\infty)\left\{1 - k\left[\sum_{i=1}^{I+1/2} C_{1,i}\ \exp\left(-R_{1,i}t\right)\right]\right\} \qquad (4)$$

$$M_2(t) = M_2(0)\left[\sum_{i=1}^{I+1/2} C_{2,i}\exp(-R_{2,i}t)\right] \qquad (5)$$

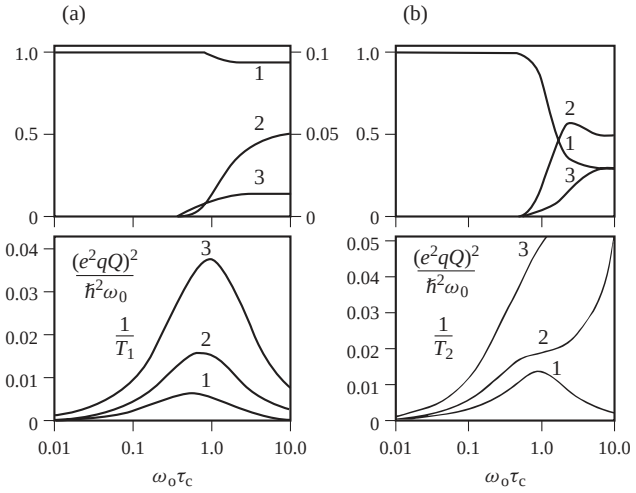

Figure 3 Longitudinal (a) and transverse (b) relaxation of spin-$\frac{5}{2}$ nuclei in the absence of chemical exchange. The upper plots show the normalized amplitudes $C_{1,i}$ and $C_{2,i}$ of the three exponential components as a function of $\omega_0\tau_c$ (coefficients 2 and 3 are plotted on the expanded scale given to the right). The lower plots show the relaxation rates as a function of the same parameter. (Adapted by permission of The American Institute of Physics from T. E. Bull, S. Forsen, and D. L. Turner, *J. Chem. Phys.*, 1979, **70**, 3106)

where $\sum_{i=1}^{I+1/2} C_{j,i}$ and $k = 2$ for an inversion–recovery experiment. Furthermore, although equation (4) is valid for the total magnetization, the decays of the individual components will normally not be exponential and will also depend on the length of the monitoring pulse. Equations (4) and (5) cannot be solved analytically, but must be solved numerically for each value of $\omega_0{}^2\tau_c{}^2$. Figure 3 illustrates the longitudinal and transverse relaxation of spin $I = \frac{5}{2}$ nuclei in the absence of chemical exchange. The longitudinal relaxation may be regarded as a single exponential, within the limits of experimental error, for all correlation times. Conversely, the transverse relaxation is governed by the three contributions and the weights of the different contributions have similar magnitudes for the longer correlation times. For values of $\omega_0{}^2\tau_c{}^2 \ll 1$, the transverse relaxation is approximately a single exponential. In the slow motion limit the rapid decay of the third component at longer correlation times may allow analysis in terms of just two exponential terms.

In addition to nonexponential relaxation for quadrupolar nuclei under conditions of nonextreme narrowing, the NMR signal will also be modified by shift changes which have been termed 'second-order dynamic frequency shifts' (see ***Quadrupolar Interactions*** and ***Dynamic Frequency Shift***). Although long recognized theoretically, the experimental demonstration of such a phenomenon is not straightforward, since the symmetry of the composite peak is in practice difficult to distinguish from small phase misadjustment and is thus usually overlooked. Furthermore, strongly relaxed transitions may decay so quickly as to be undetected if the instrument deadtime is too long. Expressions for the NMR bandshape for $I = \frac{5}{2}$ and $I = \frac{7}{2}$ nuclei have been derived, both in the presence and the absence of chemical exchange.[74] In the limit $\omega_0\tau_c \gg 1$, the $m = \frac{1}{2} \rightarrow m = -\frac{1}{2}$ component will dominate the spectrum because it is much narrower than the other components. This narrow signal will be shifted

towards lower frequency with a value proportional to χ^2/ω_0. Between these two limits the resonance will be more or less asymmetric, with an apparent shift to either high or low frequency depending on the values of ω_0, τ_c, and χ. The ratio of the dynamic shift to the linewidth $\Delta\omega_d/\Delta\omega_{\frac{1}{2}}$ in this region depends only on ω_0 and τ_c.

3.4.3 *Effects of Relaxation Mechanisms Other Than Quadrupolar*

It is evident from Figure 3 that the linewidth of the narrow component decreases as τ_c increases in the slow motion limit, while the linewidths of the intermediate and broad components increase. However, the linewidth of the narrow component does not necessarily decrease as τ_c increases if the chemical shift anisotropy is large. Such behavior has been observed in studies of the temperature and magnetic field strength dependence of ^{17}O NMR spectra of myoglobin MbC^{17}O samples.[75] For $\tau_c \simeq 14$ ns and $\sigma_{\parallel} - \sigma_{\perp} = 800$ ppm (which is the value for a model heme compound obtained from NMR studies in the solid state) a CSA contribution to the linewidth of about 100 Hz was obtained for the narrow components. This value is comparable to that of the pure quadrupolar contribution to the linewidth (about 96 Hz). The CSA contribution to T_1 was found to be negligible (about 170 ms).

4 SELECTED APPLICATIONS

4.1 Dynamic and Kinetic Studies

Numerous dynamic and kinetic studies have been performed using ^{17}O NMR. Lineshape analysis is not straightforward because the linewidth itself is temperature dependent. Nevertheless, it has been shown that dynamic ^{17}O NMR is a convenient alternative to ^{13}C NMR for studies of metal carbonyl compounds.[76] A solution of $HFeCO_3(CO)_{12}$ at $-89\,^{\circ}$C gives only two ^{13}CO signals in a ratio of 1:2 instead of the expected four signals with a 1:1:1:1 ratio. In ^{17}O NMR, the four signals are easily observed at $-11\,^{\circ}$C and a two-step exchange process averages all the sites, producing a single line at $108\,^{\circ}$C.

^{17}O NMR has been used to measure the rate of oxygen exchange in aldehydes and ketones,[77] cobaloximes,[78] and the periodate–water system.[79] It is possible to measure either the decay of a signal from a group enriched in ^{17}O or the growth of a signal that is undergoing exchange with ^{17}O labeled water.[3]

A substantial number of publications has been concerned primarily with studies of the hydration of ions in solution. The ^{17}O chemical shift of water molecules bound to Al^{3+} was found to be about 11 ppm to high frequency. Temperature dependence studies and lineshape analysis yielded the ^{17}O nuclear relaxation rates of the bound and free water molecules, the coordination number, and the rates of exchange between the bound and free water.[80] In addition, the thermodynamic parameters for activation characterizing the exchange reaction can be obtained. In cases where the chemical shift between 'bound' and 'free' water molecules is small, leading to overlapping of resonances, the resonance of the 'free' molecule can be shifted by adding small amounts of a paramagnetic salt. Estimates of 4, 6, and 6 for the hydration numbers of Be(II), Al(III), and Ga(III) were obtained from area measurements. An alternative method of determining hydration numbers, by evaluating the magnitude of the shift of the water resonances caused by the dissolved paramagnetic ion, has also been suggested.[80]

There is an extensive literature on ^{17}O NMR studies of the exchange rates of water molecules bound to paramagnetic ions.[81–84] In this case there is a much greater chance of observing separate resonances from ^{17}O nuclei in 'bound' water molecules in the solvation shells of paramagnetic cations than in the corresponding diamagnetic cations. The magnitudes and temperature dependences of the linewidths (or relaxation time measurements) of the 'bound' and 'free' resonances, and the chemical shift separations between these resonances, can in principle be used to derive information about the hyperfine splitting constant, a_N, the rate of the solvent interchange process, T_e, and the solvation number. However, because the shifted resonance of the solvated water molecules is also often very broad, it is rarely possible in practice to derive the hydration number of the paramagnetic cation from straightforward area measurements. In such cases the hydration numbers may be obtained by using the theory developed by Swift and Connick[85] who investigated a variety of systems. This type of work and the chemical significance of the results have been reviewed (see ***Paramagnetic Relaxation in Solution***).[86]

4.2 ^{17}O NMR and Torsion Angle Effects

^{17}O NMR spectroscopy is a powerful method for detecting steric effects in molecules in which the steric interactions are characterized by the rotation of functional groups about single bonds to relieve van der Waals interactions or in rigid systems in which the steric interactions are partially accommodated by bond angle and bond length distortions.[87] ^{17}O deshielding is expected when the rotation leads to greater double bond character or reduced electron density on oxygen (e.g. in an isolated carbonyl group). Shielding, however, is observed in the situation in which the carbonyl group assumes more single bond character or increased density on the oxygen atom. Studies of such steric effects have been done on aromatic and heteroaromatic nitro compounds, aryl ketones, aldehydes and 1,2-diketones, aromatic carboxylic acids, esters and amides.[88–91] For nitro aromatic compounds, a quantitative relationship was established between $\delta(^{17}O)$ of the nitro group and the torsional angle between the aromatic ring and the nitro group (Figure 4). It appears that the solid state conformational preference, and thus the angle, is in remarkably good agreement with the average angle determined in the solution state.

4.3 Hydrogen-Bonding Effects (see *Hydrogen Bonding*)

The use of ^{17}O NMR appears to be especially promising for studying hydrogen-bonding interactions, because of the large chemical shift range of the oxygen nucleus.[92–94] The dominance of intramolecular hydrogen-bonding effects over substituent effects has been clearly demonstrated in acetophenones, benzaldehydes, and hydroxynaphthoquinones.[32,95] In

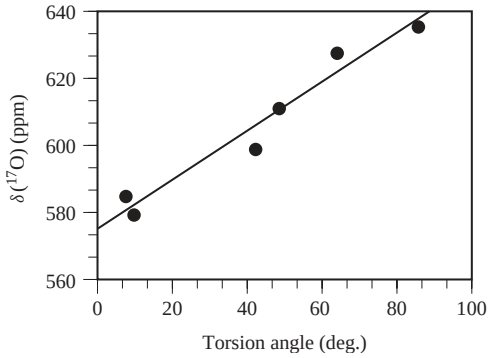

Figure 4 Plot of the torsion angles (X-ray) between aromatic rings and nitro groups versus ^{17}O chemical shift data.[87] (Reproduced by permission of CRC Press, Inc., from D. W. Boykin and A. L. Baumstark, in '^{17}O NMR Spectroscopy in Organic Chemistry', ed. D. W. Boykin, 1991, Chap. 3)

amides and peptides,[10,93,96–100] both long-range dipole–dipole interactions and specific hydrogen bonds at the amide oxygen atom induce significant and specific shielding of the ^{17}O nucleus. Thus the overall chemical shift change between an amide oxygen atom in the absence of hydrogen-bonding interactions in vacuum and one that is fully hydrated in aqueous solution is, very probably, over 95 ppm. There is a linear correlation between $\delta(^{17}O)$ and $\nu(CO)$, the infrared (IR) amide I stretching vibration, for different solvents which have varying dielectric constants and solvation abilities.[100] This demonstrates that both IR and ^{17}O NMR spectroscopy appear to be reflecting a similar type of electronic perturbation, i.e. hydrogen bonding and dipole–dipole solute–solvent interactions. Further studies include investigations of the hydration and intra- and intermolecular hydrogen bonding of the *cis*/*trans* peptide oxygen atoms in AcYOH and AcYNHMe (Y = Pro or Sar)[13,98] (Figure 1), protected dipeptides,[99] and peptide hormones.[101–103]

4.4 Oxygen Bonded to Transition Elements (Polyoxometalates)

^{17}O NMR has been employed frequently in stereochemical studies of polynuclear, anionic oxo complexes (polyoxoanions) of the early transition elements in a variety of oxidation states.[104–108] In spite of their structural complexity, these polyoxoanions often yield well resolved ^{17}O NMR spectra, since large chemical shifts are observed and samples may often be observed at elevated temperatures in nonviscous solvents. Furthermore, ^{17}O enrichment is easily obtained. A representative example is the $[V_{10}O_{28}]^{6-}$ species, the structure and spectrum of which are shown in Figure 5. Exchange of oxygen atoms in the complex ion with those of $H_2{}^{17}O$ in aqueous solution showed that all the different oxygen sites could be identified separately by their shieldings. If an oxygen atom attached to n vanadium atoms is designated as OV_n, then the observed chemical shifts are: OV $\simeq$1150; OV_2 (three different sites) $\simeq$ 900, 790 and 760; $OV_3 \simeq 390$; and $OV_4 \simeq 65$ ppm. It can be seen that there is a systematic reduction in $\delta(^{17}O)$ with an increase in the number of vanadium atoms to which the oxygen atom is bound. Other complex anions of the formula $[M_6O_{19}]^{n-}$, where M = Mo (n = 2), Nb

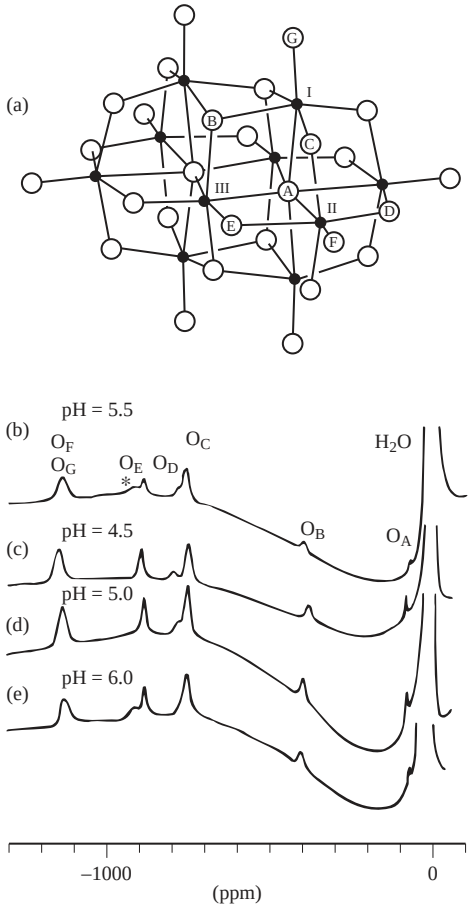

Figure 5 (a) The D_{2h} symmetrized structure of $V_{10}O_{28}{}^{6-}$. Small filled circles represent vanadium atoms and large open circles represent oxygen atoms. One member of each symmetry-equivalent set of atoms is labeled. (b–e) ^{17}O NMR spectra at 13.5 MHz of $V_{10}O_{28}{}^{6-}$ in H_2O. All spectra were measured at 25 °C with total vanadium concentrations of 1.5–1.8 M. The asterisk labels the metavanadate resonance. (Adapted by permission of The American Chemical Society from W. G. Klemperer and W. Shum, *J. Am. Chem. Soc.*, 1977, **99**, 3544)

(n = 8), or Ta (n = 8), show the same qualitative regularities in shielding, with OM > OM_2 > OM_6. These regularities have been interpreted as a correlation between increasing chemical shift and increasing π bonding from the metal to the oxygen in different sites. The regularities persist in the ^{17}O spectra of a variety of more complex anions of lower symmetry in which other metals or nonmetals are substituted within an $[M_xO_y]^{n-}$ framework. It should be noted that the resonances of oxygen nuclei in the highly symmetrical environments of the complex anions, e.g. OM_4 or OM_6, are relatively sharp. This is to be expected because the field gradient at these positions will be zero or very small; hence the normally dominant quadrupolar relaxation mechanism will be very weak and the relaxation times correspondingly long.

4.5 Heme Proteins and Model Compounds—Substrate Binding to Enzymes

The ^{17}O NMR spectra of several heme model compounds in solution have been reported.[11,109–111] Two signals at about

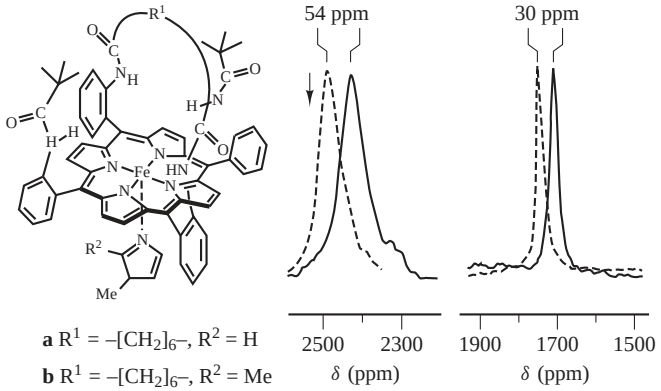

Figure 6 ^{17}O NMR spectra (54.2 MHz) of the oxygenated compounds **a**(- - - -) and **b** (—) with a preacquisition delay time Δt = 50 μs and recorded in two steps with the carrier frequency on the absorption resonances. Maximum concentration $\simeq 10^{-2}$ M in toluene solution. Concentration of 1,2-dimethylimidazole (1,2-Me_2Im) $\simeq 5.10^{-1}$ M, T = 297 K, NS = 1 080 000 (LB = 1 kHz) and 350 000 (LB = 500 Hz) for the high- and low-frequency resonances, respectively. The arrow denotes the region of the resonance position of the terminal oxygen atom of the picket-fence porphyrin model, with excess 1-MeIm, and ether models in which no hydrogen bonding interactions are expected. (Adapted by permission of the Royal Society of Chemistry from I. P. Gerothanassis, B. Look, and M. Momenteau, *J. Chem. Soc., Chem. Commun.*, 1992, 598)

1750 and 2500 ppm were observed for the FeO_2 linkage (Figure 6). The data were interpreted as ruling out sideways triangular bonding in favor of an end-on angular bonding arrangement. The data were explained in terms of bonding models in which the electrons of the FeO_2 moiety are totally paired.

Analysis of the ^{17}O relaxation and chemical shift data of $C^{17}O$ ligated hemoproteins has provided information on both the structural and the dynamic properties of the heme group.[49,75,112] Peroxidases are heme proteins with molecular weights of about 40–42 kDa that catalyze oxidations by hydrogen peroxide. They contain iron-protoporphyrin IX as a noncovalently bound prosthetic group. The ^{17}O NMR spectra of CO-horseradish peroxidase isoenzyme C (Figure 7) indicate a single hemoprotein $C^{17}O$ signal (at 358.3 ppm) below pH 10 and two separate signals at pH 10.5. The new signal, which was assigned with the alkaline form of CO-horseradish peroxidase isozyme C, is broader and at about 7 ppm to high frequency relative to that of the acidic form. A similar pH-dependent relationship of the chemical shift and linewidth was observed for CO-horseradish peroxidase isozyme A and CO-horseradish peroxidase isozyme C. It was concluded that CO-horseradish peroxidase isozyme C undergoes a transition between the acidic and alkaline forms.[112] However, unlike the case of CO-horseradish peroxidase isozyme A, the transition is slow on the NMR timescale (see ***Oxygen-17 NMR: Applications in Biochemistry***).

4.6 Hydration of Proteins: Water Orientation in Lyotropic Phases and Bilayers

Water plays a fundamental role in the conformation and activity of biological macromolecules (see ***Protein Hydration***).

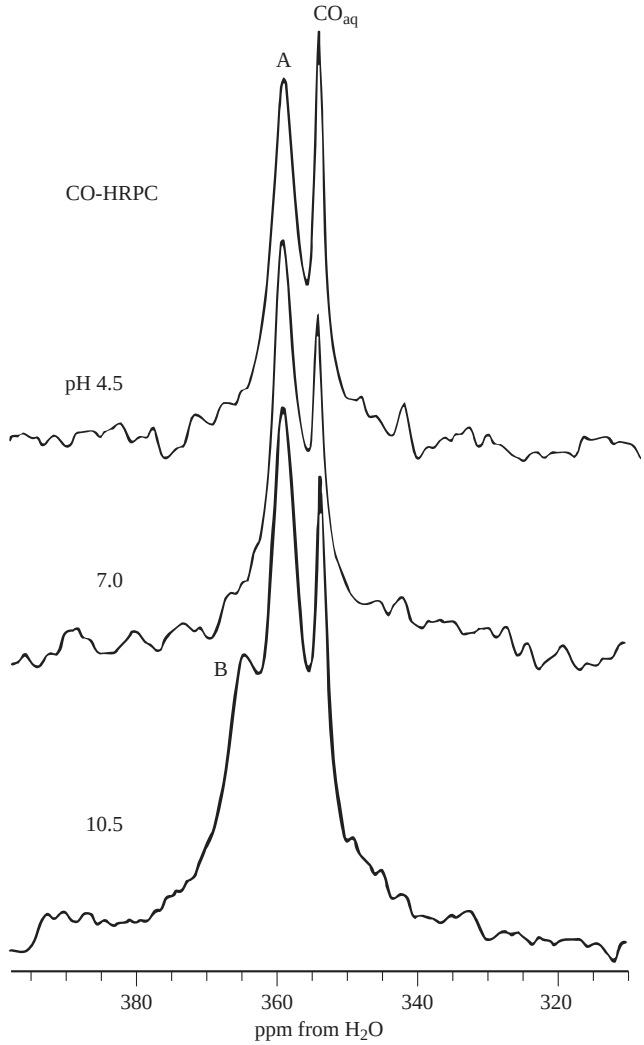

Figure 7 Oxygen-17 NMR spectra of CO-horseradish peroxidase isozyme C (CO-HRPC); concentration, 1 mM in 50 mM phosphate buffer at 11.7 T; NS = 50 000–250 000, recycle time 100–150 ms, pulse width 38 μs, LB = 100 Hz. A, B, and CO_{aq} denote the acidic form of CO-HRPC, the alkaline form of CO-HRPC, and free CO in solution, respectively. (Reprinted by permission of The American Society for Biochemistry and Molecular Biology from H. C. Lee, K. Cummings, K. Hall, L. P. Hager, and E. Oldfield, *J. Biol. Chem.*, 1988, **263**, 16 118)

^{17}O NMR studies have several advantages compared with ^{1}H and ^{2}H NMR for protein hydration:

1. The relaxation effect is large, permitting studies at low protein concentrations.
2. The ^{17}O relaxation in water is generally dominated by the quadrupolar mechanism.[113,114] The intramolecular origin of the electric field gradient makes the quadrupolar interaction virtually independent of the molecular environment.
3. The ^{17}O relaxation is not affected by proton (or deuteron) exchange with protic residues in the protein. Only T_2 can be affected by exchange within a narrow pH range near neutrality.
4. Cross relaxation that contributes to ^{1}H relaxation is unimportant for ^{17}O.[115,116]

Variable field T_1 and T_2 relaxation time measurements of several proteins[117] were interpreted in terms of two layers of

hydration having a reorientational correlation time of about 20 ps (about eight times slower than that of bulk water and independent of the nature of the protein). This rapid local motion has a small anisotropic component (corresponding to an order parameter of 0.06) which is averaged out by protein reorientation with a correlation time of the order of 10 ns.

Water molecules are important constituents of lyotropic phases and bilayers. In this case the molecular motions are strongly anisotropic and the quadrupolar interaction is not averaged out to zero and may be measured when it is small compared with the Zeeman interaction. Ordering of a water molecule results in a quadrupolar splitting which is related to the order parameter. It has been shown that important dynamic information can be obtained from ^{17}O linewidth data which complement the ordering results from ^{2}H NMR.[118] (see ***Amphiphilic Liquid Crystalline Samples: Nuclear Spin Relaxation*** and ***Liquid Crystalline Samples: Structure of Nonrigid Molecules***).

4.7 The Solid State

Under conditions of magic angle spinning (MAS) (see ***Magic Angle Spinning***), the $(\frac{1}{2}, -\frac{1}{2})$ transition of quadrupolar nuclei with nonintegral spin does not depend on first-order quadrupolar interactions or on the effects of θ (the angle between $\boldsymbol{B}_0$ and q_{zz}). The powder bandshapes depend upon second-order quadrupolar effects which do not eliminate the possibility of obtaining meaningful NMR spectra. In this case operation at very high magnetic fields will generally be most advantageous since the maximum second-order quadrupolar linewidth of the $(\frac{1}{2}, -\frac{1}{2})$ transition decreases linearly with the magnetic field.[119] Typical results are those obtained for a range of oxides, oxyanions and high temperature oxide superconductors.[120–122] For fosterite (Mg_2SiO_4), in which three crystallographically distinct oxygen sites were partly resolved, it was possible to determine the chemical shifts (61, 62, and 47 ppm), the quadrupole coupling constants (2.35, 2.35, and 2.7 MHz), and the electric field gradient tensor asymmetry parameters (0.2, 1.0, and 0.3) associated with each. From similar studies of silicate minerals and other compounds it was found that the χ values are related to the percentage ionic character of the bonds to oxygen.[120] It has also been found that VAS can be advantageous, especially for removing resonances arising from transitions other than $(\frac{1}{2}, -\frac{1}{2})$ (see ***Variable Angle Sample Spinning***). Furthermore, it has been demonstrated that ^{17}O spins can be polarized by the ^{1}H spin system, as is done for ^{13}C in CP MAS.[123]

^{17}O NMR studies on single crystals have the advantage, compared with studies on powders, that the complete principal components of the nuclear quadrupolar coupling constant and shielding tensors can be obtained and their orientation relative to the local molecular symmetry can be determined.[124]

5 RELATED ARTICLES

Amphiphilic Liquid Crystalline Samples: Nuclear Spin Relaxation; Dynamic Frequency Shift; Hydrogen Bonding; Liquid Crystalline Samples: Structure of Nonrigid Molecules; Magic Angle Spinning; Oxygen-17 NMR: Applications in Biochemistry; Paramagnetic Relaxation in Solution; Protein Hydration; Relaxation Theory for Quadrupolar Nuclei; Shielding Calculations: IGLO Method; Shielding: Overview of Theoretical Methods; Variable Angle Sample Spinning.

6 REFERENCES

1. C. Roger and N. Sheppard, in *NMR and the Periodic Table*, ed. R. K. Harris and B. E. Mann, Academic, New York, 1978, Chap. 12A.
2. W. G. Klemperer, *Angew. Chem., Int. Ed., Engl.*, 1978, **17**, 246.
3. T. St. Amour and D. Fiat, *Bull. Magn. Reson.*, 1980, **1**, 118.
4. J.-P. Kintzinger, in *NMR Basic Principles and Progress*, ed. P. Diehl, E. Fluck, and R. Kosfeld, Springer, Heidelberg, 1981, Vol. 17.
5. W. G. Klemperer, in *The Multinuclear Approach to NMR Spectroscopy*, ed. J. B. Lambert and F. G. Riddell, Reidel, Dordrecht, 1983, Chap. 11
6. J.-P. Kintzinger, in *NMR of Newly Accessible Nuclei*, ed. P. Laszlo, Academic, New York, 1983, Vol. 2.
7. M.-D. Tsai and K. Bruzik, in *Biological Magnetic Resonance*, ed. L. J. Berliner and J. Reuben, Plenum, New York, 1983, Vol. 5.
8. W. McFarlane and H. C. E. McFarlane, in *Multinuclear NMR*, ed. J. Mason, Plenum, New York, 1987, Chap. 14
9. D. W. Boykin (ed.), *^{17}O NMR Spectroscopy in Organic Chemistry*, CRC, Boston, 1991.
10. I. P. Gerothanassis, *Progr. NMR Spectrosc.*, 1994, **26**, 171.
11. I. P. Gerothanassis, *Progr. NMR Spectrosc.*, 1994, **26**, 239.
12. I. P. Gerothanassis, R. Hunston, and J. Lauterwein, *Helv. Chim. Acta*, 1982, **65**, 1764.
13. R. N. Hunston, I. P. Gerothanassis, and J. Lauterwein, *J. Am. Chem. Soc.*, 1985, **107**, 2654.
14. G. W. Kabalka, and N. M. Goudgaon, in *^{17}O NMR Spectroscopy in Organic Chemistry*, ed. D. W. Boykin, CRC, Boston, 1991, Chap. 1
15. I. P. Gerothanassis and J. Lauterwein, *Magn. Reson. Chem.*, 1986, **24**, 1034.
16. I. P. Gerothanassis, J. Lauterwein, and N. Sheppard, *J. Magn. Reson.*, 1982, **48**, 431.
17. J. Lauterwein and I. P. Gerothanassis, *J. Magn. Reson.*, 1983, **51**, 153.
18. J. Schulte and J. Lauterwein, *J. Magn. Reson., Ser. A*, 1993, **101**, 95.
19. I. P. Gerothanassis, *Progr. NMR Spectrosc.*, 1987, **19**, 267.
20. A. C. Kunwar, G. L. Turner, and E. Oldfield, *J. Magn. Reson.*, 1986, **69**, 124.
21. H. A. Christ, P. Diehl, H. R. Schneider, and H. Dahn, *Helv. Chim. Acta*, 1961, **44**, 865.
22. M. Karplus and J. A. Pople, *J. Chem. Phys.*, 1963, **38**, 2803.
23. H. A. Christ and P. Diehl, *Helv. Phys. Acta*, 1963, **36**, 170.
24. L.-O. Andersson and J. Mason, *J. Chem. Soc., Dalton Trans.*, 1974, 202.
25. E. Lippmaa, M. Magi, S. S. Novikov, L. I. Khmelnitski, A. S. Prihodko, O. V. Lebedev, and L. V. Epishina, *Org. Magn. Reson.*, 1972, **4**, 153.
26. J. A. Coderre, S. Mehdi, P. C. Demou, R. Weber, D. D. Traficante, and J. A. Gerlt, *J. Am. Chem. Soc.*, 1981, **103**, 1870.
27. I. P. Gerothanassis and N. Sheppard, *J. Magn. Reson.*, 1982, **46**, 423.
28. J. A. Gerlt, P. C. Demou, and S. Mehdi, *J. Am. Chem. Soc.*, 1982, **104**, 2848.

29. B. N. Figgis, R. G. Kidd, and R. S. Nyholm, *Proc. R. Soc. London, Ser. A*, 1962, **269**, 469.
30. W. H. De Jeu, *Mol. Phys.*, 1970, **18**, 31.
31. D. J. Sardella and J. B. Stothers, *Can. J. Chem.*, 1969, **47**, 3089.
32. T. E. St. Amour, M. I. Burgar, B. Valentine, and D. Fiat, *J. Am. Chem. Soc.*, 1981, **103**, 1128.
33. T. C. Brownlee, M. Sadek, and D. J. Craik, *Org. Magn. Reson.*, 1983, **21**, 616.
34. C. Delseth and J. P. Kintzinger, *Helv. Chim. Acta*, 1978, **61**, 1327.
35. I. J. Solomon, J. N. Keith, A. J. Kacmarek, and J. K. Raney, *J. Am. Chem. Soc.*, 1968, **90**, 5408.
36. I. J. Solomon, A. J. Kacmarek, and J. Raney, *Inorg. Chem.*, 1968, **7**, 1221.
37. I. J. Solomon, A. J. Kacmarek, W. K. Sumida, and J. K. Raney, *Inorg. Chem.*, 1972, **11**, 195.
38. R. Ditchfield, D. P. Miller, and J. A. Pople, *J. Chem. Phys.*, 1970, **53**, 613; 1971, **54**, 4186.
39. R. Ditchfield, *Mol. Phys.*, 1974, **27**, 789.
40. K. A. K. Ebraheem and G. A. Webb, *Progr. NMR Spectrosc.*, 1977, **11**, 149.
41. K. A. K. Ebraheem and G. A. Webb, *J. Magn. Reson.*, 1977, **25**, 399.
42. K. A. K. Ebraheem and G. A. Webb, *J. Magn. Reson.*, 1978, **30**, 211.
43. M. Jallali-Heravi and G. A. Webb, *J. Magn. Reson.*, 1978, **32**, 429.
44. J. Sadlej and A. J. Sadlej, *J. Magn. Reson.*, 1974, **14**, 97.
45. M. Schindler and W. Kutzelnigg, *Mol. Phys.*, 1983, **48**, 781.
46. C. J. Jameson, in *Nuclear Magnetic Resonance*, ed. G. A. Webb, Royal Society of Chemistry, London, 1985, Vol. 14, Chap. 1
47. J. D. Augspurger, C. E. Dykstra, and E. Oldfield, *J. Am. Chem. Soc.*, 1991, **113**, 2447.
48. J. D. Augspurger and C. E. Dykstra, *J. Phys. Chem.*, 1991, **95**, 9230.
49. K. D. Park, K. Guo, F. Adebodun, M. L. Chiu, S. G. Sligar, and E. Oldfield, *Biochemistry*, 1991, **30**, 2333.
50. I. Ando and G. A. Webb, *Org. Magn. Reson.*, 1981, **15**, 111.
51. G. Klopman, *Chem. Phys. Lett.*, 1967, **1**, 200.
52. M. Jallali-Heravi, B. Na Lamphun, G. A. Webb, I. Ando, M. Kondo, and S. Watanabe, *Org. Magn. Reson.*, 1980, **14**, 92.
53. F. R. Prado, C. Giessner-Prettre, A. Pullman, J. F. Hinton, D. Horspool, and K. R. Metz, *Theor. Chim. Acta*, 1981, **59**, 55.
54. Z. Luz and G. Yagil, *J. Phys. Chem.*, 1966, **70**, 554.
55. J. Reuben, A. Tzalmona, and D. Samuel, *Proc. Chem. Soc.*, 1962, 353.
56. H. Versmold, and C. Yoon, *Ber. Bunsenges. Phys. Chem.*, 1972, **76**, 1164.
57. G. A. Gray and T. A. Albright, *J. Am. Chem. Soc.*, 1977, **99**, 3243.
58. O. Lutz, W. Nepple, and A. Nolle, *Z. Naturforsch., Teil A*, 1976, **31**, 978, 1046.
59. G. D. Mateescu and G. M. Benedikt, *J. Am. Chem. Soc.*, 1979, **101**, 3959.
60. G. O. Mateescu, private communication.
61. W. L. Earl and W. Niederberger, *J. Magn. Reson.*, 1977, **27**, 351.
62. M.-D. Tsai, *Biochemistry*, 1979, **18**, 1468.
63. M.-D. Tsai, *Biochemistry*, 1980, **19**, 5310.
64. G. H. Reed and T. S. Leyh, *Biochemistry*, 1980, **19**, 5472.
65. C. P. Cheng and T. L. Brown, *J. Am. Chem. Soc.*, 1979, **101**, 2327.
66. C. P. Cheng and T. L. Brown, *J. Am. Chem. Soc.*, 1980, **102**, 6418.
67. B. H. Ruessink, and C. MacLean, *Mol. Phys.*, 1984, **53**, 421.
68. C. Chachaty and J. P. Quaegedeur, *Mol. Phys.*, 1984, **52**, 1081.
69. Y. Tricot and W. Niederberger, *Helv. Chim. Acta*, 1984, **67**, 1033.
70. G. E. Hawkes, E. W. Randall, S. Aime, and R. Gobetto, *J. Magn. Reson.*, 1986, **68**, 597.
71. R. T. C. Brownlee, M. J. O'Connor, B. P. Shehan, and A. G. Wedd, *J. Magn. Reson.*, 1985, **61**, 22.
72. S. Aime, R. Gobetto, D. Osella, G. E. Hawkes, and E. W. Randall, *J. Chem. Soc., Dalton Trans.*, 1984, 1863.
73. T. E. Bull, S. Forsen, and D. L. Turner, *J. Chem. Phys.*, 1979, **70**, 3106.
74. P. O. Westlund and H. Wennerstrom, *J. Magn. Reson.*, 1982, **50**, 451.
75. H. C. Lee and E. Oldfield, *J. Am. Chem. Soc.*, 1989, **111**, 1584.
76. S. Aime, D. Osella, L. Milone, G. E. Hawkes, and E. W. Randall, *J. Am. Chem. Soc.*, 1981, **103**, 5920.
77. P. Greenzaid, Z. Luz, and D. Samuel, *Trans. Faraday Soc.*, 1968, **64**, 2780, 2787.
78. E. H. Curzon, B. T. Golding, and A. K. Wong, *J. Chem. Soc., Chem. Commun.*, 1982, 63.
79. I. Pecht and Z. Luz, *J. Am. Chem. Soc.*, 1965, **87**, 4068.
80. J. A. Jackson, J. Lemons, and H. Taube, *J. Chem. Phys.*, 1960, **32**, 553.
81. R. E. Connick and D. N. Fiat, *J. Chem. Phys.*, 1963, **39**, 1349.
82. D. Fiat and R. E. Connick, *J. Am. Chem. Soc.*, 1966, **88**, 4754.
83. D. Fiat and A. M. Chmelnick, *J. Am. Chem. Soc.*, 1971, **93**, 2875.
84. R. E. Connick and D. Fiat, *J. Chem. Phys.*, 1966, **44**, 4103.
85. T. J. Swift and R. E. Connick, *J. Chem. Phys.*, 1962, **37**, 307; 1964, **41**, 2553.
86. J. P. Hunt, *Coord. Chem. Rev.*, 1971, **7**, 1.
87. D. W. Boykin and A. L. Baumstark, in *^{17}O NMR Spectroscopy in Organic Chemistry*, ed. D. W. Boykin, CRC, Boston, 1991, Chap. 3
88. M. G. Oakley and D. W. Boykin, *J. Chem. Soc., Chem. Commun.*, 1986, 439.
89. A. L. Baumstark, P. Balakrishnan, M. Dotrong, C. J. McCloskey, M. G. Oakley, and D. W. Boykin, *J. Am. Chem. Soc.*, 1987, **109**, 1059.
90. D. W. Boykin, G. H. Deadwyler, and A. L. Baumstark, *Magn. Reson. Chem.*, 1988, **26**, 19.
91. D. W. Boykin and A. L. Baumstark, *Tetrahedron*, 1989, **45**, 3613.
92. J. Reuben, *J. Am. Chem. Soc.*, 1969, **91**, 5725.
93. M. I. Burgar, T. E. St. Amour, and D. Fiat, *J. Phys. Chem.*, 1981, **85**, 502.
94. H. M. Schwartz, M. MacCoss, and S. S. Danyluk, *J. Am. Chem. Soc.*, 1983, **105**, 5901.
95. G. Jaccard and J. Lauterwein, *Helv. Chim. Acta*, 1986, **69**, 1469.
96. A. Steinschneider, M. I. Burgar, A. Buku, and D. Fiat, *Int. J. Peptide Protein Res.*, 1981, **18**, 324.
97. D. Fiat, *Bull. Magn. Reson.*, 1984, **6**, 30.
98. J. Lauterwein, I. P. Gerothanassis, and R. Hunston, *J. Chem. Soc., Chem. Commun.* 1984, 367.

99. N. Birlirakis, I. P. Gerothanassis, C. Sakarellos, and M. Marraud, *J. Chem. Soc., Chem. Commun.*, 1989, 1122.
100. I. P. Gerothanassis and C. Vakka, *J. Org. Chem.*, 1994, **59**, 2341.
101. H. Gilboa, A. Steinschneider, B. Valentine, D. Dhawan, and D. Fiat, *Biochim. Biophys. Acta*, 1984, **800**, 251.
102. C. Sakarellos, I. P. Gerothanassis, N. Birlirakis, T. Karayannis, M. Sakarellos-Daitsiotis, and M. Marraud, *Biopolymers*, 1989, **28**, 15.
103. I. P. Gerothanassis, N. Birlirakis, T. Karayannis, M. Sakarellos-Daitsiotis, C. Sakarellos, B. Vitoux, and M. Marraud, *Eur. J. Biochem.*, 1992, **210**, 693.
104. A. D. English, J. P. Jesson, W. G. Klemperer, T. Mamouneas, L. Messerle, W. Shum, and A. Tramontano, *J. Am. Chem. Soc.*, 1975, **97**, 4785.
105. M. Filowitz, W. G. Klemperer, L. Messerle, and W. Shum, *J. Am. Chem. Soc.*, 1976, **98**, 2345.
106. W. G. Klemperer and W. Shum, *J. Am. Chem. Soc.*, 1977, **99**, 3544.
107. M. Filowitz, R. K. C. Ho, W. G. Klemperer, and W. Shum, *Inorg. Chem.*, 1979, **18**, 93.
108. M. A. Freeman, F. A. Schultz, and C. N. Reilley, *Inorg. Chem.*, 1982, **21**, 567.
109. I. P. Gerothanassis and M. Momenteau, *J. Am. Chem. Soc.*, 1987, **109**, 6944.
110. I. P. Gerothanassis, M. Momenteau, and B. Loock, *J. Am. Chem. Soc.*, 1989, **111**, 7006.
111. I. P. Gerothanassis, B. Loock, and M. Momenteau, *J. Chem. Soc., Chem. Commun.*, 1992, 598.
112. H. C. Lee, K. Cummings, K. Hall, L. P. Hager, and E. Oldfield, *J. Biol. Chem.*, 1988, **263**, 16 118.
113. J. A. Glasel, *Proc. Natl. Acad. Sci. USA*, 1966, **55**, 479.
114. J. A. Glasel, *Nature*, 1968, **218**, 953.
115. S. H. Koenig, K. Hallenga, and M. Shporer, *Proc. Natl. Acad. Sci. USA*, 1975, **72**, 2667.
116. S. H. Koenig, R. G. Bryant, K. Hallenga, and G. S. Jacob, *Biochemistry*, 1978, **17**, 4348.
117. B. Halle, T. Andersson, S. Forsen, and B. Lindman, *J. Am. Chem. Soc.*, 1981, **103**, 500.
118. Y. Tricot and W. Niederberger, *Biophys. Chem.*, 1979, **9**, 195.
119. M. D. Meadows, K. A. Smith, R. A. Kinsey, T. M. Rothgelb, R. P. Skarjune, and E. Oldfield, *Proc. Natl. Acad. Sci. USA*, 1982, **79**, 1351.
120. S. Schramm and E. Oldfield, *J. Am. Chem. Soc.*, 1984, **106**, 2502.
121. S. Schramm, R. J. Kirkpatrick, and E. Oldfield, *J. Am. Chem. Soc.*, 1983, **105**, 2483.
122. E. Oldfield, C. Coretsopoulos, S. T. Yang, L. Reven, H. C. Lee, J. Shore, O. H. Han, E. Ramli, and D. Hinks, *Phys. Rev. B*, 1989, **40**, 6832.
123. T. H. Walter, G. L. Turner, and E. Oldfield, *J. Magn. Reson.*, 1988, **76**, 106.
124. W. Scheubel, H. Zimmermann, and U. Haeberlen, *J. Magn. Reson.*, 1985, **63**, 544.

Biographical Sketch

Ioannis P. Gerothanassis. *b* 1953. B.Sc., Aristotle University of Thessaloniki, 1974; M.Sc., School of Chemical Sciences, University of East Anglia, 1979; Ph.D. (supervisor Norman Sheppard, FRS), School of Chemical Sciences, University of East Anglia, 1981. Postdoctoral work at the Institut Chimie Organique, Universite de Lausanne. Successively, lecturer, assistant professor, and associate professor, Department of Chemistry, University of Ioannina, Greece. Approx. 60 publications. Current research specialties: multinuclear MR and multidimensional NMR and FT infrared studies of molecules of biological interest.

Phase Transitions and Critical Phenomena in Solids

Ferdinando Borsa
Iowa State University, Ames, IA, USA and Universita di Pavia, Pavia, Italy

1	Introduction	1
2	Static and Dynamic Critical Phenomena	1
3	The NMR and NQR Approach	2
4	Order Parameter Studies	3
5	Critical Dynamics Studies	5
6	Unconventional Phase Transitions	8
7	Related Articles	8
8	References	9

1 INTRODUCTION

A phase transition is a typical effect related to the collective behavior of a many-particle interacting system. Structural and magnetic phase transitions are the most common ones in solids, where in the structural phase transitions the interacting particles are the atoms and in the magnetic phase transitions the interacting entities are the atomic magnetic moments. In the ideal case of second-order phase transitions, very general statistical thermodynamic treatments are available based on macroscopic order parameters and response functions.[1] The onset of the order parameter (i.e. when it first becomes nonzero) below the transition temperature T_c marks a spontaneous symmetry breaking while the enhancement and the slowing down of its fluctuations around T_c is reflected in the critical behavior of the appropriate response function. The above characteristics are universal and largely independent of the microscopic details of the system. This universality makes the investigation of phase transitions an important chapter in physics.

NMR and Nuclear Quadrupole Resonance (NQR) measurements, both of static and dynamic parameters, provide valuable insights into the local properties at phase transitions. In these techniques, the nucleus is used as a probe of the electric and magnetic hyperfine interactions in the system at the microscopic level. A resonance experiment is normally related only indirectly to the static and dynamic properties of the system and, thus, a reliable theoretical interpretative model is necessary for analyzing the experimental data.

In Sections 2 and 3, we discuss some general properties of static and dynamic critical phenomena at second-order magnetic phase transitions and at reversible, weakly first-order, structural phase transitions.

In Sections 4 and 5, we give some representative examples of NMR/NQR investigations in model systems, while in Section 6, we give an example of an NMR study at a strongly first-order phase transition where the general thermodynamic treatment is not applicable. The material covered in this article assumes that one is familiar with the main aspects of the hyperfine interactions that couple the nuclear system to the 'lattice' in solids giving rise to the NMR/NQR lineshape, shift, and relaxation phenomena. Cross references to articles in this Encyclopedia where these interactions are treated are given in Section 7.

2 STATIC AND DYNAMIC CRITICAL PHENOMENA

The interpretation of NMR and NQR effects at phase transitions in solids is conveniently carried out in terms of local critical variables, $y(\boldsymbol{r}_1, t)$. The macroscopic order parameter is related to the time average of $y(\boldsymbol{r}_1, t)$ by

$$\eta \propto \sum_{\mathrm{l}} \mathrm{e}^{\mathrm{i}\boldsymbol{q}_c \cdot \boldsymbol{r}_\mathrm{l}} \langle y(\boldsymbol{r}_\mathrm{l}, t) \rangle \tag{1}$$

where $\boldsymbol{q}_c$ represents the periodicity of the ordering in the local critical variable. For a ferromagnet, $\boldsymbol{q}_c = 0$ and η is the spontaneous magnetization. For an antiferromagnet $|\boldsymbol{q}_c| = \pi/a$ and η is the sublattice magnetization (a = lattice parameter). For structural phase transitions $y(\boldsymbol{r}, t)$ is an atomic displacement from the equilibrium position, whereas for order–disorder ferroelectric transitions, $y(\boldsymbol{r}, t)$ is the orientation of a permanent electric dipole. The temperature dependence of the average critical variable $\langle y_1 \rangle = \langle y(\boldsymbol{r}, t) \rangle$ and, thus, of the order parameter is given by a universal law:

$$\eta \propto \left(\frac{T_c - T}{T_c} \right)^{\beta} \tag{2}$$

where $\beta = 0.5$ in mean-field theories. Close to the transition, a nonclassical critical region occurs, in which the mean-field approximation fails. This region covers a temperature interval that depends on the range of the interaction driving the phase transition and on the lattice dimensionality. The value of β in the nonclassical critical region is largely independent of the nature of the microscopic forces, depending instead on the dimensionalities and on the symmetries of the system and of the critical variables.

The dynamic properties can be described in terms of the pair correlation function

$$G(\boldsymbol{r}, t) = \langle y(\boldsymbol{r}, t) y(0, 0) \rangle \tag{3}$$

and the dynamic structure factor

$$S(\boldsymbol{q}, \omega) = \int \mathrm{e}^{\mathrm{i}(\omega t - \boldsymbol{q} \cdot \boldsymbol{r})} G(\boldsymbol{r}, t)\, \mathrm{d}^3 r\, \mathrm{d}t \tag{4}$$

which describes the spectrum of the collective fluctuations. The spectrum of the fluctuations is related to the imaginary part of the generalized susceptibility by the fluctuation–dissipation theorem:

$$S(\boldsymbol{q}, \omega) = \frac{2\hbar\, \mathrm{Im}\, \chi(\boldsymbol{q}, \omega)}{1 - \exp(-\hbar\omega / k_\mathrm{B} T)} \approx \frac{2 k_\mathrm{B} T}{\omega}\, \mathrm{Im}\, \chi(\boldsymbol{q}, \omega) \tag{5}$$

The static structure factor

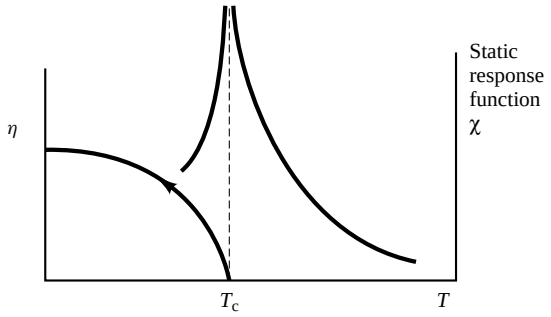

Figure 1 Sketch of the general temperature behavior of the order parameter η and of the conjugate response function χ at the transition temperature T_c for a second-order phase transition

$$S(\boldsymbol{q}) = \frac{1}{2\pi}\int S(\boldsymbol{q},\omega)\,\mathrm{d}\omega = k_B T\chi(\boldsymbol{q},0) = \langle|y_{\boldsymbol{q}}|^2\rangle \qquad (6)$$

gives the mean-square amplitude of the collective fluctuations. On approaching the critical temperature, in a second-order transition, the static response function $\chi(\boldsymbol{q}_c, 0)$ for a given critical wave vector q_c diverges, thereby reflecting the enhancement of the fluctuations of the collective variables. For a magnetic phase transition, the static response function is the uniform magnetic susceptibility (ferromagnet) or the staggered susceptibility (antiferromagnet). The slowing down of the fluctuations is reflected, instead, in the progressive increase of the low-frequency components of the normalized dynamic structure factor: $S(\boldsymbol{q}, \omega)/S(\boldsymbol{q})$ (Figure 1).

3 THE NMR AND NQR APPROACH

The coupling of the nuclei to the lattice by magnetic and electric quadrupole hyperfine interactions, is the key point that makes NMR and NQR useful tools for investigating phase transitions and critical phenomena.

The magnetic dipolar and transferred hyperfine interactions of the nucleus with the electronic moments allow one to investigate the magnetic phase transitions. We write:

$$\hat{\mathcal{H}}_{SI} = \gamma\hbar\hat{\boldsymbol{I}}\cdot\boldsymbol{B}(t) \qquad (7)$$

where γ is the nuclear gyromagnetic ratio and $\boldsymbol{B}$ is an effective local magnetic field that can be, in general, time dependent. The time average value $\langle\boldsymbol{B}(t)\rangle$ is proportional to the local average magnetic moments in the substance. Therefore, the shift in the NMR resonance frequency due to $\langle\boldsymbol{B}\rangle$ can be used to measure the temperature dependence of the static uniform susceptibility, which is the critical response function for a ferromagnet. Below the ordering temperature T_c (or T_N), the spontaneous magnetization (or staggered magnetization) may induce a local field $\langle\boldsymbol{B}\rangle$ at the nuclear site that is large enough to perform a zero field resonance experiment (see ***Zero Field NMR***). In this case, the NMR resonance frequency is proportional to the spontaneous magnetization and, thus, accurate measurements of the critical temperature behavior of the order parameter are possible in principle.

The fluctuation part of $\boldsymbol{B}(t)$, in equation (7), induces spin–spin and spin–lattice relaxation, which become useful parameters for the study of electronic spin dynamics. The structural phase transitions, on the other hand, can be investigated by using the quadrupole moment, Q, of the nucleus as a probe of the internal electric field gradients generated by the atomic charge distributions (see ***Quadrupolar Nuclei in Solids***). We write

$$\hat{\mathcal{H}}_Q = \sum_{\alpha\beta}\hat{Q}_{\alpha\beta}V_{\alpha\beta} \qquad (8)$$

where $\hat{Q}_{\alpha\beta}$ are the quadrupole operators depending on the spin coordinates only and $V_{\alpha\beta}$ are the electric field gradient (EFG) components. If $\hat{\mathcal{H}}_Q$ is a small perturbation of the Zeeman Hamiltonian $\hat{\mathcal{H}}_Z$, then the quadrupole interaction, equation (8), induces splittings and/or shifts of the NMR resonance line and also nuclear relaxation. On the other hand, if $\hat{\mathcal{H}}_Q$ is the dominant part of the total nuclear Hamiltonian, the resonance frequency is determined by the quadrupole interaction (NQR). In this case, the effect of the fluctuations of the EFG tensor is, in general, more complicated because it may also involve the modulation of the eigenstates of the main Hamiltonian.

The measurement of the static quadrupole interaction corresponds to the measurement of the time-average local EFG components. Since the EFG is related to the position in the lattice of the nuclear and electronic charges, one can measure atomic displacements and/or changes of the electronic charge density which are, in turn, related to the order parameter of structural phase transitions (see ***Field Gradients and Their Application***).

Regarding the dynamic properties, one can relate the nuclear spin–lattice relaxation rate T_1 and the nuclear spin–spin relaxation rate T_2 quite generally to the dynamic structure factor defined in equation (4), which contains the information about the critical dynamics of the system. Whenever the weak collision theory of nuclear relaxation is applicable, the relaxation rate can be expressed in terms of the spectral densities $J_\alpha(\omega_\alpha)$ at ω_α of the correlation functions for 'appropriate' lattice functions $F_L^\alpha(t)$:

$$T_i^{-1} = \sum_\alpha C_\alpha^i J_\alpha(\omega_\alpha) \qquad (i = 1, 1\rho, 2, 1\mathrm{d}) \qquad (9)$$

where the coefficients C_α^i depend on the nucleus and on the relaxation mechanism: $i = 1$ corresponds to the spin–lattice relaxation in the laboratory frame; $i = 1\rho$ to the one in the rotating frame; $i = 2$ to spin–spin relaxation; and $i = 1\mathrm{d}$ to the dipolar relaxation (see ***Relaxation: An Introduction***).

If we focus our attention on the contribution to relaxation due to fluctuations of the critical variable V_1, we can expand the lattice functions:

$$F_L^\alpha(t) = \sum_1 A_1^\alpha V_1(t) \qquad (10)$$

The above expansion is exact for certain types of system and it is only an approximation in other cases. Note that we have simplified the notation for the critical variable with respect to the notation in equations (1) and (3) by setting $y(\boldsymbol{r}_l,t) = V_1(t)$. By introducing collective variables $V_{\boldsymbol{q}}(t)$ through a Fourier transformation

$$V_{\boldsymbol{q}}(t) = \frac{1}{\sqrt{N}} \sum_{1} V_1 \mathrm{e}^{\mathrm{i}\boldsymbol{q}\cdot\boldsymbol{r}_1} \tag{11}$$

we can rewrite the spectral densities in terms of the dynamic structure factor as

$$J_\alpha(\omega_\alpha) = \frac{1}{N} \int \mathrm{e}^{-\mathrm{i}\omega_\alpha t} \sum_{\boldsymbol{q}} \sum_{11'} A_1^\alpha A_{1'}^\alpha \mathrm{e}^{\mathrm{i}\boldsymbol{q}\cdot\boldsymbol{r}_{11'}} \langle V_{\boldsymbol{q}}(0) V_{-\boldsymbol{q}}(t) \rangle \, \mathrm{d}t$$

$$= \sum_{\boldsymbol{q}} \mathcal{A}_{\boldsymbol{q}}^\alpha S(\boldsymbol{q}, \omega_\alpha) \tag{12}$$

The q summation reflects the fact that the relaxation rates are local quantities. The q components of $S(q, \omega)$ are weighted by the $\mathcal{A}_q^\alpha$ factor because the relaxation rates involve, in general, both auto and pair correlation functions for the local critical variable at the l and l' sites. The presence of the 'filter' factors $\mathcal{A}_{\boldsymbol{q}}^\alpha$ in equation (12), has the disadvantage of complicating the relationship between T_i^{-1} and $S(\boldsymbol{q}, \omega)$. On the other hand, if an explicit expression for the form factors $\mathcal{A}_{\boldsymbol{q}}$ can be obtained from theoretical considerations, one can achieve direct information on the symmetry and on the correlation properties of the fluctuations, as will be shown in Section 5. Further details about the NMR/NQR approach to the study of phase transitions are to be found in Borsa and Rigamonti.[2–4]

4 ORDER PARAMETER STUDIES

4.1 Structural Phase Transitions

As an example of an investigation of the temperature dependence of the order parameter in a structural phase transition, we consider the ^{39}K NMR study of $KMnF_3$.[5] In the perovskite-type crystal $KMnF_3$, a weakly first-order, reversible transition from cubic to tetragonal phase occurs at $T_c = 186$ K. The transition involves rotations of the MnF_6 octahedra in the opposite sense in adjacent (001) planes perpendicular to the c axis, as shown in Figure 2. This deformation corresponds to the freezing-in of the R_{25} mode of vibration at the R point of the Brillouin zone (i.e. $q = \pi/a, \pi/a, \pi/a$). The generalized order parameter can be assumed to be given by the average rotation angle $\langle\phi_1\rangle$ in a given cell l. For a uniform transition at T_c, all rotation angles are identical, i.e., $\phi_1 = \phi$, where ϕ is the order parameter. Potassium-39 has a quadrupole moment $Q = 0.07$ barns. In the cubic phase, no quadrupole effects are present. In the tetragonal phase ($T < T_c$), a nonzero EFG tensor arises at the ^{39}K site. The tensor has axial symmetry with $Z \| C$ and asymmetry parameter $\eta = (V_{xx} - V_{yy})/V_{zz} = 0$. The size of the resulting quadrupole coupling constant $\chi = eQV_{zz}/h$ (QCC) can be measured from the second-order shift of the central line transition ($\frac{1}{2} \leftrightarrow -\frac{1}{2}$) in a single crystal. The shift for $I = \frac{3}{2}$ is

$$\frac{\Delta B}{B_0} = \frac{\Delta\nu}{\nu_0} = -\frac{3\nu_Q^2}{16\nu_0^2}(1 - \cos^2\theta)(9\cos^2\theta - 1) \tag{13}$$

where θ is the angle between $\boldsymbol{B}_0$ and the Z axis of the EFG tensor, and $\nu_Q = eQV_{zz}/2h$. From a simple calculation of the EFG tensor in terms of a point ion charge approximation, one finds that $V_{zz} \propto \phi^2 \propto \epsilon^{2\beta}$. Therefore, the measurement of the QCC amounts to the measurement of the square of the order parameter. The experimental results are shown in Figure 3.

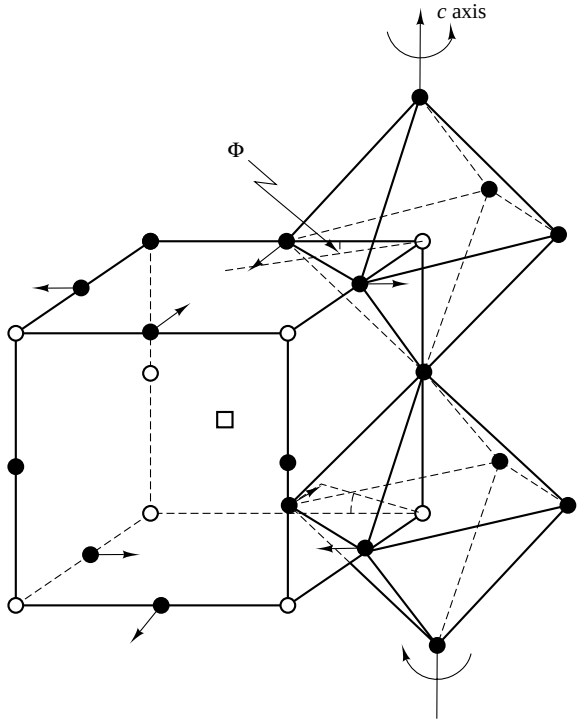

Figure 2 Perovskite structure of ABX_3 crystals. The atomic displacements corresponding to rotations of BX_6 octahedra in the opposite sense in adjacent planes are shown in the Figure with arrows. These rotations correspond to the R_{25} mode of vibration at the R point of the Brillouin zone. Its freezing is responsible for the cubic-to-tetragonal phase transition in $KMnF_3$,$SrTiO_3$, and $RbCaF_3$. (□) A; (○) B; (●) X

From the analysis of the temperature dependence of the quadrupole coupling constant, it could be concluded that for $\epsilon = (T_c - T)/T_c > 10^{-1}$ the molecular field approximation (MFA) is valid and the critical exponent is $\beta = \frac{1}{2}$. For $\epsilon < 10^{-1}$, nonclassical critical effects are present and the critical exponent crosses over to a value close to $\beta = \frac{1}{3}$. Since $\beta = \frac{1}{3}$ describes nonclassical critical effects in isotropic three-dimensional magnetic systems and in fluids, the above result is an elegant confirmation of the universality of critical effects at phase transitions. Other examples of studies of order parameter at structural phase transitions by NMR can be found in Rigamonti.[3]

4.2 Magnetic Phase Transitions

A very successful application of the NMR technique to the investigation of the critical behavior of the order parameter was performed in the antiferromagnet MnF_2.[6] In this sample the ^{19}F nuclei are strongly coupled to the nearest neighbor Mn^{2+} magnetic moments. This circumstance allows one to make precise measurements of the local internal field at the ^{19}F site by measuring the corresponding zero field NMR frequency. Actually, the measurements were performed in a single crystal with an applied magnetic field $\boldsymbol{B}_0$, and the zero field frequency

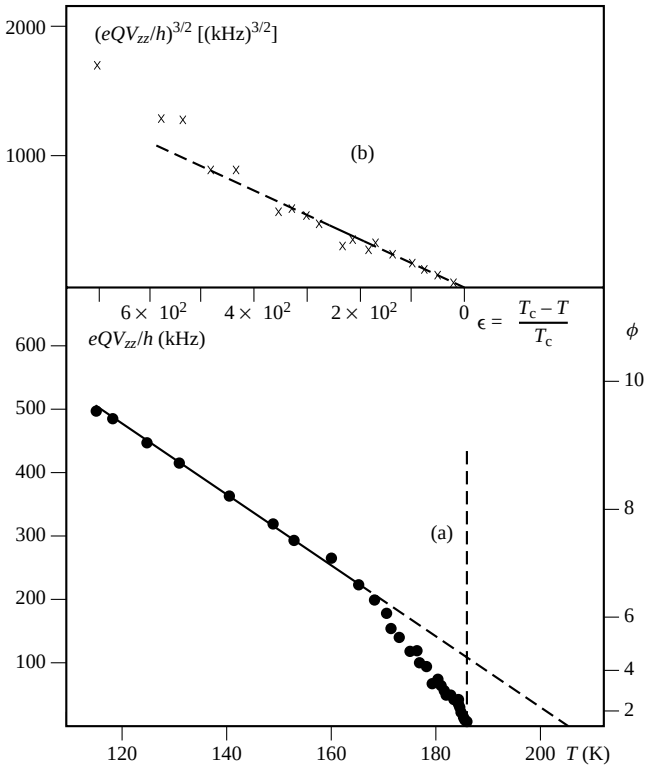

Figure 3 Temperature dependence of the ^{39}K quadrupole coupling constant in $KMnF_3$. (a) The linear T dependence of $eQV_{zz}/h \propto \phi^2 \propto \epsilon^{2\beta}$ is indicative of $\beta = 0.5$; (b) the linear T dependence of $(eQV_{zz}/h)^{3/2} \propto \phi^3 \propto \epsilon^{3\beta}$ for $T \to T_c$ is indicative of $\beta = \frac{1}{3}$

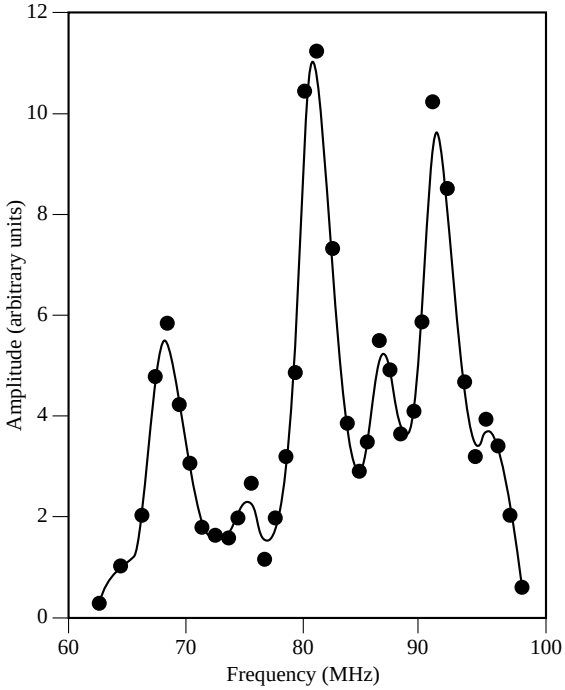

Figure 4 Copper-63 zero field antiferromagnetic spectrum in $YBa_2Cu_3O_{6.05}$ at 200 K, obtained by plotting the echo intensity vs. frequency of the irradiating radiofrequency field

$\nu_0(T)$ was derived from analysis of the ^{19}F NMR composite spectrum. The temperature dependence of $\nu_0(T)$ is a measure of the temperature dependence of the staggered magnetization $M_{st}(T)$ which, in turn, represents here the order parameter. A best fit of $\nu_0(T)/\nu_0(0) = M_{st}(T)/M_{st}(0) = (1 - T/T_c)^{\beta}$ yields a critical exponent $\beta = \frac{1}{3}$ with a very high degree of accuracy. The determination of β by NMR in MnF_2 remains one of the most accurate experiments in this field.

It is not always possible to measure the internal local field with good precision and close enough to T_c to get a reliable value for the critical exponent β. In most cases, one is limited to the study of the temperature dependence of the spontaneous magnetization well below T_c, or to the measurement of the overall temperature behavior to be compared with mean field theories. Even so, the NMR technique offers a very useful tool of investigation.

As further examples of order parameter studies, we present, in the following, results obtained in magnetic systems, which are the ceramic materials from which high-T_c superconductors evolve upon appropriate doping: $YBa_2Cu_3O_6$[7] and $La_{2-x}Sr_x$-CuO_4[8] (see ***High Temperature Superconductors***). $YBa_2Cu_3O_6$ is a planar Heisenberg antiferromagnet with T_N = 420 K. Two different Cu sites are present. The one of interest here is the Cu site in the magnetic bilayers, which experience both a quadrupole coupling to the nonzero EFG and a Zeeman interaction with the hyperfine field generated by the Cu^{2+} atomic magnetic moments. For $T < T_N$ the internal field dominates and the zero field spectrum can be analyzed in terms of a central transition ($+\frac{1}{2} \leftrightarrow -\frac{1}{2}$) and two satellite ($\pm\frac{3}{2} \leftrightarrow \pm\frac{1}{2}$) transitions whose resonance frequency is given by:

$$\nu_{1/2,-1/2} = \nu_0 \left[1 + \frac{3}{16} \left(\frac{\nu_Q}{\nu_L} \right)^2 \right] \tag{14a}$$

$$\nu_{\pm 3/2,\pm 1/2} = \nu_0 \left[1 \mp \frac{1}{2} \left(\frac{\nu_Q}{\nu_L} \right) \pm \frac{3}{64} \left(\frac{\nu_Q}{\nu_L} \right)^3 \right] \tag{14b}$$

A typical zero field spectrum at $T < T_N$ is shown in Figure 4, where a total of six lines are discernible: three lines for each of the two Cu isotopes (63, 65) according to equations (14a) and (14b). The fit of the spectrum at different temperatures to equations (14a) and (14b) allows one to derive the temperature dependence of $\nu_0(T) = \gamma B_I$, which is a measure of the internal magnetic field $B_I(T)$ and, thus, of the staggered magnetization $M_{st}(T)$, since $\nu_0(T)/\nu_0(0) = B_I(T)/B_I(0) = M_{st}(T)/M_{st}(0)$ (see Figure 5). The results were compared with the predictions of spin-wave theory.[7]

Another example of order parameter study is provided by the ^{139}La NQR in $La_{2-x}Sr_xCuO_4$.[8] The lanthanum cuprate system is a planar Heisenberg antiferromagnet with T_N = 320 K for $x = 0$ and a Neel temperature that decreases rapidly on increasing Sr substitution, whereby, for $x = 0.02$, $T_N \sim 0$. The ^{139}La nucleus, $I = \frac{7}{2}$, has an NQR spectrum above T_N, centered at about 19 MHz (for the $\frac{7}{2} \leftrightarrow \frac{5}{2}$ transition). When the temperature is lowered below T_N, an internal magnetic field arises at the La site, generating the splitting of the NQR resonance line, as shown in Figure 6.

The distance between the two peaks of the NQR spectrum is proportional to the projection of the local internal field B_z, on the direction z of the EFG tensor: $\Delta\nu = 2\gamma B_z$. Thus,

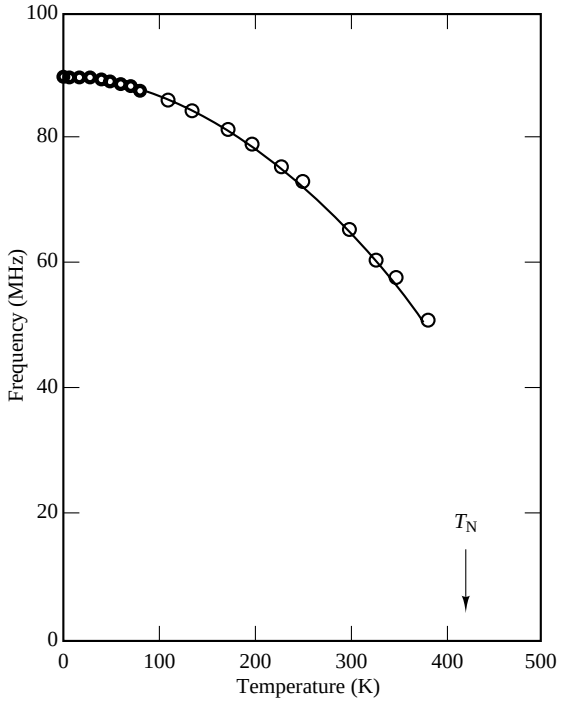

Figure 5 Temperature dependence of the ^{63}Cu nuclear resonance frequency in its internal local field below T_N. The solid line is a best fit curve discussed in Bucci et al.,[7] which gives the reduction of the order parameter upon increasing temperature due to the thermal excitation of spin waves

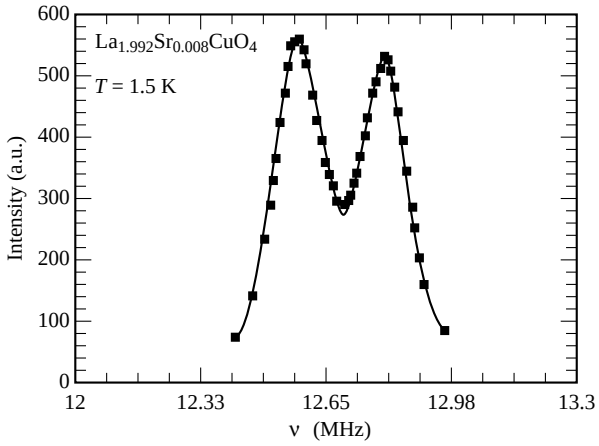

Figure 6 Lanthanum-139 NQR spectrum in zero external magnetic field in the ordered antiferromagnetic state. The NQR resonance line corresponds to the $\pm\frac{5}{2} \leftrightarrow \pm\frac{3}{2}$\$ transition. The doublet originates from the Zeeman splitting due to the internal magnetic field. The spectrum is obtained by plotting the echo intensity at different operating frequencies

a measurement of the separation of the two NQR lines is proportional to the internal field and, thus, is proportional to the spontaneous, staggered magnetization below T_N. The results are shown in Figure 7. From the departure of the experimental points at low temperatures and for $x \neq 0$, from the behavior predicted by the MFA expression, it was possible to derive information about the effect of Sr doping on the magnetic properties of the system (for details, see Chou et al.[8]).

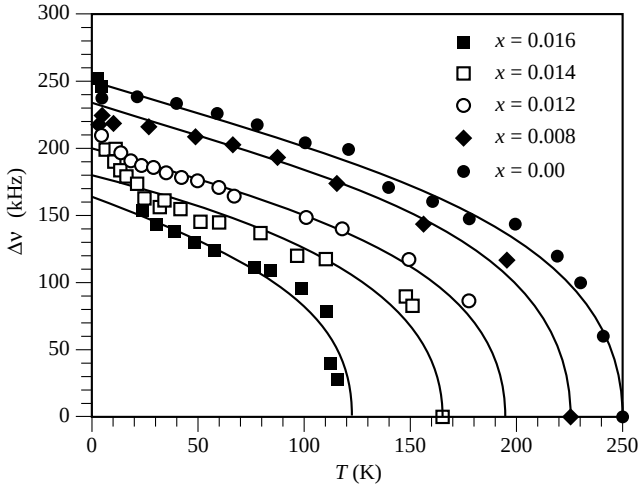

Figure 7 Zeeman splitting $\Delta\nu$ of the ^{139}La NQR line (see Figure 6 plotted vs. temperature for samples of $La_{2-x}Sr_xCuO_4$ having a different content of Sr. The full lines are the behaviors predicted for the temperature dependence of the order parameter in the MFA

5 CRITICAL DYNAMICS STUDIES

From equations (9) and (12), one can derive a general relationship connecting the NMR relaxation rate T_i^{-1} to the dynamic structure factor $S(\boldsymbol{q}, \omega)$:

$$\frac{1}{T_i} = \sum_{\alpha} \sum_{q} \mathcal{A}_q^{\alpha} S(\boldsymbol{q}, \omega_{\alpha}) \tag{15}$$

As a general rule we can expect that, on approaching the transition temperature T_c from the high-temperature side, the fluctuations of the critical collective variable, $V_{\boldsymbol{q}}$, increase in amplitude for the critical wave vector $\boldsymbol{q}_c$ and the frequency of the fluctuations approaches zero for the same wave vector. As a consequence, the relaxation rate in equation (15), which is most sensitive to the fluctuations at low frequency (ω_{α} = 0 for a T_2 process and $\omega_{\alpha} \approx \omega_L$ for a T_1 process), should be strongly enhanced. However, since the relaxation rate is a local property, only the components of $S(\boldsymbol{q}, \omega_{\alpha})$ near $\boldsymbol{q}_c$ will contribute to the enhancement of T_i^{-1}. Since a given nucleus is coupled to many neighboring critical variables (i.e. electronic spins in magnetic systems or atoms in structural transitions), the coupling parameter $\mathcal{A}_{\boldsymbol{q}}^{\alpha}$ in equation (15) is, in general, a function of $\boldsymbol{q}$. Thus, only if the coupling parameter is different from zero at $\boldsymbol{q} = \boldsymbol{q}_c$ can the NMR relaxation rate give information about the critical fluctuations near T_c. Here we present some representative examples of studies of the critical dynamics for $T \rightarrow T_c$ by means of NMR relaxation rate measurements.

5.1 Structural Transitions

The crucial role in the NMR/NQR investigation of structural phase transitions is the quadrupole coupling [equation (8)], which involves the dependence of the EFG tensor from the local critical variables $V_l(t)$. Let us consider a few representative examples of displacive-type phase transitions from the high-temperature cubic phase to the low-temperature

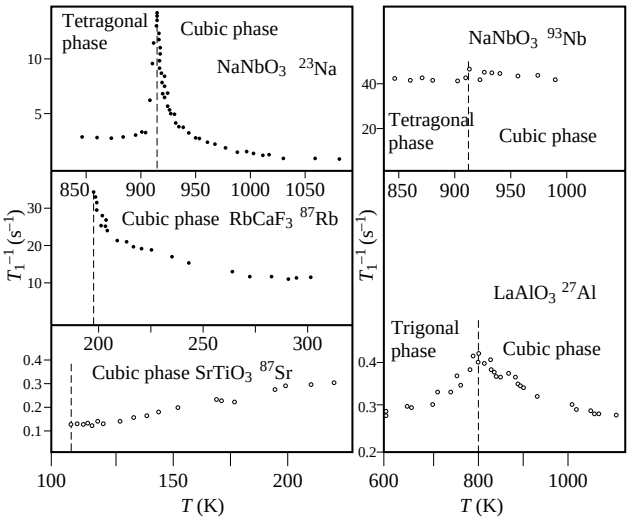

Figure 8 Experimental results for the spin—lattice relaxation rates of different nuclear probes in different crystals as a function of temperature. The broken vertical line represents the transition temperature T_c for the cubic—tetragonal structural phase transition

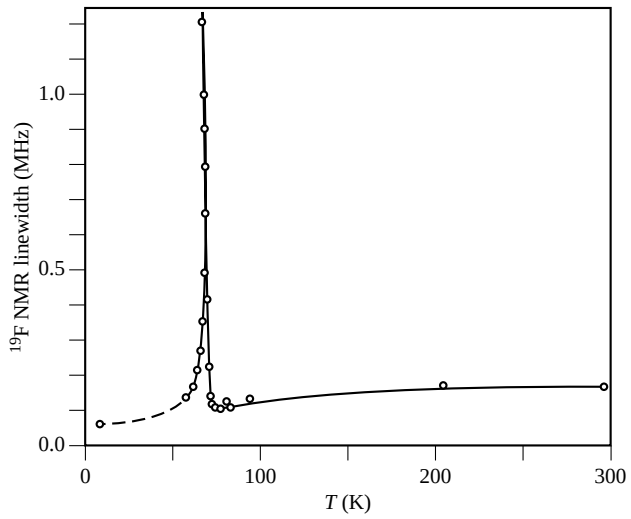

Figure 9 Fluorine-19 NMR linewidth in MnF_2 vs. temperature. The critical broadening occurs in the vicinity of the antiferromagnetic ordering temperature T_N = 67.4 K

tetragonal phase in crystals having the ABX_3 perovskite structure depicted in Figure 2. The crystals considered are $NaNbO_3$, $RbCaF_3$, $SrTiO_3$, and $LaAlO_3$, and the nuclei investigated can be either the one occupying the A site or the one occupying the B site. In the above displacive transitions, the critical variables are the rotation angles $\phi_l(t)$ of the oxygen octahedra with respect to their untilted equilibrium positions (see Figure 2). The EFG tensor components can be expressed in this case in terms of a linear combination of the critical variables: $V_{\alpha\beta} = \Sigma_1 A_1 \phi_1(t)$. The critical behavior of the nuclear spin–lattice relaxation rate, T_1^{-1}, in the crystals listed above, is illustrated in Figure 8. In some instances T_1^{-1} is strongly enhanced as $T \to T_c$, in other instances it is only weakly enhanced, and in two cases there is no enhancement at all. This represents a vivid demonstration of the role of the 'filter' parameter $\mathcal{A}_{\boldsymbol{q}}$ in equation (15). In fact, the structural transitions considered in Figure 8, involve different symmetries of the critical wave vector $\boldsymbol{q}_c$. For example, for $NaNbO_3$, the rotational fluctuations are of M_3 symmetry, whereas in $SrTiO_3$, the rotational fluctuations are of R_{25} symmetry, as in the case of $KMnF_3$ (see Figure 2). Thus, depending on the location in the lattice of the nucleus considered, and on the symmetry of the critical rotational fluctuations, the coupling parameter $A_{\boldsymbol{q}_c}$ can be either zero or different from zero and can have a different $\boldsymbol{q}$ dependence in the vicinity of $\boldsymbol{q} = \boldsymbol{q}_c$. Thus, according to equation (15), one can have different degrees of coupling to the critical fluctuations and, consequently, different degrees of enhancement. A detailed discussion of this subject can be found in Rigamonti.[3]

5.2 Magnetic Phase Transitions

A striking example of enhancement of NMR relaxation due to critical fluctuations is offered by the ^{19}F linewidth behavior in the antiferromagnet MnF_2 near T_N, as shown in Figure 9. Analysis of such an NMR linewidth experiment in MnF_2, and more accurate data from FeF_2, have yielded valuable information about critical dynamic indices.[6] In both MnF_2 and FeF_2, the ^{19}F NMR line is broadened by the 'lifetime' effect. The lineshape is Lorenzian and the linewidth is proportional to T_2^{-1}, which in turn is equal to T_1^{-1} (the same situation as found in liquids!). The critical variable $\nu_1^{\alpha}(t)$ can be identified here, with the Mn^{2+} electronic spin component $s_1^{\alpha}(t)$. From equations (9) and (12), and by using the fluctuation–dissipation theorem, one has

$$\delta\nu_{\parallel} = \sum_{\boldsymbol{q}} \mathcal{A}_{\boldsymbol{q}}^{\parallel} S(\boldsymbol{q}, 0) \propto k_B T \lim_{\omega \to 0} \int \mathrm{d}^3 q \, \mathcal{A}_{\boldsymbol{q}}^{\parallel} \frac{\mathrm{Im}\,\chi(\boldsymbol{q}, \omega)}{\omega} \quad (16)$$

By assuming that the fluctuations at the critical antiferromagnetic wave vector, $\boldsymbol{q} = \boldsymbol{q}_{AF}$, dominate, by assuming a Lorenzian shape for the generalized susceptibility $\chi(\boldsymbol{q}, \omega)$ with width $\Gamma_{\parallel}(\boldsymbol{q})$ and since $\mathcal{A}_{\boldsymbol{q}_{AF}}$ is different from zero for the coupling of ^{19}F with the three Mn^{2+} nearest neighbor spins, one finds[6]

$$\delta\nu_{\parallel} \propto \frac{\chi(\boldsymbol{q}_{AF})}{\Gamma_{\parallel}(\boldsymbol{q}_{AF})} \xi_{\parallel}^{-3} \quad (17)$$

where $\Xi_{\parallel}$ is the correlation length for the longitudinal spin correlation function. From the general theory of critical phenomena,[1] one has

$$\chi(\boldsymbol{q}_{AF}) \propto \varepsilon^{-\gamma}, \quad \xi \propto \varepsilon^{-\nu}, \quad \Gamma_{\parallel}(\boldsymbol{q}_{AF}) \propto \xi^{-z} \propto \varepsilon^{+\nu z} \quad (18)$$

with $\gamma = \nu(2 - \eta)$, leading to

$$\delta\nu_{\parallel} \propto \varepsilon^{-n} \quad [n = \gamma - 3\nu + \nu z = \nu(z - \eta - 1)] \times \left(\varepsilon = \frac{T - T_N}{T_N}\right) \quad (19)$$

The value obtained from fitting the linewidth data in FeF_2 is $n = 0.67 \pm 0.02$, which has allowed the author to infer that the dynamic critical index z should be about 2.0, since $\gamma = 2\nu = \frac{4}{3}$ and $\eta \sim 0$. Just the same as for the studies

of the order parameter, one should point out that only in a very few special cases is it possible to perform a study of the critical dynamics from NMR with the high accuracy that was possible in FeF_2. One of the main reasons is that in most cases it is impossible to separate the contributions to the relaxation from the different components of the order parameter. Nevertheless, interesting information about the critical dynamics can be obtained, as is illustrated by the ^{37}Cl NMR study in $Sr_2CuO_2Cl_2$.[9] $Sr_2CuO_2Cl_2$ is a layered perovskite with body-centered tetragonal K_2NiF_4 structure. The Cu^{2+} spins form a two-dimensional (2D) Heisenberg system with antiferromagnetic (AF) coupling which orders at T_N = 260 K. The structure and the magnetic properties of $Sr_2CuO_2Cl_2$ are similar to those of La_2CuO_4, which is the precursor of an important family of high-T_c superconductors.

The ^{35}Cl nuclear spin–lattice relaxation rate, $T_1^{-1} \equiv 2W$, displays a sharp peak at T_N = 260 K due to the enhancement and the slowing down of the AF fluctuations of the correlated Cu^{2+} spins (see Figure 10). From equations (9) and (12) one has

$$\frac{1}{T_1} \equiv 2W = \sum_{\boldsymbol{q}} \mathcal{A}_{\boldsymbol{q}} S(\boldsymbol{q}, \omega_L) = \tfrac{1}{2}\gamma^2 \frac{1}{N} \sum_{\boldsymbol{q}} |\boldsymbol{B} \cdot \boldsymbol{q}|^2 \int \langle s_{\boldsymbol{q}}^+(0) s_{\boldsymbol{q}}^-(t) \rangle \, \mathrm{d}t \quad (20)$$

where we have expressed the 'filter' parameter $\mathcal{A}_{\boldsymbol{q}}$ in terms of the effective local field $\boldsymbol{B}(t)$ at the nuclear site as defined in equation (7). Since the Larmor frequency ω_L is small compared with the electron-spin fluctuation frequency, we set ω_L = 0; also, the dynamic structural factor $S(\boldsymbol{q}, \omega)$ has been expressed in terms of the correlation function of the transverse (with respect to the applied field) spin components $s^+(t)$, which act as the critical variables. By assuming, as is done for the case of MnF_2, an exponential decay of the spin correlation function, with decay rate $\Gamma(\boldsymbol{q})$ we can write

$$\frac{1}{T_1} = \gamma^2 \sum_{q} |\boldsymbol{B} \cdot \boldsymbol{q}|^2 \frac{|s_{\boldsymbol{q}}|^2}{\Gamma(\boldsymbol{q})} \quad (21)$$

Since the hyperfine field at the ^{35}Cl site does not cancel for an AF arrangement of the Cu^{2+} spins, one expects the main contribution to the ^{35}Cl relaxation rate to come from AF fluctuations. By expanding the $\boldsymbol{B} \cdot \boldsymbol{q}$ factor around $\boldsymbol{q} = \boldsymbol{q}_{AF}$ and by using dynamic scaling arguments[1–4] for the $\boldsymbol{q}$ dependence of the inplane correlated fluctuations, equation (21) becomes

$$\frac{1}{T_1} = (\gamma B_{\mathrm{eff}})^2 \frac{1}{N} \sum_{\boldsymbol{q}} \frac{\xi^{2-\eta} f(q\xi)}{\omega_e \xi^{-z} g(q\xi)} \quad (22)$$

where B_{eff} is the static field at the ^{35}Cl site for the AF configuration of Cu^{2+} spins and ω_e is the fluctuating frequency for the uncorrelated Cu^{2+} spins coupled by the exchange constant J, i.e., $\omega_e = \frac{8}{3} J^2 n S(S+1)/\hbar$. In equation (22), we have written $|s_q|^2$ in terms of the correlation length Ξ (in lattice units) and $\Gamma(q) = \omega_e/\Xi^z \, g(q\Xi)$, where z is the dynamic scaling exponent and $f(q\Xi)$, $g(q,\Xi)$ are homogeneous functions of the product $x = q\Xi$.[1] By transforming the $\boldsymbol{q}$ summation in equation (22) into a 2D integral and taking into account the convergence of $\int f(x)/g(x) \, \mathrm{d}x$ to a number of the order of unity one has

$$\frac{1}{T_1} = 2W = (\gamma B_{\mathrm{eff}})^2 \frac{1}{\omega_e} \xi^{z-\eta} \quad (23)$$

The critical divergence of $1/T_1 \equiv 2W$ for $T \to T_N^+$ is of the form $2W \propto (T - T_N)^{-n}$ with n = 1.2 ± 0.1 as shown in Figure 10. This critical divergence is close to the one observed in the ^{19}F NMR linewidth in the 2D Heisenberg model system K_2MnF_4.[10,11] Since $\Xi \propto (T - T_N)^{-\nu}$ one has $n = \nu(z - \eta)$.

As one can see, the critical exponent n for the divergence of the relaxation rate is different for the 2D system ($Sr_2CuO_2Cl_2$)

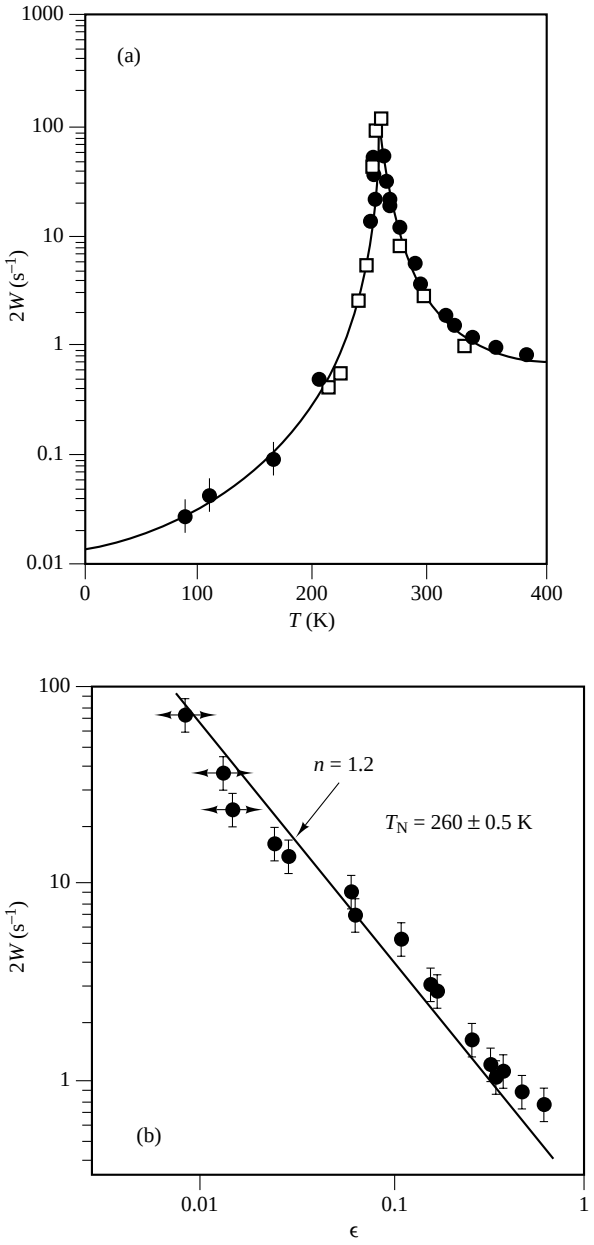

Figure 10 (a) Enhancement of the ^{35}Cl nuclear spin—lattice relaxation rate in $Sr_2CuO_2Cl_2$ in the vicinity of the antiferromagnetic ordering temperature T_N = 260 K. (b) Log—log plot of the relaxation rate vs. $\epsilon = (1 - T/T_N)$ used to determine the critical exponent n

and the 3D one (FeF_2). In the latter case, $n = \nu(z - \eta - 1)$ was derived [see equation (19)]. The difference is associated with the different integration in q space due to the different lattice dimensionality D. Furthermore, the critical indices ν, z, and η are expected to be different in the two above-mentioned magnetic systems as a consequence of the different lattice dimensionality (2D vs. 3D) and the different spin dimensionality (Heisenberg vs. Ising) leading to the different values of n in the two cases.

6 UNCONVENTIONAL PHASE TRANSITIONS

The NMR studies discussed up to this point are focused on the critical static and dynamic behavior near the transition temperature of second-order or weakly first-ordered phase transitions in solids. However, the NMR technique has also been applied widely to study phase transitions that are not amenable to the general thermodynamic treatment of second-order transitions and related to critical effects in model systems. For example, important information was obtained by NMR in the study of first-order structural phase transitions, order–disorder transitions with diffusion, semiconductor–metal phase transitions, metal–superconductor phase transitions, etc. To illustrate one of these applications, we report here the ^{113}Cd NMR study of the martensitic transformation in Ag–Cd alloys.[12]

Several noble metal-based and Ni-based metallic alloys near the equiatomic concentration display a diffusionless structural phase transformation from a high-temperature body-centered cubic structure (austenite) to a compact structure (martensite). The transformation is strongly first order and belongs to the class of the *m*artensitic *p*hase *t*ransformation (MPT). It takes place by macroscopic nucleation of martensitic regions at the temperature M_S and proceeds on lowering the temperature by the growth of the martensite within the austenite matrix until the sample is fully transformed at a temperature M_F. If the transformation is thermoelastic, the two phases coexist at thermal equilibrium at any temperature in the interval between M_S and M_F and the transformation is reversible with a small hysteresis. NMR studies of MPTs have established that the Knight shift on any nucleus in the alloy is slightly, but significantly, different in the austenitic compared with the martensitic phase. This is due to small changes of the symmetry of the conduction-electron wavefunction and/or of the density of states at the Fermi level in the two phases. Based on this circumstance, one can investigate the relative proportion of martensite over the austensite within the temperature interval of the thermoelastic transformation. Let us consider the MPT of equiatomic Cd–Ag alloy with M_S = 144 K and M_F = 120 K. The coexistence of two signals, centered at different frequencies, is evident in the ^{113}Cd NMR spectra shown in Figure 11.

A quantitative evaluation of the fraction of martensite present in thermoelastic equilibrium at each temperature can be obtained by the deconvolution of the adsorption line in the two components. The procedure requires some precautions and some assumptions which are discussed in detail in Rubini et al.[12] The results for the fraction of martensite as a function of the temperature are reported in Figure 12.

It should be stressed that the NMR method allows one to monitor the absolute quantity of martensite present and thus can detect residual parts of the sample that remain untransformed or continue to transform slowly even below M_F. In this respect, NMR proves to be complementary to dynamic measurements, such as resistivity or differential thermal analysis, which are based on the detection of relative changes of the characteristics of the whole system. For example, one can observe a small discontinuity in the growth curve in Figure 12 around the liquid nitrogen temperature (77 K). This is due to the fact that the sample was cycled several times from room temperature down to 77 K in order to stabilize the thermoelastic MPT. The 'memory' of the system to the cycling procedure is an aspect of the interesting shape memory effects associated with the MPT.

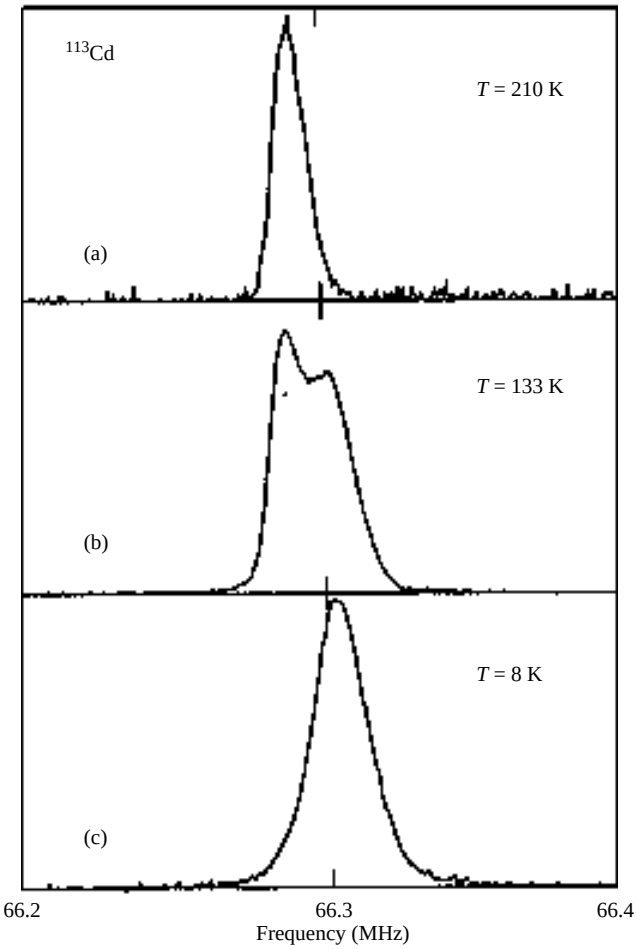

Figure 11 Cadmium-113 NMR spectrum in the Ag—Cd alloy at B_0 = 7 tesla for different temperatures: (a) $T > M_S$, (b) $M_F < T < M_S$, (c) $T < M_F$. The coexistence of two signals from the two phases is clearly visible in case (b)

7 RELATED ARTICLES

Fast Ion Conductors; Ferroelectrics and Proton Glasses; Field Gradients and Their Application; High Temperature Superconductors; Hydrogen–Metal Systems; Incommensurate Systems; Inorganic Solids; Internal Spin Interactions and Rotations in Solids; Knight Shift; Metallic Superconductors; Metals: Pure and Alloyed; Quadrupolar Interactions; Quadrupolar Nuclei in Solids; Relaxation: An Introduction; Relaxation

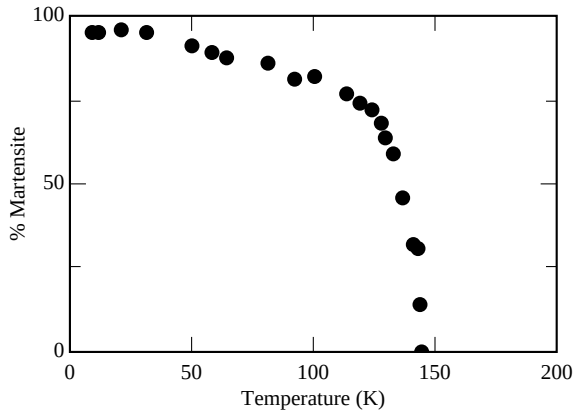

Figure 12 Fraction of martensite, present in the sample as a function of temperature, as obtained from the intensity ratio of the two signals present in the ^{113}Cd NMR spectrum (see Figure 11)

Theory: Density Matrix Formulation; Relaxation Theory for Quadrupolar Nuclei; Spin Diffusion in Solids; Wide Lines for Nonquadrupolar Nuclei; Zero Field NMR.

8 REFERENCES

1. H. E. Stanley, *Introduction to Phase Transitions and Critical Phenomena*, Clarendon, Oxford, 1971.
2. F. Borsa and A. Rigamonti, in *Magnetic Resonance of Phase Transitions*, eds. F. J. Owens, C. P. Poole, and H. A. Farach, Academic Press, New York, 1979.
3. A. Rigamonti, *Adv. Phys.*, 1984, **33**, 115.
4. F. Borsa and A. Rigamonti, in *Structural Phase Transitions II*, eds. K. A. Muller and H. Thomas, Springer, Berlin, 1990.
5. F. Borsa, *Phys. Rev. B*, 1973, **7**, 913.
6. P. Heller, in *Local Properties at Phase Transitions*, eds. K. A. Muller and A. Rigamonti, North Holland, Amsterdam, 1976, p. 447.
7. C. Bucci, P. Carretta, R. De Renzi, G. Guidi, S. G. Jang, E. Rastelli, A. Tassi, and M. Varotto, *Phys. Rev.*, 1993, **48**, 16769.
8. F. C. Chou, F. Borsa, J. H. Cho, D. C. Johnston, A. Lascialfari, D. R. Torgeson, and J. Ziolo, *Phys. Rev. Lett.*, 1993, **71**, 2323.
9. F. Borsa, M. Corti, T. Goto, A. Rigamonti, D. C. Johnston, and F. C. Chou, *Phys. Rev.*, 1992, **45**, 5756.
10. C. Bucci and G. Guidi, in *Local Properties at Phase Transitions*, eds. K. A. Muller and A. Rigamonti, North Holland, Amsterdam, 1976, p. 624.
11. P. M. Richards, in *Local Properties at Phase Transitions*, eds. K. A. Muller and A. Rigamonti, North Holland, Amsterdam, 1976, p. 539.
12. S. Rubini, C. Dimitropoulos, and F. Borsa, *Phys. Rev. B*, 1991, **44**, 2019; *Phys. Rev. B*, 1994, **49**, 12 590.

Biographical Sketch

Ferdinando Borsa. *b* 1939. Laurea in Physics, 1961, Libera Doceuza, solid state physics, 1969, Pavia, Italy. Introduced to NMR by L. Giulotto. Faculty in Physics at the University of Pavia and Iowa State University. Approx. 100 publications. Research interests include the applications of NMR and NQR to problems in solid state physics and materials science with particular emphasis on studies of collective phenomena and phase transitions.

Phosphorus-31 NMR

Konstantin Karaghiosoff

Universität München, München, Germany

1	Introduction	1
2	Nuclear Properties and Standardization	1
3	Experimental Techniques	1
4	Chemical Shifts	2
5	Coupling Constants	3
6	Applications of ^{31}P NMR Spectroscopy	4
7	Related Articles	5
8	References	5

1 INTRODUCTION

With the discovery of the phenomenon of NMR in bulk samples in 1945, a new, powerful, analytical method became available to chemists. The ^{31}P nucleus was among the first nuclei to which NMR spectroscopy was applied. Phosphorus-31 spectroscopic data have been in the literature since 1951,[1,2] and their number increased rapidly in the following years. In 1967 the first comprehensive compilation of ^{31}P NMR data of simple phosphorus compounds, as well as a presentation of the current theory of phosphorus chemical shifts, was published.[3] Another publication[4] and a review[5] cover the literature up to 1969 and to mid-1982, respectively.

With the development of pulse Fourier transform NMR spectroscopy the sensitivity of the spectrometers improved and the ^{31}P NMR experiment became routine. As a consequence the amount of published ^{31}P NMR data increased dramatically. By 1987 it was estimated that more than 40 000 ^{31}P NMR data items were available in the literature. A 'Handbook of ^{31}P NMR Data' contains extensive compilations of representative data, including coupling constants, for all types of phosphorus compounds.[6] More data can be found in a series of books dedicated partially[7,8] or entirely[9–11] to ^{31}P NMR. A number of reviews[12–14] dealing with the application of ^{31}P NMR to transition metal complexes with phosphorus ligands, and a review[15] describing the main developments in ^{31}P NMR of transition metal–phosphine complexes in the period 1970–1977, are available.

With modern spectrometers and using all instrumental and relaxation aids phosphorus compounds at 200 ppm and even 5 ppm concentration levels can be detected by ^{31}P NMR.[9] Due to this capability, ^{31}P NMR spectroscopy has also gained importance as an analytical tool in biology and medicine. The work in this area is documented by a series of reviews[16–21] and books.[22,23]

2 NUCLEAR PROPERTIES AND STANDARDIZATION

The important properties of the ^{31}P nucleus for NMR spectroscopy are given in Table 1. Since phosphorus compounds are generally reactive, no suitable internal reference compound is available for general use. Phosphorus-31 chemical shifts are referenced to 85% aqueous H_3PO_4 as an external standard. According to the present sign convention shifts are given positive for signals appearing at higher frequency (lower field) with respect to that of the standard. Great care is recommended, however, when using data from the older literature, since there was a change in sign convention in the mid-1970s.

Table 1 Properties of the ^{31}P Nucleus[7,8,10]

Natural abundance, C (%)	100
Nuclear spin, I	$\frac{1}{2}$
Magnetic moment, μ (μ_N)	1.1316
Magnetogyric ratio γ (10^7 rad T^{-1} s^{-1})	10.8394
NMR frequency at 2.35 T (MHz)	40.480
Receptivity relative to that of ^{1}H, D^P	6.63×10^{-2}
Receptivity relative to that of ^{13}C D^C	3.77×10^2

A disadvantage of 85% H_3PO_4 as a standard is its broad resonance signal. A number of secondary external standards, giving much sharper signals, are therefore in use: P_4O_6 (δ^{31}P = 112.5), $P(OMe)_3$ (δ^{31}P = 140.4), $PO(OMe)_3$ (δ^{31}P = −2.4), $[P(OH)_4]ClO_4$ (δ^{31}P = −0.1), $Na_2[CH_2(PO_3H)_2]$ in D_2O (δ^{31}P = 16.7), $(NEt_4)_2HPO_4$ in H_2O (δ^{31}P = 2.1).[8,9] In some cases D_3PO_4 (δ^{31}P = 0.3) and $(CH_3)_3PO$ (δ^{31}P = 72.6) are used as internal standards.[8,9] Alternatively the ^{2}H internal lock signal can be used to obtain accurate chemical shifts referenced to $Si(CH_3)_4$ or to an idealized shift for 85% H_3PO_4. However, there is little agreement on Ξ for 85% H_3PO_4 with values ranging from 40 480 720 to 40 480 754 Hz.[7,9] An absolute ^{31}P shielding scale is based on gas phase measurements of PH_3.[24]

Normally the reported ^{31}P chemical shifts are not corrected for diamagnetic susceptibility. In addition temperature, solvent, and concentration dependence of δ^{31}P for both the reference compound and the compounds under study, may be important. Thus variations in reported chemical shifts for the same compound of up to ±10 units can be encountered in the literature.[7–10]

Measurements of the nuclear Overhauser enhancement show a wide variation extending from zero to the theoretical maximum of 124%.[8,10,25]

Spin–lattice relaxation times T_1 of phosphorus compounds vary mostly between 1 and 30 s and can depend strongly on solvent, temperature, and concentration. Compilations of T_1 data for simple phosphorus compounds are found in Mason,[8] Verkade and Quin,[9] and Berger et al.[10] Typical values are ∼1.3 s for RPH_2, 3–9 s for $P(OR)_3$, 3–6 s for PX_3 (X = halogen), 2–9 s for $[R_4P]X$, 10–31 s for R_3P, 6–30 s for $PO(OR)_3$, and 2–11 s for R_3PO.[9] For a number of three-coordinated phosphorus compounds the spin rotation mechanism has been shown to account for T_1 at ambient temperature, while at low temperatures dipolar contributions become important.[8] However, P_2t-Bu_4 relaxes by a dipolar mechanism even at ambient temperature. Going to four-coordination the relative contribution of the spin rotation mechanism decreases and is still important in the five-coordinated species PCl_nPh_{5-n} (n = 2–4) and the PF_6^- ion. A rare example, in which chemical shift anisotropy plays an important role in relaxation, is represented by Ph_3PO.[8]

3 EXPERIMENTAL TECHNIQUES

Due to its favorable nuclear properties (I = 1/2, high NMR frequency and high receptivity), the ^{31}P nucleus is easy to observe and no particular instrumental equipment is required. Early ^{31}P NMR spectra of solutions were recorded on continuous wave instruments and were often poorly resolved. Now practically all data are obtained with modern FT NMR spectrometers, equipped either with multinuclear probes or with separate pretuned probes for ^{31}P observation, yielding highly resolved spectra with $\Delta\nu_{1/2}$ often below 1.0 Hz. The optimum pulse duration depends on the relaxation time T_1 of the ^{31}P nucleus and the acquisition time T_{ac}. It has been recommended to set the pulse duration at $\cos^{-1}(e^{-T_{ac}/T_1})$.[26] Routine ^{31}P NMR spectra are obtained with broadband proton decoupling using a rapid pulse repetition (1 s) and a short pulse angle (30°).

A large number of special experimental NMR techniques have been applied to the ^{31}P nucleus including spin tickling,[9] selective[27] and broadband[9] ^{31}P decoupling, SPT,[9] COSY,[9] reverse shift heterocorrelated NMR spectroscopy,[9,28] homonuclear[9,29] and heteronuclear[9,30] J resolved two-dimensional NMR spectroscopy, EXSY,[31] and Hahn-echo extended pulse sequences.[32] The CP MAS technique is widely used to obtain solid state ^{31}P NMR spectra.[9,33] Liquid crystal ^{31}P NMR spectra of several cyclopolyphosphines $(RP)_n$ and of other trivalent and pentavalent phosphorus compounds have been reported.[9] In a few cases reactions of phosphorus compounds have been studied by CIDNP.[34]

For ^{31}P measurements at variable temperature a 0.1 M solution of triphenylphosphine and triphenylphosphine oxide in toluene-d_8 has been recommended as a shift thermometer. At an operating frequency of 40 MHz the change in δ^{31}P is 1.3 Hz per degree.[35]

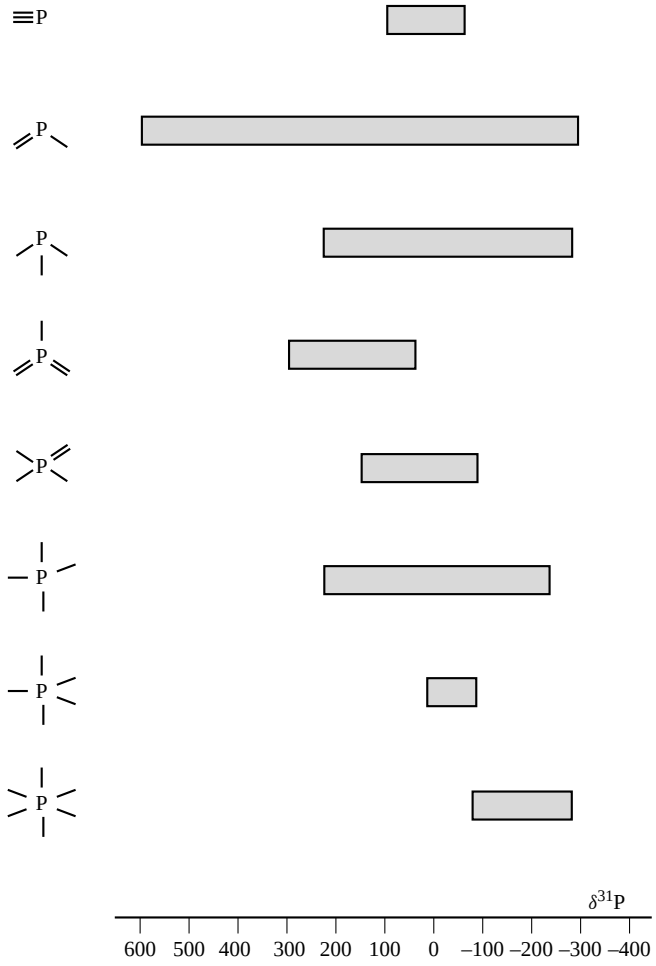

Figure 1 Typical ranges of δ^{31}P for differently coordinated phosphorus compounds

4 CHEMICAL SHIFTS

The range of ^{31}P chemical shifts for liquid, dissolved, or gaseous diamagnetic phosphorus compounds covers nearly 2000 ppm and extends from +1362 for t-BuP[Cr(CO)$_5$]$_2$ to −552 for gaseous P_4. If dissolved paramagnetic compounds are included, it widens to about 4700, with +3471 for the complex $[(C_4Me_4P)_2U(BH_4)]_2$ on the high-frequency side and −1219 for $OsCl_4(PBu_2Ph)_2$ on the low-frequency side.[9,10] The characteristic ranges of δ^{31}P for one- to six-coordinated phosphorus compounds are shown in Figure 1. For pentavalent phosphorus the shift ranges are relatively narrow, and shielding of the phosphorus nucleus increases as its coordination number increases from 3 to 6. No such dependence is found for the trivalent phosphorus and, except for one-coordinated phosphorus compounds, the shift ranges are much wider.[6,36] Detailed bar charts showing the dependence of δ^{31}P for individual classes of phosphorus compounds on the type of atoms bonded to phosphorus can be found in Tebby[6] and Mason.[8]

According to a semiempirical treatment proposed by Van Wazer and co-workers[3,37] phosphorus chemical shifts can be interpreted in terms of three contributions: the bond angles at the phosphorus atom, the electronegativity of the substituents, and the extent of π bonding. If only one parameter is being changed at a time, useful correlations within a class of compounds are obtained.[8,10] Thus for cyclopolyphosphines $(RP)_n$ the phosphorus chemical shift is almost linearly correlated with the average endocyclic PPP bond angles, and definite ranges can be established for n = 5 (δ^{31}P = +50 to −10), n = 4 (δ^{31}P = −50 to −80), and n = 3 (δ^{31}P = −30 to −180). The only known compound for n = 6, $(PhP)_6$, (δ^{31}P = −22) also fits this correlation.[8,10] Linear shift/bond angle correlations have also been reported for the basal phosphorus atoms in cage molecules of the series $P_4S_xSe_{3-x}$ (x = 0–3), $P_yAs_{4-y}S_3$, and $P_yAs_{4-y}Se_3$ (y = 0–4)[38] and for differently substituted cyclotriphosphines.[39] For δ^{31}P of *tert*-phosphines an additive relationship for the alkyl substituents is found; deshielding of phosphorus increases in the order Me < Et < i-Pr < t-Bu.[7] More additive relationships have been reported for δ^{31}P in polyphosphines P_nH_{n+2},[40] primary[41] and secondary phosphines,[42] and alkyl phosphonium salts.[42] Additive relationships often fail, however, when π bonding or electronegative substituents are involved.[7,8,10]

Theoretical calculations of ^{31}P chemical shifts for a series of simple phosphorus compounds by semiempirical methods and for PH_3 by ab initio methods have been reviewed.[9] Using the IGLO method, ab initio calculations of δ^{31}P for larger molecules have also been performed.[43]

Isotope effects on ^{31}P nuclear shielding caused by ^{2}H, ^{13}C, ^{15}N, ^{18}O, ^{34,36}S, ^{35,37}Cl, and ^{79,81}Br have been observed.[44,45]

In 2-amino-1,3,2-dioxaphosphorinane 2-chalcogenides the isotopic effect of ^{15}N on $\delta^{31}P$ is larger for the shorter equatorial than for the longer axial P–N bond.[44]

4.1 One-Coordinate Phosphorus

The range of ^{31}P chemical shifts for one-coordinated phosphorus compounds (phosphaalkynes R–C≡P[6,36,46,47] and [2,4,6-*t*-$Bu_3C_6H_2$–N≡P][$AlCl_4$][48]) extends mainly from +96 to −70. Depending on R, shielding of the phosphorus nucleus in phosphaalkynes increases generally in the order $(CH_3)_3Si$ < aryl,H < alkyl < amino < F.[36,46] A linear relationship results for $\delta^{31}P$ and δN of identically substituted phosphaalkynes and nitriles.[36] Phosphorus-31 solid state NMR investigations of 2,4,6-*t*-$Bu_3C_6H_2$–C≡P[49] and [2,4,6-*t*-$Bu_3C_6H_2$–N≡P][$AlCl_4$][50] have been published.

4.2 Two-Coordinate Phosphorus

Compilations of $\delta^{31}P$ are available for the large number of two-coordinated phosphorus compounds.[6,51–53] Values of $\delta^{31}P$ extend from +954 to −363 with most of them between +600 and −300. This wide shift range corresponds to a variation of phosphorus character from a phosphenium type with a high-frequency chemical shift to a phosphide type with a low-frequency chemical shift. The overall charge of the molecule seems not to be important.[6,51] Values of $\delta^{31}P$ of fully unsaturated phosphorus heterocycles extend from +495 to −5 with most of the shifts between +300 and +50.[6,36,52,53]

Linear correlations are found for $\delta^{31}P$ in aryl-substituted phosphaalkenes with Hammett constants and for $\delta^{31}P$ in iminophosphines with the $n \rightarrow \pi^*$ transition energies. Values of $\delta^{31}P$ of =PR in various acyclic compounds and $\delta^{13}C$ and $\delta^{77}Se$ of the corresponding $=CH_2$ and =Se compounds also give fair linear correlations. More linear correlations are found for the exchange of =P– for =N– in both acyclic and heterocyclic compounds and for =CH– in otherwise identical heterocycles.[36]

Solid state ^{31}P NMR spectra of a diphosphene,[54] a phosphaalkene,[49] and benzo-anellated heterophospholes[55] have been reported.

4.3 Three-Coordinate Phosphorus

The ^{31}P chemical shifts of three-coordinate tervalent phosphorus cover a wide range from +282 to −461 with most of the shifts between +220 and −290.[6] Ranges of $\delta^{31}P$ for individual types of P (III) compounds are found in Tebby,[6] Mason,[8] and Berger et al.[10] Values of $\delta^{31}P$ of conformationally mobile di- and polyphosphines are likely to be temperature-dependent. In alkenic-substituted phosphines the ^{31}P nucleus is more shielded in the *Z*- compared with the *E*-isomer (effect of steric compression). A nearly linear correlation is found between $\delta^{31}P$ in Ph_2P–R and $\delta^{13}C$ in CH_3–R.[8–10]

For three-coordinate pentavalent phosphorus $\delta^{31}P$ ranges (excluding extreme values) essentially from +300 to +40 and is thus found at higher frequency than $\delta^{31}P$ of higher-coordinated phosphorus(V).[6,36,56] In σ^3-phosphoranes of the type R–PXY, depending on the double bonded substituents X and Y, phosphorus shielding generally increases in the order ML_n < S < Se < CR_2 < NR < O.[36,56]

4.4 Four-Coordinate Phosphorus

The ^{31}P chemical shift range of pentavalent tetracoordinate phosphorus extends essentially between +140 and −90 with a few extreme values for phosphonium compounds of up to −308.[6] Shift ranges for individual classes of compounds can be found in Tebby,[6] Mason,[8] and Berger et al.[10]

A number of phosphonic and phosphinic acids, inorganic phosphates, and polyphosphates have been investigated by solid state ^{31}P NMR spectroscopy.[10] In the case of polyphosphates, the different $\delta^{31}P$ values of the terminal and bridging phosphate groups have been interpreted in terms of the electronegativity difference between terminal and bridging oxygen atoms (estimated at 0.4) and the difference in π-bonding order.[57] A linear relationship results between $\delta^{31}P$ and the P–O bond strength in inorganic phosphates.[58]

In phosphates and phosphate esters, as well as in their thio derivatives a clear dependence of $\delta^{31}P$ on the XPX angle (X = O,S) is observed. In phosphoric and phosphonic acids, and in mono- and dinucleotides the ^{31}P chemical shift shows a dependence on pH. Good linear Hammett correlations and a linear $\delta^{31}P/\delta^{13}C$ relationship for [Ph_3PR]X and CH_3–R have been reported.[10]

In contrast to the tetracoordinate phosphorus(V), the ^{31}P chemical shift range for the tetracoordinate tervalent phosphorus (phosphoranide-type phosphorus) is much larger and extends from +222 to −242.[6]

4.5 Five-Coordinate Phosphorus

The chemical shift of five-coordinate phosphorus covers a range between +31 and −195 with the majority of shifts between 0 and −80.[6] A temperature dependence of the NMR spectra is often encountered, due to intermolecular[9,59] or intramolecular (pseudorotation)[9,60] ligand exchange or to hindered rotation.[9,61]

4.6 Six-Coordinate Phosphorus

The chemical shifts of six-coordinate phosphorus are found between −57 and −441 with most of the shifts between −80 and −290.[6] The major factors determining the chemical shifts are electronegativity and anisotropic effects of the substituents. Increasing the overall charge of the species from +1 through zero to −1 shifts $\delta^{31}P$ to lower frequency, while incorporation of the phosphorus in a five-membered ring results in a shift of $\delta^{31}P$ in the opposite direction.[6,9]

5 COUPLING CONSTANTS

Scalar spin–spin couplings of phosphorus to almost all elements of the Periodic Table are known, and remarkably large coupling constants up to 17000 Hz (!) have been observed. Compilations of phosphorus–element coupling constants can be found in several books.[7–10,62] Representative values are contained in most of the compilations of ^{31}P chemical shift data.[4–6,51–53] Specialized reviews on phosphorus–phosphorus,[63] phosphorus–hydrogen,[64] and phosphorus–carbon[65,66] coupling constants are available.

Table 2 Observed Phosphorus–Phosphorus Coupling Constants

Coupling constant	J (Hz)	References
$^{1}J(P^{III},P^{III})$	−55 to −670	8–10,51–53,63
$^{1}J(P^{III},P^{V})$	−157 to −684	8–10,63
$^{1}J(P^{V},P^{V})$	−67 to +766	8–10,63
$^{2}J(P^{III},P^{III})$	−35 to +665	8–10,63
$^{2}J(P^{III},P^{V})$	−28 to +150	8–10,63
$^{2}J(P^{V},P^{V})$	11 to 210	8–10,63
^{3}J(P,P)	0 to 227	8–10,63
^{4}J(P,P)	2 to 35	9, 10, 63
^{5}J(P,P)	5 to 9	67
^{6}J(P,P)	3 to 12	67, 68
^{7}J(P,P)	1 to 8	67
^{8}J(P,P)	1 to 2	67
^{9}J(P,P)	4	67

More information on specific phosphorus–element coupling constants can be found in the references in Tables 2 and 3.

It is generally observed, that the values of the reduced coupling constants ^{n}K(P,X) decrease in the order $^{1}K(P,X) \gg {}^{3}K(P,X) > {}^{2}K(P,X) > {}^{4}K(P,X)$.[9] In many cases, however, the order of ^{3}K(P,X) and ^{2}K(P,X) is reversed, due to structural factors. Coupling constants over more than four bonds are normally two or more orders of magnitude smaller than ^{1}K(P,X). In special cases and particularly in compounds with a delocalized π system long-range coupling constants ^{n}J(P,P) for $n = 5–9$[67,68] and $^{n}J(^{31}P,^{13}C)$ up to $n = 7$[69] have been observed.

The presence of a lone pair of electrons at the phosphorus atom or at the atom coupled with it seems to be associated with a negative one-bond reduced coupling constant ^{1}K(P,X). An exception is provided by $^{1}K(^{31}P,^{1}H)$, however, which is positive. The magnitude of ^{1}K(P,X) increases with increasing electronegativity of the substituents regardless of its sign. Linear relationships have been found between ^{1}K(P,X) and the sum of the electronegativity of the substituents at the phosphorus atom for $^{1}K(^{183}W,^{31}P)$, $^{1}K(^{77}Se,^{31}P)$, $^{1}K(^{95}Mo,^{31}P)$, $^{1}K(^{31}P,^{31}P)$, $^{1}K(^{31}P,^{13}C)$, and $^{1}K(^{31}P,^{1}H)$.[9,10,70]

In molecules with a trigonal bipyramidal geometry ^{1}K(P,X) through the shorter equatorial bond is larger than through the longer axial bond.[9,10,71] In transition metal–phosphine complexes the one-bond phosphorus–metal coupling constant is found to increase with decreasing *trans*-effect of the ligand in the *trans*-position to the phosphorus atom in the order $MePh_2Si > Ph > Me \gg R_3P > (PhO)_3P$, $CN > Et_3As > NO_2 >$ amine, NCO, NCS > Cl, Br, I > $ONO_2 > F$.[9,10] A bond angle and dihedral angle dependence of ^{1}K(P,X) has also been discussed.[5,9,72,73]

Geminal coupling constants ^{2}K(P,X) show, in principle, the same dependences as ^{1}K(P,X); the signs are often reversed, however. For the three-coordinate trivalent phosphorus there is a dependence of ^{2}K(P,X) on the dihedral angle between the phosphorus lone pair and the X nucleus,[73] which has been investigated for $^{2}J(^{31}P,^{31}P)$, $^{2}J(^{31}P,^{13}C)$, and $^{2}J(^{31}P,^{1}H)$. For tetracoordinate phosphorus a similar dependence is found with an electronegative substituent in place of the lone pair.[9]

Of general importance is the dependence of vicinal reduced coupling constants ^{3}K(P,X) on the dihedral angle between the phosphorus and the X nucleus (Karplus relationship), which has been investigated for a number of compounds. In all cases a minimum near 90° and maxima at 0° and 180° are observed.[9,10,74]

5.1 Phosphorus–Phosphorus Coupling Constants

Typical ranges for P,P coupling constants are given in Table 2. The value of $^{1}J(^{31}P,^{31}P)$ is negative between trivalent phosphorus atoms and, where the sign is known, also between trivalent and pentavalent phosphorus atoms. Between pentavalent phosphorus atoms $^{1}J(^{31}P,^{31}P)$ is often positive. One-bond phosphorus–phosphorus coupling constants show a large stereochemical dependence on rotation about the P–P bond, especially when there are lone pairs at the phosphorus atoms.[8–10]

Geminal P(III), P(III) coupling constants are mostly positive and extend up to +665 Hz. In acyclic compounds geminal P(III), P(V) couplings range mainly between +50 Hz and +150 Hz, whereas for cyclic compounds smaller and negative values are found. The value of $^{2}J(^{31}P,^{31}P)$ between pentavalent phosphorus atoms in acyclic compounds is generally small (11–43 Hz), but can assume large values up to +210 Hz in cyclic compounds.[8]

5.2 Phosphorus Couplings to Other Nuclei

Typical ranges for the coupling constants of phosphorus to other elements of the Periodic Table are given in Table 3. The signs of the coupling constants, where known, have also been included. The value of $^{1}J(^{31}P,^{1}H)$ tends to increase with increasing oxidation state and coordination number of phosphorus; the individual ranges overlap considerably, however.[70] One-bond phosphorus–fluorine coupling constants show the opposite trend, in accord with the opposite signs of $^{1}J(^{31}P,^{1}H)$ and $^{1}J(^{31}P,^{19}F)$.[9,10] An isotope effect of ^{2}H on $^{1}J(^{31}P,^{1}H)$ has been reported.[103] The $^{1}J(^{31}P,^{15}N)$ value is positive (+24 to +105 Hz) in trivalent, generally positive (−44 to +60 Hz) in tetracovalent, and negative (−40 to −80 Hz) in pentacovalent phosphorus compounds. The $^{1}J(^{77}Se,^{31}P)$ value is larger for a phosphorus–selenium double bond (−500 to −1200 Hz) than for a single bond (−100 to −500 Hz). Similarly $^{1}J(^{125}Te,^{31}P)$ is larger for P=Te (1324–2290 Hz) than for P–Te (80–996 Hz).[8,9] Exceptionally large values, reaching orders of magnitude of the corresponding one-bond coupling constants, are observed for $^{2}J(^{77}Se,^{31}P)$,[92] $^{2}J(^{119}Sn,^{31}P)$,[10] $^{2}J(^{205}T1,^{31}P)$,[102] and $^{2}J(^{207}Pb,^{31}P)$[104] in transition metal complexes.

6 APPLICATIONS OF ^{31}P NMR SPECTROSCOPY

Phosphorus-31 NMR spectroscopy has been used to monitor the progress of chemical reactions and exchange equilibria since its early days. Today ^{31}P NMR spectroscopy is a powerful diagnostic tool in practically all areas of preparative chemistry where phosphorus is present. Alone, or in combination with the NMR spectroscopy of other nuclei, it is mostly used for the identification and structure elucidation of phosphorus compounds. The enantiomeric purity of chiral alcohols, thiols (via the corresponding phosphites and thiophosphonates), and phosphines is conveniently checked by ^{31}P NMR. Based on

Table 3 Observed Coupling Constants of Phosphorus to Other Nuclei

Coupling constant	J (Hz)	Sign	References
$^{1}J(^{31}P,^{1}H)$	110 to 1200	+	9, 10, 64
$^{2}J(^{31}P,^{1}H)$	0 to 205	±	9, 10, 36
$^{3}J(^{31}P,^{1}H)$	0 to 51	±	9, 10, 36
$^{4}J(^{31}P,^{1}H)$	0 to 18		9, 10, 75
$^{5}J(^{31}P,^{1}H)$	0 to 12		10, 75
$^{1}J(^{31}P,^{2}H)$	30 to 112		76
$^{2}J(^{31}P,^{2}H)$	6 to 10		77, 78
$^{1}J(^{31}P,^{7}Li)$	33 to 55		9, 10, 79
$^{2}J(^{31}P,^{7}Li)$	2		80
$^{2}J(^{31}P,^{9}Be)$	2 to 6		8
$^{1}J(^{31}P,^{10}B)$	9		10
$^{1}J(^{31}P,^{11}B)$	10 to 217	+	8, 9, 81
$^{1}J(^{31}P,^{13}C)$	−40 to +500	±	9, 10, 65
$^{2}J(^{31}P,^{13}C)$	−20 to +90	±	9, 10, 65
$^{3}J(^{31}P,^{13}C)$	0 to 26	+	9, 10, 65
$^{4}J(^{31}P,^{13}C)$	0 to 7		10, 69
$^{5}J(^{31}P,^{13}C)$	0 to 26		10, 69
$^{6}J(^{31}P,^{13}C)$	0 to 2		69
$^{7}J(^{31}P,^{13}C)$	0 to 2		69
$^{1}J(^{31}P,^{15}N)$	−80 to +105	±	9, 10, 36, 82, 83
$^{2}J(^{31}P,^{15}N)$	0 to 55	+	30, 82
$^{3}J(^{31}P,^{15}N)$	4 to 9		82
$^{1}J(^{31}P,^{17}O)$	48 to 220	+	8–10,84
$^{1}J(^{31}P,^{19}F)$	463 to 1555	−	4, 9, 10
$^{2}J(^{31}P,^{19}F)$	2 to 700	+	4, 10, 36
$^{3}J(^{31}P,^{19}F)$	0 to 313	+	4, 10
$^{4}J(^{31}P,^{19}F)$	6 to 64		4, 10
$^{5}J(^{31}P,^{19}F)$	4 to 33		10
$^{1}J(^{31}P,^{27}Al)$	90 to 290		8–10
$^{2}J(^{31}P,^{27}Al)$	11 to 30		8, 85
$^{1}J(^{31}P,^{29}Si)$	7 to 154	−	10, 36, 86
$^{2}J(^{31}P,^{29}Si)$	1 to 59	−	10, 36, 87
$^{3}J(^{31}P,^{29}Si)$	3 to 6		10
$^{1}J(^{35}Cl,^{31}P)$	105 to 127		88
$^{1}J(^{37}Cl,^{31}P)$	100		88
$^{2}J(^{45}Sc,^{31}P)$	30 to 40		8
$^{1}J(^{51}V,^{31}P)$	110 to 510		8, 10
$^{1}J(^{53}Cr,^{31}P)$	105 to 153		8, 89
$^{1}J(^{55}Mn,^{31}P)$	140 to 405		8
$^{1}J(^{57}Fe,^{31}P)$	10 to 149		8, 10, 77, 90
$^{1}J(^{59}Co,^{31}P)$	375 to 1222		8–10
$^{1}J(^{61}Ni,^{31}P)$	161 to 482		8–10,77
$^{1}J(^{63}Cu,^{31}P)$	1109 to 1458	+	8–10
$^{1}J(^{65}Cu,^{31}P)$	1275 to 1302		8–10
$^{2}J(^{71}Ga,^{31}P)$	38		8
$^{1}J(^{77}Se,^{31}P)$	100 to 1200	−	8–10,91
$^{2}J(^{77}Se,^{31}P)$	0 to 140		91, 92
$^{3}J(^{77}Se,^{31}P)$	0 to 18	±	91
$^{4}J(^{77}Se,^{31}P)$	0 to 1		91
$^{1}J(^{79}Br,^{31}P)$	296 to 350		88
$^{1}J(^{81}Br,^{31}P)$	315 to 380		88
$^{1}J(^{89}Y,^{31}P)$	5 to 52		90
$^{2}J(^{89}Y,^{31}P)$	5		8
$^{1}J(^{93}Nb,^{31}P)$	1050		9
$^{1}J(^{95}Mo,^{31}P)$	90 to 284		8, 9
$^{1}J(^{97}Mo,^{31}P)$	254		8
$^{1}J(^{99}Tc,^{31}P)$	400 to 909		10
$^{1}J(^{103}Rh,^{31}P)$	8 to 374	−	9, 10, 90
$^{2}J(^{103}Rh,^{31}P)$	0 to 34		9, 10
$^{3}J(^{103}Rh,^{31}P)$	1 to 24	−	9, 10
$^{1}J(^{107}Ag,^{31}P)$	212 to 1118		9, 10
$^{1}J(^{109}Ag,^{31}P)$	220 to 1217		8, 90
$^{2}J(^{109}Ag,^{31}P)$	9 to 10		8
$^{1}J(^{111}Cd,^{31}P)$	1091 − 2443		9, 93, 94
$^{1}J(^{113}Cd,^{31}P)$	1142 − 2240	−	8, 94
$^{2}J(^{113}Cd,^{31}P)$	2 − 80		8
$^{1}J(^{117}Sn,^{31}P)$	76 − 2260	+	7, 10, 95
$^{1}J(^{119}Sn,^{31}P)$	50 − 3125	+	4, 9, 10, 95, 96
$^{2}J(^{119}Sn,^{31}P)$	83 − 4269		10, 96
$^{1}J(^{125}Te,^{31}P)$	84 − 2290	+	8–10
$^{2}J(^{125}Te,^{31}P)$	11		10
$^{1}J(^{183}W,^{31}P)$	80 − 847	+	8–10,90
$^{2}J(^{183}W,^{31}P)$	2 − 24		8, 10
$^{1}J(^{187}Os,^{31}P)$	149 − 492	+	10, 90, 97
$^{1}J(^{195}Pt,^{31}P)$	62 − 9150	+	8–10
$^{2}J(^{195}Pt,^{31}P)$	36 − 1977	±	8–10,98
$^{3}J(^{195}Pt,^{31}P)$	6 − 245	−	9, 10, 99
$^{4}J(^{195}Pt,^{31}P)$	34		9
$^{1}J(^{199}Hg,^{31}P)$	143 − 17528	+	8–10,100
$^{2}J(^{199}Hg,^{31}P)$	40 − 160	−	8, 99
$^{1}J(^{203,205}Tl,^{31}P)$	3144,3203		101, 102
$^{2}J(^{205}Tl,^{31}P)$	1056 − 1202		8, 10, 102
$^{1}J(^{207}Pb,^{31}P)$	1100 − 2452	−	9, 104
$^{2}J(^{207}Pb,^{31}P)$	28 − 3460		104

the pH dependence of δ^{31}P, the pK_a values of phosphoric acids have been determined. Phosphorus-31 NMR is also extensively used for the investigation of dynamic processes.[9,10]

In biochemistry and medicine in vivo ^{31}P NMR and ^{31}P NMR imaging gain increasingly in importance.[8,105,106] Oxygen-18 isotope effects on ^{31}P nuclear shielding are extensively used to study the chirality of phosphorus compounds and the stereospecificity of enzymatic reactions.[44]

7 RELATED ARTICLES

Brain Neoplasms in Humans Studied by Phosphorus-31 NMR Spectroscopy; Inorganic Chemistry Applications; Membranes: Phosphorus-31 NMR; Nucleic Acids: Phosphorus-31 NMR; Phosphorus-31 Magnetization Transfer Studies In Vivo; Proton Decoupling During In Vivo Whole Body Phosphorus MRS; Single Voxel Whole Body Phosphorus MRS; Tissue Behavior Measurements Using Phosphorus-31 NMR.

8 REFERENCES

1. W. C. Dickinson, *Phys. Rev.*, 1951, **81**, 717.
2. H. S. Gutowsky, D. W. McCall, and C. P. Slichter, *Phys. Rev.*, 1951, **84**, 589.
3. M. M. Crutchfield, C. H. Dungan, and J. R. Van Wazer, *Top. Phosphorus Chem.*, 1967, **5**, 1.
4. G. Mavel, *Annu. Rep. NMR Spectrosc.*, 1973, **5B**, 1.
5. D. G. Gorenstein, *Prog. NMR Spectrosc.*, 1983, **16**, 1.
6. J. C. Tebby (ed.), *Handbook of Phosphorus-31 Nuclear Magnetic Resonance Data*, CRC Press, Boca Raton, FL, 1991.
7. R. K. Harris and B. E. Mann (eds.), *NMR and the Periodic Table*, Academic Press, London, 1978.
8. J. Mason (ed.), *Multinuclear NMR*, Plenum Press, New York, 1987.
9. J. G. Verkade and L. D. Quin (eds.), *Phosphorus-31 NMR Spectroscopy in Stereochemical Analysis*, VCH, Deerfield Beach, FL, 1987.

10. S. Berger, S. Braun (eds.), and H.-O. Kalinowski, *NMR-Spektroskopie von Nichtmetallen*, *Vol. 3* ^{31}*P-NMR Spektroskopie*, Thieme, Stuttgart, 1993.
11. L. D. Quin and J. Verkade (eds.), *Phosphorus-31 NMR Special Properties in Compound Characterization and Structural Analysis*, VCH, Deerfield Beach, FL, 1994.
12. J. F. Nixon and A. Pidcock, *Annu. Rep. NMR Spectrosc.*, 1969, **2**, 346.
13. P. E. Garrou, *Chem. Rev.*, 1981, **81**, 229.
14. A. Pidcock, *Adv. Chem. Ser.*, 1982, **196**, 1.
15. P. S. Pregosin and R. W. Kunz, *NMR Basic Principles Progr.*, 1979, **16**, 1.
16. C. T. Burt and A. M. Wyrwicz, *Trends Biochem. Sci.*, 1979, **4**, 244.
17. D. G. Gadian, G. K. Radda, R. E. Richards, and P. J. Seeley, in *Biological Applications of Magnetic Resonance*, ed. R. G. Schulman, Academic Press, New York, 1979, p. 463.
18. I. K. O'Neil and C. P. Richards, *Annu. Rep. NMR Spectrosc.*, 1980, **10A**, 133.
19. D. P. Hollis, in *Biological Magnetic Resonance*, eds. L. J. Berliner and J. Rouben, Plenum Press, New York, 1980, Vol. 2, p. 1.
20. E. M. Bradbury, G. K. Radda, and P. S. Allen, *Ann. Intern. Med.*, 1983, **98**, 514.
21. D. E. Gadian, *Spec. Publ. R. Soc. Chem.*, 1984, **47**, 58.
22. D. G. Gorenstein, *Phosphorus-31 NMR, Principles and Applications*, Academic Press, New York, 1984.
23. B. C. Tyler, *Phosphorus NMR in Biology*, CRC Press, Boca Raton, FL, 1987.
24. C. J. Jameson, A. De Dios, and A. K. Jameson, *Chem. Phys. Lett.*, 1990, **167**, 575.
25. P. L. Yeagle, W. C. Hutton, and R. B. Martin, *J. Am. Chem. Soc.*, 1975, **97**, 7175.
26. M. L. Martin, J. J. Delpuech, and G. J. Martin, *Practical NMR Spectroscopy*, Heyden, London, 1980.
27. I. J. Colquhoun, W. McFarlane, S. O. Grim, J. D. Mitchell, and P. H. Smith, *Inorg. Chem.*, 1981, **20**, 2516.
28. S. J. Berners-Price, P. J. Sadler, and Ch. Brevard, *Magn. Reson. Chem.*, 1990, **28**, 145.
29. C. J. Turner and P. B. Garlick, *J. Magn. Reson.*, 1984, **57**, 221.
30. P. H. Bolton and G. Bodenhausen, *J. Magn. Reson.*, 1982, **46**, 306.
31. K. G. Orrell and V. Sik, *Annu. Rep. NMR Spectrosc.*, 1993, **27**, 103.
32. B. Wrackmeyer, E. Kupce, and A. Schmidpeter, *Magn. Reson. Chem.*, 1991, **29**, 1045.
33. A. Yamasaki, *Coord. Chem. Rev.*, 1991, **109**, 107.
34. L. Jacobson, *J. Magn. Reson.*, 1982, **49**, 522.
35. F. L. Dickert and S. W. Hellmann, *JEOL (Jpn. Electron Opt. Lab.) News (Ser.) Anal. Instrum.*, 1982, **18A**, 57.
36. K. Karaghiosoff, in *Multiple Bonds and Low Coordination in Phosphorus Chemistry*, eds. M. Regitz and O. J. Scherer, Thieme, Stuttgart, 1990, p. 463.
37. J. H. Letcher and J. R. Van Wazer, *J. Chem. Phys.*, 1966, **44**, 815.
38. R. Blachnik, U. Wickel, and P. Schmitt, *Z. Naturforsch., Teil B*, 1984, **39**, 1135.
39. J. Hahn, M. Baudler, C. Krüger, and Y. H. Tsay, *Z. Naturforsch., Teil B*, 1982, **37**, 797.
40. M. Baudler, *Angew. Chem.*, 1987, **99**, 429; *Angew. Chem., Int. Ed. Engl.*, 1987, **26**, 419.
41. L. Maier, *Helv. Chim. Acta*, 1966, **49**, 1718.
42. L. D. Quin and J. J. Breen, *Org. Magn. Reson.*, 1973, **5**, 17.
43. W. Kutzelnigg, U. Fleischer, and M. Schindler, *NMR Basic Principles Progr.*, 1990, **23**, 165.
44. P. E. Hansen, *Prog. NMR Spectrosc.*, 1988, **20**, 207.
45. W. Buchner, W. Ries, and W. Malisch, *Magn. Reson. Chem.*, 1990, **28**, 515.
46. M. Regitz, in *Multiple Bonds and Low Coordination in Phosphorus Chemistry*, eds. M. Regitz and O. J. Scherer, Thieme, Stuttgart, 1990, p. 58.
47. J. Grobe, D. Le Van, B. Lüth, and M. Hegemann, *Chem. Ber.*, 1990, **123**, 2317.
48. E. Niecke, M. Nieger, and F. Reichert, *Angew. Chem.*, 1988, **100**, 1781; *Angew. Chem. Int. Ed. Engl.*, 1988, **27**, 1715.
49. J. C. Duchamp, M. Pakulski, A. H. Cowley, and K. W. Zilm, *J. Am. Chem. Soc.*, 1990, **112**, 6803.
50. R. D. Kurtis, M. J. Schriver, and R. E. Wasylishen, *J. Am. Chem. Soc.*, 1991, **113**, 1493.
51. S. Lochschmidt and A. Schmidpeter, *Phosphorus Sulfur*, 1986, **29**, 73.
52. K. Karaghiosoff and A. Schmidpeter, *Phosphorus Sulfur*, 1988, **36**, 217.
53. R. K. Bansal, K. Karaghiosoff, and A. Schmidpeter, *Tetrahedron*, 1994, **50**, 7675.
54. K. W. Zilm, G. G. Webb, A. H. Cowley, M. Pakulski, and A. Orendt, *J. Am. Chem. Soc.*, 1988, **110**, 2032.
55. R. D. Curtis, B. W. Royan, R. E. Wasylishen, M. D. Lumsden, and N. Burford, *Inorg. Chem.*, 1992, **31**, 3386.
56. H. Germa and J. Navech, *Phosphorus Sulfur*, 1986, **26**, 327.
57. U. Haubenreisser, G. Scheler, and A. R. Grimmer, *Z. Anorg. Allg. Chem.*, 1986, **532**, 157.
58. A. K. Cheetham, N. J. Clayden, C. M. Dobson, and R. J.B. Jakeman, *J. Chem. Soc., Chem. Commun.*, **1986**, 195.
59. D. Robert, C. Demay, and J. G. Riess, *Inorg. Chem.*, 1982, **21**, 1805.
60. I. Ruppert, *Z. Anorg. Allg. Chem.*, 1981, **477**, 59.
61. A. Connelly and R. K. Harris, *J. Chem. Soc., Dalton Trans.*, 1984, 1547.
62. M. Regitz and O. J. Scherer (eds.), *Multiple Bonds and Low Coordination in Phosphorus Chemistry*, Thieme, Stuttgart, 1990.
63. E. G. Finer and R. K. Harris, *Prog. NMR Spectrosc.*, 1971, **6**, 61.
64. J. F. Brazier, D. Houalla, M. Loenig, and R. Wolf, *Top. Phosphorus Chem.*, 1976, **8**, 99.
65. J. R. Llinas, E.-J. Vincent, and G. Peiffer, *Bull. Soc. Chim. Fr.*, 1973, 3209.
66. L. D. Quin, *The Heterocyclic Chemistry of Phosphorus*, Wiley, New York, 1981, Chap. 6
67. L. Ernst, *J. Chem. Soc., Chem. Commun.*, 1977, 375.
68. G. Szalontai, J. Bakos, I. Toth, and B. Heil, *Magn. Reson. Chem.*, 1987, **25**, 761.
69. L. Ernst, *Org. Magn. Reson.*, 1977, **9**, 35.
70. A. Schmidpeter, J. Ebeling, H. Stary, and C. Weingand, *Z. Anorg. Allg. Chem.*, 1972, **394**, 171.
71. J. W. Emsley, L. Phillips, and V. Wray, *Prog. NMR. Spectrosc.*, 1975, **10**, 83.
72. C. A. Tolman, *Chem. Rev.*, 1977, **77**, 313.
73. V. M. S. Gil and W. von Philipsborn, *Magn. Reson. Chem.*, 1989, **27**, 409.
74. G. Grossmann, R. Lang, G. Ohms, and D. Scheller, *Magn. Reson. Chem.*, 1990, **28**, 500.

75. M.-P. Simonnin and C. Charrier, *Org. Magn. Reson.*, 1969, **1**, 27.
76. H. H. Mantsch, H. Saito, and I. C. P. Smith, *Prog. NMR Spectrosc.*, 1977, **11**, 211.
77. R. Benn and A. Rufinska, *Magn. Reson. Chem.*, 1988, **26**, 895.
78. S. Kerschl, B. Wrackmeyer, A. Willhalm, and A. Schmidpeter, *J. Organomet. Chem.*, 1987, **319**, 49.
79. A. Zschunke, M. Riemer, E. Leissring, and K. Issleib, *Z. Anorg. Allg. Chem.*, 1985, **525**, 35.
80. P. R. Rubini, L. Rodehüser, and J.-J. Delpuech, *Inorg. Chem.*, 1979, **18**, 2962.
81. B. Wrackmeyer, *Annu. Rep. NMR. Spectrosc.*, 1988, **20**, 61.
82. M. Witanowski, L. Stefaniak, and G. A. Webb, *Annu. Rep. NMR Spectrosc.*, 1993, **25**, 1.
83. B. W. Tattershall, *J. Chem. Soc., Chem. Commun.*, 1989, 216.
84. E. L. Eliel, S. Chandrasekaran, L. E. Carpenter II, and J. G. Verkade, *J. Am. Chem. Soc.*, 1986, **108**, 6651.
85. J. W. Akitt, *Prog. NMR Spectrosc.*, 1989, **21**, 1.
86. E. A. Williams, *Annu. Rep. NMR Spectrosc.*, 1983, **15**, 235.
87. E. Niecke and W. Flick, *Angew. Chem.*, 1974, **86**, 128; *Angew. Chem., Int. Ed. Engl.*, 1974, **13**, 134.
88. V. Mlynarik, *Prog. NMR Spectrosc.*, 1986, **18**, 277.
89. M. F. A. Dove, E. M. L. Jones, and R. J. Clark, *Magn. Reson. Chem.*, 1989, **27**, 973.
90. B. E. Mann, *Annu. Rep. NMR Spectrosc.*, 1991, **23**, 141.
91. I. J. Colquhoun, H. C. E. McFarlane, W. McFarlane, J. A. Nash, R. Keat, D. R. Rycroft, and D. G. Thompson, *Org. Magn. Reson.*, 1979, **12**, 473.
92. T. Chivers, D. D. Doxsee, and R. W. Hilts, *Inorg. Chem.*, 1993, **32**, 3244.
93. P. A. W. Dean, N. C. Payne, J. J. Vittal, and Y. Wu, *Inorg. Chem.*, 1993, **32**, 4632.
94. J. S. Casas, M. S. Garcia-Tasende, A. Sanchez, J. Sordo, E. M. Vazquez-Lopez, E. E. Castellano, and J. Zukerman-Schpector, *Inorg. Chim. Acta*, 1993, **209**, 137.
95. D. Hänssgen, E. Stahlhut, H. Aldenhoven, and A. Dörr, *J. Organomet. Chem.*, 1992, **425**, 19.
96. R. Colton and D. Dakternieks, *Inorg. Chim. Acta*, 1988, **143**, 151.
97. R. Benn, H. Brenneke, E. Joussen, H. Lehmkuhl, and F. L. Ortiz, *Organometallics*, 1990, **9**, 756.
98. A. Zschunke, H. Meyer, I. Heidlas, B. Messbauer, B. Walther, and H.-D. Schädler, *Z. Anorg. Allg. Chem.*, 1983, **504**, 117.
99. P. G. Pringle and B. L. Shaw, *J. Chem. Soc., Chem. Commun.*, 1982, 81.
100. B. Wrackmeyer and R. Contreras, *Annu. Rep. NMR Spectrosc.*, 1992, **24**, 267.
101. J. F. Hinton, K. R. Metz, and R. W. Briggs, *Annu. Rep. NMR Spectrosc.*, 1982, **13**, 211.
102. J. F. Hinton, *Magn. Reson. Chem.*, 1987, **25**, 659.
103. N. M. Sergeyev, *NMR Basic Principles Progr.*, 1990, **22**, 31.
104. B. Wrackmeyer and K. Horchler, *Annu. Rep. NMR Spectrosc.*, 1990, **22**, 249.
105. G. Navon, T. Kushnir, N. Askenasy, and O. Kaplan, *NMR Basic Principles Progr.*, 1992, **27**, 237.
106. M. Rudin and A. Sauter, *NMR Basic Principles Progr.*, 1992, **28**, 161.

Biographical Sketch

Konstantin Karaghiosoff. *b* 1956. Ph. D., 1986, University of Munich. Introduced to NMR by A. Schmidpeter. Inorganic Chemistry, University of Munich, 1980–present. Approx. 50 publications. Research interests include synthesis and reactions of monocyclic and anellated heterophospholes, phosphorus–sulfur and phosphorus–selenium rings and cages, ^{31}P and ^{77}Se NMR spectroscopy, analysis and simulation of high-order spin systems.

Polymorphism and Related Phenomena

Robin K. Harris
University of Durham, Durham, UK

1	Introduction	1
2	Applicability of NMR	1
3	Molecular Polymorphs	1
4	Polymorphism and Molecular Mobility	3
5	Macromolecular Polymorphs	4
6	Related Articles	6
7	References	6

1 INTRODUCTION

Polymorphism is ubiquitous in solid state chemistry, commonly occurring for a very wide range of materials. Polymorphs are different solid forms (usually crystalline) of a given compound. The differences lie in solid state structure, i.e. in the spatial arrangement of the atoms or molecules. They may be relatively minor (e.g. variations in mutual orientations of molecules) or major (leading, for instance, to substantially different atomic arrangements). Sometimes other terms are used for the phenomenon. Thus, when concerning different forms of the elements, the word allotrope is used, instead of polymorph. Also, polymorphs which have structures differing in the stacking sequence of layers (for example, in silicon carbide) are called polytypes.

A somewhat similar phenomenon is the ability of many compounds to incorporate solvent molecules in their structure during crystallization from solution. Thus compounds frequently exist in both anhydrous and hydrated forms, the crystal structures of which may be essentially identical or profoundly different. Other solvent molecules, such as acetone and chloroform, may be similarly incorporated. Ultimately this relates to the existence of clathrates, for which the structure may only be stable when both host and guest molecules are present. Sometimes hydrates lose water readily; on other occasions anhydrous forms may be hygroscopic. Although this article will concentrate on true polymorphism, the 'pseudopolymorphism' of solvates, which can carry similar NMR connotations, will be mentioned at times.

Of course, another closely-related topic is that of phase changes and phase diagrams, together with similar matters concerning the formation and interchange of polymorphic forms. These questions will be largely ignored in the present article. Under given conditions of temperature, pressure, etc., only one polymorph will clearly be favored by thermodynamic considerations. Frequently, however, kinetics of interconversions will be slow, and several forms will exist at ambient temperature and pressure for times in excess of the minimum required to obtain NMR spectra. Such metastable forms may be obtained, for instance, by crystallization from a solvent or by quenching from a temperature at which they are stable. The present article will concentrate on NMR data obtained under standard working conditions (atmospheric pressure and ambient temperature).

Cases of polymorphism and related phenomena may be divided into those involving molecular crystals and those relating to macromolecular structures (in one, two, or three dimensions). Of course, the bonding in the latter implies that interconversion between forms (e.g. between graphite and diamond) is extremely difficult. Indeed, it might be argued that cases of macromolecular structural differences, which require bond-breaking for interconversion (as for silicon carbide) are not properly labeled as polymorphic since they are more analogous to some types of isomerism in organic compounds. However, although interconversions between molecular polymorphs are usually relatively easy, it must not be assumed that intermolecular forces are negligible. Frequently they involve hydrogen bonding, with substantial energies.

Polymorphism is particularly important, and has been extensively investigated by NMR, for pharmaceutical compounds, for silicates and zeolites, for polymers (including naturally occurring materials such as cellulose and chitosan, as well as synthetic polymers), and for ceramic materials.

2 APPLICABILITY OF NMR

Since the electronic environments of corresponding atoms in different polymorphs of the same compound differ, the NMR chemical shifts will be in principle distinguishable. Indeed, the total NMR spectrum can clearly act as a fingerprint to identify polymorphic forms. Such differences are expected to be similar in magnitude to the crystallographic splittings observed when molecules or atomic groupings of the same chemical type are in locations in the unit cell unrelated by symmetry. The 'fingerprint' is of the crystallographic asymmetric unit, and simply counting the number of resonances may, on occasion, suffice to distinguish between polymorphs.

The techniques most commonly used to distinguish polymorphs are DSC, IR, and powder XRD, but all three have disadvantages. The DSC method is very crude, since it gives little or no chemical information. IR spectroscopy often suffers from lack of resolution and from difficulties in interpreting intensities. Powder XRD is often the preferred technique, but it is not sensitive to poorly crystalline or amorphous forms. NMR does not suffer from any of these problems, and the only drawback is the cost of the equipment.

Polymorphs often differ in molecular-level mobility, and hence in NMR relaxation times, but these are unlikely to be used as distinguishing features, except perhaps for polymeric systems.

3 MOLECULAR POLYMORPHS

The principal area of investigation of molecular polymorphism is that of pharmaceutical compounds. This is for very practical reasons: polymorphs sometimes show differing physiological activity (largely as a result of differences in rates of dissolution) and government regulations therefore require pharmaceutical companies to identify carefully the polymorphic form of their products. Moreover, very small changes in

conditions of preparation can readily result in a difference in polymorphic form, and scale-up can reveal problems not found in laboratory synthesis, so that an understanding of polymorphic variations is very important in pharmaceutical chemistry.

The first application of ^{13}C CP MAS NMR to pharmaceutical polymorphism appears to be that reported by Balimann et al.[1] in 1981, which featured spectra of two forms of Nolvadex (the ICI trade name for the generic tamoxifen). In the late 1980s and early 1990s the groups of Byrn[2,3] and of Harris[4–6] were particularly active in this area.

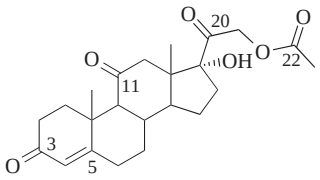

(1)

Steroids appear to be particularly prone to give rise to polymorphic forms. Cortisone acetate (**1**) is a typical example. A substantial number of polymorphs and solvated forms are known, and seven have been studied[4] by MAS NMR. Three of the polymorphs are anhydrous, and Figure 1 illustrates the ^{13}C CP MAS spectra for the high-frequency region (containing resonances from C-3, C-5, C-11, C-20 and C-22).

Immediately, two important conclusions can be made:

1. NMR readily distinguishes the three anhydrous forms (as it does the five hydrates and other solvates).
2. Whereas Forms I and II have asymmetric units consisting of a single molecule (since only five signals are seen in this region), Form III is more complex. In fact, expanded-scale spectra for all the carbon resonances show that Form III has three molecules in the asymmetric unit.

One can go further when peak assignments are firmly established. The apparent variation in the relative intensities of the two peaks on the right in Figure 1(a) and (b) arises from differing spinning sideband intensities. Complete analysis of the spinning sideband manifolds (at low spin rates) shows that C-5 and C-22 have distinguishable shielding anisotropies and asymmetries, which in turn indicates that the order of their isotropic chemical shifts is interchanged between Forms I and II. This variation can be correlated with hydrogen

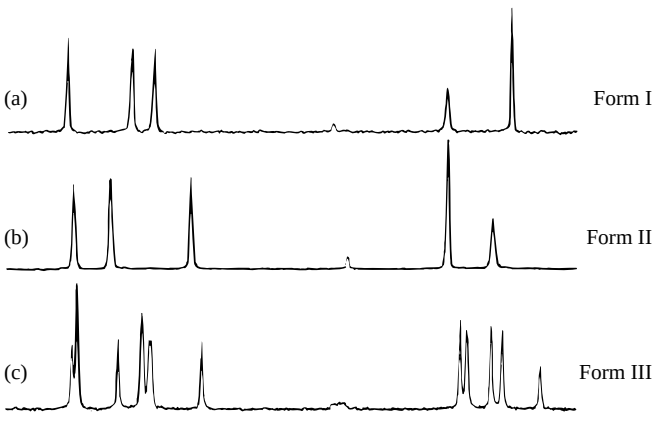

Figure 1 Carbon-13 CP MAS NMR spectra[4] (high-frequency region only) of three polymorphs of cortisone acetate (**1**) at 50.3 MHz

Table 1 Isotropic Chemical Shifts[a] for C-3, C-5, and C-22 of the Anhydrous Polymorphs of Cortisone Acetate

Carbon	Form I	Form II	Form III
C-3	202.8[b]	198.9	203.0[c], 203.0[c], 198.2
C-5	175.7	171.0	173.7, 173.7, 166.9
C-22	169.8	175.2[b]	174.3[c], 171.5, 170.3

[a]Given as δ_C (ppm).
[b]Shown by X-ray crystallography to be the acceptor site for hydrogen bonding.
[c]Concluded from the NMR evidence to be the acceptor site for hydrogen bonding.

bonding,[2,4] which causes an increase in chemical shift of 3–4 ppm at the acceptor carbonyl carbon resonance. Table 1 shows the assignments for carbons C-3, C-5 and C-22 for the three anhydrous forms, and indicates the known acceptor positions for hydrogen bonding. One can conclude that, of the three molecules in the asymmetric unit of Form III, two are hydrogen bonded at C-3 and the third, in contrast, at C-22. It may be noted that conjugation appears to relay the effect of hydrogen bonding on the chemical shift from C-3 to C-5.

This example illustrates how polymorphic form can affect chemical shifts. Unfortunately, matters are not often so simple. The differences in chemical shifts between analogous carbons for different polymorphs may arise either from *inter*molecular effects (packing, direct influence of neighboring molecules, hydrogen bonding, etc.) or *intra*molecular effects (variations in geometry and/or conformation). There is rarely any way that NMR can distinguish between the two influences. Of course, if crystal structures are known from X-ray studies, then knowledge of influences on chemical shifts obtained from solution state studies or by theory can be brought to bear. A case where intramolecular differences (but correlated with intermolecular differences!) are thought to be important is that of 4′-methyl-2′ nitroacetanilide (**2**), which exists in two forms (white and yellow), both of which have been subjected to study by single-crystal X-ray diffraction. In the white form, both the amide and nitro groups are in planes at a substantial angle (ca. 44°) to the plane of the aromatic ring, giving restricted conjugation and preventing intramolecular hydrogen bonding. On the other hand, the yellow form (with two molecules in the asymmetric unit) has more nearly coplanar groups (dihedral angles between 12° and 31°), allowing intramolecular hydrogen bonding between the amide NH and one of the nitro group oxygens. These facts suffice to explain the differences in chemical shifts between the polymorphs.[5] For example, the white form (C–NO_2 dihedral angle, 44.0°) has δ(C-2) = 144.1 ppm whereas the yellow form (C–NO_2 dihedral angles, 18.0° and 12.3°) gives δ(C-2) = 135.9 and 133.0 ppm (presumably respectively).

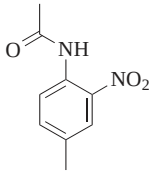

(2)

Certain simple but important measurements can be made of polymorphism via the fingerprinting ability. For example:

1. Mixtures of polymorphs can be readily studied and minor components can be quantified,[4] in favorable cases down to the 1% level.
2. NMR spectra can be used to monitor the polymorphic variations produced by different formation conditions (e.g. different rates of crystallization produced by cooling a solution quickly or slowly).[4]
3. Polymorphism can be studied directly in pharmaceutical tablets. Saindon et al.[3] have pointed out that the CP MAS technique can be used to discriminate against signals deriving from the excipient.

The combination of single-crystal XRD and CP MAS NMR for the study of polymorphism is particularly powerful. The former can give precise atomic positions but is frequently feasible for only some of the forms of a product (because of difficulties in growing suitable crystals). NMR, however, can almost always be relied upon to yield spectra of all polymorphs available in sufficient quantity, and interpretation is greatly aided by X-ray information on any one form. For example, of the two forms of fosinopril sodium, one was examined using single-crystal X-ray diffraction techniques, then both were studied[7] by CP MAS NMR of ^{13}C. The results provided by NMR enabled the conclusion to be drawn that the environment of the acetal side chain of fosinopril sodium differed in the two polymorphs. In this case ^{31}P CP MAS NMR was also used, and showed a significant chemical shift difference (2.2 ppm) between the forms.

It is possible to detect conformational disorder within polymorphs by CP MAS NMR. Thus Stoltz et al.[8] have shown that peak intensities for the monohydrate of oxyphenbutazone give a site ratio consistent with X-ray results in terms of sterically-favored isomers. However, it must be said that since CP MAS NMR spectra are obtained on microcrystalline or powdered material, it is not easy to differentiate between mixed crystals and disorder in a single type of crystal.

Differences in bonding between polymorphs can sometimes be quite startling but readily detectable by NMR. Thus, for 2-aminobenzoic acid (**3**), ^{13}C MAS NMR reveals[9] that Form I gives two signals each for C-1 and C-2. These are at chemical shifts which are characteristic of the normal and zwitterionic structures (**3**)A and (**3**)B, respectively, indicating that the unit cell contains equal proportions of each form. On the other hand, Forms II and III give spectra showing that each has an asymmetric unit containing one molecule of structure (**3**)A only.

A B

(3)

Interestingly, the ^{13}C spectra of Forms II and III are so similar as to be virtually indistinguishable. In these cases, it is necessary to turn to nuclei other than ^{13}C to differentiate. The proton CRAMP spectra of the two forms are, in fact, very different (Figure 2). Form II of the compound gives a strong signal at δ_H = 12.3 ppm, indicative of a hydrogen-bonded CO_2H group (in agreement with single-crystal X-ray results). This is not present for Form III (the crystal structure of which is unknown)—from which it can be deduced that hydrogen bonding is probably absent. However, the situation is complicated by the fact that there are proton-exchange processes occurring, involving amino and (in some cases) carboxylic acid protons, at a rate comparable with the NMR timescale, producing broad bands underlying the sharper aromatic proton signals at ambient probe temperature.

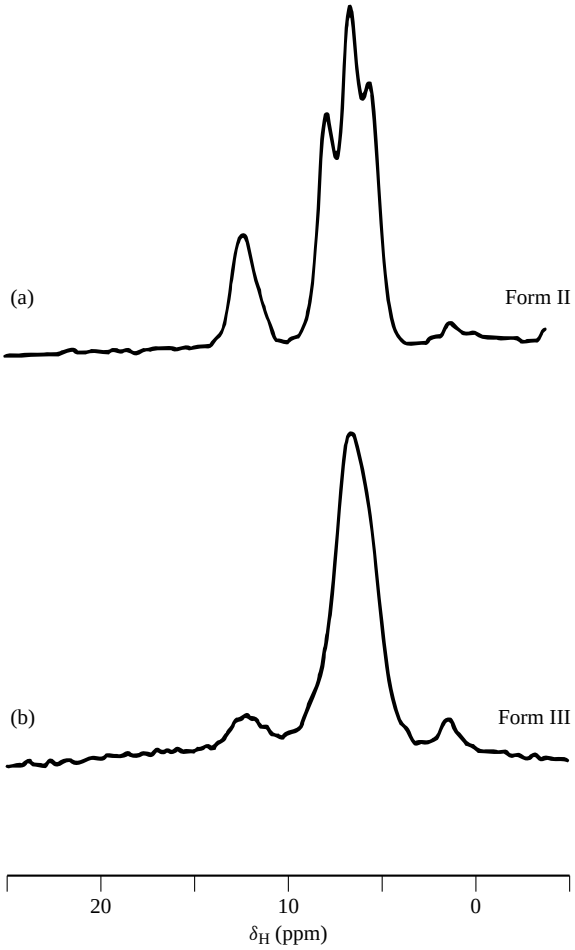

Figure 2 Proton CRAMP spectra[9] of two polymorphs of 2-aminobenzoic acid (**3**) at 200.13 MHz. The sample of Form III contains a small amount of Form II, which gives rise to the hydrogen-bonded peak at δ 12.3 ppm. The peak at $\delta \sim 1.5$ ppm in each spectrum is due to an impurity in the Kel-F rotors used. The broad line (assigned to NH_2 and CO_2H protons) underlying the spectrum of Form III is clearly visible

4 POLYMORPHISM AND MOLECULAR MOBILITY

In addition to the effects on chemical shifts arising from differences in intermolecular environment and intramolecular geometry between molecules of different polymorphs, variations in molecular level motion can often also be detected. A case in point is illustrated in Figure 3, which shows ambient probe temperature ^{13}C CP MAS spectra[10] of two forms

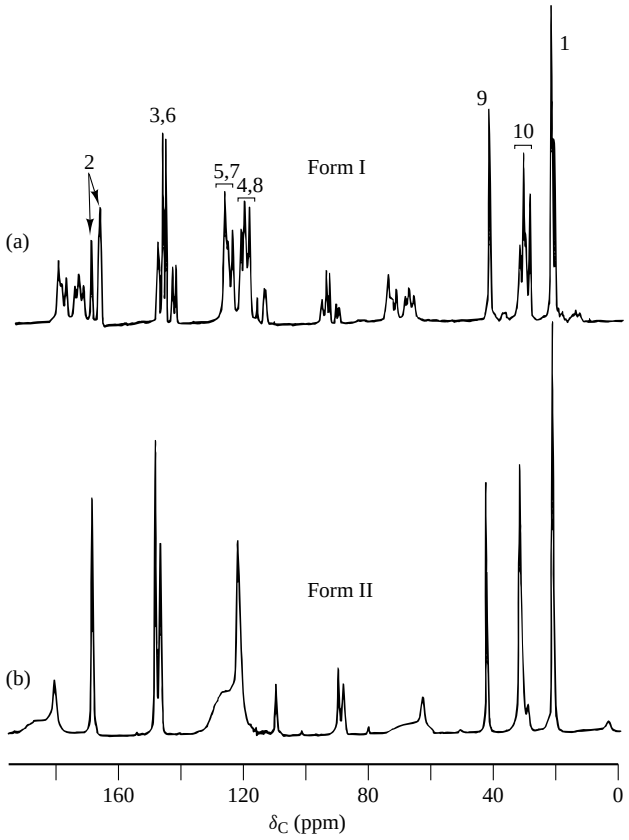

Figure 3 Carbon-13 CP MAS spectra[10] of two forms of bisphenol-A diacetate (**4**) at 50.3 MHz and ambient probe temperature. Signals not indicated by numbers in (a) [and corresponding peaks in (b)] are spinning sidebands

of bisphenol-A diacetate (**4**). Clearly, Form I gives a much more complex spectrum than Form II, as is consistent with the single-crystal X-ray results, which show that in the former case the asymmetric unit consists of two entire molecules. The second feature of importance is the breadth of the resonances for the aromatic CH carbons (C-4, C-5, C-7 and C-8) for Form II, which suggests there is substantial averaging, probably arising from 180° ring-flips of the phenylene rings (possibly by simultaneous motion of the two halves of the molecule). This suggestion is readily confirmed by variation of the temperature.

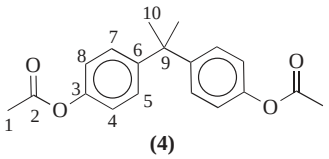

(4)

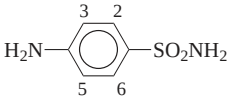

(5)

Such variable temperature ^{13}C CP MAS NMR experiments have been used[11] to study the motion of a phenylene ring about the *para* axis of one form of sulfanilamide, (**5**). Just below room temperature the C-3/C-5 resonance (but not the C-2/C-6 signal) is observably split because the SO_2NH_2 substituent is twisted with respect to the ring. An Arrhenius activation energy, E_a, of 63 ± 4 kJ mol^{-1} for the (assumed) 180° ring-flip was obtained. It should be noted that rapid motion of this type would not be detected by XRD.

An example from an entirely different area of chemistry concerns the polymorphism of phosphorus pentachloride, PCl_5. The stable form (Phase II) of this compound under normal conditions is ionic, with the structure PCl_4^+ PCl_6^-. Both ions are very mobile at ambient temperature, so that shielding anisotropy at the phosphorus nuclei is eliminated and the chlorine nuclei relax very rapidly. The latter effect causes self-decoupling of the chlorines and the net effect is that ^{31}P MAS spectra consist[12] of two sharp lines, one for each anion. However, Phase III, which can also be studied at ambient probe temperature, has the stoichiometry $[PCl_4]_2^+[PCl_6]^-Cl^-$. Since this form, like Phase II, contains PCl_4^+ and PCl_6^- ions, the ^{31}P MAS spectrum also consists of two bands, but at 81 MHz the resonances are broad and splittings arising from (Cl,P) coupling are seen at 36 MHz. Thus self-decoupling is substantially less efficient for Phase III than for Phase II, probably indicating more restricted rotational mobility for the ions in the former.

5 MACROMOLECULAR POLYMORPHS

Two types of example from widely different chemical areas should suffice to show some of the general features of polymorphism in macromolecular systems. Silicon carbide exemplifies the situation where the structure is three-dimensional so that interchange between forms is not feasible. The different polymorphs are essentially frozen-in at the time of preparation. All structures have alternating Si and C atoms, with all coordinations tetrahedral (though mostly not with the full symmetry). The structural differences between some of the forms can be appreciated from Figure 4, which shows a plane including the *c* crystallographic axis and alternating Si and C atoms in that plane for four forms of the material. It is evident that the detailed environments of all silicon atoms of the 2H form are equivalent, as is also the case for the β form (though β and 2H environments are not identical). However, the 4H form contains two types of Si and the 6H three types. The ^{29}Si spectra (Figure 5) show[13] the expected number of signals for the four forms. Similar considerations apply to the ^{13}C spectra. There is also a range of other forms. Assignment of the signals for the 4H and 6H polymorphs is not easy but has been made.[13,14] The separate signals have different relaxation times, probably as a result of the presence of impurities. Silicon carbide is a case where the amorphous material can also exist, without sizable domains of any of the potentially ordered structures. Such material gives rise to broad ^{29}Si and ^{13}C resonances, usually characterized by shorter values of T_1 than the crystalline material, probably because impurities tend to concentrate in amorphous regions.

Of course, silica provides the outstanding example of a compound with multiple polymorphs. Not only are there well-characterized crystalline forms (quartz, crystobalite, tridymite, etc.), together with the common amorphous glass, but it seems that many types of zeolites can be obtained with all aluminum atoms replaced by silicon so that they become silica polymorphs. Since zeolites are treated in other entries in this Encyclopedia they will not be discussed here. The book

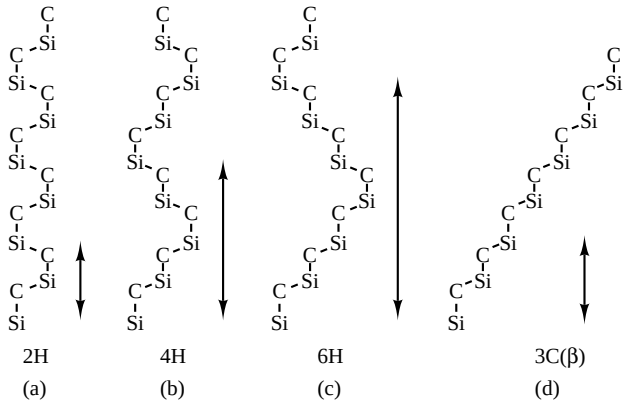

Figure 4 Schematic structures for silicon carbide polymorphs. The vertical arrows represent repeat distances

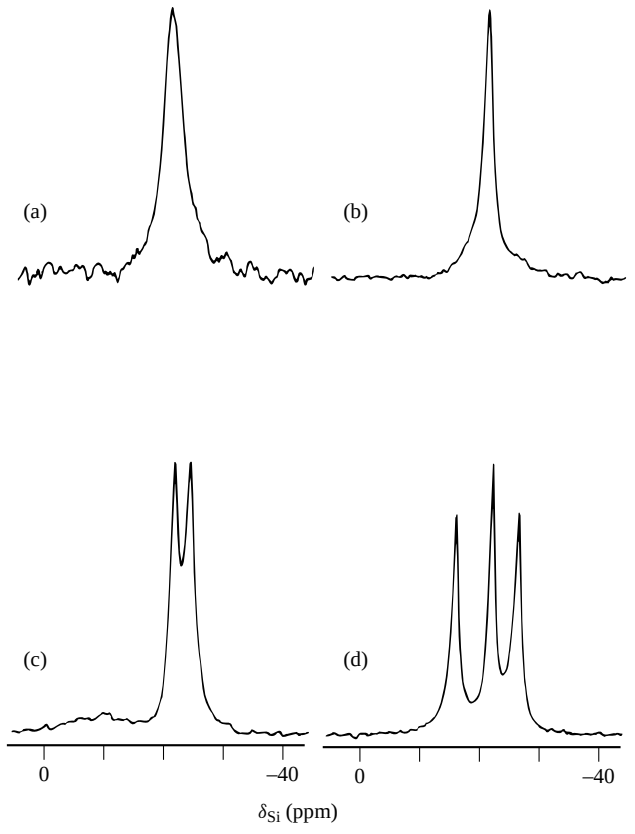

Figure 5 Silicon-29 MAS NMR spectra[13] of silicon carbide polymorphs at 59.58 MHz: (a) 3C (β); (b) 2H; (c) 4H; and (d) 6H

by Engelhardt and Michel[15] contains a useful discussion of NMR studies of nonzeolitic silica polymorphs (pp. 170–175). The ^{29}Si chemical shifts cover a wide range ($\delta_{Si} \sim -107$ to -121 ppm), the variation being attributed to differences in mean SiOSi bond angles, α, an increase in shielding resulting from widening SiOSi angles. A number of specific relationships have been proposed,[16] including (from theoretical considerations) $\delta_{Si} = -247.05\bar{\rho} + 2.19$, where $\rho = \cos\alpha/(\cos\alpha - 1)$. Of course, many of the silica polymorphs differ in the number of different crystallographic sites. Coesite, for instance, gives two widely-spaced ^{29}Si signals (δ_{Si} = 108.1 and 113.9 ppm), in accord with its structure.[16] In contrast to all the four-coordinate silica polymorphs, stishovite, which contains six-coordinate silicon, gives a signal at $\delta_{Si} = -191$ ppm.[16] As with silicon carbide, amorphous forms of silica (glass!) are well known.

Organic polymers may also show polymorphism. One of the early examples of CP MAS NMR related to the case of isotactic polypropene, which exists in several crystalline forms usually as domains separated by amorphous material. In effect, the chains constitute infinite one-dimensional bonded structures with weaker forces between the chains. The systems therefore are intermediate between the molecular polymorphs discussed in Section 3 and the infinite three-dimensional structures of SiC and SiO_2. The structure of the α form of polypropene is shown in Figure 6(a). The helical polymer units occur as pairs of interlocking chains with opposing handedness. This creates a situation where there are two distinct methyl sites, with two-thirds of the groups in a given helix facing the companion helix, and the remaining third facing outwards. Thus a 2:1 doublet is expected for the methyl carbons, and this is observed[17] in practice. A similar situation obtains for the CH carbons.

In contrast, the crystal structure of the β form contains separate groups of helices of the two types of handedness, with no pairing [Figure 6(b)]. The NMR spectrum therefore lacks the well-defined splitting shown by that of the α form.

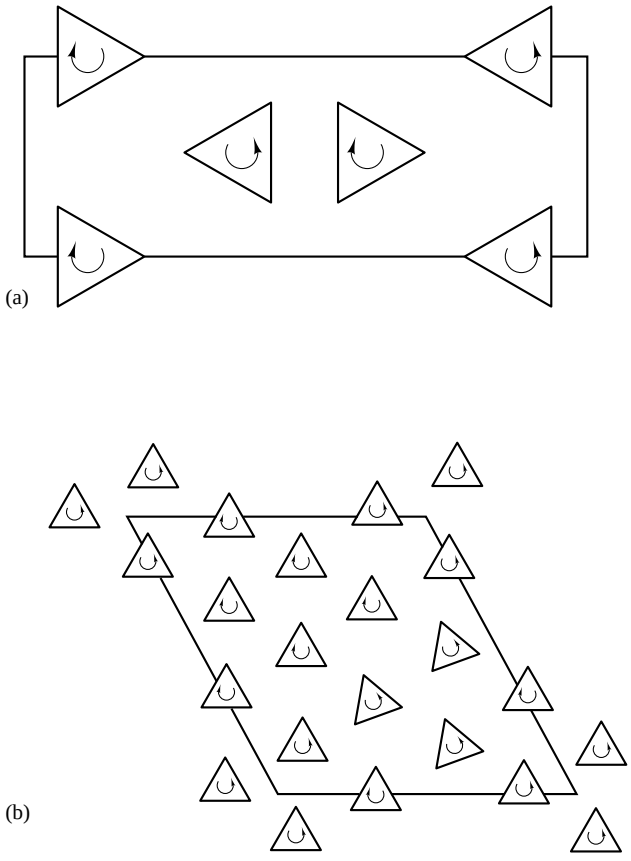

Figure 6 Diagrammatic crystal structures for two forms of isotactic polypropene: (a) α form; (b) β form. The figures show projections of the chains perpendicular to their axes, with the corners of the triangles indicating the positions of methyl groups. The arrows represent the handedness of the helices

Of course, isotactic polypropene also contains a significant proportion of amorphous material which, as usual, gives rise to somewhat broadened CP MAS ^{13}C lines. The differences between the α and β forms of isotactic polypropene arise from intermolecular packing of the polymer chains. Far greater differences occur, as expected, in NMR spectra[17,18] for polymer forms differing in tacticity (such as isotactic and syndiotactic polypropene). However, differences in tacticity are not normally classed under polymorphism.

Biochemical polymers such as cellulose and chitosan also give rise to polymorphism, which has been studied by solid state NMR methods.[19,20]

6 RELATED ARTICLES

Ceramics; Molecular Sieves: Crystalline Systems; Polysaccharide Solid State NMR; Silicon-29 NMR of Solid Silicates.

7 REFERENCES

1. G. E. Balimann, C. J. Groombridge, R. K. Harris, K. J. Packer, B. J. Say, and S. F. Tanner, *Philos. Trans. R. Soc. London, Ser. A*, 1981, **299**, 643.
2. S. R. Byrn, G. Gray, R. R. Pfeiffer, and J. Frye, *J. Pharm. Sci.*, 1985, **74**, 565; S. R. Byrn, P. A. Sutton, B. Tobias, J. Frye, and P. Main, *J. Am. Chem. Soc.*, 1988, **110**, 1609.
3. P. J. Saindon, N. S. Cauchon, P. A. Sutton, C.-J. Chang, G. E. Peck, and S. R. Byrn, *Pharm. Res.*, 1993, **10**, 197.
4. R. K. Harris, A. M. Kenwright, B. J. Say, R. R. Yeung, R. A. Fletton, R. W. Lancaster, and G. L. Hardgrove, *Spectrochim. Acta, Part A*, 1990, **46**, 927; E. A. Christopher, R. K. Harris, and R. A. Fletton, *Solid State NMR*, 1992, **1**, 93.
5. R. A. Fletton, R. W. Lancaster, R. K. Harris, A. M. Kenwright, K. J. Packer, D. N. Waters, and A. Yeadon, *J. Chem. Soc., Perkin Trans. 2*, 1986, 1705.
6. R. K. Harris, B. J. Say, R. R. Yeung, R. A. Fletton, and R. W. Lancaster, *Spectrochim. Acta, Part A*, 1989, **45**, 465; R. A. Fletton, R. K. Harris, A. M. Kenwright, R. W. Lancaster, K. J. Packer, and N. Sheppard, *Spectrochim. Acta, Part A*, 1987, **43**, 1111.
7. H. G. Brittain, K. R. Morris, D. E. Bugay, A. B. Thakur, and A. T. M. Serajuddin, *J. Pharm. Biomed. Anal.*, 1993, **11**, 1063.
8. M. Stoltz, D. W. Oliver, P. L. Wessels, and A. A. Chalmers, *J. Pharm. Sci.*, 1991, **80**, 357.
9. R. K. Harris and P. Jackson, *J. Phys. Chem. Solids*, 1987, **48**, 813.
10. D. Casarini, R. K. Harris, and A. M. Kenwright, *Magn. Reson. Chem.*, 1993, **31**, 540.
11. L. Frydman, A. C. Olivieri, L. E. Diaz, B. Frydman, A. Schmidt, and S. Vega, *Mol. Phys.*, 1990, **70**, 563.
12. E. R. Andrew, A. Bradbury, R. G. Eades, and G. J. Jenks, *Nature (London)*, 1960, **188**, 1096; R. K. Harris and A. Root, *Mol. Phys.*, 1989, **66**, 993.
13. D. C. Apperley, R. K. Harris, G. L. Marshall, and D. P. Thompson, *J. Am. Ceram. Soc.*, 1991, **74**, 777.
14. D. Guo, J. S. Hartman, and M. F. Richardson, *Can. J. Chem.*, 1992, **70**, 700; M. F. Richardson, J. S. Hartman, D. Guo, and B. G. Winsbarrow, *Chem. Mater.*, 1992, **4**, 318.
15. G. Engelhardt and D. Michel, *High-resolution Solid-state NMR of Silicates and Zeolites*, Wiley-Interscience, New York, 1987.
16. J. V. Smith and C. S. Blackwell, *Nature (London)*, 1983, **303**, 223; G. Engelhardt and R. Radeglia, *Chem. Phys. Lett.*, 1984, **108**, 271.
17. A. Bunn, M. E. A. Cudby, R. K. Harris, K. J. Packer, and B. J. Say, *Polymer*, 1982, **23**, 694; M. A. Gomez, H. Tanaka, and A. E. Tonelli, *Polymer*, 1987, **28**, 2227.
18. A. Bunn, M. E. A. Cudby, R. K. Harris, K. J. Packer, and B. J. Say, *J. Chem. Soc., Chem. Commun.*, 1981, 15.
19. R. H. Atalla, J. C. Gast, D. W. Sindorf, V. J. Bartuska, and G. E. Maciel, *J. Am. Chem. Soc.*, 1980, **102**, 3249; W. L. Earl and D. L. VanderHart, *J. Am. Chem. Soc.*, 1980, **102**, 3251.
20. H. Saito, R. Tabeta, and K. Ogawa, in *Industrial Polysaccharides: Genetic Engineering, Structure/Property Relations & Applications*, ed. M. Yalpani, Elsevier Science Publishers, Amsterdam, 1987, pp. 267–280.

Biographical Sketch

Robin K. Harris. *b* 1936. B.A. (Nat. Sci.), Ph.D. (supervisor Norman Sheppard), Sc.D., University of Cambridge, UK. Postdoctoral work at Mellon Institute, Pittsburgh, PA (with Aksel Bothner-By). Successively lecturer, senior lecturer, and professor, University of East Anglia, UK. Currently Professor of Chemistry, University of Durham, UK. Secretary-General of ISMAR, 1986–92. Approx. 350 publications. Current research specialty: solid state NMR and its applications in materials chemistry.

Quadrupolar Nuclei in Solids

Alexander J. Vega
DuPont, Wilmington, DE, USA

1	Introduction	1
2	Basic Spin Properties	1
3	Interaction with Radiofrequency Fields	7
4	Experimental Methods	10
5	Theory	14
6	Related Articles	20
7	References	20

1 INTRODUCTION

Nuclei with spin quantum number $I \geq 1$ have an electric quadrupole moment that couples with the inhomogeneous internal electric fields existing in molecules and solids. Since this quadrupolar interaction is usually stronger than other interactions such as chemical shift and dipole–dipole couplings, it dominates the NMR spectra of quadrupolar nuclei in solid materials. Liquid state NMR spectra of quadrupolar nuclei are not affected to a comparable extent, because the fast isotropic tumbling of the molecules greatly diminishes the impact of the quadrupolar interaction. While the NMR signals of quadrupolar nuclei in solids are split into multiplets that at times broaden the lineshapes of powder samples over many megahertz, the quadrupolar interaction does not split the NMR lines of liquid samples. Instead, it has a pronounced effect on the T_1 and T_2 relaxation times of nuclei in liquids (see ***Relaxation of Quadrupolar Nuclei Measured via Multiple Quantum Filtration*** and ***Relaxation Theory for Quadrupolar Nuclei***). The NMR spectra of quadrupolar nuclei in liquid crystals, where the quadrupolar splitting is partially reduced, provide a wealth of information concerning molecular orientation and dynamics (see ***Deuteron Relaxation Rates in Liquid Crystalline Samples: Experimental Methods*** and ***Liquid Crystalline Samples: Deuterium NMR***).

This article is devoted to the solid state aspects of the quadrupolar interaction. Since many subtopics from this area of NMR are discussed elsewhere in the Encyclopedia, the aim of this article is to provide a general overview rather than comprehensive discussions of each specific method. The first two sections following this introduction summarize the quantum mechanical properties of quadrupolar spins and their response to radiofrequency pulses. This survey is given without theoretical derivations and with only a few mathematical formulas. The important experimental approaches are catalogued in Section 4. Some of the fundamental theoretical concepts underlying quadrupolar spin properties are presented in Section 5.

Quadrupolar effects in NMR of solids were first reported and analyzed in 1950 by Pound.[1] Introductions to NMR of quadrupolar nuclei are provided in the classic 1957 review article by Cohen and Reif[2] and in the textbooks by Abragam[3] and Slichter.[4] Kanert and Mehring also covered the basics of quadrupole NMR in their 1971 review of quadrupole NMR of disordered cubic solids.[5] Nuclei with half-integer spins have distinctive quantum mechanical properties that have led to the development of special methods for their detection. Progress in this area was summarized in a 1993 review article by Freude and Haase.[6] NMR of integer spin nuclei is almost exclusively limited to ^{2}H and ^{14}N. Although both are $I = 1$ spins, the disparate orders of magnitude of their quadrupolar interaction energies necessitate different methodologies for their study in the solid state. Deuterium NMR spectroscopy was reviewed by Spiess[7] in 1985.

2 BASIC SPIN PROPERTIES

2.1 Nuclear Electric Quadrupolar Interaction

The nuclear quadrupolar interaction is the coupling of the electric quadrupole of the nucleus with the gradient of the electric field generated by the other charges in the system. The quadrupole moment is usually denoted by eQ and the magnitude of the electric field gradient (EFG) by eq, where e is the elementary charge. Since it is impractical to produce NMR-detectable EFGs by means of external charged conductors, the gradients are exclusively generated by the electrons and nuclei of molecules and crystals. Thus, the size of the quadrupolar interaction experienced by a particular nucleus is a constant that is characteristic of the molecular or crystalline environment. Its value in frequency units, e^2qQ/h, is called the nuclear quadrupolar coupling constant (NQCC). In this Encyclopedia, we use the letter χ as shorthand notation for e^2qQ/h. A variety of different symbols (C_q, C_Q, C_{qcc}, $\aleph_{zz}$, ...) are found in other publications (see also ***Quadrupolar Interactions***).

Closely related to the NQCC is the so-called quadrupolar frequency ν_Q (in Hz) or ω_Q (in rad s^{-1}), in this article defined as

$$\nu_Q = \frac{\omega_Q}{2\pi} = \frac{3\chi}{2I(2I-1)} \qquad (1)$$

The use of ν_Q is often preferred over that of χ, because it simplifies equations. Moreover, the quadrupolar frequency describes the actual strength of the quadrupolar interaction more closely than does the NQCC. It should be noted that equation (1) is not a universally accepted definition of ν_Q, although in literature dealing with half-integer spins it is often (but not always) found in this form. However, in the case of $I = 1$ authors usually prefer $\nu_Q = \frac{3}{4}\chi$ over the $\nu_Q = \frac{3}{2}\chi$ that follows from equation (1). For the sake of uniformity, we shall adhere to equation (1) for all values of I throughout this article.

The EFG is a three-dimensional entity with the properties of a tensor. To describe it fully, we need to specify its size, shape, and orientation. The quantity eq was introduced above as a parameter of the size. The shape is characterized by the asymmetry parameter η, which is a measure of the deviation of the EFG from axial symmetry. η can have any value between 0 and 1, with $\eta = 0$ corresponding to axial symmetry. The orientation of the EFG with respect to the molecular or crystalline structure is defined by three Euler angles. The

tensor properties are more fully defined in Section 5.1. In the literature, quadrupolar interactions are commonly reported by specification of their NQCC and η. The angular parameters are not usually provided unless orientational information is of special interest.

The quadrupolar interaction vanishes in three general cases.

1. No quadrupolar interaction is ever associated with an $I = \frac{1}{2}$ nucleus, because eQ vanishes for all subatomic particles with spin quantum number $I = 0$ or $\frac{1}{2}$.
2. The NQCC is zero when a quadrupolar nucleus is positioned at a cubic (octahedral or tetrahedral) site, because then $eq = 0$ by symmetry.
3. The quadrupolar interaction of a nucleus belonging to a molecule in an isotropic liquid or a gas is averaged to zero by the rapid tumbling motion of the molecule.

2.2 NQR and NMR Spectra of Quadrupolar Nuclei

The nature of magnetic resonance spectra of quadrupolar nuclei in solids depends to a large extent on the size of the electric quadrupolar interaction relative to that of the Zeeman interaction with the externally applied magnetic field B_0. The strength of this magnetic interaction is given by the Larmor frequency $\omega_0 = 2\pi\nu_0 = \gamma B_0$, where γ is the gyromagnetic ratio. In this subsection, we review the general features of magnetic resonance spectra for the various magnitude ranges of the ratio ν_0/ν_Q.

We begin with the case where no magnetic field is applied at all ($\nu_0 = 0$). The quadrupolar interaction then splits the magnetic energy levels of the nuclear spins into patterns like those shown in Figure 1. The energy levels are associated with particular orientations of the nuclear spin axis with respect to the EFG axes, and can thus be identified by magnetic quantum numbers m. The spectroscopic transitions among these magnetic states can be detected with the regular radiofrequency methods of magnetic resonance. This branch of spectroscopy is known as nuclear quadrupole resonance (NQR). Its first spectrum was observed by Dehmelt and Krüger in 1949.[8] Unlike the extremely broad high-field NMR spectra of quadrupolar nuclei in randomly oriented powder samples (see below), the NQR resonances are sharp. In fact, they provide the most precise measurements of the quadrupolar frequency and the NQCC. Although NQR employs the radiofrequency methods of magnetic resonance, it is not an NMR technique in the proper sense, since NMR is defined as a spectroscopy associated with a Zeeman field. NQR is therefore outside the scope of this Encyclopedia, although some aspects of it are discussed in the articles on ***SQUIDs*** and ***Zero Field NMR***. For further literature on the subject, the reader is referred to the classic monograph by Das and Hahn,[9] several other books and tabulations,[10–12] and the review articles in the series 'Advances in Nuclear Quadrupole Resonance'.[13]

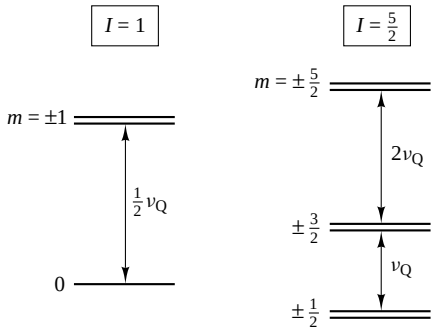

Figure 1 Quadrupolar energy levels in zero magnetic field. These two examples are for axial symmetry of the EFG. If the EFG is not axially symmetric, the transition frequencies are more complicated functions of the quadrupolar frequency ν_Q and the asymmetry parameter η, while the eigenstates are linear combinations of m states. Furthermore, the $m = \pm 1$ degeneracy of the $I = 1$ states is lifted when $\eta \neq 0$. However, the eigenstates of half-integer spins remain degenerate in pairs for any value of η

A weak magnetic field, corresponding to a Larmor frequency ν_0 smaller than ν_Q, shifts and splits the NQR lines. The frequency shifts of this so-called Zeeman effect of NQR are functions of the orientation of the magnetic field with respect to the crystal axes. Consequently, in randomly oriented powder samples, the effect is observed as a broadening of the peaks.

When ν_0 is much larger than ν_Q, we are in the regime of NMR. In the extreme limit of vanishing ν_Q, the energy levels are the $2I + 1$ Zeeman levels, $E_m = m\omega_0$, giving rise to $2I$ coinciding transitions of frequency ν_0. A relatively small quadrupolar interaction, $\nu_Q \ll \nu_0$, shifts the eigenvalues of the Zeeman levels and splits the NMR spectrum into $2I$ peaks. Examples for spins $I = 1$ and $\frac{5}{2}$ are shown schematically in Figure 2. For the theoretical description of these effects, we follow the methods of perturbation theory and express the quadrupolar corrections to the energy levels as the sums of first-order terms of order ω_Q and second-order terms of order $\omega_Q{}^2/\omega_0$ (see Section 5.3). Third- and higher-order terms do not need to be considered.

The main features of quadrupolar NMR spectra are governed by the equation describing the orientation dependence of the first-order energy corrections $\Delta E_m{}^{(1)}$ of the Zeeman levels m:

$$\Delta E_m^{(1)} = \tfrac{1}{2}\Delta\omega_Q(\theta,\phi)[m^2 - \tfrac{1}{3}I(I+1)] \qquad (2)$$

where $\Delta\omega_Q$ is a fraction of ω_Q and is a function of the polar angles θ and ϕ which relate the Zeeman field direction to the EFG principal axes system (see Section 5.1 and Figure 11):

$$\begin{aligned}\Delta\omega_Q(\theta,\phi) &= 2\pi\,\Delta\nu_Q(\theta,\phi)\\ &= \tfrac{1}{2}\omega_Q[3\cos^2\theta - 1 - \eta\sin^2\theta\cos 2\phi] \qquad (3)\end{aligned}$$

$\Delta\nu_Q$ (or $\Delta\omega_Q$) is called the quadrupolar splitting because the $2I$ lines in the spectrum are, to first order, equally spaced by $\Delta\nu_Q$. This follows from equation (2), which predicts that the first-order frequency shifts $\Delta\nu_{m\leftrightarrow m+1}^{(1)}$ of the allowed transitions $m \leftrightarrow m + 1$ are given by

$$\Delta\nu_{m\leftrightarrow m+1}^{(1)} = \Delta\nu_Q(\theta,\phi)(m+\tfrac{1}{2}) \qquad (4)$$

In powder samples, the orientation dependence of $\Delta\nu_Q$ broadens the individual transitions and causes them to overlap. However, the $-\frac{1}{2} \leftrightarrow \frac{1}{2}$ transition of noninteger spins ($I = \frac{3}{2}, \frac{5}{2}, \frac{7}{2}, \frac{9}{2}$) does not experience a first-order broadening [$m = -\frac{1}{2}$ in equation (4)]. Consequently, this 'central transition' stands out as a relatively sharp peak at the center of the 'satellite transitions'. It is clear from equation (4) that there

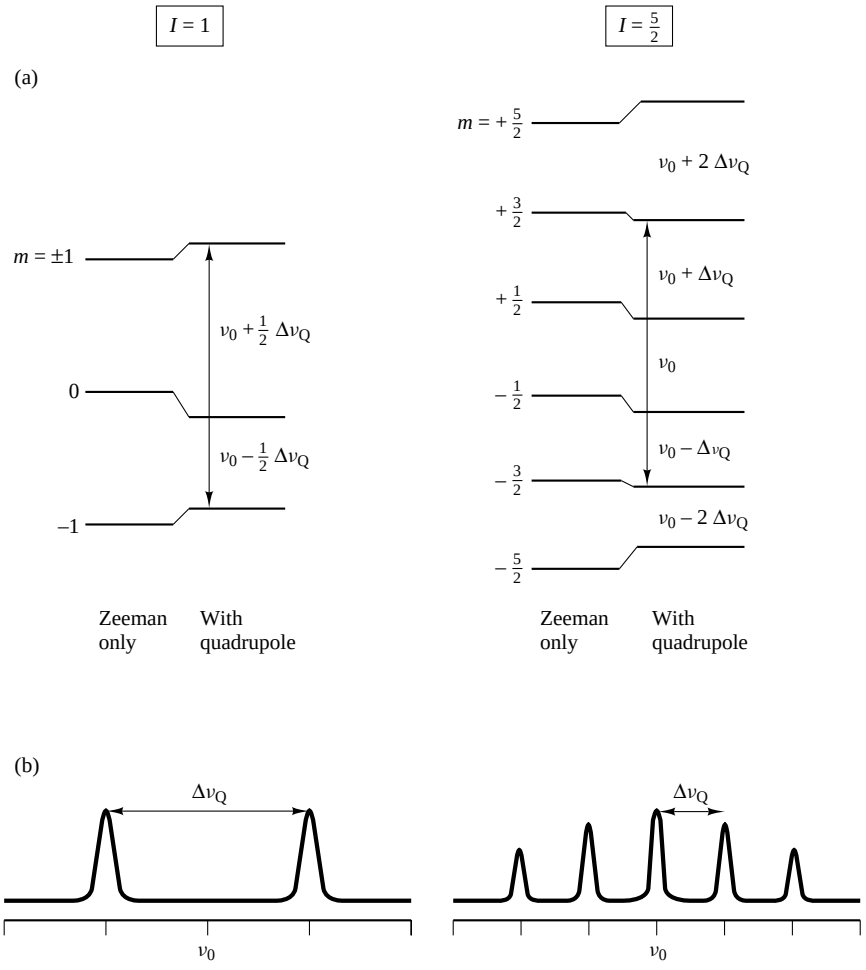

Figure 2 (a) Energy levels of spins $I = 1$ and $\frac{5}{2}$ in a Zeeman field, in the absence and in the presence of a quadrupolar interaction. The frequencies of the allowed ($\Delta m = 1$) transitions are indicated with first-order quadrupolar corrections. The arrows mark forbidden ($\Delta m = 2, 3$) transitions. (b) The corresponding quadrupole-split NMR spectra. $\omega_0 = 2\pi\nu_0$ is the Larmor frequency and $\Delta\omega_Q = 2\pi\ \Delta\nu_Q$ is the quadrupolar splitting

is no central transition associated with integer-spin nuclei. The dependence of $\Delta\nu_Q(\theta, \phi)$ on the orientation is similar to that of the anisotropic chemical shift. However, unlike the chemical shift, the first-order quadrupolar effect has no isotropic contribution, implying that the centers of gravity of the spectral distributions are not shifted. Thus, each satellite transition has a powder lineshape characteristic of the value of η, and is centered around the Larmor frequency. Figure 3 shows a few simulated examples for $I = 1$ and $\frac{5}{2}$.

The broadening of the satellites is often too large to be captured within the bandwidth of the NMR spectrometer. In such a case, we only observe the central transition, the lineshape of which is dominated by second-order quadrupolar shifts. The orientation dependence of this shift is of a different nature to that of the first-order satellite shift. A consequence of this is that it contributes to an isotropic shift of the order of $\nu_Q{}^2/\nu_0$ (see equation (15) in Section 4.3).

Equation (2) shows further that levels m and $-m$ have identical first-order energy shifts. Therefore, in addition to the central transition, there are forbidden transitions $\Delta m = 2, 3, \ldots$ (indicated in Figure 2 by arrows) with transition frequencies that are not affected to first order by the quadrupolar interaction. The experimental methods of double quantum excitation and overtone spectroscopy of $I = 1$ nuclei take advantage of this special property (see Section 4).

The energy-level diagrams of Figure 4 illustrate the transition from the NQR limit to the NMR limit. The figure shows the variation of the energy levels of a spin-$\frac{3}{2}$ when the ratio ν_0/ν_Q changes gradually from 0 to ∞. This is shown for two cases, both with an axially symmetric EFG—one with the EFG symmetry axis $\boldsymbol{q}$ parallel to the field $\boldsymbol{B}_0$, and one with $\boldsymbol{q}$ perpendicular to $\boldsymbol{B}_0$. The difference between the two sets of energy curves demonstrates the strong dependence of the transition frequencies on the relative orientations of the EFG and $\boldsymbol{B}_0$. When ν_0 is of the order of ν_Q, the powder spectra are sufficiently broad, that detection of magnetic resonance becomes impractical within the limitations of bandwidth and sensitivity of equipment currently in use.

Figure 4 also indicates the spin states in the limiting cases. Note that these eigenstates are quantized along the symmetry direction of the prevailing field, as is indicated by the Q and Z subscripts on the quantum numbers m. In general, these states are not identical. In fact, they are linear combinations of each other. A certain amount of mixing of the pure Zeeman states occurs even when the quadrupolar interaction is small in comparison with the Zeeman interaction. We say that the spins are then 'no longer quantized along the Zeeman direction'

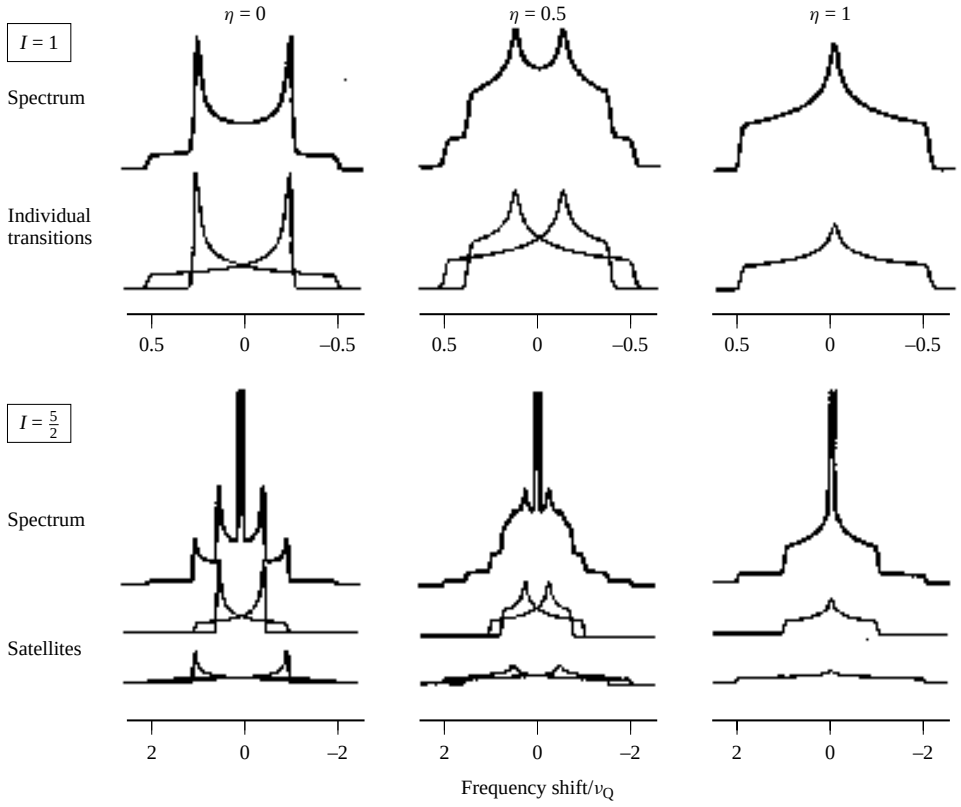

Figure 3 First-order quadrupolar spectra of powder samples simulated for $I = 1$ and $\frac{5}{2}$ and for three values of the asymmetry parameter η. The lineshapes of individual transitions are drawn below the spectra. The central transition peaks of $I = \frac{5}{2}$ are off scale. The frequency scale is in units of the quadrupolar frequency ν_Q as defined in equation (1). The Larmor frequency is at the center of the spectra

(see Section 5.3). This mixing controls a number of the NMR phenomena reviewed below, including overtone NMR, heteronuclear dipolar splittings, and zero field NMR.

2.3 Level Populations

Since $I > \frac{1}{2}$ spins have more than two Zeeman levels, it is necessary to use two or more independent parameters for the description of their relative populations. In thermal equilibrium, the high-field population pattern is as illustrated in Figure 5(a) for $I = 1$ or Figure 5(c) for $I = \frac{3}{2}$. The populations of the levels m are then given by $(1 - m\hbar\omega_0/kT)/(2I + 1)$, which is the Boltzmann distribution in the high-temperature approximation. This is called Zeeman order, because the populations are determined by the Zeeman interaction. It is characterized by uniform population increments between adjacent levels. The application of rf pulses causes deviations from the Boltzmann distribution. When these deviations are such that the Zeeman pattern is retained, we can introduce a meaningful 'spin temperature' replacing T in the distribution expression above. The distribution pattern can also be of the type depicted in Figure 5(b) and (d). This is called quadrupolar order, because the deviations from the average population follow the $m^2 - \frac{1}{3}I(I + 1)$ dependence associated with the quadrupolar interaction [equation (2)]. In general, the population distribution of spins $I = 1$ is a combination of the two. Unlike Zeeman order, quadrupolar order does not contribute to the z magnetization. In thermal equilibrium, quadrupolar order is negligible, because the population differences associated with it are ν_0/ν_Q times smaller than those of equilibrium Zeeman order.

For spins with $I \geq \frac{3}{2}$, more types of population distribution need to be considered. An important example is the $I = \frac{3}{2}$ configuration illustrated in Figure 5(e). This arrangement can be viewed as Zeeman order in which the $m = \pm\frac{1}{2}$ populations are equilibrated and do not contribute to the z magnetization (e.g., as a result of selective saturation of the central transition), whereas the equilibrium population difference of the $m = \pm\frac{3}{2}$ levels and their contribution to the z magnetization is retained. For later reference, we call this 'triple quantum order'.

2.4 Relaxation

Spin relaxation is caused by randomly fluctuating interactions (see also ***Relaxation: An Introduction*** and ***Relaxation Theory for Quadrupolar Nuclei***). In the case of quadrupolar nuclei, the fluctuations can be electric (due to a time-dependent size or orientation of the EFG) or magnetic (due to fluctuating chemical shifts, dipole–dipole interactions, or interactions with unpaired electrons). When caused by random molecular motions or lattice vibrations, the electric fluctuations usually dominate, since in most cases the quadrupolar interaction is stronger than the magnetic dipolar interactions and chemical shifts.[6] On the other hand, a magnetic relaxation mechanism mostly prevails in the presence of conduction electrons[14] or in structures containing paramagnetic centers

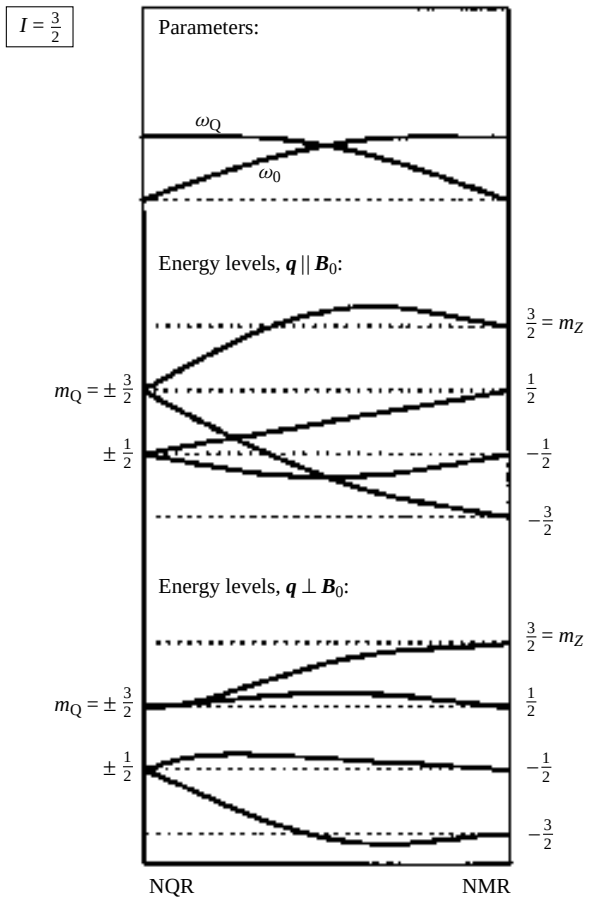

Figure 4 Energy levels of a spin $I = \frac{3}{2}$ in a coexisting electric field gradient and a magnetic Zeeman field, calculated for varying Larmor frequency ω_0 and quadrupolar frequency ω_Q. The gradual change of these parameters, from the NQR limit ($\omega_0 = 0$) on the left to the NMR limit ($\omega_Q = 0$) on the right, is shown in the curves at the top. The EFG is assumed to be axially symmetric. The corresponding energies of the spin states are shown for two relative orientations of the symmetry axis $\boldsymbol{q}$ of the EFG and the Zeeman field $\boldsymbol{B}_0$. The magnetic quantum numbers are indicated for the NQR and NMR limits (m_Q is quantized along $\boldsymbol{q}$; m_Z is quantized along $\boldsymbol{B}_0$)

such as superconducting oxide materials (see ***High Temperature Superconductors***).

Longitudinal spin–lattice relaxation is the process by which nonequilibrium level populations (see Figure 5) revert to thermal equilibrium. Unlike relaxation of spin-$\frac{1}{2}$ nuclei, which involves a single transition probability between two energy levels, relaxation of quadrupolar nuclei is generally characterized by several transition rates. Hence, the relaxation decay is multi-exponential, and cannot be quantified by a single T_1. For instance, the quadrupole-induced spin–lattice relaxation of a spin $I = 1$ has two principal spin–lattice relaxation times: the conventional T_1 for the return of Zeeman order to the equilibrium populations, and a different time T_{1Q} for the decay of quadrupolar order (see Section 2.3). Spin–lattice relaxation patterns of higher spins are more complex. Provided the initial population distribution has the form of Zeeman order, spin–lattice relaxation has one decay constant for $I = 1$, two for $I = \frac{3}{2}$ or 2, three for $I = \frac{5}{2}$ or 3, etc.[15] In powders, the complexity is compounded with

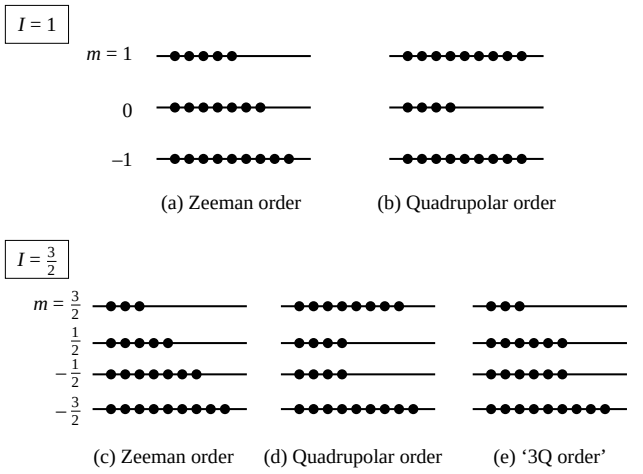

Figure 5 Level population patterns of spins 1 and $\frac{3}{2}$ according to Zeeman order, quadrupolar order, and 'triple quantum order'

a dependence of the relaxation time on the orientation of the EFG with respect to the Zeeman field. However, the transition rates are mostly of comparable magnitude, such that an approximate assessment of a global T_1 is not unwarranted. The dependence of T_1 on the correlation time τ_c of the motion follows the general Bloembergen–Purcell–Pound (BPP) or Redfield behavior (see ***Relaxation: An Introduction***) given by

$$\frac{1}{T_1} = \omega_Q^2 \left(\frac{a\tau_c}{1+\omega_0^2\tau_c^2} + \frac{b\tau_c}{1+4\omega_0^2\tau_c^2} \right) \qquad (5)$$

where the numerical coefficients a and b reflect the amplitudes of the EFG fluctuations, the geometric details of the motion, a dependence on I, and the multiexponential character of the decay. A log–log plot of T_1 versus τ_c has the familiar shape shown in Figure 6, with its minimum around ${\omega_0}^{-1}$. For relaxation due to lattice vibrations, the equation is cast in different forms reflecting the thermal behavior of the phonons.[6] A similar expression, with a hyperfine coupling constant instead of ω_Q, holds for magnetically induced relaxation.

As is usually done in BPP-type discussions of the transverse relaxation time, we define T_2 as a measure of the inverse linewidth of the spectrum. (The signal decay in echo experiments, albeit important in deuterium NMR, is outside the scope of this article.) In the slow motion limit, the powder spectra have widths and shapes like those of the examples shown in Figure 3. Hence, $1/T_2$ is approximately equal to ω_Q, except for the central transition of half-integer spins, which has $1/T_2$ of the order of ${\omega_Q}^2/\omega_0$. In the fast motion limit, the spectra are reduced to motionally narrowed Lorentzian lines having full linewidth at half-maximum equal to $1/\pi T_2$. The majority of the spectral components follow the familiar BPP pattern schematically drawn as the T_2(other) curve in Figure 6. If the relaxation mechanism is quadrupolar, the condition for motional narrowing is $\tau_c \ll {\omega_Q}^{-1}$, and the T_2 of the narrowed spectrum varies with the correlation time according to

$$\frac{1}{T_2} = c\omega_Q^2\tau_c \qquad (6)$$

where the numerical coefficient c depends on the motional model.

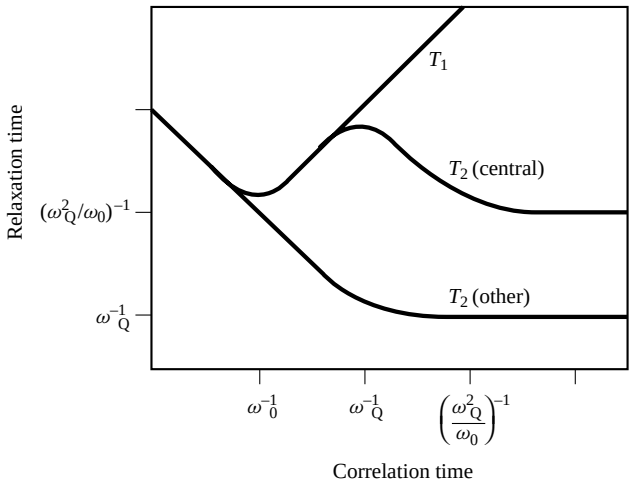

Figure 6 Idealized log–log plot of T_1 and T_2 relaxation times versus the correlation time of the motion for a model where the spin relaxation is caused by large-scale fluctuations of the EFG. T_2(central) is the inverse halfwidth of the central transition spectra of half-integer spins; T_2(other) is that of satellite transitions or transitions of integer spins

The effect of quadrupolar relaxation on T_2 of the central transition is markedly different,[16,17] as is indicated by T_2(central) in Figure 6. A gradual increase in the motional rate (decreasing correlation time) begins to narrow the rigid limit spectrum when τ_c becomes smaller than the reciprocal linewidth ($\tau_c < (\omega_Q{}^2/\omega_0)^{-1}$), but for shorter τ_c, the line broadens again, and T_2 passes through a minimum when $\tau_c \approx \omega_0{}^{-1}$. This T_2 behavior was observed for ^{23}Na in amorphous polymer electrolytes above the glass transition temperature.[18] The T_2 minimum is associated with a dynamic frequency shift[16,17] (see ***Dynamic Frequency Shift*** and ***Relaxation of Quadrupolar Nuclei Measured via Multiple Quantum Filtration***). Transverse relaxation of the central transition due to unpaired electrons does not differ substantially from the relaxation of the other transitions.

2.5 Typical Values of the Nuclear Quadrupolar Coupling Constant

Table 1 lists typical values of the NQCC (χ), the quadrupolar frequency [ν_Q as defined in equation (1)], and the Larmor frequency (ν_0 in the magnetic field of a 300 MHz spectrometer) for selected nuclei. The data were gathered from various sources in the literature. Unless the quadrupole interaction is drastically reduced by cubic symmetry, the actual NQCCs for a particular nucleus do not usually differ by more than a factor two or three from the quoted value. The multiplication factors in parentheses indicate the ratios between the NQCC of isotopes of the same element. These ratios are fixed by the ratios of their eQ values. The relative magnitudes of ν_Q and

Table 1 Typical Values of Nuclear Quadrupole Coupling Constants (NQCC), Quadrupole Frequencies (ν_Q), and Larmor Frequencies (ν_0)

Nucleus	I	Natural abundance (%)	Typical NQCC (MHz)	Typical ν_Q (MHz)	ν_0 at 7.05 T (MHz)
Integer spin:					
^{2}H	1	0.015	0.16	0.24	46.1
^{6}Li	1	7.4	0.001	0.0015	44.2
^{10}B	3	19.6	1	0.1	32.2
^{14}N	1	99.6	4	6	21.7
Half-integer spin:					
^{7}Li	3/2	92.6	0.05	0.025	116.6
^{9}Be	3/2	100	0.4	0.2	42.2
^{11}B	3/2	80.4	2	1.5	96.3
^{17}O	5/2	0.037	7	1	40.7
^{23}Na	3/2	100	2	1	79.4
^{27}Al	5/2	100	1–20	0.15–3	78.2
^{35}Cl	3/2	75.5	60	30	29.4
^{37}Cl	3/2	24.5	(× 0.788)	(× 0.788)	24.5
^{39}K	3/2	93.1	4	2	14.0
^{45}Sc	7/2	100	3	0.2	73.0
^{51}V	7/2	99.8	3	0.2	78.9
^{55}Mn	5/2	100	60	9	74.0
^{63}Cu	3/2	69.1	60	30	79.5
^{65}Cu	3/2	30.9	(× 0.925)	(× 0.925)	85.2
^{71}Ga	3/2	39.6	150	75	91.5
^{75}As	3/2	100	160	80	51.4
^{87}Rb	3/2	27.8	20	10	98.2
^{79}Br	3/2	50.5	400	200	75.2
^{81}Br	3/2	49.5	(× 0.835)	(× 0.835)	81.0
^{91}Zr	5/2	11.2	20	3	28.0
^{93}Nb	9/2	100	50	2	73.6
^{96}Mo	5/2	15.7	2	0.3	19.6
^{133}Cs	7/2	100	0.7	0.02	39.4
^{121}Sb	5/2	57.2	500	70	71.8
^{127}I	5/2	100	2000	300	60.0
^{209}Bi	9/2	100	500	20	48.2

ν_0 serve as a guide for determining whether a nucleus is better studied by NQR or by NMR.

3 INTERACTION WITH RADIOFREQUENCY FIELDS

The manner in which radiofrequency (rf) pulses affect quadrupolar spins in a high magnetic field depends strongly on the relative magnitudes (in frequency units) of three parameters. One is the rf amplitude $\omega_1 = 2\pi\nu_1 = \gamma B_1$, where B_1 is the strength of the rotating magnetic component of the rf field. The other two are the first-order quadrupolar splitting $\Delta\omega_Q = 2\pi\ \Delta\nu_Q$ and the difference $\Delta\omega_0 = 2\pi\ \Delta\nu_0$ between the resonance frequency of the spins and the carrier frequency of the rf pulse. Here, the resonance frequency is the combination of Larmor frequency, chemical shift, and second-order quadrupolar shift. While there are no other ways in which second-order quadrupolar effects impact the performance of rf pulses to a noticeable extent, first-order splittings make a large difference. Consequently, the orientation dependence of $\Delta\nu_Q$ can cause a wide range of responses to a uniform rf pulse when it is applied to a powder sample. To avoid this complication, we limit the discussion in this section to samples with a uniform $\Delta\nu_Q$ as in a single crystal. The distinct experimental conditions and their respective effects on quadrupolar spins are categorized below. The summary is descriptive in nature and is presented without theoretical explanations. For the latter, see Section 5.5. See also ***Radiofrequency Pulses: Response of Nuclear Spins***.

3.1 Nonquadrupolar Nuclei

To introduce the rf-related concepts of nutation, spin locking, and population transfer, we first consider the simple example of a vanishing NQCC ($\nu_Q = 0$). In the rotating frame (the axes system that rotates with the frequency of the rf carrier), the rf field is represented by a constant vector $\boldsymbol{\nu}_1$ of length $\boldsymbol{\nu}_1$ along x, while the Zeeman field is effectively reduced to an offset vector $\Delta\boldsymbol{\nu}_0$ of length $\Delta\nu_0$ along z (see the axis diagram in the top portion of Figure 7). The magnetization precesses about the 'effective field', which is represented by the vector $\boldsymbol{\nu}_{\text{eff}}$. We distinguish the two limiting cases of (a) irradiation close to resonance, $\Delta\nu_0 \ll \nu_1$, and (b) irradiation far off resonance, $\Delta\boldsymbol{\nu}_0 \gg \nu_1$. These cases are also represented in the more schematic illustration in the lower part of Figure 7, where the effective range of the rf field is represented in the frequency domain by a shaded rectangle of width of order ν_1 centered at the carrier frequency. In NMR terminology, the precession induced by a pulse of type (a) is referred to as 'nutation'. In general, this term relates to precessions caused by rf irradiation and that begin with the spins in thermal equilibrium. In case (a), the nutation is in the (y, z) plane, and takes place with a nutation frequency equal to the rf amplitude, $\nu_{\text{nut}} = \nu_1$. If before the application of the pulse the spins have been prepared so that they point in the x direction of the rotating frame, they will be spin locked by a pulse of type (a).

No nutation or excitation is induced by a far-off-resonance pulse, but we can speak of spin locking in its presence. Namely, the direction of the effective field $\boldsymbol{\nu}_{\text{eff}}$, which is nearly parallel to z in case (b), can be viewed formally as a spin locking field for z magnetization. This notion is a

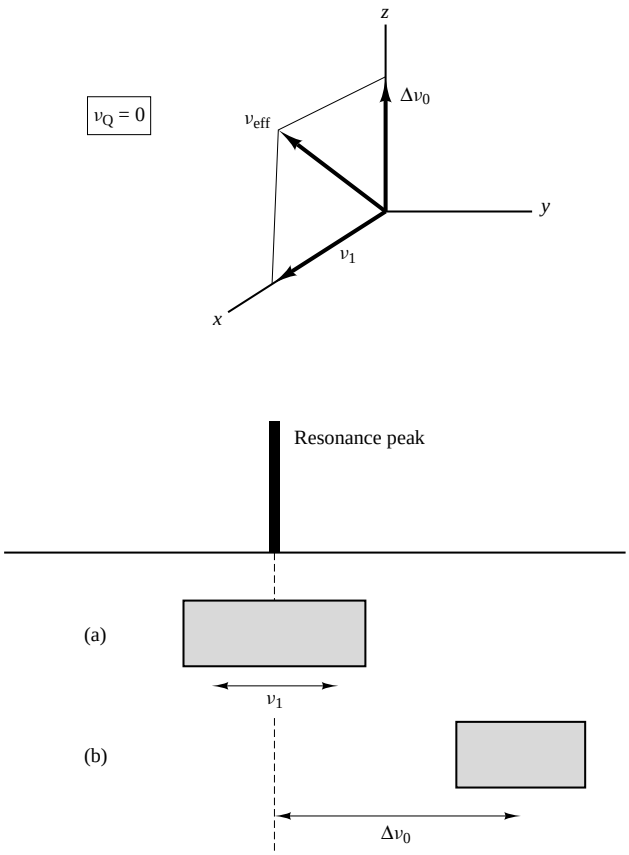

Figure 7 Top: Rotating frame representation of an rf field of ampitude ν_1 (in frequency units) and a resonance offset $\Delta\nu_0$. This representation is adequate for a nonquadrupolar spin system, either $I = \frac{1}{2}$ or $I > \frac{1}{2}$. Bottom: Schematic frequency domain representation of rf irradiation of nonquadrupolar spins. The rf excitation profile is indicated by a shaded rectangle centered at the rf carrier frequency and extending over the approximate excitation range of the rf field. The limiting cases are (a) on-resonance rf ($\Delta\nu_0 \ll \nu_1$) and (b) off-resonance rf ($\Delta\nu_0 \gg \nu_1$)

useful starting point for the description of an adiabatic passage that occurs when $\Delta\nu_0$ is slowly changed from one side of resonance to the other. During an adiabatic passage, the spins remain spin locked along $\boldsymbol{\nu}_{\text{eff}}$ and rotate together with it from z through x to $-z$. Eventually, this results in population inversion of the Zeeman levels. In the case of $I = \frac{1}{2}$ the passage transfers the population of the $\frac{1}{2}$ level to the $-\frac{1}{2}$ level and vice versa. The criterion for adiabaticity is that the parameter

$$\alpha = \frac{\omega_{\text{nut}}^2}{\mathrm{d}\Delta\omega_0/\mathrm{d}t} \tag{7}$$

must be larger than 1. If the passage is sudden ($\alpha \ll 1$), the magnetization remains in the original direction and no populations are transferred. If it is intermediate ($\alpha \approx 1$), the magnetization ends up in a direction that is not spin locked.

3.2 Spin-1 Nuclei

For the visualization of rf fields in the presence of quadrupolar interactions, we can no longer resort to a simple three-dimensional vector picture. Instead, we shall review the

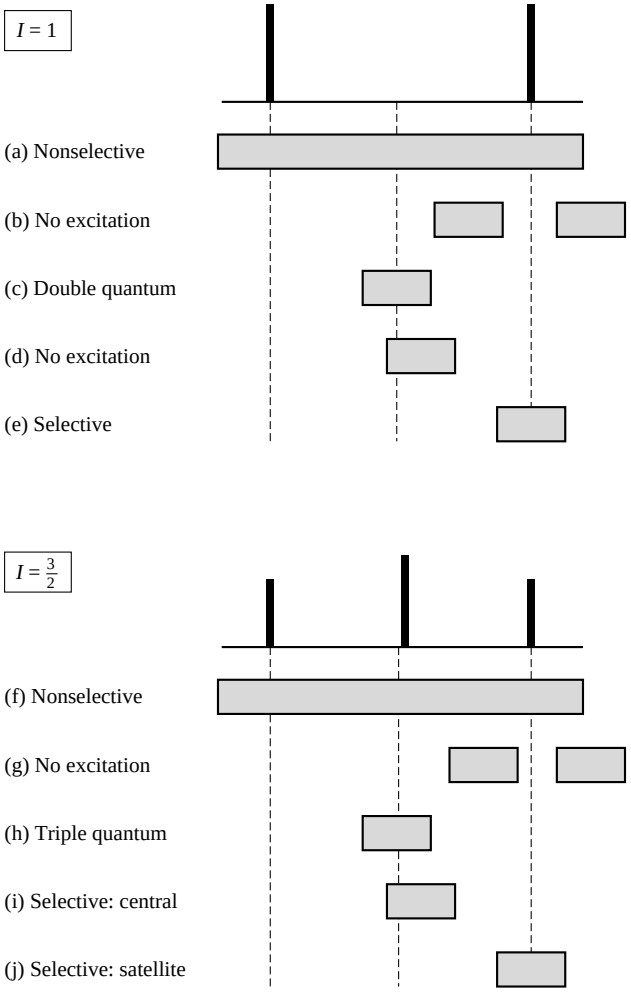

Figure 8 Schematic frequency domain representation of rf irradiation of quadrupolar spins $I = 1$ and $\frac{3}{2}$. The rf ranges are indicated as in Figure 7. The response of the spins to the irradiation depends on the position of the carrier frequency and on the width of the excitation range with respect to the quadrupole-split NMR peaks shown at the top

various aspects of rf irradiation with the help of the illustrations in the frequency domain shown in Figure 8.

3.2.1 Nutation

When $I = 1$, we distinguish five special cases denoted (a)–(e):

3.2.1.1 Case (a). The excitation is nonselective when ν_1 is larger than both $\Delta\nu_Q$ and $\Delta\nu_0$. The two allowed transitions (see the $I = 1$ portion of Figure 2) are then simultaneously excited. As in the $\nu_Q = 0$ case (Figure 7), the nonselective pulse induces nutation with frequency $\nu_{nut} = \nu_1$. However, following the pulse, the spin system will not continue to behave like a nonquadrupolar nucleus. Excitation by two or more pulses, with quadrupolar interactions acting in the intervals, can create as many as eight distinct spin state configurations, of which polarizations along x, y, and z are only three examples.

Two other kinds of spin states are of particular interest. These are 'quadrupolar order', which was discussed in the previous section (see Figure 5), and 'double quantum coherence', which is a quantum mechanical state that can be thought of as a linear combination of $m = +1$ and -1 states. Although double quantum coherence is not observable in the form of nuclear magnetization, it has some similarity to regular transverse magnetization ('single quantum coherence') in that it has x and y components that undergo precession under frequency offset. Unlike single quantum coherence, the double quantum precession frequency is twice the offset frequency. For density matrix representations of these coherences, see Section 5.4.

The most prominent nonselective pulse sequence is the quadrupolar echo sequence, also called solid echo sequence. It consists of two out-of-phase 90° pulses separated by an interval τ: $90°_x - \tau - 90°_y$. The spin dephasing due to first-order quadrupolar effects is refocused by the second pulse, and an echo is formed at time τ following the second pulse.

3.2.1.2 Case (b). When ν_1 is small ($\nu_1 \ll \Delta\nu_Q$) and the rf profile does not overlap with any of the transitions [Figure 8(b) shows two examples], the spins are not excited, except in case (c) below.

3.2.1.3 Case (c). A weak rf field ($\nu_1 \ll \Delta\nu_Q$) applied at the exact midpoint between the two spectral lines ($\Delta\nu_0 = 0$) induces $\Delta m = 2$ transitions directly between the $m = +1$ and -1 states, while leaving the $m = 0$ state unaffected. This effect was indicated in Figure 2 as the forbidden double quantum transition. It can be understood in terms of a second-order perturbation of the first-order quadrupolar interaction by the rf interaction (see Section 5.5). It results in a double quantum nutation frequency given by[19]

$$\nu_{2Q} = 2\nu_1^2/\Delta\nu_Q \tag{8}$$

A pulse of duration $\tau_p = 1/4\nu_{2Q}$ is a double quantum 90° pulse. It transforms Zeeman order into a state of double quantum coherence. A double quantum 180° pulse inverts the populations.

3.2.1.4 Case (d). When the rf carrier is slightly off resonance, no double quantum excitation occurs, despite the fact that the offset may be less than the rf amplitude ($\nu_{2Q} \ll \Delta\nu_0 < \nu_1 \ll \Delta\nu_Q$).

3.2.1.5 Case (e). Selective excitation of one of the allowed transitions ($-1 \leftrightarrow 0$ or $0 \leftrightarrow +1$) is caused by a weak rf field applied at its resonance frequency. The corresponding nutation frequency is given by $\nu_{nut} = \nu_1\sqrt{2}$.

3.2.2 Spin Locking

Each of these five forms of rf irradiation is associated with one or more spin locked spin configurations. If the rf field is applied along x in the rotating frame, the following spin states are spin locked under the various conditions: nonselective irradiation (a) spin locks transverse spin polarization along x; off-resonance irradiation (b) and (d) spin lock Zeeman and quadrupolar order; double quantum irradiation (c) spin locks double quantum coherence of type x; and selective irradiation of an allowed transition (e) spin locks the corresponding single quantum coherence.

3.2.3 Population Transfer

Adiabatic passages, similar to the population inversion described in Section 3.1, can occur for quadrupolar spins

I = 1 when the rf profile crosses over from one side of a transition to the other. For instance, a slow passage between the two situations drawn for case (b) in Figure 8 causes population exchange between the levels m = 0 and −1, and thus transforms pure Zeeman order to a combination of Zeeman and quadrupolar order. Such a passage is materialized by a slow sweep of $\Delta\nu_0$, which can in turn be done by sweeping of the carrier frequency or of the magnetic field. Another possibility is the sweeping of $\Delta\nu_Q$. Because of its orientation dependence, the quadrupolar splitting can easily be varied by simply turning the sample. The passage is adiabatic if the change in $\Delta\nu_Q$ is sufficiently slow for the condition $\alpha > 1$ to be satisfied, with the adiabaticity parameter defined as $\alpha = \omega_{nut}{}^2/(d\Delta\omega_Q/dt)$. Magic angle spinning (MAS) is a particularly effective method for $\Delta\nu_Q$ sweeping, since $\Delta\nu_Q$ of any crystallite experiences two or four zero-crossings per rotation cycle. (This is consistent with the $\Delta\nu_Q$ averaging to zero by MAS.) If the spinning rate is denoted by ν_R, the adiabaticity parameter is roughly equal to

$$\alpha \approx \frac{\nu_1^2}{\nu_R \nu_Q} \tag{9}$$

3.3 Nuclei with Half-Integer Spin

3.3.1 Nutation ($I = \frac{3}{2}$)

The response of a spin $I = \frac{3}{2}$ to the application of rf pulses is in many respects similar to that of I = 1, but there are a few differences to be pointed out. We again distinguish among five special cases illustrated in the bottom half of Figure 8.

3.3.1.1 Case (f). When ν_1 covers the entire spectrum, the excitation is nonselective and the nutation frequency is $\nu_{nut} = \nu_1$. The spin dynamics of sequences with more than one pulse is even richer than for I = 1 nuclei, since there are 15 independent spin states for $I = \frac{3}{2}$ (see Section 5.4). The nonselective solid echo sequence $90^\circ{}_x - \tau - 90^\circ{}_y$ refocuses first-order quadrupolar dephasing as in the case of I = 1.

3.3.1.2 Case (g). There is no excitation when the rf profile does not overlap with any transition (but see Section 5.5).

3.3.1.3 Case (h). A weak rf pulse applied at the exact midpoint between the satellite transitions induces a triple quantum excitation[20,21] between $m = -\frac{3}{2}$ and $\frac{3}{2}$ with a nutation frequency given by $\nu_{3Q} = \frac{3}{2}\nu_1^3/\Delta\nu_Q^2$. The resonance conditions for triple quantum transition and for the allowed central transition do not coincide exactly, because the two transitions have different second-order shifts. The triple quantum excitation is quenched when the carrier frequency is slightly off resonance ($\Delta\nu_0 > \nu_{3Q}$), but when $\Delta\nu_Q$ is not much larger than ν_1, the excitation is effective for $\Delta\nu_0 \lesssim \nu_1$.

3.3.1.4 Case (i). A weak pulse ($\nu_1 < \Delta\nu_Q$) with an rf profile that overlaps with the central transition induces selective excitation of the latter. The nutation frequency for this transition is $\nu_{nut} = 2\nu_1$.

3.3.1.5 Case (j). Selective excitation of the satellites occurs with a nutation frequency $\nu_{nut} = \nu_1\sqrt{3}$. Note that, unlike selective excitation of the narrow central transition, selective excitation of satellite transitions cannot be achieved simultaneously for all crystallites in a powder sample.

3.3.2 Spin Locking ($I = \frac{3}{2}$)

The spin states of $I = \frac{3}{2}$ nuclei that are spin locked under the various modes of rf irradiation follow a pattern similar to that of I = 1, and do not need to be discussed in detail. However, the case of selective irradiation of the central transition [case (i)] deserves some special attention. During an rf pulse of this type, two spin state configurations can be spin locked. One is the population difference of the $m = \pm\frac{3}{2}$ levels illustrated as 'triple quantum order' in Figure 5(e). For convenience, we give it the shorthand notation T_z to indicate that it is associated with the triple quantum transition and that it contributes to z magnetization. The other is single quantum coherence of the central transition, denoted by C_x, which is a linear combination of states $m = \frac{1}{2}$ and $-\frac{1}{2}$ contributing to x magnetization. Density matrix representations of T_z and C_x are given in Section 5.5. When a type (i) pulse is applied to spins $I = \frac{3}{2}$ that are initially in thermal equilibrium, two things happen simultaneously: the T_z portion of the spin state is spin locked while the central transition portion undergoes nutation. However, if the central transition portion is prepared in the C_x state by appropriately chosen preparatory pulses, simultaneous spin locking of T_z and C_x can be achieved.

3.3.3 Population Transfer ($I = \frac{3}{2}$)

An adiabatic passage caused by zero-crossing of $\Delta\nu_Q$ in a slowly rotating sample transfers a spin locked T_z state to C_x, and vice versa. As mentioned above for I = 1, magic angle spinning is an efficient method for inducing these passages. The criterion for adiabaticity is again $\alpha > 1$, with α as defined as in equation (9).[22] The populations of the $\pm\frac{3}{2}$ states can also be transferred to the $\pm\frac{1}{2}$ states by adiabatic sweeping of $\Delta\omega_0$.[23]

3.3.4 Central Transition ($I \geq \frac{3}{2}$)

Similar concepts can be applied to half-integer spins with $I > \frac{3}{2}$, but, other than the general case of central transition excitation, they will not be discussed further. The frequency of nutation of the central transition induced by nonselective irradiation, as exemplified by case (f) in Figure 8, is given by $\nu_{nut} = \nu_1$. On the other hand, when the excitation is selective as in case (i), the general formula for the nutation frequency is

$$\nu_{nut} = (I + \tfrac{1}{2})\nu_1 \tag{10}$$

This effective enhancement of the rf amplitude has obvious consequences for the choice of pulse length for obtaining optimum signal intensity in a selective single pulse excitation experiment. For $I = \frac{3}{2}$ the apparent 90° pulse is a nominal 45° pulse. Likewise, for $I = \frac{5}{2}$, it is 30°, and so on. An additional result of selective excitation is that it reduces the intensity of the resulting central transition signal. If the signal (not including the satellites) following a nonselective pulse of length τ_p can be described by

$$S(\tau_p) = S_0 \sin \omega_1 \tau_p \tag{11}$$

then the signal following a selective pulse is

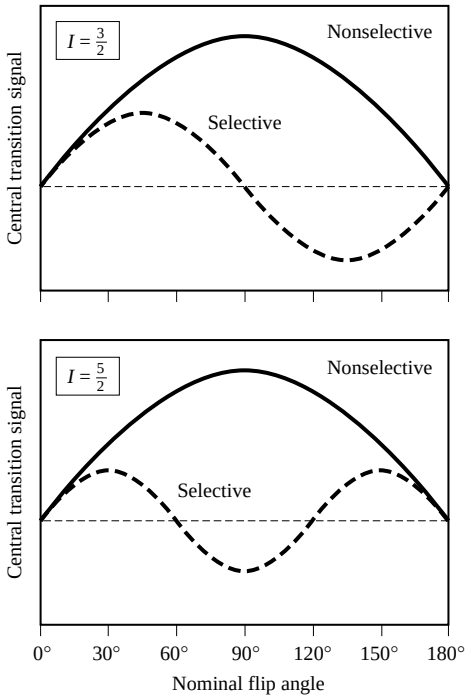

Figure 9 Central transition signal intensity following excitation by a single rf pulse of nominal flip angle $\omega_1\tau_p$, where τ_p is the duration of the pulse, plotted for the limits of nonselective ($\omega_1 \gg \Delta\omega_Q$) and selective ($\omega_1 \ll \Delta\omega_Q$) irradiation

$$S(\tau_p) = \frac{S_0}{I + \frac{1}{2}} \sin[(I + \tfrac{1}{2})\omega_1\tau_p] \qquad (12)$$

The flip angle dependence according to equations (11) and (12) is plotted in Figure 9 for $I = \frac{3}{2}$ and $\frac{5}{2}$.

So far, we have avoided discussion of rf amplitudes that are intermediate between selective and nonselective excitation ($\nu_1 \approx \nu_Q$). However, this situation is often encountered in practice. The response of the spin system to intermediate rf amplitudes is more complex than in the limiting cases. For details see ***Nutation Spectroscopy of Quadrupolar Nuclei***. A significant feature is that for relatively small flip angles ($\omega_{nut}\tau_p < \pi$), the intermediate $S(\tau_p)$ functions fall between the limits of selective and nonselective pulses. Hence, since the initial slopes of the functions of equations (10) and (11) are identical, the signal intensity following very short pulses is independent of the size of the quadrupolar interaction. This result has important implications for the quantitative interpretation of NMR signal intensities.

4 EXPERIMENTAL METHODS

Methods for NMR detection of quadrupolar nuclei in solids are surveyed in this section. The emphasis is not on the achievements of the applications of these techniques, but rather on the underlying spectroscopic principles and their interrelations. Consequently, this section frequently refers to the basic spin properties introduced in the previous sections. The survey is divided in subsections on deuterium, ^{14}N, and half-integer spins, reflecting the fact that in practical applications the choice of a workable NMR method is usually dictated by the size of the NQCC and by the presence or absence of a central transition. The section concludes with a brief introduction to zero field NMR.

4.1 Deuterium

Detailed theoretical and experimental aspects of solid state NMR of deuterium are covered in the articles ***Deuterium NMR in Solids***; ***Liquid Crystalline Samples: Deuterium NMR***; ***Liquid Crystalline Samples: Relaxation Mechanisms***; ***Membranes: Deuterium NMR***, and ***Polymer Dynamics and Order from Multidimensional Solid State NMR***. Applications to polymers were reviewed by Spiess in 1985.[7] Key references to the literature can also be found in these articles.

4.1.1 First-Order Spectra

The most intensively studied first-order quadrupolar spectra are those of deuterium. This is partially due to the chemical importance of the hydrogen atom and the advantages of selective deuteration, but there is also a fortuitous combination of spectroscopic conditions. Deuterium is among the few quadrupolar nuclei for which the total width of the spectra is never much larger than 200 kHz. This ensures that the deuterium spectrum of any chemical structure can be detected within a practical bandwidth and the spins can be excited with essentially nonselective pulses. In addition, the spectra are not appreciably affected by second-order quadrupolar shifts, dipolar broadenings, or chemical shifts, because in the case of deuterium all these contributions are at least two orders of magnitude smaller than ν_Q. Another advantage is that the powder lineshapes of the first-order spectra of spin-1 nuclei are composed of only two spectral transitions, and are thus less complex than those of higher-spin nuclei (see Figure 2 and 3). These circumstances allow the observation of the sometimes subtle lineshape changes caused by nonrandom distributions of molecular orientation (as in liquid crystalline materials) or by rapid random reorientations of the EFG tensor. In fact, the bulk of solid state deuterium NMR work is focused on the elucidation of molecular motions, particularly in polymers, liquid crystals, and adsorbed molecules. In combination with a judicious use of relaxation times and the application of two-dimensional methods (see below), motions with correlation times from nanoseconds to seconds can be characterized.

4.1.2 Zeeman Order and Quadrupolar Order

In the so-called spin-alignment experiment,[7] the spins are prepared in a state of quadrupolar order (see Section 2.3), where they can be held for a time as long as T_{1Q} permits. During that time, chemical exchange can modify the level populations. Two-dimensional methods use this and a similar Zeeman-order scheme for characterization of slow molecular dynamics.

4.1.3 Pulse Sequences

Although deuterium spins can be excited with a nonselective pulse, the FID following a single 90° excitation pulse is short and largely undetectable because of the receiver dead time.

Therefore, the signals need to be created with the solid echo sequence, $90^\circ_x - \tau - 90^\circ_y$, where the second half of the echo serves as the FID for further data processing. The dependence of the signal on τ provides an extra experimental parameter for the study of motions. Quadrupolar order is created with the Jeener–Broekaert sequence, $90^\circ_x - \tau - 45^\circ_y$,[24] and detected with a 45° read-out pulse.

4.1.4 Double Quantum Transitions

Since the double quantum transition frequency is not shifted by the quadrupolar interaction, it is useful for measurements of the chemical shift tensor[25] or, in conjunction with MAS, the isotropic chemical shift,[26] and also for achieving high resolution in imaging.[27] In fact, the double quantum coherence precesses in the rotating frame with twice the offset frequency, and thus has an enhanced sensitivity to small changes in the resonance frequency. Because double quantum coherences are not directly observable, their time dependence has to be measured in a 2D-type experiment where the spins are allowed to evolve for a stepwise incremented time t_1, at the end of which they are detected with a nonselective read-out pulse that transfers double quantum coherence to observable signals. The double quantum state can be prepared by a variety of methods:[28] a double quantum excitation pulse [Figure 8(c)], double quantum cross polarization (a method where Hartmann–Hahn contact between, say, protons and deuterons is established by adjusting ν_1 of the protons to be equal to ν_{2Q} given by equation (8)),[29] two nonselective pulses,[26] or three nonselective pulses.[27]

4.1.5 Double Quantum Decoupling

Effective dipolar decoupling of deuterium from other nuclei by nonselective irradiation of the allowed transitions requires a very high rf intensity, which is difficult to produce in practice. However, decoupling can also be achieved through stirring of the $m = +1$ and -1 states by double quantum excitation.[19] It does not matter that this method does not stir the $m = 0$ state, because the latter is magnetically 'neutral' and does not contribute to dipolar broadening. The provision that the irradiation must be close to the double quantum resonance frequency (see Section 3.2.1.4) presents no practical problem, since the resonance condition is only affected by chemical shifts and second-order quadrupolar shifts.

4.1.6 Magic Angle Spinning

The similarity between the orientational dependence of the first-order quadrupolar splitting and that of CSA implies that MAS removes quadrupolar broadening in deuterium spectra of powders in the same way in which it narrows CSA broadening. However, since rotation speeds are much smaller than the width of the spectrum, the centerband of the MAS spectrum is always accompanied by a large number of sidebands, the envelope of which resembles the static lineshape.[30,31] Owing to the absence of an isotropic first-order shift, the position of the centerband is entirely determined by isotropic chemical shifts and second-order quadrupolar shifts.

4.2 Nitrogen-14

With the exception of chemical structures where near-cubic site symmetry reduces the NQCC to small values,[32] first-order ^{14}N spectra of powders are too broad for detection by NMR. Consequently, direct measurement of ν_Q and η of most compounds is feasible only by NQR spectroscopy. The spin-$\frac{1}{2}$ isotope ^{15}N is usually preferred for solid state NMR studies, despite its low natural abundance (0.365%). (See also ***Nitrogen NMR***.) Nevertheless, ^{14}N nuclei can be detected by several indirect NMR methods that circumvent the bandwidth problems related to the first-order broadening.

4.2.1 Double Quantum Transitions

The absence of first-order quadrupolar effects on double quantum resonance frequencies reduces the spectral width to within practical detection limits. However, double quantum spectroscopy of ^{14}N is much more difficult to perform than the corresponding deuterium experiments (see above). For instance, the method of detection of double quantum coherence by way of coherence transfer to the allowed transitions is not applicable to ^{14}N, because the allowed transitions are inaccessible. Instead, double quantum coherence can be observed indirectly via cross polarization to neigboring protons.[33]

4.2.2 Overtone NMR

As was mentioned in connection with Figure 4 in Section 2.2, a strong quadrupolar interaction causes the admixture of, e.g., some $m = 0$ character in the $m = 1$ and -1 states. As a result, the nominally forbidden $\Delta m = 2$ transition between the $m = -1$ and 1 levels acquires some degree of $\Delta m = 1$ character and becomes weakly allowed. Overtone NMR is the direct excitation and observation of this transition. It is performed at twice the Larmor frequency, $2\nu_0$, which is the frequency corresponding to the energy difference between the $m = \pm 1$ levels (see Figure 2). Although both overtone excitation and double quantum excitation (Section 2.3) induce forbidden transitions between the $m = \pm 1$ levels, they are based on entirely different principles: overtone NMR makes use of the second-order quadrupolar perturbation of Zeeman levels, but is otherwise a direct detection method. On the other hand, double quantum NMR does not rely on mixing of the Zeeman levels, but rather on a second-order rf perturbation of the quadrupole energy levels (see Section 5.5). The practical incentive for overtone NMR is obviously that the resonance frequencies are not shifted by first-order quadrupolar effects, an advantage shared with double quantum NMR. For further details, see ***Overtone Spectroscopy of Quadrupolar Nuclei***.

4.2.3 Heteronuclear Dipolar Splitting

The single crystal NMR spectrum of, say, a ^{13}C nucleus coupled by dipolar interaction to a nearby ^{14}N nucleus is split into three lines corresponding to the magnetic states $m = -1$, 0, 1 of the $I = 1$ spin. In first approximation, the magnetic moments associated with these ^{14}N states are aligned with the Zeeman field and have values proportional to m. This has two consequences: the ^{13}C triplet is symmetric,

and the dependence of their spectral positions on the crystal orientation is such that MAS removes the dipolar broadening in powders. However, in the presence of a large NQCC, the ^{14}N spins are no longer quantized along the Zeeman field, as was pointed out in our discussion of Figure 4. This changes the directions and magnitudes of the magnetic moments of the three eigenstates, and, hence, the symmetry of the triplet and the orientation dependence of its peak positions. These effects were first observed in a single crystal.[34] The modified orientation dependence also prevents complete narrowing of the dipolar broadening by MAS.[35] Provided ν_Q is sufficiently small in comparison to the ^{14}N Larmor frequency ν_0, the residual splitting of the ^{13}C MAS peak can be evaluated by perturbation theory. It was shown to be of the order $\nu_D\nu_Q/\nu_0$, where ν_D is the magnitude of the dipolar interaction. The literature dealing with these phenomena is summarized in a review article by Harris and Olivieri.[36] (See ***Magic Angle Spinning Carbon-13 Lineshapes: Effect of Nitrogen-14***.)

4.2.4 Population Transfer

Slow MAS rotation under continuous rf irradiation of ^{14}N nuclei induces spin flips through adiabatic transformations among the m states (see Section 3.2). This effect has found application in a REDOR-type method for ^{13}C–^{14}N distance determination.[37] The principle of regular REDOR experiments as applied to $I = S = \frac{1}{2}$ spin pairs is as follows. The FID signal of the S spins decays as a result of the dipolar interaction between I and S, but MAS refocuses the dipolar dephasing and creates a rotational echo at the end of a full rotor period. The refocusing is undone if a 180° pulse is applied to the I spins, flipping them from one m state to another at some time during the rotor cycle. This causes a rotational echo signal reduction of S, which can be analyzed to determine the I–S atomic distance (see ***REDOR and TEDOR***). The REDOR experiment cannot be applied in this form when the I spins are ^{14}N, because the 180° pulse must be nonselective to be effective. Instead, one can bring about the desired m flips by population transfer under adiabatic sample spinning conditions (transfer of populations in double resonance or TRAPDOR).[37]

4.3 Nuclei of Half-Integer Spin

Detailed theoretical and experimental aspects of solid state NMR of half-integer spins are covered in the articles ***Double Rotation***; ***Dynamic Angle Spinning***; ***High Speed MAS of Half-Integer Quadrupolar Nuclei in Solids***; ***High Temperature Superconductors***; ***Nutation Spectroscopy of Quadrupolar Nuclei***; ***Quadrupolar Nuclei in Glasses***, and ***Variable Angle Sample Spinning***. The literature on this subject before 1993 is summarized in an extensive review article by Freude and Haase.[6] Key references to the literature can also be found in these articles.

4.3.1 Static First-Order Spectra

Examples of simulated first-order quadrupolar lineshapes of half-integer nuclei in static samples were shown in Figure 3. Experimental spectra are, however, rarely reported. Their detection necessitates excitation by more than one pulse, since the receiver deadtime renders the FID following a single pulse largely undetectable. If nonselective pulses are feasible, a quadrupolar echo sequence identical to that described above for deuterium can be applied to refocus the signal and to allow 'zero-time resolution'. This has been demonstrated for $I = \frac{3}{2}$[38] and $\frac{5}{2}$.[39] Another approach is the so-called two-pulse free induction decay.[6] It is a 2D experiment consisting of two nonselective pulses. The first creates coherences of Δm = 1 transitions that evolve with frequencies equal to multiples of $\Delta\nu_Q$. After a time t_1, the second pulse is applied to transfer the coherences to the central transition, which can easily be detected. Central transition coherences during t_1 are suppressed by phase cycling, and the 2D spectra of spins $\frac{5}{2}$ are simplified in that they are dominated by the first satellite as a result of less effective coherence transfer from the second satellites.

4.3.2 MAS of First-Order Spectra

The orientational dependence of $\Delta\nu_Q$ is such that it allows narrowing of first-order powder spectra by MAS. Compared with deuterium, this experiment is more demanding in terms of spinning stability, because the spectra are generally broader. Jakobsen and co-workers (see ***High Speed MAS of Half-Integer Quadrupolar Nuclei in Solids***) have succeeded in obtaining highly resolved sideband patterns with ν_Q as large as 1 MHz for $I = \frac{3}{2}$ and 0.5 MHz for $I = \frac{5}{2}$. Fine structure of the sidebands due to second-order shifts and sideband envelopes can be analyzed to obtain detailed information on the spin system.

4.3.3 Multiple Quantum Coherence

Triple quantum coherence can be excited with an on-resonance selective pulse,[20] as indicated in Figure 8(h). The method of pulsed multiple quantum NMR (much-practised in one- and multidimensional NMR[28]) was first demonstrated in 1975 by Hatanaka et al.,[40] who created ^{27}Al ($I = \frac{5}{2}$) double quantum coherence in a single crystal by application of two consecutive selective pulses at different allowed transition frequencies.

4.3.4 Echoes and Multiple Pulse Experiments

Numerous combinations of nonselective and selective, on- and off-resonance pulses have been reported for the excitation, refocusing, coherence transfer, or selective detection of single and multiple quantum coherences. This diverse subfield of quadrupolar NMR has been reviewed by Sanctuary and Halstead[41] and by Freude and Haase.[6]

4.3.5 Spin Counting

In NMR, the signal intensity is proportional to the number of spins that give rise to it (see ***Quantitative Measurements***). It can thus be used for quantitative analysis, provided the signals of the unknown sample and a reference sample are excited and detected under comparable conditions. In the case of NMR of half-integer spins, three complicating factors need to be considered.

1. When only the central transition is observed, the signal is reduced by a factor reflecting the relative intensities of the

central and satellite transitions. For a given spin I these are given by

$$S_{m\leftrightarrow m+1} \propto I(I+1) - m(m+1) \tag{13}$$

The relative intensities and the percentages of the total intensity represented in the central transition are listed in Table 2. The appropriate reduction factor needs to be accounted for when signal intensities of solids are compared with a liquid reference sample, because in liquids all the transitions are observed. A corresponding signal reduction is also observed when defects are introduced in cubic crystals: at perfectly cubic sites the full signal is detected because ν_Q vanishes, but defects lower the symmetry, increase ν_Q, and wipe out the satellites.[5]

2. The NQCC can be so large that even the second-order effects broaden the central transition beyond the detection limit. Aluminum-27 NMR is particularly susceptible to this effect, since minor chemical modifications can drastically enhance the NQCC (Table 1). A classic example is the disappearance of ^{27}Al signal due to atoms near the surface of high-surface-area alumina, resulting in an inverse correlation between the signal intensity and the specific surface area.[42] In studies of disordered systems, it is always good practice to supplement ^{27}Al NMR spectra with a quantitative assessment of the percentage of nuclei that are represented in the spectrum. Sometimes, more useful information on the nature of a sample is revealed by a determination of the amount of 'NMR-invisible' Al than by the interpretation of an observed but nonrepresentative lineshape.
3. For quantitative comparison between different signals, it is imperative to work with excitation pulses of sufficiently small flip angle to ensure that the signal intensity does not depend on $\Delta\nu_Q$ (compare Figure 9). The largest deviation is between purely selective and nonselective excitations. To keep it under 5%, the nominal flip angle (i.e., the nutation angle if the pulse were applied to a liquid sample) must be smaller than 18°, 11°, and 8° for $I = \frac{3}{2}, \frac{5}{2}$, and $\frac{7}{2}$, respectively. For deviations less than 10%, the flip angles must be limited to 25°, 15°, and 11°, respectively.

4.3.6 Nutation Spectroscopy

Nutation spectroscopy in its simplest form is the study of the signal intensity following a single pulse, measured as a function of the length of the pulse. Fourier transformation in 2D fashion yields a nutation spectrum that reflects the distribution of nutation frequencies ν_{nut} of the spins during the pulse. Nutation spectroscopy applied to the central transition provides indirect information on the first-order quadrupolar parameters: when $\nu_1 \gg \nu_Q$, the nutation spectrum has a peak at ν_1; when $\nu_1 \ll \Delta\nu_Q$ the peak is at $(I + \frac{1}{2})\nu_1$ [see equation (12) and Figure 9]. Nutation spectra of powders obtained with intermediate rf amplitudes ($\nu_1 \approx \nu_Q$) feature characteristic powder lineshapes that are sensitive to the ratio ν_Q/ν_1 and to η. For further details, see ***Nutation Spectroscopy of Quadrupolar Nuclei***.

Table 2 Relative Intensities of the Transitions of Half-Integer Quadrupolar Nuclei

I	Relative intensities	Central transition (%)
3/2	3 : 4 : 3	40
5/2	5 : 8 : 9 : 8 : 5	25.7
7/2	7 : 12 : 15 : 16 : 15 : 12 : 7	19.0
9/2	9 : 16 : 21 : 24 : 25 : 24 : 21 : 16 : 9	15.2

4.3.7 Second-Order Spectra: Static, MAS, and VAS

The central transition spectra of powder samples have received a great deal of attention. Figure 10 shows the spectral lineshapes for various values of η, without and with MAS. The shapes of the spectra do not depend on I, but their widths do. For that reason, the lineshapes in Figure 10 are plotted on a universal frequency scale, where one unit represents a frequency increment of

$$A = \tfrac{1}{9}[I(I+1) - \tfrac{3}{4}]\frac{\nu_Q^2}{\nu_0} \tag{14}$$

The symmetry of the orientation dependence of the second-order shift differs from that of first-order effects such as CSA, dipolar interaction, and first-order quadrupolar splitting. Consequently, complete line narrowing is not achieved with MAS, as may be seen in Figure 10. Nevertheless, MAS spectra are still preferable to static spectra, not only because the quadrupolar pattern is three to four times narrower, but also because CSA and dipolar broadenings are removed. Chemical shift resolution of MAS spectra improves dramatically when the magnetic field is increased. Since second-order broadening and chemical shift are proportional to $1/\nu_0$ and ν_0, respectively, the resolution scales as ${\nu_0}^2$. High spinning speeds also improve

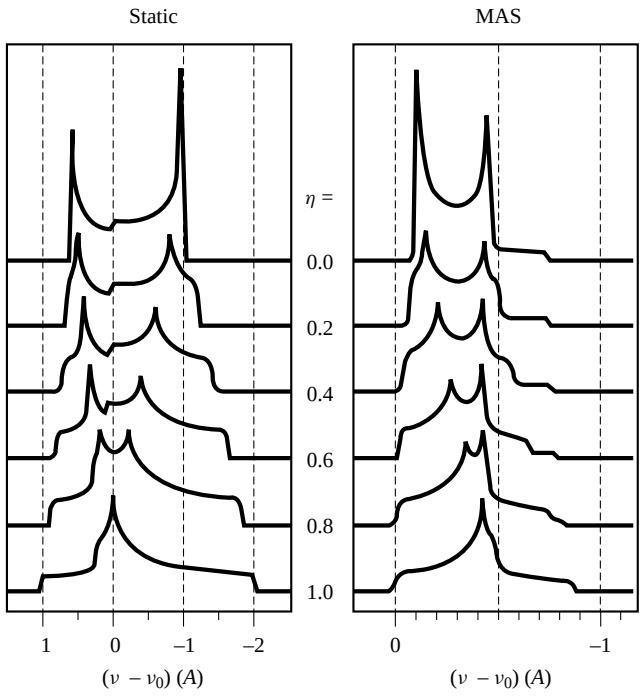

Figure 10 Central transition lineshapes of half-integer spins broadened by the second-order quadrupolar effect, calculated for static and fast MAS conditions. The frequency scale is in units of A, which is defined in equation (14)

resolution, because they prevent overlap of sidebands. Another approach is the technique of variable angle spinning (VAS), in which the samples are rotated about an axis that does not necessarily make the magic angle with the Zeeman field. Certain angles give narrower second-order spectra, but complete narrowing is not obtained. For more details, see ***Variable Angle Sample Spinning***.

4.3.8 Narrowing of Second-Order Broadening

The search for methods to remove the second-order quadrupolar broadening culminated in the inventions of two composite sample rotation techniques: DAS[43] and DOR.[44] Both methods succeed in narrowing the lines by making use of the particular orientational symmetry of the shift. For details, see ***Double Rotation*** and ***Dynamic Angle Spinning***. It should be noted that sample rotation does not change the center of gravity of the spectra. Consequently, the spectral position of the narrowed peak is the combination of a chemical shift and an isotropic second-order quadrupolar shift, where the latter is given by

$$\Delta\nu_{\mathrm{iso}}^{(2)} = -\tfrac{1}{30}[I(I+1) - \tfrac{3}{4}]\frac{\nu_{\mathrm{Q}}^2}{\nu_0}(1 + \tfrac{1}{3}\eta^2) \qquad (15)$$

More recently, line narrowing has also been achieved in a 2D multiple quantum MAS experiment which does not require composite sample rotation. In this MQMAS method the spins are first excited to a triple quantum coherence state (see Section 3.3.1.3) and are subsequently transferred to central-transition coherence where second-order dephasing is refocused.[45] See also ***Line Narrowing Methods in Solids***.

4.3.9 Heteronuclear Dipolar Splitting

Modifications of dipolar splitting patterns similar to those of nuclei coupled to ^{14}N (see Section 4.2), are also observed when the neighboring nucleus is of half-integer spin and has a large NQCC. Examples of coupling to ^{63}Cu/^{65}Cu, ^{35}Cl/^{37}Cl, and other nuclei have been documented.[36]

4.3.10 Relaxation

Spin–lattice relaxation does not usually follow a single exponential behavior for the reasons outlined in Section 2.4. Additional complications arise when the T_1 of a central transition is measured by monitoring the signal following saturation. The results depend on whether a single selective saturation pulse or a long saturation comb is applied, and on whether the measurements are done under MAS or static conditions. The apparent T_1 can vary by more than an order of magnitude, depending on the measurement method.[46] The differences are caused by variations in initial population distributions of the energy levels [compare Figure 5(c) and (e)] and by variability of the effectiveness of spin diffusion between the central transition and satellite transitions of a neighboring nucleus.[46]

4.3.11 Spin Locking and Population Transfer

The x magnetization formed by application of a selective y pulse to the central transition corresponds to the spin state C_{x} (see Section 3.3). When spin locked by rf irradiation in the x direction, it decays with the relaxation time $T_{1\rho}$. However, under MAS at slow rates [$\alpha > 1$ with α defined as in equation (9)], the relaxation decay is interrupted by adiabatic population transfer from C_{x} to T_{z} (see Section 3.3). As a result, the x magnetization of every nucleus in the sample disappears at the first zero-crossing of its oscillating quadrupolar splitting $\Delta\nu_{\mathrm{Q}}$ and then reappears again at the next zero-crossing. Since different nuclei have their zero-crossings at different times, the total signal decays gradually, but because every nucleus has an even number of zero-crossings per rotor cycle (two or four), the signal grows back toward the end of the first rotor cycle. This pattern is repeated for successive rotor cycles until $T_{1\rho}$ relaxation causes the signal to decay. However, when the rotation rate is so fast that $\alpha \ll 1$, there is no population transfer, and the signal does not decay other than by relaxation. Under rotation at intermediate rates ($\alpha \approx 1$), the passages transform C_{x} to spin states that are not spin locked, resulting in an irreversible signal decay.[22] Another method of population transfer is slow sweeping of the rf carrier frequency. For instance, it can be applied to static $I = \frac{5}{2}$ nuclei for transfer of the populations of the $m = \pm\frac{5}{2}$ states to the $m = \pm\frac{1}{2}$ states in order to obtain a fivefold increase of central transition signal intensity.[23]

4.3.12 Cross Polarization

Cross polarization (CP) is the transfer of spin locked polarization (magnetization) from nuclei S to neighboring nuclei I by simultaneous rf irradiation of the two spin systems under matched conditions of the two rf amplitudes ν_{1S} and ν_{1I}. When both I and S are spins $\frac{1}{2}$, the matching requirement is the familiar Hartmann–Hahn condition, $\nu_{1S} = \nu_{1I}$. However, if one or both are quadrupolar nuclei, the appropriate matching condition is that the two nutation frequencies be equal, $\nu_{\mathrm{nut},S} = \nu_{\mathrm{nut},I}$. Thus, for CP of the central transition of half-integer spins I from protons with spin $S = \frac{1}{2}$, the condition is $\nu_{1\mathrm{S}} = (I + \frac{1}{2})\nu_{1I}$ (see Section 3.3). The resulting I polarization has the spin locked spin configuration C_{x}. If the cross polarization is done under MAS conditions (CP MAS), complications arise as a result of the zero-crossings of $\Delta\nu_{\mathrm{Q}}$. The same rf irradiation that establishes the CP matching also serves as a spin lock field for the newly formed central transition polarization. Hence, if the adiabaticity parameter α is in the intermediate range, the signal enhancement is frustrated by the irreversible decay of C_{x} caused by the nonadiabatic passages (see the preceding paragraph). This can be a reason for poor performance of CP MAS of the central transition.[47]

4.4 Zero Field NMR

The technique of zero field NMR makes use of the connectivity, illustrated in Figure 4, between the spin states at zero Zeeman field (the NQR limit) and at high field (the NMR limit). A sample is mechanically shuttled back and forth between a position where the field is strong and another position where the field vanishes. In this way, the NQR spectrum can be indirectly detected as an NMR signal, with the combined advantages of the higher sensitivity of NMR and the higher spectroscopic resolution of NQR (see Section 2.2). For details, see ***Zero Field NMR***.

5 THEORY

5.1 Electric Field Gradient

The nuclear quadrupole interacts with an electric field gradient (EFG). This is the gradient of the electric field created by the charges other than the nucleus under consideration. The isotropic portion of the EFG, i.e., the part that originates from the s electrons, which have a nonvanishing charge density at the site of the nucleus, has no relevance to NMR, because the energy of its interaction with the nuclear charge distribution does not change when the nuclear spin axis changes orientation.[4] To be sure, the isotropic EFG contributes to isotope shifts in atomic spectra in the form of a 'volume effect' or 'field effect'.[48,49] However, in the context of NMR, it is customary to ignore its existence. The remaining EFG tensor $\boldsymbol{V}$ is thus purely anisotropic. It has three principal tensor components, V_{XX}, V_{YY}, and V_{ZZ}, which are associated with a principal axis system (PAS) X, Y, Z (in the present notation, we reserve capital indices for the PAS and let the lower case x, y, z stand for a general axis system). The off-diagonal elements V_{XY}, V_{XZ}, etc., are zero in the PAS. The diagonal elements satisfy the Laplace equation

$$V_{XX} + V_{YY} + V_{ZZ} = 0 \tag{16}$$

reflecting the fact that we ignore the isotropic component. Following the convention

$$|V_{ZZ}| \geq |V_{XX}| \geq |V_{YY}| \tag{17}$$

for the assignment of the three PAS directions, we define the quantity

$$eq = V_{ZZ} \tag{18}$$

and the asymmetry parameter

$$\eta = (V_{YY} - V_{XX})/V_{ZZ} \tag{19}$$

The convention ensures that $0 \leq \eta \leq 1$. When $\eta = 0$, the EFG tensor is axially symmetric about the Z axis: $V_{XX} = V_{YY} = -\frac{1}{2}V_{ZZ}$. For arbitrary η, equations (18) and (19) are solved to give

$$V_{XX} = -\tfrac{1}{2}(1 + \eta)eq \tag{20}$$

$$V_{YY} = -\tfrac{1}{2}(1 - \eta)eq \tag{21}$$

One should be aware that many authors prefer the convention $|V_{ZZ}| \geq |V_{YY}| \geq |V_{XX}|$ instead of equation (17) for the assignment of the X and Y axes. The appropriate definition of η is then $(V_{XX} - V_{YY})/V_{ZZ}$, and the signs of η-containing terms in formulas such as equations (3), (20), (21), and (22)–(27) are reversed.

Two kinds of local symmetry at the site of the nucleus dictate the symmetry of the EFG tensor.

1. Cubic point symmetry (including eightfold cubic, sixfold octahedral, and fourfold tetrahedral coordinations) results in $V_{XX} = V_{YY} = V_{ZZ}$, and, hence, by the Laplace equation, $eq = 0$.
2. Axial point symmetry (including structures where the nucleus lies on a threefold, fourfold, fivefold, or sixfold symmetry axis) results in $\eta = 0$.

In ionic crystals, the EFG tensor can be calculated from the known positions and charges of the surrounding ions. However, the actual EFGs experienced by the nucleus are many times larger than the calculated values as a result of distortions of the local electron cloud. The Sternheimer antishielding factor accounts for this correction (see ***Quadrupolar Interactions***).

Below are formulas for the components of the EFG tensor in a more general axis system x, y, z. To be completely general, we ought to specify three Euler angles for the orientation of x, y, z with respect to X, Y, Z. However, in most NMR experiments, we do not need to know more about the laboratory frame than the direction of the z axis specifying the $\boldsymbol{B}_0$ field orientation. In such bases, it is sufficient to define the two polar angles θ and ϕ of z with respect to the PAS. In fact, the polar angles represent two of the Euler angles, as is demonstrated in Figure 11, where the directions of x, y, and z are seen to be obtained from X, Y, and Z by rotating the system first about Z over angle ϕ and then about the new y over angle θ. The third Eulerian rotation (about z) is not executed. The transformation depicted in Figure 11 leads to

$$V_{xx} = \tfrac{1}{2}eq(3\sin^2\theta - 1 - \eta\cos^2\theta\cos 2\phi) \tag{22}$$

$$V_{yy} = \tfrac{1}{2}eq(-1 + \eta\cos 2\phi) \tag{23}$$

$$V_{zz} = \tfrac{1}{2}eq(3\cos^2\theta - 1 - \eta\sin^2\theta\cos 2\phi) \tag{24}$$

$$V_{xy} = V_{yx} = \tfrac{1}{2}eq\eta\cos\theta\sin 2\phi \tag{25}$$

$$V_{xz} = V_{zx} = -\tfrac{1}{2}eq\sin\theta\cos\theta(3 + \eta\cos 2\phi) \tag{26}$$

$$V_{yz} = V_{zy} = \tfrac{1}{2}eq\eta\sin\theta\sin 2\phi \tag{27}$$

There are, however, situations where three parameters must be specified to define the relative orientations of the PAS and

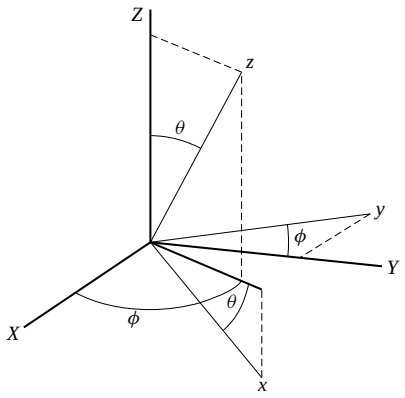

Figure 11 Transformation from a principal axis system X, Y, Z to a more general axis system x, y, z. The transformation is accomplished by a rotation through ϕ about Z followed by a rotation through θ about y. θ and ϕ are the polar and azimuthal angles of z with respect to X, Y, Z

the laboratory frame. For instance, when the EFG changes direction during the NMR experiment because of molecular motions or sample spinning, the full information concerning relative orientations at different times is generally needed for analysis of spin dynamics and relaxation rates.

5.2 Hamiltonian

The nuclear quadrupolar Hamiltonian is introduced in ***Internal Spin Interactions and Rotations in Solids*** and in ***Quadrupolar Interactions***. In the Cartesian coordinates of an arbitrary axes system, it is

$$\begin{aligned}\hat{\mathcal{H}}_{\mathrm{Q}} = \frac{eQ}{4I(2I-1)\hbar}\{&V_{zz}[3\hat{I}_z^2 - I(I+1)] \\ &+(V_{xx}-V_{yy})(\hat{I}_x^2-\hat{I}_y^2)+2V_{xy}(\hat{I}_x\hat{I}_y+\hat{I}_y\hat{I}_x) \\ &+2V_{xz}(\hat{I}_x\hat{I}_z+\hat{I}_z\hat{I}_x)+2V_{yz}(\hat{I}_y\hat{I}_z+\hat{I}_z\hat{I}_y)\}\end{aligned} \tag{28}$$

This formula contains the tensor elements of $\boldsymbol{V}$, which depend on the orientation of the axes with respect to the PAS, as was pointed out above. Another representation of the Hamiltonian is in terms of irreducible tensor operators:

$$\hat{\mathcal{H}}_{\mathrm{Q}} = \frac{1}{2\hbar}\sum_{k=-2}^{2}(-1)^k\hat{Q}_k V_{-k} \tag{29}$$

where

$$\left.\begin{aligned}\hat{Q}_0 &= \frac{eQ}{2I(2I-1)}\frac{1}{\sqrt{6}}[\hat{I}_z^2 - I(I+1)] \\ \hat{Q}_{\pm1} &= \mp\frac{eQ}{2I(2I-1)}(\hat{I}_z\hat{I}_\pm+\hat{I}_\pm\hat{I}_z) \\ \hat{Q}_{\pm2} &= \frac{eQ}{2I(2I-1)}\hat{I}_\pm^2 \\ \hat{I}_\pm &= \hat{I}_x \pm \mathrm{i}\hat{I}_y\end{aligned}\right\} \tag{30}$$

and

$$\left.\begin{aligned}V_0 &= \sqrt{\tfrac{3}{2}}V_{zz} \\ V_{\pm1} &= \mp V_{xz} - \mathrm{i}V_{yz} \\ V_{\pm2} &= \tfrac{1}{2}(V_{xx}-V_{yy}) \pm \mathrm{i}V_{xy}\end{aligned}\right\} \tag{31}$$

The transformation properties of the irreducible tensors make this form of the Hamiltonian particularly useful for description of rotations of the coordinate system. The notation of equation (29) is also helpful for writing out the Hamiltonian in matrix form.

5.3 Hamiltonian in Matrix Form

Since many aspects of the spin dynamics of quadrupolar nuclei can readily be explained by inspection of the structures of the matrices of the various contributions to the total Hamiltonian, we give here a few representative examples. The matrices are given in the standard representation of spin I, i.e., the matrix elements are $\langle m'|\hat{\mathcal{H}}_{\mathrm{Q}}|m\rangle$, where $|m\rangle$ are the $2I+1$ eigenstates of $\hat{I}_z$: $|I\rangle$, $|I-1\rangle$, ... , $|-I+1\rangle$, $|-I\rangle$. The spin operator properties of the $\hat{Q}_k$ components in equation (29) place the coefficient V_0 in the diagonal elements, $V_{\pm1}$ in elements one position removed from the diagonal, and $V_{\pm2}$ two positions removed. As two examples, we give the matrices for $I = 1$,

$$\hat{\mathcal{H}}_{\mathrm{Q}} = \frac{3eQ}{2I(2I-1)\hbar}\begin{pmatrix} \frac{1}{6}V_{zz} & \sqrt{\frac{1}{2}}V_{-1} & V_{-2} \\ -\sqrt{\frac{1}{2}}V_{+1} & -\frac{1}{3}V_{zz} & -\sqrt{\frac{1}{2}}V_{-1} \\ V_{+2} & \sqrt{\frac{1}{2}}V_{+1} & \frac{1}{6}V_{zz}\end{pmatrix} \tag{32}$$

and for $I = \frac{3}{2}$,

$$\hat{\mathcal{H}}_{\mathrm{Q}} = \frac{3eQ}{2I(2I-1)\hbar} \times \begin{pmatrix} \frac{1}{2}V_{zz} & \sqrt{\frac{1}{3}}V_{-1} & \sqrt{\frac{1}{3}}V_{-2} & 0 \\ -\sqrt{\frac{1}{3}}V_{+1} & -\frac{1}{2}V_{zz} & 0 & \sqrt{\frac{1}{3}}V_{-2} \\ \sqrt{\frac{1}{3}}V_{+2} & 0 & -\frac{1}{2}V_{zz} & -\sqrt{\frac{1}{3}}V_{-1} \\ 0 & \sqrt{\frac{1}{3}}V_{+2} & \sqrt{\frac{1}{3}}V_{+1} & \frac{1}{2}V_{zz}\end{pmatrix} \tag{33}$$

In high-field NMR, the quadrupolar Hamiltonian is considered to be a perturbation of the Zeeman Hamiltonian $\hat{\mathcal{H}}_{\mathrm{Z}} = \omega_0\hat{I}_z$. The first-order perturbation is determined by the secular part of $\hat{\mathcal{H}}_{\mathrm{Q}}$, i.e., the portion $\hat{\mathcal{H}}_{\mathrm{Q}}{}^{(1)}$ of $\hat{\mathcal{H}}_{\mathrm{Q}}$ that commutes with $\hat{\mathcal{H}}_{\mathrm{Z}}$. Since the latter is represented by a diagonal matrix with nondegenerate eigenvalues, $\hat{\mathcal{H}}_{\mathrm{Q}}{}^{(1)}$ retains only the diagonal elements of equations (32) and (33), 'truncating' $\hat{\mathcal{H}}_{\mathrm{Q}}$ to

$$\hat{\mathcal{H}}_{\mathrm{Q}}^{(1)} = \tfrac{1}{2}\Delta\omega_{\mathrm{Q}}[\hat{I}_z^2 - \tfrac{1}{3}I(I+1)] \tag{34}$$

$\hat{\mathcal{H}}_{\mathrm{Q}}{}^{(1)}$ determines the first-order energy level corrections $E_{\mathrm{m}}{}^{(1)}$ given in equation (2). The second-order corrections $E_{\mathrm{m}}{}^{(2)}$ of the eigenvalues involve double products of the off-diagonal elements of $\hat{\mathcal{H}}_{\mathrm{Q}}$ divided by differences between Zeeman energies:

$$\begin{aligned}E_m^{(2)} = -\frac{\omega_{\mathrm{Q}}^2}{9\omega_0}m\Bigg\{&2[I(I+1)-2m^2-\tfrac{1}{4}]\left(\frac{|V_1|}{eq}\right)^2 \\ &-[I(I+1)-m^2-\tfrac{1}{2}]\left(\frac{|V_2|}{eq}\right)^2\Bigg\}\end{aligned} \tag{35}$$

These eigenvalue equations are used to calculate first- and second-order quadrupolar shifts of transition frequencies. The expressions $(|V_1|/eq)^2$ and $(|V_2|/eq)^2$ in equation (35) are functions of the orientation of the Zeeman field with respect to the EFG principal axes and of η [see equations (31) and (22)–(27)]. For instance, the second-order shift of the central transition is

$$\begin{aligned}\Delta\omega_{-1/2\leftrightarrow1/2}^{(2)} = -\frac{\omega_{\mathrm{Q}}^2}{9\omega_0}&[I(I+1)-\tfrac{3}{4}] \\ &\times\left[2\left(\frac{|V_1|}{eq}\right)^2-\left(\frac{|V_2|}{eq}\right)^2\right]\end{aligned} \tag{36}$$

which for $\eta = 0$ reduces to

$$\Delta\omega^{(2)}_{-1/2\leftrightarrow 1/2} = -\frac{\omega_Q^2}{16\omega_0}[I(I+1) - \tfrac{3}{4}] \times(1-\cos^2\theta)(9\cos^2\theta - 1) \qquad (37)$$

The eigenfunctions of the Hamiltonian are also perturbed. In other words, the vectors representing them in wavefunction space are slightly tilted. The general formula for these tilted states is

$$|m\rangle \rightarrow |m\rangle + \sum_{m'\neq m} \frac{\langle m'|\hat{\mathcal{H}}_Q|m\rangle}{(m-m')\omega_0}|m'\rangle \qquad (38)$$

which can be used to evaluate the Zeeman state mixing that determines the detectability of overtone spectra and the dipolar splittings in spectra of neighboring nuclei. The correction terms have the forms $(\omega_Q/\omega_0)(V_{\pm 1}/eq)|m \pm 1\rangle$ and $(\omega_Q/\omega_0)(V_{\pm 2}/eq)|m \pm 2\rangle$ multiplied by numerical coefficients. Because the corrections involve off-diagonal elements of $\hat{\mathcal{H}}_Q$ divided by ω_0, they are considered to be second-order perturbations.

5.4 Density Matrix

The state of an ensemble of mutually noninteracting nuclei of spin I is described by a density matrix $\hat{\rho}$ having $2I + 1$ rows and columns. Since this is a Hermitian matrix, it has in addition to a unit-matrix term, $(2I + 1)^2 - 1$ independent traceless components (3 when $I = \frac{1}{2}$; 8 when $I = 1$; 15 when $I = \frac{3}{2}$; etc.). It is convenient to choose a basis set of mutually independent matrices or operators for the description of the density matrices. In the case of spin-$\frac{1}{2}$, the three operators $\hat{I}_x$, $\hat{I}_y$, and $\hat{I}_z$ are the natural selection for that purpose, but for higher spin numbers the choices are not so obvious. A number of formalisms exist. Some are based on the use of irreducible tensor operators [i.e., variations of equation (30)].[41,50,51] Others employ fictitious spin-$\frac{1}{2}$ operators[21,52] or specially adapted operators.[54] Since the spin dynamics are determined by the Liouville–von Neumann equation

$$\frac{d\hat{\rho}}{dt} = i[\hat{\rho}, \hat{\mathcal{H}}] \qquad (39)$$

the preferred formalism depends on the nature of the Hamiltonian to be analyzed, and is often the one that offers the simplest set of commutation relations. Not infrequently, however, other considerations such as ease of visualization, relaxation properties, or personal taste of the theoretician determine the choice of formalism.

Below, we give the traceless parts of the density matrices corresponding to the special spin states that were mentioned in Sections 2.3, 3.2, and 3.3. Rather than referring to a particular basis set, we reproduce here the full matrices in the standard representation. (Complete operator basis sets may be found in the respective references.)[21,41,52,53] For $I = 1$, we have mentioned Zeeman order $\hat{I}_z$ and quadrupolar order $\hat{Q}_z$,

$$\hat{I}_z = \begin{pmatrix} 1 & 0 & 0 \\ 0 & 0 & 0 \\ 0 & 0 & -1 \end{pmatrix}, \quad \hat{Q}_z = \frac{1}{\sqrt{3}}\begin{pmatrix} 1 & 0 & 0 \\ 0 & -2 & 0 \\ 0 & 0 & 1 \end{pmatrix} \qquad (40)$$

single quantum coherences $\hat{I}_x$ and $\hat{I}_y$ corresponding to x and y magnetization,

$$\hat{I}_x = \frac{1}{\sqrt{2}}\begin{pmatrix} 0 & 1 & 0 \\ 1 & 0 & 1 \\ 0 & 1 & 0 \end{pmatrix}, \quad \hat{I}_y = \frac{1}{\sqrt{2}}\begin{pmatrix} 0 & -i & 0 \\ i & 0 & -i \\ 0 & i & 0 \end{pmatrix} \qquad (41)$$

single quantum coherences $\hat{S}_x$ and $\hat{S}_y$ associated with selective excitation of the $(0, -1)$ transition,

$$\hat{S}_x = \begin{pmatrix} 0 & 0 & 0 \\ 0 & 0 & 1 \\ 0 & 1 & 0 \end{pmatrix}, \quad \hat{S}_y = \begin{pmatrix} 0 & 0 & 0 \\ 0 & 0 & -i \\ 0 & i & 0 \end{pmatrix} \qquad (42)$$

and double quantum coherences with x and y phases,

$$\hat{D}_x = \begin{pmatrix} 0 & 0 & 1 \\ 0 & 0 & 0 \\ 1 & 0 & 0 \end{pmatrix}, \quad \hat{D}_y = \begin{pmatrix} 0 & 0 & -i \\ 0 & 0 & 0 \\ i & 0 & 0 \end{pmatrix} \qquad (43)$$

The $I = \frac{3}{2}$ spin states relevant to the discussions in this article are Zeeman order $\hat{I}_z$ and quadrupolar order $\hat{Q}_z$,

$$\hat{I}_z = \frac{1}{2}\begin{pmatrix} 3 & 0 & 0 & 0 \\ 0 & 1 & 0 & 0 \\ 0 & 0 & -1 & 0 \\ 0 & 0 & 0 & -3 \end{pmatrix}, \quad \hat{Q}_z = \frac{1}{2}\begin{pmatrix} 1 & 0 & 0 & 0 \\ 0 & -1 & 0 & 0 \\ 0 & 0 & -1 & 0 \\ 0 & 0 & 0 & 1 \end{pmatrix} \qquad (44)$$

three coherences associated with the central transition,

$$\hat{C}_x = \frac{1}{2}\begin{pmatrix} 0 & 0 & 0 & 0 \\ 0 & 0 & 1 & 0 \\ 0 & 1 & 0 & 0 \\ 0 & 0 & 0 & 0 \end{pmatrix}, \quad \hat{C}_y = \frac{1}{2}\begin{pmatrix} 0 & 0 & 0 & 0 \\ 0 & 0 & -i & 0 \\ 0 & i & 0 & 0 \\ 0 & 0 & 0 & 0 \end{pmatrix}$$
$$\hat{C}_z = \frac{1}{2}\begin{pmatrix} 0 & 0 & 0 & 0 \\ 0 & 1 & 0 & 0 \\ 0 & 0 & -1 & 0 \\ 0 & 0 & 0 & 0 \end{pmatrix} \qquad (45)$$

and three coherences associated with the triple quantum transition,

$$\hat{T}_x = \frac{1}{2}\begin{pmatrix} 0 & 0 & 0 & 1 \\ 0 & 0 & 0 & 0 \\ 0 & 0 & 0 & 0 \\ 1 & 0 & 0 & 0 \end{pmatrix}, \quad \hat{T}_y = \frac{1}{2}\begin{pmatrix} 0 & 0 & 0 & -i \\ 0 & 0 & 0 & 0 \\ 0 & 0 & 0 & 0 \\ i & 0 & 0 & 0 \end{pmatrix}$$
$$\hat{T}_z = \frac{1}{2}\begin{pmatrix} 1 & 0 & 0 & 0 \\ 0 & 0 & 0 & 0 \\ 0 & 0 & 0 & 0 \\ 0 & 0 & 0 & -1 \end{pmatrix} \qquad (46)$$

Note that $\hat{T}_z$ is equivalent to the 'triple quantum order' represented in Figure 5. The nonvanishing matrix elements in equations (42), (43), (45), and (46) form 2×2 submatrices. They are examples of fictitious spin-$\frac{1}{2}$ operators.

5.5 Hamiltonian in Rotating Frame

An rf field of amplitude ω_1 and carrier frequency ω is best described in the axis frame that rotates with frequency ω with respect to the laboratory frame. The corresponding rotating-frame Hamiltonian is

$$\hat{\mathcal{H}}_{\mathrm{rf}} = \omega_1 \hat{I}_x \tag{47}$$

whose matrix elements are proportional to those of $\hat{I}_{\mathrm{x}}$:

$$\langle m|\hat{I}_x|m \pm 1\rangle = \tfrac{1}{2}\sqrt{I(I+1) - m(m \pm 1)} \tag{48}$$

In the same rotating frame, the Zeeman Hamiltonian is reduced to the resonance-offset Hamiltonian

$$\hat{\mathcal{H}}_{\mathrm{os}} = (\omega_0 - \omega)\hat{I}_z = \Delta\omega_0 \hat{I}_z \tag{49}$$

The matrix elements of the quadrupolar Hamiltonian in the rotating frame are transformed to oscillating functions obtained by replacing V_{k} in equations (29), (32), and (33) with $V_{\mathrm{k}} \exp(-\mathrm{i}k\omega t)$. In the presence of rf fields, it is usually permissible to neglect the rapidly oscillating terms. This reduces $\hat{\mathcal{H}}_{\mathrm{Q}}$ in the rotating frame to $\hat{\mathcal{H}}_{\mathrm{Q}}{}^{(1)}$ of equation (34). In summary, we consider a rotating-frame Hamiltonian consisting of three terms:

$$\hat{\mathcal{H}}_{\mathrm{R}} = \hat{\mathcal{H}}_{\mathrm{Q}}^{(1)} + \hat{\mathcal{H}}_{\mathrm{os}} + \hat{\mathcal{H}}_{\mathrm{rf}} \tag{50}$$

In matrix form, it is for $I = 1$,

$$\hat{\mathcal{H}}_{\mathrm{R}} = \frac{1}{2}\begin{pmatrix} \frac{1}{3}\Delta\omega_{\mathrm{Q}} + 2\Delta\omega_0 & \omega_1\sqrt{2} & 0 \\ \omega_1\sqrt{2} & -\frac{2}{3}\Delta\omega_{\mathrm{Q}} & \omega_1\sqrt{2} \\ 0 & \omega_1\sqrt{2} & \frac{1}{3}\Delta\omega_{\mathrm{Q}} - 2\Delta\omega_0 \end{pmatrix} \tag{51}$$

and for $I = \frac{3}{2}$,

$$\hat{\mathcal{H}}_{\mathrm{R}} = \frac{1}{2}\begin{pmatrix} \Delta\omega_{\mathrm{Q}}+3\Delta\omega_0 & \omega_1\sqrt{3} & 0 & 0 \\ \omega_1\sqrt{3} & -\Delta\omega_{\mathrm{Q}}+\Delta\omega_0 & 2\omega_1 & 0 \\ 0 & 2\omega_1 & -\Delta\omega_{\mathrm{Q}}-\Delta\omega_0 & \omega_1\sqrt{3} \\ 0 & 0 & \omega_1\sqrt{3} & \Delta\omega_{\mathrm{Q}}-3\Delta\omega_0 \end{pmatrix} \tag{52}$$

The corresponding matrices for higher values of I can be evaluated similarly. Here, we only mention that when m and $m \pm 1$ equal $-\frac{1}{2}$ and $\frac{1}{2}$, the square root in equation (48) reduces to $I + \frac{1}{2}$, resulting in

$$\langle -\tfrac{1}{2}|\hat{\mathcal{H}}_{\mathrm{rf}}|\tfrac{1}{2}\rangle = \langle \tfrac{1}{2}|\hat{\mathcal{H}}_{\mathrm{rf}}|-\tfrac{1}{2}\rangle = \tfrac{1}{2}\omega_1(I + \tfrac{1}{2}) \tag{53}$$

The nutation frequencies of selective central transition nutation, equation (10), are determined by these matrix elements.

The various ways in which rf pulses affect a quadrupolar spin system were reviewed in Section 3. In an effort to keep that presentation succinct, a quantum mechanical explanation of the effects was not given. The following discussion is intended to show how the effects are related to the Hamiltonian in the rotating frame, equation (50). As in Section 3, we begin with an example of a nonquadrupolar spin to introduce the concepts of nutation, spin locking, and population transfer. Taking $I = \frac{1}{2}$ for simplicity, we have the Hamiltonian matrix

$$\hat{\mathcal{H}}_{\mathrm{R}} = \frac{1}{2}\begin{pmatrix} \Delta\omega_0 & \omega_1 \\ \omega_1 & -\Delta\omega_0 \end{pmatrix} \tag{54}$$

If the rf field vanishes, the dependence of its eigenvalues on the offset is represented by two straight lines crossing at zero offset, as indicated by the broken lines in the top diagram of Figure 12. The associated eigenstates are $|\frac{1}{2}\rangle$ and $|-\frac{1}{2}\rangle$. Introduction of the rf term changes the eigenvalues and eigenstates provided ω_1 [occupying the off-diagonal elements in equation (54)] is not much smaller than $\Delta\omega_0$ (the difference between the diagonal elements). This leads to an avoided level crossing in the eigenvalue diagram, with a residual level splitting of ω_1 at the center. This result follows immediately from the solution of the eigenvalue equation of the matrix of equation (54) with vanishing diagonal elements. When $\Delta\omega_0 = 0$, the eigenstates of $\hat{\mathcal{H}}_{\mathrm{R}}$ are the linear combinations

$$|\mathrm{c}+\rangle = (|+\tfrac{1}{2}\rangle + |-\tfrac{1}{2}\rangle)/\sqrt{2} \tag{55}$$

$$|\mathrm{c}-\rangle = (|+\tfrac{1}{2}\rangle - |-\tfrac{1}{2}\rangle)/\sqrt{2} \tag{56}$$

Zeeman order corresponds to populations of the untilted $|\pm\frac{1}{2}\rangle$ wavefunctions. Since these are eigenstates of the Hamiltonian when $\Delta\omega_0 \gg \omega_1$, Zeeman order is spin locked far off resonance. Another way of expressing this is by saying that the density matrix $\hat{I}_{\mathrm{z}}$, which represents Zeeman order, commutes with the Hamiltonian far off resonance. On resonance, the spin locked density matrix is $\hat{I}_{\mathrm{x}}$, which corresponds to populations of the eigenstates $|\mathrm{c}\pm\rangle$. Since $\hat{I}_{\mathrm{z}}$ does not commute with the Hamiltonian on resonance, a spin system in thermal equilibrium is not spin locked on resonance, but rather undergoes nutation in the rf field with a frequency ω_{nut} equal to the level splitting, which in this case is ω_1. Population transfer occurs when $\Delta\omega_0$ is swept slowly from above to below resonance. If the passage is sufficiently slow that the adiabatic condition of equation (7) is satisfied, an eigenstate of the Hamiltonian is changed into the state that is connected to it by continuity in the level diagram. The top diagram in Figure 12 shows that, when going from above to below resonance, the $|+\frac{1}{2}\rangle$ state connects via $|\mathrm{c}+\rangle$ to $|-\frac{1}{2}\rangle$. (Compare the $z \rightarrow x \rightarrow -z$ trajectory of the magnetization vector in the axis system of Figure 7.) In this way, the density matrix is converted from $\hat{I}_{\mathrm{z}}$ to $-\hat{I}_{\mathrm{z}}$, and the populations of the Zeeman levels are exchanged.

These concepts are readily extended to quadrupolar spins. Examples of offset-dependent eigenvalues are plotted in the $I = 1$ and $I = \frac{3}{2}$ diagrams in Figure 12. They were calculated by numerical diagonalization of the matrices of equations (51) and (52) for selective rf excitation conditions ($\omega_1 < \Delta\omega_{\mathrm{Q}}$). Avoided level crossings are indicated by the circles in the figure. They occur at values of $\Delta\omega_0$ for which two diagonal elements of the Hamiltonian are equal. The numbers above the circles mark the differences Δm of the m values of the crossing states. The residual level splittings are the nutation frequencies ω_{nut} of the corresponding excitations. For single quantum crossings ($\Delta m = 1$), they are determined by the respective off-diagonal elements in the Hamiltonian. For multiple quantum transitions, the residual splittings are to be calculated by higher-order perturbation theory, resulting in the general expression

$$\omega_{\mathrm{nut}}(m' \leftrightarrow m) = M_{m' \leftrightarrow m}\omega_1 \left(\frac{\omega_1}{\Delta\omega_{\mathrm{Q}}}\right)^{\Delta m - 1} \tag{57}$$

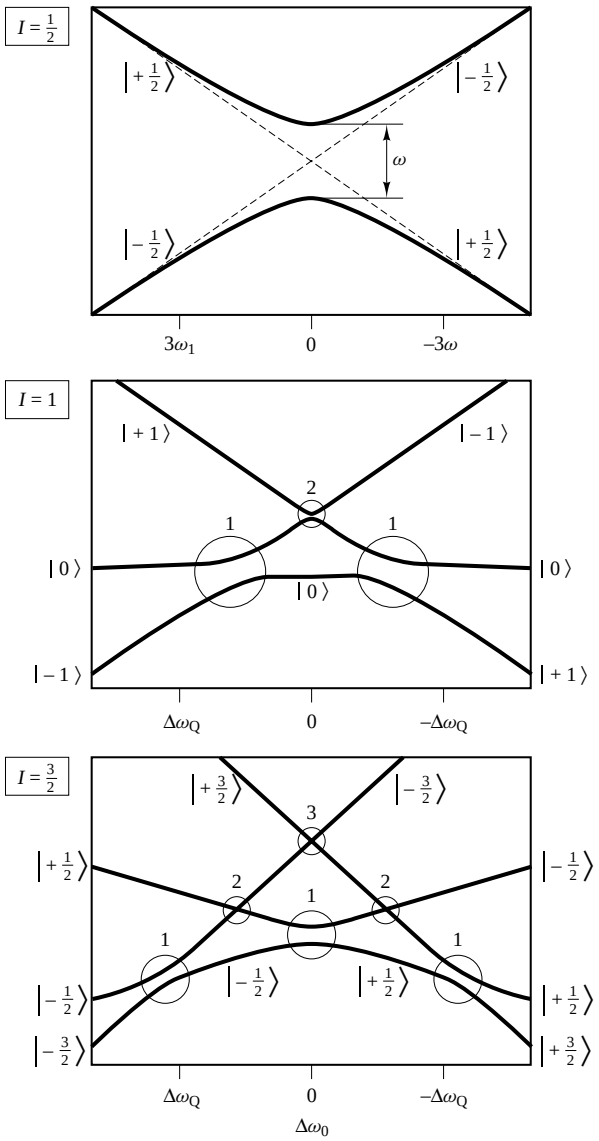

Figure 12 Eigenstate diagrams of a rotating frame Hamiltonian consisting of a first-order quadrupolar term, a frequency offset term, and an rf term. The eigenvalues are plotted versus the offset $\Delta\omega_0$. The $I = \frac{1}{2}$ diagram is representative of the case of a nonquadrupolar nucleus ($\Delta\omega_Q = 0$). The $I = 1$ and $I = \frac{3}{2}$ diagrams represent cases of weak irradiation ($\omega_1 < \Delta\omega_Q$). The actual $\Delta\omega_Q/\omega_1$ ratios used in the simulations were 5 and 10 for $I = 1$ and $\frac{3}{2}$, respectively. Eigenfuctions $|m\rangle$ outside the circled regions are indicated. The numbered circles mark regions of avoided level crossings and the respective values of Δm

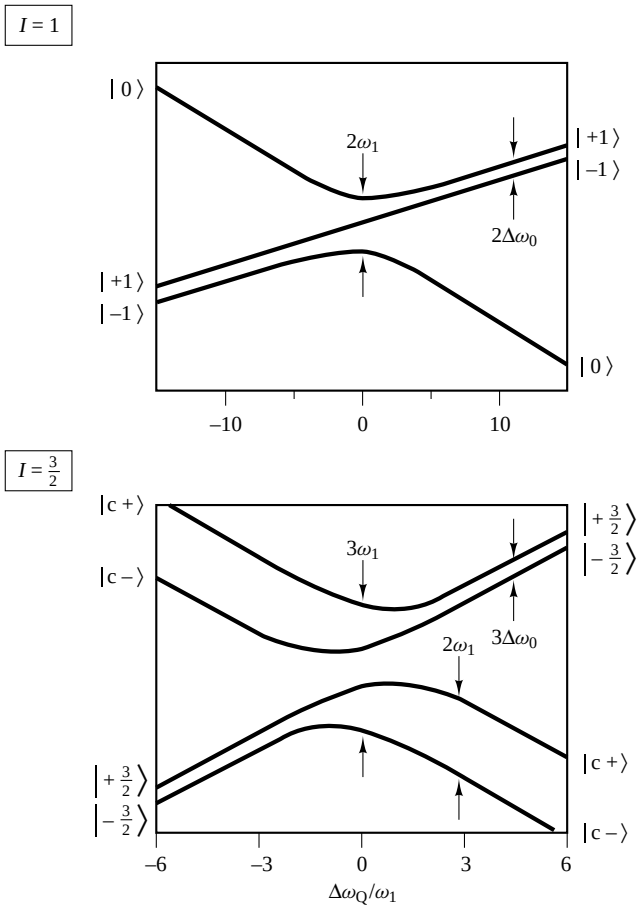

Figure 13 Eigenstate diagrams of a rotating frame Hamiltonian consisting of a first-order quadrupole term, a frequency offset term, and an rf term. The eigenvalues are plotted versus the quadrupole splitting $\Delta\omega_Q$. The diagrams represent cases of small frequency offsets ($\Delta\omega_0 < \omega_1$). The actual $\Delta\omega_0/\omega_1$ ratios used in the simulations were 0.25 and 0.15 for $I = 1$ and $\frac{3}{2}$, respectively. The eigenvalue levels for vanishing $\Delta\omega_Q$ are equally spaced by ω_1. The eigenfuctions are indicated for large $\Delta\omega_Q$. $|c\pm\rangle$ are linear combinations of $|\pm\frac{1}{2}\rangle$ (see text)

Examples of the coefficients are, for $I = 1$, $M_{0\leftrightarrow+1} = \sqrt{2}$, $M_{-1\leftrightarrow+1} = 2$; for $I = \frac{3}{2}$, $M_{-\frac{1}{2}\leftrightarrow+\frac{1}{2}} = 2$, $M_{+\frac{1}{2}\leftrightarrow+\frac{3}{2}} = \sqrt{3}$, $M_{-\frac{1}{2}\leftrightarrow+\frac{3}{2}} = 2\sqrt{3}$, $M_{-\frac{3}{2}\leftrightarrow+\frac{3}{2}} = \frac{3}{2}$. Furthermore, $M_{m'\leftrightarrow m} = M_{m\leftrightarrow m'} = M_{-m'\leftrightarrow-m}$. The coefficients for $I = \frac{5}{2}$ are tabulated elsewhere.[23] The various excitation conditions listed in Figure 8 are easily located in Figure 12. Note that the double quantum transition of $I = \frac{3}{2}$ at $\Delta\omega_0 = \frac{1}{2}\Delta\omega_Q$ was omitted in Figure 8. In the areas outside the circles, i.e. when the irradiation is off-resonance, the eigenstates are essentially pure Zeeman states $|m\rangle$. The corresponding spin locked spin configurations are populated states $|m\rangle$ (see Figure 5), which are represented by diagonal density matrices (e.g., $\hat{I}_z$, $\hat{Q}_z$, $\hat{C}_z$, and $\hat{T}_z$). An adiabatic sweep of $\Delta\omega_0$ interchanges the diagonal matrix elements by population transfer at the avoided level crossings.

Finally, examples of the dependence of the eigenvalues on $\Delta\omega_Q$ are shown in Figure 13. They were calculated for a relatively small resonance offset ($\omega_1 > \Delta\omega_0$). The case of nonselective excitation [Figure 8(a) and (f)] is represented at the centers of the diagrams ($\Delta\omega_Q \ll \omega_1$), where adjacent levels are split by ω_1. A nonselective pulse affects the entire spin system, with a nutation frequency $\omega_{nut} = \omega_1$. At large quadrupolar splittings ($\Delta\omega_Q \geq \omega_1$) all the ω_1-containing off-diagonal elements of equations (51) and (52) are nonsecular, except the central transition elements of $I = \frac{3}{2}$, which connect essentially degenerate states. Thus, the nutation frequency for the central transition is $(I + \frac{1}{2})\omega_1$, even when the quadrupolar splitting is large. The spin locked states of a spin 1 are seen to be made up of populations of Zeeman states, which can be adiabatically transferred into each other by slow sweeping of $\Delta\omega_Q$ from positive to negative values, or vice versa. In the case of half-integer spins, the situation is slightly different.

The eigenstates associated with the central transition are now the sum and difference of the Zeeman states [equations (55) and (56)] population of these eigenstates corresponds to the density matrix $\hat{C}_x$. Figure 13 further shows that an adiabatic zero-crossing of $\Delta\omega_Q$ transfers the $|c\pm\rangle$ states to the $|\pm\frac{3}{2}\rangle$ states, i.e., it transfers $\hat{C}_x$ to $\hat{T}_z$.

6 RELATED ARTICLES

Cross Polarization in Solids; Double Rotation; Dynamic Angle Spinning; Echoes in Solids; High Speed MAS of Half-Integer Quadrupolar Nuclei in Solids; Internal Spin Interactions and Rotations in Solids; Line Narrowing Methods in Solids; Liquid Crystalline Samples: Deuterium NMR; Magic Angle Spinning Carbon-13 Lineshapes: Effect of Nitrogen-14; Magic Angle Spinning: Effects of Quadrupolar Nuclei on Spin-1/2 Spectra; Membranes: Deuterium NMR; Nutation Spectroscopy of Quadrupolar Nuclei; Overtone Spectroscopy of Quadrupolar Nuclei; Quadrupolar Interactions; Quadrupolar Nuclei in Glasses; Quadrupolar Nuclei in Liquid Samples; Quadrupolar Transition Metal and Lanthanide Nuclei; Radiofrequency Pulses: Response of Nuclear Spins; Relaxation of Quadrupolar Nuclei Measured via Multiple Quantum Filtration; Relaxation Theory for Quadrupolar Nuclei; Rotating Solids; SQUIDs; Variable Angle Sample Spinning; Zero Field NMR.

7 REFERENCES

1. R. V. Pound, *Phys. Rev.*, 1950, **79**, 685.
2. M. H. Cohen and F. Reif, in *Solid State Physics*, eds. F. Seitz and D. Turnbull, Academic Press, New York, 1958, Vol. 5, p. 321.
3. A. Abragam, *Principles of Nuclear Magnetism*, Clarendon Press, Oxford, 1961, Chaps. 6 and 7.
4. C. P. Slichter, *Principles of Magnetic Resonance*, 3nd edn., Springer-Verlag, Berlin, 1990, Chap. 10
5. O. Kanert and M. Mehring, in *NMR Basic Principles and Progress*, eds. P. Diehl, E. Fluck, and R. Kosfeld, Springer-Verlag, Berlin, 1971, Vol. 3, p. 1.
6. D. Freude and J. Haase, in *NMR Basic Principles and Progress*, eds. P. Diehl, E. Fluck, and R. Kosfeld, Springer-Verlag, Berlin, 1993, Vol. 29, p. 1.
7. H. W. Spiess, *Adv. Polym. Sci.*, 1985, **66**, 23.
8. H.-G. Dehmelt and H. Krüger, *Naturwissenschaften*, 1950, **37**, 111.
9. T. P. Das and E. L. Hahn, in *Solid State Physics*, eds. F. Seitz and D. Turnbull, Academic Press, New York, 1958, Suppl. 1.
10. E. A. C. Lucken, *Nuclear Quadrupole Coupling Constants*, Academic Press, London, 1969.
11. I. P. Biriukov, M. G. Voronkov, and I. A. Safin, *Tables of Nuclear Quadrupole Resonance Frequencies*, Israel Program for Scientific Translations, Jerusalem, 1971.
12. G. K. Semin, T. A. Babushkina, and G. G. Iakobson, *Nuclear Quadrupole Resonance in Chemistry*, Wiley, New York, 1975.
13. J. A. S. Smith, ed., *Advances in Nuclear Quadrupole Resonance*, Heyden, London, 1974–1983, Vols. 1–5.
14. C. P. Slichter, *Principles of Magnetic Resonance*, 3nd edn., Springer-Verlag, Berlin, 1990, p. 157.
15. P. S. Hubbard, *J. Chem. Phys.*, 1970, **53**, 985.
16. A. Baram, Z. Luz, and S. Alexander, *J. Chem. Phys.*, 1973, **58**, 4558.
17. L. G. G. Werbelow, *J. Chem. Phys*, 1979, **70**, 5381.
18. S. G. Greenbaum, Y. S. Pak, K. J. Adamic, M. C. Wintersgill, and J. J. Fontanella, in *Solid State Ionics II*, eds. G.-A. Nazri et al., Materials Research Society Symposium Proceedings, 1991, Vol. 210, p. 237.
19. A. Pines, D. J. Ruben, S. Vega, and M. Mehring, *Phys. Rev. Lett.*, 1976, **36**, 110.
20. S. Vega, *Phys. Rev. A*, 1981, **23**, 3152.
21. A. Wokaun and R. R. Ernst, *J. Chem. Phys.*, 1977, **67**, 1752.
22. A. J. Vega, *J. Magn. Reson.*, 1992, **96**, 50.
23. J. Haase and M. Conradi, *Chem. Phys. Lett.*, 1993, **209**, 287; J. Haase, M. Conradi, C. P. Grey, and A. J. Vega, *J. Magn. Reson.*, 1994, **109**, 90.
24. J. Jeener and P. Broekaert, *Phys. Rev.*, 1967, **157**, 232.
25. S. Vega, T. W. Shattuck, and A. Pines, *Phys. Rev. Lett.*, 1976, **37**, 43.
26. R. Eckman, L. Müller, and A. Pines, *Chem. Phys. Lett.*, 1980, **74**, 376.
27. E. Günther, B. Blümich, and H. W. Spiess, *Mol. Phys.*, 1990, **71**, 477.
28. R. R. Ernst, G. Bodenhausen, and A. Wokaun, *Principles of Nuclear Magnetic Resonance in One and Two Dimensions*, Clarendon Press, Oxford, 1987, Chap. 5
29. S. Vega, T. W. Shattuck, and A. Pines, *Phys. Rev. A*, 1980, **22**, 638.
30. J. L. Ackerman, R. Eckman, and A. Pines, *Chem. Phys.*, 1979, **42**, 423.
31. J. H. Kristensen, H. Bildsøe, H. J. Jakobsen, and N. C. Nielsen, *J. Magn. Reson.*, 1991, **92**, 443.
32. J. Mason, ed., *Multinuclear NMR*, Plenum Press, New York, 1987, p. 339.
33. M. Reinhold, P. Brunner, and R. R. Ernst, *J. Chem. Phys.*, 1981, **74**, 184.
34. D. L. VanderHart, H.S. Gutowsky, and T. C. Farrar, *J. Am. Chem. Soc.*, 1967, **89**, 5056; M. E. Stoll, R. W. Vaughan, R. B. Saillant, and T. Cole, *J. Chem. Phys.*, 1974, **61**, 2896.
35. E. Lipmaa, M. Alla, H. Roude, R. Teeaar, I. Heinmaa, and E. Kundla, in *Magnetic Resonance and Related Phenomena, Proceedings of the 20th Congrès Ampère, 1979*, p. 87; S. J. Opella, M. H. Frey, and T. H. Cross, *J. Am. Chem. Soc.*, 1979, **101**, 5856.
36. R. K. Harris and A. C. Olivieri, in *Progress in Nuclear Magnetic Resonance Spectroscopy*, eds. J. W. Emsley, J. Feeney, and L. H. Sutcliffe, Pergamon Press, Oxford, 1992, Vol. 24, p. 435.
37. C. P. Grey and W. S. Veeman, *Chem. Phys. Lett.*, 1992, **192**, 379; C. P. Grey, A. J. Vega, and W. S. Veeman, *J. Chem. Phys.*, 1993, **98**, 7711.
38. K. R. Jeffrey, *J. Chem. Phys.*, 1977, **66**, 4677.
39. E. Oldfield, H. K. C. Timken, B. Montez, and R. Ramachandran, *Nature (London)*, 1985, **318**, 163.
40. H. Hatanaka, T. Terao, and T. Hashi, *J. Phys. Soc. Jpn.*, 1975, **39**, 835.
41. B. C. Sanctuary and T. K. Halstead, *Adv. Magn. Opt. Reson.*, 1990, **15**, 79.
42. D. E. O'Reilly, *Adv. Catal.*, 1960, **12**, 31.
43. A. Llor and J. Virlet, *Chem. Phys. Lett.*, 1988, **152**, 248; B. F. Chmelka, K. T. Mueller, A. Pines, J. Stebbins, Y. Wu, and J. W. Zwanziger, *Nature (London)*, 1989, **339**, 42.
44. A. Samoson, E. Lippmaa, and A. Pines, *Mol. Phys.*, 1988, **65**, 1013.

45. L. Frydman and J. S. Harwood, *J. Am. Chem. Soc.*, 1995, **117**, 5367.
46. D. E. Woessner and H. K. C. Timken, *J. Magn. Reson.*, 1990, **90**, 411.
47. A. J. Vega, *Solid State NMR*, 1993, **1**, 17.
48. H. G. Kuhns, *Atomic Spectra*, Academic Press, New York, 1962, pp. 368–380.
49. W. H. King, *Isotope Shifts in Atomic Spectra*, Plenum Press, New York, 1984.
50. H. W. Spiess, *NMR Basic Principles and Progress*, eds. P. Diehla, E. Fluck, and R. Kosfeld, Springer-Verlag, Berlin, 1987, Vol. 15, p. 55.
51. H. W. Spiess, *J. Chem. Phys.*, 1980, **72**, 6755.
52. S. Vega and A. Pines, *J. Chem. Phys.*, 1977, **66**, 5624.
53. A. J. Vega and Z. Luz, *J. Chem. Phys.*, 1987, **86**, 180.

Acknowledgments

The author wishes to thank Dr. D. Schaefer and Professor C. P Grey for helpful comments, and Dr. J. Haase and Professor B. C. Gerstein for critical reading of the manuscript.

Biographical Sketch

Alexander J. Vega. *b* 1938. B.S. (kandidaat), 1961, M.S. (doctorandus), 1967, University of Amsterdam, The Netherlands; Ph.D. (supervisor Daniel Fiat), 1974, Weizmann Institute of Science, Israel. Postdoctoral work at California Institute of Technology (with Robert W. Vaughan) 1975–77. DuPont CR&D, 1977–present. Approx. 60 publications. Research interests: solid state NMR for applications in materials research.

Quadrupolar Transition Metal and Lanthanide Nuclei

Pierre Granger

Université Louis Pasteur, CNRS, Bruker, Strasbourg, France

1	Introduction	1
2	Nuclei without Resonance Known in Solution	1
3	Nuclei with Limited Results in Solution	1
4	Nuclei with Some Potentialities	4
5	The Well-Studied Nuclei	8
6	Lanthanides	10
7	Actinides	11
8	Conclusions	11
9	Related Articles	11
10	References	11

1 INTRODUCTION

Among the 43 transition metal isotopes active in NMR, 32 have a quadrupole moment. Most of them also have paramagnetic states, which usually prevent the usual NMR observation of these nuclei in solution. All these drawbacks greatly reduce the potentialities of NMR of transition metals. Nevertheless, a large amount of data are available for some of them, and they are of prime interest for chemists.

The situation is more severe for the lanthanides, since most of them have only paramagnetic states. Some actinides have NMR potentialities, but only uranium has been observed in solution.

The quadrupole moments that condition the width of the resonances, the gyromagnetic ratios, and the natural abundances that determine the sensitivity of the experiments are the three factors that can lead from easy observation to unobservability of these nuclei. We can therefore classify transition metals according to their observability—which is generally related to the number of papers cited in the literature.

As the quadrupolar relaxation mechanism is almost the only efficient relaxation process, most transition metal nuclei are always decoupled from neighboring nuclei. Consequently, relatively few coupling constants are known. Most of those that are known are with isotopes having spin-$\frac{1}{2}$, which are often used for the measurement of these couplings. This situation usually prevents the observation of homonuclear coupling constants.

The NMR-active transition metal nuclei have been the subjects of reviews or books,[1–7] and theoretical[8,9] and spectroscopic methods[10] for such nuclei have been discussed. See also ***Inorganic Nuclei: Low Sensitivity Transition Metals***; ***Organometallic Compounds***.

2 NUCLEI WITHOUT RESONANCE KNOWN IN SOLUTION

Three elements, namely, hafnium, iridium, and gold, have NMR-active isotopes, but their large electric quadrupole moments and low gyromagnetic ratios prevent signals from being observed. (^{201}Hg is the fourth of this series, but, since mercury also has a spin-$\frac{1}{2}$ isotope, which is easy to observe, the NMR of this element is well known.) Their nuclear spin properties may be found in ***Nuclear Spin Properties and Notation***.

All these nuclei have been observed in the metallic form. A one-bond coupling constant of 200 Hz is known between gold and phosphorus in the solid state. ^{201}Hg has also been observed in $K_2Hg(CN)_4$ in the solid state.[11]

At the present level of development of NMR, none of these nuclei seem to present any prospect for solution studies.

3 NUCLEI WITH LIMITED RESULTS IN SOLUTION

Some nuclei with large quadrupole moments (e.g., ^{181}Ta, ^{185}Re, and ^{187}Re), low receptivities (e.g., ^{53}Cr, ^{61}Ni, and ^{91}Zr), or both (e.g., ^{67}Zn, ^{105}Pd, and ^{189}Os) are very difficult to observe, but in some cases of a high-symmetry environment, resonances have been detected that at least allow the determination of precise NMR parameters.

3.1 Chromium

The receptivity of ^{53}Cr is half that of ^{13}C, but its relatively large quadrupole moment of $-0.150 \times 10^{-28}\,m^2$ reduces its observability. Some reviews have appeared.[1–7,12] Only a few resonances were known before the publication of two papers giving most of the interesting data.[13,14]

3.1.1 Chemical Shifts

Only one isotope, ^{53}Cr with spin $-\frac{3}{2}$ and a natural abundance of 9.55%, is NMR-active. The Ξ value of the most used reference, K_2CrO_4 in D_2O, is 5 652 477 Hz. $Cr(CO)_6$ has also been used as a reference. The relation between the two scales is $\delta(CrO_4^{2-}) = \delta(Cr(CO)_6) - 1796.5$ ppm.

The chemical shifts range between −1900 and +700 ppm for the Cr(0) and Cr(VI) oxidation states, which are the only diamagnetic species for this element.

The influence of the counterion associated with CrO_4^{2-} shows a shielding effect from Na^+ to Cs^+, with NH^+_4 being intermediate. The shielding increases slightly with concentration. The solvent has a greater influence; for example, CH_3CN solutions are deshielded by about 17 ppm compared with D_2O solutions.

Chromium chemical shifts are also temperature-dependent. The observed range of this effect is between 0.1 ppm K^{-1} for Na_2CrO_4 to 1 ppm K^{-1} for $Cr(CO)_6$. A large isotopic shielding of −1.3 ppm is observed between solutions in H_2O and D_2O.

The resonances of Cr(VI), which appear between +700 and −10 ppm, are well separated from the Cr(0) oxidation state, which spans the range from −1600 to −1900 ppm. An inverse

halogen behavior has been noticed in the series CrO_3X^- (with X = F, Cl, Br).

Forty-six carbene complexes $(CO)_5CrL$ [with L = =C(X)(Y)] appear between −1490 and −1740 ppm, and four isonitrile complexes (with L = =C=N−R) are found between −1730 and −1775 ppm. The evolution of these chemical shifts may be interpreted according to the donor–acceptor properties of the ligand for the same type of symmetry.

3.1.2 Coupling Constants

Only a few values are reported in the literature: $^1J(^{53}Cr, ^{17}O)$ = 10 Hz in CrO_4^{2-} and $^1J(^{53}Cr, ^{31}P)$ = 153 Hz in $Cr(CO)_5\{(MeO)_2P(CH_2)_2P(OEt)_2\}$ and 105 Hz in $Cr(PF_3)_6$.

3.1.3 Relaxation and Linewidths

Linewidths are between 4 and 3500 Hz. For carbenes, it has been shown that the broader lines are associated with the more reactive molecules in photolytic reactions.

Few relaxation measurements have been reported. Values of T_1 are usually very short—below 1 ms. The longest is 37 ms for Na_2CrO_4. The evolution of T_1 with temperature for K_2CrO_4 has been published.[6]

3.2 Nickel

It is not its quadrupole moment, which is acceptable (0.162×10^{-28} m^2) that leads to difficulties in the observation of this element, but rather the low natural abundance, 1.13%, of the only NMR-active isotope: ^{61}Ni with spin $-\frac{3}{2}$.[1,2,4–6] Only relatively recently[15,16] have some publications appeared describing the resonances of some tri- and tetracoordinate complexes of Ni(0).

3.2.1 Chemical Shifts

Two references are used, and the preferred one is $Ni(CO)_4$, neat or dissolved in C_6D_6 or CD_2Cl_2. The Ξ value of this reference is 8 936 050 Hz for the neat sample. The second reference is $Ni(PMe_3)_4$ in toluene-d_8. The relation between the two scales, $\delta(Ni(CO)_4) = \delta(Ni(PMe_3)_4) + 15.2$ ppm, is only approximate.

The chemical shifts lie between −930 and +940 ppm. The values for the tricoordinate complexes are not distinct from the tetracoordinate ones. Nickel bound to four phosphorus atoms absorbs between −930 and +267 ppm. Carbonyl derivatives $Ni(CO)_3PX_3$ fall in a short range between −60 and 93 ppm. Theoretical discussion of these chemical shifts awaits more experimental results.

3.2.2 Coupling Constants

Surprisingly for a quadrupolar nucleus with such a large quadrupole moment, many values have been published. All the phosphines observed have $^1J(^{61}Ni, ^{31}P)$ values between 252 and 161 Hz. Phosphites give larger values around 400 Hz. The highest values are observed with $Ni(PCl_3)_4$, 450 Hz, and $Ni(PF_3)_4$, 482 Hz. These couplings allow indirect detection of nickel resonances using inverse experiments.[16]

3.2.3 Relaxation and Linewidths

To the best of our knowledge, only one T_1 measurement has been reported, namely, one on a degassed sample of $Ni(CO)_4$ at 25 °C. The high value of 0.218 s is surprising for a quadrupolar nucleus, but the result agrees with the narrow line observed for this compound (4 Hz). The relaxation mechanism is purely quadrupolar, and usually leads to greater linewidths of between 20 and 90 Hz.

3.3 Zinc

Zinc has only one NMR-active isotope: ^{67}Zn, with a spin $+\frac{5}{2}$.[1,2,4–6] Its low natural abundance (4.11%), its moderate quadrupole moment (0.150×10^{-28} m^2), and its low resonant frequency (Ξ = 6 256 819 Hz for $Zn(NO_3)_2$ in H_2O) lead to poor observability. This situation has been overcome by the use of enriched samples.

3.3.1 Chemical Shifts

Since the solvent and temperature effects on the resonance of zinc in $Zn(NO_3)_2$, $Zn(ClO_4)_2$, and $ZnSO_4$ in H_2O are below 2 ppm, these salts have been used as reference samples. After the first observation around 1970, publications with some chemical interest appeared with the advent of pulse NMR spectrometers and high-field instruments. About 20 resonances have been observed under different conditions.

The most interesting features are the well-separated regions for the tetra- and hexacoordinated cations. The first fall in the range from 200 to 420 ppm, the second in the range from −35 to 100 ppm. Only $ZnCl_2$ and $ZnBr_2$ in H_2O seem to be exceptions to this rule. Because of chemical exchange, salts with anions other than NO_3^-, ClO_4^-, and SO_4^{2-} are very sensitive to concentration, with temperature dependences of about 0.48 ppm K^{-1} for $ZnCl_2$ and 0.61 ppm K^{-1} for $ZnBr_2$. The large isotope effect of +13 ppm for $ZnBr_2$ when H_2O is replaced by D_2O has the same origin. Perchlorate solutions do not show an isotope effect.

Zinc NMR has been used to follow the complexation of this element by different ligands, some of them being biological molecules.

Some theoretical studies are able to predict the trend of the different observed chemical shifts.[17] No coupling constants have been observed with this nucleus.

3.3.2 Relaxation and Linewidths

The linewidths of zinc resonances have often been used in the study of complexation of zinc salts by different ligands or different biological molecules. Usually they are found between 20 and 1500 Hz, but linewidths of the order of 6000 Hz have been observed in biological complexes.

Relaxation measurements usually give $T_1 = T_2$, but the complex formed with insulin gives $T_2 < T_1$, which is explained by the conditions of non-extreme narrowing.

Zinc NMR seems to be very difficult and not very promising.

3.4 Zirconium

The only active isotope of this element, ^{91}Zr with spin $-\frac{5}{2}$ has a receptivity six times greater than ^{13}C. However, it has

not yet been the subject of much active research.[2,4–6,15] Its moderate quadrupole moment of $-0.206 \times 10^{-28}\,m^2$, which is similar to that of ^{59}Co, is not a major difficulty. It is therefore surprising that little work has been done on this nucleus.

3.4.1 Chemical Shifts

The reference sample is $(C_5H_5)_2ZrBr_2$, which has the narrowest resonance. The Ξ value is 9 296 300 Hz, but this frequency seems to be dependent on the experimental conditions: solvent, concentration, temperature, and counterions. A temperature effect of 0.5 ppm K^{-1} has been observed on $(PhCMe_2CH_2)_4Zr$, but the chemical shift of $Cp_2Zr(CH_3)[HC(SO_2CF_3)_2]$ remains constant between 25 and 80 °C.

The chemical shifts range between −390 and +900 ppm, but recently a high deshielding effect has been observed for $(PhCMe_2CH_2)_4Zr$, which appears around +2675 ppm.[17,18] Most of the observed compounds are dicyclopentadienyl derivatives, for which an inverse halogen dependence has been observed, as for all the elements of this column of the Periodic Table having a d^0 structure: the behavior of chemical shifts has been tentatively explained by the HOMO–LUMO concept, and crude additivity rules have been suggested.[15]

3.4.2 Coupling Constants

Only a few coupling constants are known. $^1J(^{91}Zr, ^{13}C)$ = 81.5 Hz was measured on a ^{13}C-enriched $Zr(CO)_6^{2-}$-sample. The results from an interesting experiment are shown in Figure 1. These allowed the measurement of $^1J(^{91}Zr, ^{11}B)$ = 18 Hz and $\frac{1}{4}[3\ ^1J(^{91}Zr, ^1H) + {}^3J(^{91}Zr, ^1H)]$ = 28 Hz which leads to $^1J(^{91}Zr, ^1H)$ = 37 Hz if the three-bond coupling constant is assumed to be negligible.

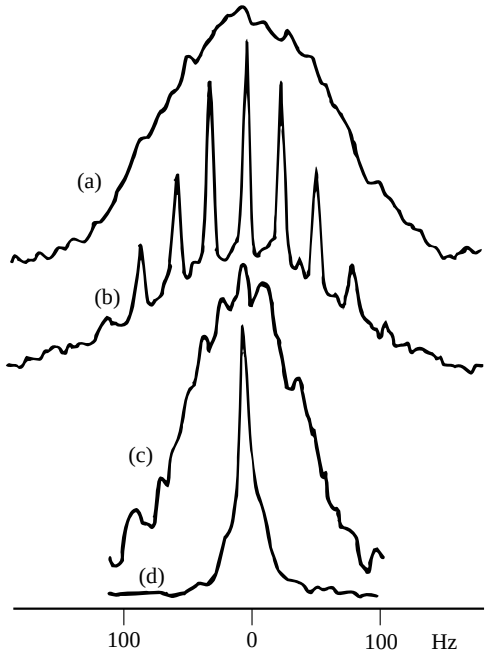

Figure 1 (a) ^{91}Zr NMR spectrum. (b) ^{11}B-decoupled. (c) ^1H-decoupled. (d) ^1H- and ^{11}B-decoupled. (Reproduced by permission of the American Chemical Society from B. G. Sayer, J. I. A. Thompson, N. Hao, T. Birchall, D. R. Eaton, and M. J. McGlinchey, *Inorg. Chem.*, 1981, **20**, 3748)

3.4.3 Relaxation and Linewidths

Only two relaxation time measurements have been performed. The earliest (1957) on $ZrF_6(NH_4)^2$ gave T_1 = 0.001 s; the most recent one on Cp_2ZrBr_2 gives 0.017 s. The linewidths range between 20 Hz for the reference to 7000 Hz for Cp_2Zr diene complexes. These linewidths may sometimes be reduced by proton decoupling, as for $(t\text{-Bu})_4Zr$, where $\Delta\nu_{\frac{1}{2}}$ decreases from 45 Hz (normal) to 20 Hz (decoupled). A decrease in the linewidth has been observed for $Cp_2Zr(CH_3)[HC(SO_2CF_3)_2]$, where $\Delta\nu_{\frac{1}{2}}$ = 7000 Hz at 25 °C and 2800 Hz at 80 °C.

This nucleus seems to be promising, with the development of high-field instruments.

3.5 Palladium

^{105}Pd is the only NMR-active isotope of this element, with a natural abundance of 22.2% and a spin of $-\frac{5}{2}$. It has a large quadrupole moment of $0.660 \times 10^{-28}\,m^2$, which has made observation almost impossible. Its receptivity is higher than that of ^{13}C. Nevertheless, one resonance has been observed for $PdCl_6^{2-}$ in solution.[2,19] The Ξ value is 4 586 100 Hz and is solvent dependent, as is the linewidth which is between 1 200 and 25 000 Hz.

3.6 Tantalum

With a natural abundance of 99.9%, ^{181}Ta, with spin $+\frac{7}{2}$, is one of the most receptive nuclei.[4–6] But its extremely large quadrupole moment of $3.170 \times 10^{-28}\,m^2$ leads almost to unobservability. It was first observed in TaF_6^- in HF/HNO_3 solution,[1] then in $KTaCl_6$ in CH_3CN,[2] from which the Ξ value of 11 989 600 Hz has been determined, the linewidth of the resonance being 4400 Hz.

In 1986, three compounds were observed:[20] $(Et_4N)(TaCl_6)$ in a $CH_3CN/(CH_3)_2CO$ 1/1 mixture and used as reference with a linewidth of 4300 Hz, $K_2(TaF_7)$ in 48% HF, which appears at −2295 ppm with $\Delta\nu_{1/2}$ = 28 700 Hz, and $(Et_4N)[Ta(CO)_6]$ in THF/CH_3CN 5/1, found at −3450 ppm and with a linewidth of 6700 Hz. The behavior seems to parallel that of ^{93}Nb and ^{183}W. The linewidth of TaF_6^- is reduced by a factor 6 from 0 °C to 80 °C.

3.7 Rhenium

This element has two active isotopes in NMR: ^{185}Re and ^{187}Re, both with spin $+\frac{5}{2}$. Their natural abundances are 37.5% and 62.5%, respectively. They have about the same resonant frequency. Consequently, ^{187}Re has a receptivity that is about twice that of ^{185}Re, and is the preferred isotope to observe. They also have similar quadrupole moments: $2.180 \times 10^{-28}\,m^2$ for the first and $2.070 \times 10^{-28}\,m^2$ for the second. Except for ^{181}Ta and ^{235}U, they have the largest quadrupole moments of all stable isotopes. This situation leads to a very difficult observability, which explains the scarcity of publications devoted to this element.[1,2,4–6]

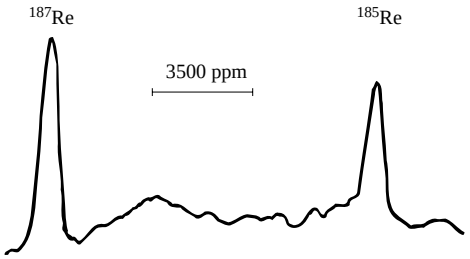

Figure 2 8 MHz $^{185/187}$Re NMR spectrum of $[(C_2H_5)_4N][ReS_4]$ in $MeCN/CH_2Cl_2/Me_2SO$ at 305 K. (Reproduced by permission of Schweitzerischen Chemiker-Verbandes from A. Müller, E. Krickemeyer, H. Bögge, M. Penk, and D. Rehder, *Chimia*, 1986, **40**, 50)

The adopted reference is ReO_4^- for which the Ξ values are Ξ(^{185}Re) = 22 524 600 Hz and Ξ(^{187}Re) = 22 751 600 Hz. As the frequencies are very near and the chemical shift ranges of the transition metal nuclei are large, the two isotopes are often observed in the same spectrum (see Figure 2). The difference between the two resonances is about 10 000 ppm. The only reported chemical shifts are for $Re(CO)_6Cl.HCl$ in CH_3CN (−3400 ppm, $\Delta\nu_{1/2}$ = 2.4 kHz) and Et_4NReS_4 in $CH_3CN/CH_2Cl_2/(CH_3)_2SO$ (+3400 ppm, $\Delta\nu_{1/2}$ = 1.96 kHz). These shifts are comparable to those of Mo and V.

The relaxation of ^{187}Re in ReO_4^- has been studied as a function of temperature.

Surprisingly, several coupling constants have been measured indirectly using ^{1}H, ^{13}C, and ^{31}P relaxation techniques: $^1J(^{187}Re, ^{31}P)$ = 1260 Hz and $^1J(^{187}Re, ^1H)$ = 440 Hz in $HRe(CO)_4PPh_3$, $^1J(^{187}Re, ^1H)$ = 385 Hz in $HRe(CO)_5$, and $^1J(^{187}Re, ^{13}C)$ = 360 Hz and 397 Hz for two carbonyls in $[Re_3(\mu\text{-}H)_4(CO)_{10}]^-$. The future prospects for spectroscopy of this element are not encouraging.

3.8 Osmium

One of the isotopes, ^{187}Os, has spin $+\frac{1}{2}$ and has the lowest receptivity of all nuclei. The other NMR-active isotope is ^{189}Os, with spin $+\frac{3}{2}$. Its natural abundance of 16.1% leads to a receptivity that is twice that of ^{13}C, but its very large quadrupole moment of 0.856×10^{-28} m^2 is a large obstacle to its observation. Consequently, the observation of ^{189}Os has been limited to OsO_4, molten or dissolved in CCl_4, where the Ξ value is 7 765 400 Hz. The observed linewidth on this compound is 860 Hz.[2]

Relaxation measurements on ^{189}Os have been performed on OsO_4 in CCl_4, for which T_1 = 370 μs, and have been used to compare the quadrupole moment of ^{189}Os with those of ^{99}Ru and ^{101}Ru.

4 NUCLEI WITH SOME POTENTIALITIES

4.1 Scandium

The only stable isotope of scandium, ^{45}Sc, has spin $+\frac{7}{2}$ and a high receptivity, equal to 0.3 that of the proton. This is a nucleus that is easy to observe. Its quadrupole moment of -0.220×10^{-28} m^2 is not too large, and facilitates the observation of scandium. The limited number of papers in the literature arises mainly from the chemistry of this element being essentially limited to ionic forms studied in solution.[1,2,4–6]

4.1.1 Chemical Shifts

The reference is $Sc(ClO_4)_3$, 0.1 M at low pH in water. The observed resonance is in fact $Sc(H_2O)_6^{3+}$ which has a Ξ value of 24 291 700 Hz. Depending on the counterion associated with Sc^{3+} in H_2O and on the concentration, the observed shifts range from −88 to +27 ppm. These variations reflect the equilibrium between the counteranion and the water molecules. Exchange studies have also been performed using temperature and pressure variations. The exchange effect leads to a large isotopic effect of −6.2 ppm between H_2O and D_2O, which may be of reverse sign +1 ppm) in 10 M NaOH solutions.

Some complex ions enlarge the chemical shift range from +288 ppm for $ScBr_6^{3-}$ to −115 ppm for $Sc(OH)_4^-$. Sc NMR has been used to identify the following species in solution: $[ScCl_{6-x-y}(SCN)_x(CH_3CN)_y]^{3-y}$ and $ScCl_{6-n}[OP(OR)_3]_n^{3-n}$.

4.1.2 Coupling Constants

Some coupling constants are known with fluorine, $^1J(^{45}Sc, ^{19}F)$ = 180 Hz in ScF_6^{3-}, with phosphorus, $^2J(^{45}Sc, ^{31}P)$ = 30–40 Hz in $ScCl_{6-n}[OP(PMe)_3]_n^{3-n}$, and with boron, $^1J(^{47}Sc, ^{11}B)$ = 15.5 Hz, and proton, $^2J(^{45}Sc, ^1H)$ = 30 Hz, both in $Sc(BH_4)_3$.

4.1.3 Relaxation and Linewidths

The linewidths range from 29 Hz, corresponding to T_1 = 7.2 ms, to 4550 Hz. The evolution of the linewidths with concentration or with the addition of other counterions has been used to probe the existence of labile complexes or contact ion pairs.

4.2 Titanium

The two isotopes, ^{47}Ti with spin $-\frac{5}{2}$, and ^{49}Ti, with spin $-\frac{7}{2}$, have resonant frequencies differing only by 267 ppm, ^{49}Ti being at higher frequency.[1,2,4–6,15] The resonances of both isotopes always appear in all spectra. When different species are present, to avoid the overlapping between the two isotope resonances, it has been suggested recently that a 140 μs delay before the acquisition be used, such that the resonances of ^{47}Ti decrease completely.[21]

Both isotopes have a moderate quadrupole moment: 0.290×10^{-28} m^2 for ^{47}Ti and 0.240×10^{-28} m^2 for ^{49}Ti, so that the higher frequencies have the narrower linewidths.

4.2.1 Chemical Shifts

The reference is $TiCl_4$ neat and its resonances seems independent of the solvent. The Ξ values are 5 637 583 Hz for ^{47}Ti and 5 639 091 Hz for ^{49}Ti; their linewidths are around 6–8 Hz.

The hexacarbonyl complex $Ti(CO)_6^{2-}$ is the most shielded derivative, and is found at −1389 ppm. On the opposite

side, TiI_4 is observed at +1278 ppm. Titanium has an inverse halogen dependence, as does zirconium, and this behavior has recently been explained theoretically.[22] The NMR applications of this element have begun to increase, and have been used to distinguish between enantiomers and to prove the existence of complexes with aromatic compounds, electron donor–acceptor ligands, and with small peptides. It has been found that the alkoxides $Ti(OR)_4$ are difficult to observe, probably because of the presence of polymeric structures.

4.2.2 Coupling Constants

Only two coupling constants have been observed: $^1J(^{49}Ti, ^{13}C) = 23$ Hz and $^1J(^{49}Ti, ^{19}F) = 34$ Hz.

4.2.3 Relaxation and Linewidths

According to their quadrupole moments, the linewidths of ^{47}Ti are about 1.5 times larger than those of ^{49}Ti. The spin–lattice relaxation time has been measured for both isotopes for TiF_6^{2-} and $TiCl_4$ at different concentrations in *n*-pentane and at different temperatures in toluene. The values for ^{49}Ti are about 0.1 s.

4.3 Manganese

The only stable isotope ^{55}Mn of this element has spin $+\frac{5}{2}$, a high receptivity, 1000 times that of ^{13}C, but a large quadrupole moment of 0.330×10^{-28} m^2, which considerably reduces the observability of the manganese resonances.[1,2,4,5] On the other hand, the only diamagnetic states correspond to the +1, 0, −1 oxidation states, which do not comprise the major part of the chemistry of this element. An exception to this rule is MnO_4^{2-}.

4.3.1 Chemical Shifts

These are all referred to $KMnO_4/H_2O$ solution, where the Ξ value is 24 789 060 Hz. This resonance depends on concentration, solvent (18 ppm from H_2O to hexamethylphosphoramide), and temperature (0.3 ppm K^{-1}). An isotope effect of −0.76 ppm is reported between H_2O and D_2O solutions. MnO_4^- is the only observed Mn(VII) oxidation state; all other molecules are mainly carbonyl or nitroxyl derivatives. The total chemical shift range is from +20 ppm (MnO_4^-) to −2953 ppm [$MnH(PF_3)_5$]. The +1 oxidation state is roughly between −1000 and −1500 ppm and the −1 oxidation state between −1700 and −3000 ppm. Several interesting correlations have been more or less established between the chemical shifts and the mean excitation energy ΔE, the σ-donor properties in the $LMn(CO)_5$ series, the Mössbauer isomer shifts for the $R_{3-n}X_n$–$Mn(CO)_5$ species, the rate of demetalation, and the ^{17}O chemical shifts.

Theoretical studies agree with the experimental results on model molecules[9] and the sensitivity of the chemical shifts is such that it allows the determination of the relative concentration of inseparable isomers in solution. High-pressure experiments up to 3×10^7 Pa at different temperatures have been performed to study the equilibrium during the hydrogenation of $Mn_2(CO)_{10}$.

4.3.2 Coupling Constants

Most of the known coupling constants are those with phosphorus in $Mn(CO)_5L$ derivatives. The values range between 140 and 405 Hz, the coupling constants to phosphites being larger than those to phosphines. Values of $^1J(^{55}Mn, ^{13}C)$ ranging from 111 to 121 Hz have been observed in $Mn(CNR)_6^+$, and MnO_4^- gives rise to a $^1J(^{55}Mn, ^{17}O) = 30$ Hz.

4.3.3 Relaxation and Linewidths

The longitudinal relaxation time is 0.84 s in MnO_4^-. This result corresponds to a linewidth of 3.5 Hz. This seems to be the only T_1 measurement.

With some exceptions, the reported linewidths are found between 1000 and 21 500 Hz. They have been used to measure the exchange rate of electrons between diamagnetic and paramagnetic states. The two species $Mn[CNC(CH_3)_3]_6^{+/2+}$ and $Mn(CNC_6H_{11})_6^{+/2+}BF_4^-$ were observed under pressures up to 20 MPa and at different temperature in many solvents. The thermodynamic parameters of the exchange were determined.

Despite its high receptivity, the use of ^{55}Mn NMR is greatly handicapped by the large ^{55}Mn quadrupole moment.

4.4 Copper

The two stable isotopes of this element have spin $+\frac{3}{2}$, with a natural abundance of 69.1% for ^{63}Cu and 30.9% for ^{65}Cu.[1–6] As they have similar resonant frequencies and similar quadrupole moments (-0.220×10^{-28} m^2 for ^{63}Cu and -0.204×10^{-28} m^2 for ^{65}Cu), ^{65}Cu is preferred, since it has a larger receptivity. A disadvantage is that the copper resonance from the probe is also observed at about 2000 ppm as a broad band with a linewidth between 7 and 14 kHz. When the observed resonances have smaller linewidth, this artifact may be suppressed using a delay before the acquisition, or by using an echo experiment. Note that Na^+ is found at −2400 ppm from the ^{63}Cu resonances.

4.4.1 Chemical Shifts

Only the Cu(I) oxidation state is observed in complexes having a high symmetry. The usual reference is $Cu(MeCN)_4^+$ in CH_3CN solution. The Ξ values are 26 515 441 Hz for ^{63}Cu and 28 403 658 Hz for ^{65}Cu. The resonances do not depend on the usual counterions. Most complexes are found between 550 and −434 ppm. Resonances of carbonyl clusters are observed at very low frequencies around −2410 ppm, as for cobalt clusters. The relative small chemical shift range arises from the d^{10} structure of these molecules.

As the complexes are strongly bonded to copper, they protect the nucleus from external perturbations. Consequently, the chemical shifts of copper in these complexes are not sensitive to the concentration, or to the nature of the solvent and of the counterions. Large effects do arise if there is chemical exchange. The temperature effect on the shifts is relatively small, ranging between −0.055 and −0.75 ppm K^{-1}. Contrary to some early observations, copper follows the normal halogen effect. This behavior has been the subject of some theoretical investigations.[17]

Copper resonances in complexes with phosphine ligands are observed at lower frequencies (90−70 ppm) than those with phosphites (250−150 ppm). Complexes with different ligands have copper resonances that fall between these ranges, but are often not observed since the disymmetry considerably broadens the lines.

4.4.2 Coupling Constants

Only a few coupling constants are known. Most are one-bond coupling constants between ^{63}Cu and ^{31}P, which range between 1100 and 1460 Hz. A lower value has been observed at 790 Hz. These couplings have been used to observe copper indirectly by MINDOR (modified internuclear double resonance) or TINDOR (transferred internuclear double resonance) techniques.[6]

Only one $^1J(^{63}\text{Cu}, ^{13}\text{C})$ of 800 Hz has been measured on a ^{13}C-enriched sample of $[\text{Cu(CO)(O-}t\text{-Bu)}]_4$.

4.4.3 Relaxation and Linewidths

The quadrupolar mechanism is always dominant. Linewidths range from 20 to 28 000 Hz. Rapid chemical exchange may also increase the widths. The lower linewidths are found in clusters, as for cobalt.

The linewidths are sensitive to solvent, temperature, and concentration, and these properties have been used to study ligand exchange. A special case is the exchange between Cu(I) and the paramagnetic Cu(II) species. Here, the linewidth of Cu(I) is a function of the exchange rate.

4.5 Niobium

The only stable isotope of this element, ^{93}Nb, with spin $+\frac{9}{2}$, has one of the highest receptivities: about half that of the proton, but its relatively large quadrupole moment of -0.320×10^{-28} m^2 seriously limits its observability.[1−6]

4.5.1 Chemical Shifts

A reference has not been definitively chosen. The most used is $NbCl_6^-$ in CH_3CN for which Ξ = 24 476 193 Hz, but NbF_6 or $NbOCl_3$ have also been proposed. The latter one is equivalent to $VOCl_3$, used as reference for vanadium, which would allow direct comparison between these two nuclei. Its drawback is its large linewidth of 700 Hz compared with the narrow band observed with the solution of $NbCl_5$ + Et_4Cl in *dry* CH_3CN. We shall use this last reference in this article. The relations with the two most used scales are $\delta(NbCl_6^-) \approx \delta(NbOCl_3) - 460$ ppm and $\delta(NbCl_6^-) \approx \delta(NbF_6^-) - 1500$ ppm. These conversion factors are not unique, since the measured values depend on the nature of the observed species, which are not always clearly identified.

The observed chemical shift range has been extended by about +2500 ppm,[23] and is now between +2600 and −4800 ppm. Niobium chemical shifts often parallel those of vanadium.[7] The Nb(V) oxidation state has a d^0 structure, and is not very sensitive to solvent, concentration, or temperature effects. Niobium NMR has been used to study the mixture of species $NbEX_{4-n}Y_n$, with E = O, S, Se, Te. The identification of species is sometimes based on a pairwise additivity rule. Deviations from this rule seem to be related to the preparation of the samples. A theoretical study has improved the understanding of the origin of the chemical shifts in these series, which is related to d−d transitions.[9,24]

Low-valent Nb(I) and Nb(−I), in contrast, have d electrons and are very sensitive to medium and temperature effects: 0.18 ppm K^{-1} for $Nb(CO)_6$ and 0.40 ppm K^{-1} for $CpNb(CO)_4$. Large isotopic effects are observed: −6 ppm for H/D substitution for $CpNb(CO)_3$ and 0.173 ppm for ^{12}C/^{13}C exchange for $Nb(CO)_6^-$. Low-valent niobium complexes usually appear at lower frequencies.

4.5.2 Coupling Constants

Only a few coupling constants are known. $^1J(^{93}\text{Nb}, ^1\text{H})$ ranges between 36 and 80 Hz in hydrides, and 281 Hz < $^1J(^{95}\text{Nb}, ^{19}\text{F})$ < 410 Hz and $^2J(^{95}\text{Nb}, ^{19}\text{F})$ = 53 Hz in $Nb(PF_3)_6^-$ where $^1J(^{95}\text{Nb}, ^{31}\text{P})$ = 1050 Hz. Coupling constants with ^{13}C are known only for $CpNb(CO)_4$: $^1J(^{95}\text{Nb}, ^{13}\text{C})$ (CO) = 236 Hz and $^1J(^{95}\text{Nb}, ^{13}\text{C})$ (Cp) = 13 Hz. A one-bond coupling constant of ±10 Hz between Nb and ^{11}B has been observed.

4.5.3 Relaxation and Linewidths

The dominant relaxation mechanism is quadrupolar. The linewidths range from a few to 13 000 Hz. As is usual for quadrupolar nuclei, the linewidths have been used for the identification of species on the basis of their symmetry. The relaxation has been studied between 270 and 320 K in $NbOF_5^{2-}$ in CH_3CN, and used for microdynamical studies.

4.6 Technetium

^{99}Tc is the most stable isotope of this element, having spin $+\frac{9}{2}$ and a quadrupole moment of -0.129×10^{-28} m^2.[1,2,4,6] The observation of this radioactive element requires special equipment for handling the samples, and for security during the measurements. As it is artificially produced, its abundance is always 100%. It is the fifth most sensitive nucleus. A test has shown[24] that a 10^{-7} M solution of TcO_4^- gives a reasonable signal-to-noise ratio after 12 h of data accumulation on a 250 MHz (^{1}H) spectrometer. Despite its radioactivity, the literature on ^{99}Tc is rapidly growing, since it is used for structural studies of complexes used in diagnostic nuclear medicine.

4.6.1 Chemical Shifts

The reference is NH_4TcO_4 for which Ξ = 22 508 314 Hz in D_2O. It seems that no detailed studies on the effects of solvent, concentration, and temperature have been reported, but according to its d^0 electronic structure, it may be anticipated that these effects are small. Except for Tc(0), the chemical shift ranges of the different oxidation states are more or less distinct. Tc(VII) derivatives are found between +396 and 0 ppm. Tc(V) compounds lead to the largest range, between +5500 and +806 ppm, with the exception of TcH_9^{2-} (observed at −3672 ppm). Tc(III) compounds are between

−78 and −1329 ppm, Tc(I) compounds between −1460 and −3517 ppm, and the ditechnetium carbonyls between −2477 and −2600 ppm. The total range is therefore about 9200 ppm. Theoretical interpretations have been published.[9]

4.6.2 Coupling Constants

TcH_9^{2-} provides the only example of a $^1J(^{99}Tc, ^1H)$ coupling constant, which has a value of 24 Hz. Three different $^1J(^{99}Tc, ^{17}O)$ values are known: 139.8, 131.6, and 87 Hz. Only one coupling constant with fluorine has been observed, with a value of 259 Hz. As usual, several $^1J(^{99}Tc, ^{31}P)$ values have been reported, with values between 400 and 1750 Hz, and even a two-bond phosphorus–technetium coupling constant of 40 Hz has been observed.

4.6.3 Relaxation and Linewidths

Some T_1 and T_2 measurements have been performed. A T_2 value of 0.4 s observed for $Tc_2(CO)_{10}$ corresponds to the smallest linewidth of 1.4 Hz. More usually, broad bands are obtained, with $\Delta\nu_{1/2} > 1000$ Hz, the largest one observed, for $TcOCl_4^-$, being about 20 000 Hz.

4.7 Ruthenium

This element has two active isotopes, ^{99}Ru and ^{101}Ru, both with spin $\frac{5}{2}$.[1–6] They have about the same natural abundance (12.7% for ^{99}Ru and 17% for ^{101}Ru), but they have large and different quadrupole moments: 0.079×10^{-28} and 0.457×10^{-28} m^2, respectively. ^{99}Ru has the same receptivity as ^{13}C, and that of ^{101}Ru is about twice that of ^{99}Ru. Nevertheless, it is ^{99}Ru that is usually observed, since its low quadrupole moment leads to sharper lines.

Although ^{99}Ru seems a good quadrupolar nucleus, it was, in fact, observed in solution only in 1981, by two independent groups. Since then, few studies have been published. The main difficulty arises from acoustic ringing, since the observation frequencies are relatively low.

Only Ru(0), Ru(II), and Ru(III) oxidation states are suitable for solution studies.

4.7.1 Chemical Shifts

The reference is $K_4Ru(CN)_6$ in D_2O, for which Ξ (^{99}Ru) = 4 605 152 Hz and $\Xi(^{101}Ru)$ = 5 161 369 Hz. The drawback of this reference is its large temperature dependence of 0.7 ppm K^{-1}. It should be noted that $^{39}K^+$ appears at +13 360 ppm from the reference.

The chemical shifts range from −1270 ppm for ruthenocene to +16 050 ppm for $Ru(H_2O)_6^{2+}$. These shifts are very sensitive to the chemical environment, and have been used to identify different stereoisomers. Consequently, they are dependent on concentration, counterions, and solvents, and there is a temperature coefficient of up to 1 ppm K^{-1}. A theoretical study of the chemical shifts[9] has been published, but more experiments are needed to find some rules to interpret their evolution.

4.7.2 Coupling Constants

Only three coupling constants are known in solution: $^1J(^{99}Ru, ^{17}O)$ = 23.4 Hz in RuO_4, $^1J(^{99}Ru, ^{13}C)$ = 44.1 Hz in $Ru(CN)_6^{4-}$, and $^1J(^{99}Ru, ^{119}Sn)$ = 843 Hz in $[Ru(SnCl_3)_5Cl]^{4-}$.

4.7.3 Relaxation and Linewidths

Two relaxation time studies on both ^{99}Ru and ^{101}Ru have been published. One is a determination of the ratio $^{101}Q/^{99}Q$; the second reports the variation of T_1 with temperature. Both have been done on RuO_4. An interesting study of the ligand exchange in $Ru(H_2O)_6^{2+}$, using ^{99}Ru, has been done as a function of temperature. The linewidths range from a few up to 800 Hz. They depend on temperature and the different extent of chemical exchange between the complexes and the solvents.

4.8 Lanthanum

Two isotopes are available for NMR spectroscopy.[1,2,4–6] The first, ^{138}La with spin +5, has a relatively high quadrupole moment of 0.450×10^{-28} m^2 and an extremely low natural abundance of 0.09%, and is cited here only for completeness. Its Ξ value is 13 194 267 Hz. The second, ^{139}La with spin $+\frac{7}{2}$, a natural abundance of 99.91%, and a quadrupole moment of 0.200×10^{-28} m^2, is the only isotope used in NMR.

As for scandium, the NMR interest of lanthanum is limited by its chemistry, which has mainly developed for La^{3+} ions.

4.8.1 Chemical Shifts

The reference is $La(H_2O)_n^{3+}$ in D_2O. The Ξ value of ^{139}La is 14 125 605 Hz. The observed chemical shift range is between +1090 and −772 ppm. The lanthanum cation gives solvated species or weak complexes, so that most of the reported studies are focused on the problem of outer and inner coordination spheres, which can be summarized by the equation

$$[La(H_2O)_n]^{3+} + xL^- \rightleftharpoons [La(H_2O)_{n-x}L_x]^{3-x} + xH_2O \quad (1)$$

For these samples, the lanthanum chemical shifts depend on concentration and solvent. An isotopic effect of −1.6 ppm has been observed between H_2O and D_2O solutions. Some tentative relationships between δ(La) and the nature of the ligand have been proposed.

Lanthanum complexes with proteins have been studied, and the exchange rates of ligands have been measured between 273 and 326 K and up to 200 MPa. Such equilibria have also been confirmed by 2D EXSY experiments.

To the best of our knowledge, no coupling constants are known.

4.8.2 Relaxation and Linewidths

Some relaxation time measurements have been performed and have been used for the study of exchange processes. T_1 values are usually less than milliseconds. The narrowest linewidth is 22 Hz, but usually they are in the range of 200–2000 Hz, with a maximum of 11 800 Hz.

5 THE WELL-STUDIED NUCLEI

5.1 Vanadium

With its high receptivity (D^P = 0.38), low quadrupole moment ($-0.052 \times 10^{-28}\,m^2$), and high natural abundance (99.76%), ^{51}V, with spin $+\frac{7}{2}$, is the most widely studied transition metal. Numerous reviews[1,3–6] have appeared, the most documented being that of the Hamburg group.[6,26]

Vanadium also has another NMR-active isotope: ^{50}V, with spin +6, a natural abundance of 0.24% (and therefore a very poor receptivity), a moderate quadrupole moment of $+0.210 \times 10^{-28}\,m^2$, and a Ξ value of 9 970 314 Hz for neat $VOCl_3$. This isotope has only been studied in some relaxation experiments to determine the ratio $^{50}Q/^{51}Q$. We shall now focus our attention only on ^{51}V.

5.1.1 Chemical Shifts

The universally adopted reference is neat $VOCl_3$, which has a Ξ value of 26 302 961 Hz. The observed chemical shift range is between +2375 and −2052 ppm. The ranges corresponding to the different oxidation states largely overlap, and cannot be used for oxidation state determination. Attention must be paid to neighboring nuclei: ^{63}Cu, +8080 ppm; ^{23}Na, +5660 ppm; ^{123}Te, −5060 ppm; and ^{27}Al, −9350 ppm. A summary of the chemical shifts according to the chemical nature of the molecule is presented in Figure 3.

Two classes may be distinguished: the V(V) compounds, with d^0 closed shell structure, and the other oxidation states +III, +I, 0 and −I, with d^4 or d^6 open shells.

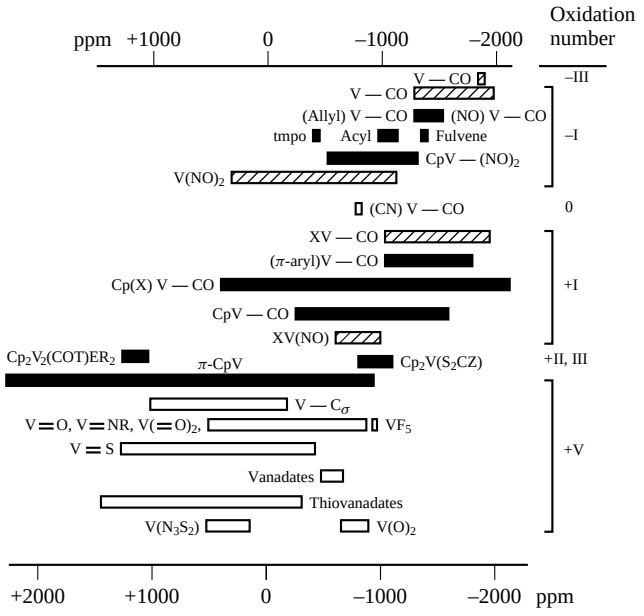

Figure 3 Chemical shift ranges of ^{51}V relative to $VOCl_3$. Open bars correspond to closed-shell d^0 and shaded bars to open-shell d^n complexes. Black bars correspond to complexes with π-bonded ligands. (Reproduced by permission of Elsevier from D. Rehder, in Transition Metal Nuclear Magnetic Resonance, ed. P. Pregosin, Elsevier, Amsterdam, 1991, Chap. 1)

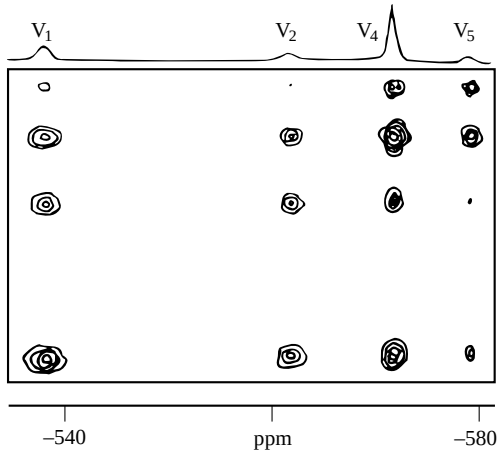

Figure 4 ^{51}V 2D EXSY NMR spectrum of a solution containing 10 mM vanadate, 1.0 M KCl, and 20% D_2O at pH 8.6. (Reproduced by permission of the American Chemical Society from D. C. Crans, C. D. Rithner, and L. A. Theisen, *J. Am. Chem. Soc.*, 1990, **112**, 2901)

The first class, V(V), comprises mainly vanadates, thiovanadates, peroxovanadates, and heterovanadates, and here ^{51}V NMR has been important in increasing the understanding of this complex chemistry. 2D COSY or EXSY experiments have been used, as shown by the example in Figure 4. The temperature effect on the chemical shifts is small, except for the cases where chemical exchange occurs. Isotope effects have been observed with $^1H/^2D$ or $^{16}O/^{18}O$ replacement, which leads to low-frequency shifts of −0.73 ppm for the former and −0.19 ppm for the latter.

The evolution of the chemical shifts according to the steric effect is not yet clear, but the electronic effect is better understood, and is related to the HOMO–LUMO splitting ΔE. The d^0 structure gives rise to what is called an 'inverse' behavior—for instance, according to the halogen effect.[9] For V(V) derivatives of biological molecules, ^{51}V NMR has been widely used.

The second class comprises all other oxidation states, which have a 'normal' behavior according to their d^4 or d^6 electronic structures. This series includes the cyclopentadienyl complexes [V(I)] and the carbonylvanadates [V(−I)]. Some V(III) complexes have been studied. Complexes of the second class have resonances that are very sensitive to temperature and isotopic substitution. Temperature coefficients of 0.3–1.5 ppm K^{-1} have been observed. The substitutions $^1H/^2D$, $^{12}C/^{13}C$, and $^{16}O/^{18}O$ lead to low-frequency shifts of −0.4 to −0.85 ppm, −0.26 to −0.5 ppm, and −0.19 ppm; these values are calculated for the substitution of one atom. The use of deuterated solvents also has an influence. All these results have been justified theoretically.[9]

5.1.2 Coupling Constants

As the relaxation processes are not very efficient, many coupling constants are known. Two coupling constants of 20.3 and 27.6 Hz are known between ^{51}V and ^1H. $^1J(^{51}V, ^{19}F)$ lies between 88 and 140 Hz; these values are temperature-dependent. $^2J(^{51}V, ^{19}F)$ = 10.3 Hz in $V(PF_3)_6^-$. $^1J(^{51}V, ^{14}N)$ ranges from 92 to 112 Hz. Using ^{17}O NMR on 5% ^{17}O-enriched compounds, $^1J(^{51}V, ^{17}O)$ has been found between

31 and 64 Hz. The greatest number of coupling constants have been measured with phosphorus, and range from 70 to 655 Hz. They have been discussed in detail.[26] An interesting relationship has been proposed between $^1J(^{51}V, ^{31}P)$ in η^5-$(C_5H_5)V(CO)_3PR_3$ and the isotropic ESR hyperfine coupling constant with ^{57}Fe in $Fe(NO)_2(PR_3)Br$.

Other one-bond coupling constants are known: $^1J(^{51}V, ^{13}C)$ = 116, 124.5 and 139 Hz in carbonyl derivatives, $^1J(^{119}Sn, ^{51}V)$ = 900 Hz in $VCp(SnCl_3)(CO)_3^{2-}$, and $^2J(^{183}W, ^{51}V)$ = 11 Hz in $(VW_5O_{19})^{3-}$.

5.1.3 Relaxation and Linewidths

There are few direct relaxation measurements apart from those used in conjunction with the observation of ^{50}V. Relaxation times are usually deduced from linewidth measurements.

As ^{51}V has a small quadrupole moment, the linewidths are narrow compared with those of most quadrupolar nuclei. $\Delta\nu_{1/2}$ ranges from 5 to more than 3000 Hz, but values are usually between 100 and 500 Hz. The quadrupolar relaxation mechanism is always dominant. It depends on the symmetry around the vanadium atom, but also on the ligand strength or the bulkiness of the ligands.

Vanadium is the best suited quadrupolar transition metal nuclei for NMR study.

5.2 Cobalt

The description here of ^{59}Co NMR is just a short summary, because this nucleus has the largest published literature among the quadrupolar transition metals. Its well-developed chemistry of complexes, especially of octahedral Co(III), is a part of the reason for this.[1–6,15]

Even with its relatively large quadrupole moment of 0.420 $\times 10^{-28}$ m^2, attenuated by the factor $(2I + 3)/I^2(2I - 1)$ = 0.163 for its spin $+\frac{7}{2}$, its high receptivity (one-third that of ^1H), and its large chemical shift range of 18 000 ppm, ^{59}Co NMR is of great interest for the chemist. Historically, it was also one of the first observed nuclei, and allowed the discovery of the chemical shift effect.

5.2.1 Chemical Shifts

^{59}Co has the largest chemical shift range of all the Periodic Table. It is then sensitive to all the small influences that a nucleus may experience from its substituents and from its surrounding. The recognized reference is $K_3Co(CN)_6$ in H_2O, for which the Ξ value is 23 727 072 Hz, a value that is dependent on temperature, pressure, and concentration. Because of the large chemical shift range, it is sometimes useful to have a secondary reference. This is often $Co(acac)_3$, for which the proposed equivalence is $\delta[Co(CN)_6^{3-}] = \delta[Co(acac)_3] + 12500$ ppm.

As cobalt is very sensitive to subtle chemical change, and as its chemical shift range is very large, an error of a few ppm is not often chemically significant. All these chemical shifts are solvent-dependent; for instance, an effect of 200 ppm is observed for $Co(acac)_3$ in different solvents. They are also highly temperature-dependent. A coefficient of -1.38 ppm K^{-1} has been observed for $K_3Co(CN)_6$, but this effect may be larger, and can reach values of -3 ppm K^{-1} with $Co(acac)_3$. Concentration has a 'reduced' influence: 20 ppm for the reference between 0.1 and 0.3 M in H_2O. It is clear that such a sensitivity leads to an isotopic effect. From $Co(NH_3)_6^{3+}$ to $Co(ND_3)_6^{3+}$, an effect of 5.6 ppm/D is observed. Isotopic shifts have also been reported between normal and deuterated solvents: -1.05 ppm H_2O/D_2O or -2 ppm CH_3OD/CD_3OD for $K_3Co(CN)_6$.

Co(III) complexes are found at high frequency, most of them between +13 000 and +2000 ppm, with the remarkable exception of the reference $K_3Co(CN)_6$. Co(I), Co(0), and Co(−I) are found at lower frequencies, generally below 2000 to −4500 ppm. The ranges of the different oxidation states overlap. A large database of observed chemical shifts has been developed by Yamasaki.[27] Several laboratories have examined the cobalt resonances in tetrahedral carbonyl clusters MCo_3 (with M = Co, Fe, Ru), which are found between 0 and −3000 ppm.

Since the beginning of NMR, the chemical shifts of cobalt have been the subject of intensive theoretical studies.[9] Linear correlations have been interpreted between $\delta[^{59}Co(III)]$ and the lowest d–d transition energy ΔE. The introduction of the nephelauxetic effect allowed Juranic to find a good linear correlation between $\delta(^{59}Co)$ and ΔE.[9] Other relations have been found between δ(Co) and catalytic activity, the relative percentage of isomers in the catalysis product, reaction temperature, and electrochemical data. Lower oxidation states have a $3d^{10}$ electronic structure, and their ΔE values are larger. Consequently, they are less sensitive to chemical changes and have a narrower chemical shift range.

The high sensitivity of cobalt chemical shifts allows determination of the relative abundance of isomers in mononuclear complexes or in clusters (Figure 5). Biological complexes have been studied, among them vitamin B_{12}.

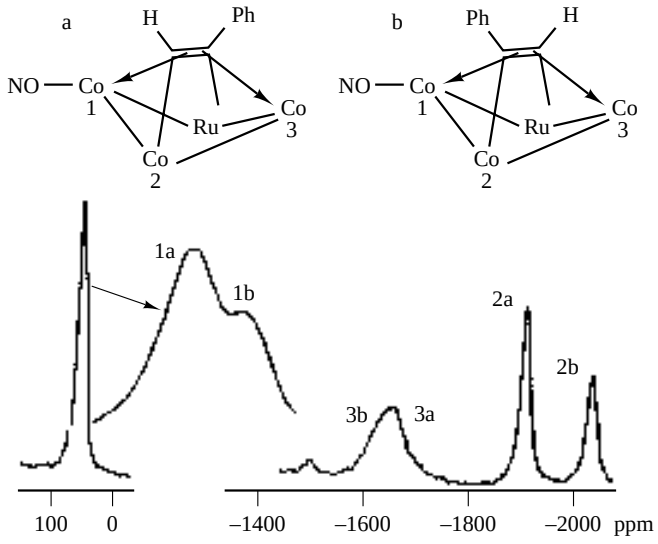

Figure 5 ^{59}Co NMR spectrum of the two isomers of $RuCo_3(CO)_9(NO)(\mu_4\text{-}\eta^2\text{-HC=CPh})$. (Adapted with permission of the Royal Society of Chemistry from P. Braunstein, F. Y. Jiao, J. Rosé, P. Granger, F. Balegroune, O. Bars, and D. Grandjean, *J. Chem. Soc., Dalton Trans.*, 1992, 2543)

5.2.2 Coupling Constants

Only a few coupling constants are known, since they are usually small and hidden by the linewidths. $^1J(^{59}Co, ^{19}F)$ is unknown, since $(CoF_6)_3^-$ is paramagnetic. $^1J(^{59}Co, ^{13}C)$ = 126 Hz in $K_3Co(CN)_6$ and 287 Hz in $NaCo(CO)_4$. $^1J(^{59}Co, ^{31}P)$ = 1222 Hz in $KCo(PF_3)_4$ and between 447 and 840 Hz in phosphine tetrahedral clusters.

5.2.3 Relaxation and Linewidths

The linewidths range from a few hertz to several kilohertz at the limit of detectability. The widths are related to the symmetry around the cobalt atom, and allow distinction between isomers. They have also been used for solvation studies.

There are a few relaxation time measurements. The $Co(CN)_6^{3-}$ ion has been investigated by several authors. It seems that the origin of the relaxation in this molecule comes from perturbation of the electric field by the asymmetric vibrational modes. For large linewidths, the quadrupolar mechanism is exclusively dominant, but this is not always the case for complexes with long relaxation times. Spin–rotation or scalar mechanisms may be sometimes involved. On high-field spectrometers, the relaxation mechanism arising from the large chemical shift anisotropies has been found to play a role.

5.3 Molybdenum

Two isotopes, ^{95}Mo and ^{97}Mo with spins $-\frac{5}{2}$, and natural abundances of 15.72% and 9.46%, respectively, are NMR-active. Having the higher sensitivity (about three times that of ^{13}C) and the lower quadrupole moment ($-0.022 \times 10^{-28}\,m^2$), ^{95}Mo is the preferred observed isotope. ^{97}Mo, having a large quadrupole moment of $0.255 \times 10^{-28}\,m^2$ and a Ξ value of 6 673 711 Hz, gives broad bands and is sometimes used in relaxation studies. A large number of results have been published and have been summarized in books[1–7] and in an excellent review.[12]

5.3.1 Chemical Shifts

The definitively adopted reference is Na_2MoO_4 in a 2 M solution at pH 11, for which Ξ = 6 516 942 Hz. At pH < 9, the lines become broader—first by chemical exchange with protons and then by polycondensation processes that give rise to a second broad band. Chemical shifts range between +4200 to −3000 ppm, and the domains corresponding to the different oxidation states largely overlap.

Mo(VI) derivatives are observed between +3200 and −620 ppm. Molybdates and polyoxymolybdates have been widely studied, as their sulfur analogs or their mixtures. A detailed review may be found elsewhere.[11,12] All these compounds have resonances that are not very sensitive to concentration, temperature or solvents, since they have d^0 electronic structures.

Mononuclear complexes of Mo(V) are paramagnetic, and are not observed, but the dimers are diamagnetic, and some chemical shifts have been reported, lying between +320 and +985 ppm. Their d^1 structure leads to a high sensitivity to the chemical environment.

Only a few results have been published on Mo(IV), and are mainly devoted to $Mo_3O_4L_9$. Consequently, the known chemical shift range is limited to between 1165 and 990 ppm. As for Mo(V), only dimers are observed for Mo(III) species, which have resonances between 3700 and 2400 ppm.

A large number of Mo(II) complexes have been studied. The surprising characteristic is that mononuclear species have chemical shifts that fall between +315 and −2100 ppm. The dimeric species are among the most deshielded molybdenum nuclei, and have resonances between +3200 and 4150 ppm. In this series, carbonyl and isocyanide complexes are the most studied compounds.

Mo(I) derivatives have resonances between −1856 and +182 ppm, and Mo(0) compounds have been widely studied and have molybdenum chemical shift ranges from −860 to −2130 ppm for the carbonyl derivatives and between +2270 to −1585 ppm for the other species. Mixed metal complexes $Cp(CO)_2LMoHgX$ have molybdenum resonances in the range −1700 to −1940 ppm. Although most molybdenum derivatives have a normal halogen effect, some Mo(VI) derivatives have an inverse behavior. As molybdenum has many electrons, only approximate theoretical calculations have been performed, which can be used to interpret the observed resonances.[9] Although for some series, the dependence on ΔE is verified, this is not always the case.

Molybdenum chemical shifts are sensitive to the isomerism of chiral centers when the linewidths are not too large. They have also been used to follow reactions and to analyze mixtures, and are now used for the study of the role of molybdenum in enzymes.

5.3.2 Coupling Constants

A large number of $^{95}Mo–^{31}P$ coupling constants are known, especially in Mo(0) complexes. Their values range between 117 and 290 Hz, phosphine ligands having the lowest values. Coupling constants with other nuclei are rare. One $^1J(^{95}Mo, ^1H)$ = 15 Hz, one $^1J(^{95}Mo, ^{19}F)$ = 48 Hz, one $^2J(^{95}Mo, ^{19}F)$ = 14 Hz, and one $^1J(^{95}Mo, ^{17}O)$ = 40 Hz are known. Several coupling constants, ranging between 39 and 46 Hz, have been observed between ^{95}Mo and ^{14}N. Using ^{13}C NMR, a $^1J(^{95}Mo, ^{13}C)$ = 68 Hz has been measured.

5.3.3 Relaxation and Linewidths

Several T_1 studies have been performed on both isotopes, mainly for the comparison of quadrupole moments. Except perhaps in some rare cases, such as $Mo(CO)_6$, where T_1 = 7 s, the quadrupolar relaxation is dominant and explains the evolution of the observed linewidths according to the symmetry around the molybdenum atom.

6 LANTHANIDES

Apart from ytterbium isotopes and thulium, all NMR-active lanthanides are quadrupolar nuclei, but most exist only in a paramagnetic state, and are not observed in solution. Some are used as paramagnetic shift reagents.

The only lanthanides giving diamagnetic species are ytterbium and lutetium. The former has been observed in solution using its spin-$\frac{1}{2}$ isotope ^{171}Yb. To the best of our knowledge, the quadrupolar isotope ^{173}Yb has never been observed

in solution. Lutetium has two active isotopes. ^{176}Lu has a low natural abundance of 2.6%, a relatively low Ξ value around 8097 kHz, and a very large quadrupole moment of 5×10^{-28} m^2. The second isotope, ^{175}Lu, has a larger natural abundance of 97.4%, a higher resonant frequency Ξ = 11 430 kHz, but a large quadrupole moment of 3.5×10^{-28} m^2. These large quadrupole moments have precluded observations.

Some other lanthanides have been observed, but only in the solid state and at low temperature.

7 ACTINIDES

These are all radionuclides, and hence require special equipment for their measurement. The only actinide observed in solution is ^{235}U. Despite its large quadrupole moment of 4.936×10^{-28} m^2, ^{235}U, with a spin $-\frac{7}{2}$ has been observed in neat liquid on a 93.5% enriched sample and on a natural sample at 380 K.[28] The Ξ value found is 1841 kHz, and the linewidth of 20 kHz proves the efficient quadrupolar relaxation.

Relaxation measurements of ^{19}F in UF_6 at different temperatures and different frequencies allow an estimation of $^1J(^{235}\text{U}, ^{19}\text{F})$ = 4000 Hz. Other studies have been performed in the solid state.

Several other actinides are potentially of interest. ^{239}Pu, with spin-$\frac{1}{2}$, has been subject to some experiments in the solid state. The others; ^{227}Ac ($\frac{3}{2}$), ^{231}Pa ($\frac{3}{2}$), ^{237}Np ($\frac{5}{2}$), ^{241}Am ($\frac{5}{2}$), and ^{243}Am ($\frac{5}{2}$), are produced at a chemical level, and may be used to prepared samples for NMR experiments. The drawback of these nuclei is, as for ^{235}U, their large quadrupole moments of around 4.5×10^{-28} m^2 and their low or very low Ξ values.

8 CONCLUSIONS

Although quadrupolar nuclei are handicapped by their quadrupole moments, this article has shown that at least half of them can be of a considerable interest for the chemist. The availability of stronger magnetic fields will improve the observability of these nuclei—not only by the consequent large increase in sensitivity but also by the fact that on high-field instruments chemical shifts expressed in hertz increase and linewidths remain approximately constant. The result is an increase in resolution. It appears likely that the use of very high fields is the future direction for studies of quadrupolar nuclei to take. As resonances are broad, accurate shimming is not necessary, and these nuclei are less demanding on magnet quality. Because of the large chemical shift range of most of these nuclei, pulse methods may become difficult to use, and new spectroscopic means may have to be found.

9 RELATED ARTICLES

Chemical Exchange Effects on Spectra; Inorganic Nuclei: Low Sensitivity Transition Metals; Nuclear Spin Properties and Notation; Nutation Spectroscopy of Quadrupolar Nuclei; Organometallic Compounds; Quadrupolar Interactions; Quadrupolar Nuclei in Liquid Samples; Quadrupolar Nuclei in Solids; Quadrupolar Nuclei in Liquid Samples; Relaxation of Quadrupolar Nuclei Measured via Multiple Quantum Filtration; Relaxation Theory for Quadrupolar Nuclei; Vanadium Catalysts: Solid State NMR.

10 REFERENCES

1. R. K. Harris and B. E. Mann, *NMR and the Periodic Table*, Academic Press, London, 1978.
2. C. Brevard and P. Granger, *Handbook of High Resolution Multinuclear NMR*, Wiley, New York, 1981.
3. P. Laszlo, *NMR of Newly Accessible Nuclei*, Academic Press, London, 1983, Vol. 2.
4. J. Mason, *Multinuclear NMR*, Plenum Press, New York, 1987.
5. T. Drakenberg, in *Annual Reports on NMR Spectroscopy*, ed. G. A. Webb, Academic Press, London, 1986, Vol. 17, p. 231.
6. P. S. Pregosin, *Transition Metal Nuclear Magnetic Resonance*, Elsevier, Amsterdam, 1991.
7. D. Rehder, *Chimia*, 1986, **40**, 186.
8. J. Mason, *Chem. Rev.*, 1987, **87**, 1299.
9. N. Juranic, *Coord. Chem. Rev.*, 1989, **96**, 253.
10. B. E. Mann, in *Advances in Organometallic Chemistry*, eds. F. G. A. Stone and R. West, Academic Press, London, 1988, Vol. 28, p. 397.
11. G. Wu and R. E. Wasylishen, *Magn. Res. Chem.*, 1993, **31**, 537.
12. M. Minelli, J. H. Enemark, R. T. C. Brownlee, M. J. O'Connor, and A. G. Wedd, *Coord. Chem. Rev.*, 1985, **68**, 169.
13. A. Hafner, L. S. Hegedus, G. de Weck, B. Hawkins, and K. H. Dötz, *J. Am. Chem. Soc.*, 1988, **110**, 8413.
14. M. F. A. Dove, E. M. Lloyd Jones, and R. J. Clark, *Magn. Res. Chem.*, 1989, **27**, 973.
15. R. Benn and A. Rufinska, *Angew. Chem., Int. Ed. Engl.*, 1986, **25**, 861.
16. R. Benn and A. Rufinska, *Magn. Res. Chem.*, 1988, **26**, 895.
17. H. Nakatsuji, K. Kanda, K. Endo, and T. Yonezawa, *J. Am. Chem. Soc.*, 1984, **106**, 4653.
18. A. R. Siedle, R. A. Newmark, W. B. Gleason, and W. M. Lamanna, *Organometallics*, 1990, **9**, 1290.
19. M. A. Fedotov and V. A. Likholobov, *Izv. Akad. Nauk. SSSR, Ser. Khim.*, 1984, 1917 (*Chem. Abstr*., 101/162447).
20. D. Rehder and W. Basler, *J. Magn. Reson.*, 1986, **68**, 157.
21. A. Hafner, R. O. Duthaler, R. Marti, G. Rihs, P. Rothe-Streit, and F. Schwarzenbach, *J. Am. Chem. Soc.*, 1992, **114**, 2321.
22. H. Nakatsuji and T. Nakao, *Chem. Phys. Lett.*, 1990, **167**, 571.
23. H. Brunner, G. Gehart, W. Meier, J. Wachter, B. Wrackmeyer, B. Nuber, and M. L. Ziegler, *J. Organomet. Chem.*, 1992, **436**, 313.
24. M. Sugimoto, M. Kanayama, and H. Nakatsuji, *J. Phys. Chem.*, 1992, **96**, 4375.
25. M. Findeisen, B. Lorenz, and M. Wahren, *Isotopenpraxis*, 1990, **26**, 520.
26. D. Rehder, *Bull. Magn. Reson.*, 1982, **4**, 33.
27. A. Yamasaki, *Anal. Chim. Acta*, 1981, **133**, 741.
28. H. Le Bail, C. Chachaty, P. Rigny, and R. Bougon, *J. Phys. Lett. (Orsay, Fr.)*, 1983, **44**, L1017.

Biographical Sketch

Pierre Granger. *b* 1936. Chemical Engineer, 1961, Doctorat, 1969 (supervisor Professor Barriol), ENSIC, Nancy, France. Professor at University of Rouen, 1975–85. Now Professor at University of Strasbourg. Approx. 100 publications. Area of interest: NMR of 'exotic' nuclei in solutions and in the solid state.

Reactions in Zeolites

Tom M. Apple

Rensselaer Polytechnic Institute, Troy, NY, USA

1	Introduction	1
2	Reactions of Olefins	1
3	Reactions of Alcohols	3
4	Coking	6
5	Related Articles	6
6	References	6

1 INTRODUCTION

Zeolites are crystalline aluminosilicates composed of tetrahedra of oxygen anions which surround either a Si^{4+} or Al^{3+} cation. These tetrahedra are arranged such that each oxygen is shared by a neighboring aluminum or silicon atom. Due to an overall stoichiometry of two oxygen anions per tetrahedral center, a net charge of -1 accrues for each aluminum in the zeolite lattice. This negative charge is compensated for by a cation, most commonly a proton or a metal ion of Group IA or IIA. The nature of the cation influences the strength of the acid/base properties of the zeolite.

A great deal of the interest in zeolites stems from the strong Brønsted acidity of the hydrogen forms. Two very important processes are currently carried out over acidic zeolites, the cracking of petroleum and the conversion of methanol to gasolines (MTG process). Petroleum cracking is carried out over hydrogen forms of the faujasite zeolite Y, a medium-pore zeolite comprised of cages with a 1300 pm diameter. Access to these cages is provided by tetrahedrally arranged windows having diameters of 740 pm. Much of the NMR work dealing with the chemistry of olefins is, in part, motivated by the need for a better understanding of the mechanisms of petroleum cracking. The MTG process provides an alternative source of gasoline from methanol, which can be obtained from synthesis gas, itself a product of coal gasification. The MTG process is a relatively recent discovery.[1,2] It is carried out over the acidic form of the zeolite ZSM-5, a pentasil zeolite having two types of slightly elliptical intersecting channels, one straight and the other sinusoidal. The channel cross-sections are 530 pm by 560 pm and 510 pm by 550 pm respectively. Where the channels intersect a larger void region results.

While both of the above catalytic processes rely on the acidic nature of the zeolites involved, they are also facilitated by the molecular sieving properties of the zeolites. The size and shape of the channels and cages leads to several types of shape selectivity, reactant selectivity, product selectivity, and selectivity caused by restriction at the active site of catalysis.

Most NMR studies of reactions in zeolites have involved the reactions of olefins or alcohols. A prime concern has been the manner in which the acid (or base) properties of the zeolites affect the intermediates and products of these reactions. Shape-selective aspects of the catalysis, particularly those relating to the MTG process, have also been intensely studied by NMR. With time, olefin and alcohol reactions are accompanied by coking of the catalyst. The formation of coke deposits during reaction has been the focus of several NMR studies. This review will focus primarily on these areas. NMR studies dealing strictly with adsorption into zeolites will not be addressed in this article.

2 REACTIONS OF OLEFINS

While many techniques can be applied to study product distributions over catalysts, very few have the capability of probing the chemistry within a zeolite catalyst. Such internal monitoring provides direct evidence for shape selectivity as well as information on the nature of the adsorbed intermediates in a chemical process. NMR is becoming a very powerful tool for obtaining this type of information.

One of the earliest studies of olefin reactions in zeolites involved low-resolution ^{13}C NMR spectra of ethylene reacting over H–ZSM-5.[3] At room temperature immobile polymeric paraffins were evident. When water was added, and the sample heated to 573 K, lighter olefins and paraffins were observed as a product of cracking of the polymeric material.

Van den Berg et al.[4] applied ^{13}C NMR to the study of a number of adsorbed olefins on H–ZSM-5. These authors adsorbed ethylene, propene, isobutene, and 2-methyl-1-butene at room temperature. The ^{13}C NMR spectra revealed that at 300 K a majority of linear oligomers were formed over the catalyst for all of the adsorbates studied. The average chain length decreased in the series $C_2H_4 \gg C_3H_6 > i\text{-}C_4H_8 >$ 2-methyl-1-butene. Some small amounts of branched hydrocarbons were observed with ethylene and isobutene. When ethylene was adsorbed into H–ZSM-5 at 373 K a significant amount of branching occurred and the average chain length decreased. When this reaction was performed over H–mordenite the products were highly branched. The formation of primarily linear chains in H–ZSM-5 was attributed to restrictions due to the pore dimensions. The authors proposed that branched oligomers originally formed at channel intersections and were then linearized through isomerization reactions. The larger pores of the mordenite allowed for branched species.

Zardkoohi et al.[5] studied the reaction of propene labeled with ^{13}C at the 2-site over both normal and ultrastable (Si/Al = 4) H–Y zeolite. In this work it was assumed that carbons scrambled via a cyclopropane intermediate prior to oligomerization. Cross polarization with magic angle spinning (CP MAS) was used to acquire the spectra. A peak at 250 ppm was assigned to formation of a carbenium ion $CH_3C^+HCH_3$. Olah's work[6] with superacids had shown that stationary secondary carbocations should resonate between 300 and 330 ppm. The carbenium ion proposed in this work interacts with zeolitic oxygen, and, because of the typical 80 ppm shift to low frequency (upfield) of oxygenated species such as RC^+OH relative to RC^+R moieties, the shift of 250 ppm was deemed a reasonable one for such a species. The methyl groups associated with the isopropyl cation should resonate at 48 ppm, but this area was obscured by peaks due to oligomers. The authors proposed the following mechanism (Scheme 1):

A peak at 160 ppm was assigned to a dynamic equilibrium between carbons in an ethyl isopropyl carbenium ion and a methyl isobutyl carbenium ion. This resonance position is an

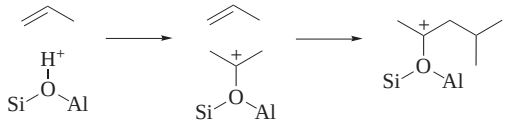

Scheme 1

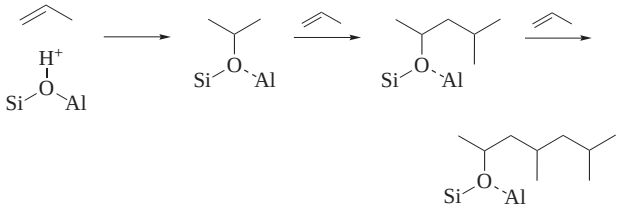

Scheme 2

average of a resonance at 330 ppm due to the carbenium ion and one at 60 ppm due to the methylene. The average value of 195 is consistent with the observed value of 160 ppm if one again considers the low-frequency shift induced by the framework oxygen. A peak also appeared at 70 ppm which was assigned to the carbon at the β position relative to the carbenium center.

Intense peaks at 40 ppm and 30 ppm were assigned to methylene and methyl groups respectively from oligomeric species and carbocations. The intensity of these peaks was higher in H–Y than in the ultrastable H–Y sample due to the blocking of pores by detrital aluminum species in the ultrastable H–Y.

In later work by this group[7] an apparatus called CAVERN (cryogenic adsorption vessel enabling rotor nestling) was employed for adsorption studies. Propene samples labeled at the 1-, 2-, and 3-positions gave different spectra on H–Y. As a result, label scrambling was not present as had been presumed in their previous study. When [2-^{13}C]propene was adsorbed, signals were observed at 250, 143, and 87 ppm. Both single pulse Bloch decays and CP MAS spectra were employed in this study. Signals in the aliphatic region and those of unreacted propene had T_1 values of approximately 80 ms, while the peak at 87 ppm had a T_1 of 2–3 s. The short T_1 values indicated mobile species while the longer T_1 was indicative of a more strongly bound species. In experiments of this type Bloch decays are more quantitative, since they do not depend upon efficiency of magnetization transfer between carbons and protons. In the Bloch decays the size of the signal at 87 ppm was greatly reduced, comprising only about 2% of the spectral intensity. Carbon-13 $T_{1\rho}$ values were equal to 5–10 ms for all species. The CAVERN was loaded and spectra were recorded at temperatures from 213 to 293 K. At 213 K very little propene had reacted. At 253 K the oligomer peak appeared. At 263 K about one-third of the propene had reacted and peaks at 87 and 140 ppm were now evident. At 273 K there was 70% conversion with increasing intensity at 87 and 140 ppm.

The peak at 87 ppm had been previously assigned to those carbons adjacent to the nonequilibrating carbenium ions, which resonated at 250 ppm. However, there was no peak observed at 250 ppm in this series of spectra; therefore, the assignment of the peak at 87 ppm to carbons adjacent to the cation had to be abandoned. A reasonable alternative explanation was to assign the resonance to an alkoxy (alkyl silyl ether) species bound to a zeolite lattice oxygen atom. The peak at 140 ppm was assigned to olefinic carbon atoms of oligomeric species. At room temperature there was complete conversion, and a peak at 250 ppm appeared, which was assigned to a carbocation. When 1-propene was used, two major changes were exhibited: no peak at 87 ppm was observed and, secondly, the aliphatic region extended further to low frequency (indicating a greater contribution of methyl groups). Thus, the carbon atoms in the 1-position ended up in more methyl groups than carbon atoms at the 2-position. No scrambling of label was observed. The authors proposed the following mechanism (Scheme 2) to explain these observations:

Upon adsorption, propene forms an alkoxy species. This is followed by Markovnikow addition of a second propene prior to cleavage of the alkoxy. A third propene adds, followed by cleavage, to form a disubstituted olefin. Probable rearrangement of the olefin to more stable olefins occurs in the acidic environment of the zeolite.

This mechanism relied heavily on the assignment of the peak at 87 ppm to the alkoxide. To support this assignment the authors noted that the intensity of this peak did not correlate at all with the peak at 250 ppm assigned to the carbocation. Also, upon exposure of the sample to moisture, there was a loss of intensity of the resonance at 87 ppm and formation of a peak at 67 ppm. A peak at 67 ppm is consistent with secondary ethers or alcohols having the hydroxyl group in the 2-position, but not from primary or tertiary alcohols. The expected product from the alkoxide would be an alcohol with the hydroxyl group in the 2-position. The peak at 67 ppm survived interrupted decoupling of 50 μs, while that at 87 ppm did not. This suggested that the species resonating at 87 ppm was an immobilized, protonated carbon. The peak at 87 ppm was never observed with 1- or 3-propene. This finding rules out a long-lived carbocation which would surely scramble. The shift of this peak was about 20 ppm to high frequency from that expected for an alkyl silyl ether. However the presence of a nearby Al atom and the incipient carbocation nature of the species may explain the high-frequency shift. Low-temperature experiments confirmed that propene itself was mobile in the zeolite at low temperatures and could diffuse to form alkoxy intermediates.

The assignment of the peak at 250 ppm to a nonequilibrating carbocation, is now believed to be incorrect. The interaction between the carbocation and the zeolitic oxygen atom is apparently so strong that an alkoxy is formed. For a long-lived carbocation to exist in the zeolite it cannot interact with an oxygen atom and must be stabilized in some way. The authors suggested that olefins are formed, and then undergo hydride abstraction and cyclization, as is observed in the conjunct polymerization of alkenes. In this process alkanes are formed at the expense of hydrogen from the olefins, which in turn are converted into alkyl cyclopentenyl cations. The proposed cations contain carbons that should resonate at 249 and 158 ppm.[8,9] If this assignment is correct there should be a correlation between intensity at 158 ppm and 250 ppm. Careful examination of their spectra show this to be the case. The peaks appear at a roughly 2:1 intensity ratio as expected. The same alkoxy intermediate was observed by Aronson et al.[10] (see below) upon adsorption of 2-methyl-2-propanol on HZSM-5.

Later work by the Haw group[11] involved studies of samples prepared at 298 K by adsorbing both 1- and 2-labeled propene. The samples were then heated in situ to 503 K. After heating, the low-frequency region showed many highly resolved resonances indicative of small mobile species. Resonance shifts and *J* couplings allowed the identification of isopentane, isobutane, 2,3-dimethylbutane, and propane. The high-temperature spectra of 1- and 2-labeled samples are identical, indicating scrambling of the labels. This is consistent with carbocation mechanisms proposed for high-temperature cracking reactions.[12] The hydrogen necessary for formation of the alkanes from the olefins comes about by coke formation. Coke is observed by CP MAS as a peak between 120 and 140 ppm.

The alkylation of isobutane with 1-butene in LaNaY zeolite was studied by ^{13}C CP MAS NMR.[13] During the initial feed, all of the butene was consumed and the products were comprised primarily of a mixture of isoalkanes. In the second stage the butene conversion dropped to about 40% and the product distribution changed drastically to isoalkenes, indicating that in the early portion of the reaction the isobutane was being alkylated by the olefin. In the latter stage, however, the olefin was oligomerizing. At higher temperatures the product distributions shifted to lower molecular weights as a result of more pronounced contributions from cracking reactions. Above 220 °C aromatics began to appear.

Butadiene reactions on H–Y and H–ZSM-5 were studied by ^{13}C MAS NMR.[14] Bloch decays were used to probe mobile species whereas CP MAS was used for immobile molecules. Butadiene oligomerizes by primarily 1,4-addition upon adsorption on H–ZSM-5. 1,4-Addition accounts for most of the oligomer in H–Y as well, although 1,2-addition was a minor contributor. As the reaction proceeded there was a loss of intensity in the olefinic region and a corresponding increase in the aliphatic region due to cyclization. These subsequent reactions were zeolite-dependent. In H–Y the linear product underwent cyclization to form fused rings, while isolated rings were formed in H–ZSM-5. Branching reactions and 1,2-enchainment resulted in oligomers with a large methyl group content in H–Y. The 1,4-addition reactions, followed by cyclization, result in pore blockage and catalyst deactivation. No reactive intermediates or carbenium ions were observed.

The Haw group[15] adsorbed acetylene on H–Y and HZSM-5 zeolite. At room temperature no reaction was observed. Upon heating to 473 K, however, two major resonances appeared under CP MAS conditions at 143 and 107 ppm, along with peaks from aliphatic and aromatic carbons (tar). The fact that these reactions were not occurring in the gas phase was confirmed by attempting the reaction over NaY. The authors suggested the species analogous to those observed by Chin and Ellis[16] on alumina (**1**). Reaction of this sample with water in

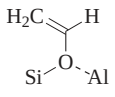

(1)

the atmosphere produced acetaldehyde. Further heating in atmosphere eventually resulted in acetic acid. Control experiments involving acetylene and water produced tars with a highly paraffinic nature. The hydrogen source for these tars appears to be water. In fact, the amount of tar formed could be correlated with the degree of hydration of the zeolite. Interrupted decoupling experiments at low and high temperature indicated that the adsorbed species probably undergoes rotation about its O–C bond at 298 K.

The reaction of ethylene over a series of cocation-exchanged Ru–Y zeolites was studied.[17] At room temperature ethylene was converted to ethane and butane on the timescale of days. 2-Butenes appear to be intermediates in the reaction. Coadsorption of hydrogen led to an increase in the initial rate, which was roughly first order with respect to hydrogen. The rate of reaction of ethylene was strongly dependent upon the cocation in the order Ru–H–Y > Ru–Ca–Y > Ru–NaY. At intermediate temperatures isomerization of butane to isobutane occurred presumably at acid sites. Above 623 K, carbon–carbon bond cleavage caused methane to be the only detectable product.

Methyl halides were found to convert to hydrocarbons over a large number of faujasite zeolites.[18] Upon adsorption of methyl iodide onto Cs–X a zeolite-bound methoxy species was formed. This species appears at 58 ppm. The assignment of this resonance was proven unequivocally by several NMR methods, including interrupted decoupling, slow MAS, and rotational resonance. Chemical verification was achieved by interacting the adsorbate with water to produce the corresponding alcohol. Ethyl iodide forms the corresponding framework-bound ethoxy species with resonances at 68 and 17 ppm. These peaks also passed all of the criteria for assignment to framework-bound species.

At higher temperatures, both the surface methoxy and the surface ethoxy groups were converted to ethylene, and subsequently to aliphatic moieties. Ethylene did not convert to aliphatic species in the absence of the alkyl iodides over these catalysts. Evidently this conversion of ethylene to aliphatics was catalyzed by HI which was released upon formation of the alkoxy from the alkyl halide.

Methyl chloride and methyl bromide also react in an analogous manner to methyl iodide; however, the concentration of methoxy groups and the reactivity to hydrocarbon synthesis was in the order $CH_3I > CH_3Br > CH_3Cl$. This order of reactivity is as expected for S_N2 reactions based upon the leaving group ability. One may consider the reaction of methyl halide with the zeolite as attack on the carbon by the nucleophilic oxygen atom of the zeolite lattice, resulting in displacement of the halogen. The basicity of a zeolite increases with the size of the cation. The activity of this reaction should, therefore, increase with increasing size of the cation.

The effect of cation nature on the reaction was investigated. Different cations affected both the activity and the selectivity of the catalysts. NaX was the most active, while K–X and Rb–X were less active than Cs–X. H–X was very unreactive, indicating that activity is not due to acidity. With the exception of NaX, the activities were in line with those predicted by consideration of zeolite basicity. Rb–X was unique in that it showed a high selectivity for olefin and aromatic products. Small shifts in the methyl resonance as a function of the cation were observed. These shifts correlated with activity of the catalyst: the higher the resonance frequency, the more active the catalyst. Cesium-133 NMR showed that the adsorbates interact with the cation sites and that this interaction may be significant in affecting catalyst activity. The framework also affected catalyst activity in the order Cs–X > Cs–Y > Cs–ZSM-5.

3 REACTIONS OF ALCOHOLS

NMR has been used extensively to investigate the mechanism of formation of the first carbon–carbon bond in the MTG process. Direct evidence for two types of shape selectivity have been revealed by NMR: product selectivity and active site selectivity.

A study of methanol and ethanol conversion over H–ZSM-5 was undertaken using ^{13}C NMR without MAS.[19] The NMR results were compared with those from gas chromatography. Below 250 °C there was nearly complete conversion of methanol to dimethyl ether. When the temperature was raised to 300 °C there was a loss of intensity in the ether range and an increase in $-CH_2-$ and $-CH_3$ resonances. With increasing temperature these peaks shifted to high frequency, indicative of formation of branched chains on aromatic residues. The aliphatic to aromatic ratio of the initially low-temperature adsorbed methanol was 5:1, while a fresh dose of methanol converted directly at 350 °C yielded a ratio of 2:1. It therefore appears that there is competition between aliphatic and aromatic product, rather than a sequential change from aliphatic to aromatic moieties.

Ethanol adsorption at 150 °C yielded diethyl ether. Between 150 and 250 °C an olefinic peak appeared and was assigned to ethylene. Above 250 °C the olefinic peak diminished and an aliphatic resonance formed between 14 and 23 ppm. No distinct aromatic peaks were visible. The authors proposed mechanisms involving carbenium ions.

Carbon-13 NMR studies of methanol on a germanic, near-faujasite zeolite[20] showed that methanol reversibly yielded dimethyl ether. Greater conversion occurred at higher temperatures. No other products were observed on the faujasite. Following prolonged heating at 300 °C, a broader resonance appeared underneath that for dimethyl ether (DME) near 60 ppm. This peak was attributed to surface methoxy formation. Peaks due to aldehydes were observed at 193 ppm during reaction of methanol on H–ZSM-5 in the presence of CO.[21] It was proposed that this signal derives from incorporation of CO via a carbenium ion mechanism.

Carbon-13 CP MAS NMR was used to study the carbonaceous residues formed in H–ZSM-5 and H–mordenite from methanol and ethylene.[22] Methanol on H–ZSM-5 yielded a broad distribution of aliphatics including propene, propane, *n*-butane, isobutane, and isopentane. In the aromatic region there was some evidence of benzene, toluene, and xylenes. Over mordenite a much narrower aliphatic product distribution was obtained: only propane, propene, and *n*-butane. The aromatic distribution was, however, broader and included fused aromatics. On both catalysts, surface methoxides were suggested as intermediates. Isoparaffins were more prevalent than linear ones on H–ZSM-5, while on mordenite isoparaffins and C_5-aliphatics were not seen. Instead, the larger pores of mordenite allowed conversion of C_4–C_6 olefins into aromatics by mechanisms similar to conjunct polymerization.

Ethylene formed linear chains on H–ZSM-5. The average chain length was 10–12 carbon atoms. Steam cracking of this sample resulted in a large number of C_5 and C_6 residues and some alkylation, as evidenced by the appearance of ethylbenzene. When an ethylene-loaded sample was heated to 573 K in the presence of water, products included the linear paraffins (propane and butane), branched paraffins (isobutane and isopentane), and aromatics (toluene, xylene, and ethylbenzene). Unlike in the steam-cracked catalyst, xylenes were quite abundant, indicating that they are formed by the conjunct polymerization of olefins.

Kotanigawa et al.[23] studied the adsorption and reaction of methanol on H–Y zeolite by ^{13}C NMR. At room temperature a signal from adsorbed methanol was observed at 48.9 ppm. When the sample was heated to 220 °C four peaks appeared, one of which was derived from the adsorbed methanol. A peak at 59.2 ppm was assigned to a surface methoxyl; however, later work by Anderson and Klinowski[24] suggests that this peak was probably due to DME. The two other resonances at 27.2 and 64.7 ppm were tentatively assigned to the methyl carbon of 2-propanol and carbons adjacent to oxygen (either the 2-carbon of 2-propanol or the carbon of a hydroxymethyl group) respectively. Higher temperatures produced surface alcohols as well as a resonance which these authors assigned to a surface epoxy based upon IR data. When 480 °C was reached, olefins were observed. Based upon these assignments the authors proposed that the formation of the first carbon–carbon bond involves a surface methoxyl reacting with a hydroxymethyl group via a carbenium ion intermediate.

Aronson et al.[10] studied the 1:1 adsorption complex of 2-methyl-2-propanol with a Brønsted site on H–ZSM-5. The 2-methylpropanol was labeled at the hydroxyl carbon. Under the conditions of the experiment the adsorbate was dehydrated and the water which was formed desorbed completely, as verified by temperature-programed description (TPD) and thermogravimetric analysis (TGA). Two broad features appeared in the Bloch decay ^{13}C spectra at 80 and 30 ppm in the ratio of 2:3. The peak at 30 ppm indicated that some additional reaction had occurred changing the hydroxyl carbon to an aliphatic one, probably through oligomerization. No peak in the area of 330 ppm was seen, thereby ruling out a carbenium ion resonating in the area reported by Olah.[6] Furthermore, no line shifts were evident with changes in temperature, thereby ruling out exchange. A small resonance at 123 ppm from carbon–carbon double bonds was observed. Heating of this sample to 373 K resulted in an increase in the intensity and complexity of the aliphatic region. There was a compensatory decrease in the intensity in the 80 ppm region associated with carbons attached to oxygen. Most of the oligomers were still attached to the zeolite in alkyl silyl ethers, since the intensity in the region above 100 ppm remained low. The peak near 80 ppm exhibited an axially symmetric powder pattern with $\sigma_{\parallel} = 93$ and $\sigma_{\perp} = 44$ ppm at 200 K. The isotropic shift was slightly to high frequency from that of the 72.6 ppm shift of the *tert*-butoxide group in bis[(2-ethylhexyl)oxy]di-*tert*-butoxysilane, but to low frequency from the *tert*-butoxide group attached to the more electropositive Ti atom in Ti(*t*-BuO)$_4$.[25] The authors presented a carbenium ion-mediated scheme for formation of some olefinic carbons as well as oligomers (Scheme 3).

The complexity of the spectra in the aliphatic region could not be explained by their scheme. In particular, the appearance of a well-resolved peak at 13 ppm indicates that the labeled carbon has been converted into methyl or methylene groups. This implies rearrangement of tertiary carbenium ions.

From a combination of their TPD–TGA, IR, and NMR work, a potential energy surface was constructed. Reaction proceeds by protonation of the alcohol to form the oxonium ion. This dehydrates to form the alkyl silyl ether via the

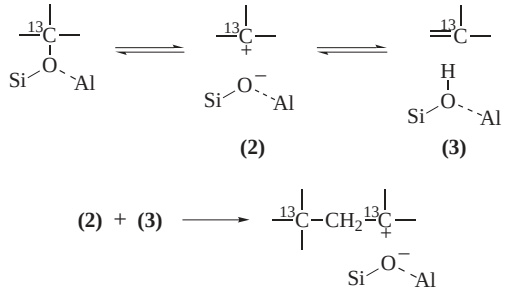

Scheme 3

carbenium ion intermediate. The reaction proceeds again through the carbenium ion to the olefin product.

Anderson and Klinowski[24,26] studied the adsorption and reaction of methanol in H−ZSM-5 zeolite. At room temperature a signal at 50 ppm was observed from adsorbed methanol. Higher pressures of methanol resulted in a second peak due to either vapor or methanol on the outer surfaces of the zeolite. Following heating at 150 °C for 5 or 20 min a resonance at 60 ppm attributable to dimethyl ether appeared. The authors showed via ^{1}H NMR that this occurs through interaction of the methanol with an acid site in the zeolite. The hydroxyl resonance was shifted to higher frequency by 7.9 ppm upon adsorption, due to formation of a methoxonium ion hydrogen bonded in the intracrystalline space. At larger coverages protonated clusters were formed.[27,28] The ratio of DME/MeOH was constant with time, indicating that an equilibrium was attained. After treatment of the methanol-loaded sample for longer than 20 min at 150 °C a new resonance appeared at 184 ppm which could be identified as CO. CO was also produced at 250 °C. The production of CO from DME by two different mechanisms has been reported.[29,30] Both mechanisms, however, involve formation of methane, which was not observed coincident with the formation of CO. CO is formed on ZSM-5 from methanol through a formaldehyde intermediate.[31]

After heating a methanol-treated sample at 250 °C for 54 min and then at 300 °C for 10 min, aliphatic resonances began to appear with a corresponding drop in the DME/MeOH ratio. It would seem that the higher hydrocarbons are either formed preferentially from DME and their formation occurs quicker than the reestablishment of equilibrium between DME and MeOH, or the equilibrium between DME and MeOH (which involves water) is affected by subsequent dehydration reactions. Further heating at this temperature caused complete conversion of methanol and DME to aliphatics and aromatics. Two narrow peaks due to mobile methane and cyclopropane were observed under Bloch decays, but not under CP. Despite spectral overlap, under MAS conditions a large number of products were readily identified, due to the multiplicity of resonances associated with most products. Because CO formed prior to hydrocarbon formation, and its resonant intensity decreased upon formation of hydrocarbon products, the authors suggested that CO was an intermediate in hydrocarbon formation. This was proposed to occur by hydrocarbonylation to ethanol at an iron impurity site, followed by dehydration of ethanol to ethylene. The authors were able to obtain ethylene as the primary olefinic product from an Fe^{3+}-exchanged catalyst in support of this suggestion. Haw's group[32] tested this hypothesis by carrying out the reaction of methanol over H−ZSM-5 in the presence of CO generated from formic acid. Carbon-13 from CO was not incorporated in the product hydrocarbon. CO also did not catalyze the reaction of methanol to hydrocarbon as had been suggested by Jackson and Bertsch.[33]

An examination of the aromatic region of the NMR spectrum following the 300 °C treatment revealed that the distribution of the adsorbed species during methanol conversion was very different from the product distribution. Product distribution data suggested that primarily *m*- and *p*-xylene, toluene and 1,2,4-trimethylbenzene would be found. The major species found by NMR in the adsorbed phase were, however, *o*- and *p*-xylene and 1,2,4,5-tetramethylbenzene, with smaller amounts of other species including some trimethylbenzenes. These trimethyl species were found in their equilibrium distribution[34] in the adsorbed phase, but the larger 1,2,3- and 1,3,5-forms were not found in the product distribution. This was a clearcut example of product selectivity. In ZSM-5 the channel dimensions are 560 × 530 pm; however, more space is available at channel intersections. The larger 1,2,3- and 1,2,5-forms must isomerize to the smaller 1,2,4-form in order to diffuse out of the zeolite. All four tetramethylbenzenes were observed in the catalyst, having been formed at channel intersections. They were not found in the product, again showing product selectivity. The tetramethylbenzenes were not formed in their equilibrium distributions, showing active site selectivity.

At 300 °C signals from the aliphatic region came predominantly from isobutane and propane. Large signals were also observed, however, from *n*-butane, *n*-hexane, *n*-heptane, isopentane, and methane. At 370 °C the number of straight-chain alkanes decreased and larger numbers of branched alkanes were evident. At higher temperatures many larger species were observed in the product distributions due to the larger channel dimensions which allowed diffusion out of the catalyst.

This group also studied methanol adsorption on SAPO-5 and H−ZSM-5 in order to determine the nature of the strong bonding of methanol to Brønsted sites in the zeolites and the conversion of methanol to DME.[35] On SAPO-5 at room temperature only mobile methanol was observed. Heating to 150 °C resulted in conversion of about one-third of the methanol to dimethyl ether which was still mobile. Further heating at 250 °C produced two species: methanol and another species exhibiting chemical shift anisotropy due to reduced mobility. The chemical shift suggested either a surface methoxyl or possibly immobile dimethyl ether.[36] Heating the sample above 300 °C produced mobile alkenes and aliphatic compounds. By contrast in H−ZSM-5 methanol adsorbed as methanol, but hydrogen bonded to a Brønsted site. The resonance shift remained at 50 ppm in the ^{13}C spectra, but the ^{1}H spectra revealed a hydroxyl resonance near 9.4 ppm. When one methanol was adsorbed per Brønsted site there was considerable line broadening indicating strong bonding. The shift indicated that methanol was still intact. Thus, in H−ZSM-5 methanol strongly adsorbs by hydrogen bonding prior to dehydration, while on SAPO-5 the dehydration precedes the strong binding to the surface. This strong bonding pursuant to dehydration is followed by formation of the C−C bond.

Two-dimensional (2D) *J*-resolved spectroscopy was used to unravel the product distribution of a sample of H−ZSM-5 reacted with methanol for 30 min at 300 °C.[37] From the 2D spectrum the authors were able to show that the resonance at 22 ppm had a contribution from the methyl resonance of

isopentane. In later work using 2D spin diffusion NMR[38] they showed that this resonance also contained intensity from carbon atoms adjacent to methyl groups in *n*-hexane and *n*-heptane. This work showed the power of 2D techniques in the solid to resolve the many lines in the aliphatic regions of a working MTG catalyst.

Methanol conversion was also studied over SAPO-34.[39] The authors discovered an interesting shape selectivity in the chabazite-like structure. At 300 °C treatments many aliphatics up to C_6 were in abundance on the catalyst. This included branched hydrocarbons. Only C_3 and smaller species were present in anything but trace amounts in the product stream, however. Due to the small 380 pm windows to the cages, two types of shape selectivity occur. C_1 and C_2 molecules have unrestricted diffusion. C_3 species are somewhat restricted by occluded hydrocarbons, and C_4 and larger species are diffusion-restricted.

The question of the formation of the first carbon–carbon bond in the MTG process has been a source of great interest. In order to test the hypothesis that the trimethoxonium ion (derived from dimethyl ether) may play a role, trimethyloxonium salts were cation-exchanged into ZSM-5 and the ^{13}C NMR spectrum was recorded under CP MAS conditions as a function of time.[40] The methyl groups of the trimethyloxonium ion resonated at 80 ppm. This signal gradually converted to two overlapping signals at 60 ppm which the authors attributed to surface methoxyl and dimethyl ether. Munson and Haw[41] adsorbed DME on H–ZSM-5. At 293 K a resonance appeared at 80 ppm which could be assigned to the trimethoxonium ion. This species was generated from two dimethyl ether molecules and formed in a 1:1 ratio with methanol. This species could not be seen in methanol adsorption studies due to the shift in the equilibrium toward DME. At high temperatures DME yielded similar products as adsorbed methanol. The observation of this species in H–ZSM-5, while not proving that it is a reaction intermediate, lends some credibility to the Chang mechanism involving deprotonation of the trimethoxonium ion to form the methylenedimethyloxonium ylide.[42]

A comparison of methanol conversion on straight channel offretites and increasingly tortuous erionite-like zeolites was undertaken.[43] The most fault-free (least tortuous) zeolite showed a proclivity for formation of long-chain polymeric hydrocarbons, which were highly branched. A chemical shift at 46 ppm due to tertiary carbons, and a peak at 58 ppm due to quaternary carbons were seen. Formation of these polymeric species was inhibited by the presence of only a few blockages in the channel structure. Channel tortuosity is, therefore, necessary to maintain selectivity to low olefins.

4 COKING

Richardson and Haw[44] coked samples with a single feed of butadiene at six different temperatures for 1 h. Carbon-13 NMR spectra generally showed two peaks, one due to aliphatics and one due to aromatic and olefinic resonances. The relative size of the aromatic peak increased drastically with treatment temperature. Over 90% of the NMR intensity observed from samples treated above 400 °C was attributed to aromatic species. A sample was heated under butadiene at 150 °C and then subjected to chemical extraction techniques. Virtually all of the coke was unrecoverable, indicating that the coke comprised large, insoluble, high molecular weight species. Interrupted decoupling experiments confirmed that few carbons were protonated. This result suggests that cross polarization may not be quantitative. Spin counting experiments confirmed that at 150 °C about 80% of the carbon was observable, but that at higher temperatures a significant fraction of the carbon in the coked samples was unobservable.

A number of rare-earth-exchanged zeolites were investigated by CP MAS NMR and relaxation analysis.[45] Cross polarization was not greatly affected by diamagnetic La^{3+} or those ions having short electron T_1 values, including Nd^{3+} and Pr^{3+}. For Gd^{3+}- and Dy^{3+}-exchanged zeolites the ^1H $T_{1\rho}$ was drastically decreased, allowing insufficient time for cross polarization. This prevents quantifying coking reactions in these zeolites by CP MAS NMR. The effect was localized. As a result, dilution of the ion concentration in the zeolite allowed spectra to be obtained.

5 RELATED ARTICLES

Adsorbed Species: Spectroscopy and Dynamics; Brønsted Acidity of Solids; Intercalation Compounds.

6 REFERENCES

1. S. Meisel, J. McCullough, C. Lechtaler, and P. Weisz, *Chem. Tech.*, 1976, **6**, 86.
2. W. Kaeding and S. Butter, *J. Catal.*, 1980, **61**, 155.
3. E. Derouane, J. Gilson, and J. Nagy, *J. Mol. Catal.*, 1981, **10**, 331.
4. J. van den Berg, J. Wolthuizen, A. Clague, G. Hays, R. Huis, and J. van Hooff, *J. Catal.*, 1983, **80**, 130.
5. M. Zardkoohi, J. Haw, and J. Lunsford, *J. Am. Chem. Soc.*, 1987, **109**, 5278.
6. G. Olah and D. Donovan, *J. Am. Chem. Soc.*, 1977, **99**, 5026.
7. J. Haw, B. Richardson, I. Oshiro, N. Lazo, and J. Speed, *J. Am. Chem. Soc.*, 1989, **111**, 2052.
8. N. Deno, H. Richey, J. Hodge, and M. Wisotsky, *J. Am. Chem. Soc.*, 1962, **84**, 1498.
9. G. Olah and G. Liang, *J. Am. Chem. Soc.*, 1972, **94**, 6434.
10. M. Aronson, R. Gorte, W. Farneth, and D. White, *J. Am. Chem. Soc.*, 1989, **111**, 840.
11. J. White, N. Lazo, B. Richardson, and J. Haw, *J. Catal.*, 1990, **125**, 260.
12. B. Gates, J. Katzer, and G. Schuit, in *Chemistry of Catalytic Processes*, McGraw-Hill, New York, 1979.
13. J. Weitkamp and S. Maixner, *Zeolites*, 1987, **7**, 6.
14. B. Richardson, N. Lazo, P. Schettler, J. White, and J. Haw, *J. Am. Chem. Soc.*, 1990, **112**, 2886.
15. N. Lazo, J. White, E. Munson, M. Lambregts, and J. Haw, *J. Am. Chem. Soc.*, 1990, **112**, 4050.
16. Y. Chin and P. Ellis, *J. Am. Chem. Soc.*, 1989, **111**, 7653.
17. Y. Kye, S. Wu, and T. Apple, *J. Phys. Chem.*, 1992, **96**, 2632.
18. D. Murray, J. Chang, and J. Haw, *J. Am. Chem. Soc.*, 1993, **115**, 4732.
19. E. Derouane, J. Nagy, P. Dejaifve, J. van Hooff, B. Spekman, J. Vedrine, and C. Naccache, *J. Catal.*, 1978, **53**, 40.
20. E. Derouane, P. Dejaifve, and J. Nagy, *J. Mol. Catal.*, 1977, **3**, 453.

21. J. Nagy, J.-P. Gilson, and E. Derouane, *J. Mol. Catal.*, 1979, **5**, 393.
22. E. Derouane, J.-P. Gilson, and J. Nagy, *Zeolites*, 1982, **2**, 42.
23. T. Kotanigawa, K. Shimokawa, and T. Yoshida, *J. Chem. Soc., Chem. Commun.*, 1982, 1185.
24. M. Anderson and J. Klinowski, *J. Am. Chem. Soc.*, 1990, **112**, 10.
25. Sadtler Indices of ^{13}C NMR Data, No. 2073, Sadtler, Philadelphia, PA, 1985.
26. M. Anderson and J. Klinowski, *Nature (London)*, 1989, **339**, 200.
27. G. Mirth, J. Lercher, M. Anderson, and J. Klinowski, *J. Chem. Soc., Faraday Trans. 1*, 1990, **86**, 3039.
28. M. Anderson, P. Barrie, and J. Klinowski, *J. Phys. Chem.*, 1991, **95**, 238.
29. C. Chu and C. Chang, *J. Catal.*, 1984, **86**, 297.
30. G. Olah, H. Doggweiler, J. Feldberg, S. Frohlich, M. Grdina, R. Karpeles, T. Keumi, S. Inaba, W. Ip, K. Lammertsma, G. Salem, and D. Tabor, *J. Am. Chem. Soc.*, 1984, **106**, 2143.
31. Y. Matsumara, K. Hashimoto, and S. Yoshida, *J. Catal.*, 1986, **100**, 392.
32. E. Munson, N. Lazo, M. Moellenhoff, and J. Haw, *J. Am. Chem. Soc.*, 1991, **113**, 2783.
33. J. Jackson and F. Bertsch, *J. Am. Chem. Soc.*, 1990, **112**, 9085.
34. S. Hastings and D. Nicholson, *J. Chem. Eng. Data*, 1961, **6**, 1.
35. M. Anderson and J. Klinowski, *J. Chem. Soc., Chem. Commun.*, 1990, 918.
36. J. Klinowski and M. Anderson, *Magn. Reson. Chem.*, 1990, **S28**, 68.
37. M. Anderson and J. Klinowski, *Chem. Phys. Lett.*, 1990, **172**, 275.
38. W. Kolodziejski and J. Klinowski, *Appl. Catal.*, 1992, **A81**, 133.
39. M. Anderson, B. Sulkowski, P. Barrie, and J. Klinowski, *J. Phys. Chem.*, 1990, **94**, 2730.
40. S. Hellring, K. Schmitt, and C. Chang, *J. Chem. Soc., Chem. Commun.*, 1987, 1320.
41. E. Munson and J. Haw, *J. Am. Chem. Soc.*, 1991, **113**, 6303.
42. C. Chang, *Catal. Rev.-Sci. Eng.*, 1983, **25**, 1.
43. M. Anderson, M. Occelli, and J. Klinowski, *J. Phys. Chem.*, 1992, **96**, 388.
44. B. Richardson and J. Haw, *Anal. Chem.*, 1989, **61**, 1821.
45. E. Munson and J. Haw, *Anal. Chem.*, 1990, **62**, 2532.

Biographical Sketch

Tom M. Apple. *b* 1954. B.S., 1976, Pennsylvania State University; Ph.D., 1981, University of Delaware. Introduced to NMR by C. R. Dybowski. Faculty in Chemistry, University of Nebraska, 1983–1991, Faculty in Chemistry, Rensselaer Polytechnic Inst., 1991–present. Approx. 40 publications. Research interests include applications of solid state NMR to catalysis and materials science.

Silica Surfaces: Characterization

Gary E. Maciel
Colorado State University, Fort Collins, CO, USA

1	Introduction	1
2	NMR Strategies for Silica Surface Selectivity	1
3	$^{1}H \rightarrow {}^{29}Si$ CP in Silicas	2
4	$^{1}H \rightarrow {}^{17}O$ Cross Polarization	5
5	Proton NMR Approaches	5
6	Correlating ^{1}H-based and ^{29}Si-based Information	11
7	Subsurface Silanols	14
8	Summary and Conclusions	14
9	Related Articles	15
10	References	15

1 INTRODUCTION

Silica (SiO_2) is one of the most abundant materials on Earth.[1] If the wide range of silicate minerals in which silica 'formally' occurs is included, one can account for more than 60% of the Earth's crust in terms of silica. From the industrial point of view, the number of applications of silica is enormous, and we make no attempt to represent them all here. These technological applications of silica include its use in separations (e.g. column chromatography), in composite materials, in consumer products (e.g. as thickening agents), in immobilized reagents (e.g. heterogeneous catalysts), and even in foods. Although a variety of high-surface-area forms of silica are important, including precipitated and fumed silicas, in this article we will focus mainly on samples originating as *silica gels*, i.e. silica samples precipitated from the products of reactions such as:

$$Si(OCH_2CH_3)_4(aq.) + 2H_2O(l) \rightarrow SiO_2(s) + 4CH_3CH_2OH(aq.) \qquad (1)$$

The materials prepared in this manner tend to have high surface areas and high porosities, although these properties depend substantially on details of the preparation conditions. Most of the technologically important properties of silica depend substantially on the characteristics of the silica *surface*, e.g. the numbers, types, distributions, and reactivities of silanols, i.e. ≡Si-OH groups, at the silica surface.

A priori, it would appear that the spin-$\frac{1}{2}$ nuclides ^{29}Si (4.7% natural abundance) and ^{1}H (∼100% natural abundance) should be useful for characterizing the silica surface, and possibly also the quadrupolar nuclides ^{17}O ($I = \frac{5}{2}$, 0.04% natural abundance) and ^{2}H (I = 1, 0.02% natural abundance). Clearly, for these quadrupolar nuclides to be useful, isotopic enrichment is required, but that has not been a major difficulty. Indeed, there has been a great deal of NMR work done on silicas and silica-based systems,[2–5] and it would be impossible to review it all comprehensively here, because of reasonable space limitations. Furthermore, because of restrictions on space, it will not be possible to list all of the worthwhile studies in this research area. For these reasons, the convenient approach of emphasizing studies from our own laboratory is adopted, with apologies to those who feel their work may have been neglected.

2 NMR STRATEGIES FOR SILICA SURFACE SELECTIVITY

2.1 The Need

With any NMR experiment on a solid, a technique that provides no major detection advantage to nuclei at the surface will generate spectra that are dominated by peaks due to nuclei that are in positions in the interior (bulk) of a particle, because the number of nuclei that constitute the bulk of a particle will typically be much larger than the number of corresponding nuclei in analogous structural sites at the surface (unless the surface area is very large, say, $\gg 100\,m^2\ g^{-1}$). This intensity dominance by peaks due to bulk sites can be overcome if (1) the nuclei being observed are located only (or largely) at the surface or (2) the method of generating the polarization to be observed discriminates strongly in favor of nuclei at the surface. The former situation often obtains for protons in a typical silica, because most of the protons in such systems exist at the surface as covalently attached −OH groups (vide infra), as physisorbed H_2O, or as covalently attached structures that result from derivatization processes.

Perhaps the most obvious strategy for preferentially or selectively polarizing surface nuclei in the presence of an overwhelmingly larger number of nuclei in analogous structural sites in the interior would be to use a relaxation reagent that can, at least briefly, interact with the surface and thereby relax the surface nuclei. Although surprisingly little effort seems to have been expended in this direction, one must note the elegant ultra-low-temperature (∼10 mK) NMR studies of Waugh and co-workers,[6] who have used the relaxation effects of ^{3}He impinging on a surface for the selective relaxation of nuclei at the surface. Other surface-selective (or preferential) relaxation mechanisms would seem possible via the dipolar mechanism of impinging species with large nuclear magnetic moments (say, ^{1}H or ^{19}F) or even the electron spin magnetic moments of paramagnetic relaxation agents. In the case of paramagnetic surface relaxants, the possibility of dynamic nuclear polarization (DNP)[7] of surface nuclei from adsorbed paramagnetic species seems attractive, possibly with the Overhauser mechanism operating if the adsorption is rapidly reversible, or the solid state mechanism if the adsorption/desorption process is very slow. Possibilities would also appear to exist for surface-selective relaxation mechanisms based on quadrupolar relaxation of a nuclide with $I > \frac{1}{2}$ (e.g. ^{2}H or ^{17}O) due to rapid, reversible adsorption/desorption causing a modulation of the local electric field gradient. Recent progress in the surface transfer of ^{129}Xe polarization that has been dramatically enhanced via electron → nuclear polarization transfer (e.g. from optically pumped rubidium) is promising for not only providing a surface-selective NMR strategy, but also for providing huge enhancements in the effective sensitivity of NMR detection at surfaces.[8]

2.2 Cross Polarization

To date, the most popular and generally successful surface-selective polarization strategies have been based on $^{1}H \rightarrow X$ cross polarization (CP),[9] where X is a nucleus present at the surface (and presumably also with the bulk).[10,11] These strategies are often based on the assumption that essentially all

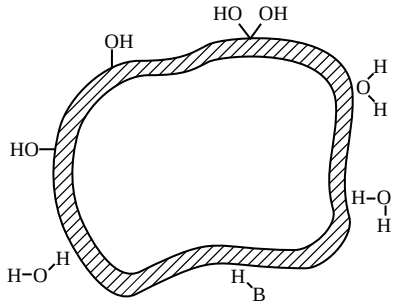

Figure 1 Cross polarization as a surface-selective strategy, showing only protons near the (hatched) surface region, as covalently attached hydroxyls, physisorbed water, or physisorbed acids (B–H) of some other type. (Taken from Maciel and Ellis[4])

(or, at least, most) of the protons in the system are present at the surface and on the fact that cross polarization depends upon a static component of the $^{1}H–X$ dipolar interaction, which has an inverse cube dependence on the $^{1}H–X$ internuclear distance (in many cases the cross polarization rate appears to have an essentially r^{-6} dependence). Cross polarization was developed during the early 1970s by Pines, Gibby, and Waugh.[9] Its early impact was primarily the dramatic increase in ^{13}C signal-to-noise ratio in NMR experiments on organic solids, which rendered such experiments especially attractive when carrried out with magic angle spinning (MAS), as demonstrated first by Schaefer and Stejskal.[12] From the point of view of surface applications, at least as important as the effective increase in sensitivity is the above-mentioned dependence of the cross-polarization rate on internuclear distances. Figure 1 displays the essence of a surface-selective CP strategy, in which only those X nuclei that are close enough to the surface (within, say, 5–6 Å, as represented by the 'cross-hatched' area) can be cross polarized by surface protons. The more remote X nuclei in the 'interior' or 'bulk' of the material are not cross polarized efficiently. Hence, the efficiency, or dynamics, of cross polarization can be used to discriminate in favor of the surface nuclei.

3 $^{1}H \rightarrow {}^{29}Si$ CP IN SILICAS

3.1 Silica Gels and Derivatized Silica Gels

In 1980, Sindorf and Maciel[10,11] published the first high-resolution example of the use of $^{1}H \rightarrow X$ cross polarization for surface-selective X detection in a demonstration of $^{1}H–{}^{29}Si$ CP in silica gel. Since that time $^{1}H \rightarrow {}^{29}Si$ CP has remained the most popular application of this strategy, although there has been significant success with applications to other types of systems. Figure 2 shows typical ^{29}Si spectra of silica gel and related samples obtained by CP MAS (cross polarization and magic angle spinning) and DP MAS (direct polarization, based on ^{29}Si spin–lattice relaxation, not CP). The DP MAS spectrum [Figure 2(a)] of an undried silica gel is dominated by the peak due to $(\equiv SiO)_4\mathbf{Si}(Q_4)$ sites, which represent the bulk (nonsurface regions) of silica particles. The ^{29}Si CP MAS spectrum of an undried silica gel [Figure 2(b)] selects primarily surface sites and shows the following three peaks: a peak at −89 ppm (relative to liquid TMS) due to

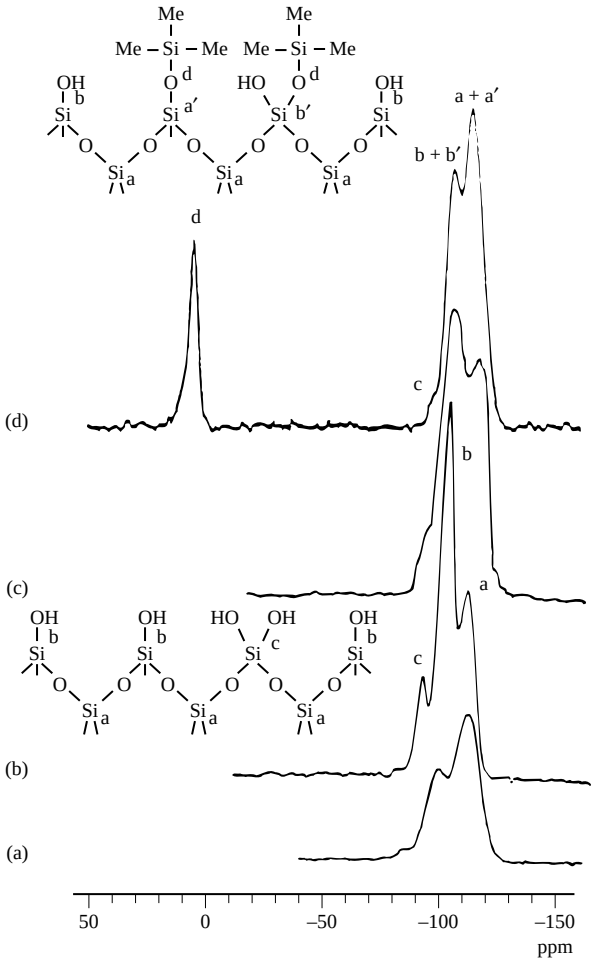

Figure 2 ^{29}Si MAS spectra of silica gel samples. (a) DP MAS spectrum of an undried sample. (b) CP MAS spectrum of the same sample as in (a). (c) CP MAS spectrum of a sample dehydrated under vacuum at 209 °C. (d) Sample derivatized with $(CH_3)_3SiCl$. (Taken from Maciel[5])

$(\equiv SiO)_2\mathbf{Si}(OH)_2$ (geminal, Q_2) sites; a peak at −99 ppm arising from $(\equiv SiO)_3\mathbf{Si}OH$ (single silanol, Q_3) sites; and a peak at −109 ppm from the Q_4 (siloxane) sites near the surface. These peak assignments can be made on the basis of the usual kinds of empirical chemical shift correlations with structure from liquid sample data on silicic acid solutions. However, the dynamics of the $^{1}H–{}^{29}Si$ CP process can also be used to make these assignments.

Figure 3 shows the results of a variable contact time CP experiment, in which the $^{1}H \rightarrow {}^{29}Si$ CP contact period (t_{cp}) is varied in order to elucidate the $^{1}H \rightarrow {}^{29}Si$ CP (relaxation) time constant (T_{HSi}) for each ^{29}Si peak. The early (small t_{cp}) part of such curves is typically dominated by the rate of CP transfer, as characterized by the rate constant $T_{HSi}{}^{-1}$, and the latter part of such curves is usually determined by the rate constant of the rotating frame spin–lattice relaxation of the protons responsible for polarization transfer to the observed silicons, as characterized by the time constant, $T_{1\rho}^{H}$ (assuming $T_{1\rho}^{H} \rangle T_{HSi}$). These curves can be analyzed mathematically in terms of equation (1),[13]

$$M(t_{cp})/M^{*} = \frac{1}{1 - T_{HSi}/T_{1\rho}^{H}}(e^{-t_{cp}/T_{1\rho}^{H}} - e^{-t_{cp}/T_{HSi}}) \qquad (2)$$

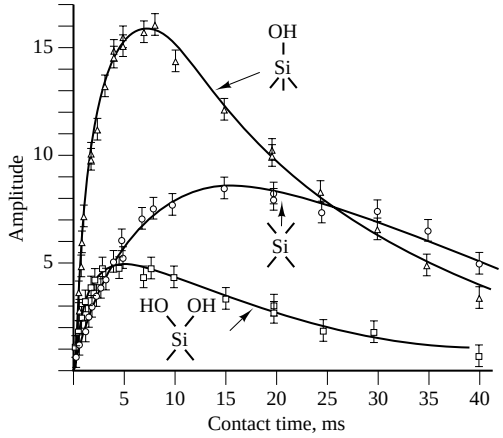

Figure 3 Variable contact time ^{29}Si CP MAS plots for silica. (Taken from Maciel and Sindorf[10])

where $M(t_{cp})$ is the ^{29}Si magnetization generated by ^{1}H–^{29}Si CP as a result of a CP contact period t_{cp}, and M^* is the 'ideal' maximum ^{29}Si magnetization that would be generated if $T_{1\rho}^{H}$ and $T_{HSi}{}^{-1}$ were both infinite. This analysis shows that $T_{HSi}{}^{-1}$ for the -89 ppm peak is roughly twice that of the -99 ppm peak, which in turn is an order of magnitude larger than the $T_{HSi}{}^{-1}$ value for the -109 ppm peak. In terms of the number and distances of nearby protons, the ^{29}Si chemical shift assignments given above in terms of Q_2, Q_3, and Q_4 sites are entirely consistent with these T_{HSi} determinations.

3.2 Dehydration of Silica

The ^{29}Si CP MAS spectra collected in Figure 2 also represent two important classes of chemical transformations of silica surfaces that were studied by ^{29}Si CP MAS spectra by Sindorf and Maciel.[10,11,14–18] Figure 2(c) shows a spectrum obtained on a silica gel sample that has been dehydrated under vacuum at 209 °C. One can see in this spectrum the subtle redistribution of peak intensity and the dramatic line broadening relative to the spectrum observed on an 'air hydrated' silica gel sample. These changes, especially the line broadening, are presumably due to a redistribution of hydrogen bonding patterns, and perhaps bond angles and bond lengths (and strains) introduced with the removal of the (predominantly physically) adsorbed water of the 'hydrated' and essentially 'annealed' silica surface represented in Figure 2(b). Such experiments carried out over a wide range of dehydration temperatures, and corresponding rehydration experiments, have revealed valuable information on the effects of dehydration and rehydration on the silica gel surface.

3.3 Silylation of Silica

The ^{29}Si CP MAS spectrum shown in Figure 2(d) represents a sample prepared by the silylation of a silica gel by $(CH_3)_3SiCl$. This silylation reaction is a member of an important class of derivatizations of the silica surface, represented by the following chemical equation:

(3)

where X represents a labile leaving group (e.g. Cl or OCH_2CH_3) and Si represents a silanol site on the reactant silica surface or a corresponding derivatized silica site in the reacted sample. Such reactions are important, or potentially important, technologically—for the preparation of stationary phases for chromatographic separations, as a means of immobilizing reactive chemical centers (e.g. catalytic sites), in coupling agents for composite materials, and for a wide range of other applications in which it is desired to anchor or 'immobilize' a chemically important moiety. Peak d in the spectrum of Figure 2(d), at ca. 10 ppm, is assigned to the trimethylsilyl group covalently attached to the silica surface. Clearly the silylation process has brought about a change of intensities of peaks a, b, and c in Figure 2(b), corresponding to the $(\equiv SiO)_2\mathbf{Si}(OH)_2$ or Q_2 sites, the $(\equiv SiO)_3\mathbf{Si}OH$ or Q_3 sites, and $(\equiv SiO)_4\mathbf{Si}$ or Q_4 sites, at the underivatized surface. At the relatively low level of structural detail represented by the Q_2, Q_3, Q_4 notation, the silylation process transforms Q_2 sites into Q_3 sites, and Q_3 sites into Q_4 sites, and these changes are seen by comparing the spectra in Figure 2(b) and (d). By examining such intensity changes systematically, it has been possible to elucidate important reactivity patterns in these systems.[10,11,14–18] Indeed, ^{29}Si CP MAS NMR, along with supporting data from ^{13}C CP MAS experiments, can serve as an analytical technique for monitoring chemical reactivity

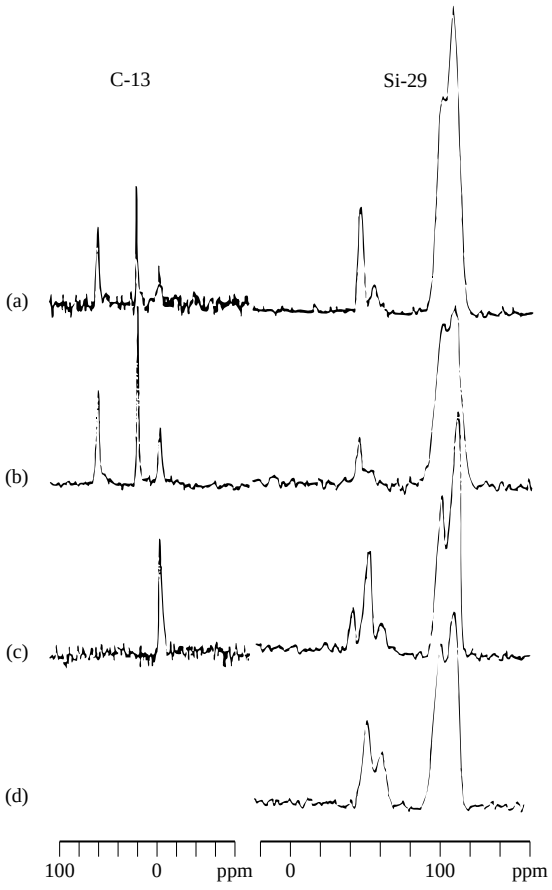

Figure 4 ^{29}Si (right) and ^{13}C (left) CP MAS spectra of silica gel derivatized with $(CH_3)_2Si(OCH_2CH_3)_2$. (a) Product of reaction with predried silica at 138 °C. (b) Product of reaction with predried silica at 240 °C. (c) Product of reaction with undried silica at 115 °C. (d) Sample (c) heated in air at 150 °C. (Taken from Sindorf and Maciel[17])

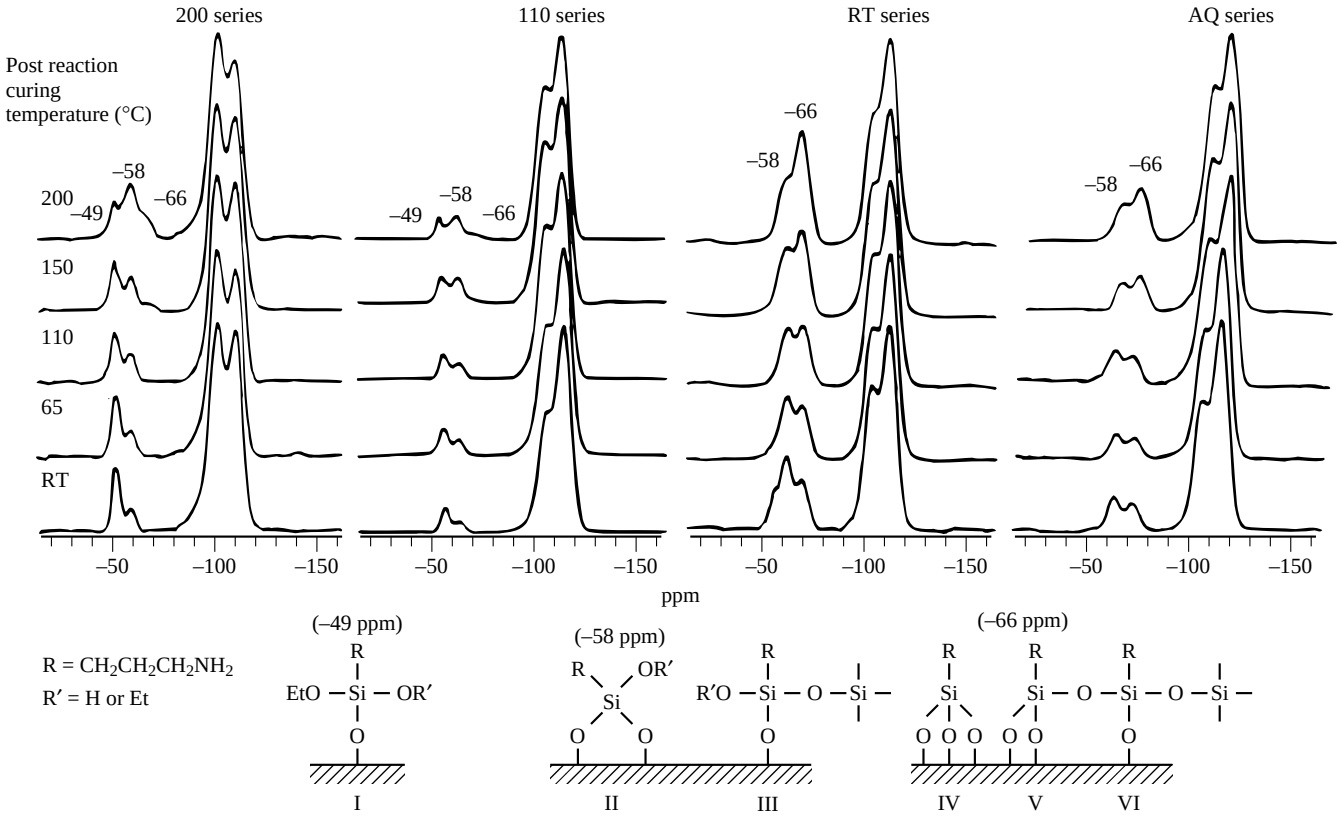

Figure 5 ^{29}Si CP MAS spectra of APTS-modified silica gels. Each column of spectra corresponds to the drying temperature of silica gel (°C; RT = room temperature) under vacuum prior to reaction in dry toluene, or aqueous reaction conditions (AQ). Postreaction treatment (curing) temperature shown on the left. Structural assignments given at the bottom. (Taken from Caravajal et al.[19])

patterns, e.g. the relative reactivities of the various types of silanols on a silica surface.

The complex chemistry that can occur on a silica surface after silylation by a reagent with more than one leaving group (X), e.g. $RR'SiX_2$ or $RSiX_3$, is also amenable to study by CP MAS NMR.[17] In the ^{29}Si CP MAS spectra shown in Figure 4 one sees that the product formed initially from the reaction of silica with $(CH_3)_2Si(OCH_2CH_3)_2$ depends on the reaction conditions and predrying of the silica, and can be converted by the moisture in air [Figure 4(c), (d)] to products in which ≻**Si**-OCH_2CH_3 moieties are replaced by ≻**Si**-OH and ultimately ≻**Si**-OSi- moieties. In this case, ^{13}C CP MAS spectra are also useful, because they detect the presence and amount of residual ≻Si-OCH_2CH_3 moieties.

The ^{29}Si CP MAS spectra shown in Figure 5 represent an even more complex derivatized silica system, a series of samples prepared by the silylation of silica with 3-aminopropyltriethoxysilane (APTS) under a variety of conditions (pretreatment temperature = 200 °C for 200 series, or 110 °C for 110 series, 25 °C for RT series, or with silylation carried out in an aqueous slurry, AQ series).[19] APTS-derivatization of the silica surface is of interest for such diverse applications as a variety of composite materials (in which APTS serves as a coupling agent between a silica-like component and, usually, an organic polymer) and for metal complexation agents. One sees from the spectra of Figure 5 that increasing the amount of water in the silylation process or increasing the postsilylation 'curing' temperature brings about changes in attached silane populations from species with one **Si**-OSi attachment (−49 ppm) to species with two such attachments (−58 ppm) to three such attachments (−66 ppm). Although ^{13}C spectra are primarily useful for monitoring the residual ≻Si-OCH_2CH_3 moieties in this system, a careful analysis of the ^{13}C CP MAS spectra of samples corresponding to those represented in Figure 5 reveals that the ^{13}C chemical shift of the central carbon of the pendant $-(CH_2)_3-$group originating from APTS is sensitive to protonation or hydrogen bonding of the amino group. ^{1}H CRAMP spectra (vide infra) and ^{15}N CP MAS spectra are also useful for studying this important issue.

3.4 Fumed Silica

Other types of silicas (and derivatized silicas), besides those based on silica gels, have also been studied by ^{29}Si CP MAS (and DP MAS) experiments, e.g. by Brinker and co-workers[20,21] and by Legrand and co-workers.[22,23] Figure 6 shows a comparison of ^{29}Si CP MAS spectra of a fumed silica (a Cab-O-Sil, formed by the vapor-phase combustion of $SiCl_4$) and a silica gel equilibrated to about the same H_2O vapor pressure.[24] The same peaks are present, but they are broader in the case of the fumed silica, and the percentage of surface silica sites that are single silanols is seen to be smaller for the fumed silica than for silica gel. The greater linewidth presumably relates to the greater dispersion of local surface geometries (and chemical shifts) in the Cab-O-Sil structure, which is formed at a higher temperature, and possibly to

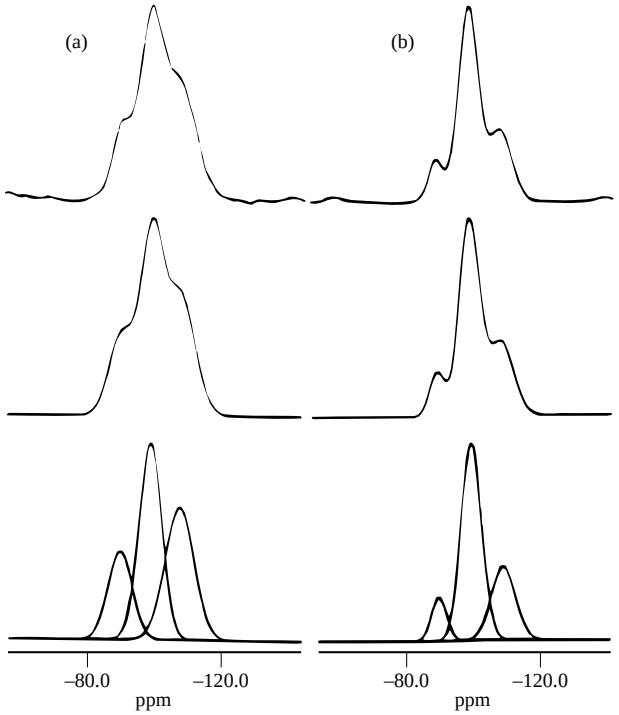

Figure 6 ^{29}Si CP MAS spectra of (a) Cab-O-Sil fumed silica and (b) silica gel. Top: experimental spectra. Bottom: individual Q_2, Q_3, and Q_4 peaks by deconvolution. Middle: computer sum of the contributions shown at the bottom. (Taken from Liu and Maciel[24])

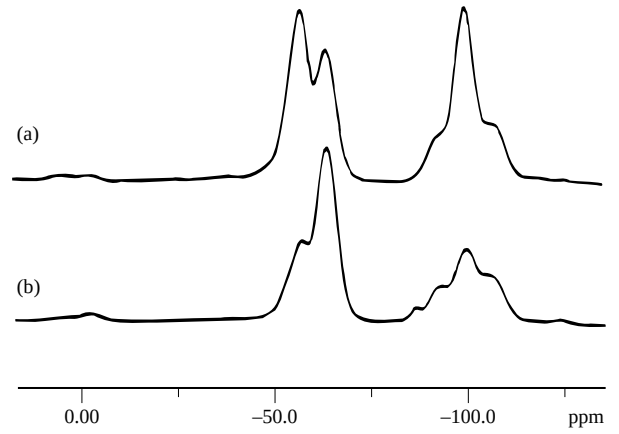

Figure 7 ^{29}Si CP MAS spectra of polysiloxane polymer prepared from $Si(OEt)_4$ and $(CH_3O)_3SiCH_2CH_2CH_2Cl$ with (a) $Bu_2Sn(OAc)_2$ or (b) 0.1 M HCl as catalyst. (Taken from Elnahhal et al.[26])

the potential effects of so-called 'interparticle sites' at the junctures of the primary particles that contribute to the overall topography of a fumed silica.[23] Detailed studies of ^{29}Si CP MAS spin dynamics of fumed silicas, especially when viewed in relationship to analogous silica gel results, appear promising for identifying the main similarities and differences between these two types of silica surfaces.[24]

3.5 Polysiloxane Systems

There has been a great deal of interest recently in a class of polysiloxane polymers prepared by the hydrolysis and gelation of mixtures of reagents of the types, $Si(OR')_4$ and $RSi(OR'')_3$, where R′ and R″ are typically methyl or ethyl and R is a 'pendant' group that contains some desired chemical moiety, e.g. a specific ligand.[25] By varying the nature of R and the ratios of the two types of starting reagents, a wide range of polysiloxane materials, with a broad variety of potentially useful properties, can be prepared. These polysiloxane materials bear a substantial similarity to derivatized (silylated) silicas, with a silica-like three-dimensional network to which the pendant (R) groups are attached. Hence, the NMR techniques that are useful for characterizing derivatized silicas are also useful for these polysiloxane systems.

Figure 7 shows ^{29}Si CP MAS spectra of polysiloxane systems with $-CH_2CH_2CH_2Cl$ as the pendant group, prepared by the reaction of $Si(OEt)_4$ with $(MeO)_3SiCH_2CH_2CH_2Cl$, using two different catalysts.[26] One notes substantially different intensity ratios for the Q_2, Q_3, and Q_4 peaks in the two spectra [and possibly a Q_1 peak at about −82 ppm in Figure 7(b)], and for the peaks due to the pendant groups (at about 60 and 65 ppm), as well as a dramatic difference in intensities between the 60 and 65 ppm peaks relative to the Q_2, Q_3, Q_4 peaks, for the products from the two catalyst systems employed.

4 ^{1}H → ^{17}O CROSS POLARIZATION

In addition to cross polarization to ^{29}Si in silica, or to ^{13}C (or ^{15}N, ^{31}P, etc.) in derivatized silicas, cross polarization to ^{17}O in isotopically-enriched silicas has also been illuminating. Oldfield and co-workers have during the past several years made significant progress in the application of solid state ^{17}O NMR techniques for the characterization of inorganic materials. Walter, Turner, and Oldfield[27] have demonstrated that ^{1}H → ^{17}O CP experiments are not only feasible, but they are also very informative from the point of view of *editing* ^{17}O spectra, by discriminating against ^{17}O signals from oxygen sites with no directly bonded hydrogen. Figure 8 shows ^{1}H → ^{17}O CP spectra of amorphous silica and a model SiOH system. From a comparison of the spectra obtained from static samples and by MAS, with and without CP, it was possible to assign the ^{17}O signal due to SiOH groups at the surface.

5 PROTON NMR APPROACHES

5.1 Dipole–Dipole Broadening

High-resolution ^{1}H NMR spectroscopy has proved to be highly useful in studying the surfaces of silicas and a variety of other solids. In order to obtain high-resolution ^{1}H NMR spectra of solids (including their surfaces), it is necessary to average not only the chemical shift anisotropy (easily done by MAS), but also ^{1}H–^{1}H dipolar interactions.[28,29] The latter can be very large (tens of kHz). Magnetic dipole–dipole interactions manifest an inverse cube dependence on internuclear distance. Therefore such interactions, and the ^{1}H–^{1}H spin–spin flip-flops that they can generate, are especially strong if the protons are situated in close proximity to each other, e.g. in a typical organic solid, but also perhaps in hydrogen-bonded clusters of hydroxy groups on a surface. Hence, a priori one can feel confident that moderate-speed MAS experiments (say, less

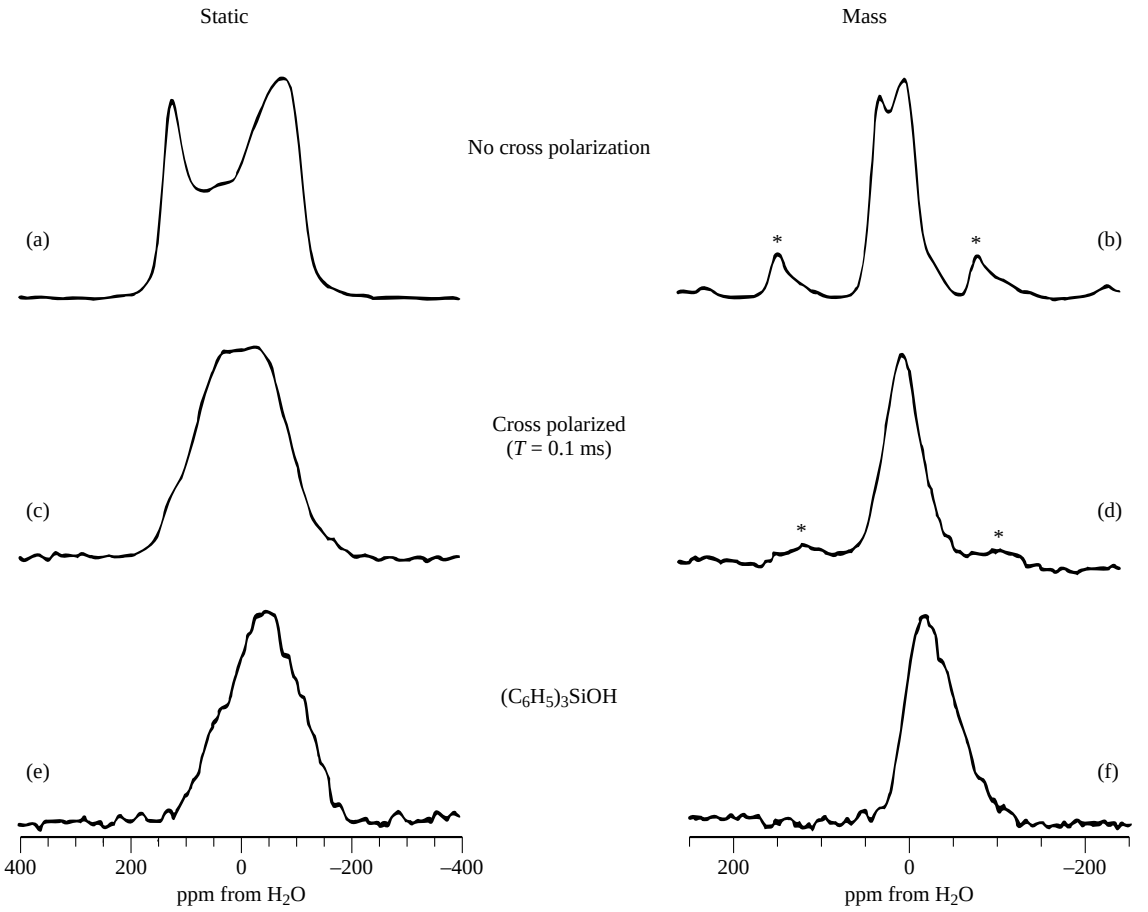

Figure 8 Static and MAS ^{17}O spectra of amorphous SiO_2 and polycrystalline $(C_6H_5)_3SiOH$ obtained at 67.8 MHz. (a) ^1H-decoupled static spectrum of SiO_2 without CP: 108 scans. (b) ^1H-decoupled MAS spectrum: 100 scans, 7.6 kHz spinning speed (*indicates spinning sidebands). (c) $^1H \rightarrow {}^{17}O$ static spectrum of SiO_2, 200 scans, 0.1 ms contact time. (d) $^1H \rightarrow {}^{17}O$ MAS spectrum of SiO_2, 200 scans, 0.1 ms contact time. (e) ^1H-decoupled static spectrum of $(C_6H_5)_3SiOH$ without CP: 500 scans. (f) ^1H-decoupled MAS spectrum of $(C_6H_5)_3SiOH$: 800 scans, 4.0 kHz spinning speed. All spectra were obtained using a 2 s recycle time. (Taken from Walter et al.[27])

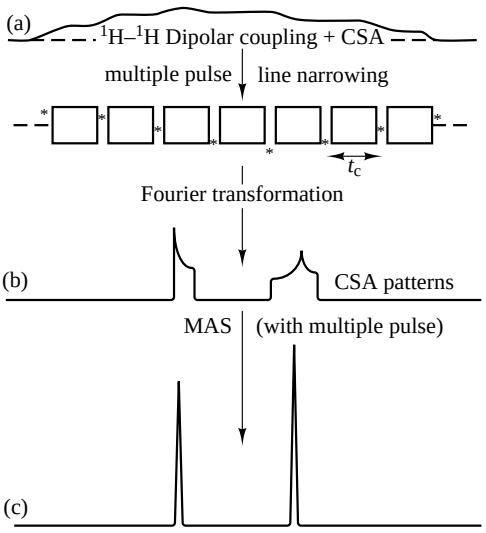

Figure 9 The multiple pulse line-narrowing strategy for averaging homonuclear dipolar interactions. Each rectangle [between (a) and (b)] represents one multiple pulse cycle (e.g. four pulses for WAHUHA, eight for MREV-8 or 24 for BR-24). There is one data acquisition point for each cycle (e.g. between each rectangle). (Taken from Maciel[5])

than 20 kHz) are adequate for studying silica surfaces only for substantially dehydrated samples. For nondehydrated or nondeuterated samples, in which the *local* surface density of protons can be substantial, multiple pulse techniques may be required for eliminating the line-broadening effects of ^1H–^1H dipolar interactions. Alternatively, a useful strategy employed by Vega and co-workers is to ensure that the ^1H concentration is small by exchanging protons at the surface with deuterons.[30]

5.2 Multiple Pulse Line Narrowing: CRAMPS

In 1968, Waugh and co-workers[31] introduced a *multiple pulse* approach for averaging strong homonuclear dipolar interactions. The strategy of this kind of approach is that, over the *entire* period of each individual multiple pulse cycle (four 90° pulses in the original work), the average Hamiltonian that governs the evolution of the spins over the entire cycle does not include the homonuclear dipolar interaction. A nonvanishing chemical shift effect, albeit scaled down, is present in the average Hamiltonian. Hence, if one acquires one data point stroboscopically between each adjacent pair of multiple pulse cycles in a long string of such cycles, the resulting time-dependent signal (analogous to a free induction decay) is

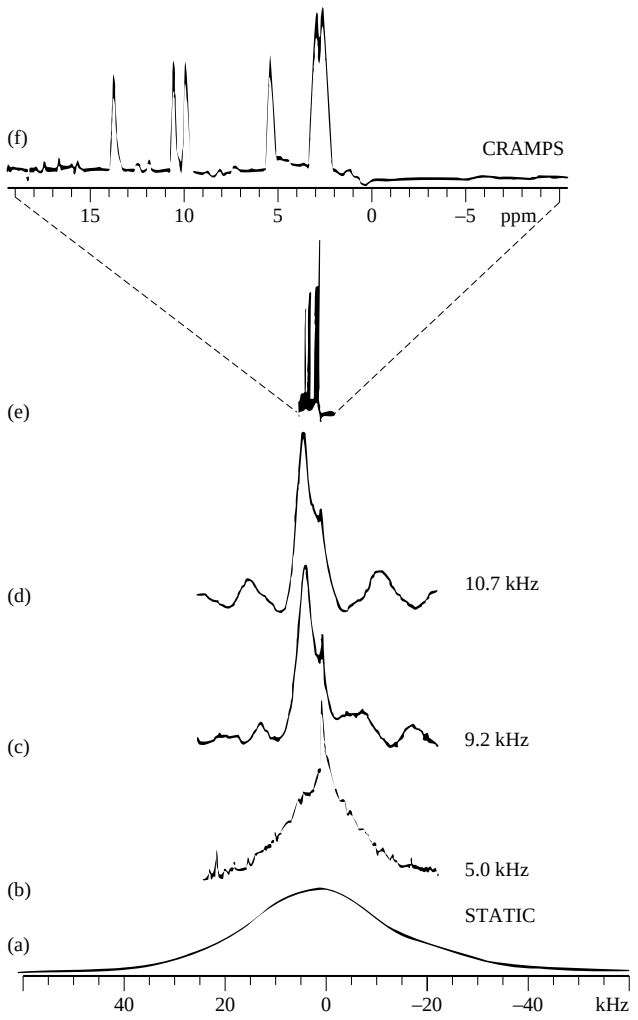

Figure 10 ^{1}H NMR spectra of citric acid. (a) Static sample, single pulse, (b),(c),(d) MAS-only with indicated MAS speed. (e) and (f) CRAMPS. (Taken from Dec et al.[35])

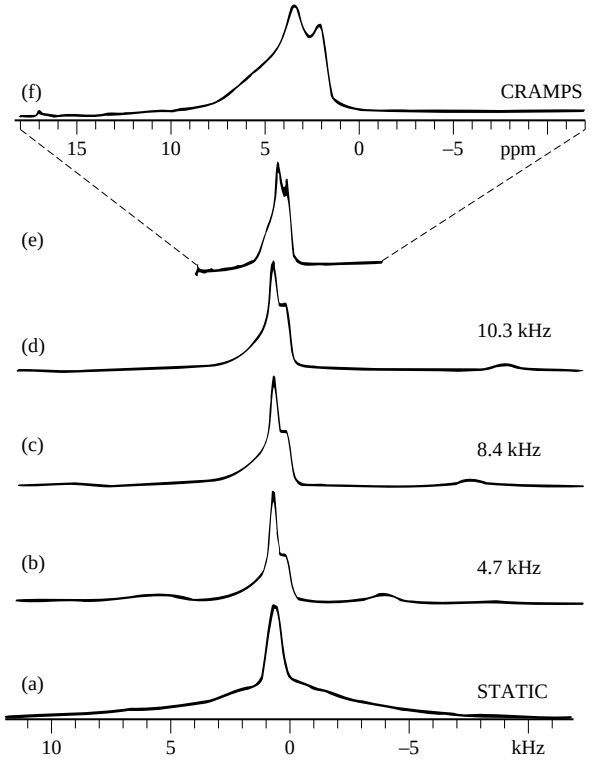

Figure 11 ^{1}H NMR spectra of untreated silica gel. (a) Static sample, single pulse. (b),(c),(d) MAS-only with indicated MAS speed. (e) CRAMPS. (f) CRAMPS on an expanded scale. (Taken from Dec et al.[35])

modulated by chemical shift effects, but not by homonuclear dipolar effects. The strategy is outlined in Figure 9 in which each rectangle represents a multiple pulse cycle and each asterisk represents a data acquisition point. The bandwidth of the experiment depends on $1/t_c$, the inverse of the multiple pulse cycle time.

The original homonuclear line-narrowing pulse sequence (WAHUHA)[31] was a four pulse sequence; later elaborations involve more pulses in the total cycle and offer compensation for pulse imperfections and/or higher order averaging of the homonuclear dipolar interaction.[32,33] In general, this class of experiments requires short ($<1.5\,\mu$s), powerful 90° pulses with precisely defined phases and until recently has been technically one of the most difficult experiments in the solid state NMR laboratory. Currently, the most popular multiple pulse sequences are the eight pulse MREV-8 sequence[32] and the 24 pulse BR-24 sequence.[33]

For powdered or amorphous samples, in order to avoid line broadening due to chemical shift anisotropy, magic angle spinning is employed (which also averages various heteronuclear dipolar couplings). Gerstein and co-workers[34] were the first to combine a multiple pulse homonuclear line-narrowing technique with magic angle spinning, and introduced the acronymn CRAMPS for Combined Rotation And Multiple-Pulse Spectroscopy.[28,29]

5.3 ^{1}H CRAMPS Studies of Silicas

Figures 10 and 11 show the difference in ^{1}H line-narrowing capabilities between CRAMPS and MAS-only (no multiple pulse sequence) with a modestly high MAS speed (10–11 kHz).[35] For powdered crystalline citric acid (Figure 10), one sees six distinctly resolved ^{1}H CRAMPS peaks, but essentially no resolution in the 10.7 kHz MAS-only ^{1}H spectrum. This difference reflects the high proton concentration (∼29 atom %) and molecular rigidity of crystalline citric acid. For the more proton-dilute (∼2.5 atom %) silica gel system (Figure 11), the ^{1}H NMR experiment yields a modestly narrowed ^{1}H spectrum even on a static sample, and 4.7 kHz MAS yields a spectrum that is superficially similar to that obtained by CRAMPS. However, close inspection reveals important details that differentiate the ^{1}H spectra obtained by these two techniques [Figure 11(d) and (e)]. All of the remaining ^{1}H spectra discussed in this article were obtained by the CRAMPS technique.

One should note that the CRAMPS technique is not necessarily a panacea for ^{1}H NMR studies on surfaces, or for any other type of sample. Dynamics associated with motion and/or chemical reactions with a time constant that is comparable to the cycle time (t_c) of the multiple pulse sequence interferes with the multiple pulse averaging of

$^1H-^1H$ dipolar interactions.[29,36] Of course, an analogous problem can also arise with magic angle spinning, for which the critical period is $\nu_{MAS}{}^{-1}$, where ν_{MAS} is the MAS frequency.[37] To quench this kind of dynamic interference with the line-narrowing efficiency of any cyclic technique, like MAS and/or a multiple pulse sequence, one can try to alter the dynamics, e.g. by changing (usually lowering) the sample temperature.

As an example of the application of the ^1H CRAMPS technique to the study of silica surfaces,[38] Figure 12 shows the ^1H CRAMPS spectra obtained on untreated [Figure 12(a), (a′), (a″)] and dried [Figure 12(b), (c), (d)] silica gel samples. Comparison of spectra (a) and (b) show that the relatively sharp peak at about 3 ppm in the spectrum of an untreated silica is removed by moderate dehydration; this peak is therefore identified as physisorbed water. The broad nonsymmetrical peak that is largely to the left of the sharp 1.9 ppm peak is unaffected by sample evacuation at 200 °C, but removed by evacuation at 500 °C; this behavior suggests that this peak can be identified tentatively with clustered (or hydrogen bonded) silanols, which are close enough together that suitable dehydration pathways are available. The sharp peak at 1.9 ppm remains after evacuation at 500 °C; this behavior implies that the silanol groups represented by this peak are sufficiently far from each other to make dehydration difficult, so it is assigned to isolated (non-hydrogen-bonded) silanols. These assignments are consistent with 35 years of literature results on liquid solution samples, which show that hydrogen bonding typically reduces proton shielding, and with the reasonable point of view that a wide range of hydrogen-bonding structures exist on a silica surface (chemical shift dispersion:broad peak). These assignments are also consistent with the results of proton dipolar-dephasing experiments, as shown in Figure 13.

5.4 CRAMPS-Based Time Domain Studies of Silicas

Figure 13(a) shows a ^1H CRAMPS version[38] of the popular 'dipolar-dephasing' experiment used routinely in ^{13}C CP MAS NMR. In this ^1H CRAMPS version, a 'dephasing period' 2τ is inserted between the initial $\pi/2$ pulse that generates transverse magnetization and the multiple pulse line-narrowing pulse train that detects the transverse magnetization. During the dephasing period, those proton magnetic moments that experience strong dipolar interactions undergo a corresponding degree of dephasing, and the resulting detected signal will be accordingly attenuated. Figure 13(b) and (c) show the results of applying the dipolar-dephasing CRAMPS experiment to untreated silica gel [Figure 13(b)] and to a silica gel sample evacuated at 200 °C [Figure 13(c)]; in both cases one sees that the broad (3.0 ppm) peak is attenuated by a dephasing period (2τ) of 160 μs, whereas the sharp (1.7 ppm) peak is largely unattenuated. From the relationship between hydrogen bonding and proximity (between atoms that participate in a hydrogen bond) and the r^{-3} dependence of dipolar interactions, this dipolar-dephasing behavior provides strong support for identifying the 1.7 ppm peak as arising from isolated (non-hydrogen-bonded) silanols and the broad 3.0 ppm peak as clustered (hydrogen bonded) silanols. This is the same conclusion regarding proximity (and hydrogen bonding) that one would reach from the dehydration behavior shown in Figure 12. It would be difficult to rationalize the elimination

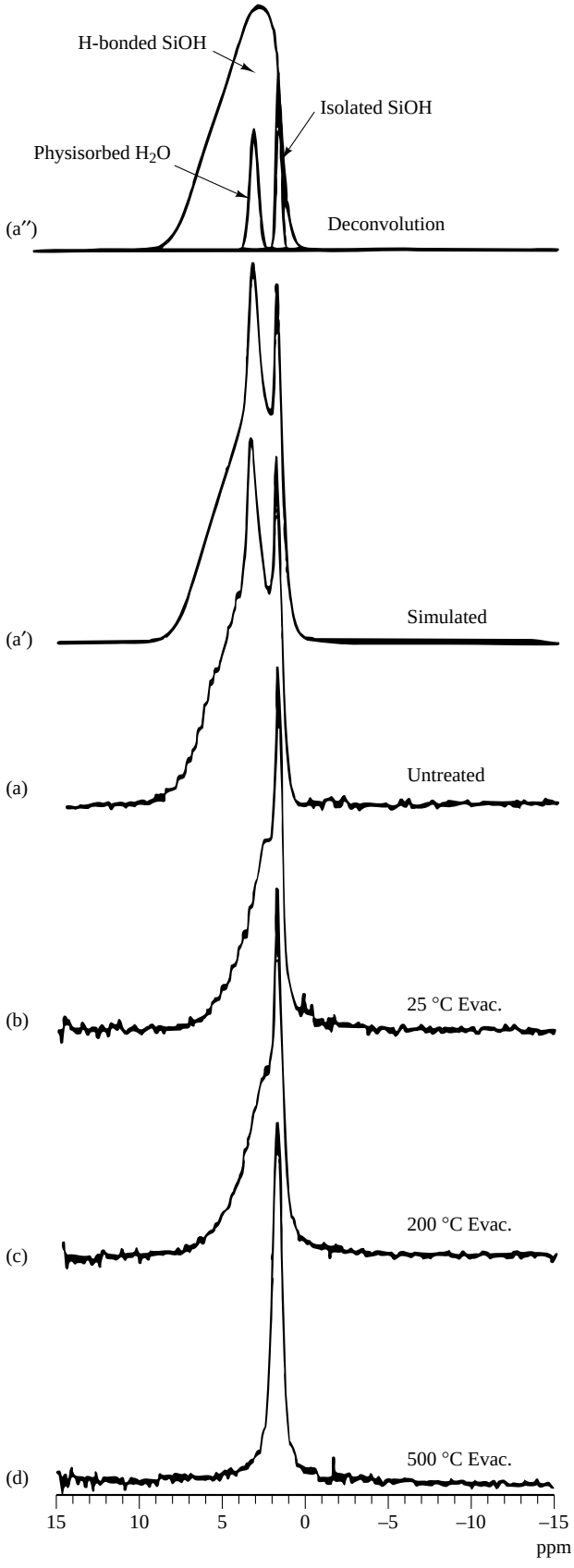

Figure 12 187-MHz ^1H CRAMPS spectra of Fisher S-679 silica gel. (a) untreated; (b) evacuated at 25 °C; (c) evacuated at 200 °C; (d) evacuated at 500 °C; (a″) deconvolution of spectrum (a); (a′) computer simulation based on (a″). (Taken from Bronnimann et al.[38])

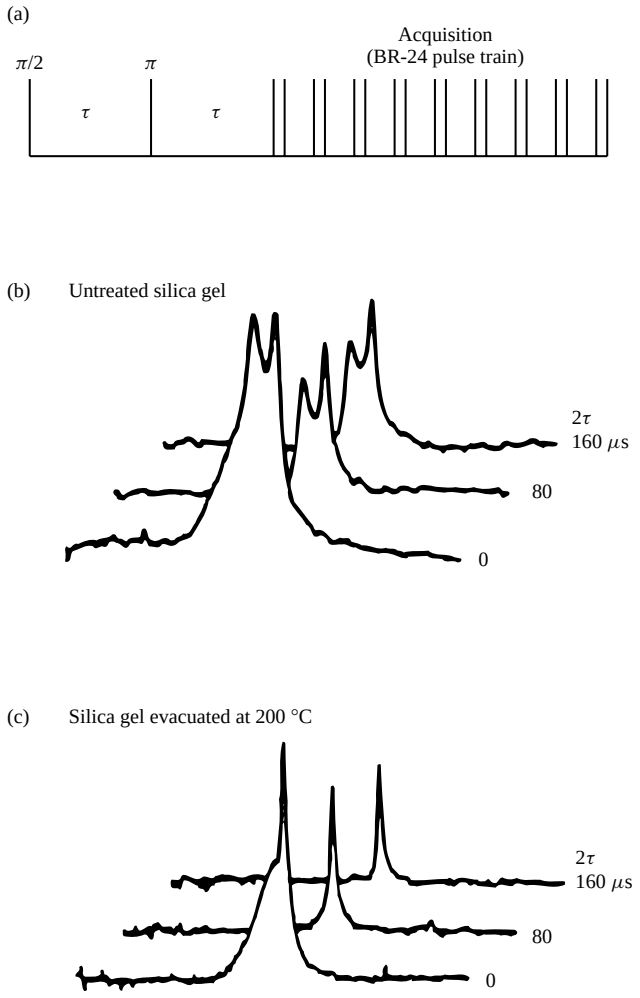

Figure 13 ^{1}H CRAMPS dipolar-dephasing experiment. (a) Pulse sequence. (b) results for untreated silica gel (showing τ values). (c) Results for sample evacuated at 200 °C (showing τ values). (Taken from Bronnimann et al.[38])

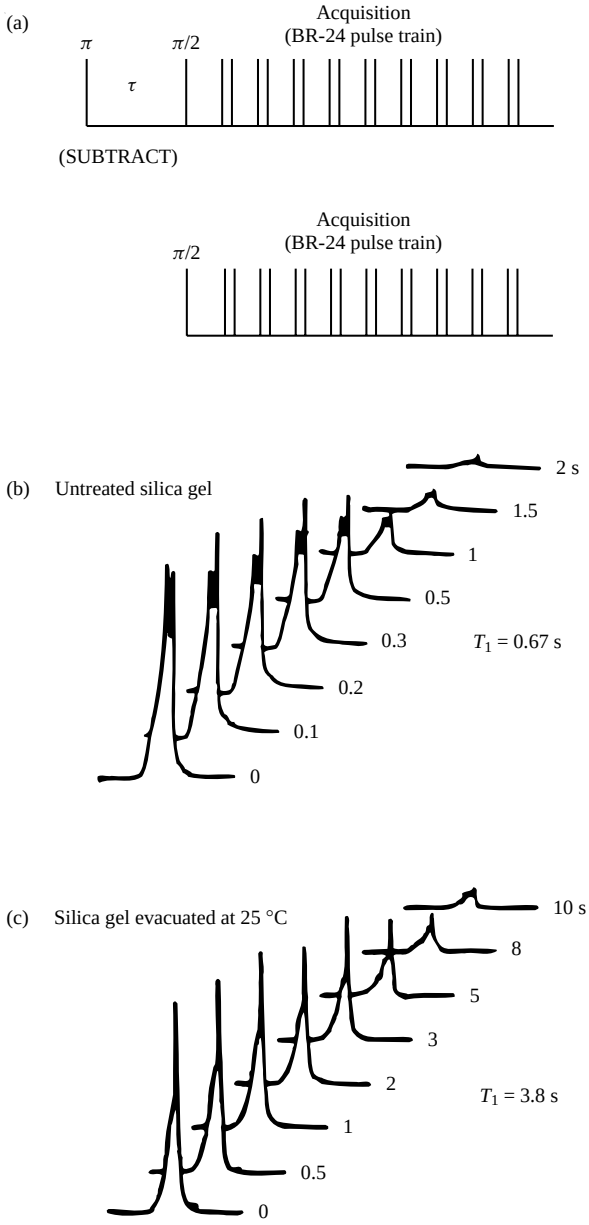

Figure 14 ^{1}H CRAMPS T_1 determination. (a) Pulse sequence, showing individual sequences employed in alternate scans (lower case subtracted from upper case in computer memory). (b) Results for untreated silica gel (showing τ values). (c) Results for sample evacuated at 25 °C. (Taken from Bronnimann et al.[38])

of water via the 'dehydration' of silanols that are *isolated* from each other. Since the physisorbed water peak (3.5 ppm) is only slightly attenuated by the 160 μs dephasing period [Figure 13(b)], one can conclude that water protons experience only weak resultant dipolar interactions, the result of efficient motional averaging.

Other CRAMPS-based ^{1}H time domain approaches have also been useful in studying silica surfaces. Figure 14 summarizes a CRAMPS-detected T_1^H determination on silica gel samples, based on an alternating, two-sequence scheme of the Freeman–Hill type.[39] One sees that for each of the two silica samples, untreated (b) and dried (c), all components of proton magnetization relax essentially homogeneously, which suggests that proton spin diffusion among the different spin isochromats is much more efficient that spin–lattice relaxation, which is characterized overall by T_1^H values of 0.7–4 s. Furthermore, the marked increase in T_1^H that results from sample drying indicates that the physisorbed water in the sample of Figure 14(b) provides an important relaxation source, and is presumably in a rapid state of motion at room temperature.[36] Having the ability to establish, via dipolar dephasing, different spin polarizations for hydrogen bonded and isolated silanols, one can explore spin exchange between these two spin sets by an experiment of the type shown in Figure 15(a).[38] One sees for the untreated silica [Figure 15(b)] that in a mixing time of a few ms after eliminating ^{1}H magnetization due to hydrogen-bonded silanols there is a substantial transfer of magnetization (spin exchange) from the isolated silanol reservoir to the hydrogen-bonded silanol protons. In any attempt to interpret or model the structure of the silica surface, the rate of this spin exchange places constraints on the spatial proximities of these two proton spin sets in terms of the dipole–dipole interactions that can be responsible for ^{1}H–^{1}H flip-flops, and/or chemical (H^+) exchange.

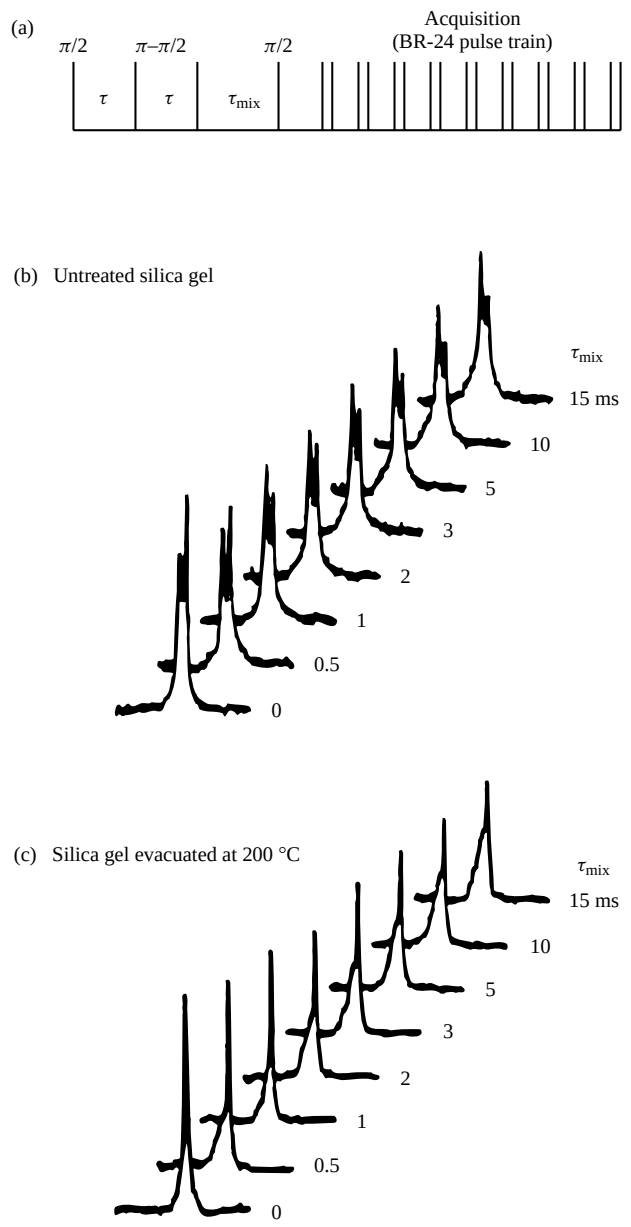

Figure 15 ^{1}H CRAMPS spin exchange experiment. (a) Pulse sequence. (b) Results for untreated silica gel (showing τ_{mix} values). (c) Results for sample evacuated at 200 °C (showing τ_{mix} values). (Taken from Bronnimann et al.[38])

A variety of CRAMPS-based ^{1}H NMR experiments of the types represented in Figures 12, 13, 14, and 15 have been carried out on silica samples in which there have been systematic variations of physisorbed water content or dehydration, and often temperature. Figure 16 shows ^{1}H CRAMPS dipolar-dephasing results obtained at room temperature on three different silica gels.[36] The behavior shown is consistent with the ideas described above. Figure 17 shows ^{1}H CRAMPS spectra of a hydrated (exposed to air) silica gel over a temperature range from 138 K to 298 K.[36] An effective freezing point depression of about 45 K can be noted from these kinds of measurements; this result is consistent with previous reports based on other types of experiments.[41]

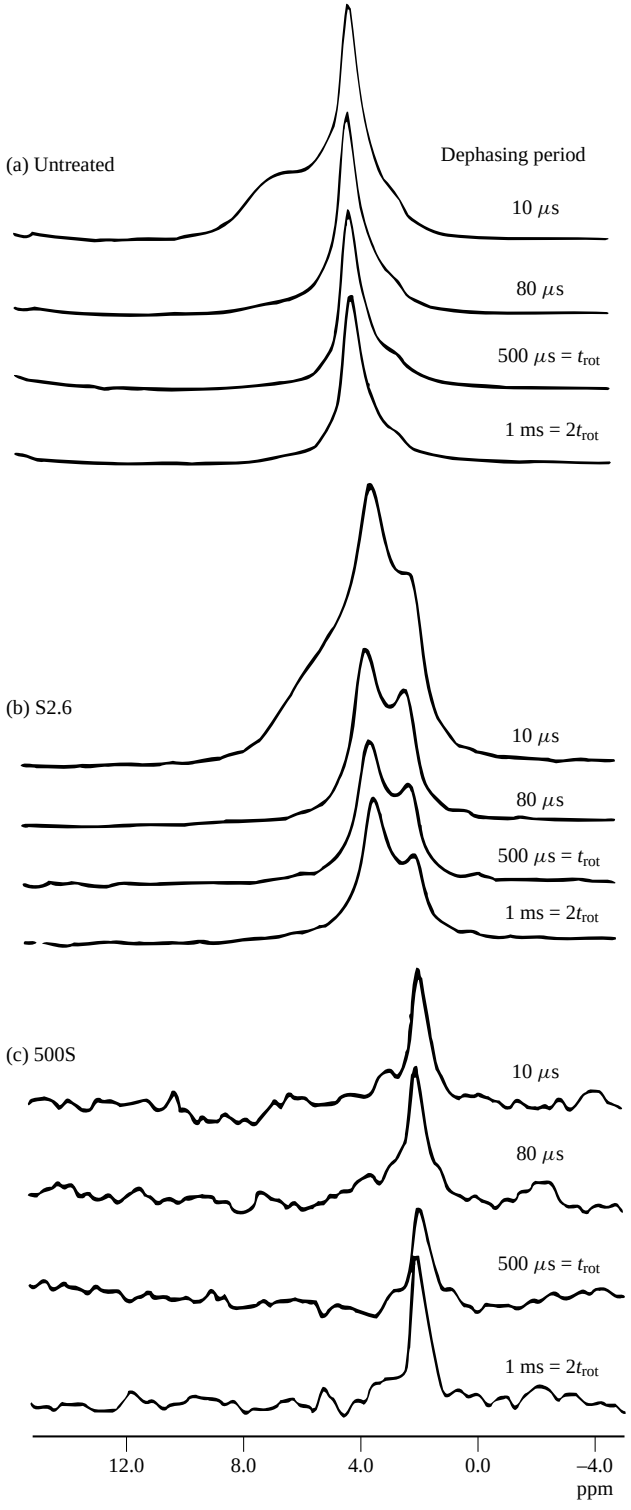

Figure 16 ^{1}H CRAMPS dipolar-dephasing spectra of three different silica gels. (a) Untreated. (b) Modestly dehydrated (2.6% weight loss). (c) Drastically dehydrated (at 500 °C)

5.5 Derivatized Silicas

Figures 18 and 19 show ^{1}H CRAMPS spectra of silica surfaces that have been derivatized with $(CH_3)_3SiCl$ and

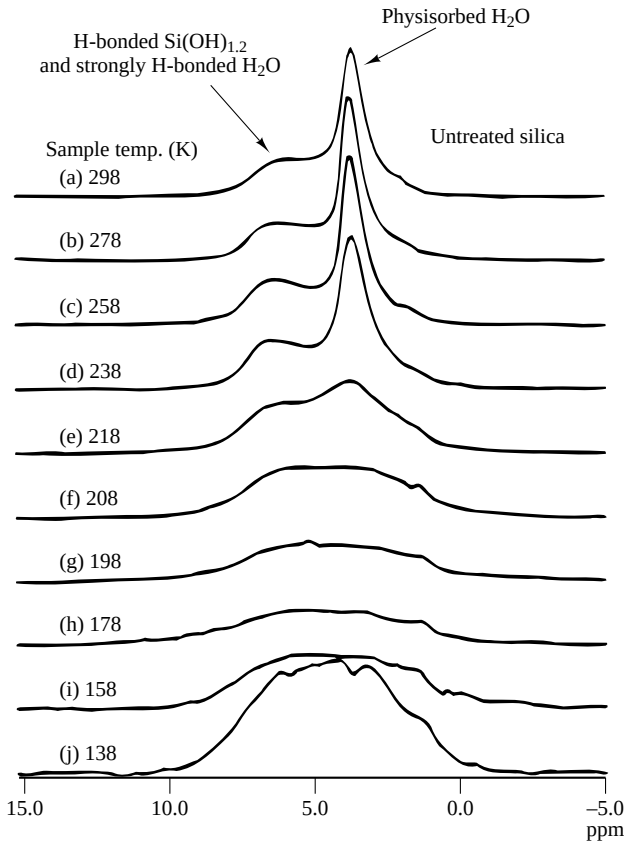

Figure 17 ^{1}H CRAMPS spectrum of an untreated silica gel as a function of temperature, as shown

$(CH_3CH_2O)_3SiCH_2CH_2CH_2NH_2$ (APTS), respectively. These spectra show that this technique can provide a rich level of structural detail on derivatized silica samples. The difference between the spectra of unprotonated and protonated APTS-derivatized samples (Figure 19) is the absence and presence, respectively, of a clearly distinct peak corresponding to the amino group of APTS.[29] This difference reflects, at least in part, the interference of ^{14}N quadrupole effects of the $-NH_2$ group with MAS averaging of $^{1}H-^{14}N$ dipolar interactions. Calculations on $=N-H$ groups show that, because of the small internuclear N–H distances for directly bonded pairs, very high NMR fields (>1000 MHz) would be required to reduce this broadening to an acceptable level by the 'brute force' approach of simply going to a higher field.[42]

6 CORRELATING ^{1}H-BASED AND ^{29}Si-BASED INFORMATION

6.1 Complementary Results

While one can distinguish between hydrogen bonded and isolated silanols by ^{1}H CRAMPS experiments and between single silanols and geminal silanols by ^{29}Si CP MAS experiments, it is important to correlate these two types of information. Ideally, one would base such a correlation on two-dimensional (2D) $^{1}H-^{29}Si$ heteronuclear chemical shift

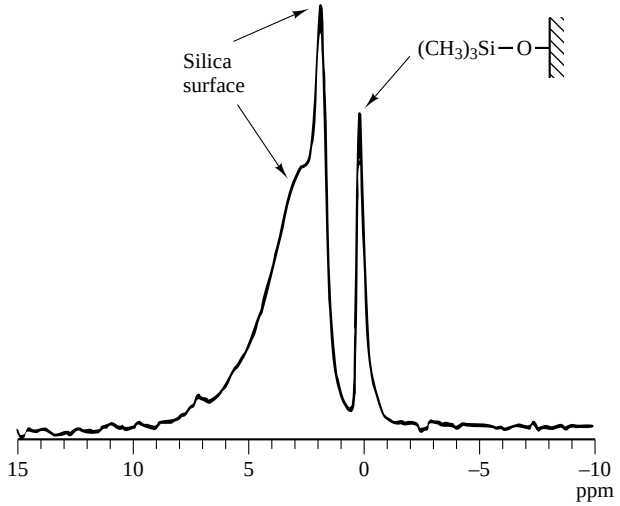

Figure 18 ^{1}H CRAMPS spectrum of trimethylsilyl-derivatized silica gel

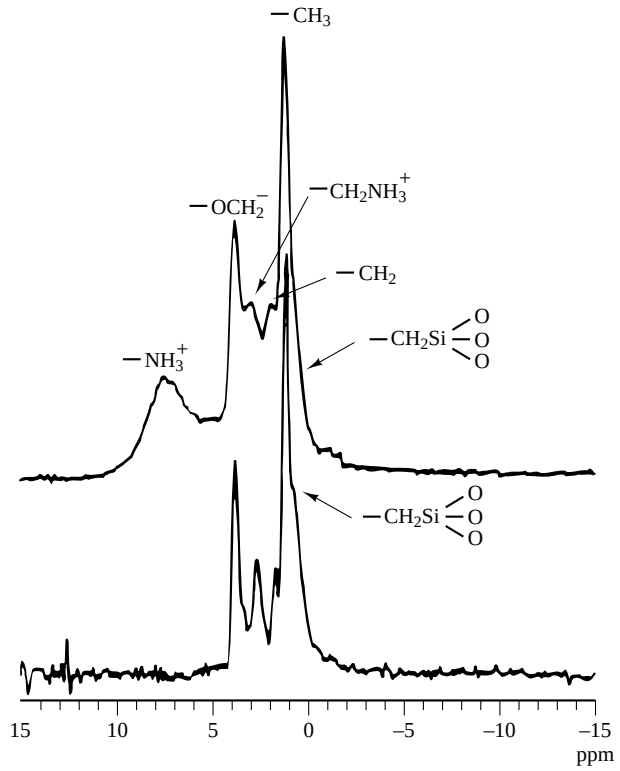

Figure 19 ^{1}H CRAMPS spectra of APTS-modified silica gel. Lower, untreated. Upper, treated with HCl. (Taken from Maciel et al.[29])

correlation (HETCOR) experiments of the general type that are employed routinely for $^{1}H-^{13}C$ correlation in liquids and more recently in solids.[43,44] Indeed, Vega has reported such experiments based on $^{1}H \rightarrow {}^{29}Si$ CP for the polarization transfer step.[45] However, as is seen below, rotating frame ^{1}H spin diffusion among the protons in a typical silica gel during the spin lock state in a $^{1}H \rightarrow {}^{29}Si$ CP experiment can substantially scramble what one would hope are discrete H $\leftrightarrow {}^{29}Si$ CP correlations in the time frame (>200 μs) required for relatively efficient CP transfer. Furthermore, the multiple

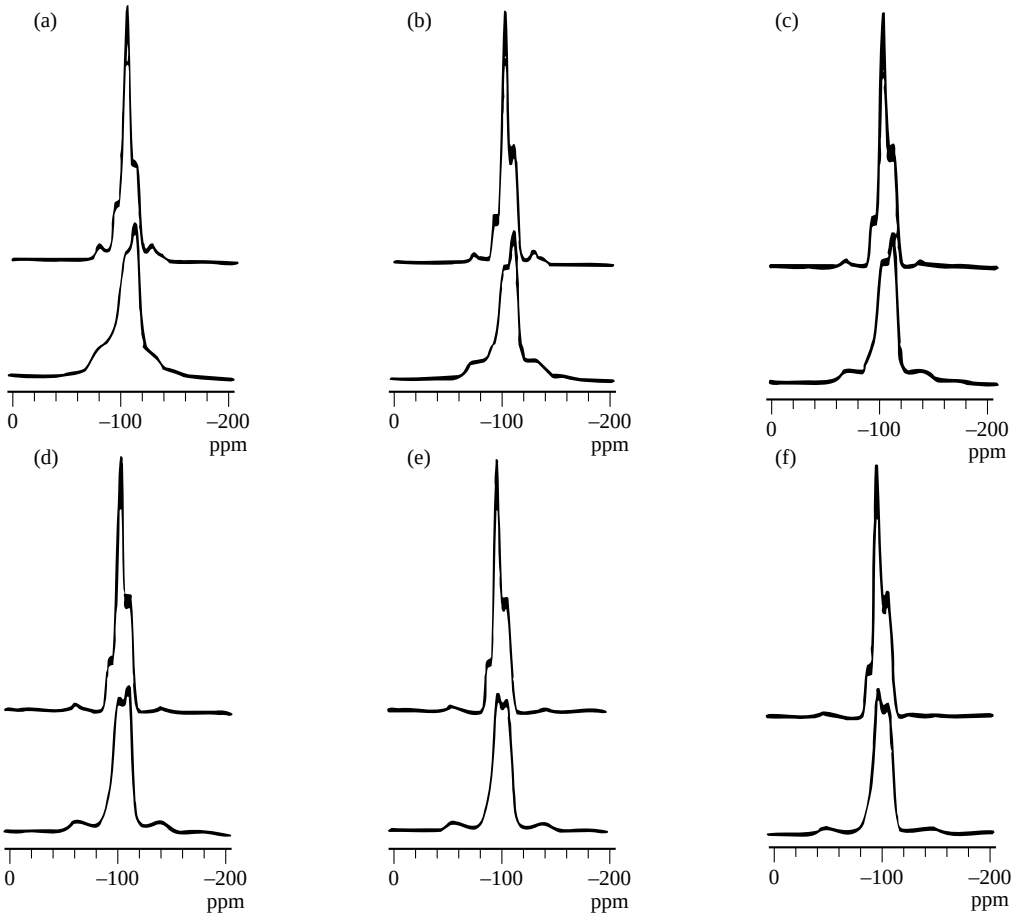

Figure 20 Proton-decoupled (top spectrum of each set) and proton-coupled (bottom spectrum of each set) 39.75 MHz ^{29}Si CP MAS NMR spectra of Fisher S-679 silica gel at six different magic angle spinning speeds. Cross polarization time, 5 ms. (a) 1.0 kHz, 1096 accumulations (b) 1.1 kHz, 3000 accumulations (c) 1.4 kHz, 720 accumulations (d) 1.6 kHz, 2000 accumulations (e) 1.8 kHz, 2000 accumulations (f) 2.0 kHz, 2000 accumulations. (Taken from Chuang et al.[47])

pulse approaches used in ^{1}H–^{13}C HETCOR experiments on solids are not very efficient in these ^{1}H–O–^{29}Si systems, although recently reported successes in ^{1}H–^{31}P 2D HETCOR experiments on P–O–H systems[46] indicate that ^{1}H–^{29}Si HETCOR in silica may be attractive. In any case, as an alternative to the 2D HETCOR approach, a variety of ^{29}Si-detected ^{1}H–^{29}Si CP experiments have been carried out, in which the behavior of protons is monitored by ^{29}Si, establishing the correlation.[47]

6.2 ^{29}Si Detection of Proton Spin Behavior

The simplest such experiment is a ^{29}Si CP MAS experiment in which ^{29}Si detection is carried out *without* proton decoupling. MAS should still average the ^{1}H–^{29}Si dipolar interaction during detection, yielding a corresponding sideband pattern to the extent that this interaction behaves inhomogeneously, i.e. to the extent that the ^{1}H–^{29}Si dipolar interaction is not altered (by chemical reaction, motion, or ^{1}H–^{1}H flip-flops) during a MAS rotor period.[47] Figure 20 shows a comparison of spectra obtained with and without ^{1}H decoupling; it is clear that the geminal silanol peak suffers most dramatically from the absence of high-power ^{1}H decoupling, implying that ^{1}H spin exchange is most efficient in the protons of geminal silanols.

Another ^{29}Si CP MAS experiment useful for correlating ^{1}H and ^{29}Si spin behaviors is the ^{1}H–^{29}Si analog of the common ^{1}H–^{13}C dipolar-dephasing experiment. In this technique, rotational and Hahn echo formation occur for a dephasing period (2τ) corresponding to two MAS rotor periods ($2\tau_{rot}$) for the isotropic ^{29}Si chemical shift, the ^{29}Si chemical shift anisotropy, and the ^{1}H–^{29}Si dipolar interaction (to the extent that it behaves inhomogenously).[47] Figure 21 shows results of the ^{1}H–^{29}Si dipolar-dephasing ^{29}Si CP MAS experiment with the dephasing period ranging over more than $4t_{rot}$. Focusing on the points at $2\tau = 0$, $2t_{rot}$ and $4t_{rot}$, one sees very little dephasing decay for the Q_4 (siloxane) signal, and more efficient decay for the Q_2 (geminal silanol) signal than for the Q_3 (single silanol) signal. This again suggests more efficient ^{1}H–^{1}H spin diffusion among the $=Si(OH)_2$ protons than among $\equiv$SiOH protons.

A very direct correlation of ^{1}H CRAMPS dipolar-dephasing behavior with ^{29}Si CP MAS signals is obtained in the experiment shown in Figure 22, in which there is a 2τ ^{1}H–^{1}H

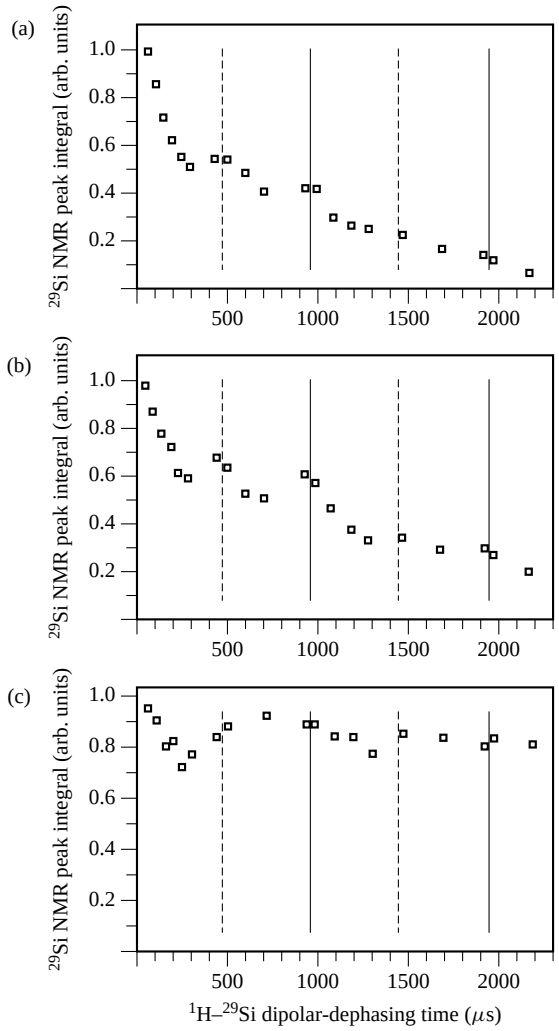

Figure 21 Plots of deconvoluted peak integrals of the 39.75-MHz ^{29}Si CP MAS NMR spectra of Fisher S-679 silica gel versus ^{1}H–^{29}Si dipolar-dephasing time up to four rotor periods. CP contact time, 5 ms; magic angle spinning speed, 2.0 kHz. Vertical dashed lines show odd numbers of rotor periods and vertical solid lines show even numbers of rotor periods. (a) −89 ppm peak (geminal silanols); (b) −99 ppm peak (single silanols); (c) −109 ppm peak (siloxane silicons). (Taken from Chuang et al.[47])

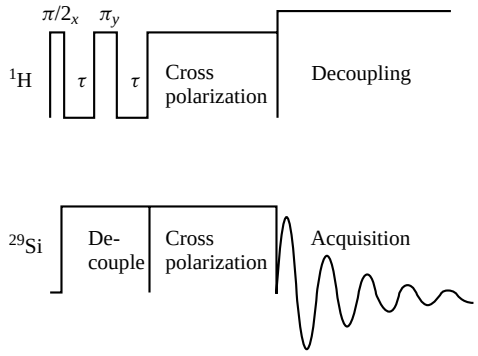

Figure 22 ^{29}Si CP MAS NMR experiment with ^{1}H–^{1}H dipolar-dephasing prior to ^{1}H → ^{29}Si cross polarization. (Taken from Chuang et al.[47])

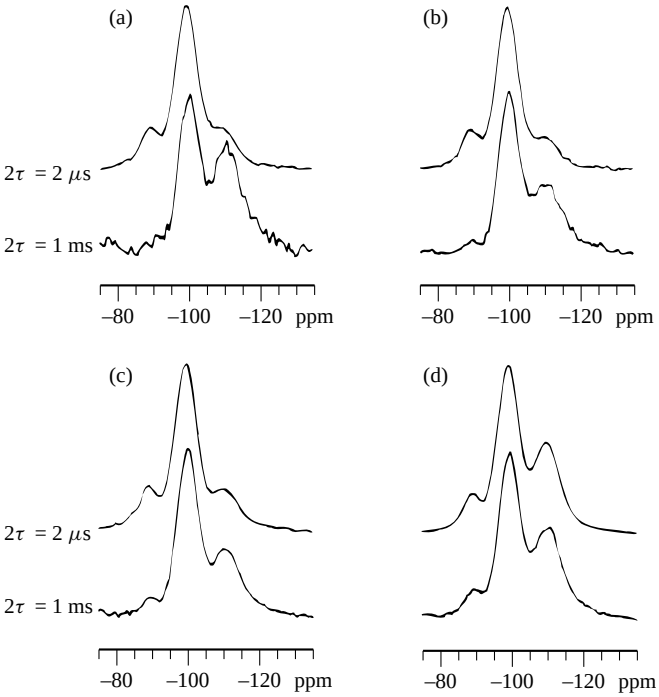

Figure 23 ^{29}Si CP MAS NMR spectra of Fisher S-679 silica gel obtained with 2 μs (top spectrum of each set) and two rotor periods (1.04 ms; bottom spectrum of each set) of ^{1}H–^{1}H dipolar-dephasing prior to four different ^{1}H–^{29}Si CP contact times. Magic angle spinning speed, 1.9 kHz. (a) t_{cp} = 100 μs (top spectrum, 7376 accumulations; bottom spectrum, 82 504 accumulations); (b) t_{cp} = 300 μs (top spectrum, 2400 accumulations; bottom spectrum, 46 200 accumulations); (c) t_{cp} = 1 ms (top spectrum, 432 accumulations; bottom spectrum, 21 232 accumulations); (d) t_{cp} = 5 ms (top spectrum, 600 accumulations; bottom spectrum, 8320 accumulations). (Taken from Chuang et al.[47])

dipolar-dephasing period *before* CP transfer to ^{29}Si.[47] Taking account of the rotational echo behavior of ^{1}H magnetization, for $2\tau = 2nt_{rot}$ essentially all relevant proton interactions refocus except the ^{1}H–^{1}H dipolar interaction. Hence, the magnetization of those protons involved in the strongest (shortest, least mobile) hydrogen bonds is most effectively dephased during $2\tau = 2nt_{rot}$ and unavailable for CP transfer to ^{29}Si. Figure 23 shows the results obtained on a silica gel sample. For a CP contact time (t_{cp}) that is small enough (100 μs) to avoid the rotating frame spin diffusion that scrambles the desired ^{1}H–^{29}Si correlation (vide supra), the geminal silanol peak at −89 ppm is the one that suffers most from ^{1}H–^{1}H dipolar dephasing for a $2t_{rot}$ period. The effect of rotating frame proton spin diffusion is also clear from the spectra in Figure 23: if a long CP contact period (e.g. 1–5 ms) is employed, essentially the same relative peak intensities are obtained whether or not the $2t_{rot}$ ^{1}H–^{1}H dipolar-dephasing period is included in the experimental sequence.

One overriding theme emerges from all the results embodied in Figures 20–23: the protons that are primarily responsible for cross polarization to geminal silanol silicons are much more extensively involved in hydrogen bonding than are the protons primarily responsible for cross polarization to single silanol silicons. This theme is consistent with structural models of the

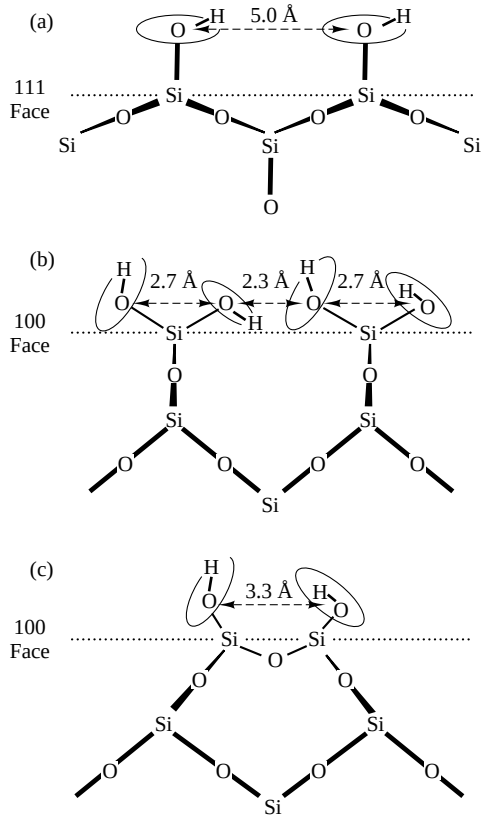

Figure 24 Side views of specific silicon planes (dashed line representing an edge of such a plane) of β-cristobalite. Drawing approximately to scale: (a) 111 face; (b) 100 face; (c) vicinal sites from dehydration of the 100 face. (Taken from Chuang et al.[47])

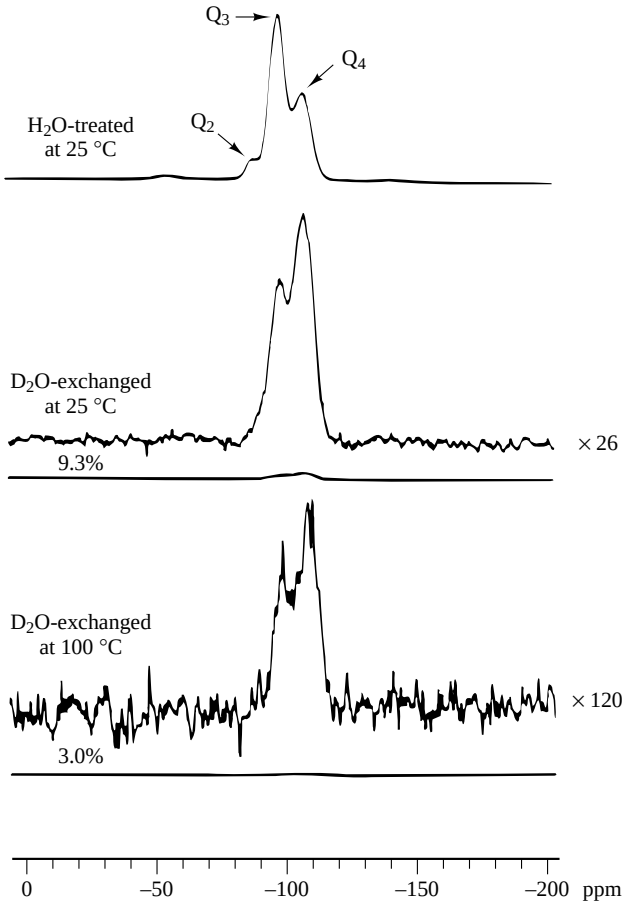

Figure 25 ^{29}Si CP MAS spectra of silica gels stirred in H_2O or D_2O at 25 °C or 100 °C, as indicated

silica surface (or, at least fragments of it) that correspond to specific faces of a β-cristobalite crystal.[47,48]

Figure 24 shows views looking 'into' the 111 and 100 faces, which contain single silanols (Q_3) and geminal silanols (Q_2), respectively. From the O–O distances between hydroxyl oxygens of these surfaces, we see that one should expect hydrogen bonding between adjacent geminal silanols, but not between adjacent single silanols; this is in agreement with the NMR results summarized above. Of course, the silica surface is not a homogeneous one, and may be describable as a composite of these two types of surfaces, with suitable interfaces. The geometrical relationship between silanols that are adjacent *across* these interfaces is important in the overall hydrogen-bonding patterns at silica surfaces. Furthermore, the presence of water on the surface dramatically changes the pattern of hydrogen bonding, including the establishment of hydrogen-bonding networks among the single silanols.

7 SUBSURFACE SILANOLS

An implicit assumption on which the use of ^{29}Si CP MAS as a kind of surface-selective technique is based is the following: essentially all (or at least most) of the protons of a sample like SiO_2 are at the surface. This assumption has been tested in a variety of ways, including ^{29}Si NMR. One NMR avenue for testing this assumption is to examine the ^{1}H and/or ^{29}Si NMR spectra of samples that have been subjected to repeated exchanges with D_2O. Figure 25 shows the ^{29}Si CP MAS spectra of silica gel samples that have been treated in this way.[40] From such studies, it has been determined that for a typical silica gel, 91–97% of the silanols are exchangeable with D_2O, the exact percentage depending on the time and temperature of the exchange. The geminal silanol signal is completely depleted by D_2O exchange, and Figure 26 shows that this signal is immediately restored to its equilibrium intensity shortly after a D_2O-exchanged silica is exposed to the moisture in air. Hence, none of the inaccessible or subsurface silanols are of the Q_2 type.

Extensive studies of spin dynamics in D_2O-exchanged samples have revealed a substantial amount of detail about the local environment and motional dynamics of 'internal' silanols in silica gel.[40] The T_{HSi} values indicate that the hydroxy groups of 'internal' silanols rotate freely about the Si–O axis in a manner similar to the rotation of non-hydrogen-bonded silanols on a dehydrated silica surface. Analogous studies have also been carried out on a fumed silica Cab-O-Sil.[24] While the D_2O-exchange behavior and various features of ^{1}H and ^{29}Si spin dynamics in Cab-O-Sil are qualitatively similar to what is discussed above for silica gel, some significant and possibly important differences are observed,[24] perhaps because of interparticle (particle bridging) silanols that have been suggested by some authors for fumed silicas.

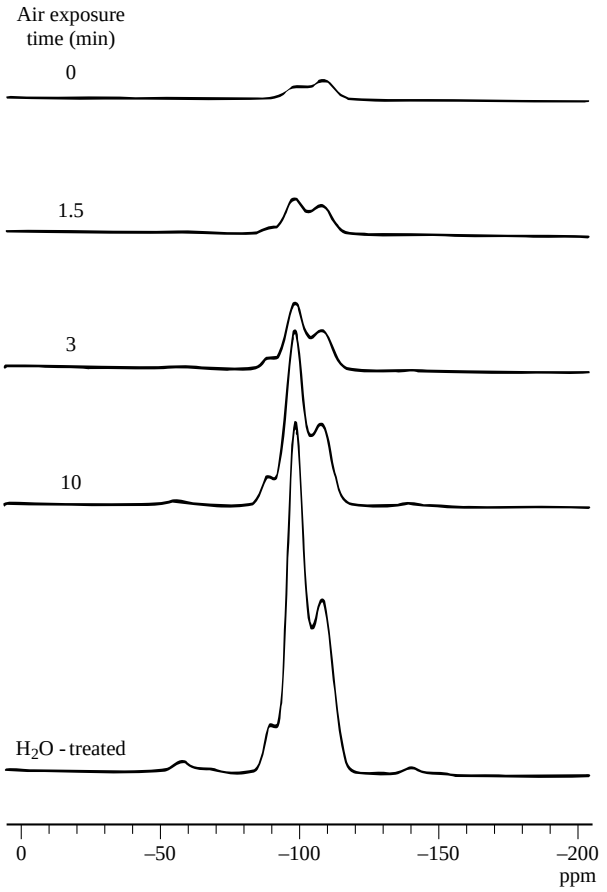

Figure 26 ^{29}Si CP MAS spectra of a D_2O-exchanged silica gel, after air exposure for the indicated times, or (bottom) stirred in H_2O

8 SUMMARY AND CONCLUSIONS

MAS NMR approaches based on ^{1}H and ^{29}Si are enormously useful in the characterization of silica surfaces, including derivatized silica surfaces. The CRAMPS technique, and especially dipolar-dephasing elaborations, provide a powerful way to distinguish between hydrogen bonding and isolated silanols. Silicon-29 CP MAS spectra clearly distinguish between Q_2, Q_3, and Q_4 sites at the surface. Via $^{1}H \rightarrow {}^{29}Si$ cross polarization, the ^{29}Si CP MAS technique provides avenues for projecting ^{1}H spin behavior onto a ^{29}Si NMR spectrum. D_2O-exchange approaches allow the use of ^{1}H and ^{29}Si NMR behavior to examine subsurface or trapped silanols.

9 RELATED ARTICLES

CRAMPS; Silicon-29 NMR of Solid Silicates.

10 REFERENCES

1. R. K. Iler, *The Chemistry of Silica. Solubility, Polymerization, Colloid and Surface Properties, and Biochemistry*, Wiley-Interscience, New York, 1979.
2. G. Engelhardt and D. Michel, *High Resolution Solid-State NMR of Silicates and Zeolites*, Wiley, New York, 1987.
3. G. E. Maciel, C. E. Bronnimann, R. C. Zeigler, I.-S. Chuang, D. R. Kinney, and E. A. Keiter, in *The Colloid Chemistry of Silica. Adv. Chem. Ser. No. 234*, ed. H. Bergna, Am. Chem. Soc., Washington, DC, 1994, p. 269.
4. G. E. Maciel and P. D. Ellis, in *NMR Techniques in Catalysis*, eds. A. T. Bell and A. Pines, Marcel Dekker, New York, 1994, pp. 231–310.
5. G. E. Maciel, in *Nuclear Magnetic Resonance in Modern Technology, NATO ASI Series C* ed. G. E. Maciel, Kluwer, Amsterdam, 1994, p. 225.
6. P. C. Hammel, P. L. Kuhns, O. Gonen, and J. S. Waugh, *Phys. Rev. B*, 1986, **34**, 6543.
7. R. A. Wind, M. J. Duijvestijn, C. Van Der Lugt, A. Manenschijn, and J. Vriend, *Prog. NMR Spectrosc.*, 1985, **17**, 33.
8. D. Raftery, H. Long, T. Meersmann, P. J. Grandinetti, L. Reven, and A. Pines, *Phys. Rev. Lett.*, 1991, **66**, 584.
9. A. Pines, W. G. Gibby, and J. S. Waugh, *J. Chem. Phys.*, 1973, **59**, 569.
10. G. E. Maciel and D. W. Sindorf, *J. Am. Chem. Soc.*, 1980, **102**, 7606.
11. D. W. Sindorf and G. E. Maciel, *J. Phys. Chem.*, 1982, **86**, 5208.
12. J. Schaefer and E. O. Stejskal, *J. Am. Chem. Soc.*, 1976, **98**, 1031.
13. M. Mehring, *High Resolution NMR in Solids*, Springer, Berlin, 1983, p. 135.
14. D. W. Sindorf and G. E. Maciel, *J. Am. Chem. Soc.*, 1983, **105**, 1487.
15. G. E. Maciel, D. W. Sindorf, and V. J. Bartuska, *J. Chromatogr.*, 1981, **205**, 438.
16. D. W. Sindorf and G. E. Maciel, *J. Am. Chem. Soc.*, 1981, **103**, 4263.
17. D. W. Sindorf and G. E. Maciel, *J. Am. Chem. Soc.*, 1983, **105**, 3767.
18. D. W. Sindorf and G. E. Maciel, *J. Phys. Chem.*, 1983, **87**, 5516.
19. G. S. Caravajal, D. E. Leyden, G. R. Quinting, and G. E. Maciel, *Anal. Chem.*, 1988, **60**, 1776.
20. C. J. Brinker, R. J. Kirkpatrick, D. R. Tallant, B. C. Bunker, and B. Montez, *J. Non-Cryst. Solids*, 1988, **99**, 418.
21. C. J. Brinker, R. K. Brow, D. R. Tallant, and R. J. Kirkpatrick, *J. Non-Cryst. Solids*, 1990, **120**, 26.
22. S. Léonardelli, L. Facchini, C. Fretigny, P. Tougne, and A. P. Legrand, *J. Am. Chem. Soc.*, 1992, **114**, 6412.
23. A. Tuel, H. Hommel, A. P. Legrand, Y. Chevallier, and J. C. Morawski, *Colloid Surf.*, 1990, **45**, 413.
24. C. Liu and G. E. Maciel, unpublished results.
25. L. L. Hench and J. K. West, *Chem. Rev.*, 1990, **90**, 33.
26. I. Elnahhal, J. Yang, I.-S. Chuang, S. F. Dec, and G. E. Maciel, *J. Non-Cryst. Solids*, submitted.
27. T. H. Walter, G. L. Turner, and E. Oldfield, *J. Magn. Reson.*, 1988, **76**, 106.
28. C. E. Bronnimann, B. L. Hawkins, M. Zhang, and G. E. Maciel, *Anal. Chem.*, 1988, **60**, 1743.
29. G. E. Maciel, C. E. Bronnimann, and B. L. Hawkins, in *Advances in Magnetic Resonance: The Waugh Symposium*, ed. W. S. Warren, Academic Press, San Diego, CA, 1990, Vol. 14, pp. 125–150.
30. Z. Luz and A. J. Vega, *J. Phys. Chem.*, 1987, **91**, 374.
31. J. S. Waugh, L. M. Huber, and V. Haeberlen, *Phys. Rev. Lett.*, 1968, **20**, 180.
32. W.-K. Rhim, D. D. Elleman, and R. W. Vaughan, *J. Chem. Phys.*, 1973, **58**, 1772.
33. D. P. Burum and W. K. Rhim, *J. Chem. Phys.*, 1979, **71**, 944.
34. B. C. Gerstein, R. G. Pembleton, R. C. Wilson, and L. M. Ryan, *J. Chem. Phys.*, 1977, **66**, 361.

35. S. F. Dec, C. E. Bronnimann, R. A. Wind, and G. E. Maciel, *J. Magn. Reson.*, 1989, **82**, 454.
36. D. R. Kinney, I.-S. Chuang, and G. E. Maciel, *J. Am. Chem. Soc.*, 1993, **115**, 6786.
37. D. Suwelack, W. P. Rothwell, and J. S. Waugh, *J. Chem. Phys.*, 1980, **73**, 2559.
38. C. E. Bronnimann, R. C. Zeigler, and G. E. Maciel, *J. Am. Chem. Soc.*, 1988, **110**, 2023.
39. R. Freeman and H. D. Hill, *J. Chem. Phys.*, 1971, **54**, 3367.
40. I.-S. Chuang, D. R. Kinney, and G. E. Maciel, *J. Am. Chem. Soc.*, 1993, **115**, 8695.
41. R. J. Wittebort, M. G. Usha, D. J. Ruben, D. E. Wemmer, and A. Pines, *J. Am. Chem. Soc.*, 1988, **110**, 5668.
42. R. A. Lewis, Ph.D. Dissertation, Colorado State University, 1994.
43. D. P. Burum and A. Bielecki, *J. Magn. Reson.*, 1991, **94**, 645.
44. C. E. Bronnimann, C. Ridenour, D. R. Kinney, and G. E. Maciel, *J. Magn. Reson.*, 1992, **97**, 522.
45. A. J. Vega, *J. Am. Chem. Soc.*, 1988, **110**, 1049.
46. R. A. Santos, R. A. Wind, and C. E. Bronnimann, *35th Exp. NMR Conf., Asilomar, CA, April 14, 1994*.
47. I.-S. Chuang, D. R. Kinney, C. E. Bronnimann, R. C. Zeigler, and G. E. Maciel, *J. Phys. Chem.*, 1992, **96**, 4027.
48. D. W. Sindorf, Ph.D. Dissertation, Colorado State University, 1982.

Acknowledgments

For that portion of the research described in this paper that was carried out at Colorado State University, the author gratefully acknowledges partial support by National Science Foundation grants during the past few years. He also acknowledges the invaluable assistance over many years of Dr. I.-Ssuer Chuang.

Biographical Sketch

Gary E. Maciel. *b* 1935. B.S., 1956, chemistry, University of California, Berkeley, Ph.D., 1960, Massachusetts Institute of Technology (MIT). Postdoctoral work at MIT (with John S. Waugh), 1960–61 which provided first hands-on experience with NMR. Assistant professor, associate professor, professor at the University of California, Davis, 1961–70. Professor of Chemistry, Colorado State University, 1971–present. Approx. 320 publications. Research specialties: development and application of NMR techniques, especially for solids and surfaces, and currently for environmental studies.

Silicon-29 NMR of Solid Silicates

Günter Engelhardt

University of Stuttgart, Stuttgart, Germany

1	Introduction	1
2	Silicate Structure Types	1
3	Experimental NMR Techniques	2
4	General Features of the Spectra and Spectral Parameters	3
5	Survey of Information on Silicate Structure Available from the Spectra	5
6	Applications	9
7	Related Articles	9
8	References	9

1 INTRODUCTION

Though static ^{29}Si CW NMR spectra of quartz, cristobalite, amorphous silica, and silicate glasses were measured as early as 1956,[1] it was more than 20 years before the first systematic study of solid silicates by ^{29}Si MAS FT NMR spectroscopy was accomplished.[2] Subsequently, the application of this method has grown rapidly and is now a powerful tool in the structural characterization of a wide range of silicate materials. The development is closely related to the great progress made in the 1980s in the instrumentation and methods for the registration of solid state ^{29}Si NMR spectra and their detailed interpretation. Nowadays, high magnetic field strengths and a wide selection of experimental NMR techniques, such as MAS, high-power dipolar decoupling, cross polarization (CP), two-dimensional experiments, and variable temperature measurements, are available on modern solid state NMR spectrometers. Moreover, it was shown even in the initial work on ^{29}Si MAS NMR of silicates and related materials, and has been further confirmed in numerous subsequent studies, that the ^{29}Si chemical shift is most sensitive to the chemical and structural surroundings of the silicon atoms. Chemically and/or crystallographically inequivalent Si sites can thus be detected by distinct resonances in the spectra. Moreover, empirical and theoretical relations have been established between the ^{29}Si chemical shift and the kind, number, and structural arrangement of the nearest and second-nearest neighbor atoms of the silicon atom. Silicon-29 MAS NMR can thus provide detailed information on the local structure around the silicon atoms and is, therefore, a valuable complement to X-ray or neutron diffraction techniques which monitor the periodic long-range order of crystalline materials.

Silicon-29 MAS NMR can also be successfully applied to amorphous or highly disordered solids, the study of which by X-ray diffraction (XRD) techniques is notoriously difficult. It should be emphasized, however, that, at least for crystalline materials, the combination of ^{29}Si NMR and XRD results is often a prerequisite for the reliable interpretation of the NMR spectra and, also, particularly appropriate for a more complete and detailed description of the structure.

Numerous papers have been published on the application of solid state ^{29}Si NMR to a wide range of crystalline and amorphous silicates and aluminosilicates, and the progress in the field has recently been summarized in several review articles.[3–5] In addition, a comprehensive review of the fundamentals and applications of ^{29}Si NMR to silicates considering the literature up to 1986 has been presented in a book.[6] Extensive compilations of ^{29}Si chemical shift data of silicates are given, for example, in Stebbins[4] and Engelhardt and Michel.[6]

In this article a concise review is given of ^{29}Si NMR spectroscopy of silicates with emphasis on the application of solid state MAS NMR techniques to powder samples. In particular, the characteristic features of the ^{29}Si MAS NMR spectra and the related information on structure and composition of silicates are considered from a general point of view and illustrated by selected examples. However, no detailed discussion on specific classes of silicate materials, such as zeolites, minerals, glasses, and amorphous silica, is presented since other articles in the Encyclopedia are devoted to these subjects (see, e.g. ***Molecular Sieves: Crystalline Systems***; ***Geological Applications***; ***Amorphous Materials***; ***Silica Surfaces: Characterization***). To facilitate the subsequent discussions, Section 2 gives a brief introduction to the general structure of silicates and aluminosilicates and the notation used for their description. Section 3 summarizes the pertinent techniques in solid state NMR of ^{29}Si. The general features of the ^{29}Si MAS NMR spectra and their intrinsic parameters are discussed in Section 4, followed, in Section 5 by a survey of the specific information available from ^{29}Si NMR on structure and composition of silicates and aluminosilicates. Finally, applications of ^{29}Si NMR to selected subjects are summarized in Section 6.

2 SILICATE STRUCTURE TYPES

The basic structural units of the silicate framework are SiO_4 tetrahedra which link together in a great variety of ways by sharing the oxygen atoms at their vertices. The resulting configurations can be classified by their topology:[7] SiO_4 tetrahedra may exist as isolated monomeric anions (nesosilicates), or may be connected by sharing one or two oxygen atoms forming dimeric and trimeric structures (sorosilicates), rings (cyclosilicates), or infinite chains (inosilicates). Single rings and chains may be put together to build up double rings or multiple chains, respectively, and, by linking an infinite number of chains, two-dimensional single layers (layer- or phyllosilicates) are formed. Connection of two or more tetrahedral layers results in the formation of double layers and finally infinite three-dimensional frameworks (tectosilicates). The number of oxygen atoms *not* shared by a second silicon atom ('nonbridging oxygens') determines the negative charge of the complex anionic silicate network, which is balanced by the positive charge of cations located within the interstices of the structure.

Aluminosilicates may be thought of as being formed from silicates by isomorphous replacement of SiO_4 with AlO_4 tetrahedra. The extra charge introduced by the negatively charged AlO_4 tetrahedra must be balanced by additional cations elsewhere in the structure. The distribution of Si and

Al atoms on the tetrahedral sites of the framework may be ordered or disordered and is, in general, governed by Loewenstein's rule,[8] which suggests that AlO_4 tetrahedra in aluminosilicate networks do not share oxygen atoms ('AlOAl avoidance principle').

Crystalline silicates and aluminosilicates play an important role as rock-forming minerals and as synthetic materials of great industrial and scientific interest. There is also a wide range of disordered or noncrystalline systems, such as amorphous silicates and silicas, gels, and glasses, the structure of which also consists of joined SiO_4 (and possibly AlO_4) tetrahedra, but lacking in any distinct long range order or lattice periodicity. A few silicate structures are known which contain sixfold coordinated silicon, i.e. SiO_6 octahedra (e.g. stichovite, thaumasite), and fivefold coordinated SiO_5 has recently been observed in quenched high-pressure silicate glasses and crystalline $CaSiO_3$ samples.[9]

For the presentation of the structure of building units or silicate anions in the following, the commonly used Q^n notation is adopted.[6] In this notation, Q represents a silicon atom bonded to four oxygen atoms forming a tetrahedron. The superscript n indicates the connectivity, i.e. the number of other Q units attached to the SiO_4 tetrahedron in question. Thus, Q^0 denotes the monomer orthosilicate anion SiO_4^{4-}, Q^1 end groups of chains, Q^2 middle groups in chains or rings, Q^3 chain branching sites, and Q^4 three-dimensionally cross-linked groups. A subscript denotes the number of equal Q^n units present in the corresponding silicate anion species. For aluminosilicates the number of AlO_4 tetrahedra bound to the central silicon of a Q^n unit is given in parentheses, e.g. $Q^n(m\mathrm{Al})$ means a SiO_4 group connected via oxygen bridges to m Al and $n - m$ other Si atoms, where $n = 0{-}4$ and $m \leq n$. In framework aluminosilicates, which are built up exclusively from $Q^4(m\mathrm{Al})$ units, the designation $\mathrm{Si}(n\mathrm{Al})$ is also used. The constitution of the basic Q^n, $\mathrm{Si}(n\mathrm{Al})$, and $Q^3(m\mathrm{Al})$ units is also depicted in Figures 5, 6, and 8 shown in a later section (Section 5.3).

To avoid confusion it should be noted that the general term 'silicate' is often used in this article in its broadest sense, i.e. it may include both silicates (only Si on tetrahedral sites) *and* aluminosilicates (Si and Al on tetrahedral sites).

3 EXPERIMENTAL NMR TECHNIQUES

Although single crystal (see ***Chemical Shift Tensors in Single Crystals***) or static powder ^{29}Si NMR can provide valuable information on local bonding and symmetry in silicates, these techniques have only been applied sparingly. Complete single crystal studies are time consuming and require, at least for work with ^{29}Si in its natural abundance (4.7%), relatively large crystals (usually about 5 mm in diameter), which are normally not available. Static powder studies yield direct information on the anisotropy of the ^{29}Si chemical shift but suffer from broad and often overlapping resonances and also need long measuring times.

The main reason for line broadening in the ^{29}Si NMR spectra of solid silicates is, in general, shielding anisotropy which can be fully averaged by the MAS technique (see ***Magic Angle Spinning***). Therefore, the overwhelming majority of solid state ^{29}Si NMR studies of silicates have been performed using MAS of powder samples. The chemical shift anisotropy for ^{29}Si in silicates is generally less than 100 ppm. Thus, narrow isotropic lineshapes without or with only weak spinning sidebands can be observed at magnetic field strengths $\boldsymbol{B}_0$ up to 9.4 T by MAS applying spinning frequencies of about 4–6 kHz. Such spinning rates are easily attainable by standard MAS probes with rotors of 7 mm diameter and, if necessary, even spinning rates up to 15 kHz and more can be achieved if smaller rotors (4 mm diameter) are used. Moreover, residual spinning sidebands may be removed by special sideband suppression techniques. If the orientational information available from chemical shift anisotropy data is of particular interest, the three components of the shielding tensor can be retrieved from the detailed analysis of MAS sideband patterns (see ***Sideband Analysis in Magic Angle Spinning NMR of Solids***) registered at moderate spinning rates. The MAS technique also averages weak heteronuclear dipolar interactions to distant protons or to other NMR-active nuclei, e.g. ^{27}Al in aluminosilicates. Stronger dipolar couplings of ^{29}Si to nearby protons can be removed by *high-power proton decoupling*.

In addition to MAS and dipolar decoupling, which by the line-narrowing effect result in a considerable improvement of the signal-to-noise ratio of the spectra, the intensities of the ^{29}Si NMR peaks may be substantially enhanced by use of the ^{1}H–^{29}Si CP technique, (see ***Cross Polarization in Solids*** and ***Cross Polarization in Rotating Solids: Spin-1/2 Nuclei***), provided that ^{1}H nuclei capable of polarization transfer to ^{29}Si are present in the sample. In silicates and related materials the most likely candidates for CP are protons of SiOH groups, but under certain conditions also protons of water or organic molecules adsorbed onto porous materials, or functional groups bonded at the silicates surface may give effective CP enhancements. Another advantage of the CP technique is that significantly shorter repetition times for spectral accumulation can be applied since the magnetization recovery of the protons is governed by the longitudinal relaxation time $T_{1\mathrm{H}}$ rather than $T_{1\mathrm{Si}}$, the former being generally much shorter. Beside the gain in sensitivity, ^{29}Si CP MAS NMR spectra may provide valuable information on specific proton–silicon coordinations, e.g. on SiOH groups or more distant Si$\cdots$H interactions (see Section 5.7). However, because the CP efficiency is determined by the cross-relaxation rate ${T_{\mathrm{HSi}}}^{-1}$ which depends strongly on the Si$\cdots$H distance (${T_{\mathrm{HSi}}}^{-1} \propto {r_{\mathrm{HSi}}}^{-6}$), the resulting intensity enhancement in the CP MAS spectra may be rather different for distinct Si sites. Therefore, ^{29}Si CP MAS NMR spectra of silicates are not always quantitatively reliable in the sense of single pulse MAS spectra. For quantitative information from ^{29}Si CP NMR spectra, detailed studies of the CP characteristics by contact time variation and relaxation measurements (T_{HSi}, $T_{1\rho\mathrm{H}}$) are required.

Substantial gains in sensitivity and resolution are further achieved by application of high magnetic field strength $\boldsymbol{B}_0$. It is thus generally advantageous to measure ^{29}Si MAS NMR spectra of silicates at high field, e.g. at $B_0 \geq 7$ T, corresponding to resonance frequencies of ν_0 (^{29}Si) $\geq$ 59.6 MHz.

Structural transformations and dynamic processes in solid silicates and their melts can be profitably studied by ^{29}Si MAS NMR experiments at varying temperatures. In principle, variable temperature MAS NMR measurements in the range of about -100 to $+200\,^\circ$C can be performed with most commercially available MAS probes by cooling or heating the sample via the flowing gas stream used for sample spinning.

However, extension of the range of temperatures applicable in MAS NMR experiments remains a technical challenge. Nevertheless, sample temperatures of up to 600–700 °C have been achieved in special designs of gas- or laser-heated MAS probes. Even higher temperatures have been reached in static NMR experiments, and temperatures up to 1250 °C have been applied to static ^{29}Si NMR investigations of solid and molten silicates.[10]

Two-dimensional (2D) NMR techniques are well established in solution studies but have found only limited use so far in solids. There have been, however, several successful studies on the connectivity patterns of tetrahedral Si sites in microporous silica polymorphs with a complex framework structure (see Fyfe et al.[11] and references therein) and glasses[12] using the well-known COSY or INADEQUATE pulse sequences. In these studies scalar coupling interactions in the ^{29}Si–O–^{29}Si connections are used to establish the three-dimensional (3D) connectivities of the silicate framework. In addition, a 2D ^{1}H–^{29}Si CP MAS NMR heteronuclear correlation experiment has been proposed which provides specific information on SiOH groups at the silicate surface.[13] In general, ^{29}Si isotopic enrichment of the samples considerably reduces the measuring times, but 2D ^{29}Si MAS NMR spectra have also been obtained from natural abundance materials, making the method quite generally applicable.

4 GENERAL FEATURES OF THE SPECTRA AND SPECTRAL PARAMETERS

4.1 From Liquids to Solids

Liquid state high-resolution ^{29}Si NMR has been used extensively to study the structure and quantitative distribution of silicate anions present in aqueous silicate solutions of a great variety of compositions (for a review see Chapter III of Engelhardt and Michel[6]). In general, sharp lines appear in the solution spectra, the chemical shifts of which depend sensitively on the specific structural surrounding of the SiO_4 tetrahedra. Characteristic chemical shift ranges were observed for the different Q^n units, and about 20 distinct silicate anion types containing up to 10 silicon atoms could be positively identified by detailed considerations of the shift effects owing to next-nearest and second-nearest Q^n connections, chain length, cyclization, and, in particular, of scalar spin–spin couplings in ^{29}Si isotopically enriched silicate solutions.[14] In addition, the incorporation of aluminum into silicate anions has been proved in highly alkaline, diluted, aluminosilicate solutions.[6,15]

Clearly, this potential of ^{29}Si NMR to provide detailed information on the silicate structure should be extremely useful if it could also be applied to solid silicates. However, line broadening in solids prevents resolution of distinct signals for structurally different Si sites in the spectra if conventional NMR techniques are used. Therefore, application of MAS and possibly dipolar decoupling is required to narrow the lines, as considered in the preceding section. Although the high resolution of liquid state NMR spectra is normally not attained in solid silicates, well-separated narrow resonances are observed in the ^{29}Si MAS NMR spectra of highly crystalline materials. Moreover, the spectra of solid silicates are often much simpler than those of silicate solutions since the variety and complexity of silicate anion types is normally greatly reduced in the crystalline solid. A striking example is shown in Figure 1 by the ^{29}Si NMR spectra of a crystalline sodium silicate hydrate and its liquid melt which corresponds to the solution of the same composition.[16] While the crystalline sample exhibits a single line of the monomeric Q^0 unit, the liquid shows a number of resonances representing different silicate anions. On the other hand, specific solid state effects may cause additional line splittings or line shifts not present in the solution spectra, which can provide valuable information on subtle details of the solid structure. This is demonstrated in Figure 2 by the ^{29}Si MAS NMR spectrum of the trimethylsilyl ester of cubic octamer silicate 'Q_8M_8' (M denotes the trimethylsilyl group). The spectrum of Q_8M_8 in benzene solution (not shown) exhibits two sharp lines at +12.4 ppm for the silicon in the M group and at −108.6 ppm for the silicon in the Q group, indicating a highly symmetric structure of the Q_8M_8 molecule in solution. In the crystalline solid, the resonances are split into three (δ = 11.76, 11.70, 11.50 ppm) and four (δ = −108.34, −108.62, −109.33, −109.68 ppm) components, respectively, owing to a slight asymmetric deformation of the Q_8 cube in the crystal lattice (resulting in four inequivalent pairs of Q sites) and nonequivalent orientations of the M groups, in full agreement with the X-ray structure.[17] Note also the excellent resolution

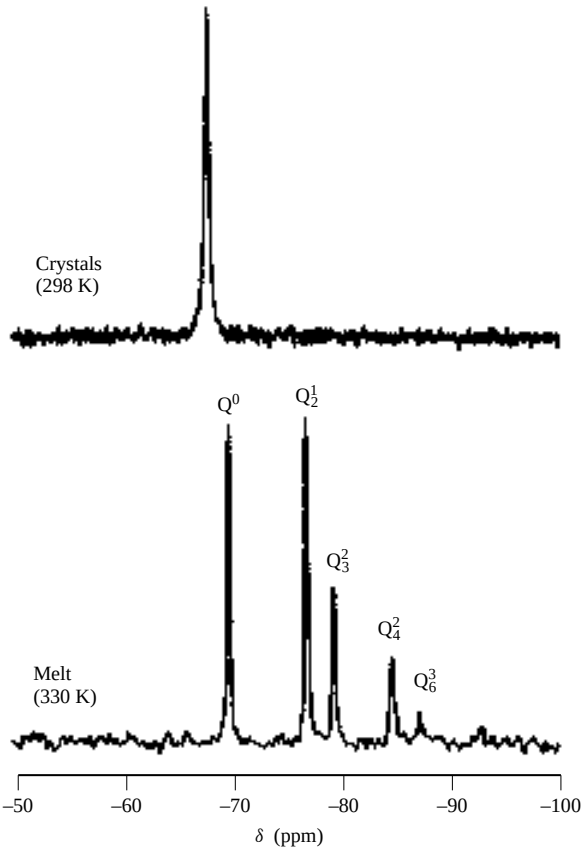

Figure 1 ^{29}Si MAS NMR spectra of crystalline sodium silicate hydrate of composition $Na_2H_2SiO_4{\cdot}8H_2O$ and its melt. The line assignment to monomer (Q^0), dimer (Q1/2), cyclotrimer (Q2/3), cyclotetramer (Q2/4), and prismatic hexamer (Q3/6) silicate anions is indicated in the spectrum of the melt.

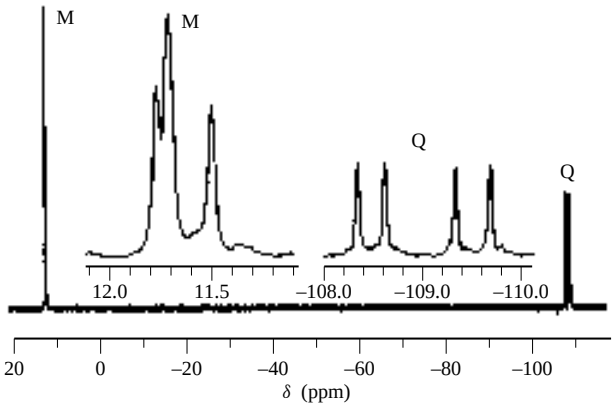

Figure 2 ^{29}Si CP MAS NMR spectrum of crystalline Q_8M_8 (the cubic octamer silicic acid trimethylsilyl ester, $[Si_8O_{20}][Si(CH_3)_3]_8$). The inserts are expanded regions of the M and Q signals.

achieved permitting the clear separation of two lines with a chemical shift difference of only 0.06 ppm in this spectrum. Owing to the sharp lines, the large dispersion of the M and Q resonances, the well-defined line splittings, and the dynamics of the CP processes, crystalline Q_8M_8 powder is particularly well suited for checking the spectrometer resolution, setting the Hartmann–Hahn match for CP experiments, and for use as a secondary chemical shift reference.

Although, as shown above, characteristic differences may appear between liquid and solid state spectra, it is important to note that the general relationships between spectral characteristics and structure deduced from the ^{29}Si NMR spectra of silicate solutions also hold for solid silicates and may, therefore, provide a first guideline for the interpretation of the solid state spectra.

4.2 Spectral Parameters

The individual peaks of a ^{29}Si NMR spectrum are characterized by three main parameters, which can be readily extracted from the spectrum: the chemical shift, δ, the intensity, I, and the linewidth, $\Delta\nu_{1/2}$. These parameters are closely related to the structure of the sample being investigated and are preferentially used in structural ^{29}Si NMR studies of silicates. Some general relationships between the NMR parameters and structural features of silicates will be considered below.

4.2.1 Chemical Shift

Most of the structural information that can be derived from ^{29}Si NMR spectra of silicates arises from the chemical shifts. Since δ is dependent on the electronic environment of the ^{29}Si nucleus, it is closely related to the type, position, and bonding characteristics of the surrounding atoms. For silicate structures and related systems, many empirical relationships between δ and structural features have been established, and, at least in part, substantiated by theoretical considerations (see below). In particular, a shift of approximately 10 ppm to lower frequency is generally observed for each newly formed SiOSi connection in a given Q^n environment, while each replacement of silicon with aluminum in a $Q^n(m\text{Al})$ environment induces a shift contribution of about 5 ppm to higher frequency. Consequently, the central Si atoms of the $Q^n(m\text{Al})$ units are more shielded with increasing connectivity, n, and decreasing number of Al atoms, m.

Besides the chemical environment, δ further depends on the particular geometry around the Si atom in question. Linear correlations have been established between δ and the mean SiOT (T = Si, Al) bond angles, α, nonbonded Si–Si distances, d_{SiSi}, Si–O bond lengths, d_{SiO}, and, for cubic structures, lattice parameters, a_0, all derived from the X-ray structures of a large number of framework silicates and aluminosilicates. The correlations indicate low-frequency shifts of δ with decreasing d_{SiO} and increasing α, d_{SiSi}, and a_0.

These dependences could be rationalized by a simple theoretical model (see Engelhardt[18] and references therein) combining quantum chemical calculations with the general shielding theory. In short, the model shows that shielding increases almost linearly with the (positive) net atomic charge, q_{Si}, at the silicon atom, which itself rises with the number of SiOT bridges, n, and decreases with the number of Al atoms, m, of the $Q^n(m\text{Al})$ environments. This result from the theoretical model is in full agreement with the experimental observations considered above. The q_{Si} value further depends on the degree of s hybridization, ρ, of the oxygen bond orbitals in the four O–Si bonds defining the SiO_4 tetrahedron. Since ρ is related to the SiOT bond angle, α, by $\rho = \cos\alpha/(\cos\alpha - 1)$, and reciprocal to d_{SiO}, the observed correlation with larger shielding at increasing α and decreasing d_{SiO} is confirmed by the theoretical model.

A simple relationship has further been derived between δ and the structures of a large number of silicate minerals and ^{29}Si chemical shifts, which is based on the magnetic susceptibility anisotropy of the bonds to second-nearest neighbors modified by the bond valence and the angle at the bridging oxygen.[19]

Finally, it should be noted that δ is further extremely sensitive to the coordination number of the silicon atom. Large, low-frequency shifts are observed in going from four- to five- to sixfold silicon coordination by oxygen (see below).

4.2.2 Line Intensity

In general, the integrated intensities of the peaks observed in a ^{29}Si NMR spectrum are directly related to the number of corresponding silicon atoms present in the sample. Thus, from relative peak intensities the quantitative proportions of the various structurally distinct Si sites can be determined. However, in order to obtain reliable signal intensities, the pulse repetition times and pulse width (flip angle) used in the spectral registration must be carefully selected to avoid saturation due to insufficient spin relaxation between the pulses. The relaxation times T_1 of ^{29}Si in silicates may be rather long in certain cases (up to several thousand seconds) and may differ for different Si sites in the sample. In such cases the pulse timing must be adjusted with regard to the longest T_1. As mentioned above, the signal intensities of CP spectra are often not quantitatively reliable owing to different CP efficiencies of Si in structurally distinct surroundings.

4.2.3 Linewidth

Provided that instrumental factors, such as inhomogeneity of the $\boldsymbol{B}_0$ field and missetting of the magic angle or rotor

instabilities, can be excluded, the most likely contributing factors to the linewidth in ^{29}Si MAS NMR spectra of silicates are (i) dispersion of chemical shifts due to structural disorder, distortion, or amorphization of the silicate framework, (ii) residual dipolar interactions of the ^{29}Si nucleus with ^{1}H, ^{27}Al, or other NMR active nuclei, and (iii) the presence of paramagnetic impurities.

Line broadening by chemical shift dispersion is a very common occurrence in the spectra and is very often the limiting factor for the linewidth. Chemical shift dispersion occurs owing to slightly different environments around nominally equivalent $Q^n(m\,Al)$-type silicon atoms characterized by small distortions of bond angles and bond lengths. The latter may be created by lattice imperfections, crystallographic inequivalence, or local distributions of second-nearest and further tetrahedral neighboring atoms, but also by localized cations or other nonframework constituents. Hence, very broad resonances ($\Delta\nu_{1/2} \approx 10-20$ ppm) are observed for highly disordered systems, such as amorphous or glassy materials, while narrow peaks ($\Delta\nu_{1/2} \approx 0.1-3$ ppm) appear in the ^{29}Si MAS NMR spectra for highly crystalline, perfectly ordered silicates. Insufficient MAS averaging of dipolar interactions with protons of water of hydration or hydroxyl groups can be overcome by high-power proton decoupling. Line broadenings due to dipolar interactions between ^{29}Si and the quadrupolar ^{27}Al nuclei in aluminosilicates may be significant for direct Si–O–Al pairings but are essentially eliminated at $\boldsymbol{B}_0$ field strengths of 4.7 T or higher. Paramagnetic centers (e.g. heavy metal cations) present in the sample as impurities or constituent parts of the structure can give rise to severe line broadening or may even render the spectrum undetectable, as, for example, observed for samples of olivine with different Fe^{2+} contents.[20]

5 SURVEY OF INFORMATION ON SILICATE STRUCTURE AVAILABLE FROM THE SPECTRA

In this section the information on local structure and chemical composition that can be derived from the ^{29}Si NMR spectra of solid silicates will be summarized from a general point of view. Unless otherwise stated the following considerations refer to ^{29}Si MAS NMR spectra of microcrystalline samples recorded at high magnetic field strengths and under optimum conditions for maximum spectral resolution and reliable line intensities.

5.1 Number and Population of Si Sites in Nonequivalent Environments

The most direct and rather fundamental information which follows immediately from the number of distinct resonances observed in the ^{29}Si MAS NMR spectra is the number of chemically and/or crystallographically inequivalent Si sites present in the silicate sample. Moreover, from the normalized peak intensities, the relative populations of the various sites can be determined. The number of inequivalent sites that can be distinguished in the spectra depends on the relationship between spectral resolution (linewidth) and chemical shift difference between the distinct resonances. As mentioned above, for highly crystalline samples with well-ordered structures, usually very narrow lines are observed, and subtle differences in the structural surrounding of the corresponding Si sites may be detected. Figure 3 shows the ^{29}Si MAS NMR spectrum of highly crystalline tricalcium silicate, Ca_3SiO_5, a major constituent of Portland cement. The X-ray structure of Ca_3SiO_5 reveals the presence of nine crystallographically distinct Si sites in isolated SiO_4^{4-} tetrahedra (Q^0). In full agreement with this structure, the spectrum exhibits seven clearly resolved lines, two of them with double intensities, for the nine Q^0 environments in the narrow range of -69 to -75 ppm.[21] In contrast, amorphous, glassy or ill-crystallized samples with highly disordered structures show, in general, broad and overlapping resonances rendering the interpretation of the spectra difficult. However, if sensible assumptions can be made on line positions and lineshapes, the spectra may be analyzed by decomposition and line fitting procedures.

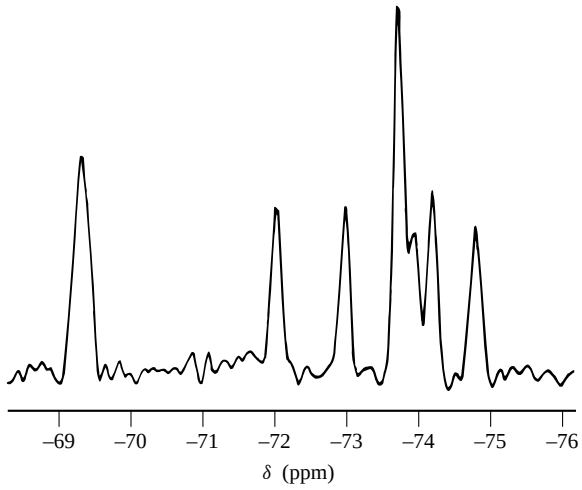

Figure 3 ^{29}Si MAS NMR spectrum of tricalcium silicate, Ca_3SiO_5. (Reproduced by permission of the American Chemical Society from Mägi et al.[21]).

5.2 Coordination Number of Si

The vast majority of silicates contain fourfold coordinated silicon but a number of structures with six-coordinated Si are also known. Silicon-29 MAS NMR can clearly distinguish between the different Si coordination numbers owing to large differences in the ^{29}Si chemical shifts. While δ values between -60 and -120 ppm are typical of four-coordinated SiO_4 in silicates,[6] the resonances of octahedral SiO_6 coordinations, as observed e.g. in thaumasite, stishovite,[22] $MgSiO_3$-rich garnets, perovskites, and other high-pressure silicate minerals[23] appear in the range between -170 and -220 ppm. The clear distinction between four- and six-coordinated Si is demonstrated in Figure 4 by the ^{29}Si MAS NMR spectrum of a high-pressure $MgSiO_3$ sample which exhibits several resonances that could be attributed to the SiO_4 and SiO_6 environments of distinct silicate phases present in this material.[23] Silicon-29 NMR has also revealed the presence of five-coordinated SiO_5 in silicate materials. Weak resonances at about -150 ppm have recently been attributed to SiO_5 in quenched high-pressure alkali silicate glasses and crystalline $CaSiO_3$ samples.[9]

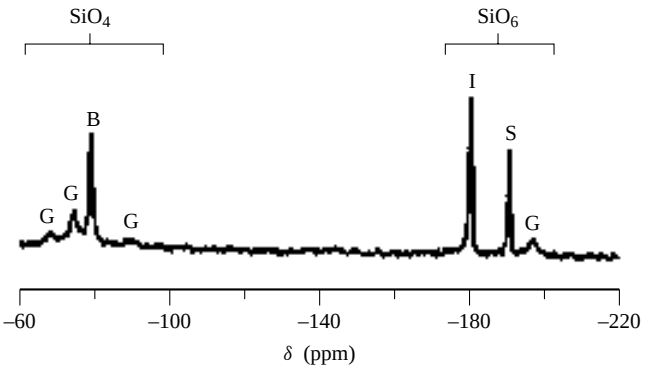

Figure 4 ^{29}Si MAS NMR spectrum of a high-pressure $MgSiO_3$ phase showing resonances of four- and six-coordinated silicon in garnet (G), β-$MgSiO_3$ (B), ilmenite (I), and stishovite (S). (Reproduced by permission of the American Association for the Advancement of Science from Stebbins and Kanzaki[23]).

5.3 Local Chemical Environment of SiO_4 Tetrahedra

It was shown in Section 4.2.1 that the ^{29}Si chemical shifts of SiO_4 tetrahedra in silicates depend sensitively on type and structural arrangement of the second nearest neighbor atoms at the silicon atom. There are, in particular, two characteristic features which affect the ^{29}Si chemical shift of a SiO_4 group: characteristic shifts to lower frequency are observed with increasing number of SiOT bridges (T = Si, Al) formed by the SiO_4 tetrahedron (SiO_4 connectivity), and typical shifts to higher frequencies follow from the replacement of Si with Al in the second coordination sphere of the central silicon (degree of tetrahedral Al substitution). Similar effects have been observed for substitution of tetrahedral Ga in gallosilicates.[6]

A large number of aluminum-free silicates of different degree of SiO_4 connectivity, i.e. neso-, soro-, cyclo-, ino-, and layer silicates and silica polymorphs, have been studied by ^{29}Si MAS NMR, and the resulting ranges of δ for the five Q^n environments are displayed in Figure 5. The increasing shielding with higher degree of SiO_4 connectivity, n, is obvious. However, with the exception of the Q^4 units, the Q^n

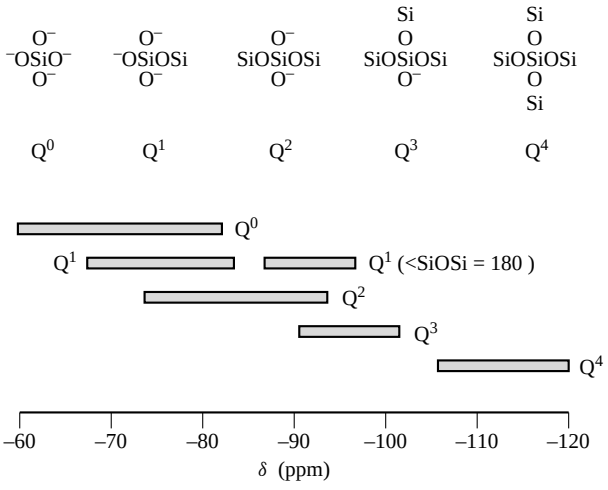

Figure 5 Ranges of ^{29}Si chemical shifts of $Si(O^-)_{4-n}(OSi)_n$ coordinations (Q^n) in silicates. (Reproduced by permission of Springer-Verlag from Engelhardt and Koller[5]).

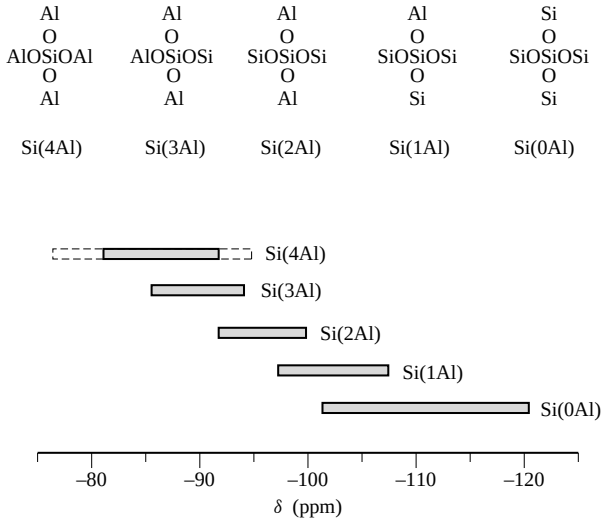

Figure 6 Ranges of ^{29}Si chemical shifts of $Si(OSi)_{4-n}(OAl)_n$ coordinations [Si(nAl)] in tectoaluminosilicates. The dotted lines for Si(4Al) designate the particularly large range observed for 1:1 aluminosilicate sodalites with different cage fillings.[18] (Reproduced by permission of Springer-Verlag from Engelhardt and Koller[5]).

shift ranges overlap significantly and a simple correlation of δ and Q^n type for a silicate of unknown structure is likely to be risky. Nevertheless, δ may be used as a guide to the Q^n units present, especially if other shift contributions originating from, e.g., cation effects or different geometry are considered.[21]

The characteristic ranges of shift for the five Si(nAl) (or Q^4(mAl) environments in framework aluminosilicates shown in Figure 6 have been established from a large body of shift data measured in various types of tectoaluminosilicates, silica polymorphs, and, in particular, zeolites. Only Q^4-type silicons are present in framework silicates but, as in the case of Q^n, the ranges of δ for the Q^4(mAl) units overlap. Nevertheless, the assignment of the usually well-separated lines to the corresponding Si(nAl) units is, in general, feasible. As an example, Figure 7 shows the MAS NMR spectrum of ^{29}Si in a microporous framework aluminosilicate with an Si/Al atomic ratio of 2.2, i.e. zeolite ZK-5. Five well-resolved resonances are observed which can easily be attributed to the five distinct Si(nAl) environments by the chemical shifts. Spectra of this type are quite typical for aluminosilicates and do not depend very much on the particular framework structure, at least if no crystallographically inequivalent Si sites are present in the structure. With decreasing Al content (i.e. increasing Si/Al ratio) the intensities shift from the high-frequency lines for Si(nAl) with higher n to those of the low-frequency Si(nAl) lines with lower n, and vice versa, i.e., single-line spectra were observed for Si/Al = 1, i.e. Si(4Al), and for Si/Al = ∞ (SiO_2), i.e. Si(0Al).

Finally, the typical ranges of δ for the four different Q^3(mAl) tetrahedral units in layer aluminosilicates are displayed in Figure 8. Similar to the tectoaluminosilicates, multiple resonances observed for a certain layer silicate can usually be attributed to the distinct Q^3(mAl) units, despite the overlap of the δ ranges. Besides the aluminum atoms incorporated in the tetrahedral silicate layer, further aluminum may be present in the octahedral sheet which, however, induces comparatively small effects on δ.

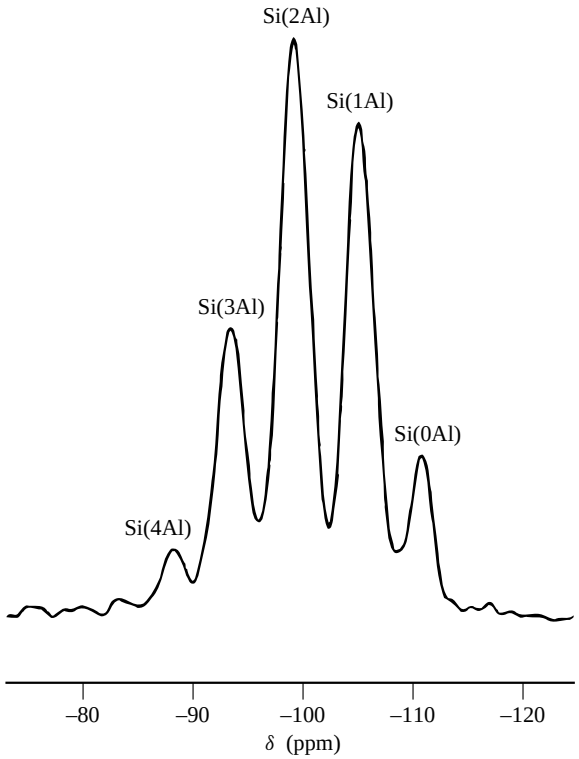

Figure 7 ^{29}Si MAS NMR spectrum of zeolite ZK-5, a microporous tectoaluminosilicate of Si/Al = 2.2. The line assignments to the five distinct Si(nAl) coordinations are indicated.

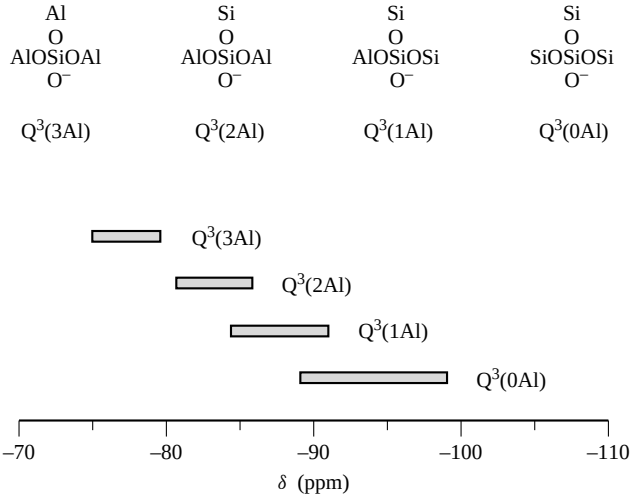

Figure 8 Ranges of ^{29}Si chemical shifts of Si(OH)(OSi)$_{3-m}$(OAl)$_m$ coordinations [Q^3(mAl)] in layer aluminosilicates. (Reproduced by permission of Springer-Verlag from Engelhardt and Koller[5]).

5.4 Atomic Ratio of Si/Al in the Aluminosilicate Framework

Provided that the NMR spectrum of ^{29}Si in an aluminosilicate is correctly interpreted in terms of the different Q^n(mAl) units, the atomic ratio of tetrahedral Si and Al in the structure can be calculated from the peak intensities according to the equation

$$\mathrm{Si/Al} = \sum_{m=0}^{n} I_{n,m} / \sum_{m=0}^{n} (m/n) I_{n,m} \qquad (1)$$

where $I_{n,m}$ are the intensities of the Q^n(mAl) peaks and summation is from $m = 0$ to $m = n$, i.e., from 0 to 3 in layer aluminosilicates and from 0 to 4 in framework aluminosilicates.[6] The above equation is independent of the specific structure of the aluminosilicate and includes the aluminum which is substitutionally incorporated into the tetrahedral framework, but excludes any nonframework aluminum frequently present, e.g. in layer aluminosilicates and in chemically or thermally treated zeolites. If the total Si/Al ratio of such samples is known from the overall chemical composition, the proportion of nonframework Al can readily be determined.

5.5 Ordering of Si and Al in the Aluminosilicate Framework

For the general case of a random distribution of Si and Al atoms on the tetrahedral sites of an aluminosilicate framework of Si/Al atomic ratio $1/p$, the probabilities of the occurrence of the various Q^n(mAl) configurations can be calculated by the binomial probability distribution

$$P_{n,m} = \frac{n!}{m!(n-m)!} p^m (1-p)^{n-m} \qquad (2)$$

It is obvious that the Si, Al distribution cannot be random if the relative Q^n(mAl) intensities measured in the ^{29}Si NMR spectrum of a certain aluminosilicate are significantly different from the calculated probabilities. If, however, the calculated populations and observed intensities are similar, then both ordering and disorder are possible. Hence ^{29}Si NMR can disprove random substitution of Si and Al but cannot prove it.

Specific information about the topological Si, Al distribution can be derived by comparing the relative Q^n(mAl) populations obtained from ^{29}Si NMR peak intensities with model-generated populations. The latter may be derived, e.g. from ordering schemes which are constructed by distributing the respective number of Si and Al atoms on the T sites of a certain repeating unit of the structure. It should be noted, however, that NMR monitors the averaged local environments of the Si atoms throughout the framework and the whole sample volume, which do not, therefore, necessarily imply any simple long-range ordering. Nevertheless, specific Si, Al distributions or, less specifically, the degree of dispersion of Al atoms over the framework has been deduced from the ^{29}Si MAS NMR spectra of a number of zeolites and layer aluminosilicates with different tetrahedral Si/Al ratios. A review of the strategies and methods applied is given in Chapter V of Engelhardt and Michel.[6] For recent applications see, for example, Herrero.[24]

5.6 Crystallographically Inequivalent Si Sites

The broad shift ranges observed for the distinct Q^n and Q^n(mAl) environments (see Figures 5, 6, and 8) indicate

the influence of different bonding geometries around the Si atom on δ, as already discussed in Section 4.2.1. Distinct resonances may thus be observed in the ^{29}Si MAS NMR spectra for Si atoms residing in chemically equivalent $Q^n(m\mathrm{Al})$ environments but occupying crystallographically nonequivalent sites which differ in SiOT bond angles and/or SiO bond lengths. Pertinent examples are the splittings of the Q^3 and M lines in the spectrum of Q_8M_8 (Figure 2), the seven Q^0 lines observed in Ca_3SiO_5 (Figure 3), and the appearance of several resonances in the ^{29}Si MAS NMR spectra of a variety of silica polymorphs and high-silica zeolites,[6] e.g. the 20 lines observed for the 24 crystallographically inequivalent Q^4 sites in the monoclinic form of silicalite.[25] The number and, from line intensities, the relative occupancies of crystallographically distinct Si sites can thus be obtained from the spectra and may be directly related to the results of diffraction experiments. Moreover, for framework silicates the mean SiOT bond angles, α, of the different Si sites can be estimated from δ by applying the quantitative correlations between δ and α considered in Section 4.2.1. These correlations reveal that δ changes by about 0.6 ppm for a 1° change in α. Since, for highly crystalline materials, a peak-to-peak resolution of 0.1 ppm can be achieved in the ^{29}Si MAS NMR spectra, differences in the mean bond angles of about 0.2° may be detected. If the mean bond angles are known from X-ray structure refinements, δ can be calculated which may be helpful in the correct assignment of multiline spectra,[18] as, for example, in the case of the above-mentioned silicalite.[26]

5.7 Characterization of SiOH Groups in Silicate Materials

It was shown in Section 3 that application of the CP technique selectively enhances the signal intensity of Si nuclei near protons and that the enhancement factor depends on the Si···H distance and the CP contact time applied. At short contact times, intense lines of SiOH (e.g. in Q^3 or Q^2 structural groups) are observed, while the signals of Si nuclei with larger Si···H distances (e.g. Q^4 adjacent to Q^3) are strongly reduced or do not appear (e.g. Q^4 surrounded only by other Q^4 groups) in the CP MAS spectra. An even more detailed discrimination of the different Si environments can be achieved by application of CP with variable contact times.[27] However, as mentioned in Section 3, CP MAS spectra are not always quantitatively reliable. But once the linewidth and position of less abundant species have been determined from the CP MAS spectrum, this information may be used for the quantitation of weak and overlapping lines in the single-pulse MAS spectrum by line fitting procedures.

5.8 Si–O–Si Framework Connectivities

The direct determination of bonding connectivities between the various crystallographically inequivalent SiO_4 sites of a 3D silicate framework has recently become feasible by application of 2D ^{29}Si MAS NMR experiments such as COSY and INADEQUATE[11] (see Section 3). The latter experiment has been proved to be particularly useful since only double quantum coherence signals, i.e. only signals due to ^{29}Si nuclei coupled via scalar spin interactions in the ^{29}Si–O–^{29}Si connection are observed in the 2D plot. This

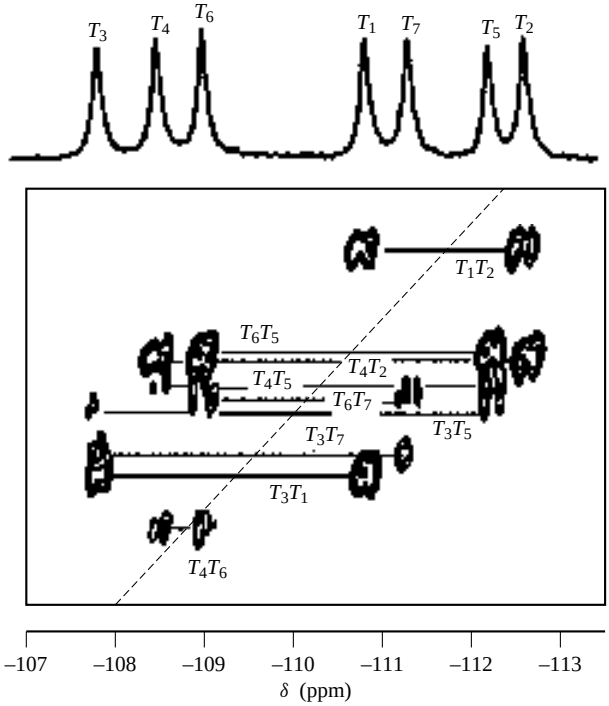

Figure 9 Contour plot of the 2D ^{29}Si MAS INADEQUATE experiment on high-silica zeolite ZSM-12 with the 1D MAS NMR spectrum shown above. The T site assignments and TOT connectivities are indicated in the spectra. (Reproduced by permission of the American Chemical Society from Fyfe et al.[11]).

is demonstrated in Figure 9 by the 2D INADEQUATE ^{29}Si MAS NMR spectrum of high-silica zeolite ZSM-12.[11] The F_2 dimension is the normal ^{29}Si chemical shift scale while the F_1 domain represents the double quantum frequencies of the resonances. Connected signals occur equally spaced on either side of the diagonal of the plot at the same frequencies in F_2 as the corresponding lines from the simple one-dimensional (1D) experiment. The ZSM-12 structure has seven crystallographically distinct Si sites with equal occupancies in the unit cell which are reflected by the seven lines of equal intensity in the 1D MAS NMR spectrum shown above the 2D plot of Figure 9. All of the nine connectivities expected for the known ZSM-12 structure are observed in the 2D spectrum. The lines may be assigned unambiguously from the expected connectivities by trial and error, but a partial assignment from other data may also be used as a starting point. Such information may be gained, for example, from the expected intensity distribution of the lines, the above-mentioned correlations between δ and SiOSi bond angles, or from different relaxation behavior of particular sites. Other than INADEQUATE, 2D plots from COSY experiments have the normal ^{29}Si chemical shift scale in both F_1 and F_2 and the connectivities appear by cross peaks. However, large intensities along the diagonal occur which may obscur cross peaks close to the diagonal.

So far, 2D ^{29}Si NMR experiments have been mostly applied to high-silica zeolite materials with known structures, and additional details of some of the structures have been revealed. In the case of unknown structures, 2D experiments will make it possible to select between different structural models and to prove or disprove proposed structures or crystallographic space

groups as, for example, shown recently for the low-temperature form of zeolite ZSM-11 and for zeolite ZSM-23.[28]

Silicon-29 COSY MAS NMR spectroscopy has also been applied to ^{29}Si isotopically enriched sodium silicate glasses and sodium phosphosilicate glasses.[12] The cross peaks observed in the COSY spectra of sodium silicate glasses suggest that a substantial portion of the Q^2 and Q^3 as well as Q^3 and Q^4 silicate sites in the glass are interconnected on a nearest neighbor level. In contrast, no cross peaks were observed for the sodium phosphosilicate glass, implying that the Q^4 and six-coordinate silicate sites present in this glass are not linked directly together.

6 APPLICATIONS

Important fields of application of solid state ^{29}Si NMR in the various branches of silicate science are listed below. For more detailed information on these topics the reader is referred to the related articles in the Encyclopedia and the selected reviews or research papers from the recent literature cited in parentheses.

1. Zeolites and related microporous materials (see ***Molecular Sieves: Crystalline Systems***; ***Microporous Materials and Xenon-129 NMR***, and Fyfe et al.,[11] Klinowski,[29] Engelhardt[30]).
2. Mineralogy and geochemistry (see ***Geological Applications*** and Kirkpatrick,[3] Stebbins,[4] Wilson,[31] Stebbins[32]).
3. Silicate and aluminosilicate glasses (see ***Amorphous Materials*** and Kirkpatrick,[3] Grimmer,[33] Dupree,[34] Eckert[35]).
4. Amorphous silica (see ***Silica Surfaces: Characterization*** and Leonardelli et al.,[27] Pfleiderer et al.,[36] Legrand et al.,[37] Chuang et al.[38]).
5. Cements (see Hjorth et al.,[39] Kirkpatrick and Jong,[40] Tong et al.,[41] Grimmer[42]).
6. Phyllosilicates and their transformations (see Kinsey et al.,[43] Weiss et al.,[44] Lambert et al.,[45] Herrero et al.[46]).

7 RELATED ARTICLES

Amorphous Materials; Cross Polarization in Rotating Solids: Spin-1/2 Nuclei; Geological Applications; Magic Angle Spinning; Molecular Sieves: Crystalline Systems; Silica Surfaces: Characterization; Silicon-29 NMR.

8 REFERENCES

1. G. R. Holzman, P. C. Lauterbur, J. H. Anderson, and W. Koth, *J. Chem. Phys.*, 1956, **25**, 172.
2. E. Lippmaa, M. Mägi, A. Samoson, G. Engelhardt, and A.-R. Grimmer, *J. Am. Chem. Soc.*, 1980, **102**, 4889.
3. R. J. Kirkpatrick, in *Spectroscopic Methods in Mineralogy and Geology*, ed. F. C. Hawthorne, Mineralogical Society of America, Washington, DC, 1988, p. 341 (*Rev. Mineral.*, 18)
4. J. F. Stebbins, in *Handbook of Physical Constants*, ed. T. H. Ahrens, American Geophysical Union, Washington, DC, 1993.
5. G. Engelhardt and H. Koller, *NMR Basic Principles Prog.*, 1994, **31**, 1.
6. G. Engelhardt and D. Michel, *High-Resolution Solid-State NMR of Silicates and Zeolites*, Wiley, Chichester, 1987.
7. F. Liebau, *Structural Chemistry of Silicates—Structure, Bonding, and Classification*, Springer, Berlin, 1985.
8. W. Loewenstein, *Am. Mineral.*, 1954, **39**, 92.
9. J. F. Stebbins, *Nature (London)*, 1991, **351**, 638.
10. I. Farnan and J. Stebbins, *J. Am. Chem. Soc.*, 1990, **112**, 32.
11. C. A. Fyfe, Y. Feng, H. Grondey, G. T. Kokotailo, and H. Gies, *Chem. Rev.*, 1991, **91**, 1525.
12. C. T. G. Knight, R. J. Kirkpatrick, and E. Oldfield, *J. Non-Cryst. Solids*, 1990, **116**, 140.
13. A. J. Vega, *J. Am. Chem. Soc.*, 1988, **110**, 1049.
14. R. K. Harris and C. T. G. Knight, *J. Chem. Soc., Faraday Trans. 2*, 1983, **79**, 1539.
15. R. F. Mortlock, A. T. Bell, and C. J. Radke, *J. Phys. Chem.*, 1991, **95**, 7847.
16. H. Koller, G. Engelhardt, and J. Felsche, *Z. Anorg. Allg. Chem.*, 1995, **621**, 301.
17. G. Engelhardt, D. Zeigan, D. Hoebbel, A. Samoson, and E. Lippmaa, *Z. Chem. (Leipzig)*, 1982, **22**, 314.
18. G. Engelhardt, *Stud. Surf. Sci. Catal.*, 1989, **52**, 151.
19. B. L. Sheriff, H. D. Grundy, and J. S. Hartman, *Eur. J. Mineral.*, 1991, **3**, 751.
20. A.-R. Grimmer, F. v. Lampe, M. Mägi, and E. Lippmaa, *Z. Chem. (Leipzig)*, 1983, **23**, 343.
21. M. Mägi, E. Lippmaa, A. Samoson, G. Engelhardt, and A.-R. Grimmer, *J. Phys. Chem.*, 1984, **88**, 1518.
22. A.-R. Grimmer, F. v. Lampe, and M. Mägi, *Chem. Phys. Lett.* 1986, **132**, 549.
23. J. F. Stebbins and M. Kanzaki, *Science*, 1991, **251**, 294.
24. C. P. Herrero, *J. Phys. Chem.*, 1991, **95**, 3282.
25. C. A. Fyfe, H. Strobl, G. T. Kokotailo, G. J. Kennedy, and G. E. Barlow, *J. Am. Chem. Soc.*, 1988, **110**, 3373.
26. G. Engelhardt and H. van Koningsveld, *Zeolites*, 1990, **10**, 650.
27. S. Leonardelli, L. Facchini, C. Fretigny, P. Tougne, and A. P. Legrand, *J. Am. Chem. Soc.*, 1992, **114**, 6412.
28. C. A. Fyfe, H. Grondey, Y. Feng, G. T. Kokotailo, S. Ernst, and J. Weitkamp, *Zeolites*, 1992, **12**, 50.
29. J. Klinowski, *Chem. Rev.*, 1991, **91**, 1459.
30. G. Engelhardt, *Stud. Surf. Sci. Catal.*, 1991, **58**, 285.
31. M. A. Wilson, *NMR Techniques and Applications in Geochemistry and Soil Chemistry*, Pergamon Press, Oxford, 1987.
32. J. F. Stebbins, in *Spectroscopic Methods in Mineralogy and Geology*, ed. F. C. Hawthorne, Mineralogical Society of America, Washington DC, 1988, p. 405 (*Rev. Mineral.*, 18).
33. A.-R. Grimmer, *Exp. Tech. Phys.*, 1988, **36**, 81.
34. R. Dupree, *Exp. Tech. Phys.*, 1988, **36**, 315.
35. H. Eckert, *Prog. NMR Spectrosc.*, 1992, **24**, 159.
36. B. Pfleiderer, K. Albert, E. Bayer, L. van de Ven, J. de Haan, and C. Cramers, *J. Phys. Chem.*, 1990, **94**, 4189.
37. A. P. Legrand, H. Taibi, H. Hommel, P. Tougne, and S. Leonardelli, *J. Non-Cryst. Solids*, 1993, **115**, 122.
38. I.-S. Chuang, D. R. Kinney, C. E. Bronnimann, R. C. Zeigler, and G. E. Maciel, *J. Phys. Chem.*, 1992, **96**, 4027.
39. J. Hjorth, J. Skibstedt, and H. J. Jacobsen, *Chem. Concr. Res.*, 1988, **18**, 789.
40. R. J. Kirkpatrick and C. D. Jong, in *Application of NMR to Cement Chemistry*, eds. A.-R. Grimmer and P. Colombet, Gordon & Breach, London, 1994, p. 55.
41. Y. Tong, H. Du, and L. Fei, *Cem. Concr. Res.*, 1990, **20**, 986.

42. A.-R. Grimmer, in *Application of NMR to Cement Chemistry*, eds. A.-R. Grimmer and P. Colombet, Gordon & Breach, London, 1994, p. 113.
43. R. A. Kinsey, R. J. Kirkpatrick, J. Hower, K. A. Smith, and E. Oldfield, *Am. Mineral.*, 1985, **70**, 537.
44. C. A. Weiss, S. P. Altaner, and R. J. Kirkpatrick, *Am. Mineral.*, 1987, **72**, 935.
45. J. F. Lambert, W. S. Millman, and J. J. Fripiat, *J. Am. Chem. Soc.*, 1989, **111**, 3517.
46. C. P. Herrero, J. Sanz, and J. M. Serratosa, *J. Phys. Chem.*, 1989, **93**, 4311.

Biographical Sketch

Günter Engelhardt. *b* 1936. Dipl.-Chem., 1960. Dr.rer.nat., 1963, Technical University of Dresden, East Germany (supervisor Heinrich Kriegsmann), Dr. habil., 1969, Humboldt University Berlin, East Germany. Central Institute of Physical Chemistry, Academy of Sciences of the GDR, Berlin-Adlershof, East Germany, 1963–86. Faculty of Chemistry, University of Konstanz, West Germany, 1987–92. Institute of Chemical Technology I, University of Stuttgart, Germany, 1992–present. Approx. 180 publications, and, with D. Michel, the book High-Resolution Solid-State NMR of Silicates and Zeolites. Current research specialty: multinuclear solid state MR and its application to zeolite catalysts and other inorganic materials.

Silicon-29 NMR

Heinrich C. Marsmann
Universität-GH Paderborn, Paderborn, Germany

1	Introduction	1
2	Practical Aspects of Silicon NMR	1
3	Chemical Shifts	1
4	Coupling constants	9
5	Spin–Lattice Relaxation	10
6	Related Articles	11
7	References	11

1 INTRODUCTION

Silicon is in many respects an important member of the elements. Silicates constitute the main material of the Earth's crust and organosilicon compounds are often found in organic chemistry. This is additional to silicon chemistry proper which has its own new and exciting fields, as for example the formation of a double bond with itself or with other elements. This is reflected in the literature concerning silicon NMR. The fastest growing section comprises the application to materials science and especially solid state silicon NMR. Of the naturally occurring isotopes ^{28}Si (92.21%), ^{29}Si (4.70%), and ^{30}Si (3.09%), only ^{29}Si has a spin $\neq 0$ and a magnetic moment. This puts it in the same league as other elements of Group 14 of the Periodic Table of the elements such as carbon, tin, and lead. There are differences between the techniques as well as the aims in obtaining silicon NMR spectra of silicon compounds in the liquid or dissolved and solid states. For solid state silicon NMR, see ***Amorphous Materials***; ***Amorphous Silicon Alloys***; ***Ceramics***; ***Silica Surfaces: Characterization***, and ***Silicon-29 NMR of Solid Silicates***.

Because of the immense published material available on silicon NMR, the discussion will be limited to that of review articles and the pertinent references should looked up there. The only exceptions are recent developments not covered adequately in the reviews. All authors whose accomplishments are only mentioned indirectly in this way are asked for forgiveness.

2 PRACTICAL ASPECTS OF SILICON NMR

The only magnetic isotope of silicon ^{29}Si has a natural abundance of 4.7%, a spin of $\frac{1}{2}$, a magnetic moment of -0.9609 and therefore a receptivity of 3.69×10^{-4} compared with ^{1}H. It can be characterized as a magnetically diluted isotope of medium sensitivity.[1] Referencing is mostly done relative to $(CH_3)_4Si$ (TMS), which has the advantage of having a high volatility, a relatively short relaxation time, and chemical stability, so that it can be added directly to the sample. However, its resonance occurs directly where the resonances of many other organosilicon compounds are found. For this reason, except for precision measurements, the tube interchange technique is mostly used. Some useful secondary reference standards are collected in Table 1. Because of their reactivity, they are not universally usable.

Table 1 Reference Compounds for Silicon NMR

$(CH_3)_4Si$	TMS	0.00 ppm
$[(CH_3)_3Si]_4C$		3.6
$[(CH_3)_3Si]_2O$	M_2	7.22
$[(CH_3)_2SiO]_4$	D_4	−19.86
$(CH_3O)_4Si$	TMOS	−78.22
$(C_2H_5O)_4Si$	TEOS	−81.65
$[(CH_3)_3SiO]_4Si$	M_4Q	+8.62
		−104.08

There are two special features in measuring silicon NMR. The first concerns the fact that silicon-containing materials such as glass and ceramics constitute a major part of the construction materials of the probehead, resulting in a broad background signal at ca. −110 ppm. There are three ways to alleviate the problem:

(a) If the signals are narrow, the smallest sweep width possible should be used.
(b) If there are couplings to protons (or fluorine), population transfer pulse programs such as DEPT or INEPT (see ***INEPT***) can be used.
(c) If the lines are broad, subtract from a blank spectrum obtained under otherwise identical conditions.

The other peculiarity concerns spectra of organosilicon compounds obtained with broadband decoupling of the protons. The nuclear Overhauser effect (NOE) can then lead to null signals, if the (^{29}Si, ^{1}H) dipole–dipole contribution $T_1{}^{DD}$ to the other longitudinal relaxation paths of the silicon is close to 2.52. Because relaxation times depend on the correlation times of a molecule, the signal intensity of a ^{29}Si spectrum with NOE varies with the temperature (see Figure 1). Again there are three methods of working around this situation:

(a) Doping the sample with a shiftless relaxation reagent, e.g. $Cr(acac)_3$ (ca. 10^{-2} mol L^{-1}), which also gives shorter relaxation times as a side benefit. There are several disadvantages to this method. The silicon compound can interact strongly with the chromium complex, the purity of the sample is impaired, and population transfer experiments are not effective any more.
(b) Inverse gated decoupling. Here proton decoupling is only active during acquisition with long waiting times (three to five times the relaxation time T_1) between scans. The advantage of not polluting the sample is offset by an ineffective use of spectrometer time which can be alleviated somewhat by using shorter pulses (40°) and shorter recovery times (20 s).
(c) Using population transfer pulse programs such as INEPT or DEPT (see ***INEPT***).

A review on the use of INEPT and DEPT in silicon NMR has been written by Blinka et al.[2] Although it appears that population transfer pulse programs provide the best method for obtaining silicon spectra, some of these experiments fail even if there is a known coupling between silicon and hydrogen. One of the reasons may be the short relaxation times of the protons. On the other hand, there may be a sizeable population transfer in the absence of a noticeable coupling between silicon and hydrogen (see Figure 2)

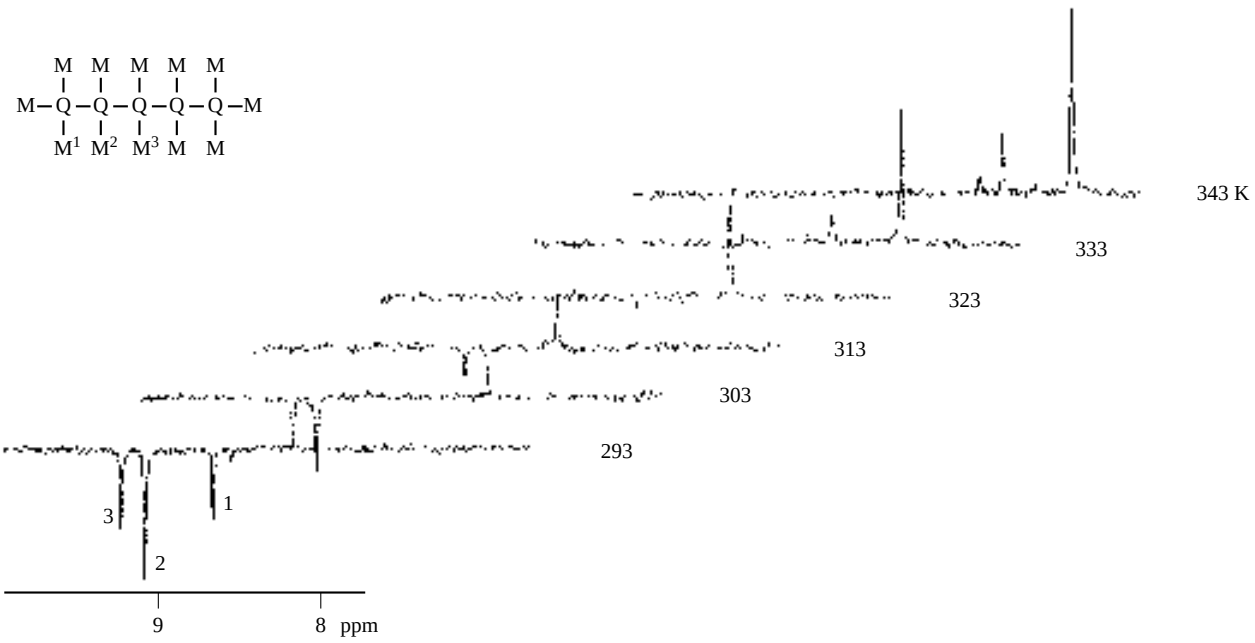

Figure 1 59.625 MHz ^{29}Si spectrum of $M_{12}Q_5$ [M = $(CH_3)_3SiO_{\frac{1}{2}}$, Q = $SiO_{\frac{4}{2}}$] with NOE at different temperatures. The rotation of the M groups is more hindered in the center than at the end of the molecule. Hence the switch from negative to positive signals occurs at higher temperatures

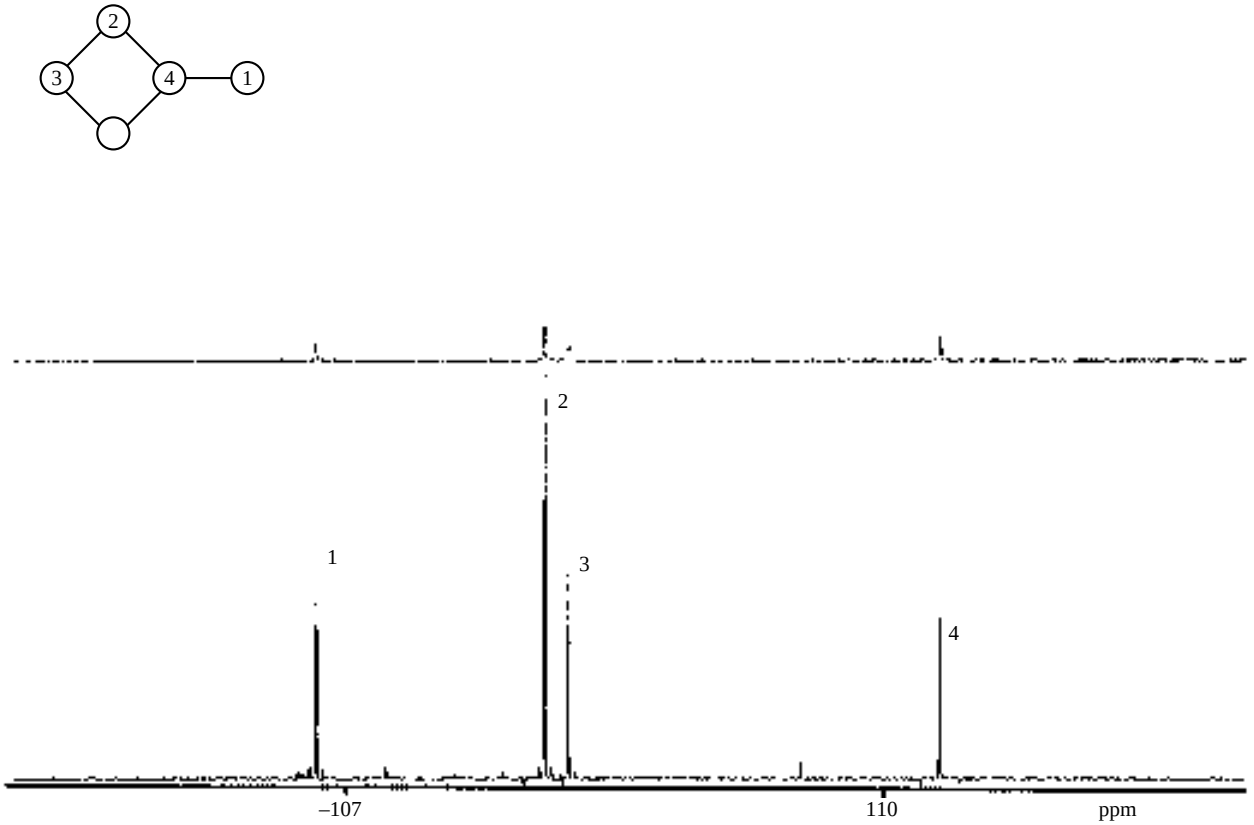

Figure 2 Comparison of the signal intensity of an inverse gated and an INEPT spectrum of the Q-part of $M_{10}Q_5$ (for M and Q, see Figure 1). The upper trace shows a 59.625 MHz ^{29}Si spectrum without proton decoupling. The ^4J(H,C,Si,O,Si) coupling is too small to be measured. Nevertheless a signal enhancement can be reached with a first empirical precession period of 1 s and a second of 0.5 s. The time necessary to obtain the spectra was 30 s in both cases

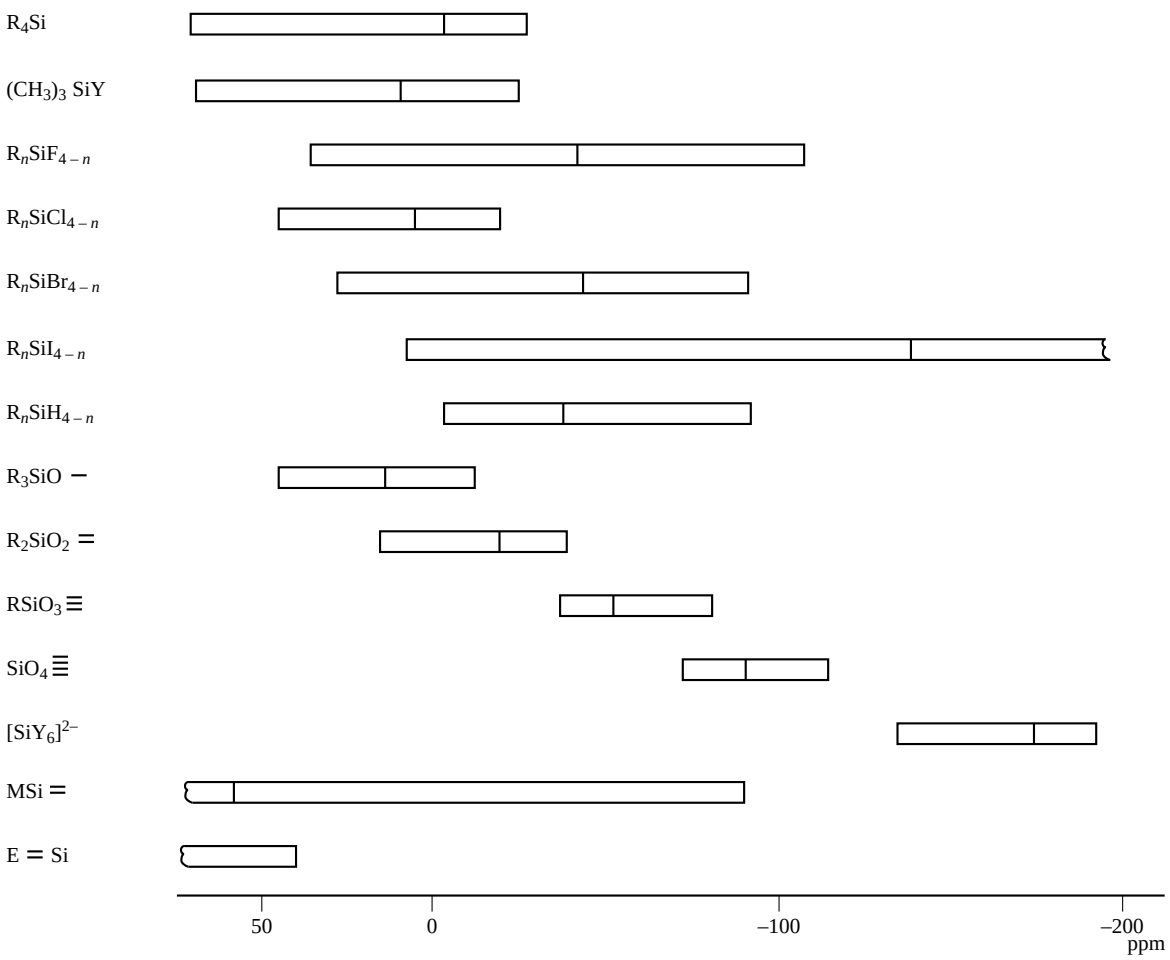

Figure 3 Chemical shift ranges for typical bonding situations in silicon compounds

3 CHEMICAL SHIFTS

3.1 General Aspects

The greatest spread of chemical shifts occur in Si(II) complexes. The current low-frequency (upfield) limit is that of decamethylsilicocene which has a shift of −577 ppm.[3] The largest high-frequency shifts are found for silylene complexes of transition metals, with (**1**) giving the most positive shift value of +268.7 ppm:[4]

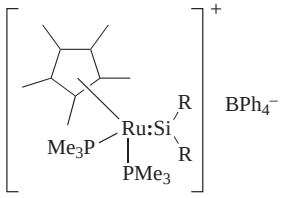

(1)

where R = c-C_6H_{11}. The majority of silicon compounds give shifts falling between +50 ppm and −200 ppm. The chemical shift ranges for typical silicon compounds are depicted in Figure 3. As is typical for most of the heavier elements, multiple substitution leads to a 'sagging behavior' as demonstrated in Figure 4 for the series $(CH_3)_{4-n}SiCl_n$ and *cis*-Os $(CO)_4[Si(CH_3)_{3-n}Cl_n]_2$. For chemical shift compilations see Williams and Cargioli[5] and Marsmann.[6]

3.2 Empirical and Semiempirical Treatment of Silicon Chemical Shifts

The first and simplest approach to the interpretation of silicon chemical shifts was based on the charge on the silicon atom. Thus Ernst et al. observed that silicon chemical shifts follow a parabola if plotted against the sum of the electronegativities of the substituents on the silicon atom. Other examples of charge dependency will be discussed in sections dealing with some selected classes of silicon compounds. A more detailed view was advanced by Radeglia et al. They used the assumption that of the contributions to the magnetic shielding σ could be subdivided into three components as:

$$\sigma = \sigma_d + \sigma_p + \sigma_n \quad (1)$$

where σ_d represents the diamagnetic component, σ_p the paramagnetic component and σ_n is the influence of neighboring atoms in the molecule, the paramagnetic contribution is responsible for the chemical shift [equation (1)] (see ***Chemical Shift Tensors***, ***Shielding: Overview of Theoretical Methods***, and ***Shielding in Small Molecules***). The approximation of

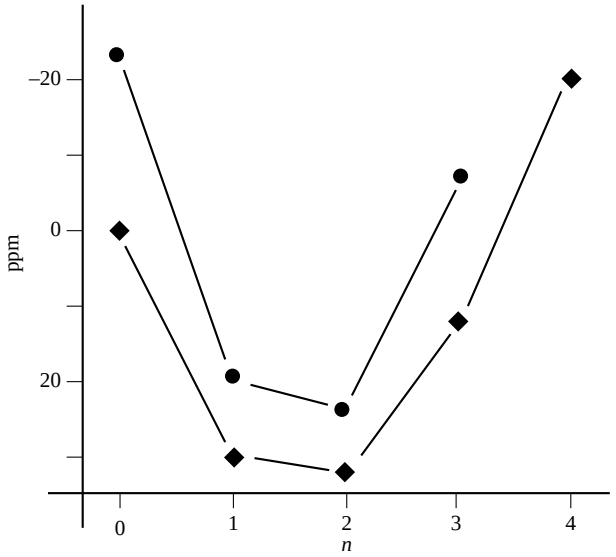

Figure 4 'Sagging behavior' of chemical shifts associated with multiple substitution of a methyl group by chlorine in the series $(CH_3)_{4-n}SiCl_n$ (♦) and *cis*-$Os(CO)_4(Si(CH_3)_{3-n}Cl_n)_2$ (●). (data from Lickiss[4])

Jameson and Gutowsky was used considering the 3p orbitals only:

$$\sigma_p = C\langle r^{-3}\rangle P_u \tag{2}$$

where C is a constant including the mean excitation energy ΔE. All magnetic shieldings are calculated relative to the situation σ_{p_0}, in which all the electrons are divided evenly between bonding partners. The calculated shielding values may then be written as relative shieldings, σ^*:

$$\sigma^* = \left(\frac{\sigma_p}{\sigma_{p_0}}\right) = \frac{P_u\langle r^{-3}\rangle_p}{P_u\langle r^{-3}\rangle_{p_0}} = P_u^* \cdot R^* \tag{3}$$

The values of P_u* and R* are then calculated using electronegativity values or by CNDO/2. A refinement was made using different bonding angles around the silicon derived from the difference in the electronegativity of ligands around the silicon. An improved fit to the data was obtained by considering the atomic number of the next neighbors on the silicon. For a detailed discussion of this field and references see Marsmann.[6]

Except for a limited set of substituents, for example the halosilanes $SiX_{4-n}Y_n$ (X, Y = halogen), linear increments usually do not apply for silicon chemical shifts. Parameters for mutual interactions can then be used if a greater variety of substituents is to be considered. Data are found in Marsmann.[6] Other substitution parameters will be discussed in the sections below.

Although the silicon chemical shift is mostly determined by elements bonded to the silicon, there are a few general features which influence it, i.e. ring strain, solvent effects, and when the coordination number of the silicon atom differs from the usual value of four. These will be discussed briefly below.

3.2.1 Ring Strain

Incorporating the silicon atom in small rings normally leads to a high-frequency shift compared with the situation in which the atom is in an open-chain compound. The topic has been fully covered[3,6] so that the few examples listed in Table 2 will be sufficient.

Table 2 The Effect of Ring Strain on the Silicon Chemical Shift (δ, ppm)

n	$[(CH_3)_2Si]_n$	$(Cl_2Si)_n$	$[(CH_3)_2SiO]_n$
3			−8.93
4	−27.6	5.86	−20.20
5	−42.1	−1.67	−22.80
6	−41.9	−2.54	−22.48
acyclic	−39.2	−1.15	−22.40

Table 3 Chemical Shifts for Some Silacyclopropenes3, 6

R^1	R^2	δ_{Si} (ppm)
CH_3–	t-C_4H_9–	−87.0
CH_3–	$(CH_3)_3Si$–	−88.6
$(CH_3)_3Si$–	t-C_4H_9–	−91.9
$H(CH_3)_2Si$–	$H(CH_3)_2Si$–	−102.1
$(CH_3)_3Si$–	$(CH_3)_3Si$–	−106.2

Before the value for a silicon in an open chain is attained, there is a small variation towards lower frequency. To date, there are two major exceptions to this rule. The first concerns three-membered rings which give shifts at rather low frequency, as shown by the examples of some silacyclopropenes (**2**) (Table 3).

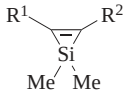

(2)

In these cases the upfield shift of ca. −90 ppm is attributed to the interaction between the π orbitals on the carbons with d orbitals on the silicon. Sterically demanding ligands on the silicon also lead to a low-frequency shift.[3]

The other exception is found for the bicyclic silanorbornenes and silanorbornadienes. The shifts of these compounds occur at very high frequencies for a silicon connected to four carbon atoms. A few examples for silanorbornadienes (**3**) from the work of Sakurai are found in Table 4.

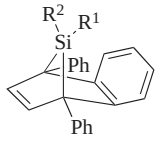

(3)

The high-frequency shift of about 80 ppm is attributed to a $\sigma-\pi$ conjugation leading to a positive charge on the silicon. Rings consisting of three silicon atoms show a chemical shift anisotropy similar to a disilene with an Si=Si double bond as observed via solid state NMR.[7]

3.2.2 Low Coordination Numbers

By using substituents with a large volume on the silicon, stable compounds in which silicon is linked via a double

Table 4 Silicon Chemical Shifts for the Bridge Silicon Atom in Silanorbornadienes[3]

	δ (ppm)
R^1=R^2= CH_3	76.9
R^1= CH_3, R^2= $Si(CH_3)_3$	82.5
R^1= CH_3, R^2= $Si(CH_3)_2(C_6H_5)$	80.2
R^1= CH_3, R^2= $Si(CH_3)_2Si(CH_3)_3$	85.7
R^1=R^2 $Si(CH_3)_3$	97.7

bond to one of its neighbors can be synthesized. In general, silicon is strongly deshielded when it is involved in a π-bond. Shift values of between 49.9 and 94.7 ppm have been reported for disilenes[2], but newer data show that 97.8 ppm can be obtained if the substituents around the silicon are of an aliphatic nature.[8] The assumption of a $p_\pi - p_\pi$ bond is supported by the chemical shift anisotropy data obtained from solid state NMR which demonstrates tensor values comparable with a $p_\pi - p_\pi$ carbon–carbon double bond.[2] Silenes with a π bond between silicon and carbon give resonances in the range 38–144 ppm.[9,10] Phosphasilenes with a silicon–phosphorus double bond give signals at an even higher frequency, namely 148–176 ppm.[11]

3.2.3 Higher Coordination Numbers

Silicon with a coordination number of four still acts as a Lewis acid provided one or more of the substituents are electronegative. Compounds with silicon of higher coordination numbers such as five and six can be formed, with donor atoms, most notably oxygen, nitrogen, and fluorine, leading to a strong low-frequency shift. Reviews have been published elsewhere.[3,6] However, it is not very easy to establish the degree of higher coordination in solution because equilibria can exist between donor atoms which are attached and those in a free state. For silatranes (**1**) and related compounds, the observation of $^{29}Si-^{15}N$ coupling (0.20–3.37 Hz) indicates the certainty of a coordination number of five.[12] In addition, the difference between the chemical shifts of silatranes in the solid state and in solution is small (−1.0 to −5.1 ppm).[13] The additional Si–N bond leads to a shift of between 10–30 ppm to low frequency, as concluded by comparison with the shifts of analogous aminotriethoxysilanes.[42] A number of complexes of silicon with chelating diols gave shifts of up to −196 ppm,[3,6] compared with the value of −180 ppm for the mineral thaumasite where the silicon atom is surrounded by six oxygen atoms.[14] This leaves a ca. 100 ppm shift to low frequency as the effect of two extra oxygens in the coordination sphere of the silicon. Silicon surrounded by five oxygens shows shifts around −120 ppm to −131 ppm, resulting in an additional low-frequency shift of about −50 ppm compared with tetraalkoxysilicates.[15] Solvents with donor atoms can also lead to low-frequency shifts.[5,16] The chemical shift difference of −24 ppm to −59 ppm occurring in the presence of a donating solvent such as 1-methylimidazole, hexamethylphosphoramide, or dimethylpropyleneurea has been interpreted as being due to the formation of a pentacoordinate complex.[16] Generally, the solvent shift appears to depend on Gutmann's donor number.[5]

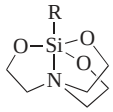

(4)

The hexafluorosilicate SiF_6^{2-} also exhibits an extremely large low-frequency shift of −191.7 ppm.[3,6] Shifts of a number of silicon–fluorine anions with silicon in a five-coordinated state have been observed in solution as well as in the solid state. The additional fluorine brings about a low-frequency shift of between −28 ppm and −80 ppm, with the larger effect being for difluorides.[17–19] The fluxional behavior of these siliconates has been studied mostly by other methods such as ^{19}F NMR, but is also visible in ^{29}Si NMR.

3.3 Chemical Shifts of Selected Classes of Silicon Compounds

3.3.1 The Trimethylsilyl Derivatives

The trimethylsilyl group, $(CH_3)_3Si-$, abbreviated as TMS, is one of the more versatile tools of chemistry. In organic chemistry, one reason for introducing such a moiety into a molecule is to obtain a certain substitution pattern.[52] Another reason may be to make substances containing labile protons such as −OH or −NH groups easier to handle. Thus, the volatility or solubility in organic solvents is much better for the derivatized compound. The TMS group is also useful for characterization by NMR methods. As several authors have pointed out, most recently Schraml in his review article about tagging with the help of the TMS moiety, the spread of chemical shifts is 0.5 ppm for the proton, 5 ppm for the ^{13}C but ca. 40 ppm for the ^{29}Si resonance of this group. For references consult Schraml.[21] A chart of the silicon chemical shifts for TMS derivatives is found in Figure 5.

The greatest variation is found for the derivatives of acids. As several authors have shown, in this case the silicon chemical shift of the TMS group depends on the p*K* value of the parent acid. This has been interpreted as an argument against an appreciable $p_\pi - d_\pi$ contribution to the Si–O bond. Furthermore, the chemical shifts of trimethylsilylalkoxides correlate with the charge at the oxygen and the polar substituent constant σ^*. As can be deduced from Figure 5, the chemical shifts of the different types of TMS alkoxides overlap somewhat, and this could be a problem if the TMS derivatives are to be used to characterize polyols, such as carbohydrates and other natural products where the resonances of the trimethylsiloxy groups appear over a very narrow region.

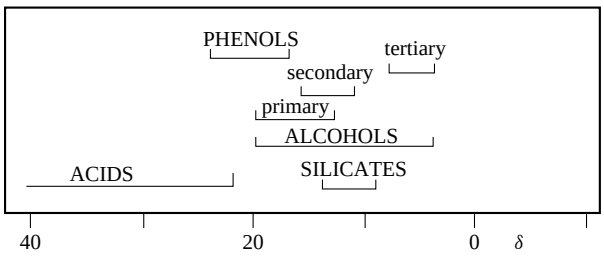

Figure 5 Chemical shift ranges of the trimethylsilyloxy group (reproduced with permission of Wiley from Schraml[21])

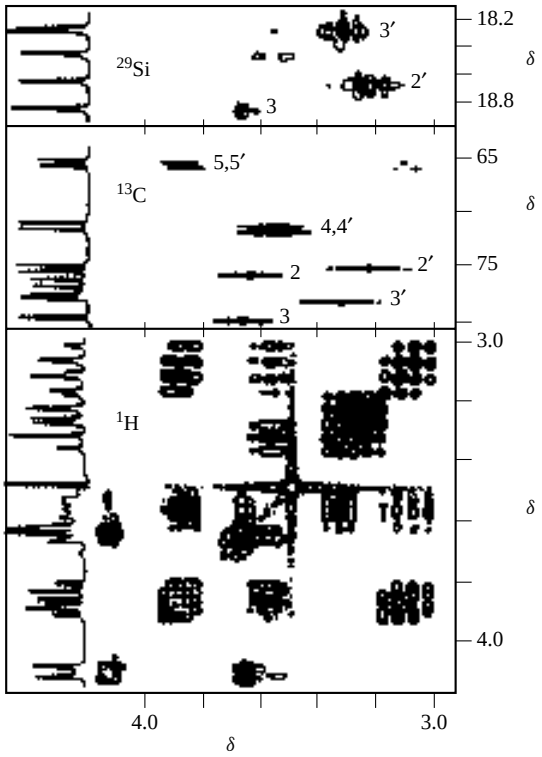

Figure 6 Partial H,H-, H,C-, and H,Si-COSY spectra of the trimethylsiloxy derivative of methyl 2-(β-D-xylopyranosyl)-β-D-xylopyranoside (reproduced with permission of Wiley from Schraml[21])

With $CDCl_3$ as solvent, the shifts of the $(CH_3)_3SiX$ group (X = O,N) depend slightly on the concentration of the solute, and so Schraml proposed a 'standard condition' in order to improve the reproducibility of the shift data. Thus if the ^{13}C resonance of $CDCl_3$ is set equal to 76.99 ppm, the ^{13}C resonance of $[(CH_3)_3Si]_2O$ (M_2) used as a secondary standard should be 2.48 $\pm$ 0.02 ppm. Otherwise, the sample should be diluted further with $CDCl_3$.

Several procedures have been suggested to give additional information needed to make such an assignment. Most of the techniques have been developed by the groups of Harris and Schraml. One of the simpler, but still difficult, methods involves the selective decoupling of the methyl protons of the TMS group. The only splittings left then arise from the $(CH_3)_3SiOCH_n-$part of the molecule. A triplet then stems from a primary, a doublet from a secondary, and a singlet from a tertiary alkoxy group. Selective deuteration can be used to distinguish between resonances from different locations in the molecule as demonstrated by Harris.

INEPT experiments with selective excitation of proton resonances also provide another valuable tool. By combining H,H-, H,C-, and H,Si- two-dimensional COSY, the task of assigning can be greatly simplified. An example is found in Figure 6. Additivity rules exist to connect chemical shifts to structural models of steroid alcohols and carbohydrates (pentoses). For data, Schraml[21] should be consulted.

While trimethylsilylated enols show marked differences for *E* and *Z* isomers, the shifts of aryloxy derivatives are far more predictable. The shift value for trimethylsiloxyphenols of the type $X-C_6H_4-OSi(CH_3)_3$ depends on the Hammett σ parameter, but the relative position of X is much less

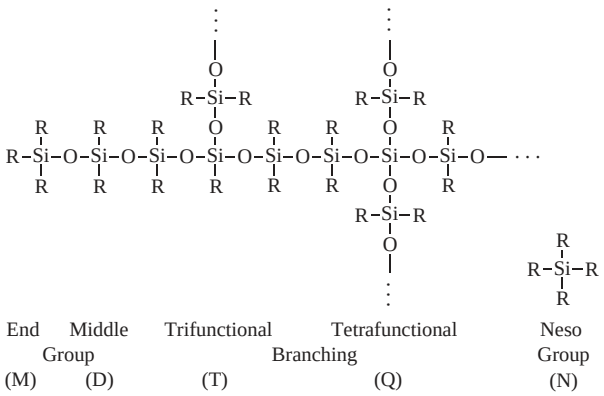

Figure 7 Structural diagram for the building units in polysiloxanes

influential. The shift of the TMS−O group is almost identical for X when in the *meta* and *para* positions. An *ortho* substitution shifts the resonance ca. 1.5 ppm to high frequency if X contains lone pairs and only a little if X has none. The temperature dependence of the shifts (ca. 1 ppm for a temperature difference of 150 °C) has been interpreted as being caused by the silicon of the TMS−O group being perpendicular to the phenyl ring in the ground state and rotated more to the plane of the ring at higher temperatures. TMS−O derivatives of multiply substituted phenols have been studied as model compounds for lignins and coals. The data for a number of potential structural components for trimethylsilylated lignins have been collected.[21]

Trimethylsilylation as a means of characterizing silicates was originally suggested by Lentz.[20] Although the silicon shifts of the silicate skeleton are used primarily for this purpose, the region 8.35−13.65 ppm is typical for TMS−O groups connected to a silicic acid skeleton.[22]

3.3.2 Oligomeric and Polymeric Siloxanes

One of the first uses of silicon NMR was its application to siloxane polymers. Although it is sometimes possible to recognize and isolate individual molecules, the main aim is to dissect the molecules into building units (see Figure 7). To distinguish between building units with different substituents at the silicon, a short notation for the substituent is added as a superscript. As the methyl group is thought to be the normal case, it is not considered in the notation. The chemical shift regions of such building units are collected in Figure 8. The main difference between the building units is the number of oxygen atoms connected to a silicon atom. Except for the M group, the exchange of an R substituent for oxygen leads to a low-frequency shift. The chemical shifts of the building units are sensitive to neighbor effects in the chain structure, thus revealing the microstructure of the polymers. This was demonstrated, for example, by Harris and Kimber, who deduced the triad and pentad structures of a mixed oligomer consisting of D and D^H groups,[23] and by Engelhardt and Jancke for the system D and D^{Ph}.[24] As stated above, the chemical shifts of all building groups are modified by ring strain.

The analysis of the silicic acid anions in aqueous solutions is a formidable feat. A status report on the different methods to achieve this has been published by Hoebbel and Ebert.[25] Fast

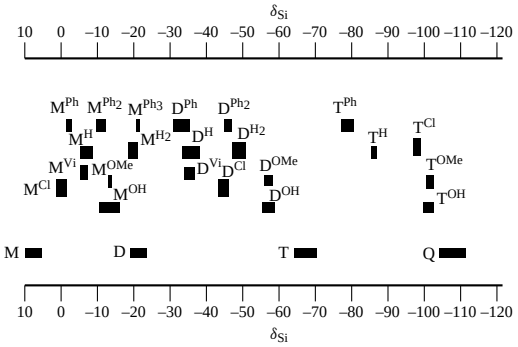

Figure 8 Silicon chemical shift regions of building units of polysiloxanes (reproduced with permission of Wiley from Williams[3])

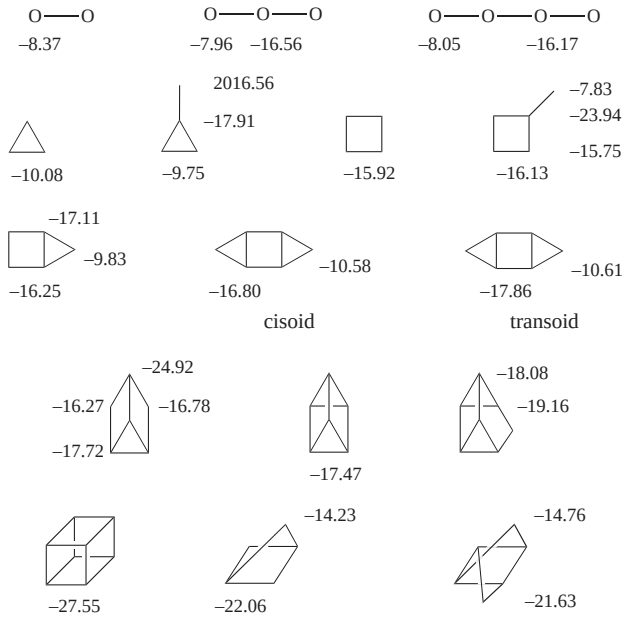

Figure 9 Structural diagrams and shift values of silicate anions identified in aqueous solution (relative to the resonance of the monosilicate δ_{TMS} ca. −71.3 ppm)

and slow hydrolysis condensation reactions between silicate anions and protonation equilibria exist depending on the pH and silicate concentration of the solution.[26–28] This makes assignments beyond the basic principles difficult (see Table 5). One way out of this dilemma has been the use of ^{29}Si-enriched material. This opens the opportunity to undertake ^{29}Si, ^{29}Si-COSY experiments or classical assignments by the selective decoupling technique. Some of the anions identified in this way are collected in Figure 9.[29–31]

Because the chemical shifts of the anions depend on the pH value, it is common practice to use the resonance of the monomeric species SiO_4^{4-} as a secondary standard, which from its own shift variation with pH and concentration makes it easier to track the signals of the other anions. A rough conversion to the shift scale based on TMS can be obtained by adding −71.3 ppm. An inspection of Figure 9 reveals the following:

(a) The shift difference of the building units is smaller than in the case of other oligomeric siloxanes.
(b) Condensed ring structures are common.

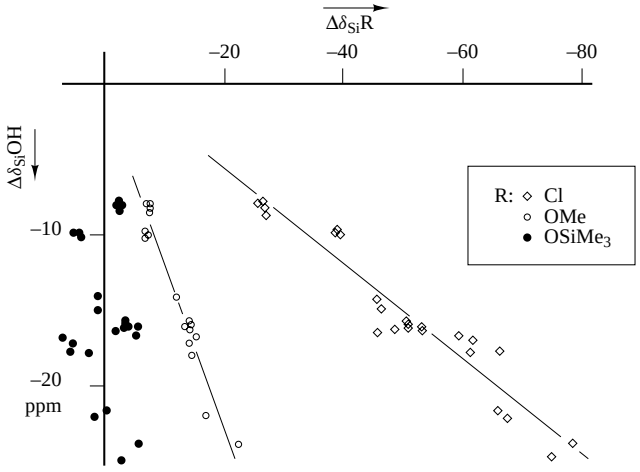

Figure 10 Comparison of chemical shifts relative to the neso group of silicate anions with the corresponding silicic acid derivatives (reproduced with permission of Springer Verlag from Bertling and Marsmann[33])

(c) Shift variations caused by ring strain can make resonances from the Q^n building unit appear in the same place as those of Q^{n-1}.

The chemical shifts of silicic acid esters are closely related to those of the silicic acid anions and this can help in assignment (Figure 10). The shift regions for the acyclic esters are given in Table 5. The exceptions are the TMS esters which are often used for the characterization of silicates. Here ring strain effects are more prominent and so a shift correlation with other species is not observed.[22]

3.3.3 Oligomeric and Polymeric Silanes

This topic has been discussed by Williams[3] and the pertinent references should be looked up there. The chemical shift ranges for the building units of some oligomeric silanes are collected in Table 6.

The skeleton of these compounds is similar to that of alkanes. Therefore, models as used by Grant and Paul for the ^{13}C resonance have been applied to rationalize the shifts of this class of compounds. Hahn fitted the empirical equation:

$$\delta_{Si} = -96.02 - 2.43a - 3.73a^2 + Bb + C \quad (4)$$

where −96.02 ppm is the idealized shift of the monosilane SiH_4, a is the number of silicon atoms in the α position, b the number of silicon atoms in the β position, and B and C are incremental chemical shifts due to β- and γ-positioned silicon atoms. West and Stanislawski used a similar approach [equation (5)] to explain the shifts of oligomeric permethylsilanes:

$$\delta_{Si(k)} = B + \Sigma A_l n_{kl} \quad (5)$$

where the constant B is 8.5 ppm and A_l represents the influence of silicon atoms in the α (−28.5 ± 0.10 ppm), β (+3.9 ± 0.05 ppm), γ (+1.2 ± 0.09 ppm), and δ positions (+0.2 ± 0.01 ppm) relative to the silicon atom considered, and n_{kl} the incidence of A_l. Substituent parameters for fluorine or chlorine could also be calculated. The model was not successful for cyclic silanes and quaternary silicon atoms. This

Table 5 Silicon Chemical Shifts[a] of Building Units of Silicic Acid Anions and Derivatives

				Branching group	
	Neso group	End group	Middle group	Trifunctional	Tetrafunctional
Silicates[b]	−70 to −72	−76 to −80	−85 to −91	−96 to −100	−104 to −112
Methyl silicates[c]	−78.5	−84 to −86	−93 to −94	−102 to −103	−110 to −111
Ethyl silicates[c]	−82.0	−88 to −90	−96 to −97	−103 to −104	−112 to −113
Chlorosiloxanes[c]	−18.5	−45 to −46	−71 to −72	−96 to −97	−119 to −120

[a]In ppm relative to TMS.
[b]See Hoebbel and Ebert,[25] building units also identified as Q^0 (neso), Q^1 (end), Q^2 (middle), Q^3 (trifunctional), Q^4 (tetrafunctional branching group).
[c]See Marsmann et al.[32]

Table 6 Silicon Chemical Shifts of Building Units for Some Oligomeric Silanes

	SiX_4	$(—)SiX_3$	$(—)_2SiX_2$	$(—)_3SiX$	$(—)_4Si$
X = H	−95.6	−90 to −103	−103 to −115	−126 to −136	(−165.9)
= CH_3	0.0	−9 to −20	−26 to −49	−78 to −88	−118 to −136
= Cl	−18.5	+4 to −6	+6 to −8	(−31.8)	−79 to −81

Table 7 Chemical Shifts for the Central Silicon in Neopentasilanes

	Si$(SiX_3)_4$ (δ, ppm)
X = Cl	−80.2
CH_3	−135.5
H	−165.9
OCH_3	−172.2

Table 8 Silicon Shift Differences[d] $\Delta[\delta(LM^{29}Si) - \delta(CH_3{}^{29}Si)]$ for Some Transition Metal Complexes

Complex type	Si_α	Si_β	Si_γ
$(\eta^5\text{-}C_5H_5)FeL_2R$[e]	25–42	7–13	−1 to 1
$(CO)_5ReR$[f]	−39 to −13	9–15	1 to 2
$(\eta^5\text{-}C_5H_5)Ru(CO)_2R$[f]	10–27	7–13	−1 to 1
$(\eta^5\text{-}CH_3C_5H_5)MnHR$[g]	40–64		

[d]In ppm.
[e]L = CO, $P(C_6H_5)_3$, R = methylsilanes.[35]
[f]R = methylsilanes.[36]
[g]$\Delta[\delta(LM^{29}Si) - \delta(H^{29}Si)]$.[37]

is not surprising considering the spread of shifts for quaternary silicon atoms in silanes and their sensitivity to substitution β to the central silicon as the few data listed in Table 7 show. The review also cites a number of studies on substituted di- and trisilanes.[3]

3.3.4 Transition Metal Complexes

The data for a number of transition metal complexes are collected in some reviews.[3,4,6,34] There is a large variety of bonding situations for the silicon atom leading to a large spread of chemical shifts. The first variable is the kind of metal involved. Complexes studied so far have central atoms belonging to Groups 6 to 12 of the Periodic Table, with iron as the most often used. Although there are still not enough data known to explain the shifts of silicon bonded to transition metals, a few trends emerge. There seems to be a low-frequency shift for a given silicon-containing ligand in going to a heavier homologous transition metal. The 'sagging pattern' found in ordinary silicon compounds is also encountered for such complexes[34] (see, for example, Figure 4). A very useful concept was suggested by Pannell and Bassindale for more conventional complexes where the silicon is linked via a single bond to the metal.[35] In Table 8 the chemical shift of a central silicon atom is compared with the shift of the silicon where the metal is replaced by a methyl group. A high-frequency shift of up to +40 ppm is observed if the metal is Fe or Ru, but a low-frequency shift of −13 to −39 ppm is obtained if the metal is Re.[36] Somewhat larger values are found if the chemical shift difference is that between the shifts of silicon in the complex and in the corresponding silane.[37] Silicon in a β position to the metal experiences a less pronounced low frequency shift of up to 20 ppm. Silicon in the γ position is only shifted by a small amount.[35–37] In π complexes where the silicon is next to the carbon–carbon double bond, the shift difference to the free ligand is between −2 and +21 ppm.[38]

Extreme high-frequency shifts are experienced by silicon atoms in nonclassical complexes containing silylenes as ligands.[4] If the silylene ligand is either doubly bonded to the metal or is attached via a single bond to two metals, then shifts between 230 and 269 ppm are observed. If the complex is stabilized by donor molecules at the silicon, then the shifts are found in the region between 58 and 127 ppm.

3.3.5 Miscellaneous

Silazanes have structures similar to siloxanes and can be rationalized by the same principles, but the spread of chemical shifts is smaller. The total region extends from −62 ppm to +18 ppm.[6] The same is true for carbosilanes where resonances are found for silicon connected to four carbons of between −4 ppm and +20 ppm.[6] A new report has appeared for silthianes.[39] Generally, the shifts are placed to higher frequencies as compared to siloxanes. For the other compounds, general collections of silicon chemical shifts should be consulted.[5,6]

4 COUPLING CONSTANTS

All magnetic nuclei in a molecule interact and the resulting splitting gives rise to typical patterns. Two cases can be distinguished:

(a) Coupling with abundant isotopes such as ^{1}H, ^{19}F, or ^{31}P gives rise to well-known splitting patterns in ^{29}Si spectra. Couplings with quadrupolar nuclei such as the isotopes of chlorine are usually not observed, but can lead to broad lines.

(b) Coupling with other rare spins such as ^{29}Si itself or ^{13}C leads to small satellite lines on each side of the main line.

The amount of data available is governed by the fact that $^{1}H-^{29}Si$ couplings are easily obtained and the discussion of these predate the advent of silicon NMR itself. Theoretical approaches and data for couplings concerning silicon are summarized in Marsmann[6] and Schraml and Bellama[40] and the arguments presented here are taken from these sources. Of the three possible pathways for transmitting information about the other spins to silicon, the Fermi contact term is assumed to be the most effective (see ***Indirect Coupling: Semiempirical Calculations***). As consequences of this, the sign of the coupling constants for $^{1}J(Si,H)$ is negative because of the negative gyromagnetic ratio of the isotope ^{29}Si. The magnitude of the couplings depends on the s orbital density between silicon and the other coupling nucleus and an average excitation energy ΔE. The latter quantity is difficult to assess. Therefore semiquantitative and empirical relationships have been found by several authors—mostly for $^{1}J(Si,H)$ and $^{1}J(Si,C)$. A few examples (J values in Hz) are:

$$^{1}J(Si,H) = 725\alpha_{Si}^{2} + 15.9 \quad (6)$$

$$^{1}J(Si,H) = 969.7\alpha_{Si}^{2} + 5.9N_{P} - 41.0 \quad (7)$$

$$^{1}J(Si,H) = 810\alpha_{Si}^{2} + 4.30N_{P} - 1.40N_{Me} \quad (8)$$

for H_nSiR_{4-n}(R = CH_3, C_6H_5; n = 1–4)

$$^{1}J(Si,C) = 555.4\alpha_{C}^{2}\alpha_{Si}^{2} + 18.2 \quad (9)$$

$$^{1}J(Si,C) = -1227.7P_{sSisC}^{2} + 26.0 \quad (10)$$

where $\alpha_E{}^2$ is the square of the s character of the hybrid used for bonding onto element E, P_{sSisC} is the bond order matrix element pertaining to the SiC bond, and N_P is the number of phenyl and N_{Me} the number of methyl groups bonded to the silicon atom.[3] A more complete collection is published elsewhere.[6,40] On a purely empirical basis, the magnitude of the coupling constant depends on the electronegativity of the substituents, but is nonlinear. Some quadratic relationships have been suggested on the basis of pairwise interaction parameters (Malinowski) or effective electronegativities (Jensen). The quantity $^{1}J(Si,H)$ can also be connected to other properties of a molecule, e.g. the H–Si, the Si–Si stretching frequencies (Hengge), or the Hammett–Taft σ^* term (Nagai).

The ranges of some coupling constants involving silicon are found in Table 9. The sign of the coupling constants over one bond is usually negative because of the negative magnetogyric ratio of the ^{29}Si. Exceptions are found if the silicon is connected to an element with tightly bonded s electrons, e.g. ^{19}F or ^{31}P.

Table 9 Ranges of Some Coupling Constants Involving Silicon

Type	Sign	Values (Hz)
$^{1}J(Si,H)$	–	420–75
$^{2}J(Si,CH_3)$	+	10–3
$^{2}J(Si,XH)$	±	13–1
$^{3}J(SiH)$		8–1
$^{1}J(Si,F)$	+	488–108
$^{2}J(Si,F)$	–	91–17
$^{3}J(Si,F)$	±	16–2
$^{1}J(P,Si)$	+	256–16
$^{2}J(P,Si)$	±	44–0.7
$^{1}J(Si,C)$	–	113–37
$^{2}J(Si,C)$	+	18–4
$^{1}J(Si,Si)$		186–23
$^{2}J(Si,Si)$		24–0.7

4.1 Silicon–Hydrogen Couplings

For the one bond hydrogen–silicon coupling a rough correlation exists with the electronegativity of the other bonding partners to the silicon. This is an application of Bent's rule that atomic s character concentrates in orbitals directed toward electropositive substituents. The exception is $H_2Si[Mn(CO)_5]_2 \cdot 4py$ where the extreme value of 420 Hz is observed. Hence the value of −381.7 Hz for $HSiF_3$ is a better upper working limit for $^{1}J(Si,H)$. H_3SiK [$^{1}J(Si,H)$ = 74.8 Hz] gives the lowest value in concordance with the low electronegativity of potassium. The coupling of silicon with the hydrogen of a methyl group runs from 6.0 Hz to 9.5 Hz in most cases. Exceptions are found if the silicon is bound to an alkali metal such as Li, e.g. $(CH_3)_3SiLi$, $^{2}J(Si,CH_3)$ = 2.8/3.5 Hz. The value between 20 and 69 Hz found for $^{2}J(Mn,Si,H)$ has been thought to arise from a direct bonding interaction between silicon and hydrogen.[37,41]

4.2 Silicon–Fluorine Couplings

The value of $^{1}J(Si,F)$ for fourfold coordinated silicon lies in the range 167–488 Hz. The lower limit is found in perfluorosilanes and the high value for the cyclic $\overline{CH_2CH_2SiF_2SiF_2}$.[40] Higher coordination numbers lead to lower values, e.g. 131–300 Hz for five-coordinated silicon[6,17,18] and 108–182 Hz for silicon with a coordination number of six.[6]

4.3 Silicon–Phosphorus Couplings

One bond couplings in silylphosphines can be calculated by the empirical equation:

$$^{1}J(P,Si) = 26.3 + 8u + 5v - Zw \quad (11)$$

where 26.3 is the value for the reference compound (H_3SiPH_2) with u the number of silyl, v the number of methyl groups substituting P–H bonds, and w the number of methyl groups substituting Si–H bonds. The quantity Z is an empirical factor with a value of 3.3–5. Coupling across a silicon–phosphorus double bond gives splittings of 149–155 Hz.[11] The two bond coupling over nitrogen enables the bonding situations between

P=N–Si and P–N–Si to be distinguished. Very low values have been found if the couplings go over triply linked nitrogen, but values of 8–42 Hz are typical for a sp^2-hybridized nitrogen between silicon and phosphorus.[6]

4.4 Silicon–Carbon and Silicon–Silicon Couplings

The range for the splittings of the satellites in a ^{29}Si spectrum due to the presence of a ^{13}C one bond away is 44–107 Hz where electronegative substituents at the silicon and sp^2-hybridized carbon favor the higher values. A coupling constant of 83.7 Hz has been reported for an Si–C double bond.[42] The silicon–silicon coupling across a double bond has been measured as 155–158 Hz[43] and is enhanced compared with values of around 85 Hz for aryldisilanes.[44] Little is known about higher bond Si–Si couplings. In stress-free linear and cyclic silanes, ^2J(Si,Si,Si) is found in the range 3–13 Hz, but in polycyclic silanes values of 14–24 Hz can be observed.[45,46] Because the magnitude of ^1J(Si,Si) in polycyclic silane rings is reduced, both types cannot be distinguished easily.[45] The value of ^2J(Si,O,Si) is generally very small with values of 3.6–9.8 being observed in silicate anions. Trimethylsilyl silicates gave slightly larger values of 6.7–13.5 Hz for the couplings between the silicon atoms of the skeleton.[22]

5 SPIN–LATTICE RELAXATION

As an isotope with a spin of $\frac{1}{2}$, ^{29}Si has five pathways to dissipate to the surroundings (lattice) any excess energy stored in its excited Zeemann level. The mechanisms for these relaxation processes are basically the same as for excitation, i.e. fluctuating magnetic fields. Such fluctuating magnetic fields can arise from other magnetic dipoles, $T_1{}^{DD}$, interaction of the spin with the molecular rotation, $T_1{}^{SR}$, the chemical shift anisotropy, $T_1{}^{CSA}$, scalar interactions, $T_1{}^{SC}$, and the presence of unpaired electrons in the sample, $T_1{}^{E}$. The total relaxation is then the reciprocal sum of all these components [equation (12)]:

$$\frac{1}{T_1} = \frac{1}{T_1^{DD}} + \frac{1}{T_1^{SR}} + \frac{1}{T_1^{CSA}} + \frac{1}{T_1^{SC}} + \frac{1}{T_1^{E}} \tag{12}$$

Results obtained up to 1981 have been summarized by Marsmann[6] and if not indicated otherwise the following discussion is based on the references cited there. In the absence of substances with unpaired electrons, Levy has shown that the dipole–dipole and the spin–rotation mechanisms are the most efficient contributions to the total ^{29}Si relaxation. The value of $T_1{}^{DD}$ is usually dominated by interaction with the magnetic moments of the protons:

$$\frac{1}{T_1^{DD}} = h^2 \tau_c \Sigma \gamma_H^2 \gamma_{Si}^2 r_{SiH}^{-6} \tag{13}$$

The silicon–hydrogen bond distance is ≈148 pm so the effectiveness is only 10% compared with the same situation with carbon. Hence hydrogens further away, both intra- as well as intermolecular, are also effective. This is important because in the usual organosilicon compounds the hydrogen is not bonded directly to the silicon but is found in a side chain.

Relaxation times are also dependent on the dilution of the silicon compound and on the concentration of proton-carrying molecules (solvents). The molecular correlation time τ_c in equation (13) describes the rotational tumbling motion. Very often a molecule cannot be considered as rigid, so an effective correlation time $\tau_c{}^{eff}$ is used. The motions of a molecule depend on the temperature of the sample and Arrhenius-type relationships between temperature and $T_1{}^{DD}$ are observed. The share of the dipole–dipole term on the total relaxation time can be obtained from the nuclear Overhauser effect (NOE) which is obtained by the change of intensity by decoupling another nucleus, usually protons:

$$\begin{aligned} \text{NOE} &= \frac{\text{signal intensity with irradiation of protons}}{\text{signal intensity without irradiation}} \\ &= 1 + \frac{\gamma_H \cdot T_1}{\gamma_{Si} T_1^{DD}} \end{aligned} \tag{14}$$

If the silicon nucleus relaxes exclusively via $T_1{}^{DD}$ then the NOE becomes −1.52. The NOE enhancement factor η is calculated as:

$$\text{NOE} = 1 + \eta \tag{15}$$

with η_0 = −2.52 being the NOE enhancement factor for exclusive relaxation by dipole–dipole interaction. For the normal case where dipole–dipole relaxation is the sole mechanism, its share is given by:

$$T_1^{DD} = -\frac{2.52 T_1}{\eta} \tag{16}$$

If η = −1 then a null signal in the ^{29}Si spectrum is the consequence. (See also ***Nuclear Overhauser Effect***.)

The spin–rotation interaction is the other effective relaxation mechanism. The rotation of a molecule or a part of it generates a ring current via the electrons connected to it. Changes in the rotational speed produce the fluctuating magnetic fields necessary for the relaxation process. If the molecule moves isotropically, the spin–rotation relaxation time is given by:

$$\frac{1}{T_1^{SR}} = \frac{2\pi I k T}{h^2} \frac{2C_\perp^2 + C_\parallel^2}{3} \tau_j \tag{17}$$

In equation (17), τ_j is the angular momentum correlation time. If the molecular reorientation occurs by small-step diffusion, then the Hubbard relationship applies:

$$\tau_c \tau_j = \frac{I}{6kT} \tag{18}$$

The practical application is that at high temperatures the relaxation is governed by the spin–rotation process and at lower temperatures by the dipole–dipole interaction, and that there is a border region where T_1 reaches a maximum value (see Figure 11). The components of the spin–rotation interaction tensor $\boldsymbol{C}$ are difficult to determine, but contain information about the paramagnetic term of the chemical shift σ_p.[6,47] (See also ***Spin–Rotation Relaxation Theory***.)

The effect of unpaired electrons can be used very effectively to shorten the total relaxation time and to suppress the NOE, because the main relaxation path no longer goes through the dipole–dipole interaction. The addition of $Cr(acac)_3$ in ca. 10^{-2} molar concentration was suggested by Levy et al. to bring relaxation times down below 10 s. In addition, the presence of molecular oxygen in a sample shortens the relaxation times.

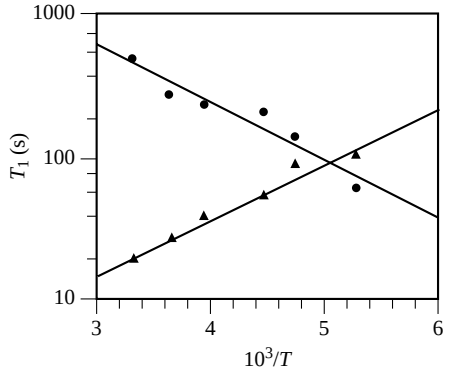

Figure 11 ^{29}Si spin–lattice relaxation in tetramethylsilane: (●) T_1^{DD}, (▲) T_1^{SR} (assumes $T_1^{CSA} \gg T_1^{DD}$) (reproduced with permission of the American Chemical Society from Levy et al.[48])

Table 10 Typical Relaxation Times for ^{29}Si at Room Temperature6, 49, 50

Compound	T_1	T_1^{DD}	T_1^{other}
$(CH_3)_3SiH$	15.9	190	175
$(C_6H_5)_3SiH$	12.0	12.5	275
Siloxanes			
M	35–52	150–320	40–61
D in chains	54–67	73–247	69–266
D in rings	80–100	102–183	142–820
D^H in chains	30–46		
Methyl silicates	73–205	320–503	
Chlorosiloxanes	53–352		
Silicates in aqueous solution			
Q^0	0.3–3.8		
Q^1	1.4–2.7		
Q^2	1.4–4.6		
$(Q^3)_8$	9.8	11.8	

The value of T_1^E was calculated to be around 37 s for an oxygen pressure of 1 atm.[48]

An inspection of the relaxation data listed in Table 10 shows that the principal pathway for dissipating energy from the spin system is the spin–rotation mechanism, because it is safe to assume that T_1^{other} consists almost exclusively of T_1^{SR}. Exceptions occur if the segmental motion in larger molecules is constricted, as in the case of small siloxane rings, or the silicon bears one or more directly connected hydrogens. The short relaxation times of silicate anions in aqueous solution have attracted much attention. An explanation may be relaxation by unpaired electrons from transition metal ions leached from the glass of the NMR tube. The equilibria between different silicate ions or protonated forms may be another factor.[26–28,51]

The longitudinal relaxation times are usually determined by inversion–recovery pulse programs modified to avoid null signals which are possible via the negative gyromagnetic ratio of ^{29}Si as suggested by Levy et al. Harris has proposed a pulse cycle using a null signal to obtain the relaxation times.[6]

6 RELATED ARTICLES

Silicon-29 NMR of Solid Silicates.

7 REFERENCES

1. R. K. Harris and B. E. Mann, *NMR and the Periodic Table*, Academic Press, New York, 1978.
2. T. A. Blinka, B. J. Helmer, and R. West, *Adv. Organomet. Chem.*, 1984, **23**, 193.
3. E. A. Williams, in *The Chemistry of Organic Silicon Compounds*, ed. S. Patai and Z. Rappoport, John Wiley & Sons, New York, 1989, Vol. 1, pp. 511–554.
4. P. D. Lickiss, *Chem. Soc. Rev.*, 1992, 271.
5. E. A. Williams and J. D. Cargioli, *Annu. Rep. NMR Spectrosc.*, 1979, **9**, 221.
6. H. C. Marsmann, *NMR Basic Principles Prog.*, 1981, **17**, 65.
7. J. D. Cavalieri, R. West, J. C. Duchamps, and K. W. Zilm, *J. Am. Chem. Soc.*, 1993, **115**, 3770.
8. R. S. Archibald, Y. van den Winkel, A. J. Millevolte, J. M. Desper, and R. West, *Organometallics*, 1992, **11**, 3276.
9. N. Wiberg, G. Wagner, and G. Muller, *Angew. Chem.*, 1985, **97**, 220; *Angew. Chem., Int. Ed. Engl.*, 1985, **24**, 229.
10. K. M. Baines, A. G. Brook, R. R. Ford, P. D. Lickiss, A. K. Saxena, W. J. Chatterton, J. F. Sawyer, and B. A. Behman, *Organometallics*, 1989, **8**, 693.
11. C. N. Smit and F. Bickelhaupt, *Organometallics*, 1987, **6**, 1156.
12. E. Kupce, E. Liepins, I. Urtäne, G. Zelcons, and E. Lukevics, *J. Organomet. Chem.*, 1985, **279**, 343; E. Kupce and E. Lukevics, *J. Organomet. Chem.*, 1988, **358**, 67.
13. M. Ya. Myagi, A. V. Somoson, E. T. Lippmaa, V. A. Pestunovich, S. N. Tandura, B. Z. Shterenberg, and M. G. Voronkov, *Dokl. Akad. Nauk SSSR*, 1980, **252**, 140.
14. A.-R. Grimmer, W. Wieker, F. von Lampe, E. Fechner, R. Peter, and G. Molgedey, *Z. Chem.*, 1980, **20**, 453.
15. K. C. Kumara Swamy, V. Chandresekhar, J. J. Harland, J. M. Holmes, R. O. Day, and R. R. Holmes, *J. Am. Chem. Soc.*, 1990, **112**, 2341.
16. A.R. Bassindale and Jianxiong Jiang, *J. Organomet. Chem.*, 1993, **446**, C3.
17. S. E. Johnson, J. A. Deiters, R. O. Day, and R. R. Holmes, *J. Am. Chem. Soc.*, 1989, **111**, 3250.
18. S. E. Johnson, R. O. Day, and R. R. Holmes, *Inorg. Chem.*, 1989, **28**, 3182.
19. K. Tamao, T. Hayashi, and Y. Ito, *Organometallics*, 1992, **11**, 2099.
20. C. W. Lentz, *Inorg. Chem.*, 1964, **3**, 574.
21. J. Schraml, *Prog. Nucl. Magn. Reson. Spectrosc.*, 1990, **22**, 289.
22. E. Bertling and H. C. Marsmann, *Z. Anorg. Allg. Chem.*, 1989, **578**, 166.
23. R. K. Harris and B. J. Kimber, *Appl. Spectrosc. Rev.*, 1975, **10**, 117.
24. G. Engelhardt and H. Jancke, *Polym. Bull.*, 1981, **5**, 577.
25. D. Hoebbel and R. Ebert, *Z. Chem.*, 1988, **28**, 41.
26. G. Engelhardt and D. Hoebbel, *J. Chem. Soc., Chem. Commun.*, 1984, 514.
27. C. J. Creswell, R. K. Harris, and P. T. Jageland, *J. Chem. Soc., Chem. Commun.*, 1984, 1261.
28. S. D. Kinrade and T. W. Swaddle, *J. Chem. Soc., Chem. Commun.*, 1986, 120.
29. R. K. Harris and C. T. G. Knight, *J. Chem. Soc., Faraday Trans. 2*, 1983, **79**, 1525.
30. R. K. Harris and C. T. G. Knight, *J. Chem. Soc., Faraday Trans. 2*, 1983, **79**, 1539.
31. R. K. Harris and M. J. O'Connor, *J. Magn. Reson.*, 1984, **57**, 115.

32. H. C. Marsmann, E. Meyer, M. Vongehr, and E. F. Weber, *Makromol. Chem.*, 1983, **184**, 1817.
33. E. Bertling and H. C. Marsmann, *Phys. Chem. Miner.*, 1988, **16**, 295.
34. R. Krentz and R. K. Pomeroy, *Inorg. Chem.*, 1985, **24**, 2976.
35. K. H. Pannell and A. R. Bassindale, *J. Organomet. Chem.*, 1982, **229**, 1.
36. K. H. Pannell, J. M. Rozell, and Woei-Min Tsai, *Organometallics*, 1987, **6**, 2085.
37. E. Colomer, R. J. P. Corriu, C. Marzin, and A. Vioux, *Inorg. Chem.*, 1982, **21**, 368.
38. K. H. Pannell, A. R. Bassindale, and J. W. Fitch, *J. Organomet. Chem.*, 1981, **209**, C65.
39. H.-G. Horn, *J. Prakt. Chem.*, 1992, **334**, 201.
40. J. Schraml and J. M. Bellama, *Determination of Organic Structures by Physical Methods*, Academic Press, New York, 1976, Vol. 6, pp. 203–269.
41. U. Schubert, G. Scholz, J. Müller, K. Ackermann, and B. Wörle, *J. Organomet. Chem.*, 1986, **306**, 303.
42. E. A. Williams, *Annu. Rep. NMR Spectrosc.*, 1983, **15**, 235.
43. H. B. Yokelson, A. J. Millevolte, B. R. Adams, and R. West, *J. Am. Chem. Soc.*, 1987, **109**, 4116.
44. R. West, *Angew. Chem.*, 1987, **99**, 1231; *Angew. Chem., Int. Ed. Engl.*, 1987, **26**, 1201.
45. M. Kuroda, Y. Kabe, M. Hashimoto, and S. Masamune, *Angew. Chem.*, 1988, **108**, 1795; *Angew. Chem., Int. Ed. Engl.*, 1988, **27**, 1227.
46. P. K. Jenkner, A. Spielberg, M. Eibl, and E. Hengge, *Spectrochim. Acta*, 1993, **49A**, 161.
47. K. M. Larsson and J. Kowalewski, *J. Magn. Reson.*, 1985, **62**, 260.
48. G. C. Levy, J. D. Cargioli, P. C. Juliano, and T. D. Mitchell, *J. Am. Chem. Soc.*, 1973, **95**, 3445.
49. Yi-Ming Pai, W. P. Weber, and K. L. Servis, *J. Organomet. Chem.*, 1985, **288**, 269.
50. H. C. Marsmann and E. Meyer, *Makromol. Chem.*, 1987, **188**, 887.
51. C. T. G. Knight and R. K. Harris, *Magn. Reson. Chem.*, 1986, **24**, 872.
52. E. Colvin, *Silicon in Organic Synthesis*, Butterworths, London, 1981.

Biographical Sketch

Heinrich C. Marsmann. *b* 1938. B.S., 1961, TU Berlin, Ph.D., 1966, Göttingen. Postdoctoral fellow (Van Wazer 1967) Dates?, Habilitation RU Bochum, 1973. Faculty in Chemistry, Paderborn, 1974–present. Approx. 80 publications. Research interests: silicon chemistry and NMR.

Sodium-23 NMR

Pierre Laszlo
Université de Liège B6, B-4000 Liège, Belgium, and École polytechnique, F-91128 Palaiseau, France

1	Introduction	1
2	Sodium Coordination and Preferential Solvation	1
3	Inclusion Complexes	1
4	Polyelectrolytes	2
5	Inorganic Solids	3
6	Ion Transport	3
7	Whole Cells	3
8	Tissues and Organs	3
9	Magnetic Resonance Imaging	4
10	Conclusions	4
11	Related Articles	4
12	References	4

1 INTRODUCTION

In order to avoid duplication with earlier reviews, I will cover only the main areas of activities during the last decade or so. This explains why fundamental aspects such as the super-Lorentzian lineshape outside of extreme narrowing–biexponential relaxation is now accessible by multiple quantum methods[1] and lineshapes for exchange kinetics are available;[2] direct determination of the attendant dynamic frequency shift is feasible[3] (but will not be repeated here), and the question of why applications such as studies of ion pairing as for instance in McCormick et al.,[4] Iida and Hata,[5]—will not be found here. Neither shall I cover the classic demonstration of the existence of the sodium anion, which is dealt with at proper length elsewhere in this Encyclopedia. In addition, space restriction does not allow coverage of applications to liquid crystalline mesophases whose heyday is now past its prime despite some excellent studies[6–8] and extensions to suspensions of clay platelets.[9] Likewise, the application to micelles[10]—a field in itself, thriving because of relevance to the industry of detergents—will not be further detailed.[11,12] I will just mention the potentially useful technique of spin-$\frac{3}{2}$ relaxation in the doubly rotating tilted frame.[13]

2 SODIUM COORDINATION AND PREFERENTIAL SOLVATION

The sodium anion Na^- with its filled 3s electronic levels has a remarkably invariant chemical shift of -62 ± 1 ppm.[14–16] By contrast, the Na^+ cation has a chemical shift ranging from -52 ppm for the tetraphenylborate salt in the solid state[17] to solution values ranging between 0 and +60 ppm, in proportion to donation from counteranion and solvent lone pairs on to the sodium 3p orbitals.[18] The calculated changes in nuclear shielding constants of Na^- (gas) with respect to Na^+ (gas) amount to shielding by only 7.7 ppm for full addition of two electrons to gaseous Na^+ (gas) to form Na^- (gas).[19] In the solid state, chemical shifts depend on ligand type (water $\approx$ 0, hydroxy ≈ -2, carbonyl -8 to -12, diethyl ether -10, ionophores -15 to -25 ppm). Some ionophore complexes (monensin, tetranactin) display near-identical chemical shifts in the solid state and in solution. Other complexes, when solvent molecules are able to get to the encapsulated sodium cation, show substantial (10–20 ppm) downfield shifts.[20]

We now select for praise a handsome study using magic angle spinning of several homoionic Llano vermiculites.[21] These are swelling clays. Each state of hydration goes with a specific value of the chemical shift, more and more to high frequency (downfield) as the number of molecules in the interlayer increases. For ^{23}Na, ^{111}Cd, and ^{133}Cs a reduced isotropic chemical shift is defined as $\delta_{iso} \times \nu_0$, where ν_0 is the Larmor frequency. This chemical shift δ is determined to first approximation by the oxygen ligands. Their donation to the empty orbitals of the cation is in proportion to their ionization enthalpy I. In the second approximation, the chemical shift depends also on the configuration of the M ligands within the N sites available to the cation. Assuming that δ/I is like the partial potential of a configurational shielding energy, Fripiat predicts that $\delta/I \propto \ln (M)/(N - M)$, as it indeed does handsomely.

Sodium-23 NMR is very good at detecting mixed solvates with their nonvanishing electrostatic field gradient leading to marked increases in linewidth. Since each discrete solvate has a characteristic chemical shift and linewidth, even under the prevailing situation of fast ligand exchange, one can often obtain and offer the full story of preferential solvation over the whole range of composition for a binary solvent mixture. It includes solvation numbers, the rate constants and the thermodynamic equilibrium constants for interconversion between the coexisting complexes, and determination of the associative or dissociative character of ligand exchange.[22]

3 INCLUSION COMPLEXES

Shchori et al. kicked off the kinetics of Na^+ exchange in 1971.[23] Decomplexation of Na^+ from its complex with dibenzo-18-crown-6 provided a favorable case, since the rate of chemical exchange is of the same magnitude as relaxation rates. In these initial studies,[24] the chemical shift difference between the free and bound states was negligible. If conversely there exists such a chemical shift difference, the transverse relaxation rate exceeds the longitudinal relaxation rate because of exchange broadening. In this latter case, under the appropriate (solvent, temperature) conditions one is looking only at the resonance for free sodium ions broadened by exchange with the underlying signal for bound sodium ions, whose intensity is too low for direct detection. A number of studies have followed this scheme.[25–43] Some address the mechanistic question of whether Na^+ exchange obeys a unimolecular (Na^+, C) $\rightarrow$ Na^+ + C dissociative or a bimolecular $*Na^+$ + (Na^+, C) $\rightarrow$ Na^+ + ($*Na^+$, C) associative mechanism.[44]

Alternatively, separate ^{23}Na resonances for free and complexed states have been observed for encapsulation by cryptands,[45–48] or with the tetraphenylborate counterion in

solvent-separated ion pairs. The reader is reminded of the distinction between tight ion pairs in which anion and cation are nearest neighbors and loose ion pairs in which at least one solvent molecule gets in between the ionic partners.

4 POLYELECTROLYTES

Exploration of the area is to be credited to the group in Lund. Early on, they examined changes in quadrupolar relaxation with concentration of a natural or synthetic polyelectrolyte.[49,50] Synthetic polyelectrolytes such as poly(acrylic acid) and poly(methacrylic acid) and also natural polyelectrolytes such as mucopolysaccharides were studied.[51,52] Before reviewing these and other contributions, we have to introduce the key relevant ideas. A conceptually and operationally useful distinction contrasts site binding (i.e. tight ion pairs) and atmospheric condensation (loose ion pairs). The former is describable by complex formation, with the attendant thermodynamic equilibrium constant. The latter, not amenable to such a description, is the generalized attraction of the counterions into the electrostatic potential well from the polyelectrolyte, so as to screen from one another the amassed charges of like sign. The polyion is characterized by high linear charge density. When it exceeds a critical value, then accumulation of the counterions occurs. Electrostatic theories provide models for atmospheric condensation. The crudest variety is an all-or-nothing two-state model devised by Manning,[53] that accounts nicely for condensation occurring as soon as the counterion concentration reaches a critical value set by the linear charge density on the polyelectrolyte. However most authors now perform a more accurate Poisson–Boltzmann calculation of the mole fraction of atmospheric ions,[54] to apply it for instance to the ^{23}Na NMR of poly(styrene sulfonate)[55] or to condensation of sodium ions around micelles.[56]

The Manning model, useful as a first approximation, defines a reduced linear charge density ξ. Its critical value is unity for a univalent counterion such as Na^+. The corresponding critical distance d_c between the adjoining like charges on the polymer is 7.1 Å in water at 25 °C, and ξ is simply the ratio to d_c of the mean actual distance between adjacent charges, projected onto the cylindrical axis of the polyanion. As soon as ξ reaches unity sodium counterions condense into the atmosphere around the polyanion. The charge fraction f of nonneutralized negative charges on the polyanion is unity whenever $\xi < 1$ and with $(\xi)^{-1}$ otherwise. For instance, in the interaction of Na^+ with polyacrylic acid, no condensation occurs at $\xi = 0.8$ but is observed at $\xi = 1.1$.[57]

Monitoring dispersion of ^{23}Na longitudinal and transverse relaxations at nominal frequencies between 8 and 64 MHz for sodium ions in poly(methacrylic acid) solutions provides in an assumption-free manner the relevant spectral densities; the procedure indicates that a simple two-state model, consisting of a simple Lorentzian density for bound ions and a white noise density for the free ions in the bulk solution, is inadequate.[58] In general, sodium cations interacting with polyanions lead to relaxation rates outside the extreme narrowing limit.[59,60] A control experiment, i.e. shielding the sodium ions with a cage-like ligand such as the [2.2.2]cryptand confirms this finding. The sodium NMR becomes immune to the proximity of the polyelectrolyte when ^{23}Na relaxation is dominated by the electrostatic field gradient from the coordinated ligand.[61]

The general situation described by many authors is a small degree of specific site binding coexisting with predominant nonspecific atmospheric condensation. Very often, the correlation time of bound sodium ions is sufficiently long that magnetization decay acquires biexponential character, as displayed in super-Lorentzian lineshapes. This served to characterize the state of sodium ions in hydrocolloid systems,[62] in aqueous solutions of sodium pectate and polyuronates,[63] and a solvent relaxation NMR bound-fraction determination for sodium poly(styrene sulfonate) at the solid–solution interface.[64] An early example will give the flavor of these studies. Glycosaminoglycans are carbohydrate biopolymers occurring at neuronal synapses, in the extracellular volume of connective tissues, etc. Examples are chondroitin sulfate and dermatan sulfate with one ionizable group alternatively $-OSO_3^-$ and $-COO^-$ on each monosaccharide unit, and hyaluronic acid with a carboxylate $-COO^-$ group on every second monosaccharide unit. The transverse relaxation rate R_2 changes in sigmoidal manner with the degree of neutralization α. Comparing longitudinal and transverse relaxation rates yields the product $p_B\chi^2$, where p_B is the mole fraction of bound Na^+ ions and χ the quadrupolar coupling constant. This product undergoes a sharp increase in the range $\alpha = 0.6–0.9$. In this range, χ is essentially independent of α, with a value of about 0.15 MHz consistent only with a full hydration shell and therefore with atmospheric condensation rather than site binding.[65]

The late Ed Gabbay pioneered the use of ^{23}Na NMR to examine the influence of DNA on counterions coexisting in solution. The DNA polyanion increases markedly the relaxation rates of the $^{23}Na^+$ counterions. By measuring longitudinal relaxation at three distinct frequencies (4.3, 8.15, 15.7 MHz), the authors determined a reorientational correlation time τ_c of 5.5 ns. The concentration dependence gave a limiting relaxation rate in the bound state of 170 Hz, that translated into a quadrupolar coupling constant $\chi = 0.1$ MHz. Such a low value rules out site binding and is nicely consistent with atmospheric condensation.[66] It remained to be shown that the linear dependence of the relaxation rate enhancement with DNA content is accountable by electrostatic theory, which the Madison group proceeded to do. One of the tenets of Manning's model is the invariance of the neutralized fraction of the DNA polyanionic charge; Anderson, Record, and Hart successfully addressed this issue.[67] Work continued at a steady pace.[68–71] In 1984, a study was made on three synthetic polynucleotides and on DNAs from four different species, calf thymus, *Clostridium perfringens*, *Escherichia coli*, and *Micrococcus lysodeikticus*: the ^{23}Na spectra (at 4.7 T) were uniformly non-Lorentzian. All of the sodium correlation times continued to be in the range of nanoseconds, and the Madison group concluded on a dominance of the relaxation process by the radial translational diffusion of sodium ions away from the nucleic acid semirigid rod.[72] A number of interesting studies followed.[73–79]

More recently, increased sophistication came into play, and ^{23}Na NMR was used to monitor intercalation of various drugs in the DNA double helix. The basic idea is very simple: intercalation extends the helix whereby the mean phosphate-to-phosphate distance increases. The overall decrease of the DNA charge density should and does lead to a lesser degree of atmospheric condensation for the counterions.[80–82] In this manner intercalation of 9-aminoacridine has been studied.[83] Intercalation mainly affects the part of the spectral density

function describing the contribution of the fast modulations to the relaxation. These fast motions may be ascribed to anisotropic fluctuations in the symmetry of the Na^+ hydration shell.[84]

5 INORGANIC SOLIDS

Since the sodium nucleus has a large quadrupole moment and a low quantum spin number I, it has a significant second-order quadrupolar shift given by $-(1/30)\cdot(\nu_Q/\nu_0)^2\cdot[I(I+1)-9m(m-1)-3]\cdot(1+\eta^{2/3})$, where $\nu_Q = 3\chi[2I(I-1)]^{-1}$, ν_0 is the Larmor frequency, and η is the asymmetry factor.[85–88] The attendant correction is in the range 0–10 ppm. Interferometric correlation of the first- and second-order shifts enhances resolution,[89] due in part to population transfers between single-quantum (SQ) and double-quantum (DQ) states.[90] Both the SQ and the DQ ^{23}Na resonances in a single crystal of sodium nitrate share lineshapes with the same second moment.[91] The length of the exciting pulse depends on the transition observed. With the central $m = +\frac{1}{2} \rightarrow -\frac{1}{2}$ coherence it is $\pi/4\gamma H_1$ (90°), whereas if one of the satellite $m = \pm\frac{3}{2} \rightarrow \pm\frac{1}{2}$ resonances is excited it is $\pi/\gamma\ H_1 2\sqrt{3}$. The amplitude of the FID following a 90° pulse thus depends on the precise resonance being excited. The FID amplitudes are in the ratio $1:\sqrt{4/10}:\sqrt{3/10}$ when the excitation is indiscriminate, applied to the sole center line, or to one of the satellites alone. Measurement of such pulse responses amounts to a measurement of the quadrupolar coupling constant χ.[92] Of course, relatively high-resolution solid state spectra result from focusing exclusively on the central $(+\frac{1}{2}, -\frac{1}{2})$ resonance. It is broadened in a solid only by dipolar, chemical shift anisotropy and second-order quadrupolar broadening. Since the latter are $\propto \boldsymbol{B}_0{}^{-1}$, the best results are achieved at the highest fields and spinning rates. Residual widths in the kHz range are typical with large 2–3 MHz quadrupolar coupling constants.[93,94]

The state of Na^+ cations inside zeolites has been monitored.[95–98] Other minerals such as β-gallate,[99] $Na^+XZR_2Si_xP_{3-x}O_{12}$,[100] lanthanide salts,[101] β-alumina,[102] the sodium phyllosilicate $Na_2Si_2O_5$,[103] and the polycrystalline salts of ADP and ATP[104,105] have also been the topics of fine work.

6 ION TRANSPORT

Active transport is of the St. Christopher variety: an ionophore molecule grabs the sodium cation, divested of most or all its hydration shell, shields it from the lipophilic interior of a cell membrane, and disgorges it on the other side of the membrane where the Na^+ ion puts back on a coordination shell.

Passive transport is a canal crossing. Singly or in a queue, the sodium ions (accompanied by the chloride anions) pass through a channel set up through a cell membrane. Nature can build these channels (for instance from gramicidin A, a pentadecapeptide) so that the electrostatic field and charges on the inner walls of the channel help to bring along the migrating ions from one side of the membrane, or wall, to the other.

After a couple of pioneering studies of the gramicidin A channel by ^{23}Na NMR[106,107] Dan Urry's group at the University of Alabama gave it their detailed and careful attention from the beginning of the 1980s.[108,109] As is often the case, the study of the natural structures prompted synthesis of artificial analogs such as that of a membrane-insertable, sodium cation conducting channel: kinetic analysis by dynamic ^{23}Na NMR was reported.[110]

Monensin-mediated[111] and nigericin-mediated[112] transport of sodium ions through phospholipid bilayers have been monitored by ^{23}Na NMR. Sodium-23 NMR measurement of the maximal rate of active sodium efflux from human red blood cells has been reported.[113] Simultaneous observation with ^{23}Na and ^{31}P NMR gave insight into the coupling between in vivo sodium transport and phosphorus metabolism in sodium-loaded yeast[114,115] and in *Streptococcus faecalis*.[116] One- and two-dimensional magnetization transfer experiments applied to monensin-mediated transport gave a coherent overall description of transmembrane cation transport and of the kinetics of the sodium pump.[117,118] The state of sodium in membranes of the sarcoplasmic reticulum was investigated.[119]

7 WHOLE CELLS

Saline aqueous solutions within organisms, as the internal medium of cells, are the remanent trace, the enduring memory, many think, of the composition of the primeval ocean: one more impetus for the determination of the concentration of these living solutions of ordinary table salt.

For determination of intracellular sodium concentration, discrimination between intra- and extracellular sodium ions is achieved by various means. One can use extracellular contrast reagents[120–125] or apply a DQ filter, so that those sodium ions with biexponential relaxation outside the extreme narrowing condition can be selected.[126,127] The contrast reagents used are lanthanide complexes either of the shift reagent[128–131] or of the relaxation agent type pioneered by Degani and Elgavish[132] and reemphasized by Riddell and Southon as diamagnetic relaxation agents.[133] The intracellular concentrations thus determined agree nicely with those determined by flame photometry. Many such determinations were made, in mammalian proximal tubule,[134] in those of diabetics,[135–137] in amphibian oocytes, ovulated eggs, and early embryos,[138] in renal brush border membrane vesicles,[139] in the halotolerant alga *Dunaliella salina*,[140] and in the halophilic bacterium *Halobacterium halobium*,[141] in *Dictyostelium discoideum* ameba,[142] in kidney tubules,[143] also in vivo[144] in a wall-less strain of *Neurospora crassa*,[145] in reticulocyte,[146] and red blood cells[147,148] submitted to drugs.[149] Sodium influxes in renal epithelial LLC-PK1/CL4 cells were monitored by ^{23}Na NMR.[150] In the late 1980s, removal of artifacts such as the invisibility of some of the sodium ions[151–154] or leakage through the DQ filter of extracellular ions led to combining the DQ filter and paramagnetic quenching of outer sodium,[155,156] or to selective detection of intracellular sodium by coherence transfer.[157] The relaxation rates gave insight into the molecular environment of intracellular sodium.[158]

8 TISSUES AND ORGANS

This is one of the earliest applications of sodium NMR. Tainted initially by misinterpretation (40% free sodium

coexisting with 60% bound sodium)[159–171] it was set right by the appearance of the theoretical paper by Hubbard and by the Monoi reinterpretation[172,173] in terms of the presence of membrane-bound sodium ions with two different transverse relaxations. The modern era of ^{23}Na studies of intact tissue was ushered in by the Chang and Woessner study[174] of skeletal muscle using T_1 and spin echo T_2 determination. The latter had both slow and fast components. Ordering by condensation around macromolecules was responsible, and more than 90% of the sodium ions were in such a 'bound' state, characterized by a small quadrupolar coupling constant < 0.17 MHz and slow tumbling with a $\tau_c > 10$ ms.[174] Another epochal paper recorded, shortly thereafter, by gated sodium NMR, the first images of a beating heart.[175] Numerous authors followed with studies of NMR measurements of intracellular and extracellular sodium in intact tissues,[176] such as muscle,[177,178] heart,[179,180] kidneys,[181] the aorta of hypertensive rats,[182] neoplastic and nonneoplastic human tissue,[183] and during ischemia and calcium-free perfusion.[184] Phosphorus-31 and ^{23}Na NMR were applied to the study of phosphate metabolites, intracellular pH, and intracellular sodium during liver hypoxia and recovery.[185,186] Their joint use was also applied to sonicated cardiolipin sodium salt.[187] Membrane depolarization was detected by continuous sodium ion monitoring of rat hearts at 4 °C,[188] and during ischemia[189] ion transport was monitored[190] which obeyed a proton–sodium ions antiport mechanism.[191]

9 MAGNETIC RESONANCE IMAGING

Given its good NMR receptivity the ^{23}Na nucleus was a natural for imaging studies. Among the numerous applications, an early one was the study of tissue following a cerebral stroke.[192] The same group also compared resected with normal organs.[193] Arthritic cartilage degradation can be followed.[194] Sodium imaging in conjunction with proton imaging of lung water[195] was performed and improved.[196] Use of surface coils and a DQ methodology monitors brain potassium and sodium.[197] Sodium chloride-rich kidney is an easy target for imaging.[198] A number of improved methodologies such as chemical shift imaging,[199] DQ filtered[200] and triple quantum filtered[201] sodium imaging have been proposed in more recent years.

10 CONCLUSIONS

Of some interest to future historians is the choice of the periodical in which a particular study appears. In each discipline, authors are acutely aware of the pecking order. While one may safely assume that investigators will push their results into the most prestigious and therefore most widely 'read' journal, the editors see to it that the material published conforms to their vision of the subject matter encompassed by their journal. We state these self-evident behaviors, at the risk of belaboring the obvious, only because preparation of this manuscript revealed the existence of (i) a bandwagon—in the 1970s and in the 1980s, the *Journal of the American Chemical Society* was extremely receptive to physicochemical characterizations of inclusion complexes between metallic ions and crown ethers or cryptands—and (ii) a preference—somewhat contradictory with the choice of the periodical of the greatest impact—for making a contribution appear as *methodological* rather than *applied*. Many a paper that could very well have appeared also in a biochemical/biophysical journal showed up instead in the *Journal of Magnetic Resonance*.

The ultraspecialization strikes this reviewer as paradigmatic science at its routine worst: to keep in the same rut, repeating similar work in order to associate one's name with a tiny portion of a vast field is a parody of free inquiry.

Thus we reach the end of this survey. Even though the picture painted is a composite, it is not unattractive. The prospects though may be somewhat grim. One can read recent history as gradual secession of the field from intrinsic scientific interest, as the money and the talent switch their allegiance to the biomedical side.

11 RELATED ARTICLES

Brownian Motion and Correlation Times; Calcium-Binding Proteins; Deuteron Relaxation Rates in Liquid Crystalline Samples: Experimental Methods; Dynamic Frequency Shift; High Speed MAS of Half-Integer Quadrupolar Nuclei in Solids; Liquid Crystalline Samples: Deuterium NMR; Lithium NMR; Magic Angle Spinning Carbon-13 Lineshapes: Effect of Nitrogen-14; Inorganic Chemistry Applications; Inorganic Nuclei: Low Sensitivity Transition Metals; Multiple Quantum Spectroscopy of Liquid Samples; Nucleic Acid Flexibility and Dynamics: Deuterium NMR; Organic Chemistry Applications; Overtone Spectroscopy of Quadrupolar Nuclei; Oxygen-17 NMR; Quadrupolar Interactions; Relaxation Processes in Coupled-Spin Systems; Relaxation Processes: Cross Correlation and Interference Terms; Relaxation Theory for Quadrupolar Nuclei; Selective Relaxation Techniques in Biological NMR.

12 REFERENCES

1. G. Jaccard, S. Wimperis, and G. Bodenhausen, *J. Chem. Phys.*, 1986, **85**, 6282.
2. U. Eliav, A. Baram, and G. Navon, *J. Chem. Phys.*, 1988, **89**, 5584.
3. A. G. Marshall, T. C. L. Wang, C. E. Cottrell, and L. G. Werbelow, *J. Am. Chem. Soc.*, 1982, **104**, 7665.
4. A. V. McCormick, A. T. Bell, and C. J. Radke, *J. Phys. Chem.*, 1989, **93**, 1733.
5. M. Iida and Y. Hata, *Bull. Chem. Soc. Jpn.*, 1992, **65**, 707.
6. A. Loewenstein and M. Brenman, *J. Phys. Chem.*, 1980, **84**, 340.
7. J. E. Bonekamp, I. Artaki, M. L. Phillips, S. Plesko, and J. Jonas, *J. Phys. Chem.*, 1983, **87**, 4991.
8. I. Furó, B. Halle, P.-O. Quist, and T. C. Wong, *J. Phys. Chem.*, 1990, **94**, 2600.
9. J. Grandjean and P. Laszlo, in *Dynamics of Solutions and Fluid Mixtures by NMR*, ed. J.-J. Delpuech, Wiley, Chichester, Chap. 5, p. 231.
10. B. Lindman, in *NMR of Newly Accessible Nuclei*, ed. P. Laszlo, Academic Press, New York, 1983, Vol.1, p. 193.

11. A. Ceglie, G. Colafemmina, M. Dellamonica, L. Burlamacchi, and M. Monduzzi, *J. Colloid Interface Sci.*, 1991, **146**, 363.
12. H. Fujii, T. Kawai, H. Nishikawa, and G. Ebert, *Colloid Polym. Sci.*, 1983, **261**, 340.
13. J. R. C. van der Maarel, *J. Chem. Phys.*, 1989, **91**, 1446.
14. R. C. Phillips, S. Khazaeli, and J. L. Dye, *J. Phys. Chem.*, 1985, **89**, 606.
15. J. L. Ceraso and J. L. Dye, *J. Chem. Phys.*, 1974, **61**, 1585.
16. J. L. Dye, C. W. Andrews, and J. M. Ceraso, *J. Phys. Chem.*, 1975, **79**, 3076.
17. R. Tabeta, M. Aida, and H. Saitô, *Bull. Chem. Soc. Jpn.*, 1986, **59**, 1957.
18. P. Laszlo, *Angew. Chem., Int. Ed. Engl.*, 1978, **17**, 254.
19. G. Malli and S. Fraga, *Theor. Chim. Acta*, 1966, **5**, 275.
20. H. Saitô and R. Tabeta, *Bull. Chem. Soc. Jpn.*, 1987, **60**, 61.
21. V. Laperche, J. F. Lambert, R. Prost, and J. J. Fripiat, *J. Phys. Chem.*, 1990, **94**, 8821.
22. H. J. Chuang, L. L. Soong, G. E. Leroi, and A. I. Popov, *J. Solution Chem.*, 1989, **18**, 759.
23. E. Shchori, J. Jagur-Grodzinski, Z. Luz, and M. Shporer, *J. Am. Chem. Soc.*, 1971, **93**, 7133.
24. E. Shchori, J. Jagur-Grodzinski, and M. Shporer, *J. Am. Chem. Soc.*, 1973, **95**, 3842.
25. M. Shporer and Z. Luz, *J. Am. Chem. Soc.*, 1975, **97**, 665.
26. E. Mei, A. I. Popov, and J. L. Dye, *J. Phys. Chem.*, 1977, **81**, 1677.
27. E. Mei, J. L. Dye, and A. I. Popov, *J. Am. Chem. Soc.*, 1977, **99**, 5308.
28. J. Grandjean, P. Laszlo, W. Offermann, and P. Rinaldi, *J. Am. Chem. Soc.*, 1981, **103**, 1380.
29. R. C. Phillips, S. Khazaeli, and J. L. Dye, *J. Phys. Chem.*, 1985, **89**, 606.
30. B. O. Strasser and A. I. Popov, *J. Am. Chem. Soc.*, 1985, **107**, 7921.
31. B. O. Strasser, K. Hallenga, and A. I. Popov, *J. Am. Chem. Soc.*, 1985, **107**, 789.
32. A. Delville, H. D. H. Stöver, and C. Detellier, *J. Am. Chem. Soc.*, 1985, **107**, 4172.
33. H. D. H. Stöver, A. Delville, and C. Detellier, *J. Am. Chem. Soc.*, 1985, **107**, 4167.
34. S. F. Lincoln, A. White, and A. M. Hounslow, *J. Chem. Soc., Faraday Trans. 1*, 1987, **83**, 2459.
35. P. Szczygiel, M. Shamsipur, K. Hallenga, and A. I. Popov, *J. Phys. Chem.*, 1987, **91**, 1252.
36. E. Amat, B. G. Cox, and H. Schneider, *J. Magn. Reson.*, 1987, **71**, 259.
37. A. Delville, H. D. H. Stöver, and C. Detellier, *J. Am. Chem. Soc.*, 1987, **109**, 7293.
38. K. M. Brière and C. Detellier, *J. Phys. Chem.*, 1987, **91**, 6097.
39. Q. H. Luo, X. D. Feng, Z. D. Li, and M. C. Shen, *Acta Chim. Sinica*, 1988, **46**, 577.
40. H. D. H. Stöver and C. Detellier, *J. Phys. Chem.*, 1989, **93**, 3174.
41. Q. H. Luo, X. D. Feng, M. C. Shen, and Q. Y. Tu, *Acta Chim. Sinica*, 1989, **47**, 727.
42. T. Jin and K. Ichikawa, *J. Phys. Chem.*, 1991, **95**, 2601.
43. M. Tanaka, H. Mizufune, and T. Shono, *Chem. Lett.*, 1990, 1419.
44. H. P. Graves and C. Detellier, *J. Am. Chem. Soc.*, 1988, **110**, 6019.
45. J. M. Ceraso, P. B. Smith, J. S. Landers, and J. L. Dye, *J. Phys. Chem.*, 1977, **81**, 760.
46. J. C. Lin and A. I. Popov, *J. Am. Chem. Soc.*, 1981, **103**, 3773.
47. J. M. Ceraso and J. L. Dye, *J. Phys. Chem.*, 1974, **61**, 1585.
48. J. L. Dye, C. W. Andrews, and J. M. Ceraso, *J. Phys. Chem.*, 1975, **79**, 3076.
49. S. Forsén and B. Lindman, *Methods Biochem. Anal.*, 1981, **27**, 289.
50. B. Lindman, in *NMR of Newly Accessible Nuclei*, ed. P. Laszlo, Academic Press, San Diego, CA, 1983, pp. 193.
51. H. Gustavsson, B. Lindman, and T. Bull, *J. Am. Chem. Soc.*, 1978, **100**, 4655.
52. H. Gustavsson, G. Siegel, B. Lindman, and L.-Å. Fransson, *Biochim. Biophys. Acta*, 1981, **677**, 23.
53. G. S. Manning, *Acc. Chem. Res.*, 1979, **12**, 443.
54. R. Fuoss, A. Katchalsky, and S. Lifson, *Proc. Natl. Acad. Sci. U.S.A.*, **37**, 579.
55. A. Delville, H. Gilboa, and P. Laszlo, *J. Chem. Phys.*, 1982, **77**, 2045.
56. A. Delville, L. Herwats, and P. Laszlo, *Nouv. J. Chim.*, 1984, **8**, 557.
57. J. J. van der Klink, L. H. Zuiderweg, and J. C. Leyte, *J. Chem. Phys.*, 1974, **60**, 2391.
58. C. W. R. Mulder, J. de Bleijser, and J. C. Leyte, *Chem. Phys. Lett.*, 1980, **69**, 354.
59. M. Levij, J. de Bleijser, and J. C. Leyte, *Chem. Phys. Lett.*, 1981, **83**, 183.
60. M. Levij, J. de Bleijser, and J. C. Leyte, *Chem. Phys. Lett.*, 1982, **87**, 34.
61. J. R. C. van der Maarel, D. van Duijn, J. de Bleijser, and J. C. Leyte, *Chem. Phys. Lett.*, 1987, **135**, 62.
62. N. Ayya, S. J. Richardson, and B. P. Klein, *Cereal Foods World*, 1987, **32**, 665.
63. H. Grasdalen and B. J. Kvam, *Macromolecules*, 1986, **19**, 1913.
64. T. Cosgrove, T. M. Obey, and M. Taylor, *Colloids Surf.*, 1992, **64**, 311.
65. H. Gustavsson, G. Siegel, B. Lindman, and L. A. Fransson, *FEBS Lett.*, 1978, **86**, 127.
66. J. Reuben, M. Shporer, and E. J. Gabbay, *Proc. Natl. Acad. Sci. U.S.A.*, 1975, **72**, 245.
67. C. F. Anderson, M. T. Record, Jr., and P. A. Hart, *Biophys. Chem.*, 1978, **7**, 301.
68. M. L. Bleam, C. F. Anderson, and M. T. Record, Jr., *Proc. Natl. Acad. Sci. U.S.A.*, 1980, **77**, 3085.
69. D. R. Burton, S. Forsén, and P. Reimarsson, *Nucleic Acids Res.*, 1981, **9**, 1219.
70. M. L. Bleam, C. F. Anderson, and M. T. Record, Jr., *Biochemistry*, 1983, **22**, 5418.
71. Y. H. Mariam and W. D. Wilson, *J. Am. Chem. Soc.*, 1983, **105**, 627.
72. L. Nordenskiöld, D. K. Chang, C. F. Anderson, and M. T. Record, Jr., *Biochemistry*, 1984, **23**, 4309.
73. W. K. Lee, Y. Gao, and E. W. Prohofsky, *Biopolymers*, 1984, **23**, 257.
74. W. H. Braunlin, C. F. Anderson, and M. T. Record, Jr., *Biopolymers*, 1986, **25**, 205.
75. A. Delville, P. Laszlo, and R. Schyns, *Biophys. Chem.*, 1986, **24**, 121.
76. W. H. Braunlin, C. F. Anderson, and M. T. Record, Jr., *Biochemistry*, 1987, **26**, 7724.

77. M. Casu, A. Lai, C. Meloni, and G. Saba, *Chem. Phys. Lett.*, 1987, **137**, 533.
78. S. Padmanabhan, B. Richey, C. F. Anderson, and M. T. Record, Jr., *Biochemistry*, 1988, **27**, 4367.
79. T. E. Strzelecka and R. L. Rill, *Biopolymers*, 1990, **30**, 803.
80. Y. H. Mariam and W. D. Wilson, *J. Am. Chem. Soc.*, 1983, **105**, 627.
81. H. Eggert, J. Dinesen, and J. P. Jacobsen, *Biochemistry*, 1989, **28**, 3332.
82. J. Dinesen, J. P. Jacobsen, F. P. Hansen, E. B. Pedersen, and H. Eggert, *J. Med. Chem.*, 1990, **33**, 93.
83. M. Hald and J. P. Jacobsen, *Biophys. Chem.*, 1991, **41**, 113.
84. M. Hald and J. P. Jacobsen, *Chem. Phys.*, 1992, **159**, 257.
85. B. C. Gerstein and C. R. Dybowski, *Transient Techniques in NMR of Solids*, Academic Press, New York, 1985.
86. E. Kundla, A. Samoson, and E. Lipmaa, *Chem. Phys. Lett.*, 1981, **83**, 229.
87. A. Samoson, E. Kundla, and E. Lipmaa, *J. Magn. Reson.*, 1982, **49**, 350.
88. E. Lipmaa, A. Samoson, and J. Mägi, *J. Am. Chem. Soc.*, 1986, **108**, 1730.
89. M. Polak, A. J. Highe, and R. W. Vaughan, *J. Magn. Reson.*, 1980, **37**, 357.
90. M. Polak and R. W. Vaughan, *Chem. Phys.*, 1980, **53**, 415.
91. P. A. Spencer and D. G. Hughes, *J. Magn. Reson.*, 1980, **38**, 1.
92. L. Pandey, S. Towta, and D. G. Hughes, *J. Chem. Phys.*, 1986, **85**, 6923.
93. M. D. Meadows, K. A. Smith, R. A. Kinsey, T. M. Rothgeb, R. P. Skarjune, and E. Oldfield, *Proc. Natl. Acad. Sci. U.S.A.*, 1982, **79**, 1351.
94. E. Oldfield, S. Schramm, M. D. Meadows, K. A. Smith, R. A. Kinsey, and J. Ackerman, *J. Am. Chem. Soc.*, 1982, **104**, 919.
95. W. D. Basler, *Colloids Surf.*, 1984, **12**, 59.
96. R. Jelinek, S. Ozkar, and G. A. Ozin, *J. Am. Chem. Soc.*, 1992, **114**, 4907.
97. R. Jelinek, S. Ozkar, and G. A. Ozin, *J. Phys. Chem.*, 1992, **96**, 5949.
98. R. Challoner and R. K. Harris, *Zeolites*, 1991, **11**, 265.
99. L. Bottyan, R. Dupree, and G. V. Chandrashekhar, *Solid State Ionics*, **1983**, 347.
100. H. Ohki and N. Nakamura, *Z. Naturforsch., Teil A*, 1992, **47** 319.
101. A. R. Brough, C. P. Grey, and C. M. Dobson, *J. Chem. Soc., Chem. Commun.*, **1992**, 742.
102. K. R. Carduner and D. White, *J. Chem. Phys.*, 1986, **85**, 3173.
103. D. Heidemann, C. Hubert, W. Schwieger, P. Grabner, K. H. Bergk, and P. Sarv, *Z. Anorg. Allg. Chem.*, 1992, **617**, 169.
104. E. C. Reynhardt, K. Jurga, and E. R. Andrew, *J. Magn. Reson.*, 1987, **74**, 480.
105. E. C. Reynhardt, S. Froneman, E. R. Andrew, and E. Szczesnik, *J. Magn. Reson.*, 1989, **84**, 110.
106. A. Cornélis and P. Laszlo, *Biochemistry* 1979, **18**, 2004.
107. H. Monoi and H. Uedaira, *Biophys. J.*, 1979, **25**, 535.
108. C. M. Venkatachalam and D. W. Urry, *J. Magn. Reson.*, 1980, **41**, 313.
109. D. W. Urry, C. M. Venkatachalam, A. Spisni, R. J. Bradley, T. L. Trapane, and K. U. Prasad, *J. Membr. Biol.*, 1980, **55**, 29.
110. A. Nakano, Q. S. Xie, J. V. Mallen, L. Echegoyen, and G. W. Gokel, *J. Am. Chem. Soc.*, 1990, **112**, 1287.
111. F. G. Riddell and M. K. Hayer, *Biochim. Biophys. Acta*, 1985, **817**, 313.
112. F. G. Riddell, S. Arumugam, P. J. Brophy, B. G. Cox, M. C. H. Payne, and T. E. Southon, *J. Am. Chem. Soc.*, 1988, **110**, 734.
113. T. L. Knubovets, A. V. Revazov, L. A. Sibeldina, and U. Eichhoff, *Magn. Reson. Med.*, 1989, **9**, 261.
114. H. Hofeler, D. Jensen, M. M. Pike, J. L. Delayre, V. P. Cirillo, C. S. Springer, E. T. Fossel, and J. A. Balschi, *Biochemistry*, 1987, **26**, 4953.
115. J. A. Balschi, D. Jensen, M. M. Pike, H. Hoefeler, V. P. Cirillo, J. Delayre, C. S. Springer, and E. T. Fossel, *Magn. Reson. Med.*, 1984, **1**, 96.
116. F. Rabaste, G. Dauphin, G. Jeminet, J. Guyot, and A.-M. Delort, *Biochem. Biophys. Res. Commun.*, 1991, **181**, 74.
117. D. C. Shungu and R. W. Briggs, *J. Magn. Reson.*, 1988, **77**, 491.
118. D. C. Shungu, D. C. Buster, and R. W. Briggs, *J. Magn. Reson.*, 1990, **89**, 102.
119. S. N. Dvoryantsev, V. V. Petrov, D. O. Levitsky, and E. K. Ruuge, *Biol. Membr.*, 1984, **1**, 1179.
120. H. Shinar and G. Navon, *Biophys. Chem.*, 1984, **20**, 275.
121. R. K. Gupta, *NMR Spectroscopy of Cells and Organisms*, CRC Press, Boca Raton, FL, 1987, Vol.II, p. 1.
122. R. K. Gupta, P. Gupta, and R. D. Moore, *Annu. Rev. Biophys. Bioeng.*, 1984, **14**, 221.
123. C. S. Springer, Jr., *Annu. Rev. Biophys. Biophys. Chem.*, 1987, **16**, 375.
124. J. W. Pettegrew, D. E. Woessner, N. J. Minshew, and T. Glonek, *J. Magn. Reson.*, 1984, **57**, 185.
125. R. Gupta and L. A. Jelicks, *Indian J. Chem.*, 1988, **27A**, 829.
126. J. Pekar, P. F. Renshaw, and J. S. Leigh, Jr., *J. Magn. Reson.*, 1987, **72**, 159.
127. W. D. Rooney, T. M. Barbara, and C. S. Springer, Jr., *J. Am. Chem. Soc.*, 1988, **110**, 674.
128. R. K. Gupta and P. Gupta, *Biophys. J.*, 1982, **37**, 76a.
129. M. M. Pike and C. S. Springer, Jr., *J. Magn. Reson.*, 1982, **46**, 348.
130. M. M. Pike, D. M. Yarmush, J. A. Balschi, R. E. Lenkinski, and C. S. Springer, Jr., *Inorg. Chem.*, 1983, **22**, 238.
131. N. A. Matwiyoff, C. Gasparovic, R. Wenk, J. D. Wicks, and A. Rath, *Magn. Reson. Med.*, 1986, **3**, 164.
132. H. Degani and G. A. Elgavish, *FEBS Lett.*, 1978, **90**, 357.
133. F. G. Riddell and T. E. Southon, *Inorg. Chim. Acta*, 1987, **136**, 133.
134. S. R. Gullans, M. J. Avison, T. Ogino, G. Giebisch, and R. G. Shulman, *Fed. Proc.*, 1984, **43**, 301.
135. A. M. Kumar, R. Gupta, and A. Spitzer, *Pediatr. Res.*, 1986, **20**.
136. A. M. Kumar, R. Gupta, and A. Spitzer, *Fed. Proc.*, 1986, **45**, 210.
137. A. M. Kumar, R. K. Gupta, and A. Spitzer, *Kidney Int.*, 1986, **29**, 356.
138. R. K. Gupta, A. B. Kostellow, and G. A. Morrill, *J. Biol. Chem.*, 1985, **260**, 9203.
139. R. K. Gupta, R. Neiberger, A. Spitzer, and M. Baracnieto, *Fed. Proc.*, 1987, **46**, 1286.
140. M. Bental, H. Degani, and M. Avron, *Plant Physiol.*, 1988, **87**, 813.
141. R. Melamud, M. Risk, and H. Gilboa, *Biochim. Biophys. Acta*, 1981, **678**, 311.
142. J. B. Martin, G. Klein, and M. Satre, *Arch. Biochem. Biophys.*, 1987, **254**, 559.
143. Y. Boulanger, P. Vinay, and M. Boulanger, *Am. J. Physiol.*, 1987, **253**(5).

144. Y. Boulanger, P. Vinay, A. Tejedor, and J. Noel, *Kidney Int.*, 1987, **31**, 430.
145. N. J. Greenfield, C. N. Cherapak, F. Adebodun, F. Jordan, and J. Lenard, *Biochim. Biophys. Acta*, 1990, **1025**, 15.
146. L. A. Jelicks, J. Weaver, S. Pollack, and R. K. Gupta, *Biochim. Biophys. Acta*, 1989, **1012**, 261.
147. C. Y. Kwan, Y. Seo, M. Murakami, H. Ito, and H. Watari, *Biochem. Arch.*, 1987, **3**, 13.
148. Y. Hotta, K. Takeya, H. Ando, M. Haruna, K. Ito, and J. Sakakibara, *Jpn. J. Pharmacol.*, 1987, **43S**.
149. Y. Hotta, H. Ando, R. Eto, K. Takeya, M. Haruna, K. Ito, and J. Sakakibara, *Fol. Pharmacol. Jpn.*, 1992, **100**, 143.
150. A. W. H. Jans, R. Willem, E. R. Kellenbach, and R. K. H. Kinne, *Magn. Reson. Med.*, 1988, **7**, 292.
151. Y. Boulanger and P. Vinay, *Kidney Int.*, 1986, **29**, 392.
152. Y. Boulanger, P. Vinay, and M. Boulanger, *Clin. Invest. Med.*, 1987, **10**(4).
153. H. Ammann, Y. Boulanger, and P. Vinay, *Magn. Reson. Med.*, 1990, **16**, 368.
154. H. Nissen, J. P. Jacobsen, and M. Horder, *Magn. Reson. Med.*, 1989, **10**, 388.
155. L. A. Jelicks and R. K. Gupta, *J. Magn. Reson.*, 1989, **81**, 586.
156. L. A. Jelicks and R. K. Gupta, *J. Magn. Reson.*, 1989, **83**, 146.
157. J. Pekar, P. F. Renshaw, and J. S. Leigh, *J. Magn. Reson.*, 1987, **72**, 159.
158. W. D. Rodney and C. S. Springer, *NMR Biomed.*, 1991, **4**, 227.
159. F. W. Cope, *Proc. Natl. Acad. Sci. U.S.A.*, 1965, **54**, 225.
160. F. W. Cope, *Biochemistry*, 1965, **54**, 225.
161. F. W. Cope, *J. Gen. Physiol.*, 1967, **50**, 1353.
162. G. N. Ling and F. W. Cope, *Science*, 1969, **163**, 1335.
163. F. W. Cope, *Physiol. Chem. Phys.*, 1970, **2**, 545.
164. J. L. Czeisler, O. G. Fritz, Jr., and T. J. Swift, *Biophys. J.*, 1970, **10**, 260.
165. J. L. Czeisler and T. J. Swift, *Ann. N.Y. Acad. Sci.*, 1973, **204**, 261.
166. C. A. Rotunno, V. Kowaleski, and M. Cereijido, *Biochim. Biophys. Acta*, 1967, **135**, 170.
167. D. Martinez, A. A. Silvidi, and R. M. Stokes, *Biophys. J.*, 1969, **9**, 1256.
168. I. L. Reisin, C. A. Rotunno, L. Corchs, V. Kowalewski, and M. Cereijido, *Physiol. Chem. Phys.*, 1970, **2**, 171.
169. G. S. Bystrov, G. I. Romanenko, N. I. Nikolaev, G. A. Grigor'eva, and L. Atamanchuk, *Biofizika*, 1972, **17**, 623; *Biophysics (USSR)*, 1972, **17**, 649.
170. H. J. C. Yeh, F.J. Brinley, Jr., and E. D. Becker, *Biophys. J.*, 1973, **13**, 56.
171. V. I. Ionov, R. K. Mazitov, and N. A. Mal'tsev, *Tsitologiya*, 1968, **10**, 903.
172. H. Monoi, *Biophys. J.*, 1974, **14**, 645.
173. H. Monoi, *Biophys. J.*, 1974, **14**, 653.
174. D. C. Chang and D. E. Woessner, *J. Magn. Reson.*, 1978, **30**, 185.
175. J. L. DeLayre, J. S. Ingwall, C. Malloy, and E. T. Fossel, *Science*, 1981, **212**, 935.
176. M. Barany and P. N. Venkatasubramanian, *Physiol. Chem. Phys. Med. NMR*, 1986, **18**, 233.
177. R. Buist, R. Deslauriers, J. K. Saunders, and G. W. Mainwood, *Biophys. J.*, 1990, **57**(2).
178. R. J. Buist, R. Deslauriers, J. K. Sunders, and G. W. Mainwood, *Can. J. Physiol. Pharmacol.*, 1991, **69**, 1663.
179. E. T. Fossel and H. Hoefeler, *Magn. Reson. Med.*, 1986, **3**, 534.
180. D. Burstein and E. T. Fossel, *Magn. Reson. Med.*, 1987, **4**, 261.
181. G. A. Elgavish and A. Elgavish, *Biochem. Biophys. Res. Commun.*, 1985, **128**, 746.
182. L. A. Jelicks and R. K. Gupta, *J. Biol. Chem.*, 1990, **265**, 1394.
183. M. S. Liebling and R. K. Gupta, *Ann. N.Y. Acad. Sci.*, 1987, **508**, 149.
184. C. J. A. Vanechteld, J. H. Kirkels, M. H. J. Eijgelshoven, P. Vandermeer, and T. J. C. Ruigrok, *J. Mol. Cell. Cardiol.*, 1991, **23**, 297.
185. A. Lanir, R. G. L. Lee and M. E. Clouse, *Hepatology*, 1987, **7**, 1084.
186. A. Lanir, R. G. L. Lee, and M. E. Clouse, *J. Clin. Chem. Clin. Biochem.*, 1988, **26**, 386.
187. A. Lai, M. Casu, C. Meloni, and U. Muscatello, *Biochem. Biophys. Res. Commun.*, 1989, **161**, 979.
188. N. Askenasy and G. Navon, *J. Mol. Cell. Cardiol.*, 1991, **23**(9).
189. R. E. Anderson, J.-F. Nedelec, P. A. Mils, and K. Clarke, *Circulation*, 1990, **82**, 759.
190. N. Askenasy, A. Vivi, M. Tassini, and G. Navon, *Magn. Reson. Med.*, 1992, **28**, 249.
191. N. Askenasy and G. Navon, *J. Mol. Cell. Cardiol.*, 1992, **2455**, 105.
192. S. K. Hilal, A. A. Maudsley, H. E. Simon, W. H. Perman, J. Bonn, M. E. Mawad, A. J. Silver, S. R. Ganti, P. Sane, and I. C. Chien, *Am. J. Neuroradiol.*, 1983, **4**, 245.
193. S. K. Hilal, A. A. Maudsley, J. Bonn, H. E. Simon, P. Cannon, and W. H. Perman, *Magn. Reson. Med.*, 1984, **1**, 165.
194. P. K. Paul, E. M. Obyrne, R. K. Gupta, and L. A. Jelicks, *Br. J. Rheumatol.*, 1991, **30**, 318.
195. H. L. Kundel, A. Shetty, P. M. Joseph, R. M. Summers, E. Kassab, and B. Moore, *Invest. Radiol.*, 1987, **22**.
196. H. L. Kundel, A. Shetty, P. M. Joseph, R. M. Summers, E. A. Kassab, and B. Moore, *Magn. Reson. Med.*, 1988, **6**, 381.
197. R. C. Lyon, J. Pekar, C. T. W. Moonen, and A. C. McLaughlin, *Magn. Reson. Med.*, 1991, **18**, 80.
198. S. D. Wolff and R. S. Balaban, *Biophys. J.*, 1988, **53**(2).
199. S. J. Kohler, E. K. Smith, and N. H. Kolodny, *J. Magn. Reson.*, 1989, **83**, 423.
200. M. D. Cockman, L. W. Jelinski, J. Katz, D. J. Sorce, L. M. Boxt, and P. J. Cannon, *J. Magn. Reson.*, 1990, **90**, 9.
201. S. Wimperis, P. Cole, and P. Styles, *J. Magn. Reson.*, 1992, **98**, 628.

Biographical Sketch

Pierre Laszlo. *b* 1938. B.S., 1961, D.Sc., 1965, University of Paris, Sorbonne. Self-taught in NMR from Pople–Schneider–Bernstein and the Abragam lectures at Collège de France, 1961–62. Postdoctoral research, Princeton University, 1962–63 (nmr of bicyclics). Assistant professor, Princeton University, 1966–70 (nmr of rate processes, critical inquiry into the origin of aromatic solvent-induced shift); Professor, University of Liège, 1970–present (^{13}C relaxation, ^{23}Na and ^{59}Co nmr, nmr of adsorbates). Professor of Chemistry, École polytechnique, 1986–present (interplay of dipolar and quadrupolar relaxations). Taught NMR courses at Hamburg, Cornell University, and University of Kansas, and NMR workshops in Europe, the United States, and Japan. Approx. 200 publications and among 14 books, Organic Spectroscopy with Peter Stang in 1970 and editing of NMR in Newly Accessible Nuclei (two volumes) in 1983. Loves nmr as an open-ended adventure into the chemical wonderlands. Current research specialty: NMR studies of molecular interactions and motions in chemical and biochemical systems.

Steady-State Techniques for Low Sensitivity and Slowly Relaxing Nuclei

Andreas Schwenk

Universität Tübingen, Tübingen, Germany

1	Introduction	1
2	Theoretical Analysis of the Steady-State Free Precession Technique	2
3	Recording of NMR Spectra with the Steady-State Technique	3
4	Measuring Techniques for Extremely Long Relaxation Times	6
5	Investigation of Nuclei with Spin–Spin Coupling	6
6	Related Articles	7
7	References	7

1 INTRODUCTION

The detection of NMR signals of low-γ nuclei with spin $I = \frac{1}{2}$ is a very difficult task in most cases, for the following reasons: owing to the low magnetic moment, the sensitivity of these nuclei is very poor, and owing to the missing electric and the small magnetic interaction of these nuclei, they are very slowly relaxing. If a sufficiently large indirect spin–spin coupling to another kind of nucleus with higher magnetogyric ratio exists, the signal of the low-γ nuclei may be enhanced by polarization transfer, or the spectrum of the low-γ nuclei may be detected indirectly by double resonance techniques; such methods are described in detail elsewhere (see ***Double Resonance*** and ***Polarization Transfer Experiments via Scalar Coupling in Liquids***). With the greater and greater static magnetic fields $\boldsymbol{B}_0$ available from superconducting magnets, the relaxation rates by chemical shift anisotropy increase proportionally to B_0^2, and the relaxation times of anisotropically shielded nuclei are sometimes reduced to a value useful for pulsed Fourier spectroscopy. In general, however, the natural widths of NMR lines $\Delta\nu_{\frac{1}{2}} = (\pi T_2)^{-1}$ of spin-$\frac{1}{2}$ low-γ nuclei are far less than the instrumental linewidth, which is due to the inhomogeneity of the magnet used for the experiment, i.e., inhomogeneously broadened lines result.

The only way to avoid such inhomogeneously broadened NMR lines and the resulting loss of signal intensity in CW spectroscopy consists in broadening the NMR lines beyond the width of the instrumental line by adding paramagnetic substances to the sample. Unfortunately, other essential properties of the sample may be changed by such paramagnetic admixtures (e.g., shifts of the NMR lines or changes in their relative intensities). Moreover, the efficiency in reduction of the relaxation times of an unknown sample by paramagnetic ingredients cannot be predicted in most cases. Pulsed Fourier spectroscopy, starting from thermal equilibrium, yields absorption lines with the same natural halfwidth, i.e., the resulting NMR lines are inhomogeneously broadened to the same instrumental linewidth. This loss of NMR signal may also be demonstrated in the time domain by the following example: the nucleus ^{109}Ag in a 1 M aqueous $AgNO_3$ solution in a field $B_0 = 2.1\,\mathrm{T}$ has a longitudinal relaxation time $T_1 > 1000\,\mathrm{s}$, whereas the decay time of the FID of such a sample contained in a cylinder of 20 mm diameter and 40 mm filling height in an optimally homogenized iron magnet is $T_2{}^* \approx 60\,\mathrm{ms}$. To observe the FID during $T_{\mathrm{ac}} \approx 200\,\mathrm{ms}$, one must wait for the build-up time of thermal equilibrium (at least $3T_1$) $T_{\mathrm{p}} \approx 1\,\mathrm{h}$; this shows clearly that the NMR signal may be received only during a small fraction $T_{\mathrm{ac}}/T_{\mathrm{p}} \approx 2 \times 10^{-4}$ of the total measuring time.

In pulsed Fourier spectroscopy, beginning with the pioneer work of Ernst and Anderson,[1] the results of a multitude of equal experiments are averaged, each of them starting from the thermal Boltzmann equilibrium, i.e. starting with the magnetization $\boldsymbol{M}_0$ in the z direction (the direction of the static field $\boldsymbol{B}_0$). In contrast to CW spectroscopy, pulsed Fourier spectroscopy offers a way to overcome the problem of these inhomogeneously broadened lines: the narrow NMR lines of very slowly relaxing nuclei may be broadened by saturation to any desired width in an exactly predictable way. To achieve this aim, the distance T_{p} between the periodically applied rf pulses must be reduced: $T_{\mathrm{p}} \ll T_2{}^*$ or $T_{\mathrm{p}} \gtrsim T_2{}^*$, with $T_2{}^* \ll T_2 \leq T_1$; then the magnetization vector $\boldsymbol{M}$ of the sample will perform a periodic motion with the period T_{p}, but $\boldsymbol{M}$ never reaches its thermal equilibrium value $\boldsymbol{M}_0$ in the z direction. In this pulsed steady state of the nuclear spin system, a refocusing effect occurs for the magnetization vectors of all different spin isochromats, which shows some analogy to the well-known spin echo techniques of Hahn[2] and Carr and Purcell,[3] with the modification by Gill and Meiboom,[4] which was also introduced to FT spectroscopy by Allerhand and Cochran[5] and called spin echo Fourier transform NMR. A spin echo technique including a steady state of the z magnetization was pointed out by Becker et al.[6] and named driven equilibrium Fourier transform spectroscopy.

In contrast to all spin echo techniques, the steady state magnetization vector $\boldsymbol{M}$ is neither in the z direction nor perpendicular to the z axis during any time interval; i.e., $\boldsymbol{M}$ shows a periodic motion with the pulse period T_{p} in all three dimensions of the space. No exact adjustment of the flip angle Θ of the periodically applied rf pulses is required; a misadjustment of Θ results in a changed steady state but it is not cumulative. But, in contrast to the normal FT spectroscopy starting from thermal equilibrium, the steady-state magnetization $\boldsymbol{M}$ depends strongly on the free precession angle of the magnetization during the pulse period in the rotating frame: $\Phi = (\omega_0 - \omega_{\mathrm{c}})T_{\mathrm{p}}$. Such a steady state of all three components of $\boldsymbol{M}$ was first observed by Bradford et al.,[7] and was analyzed in detail and demonstrated with water protons by Carr.[8] Unfortunately this steady-state technique could not be introduced into NMR spectroscopy at that time, since digital signal averagers and efficient computers to perform the Fourier transformation were not then available.

However, this situation changed when, in the second half of the 1960s signal averagers and on-line computers became available. Only a few months after the pioneer work of Ernst

and Anderson,[1] the extremely weak NMR signal of the spin-$\frac{1}{2}$ nucleus ^{187}Os, which has one of the smallest magnetic moments and which is of low natural abundance (1.64%), was detected for the first time with the aid of this steady-state free precession technique.[9,10] In the following years, the gain in sensitivity with the steady-state technique made possible the first systematic investigations or even the first detection of the NMR signal of a string of $I = \frac{1}{2}$ low-γ nuclei: ^{57}Fe, ^{107}Ag and ^{109}Ag, ^{207}Pb, ^{111}Cd and ^{113}Cd, ^{115}Sn, ^{117}Sn, and ^{119}Sn, ^{183}W, ^{89}Y, ^{103}Rh, and others (cited by Schwenk[11]).

Because of the dependence of the steady-state magnetization $\boldsymbol{M}$ on the free precession angle Φ, this simple steady-state technique cannot be used to record multiline NMR spectra; each line of such a spectrum is attenuated and distorted in a different way, as pointed out by Ernst and Anderson[1] and in more detail by Freeman and Hill.[12] To cancel these phase and intensity anomalies, the results of different experiments must be combined, in which the frequencies of the lines of the irradiated rf spectra are changed relative to the Larmor frequencies of the NMR spectrum. Two ways were proposed to reach this goal: in the scrambled steady-state technique,[12] many experiments are performed with changed pulse period T_p, i.e., the distance of the lines in the irradiated rf spectrum is changed, whereas in the Quadriga technique[13] only four experiments are performed with the carrier ν_c of the irradiated rf spectrum lowered by a quarter of the pulse repetition rate $1/T_p$ after each experiment. Ernst has pointed out a variant of the latter technique, four phase Fourier spectroscopy,[14,15] which reduces the four FT calculations, and with this the amount of data to be processed, to a single FT calculation. By an appropriate selection of the pulse period $T_p \ll T_2^*$ or $T_p \gtrsim T_2^*$, either maximum sensitivity or maximum resolution can be achieved, respectively.

Steady-state free precession techniques also offer a way to determine extremely long relaxation times T_1 and T_2 in the range from 1 s to some hours.[16] In contrast to spin echo techniques, no waiting time, either for the installation of the thermal equilibrium or for partial relaxation, is required during which no signal acquisition is possible. With the aid of these techniques the relaxation mechanisms of ^{109}Ag in the Ag^+ ion[17] and in a molecule[18] and of ^{57}Fe and ^{103}Rh in organometallic compounds[19] were detected for the first time. To separate the contributions of different relaxation mechanisms to the relaxation rate of spin-$\frac{1}{2}$ low-γ nuclei, determinations of the relaxation times T_1 in at least two quite different fields $\boldsymbol{B}_0$ must be performed. In the high fields of superconducting magnets, conventional techniques may be applied, whereas the extremely long relaxation times in the low $\boldsymbol{B}_0$ of iron magnets cannot be measured without the application of such steady-state techniques. Moreover, slowly relaxing nuclei are excellent tools to study exchange phenomena[20,21] (see ***Relaxation Effects of Chemical Exchange***).

Steady-state free precession techniques have proved to be powerful tools in NMR spectroscopy of slowly relaxing spin systems. The signal-to-noise ratio attainable in a given measuring time may be increased by orders of magnitude with the aid of such techniques. This is why steady-state techniques presently are not only applied to low-γ nuclei but also used in fast imaging techniques.[22,23] To carry out steady-state experiments on a pulsed FT NMR spectrometer requires no extra hardware—but does of course require appropriate software.

2 THEORETICAL ANALYSIS OF THE STEADY-STATE FREE PRECESSION TECHNIQUE

For the following considerations, one single species of spins with magnetogyric ratio γ may be assumed, and also the validity of the Bloch equations, i.e., the spin system can be described by the Larmor frequency $\nu_0 = \gamma B_0/2\pi$, the longitudinal relaxation time T_1, and the transverse relaxation time T_2. To establish a steady state in this spin system, equal, periodic, and coherent rf pulses of an oscillating magnetic field are applied to the sample. The repetition period T_p must be chosen to be small in comparison with the relaxation times T_1 and T_2:

$$T_p \ll T_2 \leq T_1 \tag{1}$$

In order to be able to observe the NMR signal during the most part of T_p, the duration of the rf pulses may be chosen as

$$\tau_p \ll T_p \tag{2}$$

The amplitude $2B_1$ and the carrier frequency ν_c of the oscillating rf magnetic field must fulfill the condition

$$\Delta B = \left|\frac{2\pi(\nu_0 - \nu_c)}{\gamma}\right| = \left|\frac{\omega_0 - \omega_c}{\gamma}\right| = \left|\frac{\Delta\omega}{\gamma}\right| \ll B_1 \tag{3}$$

Moreover, the rf pulses must be coherent; i.e., the rf signal necessary to produce the oscillating magnetic field must be derived with the aid of electronic switches from a generator constantly running with the frequency ν_c; the rf signal cannot be derived from an oscillator, which starts with arbitrary phase for each rf pulse. By this, it is guaranteed that one of the rotating components of the rf field is stationary (assumed in the u direction) in the coordinate system (u, v, z) rotating around the z axis with the angular velocity ω_c; during the pulse, its amplitude is B_1.

The magnetization vector $\boldsymbol{M}$ of the sample responds to these periodic, equal, and coherent rf pulses in the following ways.

1. During the rf pulse, $\boldsymbol{M}$ precesses around the u axis with angular velocity $\omega_1 = \gamma B_1$, and the total precession angle is $\Theta = \omega_1\tau_p = \gamma B_1\tau_p$. Relaxation effects may be neglected during this short time interval τ_p.
2. During the time interval of free precession (duration $T_p - \tau_p \approx T_p$), $\boldsymbol{M}$ precesses around the z axis with angular velocity $\Delta\omega = 2\pi\ \Delta\nu = 2\pi(\nu_0 - \nu_c)$; the total precession angle $\Phi = \Delta\omega\ T_p$. Superimposed on this motion are the relaxation effects: the exponential increase of the z component of $\boldsymbol{M}$ to the thermal equilibrium value $\boldsymbol{M}_0$ with the time constant T_1, and the exponential decay of the transverse component of $\boldsymbol{M}$ with the time constant T_2.

The magnetization vectors in the rotating frame (u, v, z) may be denoted as $\boldsymbol{M}(-0)$ immediately before the application of an rf pulse, $\boldsymbol{M}(+0)$ immediately after the end of this rf pulse, and $\boldsymbol{M}(-T_p)$ at the end of the following free precession period. In the steady state, which is established after a time considerably longer than T_1 [see equations (13) and (14)], $\boldsymbol{M}$ will always perform the same motion during each pulse period. In particular, the magnetization vectors immediately before the irradiation and at the end of the free precession, i.e., immediately before the next pulse, must be the same:

$$\boldsymbol{M}(-0) = \boldsymbol{M}(-T_p) \tag{4}$$

This condition leads to a linear, inhomogeneous system of equations for the steady state magnetization $\boldsymbol{M}(-0)$. The

solutions were first derived by Ernst and Anderson[1] for the general case [without the steady-state condition, equation (1)]. The special solutions for the steady state [equation (1)] and the additional condition

$$\Theta \gg T_p/T_2 \geq T_p/T_1 \tag{5}$$

are[11]

$$\left.\begin{aligned} \frac{M_u(+0)}{M_0} &= \frac{M_u(-0)}{M_0} = \frac{\sin\Theta\sin\Phi}{\Delta} \\ \frac{M_v(+0)}{M_0} &= -\frac{M_v(-0)}{M_0} = \frac{\sin\Theta(1-\cos\Phi)}{\Delta} \\ \frac{M_z(+0)}{M_0} &= \frac{M_z(-0)}{M_0} = \frac{(1+\cos\Theta)(1-\cos\Phi)}{\Delta} \end{aligned}\right\} \tag{6a}$$

where

$$\Delta = (1+\cos\Theta)(1-\cos\Phi) + 2(1-\cos\Theta)T_1/T_2 \tag{6b}$$

The steady-state transverse component of $\boldsymbol{M}$, which is responsible for the induced NMR signal, becomes

$$M_R = M_0 \frac{|\sin\Theta|\sqrt{2-2\cos\Phi}}{(1+\cos\Theta)(1-\cos\Phi) + 2(1-\cos\Theta)T_1/T_2} \tag{7}$$

The free precession angle Φ appears as argument only of harmonic functions, which are periodic in multiples of 2π; therefore, in all equations, Φ may be replaced by the excess free precession angle Φ_{ex}, which is defined by subtracting an integer multiple of 2π from Φ: $\Phi_{ex} = \Phi - 2\pi n$, so that Φ_{ex} falls in the range $0 \leq \Phi_{ex} < 2\pi$. Equation (7) shows clearly that M_R, and thus the NMR signal induced during the free precession period, depend only on the ratio T_1/T_2 but not on the absolute values of the relaxation times.

The strong dependence of M_R on the free precession angle Φ is shown in Figure 1 for the special case $T_1/T_2 = 1$. For $\Phi_{ex} = 0$, all components of the steady-state magnetization $\boldsymbol{M}$ vanish because of saturation of the spin system. This result may be seen in the frequency domain: the Fourier transform of the pulsed irradiation of the rf magnetic field is a discrete spectrum of lines with the frequencies

$$\nu_c \pm n/T_p, \quad n = 0, 1, 2, \ldots \tag{8}$$

and the amplitudes

$$A(\nu_c \pm n/T_p) \propto \frac{\sin(n\pi\tau_p/T_p)}{n\pi\tau_p/T_p} \tag{9}$$

For $\Phi_{ex} = 0$, one of the sidebands of the irradiated spectrum coincides with the Larmor frequency ν_0, the NMR transition is saturated, and all macroscopic magnetization vanishes. By considering either the frequency or time domains, it is concluded that the optimum case for a steady-state experiment is the choice of the free precession angle $\Phi_{ex} = \pi$ or the choice of the irradiation carrier frequency

$$\nu_c = \nu_0 \pm (n + \tfrac{1}{2})/T_p \tag{10}$$

This choice guarantees that the Larmor frequency ν_0 lies just in the middle between two irradiation lines, i.e., the maximum distance between ν_0 and any sideband of the irradiation spectrum.

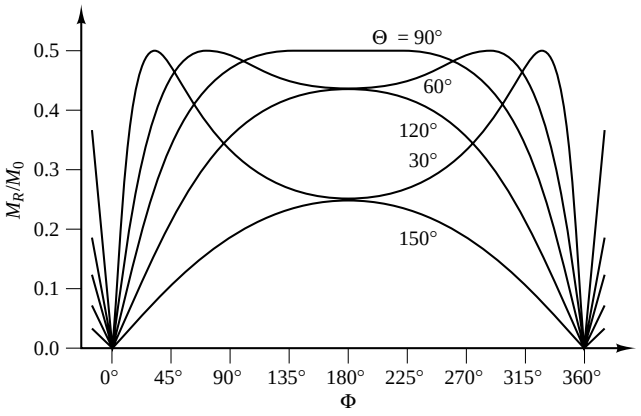

Figure 1 Steady-state transverse magnetization (proportional to the NMR signal) during the free precession period as a function of the free precession angle Φ for various flip angles Θ. A sample with T_1=T_2 is assumed

Under this optimum experimental condition, $\Phi_{ex} = \pi$ or equation (10), the maximum transverse component of the magnetization

$$M_{R,opt} = \frac{M_0}{2}\sqrt{\frac{T_2}{T_1}} \tag{11}$$

is reached, when pulses with the optimum flip angle

$$\Theta_{opt} = \arccos\frac{T_1/T_2 - 1}{T_1/T_2 + 1} \tag{12}$$

are applied.

The development of this steady state free precession [$\Phi_{ex} = \pi$ and irradiation of optimum flip angles Θ_{opt}, as given in equation (12)], starting from the unmagnetized sample $\boldsymbol{M}(t = 0) = 0$, may be described by an exponential function:[11,16]

$$M_R(t) = \frac{M_0}{2}\sqrt{\frac{T_2}{T_1}}(1 - e^{-t/T^*_{opt}}) \tag{13}$$

with the time constant

$$T^*_{opt} = \tfrac{1}{2}(T_1 + T_2) \tag{14}$$

Apart from rapidly damped oscillations, which are averaged out in a real experiment, each initial state $\boldsymbol{M}(t = 0)$ yields an exponential build-up of M_R as well as of M_z with the same time constant T^*_{opt} as given in equation (14).

3 RECORDING OF NMR SPECTRA WITH THE STEADY-STATE TECHNIQUE

In a real NMR experiment, a single species of a nucleus with one well-defined Larmor frequency is never investigated. The inhomogeneity of all magnets available today results in an inhomogeneously broadened NMR line, i.e., in a distribution of Larmor frequencies, usually characterized by its mean value $\langle\nu_0\rangle$ and the decay constant $T_2' \approx T_2^*$. Slowly relaxing spin systems are characterized by the condition $T_2^* \ll T_2$.

To achieve maximum sensitivity, the pulse period should be chosen as

$$T_p \ll T_2^* \tag{15}$$

The conditions in equations (1)–(3) are assumed to be valid, the carrier ν_c of the irradiated rf field should be chosen according to equation (10), and pulses with the optimum flip angle Θ_{opt} as given in equation (12) should be applied. Then the NMR signal is induced by a transverse magnetization M_R as described in equation (11). After mixing with the carrier ν_c, the low-frequency NMR signal is received during the free precession period:

$$S(t) = A\frac{M_0}{2}\sqrt{\frac{T_2}{T_1}}\cos[2\pi(\nu_0 - \nu_c)t + \varphi] \tag{16}$$

in the time interval $0 \le t \le \alpha T_p$, with $\alpha < 1$. A is an apparatus constant, containing all properties of the probe assembly, gain, etc. This signal is accumulated in a time-averaging computer:

$$S(n) = A'\frac{M_0}{2}\sqrt{\frac{T_2}{T_1}}\cos\left(\frac{2\pi\kappa n}{N} + \varphi\right) \tag{17}$$

where $n = 1, 2, \ldots, \alpha N$ are the computer word numbers and N is the number of words corresponding to the total pulse period T. The quantity κ, the resonance frequency in harmonics of the pulse repetition rate, is given by $\kappa = T_p(\nu_0 - \nu_c) = \Phi/2\pi$. This function $S(n)$ is Fourier transformed:

$$\tilde{I}(x) = \frac{2}{N}\int_0^{\alpha N} S(n)\cos\left(\frac{2\pi x n}{N} + \psi\right) \mathrm{d}n \tag{18}$$

Neglecting all terms with $\kappa + x$ in the denominator and adjusting the phase angle $\psi = \varphi$, the result of the Fourier transformation is the absorption curve:

$$I(x) = A'\frac{M_0}{2}\sqrt{\frac{T_2}{T_1}}\frac{\sin[2\pi\alpha(\kappa - x)]}{2\pi(\kappa - x)} \tag{19}$$

with the halfwidth $\Delta x_{\frac{1}{2}} = 0.6/\alpha$. Setting the phase adjustment ψ to be $\varphi + \frac{1}{2}\pi$ yields the corresponding dispersion curve:

$$I'(x) = A'\frac{M_0}{2}\sqrt{\frac{T_2}{T_1}}\frac{\cos[2\pi\alpha(\kappa - x)] - 1}{2\pi(\kappa - x)} \tag{20}$$

Figure 2 shows an example of a steady-state experiment of this kind with fairly good signal-to-noise ratio. Further examples with extremely low NMR signals are given by Schwenk.[11] As pointed out in detail there, the signal-to-noise ratio (S/N) attainable with the steady-state free precession technique is superior to that of the usual FID technique starting from thermal equilibrium before each pulse by a factor

$$\frac{(\mathrm{S/N})_{\text{steady state}}}{(\mathrm{S/N})_{\text{therm equil}}} = \sqrt{\frac{T_2}{T_2^*}} \tag{21}$$

i.e., all disadvantages resulting from the inhomogeneity of the static field $\boldsymbol{B}_0$ are removed.

Choosing, instead of the condition in equation (15), a pulse period

$$T_p \gtrsim T_2^* \tag{22}$$

(in practice, $T_p > 6T_2^*$), the distribution of the Larmor frequencies of all spin isochromats becomes considerably wider than the distance $1/T_p$ of the Fourier lines of the pulsed rf magnetic field; i.e., many lines of the rf spectrum fall in the range of the inhomogeneously broadened NMR line. Owing to this, the dependence of the NMR signal on the free precession angle Φ is averaged out, and the FT yields an NMR line with shape determined by the inhomogeneity of the magnet. The condition in equation (21) guarantees maximum resolution in a given magnetic field. However, the price that must be paid for this maximum resolution is a loss of signal-to-noise ratio of up to one order of magnitude in comparison with the maximum sensitivity case [the condition in equation (15)]. This approach of the steady state technique was first pointed out by Waldstein and Wallace,[24] and is described in detail with experimental hints by Schwenk.[11]

Recording a multiline NMR spectrum, the condition $\Phi_{ex} = \pi$, or equation (10), can never be fulfilled for all NMR lines simultaneously; i.e., according to equations (6) and (8) and

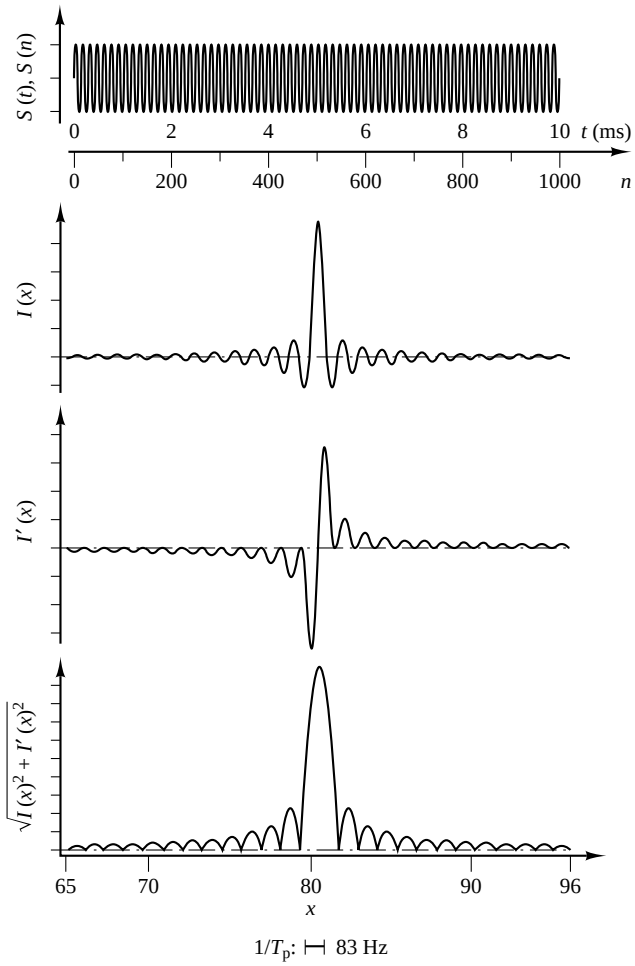

Figure 2 Steady-state ^{109}Ag NMR signal of a 8.3 M aqueous AgF solution, recorded with pulse period T_p = 12 ms, corresponding to N = 1200 channels in the time-averaging computer, i.e., α = 0.83. The carrier frequency ν_c of the irradiation spectrum was chosen $80.5/T_p$ below the Larmor frequency ν_0, i.e., κ = 80.5. The time-dependent NMR signal [equations (16) and (17)], the absorption curve $I(x)$, and the dispersion curve $I'(x)$ [equations (19} and (20)] are plotted, as well as the power spectrum

Figure 1, each line will be affected by a special phase and intensity anomaly. To get rid of these distortions in the case of maximum sensitivity [the condition in equation (15)], either the distribution $D(\Phi_{ex})$ of the free precession angles of one line of the spectrum must be enlarged far beyond the separation $1/T_p$ of the lines of the irradiation spectrum, as given in equation (8), or the irradiation spectrum must be changed sometimes during the NMR experiment, in order to average the results of experiments with different free precession angles Φ_{ex}, i.e., to give each NMR line the same chance.

The first way—the enlargement of the distribution $D(\Phi_{ex})$—may be accomplished by inserting a short homogeneity spoil pulse at an arbitrary time during the pulse period T_p. In doing this, the steady state is not destroyed at all, and all Larmor frequencies remain unchanged during the time of observation of the signal; examples and experimental hints are given by Schwenk.[11] Unfortunately, in samples of low viscosity, diffusion effects during the interval T_p between homogeneity spoil pulses may reduce the NMR signal.

The second way—the change of the irradiation spectrum—may be accomplished in two different manners. The first consists in a random variation of the pulse period T_p after a batch of pulses. In doing this, the rf spectrum [equation (8)] is stretched or compressed, with the carrier frequency ν_c as a fixed point. Outside a frequency range near ν_c, this scrambled steady-state technique[12] changes the free precession angle to be equally distributed in the range $0 \leq \Phi_{ex} \leq 2\pi$, and averaging the results of all such experiments cancels phase and intensity anomalies. The second manner of changing the irradiation spectrum consists of a linear shift of the carrier: four experiments with the carrier frequencies

$$\nu_{c,\rho} = \nu_c - \rho/4T_p, \quad \rho = 0, 1, 2, 3 \tag{23}$$

must be performed; the complete irradiation spectrum is shifted to lower frequencies by $\rho/4T_p$. The accumulated NMR signals $S_\rho(t)$ or $S_\rho(n)$, as described by equations (16) and (17), must be Fourier transformed separately to give four resonance curves $I_\rho(x)$, as described by equation (19). Shifting back these curves $I_\rho(x)$ by defining four different abscissa scales $z = x - \frac{1}{4}\rho$, the absorption curves $I_\rho(z)$ may be added, $I(z) = \sum_{\rho=0}^{3} I_\rho(z)$, to get the undistorted spectrum. This Quadriga–FT technique (QFT),[13] with only four experiments, reduces phase and intensity anomalies to less than 1% of the desired signal. Many details, experimental hints, and examples are given by Schwenk.[11] The QFT signal attainable within a given measuring time is 60% of that attainable with a normal steady-state free precession experiment ($T_p \ll T_2^*$ and $\Phi_{ex} = \pi$); this is the price to pay for the constant sensitivity throughout the total frequency range. Hence, in the case of maximum sensitivity, the QFT signal-to-noise ratio becomes

$$\frac{(S/N)_{QFT}}{(S/N)_{therm\ equil}} \approx \frac{3}{5}\sqrt{\frac{T_2}{T_2^*}} \tag{24}$$

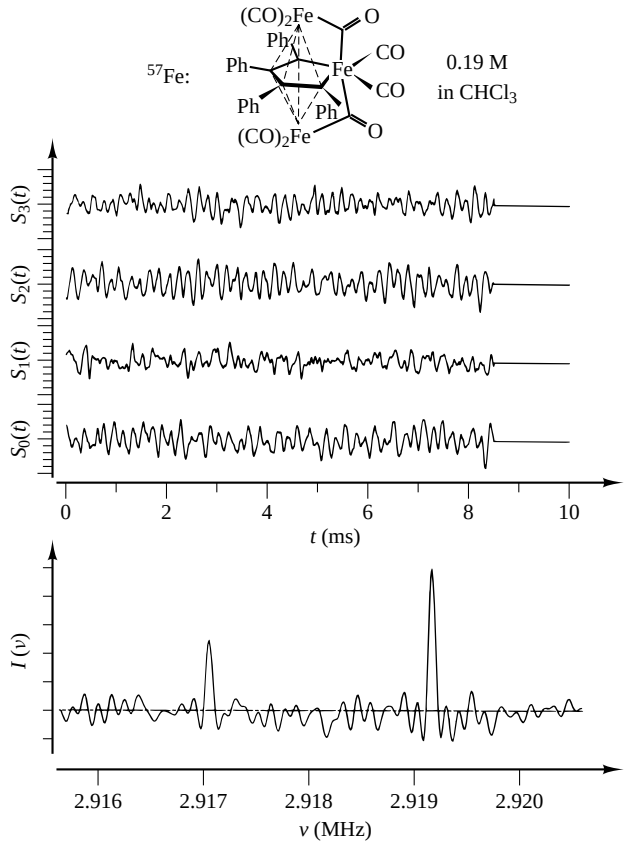

Figure 3 ^{57}Fe NMR spectrum of a three-nuclear iron complex recorded with the Quadriga–FT technique to achieve maximum sensitivity: $1/T_p$ = 83 Hz, $\Theta = 57^\circ$ (optimum for unknown ratio T_1/T_2). A measuring time of 4 × 12 h = 2 days was spent for this spectrum of the unenriched sample

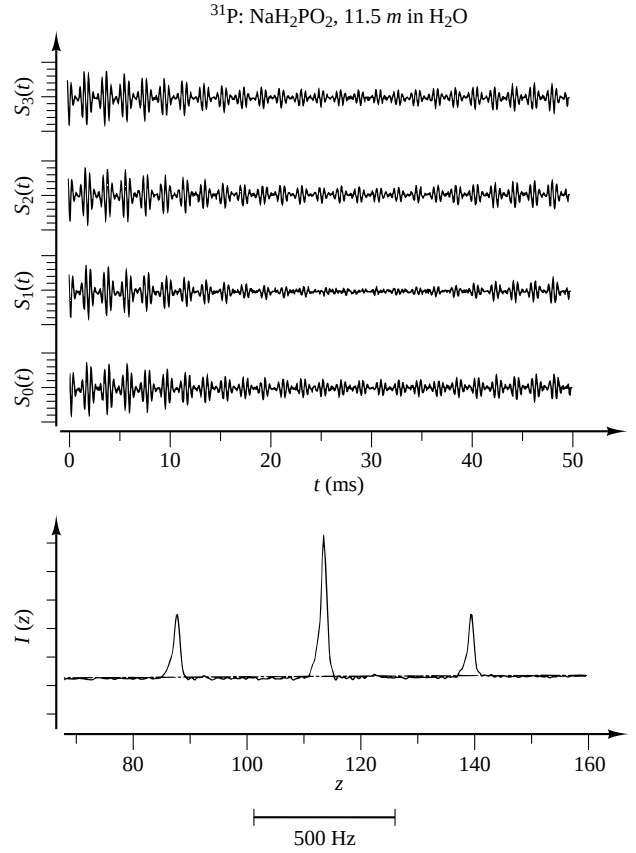

Figure 4 ^{31}P NMR spectrum of the hypophosphite ion recorded with the quadriga technique to achieve maximum resolution in a less homogeneous field $\boldsymbol{B}_0$: $1/T_p$ = 20 Hz, $\Theta = 44^\circ$ (optimum for the ^{31}P relaxation times $T_1 \approx 1$ s and $T_2 \approx 270$ ms). The total measuring time was about 4 min

Of course, this QFT technique may be applied with the condition in equation (15) to get maximum sensitivity, as well as with the condition in equation (22) to get maximum resolution. Examples of both cases are given in Figures 3 and 4.

The same four irradiation spectra may be achieved by phase shifts of the carrier signal by 0, $\frac{1}{2}\pi$, π, and $\frac{3}{2}\pi$ from pulse to pulse instead of lowering the carrier frequency ν_c. This four-phase Fourier spectroscopy, proposed by Ernst,[15] enables the coaddition of the NMR signals in time, $S_\rho(t)$, from all four experiments, and therefore requires only one Fourier transformation.

4 MEASURING TECHNIQUES FOR EXTREMELY LONG RELAXATION TIMES

The steady state magnetization $\boldsymbol{M}(t)$ is neither purely longitudinal nor purely transverse during any time interval. Therefore steady-state techniques are not suitable to study purely longitudinal or purely transverse relaxation. The results of two experiments must be combined to evaluate T_1 and T_2.

In the T_1/T_2 *experiment*, the amplitudes of the established steady state of the sample are determined for some different flip angles in the range $0° \leq \Theta \leq 90°$. Equation (7), describing the transverse component M_R of the magnetization, contains, besides the flip angle Θ and the free precession angle Φ (which should be adjusted to $\Phi_{ex} \approx \pi$), the two unknown quantities M_0 and the ratio of the relaxation times T_1/T_2. With the aid of a Gaussian least-squares fitting routine, this ratio of the relaxation times as well as the signal amplitude corresponding to the equilibrium magnetization M_0 may be evaluated. The necessary calibration of the flip angles Θ is described in detail by Kronenbitter and Schwenk[16] and Schwenk,[11] and many experimental hints and examples are given there. Figure 5 shows the results of such T_1/T_2 experiments with some nuclei in different chemical environments.

In the $T_1 + T_2$ *experiment*, the development of the transverse magnetization $M_R(t)$ starting from the totally unmagnetized state of the sample $\boldsymbol{M}(t = 0) = 0$ (or starting from any other initial state of the sample) is observed. To investigate this development of the NMR signal as a function of the time elapsed since demagnetization, the following block averaging technique is used. The signal is observed during a time interval of about $3T^*_{opt}$; this interval is split into L parts (about a dozen) of the duration T_{ac}. During the νth time interval $\nu T_{ac} \leq t \leq (\nu + 1)T_{ac}$ ($\nu = 0, \ldots, L - 1$), the NMR signal is accumulated in block ν of the memory in the time-averaging computer. Of course, this acquisition time T_{ac}, governed by the relaxation times of the sample, is far too short to achieve a sufficient signal-to-noise ratio. Therefore this development must be repeated frequently and the signal added to the corresponding block in the computer memory; i.e., a dynamic steady state is performed in the spin system. The demagnetization of the sample within the shortest time is described in detail by Kreibich and Schwenk;[25] a higher range of this dynamic steady state may be achieved by an inversion of the magnetization rather than by a destruction. This development of the transverse magnetization M_R is described in equations (13) and (14), for the special case $\Phi_{ex} = \pi$ and $\Theta = \Theta_{opt}$ [as given in equation (12)]; for the arbitrary case, see Kronenbitter and Schwenk[16] and Schwenk.[11] By a Gaussian least-squares fitting routine, the time constant T^* as well as the signal amplitude of the totally established steady state may be evaluated from the absorption maxima of $I_\nu(x = \kappa)$; equation (19), as determined by Fourier transformation of the signal in block ν of the memory. Figure 6 shows an example of such a $T_1 + T_2$ experiment.

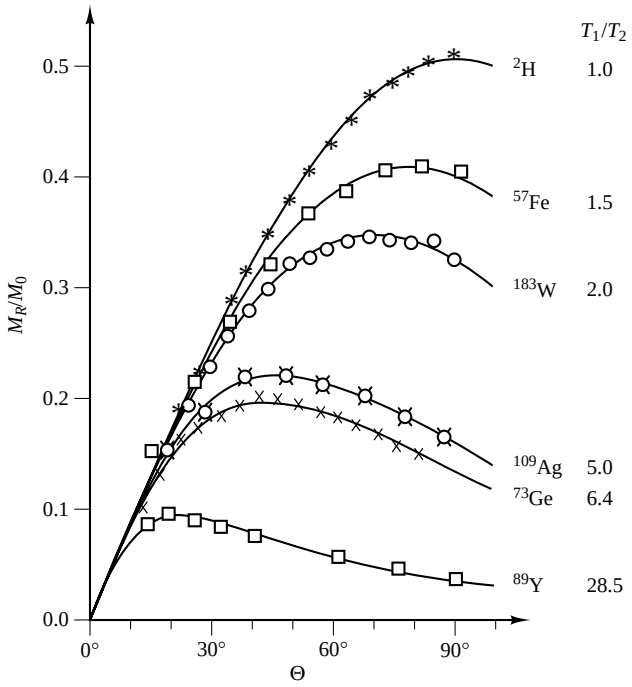

Figure 5 Results of some T_1/T_2 experiments with the following nuclei and samples: ^{2}H in D_2O; ^{57}Fe in butadiene–$Fe(CO)_3$, 2.9 M in C_6D_6; ^{183}W in WF_6, neat liquid; ^{109}Ag in a 12 M solution of $AgNO_3$ in acetonitrile at 298 K; ^{73}Ge in $GeCl_4$, neat liquid; and ^{89}Y in a 3 M aqueous solution of $Y(NO_3)_3$ with pH 1.3

A detailed description with additional examples, experimental hints and a discussion of the systematic errors caused by inhomogeneities in the fields $\boldsymbol{B}_0$ and $\boldsymbol{B}_1$ may be found in Kronenbitter and Schwenk[16] and Schwenk.[11]

5 INVESTIGATION OF NUCLEI WITH SPIN–SPIN COUPLING

Two types of scalar coupling of the $I = \frac{1}{2}$ low-γ nucleus X under investigation to another nucleus A must be distinguished.

5.1 Heteronuclear Coupling

Here, A is not the same isotope as X. In this case, nucleus A is not affected by the steady-state experiment performed with nucleus X. However, the steady state of X is affected by the longitudinal relaxation of A. A change in the eigenstate of nucleus A results in a change in the Larmor frequency of X by the coupling constant J. Owing to this, the steady state of X is disturbed, depending on the longitudinal relaxation time $T_1{}^A$ of nucleus A; the worst case is $T_1{}^A \approx T_p$. In this worst case,

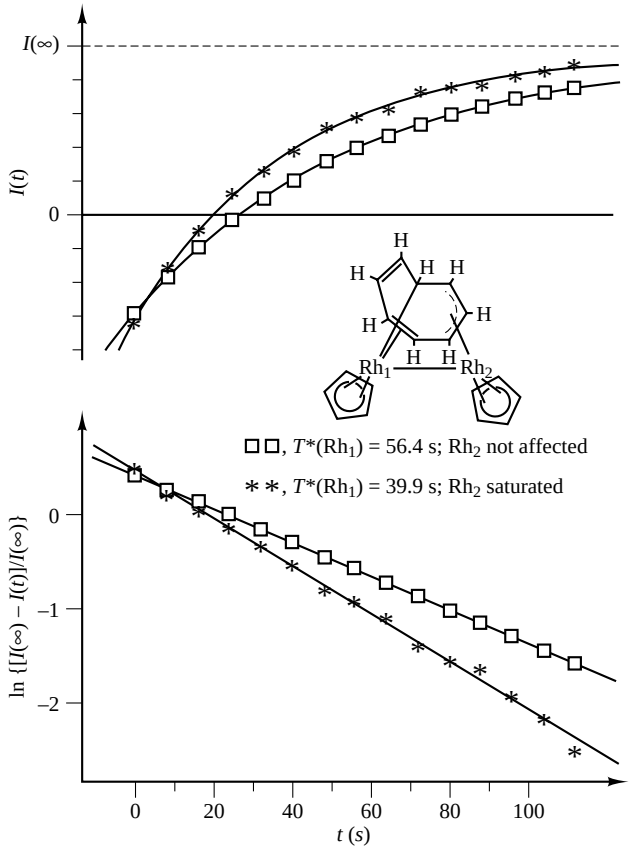

Figure 6 Results of a T_1+T_2 experiment with a binuclear Rh complex, about 0.1 M in CH_2Cl_2 at 296 K. $Rh_1 \equiv$ X and $Rh_2 \equiv$ A are weakly spin–spin coupled. Rh_1 was investigated; i.e., $\Phi_{ex}(Rh_1) = \pi$ was chosen. By application of semiselective triplet rf pulses, Rh_2 was not affected by the irradiation in the first experiment, whereas by single pulses with $\Phi_{ex}(Rh_1) = \pi$ and $\Phi_{ex}(Rh_2) = 0$ in the second experiment, the Rh_2 NMR line was saturated, resulting in a shorter $T^*(Rh_1)$ because of cross relaxation

a coupling constant J with $|J|T_p \approx 5\%$ is sufficient to destroy the steady state of X, as pointed out by Schwenk.[11] In most cases, a scalar coupling of X to an $I = \frac{1}{2}$ nucleus with high γ, e.g., to ^{19}F, ^{31}P, or a similar nucleus, destroys the steady state of nucleus X. Fortunately, such a coupling of X to an $I = \frac{1}{2}$ nucleus A with considerably stronger magnetic moment offers a way to improve the signal of spins X by spin transfer or to record the spectrum of spins X by a double resonance experiment.

5.2 Homonuclear Coupling

Here, A and X are nuclei of the same isotope in a molecule, they differ only in their chemical shifts δ_X and δ_A. In general, rf irradiation affects both nuclei X and A; i.e. a double resonance experiment is performed, which must be treated theoretically with the density matrix[26] or product operator formalism,[27] rather than with the Bloch equations. In contrast with an NMR experiment affecting only one kind of nuclei X or A, in such a double resonance experiment, not only the signal intensities of both nuclei X and A but also their relaxation times are changed. In the case of weak spin–spin coupling $|J| \ll |\delta_X - \delta_A|$, such a double resonance experiment can nearly be avoided by irradiation of semiselective rf pulses with full intensity for nuclei X and vanishing spectral intensity for nuclei A. Such semiselective pulses may be doublets[11] or triplets,[28] which (in the time domain) act on nuclei X in just the same manner as a single rf pulse, but restore the magnetization of spins A, assumed to be in the z direction immediately before the semiselective pulse, to exactly the same direction after it. Semiselective doublets allow such a restoration of $\boldsymbol{M}$ in the z direction only for one spin isochromat with distinct Larmor frequency, whereas with semiselective triplets, the same result may be achieved in a range of Larmor frequencies sufficient for a real inhomogeneously broadened NMR line. A steady state of the nuclei X stimulated with semiselective triplets consists of three pulses and three intervals of free precession and relaxation; this, of course, requires amendment of the formulas [equations (7), (13), and (14)] necessary to evaluate the relaxation experiments. Figure 6 shows two results of the T_1 + T_2 experiment performed with the ^{103}Rh nucleus shifted to lower frequency in *cis*-[$(CpRh)_2COT$] (the two ^{103}Rh Larmor frequencies differ by 960 Hz at 2.114 T and the coupling constant is $|J(Rh,Rh)| < 5$ Hz). Selective irradiation yields a considerably longer T^* than wideband irradiation, since cross relaxation is avoided (see ***Relaxation Processes in Coupled-Spin Systems*** and ***Relaxation Processes: Cross Correlation and Interference Terms***).

6 RELATED ARTICLES

Fourier Transform Spectroscopy; Germanium, Tin, and Lead NMR; Inorganic Nuclei: Low Sensitivity Transition Metals; Organometallic Compounds; Selective Pulses.

7 REFERENCES

1. R. R. Ernst and W. A. Anderson, *Rev. Sci. Instrum.*, 1966, **37**, 93.
2. E. L. Hahn, *Phys. Rev.*, 1950, **80**, 580.
3. H. Y. Carr and E. M. Purcell, *Phys. Rev.*, 1954, **94**, 630.
4. S. Meiboom and D. Gill, *Rev. Sci. Instrum.*, 1958, **29**, 688.
5. A. Allerhand and D. W. Cochran, *J. Am. Chem. Soc.*, 1970, **92**, 4482.
6. E. D. Becker, J. A. Ferretti, and T. C. Farrar, *J. Am. Chem. Soc.*, 1969, **91**, 7784.
7. R. Bradford, C. Clay, and E. Strick, *Phys. Rev.*, 1951, **84**, 157.
8. H. Y. Carr, *Phys. Rev.*, 1958, **112**, 1693.
9. J. Kaufmann and A. Schwenk, *Phys. Lett. A*, 1967, **24**, 115.
10. A. Schwenk, *Z. Phys.*, 1968, **213**, 482.
11. A. Schwenk, in *Progress in Nuclear Magnetic Resonance Spectroscopy*, eds. J. W. Emsley, J. Feeney, and L. H. Sutcliffe, Pergamon Press, Oxford, 1985, Vol. 17, p. 69.
12. R. Freeman and H. D. W. Hill, *J. Magn. Reson.*, 1971, **4**, 366.
13. A. Schwenk, *J. Magn. Reson.*, 1971, **5**, 376.
14. R. R. Ernst, personal communication, 1972.
15. R. R. Ernst, G. Bodenhausen, and A. Wokaun, *Principles of Nuclear Magnetic Resonance in One and Two Dimensions*, Clarendon Press, Oxford, 1987, p. 133.
16. J. Kronenbitter and A. Schwenk, *J. Magn. Reson.*, 1977, **25**, 147.

17. H. Pfister, A. Schwenk, and D. Zeller, *J. Magn. Reson.*, 1986, **68**, 138.
18. A. Schwenk, U. Piantini, and W. Wojnowski, *Z. Naturforsch. A*, 1991, **46**, 939.
19. A. Hafner, W. von Philipsborn, and A. Schwenk, *J. Magn. Reson.*, 1987, **74**, 433.
20. J. Kronenbitter, U. Schweizer, and A. Schwenk, *Z. Naturforsch. A*, 1980, **35**, 319.
21. L. Guinand, K. L. Hobt, E. Mittermaier, E. Rössler, A. Schwenk, and H. Schneider, *Z. Naturforsch. A*, 1984, **39**, 83.
22. A. Haase, J. Frahm, D. Matthaei, W. Hänicke, and K.-D. Merboldt, *J. Magn. Reson.*, 1986, **67**, 258.
23. P. Mansfield and P. G. Morris, *NMR Imaging in Biomedicine*, Academic Press, New York, 1982, p. 76.
24. P. Waldstein and W. E. Wallace, *Rev. Sci. Instrum.*, 1971, **42**, 437.
25. W. Kreibich and A. Schwenk, *J. Magn. Reson.*, 1987, **77**, 308.
26. R. R. Ernst, G. Bodenhausen, and A. Wokaun, *Principles of Nuclear Magnetic Resonance in One and Two Dimensions*, Clarendon Press, Oxford, 1987, Chap. 2
27. O. W. Sørensen, G. W. Eich, M. H. Levitt, G. Bodenhausen, and R. R. Ernst, in *Progress in Nuclear Magnetic Resonance Spectroscopy*, eds. J. W. Emsley, J. Feeney, and L. H. Sutcliffe, Pergamon Press, Oxford, 1983, Vol. 16, p. 163.
28. A. Melchinger and A. Schwenk, *J. Magn. Reson.*, 1991, **94**, 34.

Biographical Sketch

Andreas Schwenk. *b* 1937. Dipl.-Phys., 1963, Dr. rer. nat., 1968, Universität Tübingen. Introduced to NMR by H. Krüger. Faculty in Physics, University of Tübingen, Germany, 1977–present. Approx. 70 publications. Research specialties: investigation of slowly relaxing low-γ nuclei and development of new techniques enabling such investigations.

Sulfur, Selenium, and Tellurium NMR

Helmut Duddeck

University of Hannover, Hannover, Germany

1	NMR Spectroscopic Properties of ^{33}S, ^{77}Se, and ^{125}Te and Experimental Techniques	1
2	^{33}S NMR and Its Applications	2
3	^{77}Se NMR and its Applications	4
4	^{125}Te NMR and Its Applications	9
5	Related Articles	11
6	References	12

1 NMR SPECTROSCOPIC PROPERTIES OF ^{33}S, ^{77}Se, AND ^{125}Te AND EXPERIMENTAL TECHNIQUES

The three chalcogens sulfur, selenium, and tellurium are rare elements in NMR spectroscopy. Although sulfur is important in inorganic, organic and biochemistry, only few scattered NMR spectroscopic studies exist, a fact which is due to the rather unfavorable nuclear properties of its only NMR-active isotope ^{33}S. So, this nucleus is of interest only for specialists and will probably not see general application. On the other hand, the heavier chalcogen isotopes ^{77}Se and ^{125}Te are comparable to ^{13}C in their properties or even superior, but these elements are much less abundant in chemistry. However, during the 1980s this situation changed, at least for ^{77}Se, when organoselenium chemistry was developed into a valuable synthetic tool, especially for regio- and/or stereoselective reactions and other stereochemical applications.

This article is not intended to be a comprehensive review. NMR spectroscopy of all three nuclei has been reviewed several times.[1–9,32] In order to avoid an extensive literature list, data and facts are quoted only if they have not yet appeared in any earlier review.

1.1 Sulfur-33

As can be seen from Table 1, ^{33}S is the only quadrupolar nucleus, and so large linewidths have to be expected. Indeed, this is the main reason why applications of ^{33}S NMR spectroscopy are so rare.[1,2] The quadrupolar moment of ^{33}S makes its relaxation so effective that T_1 and T_2 values are very often in the range 10–100 ms, making ^{33}S lines several kilohertz wide.[1,2] A possible way to attenuate such signal line-broadening effects is to apply higher temperatures and to use low-viscosity solvents, because linewidths are dependent on the isotropic tumbling correlation time of the molecule (τ_c). The relatively low resonance frequency of ^{33}S leads to acoustic-ringing effects in the probehead which can cause severe baseline distortions so that the signal may even be invisible. Several methods have been proposed to overcome this problem, for example the application of high external fields and special pulse sequences (e.g. RIDE).[1,2,10] The unfavorable R_c value (Table 1) is due to the low resonance frequency and the low natural abundance, but this difficulty can be overcome. The small relaxation times allow a high repetition rate for FID sampling. In many cases, it may be possible to accumulate 10 to 100 transients per second. Nevertheless, ^{33}S signals with halfheight widths lower than 1 kHz occur only if there is high symmetry at the sulfur atom, as for example when it is surrounded tetrahedrally by four atoms as in sulfates or sulfones. There are only few exceptions, among them the cylindrical molecules CS_2 and COS. Unfortunately, symmetry is a very severe restriction to the application of ^{33}S NMR because many sulfur compounds of interest such as thiols, sulfides, disulfides and sulfoxides do not meet this condition.

Temperature and medium effects on ^{33}S chemical shifts are low compared with the experimental uncertainty associated with line broadening. ^{33}S linewidths governed by relaxation times vary with changes in concentration, solvent, and temperature. These dependences can be exploited for measuring activation energies of molecular reorientation. So, it is possible to monitor differences in the molecular association of sulfur-containing solutes and solvent molecules.[1]

1.2 Selenium-77 and Tellurium-125

The situation is much better for selenium and tellurium because all their NMR-active isotopes are spin-$\frac{1}{2}$ nuclei where extreme line broadening generally does not occur. Consequently, there are many more publications in this field, and they have been reviewed several times.[3–9] The receptivity (R_c in Table 1) of ^{77}Se is about three times larger than that of ^{13}C. If one considers that, normally, NOE signal enhancements are not observed (see below), ^{77}Se can be regarded as equivalent to ^{13}C in its sensitivity. The element tellurium offers two isotopes. However, inspection of their R_c values (Table 1) clearly shows why ^{125}Te has been used in the overwhelming majority of tellurium NMR studies. Only in compounds with more than one tellurium atom might it be rewarding to measure ^{123}Te signals in order to identify ^{123}Te–^{125}Te coupling constants. No significant differences in the chemical shifts of the two isotopes have been observed, as expected.

The longitudinal relaxation of ^{77}Se and ^{125}Te is governed by spin rotation (SR) and, particularly at higher fields, chemical shift anisotropy (CSA) mechanisms.[7] In general, dipolar relaxation does not play a significant role, and so NOE signal enhancements do not occur (except for selenols, R–SeH, where a proton is directly attached to ^{77}Se). Typically, T_1 values are in the range of 1–30 s and, consequently, repetition rates should be in the same range. In the solid state the relaxation time of ^{77}Se can become very long so that high-resolution magic angle spinning (MAS) experiments without cross polarization (CP) will generally produce signals only with very long relaxation delays.

^{77}Se and ^{125}Te may display rather strong temperature dependences of their chemical shifts, a property which they share with many other heavy nuclei. The signals may be shifted by several parts per million over a range of only a few degrees Celsius so that extreme care is necessary if high-resolution ^{77}Se or ^{125}Te NMR is required.[11] This is particularly

Table 1 Nuclear Properties of ^{33}S, ^{77}Se, ^{123}Te and ^{125}Te[1,4,5]

Isotope	Spin (%)	Natural abundance (MHz)	NMR frequency[a] (relative to ^{13}C)	Receptivity, R_c
^{33}S	$\frac{3}{2}$	0.76	7.7	0.1
^{77}Se	$\frac{1}{2}$	7.58	19.1	3.0
^{123}Te	$\frac{1}{2}$	0.87	26.2	0.9
^{125}Te	$\frac{1}{2}$	6.99	31.5	12.5

[a]At 2.35 T (^1H frequency: 100 MHz).

Table 2 Various Selected ^{33}S Chemical Shifts, ^{33}S Chemical Shift Ranges, and Linewidths (where available)[1,2]

Compound	Chemical shift, δ (ppm)	Linewidth (Hz)
Inorganic:		
H_2S	−503	
Metal sulfides (solid)	−30 to −680	>2000
Metal sulfates (solid)	+5 to −15	>1000
SO_2	+375	
$SOCl_2$	+224	
SO_2Cl_2	−45	
SF_6	−177	0.03
H_2SO_4, sulfates and related salts and esters	+110 to +35	
$[MoS_nO_{4-n}]^{2-}$ and $[WS_nO_{4-n}]^{2-}$ (n = 1 to 4)	+350 to −190	10 to 300
Organic:		
Alkylthiols and -thioethers	−330 to −510	>2000
Sulfoxides	+40 to −100	>4000
Sulfones and other related diorganyl S(VI) derivatives	+40 to −30	10 to 410
Alkyl- or arylsulfonic acids, sulfonates, and sulfonamides	+3 to −20	10 to 350
Sulfonium salts	+420 to +330	>9000
Thiophene	−111, −119[a]	650, 1450[a]
Isothiazole	54	
C=S/N=S:		
CS_2	−333	350
COS	−594	440
Et−N=C=S	−340	4300
Ph−N=S=O	+261	6800
$Me_3Si-N=S=N-SiMe_3$	+299	3400

[a]Different values are from different literature sources.

the case with diorganylselenides and -tellurides; interestingly, the temperature dependence of diorganyltellurium dihalides is much less.[11b] Concentration dependence is not severe and can even be neglected if low or moderate concentrations are used. Changing solvents, however, may shift a ^{77}Se signal considerably. For example, a shift of about 22 ppm to low frequency is observed for a 5% solution of Me_2Se when going from C_6D_{12} to $(CD_3)_2SO$.[12] Analogous effects are expected to be even more pronounced for ^{125}Te.[7]

1.3 Referencing

Correct referencing is important when documenting and comparing NMR data. The most commonly used standards are: $(NH_4)_2SO_4$ or Cs_2SO_4 in water for ^{33}S; Me_2Se in $CDCl_3$ for ^{77}Se; and Me_2Te in $CDCl_3$ for ^{125}Te; all with the chemical shift δ = 0 and used as external reference. CS_2 with a ^{33}S chemical shift of δ = −333 ppm has been recommended as an alternative for the sulfate ions. Since Me_2Se and Me_2Te are liquids with a very unpleasant smell, many workers prefer to use low concentration $CDCl_3$ solutions of commercially available and easy to handle solids such as Ph_2Se_2 [$\delta(^{77}Se)$ = 463 ppm] and Ph_2Te_2 [$\delta(^{125}Te)$ = 422 ppm], respectively, as internal or external standards. It should be noted that an absolute ^{33}S shielding scale has been proposed according to which $(NH_4)_2SO_4$ and CS_2 resonate at δ = +249 and +581 ppm, respectively.[1,2]

2 ^{33}S NMR AND ITS APPLICATIONS

2.1 ^{33}S Chemical Shifts

^{33}S chemical shifts span a range of about 1000 ppm. The δ values of some representative compounds along with their signal linewidths (where available) are listed in Table 2 together with some typical resonance ranges of certain inorganic and organic sulfur functionalities. However, it should be noted that many values are imprecise due to extensive line broadening (see Section 1).

Four regions can be identified.[1,10] In order of increasing frequency these are: (a) singly bonded sulfur, (b) multiply

bonded sulfur, (c) sulfur in a delocalized π system, and (d) S=O bonds. Although, in principle, this is correct, the four ranges do overlap severely and exceptions occasionally occur so that ^{33}S chemical shifts are by no means good parameters for indicating the bonding situation of sulfur.

Sulfuric acid and sulfates generally resonate around δ = 0 ppm. The thiosulfate anion ($S_2O_3^{2-}$) has two sulfur atoms in different positions but only one ^{33}S signal could be measured (δ = 34 ppm). ^{33}S depletion of the thiosulfur and estimation of the electric field gradients enabled the signal observed to be assigned to the internal sulfur atom.[1]

Strong diagnostic ^{33}S deshieldings have been observed when oxygen is replaced gradually by sulfur in the thiomolybdate anions (**1**)–(**4**) (Table 3).[10] Thiotungstates show the same trend, but the ^{33}S atoms are shielded by 179–199 ppm when compared with the analogous thiomolybdate ions.[10] Recently, ^{33}S chemical shifts of Cu(I) and Ag(I) complexes with MoS_4^{2-} and WS_4^{2-} have been reported.[13] ^{33}S signals of metal sulfides and sulfates in the solid state were recorded.[1] Whereas a large number of sulfates resonate uniformly between δ = −13 and 0 ppm, the resonances of sulfides vary over a wide range (more than 600 ppm), e.g. Li_2S (δ = −680 ppm), SrS (δ = −290 ppm), and BaS (δ = −42 ppm). The explanation is the existence of different bond characters and ionicities in the crystal.[1]

Whereas the sulfur nucleus in thiols and thioethers is strongly shielded (δ = −300 to −510 ppm), oxidation to sulfoxides leads to 300–400 ppm deshielding. Further oxidation to sulfones, however, does not significantly change the $\delta(^{33}S)$ values. This pattern is also seen in ^{77}Se chemical shifts (see Section 3.1). Two positively charged sulfonium salts have been measured, and their signals appear at the high-frequency end of the δ scale (*S*-methylthiolanium, +420 ± 50 ppm; *S*-methylthianium, +340 ± 50 ppm).[1,2] Interestingly, three- and four-membered ring compounds are exceptions [see, for example, (**5**–(**7**)] in that the sulfur is much more shielded than in the corresponding acyclic and cyclic analogs of larger ring sizes.[1,2] The same has been observed for other nuclei (^1H, ^{13}C, and ^{17}O) in or at three-membered rings.

(5) (δ = –574 ppm) **(6)** (δ = –214 ppm) **(7)** (δ = –89 ppm)

Substituent effects of alkyl and aryl groups on the ^{33}S chemical shift of diorganyl sulfones have been determined. In many cases good additivities of alkyl, alkenyl, and aryl group effects have been found (for details see Hinton[1]), and correlations of $\delta(^{33}S)$ values with those of ^{13}C and ^{17}O in analogous compounds as well as with Taft σ^* parameters could be established.[14] Substituents in 3- and *trans*-3,4-substituted thiolane 1,1-dioxides and 4-substituted 2-thiolene 1,1-dioxides influence the ^{33}S chemical shift according to their σ_I parameter, although the δ values vary by only 10–12 ppm for a wide range of substituents (CH_3 to SO_3Cl).[15] There is a similarity between the ^{33}S chemical shifts in sodium sulfonates ($R-^{33}SO_3^-$) and the ^{13}C shifts in carboxylates ($R-^{13}COO^-$),[1,2] and good correlation has been found between ^{33}S chemical shifts in *para* substituted benzenesulfonates and the Hammett σ constants of the substituents.[1] Other authors correlate ^{33}S chemical shifts in the same class of compounds with inductive substituent effects (ρ_I)[16] and pK_a values.[2]

Table 3 Chemical Shifts and Linewidths of the Thiomolybdate Ions (**1**)–(**4**)

	$[Mo_oSO_3]^{2-}$ (**1**)	$[Mo_oS_2O_2]^{2-}$ (**2**)	$[Mo_oS_3O]^{2-}$ (**3**)	$[Mo_oS_4]^{2-}$ (**4**)
$\delta(^{33}S)$	−25	+123	+240	+345
Linewidth (Hz)	200	250	170	38

Sulfonated naphthalene derivatives have been studied in terms of substituent effects on their ^{33}S chemical shifts.[17] An $n_X \rightarrow \sigma_{S-X}^*$ interaction in sulfonyl halides ($-SO_2X$) has been proposed.[18]

Sulfoximines [R–(O=)S(=NR″)–R′] resonate at lower frequencies than the corresponding sulfones [R–S(=O)$_2$–R′], which may be due to the lower electronegativity of the doubly bonded NR group in the sulfoximine replacing the oxygen in the sulfone. However, the opposite is seen when sulfimines [R–S(=NR″)–R′] are compared with the corresponding sulfoxides [R–S(=O)–R′].[1,2] On the other hand, ^{33}S chemical shifts in sulfonamides are quite similar to those in the sulfones.[1,2]

The absorption range of the sulphones of about 60 ppm has led to the suggestion of using ^{33}S NMR spectroscopy in the analysis of sulfur-containing oils after oxidation of all sulfur species.[1,2,19,20] In two instances, stereochemical effects on ^{33}S chemical shifts have been studied. It was shown that the diastereomeric sulfones (**8**) and (**9**) differ by 10 ppm.[1,2] The diverging stereochemical position of the phenylsulfonyl group in the conformationally fixed cyclohexanes (**10**) and (**11**) is reflected by a 3 ppm difference in the ^{33}S chemical shifts.[2] Interestingly, the sulfur atom in the axial stereoisomer (**11**) is deshielded compared with that in (**10**), which is opposite to the general finding that *γ-gauche* substituent effects are shielding, a rule with only very few exceptions.[21]

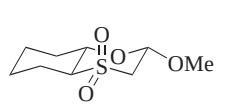

(8) (δ = –10 ppm)

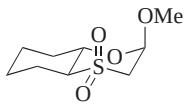

(9) (δ = –20 ppm)

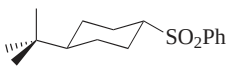

(10) (δ = –3 ppm)

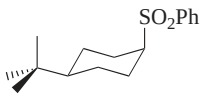

(11) (δ = 0 ppm)

2.2 ^{33}S Couplings

There are only few reported data on ^{33}S couplings. This is due to the short relaxation times associated with severely broadened signals (see below). Two-bond $^{33}S-^1H$ coupling constants of 3 and 4.5 Hz were measured for $CH_3-SO_2-CH_3$ and sulfolane,[1,2] and a $^{33}S-^1H$ coupling constant of 6 Hz extracted from the signal of 2,5-dihydrothiophene 1,1-dioxide was attributed to a vicinal (three-bond) coupling to the alkenic protons.[1,2,10] The exceptionally narrow linewidth of SF_6 (<1 Hz, corresponding to a relaxation time of T_1 = 10 ± 2 s) allowed a precise determination of the one-bond $^{33}S-^{19}F$ coupling constant: $^1J(^{33}S,^{19}F)$ = 251.8 ± 0.2 Hz.[1,2]

3 ^{77}Se NMR AND ITS APPLICATIONS

3.1 ^{77}Se Chemical Shifts

The total range of ^{77}Se chemical shifts is about 3300 ppm; the extremes are marked by selenoaldehydes and some molybdenum selenides (up to δ = 2400 ppm) on the high-frequency side and bridging (μ) selenium in tungsten complexes (δ = −900 ppm) on the low-frequency side. Figure 1 gives the resonance ranges of various selenium functionalities, and the ^{77}Se chemical shifts of selected compounds are collected in Table 4.

A number of reports have been published on elementary selenium. It is interesting to note that amorphous selenium (in a solid state ^{77}Se NMR experiment) resonates at δ = 865 ppm, whereas hexagonal selenium is shielded (δ = 809 ppm).[22] Several cyclic selenium species have been identified in solution: neutral Se_6, Se_7, and Se_8 in CS_2 have been described, and their ^{77}Se chemical shifts were found to be in a similar range to those of solid selenium (δ = 685, 998, and 615 ppm, respectively).[23] Other six- to eight-membered rings with selenium atoms replaced by sulfur and tellurium to various extents also absorb in these ranges, and again the chemical shifts of the seven-membered rings are higher than those of the others (about δ = 980 to 1100 ppm).[23,24] Se_4 dications as well as the mono-, di-, and tritellura derivatives thereof, generated in sulfuric acid or other Lewis acid solutions, were investigated. They form four-membered rings and, expectedly, their signals were found at very high frequencies (δ = 1432 to 1948 ppm).[9,25]

The ^{77}Se chemical shifts in selenium halides (SeX_2) reveal strong deshieldings with decreasing electronegativity of X in the series X = Cl (δ = 1758 ppm), Br (δ = 1474 ppm)[4,5,7] and I (δ = 814 ppm).[22] The same deshielding, but with an opposite trend in the halogen effects, is found for the oxygenated species: $SeOF_2$ (δ = 1378 ppm), $SeOCl_2$ (δ = 1479 ppm), and $SeOBr_2$ (δ = 1559 ppm).[4,6] On the other hand, electropositive substituents such as H_3E (E = Si and Ge) attached to selenium lead to very strong shieldings ($H_3E-Se-EH_3$: δ = −666 and −612 ppm, respectively),[4,6] which are only exceeded by selenide ions in alkaline aqueous solution such as K_2Se (δ = −670 ppm).[26] The highest shielding for a nonmetallic compound reported in the literature is the one due to a combination of the two influences in silicon-substituted selenides: $H_3Si-Se^-Li^+$ (δ = −736 ppm).[5] A general trend to deshielding with increasing electronegativity of substituents

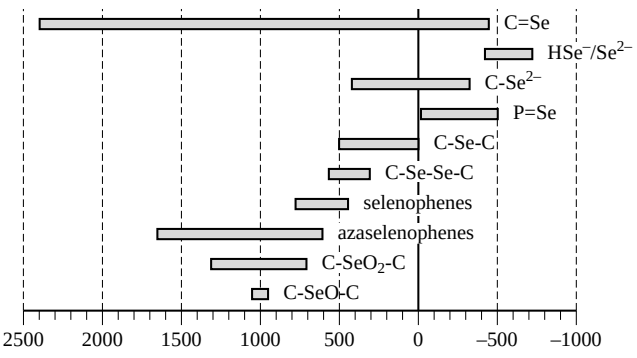

Figure 1 ^{77}Se chemical shift ranges of selected selenium functionalities (excluding metal complexes)

directly attached to selenium in R−Se−X (R = organyl) is observed [see (**12**)−(**16**)][7] although additional substituents or atomic groups play an important role and may even overrule the trend; e.g. see the C−Se−N compounds (**17**)−(**20**) where the ^{77}Se chemical shift difference between Ph−Se−NH−Bu^t and $(CF_3-Se)_3N$ is 1000 ppm![7,27]

Ph−Se−Cl **(12)** (δ = 1039 ppm)

Ph−Se−NMe_2 **(13)** (δ = 924 ppm)

Ph−Se−Br **(14)** (δ = 867 ppm)

Ph−Se−SMe **(15)** (δ = 514 ppm)

Ph−Se−SeMe **(16)** (δ = 447 ppm)

Ph−Se-NH-*t*-Bu **(17)** (δ = 617 ppm)

Ph−Se-morpholino **(18)** (δ = 926 ppm)

$F_3C-Se-NCO$ **(19)** (δ = 1104 ppm)

$(CF_3-Se)_3N$ **(20)** (δ = 1617 ppm)

The structure of alkyl substituents in dialkyl- and arylalkyl selenides has a great influence on the ^{77}Se shielding, a behaviour that is analogous to, although stronger than, what has been found for other nuclei such as ^{13}C and ^{17}O. α Effects are large, as shown by comparing PhSe−H (δ = 145 ppm) and PhSe−Me (δ = 197 ppm),[7] but β effects are even larger: replacement of a hydrogen atom at an α-methyl group leads to a 100−120 ppm deshielding. So, for example, the difference between Me_2Se (δ = 0 ppm) and Me−Se−Bu^t (δ = 294 ppm) corresponds to three methyl groups (Me → Bu^t) and that between Me_2Se and Pr^i_2Se (δ = 466 ppm) to four methyl groups (2 Me → 2 Pr^i).[6,7] Analogous trends have been detected for phenylselenenylalkanes (PhSe−R),[28] alkylselenols (RSeH), and alkylselenolates (RSe^-Na^+), but in dialkyl diselenides (RSeSeR) the deshielding is attenuated to about 65 ppm.[6,7] Fluorine atoms in the β-position lead to deshieldings similar to those of methyl groups: $(CF_3)_2Se$, δ = 698 to 725 ppm (the data in the original papers differ a little).[7] However, replacing fluorine by the less electronegative chlorine affords a further strong deshielding: $CF_3Se-CCl_3$, δ = 953 ppm.[7] This apparently paradoxical observation has been explained as being due to the differences in the hyperconjugation or polarizability of these two halogens.[7] γ Effects are substantially shielding: e.g. PhSe−Et (δ = 325 ppm) and PhSe−Pr^n (δ = 288 ppm); $\Delta\delta$ = −37.[6,7,28] An inspection of rigid cyclohexane derivatives with selenium fixed in an axial position (two γ *gauche* methylene groups) shows that the magnitudes of these γ effects are very similar (35−40 ppm).[11a] Thus it was concluded that molecular fragments such as PhSe−C−C−C prefer *gauche* conformations.[28] Substituent effects beyond the γ position are more or less negligible. The large magnitudes of α to γ effects have been discussed in terms of intramolecular polarizability effects, which act in parallel to intermolecular effects, thus causing a large solvent dependence of the ^{77}Se chemical shifts.[7]

The investigation of a number of selenoanisoles (Ph−Se−Me) substituted at the aromatic ring revealed that the ^{77}Se chemical shift can be expressed by a linear combination of parameters σ_I and σ_R, the inductive and resonance parameters, respectively, in the dual substituent parameter (DSP) approach.[29] There is a different linear relationship for each position, *ortho*, *meta*, and *para* (for details see Baiwir[6] and Luthra and Odom).[7] Selenoesters [R−C(=O)−Se−R′] have also been studied intensively.[7]

Table 4 ^{77}Se Chemical Shifts of Selected Compounds[3]emrstm0543-bib-0008

Compound	$\delta(^{77}Se)$ (ppm)	Compound	$\delta(^{77}Se)$ (ppm)	Compound	$\delta(^{77}Se)$ (ppm)
SeF_6	610	H_2Se	−226	Me_2SeCl_2	448
SeO_2F_2	948	Me−Se−H	−116	Me_2SeBr_2	389
$SeOF_2$	1378	Ph−Se−H	152	$Me-SeCl_3$	890
$SeOCl_2$	1479	C_6F_5−Se−H	287	Me_2SeO	812
$SeOBr_2$	1559	Me−Se−Me	0	$Me-SeO_2H$	1216
SeF_4	1092	Ph−Se−Me	202	$Me-SeO_3^-K^+$	1045
$SeCl_4$	1154	CF_3−Se−Me	370	$(MeO)_2SeO$	1339
$SeCl_2$	1758	CF_3−Se−CF_3	717	$(MeO)_2SeO_2$	1053
$SeBr_2$	1474	Me−SeCN	125	H_2SeO_4	1001
SeI_2	814	H_3Si−Se−SiH_3	−666	SeO_3	944
Se_2Cl_2	1274	H_3Ge−Se−GeH_3	−612	H_2SeO_3	1300
Se_2Br_2	1174	Ph−Se−Se−Ph	463		
Se (solid)	865, 809	$Me_3Se^+I^-$	253		
Se_6 (in CS_2)	685	Selenophene	605		
Se_7 (in CS_2)	998	Benzo[*b*]selenophene	526		
Se_8 (in CS_2)	615				

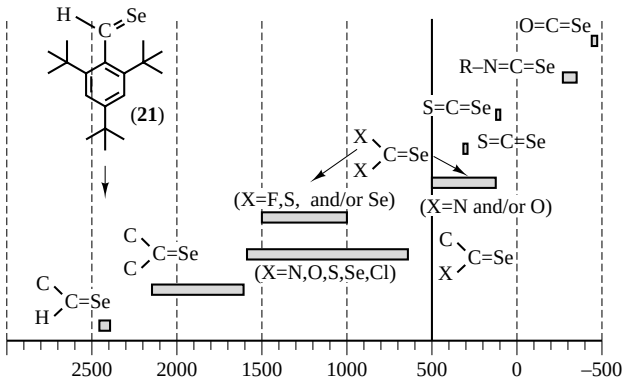

Figure 2 ^{77}Se chemical shift ranges of compounds containing C=Se groups (excluding metal complexes)

Oxidation of Se(II) to Se(IV) generally leads to considerable deshielding as can been shown in many cases: Me_2Se (δ = 0 ppm), Me_2SeBr_2 (δ = 389 ppm), and Me_2SeCl_2 (δ = 448 ppm).[7] In a series of phenylselenylalkane selenium oxides high-frequency shifts of 450–630 ppm due to oxidation have been found.[28] The magnitudes of substituent effects caused by the alkyl groups are approximately four times smaller in the selenoxides than in the corresponding selenides.[28]

Halogenated species, however, may show the opposite tendency: $SeCl_2$ (δ = 1758 ppm) and $SeOCl_2$ (δ = 1479 ppm) (see above) or CF_3SeCl (δ = 1077 ppm) and CF_3SeCl_3 (δ = 953 ppm).[7]

In general, Se(VI) species have clearly smaller δ values than the structurally related Se(IV) analogs; for example, H_2SeO_4 resonates at δ = 1001 ppm and H_2SeO_3 at δ = 1300 ppm.[4,5,7] Similarly, CF_3SeO_2H resonates at δ = 1231 ppm, whereas the ^{77}Se chemical shift of CF_3SeO_3H is only 981 ppm.[30]

Compounds containing a C=Se group show chemical shifts spread over nearly the whole known range of ^{77}Se chemical shifts. The largest value has been reported for the selenoaldehyde (**21**) (δ = 2398 ppm, Figure 2)[31] and the lowest for O=C=Se (δ = −447 ppm).[7] Figure 2 shows the various ranges, which depend strongly on the atoms and substituents attached to the carbon of the C=Se group. Correlations with $n \rightarrow \pi^*$ transitions and with ^{17}O chemical shifts in C=O analogs have been found.[7]

Hundreds of cyclic compounds with selenium in the ring(s) have been reported, but only a small selection can be presented here. A more comprehensive compilation is available.[32] Annulation of conjugated ring systems to selenophene (**22**) can cause considerable shieldings 23–26.[5–7] On the other hand, replacement of carbon by an electronegative element such as nitrogen shifts the ^{77}Se signal to high frequencies by up to 900 ppm [(**27**)–(**29**)].[5–7] Interestingly, the size of the aliphatic ring annulated to the selenadiazole (**29**) has a considerable influence on the ^{77}Se chemical shift; apparently, the selenium nucleus reacts very sensitively to minor strain effects within the heterocycle caused by the different cycloalkene rings in (**30**)–(**32**).[33] Substituent effects have a great impact as well. In monosubstituted selenophenes they range from δ = 721 ppm for 2-iodoselenophene down to δ = 513 ppm for 2-fluoroselenophene.[7] As expected, positively charged unsaturated ring systems strongly deshield selenium nuclei;[25] e.g. in (**33**), the chemical shift of which is the highest value reported so far.[34] Other interesting cyclic and caged structures such as (**34**)[35] and (**35**)[36] have been reported; here the chemical shifts follow the general trends of inductive and mesomeric influences encountered in open-chain selenium compounds. A transannular effect between the two silicon atoms in (**37**) deshields the bridging selenium atoms by more than 500 ppm as compared with (**36**) where no such through space interaction is expected.[37]

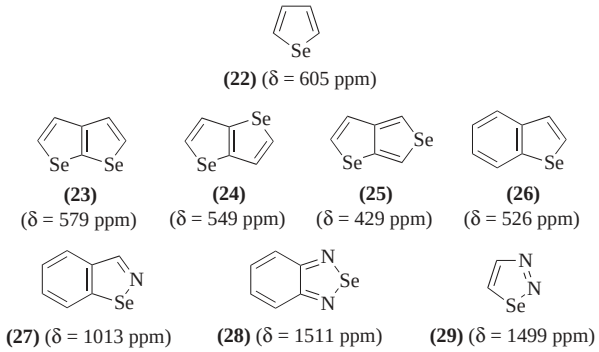

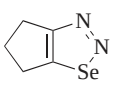

(30) (δ = 1405 ppm)

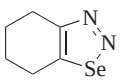

(31) (δ = 1490 ppm)

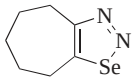

(32) (δ = 1533 ppm)

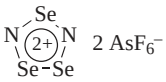

(33) (δ = 2434 ppm)

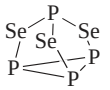

(34) (δ = 741 ppm)

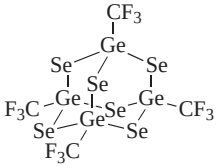

(35) (δ = 113 ppm)

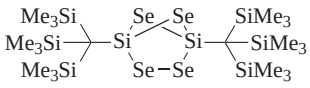

(36) (δ = 321 and 273 ppm)

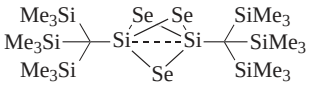

(37) (δ = 830 ppm)

Some hypervalent tetraarylselenium compounds, e.g. (**38**) and (**39**), have been measured at −100 °C.[38] Surprisingly, their ^{77}Se chemical shifts do not deviate much from those of other divalent diaryl selenides (Ph−Se−Ph: δ = 402 ppm).[5–7]

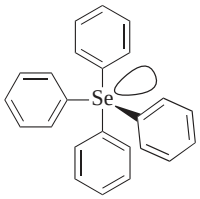

(38) (δ = 377 ppm)

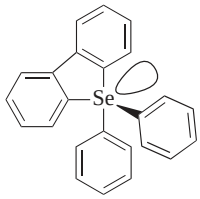

(39) (δ = 397 ppm)

The δ values of selenium in P=Se bonds are negative ((**40**)–(**53**)). This indicates a substantial contribution of the dipolar mesomeric form (**II**): –P=Se (**I**) ↔ –P$^+$–Se$^-$ (**II**). Only very few exceptions exist, e.g. Ph–P(=Se)Cl$_2$ (δ = 149 ppm)[39] and (NC)$_2$P(=Se)–Se$^-$ K$^+$ (δ = 172 ppm).[40] The chemical shifts depend strongly on the nature of the substituent at phosphorus (carbon or hetero atom), and the branching of carbon substituents also plays a significant role; for example, there is a nearly 100 ppm difference for the isomeric tripropylphosphine selenides (**42**) and (**43**).[41] Very little is known about the stereochemical dependence of ^{77}Se chemical shifts in P=Se groups, in contrast to the one-bond ^{31}P–^{77}Se coupling constant (see Section 3.2) which has been studied extensively, but mainly by recording ^{31}P NMR. The diastereomeric pair (**52**) and (**53**), however, clearly shows that selenium experiences a strong shielding in the axial position [(**53**), γ *gauche* effect].[42]

$Me_3P{=}Se$

(40) (δ = –235 ppm)

$Et_3P{=}Se$

(41) (δ = –419 ppm)

$(n\text{-Pr})_3P{=}Se$

(42) (δ = –398 ppm)

$(i\text{-Pr})_3P{=}Se$

(43) (δ = –497 ppm)

$(t\text{-Bu})_3P{=}Se$

(44) (δ = –385 ppm)

$Me_2(MeO)P{=}Se$

(45) (δ = –219 ppm)

$Me(MeO)_2P{=}Se$

(46) (δ = –269 ppm)

$(MeO)_3P{=}Se$

(47) (δ = –396 ppm)

$(Me_2N)_3P{=}Se$

(48) (δ = –275 ppm)

$F_2HP{=}Se$

(49) (δ = –283 ppm)

$Ph_3P{=}Se$

(50) (δ = –275 ppm)

$(PhO)_3P{=}Se$

(51) (δ = –283 ppm)

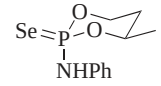

(52) (δ = –210 ppm)

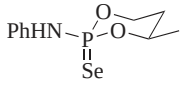

(53) (δ = –285 ppm)

^{77}Se NMR data for many selenium–metal compounds have been published and their appearance is rapidly increasing.[32] These compounds can be classified into three different types: (a) selenium with covalent bonds to main group metals, (b) selenium σ-, π-, μ-, or η-coordinated to transition metal atoms, and (c) selenium being a member atom of ligands, but with other atoms (mostly phosphorus or nitrogen) coordinated to the metal atom.

3.1.1 Type (a) Compounds

Deshieldings, as compared to the corresponding selenide anions, are often observed when selenium is bonded to group 13, 14, or 15 elements: Sn(SeMe)$_4$, δ = −127 (MeSe$^-$, δ = −330); [Pb(SePh)$_3$]$^-$ Na$^+$, δ = 127 (PhSe$^-$, δ = 104); or M(SePh)$_3$ with M = As (δ = 266), M = Sb (δ = 397), or M = Bi (δ = 311 ppm).[43] But the reverse has also been reported (In(SePh)$_3$, δ = 39 ppm),[44] and high shieldings are found if selenium carries two metal atoms: Ph$_3$Pb–Se–PbPh$_3$ (δ = −454 ppm).[45]

3.1.2 Type (b) Compounds

^{77}Se chemical shifts of these complexes cover the whole shift range. In most cases the selenium atom is deshielded (δ = 200 to 1500 ppm) as compared with the free selenium-containing ligand. The δ value of the terminal selenium atom (c) in the molybdenum complex (**54**) is one of the largest ever recorded; in the corresponding tungsten analog it is only δ = 1787 ppm.[46] On the other hand, the spectra of the adamantane-like caged selenides (**55**) and (**56**) display rather low δ values.[47] Extremely strong shieldings have been observed in the case of the η^4-cobalt complex (**57**) (δ = −727 ppm) as compared with the free heterocycle with δ = −95 ppm,[48] and a complex with selenium atoms linking two tungsten atoms, [η^5-Cp-W(CO$_3$)]$_2$(μ-Se), δ = −900 ppm, seems to have the smallest ^{77}Se chemical shift reported so far.[49] The π-complex (**58**) has a surprisingly low δ value;[50] one expects ^{77}Se chemical shifts of selenoaldehydes to be above 2000. Stereochemical assignments seem to be possible in platinum complexes. For example, the difference in ^{77}Se chemical shifts of the isomeric structures (**59**) (*cis*) and (**60**) (*trans*) is 83 ppm.[51]

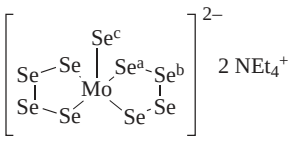

(54) [δ = 1163 (a), 403 (b), 2357 (c) ppm]

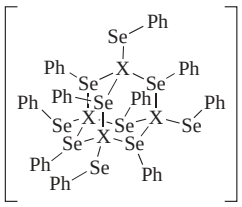

(55) [X = Cd, δ = 28 ppm (terminal), –64 ppm (bridging)]
(56) [X = Zn, δ = 46 ppm (terminal), –7 ppm (bridging)]

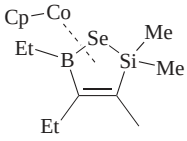

(57) (δ = 727 ppm)
(Cp ≡ η^5-cyclopentadienyl)

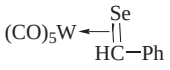

(58) (δ = 211 ppm)

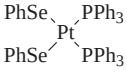

(59) (δ = 321 ppm)

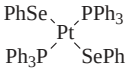

(60) (δ = 238 ppm)

3.1.3 Type (c) Compounds

The ^{77}Se chemical shifts in this type of metal complex do not differ significantly from those of the free ligands unless the selenium is involved in some interaction with the metal atom.

3.2 ^{77}Se Couplings

Coupling constants [$^nJ(X,^{77}\mathrm{Se})$] can be extracted quite easily from the spectra of the coupling partner (e.g. ^{1}H, ^{13}C, ^{31}P, or others) by inspecting the ^{77}Se satellites; each has about 4% intensity compared with the corresponding main signal. These J values have been reviewed extensively,[5,7,8] so in this article we concentrate on some general outlines.

3.2.1 $^nJ(^{77}Se,^1H)$

One-bond coupling constants $^1J(^{77}\mathrm{Se},^1\mathrm{H})$ are rather rare in the literature since they require a Se–H fragment in the molecule. Presumably, they are positive, and values between 65.4 (H_2Se) and 38 ± 1 Hz (Bu^tSeH) have been reported.[5,7] An exception is Cp–W(CO)$_3$SeH for which $^1J(^{77}\mathrm{Se},^1\mathrm{H})$ = 5.3 Hz.[49] $^2J(^{77}\mathrm{Se},^1\mathrm{H})$ values (geminal coupling) are mostly positive. They are between 4 and 16 Hz for hydrogen atoms in aliphatic fragments, but can increase to 50 Hz if the fragment has further geminal heteroatoms or if it is in an aromatic ring (selenophene 47.5 Hz).[5] Only in molecules in which selenium bears no free electron pairs do the coupling constants become negative, e.g. in $MeSeO_3^-$, −17.4 Hz.[5] There seems to be some stereochemical dependence in two-[5] and in three-bond (vicinal) couplings, $^3J(^{77}\mathrm{Se},^1\mathrm{H})$.[5,52]

3.2.2 $^nJ(^{77}Se,^{13}C)$

One-bond couplings ($^1J(^{77}\mathrm{Se},^{13}\mathrm{C})$ are negative and strongly depend on the hybridization state of the carbon atom.[5] Typical ranges are −45 to −100 Hz for Csp^3–Se [The values are larger if heteroatoms are attached to carbon: −90 to −162 Hz for C=**C**–Se (aromatic or alkenic); −203 to −249 Hz for C=Se; −184 to −193 Hz for C≡**C**–Se; −240 to −292 Hz for N≡**C**–Se–; −274 Hz for –N=**C**=Se; and −287 Hz for O=C=Se].[5,32] Exceptionally low values are found for selenonic acids, e.g. −13 Hz for Me–SeO_3^-.[5] Two-bond couplings [$^2J(^{77}\mathrm{Se},^{13}\mathrm{C})$] have not been studied intensively. Generally, they are positive, much smaller than $^1J(^{77}\mathrm{Se},^{13}\mathrm{C})$, and rarely larger than 15 Hz for aliphatic carbons. However, values up to 34 Hz have been detected in heteroaromatics,[5,53] but these cannot be confused with one-bond couplings.[5] Very little is known about $^3J(^{77}\mathrm{Se},^{13}\mathrm{C})$ values. They seem to be in the range 3–12 Hz,[53,54] but decrease to less than 3 Hz if the selenium atom is oxygenated.[53] Further investigation is needed to explore whether a Karplus-type dependence exists.

3.2.3 $^nJ(^{77}Se,^{15}N)$

Only two reports on ^{77}Se–^{15}N couplings seem to exist, and only one-bond coupling constants [$^1J(^{77}\mathrm{Se},^{15}\mathrm{N})$] are known: +60.1 Hz for $CF_3Se–NH_2$,[55] 83.4 Hz for (**30**), 89.8 Hz for (**31**), and 92.2 Hz for (**32**).[33]

3.2.4 $^nJ(^{77}Se,^{19}F)$

One-bond ^{77}Se–^{19}F coupling constants [$^1J(^{77}\mathrm{Se},^{19}\mathrm{F})$] are generally very large and can considerably exceed 1000 Hz. If fluorine atoms are in different stereochemical positions, they can be discerned easily. For example, the coupling to the axial fluorine atom in SeF_4 (trigonal bipyramid) is 284 Hz and that to the equatorial one 1206 Hz.[5,8] Values between 1200 and 1500 Hz are reached in SeF_6 and related Se(VI) derivatives, but stereochemical differences are much smaller and it is not possible to make reliable assignments on this basis.[5] $^2J(^{77}\mathrm{Se},^{19}\mathrm{F})$ values can be substantial; 120 and 117 Hz have been measured in fluorinated 1,3-diselenetanes, and even four-bond coupling constants of 11 and 12 Hz exist in these molecules.[56]

3.2.5 $^nJ(^{77}Se,^{29}Si)$

Few data have been published, and these are exclusively one-bond couplings. The largest is +110.6 Hz for $H_3Si–Se–SiH_3$[5] and the smallest is 48.5 Hz for (**37**).

3.2.6 $^nJ(^{77}Se,^{31}P)$

One-bond couplings [$^1J(^{77}\mathrm{Se},^{31}\mathrm{P})$] are negative and can have high values.[5,8] The magnitude of this coupling constant is an excellent indicator of the bond order between phosphorus and selenium. Values between −800 and −1200 Hz are normal for P=Se double bonds, whereas the values are much smaller for single bonds (−200 to −620 Hz).[5,8] Moreover, the coupling constants contain information about the stereochemistry of the compounds investigated. In both pairs (**61**)/(**62**) and (**63**)/(**64**) the absolute values of the coupling is larger for equatorially positioned selenium atoms,[57] and this is a general rule.

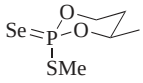

(61) [^1J(Se,P) = –960]

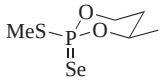

(62) [^1J(Se,P) = –895]

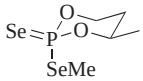

(63) [^1J(Se,P) = –435]

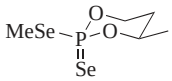

(64) [^1J(Se,P) = –510]

3.2.7 $^nJ(^{77}Se,^{77}Se)$

^{77}Se–^{77}Se couplings have not received much attention as their observation requires compounds with at least two selenium atoms in unsymmetrical positions. One-bond couplings have been measured for a number of diselenides and δ values between +22 Hz (Ph–Se–Se–Me)[7] and −66.5 Hz (CF_2Cl–Se–Se–CF_2Cl)[58] have been found. $^1J(^{77}Se,^{77}Se)$ values in various polyselenide anions are 250 ± 20 Hz if a charged selenium atom is involved.[59] Neutral cyclic sulfur–selenium compounds, however, have much smaller values (−17 to −65 Hz).[24a,60] The largest one-bond ^{77}Se–^{77}Se coupling so far reported seems to be 391 Hz (sign unknown) for (**65**).[61] Two-bond couplings can adopt large values. In cyclic sulfur–selenium compounds their absolute values are even larger than $^1J(^{77}Se,^{77}Se)$: 95–114 Hz.[24a,60] In the same class of compounds three-bond couplings are noticeable (3–16 Hz).[24a,60] An interesting case of a clear stereochemical differentiation by means of $^3J(^{77}Se,^{77}Se)$ values is for the pair (**66**) and (**67**).[52] Four-bond couplings vary between 0 and 16 Hz in sulfur–selenium cycles.[24a,60]

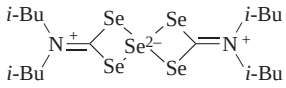

(65) [^1J(Se,Se) = 391]

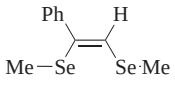

(66) [^3J(Se,Se) = 96]

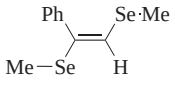

(67) [^3J(Se,Se) = 12]

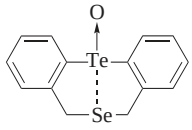

(68) [^3J(Se,Te) = 467]

3.2.8 $^nJ(^{125}Te,^{77}Se)$

One-bond couplings have been reported for Me–Se–Te–Me (−169 Hz)[5] and some polychalcogen cations and anions, for which the values can be substantial (189–670 Hz).[5,8] In compound (**68**) a very strong coupling between selenium and tellurium indicates the existence of a transannular interaction between these atoms.[62]

3.2.9 $^nJ(^{129}Xe,^{77}Se)$

A two-bond coupling to ^{129}Xe has been reported for $Xe(OSeF_5)_2$ (153.8 Hz).[63]

3.2.10 Couplings to Metal Nuclei

One-bond couplings to ^{119}Sn are generally between 500 and 1700 Hz,[5] whereas the two reported ^{207}Pb–^{77}Se couplings are

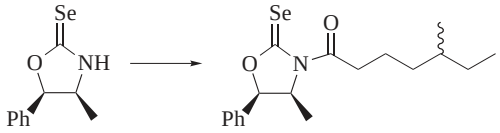

(69) **(70)**

Scheme 1

780 Hz (Ph_3Pb–Se–$PbPh_3$)[45] and 149 Hz ($K_2Pb_2Se_3$).[64] Typical couplings to transition metals[5,8] are: ^{103}Rh, 20–44 Hz;[65] ^{113}Cd, 126–195 Hz; ^{183}W, 14–109 Hz;[46,66] ^{195}Pt, 74–630 Hz; and ^{199}Hg, −751 to −1270 Hz. Strong diagnostic dependences of $^1J(^{195}Pt,^{77}Se)$ on the substituents and the stereochemistry have been noted.[5,8]

3.3 Special NMR Techniques and Applications

Conformational analysis of selenium-containing compounds by variable temperature NMR spectroscopy (DNMR) is facilitated by the high sensitivity of ^{77}Se chemical shifts because the coalescence temperature is generally much higher than in ^{1}H or ^{13}C NMR spectra. For example, the coalescence of ^{77}Se signals for the ring inversion process of phenylselenenylcyclohexane occurs at about 10 °C, whereas that of ^{1}H or ^{13}C signals appears at least 60 °C lower at the same external field strength.[11a,67] Analyses of other molecular systems such as 2,11-diselena[3.3]metacyclophane,[68] [3.3]diselena- and [4.4]tetraselenacyclo-phanes,[69] and 1,4,5,7-tetrahydro-3*H*-2,6-benzodiselenines[70] have been undertaken. The study of 2-arylseleno-1,3-dithianes shed some light on the question of an anomeric effect of arylselenenyl substituents.[71]

Gronowitz and coworkers[72] were the first to report that ^{77}Se NMR is an excellent tool for chiral recognition. They found noticeable differences in the spectra of diastereomeric α-phenylselenenylpropionic esters.[27] In 1990, the first derivatizing agent, (4*S*,5*R*)-(−)-4-methyl-5-phenyloxazolidine-2-selone (**69**), for the determination of enantiomeric purities by ^{77}Se NMR was published.[73] The authors showed that the ^{77}Se signal is split into two with a separation of 5.3 Hz (external field 7.05 T) when (**69**) was reacted with the racemic mixture of 5-methylheptanoic acid to produce (**70**) (Scheme 1). This is a chiral recognition across seven bonds. Moreover, the presence of deuterium five bonds away from the selenium atom (**71**), could clearly be recognized by a deuterium isotope shift.[73a]

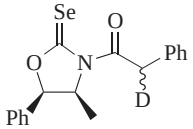

(71)

High-resolution solid state CP MAS ^{77}Se NMR has been applied to some selenium-containing molecules. The ^{77}Se chemical shift tensors σ_{11}, σ_{22}, and σ_{33} of a number of inorganic and organic compounds have been determined and their isotropic shifts δ_{iso} compared with the chemical shifts in liquid or solution δ.[74] It was found that δ and δ_{iso} are rather similar but in some cases there is more than one signal,

due to crystallographic nonequivalences in the unit cell. So, for example, selenourea [$(NH_2)_2C{=}Se$] gives five lines spread over a range of 36 ppm.[74] Two signals have been recorded for the cyclic $(Me_2SnSe)_3$, $\delta = -266$ ppm [$^1J(^{119}Sn,^{77}Se) = 1191$] and $\delta = -352$ ppm [$^1J(^{119}Sn,^{77}Se) = 1264$], with an intensity ratio of 1 : 2, indicating that the molecule adopts a twist–boat conformation with a two-fold symmetry axis.[75] The results of CP MAS NMR spectra of tetra- and hexaselenacoronands with 12-, 16-, 18-, and 24-membered rings have been compared with X-ray structures and discussed in terms of conformational properties.[76] Some borylselenides[77] and Ag_7PSe_6[78] have also been studied by means of MAS ^{77}Se NMR.

4 ^{125}Te NMR AND ITS APPLICATIONS

4.1 ^{125}Te Chemical Shifts

The total range of ^{125}Te chemical shifts is nearly 5000 ppm. The data for some selected compounds are compiled in Table 5.[4–9] Novel inorganic anions with high coordination numbers have recently been introduced, e.g. TeF_7^- (δ = 327 ppm, Table 5) which has a pentagonal bipyramidal structure.[79] TeF_5Cl and some of its hydrolysis products have also been investigated (Table 5).[80] Other tellurium compounds with six ligands, three phenyl groups, and three halogens, resonate between δ = 776 and 896 ppm.[81] The ^{125}Te chemical shifts of dithiotellurides [$Te(SR)_2$, R = alkyl or Ph] are between δ = 63 and 749 ppm (Table 5).[82]

Table 5 contains the ^{125}Te chemical shifts of basic dialkyl, alkylaryl, and diaryl tellurides, and ditellurides; more detailed information about the effects of various of these substituents may be obtained from the extensive compilations given by Luthra and Odom.[7] Since, in contrast to the diselenides, diorganyl ditellurides have a tendency to undergo exchange reactions, a number of unsymmetrical derivatives have been studied.[7,83] The effects of replacing α-hydrogen atoms of dimethyl telluride and phenylmethyl tellurides or ditellurides are in close analogy to those seen with the corresponding selenides. An example is shown in Figure 3, correlation (a).[84] The two other correlations in Figure 3 reveal that the same holds for diorganyltellurium dichlorides (b) and difluorides (c), although the magnitudes of the substituent effects decrease gradually.[11b]

Similarly, ^{125}Te chemical shifts in *ortho*-substituted tellurophenetols can be correlated with analogous selenophenetols.[85] Lithium salts of tellurocarboxylates [R–C(=O)–Te^-Li^+] have been described.[86] The ^{125}Te chemical shifts of bis(alkyltelluro)ethynes (R–Te–C≡C–Te–R) are δ = 215 (R = Me) and 404 ppm (R = Et).[87] Bis(organyltelluro)methanes (R–Te–CH_2–Te–R, R = alkyl or Ph) and their halide derivatives have been described, and the substituent effects of alkyl groups were determined.[88]

Hypervalent tellurium compounds with organic ligands have been described recently: Me_4Te and $(H_2C{=}CH)_4Te$,[89] triarylate complexes Ar_3Te^-,[90] triaryltelluronium cations Ar_3Te^+ (Table 5),[91] and some aromatic compounds with structures analogous to the selenium compounds (**38**) and (**39**), for example Ph_4Te, (δ = 509 ppm).[91]

Halogenation of tellurium to diorganyltellurium dihalides [R–$Te(Hal)_2$–R] and organyltellurium trihalides (R–$TeHal_3$)[92] leads to substantial deshieldings, and large solvent shifts have been noticed in this class of compounds which, at least in part, may be due to the formation of dimers.[7] The first aliphatic tellurenyl halogenides reported are $(Me_3Si)_3C$–Te–X with X = Cl (δ = 1693 ppm), X = Br (δ = 1347 ppm), and X = I (δ = 1185 ppm).[93]

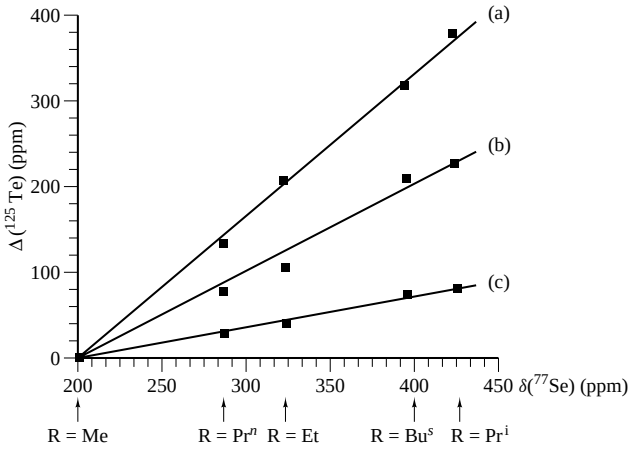

Figure 3 ^{125}Te chemical shifts of some alkanes substituted with three different kinds of tellurium functionalities plotted against ^{77}Se chemical shifts of corresponding selenium analogs (PhSe–R[84]): (a) PhTe–R,[84] (b) $PhTe(Cl_2)$–R, (c) $PhTe(F_2)$–R. For better comparability the ^{125}Te chemical shifts are referred to the methyl derivative (R = Me) in each series. In order not to confuse these values with ^{125}Te chemical shifts, the symbol $\Delta(^{125}Te)$ is used

^{125}Te chemical shifts of phosphine tellurides (tellurophosphoranes, R_3PTe) are between $\delta = -513$ (R = Me) and -1000 ppm (R = Pr^i) and have been interpreted in terms of bond characters within the P–Te bond.[94]

Recently, the first stable telluroketone (**72**) has been reported, and, as expected, its chemical shift (δ = 2858 ppm) is one of the highest ever recorded in a neutral organotellurium compound.[95] If one heteroatom is attached to the tellurocarbonyl group, the chemical shift is considerably smaller; for example, (**73**) (δ = 1418 ppm).[96] The 2-telluroimidazoline (**74**) has an unusually high shielding ($\delta = -168$ ppm), and this has been ascribed to a considerable contribution of the dipolar canonical form.[97]

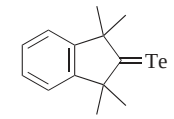

(72) (δ = 2858 ppm)

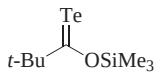

(73) (δ = 1418 ppm)

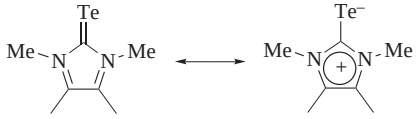

(74) (δ = –168 ppm)

Many cyclic tellurium compounds have been summarized previously.[5,7,9] Similar to the trends shown by the selenium analogs, the ^{125}Te chemical shift of benzo[*b*]tellurophene (**76**, δ = 727 ppm) is significantly smaller than that of tellurophene (**75**, δ = 782 ppm). Halogenation of the tellurium atom in

Table 5 ^{125}Te Chemical Shifts of Selected Compounds[4]emrstm0543-bib-0009

Compound	$\delta(^{125}Te)$ (ppm)	Compound	$\delta(^{125}Te)$ (ppm)
TeF_6	545	$Ph-TeCl_3$	917, 1229[a]
TeF_5Cl	592	$Ph-TeBr_3$	892, 1193[a]
trans-$(HO)_2TeF_4$	649	$Ph-TeI_3$	1101
cis-$(HO)_2TeF_4$	651	$Me-Te-Me$	0
$Te(OH)_6$	707	$Ph-Te-Me$	330
H_2TeCl_6	1403	$CF_3-Te-CF_3$	1368
H_2TeBr_6	1356	$Ph-Te-CH=CH_2$	615
H_2TeI_6	857	$Ph-Te-C\equiv C-Ph$	475
TeF_7^- Me_4N^+	327	$Me_3Si-Te-SiMe_3$	−60
$TeCl_4$	1138,1237[a]	$Me_3Sn-Te-SnMe_3$	−1214
$TeBr_4$	1442,1282[a]	$Ph-Te-Te-Ph$	422
TeI_4	845	$CF_3-Te-Te-CF_3$	686
$Te(OMe)_4$	1510	$Me-Te-Se-Ph$	512
K_2TeO_3	1732	$Me_3Te^+I^-$	443
Te_4^{2+}	2811	$Ph_3Te^+I^-$	788
$Te_2Se_2^{2+}$	3102	$Ph_3Te^-Li^+$	311
Te_6^{4+}	152	$Bu_3^tP=Te$	−80
TeI_2	3129	$(Bu^t_2P)_2Te$	−174
$Te(S-Bu^t)_2$	63	Me_2TeCl_2	749
$Te(S-Ph)_2$	749	Me_2TeBr_2	669, 858[a]
Te^{2-}	−1748	Me_4Te	−67
		$(CH_2=CH)_4Te$	412

[a]Different chemical shift values are from different literature sources and might be due to medium effects.

(**77**) is accompanied by a strong deshielding; the higher the electronegativity of the halogen, the larger the ^{125}Te chemical shift; compare (**78**)–(**81**). Replacement of the methylene group in (**82**) by oxygen (**83**), tellurium (**84**), or C=O (**85**) results in large chemical shift alterations. Some tellurapyran derivatives [(**86**)–(**88**)] have been reported.[98] The oxidation of (**89**) results in a bicyclic dication (**90**) associated with an enormous deshielding of the tellurium atoms.[99]

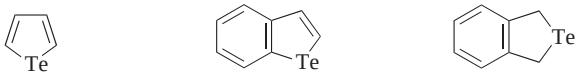

(75) (δ = 782 ppm) **(76)** (δ = 727 ppm) **(77)** (δ =269 ppm)

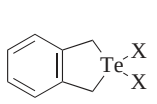

(78) (X = Cl; δ = 994 ppm)
(79) (X = Br; δ = 940 ppm)
(80) (X = I; δ = 831 ppm)

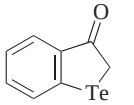

(81) (δ = 383 ppm)

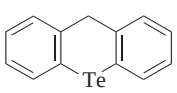

(82) (δ = 512 ppm)

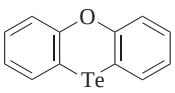

(83) (δ = 424 ppm)

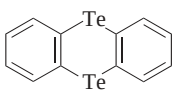

(84) (δ = 888 ppm)

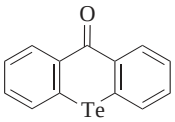

(85) (δ = 468 ppm)

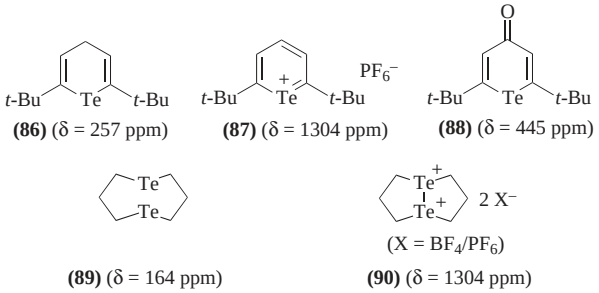

(86) (δ = 257 ppm) **(87)** (δ = 1304 ppm) **(88)** (δ = 445 ppm)

(89) (δ = 164 ppm) **(90)** (δ = 1304 ppm)

During recent years, many papers dealing with tellurium-containing metal complexes have appeared. Only two, arbitrarily chosen examples are discussed here. The stereoisomeric platinum complexes (**91**) and (**92**) differ in their ^{125}Te chemical shifts; however, it was shown in a series of related platinum and palladium complexes with ligands Me_2Te or Ph_2Te and Cl, Br, or I that, in contrast to the ^{125}Te–^{195}Pt coupling constants (see below), the ^{125}Te chemical shift is not a safe indicator of the isomerism.[100] The first example of a complex with a terminal transition metal–tellurium double bond reported in the literature is (**93**), which has a remarkably large $\delta(^{125}Te)$ value.[101]

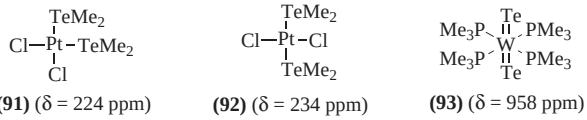

(91) (δ = 224 ppm) **(92)** (δ = 234 ppm) **(93)** (δ = 958 ppm)

4.2 ^{125}Te Coupling Constants

^{125}Te coupling constants are much less abundant in the literature than those involving ^{77}Se, and mostly they are associated with one-bond couplings. Assuming that scalar

couplings involving ^{125}Te and ^{77}Se are both governed by the Fermi contact interaction, it can be expected that ^{125}Te–X coupling constants are approximately two times larger than the corresponding ^{77}Se–X coupling constants. Due to the negative magnetogyric ratio of ^{125}Te, the signs of the respective J values should be opposite (unless their magnitudes are small).[5] In fact, the ratio $J(^{125}\text{Te,X})/J(^{77}\text{Se,X})$ is 2–3 (in absolute value).[5,7]

4.2.1 $^{n}J(^{125}Te,^{1}H)$

One-bond coupling constants [$^{1}J(^{125}\text{Te},^{1}\text{H})$] are negative; e.g. −59 Hz for H_2Te.[5] $^{2}J(^{125}\text{Te},^{1}\text{H})$ in dialkyl tellurides are approximately −20 Hz, but larger if tellurium is incorporated in a heteroaromatic (tellurophene −90 Hz) or in tellurium dihalides (−40 Hz).[5] $^{3}J(^{125}\text{Te},^{1}\text{H})$ values are smaller, but still significant: Et_2Te, −22.7 Hz; and tellurophene, −12 Hz.[5]

4.2.2 $^{n}J(^{125}Te,^{13}C)$

One-bond coupling constants [$^{1}J(^{125}\text{Te},^{13}\text{C})$] are positive and show a strong dependence on the hybridization state of the carbon atom involved. Examples are: Me_2Te, 162 Hz; $(H_2C{=}CH)_2Te$, 285 Hz; and Me–Te–C≡C–Bu, 531 Hz.[6]

4.2.3 $^{1}J(^{125}Te,^{19}F)$

Very large (probably positive) values have been noticed, for example: TeF_6, 3688 Hz; $(HO)_5TeF$, 2754 Hz;[5] TeF_5Cl, 3601/3444 Hz;[80] and TeF_7^-, 2876 Hz.[79] In some diorganyltellurium difluorides, (Ph–TeF_2–R), values between 695 and 735 Hz have been observed.[11b] If R is chiral, the two fluorine atoms are diastereotopic and differ considerably in their ^{19}F chemical shifts and $^{1}J(^{125}\text{Te},^{19}\text{F})$ values.[11b] In Ph_2TeF_2, the $^{1}J(^{125}\text{Te},^{19}\text{F})$ coupling is only 530 Hz.[11b]

4.2.4 $^{1}J(^{125}Te,^{31}P)$

These couplings are assumed to be positive, and their value depends strongly on the bond order: in compounds $R_3P{=}Te$ they are 1548–1743 Hz[5,94] whereas they are much smaller in compounds like $(Bu^t)_2P–Te–P(Bu^t)_2$ (451 Hz).[5]

4.2.5 $^{1}J(^{125}Te,^{77}Se)$

These couplings have been discussed in Section 3.2.8.

4.2.6 $^{1}J(^{125}Te,^{123}Te)$

These couplings have been recorded occasionally in compounds with more than one tellurium atom, e.g. in polyatomic cations (600–1200 Hz) and diorganyl ditellurides (213–269 Hz).[5]

4.2.7 $^{1}J(^{183}W,^{125}Te)$

The one-bond ^{183}W–^{125}Te coupling constant in (**93**) is 190 Hz.[101]

4.2.8 $^{1}J(^{195}Pt,^{125}Te)$

In platinum complexes the one-bond ^{195}Pt–^{125}Te; coupling constants are often strongly dependent on the stereochemistry.[5] For example, a value of 824 Hz was found for the *cis* isomer (**91**), whereas that of the *trans* isomer (**92**) is 489 Hz.[100] This sequence seems to be a rule, and the large differences in their magnitudes allow stereochemical assignments.

More ^{125}Te coupling data are given by Rodger et al.,[4] McFarlane and McFarlane,[5] and Luthra and Odum.[7]

4.3 Special NMR Techniques and Applications

Temperature-variable ^{125}Te NMR (DNMR) of phenyltellurenyl-substituted cyclohexane and related derivatives showed that the coalescence temperature associated with the ring inversion is even higher that in ^{77}Se DNMR of analogous selenides.[11] The ^{125}Te chemical shift difference in the axial and the equatorial phenyltellurenylcyclohexane (at −30 °C) is 130 ppm.[11]

Only a very few stereochemical applications of ^{125}Te NMR spectroscopy have been published. The stereoisomeric bicyclic compounds (**94**) and (**95**) differ by 34 ppm in their ^{125}Te chemical shifts.[7] The difference in the chemical shifts of the two diastereomeric camphor derivatives (**96**) and (**97**) is much larger (177 ppm).[102] In spite of the rather long distance from the menthyl residue in (**98**)–(**100**), the tellurium atom is able to reflect differential stereochemical positions of the vicinal methyl group by a ^{125}Te chemical shift difference of 5–7 ppm.[11b] This allows one to conclude that tellurium is an excellent nucleus for chiral recognition.

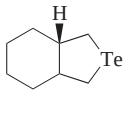

(94) (δ = 175 ppm)

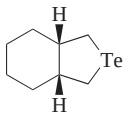

(95) (δ = 209 ppm)

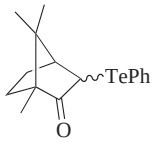

(96) (*endo*; δ = 598 ppm)
(97) (*exo*; δ = 775 ppm)

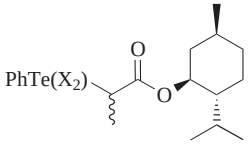

(98) (X = l.p.; δ = 810/803 ppm)
(99) (X = Cl; δ = 989/983 ppm)
(100) (X = F; δ = 1224/1219 ppm)

Little is known about solid state CP MAS ^{125}Te NMR spectroscopy. In a pioneering paper, it has been shown that $Te(OH)_6$ has two resonances, δ_{iso} = 692 and 686 ppm, reflecting the great sensitivity of this method to even minor distortions from the octahedral symmetry in the monoclinic crystal.[103] Surprisingly, the scalar coupling of ^{125}Te to two equivalent chlorine atoms [$^{1}J(^{125}\text{Te},^{35}\text{Cl}) = 106 \pm 5$ Hz] could be detected in the solid state CP MAS ^{125}Te NMR spectrum of $Me_3TeCl{\cdot}H_2O$.[103] In a series of salts with Me_3Te^+ and Ph_3Te^+ cations it was demonstrated that there are long-range covalent interactions between these cations and their anions (Cl^-, I^-, and NO_3^-).[104]

5 RELATED ARTICLES

Oxygen-17 NMR; Oxygen-17 NMR: Applications in Biochemistry.

6 REFERENCES

1. J. F. Hinton, *Annu. Rep. NMR Spectrosc.*, 1987, **19**, 1.
2. S. Berger, S. Braun, and H.-O. Kalinowski, *NMR-Spektroskopie von Nichtmetallen*, Thieme, Stuttgart, 1992, Vol. 1, Chap. 5, p. 119 (in German).
3. M. A. Lardon, in *Organic Selenium Compounds: Their Chemistry and Biology*, ed. D. L. Klayman and W. H. H. Günther, Wiley, New York, 1973, p. 933.
4. C. Rodger, N. Sheppard, H. C. E. McFarlane, and W. McFarlane, in *NMR and the Periodic Table*, ed. R. K. Harris and B. E. Mann, Academic, London, 1978, p. 383.
5. H. C. E. McFarlane and W. McFarlane, in *NMR of Newly Accessible Nuclei*, ed. P. Laszlo, Academic, New York, 1983, Vol. 2, p. 275.
6. M. Baiwir, in *Proceedings of the 9th International Conference on the Organic Chemistry of Selenium and Tellurium*, ed. B. Frank and W. R. McWhinnie, University of Aston, Birmingham, UK, 1983, p. 406.
7. N. P. Luthra and J. D. Odom, in *The Chemistry of Organic Selenium and Tellurium Compounds*, ed. S. Patai and Z. Rappoport, Wiley, Chichester, 1986, Vol. 1, p. 189.
8. H. C. E. McFarlane and W. McFarlane, in *Multinuclear NMR*, ed. J. Mason, Plenum, New York, 1987, p. 417.
9. D. H. O'Brien, K. J. Irgolic, and C.-K. Huang, in *Proceedings of the 4th International Conference on the Organic Chemistry of Selenium and Tellurium*, ed. B. Frank and W. R. McWhinnie, University of Aston, Birmingham, UK, 1983, p. 468.
10. P. S. Belton, I. J. Cox, and R. K. Harris, *J. Chem. Soc. Faraday Trans. 2*, 1985, **81**, 63.
11. (a) H. Duddeck, P. Wagner, and A. Biallass, *Magn. Reson. Chem.*, 1991, **29**, 248; (b) H. Duddeck and A. Biallass, *Magn. Reson. Chem.*, 1994, **32**, 303.
12. J. Milne, *Magn. Reson. Chem.*, 1993, **31**, 652.
13. M. Kony, R. T. C. Brownlee, and A. G. Wedd, *Inorg. Chem.*, 1992, **31**, 2281.
14. J. Hoyle, J. S. Grossert, D. L. Hooper, and S. Sotheeswaran, *Can. J. Chem.*, 1986, **64**, 1581.
15. (a) A. B. Rozhenko, V. M. Bzhezovskii, N. I. Kulik, G. A. Kalabin, and T. É. Bezmenova, *Zh. Org. Khim.*, 1990, **26**, 1079; *J. Org. Chem. USSR*, 1990, **26**, 929 (*Chem. Abstr.*, **113**, 151 700f); (b) A. B. Rozhenko, and V. M. Bzhezovskii, *Khim. Geterosikl. Soedin.*, 1990, 993; *Chem. Heterocycl. Comp.*, 1990, **26**, 832 (*Chem. Abstr.*, **114**, 100 962f); (c) A. B. Rozhenko, V. M. Bzhezovskii, and V. I. Slutskii, *Zh. Org. Khim.*, 1991, **27**, 2254; *J. Org. Chem. USSR*, 1991, **27**, 1996 (*Chem. Abstr.*, **116**, 234 983p).
16. R. Musio and O. Sciacovelli, *J. Org. Chem.*, 1992, **57**, 1195.
17. (a) J. Jirman and A. Lycka, *Collect. Czech. Chem. Commun.*, 1990, **55**, 446 (*Chem. Abstr.*, **114**, 80 892c); (b) Y. Kosugi, *Anal. Sci.*, 1991, **7**, 209 (*Chem. Abstr.*, **114**, 23 9604j).
18. (a) G. Barbarella, C. Chatgilialoglu, S. Rossini, and V. Tugnoli, *J. Magn. Reson.*, 1986, **70**, 204; (b) G. Barbarella, C. Chatgilialoglu, and V. Tugnoli, *J. Magn. Reson.*, 1990, **88**, 277; (c) G. Barbarella, A. Bongini, C. Chatgilialoglu, and M. Zambianchi, *Phosphorus, Sulfur Silicon Relat. Elem.*, 1991, **59**, 491.
19. M. B. Ngassoum, R. Faure, J. M. Ruiz, L. Lena, E. J. Vincent, and B. Neff, *Fuel*, 1986, **65**, 142.
20. G. A. Kalabin, L. V. Kanitskaya, D. F. Kushnarev, F. N. Mazitova, and N. A. Iglamova, *Dokl. Akad. Nauk. SSSR (Khim.)*, 1989, **305**, 1133; *Dokl. Chem.*, 1989, **305**, 121 (*Chem. Abstr.*, **111**, 25 993z).
21. H. Duddeck, *Top. Stereochem.*, 1986, **16**, 219.
22. M. Gopal and J. Milne, *Inorg. Chem.*, 1992, **31**, 4530.
23. R. S. Laitinen, P. Pekonen, Y. Hiltunen, and T. A. Pakkanen, *Acta Chem. Scand.*, 1989, **43**, 436.
24. (a) R. S. Laitinen, *Acta Chem. Scand., Ser. A*, 1987, **41**, 361; (b) T. Chivers, R. S. Laitinen, and K. J. Schmidt, *Can. J. Chem.*, 1992, **70**, 719; (c) J. Siivari, R. S. Laitinen, and Y. Hiltunen, *Phosphorus, Sulfur Silicon Relat. Elem.*, 1992, **65**, 177; (d) R. Steudel, D. Jensen, and F. Baumgart, *Polyhedron*, 1990, **9**, 1199; (e) R. Steudel, B. Plinke, and D. Jensen, *Polyhedron*, 1991, **10**, 1037.
25. G. J. Schrobilgen, R. C. Burns, and P. Granger, *J. Chem. Soc., Chem. Commun.*, 1978, 957.
26. J. Cusick and I. Dance, *Polyhedron*, 1991, **10**, 2629.
27. C. Paulmier, P. Lerouge, F. Outurquin, S. Chapelle, and P. Granger, *Magn. Reson. Chem.*, 1987, **25**, 955.
28. H. Duddeck, P. Wagner, and B. Rys, *Magn. Reson. Chem.*, 1993, **31**, 736.
29. M. Charton, *Prog. Phys. Org. Chem.*, 1981, **13**, 119.
30. (a) A. Haas and K. Schinkel, *Chem. Ber.*, 1990, **123**, 685; (b) K. Schinkel, Dissertation, Bochum, 1989.
31. R. Okazaki, N. Tokitoh, A. Ishii, N. Ishii, Y. Matsuhashi, T. Matsumoto, and H. Suzuki, *Phosphorus, Sulfur Silicon Relat. Elem.*, 1992, **67**, 49.
32. H. Duddeck, *Prog. NMR Spectrosc.*, 1995, **27**, 1.
33. H. Duddeck, P. Wagner, D. Müller, and J. Cs. Jaszberenyi, *Magn. Reson. Chem.*, 1990, **28**, 549.
34. E. G. Awere, J. Passmore, and P. S. White, *J. Chem. Soc., Dalton Trans.*, 1993, 299.
35. B. W. Tattershall, R. Blachnik, and H. P. Baldus, *J. Chem. Soc., Dalton Trans.*, 1989, 977, and references cited therein.
36. A. Haas, H.-J. Kutsch, and C. Krüger, *Chem. Ber.*, 1987, **120**, 1045.
37. H. Yoshida, Y. Takahara, T. Erata, and W. Ando, *J. Am. Chem. Soc.*, 1992, **114**, 1098.
38. (a) S. Ogawa, S. Sato, T. Erata, and N. Furukawa, *Tetrahedron Lett.*, 1991, **32**, 3179; (b) S. Ogawa, S. Sato, Y. Masutomi, and N. Furukawa, *Phosphorus, Sulfur Silicon Relat. Elem.*, 1992, **67**, 99.
39. K. M. Enikeev, E. V. Bayandina, I. É. Ismaev, N. A. Buina, A. V. Il'yasov, and I. A. Nuretdinov, *Zh. Obshch. Khim.*, 1983, **53**, 2143 (*Chem. Abstr.*, **100**, 22 721w).
40. A. Schmidpeter and G. Burget, *Z. Naturforsch. B*, 1985, **40**, 1306.
41. N. Kuhn, G. Henkel, H. Schumann, and R. Fröhlich, *Z. Naturforsch. B*, 1990, **45**, 1010.
42. W. Gombler, R. W. Kinas, and W. J. Stec, *Z. Naturforsch. B*, 1983, **38**, 815.
43. J. J. I. Arsenault and P. A. W. Dean, *Can. J. Chem.*, 1983, **61**, 1516.
44. R. Kumar and D. G. Tuck, *Can. J. Chem.*, 1989, **67**, 127.
45. S. R. Bahr and P. Boudjouk, *Inorg. Chem.*, 1992, **31**, 4015.
46. R. W. M. Wardle, C. H. Mahler, C.-N. Chau, and J. A. Ibers, *Inorg. Chem.*, 1988, **27**, 2790.
47. (a) P. A. W. Dean, J. J. Vittal, and N. C. Payne, *Inorg. Chem.*, 1987, **26**, 1683; (b) P. A. W. Dean and V. Manivannan, *Inorg. Chem.*, 1990, **29**, 2997.
48. R. Köster, G. Seidel, R. Boese, and B. Wrackmeyer, *Chem. Ber.*, 1988, **121**, 1955.
49. W. A. Herrmann and H.-J. Kneuper, *J. Organomet. Chem.*, 1988, **348**, 193.
50. H. Fischer, S. Zeuner, U. Gerbing, J. Riede, and C. G. Kreiter, *J. Organomet. Chem.*, 1989, **377**, 105.
51. V. W. Day, D. A. Lesch, and Th. B. Rauchfuss, *J. Am. Chem. Soc.*, 1982, **104**, 1290.

52. I. Johannsen, L. Henriksen, and H. Eggert, *J. Org. Chem.*, 1986, **51**, 1657.
53. W. Nakanishi and Y. Ikeda, *Bull. Chem. Soc. Jpn*, 1983, **56**, 1661.
54. C. D. Habben, *Chem. Ber.*, 1988, **121**, 1967.
55. W. Gombler, *Phosphorus, Sulfur Silicon Relat. Elem*. 1988, **38**, 231.
56. (a) A. Haas and M. Spehr, *Chimia*, 1988, **42**, 265; (b) R. Boese, A. Haas, and M. Spehr, *Chem. Ber*., 1991, **124**, 51.
57. W. J. Stec, R. Kinas, and A. Okruszek, *Z. Naturforsch., B*, 1976, **31**, 393.
58. (a) W. Gombler and G. Bollmann, *J. Fluorine Chem.*, 1987, **37**, 15; (b) W. Gombler, *Magn. Reson. Chem.*, 1991, **29**, 73.
59. (a) M. M. Carnell, F. Grein, M. Murchie, J. Passmore, and C. Wong, *J. Chem. Soc., Chem. Commun.*, 1986, 225; (b) M. Björgvinsson and G. J. Schrobilgen, *Inorg. Chem.*, 1991, **30**, 2540.
60. (a) R. S. Laitinen and T. A. Pakkanen, *Inorg. Chem.*, 1987, **26**, 2598; (b) P. Pekonen, Y. Hiltunen, R. S. Laitinen, and T. A. Pakkanen, *Inorg. Chem.*, 1990, **29**, 2770.
61. Y. Mazaki and K. Kobayashi, *Tetrahedron Lett.*, 1989, **30**, 2813.
62. H. Fujihara, T. Uehara, T. Erata, and N. Furukawa, *Chem. Lett.*, 1993, 263.
63. R. Damerius, P. Huppmann, D. Lentz, and K. Seppelt, *J. Chem. Soc., Dalton Trans.*, 1984, 2821.
64. M. Björgvinsson, J. F. Sawyer, and G. J. Schrobilgen, *Inorg. Chem.*, 1987, **26**, 741.
65. E. G. Hope, W. Levason, S. G. Murray, and G. L. Marshall, *J. Chem. Soc., Dalton Trans.*, 1985, 2185.
66. M. A. Ansari, C. N. Chau, C. H. Mahler, and J. A. Ibers, *Inorg. Chem.*, 1989, **28**, 650.
67. H. Duddeck, P. Wagner, and S. Gegner, *Tetrahedron Lett.*, 1985, **26**, 1205.
68. R. H. Mitchell and K. S. Weerawarna, *Tetrahedron Lett.*, 1988, **29**, 5587.
69. M. Hojjatie, S. Muralidharan, and H. Freiser, *Tetrahedron*, 1989, **45**, 1611.
70. B. Rys, H. Duddeck and M. Hiegemann, *J. Heterocycl. Chem.*, 1992, **29**, 967.
71. (a) B. M. Pinto, J. Sandoval-Ramirez, and R. D. Sharma, *Tetrahedron Lett.*, 1985, **26**, 5235; (b) B. M. Pinto, B. D. Johnston, J. Sandoval-Ramirez, and R. D. Sharman, *J. Org. Chem.*, 1988, **53**, 3766; (c) B. M. Pinto, B. D. Johnston, and R. Nagelkerke, *J. Org. Chem.*, 1988, **53**, 5668; (d) B. M. Pinto, B. D. Johnston, and R. Nagelkerke, *Heterocycles*, 1989, **28**, 389.
72. P. Michelsen, U. Annby, and S. Gronowitz, *Chem. Scr.*, 1984, **24**, 251.
73. (a) L. A. Silks, III, R. B. Dunlap, and J. D. Odom, *J. Am. Chem. Soc.*, 1990, **112**, 4979; (b) L. A. Silks, III, J. Peng, J. D. Odom, and R. B. Dunlap, *J. Chem. Soc., Perkin Trans. 1*, 1991, 2495; (c) L. A. Silks, III, J. Peng, J. D. Odom, and R. B. Dunlap, *J. Org. Chem.*, 1991, **56**, 6733.
74. M. J. Collins, C. I. Ratcliffe, and J. A. Ripmeester, *J. Magn. Reson.*, 1986, **68**, 172.
75. R. K. Harris and A. Sebald, *Magn. Reson. Chem.*, 1987, **25**, 1058; 1989, **27**, 81.
76. (a) B. M. Pinto, B. D. Johnston, R. J. Batchelor, F. W. B. Einstein, and I. D. Gay, *Can. J. Chem.*, 1988, **66**, 2956; (b) B. M. Pinto, R. J. Batchelor, B. D. Johnston, F. W. B. Einstein, and I. D. Gay, *J. Am. Chem. Soc.*, 1988, **110**, 2990; (c) R. J. Batchelor, F. W. B. Einstein, I. D. Gay, J. H. Gu, and B. M. Pinto, *J. Organomet. Chem.*, 1991, **411**, 147.
77. R. Köster, G. Seidel, and M. Yalpani, *Chem. Ber.*, 1989, **122**, 1815.
78. R. Maxwell, D. Lathrop, D. Franke, and H. Eckert, *Angew. Chem. Int. Ed. Engl.*, 1990, **29**, 882.
79. (a) K. O. Christe, J. C. P. Sanders, G. J. Schrobilgen, and W. W. Wilson, *J. Chem. Soc., Chem. Commun.*, 1991, 837; (b) A.-R. Mahjoub and K. Seppelt, *J. Chem. Soc., Chem. Commun.*, 1991, 840.
80. L. J. Lawlor, A. Martin, M. P. Murchie, J. Passmore, and J. C. P. Sanders, *Can. J. Chem.*, 1989, **67**, 1501.
81. A. F. Janzen and M. Jang, *Can. J. Chem.*, 1989, **67**, 71.
82. W. Mazurek, A. G. Moritz, and M. J. O'Connor, *Inorg. Chim. Acta*, 1986, **113**, 143.
83. R. U. Kirss and D. W. Brown, *Organometallics*, 1991, **10**, 3597.
84. D. H. O'Brien, N. Dereu, C.-K. Huang, K. J. Irgolic, and F. F. Knapp, Jr., *Organometallics*, 1983, **2**, 305.
85. (a) M. Baiwir, G. Llabrès, A. Luxen, L. Christiaens, and J.-L. Piette, *Org, Magn. Reson.*, 1984, **22**, 312; (b) M. Baiwir, G. Llabrès, L. Christiaens, A. Luxen, and J.-L. Piette, *Magn. Reson. Chem.*, 1986, **24**, 362.
86. S. Kato, H. Sasaki, and M. Yagihara, *Phosphorus, Sulfur Silicon Relat. Elem.*, 1992, **67**, 27.
87. R. W. Gedridge, Jr., K. T. Higa, D. C. Harris, R. A. Nissan, and M. P. Nadler, *Organometallics*, 1989, **8**, 2812.
88. C. H. W. Jones and R. D. Sharma, *Organometallics*, 1986, **5**, 805.
89. R. W. Gedridge, Jr, D. C. Harris, K. T. Higa, and R. A. Nissan, *Organometallics*, 1989, **8**, 2817.
90. (a) H. J. Reich, D. P. Green, N. H. Phillips, J. P. Borst, and I. L. Reich, *Phosphorus, Sulfur Silicon Relat. Elem.*, 1992, **67**, 83; (b) S. Ogawa, Y. Masutomi, N. Furukawa, and T. Erata, *Heteroatom Chem.*, 1992, **3**, 423.
91. C. H. W. Jones and R. D. Sharma, *J. Organomet. Chem.*, 1987, **332**, 115.
92. (a) H. Schumann and M. Magerstädt, *J. Organomet. Chem.*, 1982, **232**, 147; (b) M. Feikus and P. H. Laur, *Phosphorus, Sulfur Silicon Relat. Elem.*, 1992, **67**, 73.
93. K. Giselbrecht, B. Bildstein, and F. Sladky, *Chem. Ber*., 1989, **122**, 1255.
94. N. Kuhn, G. Henkel, H. Schumann, and R. Fröhlich, *Z. Naturforsch., B*, 1990, **45**, 1010.
95. M. Minoura, T. Kawashima, and R. Okazaki, *J. Am. Chem. Soc*., 1993, **115**, 7019.
96. T. Severengiz and W.-W. Du Mont, *J. Chem. Soc., Chem. Commun.*, 1987, 820.
97. N. Kuhn, G. Henkel, and T. Kratz, *Chem. Ber*., 1993, **126**, 2047.
98. M. R. Detty, W. C. Lenhart, P. G. Gassman, and M. C. Callstrom, *Organometallics*, 1989, **8**, 861.
99. H. Fujihara, T. Ninoi, R. Akaishi, T. Erata, and N. Furukawa, *Tetrahedron Lett.*, 1991, **32**, 4537.
100. T. Kemmitt and W. Levason, *Inorg. Chem.*, 1990, **29**, 731.
101. D. Rabinovich and G. Parkin, *J. Am. Chem. Soc.*, 1991, **113**, 9421.
102. L. A. Silks III, J. D. Odom, and R. B. Dunlap, *Synth. Commun.*, 1991, **21**, 1105.
103. M. J. Collins and J. A. Ripmeester, *J. Am. Chem. Soc*., 1987, **109**, 4113.
104. M. J. Collins, J. A. Ripmeester, and J. F. Sawyer, *J. Am. Chem. Soc*., 1988, **110**, 8583.

Biographical Sketch

Helmut Duddeck. *b* 1946. Dipl.-Chem., 1970, Ph.D., 1972, Bonn University. Began NMR investigations at Ruhr-University Bochum, 1973; Habilitation Bochum, 1979; Professor at Bochum University, 1985–92; Professor at Hannover University, 1992–present. Approx. 200 publications, including several reviews on NMR applications in organic and natural products chemistry. Research specialties: structural elucidation of natural products and other organic compounds by one- and two-dimensional ^{1}H and ^{13}C NMR methods; heteronuclear magnetic resonance, especially of Group 16 elements ^{17}O, ^{33}S, ^{77}Se, and ^{125}Te; high-resolution solid state NMR of organic compounds.

Thallium NMR

James F. Hinton

University of Arkansas, Fayetteville, AR, USA

1	Introduction	1
2	General Characteristics	1
3	Chemical Applications	2
4	Biochemical Applications	5
5	References	6

1 INTRODUCTION

During the decade following the landmark papers of Bloch et al.[1] and Purcell et al.[2] NMR experiments were performed with about 30 elements in the solid, liquid, or gas phase. One of the elements studied during this early development period of NMR spectroscopy was thallium. By 1953, solid[3] and liquid[4] state spectra had been obtained for the thallium nucleus. The availability of high-field magnets, multinuclear spectrometers, pulsed Fourier transform techniques, and an expanded chemistry have caused a 'rediscovery' of this element.

The nuclear properties of thallium and the sensitivity of the NMR parameters, chemical shift, spin–spin coupling constant, and relaxation time to the chemical environment into which the element is placed make thallium well suited for the NMR experiment and an excellent probe for studying a variety of chemical and physical phenomena. The intent of this review is not to present an extensive survey of thallium NMR spectroscopy but to emphasize the general characteristics of thallium NMR spectroscopy with selected applications to the solid and liquid states. An extensive review of the thallium NMR literature has been published previously.[5]

2 GENERAL CHARACTERISTICS

Because of their intrinsic nuclear properties, both isotopes of thallium are well suited for NMR experiments. Thallium-205 (70.5% natural abundance) and ^{203}Tl (29.5% natural abundance) have spins of $I = \frac{1}{2}$. The magnetic moments ($\mu/\mu N$) for ^{205}Tl and ^{203}Tl are 2.7914 and 2.7646, respectively. The resonance frequencies of ^{205}Tl at a magnet field strength of 11.75 T, 7.05 T, and 2.3488 T are 288.474 MHz, 173.108 MHz, and 57.708 MHz, respectively. For the ^{203}Tl nucleus the resonance frequencies at the same magnetic field strengths are 285.805 MHz, 171.506 MHz, and 57.149 MHz. The relative receptivity of the more abundant isotope, ^{205}Tl, is 0.1355 with respect to the proton which is assigned a value of 1. This makes the ^{205}Tl nucleus the fourth most receptive spin $I = \frac{1}{2}$ nuclide. The very high receptivity of both ^{205}Tl and ^{203}Tl nuclei allows them to be directly observed with very little difficulty. Spectra of ^{205}Tl in solution can be obtained from samples with thallium concentrations in the submillimolar range.

Although the variety of thallium compounds is not as extensive as that of other metals, such as cobalt, the available oxidation states of (I) and (III) provide an interesting array of electronic environments for thallium and concomitant chemical shift groupings. For example, the resonance frequency of Tl(III) is normally higher than that of Tl(I). The chemical shift range of thallium is extremely large, covering approximately 7000 ppm for Tl(III) species and over 3400 ppm for Tl(I) species. The origin of this large chemical shift range lies within the paramagnetic term of the nuclear screening constant. The total diamagnetic shielding of the thallium atom is quite appreciable, being about 10 000 ppm. However, in chemical bonding the core electrons are relatively unperturbed, the valence electrons being most affected. Therefore, the important quantity in determining the chemical shift is not the total shielding but the shielding per valence electron. For thallium, the diamagnetic contribution per valence electron is of the order of 10–250 ppm. This is relatively small compared with the observed chemical shift range of approximately 7000 ppm. This means that the paramagnetic term must be responsible for about 90% of the variation observed in the thallium chemical shift. A value of 5550 ppm for the paramagnetic term has been obtained for the linear dimethylthallium cation.[6]

Whereas the ^{59}Co nucleus, with a chemical shift range of 18 000 ppm, appears to be more sensitive to electronic effects that ^{205}Tl, the greater chemical shift range of ^{205}Tl in compounds in which Co and Tl are in similar environments suggests that ^{205}Tl has the greatest NMR 'shiftability' of all the elements. The magnitude of this chemical shift range can be appreciated from a consideration of the solvent, phase change, substituent change, and temperature effects on the ^{205}Tl chemical shift. The chemical shift of the ^{205}Tl(I) ion increases by about 2000 ppm as the solvent is changed from water to liquid ammonia. The chemical shift of Me_2TlNO_3 increases by 240 ppm as the solvent is changed from hexamethylphosphoramide to *n*-butylamine. The effect of environmental alteration, by phase change, on the chemical shift can also be equally dramatic. For example, the chemical shift of TlCl increases by 925 ppm in progressing from the melt to the solid phase. Substituent changes produce large chemical shifts: (1) the difference in chemical shift between $TlCl_{solid}$ and TlI_{solid} is 920 ppm; (2) the difference in chemical shift between Me_3Tl and Et_3Tl is 130 ppm and; (3) the chemical shifts of $C_6H_5Tl(TFA)_2$, 4-Bu^{t}C$_6$H$_4$Tl(TFA)$_2$, 4-Pr^{i}C$_6$H$_4$Tl(TFA)$_2$ and 4-Pr^{n}C$_6$H$_4$Tl(TFA)$_2$ (where TFA = trifluoroacetic acid) are +2790 ppm, +2818 ppm, +2823, and +2816 ppm, respectively. The chemical shift can also be very temperature dependent, as illustrated by the fact that, in liquid methylamine solutions, the resonance frequency of the Tl(I) ion changes at 5 ppm K^{-1}. The temperature dependence of the ^{205}Tl resonance frequency of the dimethylthallium cation in aqueous solution has been shown to be an accurate, convenient thermometer for determining the temperature of samples within the magnetic field of an NMR spectrometer.[7] These examples serve to illustrate the fact that the ^{205}Tl chemical shift is an exquisitely sensitive probe for subtle changes in environment. This feature of the NMR properties of ^{205}Tl makes it quite useful for investigating such phenomena as ion-pairing, solvent–solute interaction, phase changes, long-range substituent effects, and binding constants.

The chemical shift anisotropy has been measured for the ^{205}Tl nucleus in a number of chemical environments. The

values extend from 55 ppm for 7.5% $TlNO_3$ in KNO_3 to 5550 ppm for Me_2TlBr. Again, the magnitude of this range of this chemical shift property epitomizes the sensitivity of the ^{205}Tl nucleus to the chemical environment in which it is placed.

Just as the ^{205}Tl nucleus exhibits a large chemical shift range, the range in magnitude of the spin–spin coupling constants involving this nucleus is also very large. For example, $^1J(^{205}Tl,^{31}P) = 3203$ Hz, $^1J(^{205}Tl,^{13}C) > 10\,000$ Hz, and $^1J(^{205}Tl,^1H) = 6144$ Hz. Long-range coupling constants $^{5or6}J(^{205}Tl,^1H)$ can be about 100 Hz. Substituent effects are very pronounced. For example, $^2J(^{205}Tl,^1H)$ changes by 70 Hz if the methyl groups in Me_3Tl are replaced by ethyl groups and the $^1J(^{205}Tl,^{13}C)$ coupling constant changes from 10 718 Hz in $C_6H_5Tl(OAc)_2$ to 8841 Hz in 2,4,6-$Me_3PhTl(OAc)_2$. The effect of change in isotope from ^{205}Tl to ^{203}Tl can also be observed. The ^{203}Tl coupling constants are less than those of ^{205}Tl [$^3J(^{205}Tl,^1H) = 387$ Hz and $^3J(^{203}Tl,^1H) = 384$ Hz in the compound, $TlN(CH_2CO_2^-)_3$], as dictated by the difference in magnetogyric ratio. Thallium coupling constants can also be solvent- and temperature-dependent. The value of $^2J(^{205}Tl,^1H)$ for Me_3Tl in acetone is -268.8 Hz and -250.8 Hz when CH_2Cl_2 is the solvent. The value of $^2J(^{205}Tl,^1H)$ for Me_3Tl dissolved in CH_2Cl_2 at $-30\,^\circ C$, $-50\,^\circ C$, and $-70\,^\circ C$ is -232.8 Hz, -243 Hz, and -250.8 Hz, respectively. Because of the highly ionic nature of Tl(I) complexes, few coupling constants have been observed for this oxidation state. An example of spin–spin coupling with Tl(I) is found in the Tl(I)–valinomycin complex where $^2J(^{205}Tl,^{13}C) = 96$ and 101 Hz.[8] The large coupling constants associated with thallium NMR spectroscopy can, in some instances, present experimental problems because of insufficiently large spectral window, aliased peaks, and computer-limited resolution. In the observation of nuclei to which thallium is coupled, it must be remembered that there are two isotopes and that decoupling of one might still leave a relatively complex spectrum.

Several linewidth and relaxation studies have been conducted on ^{205}Tl and ^{203}Tl in the solid state. Because ^{205}Tl and ^{203}Tl nuclides have large magnetogyric ratios, direct dipole–dipole interaction is expected to contribute significantly to the NMR linewidths of these nuclides. The solid state spectra of thallium frequently exhibit line broadening as the result of indirect spin–spin coupling. This spin–spin interaction is independent of the magnetic field but depends on the transmission of nuclear spin information directly through intervening electrons. Although the indirect coupling may be negligible for light nuclides, the large hyperfine interaction is an important source of line broadening in many cases for thallium. The ^{205}Tl and ^{203}Tl linewidths of thallium metal and Tl_2O as a function of the percentage of abundance of ^{205}Tl have been investigated.[9] It was found that the ^{205}Tl line was relatively narrow in highly enriched ^{205}Tl samples, whereas the ^{203}Tl line was broad. The opposite effect was observed with samples enriched with ^{203}Tl. It was concluded that spin exchange between unlike nuclei (^{205}Tl and ^{203}Tl) contributes to the second moment or the linewidth, while spin exchange between like nuclei (^{205}Tl and ^{205}Tl or ^{203}Tl and ^{203}Tl) does not affect the second moment. One, therefore, has a very good method for detecting the contribution to the second moment or line broadening from exchange interaction in samples containing thallium at the natural abundance level. Because ^{203}Tl, whose natural abundance is 29.5%, is surrounded primarily by the unlike ^{205}Tl nucleus in the solid, exchange interactions, if present, broaden this line more than the line of ^{205}Tl which is surrounded primarily by other ^{205}Tl nuclei. The favorable natural abundance and magnetogyric ratio of ^{205}Tl make this a simple and effective method for detecting the presence of exchange broadening.

Line broadening resulting primarily from exchange interactions frequently prevents one from observing the chemical shift anisotropy (CSA) in the powder spectrum of thallium compounds. One method of eliminating this line-broadening mechanism is by dilution of the spin of interest in a magnetically inert matrix. An example of this technique can be illustrated with solid $TlNO_3$. Since the main source of line broadening in pure $TlNO_3$ arises from spin exchange between Tl(I) ions, the dilution of $TlNO_3$ in a matrix of KNO_3 should produce significant line narrowing of the thallium resonance line due to the presence of the small magnetic moments of the potassium nuclides.

In solution, the spin–lattice relaxation time of the Tl(I) ion has been found to be very sensitive to environmental effects. In an aqueous solution the spin–lattice relaxation time for the Tl(I) ion changes from 1.8 s in the absence of dissolved oxygen to 0.024 s in the presence of 101.3 kPa (1 atm) of oxygen.[10] This dependence of relaxation time upon oxygen can be advantageous because it permits faster pulsing and, therefore, more rapid spectral accumulation. The spin–lattice relaxation time of the Tl(I) ion is also solvent-dependent.[11] In aqueous solution, the Tl(I) spin–lattice relaxation time is dominated by the spin–rotation mechanism.[10,12] The $^{205}Tl(I)$ and $^{203}Tl(I)$ relaxation times are equal and are independent of solvent isotopic substitution (H_2O, D_2O), concentration (0.03–2.0 M), anion, and resonance frequency.[10,12] However, in nonaqueous solution the spin–lattice relaxation time of Tl(I) can be very dependent upon the CSA mechanism.[13] In the case of Tl(I)–antibiotic complexes, the spin–lattice relaxation time is determined by contributions from spin–rotation, dipolar, and CSA mechanisms.[14–16]

An excellent study of the relaxation of the $(CH_3)_2Tl^+$ cation as a function of temperature and magnetic field strength has been published.[17] Although the relaxation is dominated by the CSA mechanism, a contribution from the spin–rotation mechanism was also found to be present. Activation energies for the reorientational correlation time and the angular momentum correlation time were determined to be 19.7 kJ mol^{-1} and 17.7 kJ mol^{-1}, respectively. At 298 K, the reorientational correlation time was found to be 39.1 ps and a value of 5.05×10^{-15} s was obtained for the angular momentum correlation time. The ^{205}Tl spin–lattice relaxation time of the $(CH_3)_2Tl^+$ cation in an aqueous glycerol solution has been studied as a function of temperature and magnetic field strength. In this solution medium, the CSA relaxation mechanism was the only effective relaxation mechanism.[18] Theoretical investigations of the importance of the CSA and spin–rotation mechanisms[19] and other mechanisms[20] for thallium relaxation have been made. The spin–lattice relaxation time of the $(CH_3)_2Tl^+$ cation is sensitive to the presence of oxygen in solution, however, this dependence is not as great as that found for the Tl(I) cation.[10]

3 CHEMICAL APPLICATIONS

One of the most fundamental types of solution systems to be investigated involves the interaction between a thallium ion, Tl(I) or Tl(III), and a single type of solvent molecule. In practice, this type of investigation can be very difficult due to the proclivity of the thallium ion to form ion-pairs or higher order aggregates. To eliminate this problem, one must obtain the infinite dilution chemical shift of the ion from an extrapolation to infinite dilution of the curve representing the relationship between the chemical shift and ion concentration. The extreme sensitivity of the thallium chemical shift to the chemical and physical environment means that one must exercise the utmost care in temperature control of the NMR probe, the solvent purity, and the determination of the ionic concentration. For a given solvent, it is advisable to use several thallium salts whose anions are different to approach the infinite dilution point from more than one position on the chemical shift–concentration curve. A computer analysis of the curves can then be used to determine the infinite dilution chemical shift for a solvent.

The ion-pair formation constant (K_{ip}) for a process such as ($Tl^+ + X^- \rightleftharpoons Tl^+X^-$) can be determined from the thallium chemical shift–salt concentration relationship. The value of K_{ip} has been determined for a number of solvents[21] and found to increase with decreasing dielectric constant of the solvent. A correlation between the infinite dilution chemical shift of the Tl(I) ion and the Gutman donor number, a measure of the basicity of the solvent, has been made for a number of solvents.[22] This relationship suggests that the more basic the solvent, the higher the resonance frequency of the Tl(I) ion. The increase in resonance frequency with increasing solvent basicity may be interpreted as a measure of the strength of the interaction between the ion and the solvent molecules, with the solvent acting as a Lewis base and interacting both covalently and electrostatically with ions. Transient orbital mixing created by ion–solvent collision-induced polarization of the ion electron cloud may also contribute to the observed change in resonance frequency.

The thermodynamic parameters for the ion-pairing process, ΔH and ΔS, can also be determined by obtaining K_{ip} as a function of temperature.[23] The anion and concentration dependence of the Tl(I) chemical shift in aqueous solution and in nonaqueous solvents[4,24–37] has been extensively investigated, and chemical shift changes of 10–100 ppm observed. The exceptional dependence of the Tl(I) chemical shift on solvent makes thallium NMR spectroscopy a very good probe for the study of preferential solvation in mixed solvent systems. The chemical shift of 5 mM $TlNO_3$ in nine binary solvent systems has been analyzed using a nonstatistical distribution of solvate species to describe preferential solvation.[38–42] Thallium chemical shift, spin–spin coupling and spin–lattice relaxation time studies of Tl(I) complexes with crown ethers[14–16,28,43–48] and cryptands[46–48] have been used to obtain information concerning ion–ligand binding and solution structure of these complexes.

Although the Tl(III) ion tends to hydrolyze in aqueous solution, a number of ^{205}Tl(III) NMR investigations, many involving ligand exchange kinetics, have been conducted.[4,25,49–53] A combination of solution and solid state ^{205}Tl NMR experiments have been used to study the formation and geometry of $(TlX_n)^{3-n}$ complexes, where X = Cl, Br.[50] Stability constants and the chemical shifts of the individual species were also determined. This study emphasizes the importance of using solid state NMR data to understand solution results better. The chemical shift range for pH, concentration, and anion effects is about 2000 ppm. Although no specific spin–lattice relaxation time measurements have been made with the Tl(III) ion, a number of linewidths have been reported for nondegassed solution and they range from 10 to 5000 Hz.[49,50] The measurement of ^{205}Tl(III) NMR linewidths were used to study the kinetics of ligand exchange in the $TlCl_3$–$HClO_4$ (3 M) system.[52] Rate constants were obtained and the activation energy parameters for the dissociatively activated and associatively activated interchange processes determined.

The concentration, anion, temperature, and solvent dependences of the NMR parameters of the monomethyl and dimethylthallium(III) cations have been investigated. In general, the temperature dependence of the chemical shift is greater than that resulting from changes in anion or concentration for the compounds, $(CH_3)_2TlX$ (X = NO_3, BF_4, O_2CCH_3). For a number of the $(CH_3)_2Tl$(III) derivatives, a linear correlation was observed between the ^{205}Tl chemical shift and the Drago solvent base parameters.[54] Solvent isotope effects on the chemical shift of the $(CH_3)_2Tl$(III) cation in H_2O and D_2O have been found to be concentration-dependent.[10] Thallium chemical shifts have been obtained for phenylthallium(III) dichloride and its complexes with PPh_3 and dipyridine in methanol and pyridine,[25] diphenylthallium(III) chloride in liquid ammonia,[55] diphenylthallium(III) bromide in dimethyl sulfoxide,[25] a series of substituted arylthallium(III) bis(trifluoroacetates) in a number of solvents,[56] and triphenylthallium(III) in diethyl ether.[25] In general, the diaryls resonate at approximately 200 ppm to high frequency (low field) of the monoaryls and approximately 600 ppm to low frequency of the triaryls.

A proton NMR investigation of the Tl(III) complex with the nitrilotriacetate ion revealed a difference in ^{205}Tl and ^{203}Tl spin–spin coupling constants with the methylene protons, ^{205}Tl–^{1}H = 387 Hz and ^{203}Tl–^{1}H = 384 Hz.

In 1953, 7 years after the papers of Bloch et al.[1] and Purcell et al.,[2] the first solid state thallium NMR paper was published.[3] The types of compounds studied by solid state thallium NMR spectroscopy range from simple inorganic salts, to thallium antibiotic complexes, thallium species contained within zeolites, and high-temperature superconductors.

The dominant factors that determine the chemical shift of the thallium nucleus are oxidation state and electronic interactions with the environment. In solids, the presence of greater covalency might be expected to result in large shifts to high frequency of solvated, ionic thallium species. This has been observed in a number of cases: however, this is in no way an inviolable rule since the thallium resonance in a crystalline salt may be shifted to low frequency of that in solution by several hundred ppm. The relative shifts are determined by the strength of the electronic interactions in the solid compared with those in solution, which may be substantial. Within a series of solids, the highly ionic systems exhibit low-frequency shifts while more covalent systems have resonances at higher frequencies.

Several factors determine thallium linewidths and second moments in polycrystalline solids. The most important factors are the CSA, direct through-space–dipolar interactions, indirect spin–spin interactions, coupling to quadrupolar nuclei,

and motional averaging. In some cases, the CSA will be significantly larger than the total line broadening from all other sources. In such cases, NMR spectra of powders or glasses are characteristic of powder patterns from which the value of the CSA and the values of the principal elements of the shielding tensor can be determined. If the line broadening from chemical shift anisotropy is smaller than that resulting from other factors, then broad, symmetrical NMR lines are observed. The magnitude of the CSA can still be determined in this case from the slope of a plot of the second moment as a function of the square of the applied magnetic field strength.

Direct dipole–dipole interaction might be expected to contribute significantly to thallium NMR linewidths since the magnetogyric ratios of ^{205}Tl and ^{203}Tl are large. If the structure of the sample is known, the contribution of the direct dipole–dipole interaction to the second moment can be determined using the method of Van Vleck.[57] For those cases in which structural details are unknown, the absence of an orientation-dependence of the linewidth of a single crystal suggests the absence of dipolar broadening. Dipolar broadening is independent of the magnetic field strength.

Line broadening, as the result of indirect spin–spin coupling, has been found to make a significant contribution to the total linewidth of thallium NMR lines. This type of interaction is independent of the magnetic field strength but depends upon the transmission of nuclear spin information indirectly through intervening electrons. The electrons couple with the nuclear spins via dipolar or hyperfine interactions, and correlation between the electrons then results in the indirect nuclear interactions. Two types of indirect interactions are possible. When only s electrons transmit nuclear spin information, the interaction is of the scalar exchange type. When s and p electrons are involved, the interaction becomes a tensor quantity and is of the pseudodipolar type. If both electrons are in p orbitals, both exchange and pseudodipolar interactions exist. In the single crystal rotation experiment, it is not possible to separate directly the orientation dependence of the second moment into dipolar and pseudodipolar contributions. However, since the total orientation dependence represents the sum of these, calculation of the dipolar second moment using the Van Vleck[57] approach allows the pseudodipolar contribution to be estimated. Scalar-exchange broadening is, of course, independent of orientation.

The effect of quadrupole coupling on the linewidth of spin-$\frac{1}{2}$ nuclei in the solid state has been investigated.[58] It has been shown that quadrupole broadening may add a factor of up to 1.84 times the dipolar contribution to the second moment. Quadrupolar interaction will have the same effect on both ^{205}Tl and ^{203}Tl.

Motional narrowing can occur in both the melt and the solid state. Chemical shift anisotropy is averaged by fast rotational reorientation, as are dipolar and pseudodipolar interactions. Exchange-broadened lines may also be narrowed at the onset of molecular motion. In this case, the narrowing results from the modulation of the distance between interacting nuclei rather than from angular motion. The abrupt narrowing of thallium NMR lines is usually taken as evidence of a phase transition in a solid.

The NMR properties of metals are determined predominantly by the interactions of nuclei with conduction electrons. The NMR shift of thallium in a metallic sample arises from the coupling with the magnetic moments which derive from the spins of the conduction electrons themselves. This type of NMR shift found in metals is known as the Knight shift.[59] The Knight shift for thallium in a variety of metallic systems has been measured. The Knight shift can exhibit an anisotropy just as the chemical shift can.[60–62] Spin–lattice relaxation in metals and alloys is usually the result of mutual spin flips between nuclear magnetic dipole moments and the magnetic moments of conduction electrons at the Fermi level. When these electrons are highly localized, the relaxation time is related to the Knight shift by the Korringa equation.[63] For the case where conduction electrons localize on a particular thallium site, the relaxation rate will increase proportionally above that predicted by the Korringa equation. Comparison of the experimentally determined relaxation time with that predicted by the Korringa equation provides a useful method of obtaining information about internal electronic structure in the metal or alloy.

A number of NMR investigations of the Knight shift and relaxation of thallium metal in the solid state and melt have been performed.[3,9,61,64–70] NMR studies of thallium in a number of alloys and intermetallic compounds such as $LiCd_{1-x}Tl_x$, $CaCd_{1-x}Tl_x (0 \leq x \leq 1)$, La_3TlC, $La_3Tl_{0.5}In_{0.5}$, $La_3Tl_{0.8}Pb_{0.2}$, $Tl_{1-x}Te_x$, TlSe, Tl_2Se_3, $TlAsSe_2$, $PSe_{2.5}Tl$, PSe_4Tl, $As_2Se_3–Tl_2Se_3$, $(Tl_2Se)_x–(As_2Se_3)_{1-x}$, $In_{0.5}Tl_{0.5}$, $Tl_{0.3}WO_3$, $TlGaSe_2$, $TlNb_2O_5F$, $Tl_xNbO_{2+x}F_{1-x}$, $Tl_{3.5}TaO_{2.5}F_{0.5}$, $TlPbI_3$, NaTl, and Na_2Tl, have been reported.[71–105] A number of thallium NMR studies of the thallium barium calcium copper oxide superconductor have been made[106–120] as well as that of the superconductor type, La_3Tl.[72] The investigations with the superconductors involved the determination of the shift, spin–lattice relaxation time, lineshape, and vortex lattice formation.

The favorable NMR properties of thallium have permitted a number of investigations of thallium ions adsorbed on surfaces and contained in zeolites.[121–127] The structures of thallium silicate, germanate, borate, and phosphate glasses of varying thallium content have been investigated using thallium chemical shifts and linewidths.[128–136] The thallium CSA in $TlPO_3$ glass has been determined to be 560 ppm although the isotropic chemical shift is −50 ppm to low frequency Thallium sites in $TlPO_3$ glasses are moderately ionic but not as ionic as that found in the polycrystalline form.

Thallium NMR spectroscopy has be used to study a number of paramagnetic compounds such as $TlCoF_3$, $TlMnF_3$, $TlMnCl_3$, $TlNiCl_3$, $Tl_3Fe(CN)_6$, $TlFe(SO_4)_2$, and $Tl_3Co(CN)_6$.[24,137–139] Unpaired electron spin density on thallium in these compounds produce very large shifts to high frequency, as much as +14 000 ppm for $Tl_3Fe(CN)_6$. As might be expected, thallium linewidths are very large in these compounds, ranging from 2.5 to 74 kHz.

Solid state and melt thallium NMR studies of many of the common Tl(I) salts have been performed. A number of Tl(III) compounds and a few organothallium compounds have been investigated. In general, the effect of changes in temperature on the thallium chemical shift in solids and melts is often very pronounced. For example, the ^{205}Tl chemical shift in solid Tl(I) acetate varies by 5 ppm $^{\circ}C^{-1}$. It must be mentioned that for the large number of compounds studied, none exhibits a shift that has a negative temperature dependence. The positive dependence of the chemical shift upon temperature arises from the enhanced vibrational overlap of the thallium anion wavefunctions, resulting in additional paramagnetic shielding with increasing temperature. Because

of the extreme sensitivity of the thallium chemical shift to changes in chemical environment, a change in the chemical shift would be expected to occur at the temperature of a phase transition. In fact, a change in chemical shift of several hundred ppm can occur at the phase transition. If sufficient data are available, the shift discontinuity and temperature dependence of the chemical shift can be used to calculate the distance of closest approach of ions in melts.[140,141] The magnitude of the chemical shift discontinuity may be used as a measure of the overall difference in the two phases, where large discontinuities are associated with the greatest dissimilarities. For this reason it appears that the thallium environments in melts of Tl(III) salts may be more like those in the solids. It seems likely that strong cation–anion interactions in these salts persist upon fusion and that the basic units in the melt may be relatively covalent. Thallium(I) carboxylates also exhibit little discontinuity at the melting point.[140,142] The absence of linewidth discontinuity at the melting point also suggests great similarities between the structures of the solid and the melt in these compounds (i.e., the carboxylate anions bind tightly to the thallium cations in both the solid and the melt).

There are cases where thallium linewidths are very sensitive to phase changes. An excellent example of this is observed with $TlNO_3$. The ^{205}Tl linewidth in this compound is essentially independent of temperature for a given phase, α, β, or γ. However, a sudden narrowing of the resonance line occurs at the transition from orthorhombic γ to hexagonal β and again at the transition from β to cubic α.[136,143,144] The β to α transition is accompanied by a 100-fold increase in electrical conductivity and marks the onset of Tl(I) diffusion in the solid.[143] Further support for this was obtained from thallium relaxation time studies.[145,146] Ions, by their very nature, exhibit only weak electronic interactions with their surroundings. Therefore, the degree of ionic character limits the magnitude of the CSA that can be observed for an ion. Comparatively small CSAs are anticipated for highly ionic systems, while the potential exists for much greater anisotropies if stronger ionic interactions are present. There is little doubt as to the highly ionic nature of ^{205}Tl in pure $TlNO_3$ since its resonance line lies some 135 ppm to low frequency of that of aqueous $^{205}Tl^+$. The covalency of this salt has been estimated to be only 0.6%.[15] The chemical shift of -300 ppm indicates even greater ionic character for Tl(I) isolated in the KNO_3. Yet, at high temperatures even this very ionic Tl(I) ion exhibits a rather remarkable CSA of 91 ppm. The isotropic chemical shift of ^{205}Tl in $TlClO_4$ is quite far to low frequency, suggesting that this is a very ionic salt. Nevertheless, polycrystalline $TlClO_4$ was found to present a classic powder pattern characteristic of axial symmetry with a CSA of 117 ppm.[147] Dilution of $TlClO_4$ in a $KClO_4$ matrix causes the anisotropy to increase to 149 ppm. That a salt with such high ionic character can still exhibit a CSA of that magnitude testifies to the extreme sensitivity of the thallium chemical shift to small electronic effects.

A number of thallium NMR studies have been made of the Tl(I) halides. In addition to the determination of the chemical shift of ^{205}Tl in TlF, it has been shown that the ^{205}Tl linewidth is due mainly to direct dipolar interactions between ^{205}Tl and ^{19}F.[26,140,148–150] Thallium NMR studies of TlCl suggest that the thallium linewidth results mainly from scalar interactions between thallium nuclei. For TlBr the thallium NMR linewidth is significantly larger than that observed for TlCl. Indirect spin exchange has been shown to be a very important source of line broadening for TlBr.[148,149,151] Thallium(I) iodide exhibits a phase transition from orthorhombic to cubic form at about 160 °C. Thallium NMR spectra of the two forms are significantly different. The ^{205}Tl resonance lines in both modifications are shifted well to high frequency of aqueous Tl(I), with the cubic form to higher frequency.[152] The thallium linewidths of orthorhombic and cubic TlI are quite different. It has been suggested that Tl–Tl exchange interactions are important in cubic TlI but not in the orthorhombic form.[152,153] Indirect Tl–I spin exchange has been suggested as a major source of line broadening in both forms of solid TlI, in addition to quadrupole broadening and CSA.[152] Thallium-205 chemical shifts have been obtained for molten Tl_2Cl_4[37,154] and Tl_2Br_2.[37] In both cases, two signals were observed which were attributed to equal amounts of TlX and TlX_3. For the compound, Tl_2Cl_3, two signals of relative intensity 3:1 were observed which were attributed to the presence of $Tl_3(TlCl_6)$.[26] Thallium-205 NMR studies of mixed-salt halides in the solid and melt state have been performed to explore the effect of covalency on the thallium chemical shift.[37,155,156]

The effect of phase change on the NMR parameters of thallium in the carbonate,[14,188] formate,[26,157,158] acetate,[158,159] cyanide,[160] and thiocyanate[161] salts has been extensively studied.

A number of Tl(III) salts have been studied in the melt and solid state using ^{205}Tl NMR spectroscopy. The chemical shift of $Tl(ClO_4)_3$ has been determined as a function of temperature in the melt and the solid state.[140] This salt exhibits the only known negative change in chemical shift upon fusion, implying a decrease in covalency in the melt. Chemical shift and linewidth measurements have been made on $Tl(ClO_4)_3{\cdot}6H_2O$,[140] $TlCl_3$,[140,162] and $TlCl_3{\cdot}4H_2O$[50] salts. Solids containing the TlX_4^- and TlX_5^{2-} moiety, such as $Zn(TlCl_4)_2$, $KTlCl_4$, $KTlBr_4{\cdot}2H_2O$, $Na_2TlCl_5{\cdot}4H_2O$, $Cs_2TlCl_5{\cdot}H_2O$, and $[NBu_4]TlI_4$ have been studied.[50] The $[NBu_4]TlI_4$ salt exhibits a remarkable chemical shift of -1560 ppm, which is about 1000 ppm to low frequency of the nearest Tl(I) salt. Compounds containing the TlX_6^{3-} and $Tl_2X_9^{3-}$ anions have also been studied, where X is a halogen atom.[50]

4 BIOCHEMICAL APPLICATIONS

Alkali cations participate in a variety of biological processes. These include transmission of nerve impulses, initiation and maintenance of muscular activity, synthesis of proteins, regulation of metabolism, and activation and regulation of enzymes. Most knowledge concerning the biological chemistry of sodium and potassium has come from standard biochemical assays, electrochemical experiments, and the use of radioactive tracers. With the very high magnetic field NMR spectrometers currently available, NMR spectroscopy of the alkali cations in biological systems is quite feasible. However, there are cases for which the direct observation of some of these cations is not sufficient to solve the biochemical problem of interest because of the presence of very low concentrations or because the process of interest does not produce an adequate response in the observed NMR property. A number of probe ions with more favorable spectroscopic properties can be successfully substituted for investigative purposes.[163]

A number of investigations indicate that thallium is a good surrogate for potassium and, to a lesser extent, sodium in biochemical systems.[163] The relative receptivities to the NMR experiment for ^{39}K(I) and ^{205}Tl are 0.000473 and 0.1355, respectively. The sensitivity of the chemical shift to environmental changes of thallium is much greater than that of potassium or sodium. These facts suggest that ^{205}Tl(I) is a good spectroscopic replacement probe for potassium and sodium in biochemical systems.

The structure of the binding site for the monovalent cation activator of *S*-adenosylmethionine synthetase from *Escherichia coli* has been characterized by ^{205}Tl(I) NMR spectroscopy.[164] Thallium-205 NMR spectroscopy has been used to determine that the monovalent cation binding site in (Na/K)-ATPase is very near the divalent cation binding site.[165,166] The effect of the presence of pyruvate kinase and its substrates on the chemical shift and relaxation of ^{205}Tl(I) has been investigated[167,168] as well as the interaction of Tl(I) with dipalmitoylphosphatidylcholine.[169] The interaction between the Tl(I) ion and antibiotic molecules, such as gramicidin, which acts as ion-transporting agents in membranes, has been studied with ^{205}Tl NMR spectroscopy.[170–175] The equilibrium binding constants of the group I and II cations with gramicidin A incorporated into model membranes have been determined with a combination of ^{205}Tl NMR spectroscopy and competition binding.[176–178] Thallium(III)-205 NMR spectroscopy has also been used to study the two binding sites for Fe(III) in transferrin.[179,180]

5 REFERENCES

1. F. Bloch, W. W. Hansen, and M. Packard, *Phys. Rev.*, 1946, **69**, 127.
2. E. M. Purcell, H. C. Torrey, and R. V. Pound, *Phys. Rev.*, 1946, **69**, 37.
3. N. Bloembergen and T. J. Rowland, *Acta Metall.*, 1953, **1**, 731.
4. H. S. Gutowsky and B. R. McGarvey, *Phys. Rev.*, 1953, **91**, 81.
5. J. F. Hinton, K. R. Metz, and R. W. Briggs, *Prog. Nucl. Magn. Reson. Spectrosc.*, 1988, **20**(5), 423.
6. M. J. Forster, Ph.D. thesis, University of London, 1984.
7. M. J. Forster, D. G. Gillies, and R. W. Matthews, *J. Magn. Reson.*, 1985, **65**, 497.
8. V. F. Bystrov, Yu. D. Gavilov, V. T. Ivanov, and A. Yu, *Eur. J. Biochem*, 1977, **78**, 63.
9. N. Bloembergen and T. J. Rowland, *Phys. Rev.*, 1955, **97**, 1679.
10. S. O. Chan and L. W. Reeves, *J. Am. Chem. Soc.*, 1974, **96**, 404.
11. J. F. Hinton and R. W. Briggs, *J. Magn. Reson.*, 1977, **25**, 379.
12. M. Bacon and L. W. Reeves, *J. Am. Chem. Soc.*, 1973, **95**, 272.
13. J. F. Hinton and K. H. Ladner, *J. Magn. Reson.*, 1978, **32**, 303.
14. R. W. Briggs and J. F. Hinton, *J. Magn. Reson.*, 1978, **32**, 155.
15. R. W. Briggs and J. F. Hinton, *J. Magn. Reson.*, 1979, **33**, 363.
16. R. W. Briggs, F. A. Etzkorn, and J. F. Hinton, *J. Magn. Reson.*, 1980, **37**, 523.
17. M. J. Forster, D. G. Gillies, and R. W. Matthews, *Mol. Phys.*, 1987, **60**, 129.
18. M. J. Forster and D. G. Gillies, *Mol. Phys.*, 1987, **62**, 439.
19. R. N. Schwartz, *J. Magn. Reson.*, 1981, **24**, 205.
20. B. W. Bangerter and R. N. Schwartz, *J. Chem. Phys.*, 1974, **60**, 33.
21. R. W. Briggs, K. R. Metz, and J. F. Hinton, *J. Solution Chem.*, 1979, **8**, 479.
22. R. W. Briggs and J. F. Hinton, *J. Solution Chem.*, 1977, **6**, 827.
23. K. R. Metz, J. F. Hinton, and T. L. Goforth, *J. Phys. Chem.*, 1985, **89**, 2097.
24. D. Herbison-Evans, P. B. P. Phillips, and R. J. P. Williams, *J. Chem. Soc.*, 1965, 6170.
25. H. Koppel, J. Dallorso, G. Hoffman, and B. Walther, *Z. Anorg. Allg. Chem.*, 1976, **427**, 24.
26. R. Freeman, R. P. H. Gasser, and R. E. Richards, *Mol. Phys.*, 1959, **2**, 301.
27. J. J. Dechter and J. I. Zink, *Inorg. Chem.*, 1976, **15**, 1690.
28. J. J. Dechter and J. I. Zink, *J. Am. Chem. Soc.*, 1975, **97**, 2937.
29. J. J. Dechter and J. I. Zink, *J. Chem. Soc., Chem. Commun.*, 1974, 96.
30. J. F. Hinton and R. W. Briggs, *J. Magn. Reson.*, 1975, **19**, 393.
31. J. J. Dechter and J. I. Zink, *J. Am. Chem. Soc.*, 1976, **98**, 845.
32. J. F. Hinton and R. W. Briggs, *J. Magn. Reson.*, 1977, **25**, 379.
33. J. F. Hinton and K. R. Metz, *J. Solution Chem.*, 1980, **9**, 197.
34. R. P. H. Gasser and R. E. Richards, *Mol. Phys.*, 1959, **2**, 357.
35. R. Freeman, R. P. H. Gasser, R. E. Richards, and D. H. Wheeler, *Mol. Phys.*, 1959, **2**, 75.
36. W. G. Proctor, *Phys. Rev.*, 1949, **75**, 522.
37. S. Hafner and N. H. Nachtrieb, *J. Chem. Phys.*, 1965, **42**, 631.
38. R. W. Briggs and J. F. Hinton, *J. Solution Chem.*, 1978, **7**, 1.
39. R. W. Briggs and J. F. Hinton, *J. Solution Chem.*, 1979, **8**, 519.
40. A. K. Covington, T. H. Lilley, K. E. Newman, and G. A. Porthouse, *J. Chem. Soc., Faraday Trans.*, 1973, **69**, 963.
41. A. K. Covington, I. R. Lantzke, and J. M. Thain, *J. Chem. Soc., Faraday Trans. 1*, 1974, **70**, 1869.
42. A. K. Covington and K. E. Newman, *Adv. Chem. Ser.*, 1976, **155**, 153.
43. M. Shamsipur, G. Rounaghi, and A. Popov, *J. Solution Chem.*, 1980, **9**, 701.
44. C. Srivanavit, J. I. Zink, and J. J. Dechter, *J. Am. Chem. Soc.*, 1977, **99**, 5876.
45. R. W. Briggs and J. F. Hinton, *Biochemistry*, 1978, **17**, 5576.
46. R. D. Boss and A. I. Popov, *Inorg. Chem.*, 1986, **25**, 1747.
47. H. G. Forster and J. D. Roberts, *J. Am. Chem. Soc.*, 1980, **102**, 6984.
48. J. M. Lehn, J. P. Sauvage, and B. Dietrich, *J. Am. Chem. Soc.*, 1970, **92**, 2916.
49. B. N. Figgis, *Trans. Faraday Soc.*, 1959, **55**, 1075.
50. J. Glaser and U. Henriksson, *J. Am. Chem. Soc.*, 1981, **103**, 6642.
51. T. Sidei, S. Yano, and S. Sasaki, *Oyo Butsuri*, 1958, **27**, 513.
52. I. Banyai and J. Glaser, *J. Am. Chem. Soc.*, 1989, **111**, 3186.
53. G. Batta, I. Banyai, and J. Glaser, *J. Am. Chem. Soc.*, 1993, **115**, 6782.
54. P. J. Burke, D. G. Gillies, and R. W. Matthews, *J. Chem. Res. (S)*, 1981, 124.
55. K. Hildenbrand and N. Dreeskamp, *Z. Phys. Chem. (Leipzig)*, 1970, **69**, 171.
56. J. F. Hinton and R. W. Briggs, *J. Magn. Reson.*, 1976, **22**, 447.
57. J. H. Van Vleck, *Phys. Rev.*, 1948, **74**, 1168.
58. D. L. Vanderhart, H. S. Gutowsky, and T. C. Farrar, *J. Am. Chem. Soc.*, 1967, **89**, 5056.
59. W. D. Knight, *Phys. Rev.*, 1949, **76**, 1259.
60. C. P. Slichter, *Principles of Magnetic Resonance*, 2nd edn., Springer, Berlin, 1980.

61. J. J. Schratter and D. L. Williams, *Phys. Lett. A*, 1967, **26**, 79.
62. J. Schratter, *Diss. Abstr. Int. B*, 1974, **34**, 6170.
63. J. Korringa, *Physica*, 1950, **16**, 601.
64. W. D. Knight, *Solid State Phys.*, 1956, **2**, 93.
65. D. J. Moulson and E. F. W. Seymour, *Adv. Phys.*, 1967, **16**, 449.
66. J. J. Schratter and D. L. Williams, *Can. J. Phys.*, 1974, **52**, 678.
67. G. Eska and E. Schuberth, *Jpn. J. Appl. Phys.*, 1987, Part 1, 26.
68. B. G. Turrell, G. Eska, N. Masuhara, and E. Schuberth, *J. Low Temp. Phys.*, 1988, **70**, 151.
69. G. Eska, *AIP Conf. Proc.*, 1989, **194**, 316.
70. N. Karnezos and L. B. Welsh, *Phys. Rev. B*, 1975, **12**, 4790.
71. W. Baden, P. C. Schmidt, and A. Weiss, *Phys. Status. Solidi A*, 1979, **51**, 183.
72. P. Descouts, B. Perrin, A. Dupanloup, and A. Treyvaud, *J. Phys. Chem. Solids*, 1978, **39**, 161.
73. P. Descouts, B. Perrin, and A. Dupanloup, *Proc. Colloq. AMPERE*, 1974, **2**, 335.
74. P. C. Schmidt and A. Weiss, *Z. Naturforsch., Teil A*, 1974, **29**, 477.
75. J. D. Marcoll, P. C. Schmidt, and A. Weiss, *Z. Naturforsch., Teil A*, 1974, **29**, 473.
76. P. C. Schmidt, *Ber. Bunsenges. Phys. Chem.*, 1975, **79**, 1064.
77. N. C. Halder, *Phys. Rev.*, 1969, **177**, 471.
78. W. W. Warren, *J. Non-Cryst. Solids*, 1972, **8**, 241.
79. J. Friedel, *J. Phys. Radium*, 1955, **16**, 444.
80. J. E. Enderby, R. L. Havill, and J. M. Titman, *Proc. Colloq. AMPERE*, 1966, **14**, 1072.
81. L. H. Bennett, R. M. Cotts, and R. J. Snodgrass, *Proc. Colloq. AMPERE*, 1964, **13**, 171.
82. J. Beene, O. Haeusser, A. B. McDonald, T. K. Alexander, A. J. Ferguson, and B. Herskind, *Hyperfine Interact.*, 1977, **3**, 397.
83. W. H. Jones, E. A. Garbaty, and R. G. Barnes, *J. Chem. Phys.*, 1962, **36**, 494.
84. M. S. Wittingham and L. D. Clark, *J. Chem. Phys.*, 1970, **53**, 4114.
85. A. M. Panich, S. P. Gabuda, N. T. Mamedov, and S. N. Aliev, *Fiz. Tverd. Tela (Leningrad)*, 1987, **29**, 3694.
86. N. T. Mamedov, E. S. Krupnikov, and A. M. Panich, *Fiz. Tverd. Tela (Leningrad)*, 1989, **31**, 290.
87. P. P. Man Thevenaeu, P. Papon, and J. L. Fourquet, *J. Chem. Phys.*, 1984, **80**, 1272.
88. S. Sharma and N. Weiden, *Z. Naturforsch., Teil A*, 1987, **42**, 1313.
89. H. E. Stone and W. P. Knight, *Acta Metall.*, 1963, **11**, 179.
90. R. E. Watson, L. H. Bennett, G. C. Carter, and I. D. Weisman, *Phys. Rev. B*, 1971, **3**, 222.
91. L. H. Bennett, *Acta Metall.*, 1966, **14**, 997.
92. G. C. Carter, L. H. Bennett, and D. J. Kahan, *Prog. Mater. Sci.*, 1977, **20**, 3.
93. G. C. Carter, L. H. Bennett, and D. J. Kahan, *Prog. Mater. Sci.*, 1977, **20**, 1742.
94. H. Klever and M. Schlaak, *Rev. Sci. Instrum.*, 1973, **44**, 25.
95. L. A. Baidakov and A. N. Kudryavtsev, *Izv. Akad. Nauk SSSR, Neorg. Mater.*, 1973, **9**, 1055.
96. G. E. Jellison and S. G. Bishop, *Phys. Rev. B*, 1979, **19**, 6418.
97. L. A. Baidakov and Z. U. Borisova, *Amorphous Liquid Semiconductors, Proceedings of the International Conference, 1973*, Vol. 2, p. 1035.
98. L. A. Baidakov, A. N. Kudryavtsev, and S. K. Novoselov, *Izv. Akad. Nauk SSSR, Neorg. Mater.*, 1973, **9**, 1640.
99. L. A. Baidakov and A. N. Kudryavtsev, *Vestn. Leningr. Univ., Fiz., Khim.*, 1973, 114.
100. S. Ueda and T. Shimizu, *Phys. Status Solidi B*, 1979, **95**, 279.
101. L. A. Baidakov, A. N. Katruzov, and Kh. M. El Labani, *Izv. Akad. Nauk SSSR, Neorg. Mater.*, 1978, **14**, 1810.
102. S. G. Bishop, P. C. Taylor and D. L. Mitchell, *J. Non-Cryst. Solids*, 1972, **8**, 106.
103. G. E. Jellison and S. G. Bishop, *Phys. Rev. Lett.*, 1978, **40**, 1204.
104. G. E. Jellison and S. G. Bishop, *Amorphous Liquid Semiconductors, Proceedings of the International Conference, 1977*, p. 607.
105. A. D. English, A. W. Sleight, J. L. Fourquet, and R. De Pape, *Mater. Res. Bull.*, 1980, **15**, 1727.
106. K. Tompa, I. Bakonyi, P. Banki, I. Furo, S. Pekker, J. Vandlik, G. Oszlanyi, and L. Mihaly, *Physica C (Amsterdam)*, 1988, **152**, 486.
107. A. K. Rajarajan, V. K. Gopalakrishnan, R. Vijayaraghavan, and L. C. Gupta, *Solid State Commun.*, 1989, **69**, 213.
108. M. Lee, Y. Q. Song, W. P. Halperin, L. M. Tonge, T. J. Marks, H. O. Marcy, and C. R. Kannewurf, *Phys. Rev. B, Condens. Matter*, 1989, **40**, 817.
109. M. Mehring, F. Hentsch, H. Mattausch, and A. Simon, *Z. Phys. B, Condens. Matter*, 1989, **77**, 355.
110. A. Poddar, P. Mandal, K. Ray, A. N. Das, B. Gosh, P. Choudhury, and S. K. Lahiri, *Physica C (Amsterdam)*, 1989, **159**, 226.
111. D. M. De Leeuw, W. A. Groen, J. C. Jol, H. B. Brom, and H. W. Zandbergen, *Physica C (Amsterdam)*, 1990, **166**, 349.
112. M. Mehring, F. Hentsch, H. Mattausch, and A. Simon, *Solid State Commun.*, 1990, **75**, 753.
113. V. E. Volkov, S. P. Gabuda, S. G. Kozlova, Yu. G. Kovalev, and N. K. Moroz, *Izv. Sib. Otd. Akad. Nauk SSSR, Ser. Khim. Nauk*, 1990, **2**, 15.
114. H. B. Brom, D. Reefman, J. C. Jol, D. M. De Leeuw, and W. A. Groen, *Phys. Rev. B, Condens. Matter*, 1990, **41**, 7261.
115. B. G. Turrell, G. Eska, N. Masuhara, and E. Schuberth, *J. Low Temp. Phys.*, 1988, **70**, 151.
116. Yu. Zhdanov, K. N. Mikhalev, B. A. Aleksashin, S. V. Verkhovskii, K. A. Okulova, V. I. Voronin, L. D. Shustov, A. Yu. Yakubovskii, and A. I. Akimov, *Sverkhprovodimost: Fiz. Khim. Tekkh.*, 1990, **3**, 194.
117. N. Winzek, Hj. Mattausch, S.-G. Eriksson, C. Stroem, R. Kremer, A. Simon, and M. Mehring, *Physica C (Amsterdam)*, 1993, **205**, 45.
118. S. Kambe, H. Yasuoka, A. Hayashi, and Y. Ueda, *Phys. Rev. B, Condens. Matter*, 1993, **47**, 2825.
119. N. Winzek and M. Mehring, *Appl. Magn. Reson.*, 1992, **3**, 535.
120. H. B. Brom, J. T. Moonen, and D. Reefman, *Appl. Magn. Reson.*, 1992, **3**, 597.
121. V. V. Morariu and A. Chifu, *Stud. Cercet. Fiz.*, 1979, **31**, 391.
122. T. Wada and A. P. Cohen-Addad, *Bull. Soc. Fr. Mineral. Cristallogr.*, 1969, **92**, 238.
123. H. Bittner and E. Hauser, *Monatsh. Chem.*, 1970, **101**, 1471.
124. D. Freude, A. Hauser, H. Penkaw, and H. Schmiedel, *Z. Phys. Chem. (Leipzig)*, 1972, **13**, 251.
125. D. Freude, V. Lohse, H. Pfeifer, W. Schirmer, H. Schmiedel, and H. Stach, *Z. Phys. Chem. (Leipzig)*, 1974, **255**, 443.
126. G. W. West, *Zeolites*, 1981, **1**, 150.
127. V. V. Morariu, *Chem. Phys. Lett.*, 1978, **56**, 272.
128. L. W. Panek, G. J. Exarhos, P. J. Bray, and W. M. Risen, *J. Non-Cryst. Solids*, 1977, **24**, 51.
129. L. W. Panek and P. J. Bray, *J. Chem. Phys.*, 1977, **66**, 3822.

130. L. W. Panek, *Diss. Abstr. Int. B*, 1978, **38**, 3019.
131. K. Otto and M. E. Milberg, *J. Am. Ceram. Soc.*, 1967, **50**, 513.
132. J. F. Baugher and P. J. Bray, *Phys. Chem. Glasses*, 1969, **10**, 77.
133. J. F. Baugher, *Diss. Abstr. Int. B*, 1970, **31**, 347.
134. R. K. Momii and N. H. Nachtrieb, *J. Phys. Chem.*, 1968, **72**, 3416.
135. N. H. Nachtrieb and R. K. Momii, *Reactivity of Solids*, *Proceedings of an International Symposium*, ed. J. W. Mitchell, Wiley-Interscience, New York, 1969, p. 675.
136. L. Kolditz and E. Wahner, *Z. Anorg. Allg. Chem.*, 1973, **400**, 161.
137. V. M. Buznik, E. A. Vopilov, and V. N. Voronov, *Fiz. Tverd. Tela (Leningrad)*, 1979, **21**, 1593.
138. M. P. Petrov and G. A. Smolenskii, *Fiz. Tverd. Tela (Leningrad)*, 1965, **7**, 2156.
139. D. A. Zhogolve, *Fiz. Tverd. Tela (Leningrad)*, 1966, **8**, 2798.
140. S. Hafner and N. H. Nachtrieb, *J. Chem. Phys.*, 1964, **40**, 2891.
141. N. H. Nachtrieb and S. Hafner, *Z. Naturforsch., Teil A*, 1965, **20**, 321.
142. J. F. Hinton and K. R. Metz, *J. Magn. Reson.*, 1983, **53**, 117.
143. P. C. Bury and A. C. McLaren, *Phys. Status Solidi*, 1969, **31**, K5.
144. K. R. Metz and J. F. Hinton, *J. Am. Chem. Soc.*, 1982, **104**, 6206.
145. M. Villa and A. Avogadro, *Phys. Status Solidi B*, 1976, **75**, 179.
146. A. Avogadro, M. Villa, and G. Chiodelli, *Gazz. Chim. Ital.*, 1976, **106**, 413.
147. K. R. Metz and J. F. Hinton, *J. Am. Chem. Soc.*, 1982, **104**, 6206.
148. Y. Saito, *J. Phys. Soc. Jpn.*, 1966, **21**, 1072.
149. Y. Saito, *J. Phys. Soc. Jpn.*, 1958, **13**, 72.
150. J. S. Blicharski, *Z. Naturforsch., Teil A*, 1972, **27**, 1355.
151. J. P. Mathur, *Diss. Abstr. Int. B*, 1972, **32**, 7219.
152. R. W. Vaughn and D. H. Anderson, *J. Chem. Phys.*, 1970, **52**, 5287.
153. S. K. Novoselov, L. A. Baidakov and L. P. Strakhov, *Fiz. Tverd. Tela (Leningrad)*, 1970, **12**, 1173.
154. T. J. Rowland and J. P. Bromberg, *J. Chem. Phys.*, 1958, **29**, 626.
155. Y. Nakamura, Y. Kitazawa, M. Shimoji, and S. Shimokawa, *J. Phys. Chem.*, 1983, **87**, 5117.
156. S. Hafner, *J. Phys. Chem. Solids*, 1966, **27**, 1881.
157. N. M. Sokolov, *Zh. Neorg. Khim.*, 1979, **24**, 3125.
158. J. F. Hinton and K. R. Metz, *J. Magn. Reson.*, 1983, **53**, 117.
159. M. Hanabusa and N. Bloembergen, *J. Phys. Chem. Solids*, 1966, **27**, 363.
160. T. Matsuo, M. Sugisaki, H. Suga, and S. Seki, *Bull. Chem. Soc. Jpn.*, 1969, **42**, 1271.
161. Y. Furukawa and D. Nakamura, *Z. Naturforsch., Teil A*, 1990, **45**, 1121.
162. W. G. Schneider and A. D. Buckingham, *Discuss. Faraday Soc.*, 1962, **34**, 147.
163. R. J. P. Williams, *Q. Rev., Chem. Soc.*, 1970, **24**, 331.
164. G. D. Markham, *J. Biol. Chem.*, 1986, **261**, 1507.
165. C. M. Grisham, R. K. Gupta, R. E. Barnett, and A. S. Mildvan, *J. Biol. Chem.*, 1974, **249**, 6738.
166. C. M. Grisham and A. S. Mildvan, *Fed. Proc., Fed. Am. Soc. Exp. Biol.*, 1974, **23**, 1331.
167. J. Reuben and F. J. Kayne, *J. Biol. Chem.*, 1971, **246**, 6227.
168. F. J. Kayne and J. Reuben, *J. Am. Chem. Soc.*, 1970, **92**, 220.
169. K. Arnold and R. Scholl, *Stud. Biophys.*, 1976, **59**, 47.
170. R. W. Briggs, F. A. Etzkorn, and J. F. Hinton, *J. Magn. Reson.*, 1980, **37**, 523.
171. J. F. Hinton, G. Young, and F. S. Millett, *Biochemistry*, 1982, **21**, 651.
172. G. L. Turner, J. F. Hinton, and F. S. Millett, *Biochemistry*, 1982, **21**, 646.
173. J. F. Hinton, G. L. Turner, and F. S. Millett, *J. Magn. Reson.*, 1981, **45**, 42.
174. J. F. Hinton, R. E. Koeppe, D. Shungu, W. L. Whaley, J. A. Paczkowski, and F. S. Millett, *Biophys. J.*, 1986, **49**, 571.
175. D. C. Shungu, J. F. Hinton, R. E. Koeppe, and F. S. Millett, *Biochemistry*, 1986, **25**, 6103.
176. J. F. Hinton, W. L. Whaley, D. C. Shungu, R. E. Koeppe, and F. S. Millett, *Biophys. J.*, 1986, **50**, 539.
177. J. F. Hinton, J. Q. Fernandez, D. C. Shungu, W. L. Whaley, R. E. Koeppe, and F. S. Millett, *Biophys. J.*, 1988, **54**, 527.
178. J. F. Hinton, J. Q. Fernandez, D. C. Shungu, and F. S. Millett, *Biophys. J.*, 1989, **55**, 327.
179. I. Bertini, C. Luchinat, and L. Messori, *J. Am. Chem. Soc.*, 1983, **105**, 1347.
180. I. Bertini, L. Messori, G. C. Pellacani, and M. Sola, *Inorg. Chem.*, 1988, **27**, 761.

Biographical Sketch

James F. Hinton. *b* 1938. B.S., 1960, University of Alabama; Ph.D., 1964, University of Georgia. Faculty in Chemistry University of Arkansas, 1965–present. Approx. 130 publications. Research interests: the application of NMR to solution structure, solvation, biophysics, and theoretical calculations of NMR chemical shielding.

Tritium NMR

Mark G. Kubinec and Philip G. Williams

Lawrence Berkeley National Laboratory, Berkeley, CA, USA

1	Background	1
2	Safety	1
3	Features and Parameters	2
4	Applications	5
5	Conclusion	11
6	Related Articles	11
7	References	11

1 BACKGROUND

The fundamental magnetic properties of tritium (^{3}H) were first reported in 1947[1–3] in a series of NMR measurements which demonstrated the triton to be a spin-$\frac{1}{2}$ nucleus, with a positive magnetic moment about 6.66% larger than that of the proton. Despite the fact that these measurements established tritium as the most sensitive NMR-active nucleus, very little research was conducted over the next two decades. In short, we have found only 24 reports of tritium spectra in the first 30 years, and 14 of those were published in the period 1974–76. The lack of activity in the early years of tritium NMR development is readily rationalized—tritium is a radioactive nucleus and, with the limited sensitivity of early spectrometers, the quantities required to make the 1947 measurements were enormous. [No specific details of sample sizes were given, but 50 μL of HTO with 50% abundance of ^{3}H contains ca. 3000 GBq of radioactivity, and we estimate that the samples must have been of this order, i.e. 1850–18 500 GBq (50–500 Ci).] Hence, applications were limited to US National Laboratories, where facilities existed for obtaining and handling large quantities of tritium.

The first liquids ^{3}H NMR spectrum other than HTO was described in 1964,[4] and set several important precedents for the newly developing field: (i) samples required large amounts of tritium (ca. 370 GBq in this instance); (ii) instrumental modification for ^{3}H detection was simple; (iii) proton–tritium couplings were obvious and readily measured; and (iv) the labeling pattern (or percentage of ^{3}H in various positions) was accessible from the spectrum. The sample used in this experiment was ethylbenzene prepared by metal-catalyzed reduction of phenylacetylene with tritium gas, and interestingly, the integrated ratio of methylene to methyl tritium was 1:1.5, not 1:1 as predicted. This result established high-resolution ^{3}H NMR as the tool of choice for analysis of tritiated products. The 'nontextbook' labeling pattern would have been difficult to detect and almost certainly overlooked using the conventional methods of the time, and incorrect assumptions about the labeling pattern would have affected downstream uses of the product. Indeed, biochemical applications of tritium have been slow to recover from the poorly characterized materials used in the 1950s and 1960s, when ^{3}H NMR was not available for product analysis.

Such demonstrations of the power of ^{3}H NMR spectroscopy led to a renewed interest in technical development in the late 1960s and early 1970s. Fortunately, the resurgence coincided with advances in instrumentation that allowed many other low abundance and/or low sensitivity nuclei to be routinely observed. This revolution in NMR spectrometer sensitivity was crucial. Since tritium sensitivity is $>$ 75-times that of ^{13}C, the ability to collect ^{13}C spectra at natural abundance clearly implies that tritium spectra could be obtained at the very low ^{3}H concentrations necessary to ensure the technique is safe and accessible to laboratories around the world. During this period, the sample requirement of 370–3700 GBq was drastically reduced to the range of 3.7–3700 MBq, depending on the complexity of the signals and the S/N level required. Of course, tritium detection by NMR still suffers from the inherent insensitivity of the technique, and some perspective can be gained from the fact that liquid scintillation counting (LSC) techniques can detect tritium at a level 10^{-7} lower than the highest field spectrometers of today. Yet, the detailed information which NMR yields about the chemical and magnetic environment of the nuclei makes this loss of sensitivity easy to justify.

The most influential force in the promotion of ^{3}H NMR spectroscopy as a routine research tool came from a fruitful collaboration between the University of Surrey and Amersham International. The early published work (1971–76) concentrated on methodology and proof of principle, and in the late 1970s a host of applications were reported. A number of other groups adopted the ^{3}H NMR approach, and by 1985 the Surrey group was able to publish an excellent compilation of techniques and results, describing a mature field.[5] In this article, we will discuss the major features of ^{3}H NMR spectroscopy, and address the more recent, popular, and significant chemical applications.

2 SAFETY

Tritium is the very rare, but naturally occurring, radioactive isotope of hydrogen. It is a pure β-emitter and its 12.4 year halflife is convenient for most chemical or biological experiments. In Table 1 we list a variety of chemical and physical properties of tritium and elementary tritiated compounds.

As mentioned above, the large amounts of tritium necessary for early experiments made containment of tritiated NMR samples a point of major concern, and a number of convenient containment systems have evolved.[5] Since tritium is a 'soft' β emitter, i.e. the energy of the β particle associated with its radioactive decay has very little penetrating power (Table 1, $E_{\max}$ = 18.6 keV, 6 μm range in water), it is readily contained by a thin surface of plastic, Teflon, or glass. The major hazard is from ingestion, so care should be taken to keep samples sealed and clean on the exterior. We favor a double encapsulation approach using either a 3-mm glass tube inside a regular NMR tube, or a capped Teflon liner inside a sealed glass tube. These components are all commercially available.

Since the number of tritium nuclei needed for NMR detection exceeds that required for liquid scintillation counting by a factor of ca. 10^7, the monitoring of equipment or personnel for contamination is readily accomplished by standard radiochemical techniques. At the minimum level readily detectable by liquid scintillation counting (LSC) (37 Bq L^{-1}) in a conventional urine analysis, the radiation exposure for an individual is less than 0.001 mSv y^{-1}. The sensitivity

Table 1 General Physical and Chemical Data for Tritium, and Common Radioactivity Units[a]

Production	^{6}Li(n, α)^{3}H
Radiation	β(100%); range = 4.5–6 mm in air, 6 μm in H_2O
β Energy	E_{max} = 18.6 keV, E_{mean} = 5.7 keV
Radioactive halflife	12.43 y (4540 d)
Biological halflife	ca. 10 d
Decay product	^{3}He
Maximum specific activity	1064 GBq milliatom^{-1} (28.76 Ci milliatom^{-1})
Detection limit (in 24 h): LSC	0.037 Bq = 2.09 $\times$ 10^7 atoms (ca. 0.1 fmol)
NMR	1064 kBq = 6.02 $\times$ 10^{14} atoms (ca. 1 nmol)
Diameter of tritium atom (approx.)	1.1 Å
Volume of 37 GBq (1 Ci) of tritium gas at standard temperature and pressure	0.385 mL
Radiation produced by 37 MBq (1 mCi) in a man (70 kg = 40 L, i.e. 25 μCi L^{-1})	0.044 mSv d^{-1} (= 4.4 mrem d^{-1}, or 1.6 rem y^{-1})
Density, triple point, and boiling point of	H_2O: 1.000 g mL^{-1}; 0.01°C; 100.00°C
isotopic water molecules	D_2O: 1.106 g mL^{-1}; 3.82°C; 101.42°C
	T_2O: 1.214 g mL^{-1}; 4.49°C; 101.51°C
Tritium content of pure T_2O at STP	117.4 TBq mL^{-1} (3173 Ci mL^{-1})
	96.7 TBq g^{-1} (2614 Ci g^{-1})

[a]37 gigabecquerels (GBq) = 1 curie (Ci) = 3.7 $\times$ 10^{10} disintegrations per second; 1 gray (Gy) = 10 000 erg g^{-1} = 100 rad (units of absorbed dose); 1 sievert (Sv) = 100 rem (units of radiation exposure).

of LSC thus provides a level of detection well below the average exposure from background, medical, and terrestrial sources (3 mSv y^{-1}) or the current recommendation for a US Department of Energy radiation worker (<20 mSv y^{-1}). In addition, tritium uptake in the body is cleared as tritiated water (HTO) with a 10 day biological halflife, and this period can be drastically reduced by increasing fluid intake or by diuretics (e.g. water, beer, or coffee).

The hazards associated with analyzing ^{3}H samples are real, but have been grossly overemphasized in the past. A rational assessment of the risks involved is in order. Tritium is readily contained and is physiologically benign at the levels used in most high-resolution NMR experiments. When making a benefit/hazard judgement of conducting research on a 2220 MBq (60 mCi) sample contained as described above, it is reasonable to remember that safety lights in aircraft contain up to 370 GBq (10 Ci) of tritium, a marine compass may have as much as 28 GBq (0.75 Ci), and commonly available night sights for rifles contain 2 GBq (50 mCi) of tritium. The spectroscopist may be at greater risk from the lock solvent or other chemical entity in the sample than from the radioactivity, e.g. in a 0.25 mL sample containing 2220 MBq of a tritiated compound in C_6D_6, there are 2 μmol of ^{3}H but 2.75 mmol of benzene. It is clearly less hazardous to handle a well-contained tritium sample than milligram quantities of neurotoxins and other biologically active compounds routinely analyzed in normal glass NMR tubes in many laboratories.

In summary, the handling and health physics of analyzing tritiated samples is an important but trivially solved consideration, allowing ^{3}H NMR spectroscopy to be readily executed in most laboratories having a pulsed Fourier transform NMR spectrometer.

3 FEATURES AND PARAMETERS

The characteristics of ^{3}H are compared with other common NMR active nuclei in Table 2. Tritium enjoys all the spectral advantages normally associated with spin-$\frac{1}{2}$ nuclei of high γ: narrow lines, high sensitivity, and good dispersion. A brief perusal of Table 2 indicates the strong similarity between triton and proton magnetic properties, with tritium having slightly higher sensitivity and dispersion, and similar relaxation characteristics. The similarity between nuclei extends to chemical shifts, allowing one to use the extensive library of proton chemical shifts when making tritium resonance assignments. Since tritium also has extremely low natural abundance, spectra are free of background signals and this, combined with the a priori knowledge of chemical shifts from analogous protons, makes assignment of tritium spectra particularly straightforward.

Many of the favorable properties of tritium are illustrated in the spectra in Figure 1, where a comparison of proton, deuterium, and tritium NMR spectra of labeled glucose is shown. The superior resolution and dispersion of tritium over deuterium, a spin-1 nucleus, is obvious. Note that this labeled molecule is low molecular weight, and the line broadening of deuterium signals for larger molecules is even more striking, hence eliminating deuterium NMR as a useful technique for the structural analysis of large molecules in solution. In addition, since the dominant relaxation mechanism for deuterium is quadrupolar, NOE determinations are impossible, and sensitivity in saturation transfer is reduced due to rapid spin–lattice relaxation. In contrast, tritium analysis greatly simplifies the proton spectrum in Figure 1(a), particularly around the solvent where a less fortuitous proton chemical shift (or sample temperature) would have completely obscured one of the glucose signals under the HDO peak. Even in H_2O, tritium spectra require no solvent suppression and are much more easily assigned than the generally more crowded proton analog.

To understand the quantities involved in a tritium NMR experiment, one must be aware of the common units and conversion factors which are listed in Table 1. One of the most important benchmarks is that complete replacement of hydrogen by tritium in one position of a molecule gives a specific activity (*SA*) of 1064 GBq mmol^{-1} (28.76 Ci mmol^{-1}). Obviously, for lower percentages of tritium replacement the *SA* value is proportionately reduced and this relationship,

Table 2 NMR Properties of ^{3}H and Common NMR Nuclei[a]

Nucleus	Natural abundance	Spin	γ	Resonant frequency	Relative sensitivity[b]
^{1}H	99.984	$\frac{1}{2}$	26.7510	300.13	1.00
^{2}H	0.0156	1	4.1064	46.07	9.65×10^{-3}
^{3}H	$<$**10^{-16}**	$\frac{1}{2}$	**28.5335**	**320.13**	**1.21**
^{13}C	1.10	$\frac{1}{2}$	6.7263	75.46	1.59×10^{-2}
^{15}N	0.37	$\frac{1}{2}$	-2.7116	30.40	1.04×10^{-3}
^{19}F	100	$\frac{1}{2}$	25.1665	282.23	0.83
^{31}P	100	$\frac{1}{2}$	10.8289	121.43	6.63×10^{-2}

Chemical shift (δ) range:	20 ppm
Isotope effects:	^{3}H primary, $1^\circ \approx 0.028$ ppm; 9.0 Hz at 7.1 T
	^{3}H secondary, $2^\circ \approx 0.013$ ppm; 4.2 Hz at 7.1 T
	^{2}H primary, $1^\circ \approx 0.020$ ppm; 6.7 Hz at 7.1 T
Coupling constant (J) range:	0–20 Hz
	$J(\mathrm{T,H}) = J(\mathrm{H,H}) \times \gamma_\mathrm{T}/\gamma_\mathrm{H}$
	$J(\mathrm{T,T}) = J(\mathrm{H,H}) \times (\gamma_\mathrm{T})^2 \times (1/\gamma_\mathrm{H})^2$
T_1	0–10 s
T_2	0–10 s

[a]7.1 T field.
[b]Sensitivity given for equal numbers of nuclei in the same field.

combined with a knowledge of the total number of millimoles of labeled substrate, readily yields the amount of radioactivity involved in the experiment.

3.1 Chemical Shifts and Referencing

Early measurements established that the ratios of nuclear screenings among the hydrogen isotopes was very close to unity. This implies that the chemical shift for a triton is essentially identical to that of a proton or deuteron in the analogous molecular environment. Thus tritium spectra can be referenced to, say, monotritiated TMS and chemical shifts will be nearly identical to proton chemical shifts. Since the tritium/proton Larmor frequency ratio is very well determined for TMS[6] (1.066 639 739 $\pm$ 2 $\times$ 10^{-9}), in practice it is not necessary to add a tritiated reference material to a sample to achieve accurate referencing. Instead, a simple measurement of the *proton* frequency of a reference material and multiplication by the figure above gives the tritium resonance frequency for the reference. This procedure is known as ghost referencing. Some care must be taken in very precise work when using ghost referencing because more careful studies of the Larmor frequency ratio for a variety of tritium-labeled materials[6,7] have shown that nuclear screenings are not identical, but vary slightly with carbon–hydrogen (tritium) bond hybridization. Thus, when referencing tritiated methyl groups a TMS ghost may be appropriate, but a tritiated phenyl position is more accurately referenced by a phenyl proton and a slightly different Larmor frequency ratio. These differences are usually so small that they do not interfere with routine analysis, and are not discerned in a wide display (0–6 ppm), such as that in Figure 1.

3.2 Coupling Constants and Isotope Effects

Coupling constants between tritium and other nuclei may be calculated from the analogous proton coupling constants. In particular, J(T,T) and J(T,H) are given by the relationships in Table 2, i.e. tritium–proton spin–spin coupling constants may be calculated as ca. 6.664% larger than the analogous proton constant. There is a small isotope effect on the coupling constant,[8] and measurements have been reported for tritium coupled to a number of other nuclei besides protons including carbon, tin, silicon, and boron.

Although there are isotope effects, measurement of a J(T,H) value is still an accurate way of predicting a proton–proton coupling constant, since the calculation involves division by 1.06664 rather than multiplication by 6.5144, as required by prediction from J(D,H). For isochronous protons (e.g. methyl protons having degenerate chemical shifts), measurement of the J(T,H) value readily yields a usually 'invisible' coupling constant (see Figure 2, below).

Besides the small isotope effects on nuclear screening and on coupling constants discussed above, there are also more commonly observed isotope effects on tritium chemical shifts caused by substitution of a heavy isotope in place of a proton. These are largest and therefore most easily observed when a geminal proton is replaced by a triton. This effect was first reported in analyses of highly tritiated methyl groups,[9] where the R–CT_3 singlet was resolved from the R–CT_2H doublet in the proton coupled tritium spectrum. The proton-decoupled spectrum was used to show that this primary isotope effect is ca. 0.025 ppm (i.e. 2.4 Hz at 96 MHz).

Figure 2 illustrates tritium isotope effects on chemical shifts and demonstrates how the methyl J(H,H) may be calculated from measured J(T,H) values, as discussed above. A sample of *m*-xylene was tritium-labeled by Raney nickel catalyzed exchange with T_2, which is known to give almost exclusive methyl tritiation. All three tritio-methyl species are produced, as shown in the proton-decoupled tritium spectrum in Figure 2(a), where these species are separated by the primary isotope effect ($\Delta\delta$) on the tritium chemical shift. At 320 MHz, tritium signals from methyl groups have a proton–tritium coupling constant which is double $\Delta\delta$, so that the proton-coupled tritium spectrum in Figure 2(b) has a deceptively simple

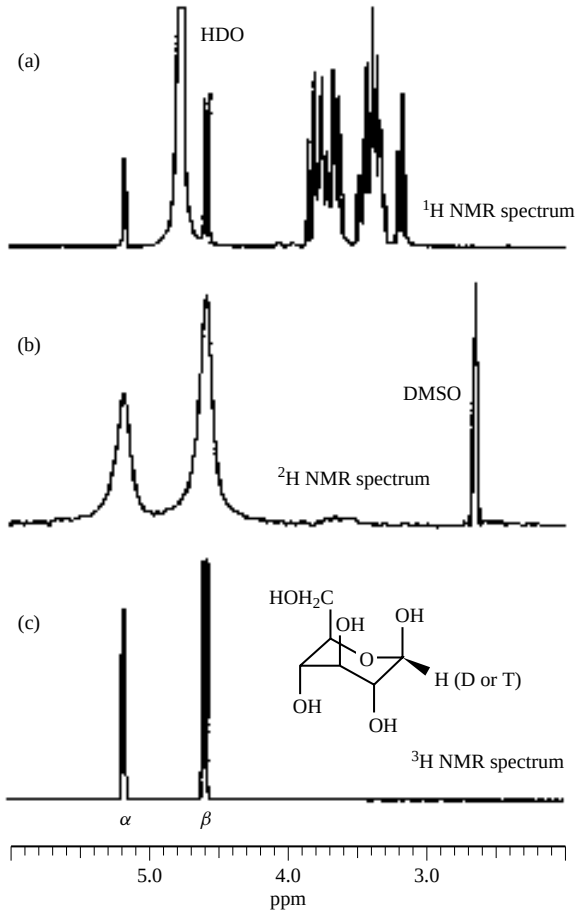

Figure 1 Hydrogen NMR spectra of D-glucose in water. (a) Proton spectrum of C-1 tritiated D-glucose; the large peak is due to HDO. (b) Proton decoupled deuterium NMR spectrum of C-1 deuterated glucose; DMSO is an integration marker. (c) Proton-coupled tritium spectrum of C-1 tritiated glucose, labeled by the same catalytic technique as in (b)

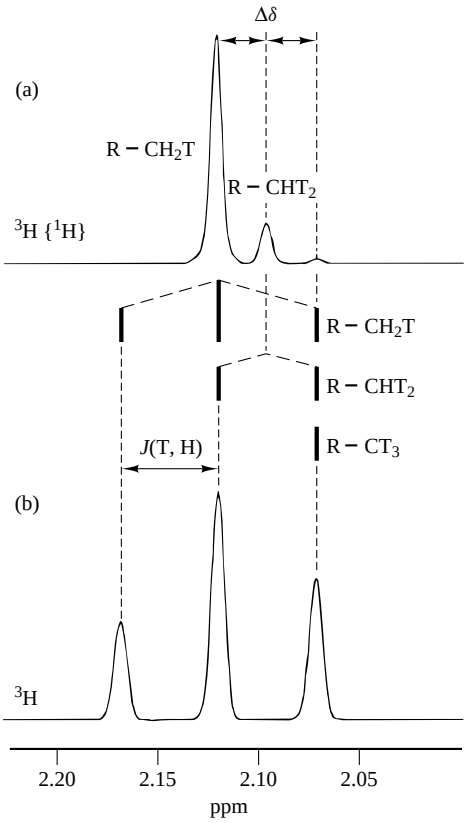

Figure 2 Deceptively simple tritium NMR spectra in C_6D_6 of *m*-xylene labeled by T_2 gas exchange over Raney nickel catalyst. (a) Proton-decoupled tritium spectrum showing peaks for R−CH_2T, R−CHT_2, and R−CT_3 species separated by $\Delta\delta = 0.025 \pm 0.001$ ppm (7.89 ± 0.21 Hz at 7.1 T). (b) Proton-coupled spectrum showing overlapped tritium multiplets separated by J(H,T) = 15.58 ± 0.21 Hz

appearance. The splitting patterns are shown on the figure, and our assignments are readily verified by integration of the signals in each of the spectra. The methyl J(H,H) for *m*-xylene methyl groups may be calculated from the observed J(T,H) value.

Secondary tritium isotope effects on chemical shifts have also been well quantified,[10] and the primary deuterium isotope effect on tritium chemical shifts is also easily measured (Table 2).

3.3 Tritium NMR Intensity and the NOE

One of the major advantages of tritium NMR spectroscopy is that the labeling pattern in a sample may be determined without the time-consuming and laborious degradative determinations previously required.[11] Indeed, a tritium spectrum gives nondestructive, quantitative information on relative tritium abundance at different sites in a molecule. Of course, care must be exercised in any measurement of NMR peak intensities so that accumulation of the data does not *differentially* affect the various peaks. When proton decoupling is used, for example, the tritium intensities will be affected by the Nuclear Overhauser Effect (NOE). Because of the frequent use of proton decoupling in tritium experiments, the importance of this effect has been the subject of several studies and discussions.[12] While the maximum theoretical NOE enhancement to tritons from proton irradiation is 47%, the observed enhancements vary from 10−35%. More importantly, there are situations where differential NOEs may prejudice tritium spectral intensities, such as a labeled molecule with a high abundance of tritium in a position without neighboring protons and a second tritiated position which has many relaxation partners, and integrals should only be compared when these issues have been considered.

3.4 Relaxation

The similarity of tritium and proton nuclei means that their pathways for relaxation are nearly identical. A feature of tritium NMR is that the simple spectra allow straightforward relaxation measurements. The analogous measurements in proton spectra can be difficult due to spectral crowding, solvent suppression, or the complexity of the physical system. Hence tritium relaxation can be the more useful probe of molecular interactions. A classic example is the use of proton and tritium relaxation measurements combined with homo- and heteronuclear saturation transfer experiments to study the relaxation of water molecules in the presence of a macromolecular suspension.[13] A rather simple suspension was created

by the formation of egg phosphatidylcholine/cholesterol lipid bilayers in solution. In a lipid suspension the water can exist in two distinct environments, a 'free' state exhibiting bulk water properties, and a motionally hindered or 'bound' state that is associated with the lipid in a hydration shell. Nuclei in these populations relax differently. The free water has the familiar characteristics of small rapidly tumbling molecules in solution, while the bound water has an additional slow component of tumbling due to its association with the lipid. This lipid-induced hydrodynamic effect causes a more rapid relaxation in the bound state and the presence of two water populations with different relaxation rates makes the overall relaxation behavior of the water signal complex. In general, it will depend on a combination of processes including the hydrodynamic effect, chemical exchange between free and bound environments, and the dipolar interaction (cross relaxation).

In the investigation of these processes, tritium doped water was used to separate the exchange contribution from other relaxation processes in the heteronuclear tritium–proton experiments. The measurements made on this rather complicated system were thus simplified to an analysis of several single-line spectra using inversion–recovery and saturation transfer experiments. The results indicated that the dipolar interaction (in the spin diffusion limit) dominates the relaxation of the water, and two models of this limit were proposed which accurately predicted the results, including a rigid and dynamic description of the lattice in the lipid solution. A complete model of the relaxation behavior of water is very desirable since the difference in relaxation properties of free and bound water populations is the basis for contrast and tissue characterization techniques in magnetic resonance imaging.

4 APPLICATIONS

We will limit the discussion here to chemical applications: (i) analysis of labeled materials for chemical and radiochemical purity; (ii) reaction mechanisms and tritium NMR techniques; (iii) specific activity measurements; (iv) solution conformation, stereochemistry, and optical purity; (v) proton exchange studies; and (vi) miscellaneous tritium NMR studies. Biological applications of ^{3}H NMR, e.g. ligand binding, metabolism studies, etc., are discussed elsewhere (see ***Tritium NMR in Biology***).

4.1 Analysis of Labeled Materials

The vast majority of reports involving ^{3}H NMR spectroscopy describe the products of tritium-labeling reactions, and in this application the technique is invaluable. Tritium NMR has been used extensively for the investigation of many tritium exchange techniques, including radiation-induced and acid-, base-, metal-, or zeolite-catalyzed reactions.[14] In general, these techniques rely on the replacement of a hydrogen atom by a tritium (i.e. exchange) in the native structure, and give low specific activity products which may contain tritium in one of several distinct sites.

In contrast, high level tritium labeling usually involves a synthetic transformation such as dehalogenation, hydrogenation, or hydride reduction of a suitable precursor. Dehalogenation reactions are an attractive method for introducing tritium into a compound, but surprisingly these reactions rarely give quantitative replacement of halogen by tritium, even when 100% T_2 gas is used. Our experience is that 10–30% of product molecules will incorporate adventitious hydrogen (^{1}H) rather than ^{3}H. In general, the shorter the reaction time, the less hydrogen incorporated (i.e. the higher the *SA* value obtained), and it is advisable to use an iodo derivative as the substrate since the facility of halogen removal is I > Br > Cl > F. Also, 1 equiv. of organic base (e.g. triethylamine) enhances the reaction rate and neutralizes the acid formed.

The power of tritium NMR in the analysis of a tritiodehalogenation reaction product is best illustrated by an example. Figure 3(a)–(e) show a full proton and ^{3}H NMR analysis of a peptide labeled by catalytic dehalogenation of the analogous 3,5-diiodotyrosyl peptide. The aromatic portion of the proton spectrum of the tritiated material [Figure 3(a)] shows ca. 15% proton intensity at the tyrosine 3 & 5 chemical shift, with the usual tyrosine 2 & 6 and Phe aromatic signals. Note that the splitting of the tyrosine 2 & 6 doublet reflects J(T,H), not coupling to the 3 & 5 protons. The proton-coupled tritium spectrum in Figure 3(b) shows a clean doublet at the tyrosine 3 & 5 chemical shift for the incorporated tritium. Broadband decoupling of the protons yields the singlet tritium signal in Figure 3(c), as expected. Selective irradiation at the tritium tyrosine 3 & 5 frequency causes the tyrosine 2 & 6 doublet to collapse, as shown in the proton spectrum in Figure 3(d) [cf. Figure 3(a)]. Similarly, selective ^{1}H decoupling at the tyrosine 2 & 6 frequency yields a singlet tritium signal at the tyrosine 3 & 5 chemical shift [Figure 3(e)]. These experiments are readily performed and characterize the product beyond any doubt.

The other most common method for introducing high levels of tritium is catalytic hydrogenation of an unsaturated site on a suitable precursor. Interestingly, heterogeneous metal-catalyzed hydrogenation reactions often do not yield 'textbook' results, and it is remarkable that so few researchers are aware of these details, despite their repeated demonstration.[5] Two effects contribute to the complicated mixture of isotopomers obtained from these reactions:[10] (i) there is an inventory of hydrogen ($^1H_1$) in the catalyst, solvent, substrate, and reaction vessel which serves to **decrease** the maximum level of tritium which may be incorporated into the labeled material; and (ii) vinylic and allylic protons may undergo metal-catalyzed exchange prior to saturation of the multiple bond, thus leading to **increased** specific activity.[15] As a result, the products of a hydrogenation reaction often have (a) lower than theoretical incorporation of tritium, (b) tritium in positions remote from the original site of unsaturation, and (c) unequal amounts of tritium on each side of the original multiple bond.

When ^{3}H NMR is used to analyze the products of both heterogeneous and homogeneous catalysis of an identical reduction, the complexities of heterogeneous catalysis are clear. Such a comparison of tritiation techniques for the labeling of an unsaturated phospholipid molecule is shown in Figure 4. All the problems described above for heterogeneous catalysis complicate the spectrum shown in Figure 4(a), including small amounts of tritium incorporated at the positions adjacent to the double bond. In contrast, the product of the homogeneous tritiation using Wilkinson's catalyst [Figure 4(b)] shows clean addition of tritium, with a 1:1 ratio at the C-7 and C-8 positions. A ^{3}H–^{3}H COSY analysis of this product [Figure 4(c)] showed that the two

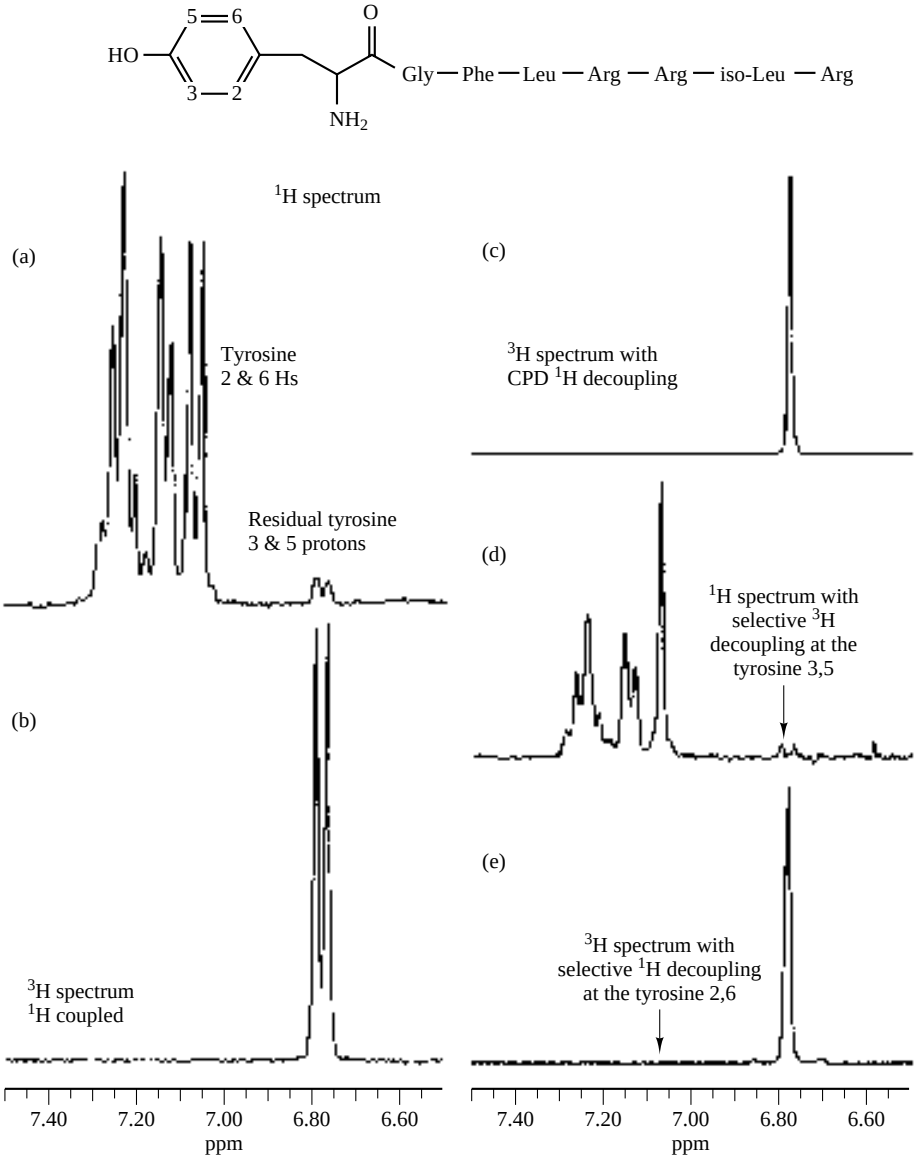

Figure 3 Proton and tritium NMR spectra in D_2O of a peptide labeled by catalytic tritio-dehalogenation of the appropriate diiodotyrosyl peptide. (a) Aromatic region of the proton spectrum showing signals from the phenylalanine residue and a clean doublet from the tyrosine 2 and 6 protons. Residual proton signals are obvious from the tyrosine 3 and 5 position. (b) Tritium spectrum showing the doublet of the tyrosine 3 and 5 tritons coupled to the 2/6 protons. (c) Proton-decoupled tritium spectrum showing the tritium singlet from the 3 & 5 tritium atoms. (d) Selectively tritium-decoupled proton spectrum: comparison with the spectrum in (a) shows the collapse of the tyrosine 2 & 6 doublet. (e) Selectively proton decoupled tritium spectrum, with irradiation only at the tyrosine 2 & 6 doublet

expected diastereotopic products were obtained, in a 1:1 ratio.[16] Although this tritium analysis shows that Wilkinson's catalyst gives a very clean product, it is not applicable in all circumstances. Such mundane issues as sample solubility and recovery of the labeled material from the reaction mixture often affect the decision of which catalyst is used. Heterogeneous catalysts have the advantages that they are tolerant of a variety of solvent systems and are easily filtered away after the reaction. Wilkinson's catalyst is usually employed as a benzene solution and may not perform well in a binary mixture if the substrate is insoluble in benzene. In addition, Wilkinson's catalyst is designed to form an intimate mixture with the substrate, and postreaction separation steps need to be optimized for each new substrate.

4.2 Reaction Mechanisms and Tritium NMR Techniques

Tritium spectra are almost always simple, hence there has been no strong drive to apply more sophisticated NMR techniques to tritium analyses. However, the subtleties of exchange effects in heterogeneous catalysis and the complex products from enzymatic reactions often require careful interpretation, and such studies may be greatly enhanced by the use of modern multipulse approaches.

The following techniques have been applied to tritium analyses over the past decade: double quantum filtering, DEPT, 2D homonuclear COSY, 2D tritium/proton correlation, 2D *J*-resolved, and 2D NOESY and EXSY experiments. The NOESY and EXSY approaches have been used for macromolecular structure studies and are discussed elsewhere

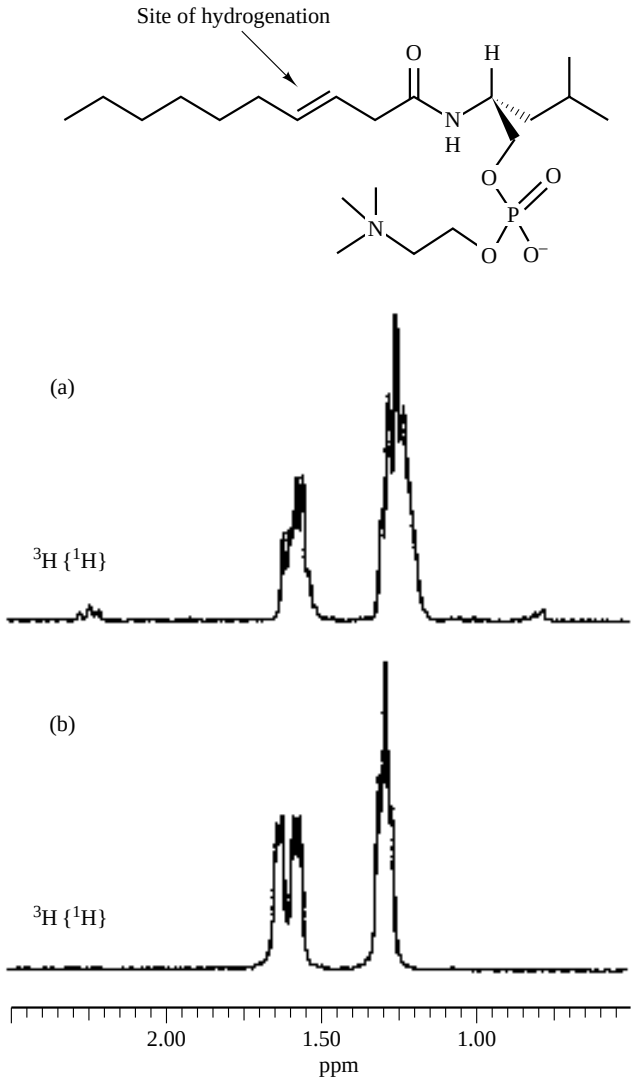

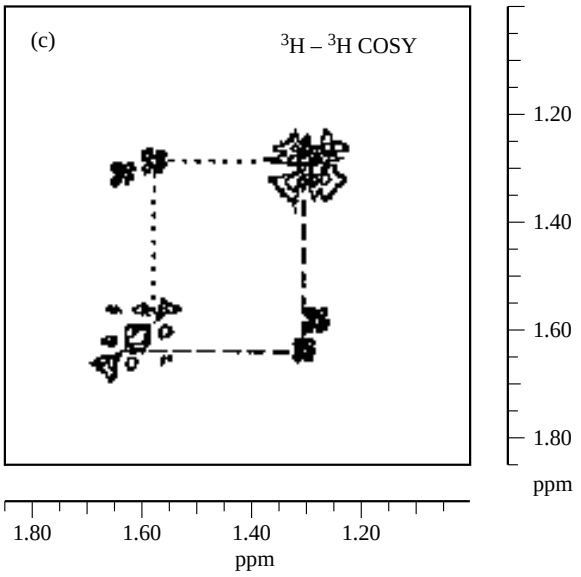

Figure 4 Proton-decoupled tritium NMR spectra of a labeled phospholipid in D_2O. (a) Product of a heterogeneous catalytic hydrogenation reaction. (b) Product from catalytic hydrogenation in the presence of Wilkinson's catalyst. (c) {^{1}H} ^{3}H–^{3}H COSY of the product in (b)

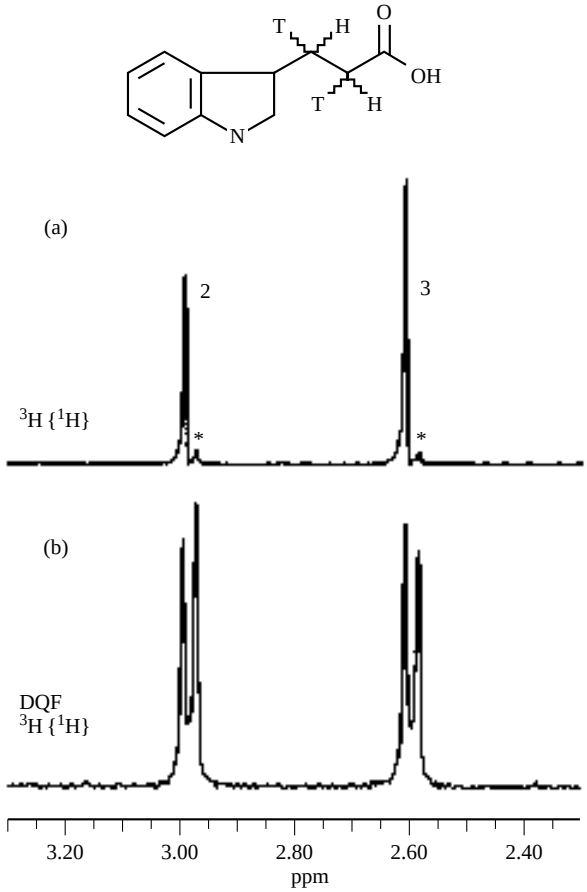

Figure 5 Tritium NMR spectra of tritiated 3-indolepropionic acid in CD_3OD. (a) Proton-decoupled tritium spectrum of the product of a heterogeneous catalytic hydrogenation reaction using 15% T/H. (b) Double quantum filtered proton-decoupled tritium spectrum of the same product as shown in (a). The observed J(T,T) = 7.32 ± 0.12 Hz, suggesting a J(H,H) value of ca. 6.4 Hz

(see ***Tritium NMR in Biology***). The pulse sequences we regard as most useful for analytical applications are the DQF and 2D J-resolved experiments. These have been used for detailed investigation of the 'nontextbook' results typically encountered in tritiation reactions, which are usually invisible in the corresponding reaction with $^1H_2$. Hence tritiation and tritium NMR spectroscopy provide an excellent approach for investigation of these imperfectly understood reaction mechanisms, as discussed below.

The research staff at Berkeley routinely use a mixture of 5–15% T_2 in H_2 for exploratory labeling reactions and in a training program. In the hydrogenation of 3-indoleacrylic acid using a 10% Pd/C catalyst and 15% T_2 in H_2 gas, simple statistics predict that 2.25% of labeled 3-indolepropionic acid product molecules will contain two ^{3}H atoms, 25.5% will have a tritium at one carbon or the other, and 72.25% will contain no tritium. The ^{1}H-decoupled tritium NMR spectrum in Figure 5(a) shows several features: (i) the large singlet signals arise from molecules containing one tritium atom, and it is obvious that unequal amounts of ^{3}H are incorporated across the double bond, and (ii) one signal from a small doublet can be discerned at the base of each singlet (asterisked), presumably arising from the doubly tritiated species. The unequal substitution pattern in the singly tritiated species is thought to arise from

exchange at those carbons prior to saturation of the double bond, and tritium NMR represents the best method for the further study of the mechanism of such exchange.[15] The doubly tritiated species can be observed simply and directly by the application of a familiar multiple pulse technique, a double quantum filtered (DQF) experiment. The results of the DQF experiment on this molecule are remarkably clean, as shown in Figure 5(b). The spectrum is simple because the doubly tritiated species is the only one present with tritium homonuclear double quantum transitions, and is further simplified because all couplings to protons are heteronuclear and have been removed by broadband decoupling. This result has tremendous potential for the study of the mechanism of this type of addition and would not have been possible without the use of tritium NMR. Clearly this unique ability to separate labeled species and perform careful analysis of complex mixtures of isotopomers resulting from a theoretically simple tritiation reaction is essential for understanding the mechanism of these reactions.

Two-dimensional *J*-resolved ^{3}H NMR[10] can be an even more powerful tool for the analysis of complex isotopic mixtures. β-Methylstyrene was tritiated by catalytic reduction with 100% T_2 over 5% Pd/C catalyst, to give highly tritiated *n*-propylbenzene with ca. 40% of the tritium on the α-methylene carbon, 50% on the β-methylene, and 10% in the methyl group. In addition, all of the multiplets for these tritiated positions showed a complex structure, not at all like the simple doublet of doublets which might have been proposed assuming clean addition of a tritium atom to each end of the double bond.

The methyl region of the proton-decoupled tritium *J*-resolved analysis of this sample (Figure 6) provided most insight into the species giving rise to the various signals. There is a repeating and slightly overlapped singlet–doublet–triplet pattern, with each repetition moved successively to lower frequency by ^{3}H isotope effects. These first of these patterns (group A, Figure 6) is due to the species X–CH_2–CH_2T, singlet; X–CHT–CH_2T, doublet; and X–CT_2–CH_2T, triplet (species 1, 2, and 3), and the small change in chemical shift between these signals is the secondary tritium isotope effect induced by addition of a T at the β-CH_2. There are similar patterns for the –CHT_2 (B) and –CT_3 (C) methyl species, successively moved to lower frequency by the primary tritium isotope effect on the methyl chemical shift. Inspection of several slices along the ω_2 dimension (submatrix, or .smx plots shown in Figure 6) show the relative abundance of each species in this mixture, and analysis of ω_1 slices allows us to extract all the ^{3}H–^{3}H coupling constants. Similar detailed analysis of the α-CH_2 and β-CH_2 regions of the *J*-resolved spectrum is also possible, and evidence was found for almost all of the 35 statistically possible, tritium-containing isotopomers. While the theoretical product, Ph–CHT–CHT–CH_3, was the most abundant species, the presence of another 34 tritiated isotopomers makes it clear that the mechanism of heterogeneous metal-catalyzed hydrogenation reactions is not as simple as commonly thought.

4.3 Specific Activity Measurements

The molar specific activity (i.e. radioactivity per unit weight) of tritium-labeled molecules is an important property, and tritium NMR may be used to determine this quantity.[5] This approach is essential when the labeled material has no UV

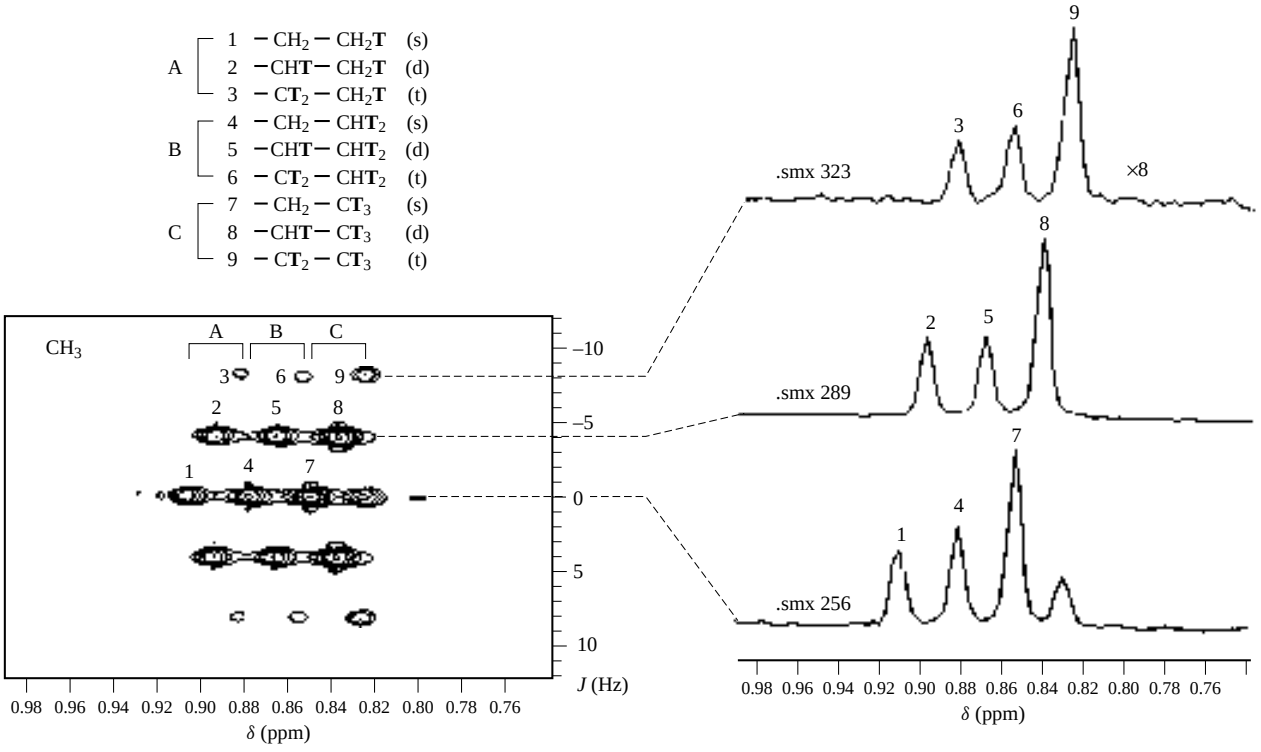

Figure 6 The methyl section (0.68–0.93 ppm) of the contour plot of the proton-decoupled tritium *J*-resolved spectrum of *n*-propylbenzene, labeled by catalytic tritiation of β-methylstyrene. Sine-bell window functions were applied in both dimensions, 2k × 512 W transform, with magnitude calculation of peak intensities. The data were 'tilted' and 'symmetrized'

spectrum, or the high specific activity precludes weighing to determine sample concentration. An example of the latter was the determination of the *SA* value for a series of $NaBT_4$ preparations.[17] Boron has two NMR active isotopes (^{10}B, 20%, $I = 3$ and ^{11}B, 80%, $I = \frac{3}{2}$), so the proton spectrum of sodium borohydride in basic CD_3OD shows a large quartet ($Na^{11}BH_4$, $\delta = -0.168$ ppm, $J = 80.6$ Hz) and a small septet ($Na^{10}BH_4$, $\delta = -0.166$ ppm, $J = 26.98$ Hz). The proton-decoupled tritium spectrum of exchange labeled $NaBH(T)_4$ shows a similar spectrum for each isotopomer, i.e. $NaBH_3T$, $NaBH_2T_2$, $NaBHT_3$, $NaBT_4$, shifted to lower frequency for each additional T. The multiplicity (redundancy) of the peaks is useful since peak overlap does not occur for all the species, and the isotopomer ratios may be compared between large quartet signals and the smaller septets. The amount of unlabeled ($NaBH_4$) material present was estimated by comparison with $NaBH_3T$ signals in the proton spectrum. Knowing the mole ratio of all the isotopomers yields the *SA* value, and this property was compared for several production 'lots' of tritiated borohydride.

Even when determination of *SA* by UV spectroscopy and LSC counting, or by mass spectrometry, is possible, the NMR technique provides a useful cross check. In comparison to the sodium borohydride case above, a very simple example of using ^3H and ^1H NMR to determine specific activity is given in Figure 7. Pinoline (6-methoxy-1,2,3,4-tetrahydro-9*H*-pyrido[3,4-*b*]indole) was labeled by catalytic hydrogenation of the unsaturated 3,4-dihydro analog. The product consisted of a mixture of three isotopomers containing zero, one, or two tritium atoms per molecule. Obviously, at the chemical shift of the C-1-methylene, one of these species has only a proton spectrum, one has a tritium spectrum, and one [R–CHT, δ = 4.39 ppm, Figure 7(a) and (b)] has both a tritium and a proton NMR spectrum. In this case, the use of selective tritium [Figure 7(a)] or proton [Figure 7(b)] decoupling allows the observation of single lines for each of the isotopomers in the proton or tritium spectrum. Since the R–CHT signal occurs in both spectra, the molar ratio of the three species may be extracted from these spectra and the specific activity calculated.

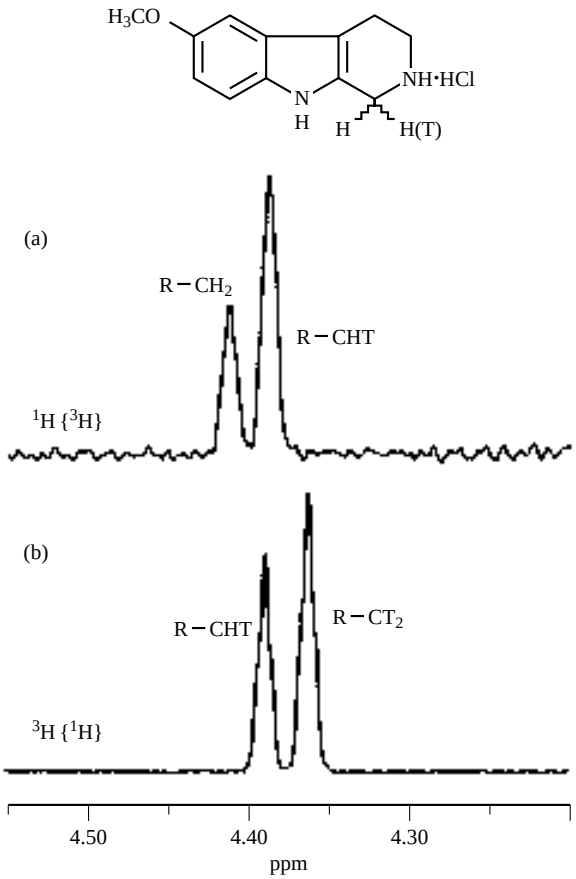

Figure 7 Proton and tritium NMR spectra of tritiated pinoline in CD_3OD. (a) Selectively tritium-decoupled proton spectrum. (b) Selectively proton-decoupled tritium spectrum

4.4 Solution Conformation, Stereochemistry, and Optical Purity

Tritium NMR has been used to obtain the axial–equatorial conformational preference of tritium in [^3H]cyclohexane.[18] Tritium has the advantage of giving sharp and well-separated peaks that are well suited for high-accuracy integration at low temperatures, i.e. the peak separation in these experiments was ca. 150 Hz at 7.1 T, whereas the analogous deuterium experiment at 11.7 T gave a separation of only 36 Hz. [^3H]Cyclohexane was made from cyclohexylmagnesium chloride in diethyl ether by the addition of HTO (5% tritium) followed by distillation of the tritiated product. A sample (ca. 0.9 GBq, 33 mCi) in CS_2 containing some CD_2Cl_2 for lock purposes was transferred into a standard thin-wall glass 5-mm NMR tube and ^3H {^1H} NMR spectra were obtained at 320 MHz (300-MHz ^1H frequency). Narrow lines (ca. 2 Hz at halfheight) with good lineshapes were obtained at $-88\,^\circ C$ by using the tritium FID as well as the ^2H lock signal for shimming. For accurate integration it is essential that the base of the peaks be narrow and symmetrical, and that the baseline is flat. A number of data sets, each consisting of the sum of 512 FIDs were acquired, several with the carrier at a higher frequency than the sample signals, some with the carrier at a lower frequency, and others with the carrier centered between the signals. The ^{13}C satellites of both the axial and equatorial ^3H signals ($\delta\nu = 0.471$ ppm) were visible in each set of spectra and gave $J(^{13}C,^3H_{ax}) = 131.1$ Hz and $J(^{13}C,^3H_{eq}) = 135.2$ Hz. Integration of the spectra showed that tritium prefers the equatorial over the axial site by about 46.9 J mol^{-1} and a ^3H EXSY experiment showed that the axial and equatorial tritium atoms are undergoing (slow) exchange at $-88\,^\circ C$. Conformational analysis by ^3H NMR relaxation has also been used in enzyme ligand studies (see NT497-***Tritium NMR in Biology***).

The absolute stereochemistry of a tritium atom on a carbon may be determined by tritium NMR if there is another chiral center in the molecule. If this is not the case on the parent molecule, it can often be created by esterification or some other derivatization. This feature was exploited in analysis of tritiated ethanol produced by enzymatic oxidation of 'chiral ethane', i.e. $CH_3–CHDT$, as part of a study of the mechanism of methane monooxygenase.[19] Tritium NMR analysis of the methylene region of the ethanol product showed signals from $CH_3–CHT–OH$ and $CH_3–CDT–OH$, separated by the ^2H isotope effect on the tritium chemical shift [Figure 8(a)]. Whereas this spectrum gives information on the relative rate of removal of an H or D atom in the oxidation process, it gives no stereochemical data. A simple derivatization with

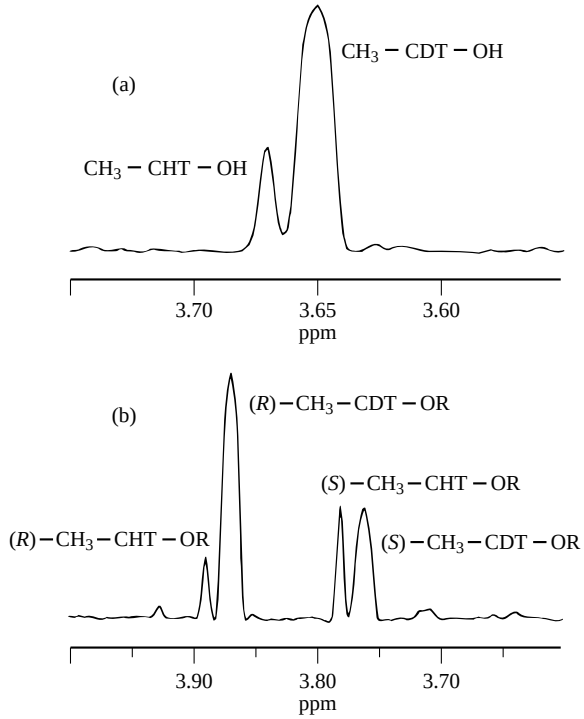

Figure 8 Proton-decoupled tritium NMR spectra of the products from enzymatic oxidation of chiral ethane. (a) Ethanol in H_2O. (b) Derivatized ethanol in C_6D_6, where R = (2*R*)-2-acetoxy-2-phenylethanoic acid

(2*R*)-2-acetoxy-2-phenylethanoic (mandelic) acid yields ethyl mandelate, and the four possible species can be readily separated and quantitated by ^3H $\{^1H\}$ NMR, as shown in Figure 8(b). The *absolute* stereochemistry was previously established by a known synthesis of the deuterium-substituted molecules and proton NMR analysis.

Tritium NMR has been used to determine the optical purity of labeled materials. The use of a lanthanide shift reagent[20] or Pirkle's alcohol[21] is a more general technique than the careful stereochemical determinations discussed above, and does not require the presence of an alcohol or amine functionality for derivatization to the appropriate ester or amide. This general approach is especially important for materials labeled at low tritium abundance because the optical properties of the bulk material may not be the same as the small subpopulation of labeled molecules.

4.5 Proton Exchange Studies

The NMR properties of tritium make it particularly well suited for in situ measurements of acid- and base-catalyzed proton exchange kinetics using tritium NMR spectroscopy.[22] Despite the great sensitivity and simplicity of this approach,[5] previous tritium NMR mechanistic studies of proton exchange have been confined to a static approach, i.e. the analysis of aliquots of a kinetic experiment.[23] In most circumstances, it is desirable to perform one-tube, accurate, kinetic experiments, especially for compounds which are only available in small amounts or have several exchanging positions with similar rates. Use of deuterium NMR spectroscopy, hampered by its low sensitivity and resolution, is inherently limited to initial rates,[24] and if several positions are measured simultaneously, relative rates for the positions must lie within a small range. In contrast, tritium NMR spectroscopy allows one to measure the proton exchange kinetics of several compounds which may have similar rates or vary by a factor of 1000. Since tritium is a highly sensitive nucleus, the sample need not contain high levels of tritium for detection (especially compared with deuterium) and tritium therefore functions as a true tracer in the reaction kinetics. Only 20–180 MBq (0.5–5 mCi) per position (1.5×10^{-5}% incorporation) is necessary for an adequate S/N ratio. This low tritium concentration also ensures the absence of tritium–tritium coupling, and the high γ and excellent relaxation characteristics of the nucleus lead to sharp resonance lines. The integrity of the reactant mixture may be monitored by proton NMR spectroscopy at any stage of the experiment. An inverse-gated proton-decoupling scheme may be used to ensure that single peaks are observed for each magnetic environment and that the relative peak integrals are not affected by NOE build-up. The quality of the kinetic data obtained by this technique suggests that it may be readily applied to other chemical proton-transfer systems.

As an example, this technique has been applied to the measurement of detritiation rates for the characterization of isotope effects. The Swain–Schaad relationship predicts that the deuterium and tritium isotope effects on the rate of a reaction are related as follows: $(k_H/k_D)^x = k_H/k_T$. Theoretical calculations put x in the range 1.33–1.58, and a simple zero-point energy formulation of isotope effects gives x = 1.44. Deviations from this range have recently been used as evidence of tunneling in enzyme-catalyzed reactions, so the accuracy of experimental results in simple chemical systems is important. Such a simple system is the hydroxide ion-catalyzed enolization of acetone (a prototype ketone ionization reaction), but the originally published measurements give an anomalously low exponent, x = 1.08.[25] This exponent was based upon rates of detritiation of labeled acetone, which were determined by a technique that involved a difficult separation of acetone from water.

This reaction was reinvestigated[26] using tritium NMR to monitor the exchange of tritium between acetone and water in situ,[22] thus avoiding the troublesome acetone–water separation. In NMR experiments using a range of base concentrations, the tritium signal from the acetone at δ = 2.1 ppm was seen to decay while another resonance at δ = 4.7 ppm, attributable to HTO, appeared (Figure 9). Least-squares fitting of the observed exponential rise and decay gave first-order rate constants that agreed well with each other.

When the NMR result was combined with k_H and a literature value of k_D determined by mass spectrometric measurements, it yielded k_H/k_D = 7.2 and k_H/k_T = 19.2. These isotope effects provide the Swain–Schaad exponent x = 1.49 $\pm$ 0.07, which is in complete agreement with theory. Thus, tritium NMR provided a simple method for the measurement of an important exchange rate which was essentially inaccessible by chemical techniques.

4.6 Miscellaneous

Tritium NMR spectroscopy has been used in a number of other very specific chemical and physical investigations, most of which have been comprehensively reviewed elsewhere.[5]

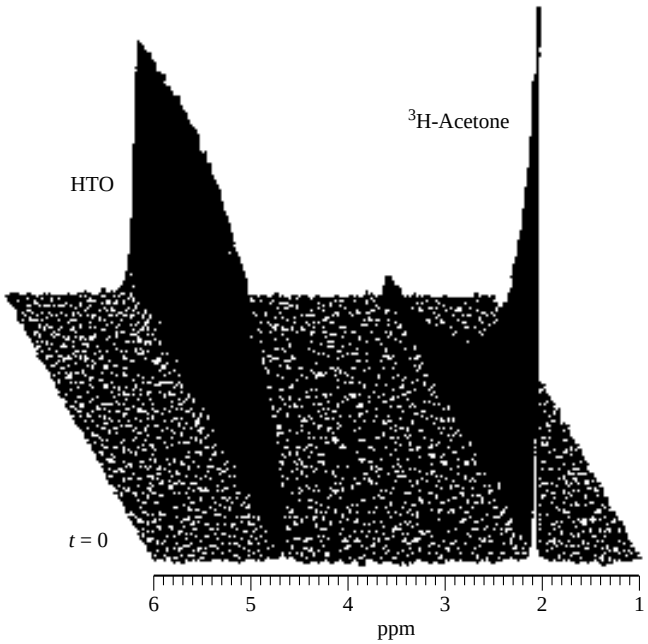

Figure 9 A stacked plot of the proton-decoupled tritium NMR spectra of the base-catalyzed detritiation of acetone (δ = 2.1 ppm) with exchange into the solvent (HTO, 4.7 ppm). The experimental parameters were: 500 μL, 0.04 M, NaOH; 5 μL, ^{3}H-acetone; T = 298 K; 120 transients; 100 experiments over 10.5 h (ca. 4-min interval for the first 50, then 8-min interval); spectrometer unlocked; t = 0 when the acetone was added, and the first spectrum was finished at t = 20 min. Seventy-seven spectra are plotted

These applications have included: (i) the observation of hydrogen-bonding effects on the chemical shift of proton versus tritium NMR signals; (ii) determination of solvent isotope effects and fractionation factors; (iii) aspects of radiation chemistry including sample radiolysis, studies of DNA hydration, and in situ production of labeled carbocations; (iv) investigations of labeled molecules in a liquid crystal environment; (v) solids tritium NMR and characterization of trapped gases in irradiated lithium hydride (tritide) samples;[27] and (vi) study of the origin of an anomalously large proton–proton coupling in transition metal polyhydrides.[28]

5 CONCLUSION

We have discussed a wide range of applications where the use of tritium NMR has been useful, and some instances where it was essential. The similarity in NMR properties between protons and tritons means that many systems may be studied using either nucleus. Moreover, when proton systems become too complex, the spectral simplification of tritium spectroscopy suggests that tritium NMR should be considered. Radioactivity is the only issue hindering the universal application of tritium in many more general NMR studies.

6 RELATED ARTICLES

Enzymatic Transformations: Isotope Probes; Multidimensional Spectroscopy: Concepts; Tritium NMR in Biology.

7 REFERENCES

1. H. L. Anderson and A. Novick, *Phys. Rev.*, 1947, **71**, 372.
2. F. Bloch, A. C. Graves, M. Packard, and R. W. Spence, *Phys. Rev.*, 1947, **71**, 373.
3. F. Bloch, A. C. Graves, M. Packard, and R. W. Spence, *Phys. Rev.*, 1947, **71**, 551.
4. G. V. D. Tiers, C. A. Brown, R. A. Jackson, and T. N. Lahr, *J. Am. Chem. Soc.*, 1964, **86**, 2526.
5. E. A. Evans, D. C. Warrell, J. A. Elvidge, and J. R. Jones, *Handbook of Tritium NMR Spectroscopy and Applications*, Wiley, Chichester, 1985, pp. 1–249.
6. J. P. Bloxsidge, J. A. Elvidge, J. R. Jones, R. B. Mane, and M. Saljoughian, *Org. Magn. Reson.*, 1979, **12**, 574.
7. J. M. A. Al-Rawi, J. P. Bloxsidge, C. O'Brien, D. E. Caddy, J. A. Elvidge, J. R. Jones, and E. A. Evans, *J. Chem. Soc., Perkin Trans. 2*, 1974, 1635.
8. J. M. A. Al-Rawi, J. A. Elvidge, J. R. Jones, and E. A. Evans, *J. Chem. Soc., Perkin Trans. 2*, **1975**, 449.
9. J. P. Bloxsidge, J. A. Elvidge, J. R. Jones, E. A. Evans, J. P. Kitcher, and D. C. Warrell, *Org. Magn. Reson.*, 1981, **15**, 214.
10. P. G. Williams, H. Morimoto, and D. E. Wemmer, *J. Am. Chem. Soc.*, 1988, **110**, 8038.
11. J. M. A. Al-Rawi, J. P. Bloxsidge, J. A. Elvidge, J. R. Jones, V. E. M. Chambers, V. M. A. Chambers, and E. A. Evans, *Steroids*, 1976, **28**, 359.
12. F. M. Kaspersen, C. W. Funke, E. M. G. Sperling, and G. N. Wagenaars, *J. Labelled Compds. Radiopharm.*, 1987, **24**, 219.
13. T. L. Ceckler and R. S. Balaban, *J. Magn. Reson.*, 1991, **93**, 572.
14. P. G. Williams, in *Isotopes in the Physical and Biomedical Sciences*, ed. E. Buncel and J. R. Jones, Elsevier, Amsterdam, 1991, Vol. 2, p. 55.
15. J. A. Elvidge, J. R. Jones, R. M. Lenk, Y. S. Tang, E. A. Evans, G. L. Guilford, and D. C. Warrell, *J. Chem. Res. (S)*, 1982, 82.
16. A. S. Culf, Ph.D. Thesis, University of Surrey, UK, 1994.
17. L. J. Altman and L. Thomas, *Anal. Chem.*, 1980, **52**, 992.
18. F. A. L. Anet, D. J. O'Leary, and P. G. Williams, *J. Chem. Soc., Chem. Commun.*, 1990, 1427.
19. N. D. Priestley, H. G. Floss, W. A. Froland, J. D. Lipscomb, P. G. Williams, and H. Morimoto, *J. Am. Chem. Soc.*, 1992, **114**, 7561.
20. J. A. Elvidge, E. A. Evans, J. R. Jones, and L. M. Zhang, *Synth. Appl. Isot. Labeled Compd., Proc. 2nd Int. Symp.*, ed. R. R. Muccino, Elsevier, Amsterdam, 1986, p. 401.
21. F. M. Kaspersen, C. W. Funke, E. M. G. Sperling, F. A. M. Van Rooy, and G. N. Wagenaars, *J. Chem. Soc., Perkin Trans. 2*, 1986, 585.
22. R. E. Dixon, P. G. Williams, M. Saljoughian, M. A. Long, and A. Streitwieser, *Magn. Reson. Chem.*, 1991, **29**, 509.
23. E. Buncel, J. P. Davey, G. J. Buist, J. R. Jones, and K. D. Perring, *J. Chem. Soc., Perkin Trans. 2*, 1990, 169.
24. D. W. Boerth, and A. Streitwieser, Jr., *J. Am. Chem. Soc.*, 1981, **103**, 6443.
25. J. R. Jones, *Trans. Faraday Soc.*, 1969, **65**, 2138.
26. Y. Chiang, A. J. Kresge, H. Morimoto, and P. G. Williams, *J. Am. Chem. Soc.*, 1992, **114**, 3981.
27. R. C. Bowman, Jr., A. Attalla, P. C. Souers, C. L. Folkers, T. McCreary, G. D. Snider, F. Vanderhoofven, and R. T. Tsugawa, *J. Nucl. Mater.*, 1988, **154**, 318.
28. K. W. Zilm, D. M. Heinekey, J. M. Millar, N. G. Payne, and P. Demou, *J. Am. Chem. Soc.*, 1989, **111**, 3088.

Acknowledgments

M.G.K. is supported by the Office of Energy Research, Office of Health and Environmental Research, Health Effects Research Division of the US Department of Energy under Contract DE-AC03-76SF00098, and through Instrumentation Grants from the US Department of Energy, DE FG05-86ER75281, and the National Science Foundation, DMB 86-09035. P.G.W. is supported by the Biomedical Research Technology Program, National Center for Research Resources, US National Institutes of Health, under Grant P41 RR01237, through Contract DE-AC03-76SF00098 with the US Department of Energy.

Biographical Sketches

Mark G. Kubinec. *b* 1964. B.S., 1986, biochemistry, B.S., 1987, chemistry, Michigan State University, USA, Ph.D., 1994, Chemistry, University of California, Berkeley, USA. Postdoctoral fellow, Lawrence Berkeley National Laboratory, 1995–present.

Philip G. Williams. *b* 1956. B.Sc., 1980, chemistry, Ph.D., 1984, chemistry, University of New South Wales, Australia. Research Fellow, Ludwig Institute for Cancer Research, Sydney, Australia, 1984–85; staff scientist, Lawrence Berkeley National Laboratory, USA, 1986–present. Approx. 70 publications Current research specialties: tritium labeling, tritium NMR.

Vanadium Catalysts: Solid State NMR

Vjatcheslav M. Mastikhin and Olga B. Lapina
Boreskov Institute of Catalysis, Siberian Branch of Russian Academy of Sciences, Novosibirsk, Russia

1 Introduction 1
2 Vanadium-51 NMR Spectra of Solids With a Well-Characterized Structure. Interrelation Between ^{51}V NMR Parameters and the Local Environment of V Nuclei 1
3 Study of Vanadium Catalysts 4
4 Related Articles 12
5 References 12

1 INTRODUCTION

Measurements of ^{51}V NMR spectra of solids (see ***Quadrupolar Nuclei in Glasses***; ***Quadrupolar Nuclei in Solids***) with the use of modern NMR spectrometers (see ***Spectrometers: A General Overview***) equipped with line-narrowing techniques for obtaining high-resolution spectra of solids (see ***Double Rotation***; ***High Speed MAS of Half-Integer Quadrupolar Nuclei in Solids***; ***Magic Angle Spinning***; ***Variable Angle Sample Spinning***) provide important information on the local environment of V nuclei.[1] The latter is known to be a key factor determining the activity and selectivity of heterogeneous catalysts. Due to this fact ^{51}V NMR solid state spectroscopy is successfully used for the studies of vanadia-based catalysts. The latter are used for the production of sulfuric acid, the selective oxidation of hydrocarbons, and also for reduction of atmospheric pollution.[2]

The results presented below show that ^{51}V NMR provides important information concerning the structure and reactivity of surface V sites. Herein will be discussed the main features of ^{51}V NMR in solids and its application for the studies of vanadium catalysts.

The vanadium-51 nucleus (natural abundance 99.76%) has a spin $I = \frac{7}{2}$, its electric quadrupole moment being $-4 \times 10^{-2} \times 10^{-24}\,\mathrm{cm}^2$; the relative intensity of ^{51}V NMR is 0.38 compared with an equal number of protons.

In general, three different types of interactions influence the ^{51}V NMR spectra of solid diamagnetic samples (see ***Internal Spin Interactions and Rotations in Solids***): (1) the dipole interaction (see ***Dipolar and Indirect Coupling Tensors in Solids***) of the magnetic moment of the ^{51}V nucleus with the magnetic moments of other nuclei that broadens the lines; (2) the quadrupole interaction (see ***Quadrupolar Interactions***) of the ^{51}V nucleus with the electric field gradient that splits the lines and contributes to the shift of the central ($m_I = \frac{1}{2} \leftrightarrow m_I = -\frac{1}{2}$) line; and (3) the chemical shielding interaction (see ***Chemical Shift Tensors***) that changes the position of the lines and makes them asymmetric.

In general, the lineshape might be rather complicated due to the simultaneous action of all types of interactions. For powdered samples (the case typically met in heterogeneous catalysts) only the central transition ($m_I = \frac{1}{2} \leftrightarrow m_I = -\frac{1}{2}$) can most commonly be observed, while other transitions are too broad to be recorded. The line from the central transition is typically anisotropic, i.e. it has a rather complicated shape. This complicated shape reflects the fact that the observed line is actually a superposition of individual lines from vanadium sites having various orientations with respect to the external magnetic field. When these individual lines are narrow enough, the positions of the so-called discontinuity points can be readily identified in the overall ^{51}V NMR spectrum. From the position of the discontinuity points one can easily obtain the quadrupole coupling constant, χ, the asymmetry parameter, η, and the shielding anisotropy parameters σ_{11}, σ_{22}, and σ_{33}.[3]

Unfortunately, in the ^{51}V NMR spectra of many solid catalysts the effects from the discontinuity points are often completely or partially obscured due to the large broadening of individual lines. In this case computer analysis of the spectra recorded at various frequencies becomes necessary if one wishes to obtain the above-mentioned values. Note, that interactions affecting ^{51}V NMR spectra exhibit different frequency dependences. Indeed, the dipole interaction and the first-order quadrupole interaction do not depend on the spectrometer frequency ν_0, while the second-order quadrupole effects are inversely proportional to ν_0. The effects of the shielding anisotropy are directly proportional to ν_0. Thus, at a sufficiently high ν_0, the second-order quadrupole effects are suppressed and can be neglected, while the effects of the chemical shielding anisotropy become more pronounced and can be measured more precisely (***Chemical Shift Tensor Measurement in Solids***). A comparison of ^{51}V NMR spectra recorded at various ν_0 with computer simulated spectra has been demonstrated to allow sufficiently precise measurements of the spectral parameters characterizing vanadium sites in the solid catalysts.[1]

Typical examples of computer simulated ^{51}V NMR spectra of V(V) sites in solid V_2O_5 are presented in Figure 1. Calculations were performed using the program for high magnetic fields ($B_0 > 7\,\mathrm{T}$) when the perturbation theory approach can be applied, i.e. the values of the quadrupole and nuclear shielding terms are small when compared with the nuclear Zeeman energy.[1,4]

Figure 1(a) and (b) show the influence of the first-order quadrupole effects on the calculated spectra of solid V_2O_5 at $\nu_0 = 105.15\,\mathrm{MHz}$. Figure 1(c) demonstrates the spectral broadening in powdered or polycrystalline samples due to the distribution of quadrupole coupling constant.

2 VANADIUM-51 NMR SPECTRA OF SOLIDS WITH A WELL-CHARACTERIZED STRUCTURE. INTERRELATION BETWEEN ^{51}V NMR PARAMETERS AND THE LOCAL ENVIRONMENT OF V NUCLEI

To analyze the spectra of real catalytic systems one needs information on the spectra of vanadium compounds that might be present in the catalysts, as well as data on the interrelation between ^{51}V NMR parameters and the characteristics of the local environment of the V nuclei.

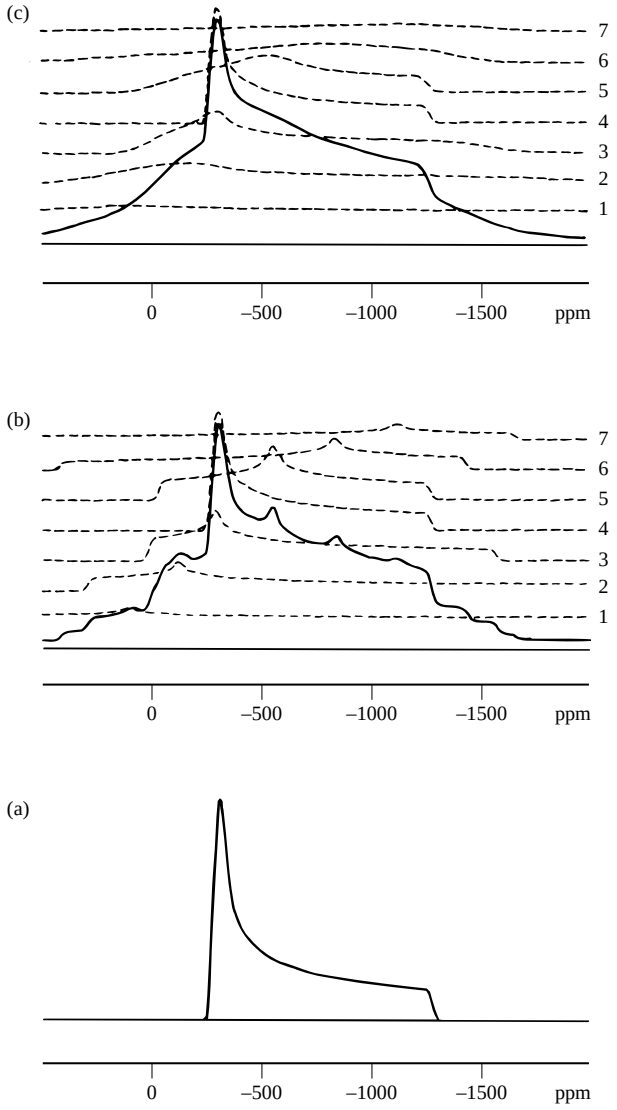

Figure 1 Computer simulated ^{51}V NMR spectra demonstrating the influence of the first-order quadrupole effects and line broadening on the spectra of solid V_2O_5 (at the frequency 105.15 MHz). The following parameters were used: χ = 0.805 MHz, η = 0.04;[5] σ_{11} = 310, σ_{22} = 1280, σ_{33} = 270 ppm. (a): The lineshape for the central transition ($\frac{1}{2}$, $-\frac{1}{2}$). (b) (Dotted lines): the lineshapes for all possible transitions: 1 ($-\frac{5}{2}$, $-\frac{7}{2}$), 2 ($-\frac{3}{2}$, $-\frac{5}{2}$), 3 ($-\frac{1}{2}$, $-\frac{3}{2}$), 4 ($\frac{1}{2}$, $-\frac{1}{2}$), the central transition, 5 ($\frac{3}{2}$, $\frac{1}{2}$), 6 ($\frac{5}{2}$, $\frac{3}{2}$), 7 ($\frac{7}{2}$, $\frac{5}{2}$). (b) (Solid line): the overall spectrum from all transitions. (c): Spectrum demonstrating the broadening of the lines from all transitions [dotted lines, numbered exactly as in (b)] and the overall spectrum from all transitions (solid line) due to the Gaussian distribution of quadrupole coupling constant χ. Dipolar linewidth *DF* = 1.5 kHz

The ^{51}V NMR spectra of various solid vanadium compounds[1,3,5–8] with well-characterized structures[9] and of the vanadates of alkali metals, which are often used for the preparation of catalysts, have been studied.

In Table 1 the ^{51}V NMR chemical shielding parameters[1,3,5,7,8] for vanadates are listed.

The ^{51}V NMR parameters of the large number of V compounds with a well-characterized crystal structure presented in Table 1 prove the high sensitivity of NMR spectra toward details of the local environment of V nuclei.

In most cases the shape of ^{51}V NMR spectra measured in high magnetic fields ($B_0 > 7$ T) depends on the anisotropy of the chemical shielding tensor. The influence of the second-order quadrupole effects is typically smaller and often is quite negligible.[10]

The following conclusions on V coordination (tetrahedral or octahedral, regular or distorted) and the extent of association of vanadium–oxygen polyhedra can be drawn based on the type and magnitude of the chemical shielding anisotropy.[1,7,10]

(a) For vanadium in regular tetrahedral sites (sites of the Q^0 type), the isotropic spectra with close values of the chemical shielding tensor components ($\sigma_{11} \approx \sigma_{22} \approx \sigma_{33}$) typically have $\Delta\sigma < 100$ ppm.

(b) For vanadium in slightly distorted tetrahedral sites with adjacent VO_4 tetrahedra sharing one common oxygen atom (sites of the Q^1 type), a fully anisotropic shielding tensor ($\sigma_{11} \neq \sigma_{22} \neq \sigma_{33}$) is typical, but with a larger $\Delta\sigma$ value ($\Delta\sigma$ = 70–300 ppm).

(c) For vanadium in strongly distorted tetrahedral sites with adjacent VO_4 tetrahedra sharing two common oxygen atoms (sites of the Q^2 type), a fully anisotropic shielding tensor ($\sigma_{11} \neq \sigma_{22} \neq \sigma_{33}$) is typical with $\Delta\sigma$ = 300–375 ppm).

(d) For vanadium in distorted octahedral sites (i.e. in a distorted octahedral environment of oxygen atoms), a nearly axial shielding anisotropy is typical with $\sigma_{11} \approx \sigma_{22} < \sigma_{33}$ ($\Delta\sigma$ = 450–900 ppm for structures 4 in Figure 2 and $\Delta\sigma$ = 900–1300 ppm for structures 5 in Figure 2).

Conclusions (a) to (d) are illustrated in Figure 2 for a family of Tl vanadates and V_2O_5.

Note, that ^{51}V NMR spectra with approximate axial symmetry of the σ tensor should also be expected for VO_4 tetrahedra with symmetry close to C_{3v}, i.e. when one V–O bond differs significantly from the other three (which have about the same length) (sites of the Q^1 type). In this case the direction of $\sigma_\parallel$ will coincide with the direction of the V–O bond which differs from the three others, with $|\sigma_\perp| < |\sigma_\parallel|$ if this bond is shorter than the three others and $|\sigma_\perp| > |\sigma_\parallel|$ if this bond is the longest one.

A comparison of the shielding anisotropy $\Delta\sigma = |\sigma_{33} - \frac{1}{2}(\sigma_{11} + \sigma_{22})|$ for metavanadates whose structural data are known shows a good correlation between $\Delta\sigma$, on the one hand, and the angle O_3–V–O_3' on the other hand [Figure 3(a)]. According to the structures of the metavanadates schematically presented in Figure 3(a) this angle characterizes the distortion of the tetrahedral environment of V. The larger the deviation of angle O_3–V–O_3' from that in the regular tetrahedron (109°28′), the larger is $\Delta\sigma$.

Distortion of the VO_4 tetrahedra also results in an increase in the electric field gradient on the V nucleus. It seems natural to expect a correlation between $\Delta\sigma$ and the quadrupole interaction parameters, χ and η. Indeed, such a correlation has been found for metavanadates [Figure 3(b)].

In contrast to ^{27}Al[11] and ^{29}Si[12] (see ***Aluminum-27 NMR of Solutions***; ***Molecular Sieves: Crystalline Systems***; ***Silicon-29 NMR***), the isotropic chemical shifts σ_{iso} for ^{51}V nuclei in vanadates are not too sensitive to V coordination (octahedral or tetrahedral). Compounds with rather different coordination may have very close σ_{iso} values. Thus, for vanadates, the anisotropy of the ^{51}V chemical shift is much more sensitive

Table 1 Components of ^{51}V Chemical Shieldings (Measured in ppm With Respect to $VOCl_3$ With An Accuracy of ±10 ppm) and Quadrupole Constants χ and η for Vanadates

Compound	Site	σ_{11}	σ_{22}	σ_{33}	σ_{iso}	$\Delta\sigma$	χ(MHz)	η
Virtually regular tetrahedra VO_4, Q^0 type								
Li_3VO_4[1]					544	50	1.52	
							1.51[3]	
Na_3VO_4[7]					545			
							1.05[3]	
K_3VO_4[1]					560	100		
Cs_3VO_4[1]		520	580	626	576	70		
Tl_3VO_4[1]					480	30		
$Mg_3(VO_4)_2$[1]					557	40		
$Ca_3(VO_4)_2$[1]					615	100		
							2.05[3]	
$Sr_3(VO_4)_2$[1]					610	20		
							0.53[3]	
$Ba_3(VO_4)_2$[1]					605	20		
							0.75[3]	
$Zn_3(VO_4)_2$[7]					522			
$Pb_3(VO_4)_2$[22]		521	508	467	486	48		0.41
$AlVO_4$[1]	V1	630	640	730	668	95		
	V2	605	745	800	747	55		
	V3	710	800	830	780	75		
$BiVO_4$[1]		355	405	500	420	120		
YVO_4[1]					664	30		
							4.75[3]	0.00[3]
$LaVO_4$[1]		555	616	657	609	72		
							5.21[3]	0.69[3]
$LuVO_4$[1]					663	30		
							4.23[3]	0.00[3]
Slightly distorted tetrahedra, Q^1 type								
$Na_4V_2O_7$[1]	V1				560			
	V2				575			
$K_4V_2O_7$[1]		500	582	642	578	100		
$Cs_4V_2O_7$[1]	V1				543			
	V2				567			
$Tl_4V_2O_7$[1]		443	512	556	504	89		
α-$Mg_2V_2O_7$[1]	V1	510	570	585	555	45		
	V2	570	580	700	617	125		
β-$Mg_2V_2O_7$[1]	V1	460	560	680	560	170		
	V2	590	660	700	650	75		
$Ca_2V_2O_7$[1]	V1	528	564	630	574	84		
	V2	530	564	640	578	93		
$Sr_2V_2O_7$[1]	V1	523	548	600	557	65		
	V2	480	620	650	582	155		
	V3	480	632	652	588	160		
	V4	480	638	658	592	168		
$Ba_2V_2O_7$[1]	V1	530	555	652	579	109		
	V2	575	574	615	588	140		
	V3	535	625	640	600	100		
$Zn_2V_2O_7$[7]		500	640	720	625	150		
$Cd_2V_2O_7$[7]		370	660	660	579	290		
$Pb_2V_2O_7$[7]		430	480	620	522	165		
ZrV_2O_7[1]		710	802	824	774	110		
Distorted tetrahedra, Q^2 type								
$LiVO_3$[8]		385	540	794	573	332	3.18	0.87
NH_4VO_3[1]		380	530	807	572	352		
		366[8]	534[8]	810[8]	570[8]	360[8]	2.95[8]	0.30[8]
							2.88[3]	0.30[3]
							2.95[3]	0.19[3]
							2.76[3]	0.37[3]
β-$AgVO_3$[22]		202	285	609	364	366		0.34
α-$NaVO_3$[1]		368	530	820	582	371		
		355[8]	531[8]	833[8]	573[8]	390[8]	3.80[8]	0.46[8]
							3.70[3]	0.52[3]

						3.65[3]	0.60[3]
						3.15[3]	0.64[3]
						3.94[3]	0.64[3]
$TlVO_3$[1]	300	490	793	528	398		
	296[8]	497[8]	794[8]	529[8]	398[8]	3.67[8]	0.71[8]
$CsVO_3$[1]	330	522	863	583	437		
						3.92[3]	0.62[3]
						3.84[3]	0.63[3]
$RbVO_3$[1]	313	508	863	570	453		
						4.33[3]	0.72[3]
KVO_3[1]	294	490	856	548	464		
	313[8]	501[8]	842[8]	552[8]	435[8]	4.20[8]	0.80[8]
						4.21[3]	0.65[3]
						4.35[3]	0.75[3]
						4.06[3]	0.76[3]
						4.34[3]	0.77[3]
Distorted octahedra							
$K_2V_6O_{16}$[1]	290	290	935	503	630		
$Rb_2V_6O_{16}$[1]	290	290	935	503	630		
$Cs_2V_6O_{16}$[1]	296	296	953	508	645		
$Tl_2V_6O_{16}$[1]	485	485	1165	700	680		
α-$Mg(VO_3)_2$[1]	310	470	950	576	560		
						6.79[3]	0.63[3]
$Ca(VO_3)_2$[1]	278	355	1080	575	764		
						3.30[3]	0.8[3]
						3.16[3]	0.60[3]
						2.81[3]	0.60[3]
$Sr(VO_3)_2$[22]	533	577	833	643	283		0.29
$Ba(VO_3)_2$[1]	540	614	950	660	373		
$Zn(VO_3)_2$[7]	270	410	920	517	580		
$Pb(VO_3)_2$[7]	310	320	1000	533	685		
$Cd(VO_3)_2$[1]	305	365	830	500	495		
V_2O_5[1]	310	310	1270	610	960		
						0.8[5]	0.04[5]
$VOAsO_4$[1]	218	255	1370	617	1134		
$VOPO_4$[1]	285	285	1547	734	1260		

to the character of the local arrangement of oxygen atoms around V than the isotropic chemical shift σ_{iso}. At the same time, for compounds with the same type of first coordination sphere, σ_{iso} depends notably on the type of atoms in the second coordination sphere of V, as also found for ^{27}Al and ^{29}Si atoms.[11,12]

3 STUDY OF VANADIUM CATALYSTS

Typically, other techniques and approaches are used for identification of individual surface V species, in addition to ^{51}V NMR. These include studies with magic angle spinning (MAS), NMR of nuclei of elements other than V and other spectroscopic methods, as well as chemical approaches. A combination of spectroscopic data with the measurements of catalytic activity allows one to identify the catalytically active sites.

3.1 V_2O_5/SiO_2 Catalysts

3.1.1 Prepared by Impregnation

Spectra of V_2O_5/SiO_2 samples prepared via impregnation of SiO_2 with NH_4VO_3 solution are presented in Figure 4. The spectrum of the sample dried at 120 °C indicates only a slight change in the vanadium surroundings in comparison to that in NH_4VO_3 (spectrum 1a) and can be ascribed to (VO_4) species adsorbed on the SiO_2 surface. Calcination in vacuum provides a species that may differ both in the number of bonds with the surface and with neighboring vanadium species (spectra 2, 3, and 4 in Figure 4). Thus, lines present in spectra 2, 3, and 4 (calcination at 200 °C, 500 °C, and 700 °C) may be assigned to V species bonded to the surface via one, two, or three V–O bonds, respectively, as well as to V species bonded to neighboring vanadium species via one or two bonds.

Spectra of samples with high V concentrations (spectra 5 and 6) suggest the formation of the amorphous (nonregular) precursor of V_2O_5, since no sidebands are observed in the MAS spectra of these samples. Increasing the treatment temperature up to 700 °C results in the appearance of a line with highly resolved sidebands, due to rearrangement of the amorphous V_2O_5 structure to the crystalline one.

3.1.2 Prepared by $VOCl_3$ Interaction With SiO_2

The spectrum of the sample after $VOCl_3$ deposition suggests the presence of physically adsorbed $VOCl_3$ (narrow line with $\delta = -6$ ppm) and of $VOCl_{3-n}(OSi)_n$ species bonded with the SiO_2 surface [a line with an axial anisotropy, Figure 4(b),

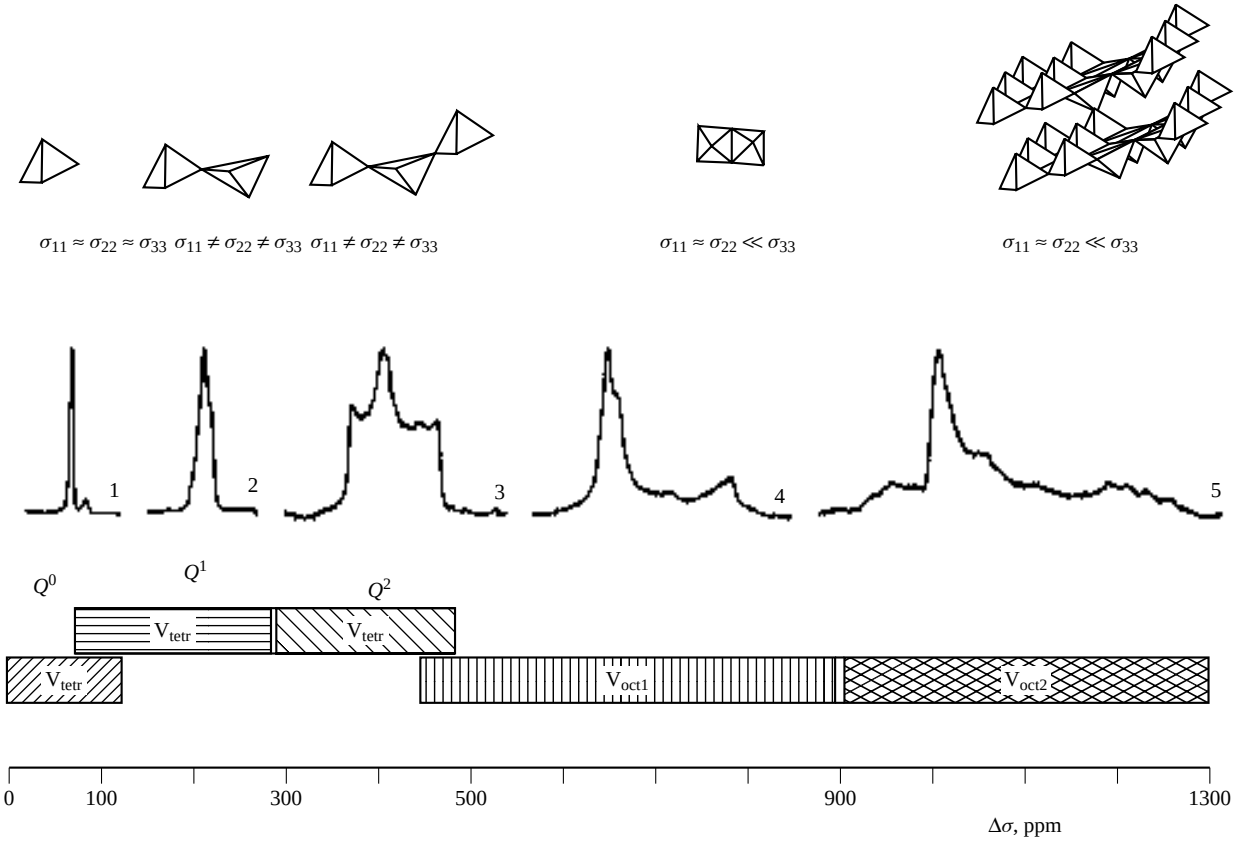

Figure 2 Relationship between the type of V coordination (tetrahedral or octahedral), the extent of polyhedra association (Q), and the shielding anisotropy $\Delta\sigma$. [As an example, the ^{51}V NMR spectra of Tl vanadates and V_2O_5 are presented: 1, Tl_3VO_4 (regular tetrahedra, Q^0); 2, $Tl_4V_2O_7$ (slightly distorted tetrahedra, Q^1); 3, $TlVO_3$ (strongly distorted tetrahedra, Q^2); 4, $Tl_2V_6O_{16}$ (distorted octahedra); 5, V_2O_5 (strongly distorted octahedron or square-pyramid)]

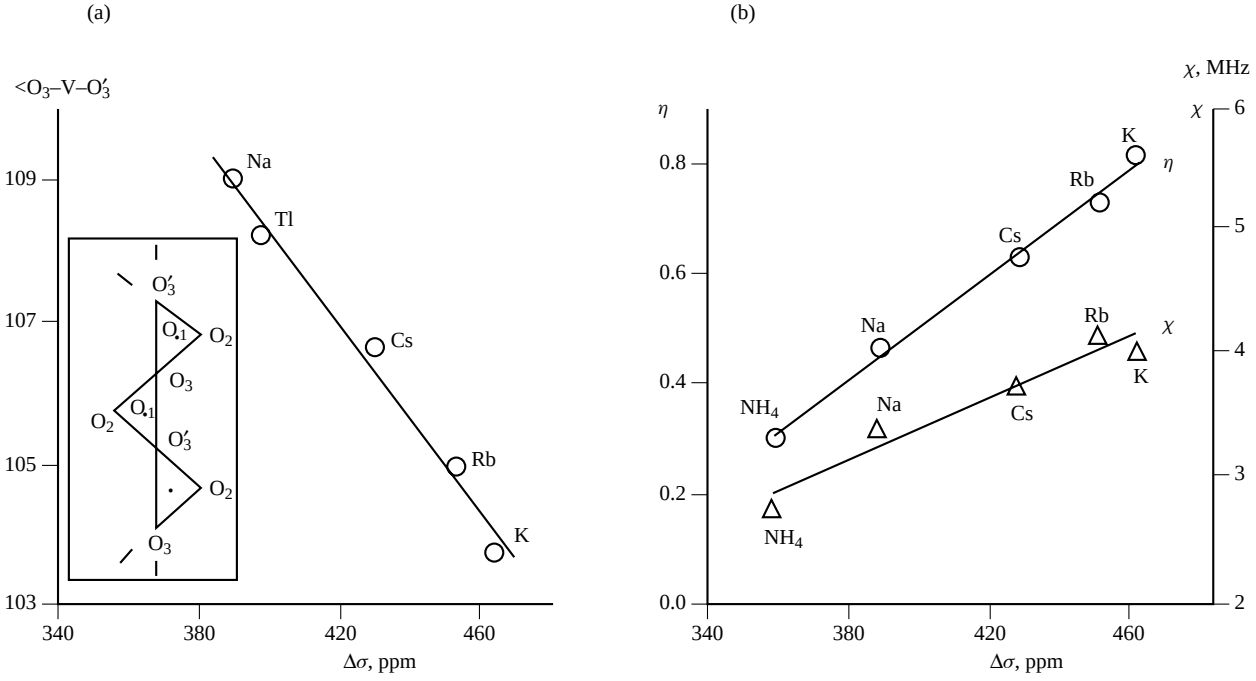

Figure 3 (a) Schematic representation of the structure of metavanadates of Na, Tl, Cs, Rb, and K and the dependence of the shielding anisotropy ($\Delta\sigma$) of their ^{51}V NMR spectra upon the $O_3–V–O_3'$ angle. This angle characterizes the distortion of the VO_4 tetrahedron from the regular form where $O_3–V–O_3' = 109°28'$. (b) Correlation between the shielding anisotropy $\Delta\sigma$ (data of Table 1) and the quadrupole coupling parameters χ and η (the latter taken from Pletnev et al.3 and Eckert and Wachs7) for metavanadates

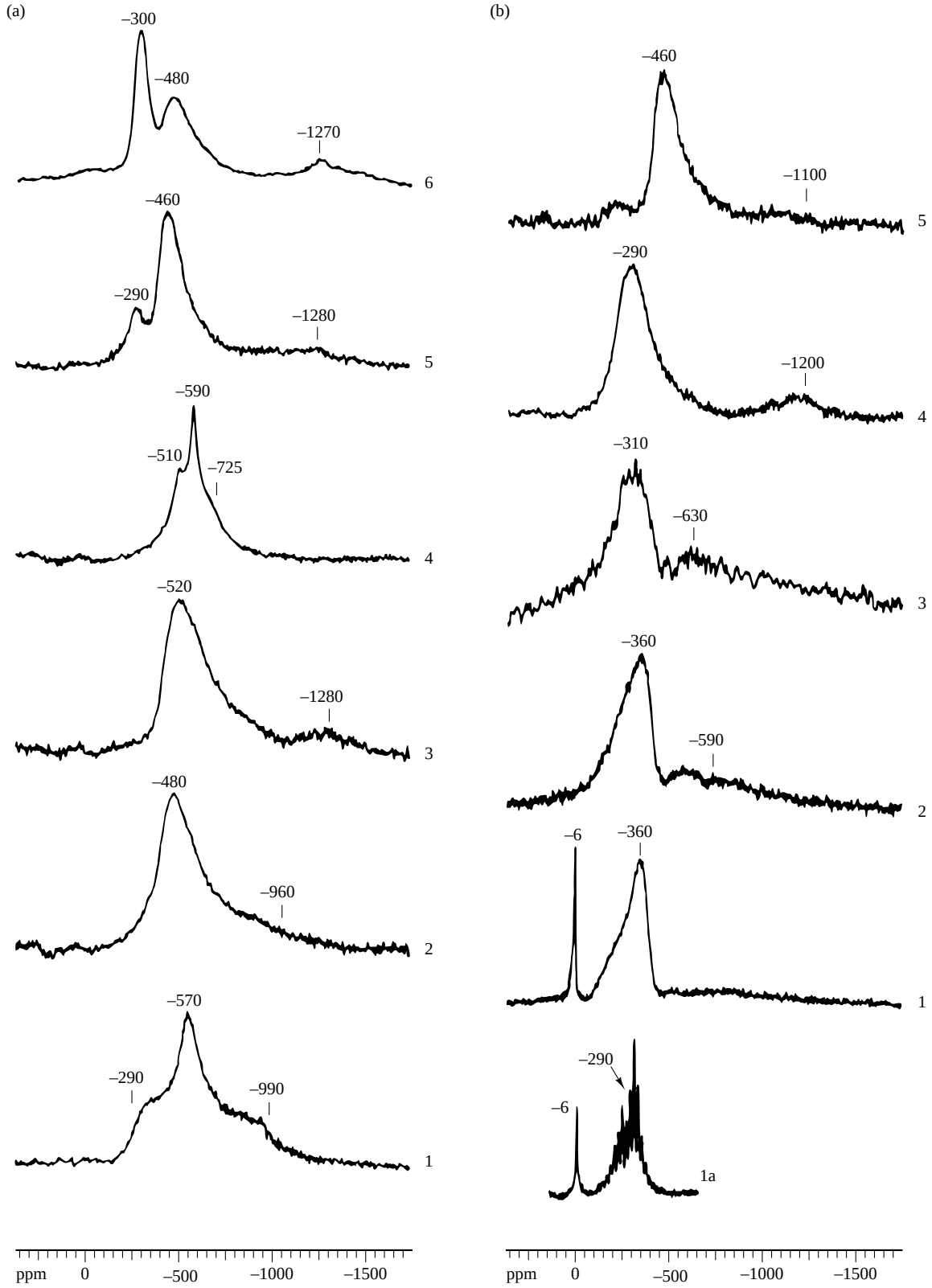

Figure 4 (a) ^{51}V NMR spectra of V_2O_5/SiO_2 samples prepared via impregnation of SiO_2 with NH_4VO_3 (pH 7, 2.6 wt.% V_2O_5) 1, after treatment in vacuum at 120 °C; 2, at 200 °C; 3, at 500 °C; 4, at 700 °C. Spectra 5 and 6 correspond to samples with a V content of 5.5 and 6.4 wt.% V_2O_5, respectively, calcined at 500 °C. (b) ^{51}V NMR spectra of $VOCl_3/SiO_2$ samples prepared by interaction of $VOCl_3$ from the gas phase with SiO_2: 1, after $VOCl_3$ deposition; 1a, MAS spectrum of the same sample [line at 6 ppm corresponds to physically adsorbed $VOCl_3$, anisotropic line with σ_{iso} = 290 ppm corresponds to $VOCl_2$(OSi) surface species]; 2, 3, 4, and 5, increase of H_2O content (replacement of Cl atoms to OH groups takes place during the first stage of hydration, then interaction of V species with the next H_2O molecules occurs); 6, spectrum 5 after evacuation at 100 °C. All the spectra here and in the remaining figures were recorded at 105.15 MHz, pulse duration = 0.5 μs, pulse repetition frequency = 1 Hz. Chemical shifts are presented with respect to $VOCl_3$ as external reference

spectrum 1]. Deposition of $VOCl_3$ at room temperature yields complexes with $n = 1$ (a line with $\sigma_{iso} = 290$ ppm, spectrum 1a). Increasing the deposition temperature to 400 °C leads to complexes with $n = 2$ or 3. The first additions of water cause the disappearance of physically adsorbed $VOCl_3$ [Figure 4(b), spectrum 2], then water interacts with the $VOCl_{3-n}(OSi)_n$ surface species producing partially hydrated $VO(OH)_y$-$Cl_{3-n-y}(OSi)_n$ ($y \leq n$, $n = 1$, 2, or 3) species (spectra 2 and 3) and fully hydrated $VO(OH)_{3-n} \cdot 2H_2O(OSi)_n$ species (for these species the sign of the anisotropy is opposite to that for species containing Cl in their coordination sphere, $\sigma_{\parallel} > \sigma_{\perp}$). Dehydration under mild conditions (100 °C) results in the removal of water from the first coordination sphere and in the formation of associated tetrahedral complexes (spectrum 5). The latter was ascribed to $VO(OSi)_3$ by Das et al.[13]

Application of magic angle spinning does not improve the resolution, unlike the situation when complexes contain Cl in the first coordination sphere. This indicates a nonregularity in the structure of the surface oxide complexes.

These data along with results presented by Lapina et al.[14] show that after calcination at 400–500 °C similar complexes are formed on the SiO_2 surface by the different deposition procedures.

3.2 V_2O_5/Al_2O_3 Catalysts

Vanadium-51 NMR spectra of V_2O_5/Al_2O_3 catalysts prepared by interaction of Al_2O_3 with $VOCl_3$, impregnation of Al_2O_3 with NH_4VO_3, and ultra-high-intensity grinding (UHIG) of V_2O_5-Al_2O_3 mixtures are shown in Figures 5 and 6.

3.2.1 Prepared by Impregnation

The various ^{51}V NMR spectra of these catalysts can be classified in terms of the five different types of lines contained[15,16] (Figure 5). Line A [spectrum (a)-1] observed for wet samples of low V content (1 wt.%) has been attributed to tetrahedral VO_4 species relatively loosely bound to the Al_2O_3 surface via one or two oxygen atoms. Line B, which was detected for calcined samples of low V content (1 wt.%) [spectrum (a)-2] was attributed to VO_4 tetrahedra bound more firmly to the Al_2O_3 surface via two or more oxygen atoms. Line C observed for samples with a large V content either dried or calcined [spectrum (a)-3] has been attributed to polynuclear V species of the decavanadate type on the Al_2O_3 surface. Line D is attributed to the $AlVO_4$ phase. It has been detected in calcined samples with a large V concentration [spectrum (a)-4]. From the MAS spectra, the σ_{iso} values for each of the three nonequivalent V sites in the structure of this compound were as follows: $\sigma_{iso1} = 668 \pm 5$; $\sigma_{iso2} = 747 \pm 5$; $\sigma_{iso3} = 780 \pm 5$ ppm. Line E ($\sigma_{\perp} = 310$ ppm, $\sigma_{\parallel} = 1270$ ppm) relates to V_2O_5 [spectrum (a)-5]. In the spectra of real catalysts, superposition of lines from different V sites occurs as shown in Figure 5(b).

3.2.2 Prepared by Interaction of Al_2O_3 With $VOCl_3$

Figure 6(a) shows that at least four types of particles are formed on the Al_2O_3 surface after $VOCl_3$ deposition: physically adsorbed $VOCl_3$ (narrow line with $\delta \approx 0$ ppm) and particles containing Cl atoms in the first coordination sphere, i.e. $VOCl_{3-n}(OAl)_n$, where $n = 1$, 2, or 3 (broad lines in the range from 0 to −1000 ppm, spectrum 1). The process of hydration occurs initially by hydration of the physically adsorbed $VOCl_3$ (disappearance of the signal at $\delta \approx 0$ ppm) and then exchange of Cl atoms in the first coordination sphere of V by OH groups takes place; after sample treatment at 500 °C, the formation of V sites typical for catalysts prepared by impregnation are also formed [cf. Figure 6(a), spectrum 5 and Figure 6(b), spectrum 3].

3.2.3 Prepared by UHIG Treatment

The ultra-high-intensity grinding (UHIG) of V_2O_5-Al_2O_3 mixtures was found to induce a heterogeneous chemical reaction between these oxides producing highly dispersed V species on the support surface.[17] The ^{51}V NMR spectrum of V_2O_5 after UHIG treatment demonstrates the broadening of the peaks from first-order quadrupole effects due to distortion of the local vanadium environment while the general crystal structure of V_2O_5 is retained [spectra 1 and 2 in Figure 6(c)]. Only a small part of the V_2O_5 reacts with Al_2O_3 when a V_2O_5-Al_2O_3 mixture is calcined for 14 h at 500 °C (peak at −570 ppm) (spectrum 3). A more complete interaction between V_2O_5 and Al_2O_3 takes place in the samples after UHIG treatment at room temperature (spectrum 4). As the concentration of V increases, the other tetrahedral V state (peak near −750 ppm) appears. Subsequent calcination at 500 °C produces V in octahedral coordination. In general, ^{51}V NMR spectra of the samples treated at 500 °C after UHIG treatment show the formation of surface structures that are similar to those for V_2O_5/Al_2O_3 catalysts prepared by the conventional impregnation/calcination method.

Thus, the types of surface V species on Al_2O_3 are the same for all three preparation procedures discussed above. Their relative amounts depend in a similar way on the total V concentration on the Al_2O_3 surface and on the treatment temperature. At low V concentration species A prevail, while at the increased V concentration species B and C appear on the catalyst surface. At still larger amounts of supported V (>10 wt.%), V_2O_5 and $AlVO_4$ also form.

3.3 V_2O_5/MgO Catalysts

Vanadium-51 NMR spectra of V_2O_5/MgO catalysts, recorded at various vanadium content, show four different V sites on the MgO surface (Figure 7).[18] Only one of them can be attributed to magnesium vanadate, $Mg_3(VO_4)_2$. Other V sites have been identified on the basis of correlations between the structure of the local environment of the V nuclei and the shielding anisotropy.

The narrow isotropic line with $\sigma_{iso} = 480$ ppm observed at low vanadium concentration (from 1.6–2.6 wt.% V) [spectra 1 and 2 in Figure 7(a)] has been attributed to isolated surface V atoms which have a virtually regular tetrahedral oxygen environment. Two broadened lines, i.e. an almost isotropic line with $\sigma_{iso} = 570$ ppm and a line with $\sigma_{\perp} = 510$ ppm, $\sigma = 720$ ppm have been assigned to surface clusters with V atoms in a tetrahedral environment (spectra 2, 3, and 4). At large V content, orthovanadate $Mg_3(VO_4)_2$ ($\sigma_{iso} = 560$ ppm) is formed in the catalysts (spectrum 4). The calculated shapes of the individual lines for various V sites in V_2O_5/MgO catalysts and

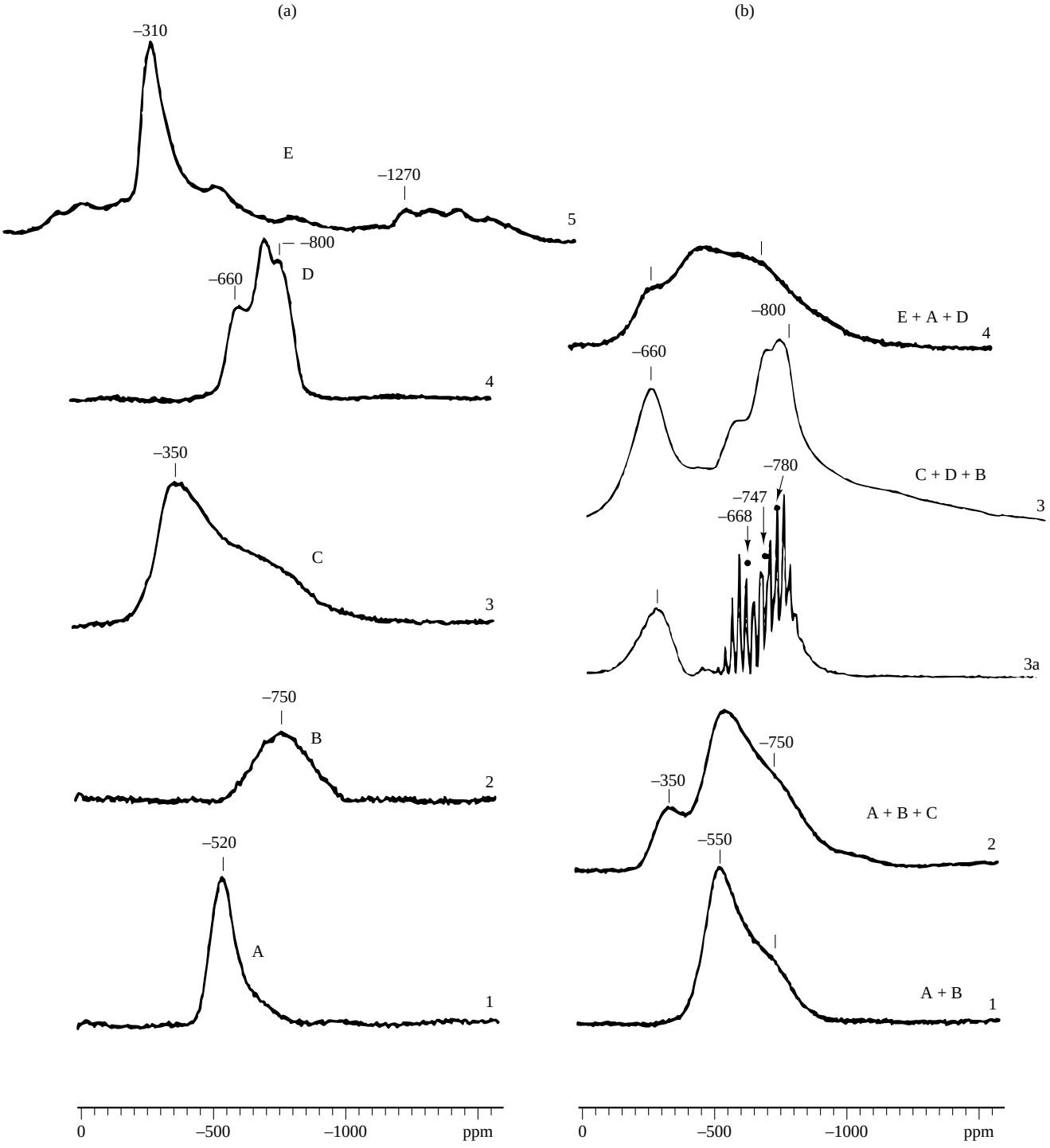

Figure 5 Classification of ^{51}V NMR lines observed in V_2O_5/Al_2O_3 catalysts prepared by Al_2O_3 impregnation with NH_4VO_3 solution. (a) Individual lines: 1, line A, σ_{iso} = 520–590 ppm, observed in wet samples at a V content from 1–2 wt.%; 2, line B, σ_{iso} = 750 ppm observed at a V content of 1 wt.% for samples calcined at 500 °C; 3, line C, $\sigma_{\perp}$ = 350 ppm observed for wet samples at high V content; 4, line D from polycrystalline $AlVO_4$; 5, line E from polycrystalline V_2O_5. (b) Spectra of various catalysts: 1, prepared by impregnation with NH_4VO_3 (pH 12, 2.2 wt.% V) dried at 110 °C, superposition of lines A and B; 2, the same sample calcined at 550 °C, superposition of lines A, B, and C; 3a, MAS spectrum of sample 3; 3, catalyst prepared via impregnation with VOC_2O_4 (pH 0.4, 14 wt.% V) calcined at 500 °C, superposition of lines B, C, and D (line D gives well-resolved sidebands with MAS); 4, catalyst prepared via impregnation with NH_4VO_3 (pH 7, 14.8 wt.% V), the superposition of lines A, D, and E

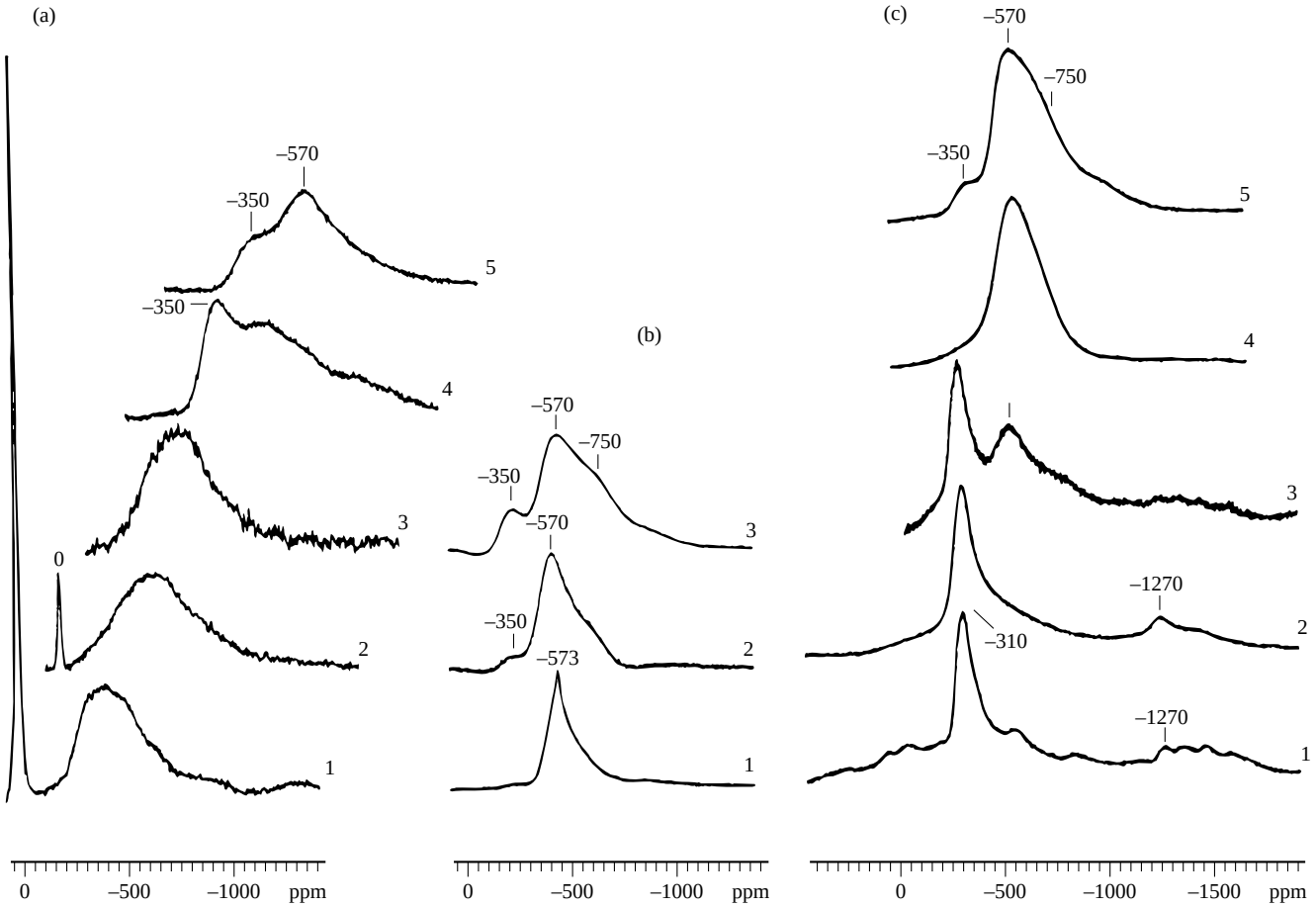

Figure 6 Vanadium-51 NMR spectra of V_2O_5/Al_2O_3 catalysts at different stages in their preparation: (a) Catalysts prepared by interaction with gaseous $VOCl_3$: 1, spectrum after $VOCl_3$ deposition; 2, 3, and 4, increase of H_2O content; 5, sample 4 after calcination at 500 °C. (b) Catalysts prepared by impregnation with NH_4VO_3 (pH 12, 3.8 wt.% V): 1, wet sample; 2, sample dried at 120 °C; 3, sample calcined at 500 °C. (c) Catalysts prepared by ultra-high-intensity grinding (UHIG): 1, V_2O_5; 2, V_2O_5 after UHIG; 3, V_2O_5-Al_2O_3 mixture (5 wt.% V_2O_5) calcined at 500 °C for 14 h; 4, after UHIG treatment at room temperature; 5, UHIG with subsequent calcination of the samples at 500 °C for 2 h

deconvolution of the experimental spectrum into individual lines are also shown in Figure 7(b) and (c). Figure 7(c) also presents the relative amounts of the various V species as measured by deconvolution of the experimental spectra.

Hence, the ^{51}V NMR spectra of V_2O_5/MgO catalysts allow one to form certain conclusions on the structure of surface V species and their concentration as a function of the total vanadium content.

3.4 V_2O_5/TiO_2 Catalysts

The influence of the admixtures on the structure of the supported species has been demonstrated for V_2O_5/TiO_2 supported catalysts[1,19] (Figure 8). Spectra of catalysts prepared via the gas-phase reaction of $VOCl_3$ with TiO_2 followed by subsequent hydration and H_2O removal at 350 °C are shown in Figure 8(a). The catalyst prepared from the most pure anatase (impurities less than 0.1 wt.%) contains two tetrahedral (peaks at $\delta = -440$ and -560 ppm) and one octahedral species (peak at $\delta = -320$ ppm) as follows from spectrum 1 in Figure 8(a). An admixture containing sulfate anions (3.9 wt.%) increases the content of the octahedral vanadium species (spectrum 2). The presence of 3 wt.% Si leads to tetrahedral vanadium complexes typical for V_2O_5/SiO_2 samples (peak at $\delta = -490$ ppm, spectrum 3) and with anatase containing Na (2.3 wt.%) the formation of Na_3VO_4 was observed (line with $\delta = -535$ ppm, spectrum 4). Similar surface species have also been identified for the same catalysts prepared by impregnation of the same anatase samples with a solution of vanadyl oxalate [cf. Figure 8(a) and (b)].

Thus, the type of surface V species on TiO_2 depends mainly on the presence of the impurities in anatase with the preparation procedure having a considerably smaller effect on the type of V sites on the catalyst surface.

Data analysis presented above and by Lapina et al.[1] shows that the structure of surface V species depends mainly on the type of support. The preparation procedure (impregnation, grafting, UHIG treatment) appears to have much less of an effect on the type of V sites on the catalyst surface provided that the concentration of vanadium and the treatment temperatures are the same.

At a V concentration less than 0.5 monolayer, surface tetrahedral species with different extents of distortion of the oxygen environment are formed, with the distortion depending on the type of the support used.

(a) For MgO and $AlPO_4$, the surface vanadium species has an almost regular tetrahedral environment with σ_{iso} depending

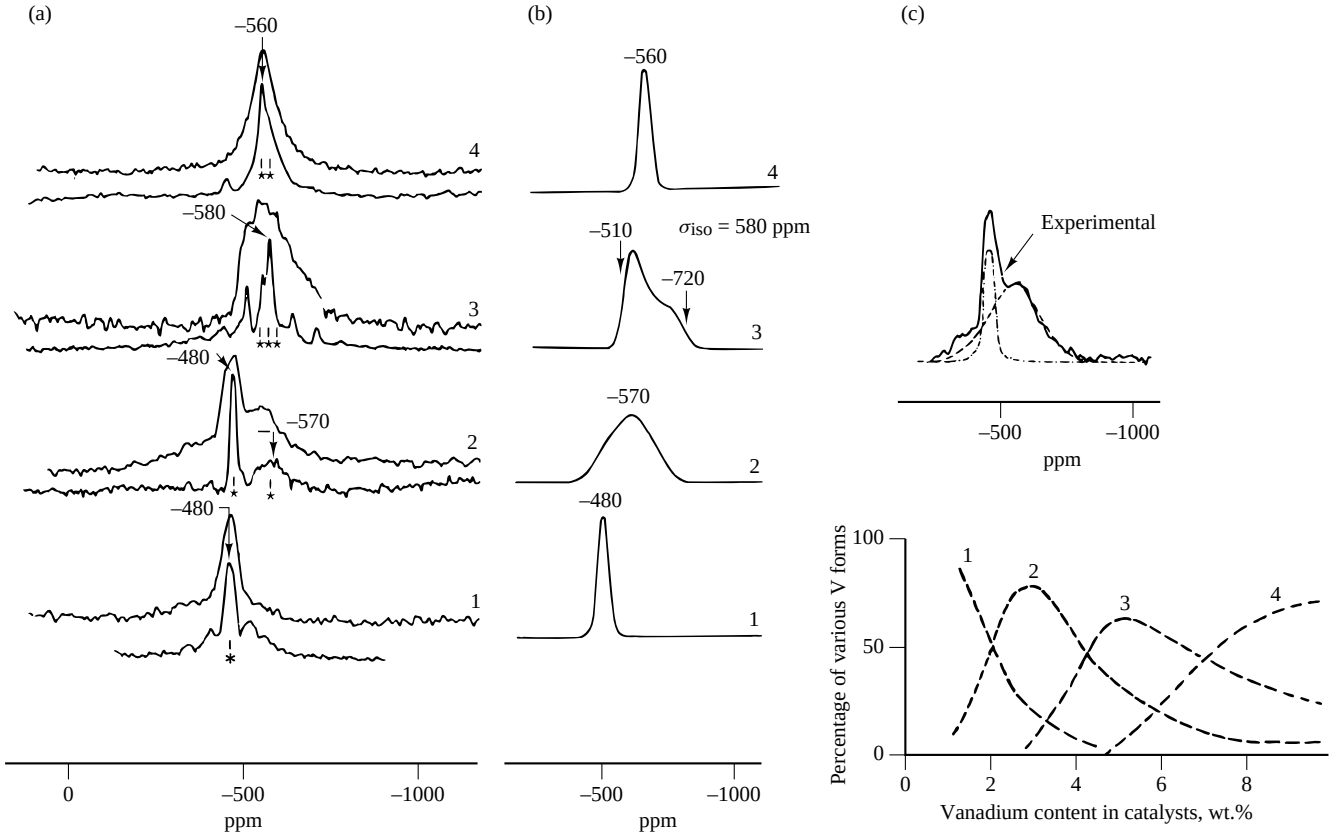

Figure 7 (a) ^{51}V NMR spectra of V_2O_5/MgO catalysts of various vanadium content: 1, 1.6 wt.%; 2, 2.6 wt.%; 3, 5.0 wt.%; 4, 9.6 wt.%. The upper spectra were recorded without MAS; the MAS spectra are shown below. The isotropic chemical shifts are indicated by asterisks (*). (b) The simulated lineshapes of ^{51}V NMR spectra for various V species found in V_2O_5/MgO catalysts: 1, isolated tetrahedral surface species; 2, tetrahedral surface clusters; 3, tetrahedral surface clusters of another type; 4, $Mg_3(VO_4)_2$. (c) Deconvolution of an experimental spectrum (2.6 wt.% V) into individual lines and the percentage of various V species on the MgO surface as a function of the total V content in V_2O_5/MgO catalysts: 1, isolated tetrahedral surface species; 2, tetrahedral surface clusters; 3, tetrahedral surface clusters of another type; 4, $Mg_3(VO_4)_2$

on the type of support employed (σ_{iso} = 480 and 880 ppm for MgO and $AlPO_4$, respectively) and $\Delta\sigma < 100$ ppm.

(b) For Al_2O_3, ZrO_2, ZrO_2/TiO_2, and SnO_2, slightly distorted tetrahedral V species exist with σ_{iso} values ranging from 500–600 ppm and $\Delta\sigma < 200$ ppm.

(c) For SiO_2 and TiO_2, distorted tetrahedral V species with one short V–O bond are formed. They exhibit axial anisotropy of chemical shielding with $\Delta\sigma < 600$ ppm.

An increase in V concentration (up to monolayer coverage) results in association of surface species. The following features associated with their ^{51}V NMR spectra can be noted.

(a) On MgO, $AlPO_4$ associated tetrahedral surface V species exhibit spectra with a fully anisotropic σ tensor, which points to a distortion of the VO_4 tetrahedra in these species (σ_{iso} = 560–570 ppm). The lines for such associated species are usually broader when compared with those for isolated species.

(b) For associated V species on Al_2O_3, ZrO_2, SnO_2, and TiO_2/ZrO_2, fully anisotropic lines from distorted VO_4 surface tetrahedra are also observed (σ = 700–800 ppm). The widths of the lines are close to those for isolated V species on this surface.

(c) For associated V species on Al_2O_3, ZrO_2, TiO_2/ZrO_2, and SnO_2 of another type, lines with an axial anisotropy of the shielding tensor arising from distorted octahedral V sites are observed ($\sigma_\perp$ = 320–330 ppm, $\Delta\sigma$ = 600 ppm).

(d) For associated V species on SiO_2 and TiO_2, lines with an axial anisotropy of the shielding tensor arising from distorted octahedral V sites are observed ($\sigma_\perp$ = 290–300 ppm, $\Delta\sigma > 900$ ppm).

A further increase of V concentration above monolayer coverage provides crystalline compounds [V_2O_5 on SiO_2, TiO_2, $AlPO_4$, TiO_2/ZrO_2, and SnO_2; $AlVO_4$ on Al_2O_3; and $Mg_3(VO_4)_2$ on MgO].

Water adsorption changes the V coordination from tetrahedral to octahedral on SiO_2 and TiO_2. In these cases, water molecules insert into the first coordination sphere of V. For V sites on ZrO_2, $AlPO_4$, TiO_2/ZrO_2, and SnO_2, water molecules adsorb in the second coordination sphere, providing slight shifts of the ^{51}V NMR lines upon adsorption.

Addition of promoters, such as rhodium, titania, or zirconia (or impurities), results in notable changes in both the structure of the surface V species and their redistribution on the surface.

3.5 Vanadium Catalysts for SO_2 Oxidation

The active component of vanadium catalysts for SO_2 oxidation is known to consist of vanadium oxide and sulfates or pyrosulfates of alkali metals (K, Na, Cs are most commonly

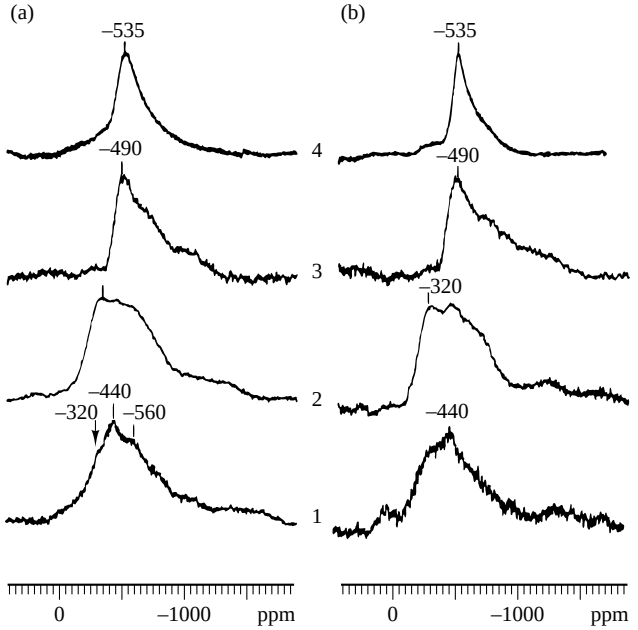

Figure 8 Vanadium-51 NMR spectra of V_2O_5/TiO_2 catalysts (a) prepared by gas phase reaction of $VOCl_3$ with TiO_2 followed by subsequent hydration and removal of H_2O with a stream of He at 350 °C and (b) prepared via impregnation with a solution of VOC_2O_4: 1, anatase (all impurities less 0.1 wt.%); 2, TiO_2 (3.9 wt.% SO_4); 3, TiO_2 (3 wt.% Si); 4, TiO_2 (2.3 wt.% Na)

used) supported on porous materials such as silica or silica alumina. At ambient temperature the active component forms a thin vitreous film dispersed over the support. Under the reaction conditions (400–500 °C), the active component exists as a melt forming a very thin liquid layer on the support surface.

We present here the results of ^{51}V NMR studies of oxosulfatovanadates(V), chemical compounds formed between V_2O_5 and alkali pyrosulfates that are assumed to be present in the active component of these catalysts, as well as of V_2O_5-$K_2S_2O_7$ alloys and of commercial catalysts. Combined with other spectroscopic methods and kinetic studies, these results have helped to reveal the active sites in SO_2 oxidation and the mechanism of this catalytic reaction.[1,20,21]

The spectra of oxosulfatovanadate(V) $K_3VO_2(SO_4)_2$, the alloy $V_2O_5 \cdot 3K_2S_2O_7$, and a commercial catalyst are presented in Figure 9. All oxosulfatovanadates(V) exhibit axial anisotropy of the chemical shielding tensor with parameters close to those for V_2O_5. Thus the local environment of the vanadium atom in oxosulfatovanadates(V) is similar to that in V_2O_5, where vanadium has a distorted octahedral (bipyramidal) oxygen atom environment with one V–O bond being considerably shorter than the others. Comparison of the spectrum of $V_2O_5 \cdot 3K_2S_2O_7$ alloy (Figure 9) with that for oxosulfatovanadate(V) $K_3VO_2(SO_4)_2$ shows that the former exhibits σ values close to those for oxosulfatovanadate(V). This indicates the same local environment for the V atoms in the glassy alloy and in crystalline oxosulfatovanadate(V).

The ^{51}V NMR spectra for various catalysts after treatment with a reaction gas mixture become quite similar and exhibit the same two lines, namely an almost isotropic line with σ_{iso} = 520–560 ppm and a line with axial anisotropy of the shielding tensor. Only the relative intensities of the

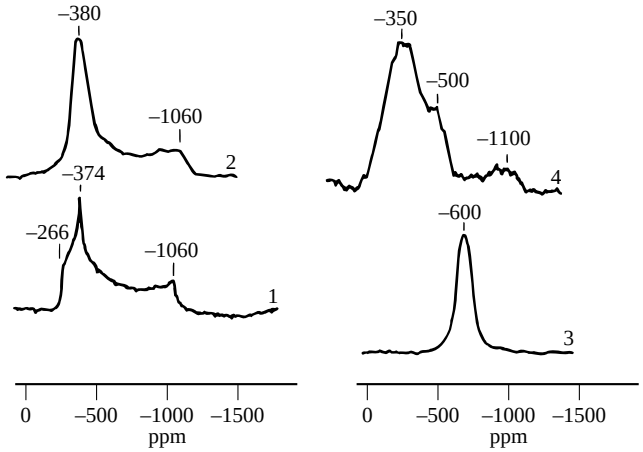

Figure 9 Vanadium-51 NMR spectra of (1) oxosulfatovanadate(V) $K_3VO_2(SO_4)_2$; (2) the solid alloy $V_2O_5 \cdot 3K_2S_2O_7$; (3) the industrial catalyst BAV before treatment under the reaction conditions; (4) the same after treatment

two lines but not their character vary from one catalyst to another. In particular, the average chemical shifts for both the isotropic and anisotropic lines ($\sigma_\perp$ = 320–350 ppm, $\sigma_\parallel$ = 1200–1300 ppm) are almost the same for all the catalysts studied. This indicates that the active component in these catalysts is the same and is actually formed during the course of catalytic reaction.[2] Initially, catalysts arising from different preparations contain a variety of V sites. However, on interaction with the components of the reaction media only the two sites mentioned above are formed. The nearly isotropic line belongs to V atoms in a slightly distorted tetrahedral environment and can be attributed to vanadium bonded to the support. This line exhibits an increase in relative intensity with a decrease in the overall V content of the sample. Thus, the isotropic line belongs to V complexes on the SiO_2 surface.

Measurement of the catalytic activity for a series of samples with different contents of surface tetrahedral V has showed the latter to be inactive in SO_2 oxidation.[20]

To elucidate the nature of the vanadium complexes which are active in SO_2 oxidation, ^{51}V, ^{17}O, ^{23}Na, ^{39}K, and ^{133}Cs NMR were combined with catalytic activity measurements of V_2O_5-$K_2S_2O_7$ melts and of catalysts with different amounts of the active component on SiO_2.[1,20,21]

Vanadium-51 NMR spectra of V_2O_5 and $V_2O_5 \cdot 3Cs_2S_2O_7$ alloy at temperatures below and above their melting points (Figure 10) demonstrate the spectrum of molten $V_2O_5 \cdot 3Cs_2S_2O_7$ (see ***Molten Salts***) to be substantially broader than that of V_2O_5. This means, that unlike V_2O_5, where melting leads to a separation of the vanadium–oxygen layers and breaks them into relatively short fragments, in molten $V_2O_5 \cdot 3Cs_2S_2O_7$ substantially larger particles are formed.

Oxygen-17 NMR (see ***Oxygen-17 NMR***) has also been used to characterize the melt of the active component in SO_2 oxidation at 500 °C in the presence of an SO_3 + SO_2 + O_2 mixture, i.e. under typical conditions for the catalytic process in industry.[1,20,21] Addition of V_2O_5 to $K_2S_2O_7$ leads to a shift and a broadening of the ^{17}O line, indicating V coordination with pyrosulfate anions. A more sophisticated analysis using a thermodynamic model of the ^{17}O linewidths has shown that at small vanadium concentrations approximately two to three pyrosulfate anions are coordinated to one V atom.

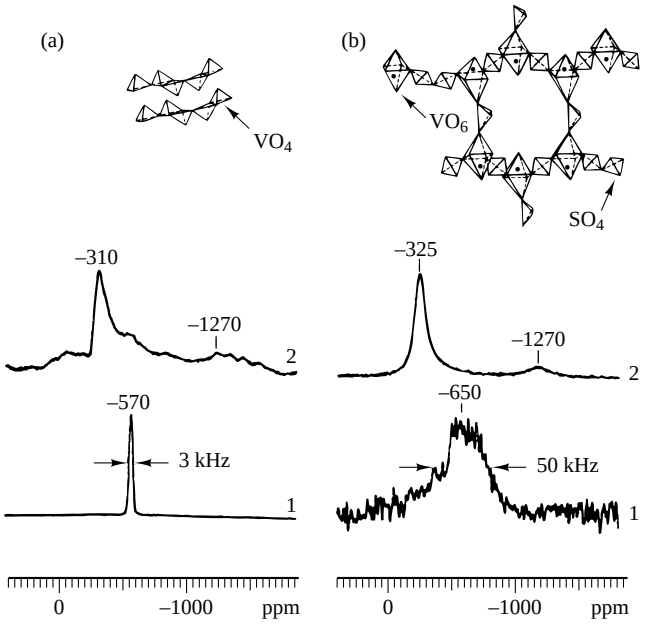

Figure 10 Vanadium-51 NMR spectra of (a) V_2O_5 and (b) of the alloy $V_2O_5 \cdot 3Cs_2S_2O_7$ (1) below the melting point (i.e. at 20 °C) and (2) above the melting point (670 °C and 370 °C for (a) and (b), respectively). Above: the structures formed in molten V_2O_5 and $V_2O_5 \cdot 3Cs_2S_2O_7$ alloy

Oxygen-17 NMR data also suggest a fast exchange between terminal and bridging oxygen atoms in the pyrosulfate anion which may occur via the reaction $S_2O_7^{2-} \rightleftarrows SO_4^{2-} + SO_3$. The characteristic time τ during which this equilibrium is established is less than 10^{-3} s. Oxygen-17 and ^{51}V NMR data show that on addition of V_2O_5 to $K_2S_2O_7$, complexes are formed according to the reaction: $V_2O_5 + 3K_2S_2O_7 \rightleftarrows 2K_3VO(SO_4)_3$. The increase in the ^{51}V and ^{17}O linewidths on increasing the V concentration suggests a further association of the V species leading to larger oligomers of the type shown in Figure 10. The large size of these oligomers makes their rotational diffusion very slow. Internal rotation of their fragments can also be hindered because of branching and linking of the oligomeric chains. Because of these factors, the ^{17}O and ^{51}V NMR lines of these species are too broad to be detected.

When supported on SiO_2, the dimeric or oligomeric vanadium species can be more stabilized on the surface due to their interaction with Si–OH groups. These results agree well with studies of the catalytic activity of thin films of active melts on Pyrex glass and on SiO_2, as well as with kinetic studies of SO_2 oxidation.[20]

4 RELATED ARTICLES

Aluminum-27 NMR of Solutions; Chemical Shift Tensor Measurement in Solids; Anisotropy of Shielding and Coupling in Liquid Crystalline Solutions; Chemical Shift Tensors; Dipolar and Indirect Coupling Tensors in Solids; Internal Spin Interactions and Rotations in Solids; High Speed MAS of Half-Integer Quadrupolar Nuclei in Solids; Internal Spin Interactions and Rotations in Solids; Magic Angle Spinning; Molecular Sieves: Crystalline Systems; Molten Salts; Oxygen-17 NMR; Quadrupolar Interactions; Quadrupolar Nuclei in Glasses; Quadrupolar Nuclei in Solids; Silicon-29 NMR; Variable Angle Sample Spinning.

5 REFERENCES

1. O. B. Lapina, V. M. Mastikhin, A. A. Shubin, V. N. Krasilnikov, and K. I. Zamaraev, *Prog. Nucl. Magn. Reson. Spectrosc.*, 1992, **24**, 457.
2. B. E. Leach (ed.), *Applied Industrial Catalysis*, Academic Press, New York, 1983.
3. R. N. Pletnev, V. A. Gubanov, and A. A. Fotiev, *NMR in Oxide Vanadium Compounds*, Nauka, Moscow, 1979 (in Russian); [*Chem Abs.*, 1980, **92**, 159 005x].
4. M. H. Cohen and F. Reif, *Solid State Phys.*, 1957, **5**, 321.
5. S. D. Gornostansky and G. V. Stager, *J. Chem. Phys.*, 1967, **46**, 4959.
6. D. Rehder, *Bull. Magn. Reson.*, 1982, **4**, 33.
7. H. Eckert and I. E. Wachs, *J. Phys. Chem.*, 1989, **93**, 6796.
8. J. Skibsted, N. C. Nielsen, H. Bildsoe, and H. J. Jakobsen, *J. Am. Chem. Soc.*, 1993, **115**, 7351.
9. A. A. Fotiev, B. V. Slobodin, and M. Ya. Hodos, *Vanadates, their Synthesis, Composition and Properties*, Nauka, Moscow, 1988 (in Russian); [*Chem. Abs.*, 1989, **110**, 68 625c].
10. V. M. Mastikhin, O. B. Lapina, V. N. Krasilnikov, and A. A. Ivakin, *React. Kinet. Catal. Lett.*, 1984, **24**, 119.
11. D. Muller, W. Gessner, and A. R. Grimmer, *Z. Chem.*, 1977, **B12**, 453.
12. J. Klinowsky, *Prog. Nucl. Magn. Reson. Spectrosc.*, 1984, **16**, 237.
13. N. Das, H. Eckert, H. Hu, I. E. Wachs, J. F. Walzer, and F. J. Feher, *J. Phys. Chem.*, 1993, **97**, 8240.
14. J. B. Lapina, V. M. Mastikhin, A. V. Nosov, T. Beutel, and H. Knozinger, *Catal. Lett.*, 1992, **13**, 203.
15. J. B. Lapina, V. M. Mastikhin, L. G. Simonova, and Yu. O. Bulgakova, *J. Mol. Catal.*, 1991, **69**, 61.
16. L. R. Le Costumer, B. Taouk, M. Le Meur, E. Payen, M. Guelton, and J. Grimblot, *J. Phys. Chem.*, 1988, **92**, 1230.
17. Z. Sobalik, O. B. Lapina, O. N. Novgorodova, and V. M. Mastikhin, *Appl. Catal.*, 1990, **63**, 191.
18. O. B. Lapina, A. V. Simakov, V. M. Mastikhin, S. A. Veniaminov, and A. A. Shubin, *J. Mol. Catal.*, 1989, **50**, 55.
19. H. Eckert, G. Deo, I. E. Wachs, and A. M. Hirt, *Colloids Surf.*, 1990, **45**, 347.
20. V. M. Mastikhin, O. B. Lapina, B. S. Balzhinimaev, L. G. Simonova, L. M. Karnatovskaya, and A. A. Ivanov, *J. Catal.*, 1987, **103**, 160.
21. B. S. Balzhinimaev, A. A. Ivanov, O. B. Lapina, V. M. Mastikhin, and K. I. Zamaraev, *Faraday Discuss. Chem. Soc.*, 1989, **87/88**, 133.
22. S. Hayakawa, T. Yoko, and S. Sakka, *J. Solid State Chem.*, 1994, **112**, 329.

Biographical Sketches

Vjatcheslav M. Mastikhin. *b* 1937. Graduated 1959, Kharkov University, Ph.D. 1969, Dr.S., 1986, Boreskov Institute of Catalysis. Leading Scientist, Boreskov Institute of Catalysis, Novosibirsk, 1986–1995.

Approx. 200 publications. Research interests: application of solid state NMR to problems of heterogeneous catalysis.

Olga B. Lapina. *b* 1953. Graduated 1976, from Novosibirsk University, Ph.D., 1984, Dr.S., 1995, Boreskov Institute of Catalysis. Senior Scientist, Boreskov Institute of Catalysis, Novosibirsk, 1990–present. Approx. 100 publications. Research interests: application of solid state NMR to problems of heterogeneous catalysis.

Adsorbed Species: Spectroscopy and Dynamics

Ian D. Gay
Department of Chemistry, Simon Fraser University, Burnaby, B.C., Canada

1	Introduction	1
2	Early Results	2
3	Multinuclear Magnetic Resonance	2
4	High-Resolution Solid State Techniques	3
5	Adsorbates on Metals	3
6	Adsorption Probes of Surface Sites	3
7	Surface Hydroxyl Groups	4
8	Chemical Reaction in Adsorbed Layers	4
9	Structure of Adsorbed Species	4
10	Motion in Adsorbed Layers	4
11	Related Articles	5
12	References	5

1 INTRODUCTION

The term 'adsorbed' implies concentrated at an interface. This article deals with the NMR of small molecules adsorbed, i.e. bound, to solid sufaces. (For a general introduction to adsorption and the properties of surfaces, see Adamson[1] or Somorjai.[2]) In addition to being of intrinsic scientific interest, adsorbed layers are of great practical importance in the areas of heterogeneous catalysis, separation science, and chromatography.

Molecules may bind to surfaces by any type of interaction, ranging from chemical bonding to van der Waals interaction. The case of chemical bonding is often called 'chemisorption', while the term 'physisorption' is sometimes used for weaker interactions. An adsorbed layer one molecule thick is called a 'monolayer' and thicker adsorbed deposits are called 'multilayers'. Clearly temperature is a major factor in determining the extent of adsorption, and appreciable adsorption will only be found when the interaction energy is greater in magnitude than *kT*.

NMR is the least sensitive of the common spectroscopic techniques, and thus the observation of adsorbed monolayers is dependent upon having a large amount of surface area in the NMR sample. The surfaces of highest specific area are those of activated carbon, and refractory oxides such as SiO_2 and Al_2O_3. Because of their great importance as adsorbents, catalysts, and catalyst supports, the preparation of these has been much studied.[3,4] These substances are readily prepared with specific surface areas of the order of hundreds of square meters per gram ($m^2\ g^{-1}$). Their densities as powders are typically about $1\ g\ cm^{-3}$, so an NMR sample may contain hundreds of $m^2\ cm^{-3}$. A monolayer of moderate sized molecules might contain 5 μmol m^{-2}, so that the bulk concentration of an adsorbed monolayer can be of the order of 0.5 M. Such concentrations of sensitive high-abundance nuclei, e.g. ^1H, ^{19}F, and ^{31}P, can be observed in a single scan with modern instrumentation. Those familiar with liquid NMR will find the effective sensitivity for adsorbed species to be considerably less, due to the much broader lines which arise for reasons noted below. None the less, high sensitivity nuclei are easily observed on such solids, and more difficult nuclei such as natural abundance ^{13}C can typically be observed in thousands or tens of thousands of scans. Often spin–lattice relaxation times for adsorbed molecules are appreciably shorter than for the same molecules in the liquid phase. This can make the signal averaging of large numbers of scans more feasible than might have been expected.

Another family of high area solids is the zeolites,[5] crystals with internal pores of molecular size. The interior of these pores is equivalent to a high surface area, again typically of the order of hundreds of $m^2\ g^{-1}$. Whether guest molecules inhabiting these pores can be said to be adsorbed is a matter of semantic convention. In this article the NMR of such guest molecules will be only briefly touched upon.

A large number of substances can be prepared in the $10\ m^2\ g^{-1}$ range, and almost any solid can be prepared with $1\ m^2\ g^{-1}$. Whether a high area preparation is stable with respect to loss of area by sintering depends mainly on the temperature. Typically the temperature must be kept below about one-half of the melting point to prevent substantial loss of area. A system of great practical interest is the supported metal catalyst.[6] These catalysts consist of metal crystallites dispersed on a refractory oxide, such as silica or alumina. This technique permits a very high dispersion of the metal, with reduced tendency to sinter, and makes the most effective use of expensive platinum group metals. While the metal dispersion is extremely high, such catalysts typically contain a few per cent of metal by mass and have metal areas of 1 to $10\ m^2\ g^{-1}$ of catalyst. Monolayers of high sensitivity nuclei are straightforward even at $1\ m^2\ g^{-1}$; however, if one wishes to explore nuclei of low sensitivity, or small fractions of a monolayer, severe sensitivity problems eventually arise. One possible approach to this problem is to use the Curie law enhancement of NMR sensitivity at extremely low temperatures in the millikelvin range.[7]

In general, the preparation of high-area solids will result in an aggregate of randomly oriented crystallites. Some preparations, e.g. silica gels, will lack long-range order entirely. In a few favorable cases, high-area oriented samples can be prepared, e.g. in the case of lamellar clay particles by sedimentation.[8]

If one imagines a surface prepared by the sudden cleavage of a solid, it is evident that the surface may be viewed as a macroscopic radical with large numbers of 'dangling bonds', resulting from the disruption of the chemical bonds responsible for the integrity of the solid. Such a surface will be a very reactive entity and will be subject to structural rearrangement, which can lower its free energy, and to chemical reaction with its environment. Thus all metal surfaces (with the possible exception of Au) that have been in contact with the atmosphere will be covered by a layer of oxide. This layer may be a monolayer, or may be many layers thick. Similarly, oxide surfaces that have been exposed to the atmosphere normally have a monolayer of –OH groups, resulting from their reaction with H_2O. This surface OH may be regarded either as the result of chemisorption of H_2O or as a normal constituent of oxide surface.

A 'clean' surface is one whose properties approximate the idealized cleaved crystal, at least as regards chemical

composition. (Many clean surfaces undergo rearrangement of their atoms to positions different from the bulk crystal.[2]) Clean surfaces are of much interest in fundamental surface science studies. In general, really clean surfaces are achieved only under ultrahigh vacuum conditions on areas of the order of 1 cm^2; adsorption on such surfaces is inaccessible to conventional NMR study at the present time. A possible exception to this statement is scattering experiments involving polarized atomic beams,[9,10] which can yield nuclear relaxation data and possibly other NMR-like parameters. For the most part, however, present NMR studies involve surfaces that are at best partially clean. Thus, surface oxide can be removed from the noble metals by H_2 reduction, followed by thermal desorption of the resulting adsorbed H; surface OH can be largely removed from oxide surfaces by thermal treatment under vacuum. While not too attractive from the point of view of fundamental studies, the surfaces studied by NMR can easily be kept in a state similar to those used in practical applications for adsorption and catalysis, and NMR has substantial contributions to make to these fields.

The main features of the NMR of any sample will be determined by the mobility of the molecules studied. In this context, adsorbed layers are somewhat intermediate between liquid and solid samples. For many strongly chemisorbed samples, the adsorbed species are held in place by strong chemical bonds and are solids for NMR purposes. However, strong bonding to the surface does not necessarily imply localized bonding. For example, H atoms bind to most metal surfaces with an energy in excess of 200 kJ mol^{-1}, but in the case of the platinum group metals at room temperature they are mobile parallel to the surface on the NMR timescale, and are in some sense a two-dimensional fluid. Rotational motion of adsorbed molecules is also common, but the presence of the surface is likely to introduce greater anisotropy in this motion than would be observed in a liquid. Weakly bound physisorbed molecules are typically in rapid exchange with the gas phase, and average NMR properties will be observed. For high-area solids it will usually be the case that the adsorbed population is much larger than the gas-phase population, so that properties like chemical shifts will be dominated by those of the adsorbed phase, while the rapid exchange ensures that the motional properties of the layer appear liquid-like, both translationally and rotationally.

2 EARLY RESULTS

Not surprisingly, the first NMR studies of adsorbed species involved proton NMR[11,12]. Since these predated high resolution solid state techniques, the possible experiments were broadline studies of immobile species, 'high-resolution' studies of mobile adsorbates, relaxation/linewidth measurements, and diffusion measurements by field gradient techniques. Examples of most of these exist from before 1960. For example, O'Reilly et al.[13] observed that surface OH on silica and silica–alumina is chemically shifted with respect to liquid H_2O, and inferred from the temperature-independent Lorentzian lineshape that the OH forms a dilute randomly populated dipolar coupled system. Hickmott and Selwood[14] studied the relaxation of water and several organics on various oxides, and showed the importance of surface paramagnetic species as relaxation agents. Fuschillo and Renton[15] studied the linewidth of methane on TiO_2 at low temperatures, and demonstrated the now well-known result that submonolayer amounts of physisorbed species do not become immobile until the temperature is well below the bulk freezing point.

In spite of these early successes, surface NMR in succeeding years proved somewhat disappointing. In general, very few chemical shifts proved to be measurable because of the large linewidths found for proton resonances. The sources of these linewidths were eventually realized to be rapid relaxation, especially by surface paramagnetic species, exchange with surface protons, heterogeneity of surface with respect to adsorption energetics, and inhomogeneous broadening from the nonzero magnetic susceptibility of irregular adsorbent particles; no proton linewidths less than 1 ppm were observed and much larger linewidths were common. Given the limited range of proton shifts, little of interest was shown regarding the structure and bonding of adsorbed molecules. Furthermore, with some notable exceptions,[16] it turned out to be difficult to obtain information regarding molecular motion from relaxation studies. This was largely because of the difficulties of disentangling different relaxation processes, and the often dominant effect of paramagnetic surface species, in the presence of which correlation times may be determined more by electron relaxation than by adsorbate motions. The results of this early period are well summarized in the reviews by Packer[17] and Pfeifer.[18] Diffusion measurements, particularly in the context of guest molecules in zeolites, have recently been reviewed by Kärger et al.[19]

3 MULTINUCLEAR MAGNETIC RESONANCE

More possibilities were opened by the increasing availability of multinuclear and Fourier transform NMR equipment beginning in the 1970s. If, as it turns out, lines from adsorbed species will be at least a few ppm in width, chemical shifts should be observable for nuclei whose shift range is of the order of hundreds of ppm or more. An extreme example of this is the observation[20] of an 80 ppm shift for Tl^+ adsorbed from H_2O onto silica. In a more practical vein, the early 1970s saw the first natural abundance ^{13}C spectra of molecules in zeolites[21] and physisorbed on silica[22]. Linewidths were a few ppm and it was possible to observe chemical shifts due, for example, to the hydrogen-bonding interaction of adsorbed acetone with surface hydroxyls. These works also demonstrated the possibility of measuring relaxation times separately for chemically different groups within a molecule. This could lead to simpler analysis of relaxation experiments for rigid molecules and the study of internal motions for others. In the early 1980s spectra were obtained for ^{15}N in a variety of molecules in zeolites[23] and adsorbed on SiO_2,[24] showing the advantages of studying the NMR of the atom which is the site of interaction between adsorbate and adsorbent. Relaxation studies of ^{17}O in H_2O on montmorillonite and kaolinite were performed.[25] These showed the desirability of measuring adsorbate correlation times in a system where strong quadrupolar interaction dominates the relaxation, and yielded surprisingly short correlation times for water in these systems, on the order of 10^{-11} s. Results to 1985 on multinuclear spectroscopy and relaxation measurements on adsorbed mobile molecules are comprehensively reviewed by Nagy, Engelhardt, and Michel.[26]

4 HIGH-RESOLUTION SOLID STATE TECHNIQUES

The advent of high-resolution solid state NMR techniques in the 1960s and 1970s opened up new possibilities for the study of adsorbate systems. The most obvious of these is the identification of immobile chemisorbed species. The first use of these techniques by Kaplan et al.[27] was however a CP study of physisorbed benzene and toluene at low temperatures. Observation of an axially symmetric CSA powder pattern showed that benzene undergoes rapid rotation about the hexad axis, even at 77 K. Further experiments demonstrated that rapid cooling can trap molecules in a metastable isotropically rotating state at this temperature.

Magic angle spinning was first applied to surface problems by Stejskal et al.[28] in their study of CO_2 in zeolites. This showed that substantial line broadening which may arise from microscopic susceptibility variations in the adsorbate can be removed by MAS. Use of MAS in surface problems suffers from the conflicting requirements of atmospheric integrity, best achieved with sealed samples, and of excellent mechanical balance, which is likely to be degraded by the sealing process. This conflict was resolved in a semisatisfactory way in 1984.[29]

The first use of multiple pulse line narrowing in surface studies was by Schreiber and Vaughan.[30] This permitted the measurement of the shielding anisotropy of surface protons on SiO_2; strong dipolar coupling to ^{27}Al prevented similar measurements on Al_2O_3. The combination of multiple pulse narrowing with MAS (CRAMPS), together with the use of higher magnetic fields, has recently been leading to growing success in the proton spectroscopy of adsorbed species.

5 ADSORBATES ON METALS

The resonance of hydrogen chemisorbed on platinum was first observed by Ito et al.[31] Subsequently, the resonance of hydrogen has been observed on Cu, W, Ru, Rh, Pd, Os, Ir, and a few alloys, by these and other workers. (In the case of W, the cleanliness of the surface is questionable.) For all of the metals, large shifts are observed which cannot reasonably be chemical shifts and must therefore be Knight shifts. For Cu the shift is to high frequency, for the others to low frequency. With Ru–Cu bimetallic clusters[32] the Knight shift of H on Ru decreases steadily as the Cu content is increased.

Platinum has been the most studied of these metals and it has been established that there is little difference between metallic powders and supported Pt catalysts. It has also been found that Knight shifts are smaller when the Pt particles are very small and when the adsorbed H covers a large fraction of the metal surface. As yet these trends have not received a satisfactory quantitative explanation in terms of the bonding between H and the metal surface. For all of the above metals the linewidth of the H resonance indicates that the hydrogen is mobile at room temperature. For those which have been studied to lower temperatures, motion generally ceases before liquid nitrogen temperature is reached.

^{13}C NMR of CO chemisorbed on a metal was first studied by Duncan et al. on Rh.[33] Since then it has been studied on the remaining noble metals, and on bimetallic Pt–Rh particles. Much of this work is described in the reviews by Slichter[34] and Duncan.[35] On Ru and Rh an average shift is observed that corresponds to the known shifts of metal carbonyl complexes. In static samples a broad powder pattern is observed with an anisotropy of some 400 ppm, corresponding to a linear carbonyl. On Rh, bridging carbonyl has also been observed. At room temperature, with the highest CO loadings, a narrow line appears from CO that is rotating isotropically on the NMR timescale. Thus the NMR of CO on Rh and Ru can be interpreted in terms of chemical shifts which are completely analogous to those observed in diamagnetic metal carbonyl complexes.

On the other hand, CO on supported Pt and Pd shows large high-frequency Knight shifts. Knight shifts are not observed for CO on colloidal platinum,[36] but it is not clear whether this is due to loss of metallic properties in the smaller particles or to interactions with the reagents used to stabilize the colloid. Supported Os and Ir show smaller high-frequency shifts and it is hard to be certain whether these are chemical or Knight shifts. Observations on Pt–Rh clusters[37] show that the Knight shift disappears above about 50% Rh, even though SEDOR measurements clearly show the presence of Pt in the surface layer of the particles.

The above results indicate that one must proceed with caution in interpreting the observed line positions of chemisorbed species on metals. For example, the metal (Rh) giving the largest Knight shift for adsorbed H gives no Knight shift for adsorbed CO. Thus in the absence of a reliable and comprehensive theory for Knight shifts of adsorbed species, every adsorption system must be examined carefully on its own merits.

6 ADSORPTION PROBES OF SURFACE SITES

The nature and concentration of specific types of site on solid surfaces has long been an area of interest, especially from the point of view of catalytic activity. These features can be probed spectroscopically by observing changes in the spectrum of a small molecule upon its binding to the surface. The archetypal example is the study of acid sites on oxide surfaces by IR spectroscopy of adsorbed amines;[38] pyridine, for example, gives distinct lines when physisorbed, protonated by a surface Brønsted acid, or coordinated to a surface Lewis acid.

This type of probing can obviously be done by NMR, which has the advantage that quantitative accuracy is in principle better. With IR spectroscopy it is generally difficult to be confident regarding the extinction coefficient of chemisorbed species, and there are often considerable uncertainties regarding path length and adsorbate concentration. Surface acids have thus been probed by direct proton NMR and by ^{13}C, ^{15}N, and ^{31}P NMR of adsorbed amines and phosphines. Such attempts have been generally successful and are complementary to IR studies. Much of the work in this area has been reviewed by Freude.[39]

Proton NMR cannot of course detect Lewis acids directly. For quantitative assessment of differing types of acid, ^{31}P spectroscopy seems the most desirable. The high sensitivity of this nucleus permits spectra to be obtained in reasonable time periods by 90° pulse excitation, avoiding the need for cross polarization which may compromise quantitative accuracy. Most results have so far been obtained with trimethylphosphine as a probe; studies of a wider range of phosphorus bases seem likely in the future.

Solid surfaces may also contain basic sites; indeed, the same surface may simultaneously contain both strong acid and strong base sites. Probing these surfaces by NMR is less well developed, but a few results are available. For example, ^{13}C spectroscopy has been used to demonstrate, through the formation of surface bicarbonate from CO_2, the unsurprising result that surface OH on MgO is basic.

7 SURFACE HYDROXYL GROUPS

As mentioned above, all oxides are covered with a layer of –OH groups, which may in a formal sense be regarded as the result of water chemisorption on an ideal oxide surface. The surface chemistry of oxides in their normal state is largely determined by the properties of these hydroxyl groups. The properties of these hydroxyl groups vary from one oxide to another, and the same oxide may show differing types of –OH groups, reflecting different exposed crystal planes, or different structural arrangements. Many of the classic NMR investigations[13,30] have dealt with these groups, and the literature of studies by IR spectroscopy is particularly voluminous. Much of the IR literauture and some of the NMR investigations have been reviewed by Morrow.[40] A recent review by Mastikhin et al.[41] is devoted to NMR studies, particularly of recent results obtained through magic angle spinning.

8 CHEMICAL REACTION IN ADSORBED LAYERS

Adsorbed layers are the site of heterogeneous catalysis and hence reaction in these layers is a topic of immense scientific, technical, and economic interest. NMR studies of such reactions may proceed in two rather different ways. For reasonably rapid reactions of systems that are in equilibrium under NMR conditions, the familiar methods of shift, relaxation, and lineshape analysis may be employed, as in solution NMR. The possibilities for this type of study of adsorbed systems have been reviewed by Resing.[42] On the other hand, slow reactions may easily be studied by recording NMR spectra as a function of time. A sealed NMR tube is in many ways an ideal contamination-free reactor. Reaction studies have been greatly advanced by CP MAS techniques, which permit the potential observation of a wide range of reaction products and intermediates.

For species reacting at a convenient rate at room temperature, e.g. the reaction of trimethyl phosphite with the silica surface,[43] straightforward MAS spectroscopy as a function of time can provide kinetic data for the surface reaction processes. For systems that are only reactive above room temperature, a ‘quick and dirty’ technique is to heat samples for controlled periods of time at the reaction temperature, and then cool to room temperature for NMR observation.[44] While this method provides useful insights, it suffers from uncontrolled conditions during the heating and cooling phases, together with uncertainties about desorption.

Clearly this type of study awaits the development of reliable high-temperature sealable MAS equipment, and recent progress has been made in this direction by Haw and coworkers.[45] Unfortunately, sealed-sample MAS is always open to uncertainties arising from the possibility of desorption when the sample is heated above its preparation temperature. There seems no obvious way of combining the traditional catalytic flow reactor with MAS NMR. For the case of static samples, an NMR-compatible flow reactor has been designed by Reimer and co-workers.[46]

9 STRUCTURE OF ADSORBED SPECIES

NMR of solids has the possibility of yielding direct structural information through measurement of dipolar interactions. Since the structures of chemisorbed species are in general not readily determined, this is a powerful possibility. The fundamental problem is that the motional state of observed species is not known a priori, and it will be unclear whether an observed dipolar coupling should be corrected for motional averaging. Thus, early observations of Pake doublets from adsorbed water[8] (see also bibliography in Pfeifer[18]) generally gave splittings much too small to correspond to static H_2O molecules. These results were therefore not used to infer structural information, but were instead interpreted to give motional information based on the assumption of the known structure of isolated water molecules. In a system where significant structural changes have occurred due to chemical reaction, it seems necessary to demonstrate that observed dipole couplings are independent of temperature, or to give some other evidence for lack of motion, before inferring structural parameters.

Duncan and Vaughan[47] were among the first to use modern solid state methods to determine dipolar couplings in adsorbed layers. Their H–C dipolar modulation studies of adsorbed formic acid gave essentially the same coupling as observed in crystalline formates. A deviation from the expected bond length based on X-ray measurements of calcium formate was attributed to motion, even though the couplings in the adsorbed layer appeared temperature independent.

More recently, Slichter and co-workers[34] have applied spin echoes and SEDOR to measure homonuclear and heteronuclear dipole couplings in adsorbed layers, and to attempt to measure the bond length between adsorbate and surface. The latter endeavor is complicated by the possibility, with heavy nuclei such as ^{195}Pt, of indirect (‘scalar’) couplings of magnitudes comparable to the dipolar couplings.

In principle, dipolar couplings could be estimated from relaxation or NOE measurements. In practice, the often dominant effects of surface paramagnetic impurities, and the general anisotropy of motion in adsorbed layers, render this a complicated and unattractive prospect.

A less direct way of obtaining structural information from dipolar couplings is by the observation of multiple quantum coherence, from which the size of coupled spin aggregations may be inferred. This was first applied to surface problems by Slichter and co-workers,[48] and has recently been reviewed by Hwang and Gerstein.[49]

10 MOTION IN ADSORBED LAYERS

As mentioned in the previous section, structural and motional determinations are a coupled problem pair. In general

the study of motions is simpler, because for many adsorbed systems the assumption of known structures in the adsorbed layer will be chemically tenable.

As indicated above, interpretation of relaxation is difficult in adsorbed systems. More reliable motional information is likely to be obtained by the observation of approximately local molecular properties, such as chemical shift anisotropies, dipolar splittings, and quadrupolar couplings. Thus the first CP study[27] of an adsorbed layer revealed an axially symmetric CSA powder pattern for physisorbed benzene at 77 K. This indicated rapid rotation about the sixfold axis at a temperature well below that at which such rotation occurs in the solid.

Subsequently, Resing and co-workers used analysis of CSA powder patterns to determine the motions of various adsorbed species, such as anchored phenyl groups.[50] Sindorf and Maciel[51] used cross polarization rates as an indicator of average C–H dipolar coupling to study the dynamics of long alkyl chains bound to silica surfaces. Yannoni et al.[52] observed C–C dipolar splittings in doubly-labeled benzene to study its structure and motions on a $Pt–Al_2O_3$ catalyst. The use of deuterium quadrupolar powder patterns to study motions in adsorbed phases is exemplified by the elegant studies of Luz et al.[53] on methyl amines sorbed in zeolites.

11 RELATED ARTICLES

CRAMPS; Cross Polarization in Solids; Deuterium NMR in Solids; Diffusion in Porous Media; Knight Shift; Line Narrowing Methods in Solids; Magic Angle Spinning: Effects of Quadrupolar Nuclei on Spin-1/2 Spectra; Multiple Quantum NMR in Solids; Reactions in Zeolites; Silica Surfaces: Characterization; Supported Metal Catalysts.

12 REFERENCES

1. A. W. Adamson, *Physical Chemistry of Surfaces*, 5th edn., Wiley, New York, 1990.
2. G. A. Somorjai, *Chemistry in Two Dimensions: Surfaces*, Cornell University Press, Ithaca, N.Y., 1981.
3. *Physical and Chemical Aspects of Adsorbents and Catalysts*, ed. B. G. Linsen, Academic, London, 1970.
4. A. B. Stiles, *Catalyst Supports and Supported Catalysts*, Butterworths, Boston, 1987.
5. R. M. Barrer, *Zeolites and Clay Minerals as Sorbents and Molecular Sieves*, Academic, London, 1978.
6. J. R. Anderson, *Structure of Metallic Catalysts*, Academic, London, 1975.
7. Q. Geng, O. Gonen, P. Kuhns, C. Zuo, and J. Waugh, *Bull. Magn. Reson.*, 1989, **11**, 154.
8. D. E. Woessner, in *Mass Spectrometry and NMR Spectroscopy in Pesticide Chemistry*, eds. R. Haque and F. J. Biros, Plenum, New York, 1974, p. 279.
9. B. Horn, E. Koch, and D. Fick, *Phys. Rev. Lett.*, 1984, **53**, 364.
10. R. F. Haglund, Jr., *Chem. Rev.*, 1988, **88**, 697.
11. T. M. Shaw and R. H. Elsken, *J. Chem. Phys.*, 1953, **21**, 565.
12. N. Fuschillo and J. G. Aston, *J. Chem. Phys.*, 1956, **24**, 1277.
13. D. E. O'Reilly, H. P. Leftin, and W. K. Hall, *J. Chem. Phys.*, 1958, **29**, 970.
14. T. W. Hickmott and P. W. Selwood, *J. Phys. Chem.*, 1956, **60**, 452.
15. N. Fuschillo and C. A. Renton, *Nature (London)*, 1957, **180**, 1063.
16. D. Michel and H. Pfeifer, *Z. Naturforsch.*, 1968, **23a**, 339.
17. K. J. Packer, *Prog. Nucl. Magn. Reson. Spectrosc.*, 1967, **3**, 87.
18. H. Pfeifer, *NMR Basic Principles and Progress*, Springer, New York, 1972, Vol. 7, p. 53.
19. J. Caro, M. Bülow, H. Jobic, J. Käger, and B. Zibrowius, *Adv. Catal.*, 1993, **39**, 351.
20. V. V. Morariu, *Chem. Phys. Lett.*, 1978, **56**, 272.
21. D. Michel, *Z. Phys. Chem. (Leipzig)*, 1973, **252**, 263.
22. I. D. Gay, *J. Phys. Chem.*, 1974, **78**, 38.
23. D. Michel, A. Germanus, and H. Pfeifer, *J. Chem. Soc., Faraday Trans. 1*, 1982, **78**, 237.
24. T. Bernstein, L. Kitaev, D. Michel, H. Pfeifer, and P. Fink, *J. Chem. Soc., Faraday Trans. 1*, 1982, **78**, 761.
25. V. I. Kvlividze and A. V. Krasnushkin, *Dokl. Akad. Nauk SSSR, Ser. Khim.*, 1975, **222**, 388.
26. J. B. Nagy, G. Engelhardt, and D. Michel, *Adv. Colloid Interface Sci.*, 1985, **23**, 67.
27. S. Kaplan, H. A. Resing, and J. S. Waugh, *J. Chem. Phys.*, 1973, **59**, 5681.
28. E. O. Stejskal, J. Schaefer, J. M. S. Henis, and M. K. Tripodi, *J. Chem. Phys.*, 1974, **61**, 2351.
29. I. D. Gay, *J. Magn. Reson.*, 1984, **58**, 413.
30. L. B. Schreiber and R. W. Vaughan, *J. Catal.*, 1975, **40**, 226.
31. T. Ito, T. Kadowaki, and T. Toya, *Jpn. J. Appl. Phys. Suppl. 2*, **1974**, 257.
32. X. Wu, B. C. Gerstein, and T. S. King, *J. Catal.*, 1990, **121**, 271.
33. T. M. Duncan, J. T. Yates, Jr., and R. W. Vaughan, *J. Phys. Chem.*, 1979, **71**, 3129.
34. C. P. Slichter, *Annu. Rev. Phys. Chem.*, 1986, **37**, 25.
35. T. M. Duncan, *Colloid Surf.*, 1990, **45**, 11.
36. J. S. Bradley, J. M. Millar, E. W. Hill, and S. Behal, *J. Catal.*, 1991, **129**, 530.
37. Z. Wang, J.-P. Ansermet, and C. P. Slichter, *J. Chem. Soc., Faraday Trans. 1*, 1988, **84**, 3785.
38. A. Zecchina, S. Coluccia, and C. Morterra, *Appl. Spectrosc. Rev.*, 1985, **21**, 259.
39. D. Freude, *Adv. Colloid Interface Sci.*, 1985, **23**, 21.
40. B. A. Morrow, *Stud. Surf. Sci. Catal.*, 1990, **57A**, 161.
41. V. M. Mastikhin, I. L. Mudrakovsky, and A. V. Nosov, *Prog. Nucl. Magn. Reson. Spectrosc.*, 1991, **23**, 259.
42. H. A. Resing, in *Magnetic Resonance in Colloid and Interface Science, Int. Symp. Menton, 1979, Reidel, Dordrecht*, 1980, p. 219.
43. I. D. Gay, A. J. McFarlan, and B. A. Morrow, *J. Phys. Chem.*, 1991, **95**, 1360.
44. S. H. C. Liang and I. D. Gay, *J. Catal.*, 1986, **101**, 293.
45. F. G. Oliver, E. J. Munson, and J. F. Haw, *J. Phys. Chem.*, 1992, **96**, 8106.
46. G. W. Haddix, J. A. Reimer, and A. T. Bell, *J. Catal.*, 1987, **106**, 111.
47. T. M. Duncan and R. W. Vaughan, *J. Catal.*, 1981, **67**, 49.
48. P.-K. Wang, C. P. Slichter, and J. H. Sinfelt, *Phys. Rev. Lett.*, 1984, **53**, 82.
49. S.-J. Hwang and B. C. Gerstein, *Bull. Magn. Reson.*, 1993, **15**, 211.
50. D. Slotfeldt-Ellingsen and H. A. Resing, *J. Phys. Chem.*, 1980, **84**, 2204.

51. D. W. Sindorf and G. E. Maciel, *J. Am. Chem. Soc.*, 1983, **105**, 1848.
52. M. Engelsberg, C. S. Yannoni, M. A. Jacintha, and C. Dybowski, *J. Am. Chem. Soc.*, 1992, **114**, 8319.
53. I. Kustanovich, Z. Luz, S. Vega, and A. J. Vega, *J. Phys. Chem.*, 1990, **94**, 3138.

Biographical Sketches

Ian D. Gay, *b* 1939, B.Sc., 1959, M.Sc., 1960 Dalhousie; Ph.D., D.I.C., 1964, London. Member of Faculty, Simon Fraser University, 1966–present. Research specialties: application of NMR to surface chemical problems.

Amphiphilic Liquid Crystalline Samples: Nuclear Spin Relaxation

Bertil Halle

Lund University, Lund, Sweden

1	Introduction	1
2	Relaxation Mechanisms and Experimental Methods	1
3	Order and Dynamics at the Molecular Level	4
4	Microstructure and Diffusion	5
5	Long-Wavelength Director Fluctuations	6
6	Related Articles	7
7	References	8

1 INTRODUCTION

Amphiphilic molecules (surfactants) consist of a polar, often charged, headgroup linked to one or two hydrocarbon, usually alkyl, chains. In the presence of water and possibly additional components, such as long-chain alcohols, alkanes, or simple electrolytes, surfactants spontaneously assemble into finite aggregates (micelles) or build up structures that extend indefinitely in one, two, or three dimensions. This gives rise to numerous liquid crystalline phases, differing in their macroscopic translational and rotational symmetries and displaying a fascinating geometrical and topological variety in their self-assembled microstructure.[1–6] The structural and dynamic characterization of these phases and the rationalization of their microstructure and phase behavior in terms of intermolecular and interaggregate forces is a challenging task. The importance of amphiphilic liquid crystals derives partly from their biological significance and diverse technical applications. In a more general context, amphiphilic liquid crystals are prime examples of complex fluids (soft matter) and their study has proven to be a rich source of fundamental knowledge.

Nuclear magnetic resonance has contributed more than any other technique to the understanding of amphiphilic liquid crystals. The NMR experiments used in this field are basically of three kinds: lineshape, diffusion, and relaxation studies. Spectral lineshapes from powder samples are now used routinely to distinguish among cubic, uniaxial, and biaxial phases (see ***Lyotropic Liquid Crystalline Samples***). Pulsed field gradient spin echo experiments can, under favorable conditions, provide the principal components of the macroscopic diffusion tensor for various molecular components (see ***Liquid Crystalline Samples: Diffusion***). Nuclear spin relaxation can provide detailed information about structure and dynamics on a wide range of length and time scales. As compared with lineshapes and diffusion, spin relaxation is a less direct source of information and therefore requires a more elaborate theoretical framework for its interpretation. On the other hand, liquid crystals can yield a large amount of relaxation data, including a variety of spin relaxation rates associated with high-rank polarization modes, and their dependence on Larmor frequency and sample orientation.

The first spin relaxation studies of amphiphilic liquid crystals appeared in the late 1960s. In a seminal contribution from the early years, Charvolin and Rigny[7] identified the three main sources of spin relaxation as: (i) local, orientationally restricted motions (rotational isomerization in the case of surfactant chains); (ii) molecular diffusion over curved interfaces; and (iii) collective director fluctuations. It was not until the 1980s, however, that improved instrumental capabilities, new pulse techniques, and advances in relaxation theory established nuclear spin relaxation as a major source of quantitative information about amphiphilic liquid crystals.[8,9] This is a highly interdisciplinary field of study where ideas and methods are continuously exchanged with several related fields, most notably molecular (thermotropic) liquid crystals and phospholipid bilayers (see Related Articles in Section 6).

2 RELAXATION MECHANISMS AND EXPERIMENTAL METHODS

2.1 General Considerations

The proton is not an ideal nucleus for relaxation studies of amphiphilic liquid crystals due to the complex relaxation behavior of the strongly coupled aliphatic chain protons, the rapid exchange of labile headgroup protons, and the contribution from intermolecular dipole–dipole couplings. Fortunately, there are several other nuclei more suitable for relaxation studies, e.g. ^{2}H or ^{13}C in surfactant chains, and ^{2}H or ^{17}O in water. For studies of microstructure, the choice is restricted to nuclei that are effectively confined to the interface, i.e. surfactant headgroup nuclei (e.g. ^{14}N), counterion nuclei (e.g. ^{23}Na), or ^{2}H nuclei in the α-position of the surfactant chain.

Despite important advances in recent years, the complex spin-dynamical behavior of quadrupolar nuclei and coupled spin-$\frac{1}{2}$ nuclei (such as $^{13}C^1H_2$) in liquid crystals has not yet been fully explored. Since most of the relevant nuclei have spin $I > \frac{1}{2}$, we emphasize quadrupolar relaxation. With the exception of $I \geq \frac{3}{2}$ nuclei, most pulse techniques for relaxation studies of anisotropic systems have been developed in other fields (see ***Deuteron Relaxation Rates in Liquid Crystalline Samples: Experimental Methods***); only a brief discussion is included here.

2.2 Quadrupolar Relaxation

Nuclei with $I \geq 1$ are coupled to the molecular degrees of freedom via the interaction of their electric quadrupole moment with the electric field gradient (EFG) generated by the surrounding charge distribution (see ***Quadrupolar Interactions***). The first-order effect of the quadrupole coupling is to split the resonance into $2I$ equidistant lines (see ***Quadrupolar Nuclei in Solids***). The quadrupole splitting occurs in all noncubic phases and contains information about the orientational order in the phase. In all but the simplest cases, however, the quadrupole splitting yields a product of order parameters, associated with different orientational

degrees of freedom, which cannot be separated without recourse to additional (e.g. relaxation) data.

The principal second-order effect of the quadrupole coupling is to induce spin relaxation (see ***Relaxation Theory for Quadrupolar Nuclei***). All information about liquid crystal structure and dynamics that can be derived from quadrupolar relaxation rates is contained in the three lab-frame spectral densities (LFSDs) $J^{\mathrm{L}}_{kk}(k\omega_0; \Omega)$ with $k = 0, 1, 2$:

$$J^{\mathrm{L}}_{kk}(k\omega_0; \Omega) = \int_0^\infty \mathrm{d}\tau \cos(k\omega_0\tau)[\langle V^{\mathrm{L}*}_k(0) V^{\mathrm{L}}_k(\tau)\rangle - |\langle V^{\mathrm{L}}_k\rangle|^2] \quad (1)$$

which are functions of the magnitude $B_0 = \omega_0/\gamma$ and orientation Ω (with respect to the liquid crystal) of the external magnetic field. The quantity within brackets in equation (1) is the time autocorrelation function of the kth spherical component V^{L}_k (in the lab frame) of the EFG tensor. The secular ($k = 0$) spectral density contains information about motions on all timescales (within the motional narrowing regime), while the nonsecular ($k = 1, 2$) spectral densities are affected only by motions on the timescale $1/\omega_0$ or faster. To determine the three individual LFSDs at a given magnetic field, one needs to measure at least three independent relaxation rates.

A system of spin I nuclei admits nonequilibrium states with magnetic tensor polarization of rank $k = 1, 2, \ldots 2I$ and coherence order $q = 0, \pm 1, \ldots \pm k$. The spin system can thus be described in terms of $(2I + 1)^2 - 1$ state multipoles[10] of rank k and projection index q. The axial ($q = 0$) multipole components, referred to as polarizations or alignments, are the generalizations of longitudinal magnetization ($k = 1$, $q = 0$). The remaining ($q \neq 0$) multipole components, referred to as q quantum coherences, are the generalizations of transverse magnetization ($k = 1$, $q = \pm 1$). The effect of hard radiofrequency pulses is simply to rotate the state multipoles, i.e. to mix the quantum order q without affecting the tensor rank k, whereas evolution under the (fluctuating) quadrupolar Hamiltonian mixes the rank without affecting the quantum order.[11]

In noncubic liquid crystals, the evolution of the polarizations involves $2I$ generalized longitudinal relaxation rates which depend on the two nonsecular LFSDs. (This dependence is linear for $I = 1$ and $I = \frac{3}{2}$, but nonlinear for $I \geq \frac{5}{2}$). The principal longitudinal relaxation experiments are the classical inversion–recovery and Jeener–Broekaert experiments[12] and their generalizations.[13]

The evolution of the coherences involves $I(2I + 1)$ generalized transverse relaxation rates, some of which may be degenerate. The homogeneous linewidths of satellite peaks, i.e. spectral lines that exhibit a first-order quadrupolar shift, are linear combinations of all three LFSDs, whereas the widths of the unshifted central peaks are linear combinations of the two nonsecular LFSDs. (This linear dependence of the linewidths on the LFSDs holds only if the quadrupole splitting is large compared with the nonsecular linewidth.)

Accurate measurements of homogeneous linewidths require echo experiments to refocus dephasing due to spatial inhomogeneities in the magnetic field and in the (static) quadrupole coupling (usually due to imperfect alignment). Whereas either 1D or 2D experiments can be performed on $I = 1$ nuclei, 2D experiments are indispensible for $I \geq \frac{3}{2}$ nuclei. The nonsecular central linewidths, associated with the $-q/2 \leftrightarrow q/2$ transitions, are obtained from 2D spin echo experiments, while the secular satellite linewidths are obtained from 2D quadrupolar echo experiments.[14–16] Table 1 lists the number of distinct relaxation rates that can be measured for different quadrupolar nuclei.

Table 1 Number of Independent Spin Relaxation Rates for Quadrupolar Nuclei in Non-Cubic Liquid Crystals

Relaxation rate	$I = 1$	$I = \frac{3}{2}$	$I = \frac{5}{2}$	$I = \frac{7}{2}$
Longitudinal	2	3	5	7
Transverse[a]	2	2	6	10
secular	1	1	3	6
nonsecular	1	1	3	4

[a]From homogeneous linewidths only.

2.3 Dipolar Relaxation

For studies of local surfactant dynamics one can use the ^{13}C nuclei in the alkyl chain, which are relaxed by the dipole–dipole coupling to directly bonded protons. The relaxation behavior of a weakly coupled AX_2 spin system such as $^{13}C^1H_2$ is complicated by $^{13}C-^1H$ cross relaxation, which is the basis of the nuclear Overhauser effect (NOE), and by cross correlation (interference) between the two C–H pairs which leads to the formation of high-rank polarization (three-spin order).[17] The ^{13}C longitudinal relaxation becomes effectively exponential, however, if the protons are decoupled by strong irradiation and if relaxation within the (strongly coupled) proton spin system quenches the development of high-rank polarization.[18] The ^{13}C inversion–recovery and steady-state NOE are then determined by the three LFSDs $J^{\mathrm{L}}_{kk}(\omega_{\mathrm{C}} + (k - 1)\omega_{\mathrm{H}}; \Omega)$ with $k = 0, 1, 2$, defined as in equation (1) but with V^{L}_k now denoting the spherical components of the $^{13}C-^1H$ dipole–dipole interaction tensor.

2.4 Relaxation Anisotropy and Phase Symmetry

For a system as complex as an amphiphilic liquid crystal, the LFSDs obtained from spin relaxation experiments are usually not amenable to direct physical interpretation without recourse to detailed structural and dynamic models. However, by transforming the lab-frame components V^{L}_k of the interaction tensor to a crystal-fixed frame, the LFSDs can be decomposed as

$$J^{\mathrm{L}}_{kk}(\omega_k; \Omega) = \sum_{n,p} F_{knp}(\Omega) J^{\mathrm{C}}_{np}(\omega_k) \quad (2)$$

where $\omega_k = k\omega_0$ for quadrupolar relaxation and $\omega_k = \omega_{\mathrm{A}} + (k - 1)\omega_{\mathrm{X}}$ for longitudinal dipolar relaxation of nucleus A coupled to nucleus X. When the time reversal invariance present in all dynamic models of interest has been taken into account there are 15 crystal-frame spectral densities (CFSDs) $J^{\mathrm{C}}_{np}(\omega_k)$, defined in analogy with equation (1). Depending on the rotational symmetry of the liquid crystal, some of these CFSDs

Table 2 Number of Independent Crystal-frame Spectral Density Functions (N) and Second-rank Order Parameters (n_2) for Different Crystallographic Point Groups

Phase	Point group	N	n_2
Isotropic fluid	K_h	1	0
Cubic	O_h	2	0
Lamellar, nematic U, hexagonal	$D_{\infty h}$, D_{6h}	3	1
Tetragonal, rhombohedral	D_{4h}, D_{3d}	4	1
Rectangular, orthorhombic, nematic B	D_{2h}	6	2
Oblique	C_{2h}	9	3
Monoclinic	C_i	15	5

may vanish or be linearly dependent. Taking the rotational symmetry into account, equation (2) can be expressed as[19]

$$J^{\mathrm{L}}_{kk}(\omega_k;\Omega) = \sum_{\lambda} F_{k\lambda}(\Omega) J^{\mathrm{C}}_{\lambda}(\omega_k) \tag{3}$$

with the composite index $\lambda = (\alpha,\mu,\mu')$ labeling the irreducible representations α of the liquid crystal point group and the independent subspaces μ of α. The irreducible CFSDs $J^{\mathrm{C}}_{\lambda}(\omega_k)$, constructed from symmetry-adapted tensor components, constitute the complete model-independent information content of a fixed-field spin relaxation study of a liquid crystal.[19] The number N of independent CFSD functions is given in Table 2 for liquid crystals of different symmetry. By measuring three linearly independent spin relaxation rates at N different orientations Ω of the (homeotropically aligned) liquid crystal, one can thus determine the $3N$ quantities $J^{\mathrm{C}}_{\lambda}(\omega_k)$. This relative wealth of model-independent information (as compared to isotropic fluids) imposes severe constraints on models of structure and dynamics.

In isotropic powder samples, the relaxation of the central peak ($-q/2 \leftrightarrow q/2$ transition) for noncubic phases and of the single peak for cubic phases is governed by the isotropically averaged (by interdomain exchange) LFSD:[19]

$$J^{\mathrm{L}}_{\mathrm{iso}}(\omega_k) = \frac{1}{5}\sum_{\alpha} d_{\alpha} \sum_{\mu} J^{\mathrm{C}}_{\alpha\mu\mu}(\omega_k) \tag{4}$$

with d_{α} being the dimension of the irreducible representation α.

While the rotational symmetry of a liquid crystal is determined by its crystallographic point group, the observable manifestations of this symmetry depend on the tensor rank of the measured physical property. The powder lineshape, being determined by the (motionally averaged) second-rank EFG tensor, can only distinguish between effectively isotropic, uniaxial, and biaxial symmetries. This is reflected in the number n_2 of independent second-rank order parameters (see Table 2). The CFSDs, involving products of two components V^{L}_k of a second-rank tensor, can be decomposed into terms transforming as tensors of rank 0, 2, and 4; hence there are $N = 1 + n_2 + n_4$ independent CFSDs.[19] Phases with the same 'second-rank symmetry' can thus have different relaxation behavior (see Table 2). On the other hand, since spin relaxation does not involve a higher tensor rank than 4, the relaxation anisotropy is of the same form for hexagonal phases (sixfold symmetry) as for lamellar and uniaxial nematic phases (full cylindrical symmetry). Since the second-rank spherical components V_n transform according to the

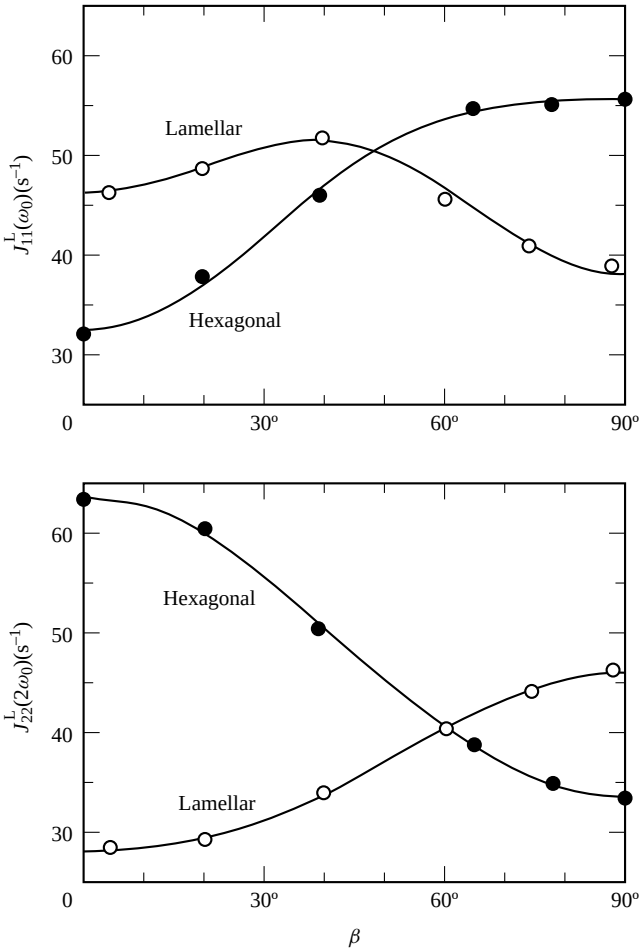

Figure 1 Anisotropy of the nonsecular lab-frame spectral densities obtained from the counterion ^{23}Na relaxation in the hexagonal[20] and (nonclassical) lamellar[21] phases of the sodium dodecyl sulfate/decanol/water system at 25 °C. The curves are fits according to equation (5)

irreducible representations (A_1, E_1, and E_2) of the point group $D_{\infty\mathrm{h}}$, the relaxation anisotropy for these phases takes the form:

$$J^{\mathrm{L}}_{kk}(\omega_k;\beta) = \sum_{n=0}^{2}(1-\delta_{n0}/2)\{[d^2_{kn}(\beta)]^2 + [d^2_{k-n}(\beta)]^2\} J^{\mathrm{C}}_{nn}(\omega_k) \tag{5}$$

where the $d^2_{kn}(\beta)$ are reduced Wigner functions and β is the angle between the magnetic field and the symmetry axis of the phase. Figure 1 shows the nonsecular ^{23}Na relaxation anisotropy of counterions in a hexagonal phase[20] and in a lamellar phase with disrupted bilayers.[21] In each case, the fit of equation (5) to the LFSD data yields the six model-independent CFSDs $J^{\mathrm{C}}_{nn}(k\omega_0)$ with $k = 1, 2$ and $n = 0, 1, 2$.

2.5 Relaxation Dispersion and Low-Frequency Dynamics

The dynamic processes responsible for spin relaxation in amphiphilic liquid crystals take place mainly on three time scales: local, restricted motions (1–100 ps), molecular

diffusion over curved interfaces (1–10 ns), and collective processes (> 100 ns). While the local motions are usually in the extreme narrowing limit, the dispersion of the surface diffusion contribution to the nonsecular spectral densities is in the frequency range ($\omega_0/2\pi \approx 1$–100 MHz) accessible by conventional relaxation experiments. While the secular spectral density $J^{\mathrm{L}}_{00}(0)$ reflects motions on all timescales, special techniques are required to investigate the low-frequency dispersion associated with collective processes.

Two methods are available for probing the secular LFSD $J^{\mathrm{L}}_{00}(\omega)$ in the kHz frequency range. For $I = 1$ nuclei, the quadrupolar echo train $(\pi/2)_x - [\tau - (\pi/2)_y - \tau]_n$ yields an effective spectral density[22]

$$\frac{8}{\pi^2}\sum_{n=0}^{\infty}(2n+1)^{-2}J^{\mathrm{L}}_{00}\left((2n+1)\frac{\pi}{2}\omega_{\mathrm{p}}\right) = J^{\mathrm{L}}_{00}(0)\left[1-\omega_{\mathrm{p}}\tau_{\mathrm{c}}\tanh\left(\frac{1}{\omega_{\mathrm{p}}\tau_{\mathrm{c}}}\right)\right] \quad (6)$$

with $\omega_{\mathrm{p}} = 1/\tau$ the pulse train frequency. The second form in equation (6) holds only if $J^{\mathrm{L}}_{00}(\omega)$ is Lorentzian, with correlation time τ_{c}. Relaxation in the presence of a spin lock field B_1 yields, in a $T_{1\rho}$ experiment on $I = 1$ nuclei, an effective spectral density given approximately by[23]

$$\frac{(2\Omega_1)^2}{\omega_Q^2+(2\Omega_1)^2}J^{\mathrm{L}}_{00}\left(\sqrt{\omega_Q^2+(2\Omega_1)^2}\right) \quad (7)$$

with $\Omega_1 = \gamma B_1$ and ω_{Q} the static (residual) quadrupole frequency. If $J^{\mathrm{L}}_{00}(\omega)$ is Lorentzian, equation (7) has a maximum of $J^{\mathrm{L}}_{00}(0)(\sqrt{1+x^2}+x)^{-2}$ at $\Omega_1 = (\omega_Q/2)(1 + x^{-2})^{1/4}$, with $x = \omega_Q\tau_{\mathrm{c}}$

A much wider frequency range, from the conventional MHz range down to ca. 100 Hz, can be explored by the field cycling technique[24] (see ***Field Cycling Experiments***). Unfortunately, this technique is not applicable to rapidly relaxing quadrupolar nuclei; so far only ^{1}H field cycling studies of amphiphilic liquid crystals have been reported. As seen from Figure 2, the entire dispersion due to collective processes can be obtained in this way.[25]

3 ORDER AND DYNAMICS AT THE MOLECULAR LEVEL

3.1 Water and Counterions

Amphiphilic interfaces induce only small and short-ranged perturbations of the strongly hydrogen-bonded network in liquid water. Since the surface-induced orientational order and reorientational anisotropy are weak, the three LFSDs are equal, $J^{\mathrm{L}}_{kk}(\omega_k) = J^{\mathrm{L}}_{00}(0)$, and the spin relaxation exhibits neither anisotropy nor dispersion. Water reorientation in the first molecular 'layer' is typically slowed down by a factor of two to three, and there is no evidence for long (> 100 ps) water residence times in any amphiphilic system. Water ^{2}H and ^{17}O relaxation rates thus report essentially on the fast, local water dynamics, which are insensitive to variations in microstructure.[26,27]

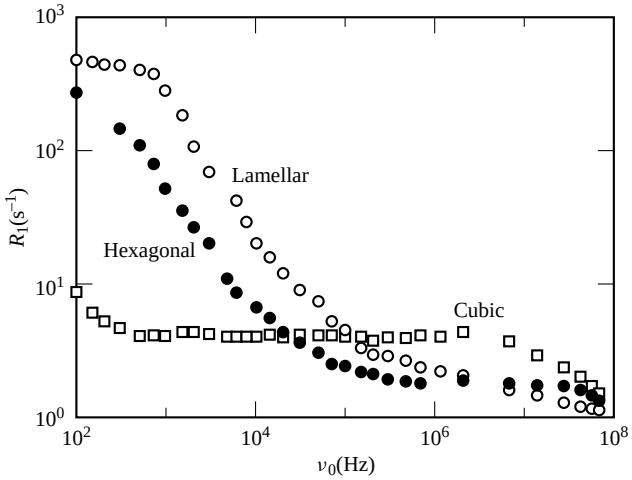

Figure 2 Dispersion of the longitudinal relaxation rate R_1 of surfactant chain protons in powder samples of the lamellar, hexagonal, and cubic phases of the potassium dodecanoate/D_2O system at 70 °C[25]

Counterion relaxation rates reflect fast, local motions as well as slower motions, e.g. diffusion over curved interfaces. The relative contributions from fast and slow motions can be estimated[26] as $\langle\chi^2\rangle\tau_{\mathrm{f}}$ and $\langle\chi\rangle^2\tau_{\mathrm{s}}$, respectively, where $\langle\chi^2\rangle$ is the mean square quadrupole coupling constant (QCC), $\langle\chi\rangle$ the residual QCC (averaged by the fast motions), and τ_{f} and τ_{s} the effective correlation times. As in the case of water, the residual anisotropy is weak ($\langle\chi\rangle^2 \ll \langle\chi\rangle^2$), and the fast-motion contribution to the LFSDs is independent of orientation and frequency.[20] However, the ratio $\tau_{\mathrm{s}}/\tau_{\mathrm{f}}$ is typically (in the presence of curved interfaces) an order of magnitude larger for counterions than for water, making the fast and slow contributions comparable. For atomic counterions, where the EFG is of intermolecular origin, the local motion contribution $\langle\chi^2\rangle\tau_{\mathrm{f}}$ and the residual QCC $\langle\chi\rangle$ depend markedly on the molecular details of the interface region, but in a way that is not readily captured by simple models.

3.2 Surfactant Molecules

Rotational isomerization in surfactant alkyl chains is too fast (< 10 ps) to produce a dispersion in the ^{2}H or ^{13}C relaxation.[8,28] This introduces a certain model dependence in the interpretation,[28–30] although constraints are imposed by the individual bond order parameters deduced from static dipole or quadrupole couplings.[8] On a longer timescale (typically, 0.1–1 ns), the conformationally averaged surfactant molecule undergoes restricted reorientation within the aggregate. This motion can produce a high-field dispersion in the ^{13}C relaxation (which involves the Larmor frequency of ^{1}H), whereas the ^{2}H relaxation is usually in the extreme narrowing limit.[28] The relaxation anisotropy is expected to be weak for alkyl chain nuclei, but can be substantial for headgroup nuclei in double-chain surfactants.[28] The overall motion of surfactants is usually modeled as rotational diffusion of a symmetric top in a uniaxial potential of mean torque (see ***Liquid Crystalline Samples: Relaxation Mechanisms***).

The relaxation of a surfactant nucleus induced by the intermolecular dipole coupling with a nuclear or electron spin in a counterion can, in certain cases, provide information about

Table 3 Relaxation Processes in Amphiphilic Liquid Crystals

Dynamics	Order fluctuations	Director fluctuations
Single-molecule	Diffusion in order gradient	Diffusion on curved interface
		Diffusion in nematic director field
Collective	Critical fluctuations	Micelle reorientation
		Nematic director fluctuations
		Interface shape fluctuations

the spatial distribution of the surfactant nucleus with respect to the interface.[8,31] The interpretation of such relaxation data is, however, strongly model dependent.[32]

4 MICROSTRUCTURE AND DIFFUSION

4.1 Fluctuating Local Anisotropy

Much of the intricate spin relaxation behavior of complex fluids such as amphiphilic liquid crystals can be rationalized in terms of a unifying concept: the fluctuating local anisotropy. On longer timescales, the net effect of the fast, local motions (see Section 3) is to project the quadrupole (or dipole–dipole) interaction tensor onto an axis, the (local) director, which usually coincides with the local interface normal. The motionally averaged, or projected, interaction tensor is proportional to the second-rank ordering tensor $\boldsymbol{S}$, with three independent components in the usual case of local uniaxial symmetry. In the director frame, $\boldsymbol{S}$ is diagonal and the three independent variables are the principal order parameter S and the set Ω of two angles that specify the director orientation (with respect to the crystal axes).

All relaxation processes, apart from the local motions, can be classified as either local order fluctuations, which modulate the order parameter $S(t)$, or local director fluctuations, which modulate the director orientation $\Omega(t)$. Each of these classes can be further subdivided according to whether the fluctuations are due to single-molecule dynamics (translational diffusion) or to collective processes, involving many molecules. Among the relaxation processes listed in Table 3, those in the director fluctuation class are generally most important. Diffusion of water or counterions between interface ($S \neq 0$) and bulk ($S = 0$) regions[33] is usually an inefficient relaxation process,[21,34] and critical order fluctuations[35] occur only near phase transitions.

4.2 Diffusion on Curved Interfaces

All amphiphilic liquid crystalline phases, save the lamellar one, are built from curved interfaces, over which surfactants and counterions diffuse freely. (The long-range Coulomb interaction effectively reduces the dimensionality of the diffusion space for counterions to two.[21,33,34]) This constitutes an efficient relaxation process of the director fluctuation type, which can yield quantitative information about the interface geometry (microstructure) and the surface diffusion coefficient, D_s. Typically, the microstructure involves radii of curvature of the order 1–2 nm, while $D_s \approx (0.1\text{–}1) \times 10^{-9}\,\mathrm{m^2\ s^{-1}}$. The associated correlation times are thus in the 1–10 ns range, which places the relaxation dispersion in the conventional MHz range of Larmor frequencies. We now consider how surface diffusion induced quadrupolar spin relaxation can be exploited in the various phases.

4.3 Hexagonal Phases

The normal hexagonal phase is built from cylindrical surfactant aggregates of indefinite length, arranged on a two-dimensional hexagonal lattice. Since the director, i.e. the cylinder surface normal, is everywhere perpendicular to the sixfold symmetry axis of the phase, surface diffusion around the cylinder contributes to only one of the three CFSDs, i.e.

$$J^{C}_{nn}(k\omega_0) = J_{loc} + \delta_{n2}\langle\chi\rangle^2 \frac{3}{8}\frac{\tau_s}{1+(k\omega_0\tau_s)^2} \qquad (8)$$

with the correlation time $\tau_s = R^2/(4D_s)$, and R the diffusion radius. In addition, the adiabatic ($k = 0$) CFSDs have contributions from long-wavelength cylinder undulations.

With R obtained from the X-ray Bragg spacing, the surface diffusion coefficients D_s of surfactants and counterions can be accurately ($\pm$ 10%) determined from the nonadiabatic ($k = 1$, 2) CFSDs obtained from the nonsecular relaxation anisotropy (see Figure 1) at a single magnetic field.[20,36] In reversed hexagonal phases, the radius of the aqueous cylinders can be varied in a controlled way, allowing a direct verification of the R^2 scaling of the correlation time.[34]

4.4 Lamellar Phases

In a classical lamellar phase, with periodically stacked, planar surfactant bilayers of indefinite lateral extent, one expects neither anisotropy nor dispersion in the nonsecular LFSDs, since in the absence of interface curvature, $J^{C}_{nn}(k\omega_0) = J_{1oc}$ for $k = 1$, 2. (The secular LFSD, however, should exhibit anisotropy due to long-wavelength bilayer undulations; see Section 5.3). Spin relaxation is therefore a sensitive curvature probe for lamellar phases; any deviation from the classical microstructure is unambiguously revealed by the relaxation anisotropy and dispersion produced by molecular diffusion over curved interfaces.

In the lamellar phase of the sodium dodecyl sulfate/decanol /water system, the ^{23}Na relaxation (see Figure 1) provides direct evidence for a highly curved interface at low decanol content,[21] whereas at higher decanol content the microstructure is classical. The relaxation behavior is consistent with a microstructure of ribbon-like aggregates, arranged on the smectic planes so as to preserve the uniaxial symmetry of the lamellar phase. The three CFSD functions $J^{C}_{nn}(\omega)$ can then be related to two irreducible (D_{2h}) ribbon-frame spectral density functions associated with surface diffusion around the ribbon-like aggregate.

4.5 Uniaxial Nematic Phases

Two types of uniaxial nematic phase occur in amphiphilic systems:[4] the calamitic (N_C) and discotic (N_D) phases, built from orientationally ordered nonspherical micellar aggregates of approximately prolate and oblate spheroidal shape, respectively. To understand these phases, one needs to quantify the size of the micelles and their long-range orientational order.

Nuclear spin relaxation studies can, in principle, yield the micelle dimensions as well as the second-rank nematic order parameter.[37] Two difficulties are encountered, however. First, the fast magnetic alignment of nematic fluids precludes relaxation anisotropy measurements with conventional methods. This experimental problem can be partly overcome by sample spinning techniques (see ***Spinning Liquid Crystalline Samples***). The second difficulty is intrinsic: spin relaxation is induced not only by molecular diffusion over the micelle surface, but also by rotation of the micelle around its symmetry axis and restricted tumbling of this axis. While the three CFSDs associated with spheroidal surface diffusion and single-micelle reorientation (in a uniaxial potential of mean torque) can be accurately calculated,[38] it is more difficult to describe the cooperative reorientation modes in the transition zone between the single-micelle and viscoelastic continuum behaviors (see Section 5.2). However, in the frequency range (typically > 10 MHz) where the cooperative modes are unimportant, quadrupolar relaxation of counterion and surfactant nuclei can yield useful, albeit somewhat model-dependent, information about micelle size and nematic order.[37,39]

4.6 Cubic Phases

According to the topology of their microstructure, amphiphilic cubic phases are either of the micellar type with a three-dimensional periodic arrangement of nonspherical surfactant aggregates, or of the bicontinuous type with both aqueous and nonpolar regions connected over macroscopic distances in all three dimensions.[5] In both types of cubic phase, surface diffusion is the major relaxation process. For micellar cubic phases, the spectral densities can be calculated as for nematic phases, also including molecular exchange between differently oriented micelles.[40]

The microstructure of bicontinuous cubic phases is usually modeled in terms of certain triply periodic minimal surfaces. Due to the high symmetry of these surfaces, the surface-diffusion spectral densities should be nearly Lorentzian (as for diffusion on a sphere). The effective correlation times can then be expressed as[41]

$$\tau_s = -\frac{1 - cQ}{6D_s\langle K\rangle} \tag{9}$$

with c a numerical constant, Q the fourth-rank cubic order parameter, and $\langle K\rangle$ the (negative) average Gaussian curvature of the minimal surface, related via the Gauss–Bonnet theorem to the unit cell surface area and topology (Euler–Poincaré characteristic). The correlation time τ_s decreases strongly with increasing topological complexity and can therefore, in contrast to X-ray diffraction, distinguish among different microstructures that belong to the same crystallographic space group.[41]

The quadrupolar relaxation dispersion of surfactant chain and headgroup nuclei has been used to determine micelle dimensions in cubic phases.[42,43] Since only powder samples of cubic phases have been studied so far,[25,42,43] the full model-independent information content of the relaxation has not been extracted. Although sometimes referred to as the 'viscous isotropic phase', the cubic phase has an inherently anisotropic relaxation behavior (see Section 2.4) and the two irreducible CFSDs can be determined from single crystal relaxation data.[40]

4.7 Low-Symmetry Phases

Although attractive with regard to their rich model-independent information content (see Table 2), amphiphilic phases of lower than hexagonal symmetry have not yet been subjected to spin relaxation studies. The four irreducible CFSDs from triply periodic tetragonal and rhombohedral phases might be analyzed in terms of surface diffusion on minimal surfaces, as for bicontinuous cubic phases. For two-dimensional rectangular phases, the ribbon-frame spectral densities discussed in Section 4.4 should be appropriate. Biaxial nematic phases pose a greater challenge however, in view of the large number of model parameters needed to describe surface diffusion on biaxial micelles undergoing asymmetric-top reorientation in a biaxial potential of mean torque.

5 LONG-WAVELENGTH DIRECTOR FLUCTUATIONS

5.1 General Considerations

For noncubic phases, spin relaxation in the sub-MHz frequency range is usually dominated by slow director fluctuations. The actual dynamic process inducing spin relaxation can be either long-range molecular diffusion or the intrinsic dynamics of collective modes. The theory of spin relaxation due to such processes is based on a phenomenological continuum description of liquid crystal mechanics, carried to second order in the elastic deformations.[44] The relaxation theory has so far been developed only for the uniaxial nematic and lamellar phases. Information about long-wavelength director fluctuations is contained in the anisotropic, secular LFSD $J^L_{00}(0;\beta)$ and in the low-frequency relaxation dispersion accessible by field cycling, echo train, and spin lock techniques (see Section 2.5).

5.2 Uniaxial Nematic Phases

The orientational state of a uniaxial nematic phase is specified at the continuum level by the director field $\boldsymbol{n}(\boldsymbol{r})$, where $\boldsymbol{n}$ is the unit vector along the principal axis of the micelle ordering tensor averaged over a macroscopically small volume of order λ_c^3 around the point $\boldsymbol{r}$. The three CFSDs involve time correlation functions of the transverse director components $\boldsymbol{n}_\perp = (n_x, n_y)$, which measure the orientational deviation of the director from the symmetry axis of the phase.

The CFSD $J^{C}_{11}(\omega_0)$, which is of second order in $n_\perp$, has a complicated dispersion with three regimes (equations (10a)–(10c)):

$$J^{C}_{11}(\omega_0) = \alpha_N \frac{\xi_m}{D_e}\left[1 - \left(\frac{\omega_0}{2\omega_m}\right)^{1/2}\right], \quad \omega_0 \ll \omega_m \qquad (10a)$$

$$J^{C}_{11}(\omega_0) = \frac{\alpha_N}{(2D_e\omega_0)^{1/2}}, \quad \omega_m \ll \omega_0 \ll \omega_c \qquad (10b)$$

$$J^{C}_{11}(\omega_0) = \alpha_N \frac{(4\pi)^2 D_e}{\lambda_c^3 \omega_0^2}, \quad \omega_c \ll \omega_0 \qquad (10c)$$

with $\alpha_N = \frac{3}{4}\pi \langle\chi\rangle^2 k_B T/K$, $D_e = D + K/\eta$, K and η the effective curvature-elasticity and viscosity of the nematic fluid,[44] and D the long-range diffusion coefficient of the spin-bearing species. Further, $\omega_c = D_e (2\pi/\lambda_c)^2$ and $\omega_m = D_e/\xi^2_m$, with $\xi_m = \sqrt{\mu_0 K \Delta\chi}\ /B_0$ the magnetic coherence length.[44] Since, in amphiphilic nematic phases, $\omega_c/2\pi$ is typically of order 1 MHz, the classical[45] $1/\sqrt{\omega_0}$ dispersion regime in equation (10b) is accessible only with special techniques such as field cycling. In the conventional MHz range, only the high-frequency $1/\omega_0^2$ tail contributes to the relaxation (at $<$ 10 MHz). In this frequency range, however, the theory may be inaccurate since short-wavelength (of order λ_c) continuum modes and single-micelle restricted tumbling modes make comparable contributions.

In the presence of a magnetic field, a stationary nematic sample (of thickness $\gg \xi_m$) adopts either a parallel or a perpendicular phase orientation with respect to the field. According to equation (5), the secular LFSD then involves only the CFSDs $J^{C}_{00}(0)$ and $J^{C}_{22}(0)$. Since these are of fourth order in $n_\perp$, the rates of molecular diffusion (D) and viscoelastic mode relaxation (K/η) are no longer additive.[46] For the case $D \gg K/\eta$ which usually applies to counterions, the result is[46]

$$J^{C}_{00}(0) = 3J^{C}_{22}(0) = \langle\chi\rangle^2 \left(\frac{3k_B T}{4\pi K}\right)^2 \frac{1}{D}[\ln(2\pi\xi_m/\lambda_c) - 1.119] \qquad (11)$$

The secular LFSD can thus be used to determine either the curvature-elasticity K or the long-range diffusion coefficient D.[46]

The second-order adiabatic CFSD $J^{C}_{11}(0)$ in equation (10) can be obtained from relaxation studies at oblique phase orientations, achievable by sample spinning techniques. Two complications then arise. First, the magnetic field breaks the intrinsic uniaxial symmetry of the nematic phase, thus altering the low-frequency ($\omega_0 < \omega_m$) relaxation behavior.[47] Due to the orientation-dependent magnetic quenching of long-wavelength elastic fluctuation modes, the relaxation anisotropy involves CFSDs $J^{C}_{np}(0)$ with $n \neq p$, and hence no longer obeys equation (5).[47] (equation (10a) and equation (11) are strictly valid only for parallel alignment.) Second, since $J^{C}_{11}(0)$ exceeds $J^{C}_{00}(0)$ by a factor $\xi_m K/k_B T$ of order 10^3, the conventional perturbation theory of spin relaxation may break down.

5.3 Lamellar Phases

Due to its layered microstructure, the lamellar phase differs fundamentally from a nematic fluid in its mechanical properties. Since the orientation of the bilayer normal (the director) is coupled to the position of the bilayer, director fluctuations in lamellar phases are suppressed not only by the bending rigidity of the bilayers but also by the (osmotic) forces that maintain the bilayer spacing. The continuum-mechanical description of the lamellar phase thus involves two elastic constants:[44] the splay-curvature modulus K_1 and the osmotic compression modulus $\overline{B}$. These are related to the average bilayer spacing d, the bilayer bending rigidity κ, and the curvature $V''(d)$ of the bilayer interaction as: $K_1 = \kappa/d$ and $\overline{B} = d\ V''(d)$. The lateral orientational correlation length $\xi_p = (d^2 K_1/\overline{B})^{1/4}$, also called the patch length, defines the crossover from a short-wavelength regime with independent bilayer fluctuations to a long-wavelength regime with highly coupled bilayer fluctuations. Since interbilayer forces limit the amplitude of long-wavelength fluctuation modes, magnetic quenching is unimportant in lamellar phases.

As in the nematic case, the dispersion of the second-order CFSD $J^{C}_{11}(\omega_0)$ exhibits three regimes (equations (12a)–(12c)):[48]

$$J^{C}_{11}(\omega_0) = \alpha_L \frac{\xi_p^2}{D_e}\left[\ln\left(\frac{d}{L_z} + \frac{\omega_0}{\omega_p}\right)^{-1} + \frac{\omega_0}{\omega_p}\right], \quad \omega_0 \ll \omega_p \qquad (12a)$$

$$J^{C}_{11}(\omega_0) = \alpha_L \frac{\pi}{\omega_0}, \quad \omega_p \ll \omega_0 \ll \omega_a \qquad (12b)$$

$$J^{C}_{11}(\omega_0) = \alpha_L \frac{2\pi^2 D_e}{a^2 \omega_0^2}, \quad \omega_a \ll \omega_0 \qquad (12c)$$

with $\alpha_L = (3/16\pi)\langle\chi\rangle^2 k_B T/\kappa$, $D_e = D_\perp + K_1/\eta$, $\omega_a = D_e(\pi/a)^2$, and $\omega_p = D_e\pi/\xi_p^2$. Further, L_z is the sample thickness and a is a lateral cut-off length, with a^2 of the order of the surfactant cross-section.

The adiabatic CFSD $J^{C}_{11}(0)$ is proportional to $\langle u^2\rangle$, with u the vertical bilayer displacement, and hence exhibits a logarithmic divergence with sample size, characteristic of one-dimensional crystals.[44] At frequencies $\omega_0 \gg \omega_p$, $J^{C}_{11}(\omega_0)$ reflects independent bilayer fluctuations and the range $\omega_p \ll \omega_0 \ll \omega_a$ corresponds to the classical $1/\omega_0$ dispersion regime,[49] where $J^{C}_{11}(\omega_0)$ depends neither on the inter-bilayer forces (ξ_p) nor on the fluctuation rate (D_e). Since ξ_p is generally of the same order as the bilayer spacing d, $\omega_p/2\pi$ is of order 10 MHz for typical lamellar phases (but lower for very dilute samples). The experimentally accessible low-frequency dispersion (see Section 2.5) then reflects coupled bilayer fluctuations and can thus, like the adiabatic CFSD $J^{C}_{11}(0)$, provide information about inter-bilayer forces.

6 RELATED ARTICLES

Bilayer Membranes: Deuterium and Carbon-13 NMR; Bilayer Membranes: Proton and Fluorine-19 NMR; Deuteron Relaxation Rates in Liquid Crystalline Samples: Experimental

Methods; Liquid Crystalline Samples: Deuterium NMR; Liquid Crystalline Samples: Relaxation Mechanisms; Lyotropic Liquid Crystalline Samples; Membranes: Deuterium NMR; Micellar Solutions and Microemulsions; Relaxation Theory for Quadrupolar Nuclei.

7 REFERENCES

1. V. Luzzati, in *Biological Membranes*, ed. D. Chapman, Academic Press, New York, 1968, Vol. 1, p. 71
2. P. Ekwall, in *Advances in Liquid Crystals*, ed. G. H. Brown, Academic Press, New York, 1975, Vol. 1, p. 1.
3. G. J. T. Tiddy, *Phys. Rep.*, 1980, **57**, 1.
4. B. J. Forrest and L. W. Reeves, *Chem. Rev.*, 1981, **81**, 1.
5. K. Fontell, *Colloid Polym. Sci.*, 1990, **268**, 264.
6. J. Charvolin, *Contemp. Phys.*, 1990, **31**, 1.
7. J. Charvolin and P. Rigny, *J. Chem. Phys.*, 1973, **58**, 3999.
8. C. Chachaty, *Mol. Eng.*, 1992, **2**, 65.
9. B. Halle, P.-O. Quist, and I. Furó, *Liq. Cryst.*, 1993, **14**, 227.
10. K. Blum, *Density Matrix Theory and Applications*, Plenum Press, New York, 1981.
11. B. C. Sanctuary and T. K. Halstead, *Adv. Magn. Opt. Reson.*, 1990, **15**, 79.
12. R. R. Vold, in *Nuclear Magnetic Resonance of Liquid Crystals*, ed. J. W. Emsley, Reidel, Dordrecht, 1985, p. 253.
13. I. Furó and B. Halle, *J. Chem. Phys.*, 1989, **91**, 42.
14. I. Furó, B. Halle, and T. C. Wong, *J. Chem. Phys.*, 1988, **89**, 5382.
15. I. Furó and B. Halle, *J. Magn. Reson.*, 1992, **98**, 388.
16. I. Furó and B. Halle, *Mol. Phys.*, 1992, **76**, 1169.
17. L. G. Werbelow and D. M. Grant, *Adv. Magn. Reson.*, 1977, **9**, 189.
18. D. Canet, *Prog. NMR Spectrosc.*, 1989, **21**, 237.
19. S. Gustafsson and B. Halle, *Mol. Phys.*, 1993, **80**, 549.
20. P.-O. Quist, I. Blom, and B. Halle, *J. Magn. Reson.*, 1992, **100**, 267.
21. P.-O. Quist and B. Halle, *Phys. Rev. E*, 1993, **47**, 3374.
22. J. S. Blicharski, *Can. J. Phys.*, 1986, **64**, 733.
23. J. R. C. van der Maarel, *J. Chem. Phys.*, 1993, **99**, 6546.
24. F. Noack, *Prog. NMR Spectrosc.*, 1986, **18**, 171.
25. W. Kühner, E. Rommel, F. Noack, and P. Meier, *Z. Naturforsch.*, 1987, **42a**, 127.
26. B. Halle and H. Wennerström, *J. Chem. Phys.*, 1981, **75**, 1928.
27. M. P. Bozonnet-Frenot, J. P. Marchal, and D. Canet, *J. Phys. Chem.*, 1987, **91**, 89.
28. C. Chachaty and T. Bredel, *J. Phys. Chem.*, 1991, **95**, 5335.
29. A. Ferrarini, G. J. Moro, and P. L. Nordio, *Liq. Cryst.*, 1990, **8**, 593.
30. R. Y. Dong, *Phys. Rev. A*, 1991, **43**, 4310.
31. Ph. Brûlet and H. McConnell, *Proc. Natl. Acad. Sci. USA*, 1975, **72**, 1451.
32. J. P. Korb, Th. Bredel, C. Chachaty, and J. R. C. van der Maarel, *J. Chem. Phys.*, 1990, **93**, 1964.
33. B. Halle, *Mol. Phys.*, 1984, **53**, 1427; 1987, **60**, 319.
34. I. Furó, B. Halle, P. O. Quist, and T. C. Wong, *J. Phys. Chem.*, 1990, **94**, 2600.
35. J. H. Freed, *J. Chem. Phys.*, 1992, **96**, 3901.
36. P. O. Quist, B. Halle, and I. Furo, *J. Chem. Phys.*, 1991, **95**, 6945.
37. P. O. Quist, B. Halle, and I. Furo, *J. Chem. Phys.*, 1992, **96**, 3875.
38. B. Halle, *J. Chem. Phys.*, 1991, **94**, 3150.
39. I. Furó and B. Halle, *Phys. Rev. E*, 1995, **51**, 466.
40. B. Halle, *Liq. Cryst.*, 1992, **12**, 625.
41. B. Halle, S. Ljunggren, and S. Lidin, *J. Chem. Phys.*, 1992, **97**, 1401.
42. O. Söderman, H. Walderhaug, U. Henriksson, and P. Stilbs, *J. Phys. Chem.*, 1985, **89**, 3693.
43. O. Söderman and U. Henriksson, *J. Chem. Soc., Faraday Trans. 1*, 1987, **83**, 1515.
44. P. G. de Gennes, *The Physics of Liquid Crystals*, Clarendon Press, Oxford, 1974.
45. P. Pincus, *Solid State Commun.*, 1969, **7**, 415.
46. B. Halle, P. O. Quist, and I. Furo, *Phys. Rev. A*, 1992, **45**, 3763.
47. B. Halle, *Liq. Cryst.*, 1994, **17**, 759.
48. B. Halle, *Phys. Rev. E*, 1994, **50**, R2415.
49. J. A. Marqusee, M. Warner, and K. A. Dill, *J. Chem. Phys.*, 1984, **81**, 6404.

Biographical Sketches

Bertil Halle. *b* 1951. M.Sc. (Civilingenjör), 1977, Ph.D., 1981, Physical Chemistry, Lund University, Sweden. Postdoctoral work in Department of Applied Mathematics, Australian National University, Canberra, 1982–84. Faculty of Physical Chemistry, Lund University, 1984–present. Approx. 75 publications. Research specialties: theory of nuclear spin relaxation, physics of complex fluids (especially amphiphilic liquid crystals), hydration and dynamics of biomolecules.

Centerband-Only Detection of Exchange (CODEX): Efficient NMR Analysis of Slow Motions in Solids

Klaus Schmidt-Rohr

Iowa State University, Ames, IA, USA

&

Eduardo R. deAzevedo and Tito J. Bonagamba

Instituto de Física de São Carlos, Universidade de São Paulo, São Carlos, São Paulo, Brazil

1	Introduction	1
2	Exchange NMR Under MAS, and Rotor Synchronization	1
3	Explanation of the CODEX Pulse Sequence	2
4	Analysis and Simulation of CODEX Curves	3
5	Practical Considerations	7
6	Applications of CODEX	8
7	Outlook	8
8	Related Articles in Volumes 1–8	9
9	References	9

1 INTRODUCTION

Solid-state NMR provides some of the most powerful techniques for elucidating details of segmental dynamics in solid materials.[1] Such dynamics have important effects on mechanical and conduction properties of polymers, activity of proteins, stability of pharmaceuticals, transport properties in zeolites, and behavior of amorphous materials near the glass transition.[2–7] While fast dynamics can be characterized to some extent by NMR lineshape analysis and relaxation-time measurements can characterize correlation times over a wide range (see also **Ultraslow Motions in Solids,** Volume 8), the most specific information is obtained in exchange NMR experiments, where relatively slow segmental reorientations with rates of $0.1-10\,000\,s^{-1}$ are observed in terms of changes of orientation-dependent NMR frequencies.[1,8–11] Correlation times and their distributions, reorientation-angle distributions, orientational memory, rate memory, the existence of dynamic heterogeneities, and their size can be characterized by 1D, 2D, 3D, and reduced 4D exchange NMR (see **Polymer Dynamics & Order from Multidimensional Solid State NMR,** Volume 6).[1,12–20] However, the sensitivity and resolution of these traditional exchange-NMR techniques have been limited, since anisotropy-broadened lineshapes or strong sidebands in magic-angle spinning spectra were required. Only by specific isotopic labeling could these limitations be eliminated in part.

The centerband-only detection of exchange (CODEX) NMR technique has overcome these problems, making it possible to observe and characterize slow ($k = 0.1\,s^{-1}$ to $3000\,s^{-1}$) segmental reorientations with the highest available NMR sensitivity and site resolution, in sideband-free magic-angle spinning spectra.[21,22] From short series of one-dimensional macroscopic rotation of the sample (MAS) spectra, the correlation function and correlation time can be determined, and it can be established whether the motion is diffusive or whether it involves jumps between discrete sites, whose number can be measured precisely if all segments are mobile. In addition, motional amplitudes can be estimated, with relatively high sensitivity to small-angle motions. This information is obtained for each site with a resolved line in the sideband-free MAS spectrum.

2 EXCHANGE NMR UNDER MAS, AND ROTOR SYNCHRONIZATION

Figure 1(a) shows the principle of stimulated-echo and exchange-NMR experiments, of which CODEX is an example.[13,16,23–26] After evolution of transverse magnetization during a time t_1, one component of the magnetization is stored along the z-direction during the long mixing time t_m. After a 90° read-out pulse, a stimulated echo forms at $t_2 = t_1$ for segments that did not change frequency during t_m. A pure stimulated echo is obtained by storing the two orthogonal components of the magnetization before t_m in alternate transients and combining their signals after read-out pulses of suitable phase (see Figure 1(a)). In a 2D exchange experiment, the time signal during the period t_2 is observed, and the t_1 period is incremented systematically.

The first exchange NMR experiments to measure reorientations under MAS were performed by Kentgens et al.[27] Their crucial innovation was the introduction of 'rotor synchronization' of the pulse sequence, i.e., making sure that t_m is an integer number of rotation periods, so that the precession of the magnetization resumes at the same rotor orientation where it stopped at the beginning of the mixing time. Otherwise, reorientations of segments relative to the external field occur due to the MAS and overwhelm the more subtle effects of intrinsic segmental reorientations. In later experiments, synchronization with the beginning of the evolution period was also used, in order to achieve pure-phase 2D MAS exchange spectra.[28] Recently introduced one-dimensional versions of the sideband-exchange experiment use similar rotor synchronization.[29,30]

Rotor synchronization for short mixing times can be achieved simply by precise timing of the mixing time. However, for long mixing times, this is not sufficient. For instance, a ±1-Hz deviation from the rotation rate results in a ±36°-deviation in the rotor phase after 100 ms, and complete uncertainty of the rotor phase after $t_m = 1$ s. Therefore, trigger-based active rotor synchronization is necessary. The optical signal of the spinning-speed detector, usually made discrete into 'high' and 'low' states by a Schmitt trigger, is used to start the pulse sequence at a certain rotor orientation, namely at the transition from high to low or low to high. Based on the trigger, one can resume pulsing at the same rotor orientation tens or hundreds of rotations later. In practice, triggering during a pulse such

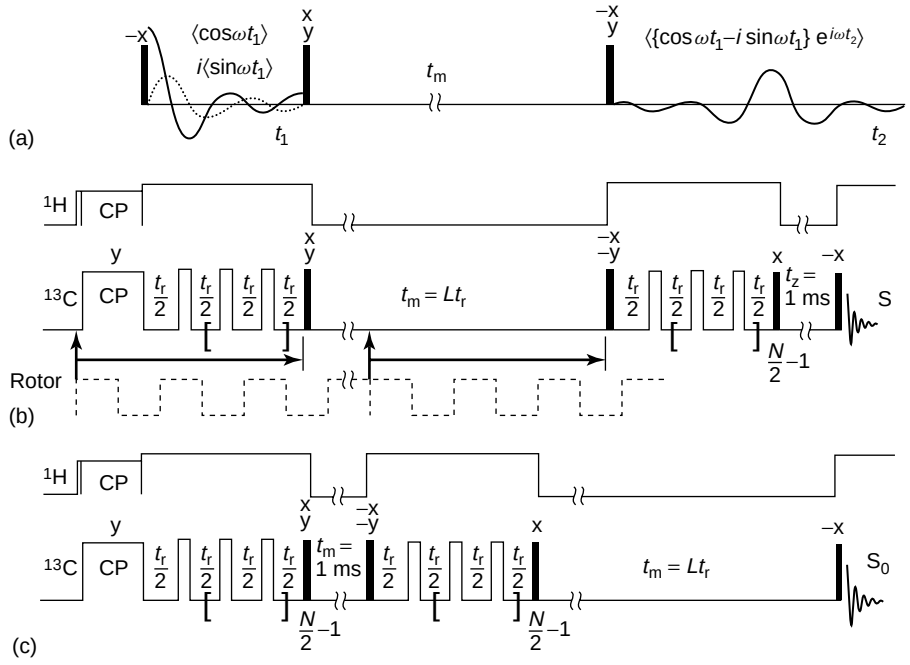

Figure 1 (a) Basic stimulated-echo and exchange-NMR pulse sequence. The fundamental time signals that produce the stimulated echo are indicated. Pointed brackets indicate powder averaging. Cosine and sine components measured with the indicated pulse phases are added in subsequent transients. (b) Basic CODEX pulse sequence and its synchronization with the sample rotation. 90° pulses are shown filled. The series of 180° pulses (short open boxes) during t_1 and t_2 recouple the anisotropic chemical shift, while removing the isotropic shift. The xy-8 phase sequence is used for the 180°-pulse trains. Note the change in the phase of the read-out pulse for the sine-component (+y in (a), −y here); it is required to achieve the correct chemical-shift recoupling. (c) Pulse sequence for obtaining the reference signal S_0, produced by interchanging t_m and t_z in the sequence (b)

as cross polarization should be avoided – in case the trigger signal is absent, the pulse would last indefinitely. To ensure the same rotor orientation at the beginning and end of t_m, the (relatively short) time period between the trigger signal and the start of t_m is reproduced after a trigger signal near the end of t_m. This is indicated by the bold arrows at the bottom of Figure 1(b). Consistent triggering requires the trigger mark on the rotor to be sharp; in practice, a straight pen mark is found to be sufficient.

3 EXPLANATION OF THE CODEX PULSE SEQUENCE

Simply put, CODEX is a stimulated-echo experiment under MAS conditions, with chemical-shift-anisotropy recoupling and intensity referencing in the tradition of REDOR.[31] Figure 1(b) shows the CODEX pulse sequence. After cross-polarization (or single-pulse excitation), the magnetization evolves under the anisotropic chemical shift, recoupled by a series of 180° pulses spaced by $t_r/2$.[22,32] Then, one component of the magnetization is stored for the mixing time t_m, during which motion can occur. The mixing time is a multiple of the rotation period t_r. In successive transients, the phases of the 90°-pulses that bracket the mixing time are changed together by 90°, so that both components, $\cos\Phi_1$ and $\sin\Phi_1$, of the magnetization are retained alternately. If the storage pulse and the read-out pulse always have opposite signs, the sum of two transients yields $\cos\Phi_1 + i\sin\Phi_1$. Except for a scaling factor of 0.5, the signal is effectively the same as if no 90°-pulses and mixing time had been applied, and a rotor echo forms at the end of the second recoupling period ($t_2 = t_1$).

The total phase $\Phi_1 + \Phi_2 = |\Phi_2| - |\Phi_1|$ of the magnetization at the end of the second recoupling period of duration $N/2\ t_r$ is obtained from

$$\Phi_1 = \frac{N}{2}\left(-\int_0^{t_r/2}\omega_1(t)\,\mathrm{d}t + \int_{t_r/2}^{t_r}\omega_1(t)\,\mathrm{d}t\right) = -N\int_0^{t_r/2}\omega_1(t)\,\mathrm{d}t \quad (1a)$$

$$\Phi_2 = \frac{N}{2}\left(\int_0^{t_r/2}\omega_2(t)\,\mathrm{d}t - \int_{t_r/2}^{t_r}\omega_2(t)\,\mathrm{d}t\right) = N\int_0^{t_r/2}\omega_2(t)\,\mathrm{d}t \quad (1b)$$

with the frequencies $\omega_1(t)$ and $\omega_2(t)$ before and after t_m, respectively.[22] In the second step of equation (1a), a standard result of recoupling of inhomogeneous NMR interactions (e.g., chemical shift anisotropy or spin-pair dipolar couplings) was used.[31,32] If $\omega_1(t) = \omega_2(t)$, i.e., if no exchange occurs, equation (1) leads to $\Phi_1 + \Phi_2 = |\Phi_2| - |\Phi_1| = 0$; in other words, the magnetization is refocused in a stimulated echo along its original direction.

At the end of the second recoupling period, the total magnetization is along the original direction that it had during CP. The full magnetization is stored along the z-axis during the period t_z, and subsequently read out for detection. To suppress spinning sidebands during detection, the total suppression of sidebands (TOSS) sequence can be used before detection.[33] Since motion-induced dephasing can break the cylindrical symmetry around the rotor axis required for TOSS, the duration of t_z is incremented in K steps over a full rotation period.[1] This ensures that TOSS suppresses all sidebands except for orders nK (for details see deAzevedo et al.).[22]

In a simple CODEX experiment, the signal intensity S(t_m, $\delta N t_r$) is observed; here we have normalized the time $N t_r$ with the chemical-shift anisotropy parameter δ.[1] To remove effects of T_1 relaxation during t_m and of T_2 relaxation during $N t_r$, a reference spectrum $S_0 = S(0, \delta N t_r)$ is required that has all the same relaxation factors but no motion during t_m. This is achieved by simply interchanging the durations of t_m and t_z, see Figure 1(c). More generally, the requirement is that in the reference experiment t_m is sufficiently short ($t_m = t_r < 1$ ms) while the sum $t_m + t_z$ is the same as in the actual CODEX spectrum. In practice, effects of spectrometer drift are minimized by alternating measurements between CODEX signal S and reference signal S_0 approximately every five minutes. The ratio S(t_m, $\delta N t_r$)/S(0, $\delta N t_r$) can be plotted as a function of t_m or $\delta N t_r$, to characterize the correlation function or the motional geometry, respectively.

Often, it is advantageous to subtract the CODEX spectrum $S = S(t_m, \delta N t_r)$ from the reference spectrum $S_0 = S(0, \delta N t_r)$, to obtain a pure-exchange CODEX spectrum $\Delta S = S_0 - S$. In this difference spectrum, the signals of non-exchanging components are removed from the spectrum. Figure 2(a) shows an example of this procedure for glassy poly(methyl methacrylate), PMMA, measured near ambient temperature. In Figure 2(b), a series of pure-exchange CODEX spectra of PMMA are plotted as a function of the mixing time; they show that some of the sidegroups of this polymer are undergoing large-amplitude motions in the glassy state.[17,34]

The pure-exchange approach can also serve as a useful 'filter' for the signals of slowly-moving groups in a multi-component system.

The normalized pure-exchange CODEX intensity is given by

$$E(t_m, \delta N t_r) = \frac{\Delta S(t_m, \delta N t_r)}{S(0, \delta N t_r)} = \frac{S(0, \delta N t_r) - S(t_m, \delta N t_r)}{S(0, \delta N t_r)} \quad (2)$$

The nomenclature was chosen in analogy to REDOR, where the normalized dephasing provides information on internuclear distances.[31,22]

The t_m-dependence of the pure-exchange CODEX intensity for PMMA and two crystalline model compounds, dimethyl sulfone (DMS) and methylmalonic acid, is plotted in Figure 3(a). The resulting curves correspond to the correlation functions of these dynamics on the millisecond time scale. For DMS, a single-exponential curve is obtained, while PMMA shows some non-exponentiality. Methylmalonic acid shows no exchange except for ^{13}C spin diffusion (see Section 5.1). In Figure 3(b), exchange due to helical jumps in the crystallites of isotactic polypropylene is shown.[28,21]

4 ANALYSIS AND SIMULATION OF CODEX CURVES

4.1 Reorientation-Angle Analysis Based on the Difference Tensor

CODEX can give more information than just the correlation function obtained by recording the intensity as a function of t_m. Through variation of the duration $N t_r$ of the evolution under the recoupled CSA, the amplitude of the reorientations during t_m can be determined. The nuclear spins evolve for N/2 rotor periods with the phase Φ_1 before t_m, and for N/2 rotor periods with the corresponding phase Φ_2 after t_m. The dephasing factor

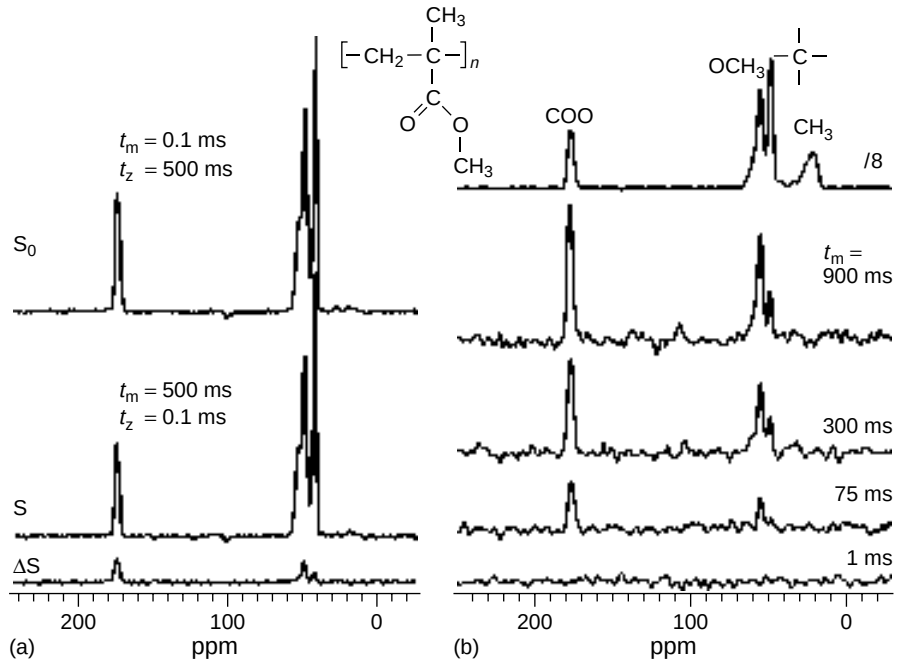

Figure 2 (a) Full reference spectrum S_0, spectrum S after CODEX dephasing and pure-exchange CODEX spectrum $\Delta S = S_0 - S$ of unlabeled PMMA at 300 K, for $t_m = 500$ ms and $N t_r = 800\,\mu$s. The intensity of ΔS is low since only a minority of the sidegroups (35%) are undergoing flips. (b) Series of pure-exchange CODEX spectra of PMMA at 300 K, $\nu_r = 6.5$ kHz, and $N t_r = 615\,\mu$s, as a function of t_m as indicated. For the COO carbon, $\delta N t_r = 8\pi$; for the OCH_3 group, $\delta N t_r = 3.8\pi$. Large-amplitude side-group and smaller-amplitude backbone motions are observed

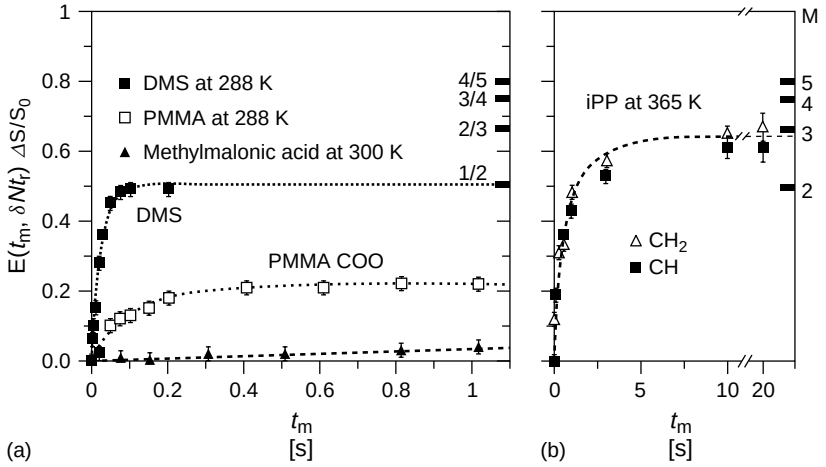

Figure 3 Correlation functions of slow segmental motions obtained from the normalized pure-exchange CODEX intensities $\Delta S/S_0 = E(t_m, \delta N t_r)$ as a function of t_m for (a) COO groups in methylmalonic acid ($T = 300\,K$, $\delta N t_r = 7.6\,\pi$); COO groups in PMMA ($T = 288\,K$, $\delta N t_r = 8\,\pi$); CH_3 groups in DMS ($T = 288\,K$, $\delta N t_r = 12.4\,\pi$); and (b) CH and CH_2 groups in iPP ($T = 365\,K$; $\delta N t_r = 3.6\,\pi$ and $8.5\,\pi$, respectively). On the right, the expected final intensity values for M-site jumps are marked

modulating the amplitude of the signal component detected in the CODEX MAS signal is therefore

$$\frac{S(t_m, \delta N t_r)}{S(0, \delta N t_r)} = \mathrm{Re}\langle \exp(i(\Phi_1 + \Phi_2))\rangle = \langle \cos(|\Phi_2| - |\Phi_1|)\rangle$$
$$= \left\langle \cos\left(N \int_0^{t_r/2} (\omega_2(t) - \omega_1(t))\,\mathrm{d}t \right) \right\rangle \quad (3)$$

The pointed brackets indicate the powder average, which also contains the effect of the correlation time τ_c and mixing time t_m. Note that according to equations (2) and (3), the pure-exchange signal is related directly to the dephasing factor, $E(t_m, \delta N t_r) = 1 - S(t_m, \delta N t_r)/S_0$. In equation (3), the phase $|\Phi_2| - |\Phi_1|$, which depends on $\delta N t_r$ and the reorientation angles (α_R, β_R, γ_R), can be considered as the phase acquired within a time of $N/2\ t_r$ under the action of the chemical-shift difference tensor

$$\overleftrightarrow{\sigma}^{\Delta} = (\overleftrightarrow{\sigma}_2 - \overleftrightarrow{\sigma}_1) \quad (4a)$$

since

$$\omega_2 - \omega_1 = -\gamma B_0 \frac{\vec{B}_0^T}{B_0} (\overleftrightarrow{\sigma}_2 - \overleftrightarrow{\sigma}_1) \frac{\vec{B}_0}{B_0} \quad (4b)$$

The 'width' (principal-value range) $\gamma B_0 N |\sigma_{33}^{\Delta} - \sigma_{11}^{\Delta}|$ of the scaled chemical-shift difference tensor $\gamma B_0 N \overleftrightarrow{\sigma}^{\Delta}$ relative to the spinning speed ω_r determines whether there is significant dephasing due to the anisotropy, i.e., whether the experiment is sensitive to the segmental reorientation. By increasing the number of rotor cycles N, we can enhance the anisotropy to large values $\gamma B_0 N |\sigma_{33}^{\Delta} - \sigma_{11}^{\Delta}| \gg \omega_r$. The useful role of the difference tensor in CODEX simulations will be discussed in Section 4.3 below.

Uniaxial interactions, i.e., with $\eta = 0$, are particularly convenient to treat analytically, because only the unique principal axis needs to be considered. This case is also quite commonly found, e.g., for dipolar couplings in a spin pair or for the ^2H quadrupolar coupling. Therefore, it is instructive to calculate the difference tensor analytically for $\eta = 0$. Due to the uniaxiality, the reorientation is fully characterized by a single reorientation angle β_R between the unique principal axis before and after the mixing time. In the specific case of $\eta = 0$, the principal values of the difference tensor are $\sigma_{22}^{\Delta} = 0$ and the full-width anisotropy $|\sigma_{33}^{\Delta} - \sigma_{11}^{\Delta}|$ of the difference tensor, i.e., the range of possible frequency differences, is[22,35]

$$|\sigma_{33}^{\Delta} - \sigma_{11}^{\Delta}| = |(\sigma_{33} - \sigma_{11}) 2 \sin \beta_R| \quad (5)$$

This represents a strong linear dependence on the reorientation angle for $\beta_R < 45°$, which permits relatively easy detection of small-angle motions. It compares favorably with the more common $(3\cos^2 \beta_R - 1)/2$ angle dependence, which is insensitive to β_R for $\beta_R < 15°$.

Figure 4(a) shows simulated pure-exchange CODEX curves as a function of $\delta N t_r$ for different reorientation angles β_R. The predicted sensitivity to small-angle motions is clearly recognizable. Experimental data points for DMS are also shown. In Figure 4(b), the pure-exchange CODEX intensity $E(\delta N t_r)$ for helical jumps in the crystallites of isotactic polypropylene (iPP) at 365 K and for backbone motion in glassy PMMA at 293 K are shown.[21,28,36] Based on the unitless variable $\delta N t_r$, the motion of iPP is immediately recognized as being of large amplitude, while the methylene groups in the backbone of PMMA reorient by approximately 10°.[22]

For a non-uniaxial interaction, the reorientation of a principal-axes system must be described in terms of three transformation coordinates. As already indicated above, these are usually chosen as the Euler angles α_R, β_R, γ_R between the initial and final PAS orientations. As in the case of $\eta = 0$, calculations of the width of the difference tensor $|\omega_{33}^{\Delta} - \omega_{11}^{\Delta}|$ for general values of η show an initial linear dependence on the reorientation angles β_R and $\varepsilon_R = \alpha_R + \gamma_R$. This can be generally proved by calculating the eigenvalues of the difference tensor for small values of β_R and ε_R.[22]

A simple result is also found for the case of a rotation by an angle β_R' around the n'th principal axis of the interaction tensor $\overleftrightarrow{\sigma}$. Here, $\sigma_{22}^{\Delta} = 0$ and

$$|\sigma_{33}^{\Delta} - \sigma_{11}^{\Delta}| = |(\sigma_{kk} - \sigma_{mm}) 2 \sin \beta_R'| \quad (6)$$

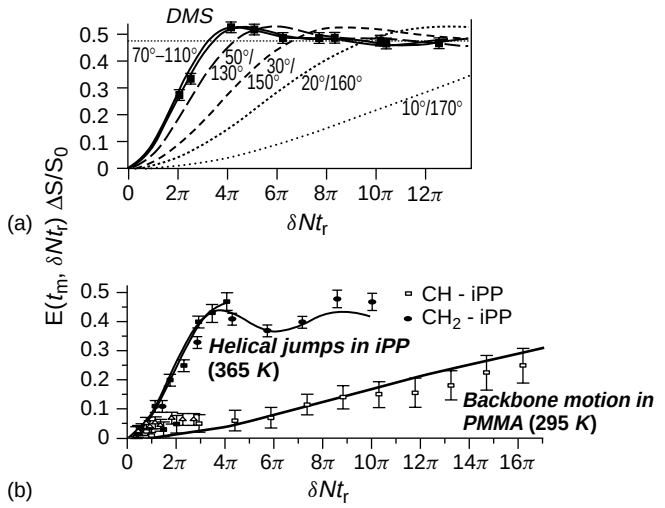

Figure 4 Measurement of the motional amplitude by recording normalized pure-exchange CODEX intensities $\Delta S/S_0 = E(t_m, \delta Nt_r)$ as a function of δNt_r. (a) DMS at 288 K, $t_m = 75$ ms, and $\nu_r = 5.5$ kHz. Also shown are simulations, for $\eta = 0$, of reorientations of the unique principal axis by 10° or 170°, 20° or 160°, 30° or 150°, 50° or 130°, and 70° to 110° (curves in this large-amplitude range are virtually indistinguishable). (b) CODEX intensities $E(t_m, \delta Nt_r)$ as a function of δNt_r for isotactic polypropylene (iPP) at 365 K, $t_m = 1$ s, and for the backbone of glassy PMMA at 293 K, $t_m = 0.5$ s. Comparison with (a) immediately shows that the motions in iPP are of large amplitude, while those of the PMMA backbone are restricted

where n, k, and m label the three principal axes of $\overleftrightarrow{\sigma}$. This is completely analogous to equation (5).

The quantitative analysis of CODEX data requires knowledge of three principal values of the chemical shift tensor, or at least of the chemical-shift anisotropy parameter δ. These values can obtained in a variety of ways. A first estimate can be obtained based on the tabulated CSA principal values of similar chemical groups.[37] Various methods of experimental CSA measurements have been described in the literature.[38–40] The estimation of $|\delta|$ by CSA recoupling under MAS very similar to CODEX has been demonstrated by deAzevedo et al.[22]

In a view traditionally taken in REDOR, rather than considering N as scaling the difference tensor relative to the spinning speed, it is considered that Nt_r is the total time of evolution under the influence of the anisotropic interaction.[32] Then it is found that the dephasing is independent of the spinning speed and only depends on the total time Nt_r.[22] Due to this ω_r-independence, the CODEX pulse sequence works up to very high spinning speeds.

4.2 The Role of the Reorientation-Angle Distribution

In the case of a uniaxial NMR interaction, i.e., $\eta = 0$, the information content of an exchange experiment at a given mixing time t_m can be summarized in terms of the reorientation-angle distribution $R(\beta_R, t_m/\tau_c)$, i.e., the probability density of finding a reorientation angle β_R after a mixing time t_m.[1,14,16,41] Since the correlation time τ_c is the natural reference for t_m, only their ratio, t_m/τ_c, is relevant for the reorientation-angle distribution. The dephasing or pure-exchange intensity CODEX curves are simply $R(\beta_R, t_m/\tau_c)$-weighted superpositions of the CODEX curves $\varepsilon(\delta Nt_r; \beta_R)$ for specific β_R values:[16,42]

$$E(t_m, \delta Nt_r) = \int_0^{90p} R\left(\beta_R, \frac{t_m}{\tau_c}\right) \varepsilon(\delta Nt_r; \beta_R)\, d\beta_R \qquad (7)$$

The integration weighting by $\sin\beta_R$ is contained in $R(\beta_R, t_m/\tau_c)$. The calculation of $\varepsilon(\delta Nt_r; \beta_R)$ is outlined in equation (10) below. Note that while all $\varepsilon(\delta Nt_r; \beta_R)$ have the same shape except for the $\sin\beta_R$ – scaling of their x-axes, their superposition $E(t_m, \delta Nt_r)$ in general has a different shape (to visualize this, consider that similarly the sum of Gaussian bell curves of different widths, even when they have the same center, is not a Gaussian). For a few motional models, the reorientation-angle distributions $R(\beta_R, t_m/\tau_c)$ and corresponding $E(\delta Nt_r; t_m)$ curves are shown in Figure 6. They will be discussed in more detail below.

For non-uniaxial interactions, β_R in this discussion and in equation (7) should be replaced with the full set of reorientation angles $(\alpha_R, \beta_R, \gamma_R)$. For specific motions, other angular variables may be more convenient. For rotations around a given axis, such as the helix axis in helical jumps or the invariant axis in uniaxial rotational diffusion, the angle ψ of rotation around that axis is most convenient.

4.3 Simulation Procedure

For simulations of CODEX curves, each subcurve $\varepsilon(\delta Nt_r; \alpha_R, \beta_R, \gamma_R)$ needed for equation (7) is calculated based on equation (3), using the following steps:

(i) Choose a convenient frame to rotate $\overleftrightarrow{\sigma}_1$ to $\overleftrightarrow{\sigma}_2$. In this frame, $\overleftrightarrow{\sigma}_1$ is expressed by a 3×3 matrix, and the rotation can be performed using Cartesian rotation matrices,

$$\overleftrightarrow{\sigma}_2 = \overleftrightarrow{R}(\alpha_R, \beta_R, \gamma_R)\overleftrightarrow{\sigma}_1\overleftrightarrow{R}^T(\alpha_R, \beta_R, \gamma_R) \qquad (8)$$

or, alternatively, Wigner rotation matrices. The rotation is defined by the Euler angles α_R, β_R, γ_R or by other angles specifying the motion that the segment is supposed to undergo (e.g., the rotation angle around a given axis).

(ii) Calculate the difference tensor (3×3 matrix) $\overleftrightarrow{\sigma}^\Delta = (\overleftrightarrow{\sigma}_2 - \overleftrightarrow{\sigma}_1)$.

(iii) Determine the principal values of $\overleftrightarrow{\sigma}^\Delta$ (i.e., diagonalize $\overleftrightarrow{\sigma}^\Delta$). Calculate its anisotropy parameter δ_Δ and asymmetry parameter η_Δ.

(iv) We can evaluate the integral in equation (3) as follows,

$$\begin{aligned}\int_0^{t_r/2} (\omega_2(t) - \omega_1(t))\, dt &= \int_0^{t_r/2} \omega^\Delta(t)\, dt \\ &= \tilde{S}_1(\delta_\Delta, \eta_\Delta, \alpha_\Delta, \beta_\Delta, \gamma_\Delta)\frac{t_r}{2} \\ &= \delta_\Delta\sqrt{2}\left\{\tfrac{1}{3}\eta_\Delta \sin 2\alpha_\Delta \sin\beta_\Delta \cos\gamma_\Delta \right. \\ &\quad + \tfrac{1}{2}\sin 2\beta_\Delta\left(1 + \tfrac{1}{3}\eta_\Delta \cos 2\alpha_\Delta\right) \\ &\quad \left. \times \sin\gamma_\Delta\right\}\frac{t_r}{2} \qquad (9)\end{aligned}$$

using the Euler angles α_Δ, β_Δ, γ_Δ that specify the orientation of the principal-axes system of the difference

tensor in the rotor-fixed frame. The subcurve $\varepsilon(\delta N t_r; \alpha_R, \beta_R, \gamma_R)$ can now be expressed as

$$\begin{aligned}\varepsilon(\delta N t_r, \alpha_R, \beta_R, \gamma_R) &= 1 - \left\langle \cos\left(N \int_0^{t_r/2} (\omega_2(t) - \omega_1(t))\, dt \right) \right\rangle \\ &= 1 - \left\langle \cos\left[\frac{\tilde{S}(\delta_\Delta, \eta_\Delta, \alpha_\Delta, \beta_\Delta, \gamma_\Delta) N t_r}{2} \right] \right\rangle_{\alpha_\Delta, \beta_\Delta, \gamma_\Delta}\end{aligned} \quad (10)$$

with $\tilde{S}(\delta_\Delta, \eta_\Delta, \alpha_\Delta, \beta_\Delta, \gamma_\Delta)$ as given in equation (9). The pointed brackets represent only the powder average over α_Δ, β_Δ, γ_Δ, i.e., the orientation of the chemical-shift difference tensor. In contrast, in equation (3) the average also included a summation over all reorientation angles. The powder average in equation (10) is calculated numerically.

(v) Go back to (i) to repeat the calculation for a different set of reorientation angles, yielding a different CODEX subcurve.

(vi) Obtain the CODEX curve $E(t_m, \delta N t_r)$ by superimposing the $\varepsilon(\delta N t_r; \alpha_R, \beta_R, \gamma_R)$ subcurves weighted with the reorientation angle distribution $R(\alpha_R, \beta_R, \gamma_R, t_m/\tau_c)$ for the t_m under consideration, according to equation (7).

4.4 Number of Accessible Orientations and Fraction of Mobile Segments

In complex systems such as amorphous polymers, broad distributions of correlation times and motional amplitudes often result in a complex exchange behavior. It is often a good approximation to analyze such situations in terms of a fraction f_m of significantly exchanging segments, and a component $(1 - f_m)$ that does not exchange significantly and therefore can be treated as immobile. The case of a homogeneous system in which all equivalent segments are moving similarly, as is true for most crystals, is obtained by setting $f_m = 1$.

Information about the fraction f_m and the number M of equivalent orientational sites accessible to the mobile segments is obtained from the long-time exchange intensity E_∞. Since a fraction 1/M of the mobile species will reside in the originally selected site, see Figure 5, we have

$$E_\infty = E(t_m \gg \tau_c, \delta N t_r \gg 1) = f_m \left(1 - \frac{1}{M}\right) \quad (11)$$

For $f_m = 1$, the minimum E_∞ is 1/2, obtained for M = 2. For diffusive reorientations of all segments, $M \gg 1$ and $E_\infty \sim 1$; note, however, that for restricted diffusion, very large phases

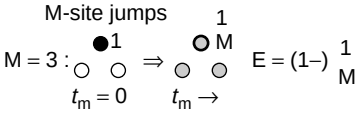

Figure 5 Relation between the final exchange intensity and the number of sites in an M-site jump process. At long times ($t_m \rightarrow \infty$), 1/M of the segments reside in the original site. Thus, the final exchange intensity E_∞ deviates from unity by 1/M

$\delta N t_r$ will be required to reach the final state. Also, if $E_\infty < 1/2$, $f_m < 1$. In fact, equation (11), with M = 2 and $M \rightarrow \infty$, yields rigorous limits for f_m in terms of E_∞:

$$E_\infty < f_m \leq 2E_\infty \quad (12)$$

From E_∞ alone, f_m and M cannot be determined unambiguously. Fortunately, the number of sites M can be measured in a four-time CODEX experiment, which is produced by concatenating two CODEX pulse sequences.[22] In the first CODEX difference experiment with mixing time t_{ma}, the mobile groups are selected; then their exchange behavior, with a final value of 1/M, is characterized selectively in another CODEX MAS section by changing the mixing time t_{mc}. Effects of T_1 relaxation decay can be eliminated by keeping the total z-period $t_{mc} + t_z$ constant. Therefore, no difference is required in the second half of the experiment. The four-time CODEX experiment has close analogies to a reduced four-dimensional (4D) exchange NMR experiment, where the orientation-dependent frequency is probed at four different times.[18] The reduced 4D exchange method, and the closely related four-time exchange experiment have been used to identify the origins of the non-exponential loss of correlation above the glass-transition temperature and to estimate the size of dynamic heterogeneities.[18–20] Four-time CODEX will make such studies much more sensitive and quantitative.

4.5 Jumps vs. Diffusive Motions

A variety of different motional models have been considered in the literature.[1,14] They can be grouped into jump processes and diffusive motions. For instance, symmetric N-site exchange is a common jump process, while isotropic rotational diffusion is the most important example of a diffusive reorientation. Defining distinctions between pure jumps and pure diffusion are seen in the evolutions of their reorientation-angle distributions $R(\beta_R, t_m/\tau_c)$ with time t_m; this behavior can be used in CODEX NMR to identify pure jump motions and diffusive motions. The $R(\beta_R, t_m/\tau_c)$ of four classical motional models and the corresponding CODEX curves $E(\delta N t_r, t_m)$ are shown in Figure 6.

All diffusive motions produce a characteristic change in the shape of $R(\beta_R, t_m/\tau_c)$ with increasing t_m. The sharp peak at $\beta_R = 0°$ gradually broadens and approaches the wide distribution characteristic of the final stage, such as $\sin\beta_R$ for isotropic diffusion. As a result, the shape of the $E(\delta N t_r)$ CODEX curves depends strongly on t_m: For short t_m, the curves rise quite slowly because only small reorientation angles have been reached, while an earlier and faster increase in $E(\delta N t_r)$ (plotted as a function of $\delta N t_r$, with t_m only as a parameter) occurs at long t_m when larger reorientation angles have been attained. These features are clearly visible in Figures 6(c) and 6(d), where isotropic and uniaxial rotational diffusion, respectively, have been simulated.

In contrast, for many pure jump motions the only change in the reorientation-angle distribution is the relative intensity of the reorientation-angle distribution at $\beta_R = 0$ and at $\beta_R \neq 0$. This holds for all two-site jumps, circular three-site jumps, random N-site jumps, and the isotropic random-jump model. As a result, the shape of the $E(\delta N t_r, t_m)$ curves does not change

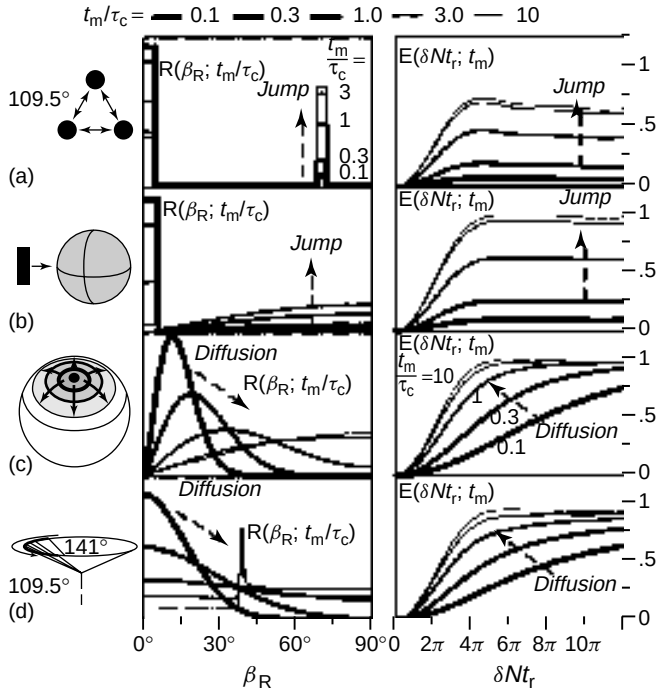

Figure 6 Time evolution of the reorientation-angle distributions $R(\beta_R, t_m/\tau_c)$ for four important motional models, and the corresponding CODEX $E(\delta N t_r, t_m)$ curves (for a uniaxial interaction, $\eta = 0$). As indicated at the top, the line thickness decreases with increasing t_m/τ_c (=0.1, 0.3, 1.0, 3.0, and 10). (a) Three-site jumps, with a 109° (or equivalently 71°) jump angle. (b) Random isotropic jumps. In this model, all orientations are equally likely after the jump. (c) Isotropic rotational diffusion, without amplitude limitation. (d) Uniaxial rotational diffusion on a cone with an apex angle of 141° (or equivalently $2 \cdot 109.5°$). The dashed arrows in the plots indicate the characteristic differences between the t_m/τ_c dependences for jump motions (a,b) and diffusion (c,d)

with t_m. Only its height (y-scale) increases. This is clearly visible in Figures 6(a) and (b).

Helical jumps, where sites along a helical chain are accessed sequentially, do not fall under this category, if the chain forms a 4_n helix (i.e., 4 repeat units in n turns) or more complex helix.[1,27] Nevertheless, their change in reorientation-angle distribution is still characteristically different from that of diffusive motions. The peak at $\beta_R = 0$ does not broaden, and $R(\beta_R, t_m/\tau_c)$ consists only of a few sharp peaks whose relative height changes only slowly. The rise for short t_m will be fast and unchanged, being due to large-angle jumps between neighboring sites; only at long t_m will changes be observed due to the contribution of non-neighboring sites.

Another characteristic aspect of diffusive motions is that the number of sites M is infinite. Thus, at sufficiently large $\delta N t_r$ and t_m, full exchange will be observed. This property is shared with only a very small number of pure jump processes; the isotropic random-jump model, Figure 6(b), is the only prominent example.

However, it should be noted that $M \rightarrow \infty$ is also a property of limited diffusion superimposed on jumps. Such a combined process may still be relatively difficult to distinguish from pure diffusion, in particular if the diffusion has a broad distribution of correlation times.

5 PRACTICAL CONSIDERATIONS

5.1 Spin Exchange by Dipolar Couplings

Segmental dynamics is not the only possible exchange process. Two effects based on dipolar couplings also lead to exchange of anisotropic interactions and intensity changes in the CODEX experiment. The first is relaxation-induced dipolar exchange due to dipolar couplings to heteronuclei, in particular ^{14}N and ^{15}N, that undergo significant longitudinal relaxation during t_m.[43,44] The relaxation removes a heteronuclear coherence term from the density operator and thus reduces the stimulated echo. This effect has been described in detail by Saalwächter and Schmidt-Rohr.[44] Due to the small value of the nitrogen-carbon dipolar coupling, it is a significant problem only for CODEX experiments involving nitrogen-bonded carbon sites with small chemical-shift anisotropies. On the other hand, this relaxation-induced dipolar exchange with recoupling can be exploited to measure internuclear distances between heteronuclei.[44]

The more common second effect is ^{13}C spin diffusion or spin exchange generated by homonuclear dipolar couplings and affected by the ^1H–^{13}C dipolar coupling.[45–48] For ^{13}C in natural abundance, it typically generates 4% exchange intensity within 0.5 s. In isotopically labeled materials, it can occur significantly within 50 ms. Apart from isotopic dilution, the only known procedure for slowing down ^{13}C spin exchange between sites with similar isotropic chemical shifts is to increase the spinning speed. Among the experiments for measuring exchange by segmental reorientation, CODEX is the only one that is compatible with high spinning speeds. We have recently shown that for unprotonated sites, an increase of the spinning speed from 8 to 28 kHz indeed decreases the spin exchange rate by a factor of 3–10.[49] Thus, CODEX under fast MAS can significantly extend the range of correlation times accessible to exchange NMR measurements.

In ^{13}C-enriched proteins, Hong et al. have circumvented the ^{13}C spin diffusion problem by performing a ^{15}N CODEX experiment followed by ^{15}N–^{13}C transfer and ^{13}C detection.[50] The dipolar couplings between the ^{15}N nuclei, which are separated by three bonds and have smaller gyromagnetic ratios, are more than an order of magnitude reduced relative to those of ^{13}C in a uniformly labeled protein.

5.2 Accessible Range of Correlation Times

The rates for which dephasing is observed in CODEX NMR range from ~0.1 to ~5000 s^{-1}. Very slow motions, which require long mixing times, can be studied better by CODEX than by any other NMR technique. The high sensitivity and good dynamic range of CODEX NMR enables detection of the ~10% exchange intensity that arises already within $t_m = 0.1\,\tau_c$, and makes it less sensitive to signal reduction by T_1-relaxation and the increased experiment duration when the mixing time exceeds the recycle delay. Exchange due to ^{13}C spin exchange (see above) which competes with motional exchange, is the main limitation for detecting very slow motions. Even in this aspect, CODEX is often superior. Not only can CODEX under fast MAS slow down spin diffusion among unprotonated carbons but its superior sensitivity also permits a reduction in the isotopic labeling level, or even measurements on ^{13}C in natural abundance.[49] This is

particularly relevant for systems that previously required ^{13}C enrichment for achieving sufficient sensitivity, e.g., benzene undergoing jumps and diffusion in zeolites.[6]

To understand the effect of motions on the 100-μs time scale on CODEX, consider that a clean exchange experiment requires that no motion occurs during the dephasing and rephasing periods Nt_r (i.e., $k < 1000\,s^{-1}$). Nevertheless, even with frequency changes during those periods, some motional dephasing will occur. Its strong dependence on the dephasing time and near independence from the mixing time will identify its high rate.

Finally, motions with rates exceeding the chemical-shift anisotropy significantly will not be detected by CODEX, since the motionally averaged frequencies do not change during the course of the experiment. This will lead to a reduction in E_∞, and care must be taken not to interpret these fast-moving segments as immobile. Fortunately, significant motions with rates exceeding $10\,000\,s^{-1}$ can be detected by other NMR experiments.[9–11,51,52]

5.3 Implementation of the CODEX Pulse Sequence

Due to the simplicity of the CODEX pulse sequence, the implementation of the technique is mostly straightforward. However, since the method relies on measuring signal amplitudes rather than frequency positions, some care should be taken to avoid artifacts. A fixed xy-8 phase sequence is used for the train of 180° pulses that recouple the CSA.[53] Effects of pulse imperfections and T_1 relaxation are minimized or eliminated using the phase cycling given by Reichert et al.[49]

For protonated carbon sites, in particular CH_2 groups, the residual C–H dipolar coupling during the multiple 180° pulses leads to significant dephasing. Fortunately, this does not affect the normalized CODEX data, since the same dephasing occurs in the reference experiment. However, the intensity is degraded. The decoupling is excellent if the ^1H B_1 field strength during the ^{13}C pulses is so high that the duration of a ^{13}C 180° pulse corresponds to a 3*180° pulse length on protons.[54] In order to reduce the ^1H power required to achieve this condition, it can be advantageous to increase the duration of the ^{13}C 180° pulses, i.e., to *reduce* the ^{13}C pulse power.

6 APPLICATIONS OF CODEX

6.1 Dynamics in Complex Glassy Polymers

So far, NMR studies of slow segmental motions of unlabeled polymers in the glassy state have been virtually impossible, due to sensitivity and line-overlap problems. CODEX and its non-spinning analog, 1D PUREX, enable detailed, quantitative studies of these dynamics.[25] The selective observation of exchanging sites in pure-exchange CODEX and 1D PUREX spectra leads to a great increase in resolution and in the dynamic range, which in turn reduces artifacts arising from the often dominant signals of immobile sites.

Examples for the detection of flipping sidegroups in PMMA by CODEX are shown in Figures 2 and 3. The characterization of the motion as a jump process between $M = 2$ sites was confirmed in PMMA by 4-time CODEX.[22] Extending these experiments to a series of glassy poly(*n*-alkyl methacrylates) with COOR sidegroups of various sizes, CODEX has revealed that even some large cyclohexyl sidegroups can flip, but that the flipping fraction is only 9%.[55] Surprisingly, the fraction of flipping sidegroups was found to remain temperature-independent in PMMA with its small methylester sidegroup, while it increases significantly with temperature in polymers with longer sidegroups.[55] In polyphenylene dendrimers, slow dynamics in the highest-generation phenylene rings has been observed by CODEX.[56] Generally, CODEX enables us to study almost any slow dynamic process in polymers and thus learn more about the relation between chain motions and mechanical properties.

6.2 Dynamics in Peptides and Proteins

In biological systems, knowledge of the three-dimensional molecular structure is important, but further insight into the segmental dynamics is also highly valuable. Segmental mobility and function in enzymes are thought to be particularly closely related. Due to the large number of sites that may be distinguished in proteins, the sensitivity and site resolution of CODEX is indispensable for studies of slow motions. Hong and coworkers have introduced ^{13}C-detected ^{15}N CODEX for studies of slow motions in ^{13}C-labeled globular proteins.[50] In a triblock protein hydrogel, the experiments revealed large-amplitude reorientations of the α-helical segments that form the reversible cross-links.[57]

7 OUTLOOK

7.1 Perspective on CODEX, PUREX, and 2D Exchange Spectra

Overall, CODEX is complementary to detailed 2D exchange NMR studies without sample rotation. The CODEX MAS approach makes it easy to identify groups with interesting dynamics, characterize their correlation times, estimate the motional amplitude, obtain information on the mobile fraction and the number of accessible sites, and identify simple jumps or more complex motions. The lineshapes of 1D PUREX spectra, which can be regarded as CODEX without sample rotation, can give valuable hints about the motional geometry.[25] Given enough interest, these sites can then be isotopically labeled by ^2H or ^{13}C to determine the details of the reorientation process by 2D and 3D exchange NMR; the information on the reorientation angle that is contained in 2D exchange patterns is still unparalleled, in particular for distributions of reorientation angles, and for large reorientation angles.[1]

7.2 Summary

Detailed analysis of slow dynamics in complex solids is enabled by centerband-only detection of exchange (CODEX), which combines chemical-shift recoupling by 180°-pulses with exchange NMR. The analysis in terms of the chemical-shift difference tensor explains the surprising sensitivity of the experiment to small-amplitude motions. For uniaxial interactions ($\eta = 0$), this can be expressed by a simple analytical relation. The number of orientational sites accessible to the mobile segments and the fraction of mobile units are reflected in the long-time exchange intensity. Jumps and diffusive motions are distinguishable from the effect of mixing

time on the recoupling-time dependence of their exchange intensity, which reflects the characteristic changes of the reorientation-angle distributions. Pure-exchange CODEX can also be used as a dynamic filter to observe slow-moving groups selectively.

8 RELATED ARTICLES IN VOLUMES 1–8

Brownian Motion & Correlation Times, Volume 2, Chemical Shift Tensor Measurement in Solids, Volume 2, Chemical Shift Tensors, Volume 2, Internal Spin Interactions & Rotations in Solids, Volume 4, Magic Angle Spinning, Volume 5, Multidimensional Spectroscopy: Concepts, Volume 5, Polymer Dynamics & Order from Multidimensional Solid State NMR, Volume 6, Polymer Physics, Volume 6, Protein Dynamics from Solid State NMR, Volume 6, REDOR & TEDOR, Volume 6, Slow & Ultraslow Motions in Biology, Volume 7, Two-Dimensional Methods of Monitoring Exchange, Volume 8, Two-Dimensional Powder Correlation Methods, Volume 8, Ultraslow Motions in Solids, Volume 8.

9 REFERENCES

1. K. Schmidt-Rohr and H. W. Spiess, 'Multidimensional Solid-State NMR and Polymers', Academic Press: London, 1994.
2. T. M. Connor, B. E. Read, and G. Willians, *J. Appl. Chem.*, 1964, **14**, 74.
3. W.-G. Hu and K. Schmidt-Rohr, *Act. Polymer*, 1999.
4. A. G. Palmer, J. Williams, and A. McDermott, *J. Phys. Chem.*, 1996, **100**, 13 293.
5. V. Andronis and G. Zografi, *Pharm. Res.*, 1998, **15**, 835.
6. D. E. Favre, D. J. Schaefer, S. M. Auerbach, and B. F. Chmelka, *Phys. Rev. Lett.*, 1998, **81**, 5852.
7. G. B. McKenna, *Comp. Mater. Sci.*, 1995, **4**, 349.
8. J. Schaefer, R. A. McKay, E. O. Stejskal, and W. T. Dixon, *J. Magn. Reson.*, 1983, **52**, 123.
9. H. W. Spiess, in 'Deuteron NMR – A New Tool for Studying Chain Mobility and Orientation in Polymers', ed H. W. Spiess, Springer: Berlin, 1985, Vol. 66, p. 24.
10. K. Schmidt-Rohr, J. Clauss, and H. W. Spiess, *Macromolecules*, 1992, **25**, 3273.
11. J. Schaefer, M. D. Sefcik, E. O. Stejskal, R. A. McKay, W. T. Dixon, and R. E. Cais, *Macromolecules*, 1984, **17**, 1107.
12. H. W. Spiess, *J. Chem. Phys.*, 1980, **72**, 6755.
13. E. Roessler, *Chem. Phys. Lett.*, 1986, **128**, 330.
14. S. Wefing, S. Kaufmann, and H. W. Spiess, *J. Chem. Phys.*, 1988, **89**, 1234.
15. C. Schmidt, S. Wefing, B. Blumich, and H. W. Spiess, *Chem. Phys. Lett.*, 1986, **130**, 84.
16. S. Wefing and H. W. Spiess, *J. Chem. Phys.*, 1988, **89**, 1219.
17. K. Schmidt-Rohr, A. S. Kulik, H. W. Beckham, A. Ohlemacher, U. Pawelzik, C. Boeffel, and H. W. Spiess, *Macromolecules*, 1994, **27**, 4733.
18. K. Schmidt-Rohr and H. W. Spiess, *Phys. Rev. Lett.*, 1991, **66**, 3020.
19. A. Heuer, M. Wilhelm, H. Zimmermann, and H. W. Spiess, *Phys. Rev. Lett.*, 1995, **75**, 2851.
20. U. Tracht, M. Wilhelm, A. Heuer, H. Feng, K. Schmidt-Rohr, and H. Spiess, *Phys. Rev. Lett.*, 1998, **81**, 2727.
21. E. R. deAzevedo, W.-G. Hu, T. J. Bonagamba, and K. Schmidt-Rohr, *J. Am. Chem. Soc.*, 1999, **121**, 8411.
22. E. R. deAzevedo, W.-G. Hu, T. J. Bonagamba, and K. Schmidt-Rohr, *J. Chem. Phys.*, 2000, **112**, 8988.
23. F. Fujara, S. Wefing, and W. H. Spiess, *J. Chem. Phys.*, 1986, **97**, 2928.
24. B. Geil, F. Fujara, and H. Sillescu, *J. Magn. Reson.*, 1998, **130**, 18.
25. E. R. deAzevedo, T. J. Bonagamba, and K. Schmidt-Rohr, *J. Magn. Reson.*, 2000, **142**, 86.
26. J. Jeener, B. H. Meier, P. Bachmann, and R. R. Ernst, *J. Chem. Phys.*, 1979, **71**, 4546.
27. A. P. M. Kentgens, E. de Boer, and W. S. Veeman, *J. Chem. Phys.*, 1987, **87**, 6859.
28. A. Hagemeyer, K. Schmidt-Rohr, and H. W. Spiess, *Adv. Magn. Reson.*, 1989, **13**, 85.
29. D. Reichert, H. Zimmermann, P. Tekely, R. Poupko, and Z. Luz, *J. Magn. Reson.*, 1997, **125**, 245.
30. V. Gerardy-Montouillout, C. Malveau, P. Tekely, Z. Olender, and Z. Luz, *J. Magn. Reson.*, 1996, **123**, 7.
31. T. Gullion and J. Schaefer, *J. Magn. Reson.*, 1989, **81**, 196.
32. T. Gullion and J. Schaefer, *Adv. Magn. Reson.*, 1989, **13**, 57.
33. W. T. Dixon, *J. Chem. Phys.*, 1982, **77**, 1800.
34. S. C. Kuebler, D. J. Schaefer, and C. Boeffel, *Macromolecules*, 1997, **30**, 6597.
35. T. Terao, H. Miura, and A. Saika, *J. Chem. Phys.*, 1986, **85**, 3816.
36. D. Schaefer, H. W. Spiess, U. W. Suter, and W. W. Fleming, *Macromolecules*, 1990, **23**, 3431.
37. T. M. Duncan, 'A Compilation of Chemical Shift Anisotropies', Farragut: Chicago, 1990.
38. R. Tycko, G. Dabbagh, and P. Mirau, *J. Magn. Reson.*, 1989, **85**, 265.
39. J. Z. Hu, C. Ye, R. J. Pugmire, and D. M. Grant, *J. Magn. Reson.*, 2000, **145**, 230.
40. M. Hong, *J. Am. Chem. Soc.*, 2000, **122**, 3762.
41. C. Schmidt, B. Blümich, and H. W. Spiess, *J. Magn. Reson.*, 1988, **79**, 269.
42. F. Fujara, S. Wefing, and W. F. Kuhs, *J. Chem. Phys.*, 1988, **88**, 6801.
43. J. R. Sachleben, V. Frydman, and L. Frydman, *J. Am. Chem. Soc.*, 1996, **118**, 9786.
44. K. Saalwächter and K. Schmidt-Rohr, *J. Magn. Reson.*, 2000, **145**, 161.
45. C. E. Bronniman, N. M. Szeverenyi, and G. E. Maciel, *J. Chem. Phys.*, 1983, **79**, 3694.
46. H. T. Edzes and J. P. C. Bernards, *J. Am. Chem. Soc.*, 1984, **106**, 1515.
47. D. L. VanderHart, *J. Magn. Reson.*, 1987, **72**, 13.
48. B. H. Meier, *Adv. Magn. Opt. Reson.*, 1994, **18**, 1.
49. D. Reichert, T. J. Bonagamba, and K. Schmidt-Rohr, *J. Magn. Reson.*, 2001, **150**, 1.
50. E. R. deAzevedo, S. B. Kennedy, and M. Hong, *Chem. Phys. Lett.*, 2000, **321**, 43.
51. K. J. McGrath, K. L. Ngai, and C. M. Roland, *Macromolecules*, 1992, **25**, 4911.
52. A. S. Maxwell, I. M. Ward, F. Laupretre, and L. Monnerie, *Polymer*, 1998, **39**, 6835.
53. T. Gullion, D. B. Baker, and M. S. Conradi, *J. Magn. Reson.*, 1990, **89**, 479.
54. Y. Ishii, J. Ashida, and T. Terao, *Chem. Phys. Letters*, 1995, **246**, 439.
55. T. J. Bonagamba, F. Becker-Guedes, E. R. deAzevedo, and K. Schmidt-Rohr, *J. Polymer Sci. B: Phys. Ed.*, 2001, **39**, 2444.
56. M. Wind, U.-M. Wiesler, K. Saalwächter, K. Müllen, and H. W. Spiess, *Angewandte Chemie*, 2001, **13**, 752.
57. S. B. Kennedy, E. R. deAzevedo, W. A. Petka, D. A. Tirrell, T. P. Russell, and M. Hong, *Macromolecules*, 2001, **34**, 8675.

Biographical Sketches

Klaus Schmidt-Rohr, *b* 1967. Diploma (Physics), 1989; Ph.D., 1991, Mainz (Germany), with Prof. H. W. Spiess,

Max-Planck-Institute for Polymer Research. Postdoc with Alex Pines, UC Berkeley, 1993-94. Assistant/Associate Prof., Dept. of Polymer Science & Engineering, UMass–Amherst, 1995–1999. Associate Prof., Dept. of Chemistry, Iowa State University, 2000-present. 1 book & approx. 80 publications on solid-state NMR. Research interests: Development of NMR techniques for studying complex macromolecular solids.

Eduardo Ribeiro de Azevedo, *b* 1974. PhD Phys., 2001, Instituto de Física de São Carlos (IFSC) – Universidade de São Paulo (USP), Brazil, with Prof. Tito José Bonagamba. Visiting Scholar, Polymer Science and Engineering Department, University of Massachusetts, USA, with Prof. Klaus Schmidt-Rohr and Prof. Mei Hong, 1998–1999; Research interests include development or utilization of solid-state NMR methods and their application to study materials.

Tito José Bonagamba, *b* 1960. PhD Phys., 1991, Instituto de Física de São Carlos (IFSC) – Universidade de São Paulo (USP), Brazil, with Prof. H. Panepucci. Professor of Physics, IFSC-USP, 1988-present. Visiting Scientist, Dept. of Polymer Science & Engineering, University of Massachusetts, USA, with Prof. Klaus Schmidt-Rohr, 1998–2000; Visiting Scientist, Ames Laboratory & Dept. of Chemistry, Iowa State University, USA, with Prof. Klaus Schmidt-Rohr, 2000. Research interests include development or utilization of multidimensional solid-state NMR methods and their application to study materials and instrumentation for NMR.

Deuteron Relaxation Rates in Liquid Crystalline Samples: Experimental Methods

Gina L. Hoatson and Robert L. Vold
College of William and Mary, Williamsburg, VA, USA

1	Introduction	1
2	Spin Dynamics	1
3	Experimental Design	3
4	Site Specific Spectral Densities	7
5	Sample Rotation Experiments	9
6	Conclusions	10
7	Related Articles	10
8	References	11

1 INTRODUCTION

Deuteron NMR spectroscopy (^{2}H NMR) is an extremely powerful technique for investigating molecular order and dynamics. The usefulness and uniqueness of this method lies in the wide range of timescales that are accessible for quantitative investigation. Fast molecular motion, with correlation times in the picosecond range, can be investigated by using relaxation rates to determine the orientation and temperature dependence of individual spectral density functions.[1] In the intermediate regime, processes with correlation times in the range $\tau_c \approx 10^{-4}$–10^{-8} s are characterized by motional narrowing effects on quadrupole echo lineshapes.[2] For slow motions, decay of quadrupolar order,[3] selective inversion,[4] or 2D exchange spectroscopy[5] permit investigation of rotational dynamics with correlation times approaching the spin–lattice relaxation time, which can vary from milliseconds to several hundred seconds. This article is focused on describing ^{2}H NMR experiments which can be used to measure specific relaxation times, T_j, in oriented media. The primary motivation is to provide information which is essential to improving the understanding of molecular motion in thermotropic liquid crystals. Many experiments have been developed to measure different relaxation rates ($R_j = 1/T_j$); these will be summarized and their sensitivity to random and systematic errors will be considered.

The utility of ^{2}H NMR is enhanced by the fact that the dominant quadrupole interaction is both small enough to permit recording of undistorted spectra and sufficiently large to be a sensitive probe of local structure and dynamics. Dipolar interactions and associated many-body complications are usually negligible, and the interaction between the nuclear quadrupole moment and the local electric field gradient (EFG) tensor is described by a one-particle Hamiltonian. As a result the spin dynamics of deuterons, in realistically complicated systems, is simple enough to allow rigorous density matrix analysis of multiple pulse sequences and relaxation behavior. This greatly facilitates the development of new NMR techniques and simplifies the interpretation of relaxation behavior, thereby providing stringent tests of theoretical descriptions of ordering and dynamics.

In discussing motion in ordered environments, it is necessary to distinguish between studies on nonmesogenic solutes dissolved in anisotropic fluids, and studies of the liquid crystal molecules themselves. Measurements of spin relaxation of small, rigid solute molecules can be interpreted without the uncertain approximations inherent in descriptions of internal motion, and provide useful tests for general theories of how an ordering potential affects the dynamic processes of small solutes. However, the weak ordering and fast motion of solutes make them unreliable probes of liquid crystal dynamics. An understanding of the basic physics of liquid crystals is better achieved through direct investigations of carefully chosen liquid crystalline materials.

In the nematic phase, the motion of liquid crystal molecules is assumed to be fast enough to be in the motional narrowing regime. Thus, the fluctuating Hamiltonian $\hat{\mathcal{H}}'(t)$ responsible for relaxation varies rapidly compared with precession under the static Hamiltonian $\hat{\mathcal{H}}_0$, i.e. the motion is fast compared with the rigid lattice linewidth. Under these circumstances, Redfield theory[6] can be used to express the measured relaxation rates in terms of spectral densities of motion. The long-range order, which leads to a nonzero average value of the anisotropic quadrupole interaction, has profound effects on the motional spectral densities which govern spin relaxation. It is now well established that in the nematic phase, contributions to nuclear spin relaxation are made by restricted reorientation of individual molecules, internal rotations within the molecule, and by long-range quasi-coherent hydrodynamic modes such as order director fluctuations (ODFs).

In the more ordered liquid crystal phases, including smectics, lyotropics, and discotics, there is more uncertainty about the dominant motional processes. Spin relaxation studies can be used to help clarify the details of molecular dynamics in these systems. Throughout this article, Redfield theory will be used to describe the effects of molecular reorientation on spin relaxation. It should be appreciated that such motional narrowing approximations may not remain valid for these more complicated mesophases. For ultraslow motions, the concept of spectral densities is not sufficiently general to describe spin relaxation, and more rigorous approaches based on the stochastic Liouville equation must be used.

2 SPIN DYNAMICS

The time-independent Hamiltonian for a deuteron in an anisotropic environment is given by

$$\hat{\mathcal{H}}_0 = -\omega_0 \hat{I}_Z + \tfrac{1}{3}\omega_Q(3\hat{I}_Z^2 - \hat{\boldsymbol{I}} \cdot \hat{\boldsymbol{I}}) \qquad (1)$$

Here $\omega_0 = 2\pi\nu_0$ is the Larmor frequency (in radians per second), $2\omega_Q = 4\pi\nu_Q$ is the quadrupole splitting, and $\hat{\boldsymbol{I}}_Z$ is the operator for spin angular momentum about the space-fixed Z axis. Energy levels and transition frequencies associated with this Hamiltonian are illustrated in Figure 1. In isotropic liquids, where $\nu_Q = 0$, the two transitions are degenerate and occur at the Larmor frequency. In an oriented medium the quadrupolar

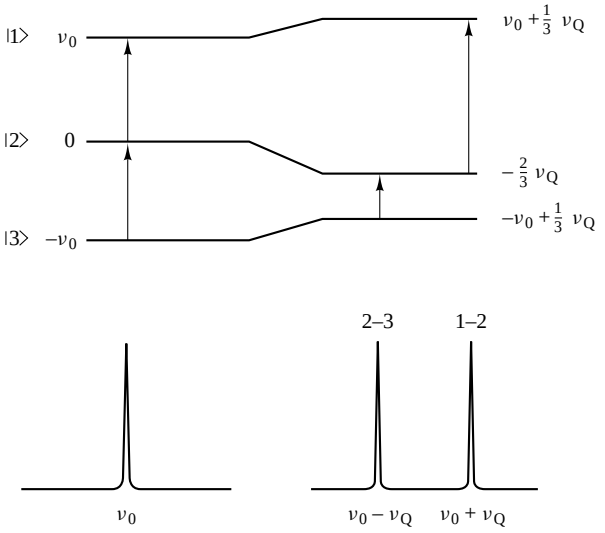

Figure 1 The energy level diagram for a spin-1 deuteron in a static magnetic field (left), and including the first-order quadrupolar interaction (right). Single quantum transition frequencies are indicated by vertical arrows on the diagram, and the corresponding NMR spectra are sketched

splitting between the $1 \rightarrow 2$ and $2 \rightarrow 3$ transitions ($2\nu_Q$) depends on the order parameters. Detailed discussions of the effects of orientational order on the NMR spectra of liquid crystals are available in the literature.[7,8]

Relaxation of deuterons in an ordered medium is best described using density matrix formalism. In the Redfield limit, in the absence of rf irradiation, the spin density matrix element, $\rho_{ij}(t)$, for an ensemble of deuterons evolves according to the equation

$$\frac{\partial \rho_{ij}(t)}{\partial t} = \mathrm{i}\omega_{ij}\rho_{ij} + \sum_{kl} R_{ijkl}[\rho_{kl}(t) - \rho_{kl}(\infty)] \qquad (2)$$

Here $\omega_{ij} = (\omega_j - \omega_i)$ is the transition frequency between the eigenstates $|i\rangle$ and $|j\rangle$ of the time-independent spin Hamiltonian, the R_{ijkl} are elements of the Redfield relaxation supermatrix, and $\rho_{kl}(\infty)$ is element kl of the thermal equilibrium density matrix. There are two fundamentally different types of states of the density matrix: diagonal elements ($i = j$), which correspond to populations of the eigenstates, and coherences ($i \neq j$), which correspond to phase coherence in the wavefunctions of the eigenstates. For a single deuteron the off-diagonal density matrix elements include two single quantum coherences $\rho_{12}(t)$ and $\rho_{23}(t)$ with precession frequencies $\nu_{12} = (\Delta + \nu_Q)$ and $\nu_{23} = (\Delta - \nu_Q)$, respectively, and one double quantum coherence $\rho_{13}(t)$ with precession frequency 2Δ. In this notation, Δ is the offset from resonance. The precession frequencies of the single quantum coherences correspond to the transition frequencies illustrated in Figure 1. Diagonal density matrix elements can be used to construct two linearly independent combinations of eigenstate populations: $(\rho_{11} - \rho_{33}) = \langle \hat{I}_Z \rangle$ is the expectation value of Zeeman polarization, and $(\rho_{11} - 2\rho_{22} + \rho_{33}) = \langle \hat{Q}_Z \rangle$ is the expectation value of quadrupole order. Theoretical expressions for the relaxation behavior of the five independent density matrix elements are easy to calculate in terms of the Redfield elements R_{ijkl}, which are in turn expressed in terms of spectral densities for molecular motion using the equations

$$R_{ijkl} = \int_0^\infty \exp[\mathrm{i}\tau(\omega_{ik} - \omega_{jl})]\langle \mathrm{i}|\hat{\mathcal{H}}'(t)|\ j\ \rangle \times \langle k|\hat{\mathcal{H}}'(t+\tau)|l\rangle^*\,\mathrm{d}\tau \qquad (3)$$

$$\hat{\mathcal{H}}'(t) = \sum_{m=-2}^{2} (-1)^m A^{(2)}_{-m} \sum_{k=-2}^{2} [D^{(2)*}_{mk}(t) - \langle D^{(2)*}_{mk}(0)\rangle] T^{(2)}_k(\mathrm{PAS}) \qquad (4)$$

Here the $A^{(2)}_{-m}$ are second rank spherical tensor spin operators, the $D^{(2)}_{mk}(t)$ are the time-dependent Wigner rotation matrix elements, the $T_k{}^{(2)}(\mathrm{PAS})$ are spherical components of the quadrupole coupling tensor, expressed in its principal axis system (PAS), and the angular brackets $\langle\ \rangle$ denote an ensemble average. The $D^{(2)}_{mk}(t)$ depend on Euler angles, $\alpha(t)$, $\beta(t)$, and $\gamma(t)$, which define the time-dependent orientation of the PAS relative to a laboratory-fixed frame. The inclusion of the term $\langle D^{(2)*}_{mk}(0)\rangle$ is necessary to ensure that the relaxation Hamiltonian fluctuates about a mean value of zero, so that the Fourier transform, defined in equation (3), is convergent. In isotropic liquids the $\langle D^{(2)*}_{mk}(0)\rangle$ are zero, but in liquid crystals they define characteristic order parameters of the anisotropic phase.

Without further analysis, several implications of the theory embodied in equations (2)–(4) are apparent. First of all, since $\mathcal{H}'(t)$ gains its time dependence exclusively through orientational variables, deuteron relaxation is sensitive only to rotational motion. This implies that the spatial order characteristic of complex mesophases is not directly probed by deuteron relaxation measurements. Instead, it is necessary to rely on theories which approximate the coupling between translation and rotation. Partially for this reason, most detailed interpretations of deuteron relaxation have been confined to the nematic phase, where translational order is unimportant. Secondly, the appearance of order parameters in the fluctuating Hamiltonian leads ultimately to expressions for measurable relaxation rates which also depend on the orientational order. This implies that the spectral density functions for motion in ordered environments are fundamentally different from those for isotropic liquids. Finally, since the Redfield relaxation matrix elements depend on the average of the product of elements of $\mathcal{H}'(t)$, they include higher-rank order parameters of the form $\langle D^{(2)*}_{mk}(0) D^{(2)*}_{mk}(0)\rangle$. In principle such quantities can be derived from relaxation studies, but they do not influence the equilibrium spectra.

In oriented nematic phases the observed quadrupole splitting is proportional to $\frac{1}{2}(3\cos^2\beta_{\mathrm{MP}} - 1)$, where β_{MP} is the angle between the largest component of the electric field gradient (EFG) tensor, q_{zz}, and the molecule fixed Z axis. Typically, in organic molecules, deuteron quadrupole coupling tensors have the largest component coincident with the C–D bond direction. Hence, C–D bonds which make different angles with the molecular Z axis give rise to resolved quadrupolar doublets, whose relaxation behavior can be determined independently. This provides a uniquely powerful way to investigate rotational anisotropy, but requires that the relaxation rates for each

deuteron be expressed in terms of spectral densities for the overall rotation of the molecule-fixed coordinate system. Thus, it is useful to decompose the Euler rotation from laboratory to PAS frames, Ω_{LP}, into separate transformations: a time-dependent transformation from laboratory to molecule-fixed coordinates [$\alpha_{LM}(t)$, $\beta_{LM}(t)$, $\gamma_{LM}(t)$], followed by a time-independent transformation to the PAS of each individual deuterated site (α_{MP}, β_{MP}, γ_{MP}). It can be shown[1] that there are then just three distinct spectral density functions, given by the equations

$$J_m(m\omega_0) = \frac{1}{(T_0^{(2)})^2} \sum_{k=-2}^{2} \sum_{k'=-2}^{2} \sum_{n=-2}^{2} \sum_{n'=-2}^{2} T_n^{(2)} T_{n'}^{(2)*} \times D_{kn}^{(2)}(\Omega_{MP})\, D_{k'n'}^{(2)*}(\Omega_{MP})\, J_{mkk'}(m\omega_0) \quad (5)$$

where m = 0, 1, or 2, and

$$T_0^{(2)} = \frac{\sqrt{6}}{4} \frac{e^2 q_{zz} Q}{\hbar} \quad (6a)$$

$$T_{\pm 1}^{(2)} = 0 \quad (6b)$$

$$T_{\pm 2}^{(2)} = \frac{\eta}{4} \frac{e^2 q_{zz} Q}{\hbar} \quad (6c)$$

Here $\eta = (q_{xx} - q_{yy})/q_{zz}$ is the asymmetry parameter of the deuteron EFG tensor. In most cases, η is small enough to ignore, and this greatly simplifies the evaluation of equation (5). Molecular motion appears in this expression through the Fourier transforms of correlation functions of time-dependent Wigner rotation matrix elements:

$$J_{mkk'}(m\omega_0) = \int_0^\infty \exp(-\mathrm{i}m\omega_0\tau) C_{mkmk'}(\tau)\, \mathrm{d}\tau \quad (7a)$$

$$C_{mkmk'}(\tau) = \langle E_{mk}^{(2)*}[\Omega_{LM}(t)) E_{mk'}^{(2)}(\Omega_{LM}(t+\tau))] \rangle \quad (7b)$$

$$E_{mk}^{(2)}[\Omega_{LM}(t)] = D_{mk}^{(2)}[\Omega_{LM}(t)] - \langle D_{mk}^{(2)}[\Omega_{LM}(0)] \rangle \quad (7c)$$

In essence, the spectral densities, J_m $(m\omega_0)$ are Fourier transforms of certain correlation functions which relate the orientation of a molecule at time t to the orientation at a later time $t + \tau$. The key idea is that by the appropriate selection of relaxation experiments, the different spectral densities for individual deuterons can be determined as a function of temperature, Larmor frequency ω_0 (magnetic field strength), and orientation with respect to the static field (for sufficiently rigid mesophases). This constitutes the maximum amount of information available from deuteron relaxation experiments.

It is implicit in the formalism presented here that relaxation during rf pulses can be ignored. When this is not the case, for example in spin lock measurements in the rotating frame ($T_{1\rho}$), the same spectral densities arise but some must be evaluated at the rf field amplitude, ω_1, rather than integer multiples of the Larmor frequency.[9]

3 EXPERIMENTAL DESIGN

Designing experiments to determine spectral densities amounts to choosing a particular state of the density matrix, calculating its relaxation rate in terms of spectral densities, designing a rf pulse sequence that creates the desired state, and measuring the relaxation time. Pulse sequences that are currently being used to create specific population distributions or coherences are summarized in Table 1. Strategies for using combinations of experiments to determine the individual spectral densities from these measurements will be described in this section. Salient practical aspects will also be discussed: which techniques give the most reliable results and where potential problems in implementation are anticipated. To a certain extent this depends on the details of the spin system, i.e. the number and relative order of magnitude of quadrupolar splittings, and the degree of orientational order of the liquid crystal, S_{zz} and $(S_{xx} - S_{yy})$.

To date, most relaxation experiments have focused on determining $J_1(\omega_0)$ and $J_2(2\omega_0)$ from the recovery of nonequilibrium population distributions. These are the simplest, most reliable and accurate experiments. In principle, $J_1(\omega_0)$ and $J_2(2\omega_0)$ can be obtained from any two relaxation experiments which depend on linearly independent combinations of these two spectral densities. These include nonselective and selective inversion recovery measurements of Zeeman polarization, conventional (JB) and broadband (BBJB) Jeener–Broekaert excitation of quadrupole order, and two-dimensional measurements of the decay rate of double quantum coherence. In practice, the accuracy of selective inversion recovery experiments is limited because the recovery curves are biexponential. The formulae given in Table 1 refer to the initial slope of the recovery, but this is difficult to measure without introducing systematic errors. Nonselective inversion recovery with quadrupolar echo detection (IRQE) does not suffer from this disadvantage, and is the method of choice for measuring T_{1Z}. Because deuteron relaxation times in liquid crystals are short there is no need to resort to inherently less accurate methods such as saturation recovery or progressive saturation.

For studies of thermotropic liquid crystals two potentially serious instrumental problems arise. The first is temperature control: the quadrupole splitting is directly proportional to order parameters which can be strongly temperature dependent. Close to the nematic–isotropic phase transition, where the order parameter changes most rapidly, temperature coefficients as large as 5 kHz K^{-1} have been observed.[10] Temperature drifts, gradients and instabilities as small as a few millidegrees can then lead to severe line broadening. Moreover, in frequency-selective preparation sequences, such as the conventional two-pulse JB sequence, a temperature drift translates into irreproducible changes in the amount of quadrupole order created. In general, accurate measurements of T_{1Z} and T_{1Q} require temperature control and gradients to less than 0.1 K, preferably to within 0.01 K. Secondly, in nematic liquid crystals, quadrupolar splittings approaching 100 kHz are common. In order to achieve uniform inversion over such large spectral widths, rf field strengths of $\nu_1 \approx 150$ kHz are required (typical 90° pulse lengths of 1.5–2.0 μs in a 5 mm coil). Thus, high-power amplifiers similar to those required for solid state ^{2}H NMR are essential. Fortunately, instrumentation with the necessary capabilities is now commercially available.

It has been shown[11] that the best procedure for determining $J_1(\omega_0)$ and $J_2(2\omega_0)$ is not the conventional JB experiment designed to retain both quadrupole and Zeeman order. Rather, two separate IRQE and BBJB experiments are performed which can be optimized independently for maximum

Table 1 Relaxation Experiments and Measured Spectral Densities

	Spectral Density[a]
Populations	
Nonselective T_{1Z} (IRQE)	
$180-T^{b}-90_x-\tau-90_y$	$2J_1(\omega_0) + 8J_2(2\omega_0)$
Broadband T_{1Q} (BBJB)	
$(90_x-2\tau-67.5_{-y}-2\tau-45_y-\tau-45_y-)-T-45_x-t-90_x-$	$6J_1\ (\omega_0)$
Conventional Jeener–Broekaert (JB)	
$90_x-\tau-45_y-T-45_y$	Sum: $2J_1(\omega_0) + 8J_2(2\omega_0)$ Difference: $6J_1(\omega_0)$
Selective T_{1Z}[c]	
$180_x^{A}-T-90^{A}$	$5J_1(\omega_0) + 2J_2(2\omega_0)$
Coherences	
Quadrupolar echo T_{2e}	
90_x-T-90_y	$3J_0\ (0) + 3J_1(\omega_0) + 2J_2(2\omega_0)$
Multipulse quadrupolar echo T_2 (MQE)	
$90_x-\tau-(90_y-2\tau-)_n$	Short τ: $3J_0(0) + 5J_1\ (\omega_0) + 2J_2(2\omega_0)$
$(T = 2n\tau)$	Long τ: $3J_0(0) + 3J_1(\omega_0) + 2J_2(2\omega_0)$
Selective single quantum T_2[c]	
$90_x^{A}-T/2-180^{A}-T/2-$	$3J_0(0) + 3J_1(\omega_0) + 2J_2(2\omega_0)$
Double quantum T_{DQ}	
$90_x-\tau-90_x-T/2-180-T/2-90$	$2J_1(\omega_0) + 4J_2(2\omega_0)$

[a]Units of $(3\pi^2/4)(e^2q_{zz}Q/\hbar)^2$.
[b]T denotes the relaxation delay.
[c]The superscript A indicates that the pulse is applied selectively at the frequency of peak A.

precision and accuracy. In particular, the use of broadband (frequency-independent) procedures for exciting quadrupole order, combined with echo detection to avoid pulse recovery problems, was shown to increase greatly the accuracy with which T_{1Q} can be determined.[11] This is important because small uncertainties in measured values of the relaxation times propagate into larger errors in determining $J_2(2\omega_0)$.

Figure 2 illustrates the difference between conventional (JB) and broadband (BBJB) excitation of quadrupole order. The sample is pure 4-*n*-pentyl-4′-cyanobiphenyl selectively deuterated (5CB-d_6) in the 1,4- and 5-positions of the alkyl chain. Figure 2(a) shows the pulse sequence, spectrum, and quadrupolar order excitation profile for the conventional JB pulse pair, $90_x-\tau-45_y$. This sequence is inherently frequency selective, with efficiency proportional to $\sin \nu_Q\tau$. The excitation delay of $\tau = 46\,\mu$s is a particularly unfortunate choice: the spectrum shows that the sign of the quadrupole order is opposite for the C-1 and C-2 methylene deuterons and there is little excitation of quadrupole order for the methyl deuterons (C-5). It is impossible to achieve full excitation of quadrupole order for all the transitions with any single τ value. The BBJB sequence does not suffer from this limitation. Figure 2(b) shows that uniform excitation is achieved by this sequence, with total excitation time $5\tau = 46\,\mu$s. Thus, for materials with several different quadrupole splittings, broadband procedures for exciting quadrupole order are definitely preferable to the simple JB pulse pair. In practice, the choice of τ in the BBJB sequence is not very critical. It is usually sufficient to use a small enough value to excite full quadrupole order for the largest splitting, and this ensures that all others will be uniformly excited. However, it must be noted that all methods of exciting quadrupole order fail as the quadrupole splitting tends to zero. For splittings less than a few kilohertz, the BBJB sequence described here is somewhat less efficient than the simple two-pulse (JB) excitation sequence. This is demonstrated by the excitation profiles shown for the JB and BBJB sequences in the lower traces of Figures 2(a) and 2(b), respectively. Computer-optimized broadband sequences have now been developed to deal with this problem.[12] In summary, the BBJB experiment has many advantages and is rapidly superseding the conventional JB experiment as the method of choice for measuring T_{1Q}. Moreover, since this technique can be applied successfully to powder patterns (which have a continuous distribution of quadrupolar splittings), it will be useful for measuring the orientation dependence of T_{1Q} in smectic and lyotropic mesophases.

To demonstrate procedures for determining individual spectral densities measurements of relaxation times of a liquid crystal mixture, consisting of 25 mol% of perdeuterated 4-methyl-4′-cyanobiphenyl (1CB-d_{11}) and 75 mol% 5CB-d_6, will be outlined as a case study.[13] 5CB-d_6 is selectively deuterated on the alkyl chain carbon at positions C-1, C-4 and C-5, as shown in the molecular structure. Figure 3 illustrates the measurement of T_{1Z} using a nonselective inversion pulse followed by quadrupole echo detection. The bottom trace is an equilibrium spectrum, and spectral assignments for each of the quadrupolar doublets are indicated. Dipolar fine structure is apparent on the 1CB transitions, but it can be shown that this does not interfere with the T_{1Z} measurements.

The top trace in Figure 3 shows a partially relaxed spectrum with relaxation delay $T = 1$ ms, and all the transitions are inverted. After 10 ms the aromatic doublet of 1CB (peak 5) has recovered substantially while the other lines remain inverted. After 45 ms, the 1CB methyl lines (peak 2) are nulled while the methyl (C-5) deuterons of 5CB (peak 4), which have the longest T_{1Z}, are still inverted. In order to obtain accurate T_{1Z} values from these data, it is necessary to choose a set

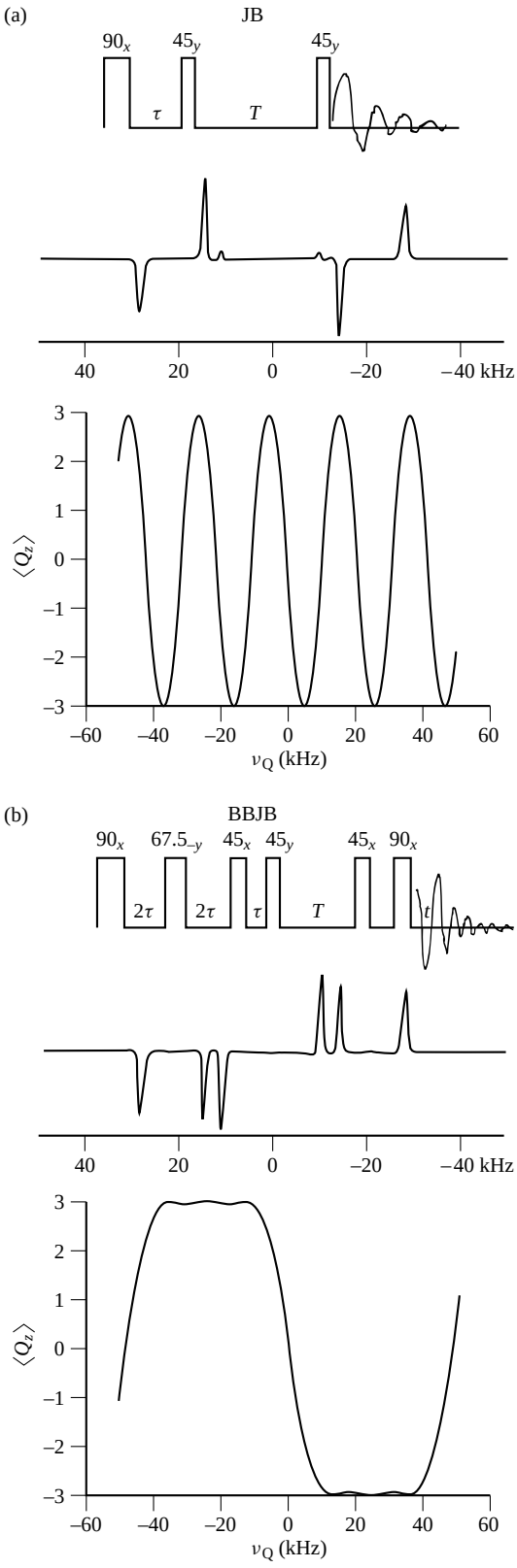

Figure 2 Pulse sequences, 5CB-d_6 spectra, and quadrupolar order excitation profiles for (a) the conventional JB pulse pair and (b) the BBJB sequence. For (a) the pulse delay was τ = 46 μs, and in (b) the total excitation time 5τ = 46 μs. The simulated quadrupolar order excitation profiles include the effects of finite pulse lengths (90° pulse width of 1.6 μs). The spectra were recorded at 46.06 MHz

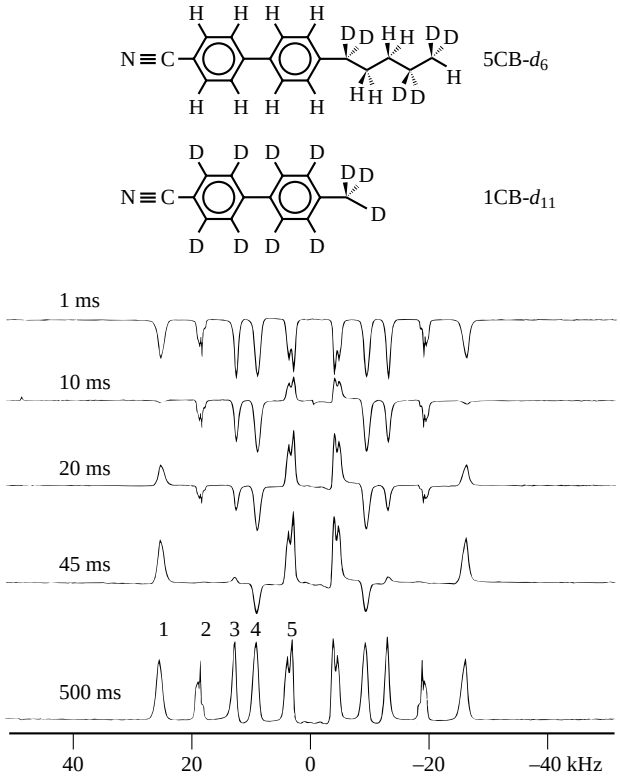

Figure 3 Molecular structures of the binary mixture of 1CB-d_{11} (25 mol%) and 5CB-d_6. Partially relaxed spectra at 46.06 MHz from the inversion–recovery experiment with quadrupolar echo detection (IRQE) were taken in the nematic phase at 28.2°C. Relaxation delay times are indicated on the left of each trace. Spectral assignments for the labeled peaks in the equilibrium spectrum, shown in the bottom trace, are: (1) deuterons on the first methylene carbon on the alkyl chain of 5CB; (2) methyl deuterons of 1CB; (3) deuterons on the fourth alkyl chain carbon of 5CB; (4) methyl deuterons of 5CB; and (5) aromatic ring deuterons of 1CB

of relaxation delays which span at least one full decade of recovery for every line. T_{1Z} for each deuteron is then obtained by fitting to the equation

$$M(\infty) - M(T) = [M(\infty) - M(0)] \exp(-T/T_{1Z}) \quad (8)$$

Here $M(T)$ is the sum intensity of the quadrupolar doublet at time T, $M(\infty)$ is its thermal equilibrium value, and $M(0)$ is the intensity immediately after inversion. In principle, perfect inversion should give $M(0) = -M(\infty)$. However, erroneous T_{1Z} values are obtained if this is assumed and the data are fitted to a two-parameter equation. A nonlinear fit in which $M(0)$, $M(\infty)$, and T_{1Z} are simultaneously adjusted is more reliable. Typically, 10 or more T values are needed for accurate results.

In the 1CB/5CB mixture, at 28.2 °C, T_{1Z} ranges from 9.8 ms for the 1CB aromatic deuterons to 209 ms for the 5CB methyl deuterons. Thus, it is not possible to construct one set of relaxation delays which is appropriate for every transition. Instead, the list must be expanded to include T values which are appropriate for all the relaxation times. In practice, this requires a few preliminary experiments to establish the approximate range of T_{1Z} values, and when the range is large, as many as 20–30 delays may be required. A common source of error in this type of experiment is failure

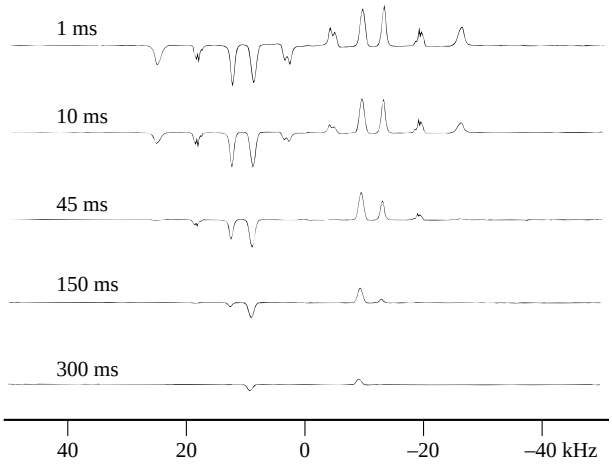

Figure 4 Partially relaxed spectra at 46.06 MHz from a BBJB experiment on the nematic phase of the binary mixture of 1CB-d_{11} (25 mol%) and 5CB-d_6 at 28.2°C. Relaxation delay times are indicated on the left of each trace. Spectral assignments are identical to those given in Figure 3

to wait for full equilibrium between successive scans: it is essential to wait at least five times the longest T_{1Z} value if systematic errors are to be avoided. Thus for the 1CB/5CB mixture, where 2048 scans were accumulated for each of 20 T values, the recycle delay was 1 s and the total experiment time was approximately 12 h.

Next, the BBJB sequence is used to excite quadrupole order uniformly. The relaxation time T_{1Q} can be measured by monitoring the decay of the difference magnetization for each doublet. Typical partially relaxed spectra for the 1CB/5CB binary mixture are shown in Figure 4. Since the difference magnetization for each doublet decays rigorously toward zero, the exponential decay function can be fitted with just two adjustable parameters (the initial intensity and T_{1Q}). Construction of an appropriate list of relaxation delays is as important as for T_{1Z} measurements, and the total experimental time is usually comparable.

Spectral densities may be calculated from the relationships

$$J_1(\omega_0) = \frac{2R_{1Q}}{9\pi^2(e^2q_{zz}Q/h)^2} \tag{9}$$

and

$$J_2(2\omega_0) = \frac{1}{18\pi^2(e^2q_{zz}Q/h)^2}(3R_{1Z} - R_{1Q}) \tag{10}$$

Here $e^2q_{zz}Q/h$ is the quadrupole coupling constant in hertz. When proper precautions are taken, and the signal-to-noise ratio is favorable, it is possible to determine the relaxation rates, $R_{1Z} = 1/T_{1Z}$ and $R_{1Q} = 1/T_{1Q}$, with a precision of 2–5%. This is sufficiently accurate that the use of approximate values for the quadrupole coupling constant should be avoided. Estimated values, from data reported for more or less similar materials, can lead to significant uncertainty in the spectral densities. Wherever possible, low-temperature quadrupole echo lineshapes should be analyzed to determine static values of the relevant quadrupole coupling constants.

While numerous measurements of $J_1(\omega_0)$ and $J_2(2\omega_0)$ have been reported, determinations of $J_0(0)$ are relatively scarce. Potential dynamic information inherent in this spectral density is very important in the study of liquid crystals. In particular, the spectral density at zero frequency should be exquisitely sensitive to long-wavelength modes of order director fluctuations. Even though this small-angle process contributes in first order only to $J_1(\omega_0)$, higher order calculations[14] reveal contributions to $J_0(\omega)$ which can be large as ω tends to zero.

All methods for determining $J_0(0)$ rely on measuring the dephasing rate of one quantum coherence, and subtracting contributions from $J_1(\omega_0)$ and $J_2(2\omega_0)$. For example, making use of the spectral densities listed in Table 1, it can be shown that $J_0(0)$ is given by

$$J_0(0) = \frac{1}{9\pi^2(e^2q_{zz}Q/h)^2}(4R_2^0 - 2R_{1Z} - 3R_{1Q}) \tag{11}$$

where $R_2{}^0$ is the limiting decay rate obtained in a multiple-pulse quadrupole echo sequence in the limit of zero pulse spacing ($2\tau \rightarrow 0$), much smaller than $(e^2q_{zz}Q/h)^{-1}$.[15] Alternatively, if the transverse relaxation rate R_2(sel) of one line of the quadrupolar doublet is measured using a selective Carr–Purcell sequence, $J_0(0)$ is given by

$$J_0(0) = \frac{1}{27\pi^2(e^2q_{zz}Q/h)^2}[12R_2(\text{sel}) - 3R_{1Z} - 5R_{1Q}] \tag{12}$$

To date, there is no single method that is successful for measuring T_2 in all liquid crystalline systems. Figure 5 illustrates an efficient 2D procedure appropriate for spectra with many lines. The sample is perdeuterated fluorene dissolved in the nematic phase of 5CB. In this experiment a train of n equally spaced 90_y° refocusing pulses are applied during the evolution period and the acquisition is started at the top of the last echo. The evolution time must therefore be incremented in integral multiples of the echo spacing. For the 2D spectrum shown in Figure 5, the spacing was $2\tau = 300\,\mu$s, and every fifth echo was recorded (n = 1, 6, 11, ... , 76). Thus the spectral width in the f_1 frequency domain is $\pm 1/(20\tau) = \pm 333$ Hz. The ordinary spectrum is recovered as a slice along $f_1 = 0$, and is displayed at the right edge of the contour plot (spectral assignments are indicated). Each peak has a Lorenztian profile in f_1, and its T_2 can be determined simply from the linewidth at half maximum. However, before relying on these T_2 values to determine $J_0(0)$ it is necessary to consider the pulse spacing dependence of the relaxation time,[15] and potential sources of systematic errors. In some cases, T_2 may be so short that only a few echoes can be observed, and the digital resolution in f_1 is then insufficient for accurate linewidth measurements. It is encouraging that the T_2 values determined in the frequency domain, from the 2D linewidths, are found to agree (within experimental error) with those determined in the time domain by fitting the line intensities as a function of relaxation delay.

Unresolved dipolar interactions are a potentially serious source of error in multiple pulse quadrupolar echo measurements of T_2 in liquid crystals. Dipolar precession is not refocused by the nonselective 90_y° pulses, and unresolved dipolar couplings produce apparent dephasing which can be confused with a true T_2 process. This problem is also unavoidable in nonselective two-pulse procedures where the echo amplitude

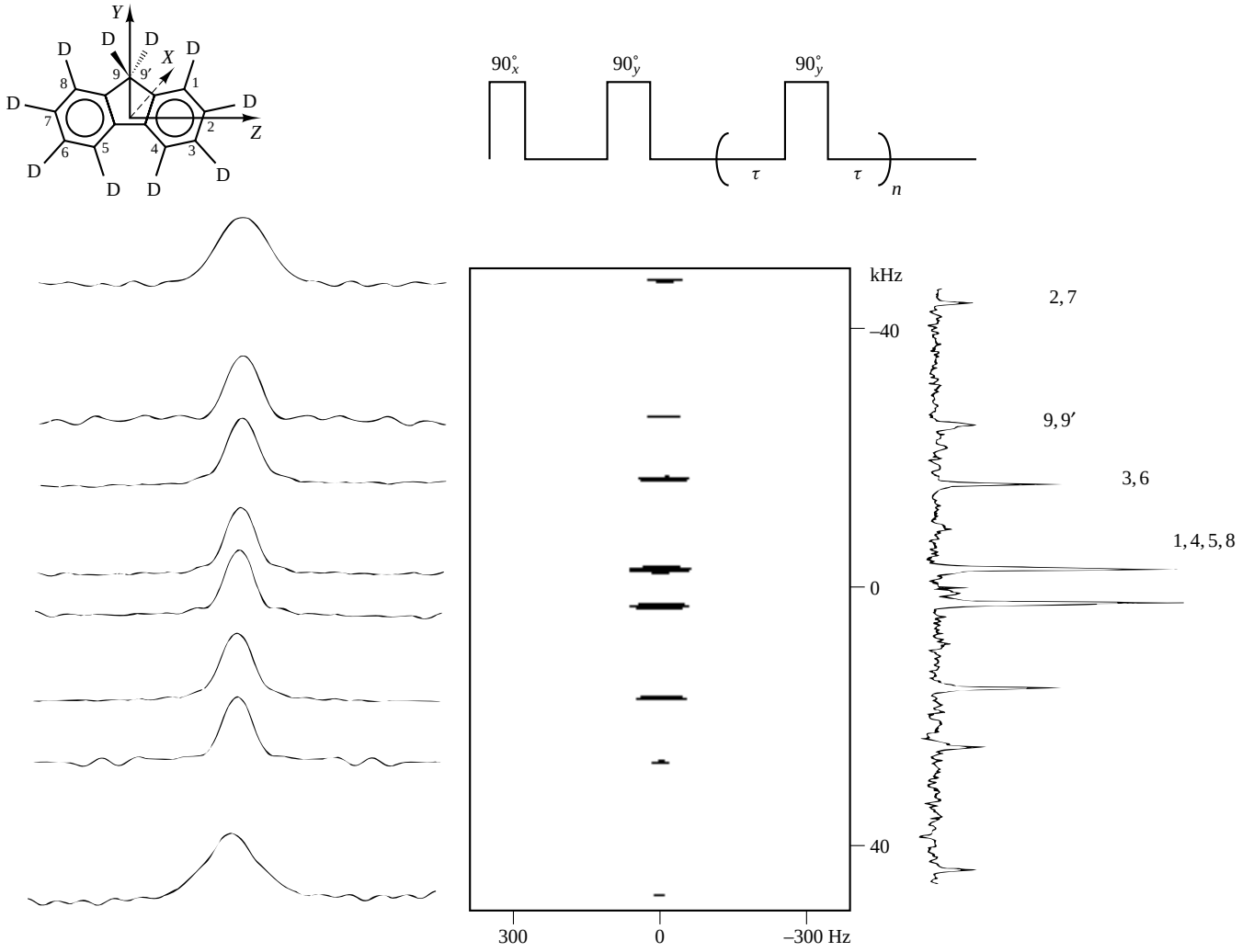

Figure 5 A 2D method for determining T_2s in a multiline spectrum. The sample is perdeuterated fluorene-d_{10} in the nematic phase of 5CB. The normal ^{2}H NMR spectra (46.06 MHz) is obtained from the $f_1 = 0$ slice through the data matrix, and is shown to the right of the contour plot. T_2 of each line is obtained from the full width at half maximum of the Lorenztian lineshape for the corresponding slice in f_2, as shown on the left. The pulse sequence for this experiment is shown, and for this data set the pulse spacing was $2\tau = 300\,\mu$s, and every fifth echo was recorded

is monitored as a function of pulse spacing to give T_{2e}. The use of selective pulses, designed to monitor spin echoes from one-half of the quadrupolar doublet, circumvents this difficulty. However, in samples with small quadrupolar splittings and many lines it may not be possible to achieve adequately selective pulses. Alternatively, all precession of the transverse magnetization can be suppressed by using the multiple quadrupolar echo experiment with closely spaced 90_y° pulses. This achieves effective spin locking when the pulse spacing is smaller than the inverse of the largest quadrupole splitting. In practice, this procedure requires a very robust temperature controller to avoid overheating the sample. A general, accurate method of measuring $J_0(0)$ in liquid crystals remains to be established, and this continues to be a topic of current research.

The decay rate of double quantum coherence for a single deuteron depends exclusively on $J_1(\omega_0)$ and $J_2(2\omega_0)$. Thus there is no additional information to be gained by measuring this relaxation rate that cannot be obtained more accurately from simple measurements of T_{1Z} and T_{1Q}. In a few carefully chosen systems, with well-resolved deuteron dipolar coupling, it has been possible to create and monitor the decay of both double- (R_{1313}) and four-quantum (R_{1414}) coherences.[16] This permitted determination of the cross-correlation terms in the motion of two different quadrupole coupling tensors, and provided insight into rotational anisotropy of small rigid solutes in liquid crystalline solvents. Unfortunately, this method cannot be readily extended to typical liquid crystal molecules because of extensive dipolar couplings, which are usually too small to be resolved and thus contribute to the apparent multiple-quantum linewidth.

4 SITE SPECIFIC SPECTRAL DENSITIES

Deuteron relaxation in liquid crystals gains much of its utility from the unambiguous way in which the spectral densities depend on the orientation of the EFG tensor with respect to molecule-fixed coordinates. By measuring spectral densities for deuterons with several different orientations, it is possible to obtain a very stringent test of models of rotational motion. The general orientation dependence, expressed in

equation (5), can be quite complex, and it is useful to consider the special case of a linear molecule. In this case, the EFG tensor has zero asymmetry parameter, and the largest component is collinear with the molecule-fixed Z axis ($\beta_{MP} = 0$). The fourfold summation in equation (5) then collapses to a single term:

$$J_m(m\omega_0) = J_{m00}(m\omega_0) \tag{13}$$

It can be shown that the spectral densities $J_{m00}(m\omega_0)$ are determined exclusively by processes which reorient the long molecular axis. These include order director fluctuations, which make a large contribution only to $J_{100}(\omega_0)$, and molecular reorientation which contributes to both $J_{100}(\omega_0)$ and $J_{200}(2\omega_0)$. Illustrative data for cyanoacetylene-*d* dissolved in a commercial nematic liquid crystal mixture (Merck Phase V)[17] are shown in Figure 6. $J_1(\omega_0)$ clearly includes a frequency-dependent contribution which is absent from $J_2(2\omega_0)$. Numerous investigations of the deuteron relaxation of small rigid solutes in nematic phases have made use of this frequency dispersion to isolate the contributions from director fluctuations.

Measurements[18] have demonstrated that director fluctuations do not play a major role in the deuteron relaxation of the liquid crystal molecules themselves. The rotational motion of typical nematogens is apparently slow enough to occur on approximately the same timescale as director fluctuations. It can then be shown that cross-correlation effects act to quench the contribution of director fluctuations, so that the spectral densities can be interpreted exclusively in terms of single-molecule rotation.[19]

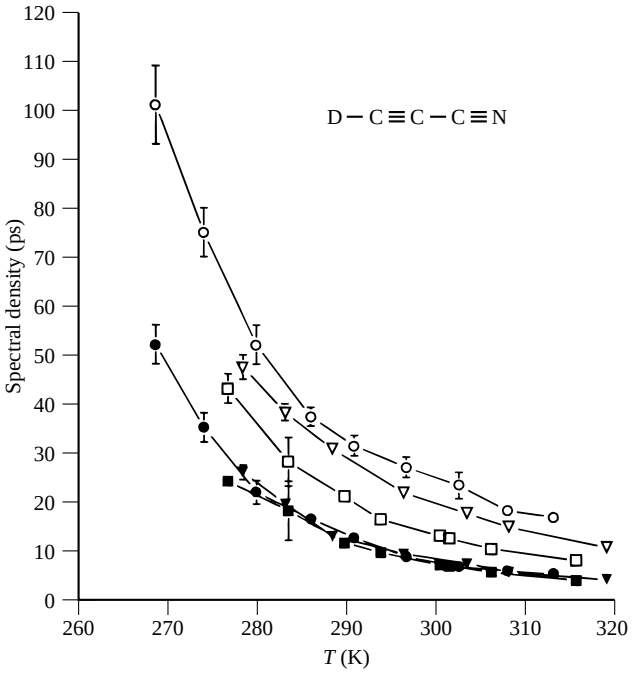

Figure 6 Spectral densities $J_1(\omega_0)$ (open symbols) and $J_2(2\omega_0)$ (solid symbols) for cyanoacetylene-*d* in nematic Merck Phase V.[17] Data were acquired at several Larmor frequencies: triangles, ν_0 = 4.6 MHz; circles, ν_0 = 9.2 MHz; squares, ν_0 = 38.4 MHz. The experimental points are joined by lines to guide the eye. For reasons discussed in the text, $J_1(\omega_0)$ depends on the Larmor frequency while $J_2(2\omega_0)$ does not

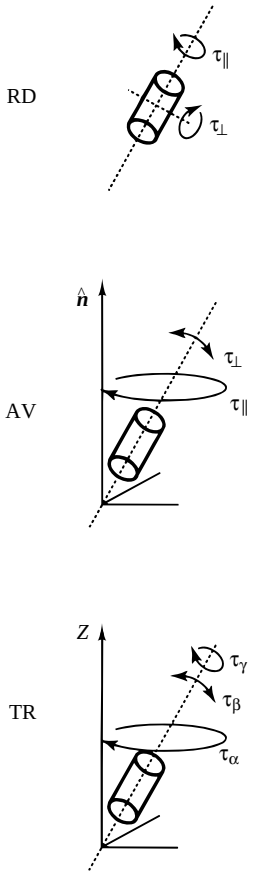

Figure 7 Models used to describe molecular motion in oriented environments. (a) rotational diffusion (RD), (b) anisotropic viscosity (AV) and (c) the 'third rate' (TR) model

While a full discussion of molecular motion is beyond the scope of this article, three popular rotational models are illustrated in Figure 7: rotational diffusion (RD),[20] anisotropic viscosity (AV),[21] and the 'third rate' (TR) model.[22]

Small-step rotational diffusion of a symmetric rotor is fully characterized by two correlation times, $\tau_\perp = 1/(6D_\perp)$ and $\tau_\parallel = 1/(6D_\parallel)$, where $D_\perp$ and $D_\parallel$ are rotational diffusion constants. If the diffusion tensor is assumed to be diagonal in laboratory-fixed coordinates, where its principal components are related to anisotropic viscosity coefficients, the relevant correlation times for this 'anisotropic viscosity' model are still labeled $\tau_\perp$ and $\tau_\parallel$ but their physical meaning is different. Assuming that the nematic director remains parallel to the magnetic field, τ_β and τ_α in the TR model have the same physical significance as $\tau_\perp$ and $\tau_\parallel$ (respectively) in the AV model. The third rate is characterized by a correlation time τ_γ for rotation about the long molecular axis, which can occur in steps of arbitrary size as specified by a collision parameter p, where $0 \leq p \leq 1$.

The nematogen 2-fluorenyl 4′-tetradecyloxybenzoate-d_9 (FLOC$_{14}$-d_9) provides an excellent example of how spectral densities can be used to test these rotational models. Figure 8 shows the molecular structures and the assigned NMR spectrum in the nematic phase of a binary mixture of FLOC$_{14}$-d_9 and *p*-xylene-d_{10} (~10 mol%). The temperature dependence of the spectra gives the orientational order parameters of both molecules.[23] By measuring and analyzing T_{1Z} and T_{1Q} for all

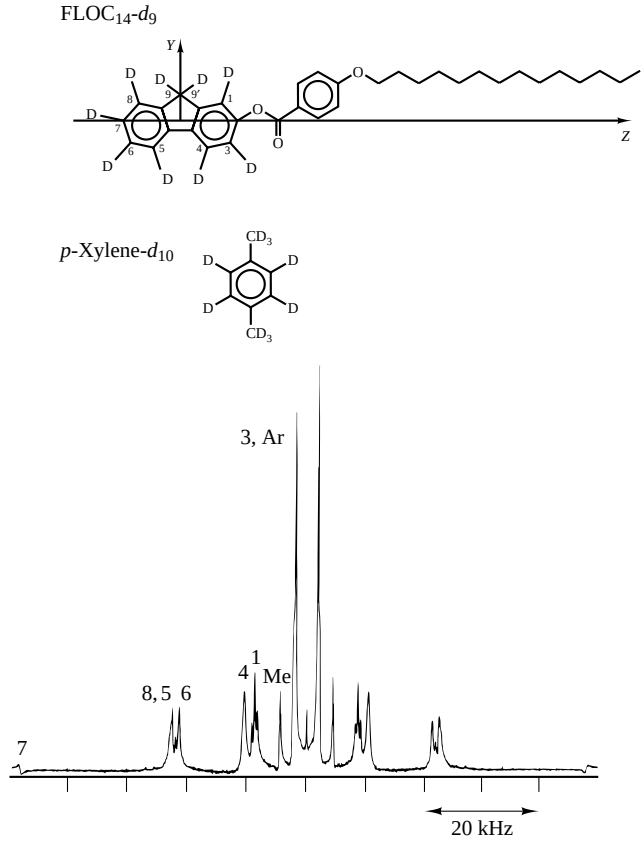

Figure 8 Quadrupole echo spectrum at 32.8 MHz with spectral assignments for a binary mixture of $FLOC_{14}$-d_9 and *p*-xylene-d_{10} in the nematic phase. Analysis of relaxation data for this sample using the TR model provided correlation times for both the rigid solute and the flexible liquid crystal molecule[24]

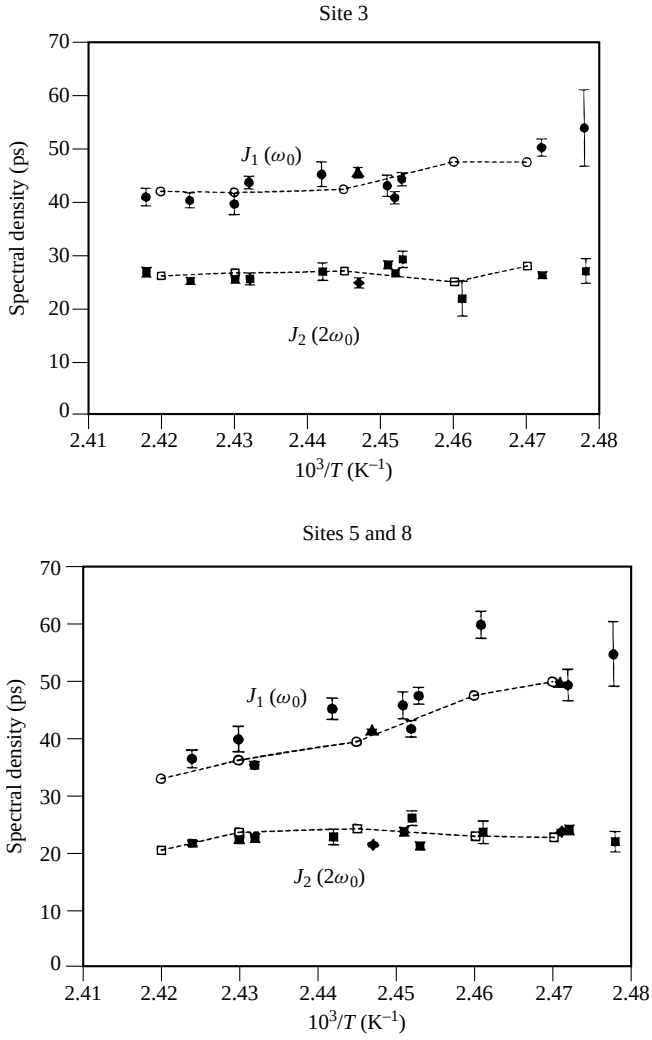

Figure 9 Individual spectral densities, $J_1(\omega_0)$ and $J_2(2\omega_0)$, for positions 3 and 5,8 of $FLOC_{14}$-d_9, as a function of inverse temperature. Closed circles are $J_1(\omega_0)$ measured at 46 MHz, closed triangles are $J_1(\omega_0)$ at 38.4 MHz, closed squares are $J_2(2\omega_0)$ at 46 MHz and closed diamonds are $J_2(2\omega_0)$ at 38.4 MHz. The open symbols, which are connected by dotted lines to guide the eye, are fits of the 46 MHz data, from all positions, to the third rate model of molecular reorientation. (Adapted from Goetz et al.[18])

the lines as a function of temperature, it was possible to determine rotational correlation times for both components of the mixture.[24]

Measurements on pure $FLOC_{14}$-d_9, which has deuterons at five different orientations of the EFG tensor, yielded 10 independent spectral densities at each temperature.[18] A representative selection of the extensive data is shown in Figure 9 which gives the spectral densities for two molecular sites—the 3 (β_{MP} = 54.65°) and 5,8 (β_{MP} = 78.15°) positions. The points are experimental spectral densities, and the lines represent a nonlinear least-squares fit of the data from all positions to the TR model.

The problem of fitting the spectral densities to the various motional models is highly overdetermined, and the quality of the fit can be used to assess the validity of each model. Not surprisingly, it was found that no two-parameter model was capable of simultaneously fitting the spectral density data for all the sites. The TR model, with four independently adjustable parameters, provided by far the best fit. Figure 10(a) shows a 3D minimum $\Delta\chi^2$ surface (68% confidence boundaries) in the correlation time phase space (τ_α, τ_β, τ_γ), for $FLOC_{14}$-d_9 at 135.7 °C.[18] At this temperature the order parameter S_{zz} = 0.523, and the correlation times are τ_α = 610 ± 300 ps, τ_β = 1050 ± 250 ps, and τ_γ = 266 ± 20 ps. Measuring the temperature dependence of the correlation times allowed activation energies for the three independent rotations to be determined.

5 SAMPLE ROTATION EXPERIMENTS

When a liquid crystal sample is rotated in a magnetic field, the diamagnetic susceptibility anisotropy results in a torque on the director which tends to align it either parallel or perpendicular to the field. In nematic mesophases, the opposing viscous forces are too weak, and spontaneous realignment of the director occurs. This is unfortunate, because when the director can be rotated, profound changes are observed in both the NMR spectrum and relaxation times. Deuteron spectra with well-resolved doublets are observed only when the director is aligned with respect to the field. If it is not so aligned, the distribution of molecular orientations about the director

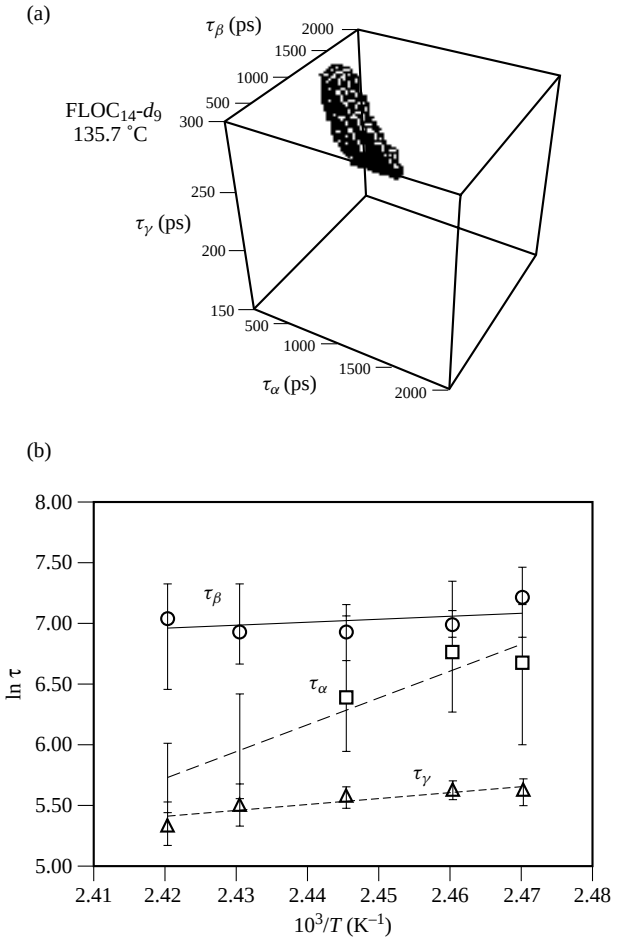

Figure 10 TR model parameters for pure FLOC$_{14}$-d_9 in the nematic phase at 135.7°C. (a) Constant $\Delta\chi^2$ boundary of 68% confidence in the 3D parameter space of the TR model, (τ_α, τ_β, τ_γ). (b) Arrhenius plots of the temperature dependence of the motional correlation times; τ_α data are shown as squares, τ_β as circles, and τ_γ as triangles. The error bars correspond to the 68% confidence boundaries, and the lines are least squares fits of the data which give the activation energies. (Adapted from Goetz et al.[18])

produces a distribution of doublet splittings, and the resulting characteristic spectra are reminiscent of the powder patterns observed in solid state ^{2}H NMR. Analysis of these lineshapes and rotation patterns can provide a wealth of information about the orientational distribution function. This technique has been especially successful in elucidating structure and organization in a magneto-aligned chiral smectic C phase, S_C*.[25]

Relaxation measurements as a function of sample orientation are relatively scarce, in part because methods for obtaining individual spectral densities from complex powder patterns have only been devised in the 1990s.[26] The information available from such experiments can be appreciated by considering the simple case of a uniaxial phase, such as smectic A or hexatic smectic B. It can then be shown[27] that the spectral densities are given by

$$J_0(\beta, 0) = \tfrac{1}{4}(1 - 3\cos^2\beta)^2 J_0(0) + 3\cos^2\beta \times \sin^2\beta\, J_1(0) + \tfrac{3}{4}(1 - \cos^2\beta)^2 J_2(0) \quad (14a)$$

$$J_1(\beta, \omega_0) = \tfrac{3}{2}\cos^2\beta \sin^2\beta\, J_0(\omega_0) + \tfrac{1}{2}(1 - 3\cos^2\beta + \cos^4\beta) J_1(\omega_0) + \tfrac{1}{2}(1 - \cos^4\beta) J_2(\omega_0) \quad (14b)$$

$$J_2(\beta, 2\omega_0) = \tfrac{3}{8}(1 - \cos^2\beta)^2 J_0(2\omega_0) + \tfrac{1}{2}(1 - \cos^4\beta) \times J_1(2\omega_0) + \tfrac{1}{8}(1 + 6\cos^2\beta + \cos^4\beta) J_2(2\omega_0) \quad (14c)$$

If T_{1Z} and T_{1Q} are analyzed to yield $J_1(\beta, \omega_0)$ and $J_2(\beta, 2\omega_0)$ as functions of sample rotation angle β, inversion of equations (14b) and (14c) will yield six spectral densities: $J_0(\omega_0)$, $J_1(\omega_0)$, $J_2(\omega_0)$, $J_0(2\omega_0)$, $J_1(2\omega_0)$, and $J_2(2\omega_0)$. It must be noted that these results are applicable only for uniaxial phases, and most phases which are rigid enough to support sample rotation have more complicated, biaxial symmetry. While this further complicates the orientation dependence of the spectral densities, it should not preclude using them to test motional models.

6 CONCLUSIONS

This article has discussed and summarized the existing experimental methods which are used to measure various deuteron relaxation times in liquid crystals. Accurate determination of appropriate combinations of relaxation rates allows the derivation of the individual spectral density functions $J_1(\omega_0)$, $J_2(2\omega_0)$, and, occasionally, $J_0(0)$. These spectral densities are Fourier transforms of rotational correlation functions and can be interpreted in terms of models of molecular motion. Currently, when appropriate precautions are taken, it is possible to measure spectral densities with an accuracy of 2–5%. This places very tight constraints on acceptable theoretical descriptions of molecular dynamics. In the nematic phase of thermotropic liquid crystals, performing these experiments as a function of temperature and magnetic field strength (ω_0) provides a rigorous test for models of molecular motion in the presence of an orientating potential. Extension of the measurements to more complex ordered smectic, lyotropic, and discotic mesophases offers the possibility of determining the orientation dependence of the relaxation rates, and represents a dramatic increase in the available information.

In conclusion, measuring ^{2}H NMR relaxation rates is a powerful and important method for investigating and understanding molecular dynamics in liquid crystal samples.

7 RELATED ARTICLES

Amphiphilic Liquid Crystalline Samples: Nuclear Spin Relaxation; Bilayer Membranes: Deuterium and Carbon-13 NMR; Brownian Motion and Correlation Times; Deuterium NMR in Solids; Double Quantum Coherence; Dynamic NMR in Liquid Crystalline Solvents; Echoes in Solids; Field Cycling

Experiments; Liouville Equation of Motion; Liquid Crystalline Samples: Carbon-13 NMR; Liquid Crystalline Samples: Deuterium NMR; Liquid Crystalline Samples: Diffusion; Liquid Crystalline Samples: Relaxation Mechanisms; Liquid Crystalline Samples: Structure of Nonrigid Molecules; Liquid Crystals: General Considerations; Lyotropic Liquid Crystalline Samples; Membranes: Deuterium NMR; Molecular Motions: T_1 Frequency Dispersion in Biological Systems; Multiple Quantum Spectroscopy in Liquid Crystalline Solvents; Polymer Dispersed Liquid Crystals; Protein Dynamics from NMR Relaxation; Relaxation of Coupled Spins from Rotational Diffusion; Relaxation Processes in Coupled-Spin Systems; Relaxation Processes: Cross Correlation and Interference Terms; Relaxation Theory: Density Matrix Formulation; Relaxation Theory for Quadrupolar Nuclei; Two-Dimensional NMR of Molecules Oriented in Liquid Crystalline Phases.

8 REFERENCES

1. R. R. Vold and R. L. Vold, *Adv. Magn. Opt. Reson.*, 1991, **16**, 85.
2. H. W. Spiess and H. Sillescu, *J. Magn. Reson.*, 1981, **42**, 381.
3. H. W. Spiess, *J. Chem. Phys.*, 1980, **72**, 6755.
4. T. M. Duncan, A. M. Thayer, and T. W. Root, *J. Chem. Phys.*, 1990, **92**, 2663.
5. C. Schmidt, B. Blümich, S. Wefing, S. Kaufmann, and H. W. Spiess, *Ber. Bunsenges. Phys. Chem.*, 1987, **91**, 1141.
6. A. G. Redfield, *Adv. Magn. Reson.*, 1965, **1**, 1.
7. J. W. Emsley and L. C. Lindon, *NMR Spectroscopy Using Liquid Crystal Solvents*, Pergamon Press, New York, 1975.
8. C. A. Veracini, in *NMR of Liquid Crystals*, ed. J. W. Emsley, D. Reidel, Boston, 1985, p. 99.
9. J. R. C. van der Maarel, *J. Chem. Phys.*, 1984, **80**, 5646.
10. L. S. Selwyn, R. L. Vold, and R. R. Vold, *J. Chem. Phys.*, 1984, **80**, 5418.
11. G. L. Hoatson, *J. Magn. Reson.*, 1991, **94**, 152.
12. G. P. Drobny, *J. Magn. Reson.*, 1993, **103**, 313.
13. G. L. Hoatson, T. Y. Tse, and R. L. Vold, *J. Magn. Reson.*, 1992, **98**, 342.
14. R. L. Vold, R. R. Vold, and M. Warner, *J. Chem. Soc. Faraday Trans.*, 1988, **84**, 997.
15. S. B. Ahmad and K. J. Packer, *Mol. Phys.*, 1979, **37**, 47.
16. D. Jaffe, R. R. Vold, and R. L. Vold, *J. Magn. Reson.*, 1982, **46**, 475.
17. R. R. Vold, R. L. Vold, and N. M. Szeverenyl, *J. Phys. Chem.*, 1981, **85**, 1934.
18. J. M. Goetz, G. L. Hoatson, and R. L. Vold, *J. Chem. Phys.*, 1992, **97**, 1306.
19. B. J. Gertner and K. Lindenberg, *J. Chem. Phys.*, 1991, **94**, 5143.
20. P. L. Nordio, G. Rigatti, and U. Segre, *J. Chem. Phys.*, 1972, **56**, 2117.
21. J. H. Freed, *J. Chem. Phys.*, 1977, **66**, 4183.
22. R. R. Vold and R. L. Vold, *J. Chem. Phys.*, 1988, **88**, 1443.
23. G. L. Hoatson and J. M. Goetz, *J. Chem. Phys.*, 1991, **94**, 3885.
24. J. M. Goetz, Ph.D. Thesis, College of William and Mary, 1993.
25. B.-G. Wu and J. W. Doane, *J. Magn. Reson.*, 1987, **75**, 39.
26. G. L. Hoatson, R. L. Vold, and T. Y. Tse, *J. Chem. Phys.*, 1994, **100**, 4756.
27. T. M. Barbara, R. R. Vold, and R. L. Vold, *J. Chem. Phys.*, 1983, **79**, 6338.

Biographical Sketches

Gina L. Hoatson. *b* 1955. B.Sc., 1977, Ph.D., 1980 (supervisor K. J. Packer), University of East Anglia, UK. Postdoctoral work: Iowa State University, USA (B. C. Gerstein), 1981–82, and University of British Columbia, USA (M. Bloom and E. E. Burnell), 1982–86. Assistant and Associate Professor of Physics, College of William and Mary, USA, 1986–present. Current research specialty: NMR studies of order and dynamics in solids and liquid crystals.

Robert L. Vold. *b* 1942. B.Sc., 1963, University of California, Berkeley, Ph.D. (supervisor H. S. Gutowsky), 1966, University of Illinois, USA. Postdoctoral work at Massachusetts Institute of Technology, 1966–67 (J. S. Waugh). Assistant, associate, and full professor of Chemistry, University of California, San Diego, 1968–91; Program Officer, National Science Foundation, 1992; National Research Council Fellow, NASA Langley Research Center, 1993; Professor of Applied Science and Physics, College of William and Mary, Virginia, 1994–present. Current research specialty: NMR studies of order and dynamics in solids.

Liquid Crystalline Samples: Deuterium NMR

Ronald Y. Dong
Brandon University, Brandon, Manitoba, Canada

1	Introduction	1
2	Orientational Ordering	2
3	Spin Relaxation and Molecular Motion	4
4	Novel NMR Experiments	6
5	Related Articles	7
6	References	8

1 INTRODUCTION

Rowell and co-workers[1,2] were first to demonstrate that deuterium is an excellent spin probe for studying liquid crystalline samples. They also used selectively deuterated compounds to simplify the proton NMR spectra. Early work in this field was devoted to measuring and interpreting spin–lattice relaxation rates[3] of protons, and to revealing orientational ordering in various mesophases[4] by means of deuterium splittings and spectral patterns. While proton NMR of liquid crystals shows broad partially resolved spectra, the deuteron NMR spectra are often characterized by well resolved quadrupolar doublets[5,6] that may contain some dipolar fine structures [Figure 1(a)]. The deuteron ($I = 1$) Zeeman levels [Figure 1(b)] are perturbed by interaction of its nuclear quadrupolar moment Q with the asymmetric EFG at the deuteron site. The static Hamiltonian $\hat{\mathcal{H}}_0$ of the system is defined by

$$\hat{\mathcal{H}}_0 = \hat{\mathcal{H}}_Z + \langle \hat{\mathcal{H}}_Q(t) \rangle \tag{1}$$

where $\hat{\mathcal{H}}_Z$ is the Zeeman Hamiltonian and $\hat{\mathcal{H}}_Q$, the quadrupolar Hamiltonian, is time dependent due to thermally driven, randomly fluctuating molecular processes. Due to a nonzero $\langle \hat{\mathcal{H}}_Q(t) \rangle$ in a partially ordered system, the two nuclear transitions are displaced at equal distances from the Larmor frequency ($\omega_0/2\pi$) as shown in Figure 1. The EFG tensor for most C–D bonds is axially symmetric, with the unique principal axis along the C–D bond direction. The quadrupolar splitting for a static C–D bond can take a maximum value of $\frac{3}{2}\chi$ or about 260 kHz, which is much less than its Larmor frequency of 46 MHz in a magnetic field of 7.1 T. For comparison, dipolar splitting between two deuterons in a methylene group is at most a few kilohertz, D–H dipolar splitting for a similar geometry is about 10 kHz, and the chemical shift is of the order of 1 kHz. It is therefore possible to neglect the chemical shift dispersion and the dipolar interaction with other nuclei and to treat the deuteron as an isolated spin-1 nucleus. The theoretical analysis of such a system is relatively simple. The quadrupolar splitting $\Delta\nu_i$ of the ith C–D bond may be approximated by[7,8]

$$\Delta\nu_i = \tfrac{3}{2}\chi S_{zz} \langle 3\cos^2\theta_i - 1 \rangle / 2 \tag{2}$$

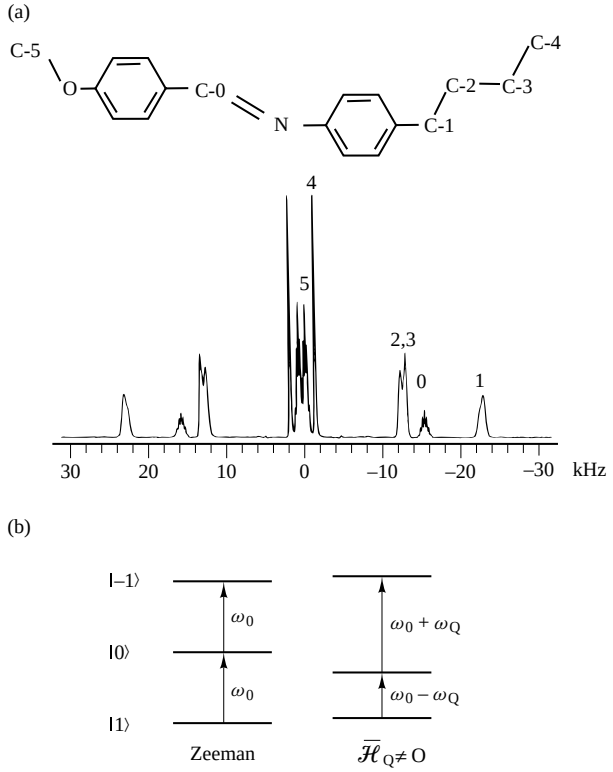

Figure 1 (a) The structure of MBBA and a typical deuterium NMR spectrum of MBBA-d_{13} in its nematic phase. (b) Energy level diagram of a deuteron spin ($\eta = 0$) in a large magnetic field. $\omega_0/2\pi$ is the Larmor frequency

where the contribution from the $S_{xx} - S_{yy}$ term is neglected, S_{zz} is the orientational order parameter of the long molecular axis with respect to the nematic director (see below), and θ_i represents the angle between the C_i–D bond and the molecular z axis. The angular brackets denote a statistical average over all allowed conformations in a flexible mesogen.

Spin relaxation has long been recognized as a useful technique for studying dynamic processes in liquid crystals.[7,8] A partial list of such processes[8] includes the order director fluctuations (ODFs), translational diffusion, order parameter fluctuations near phase transitions, molecular reorientation, and internal rotations of alkyl end chains. Deuteron is particularly suitable for getting detailed information about molecular motion in liquid crystals, since its relaxation is governed by intramolecular mechanisms, and multipulse techniques[7] may be used to determine individual spectral densities of motion from partially relaxed deuteron NMR spectra for all the resolved doublets. The quadrupolar relaxation Hamiltonian for a spin-1 system is defined by the time dependent part of $\hat{\mathcal{H}}_G(t)$ with respect to its average value $\langle \hat{\mathcal{H}}_Q(t) \rangle$:

$$\hat{\mathcal{H}}'_Q(t) = \hat{\mathcal{H}}_Q(t) - \langle \hat{\mathcal{H}}_Q(t) \rangle \tag{3}$$

The deuterium spin–lattice relaxation rates are given by[9,12]

$$\begin{aligned} \frac{1}{T_{1Z}} &= J_1(\omega_0) + 4J_2(2\omega_0) \\ \frac{1}{T_{1Q}} &= 3J_1(\omega_0) \end{aligned} \tag{4}$$

where an axially symmetric quadrupolar interaction ($\eta = 0$) is assumed. The spectral densities of motion $J_{m\mathrm{L}}$ ($m_\mathrm{L}\omega_0$) are Fourier transforms of the autocorrelation functions $G_{m_\mathrm{L}}(t)$ which involve second-rank tensor components $D^2_{m_\mathrm{L}0}(\Omega(t))$ in the relaxation Hamiltonian. The part of $\hat{\mathcal{H}}'_\mathrm{Q}(t)$ that connects spin states with $\Delta m_I = 1$ has a fluctuation spectrum described by $J_1(\omega_0)$, while the part that connects states with $\Delta m_I = 2$ is described by $J_2(2\omega_0)$. These spectral parameters and $J_0(0)$ at zero frequency (obtained in principle from one quantum spin echo or quadrupolar echo experiments) are determined without a particular choice of motional model. They must be accurately measured as a function of temperature at different Larmor frequencies, and may be used to provide critical tests of any proposed model of molecular motion. For systems with coupled deuterons, there are additional terms[13,14] in the relaxation expressions that arise from cross-correlation functions describing pairwise correlation in the motion of EFG tensor components at each deuteron. This additional information may serve as a further check of the proposed motional model.

2 ORIENTATIONAL ORDERING

One of the common features in liquid crystals is the existence of a preferred orientation of molecules along a spatial direction specified by a unit vector known as the director ***n***. Deuteron NMR spectroscopy has played a major role in establishing molecular field theories[8,15,16] for liquid crystals. These mean field theories can predict the temperature dependences of order parameters of rigid solutes and solvent molecules. The ordering of molecules in mesophases may in general be described by an orientational distribution function $f(\Omega)$ which depends on Eulerian angles $\Omega(\equiv \phi, \theta, \psi)$. The $f(\Omega)$ can be expanded in terms of Wigner rotation matrices of rank L

$$f(\Omega) = \sum_{L=0}^{\infty} \sum_{m,m'=-L}^{L} \frac{2L+1}{8\pi^2} a_{Lm'm} D^L_{m'm}(\Omega) \qquad (5)$$

where the expansion coefficients $a_{Lm'm} = \langle D^{L*}_{m'm}(\Omega)\rangle$ are the microscopic order parameters of rank L. The order parameters of rank two and four can in principle be measured, but higher rank order parameters are not as easily accessible by experiments. The potential of mean torque $V(\Omega)$ can be defined by writing $f(\Omega)$ as

$$f(\Omega) = \exp[-\beta V(\Omega)] / \int \mathrm{d}\Omega \exp[-\beta V(\Omega)] \qquad (6)$$

where $\beta = 1/k_\mathrm{B}T$. $V(\Omega)$ represents the orientational potential of a single molecule. In the Maier–Saupe theory[17,18] of nematics, $V(\Omega)$ takes on a simple form:

$$V(\cos\theta) = -\epsilon \langle P_2(\cos\theta)\rangle P_2(\cos\theta) \qquad (7)$$

where the parameter ϵ scales the strength of intermolecular interaction. The theory used a mean field approach and assumed that attractive dispersion forces among molecules are responsible for the nematic order. It was successful in predicting a first-order phase transition between a nematic and an isotropic phase, as well as the temperature dependence of the nematic order parameter $\langle P_2\rangle$ ($\equiv S_{zz}$). Using equation (2) as a first approximation, $\langle P_2\rangle$ can be calculated[1,2] from the observed quadrupolar splittings in liquid crystals. A general set of 25 rank-two order parameters[8] was defined by Saupe:

$$S^{\alpha\beta}_{ij} = \tfrac{1}{2}\langle 3 i_\alpha j_\beta - \delta_{\alpha\beta}\delta_{ij}\rangle \qquad (8)$$

where (α,β) refer to a space-fixed axis system (X,Y,Z), (i,j) refer to a molecule-fixed axis system (x,y,z), i_α denotes the projection of a unit vector ***i*** along the α axis, and the angular brackets represent an ensemble average. For uniaxial phases where ***n*** $\parallel Z$ axis, equation (8) gives the simple Saupe order matrix S_{ij} ($= \frac{1}{2}\langle 3 i_z j_z - \delta_{ij}\rangle$).

2.1 Rigid Molecules in Uniaxial Phases

For a rigid molecule (or a rigid fragment of a molecule) ordered in a uniaxial liquid crystalline phase, the partially averaged component ($\langle A_\parallel\rangle$) parallel to the director of any second rank tensor ***A*** is given by

$$\langle A_\parallel\rangle = A_0 + \tfrac{2}{3}\sum_{ij} A_{ij} S_{ij} \qquad (9)$$

where A_0 is the isotropic average of ***A***. For the EFG tensor ***q***, A_0 is zero and the splitting $\Delta\nu = \frac{3}{2}e^2Q/h\langle q_\parallel\rangle$ can be calculated using equation (9). The unknown S_{ij} elements can be determined from measuring enough independent values of $\langle q^i_\parallel\rangle$ where the superscript refers to sites in a molecule. This is usually possible for a rigid solute dissolved in a liquid crystal, where the principal axes of symmetry of the solute may be located with certainty based on its molecular symmetry. Hence deuterium NMR can provide precise measurements of S_{zz} and $S_{xx} - S_{yy}$ for a rigid molecule. Figure 2 illustrates the determination of $S_{xx} - S_{yy}$ and S_{zz} for anthracene-d_{10} in several nematogens. The solid curves are predictions based on the mean field theory of biaxial solutes where the λ parameter is a measure of the deviation in molecular symmetry of the solute from cylindrical symmetry. That the solute ordering depends on the solvent is an indication that the solute–solvent interactions cannot be dominated only by dispersion forces. For flexible mesogens, it may be possible to determine a local order matrix for a rigid fragment of the molecule provided the principal axes can be located on the fragment based on its symmetry. This is often difficult due to a lack of measurable nuclear couplings. A clear exception to this is the study of a perdeuterated fluorene group in the mesogen 2-fluorenyl-4′-tetradecyloxy benzoate-d_9 (FLOG$_4$).[20] Because of the large number (eight) of distinct deuteron sites, the location of the long molecular axis could be adjusted for the average conformer in a frame fixed to the fluorene group, and the local order parameters were unambiguously determined.

2.2 Flexible Molecules in Uniaxial Phases

Mesogenic molecules are usually composed of an aromatic core and one or more flexible alkyl chains. Due to internal

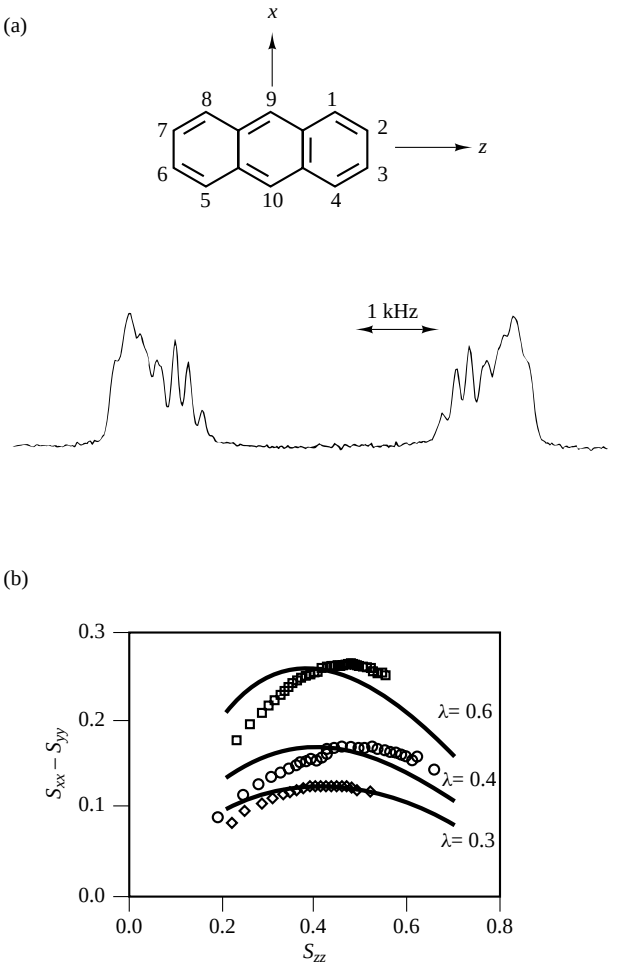

Figure 2 (a) Molecular structure of anthracene-d_{10} and the deuterium spectrum at 30.7 MHz from deuterons 1, 4, 5, 8, 9, and 10 in anthracene-d_{10} dissolved in Phase V. (b) Variation of S_{zz} with $S_{xx} - S_{yy}$ for anthracene-d_{10} dissolved in ZLI 1167 (□), E9 (○) and Phase V (◇).[19]

rotations, the chain does not always exist in an all-*trans* conformation. It is generally accepted that a single order tensor may not be enough to describe orientational ordering of different configurations. In equation (9), the average of $A_{\|}$ must also be carried out over an ensemble of molecules having all allowed configurations. The rotational isomeric state (RIS) model of Flory[21] is used to generate all chain configurations. Since a single $A_{\|}$ value would not provide quantitative information on the orientational order of the molecules, a molecular model is therefore required. Such a model using the additive potential method[15–19] was pioneered by Marcelja and later improved by Emsley and Luckhurst. The potential of mean torque which is responsible for the alignment of a conformer has its origin from the molecular field of its neighbors. It is constructed by adding up local interaction tensors of the carbon–carbon segments and the rigid aromatic core segment, which are specified by model parameters X_c and X_a, respectively. Each rigid (nth) conformer has its own order matrix $\mathbf{S}^n$ and its equilibrium probability of occurrence $P_{eq}(n)$. Equilibrium statistical mechanics is used to do the ensemble average in calculating the quadrupolar splittings $\Delta\nu_i$. The parameters X_c, X_a and E_{tg} (the energy difference between a *gauche* and a *trans* state) are varied to optimize the fits to the

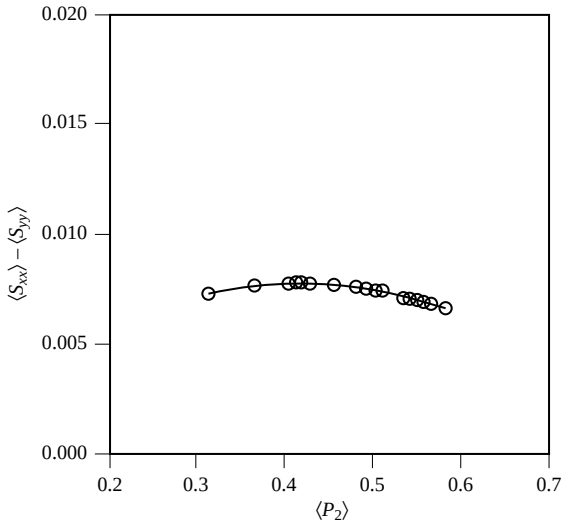

Figure 3 Plot of $\langle P_2\rangle$ versus $\langle S_{xx}\rangle - \langle S_{yy}\rangle$ for the averaged MBBA molecule.[22]

experimental splittings.[8] For example, such analysis[22] has been carried out for the splittings of MBBA (Figure 1). Knowing $S^n_{\alpha\beta}$ and $P_{eq}(n)$, it is possible to find a conformationally average order matrix $\langle\mathbf{S}\rangle$ by doing the statistical average in a common molecular frame. The principal components $\langle P_2\rangle$ and $\langle S_{xx}\rangle - \langle S_{yy}\rangle$ of the 'average' molecule can be obtained by diagonalizing the $\langle\mathbf{S}\rangle$ matrix. Figure 3 shows the plot of $\langle S_{xx}\rangle - \langle S_{yy}\rangle$ versus $\langle P_2\rangle$ of MBBA. It is interesting to note that the molecular biaxial order parameter, $\langle S_{xx}\rangle - \langle S_{yy}\rangle$, of the 'average' molecule is quite small for this flexible mesogen.

2.3 NMR in Biaxial Phases

Biaxial nematics, some smectic phases, such as S_G, and certain discotic phases[8] show phase biaxiality. Deuterium NMR may be used to detect phase biaxiality through the measurement of a nonzero motionally induced asymmetry parameter η^{LC} in the nuclear quadrupolar interaction whose EFG may have $\eta = 0$ in the solid state. Suppose that the molecule is rigid and the principal axes (X,Y,Z) of the liquid crystalline phase are chosen to coincide with the principal axes of the average EFG tensor. Letting the polar angles of the magnetic field in the (X,Y,Z) system be (θ_0, ϕ_0), the splitting is given by[8]

$$\delta\nu(\theta_0,\phi_0) = \tfrac{3}{4}\chi^{LC}\{(3\cos^2\theta_0 - 1) + \eta^{LC}\sin^2\theta_0\cos 2\phi_0\} \quad (10)$$

where χ^{LC}, a motionally averaged quadrupole coupling constant, and η^{LC} are defined by

$$\chi^{LC} = \chi\sum_m \overline{D^2_{0,m}(\theta,\psi)}D^2_{m,0}(\beta,\alpha)$$
$$\eta^{LC} = \sqrt{\tfrac{3}{2}}\frac{\chi}{\chi^{LC}}\sum_m[\overline{D^2_{2,m}(\phi,\theta,\psi)} + \overline{D^2_{-2,m}(\phi,\theta,\psi)}]D^2_{m,0}(\beta,\alpha) \quad (11)$$

where (ϕ,θ,ψ) are Euler angles that transform between a molecular frame (x,y,z) and the liquid crystalline (X,Y,Z)

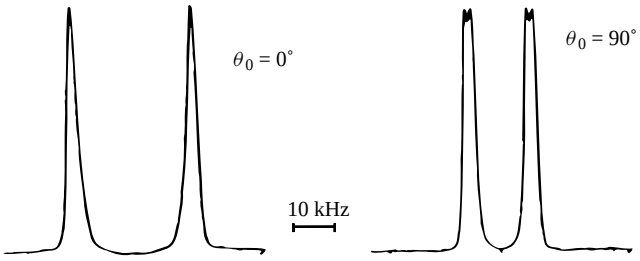

Figure 4 Experimental angular dependence of the deuterium NMR spectrum in the S_G phase of 5O.7-d_4 (aniline ring deuterated) at 31 °C.[24]

frame, and (β,α) are the polar angles of the C–D bond in the molecular frame. Phase biaxiality is reflected by $\overline{D^2_{\pm 2,m}}$ in η^{LC}, and the effect of η^{LC} on $\Delta\nu$ is maximum when the director is oriented normal to the magnetic field (i.e. $\theta_0 = 90^\circ$). It is noted that symmetry considerations involving both the nature of the molecules and of the liquid crystalline phases can considerably simplify the evaluation of the order parameters $\overline{D^2_{m',m}(\phi, \theta, \psi)}$. η^{LC} takes on a simple form if the (x,y,z) frame is chosen to be the principal frame of the order matrix. Further simplification can be made if the molecule is a cylindrical rod [$m = 0$ in equation (11)]. Then

$$\chi^{LC} = \chi S^{ZZ}_{zz}(3\cos^2\beta - 1)/2$$

$$\eta^{LC} = \sqrt{\tfrac{3}{2}}[\overline{D^2_{2,0}} + \overline{D^2_{-2,0}}]/S^{ZZ}_{zz} = (S^{XX}_{zz} - S^{YY}_{zz})/S^{ZZ}_{zz} \quad (12)$$

The $S^{XX}_{zz} - S^{YY}_{zz}$ term represents anisotropic fluctuations of the molecular z axis relative to the principal axes (X,Y,Z) of the average EFG tensor. Edge singularities (Figure 4) are predicted for the spectral pattern when $\theta_0 \neq 0$. The separation between edge singularities at $\theta_0 = 90^\circ$ is a direct measure of η^{LC}. Such a spectral pattern was first observed in an S_G phase[23] with a deuterated solute in the mesogen 6O.6. A η^{LC} value of 0.2 was obtained[24] in the S_G phase of 5O.7-d_4 (Figure 4). Phase biaxiality had been investigated in other smectic phases by Doane[25] and in discotics by Luz.[26]

3 SPIN RELAXATION AND MOLECULAR MOTION

Both nuclear spin–lattice and spin–spin relaxation rates are governed by random motion of spin-bearing molecules. Typically, a molecule remains in one state of motion for a short time (10^{-10}–10^{-12} s). After this time, it suffers a collision with one of its neighbors, which changes its state of motion. When the molecule persists in some state of motion for a time of 10^{-10} s, its motional frequency spectrum is expected to contain components ranging from zero to 10^{10} Hz, which are covered by typical NMR experiments. Several dynamic processes are known to cause deuteron spin relaxation in liquid crystals. The process known as director fluctuations is unique to liquid crystals and was first used to explain light scattering from liquid crystals. Other processes include order parameter fluctuations, molecular reorientation, and internal rotations. The latter two motions involve individual molecules as in normal liquids, while director fluctuations involve collective motions of a large number of molecules. These collective motions are influenced by macroscopic properties like elastic constants and anisotropic viscosities of the liquid crystalline medium. At best, director fluctuations can provide indirect information on the anisotropic interactions among molecules. On the contrary, molecular motion must reflect the shape of the instantaneous potential of mean torque on each molecule. Thus, it is sensitive to the nature of anisotropic interactions. Here, spin relaxation due to small cross terms between different processes will be ignored[8] for simplicity.

3.1 Solute Dynamics

To avoid dealing with internal rotations, deuterated rigid solutes dissolved in thermotropic liquid crystals were studied[7,27] by spectral density measurements. Solute reorientation and director fluctuations were used to account for the observed frequency and temperature dependences of $J_1(\omega)$ and $J_2(2\omega)$. It is now well known that director fluctuations under the small-angle approximation produce a characteristic $\omega^{-1/2}$ dependence in $J_1(\omega)$ only. Reorientation motion is often described in terms of a symmetric top reorienting in an anisotropic potential of Maier–Saupe type using a small-step rotational diffusion model.[8] This model uses a rotational diffusion tensor for the molecule which is diagonalized in a molecule-fixed frame. For weakly ordered solutes, their reorientation in a nematic solvent is often rapid to give frequency-independent spectral densities. For example, deuteron spin relaxation of p-diethynylbenzene (DEB-d_2, deuterated in the two alkynic sites) in the nematic phase of Phase V[7] clearly showed that $J_1(\omega)$ has a pronounced frequency dependence, while $J_2(2\omega)$ is essentially independent of frequency. This observation provides compelling evidence of director fluctuations in relaxing the deuterons in DEB-d_2. Smectic phases can be used to provide higher ordering of solute molecules. Similar frequency behaviors for J_1 and J_2 were obtained for DEB-d_2 in the four mesophases of 4O.8. However, J_2 showed more frequency dependence when DEB-d_2 was dissolved in 8CB.[8] A definitive explanation of the differences in these J_2 values has not yet been found. In general, analyses of experimental spectral density data would lead to rotational diffusion constants (or rotational correlation times $\tau_\parallel$, $\tau_\perp$) and a material factor A_{DF} that characterizes the strength of director fluctuations. For example, the ratio $\tau_\perp/\tau_\parallel$ is about 10 for DEB-d_2 in the nematic phase of Phase V.

3.2 Solvent Dynamics

The detection of director fluctuations in liquid crystals by means of deuteron spin relaxation in mesogens at conventional frequencies (10–50 MHz) has not met with success. This can be attributed to two factors: (1) the numerical value A_{DF} is small because most C–D bonds are oriented at an unfavorable angle to the long molecular axis; this is true for aromatic deuterons in mesogens such as 4-pentyl-4′-cyanobiphenyl (5CB), MBBA, etc., and (2) the contribution from director fluctuations to deuteron relaxation is masked by a much larger contribution due to relatively slow motions of large, sluggish molecules and fast internal motions within these molecules. To alleviate the difficulty associated with a small contribution from director fluctuations in the megahertz region, deuteron field cycling techniques have been applied[28]

to several nematogens. The techniques involve fast switching of the Zeeman field between high- and low-field levels so that detection of the NMR signal is done at a high magnetic field while the spin system is allowed to relax in a low field (in the kilohertz region). These data seem to support the findings based on the proton field cycling studies of liquid crystals that director fluctuations are slow motional processes and are effective for spin relaxation only in the kilohertz region.

To treat deuteron spin relaxation of solvent molecules in the megahertz region it is often possible to ignore the small contribution from director fluctuations. This assumption is probably necessary in modeling spectral densities of motion for various deuterated sites in flexible mesogens. In particular, correlated internal rotations in flexible chains of liquid crystals are complex to treat theoretically. Furthermore, different motional models[8] for reorientation of solvent molecules are possible. Besides the commonly used small-step rotational diffusion model, the anisotropic viscosity model of Freed and co-workers[8] is a distinct alternative. Freed used a rotational diffusion tensor that is diagonalized in the director frame to reflect the anisotropic viscosity of the liquid crystalline medium. Another motional model known as the 'third-rate' model is a simple extension of the Freed model. It has a fast rotation around the long molecular axis in addition to its motions around and toward the director. Numerous deuteron relaxation studies have been carried out in recent years to investigate molecular motion in liquid crystals. Table 1 briefly summarizes thermotropic liquid crystals in which spectral density measurements were reported.

As an example, the spectral density data of MBBA at 15.3 and 46 MHz are reproduced in Figure 5. The data are typical for thermotropic liquid crystals studied thus far. Both $J_1(\omega)$ and $J_2(2\omega)$ decrease with increasing temperature and are frequency dependent with a weaker dependence in $J_2(2\omega)$. To account for the observed site dependences of $J_1(\omega)$ and $J_2(2\omega)$, a model is required to treat internal motions in the butyl chain. A superimposed rotations model[33] was used to describe fluctuations in the orientations of the C–D bonds due to overall and internal modes of motion in the chain-deuterated nematogen 5CB. Here the internal dynamics of the pentyl chain was treated by assuming that rotations about each C–C bond are independent of each other and could be superimposed onto the rotational diffusion of the whole molecule. This motional model is, however, unrealistic and inconsistent with how quadrupolar splittings were modeled using the RIS model of Flory. The RIS model has been extended[42–44] to the time domain for liquid crystalline samples. A master equation may be used to describe transitions among all allowed configurations in the alkyl chain. The model of Nordio and co-workers[44] is inherently complex because their master equation includes configuration dependent frictional effects. The solution of the rotational diffusion problem requires a matrix representation in the full space of angular and site functions. Because of the large dimensionality of their matrix representation, the computational effort was extremely demanding. The decoupled model[42] of Dong uses three phenomenological rate constants to describe elementary jump modes: one-bond (k_1), two-bond (k_2), and three-bond (k_3) motions. The dimension of the rate matrix which is constructed in terms of these jump rate constants has the advantage of being much smaller. Both approaches,[34,42–44] however, give similar theoretical predictions for 5CB regarding site and frequency dependences of $J_1(\omega)$ and $J_2(\omega)$ as well as the observed discontinuity[33] in the spin–lattice relaxation rates at the nematic–isotropic phase transition.

The decoupled model has been successfully applied[22] to interpret the spectral densities of methylene deuterons (Figure 5) in MBBA, which are given by

$$J^{(i)}_{m_L}(m_L\omega) = \frac{3\pi^2}{2}\chi_i^2 \sum_{m_M}\sum_{n=1}^{27} c_{m_L m_M} \Big| \sum_{l=1}^{27} d^2_{m_M 0}(\beta^{(i)l}_{M,Q}) \exp[-i m_M \alpha^{(i)l}_{M,Q}] x_l^{(1)} x_l^{(n)} \Big|^2 \sum_j a^{(j)}_{m_L m_M} [(\tau^{(j)}_{m_L m_M})^{-1} + |\lambda_n|] / \{(m_L\omega)^2 + [(\tau^{(j)}_{m_L m_M})^{-1} + |\lambda_n|]^2\} \quad (13)$$

where $\beta^{(i)l}_{M,Q}$ and $\alpha^{(i)l}_{M,Q}$ are the polar angles of the C-i–D bond of the conformer l (there are 3^3 conformers in the butyl chain when the first dihedral angle at the junction of the aniline ring is allowed to sample three RISs) in a molecule-fixed frame whose z_M axis is along the ring *para* axis, λ_n and $\boldsymbol{x}^{(n)}$ are the eigenvalues and eigenvectors from diagonalizing a symmetrized rate matrix, $c_{m_L m_M}$ are the mean square of the Wigner rotation matrices, and the a, b and c coefficients are tabulated as functions of $\langle P_2 \rangle$ for a Maier–Saupe potential.[45] The correlation times $\tau^{(j)}_{m_L m_M}$ take on slightly different forms; the small-step rotational diffusion model uses

$$(\tau^{(j)}_{m_L m_M})^{-1} = [6D_\perp / b^{(j)}_{m_L m_M} + m_M^2 (D_\parallel - D_\perp)] \quad (14)$$

and the third-rate model uses

$$(\tau^{(j)}_{m_L m_M})^{-1} = h_{m_M} + [6D_\beta / b^{(j)}_{m_L m_M} + m_L^2 (D_\alpha - D_\beta)] \quad (15)$$

Table 1 Summary of Deuterium Spectral Density Measurement in Thermotropic Liquid Crystals

System	Phase	T (°C)	ν_0 (MHz)	References
1O.4 (MBBA)	N	15–40	15.3, 46	22
4O.8	N, S_A, S_B	30–79	9.2–38.4	29,30
5O.7	N, S_A, S_C, S_B	38–78	15.3, 46	31,32
5CB	N	23–35	12–46	33,34
6OCB	N	57–75.5	15.3–46	35
6OCB/8OCB	N, S_A, RN	25–78	13.8	36
1CB/5CB	N	2–28	46	37
CCH3	N	57–80	30.7	38
$FLOC_{14}$	N	130–140	38.4, 46	39
THE6	D_{h0}	68–99	46	40
8OBCAB/*n*TPCHB	N, S_A, RN	90–258	46	41

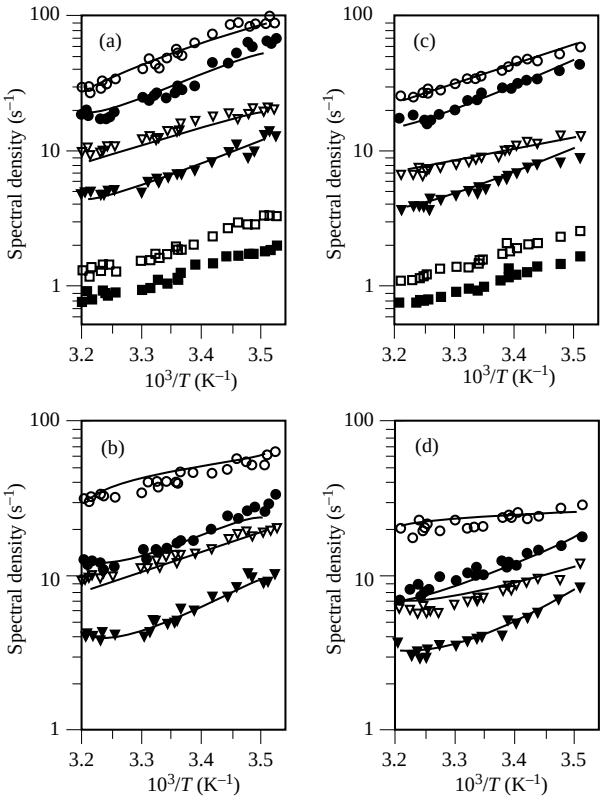

Figure 5 Plots of spectral densities versus the reciprocal temperature in the nematic phase of MBBA-d_{13}. Open symbols denote spectral densities $J_1(\omega_0)$, while solid symbols denote the corresponding $J_2(2\omega_0)$. ○ and ▽ and □ denote the C-0 and C-2 and C-4 data at (a) 15.3 MHz and (c) 46 MHz. • and ▼ denote the C-1 and C-3 data at (b) 15.3 MHz and (d) 46 MHz. Solid curves denote theoretical predictions based on the third-rate model and three jump rates for internal rotation.[22]

where $h_0 = 0$, $h_1 = D_\gamma$, and $h_2 = (3p + 1)D_\gamma$, with $p = 0$ corresponding to strong collision and $p = 1$ to small-step rotational diffusion for the γ motion. The Ds are rotational diffusion constants that are principal components of the rotational diffusion tensor of an 'average' molecule. The methine (C-0) deuteron has no internal motion, and the C-0–D bond reflects the motion of the aromatic core, giving

$$J^{(0)}_{m_L}(m_L\omega) = \frac{3\pi^2}{2}\chi_0^2 \sum_{m_M} c_{m_L m_M}[d^2_{m_M 0}(\beta_{M,Q})]^2 \times \sum_j a^{(j)}_{m_L m_M}[\tau^{(j)}_{m_L m_M}]^{-1}/[(m_L\omega)^2 + (\tau^{(j)}_{m_L m_M})^{-2}] \quad (16)$$

where $\beta_{M,Q}$ is the angle between the C–D bond and the z_M axis. Using equations (13) and (16), the fits between the calculated and experimental spectral densities are optimized by varying the rotational diffusion constants and the jump rate constants at each temperature.

Both the small-step rotational diffusion and third-rate models were examined. Both models were found to describe molecular reorientation of MBBA. The solid curves in Figure 5 are theoretical spectral densities based on equations (13) and (16) using $\tau^{(j)}_{m_L m_M}$ given by the third-rate model [equation (15)], X_a, X_c, and $\langle P_2\rangle$ given by modeling the quadrupolar splittings (E_{tg} = 2550 J mol^{-1}, $E_{g\pm g\pm}$ = 6000 J mol^{-1}). D_α and D_β are roughly the same ($\simeq 5 \times 10^7$ s^{-1} in the middle of the nematic phase), while D_γ is two orders of magnitude larger. D_α refers to the motion of the long molecular axis around the director, while D_β refers to its motion toward the director. These rotational diffusion constants decrease with decreasing temperature as expected for a thermally activated rotational process. The Nordio model has been used to derive motional parameters at different temperatures in 5CB[34] and 4-*n*-hexyloxy-4′-cyanobiphenyl (6OCB).[35] In studying the reorientation process in the smectogen 5O.7, the spectral densities of the methine and ring deuterons were measured as a function of temperature at two different Larmor frequencies in the megahertz region.[31] It was found that the large frequency dependence in $J_1(\omega)$ can only be rationalized by including director fluctuations. The third-rate model seems to produce physical rotational diffusion constants in the nematic, smectic A, and smectic C phases of 5O.7.

4 NOVEL NMR EXPERIMENTS

Some applications of newer NMR techniques to the study of liquid crystalline samples are now outlined. The proton NMR spectra of solute molecules dissolved in liquid crystals are usually complex, and iterative fitting of the NMR spectra must be used to extract dipolar couplings. Spectral simplification is possible by using partially deuterated solutes instead. When this is not practical, multiple quantum NMR spectroscopy[46] can greatly simplify spectra of complex spin systems. Multiple quantum NMR is concerned with the observation of forbidden nuclear transitions, i.e. $\Delta m_I \neq 1$. Multiple quantum coherences can only be detected indirectly. To detect all orders of multiple quantum transitions, special forms of two-dimensional NMR (2D NMR) spectroscopy are required. The high-order multiple quantum spectrum is simple due to the decrease in number of nuclear transitions with increasing order. Multiple quantum transitions of deuterons are now described.

In oriented systems, the quadrupole Hamiltonian leads to a splitting of the single quantum transitions [see Figure 1(b)]. Double quantum spectra of a deuteron (Δm_I = 2) have the advantage of eliminating quadrupolar effects. This is obvious from the deuterium energy diagram for a spin-1 system, since the quadrupolar shifts on $m_I = 1$ and $m_I = -1$ energy levels are equal. Any coherence established between these two levels will evolve at twice the Larmor frequency (as modified by chemical shift). Single- and double-quantum spectra were used[6] to study chain conformation in four members of the *n*O.7 series. It was noted that the distribution in the quadrupolar splitting is the dominant contribution to the deuteron linewidth of the single quantum spectrum. The distribution is due to a spread in the orientation of the long molecular axes in the liquid crystalline sample. Because a double quantum spectrum is not affected by quadrupolar effects, it has better spectral resolution and therefore may yield long-range dipole–dipole couplings among deuterons. Figure 6 shows a comparison of single- and double-quantum spectra of the α signal of 5O.7-αd_2 [Figure 6(a)] and the γ signal of 5O.7-$\alpha d_2 \gamma d_1$ [Figure 6(b) and (c)]. The improved resolution of the γ signal in the double quantum spectra is remarkable, and allows measurements of long-range deuterium dipolar couplings. For a two-coupled deuteron system, multiple quantum transitions can

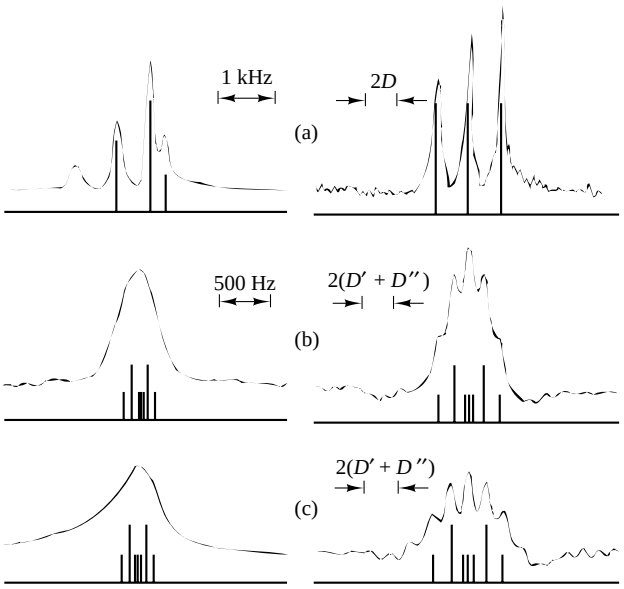

Figure 6 Single quantum (left) and double quantum (right) spectra for (a) the α signal of 5O.7-αd_2 at 57 °C, and the γ signal in 5O.7-$\alpha d_2 \gamma d_1$ at (b) 57 °C and (c) 41 °C, respectively. The stick diagrams give the corresponding theoretical spectra[6]

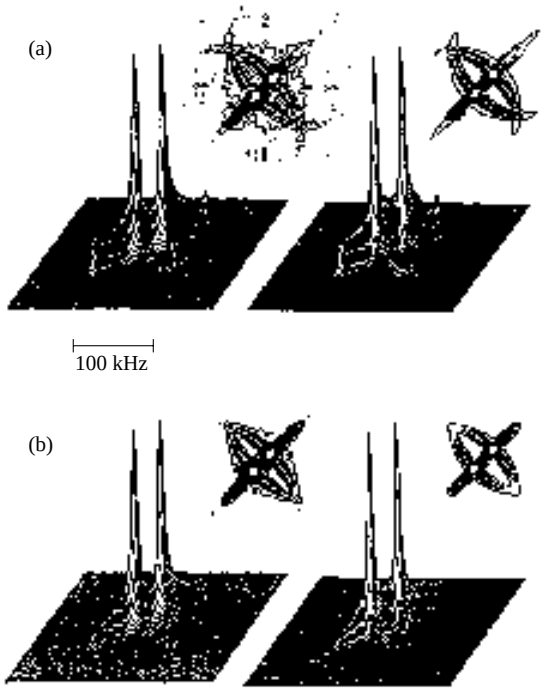

Figure 7 Experimental (left) and stimulated (right) spectra for (a) PS3 and (b) PS6 taken at 250 K with a mixing time of 100 ms. Contour plots are shown as insets[52]

reveal the correlation of relaxation mechanisms acting on two deuterium nuclei. Besides the three autocorrelation terms $J_0^{\mathrm{A}}(0)$, $J_1^{\mathrm{A}}(\omega)$, and $J_2^{\mathrm{A}}(2\omega)$, which describe the motion of the EFG tensor of either deuteron, the three cross-correlation terms $J_0^{\mathrm{C}}(0)$, $J_1^{\mathrm{C}}(\omega)$, and $J_2^{\mathrm{C}}(2\omega)$ describe correlation between the motion of the two EFG tensors. There are many relaxation studies of deuterated solutes in thermotropic liquid crystals.[13,14,27] For example, zero-, two-, and four-quantum linewidths may be used to determine the three cross-correlation terms[13,14] in acetonitrile-d_3.

2D NMR spectroscopy is now common in the study of liquid crystals. Using ^{13}C nuclei, the carbon–proton dipolar couplings can be obtained by means of the near magic angle spinning and the separated local field spectroscopy. Rapid sample spinning near the magic angle (54.7°) was incorporated to improve spectral resolution[47] so that coupling between indirectly bonded C–H pairs could be observed. A sample that has a chiral fluorinated solute dissolved in a liquid crystal was used to carry out a 2D ^{19}F spin echo[47] experiment in conjunction with the near magic angle spinning. This allows spectral analysis of small molecules to give residual dipolar coupling D_{ij} between nuclei i and j, and the isotropic spin–spin coupling J_{ij}. A deuteron 2D spin echo experiment on PAA-d_{14} allows assignment[19] of quadrupolar splittings in the NMR spectrum of perdeuterated *p*-azoxyanisole. The same technique has been used in the nematic phase of β-deuterated 5CB dispersed in polymers[48] and in model bilayer membranes[49] to determine the homogeneous linewidth of the individual lines. Another form of deuteron 2D experiment is 2D exchange spectroscopy,[50–52] which is capable of detecting slow molecular processes by monitoring the orientation of a C–D bond via its NMR frequency. A typical 2D time domain spectroscopy experiment involves four distinct periods [preparation, evolution (t_1), mixing, and detection (t_2)], leading to a time domain signal $s(t_1, t_2)$. Fourier transform of $s(t_1, t_2)$ gives $s(\omega_1, \omega_2)$, a 2D frequency spectrum. The spectrum provides information relating the frequency ω_{e} in the evolution period just before mixing and the frequency ω_{d} in the detection period just after mixing. When ω_{e} is identical to ω_{d}, this gives rise to a spectrum on the diagonal of a 2D spectrum; otherwise, off-diagonal intensity can be formed in the form of straight ridges and ellipses.[50,52] The detection of off-diagonal intensity is practical for motions that have a correlation time of the order of milliseconds or longer. As an example, deuteron 2D exchange spectroscopy in glass-forming liquid crystalline side-group polymers is described.[52] Figure 7 shows the experimental and simulated 2D spectra for poly(4-alkyloxybenzoic acid 4′-methoxyphenyl-d_4 ester)siloxane (PS*n*) with n = 3 and 6. Both PS3 and PS6 were magnetoaligned in a strong magnetic field by slow cooling from the isotropic melt into the glassy state. The glassy state of the PS6 is a frozen smectic C phase, while the glassy state of the PS3 is a frozen nematic phase. Off-diagonal intensity in the form of a partial elliptical pattern can be simulated by assuming a Gaussian distribution for the orientation distribution of the long axis of the mesogenic unit. Because the orientational order $\langle P_2 \rangle$ of PS3 is lower, the partial elliptical pattern is more pronounced for PS3 than for PS6 as seen in Figure 7. It was also found that the ring flip of 180° in PS*n* has a rather narrow angular distribution. The same technique has been used to study molecular dynamics in glass-forming discotic liquid crystals.[8]

5 RELATED ARTICLES

Amphiphilic Liquid Crystalline Samples: Nuclear Spin Relaxation; Bilayer Membranes: Deuterium and Carbon-13 NMR; Deuterium NMR in Solids; Deuteron Relaxation

Rates in Liquid Crystalline Samples: Experimental Methods; Dynamic NMR in Liquid Crystalline Solvents; Field Cycling Experiments; Liquid Crystalline Samples: Carbon-13 NMR; Liquid Crystalline Samples: Relaxation Mechanisms; Liquid Crystals: General Considerations; Lyotropic Liquid Crystalline Samples; Membranes: Deuterium NMR; Multiple Quantum Spectroscopy in Liquid Crystalline Solvents; Polymer Dispersed Liquid Crystals; Relaxation Theory: Density Matrix Formulation; Relaxation Theory for Quadrupolar Nuclei; Spinning Liquid Crystalline Samples; Two-Dimensional NMR of Molecules Oriented in Liquid Crystalline Phases.

6 REFERENCES

1. J. C. Rowell, W. D. Phillips, L. R. Melby, and M. Panar, *J. Chem. Phys.*, 1965, **43**, 3442.
2. W. D. Phillips, J. C. Rowell, and L. R. Melby, *J. Chem. Phys.*, 1964, **41**, 2551.
3. C. G. Wade, *Ann. Rev. Phys. Chem.*, 1977, **28**, 47.
4. J. W. Doane, in *Magnetic Resonance of Phase Transitions*, ed. F. J. Owens, C. P. Poole, Jr., and H. A. Farach, Academic Press, New York, 1979, Chap. 4
5. R. Y. Dong, J. Lewis, E. Tomchuk, and E. Bock, *J. Chem. Phys.*, 1978, **69**, 5314.
6. S. Hsi, H. Zimmermann, and Z. Luz, *J. Chem. Phys.*, 1978, **69**, 4126.
7. R. R. Vold, in *Nuclear Magnetic Resonance of Liquid Crystals*, ed. J. W. Emsley, Reidel, Dordrecht, 1985, Chap. 11
8. R. Y. Dong, *Nuclear Magnetic Resonance of Liquid Crystals*, Springer-Verlag, New York, 1994.
9. A. Abragam, *Principles of Nuclear Magnetism*, Oxford University Press, Oxford, 1961, Chap. 8
10. C. P. Slichter, *Principles of Magnetic Resonance*, 3rd edn., Springer-Verlag, Berlin, 1990.
11. J. P. Jacobsen, H. K. Bildsoe, and S. Schaumburg, *J. Magn. Reson.*, 1978, **23**, 153.
12. R. R. Vold and R. L. Vold, *J. Chem. Phys.*, 1977, **66**, 4018.
13. R. Poupko, R. L. Vold, and R. R. Vold, *J. Magn. Reson.*, 1979, **34**, 67.
14. D. Jaffe, R. R. Vold, and R. L. Vold, *J. Magn. Reson.*, 1982, **46**, 475.
15. G. R. Luckhurst, in *The Molecular Physics of Liquid Crystals*, ed. G. R. Luckhurst and G. W. Gray, Academic Press, London, 1979, Chap. 4
16. G. R. Luckhurst, in *Nuclear Magnetic Resonance of Liquid Crystals*, ed. J. W. Emsley, Reidel, Dordrecht, 1985, Chap. 3
17. W. Maier and A. Saupe, *Z. Naturforsch., Teil A*, 1959, **14**, 882.
18. W. Maier and A. Saupe, *Z. Naturforsch., Teil A*, 1960, **15**, 287.
19. J. W. Emsley, in *Nuclear Magnetic Resonance of Liquid Crystals*, ed. J. W. Emsley, Reidel, Dordrecht, 1985, Chap. 15
20. B. G. Wu, B. Ziemnicka, and J. W. Doane, *J. Chem. Phys.*, 1988, **88**, 1373.
21. P. J. Flory, *Statistical Mechanics of Chain Molecules*, Interscience, New York, 1969.
22. R. Y. Dong, L. Friesen, and G. M. Richards, *Mol. Phys.*, 1994, **81**, 1017.
23. T. M. Barbara and B. P. Dailey, *Mol. Cryst. Liq. Cryst.*, 1982, **87**, 239.
24. R. Y. Dong, H. Schmiedel, N. A. P. Vaz, Z. Yaniv, M. E. Neubert, and J. W. Doane, *Mol. Cryst. Liq. Cryst.*, 1993, **98**, 411.
25. J. W. Doane, in *Nuclear Magnetic Resonance of Liquid Crystals*, ed. J. W. Emsley, Reidel, Dordrecht, 1985, Chaps. 18 and 19.
26. Z. Luz, D. Goldfarb, and H. Zimmermann, in *Nuclear Magnetic Resonance of Liquid Crystals*, ed. J. W. Emsley, Reidel, Dordrecht, 1985, Chap. 14
27. R. L. Vold and R. R. Vold, *Isr. J. Chem.*, 1983, **23**, 315.
28. R. Köllner, K. H. Schweikert, F. Noack, and H. Zimmermann, *Liq. Cryst.*, 1993, **13**, 483.
29. T. M. Barbara, R. R. Vold, and R. L. Vold, *J. Chem. Phys.*, 1983, **79**, 6338.
30. T. M. Barbara, R. R. Vold, R. L. Vold, and M. E. Neubert, *J. Chem. Phys.* 1985, **82**, 1612.
31. R. Y. Dong and X. Shen, *Phys. Rev. E*, 1994, **49**, 538.
32. R. Y. Dong, *Liq. Cryst.*, 1989, **4**, 505.
33. P. A. Beckmann, J. W. Emsley, G. R. Luckhurst, and D. L. Turner, *Mol. Phys.*, 1986, **59**, 97.
34. R. Y. Dong and G. M. Richards, *J. Chem. Soc. Faraday Trans.*, 1992, **88**, 1885.
35. R. Y. Dong and G. Ravindranath, *Liq. Cryst.*, 1994, **17**, 47.
36. R. Y. Dong, G. M. Richards, J. S. Lewis, E. Tomchuk, and E. Bock, *Mol. Cryst. Liq. Cryst.*, 1987, **144**, 33.
37. G. L. Hoatson, T. Y. Tse, and R. L. Vold, *J. Magn. Reson.*, 1992, **98**, 342.
38. R. Y. Dong, J. W. Emsley, and K. Hamilton, *Liq. Cryst.*, 1989, **5**, 1019.
39. J. M. Goetz, G. L. Hoatson, and R. L. Vold, *J. Chem. Phys.*, 1992, **97**, 1306.
40. D. Goldfarb, R. Y. Dong, Z. Luz, and H. Zimmermann, *Mol. Phys.*, 1985, **54**, 1185.
41. D. Imbardelli, B. Wazynska, A. Golemme, G. Chidichimo, and R. Dabrowski, *Mol. Phys.*, 1993, **79**, 1275.
42. R. Y. Dong, *Phys. Rev. A*, 1991, **43**, 4310.
43. R. Y. Dong and G. M. Richards, *Chem. Phys. Lett.*, 1992, **200**, 541.
44. A. Ferrarini, G. J. Moro, and P. L. Nordio, *Liq. Cryst.*, 1990, **8**, 593.
45. R. R. Vold and R. L. Vold, *J. Chem. Phys.*, 1988, **88**, 1443.
46. G. P. Drobny, *Annu. Rev. Phys. Chem.*, 1985, **36**, 451.
47. J. Courtieu, J. P. Bayle, and B. M. Fung, *Prog. Nucl. Magn. Reson. Spectrosc.*, 1994, **26**, 141.
48. J. Dolinsek, O. Jarh, M. Vilfan, S. Zumer, R. Blinc, J. W. Doane, and G. Crawford, *J. Chem. Phys.*, 1991, **95**, 2154.
49. L. Müller and S. I. Chan, *J. Chem. Phys.*, 1983, **78**, 4341.
50. J. Jeener, B. H. Meier, P. Bachmann, and R. R. Ernst, *J. Chem. Phys.*, 1979, **71**, 4546.
51. C. Schmidt, B. Blümich, S. Wefing, and H. W. Spiess, *Chem. Phys. Lett.*, 1986, **130**, 84.
52. J. Leisen, C. Boeffel, R. Y. Dong, and H. W. Spiess, *Liq. Cryst.*, 1993, **14**, 215.

Acknowledgments

The financial support of the Natural Sciences and Engineering Council of Canada is gratefully acknowledged.

Biographical Sketch

Ronald Y. Dong. *b* 1942. B.A.Sc., 1966, Toronto. Ph.D. (Supervisor, Myer Bloom), 1969, University of British Columbia. Postdoctoral

work at the University of Waterloo, 1970–71, and at the National Research Council of Canada, 1971–73. Faculty in Physics, University of Winnipeg 1974–78. Faculty in Physics and Astronomy, Brandon University, 1978–present. Adjunct faculty in Physics, University of Manitoba, 1989–present. Approx. 100 publications. Research interests include solid state NMR, molecular dynamics, molecular crystals and liquid crystals.

Liquid Crystalline Samples: Relaxation Mechanisms

Pier Luigi Nordio and Alberta Ferrarini
University of Padova, Padova, Italy

1	Introduction	1
2	Experimental Observables	1
3	Dynamic Models	2
4	Related Articles	6
5	References	6

1 INTRODUCTION

In the liquid state, spin relaxation is caused by the random fluctuations of magnetic interactions resulting from Brownian rotational and translational diffusion of molecules, conformational transitions, or solvation effects. These motions act as random time-dependent perturbations, which induce transitions among the spin states and ultimately lead to Boltzmann equilibrium values of macroscopic magnetization vector components, altered by application of the excitation field in relaxation experiments. Random magnetic perturbations are characterized by the equilibrium average $\overline{\Delta}$, the mean-square value $\overline{\Delta^2}$, and the persistence or correlation time τ. It is convenient to express Δ in frequency units rather than in energy units; the strength of the interaction is therefore divided by the Planck constant $\hbar$.

In high-resolution NMR spectroscopy, a fast motional regime, characterized by the condition $(\overline{\Delta^2} - \overline{\Delta}^2)\tau^2 \ll 1$, often holds. This situation is the simplest to analyze by time-dependent perturbation theories and is generally referred to as the Redfield limit.[1] In this condition, both the longitudinal component of the macroscopic magnetization along the static field $\boldsymbol{B}_0$, and the transverse component created by the observing field $\boldsymbol{B}_1$, relax as simple exponentials, with characteristic times T_1 and T_2, respectively. The theoretical expressions predicted by the theory for T_1^{-1} and T_2^{-1} are very simple and the relaxation times come out to be of the order of $(\overline{\Delta^2} - \overline{\Delta}^2)\tau$. Thus, if the dominant relaxation mechanism is provided by modulation due to rotational diffusion of an intramolecular interaction described by an axially symmetric second-rank tensor $\boldsymbol{T}$ with principal components $T_{zz} = T_\parallel$ and $T_{xx} = T_{yy} = T_\perp$, spin relaxation times of the order of 1 s will result for $\Delta = T_\parallel - T_\perp = 10^5\,\mathrm{s}^{-1}$ (a value appropriate for the ^{13}C–H spin dipole interaction) and $\tau = 10^{-10}$ s, corresponding to the rotational correlation time of most liquids under normal conditions.

The motional processes responsible for spin relaxation in liquids are almost invariably interpreted in terms of diffusion models, so that a few comments on the underlying theoretical treatments are in order. A diffusional regime for molecular translations and rotations applies when strong impulsive interactions with the surrounding molecules interrupt the inertial motion of the particle so frequently that a random walk of infinitesimally short steps actually results. To interpret these dynamic processes, an equation of motion for the test particle can be set up, including a dissipative term in the form of a frictional force. In fact, the resulting equation is the basis of the method for describing molecular motions in fluids known as 'Brownian dynamics'.[2] (see ***Brownian Motion and Correlation Times***.)

Alternatively, a stochastic equation can be derived to interpret the time evolution of the probability distribution function specifying molecular coordinates. The treatment leading to this equation, often referred to as the 'diffusion (or Smoluchowski) equation' when inertial effects are completely quenched, is reported in specialized texts.[3] (We reserve the term 'Fokker–Planck equation' for the more general formalism which takes into account translational and angular velocity of the particle, in addition to translational and angular coordinates. According to this description, the diffusional behavior is recovered if velocities are quenched within a time shorter than the decay time for the spatial variables.) The diffusion equation is a differential equation formally similar to a time-dependent Schrödinger equation and it can solved by similar methods. In fact, after separating the time variable, the solution of the resulting second-order differential equation is reduced to the determination of eigenvalues and eigenvectors of the matrix representation of the diffusion operator on a suitable set of functions. The mathematical details are given elsewhere,[4,5] so we give here only the relevant physical factors in the diffusion equation. These are:

1. The potential function arising from forces and torques exerted on the test particle, including terms accounting for hindered internal motions.
2. Diffusion coefficients (or, more generally, diffusion tensors) which take into account frictional effects. Diffusion coefficients are determined by the molecular geometry and viscosity of the medium by the Stokes–Einstein relationships.[6,7]

The general considerations given above hold for both isotropic and anisotropic liquid phases. We will see in the following discussion how the specific nature of the liquid crystal environment may not only alter the characteristics of dynamic processes that occur in normal liquids (e.g. features of rotational and translational diffusion, or static and dynamic parameters of conformational changes), but also introduce novel relaxation mechanisms which are absent in isotropic fluids.

2 EXPERIMENTAL OBSERVABLES

NMR relaxation experiments in liquid crystals can be performed both on the molecules forming the mesophase and on solutes suitably chosen to probe the dynamic properties of the environment. Under normal experimental conditions, fast motional regimes hold, providing well-resolved spectra. Measurements on specific nuclear positions of the molecule can therefore be performed to give data which can then be processed theoretically in order to extract dynamic information. For this reason, ^{13}C (either in natural abundance or chemically enriched) and ^{2}H (introduced by specific deuteration) are the favored nuclei for use in relaxation experiments on liquid crystals. For ^{13}C and ^{2}H nuclear spins, the dominant source of spin relaxation is provided by the ^{13}C–H dipole and ^{2}H quadrupole interactions, respectively. With the very high fields used in modern spectrometers, shielding anisotropies may also have

relevant effects. In all cases, these interactions are described by second-rank Cartesian tensors.

According to the Redfield theory (see ***Relaxation Theory: Density Matrix Formulation***), the equations for ^{13}C (under proton decoupling) and ^{2}H longitudinal relaxation times are

$$1/T_1^{C} = (\tfrac{1}{12})[J_0(\omega_H - \omega_C) + 3J_1(\omega_C) + 6J_2(\omega_H + \omega_C)] \quad (1)$$

and

$$1/T_1^{D} = (\tfrac{1}{4})[J_1(\omega_D) + 4J_2(2\omega_D)] \quad (2)$$

where $J_p(\omega)$ are spectral densities, i.e. the Fourier transforms (FTs) of the correlation functions describing the time evolution of the irreducible spherical components[8] of the second-rank magnetic interactions in a laboratory reference frame. In fact, the magnetic tensor components are defined in a molecular axis system, and therefore appear to vary in time when viewed from the laboratory system, because of molecular tumbling in the liquid. The FTs are calculated at frequency values related to ^{1}H, ^{13}C, and ^{2}H resonance frequencies in the experiment. Spectral densities can be expressed in terms of the magnitude of the interactions, and of the time decay of angular functions (Wigner rotation matrix components[8]) which define the molecular orientation with respect to the laboratory fixed reference frame. The FT $j(\omega)$ of an exponential function characterized by time constant τ is

$$j(\omega) = \frac{\tau}{1 + \omega^2\tau^2} \quad (3)$$

Complete dynamic information on a system should be achieved by relaxation experiments capable of providing the various spectral densities at different frequencies. Modern experiments are actually performed at a number of working frequencies.[9,10] It is also interesting to note that equations (1) and (2) refer to standard experiments of saturation or inversion–recovery of the total longitudinal component of magnetization. In this way, individual spectral densities cannot be obtained directly from experimental data. However, they can be provided by applying appropriate sequences of radiofrequency (rf) pulses to the spin system. Equations for relaxation rates determined by various pulse experiments on a single spin $I = 1$ in ordered phases are reported in Table 3 of Vold[11] (see also ***Deuteron Relaxation Rates in Liquid Crystalline Samples: Experimental Methods***).

Experiments in liquid crystal phases are performed on samples which are macroscopically oriented by means of magnetic fields, surface effects or electric fields. In some instances, it is also possible to measure the angular dependence of the spectral densities when the axis of preferential alignment of the mesophase (the optical axis, or director) can be rotated away from the magnetic field direction. This can be easily done with uniaxial smectic-A phases. Again, explicit equations for the angular dependence of the spectral densities appropriate for this case may be found in Vold.[11]

3 DYNAMIC MODELS

In a liquid sample at thermodynamic equilibrium, the dynamic processes which cause thermal motions of the molecules are defined as random stationary. Although the system is macroscopically in equilibrium, the coordinates specifying the position and orientation of any molecule, here collectively denoted by $\boldsymbol{x}$, exhibit random walk in time. Any function of these coordinates will behave as a function $f[\boldsymbol{x}(t)]$ randomly varying in time. If a physical property of the system is related to the function $f(\boldsymbol{x})$, experimental measurements can be made to determine directly the equilibrium average:

$$\bar{f} = \int \mathrm{d}\boldsymbol{x}\ f(\boldsymbol{x})P(\boldsymbol{x}) \quad (4)$$

thus providing information on equilibrium distribution $P(\boldsymbol{x})$.

The main result of the stochastic theories is that, for random-stationary processes, knowledge of the random events occurring at the molecular level is entirely contained in a statistical property called the correlation function of $f(\boldsymbol{x})$:

$$\overline{f^*(t)f(0)} = \iint \mathrm{d}\boldsymbol{x}\,\mathrm{d}\boldsymbol{x}_0\ f^*(\boldsymbol{x})f(\boldsymbol{x}_0)P(\boldsymbol{x}, t; \boldsymbol{x}_0, 0) \quad (5)$$

where $P(\boldsymbol{x}, t; \boldsymbol{x}_0, 0)$ is the joint probability of finding the molecule in $\boldsymbol{x}_0$ at an arbitrary initial time $t_0 = 0$, and in $\boldsymbol{x}$ at the later time t. It follows from the properties of the joint probability that this function becomes equal to $P(\boldsymbol{x})\delta(\boldsymbol{x} - \boldsymbol{x}_0)$ at time zero and to the product $P(\boldsymbol{x})P(\boldsymbol{x}_0)$ at infinite time, when correlation can no longer exist. Therefore, the correlation function varies between limits $|\overline{f^2}|$ at $t = 0$ and $|\bar{f}|^2$ at $t \to \infty$. It is often convenient to define the correlation function $g(t)$ for the deviation of $f(t)$ from the equilibrium value $\bar{f}$, thus obtaining

$$g(t) = \overline{f^*(t)f(0)} - |\bar{f}|^2 \quad (6)$$

The mean square value $|\overline{f^2}|$ and average $\bar{f}$ can be calculated from the equilibrium distribution $P(\boldsymbol{x})$, but the time evolution of the joint probability function requires a mathematical model derived on the basis of a physically reasonable picture, and this is provided by solution of the diffusion equation.

The above considerations may immediately be applied to the problem of reorientational motions, which cause random fluctuations of the intramolecular anisotropic magnetic interactions, and are of particular importance for ^{13}C and ^{2}H spin relaxation in any liquid phase.

The irreducible spherical components of second-rank tensorial interactions $\boldsymbol{T}$, expressed in a laboratory frame having the Z axis parallel to the static magnetic field $\boldsymbol{B}_0$, are given by[8]

$$T_{lab}^{(2,p)} = \sum_q \mathcal{D}_{pq}^{2*}(\Omega)T_{mol}^{(2,q)} \quad (7)$$

where $T_{mol}^{(2,q)}$ are the components in a molecular frame and $\mathcal{D}_{pq}^{2}(\Omega)$ are Wigner rotation matrix elements carrying the transformation from the laboratory system (X, Y, Z) to the molecular frame (x, y, z), described by the set of Euler angles $\Omega \equiv (\alpha, \beta, \gamma)$. The time dependence of the quantities $T_{lab}^{(2,p)}$ is contained in that of the Euler angles Ω, which change randomly in time as a consequence of rotational motions. The effective perturbation induced by modulation of the $\boldsymbol{T}$

tensor components is determined by the deviation from the equilibrium value:

$$\delta T_{\text{lab}}^{(2,p)}[\Omega(t)] = \sum_q \{\mathcal{D}_{pq}^{2*}[\Omega(t)] - \overline{\mathcal{D}_{pq}^{2*}}\} T_{\text{mol}}^{(2,q)} \tag{8}$$

Of special interest, therefore, are the autocorrelation functions $g_{pq}(t)$ of the Wigner components $\mathcal{D}_{pq}^2(\Omega)$, defined as

$$g_{pq}(t) = \overline{\mathcal{D}_{pq}^{2*}(t)\mathcal{D}_{pq}^2(0)} - |\overline{\mathcal{D}_{pq}^2}|^2 \tag{9}$$

the overbar now denoting an average over the orientational degrees of freedom. The time behavior of the correlation functions $g_{pq}(t)$ is determined by the reorientational process undergone by the molecules, and the thermal averages $\overline{\mathcal{D}_{pq}^2}$ are determined by the nature of the liquid phase.

The spectral densities $J_p(\omega)$ which appear in the equations for the spin relaxation rates are

$$\begin{aligned} J_p(\omega) &= \frac{1}{2}\int_{-\infty}^{\infty} \mathrm{d}t\, \mathrm{e}^{-\mathrm{i}\omega t} \overline{\delta T_{\text{lab}}^{(2,p)*}(t)\delta T_{\text{lab}}^{(2,p)}(0)} \\ &= \sum_q |T_{\text{mol}}^{(2,q)}|^2 j_{pq}(\omega) \end{aligned} \tag{10}$$

where $j_{pq}(\omega)$ are the FTs of the correlation functions $g_{pq}(t)$.

In the case of molecules with internal degrees of freedom, the additional transformation from a fixed molecular frame to a reference system located in each molecular moiety must be considered explicitly. For a tensorial interaction located in the ith unit, equation (7) is rewritten as

$$T_{i,\text{lab}}^{(2,p)} = \sum_{q,n} \mathcal{D}_{pn}^{2*}(\Omega)\mathcal{D}_{nq}^{2*}(\Omega_i) T_i^{(2,q)} \tag{11}$$

The complex expressions resulting for correlation functions and spectral densities are given by Ferrarini et al.[12,13]

3.1 Rotational Diffusion

In isotropic media, i.e. in the case of a spherically symmetric orientational distribution, it follows from the orthogonality properties of the Wigner functions that

$$\overline{\mathcal{D}_{pq}^2} = 0, \quad \overline{|\mathcal{D}_{pq}^2|^2} = \tfrac{1}{5} \tag{12}$$

and the solution of the diffusion equation for axially symmetric molecules characterized by the principal values $D_\parallel$ and $D_\perp$ of the diffusion tensor gives

$$g_{pq}(t) = (\tfrac{1}{5}) \exp(-t/\tau_{pq}) \tag{13}$$

$$1/\tau_{pq} = 6D_\perp + (D_\parallel - D_\perp)q^2 \tag{14}$$

Since the orientational correlation time in equation (14) is independent of the index p, the spectral densities $J_p(\omega)$ all turn out to be identical.

In ordered phases, as a consequence of anisotropic interactions with the environment, the molecules are subjected to an effective orientational potential $U(\Omega)$ which, unlike the isotropic case, determines the nonuniform equilibrium distribution of orientations.

As the diffusion model is appropriate for describing the rotational dynamics of molecules in a liquid of normal density and viscosity, it is also suitable for use for liquid crystals. However, the motion in this case is better termed 'anisotropic' rotational diffusion, because of the orientational torques exerted on the molecules.

In nematics, rod-like or disk-like molecules tend to orient the symmetry axis to the director, giving rise to calamitic or discotic nematic phases, respectively. The condition of axial symmetry for the phase implies free rotations around the laboratory Z axis, and therefore $\overline{D_{pq}^2}$ must be zero for $p \neq 0$. Nematic phases are generally expected to be uniaxial, although biaxiality cannot in principle be excluded. If the molecules themselves are assumed to be uniaxial, rotations about the molecular z axis are unhindered and only terms with $q = 0$ remain. For uniaxial molecules in uniaxial phases, the only order parameter directly measured by NMR is $\overline{\mathcal{D}_{00}^2}$, which coincides with the Legendre polynomial $\overline{P}_2$.[8] The simple Maier–Saupe form

$$U(\beta)/k_{\text{B}}T = -\lambda P_2(\cos\beta) \tag{15}$$

is appropriate for this particular case, β denoting the angle between the director and the molecular symmetry axis.

The potential of the mean torque acting in nematics has two important effects on the efficiency of rotational motions as a source of spin relaxation. First, the magnitude of time-dependent perturbation is reduced with respect to the isotropic case, as the angular functions $\mathcal{D}_{pq}^2(\Omega)$ average now to non-zero values. Thermal averages $\overline{\mathcal{D}_{pq}^2}$ are called 'order parameters', because they measure the anisotropy of the orientational distribution. A second consequence of the orientational potential is to alter the features of rotational motion. Since the particles are preferentially oriented with the symmetry axis (assuming a uniaxially symmetric molecule) parallel to the director, motions can be roughly separated into fast fluctuations about the preferred orientation (with the characteristic frequencies expected to increase with the strength of the orienting field, according to the simple picture of motions in a potential well), essentially free rotations about the symmetry axis, and flippings of the long axis, which, being hindered by the orienting potential, become slower with increasing ordering. The latter motion, however, is a very important relaxation mechanism for vectorial properties, e.g. dielectric relaxation, but it is ineffective for second-rank tensorial properties. The decay of correlation functions $g_{pq}(t)$ can be calculated by solving a diffusion equation for the rotational degrees of freedom, in which the effect of the orienting potential is included.[4,5] The full solution of the diffusion equation requires expansion on the basis of the Wigner functions $\mathcal{D}_{pq}^j(\Omega)$, which are eigensolutions of the diffusional problem for the isotropic case. Correlation functions $g_{pq}(t)$ can, in most cases, be approximated by single exponentials:

$$g_{pq}(t) = C_{pq} \exp(-\alpha_{pq} t) \tag{16}$$

with the preexponential factors C_{pq} and decay rate constants α_{pq} now being dependent on the order parameters $\overline{P}_2$ and

$\overline{P_4}$, in addition to the diffusion coefficients $D_\perp$ and $D_\parallel$. Particularly simple expressions are obtained by an asymptotic solution of the diffusion problem for very highly ordered systems; these are reported in Table 2 of Chap. 18 of Nordio and Segre[4] in terms of the parameter $\delta = 1 - \overline{P_2}$, which is a measure of the deviation from perfect alignment. In the limiting case of very high ordering, the only important motion is free rotation about the molecular symmetry axis, the other motions being too rapid to produce any effective spin relaxation.

The considerations given here hold whenever uniaxial orientational order is present, such as in nematic and smectic-A phases. However, they are essentially correct also for cholesteric and smectic-C phases, because a uniaxial environment is experienced at the molecular level.

3.2 Rototranslational Couplings

In phases where both spatial and orientational order are set up, a reorientational process, which is peculiar to liquid crystal phases with spatial inhomogeneity and cannot occur in normal liquids, may result from the translational motions. We consider here the cases of smectic and cholesteric phases. In the former case, elongated molecules tend not only to orient parallel to each other, but also to organize themselves in parallel planes. In uniaxial smectic-A phases, the anisotropic potential acting on a rod-like molecule depends both on the spatial coordinate Z along the director, perpendicular to the smectic layers, and the angle β formed by the director and the molecular axis.[5,14] Because of the particular form of the potential, usually referred to as the 'McMillan potential',[15,16] the translational and rotational motions of the test molecule are coupled. Physically, a molecule traveling along the Z direction perpendicular to the smectic planes will be subjected to different orientational forces, and therefore the average value of any orientation-dependent interaction will be modulated by the translational motion. In fact, we expect that probe molecules in typical smectic systems are more oriented when surrounded by aromatic cores than when surrounded by aliphatic tails.

Modulation of intramolecular magnetic interactions by translational motion, in addition to that resulting from rotational motion, gives rise to a mechanism reminiscent of scalar relaxation of the first kind,[17] and ultimately produces similar effects. A simple interpretation of this relaxation mechanism can be given in the following way. The translational motion of the molecules is strongly anisotropic, with free diffusion within layers, and hindered diffusion across them. Translations parallel to the layers do not cause spin relaxation, because the orientational order is essentially constant. Spin relaxation results, of course, from anisotropic rotational diffusion, as in nematics. Translations perpendicular to the layers, which explore regions of a different order, are hindered by the anisotropic potential, and could be described by a diffusion equation including the McMillan potential. However, this motion can be visualized as an activated random jump process, with a correlation time given by the mean time required for the molecule to travel across layers of spacing d. The correlation time for the jump process is d^2/D_T, where D_T is the diffusion coefficient for translations perpendicular to the smectic planes. The contribution to the spin-relaxation time is proportional to

$$(\overline{P_{2\max}} - \overline{P_{2\min}})^2 (d^2/D_T) \tag{17}$$

where $\overline{P_{2\max}} - \overline{P_{2\min}}$ is the range of order parameters along Z.

In cholesteric phases too, a novel relaxation mechanism may occur, in addition to those already present in nematics, as a consequence of coupling between rotations and translations.

A simple picture of a single-domain cholesteric phase is that of a nematic in which the director moves along a helical structure, the axis of which is always perpendicular to the director itself. It follows that translation along the helical axis induces rotation of a rod-like molecule, so as to keep the long molecular axis parallel to the director. This motion gives rise to an important contribution to spin relaxation[18] by modulating the residual magnetic anisotropies left by local ordering. The correlation time for this process is the mean time required for the molecule to undergo angular displacement of the director by one radian; this time is of the order of $(p^2/4\pi^2\, D_T)$, where p is the helical pitch and D_T the diffusion coefficient for translations perpendicular to the director.

3.3 Internal Motions

The rigid rotor model is only a rough approximation for the dynamics of mesogenic molecules. Actually, molecular flexibility appears to be an important requirement for the achievement of mesomorphic states. Thus, thermotropic liquid crystals are generally made up of aromatic groups linked to flexible chains. The length and the chemical structure of the chains are important in determining their transitional properties and the nature of their mesophases. Very mobile units also characterize the lyotropics, which are water dispersions of molecules with a polar headgroup attached to long aliphatic tails. These species can be organized into structures in which regions with different characteristics can be distinguished: strong interactions of an electrostatic nature maintain the polar headgroups in hydrophilic layers separate from the hydrophobic domains of the alkyl chains. At appropriate temperatures and water concentrations, these systems may undergo transition to liquid crystal phases of different kinds, with the common feature that the chains are well aligned despite the high fluidity of the phase.

The NMR relaxation technique on specifically deuterated molecules was recognized early on as an essential tool in monitoring chain mobility, so that a large amount of experimental data is available. The timescales characterizing bond rotations depend on the specific molecule, but in most cases they range between 10^{-10} and 10^{-8} s. This means that internal motion must be an effective NMR relaxation mechanism, competing with the overall rotation of the molecule.

In the case of mesogenic molecules having a number of torsional degrees of freedom, collectively denoted by φ, the total potential undergone in the oriented phase is

$$U(\Omega, \varphi) = U^{\text{tors}}(\varphi) + U^{\text{or}}(\Omega, \varphi) \tag{18}$$

where $U^{\text{tors}}(\varphi)$ represents the torsional potential, and $U^{\text{or}}(\Omega, \varphi)$ the orientational contribution, which is now expected to depend upon the conformation assumed by the molecule.[19]

A multidimensional diffusion equation for both the orientational and the torsional degrees of freedom must be solved

in general but, under the hypothesis that internal and overall motions are decoupled, the two dynamic problems can be treated separately. Molecular reorientations are described by the diffusion model appropriate for uniaxial phases. In an analogous way, the conformational dynamics can be analyzed by solving a diffusion equation for the torsional variables. However, this procedure becomes impracticable when the number of internal degrees of freedom is greater than 3 or 4. An alternative method is based on the consideration that bond rotations are generally strongly hindered by intramolecular interactions, so that the internal potential has deep wells corresponding to a limited number of conformations. This is equivalent to assuming the so-called 'rotational isomeric state (RIS) approximation'.[20] It is therefore possible to resort to a kinetic description in terms of a master equation, for the random walk between stable conformers. This master equation can be set up phenomenologically, or be rigorously derived by asymptotic expansion of the diffusion equation in the potential minima.[21,12] The following equation is obtained for the time evolution of $P_J(t)$, the Jth conformer population:

$$\partial P_J(t)/\partial t = -\sum_{J'} W_{JJ'} P_{J'}(t) \qquad (19)$$

where $W_{JJ'}$ is the rate constant for the $J' \rightarrow J$ transition. It is calculated by generalizing to the multidimensional case the Kramers result for barrier crossing in an overdamped regime.[22] For the simple case of a single degree of freedom, as in the biphenyl molecule in which rotation about the phenyl–phenyl bond is hindered,[23] the rate constant k for a conformational jump is given by

$$k = (k_B T/2\pi\xi)\omega_m\omega_M \exp\left\{-\frac{\Delta E}{k_B T}\right\} \qquad (20)$$

where ΔE is the barrier height, ξ is the friction exerted by the viscous medium, and ω_m and ω_M are the square roots of the potential curvature along the torsional coordinate, corresponding to the starting minimum and the top of the barrier, respectively.

The structure of the master equation and the expression of the transition rate remain essentially the same in isotropic or anisotropic liquids, but the presence of the orienting potential has a twofold effect:[24]

1. A purely static effect, consisting in changes in the statistical weights of the various conformations. In calamitic nematics, the most elongated conformers can be more easily accommodated, and they are therefore stabilized at the expense of the most folded ones.
2. A dynamic effect, due to changes in the potential profile along the path of the conformational transitions, which modify the rates of such processes by altering the curvatures and activation energies.

Let us now consider mesogenic molecules formed by an elongated core and an aliphatic chain, such as those belonging to the alkylcyanobiphenyl series.[25] Conformational motions cause fast reorientations of the chain segments about the all-*trans* axis, and the whole molecule undergoes anisotropic rotational diffusion. Because of the inequivalence of the conformational sites, isomerization processes alone do not allow the chain segments to be isotropically distributed in space, and so a residual order with respect to the molecular frame is left, even in isotropic phases. The liquid crystal environment enhances the segmental order by aligning the molecular axes. If there is a timescale separation between the conformational and the overall motions, two distinct processes contributing to spin relaxation can be easily identified. Fast internal motions partially average the interaction tensors located on the various molecular segments, at rates determined by the isomerization frequencies. The partially averaged magnetic tensors are then modulated by the slow anisotropic diffusion. The same conclusions apply to the case of chains anchored to surfaces and undergoing internal and wobbling motions, and thus this can be used as a model system for studies on micelles and membranes.[13]

For illustrative purposes, we report some results obtained for a model 12-bond chain with a fixed end. Each segment of the chain can exist in one of the three states called *gauche*$_+$ (g_+), *trans*, and *gauche*$_-$ (g_-). According to the RIS approximation,[20] 531 441 different conformers are possible for this system, but only about 257 000 are physically significant, the others being rejected for steric reasons. In an isotropic liquid, the statistical weight of any conformer is never larger than 0.001. Calculations for a liquid crystalline phase of intermediate ordering show that less than 40 conformers have a global statistical weight greater than 10%. These conformers obviously include the all-*trans* configuration, the others having a single *gauche* state at chain positions not far from the free end (a *gauche* state close to the headgroup would dramatically perturb the ordered environment), and the so-called kinks, i.e. conformers with $g_\pm\ t\ g_\pm$ sequences. In all these cases an approximately cylindrical molecular shape is retained. Figure 1 shows the order parameter for the C–H (or C–D) bond and the *gauche* $\rightarrow$ *trans* isomerization rate at each chain segment of the 12-bond chain, in the isotropic and the ordered phases. The anisotropic environment significantly increases the transition rates, and dramatically changes the order parameters. Modulation of the local ordering by slow wobbling motion of the chain axis may become the most relevant mechanism for spin relaxation in the liquid crystalline phase.

3.4 Translational Diffusion and Director Fluctuations

In principle, other kinds of motion, in addition to those described so far, may operate as relaxation mechanisms in

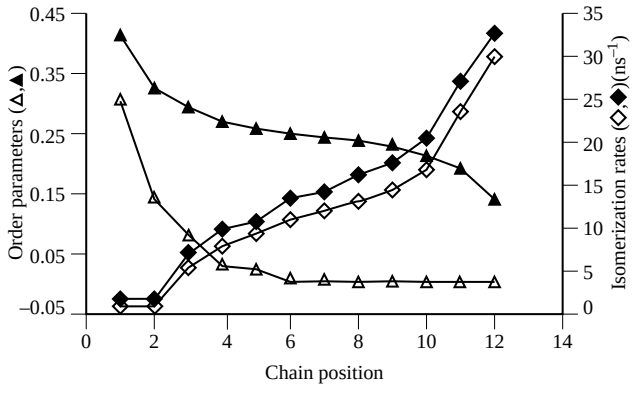

Figure 1 Order parameters and *gauche* $\rightarrow$ *trans* isomerization rates at the various segments of a substrate-supported 12-bond chain, in the isotropic (open symbols) and nematic (filled symbols) phase

liquid crystals. Since rotational diffusion and internal motion are dominant mechanisms for ^{13}C and ^{2}H spin probes at the high working frequency of standard spectrometers, they will be mentioned only briefly here.

One motional process common to all liquids is translational diffusion. This motion modulates intermolecular dipole–dipole interactions, and efficient spin relaxation results for proton nuclei, because of the abundance of hydrogen atoms in organic molecules. In the case of deuterated compounds, dipole interactions are reduced and intramolecular interactions remain, in practice, the only source of relaxation.

Another interesting process, which is specific to liquid crystal phases, results from elastic deformations of the ordered structures generated by collective thermal motions, which give rise to spontaneous alignment fluctuations. This process is responsible for the scattering of visible light, which in turn causes the turbid appearance of nematics. It also affects the spin relaxation, since it modulates the director orientation in the magnetic field. The corresponding spectral densities display characteristic frequency dependences. Director fluctuations may become the dominant relaxation mechanism at low-frequency regimes, but are relatively unimportant in high-field experiments.

4 RELATED ARTICLES

Amphiphilic Liquid Crystalline Samples: Nuclear Spin Relaxation; Bilayer Membranes: Deuterium and Carbon-13 NMR; Brownian Motion and Correlation Times; Deuteron Relaxation Rates in Liquid Crystalline Samples: Experimental Methods; Dynamic NMR in Liquid Crystalline Solvents; Liouville Equation of Motion; Liquid Crystalline Samples: Carbon-13 NMR; Liquid Crystalline Samples: Deuterium NMR; Liquid Crystalline Samples: Diffusion; Liquid Crystalline Samples: Spectral Analysis; Liquid Crystalline Samples: Structure of Nonrigid Molecules; Liquid Crystals: General Considerations; Relaxation of Coupled Spins from Rotational Diffusion; Relaxation Theory: Density Matrix Formulation.

5 REFERENCES

1. A. G. Redfield, *Adv. Magn. Reson.*, 1965, **1**, 1.
2. See, for example, R. W. Pastor, in *Molecular Description of Biological Membrane Components by Computer Aided Conformational Analysis*, ed. R. Brasseur, CRC, Boca Raton, FL, 1990.
3. N. G. van Kampen, *Stochastic Processes in Chemistry and Physics*, North-Holland, Amsterdam, 1981.
4. P. L. Nordio and U. Segre, in *The Molecular Physics of Liquid Crystals*, ed. G. R. Luckhurst and G. W. Gray, Academic, London, 1979, Chaps. 16, 18, 19.
5. G. Moro, U. Segre, and P. L. Nordio, in *Nuclear Magnetic Resonance of Liquid Crystals*, ed. J. W. Emsley, Reidel, Dordrecht, 1985, Chap. 9
6. P. Debye, *Polar Molecules*, Dover, New York, 1945.
7. J. Happel and H. Brenner, *Low Reynolds Number Hydrodynamics*, Prentice-Hall, Englewood Cliffs, NJ, 1965.
8. M. E. Rose, *Elementary Theory of Angular Momentum*, Wiley, New York, 1957.
9. W. H. Dickerson, R. R. Vold, and R. L. Vold, *J. Phys. Chem.*, 1983, **87**, 166.
10. C. R. J. Counsell, J. W. Emsley, G. R. Luckhurst, D. L. Turner, and J. Charvolin, *Mol. Phys.*, 1984, **52**, 499.
11. R. R. Vold, in *Nuclear Magnetic Resonance of Liquid Crystals*, ed. J. W. Emsley, Reidel, Dordrecht, 1985, Chap. 11
12. A. Ferrarini, G. Moro, and P. L. Nordio, *Mol. Phys.*, 1988, **63**, 225.
13. A. Ferrarini, P. L. Nordio, G. J. Moro, R. H. Crepeau, and J. H. Freed, *J. Chem. Phys.*, 1989, **91**, 5707.
14. G. Moro and P. L. Nordio, *J. Phys. Chem.*, 1985, **89**, 997.
15. W. L. McMillan, *Phys. Rev. A*, 1971, **4**, 1238; 1972, **6**, 936.
16. R. L. Humphries and G. R. Luckhurst, *Mol. Phys.*, 1978, **35**, 1201.
17. A. Abragam, *The Principles of Nuclear Magnetism*, Clarendon, Oxford, 1961.
18. Z. Luz, R. Poupko, and E. T. Samulski, *J. Chem. Phys.*, 1981, **74**, 5825.
19. A. Ferrarini, G. J. Moro, P. L. Nordio, and G. R. Luckhurst, *Mol. Phys.*, 1992, **77**, 1.
20. P. J. Flory, *Statistical Mechanics of Chain Molecules*, Interscience, New York, 1969.
21. G. Moro and P. L. Nordio, *Mol. Phys.*, 1986, **57**, 947.
22. H. Kramers, *Physica*, 1940, **7**, 284.
23. A. Ferrarini and P. L. Nordio, *J. Chem. Soc. Faraday Trans.*, 1992, **88**, 1733.
24. A. Ferrarini, A. Polimeno, and P. L. Nordio, *Liquid Cryst.*, 1993, **14**, 169.
25. A. Ferrarini, P. L. Nordio, and G. J. Moro, *Mol. Cryst. Liquid Cryst.*, 1991, **198**, 159.

Biographical Sketches

Pier Luigi Nordio. *b* 1936. Degree in Chemistry, University of Padova, 1961. Postdoctoral fellow at Stanford University, with H. M. McConnell. Associate Professor of Physical Chemistry 1968, Full Professor of Theoretical Chemistry, University of Padova, 1975–present. 100 scientific publications. Current interests include stochastic theories for molecular dynamics and conformational kinetics, interpretation of ordering in liquid crystals through molecular shape, solvation effects and photophysics of electron transfer.

Alberta Ferrarini. *b* 1957. Degree in Chemistry, 1983, Ph.D., 1989, Physical Chemistry, University of Padova, Italy. Fellowships with G. Kothe, Stuttgart University, Germany and J. H. Freed, Cornell University, USA. Presently research assistant in the Physical Chemistry Department, University of Padova. Approx. 25 publications. Current research interests: dynamics of molecules with torsional degrees of freedom, theoretical models for ordering and transitional properties in liquid crystal phases.

Relaxation of Quadrupolar Nuclei Measured via Multiple Quantum Filtration

Stephen Wimperis
University of Oxford, UK

1	Introduction	1
2	Tensor Operator Description of Spin-$\frac{3}{2}$ Quadrupolar Relaxation	1
3	Multiple Quantum Filtration Experiments for Spin-$\frac{3}{2}$ Nuclei	2
4	Measurement of Spin-$\frac{3}{2}$ Relaxation Parameters	3
5	Discrimination of Intra- and Extracellular Spin-$\frac{3}{2}$ Nuclei	5
6	Residual Spin-$\frac{3}{2}$ Quadrupolar Splittings	5
7	Discussion and Summary	6
8	Related Articles	7
9	References	7

1 INTRODUCTION

Metal ions play a vital role in a large number of biological processes. For this reason, there is widespread interest in NMR of the spin-$\frac{3}{2}$ nuclei ^{7}Li, ^{23}Na, ^{39}K, and ^{87}Rb, the spin-$\frac{5}{2}$ nuclei ^{25}Mg and ^{85}Rb, and the spin-$\frac{7}{2}$ nuclei ^{43}Ca and ^{133}Cs. In particular, ^{23}Na is one of the most widely studied of all quadrupolar nuclei, especially in vivo. Even in the most heterogeneous biological tissues, however, the NMR spectra of these metal ions usually exhibit only a single resonance at a chemical shift that is characteristic of the aqueous ion. This apparent lack of structure in the spectra is compensated for by the wealth of information about the environment of the ions yielded by the spin relaxation parameters.

It has long been known that both the transverse and longitudinal relaxation of spin $S \geq \frac{3}{2}$ nuclei are multiexponential if the extreme-narrowing condition is not fulfilled.[1] For example, the transverse relaxation of spin-$\frac{3}{2}$ nuclei is described by two distinct relaxation rates, $R_{\mathrm{f}}^{(1)}$ and $R_{\mathrm{s}}^{(1)}$ [the superscript (1) denotes relaxation of single quantum coherences, $p = \pm 1$], if the product of the Larmor frequency ω_0 and correlation time τ_{c} is unity or greater, $\omega_0\tau_{\mathrm{c}} \gtrsim 1$. As a result of this biexponential relaxation, the NMR spectrum of slowly tumbling spin-$\frac{3}{2}$ nuclei is a superposition of two Lorentzian lines with full widths (in Hz) at halfheight of $R_{\mathrm{f}}^{(1)}/\pi$ and $R_{\mathrm{s}}^{(1)}/\pi$. Figure 1 shows the normal free induction decay and the corresponding spectrum of sodium ions in an agarose gel. The ^{23}Na lineshape can be seen to be bi-Lorentzian, with 60% of the total intensity in the broader component and 40% in the narrower component. Full analysis of the spectrum of a spin-$\frac{3}{2}$ nucleus requires measurement of both the fast, $R_{\mathrm{f}}^{(1)}$, and slow, $R_{\mathrm{s}}^{(1)}$, transverse relaxation rates. This is a difficult task, especially if (a) the two relaxation rates are very similar or (b) the relaxation rate $R_{\mathrm{f}}^{(1)}$ is so fast that the broader of the two lines cannot be observed.

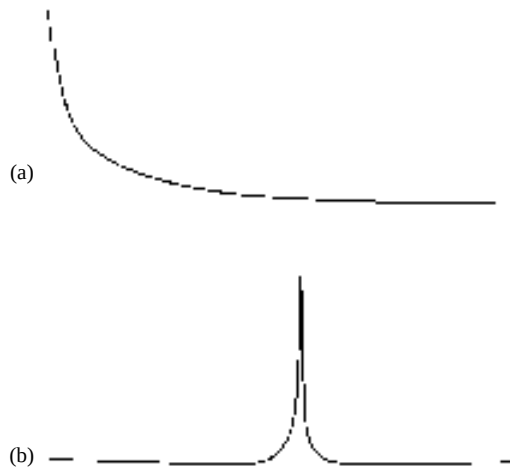

Figure 1 Magnitude mode free induction decay (a) and ^{23}Na spectrum (b) of 2 M NaCl in an agarose gel. Acquisition parameters: 2500 Hz spectral width, 48 transients coadded, 105.8 MHz Larmor frequency, 256 points in (a) zero filled to 1024 in (b)

In 1986, both Pekar and Leigh[2] and Jaccard et al.[3] showed that multiple quantum coherences could be excited in isolated spin $S \geq \frac{3}{2}$ nuclei in liquids if, but only if, their relaxation was multiexponential. This discovery helped overturn the orthodox view that excitation of multiple quantum coherence required the presence of splittings due to scalar, dipolar, or quadrupolar couplings, and so could not be achieved in a spectrum that consisted of only a single resonance. The aim of this article is to show how multiple quantum NMR is currently being used to measure the relaxation parameters of spin $S \geq \frac{3}{2}$ nuclei in liquid environments. This article will concentrate on spin-$\frac{3}{2}$ nuclei, while multiple quantum NMR of the much less important spin-$\frac{5}{2}$ and spin-$\frac{7}{2}$ nuclei will be mentioned briefly in Section 7.

2 TENSOR OPERATOR DESCRIPTION OF SPIN-$\frac{3}{2}$ QUADRUPOLAR RELAXATION

Jaccard et al.[3] have shown that a tensor operator description of multiexponential quadrupolar relaxation is particularly convenient for discussing multiple quantum NMR experiments. In this formulation, the density operator $\sigma(t)$ is expanded as a linear combination of tensor operators:

$$\sigma(t) = \sum_{l=0}^{2S} \sum_{p=-l}^{l} b_{l,p}(t) T_{l,p} \qquad (1)$$

where $T_{l,p}$ is an irreducible spherical tensor operator of rank l and order p. These two concepts have clear meanings in this usage. For example, an operator $T_{1,-1}$ represents an in-phase coherence of order $p = -1$ (i.e., one of the two components of in-phase single quantum coherence), $T_{3,+1}$ represents a doubly

antiphase coherence of order $p = +1$, $T_{3,-2}$ represents a singly antiphase coherence of order $p = -2$ (i.e., a singly antiphase double quantum coherence), and so on. The fact that the rank and coherence order of each term in the expansion of equation (1) are readily identifiable is a major asset in the description of multiple quantum NMR experiments.

A 90°_y pulse applied to a system of spin-$\frac{3}{2}$ nuclei at thermal equilibrium creates in-phase single quantum coherence. If a number of uninteresting constants are ignored, this initial state can be written in tensor form as

$$\sigma(t=0) = T_{1,-1} - T_{1,+1} \tag{2}$$

Jaccard et al.[3] have shown that if the time evolution of the density operator occurs solely as a result of biexponential transverse relaxation then the new density operator $\sigma(t)$ is given in tensor operator form by

$$\sigma(t) = f_{11}^{(1)}(t)(T_{1,-1} - T_{1,+1}) + f_{31}^{(1)}(t)(T_{3,-1} - T_{3,+1}) \tag{3}$$

where

$$f_{11}^{(1)}(t) = \tfrac{1}{5}[3\exp(-R_{\mathrm{f}}^{(1)}t) + 2\exp(-R_{\mathrm{s}}^{(1)}t)] \tag{4a}$$

$$f_{31}^{(1)}(t) = \tfrac{1}{5}\sqrt{6}[\exp(-R_{\mathrm{f}}^{(1)}t) - \exp(-R_{\mathrm{s}}^{(1)}t)] \tag{4b}$$

For pure quadrupolar relaxation in the absence of exchange, the fast and slow transverse relaxation rates can be calculated as

$$R_{\mathrm{f}}^{(1)} = C(J_0 + J_1) \tag{5a}$$

$$R_{\mathrm{s}}^{(1)} = C(J_1 + J_2) \tag{5b}$$

where the spectral densities J_n and the constant C are given by

$$J_n = \frac{2\tau_{\mathrm{c}}}{1 + n^2\omega_0^2\tau_{\mathrm{c}}^2} \tag{6}$$

$$C = \tfrac{1}{40}(e^2qQ/\hbar)^2(1 + \tfrac{1}{3}\eta^2) \tag{7}$$

In the extreme-narrowing limit, $\omega_0\tau_{\mathrm{c}} \ll 1$, the two relaxation rates are equal, $R_{\mathrm{f}}^{(1)} = R_{\mathrm{s}}^{(1)} = 4C\tau_{\mathrm{c}}$; hence, the function $f_{31}^{(1)}(t)$ is zero at all times, and spin-$\frac{3}{2}$ transverse relaxation is monoexponential. However, when the ions are tumbling slowly, $\omega_0\tau_{\mathrm{c}} \gtrsim 1$, the two rates are unequal, with $R_{\mathrm{f}}^{(1)} \rangle R_{\mathrm{s}}^{(1)}$, and both the biexponential functions $f_{11}^{(1)}(t)$ and $f_{31}^{(1)}(t)$ are needed for a full description of transverse relaxation.

The function $f_{11}^{(1)}(t)$ in equations (3), (4a), and (4b) describes the biexponential decay of in-phase single quantum coherence, $T_{1,\pm1}$, with the two components having relative intensities of 60% and 40%. As mentioned in Section 1, this behavior has been known for a long time, and the tensor operator description has here revealed nothing new. Equations (3), (4a), and (4b) also show, however, the biexponential growth and decay of doubly antiphase single quantum coherence, $T_{3,\pm1}$, according to the function $f_{31}^{(1)}(t)$. Only coherences described by the tensor operator $T_{1,-1}$ give rise to magnetization that is observable as a free induction decay, so these third-rank single quantum coherences cannot be detected directly.[3] It will be shown in the next section, however, that the function $f_{31}^{(1)}(t)$ can be measured using multiple quantum filtration.

The tensor operator description of spin-$\frac{3}{2}$ longitudinal relaxation is broadly similar to that of transverse relaxation.[3] If a 180° pulse is applied to a system of spin-$\frac{3}{2}$ nuclei at thermal equilibrium, the resulting deviation from thermal equilibrium can be written in tensor operator form [normalized to equation (2)] as

$$\sigma(t=0) - \sigma^{\mathrm{eq}} = -2\sqrt{2}\,T_{1,0} \tag{8}$$

If biexponential longitudinal relaxation occurs for a time t, then the new density operator $\sigma(t)$ is given by

$$\sigma(t) - \sigma^{\mathrm{eq}} = -2\sqrt{2}[T_{1,0}\,f_{11}^{(0)}(t) + T_{3,0}\,f_{31}^{(0)}(t)] \tag{9}$$

where

$$f_{11}^{(0)}(t) = \tfrac{1}{5}[\exp(-R_{\mathrm{f}}^{(0)}t) + 4\exp(-R_{\mathrm{s}}^{(0)}t)] \tag{10a}$$

$$f_{31}^{(0)}(t) = \tfrac{2}{5}[\exp(-R_{\mathrm{f}}^{(0)}t) - \exp(-R_{\mathrm{s}}^{(0)}t)] \tag{10b}$$

The fast and slow longitudinal relaxation rates for pure quadrupolar relaxation are given by [the superscript (0) denotes relaxation of spin populations, $p = 0$]

$$R_{\mathrm{f}}^{(0)} = 2CJ_1 \tag{11a}$$

$$R_{\mathrm{s}}^{(0)} = 2CJ_2 \tag{11b}$$

As with transverse relaxation, equations (9)–(11b) show that in the extreme-narrowing limit, $R_{\mathrm{f}}^{(0)} = R_s^{(0)} = 4C\tau_{\mathrm{c}}$, so that longitudinal relaxation is monoexponential. Outside this limit, the relaxation is again biexponential, with $R_{\mathrm{f}}^{(0)} \rangle R_{\mathrm{s}}^{(0)}$. Multiple quantum filtration experiments that allow the function $f_{31}^{(0)}(t)$ to be measured will be discussed in the next section.

3 MULTIPLE QUANTUM FILTRATION EXPERIMENTS FOR SPIN-$\frac{3}{2}$ NUCLEI

A tensor operator $T_{l,p}$ transforms under a radiofrequency pulse of flip angle β and phase ϕ according to

$$T_{l,p} \xrightarrow{\beta(\hat{I}_y\cos\phi - \hat{I}_x\sin\phi)} \sum_{p'=-l}^{l} T_{l,p'} d_{p',p}^{l}(\beta)\exp(-\mathrm{i}\Delta p\phi) \tag{12}$$

where p' is the new coherence order, and $\Delta p = p' - p$ is the change in coherence order under the pulse.[3] The amplitude of the transfer $T_{l,p} \rightarrow T_{l,p'}$ is given by the reduced rotation matrix element $d_{p',p}^{l}(\beta)$. These elements are defined to be real; hence, the phase ϕ represents a positive excursion with respect to the rotating frame y axis (i.e., $\phi = 0^\circ$ for a y pulse, $\phi = 90^\circ$ for a $-x$ pulse, and so on).

The important feature revealed by equation (12) is that a pulse cannot change the rank l of a tensor operator (or the coherence it represents), but will, in general, produce operators of all possible coherence orders p. Thus, while the $T_{1,\pm1}$ terms

in equation (3) cannot be transformed by a pulse into multiple quantum coherences ($|p| \geq 2$), the $T_{3,\pm1}$ terms that appear as a result of biexponential spin-$\frac{3}{2}$ transverse relaxation can be transformed into triple quantum coherences, $T_{3,\pm3}$, and antiphase double quantum coherences, $T_{3,\pm2}$. Therefore, it is the appearance of the third-rank terms in equations (3) and (9) that makes the excitation of multiple quantum coherence possible.

Figure 2 shows two pulse sequences for multiple quantum filtration of spin-$\frac{3}{2}$ nuclei and their corresponding coherence pathway diagrams.[4] The standard multiple quantum filtration experiment in Figure 2(a) allows the transverse relaxation function $f_{31}^{(1)}(t)$ to be measured.[2,3] At the end of the τ_e evolution interval, both $T_{1,\pm1}$ and $T_{3,\pm1}$ operators will be present as result of biexponential transverse relaxation (the 180° pulse merely refocuses any offsets). Depending on its phase ϕ', the $\beta = 90°$ pulse then converts the $T_{3,\pm1}$ coherences into either double ($T_{3,\pm2}$) or triple ($T_{3,\pm3}$) quantum coherences, which can be selected by an appropriate phase cycling of the receiver and the pulse phase ϕ. The final $\beta' = 90°$ pulse then reconverts these multiple quantum coherences into a single quantum coherence, $T_{3,\pm1}$, at the start of acquisition of the free induction decay. As mentioned

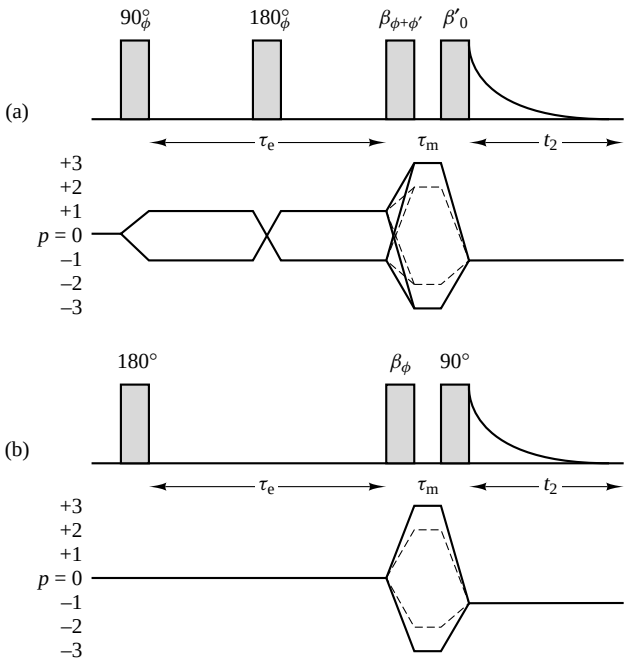

Figure 2 Pulse sequences and coherence pathway diagrams for multiple quantum filtration of spin-$\frac{3}{2}$ nuclei. Sequence (a) is used to study biexponential transverse relaxation, while sequence (b) is used to study longitudinal relaxation. The pulse phase ϕ in (a) and (b) is stepped through the values 0°, 90°, 180°, and 270° for double quantum filtration (dashed coherence pathways), and through 30°, 90°, 150°, 210°, 270°, and 330° for triple quantum filtration (solid pathways), while the receiver phase alternates between 0° and 180°. The pulse phase ϕ' in (a) is 0° for double quantum and 90° for triple quantum filtration. Maximum sensitivity is achieved with flip angles $\beta = \beta' = 90°$, except for the double quantum filtration version of (b), where $\beta = 54.7°$. The interval τ_m is a few microseconds to allow for phase shifting of the pulses, unless multiple quantum relaxation rates are being measured. The double quantum filtration version of (a) can be used selectively to observe spin-$\frac{3}{2}$ nuclei in ordered environments if $\beta = \beta' = 54.7°$

above, this third-rank single quantum coherence is not directly observable. However, further biexponential transverse relaxation during the free induction decay will convert the $T_{3,-1}$ coherence into an observable $T_{1,-1}$ coherence. The function that describes this conversion can be written as $f_{13}^{(1)}(t)$ in analogy to equation (3), and it is easily shown that $f_{13}^{(1)}(t) = f_{31}^{(1)}(t)$. Using equations (3) and (12), the observable components of the density operators produced by the double and triple quantum filters in Figure 2(a) can be calculated as[3]

$$\sigma^{DQF}(t_2) = \tfrac{10}{16}\, T_{1,-1}\, f_{31}^{(1)}(\tau_e)\, f_{31}^{(1)}(t_2) \cos 2\phi \qquad (13a)$$

$$\sigma^{TQF}(t_2) = \tfrac{15}{16}\, T_{1,-1}\, f_{31}^{(1)}(\tau_e)\, f_{31}^{(1)}(t_2) \mathrm{i} \sin 3\phi \qquad (13b)$$

where evolution solely as a result of transverse relaxation has been assumed. The dependence on the pulse phase ϕ in equations (13a) and (13b) is the basis for selection of these components by phase cycling. Note that either double or triple quantum filtration can be used to measure the function $f_{31}^{(1)}(t)$, either as a function of the evolution interval τ_e or in 'real time' as the envelope of the free induction decay. The only difference between the results of the two experiments is that the spin-$\frac{3}{2}$ triple quantum filter is 50% more sensitive than the double quantum filter.[5]

The pulse sequence in Figure 2(b) can be viewed as a multiple quantum filtered inversion–recovery experiment, and allows the longitudinal relaxation function $f_{31}^{(0)}(t)$ to be measured.[3] Again, either double (with $\beta = 54.7°$) or triple (with $\beta = 90°$) quantum filtration are possible. Using equations (9) and (12), the observable component of the density operator for each alternative can be written as

$$\sigma^{DQF}(t_2) = \tfrac{5}{6}\sqrt{2}\, T_{1,-1}\, f_{31}^{(0)}(\tau_e)\, f_{13}^{(1)}(t_2) \cos 2\phi \qquad (14a)$$

$$\sigma^{TQF}(t_2) = \tfrac{5}{8}\sqrt{6}\, T_{1,-1}\, f_{31}^{(0)}(\tau_e)\, f_{13}^{(1)}(t_2) \mathrm{i} \sin 3\phi. \qquad (14b)$$

Thus, either double or triple quantum filtration can be used to measure $f_{31}^{(0)}(t)$ as a function of the evolution interval τ_e. The envelope of the free induction decay is again described by the transverse biexponential function $f_{31}^{(1)}(t)$.

4 MEASUREMENT OF SPIN-$\frac{3}{2}$ RELAXATION PARAMETERS

The free induction decay produced by the triple quantum filter of Figure 2(a) from sodium ions in an agarose gel is shown in Figure 3(a). As predicted, the envelope of the free induction decay is the difference of two exponentials, and corresponds to the function $f_{31}^{(1)}(t_2)$. Fourier transformation of this free induction decay in the normal way yields the triple quantum filtered ^{23}Na spectrum in Figure 3(b). This spectrum corresponds to a function $F_{31}^{(1)}(\omega)$, the Fourier transform of $f_{31}^{(1)}(t)$, and is the difference of two Lorentzian lines with widths $R_f^{(1)}/\pi$ and $R_s^{(1)}/\pi$.

The experimental results in Figure 3(a) and (b) are described by exactly the same two relaxation rates, $R_f^{(1)}$ and $R_s^{(1)}$, as the results in Figure 1. However, the use of multiple quantum filtration has conferred a number of advantages. First, the very fact that a multiple quantum filtered spectrum can be recorded

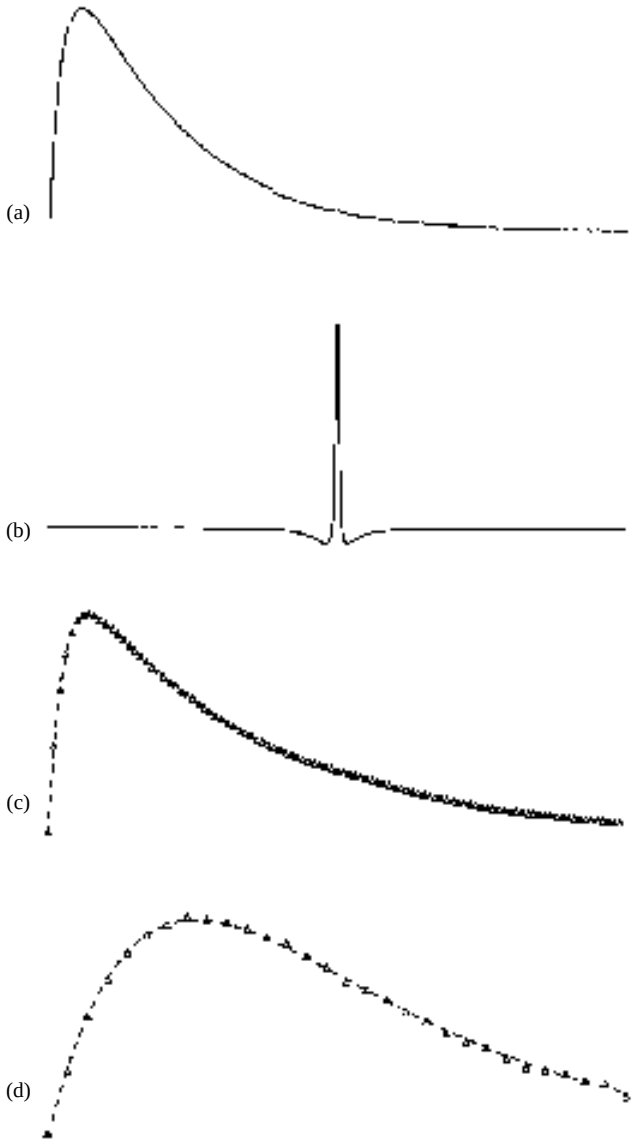

Figure 3 Magnitude mode free induction decay (a) and ^{23}Na spectrum (b) of 2 M NaCl in an agarose gel recorded with the triple quantum filter of Figure 2(a). The amplitudes of ^{23}Na spectra recorded with the triple quantum filter of Figure 2(a) are plotted in (c) as a function of the evolution interval τ_e (triangles represent 100 amplitudes between τ_e = 0 and 99 ms). Computer fitting (dashed line) of the points in (c) yielded the relaxation rates $R(1)/f = 409\,s^{-1}$ and $R(1)/s = 30.7\,s^{-1}$. Similarly, the amplitudes of ^{23}Na spectra recorded with the triple quantum filter of Figure 2(b) are plotted in (d) as a function of τ_e (triangles represent 30 amplitudes between τ_e = 0 and 116 ms). Computer fitting (dashed line) of the points in (c) yielded the relaxation rates $R(0)/f = 38.5\,s^{-1}$ and $R(0)/s = 29.7\,s^{-1}$. Acquisition parameters for all spectra: 2500 Hz spectral width, 48 transients co-added, 105.8 MHz Larmor frequency, 256 points acquired and zero filled to 1024

is significant, since it constitutes unambiguous proof that the ^{23}Na nuclei are tumbling outside the extreme-narrowing limit. Second, both the conventional and multiple quantum filtered data are now available for computer fitting, and this should result in increased accuracy. Third, it is believed that, owing to its greater number of turning points, the $F_{31}^{(1)}(\omega)$ lineshape should yield more reliable fittings than the conventional lineshape $F_{11}^{(1)}(\omega)$, especially when the two relaxation rates are similar. And finally, because the first point of the free induction decay is zero, the multiple quantum filtered spectrum shows less baseline distortion than the conventional spectrum.

The use of multiple quantum filtration is particularly favorable when the broad component of the spin-$\frac{3}{2}$ lineshape cannot be observed because it has relaxed completely in the 'dead time' between the end of the last pulse and the start of data acquisition. Clearly, this 'visibility' problem will be the same in both conventional and multiple quantum filtered spectra. Equations (13a) and (13b) show, however, that the function $f_{31}^{(1)}(t)$ can also be measured by recording the intensity of the filtered spectrum as a function of the evolution interval τ_e. This measurement suffers from no dead time problems, and, in addition, the presence of the 180° pulse means that the effects of B_0 inhomogeneity are refocused. Figure 3(c) shows the experimental function $f_{31}^{(1)}(t)$ measured in this way for the gel sample used previously. The computer fitting of these points yielded the ^{23}Na relaxation rates $R_f^{(1)} = 409\,s^{-1}$ and $R_s^{(1)} = 30.7\,s^{-1}$.

The longitudinal relaxation function $f_{31}^{(0)}(t)$ can be measured as a function of the τ_e interval in the experiment of Figure 2(b) in much the same way as the transverse function.[3] Figure 3(d) shows a computer fitting of results from the agarose gel that yielded the ^{23}Na relaxation rates $R_f^{(0)} = 38.5\,s^{-1}$ and $R_s^{(0)} = 29.7\,s^{-1}$. In general, however, the longitudinal triple quantum filter is much less sensitive and informative than the transverse experiment, and has not attained the same widespread popularity in spin-$\frac{3}{2}$ NMR.

In addition to the methods discussed so far, it is also possible to measure the spin-$\frac{3}{2}$ multiple quantum relaxation rates using a minor modification of the pulse sequence of Figure 2(a).[3,6] The decays of $T_{3,\pm2}$ and $T_{3,\pm3}$ are monoexponential and can be measured as functions of the τ_m interval (previously assumed to be of negligible duration) in the double and triple quantum filtration experiments, respectively. A 180° refocusing pulse can be inserted into the middle of the τ_m interval if required.

A full discussion of the analysis of spin-$\frac{3}{2}$ relaxation rates measured using multiple quantum filtration experiments is beyond the scope of this article, and only a brief summary can be given here. The relaxation rates given in equations (5a), (5b), (11a), and (11b) were derived on the assumption that relaxation is purely quadrupolar and is described by a single correlation time τ_c. In this case, the correlation time τ_c and the constant C can be easily extracted from the ratio of any two of the measured relaxation rates. In systems where rapid chemical exchange is occurring, however, the assumption of a single correlation time is clearly invalid. This applies to spin-$\frac{3}{2}$ ions in agarose gels, in aqueous solutions of proteins, and in both intra- and extracellular environments in cell suspensions and tissues.[7–9] In 1972, Bull[10] proposed a two-site exchange model for spin-$\frac{3}{2}$ nuclei in such systems. In this model, an observed relaxation rate is the weighted sum of the relaxation rate of ions bound to macromolecules and of those in free solution, the weights being the probabilities of the ions being found in each environment. The Bull model is attractive, since the free relaxation rates can easily be estimated and the free site probability can be taken as approximately unity. Thus, the bound relaxation rates can be easily derived and then treated according to the single correlation time model. Unfortunately,

in spite of its elegance, the Bull model does not seem to be very successful in explaining the majority of experimental data. If, using the full range of experimental techniques available, the six possible relaxation rates are measured for a spin-$\frac{3}{2}$ nucleus in, say, a protein solution then it is usually found that the value of τ_c calculated by taking the ratio of a pair of relaxation rates can differ by an order of magnitude according to which pair is chosen.[7,8] For example, using $R_{free} = 25\,s^{-1}$, a Bull analysis of the rates $R_f^{(1)}$ and $R_s^{(1)}$ measured in Figure 3(c) yields $\omega_0\tau_c = 9.1$, while the analysis of $R_f^{(0)}$ and $R_s^{(0)}$ measured in Figure 3(d) yields $\omega_0\tau_c = 1.3$. Although the error on the latter figure may be very large because of the closeness of $R_f^{(0)}$ and $R_s^{(0)}$, the failure of the two-site Bull model is clear. Attempts to extend the Bull model to include multisite exchange would seem to be futile, since (a) the number of parameters would soon become too large for any meaningful fitting, and (b) it is unlikely that monovalent metal ions bind in any discrete manner to the majority of macromolecules. In a more promising development, however, Rooney and Springer[7,8] have successfully fitted ^{23}Na relaxation data from both protein solutions and cell suspensions by using a model that allowed for a continuous distribution of correlation times.

5 DISCRIMINATION OF INTRA- AND EXTRACELLULAR SPIN-$\frac{3}{2}$ NUCLEI

As mentioned in Section 1, the ^{23}Na or ^{39}K NMR spectra of heterogeneous biological tissues or cell suspensions, either in vivo or in vitro, exhibit only a single resonance at a chemical shift characteristic of the aqueous ion. This is unfortunate, since a key aim of such studies is to determine selectively the relaxation parameters of the ions in the individual tissue compartments. One solution to this problem involves the use of lanthanide shift reagents,[11,12] such as $Dy(PPP)_2^{7-}$ or $TmDOTP^{5-}$. These are too large to cross the cell membrane, and so produce a paramagnetic shift of only the extracellular resonance. The main disadvantage of shift reagents is their toxicity. Nevertheless, they have proved popular for in vitro work and have occasionally been used in vivo, although never, of course, for studies on humans.

In 1987, Pekar et al.[13] suggested that multiple quantum filtration could be used to observe selectively the resonance from intracellular spin-$\frac{3}{2}$ metal ions. The idea was that the intracellular ions would be slowly tumbling and would thus exhibit biexponential transverse relaxation, while the extracellular ions would be in the extreme-narrowing limit. A double or triple quantum filter would, therefore, fail to excite any multiple quantum coherences in the extracellular nuclei, and only signal from the intracellular ions would appear in the spectrum. This technique has proved only a partial success, however, since it has been found that, in general, the extracellular ions also exhibit biexponential relaxation.[14,15] In spite of this, the relaxation behavior of spin-$\frac{3}{2}$ nuclei does differ widely between the various tissue compartments, and multiple quantum filters have been used to achieve partial discrimination between compartments in situations where shift reagents are not appropriate.

As an example of the degree of discrimination achieved, Figure 4(a) and (b) show the conventional and triple quantum filtered ^{23}Na NMR spectra of packed human red blood cells, while Figure 4(c) and (d) show the corresponding spectra of human red blood cells suspended in a solution containing 50 mM NaCl, 100 mM choline chloride, and 6 mM $DyTTHA^{3-}$. The triple quantum filtered lineshape of the intracellular ions in Figure 4(d) corresponds closely to that of Figure 4(b), while the intensity of the extracellular resonance relative to the intracellular resonance is clearly much reduced in Figure 4(d) compared with Figure 4(c).

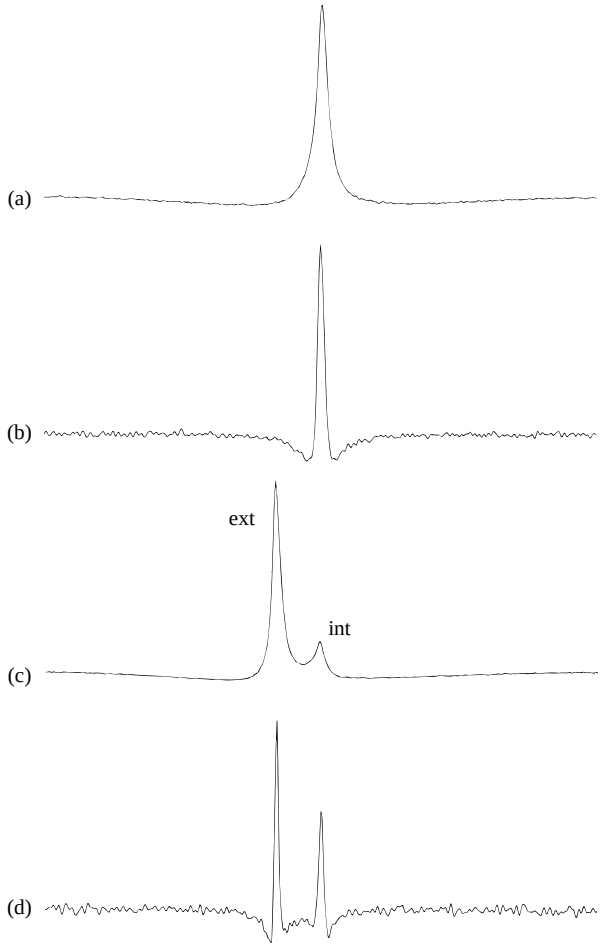

Figure 4 Conventional, (a) and (c), and triple quantum filtered, (b) and (d), ^{23}Na spectra of human red blood cells. Packed cells were used in (a) and (b), and cells suspended in a solution of 50 mM NaCl, 100 mM choline chloride, and 6 mM $DyTTHA^{3-}$ were used in (c) and (d). The pulse sequence of Figure 2(a) was used in (b) and (d). Acquisition parameters: 2500 Hz spectral width, 240 transients coadded for (a) and (c), 2400 transients coadded for (b) and (d), 105.8 MHz Larmor frequency, 128 points acquired and zero filled to 512, 5 ms evolution interval τ_e in (b) and (d). Fresh blood was drawn from the author on the day of the experiments

6 RESIDUAL SPIN-$\frac{3}{2}$ QUADRUPOLAR SPLITTINGS

The discussion in this article of the use of multiple quantum filtration in the study of spin-$\frac{3}{2}$ quadrupolar relaxation has so far assumed that the ions occur in purely isotropic, liquid-type environments; hence, their spectra exhibit no quadrupolar splittings. In 1986, however, Jaccard et al.[3] noted that if residual quadrupolar splittings were present but were

not apparent in the lineshape then these would provide an alternative pathway for the excitation of multiple quantum coherence. If, starting from the initial state of equation (2), free precession occurs solely as a result of the residual quadrupolar splitting $2\omega_Q$ for a time t then the new density operator is given by

$$\sigma(t) = g_{11}^{(1)}(t)(T_{1,-1} - T_{1,+1}) + g_{21}^{(1)}(t)(T_{2,-1} + T_{2,+1}) + g_{31}^{(1)}(t)(T_{3,-1} - T_{3,+1}) \quad (15)$$

where

$$g_{11}^{(1)}(t) = \tfrac{1}{5}(2 + 3\cos 2\omega_Q t) \quad (16a)$$

$$g_{21}^{(1)}(t) = \mathrm{i}\sqrt{\tfrac{3}{5}}\sin 2\omega_Q t \quad (16b)$$

$$g_{31}^{(1)}(t) = -\tfrac{1}{5}\sqrt{6}(1 - \cos 2\omega_Q t) \quad (16c)$$

The functions $g_{l'l}^{(1)}(t)$ in equations (15)–(16c) describe the evolution of in-phase single quantum coherence, $T_{1,\pm1}$, into antiphase single quantum coherence, $T_{2,\pm1}$, and doubly antiphase single quantum coherence, $T_{3,\pm1}$. The major difference between evolution as a result of biexponential relaxation and residual quadrupolar splittings, therefore, is that only in the latter case do singly antiphase coherences, $T_{2,\pm1}$, appear.

The appearance of the operator $T_{2,\pm1}$ as a result of a quadrupolar splitting forms the basis of a method of distinguishing this effect from biexponential relaxation. If the double quantum filter of Figure 2(a) is performed on a system that exhibits a residual quadrupolar splitting then both in-phase double quantum coherence, $T_{2,\pm2}$, and antiphase double quantum coherence, $T_{3,\pm2}$, will be selected. This does not achieve the desired discrimination, since $T_{3,\pm2}$ coherence arising as a result of pure transverse relaxation will also be selected by the filter. Jaccard et al.[3] and Eliav et al.[16] have shown, however, that if either or both of the flip angles β or β' in the double quantum filter is set to 54.7° then third-rank coherences are suppressed and only second-rank coherences will appear. Thus, the resulting spectrum will feature only those ^{23}Na nuclei that exhibit a residual quadrupolar splitting. The Jeener–Broekaert experiment can be used to achieve the same result with slightly higher sensitivity.[17]

Figure 5(a) shows the double quantum filtered ^{23}Na spectrum (with $\beta = \beta' = 90°$) of the suspension of human red blood cells used in Figure 4(c) and (d). If biexponential relaxation were solely responsible for this spectrum then equations (13a) and (13b) show that these lineshapes would be identical to those in the triple quantum filtered spectrum in Figure 4(d). Clearly, however, both intra- and extracellular lineshapes are very different, and this is because those in Figure 5(a) contain a $T_{2,-1}$ component that has arisen from residual quadrupolar splittings hidden within the linewidth. Figure 5(b) shows the result of using the double quantum filter of Figure 2(a) with $\beta = \beta' = 54.7°$ to record a spectrum arising solely from ^{23}Na nuclei that exhibit residual quadrupolar splittings (presumably those associated with the cell membrane[18,19]). The lineshapes here consist of antiphase spin-$\frac{3}{2}$ powder patterns, except that, using the same phasing parameters as in Figure 5(a), they appear in dispersive mode.[16,17]

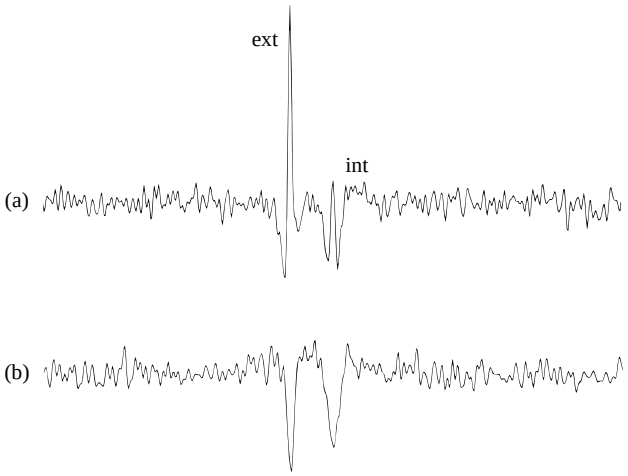

Figure 5 Double quantum filtered ^{23}Na spectra of the red blood cell suspension used in Figure 4(c) and (d). The experiment of Figure 2(a) was used with $\beta = \beta' = 90°$ (a) and $\beta = \beta' = 54.7°$ (b). Acquisition parameters: 2500 Hz spectral width, 2400 transients coadded, 105.8 MHz Larmor frequency, 128 points acquired and zero filled to 512, 5 ms evolution interval τ_e

7 DISCUSSION AND SUMMARY

This article has concentrated on spin-$\frac{3}{2}$ nuclei. This is inevitable, since nuclei such as ^{7}Li, ^{39}K, ^{87}Rb, and, in particular, ^{23}Na are studied very frequently, while higher spin nuclei such as ^{25}Mg, ^{43}Ca, ^{85}Rb, and ^{133}Cs have less favorable NMR parameters and are only rarely studied. Multiple quantum filtration has been used, however, in ^{25}Mg NMR of MgCl in bovine albumin solutions.[20,21] The relaxation of spin-$\frac{5}{2}$ nuclei is triexponential outside the extreme narrowing limit, and is described by transverse and longitudinal functions of the type $f_{11}^{(n)}(t)$, $f_{31}^{(n)}(t)$, and $f_{51}^{(n)}(t)$. Thus, excitation of multiple quantum coherences up to $p = \pm5$ is possible. The most straightforward method of determining the relaxation parameters of spin-$\frac{5}{2}$ nuclei is probably measurement of the four- and five-quantum relaxation rates in an analogous way to which the double and triple quantum relaxation rates can be measured for spin-$\frac{3}{2}$ nuclei.[21]

In summary, since being introduced only in 1986, multiple quantum filtration studies of quadrupolar relaxation have proved highly rewarding, especially in biological systems. Multiple quantum filters allow the biexponential relaxation of spin-$\frac{3}{2}$ nuclei to be measured with great accuracy, and have also been used to obtain partial discrimination of sodium and potassium ions in the various compartments of tissues and cell suspensions. A relatively new application of multiple quantum filtration has been the selective observation and study of spin-$\frac{3}{2}$ nuclei that exhibit residual quadrupolar splittings as a result of their association with ordered structures in cells and tissues. In addition to the applications discussed here, multiple quantum filters have also been used as a method of reversing contrast in ^{23}Na magnetic resonance imaging[22–24] and as a method of accurately measuring spin-$\frac{3}{2}$ dynamic shifts.[25] It seems likely that interest in all these areas will continue to grow in the next few years.

8 RELATED ARTICLES

Biological Systems: Spin-3/2 Nuclei; Cation Movements Across Cell Walls of Intact Tissues using MRS; Multiple Quantum Spectroscopy of Liquid Samples; Quadrupolar Nuclei in Liquid Samples; Relaxation Theory for Quadrupolar Nuclei; Sodium-23 Magnetic Resonance of Human Subjects; Sodium-23 NMR.

9 REFERENCES

1. P. S. Hubbard, *J. Chem. Phys.*, 1970, **53**, 985.
2. J. Pekar and J. S. Leigh, Jr., *J. Magn. Reson.*, 1986, **69**, 582.
3. G. Jaccard, S. Wimperis, and G. Bodenhausen, *J. Chem. Phys.*, 1986, **85**, 6282.
4. G. Bodenhausen, H. Kogler, and R. R. Ernst, *J. Magn. Reson.*, 1984, **58**, 370.
5. C.-W. Chung and S. Wimperis, *J. Magn. Reson.*, 1990, **88**, 440.
6. W. D. Rooney, T. M. Barbara, and C. S. Springer, Jr., *J. Am. Chem. Soc.*, 1988, **110**, 674.
7. W. D. Rooney and C. S. Springer, Jr., *NMR Biomed.*, 1991, **4**, 209.
8. W. D. Rooney and C. S. Springer, Jr., *NMR Biomed.*, 1991, **4**, 227.
9. G. S. Payne and P. Styles, *J. Magn. Reson.*, 1991, **95**, 253.
10. T. E. Bull, *J. Magn. Reson.*, 1972, **8**, 344.
11. M. M. Pike and C. S. Springer, Jr., *J. Magn. Reson.*, 1982, **46**, 348.
12. R. K. Gupta and P. Gupta, *J. Magn. Reson.*, 1982, **47**, 344.
13. J. Pekar, P. F. Renshaw, and J. S. Leigh, Jr., *J. Magn. Reson.*, 1987, **72**, 159.
14. L. A. Jelicks and R. K. Gupta, *J. Magn. Reson.*, 1989, **81**, 586.
15. L. A. Jelicks and R. K. Gupta, *J. Magn. Reson.*, 1989, **83**, 146.
16. U. Eliav, H. Shinar, and G. Navon, *J. Magn. Reson.*, 1992, **98**, 223.
17. R. Kemp-Harper and S. Wimperis, *J. Magn. Reson. B*, 1993, **102**, 326.
18. H. Shinar, T. Knubovets, U. Eliav, and G. Navon, *Biophys. J.*, 1993, **64**, 1273.
19. J. S. Tauskela and E. A. Shoubridge, *Biochim. Biophys. Acta*, 1993, **1158**, 155.
20. C.-W. Chung and S. Wimperis, *Chem. Phys. Lett.*, 1990, **172**, 94.
21. C.-W. Chung and S. Wimperis, *Mol. Phys.*, 1992, **76**, 47.
22. R. H. Griffey, B. V. Griffey, and N. A. Matwiyoff, *Magn. Reson. Med.*, 1990, **13**, 305.
23. S. Wimperis and B. Wood, *J. Magn. Reson.*, 1991, **95**, 428.
24. S. Wimperis, P. Cole, and P. Styles, *J. Magn. Reson.*, 1992, **98**, 628.
25. U. Eliav, H. Shinar, and G. Navon, *J. Magn. Reson.*, 1991, **94**, 439.

Biographical Sketch

Stephen Carl Wimperis. *b* 1962. B.A., 1984 (Chemistry), University of Oxford, UK. Doctorat ès Sciences, 1988 (supervisor Geoffrey Bodenhausen), Université de Lausanne. Research Fellow at Darwin College, Cambridge, 1988–90. Temporary lecturer at University of Manchester, 1990–91. Currently Royal Society University Research Fellow at University of Oxford and R. J. P. Williams Junior Research Fellow at Wadham College, Oxford, 1991–present. Approx. 35 publications. Current research specialties: multiple quantum NMR, spin relaxation, quadrupolar nuclei, NMR imaging, composite pulses, average Hamiltonian theory, two-dimensional NMR, selective excitation.

Supercritical Fluids

Craig M. V. Taylor and Gunilla B. Jacobson

Los Alamos National Laboratory, Los Alamos, NM, USA

1 Introduction to Supercritical Fluids 1
2 Supercritical Fluids 1
3 Instrument Requirements for High-Pressure NMR 7
4 Supercritical Fluid Applications 8
5 References 9

1 INTRODUCTION TO SUPERCRITICAL FLUIDS

While the existence of the supercritical 'phase' has been known for over 150 years it has been only in the last 20 years that the value of supercritical fluids (SCFs) as a medium for extraction, cleaning and synthesis has been recognized. It is now clear that SCF processes are often constrained to very narrow regions of economic feasibility due to the phase behavior of the solute-solvent system. As a result, there needs to be very tight controls over any industrial process employing SCFs. If the process parameters must be more exact, then so does the information required to generate the design parameters, which includes experimental measurements, theories, and the correlations that result in predictability in a given system. In an effort to expand the current understanding of SCFs and their applications, intensive studies are ongoing using nuclear magnetic resonance (NMR). In an effort to further explain the physical chemistry inherent to possible applications of SCFs, a brief introduction is given to this odd and often ignored 'phase' of substances. Following that is an introduction to NMR as it pertains to the study of SCF applications.

2 SUPERCRITICAL FLUIDS

2.1 General Properties

The supercritical state is defined by the critical pressure (P_c) and critical temperature (T_c). One of the most common phenomenological definitions describes critical pressure as the pressure above which, regardless of the applied temperature, a liquid cannot be made to boil. In a similar way, the critical temperature can be thought of as the temperature above which, regardless of the applied pressure, a gas cannot be converted into a liquid. Hence, above the critical point there is no longer a phase boundary between the liquid and the vapor. A liquid/vapor phase boundary represents a coexistence line so that material crossing it requires the expenditure of the latent heat of vaporization.

The concept of the supercritical state can be illustrated by a physical example. Consider a closed container of constant volume. Inside the container we start with some amount of pure liquid. The space above this pure liquid will be filled with pure vapor at the liquid's equilibrium vapor pressure. Now assume that we begin to heat up this container slowly and uniformly. The density of the liquid will begin to decrease through normal thermal expansion. Meanwhile, the density of the vapor phase begins to increase since more molecules are leaving the liquid to enter the vapor phase. Continued heating results in a further decrease of the liquid density and an increase in the vapor density. Eventually, at some temperature, T_c (and resulting, uniform pressure, P_c), the density of the liquid and vapor phases reach the same value, and the vapor and liquid 'phases' have identical compositions and identical densities.

Is this supercritical fluid phase to be considered a liquid or a gas? The answer is that a supercritical fluid reflects properties of both. Table 1 shows relative values of the density, diffusion coefficient, and viscosity for a typical liquid, gas, and supercritical fluid. These values indicate the mass transport properties (i.e., diffusivity) are similar to a gas, while the mechanical properties (viscosity and density) are similar to those of a liquid. This unique combination of properties makes supercritical fluids attractive for use as solvents. The high diffusivity and low viscosity allows the fluid to penetrate easily into matrices which are in the form of loose powders, compacted powders, or even fully cemented pre-forms. Further, the ability of a solvent to dissolve other liquids is, to a first approximation, related to the density of the solvent. The relatively high density of supercritical fluids, relative to gases, increases the useful levels of solubility that may be attained.

2.2 Supercritical CO_2

As a result of the law of corresponding states the physical properties of supercritical CO_2 apply to all fluids in the supercritical state. The critical values of temperature and pressure are unique for each gas/liquid and are determined by the type of intermolecular interactions occurring between

Table 1 Comparison of physico-chemical properties of a typical organic fluid in the liquid, gas, and supercritical fluid state

	Liquid	Supercritical fluid	Gas
Density ($g\,cm^{-3}$)	1	0.1–1	10^{-3}
Viscosity (Pa·s)	10^{-3}	10^{-4}–10^{-5}	10^{-5}
Diffusivity ($cm^2\,s^{-1}$)	10^{-5}	10^{-3}	10^{-1}

Table 2 Critical temperature, T_c, and Pressure, P_c, for some common fluids

Fluid	T_c (°C)	P_c (psi)
Neon, Ne	−229	400
Nitrogen, N_2	−147	492
Argon, Ar	−122	706
Xenon, Xe	17	858
Carbon dioxide, CO_2	31	1072
Sulfur hexafluoride, SF_6	46	545
Propane, C_3H_8	97	617
Ammonia, NH_3	133	1654
Water, H_2O	374	3209

the individual molecules. Table 2 gives the critical temperature and pressure of some common fluids. For example, the critical temperature and pressure required to transform water (H_2O) into a supercritical fluid are 374 °C and 218 atmospheres. These values are much higher than those for CO_2 because the water molecules exert an attractive force on each other, making the solid and liquid phases particularly stable. CO_2 molecules, on the other hand, have much weaker intermolecular attractive forces. It is important to note that, in the SCF region, attractive forces between molecules are minimized.

In the solid form CO_2 has a high density and a very high viscosity. Similarly, the liquid has a high density and a reasonably high viscosity, and the gas has a low density and low viscosity. Conversely, the supercritical fluid phase has a high density but a relatively low viscosity. The density of supercritical CO_2 can vary over a wide range from gas values, around 0.1 g cm^{-3}, to liquid values of about 2.0 g cm^{-3}. In other words, the density of supercritical CO_2 can be changed by over 2000% simply by varying the temperature and pressure within the supercritical region. A supercritical fluid is by definition both liquid and gas-like, and hence it is compressible. Thus, relatively small changes in temperature and/or pressure can significantly affect the density, as seen in Figure 1.

As the density of the CO_2 becomes more liquid-like, so do the solvent properties of the fluid. To a first approximation, the ability of a supercritical fluid to dissolve other fluids can be related to its density in the supercritical region. When operating in the supercritical region, therefore, both temperature and pressure can be used to vary the density, and therefore, the dissolving power of the fluid. It is this ability to alter the solvent power that makes supercritical CO_2 such an attractive solvent. To make the potential for SCFs even more promising, small additions of other components, called co-solvents or entrainers, often modify the observed phase equilibria dramatically. Again this special property affords the chemist the opportunity to *tailor* solvents to achieve a variety of goals, either in separations or reactions.

The viscosity of carbon dioxide is observed to change rapidly in the critical region, as is the case also for diffusivity. Even at high pressures of 300–400 atm it is still only about 0.09 centipoise, an order of magnitude below typical organic solvents. Because of these density and viscosity properties, supercritical CO_2 possesses certain other characteristics, which enhance its attractiveness as a solvent. In addition to possessing liquid-like densities over much of the temperature and pressure range of interest to industry, it exhibits the gas-like property of diffusivity with a zero value for the surface tension. These features alter the transport to allow for easy penetration of SCFs into nano-dimensional spaces.

The self-diffusion coefficient for carbon dioxide (which is approximately the same for similar sized molecules diffusing through carbon dioxide) is about one to two orders of magnitude higher than the diffusivities of comparable solutes in typical organic liquids.

2.3 NMR of Supercritical Fluids

The interactions of a nuclear moment with other nuclei and the electrons surrounding it provide a very sensitive site specific probe into the structure and dynamics in the solid, liquid, and gas phase. This work will concern itself with NMR in the supercritical fluid state of carbon dioxide. As mentioned above, these states exhibit properties of both the liquid and the gas phases. Thus, techniques and theory from work in both phases combine in these unique applications. Thorough reviews have been published on the unique information which can be obtained in the gas phase.[1,2] Other reviews have been published on experimental techniques and applications of high pressure NMR.[3,4] These reviews were published on or before

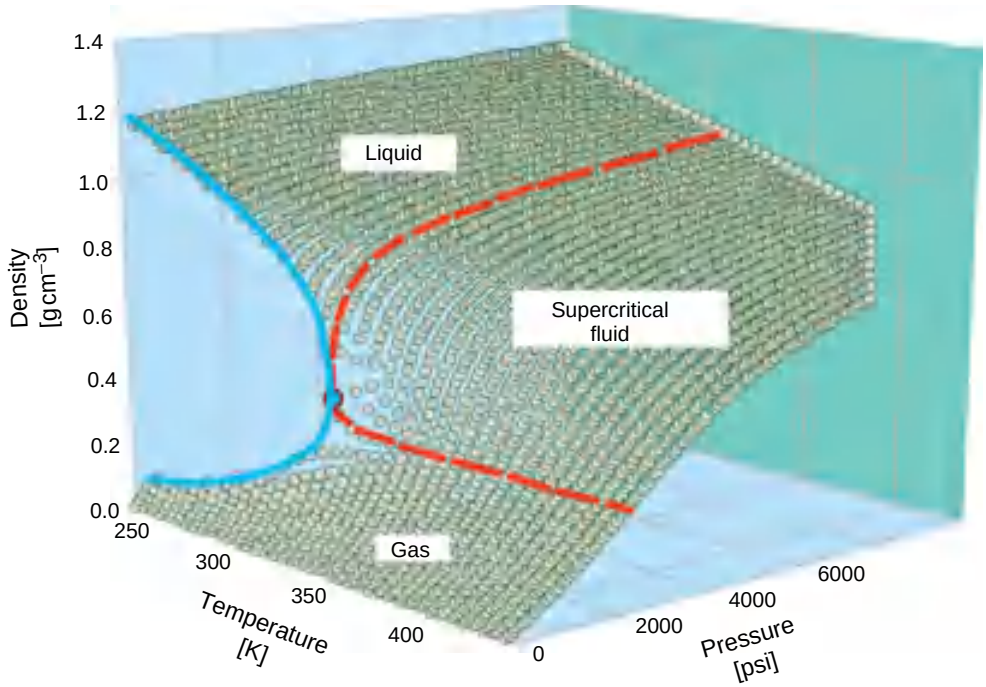

Figure 1 Pressure–temperature–density surface of pure CO_2

1991. We will discuss primarily studies published later, with information as it relates specifically to NMR determination of the dynamics and structure in the SCF state.

Although the application of high pressure NMR to simple fluids leads to some interesting additional complications, the information gained from the technique more than justifies its use. The pressure axis provides an additional dimension to the experimental matrix. For a liquid it is commonly known that temperature changes at constant pressure will effect the molecular motion via kinetic energy and molecular average volume collisional arguments. One can separate the effects of density and temperature on the molecular motion only if both the temperature and pressure are controlled variables in the NMR experiment. Increased pressure also allows for the experimental range to expand well above the normal boiling point and into the compressible supercritical fluid regime. Some examples of the usefulness of high pressure NMR will be given.

2.4 Introduction to the Basics of High-pressure NMR

The motions of molecules in liquids is accessible only through a large number of various models that depend upon phenomenological parameters such as the coefficient of rotational diffusion, the frequency of collisions, the time between jumps, etc. Three such theories: the random walk theory of Torrey,[5] the rotational diffusion theory of Abragam,[6] and the rotational Brownian motion of McConnell[7] form the basis upon which most NMR relaxation models in liquids are based. Other methods of studying molecular motion (optical, dielectric, neutron scattering, etc.) can in principal give additional detailed information. However, as a consequence of the many-particle effects present in these methods, the interpretation of the experimental results for liquids is often ambiguous. In NMR, the weak coupling of the spin system with the lattice allows one to focus better on isolated molecular motions to describe relaxation in liquids.[8] Information on the rotational motion of molecules in liquids of low viscosity, given by NMR, is obtained in the form of the integrals of the time correlation functions, i.e., the correlation times. This section will discuss the effects of dense gas and supercritical fluid states on the correlation times, and what this means to the NMR spectroscopist.

2.5 The Origin of Nuclear Spin Relaxation

Direct time dependant interactions have been shown to cause spin relaxation. However any static interaction can simply be treated as part of the normal spin Hamiltonian, altering the positions and intensities of the spectral lines. For example, a nuclear spin may experience a local magnetic field from the spins of other nuclei moving in its vicinity, from an unpaired electron, or from a variety of other mechanisms, such as the spin–rotation interaction in which the rotation of the molecular electrons generates a magnetic field at the nucleus. In general, rotational and diffusional motions are important sources of relaxation in fluids. Some mechanisms that make contributions to spin–lattice relaxation will be discussed.

2.5.1 Nuclear Spin Relaxation Mechanisms

There are a number of processes that provide the basis for nuclear spin relaxation. These include the nuclear magnetic dipole–dipole interactions (DD), the spin–rotation interactions (SR), the quadrupolar interactions (Q), and the chemical shift interactions, (CSA). The overall relaxation rate can be expressed as a sum of contributions from each mechanism.

2.5.2 Dipole–Dipole Interaction

The magnetic nuclei in molecules provide magnetic dipole fields that are proportional to the magnetic moments of the nuclei. These fields fluctuate in magnitude and direction as the molecule tumbles through space. When these random oscillating fields have magnetic field components at the Larmour frequency, the nuclear spin relaxes. This interaction depends upon the correlation time of the tumbling molecule as well as the distance between the interacting nuclei. The dipole interactions can be divided into intramolecular and intermolecular interactions. For both of these types of interactions there is a homo, and hetero-nuclear sub-interaction. These are reflected in the following equations

$$\text{For intra-homo:} \quad \frac{1}{T_1^{\mathrm{DD}}} = \frac{3\gamma_A^4\hbar^2\tau_c}{2r^6}$$

$$\text{For intra-hetero:} \quad \frac{1}{T_1^{\mathrm{DD}}} = \frac{\gamma_A^2\gamma_X^2\hbar^2\tau_c}{r^6} \tag{1}$$

$$\text{For inter-hetero:} \quad \frac{1}{T_1^{\mathrm{DD}}} = \frac{2N_x\gamma_A^2\gamma_X^2\hbar^2}{Da}$$

where r is the distance between the interacting nuclei, D is a mutual translational self-diffusion coefficient for the molecules containing A and X, and a is the distance of closest approach between A and X. τ_c is a rotational diffusion correlation time for molecular tumbling. This corresponds to the average time it takes for a molecule to rotate through one radian.

2.5.3 The Spin–Rotation (SR) Interaction

Spin–rotation relaxation of the nuclear magnetization in molecules is due to the intramolecular coupling of the individual nuclear spins to the molecular angular momentum. A fluctuating local magnetic field, which relaxes the nuclear spins, is the result of the collisional reorientation of the molecular rotational angular momentum. For linear molecules such as CO_2, the spin–rotation contribution to the total spin–lattice relaxation can be expressed as

$$\frac{1}{T_1^{\mathrm{SR}}} = \frac{4C_\perp^2 IkT\tau_j}{3\hbar^2} \tag{2}$$

$C_\perp$ is the spin–rotation constant and I is the moment of inertia. For a spherical top molecule, the relaxation rate has the form

$$\frac{1}{T_1^{\mathrm{SR}}} = \frac{2C_{\mathrm{eff}}^2 IkT\tau_j}{\hbar^2} \tag{3}$$

C_{eff} is the effective spin–rotation tensor. The τ_j is the correlation time for angular momentum transfer and therefore is closely related to the average time between collisions. The higher the temperature the faster the molecule reorients in accordance with the kT term. The result is that the spin–rotation contribution to the total spin–lattice relaxation

increases with temperature. This is quite the opposite in all other mechanisms examined in this work.

2.5.4 Quadrupolar Relaxation

Quadrupolar occurs when the nuclear electric quadrupole moment, interacts with electric field gradients to provide a very efficient nuclear relaxation process. The equation for these interactions is similar in form to that of the dipole interaction. The electric quadrupolar interaction between spin I and an electric field gradient can be written in the form given in equation (4).

$$\frac{1}{T_1^{\mathrm{Q}}} = \frac{3\pi^2(2I+3)\chi^2\tau_{\mathrm{c}}}{10[I^2(2I-1)]} \tag{4}$$

where χ is known as the nuclear quadrupolar coupling constant and is in units of frequency. The τ_{c} here is the rotational diffusion correlation time as it appeared in the dipolar equation. Because of its relative efficiency the quadrupolar interaction nearly dominates when quadrupolar nuclei are present.

2.5.5 Chemical Shift Anisotropy

Anisotropic shielding at the nucleus changes with the orientation of the molecule in a static field. Therefore the molecular tumbling modulates the local magnetic field resulting in relaxation. The spin–lattice relaxation rate due to this interaction is proportional to the square of the magnetic field:

$$\frac{1}{T_1^{\mathrm{CSA}}} = \frac{2}{15}\gamma_A^2 B^2 \Delta\sigma^2 \tau_{\mathrm{c}} \tag{5}$$

where Δ is the chemical shielding anisotropy of the nucleus and τ_{c} has the same meaning as before.

The spin–lattice relaxation can be measured and contributions from each of the mechanisms decoupled to yield dynamic and structural information pertaining to the species of interest. Each of the following sections will contain specific observation techniques and theoretical treatments used to provide insight into the often strange and unpredictable world of supercritical fluids.

Extensive studies have been performed on nuclear magnetic spin lattice relaxation and its dependence on molecular structure and dynamics. This is the subject of several review articles.[9–12] Decoupling techniques are often used to enhance the signal and to simplify the resulting spectrum. Such decoupling studies also yield the nuclear Overhauser enhancement (NOE), which allows the unique separation of the dipolar interaction from other relaxation interactions. However, decoupling also eliminates multiplet splittings from scalar couplings, thereby preventing direct measurement of some of the spectral features that are required to completely describe the relaxation of coupled nuclear spin systems.

Spin-coherent double-resonance experiments, which avoid this loss of information, and a general numerical method for analyzing the data obtained in relaxation studies of this type may be used.[13,14] Relaxation processes, described by a system of coupled linear differential equations, determine a variety of time-independent relaxation parameters that contain information on the molecular structure, and dynamic features of the motion. The relaxation parameters in the equations of motion can then be extracted from the experimental data using standard least squares methods.[13,14]

For polyatomic gases, nuclear spin relaxation proceeds primarily from the collisional modulation of the molecular rotational angular momentum coupled to the angular momentum of the nuclear spins. Reorientations of molecular angular momentum by collision then give rise to fluctuating internal magnetic fields, that effect the nuclear spins through intramolecular spin–rotation couplings. In addition to the spin–rotation mechanism molecular motional modulation of the chemical shift anisotropy, dipole-dipole and quadrupolar couplings also affect the relaxation rates.

In low-viscosity liquids and gases, spin–lattice relaxation may be treated as a temporal modulation associated with the thermal reorientation of the molecule. The study of spin lattice relaxation contributes to an understanding of molecular dynamics.[15] In dilute gaseous samples of small molecules where the interactions mediating spin relaxation are primarily intermolecular,[16,17] and the various interaction parameters are known accurately,[18–21] the study of relaxation reveals features of collisional processes responsible for reorientation of the molecules.[22–24]

2.6 Line Narrowing

All polyatomic gases possess more than one intramolecular relaxation mechanism. Even the molecule H_2, for instance, has two competing mechanisms: the spin–rotation and the direct dipole–dipole interaction. In condensed phase molecular hydrogen the contribution of the dipole–dipole mechanism is comparable to that of spin rotation because the distance between the protons is short enough for the dipole–dipole relaxation to be appreciable. In a gaseous system, however, spin rotation is normally the dominant relaxation mechanism. In such experiments high density carbon dioxide can be added to hydrogen isotopomers such as hydrogen deuteride, as suggested by Johnson and Waugh,[23] to shorten the rotational correlation times and thereby lengthen the spin–rotation relaxation time and narrow the resonances in the high-resolution spectra. The H_2 system is difficult to study because of the indistinguishability of the two particles. Thus research on the lower HD symmetry[18,19,21–23,25–28] provides more information from both the proton and deuteron resonances arising from indirect spin-spin couplings.

Supercritical fluids generally have viscosities 10–100 times lower than that of the normal liquid phase and self diffusion coefficients 10–100 times greater. To the NMR spectroscopist, these properties are of significant benefit in studying quadrupolar nuclei, since the quadrupolar linewidth is proportional to the rotational correlation time. The utility of NMR to study many quadrupolar nuclei has been somewhat limited. Quadrupolar relaxation can be very efficient, leading to broad lines and low sensitivities. In the extreme narrowing limit, the linewidth of these nuclei,$(1/\pi T_2)$ can be written as

$$\frac{1}{\pi T_2} = \frac{3}{8}\left(\frac{e^2qQ}{h}\right)^2\left(1+\frac{\eta^2}{3}\right)\tau \tag{6}$$

where e^2qQ/h is the quadrupolar coupling constant, τ is the rotational correlation time for the molecular motion, and η is the asymmetry parameter of the electric field gradient

tensor. Various studies have demonstrated the validity of the Stokes–Einstein–Debye equation.[29]

$$\tau = \frac{A\eta}{T + \tau_0} \tag{7}$$

in which τ is the rotational correlation time, η is the solvent viscosity, T is the temperature and τ_0 is the high temperature intercept. This equation predicts a linear relation between τ and η/T to a limiting value τ_0 attained in the limit as $\eta/T \rightarrow 0$. Comparisons with above equation show that NMR line widths should decrease with decreasing viscosity to a limiting value expected to be related to the free rotor correlation time given by

$$\tau_{\mathrm{FR}} = \left(\frac{2\pi I}{9kT}\right)^{1/2} \tag{8}$$

where I is the moment of inertia about the rotational axis.

2.7 NMR Determination of Structural Dynamics in High-Pressure Fluids

There have been direct spectroscopic probes of the local solvent structure around solutes in supercritical fluids. These include using the solvatochromic scales as in the ultraviolet-visible (UV) absorption of phenol blue in ethylene[30] and the fluorescence spectroscopy of pyrene in carbon dioxide.[31] The use of spectroscopic methods to study the local environment surrounding solute molecules in dilute supercritical fluid mixtures has been reviewed.[32] However the use of NMR to determine the local structure within supercritical fluids has thus far been sparse in the literature.

2.7.1 High Pressure NMR Studies of Hydrogen Bonded Liquids

An understanding of molecular interactions between solute and solvent molecules in supercritical fluids (SCF) is essential to an explanation of clustering phenomena, considered responsible for the unique SCF solvating characteristics compared to gases.[33–35] Although both theoretical[36–38] and experimental efforts[39–46] have been made to increase the understanding of these phenomena, a complete picture of clustering in SCFs is still evolving. The accumulation of experimental NMR relaxation data is expected to improve our physical picture of solvent clustering in SCF. Because the nuclear spin–lattice relaxation rates depend on the fluctuating molecular reorientation and molecular collision frequency, their measurement proves to be an effective method for studying such molecular interactions and dynamics in fluids.[47] One of the advantages of utilizing NMR relaxation data is that they provide not only information, similar to optical methods, on overall molecular motions but also site-specific information on intramolecular motions. The ^{13}C spin–lattice relaxation processes in CO_2 are dominated by spin–rotation interactions.[48–50] Nuclear spin–lattice relaxation rates have been measured under SCF conditions by Lamb et al.[51] and Etesse et al.[52–54] for various SCF mixtures. NMR chemical shift measurements[55] were also used to relate ^{129}Xe chemical shift data to the local solvent structures of SCF Xe. SCF fluid structures in pure methanol,[56] CO_2–methane,[39] CO_2–methanol,[40] and CO_2–decanol[40] mixtures have recently been made. The function of the hydroxyl group in solute-induced solvent clustering in SCF CO_2 appears to be especially important. Earlier developments in high pressure NMR studies of hydrogen bonded liquids may be found in a review article by Lang and Ludemann.[57]

Information on the nature and average rate of molecular motions may be obtained by determining the nuclear spin–lattice relaxation rates of nuclei in the molecules under investigation. The nuclear spin relaxation rate, $1/T_1$, depends on fluctuations in molecular reorientations as a consequence of molecular collisions, where T_1 is the time constant defining the exponential return of a perturbed nuclear spin to its equilibrium state. Many nuclear spin interaction mechanisms affect T_1 values. Among them, spin–rotation, quadrupolar and dipolar interactions are the most important ones at sub- and supercritical densities. Detailed descriptions of spin–rotation, quadrupolar and dipolar interactions may be found in the review articles by Grant et al.[58] and Jameson.[59] Briefly, determination of NMR nuclear relaxation rates provides the angular momentum[59] and rotational reorientation correlation times[58] from the spin–rotation and quadrupolar/dipolar interactions, respectively. Spin–rotation interactions are directly related to molecular collision frequencies and depend on macroscopic properties such as fluid density and temperature. Dipolar and quadrupolar interactions, however, are often related to fluid viscosity and temperature. Since the fluid viscosity may be treated as a function of local density in the compressible regions of CO_2, both correlation times may be considered as functions of local densities. Therefore, clustering phenomena in SCF resulting in fluctuations of local density may in principle be observed by NMR relaxation measurements.

The magnitude of the NOE effect is given by[60]

$$\mathrm{NOE}(A\{X\}) = \frac{I_A^*}{I_A^0} \tag{9}$$

where I_A^* is the integrated intensity of a decoupled spectrum with saturation of the nucleus X, and I_A^0 is the equilibrium intensity of A in the coupled spectrum. The maximum possible NOE of ^{13}C{^{1}H} occurs when ^{13}C and ^{1}H relax only by the dipolar mechanism given by[60] and is given by

$$\mathrm{NOE(max)} = 1 + \left(\frac{\gamma_{\mathrm{H}}}{2\gamma_{\mathrm{C}}}\right) = 2.988 \tag{10}$$

where γ_{H} and γ_{C} are the magnetogyric ratios for ^{1}H and ^{13}C, respectively. The NOE effect may be determined as a ratio of spectral intensities with proton decoupling to that of gated proton decoupling. Since the ^{13}C in CO_2 does not exhibit an NOE, its signal intensity may be used as a fiducial reference.

2.8 Significant Mechanism in Spin–Lattice Relaxation: Overall Rotational Motion

In general, the overall rotational motions of solute molecules depend on the intermolecular frictional forces between the solute and solvent molecules and, therefore, are dependent upon the solvent viscosity. The solvent viscoelastic response, in turn, is also dependent on various relaxation mechanisms of solvent molecules. Internal rotational motions including various local isomerization movements are driven by torsional forces.[61]

The rotational reorientation correlation time, τ_c, may be extracted from NMR spin–lattice relaxation time measurements, within the *extreme narrowing* limit, using the following expression[60]

$$T_{1,\mathrm{DD}}^{-1}(^{13}\mathrm{C}) = \frac{\upsilon\gamma_C^2\gamma_H^2\hbar^2\tau_c}{r^6} \tag{11}$$

where r is the bond distance between ^{1}H and ^{13}C (measured as 1.085 Å), and υ is the number of protons directly attached to the ^{13}C nucleus. The dipole–dipole relaxation rate, may be obtained from the standard relationship between the overall T_1 and NOE measurements:[60]

$$\mathrm{NOE} = 1 + \frac{\gamma_H}{2\gamma_C}\frac{T_{1,\mathrm{DD}}^{-1}(^{13}\mathrm{C})}{T_{1,\mathrm{Tot}}^{-1}(^{13}\mathrm{C})} \tag{12}$$

The reorientation correlation time obtained in this manner is an average assuming isotropic reorientation. This correlation time may be related to a rotational diffusion coefficient by assuming that each nuclear environment is roughly spherical and rotates randomly.[62]

$$\tau_c = \frac{1}{6D} \tag{13}$$

From the temperature dependence of rotational diffusion coefficients at fixed viscosity, one can determine effective rotational activation energies.

2.9 CO_2 Clustering

The rotational reorientation correlation time, τ_c, can be expressed by a modified Stokes–Einstein–Debye (SED) equation[63]

$$\tau_c = \frac{\eta V_p}{kT} f_{\mathrm{stick}} C + \tau_0 \tag{14}$$

where η is the fluid viscosity, V_p is the volume of solute molecule, f_{stick} is a well-defined shape parameter dependent only on the structure of solute molecules,[64] C is a boundary parameter dependent on the nature of the solute and solvent and upon their concentration, and finally τ_0 is the free-rotor correlation time. The success of this model strongly depends on the selection of parameters C and f_{stick}. Recently, Roy et al.[64] noted that the Dote, Kivelson, and Schwartz (DKS) model[63] is the best model for predicting reorientational correlation times for solutes with radii up to about 4.5 Å. Anderson and Kauffman[65] further modified the calculation of the smallest volume of free space per solvent molecule, ΔV, in the DKS model, and more recently, these two workers[66] related fluid viscosity and the parameter C in the SED model to the local density by introducing a radial distribution function into the hydrodynamic model. These modifications[65,66] by Anderson and Kauffman are referred to as the AK model.

In the AK model, the viscosity for a fluid is expressed as a function of local density ρ_{12}^1 by equation 4.7 described by Jossi et al.[67]

$$[(\eta - \eta_0)\xi_T^y + 1]^{1/4} = 1.023 + 0.23364\rho_r + 0.58533\rho_r^2 - 0.40758\rho_r^3 + 0.09324\rho_r^4 \tag{15}$$

where $\rho_r = \rho_{12}^1/\rho_c$ and $\xi_T = (T_c/M^3P_c^4)^{1/6}$. ρ_c, T_c, and P_c represent the critical density, temperature, and pressure, respectively. M is the molecular weight in the unit of g mol^{-1}. The local density of is related to the bulk density ρ by a radial distribution formalism

$$\rho_{12}^1 = \rho\{1 + F[g_{12}(r)]\} \tag{16}$$

where $F[g_{12}(r)]$ is an integral equation in the pair distribution function, $g_{12}(r)$, over the spatial coordinates and r is the distance between solvent and solute molecules. $F[g_{12}(r)]$ is a measure of the excess solvent density near the solute molecule and is treated as an adjustable parameter in the AK model. When $F[g_{12}(r)] = 0$, the local density equals the bulk density, and when $F[g_{12}(r)] = 1.0$, the local density is twice the bulk density.

In the AK model, the parameter $C(\rho_{12}^1)$ equivalent to C in the SED model, is also treated as a function of local density. According to the DKS model

$$C(\rho_{12}^1) = \frac{f_{\mathrm{slip}}V_p}{f_{\mathrm{slip}}V_p + \gamma V_p} \tag{17}$$

where f_{slip} is a factor for the slip boundary condition whose value estimated from f_{stick} by the method reported by Hu and Zwanzig[68] and γ is defined as

$$\gamma = \left(\frac{\Delta V}{V_p}\right)\left[4\left(\frac{V_p}{V_s}\right)^{\frac{2}{3}} + 1\right] \tag{18}$$

In equation (18), V_s is the solute molecular volume and ΔV is the free space volume for a solvent molecule. For supercritical fluids in their compressible regions, a large variation in the free space is expected, and ΔV is given by equation (19) relating molecular weight (MW) and local density:

$$\Delta V = \frac{\mathrm{MW}}{\rho_{12}^1} - V_s \tag{19}$$

Therefore, the parameter $C(\rho_{12}^1)$ is expressed as a function of local density ρ_{12}^1 though the free space volume ΔV.

Combining equations (18) and (19), the AK version of the SED equation may be expressed as[66]

$$\tau_c \equiv \frac{\eta(\rho_{12}^1)V_p}{kT} f_{\mathrm{stick}} C(\rho_{12}^1) + \tau_0 \tag{20}$$

Equation (20) relates the reorientation correlation time, τ_c, to the solvent local density at a given temperature. By performing a comparison experiment on *trans*,*trans*-1,4-diphenylbutadiene (DPB) solute in CO_2, Anderson and Kauffman[66] also observed that CO_2 solvent clustering only occurs in the vicinity of *trans*-4-(hydroxymethyl)stilbene (HMS) molecules. Because the extended π-electron systems existing in DPB and HMS are similar, Anderson and Kauffman concluded that the OH group in HMS is responsible for the association between the solute and solvent molecules. The one-to-one association between solute and solvent molecules may initiate further CO_2 clustering whenever strong many-body interactions affect the solvent structure in supercritical

fluids in the compressible density region. The CO_2 clustering gradients observed along the aliphatic chain of l-decanol molecules in the Bai et al.[39] study appear to support the observations by Anderson and Kauffman.

To verify further the importance of alcohol enhanced clustering, the same procedure was applied to a CO_2–methanol mixture,[69] where a specific association between CO_2 and CH_3OH has been observed also by the IR studies.[42] Such solvent-solute interactions may initiate CO_2 solvent clustering.[66] The low-pressure limit free-rotor correlation time can be calculated using the following expression[70]

$$\tau_0 = \frac{2\pi}{9}\left(\frac{I_\perp}{kT}\right)^{1/2} \tag{21}$$

where is the perpendicular component of the moment of inertia for methanol molecules. The calculated τ_0 from equation (21) is 0.20 ps, which agrees well with the 0.17 ps from fitting the low-density data.

2.10 More Evidence for the Formation of CO_2 Clusters in the Vicinity of Methanol

As stated above, NOE measurements allow the separation of the dipole–dipole contributions to spin–lattice relaxation rates from other mechanistic contributions. For methanol, the remaining relaxation contributions result essentially from the spin–rotation mechanisms described previously.[69] These spin–rotation relaxation rates allow one to calculate an angular momentum exchange correlation time, τ_J, which is strongly dependent on the fluid density. Methanol is a quasi-symmetric top molecule, but the relation between ρ, and spin–rotation relaxation rates for symmetric top molecules may be used as a good approximation for T_1^{SR}. The expression[71] is

$$\frac{1}{T_1^{SR}} = \frac{2\pi^2}{\alpha} C_{\text{eff}}{}^2 \tau_J \tag{22}$$

where pull down $\alpha = \hbar^2/(2kTI_\perp)$ and $I_\perp$ is the perpendicular part of the moment of inertia for methanol. The effective spin–rotation, C_{eff}, may be expressed as

$$C_{\text{eff}}{}^2 = k_1 C_a^2 + k_2 C_a C_d + k_3 C_d^2 \tag{23}$$

In equation (23), the structure parameters, k_i, only depend on molecular structure. C_a and C_d are the isotropic and anisotropic components of the spin–rotation tensor. Therefore, in principle, an experimental angular momentum correlation time, τ_J, may be estimated using equation (22). Since τ_J is linearly related to the time between molecular collisions, τ_{BC}, one may calculate τ_J using a gas kinetic theory. The slope of this linear relationship, called an effective collision number and referred to as Z,[72] provides the average number of collisions needed for an effective molecular angular momentum exchange. This number is found to be between 1.4 and 3.4 for many collision pairs (cf. Table 3 in Ref.[72]). In the use of a hard-sphere model (HSM) for calculating cross sections, choosing the effective collision number of two appeared to be a good approximation in the work of Maryott, Malmberg, and Gillen,[72] and therefore, this value is used in the following discussion. The expression for computing τ_J is given by[73]

$$\tau_J = \frac{Z}{\rho \overline{v} \sigma_K} \tag{24}$$

where ρ is fluid density, $\overline{v}$ is the average velocity of molecules, and ρ_K is the kinetic collisional cross section between solute and solvent molecules. Both $\overline{v}$ and σ_K may be estimated from molecular properties of the solute and solvent. If the density term, ρ, in equation (24) is replaced by a local density [cf. equation (16)], the estimated τ_J becomes a function of the excess solvent density parameter, $F[g_{12}(r)]$. In this case, equation (24) becomes

$$\tau_J = \frac{Z}{\rho\{1 + F[g_{12}(r)]\}\overline{v}\sigma_K} \tag{25}$$

There is good agreement between theoretical and experimental data when an increase in local density is employed in the predictions of τ_J. This provides additional evidence for the formation of SCF solvent clustering in the vicinity of hydrogen bonding solute molecules. Supposedly, these interactions are induced by the hydroxyl functional group present in alcohol molecules.

2.11 NMR Determination of Self-diffusion Coefficients in High-pressure Fluids

Many methods exist for measuring the diffusion coefficients of fluids. However, the experimental accuracy of many of these is quite limited.[74,75] Furthermore, methods that give reliable results in the low pressure regime are not always suitable at high pressures because the inverse dependence of the diffusion coefficient on pressure makes for experiments that take an inordinately long time. The most widely reported method for the measurement of diffusion coefficients in the SCF state is a gas chromatographic method based on Taylor dispersion, which has proven unreliable at lower pressures.[76–78]

The only other methods that can be utilized for this measurement in SCFs are photon correlation spectroscopy[79,80] and NMR.[81,82] They are not widely used at this time because the equipment is very expensive and their application to industrially important SCF's is still in its infancy. The use of the NMR technique has been confined to the measurement of self diffusion coefficients.[81,82]

3 INSTRUMENT REQUIREMENTS FOR HIGH-PRESSURE NMR

In order to perform NMR experiments under high pressure, it is necessary to devise a convenient means to control the pressure, temperature and sample concentration while it is inside the magnet. Two basic approaches to the design of high pressure NMR experiments have been reported: (1) construction of a probe which is capable of achieving the necessary pressures, referred to as the *high pressure probe technique*,[83] or (2) fabrication of a high pressure cell which can be used in a standard commercial NMR probe, referred to as the *high pressure cell technique*.

The very first high pressure NMR experiment was performed in 1954 by Benedek and Purcell.[84] They used a

hydrostatic high pressure probe capable of holding pressures up to 10 000 atm. For deformable samples the high pressure probe technique requires a sealed sample cell which incorporates a volume change mechanism such as bellows or a mercury column.[85] The cell is surrounded by a RF coil and is located inside a pressure vessel small enough to fit inside the NMR magnet. The high pressure probe technique usually offers higher sensitivity because of a better filling factor for the receiver coil. It also allows for higher pressures and is usually safer to work with. The disadvantages are that they require a more elaborate and expensive design and are therefore not suitable for a routine NMR laboratory. The approach to a high pressure probe has continually been developed by Jonas et al.[86] with improvements to pressure vessel design and electrical feed-throughs. The most recent advances to the probe design for studying supercritical fluids include the toroidal coil[87] and cavity[88] design by Rathke et al.

The high pressure cell technique allows the experiments to be performed in a commercial NMR probehead, thereby eliminating the need to alter the basic probe design. The earlier versions of high pressure cells experienced lower sensitivity and reduced working pressures. Yonker et al. designed a simple and safe method by coiling a fused silica capillary tube inside a commercial 5-mm NMR tube.[89] Newer cell designs have improved these limitations providing a more convenient and cost-effective means of carrying out high pressure NMR experiments. Roe et al.[90] designed the first cell made of single crystal sapphire and Horvath et al. later improved this design.[91,92] Pressure control while the cell is in the magnet is a major issue in the cell design. The previously reported designs of the sapphire NMR cells were unable to independently control both the sample temperature and pressure. In the Bai et al. design[93] a movable piston is used to control the sample pressure (see Figure 2). With this design it is possible to control temperature and pressure independently over a wide range of conditions while keeping the relative molar concentration ratios of the sample mixture intact. The sample volume must be restricted to the active coil in order to eliminate errors introduced through molecular diffusion between polarized and nonpolarized volume elements within the cell. Recently a high pressure cell constructed of high-performance polymers, such as poly(etherether ketone) (PEEK), was developed by Wallen et al.[94] with the purpose of simplifying the cell design to allow for more routine experiments on supercritical fluids.

The very first high pressure probe was made of a beryllium copper alloy (Berylco 25). This alloy was used due its strength and nonmagnetic properties, but does require special heat treatment and can have significant variations in the level of paramagnetic impurities. Berylco 25 is stable up to 10 000 atm and permits a temperature range of $-10\,^{\circ}\mathrm{C}$–$80\,^{\circ}\mathrm{C}$. Titanium alloys (IMI-680) are now more commonly used as they require no special heat treatment during machining and retain their strength up to 400 °C and 5000 atm. For even higher pressures, up to 100 kbar, the diamond anvil method can be used.[95] This method can only be used with very small samples so most studies concern sensitive nuclei, although a study on ^{13}C has been reported.

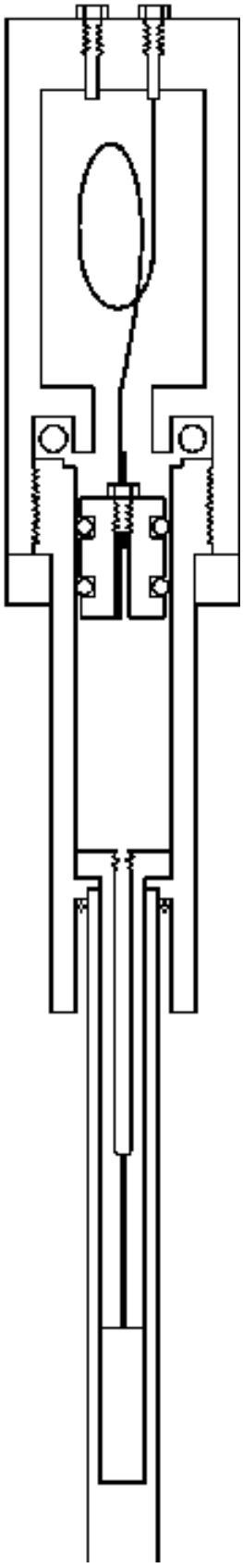

Figure 2 Schematic diagram of the high pressure piston NMR cell capable of independently controlling temperature, pressure and sample concentration

4 SUPERCRITICAL FLUID APPLICATIONS

Most of the high pressure NMR studies of supercritical fluids have involved measuring chemical shifts, such as ^{1}H,[96]

of both polar and nonpolar solute molecules in the dense phase fluid. Increased reaction rates of certain reactions in supercritical fluids has been attributed to specific solvent-solute and solute–solute interactions. By studying these specific interactions by NMR further insight into the variation of the surroundings of the solute molecules with the density of the supercritical fluid is obtained and can be compared to other experimental techniques, such as UV and vibrational spectroscopy.

Using a fused silica capillary cell an in situ photolysis study of organometallics in supercritical fluids was performed where the ligand exchange with the metal center was directly observed.[97] High pressure NMR was also used to determine the fundamental dynamic and electronic properties of the organometallic complexes in the SCF through the investigation of the spin–lattice relaxation times, T_1, and NMR magnetic shielding constants, σ.

Another interesting application of supercritical fluids is to use them as solvents for comprehensive NMR studies of large proteins. In conventional solvents large proteins (over 30 kDa) tumble too slowly and correspondingly the spin–spin relaxation times (T_2) become shorter, making some standard experiments unreliable. By encapsulating the protein in a reverse micelle dispersed in a low viscosity fluid, such as a supercritical fluid, the tumbling correlation time (τ_m) of the protein is reduced thereby increasing T_2.[98] This results in narrower lines in the spectrum.

High pressure NMR has also been used to investigate phase behavior of binary solvent systems in order to obtain vapor–liquid equilibrium (VLE) values. Usually VLE values of supercritical fluid solutions are obtained using variable volume view cells and off-line analysis techniques. By using NMR, this process can be simplified and made more efficient for numerous solvent systems. This technique is especially suitable for hydrocarbon containing solvent molecules as detection of solvent protons in both the liquid and vapor phase can be detected simultaneously.[99]

An advantage of using supercritical fluids as reaction media for chemical reactions is that gaseous reagents are completely miscible with the solvent. In catalytic reactions such as hydrogenations and hydroformylations where H_2 and CO are reactants this can have a significant impact on both the yield and selectivity of the desired products. Since only one phase is present in the supercritical system, stirring to achieve gas–liquid mixing is unnecessary. By studying these reactions in situ by NMR valuable information regarding the mechanism can be obtained.[100] In situ NMR was used to optimize the iridium catalyzed enantioselective hydrogenation of imines in supercritical CO_2. By studying the specific interactions between substrates and products with CO_2 conclusions about the different reactivities of structurally similar substrates were obtained.[101]

5 REFERENCES

1. C. J. Jameson, *Chem. Rev.*, 1991, **91**, 1375–1395.
2. R. L. Armstrong, *Magn. Reson. Rev.*, 1987, **12**, 91.
3. J. Jonas, ed, 'NMR Basic Principles and Progress', Springer Verlag: Berlin, 1991, Vol. 24 of High Pressure NMR.
4. I. T. Horvath and J. M. Millar, *Chem. Rev.*, 1991, **91**, 1339–1351.
5. H. C. Torrey, *Phys. Rev.*, 1953, **92**, 962.
6. A. Abragam, 'The Principals of Nuclear Magnetism', The Clarendon Press: Oxford, 1961.
7. J. McConnell, 'Rotational Brownian Motion and Dielectric Theory', Academic Press: London, 1980.
8. J. McConnell, 'The Theory of Nuclear Magnetic Resonance Relaxation in Liquids', Cambridge University Press: Cambridge, 1987.
9. S. W. Collins, T. D. Alger, D. M. Grant, K. F. Kuhlman, and J. C. Smith, *J. Phys. Chem.*, 1975, **79**, 2031.
10. C. L. Mayne, D. W. Alderman, and D. M. Grant, *J. Chem. Phys.*, 1975, **63**, 2514.
11. G. A. Gray and S. E. Cremer, *J. Magn. Reson.*, 1973, **12**, 5.
12. D. M. Grant, R. J. Pugmire, E. P. Black, and K. A. Christensen, *J. Phys. Chem.*, 1973, **95**, 8465.
13. D. M. Grant, C. L. Mayne, F. Liu, and T.-X. Xiang, *Chem. Rev.*, 1991, **91**, 1591–1624.
14. D. Canet, *Prog. NMR Spectrosc.*, 1989, **21**, 237.
15. D. M. Grant, C. L. Mayne, F. Liu, and T.-X. Xiang, *Chem. Rev.*, 1991, **91**, l591–1624.
16. N. Bloembergen, E. M. Purcell, and R. V. Pound, *Phys. Rev.*, 1948, **73**, 679.
17. A. Abragam, 'Principles of Nuclear Magnetism', Clarendon Press: Oxford, 1961, p. 1581.
18. N. F. Ramsey and H. R. Lewis, *Phys. Rev.*, 1957, **108**, 1246.
19. N. J. Harrick, R. G. Barnes, P. J. Bray, and N. F. Ramsey, *Phys. Rev.*, 1953, **90**, 260.
20. N. F. Ramsey, 'Molecular Beams', Clarendon Press: Oxford, 1956, p. 1454.
21. W. E. Quinn, J. M. Baker, J. T. LaTourrette, and N. F. Ramsey, *Phys. Rev.*, 1958, **112**, 1929.
22. J. R. Gains, P. C. Souers, E. M. Fearon, J. D. Sater, and E. R. Mapoles, *Phys. Rev. B*, 1989, **39**, 3943.
23. C. S. Johnson, Jr. and J. S. Waugh, *J. Chem. Phys.*, 1962, **36**, 2266.
24. P. R. McCourt, in 'NMR Basic Principles and Progress', eds P. Diehl, B. Fluck, and R. Kosfeld, Springer Verlag: Berlin, 1976, p. 56.
25. B. D. Nageswara Rao and L. R. Anders, *Phys. Rev.*, 1967, **140**, A112.
26. P. C. Souers, E. M. Fearon, J. D. Sater, E. R. Mapoles, J. R. Gaines, and P. A. Fedders, *J. Voc. Sci. Tec. A.*, 1991, **9**, 232.
27. R. S. Wagner, R. L. Armstrong, E. C. Bissonette, and F. R. W. McCourt, *J. Chem. Phys.*, 1990, **92**, 5907.
28. J. M. Deutch and I. Oppenheim, in 'Advances in Magnetic Resonance', ed J. S. Waugh, Academic Press: New York, 1966, p. 225.
29. R. B. Bird, W. E. Stewart, and L. N. Lightfoot, 'Transport Phenomena', Wiley: New York, 1960, Chapter 16.
30. S. Kim and K. P. Johnston, *Ind. Eng. Chem. Res.*, 1987, **26**, 1206.
31. J. F. Brennecke and C. A. Eckert, in *Proceedings of the International Symposium on Supercritical Fluids*, Nice, October, 1988.
32. K. P. Johnston, S. Kim, and J. Coombes, in 'Supercritical Fluid Science and Technology', eds K. P. Johnston and J. Penninger, ACS Symposium Series No. 406, American Chemical Society: Washington, DC, 1989.
33. P. G. Jessop, T. Ikariya, and R. Noyori, *Science*, 1995, **269**, 1065–1069.
34. T. J. Bruno and J. F. Ely, eds, 'Supercritical Fluid Technology – Reviews in Modern Theory and Applications', CRC Press: Boca Raton, FL, 1991.
35. E. Klesper, *Angew. Chem. Int. Ed. Engl.*, 1978, **17**, 738–746.
36. (a) J. W. Tom and P. G. Debenedetti, *Ind. Eng. Chem. Res.*, 1993, **32**, 2118–2128; (b) P. G. Debenedetti, *Chem. Eng. Sci.*, 1987, **42**, 2203–2212.
37. S. Kim and K. P. Johnston, *Ind. Eng. Chem. Res.*, 1987, **26**, 1206–1213.

38. (a) H. D. Cochran and L. L. Lee, in 'Supercritical Fluid Science and Technology – Reviews in Modern Theory and Applications', eds T. J. Bruno and J. F. Ely, CRC Press: Boca Raton, FL, 1991; (b) K. P. Johnston and J. Penninger, eds, 'Supercritical Fluid Science and Technology', ACS Symposium Series No. 406, American Chemical Society: Washington, DC, 1989, Chapter 3.
39. S. Bai, C. M. V. Taylor, F. Liu, C. L. Mayne, R. J. Pugmire, and D. M. Grant, *J. Phys. Chem. B*, 1997, **101**, 2923–2928.
40. C. M. V. Taylor, S. Bai, C. L. Mayne, and D. M. Grant, *J. Phys. Chem. B*, 1997, **101**, 5652–5658.
41. J. P. Blitz, C. R. Yonker, and R. D. Smith, *J. Phys. Chem.*, 1989, **93**, 6661–6665.
42. J. L. Fulton, G. G. Yee, and R. D. Smith, *J. Am. Chem. Soc.*, 1991, **113**, 8327–8334.
43. C. R. Yonker, S. L. Frye, D. R. Kalkwarf, and R. D. Smith, *J. Phys. Chem.*, 1986, **90**, 3022–3026.
44. C. R. Yonker and R. D. Smith, *J. Phys. Chem.*, 1988, **92**, 2374–2378.
45. J. Zagrobelny and F. V. Bright, *J. Am. Chem. Soc.*, 1993, **115**, 701–707.
46. T. A. Betts, J. Zagrobelny, and F. V. Bright, *J. Am. Chem. Soc.*, 1992, **114**, 8163–8171.
47. D. M. Grant, C. L. Mayne, F. Liu, and T. X. Xiang, *Chem. Rev.*, 1991, **91**, 1591–1624.
48. P. Etesse, J. A. Zega, and R. Kobayashi, *J. Chem. Phys.*, 1992, **97**, 2022–2029.
49. S. Bai, C. L. Mayne, R. J. Pugmire, and D. M. Grant, *J. Chem. Phys.*, 1997, **101**, 2923–2928.
50. C. J. Jameson, A. K. Jameson, N. C. Smith, and K. Jackowski, *J. Chem. Phys.*, 1987, **86**, 2717–2722.
51. D. M. Lamb, S. T. Adamy, K. W. Woo, and J. Jonas, *J. Phys. Chem.*, 1989, **93**, 5002–5005.
52. P. Etesse, J. A. Zega, and R. Kobayashi, *J. Chem. Phys.*, 1992, **97**, 2022–2029.
53. P. Etesse, A. M. Ward, and R. Kobayashi, *Physica B*, 1993, **183**, 45–52.
54. P. Etesse, W. G. Chapman, and R. Kobayashi, *Mol. Phys.*, 1993, **80**, 1145–1164.
55. D. M. Pfund, T. S. Zemanian, J. C. Linehan, J. L. Fulton, and C. R. Yonker, *J. Phys. Chem.*, 1994, **98**, 11 846–11 857.
56. S. Bai and C. R. Yonker, *J. Phys. Chem. A*, 1998, **102**, 8641–8647.
57. E. W. Lang and H. D. Ludemann, *Prog. NMR Spectrosc.*, 1993, **25**, 507.
58. D. M. Grant, C. L. Mayne, F. Liu, and T. X. Xiang, *Chem. Rev.*, 1991, **91**, 1591–1624.
59. C. J. Jameson, *Chem. Rev.*, 1991, **91**, 1375–1395.
60. R. K. Harris, 'Nuclear Magnetic Resonance Spectroscopy', The Bath Press: Avon, UK, 1986, Chapter 4.
61. F. Liu, W. J. Horton, C. L. Mayne, T. X. Xiang, and D. M. Grant, *J. Am. Chem. Soc.*, 1992, **114**, 5281–5294.
62. Y. J. Kim and J. Jonas, *J. Phys. Chem.*, 1995, **99**, 6777–6788.
63. J. L. Dote, D. Kivelson, and R. N. Schwartz, *J. Phys. Chem.*, 1981, **85**, 2169–2180.
64. M. Roy and S. Doraiswamy, *J. Chem. Phys.*, 1993, **98**, 3213–3223.
65. R. M. Anderson and J. F. Kauffman, *J. Phys. Chem.*, 1994, **98**, 12 117–12 124.
66. R. M. Anderson and J. F. Kauffman, *J. Phys. Chem.*, 1995, **99**, 13 759–13 762.
67. J. A. Jossi, L. I. Stiel, and G. Thodos, *AIChE J.*, 1961, **7**, 625.
68. C.-M. Hu and R. Zwanzig, *J. Chem. Phys.*, 1974, **60**, 4354–4357.
69. S. Bai, C. M. V. Taylor, F. Liu, C. L. Mayne, R. J. Pugmire, and D. M. Grant, *J. Phys. Chem. B.*, 1997, **101**, 2923–2928; C. M. V. Taylor, S. Bai, C. L. Mayne, and D. M. Grant, *J. Phys. Chem. B*, 1997, **101**, 5652–5658.
70. D. Ben-Amotz and T. W. Scott, *J. Chem. Phys.*, 1987, **87**, 3739.
71. B. L. Armstrong and J. Courtney, *Can. J. Phys.*, 1972, **50**, 1262–1272.
72. A. A. Maryott, M. S. Malmberg, and K. T. Gillen, *Chem. Phys. Lett.*, 1974, **25**, 169–174.
73. P. Etesse, J. A. Zega, and R. Kobayashi, *J. Chem. Phys.*, 1992, **97**, 2022–2029.
74. J. Kestin and W. A. Wakeham, in 'Transport Properties of Fluids: Thermal Conductivity, Viscosity and Diffusion Coefficients', CINDAS Data Series Material Properties, ed C. Y. Ho, Hemisphere Publishing: New York, 1988, Vol. 1.
75. T. R. Marrero and E. A. Mason, *J. Phys. Chem. Ref. Data*, 1972, **1**, 1.
76. I. Swaid and G. M. Schneider, *Ber. Bunsenges. Phys. Chem.*, 1979, **83**, 969.
77. R. Feist and G. M. Schneider, *Sep. Sci. Technol.*, 1980, **17**, 261.
78. Z. Balenovic, M. Myers, and J. C. Giddings, *J. Chem. Phys.*, 1970, **52**, 915.
79. H. Saad and E. Gulari, *Ber. Bunsenges. Phys. Chem.*, 1984, **88**, 834.
80. H. Saad and E. Gulari, *J. Phys. Chem.*, 1984, **88**, 136.
81. J. Jonas and D. M. Lamb, in 'ACS Symposium Series No. 329', eds T. G. Squires and M. E. Paulaitis, American Chemical Society: Washington, DC, 1987.
82. W. J. Lamb, G. A. Hoffmann, and J. Jonas, *J. Chem. Phys.*, 1981, **74**, 6875.
83. I. T. Horváth and J. M. Millar, *Chem. Rev.*, 1991, **91**, 1339–1351.
84. G. B. Benedek and E. M. Purcell, *J. Chem. Phys.*, 1954, **22**, 2003.
85. M. E. Smith and J. H. Strange, *Meas. Sci. Technol.*, 1997, **7**, 449–475.
86. B. Lance and J. Jonas, *Annu. Rep. NMR Spectrosc.*, 1997, **33**, 115–150.
87. J. W. Rathke, *J. Magn. Reson.*, 1989, **85**, 150–155.
88. K. Woelk, R. W. Rathke, and R. J. Klinger, *J. Magn. Reson. A*, 1994, **109**, 137–146.
89. C. R. Yonker, T. S. Zemanian, S. L. Wallen, J. C. Linehan, and J. A. Franz, *J. Magn. Reson. A*, 1995, **113**, 102.
90. D. C. Roe, *J. Magn. Reson.*, 1985, **63**, 388.
91. I. T. Horvath and E. C. Ponce, *Rev. Sci. Instrum.*, 1991, **62**, 1104.
92. I. T. Horvath and J. M. Millar, *Chem. Rev.*, 1991, **91**, 1339.
93. S. Bai, C. M. Taylor, C. L. Mayne, R. J. Pugmire, and D. M. Grant, *Rev. Sci. Instrum.*, 1996, **76**, 240–243.
94. S. L. Wallen, L. K. Schoenbachler, E. D. Dawson, and M. A. Blatchford, *Anal. Chem.*, 2000, **72**, 4230–4234.
95. R. Bertani, M. Mali, J. Roos, and D. Brinkmann, *Rev. Sci. Instrum.*, 1992, **63**, 3303.
96. M. Kanakubo, T. Aizawa, T. Kawakami, O. Sato, Y. Ikushima, K. Hatakeda, and N. Saito, *J. Phys. Chem. B*, 2000, **104**, 2749–2758.
97. J. C. Linehan, S. L. Wallen, C. R. Yonker, T. E. Bitterwolf, and J. T. Bays, *J. Am. Chem. Soc.*, 1997, **119**, 10 170–10 177.
98. M. R. Ehrhardt, P. F. Flynn, and A. J. Wand, *J. Biomol. NMR*, 1999, **14**, 75–78.
99. C. R. Yonker, J. C. Linehan, and J. L. Fulton, *J. Supercrit. Fluids*, 1998, **14**, 9–16.
100. J. W. Rathke, R. J. Klinger, R. E. Gerald II, K. W. Kramarz, and K. Woelk, *Prog. NMR Spectrosc.*, 1997, **30**, 209.
101. S. Kainz, A. Brinkmann, W. Leitner, and A. Pfalz, *J. Am. Chem. Soc.*, 1999, **121**, 6421–6429.

Biographical Sketches

Gunilla B. Jacobson, *b* 1969. Ph.D. 1996, Organic Chemistry, University of Uppsala, Sweden. Postdoctoral Research Associate with Keith P. Johnston, Univ. of Texas, Austin, 1997–1998. Research

Associate with William Tumas, Los Alamos National Laboratory, 1998–1999. Technical Staff Member, Los Alamos National Laboratory, 2000–present. Approx 30 publications. Current research interests: reactions, separations, and materials modifications using supercritical fluid technology.

Craig M. V. Taylor, *b* 1962. M.S., 1987 Organometallic Chemistry, New Mexico Institute of Mining and Technology, Ph.D. 1999, Physical Chemistry, University of Utah (supervisor David M. Grant) 1985–87 Research Associate on Supercritical Fluid Tertiary Oil Recovery, Petroleum Recovery Research Center Socorro New Mexico. 1987–94 Scientist Los Alamos National Laboratory (LANL). 1994–98 Principal Investigator Supercritical Fluids Facility, LANL. Leader of Applied Chemical Technologies Group, Chemistry Division, LANL 1998–present. Approx 25 publications. Current research interests: Supercritical Fluids Applications.

Amino Acids, Peptides and Proteins: Chemical Shifts

David A. Case

The Scripps Research Institute, La Jolla, CA, USA

1	Introduction	1
2	Empirical Surveys of Chemical Shifts in Peptides and Proteins	1
3	Chemical Shifts and Secondary Structure	2
4	Chemical Shifts and Tertiary Structure	3
5	Conclusions	4
6	Related Articles	4
7	References	4

1 INTRODUCTION

Perhaps the most direct observables in NMR spectra are the positions of the resonances, which are generally reported as chemical shifts relative to a standard position. The very existence of useful spectra depends upon chemical shift dispersion, so that nuclei in chemically distinct positions resonate at different frequencies. For peptides and proteins it is convenient to divide the origins of chemical shift differences into two components: the first arises from variations in the local electronic environment, so that aromatic and aliphatic protons, for example, have characteristic shifts that differ from each other and from amide protons. A second component of chemical shift dispersion occurs with nominally identical protons, such as valine Hα, due to variations in the nature of adjoining residues and especially to conformational differences in secondary and tertiary structure. While there is no sharp distinction between these two components, the 'local' effects usually arise from variations in shielding by electrons in the bonds that contain (or are adjacent to) the resonating nucleus, whereas the longer range effects are generally 'through-space' interactions involving functional groups separated by many chemical bonds from the nucleus in question.

This article surveys both empirical trends and theoretical approaches to understanding chemical shift trends in amino acids, peptides and proteins. The main emphasis is on connections between conformation (especially secondary and tertiary structure) and chemical shift. It has been clear for some time that chemical shifts in proteins and peptides depend upon structure in a reasonably regular way, so that, for example, the shifts in structurally homologous proteins are themselves homologous.[1,2] One force driving recent reexaminations of the origins of chemical shift dispersion has been the rapid growth in the number of protein and peptide assignments. Many of these are now available in a relational database that contains about 140 000 assignments.[3] While much of the 'information content' of these data remains to be discovered, the following two sections outline some of the clear trends that emerge from surveys of shift distributions

2 EMPIRICAL SURVEYS OF CHEMICAL SHIFTS IN PEPTIDES AND PROTEINS

2.1 Peptides

Short, unstructured peptides provide a useful reference point for many examinations of protein shifts, since they embody most of the local contributions that depend upon the chemical nature of the amino acid side chain, but lack the longer range contributions characteristic of folded proteins. The values most often cited are those of Bundi and Wüthrich (for protons),[4] and Richarz and Wüthrich (for ^{13}C),[5] based on the peptide H-Gly-Gly-X-Ala-OH, where X represents any of the 20 common amino acids. Table 1 lists these values for the backbone nuclei. It is common practice to define a 'structural' shift as the difference between an observed resonance position in a protein or structured peptide and these 'random coil' values.

In principle, peptide shifts like these could be computed from first principles using quantum chemistry calculations. At present such calculations are limited to relatively small molecules in the gas phase, and are generally not of routine 'chemical' accuracy, at least when one is considering nuclei in different bonding environments.[6] The situation is changing rapidly, however, and ab initio calculations with reasonable basis sets are now feasible for protein fragments such as amino acids and dipeptides.[7–11] Such calculations appear to be able to rationalize the dependence of some shifts on backbone dihedral angles, and point the way to the exploration of other effects such as hydrogen bonding and external electric fields. Because a variety of effects are important in influencing shifts, reliable computational studies on amino acids and peptides could have an important impact in the next few years.

2.2 Proteins

The primary empirical study of chemical shifts in proteins is that of Wishart et al.[12] who correlated observed chemical shifts and secondary-structure assignments in over 70 proteins, and computed averages and distributions for shifts in helix, β-strand, and coil configurations. Table 1 gives the results (not sorted by secondary structure) for a larger sample drawn from the BioMagResBank database.[3] There are only minor differences between the proton averages given in Table 1 and the earlier results; for the amide ^{15}N shifts, results for M, P and T differ by more than 1 ppm between the two compilations; for ^{13}Cα, C, M, N, Q and W differ by at least 1 ppm; the majority of values for the carbonyl ^{13}C shift differ by at least this much, perhaps reflecting the small number of available shifts even now. As might be expected, the Cα and Hα nuclei, which are closest to the side chain, show a strong correlation between the median shift observed in proteins and the 'random coil' peptide value: linear correlation coefficients are 0.95 and 0.99 for Hα and Cα respectively. On the other hand, median shifts in proteins for the amide proton and carbonyl carbon are only weakly related to the peptide random coil shifts, with correlation coefficients of 0.11, and 0.56, respectively. This suggests that longer range interactions, such as hydrogen bonding, may be important in influencing these shifts.

Table 1 Backbone Shift Distributions in protein[a]

	HN				Hα			
Res.	No.	Median	SD	rc	No.	Median	SD	rc
A	1446	8.16	0.61	8.25	1429	4.18	0.50	4.35
C	882	8.44	0.66	8.31	942	4.72	0.63	4.69
D	975	8.34	0.62	8.41	936	4.59	0.32	4.76
E	1225	8.30	0.68	8.37	1167	4.17	0.45	4.29
F	668	8.40	0.76	8.23	694	4.61	0.61	4.66
G	1485	8.33	1.31	8.39	2295	3.92	0.68	3.97
H	421	8.27	0.96	8.41	450	4.61	1.02	4.63
I	789	8.24	0.68	8.19	807	4.15	0.62	4.23
K	1593	8.17	0.75	8.41	1500	4.20	0.48	4.36
L	1447	8.19	0.73	8.42	1426	4.24	0.51	4.38
M	326	8.30	0.63	8.42	325	4.29	0.49	4.52
N	862	8.33	0.84	8.42	827	4.67	0.46	4.75
P	–	–	–	–	683	4.42	0.40	4.44
Q	730	8.16	0.65	8.41	683	4.25	0.46	4.37
R	892	8.23	0.58	8.27	848	4.25	0.46	4.38
S	1113	8.27	1.43	8.38	1118	4.45	0.44	4.50
T	1082	8.16	0.82	8.24	1087	4.40	0.57	4.35
V	1157	8.21	0.82	8.44	1202	4.08	0.86	4.18
W	227	8.26	0.86	8.09	220	4.63	0.61	4.70
Y	685	8.26	0.81	8.18	717	4.58	0.61	4.60

	N			Cα				C			
Res.	No.	Median	SD	No.	Median	SD	rc	No.	Median	SD	rc
A	335	122.8	8.7	118	52.1	2.1	50.8	40	177.8	2.4	175.8
C	62	117.8	3.7	35	55.0	3.1	53.9	40	172.2	2.0	173.9
D	216	120.3	4.1	77	53.0	2.1	52.7	31	176.9	1.4	174.2
E	258	120.9	3.2	112	56.7	2.6	55.4	42	177.2	2.1	173.7
F	136	121.3	4.4	79	56.2	2.6	56.2	38	174.7	2.5	172.9
G	277	109.1	4.0	171	44.0	1.9	43.9	52	172.7	2.1	171.8
H	59	119.5	3.5	30	53.8	5.7	53.6	6	175.8	1.8	172.2
I	169	123.6	4.6	59	60.0	3.0	59.6	22	175.8	1.9	174.2
K	364	120.7	4.0	153	56.0	2.1	54.6	30	175.7	2.2	174.5
L	289	122.0	4.4	115	53.7	1.9	53.8	26	176.5	1.8	174.7
M	79	120.9	4.8	42	54.7	2.2	54.0	19	177.4	1.8	173.4
N	172	118.9	5.1	65	52.7	1.9	53.8	26	173.7	1.9	173.1
P	34	137.7	3.8	61	62.3	1.6	61.9	19	175.0	2.1	174.1
Q	179	120.2	3.8	64	55.4	2.1	54.1	19	175.1	1.8	174.0
R	128	120.7	3.7	57	55.6	2.5	54.6	31	174.7	3.7	173.4
S	166	116.9	3.6	78	57.0	1.9	56.6	19	173.7	1.6	172.6
T	200	115.7	5.6	111	60.3	2.6	60.1	38	174.8	1.9	172.5
V	237	121.3	6.0	92	60.8	2.9	60.7	24	174.8	2.1	173.9
W	41	120.3	4.0	16	55.7	2.2	55.7	0	–	–	173.4
Y	114	121.2	5.5	69	55.7	1.7	56.3	14	173.9	1.9	172.9

[a]Data extracted from version 1.0 of the BioMagResBank database.[3] For each shift, the first three columns list the number of shifts, the median value and the standard deviation SD about the mean Column labeled 'rc' gives peptide shifts for H-Gly-Gly-X-Ala-OH from Bundi and Wüthrich[4] and Richarz and Wüthrich.[5]

3 CHEMICAL SHIFTS AND SECONDARY STRUCTURE

Considerable attention has been paid to ways in which the Hα shift reflects local secondary structure. It has been recognized for some time that β-sheet regions show high-frequency shifts for this resonance, while helical regions show low-frequency shifts. In the Wishart et al.[12] survey, the mean Hα positions in helices and sheets differ by nearly 0.8 ppm, and there is remarkably little overlap between the two distributions. The same general trend is found for amide protons, whereas Hβ shifts move in the opposite direction by a smaller amount. Amide protons at the N-terminus of helices tend to be shifted to high frequency compared with those at the C-terminus. These relationships are in many cases clear enough to drive secondary-structure assignments in proteins,[13,14] and to gain a qualitative idea of structural differences among homologous systems. It has been shown that this dependence of Hα and Hβ shifts on secondary structure can be explained in terms of peptide group contributions, as outlined below.[15]

These ideas may also be of use for linear peptides, where conformational heterogeneity hampers quantitative NOE-based structure calculations. For example, amide proton shifts in model helical peptides are often periodic (with a 3–4 residue repeat pattern);[16,17] amphipathic helices show a periodic behavior that appears to be related to curving of the helix axis;[18,19] and it may be possible to characterize helices of marginal stability through an analysis of the solvent dependence of backbone shifts.[20]

The relationship of ^{15}N and ^{13}C shifts to secondary structure is also of considerable current interest.[9–12,21] Cα and carbonyl shifts exhibit a strong correlation with secondary structure, both moving to higher frequency in helical conformations and to lower frequency in β-strand or extended configurations. As with Hα shifts, there is surprisingly little overlap between the distributions, which suggests that reliable conformational conclusions may be drawn, and the Cα shift has been used as a site-specific probe of the helix/coil transition in linear peptides.[22] There are also indications from solid state studies of peptides that the carbonyl ^{13}C resonance moves to higher frequency with decreasing CO$\cdots$HN hydrogen-bond length,[23–27] a result that is in rough accord with quantum chemical calculations.[26] Cβ shifts also show systematic differences between helices and sheets, but with much more overlap in the observed distributions.

The situation for amide ^{15}N shifts in proteins (as with amide protons) is less clear. There are general differences between shifts in helix and sheet structures of about 3 ppm, but the overlap between the two distributions is often greater than this, so that it is difficult to draw simple conclusions from a given set of shifts.[12,28,29] There is a correlation between amide proton and amide ^{15}N shifts, suggesting that similar physical effects are influencing both. There is some evidence that ^{15}N shifts may be periodic in helices, reflecting the local structure, but the relationship does not appear to be a simple one.[16,30]

4 CHEMICAL SHIFTS AND TERTIARY STRUCTURE

In both organic chemistry and biochemistry, empirical analyses of the effects of 'distant' substituents on chemical shifts have played an important role for many years.[31] There are generally two such types of interaction: magnetic fields arising from anisotropies in the magnetic susceptibilities of distant functional groups, and electric fields created by distant dipoles or charges. The former are strongest with conjugated or partially delocalized electrons (such as in aromatic rings or peptide groups) where there are significant anisotropies in group magnetic susceptibilities.[32–34] These groups then respond to an external spectrometer field $\boldsymbol{B}_0$ to create a local magnetic field which can augment or oppose $\boldsymbol{B}_0$.[35] The electrostatic fields of distant groups influence chemical shifts indirectly, by polarizing chemical bonds, and thus contributing to shielding or deshielding of the nuclei.[36] These mechanisms are considered in more detail in the following paragraphs.

4.1 Ring Current Calculations

The general form of empirical theories is $\sigma_{rc} = iBG(\boldsymbol{r})$ where $\boldsymbol{r}$ is the vector from the observed proton to the aromatic ring, $G(\boldsymbol{r})$ is a geometric factor, and i and B are constants.[31,34] It is conventional to incorporate in B those constants that would yield the expected contribution from a benzene ring, and to use i# (the 'ring current intensity' factor) to represent the ratio of the intensity expected for the ring in question to that of a benzene ring. There have been several attempts to estimate these factors, based on both quantum mechanical and empirical calculations[37,38]

Two commonly used parameterizations of the geometric factors were proposed by Johnson and Bovey[39] and by Haigh and Mallion.[34] In the latter model, which is one of the simplest to implement, the geometric factor is

$$G(\boldsymbol{r}) = \sum_{ij} s_{ij} \left\{ \frac{1}{r_i^3} + \frac{1}{r_j^3} \right\} \qquad (1)$$

Here r_i and r_j are the distances from ring atoms i and j to the proton, and s_{ij} is the area of the triangle formed by atoms i and j and the proton projected onto the plane of the aromatic ring. The sum is over the bonds in the ring. The Johnson–Bovey model sets up 'rings' of current above and below the plane of the atoms, and computes fields from this model. There appears to be very little difference between the two models, except at very short distances.

The heme group is an important special case for ring current calculations, and a variety of empirical calculations have been carried out.[40–43] A simple model that gives good results treats the heme as five rings: four for the pyrroles, and one 'macrocycle' that traverses the large conjugated ring in the canonical valence-bond structure. Cross and Wright[43] compared the results of this and other models with a dataset composed of protein and model compound shifts, and Ösapay and Case[38] used a larger heme protein database, including cytochromes c, b_5, and c_{551} and myoglobin. The empirical formulas appear to reproduce the observed behavior quite well.

4.2 Peptide Group Contributions

It has been recognized for some time that the magnetic anisotropy of the peptide group is likely to contribute significantly to chemical shifts in proteins. McConnell[35] has shown that when the observed proton and the 'source' of the magnetic anisotropy are far apart, the contribution to the local shielding tensor depends upon the magnetic anisotropy of the distant group:

$$\sigma_m = (3L_0R^3)^{-1} \sum_{i=x,y,z} \chi_{ii}(1 - 3\cos^2\theta_i) \qquad (2)$$

Here L_0 is the Avogadro constant, R is the distance from the proton to the distant group, χ_{ii} is a component of the magnetic susceptibility tensor, and θ_i is the angle between the i axis and the radius vector $\boldsymbol{R}$. Since there is no direct method for measuring the magnetic anisotropy of a peptide group within a protein, all estimates of these effects are to some extent empirical. Data for formamide[44] suggest that the peptide group is nearly axially symmetric about the out-of-plane axis, with an anisotropy $\Delta\chi$ of $-5.1 \pm 0.6 \times 10^{-6}$ erg (G^2-mol)$^{-1}$. This value is in good agreement with the one obtained using an empirical theoretical approach developed by Pauling:[33] -5.4×10^{-6} erg (G^2-mol)$^{-1}$.

Alternative models for peptide groups can be constructed by adding contributions from individual atoms[45] or bonds,[46–48] rather than using parameters for the peptide group as a whole. These alternative methods give generally similar results.[49,50]

Contributions from peptide groups calculated in this way can explain to a large extent the observed behavior of Hα chemical shifts as a function of local secondary structure.[15] Because of the R^{-3} distance dependence in equation (2), the neighboring peptide groups have the greatest influence, so that the shift depends to a large extent on the backbone dihedral angles ϕ and ψ, which determine the geometric relationship between the peptide planes and the Hα position.

4.3 Electrostatic Contributions

A significant contribution to chemical shifts can also arise from distant charges and dipoles, which can polarize the C–H bond and thereby increase or decrease the local shielding by electrons. The most significant term is expected to be proportional to the projection of the local electric field onto the C–H vector:

$$\sigma_{\mathrm{el}} = AE(\mathrm{C\text{–}H}) \qquad (3)$$

Buckingham[36] suggested that an appropriate value for A would be -2×10^{-12} esu^{-1}, but this magnitude clearly depends upon the way in which local electric fields are estimated. Most estimates to date have been based on Coulomb's law using partial charge models from molecular mechanics force fields, but this approach ignores important solvent effects that screen charge interactions, and further work in this area is needed.

The relative importance of various contributions is expected to be different for protons than for heavier nuclei. Ring current and magnetic anisotropy contributions will contribute the same absolute shift for all nuclei, and hence should be less important for nuclei like ^{13}C or ^{15}N that have large chemical shift ranges (compared with protons). These heavier nuclei, on the other hand, are more sensitive to electrostatic effects than are protons, probably because of the ability of electric fields to polarize their occupied p shells, which are unoccupied for hydrogen,[51] and some interesting attempts have been made to correlate shifts in proteins with estimates of the local electric fields.[52,53]

The analysis of chemical shift patterns using these ideas has a long history in organic chemistry.[31,34,46] Recently, several groups have shown that such calculations can explain a large portion of the chemical shift dispersion seen in globular proteins.[38,47,48,54,55] For example, Ösapay and Case[38] analyzed proton shifts from 17 proteins whose X-ray crystal structures had been determined; for 5678 protons bonded to carbon they obtained a linear correlation coefficient of 0.88 between the calculated and observed structural shifts, with an rms error of 0.23 ppm; for side-chain protons in nonheme proteins the rms error was 0.18 ppm, and for methyl groups it was 0.13 ppm. Computer codes that implement these ideas are available from the author, and equivalent code is part of the AMBER molecular modeling package, which also allows refinement of structures using penalty functions based on chemical shift formulas.[56] Initial applications to myoglobin[57] suggest that this idea may be a feasible and useful approach.

5 CONCLUSIONS

There is little doubt that the use of chemical shift information for peptides and proteins will continue to grow as a source of structural information. The Hα and Cα shifts appear to provide a reliable indicator of local secondary structure, and useful theories are available for magnetic interactions with aromatic rings and peptide groups. Electrostatic interactions (including hydrogen bonding and solvation effects) are less well understood. Ab initio electronic structure calculations are beginning to address problems of interest to peptide and protein chemists, and this, together with empirical analyses of larger numbers of shifts, should provide new insight into the origins of chemical shift dispersion.

6 RELATED ARTICLES

Carbon-13 Spectral Simulation; Shielding Calculations: LORG and SOLO Approaches; Chemical Shifts in Biochemical Systems; Shielding: Overview of Theoretical Methods; Shielding in Small Molecules.

7 REFERENCES

1. C. Redfield and J. P. Robertson, in *Computational Aspects of the Study of Biological Macromolecules by NMR Spectroscopy*, ed. J. Hoch, F. M. Poulsen, and C. Redfield, Plenum, New York, 1991, pp. 303–316.
2. B. J. Stockman, T. A. Scahill, N. A. Strakalaitis, D. P. Brunner, A. W. Yem, and M. R. Deibel, Jr., *J. Biomol. NMR*, 1992, **2**, 591.
3. B. R. Seavey, E. A. Farr, W. M. Westler, and J. L. Markley, *J. Biomol. NMR*, 1991, **1**, 217.
4. A. Bundi and K. Wüthrich, *Biopolymers*, 1979, **18**, 285.
5. R. Richarz and K. Wüthrich, *Biopolymers*, 1978, **17**, 2133.
6. G. A. Webb, in *Nuclear Magnetic Shieldings and Molecular Structure*, ed. J. A. Tossell, Kluwer, Dordrecht, 1993, pp. 1–25.
7. D. B. Chestnut and C. G. Phung, *Chem. Phys. Lett.*, 1991, **183**, 505.
8. D. B. Chestnut and C. G. Phung, in *Nuclear Magnetic Shieldings and Molecular Structure*, ed. J. A. Tossell, Kluwer, Dordrecht, 1993, pp. 221–241.
9. D. Jiao, M. Barfield, and V. J. Hruby, *J. Am. Chem. Soc.*, 1993, **115**, 10883.
10. A. C. de Dios, J. G. Pearson, and E. Oldfield, *J. Am. Chem. Soc.*, 1993, **115**, 9768.
11. A. C. de Dios, J. G. Pearson, and E. Oldfield, *Science*, 1993, **260**, 1491.
12. D. S. Wishart, B. D. Sykes, and F. M. Richards, *J. Mol. Biol.*, 1991, **222**, 311.
13. D. S. Wishart, B. D. Sykes, and F. M. Richards, *Biochemistry*, 1992, **31**, 1647.
14. N. H. Andersen, B. Cao, and C. Chen, *Biochem. Biophys. Res. Commun.*, 1992, **184**, 1008.
15. K. Ösapay and D. A. Case, *J. Biomol. NMR*, 1994, **4**, 215.
16. I. D. Kuntz, P. A. Kosen, and E. C. Craig, *J. Am. Chem. Soc.*, 1991, **113**, 1406.
17. M. A. Jiménez, F. J. Blanco, M. Rico, J. Santoro, J. Herranz, and J. L. Nieto, *Eur. J. Biochem.*, 1992, **207**, 39.

18. N. E. Zhou, B. -Y. Zhu, B. D. Sykes, and R. S. Hodges, *J. Am. Chem. Soc.*, 1992, **114**, 4320.
19. F. J. Blanco, J. Herranz, C. González, M. A. Jiménez, M. Rico, J. Santoro, and J. L. Nieto, *J. Am. Chem. Soc.*, 1992, **114**, 9676.
20. M. Bruix, M. Perello, J. Herranz, M. Rico, and J. L. Nieto, *Biochem. Biophys. Res. Commun.*, 1990, **167**, 1009.
21. S. Spera and A. Bax, *J. Am. Chem. Soc.*, 1991, **113**, 5490.
22. M. D. Reily, V. Thanabal, and D. O. Omecinsky, *J. Am. Chem. Soc.*, 1992, **114**, 6251.
23. D. W. Urry, L. W. Mitchell, and T. Ohnishi, *Proc. Natl. Acad. Sci. USA*, 1974, **71**, 3265.
24. T. Asakura, M. Kamio, and A. Nishioka, *Biopolymers*, 1979, **18**, 467.
25. S. Ando, I. Ando, A. Shoji, and T. Ozaki, *J. Am. Chem. Soc.*, 1988, **110**, 3380.
26. N. Asakawa, S. Kuroki, H. Kurosu, I. Ando, A. Shoji, and T. Ozaki, *J. Am. Chem. Soc.*, 1992, **114**, 3261.
27. E. Tüchsen and P. E. Hansen, *Int. J. Biol. Macromol.*, 1991, **13**, 2.
28. J. Glushka, M. Lee, S. Coffin, and D. Cowburn, *J. Am. Chem. Soc.*, 1989, **111**, 7716.
29. J. Glushka, M. Lee, S. Coffin, and D. Cowburn, *J. Am. Chem. Soc.*, 1990, **112**, 2843.
30. N. J. Skelton, M. Akke, J. Kördel, E. Thulin, S. Forsén, and W. J. Chazin, *FEBS Lett.*, 1992, **303**, 136.
31. R. K. Harris, *Nuclear Magnetic Resonance Spectroscopy, A Physicochemical View*, Longman, Harlow, 1986.
32. W. H. Flygare, *Chem. Rev.*, 1974, **74**, 653.
33. L. Pauling, *Proc. Natl. Acad. Sci. USA*, 1979, **76**, 2293.
34. C. W. Haigh and R. B. Mallion, *Prog. Nucl. Magn. Reson. Spectrosc.*, 1980, **13**, 303.
35. H. M. McConnell, *J. Chem. Phys.*, 1957, **27**, 226.
36. A. D. Buckingham, *Can. J. Chem.*, 1960, **38**, 300.
37. C. Giessner-Prettre and B. Pullman, *C. R. Hebd. Seances Acad., Sci., Ser. D*, 1969, **268**, 1115.
38. K. Ösapay and D. A. Case, *J. Am. Chem. Soc.*, 1991, **113**, 9436.
39. C. E. Johnson and F. A. Bovey, *J. Chem. Phys.*, 1958, **29**, 1012.
40. R. J. Abraham, *Mol. Phys.*, 1961, **4**, 145.
41. R. J. Abraham, G. R. Bedford, D. McNeillie, and B. Wright, *Org. Magn. Reson.*, 1980, **14**, 418.
42. R. J. Abraham, *J. Magn. Reson.*, 1981, **43**, 491.
43. K. J. Cross and P. E. Wright, *J. Magn. Reson.*, 1985, **64**, 220.
44. H. L. Tigelaar and W. H. Flygare, *J. Am. Chem. Soc.*, 1972, **94**, 343.
45. T. Asakura, Y. Niizawa, and M. P. Williamson, *J. Magn. Reson.*, 1992, **98**, 646.
46. R. F. Zürcher, *Prog. Nucl. Magn. Reson. Spectrosc.*, 1967, **2**, 205.
47. M. P. Williamson and T. Asakura, *J. Magn. Reson.*, 1991, **94**, 557.
48. M. P. Williamson, T. Asakura, E. Nakamura, and M. Demura, *J. Biomol. NMR*, 1992, **2**, 83.
49. J. Herranz, C. González, M. Rico, J. L. Nieto, J. Santoro, M. A. Jiménez, M. Bruix, J. L. Neira, and F. J. Blanco, *Magn. Reson. Chem.*, 1992, **30**, 1012.
50. M. P. Williamson and T. Asakura, *J. Magn. Reson., Ser. B*, 1993, **101**, 63.
51. J. Augspurger, J. G. Pearson, E. Oldfield, C. E. Dykstra, K. D. Park, and D. Schwartz, *J. Magn. Reson.*, 1992, **100**, 342.
52. J. D. Augspurger, A. C. de Dios, E. Oldfield, and C. E. Dykstra, *Chem. Phys. Lett.*, 1993, **213**, 211.
53. J. G. Pearson, E. Oldfield, F. S. Lee, and A. Warshel, *J. Am. Chem. Soc.*, 1993, **115**, 6851.
54. C. Giessner-Prettre, M. T. Cung, and M. Marraud, *Eur. J. Biochem.*, 1987, **163**, 79.
55. N. Gresh and C. Giessner-Prettre, *Biochem. Biophys. Res. Commun.*, 1990, **171**, 1211.
56. D. A. Pearlman, D. A. Case, J. C. Caldwell, G. L. Seibel, U. C. Singh, P. Weiner, and P. A. Kollman, *AMBER 4.0*, University of California, San Francisco, CA, 1991.
57. D. A. Case and P. E. Wright, in *NMR in Proteins*, ed. G. M. Clore and A. Gronenborn, MacMillan, New York, 1993, pp. 53–91.

Acknowledgments

This work was supported by NIH Grant GM45811. I thank Beverley Seavey and John Markley for providing access to the BioMagResBank database, and Gene Merutka, Jane Dyson, Peter Wright, and Klara Ösapay for helpful discussions.

Biographical Sketches

David A. Case, b 1948. B.S., 1970, Michigan State, A.M., 1972, Harvard, Ph.D., 1977, Harvard, USA. Approx. 90 publications. Research interests include modeling of proteins and nucleic acids, quantum mechanical studies of the active sites of metalloenzymes, and computational aspects of NMR.

Bacteriorhodopsin and Rhodopsin

Judith Herzfeld and Jingui G. Hu
Brandeis University, Waltham, MA, USA

1	Introduction	1
2	NMR Strategies	2
3	Structure	3
4	Protonation and Hydrogen Bonding	7
5	Proton Diffusion	8
6	Related Articles	8
7	References	9

1 INTRODUCTION

Situated at the barrier between the interior and exterior of a cell or organelle, membrane proteins execute a variety of vital functions, including energy transduction (i.e. conversion of energy between different forms) and signal transduction (i.e. triggering a cascade of events in response to an environmental effector). The rhodopsins are light-transducing membrane proteins with a chromophore formed by a retinal molecule linked to the protein (known as the opsin) via a Schiff base with a lysine residue (Figure 1). Most rhodopsins are signal transducers: absorption of a proton induces a change in the rhodopsin that activates a primed system, leading to a visual response (e.g. in mammals) or phototactic response (e.g. in algae and archaeobacteria). However, two energy-transducing rhodopsins have been found in halophilic archaeobacteria: in these cases, absorption of a photon results in transport of an ion across the membrane, against its gradient, resulting in conversion of radiant energy into electrochemical energy which can be stored. One of these energy-transducing rhodopsins, known as bacteriorhodopsin because it was the first rhodopsin discovered in a unicellular organism, pumps protons and the other, known as halorhodopsin, pumps halide ions.

Bacteriorhodopsin (248 amino acids, 26 kDa) is the most thoroughly studied membrane protein. This is because it is a major product of *Halobacterium salinarium* (previously also known as *Halobacterium halobium*), and crystallizes in the plane of the membrane to form patches with 2D hexagonal order, from which all other proteins are excluded.[1] These patches (known as 'purple membranes' due to the color of the pigment) are readily separated from the rest of the cell membrane and are stable and functional over an exceptionally wide range of conditions (including pH values, ionic strengths, and temperatures). Thus, it is relatively easy to prepare large samples of the protein in its native form. Due to the 2D crystalline order in the membranes, it has been possible to construct 3D electron density maps from electron micrographs taken over a range of tilt angles.[2] These studies show that the protein folds into a bundle of seven transmembrane helices that encapsulates the retinal chromophore. Chemical studies have shown that the retinal Schiff base is formed with Lys216.[3] Neutron diffraction studies find that the retinal is located near the center of the membrane with the ionone ring closer to the extracellular side than the Schiff base.

Figure 2 shows the relationships between the functionally important forms of bacteriorhodopsin. In the dark, there is a thermal equilibrium between bR_{555} and bR_{568}, where the subscript indicates the wavelength of maximum visible absorbance. The photoproducts of bR_{555} (not shown) decay to bR_{568}, so that bR_{555} disappears upon light adaptation. The photocycle of bR_{568} is responsible for proton transport. The initial photoreaction is the isomerization of the chromophore from all-*trans* in bR_{568} to 13-*cis* in J_{625}. The proton on the Schiff base is lost in the $L_{550}-M_{412}$ transition, and restored in the $M_{412}-N_{520}$ transition. FTIR and kinetic studies, of wild-type and mutant samples, indicate that the immediate proton acceptor is Asp85, and the immediate proton donor is Asp96. However, the proton pathway traverses the entire membrane, and pumping occurs because a proton is released into the extracellular medium in the first half of the photocycle and taken up from the cytoplasm in the second half of the photocycle. The central question regarding the mechanism of bacteriorhodopsin is how this switch occurs: what prevents the system from being reprotonated from the extracellular side? For *Halobacterium*, bacteriorhodopsin

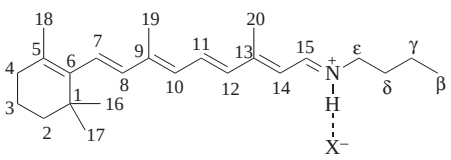

Figure 1 Protonated Schiff base of all-*trans*-retinal with a Lys side chain. X^- is the Schiff base counterion. The carbons atoms are identified according to convention by numbers on the retinal and Greek letters on the Lys residue

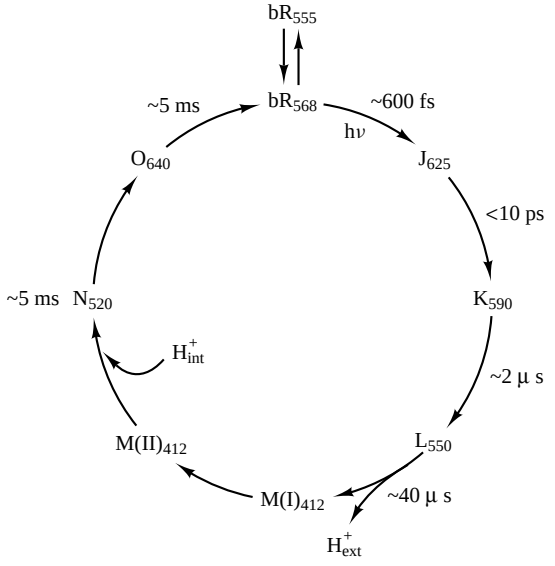

Figure 2 Relationships among the functionally important forms of bacteriorhodopsin. Subscripts indicate the wavelength of maximum visible absorbance. The chromophore is photoisomerized from all-*trans* to 13-*cis* in the bR_{568} to L_{625} photoreaction. The Schiff base is protonated in all but the M-states

provides a solar-powered alternative to respiration for creating the proton electrochemical potential gradient that is required for regeneration of ATP from ADP (the 'proton motive' force of the chemiosmotic mechanism).

Bovine rhodopsin (348 amino acids, 40 kDa) is the most thoroughly studied visual pigment, due to Western dietary habits. Rhodopsin is solubilized and purified from the rod cells of the retina, and then reconstituted into lipid bilayers. Although it does not naturally form a crystalline lattice, it can be induced to do so, and electron cryomicroscopy of such preparations indicates that rhodopsin also forms a bundle of seven transmembrane helices.[4] The retinal Schiff base is formed with Lys296,[5] and the Schiff base counterion is Glu113.[6,7] Figure 3 shows the photointermediates of rhodopsin. In the initial photoreaction, the 11-*cis*-retinal in rhodopsin is isomerized to the all-*trans* form. The following thermal steps lead to the release of the retinal from the protein. Photoactivation of rhodopsin leads to interaction with a heterotrimeric guanine nucleotide-binding protein (G-protein) on the intracellular side of the membrane. The activated G-protein then triggers the further steps that ultimately lead to the hyperpolarization of the plasma membrane that initiates a nerve impulse. In its seven-helix structure and embedded ligand, rhodopsin is believed to be representative of G-protein-coupled receptors generally, a class which includes the signal transducers for acetylcholine, dopamine, glycoprotein hormones, and peptides.[8] While rhodopsin is the rod cell pigment responsible for low-light vision, other retinal proteins in the cone cells are responsible for color vision. For these pigments the action spectrum is of obvious functional importance. In general, the visible spectra of rhodopsins are red shifted relative to the 440 nm absorption maximum of protonated retinal Schiff bases in methanol. Because this bathochromic shift is due to the protein environment, it is known as the 'opsin shift'.[9] The mechanisms by which the opsins 'tune' the chromophore has been one of the central issues in research on retinal proteins. The particularly large opsin shift in bacteriorhodopsin (to 568 nm) has made it a particularly interesting case even though it is not a visual pigment.

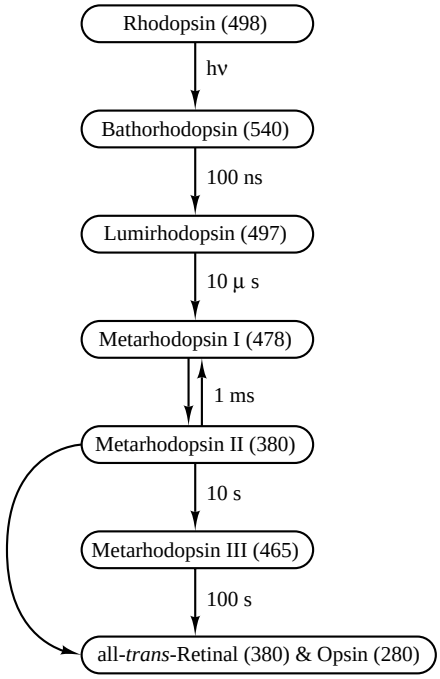

Figure 3 Photoproducts of bovine rhodopsin and their wavelengths of maximum visible absorbance. The chromophore is isomerized from 11-*cis* to all-*trans* in the initial photoreaction. Metarhodopsin II is the form that activates the G-protein. The isomerized chromophore is subsequently released and recycled by the cell

2 NMR STRATEGIES

Although NMR studies have also been made of fragments, here we will focus on studies of intact retinal proteins. These large integral membrane proteins are amenable to different NMR approaches depending on their manner of preparation. In solubilized form, they can be studied by solution techniques, with the caveats that the large protein–detergent complexes have relatively long rotational correlation times and that functional integrity cannot be assayed in the absence of a membrane. For membrane preparations, solid state techniques are required and have the potential of providing additional information from anisotropic interactions. In the crystalline native membrane, bacteriorhodopsin does not diffuse, which is ideal for solid state spectroscopy. With the exception of a few initial studies of lyophilized samples, purple membranes are normally studied as wet ultracentrifuge pellets which are frozen as needed to trap photointermediates (see below) or improve the signal-to-noise ratio. Rhodopsin, reconstituted in lipids after purification, undergoes slow rotational diffusion about an axis perpendicular to the plane of the bilayer. Since such motion interferes with cross polarization and decoupling, it is quenched for solid state NMR studies by lyophilization or freezing.

The large size of these systems makes selective isotopic labeling essential. For studies of the chromophore, the native retinal can be replaced by a synthetic isotopomer:[10] the sample is bleached by treatment with hydroxylamine (which breaks the Schiff base linkage and releases retinal oxime) and then the pigment is regenerated by incubation of the sample with synthetic retinal in the appropriate conformation. Labeling of the opsins relies on bacterial or in vitro expression systems. In the case of bacteriorhodopsin, biosynthetic labeling is practical for those amino acids that the *Halobacteria* do not synthesize in excess. Attempts to isolate auxotrophic strains for the other amino acids have been successful only for arginine.[11] In one NMR study, an auxotroph of *Escherichia coil* was used to express selectively labeled bacteriorhodopsin, which was then purified and reconstituted in lipids.[12] So far, in vitro expression of bacteriorhodopsin[13] has not been achieved on a scale relevant for NMR. For rhodopsin, it has so far proved impossible to prepare NMR quantities of properly folded protein either in cultures or in vitro. NMR studies of rhodopsin have therefore been restricted to the chromophore, with the exception of a recent study of a labeled fragment of G-protein bound to rhodopsin.[14]

For the most part, isotopic labeling of retinal proteins has taken the form of selective enrichment of naturally rare isotopes. This has the advantage of minimizing perturbation of the molecule. Thus, most NMR studies have made use of selective substitution of ^{13}C for ^{12}C, ^{15}N for ^{14}N, and ^{2}H for ^{1}H. However, NMR nuclei have occasionally been

introduced less conservatively, by substitution of ^{19}F for ^{1}H.[15] Most studies up to this point have made use of dilute spin systems; however, increasing attention is now being given to measurements of dipolar interactions between spin pairs to obtain internuclear distances. In ^{13}C studies the large natural-abundance signal generally makes the spectrum difficult to interpret, even with selective isotopic enrichment. Thus, in ^{13}C studies, it has become routine to subtract the spectrum of a natural-abundance sample from the spectrum of the labeled sample obtained under the same conditions (particularly spinning speed).[16]

In order to understand the molecular mechanisms of light transduction in retinal proteins, it is necessary to study their photointermediates. Time-resolved NMR studies have not been possible because of the very high optical density of the large samples required. Thus, NMR studies of photointermediates have relied on cryotrapping. In bacteriorhodopsin, pure bR_{568} obtained by light adaptation can be stabilized for the duration of an NMR experiment by cooling to $-5^{\circ}C$. The only intermediates of the bR_{568} photocycle that have so far proven accessible are one of the M-intermediates and the N-intermediate. The M-intermediate is trapped alone in guanidinium hydrochloride at pH 10, which slows the M to N transition of the photocycle. These conditions are justified by the fact that the proton pump, which is the focus of interest, still functions, albeit relatively slowly. In NaCl at pH 10, the N-intermediate accumulates along with the M-intermediate. In both of these preparations, cooling to $-40^{\circ}C$ suffices to stabilize the intermediates for the duration of an NMR experiment. In rhodopsin, NMR studies have been conducted on the bathorhodopsin[17] and metarhodopsin II[18] intermediates, by cooling below 120 and 130 K, respectively.

3 STRUCTURE

3.1 Chromophore

In the earliest studies, retinal conformations were determined by analysis after chemical extraction. Although this procedure is relatively safe for the C=C configurations, it is not useful for single bonds, which are free to rotate when the chromophore is liberated from its binding pocket. It is also not useful for the C=N bond, which is broken on extraction. In situ studies have made use of resonance Raman spectroscopy and NMR spectroscopy. Of these, NMR has the advantage of avoiding any possible perturbation by light.

Initial NMR studies made use of the sensitivity of ^{13}C chemical shifts to steric interactions of directly bonded protons: electron density driven from the proton produces a low-frequency shift at the carbon. This effect was first identified for a retinal pigment in [12-^{13}C] retinal-labeled bacteriorhodopsin. In the dark-adapted state, the spectrum showed a doublet with a low-frequency:high-frequency stoichiometry similar to the accepted 60:40 stoichiometry of bR_{555}:bR_{568}.[19] Upon light adaptation to form pure bR_{568}, the low-frequency signal disappeared, confirming the assignment of signals originally made by stoichiometry.[20] These observations supported previous evidence for 13-*cis* and all-*trans* chromophores in bR_{555} and bR_{568}, respectively. However, a doublet with similar stoichiometry was also seen in dark-adapted [14-^{13}C]retinal-labeled bacteriorhodopsin.[21] Again, the low-frequency signal disappeared on light adaptation.[20] These observations suggested that the chromophores of bR_{555} and bR_{568} are 13-*cis*,15-*syn* and all-*trans*,15-*anti*, respectively. According to this interpretation, a corresponding steric effect should also be seen at C-ϵ of Lys216. These expectations have recently been confirmed in studies of [ϵ-^{13}C]Lys-labeled bacteriorhodopsin, with a doublet in the dark-adapted state and disappearance of the low-frequency signal on light adaptation.[22] Although the chemical shift data are thoroughly self-consistent, the most unambiguous determination of the C=N configuration has been made by rotational resonance studies of [14-^{13}C]retinal,[ϵ-^{13}C]Lys-labeled bacteriorhodopsin. The rate of magnetization exchange between the two carbons indicated an internuclear distance of 0.3 ± 0.02 nm in bR_{555} and 0.41 ± 0.03 nm in bR_{568}, as expected for C=N *syn* and *anti* configurations, respectively.[23] This spin pair has also been revisited recently in a 2D rf-driven recoupling (RFDR) experiment in which the interactions can be observed in bR_{555} and bR_{568} simultaneously.[24] In this case, the more rapid development of cross-peak intensity for the low-frequency signals clearly demonstrates that these are associated with the shorter internuclear distance and steric interaction.

Steric interactions also play an important role at the other end of the chromophore. Retinal in solution comprises a rapidly exchanging mixture of the skewed 6-*s*-*cis* and planar 6-*s*-*trans* conformations, with the former dominating. The planar 6-*s*-*trans* conformation (shown in Figure 1) has the advantage of the extended planar π-system, but it has two methyl groups in close proximity to C-8. In the skewed 6-*s*-*cis* conformation the planar π-system is truncated, but only one methyl group is near C-8. Since the length of the π-system is an important factor for color discrimination, the 6-*s* conformation of the bound chromophore has received considerable attention. Studies of the 6-*s*-*cis* and 6-*s*-*trans* crystal forms of retinoic acid demonstrated that the ^{13}C-5 shift is sensitive to isomerization of the 6-*s* bond, as expected given the changes in steric interactions.[25] Interestingly the effect is entirely in the most high-frequency tensor element which moves 20 ppm to high frequency on 6-*s*-*cis* to 6-*s*-*trans* isomerization.

In [5-^{13}C]retinal-labeled bacteriorhodopsin, the most high-frequency and most low-frequency tensor elements were found to correspond exactly to that of 6-*s*-*trans*-retinoic acid, suggesting that the chromophore in bacteriorhodopsin is the 6-*s*-*trans* form.[26] (The middle tensor element will be discussed in Section 4.1.) Complementary evidence for a 6-*s*-*trans* conformation in bacteriorhodopsin was obtained from the ^{13}C-8 chemical shift, which is also affected by the changes in steric interactions.[26] Steric interactions also influence the dynamics of the methyl groups, and the ^{13}C-18 longitudinal relaxation time in bacteriorhodopsin was found to be more typical of a 6-*s*-*trans* chromophore than a 6-*s*-*cis* conformation.[26] More recent ^{2}H NMR measurements of the activation energy for threefold hopping of the C-18 methyl group are also consistent with a 6-*s*-*trans* chromophore and inconsistent with a 6-*s*-*cis* chromophore.[27] Again, however, the most unambiguous determination of the 6-*s* conformation has been made by rotational resonance studies of doubly labeled bacteriorhodopsin. In [8,18-^{13}C]retinal-labeled bacteriorhodopsin, the slow rate of magnetization exchange indicated a 6-*s*-*trans*

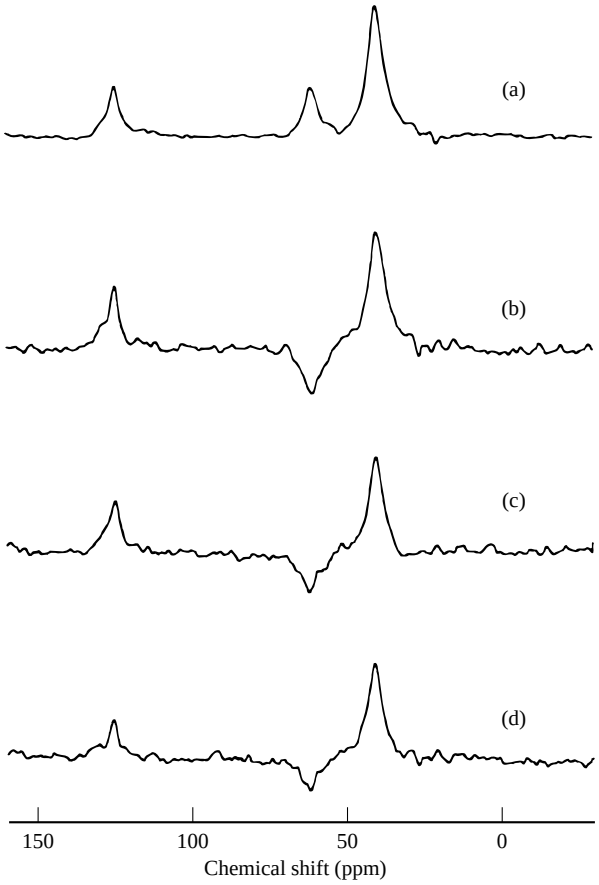

Figure 4 Solid state ^{13}C MAS difference spectra obtained by subtraction of a spectrum of natural-abundance bacteriorhodopsin from spectra of [ϵ-^{13}C]Lys[14-^{13}C]retinal-labeled bacteriorhodopsin in the M-state.[31] (a) The CP MAS difference spectrum. The ^{13}C-14 signal is to high frequency. There are two ^{13}C-ϵ signals, the stronger low-frequency signal is from the six free lysine residues. The smaller signal is from Lys216, which forms the Schiff base with the retinal. (b)–(d) The n = 1 rotational resonance difference spectra for magnetization exchange between [ϵ-^{13}C]Lys216 and [14-^{13}C]retinal at mixing times of 0.2, 5.0 and 20.0 ms, respectively

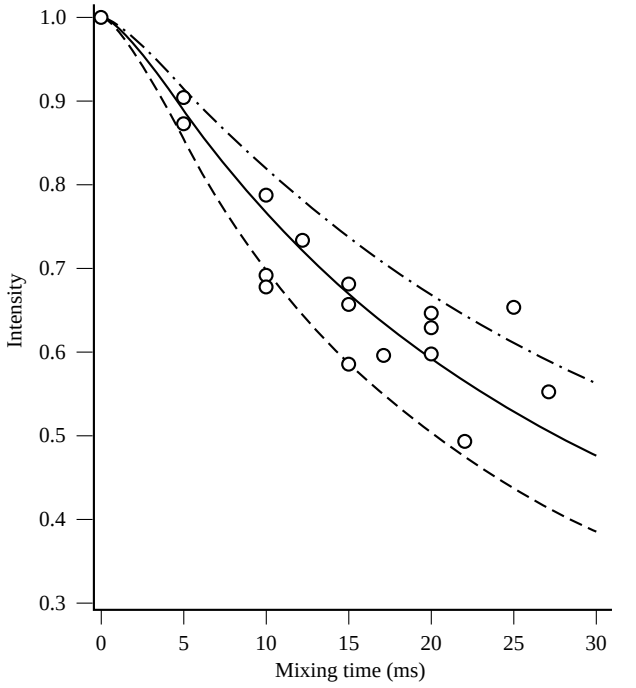

Figure 5 The observed and simulated magnetization exchange between [ϵ-^{13}C]Lys216 and [14-^{13}C]retinal in the M-state, under the n = 1 rotational resonance condition.[31] - - - -, 0.38 nm; ——, 0.39 nm; —·—, 0.40 nm

conformation[28] with an internuclear distance of 0.41 nm.[29] In [8,16/17-^{13}C]retinal-labeled bacteriorhodopsin the average internuclear distance was found to be 0.33–0.35 nm, also consistent with a 6-*s*-*trans* conformation.[29]

Analogous studies have been conducted of the M-state that is trapped at pH 10, in 0.3–0.5 M guanidinium hydrochloride or 0.1 M NaCl, when bR_{568} is illuminated with light of wavelengths > 540 nm, at low temperatures.[22,30,31] The ^{13}C-5 chemical shift indicates that the 6-*s* bond is still *trans*.[30] The ^{13}C-12 chemical shift confirms that the chromophore is 13-*cis*. The ^{13}C-14 and [ϵ-^{13}C]Lys216 chemical shifts indicate that the Schiff base configuration is still *anti*.[22,30] This was confirmed by rotational resonance (Figures 4 and 5), which gave a 14-ϵ internuclear distance of 0.39 ± 0.01 nm, as expected for a C=N *anti* configuration and 0.1 nm larger than expected for a *syn* configuration.[31] These results are consistent with interpretations made of resonance Raman spectra.[32]

Similar studies have been made of the N-intermediate, cryotrapped with the M-intermediate in 0.1 M NaCl at pH 10.[33] The 6-*s* conformation was not investigated, but the ^{13}C-12 chemical shift showed that the chromophore is still 13-*cis*, and the ^{13}C-14 and [ϵ-^{13}C]Lys216 chemical shifts showed that the Schiff base remains in the C=N *anti* configuration. These results agree with the conclusions of time-resolved resonance Raman studies of the N-intermediate at room temperature.[34]

Carbon-13 chemical shifts have also been used to characterize the rhodopsin chromophore. As in bacteriorhodopsin, the ^{13}C-14 chemical shift indicates that the Schiff base is C=N *anti* in rhodopsin[35] and bathorhodopsin.[17] Whereas the bacteriorhodopsin chromophore has been found to be 6-*s*-*trans*, a 6-*s*-*cis* conformation is indicated by the ^{13}C-5 chemical shift in rhodopsin,[35–37] and the ^{13}C-8 chemical shift in bathorhodopsin.[17] Other ^{13}C chemical shifts are generally similar to those in the corresponding retinal Schiff base model compounds (11-*cis* for rhodopsin and all-*trans* for bathorhodopsin). Interestingly, those deviations that are observed are localized in the region of the chromophore that was identified in retinal analog studies as interacting with a protein charge.[17,36,37] Perturbations in this region have also been detected by ^{19}F NMR of rhodopsin-containing fluorinated retinals.[15]

While bond isomerization determines the orientations of different parts of the chromophore relative to each other, it is also important to determine absolute orientations, especially for vectorial transport. Ulrich et al.[38] have used the quadrupole splittings of ^{2}H labels in uniaxially oriented films of bacteriorhodopsin to examine the orientation of the ionone ring relative to the membrane normal. Using the ^{31}P NMR spectral lineshape to determine the mosaic spread of the sample, and treating the ionone ring as a rigid unit, ^{2}H spectral lineshapes of oriented [2,4,4,16,16,16,17,17,17,18,18-$^{2}H_{11}$] retinal-labeled bacteriorhodopsin, at various inclinations to the magnetic field,

were simulated for various ionone ring orientations. The fit to the experimental series of ^{2}H spectra was optimal for an ionone ring orientation that places the methyl groups on C-16, C-17, and C-18 at angles of 94, 75, and 46°, respectively, relative to the membrane normal. Given the known tilt of the chromophore, with the Schiff base closer to the cytoplasmic side and the ionone ring closer to the extracellular side, the ^{2}H analysis indicates that the C-18 methyl group points toward the cytoplasmic side of the membrane. This means that, for a fully planar all-*trans*,15-*anti* or 13-*cis*,15-*syn* chromophore the Schiff base proton or lone pair points toward the extracellular surface (as found for bR_{568} in linear dichroism experiments[39]), while for a fully planar 13-*cis*,15-*anti* chromophore the Schiff base proton or lone pair points toward the cytoplasmic surface.

3.2 Protein

Isotopic labeling of the opsin in NMR quantities has so far only been possible for bacteriorhodopsin. In this system, both secondary structure and tertiary structure have been addressed in a variety of ways.

The peptide backbone was first labeled by Lewis et al.,[40] in the carbonyls of the leucine residues, because these hydrophobic residues were expected to be buried in the membrane on the basis of their location in the hydrophobic stretches of the peptide sequence that were expected to form the transmembrane segments. The spectrum of intact [1-^{13}C]Leu-labeled purple membrane showed a rigid-lattice carbonyl powder pattern which indicated that, at the Leu residues, the peptide backbone was immobile on the ^{13}C NMR timescale even at 40°C. When the labeled bacteriorhodopsin was solubilized and reconstituted in DMPC (dimyristoyl phosphatidylcholine) vesicles above the lipid phase transition temperature, the spectrum was narrowed by fast rotational diffusion. Analysis of the motionally averaged lineshape was used to determine the possible orientations of the Leu peptide bonds relative to the diffusion axis. The data were found to be consistent with α_I helices tilted at 20° from the membrane normal, a model that is congruent with electron density information.[2]

Bowers and Oldfield[41] also studied [1-^{13}C]Leu-labeled purple membrane, and found a mobile component. Mobile components were also found for purple membranes 1-^{13}C labeled in Gly, Ile, Lys, Phe, and Val residues. For each amino acid except Val, the proportion of mobile residues was correlated with the proportion of residues in the C-terminus, suggesting that the C-terminus is mobile on the ^{13}C NMR timescale. Since the C-terminus does not contain any Val residues, it was suggested that the observation of mobile Val residues indicates another mobile region in protein. The discrepancy between these results for Leu and those of Lewis et al., described above, has not been solved.

Helgerson et al.[42] have considered the chemical shifts of peptide carbonyl atoms. Based on homopolymers, in which the carbonyl carbon resonance is found at 176 ± 1 ppm for helical structures and 171 ± 1.5 ppm for nonhelical structures, they concluded that about 85% of Leu, 75% of Val, and 80% of Lys residues in bacteriorhodopsin are in helical regions. Less quantitatively, but more generally, Engelhard et al.[43] have noted that the chemical shift of the peak of the natural-abundance peptide signal in bacteriorhodopsin suggests a largely α-helical secondary structure. These results are consistent with the electron density distribution in bacteriorhodopsin.[2]

Seigneuret and co-workers have labeled the peptide backbone at the carbonyl carbons of the Phe[44] and Met[45] residues. Narrow, well-resolved signals were obtained by solubilizing in *n*-dodecylmaltoside. For the [1-^{13}C]Met-labeled bacteriorhodopsin, sequence specific assignments were obtained by selective colabeling of neighboring amino acid residues with ^{15}N and by papain proteolysis. Using these assignments, it was determined that, of the nine Met residues, only Met32, Met68, and Met163 are water exposed (as reflected in susceptibility to H_2O_2 oxidation) and weakly hydrogen bonded (as indicated by deuterium exchange from ^2H_2O). These results are also consistent with the current structural model of bacteriorhodopsin.[2]

Deber et al.[46] focused on the secondary structure at proline peptide bonds, which are thought to play an important role in transport proteins. [γ-^{13}C]Pro-labeled bacteriorhodopsin was solubilized in $CHCl_3$:CD_3OD (1:1) with 0.1 M $LiClO_4$. Sufficient resolution was achieved to distinguish the 2 ppm difference in ^{13}C chemical shift between a *cis* and a *trans* X-Pro peptide bond. No *cis* signal was observed, and it was concluded that all 11 X-Pro peptide bonds in the solubilized bacteriorhodopsin are in the *trans* conformation. Further evidence has been supplied by an analogous solid state NMR study.[47] The chemical shift difference between C-β and C-γ of a proline residue is 7−11 and 3−5 ppm when the X−Pro peptide bond is *cis* and *trans*, respectively. The MAS spectrum of [β,γ-^{13}C]Pro-labeled bacteriorhodopsin showed only *trans*-configured X−Pro peptide bonds.

The Pro peptide bonds have also been studied by ^{15}N solid state NMR of [^{15}N]Pro-labeled purple membranes. Five well-resolved peaks are obtained at room temperature for the 11 Pro residues.[48] Less resolution is obtained at lower temperatures, suggesting that disorder is being frozen in. In order to assign the Pro91 signal, a REDOR experiment was carried out on a [1-^{13}C]Thr,[^{15}N]Pro-labeled sample, which has only one ^{13}C−^{15}N spin pair, between Thr90 and Pro91.[49] As shown in Figure 6, a single signal is obtained for Pro91 in bR_{568}. Figure 6 also shows a REDOR difference spectrum for a mixture of the bR_{568} and M forms of bacteriorhodopsin. The spectrum clearly reveals a difference in the Pro91 ^{15}N chemical shift, providing direct evidence for a structural change in that part of the protein.

Nitrogen-15-labeled bacteriorhodopsin was also studied by heteronuclear ^{1}H−^{15}N coherence spectroscopy in methanol/chloroform (1:1) solution with 0.1 M NH_4CHO_2.[50] In a uniformly ^{15}N-enriched sample, less than half of the cross peaks expected from the amino acid sequence were observed. By selective labeling and proteolytic cleavage, it was determined that the ^{1}H−^{15}N cross peaks were exclusively from the first two and the last helices in the sequence. Dynamic processes were inferred in the other four helices of the solubilized protein.

The protein structure has also been studied from the vantage point of the amino acid side chains. Initial studies of the mobilities of different side chains using ^{2}H NMR found a significant proportion of mobile residues that were attributed to surface groups.[51−54] However, other investigations suggested that the mobile residues were largely due to contamination by residual plasma membrane.[55] More direct measures of surface exposure have made use of paramagnetic broadening in solubilized [^{13}C]methyl-labeled bacteriorhodopsin[56] and photochemically induced dynamic nuclear polarization of aromatic signals in ^{1}H NMR studies of solubilized natural-abundance

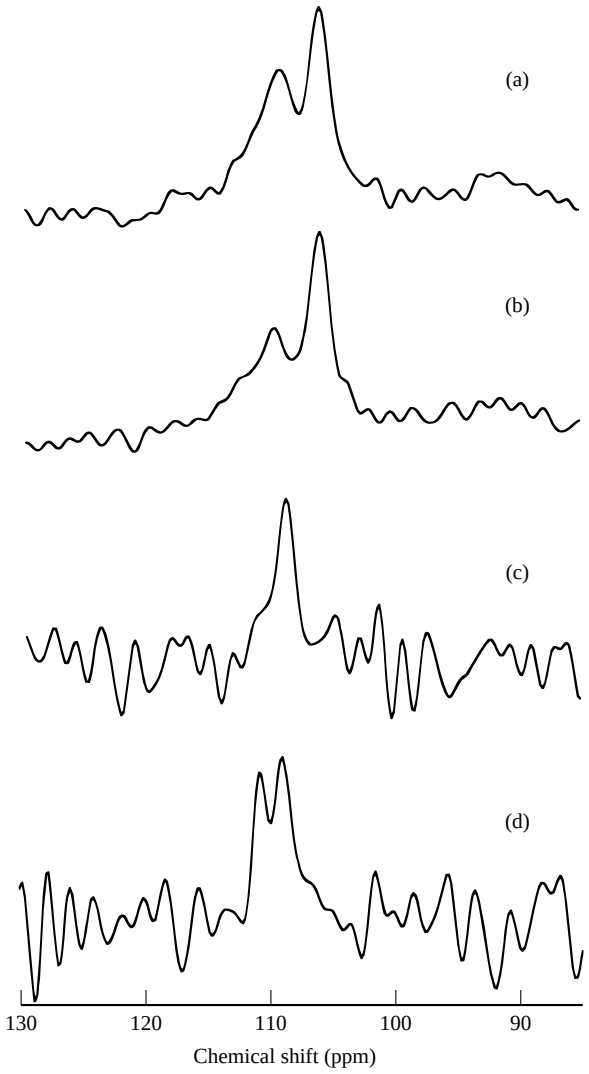

Figure 6 Nitrogen-15 MAS spectra for [1-^{13}C]Thr,[^{15}N]Pro-labeled bacteriorhodopsin.[49] (a) CP MAS spectrum in the light-adapted state. (b) REDOR MAS spectrum in the light-adapted state. (c) The difference between spectra (a) and (b), showing only the signal from Pro91 (the only Pro bound to Thr) in the light-adapted state. (d) REDOR difference spectrum as in part (c) but for a mixture of the light-adapted and M states to show the change in the Pro91 chemical shift

bacteriorhodopsin.[57] Arseniev et al.[58] attempted to detect interactions between tryptophan residues in [5-^{19}F]Trp-labeled bacteriorhodopsin solubilized in $CD_3OH//CHCl_3$ (1:1) with 0.1 M $LiClO_4$. No such interactions were observed, but effects on different signals in the ^{19}F spectrum were noted upon addition of formic acid, reduction of the Schiff base, and modification of the retinal ionone ring. In similar studies of [3-^{19}F]Phe-labeled bacteriorhodopsin, a distance of 1.3 $\pm$ 0.1 nm was measured between Phe230 and a spin label introduced at Met163.[59]

4 PROTONATION AND HYDROGEN BONDING

Changes in protonation are obviously critical along the proton transport pathway in bacteriorhodopsin. As it happens, a protonation change is also at the heart of signal transduction in rhodopsin.[60] Chemical shifts are excellent probes of protonation, and have been used to good advantage in studies of both bacteriorhodopsin and rhodopsin.

4.1 Schiff Base

Model compound studies show that chemical shifts of the odd-numbered carbon atoms of a retinal Schiff base are sensitive to the protonation of the Schiff base,[25] as expected based on the resonance structures which redistribute the positive charge from the Schiff base to the odd-numbered carbon atoms. The sensitivity is greatest at the C-13 position and, for rhodopsin studies which are so far limited to labels on the retinal, the ^{13}C-13 chemical shift is the clearest indicator of the protonation of the Schiff base. After some early false starts due to difficulties in replacing natural-abundance retinal with labeled retinal,[61–63] Mateescu obtained the first ^{13}C NMR spectra for [13-^{13}C]retinal-labeled samples of rhodopsin and bacteriorhodopsin.[64,65] In both proteins, the ^{13}C-13 chemical shift indicated a protonated Schiff base. The ^{13}C-11 chemical shift also provided evidence for a protonated Schiff base in bacteriorhodopsin.[19] In more recent work, the ^{13}C-13 and ^{13}C-15 chemical shifts obtained for bathorhodopsin are consistent with a protonated Schiff base in this photointermediate,[17] and those obtained for metarhodopsin II indicate a deprotonated Schiff base in this activated state.[18] In bacteriorhodopsin, the ^{13}C-13 chemical shifts correspond to a deprotonated Schiff base in the M-state[30] and a reprotonated Schiff base in the N-state.[33]

However, the ^{15}N chemical shift of the Schiff base is by far the most sensitive probe of protonation,[66] and in bacteriorhodopsin, where it is possible to label the protein, the solid state ^{15}N NMR spectrum of [ϵ-^{15}N]Lys-labeled bacteriorhodopsin provides the definitive determination of the protonation state of the Schiff base. Such spectra for dark-adapted bacteriorhodopsin were reported independently by Mateescu et al.[65] and by Harbison and co-workers.[66–69] With a good signal-to-noise ratio, the spectrum shows a doublet due to the coexistence of bR_{568} and bR_{555} in a dark-adapted sample.[66–69] Solid state ^{15}N NMR spectra have also been obtained for [ϵ-^{15}N]Lys-labeled bacteriorhodopsin cryotrapped in the M- and N-states. The [ϵ-^{15}N]Lys chemical shifts indicate that the Schiff base is deprotonated in the M-state and reprotonated in the N-state.[33]

From the start, it was noted that the ^{15}N chemical shifts in bR_{568} and bR_{555} are still further to low frequency than normal for protonated retinal Schiff bases, and it was suggested that this is due to an unusually weak counterion.[66] Comparison of the shift tensor elements for different retinylidenebutylimine salts[70] and retinylideneanilinimine salts[71] has shown that the lowest-frequency element is insensitive to counterion strength, and the two high-frequency elements vary proportionately. The same relationship is observed between the tensor elements for bacteriorhodopsin, strengthening the association of the ^{15}N chemical shift with counterion strength.[70] However, the effect is more extreme in bacteriorhodopsin, indicating a counterion that is weaker than any halide, carboxylate, or phenolate moiety that might be available as a simple counterion in a protein. In order to explain the data it became necessary to postulate a complex counterion, involving water-mediated hydrogen bonding between the Schiff base and protic amino

acid residues.[70] Such a hydrogen-bonded complex would diffuse the counterion charge over several bonds. The complex counterion is consistent with the current structural model of bacteriorhodopsin, which locates water, two Asp residues and one Arg residue in the vicinity of the Schiff base.[2]

Interestingly, weakening the strength of the Schiff base counterion also affects the ^{13}C-5 chemical shift at the other end of the polyene chain.[71,72] In the retinylideneanilinimine salts, which crystallize in the planar 6-*s*-*trans* conformation, the effect shows up essentially exclusively in the middle element of the ^{13}C-5 chemical shift tensor, and the unusually weak Schiff base counterion in bacteriorhodopsin completely explains the unusual value of the middle element of the ^{13}C-5 chemical shift tensor in bacteriorhodopsin.[71] A weak Schiff base counterion also destabilizes the ground electronic state of the chromophore relative to the excited state, and thereby constitutes an important mechanism for the bathochromic opsin shift. This effect is larger in the retinylideneanilinimine salts, which crystallize in the planar 6-*s*-*trans* conformation, than in the retinylidenebutylimine salts, which crystallize in the skewed 6-*s*-*cis* conformation.[71] This enhancement is also seen in solution in 1,1-didemethylretinal Schiff bases, which adopt a planar 6-*s*-*trans* conformation, compared with retinal Schiff bases in which the planar 6-*s*-*trans* conformation is sterically disfavored.[72] The synergistic effects of the extended π system, due to ring–chain planarization, and the weak Schiff base hydrogen bonding, due to the complex counterion, are sufficient to explain completely the very large opsin shift in bacteriorhodopsin.[71]

With HCl titration, the visible absorption maximum of bacteriorhodopsin shifts from 568 nm (at pH ~7) to 605 nm (at pH ~2), and then reverts to 565 nm (at pH ~0). Spectra of [ϵ-^{15}N]Lys-labeled samples indicated that the ^{15}N chemical shift is closely correlated with the color.[73] A 16 ppm low-frequency shift in the blue species indicates an even weaker Schiff base counterion than in the two purple species. This is consistent with the expected protonation of an acidic residue in the complex counterion at low pH. The recovery of the color and ^{15}N chemical shift at still lower pH is thought to be due to the replacement of a water molecule in the complex counterion by chloride from the bulk acid. Carbon-13 NMR results for selectively enriched polyene carbons in bR_{605} revealed that the chromophore conformation is generally not very different from that of bR_{568}, although the spectrum of [14-^{13}C]retinal bR_{605} showed doublets for the 15-*syn* and 15-*anti* forms that may reflect the coexistence of 13-*cis* and all-*trans* conformers in each case.[73]

4.2 Polar Amino Acid Residues

Amino acids capable of ionization or hydrogen bonding could participate in proton transport in bacteriorhodopsin. Roles proposed for Tyr and Asp residues have motivated NMR studies of these groups.

Tyrosinate is an unusual species, but FTIR and UV studies suggested that it existed in bacteriorhodopsin. Since the [4′-^{13}C]Tyr chemical shift is sensitive to deprotonation of the adjoining oxygen, it provides an unambiguous probe for long-lived tyrosinate. However, MAS NMR spectra of [4′-^{13}C]Tyr-labeled bacteriorhodopsin showed no detectable long-lived tyrosinate in dark-adapted bacteriorhodopsin at pH bulk values below 13,[74] light-adapted bacteriorhodopsin at pH = 7 or 10,[75] or the M-state at pH = 10.[75] It was concluded that the changes in Tyr residues detected by FTIR and UV spectroscopy represented changes in hydrogen bonding rather than deprotonation.

Internal Asp residues certainly do play a direct role in proton transport. Engelhard et al.[43] biosynthetically labeled bacteriorhodopsin with [4-^{13}C]Asp. Unexpected scrambling of the label to Trp was found, but this signal causes no problem because it appears in a distinct region of the spectrum. On the other hand, the signals of the nine labeled Asp residues and the three labeled Asn residues are superimposed on peptide backbone signals due to natural-abundance ^{13}C and some scrambling through the tricarboxylic acid cycle to [1-^{13}C]Glu. Nevertheless, six resonances were resolved. These were considered in terms of five categories: exposed Asp residues which must be deprotonated, buried Asp residues that are not protonated, buried Asp residues that are protonated, Asn residues in polar environments, and Asn residues in nonpolar environments. The signals due to surface Asp residues were assigned to high-frequency resonances by comparison of the spectrum of the native membrane with that obtained after 'deionization' (ion exchange chromatography to replace the intrinsic cations of the purple membrane with protons). Based initially on chemical shifts and ^{14}N line-broadening effects in model compounds, the two most narrow, lowest frequency lines were assigned to protonated Asp residues which must be buried. The protonated state of these low-frequency resonances was later confirmed by estimation of the middle chemical shift tensor element from sideband intensities.[76] Specific assignments for the Asp96 and Asp85 signals were subsequently obtained by studies of site-specific mutants.[77] By elimination, based on the current structural model of bacteriorhodopsin and FTIR studies of Asp residues, the other narrow low-frequency signal was assigned to Asp115.[76] Based on the current structural model of bacteriorhodopsin and the functional properties of site-specific mutants, Asp85 and Asp212 are expected to be influenced by light adaptation. This prediction was borne out: two signals shifted on light adaptation, including the previously assigned Asp85 signal and a signal further to high frequency which was assigned to Asp212 by elimination.[76] The signals of all four internal Asp residues have thus been assigned in bR_{555} and bR_{568}. Using these assignments to interpret the spectrum of the M-intermediate in the D96 N mutant, deprotonation of the Schiff base is seen to lead to protonation of Asp85 while Asp212 remains protonated.[78] Deionization of the membranes was also found to induce protonation of Asp85.[78]

5 PROTON DIFFUSION

Among the various forms of spectroscopy that have been applied to bacteriorhodopsin, NMR has the unique potential to chart the movement of protons, which is central to the energy transduction process. One approach makes use of the relatively fast relaxation of the immobile protons of the protein.[79] In this CP MAS experiment, cross polarization is delayed until ^{1}H magnetization remains only in the bulk water. Under these circumstances, the only nuclei that are cross polarized effectively are those that exchange protons with bulk water on the submillisecond timescale. Using this

selection technique for [ϵ-^{15}N]Lys-labeled bacteriorhodopsin, Harbison et al.[79] observed cross polarization of the Schiff base and the six free Lys residues, although there was no longer any cross polarization of the natural-abundance ^{15}N in the peptide backbone. By varying the delay, it was demonstrated that proton exchange between the Schiff base and bulk water is essentially complete in about 0.5 ms. Delayed cross polarization has also been applied to [^{15}N]Arg-labeled bacteriorhodopsin.[80,81] In this case, rapid proton exchange was only observed at high pH.[81]

Proton NMR provides a more direct means of following proton movement. Zheng et al.[82] have shown that high-resolution 2D ^{1}H MAS NMR spectra can be obtained by using ^{2}H to dilute and cross polarize the protons. This approach was used to obtain 2D ^{1}H NOESY spectra of chemically exchanging solids, and the development of cross-peak intensities was analyzed to extract the kinetic constants for exchange. Proton exchange was found to occur preferentially along hydrogen bonds. Initial 2D ^{1}H NOESY spectra have also been obtained for perdeuterated bacteriorhodopsin.[83] Signal intensity from the residual nonexchanging protons on the protein prevents detailed examination of the signals of the exchanging protons. However, the 2D spectrum shows the expected exchange among high-frequency absorbing protons and, on a somewhat longer timescale, unexpected exchange between high-frequency and low-frequency protons. The latter are believed to be water molecules in nonpolar pockets. This interpretation is supported by parallel ^{2}H studies of water dynamics, which show a small population of freely rotating water molecules even at very low temperatures where hydrogen bonding would inhibit rotation.[83] Although these experiments are the first to find evidence for water in hydrophobic regions of purple membranes, such water has been suggested to fill gaps between polar amino acids along the proton transport pathway.

6 RELATED ARTICLES

Amino Acids, Peptides and Proteins: Chemical Shifts; Carbon and Nitrogen Chemical Shifts of Solid State Enzymes; Cross Polarization in Rotating Solids: Spin-1/2 Nuclei; Chemical Exchange on Solid Metal Surfaces; Deuterium NMR in Solids; Dipolar and Indirect Coupling Tensors in Solids; Homonuclear Recoupling Schemes in MAS NMR; Hydrogen Bonding; Magic Angle Spinning; Membrane Proteins; Membranes: Carbon-13 NMR; Protein Dynamics from Solid State NMR; REDOR and TEDOR; Rotational Resonance in Biology.

7 REFERENCES

1. W. Stoeckenius, *Sci. Am.*, 1976, **234**(6), 38.
2. R. Henderson, J. M. Baldwin, T. A. Ceska, F. Zemlin, E. Beckmann, and K. H. Downing, *J. Mol. Biol.*, 1990, **213**, 899.
3. H. Bayley, K.-S. Huang, R. Radharkrishnan, A. H. Ross, Y. Takayaki, and H. G. Khorana, *Proc. Natl. Acad. Sci. USA*, 1981, **78**, 2225.
4. G. F. X. Schertler, C. Villa, and R. Henderson, *Nature*, 1993, **362**, 770
5. M. L. Applebury and P. A. Hargrave, *Vision Res.*, 1986, **26**, 1881.
6. E. A. Zhukovsky and D. D. Oprian, *Science*, 1989, **246**, 928.
7. T. P. Sakmar, R. R. Franke, and H. G. Khorana, *Proc. Natl. Acad. Sci. USA*, 1989, **86**, 8309.
8. J. M. Baldwin, *EMBO J.*, 1993, **12**, 1693.
9. K. Nakanishi, V. Balogh-Nair, M. Arnabaldi, K. Tsujimoto, and B. Honig, *J. Am. Chem. Soc.*, 1980, **102**, 7945.
10. J. Lugtenburg, *Pure Appl. Chem.*, 1985, **57**, 753.
11. M. B. Bizounok, M. M. Simpson, and J. Herzfeld, To be submitted.
12. M. Auger, K. V. Lakshmi, E. van den Berg, S. Roesselet, H. G. Khorana, S. K. Das Gupta, W. B. D. van Liemt, J. Raap, J. Lugtenburg, J. Herzfeld, and R. G. Griffin, *Biophys. J.*, 1992, **61**, A532.
13. S. Sonar, N. Patel, W. Fischer, and K. J. Rothschild, *Biochemistry*, 1993, **32**, 13 777.
14. E. A. Dratz, J. E. Furstenau, C. G. Lambert, D. L. Thireault, H. Rarick, T. Schepers, S. Pakhlevaniants, and H. E. Hamm, *Nature*, 1993, **363**, 276.
15. L. U. Colmenares, A. E. Asato, M. Denny, D. Mead, J. P. Zingoni, and R. S. H. Liu, *Biochem. Biophys. Res. Commun.*, 1991, **179**, 1337.
16. H. J. M. de Groot, V. Copié, S. O. Smith, P. J. Allen, C. Winkel, J. Lugtenburg, J. Herzfeld, and R. G. Griffin, *J. Magn. Reson.*, 1988, **77**, 251.
17. S. O. Smith, J. Courtin, H. De Groot, R. Gebhard, and J. Lugtenburg, *Biochemistry*, 1991, **30**, 7409.
18. S. O. Smith, H. J. M. de Groot, R. Gebhard, and J. Lugtenburg, *Photochem. Photobiol.*, 1992, **56**, 1035.
19. G. S. Harbison, S. O. Smith, J. A. Pardoen, P. P. J. Mulder, J. Lugtenburg, J. Herzfeld, R. Mathies, and R. G. Griffin, *Biochemistry*, 1984, **23**, 2662.
20. S. O. Smith, H. J. M. de Groot, R. Gebhard, J. M. L. Courtin, J. Lugtenburg, J. Herzfeld, and R. G. Griffin, *Biochemistry*, 1989, **28**, 8897.
21. G. S. Harbison, S. O. Smith, J. A. Pardoen, C. Winkel, J. Lugtenburg, J. Herzfeld, R. Mathies, and R. G. Griffin, *Proc. Natl. Acad. Sci. USA*, 1984, **81**, 1706.
22. M. R. Farrar, K. V. Lakshmi, S. O. Smith, R. S. Brown, J. Rapp, J. Lugtenburg, R. G. Griffin, and J. Herzfeld, *Biophys. J*, 1993, **65**, 310.
23. L. K. Thompson, A. E. McDermott, J. Raap, C. M. van der Wielen, J Lugtenburg, J. Herzfeld, and R. G. Griffin, *Biochemistry*, 1992, **31**, 7931.
24. J. M. Griffiths, K. V. Lakshmi, A. E. Bennett, J. Raap, C. M. van der Wielen, J. Lugtenburg, J. Herzfeld, and R. G. Griffin, *J. Am. Chem. Soc.*, 1994, **116**, 10 178.
25. G. S. Harbison, P. P. J. Mulder, H. Pardoen, J. Lugtenburg, J. Herzfeld, and R. G. Griffin, *J. Am. Chem. Soc.*, 1985, **107**, 4809.
26. G. S. Harbison, S. O. Smith, J. A. Pardoen, J. M. L. Courtin, J. Lugtenburg, J. Herzfeld, R. A. Mathies, and R. G. Griffin, *Biochemistry*, 1985, **24**, 6955.
27. V. Copié, A. E. McDermott, K. Beshah, J. C. Williams, M. Spijker-Assink, R. Gebhard, J. Lugtenburg, J. Herzfeld, and R. G. Griffin, *Biochemistry*, 1994, **33**, 3280.
28. F. Creuzet, A. McDermott, R. Gebhard, K. van der Hoef, M. B. Spijker-Assin, J. Herzfeld, J. Lugtenburg, M. H. Levitt, and R. G. Griffin, *Science*, 1991, **251**, 783.
29. A. E. McDermott, F. Creuzet, R. Gebhard, K. van der Hoef, M. H. Levitt, J. Herzfeld, J. Lugtenburg, and R. G. Griffin, *Biochemistry*, 1994, **33**, 6129.

30. S. O. Smith, J. Courtin, E. van den Berg, C. Winkel, J. Lugtenburg, J. Herzfeld, and R. G. Griffin, *Biochemistry*, 1989, **28**, 237.
31. K. V. Lakshmi, M. Auger, J. Raap, J. Lugtenburg, R. G. Griffin, and J. Herzfeld, *J. Am. Chem. Soc.*, 1993, **115**, 8515.
32. J. B. Ames, S. P. A. Fodor, R. Gebhard, J. Raap, E. M. M. van den Berg, J. Lugtenburg, and R. A. Mathies, *Biochemistry*, 1989, **28**, 3681.
33. K. V. Lakshmi, M. R. Farrar, J. Raap, J. Lugtenburg, R. G. Griffin, and J. Herzfeld, *Biochemistry*, 1994, **33**, 8853.
34. S. P. A. Fodor, J. B. Ames, R. Gebhard, E. M. M. van den Berg, W. Stoeckenius, J. Lugtenburg, and R. A. Mathies, *Biochemistry*, 1988, **27**, 7097.
35. S. O. Smith, I. Palings, V. Copie, D. P. Raleigh, J. Courtin, J. A. Pardoen, J. Lugtenburg, R. A. Mathies, and R. G. Griffin, *Biochemistry*, 1987, **26**, 1606.
36. L. C. P. J. Mollevanger, A. P. M. Kentgens, J. A. Pardoen, J. M. L. Courtin, W. S. Veeman, J. Lugtenburg, and W. J. De Grip, *Eur. J. Biochem.*, 1987, **163**, 9.
37. S. O. Smith, I. Palings, M. E. Miley, J. Courtin, H. J. M. de Groot, J. Lugtenburg, R. A. Mathies, and R. G. Griffin, *Biochemistry*, 1990, **29**, 8158.
38. A. S. Ulrich, M. P. Heyn, and A. Watts, *Biochemistry*, 1992, **31**, 10 390.
39. S. W. Lin and R. A. Mathies, *Biophys. J.*, 1989, **56**, 653.
40. B. A. Lewis, G. S. Harbison, J. Herzfeld, and R. G. Griffin, *Biochemistry*, 1985, **24**, 4671.
41. J. L. Bowers and E. Oldfield, *Biochemistry*, 1988, **27**, 5156.
42. S. L. Helgerson, S. L. Slemson, E. A. Adams, R. D. Renthal, and E. A. Dratz, *Biophys. J.*, 1991, **59**, 475 a.
43. M. Engelhard, B. Hess, D. Emeis, G. Metz, W. Kreutz, and F. Siebert, *Biochemistry*, 1989, **28**, 3967.
44. M. Seigneuret, J. M. Neumann, and J. L. Rigaud, *J. Biol. Chem*., 1991, **266**, 10 066.
45. M. Seigneuret and M. Kainosho, *FEBS Lett.*, 1993, **327**, 7.
46. C. M. Deber, B. J. Sorrell, and G. Y. Xu, *Biochem. Biophys. Res. Commun.*, 1990, **172**, 862.
47. M. Engelhard, S. Finkler, G. Metz, and F. Siebert, *Biophys. J.*, 1992, **61**, A532.
48. M. R. Farrar, L. K. Thompson, R. S. Brown, R. G. Griffin, and J. Herzfeld, *Biophys. J.*, 1991, **59**, 326a.
49. J. G. Hu, B. Q. Sun, M. B. Bizounok, R. G. Griffin, and J. Herzfeld, To be submitted.
50. V. Yu. Orekhov, G. V. Abdulaeva, L. Yu. Musina, and A. S. Arseniev, *Eur. J. Biochem.*, 1992, **210**, 223.
51. R. A. Kinsey, A. Kintanar, and E. Oldfield, *J. Biol. Chem.*, 1981, **256**, 9028.
52. R. A. Kinsey, A. Kintanar, M. D. Tsai, R. L. Smith, N. Janes, and E. Oldfield, *J. Biol. Chem.*, 1981, **256**, 4146.
53. M. A. Keniry, H. S. Gutowsky, and E. Oldfield, *Nature (London)*, 1984, **307**, 383.
54. I. C. Baianu, H. S. Gutowsky, E. Oldfield, *Biochemistry*, 1984, **23**, 3105.
55. J. Herzfeld, C. M. Mulliken, D. J. Siminovitch, and R. G. Griffin, *Biophys. J.*, 1987, **52**, 855.
56. M. Seigneuret, J. M. Neumann, D. Levy, and J. L. Rigaud, *Biochemistry*, 1991, **30**, 3885.
57. K. H. Mayo, A. Schussheim, G. W. Vuiter, R. Boelens, R. Kaptein, M. Engelhard, and B. Hess, *FEBS Lett.*, 1988, **235**, 163.
58. A. S. Arseniev, A. B. Kuryatov, V. I. Tsetlin, V. F. Bystrov, V. T. Ivanov, and Yu. A. Ovchinnikov, *FEBS Lett.*, 1987, **213**, 283.
59. G. V. Abdulaeva, A. G. Sobol, A. S. Arseniev, V. I. Tsetlin, and V. F. Bystrov, *Biol. Membr.*, 1991, **8**, 30.
60. G. B. Cohen, D. D. Oprian, and P. R. Robinson, *Biochemistry*, 1992, **31**, 12 592.
61. J. Shriver, G. Mateescu, R. Fager, D. Torchia, and E. W. Abrahamson, *Nature (London)*, 1977, **270**, 271.
62. J. Shriver, G. D. Mateescu, and E. W. Abrahamson, *Methods Enzymol.*, 1982, **81**, 698.
63. A. Yamaguchi, T. Unemoto, and A. Ikegami, *Photochem. Photobiol.*, 1981, **33**, 511.
64. G. D. Mateescu, W. G. Copan, D. D. Muccio, D. V. Waterhous, and E. W. Abrahamson, in *Synthesis and Applications of Isotopically Labeled Compounds: Proceedings of the First International Symposium*, ed. W. P. Duncan and A. B. Susan, Elsevier, Amsterdam, 1982, p. 123.
65. G. D. Mateescu, E. W. Abrahamson, J. W. Shriver, W. Copan, D. Muccio, M. Iqbal, and D. V. Waterhous, *NATO ASI Ser., Ser. C.*, 1984, **139**, 257.
66. G. S. Harbison, J. Herzfeld, and R. G. Griffin, *Biochemistry*, 1983, **22**, 1.
67. S. O. Smith, G. S. Harbison, D. P. Raleigh, J. E. Roberts, J. A. Pardoen, S. K. Das Gupta, C. Mulliken, R. A. Mathies, J. Lugtenburg, J. Herzfeld, and R. G. Griffin, in *Biomolecular Stereodynamics: Proceedings of the Fourth Conversation in the Discipline Biomolecular Stereodynamics*, 4th edn., ed. R. H. Sarma and M. H. Sarma, Adenine Press, Guilderland, NY, 1986, Vol. 3, p. 159.
68. S. O. Smith, G. S. Harbison, D. P. Raleigh, J. E. Roberts, J. A. Pardoen, S. K. Das Gupta, R. A. Mathies, J. Lugtenburg, J. Herzfeld, and R. G. Griffin, in *Synthesis and Applications of Isotopically Labeled Compounds: Proceedings of the Second International Symposium*, ed. R. R. Muccino, Elsevier, Amsterdam, 1985, p. 239.
69. G. S. Harbison, J. Herzfeld, S. O. Smith, R. Mathies, J. A. Pardoen, P. P. J. Mulder, C. Winkel, J. Lugtenburg, and R. G. Griffin, In *XXIInd Congress AMPERE Magnetic Resonance and Related Phenomena, Proceedings*, ed. K. A. Mueller, R. Kind, and J. Roos, 22nd Zurich AMPERE Commun., Zurich, 1984, p. 461.
70. H. J. M. de Groot, G. S. Harbison, J. Herzfeld, and R. G. Griffin, *Biochemistry*, 1989, **28**, 3346.
71. J. G. Hu, R. G. Griffin, and J. Herzfeld, *Proc. Natl. Acad. Sci. USA*, in press.
72. A. Albeck, N. Livnah, H. Gottlieb, and M. Sheves, *J. Am. Chem. Soc.*, 1992, **114**, 2400.
73. H. J. M. de Groot, S. O. Smith, J. Courtin, E. Van den Berg, C. Winkel, J. Lugtenburg, R. G. Griffin, and J. Herzfeld, *Biochemistry*, 1990, **29**, 6873.
74. J. Herzfeld, S. K. Das Gupta, M. R. Farrar, G. S. Harbison, A. E. McDermott, S. L. Pelletier, D. P. Raleigh, S. O. Smith, C. Winkel, J. Lugtenburg, and R. G. Griffin, *Biochemistry*, 1990, **29**, 5567.
75. A. E. McDermott, L. K. Thompson, C. Winkel, M. R. Farrar, S. Pelletier, J. Lugtenburg, J. Herzfeld, and R. G. Griffin, *Biochemistry*, 1991, **30**, 8366.
76. G. Metz, F. Siebert, and M. Engelhard, *Biochemistry*, 1992, **31**, 455.
77. M. Engelhard, B. Hess, G. Metz, W. Kreutz, F. Siebert, J. Soppa, and D. Oesterhelt, *Eur. Biophys. J.*, 1990, **18**, 17.
78. G. Metz, F. Siebert, and M. Engelhard, *FEBS Lett.*, 1992, **303**, 237.
79. G. S. Harbison, J. E. Roberts, J. Herzfeld, and R. G. Griffin, *J. Am. Chem. Soc.*, 1988, **110**, 7221.
80. M. Engelhard, B. Hess, G. Metz, and F. Siebert, *Biophys. J.*, 1990, **57**, 361a.

81. K. V. Lakshmi, A. E. McDermott, J. Herzfeld, and R. G. Griffin, *Biophys. J.*, 1991, **59**, 327a.
82. L. Zheng, K. W. Fishbein, R. G. Griffin, and J. Herzfeld, *J. Am. Chem. Soc.*, 1993, **115**, 6254.
83. L. L. Z. Cheng, R. G. Griffin, and J. Herzfeld, Submitted.

Biographical Sketches

Judith Herzfeld. *b* 1948. A.B. 1967, Barnard College, Columbia University, USA, Ph.D., 1972, Massachusetts Institute of Technology, USA, M.P.P., 1973, John F. Kennedy School of Government, Harvard University, USA, Faculty in Chemistry, Amherst College, USA, 1973–74, Faculty in Physiology and Biophysics, Harvard Medical School USA, 1975–85, Faculty in Chemistry, Brandeis University, USA, 1985–present. Currently Professor of Biophysical Chemistry and Chair of the Department of Chemistry. Approx. 115 publications. Research specialties: solid state NMR studies of the structure and function of membrane proteins, statistical mechanical studies of entropically driven long-range order in crowded solutions of self-assembling amphiphiles.Jingui G. Hu. *b* 1962. B.S., 1984, M.S. 1987, Tsinghua University, People's Republic of China. Assistant Professor, Tsinghua University, 1987–90. As a Ph.D. candidate in chemistry at Brandeis University, USA, he is conducting solid state NMR studies of bacteriorhodopsin and related model compounds.

Biological Macromolecules

Oleg Jardetzky
Stanford University, CA, USA

1 Introduction 1
2 Macromolecular Structure from NMR Data—General Strategy 1
3 Macromolecular Dynamics 13
4 Molecular Interactions 17
5 Protein Function 18
6 Conclusions 18
7 Appendix: Definition of Symbols Used in Equation (16) 18
8 References 19

1 INTRODUCTION

High-resolution NMR spectroscopy has become, alongside X-ray crystallography, one of the two most important physical methods for the study of the *structure, dynamics, interactions* and *function* of biological macromolecules—in particular proteins and nucleic acids and, to a lesser extent, polysaccharides. This article summarizes under each of these headings the general framework, the essential techniques and classical paradigms for the application of NMR in molecular biology, illustrated by the key original findings. More specialized accounts can be found under specific topics. The historical development of this field has been described in volume I of this Encyclopedia.

High-resolution NMR shares a common feature with X-ray diffraction in that both methods—in contrast to all other physical methods—permit the study of biological macromolecules at *atomic resolution*. Beyond that, the two methods are in many ways complementary. NMR offers the advantage that it allows the study of macromolecules in solution, their natural environment, while X-ray diffraction requires crystallization. Structures with molecular weights up to 37 kDa can now be determined by NMR, and the molecular weight range is likely to be soon extended upwards. Structures approaching the 1000 kDa range are already amenable to study by X-ray diffraction. Yet crystallography yields a static picture, whereas NMR provides, in addition to the structure, information on its dynamics. Such information is particularly important for the understanding of biological function. NMR is also the method of choice for the study of ligand interactions. It lends itself more easily to the determination of informative partial structures and allows estimates of ligand exchange rates, rates of structural changes in the macromolecule and observations of the modulation of macromolecular dynamics by ligand binding.

There is, however, a fundamental difference between structural information that can be derived from NMR data and that obtainable by X-ray diffraction. The experimental diffraction pattern is a simple function of geometric parameters and can be converted by Fourier transformation directly into an electron density map and hence, in principle, into a set of coordinates. In practice, for macromolecular structures, resolution is never sufficient, and model building becomes an essential part of structure determination. On the other hand, direct transformation from data to a set of coordinates is, even in principle, impossible in NMR. Measurable NMR parameters depend simultaneously on several internuclear distances, rates of motion and rates of conformational averaging. To obtain geometric parameters (internuclear distances or angles) from a set of NMR data, it is necessary to make assumptions about the dynamics and other features of the structure. To then obtain a set of coordinates, it is necessary to search the conformational space accessible to the macromolecular chain, usually adding information not obtainable directly from NMR experiments. Both the subjective judgments required and the methods of searching conformational space are important potential sources of error. These are discussed further in the sections devoted to specific methods of structure calculation.

2 MACROMOLECULAR STRUCTURE FROM NMR DATA—GENERAL STRATEGY

Defining the structure and dynamics of a biological macromolecule (protein or nucleic acid fragment) from NMR data requires four steps: (1) experimental *resolution* and (2) *assignment* of the macromolecular spectrum; (3) *interpretation* of the observed spectra in terms of *geometric parameters* and their changes in time; and (4) *structure calculation or model building*, for which a variety of computer algorithms are available.

The limiting steps are usually the resolution and the assignment of the NMR spectrum. NMR spectra of a macromolecule typically consist of a few hundred to a few thousand overlapping lines. The first experimental task is then to resolve all spectral lines and to assign each spectral line to a specific nucleus in a specific residue in the sequence. For linear polymers, such as proteins and nucleic acids (with few exceptions), the task has become manageable. The situation for polysaccharides, where branching is frequent, is more complicated, and the assignment problem has not been completely solved.

The geometric parameters necessary for building models of a macromolecular structure are[1] estimates of internuclear distances, derived from relaxation parameters, in particular from the Nuclear Overhauser Effect (NOE)[2] estimates of dihedral angles, derived from coupling constants, and auxiliary constraints,[3] which can sometimes be derived from chemical shifts (e.g. ring current shifts in nucleic acids, charateristic shifts in α-helices), proton exchange rates (slow rates are often taken to be indicative of hydrogen bonding), or other spectroscopic measure-ments. NMR spectroscopic data are by themselves never sufficient to define a macromolecular structure. Any structural interpretation of NMR data is, in practice, though not in principle, predicated on prior knowledge of the primary sequence of the macromolecule, of the covalent distances, chirality and bond angles within it and of the van der Waals radii of the constituent atoms.

Model building thus relies on the geometric parameters contained in the known primary structure and on the additional geometric constraints derived from NMR, which play a determining role in the definition of the three-dimensional

folding. It is the only one of the steps that has been largely automated, but it will always require considerable judgment. As will be discussed below, 'calculation' of NMR structures assumes that the structure is rigid. The extent to which this assumption applies varies from one macromolecule to another, and choosing the wrong assumption can lead to a wrong structure.

2.1 Solution Structures of Proteins

Resolution and assignment usually go hand in hand. The specific techniques that can be used at each step of an NMR structure determination differ, depending on the molecular weight of the protein. Simple, purely spectroscopic procedures for obtaining resolution and assignment, applicable to small structures (<10 kDa), break down at higher molecular weights, whereas the more elaborate isotope labeling techniques needed for larger structures are rarely needed for proteins of lower molecular weight.

2.1.1 Resolution

Sufficient resolution of protein NMR spectra to allow their interpretation in atomic detail has become possible by the development of three technologies: (1) high frequency NMR spectrometers, at 500–750 MHz for ^{1}H, allowing a high degree of chemical shift dispersion; (2) multidimensional (initially two-dimensional) spectroscopy, which allows further separation of lines overlapping in a one-dimensional spectrum by cross peaks to other lines representing physically interacting nuclei; and (3) isotopic spectral editing, or the simplification of protein NMR spectra by prior isotopic (^{2}H, ^{13}C or ^{15}N) labeling of the protein. As noted, purely spectroscopic methods [(1) and (2)] usually suffice to resolve the spectra of small proteins (<10 kDa). For larger proteins (>20 kDa), isotopic spectral editing is indispensable, and for the intermediate molecular weight range (10–20 kDa), the methodological requirements depend on the extent of overlap of spectral lines, which in turn depends on the specific structure.

The contributions of each of the three technologies to the resolution of protein spectra are best illustrated graphically. Figure 1 compares the one-dimensional spectra of ribonuclease at 40 MHz[1] and 750 MHz. Figure 2 shows the relationship between two-, three-, and four-dimensional spectra.[2] Figure 3 illustrates the simplification of a two-dimensional proton spectrum by selective deuteration[3] and Figure 4 shows the two-dimensional resolution of an overlapping ^{1}H spectrum by adding a heteronuclear dimension through ^{15}N labeling.[4] Many multidimensional and isotopic spectral editing schemes are now available. Inasmuch as they not only improve resolution but also allow different assignment strategies, they are discussed below under assignment.

2.1.2 Assignment. Sequential Assignment Methods

The basic idea underlying all *sequential assignment methods* is to establish a connectivity between the spectrum of an amino acid residue with that of its sequential neighbors. Two types of connectivities are generally observable in NMR spectra: (1) through-bond connectivity reflected in spin–spin coupling, possible only between covalently linked atoms;

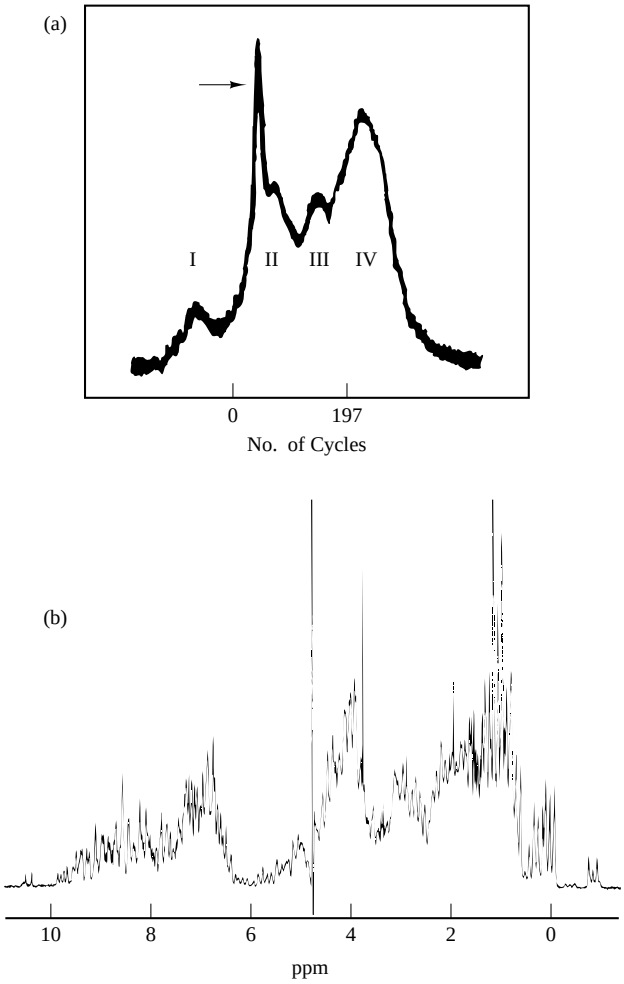

Figure 1 (a) Ribonuclease spectra taken at 40 MHz. (Reproduced from M. Saunders, A. Wishnia and J. G. Kirkwood, *J. Am. Chem. Soc.*, 1957, **79**, 3289). (b) Ribonuclease spectra (2 mmol double-labeled RNAse in 90% H_2O/10% D_2O, ^{1}H NOESY, 16 scans) taken at 750 MHz. (Courtesy of Bruker Instruments, Inc.)

and (2) through-space connectivity reflected in relaxation parameters—in particular the NOE, i.e. the connectivity between any two atoms in spatial proximity. Either can be used for sequential assignment, and different assignment strategies now use different combinations of either or both. The classical paradigm for sequential assignment emerged gradually. The use of coupling constants to identify amino acid residues in peptides by residue type was introduced in 1957 in the very first systematic study of amino acid and peptide spectra by Takeda and Jardetzky.[5] The use of relaxation parameters to evaluate distances in macromolecules was first suggested in 1964.[6] The usefulness of the combination was first demonstrated in 1976 by Gibbons[7] on one-dimensional (1D) spectra of the cyclic peptide, gramicidin S. In this paradigm the peptide NH of each residue is identified by its (small, $J \leq 10$ Hz) coupling to the α-CH of the same residue, and the connectivity between the NH group of residue i and the NH and α-CH groups of residue $i \pm 1$ by a NOE. This 'jumps' the peptide bond, across which spin–spin coupling is too small to be useful, with the help of a relaxation parameter. In this manner, it is, in principle, possible to assign the entire spectrum of a protein, beginning with a residue

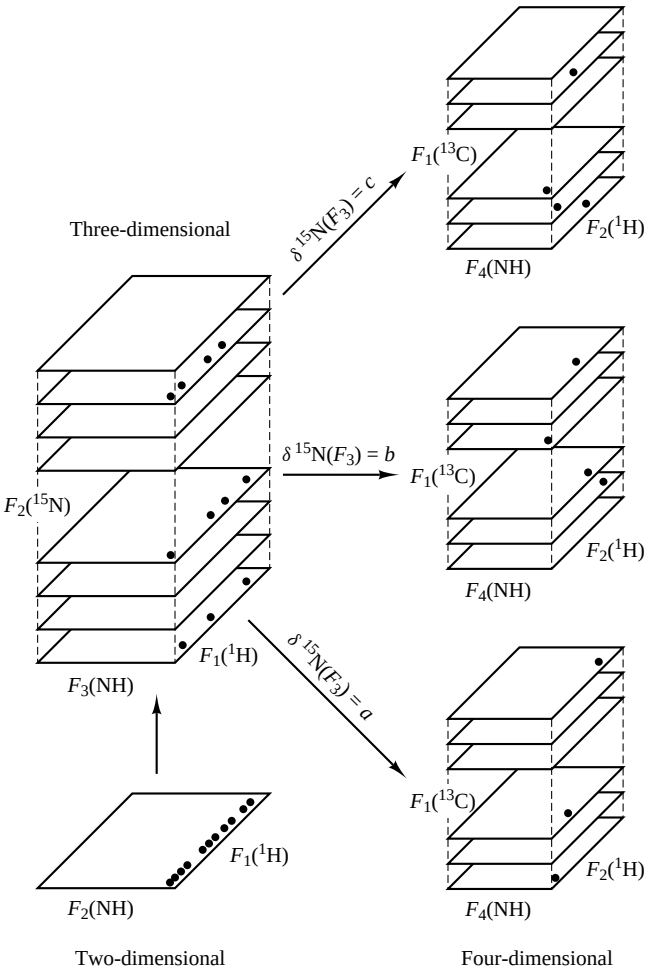

Figure 2 Illustration of relationships between heteronuclear $^{15}N/^{13}C$-edited two-, three-, and four-dimensional (^{13}C or ^{15}N) NOESY spectra. (Modified from Clore and Gronenborn[2])

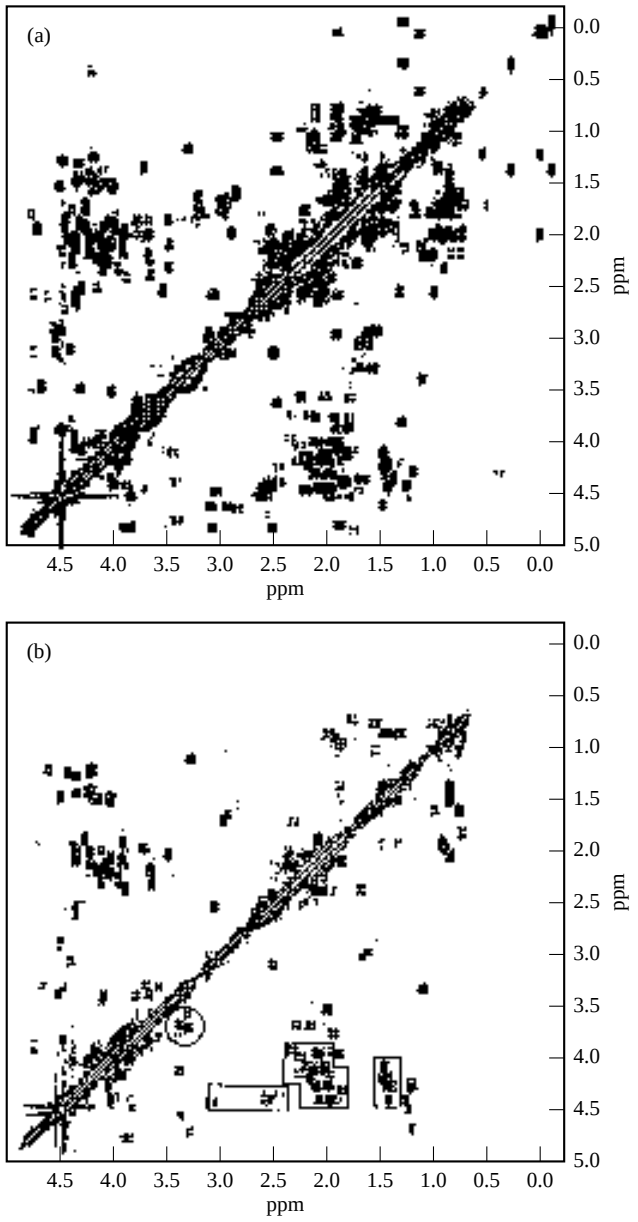

Figure 3 Comparison of the aliphatic region of (a) the natural abundance or wild-type *trp*-repressor DQF (double quantum filtered) COSY spectrum with (b) the spectrum of selectively deuterated *trp*-repressor analog (A5). (Reproduced from C. H. Arrowsmith, L. Treat Clemons, L. Szilágyi, R. Pachter and O. Jardetzky, *Makromol. Chem., Macromol. Symp.*, 1990, **34**, 33)

whose assignment is easily established (e.g. an N- or C-terminal, or with a unique residue in a protein) and then sequentially tracing all connectivities along the polypeptide chain. The Gibbons paradigm is illustrated in Figure 5. The tracing is much more easily done in 2D spectra, where the connectivities are seen directly as cross peaks in the spectrum. Two types of 2D spectra are required as a minimum for this purpose: a COSY-type spectrum to establish through-bond connectivities, thereby at least identifying the side chains; and a NOESY-type spectrum to establish through-space connectivities. For peptides and small proteins studied at 500–600 MHz, stumbling blocks are rare, and a complete assignment of the ^1H spectrum using this paradigm can, as a rule, be obtained. Since other characteristics distances can be defined for specific types of secondary structure (e.g., for the NH $i \rightarrow$ NH $i + 3$ for α-helices, or NH $i \rightarrow$ NH $i + 2$ for β-sheets), the assignment procedure simultaneously yields the secondary structure pattern of the protein.

Although the paradigm is applicable, in principle, to any polypeptide chain regardless of length, practical limitations preclude its use for larger proteins. For structures larger than 10 kDa the overlap makes it difficult to distinguish between different sequential assignment possibilities and, in addition, at higher molecular weights (15–20 kDa) line broadening is usually sufficient to obliterate most NH–α-CH couplings. A scheme based entirely on NOEs along the peptide chain and a combination of coupling constants and NOEs within side chains can sometimes be used instead.[8] However, for unedited spectra the usefulness of this technique is still limited by overlap: increasing overlap with increasing molecular weight leads to exponentially growing ambiguities in following the sequence. Therefore, for larger molecules, isotopic spectral editing is required for both resolution and assignment.

Isotopic Spectral Editing in its simplest form, as proposed by us in 1965, is achieved by selective deuteration. Biosynthesis of proteins from a mixture of deuterated and protonated amino acids allows the preparation of a series of labeled

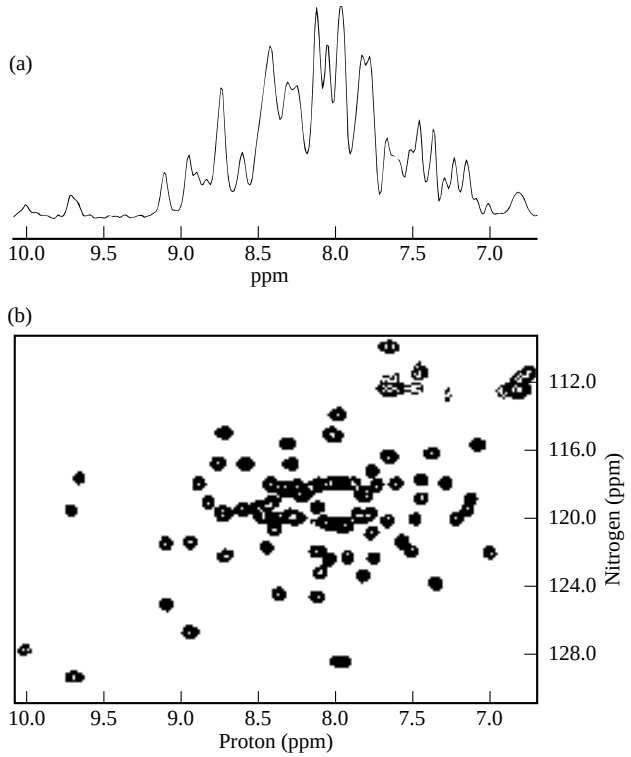

Figure 4 (a) Two-dimensional homonuclear spectrum of *trp*-repressor. (b) The ^{15}N-labeled HMQC spectrum of the same region of the *trp*-repressor

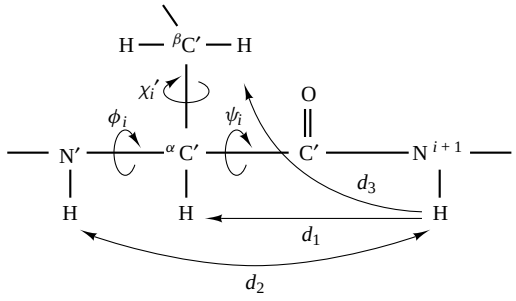

Figure 5 Gibbons's paradigm: magnetization transfer pathways and scalar connectivities in the peptide backbone. Arrows denote distances from the amide proton that can be defined. (Reproduced from O. Jardetzky, A. Lane, J.-F. Lefèvre, O. Lichtarge, B. Hayes-Roth, and B. Buchanan, in 'NMR in the Life Sciences', eds. E. M. Bradbury and C. Nicolini, Plenum, New York, 1986, pp. 49–72)

analogs in which only the desired combinations of amino acids remain visible to ^{1}H spectroscopy. Even though the labeling is by residue type (e.g. all leucines protonated, or all isoleucines deuterated), this type of editing reduces the problems of overlap sufficiently to allow, by itself, complete sequential assignment in larger proteins. Its largest drawback is the expense of preparing a sufficient number of deuterated analogs. Selective deuteration also narrows the linewidths by reducing the number of interacting neighbors and hence the number of alternative pathways for magnetization transfer or 'spin diffusion'. This may in some cases allow the observation of coupling constants not observable in a fully protonated species and the use of such constants for sequential assignment. In other cases, however, line broadening by the nearest neighbor will be sufficient to limit the assignment options to those relying on through-space (NOE) connectivities.

Heteronuclear spectral editing schemes for resolution and assignment using multidimensional spectroscopy based on uniform ^{15}N or combined ^{15}N and ^{13}C labeling have been devised, and their usefulness for assigning the spectra of proteins in the intermediate molecular weight range (20–30 kDa) has been demonstrated. The simplest among these are heteronuclear three-dimensional 3D HMQC (heteronuclear multiple quantum coherence)-NOESY or HSQC (heteronuclear single quantum coherence)-NOESY experiments on uniformly ^{15}N labeled peptide chains. In this experiment, the backbone NH resonances are spread out in two dimensions (^{1}H and ^{15}N) and their connectivities to each other and to their respective side chains are established by a NOESY experiment in an additional (^{1}H) dimension. In favorable cases the overlap is reduced sufficiently to allow a complete, or nearly complete, set of sequential assignments needed for a structure determination. At higher molecular weights, however, this is not always sufficient to eliminate overlap, and selective labeling becomes necessary.

A very general triple-resonance sequential assignment strategy based on ^{13}C and ^{15}N double labeling of the peptide chain has been developed.[9,10] The connectivities that can be established using this strategy, and the 3D experiments required for this purpose are summarized in Figure 6.[9,11] The crucial interresidue connectivity bridging the peptide bond can be obtained in several different ways, relying on each of the following correlations: (1) HNCO relying on the across-the-amide bond ^{13}CO–^{15}N coupling J(NCO) $\approx$ 15 Hz; (2) HNCA identifying each NH with the C-α of its side chain by the ^{15}N–^{13}C-α coupling constant J(NC-α) $\approx$ 7–11 Hz; (3) HCACO identifying each carbonyl with the C-α of its side chain by the large ^{13}C-α–^{13}CO coupling constant J(C-αCO) $\approx$ 55 Hz; (4) ^{15}N HOHAHA-HMQC providing the same identification of the ^{15}NH group with its side chain as (2), but relying on proton couplings, J(NC-αH) $\approx$ 5–10 Hz; and (5) HCA(CO)N, again bridging the peptide bond using the two-bond ^{13}C-$\alpha(i+1)$–^{15}N$_{(i)}$ constant J(C-αN) $\leq$ 7 Hz.

Additional and alternative correlation pathways for the triple resonance correlations can also be defined, and the technique has been successfully used to establish the structures of calmodulin and of its complex with a 2 kDa calmodulin receptor binding domain (16.7 kDa; 19.4 kDa in the complex),[12] the ribonuclease domain of HIV-reverse transcriptase (18 kDa),[13] *Escherichia coli* enzyme III(glc) (18.1 kDa),[14] and human interleukin-4 (15.4 kDa).[15] The details of these and many other possible similar experiments are described in more detail elsewhere in this Encyclopedia. Although they are very useful extensions of the existing technology for the study of intermediate-size proteins (up to 30 kDa), as a class the heteronuclear multidimensional assignment strategies do not escape the problems posed by increasing molecular weight, for two reasons. First, they require relatively long pulse sequences, which lower the sensitivity of the NMR experiment, and as the T_2 becomes shorter with increasing molecular weight, this effect becomes more prominent. Second, they rely on heteronuclear coupling constants of the order of 10–15 Hz, and in a fully protonated protein at molecular weights above the range 30–40 kDa most of these will be obliterated by line

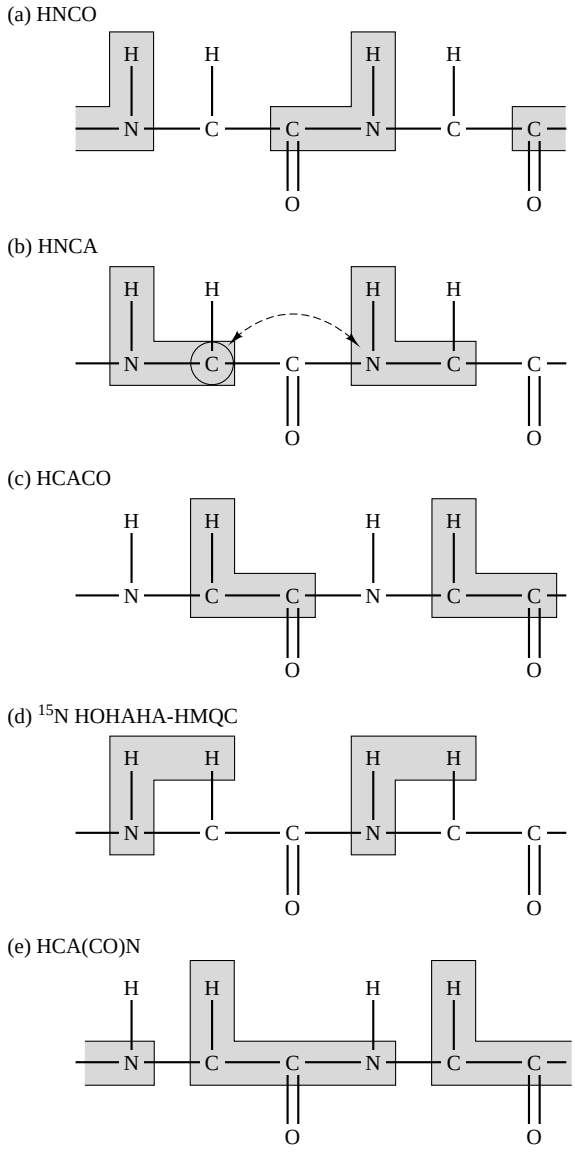

Figure 6 Connectivities observed in the five different types of three-dimensional NMR experiments. (a) The HNCO experiment correlates the peptide bond C′ and ^{15}N resonances with the NH chemical shift. (b) The HNCA experiment correlate the NH and ^{15}N shifts with the intraresidue C-α shift. For $\approx$ 60% of the residues in calmodulin, a two-bond connectivity to the C-α resonance of the preceding residue is also observed (broken line). (c) The HCACO experiment correlates intraresidue H-α, C-α, and C′ chemical shifts. (d) The ^{15}N HOHAHA-HMQC experiment correlate intraresidue ^{15}N, NH and H-α shifts. (e) The HCA(CO)N experiment correlates the H-α and C-α shifts of one residue with the ^{15}N shift of the next residue. (Reproduced from M. Ikura, L. E. Kay and A. Bax, *Biochemistry*, 1990, **29**, 4659)

broadening. Their usefulness can be extended by combination with selective deuteration, and the combination has been used successfully in the determination of the structure of the *trp*-repressor–DNA complex (37 kDa).[16] It can be expected that the very significant reduction of the relaxation rate in selectively deuterated proteins will allow even further extension of the usefulness of the combined homo/heteronuclear labeling methods to achieve complete resolution and assignment for proteins of still higher molecular weight. At the time of writing, the potential of the combined isotope editing techniques has not yet been fully realized. A more detailed discussion of the possibilities and limitations is available.[17]

2.1.3 Interpretation of NMR Data to Obtain Geometric Constraints

The conversion of the experimentally observed parameters (mostly intensities of cross peaks in multidimensional spectra) into geometric parameters that can be used for structure calculation (i.e. internuclear distances and dihedral angles) requires a series of subjective judgments.

The simplest model for obtaining a distance from cross peak intensities in a NOESY spectrum is the well known and widely used 'two-spin approximation', relating the observed cross-peak intensity (in this case equal to the cross-relaxation rate) to a single internuclear distance, r:

$$\sigma = \frac{K\tau}{r^6} \tag{1a}$$

where K is a constant and τ is the single (rigid body) correlation time. This equation holds *approximately* for small structures observed at short mixing times. For larger structures (above 15 kDa), equation (1a) does not hold even approximately. Even in the simplest case there exists an uncertainty in the relationship between distance and peak intensity, because the value of τ(the local correlation time of the internuclear vector in question) is unknown. The most commonly made assumption is that the macromolecule is rigid and that the overall rotational tumbling time can be used for all internuclear vectors. As noted, this assumption has proved very useful as a first approximation, even though it generally does not hold. The reason for the success of the assumption, even in some cases where its applicability is doubtful, is that the sixth-power relationship between peak intensity or correlation time and distance substantially reduces the error in the distance that results from an erroneous estimate of either peak intensity or correlation time: an error of a factor of 10 in either of the latter results in only a 46% error in the estimated distance. For the determination of the overall topology such errors can be tolerated. To account for them, as well as for the experimental errors of intensity measurements, it is customary to interpret each observed NOE not in terms of a single distance, but in terms of a distance range. A commonly used classification is into ranges allowed for 'strong', 'medium', and 'weak' NOEs. Many different calibrations of appropriate distance ranges, some differentiating between 'very strong' and 'strong', and 'weak' and 'very weak', have now been carried out. It can be said that for the first structure calculation, the differences between them are not significant. A set of typical values is given in Table 1, and the issues are discussed in more detail elsewhere.[18,19]

Some workers have attempted to reduce the uncertainties of relating observed intensities to distance by using an empirical calibration in the form:

$$r_{\mathrm{u}}^6 = \frac{(\mathrm{NOE})_{\mathrm{k}}}{(\mathrm{NOE})_{\mathrm{u}}} \cdot r_{\mathrm{k}}^6 \tag{1b}$$

where $(\mathrm{NOE})_{\mathrm{u}}$ is the intensity of the NOE for the spin pair at an unknown distance, r_{u}, and $(\mathrm{NOE})_{\mathrm{k}}$ is the NOE intensity

Table 1 Distance between Residues as Determined by NOE Intensity

NOE Intensity	Distance Range (nm)
Strong	0.18–0.27
Medium	0.18–0.33
Weak	0.18–0.50
Very Weak	0.30–0.60

for a spin pair for which the distance r_k is known. However, the use of this calibration implies strictly that the molecule is rigid and that the two-spin approximation applies. Use of distance *ranges* is equivalent to loosening these constraints in order to take the reality of internal flexibility in proteins at least partially into account. The precision of a calibration is therefore deceptive. Given that differences in local correlation times and the limits of the applicability of equation (1a) are now well known, it is doubtful that distances derived by calibration can be considered accurate. Better accuracy is still achieved by using a reasonable estimate of the allowed distance ranges.

A more significant source of error is the fact that equation (1a) does not hold, except for small structures and mixing times that are too short to obtain good spectra on larger molecules. Under these conditions one must take into account that magnetization transfer during the experiment is not limited to the two spins, but occurs between all neighboring spins in the structure. This phenomenon is known as spin diffusion, and the evolution of magnetization (peak intensity) in the presence of spin diffusion is given by the generalized Bloch equations:

$$\frac{dM_i}{dt} = -\rho_i[M_i - M_i(0)] - \sum_{j \neq i} \sigma_{ij}[M_j - M_j(0)]; i \neq j \quad (2)$$

where ρ_i is the spin–lattice relaxation rate of the ith nucleus, and σ_{ij} is the cross-relaxation rate between the two nuclei i and j, as defined in equation (1a).

To solve the generalized Bloch equations, one obviously has to know already the structure that one is trying to determine. The initial structure calculation therefore *always* has to rely on the assumption that equation (1a) holds as a first approximation. To compensate for the additional (and often substantial) errors resulting from spin diffusion, it is necessary to widen the limits for the distance estimates for purposes of the initial calculations on larger molecules. The effects (and errors) due to spin diffusion can be greatly reduced by selective deuteration of the protein, as noted above. The ultimate molecular weight limit for structure determination by NMR remains to be explored, but given the dramatic reduction of linewidths by selective deuteration, probably lies much higher that originally expected. Good local spectra have now been obtained for structures as large as 150 kDa.[20] It must be noted that using the solution of equation (2), or of its equivalent, the relaxation matrix equation for the back-calculation of spectra from an initial structure again usually involves the assumption that the structure is rigid and a single correlation time can be used in the structure calculation. Back-calculation based on this assumption may not significantly increase the accuracy of the structure over the crude initial model—as discussed below. The important point to bear in mind is that the geometric parameters derived from NMR experiments are always approximate, and the quality of the approximations used is an important determinant of the accuracy of the resulting structure.

The magnitude of the errors that can be introduced by neglecting spin diffusion can be well illustrated by an early model calculation on sperm whale myoglobin.[18] Distances derived from the X-ray structure and a correlation time of 8 ns were used to calculate cross-peak intensities by solving the generalized Bloch equations [equation (2)]. These intensities were then analyzed using equation (1a) and the same correlation time to estimate (apparent) 'NOE distances'. A plot of the apparent distances versus actual crystallographic distances (Figure 7),[18] indicates that the error in the distances calculated from equation (1a) depends on the details of the surrounding structure and may be as high as ±50% for distances >0.3 nm. Very precise distance calibrations of NOEs on an unknown structure [equation (1a) or equation (1b)] are apt to introduce significant distortions into the calculated structure.[21]

The dihedral angles, which can be derived from coupling constants in COSY-type spectra and used to define the conformations of both the protein backbone and of the side chains, are subject to similar uncertainties. In the presence of free rotation around side-chain bonds, the observed values

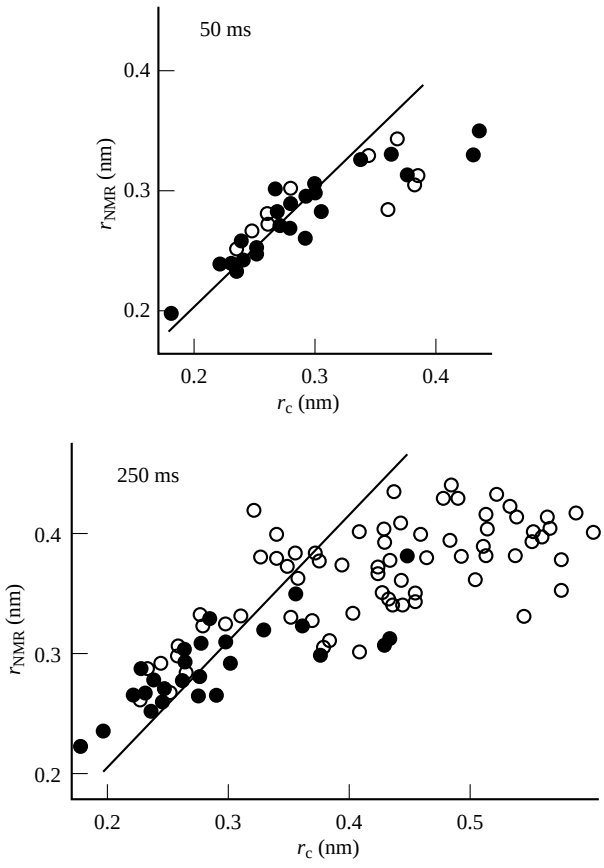

Figure 7 Apparent $^1H-^1H$ distances calculated from NOEs (r_{NMR}) plotted versus actual crystallographic distances (r_c) for helix 4 of myoglobin. NOE cut-off: 2%. (•) Intramolecular distances; (○) intermolecular distances. (Reproduced from O. Jardetzky and A. N. Lane, in 'Physics of NMR Spectroscopy in Biology and Medicine,' ed. B. Maraviglia, Italian Physical Society, North-Holland, Amsterdam, 1988, pp. 267–301)

are averages over several conformations and do not permit a unique interpretation. Dihedral angles are most useful along the backbone, where the rotation is hindered, and stereospecific assignments, e.g. those of individual methylene protons, β-CH$'$ and CH$''$, are possible. In that case, a unique value of the angle (more precisely, a narrow range of angles allowed by the coupling constant) can often be derived from the Karplus relation.[22] Since the coupling constant has a strong dependence on the dihedral angle, experimentally derived angles are powerful constraints in a structure calculation. The largest limitation to their use is the fact that the small coupling constants involved (often $<10-15$ Hz) become largely unresolvable at molecular weights above 15 kDa. For larger molecules, only broad ranges of dihedral angles, inferred from indirect evidence on the secondary structure, can be used (as relatively loose constraints) in the structure calculation.

It is still best to make the choice of assumptions explicitly, on the basis of prior experience and with additional knowledge of the specific system on which the structure is to be determined, although there is an increasing tendency to make them implicitly in an iterative back-calculation of spectral intensities using one of the several computer programs available for this purpose. The danger of such implicit decision-making is that each program has specific assumptions built into it, of which the user may or may not be aware. Almost all programs are built on the assumption that the protein is rigid (or undergoes only averaging of the first kind, i.e. in a potential well about a single energy minimum, but does not undergo any averaging of the second kind, i.e. between different metastable conformations). This assumption holds reasonably well as a zero-order approximation in many cases, especially for smaller, well chosen globular proteins, but the cases of the *trp*-repressor and several other larger proteins have clearly shown that it is not universally applicable. *There exists no general, universally applicable, set of assumptions for the exact geometric interpretation of spectroscopic parameters in macromolecular spectra.* Obviously, the calculated structure will be wrong if the assumptions made at this step are not appropriate for the molecule under study.

2.1.4 Model Building and the Calculation of Protein Structures

There are several options for defining a three-dimensional structure of a protein from the geometric constraints implied by NMR data. The basic paradigm is straightforward: given the primary sequence (with all covalent bond lengths and angles and van der Waals radii implied by it, which must be determined by other methods and known to begin with), and given a set of distance and angular constraints derived from NMR experiments, as outlined above, find the family of all three-dimensional configurations that satisfy the given set of experimental constraints. The essential step here is to search the conformational space available to the polypeptide chain, selecting only those configurations that are allowed by the NMR constraints. The first 3D structure derived from NMR data, that of the *lac*-repressor headpiece (MW $\approx$ 6 kDa) was built by hand, using Pauling-Corey space-filing models.[23] At the time of writing, several classes of search procedures have been implemented in computer programs and are generally available. A major consideration in choosing the procedure is that the search must be sufficiently representative to ascertain that alternative configurations equally compatible with the experimental data set are included in the final result. This is more easily said than done. The conformational space available to a polypeptide chain is very large (for the two Ramachandran angles, each allowed only two values, it is of the order of 2^{2N}, where N is the number of amino acid residues in the chain; i.e. for 100 residues, it is of the order of 2^{200} or 10^{60}). A systematic search of all possible configurations is therefore computationally out of the question. Even exhaustive random sampling, starting with a variety of randomly chosen arbitrary configurations, is possible only for relatively short peptide chains (up to 10–12 kDa). Consequently, all search procedures have to rely on approximations and it remains important to ascertain that the approximations made in each applicable algorithm are valid for the specific system under investigation. The derivation of three-dimensional structures from NMR data is only possible because some of the experimental distance constraints—in particular NOE constraints between residues distant in the primary sequence (e.g. between residues 6 and 42, or 24 and 98)—at once eliminate large segments of the conformational space. Furthermore, a not very large number of imprecise constraints can define the folding of a polypeptide chain rather accurately, as originally pointed out by Kuntz and coworkers.[24] The human mind remains by far the most efficient instrument for recognizing and applying this hierarchy of constraints in order to reduce the search space. For this reason, model building, which had at first been all but abandoned in favor of 'more objective' search procedures that treat all constraints alike, is again gaining in importance as the molecular size of the structures being determined increases, making 'objective' random searches computationally intractable.

Among the available algorithms for searching conformational space and selecting structures compatible with the experimental constraints, it is useful to distinguish between methods that (a) rely on geometric information alone, and (b) those that bring to bear additional information on the search in the form of energy potentials. In the first category of purely geometric methods, there are three classes of algorithms: (1) computer model building, (2) distance geometry, and (3) optimal filtering. In the second category—there is one class: (4) restrained molecular dynamics (RMD). In practice, a combination of a geometric and a dynamic method[25] is now almost universally used, and molecular dynamics can be considered indispensable for the refinement of NMR as well as of X-ray structures. At the same time, molecular dynamics is most effective if a starting structure not very far from the final structure is provided. Only for rather small structures is it practical to fold a random polypeptide chain into its final configuration by using an RMD algorithm.

(1) Computer model building programs are either entirely manual (e.g. Frodo, Quanta, and MacImDad) or have a built-in routine for conformational-space searches under geometric constraints (e.g. PROTEAN). In the manual programs, the application of covalent, bond angle and van der Waals constraints is often automated, but the application of NMR-derived distance and angular constraints is under the complete control of the experimenter. Application of constraints is usually sequential, with those deemed most constraining (i.e. those connecting two structures, as in the case of protein–DNA complexes, or two distant parts of a protein chain) being applied first. Even though the procedure is subjective, it

is generally valid because all conformations violating these key constraints can be ruled out. As in all initial model building, the assumption is made that averaging between two or more distinct conformations (averaging of the second kind) does not occur. The typical result is a topologically accurate, but imprecise, model that can be used as a starting structure for refinement by RMD. In the case of constraint satisfaction programs, such as PROTEAN, which build models automatically under a given set of constraints, a *systematic* search of the space available for the mutual positioning of units of secondary structure is possible. By considering each unit of secondary structure as a rigid entity and representing it at a higher level of geometrical abstraction (e.g. cylinders for α-helices or β-strands), the number of conformational variables is reduced to a manageable size. This makes a systematic search of the conformational space available to define the main topological features (with the reduced set of key variables) computationally tractable. Since the space to be searched grows exponentially with the number of variables (e.g. rotatable bonds), systematic sampling of conformational space using the complete set of variables is otherwise only possible for very small peptides. If the output of such a systematic search, which generally defines the overall topology rather well, is used as a set of starting structures for molecular-dynamic refinement at atomic resolution, it is possible to minimize the danger of having the refined structure represent a single local minimum. This is difficult, if not impossible, when only a smaller set of starting structures is used, whether such a set is derived from manual model building or random sampling by distance geometry. Adequate sampling of random structures is at present limited to proteins smaller than ~12 kDa. For larger structures, random sampling that could safely be considered extensive enough is prohibitively expensive in computer time, and the danger that the reported structure represents only a local minimum remains ever present. Computer model building is hardly necessary for the smaller structures where adequate random sampling is computationally feasible. For larger structures, some degree of preliminary model building is unavoidable. A typical PROTEAN output, defining the topology of the helix–turn–helix *lac*-repressor DNA binding domain (headpiece), along with the uncertainty in the positioning of the different units of secondary structure, is shown in Figure 8.[26]

(2) Distance geometry (DG)[27] is a general method for calculating the atomic coordinates of a structure from an arbitrary set of internal distance and/or angular constraints. It has two highly attractive characteristics: (1) it is a simple and rigorous mathematical theory containing the proof that if all the distances between all points within a structure are known precisely, an exact calculation of the coordinates of each point in the structure is possible; and (2) computational efficiency. In applications to NMR structure determination—where only a fraction of all distances that rigorously define the structure can be obtained experimentally—theoretical rigor is lost, but the efficiency of the method for randomly searching conformational space remains.

The input to a DG calculation is: the *distance matrix* derived from experiment—in principle the square matrix of $N(N-1)/2$ distances between all N atoms (points), in practice a (usually asymmetric) matrix of the distances available from experiment; and an *initial coordinate matrix*, preferably consisting of a random arrangement of points.

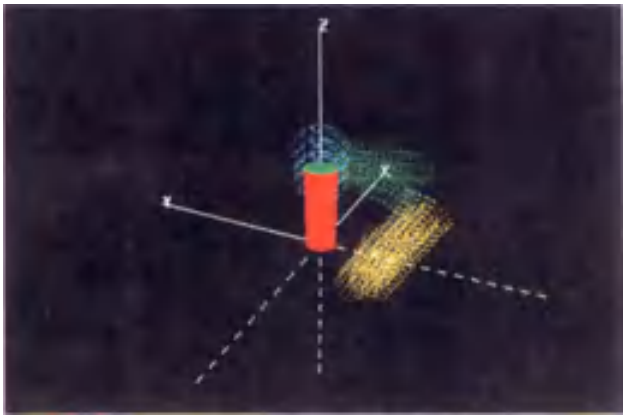

Figure 8 *Lac*-Repressor headpiece structure calculated by PROTEAN, showing the uncertainty in the positioning of the different units of secondary structure. (Reproduced from R. B. Altman and O. Jardetzky, *J. Biochem.*, 1986, **100**, 1403)

This represents the 'starting structure' for the search of the conformational space. The first step in a DG calculation, called *embedding*, calculates a set of coordinates that represents a multidimensional best fit of the coordinates to all the distances considered simultaneously. As allowed distance ranges rather than precise distances have to be used, and because the number of observable distances is too small to define the structure precisely, the resulting structures that at first seem to satisfy the constraints in fact usually contain a large number of constraint violations—and also violate constraints at first not considered, such as van der Waals radii. A second *optimization* step is therefore necessary to minimize the errors by iterative adjustments, using a scoring function that reflects the number and severity of the violations as a criterion for the goodness of fit.

There are many different algorithms for carrying out the embedding step and many different formulations of the optimization function, a detailed description of which is beyond the scope of this article, but can be found elsewhere.[28] The essential mathematical features of the two steps are given by equations (3) and (4). In the first step

$$\mathbf{S} = \boldsymbol{\lambda}\mathbf{M} \tag{3a}$$

where **S** is the coordinate matrix and **M** is the metric (distance) matrix, calculated from the initially set up distance matrix by a coordinate transformation to refer all distances to the geometric center of the structure which can be calculated from the distance matrix. The elements of **M** are:

$$M_{ij} = \frac{1}{2}(D_{io}^2 + D_{jo}^2 - D_{ij}^2) \tag{3b}$$

where D_{io} is the distance of the atom i from the origin and D_{ij} the internuclear distance between i and j. $\boldsymbol{\lambda}$ is the matrix of coefficients relating the two.

The embedding process itself is thus seen from equation (3a) to be an eigenvalue problem (finding the values of $\boldsymbol{\lambda}$ to yield the values of **S**), for the solution of which a variety of techniques is available.[29] A typical error function useful for

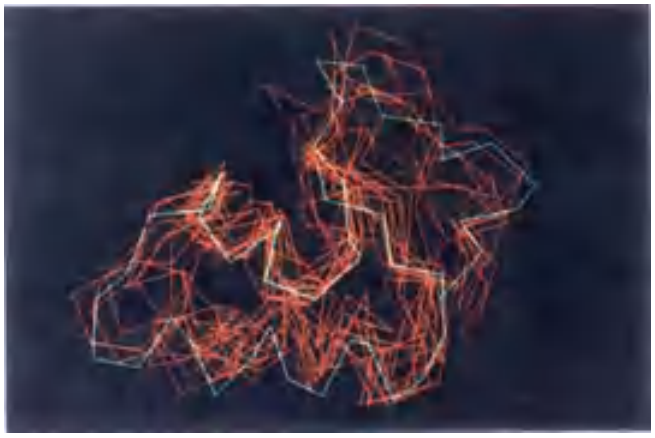

Figure 9 C-α traces of a family of crambin structures computed using the distance geometry protocol. The target structure is shown in green. (Reproduced from J. C. Hoch and A. S. Stern, *J. Biomol. NMR*, 1992, **2**, 535)

optimization in distance space is:

$$F_E(R) = \sum_{i<j}(|R_{ij}| - U_{ij})^2 + \sum_{k<l}(L_{kl} - |R_{kl}|)^2 \qquad (4)$$

where $F_E(R)$ is the distance error, L_{ij} and U_{ij} the lower and upper distance boundaries, respectively, and R_{ij} the actual distance in the proposed structure. Similar error functions can be introduced for dihedral angles and chiral constraints (to distinguish between L- and D-amino acid configurations). The result of each calculation is a single optimized structure. Experience shows that repeated calculations with the same set of initial constraints but different starting structures do not exactly reproduce the same structure. Therefore, a family of structures is usually obtained by repeated runs of the DG algorithm. Published structure determinations report anywhere from 30 to over 100 closely related but different structures, and the precision of the structure can be measured by taking the root-mean-square deviation (RMSD) of the individual atomic coordinates. A typical family of structures calculated by repeated optimization using a DG algorithm is shown in Figure 9.[30]

Important to note is that all non systematic search procedures contain several potential sources of bias. Among the most important in the case of DG are: (1) the algorithms used for the generation of starting structures; (2) the adequacy of their use in an individual case; and (3) the choice of weighting factors for the error function when forms more complex than equation (6) are chosen, as they now usually are. Comparisons of different programs are therefore of utmost importance, but thus far have been carried out only sporadically, as discussed below.

(3) Optimal filtering is a probabilistic method widely used in signal processing. Its application to the search of conformational space in the course of an NMR structure determination has the advantage that a set of coordinates, and the uncertainty limits of each coordinate, can be obtained in a single calculation from the starting set of distance and angular constraints and the estimated uncertainties of these constraints. This eliminates the need for repeated optimization runs with different starting structures and the bias potentially introduced by limiting the calculation to an inadequate number of runs. All data relevant to the uncertainty of the final structure are introduced into the calculation and used throughout the calculation at once.

The principle of the method is to represent the system (structure) by a coordinate 'state vector' of length $3N$, where N is the number of atoms in the structure, and of the form:

$$\mathbf{x} = [x_1\ y_1\ z_1\ x_2\ y_2\ z_2\ x_3\ y_3\ z_3 \ldots] \qquad (5)$$

x_1,y_1,z_1, etc., denote the x,y,z coordinates of all individual atoms. The uncertainty of the structure is contained in the covariance matrix of $\mathbf{x}$:

$$\mathbf{C}(\mathbf{x}) = \begin{bmatrix} \mathbf{C}(x_{1,1}) & \mathbf{C}(x_{1,2}) & \ldots & \mathbf{C}(x_{1,N}) \\ \mathbf{C}(x_{2,1}) & \mathbf{C}(x_{2,2}) & & \\ \vdots & & \ddots & \vdots \\ \mathbf{C}(x_{N,1}) & \ldots & & \mathbf{C}(x_{N,N}) \end{bmatrix} \qquad (6a)$$

where

$$\mathbf{C}(x_{i,j}) = \begin{bmatrix} \sigma_{x_i x_j} & \sigma_{x_i y_j} & \sigma_{x_i z_j} \\ \sigma_{y_i x_j} & \sigma_{y_i y_j} & \sigma_{y_i z_j} \\ \sigma_{z_i x_j} & \sigma_{z_i y_j} & \sigma_{z_i z_j} \end{bmatrix} \qquad (6b)$$

is the covariance matrix for an individual atom with the variance $\sigma_{xy} = E_{(xy)} - E_{(x)}E_y$ is defined as usual in terms of the expectation values. The diagonal terms of equation (6b) measure the uncertainty in each coordinate, and the off-diagonal terms determine the shape of the spatial distribution of the uncertainty. A common assumption is that this distribution is normal, in which case the uncertainty in the position is given by an ellipsoid. However, asymmetry in the uncertainty distribution of the initial constraints can be taken into account by the use of higher order moments to describe the distribution.

In the first order calculation, distance constraints are used in the form

$$z = |x_i - x_j| + v, \text{ or, generally, } z = h(\mathbf{x}) + v \qquad (7)$$

where v is the uncertainty range in the measurement of the distance. A similar equation applies to angular constraints.

The constraints are introduced to update an initial structure given by an initial state vector $\mathbf{x}_o$ to a new structure that better fits the constraints by calculating a new set of coordinates from the Kalman filter formula:

$$\mathbf{x}_{new} = \mathbf{x}_{old} + \mathbf{K}[z - h(\mathbf{x}_{old})] \qquad (8)$$

where

$$\mathbf{K} = \mathbf{C}(\mathbf{x}_{old})H^T[\mathbf{H}\mathbf{C}(\mathbf{x}_{old})\mathbf{H}^T + \mathbf{C}(v)]^{-1} \qquad (9)$$

where T denotes the transpose and $\mathbf{H}$ is given by:

$$H = \frac{\partial h(\mathbf{x})}{\partial x}|\mathbf{x}_{old} \qquad (10)$$

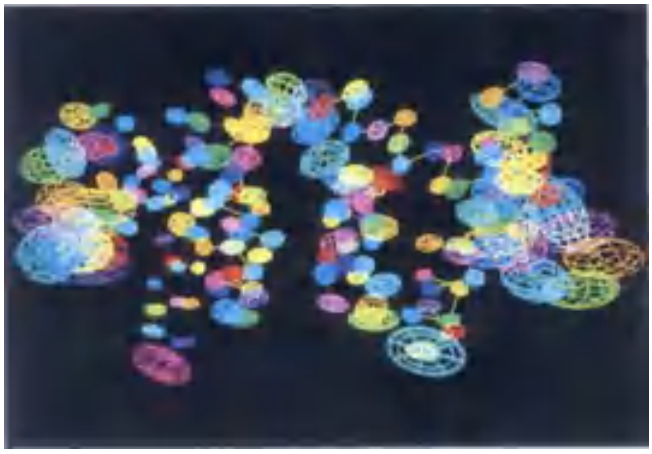

Figure 10 Tertiary structure of the *trp*-holorepressor calculated using the Kalman filter. The α-carbon trace is displayed (at 2 SD) with ellipsoids of uncertainty for each α-carbon, the larger ellipsoids at the extreme left and right indicating the larger uncertainty for region D. (Reproduced from C. Arrowsmith, R. Pachter, R. Altman and O. Jardetzky, *Eur. J. Biochem.*, 1991, **202**, 53)

The covariance matrix **C** is updated by a formula analogous to equation ((8)). Programs have been written for either a sequential or a simultaneous introduction of constraints, and for calculations in either cartesian (PROTEAN2)[31] or dihedral angle space (FILMAN).[32] The calculation must be iterated for nonlinear systems, hence the occasionally used name, 'Doubly Iterated Kalman Filter' (DIKF). As in the case of DG, for small structures the initial 'structure' can be a random distribution of points (or all points placed at the origin) with very large initial variances. In both cases, starting structures more closely resembling the final result (and obtained by initial model building) are required for larger proteins to make the structure calculation feasible computationally. Also, in both cases, the definition of the uncertainty in the distance constraints used for the conformational space search remains subjective, as discussed in the section on the conversion of spectral intensities into distances. The topology of the *trp*-repressor backbone, determined by optimal filtering, together with the uncertainty ellipsoids of the α-carbon atoms is shown in Figure 10.[33]

The model-building methods described thus far rely on purely geometric information. Because the geometric constraints derived from NMR experiments are generally imprecise and too few in number to give an exact definition of the protein structure, the resulting structures generally represent the overall topology rather well, but contain numerous energetically unfavorable, and sometimes impossible, features. For this reason, refinement of the crude structure by energy minimization is generally necessary, and molecular dynamics algorithms have become the method of choice for this purpose.

(4) Molecular dynamics, as a method for search of the conformational space under a given set of geometric constraints, differs from the purely geometric methods of model building, distance geometry and optimal filtering in that energy potentials, representing both attractive and repulsive interactions between atoms, are introduced into the calculation in addition to the experimental constraints.

The technique is based on the solution of Newton's equations of motion for all atoms in the structure simultaneously:

$$\frac{\partial^2 \boldsymbol{r}_i}{\partial t^2} = \frac{\partial \boldsymbol{v}_i}{\partial t} = \frac{\nabla E(\boldsymbol{r}_i)}{m_i} \tag{11}$$

where $\partial\ ^2\boldsymbol{r}_i/\partial\ t^2$ is the acceleration and $\boldsymbol{v}_i$ is the velocity of atom i. This mass, m_i, of each atom is known. The force is taken to be the gradient of an empirically defined set of potentials, which is the weighted sum of all relevant terms:

$$\begin{aligned} E_{(xi)\text{empirical}} = {} & \textstyle\sum_{P=1}^{N} N_1 E_{\text{bond}} + w_2^P E_{\text{angle}} + w_3^P E_{\text{dihedral}} \\ & + w_4^P E_{\text{van der Waals}} + w_5^P E_{\text{electrostatic}} \\ & + w_6^P E_{\text{H bond}} \end{aligned} \tag{12}$$

In *restrained molecular dynamics* (RMD), experimental distance and angular constraints are usually introduced as pseudopotentials of the form

$$E_{\text{NOE}} = S\frac{kT}{2d^2}(R-d)^2 \tag{13}$$

where S is a scaling factor, k is the Boltzmann constant, T is the absolute temperature, R is the averaged internuclear distance, and d is the allowed distance bounds.

The solution of Newton's equations proceeds by numerical integration over very small time steps, Δt, over which the forces are assumed to remain constant:

$$\boldsymbol{r}_{n+1} = 2\boldsymbol{r}_n - \boldsymbol{r}_{n-1} - \frac{\nabla_{\mathbf{r}_n} E(\boldsymbol{r}_n)}{m}\Delta t^2$$

$$\boldsymbol{V}_n = \frac{1}{2\Delta t}(\boldsymbol{r}_{n+1} - \boldsymbol{r}_{n-1}) \tag{14}$$

This is the so-called *Verlet algorithm*. The choice of a sufficiently small time step (by comparison to the timescale of the fastest motion in the system) is critical, and values of the order of Δt = 0.001–0.002 ps are normally used.

A large amount of literature exists on the best choice of potentials, number of terms and weighting factors,[34–36] and different programs incorporate sometimes very different sets of potentials. Similarly, the choice of initial velocities, usually based on a Maxwell distribution at a chosen temperature, can be made at will. Both an energy minimum and a trajectory for the motions of individual atoms over the period of the calculation can be calculated for any starting structure.

It is possible to use RMD as a purely geometric method for the search of the conformational space by assigning very high values to the pseudopotentials representing the experimental constraints and making all other potentials negligible by comparison. As in the case of DG and DIKF, the topology of small structures can be calculated successfully by starting with an arbitrary arrangement of atoms (usually given the correct covalent and bond angle constraints). As

the molecular size increases, it rapidly becomes necessary to start with a structure resembling the final result if the computational time is to be kept within manageable limits. This is much more important for RMD than for DG or DIKF calculations because of the larger number of arbitrarily adjustable parameters. The large number of adjustable parameters also makes the method subject to stronger built-in systematic bias. Fortunately, several programs have been tested extensively—notably X-PLOR, CHARMm, GROMOS and AMBER—and even though none of these are foolproof or free of all bias, internally consistent results can be obtained in most cases. Credible refinement of NMR structures to an 'effective resolution', i.e. precision of 0.05 nm, is possible in many cases. This 'resolution' is obtained, as in the case of DG, by calculating a family of structures, each representing a complete RMD calculation beginning with a different starting structure each time, and then determining the RMSDs of the atomic coordinates within the family. Of particular interest for structure calculations using molecular dynamics is the simulated annealing protocol (sometimes even discussed as a separate method of structure calculation). In this protocol the temperature is repeatedly raised in the course of each molecular dynamics simulation, in order to reduce systematic bias by randomizing the structure, and then allowed to converge onto a new configuration. For the largest structures refined thus far (37 kDa), the computer time required for the calculation of an RMD family by this procedure can be prohibitively long. For such structures, however, it is possible to invoke the ergodic theorem (equality of the time average to the ensemble average) and use the Sequential simulated annealing protocol[37] to obtain a family of structures from a single calculation. A typical family of structures obtained by RMD has the same appearance as a family calculated by DG (see Figure 9).

2.1.5 Back-Calculation of NMR Spectra

Back-calculation of NMR spectra from a given structure has long been recognized as a desirable step for the validation and refinement of the proposed structure,[38] regardless of the method initially used to derive the structure. The back-calculation for NOESY-type spectra is based on the numerical integration of the set of generalized Bloch equations [equation (2)] or, as an equivalent, the inversion of the relaxation matrix[37,39] using the coordinates of the proposed structure to calculate the required interproton distances.[40,41] Several programs—including BLOCH, CORMA, IRMA, MARDIGRAS—are available for this purpose. Direct refinement of the structure against experimental NOE intensities has also been developed and implemented in X-PLOR. The use of time-averaged distances, with the averaging based on a molecular dynamics trajectory, has been suggested as an improvement to the accuracy of such calculations.[42] Iterative protocols are part of most suggested procedures. Back-calculation and its applications to both protein and nucleic acid structures are described elsewhere in this Encyclopedia. Of importance in the general context is the fact that a completely correct back-calculation is not possible without detailed knowledge of the spectral density functions (correlation times) needed to describe internal motions in the protein. Good predictions of spectra from proposed structures are possible when the structure can be taken as rigid and the spectral density functions to be the same throughout the molecule. Unfortunately, spurious agreement between calculated and observed spectra can also occur. In an iterative calculation based on inaccurate (or even wrong) values of the spectral density function, the internuclear distances (and hence the coordinates) can be adjusted until 'the best fit' is obtained, even though the adjusted distances would give poor agreement, and hence be judged incorrect, if correct values of the spectral density function were known. The use of time-averaged distances in the back-calculation is also not unproblematic, since molecular dynamics simulations generate predominantly averages of the first kind (around a single major energy minimum), with major conformational averaging being largely left out. With the inherent imprecision of the data, the indeterminacy of the generalized Bloch equations, and the limitations of the proposed remedies of this indeterminacy, the observation has been made on several occasions that back-calculation with existing methods does not significantly improve the 'quality' of the reported structures.[43] Although a completely rigorous test of this observation is lacking, the observation is likely to remain correct, unless, or until, back-calculations using a correct set of spectral density functions become possible and the obtainable raw NMR data become more precise.

2.1.6 Accuracy and Precision of Protein Structures Determined by NMR

Given the uncertainties and potential sources of bias in each exploration of the conformational space, with each method and each program potentially subject to its own limitations and bias, the use of combined search methods has gained wide popularity. Particularly common are protocols combining DG and RMD into a single program package (e.g. DIANA and DADAS) and those combining either DG or RMD structure calculations with the back-calculation of spectra. It is thought that the bias of each of the constituent search methods will be canceled by the other. The possibility that the errors will be additive has, regrettably, not been properly tested.

Before it becomes possible to assess the validity of individual structures calculated by any particular method or combination of methods, it is necessary to evaluate the *accuracy*, as well as the *precision*, of NMR structure calculations by a comparison of the families of structures calculated by different methods. Accuracy, in this as in other contexts, means the faithfulness of the reproduction of the 'true' structure and is only measurable with respect to a 'gold standard', i.e. a structure independently determined by another method. Precision, in its usual definition, measures the reproducibility of repeated measurements or calculations. Most of the NMR literature published to date is confused on this issue, and all too often one sees measures of precision offered as a measure of accuracy. The 'first-order answer'—that protein structures built from NMR constraints, by whatever method, rather faithfully reproduce the main topological features of a protein molecule —can be considered to have been demonstrated beyond any doubt. An exact answer with regard to how accurate NMR structures are is more difficult to give. Only a few rigorous comparisons of the accuracy of NMR structures calculated by different methods have been made thus far.[21,44] The principal finding is that the mean

structures calculated by different methods from the same set of data differ by an RMSD of 0.1–0.2 nm from each other and from a 'true' structure independently determined by X-ray diffraction. Claims that an accuracy of 0.025 nm can be achieved for NMR structures[45] were not based on a rigorous study of accuracy, but on a comparison of the relative precision of structures calculated by the same method using two different protocols. In such a procedure, the reference ('true') structure and the test structures are subject to the same systematic error. The calculated estimates are still estimates of precision and not of accuracy, and the claim is therefore not valid. The accuracy of NMR structures determined by now existing methods cannot be taken to be higher than 0.1–0.2 nm, although the precision of the family of structures calculated by any one method can be considerably higher (of the order of 0.03–0.05 nm). If one remembers that proteins in solution are subject to Brownian and internal motions, it is not too surprising that the family of structures reflected in the NMR data may be appreciably larger than any one particular structure calculation may show.

2.2 Solution Structures of Nucleic Acids

These can be defined by using the same procedures as for the structures of proteins. The structure determination involves the same four steps: resolution and assignment of the spectrum, derivation of geometric parameters from spectroscopic data, and model building. For reasons of resolution, limited by spectral overlap, the possibilities of NMR structure determination are for the present limited to relatively short stretches of oligonucleotides (up to 20–30 mers for double-stranded DNA). For such structures an additional serious limitation comes into play in that only short-range distances, i.e. between adjacent bases and base pairs, can be found. Long range interactions, so useful in defining the tertiary fold of a polypeptide chain, are not found in the short, rod-like structures. It is conceivable that for larger circular and supercoiled DNAs, where long-range interactions occur, they could also be detected and used, as in the case of polypeptides to define the tertiary structure. However, the resolution of the spectra of larger DNA structures is beyond the limits of current methodology. Thus only local structural features in nucleic acids—for di- or trinucleotide stretches— can, for the present, be studied by NMR. An exception is the structure of DNA fragments in complexes with proteins, exemplified by the operator–*trp*-repressor complex. In such cases the long-range interactions are provided by protein contacts, allowing the detection of longer range structural features, such as bends and twists of the double helix.

Details of NMR studies of oligonucleotide structures, of their complexes with a variety of drug molecules and of the methods developed for this purpose are given in several articles elsewhere in this Encyclopedia. A critical evaluation of the applicability of NMR methods to solution structure of nucleic acids, published in 1991 by Wemmer,[46] should be read by anyone concerned with the significance of published oligonucleotide structures derived from NMR data. In no other field of biological applications of NMR has the disregard for the principles and pitfalls of NMR structure determination outlined in the preceding section produced as much questionable, and outright erroneous, published information. A dramatic claim for the existence of highly bent, twisted and otherwise distorted, nearly doughnut-shaped DNA segments had already been published in 1988.[47] A re-examination of the method of analysis used in these studies brings to light the danger of overinterpreting the precision of distance constraints by calibrations that do not take either spin diffusion or internal motions into account and using a global optimization procedure with a set of only local constraints. Structures calculated by such oversimplified procedures are not likely to be correct. The extent to which the use of NMR methods for studies of nucleic acid structures is meaningful has not changed since it was succinctly summarized by Wemmer: 'Aspects of secondary structure and the general positioning of bases can be determined readily from NMR data. Highly quantitative structure analyses must be viewed as quite questionable at this time.'

2.3 Solution Structures of Noncovalent Complexes

The solution structure of noncovalent complexes (in particular DNA–protein and small ligand–protein complexes) can also be defined by the procedures described above. The only difference is that docking constraints (e.g. NOEs between the ligand and the protein or between two macromolecules) have to be used in addition to the usual set of constraints defining the geometry of each of the components. The docking constraints play a crucial role in defining both the topology of the complex and the structural changes that occur upon complex formation. For DNA–protein complexes, relatively few docking constraints will define the geometry and, where applicable, the symmetry of the complex, and identify the regions of contact. Many such constraints are required to define the fine structure of the interface and the structural changes resulting from complex formation. In the case of the operator–*trp*-repressor complex already mentioned as the largest NMR structure to have been determined so far, a considerable distortion of both the DNA and the protein structure occurs upon binding in the presence of tryptophan, so that simple docking of the independently determined operator and repressor structures using only experimental docking constraints gives only an approximate structure, although its symmetry is correct. A complete de novo structure determination was necessary in this case to account for all of the data in detail. The resulting structure is shown in Figure 11.[16]

Two considerations are of importance when viewing reported ligand–protein structures. First, several of the structures that are found in the literature are based on model building only—i.e. on rigid body docking of independently determined ligand and protein structures (in the case of DNA based on a standard B-DNA model).[48] Such structures must be regarded as hypothetical and must be distinguished from structures obtained by a bona fide complete structure determination, to which, as the *trp*-system example shows, they are by no means equivalent. Second, discrepancies between NMR structures and crystal structures of the same complex must be examined with care, as they may provide important information. In the case of the *trp*-repressor–operator complex, direct hydrogen bonding contacts between the DNA and the protein are compatible with all observed NMR constraints. In the crystal structures of the same complex, several protein–DNA contacts are mediated by water molecules, a rather unusual

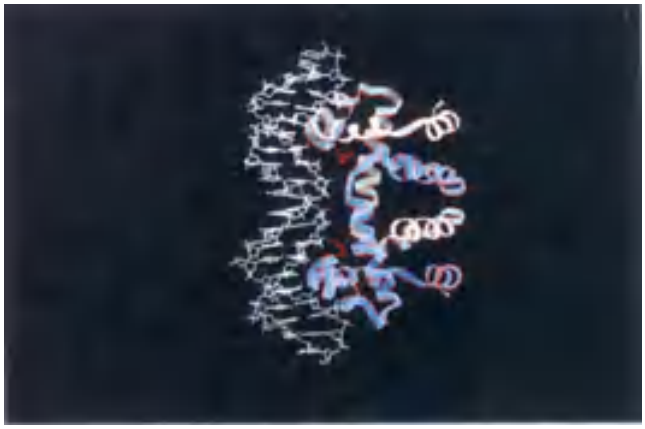

Figure 11 Solution structure of the *trp*-repressor–ODNA complex. The view shows the repressor backbone with DNA at full atomic representation. (Reproduced from H. Zhang, D. Zhao, M. Revington, W. Lee, X. Jia, C. Arrowsmith and O. Jardetzky, *J. Mol. Biol.*, 1994, **238**, 592)

feature even among protein–DNA complexes determined by X-ray diffraction. For the study of noncovalent complexes, NMR may prove to be the better method. In several reported cases it is apparent that flexible protein segments are involved in the interaction with DNA,[49] and flexible peptides are found at protein binding sites.[50,51] The flexibility of such structures means that they are particularly vulnerable to the action of external forces, and specifically those that are responsible for crystallization. Whereas distortion of tightly packed covalent protein structures upon crystallization is generally regarded as minimal, this is not necessarily the case when the much weaker noncovalent complexes are examined. One should therefore expect to encounter artifacts resulting from crystallization which would not occur in the solution structure. Only a minor distortion of specific contacts is required to allow water molecules in the crystallized complex where they would not normally occur in solution, creating the potentially erroneous impression that they play a functional role.

3 MACROMOLECULAR DYNAMICS

NMR spectra are sensitive to molecular motions over a wide range of frequencies. The timescales on which each of the principal measurable NMR parameters—chemical shifts, line intensities, coupling constants and relaxation rate constants (including linewidths and NOEs), and proton exchange rates —provide dynamic information are summarized in Figure 12.[52] The total range spans from picoseconds to hours, days and weeks, making NMR a uniquely useful method for the study of dynamic processes in molecules (as in the case of structure) at atomic resolution. Although other spectroscopic methods allow the study of dynamic processes at selected points in a protein structure, focusing on a single atom or a group of atoms, no other method allows the *simultaneous* observation of dynamic phenomena in different parts of the molecule at atomic resolution. Application of high resolution NMR to the study of proteins has led to the discovery of several types of dynamic phenomena in protein molecules, most of which are as yet not fully understood. We can distinguish at least five categories of such phenomena: (1) variation of fast (i.e. nanosecond) motional frequencies along the polypeptide backbone; (2) enhanced conformational flexibility of longer backbone segments on different timescales (nanoseconds to seconds); (3) 'breathing' of folded protein made evident by the free rotation of aromatic amino acid side chains in the tightly packed core of many proteins or by rapid exchange of backbone NH protons with the solvent (micromillisecond); (4) conformational equilibria involving entire domains (usually on a millisecond to second timescale); and (5) dynamic states of partially folded structures observed under denaturing conditions. Variations of motional (rotational) frequencies along an amino acid side chain on the protein surface might be considered as a sixth category, but they are relatively well understood and of interest for the understanding of protein function only in the special cases when the motion becomes hindered by interactions.

3.1 Protein Dynamics

3.1.1 Fast Motional Frequencies along the Backbone

The possibility of resolving and assigning individual resonances for most atomic groups in the protein has brought with it the possibility of mapping the motional frequencies, which are reflected in relaxation parameters, for each individual group. Generally, a combination of relaxation parameters—T_1, T_2 and $T_{1\rho}$, and for ^{13}C and ^{15}N atoms with covalently bonded protons, also the NOE—has to be used to define the motions of interest and their frequencies. A most exact analysis of the motions along the peptide backbone allows the direct calculation of individual spectral density functions for individual interatomic vectors from experimental data without recourse to any (always arbitrary) model for their analysis. This type of analysis does not directly define a physical picture of the motions—a motional model giving a correct prediction of the spectral density functions is required for this purpose. However, *variations* in motional frequencies and amplitudes along the backbone can be mapped, although it should be said that they are also evident from the raw relaxation data themselves, independently of any method of analysis. The experimental results reported so far reflect two types of situation: (a) relatively rigid proteins, e.g. the IIA domain of glucose permease,[53] for which the variation in the magnitude of measured relaxation parameters along the polypeptide backbone is minimal; and (b) proteins containing segments of varying flexibility, e.g. staphylococcal nuclease, eglinC, gal4, calmodulin[54] and others. Larger amplitude motions are frequently observed in loops and at hinges between compact domains. In some cases these motions may involve the entire loop, leading to a poor definition of the NMR structure, whilst in others they are limited to one or a few residues at each end of the loop, the remainder of the loop appearing well structured. In other cases large-amplitude motions affect a group of residues within a unit of secondary structure, as in the case of interleukin or staphylococcal nuclease. There is as yet no clearly recognizable pattern to the distribution of amplitudes and frequencies of these fast motions, and it is not yet clear whether they play any role in protein function or are irrelevant byproducts of protein architecture.

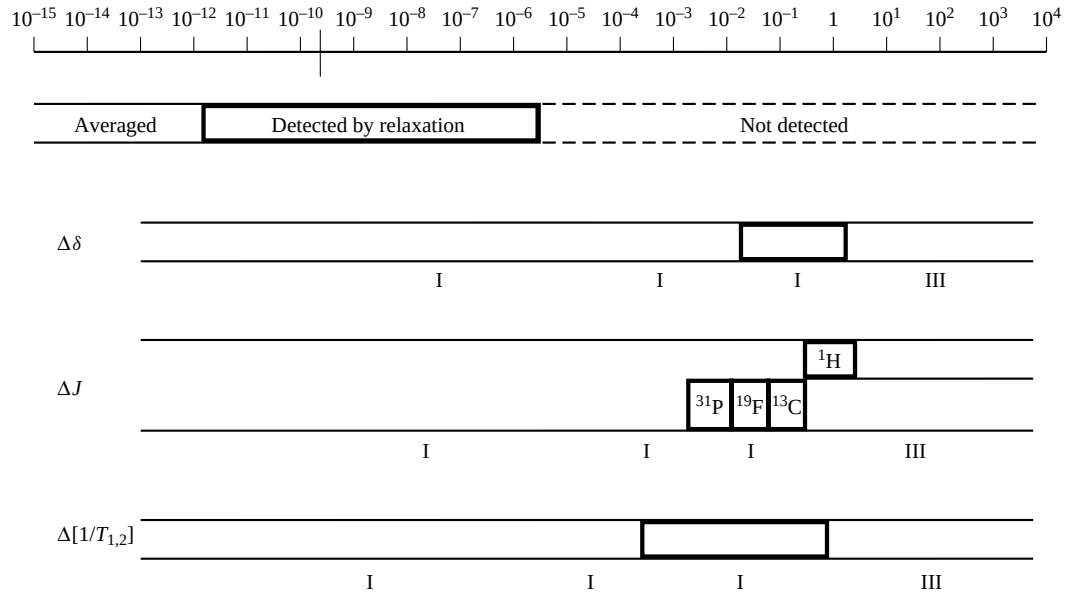

Figure 12 Timescales in seconds defined by NMR parameters. (I) Region of fast exchange; (II) region of intermediate exchange; (III) region of slow exchange. (Reproduced from O. Jardetzky and G. C. K. Roberts, 'NMR in Molecular Biology', Academic Press, New York, 1981)

The interpretation of the observed spectral density functions in terms of motional parameters, i.e. amplitudes and frequencies, depends of course on the construction of an appropriate model. Such models are necessarily complex and are only now beginning to emerge. The models used initially—anisotropic rigid body rotation, fast rigid rotor on a slower rigid rotor, wobbling on a cone[55,56]—were too simplistic to account for more than a few data points. Model-free approaches, which have enjoyed some popularity, can generate detailed motional maps, but fail to provide a complete insight into their nature. The original model-free approach of King and Jardetzky[57] can account for the observed motional frequencies, but not for the detailed amplitude characteristics of the motion. The model-free approach of Lipari and Szabo[58] actually represents a very restrictive model, equivalent to rigid body rotation with one degree of internal motional freedom or a two-term expansion of the King–Jardetzky formalism. Not surprisingly, it fails to account for the more detailed motional maps now obtainable experimentally,[59] just as any other of the oversimplified models. In the experimental maps, one can frequently see regions affected by slower motions of some kind, largely reflected in anomalous values of T_2. No fully satisfactory treatment of such slow motions has as yet been developed, although it has been suggested that they represent concerted motions, such as solitons.[60] Molecular dynamics simulations have shown promise in accounting for fast rotations in protein side chains.[42] Their great attraction is that they allow an independent, rigorous, a priori calculation of spectral density functions, which can then be compared with those obtained from experiments. In principle, molecular dynamics can provide a complete explanation of all dynamic processes observed in proteins, including the slower (micro- to millisecond) motions. Unfortunately for the nanosecond and slower motions observed along the backbone, rigorous molecular dynamics simulations are not yet practical. A complete and correct description of the patterns of the motions observed along the polypeptide chain remains a subject for future research, as does the evaluation of their functional significance.

3.1.2 Conformational Flexibility

Conformational flexibility of a longer contiguous segment of the peptide backbone may occur on any timescale and can be reflected in a different set of NMR parameters in different cases. Many examples of flexible segments varying in length from 7 to 25 or even more amino acid residues are now known. Some occur at the *N*- and *C*-terminals of peptide chains and some in their interior. The earliest discoveries of flexible segments—those of the RNA-binding site in Tobacco Mosaic Virus (TMV),[61] the DNA-binding domain of the *lac*-repressor,[62] histones,[63] and the S1 domain of myosin[64]—were based on the finding of anomalously narrow lines (long T_2) reflecting free rotation on a nanosecond timescale. In the crystal structure of TMV the corresponding segment was found to be disordered. In the more recent examples—the DNA-binding domains of the *trp*-repressor[65] and antennapedia homeodomain,[66] and the B-chain of insulin analogs[67]—fast motions do not play a prominent role, and the most striking finding is the absence of NOEs needed to define the structure of the segment. This finding is usually accompanied by the finding of unusually rapid exchange rates for the peptide backbone protons. Structure calculations on molecules containing such segments lead to the conclusion that the segments are disordered in solution. However, the apparent disorder may reflect averaging between two or more well-defined conformations. In the absence of line narrowing and other anomalies in the relaxation parameters, the conclusion must be drawn that the conformational averaging occurs on timescales longer than nanoseconds. In favorable cases, where the segment undergoes transitions between a closed and an open form of a secondary structure (e.g. a helix-coil transition), the rates of conformational averaging can be estimated from rates of backbone proton exchange. A very detailed study

of conformational flexibility in the DNA-binding domain of the *trp*-repressor has led to the conclusion that the interplay of dynamic processes in peptide segments can be quite complicated. It is thus necessary to distinguish between *true flexibility*, or *true disorder*, and *apparent flexibility*, or *apparent disorder*. In the case of true flexibility one will find 'random coil' behavior by all NMR criteria—rapid averaging of chemical shifts and coupling constants, rapid proton exchange and rapid motions reflected in narrow lines, as well as disappearance of NOEs and other cross peaks in multidimensional spectra. These are findings typical of the N- and C-terminal peptide segments in several proteins. On the other hand, in cases of apparent disorder or flexibility the findings tend to be contradictory, as they are in the case of the *trp*-repressor. The DNA binding segment appears disordered if one relies on the observations of sequential NOEs, backbone proton exchange rates and backbone ^{1}H T_1 measurements. At the same time, it appears ordered from the ^{15}N relaxation profile and from the finding of α-CH shifts typical of α-helical structures. The findings can be reconciled if one infers that the segments are largely helical on a nanosecond timescale, but the helices are unstable on longer (in this case millisecond) timescales, and the closed state (corresponding to the formation of a hydrogen bond) at all sites exists less than 100% of the time. One is thus dealing not with a continuum of conformational states, which defines true flexibility, but rather with a structure that is unstable and hence 'flexible' only on a much longer timescale. A similar phenomenon is known to occur in the ready unfolding of the *lac*-repressor DNA-binding domain. In this case sufficient NOEs were found initially to define a helical structure, but the structure was shown to be unstable under a variety of ambient conditions.[68]

The quantitative analysis of the apparent disorder cases requires a wide range of NMR measurements and can be rather complicated. Selective attention to only some of the NMR parameters (e.g. only the set of observable NOEs, which has become common practice in NMR structure determination) will confuse true and apparent disorder and lead to erroneous conclusions, as will the uncritical application of commonly used theoretical treatments [e.g., those for backbone proton exchange, which are based on simplified assumptions of relatively stable secondary structures (see ***Hydrogen Exchange and Macromolecular Dynamics***), and do not apply in the general case]. The paradigm for the analysis of the general case was first worked out for the *trp*-repressor and is briefly summarized here because of its wide applicability. The picture of the repressor helix–turn–helix DNA-binding domain that has emerged from this analysis is as follows: the region consists of two helices which retain their overall helical shape at all times, but with hydrogen bonds opening, one at a time, on a millisecond time scale.

Three types of experiment are necessary to calculate the exchange rates (or lifetimes) between the different states in this type of situation. First, the classical hydrogen–deuterium exchange experiments can identify hydrogen bonds that are stable on timescales from minutes to years. Second, proton T_1 relaxation, with and without solvent presaturation, will identify those hydrogen bonds undergoing an exchange on a millisecond to second timescale. Third, the pH dependence of the T_1 will allow calculation of opening and closing rates, since the intrinsic exchange rate is known to be pH dependent and can be independently evaluated from the amino

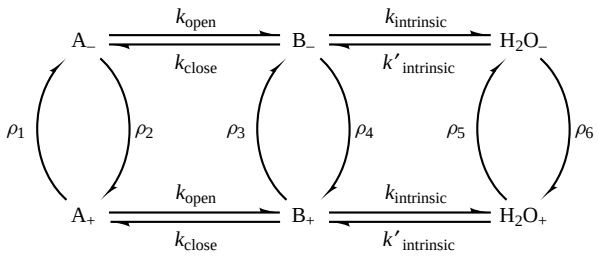

Figure 13 The generalized Linderstrøm–Lang model

acid sequence (see ***Hydrogen Exchange and Macromolecular Dynamics***).

The simplest model that can account for the observation is the generalized Linderstrøm–Lang model, which is free of all of the usual assumptions about the relative magnitudes of helix opening, helix closing and intrinsic exchange rates[69,70] (Figure 13). The magnetization transfer equations describing this model without arbitrary simplification are the generalized McConnell equations:

$$\left.\begin{aligned}
\frac{dM_A}{dt} &= -R_{1A}(M_A - M_A^{EQ}) - k_{open}M_A + k_{close}M_B \\
\frac{dM_B}{dt} &= -R_{1B}(M_B - M_B^{EQ}) + k_{open}M_A - k_{close}M_B \\
&\quad - k_{intr}M_B + k'_{intr}M_{H_2O} \\
\frac{dM_{H_2O}}{dt} &= -R_{1H_2O}(M_{H_2O} - M_{H_2O}^{EQ}) - k'_{intr}M_{H_2O} + k_{intr}M_B
\end{aligned}\right\} \quad (15)$$

whose solution is:

$$\begin{aligned}
M_A &= C_1 e^{\lambda_1 t} + C_2 e^{\lambda_2 t} + C_3 \\
M_B &= D_1 e^{\lambda_1 t} + D_2 e^{\lambda_2 t} + D_3
\end{aligned} \quad (16)$$

The symbols are defined in the Appendix at the end of this article.

The solution of these equations predicts pH independent single exponential behavior for the NHs of slowly exchanging (stable) hydrogen bonds, and pH dependent double exponential behavior for hydrogen bonds exchanging on a timescale comparable to the intrinsic relaxation rate, T_1 (milliseconds to seconds).[71,72]

In the study of the pH dependence of relaxation in the *trp*-repressor, the observation was made that, even though the data could be accounted for by this model, the conclusions drawn about the percentage helicity and opening and closing of helices were contradicted by other experimental findings. The contradictions are summarized in Table 2.

To account for all the data simultaneously, one either has to assume that the 'open' state in the Linderstrøm-Lang model is not completely open, characterized by $k_{intrinsic}$ slower than the rate observed in a free peptide, or alternatively, invoke a three-state model allowing for the observed slow exchange between

Table 2 Contradictory Evidence on the Percentage Helicity and Opening and Closing of Helices

Helix–Coil Transition	Process Monitored by T_1
$\geq$90% helicity (δ, ^{15}N)	20–40% 'helicity'
$k_{ex} > 100$ Hz ($\Delta\delta$, temperature dependent)	$0.4 < k_{ex} < 4$ Hz

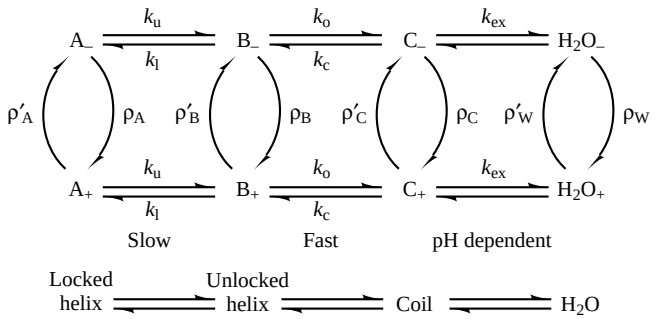

Figure 14 The three-state model

'locked' and 'unlocked' states of the DNA-binding helices, and a rapid helix–coil equilibrium (Figure 14). The equations for this model, too complex to be reproduced here, reduce to the form of equations (15) and (16) if the helix–coil equilibrium is rapid. The physical meaning of the observed rates is, however, in either case different than that originally envisioned. This underscores the importance of comparing different types of NMR and other data if one is to arrive at a correct description of solution structures and their dynamics.

The functional significance of segmental flexibility—either true or apparent—may well be to facilitate conformational adjustments on binding to ligands. It is probably no accident that segmental flexibility appears prevalent in the binding domains of DNA (and RNA) binding proteins. Especially in the case of repressors, such as the *trp*-repressor, which are known to interact with more than one DNA sequence, such conformational flexibility could be necessary to make the optimal contacts in each case, using the same amino acid sequence and the same secondary structure. Similarly, in the case of insulin, flexibility of residues 20–30 in the B chain could facilitate conformational adjustments upon receptor binding. A very interesting example of flexibility associated with the ability of a segment to assume a helical conformation in the crystal and a β-turn conformation in solution has been described for chicken egg-white cystatin.[73] The function of this segment is as yet unknown, and much remains to be learned about protein function from the NMR study of similar phenomena in other proteins.

3.1.3 'Breathing' Motions

Breathing motions first became apparent in the spectra of selectively deuterated staphylococcal nuclease, which showed that the tyrosines in the interior of the molecule had motionally averaged spectral lines.[74] This phenomenon was extensively studied on several proteins in the 1970s, and the rates for the 180° flip were estimated to lie between 102 and 104 s^{-1}. A temperature dependent transition from the 'frozen' configuration at low temperatures to the freely rotating state at room temperature was described for ferrocytochrome *C*.[75] In the case of parvalbumin, low amplitude librations of phenylalanine rings in the core on a nanosecond timescale, detectable by ^{13}C relaxation, could be shown to precede the relatively rare 180° flips on a microsecond timescale, evident from chemical shift averaging.[76] Rotation of rings in the interior of the protein has been and always needs to be considered in the interpretation of NOEs used for a protein structure determination.[18] The relationships of such 'breathing' motions to backbone motions and segmental flexibility have not yet been sufficiently studied, but it may be expected that they will emerge from comparisons of the relative timescales, directions, and amplitudes. Ideally, the relationship should be given by molecular dynamics calculations, but molecular dynamics simulations on the required micromillisecond timescales are impractical at present.

3.1.4 Conformational Transitions

Conformational transitions usually manifest themselves as changes of local structure. The ease of detecting and describing them depends on the lifetimes of the conformational states involved. If the exchange between the states is slow on the chemical shift timescale, i.e. the lifetimes of the states are long compared to the inverse of the chemical shift difference between the peaks representing the two states, the states can be observed and described separately by standard structure determination methods. Into this category fall the conformational readjustments occurring in Ca^{2+} binding proteins upon addition of Ca^{2+}, which have been studied extensively and are described elsewhere in this Encyclopedia, and many others. If the exchange rate is of the same order as the frequency difference of chemical shifts between the two states, the transition is often observable as a selective line broadening. The early NMR detection of conformational equilibria, even in simple enzymes such as pancreatic ribonuclease A,[77] was based on this phenomenon. As the exchange rate becomes more rapid on the chemical shift timescale, the individual conformational states can no longer be resolved. In the intermediate exchange range it is possible to infer from the data that an exchange process is occurring, but not the nature of the conformers or their number. In the rapid exchange case, even the existence of the exchange process itself is not directly detectable. This leads to the well-known problem that a structure determination on a system undergoing rapid averaging between two or more distinct conformations leads to a structure that has no physical meaning.[52,78] Attempts to resolve this dilemma by modeling the individual conformers and calculating the pattern of NMR parameters that would correspond to a dynamic average of the multiple states have been published.[79] A residual of uncertainty as to the adequacy of the dynamic model invoked will always remain for structures determined on systems undergoing conformational averaging. In formulating and testing such a dynamic model, it is therefore advisable to invoke a wide range of NMR experiments and test the interpretation of results for internal consistency.

3.1.5 Dynamic States of Partially Folded Structures and the Problem of Protein Folding

These topics are an active area of current research, and NMR approaches to this problem are discussed in detail elsewhere in this Encyclopedia. Suffice it to say here that studies of this type—conducted on objects known to be unstable—are especially vulnerable to the problems of conformational averaging discussed above. At the same time, it must be pointed out that even NMR 'structures' of intermediates which have no physical existence ('apparent structures') may be useful as indicators of the trends of changes occurring in

the structure as it folds or unfolds, respectively, and thus point to the deciphering of the folding pathway. An interesting recent example has been provided by the work of Dobson and coworkers[80] on the folding pathway for the assembly of hen egg-white lysozyme. The pathway appears to proceed from: (1) the formation of α-helices; to (2) the formation of two-helix bundles; to (3) the addition of a β-structure to form a 'molten globule' that topologically resembles the final structure, but is not well defined in detailed contacts and must undergo a rearrangement to yield, (4) the fully folded lysozyme.[73] A caveat emerging from this study is that alternative pathways are also compatible with all of the available NMR data. This reflects the ambiguity of the NMR data, but may also reflect the actual existence of multiple folding pathways. In a case of this kind, extensive correlation of the NMR findings with findings obtained by other physical methods is essential for the resolution of ambiguities.

3.1.6 Implications of Internal Motions and Flexibility for Structure Determination by NMR

The most serious problem to be considered when deriving solution structures of proteins from NMR data is that of conformational averaging, as discussed above. The problem is ubiquitous, and the burden of proof that the reported structure is rigid as calculated, remains on the investigator. For small compact globular proteins the problem is minimal. Averaging in a single potential well around a single set of coordinates is, for all practical purposes, indistinguishable from the case of a rigid structure, and corrections for this type of averaging have been proposed.[42] Short disordered regions are easily detected by the absence of NOEs, as in the case of insulin. The problem is much more serious for larger proteins, where averaging between ordered local structures may occur, as in the case of the *trp*-repressor. In such cases a detailed study of the dynamics becomes necessary, before the proposed structure can be given full credence. As has been pointed out already, many years ago,[23,78] to derive correctly a protein solution structure from NMR data, it is necessary to understand the dynamics of the protein in detail, and vice versa. Simple NMR structure determination is limited to simple objects. For most proteins, the study of structure and dynamics must, of necessity, go hand in hand.

3.2 Nucleic Acid Dynamics

Two types of rapid motion are known to occur in nucleic acid structures: (1) puckering of the phosphate backbone, reflected in the rapid averaging of ^{31}P chemical shifts so that typically, with few exceptions, only a single phosphate NMR signal is observed in both short oligonucleotide double helices and long (300–600 base pair) stretches of DNA; and (2) puckering of the sugar rings (deoxyribose in DNA and ribose in RNA, respectively), usually described as an exchange between a 2′-*endo* and a 3′-*endo* conformation.[81] Since the exchange rate is rapid on both the chemical shift and the coupling constant timescales (so that only time-averaged parameters are observed and individual states can not be resolved), it remains possible, but unprovable, that the exchange involves more than two states. Both of these motions clearly reflect thermal fluctuations. If they have any functional significance, it is to reflect the inherent flexibility of nucleic acid strands, necessary for the unwinding of double-stranded structures in the processes of replication, transcription and translation. It has been proposed that these motions may be accompanied by changes in helical twist.[82] On the other hand, wobbling of bases in double-stranded structures is rarely of sufficient amplitude to be reflected in NMR parameters, except at the fraying ends of oligonucleotide sequences.[83] Motions within the DNA double strand can be modulated and damped by the binding of intercalating agents. For purposes of structure calculations, short double-helical oligonucleotide strands can be treated as if they were rigid, since all of the described motions result only in averaging about a single energy minimum, i.e. within a single potential well. As yet, insufficient NMR data on the structure and dynamics of RNA are available to judge whether the more complex RNA structures found in crystallographic studies also undergo more complex and functionally significant motions. The existence of such motions can for the present only be inferred from the diversity of binding and catalytic interactions within the RNA family, observed in biological experiments. Conformational flexibility is a prerequisite for such diversity. Specific examples of nucleic acid dynamics are discussed elsewhere in this Encyclopedia (see ***Nucleic Acids: Spectra, Structures, and Dynamics***).

4 MOLECULAR INTERACTIONS

Molecular interactions of small ligands with macromolecules were among the first biological problems to be successfully studied by NMR. As early as 1961 a relaxation method for the determination of the groups involved in ligand–protein interactions had been developed in the author's laboratory.[84,85] With the methods then available, it was possible to infer which part of the flexible ligand—e.g. the phenyl ring of penicillin, rather than the penicillanic acid moiety—was bound to the protein. Interesting observations on different modes of binding in the sulfonamide family could be made, distinguishing binding by the sulfonamide ring from binding of an aromatic substituent to the same protein.[86] Later, it became possible to infer structures of inhibitor binding sites from a combination of NMR observations of ligand and protein side chains, as in the cases of pancreatic ribonuclease[87] and staphylococcal nuclease.[88] The binding of a transition state analog to lysozyme was also the subject of one of the early studies.[89] With modern technology it is possible to obtain detailed structures of binding sites, even for proteins that are for the time being too large to be amenable to a complete structure determination. A classic example is the detailed study of the binding of substrates and cofactors to dihydrofolate reductase, carried out by Roberts and coworkers.[90] In these studies it was found, long before a complete structure determination, that the cofactors NAD and NADH bound in different orientations, and, in a corresponding study of the dynamics, that the bound heterocyclic rings were able to undergo 180° flips in the bound state. A similar detailed study of the anti-TEMPO hapten antibody Fab fragment binding site by McConnell and coworkers[91] revealed that hapten binding caused a conformational change involving the displacement of a tyrosine side chain near the binding site to accommodate the hapten moiety. A detailed NMR structure of the Fab

fragment is not yet available. A complete structure of the tryptophan binding site in the *trp*-repressor was obtained in the course of the structure determination. It must be said, however, that the precision with which noncovalent structures can be defined from NMR data still leaves something to be desired, although the general configuration of the complex can be clearly outlined and the possibilities of forming different contacts evaluated. In dynamic NMR studies of ligand–protein interactions, the lifetimes of the bound and free states and the binding constants can be estimated. For typical small molecule ligands, the dwelling time on a protein falls in the millisecond range.

NMR studies of binding sites are particularly attractive when a comparison of the binding modes of different ligands (e.g., in a series of analogs) are needed, because of the relative speed and efficiency with which comparisons can be made. For ligands binding in a similar manner, the spectral changes (e.g., in the observed NOE pattern) from one compound to the next will be minor, and similarity of binding can be inferred from the similarity of the spectra without a complete reanalysis of the spectra in each case. Only when the binding patterns are different will the spectral changes be marked and require a de novo interpretation. A further advantage of NMR studies in this context is that comparative kinetic information on the exchange rates between the bound and free states is readily obtainable.

5 PROTEIN FUNCTION

Studies of protein function made possible by NMR fall into several categories. Very few detailed studies of this kind have as yet been carried out, but the possibilities have been clearly recognized.

The function of enzymes can be studied at several levels. Rates of enzymatic catalysis can be followed by observing the disappearance of substrates and appearance of products in (real) time. Structures of enzyme–inhibitor, enzyme–substrate or enzyme–transition-state analog complexes can be determined and examined for clues concerning the involvement of different groups at the binding site in the process. The first successful example of such a study was that of pancreatic ribonuclease A,[77,87] leading to a proposed mechanism that has since been confirmed by several kinetic and structural methods. Conformational changes and conformational equilibria involved in allosteric regulation can be defined, as described above. The obvious advantage of NMR over X-ray diffraction in this context is that the enzyme can be studied in its natural environment in solution, and that the dynamic processes involved can in many cases (though not always) be observed directly rather than being inferred from the initial and final states that can be crystallized.

The function of regulatory proteins, in which points of contact between the protein and DNA can be altered by a small molecule ligand, can be examined in much the same way as the function of allosteric enzymes. The study of the operator–*trp*-repressor complex, which forms in the presence of tryptophan and dissociates in its absence, can serve as the prototype for all studies of this type. This system is not only, as already noted, the largest molecular entity determined by NMR, but also the only complete allosteric regulatory complex analyzed by NMR methods in detail. All other NMR studies of protein–DNA interactions that have been reported involve binary complexes between the two macromolecules, with the regulatory function and ligand binding sites having been lost in the preparation of DNA-binding domains small enough to be easily studied by NMR. Structural studies of the complete system, including the ternary ligand–protein–DNA complex revealed a first conformational change on corepressor tryptophan binding and a further conformational change on the formation of the ternary complex with operator DNA. Dynamic studies revealed a stabilization of the DNA binding region by the binding of tryptophan and a further stabilization upon the formation of the ternary complex. The actual process is therefore more complex than the simple model commonly used for regulatory proteins—a single ligand induced conformational transition which aligns the DNA binding sites for better docking. It is to be expected that further, as yet unanticipated, variants of regulation by structural change will be uncovered in the course of studies on other systems.

Proteins involved in signal transduction and information transfer are also thought to function by undergoing structural transitions and, therefore, can be studied by the same techniques as those applied to the *trp*-repressor system, as can transport proteins functioning by an allosteric mechanism.

6 CONCLUSIONS

In summary, it can be said that the biological-NMR literature to date has laid all the necessary foundations for the study of protein structure, dynamics, interactions and function, devising and testing the required techniques and prototype experimental protocols on selected prototype systems. To a lesser extent, this can also be said of nucleic acids. Some technical development still remains to be done, in particular testing combinations of techniques to solve specific problems. The full range of potential applications remains in the future.

7 APPENDIX: DEFINITION OF SYMBOLS USED IN EQUATION (16)

$$\lambda_1 = \frac{-\frac{1}{T_{1A}} - k_{open} - \frac{1}{T_{1B}} - k_{close} - k_{intrinsic} + \sqrt{\left(\frac{1}{T_{1A}} + k_{open} - \frac{1}{T_{1B}} - k_{close} - k_{intrinsic}\right)^2 + 4k_{close}k_{open}}}{2}$$

$$\lambda_2 = \frac{-\frac{1}{T_{1A}} - k_{open} - \frac{1}{T_{1B}} - k_{close} - k_{intrinsic} - \sqrt{\left(\frac{1}{T_{1A}} + k_{open} - \frac{1}{T_{1B}} - k_{close} - k_{intrinsic}\right)^2 + 4k_{close}k_{open}}}{2}$$

$$C_1 = \left(\lambda_1 + \frac{1}{T_{1B}} + k_{close} + k_{intrinsic}\right)\left\{\frac{(M_A^i - C_3)\left(\lambda_2 + \frac{1}{T_{1A}} + k_{open}\right) - k_{close}(M_B^i - D_3)}{\left(\lambda_2 + \frac{1}{T_{1A}} + k_{open}\right)\left(\lambda_1 + \frac{1}{T_{1B}} + k_{close} + k_{intrinsic}\right) - k_{open}k_{close}}\right\}$$

$$C_2 = k_{open}\left\{\frac{(M_B^i - D_3)\left(\lambda_1 + \frac{1}{T_{1B}} + k_{close} + k_{intrinsic}\right) - k_{open}(M_A^i - C_3)}{\left(\lambda_z + \frac{1}{T_A} + k_{open}\right)\left(\lambda_1 + \frac{1}{T_{1B}} + k_{close} + k_{intrinsic}\right) - k_{open}k_{close}}\right\}$$

$$D_1 = k_{close}\left\{\frac{(M_A^i - C_3)\left(\lambda_2 + \frac{1}{T_{1A}} + k_{open}\right) - k_{close}(M_B^i - D_3)}{\left(\lambda_2 + \frac{1}{T_{1A}} + k_{open}\right)\left(\lambda_1 + \frac{1}{T_{1B}} + k_{close} + k_{intrinsic}\right) - k_{open}k_{close}}\right\}$$

$$D_2 = \left(\lambda_2 + \frac{1}{T_{1A}} + k_{open}\right)\left\{\frac{(M_B^i - D_3)\left(\lambda_1 + \frac{1}{T_{1B}} + k_{close} + k_{intrinsic}\right) - k_{open}(M_A^i - C_3)}{\left(\lambda_2 + \frac{1}{T_{1A}} + k_{open}\right)\left(\lambda_1 + \frac{1}{T_{1B}} + k_{close} + k_{intrinsic}\right) - k_{open}k_{close}}\right\}$$

$$C_3 = M_A^{EQ} + \frac{f k_{close}}{\left(\frac{1}{T_{1A}} + k_{open}\right)\left(\frac{1}{T_{1B}} + k_{close} + k_{intrinsic}\right) - k_{open}k_{close}}$$

$$D_3 = M_B^{EQ} + \frac{f\left(\frac{1}{T_{1A}} + k_{open}\right)}{\left(\frac{1}{T_{1A}} + k_{open}\right)\left(\frac{1}{T_{1B}} + k_{close} + k_{intrinsic}\right) - k_{open}k_{close}}$$

For presaturation experiments: $f = -k_{intrinsic}\boldsymbol{M}_B^{EQ}$. For no-presaturation experiments: $f = 0$.

8 REFERENCES

1. M. Saunders, A. Wishnia, and J. G. Kirkwood, *J. Am. Chem. Soc.*, 1957, **79**, 3289.
2. G. M. Clore and A. M. Gronenborn, *Prog. NMR Spectrosc.*, 1991, **23**, 43.
3. C. H. Arrowsmith, L. Treat-Clemons, L. Szilágyi, R. Pachter, and O. Jardetzky, *Makromol. Chem., Macromol. Symp.*, 1990, **34**, 33.
4. J. Czaplicki, C. Arrowsmith, and O. Jardetzky, *J. Biomol. NMR*, 1991, **1**, 349.
5. M. Takeda and O. Jardetzky, *J. Chem. Phys.*, 1957, **26**, 1346; see also O. Jardetzky and C. D. Jardetzky, *J. Am. Chem. Soc.*, 1957, **79**, 5322.
6. O. Jardetzky, *Adv. Chem. Phys.*, 1964, **7**, 499.
7. W. A. Gibbons, D. Crepaux, J. Delayre, J.-J. Dunand, G. Hajdukovic, and H. R. Wyssbrod, in *Peptides: Chemistry, Structure and Biology*, eds. R. Walter and J. Meienhofer, Ann Arbor, New York, 1976, pp. 127–137.
8. C. H. Arrowsmith, R. Pachter, R. B. Altman, S. B. Iyer, and O. Jardetzky, *Biochemistry*, 1990, **29**, 6332.
9. M. Ikura, L. E. Kay, and A. Bax, *Biochemistry*, 1990, **29**, 4659.
10. G. T. Montelione and G. Wagner, *J. Magn. Reson.*, 1990, **87**, 183.
11. R. Powers, D. S. Garrett, C. J. March, E. A. Frieden, A. M. Gronenborn, and G. M. Clore, *Biochemistry*, 1992, **31**, 4334.
12. M. Ikura, G. M. Clore, A. M. Gronenborn, G. Zhu, C. B. Klee, and A. Bax, *Science*, 1992, **256**, 632.
13. R. Powers, G. M. Clore, A. Bax, D. S. Garrett, S. J. Stahl, P. T. Wingfield, and A. M. Gronenborn, *J. Mol. Biol.*, 1991, **221**, 1081.
14. W. J. Fairbrother, J. Cavanaugh, H. J. Dyson, A. G. Palmer, S. L. Sutrina, J. Reizer, M. H. Saier, Jr, and P. E. Wright, *Biochemistry*, 1991, **30**, 6896.
15. R. Powers, D. S. Garrett, C. J. March, E. A. Frieden, A. M. Gronenborn, and G. M. Clore, *Science*, 1992, **256**, 1673.
16. H. Zhang, D. Zhao, M. Revington, W. Lee, X. Jia, C. Arrowsmith, and O. Jardetzky, *J. Mol. Biol.*, 1994, **238**, 592.
17. D. M. LeMaster, *Prog. NMR Spectrosc.*, 1994, **26**, 371.
18. O. Jardetzky and A. N. Lane, in *Physics of NMR Spectroscopy in Biology and Medicine*, ed. B. Maraviglia, Italian Physical Society/North-Holland Physics, Amsterdam, 1988, pp. 267–301.
19. J. D. Forman-Kay, G. M. Clore, P. T. Wingfield, and A. M. Gronenborn, *Biochemistry*, 1991, **30**, 2685.
20. K. Kato, C. Matsunaga, T. Igarashi, H.-H. Kim, A. Odaka, I. Shimada, and Y. Arata, *Biochemistry*, 1991, **30**, 270.
21. D. Zhao and O. Jardetzky, *J. Mol. Biol.*, 1994, **239**, 601.
22. M. Karplus, *J. Chem. Phys.*, 1959, **30**, 11.
23. O. Jardetzky, in *Progress in Bioorganic Chemistry and Molecular Biology. Proceedings of the International Conference on the Frontiers of Bio-organic Chemistry and Molecular Biology, Moscow-Alma Ata*, ed. Yu. A. Ovchinnikov, Elsevier Science, Amsterdam, 1984, pp. 55–63.
24. T. F. Havel, G. M. Crippen, and I. D. Kuntz, *Biopolymers*, 1979, **18**, 73.
25. T. A. Holak, J. H. Prestegard, and J. D. Forman, *Biochemistry*, 1987, **26**, 4652.
26. R. B. Altman and O. Jardetzky, *J. Biochem.*, 1986, **100**, 1403.
27. I. D. Kuntz, J. F. Thomason, and C. M. Oshiro, *Methods Enzymol.*, 1989, **177**, 159.
28. G. M. Crippen, *Distance Geometry and Molecular Conformation*, Wiley, Chichester, 1988.
29. E. Madelung, *Die Mathematischen Hilfsmittel des Physikers*, Dover, New York, 1943.

30. J. C. Hoch and A. S. Stern, *J. Biomol. NMR*, 1992, **2**, 535.
31. R. B. Altman, R. Pachter, E. A. Carrara, and O. Jardetzky, *QCPE Bull.*, 1990, **10**(4), Program 596.
32. P. Koehl, J.-F. Lefèvre, and O. Jardetzky, *J. Mol. Biol.*, 1992, **223**, 299.
33. C. Arrowsmith, R. Pachter, R. Altman, and O. Jardetzky, *Eur. J. Biochem.*, 1991, **202**, 53.
34. B. R. Brooks, R. E. Bruccoleri, B. D. Olafson, D. J. States, S. Swaminathan, and M. Karplus, *J. Comput. Chem.*, 1983, **4**, 187.
35. A. T. Brünger, *X-PLOR Software Manual Version 2.1*, Yale University, New Haven, CT, 1990.
36. A. T. Brünger and M. Karplus, *Acc. Chem. Res.*, 1991, **24**, 54, (and references therein).
37. D. Zhao and O. Jardetzky, *J. Phys. Chem.*, 1993, **97**, 3007.
38. J. W. Keepers and T. L. James, *J. Magn. Reson.*, 1984, **57**, 404.
39. S. Macura and R. R. Ernst, *Mol. Phys.*, 1980, **41**, 95.
40. M. Nilges, J. Habazettl, A. T. Brünger, and T. A. Holak, *J. Mol. Biol.*, 1991, **219**, 499.
41. P. Yip and D. A. Case, *J. Magn. Reson.*, 1989, **83**, 643.
42. A. E. Torda, R. M. Scheek, and W. F. van Gunsteren, *Chem. Phys. Lett.*, 1989, **157**, 289.
43. G. M. Clore and A. M. Gronenborn, *J. Magn. Reson.*, 1989, **84**, 398.
44. Y. Liu, D. Zhao, R. Altman, and O. Jardetzky, *J. Biomol. NMR*, 1992, **2**, 373.
45. G. M. Clore, M. A. Robien, and A. M. Gronenborn, *J. Mol. Biol.*, 1993, **231**, 82.
46. D. E. Wemmer, *Curr. Opin. Struct. Biol.*, 1991, **1**, 452.
47. A. S. Benight, J. M. Schurr, P. F. Flynn, B. R. Reid, and D. E. Wemmer, *J. Mol. Biol.*, 1988, **200**, 377.
48. T. Hard, E. Kellenbach, R. Boelens, B. A. Maler, K. Dahlman, L. P. Freedman, J. Carlstedt-Duke, K. R. Yamamoto, J.-A. Gustafson, and R. Kaptein, *Science*, 1991, **249**, 157.
49. O. Jardetzky and J.-F. Lefèvre, *FEBS Lett.*, 1994, **338**, 246.
50. H.-C. Guo, T. S. Jardetzky, T. P. J. Garrett, W. S. Lane, J. L. Strominger, and D. C. Wiley, *Nature*, 1992, **360**, 364.
51. T. S. Jardetzky, J. C. Gorga, R. Busch, J. Rothbard, J. L. Strominger, and D. C. Wiley, *EMBO J.*, 1990, **9**, 1797.
52. O. Jardetzky and G. C. K. Roberts, *NMR in Molecular Biology*, Academic Press, New York, 1981, Chap. 4
53. M. J. Stone, W. J. Fairbrother, A. G. Palmer, III, J. Reizer, M. H. Saier, Jr., and P. E. Wright, *Biochemistry*, 1992, **31**, 4394.
54. G. Barbato, M. Ikura, L. E. Kay, R. W. Pastor, and A. Bax, *Biochemistry*, 1992, **31**, 5269.
55. O. W. Howarth, *J. Chem. Soc., Faraday Trans. II*, 1978, **74**, 1031.
56. O. W. Howarth, *J. Chem. Soc., Faraday Trans. II*, 1979, **75**, 863.
57. R. King and O. Jardetzky, *Chem. Phys. Lett.*, 1978, **55**, 15.
58. G. Lipari and A. Szabo, *J. Am. Chem. Soc.*, 1982, **104**, 4546.
59. J. W. Peng and G. Wagner, *J. Magn. Res.*, 1992, **98**, 308.
60. O. Jardetzky and R. King, in *Mobility & Function in Proteins & Nucleic Acids (Ciba Foundation Symposium 93)*, Pitman, London, 1982, p. 291.
61. O. Jardetzky, K. Akasaka, D. Vogel, S. Morris, and K. C. Holmes, *Nature*, 1978, **273**, 564.
62. N. Wade-Jardetzky, R. P. Bray, W. W. Conover, O. Jardetzky, N. Geisler, and K. Weber, *J. Mol. Biol.*, 1979, **128**, 259.
63. E. M. Bradbury and H. W. E. Rattle, *Eur. J. Biochem.*, 1972, **27**, 270.
64. S. Highsmith and O. Jardetzky, in *Mobility & Function in Proteins & Nucleic Acids (Ciba Foundation Symposium 93)*, Pitman, London, 1982, pp. 156–168.
65. C. H. Arrowsmith, J. Carey, L. Treat-Clemons, and O. Jardetzky, *Biochemistry*, 1989, **28**, 3875.
66. Y. Q. Qian, G. Otting, K. Furukubo-Tokunaga, M. Affolter, W. J. Gehring, and K. Wüthrich, *Proc. Natl. Acad. Sci. U.S.A.*, 1992, **89**, 10738.
67. Q. X. Hua, S. E. Shoelson, and M. A. Weiss, *Biochemistry*, 1992, **31**, 1 1940.
68. D. Wemmer, A. A. Ribeiro, R. P. Bray, N. G. Wade-Jardetzky, and O. Jardetzky, *Biochemistry*, 1981, **20**, 829.
69. A. Hvidt and S. O. Nielsen, *Adv. Protein Chem.*, 1966, **21**, 287.
70. S. Spera, M. Ikura, and A. Bax, *J. Biomol. NMR*, 1991, **1**, 155.
71. Z. Zheng, M. R. Gryk, M. D. Finucane, and O. Jardetzky, *J. Magn. Res., Ser. B*, 1995, **108**, in press.
72. M. R. Gryk, M. D. Finucane, Z. Zheng, and O. Jardetzky, *J. Mol. Biol.*, 1995, **246**, 618.
73. E. A. Auerswald, G. Genenger, R. Mentele, S. Lenzen, I. Assfalg-Machleidt, L. Mitschang, H. Oschkinat, and H. Fritz, *Eur. J. Biochem.*, 1991, **200**, 131.
74. O. Jardetzky, in *Molecular Properties of Drug Receptors*, eds. R. Porter and M. O'Connor, J. & A. Churchill, London, 1970, pp. 113–132.
75. I. D. Campbell and C. M. Dobson, *Methods Biochem. Anal.*, 1979, **25**, 1.
76. D. J. Nelson, S. J. Opella, and O. Jardetzky, *Biochemistry*, 1976, **15**, 5552.
77. D. H. Meadows, O. Jardetzky, R. M. Epand, H. H. Ruterjans, and H. A. Scheraga, *Proc. Natl. Acad. Sci. U.S.A.*, 1968, **60**, 766.
78. O. Jardetzky, *Biochim. Biophys. Acta*, 1980, **621**, 227.
79. Y. Kim and J. H. Prestegard, *Biochemistry*, 1989, **28**, 8792.
80. S. E. Radford, C. M. Dobson, and P. A. Evans, *Nature*, 1992, **358**, 302.
81. O. Jardetzky and G. C. K. Roberts, *NMR in Molecular Biology*, Academic Press, New York, 1981, Chap. 6
82. M. E. Hogan and O. Jardetzky, *Proc. Natl. Acad. Sci. U.S.A.*, 1979, **76**, 6341.
83. J.-F. Leféyre, A. N. Lane, and O. Jardetzky, *Biochemistry*, 1987, **26**, 5076.
84. O. Jardetzky and J. J. Fischer, in *Proceedings of the 4th International Conference on Medical Electronics New York, 1961*, p. 46.
85. O. Jardetzky, J. J. Fischer, and P. Pappas, *Biochem. Pharmacol.*, 1961, **8**, 387.
86. O. Jardetzky and N. G. Wade-Jardetzky, *Mol. Pharmacol.*, 1965, **1**, 214.
87. D. H. Meadows, G. C. K. Roberts, and O. Jardetzky, *J. Mol. Biol.*, 1969, **45**, 491.
88. J. L. Markley and O. Jardetzky, *J. Mol. Biol.*, 1970, **50**, 223.
89. S. L. Patt, J. H. Baldo, K. Boekelheide, G. Weisz, and B. D. Sykes, *Can. J. Biochem.*, 1978, **56**, 624.
90. G. C. K. Roberts, in *Protein Structure and Engineering*, ed. O. Jardetzky, Plenum, New York, 1989, pp. 209–220, and references therein.
91. P. P. Theriault, D. J. Leahy, M. Levitt, H. M. McConnell, and G. S. Rule, *J. Mol. Biol.*, 1991, **221**, 257.

Biographical Sketches

Oleg Jardetzky. *b* 1929. B.A., 1950, Chemistry & Biology, Macalester College, St. Paul MN, M.S., 1953, Physiological Chemistry, M.D., 1954, Medicine, Ph.D., 1956, Physiology & Physical Chemistry, University of Minnesota, St. Paul, MN. National Research Council Fellow, Department of Chemistry, CalTech, 1956–57; Associate in Pharmacology, 1957–59, Assistant Professor of Pharmacology, Harvard Medical School, 1959–66; Director, Department of Biophysics & Pharmacology, Merck, Sharp & Dohme, 1966–68; Executive Director of Basic Medical Science, Merck Institute for Therapeutic Research, 1968–69; Professor of Pharmacology, 1969–present, Director, Stanford Magnetic Resonance Laboratory, Stanford University, 1975–present. Approx. 230 publications. Current research interests: structure dynamics and function of proteins involved in regulatory processes; the mechanism of action of *trp*-repressor; use of high-resolution NMR spectroscopy and other physical methods to define mechanisms of conformational transition and protein folding.

Calmodulin

Mitsuhiko Ikura

University of Toronto, Canada

1	Introduction	1
2	Interactions with Metal Ions and Drugs	2
3	Calcium–Calmodulin Complex	4
4	Calcium–Calmodulin–Peptide Ternary Complexes	4
5	Related Articles	6
6	References	6

1 INTRODUCTION

Calmodulin (CaM) was discovered as an activator of cyclic nucleotide phosphodiesterase in brain by Cheung[1] and by Kakiuchi and Yamazaki[2] in 1970. Since then, it has became clear that CaM is a ubiquitous intracellular calcium receptor present in eukaryotic cells and that its structure has been highly conserved during evolution.[3] The amino acid and gene sequences of CaM from various species have been determined.[4–6] Figure 1 shows the amino acid sequence of bovine brain CaM.[4] The molecular weight of CaM is ca. 16 700. The amino terminal is acetylated and lysine-115 is trimethylated at the ϵ position. CaM consists of four repeated sequences of about 35 amino acid residues, each of which forms a helix–loop–helix Ca^{2+}-binding motif of the EF-hand type, first discovered in parvalbumin by Kretsinger and co-workers.[7] The biophysical properties of CaM have been extensively studied (for reviews, see Cohen and Klee[5]). CaM is an acidic (pI = 4.3) and heat stable protein which binds four Ca^{2+} ions. The four Ca^{2+}-binding motifs can be classified into the high affinity sites III and IV in the C-terminal region ($K_d \approx 10^{-6}$ M) and the low affinity sites I and II in the N-terminal region ($K_d \approx 10^{-5}$ M).[8]

A number of enzymes and proteins have been reported to date to be stimulated by CaM.[4] These include myosin light chain kinase (MLCK), CaM kinase II, phosphorylase kinase, calcineurin, myristoylated alanine-rich C kinase substrate (MARCKS), and many others (for reviews, see Cohen and Klee[5] and Crivici and Ikura[6]). Thus, CaM plays a role as a multifunctional activator or regulator in various Ca^{2+}-dependent cellular processes. CaM-binding regions in many target enzymes and proteins have been mapped. These regions are generally small (14–27 amino acid residues) and rich in basic and hydrophobic residues. Most of the CaM-binding sequences identified so far appear to have a propensity for helix formation. A number of naturally occurring peptides are also known to bind CaM in a Ca^{2+}-dependent manner.[9] These peptides include insect venom peptides such as mastoparans and melittin, and certain hormones and opioids such as ACTH, VIP, glucagon, and substance P. In addition, phenothiazines and other hydrophobic drugs including trifluroperazine (TFP), chlorpromazine, and W-7, bind CaM and inhibit the CaM-mediated activation of enzymes.[10] Proteolytic fragments and synthetic peptides comprising the CaM-binding regions of target proteins, as well as the insect and hormone peptides and the hydrophobic drugs, have been extensively used to study the structural and biochemical properties of the interaction of CaM with targets.

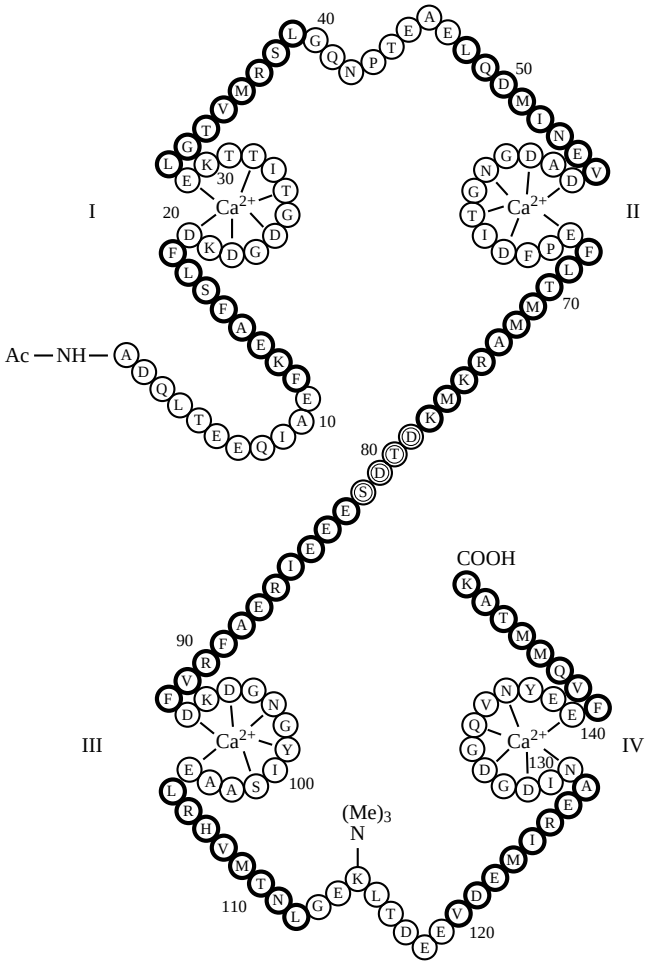

Figure 1 The amino acid sequence of bovine brain calmodulin[4] [Courtesy of C. B. Klee]

The crystal structures of Ca^{2+}-loaded CaM were reported by Babu et al.[11] in 1985 and by Kretsinger et al.[12] in 1986. The structures have an unusual dumbbell shape [Figure 2(a)] in which the N- and C-terminal globular domains are connected by a long α-helix. The length of the molecule is about 65 Å, with each lobe having approximate dimensions of 25 × 20 × 20 Å.[3] Each domain possesses a hydrophobic patch, which is considered to be responsible for target binding. Similar structural features were found in the crystal structure of a homologous Ca^{2+}-binding protein, skeletal muscle troponin C[13] (see ***Calcium-Binding Proteins*** and ***Muscle Proteins***). In 1992, an NMR structure of CaM complexed with a 26-residue CaM-binding peptide derived from skeletal muscle MLCK was determined[14] [Figure 2(b)]. Subsequently, a crystal structure of CaM complexed with a smooth muscle MLCK peptide was also solved at 2.4 Å. More recently, a crystal structure of CaM complexed with a CaM kinase II peptide has been reported.[16]

Detailed mechanisms by which CaM regulates the activity of target enzymes and proteins are still not yet fully understood even for a single case. Nevertheless, NMR spectroscopy has contributed tremendously to our understanding of the structural basis of the action of CaM in the context of interactions with

Ca^{2+}, and peptides and drugs. In the following discussion NMR studies on CaM reported during the period of 1979–93 will be summarized.

2 INTERACTIONS WITH METAL IONS AND DRUGS

The first 250- and 360-MHz ^{1}H NMR spectra of bovine brain CaM were reported by Seamon[17,18] in 1979 and 1980, who demonstrated that dramatic Ca^{2+}-dependent spectral changes could be monitored by ^{1}H NMR. Aromatic proton resonances of Tyr-99, His-107, and Tyr-138, and a unique trimethyl group of ϵ-trimethylated Lys-115 were identified. Klevit et al.[19] and Krebs and Carafoli[20] studied the interaction of bovine brain CaM with TFP using ^{1}H NMR. Shimizu et al.[21,22] used ^{19}F NMR to study the interactions of porcine brain and *Tetraphymena pyriformis* CaM with TFP. All these studies indicate that one CaM molecule binds two TFP molecules.

More detailed assignments for aromatic ring and methyl protons in scallop testis CaM were reported by Ikura et al.[23] in 1983. Using those resonance assignments, Ca^{2+}-induced conformational changes have been examined.[24] Figure 3 illustrates Ca^{2+}-induced changes in the aromatic region of the ^{1}H NMR spectra. The results show that many resonances C-terminal domain (Phe-99, His-107, trimethyl Lys-115, and Tyr-138) are shifted in an early stage of Ca^{2+} titration (0–2 mol Ca^{2+} per mol of CaM), thus concluding that the C-terminal domain contains the high affinity sites for Ca^{2+}. Forsén and co-workers independently reached the same conclusion from ^{43}Ca and ^{113}Cd NMR studies[25,26] using two tryptic fragments

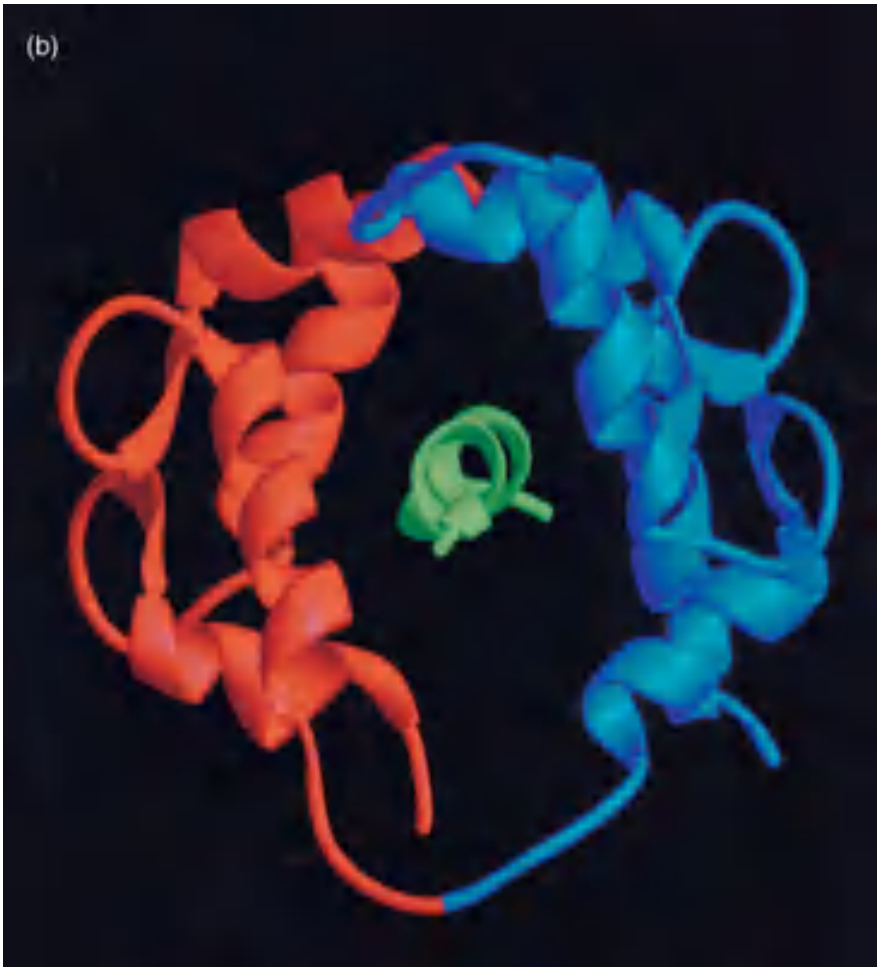

Figure 2 Ribbon diagram representations of (a) Ca^{2+}–CaM[11] and (b) the Ca^{2+}–CaM–M13 complex[14] as generated by the program ribbons. The CaM N-terminal domain is shown in blue and the C-terminal domain in red. In Figure 2(b), the structure is viewed parallel to the M13 peptide helix axis

of CaM (TR_1C, fragment 1–75; TR_2C, fragment 78–148). These half-fragments were found to be extremely useful for NMR studies of CaM. In 1984, ^1H NMR studies on the half-fragments were reported by three groups[27–30] almost at the same time. Two uniquely low-frequency shifted ring proton resonances at 6.46 and 6.50 ppm of apo-CaM were assigned to phenylalanines in the N-terminal domain. All these studies provided further evidence for the order of Ca^{2+} binding to four sites in CaM. Together with ^{43}Ca and ^{113}Cd NMR[25,26] and other biophysical studies,[4,5,8] it became clear that the two tryptic half-fragments retain the conformations which they assume in whole CaM. The property was shown for both the Ca^{2+}-free and Ca^{2+}-bound forms.

Because of the complexity of the ^1H NMR spectra of whole CaM, several groups used the tryptic half-fragments to elucidate the structural details of CaM. In 1984, Aulabaugh et al.[31] applied 2D ^1H NMR at 600 MHz to fragment TR_2C in the absence of Ca^{2+} and obtained assignments for many side-chain proton resonances to particular amino acid types. In 1985, Ikura et al.[32] applied 2D ^1H NMR techniques to the TR_2C fragment both in the presence and the absence of Ca^{2+}, and obtained about 30% backbone and side-chain proton assignments in each state using the sequential assignment procedure proposed by Wüthrich and co-workers (see ***Biological Macromolecules: Structure Determination in Solution*** and ***Structures of Larger Proteins, Protein-Ligand, and Protein-DNA Complexes by Multi-Dimensional Heteronuclear NMR***). Extremely high-frequency shifted amide proton resonances (10.0–11.0 ppm) were assigned to the glycine residues at the fifth position of the Ca^{2+}-binding loops. These uniquely shifted glycine amide resonances were further characterized using both TR_1C and TR_2C fragments.[33] Such large shifts of the amide protons of this conserved glycine residues in EF-hand Ca^{2+}-binding loops were also found in troponin C[34] and calbindin[35] (see ***Calcium-Binding Proteins***), suggesting that this feature is universal among the members of the EF-hand superfamily. Hoffman and Klevit[36] reported 2D ^1H NMR analysis of the Ca^{2+}-free TR_1C fragment in the absence of Ca^{2+}, indicating hydrophobic contacts between Phe-16 and Val-35 which are absent in the Ca^{2+}-bound form of the crystal structure.[11,12] More recently, Finn et al.[37] obtained the complete backbone ^1H resonance assignments of the Ca^{2+}-free TRC fragment, indicating that the Ca^{2+}-free state retains the helix–loop–helix secondary structure similar to that observed in the Ca^{2+}-bound form.[11,12,38]

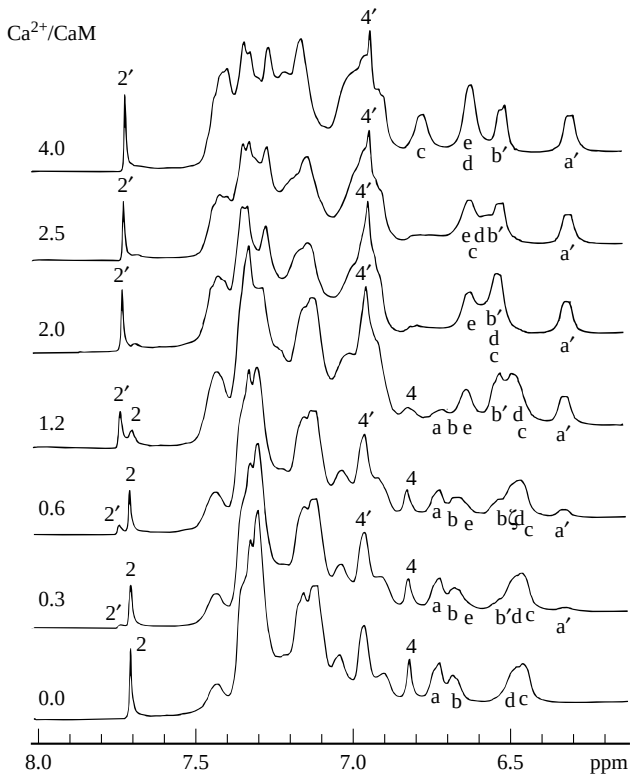

Figure 3 The aromatic region of the 400 MHz ^{1}H NMR spectra of scallop testis calmodulin at various Ca^{2+} concentrations. (Reproduced by permission of the American Chemical Society from Ikura et al.[24])

Several different NMR techniques were used to study the kinetics of Ca^{2+} binding to CaM and its fragments. Calcium-43 and ^{113}Cd NMR studies[25,26] indicate that the resonances from metal ions bound to sites III and IV show much slower exchange on the NMR timescale than those from metal ions bound to sites I and II. ^{1}H NMR saturation transfer and spectral simulation methods were employed to obtain the exchange rate constants and activation parameters between Ca^{2+}-free and Ca^{2+}-bound forms of two half-fragments.[39] Two distinct rate constants of $3-10\,s^{-1}$ and $300-500\,s^{-1}$ were found at 22 °C for the C-terminal and the N-terminal fragments, respectively. All these results confirm the identification of sites III and IV as being the high affinity sites.

Starovasnik et al[40] studied the Ca^{2+} binding and structural properties of CaM from the yeast *Saccharomyces cerevisiae* using flow dialysis and ^{1}H NMR. The amino acid sequence of yeast CaM is 60% identical to that of vertebrate CaM, whereas all known vertebrate CaM sequences are totally identical. The results indicate that, unlike vertebrate CaM, yeast CaM binds only three Ca^{2+} ions and that all three sites exhibit slow-exchange behavior upon Ca^{2+} binding. Thermal denaturation properties of yeast CaM as well as of its half-fragments were also studied. Starovasnik et al.[41] studied a series of four site-directed mutants using the same techniques, demonstrating interactions between the Ca^{2+}-binding sites in CaM.

Vogel and co-workers have extensively studied lysine residues in CaM using ^{1}H and ^{13}C NMR. The pK_a values of *N*-dimethylated lysine residues were obtained both in apo and Ca^{2+}-bound forms, as well as in a complex with a 22-residue peptide comprising the CaM-binding region of skeletal muscle MLCK.[42,43] Zhang et al.[44] applied ^{14}N NMR to ϵ-trimethyl Lys-115 in both vertebrate and yeast CaMs. The ϵ-trimethyl group of this posttranslated lysine gives rise to a sharp ^{14}N NMR resonance because of its unique tetrahedral symmetry. Selenium-77 NMR was used to study the microenvironments of the nine methionine residues in CaM, all of which were biosynthetically substituted with selenomethionine.[45]

3 CALCIUM–CALMODULIN COMPLEX

During the period 1989–93, CaM was extensively used by Bax's group at the NIH to develop multidimensional heteronuclear MR methods (see ***Multidimensional Spectroscopy: Concepts***, and ***Three- and Four-Dimensional Heteronuclear Magnetic Resonance***). This methodology requires isotope enrichment of proteins with ^{15}N and ^{13}C. Uniformly ^{15}N- and ^{13}C-labeled CaM was obtained using an *E. coli* expression system.[46] Figure 4 shows a ^{1}H–^{15}N heteronuclear single quantum coherence (HSQC) spectrum of Ca^{2+}-loaded recombinant CaM labeled uniformly with ^{15}N, illustrating that a high-quality ^{1}H–^{15}N shift correlation spectrum can be obtained at 1 mM protein concentration. Ikura et al.[38,47] reported complete backbone and side-chain ^{1}H, ^{13}C, and ^{15}N assignments of Ca^{2+}-loaded recombinant *Drosophila* CaM using a series of triple- and double-resonance 3D and 4D experiments. The secondary structure in solution was then characterized using NOE, $^3J_{NH\alpha}$ coupling constants, and ^{13}C chemical shift data.[38] These results confirm the crystal structure[11,12] in that both the N- and C-terminal globular domains assume a pair of the EF-hand type helix–loop–helix motifs. However, the central helix portion (residues 65–92), found in the crystal structure, appears to contain a nonhelical region at residues 78–81 in solution. Nitrogen-15 relaxation studies reported by Barbato et al.[48] further indicate that this nonhelical portion has considerable flexibility, consistent with other studies using solution techniques such as small angle X-ray or neutron scattering.[49] The ^{15}N relaxation studies[48] (see ***Protein Dynamics from NMR Relaxation***) provide additional interesting insights into the structure and dynamics of Ca^{2+}–CaM. The rotational correlation times obtained for the N- and C-terminal domain (7.1 ns and 6.3 ns, respectively) do not reflect the overall motion of a 16.7 kDa protein, but rather correspond to that of a smaller protein (ca. 12 kDa). Further, the correlation times for the individual amide bond vectors vary to a much lesser degree than predicted by hydrodynamic calculations for rigid dumbbell models. These results indicate that the two domains move independently in solution.

4 CALCIUM–CALMODULIN–PEPTIDE TERNARY COMPLEXES

In 1985, Klevit et al.[50] using ^{1}H NMR studied the interaction of CaM with a 26-residue synthetic peptide (known as M13) comprising the CaM-binding domain of skeletal muscle myosin light chain kinase. These data indicate that both the N- and C-terminal domains must participate in the interaction with the M13 peptide. The ^{113}Cd NMR studies of mastoparan binding to Cd_4CaM have shown that both the N- and C-terminal domains undergo conformational

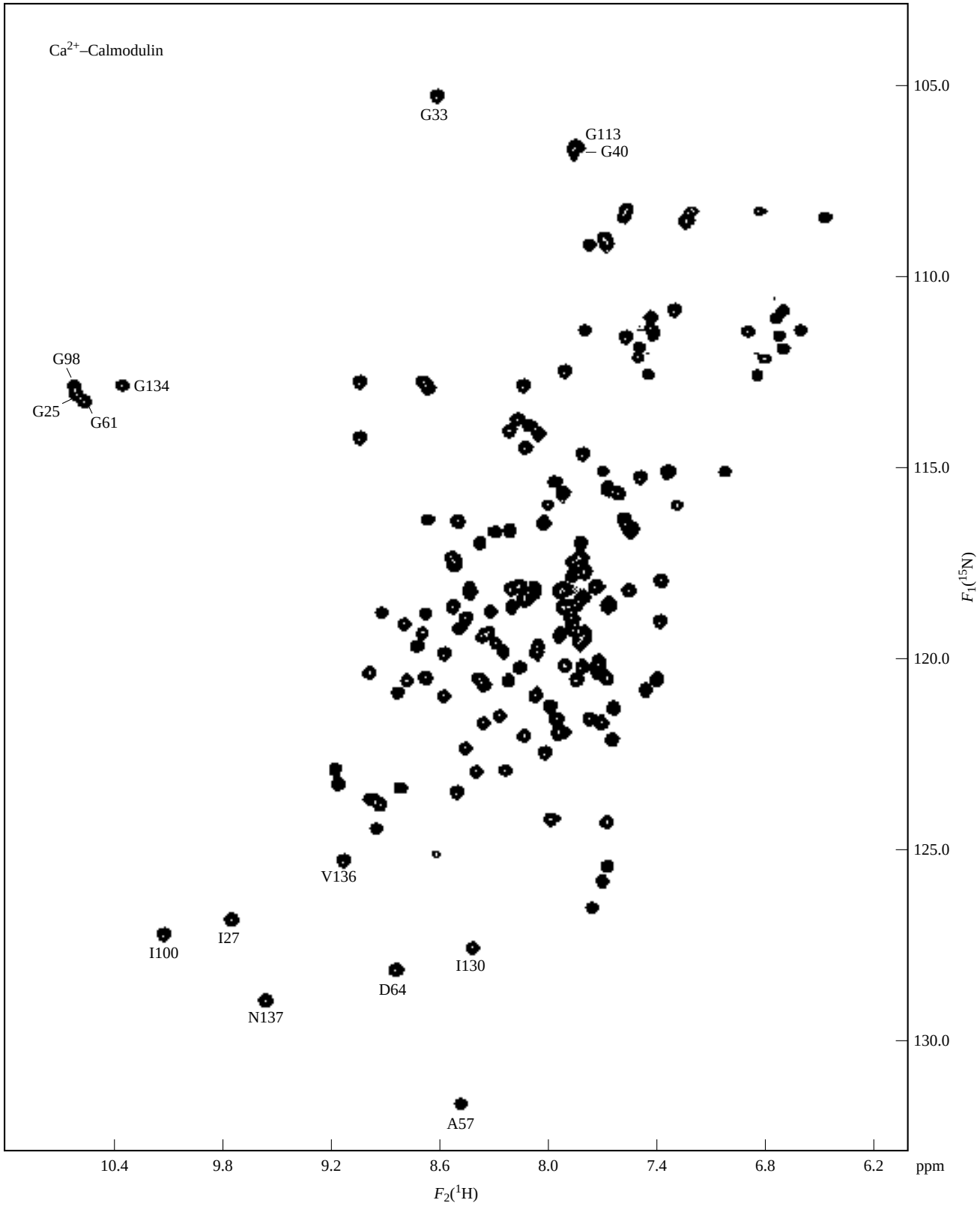

Figure 4 The 500 MHz $^{1}H-^{15}N$ HSQC shift correlation spectrum of *Xenopus laevis* calmodulin. The spectrum was recorded using a pulse sequence combined with the pulse field gradient technique described by Kay et al.[66] The full backbone amide assignment of *Xenopus* calmodulin is available from the author

changes upon binding of the peptide (see ***Calcium-Binding Proteins***). Seeholzer et al.[51] also used ^{1}H NMR to study the interaction of melittin with [^{1}H]- and [^{2}H]-CaM, suggesting that melittin assumes an α-helical conformation upon binding CaM, consistent with earlier conclusions based on circular dichroism spectra. Yazawa et al.,[52] using the ^{1}H NMR signal of His-107, showed that in the presence of M13 the Ca^{2+}-dependent conformational change becomes completely cooperative between the N- and C-terminal domains. Ikura et al.[53] studied the Cd^{2+} dependence of the interactions of CaM with M13 and mastoparan using ^{113}Cd NMR, supporting the notion of the higher cooperativity of metal binding in the presence of these peptides. Ohki et al.[54,55] studied the interaction of mastoparan with CaM under various solution conditions using ^{1}H NMR. It was shown that the N-terminal domain may interact with a second mastoparan molecule with a lower affinity, and that Mg^{2+} reduces the cooperative Ca^{2+} binding to CaM in the presence of mastoparan.

In 1991, Ikura et al.[56] completed ^{1}H, ^{13}C, and ^{15}N backbone assignments of Ca^{2+}–CaM complexed with M13 by using multidimensional heteronuclear MR methods. Proton assignments of M13 in the complex were also obtained using ^{15}N/^{13}C-filtered techniques[57] (see ***Half-Filter Experiments: Proton–Carbon-13***). Based on these assignments, the three-dimensional NMR structure of the Ca^{2+}–CaM–M13 ternary complex was determined.[14] Figure 2(b) shows a schematic ribbon model of the restrained minimized mean structure. A striking difference in conformation can be seen as compared with the crystal structure of Ca^{2+}–CaM[11] [Figure 2(a)]. The N- and C-terminal domains of CaM (residues 6–73 and 83–146) remain essentially unchanged upon complexation. The long central helix, (residues 65–93), however, which connects the two domains in the crystal structure of Ca^{2+}–CaM [Figure 4(a)], is disrupted into two helices connected by a long flexible loop (residues 74–82), thereby enabling the two domains to clamp residues 3–21 of the bound peptide which adopt a helical conformation. Key residues of the peptide are Trp-4 and Phe-17, which serve to anchor the N- and C-terminal halves of the peptide to the C- and N-terminal domains of CaM, respectively. This characteristic structure of Ca^{2+}–CaM complexed with the M13 peptide was confirmed by a crystallographic study on Ca^{2+}–CaM complexed with a similar peptide derived from smooth muscle MLCK.[15] Based on the knowledge of the structural features of these Ca^{2+}–CaM–peptide complexes, Prumb et al.[58] produced a hybrid CaM–peptide molecule and characterized the structural and Ca^{2+}-binding properties using ^{1}H–^{15}N HSQC and flow dialysis experiments.

Roth et al.[59,60] revealed the secondary structure of a 19-residue smooth muscle MLCK peptide and CaM in their complex using heteronuclear multidimensional NMR techniques. Most of the backbone amide nitrogen nuclei in the MLCK peptide were labeled with ^{15}N, which allowed the characterization of the α-helix structure of the peptide. Precheur et al.[61] also used a similar labeling technique on a 17-residue model peptide proposed by DeGrado et al.,[62] and showed a stable α-helical structure in the N-terminal 11 residues of the complex. Zhang et al.,[63,64] using 2D ^{1}H NMR, studied three synthetic CaM binding peptides which are derived from skeletal muscle MLCK, rat cerebellar nitric oxide synthase, and smooth muscle caldesmon. The MLCK[63] and caldesmon[64] peptides were found to assume an α-helical conformation in an aqueous trifluoroethanol mixture (75%/25%) The nitric oxide synthase peptide[66] also adopts an α-helical structure in aqueous solution at pH 5.5 and 5 °C.

In summary, CaM has provided an excellent example of the power of the high-resolution multinuclear magnetic resonance approach. Various NMR studies have provided valuable information on the structural and physical properties of CaM as a Ca^{2+}-sensitive molecular switch in cells. Yet, further studies have to come in order to elucidate secrets involved in multitarget recognition of this amazing molecule.

5 RELATED ARTICLES

Biological Macromolecules; Biological Macromolecules: NMR Parameters; Calcium-Binding Proteins; Half-Filter Experiments: Proton–Carbon-13; Multidimensional Spectroscopy: Concepts; Muscle Proteins; Protein Dynamics from NMR Relaxation; Structures of Larger Proteins, Protein-Ligand, and Protein-DNA Complexes by Multi-Dimensional Heteronuclear NMR; Three- and Four-Dimensional Heteronuclear Magnetic Resonance

6 REFERENCES

1. W. Y. Cheung, *Biochem. Biophys. Res. Commun.*, 1970, **38**, 533.
2. S. Kakiuchi and R. Yamazaki, *Biochem. Biophys. Res. Commun.*, 1970, **41**, 1104.
3. A. R. Means, J. S. Tash, and J. G. Chafouleas, *Physiol. Rev.*, 1982, **62**, 1.
4. D. M. Watterson, F. Sharief, and T. Vanaman, *J. Biol. Chem.*, 1980, **255**, 962.
5. P. Cohen and C. B. Klee (eds.), *Calmodulin*, Elsevier, Amsterdam, 1988.
6. A. Crivici and M. Ikura, *Annu. Rev. Biophys. Biomol. Struct.*, 1995, **24**, 85.
7. P. C. Moews and R. H. Kretsinger, *J. Mol. Biol.*, 1975, **91**, 201; *Cell Calcium*, 1992, **13**, 353.
8. O. Minowa and K. Yagi, *J. Biochem. (Tokyo)*, 1984, **96**, 1175.
9. S. R. Anderson and D. A. Malencik, in *Calcium and Cell Function*, Academic Press, New York, 1986, Vol. 6, pp. 1–42.
10. H. Hidaka, T. Yamaki, T. Totsuka, and M. Asano, *Mol. Pharmacol.*, 1979, **15**, 49.
11. Y. S. Babu, J. S. Sack, T. J. Greenhough, C. E. Bugg, A. R. Means, and W. J. Cook, *Nature (London)*, 1985, **315**, 37.
12. R. H. Kretsinger, S. E. Rudnick, and L. J. Weissman, *J. Inorg. Biochem.*, 1986, **28**, 289.
13. O. Herzberg and M. N. G. James, *Nature (London)*, 1985, **313**, 653.
14. M. Ikura, G. M. Clore, A. M. Gronenborn, G. Zhu, C. B. Klee, and A. Bax, *Science*, 1992, **256**, 632.
15. W. E. Meador, A. R. Means, and F. A. Quiocho, *Science*, 1992, **257**, 1251.
16. W. E. Meador, A. R. Means, and F. A. Quiocho, *Nature*, **262**, 1718.
17. K. B. Seamon, *Biochem. Biophys. Res. Commun.*, 1979, **86**, 1256.
18. K. B. Seamon, *Biochemistry*, 1980, **19**, 207.
19. R. E. Klevit, B. A. Levine, and R. J. P. Williams, *FEBS Lett.*, 1981, **123**, 25.
20. J. Krebs and E. Carafoli, *Eur. J. Biochem*, 1982, **124**, 619.

21. T. Shimizu and M Hatano, *FEBS Lett.*, 1983, **160**, 182.
22. T. Shimizu, M. Hatano, S. Nagao, and Y. Nozawa, *Biochem. Biophys. Res.* Commun., 1982, **106**, 1112.
23. M. Ikura, T. Hiraoki, K. Hikichi, T. Mikuni, M. Yazawa, and K. Yagi, *Biochemistry*, 1983, **22**, 2568.
24. M. Ikura, T. Hiraoki, K. Hikichi, T. Mikuni, M. Yazawa, and K. Yagi, *Biochemistry*, 1983, **22**, 2573.
25. S. Forsén A. Andersson, T. Drakenberg, O. Teleman, E. Thulin, and H. J. Vogel, *Calcium-Binding Proteins* Elsevier, Amsterdam, 1983, p.# 121.
26. A. Andersson, S. Forsén, E. Thulin, and H. J. Vogel, *Biochemistry*, 1983, **22**, 2309.
27. E. Thulin, A. Andersson, T. Drakenberg, S. Forsen, and H. J. Vogel, *Biochemistry*, 1984, **23**, 1862.
28. M. Ikura, T. Hiraoki, K. Hikichi, O. Minowa, H. Yamaguchi, M. Yazawa, and K. Yagi, *Biochemistry*, 1984, **23**, 3124.
29. D. C. Dalgarno, B. A. Levine, R. J. P. Williams, C. S. Fullmer, and R. H. Wasserman, *Eur. J. Biochem.*, 1983, **137**, 523.
30. R. E. Klevit, D. C. Dalgarno, B. A. Levine, and R. J. P. Williams, *Eur. J. Biochem.*, 1984, **139**, 109.
31. A. Aulabaugh, W. P. Niemczura, T. L. Blundell, and W. A. Gibbons, *Eur. J. Biochem.*, 1984, **143**, 409.
32. M. Ikura, O. Minowa, and K. Hikichi, *Biochemistry*, 1985, **24**, 4264.
33. M. Ikura, O. Minowa, M. Yazawa, K. Yagi, and K. Hikichi, *FEBS Lett.*, 1987, **219**, 17.
34. S. Tsuda, K. Ogura, Y. Hasegawa, K. Yagi, and K. Hikichi, *Biochemistry*, 1990, **29**, 4951.
35. J. Kördel, S. Forsén, T. Drakenberg, and W. J. Chazin, *Biochemistry*, 1990, **29**, 4400.
36. R. Hoffman and R. E. Klevit, in *Techniques in Protein Chemistry II*, Academic Press, New York, 1991, p. 383.
37. B. E. Finn, T. Drakenberg, and S. Forsén, *FEBS Lett.*, 1994, **336**, 368.
38. M. Ikura, S. Spera, G. Barbato, L. E. Kay, M. Krinks, and A. Bax, *Biochemistry*, 1991, **30**, 9216.
39. M. Ikura, *Biochem. Biophys. Acta*, 1986, **872**, 195.
40. M. A. Starovasnik, T. N. Davis, and R. E. Klevit, *Biochemistry*, 1993, **32**, 3261.
41. M. A. Starovasnik, D.-R. Su, K. Beckingham, and R. E. Klevit, *Protein Sci.*, 1992, **1**, 245.
42. M. E. Huque and H. J. Vogel, *J. Protein Chem.*, 1993, **12**, 693.
43. M. Zhang and H. J. Vogel, *J. Biol. Chem.*, 1993, **268**, 22420.
44. M. Zhang, M. E. Huque, and H. Vogel, *J. Biol. Chem.*, 1994, **269**, 5099.
45. M. Zhang and H. J. Vogel, *J. Mol. Biol.*, submitted for publication.
46. M. Ikura, D. Marion, L. E. Kay, H. Shih, M. Krinks, C. B. Klee, and A. Bax, *Biochem. Pharmacol.*, 1990, **40**, 153.
47. M. Ikura, L. E. Kay, and A. Bax, *Biochemistry*, 1990, **29**, 4659.
48. G. Barbato, M. Ikura, L. E. Kay, R. W. Pastor, and A. Bax, *Biochemistry*, 1992, **31**, 5269.
49. T. Trewhella, *Cell Calcium*, 1992, **13**, 377, and references cited therein.
50. R. E. Klevit, D. K. Blumenthal, D. E. Wemmer, and E. G. Krebs, *Biochemistry*, 1985, **24**, 8152.
51. S. H. Seeholzer, M. Cohn, J. A. Putkey, A. R. Means, and H. L. Crespi, *Proc. Natl. Acad. Sci. USA*, 1986, **83**, 3634.
52. M. Yazawa, M. Ikura, K. Hikichi, L. Ying. and K. Yagi, *J. Biol. Chem.*, 1987, **262**, 10 951.
53. M. Ikura, N. Hasegawa, S. Aimoto, M. Yazawa, and K. Yagi, and K. Hikichi, *Biochem. Biophys. Res. Commun.*, 1989, **161**, 1233.
54. S. Ohki, M. Yazawa, K. Yagi, and K. Hikichi, *J. Biochem.*, 1991, **110**, 737.
55. S. Ohki, U. Iwamoto, S. Aimoto, M. Yazawa, and K. Hikichi, *J. Biol. Chem.*, 1993, **268**, 12 388.
56. M. Ikura, L. E. Kay, M. Krinks, and A. Bax, *Biochemistry*, 1991, **30**, 5498.
57. M. Ikura and A. Bax. *J. Am. Chem. Soc.*, 1992, **114**, 2433.
58. T. Prumb, P. Yau, T. S. Harvey, and M. Ikura, *Protein Eng.*, 1994, **7**, 109.
59. S. M. Roth, D. M. Schneider, L. A. Strobel, M. F. A. van Berkum, A. R. Means, and A. J. Wand, *Biochemistry*, 1991, **30**, 10 078.
60. S. M. Roth, D. M. Schneider, L. A. Strobel, M. F. A. van Berkum, A. R. Means, and A. J. Wand, *Biochemistry*, 1992, **31**, 1443.
61. B. Precheur, H. Munier, J. Mispelter, O. Barzu, and C. T. Craescu, *Biochemistry*, 1992, **31**, 229.
62. W. F. DeGrado, F. G. Prendergast, H. R. Wolfe, Jr., and J. A. Cox, *J. Cell. Biochem.*, 1985, **29**, 83.
63. M. Zhang, T. Yuan, and H. J. Vogel, *Protein Sci.*, 1993, **2**, 1931.
64. M. Zhang and H. J. Vogel, *Biochemistry*, 1994, **33**, 1163.
65. M. Zhang and H. J. Vogel, *J. Biol. Chem.*, 1994, **269**, 981.
66. L. E. Kay, P. Keifer, and T. Saarinen, *J. Am. Chem. Soc.*, 1992, **114**, 10 663.

Biographical Sketches

Mitsuhiko Ikura. *b* 1956. B.S., 1979, Ph.D., 1986, Hokkaido University, Japan, where he was introduced to NMR by Kunio Hikichi. Postdoctoral work with Ad Bax at National Institutes of Health, USA, 1988–91. Senior scientist, Ontario Cancer Institute University of Toronto, Canada, 1991–present. Approx. 80 publications. Current research specialty: structural biology of calcium binding proteins and other biological macromolecules.

Carbohydrates and Glycoconjugates

Herman van Halbeek
The University of Georgia, Athens, GA, USA

1	Introduction	1
2	Carbohydrates and Glycoconjugates: Structure and Function	1
3	The Past: Primary Structure	3
4	The Present: Solution Conformation and Dynamics	9
5	The Future: Glycoconjugates in (Inter-)Action at the Membrane Surface	23
6	Conclusions	26
7	Related Articles	26
8	Abbreviations	26
9	References	26

1 INTRODUCTION

The expansion of glycobiology into the realm of the structure–function relationships of carbohydrates is strongly dependent upon advances in technology. Unquestionably, nuclear magnetic resonance (NMR) spectroscopy has made the most significant impact on structural studies of oligosaccharides and glycoconjugates. While researchers in the past (1960–84) concerned themselves in the first place with the study of primary carbohydrate structures, NMR spectroscopy has recently (1985–94) reached a level of sophistication which allows the conformational analysis of oligosaccharides, glycopeptides, and glycolipids in solution. This article briefly summarizes the early days of carbohydrate NMR, reviews the application of current NMR spectroscopic techniques to the structural and conformational characterization of oligosaccharides from glycoproteins and glycolipids, and ends with a discussion of some questions about carbohydrate structure, dynamics, and function that can be addressed by NMR in the near future.

2 CARBOHYDRATES AND GLYCOCONJUGATES: STRUCTURE AND FUNCTION

The carbohydrate moieties of glycoconjugates, i.e., glycoproteins and glycolipids, generally have complex structures featuring highly varied chemical functionalities. These oligosaccharide chains, varying in size from two to 20 or more residues, are composed of neutral monosaccharides such as d-mannose (Man) and d-galactose (Gal), amino sugars such as *N*-acetyl-d-glucosamine (GlcNAc) and *N*-acetyl-d-galactosamine (GalNAc), the C-6-deoxy sugar l-fucose (Fuc), and the nine-carbon-atom acidic sugars of the sialic acid family of which *N*-acetylneuraminic acid (Neu5Ac) is the most commonly found representative (for structures, see Figure 1). In glycoproteins, these oligosaccharide chains are covalently attached to the side chains of specific amino acids such as Asn, Ser, and Thr. Glycoproteins are anchored to the outer surface of the cell's plasma membrane by either a transmembrane peptide fragment or by a phosphatidyl-inositol anchoring lipid. Complex carbohydrate chains similar to those of glycoproteins may also be found attached to lipids similarly inserted in the plasma membrane where they present the hydrophilic carbohydrate chain to the extracellular environment (Figure 1).

Because of their structural diversity, glycoconjugate oligosaccharides are potentially rich sources of biological information. Although the precise function of the carbohydrate chains of glycoproteins and glycolipids is not fully understood, it has been proposed that they are informational macromolecules with signals encoded in their structure that are crucial to the biological functions of the cells carrying them.[1] As this information apparently relates to intercellular communication and control of cellular growth and differentiation, it is possible that complex carbohydrates play an important role in such important processes as developmental biology and tumor metastasis. Areas of focus in current glycobiology research include the importance of oligosaccharides to immune mechanisms, the association of certain structural changes with diseases such as malignant cancer growth and rheumatoid arthritis, and the potential for the development of novel therapeutic strategies [recombinant glycoproteins such as erythropoietin and tissue plasminogen activator are already in widespread clinical use for the treatment of anemia and myocardial infarction, respectively, while the glycolipid 'ganglioside G_{M1}' (Figure 1) is administered to alleviate the symptoms of cholera].

From a structure–function point of view, the 20th century has come full circle: Landsteiner's discovery, around 1900, of the ABH blood group antigens inspired structural studies that culminated in the identification of the antigens as tri- and tetrasaccharide epitopes at the nonreducing termini of the glycoprotein and glycolipid carbohydrate chains found on the cell surface of erythrocytes and many other mammalian tissues (Figure 1). Landsteiner's pioneering work sparked investigations into the involvement of carbohydrates in immune protection and in graft versus host reactions in blood transfusions and other organ transplants. The presence of sialic acid on erythrocyte surfaces proved to be a necessary requirement for their infection by the influenza virus. Malignant tumor cells were found to exhibit certain tumor-associated antigens (TAA), carbohydrate sequences not found on membrane glycoproteins and glycolipids of normal cells. TAA-like epitopes were discovered on cell surfaces in the early stages of embryonic development (hence, they are known as onco-fetal antigens).[2–4] Around 1990, the discovery and identification of sialylated Lewis blood group carbohydrates (sLe^a and sLe^x, Figure 1) as ligands for selectins (cell adhesion molecules)[5,6] added the latest exciting chapter to the involvement of oligosaccharides in an important biological process, in this case endothelial leukocyte adhesion being the key to inflammation.

From the beginning it was understood that an insight into the biological and physicochemical functions of complex carbohydrates at the molecular level would require a precise knowledge of the primary and secondary structures of these often highly branched polymers with their intriguing blend of segmental rigidity and flexibility. The complete structural characterization of complex carbohydrates involves

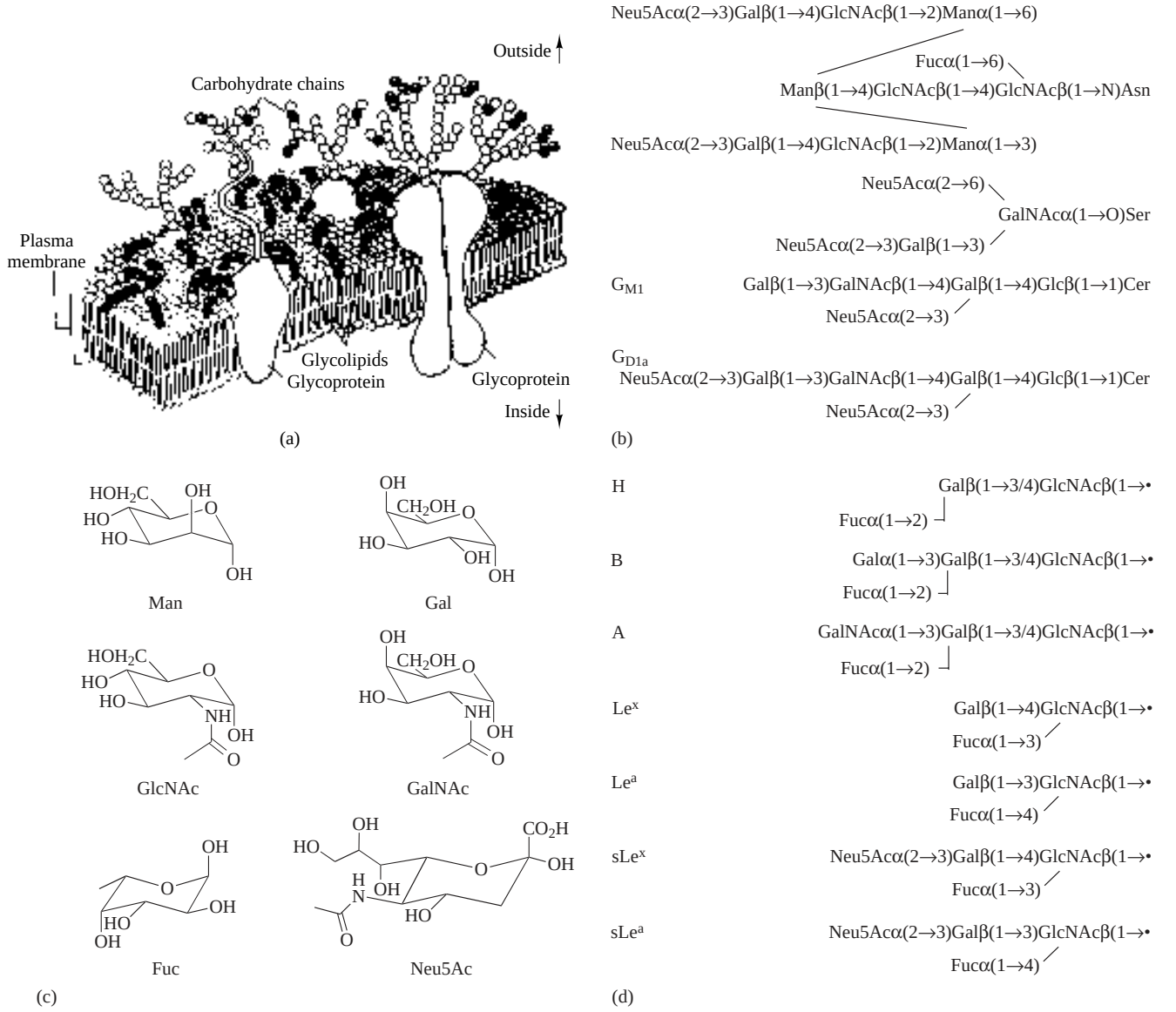

Figure 1 (a) Schematic representation of a cell's plasma membrane with an emphasis on the glycoprotein and glycolipid carbohydrate chains, the cell's communication organelles. (b) Primary structures of some commonly found glycoprotein and glycolipid carbohydrate chains. Represented from top to bottom: a diantennary *N*-type glycoprotein oligosaccharide, an *O*-type glycoprotein tetrasaccharide, and the monosialo and disialo gangliosides G_{M1} and G_{D1a} (Asn = l-asparagine; Ser = l-serine; Cer = ceramide, the generic name for an *N*-acylated sphingosine). (c) Structures of typical constituent monosaccharides of glycoprotein and glycolipid oligosaccharide chains (Man, Gal, GlcNAc, GalNAc, Fuc, and Neu5Ac, drawn in the α-configuration of their thermodynamically most stable pyranose ring forms). (d) Structures of selected blood group and differentiation antigens

determining (i) the type, number, and primary sequence of the constituting glycosyl residues, including the occurrence of branch points and the location of appended noncarbohydrate groups and (ii) their three-dimensional (3D) conformation(s) and dynamics in solution. Although determining the complete structure of a carbohydrate usually requires the application of a combination of chemical, enzymatic, and spectrometric methods,[7,8] NMR spectroscopy has emerged as the single most powerful technique for the accomplishment of this task. The nuclei of predominant interest in NMR studies of carbohydrates are ^{1}H and ^{13}C. The natural allocation of hydrogen and carbon atoms in carbohydrate molecules lends itself to the revelation of their complete primary structure through ^{1}H and ^{13}C NMR analysis. Whereas the primary structural characterization of carbohydrates relies on a combination of techniques, only one of which is NMR spectroscopy, solution conformation analysis is almost entirely the domain of NMR spectroscopy. X-ray structures of glycoconjugates are not commonly available (and if they are, carbohydrates are usually not well-defined), and molecular modeling of carbohydrates, although a hotly contested area of research, is still in its infancy and, therefore, of little help to the experimentalist to date.

The purpose of this review is to put NMR of carbohydrates and glycoconjugates in its historical perspective; not surprisingly, a chronological account shows a remarkable parallel with primary and three-dimensional structure analysis. It should be noted that NMR of carbohydrates covers a much

broader area than solution-state ^{1}H and ^{13}C NMR of monosaccharides, oligosaccharides, and glycoconjugates. Polysaccharides are the topic of the article by Bush (***Polysaccharides and Complex Oligosaccharides***), and ^{2}H NMR of glycolipids is covered in Jarrell's article (***Glycolipids***). Here we will cover neither the application of solid state NMR to carbohydrates nor touch upon ^{31}P NMR of sugar phosphates, ^{15}N NMR of amino sugars, ^{17}O NMR of carbohydrates, and NMR of X-nuclei (^{11}B, ^{119}Sn, etc.) in carbohydrate adducts (see, for example, Bush[9]). We will further limit the discussion in this article largely to pyranose ring systems. For the discussion of furanose rings and their flexibility, the reader is referred to articles by Altona (***Vicinal Coupling Constants and Conformation of Biomolecules***), Hilbers (***Nucleic Acids: Spectra, Structures, and Dynamics***), and others covering NMR of nucleic acids. Furthermore, the molecules (peptides/proteins, lipids) that serve as appended groups of carbohydrates in glycoconjugates are discussed elsewhere throughout this Encyclopedia.

3 THE PAST: PRIMARY STRUCTURE

The initial discovery of the potential value of NMR spectroscopy for carbohydrate structural and conformational analysis is described by Lemieux in his book entitled 'Explorations with Sugars: How Sweet It Was'.[10] We quote:

> In spite of the difficulties and shortcomings of the NMR technique [in 1955], it became evident that acetylated sugars, because of large differences in chemical shifts, were very interesting substances with which to explore the possible use of ^{1}H NMR spectroscopy in organic chemistry. It soon became apparent that an equatorially oriented hydrogen generally gave rise to a signal at a lower field compared with that of a chemically similar but axial hydrogen.[11] This discovery was very encouraging. However, the big excitement came when [...] significant improvements in resolution were made. Examination of the spectra of [...] cyclohexanol acetates firmly established that the spin–spin coupling constants for vicinal hydrogens in antiperiplanar orientation were two to three times larger than those for vicinal hydrogens in a synclinal relationship.[12] [...] The discovery provided the long-sought definitive basis for the assessment of the preferred conformations of the sugar acetates in solution. [...] The spectra of *trans*,*trans*- and *cis*,*trans*-di-*O*-methylcyclohexanol acetate, shown in Figure 2, represent the first application of NMR for the establishment of the relative configurations of chiral centers in organic compounds. Thus, the experimental foundation was laid for the Karplus relationship[13] between the vicinal coupling constant and the torsion angle and for the use of the time-averaged coupling constants to estimate conformer populations.

The stereochemistry of a particular monosaccharide provides its signature in the ^{1}H NMR spectrum; the ^{1}H signals of most monosaccharides can readily be assigned to the appropriate (aliphatic) protons by making use of the observed chemical shifts and splitting patterns. Thus, the foundation for the identification of carbohydrates by ^{1}H NMR spectroscopy had been laid.

Section 3.1 below elaborates on the empirical rules that emerged from the inspection of ^{1}H and ^{13}C NMR spectra of monosaccharides and simple oligosaccharides of known primary structure. Sections 3.2 and 3.3 below summarize 1D ^{1}H NMR spectroscopy as a fingerprinting method for

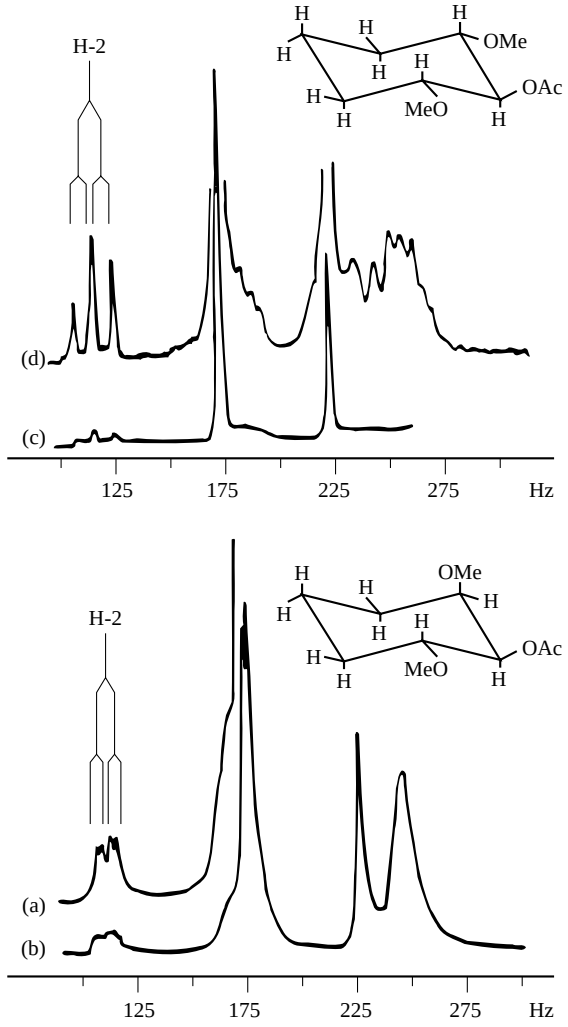

Figure 2 The first application of ^{1}H NMR spectroscopy, at 40 MHz, for the determination of stereochemical configuration (adapted from Lemieux et al.;[14] spectra reproduced with permission from the American Chemical Society). For the *cis*,*trans* isomer, ^{3}J(H-1,H-2) = 3 Hz and ^{3}J(H-2,H-3) = 7 Hz (traces a and b); for the *trans*,*trans* isomer, ^{3}J(H-1,H-2) = ^{3}J(H-2,H-3) = 7 Hz (traces c and d)

the characterization of the primary structure of glycoprotein and glycolipid oligosaccharide chains, respectively, and the usefulness of an empirical concept that emerged during the 1980s for the interpretation of the ^{1}H NMR spectrum of a glycoprotein or glycolipid carbohydrate in terms of its primary structure is outlined. Ongoing efforts aimed at computer-assisted carbohydrate NMR spectral 'interpretation' are mentioned as well. Finally, Section 3.4 takes the concepts developed in previous sections to the level of de novo primary structural elucidation of glycoconjugate carbohydrates by 1D and 2D ^{1}H and ^{13}C NMR spectroscopy.

3.1 Monosaccharides and Simple Oligosaccharides

As their generic name implies, carbohydrate molecules contain numerous carbon and hydrogen nuclei. It follows that the magnetically active nuclei in carbohydrates that are of practical interest to NMR spectroscopists are those of ^{1}H

and ^{13}C atoms. For example, each hexosyl residue [such as the galactosyl residue in Figure 3(a)] has six carbon atoms, seven hydrogens that are involved in CH linkages, and four hydrogens in OH groups. Each of these nuclei in a glycosyl residue has its own characteristic environment and, thus, its own chemical shift. For primary structural characterization of a carbohydrate by ^1H NMR spectroscopy, the observation of the aliphatic protons suffices. Observation of hydrogens in OH groups would unnecessarily complicate spectra aimed at primary structural characterization. Therefore, the carbohydrate sample is typically dissolved in D_2O (no chemical derivatization is necessary), effectively removing any OH signals from the spectrum. Chemical shifts are referenced to the methyl signal of DSS (sodium 4,4-dimethyl-4-silapentane-1-sulfonate). The ^1H NMR spectrum of an oligosaccharide is essentially a superposition of the spectra of the individual glycosyl residues which are slightly modified because of their linkages to each other. For example, the ^1H NMR spectra of typical glycoprotein Ser-linked tri- and tetrasaccharides are shown in Figures 3(b) and 3(c).[15] The subspectrum of the β-galactosyl residue is recognizable in the spectra of both the linear trisaccharide and the branched tetrasaccharide. Furthermore, Figure 3(c) clearly illustrates the difference in the NMR appearance of an $\alpha(2\rightarrow3)$- versus an $\alpha(2\rightarrow6)$-linked sialic acid.

The following empirical 'rules' have emerged to guide the interpretation of ^1H NMR spectra of simple carbohydrates:

1. The nonanomeric ring-skeleton protons in a glycosyl residue have very similar electron densities and, thus, chemical shifts; all of their signals appear between 3 and 4 ppm (Figures 3 and 4). In the spectrum of an oligosaccharide, the signals of the nonanomeric protons partially overlap; they constitute a broad envelope of signals in the middle of the spectrum having little fine structure and, therefore, almost no readily accessible structural information. However, anomeric protons (H-1) show signals at significantly higher chemical shifts due to their neighboring glycosidic and ring oxygens. Anomeric proton doublets are typically found between δ 4.3–5.6 ppm.

2. A proton in an equatorial position at a certain carbon atom in a pyranose ring has a chemical shift ~0.5 ppm higher than the corresponding axial proton attached to the same carbon. Therefore, for d-residues involved in α-glycosidic linkages (H-1 equatorial), δ(H-1) ~ 4.9–5.6 ppm, while for β-anomeric linkages (H-1 axial), δ(H-1) ~ 4.3–4.7 ppm. For carbohydrates in D_2O at ambient temperature, these positions correspond to the near left and right of the HDO signal (at δ ~ 4.80), respectively. Further illustrating this rule, the equatorial Man H-2 signals are typically found ~0.5 ppm further to the left than the axial GlcNAc or Gal H-2 signals (Figure 4). Also, Gal H-4 protons resonate ~0.5 ppm further to the left than GlcNAc H-4 protons (compare Figure 3).

3. Each anomeric proton, by virtue of its ^3J(H,H) scalar coupling to H-2, resonates as a doublet. The magnitude of the coupling constant reflects the relative orientation of neighboring protons. The coupling constant ^3J(H-1,H-2) for two neighboring protons (H-1 and H-2, separated from each other by three covalent bonds) that are both in axial orientation is 7–8 Hz (i.e., relatively large), while coupling constants ^3J(H-1,H-2) between two neighboring protons, one of which is axial and the other equatorial, or between two equatorial protons, are 3–4 Hz (relatively small). Thus, the anomeric configuration of a glycosyl residue can be inferred both from

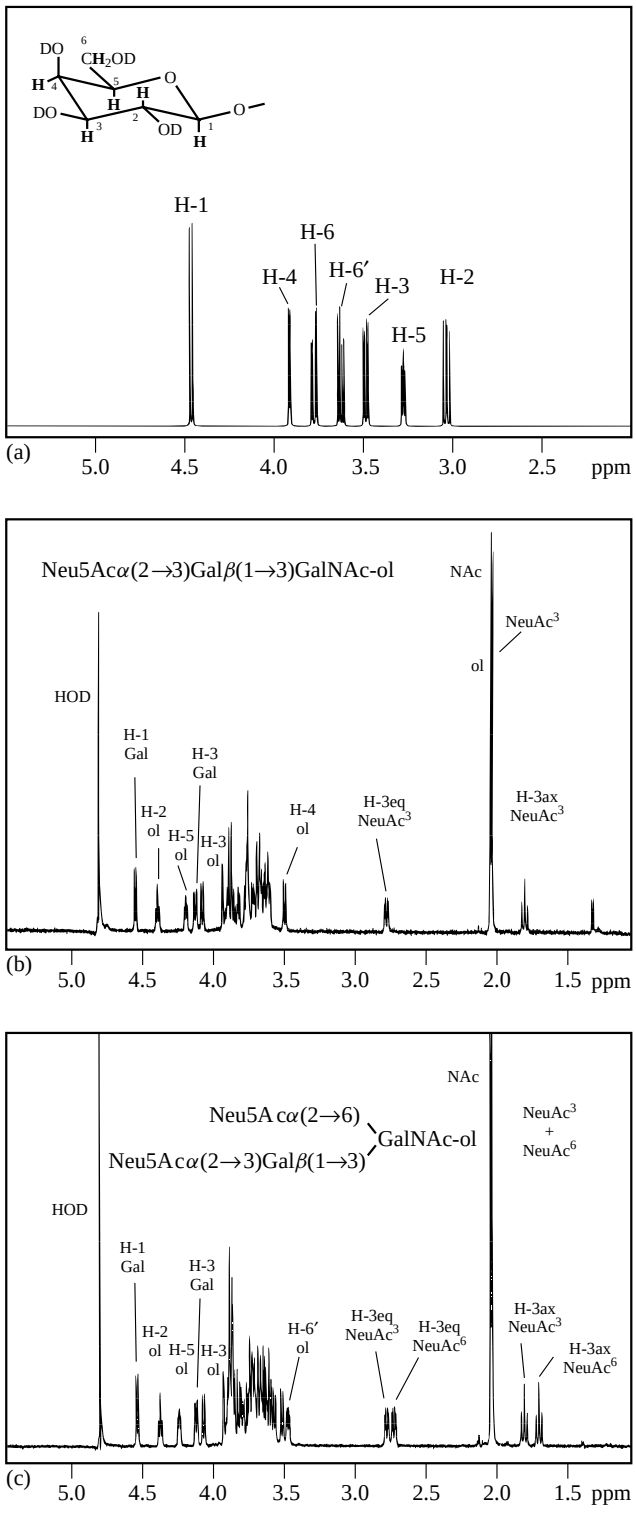

Figure 3 (a) The computer-simulated ^1H NMR spectrum of a β-linked galactopyranosyl residue in D_2O. (b) The 600 MHz ^1H NMR spectrum (D_2O, pD = 6, 23 °C) of a linear *O*-type trisaccharide-alditol (70 μg) obtained from a glycoprotein via reductive alkalinolysis.[15] (c) The 600 MHz ^1H NMR spectrum (D_2O, pD = 6, 23 °C) of an *O*-type tetrasaccharide-alditol (75 μg) released from a glycoprotein via reductive alkalinolysis.[15] Superscripts in $NeuAc^3$ and $NeuAc^6$ refer to the position of the linkage in which these residues are involved

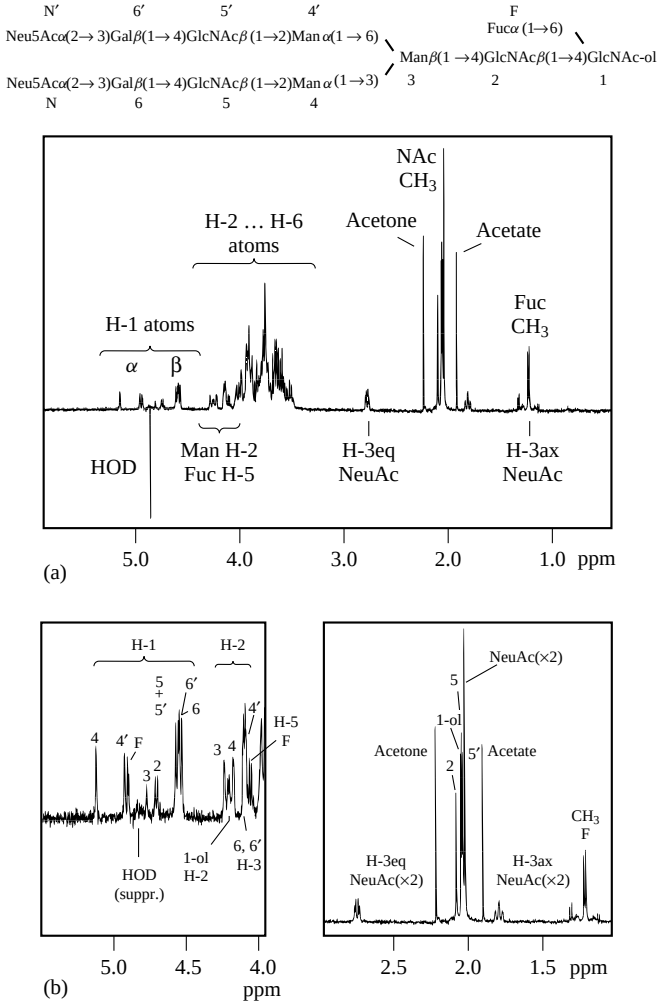

Figure 4 (a) The 500 MHz ^{1}H NMR spectrum (D_2O, pD = 6, 21 °C) of a typical diantennary *N*-type oligosaccharide side chain of a glycoprotein (250 μg, examined as oligosaccharide-alditol, obtained by *N*-glycanase digestion of the glycoprotein and subsequent chemical reduction). The residual HOD signal was suppressed by low-power presaturation. (b) Structural-reporter-group regions of spectrum (a). The numbers in the spectra refer to the corresponding glycosyl residues in the structure

the chemical shift and the coupling constant of its anomeric-proton signal in the ^{1}H NMR spectrum.

4. When a glycosyl residue has either an additional glycosyl residue or a noncarbohydrate group attached at a certain carbon position, the signal of the proton attached to this carbon tends to shift ~0.2–0.5 ppm to the left in the spectrum. Therefore, signals of nonanomeric protons that are attached to linkage sites usually appear just outside the envelope resonance of skeleton protons ($3.9 < \delta < 4.4$) (Figure 4); they become individually observable 'structural-reporter' signals (Section 3.2). Thus, if the nonanomeric proton signals that emerge in the region between δ 3.9 and 4.4 ppm can be assigned, linkage positions can be deduced from a ^{1}H NMR spectrum.

These rules are the result of the extrapolation and rationalization of numerous NMR data obtained on mono- and disaccharides of known primary structure. Noteworthy review articles on general applications of NMR to carbohydrates, developing interalia the above concepts, have appeared[2,16,17] including one recently.[18] Additionally, the scientific literature includes extensive ^{1}H databases of chemical shifts for mono- and small oligosaccharides.[19,20]

The first reports on ^{13}C NMR spectroscopy of carbohydrates appeared in the late 1960s.[21,22] It was found that the ring ^{13}C methine signals of pyranosyl residues are typically observed between 65 and 110 ppm downfield from DSS. Anomeric carbons usually resonate between 90 and 110 ppm. The magnitude of the one-bond ^1J(C-1,H-1) coupling for the anomeric carbon atoms reflects the configuration at the anomeric center. As a rule of thumb, ^1J(C-1,H-1) ~ 170 Hz indicates the α-anomeric configuration, whereas ^1J(C-1,H-1) ~ 160 Hz indicates the β-anomeric configuration. The exocyclic methylene signals of monosaccharides (in CH_2OH groups) are observed at ~60–70 ppm [unless the glycosyl residue is involved in a (1→6) linkage]. Extensive ^{13}C databases for mono- and simple oligosaccharides are found in the literature.[23–28] Glycosylation shifts ($\Delta\delta$ ~10 ppm for ^{13}C at the site of substitution, $\Delta\delta$ −1 to −2 ppm for the adjacent ^{13}C atoms) are more reproducible in ^{13}C NMR than in ^{1}H NMR of carbohydrates. Computer-assisted interpretation of NMR spectra of carbohydrates in terms of primary sequence based solely on ^{13}C chemical shifts[29–31] preceded that of ^{1}H NMR spectra.[32–34]

3.2 Complex Oligosaccharides Related to Glycoproteins

The carbohydrate side chains of glycoproteins are amenable to high-resolution ^{1}H NMR spectroscopy either as glycopeptides or as free oligosaccharides. These can be obtained from the glycoprotein by enzymatic or chemical procedures.[7,8] A typical example of a ^{1}H NMR spectrum of a glycoprotein-derived *N*-type oligosaccharide is shown in Figure 4(a). In the early 1970s, when the complete interpretation of ^{1}H NMR spectra of carbohydrates of this size seemed impossible, the spectrum of an oligosaccharide was regarded by the glycobiologist primarily as a fingerprint, a readily obtainable 'identity card' of a carbohydrate. A mere comparison of the ^{1}H NMR spectra of compounds (without detailed interpretation) was used to demonstrate whether they were identical and/or pure substances. Thus, at first, a 1D ^{1}H NMR study appeared valuable for the primary structure determination of glycoprotein carbohydrates only if the oligosaccharide had been characterized previously by ^{1}H NMR in conjunction with chemical and other spectrometric methods.

However, in the late 1970s the first successful attempts were made to interpret the ^{1}H NMR spectra of glycoprotein oligosaccharides, even when the spectra did not match exactly any of the spectra in existing databases. Using the *structural-reporter-group concept*,[15,35,36] the spectra were interpreted in terms of (partial elements of) carbohydrate primary structure, including anomeric configurations and positions of glycosidic linkages. The crux of this concept is that it appeared sufficient to inspect only certain regions in the spectrum [see Figure 4(b)] in order to ascertain the primary structure of the glycoprotein carbohydrate from its NMR spectrum. Perceived by some in the field as 'mystical' or 'voodoo NMR', the structural-reporter-group concept is merely an extrapolation of the empirical rules listed in Section 3.1 to larger oligosaccharides. The concept ignores the crowded region in the center of the spectrum (between 3–4 ppm, see

Figure 4); only the positions and patterns of those signals that are more or less individually observable are examined. Particularly useful structural-reporter groups are (i) the anomeric (H-1) protons, (ii) the protons attached to the carbon atoms in the direct vicinity of a linkage position, (iii) the protons attached to deoxy carbon atoms and (iv) methyl protons, e.g., in *N*-acetyl groups. The structural-reporter-group regions of the spectrum in Figure 4(a) are expanded in Figure 4(b). For the interpretation of a ^{1}H NMR spectrum such as depicted in Figure 4, structural-reporter-group signals are cataloged by chemical shift and coupling constants; these values are then compared with literature data on similar oligosaccharides and/or glycopeptides. A highly refined set of empirical rules was developed to rationalize the effects of structural elongations, as typically found in glycoprotein oligosaccharides, on structural-reporter-group chemical shifts. For example, the structural-reporter-group concept developed rules to identify the degree of branching as well as the type of linkage and branch location of sialic acid and fucosyl residues.[15,35,36] Several glycoprotein carbohydrate structural-reporter-group ^{1}H chemical shift databases are currently available for *N*-type glycopeptides and oligosaccharides[36–38] and *O*-type oligosaccharide-alditols[39] in D_2O; other noteworthy databases are also available.[40–43] The structural-reporter-group approach continues to enjoy considerable popularity as a method for the primary structural characterization of glycoprotein and glycolipid (for gangliosides, see Section 3.3) carbohydrates by NMR spectroscopy.

An important advantage of NMR spectroscopy over other techniques used for structural analysis of carbohydrates is its nondestructive nature. Oligosaccharide and glycopeptide samples, after NMR analysis, can be recovered unimpaired and used for other analyses, biological activity tests, etc. Glycoprotein oligosaccharides with 15–20 constituent glycosyl residues have been successfully characterized by 500 MHz one-dimensional (1D) ^{1}H NMR spectroscopy. Also, mixtures of components with closely related structures have been analyzed successfully. The most important limitation of NMR spectroscopy lies in its relatively low level of sensitivity. At least 10 nmol of pure carbohydrate is required to record an NMR spectrum and, even at 600 MHz, heterogeneity occurring in low abundance in the sample may escape attention. NMR spectroscopy, by its very nature, may also fail to detect the presence of nonmagnetically active nuclei, e.g. the occurrence of sulfate esters, in the carbohydrate.

Until now, the most laborious part of the NMR structural analysis of carbohydrates has been spectral interpretation. Partial or even complete primary structure determination is possible from the structural-reporter-group regions of a 1D ^{1}H NMR spectrum only if structurally closely related compounds have been previously characterized by ^{1}H NMR spectroscopy. The multitude of extremely refined rules resulting from the structural-reporter-group inspection of spectra makes interpretation of spectra of novel compounds a tedious effort. Even the basically simple process of retrieving previously recorded spectra and comparing them with a newly recorded spectrum becomes a considerable task, given the exponential growth of the amount of ^{1}H NMR data collected on glycoprotein and glycolipid oligosaccharides from 1980 to 1994. Assistance from computers to facilitate this aspect of the method is being sought along two different lines. The use of a computer search algorithm to compare a list of structural-reporter-group chemical shifts with those in a database appears rather straightforward. Indeed, several such computer programs have been written to assist the interpretation of glycoprotein oligosaccharide ^{1}H NMR spectra.[33,34,44] A more elegant and much faster method involves the use of the entire spectrum (including the 3–4 ppm envelope region with its high information density) for pattern recognition by artificial intelligence techniques. The NMR spectrum, already available in digital format, need not be reduced to a list of chemical shifts, as is commonly done for human interpretation. Artificial neural networks (ANN) have been successfully applied for pattern recognition of NMR spectra.[45,46] Recently, this work has been extended to include the 500 MHz ^{1}H NMR spectra of glycoprotein carbohydrates.[47] In the foreseeable future, NMR spectral databases will be linked to the complex carbohydrate structure database (CCSD),[48] and the neural network search algorithms will be incorporated into CarbBank. This approach will not only render much of the previously necessary laborious supporting structural analysis work superfluous for oligosaccharides already in the database, it will also allow the interpretation of spectra by the rules resulting from the structural-reporter-group concept, thus 'automating' empirical NMR spectral interpretation.

An unexpected but welcome development in the application of the ANN technology for the analysis of ^{1}H NMR spectra lies in the potential increase in sensitivity of the method by two or three orders of magnitude. For a spectrum of a given oligosaccharide with fairly good signal-to-noise ratio (S/N) already in the database (i.e., when a neural network has been trained to recognize this spectrum in terms of the associated carbohydrate structure), the oligosaccharide can be recognized again from its ^{1}H NMR spectrum with a 100 to 1000-fold less S/N than the original spectrum (such as would be obtainable for subnanomole amounts of carbohydrate).[47] In the very near future, the ANN technology will make NMR competitive in terms of sensitivity with any other technique in the primary structural determination of carbohydrates related to glycoproteins and glycolipids.

In principle, ^{13}C NMR spectra can also be used for the fingerprinting of glycoprotein carbohydrates.[49] The ^{13}C spectra, recorded under ^{1}H decoupling conditions, consist exclusively of singlets. Further favored by the large chemical shift dispersion ($\Delta\delta \sim 100$ ppm), ^{13}C NMR spectra [even for intact glycoproteins (Section 5.1)] are often characterized by high resolution. Attempts were made to develop ^{13}C chemical shift databases for glycoprotein carbohydrate chains,[50] and to derive rules for the interpretation of spectra of novel compounds based on those of observed larger or smaller related structures. However, these efforts met with little success because of the higher demands on amounts of material needed for recording spectra and the much greater ease with which the same goal of primary structure characterization was achievable by ^{1}H NMR spectroscopy.

3.3 Complex Oligosaccharides Related to Glycolipids

The ^{1}H NMR spectroscopy principles and methodology discussed in the previous section are not only valid for glycoprotein-related carbohydrates. They apply equally well to glycolipids[51,52] and glycosyl phosphatidyl-inositol (GPI)

anchors,[53] polysaccharides,[24] and proteoglycans.[54] Here we will limit the discussion to glycolipids. Unlike glycoproteins, glycolipids are amenable to high-resolution ^{1}H NMR analysis in their native state; however, they cannot be investigated in aqueous solution. Solvents such as DMSO and DMF have been successfully applied, and volumes of data that are valuable for primary structural analysis have been collected over the years. Examples of ^{1}H NMR databases of glycolipids in DMSO are given elsewhere.[51,55–59]

To take advantage of the massive amount of NMR data on glycoprotein-related oligosaccharides in water, the removal of the lipid by enzymatic (endoglycoceramidase) or chemical (ozonolysis) procedures is currently employed as a standard technique for allowing the glycolipid oligosaccharides to be examined under the same circumstances as glycoprotein/glycopeptide carbohydrates and free oligosaccharides [see, for example, Figure 5(b) versus Figure 5(a)].[60]

3.4 De Novo Sequencing of Glycoconjugate Carbohydrates

Although useful for the primary structural analysis of carbohydrates within the closely knit framework of structures presented abundantly by Nature for glycoprotein and glycolipid oligosaccharides, collections of chemical shifts contribute little to our understanding of NMR. However, as of the early 1980s, NMR spectroscopy provides the tools necessary to determine any novel carbohydrate structure de novo, without significant help from other techniques.

When the 1D ^{1}H spectrum does not resemble that of a known oligosaccharide structure, a combination of multiple pulse ^{1}H NMR spectroscopic techniques, primarily two-dimensional (2D) COSY, TOCSY, and NOESY or ROESY, may be applied for the de novo sequencing of the carbohydrate[9,55,58] provided that 20–50 nmol of pure substance (2–5-times the amount of sample mentioned for the 1D analysis) is available for the analysis. The TOCSY technique permits subspectral editing of the ^{1}H spectrum for each constituting glycosyl residue[61,62] and, consequently, the virtually complete assignment of all of the multiplet patterns in the ^{1}H NMR spectrum (including those in the envelope region between 3–4 ppm). Subsequently, depending on the size of the oligosaccharide and the magnetic field strength of the spectrometer used, NOESY or ROESY spectra enable the inference of the glycosyl-residue sequence, including the positions of glycosidic linkages, based on the detection of through-space connectivities.[63]

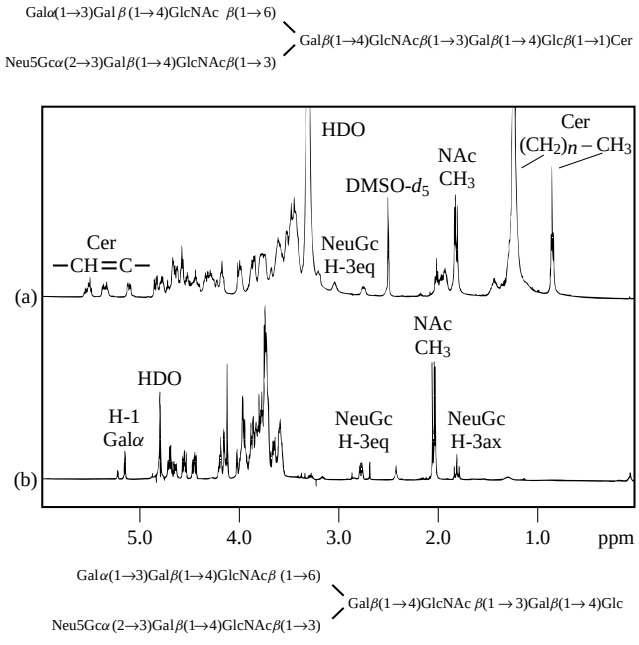

Figure 5 (a) The 500 MHz ^{1}H NMR spectrum (DMSO-d_6/D_2O, 98:2, v/v; 27 °C) of an intact ganglioside. (b) The 500 MHz ^{1}H NMR spectrum (D_2O, pD = 6, 23 °C) of the oligosaccharide released from the ganglioside by endoglycoceramidase digestion[60]

Examples of the application of this general strategy are manifold.[18,64–68] Because of its importance, we will briefly illustrate the strategy for a novel tetrasaccharide found *O*-linked to Ser_{61} in Factor IX, a serum glycoprotein involved in the human blood clotting cascade.[69,70] Figure 6(a) shows the 1D ^{1}H NMR spectrum of a glycopeptide (20 nmol) obtained from human Factor IX consisting of four glycosyl residues and nine amino acids. At the start of the NMR studies, the peptide sequence was known to be Leu_{57}–Asn–Gly–Gly–Ser–Cys*–Lys–Asp–Asp_{65} (where Cys* indicates an *S*-carboxymethylated Cys residue). Also, it was known that the carbohydrate portion of the glycopeptide contained Gal, GlcNAc, Fuc, and Neu5Ac in equimolar ratios. In order to decipher the primary sequence of the tetrasaccharide, to pinpoint the side chain of Ser_{61} as the site of glycosylation in the peptide, and to elucidate which of the four sugar residues was involved in the linkage to Ser_{61}, the complete assignment of the ^{1}H NMR spectrum of the glycopeptide was required. However, not only did the presence of the nonapeptide obscure many of the saccharide ^{1}H signals, it was not even possible (unlike for many other glycopeptide NMR spectra) to assign any signals in the 1D spectrum of the Factor IX glycopeptide simply by inspection. Neither the usually well-resolved structural-reporter-group signals of sugar anomeric and deoxy protons nor the amino acid H-α protons were recognizable off-hand. However, 2D correlated spectroscopy (in particular, COSY and TOCSY) was successfully applied for the identification of the spin systems of the individual sugar and amino acid residues. Figure 6(b) shows the relevant portion of the TOCSY spectrum. The resulting connectivity patterns in the COSY and TOCSY spectra were assigned to sugar and amino acid residue types based on their comparison with literature data for the individual spin systems. Subspectra for the sugar residues were traced starting from their H-1 signals (found between 4.4 and 5.5 ppm) or, in the case of Neu5Ac, from the H-3ax and H-3eq protons (expected around 1.8 and 2.7 ppm, respectively; see Figure 3). The H-1,H-2 connectivities for Gal, GlcNAc, and Fuc were particularly clear in the COSY spectrum. The TOCSY subspectra through H-1 included (in addition to the H-2 signals) the Fuc H-3, Gal H-3 and H-4, and GlcNAc H-3, H-4, H-5, and H-6/6′ [Figure 6(b)].

Once the chemical shifts of 80% of the sugar protons had been established, the structural-reporter-group concept (Section 3.2) enabled the assignment of the linkage configurations and partial sequence of the four residues. The combination of chemical shifts for Neu5Ac H-3ax and H-3eq

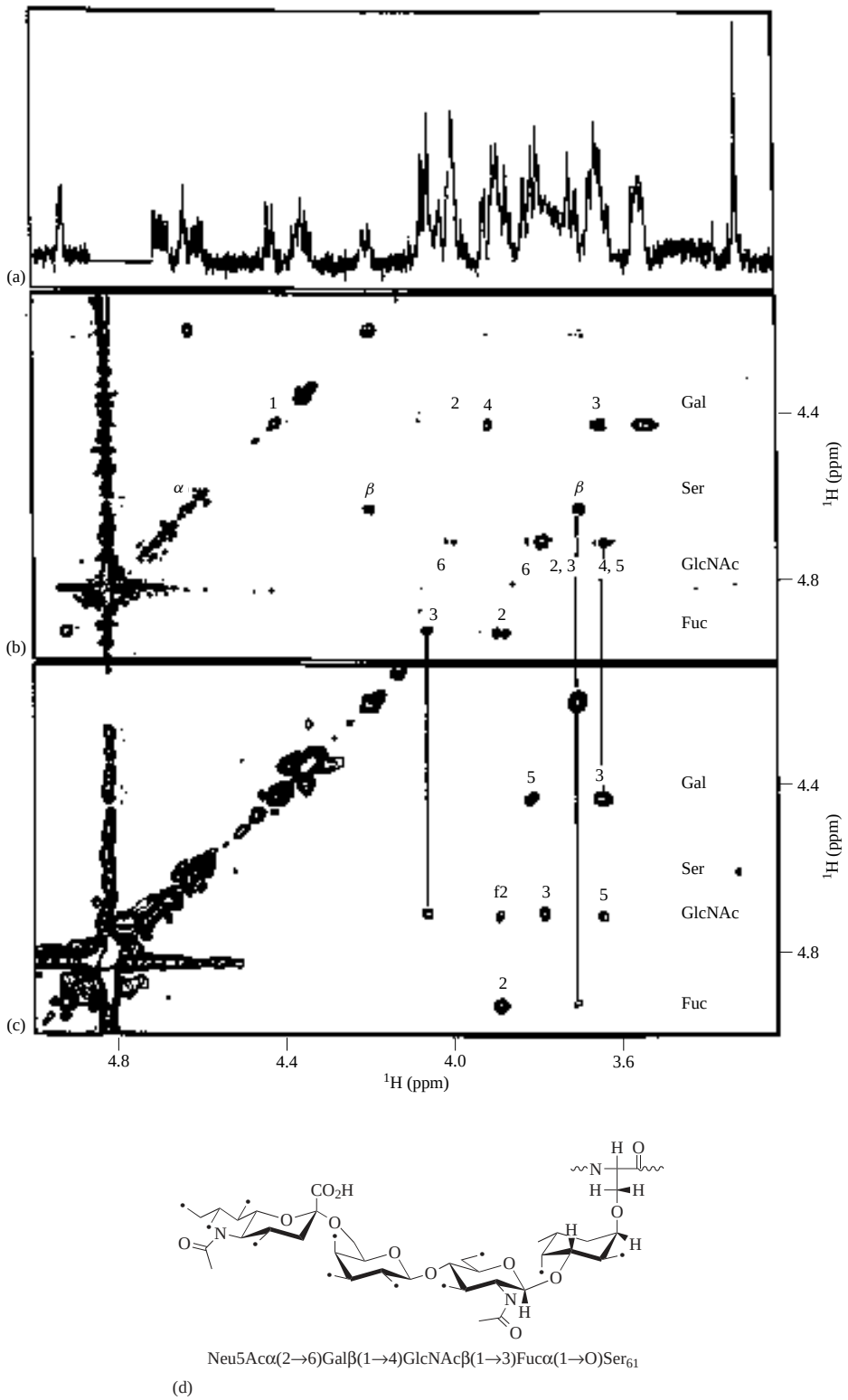

Figure 6 (a) The 600 MHz 1D ^{1}H NMR spectrum (D_2O, pD = 7.2, 23 °C) of the Factor IX glyco-nonapeptide (~20 nmol).[69] (b) Regions of the 2D ^{1}H TOCSY (mixing time 108 ms) and (c) ROESY (mixing time 200 ms) spectra of Factor IX glyco-nonapeptide. The sequence of the structural entities Galβ(1→4)GlcNAc, GlcNAcβ(1→3)Fuc, and Fucα(1→O)Ser is indicated by the vertical lines that connect ROESY and TOCSY cross peaks. The numbers in the spectra refer to the protons in the respective glycosyl residues. (d) Schematic structure of the tetrasaccharide Neu5Acα(2→6)Galβ(1→4)GlcNAcβ(1→3)Fuc α-linked to Ser$_{61}$ of human Factor IX. The • —— symbolizes an OH group. Sugar ring H atoms are not shown, with the exception of the GlcNAc H-1, Fuc H-3, Fuc H-1, and Ser H-β protons in order to illustrate their spatial arrangement relevant to the observed NOE effects

at 1.72 and 2.67 ppm, known to be sensitive to the linkage in which the residue is involved and the type of sugar to which it is attached, indicated that the Neu5Ac residue was $\alpha(2\rightarrow6)$-linked to the Gal residue (compare Figure 3). Furthermore, the Gal H-1 chemical shift of 4.43 ppm and its coupling ^3J(H-1,H-2) of 7.8 Hz were characteristic of its involvement in a $\beta(1\rightarrow4)$ linkage to GlcNAc in a sialyl-*N*-acetyllactosamine moiety. Likewise, the positions and coupling constants for the Fuc [4.92 ppm; ^3J(H-1,H-2) = 4.2 Hz] and GlcNAc H-1 [4.71 ppm; ^3J(H-1,H-2) = 8.0 Hz] signals indicated the involvement of these residues in α- and β-glycosidic linkages, respectively. At this point, it was evident from the NMR data that the tetrasaccharide consisted of a terminal Neu5Ac$\alpha(2\rightarrow6)$Gal$\beta(1\rightarrow4)$GlcNAc$\beta(1\rightarrow\bullet)$ moiety and an α-linked Fuc residue.

To complete the structural analysis of the tetrasaccharide, 2D NOE experiments were performed in order to gather information about the distance between pairs of protons and, thus, sequence information. A ROESY spectrum of the glycopeptide provided a number of transglycosidic NOEs [Figure 6(c)]. Among them were a NOE between GlcNAc H-1 and the proton resonating at 4.06 ppm assigned to Fuc H-3 by TOCSY, and a NOE between Fuc H-1 and a proton at 3.72 ppm, i.e., one of the β-protons on Ser_{61}. The aforementioned interresidue NOE effects [between the protons highlighted in the schematic structure in Figure 6(d)] pointed to GlcNAc(1 $\rightarrow$ 3)Fuc and Fuc(1 $\rightarrow$ O)Ser linkages, respectively. Thus, NMR spectroscopy allowed the unambiguous establishment of the linearity of the tetrasaccharide's structure. Fuc was found present in this tetrasaccharide as an internal residue, providing the 'bridge' between GlcNAc in the sialyl-*N*-acetyllactosamine moiety and Ser in the peptide. The NMR data are therefore compatible with the structure Neu5Ac$\alpha(2 \rightarrow 6)$Gal$\beta(1 \rightarrow 4)$GlcNAc$\beta(1 \rightarrow 3)$Fuc$\alpha(1 \rightarrow$ O)Ser_{61}.

The methodology described here is generally applicable for the complete primary structure analysis of carbohydrates as free oligosaccharides and as constituents of glycoconjugates; anomeric configurations and positions of all glycosidic linkages and, indeed, full sequences can be unraveled. The only potential problem is that ^{1}H/^{1}H transglycosidic NOEs are not always the largest magnitude interresidue NOEs. The resulting ambiguity in the definition of the linkage position, however, can be solved by ^{1}H-detected ^{13}C,^{1}H multiple-bond correlation (HMBC) spectroscopy.[71] Detailed applications of this technique for glycoprotein oligosaccharides have been described.[72] Briefly, when ^{13}C and ^{1}H NMR spectroscopy are used together, NMR demonstrates its real power in the de novo delineation of carbohydrate structures from first principles. Heteronuclear ^{13}C,^{1}H correlation NMR techniques are the most informative NMR experiments for carbohydrate primary structures.[72,73] The sensitivity limitations for these types of experiments were overcome by the introduction of the ^{1}H-detected versions of many ^{13}C,^{1}H correlated spectroscopies. The HMQC experiment, providing a one-bond ^{13}C,^{1}H correlation map, is generally sufficient to assign unambiguously all resonances in the ^{13}C NMR spectrum, provided that the entire ^{1}H spectrum is assigned by the COSY/TOCSY approach. The tracing of long-range transglycosidic ^3J(C,H) values from the HMBC spectrum completes the primary structural analysis by unambiguously providing the linkage positions and the sequence of the glycosyl residues in the complex carbohydrate. Heteronuclear correlation experiments also allow the location of appended noncarbohydrate groups (such as acetates[74] and phosphates[75]) in oligosaccharides. For further examples, see the article by Bush (***Polysaccharides and Complex Oligosaccharides***) in this Encyclopedia.

At the present time, the NMR methodology for nondestructively deciphering any unknown carbohydrate primary structure is available. Isolating and purifying carbohydrates in amounts sufficient to perform these analyses is currently the bottleneck to their structural characterization.

4 THE PRESENT: SOLUTION CONFORMATION AND DYNAMICS

Due to the competition of more sensitive procedures, NMR spectroscopy may not always be the method of choice for the de novo determination of oligosaccharide primary structures. However, NMR spectroscopy easily outperforms any other available method of structural analysis when molecular conformation and motional characteristics are the focus of attention, and it yields the most complete picture of oligosaccharide structure and dynamic behavior in solution. A knowledge of conformation and dynamics is essential to understanding how oligosaccharides mediate biological recognition on cell surfaces. The NMR parameters holding the key information regarding oligosaccharide conformation and flexibility include scalar and dipolar couplings, relaxation times, and chemical exchange rates. Section 4.1 discusses how these parameters can be related to internuclear distance and torsion angle information and, therefore, to pyranose ring pucker, ensembles of rotamers around bonds that allow for certain flexibility, glycosidic linkage conformation, hydrogen bonding, and rotational correlation times for molecular tumbling and internal motions. Section 4.2 highlights some of the multipulse NMR spectroscopic techniques currently used to gather the constraints required to define the conformation and dynamics of an oligosaccharide in aqueous solution. Noteworthy review articles dealing with the application of multipulse *n*D NMR for carbohydrate conformational analysis are available.[9,18,55,58,59,64,66,72,76–78] Most of the NMR methodology reviewed in this section will be concerned with selective excitation experiments[79,80] which, for carbohydrates, are extremely useful in the retrieval of any desired information from NMR spectra. Upon critical evaluation of this information, it becomes clear that all oligosaccharides are, to a greater or lesser extent, flexible. The number of conformers adopted by small oligosaccharides is, however, not infinitely large; even oligosaccharides that include a $(1\rightarrow6)$ linkage fluctuate between a relatively small number of rather well-defined conformations. As an example, the process of deriving an ensemble of conformations from a sufficiently large set of NMR constraints is illustrated for sialyl-$\alpha(2\rightarrow$b)lactose. This discussion will be followed immediately by the description of NMR experiments which are capable of revealing internal motion in an oligosaccharide for which, at first glance, all measured NMR constraints seem to favor a rigid-body model. For example, we demonstrate that sucrose, the disaccharide that for years has been the paradigm of carbohydrate rigidity in solution, more than likely experiences fast internal motion around its glycosidic bond. Finally, Sections 4.3 and 4.4 will summarize the current knowledge on glycoprotein and glycolipid carbohydrate conformations and dynamics.

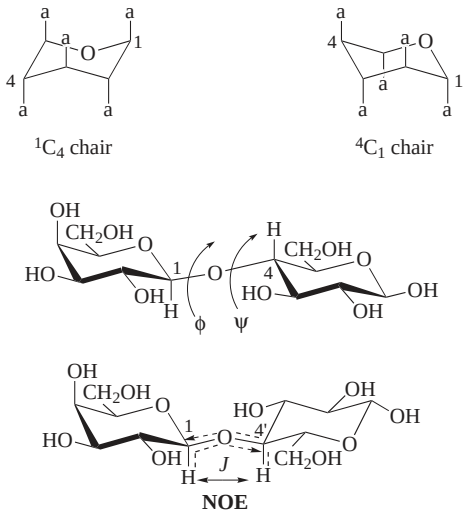

Figure 7 (a) Definition of the chair conformations of d-hexopyranose rings (a = axial substituent). For most monosaccharides, the $^1C_4$ and $^4C_1$ chairs are energetically favored over any boat conformers. For example, Man and Gal typically adopt the $^4C_1$ chair conformation, while Fuc and Neu5Ac adopt the $^1C_4$ chair (called the $^2C_5$ chair for Neu5Ac) [see Figure 1(c)]. (b) Definition of the torsion angles ϕ and ψ around a typical glycosidic linkage [in this case, the (1→4) linkage in lactose]: ϕ = H-1−C-1−O-1−C-4′ and ψ = C-1−O-1−C-4′−H-4′. In conjunction with ^3J(H-1,C-4′) and ^3J(C-1,H-4′) the NOE between H-1 and H-4′ across the glycosidic bond is used for linkage conformation analysis

4.1 Three-Dimensional Carbohydrate Structure

Once an oligosaccharide's primary sequence has been elucidated, its 3D structural characterization is typically approached in the following steps: (i) the ring conformation for each of the constituent glycosyl residues is defined [see Figure 7(a)]; (ii) the intraresidue conformation is completed by attempting to define, relative to the ring, the conformation(s) of any pendant (CH_2OH and OH) groups; (iii) the conformations of each of the glycosidic linkages in the oligosaccharide are characterized [see Figure 7(b)]; and (iv) additional distance constraints which could be indicative of hydrogen bonding or other types of interaction between residues, both adjacent and nonadjacent in the primary structure, are sought. Oligosaccharide conformations are ultimately defined in terms of the relative (Cartesian or spherical) coordinates of the atoms in 3D space; these coordinates are obtained via the measurement of internuclear distances and torsion angles around bonds. The pioneering work of Solomon[81] and Karplus[13,82] has demonstrated the possibility of probing the geometry of molecules in solution via NMR by measurements of NOE effects and scalar couplings, respectively. NOE effects are dependent on internuclear distance, while scalar couplings between nuclei separated by three chemical bonds (^3J) depend on the dihedral angle between two planes containing those nuclei. The advent of multidimensional and multinuclear spectroscopy enabled the measurement of a large number of homo- and heteronuclear NOE contacts and vicinal coupling constants, including those from extremely overlapped oligosaccharide NMR spectra. If a sufficient number of constraints can be obtained from NMR, the 3D structure(s) of the carbohydrate can be computed.[66,76,83] Carbohydrate NMR has reached a level of sophistication at which the number of detectable constraints is sometimes large enough to be incompatible with a single rigid conformer, prompting the consideration of ensemble average models. Help is then sought from molecular modeling (potential energy calculations) to provide candidate low-energy structures that may contribute to the ensemble average. Sometimes, rather deceptively, all measured constraints seem to favor one rigid conformation for the oligosaccharide in question. In these cases, it is particularly important to remember to take into consideration that J and NOE values are intrinsically motionally averaged. Perhaps more often, modeling of carbohydrates is hampered by the existence of very few detectable NOE contacts. Unfortunately, the number of detectable structural constraints usually proves insufficient to unambiguously define the carbohydrate's conformation. The latter phenomenon is most often attributed to more pronounced conformational flexibility.[58] As soon as carbohydrate NMR spectroscopists became aware of the dynamic nature of oligosaccharides, they attempted to measure NMR parameters which could be used to characterize internal motions more quantitatively. Internal motion in biomolecules can be detected and quantified by NMR spectroscopy if it occurs relatively slowly or relatively quickly compared with the overall motion of the molecule.[84] NMR parameters that can be related to internal dynamics include the temperature and magnetic-field-strength dependences of relaxation times (T_1 and $T_{1\rho}$) and cross-relaxation rates (homo- and heteronuclear NOEs).[85]

4.1.1 Conformation

For the determination of pyranoid ring conformations, a complete set of vicinal ^3J(H,H) couplings for the spin system suffices due to the relative rigidity of this type of ring structure. One or more intraresidue $^1H/^1H$ NOEs may be useful in refining the pyranose ring pucker. Conformations of pendant groups require the measurement of all pertinent vicinal J(H,H) scalar couplings [for example, ^3J(H-5,H-6) and ^3J(H-5,H-6′) for CH_2OH in hexopyranoses; ^3J(HOCH) couplings for OH groups]. Additionally, $^1H/^1H$ NOEs and heteronuclear scalar couplings may be measured. For the conversion of ^3J(H,H′) scalar couplings into torsion angles, carbohydrate spectroscopists use the Karplus equation as parameterized by Haasnoot et al. to account for substitution and electronegativity effects along the H−C−C′−H′ pathway[86,87] [see also Altona (***Vicinal Coupling Constants and Conformation of Biomolecules***) in this Encyclopedia]:

$$^3J(\mathrm{H,H'}) = 13.22\cos^2\theta - 0.99\cos\theta + \sum_i \Delta\chi_i[0.87 - 2.46\cos^2(\xi_i\theta)] \qquad (1)$$

where θ is the H−C−C′−H′ torsion angle, and $\Delta\chi_i$ are the Huggins electronegativities of substituent i relative to that of H. The value of ξ_i is either +1 or −1, depending on the orientation of the substituents.[86] As for the pendant groups, the conformation of the hydroxymethyl group in hexopyranoses is predominantly determined by the rotation around the C-5−C-6 bond described by the dihedral angle ω_H (Figure 8). As was reviewed by Bock and Duus,[88] information about the

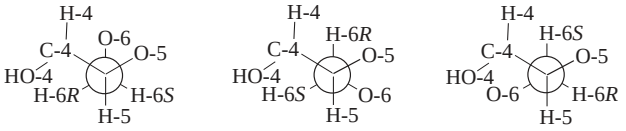

Figure 8 Definition of the three staggered conformations for the hydroxymethyl group in d-glucopyranose. For NMR spectroscopy, ω_H is defined as the dihedral angle H-5–C-5–C-6–O-6. (In crystallography, ω is commonly defined as O-5–C-5–C-6–O-6; hence, the subscript H in ω_H when using H-5 as the reference atom.) The three staggered conformers are described as *gg*, *gt*, and *tg* (*g* = *gauche*, *t* = *trans*; the first letter in the pair refers to the O-6 position relative to O-5, the second to the orientation of O-6 with respect to C-4). Thus, *gg*, *gt*, and *tg* correspond to ω_H = 180°, 60°, and −60°, respectively

conformational preferences of the hydroxymethyl group can be obtained via NMR using ^3J(H-5,H-6*R*) and ^3J(H-5,H-6*S*) provided that the stereospecific assignment of the H-6 atoms is either known or can be achieved via NMR:[89]

$$^3J(\text{H-5, H-6}R) = 13.22\cos^2\theta - 0.99\cos\theta - 6.4\cos^2(25.87-\theta) - 0.96\cos^2(7.96+\theta) + 2.61 \quad (2a)$$

$$^3J(\text{H-5, H-6S}) = 13.22\cos^2\theta - 0.99\cos\theta - 3.2\cos^2(25.87-\theta) - 3.2\cos^2(25.87+\theta) - 0.96\cos^2(7.96+\theta) + 2.61 \quad (2b)$$

If one assumes that the three low-energy staggered rotamers (ω_H = 60°, −60°, and 180°) (Figure 8) are the exclusive contributors to the average conformer, the measured values $[^3J(\text{H-5,H-6}R)]_{exp}$ and $[^3J(\text{H-5,H-6}S)]_{exp}$ are analyzed as linear combinations of the calculated values of these couplings for the pure *gg*, *gt*, and *tg* rotamers; the coefficients p_{gg}, p_{gt}, and p_{tg} in these equations are interpreted as relative populations, i.e., the mole fractions in which the respective staggered rotamers contribute to the time-averaged conformation as measured by NMR:

$$J_{exp} = p_{gg}\cdot J_{gg} + p_{gt}\cdot J_{gt} + p_{tg}\cdot J_{tg} \quad (3a,b)$$

(where J_{exp} is ^3J(H-5, H-6*R*) or ^3J(H-5, H-6*S*)

$$p_{gg} + p_{gt} + p_{tg} = 1 \quad (3c)$$

However, if constraints other than the two ^3J(H-5,H-6) homonuclear couplings are available, it is not necessary to make the aforementioned assumption. More advanced methods applied to the analysis of the rotamer population around the C-5–C-6 bond use the conformational entropy (S) associated with an ensemble; S can be calculated as:

$$S = -R\sum_i p_i \ln p_i \quad (4)$$

where the sum is over all the conformations, p_i is the probability of the ith conformation occurring in the ensemble, and R is the gas constant. Given the number of measurable NMR constraints, computerized methods attempt to maximize the conformational entropy.[90,91]

Linkage conformations cannot be defined by ^nJ(H,H′) measurements; their analysis requires the measurement of interglycosidic NOEs and ROEs (both ^{1}H/^{1}H NOE and ROE, and ^{13}C/^{1}H NOE, if possible), in combination with transglycosidic ^3J(C,H) couplings. Distances are typically calculated as $r_{ij} = (igma_{ref}/\sigma_{ij})^{\frac{1}{6}} r_{ref}$, where σ_{ref} and r_{ref} are the cross-relaxation rate and the distance, respectively, of a pair of reference protons within the rigid pyranose ring system. Glycosidic bond angles are calculated from ^3J(C,H) values according to the Karplus equation as parameterized by Tvaroska et al.[92] (see also Mulloy et al.[93]) based on seminal work by Perlin and co-workers:[94]

$$^3J(\text{C, H}) = 5.7\cos^2\theta - 0.6\cos\theta + 0.5 \quad (5)$$

where θ is the H–C–O–C torsion angle. In addition, ^1J(C,H) values may be used to assist in the determination of bond conformations.[95,96] If carbohydrates can be obtained uniformly or selectively ^{13}C isotopically-enriched,[97] long-range ^{13}C,^{1}H couplings become easier to measure. In addition, ^1J(C,C), ^2J(C,C), and ^3J(C,C) become detectable as conformational constraints. However, notwithstanding the advances that are being made in combining chemical and enzymatic syntheses, procedures to obtain uniformly ^{13}C isotopically-enriched ('labeled') carbohydrates, particularly glycoconjugate side chains, are by no means straightforward.

4.1.2 Hydrogen Bonding

Hydroxyl resonances in the ^{1}H NMR spectra of oligosaccharides in aprotic solvents such as DMSO have long been used as structural probes. However, as most biologists are primarily interested in carbohydrate conformations in aqueous solutions, only glycolipid NMR researchers have put any significant effort into investigating these signals in DMSO (Section 3.3). Although hydroxyl proton resonances in aqueous solutions of sugars were first observed over 14 years ago,[98] the utility of these protons in the conformational analysis of carbohydrates has been demonstrated only recently.[99–103] Hydroxyl resonances potentially provide a wealth of structural information in the form of chemical shifts, J couplings, NOEs, exchange rates, and isotope shifts. However, this information is accessible only if the intermolecular exchange of OH protons with H_2O in the aqueous solvent can be slowed sufficiently. At room temperature, hydroxyl protons in aqueous solutions of carbohydrates engage in fast chemical exchange with water. Several researchers have applied mixed solvents (water/acetone and water/methanol) to study OH groups at low temperatures (−5 °C to −10 °C) (see, e.g., Poppe and Van Halbeek).[99] Recently, ^{1}H NMR studies of hydroxyl groups in dilute solutions of mono- and disaccharides in pure H_2O under supercooled (−15 °C to −20 °C) conditions have been reported.[101] The chemical exchange effects under these conditions are reduced to such an extent that separate signals can be observed for each hydroxyl site; thus, all hydroxyl proton resonances can be assigned on the basis of scalar connectivities to nonlabile aliphatic protons. The scalar ^3J(HOCH) couplings can be analyzed[103] by equations (1) and (3)[3,4]3, in conjunction with more advanced statistical methods. The linewidths,

temperature-shift coefficients, and coupling constants of OH protons are valuable hydration and hydrogen-bonding probes in NMR studies. H/D isotope effects of hydroxyl protons on ^{13}C resonances may be used to obtain additional evidence of the involvement of OH groups in intra- or interresidue hydrogen bonds.104 Protruding farther from the glycosyl ring systems, OH protons may additionally serve as long-range sensor conformational probes which can be interrogated by NOESY and ROESY experiments of the carbohydrate in aqueous solution.[99,105,106]

4.1.3 Dynamics

NOEs and ROEs (or, more strictly speaking, the cross-relaxation rates $\sigma^{\parallel}$ and $\sigma^{\perp}$), as well as scalar coupling constants, are time-averaged parameters when the interconversion of conformers is fast on the NMR timescale.[107] However, interpretation of the measured NMR constraints in terms of the existence of several conformers and their interconversion rates is not easily accomplished. An extensive use of molecular modeling is usually required.[66,76,83,107,108] The experimental approach to the problem of flexibility involves the measurement of different relaxation rates (^{13}C and ^{1}H T_1 and $T_{1\rho}$, as well as $^{1}H/^{1}H$ and $^{13}C/^{1}H$ NOE) at a number of different frequencies (ω) in order to sample the spectral density $J(n\omega)$:[109–112]

$$J(n\omega) = \left(\frac{2}{5}\right) \cdot \frac{\tau_c}{1 + (n\omega\tau_c)^2} \tag{6}$$

where n = 0, 1, or 2, and τ_c, the rotational correlation time, is directly related to relaxation times T_1 and $T_{1\rho}$ (see, for example, Wagner and others).[112–115] The laboratory and rotating frame homonuclear cross-relaxation rates, $\sigma^{\parallel}$ and $\sigma^{\perp}$, respectively, are expressed by equations (7a) and (7b):

$$\sigma^{\parallel} = K[6J(2\omega) - J(0)] \tag{7a}$$

$$\sigma^{\perp} = K[3J(\omega) + 2J(0)] \tag{7b}$$

where $K = 0.1\ \Sigma_1 \gamma^4 h^2/4\pi^2 r_{kl}^6$, γ is the ^{1}H gyromagnetic ratio, h is Planck's constant, r is the internuclear distance between nuclei k and l, and the summation index runs over all interactions.[113,114,116] Similar expressions for $^{13}C/^{1}H$ cross-relaxation rates have been documented.[112]

Spectral density is most conveniently interpreted at the molecular level by the model-free approach of Lipari and Szabo[117,118] in which the types of molecular motion of an oligosaccharide are distinguished by their different timescales. The total motion of the molecule is separated into the tumbling of the entire molecule (with rotation correlation time τ_o) modulated by more rapid internal (segmental) motion with characteristic correlation time (τ_i) and amplitude expressed by an order parameter (S^2):

$$J(n\omega) = S^2 \left(\frac{2}{5}\right) \cdot \frac{\tau_o}{1 + (n\omega\tau_o)^2} + (\langle r^{-6} \rangle - S^2) \left(\frac{2}{5}\right) \cdot \frac{\tau}{1 + (n\omega\tau)^2} \tag{8a}$$

where n = 0, 1, or 2, $S^2 = \sum_{m=-2}^{m=2} |\langle (5/4\pi)^{-1/2} Y_{2m}(\Omega)/r^3 \rangle|^2$, $Y_{2m}(\Omega)$ are spherical harmonics functions with r and Ω corresponding to the distance and polar angle of a given proton pair in the molecular frame; $\langle \ldots \rangle$ denotes ensemble average; and $\tau^{-1} = \tau_o{}^{-1} + \tau_i{}^{-1}$. A slightly more simplified expression for $J(n\omega)$ may be used when taking only fluctuations due to molecular reorientation, but not internuclear separation, into account (Section 5.2); S^2 becomes distance independent, and equation (8a) becomes equation (8b):

$$J(n\omega) = S^2 \left(\frac{2}{5}\right) \cdot \frac{\tau_o}{1 + (n\omega\tau_o)^2} + (1 - S^2) \left(\frac{2}{5}\right) \cdot \frac{\tau}{1 + (n\omega\tau)^2} \tag{8b}$$

Either way, the generalized order parameter is a measure of the spatial restriction of the internal reorientation ($S^2 = 1$ in the absence of internal motion; $S^2 = 0$ in the presence of complete, isotropic reorientation).

Often applicable to oligosaccharides, this model predicts that, if there is significant relaxation through internal motion in the saccharide, the ratio of the NOEs (and the T_1 values) at different field strengths should differ for those protons relaxing with neighboring protons within fixed distances (i.e., neighbors on the same pyranose ring) versus those relaxing with neighbors at fluctuating distances (i.e., across the glycosidic linkage). The separation of the motions into distinct regimes is crucial to the success of this method. For internal motions to contribute significantly to the relaxation, their time scale must be fast compared with that of the overall tumbling (i.e., $\tau_o \sim 0.1$ ns for a disaccharide). Thus the internal dynamics (segmental motions) of carbohydrate molecules in solution can be assessed by NMR spectroscopy if the rearrangements occur much faster (or much slower) than the overall molecular tumbling. Physical models for the temperature dependences of τ_o, τ_i, and NOEs are in existence as well, but they are less successful in reproducing the dynamic behavior of oligosaccharides.

4.2 Di- and Trisaccharides

Analyses of the solution conformation and dynamics of carbohydrates encompass the following steps: (i) the complete assignment of ^{1}H and ^{13}C NMR spectra of the carbohydrate, (ii) the measurement of NOEs and vicinal couplings in order to establish spatial (distance and/or torsion angle) constraints between atoms, (iii) the measurement of ^{1}H and ^{13}C relaxation parameters (T_1, $T_{1\rho}$, homo- and heteronuclear NOEs) as a function of temperature and field strength, and (iv) the evaluation of experimental data with the use of computational strategies, including statistical methods, potential energy calculations, and molecular dynamics (MD) or Monte Carlo (MC) simulations (as well as comparison with crystal structures, if available). With the application of at least two of the aforementioned steps, a large number of di- and trisaccharides have been examined, including sucrose (see below), maltose [Glcα(1→4)Glc],[119] cellobiose [Glcβ(1→4)Glc],[120] lactose [Galβ(1→4)Glc],[97,121] melibiose [Galα(1→6)Glc],[122] gentiobiose [Glcβ(1→6)Glc] (see below), xylobiose [Xylβ(1→4)Xyl],[123] mannobioses [Manα(1→3)Man and Manα(1→2)Man],[108,124] chitobiose [GlcNAcβ(1→4)GlcNAc], and chitotriose. For an overview of

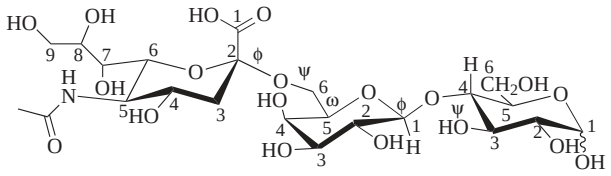

Figure 9 Schematic structure of sialyl-$\alpha(2\rightarrow6)$-lactose. The numbering of the carbon atoms and their substituents is indicated. The torsion angles ϕ and ψ around the $(1\rightarrow4)$ glycosidic bond are defined as in Figure 7(b): ϕ(H-1′–C-1′–O-1′–C-4) and ψ(C-1′–O-1′–C-4–H-4). The angles ϕ and ψ around the $(2\rightarrow6)$ glycosidic linkage are defined as ϕ(C-1′–C-2′–O-2′–C-6) and ψ(C-2′–O-2′–C-6–C-5), while ω is (O-5–C-5–C-6–O-2′); the definition of ϕ differs from that given in the legend to Figure 7(b) due to the absence of an anomeric proton in Neu5Ac. The conformation of the $(1\rightarrow4)$ linkage was studied by measuring ^3J(H-1′,C-4) and ^3J(C-1′,H-4) (compare Figure 14), as well as interglycosidic NOEs. Angle ϕ for the $(2\rightarrow6)$ linkage was studied by ^{1}H/^{1}H ROE and ^{13}C/^{1}H NOE experiments, while ψ for the $(2\rightarrow6)$ linkage was deduced from ^3J(C-2′,H-6*R*) and ^3J(C-2′,H-6*S*) measurements (Table 2). For ω around the $(2\rightarrow6)$ linkage, the Gal ^3J(H-5,H-6*R*) and ^3J(H-5,H-6*S*) were measured (Figure 13 and Table 1).[106] The Neu5Ac glycerol side-chain conformation was defined by the ^3J(H-6,H-7), ^3J(H-7,H-8), ^3J(H-8,H-9) and ^3J(H-8,H-9′) couplings (for the latter two, see Figure 12) in conjunction with the existence of a hydrogen bond between O-8 and the C–O bond of the C-1 carboxyl group[106]

di- and trisaccharide structures determined by X-ray crystallography, NMR spectroscopy and/or theoretical computations, the reader is referred elsewhere.[77,125–128] Because of the importance of sialyl oligosaccharides in the biology of glycoproteins and glycolipids, an illustration is provided of the typical procedures involved in the NMR conformational analysis of a trisaccharide similar to the terminal entity found on various glycoprotein and ganglioside oligosaccharides, namely, sialyl-$\alpha(2\rightarrow6)$-lactose [Neu5Ac$\alpha(2\rightarrow6)$Gal$\beta(1\rightarrow4)$Glc].[106] Comparisons are drawn with the conformations of Neu5Ac$\alpha(2\rightarrow3)$Gal[129] and sialyl-$\alpha(2\rightarrow3)$-lactose.[130] A schematic drawing of the structure of sialyl-$\alpha(2\rightarrow6)$-lactose is shown in Figure 9, and definitions of torsion angles ϕ, ψ, ω, and other pertinent parameters are included in the legend to that figure.

4.2.1 ^{1}H and ^{13}C Spectral Assignments

Attractive alternatives to the 2D COSY and TOCSY techniques currently used for the complete assignment of the ^{1}H NMR spectrum of an oligosaccharide (Section 3.4) are their 1D selective analogs.[79,131] Despite the overlap of ~85% of the aliphatic proton resonances within approximately 1 ppm in a typical carbohydrate spectrum, the resonances of the structural-reporter groups, including those of the anomeric protons, are separated and accessible for selective excitation, providing suitable entries for transfer of magnetization through scalar couplings to other protons in the spin system of a glycosyl residue. In fact, carbohydrates are often cited in the magnetic resonance literature as being used as toy systems for new selective excitation sequences (see Kupce and Freeman,[132] for example). To reveal the entire spin system, i.e., trace the scalar connectivity from H-1 through H-6 for a hexosyl residue, two methods are currently being applied; (i) multistep correlated (relayed COSY) experiments[133,134] in which magnetization is transferred in successive steps from the selectively excited resonance, and (ii) isotropic mixing (TOCSY) pulse sequences[62,135] that distribute selectively excited magnetization in a more uniform manner among coupled spins. Magnetization transfer in TOCSY experiments is more efficient than in relayed COSY experiments, which suffer from larger losses of magnetization due to T_2 relaxation; also, TOCSY signals occur as in-phase multiplets. The major obstacles to tracing glycosyl spin systems are small coupling constants (e.g., those between H-1 and H-2 in mannosyl, H-4 and H-5 in galactosyl, and H-6 and H-7 in Neu5Ac residues). In order to overcome these 'bottlenecks' in TOCSY experiments, researchers have applied a number of different schemes which rely on multiple selective excitation, e.g. double-TOCSY[136] or double-DANTE TOCSY[137] or relayed TOCSY[138] (where isotropic mixing is followed by a COSY step). Parenthetically, it should be mentioned that extensions of ^{1}H 1D and 2D techniques to 3D and 4D NMR techniques have been described for carbohydrates;[139,140] however, full-blown 3D and 4D data acquisition is time-consuming and rarely necessary to solve a carbohydrate structural problem. (Multi-)selective 1D and 2D analogs of 3D and 4D NMR experiments[80,141] are far more efficient methods of obtaining the desired information from a carbohydrate ^{1}H NMR spectrum. For example, the 2D selective analog of the 3D TOCSY–COSY experiment and the 3D selective analog of the 4D TOCSY–TOCSY–COSY experiment have been applied for tracing scalar connectivities in GlcNAc residues for medium-sized oligosaccharides.[140,142] Pulse sequences which are successfully utilized for isotropic mixing include: MLEV-17,[62] WALTZ-16,[143] DIPSI-2,[144] clean-CITY,[145] and mixing sequences proposed by Glaser and Drobny.[146] Selective excitation is accomplished by DANTE pulse trains[147] or any one of a variety of shaped pulses.[79,80,148]

Once the ^{1}H NMR spectrum of an oligosaccharide has been assigned, the assignment of the protonated ^{13}C resonances on the basis of one-bond ^{13}C,^{1}H correlation spectroscopy (e.g., HMQC) is relatively straightforward (Section 3.4). Nonprotonated ^{13}C signals can be assigned by an HMBC experiment. These ^{1}H-detected (or 'inverse-detected') schemes[149] allow the acquisition of correlation spectra for submillimolar amounts of carbohydrate sample within a few hours of data acquisition. Employing the combination of TOCSY and HMQC/HMBC spectroscopy, the ^{1}H and ^{13}C spectra of sialyl-$\alpha(2\rightarrow6)$-lactose in D_2O have been fully assigned.[106]

4.2.2 Distance and Torsion Angle Constraints

4.2.2.1 Ring Conformation. The establishment of pyranose ring pucker involves the accurate measurement of homonuclear vicinal scalar couplings; this is best accomplished with the use of ^{1}H selective excitation experiments such as 1D TOCSY [Figure 10(a)]. The signals in 1D TOCSY spectra are obtained in pure absorption if the admixture of antiphase dispersive lines is averaged out by stepwise incrementation of the isotropic mixing time[135] or by incorporation of a *z* filter.[62] The values of the ^3J(H,H′) couplings acquired for sialyl-$\alpha(2\rightarrow6)$-lactose[106] show each of the ring systems in the trisaccharide to be in its typical pyranose chair conformation, i.e., $^4C_1$ for Glc and Gal, $^2C_5$ for Neu5Ac [compare Figures 1(c) and 7, and Sabesan et al.].[158]

4.2.2.2 Exocyclic Groups. In order to evaluate rotamer populations around the C-5–C-6 bond in hexopyranoses, the

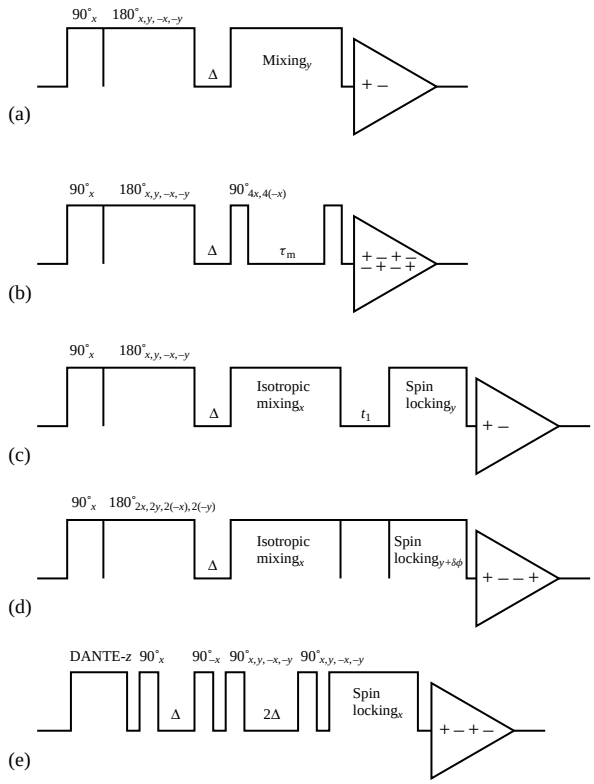

Figure 10 Pulse sequences commonly used for ^{1}H selective excitation experiments on carbohydrates. Selective excitation uses either a composite 90° pulse[150] consisting of two consecutive DANTE pulse trains,[147] traces (a)–(d) or a DANTE-*z* sequence[151] consisting of two interleaved pulse trains with different phase properties, trace (e). In all cases, $\Delta \sim 0.63t_{90}$, where t_{90} is the duration of the selective 90° pulse. The basic phase cyclings, as listed, may be extended following CYCLOPS and EXORCYCLE procedures.[152] (a) 1D TOCSY or 1D ROESY experiment. Isotropic mixing is performed with[146] composite pulses R = (290°_x,330°_{-x},290°_x) arranged into the supercycle (R*RR*R RR*RR* *RRR*R *RR*RR, 180°_y) analogous to the MLEV-17 sequence;[153] italicized letters indicate phase inversion of the element. The mixing time is flanked by two short (~2 ms) trim pulses. For mixing in the ROESY experiment, a train of short (~20°) pulses is used.[154] (b) 1D NOESY experiment. (c) Selective 3D TOCSY–ROESY experiment.[150,155] (d) Double selective 3D TOCSY–ROESY experiment. The selective α pulse, when achieved with a DANTE pulse train,[156] can have any tilt angle in the range of 60° to 180°. The phase increment $\delta\phi$, associated with the change of offset during a finite time interval, is determined experimentally. (e) 1D experiments in H_2O solution utilizing 1–1 echo water suppression.[157] The DANTE-*z* pulse train can be used either for spin inversion or presaturation. The delay Δ determines the width of the excitation profile; typical values of Δ tailored for carbohydrate NMR spectra are 200–400 μs. A short (~2 ms) spin lock pulse may serve to purge the dispersive part of the residual water signal. The experiments are typically performed in the difference mode, with pertinent shift of carrier frequencies, using a single power level of excitation (typically $t_{90} \sim 60$ μs)

protons in the exocyclic CH_2OH group must be assigned stereospecifically. Since the methylene protons, together with ring proton H-5, form a mutually coupled three-spin system, they can be recognized with, for example, a 2D triple quantum filtered COSY[76] or triple quantum correlated spectroscopy experiment.[64,78,159,160] Proton multiplets from exocyclic groups are more readily retrievable from selective 1D TOCSY spectra or, alternatively, from 1D COSY spectra recorded with a chemical-shift-selective filter.[161,162] If the pertinent coupling constants cannot be accurately measured from such ^{1}H spectra, either due to extreme spectral overlap or second-order effects, then the goal can be attained with inverse ^{13}C,^{1}H correlation experiments in which the proton multiplets are more likely to occur separately due to the larger chemical shift dispersion in the ^{13}C spectrum. Usually, the method of choice is the modified over-Bodenhausen experiment[163] as depicted in Figure 11(a); this selective 1D heteronuclear single quantum coherence (HSQC) experiment gives pure absorptive ^{1}H lineshapes. An additional advantage of this pulse sequence lies in the ease with which it can be applied selectively; this is accomplished by either replacing the first ^{13}C 180° pulse with its selective analog[169] or by performing t_1 incrementation in analogy to a chemical-shift-selective filter (by jittering of delay, δ).[161,166] Application of this method to sialyl-α(2→6)-lactose yields well separated, first-order H-9*R* and H-9*S* multiplets for the Neu5Ac side chain (Figure 12).

The stereospecific assignment of the exocyclic methylene protons is particularly critical when analyzing the conformation of a (1→6) linkage between two glycosyl residues [for example, the linkage between Neu5Ac and Gal in sialyl-α(2→6)-lactose (Figure 9)]. When the stereospecifically mono-C-6 (or mono-C-9, if Neu5Ac is concerned) deuterated analogs of the oligosaccharide are available, the assignment of H-6*R* (H-9*R*) and H-6*S* (H-9*S*) is readily accomplished. However, the stereospecific chemical synthesis of a mono-C-6-deuterated analog of a mono- or disaccharide is usually a rather laborious procedure. Fortunately, NMR spectroscopy can, for some oligosaccharides, assign the C-6 methylene protons stereospecifically without the aid of deuteration. To accomplish this, one needs to be able to measure the pertinent vicinal ^3J(H-5,H-6) and ^3J(H-5,H-6′) coupling constants in conjunction with either the H-4/H-6,6′ NOE effects[78] or the ^3J(C-4,H-6) and ^3J(C-4,H-6′) scalar couplings.[89,170] The measurement of heteronuclear coupling constants will be discussed later in this section. As to the stereospecific assignment of H-6*R* and H-6*S* based on 'NOE-labeling', valuable spectral information can be obtained from selective analogs of 3D NOE-labeling experiments in many cases.[80,150,171] Figure 13 shows a selective 3D TOCSY–ROESY spectrum obtained for sialyl-α(2→6)-lactose with the pulse sequence shown in Figure 10(d). The NOE connectivities originating from Gal H-4 appear well-resolved. The values of the Gal ^3J(H-5,H-6) coupling constants (Table 1), along with the observation of NOE between Gal H-4 and only one of the H-6 protons (Figure 13), enabled the stereospecific assignment of Gal H-6*R* and Gal H-6*S*.[106] Subsequent analysis of the vicinal ^3J(H-5,H-6*R*) and ^3J(H-5,H-6*S*) coupling constants using equations (3a)–(3c) provided the rotamer populations around ω for sialyl-α(2→6)-lactose (Table 1). This interpretation was refined by the application of the maximum entropy method.[90] The availability of a relatively large set of structural constraints is required for this approach [for example, the values of the Gal ^3J(H-5,H-6*R*′), ^3J(H-5,H-6*S*′), ^3J(C-4,H-6*R*) and ^3J(C-4,H-6*S*) scalar couplings and the H-5/H-6*R*, H-5/H-6*S*, H-4/H-6*R*, and H-4/H-6*S* NOEs were used in the analysis of the rotameric distribution; see Table 2]. When applied to gentiobiose [Glcβ(1→6)Glc] to characterize the conformational flexibility around the C-5–C-6 bond which is part of the disaccharide's glycosidic linkage,

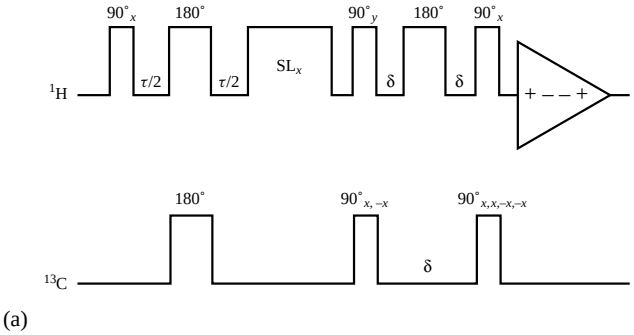

(a)

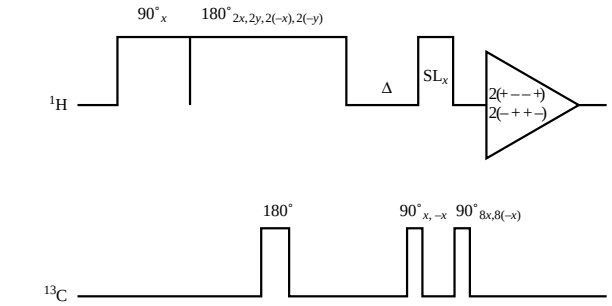

(b)

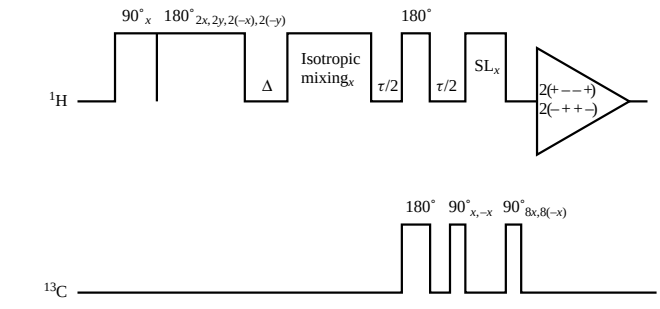

(c)

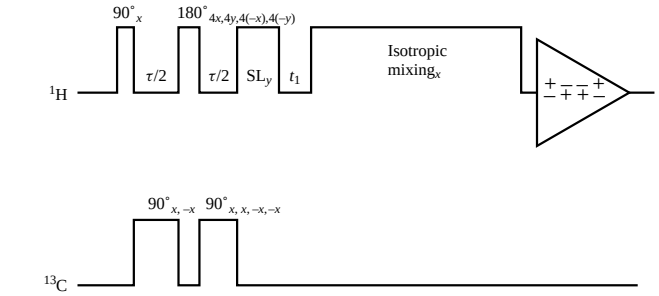

(d)

Figure 11 Pulse sequences for measuring long-range nJ(C,H) (n = 2, 3, 4, . . .) with ^{1}H detection. SL denotes spin lock; the other symbols are as defined in Figure 10. (a) Modified HSQC experiment.[163–165] The pulse marked with is either selective or nonselective. The delay δ is either systematically or stochastically incremented[166] to obtain selectivity in the carbon domain. The delay τ is taken long enough for the evolution due to heteronuclear long-range couplings to become manifest. The resulting proton multiplets are in antiphase with respect to one- or multibond ^{13}C,^{1}H couplings and in-phase with respect to homonuclear couplings. (b) Modified HSQC and (c) relay TOCSY–HSQC experiments[167] tailored for measuring interglycosidic ^{3}J(C,H) in oligosaccharides. (d) ^{13}C-selective 2D analog of a 3D exclusive-type ^{13}C,^{1}H correlation experiment.[168] The ^{13}C 90° pulses are 1–2 ms long; $\tau \sim [2^{1}J(\mathrm{C,H})]^{-1}$

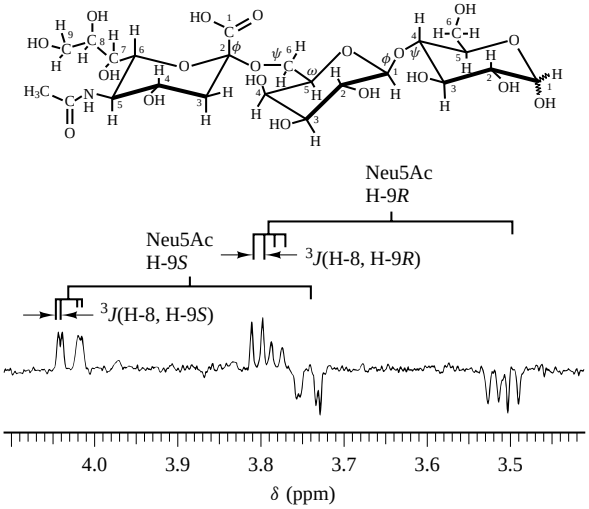

Figure 12 Editing ^{1}H multiplets according to their ^{13}C chemical shift. Spectrum of sialyl-$\alpha(2\rightarrow6)$-lactose in D_2O solution obtained with the pulse sequence shown in Figure 11(a); τ is set to 3 ms. The Neu5Ac C-9 frequency was selected by randomly jittering the delay δ. In the ^{1}H spectrum of the ^{12}C-9 isotopomer, H-8–H-9*S*–H-9*R* constitute a second-order ABX spin system; no value for the homonuclear coupling ^{3}J(H-8,H-9*S*) can be derived from that spectrum (reproduced with permission from Escom Science Publishers)[106]

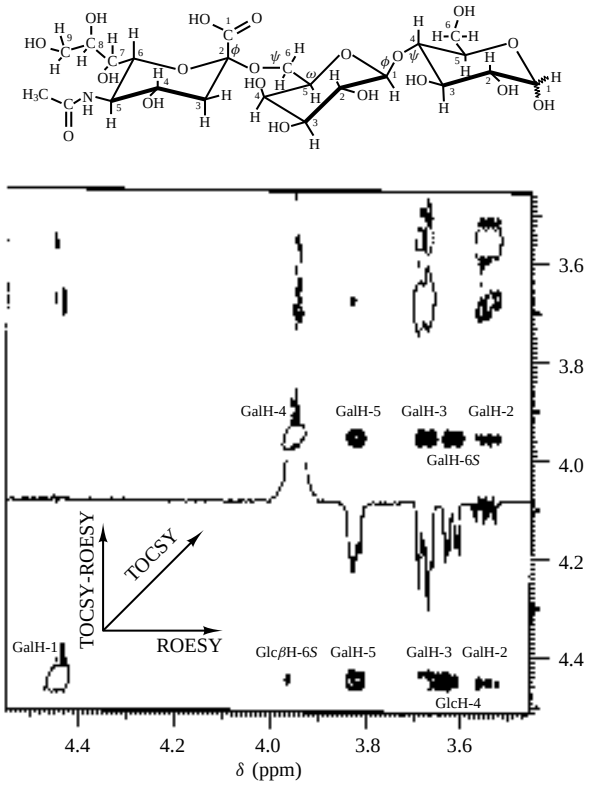

Figure 13 Selective 3D TOCSY–ROESY spectrum of sialyl-$\alpha(2\rightarrow6)$-lactose in D_2O solution (~30 mM) obtained with the pulse sequence shown in Figure 10(c) at 500 MHz and ambient temperature. The Gal H-1 proton was selectively excited (for 60 ms), followed by 77 ms of TOCSY and 140 ms of ROESY mixing. The digital resolution in the resulting 2D spectrum is 0.73 Hz pt^{-1} and 4.3 Hz pt^{-1} in the ω_2 and ω_1 dimensions, respectively; the total acquisition time was less than 5 h (reproduced with permission from Escom Science Publishers)[106]

the maximum entropy method yields results that differ significantly from the results of traditional rotameric distribution calculations employing force-field-based analysis of the ^{3}J(H-5,H-6) couplings by a Karplus-type equation;[90] however, for sialyl-$\alpha(2\rightarrow6)$-lactose that difference was insignificant.

4.2.2.3 Linkage Conformations from ^{3}J(C,H). Long-range heteronuclear scalar couplings [^{3}J(C,H)] through the glycosidic bonds (H–C–O–C′ and C–O–C′–H′) [Figure 7(b)] provide spatial constraints for the torsion angles ϕ and ψ, respectively, around the glycosidic linkages. Most of the NMR pulse sequences developed for the sensitive and accurate measurement of ^{3}J(C,H) values for carbohydrates are based on the ^{1}H-detected HSQC experiment.[163,164] The experiments can be conducted in true 2D or selective 2D mode by selective excitation and/or chemical-shift filtering of the protons and/or carbons of interest[167,169,172] (Figure 11). If the proton of interest is not accessible for selective excitation, the anomeric proton of the relevant monosaccharide is excited first, and the magnetization is transferred to the desired proton by a TOCSY step preceding the HSQC experiment [Figures 11(c) and 14].[167] With the aid of these methods, the pertinent ^{3}J(Glc C-4, Gal H-1) and ^{3}J(Glc H-4, Gal C-1) couplings in sialyl-$\alpha(2\rightarrow6)$-lactose were determined to be 4.2 and 5.1 Hz, respectively (Table 2).

As a valuable alternative to HSQC, a double INEPT type polarization transfer step may be used in the ^{1}H-detected measurement of long-range ^{13}C,^{1}H couplings; examples of such ^{1}H- and ^{13}C-selective, ^{1}H-detected 2D and pseudo 2D experiments have been reported.[173] Selective and nonselective measurements of interglycosidic ^{3}J(C,H) are greatly facilitated by the incorporation of ^{13}C labels at the positions involved in glycosidic linkages, as was demonstrated for sucrose.[174]

The elusive long-range heteronuclear scalar coupling parameters are also present in 2D ^{13}C-filtered ^{1}H,^{1}H correlation spectra, e.g., TOCSY[175] and NOESY/ROESY spectra,[176] which exhibit an exclusive type cross-peak structure. In these spectra, the long-range coupling constants are measured in the ω_2 dimension as a displacement of the proton multiplets that are resolved in the ω_1 dimension by the (large) ^{1}J(C,H) coupling. One-dimensional versions of this experiment have been applied to carbohydrates[89,177] to measure, for example, the ^{3}J(C-4,H-6*R*) and ^{3}J(C-4,H-6*S*) scalar couplings in glucose and galactose residues. Alternatively, a ^{13}C-filtered ROESY experiment has been introduced to measure ^{3}J(C,H) coupling constants through the glycosidic bonds of a cyclic glucan.[178]

Table 1 Rotamer Distribution around Gal C-5–C-6 in Sialyl-$\alpha(2\rightarrow6)$-Lactose

Coupling constant	4 °C	21 °C	77 °C
^{3}J(H-5,H-6*R*)	8.5 ± 0.2	8.3 ± 0.2	7.8 ± 0.2
^{3}J(H-5,H-6*S*)	3.7 ± 0.2	3.8 ± 0.2	4.2 ± 0.2
Population[a]	4 °C	21 °C	77 °C
p_{gg}	0.18 ± 0.03	0.20 ± 0.03	0.22 ± 0.02
p_{gt}	0.74 ± 0.03	0.71 ± 0.03	0.64 ± 0.02
p_{tg}	0.08 ± 0.03	0.08 ± 0.03	0.14 ± 0.02

[a]Calculated from the vicinal coupling constants ^{3}J(H-5,H-6*R*) and ^{3}J(H-5,H-6*S*) using equations (3a)–(3c). See Figure 8 for explanation of *gg*, *gt*, *tg* notation.

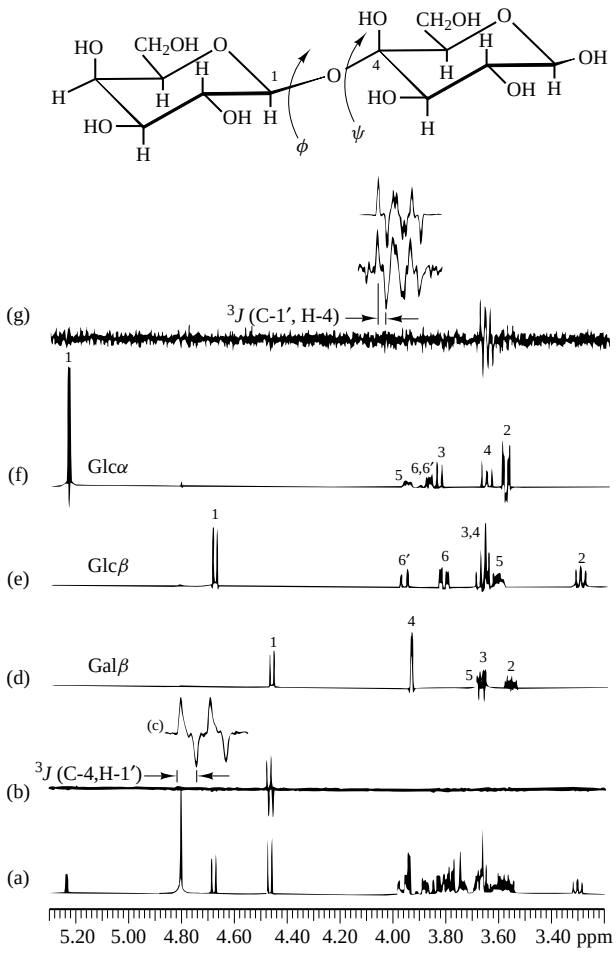

Figure 14 The measurement of heteronuclear long-range coupling constants across a glycosidic linkage illustrated for lactose in D_2O (50 mg mL^{-1}). (a) Reference spectrum. (b) Spectrum obtained with the pulse sequence shown in Figure 11(b). A ^1H composite pulse of 60 ms was applied selectively at Gal H-1, while the Glc ^{13}C-4 selective pulse was 2 ms long. (c) The heteronuclear coupling ^3J(C-4,H-1′) causes the antiphase pattern of the observed Gal H-1 multiplet. It is evident from the 1D TOCSY traces (d), (e), and (f) that ^3J(C-1′,H-4) cannot be obtained via the experiment shown in Figure 11(b) (note the overlap of Glc H-4 with Gal H-3); therefore, a relay TOCSY–HSQC experiment [Figure 11(c)] in which magnetization was selectively transferred from Glcα H-1 to H-4 was necessary (trace g). The duration of the entire pulse sequence in Figure 11(c) was close to 200 ms; 5500 scans were accumulated. (h) The heteronuclear coupling ^3J(C-1′,H-4) is read from the antiphase structure of the observed Glcα H-4 multiplet, computer-simulated in trace (i). The values ^3J(C-4,H-1′) and ^3J(C-1′,H-4) are 4.0 and 5.1 Hz, respectively (reproduced with permission from Academic Press)[167]

These methods, successfully applied to oligosaccharides with a natural abundance of ^{13}C, show their greatest potential in the measurement of long-range heteronuclear scalar couplings in ^{13}C isotopically-enriched carbohydrates (cf. Montelione et al.).[179] The pulse sequence in Figure 11(d) presents the selective version of 3D experiments originally designed for measurements of heteronuclear couplings in isotopically-enriched proteins.[179,180] The long-range carbon–proton coupling constants are measured independently of the linewidth from the exclusive-type scalar couplings correlation patterns,[168,179,180] as demonstrated (Figure 15) for glucose, 99% ^{13}C-labeled at C-1. Furthermore, the direction of the multiplet displacements allows the determination of the signs of the relevant coupling constants (cf. Serianni and Podlasek).[181]

Table 2 Average Distances and Vicinal Coupling Constants for Sialyl-$\alpha(2\rightarrow6)$-Lactose in Aqueous Solution[106]

Atom pair	$\langle r_{app}\rangle$ (Å)[a] or J_{exp} (Hz)[b]	$\langle r_{sim}\rangle$ or J^c_{sim} Family I[d]	Family II[d]
Neu5Ac/Gal			
H-3_{ax}/H-6*R*	3.3	4.35	2.35
H-3_{ax}/H-6*S*	3.3	4.63	2.53
H-3_{ax}/H-4	>5	6.34	4.78
H-3_{eq}/H-6*R*	5	4.54	3.37
H-3_{eq}/H-6*S*	4	4.33	3.84
H-3_{eq}/H-5	5	5.15	4.62
H-3_{eq}/H-4	>5	6.53	5.62
OH-8/H-6*R*	3.5	3.58	6.56
OH-8/H-6*S*	>4	5.07	5.67
O-7/Glc O-3	3[e]	3.43	5.64
C-2/H-6*R*	2.6	2.56	2.79
C-2/H-6*S*	>2.6	2.90	2.67
^3J(C-2,H-6*S*)	1.8	1.22	3.42
^3J(C-2,H-6*R*)	2.8	3.95	3.01
Gal/Gal			
^3J(H-5,H-6*R*)	8.5[f]	9.25	6.46
^3J(H-5,H-6*S*)	3.7[f]	3.97	4.17
^3J(C-4,H-6*R*)	2.9	2.48	2.39
^3J(C-4,H-6*S*)	1.8	1.75	3.07
H-4/H-6*R*	3.3	3.02	2.88
H-4/H-6*S*	2.6	2.65	2.75
Gal/Glc			
H-1/H-4	2.5	2.39	2.48
H-1/H-6*S*	3.5	2.72	2.69
H-6*R*/OH-3	3.5	4.17	4.39
^3J(H-1,C-4)	4.2[g]	2.58	2.08
^3J(C-1,H-4)	5.1[g]	5.07	5.22
H-6*R*/O-3	[h]	4.28	4.43
H-6*S*/O-3	[h]	5.09	5.01

[a]The distances r_{app} were evaluated with the formula $r_{ij} = r_{kl}(I_{kl}/I_{ij})^{\frac{1}{6}}$, in which I_{ij} and I_{kl} are the integrated signal intensities; I_{kl} corresponds to a reference interaction. For ROESY spectra, the intensities were scaled by the offset dependent factors $(\sin\theta_i \cdot \sin\theta_j)^{-2}$, in which $\theta_i = \arctan(\omega_i/\langle\gamma B_1\rangle)$; ω_i represents the offset from the carrier frequency and $\langle\gamma B_1\rangle$ the effective field strength in Hz. The precision of the distances is estimated to be $\sim 0.1r$.

[b]The precisions of the J_{exp} values are ±0.2 Hz, except those of ^3J(C-1,H-4) (±0.4 Hz) and ^3J(C-4,H-6*R*) and ^3J(C-4,H-6*S*) (±0.2 Hz).

[c]MMC simulated distances[106] were calculated according to the formula $\langle r^{-3}\rangle^{-\frac{1}{3}}$. The $\langle r_{sim}\rangle$ and J_{sim} values were scaled to 27 °C.

[d]Family I corresponds to the MMC simulation that started with ϕ of the (2→6)-linkage being set to −60°; for family II, the pertinent angle was set to 180°.

[e]This distance reflects the occurrence of a hydrogen bond between Neu5Ac OH-7 and Glc O-3.

[f]See Table 1.

[g]Compare with Figure 14.

[h]An anomerization effect ($\Delta\delta_{\alpha-\beta}$) was observed for Gal H-6*R*, but not for Gal H-6*S*, indicating that the former proton is closer to the Glc reducing end, i.e. near O-3 of the Glc residue; see Figure 16.

4.2.2.4 Linkage Conformations from Interresidue $^1H/^1H$ NOE. Early in the history of carbohydrate NMR, conformational studies of small and medium-sized oligosaccharides in solution were based on steady-state NOE measurements.[113]

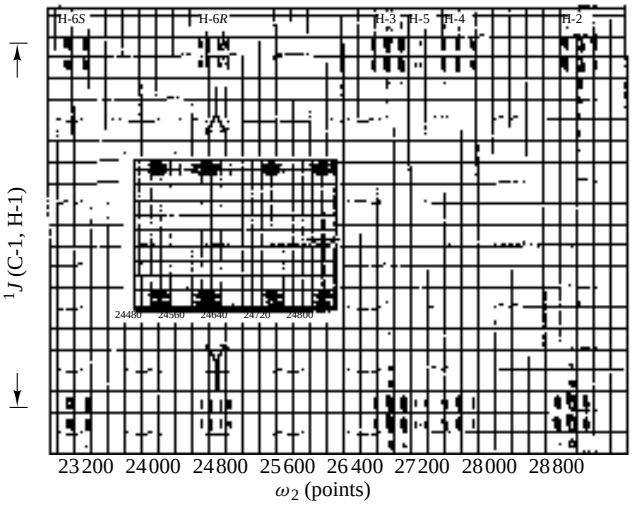

Figure 15 The measurement of heteronuclear coupling constants nJ(C-1,H) within glucose, ^{13}C-labeled at C-1, utilizing the pulse sequence shown in Figure 11(d). The heteronuclear couplings are read from the chemical shift difference between corresponding upper and lower multiplets. The digital resolution in the ω_2 domain is 0.055 Hz pt^{-1}, allowing the ^4J(C-1,H-6*R*) and ^4J(C-1,H-6*S*) couplings to be determined as 0.2 ± 0.05 and 0.4 ± 0.1 Hz, respectively

The major disadvantage of this approach lies in the fact that weak, direct interactions are frequently obscured by indirect effects and, thus, escape observation. More recent studies are based on measurements of cross-relaxation rates between two nuclei. Values for these parameters can be obtained either from multiselective relaxation time measurements[115] or analyses of 1D transient or 2D NOESY spectra.[114] The cross-relaxation rates are extracted from NOESY experiments on the basis of the two-spin approximation[182] or by 'full relaxation matrix analysis'.[183] The latter method has proven to be the most reliable in conformational analyses of carbohydrates.[66] Selective 1D NOESY experiments can give accurate (within 3%) estimations for cross-relaxation rates in small and medium-sized oligosaccharides, even at long mixing times. Moreover, selective spectra are free from zero quantum interferences which particularly obscure analysis of 2D NOESY spectra at short mixing times. Another crucial issue in quantitatively analyzing NOE data lies in their avoidance of contamination by indirect magnetization transfers. Undesired three-spin effects can be eliminated by (multi-)selective irradiation of potential mediators of spin diffusion during the NOESY mixing time.[184]

In order to overcome the problem of trying to detect vanishingly small NOE effects for tri- and tetrasaccharides at ~400–500 MHz, a novel technique for measuring cross-relaxation rates in the rotating frame was proposed. After its first application to a tetrasaccharide,[63] the technique's name was changed from CAMELSPIN to ROESY[185] spectroscopy and steadily gained the confidence of NMR spectroscopists as being an invaluable addition to the assortment of techniques used for the conformational analysis of molecules of all sizes. A major problem in the quantitative analysis of ROESY spectra are Hartmann–Hahn effects which occur in coupled spin systems.[154,186] These effects can, however, be minimized experimentally by a judicious choice of the carrier frequency.[154] An important feature of ROESY spectra is that NOE and chemical-exchange-mediated magnetization transfers can be readily distinguished.[187,188] Sialyl-$\alpha(2\rightarrow6)$-lactose, when investigated at 500 MHz and ambient temperature, is characterized by laboratory frame ^{1}H/^{1}H NOEs close to zero. Therefore, most of the distance constraints listed for the trisaccharide in Table 2 were obtained via 1D selective ROESY experiments.[106]

4.2.2.5 Hydrogen Bonding. The detection of intramolecular hydrogen bonds requires the observation of chemical shifts, linewidths, temperature shift coefficients, NOEs, and, if possible, ^3J(HOCH) couplings and exchange rates of assigned OH signals. In order to use OH protons as conformational probes for oligosaccharides, special techniques for water suppression must be utilized.[157,189–191] Additionally, isotope effects on ^{13}C chemical shifts examined in H_2O/D_2O (1:1, v/v) may be interpreted in terms of hydrogen bonding.[104]

If chemical exchange rates are of the same order of magnitude as the vicinal coupling constants, the assignment of hydroxyl protons on the basis of scalar correlation spectroscopy will not be possible. In these cases, assignments can be based on spatial proximities to the ring protons gained from steady-state NOE spectra [see Figure 10(c) for the pulse sequence]. This procedure requires, however, a good deal of caution, as spin diffusion and NOE enhancements mediated by chemical exchange could lead to erroneous assignments. In mixed solvents at temperatures well below 0 °C, chemical exchange is often retarded to an extent that transient NOE techniques can be utilized. As may be expected, even at low temperatures, the ^3J(HOCH) couplings for mono- and disaccharides obtained are found to be indicative of rotational averaging of the 'dangling' hydroxyl groups in most cases.[103] However, NOESY experiments performed on supercooled di- and trisaccharides strongly suggest that the majority of the intramolecular hydrogen bonds inferred from their crystal structures persist in solution.[101]

Most of the OH signals of sialyl-$\alpha(2\rightarrow6)$-lactose, investigated in mixed solvent systems at temperatures as low as −12 °C and in H_2O/D_2O at 1 °C, were assigned by 1D steady-state NOE experiments. Based on their linewidths and temperature shift coefficients (in conjunction with isotope shift effects observed in the ^{13}C spectra of the trisaccharide in H_2O/D_2O), three OH groups were found to be involved in intramolecular hydrogen bonds. First, Neu5Ac OH-8 is involved in an intraresidue hydrogen bond to the C-1 carboxyl group;[99] secondly, the hydrogen bond between Glc OH-3 and Gal O-5 is reminiscent of that found in lactose,[101] both in solution and in the crystal structure. Finally, the hydrogen bond observed between Neu5Ac OH-7 and Glc O-3 is an example of a long-range structural constraint of great value in the construction of the preferred conformation of sialyl-$\alpha(2\rightarrow6)$-lactose in aqueous solution. Modeling of the trisaccharide was based on 25 interresidue NMR constraints (Table 2). Analysis by MMC simulations[106,192] has shown that sialyl-$\alpha(2\rightarrow6)$-lactose occurs predominantly in two families of conformers that differ in the ϕ angle around the (2→6)-linkage (−60° versus 180°). The average structure of the predominant (>80%) family of conformers is depicted in Figure 16; it is the family stabilized by the three intramolecular hydrogen bonds.

4.2.3 Dynamics

The 3D structure of the disaccharide sucrose [Fru$\beta(2\leftrightarrow1)$ αGlc] (Figure 17), particularly the conformation of its glycosidic linkage, has been the subject of numerous investigations.

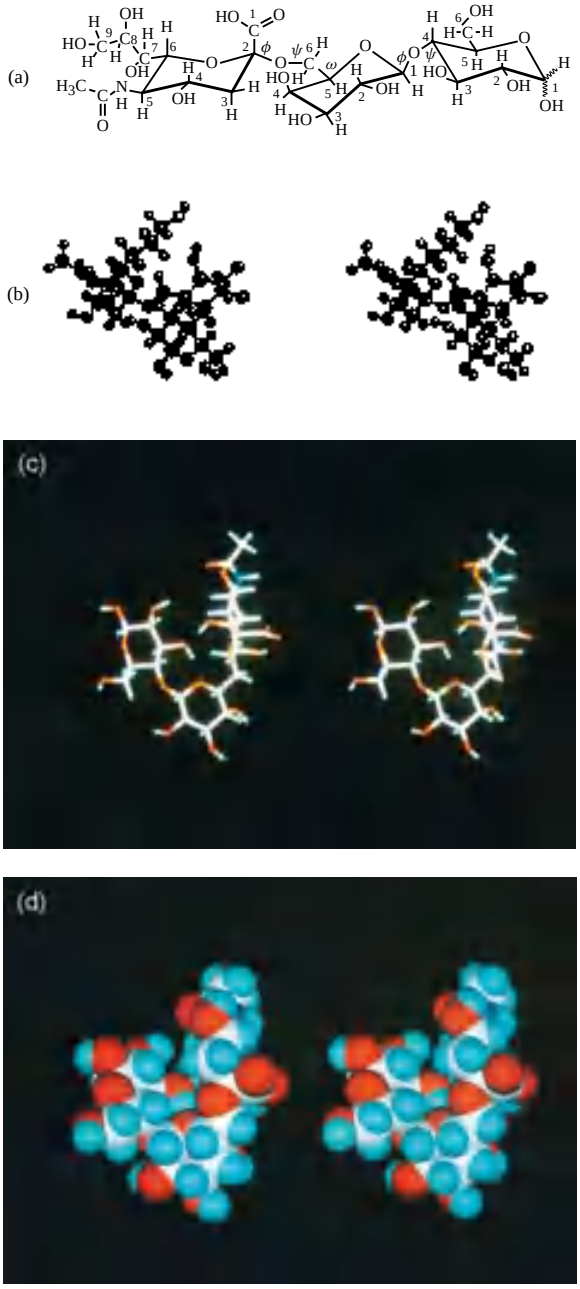

Figure 16 Stereo plots [ball-and-stick (b), Dreiding models (c), CPK models (d)] of the predominant conformer ('family I', Table 2) of sialyl-$\alpha(2\rightarrow6)$-lactose (a) in aqueous solution as derived from NMR data.[106] The Neu5Ac O-7:::H:::Glc O-3 and Glc O-3:::H:::Gal O-5 hydrogen bonds are clearly visible

Data obtained on sucrose in the crystalline[193,194] and solution states[93,174,195] have led to uncertainties concerning the degree of rigidity of the linkage conformation in solution, thus posing the question whether it is the same as in the crystal structure. A great deal of effort was spent examining intramolecular hydrogen bonding[196,197] and its effect, if any, on the overall conformation of sucrose in solution. McCain and Markley[198] were the first to measure ^{13}C T_1 relaxation times on sucrose as a function of the magnetic field strength. They realized the importance of knowing the timescale of internal motion when modeling carbohydrate conformations. As discussed in Section 4.1.3, this information can, in principle, be gained from nuclear relaxation rate measurements, preferably at different field strengths and different temperatures. The number of such studies performed on carbohydrates is remarkably small, and a model rigid on the timescale of molecular reorientation is often assumed on the basis of ^{13}C T_1 relaxation times. Accordingly, McCain and Markley's careful ^{13}C T_1 measurements for sucrose revealed very fast and small amplitude torsional and vibrational motions[198–200] and different mobility of exocyclic groups;[200] however, the glycosidic linkage was judged to be rigid on the basis of this type of measurements, and similar in conformation to that observed in the crystalline state. Presenting a quantitative analysis of the field strength dependence of $^1H/^1H$ NOE data, Poppe and Van Halbeek[105] questioned the rigidity of the sucrose glycosidic bond in solution and explained the reasons why this type of flexibility was not revealed by McCain and Markley's data. The evidence is briefly reviewed below.

Seeking to reveal as large a set of interresidue distance constraints as possible and to shed light on the existence of any hydrogen bonds in sucrose in aqueous solution, sucrose was investigated at low temperatures in aqueous solutions with the purpose of including the OH signals in the analyses. All of the sucrose OH signals were indeed observed in 1–1 echo experiments [Figure 17(a)], and had lines sufficiently narrow to be assigned by 2D and selective 1D TOCSY experiments. To measure interresidue distance constraints, 1D ROESY [Figure 10(a)] and multiselective TOCSY–ROESY [Figure 10(d)] experiments were performed; these experiments benefited from the excellent water suppression by an inhomogeneous, transverse $\boldsymbol{B}_1$ field [see Figure 17(b–f)]. The concept of selective 3D TOCSY–NOESY and TOCSY–ROESY spectroscopy [as mentioned for the assignment of the Gal H-6 protons in sialyl-$\alpha(2\rightarrow6)$-lactose, Figure 13] was extended to include multiple selective excitations. In an analogous manner to a 1D NOE experiment, these experiments allowed the measurement of NOEs between H-5 g and its spatial neighbors, in addition to NOEs between H-1 g and its neighbors ('g' denotes the glucose, 'f' the fructose moiety in sucrose). An example of a double selective pseudo 3D TOCSY–ROESY spectrum of sucrose is shown in Figure 17(c). Selective excitation of the H-4 g resonance was followed by a TOCSY step, a second selective pulse applied to the H-5 g resonance, and finally a ROESY step. Thus, NOE connectivities originating from H-5 g, which could not have been excited in a single selective experiment, were successfully measured. Special care was taken to ensure that NOEs were free of spin diffusion artifacts before converting them into distances. The standard 1D NOESY spectrum of sucrose after selective excitation of the H-1 g resonance [Figure 18(a)] revealed NOE enhancements to H-11′f, H-66′f, H-4f, H-5f, and H-3f. To determine the amount of the H-1 g/H-3f NOE due to direct magnetization transfer, H-11′f, H-4f, and H-5f were selectively and simultaneously spin locked during the mixing time of a second experiment [Figure 18(b)], thereby cutting off all possible indirect magnetization transfer pathways from H-1 g to H-3f. The results of the quantitative NOE measurements are compiled in Table 3. Interestingly, all NOE connectivities (and the lone exchange interaction, see below) found for sucrose in water solution

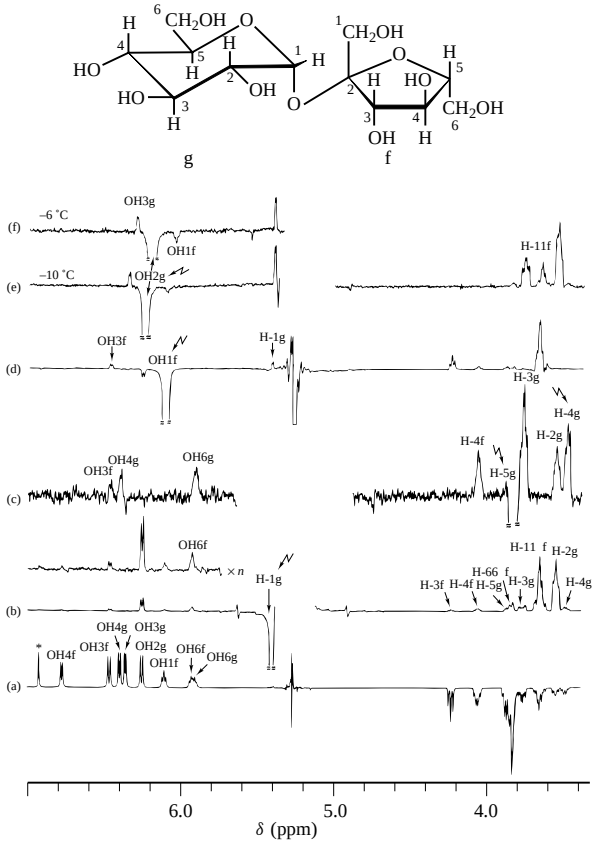

Figure 17 500 MHz ^{1}H NMR spectra of sucrose [Fru$\beta(2\rightleftarrows1)\alpha$Glc; g = Glc, f = Fru] (5 mg in 0.5 ml of $H_2O/(CH_3)_2CO$, 6:1, v/v) obtained at $-10\,^\circ$C (except trace f). (a) Spectrum obtained with a 1–1 echo pulse sequence. (b) 1D ROESY spectrum (320 scans) obtained with the pulse sequence shown in Figure 10(a); selective excitation of the H-1 g resonance was followed by a 200 ms spin lock pulse train. (c) Double-selective 3D TOCSY–ROESY spectrum obtained with the pulse sequence shown in Figure 10(d). Selective irradiation of H-4 g was followed by 30 ms of isotropic mixing, the selective irradiation of H-5 g, and a 200 ms spin lock pulse train; 640 scans were accumulated. (d, e) 1D ROESY spectra (320 scans) with selective irradiation of OH-1f and OH-2 g, respectively. (f) 1D ROESY spectrum, recorded at $-6\,^\circ$C, with selective irradiation of OH-2 g. A comparison of traces (e) and (f) reveals an OH-2 g/OH-1f chemical exchange interaction, suggesting the existence of an O-1f:::H:::O-2 g hydrogen bond in solution under the applied conditions[105]

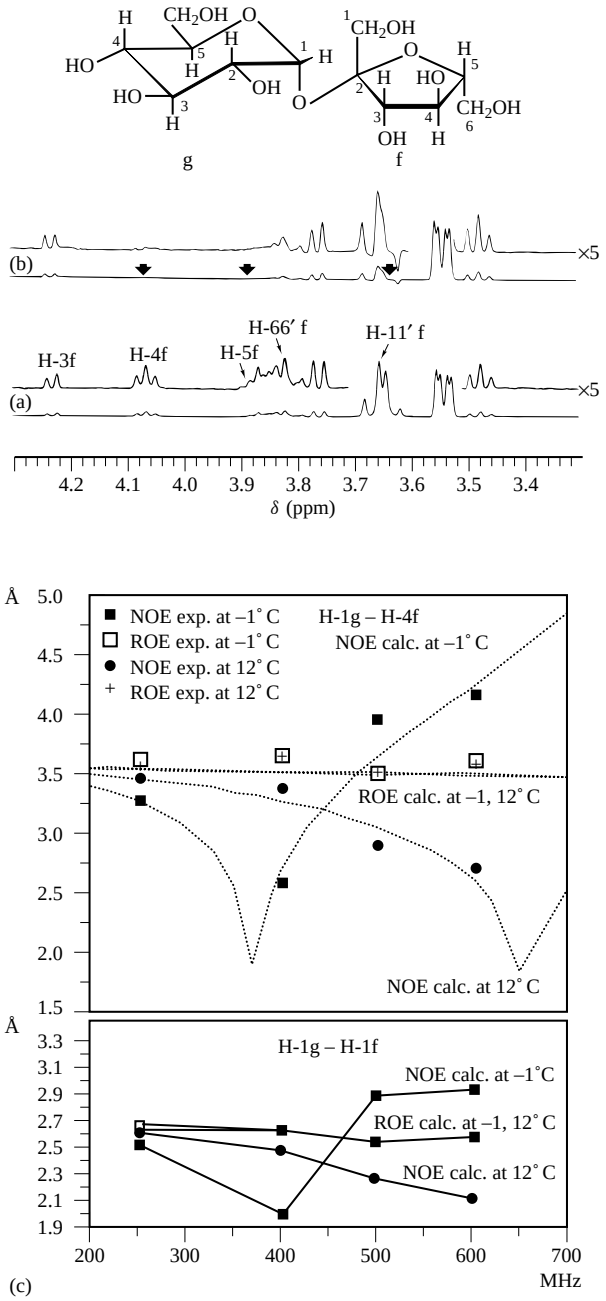

Figure 18 (a) 1D NOESY spectrum (500 MHz; τ_{mix} = 0.4 s) of sucrose [Fru$\beta(2\rightleftarrows1)\alpha$Glc; g = Glc, f = Fru] in a $D_2O/(CH_3)_2CO$ (6:1, v/v solution) at $-5\,^\circ$C. The interresidue NOE enhancements of fructose ring protons obtained after selective excitation of Glc H-1 are indicated [see the pulse sequence in Figure 10(b)]. (b) Identical to (a), with the addition of the triple-selective spin locking of H-4f, H-5f, and H-11′f (marked with arrows) during the mixing time using a triple-DANTE pulse train. As all possible indirect magnetization transfer pathways from spin H-1 g to spin H-3f are cut off in experiment (b), the measured H-1 g/H-3f NOE enhancement is solely the result of direct dipolar interaction between these two spins. (c) Distances $r_{H-1\,g-H-4f}$ and $r_{H-1\,g-H-1f}$ as determined from 1D NOESY and 1D ROESY measurements on sucrose in H_2O solution at two different temperatures ($-1\,^\circ$C and $12\,^\circ$C) and four magnetic field strengths (250, 400, 500, and 600 MHz). Theoretical values for $r_{H-1\,g-H-4f}$ (dotted lines) were predicted from a model described by Poppe and Van Halbeek,[105] assuming rapid interconversion of three different rotameric conformations around the glycosidic linkage

can be explained in terms of a single conformation, which is virtually identical to that in its crystal structure.

However, when measuring specific $^1H/^1H$ cross-relaxation rates as a function of magnetic field strength and temperature, large conformational changes occurring much faster than the overall motion were revealed around the glycosidic bond.[105] Selective excitation at the H-1 g resonance was followed by the detection of NOEs at H-11′f, H-4f, and several protons in the glucopyranose ring. The NOEs between protons on different rings proved to be field-strength-dependent, while this did not seem to be the case for NOEs between protons in the glucopyranose ring [Figure 18(c)]. This observation is interpreted as evidence for the occurrence of rearrangements around the glycosidic bond between the glucosyl and fructosyl residue which are much faster than the tumbling time of the molecule in solution ($\tau_o \sim 0.2$ ns). This type of internal motion is transparent

Table 3 $^{1}H/^{1}H$ Distances for Sucrose in Aqueous Solution Derived from Interglycosidic NOE Contacts[105]

Proton pair[a]	Distance[b] (Å)
H-1g/H-1f	2.6[c]
H-1g/H-3f	4.6
H-1g/ H-4f	3.5[c]
H-1g/H-6f	4.0
H-5g/H-4f	3.0
H-1g/OH-1f	3.6
H-1g/OH-6f	3.4
H-1g/OH-3f	4.0
H-5g/OH-3f	3.8
OH-2g/H-1f	3.2

[a]Data for aliphatic protons were acquired at 27 °C, data for hydroxyl protons at −10 °C; 'g' denotes the glucosyl, 'f' the fructosyl ring.

[b]Distances were calculated using the formula $r_{ij} = (\sigma_{\mathrm{ref}}/\sigma_{ij})^{\frac{1}{6}} r_{\mathrm{ref}}$ in which σ_{ref} and r_{ref} represent the cross-relaxation rate of and the distance between a reference pair of protons. Intraglucosyl distances H-1g/H-2g (2.4 Å), H-1g/H-3g (3.7 Å), and H-1g/H-4g (4.0 Å) were used as references. The precision of the distances r_{ij} is estimated to be $0.1r$.

[c]See Figure 18(c).

to relaxation parameters, including ^{13}C T_1, if it occurs on the timescale of overall molecular tumbling; this seems to be the case for sucrose at ambient temperature. Thus, the accurate measurement of ^{1}H cross-relaxation rates ($\sigma_{\mathrm{H,H}}$) has the following advantages over traditional ^{13}C T_1 measurements: (i) a higher spectral sensitivity; (ii) an increased ability to detect internuclear fluctuations; (iii) a dependence on spectral density at zero frequency and, therefore, sensitivity to slow motions, and (iv) the greater diversity of geometric orientations of the H−H vectors in a rigid pyranose ring, as compared with the parallel orientation of most of the C−H vectors, allowing more efficient sampling of spectral densities.

Additionally, the observation of chemical exchange between OH-1f and OH-2 g [Figures 17 (e) and (f)] provides reasonable evidence for the existence of an OH-1f:::O-2 g hydrogen bond in solution under the applied conditions. In summary, it appears that intramolecular hydrogen bonding in sucrose is concentration-dependent; the existence of hydrogen bonds OH-1f:::O-2 g, OH-3f:::O-2 g, and OH-6f:::O-5 g at higher concentrations has been postulated, based interalia on ^{13}C isotope effects.[196] The existence of the first two hydrogen bonds at high concentration in solution implies flexibility and fast interconversion between two conformers around the glycosidic linkage in solution (in the crystal only OH-1f:::O-2 g and OH-6f:::O-5 g are observed).

Once fast internal motion in sucrose was detected by measuring a number of interglycosidic NOEs as a function of magnetic field strength and temperature of the solution,[105] similar observations were reported for other di- and trisaccharides.[201–204] It is now widely accepted that small oligosaccharides are flexible molecules, experiencing intramolecular rearrangements that are fast compared with the overall tumbling of the molecules.

4.3 Glycoprotein Oligosaccharides

Although, during the past decade, NMR spectroscopy has become sophisticated enough to handle conformational analysis of glycoprotein-related oligosaccharides and glycopeptides in solution, few of these oligosaccharides have yet been examined as rigorously as the di- and trisaccharides mentioned in Section 4.2. In hindsight, the relatively slow pace in which oligosaccharide conformational analysis has developed is primarily due to glycobiologists' expectations concerning the models for glycoprotein carbohydrates; they expected a single, rigid 3D shape for an oligosaccharide of any given primary structure. This school of thought was based on pioneering investigations of the ABH and Lewis blood group determinants [for primary structures see Figure 1(d)]. However, as it turned out later, these branched tri- and tetrasaccharide epitopes happened to be far more rigid than most small oligosaccharides, leading to the misguided concept of carbohydrate 3D structural rigidity and the resultant overconfidence that modeling of any carbohydrate could be handled by the HSEA approach (hard-sphere representation of nonbonded interactions dominated by the *exo*-anomeric effect). Most glycoprotein oligosaccharides are flexible to some degree and are continually experiencing dynamic fluctuations in structure. Their flexibility is important because it may allow them to fit into the binding sites of carbohydrate-binding proteins (lectins, antibodies, receptors) (Section 5.3). In chronological order, we will summarize the work on blood group oligosaccharides which are known to occur in the peripheral portions of glycoprotein and ganglioside carbohydrate chains, followed by more typical *N*-type and *O*-type glycoprotein carbohydrate structures (Figure 1).

4.3.1 Peripheral Epitopes

The conformations of blood group oligosaccharides were first investigated by Lemieux et al.,[205] who reported ^{1}H and ^{13}C NMR assignments for trisaccharide fragments of the oligosaccharides denoted A, B, H, Le^x, and Le^y in Figure 1(d). Qualitative NOE data, along with primitive conformational energy calculations, were thought to indicate single conformations for each of these oligosaccharides. The influence of hydrogen bonding and other electrostatic effects was proposed to be unimportant; the rigid conformations were thought to be mainly determined by steric or nonbonded interactions and by torsional potentials.[206]

With the advent of more sophisticated NMR techniques, as well as a less naive approach to oligosaccharide modeling, Bush and co-workers set out to apply much more rigorous tests to these proposals in the late 1980s. This group of investigators acquired large collections of carefully measured NOE data on blood group and related oligosaccharides in various solvents at a number of sample temperatures.[207–215] Full relaxation matrix analysis of those data, along with MD simulations, revealed that the blood group epitopes found on glycoproteins and glycolipids assume relatively rigid conformations. The latest results obtained by Bush and co-workers on the Le^x trisaccharide and sialyl-Le^x tetrasaccharide[208,216] indicate that the Le^x portions of the molecules are rigid, but the Neu5Acα(2→3)-linkage shows transitions between two predominant conformational states [experimentally defined by ROE and ^{3}J(C,H) values]. Other investigators[217,218] concur with these findings on the issue of the rigidity of the Le^x portion of the molecule [i.e., the conformation can be described by one set of ϕ,ψ-values for the Fucα(1→3)GlcNAc and Galβ(1→4)GlcNAc linkages each] and support a model featuring fast exchange between two different conformations

of the Neu5Acα(2→3)Gal-linkage. The dynamics of fucosyl-α(1→2)-lactose and related oligosaccharides are currently being reinvestigated along the lines discussed in Section 4.2[203,204]

4.3.2 N- and O-Type Glycoprotein Oligosaccharides

The NOE-based conformational analysis of *N*-type glycoprotein oligosaccharides began simultaneously and independently in Toronto[219–222] and Oxford.[223] The conformations of the various linkages in the diantennary *N*-acetyllactosamine-type oligosaccharide [Figure 1(b)] and its high-mannose analogs were evaluated and, at first, judged to be fairly rigid with the exception of the α(1→6)-linkage. In 1987, however, both the Toronto[224–226] and the Oxford[227–229] groups realized that they had proposed 'virtual conformations' for the *N*-type core structures up to that point. When carefully scrutinized, the increased amount of NOE constraints available at that time appeared to be inconsistent with one conformation per linkage and prompted a reevaluation of the concept of carbohydrate structure rigidity. The ensemble representation was introduced for the oligosaccharides, as NMR observables calculated as ensemble averages gave better agreement with experimental values than those derived from single structures. Since then, MD simulations and NOE measurements at different field strengths have been helping each other over a number of 'barriers' to the further understanding of glycoprotein carbohydrate dynamics. Both the Oxford and the Toronto groups have recently resorted to small di-, tri- and tetrasaccharide building elements of the *N*-type oligosaccharides in order to assess carefully their dynamic behavior, while simultaneously attempting to improve the molecular modeling methods for carbohydrates.[76,107,108,201,230–234] Currently, detailed NMR studies on larger *N*-type oligosaccharides covalently linked to proteins are being conducted as well (Section 5.1). Impartial review articles[18,66,83,235] keep the glycobiology community abreast of continuing developments in this area of research.

Additional insight into the conformation of the core pentasaccharide $Man_3GlcNAc_2$ in an *N*-type glycopeptide was provided by a study of a hen ovomucoid glycodecapeptide.[236] TOCSY and NOESY experiments on the glycopeptide in H_2O, supported by ^3J(N,H) data, provided evidence that the C-2–N-2 bond in Asn-linked GlcNAc is rigid; however, this rigidity could not be attributed to any intramolecular hydrogen bond. Although these and other sophisticated tricks of the NMR trade are just beginning to be applied to larger oligosaccharides and glycopeptides, we now have a reasonable picture of the conformation and flexibility of *N*-type oligosaccharides of the high-mannose and the *N*-acetyllactosamine type. Similar investigations of *O*-type Ser/Thr-linked oligosaccharides[78,237,238] and small sialyl oligosaccharides (Section 4.2) are currently being conducted. Given the similarities of the backbone and peripheral structural elements of *N*-type and *O*-type oligosaccharides, the results should be applicable to both classes of glycoprotein carbohydrates.

4.4 Glycolipids and Glycolipid-Related Oligosaccharides

Oligosaccharides released from gangliosides and other glycolipids (by endoglycoceramidase digestion or ozonolysis) are amenable to, and have been investigated by, the same NMR techniques as mentioned for glycoprotein oligosaccharides (Section 4.3). For example, the 1D TOCSY subspectra of the Gal and Neu5Ac residues in the G_{D1a} oligosaccharide (Figure 19) serve to illustrate that, despite the abundance of small couplings, magnetization can be propagated over the entire spin system of each residue allowing the complete assignment of these spectra. The conformations of the oligosaccharide portions of gangliosides such as G_{M1}, G_{M2}, G_{D1a} (for primary structures, see Figure 1), and GPI anchors[239,240] have been studied in aqueous environments by $^1H/^1H$ NOESY methods in combination with molecular modeling.[241,242] Frequently, the results obtained on the free oligosaccharides have been compared to those obtained by examinations of the intact glycolipids in DMSO solutions and other aprotic solvents.[51,55–57,64,187,188,243–247] In particular, the study of peripheral blood group elements which are so abundant on glycolipids features prominently in this work; not unexpectedly (see Section 4.3.1), the conformations of these epitopes are independent of the solvent. Although the results of these studies in DMSO are interesting from a basic science point of view, we will not review their details because of their relative lack of biological significance. Instead, we will turn to micellar systems formed by glycolipids in aqueous solutions (Section 5.2), emulating the cell's plasma membrane, and compare the carbohydrate's structures under those circumstances to the structures of the free glycolipid oligosaccharides in water.

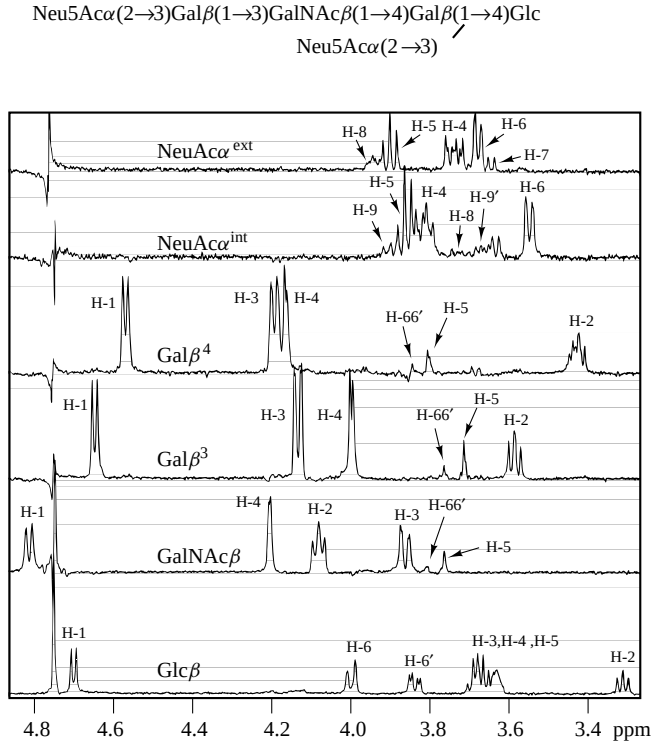

Figure 19 Subspectral editing of the ^1H NMR spectrum (600 MHz) of the G_{D1a} oligosaccharide in D_2O [16 mg mL^{-1}] by 1D TOCSY [see the pulse sequence in Figure 10(a)]. The H-1 signals of the hexosyl residues and the H-3ax signals of the Neu5Ac residues, respectively, were selectively excited. Superscripts in Gal^3 and Gal^4 refer to the position of the linkage in which these residues are involved (ext = external; int = internal). The constant isotropic mixing time was 370 ms; 160 scans were accumulated per spectrum

Due to the relative ease with which they can be ^{13}C-enriched, glycolipids have recently inspired the development of several new NMR spectroscopic techniques. Heteronuclear 3D NMR experiments, employing ^{13}C chemical shift editing of homonuclear correlation spectra, are an effective means of reducing spectral overlap for larger carbohydrates, particularly when ^{13}C-enriched carbohydrates are available for investigation.[235,248] Complete ^{1}H assignments for uniformly ^{13}C-labeled carbohydrates have been obtained with the use of HCCH–COSY and HCCH–TOCSY experiments.[249] By employing the ^{13}C,^{13}C coupling pathway [^{1}J(C,C) $\sim$ 40 Hz] for magnetization transfer, these techniques overcome the T_2 relaxation [^{3}J(H,H) $\ll$ linewidth] problems observed in ^{3}J(H,H)-mediated ^{1}H,^{1}H COSY and TOCSY spectra of glycoconjugates of high molecular weights and yield well-resolved spectra for polysaccharides and glycolipids. The 2D constant evolution time HCCH–COSY and HCCH–TOCSY experiments are particularly useful for the study of carbohydrates due to the relatively constant value of ^{1}J(C,C) couplings around the carbohydrate ring (36–45 Hz) which facilitates optimization of the fixed delay for ^{13}C,^{13}C magnetization transfer. The resulting ^{13}C,^{13}C decoupling simplifies the analysis of the ^{1}H spectra as traces in the 2D plots. Alternatively, ^{1}H-detected ^{13}C,^{13}C COSY experiments may be performed for complete ^{1}H and ^{13}C assignments of ^{13}C-enriched oligosaccharides (as was illustrated for the uniformly ^{13}C-labeled carbohydrate headgroup in a sulfolipid[250]). The sensitivity and resolution of the ^{1}H-detected 3D ^{13}C COSY experiments can be considerably improved by the implementation of pulsed field gradients, as demonstrated for a digalactosyl diacylglyceride which was biosynthetically uniformly ^{13}C-enriched to $\sim$15%.[251]

5 THE FUTURE: GLYCOCONJUGATES IN (INTER-)ACTION AT THE MEMBRANE SURFACE

The molecular behavior of an oligosaccharide chain isolated from a glycoprotein or glycolipid differs considerably from the behavior of the chain when bound to a protein or lipid. For example, the molecular motion of a freely tumbling oligosaccharide will be substantially different from that of the same oligosaccharide anchored to a protein backbone and/or in a lipid bilayer. It is quite conceivable that both molecular conformation and internal dynamics are affected upon the covalent binding of an oligosaccharide to a protein. Thus, appropriate caution must be exercised when extrapolating NMR-derived results concerning conformation and dynamics of isolated oligosaccharides to similar structures linked to proteins or lipids. NMR efforts are now underway to examine the conformation and dynamics of oligosaccharides as covalent parts of larger molecular weight glycoconjugates, both intact glycoproteins (Section 5.1) and glycolipids dispersed in lipid bilayers (Section 5.2). Also, the study of noncovalent carbohydrate–protein interactions via NMR methods is producing its first encouraging results (Section 5.3).

5.1 Glycoproteins

It has been known for quite some time[252] that the ^{13}C NMR spectra of intact glycoproteins in solution display signals arising from the oligosaccharide component that are considerably sharper than those arising from the polypeptide backbone. This observation suggests that the oligosaccharides of at least some intact glycoproteins possess motional characteristics other than those conferred on them by the tumbling of the protein; in other words, local (segmental) motion is experienced by the oligosaccharide chain. In 1982, Goux et al.[253] reported on ovalbumin in which nonreducing Gal was enriched in ^{13}C. Off-resonance rotating frame relaxation data showed that the carbohydrate had a 40–80 ps motion superimposed on the slow overall tumbling ($\tau_o \sim 25$ ns) of the protein.

Several NMR studies are currently being designed to elucidate the conformational effects of covalently linked carbohydrates on peptides in glycoproteins and vice versa. The glycoprotein ribonuclease B (RNase B) has most often served as the 'guinea pig'. The consensus with regard to this glycoprotein and several others seems to be that oligosaccharide and peptide do not mutually affect each other's conformation; instead, the oligosaccharide causes a decrease in the peptide's conformational mobility near the glycosylation site and vice versa. Thus, mutual effects have been observed on the local dynamics of peptide and oligosaccharide rather than on their conformation per se. For example, NMR measurements of amide H/D exchange rates on RNase A and B revealed that glycosylation of the protein leads to the protection of amide proton resonances from solvent exchange for a large number of amino acid residues in the vicinity of the glycosylation site and in more remote locations.[254,255] The detailed influence of a high-mannose oligosaccharide on the enzyme's properties was also explored with a combination of MD simulations of the carbohydrate, employing a novel force field parameterization for glycoproteins (GLYCAM-93), and structural model building based on the 2.5 Å X-ray crystal structure of the enzyme;[256] the results are currently awaiting NMR experimental verification.

Studies[108,231] focusing on the local dynamics of the $Man_5GlcNAc_2$ carbohydrate chain in RNase B took advantage of the protein's presence; the protein is, in essence, a large mass which, relative to the timescale of the internal motions, tethers the reducing end of the glycan. This causes the relaxation parameters to become much more sensitive to differential motion along the glycan chain. In addition, the overall motion of the glycoprotein can be considered to be isotropic, considerably simplifying data analysis. The order parameter S^2 was measured for reorientation of the C-1–H-1 vector of each glycosyl residue. As computed from ^{13}C T_1 values, S^2 was found to be $\sim$0.5 for internal residues and $\sim$0.1 for terminal residues (most distal to the protein). The rate of internal motion was found to be an order of magnitude higher for the distal than for the proximal residues. These data strongly support the existence of significant torsional oscillations about glycosidic bonds in high-mannose oligosaccharides.

However, there is at least one well-characterized glycoprotein in which carbohydrate and protein conformation do affect each other considerably: the F_c fragment of immunoglobulin G (IgG) containing an *N*-linked carbohydrate chain at Asn_{297} in the hinge region. There is compelling evidence, both from X-ray structural data and molecular modeling,[77,257] that the (1→6)-arm of the diantennary oligosaccharide interacts with Phe_{243}, Pro_{244}, and Thr_{260} residues of the protein. These interactions result not only in the loss of the flexibility associated with the (1→6)-arm, but also in a conformation of the

diantenna very different from that of the free oligosaccharide in solution. Recently, the F_c fragment in which ^{13}C-labeled Gal had been biosynthetically incorporated in terminal position of both arms of the diantenna in a similar way to the aforementioned studies on ovalbumin, was probed by ^1H-detected $^{13}C,^1H$ NMR. The two Gal residues were distinctly different in their NMR parameters (chemical shifts, linewidth), providing evidence for the strong interaction in solution of one arm of the diantenna with the peptide backbone.

5.2 Dynamics of Membrane-Bound Carbohydrates

Due to their amphipathic nature, isolated glycolipids aggregate in aqueous solution to form micelles. With their long overall rotational correlation times, these systems lend themselves to high-resolution NMR studies and are the most revealing probes currently used for the study of internal motions in lipid-linked oligosaccharides. Poppe and coworkers have studied the conformation and dynamics of the carbohydrate headgroups of a number of glycolipids inserted in deuterated dodecylphosphocholine (DPC) micelles in D_2O and/or H_2O, including globoside,[129,187] Forssman antigen,[162] and the gangliosides G_{M4},[258] G_{M3} and Neu4Ac5Gc-G_{M3},[259] G_{M1},[188] and G_{D1a}.[260] The researchers typically measured interglycosidic $^1H/^1H$ NOEs and used these to build tentative 3D structures of the oligosaccharide using a distance mapping procedure.[188] Figure 20 shows 1D NOESY spectra for one of the galactose residues in the G_{D1a} ganglioside/micelle system in D_2O solution. Selective spin locking during the mixing time, obtained with a double-DANTE pulse sequence,[261] allowed the calculation of, for example, the intraring Gal H-1–H-4 distance based upon a spin-diffusion-free NOE effect.

Figure 21 shows that G_{D1a} in a micellar membrane in H_2O is singularly suited for high-resolution NMR studies, particularly those focusing on its OH signals at low temperature, without the use of organic solvents. It appeared[260] that the observed NOEs could not be explained by the occurrence of the G_{D1a} oligosaccharide in a single conformation such as the reasonably rigid structures proposed for the G_{D1a}-free oligosaccharide[242] in D_2O and glycolipid[245] in DMSO on the basis of ^{13}C T_1 data. At least two families of carbohydrate conformers, differing in the relative orientation of the Neu5Acα(2→3)Galβ(1→3) external disaccharide arm, must exist in this model membrane system to account for the NOE constraints. The internal dynamics of the oligosaccharide were probed by ^1H detection of the ^{13}C relaxation parameters (T_1, $T_{1\rho}$, and heteronuclear NOEs) of the micellar system at ^{13}C natural abundance. The internal reorientations were found to occur with a rotation correlation time of 0.35 ns. The slow tumbling of the micelle ($M_r \sim 8$ kDa) provided the distinct timescale (τ_o = 2.8 ns), facilitating the discovery of the faster internal motion of two flexible glycosidic linkages in the carbohydrate headgroup.[260]

Applications of these methods to larger complex oligosaccharides, as well as to those tethered to proteins or lipid membranes, will continue to provide valuable evidence with which to address the question of internal motions on a timescale of the reciprocal of the NMR frequency range used in the experiment (0.1–1 ns). Motions on a slower timescale, which would not be detectable by ^{13}C T_1 experiments, can be studied with rotating frame relaxation data ($T_{1\rho}$). With control of the spin locking field strength, the latter parameter can reveal motions on the μs timescale.

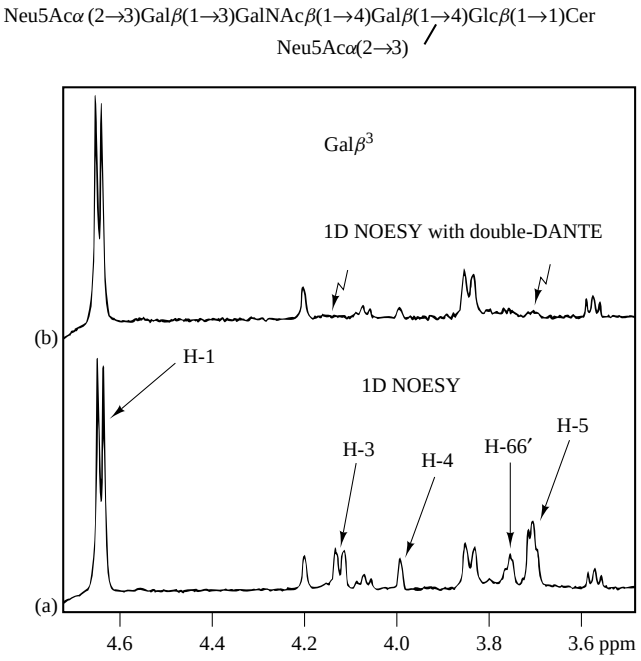

Figure 20 1D NOESY spectra (600 MHz, 25 °C) of G_{D1a}/DPC-d_{38} micelles in D_2O solution. Mixing time 0.4 s. (a) Selective irradiation of Gal^3 H-1. The labels indicate intraresidue NOEs that are significantly compromised by spin diffusion. (b) Selective irradiation of Gal^3 H-1 with double-selective spin locking of Gal^3 H-3 and H-5 during the mixing time. The resulting H-1/H-4 NOE intensity is devoid of indirect magnetization transfers

Alternative approaches to unmasking the conformation and dynamics of glycolipids embedded in model membranes include the study of the angular dependence of NOE in oriented systems of G_{M3} ganglioside with partially ^{13}C-labeled sialic acid[262] at the surface of magnetically oriented membranes. Dipolar interactions measured between $^{13}C,^{13}C$ and $^{13}C,^1H$ pairs located in the ^{13}C-labeled sialic acid moiety of G_{M3} are interpreted as indications that the G_{M3} structure is well extended from the membrane surface. In fact, membrane-bound G_{M3} was shown to bind wheat germ agglutinin (WGA), leading to the conclusion that the dominant G_{M3} structure at the membrane surface is favored for binding by the lectin. These and other aspects of NMR studies of glycolipids at model membrane surfaces are covered in detail by Jarrell (***Glycolipids***) in this Encyclopedia.

5.3 Carbohydrate–Protein Interactions

The general argument made in Section 2 for the role of complex carbohydrates as informational macromolecules implies that there must be a mechanism for decoding the information which is stored in their structures. Apparently, this decoding depends on a group of multivalent carbohydrate-binding proteins known as (se)lectins. Lectins are widely distributed in animal tissues (albeit in small quantities) and bind simultaneously to at least two carbohydrate determinants (epitopes). Some lectins are membrane-bound, others are soluble; both are thought to function by facilitating communication between

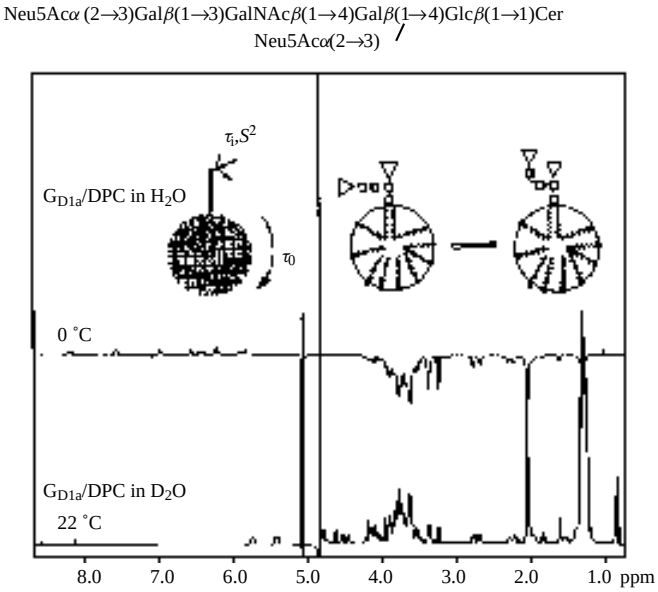

Figure 21 ^{1}H NMR spectra of G_{D1a}/DPC-d_{38} micelles in aqueous solutions; (bottom trace) spectrum in D_2O at 22 °C; (top trace) spectrum in 90% H_2O/10% D_2O at 0 °C, obtained with the 1–1 echo water suppression technique. The experimental data obtained on the micellar G_{D1a} system are compatible with the existence of two conformations of the external Neu5Ac–Gal portion of the oligosaccharide relative to the core tetrasaccharide anchored into the micelle. Interconversion between the two conformers is fast (τ_i = 0.35 ns; S^2 = 0.55 for the external disaccharide unit) relative to the overall tumbling of the micellar system ($M_r \sim 8$ kDa; τ_o = 2.8 ns; S^2 = 1)[260]

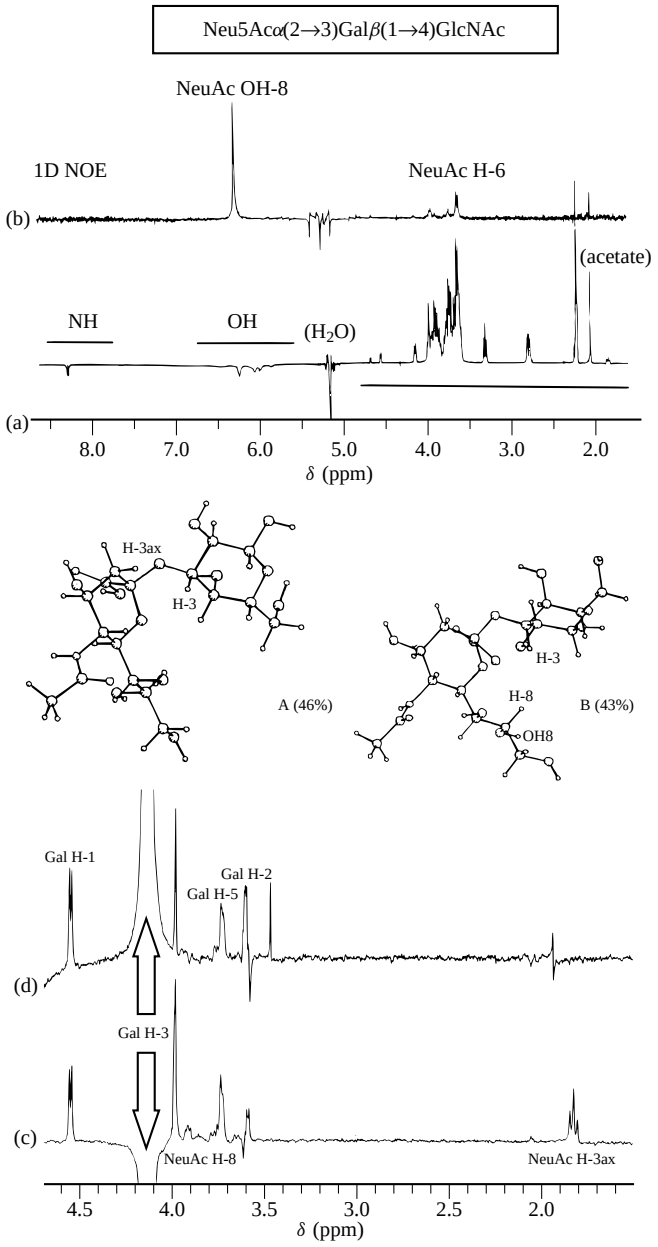

Figure 22 (a) The 500 MHz ^{1}H NMR spectrum of sialyl-α(2→3)-lactose [5 mM in H_2O/$(CD_3)_2CO$, 8:1, v/v] obtained at −12 °C with the 1–1 echo water suppression technique. Among the OH signals, the Neu5Ac OH-8 signal is characterized by the smallest exchange contribution to the linewidth and the smallest temperature variation of chemical shift (~0.001 ppm °C^{-1}). (b) 1D pre-steady-state NOE difference spectrum obtained subsequent to presaturation of OH-8 under the conditions described in (a); a strong NOE contact to Neu5Ac H-6 is observed. (c) 1D clean-ROESY[272] spectrum of sialyl-α(2→3)-lactose (5 mM in D_2O, 25 °C, 600 MHz). (d) 1D transferred NOESY spectrum of sialyl-α(2→3)-lactose in complex with wheat germ agglutinin (4 mM trisaccharide; 0.08 mM WGA; pD = 7, D_2O, 25 °C, 600 MHz). Note the absence of an NOE between GalH-3 and Neu5Ac H-3ax in trace (d) while Neu5Ac H-8 experiences a NOE, suggesting that the conformation of sialyl-α(2→3)-lactose that binds to WGA is the less populated[129] conformation free in solution (conformation B; middle right)

cells by linking them together. Antibodies are another class of soluble proteins involved in biological interactions with carbohydrates.

NMR spectroscopy is beginning to emerge as an experimental approach to the study of carbohydrate–protein interactions. Although limited by the size (molecular weight) and solubility of the protein, NMR spectroscopy is particularly useful for detailed studies of protein–carbohydrate interactions in solution when the complex has a molecular weight less than 35 kDa; under favorable circumstances, NMR can provide information about larger molecular weight systems as well. In general, if detailed information about conformation is sought, it is preferable that the ligand or the protein be ^{15}N, ^{13}C and ^{13}C,^{15}N doubly labeled in order to provide a sufficient amount of structural constraints. For the larger M_r protein–carbohydrate complexes this is a necessity; for the smaller M_r complexes it is highly desirable (cf. Otting[263]).

NMR spectroscopic studies on the interactions between proteins and carbohydrates have focused on several systems, including the lectins wheat germ agglutinin[264,265], concanavalin A, *Sambucus nigra* agglutinin, *Ricinus communis* B,[122] and *Aleuria aurantia* agglutinin[266] with their respective ligands, and several monoclonal antibodies with their oligosaccharide antigenic counterparts.[267–269] The typically weak carbohydrate–protein binding and intermediate-to-fast exchange between the free and the bound ligand permit transferred NOE (TrNOE) studies[108,263,270,271] and lineshape analysis. The aim of a TrNOE experiment is to measure *negative*

NOEs on easily detectable free or averaged carbohydrate resonances following the irradiation of other carbohydrate resonances in order to obtain conformational information on the *bound* ligand. The true advantage of studying TrNOEs is that the effect is not restricted by the M_r value of the complex; instead, it continues to be favorable as the protein size increases. The TrNOE experiment is one of the few experiments capable of yielding information on the conformation of bound ligands in complex with large-size proteins. In general, the amount of information gained about the system will not be as large as from ^{13}C-labeled systems in the tight-binding/slow-exchange regime, and extreme care must be given to the analysis of the NOE-derived distances. For exchange rates $>100\,s^{-1}$, one can analyze the data with relative ease; for rates between $10-100\ s^{-1}$, the use of an extended relaxation matrix is necessary, as was demonstrated for the analysis of the binding of β-methylmelibiose to ricin B.[122] The lectin preferentially selects one of the two conformations that melibiose adopts when free in solution. Similarly, WGA preferentially binds one of the two major conformations that sialyl-$\alpha(2\rightarrow3)$-lactose adopts around the Neu5Ac−Gal linkage when free in solution. A preliminary TrNOE study of WGA isolectin 1 in complex with sialyl-$\alpha(2\rightarrow3)$-lactose (Figure 22) suggests that conformation B is the one which preferentially binds to the lectin, in accordance with the crystal structure of the complex of WGA isolectin 1 with sialyl-$\alpha(2\rightarrow3)$-lactose.[273] More detailed studies are in progress to confirm this hypothesis. The studies follow the protocol of a recent NMR and X-ray study of the complex of a monoclonal antibody with a branched trisaccharide epitope.[269] For this complex, Bundle and co-workers measured NOE build-up rates from TrNOE experiments which show that the trisaccharide undergoes a protein-induced conformational shift around a specific glycosidic linkage when bound in solution. Distance constraints derived from the TrNOE studies are consistent with two bound trisaccharide conformations, one of which correlates with the ligand conformation in the crystalline trisaccharide−antibody complex.

6 CONCLUSIONS

Since its first application to monosaccharide derivatives in the late 1950s, NMR spectroscopy has greatly contributed to our current knowledge of the structures and functions of complex carbohydrates. The importance of oligosaccharides in their own right and as the 'business ends' of glycoconjugates are becoming increasingly appreciated, and the role that NMR has played in this accomplishment cannot easily be overestimated. First of all, NMR spectroscopy provides a powerful nondestructive means with which to characterize the primary structures of carbohydrates and has, therefore, become an integral part of the current methodology of protein glycosylation site mapping. Moreover, the vast potential of NMR to unravel 3D carbohydrate structures and dynamics, as well as to study carbohydrate−protein interactions, is just beginning to penetrate into the collective mind of the glycobiology community. At the same time, NMR spectroscopists long preoccupied with the study of protein−peptide and protein−nucleic acid interactions are beginning to see the merits of investigating protein−carbohydrate interactions. Biological data point to a pivotal function for glycoproteins in the control of growth and differentiation in the complex cell organization of eukaryotic systems. In fact, some complex oligosaccharides are implicated as onco-fetal antigens. Thus, the biological function of the complex carbohydrate chains of glycoproteins and glycolipids in animals is perhaps one of the most interesting unanswered fundamental questions in modern biochemistry. Unmasking carbohydrate structure−function relationships has been marked as the next frontier in molecular biology; the glycobiology community now finds itself turning to NMR spectroscopy to provide the instrumental means with which to enter this 'promised land'.

7 RELATED ARTICLES

Glycolipids; Nucleic Acids: Spectra, Structures, and Dynamics; Polysaccharides and Complex Oligosaccharides; Protein Structures: Relaxation Matrix Refinement; Vicinal Coupling Constants and Conformation of Biomolecules.

8 ABBREVIATIONS

The abbreviations used for monosaccharides, blood group determinants, and gangliosides are defined in the legend to Figure 1. Other abbreviations are: ANN, artificial neural network; CCSD, complex carbohydrate structure database; DANTE, delays alternated with nutations for tailored excitation; DIPSI, decoupling in the presence of scalar interaction; DPC, dodecylphosphocholine; DSS, 4,4-dimethyl-4-silapentane-1-sulfonate; GPI, glycosyl phosphatidyl-inositol; HMBC, heteronuclear multiple-bond connectivity; HMQC, heteronuclear multiple quantum coherence; HSEA, hard-sphere *exo*-anomeric; HSQC, heteronuclear single quantum coherence; Le^a, Lewis a; (M)MC, (Metropolis) Monte Carlo; MD, molecular dynamics; MLEV, pulse sequence first proposed by Malcolm Levitt; *n*D, *n*-dimensional (where n = 1, 2, 3, or 4); sLe^x, sialyl-Lewis x; TAA, tumor-associated antigens; TrNOE, transferred NOE; UGA, The University of Georgia; WGA, wheat germ agglutinin.

9 REFERENCES

1. A. Varki, *Glycobiology*, 1993, **3**, 97.
2. R. C. Hughes, *Glycoproteins*, Chapman and Hall, London, 1983.
3. M. Fukuda (ed.), *Cell Surface Carbohydrates and Cell Development*, CRC Press, Boca Raton, FL, 1992.
4. N. Sharon and H. Lis, *Lectins*, Chapman and Hall, London, 1989.
5. R. P. McEver, *Thromb. Haemost.*, 1991, **65**, 223.
6. L. A. Lasky, *Science*, 1992, **258**, 964.
7. W. J. Lennarz and G. W. Hart (eds.), *Methods in Enzymology*, Academic Press, San Diego, 1994, Vol. 230.
8. E. F. Hounsell (ed.), *Methods in Molecular Biology*, Humana Press, Totowa, NJ, 1993, Vol. 14.
9. C. A. Bush, *Bull. Magn. Reson.*, 1988, **10**, 73.
10. R. U. Lemieux, *Explorations with Sugars: How Sweet It Was*, American Chemical Society, Washington, DC, 1990.

11. R. U. Lemieux, R. K. Kullnig, H. J. Bernstein, and W. G. Schneider, *J. Am. Chem. Soc.*, 1957, **79**, 1005.
12. R. U. Lemieux, R. K. Kullnig, H. J. Bernstein, and W. G. Schneider, *J. Am. Chem. Soc.*, 1958, **80**, 6098.
13. M. Karplus, *J. Chem. Phys.*, 1959, **30**, 11.
14. R. U. Lemieux, R. K. Kullnig, and R. Y. Moir, *J. Am. Chem. Soc.*, 1958, **80**, 2237.
15. H. van Halbeek, *Methods Enzymol.*, 1994, **230**, 132.
16. G. Kotowycz and R. U. Lemieux, *Chem. Rev.*, 1973, **73**, 669.
17. A. S. Perlin and B. Casu, in *The Polysaccharides*, ed. G. O. Aspinall, Academic Press, New York, 1982, Vol. I, p. 133.
18. A. S. Serianni, in *Glycoconjugates: Composition, Structure, and Function*, eds. H. J. Allen and E. C. Kisailus, Marcel Dekker, New York, 1992, p. 71.
19. K. Bock and H. Thøgersen, *Annu. Rep. NMR Spectrosc.*, 1982, **13**, 1.
20. A. S. Shashkov, N. E. Nifant'ev, V. Y. Amochaeva, and N. K. Kochetkov, *Magn. Reson. Chem.*, 1993, **31**, 599.
21. F. J. Weighert, M. Jautelat, and J. D. Roberts, *Proc. Natl. Acad. Sci. USA*, 1968, **60**, 1152.
22. A. S. Perlin and B. Casu, *Tetrahedron Lett.*, **1969**, 2921.
23. K. Bock and C. Pedersen, *Adv. Carbohydr. Chem. Biochem.*, 1983, **41**, 27.
24. K. Bock, C. Pedersen, and H. Pedersen, *Adv. Carbohydr. Chem. Biochem.*, 1984, **42**, 193.
25. J. H. Bradbury and G. A. Jenkins, *Carbohydr. Res.*, 1984, **126**, 125.
26. G. Strecker, S. Fièvre, J.-M. Wieruszeski, J.-C. Michalski, and J. Montreuil, *Carbohydr. Res.*, 1992, **226**, 1.
27. J.-M. Wieruszeski, J.-C. Michalski, J. Montreuil, and G. Strecker, *Glycoconjugate J.*, 1990, **7**, 13.
28. G. Strecker, J.-M. Wieruszeski, J.-C. Michalski, and J. Montreuil, *Glycoconjugate J.*, 1989, **6**, 271.
29. K. Hermansson, P.-E. Jansson, L. Kenne, G. Widmalm, and F. Lindh, *Carbohydr. Res.*, 1992, **235**, 69.
30. P.-E. Jansson, L. Kenne, and G. Widmalm, *Carbohydr. Res.*, 1989, **188**, 169.
31. P.-E. Jansson, L. Kenne, and G. Widmalm, *Anal. Biochem.*, 1991, **199**, 11.
32. E. F. Hounsell, D. J. Wright, A. S. R. Donald, and J. Feeney, *Biochem. J.*, 1984, **223**, 129.
33. D. S. M. Bot, P. Cleij, H. A. van 't Klooster, H. van Halbeek, G. A. Veldink, and J. F. G. Vliegenthart, *J. Chemometrics*, 1988, **2**, 11.
34. J. A. van Kuik, K. Hård, and J. F. G. Vliegenthart, *Carbohydr. Res.*, 1992, **235**, 53.
35. H. van Halbeek, in *Methods in Molecular Biology*, eds. C. Jones, B. Mulloy, and A. H. Thomas, Humana Press, Totowa, NJ, 1993, Vol. 17, p. 115.
36. J. F. G. Vliegenthart, L. Dorland, and H. van Halbeek, *Adv. Carbohydr. Chem. Biochem.*, 1983, **41**, 209.
37. J. P. Carver and A. A. Grey, *Biochemistry*, 1981, **20**, 6607.
38. I. Brockhausen, A. A. Grey, H. Pang, H. Schachter, and J. P. Carver, *Glycoconjugate J.*, 1988, **5**, 419.
39. J. P. Kamerling and J. F. G. Vliegenthart, in *Biological Magnetic Resonance*, eds. L. J. Berliner and J. Reuben, Plenum Press, New York, 1992, Vol. 10, p. 1.
40. J. F. G. Vliegenthart, L. Dorland, H. van Halbeek, and J. Haverkamp, in *Sialic Acids: Chemistry, Metabolism and Function*, ed. R. Schauer, Springer, Vienna/New York, 1982, p. 127.
41. J. F. G. Vliegenthart, H. van Halbeek, and L. Dorland, *Pure Appl. Chem.*, 1981, **53**, 45.
42. G. Grönberg, P. Lipniunas, T. Lundgren, K. Erlansson, F. Lindh, and B. Nilsson, *Carbohydr. Res.*, 1989, **191**, 261.
43. H. van Halbeek, *Biochem. Soc. Trans.*, 1984, **12**, 601.
44. E. F. Hounsell and D. J. Wright, *Carbohydr. Res.*, 1990, **205**, 19.
45. J. U. Thomsen and B. Meyer, *J. Magn. Reson.*, 1989, **84**, 212.
46. B. Meyer, T. Hansen, D. Nute, P. Albersheim, A. Darvill, W. York, and J. Sellers, *Science*, 1991, **251**, 542.
47. J. P. Radomski, H. van Halbeek, and B. Meyer, *Nature Struct. Biol.*, 1994, **1**, 217.
48. S. Doubet, K. Bock, D. Smith, A. Darvill, and P. Albersheim, *Trends Biochem. Sci.*, 1989, **14**, 475.
49. D. A. Cumming, C. Hellerqvist, and O. Touster, *Carbohydr. Res.*, 1988, **179**, 369.
50. A. Allerhand and E. Berman, *J. Am. Chem. Soc.*, 1984, **106**, 2400.
51. R. K. Yu, T. A. W. Koerner, Jr., J. N. Scarsdale, and J. H. Prestegard, *Chem. Phys. Lipids*, 1986, **42**, 27.
52. F. Inagaki, *Magn. Reson. Chem.*, 1992, **30**, S125.
53. S. W. Homans, M. A. J. Ferguson, R. A. Dwek, T. W. Rademacher, R. Anand, and A. F. Williams, *Nature (London)*, 1988, **333**, 269.
54. A. S. Perlin, in *NMR Applications in Biopolymers*, eds. J. W. Finley, S. Schmidt, and A. S. Serianni, Plenum Press, New York, 1990, p. 7.
55. T. A. W. Koerner, Jr., J. H. Prestegard, and R. K. Yu, *Methods Enzymol.*, 1987, **138**, 38.
56. T. A. W. Koerner, Jr., J. H. Prestegard, P. C. Demou, and R. K. Yu, *Biochemistry*, 1983, **22**, 2676.
57. T. A. W. Koerner, Jr., J. H. Prestegard, P. C. Demou, and R. K. Yu, *Biochemistry*, 1983, **22**, 2687.
58. J. Dabrowski, *Methods Enzymol.*, 1989, **179**, 122.
59. J. Dabrowski, in *Methods in Stereochemical Analysis*, eds. W. R. Croasmun and R. M. K. Carlson, VCH, New York, 1987, Vol. 9, p. 349.
60. S. Dasgupta, E. L. Hogan, J. Glushka, and H. van Halbeek, *Arch. Biochem. Biophys.*, 1994, **310**, 373.
61. S. W. Homans, R. A. Dwek, J. Boyd, N. Soffe, and T. W. Rademacher, *Proc. Natl. Acad. Sci. USA*, 1987, **84**, 1202.
62. S. Subramanian and A. Bax, *J. Magn. Reson.*, 1987, **71**, 325.
63. A. A. Bothner-By, R. L. Stephens, J.-M. Lee, C. D. Warren, and R. W. Jeanloz, *J. Am. Chem. Soc.*, 1984, **106**, 811.
64. J. Dabrowski, in *Methods in Stereochemical Analysis*, 2nd edn., eds. W. R. Croasmun and R. M. K. Carlson, VCH, New York, 1994, Vol. 9, p. 741.
65. S. W. Homans, in *NMR of Macromolecules. A Practical Approach*, ed. G. C. K. Roberts, Oxford University Press, New York, 1993, p. 289.
66. C. A. Bush and P. Cagas, in *Advances in Biophysical Chemistry*, ed. C. A. Bush, JAI Press, Greenwich, Ct, 1992, Vol. 2, p. 149.
67. F. Inagaki, S. Tate, H. Kubo, and M. Hoshi, *J. Biochem. (Tokyo)*, 1992, **112**, 286.
68. F. J. Cassels and H. van Halbeek, *Methods Enzymol.*, 1995, **253**, 69.
69. R. J. Harris, H. van Halbeek, J. Glushka, L. J. Basa, V. T. Ling, K. J. Smith, and M. W. Spellman, *Biochemistry*, 1993, **32**, 6539.
70. R. J. Harris, L. J. Basa, V. T. Ling, M. W. Spellman, K. J. Smith, J. Glushka, R. W. Carlson, and H. van Halbeek, in *Techniques in Protein Chemistry V*, ed. J. W. Crabb, Academic Press, New York, 1994, p. 71.

71. A. Bax and M. F. Summers, *J. Am. Chem. Soc.*, 1986, **108**, 2093.
72. H. van Halbeek, in *Frontiers of NMR in Molecular Biology (UCLA Symposia Series*, Vol. 109), eds. D. Live, I. M. Armitage, and D. Patel, Alan R. Liss Inc., New York, 1990, p. 195.
73. C. Abeygunawardana and C. A. Bush, in *Advances in Biophysical Chemistry*, ed. C. A. Bush, JAI Press, Greenwich, CT, 1993, Vol. 3, p. 199.
74. D. A. Powell, W. S. York, H. van Halbeek, J. T. Etse, A. I. Gray, and P. G. Waterman, *Can. J. Chem.*, 1990, **68**, 1044.
75. J. Glushka, F. J. Cassels, R. W. Carlson, and H. van Halbeek, *Biochemistry*, 1992, **31**, 10 741.
76. S. W. Homans, *Prog. NMR Spectrosc.*, 1990, **22**, 55.
77. B. Meyer, *Top. Curr. Chem.*, 1990, **154**, 141.
78. H. van Halbeek and L. Poppe, *Magn. Reson. Chem.*, 1992, **30**, S74.
79. R. Freeman, *Chem. Rev.*, 1991, **91**, 1397.
80. H. Kessler, S. Mronga, and G. Gemmecker, *Magn. Reson. Chem.*, 1991, **29**, 527.
81. I. Solomon, *Phys. Rev.*, 1955, **99**, 559.
82. M. Karplus, *J. Am. Chem. Soc.*, 1963, **85**, 2870.
83. C. A. Bush, *Curr. Opin. Struct. Biol.*, 1992, **2**, 655.
84. J. McConnell, *The Theory of Nuclear Magnetic Relaxation in Liquids*, Cambridge University Press, Cambridge, UK, 1987.
85. J. H. Prestegard and Y. M. Kim, in *Computational Aspects of the Study of Biological Macromolecules by Nuclear Magnetic Resonance Spectroscopy*, eds. J. C. Hoch, F. M. Poulsen, and C. Redfield, Plenum Press, New York, 1991, p. 269.
86. C. A. G. Haasnoot, F. A. A. M. De Leeuw, and C. Altona, *Tetrahedron*, 1980, **36**, 2783.
87. L. A. Donders, F. A. A. M. De Leeuw, and C. Altona, *Magn. Reson. Chem.*, 1989, **27**, 556.
88. K. Bock and J. Ø. Duus, *J. Carbohydr. Chem.*, 1994, **13**, 513.
89. L. Poppe, S. Sheng, and H. van Halbeek, *Magn. Reson. Chem.*, 1994, **32**, 97.
90. L. Poppe, *J. Am. Chem. Soc.*, 1993, **115**, 8421.
91. Z. Dzakula, W. M. Westler, A. S. Edison, and J. L. Markley, *J. Am. Chem. Soc.*, 1992, **114**, 6195.
92. I. Tvaroska, M. Hricovíni, and E. Petráková, *Carbohydr. Res.*, 1989, **189**, 359.
93. B. Mulloy, T. A. Frenkiel, and D. B. Davies, *Carbohydr. Res.*, 1988, **184**, 39.
94. J. A. Schwarcz and A. S. Perlin, *Can. J. Chem.*, 1972, **50**, 3667.
95. M. Hricovíni and I. Tvaroska, *Magn. Reson. Chem.*, 1990, **28**, 862.
96. S. Uhrínová, D. Uhrín, T. Liptaj, J. Bella, and J. Hirsch, *Magn. Reson. Chem.*, 1991, **29**, 912.
97. R. Barker and A. S. Serianni, *Acc. Chem. Res.*, 1986, **19**, 307.
98. M. C. R. Symons, J. A. Benbow, and J. M. Harvey, *Carbohydr. Res.*, 1980, **83**, 9.
99. L. Poppe and H. van Halbeek, *J. Am. Chem. Soc.*, 1991, **113**, 363.
100. B. R. Leeflang and J. F. G. Vliegenthart, *J. Magn. Reson.*, 1990, **89**, 615.
101. L. Poppe and H. van Halbeek, *Nature Struct. Biol.*, 1994, **1**, 215.
102. J. Dabrowski and L. Poppe, *J. Am. Chem. Soc.*, 1989, **111**, 1510.
103. B. Adams and L. E. Lerner, *Magn. Reson. Chem.*, 1994, **32**, 225.
104. J. C. Christofides and D. B. Davies, *J. Am. Chem. Soc.*, 1983, **105**, 5099.
105. L. Poppe and H. van Halbeek, *J. Am. Chem. Soc.*, 1992, **114**, 1092.
106. L. Poppe, R. Stuike-Prill, B. Meyer, and H. van Halbeek, *J. Biomol. NMR*, 1992, **2**, 109.
107. J. P. Carver, *Curr. Opin. Struct. Biol.*, 1991, **1**, 716.
108. S. W. Homans, *Glycobiology*, 1993, **3**, 551.
109. S. Bagley, H. Kovacs, J. Kowalewski, and G. Widmalm, *Magn. Reson. Chem.*, 1992, **30**, 733.
110. P. J. Hajduk, D. A. Horita, and L. E. Lerner, *J. Am. Chem. Soc.*, 1993, **115**, 9196.
111. J. Kowalewski and G. Widmalm, *J. Phys. Chem.*, 1994, **98**, 28.
112. G. Wagner, *Curr. Opin. Struct. Biol.*, 1993, **3**, 748.
113. J. H. Noggle and R. E. Schirmer, *The Nuclear Overhauser Effect*, Academic Press, New York, 1971.
114. D. Neuhaus and M. P. Williamson, *The Nuclear Overhauser Effect in Structural and Conformational Analysis*, VCH, New York, 1989.
115. P. Dais and A. S. Perlin, *Adv. Carbohydr. Chem. Biochem.*, 1987, **45**, 125.
116. T. E. Bull, *Prog. NMR Spectrosc.*, 1992, **24**, 377.
117. G. Lipari and A. Szabo, *J. Am. Chem. Soc.*, 1982, **104**, 4546.
118. G. Lipari and A. Szabo, *J. Am. Chem. Soc.*, 1982, **104**, 4559.
119. A. S. Shashkov, G. M. Lipkind, and N. K. Kochetkov, *Carbohydr. Res.*, 1986, **147**, 175.
120. L. M. J. Kroon-Batenburg, J. Kroon, B. R. Leeflang, and J. F. G. Vliegenthart, *Carbohydr. Res.*, 1993, **245**, 21.
121. M. L. Hayes, A. S. Serianni, and R. Barker, *Carbohydr. Res.*, 1982, **100**, 87.
122. V. L. Bevilacqua, Y. Kim, and J. H. Prestegard, *Biochemistry*, 1992, **31**, 9339.
123. A. J. Duben, M. Hricovíni, and I. Tvaroska, *Carbohydr. Res.*, 1993, **247**, 71.
124. S. W. Homans and T. Rutherford, *Biochem. Soc. Trans.*, 1993, **21**, 449.
125. G. M. Lipkind, A. S. Shashkov, S. S. Mamyan, and N. K. Kochetkov, *Carbohydr. Res.*, 1988, **181**, 1.
126. A. D. French and J. W. Brady (eds.), *No. 43 of ACS Symp. Ser. 43*, Am. Chem. Soc., Washington, DC, 1990.
127. A. Imberty, S. Gerber, V. Tran, and S. Pérez, *Glycoconjugate J.*, 1990, **7**, 27.
128. A. Imberty, M.-M. Delage, Y. Bourne, C. Cambillau, and S. Pérez, *Glycoconjugate J.*, 1991, **8**, 456.
129. L. Poppe, J. Dabrowski, C.-W. von der Lieth, K. Koike, and T. Ogawa, *Eur. J. Biochem.*, 1990, **189**, 313.
130. C. Mukhopadhyay and C. A. Bush, *Biopolymers*, 1994, **34**, 11.
131. H. Kessler, M. Gehrke, and C. Griesinger, *Angew. Chem., Int. Ed. Engl.*, 1988, **27**, 490.
132. E. Kupce and R. Freeman, *J. Magn. Reson.*, 1992, **100**, 208.
133. P. Berthault, F. Djedaini, and B. Perly, *J. Magn. Reson.*, 1991, **91**, 102.
134. G. Batta and K. E. Kövér, *Tetrahedron*, 1991, **47**, 3535.
135. L. Braunschweiler and R. R. Ernst, *J. Magn. Reson.*, 1983, **53**, 521.
136. R. Bazzo, C. J. Edge, R. A. Dwek, and T. W. Rademacher, *J. Magn. Reson.*, 1990, **86**, 199.
137. L. Poppe and H. van Halbeek, *Magn. Reson. Chem.*, 1991, **29**, 355.
138. F. Inagaki, I. Shimada, D. Kohda, A. Suzuki, and A. Bax, *J. Magn. Reson.*, 1989, **81**, 186.

139. G. W. Vuister, P. De Waard, R. Boelens, J. F. G. Vliegenthart, and R. Kaptein, *J. Am. Chem. Soc.*, 1989, **111**, 772.
140. T. J. Rutherford and S. W. Homans, *Glycobiology*, 1992, **2**, 293.
141. D. Uhrín, J.-R. Brisson, and D. R. Bundle, *J. Biomol. NMR*, 1993, **3**, 367.
142. S. W. Homans, *J. Magn. Reson.* 1990, **90**, 557.
143. A. Bax, *Isr. J. Chem.*, 1988, **28**, 309.
144. S. P. Rucker and A. J. Shaka, *Mol. Phys.*, 1989, **68**, 509.
145. J. Briand and R. R. Ernst, *Chem. Phys. Lett.*, 1991, **185**, 276.
146. S. J. Glaser and G. P. Drobny, *Adv. Magn. Reson.*, 1990, **14**, 35.
147. G. A. Morris and R. Freeman, *J. Magn. Reson.*, 1978, **29**, 433.
148. E. Gaggelli and G. Valensin, *Concepts Magn. Reson.*, 1993, **5**, 19.
149. L. Lerner and A. Bax, *Carbohydr. Res.*, 1987, **166**, 35.
150. V. Sklenár and J. Feigon, *J. Am. Chem. Soc.*, 1990, **112**, 5644.
151. D. Boudot, D. Canet, J. Brondeau, and J. C. Boubel, *J. Magn. Reson.*, 1989, **83**, 428.
152. G. Bodenhausen, R. Freeman, and D. L. Turner, *J. Magn. Reson.*, 1977, **27**, 511.
153. A. Bax and D. G. Davis, *J. Magn. Reson.*, 1985, **63**, 207.
154. A. Bax, *J. Magn. Reson.*, 1988, **77**, 134.
155. L. Poppe and H. van Halbeek, *J. Magn. Reson.*, 1992, **96**, 185.
156. X.-L. Wu, P. Xu, and R. Freeman, *J. Magn. Reson.*, 1989, **83**, 404.
157. V. Sklenár and A. Bax, *J. Magn. Reson.*, 1987, **74**, 469.
158. S. Sabesan, K. Bock, and J. C. Paulson, *Carbohydr. Res.*, 1991, **218**, 27.
159. P. J. Hore, R. M. Scheek, and R. Kaptein, *J. Magn. Reson.*, 1983, **52**, 339.
160. S. Brownstein and J. Bornais, *J. Magn. Reson.*, 1990, **86**, 247.
161. L. D. Hall and T. J. Norwood, *J. Magn. Reson.*, 1988, **76**, 548.
162. L. Poppe, J. Dabrowski, and C.-W. von der Lieth, *Biochem. Biophys. Res. Commun.*, 1991, **174**, 1169.
163. G. Otting and K. Wüthrich, *J. Magn. Reson.*, 1988, **76**, 569.
164. G. Bodenhausen and D. J. Ruben, *Chem. Phys. Lett.*, 1980, **69**, 185.
165. L. Poppe and H. van Halbeek, *J. Magn. Reson.*, 1991, **92**, 636.
166. M.-A. Delsuc, E. Guittet, and J.-Y. Lallemand, *Magn. Reson. Chem.*, 1985, **23**, 213.
167. L. Poppe and H. van Halbeek, *J. Magn. Reson.*, 1991, **93**, 214.
168. A. S. Edison, W. M. Westler, and J. L. Markley, *J. Magn. Reson.*, 1991, **92**, 434.
169. L. Poppe and H. van Halbeek, *Magn. Reson. Chem.*, 1991, **29**, 848.
170. C. Morat, F. R. Taravel, and M. R. Vignon, *Magn. Reson. Chem.*, 1988, **26**, 264.
171. R. Brüschweiler, J. C. Madsen, C. Griesinger, O. W. Sørensen, and R. R. Ernst, *J. Magn. Reson.*, 1987, **73**, 380.
172. D. Uhrín, A. Mele, J. Boyd, M. R. Wormald, and R. A. Dwek, *J. Magn. Reson.*, 1992, **97**, 411.
173. D. Uhrín, A. Mele, K. E. Kövér, J. Boyd, and R. A. Dwek, *J. Magn. Reson., Ser. A*, 1994, **108**, 160.
174. J. M. Duker and A. S. Serianni, *Carbohydr. Res.*, 1993, **249**, 281.
175. U. Wollborn and D. Leibfritz, *J. Magn. Reson.*, 1992, **98**, 142.
176. G. Otting and K. Wüthrich, *Q. Rev. Biophys.*, 1990, **23**, 39.
177. J.-M. Nuzillard and J.-M. Bernassau, *J. Magn. Reson., Ser. B*, 1994, **103**, 284.
178. L. Poppe, W. S. York, and H. van Halbeek, *J. Biomol. NMR*, 1993, **3**, 81.
179. G. T. Montelione, M. E. Winkler, P. Rauenbuehler, and G. Wagner, *J. Magn. Reson.*, 1989, **82**, 198.
180. G. Wider, D. Neri, G. Otting, and K. Wüthrich, *J. Magn. Reson.*, 1989, **85**, 426.
181. A. S. Serianni and C. A. Podlasek, *Carbohydr. Res.*, 1994, **259**, 277.
182. G. M. Clore and A. M. Gronenborn, *J. Magn. Reson.*, 1985, **61**, 158.
183. B. A. Borgias, M. Gochin, D. J. Kerwood, and T. L. James, *Prog. NMR Spectrosc.*, 1990, **22**, 83.
184. W. Massefski, Jr.and A. G. Redfield, *J. Magn. Reson.*, 1988, **78**, 150.
185. D. G. Davis and A. Bax, *J. Magn. Reson.*, 1985, **64**, 533.
186. A. A. Bothner-By and R. Shukla, *J. Magn. Reson.*, 1988, **77**, 524.
187. L. Poppe, C.-W. von der Lieth, and J. Dabrowski, *J. Am. Chem. Soc.*, 1990, **112**, 7762.
188. D. Acquotti, L. Poppe, J. Dabrowski, C.-W. von der Lieth, S. Sonnino, and G. Tettamanti, *J. Am. Chem. Soc.*, 1990, **112**, 7772.
189. V. Sklenár, R. Tschudin, and A. Bax, *J. Magn. Reson.*, 1987, **75**, 352.
190. V. Sklenár and A. Bax, *J. Magn. Reson.*, 1987, **75**, 378.
191. M. Guéron, P. Plateau, and M. Decorps, *Prog. NMR Spectrosc.*, 1991, **23**, 135.
192. T. Peters, B. Meyer, R. Stuike-Prill, R. Somorjai, and J.-R. Brisson, *Carbohydr. Res.*, 1993, **238**, 49.
193. V. H. Tran and J. W. Brady, *Biopolymers*, 1990, **29**, 961.
194. V. H. Tran and J. W. Brady, *Biopolymers*, 1990, **29**, 977.
195. C. Hervé du Penhoat, A. Imberty, N. Roques, V. Michon, J. Mentech, G. Descotes, and S. Pérez, *J. Am. Chem. Soc.*, 1991, **113**, 3720.
196. D. B. Davies and J. C. Christofides, *Carbohydr. Res.*, 1987, **163**, 269.
197. B. Adams and L. Lerner, *J. Am. Chem. Soc.*, 1992, **114**, 4827.
198. D. C. McCain and J. L. Markley, *Carbohydr. Res.*, 1986, **152**, 73.
199. D. C. McCain and J. L. Markley, *J. Am. Chem. Soc.*, 1986, **108**, 4259.
200. D. C. McCain and J. L. Markley, *J. Magn. Reson.*, 1987, **73**, 244.
201. M. Hricovíni, R. N. Shah, and J. P. Carver, *Biochemistry*, 1992, **31**, 10 018.
202. I. Braccini, V. Michon, C. Hervé du Penhoat, A. Imberty, and S. Pérez, *Int. J. Biol. Macromol.*, 1993, **15**, 52.
203. A. Ejchart, J. Dabrowski, and C.-W. von der Lieth, *Magn. Reson. Chem.*, 1992, **30**, S105.
204. A. Ejchart and J. Dabrowski, *Magn. Reson. Chem.*, 1992, **30**, S115.
205. R. U. Lemieux, K. Bock, L. T. J. Delbaere, S. Koto, and V. S. R. Rao, *Can. J. Chem.*, 1980, **58**, 631.
206. H. Thøgersen, R. U. Lemieux, K. Bock, and B. Meyer, *Can. J. Chem.*, 1982, **60**, 44.
207. P. Cagas and C. A. Bush, *Biopolymers*, 1992, **32**, 277.
208. K. E. Miller, C. Mukhopadhyay, P. Cagas, and C. A. Bush, *Biochemistry*, 1992, **31**, 6703.
209. C. Mukhopadhyay and C. A. Bush, *Biopolymers*, 1991, **31**, 1737.
210. P. Cagas and C. A. Bush, *Biopolymers*, 1990, **30**, 1123.
211. Z.-Y. Yan and C. A. Bush, *Biopolymers*, 1990, **29**, 799.

212. B. N. N. Rao and C. A. Bush, *Carbohydr. Res.*, 1988, **180**, 111.
213. Z.-Y. Yan, B. N. N. Rao, and C. A. Bush, *J. Am. Chem. Soc.*, 1987, **109**, 7663.
214. C. A. Bush, Z.-Y. Yan, and B. N. N. Rao, *J. Am. Chem. Soc.*, 1986, **108**, 6168.
215. B. N. N. Rao, V. K. Dua, and C. A. Bush, *Biopolymers*, 1985, **24**, 2207.
216. C. Mukhopadhyay, K. E. Miller, and C. A. Bush, *Biopolymers*, 1994, **34**, 21.
217. T. J. Rutherford, D. G. Spackman, P. J. Simpson, and S. W. Homans, *Glycobiology*, 1994, **4**, 59.
218. H. Kogelberg and T. J. Rutherford, *Glycobiology*, 1994, **4**, 49.
219. J.-R. Brisson and J. P. Carver, *J. Biol. Chem.*, 1983, **258**, 1431.
220. J.-R. Brisson and J. P. Carver, *Biochemistry*, 1983, **22**, 3671.
221. J.-R. Brisson and J. P. Carver, *Biochemistry*, 1983, **22**, 3680.
222. J. P. Carver and J.-R. Brisson, in *Biology of Carbohydrates*, eds. V. Ginsburg and P. W. Robbins, Wiley, New York, 1984, Vol. 2, p. 289.
223. S. W. Homans, R. A. Dwek, D. L. Fernandes, and T. W. Rademacher, *FEBS Lett.*, 1983, **164**, 231.
224. D. A. Cumming, R. N. Shah, J. J. Krepinsky, A. A. Grey, and J. P. Carver, *Biochemistry*, 1987, **26**, 6655.
225. D. A. Cumming and J. P. Carver, *Biochemistry*, 1987, **26**, 6664.
226. D. A. Cumming and J. P. Carver, *Biochemistry*, 1987, **26**, 6676.
227. S. W. Homans, R. A. Dwek, and T. W. Rademacher, *Biochemistry*, 1987, **26**, 6553.
228. S. W. Homans, R. A. Dwek, and T. W. Rademacher, *Biochemistry*, 1987, **26**, 6571.
229. S. W. Homans, A. Pastore, R. A. Dwek, and T. W. Rademacher, *Biochemistry*, 1987, **26**, 6649.
230. S. W. Homans, *Biochemistry*, 1990, **29**, 9110.
231. T. J. Rutherford, J. Partridge, C. T. Weller, and S. W. Homans, *Biochemistry*, 1993, **32**, 12 715.
232. J. P. Carver, D. Mandel, S. W. Michnick, A. Imberty, and J. W. Brady, *ACS Symp. Ser., No. 430*, Am. Chem. Soc., Washington, DC, 1990, p. 266.
233. J. P. Carver, *Pure Appl. Chem.*, 1993, **65**, 763.
234. A. Imberty, S. Pérez, M. Hricovíni, R. N. Shah, and J. P. Carver, *Int. J. Biol. Macromol.*, 1993, **15**, 17.
235. H. van Halbeek, *Curr. Opin. Struct. Biol.*, 1994, **4**, 697.
236. J. T. Davis, S. Hirani, C. Bartlett, and B. R. Reid, *J. Biol. Chem.*, 1994, **269**, 3331.
237. A. Pollex-Krüger, B. Meyer, R. Stuike-Prill, V. Sinnwell, K. L. Matta, and I. Brockhausen, *Glycoconjugate J.*, 1993, **10**, 365.
238. D. V. Renouf and E. F. Hounsell, *Int. J. Biol. Macromol.*, 1993, **15**, 37.
239. S. W. Homans, C. J. Edge, M. A. J. Ferguson, R. A. Dwek, and T. W. Rademacher, *Biochemistry*, 1989, **28**, 2881.
240. S. W. Homans, A. Mehlert, and S. J. Turco, *Biochemistry*, 1992, **31**, 654.
241. S. Sabesan, K. Bock, and R. U. Lemieux, *Can. J. Chem.*, 1984, **62**, 1034.
242. S. Sabesan, J. Ø. Duus, T. Fukunaga, K. Bock, and S. Ludvigsen, *J. Am. Chem. Soc.*, 1991, **113**, 3236.
243. J. Dabrowski, P. Hanfland, and H. Egge, *Biochemistry*, 1980, **19**, 5652.
244. T. A. W. Koerner, Jr., J. N. Scarsdale, J. H. Prestegard, and R. K. Yu, *J. Carbohydr. Chem.*, 1984, **3**, 565.
245. J. N. Scarsdale, J. H. Prestegard, and R. K. Yu, *Biochemistry*, 1990, **29**, 9843.
246. S. B. Levery, *Glycoconjugate J.*, 1991, **8**, 484.
247. S. B. Levery, E. H. Holmes, D. D. Harris, and S. I. Hakomori, *Biochemistry*, 1992, **31**, 1069.
248. C. Griesinger, H. Schwalbe, J. Schleucher, and M. Sattler, in *Two-Dimensional NMR Spectroscopy. Applications for Chemists and Biochemists*, 2nd edn., eds. W. R. Croasmun and R. M. K. Carlson, VCH, New York, 1994, p. 457.
249. L. Yu, R. Goldman, P. Sullivan, G. F. Walker, and S. W. Fesik, *J. Biomol. NMR*, 1993, **3**, 429.
250. Y. Q. Gosser, K. P. Howard, and J. H. Prestegard, *J. Magn. Reson., Ser. B*, 1993, **101**, 126.
251. J. Chung, J. R. Tolman, K. P. Howard, and J. H. Prestegard, *J. Magn. Reson., Ser. B*, 1993, **102**, 137.
252. K. Dill, E. Berman, and A. A. Pavia, *Adv. Carbohydr. Chem. Biochem.*, 1985, **43**, 1.
253. W. J. Goux, C. Perry, and T. L. James, *J. Biol. Chem.*, 1982, **257**, 1829.
254. H. C. Joao and R. A. Dwek, *Eur. J. Biochem.*, 1993, **218**, 239.
255. P. M. Rudd, H. C. Joao, E. Coghill, P. Fiten, M. R. Saunders, G. Opdenakker, and R. A. Dwek, *Biochemistry*, 1994, **33**, 17.
256. R. J. Woods, C. J. Edge, and R. A. Dwek, *Nature, Struct. Biol.*, 1995, **1**, 499.
257. R. Stuike-Prill and B. Meyer, *Eur. J. Biochem.*, 1990, **194**, 903.
258. L. Poppe, J. Dabrowski, C.-W. von der Lieth, M. Numata, and T. Ogawa, *Eur. J. Biochem.*, 1989, **180**, 337.
259. H.-C. Siebert, G. Reuter, R. Schauer, C.-W. von der Lieth, and J. Dabrowski, *Biochemistry*, 1992, **31**, 6962.
260. L. Poppe, H. van Halbeek, D. Acquotti, and S. Sonnino, *Biophys. J.*, 1994, **66**, 1642.
261. H. Geen, X.-L. Wu, P. Xu, J. Friedrich, and R. Freeman, *J. Magn. Reson.*, 1989, **81**, 646.
262. Y. Aubin, Y. Ito, J. C. Paulson, and J. H. Prestegard, *Biochemistry*, 1993, **32**, 13 405.
263. G. Otting, *Curr. Opin. Struct. Biol.*, 1993, **3**, 760.
264. K. A. Kronis and J. P. Carver, *Biochemistry*, 1982, **21**, 3050.
265. K. A. Kronis and J. P. Carver, *Biochemistry*, 1985, **24**, 826.
266. T. Weimar and T. Peters, *Angew. Chem., Int. Ed. Engl.*, 1994, **33**, 88.
267. C. P. J. Glaudemans, L. Lerner, G. D. Daves, Jr., P. Kovác, R. Venable, and A. Bax, *Biochemistry*, 1990, **29**, 10 906.
268. B. Bechtel, A. J. Wand, K. Wróblewski, H. Koprowski, and J. Thurin, *J. Biol. Chem.*, 1990, **265**, 2028.
269. D. R. Bundle, H. Baumann, J.-R. Brisson, S. M. Gagné, A. Zdanov, and M. Cygler, *Biochemistry*, 1994, **33**, 5183.
270. A. P. Campbell and B. D. Sykes, *Annu. Rev. Biophys. Biomol. Struct.*, 1993, **22**, 99.
271. B. D. Sykes, *Curr. Opin. Biotechnol.*, 1993, **4**, 392.
272. T.-L. Hwang and A. J. Shaka, *J. Am. Chem. Soc.*, 1992, **114**, 3157.
273. C. S. Wright, *J. Mol. Biol.*, 1990, **215**, 635.

Acknowledgments

Research in the author's laboratory is supported by National Institutes of Health Grants P41-RR-05351, R01-AI-29751, and R01-AI-32899. The author thanks Drs. Leszek Poppe, John Glushka, and Shuqun Sheng for fruitful collaborations and stimulating discussions enjoyed over the course of many years, and Ms. Traci Swanson for editing the manuscript.

Biographical Sketch

Herman van Halbeek. *b* 1953. B.Sc., 1978, Ph.D., 1982, Bioorganic Chemistry, University of Utrecht, The Netherlands. Introduced to NMR by Robert Kaptein and Cornelis A. G. Haasnoot at the National NMR Facilities in Groningen and Nijmegen, The Netherlands. Postdoctoral fellow of the Dutch Cancer Foundation (Koningin Wilhelmina Fonds), 1982–85. Member of the Faculty in the Complex Carbohydrate Research Center at the University of Georgia (UGA), 1985–present. Currently Professor of Biochemistry and Chemistry at UGA. Approx. 185 publications. Research specialty: solution state NMR and its application to problems in glycobiology.

Cobalt(II)- and Nickel(II)-Substituted Proteins

Lucia Banci and Mario Piccioli
University of Florence, Florence, Italy

1	Introduction	1
2	The Electronic Properties of High Spin Cobalt(II) and Nickel(II) Ions	1
3	Metal Substitution and NMR Parameters	1
4	Cobalt(II)-Substituted Proteins	3
5	Nickel(II)-Substituted Proteins	5
6	Cobalt(II)- and Nickel(II)-Substitution in Magnetically Coupled Dimers	6
7	Conclusions	7
8	Related Articles	7
9	References	7

1 INTRODUCTION

Why is there a need for metal substitution? This approach in the investigation of metalloproteins has been, and is being, widely used in order to exploit the favorable spectroscopic properties of a suitable metal ion.[1–6] With regard to NMR, paramagnetic metal ions are used because they produce additional contributions to both the shift and relaxation parameters of the nuclei coupled to them [7–9] (see ***Electron–Nuclear Hyperfine Interactions***, ***Electron–Nuclear Multiple Resonance Spectroscopy***). The effect on the shift can be of sufficient size that, under certain circumstances, the signals due to such nuclei are well resolved from those of the rest of the protein. This increases the spectral resolution for those nuclei coupled with the paramagnetic center and, when the latter is in the active center of the molecule, very valuable biochemical information can be obtained.

Paramagnetic metal ions can be exploited as relaxation probes or shift probes depending essentially on their electron relaxation times. When the electron relaxation times are long, NMR lines are broad and the metal ion acts as relaxation probe (see ***Paramagnetic Relaxation in Solution***). When electron relaxation times are short, NMR lines are relatively sharp and the metal ion acts as a shift probe. We are only interested in shift probes here.

In order to have little line broadening, the coupling between the electron spin S and the nuclear spin I should be modulated by correlation times τ_c in the range 10^{-11}–10^{-13} s, depending on the number of unpaired electrons. As the rotational correlation times, τ_r, in macromolecules with molecular weights in the range 6000–50 000 are of the order of 10^{-8}–10^{-9} s, it follows that the possibility of obtaining high-resolution NMR spectra depends on the efficiency of the electron relaxation of the metal ion.

If a diamagnetic metal ion (typically Zn^{2+} but also Ca^{2+}, Cd^{2+}) or a paramagnetic metal ion with unfavorable relaxation properties (Cu^{2+}, Mn^{3+}, Mn^{2+}, high-spin Fe^{3+}) is present in a metalloprotein, its replacement with another metal ion with a similar ionic radius and similar coordination properties but favorable electron relaxation times gives rise to a metal-substituted protein whose metal ion surroundings can be investigated by NMR. Because of their favorable electronic properties with respect to NMR and their coordination chemistry, high-spin Co^{2+} and Ni^{2+} are among the most used and most suitable metal ions for substituting other metal ions, particularly Zn^{2+}. They are always high spin in tetrahedral geometry and, for Ni^{2+}, in octahedral geometry. Penta-coordinate ions are often high spin with oxygen and nitrogen donor atoms. In addition, octahedral Co^{2+} is often high spin.

The goal in the use of metal substitution is that of obtaining local information on the metal site through the analysis of the hyperfine (paramagnetic) shifts and of the nuclear relaxation rates of the nuclei of the metal ion ligands and of nearby residues. Furthermore, in the presence of inhibitors and pseudosubstrates, the NMR parameters provide information on the rearrangements induced by the binding of the molecule to the protein.

2 THE ELECTRONIC PROPERTIES OF HIGH SPIN COBALT(II) AND NICKEL(II) IONS

The Co^{2+} ion is a d^7 metal ion, the free ion having the ground state ^4F. In octahedral symmetry the ground state splits into $^4T_{1g}$, $^4T_{2g}$, $^4A_{2g}$, the ground state being $^4T_{1g}$. In the presence of low-symmetry components, spin–orbit coupling provides six Kramers doublets which are slightly separated. Conversely, in tetrahedral symmetry the ground state is the nondegenerate $^4A_2$ state. Hence, in O_h symmetry, low energy levels are available while in T_d symmetry the ground state is nondegenerate and excited levels are higher in energy. The presence of low-lying excited states in octahedral symmetry, arising from the splitting of the $^4T_{1g}$ ground level due to low-symmetry components, contributes to making electron relaxation more efficient in this geometry with respect to tetrahedral coordination and hence to shortening the electron relaxation times. Consequently, the τ_s values of a metal ion are dependent on the coordination geometry of the metal ion itself. For Co^{2+}, τ_s values of 10^{-13}–10^{-12} s have been found for hexa-coordinate ions, of around 10^{-12} s for penta-coordinate, and of around 10^{-11} s for tetrahedral chromophores.[9]

In the case of the Ni^{2+} (d^8) metal ion, the splitting of the free ion term ^3F provides a nondegenerate ($^3A_{2g}$) ground state for octahedral chromophores and, therefore electron relaxation mechanisms are not very efficient. In contrast, in tetrahedral chromophores a degenerate ($^3T_2$) ground state is available and therefore more efficient electron relaxation pathways are operative. Thus τ_s values of 3×10^{-12} s have been estimated for $Ni(H_2O)_6^{2+}$ [9] while tetrahedral Ni^{2+} experiences τ_s values in the range 10^{-12}–10^{-13} s at low magnetic fields. As a consequence, Ni^{2+} is a better probe for metal substitution in tetrahedral systems, while Co^{2+} is more suitable for penta- and hexa-coordinate chromophores. In the next sections we will provide examples of metalloproteins in which the native metal ion has been replaced with Co^{2+} and/or Ni^{2+} and we will illustrate the valuable information thus obtained.

3 METAL SUBSTITUTION AND NMR PARAMETERS

One large and relevant class of metalloproteins is that of the zinc enzymes[1–3] (see ***Carbonic Anhydrase***; ***Zinc Fingers***). Due to the similar coordination properties of the two metal ions, in many cases the cobalt(II)-substituted zinc proteins retain most of the biological properties of the native protein. Usually, substitution with Ni^{2+} produces derivatives with reduced biological activity. In addition, Fe^{2+}, Mn^{2+}, and Cu^{2+} have been replaced by Co^{2+} and also sometimes by Ni^{2+}.[6,10]

The extent of hyperfine shifts on the nuclei of residues directly bound to the paramagnetic metal ion depends on the metal ion itself and on the nature of the ligands (see ***Electron–Nuclear Hyperfine Interactions***). The contact contribution is related to the spin delocalization on the ligand nuclei, while the pseudocontact contribution depends on the magnetic susceptibility anisotropy of the metal ion which, in turn, is determined by the nature of the metal ion and by its coordination geometry. Table 1 reports the range of observed chemical shifts for protons of various ligands to cobalt(II) and nickel(II) in different coordination geometries and in biological molecules. In a few cases the two contributions, i.e. contact and pseudocontact contributions, have been factored out. However, for the nuclei of ligands directly coordinated to the metal ion, the contact contribution is, by far, the dominant. From Table 1, it appears that shifts of up to +300 ppm have been observed for the H-β protons of cysteines coordinated to Co^{2+} and Ni^{2+}.

The pseudocontact contribution to the shift in penta- and hexa-coordinate Co^{2+} chromophores is considerably larger than in tetrahedral coordination. The opposite occurs for Ni^{2+}, where large pseudocontact shifts are observed for tetrahedral coordination and negligible pseudocontact contributions are observed in hexa-coordinate systems. The presence of sizable pseudocontact contributions to the shift causes the appearance of several relatively sharp resonances in the +25 to −20 ppm region of penta- and hexa-coordinate Co^{2+} systems arising from protons up to 7–8 Å apart from the metal ion and not belonging to metal-coordinated residues. The hyperfine shifted signals can be investigated via 1D NOE (see ***Nuclear Overhauser Effect***) and/or 2D NMR spectroscopy in order to assign them unambiguously.

The increase in the nuclear relaxation rates due to coupling with the paramagnetic metal center occurs essentially through dipolar coupling for protons, while contact coupling can also appreciably affect nuclear relaxation in the case of other nuclei. In macromolecules, in the absence of chemical exchange, both couplings are modulated by the electron correlation times of the paramagnetic center.

A limitation in the application of high-resolution NMR in cobalt(II)- and nickel(II)-substituted proteins arises from the occurrence of substantial line broadening with increasing magnetic fields. Indeed, the contribution to transverse relaxation due to coupling of the nuclei with the static magnetic moment (Curie spin relaxation) (see ***Paramagnetic Relaxation in Solution***) must be taken into account.[11] This contribution can be relevant in metalloproteins, and its relevance increases with the number of unpaired electrons and, consequently, with the magnetic moment of the metal ion.[9] The spin state $S = \frac{3}{2}$ of cobalt(II) produces a sizable Curie spin relaxation contribution to the linewidth at high magnetic fields. The Curie spin relaxation term is modulated by τ_r and, therefore, increases with increasing molecular size. Furthermore, it depends on the square of the magnetic field. Hence, in unfavorable cases, i.e. large molecules at high magnetic fields, this contribution easily dominates transverse relaxation. As an example, consider a cobalt(II)-substituted protein of molecular weight 30 000 with τ_r of 1×10^{-8} s and a τ_s value of 5×10^{-12} s for Co^{2+}. For a proton 5 Å from the metal ion, the overall (dipolar + Curie) linewidth at 200 MHz is 78 Hz and the Curie spin contribution is 28 Hz (i.e. the latter accounts for 37% of the overall linewidth). At 600 MHz the overall linewidth for the same proton is 293 Hz and the Curie contribution is 249 Hz (85% of the overall linewidth). This example shows why, due to the strong field dependence of signal linewidths in cobalt(II)-containing proteins, the use of lower field spectrometers can be convenient and, sometimes, necessary.

The ^{1}H NMR spectra of an inhibitor (thiocyanate) adduct of cobalt(II)-substituted carbonic anhydrase (molecular weight, 32 000) (see later), shown in Figure 1 at different magnetic fields, provide a nice example of the above considerations. It can be seen, for example, that signal A′ is only detectable at 90 MHz, while signal E is still observable at 200 MHz but is broadened beyond detection at 600 MHz.

Two-dimensional experiments have been carried out on several cobalt(II)-substituted and nickel(II)-substituted macromolecules (see ***Multidimensional Spectroscopy: Concepts***), despite the presence of a paramagnetic center (see later for examples). In these experiments the mixing times were relatively short with respect to the relaxation of the nuclei but long enough such that transfer of magnetization or coherence occurred. The recycle times can also be set to be relatively short in order to increase the number of transients in the experiment time, thus improving the signal-to-noise ratio.

Recently, it has been pointed out[12] that cross correlation between dipolar relaxation and Curie spin relaxation [which can be sizable in cobalt(II)-containing macromolecules] can

Table 1 Chemical Shift Ranges (ppm) Experienced at Room Temperature in Solution by Protons of Residues Bound to a Cobalt(II) or a Nickel(II) in the Active Site of Metalloproteins with Different Coordination Geometries

Coordination geometry	Ligand and proton type			
	Cys G-β	His *ortho*-like	His *meta*-like	Asp H-β, Glu H-γ
Cobalt(II)				
Tetrahedral	300–200	150–40	70–35	80–30
Penta-coordinate	300–200	130–30	80–50	
Octahedral			70–50	
Nickel(II)				
Tetrahedral	300–150		80–20	
Penta-coordinate	240–190		80–35	

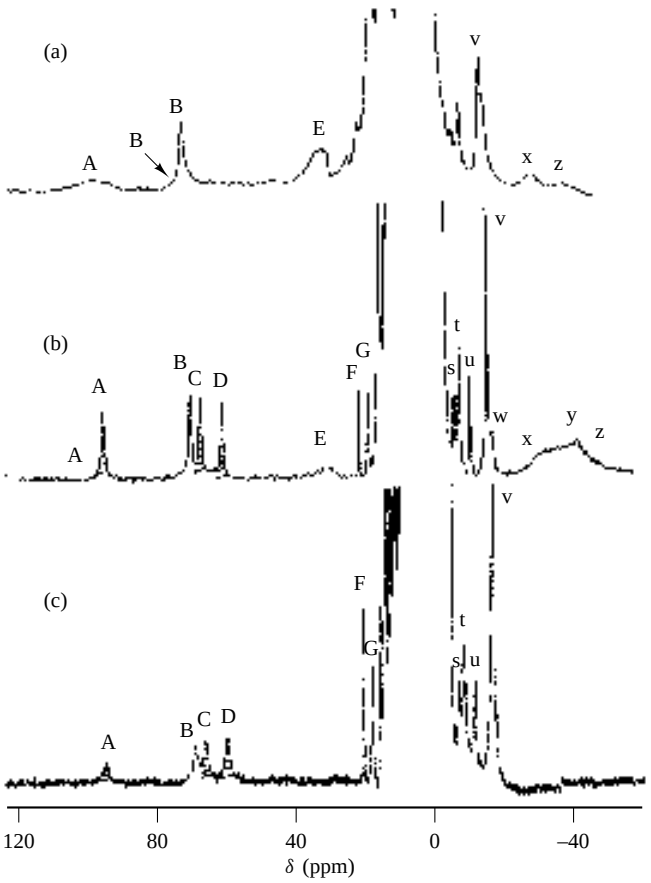

Figure 1 ^{1}H NMR spectra of the thiocyanate adduct of cobalt(II)-substituted carbonic anhydrase recorded at different magnetic fields: (a) 90 MHz, (b) 200 MHz, (c) 600 MHz. The spectrum shown in (a) was recorded in D_2O in order to detect the broad A′ signal otherwise covered by the A signal. 'Hatched' signals disappeared when the spectra were recorded in D_2O

give rise to cross peaks in COSY experiments even in the absence of scalar interaction between the protons. This mechanism is called relaxation allowed coherence transfer (RACT); it is absent in in-phase COSY or superCOSY experiments (see ***Relaxation Processes: Cross Correlation and Interference Terms***).

4 COBALT(II)-SUBSTITUTED PROTEINS

The first spectrum of a cobalt(II)-substituted protein for which an attempt at sequence specific assignment was reported was that of cobalt(II)-substituted carbonic anhydrase (CA).[13] CA is a zinc enzyme (see ***Carbonic Anhydrase***) which catalyzes the hydration of carbon dioxide.[14] The zinc ion is bound to three histidines with a roughly tetrahedral geometry. The fourth coordination position is accessible to the solvent or occupied by a water molecule. The latter molecule is transformed into a hydroxide group with a relatively low pK_a value. Substitution of the native zinc ion with cobalt(II) maintains about 50% of the enzymatic activity of the native protein. The cobalt(II)-substituted protein provides an NMR spectrum which shows some well resolved, high-frequency-shifted signals. They are due to the histidine protons in *meta*-like positions with respect to the cobalt. Some of these signals have been readily assigned to the NH protons of the histidine rings due to their exchange with the bulk solvent.

As can be seen from the spectrum of the native cobalt(II)-substituted protein, reported at the bottom of Figure 2, the ^{1}H NMR signals due to the protons of the cobalt ligands are relatively broad (ca. 300 Hz at 200 MHz) and shifted within a relatively narrow shift range (+53 to +63 ppm). In addition, very few signals of protons not belonging to metal ligands are resolved outside the diamagnetic envelope. This is due to the tetrahedral geometry of the cobalt ion in the native form of this enzyme, which is characterized by small magnetic anisotropy and relatively long electron relaxation times. Hence the pseudocontact contribution to the shift is small and only protons belonging to the metal ion ligands experience sizable hyperfine shifts. This means that information remains substantially limited to the coordinated residues.

When inhibitors bind cobalt(II) without displacing the coordinated solvent molecule, a five-coordinate adduct is obtained in which cobalt(II) experiences a much larger magnetic anisotropy and shorter electron relaxation times. This means that several protons belonging to residues close to the cobalt ion, but not directly coordinated to it, are shifted substantially and well resolved outside the diamagnetic envelope. Furthermore the lines are sharper (ca. 200 Hz at 200 MHz) than in the spectrum of the native form. ^{1}H NMR spectra of adducts with several inhibitors are reported in Figure 2. On these spectra, classical NMR techniques for spectral assignment such as NOE (see ***Nuclear Overhauser Effect***) and 2D NMR experiments (***COSY Two-Dimensional Experiments***; ***Multidimensional Spectroscopy: Concepts***; ***NOESY***) have been performed. They have led, for the adducts with nitrate, perchlorate and thiocyanate, to the assignment of the signals of the metal ligands and of several residues present around the active site.[13,16] Some of these assignments have been confirmed by analysis of the spectra of samples produced with selectively deuterated amino acids.[16]

The assignment of several protons experiencing only pseudocontact shifts has allowed the calculation, using a best-fitting procedure and the knowledge of the X-ray structure of the protein, of the anisotropy and the orientation of the magnetic susceptibility (χ) tensor. The latter information is relevant for the knowledge of the electronic structure of the cobalt ion in the adduct. Furthermore, it allows the calculation of the shifts for all the protons sensing some coupling with the metal ion, which can help in further assigning other signals.[13,16]

Extensive studies have also been performed on cobalt(II)-substituted carboxypeptidase (CPA) which is a zinc enzyme[17] where the five-coordinate metal ion is bound to two histidines, a water molecule, and a bidentate glutamate. Cobalt substitution increases the enzymatic activity of native CPA. The protein is soluble only at high ionic strengths, i.e. in viscous solutions. This provides long τ_r values and consequently large line broadening due to Curie spin relaxation. Indeed, no high-field NMR experiments have been performed on this system.

Despite these problems, cobalt(II)-substitution in CPA has provided useful information on the local structural features at the metal ion and on the enzyme reactivity. The ^{1}H NMR

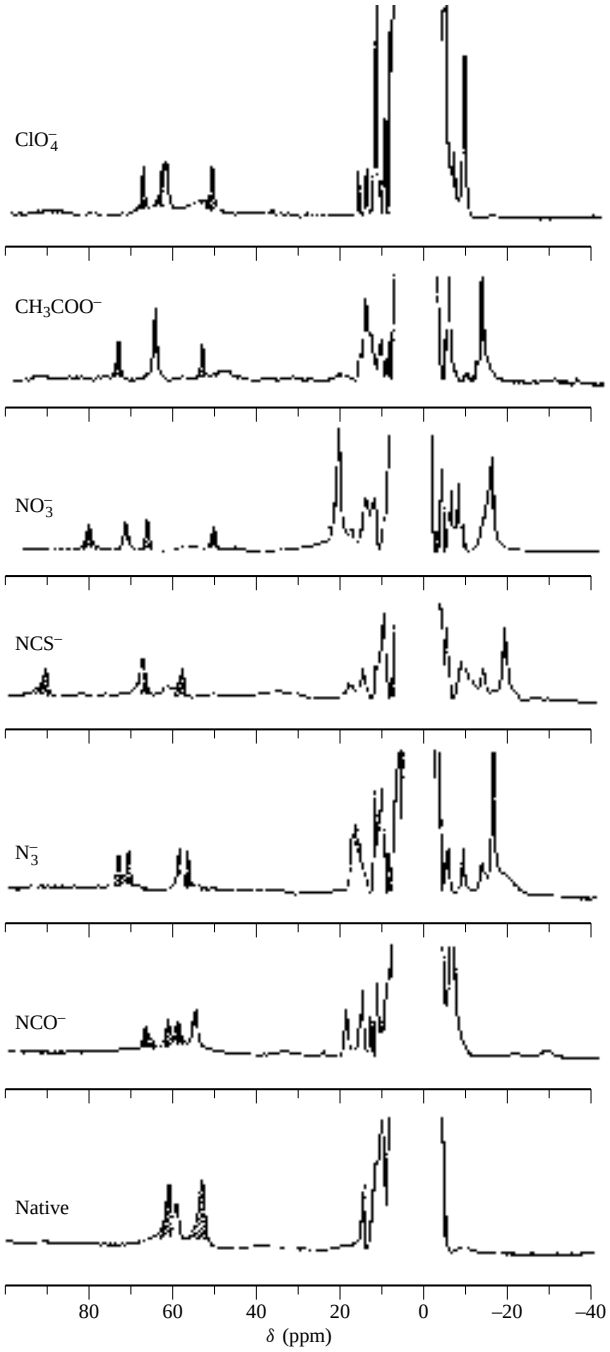

Figure 2 ^{1}H NMR spectra at 200 MHz of native and some anion adducts of cobalt-substituted carbonic anhydrase. 'Hatched' signals disappeared when the spectra were recorded in D_2O. (Reproduced by permission of Kluwer Academic Publishers from L. Banci, I. Bertini, C. Luchinat, and J. M. Moratal, in Enzymatic and Model Carboxylation and Reduction Reactions for Carbon Dioxide Utilization, eds. M. Aresta and J. V. Schloss, 1990, pp. 181–197)

spectrum of CoCPA (optimal field 90–200 MHz) shows three relatively sharp signals which have been assigned, through 1D NOE measurements, to *meta*-like protons of the two histidines. Two broader peaks have also been observed in the ^{1}H NMR spectrum of CoCPA and assigned, on the basis of their T_1 and T_2 values, to the two H-γ protons of the Co^{2+}-bound glutamate.

Information on the biochemistry of the enzyme was obtained by monitoring the changes in the ^{1}H NMR spectrum upon addition of inhibitors and substrate analogs.[18] For instance, it has been observed that some inhibitors such as carboxylic acids bind the enzyme in a 2:1 ratio. The first inhibitor molecule binds through its carboxylate group to an Arg residue (Arg-145) present in the catalytic cavity. The binding of this molecule in the cavity breaks the strong H-bond present between the zinc-bound water molecule and a Glu residue (Glu-270) present in the cavity, and makes the water molecule easily displaceable by a second molecule of inhibitor which binds the metal ion directly.

Cobalt substitution has been successfully performed on Cu_2Zn_2 superoxide dismutase (SOD hereafter).[19] This enzyme contains two metal centers connected by a histidinate bridge. Cobalt(II) can substitute zinc in its native site. Several systems, with no metal or with diamagnetic metal ions [Ag(I) or Cu(I)] in the copper site, have been investigated with the aim of characterizing the zinc ion-binding site. In such systems, cobalt(II) is coordinated by three histidines and a unidentate aspartate. The spectra of such derivatives are all similar to each other. Eight signals are hyperfine-shifted in the high-frequency region, i.e. the three *meta*-like exchangeable HN-ϵ2, the three nonexchangeable H-δ2 protons of the imidazole rings and the signals of the two H-β protons of the bound aspartate. The observation of three HN signals in the case of $Cu^I_2Co_2SOD$ provided the first direct evidence that the imidazole bridge between the two metal ions is broken when the copper ion is reduced.[20] Indeed, this finding is particularly remarkable in the light of recent X-ray studies on the reduced form of the native ($Cu^I_2Zn_2SOD$) protein which show, in the solid state, no bridge-breaking in this form of the enzyme. The spectrum of $Cu^I_2Co_2SOD$ has been investigated through 1D NOE and 2D NMR experiments at different magnetic fields[20] in order to: (i) assign the far-hyperfine-shifted signals (1D NOE at 200 MHz), (ii) assign the signals of residues belonging to the active site but not bound to the Co^{2+} ion (2D NOESY, 600 MHz), and (iii) use the pseudocontact shifts [available because of the assignment at point (ii)] to obtain information on the χ tensor anisotropy and directions of the Co^{2+} ion in the zinc site, analogous to the case of cobalt(II)-substituted CA.

An interesting example of the utility of metal substitution in proteins with large molecular weight (MW) is provided by cobalt substitution of the native zinc ion in liver alcohol dehydrogenase (LADH), a dimeric protein of MW ca. 80 000. The metal ligands are two cysteines, one histidine, and a water molecule. Even in the case of this large molecule, the signals of the two Cys H-β protons and of the three histidine protons (including the *ortho*-like proton) have been observed. Of course, the higher the molecular weight, the larger is the Curie spin relaxation term. Hence, such signals are best detected at 60 MHz![21]

Another example of a large protein for which cobalt substitution turned out to be useful with respect to obtaining information on the metal site is alkaline phosphatase (AP). AP is a large dimeric protein (MW 94 000) consisting of two identical subunits. Each contains three metal binding sites; in the native form two of these sites bind zinc while the third is specific for magnesium. Zinc has been substituted by cobalt(II) in its binding sites. Information on the metal ion ligands as well as on the metal uptake pathways has been obtained even on this large molecule.[22]

One of the most recent applications of cobalt(II) substitution has been performed on zinc finger peptide CP-1.[23] At variance with the previously reported cases, zinc finger proteins have already been studied extensively through high-resolution ^{1}H NMR in their native form due to their relatively low molecular weight (see ***Zinc Fingers***). However, cobalt(II) substitution has provided useful insights. Knowledge of the pseudocontact shifts of several resonances in the cobalt(II)-substituted protein has led the authors to calculate the χ tensor of the system. For a correct determination of the pseudocontact shifts, it is important to know the diamagnetic contributions to the shifts. The latter have been obtained by taking advantage of the assignment of the signals of the native protein.

Zinc proteins are not the only systems in which cobalt(II) substitution was successfully attempted. Iron has been substituted by cobalt(II) in several systems (see ***Iron—Sulfur Proteins***, ***Nonheme Iron Proteins***, ***Transferrins***). Indeed, in the absence of magnetic coupling with fast relaxing metal ions and in nonheme proteins, both high spin iron(III) and high spin iron(II) give rise to relatively broad ^{1}H NMR signals.[9] For this reason, although the ^{1}H NMR spectra of the iron(III)-containing protein Isopenicillin Synthase (INPS) have been recorded and several hyperfine-shifted signals observed, cobalt(II)-substituted INPS has been prepared in order to obtain hyperfine-shifted signals sharp enough to perform 1D NOE experiments. These have led to the tentative proposal of the structure of the active site (no X-ray data are available) and of a catalytic mechanism.[24] Similar considerations hold also for the signal linewidths in rubredoxin (Rd) (see ***Iron—Sulfur Proteins***) where the iron ion has a tetrahedral geometry and is coordinated to the sulfur atoms of the four cysteines. In this system, cobalt(II) and nickel(II) substitution was also performed. The ^{1}H NMR spectra are characterized by sharp and well-resolved signals, although no firm assignment is available for the spectra.[25]

Metallothioneins (MT) constitute a class of small proteins containing clusters of the type Cd_4S_{11} and Cd_3S_9. Titration of the apoprotein with cobalt(II) has been followed using NMR and has allowed the authors to study the uptake pathway of the metal ions. The Co_3S_9 cluster was first formed. The protein containing this cluster shows broad hyperfine signals, probably because the Co_3S_9 cluster experiences some fluxionality that broadens the lines beyond detection.[26] The ^{1}H NMR spectrum of the fully-substituted protein (Co_7MT) shows a large number of sharp, very high-frequency-shifted signals arising from the H-β protons of the cobalt(II)-coordinated cysteines. Such signals are shifted by up to +400 ppm. Detection of ^{1}H NMR signals at 600 MHz over such a large spectral width required the use of a fast ADC (9-bit digitizer over 10 MHz) (see ***Spectrometers: A General Overview***). An extensive pairwise assignment of the H-β cysteine protons was performed by 1D NOE and 2D NOESY experiments as well as by observing the temperature dependence of the shifts, interpreted on the basis of a magnetic coupling scheme among the metal ions.[26]

Substitution of the native iron(III) ion in transferrins (TRN, MW 90 000) (see ***Transferrins***) with cobalt(II) provided derivatives which showed, at 90 MHz, several high-frequency-shifted signals despite the large molecular weight of the protein.[27] The protein contains two metal binding sites which are not equivalent as revealed by ^{1}H NMR spectra. The observed signals were attributed to the presence of histidine and tyrosine residues as ligands to the metal ions. This example shows that the presence of a suitable metal ion can aid the characterization through NMR of even large proteins.

The blue copper protein azurin (Az) (see ***Copper Proteins***) has been investigated through ^{1}H NMR of the cobalt(II)- and nickel(II)-substituted derivatives.[28] The metal ion is pentacoordinate, its ligands being two histidines, one cysteine, one methionine, and the oxygen of the carbonyl group of a glycine residue. This protein has a relatively small molecular weight (16 000) which makes the Curie spin relaxation less efficient than in the systems previously described. The signals of the protons of the metal ion ligands are therefore relatively sharp. The H-β proton signals of the coordinated cysteine are shifted by more than +200 ppm while the signals of the ring protons of the two histidines fall in the usual 60–30 ppm region. The signals of two geminal proton pairs, which were tentatively assigned to the H-α protons of the metal-coordinated glycine and to the H-γ protons of the coordinated methionine, are observed with one signal shifted at low frequency and its geminal partner at high frequency for both pairs.[29] This behavior has not yet been rationalized, but it could be due to the different M–S(O)–C–H dihedral angles experienced by the two protons in each pair. This would make the spin density different on each of the two protons.

Experiments involving nuclei other than protons are much less common, even if quite promising. Heteronuclear multiple quantum coherence (HMQC) experiments (see ***Heteronuclear Shift Correlation Spectroscopy***) on ^{15}N-enriched samples have been performed on cobalt(II)-substituted CA,[6] and several scalar ^{15}N–^{1}H couplings between residues close to the cobalt ion have been detected.

5 NICKEL(II)-SUBSTITUTED PROTEINS

There are several examples in which nickel substitution has been performed on the same proteins where the native metal ion has also been replaced by cobalt. As previously discussed, nickel(II) is, in principle, more suitable for the investigation of tetrahedral centers and less useful in the case of hexacoordinate chromophores. Indeed, the nickel(II) ion in NiCPA in the presence of two moieties of D-phenylalanine induces broad lines and small pseudocontact shifts due to the small magnetic anisotropy.[30] In contrast, the ^{1}H NMR spectrum of NiCPA without any inhibitor shows sharp lines for the *meta*-like protons of the bound histidines,[30] the opposite of that observed for cobalt(II)-substituted CPA.

Nickel(II)-substituted CA has also been investigated through ^{1}H NMR, although the interest in such derivatives from the biochemical point of view is limited due to the severe reduction of activity. For those adducts of NiCA for which NMR studies have been performed, information similar to that obtained upon cobalt(II) substitution was achieved.[31]

In the case of tetrahedral chromophores such as Fe^{III}Rd and Cu^{II}Az, nickel(II) substitution produces derivatives with narrower lines relative to the corresponding cobalt(II) substituted derivatives.[32] In the case of zinc fingers, also, nickel(II) substitution produces narrower hyperfine-shifted ^{1}H NMR signals with respect to those observed in the cobalt(II) derivative. However, no assignment of the hyperfine-shifted signals has been attempted for the nickel derivative.[33]

Finally, a derivative with a nickel(II) in the zinc site of SOD and no metal in the copper site has been prepared and

characterized through NMR,[20] again obtaining information similar to that on the analogous cobalt(II) derivative.

6 COBALT(II)- AND NICKEL(II)-SUBSTITUTION IN MAGNETICALLY COUPLED DIMERS

Cobalt(II) and nickel(II) are not only efficient probes for NMR investigation in themselves, but they can also drastically reduce the electron relaxation rates of a slow-relaxing metal ion through magnetic coupling.[9] This coupling allows the slow-relaxing ion to relax through the efficient mechanisms of the fast-relaxing metal ion. The effect depends on the extent of the magnetic coupling constant; in the limit of $J/\hbar >> \tau_s{}^{-1}$ (where τ_s is referred to the fast-relaxing metal ion) the relaxation rate of the slow-relaxing metal ion approaches that of the fast-relaxing ion[9,34] (see ***Paramagnetic Relaxation in Solution***, ***Relaxation Theory: Density Matrix Formulation***). Under such conditions, even the signals of nuclei coupled to a slow-relaxing metal ion which, when isolated, would induce a dramatic increase in the linewidth, can be easily detected because they are sharp enough for the application of standard high-resolution NMR techniques.

An elegant application of the above considerations is provided by the replacement of native zinc ion in $Cu^{II}{}_2Zn_2SOD$ by cobalt(II) and nickel(II). The copper(II) ion is characterized by τ_s values of the order of 10^{-9} s which produce a dipolar contribution to the linewidth of a proton at 5 Å from copper (as for the *meta*-like protons of the coordinated histidines) of 2000 Hz. However, the magnetic coupling of copper with cobalt(II) or nickel(II), which relax much faster than copper(II), produces a drastic reduction of the relaxation times of the latter metal ion. The ^{1}H NMR spectra of Cu_2Co_2SOD and of Cu_2Ni_2SOD are reported as the upper traces in Figure 3.[20]

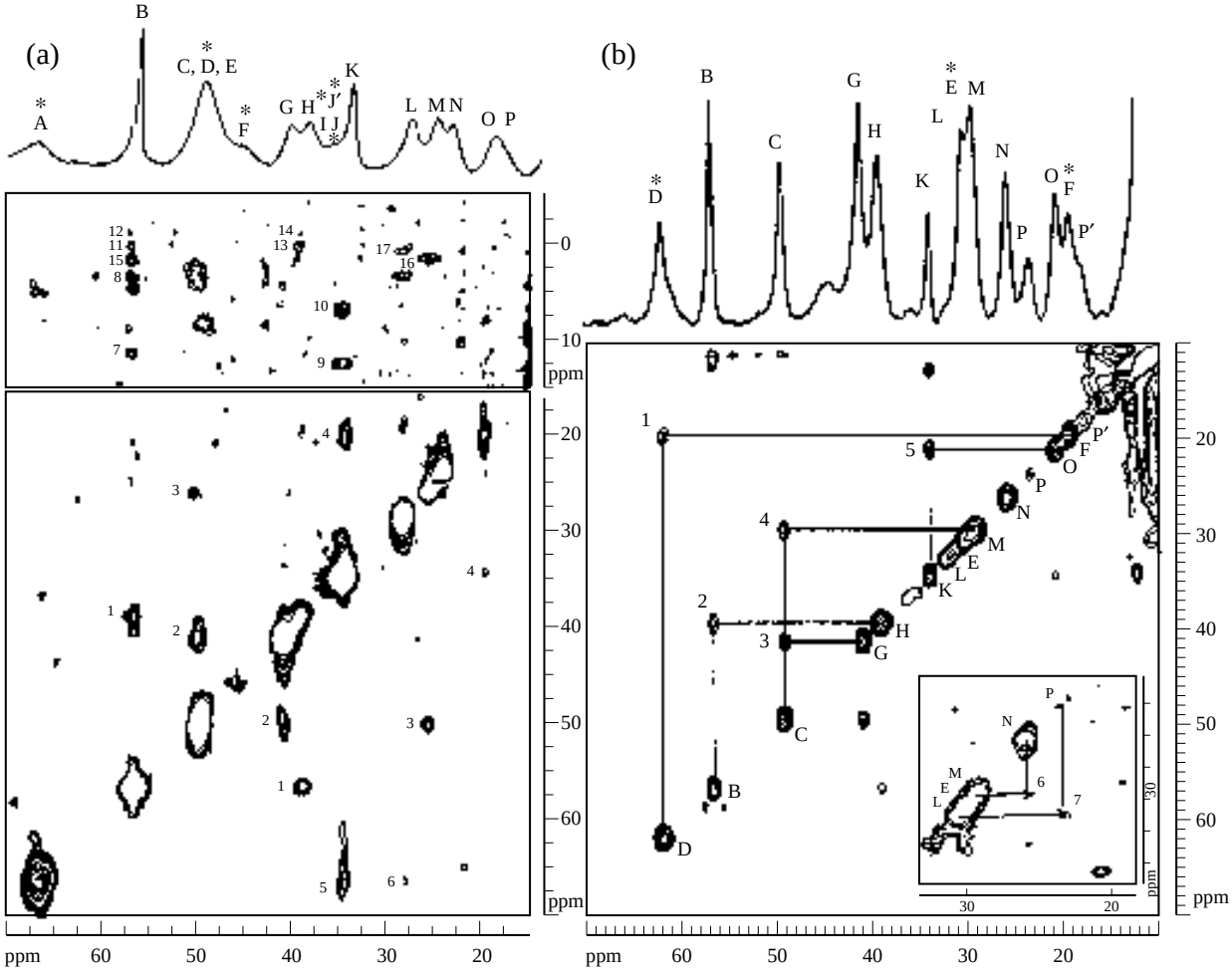

Figure 3 600 MHz NOESY spectra of Cu_2Co_2SOD (a) and Cu_2Ni_2SOD (b) in the region of hyperfine, high-frequency-shifted signals. The 1D spectra are also reported on the top of the NOESY maps. Signals marked by asterisks arise from protons of residues bound to the cobalt(II) or nickel(II) ions. Signal and cross peak labeling refer to the assignments summarized by Bertini et al.[20] Experimental conditions were: (a), lower map mixing time 4 ms, relaxation delay 80 ms, 256 experiments in F_1 and 512 experiment in F_2; upper map mixing time 15 ms, relaxation delay 150 ms (in order to better detect connectivities between hyperfine shifted signals and diamagnetic signals): (b), mixing time 15 ms, relaxation delay 80 ms, 512 experiments in F_1 and 1024 experiments in F_2. The inset in (b) shows a region of a NOESY spectrum recorded under the same experimental conditions at 300 MHz. All the observed connectivities in Cu_2Co_2SOD involve signals of copper-coordinated residues. In the NOESY map of Cu_2Ni_2SOD, connectivities 1–5 arise from intraresidue connectivities involving imidazole protons of residues bound either to Ni(II) (1) or Cu(II) (2–5). Connectivities 6 and 7 arise from interresidue contacts involving copper-coordinated histidines

It should be noted that the signals of the protons of the copper ligands are even sharper [due to the lower S value of copper(II) than of cobalt(II) and nickel(II)] than those of the cobalt or nickel ligands. All the metal–ligand proton signals, as well as several signals due to protons of residues located close to the two paramagnetic centers, have been firmly assigned through 1D NOE (see ***Nuclear Overhauser Effect***) and/or 2D NOESY (see ***NOESY*** experiments). In Figure 3 the NOESY spectra of Cu_2Co_2SOD and Cu_2Ni_2SOD are reported.[20,35,36] In these maps, besides many intraresidue connectivities, some interresidue connectivities are also detected between the copper ligand protons. In Cu_2Ni_2SOD some intraresidue connectivities have also been detected for nickel(II) ligand protons (see inset in Figure 3), while no connectivities between protons of residues coordinated to the cobalt(II) ion in Cu_2Co_2SOD could be observed. The latter effect is due to the very short T_2 values of the signals which render the broad NOESY cross peaks expected in these cases difficult to detect.

The signals of the protons in the copper site are sharper in Cu_2Ni_2SOD than in Cu_2Co_2SOD. This is the result of the shorter electron relaxation times of nickel(II) than of cobalt(II) in tetrahedral geometry. For the signals of the ligands of the zinc site, the spin state of Ni^{2+}, $S = 1$, makes the Curie contribution to their linewidth smaller than for those in the cobalt(II)-substituted derivative.

Cobalt(II) has also been used to replace the native copper(II) to obtain either Co_2Zn_2SOD or Co_2Co_2SOD; the above derivatives have been investigated through NMR and the signals of the metal-coordinated residues have been observed even if no detailed assignment was attempted.[20]

The ^{1}H NMR signals for metal–ligand protons have also been detected in Co_2Cu_2AP, for the ligands of copper ion,[22] and in iron(II)–cobalt(II) uteroferrin[37] (see ***Nonheme Iron Proteins***) for the ligands of the iron(II) ion. Indeed, the effect of the coupling is quite general. In all the proteins which contain two metal binding sites close enough that magnetic coupling can occur, NMR characterization of the metal sites can be successfully performed provided that one of the metal ions has short electron relaxation times.

Heteronuclear NMR spectroscopy has been rarely applied in the case of dimers. ^{15}N–^{1}H HMQC spectra (see ***Heteronuclear Shift Correlation Spectroscopy***) have been recorded on Cu_2Co_2SOD, detecting the ^{15}N–^{1}H scalar couplings for the copper-bound histidines.[38] This is the first case in which ^{15}N–^{1}H connectivities involving residues directly coordinated to the metal center of a paramagnetic protein have been observed.

7 CONCLUSIONS

Some of the examples discussed above clearly indicate that cobalt(II) substitution is *still* a powerful technique for the ^{1}H NMR spectroscopy of metalloproteins, although the actual capabilities of 'standard' multidimensional experiments are such that the 3D structure of proteins up to MW 30 000 can now be determined (see ***Biological Macromolecules: Structure Determination in Solution***, ***Structures of Larger Proteins, Protein-Ligand, and Protein-DNA Complexes by Multi-Dimensional Heteronuclear NMR***). In the case of proteins containing paramagnetic metal ions, which provide hyperfine-shifted signals which are too broad, Co^{2+} and/or Ni^{2+} substitutions allow a good structural characterization of the protein region around the metal center. In the case of relatively small proteins, standard NMR experimental procedures for diamagnetic systems can be successfully combined with the analysis of 2D NOESY and COSY maps designed for the detection of connectivities between the hyperfine shifted signals to obtain the overall 3D protein structure in solution. Hence, the 'paramagnetism' of the system is no longer a drawback for the complete characterization and for the determination of the solution structure. In the case of large proteins such results cannot be achieved, but valuable local information on the active site can be obtained. Finally, we would like to stress the relevance of the evaluation of the χ tensor anisotropy and directions in cobalt(II)-substituted systems. Analysis of pseudocontact shifts, as formerly performed in the case of heme proteins, has also provided satisfactory results in cobalt(II)-substituted systems. More frequent utilization of such an approach is expected in the future.

8 RELATED ARTICLES

Calcium-Binding Proteins; Carbonic Anhydrase; Copper Proteins; Electron–Nuclear Hyperfine Interactions; Iron—Sulfur Proteins; Metallothioneins; Nonheme Iron Proteins; Paramagnetic Relaxation in Solution; Transferrins; Zinc Fingers.

9 REFERENCES

1. I. Bertini and C. Luchinat, in *Metal Ions in Biological Systems*, ed. H. Sigel, Marcel Dekker, New York, 1983, 15, p. 101
2. I. Bertini, C. Luchinat, W. Maret, and M. Zeppezauer (eds.), *Zinc Enzymes*, Birkhauser, Boston, MA, 1986.
3. B. L. Vallee, A. Galdes, D. S. Auld, and J. F. Riordan, in *Zinc Enzymes*, ed. T. G. Spiro, Wiley-Interscience, New York, 1983, p. 25.
4. I. Bertini, H. B. Gray, S. J. Lippard, and J. S. Valentine (eds.) *Bioinorganic Chemistry*, University Science Books, Mill Valley, CA, 1994.
5. J. J. R. Frausto da Silva and R. J. P. Williams, *The Biological Chemistry of the Elements*, Oxford University Press, Oxford, UK, 1991.
6. J. S. Valentine and M. W. Pantoliano, in *Metal Ions in Biological Systems*, ed. H. Sigel, Marcel Dekker, New York, 1981, Vol. 3, p. 291.
7. G. N. La Mar, W. DeW Horrocks, Jr., and R. H. Holm (eds.), *NMR of Paramagnetic Molecules Principles and Applications*, Academic Press, New York, 1973.
8. I. Bertini and C. Luchinat, *NMR of Paramagnetic Molecules in Biological Systems*, Benjamin/Cummings, Menlo Park, CA, 1986.
9. L. Banci, I. Bertini, and C. Luchinat, *Nuclear and Electron Relaxation. The Magnetic Nucleus–Unpaired Electron Coupling in Solution*, VCH, Weinheim, 1991.
10. I. Bertini, P. Turano, and A. J. Vila, *Chem. Rev.*, 1993, **93**, 2833.
11. M. Gueron, *J. Magn. Reson.*, 1975, **19**, 58.
12. I. Bertini, C. Luchinat, and D. Tarchi, *Chem. Phys. Lett.*, 1993, **203**, 445.
13. L. Banci, L. B. Dugad, G. N. La Mar, K. A. Keating, C. Luchinat, and R. Pierattelli, *Biophys. J.*, 1992, **63**, 530.

14. S. Lindskog, in *Zinc Enzymes*, ed. T. G. Spiro, Wiley-Interscience, New York, 1983, p. 77.
15. L. Banci, I. Bertini, C. Luchinat, A. Donaire, M.-J. Martinez, and J. M. Moratal Mascarell, *Comments Inorg. Chem.*, 1990, **9**, 245.
16. I. Bertini, B.-H. Jonsson, C. Luchinat, R. Pierattelli, and A. J. Vila, *J. Magn. Reson. Ser. B*, 1994, **104**, 230
17. D. W. Christianson and J. D. Lipscomb, *Acc. Chem. Res.*, 1989, **22**, 62.
18. I. Bertini, C. Luchinat, L. Messori, R. Monnanni, D. S. Auld, and J. F. Riordan, *Biochemistry*, 1988, **27**, 8318.
19. (a) J. S. Valentine and M. W. Pantoliano, in *Copper Proteins*, ed. T. G. Spiro, Wiley, New York, 1981, p. 291; (b) I. Fridovich, *Adv. Enzymol. Relat. Areas Mol. Biol.*, 1986, **58**, 61.
20. I. Bertini, C. Luchinat, and M. Piccioli, *Prog. Nucl. Magn. Reson. Spectrosc.*, 1994, **26**, 91.
21. I. Bertini, M. Gerber, G. Lanini, C. Luchinat, W. Maret, S. Rawer, and M. Zeppezauer, *J. Am. Chem. Soc.*, 1984, **106**, 1826.
22. L. Banci, I. Bertini, C. Luchinat, M. S. Viezzoli, and Y. Wang, *Inorg. Chem.*, 1988, **27**, 1442.
23. L. V. Harper, B. T. Amann, V. K. Vinson, and J. M. Berg, *J. Am. Chem. Soc.*, 1993, **115**, 2577.
24. L. J. Ming, L. Que, Jr., A. Kriauciunas, C. A. Frolik, and V. J. Chen, *Biochemistry*, 1991, **30**, 11 653.
25. I. Moura, M. Teixeira, J. LeGall, and J. J. G. Moura, *J. Inorg. Biochem.*, 1991, **44**, 127.
26. I. Bertini, C. Luchinat, L. Messori, and M. Vašak, (a) *J. Am. Chem. Soc.*, 1989, **111**, 7296; (b) *J. Am. Chem. Soc.*, 1989, **111**, 7300; (c) *Eur. J. Biochem.*, 1993, **211**, 235.
27. L. Messori and M. Piccioli, *Inorg. Chim. Acta*, 1990, **174**, 137.
28. H. A. O. Hill, C. B. Storm, and R. P. Ambler, *Biochem. Biophys. Res. Commun.*, 1976, **70**, 783.
29. J. M. Moratal Mascarell, J. Salgado, A. Donaire, H. R. Jimenez, and J. Castells, *Inorg. Chem.*, 1993, **32**, 3587.
30. I. Bertini, A. Donaire, R. Monnanni, J. M. Moratal, and J. Salgado, *J. Chem. Soc., Dalton Trans.*, 1992, 1443.
31. J. M. Moratal, M.-J. Martinez Ferrer, A. Donaire, J. Castells, J. Salgado, and H. R. Jimenez, *J. Chem. Soc., Dalton Trans.*, 1991, 3393.
32. J. M. Moratal Mascarell, J. Salgado, A. Donaire, H. R. Jimenez, J. Castells, and M.-J. Martinez Ferrer, *Magn. Reson. Chem.*, 1993, **31**, S41.
33. B. A. Krizek and J. M. Berg, *Inorg. Chem.*, 1992, **31**, 2984.
34. L. Banci, I. Bertini, and C. Luchinat, *Struct. Bonding (Berlin)*, 1990, **72**, 113.
35. L. Banci, I. Bertini, C. Luchinat, M. Piccioli, and A. Scozzafava, *Gazz. Chim. Ital.*, 1993, **123**, 95.
36. I. Bertini, C. Luchinat, L. J. Ming, M. Piccioli, M. Sola, and J. S. Valentine, *Inorg. Chem.*, 1992, **31**, 4433.
37. R. C. Holz, L. Que, Jr., and L. J. Ming, *J. Am. Chem. Soc.*, 1992, **114**, 4434.
38. I. Bertini, C. Luchinat, R. Macinai, M. Piccioli, A. Scozzafava, and M. S. Viezzoli, *J. Magn. Reson. Series B*, 1994, **104**, 95.

Biographical Sketches

Lucia Banci. *b* 1954. Doctor in Chemistry, 1978, University of Florence. Faculty positions at University of Florence, 1982–present; Associate Professor of Nuclear Magnetic Resonance, 1987–present. More than 100 publications. Research fields: NMR of paramagnetic species, biological applications of NMR, molecular dynamics calculations on metalloproteins, bioinorganic and biophysical chemistry, theory of nuclear and electron relaxation.

Mario Piccioli. *b* 1960. Doctor in Chemistry, 1987, Ph.D. 1991, University of Florence (supervisor Lucia Banci). Researcher at University of Florence since 1991. Introduced to NMR by Ivano Bertini. 40 publications. Research fields: NMR of paramagnetic macromolecules, magnetic coupled systems, iron–sulfur proteins, solution structure of proteins, bioinorganic chemistry, biophysics.

Copper Proteins

Gerard W. Canters
Leiden University, Leiden, The Netherlands
and
Mart van de Kamp
Nijmegen University, Nijmegen, The Netherlands

1	Introduction	1
2	Blue Copper Proteins	1
3	Nonblue Copper Proteins	4
4	Related Articles	5
5	References	5

1 INTRODUCTION

The presence of a 3d transition metal in their interior makes Cu proteins challenging and interesting subjects of study by NMR techniques. In addition, in a number of cases the properties of the protein matrix make them eminently suitable for the application of advanced NMR spectroscopic techniques, despite the occasional inconvenience caused by the presence of a redox-active metal.

Although copper itself is NMR-visible this property has hardly been used in the study of copper proteins.[1] The two naturally occurring stable copper isotopes (^{63}Cu and ^{65}Cu, natural abundances 69.2% and 30.8%) have nonzero spin ($I = \frac{3}{2}$ for both isotopes), but the accompanying nuclear quadrupole moment is large enough to cause considerable relaxation and line broadening, except for cases where the metal environment is highly symmetric and the electrical field gradient is consequently zero. For coordination compounds the latter may sometimes be the case, but protein environments are usually of low symmetry and Cu NMR spectroscopy, therefore, has been of little practical value in the study of Cu proteins.

Copper in proteins may occur in more than one redox state: Cu(I) or Cu(II). Copper(I) is diamagnetic and produces no problems in the measurement and interpretation of NMR spectra. However, the metal is easily oxidized and changes over to the (paramagnetic) Cu(II) state, which may cause complications from a spectroscopic point of view. The electronic spin–lattice relaxation of Cu(II) is too slow (relaxation times of 1–3 ns) for Cu to be useful as a shift reagent. Instead, resonances from nuclei close to the metal are broadened beyond detection. This is often a nuisance, but it can be used to advantage in kinetic experiments where the rate of electron transfer to and from the Cu is measured (vide infra). The broadening effect may also be used as an additional help in the assignment of some peaks in the NMR spectrum of the protein. The metal then serves as a relaxation probe.

Thus the presence of Cu may impart some experimental obstacles to high-resolution studies of Cu proteins. NMR spectroscopists have tried to circumvent these by replacing the Cu with paramagnetic shift probes such as Ni(II) and Co(II), which have shorter electron spin relaxation times, or with diamagnetic redox-inactive metals such as Ag(I), Zn(II), Cd(II), and Hg(II).[2–5] Some of the latter nuclei are directly accessible to NMR spectroscopy (^{109}Ag, ^{113}Cd, ^{199}Hg).

Copper proteins have been distinguished on the basis of the structural and spectroscopic characteristics of their metal sites.[6,7] Type-I sites contain a single copper ion covalently anchored to the protein by three metal–ligand bonds, two of them provided by histidines that act as N-donors, and one by a cysteine that coordinates to the Cu via its S-γ atom. The Cu is located almost in the plane of the three ligands. A fourth ligand, usually a methionine, sometimes a glutamine, occupies one of the axial positions, while in the azurins an additional main-chain carbonyl oxygen may coordinate weakly at the opposite axial position. Type-I sites invariably function in electron transfer.

Type-II sites also contain a single Cu atom, often coordinated in a square planar configuration by four nitrogen/oxygen donors and one or two axial ligands, one of which may be a water molecule or the substrate. They are found, for instance, in various oxidases, often in conjunction with an organic cofactor.

Type-III sites contain a Cu_2 dimer which is fixed within the protein framework by six histidines. They function in the transport of oxygen (hemocyanins) or the activation of oxygen in oxidase or oxygenase reactions (tyrosinase).

For a long time the copper sites in the blue oxidases like ascorbate oxidase and laccase were thought to be of a composite of type-I, -II, and -III sites. Crystal structure determination of ascorbate oxidase has made it clear that at least in this oxidase the Cu atoms occur in the form of a single type-I site plus a trimer of Cu atoms arranged in an equilateral triangle, which may be considered as a new type of site (type-IV).

Finally, recent work on cytochrome a,a_3 oxidase and nitrous oxide reductase has provided evidence for the occurrence of a new type of Cu_2 dimer in which the Cu atoms are possibly bridged by a cysteine.[8,9]

Until very recently the size of most copper proteins precluded the study of their structure by means of high-resolution ^{1}H NMR techniques. Investigations were thus limited to studies of the metal site and its immediate surroundings, as in the case of proteins containing a type-I or a type-II Cu center. Only in the case of the so-called blue (type-I) copper proteins did the size of the proteins appear sufficiently small to allow extensive structural and mechanistic studies by high-resolution 2D and 3D NMR techniques. No elaborate NMR studies of proteins with type-III or type-IV sites seem to have been reported to date. Very recently the application of *rec*-DNA techniques has allowed the isolation of single domains of larger Cu-containing proteins, and the study of these domains by NMR techniques is presently being pursued by various groups.

In the following sections the progress achieved over the past two decades in the NMR study of Cu proteins is briefly reviewed.

2 BLUE COPPER PROTEINS

2.1 Introduction

The so-called small blue copper proteins (96–155 residues), which invariably contain a type-I Cu site, were described

for the first time at the end of the 1950s/beginning of the 1960s (for recent reviews see References 10 and 11).[10,11] The following subclasses are distinguished at present: proteins involved in bacterial respiratory electron transport (azurin, pseudoazurin, amicyanin, rusticyanin, and auracyanin),
photosynthetic plant and algal proteins (plastocyanin), and plant proteins with unknown function [either nonglycosylated: 'cucumber basic blue protein' (CBP) and plantacyanin; or glycosylated: stellacyanin, umecyanin, mavicyanin, and cucumber peeling cupredoxin (CPC)]. During the course of time it gradually transpired that their relatively small size (10–15 kDa), robustness under extremes of pH and temperature, ease of isolation and purification, and stability in solution at high concentrations made the blue copper proteins excellently suitable for detailed NMR investigations. Their attractiveness was further enhanced when the crystal structures of a number of them were solved at the end of the 1970s/beginning of the 1980s (plastocyanin,[12] azurin[13]). Later the structures of amicyanins (Amcs),[14,15] CBP,[16] and pseudoazurin were reported.[17,18]

The presence inside the protein of a metal capable of occurring in two oxidation states, one of which is paramagnetic, further heightened the appetite of NMR spectroscopists towards applying the tricks of their trade in unraveling the effect of the metal on the appearance of the NMR spectra. Most of the NMR studies have been performed on the azurins (Azus) from *Pseudomonas aeruginosa* and *Alcaligenes denitrificans*,[19,20] the plastocyanins (Pcs) from *Phaseolus vulgaris* (French bean),[21] spinach and *Scenedesmus obliquus*,[22,23] amicyanin (Amc) from *Thiobacillus versutus*,[24] and stellacyanin from *Rhus vernicifera*,[25] but brief reports have also been published of various other blue copper proteins.[26–30] Finally, it has recently been shown that the small blue copper proteins yield fairly easily to the application of *rec*-DNA and site-directed mutagenesis techniques and this has added a new dimension to their study.[11] For instance, the application of multidimensional heteronuclear MR techniques on isotopically-enriched (^{13}C and ^{15}N) proteins has now become available.

2.2 Copper Site Structure

Some of the first investigators to study copper proteins by NMR techniques were Blumberg et al.,[31] who around 1965 tried to assess the accessibility of the metal towards water molecules. They measured the relaxation enhancement of the bulk water protons as a function of the protein concentration and the oxidation state of the metal(s). In Pc, for instance, the Cu appeared inaccessible towards water. Application of this technique only required the study of the easily observable bulk water signal and not that of the protein. It would take 10 more years before spectrometers of sufficient resolution and sensitivity would become available to enable the successful tackling of the latter task. In the second half of the 1970s the first reports on the ^{1}H NMR spectra of various Pcs,[32–35] of *P. aeruginosa* Azu,[36–38] and of *R. vernicifera* stellacyanin appeared.[39] Also natural abundance ^{13}C NMR studies of Azu and Pc were reported around this time.[40,41] The spectra were much too complex to allow a detailed assignment of the signals, and attention primarily focused on the assignment by type of a few amino acids such as histidines and methionines, which give rise to easily identifiable singlet signals and (in the case of histidine) a characteristic pH titration behavior.

Since the four canonical ligands of a type-I Cu site comprise (apart from a cysteine) two histidines and a methionine, the structure of the Cu site in blue copper proteins rapidly became a popular subject of study by NMR techniques. By comparing the spectra of the Cu(II), Cu(I), apo-, and Hg(II)-substituted forms,[37] the ligands of the Cu could be identified correctly in Azu and Pc. Later on, these assignments were elaborated by 1D and 2D ^{1}H NMR and 2D $^{1}H\{^{113}Cd\}$ and $^{1}H\{^{13}C\}$ NMR studies.[42–48] The ^{1}H NMR signals of the metal ligands could be shifted outside the envelope of the regular NMR spectrum by replacing the Cu by paramagnetic shift probes such as the 3 d metal ions Co(II) and Ni(II).[48,49] This essentially provided clearly resolved signals from protons in the first coordination shell of the metal, but the unraveling of the various contact and pseudocontact contributions to the paramagnetic shifts proved too complicated to make this subterfuge much use in the analysis of the behavior and structure of the Cu site.

An illustration of the difficulties of this approach is provided by the study of Dahlin et al.[25] who made an elaborate attempt to identify the Cu ligands in the plant blue copper protein stellacyanin. The nature and coordinating properties of the fourth Cu ligand in this protein had long been an enigma, since the lack of methionines in the amino acid sequence provided indelible proof that the metal-binding site in stellacyanin was at least different in one respect from that in the Azus and Pcs. Despite careful analysis, the NMR results obtained on the Co(II)-substituted form of stellacyanin remained ambiguous. Subsequently, structural research on the related 'cucumber blue protein',[50] and site-directed mutagenesis studies on Azus,[51] have made it clear that the fourth ligand in stellacyanin is probably a glutamine.

The study of Ni(II) and Co(II)-substituted Azus has recently been taken up again by Moratal et al.[52,53] who are applying multidimensional NMR techniques to study paramagnetically shifted signals. This work may provide further insight into the malleability of the metal site, as probed already by NMR and XRD (X-ray diffraction) studies of wild-type and mutant blue copper proteins in their apo and holo forms, or with Cd(II), Hg(II), or Zn(II) substituted at the metal site.[10,11] The latter investigations have demonstrated that the metal site is preformed by the protein matrix, but does still retain some flexibility and is able to adapt somewhat to the metal that is substituted for the Cu.

Several attempts have been made to identify differences in structure and the Cu-binding mode of the metal sites between the Azus and the Pcs. Additional inspiration for this work came from XRD reports showing that the Cu site in Pc more closely resembled a distorted tetrahedron, while the coordination of the Cu in Azu was more like that of a trigonal bipyramid, with three strong almost in-plane ligands (two histidines and a cysteine) and two axial ligands, provided by a methionine sulfur (Met-121) and a backbone carbonyl oxygen (Gly-45).[6,11] Differences in chemical shift of the ^{113}Cd NMR signal of Cd-substituted Azu and Pc seemed diagnostic of a difference in electronic structure,[54,55] but the difference was not easy to interpret. Further, the early ^{13}C NMR studies of Azu implicated close proximity or possibly binding of a backbone carbonyl oxygen to the Cu.[40] Debate is still continuing regarding the amount of covalency involved in the Cu–S(Met) bond and the actual involvement of the Gly-45 carbonyl in determining the Cu-site properties in the Azus.

2.3 The Effects of pH

A clear difference between Pcs and Azus was provided by the pH titration behavior of the metal site. While the Cu site in the Azus is insensitive to pH, the geometry of the Cu site in the reduced form of the Pcs changes from fourfold to threefold towards low pH as one of the histidine ligands (His-87, *P. nigra* numbering) becomes protonated and dissociates from the Cu. This was beautifully documented by a series of XRD studies by Freeman et al.,[56] and confirmed later by ^{1}H NMR studies.[42,57,58] A similar effect is seen to occur in the Amcs described for the first time in the early 1980s, i.e. the blue copper proteins that act as electron acceptors of methylamine dehydrogenases in C_1 organisms. Thus the Amc from *T. versutus* was studied in detail by NMR spectroscopy, and the dissociation of the histidine ligand at low pH (His-96, *T. versutus* numbering) was shown to occur in two steps with different timescales.[59] As the change in coordination with pH is seen only for the reduced and not for the oxidized form of the protein, electron transfer at low pH is accompanied by a large change in conformation around the Cu. It is not surprising, therefore, that a slowing down of the electron transfer as catalyzed by Amc or Pc is observed under acidic conditions.[59] A similar lability of the Cu site probably occurs in the pseudoazurins.[60] It appears, therefore, as what was initially considered an anomaly in the case of Pc (a pH-dependent Cu-site structure) relative to Azus, seems to be the rule for small blue copper proteins and that the pH-insensitive Cu site of the Azus constitutes the anomaly.

A pH effect of a different kind was observed for Azu from *P. aeruginosa*, and for a long time its precise nature and mechanistic relevance remained a source of speculation. Almost from the very beginning of the NMR studies on the Azus it appeared that Azu from *P. aeruginosa* is involved in a pH-dependent equilibrium between two conformations which on the NMR timescale are in slow exchange.[37,46] From successive NMR studies it transpired that residue His-35 is responsible for this phenomenon and that the two conformations of the protein are related to the different states of protonation of His-35. Subsequent studies of the kinetics of the electron exchange between Azu and cytochrome C_{551} seemed to necessitate the assumption that Azu may occur in two states, one redox-active and the other one redox-inactive, and that the equilibrium between them was pH-dependent. The pK_a of this transition appeared to be the same as that of His-35. Since in the crystal structure His-35 is in van der Waals contact with the Cu ligand His-46, the hypothesis was advanced that (one of) the electron transfer pathway(s) in Azu runs through His-35 and His-46, and that His-35 might act as a switch depending on the pH of the surrounding medium. This hypothesis was subsequently tested by a large number of groups.[61]

Eventually, a combination of (a) NMR studies of the electron self-exchange (ESE) reaction of wild-type Azu and of Azus with mutations at residue 35 and in the hydrophobic patch surrounding the other histidine ligand (His-117),[62,63] (b) kinetic studies of the electron exchange between Azu mutants and physiological partners such as cytochrome C_{551} and nitrite reductase,[64] and (c) XRD studies of wild-type and mutant Azus[65,66] have led to the conclusion that His-35 is not in the electron transfer path to and from the Cu. Instead, Cu-ligand His-117, which pierces the protein surface at the position of the hydrophobic patch, provides the sole port of exit and entry for the electrons. Small changes in the chemical shifts of the protons in the first and second coordination shell of the metal as a function of protonation state of His-35 reflect a 180° flip in the Pro-36/Gly-37 peptide bond which is at H-bonding distance of the N-δ of His-35. The position of His-35 relative to the Cu site is hardly affected. Finally, the redox activity of the protein appears to be independent of pH.

The only parameter relevant to the redox properties of the Azu affected by the change in protonation of His-35 is the midpoint potential which drops by 60 mV if His-35 is deprotonated.[63] It is interesting to note that in Pc a pathway running through Cu ligand His-87 (*P. nigra* numbering) similar to the His-117 pathway in the Azus has been delineated, but that here a second, albeit less efficient route for electron transfer has been identified starting at the 'eastern side' of the protein at the Tyr-83 residue.[10,67,68]

2.4 Electron Transfer

The ESE rates of the blue copper proteins have attracted considerable attention apart from the metal site. It turned out that NMR methods are particularly suitable for the determination of these rates.[3,69,70] Due to small conformational differences the NMR spectra of the oxidised and reduced forms of a blue copper protein show numerous small differences. In addition, in the paramagnetic [Cu(II)] species, the signals from nuclei close to the Cu are broadened beyond detection. In a solution containing a mixture of the reduced and oxidized form, exchange of an electron may occur when an oxidized and a reduced molecule collide. As a result two observations can be made. First, as the exchange becomes faster, signals from the same proton which occur at different positions in the spectra of the oxidized and reduced protein begin to merge. Secondly, signals that are only observed for the diamagnetic species may begin to broaden.

The first phenomenon may be adequately analyzed with customary 'chemical exchange' theory and information about the ESE rate can be obtained directly. The second phenomenon can be analyzed most readily in the so-called strong pulse or slow exchange limit. This limit applies if during the time the protein is in the paramagnetic state the nuclear spins are dephased to a sufficient extent that any phase coherence left over from the period the protein was diamagnetic is wiped out. Thus, effectively only the (lifetime broadened) signal deriving from the diamagnetic protein is observed and the broadening in (rad s^{-1}) is directly equal to the inverse lifetime of the diamagnetic state. For the paramagnetic dephasing to be strong enough, the nucleus whose signal is studied should be close enough to the copper. In practice, the strong pulse condition is met for nuclei which are located on side chains of the Cu ligands. When nuclei further away from the Cu are used for this technique erroneous results may be obtained, as is illustrated by a study of Azu where the ESE-induced broadening of the His-35 proton signals was used to determine an ESE rate which was two orders of magnitude off the correct value.[71,72]

The high second order ESE rates (8×10^5 M^{-1} s^{-1}) observed for the Azus have been interpreted as indicating that formation of the association complex is thermodynamically favorable.[71,73,74] Current ideas are that the edges of the His-117 side chains in both Azus in the association complex

have to come sufficiently close for efficient electron transfer to occur, this being achieved when the two Azu molecules associate with their hydrophobic patches along each other. In the case of the Pcs a similar association complex has to be formed, but here the association is hampered by the presence of charged residues in or close to the hydrophobic ('northern') patch of the protein surface, which for most plant Pcs results in ESE rates of less than $1 \times 10^3\ M^{-1}\ s^{-1}$.[75,76] For the algal Pcs, which lack these charged residues in the hydrophobic patch, the ESE rates may reach values of $10^5\ M^{-1}\ s^{-1}$.[70] For Amc, which in some respects resembles the algal Pcs, rates on the order of $1 \times 10^5\ M^{-1}\ s^{-1}$ have been measured.[59] In line with these observations is that the ESE rates of the Azus are independent of ionic strength,[73] while those of the Pcs,[75] and to a smaller extent those of the Amcs,[59] increase when salts are added to the sample solution. Multivalent cations such as Mg(II) have appeared especially effective in promoting ESE.[75] Interestingly, redox-active compounds, such as ferricyanide, may catalyze the protein ESE reaction.[35,77]

To identify areas on the protein surface where other electron transfer proteins might possibly associate, the complexation of blue copper proteins with redox-inert paramagnetic transition metal compounds serving as charged analogs of protein partners have been studied.[22,57,58,78–80] By identifying and assigning the affected signals in the NMR spectrum, the location of the complex on the protein surface could sometimes be identified. In a similar way the association of blue copper proteins with proteins such as cytochrome *c* and cytochrome *f* have been studied directly. For this, the perturbation of the NMR spectrum of the blue copper protein that resulted from the admixture of the cytochrome and vice versa was investigated.[81–83] The inhibition of protein/protein complex formation by transition metal complexes was also studied in this manner. For this method to be successful it is of importance to dispose of a complete assignment of the NMR spectrum of the protein under study. Such assignments are now available for a number of cases.

2.5 Structural Studies

Complete NMR assignments for blue copper proteins started to become available in the second half of the 1980s. Two-dimensional ^{1}H NMR assignment studies have been performed on the Pcs from spinach,[22] *P. vulgaris* (French bean),[84,85] and the alga *S. obliquus*.[86] The assignment of the ^{1}H NMR spectrum of Amc from *T. versutus* has also been accomplished using 2D NMR techniques.[24] Finally from the analysis of 2D and 3D homo- and heteronuclear NMR experiments, complete ^{1}H and ^{15}N NMR assignments have become available for the Azus from *P. aeruginosa*[19] and *A. denitrificans*.[20] An interesting observation for the latter two proteins was that the differences in C-α–H chemical shifts did not average out to zero, contrary to the differences in amide proton chemical shifts. This is the subject of further study at the moment.

The secondary structures derived from the NMR results compared well with the published XRD structures in the case of the Pcs and Azus. For the Amc no XRD results were available initially, and the NMR results (later confirmed by more elaborate NMR studies and XRD investigations) showed an unusual extension of the N-terminus compared with the Pcs and Azus. Subsequent determination of the 3D structures of the Pcs from *S. obliquus*[23] and *P. vulgaris*[21] on the basis of the NMR results showed extensive similarity with the XRD-derived 3D structure of Pc from *P. nigra*. The NMR results formed a nice starting point for further structural investigations. Wright and coworkers studied the denaturation and refolding of Pc as well as the folding behavior of peptide fragments that were synthesized according to the natural amino acid sequence of the Pc. In this way a beginning could be made with the tentative delineation of the natural folding pathway(s) of Pc.[87,88] The 3D structure in solution of Amc from *T. versutus* was determined by NMR methods at the same time that an XRD study could be completed.[14,89] A detailed comparison of the two structures still has to be performed, but the overall structures do show a great deal of similarity.

3 NONBLUE COPPER PROTEINS

3.1 Superoxide Dismutase (SOD)

SOD is a eukaryotic homodimeric metalloenzyme (M_r approx. 30 kDa) which catalyzes the disproportionation of O_2^- to O_2 and H_2O_2.[90] Each monomer contains a structural Zn(II) site and a catalytic type-II Cu(II) site. An imidazolate bridges the two metal ions which are about 6 Å apart. The metal ions in the native enzyme $Cu(II)_2Zn(II)_2SOD$ can be readily removed or substituted. The crystal structures of bovine and spinach $Cu(II)_2Zn(II)_2SOD$[91,92] and of the $Cu(II)_2Co(II)_2$ derivative of bovine SOD[93] have been determined by X-ray crystallography. NMR experiments have been performed with bovine, human, and yeast SODs, which have similar catalytic, spectroscopic, and structural properties.

Because of their relatively large size, the assignment of all resonances in the ^{1}H NMR spectrum has not been achieved to date for any SOD. NMR experiments have been directed mainly at the study of the metal sites and their environment, including the interaction with exogenously added molecules like small anions and water. In the 1970s, work on SOD commenced by looking at the C-δ H and C-ϵ H resonances of His residues. The resonances of His ligands of the metal ions were tentatively identified by their broadening in the ^{1}H NMR spectrum of paramagnetic $Cu(II)_2Zn(II)_2SOD$ when compared with the spectrum of diamagnetic $Cu(I)_2Zn(II)_2SOD$,[94–96] and by the reduction of their C-α,H exchange rate.[97] His resonances were also investigated in the spectra of the diamagnetic forms E_2E_2SOD (E denotes an empty metal site), $E_2Zn(II)_2SOD$, and $Zn(II)_2Zn(II)_2SOD$. It appears that the metal-site conformation is preserved among these derivatives.

A breakthrough in the study of the metal sites of SOD was achieved when Bertini et al. investigated the metal derivative $Cu(II)_2Co(II)_2SOD$ by NMR spectroscopy.[90,98] Because of the magnetic coupling between Cu(II) and Co(II), which reduces the electron relaxation time of Cu(II), the resonances of protons near the Cu(II) ion are much less broadened than for $Cu(II)_2Zn(II)_2SOD$, and moreover experience large isotropic hyperfine shifts like the resonances of protons near the Co(II) ion. Similar observations have been made for $Cu(II)_2Ni(II)_2SOD$.[99] The metal-site ^{1}H resonances have been assigned, firstly by studying the effects of ^{1}H/^{2}H exchange on the 1D ^{1}H NMR spectrum and by analyzing 1D T_1, T_2 and ^{1}H NOE measurements,[90,99] and

secondly by the recent application of 2D ^{1}H NMR techniques (COSY, NOESY).[2,100–102] Using $Cu(II)_2Co(II)_2SOD$ and $Cu(I)_2Co(II)_2SOD$, it was shown that the breakage of the imidazolate bridge between the metal ions upon reduction of the copper occurs at the Cu side,[103] a result that had already been anticipated on the basis of ^{113}Cd NMR spectroscopy of $Cu(II)_2Cd(II)_2SOD$ and $Cu(I)_2Cd(II)_2SOD$.[104] From NMR experiments involving both protons and nuclei such as ^{13}C, ^{19}F, ^{31}P, and ^{35}Cl on SOD metal derivatives and SOD with mutations in the substrate-binding cavity, valuable insights were obtained regarding the interaction of the protein with substrate-mimicking and other anionic compounds such as CN^-, N_3^-, NCO^-, NCS^-, F^-, Cl^-, $H_2PO_4^-$, and HCO_2^-.[2,90,100,101,105–110] The accessibility of the Cu site in native and mutant $Cu(II)_2Zn(II)_2SOD$, and the effect of anion binding on it, has also been studied by measurements of the paramagnetic effect on the relaxation properties of solvent water.[90] The picture that arises from these studies is that some anions (in order of decreasing efficiency $CN^- > N_3^- > NCO^- > NCS^-$) bind to the Cu ion and displace a semicoordinated water molecule, thus reducing the solvent accessibility and affecting one of the Cu–His bonds. The effects of F^- and Cl^- binding are still smaller, making it questionable whether they bind to the Cu ion or to residues in its environment; phosphate and formate do not bind to the Cu ion but to residues near the copper. In addition to the Cu ion, one Arg and two Lys residues in the substrate-binding cavity have a particular effect in determining the affinity of SOD for anions.

3.2 Amine Oxidase (AO)

The eukaryotic copper-containing amine oxidases are dimeric metalloenzymes (M_r 170–190 kDa)[111] that have various functions, amongst others, in the metabolism of biogenic primary amines. Per dimer they contain two type-II Cu sites and one covalently bound organic cofactor with a quinone functionality. NMR studies of the protein have been confined to this cofactor and its orientation relative to the Cu site(s). ^{1}H NMR characterization of a small peptide from bovine serum AO that contained the phenylhydrazone-derivatized cofactor revealed it to be 6-hydroxydopa.[112] Using several fluorine-labeled phenylhydrazine derivatives, the distance between the organic cofactor at the amine-substrate-binding site of porcine plasma AO and one of its Cu(II) ions was inferred from the effect the paramagnetic Cu(II) exerts on the relaxation behavior of the fluorine nuclei as measured by ^{19}F NMR spectroscopy.[113] The organic cofactor and the Cu(II) ion appear to be within approximately 9 Å from each other.

3.3 Copper-Storage, -Transport and -Resistance Proteins

Several proteins involved in the storage and delivery of Cu ions, as well as in protection against Cu overload, are known. NMR reports concerning the Cu-containing forms of these proteins are scarce. Two examples which have been studied by NMR spectroscopy may be mentioned. In yeast, a 53-residue metallothionein (MT) involved in Cu resistance binds copper as Cu(I). Complete sequential ^{1}H NMR assignments have been made for the Cu(I)-containing MT as well as for the Ag(I)-substituted form.[114] The ligation pattern of the metal ions was derived from heteronuclear ^{1}H{^{109}Ag} HMQC spectroscopy.[114,115] It is noted that the 3D structures of several mammalian MTs have been determined with homo- and heteronuclear 2D NMR spectroscopy using the ^{112}Cd- or ^{113}Cd-substituted proteins.[116]

As a second example, the interaction of the high-M_r blood plasma protein albumin (67 kDa) with Cu(II), Co(II), and Ni(II) ions has been investigated by 1D and 2D ^{1}H NMR spectroscopy.[117,118] It appeared to be possible to detect such interactions at the mobile N-terminus, for which relatively sharp resonances are observed in the ^{1}H NMR spectrum of the metal-free protein.[119]

3.4 Other Cu Proteins

A very limited number of NMR reports on other Cu proteins or related model compounds has appeared in the literature. Here we mention two NMR studies that are concerned with Cu sites that have not been dealt with so far in this review. First, crystalline bovine heart cytochrome *c* oxidase (M_r 200 kDa), that contains so-called Cu_A and Cu_B sites, has been studied by solid state ^{13}C NMR spectroscopy.[120] The spectral resolution appeared to be better than that of dissolved or lyophilised samples and to be comparable with that of crystals of the much smaller protein lysozyme, without severe interference from the paramagnetic metal ions. Measurements of T_1 indicated that the backbone of cytochrome *c* oxidase is more flexible than that of lysozyme. Second, it has been reported that a dicopper dioxygen model compound for the dinuclear type-III Cu site in high-M_r metalloproteins such as hemocyanin exhibits very normal looking ^{1}H and ^{13}C NMR spectra, indicating strong coupling between the Cu(II) ions.[121]

4 RELATED ARTICLES

Biological Macromolecules: Structure Determination in Solution; Cadmium-113 NMR: A Surrogate Probe for Zinc and Calcium in Proteins; Cobalt(II)- and Nickel(II)-Substituted Proteins; Inorganic Nuclei: Low Sensitivity Transition Metals; Metallothioneins; Paramagnetic Relaxation in Solution; Quadrupolar Nuclei in Liquid Samples; Quadrupolar Transition Metal and Lanthanide Nuclei.

5 REFERENCES

1. J. Mason (ed.), *Multinuclear NMR*, Plenum Press, New York, 1987.
2. I. Bertini, P. Turano, and A. J. Vila, *Chem. Rev.*, 1993, **93**, 2833.
3. G. W. Canters, C. W. Hilbers, M. van de Kamp, and S. S. Wijmenga, *Methods Enzymol.*, 1993, **227**, 244.
4. L. M. Utschig, J. G. Wright, and T. V. O'Halloran, *Methods Enzymol.*, 1993, **226**, 71.
5. J. E. Coleman, *Methods Enzymol.*, 1993, **227**, 16.
6. E. T. Adman, *Adv. Protein Chem.*, 1991, **42**, 145.
7. N. Kitajima, *Adv. Inorg. Chem.*, 1992, **39**, 1.
8. W. E. Antholine, D. H. W. Kastrau, G. C. M. Steffens, G. Buse, W. G. Zumft, and P. H. M. Kroneck, *Eur. J. Biochem.*, 1992, **209**, 875.

9. B. G. Malmström and R. Aasa, *FEBS Lett.*, 1993, **325**, 49.
10. A. G. Sykes, *Adv. Inorg. Chem.*, 1991, **36**, 377.
11. G. W. Canters and G. Gilardi, *FEBS Lett.*, 1993, **325**, 39.
12. P. M. Colman, H. C. Freeman, J. M. Guss, M. Murata, V. A. Norris, J. A. M. Ramshaw, and M. P. Venkatappa, *Nature (London)*, 1978, **272**, 319.
13. E. T. Adman, R. E. Stenkamp, L. C. Sieker, and L. H. Jensen, *J. Mol. Biol.*, 1978, **123**, 35.
14. A. Romero, H. Nar, R. Huber, A. Messerschmidt, A. P. Kalverda, G. W. Canters, R. Durley, and F. S. Mathews, *J. Mol. Biol.*, 1994, **236**, 1196.
15. R. Durley, L. Chen, L. W. Lim, F. S. Mathews, and V. L. Davidson, *Protein Sci.*, 1993, **2**, 739.
16. J. M. Guss, E. A. Merritt, R. P. Phizackerley, B. Hedman, M. Murata, K. O. Hodgson, and H. C. Freeman, *Science*, 1988, **241**, 806.
17. E. T. Adman, S. Turley, R. Bramson, K. Petratos, D. Banner, D. Tsernoglou, T. Beppu, and H. Watanabe, *J. Biol. Chem.*, 1989, **264**, 87.
18. K. Petratos, Z. Dauter, and K. S. Wilson, *Acta Crystallogr.*, 1988, **B44**, 628.
19. M. van de Kamp, G. W. Canters, S. S. Wijmenga, A. Lommen, C. W. Hilbers, H. Nar, A. Messerschmidt, and R. Huber, *Biochemistry*, 1992, **31**, 10 194.
20. C. W. G. Hoitink, P. C. Driscoll, H. A. O. Hill, and G. W. Canters, *Biochemistry*, 1994, **33**, 3560.
21. J. M. Moore, C. A. Lepre, G. P. Gippert, W. J. Chazin, D. A. Case, and P. E. Wright, *J. Mol. Biol.*, 1991, **221**, 533.
22. P. C. Driscoll, H. A. O. Hill, and C. Redfield, *Eur. J. Biochem.*, 1987, **170**, 279.
23. J. M. Moore, D. A. Case, W. J. Chazin, G. P. Gippert, T. F. Havel, R. Powls, and P. E. Wright, *Science*, 1988, **240**, 314.
24. A. Lommen, S. Sijmenga, C. W. Hilbers, and G. W. Canters, *Eur. J. Biochem.*, 1991, **201**, 695.
25. S. Dahlin, B. Reinhammer, and J. Ångström, *Biochemistry*, 1989, **28**, 7224.
26. S. Mitra and R. Bersohn, *Proc. Natl. Acad. Sci. USA*, 1982, **79**, 6807.
27. G. King, T. A. Andary, H. C. Freeman, L. Gavrilovic, and P. E. Wright, *FEBS Lett.*, 1984, **166**, 288.
28. M. A. Babayan, L. Kh. Sarkissian, A. M. Nersissian, E. G. Sarukhanian, and R. M. Nalbandyan, *Biochem. Biophys. Res. Commun.*, 1983, **117**, 385.
29. A. M. Nersissian, M. A. Babayan, L. Kh. Sarkissian, E. G. Sarukhanian, and R. M. Nalbandyan, *Biochim. Biophys. Acta*, 1985, **830**, 195.
30. M. A. Babayan, A. M. Nersissian, and R. M. Nalbandyan, *FEBS Lett.*, 1988, **238**, 167.
31. W. E. Blumberg, J. Eisinger, P. Aisen, A. G. Morell, and I. H. Scheinberg, *J. Biol. Chem.*, 1963, **238**, 1675.
32. J. L. Markley, E. L. Ulrich, S. P. Berg, and D. W. Krogmann, *Biochemistry*, 1975, **14**, 4428.
33. H. C. Freeman, V. A. Norris, J. A. M. Ramshaw, and P. E. Wright, *FEBS Lett.*, 1978, **86**, 131.
34. H. A. O. Hill and B. E. Smith, *Biochem. Biophys. Res. Commun.*, 1978, **81**, 1201.
35. J. K. Beattie, D. J. Fensom, H. C. Freeman, E. Woodcock, H. A. O. Hill, and A. M. Stokes, *Biochim. Biophys. Acta*, 1975, **405**, 109.
36. K. Ugurbil and R. Bersohn, *Biochemistry*, 1977, **16**, 3016.
37. H. A. O. Hill and B. E. Smith, *J. Inorg. Biochem.*, 1979, **11**, 79.
38. H. A. O. Hill, J. C. Leer, B. E. Smith, C. B. Storm, and R. P. Ambler, *Biochem. Biophys. Res. Commun.*, 1976, **70**, 331.
39. H. A. O. Hill and W. K. Lee, *J. Inorg. Biochem.*, 1979, **11**, 101.
40. K. Ugurbil, R. S. Norton, A. Allerhand, and R. Bersohn, *Biochemistry*, 1977, **16**, 886.
41. J. L. Markley, E. L. Ulrich, and D. W. Krogmann, *Biochem. Biophys. Res. Commun.*, 1977, **78**, 106.
42. C. L. Kojiro and J. L. Markley, *FEBS Lett.*, 1983, **162**, 52.
43. G. King and P. E. Wright, *Biochem. Biophys. Res. Commun.*, 1982, **106**, 559.
44. D. H. Live, C. L. Kojiro, D. Cowbum, and J. L. Markley, *J. Am. Chem. Soc.*, 1985, **107**, 3043.
45. G. C. King and P. E. Wright, *Biochemistry*, 1986, **25**, 2364.
46. E. T. Adman, G. W. Canters, H. A. O. Hill, and N. A. Kitchen, *FEBS Lett.*, 1982, **143**, 287.
47. G. W. Canters, H. A. O. Hill, N. A. Kitchen, and E. T. Adman, *Eur. J. Biochem.*, 1984, **138**, 141.
48. H. A. O. Hill, B. E. Smith, C. B. Storm, and R. P. Ambler, *Biochem. Biophys. Res. Commun.*, 1976, **70**, 783.
49. J. A. Blaszak, E. L. Ulrich, J. L. Markley, and D. R. McMillin, *Biochemistry*, 1982, **21**, 6253.
50. B. A. Fields, J. M. Guss, and H. C. Freeman, *J. Mol. Biol.*, 1991, **222**, 1053.
51. A. Romero, C. W. G. Hoitink, H. Nar, R. Huber, A. Messerschmidt, and G. W. Canters, *J. Mol. Biol.*, 1993, **229**, 1007.
52. J.-M. Moratal, J. Salgado, A. Donaire, H. R. Jiménez, and J. Castells, *J. Chem. Soc., Chem. Commun.*, **1993**, 110.
53. J.-M. Moratal, J. Salgado, A. Donaire, H. R. Jiménez, and J. Castells, *Inorg. Chem.*, 1993, **32**, 3587.
54. H. R. Engeseth, D. R. McMillin, and J. D. Otvos, *J. Biol. Chem.*, 1984, **259**, 4822.
55. M. F. Summers, *Coord. Chem. Rev.*, 1988, **86**, 43.
56. J. M. Guss, P. R. Harrowell, M. Murata, V. A. Norris, and H. C. Freeman, *J. Mol. Biol.*, 1986, **192**, 361.
57. J. McGinnis, J. D. Sinclair-Day, A. G. Sykes, R. Powls, J. Moore, and P. E. Wright, *Inorg. Chem.*, 1988, **27**, 2306.
58. M. P. Jackman, J. D. Sinclair-Day, M. J. Sisley, A. G. Sykes, L. A. Denys, and P. E. Wright, *J. Am. Chem. Soc.*, 1987, **109**, 6443.
59. A. Lommen and G. W. Canters, *J. Biol. Chem.*, 1990, **265**, 2768.
60. E. T. Adman, personal communication.
61. E. T. Adman, *Top. Mol. Struct. Biol.*, 1985, **6**, 1.
62. M. van de Kamp, R. Floris, F. C. Hali, and G. W. Canters, *J. Am. Chem. Soc.*, 1990, **112**, 907.
63. M. van de Kamp, G. W. Canters, C. R. Andrew, J. Sanders-Loehr, C. J. Bender, J. Peisach, and I. Pecht, *Eur. J. Biochem.*, 1993, **218**, 229.
64. M. van de Kamp, M. C. Silvestrini, M. Brunori, J. Van Beeumen, F. C. Hali, and G. W. Canters, *Eur. J. Biochem.*, 1990, **194**, 109.
65. H. Nar, A. Messerschmidt, R. Huber, M. van de Kamp, and G. W. Canters, *J. Mol. Biol.*, 1991, **218**, 427.
66. H. Nar, A. Messerschmidt, R. Huber, M. van de Kamp, and G. W. Canters, *J. Mol. Biol.*, 1991, **221**, 765.
67. S. He, S. Modi, D. S. Bendall, and J. C. Gray, *EMBO J.*, 1991, **10**, 4011.
68. S. Modi, M. Nordling, L. G. Lundberg, O. Hansson, and D. S. Bendall, *Biochim. Biophys. Acta*, 1992, **1102**, 85.
69. G. W. Canters, H. A. O. Hill, N. A. Kitchen, and E. T. Adman, *J. Magn. Reson.*, 1984, **57**, 1.

70. C. Dennison, P. Kyritsis, W. McFarlane, and A. G. Sykes, *J. Chem. Soc., Dalton Trans.*, **1993**, 1959.
71. C. M. Groeneveld and G. W. Canters, *J. Biol. Chem.*, 1988, **263**, 167.
72. K. Ugurbil and S. Mitra, *Proc. Natl. Acad. Sci. USA*, 1985, **82**, 2039.
73. C. M. Groeneveld and G. W. Canters, *Eur. J. Biochem.*, 1985. **153**, 559.
74. C. M. Groeneveld, M. C. Ouwerling, C. Erkelens, and G. W. Canters, *J. Mol. Biol.*, 1988, **200**, 189.
75. F. A. Armstrong, P. C. Driscoll, and H. A. O. Hill, *FEBS Lett.*, 1985, **190**, 242.
76. D. G. A. H. de Silva, D. Beoku-Betts, P. Kyritsis, K. Govindaraju, R. Powls, N. P. Tomkinson, and A. G. Sykes, *J. Chem. Soc., Dalton Trans.*, **1992**, 2145.
77. A. Lommen, G. W. Canters, and J. van Beeumen, *Eur. J. Biochem.*, 1988, **176**, 213.
78. K. C. Cho, D. F. Blair, U. Banerjee, J. J. Hopfield, H. B. Gray, I. Pecht, and S. I. Chan, *Biochemistry*, 1984, **23**, 1858.
79. D. J. Cookson, M. T. Hayes, and P. E. Wright, *Nature (London)*, 1980, **283**, 682.
80. D. J. Cookson, M. T. Hayes, and P. E. Wright, *Biochim. Biophys. Acta*, 1980, **591**, 162.
81. L. Qin and N. M. Kostic, *Biochemistry*, 1993, **32**, 6073.
82. S. Bagby, P. C. Driscoll, K. G. Goodall, C. Redfield, and H. A. O. Hill, *Eur. J. Biochem.* 1990, **188**, 413.
83. G. C. King, R. A. Binstead, and P. E. Wright, *Biochim. Biophys. Acta*, 1985, **806**, 262.
84. W. J. Chazin, M. Rance, and P. E. Wright, *J. Mol. Biol.*, 1988, **202**, 603.
85. W. J. Chazin and P. E. Wright, *J. Mol. Biol.*, 1988, **202**, 623.
86. J. M. Moore, W. J. Chazin, R. Powls, and P. E. Wright, *Biochemistry*, 1988, **27**, 7806.
87. H. J. Dyson, J. R. Sayre, G. Merutka, H.-C. Shin, R. A. Lerner, and P. E. Wright, *J. Mol. Biol.*, 1992, **226**, 819.
88. S. Koide, H. J. Dyson, and P. E. Wright, *Biochemistry*, 1993, **32**, 12 299.
89. A. P. Kalverda, S. S. Wymenga, A. Lommen, F. J. M. van de Ven, C. W. Hilbers, and G. W. Canters, *J. Mol. Biol.*, 1994, **240**, 358.
90. I. Bertini, L. Banci, M. Piccioli, and C. Luchinat, *Coord. Chem. Rev.*, 1990, **100**, 67.
91. J. A. Tainer, E. D. Getzoff, K. M. Beem, J. S. Richardson, and D. C. Richardson, *J. Mol. Biol.*, 1982, **160**, 181.
92. Y. Kitagawa, N. Tanaka, Y. Hata, M. Kusunoki, G.-P. Lee, Y. Katsube, K. Asada, S. Aibara, and Y. Morita, *J. Biochemistry*, 1991, **109**, 477.
93. K. Djinovic, A. Coda, L. Antolini, G. Pelosi, A. Desideri, M. Falconi, G. Rotilio, and M. Bolognesi, *J. Mol. Biol.*, 1992, **226**, 227.
94. A. E. G. Cass, H. A. O. Hill, B. E. Smith, J. V. Bannister, and W. H. Bannister, *Biochemistry*, 1977, **16**, 3061.
95. J. D. Stoesz, D. P. Malinowski, and A. G. Redfield, *Biochemistry*, 1979, **18**, 4669.
96. H. A. O. Hill, W.-K. Lee, J. V. Bannister, and W. H. Bannister, *Biochem. J.*, 1980, **185**, 245.
97. A. E. G. Cass, H. A. O. Hill, J. V. Bannister, W. H. Bannister, V. Hasemann, and J. T. Johansen, *Biochem. J.*, 1979, **183**, 127.
98. I. Bertini, G. Lanini, C. Luchinat, L. Messori, R. Monnanni, and A. Scozzafava, *J. Am. Chem. Soc.*, 1985, **107**, 4391.
99. L.-J. Ming, L. Banci, C. Luchinat, I. Bertini, and J. S. Valentine, *Inorg. Chem.*, 1988, **27**, 4458.
100. I. Bertini, F. Capozzi, C. Luchinat, M. Piccioli, and M. S. Viezzoli, *Eur. J. Biochem.*, 1991, **197**, 691.
101. I. Bertini, C. Luchinat, L.-J. Ming, M. Piccioli, M. Sola, and J. S. Valentine, *Inorg. Chem.*, 1992, **31**, 4433.
102. M. Sette, M. Paci, A. Desideri, and G. Rotilio, *Eur. J. Biochem.*, 1993, **213**, 391.
103. I. Bertini, C. Luchinat, and R. Monnanni, *J. Am. Chem. Soc.* 1985, **107**, 2178.
104. D. B. Bailey, P. D. Ellis, and J. A. Fee, *Biochemistry*, 1980, **19**, 591.
105. L. Banci, I. Bertini, D. Cabelli, R. A. Hallewell, C. Luchinat, and M. S. Viezzoli, *Inorg. Chem.*, 1990, **29**, 2398.
106. L.-J. Ming and J. S. Valentine, *J. Am. Chem. Soc.*, 1990, **112**, 4256.
107. L.-J. Ming, and J. S. Valentine, *J. Am. Chem. Soc.*, 1990, **112**, 6374.
108. D. Mota de Freitas, L.-J. Ming, R. Ramasamy, and J. S. Valentine, *Inorg. Chem.*, 1990, **29**, 3512.
109. M. Paci, A. Desideri, M. Sette, and G. Rotilio, *Arch. Biochem. Biophys.*, 1991, **286**, 222.
110. M. Sette, M. Paci, A. Desideri, and G. Rotilio, *Biochemistry*, 1992, **31**, 12 410.
111. U. Bachrach, in *Structure and Function of Amine Oxidases*, ed. B. Mondovi, CRC Press, Boca Raton, FL, 1985, pp. 5–20.
112. S. M. Janes, D. Mu, D. Wemmer, A. J. Smith, S. Kaur, D. Maltby, A. L. Burlingame, and J. P. Klinman, *Science*, 1990, **248**, 981.
113. T. J. Williams and M. C. Falk, *J. Biol. Chem.*, 1986, **261**, 15 949.
114. S. S. Narula. D. R. Winge, and I. M. Armitage, *Biochemistry*, 1993, **32**, 6773.
115. S. S. Narula, R. K. Mehra, D. R. Winge, and I. M. Armitage, *J. Am. Chem. Soc.*, 1991, **113**, 9354.
116. K. Wüthrich, *Methods Enzymol.*, 1991, **205**, 502.
117. S. U. Patel, P. J. Sadler, A. Tucker, and J. H. Viles, *J. Am. Chem. Soc.*, 1993, **115**, 9285.
118. P. J. Sadler, A. Tucker, and J. H. Viles, *Eur. J. Biochem.*, 1994, **220**, 193.
119. P. J. Sadler and A. Tucker, *Eur. J. Biochem.*, 1992, **205**, 631.
120. S. Tuzi, S. K. Shinzawa-Itoh, T. Erata, A. Naito, S. Yoshikawa, and H. Saitô, *Eur. J. Biochem.*, 1992, **208**, 713.
121. Z. Tyeklár, R. R. Jacobson, N. Wei, N. N. Murthy, J. Zubieta, and K. D. Karlin, *J. Am. Chem. Soc.*, 1993, **115**, 2677.

Biographical Sketches

Gerard W. Canters. *b* 1940. M.A., 1966, Amsterdam University (with G.J. Hoitink), Ph.D., 1969, University of Nijmegen, The Netherlands (supervisor Bert de Boer). Postdoctoral work with Charles. S. Johnson, Jr. at University of North Carolina, Chapel Hill, NC, USA and with John van der Waals, Physics Department Leiden University. Lecturer, senior lecturer and Professor of Biophysical Chemistry subsequently at the Physics, Organic Chemistry, Inorganic Chemistry, and Biochemistry Departments of Leiden University, 1973–present. Visiting scientist, Oxford University, UK, 1981–82. Approx. 125 publications. Current research interest: structure/function of metalloproteins and engineering of metal sites in proteins.

Mart van de Kamp. *b* 1963. Ph.D. (supervisor Gerard W. Canters) 1993, Leiden University, The Netherlands. Postdoctoral work at the Nijmegen SON Research Centre with Cornelis W. Hilbers and Frank J. M. van de Ven. Approx. 20 publications. Research specialties: application of high-frequency NMR spectroscopy to the study of copper-containing proteins and modified polypeptides in solution.

Natural Products

Koji Nakanishi
Columbia University, New York City, NY, USA

and

Takashi Iwashita
Suntory Institute for Bioorganic Research, Osaka, Japan

1	Introduction	1
2	Sample Preparation	1
3	Chemical Shift and Spin–Spin Coupling	1
4	Nuclear Overhauser Effect	4
5	Multidimensional NMR	6
6	Solid State NMR	6
7	Related Articles	8
8	References	8

1 INTRODUCTION

In this article, we deal with organic compounds which, unlike amino acids or nucleic acids, have no repeating units. By far the major objective in this area evolves around structure determination using all available modern NMR techniques to gain maximum structural information, frequently on microgram scales. In the solution NMR of natural products, the spin system to be elucidated has many spins coupled to each other via the various spin–spin coupling pathways. UV and IR, the first spectroscopic tools used in structure determination of natural products, were introduced in the 1940s. Prior to this period, structural studies were performed by a combination of chemical derivatization, degradation, and synthesis; these reactions always had to be submitted to elementary analyses and determination of molecular weights in order to check whether the reactions had proceeded as expected. Hence, proof for the presence of a hindered ketone or hydroxyl group could be time-consuming and was frequently the subject of a full communication. The structure determination of cholesterol required several decades until it was finally solved in the early 1930s with the help of X-ray, one of its earliest applications.

In the 1950s, solution ^{1}H NMR became available to organic chemists, and soon became the most popular and important method for determining organic structures because it readily provided much information about connectivities between hydrogen atoms, usually the most abundant nucleus in organic compounds. Subsequent developments of Fourier-transform NMR facilitated measurements of insensitive nuclei present in low natural abundance, e.g., carbon-13 or nitrogen-15.[1] Two-dimensional Fourier transform NMR, which correlates spin pairs through various kinds of interactions, drastically increased the amount of structural information one could secure.[2,3]

Topics in natural products are increasingly expanding into interdisciplinary areas such as elucidating the mode of action of bioactive compounds, which in turn almost invariably requires an understanding of the interaction between ligand and biopolymeric receptors on a molecular structural basis. The recent techniques of multidimensional NMR and solid state NMR will play crucial roles in such studies. This article describes some general approaches and examples in natural products NMR from a methodological point of view.

2 SAMPLE PREPARATION

Natural products are usually analyzed by solution NMR, some of the common solvents being deuterated chloroform, benzene, and deuterium oxide. When carbon tetrachloride or water is the solvent, it is advisable to add about 5% of a deuterated solvent, which maintains a high stability and homogeneity of the magnetic field by the so-called deuterium 'lock system'.

In order to obtain high-resolution spectra, undissolved material and contaminants such as fibers must be removed by filtration upon addition of the solution to the sample tube. It is also critical to have a homogeneous solution and to pay attention to minuscule iron particles coming from spatulas because of their deleterious effects on spectral resolution. When measuring nuclear Overhauser effects (NOE), a preliminary degassing step is essential because it removes interfering paramagnetic species such as oxygen gas. The degassing process is performed by repetition of the steps of (i) submitting the frozen solution to reduced pressure, and (ii) bringing the solution to room temperature. If possible, it is advisable to seal the sample tube under high vacuum. However, it is very difficult to carry out protocols (i) and (ii) with water or deuterium oxide solutions due to the big difference in volume between the frozen state and solution. Without proper precaution this may lead to breaking the NMR sample tubes.

The selection of the solvent is particularly important for NMR measurements. Usually the sample can be recovered from the NMR tube without decomposition, but this naturally depends on the stability of the compound in the solvent. For example, traces of HCl and phosgene are generated by the decomposition of chloroform, and this often initiates chemical reactions or sample decomposition. Especially if tube-sealing has not been done properly, chloroform vapor at the tube tip generates considerable acid by heat. When using chloroform for an unstable sample, the solvent should be filtered through a neutral aluminum oxide column just before sample dissolution, and the sample removed as soon as possible after measuring. Other solvents such as benzene-d_6 or dimethyl sulfoxide-d_6 (DMSO-d_6) are also common solvents. Benzene-d_6 has less solubilizing properties than chloroform but exhibits unique solvent effects in that the chemical shifts of the protons are drastically shifted. Hydroxyl and amide protons, including the coupling pattern, can be observed in strongly solvating solvents such as DMSO-d_6 and tetrahydrofuran; however, recovery of the sample from DMSO-d_6 is more tedious.

The common chemical shift references in both ^{1}H and ^{13}C NMR are usually tetramethylsilane (TMS), 3-trimethylsilylpropionic acid-d_4 sodium salt (TSP), etc. The residual proton or the carbon peak in the solvent can also be used as a reference. However, since this chemical shift changes slightly according to sample concentration or temperature, the use of an internal standard is strongly recommended.

3 CHEMICAL SHIFT AND SPIN–SPIN COUPLING

In structure determinations of natural products, the chemical shift is one of the most important pieces of information.[4] For example, a peak around δ 9.5 in the ^{1}H NMR spectrum strongly suggests the existence of an aldehyde or a formyl group, which can be readily checked by other routine NMR techniques such as ^{13}C NMR and ^{1}H/^{13}C decoupling. Spin–spin coupling also provides vital information regarding the connectivities of protons.

3.1 ^{1}H NMR

Many ^{1}H NMR peaks have chemical shifts or shapes characteristic of a particular functional group. For example, a *t*-butyl group exhibits an intense nine-proton singlet, whereas three-proton singlets are exhibited by freely rotating (methyl) Me groups (on the NMR timescale) which are present in methyl, methoxyl, and acetate groups; a Me group shows simple and distinguishable signals because it has only three types of spin–spin coupling patterns, i.e., singlet, doublet, and triplet. The chemical shifts of steroidal 10- and 13-Me groups were studied extensively in the early days leading to additivity rules reflecting nearby substituents.[5] Methylene and methine spectra give rise to far more complex features due to the broad range of chemical shifts and various spin–spin coupling patterns.[6] The chemical shifts of protons in a cyclic compound show subtle differences depending on ring current and conformational effects. For example, the protons in cyclohexane absorb at δ 1.44. However, if the ring is fixed in the chair conformation, the equatorial protons absorb at δ 1.6, whereas the axial protons absorb at the lower frequency (higher field) of δ 1.2 because of the ring current. Olefinic and aromatic protons also cover a wide range of chemical shifts, some being predictable by empirical rules.[7,8]

NMR techniques such as COSY and HOHAHA (TOCSY) enable one to clarify the correlation between chemical structure and spin systems starting from a specific peak. Furthermore, the nuclear Overhauser effect provides information regarding proximate protons.

3.2 ^{13}C NMR

The ^{13}C NMR chemical shift covers a wide range exceeding 250 ppm and is dominated by a paramagnetic term arising from the asymmetric p-orbital in chemical bonding. The decoupling of protons leads to simple singlet peaks, because the natural abundance of ^{13}C is 1.1% and the height of doublet peaks due to ^{13}C–^{13}C spin–spin coupling is only 0.55% for the center peak. On the other hand, the low natural abundance of ^{13}C is advantageous for biosynthetic studies since the use of precursors specifically enriched with ^{13}C allows one to locate its position; when two ^{13}C atoms become incorporated in adjacent positions, this can also be readily detected and analyzed through the characteristic coupling pattern. Because of the difficulty in theoretical calculations of ^{13}C chemical shifts, certain empirical rules or comparisons with known compounds are used for chemical shift predictions.[9]

Determination of the multiplicities of respective carbon signals is an important first step in the assignment of signals and structure determination of natural products. Proton-coupled carbon spectra and off-resonance techniques have been used for such purposes. However, because these methods have resolution problems, polarization transfer techniques, such as INEPT or DEPT, are more commonly used.[10–13] Furthermore, an almost complete correlation between protons and carbons can be obtained from two-dimensional NMR techniques, ^{1}H–^{13}C COSY (HETCOR), HMQC (^{1}H-detected heteronuclear multiple quantum coherence), or HSQC (^{1}H-detected heteronuclear single quantum coherence).[2,3,14–16] The next step is to clarify the arrangement of carbons and protons in the molecule. Long-range proton/carbon spin–spin coupling provides this kind of information; for this purpose, many techniques such as LSPD (long range selective proton decoupling), COLOC (correlation spectroscopy via long range coupling), and HMBC (^{1}H-detected multiple bond heteronuclear multiple quantum coherence) have been developed.[17–19]

3.3 Other Nuclei

Natural products contain oxygen, nitrogen, phosphorus, sulfur, and metals. Generally, oxygen and nitrogen are not detected because of their low sensitivity. However, phosphorus has good sensitivity and a spin quantum number of $\frac{1}{2}$, so that ^{31}P NMR is commonly used for the characterization of phosphorus groups.

3.4 Chemical Manipulations

The combination of chemical manipulations with NMR measurements is an important aspect that greatly simplifies structure determination, but is frequently underutilized. Taking the hydroxyl group as an example, manipulations involve acetylations, substitution of the hydroxyl proton with deuterium oxide, usage of solvating solvents to differentiate among primary/secondary/tertiary hydroxyl groups, addition of shift reagents, etc.

The addition of deuterium oxide in ^{1}H NMR often causes the disappearance of spin–spin coupling between the hydroxyl proton and its adjoining proton. In ^{13}C NMR it induces an isotope shift on the OH-bearing carbon; such data readily differentiate hydroxyl and ether groups.[20] However, since the isotope shift in ^{13}C NMR is rather small, an internal reference or a coaxial tube is required.

Acetylation induces a ca. 1 ppm high-frequency shift on the adjoining proton of a hydroxyl group; acetylation using deuterated acetic anhydride prevents interference from the intense acetate methyl peaks around δ 2 so that other weaker signals can be analyzed. Benzoylation can also be used for similar purposes; an advantage of using benzoate derivatives is that whenever applicable, measurements of CD spectra will determine the absolute configuration through exciton coupling.[21]

When the solvent is changed from chloroform-*d* to benzene-d_6, some protons undergo large low- or high-frequency shifts. This shift, the ASIS effect (aromatic solvent induced shift), is due to the diamagnetic current effect of the solvent. ASIS and shift reagents are used to separate overlapping proton peaks.

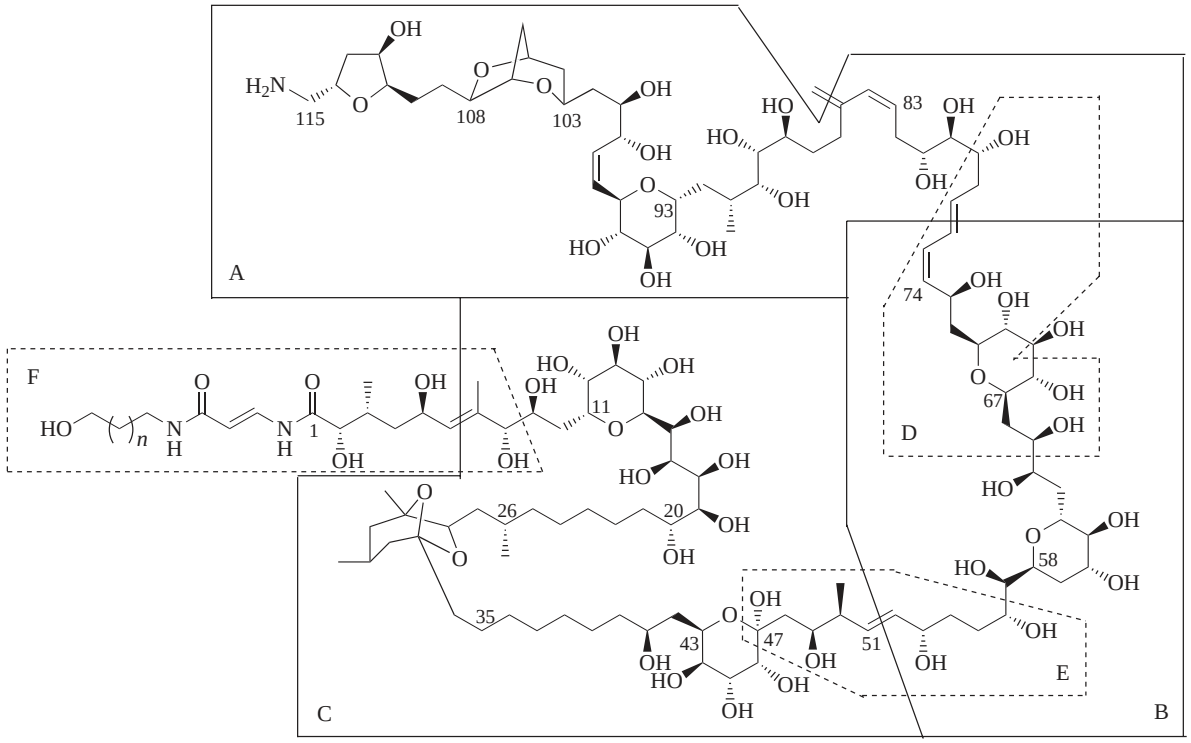

(1)

Figure 1 Structure of palytoxin (**1**) and oxidative cleavage fragments. Fragments resulting from ozonolysis and periodate cleavage are bracketed with solid and dotted lines, respectively. A, B fragments: $NaBH_4$ reduction of the partial ozonolysis products of *N*-(*p*-bromobenzoyl)palytoxin. C fragment: $NaBH_4$ reduction of the complete ozonolysis product of palytoxin. D, E fragments: $NaBH_4$ reduction of the $NaIO_4$ degradation products of palytoxin. F fragment: $NaIO_4$ degradation of palytoxin

3.5 Example 1: Palytoxin

Palytoxin (**1**) is a marine toxin obtained from *Palythoa* soft corals, and is one of the strongest neurotoxins. The biological activity of this toxin is thought to be related to the sodium channel. The structure determination was carried out by two groups, Uemura/Hirata in Nagoya (Japan)[22] and Moore in Hawaii (US).[23] Its complex structure is shown in Figure 1.

Uemura and Hirata secured the smaller fragments more suited for structure determination by ozonolysis and periodate oxidation; the terminal aldehyde groups in the resultant mixture were reduced by sodium borohydride to obtain stable fragments. After acetylation and purification, these fragments were mainly analyzed by ^1H NMR. It was not easy to establish the structure around C-47, i.e., to differentiate between (**1a**) and (**1b**) (Figure 2); this was finally solved by comparing the ^{13}C chemical shifts with those of the model compounds (**2**) and (**3**), which led to the six-membered hemiketal moiety. The Moore group also carried out extensive NMR studies.[23]

This molecule has 64 asymmetric centers, in which 13 centers were determined by X-ray crystallography. However, the preparation of derivatives with fixed conformations would have been necessary in order to determine the relative configurations of the remaining 51 asymmetric centers, an almost impossible task to perform because of the availability of the sample. The configurations of these asymmetric centers were finally established by synthesis of the fragments.[24]

3.6 Example 2: Brevetoxin A

Brevetoxins (BTX) are potent neurotoxins produced by blooms or explosive growth of the dinoflagellate, *Gymnodinium breve* Davis (*Ptychodiscus breves* Davis), the 'red tide'. The toxins have led to massive fish kills, mollusk poisoning, and human food poisoning along the Florida coast and the Gulf

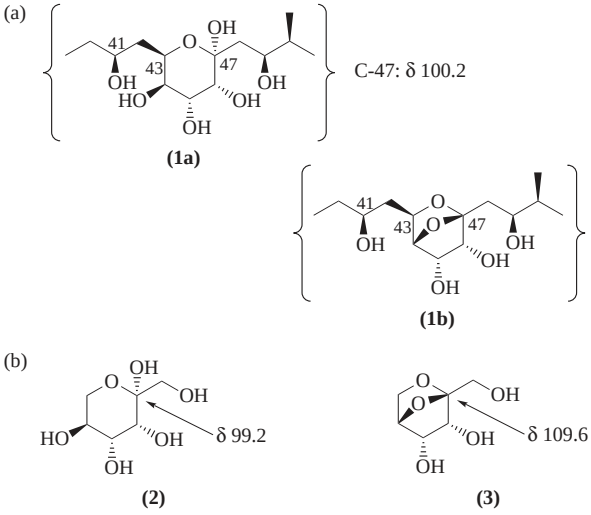

Figure 2 ^{13}C NMR of C-47 in palytoxin: (a) structural alternatives (**1a**) and (**1b**) of the hemiketal portion in palytoxin; (b) model compounds (**2**) and (**3**)

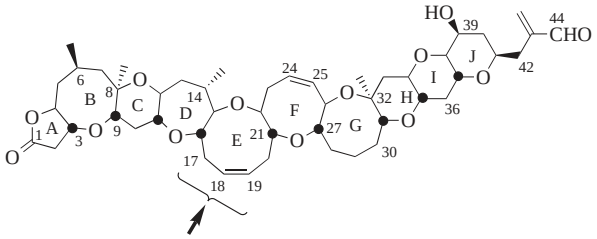

(4) Brevetoxin A

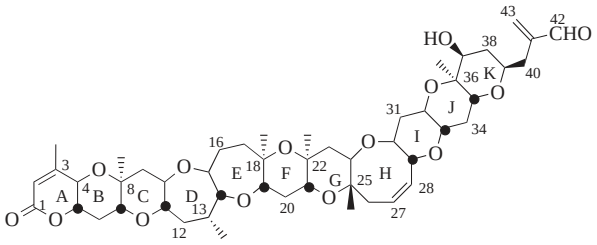

(5) Brevetoxin B

Figure 3 Structures of brevetoxin (BTX)- A (**4**) and -B(**5**): protons of ring E of BTX-A (indicated by the arrow) were detected by a HOHAHA experiment

of Mexico. Structures of two of the isolated toxins BTX-A (**4**) and BTX-B (**5**) are shown in Figure 3.

A variety of two-dimensional NMR techniques were used in the structural studies of 10 mg BTX-A, $C_{49}H_{70}O_{13}$.[25] COSY is a popular method for clarifying spin–spin coupled systems, and many variations have been developed. TOCSY or HOHAHA, related to the spin lock method, is a further method developed to observe broad or weak signals as well as relay peaks. The COSY pulse sequence used during the early stages of BTX-A structural studies provided good spectra of the terminal parts of the molecule. However, the mobile conformation of the eight- and nine-membered rings E/F/G in the middle of the molecule broadens the proximate proton signals, and it was difficult to observe the broad peaks in the COSY spectrum. These difficulties were overcome in the HOHAHA spectrum which now showed cross peaks related to the broad signals and the various kinds of relay peaks. Such NMR data, coupled with systematic analysis of the MS data, led to structure (**4**) (however, with a 6α-Me).[25] Independently, Shimizu, Clardy and co-workers determined the structure of BTX-A (**4**) by X-ray crystallography;[26] the NMR and MS-deduced structure had only to be corrected for the 6-Me configuration.

3.7 Example 3: Brevetoxin B

The ^{13}C labeling technique is extremely powerful for investigating the biosynthesis of natural products, because the labeled position is easily determined from the assigned ^{13}C NMR spectrum. Generally, it is necessary to use several kinds of carbon-13 labeled precursors for the elucidation of biosynthetic pathways. If a doubly-labeled compound with two adjacent carbon-13 nuclei is available, such as $^{13}CH_3{}^{13}COOH$, the position of the incorporated precursor can be recognized through spin–spin coupling. The ^{13}C INADEQUATE technique is very useful for such purposes because the intense singlet peaks which arise from single quantum transitions are

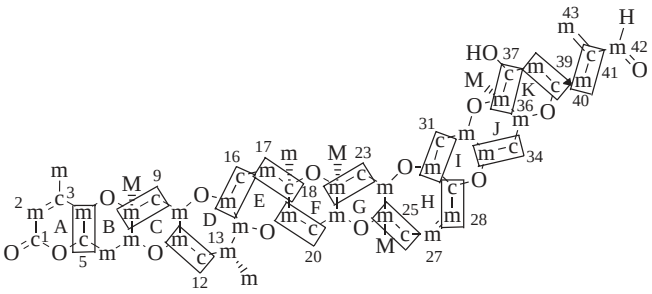

Figure 4 Biogenesis of brevetoxin B (**5**): the C_2 units that originate from the same acetates are enclosed in squares; m and c denote, respectively, the carbons derived from the methyl and carboxy carbons of acetic acid

suppressed by double quantum filtering. ^{13}C INADEQUATE is one of the ideal techniques to trace the connectivities of the carbon skeleton in a molecule. A major problem, however, is that the sensitivity level of this experiment is too low for this pulse sequence to be used routinely because of the low natural abundance of carbon-13; about 100 mg of sample would be necessary for mapping out the skeleton of a steroid using currently available instruments. However, the method becomes extremely powerful with ^{13}C-labeled compounds even if the incorporation level is low (several per cent).

Brevetoxin B (BTX-B) (**5**) also has a linear polycyclic structure which is related to, but different from, the carbon skeleton of BTX-A (Example 2). The assignment of the ^{13}C NMR spectrum of BTX-B was performed by a combination of the $^1H-{}^1H$ COSY, DEPT, $^1H-{}^{13}C$ COSY (HETCOR) and COLOC techniques.[27]

The biosynthesis was studied by ^{13}C NMR measurements of samples enriched with [1-^{13}C]-, [2-^{13}C]-, [1,2-$^{13}C_2$]-acetates and methyl-^{13}C-methionine.[27] The *Gymnodinium breve* Davis (*Ptychodiscus breves* Davis) culture (18 L) yielded approximately 1–2 mg of BTX-B and 0.5–0.8 mg of BTX-A. From the ^{13}C NMR peak heights, the incorporation level of acetates in BTX-B was estimated to be 2.0–2.5%. The 2D INADEQUATE measurements on BTX-B (**5**) incorporating [1,2-$^{13}C_2$]acetate enabled one to confirm assignments of many carbons as well as to elucidate their biosynthetic origins as shown in Figure 4. In this case, the ^{13}C-incorporation pattern shows that the single carbon chain which constitutes the backbone of the ladder-like oxacyclic skeleton is not a simple polyketide. Chou and Shimizu carried out extensive biosynthetic studies of BTX-B using ^{13}C NMR, and obtained evidence for the mixed origin of the backbone carbon chain.[28]

4 NUCLEAR OVERHAUSER EFFECT

When an appropriate nucleus is perturbed by saturation or inversion, the intensity of other nuclei which are close to that perturbed may be changed. This is a relaxation phenomenon based on the dipole–dipole interaction, and is called the nuclear Overhauser effect (NOE).[29] It has become an indispensable technique in structural studies of natural products because it yields information on a pair of proximate nuclei. The sign of the intensity change depends on the relationship between the molecular motion and the observing

frequency. Thus, a small molecule in a low viscosity solvent is usually in the 'extremely narrowing condition', and shows a strong positive NOE, i.e., enhancement in signal intensity. However, the combination of a bigger molecule (MW > 1000 Da), a viscous solvent, and a high observation frequency results in a 'diffusion limit condition', and gives rise to a negative NOE. The intermediate state of these conditions is a no NOE. Under such conditions, the temperature, solvent, or magnetic field strength should be changed. The use of the ROESY experiment is also a good solution.[30]

4.1 Steady-State NOE and Difference Spectroscopy

Steady-state NOE is usually used for small molecules because the intensity of the NOE is positive and weak. In such cases, it is usually unnecessary to consider spin diffusion, and one secures qualitative data that disclose the spatial relationships of certain groups within the molecule. The NOE difference spectroscopy technique is used to observe explicit intensity changes.

4.2 NOESY

For the global search of NOE pairs and quantitative treatment, the NOESY experiment which is related to the transient NOE method is used.[31,32] The cross-relaxation term can be obtained upon changing the mixing time. A positive NOE spectrum shows opposite phases between diagonal peaks and cross peaks, so that the chemical exchange peaks are easily distinguished from NOE peaks. On the other hand, a negative NOE and a chemical exchange spectrum show the same phase in the diagonal and cross peaks. To distinguish these, the ROESY experiment is used.

4.3 Example 4: Ginkgolide

Ginkgolides are diterpenoids obtained from the root bark of *Ginkgo biloba* L. (ginkgo tree) which is the last surviving member of a family of trees that appeared more than 200 million years ago.[33] The compounds have a unique cage structure possessing a *t*-Bu group in the molecule. The ginkgolides were the first example of the use of NOE in the structure determination of natural products. The NOE was first discovered by Solomon in his study of the relaxation mechanism of the two-spin system HF.[34] Then, Anet and Bourn demonstrated the first example of intramolecular homonuclear NOE in simple organic compounds in 1965.[35] At about the same time, during the course of scrutinizing small spin–spin couplings in the ginkgolides, Woods and co-workers observed that irradiation of the *t*-Bu group led to an increase in the intensities of certain proton peaks.[36]

As shown in Figure 5, four protons were affected by saturation of the *t*-Bu group in ginkgolide C (**6**). Later, this phenomenon was interpreted to be the same as Anet's finding. The affected protons were identified as being close to the *t*-Bu group, and this finding culminated in the structure determination of the ginkgolides.[34]

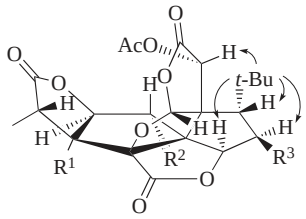

(6) Ginkgolide C: $R^1 = R^2 = R^3 = OH$

Figure 5 NOEs of ginkgolide C (**6**): NOEs (indicated by arrows in the structure) observed upon irradiation of the *t*-Bu group

4.4 Example 5: Taxane Derivatives

Soon after the initial observations of NOE, it was applied in the structure determination of various naturally occurring taxanes [TB (**8**), TE (**9**), TJ (**10**)].[37] These compounds are diterpenoids isolated in only very small amounts from the leaves of *Taxus cuspidata* Sieb. *et* Zucc. The molecular weight of the compounds is in the range of 664–704 Da, so that the compounds fall within the extreme narrowing condition and the NOEs are positive.

As shown in Figure 6, the NOEs between H-2/H-5 and 15-Me, and between H-10/12-Me and H-10/H-7 clearly distinguish orientations of the protons with respect to the taxane skeleton. The remarkable NOE observed between 12-Me and the cinnamate H-21 not only determined the configuration at C-5 but also demonstrated that the ester group was tucked under, like the tail of a shrimp. This example shows that proximate pairs may exist in a molecule, even when they are distant from each other in the planar structure.

4.5 Example 6: Vancomycin

Vancomycin (**11**) is a broad-spectrum antibiotic produced by *Streptomyces orientalis*, which inhibits the growth of cell walls

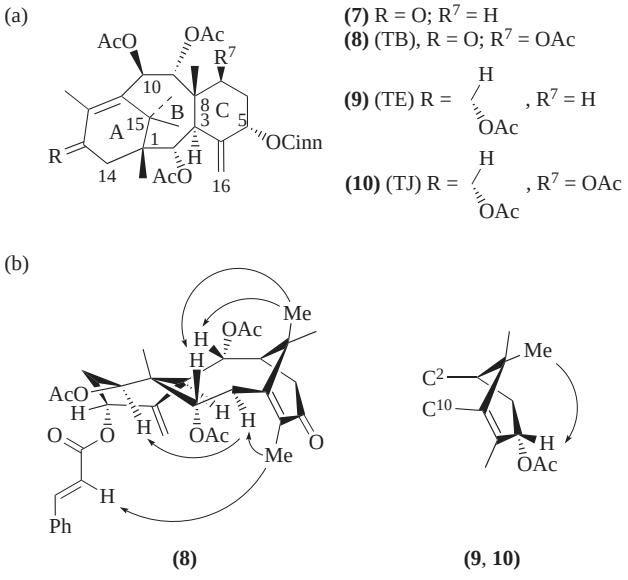

Figure 6 (a) Planar structures of taxinine (**7**), and taxinines B (**8**), E (**9**), and J (**10**); (b) NOEs (indicated by arrows) observed in taxinines B, J, and E

by the recognition of a terminal D-alanyl-D-alanine functional group. This 1449 Da molecule contains disaccharide, phenol, and amino acid groups and also chlorine atoms. At first, the structure was analyzed by X-ray crystallography using the degradation product of vancomycin, CDP-1 (**12**).[38] The observed NOEs were negative because the sample was dissolved in the viscous solvent DMSO and measured at high frequencies (270 MHz or 400 MHz) which matched the spin diffusion limit condition.[39] This is probably the first example of the observation of a negative NOE in the natural products.

Williamson and Williams paid careful attention to spin diffusion and spin migration (chemical exchange), and measured the build-up rate of NOEs. From such data, the distances between protons in some pairs of protons were estimated; it was determined that one of the aromatic rings containing chlorine (ring C) had an inverted conformation (Figure 7). In this study, it was found that CDP-I (**12**) (structure determined by X-ray diffraction) had an isomer in which the conformation of ring C was the same as that in vancomycin, from which it was interpreted that the strong steric hindrance present in ring C resulted in bond-breaking and bond-reforming at the P6–α2 bond to yield the conformational isomer of CDP-1.

5 MULTIDIMENSIONAL NMR

Two-dimensional NMR was developed by the addition of evolution and mixing times; the detection period is one of the time dimensions.[40] The substitution of the detection period by a two-dimensional pulse sequence leads to three-dimensional NMR. Repetition of the same procedure results in higher-dimensional NMR. The multidimensional technique is expected to improve the separation of overlapping peaks, thus leading to greater facilitation in complex signal assignments. However, in this technique, since multiple evolution and mixing periods are present, the signal-to-noise (S/N) ratio problem becomes severe and requires the use of labeled samples. If the problem of low S/N ratio is solved, the technique promises to be a very powerful tool for the structure determination of complex natural products (and especially biopolymers).

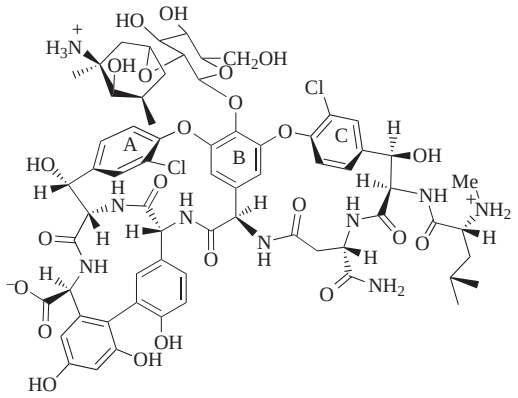

(11) Vancomycin

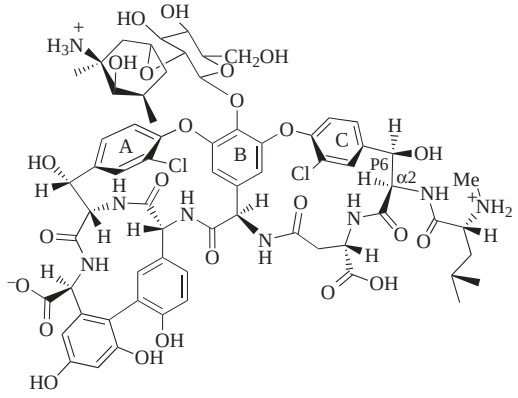

(12) CDP-1

Figure 7 Structures of vancomycin (**11**) and CDP-I (**12**)

5.1 Example 7: Maitotoxin

Maitotoxin (MTX) (**13**) with a molecular weight of 3422 Da and an empirical formula of $C_{164}H_{256}O_{68}S_2Na_2$ is one of the largest natural products.[41] The toxicity of MTX, which is related to the stimulation of calcium influx into cells, is also remarkably strong (1 mg of MTX kills 1×10^6 mice). MTX was first identified as a toxic substance of the cigatera of surgeon fish collected in French Polynesia, but it was subsequently found that *Gambierdiscus toxicus* produced this toxin in cultures.

Structural determination was carried out relying mainly on modern physicochemical methods such as MS/MS and multidimensional NMR (Figure 8). Various kinds of two-dimensional techniques, e.g., double quantum filtered correlated spectroscopy (DQF–COSY), NOESY, ^{1}H–^{13}C COSY(HETCOR), HMQC, and HSQC, were used to obtain valuable information. However, the signal overlap was so severe that a three-dimensional NMR technique was used for spectral editing and resolution enhancement. Murata et al.[41] cultured *G. toxicus* in a medium containing 0.01% (w/v) of 99% ^{13}C-enriched sodium carbonate, to produce 9 mg of 4% ^{13}C-enriched MTX from 2000 L of the culture.

The NOESY–HMQC data were acquired as a three-dimensional matrix [t_1(^{1}H) 128, t_2(^{13}C) 32, t_3(^{1}H) 512] during a period of 6 d. The region which has over 1000 NOE peaks in the two-dimensional spectrum is resolved in 64 2D sheets, in which only 70 nonoverlapping cross peaks were obtained at 77.5 ppm (carbon chemical shift) as shown in Figure 9. These data were extremely helpful in elucidating the NOE correlation.[42] The experiment was performed with the pulsed field gradient technique, which simplified the pulse sequence and reduced the running time.

6 SOLID STATE NMR

Solid state NMR has not been used in structure determinations of natural products because of experimental difficulties. However, recent progress has made it possible to obtain unique information such as nuclear distances and dynamics of the molecule. Furthermore, as more attention is being paid to elucidating the function of natural products in the biological system, solid state NMR will undoubtedly become an increasingly useful tool in the chemistry of natural products.

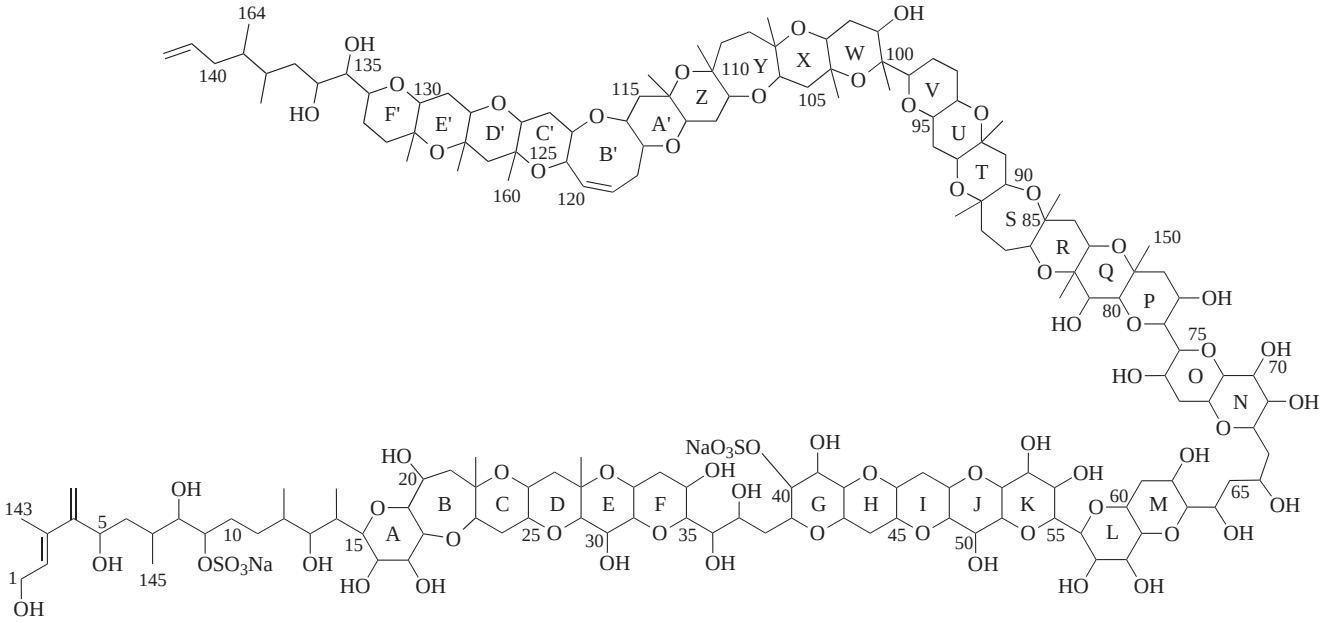

(13)

Figure 8 Structure of maitotoxin (**13**)

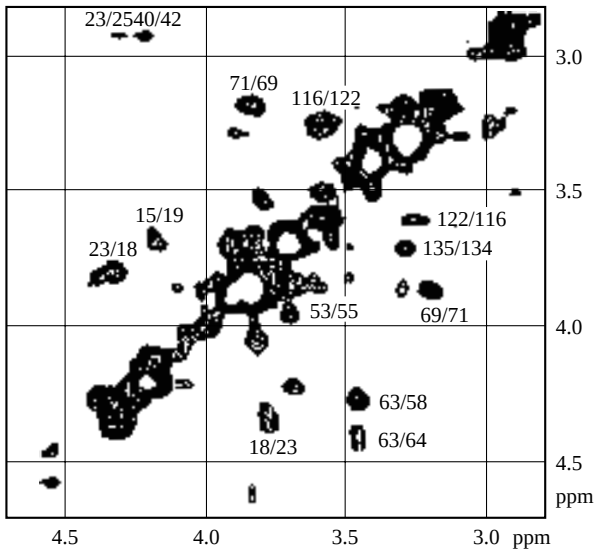

Figure 9 3D PFG NOESY–HMQC partial spectra of maitotoxin: one NOESY plane at 77.5 ppm in the carbon dimension

6.1 Example 8: Retinal (1)

Bacteriorhodopsin (bR) is a transmembrane protein possessing a light-driven proton pump function, and is produced by *Halobacterium halobium*. The protein has a retinal chromophore which binds to lysine 216 (Lys-216) via a protonated Schiff base linkage. Because bR can be readily grown, is a light-driven proton pump, and is one of the simplest of the membrane proteins, it has been the subject of extensive investigations in all fields of science. In natural product chemistry, numerous retinal analogs have been incorporated into bR in order to elucidate its function in the protein. Recently carbon-13 labeling and solid state NMR methods have been applied to bR to determine the configurations and conformations of the chromophore. The retinal chromophore labeled by ^{13}C at C-8 and 5-Me is bound to the protein. Magnetization transfer experiments under rotational resonance conditions ($\delta = n\omega_\tau$, where δ is the isotropic shift difference, ω_τ is the magic angle spinning speed, and n is a small integer) were used to determine the distance between the ^{13}C atoms at C-8 and 5-Me [indicated by large black dots in (**14**) in Figure 10]. The 4.2 Å distance established the 6-*s*-*trans* conformation (**14**) of the retinal moiety (Figure 10); if it were 6-*s*-*cis* (**15**), the distance would have been 3.1 Å.[43]

The C-14 carbon of retinal and the ϵ carbon of Lys-216 in the protein were labeled with ^{13}C, and the distance between these carbons was measured by the same method. The distances were 3.0 ± 0.2 Å for the dark-adapted bR_{555} (**16**) which leads to a *syn* C=N bond, and a 4.1 ± 0.3 Å distance for the light-adapted bR_{568} (**17**) which leads to an *anti* C=N bond (Figure 11).[44]

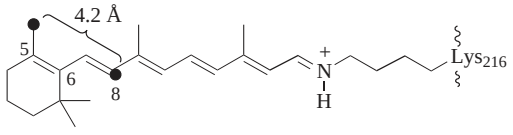

(14) 6-*s*-*trans*

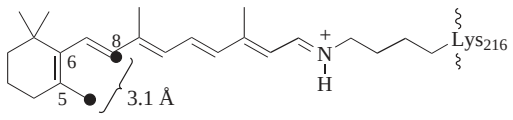

(15) 6-*s*-*cis*

Figure 10 The ring-polyene conformation of the retinal chromophore in bR: magnetization transfer data at −30°C fitted with the 6-*s*-*trans* conformation (**14**) but not with the 6-*s*-*cis* conformation (**15**)

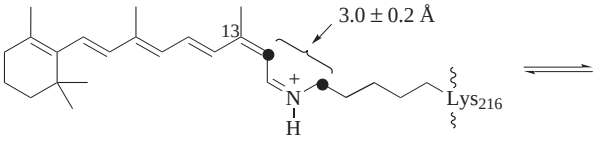

(16) bR_{555}

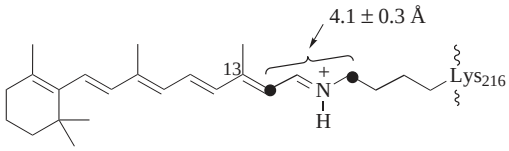

(17) bR_{568}

Figure 11 Structures of the retinal chromophore in dark-adapted bR_{555} (**16**) and light-adapted bR_{568} (**17**)

6.2 Example 9: Retinal (2)

Solid state deuterium NMR yields information on molecular conformation and dynamics through quadrupole coupling. A bR sample was regenerated from a $^2H_{11}$-retinal carrying the multiple labels 1-CD_3, 1-CD_3, 2-D, 4-D, 4-D, and 5-CD_2H. The sample was prepared as an uniaxially oriented membrane patch, and the axis was systematically changed with respect to the magnetic field. The quadrupole splittings showed that the two Me groups on C-1 have angles of 94 ± 2° and 75 ± 2° with respect to the membrane, respectively, and that the third Me group on C-5 is directed toward the cytoplasmic side with an angle of 46 ± 3°. This indicates that the orientation of the cyclohexene ring is almost perpendicular to the membrane surface and has a 6-*s*-*trans* conformation around the C-6/C-7 bond (Figure 12).[45]

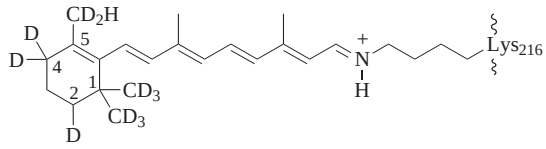

(18) bR from $^2H_{11}$-retinal

Figure 12 The $^2H_{11}$-retinal chromophore incorporated into bR

7 RELATED ARTICLES

Analysis of High-Resolution Solution State Spectra; Bacteriorhodopsin and Rhodopsin; Biological Macromolecules: Structure Determination in Solution; Biological Macromolecules: NMR Parameters; Biosynthesis and Metabolic Pathways: Carbon-13 and Nitrogen-15 NMR; Biosynthesis and Metabolic Pathways: Deuterium NMR; Carbon-13 Spectral Simulation; Chemical Exchange Effects on Spectra; COSY Spectra: Quantitative Analysis; COSY Two-Dimensional Experiments; Coupling Constants Determined by ECOSY; Decoupling Methods; Deuterium NMR in Solids; Double Resonance; Field Gradients and Their Application; Heteronuclear Shift Correlation Spectroscopy; Homonuclear Recoupling Schemes in MAS NMR; INADEQUATE Experiment; Indirect Coupling: Theory and Applications in Organic Chemistry; INEPT; Isotope Effects on Chemical Shifts and Coupling Constants; Multidimensional Spectroscopy: Concepts; Multiple Quantum Spectroscopy of Liquid Samples; NOESY; Nuclear Overhauser Effect; Organic Chemistry Applications; Polarization Transfer Experiments via Scalar Coupling in Liquids; Quantitative Measurements; Relayed Coherence Transfer Experiments; ROESY; Rotational Resonance in Biology; Spin Echo Spectroscopy of Liquid Samples; Stereochemistry and Long Range Coupling Constants; Three-Dimensional HMQC-NOESY, NOESY-HMQC, and NOESY-HSQC; Three- and Four-Dimensional Heteronuclear Magnetic Resonance; TOCSY in ROESY and ROESY in TOCSY; Two-Dimensional J-Resolved Spectroscopy; Vicinal Coupling Constants and Conformation of Biomolecules.

8 REFERENCES

1. R. R. Ernst and W. A. Anderson, *Rev. Sci. Instrum.*, 1966, **37**, 93.
2. A. Bax, *Two-Dimensional Nuclear Magnetic Resonance in Liquids*, Delft Unversity Press, Delft, The Netherlands, 1982.
3. R. R. Ernst, G. Bodenhausen, and A. Wokaun, *Principles of Nuclear Magnetic Resonance in One and Two Dimensions*, Oxford University Press, Oxford, UK, 1987.
4. A. Saika and C. P. Slichter, *J. Chem. Phys.*, 1954, **22**, 26.
5. J. N. Shoolery and M. T. Rogers, *J. Am. Chem. Soc.*, 1958, **80**, 5121; R. F. Zürcher, *Helv. Chim. Acta*, 1961, **44**, 1380.
6. J. N. Shoolery, *Tech. Inform. Bull. (Varian Assoc.)*, 2 (No.3) (1959); L. M. Jackman and S. Sternhell, *Applications of Nuclear Magnetic Resonance Spectroscopy in Organic Chemistry*, 2nd edn., Pergamon Press, Oxford, UK, 1969.
7. C. Pascual, J. Meier, and W. Simon, *Helv. Chim. Acta*, 1966, **49**, 164.
8. P. L. Corio and B. P. Dailey, *J. Am. Chem. Soc.*, 1956, **78**, 3040; P. Diehl, *Helv. Chim. Acta*, 1961, **44**, 829; G. W. Smith, *J. Mol. Spectrosc.*, 1964, **12**, 146.
9. J. B. Stothers, *Carbon-13 NMR Spectroscopy*, Academic Press, New York, 1972; E. Breitmaier and W. Voelter, *Carbon-13 NMR Spectroscopy: High Resolution Methods and Applications in Organic Chemistry and Biochemistry*, VCH, New York, 1987.
10. C. Le Cooq and J.-Y. Lallemand, *J. Chem. Soc., Chem. Commun.*, 1981, 150; D. J. Cookson and B. E. Smith, *Org. Magn. Reson.*, 1981, **16**, 111.
11. S. L. Patt and J. N. Shoolery, *J. Magn. Reson.*, 1982, **46**, 535.
12. D. P. Burum and R. R. Ernst, *J. Magn. Reson.*, 1980, **39**, 163.
13. D. T. Pegg, M. R. Bendall, and D. M. Doddrell, *J. Magn. Reson.*, 1981, **44**, 238; M. R. Bendall, D. T. Pegg, D. M. Doddrell, and D. M. Thomas, *J. Magn. Reson.*, 1982, **46**, 43; D. M. Doddrell, D. T. Pegg, and M. R. Bendall, *J. Magn. Reson.*, 1982, **48**, 323.
14. A. Bax and S. Sarkar, *J. Magn. Reson.*, 1984, **60**, 170.
15. A. Bax, R. H. Griffey, and B. L. Hawkins, *J. Magn. Reson.*, 1983, **55**, 301; A. Bax and S. Subramanian, *J. Magn. Reson.*, 1986, **67**, 565; M. F. Summers, L. G. Marzilli, and A. Bax, *J. Am. Chem. Soc.*, 1986, **108**, 4285.
16. L. Müller, *J. Am. Chem. Soc.*, 1979, **101**, 4481; G. Bodenhausen and D. J. Ruben, *Chem. Phys. Lett.*, 1980, **69**, 185.
17. S. Takeuchi, J. Uzawa, H. Seto, and H. Yonehara, *Tetrahedron Lett.*, 1977, 2943; J. Uzawa and S. Takeuchi, *Org. Magn. Reson.*, 1978, **11**, 502.
18. H. Kessler, C. Griesinger, J. Zarbock, and H. R. Loosli, *J. Magn. Reson.*, 1984, **57**, 331.

19. A. Bax and M. F. Summers, *J. Am. Chem. Soc.*, 1986, **108**, 2093; M. F. Summers, L. G. Marzilli, and A. Bax, *J. Am. Chem. Soc.*, 1986, **108**, 4285.
20. P. E. Pfeffer, K. M. Valentine, and F. W. Parrish, *J. Am. Chem. Soc.*, 1979, **101**, 1265.
21. K. Nakanishi and N. Harada, *Circular Dichroic Spectroscopy–Exciton Coupling in Organic Stereochemistry*, University Science Books, California, 1983.
22. D. Uemura, K. Ueda, Y. Hirata, H. Naoki, and T. Iwashita, *Tetrahedron Lett.*, 1981, **22**, 1909; *ibid.*, 1981, **22**, 2781; D. Uemura, Y. Hirata, T. Iwashita, and H. Naoki, *Tetrahedron*, 1985, **41**, 1007; Atta-ur-Rahman (ed.), *Studies in Natural Products Chemistry*, Elsevier, Amsterdam, Vol. 5, p. 377.
23. R. E. Moore and G. Bartolini, *J. Am. Chem. Soc.*, 1983, **103**, 2491.
24. J. K. Cha, W. J. Christ, J. M. Finan, H. Fujioka, Y. Kishi, L. L. Klein, S. S. Ko, J. Leder, W. W. McWhorter, Jr., K.-P. Pfaff, M. Yonaga, D. Uemura, and Y. Hirata, *J. Am. Chem. Soc.*, 1982, **104**, 7369; H. Fujioka, W. J. Christ, J. K. Cha, J. Leder, Y. Kishi, D. Uemura, and Y. Hirata, *J. Am. Chem. Soc.*, 1982, **104**, 7367; S. S. Ko, J. M. Finan, M. Yonaga, Y. Kishi, D. Uemura, and Y. Hirata, *J. Am. Chem. Soc.*, 1982, **104**, 7364; L. L. Klein, M. M. McWhorter, Jr., S. S. Ko, K.-P. Pfaff, Y. Kishi, D. Uemura, and Y. Hirata, *J. Am. Chem. Soc.*, 1982, **104**, 7362.
25. J. Pawlak, M. S. Tempesta, J. Golik, M. G. Zagorski, M. S. Lee, K. Nakanishi, T. Iwashita, M. L. Gross, and K. B. Tomer, *J. Am. Chem. Soc.*, 1987, **109**, 1144; M. S. Lee, K. Nakanishi, and M. G. Zagorski, *New J. Chem.*, 1987, **11**, 753.
26. Y. Shimizu, H.-N. Chou, H. Bando, G. Van Buyne, and J. C. Clardy, *J. Am. Chem. Soc.*, 1986, **108**, 514.
27. M. S. Lee, D. J. Repeta, K. Nakanishi, and M. G. Zagorski, *J. Am. Chem. Soc.*, 1986, **108**, 7855.
28. H.-N. Chou and Y. Shimizu, *J. Am. Chem. Soc.*, 1987, **109**, 2184.
29. J. H. Noggle and R. E. Schirmer, *The Nuclear Overhauser Effect–Chemical Applications*, Academic Press, New York, 1971; D. Neuhaus and M. P. Williamson, *The Nuclear Overhauser Effect in Structural and Conformational Analysis*, VCH, New York, 1989.
30. A. A. Bothner-By, R. L. Stephens, J.-M. Lee, C. D. Warren, and R. W. Jeanloz, *J. Am. Chem. Soc.*, 1984, **106**, 811; A. Bax and D. G. Davis, *J. Magn. Reson.*, 1985, **63**, 207; H. Kessler, C. Griesinger, R. Kerssebaum, K. Wagner, and R. R. Ernst, *J. Am. Chem. Soc.*, 1987, **109**, 607.
31. J. Jeener, B. Meier, P. Bachmann, and R. R. Ernst, *J. Chem. Phys.*, 1979, **71**, 4546; S. Macura and R. R. Ernst, *Mol. Phys.*, 1980, **41**, 95.
32. S. Macura, B. T. Farmer, II, and L. R. Brown, *J. Magn. Reson.*, 1986, **70**, 493.
33. K. Nakanishi, *Ginkgolides—Chemistry, Biology, Pharmacology and Clinical Perspectives*, ed. P. Braquet, J. R. Prous Science Publishers, 1988, p. 27; K. Nakanishi, *Pure Appl. Chem.*, 1967, **14**, 89.
34. I. Solomon, *Phys. Rev.*, 1955, **99**, 559; I. Solomon and N. Bloembergen, *J. Chem. Phys.*, 1956, **25**, 261.
35. F. A. L. Anet and A. J. R. Bourn, *J. Am. Chem. Soc.*, 1965, **87**, 5250.
36. M. Maruyama, A. Terahara, Y. Itagaki, and K. Nakanishi, *Tetrahedron Lett.*, 1967, 299; M. Maruyama, A. Terahara, Y. Itagaki, and K. Nakanishi, *Tetrahedron Lett.*, 1967, 303; M. Maruyama, A. Terahara, Y. Nakadaira, M. C. Woods, and K. Nakanishi, *Tetrahedron Lett.*, 1967, 309; M. Maruyama, A. Terahara, Y. Nakadaira, M. C. Woods, Y. Takagi, and K. Nakanishi, *Tetrahedron Lett.*, 1967, 315; M. C. Woods, I. Miura, Y. Nakadaira, A. Terahara, M. Murayama, and K. Nakanishi, *Tetrahedron Lett.*, 1967, 321.
37. M. C. Woods, H.-C. Chiang, Y. Nakadaira, and K. Nakanishi, *J. Am. Chem. Soc.*, 1968, **90**, 522.
38. G. M. Sheldrick, P. G. Jones, O. Kennard, D. H. Williams, and G. A. Smith, *Nature (London)*, 1978, **271**, 223.
39. M. P. Williamson and D. H. Williams, *J. Am. Chem. Soc.*, 1981, **103**, 6580.
40. H. Oschkinat, C. Griesinger, P. J. Kraulis, O. W. Sørensen, R. R. Ernst, A. M. Gronenborn, and G. M. Clore, *Nature (London)*, 1988, **332**, 375; A. M. Gronenborn and G. M. Clore, *Anal. Chem.*, 1990, **62**, 2.
41. M. Murata, H. Naoki, T. Iwashita, S. Matsunaga, M. Sasaki, A. Yokoyama, and T. Yasumoto, *J. Am. Chem. Soc.*, 1993, **115**, 2060.
42. M. Murata, personal communication, 1993.
43. F. Creuzet, A. McDermott, R. Gebhard, K. van der Hoff, M. B. Spijker-Assink, J. Herzfeld, J. Lugtenburg, M. H. Levitt, and R. G. Griffin, *Science*, 1991, **251**, 783.
44. L. K. Thompson, A. E. McDermott, J. Raap, C. M. van der Wielen, J. Lugtenburg, J. Herzfeld, and R. G. Griffin, *Biochemistry*, 1992, **31**, 7931.
45. A. S. Ulrich, M. P. Heyn, and A. Watts, *Biochemistry*, 1992, **31**, 10 390.

Biographical Sketches

Koji Nakanishi. *b* 1925. B.S., 1947, Ph.D., 1954, Nagoya University. Assistant Professor, Dept. of Chemistry, Nagoya University 1955–58; Professor, Dept. of Chemistry, Tokyo Kyoiku University 1958–63; Professor, Dept. of Chemistry, Tohoku University 1963–69; Professor, Dept. of Chemistry, Columbia University, 1969–80; Centennial Professor, Dept. of Chemistry, Columbia University, 1980–present; Chairman, Dept. of Chemistry, Columbia University, 1987–90; Director of Research, The International Centre of Insect Physiology and Ecology in Kenya, 1969–77; Director, Suntory Institute for Bioorganic Research in Osaka, 1978–91. Approx. 600 publications. Research interests include isolation, structural and bioorganic studies of bioactive compounds, retinal proteins, interaction between ligands and neuroreceptors, structural studies of oligosaccharides, and application of various spectroscopic methods, especially circular dichroic spectroscopy.

Takashi Iwashita. *b* 1950. B.S., 1975, Tokyo Kyoiku University, Ph.D., 1980, University of Tsukuba. Researcher in Suntory Institute for Bioorganic Research, 1980–present. Approx. 70 publications. Research interests: three-dimensional structure of natural products, interaction and function between bioactive compounds and receptor proteins.

Nitrogen-15 Chemical Shift Tensors and Organic Structure

Ronald J. Pugmire

Department of Chemical and Fuels Engineering, University of Utah, Salt Lake City, UT, USA

1 Introduction 1
2 Chemical Shielding 1
3 Experimental Techniques 3
4 Results 4
5 Conclusions 7
6 References 7

1 INTRODUCTION

During the past two decades solid state NMR spectroscopy and its applications have grown rapidly among the chemistry and biochemistry community. The availability of increasingly sophisticated instrumentation and software has created opportunities for conducting experiments in areas that have not previously been available to the general chemical community. These new opportunities have been especially helpful in the study of solids. While the majority of such solid state applications have utilized ^{13}C nuclei, a much broader range of interesting nuclei (e.g., ^{11}B, ^{14}N, ^{15}N, ^{17}O, ^{19}F, ^{23}Na, ^{27}Al, ^{29}Si, ^{31}P, ^{113}Cd, ^{209}Pb, etc.) has emerged for use by solid state scientists and engineers.

Interest in magnetic resonance studies of nitrogen has increased significantly in the past decade. The distribution of nitrogen containing substances in materials important to the chemical, biological, medical, agricultural, and environmental sciences is well documented. The ^{14}N nucleus (99.6% natural abundance, nuclear spin 1) is quadrupolar giving rise to a broad signal while the ^{15}N nucleus has spin 1/2. The relative sensitivity of both nuclei is approximately 1×10^{-3} compared to ^{1}H. Nitrogen NMR data have been extensively reviewed by Witanowski et al.[1] and by Mason.[2] Most of the literature describes liquid state isotropic shifts and their relationship to structure elucidation, the importance of solvent effects, and tautomeric equilibria. The combination of a large isotropic shift range, approximately 1350 ppm,[1] and sensitivity to electronic interactions involving the lone pair of electrons make ^{15}N shifts a very sensitive probe of both structural changes and intermolecular interaction.[3] These attractive features of the ^{15}N nucleus are off-set by the sensitivity challenges arising from a low natural abundance (0.365%), long relaxation times, small magnetogyric ratio, and a subsequent receptivity factor 2.19×10^{-2} relative to ^{13}C for an equivalent number of nuclei. Hence, much of the data reported has been obtained from ^{15}N labeled materials although modern high field spectrometers have proven their value in studies at the natural abundance level. A significant amount of attention has recently been focused on the role of nitrogen in biological structures[4] because of its sensitivity to both hydrogen bonding and intermolecular and long-range interactions. In this document the discussion will be restricted to the ^{15}N nucleus.

2 CHEMICAL SHIELDING

The well known relationship between magnetic field strength B_o(arbitrary orientation in the z direction), the magnetogyric ratio γ_I of nuclear spin I, and the NMR Larmor frequency ν_o (in frequency units, Hz) is given in equation (1)

$$\nu_o = \frac{\gamma_I B_o}{2\pi} \tag{1}$$

where ν_o is the difference in energy between any two of the allowed states. The magnetic inductive affect at the nucleus is equal to the vector sum of the static magnetic field and an induced magnetization vector arising from electronic currents that exist in the sample. The induced magnetization is proportional to B_o and the proportionality constant is the sum of the chemical shielding and the magnetic susceptibility of the material surrounding the nucleus of interest. In solids, where rapid motional averaging is absent, all intramolecular currents within the molecule of interest are assigned to chemical shielding. Electronic currents arising from neighboring molecules are assigned to magnetic susceptibility. A more detailed and very useful outline of these interactions is provided by Grant.[5]

The electronic circulation set up by the magnetic induction of the applied field perturbs the effects of B_o at the nucleus of interest. These electronic currents induce a shielding field, B_s, which may be either paramagnetic or diamagnetic (deshielding or shielding) and this induced field must be added to B_o in order to obtain the effective field, B_{eff}, experienced by the nucleus of interest (equation (2)).

$$B_{eff} = B_s + B_o \tag{2}$$

This effect is portrayed in vector form in Figure 1.

The shielding of the nuclear spin is a tensor quantity, described below, that depends on the electronic environment as well as the molecular orientation in the magnetic field. In solids the molecular orientation is locked into a powder pattern in which the nuclear resonance frequency is a function of the orientation of the microcrystalline particles. The random orientation of these particles leads to broad resonance patterns for each unique nuclear spin. The rich informational content of these powder patterns provides more information about electronic structure than the isotropic shifts observed in rapidly tumbling liquid molecules. Unfortunately, the diversity of the banding arising from multiple unique chemical environments in these broad powder patterns obscures the information content that is available in the isotropic chemical shift. However, the components of the shift tensor in the solid state reveal even more information regarding the subtle differences in electronic and geometrical structural characteristics and

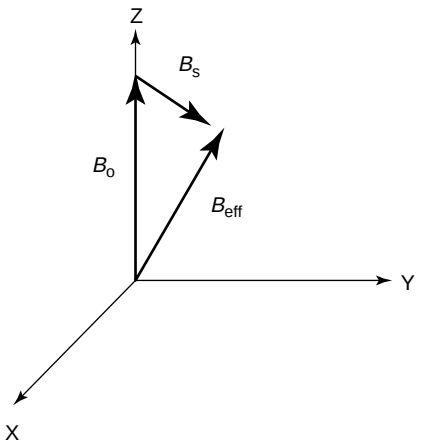

Figure 1 Relationship between the applied field, B_o, and the shielding field and effective fields (not drawn to scale) B_s and B_{eff}

the various experimental techniques employed to extract this information from solid samples is summarized in Section 3.

The shielding interaction with a nucleus is different for each unique chemical environment or symmetry position relative to the remainder of the lattice structure. Furthermore, the orientation dependence of the magnetic field to the screening currents induced around the nucleus presents an anisotropic environment that can be described by the chemical shift tensor. In principal, a different resonance frequency will be observed for each orientation of the nuclear spin with respect to the external magnetic field and the difference in this screening effect from that of a reference material is defined as the chemical shift. The reference that has emerged in the field is

$$\delta = \begin{bmatrix} \delta_{xx} & \delta_{xy} & \delta_{xz} \\ \delta_{yx} & \delta_{yy} & \delta_{yz} \\ \delta_{zx} & \delta_{zx} & \delta_{zz} \end{bmatrix} \tag{3}$$

external nitromethane ($\delta = 0$) with the convention of negative values for more shielded resonance positions. The chemical shift tensor δ in a general reference frame may be represented by a 3×3 Cartesian matrix that is called a second rank tensor (equation (3)) which can be decomposed into three individual tensors of rank zero, one, and two which are defined as the scalar isotropic chemical shift, the symmetric, and antisymmetric chemical shifts denoted (equation (4)) as

$$\delta = \delta_o + \delta_{sym} + \delta_{anti} \tag{4}$$

The isotropic shift, δ_o, of zeroeth rank, is the trace of the Cartesian tensor, e.g., $1/3(\delta_{xx} + \delta_{yy} + \delta_{zz})$, and is invariant to any rotational transformation of the coordinate frame. Hence, δ_o is the only part of the chemical shift tensor that can be measured in solution samples; this the result of rapid tumbling motion of the molecules. The antisymmetric (first rank) and symmetric (second rank,) chemical shifts are given in equations (5) and (6), respectively.

$$\delta_{ij}^{(a)} = \tfrac{1}{2}(\delta_{ij} - \delta_{ji}) \tag{5}$$

$$\delta_{ij}^{(s)} = \tfrac{1}{2}(\delta_{ij} + \delta_{ji}) \tag{6}$$

The absence of diagonal elements in the first rank tensor renders these second order infinitesimal shift frequencies immeasurable. The traceless second-rank symmetric matrix contains diagonal elements that can provide first-order anisotropic shifts that add to or subtract from the Zeeman frequencies and are measurable in the NMR spectrum of solids. In the symmetric matrix any change in orientation of the magnetic field in the molecular frame will still leave anisotropic shifts along the diagonal of the transformed second-rank matrix. Unlike the antisymmetric components, the off-diagonal shifts in the symmetric portion of the chemical shift tensor will affect the principal values under the transformations associated with matrix diagonalization.

There always exists some frame in which the matrix in equation (3) is diagonal, in which case the three diagonal elements of the chemical shift tensor are designated as the principal values, δ_{11}, δ_{22}, and δ_{33}. By convention the order of the principal values are given as $\delta_{11} \geq \delta_{22} \geq \delta_{33}$, with δ_{11} representing the highest frequency (least shielded) component. The axis system in which the symmetric chemical shift matrix is diagonal is designated the principal axis system (PAS). The diagonal components are the principle values in the PAS while the remaining three (off-diagonal) terms are the Euler angles which define the directions of these principal values in the molecular frame. Hence, the complete description of the chemical shift tensor requires six elements of the shift tensor. The breakpoints in a powder pattern provide the principal values of the chemical shift tensor. The off-diagonal terms can only be obtained experimentally by tracking the chemical shift of each unique nucleus as a molecule (e.g., a molecule in a single crystal) is rotated in the magnetic field. These data can then be transformed into any of a number of reference frames that can be used to determine the orientation of the tensor in the molecular frame. The details of these experiments and transformations are described in a general outline by Orendt[6] and in detail by Grant[5] and Sherwood.[7]

The difficulties associated with growing single crystals and then acquiring the necessary orientational data is daunting, time consuming, and complicated by the reality that acquiring a single crystal of sufficient size for NMR experiments is usually not practical. However, sufficient single crystal data, together with theoretical simulations of the shift tensors, have been acquired to demonstrate that quite good approximations can be obtained for the orientation of the shift tensor principal axis system on the molecular frame.[8,9] Hence, the various types of experiments that provide only the principal values of the shift tensor on powder samples[6,10] are sufficient, when combined with appropriate theoretical calculations, to describe the off-diagonal elements which fix the orientation in the molecular frame with reasonable accuracy (see Section 4.3). To date, the majority of chemical shift tensor data appearing in the literature has been restricted to the ^{13}C nucleus and the latest, but somewhat dated, compilation of these data together with available data on ^{15}N shift tensor principal values has been provided by Duncan.[11] The acquisition of shift tensor data on solid materials, however, has expanded considerably in the past 10–15 years as line narrowing methods and techniques have become available. A review has described these experimental advances[6] but additional major advances in multidimensional experiments have recently appeared[12–14] and are described in another article in this encyclopedia,

Magic-angle Turning Spectra of Solids Involving 5π-pulse Sequences.

Despite the challenges faced with obtaining shift tensor data, new experimental techniques now enable investigators to obtain high quality ^{13}C shift tensor data on molecules containing more than sixty unique carbon atoms[10] and ^{15}N shift tensors at the natural abundance level on molecules containing as many as five nitrogens (guanine)[15] and eight non-equivalent nitrogens in potassium penicillin V.[13]

3 EXPERIMENTAL TECHNIQUES

^{15}N chemical shift tensor data have been reported using five different types of experimental techniques: (1) single crystal studies; (2) analysis of static powder patterns and off-magic-angle spinning on simple ^{15}N enriched heterocycles; (3) analysis of powder patterns utilizing the dipolar interaction between ^{1}H–^{5}N or adjacent ^{13}C–^{15}N labeled pairs; (4) powder patterns obtained by means of dynamic nuclear polarization experiments; (5) two-dimensional experiments such as polarization inversion spin exchange at the magic angle (PISEMA), and the five-π pulse experiment five pi replicated magic angle turning (FIREMAT).

3.1 Single Crystals

A single crystal study of L-hystidine·HCl·H_2O[16] reported the full tensor of the two imidazole nitrogens in the amino acid while a single crystal study of [1-^{13}C]glycyl[^{15}N]glycine provided the principal values of the ^{15}N tensor and its orientation in the molecular frame.[17]

3.2 Static Powders and Off-Magic Angle Spinning

The major portion of the ^{15}N shift tensor data has been obtained by static powder pattern analysis. Illustrative examples of static experiments on ^{15}N-enriched materials include: studies of the various phases of NH_4NO_3,[18] protonated and non-protonated species in simple five- and six-member nitrogen heterocycles,[19] porphyrin complexes,[20] cation binding in a membrane-bound polypeptide,[21] substituted benzonitriles,[22] off-angle fast sample spinning of an isolated ^{15}N–^{15}N diazo system,[23] static and off-angle fast sample spinning of substituted pyrazoles,[24] secondary structure of peptides containing L-alanine[25] and poly(β-benzyl L-aspartate),[26] substituted benzonitriles,[27] the amide fragment of acetanilide and *N*-methylacetanilide,[28] and the relationship of the δ_{33} principal value to the hydrogen bond length in the glycine residue of some oligopeptides.[29]

3.3 Dipolar Interactions in Powders

^{15}N shift tensor principal values and their orientation in the molecular frame have been determined through the dipolar interaction between proton and nitrogen dipolar coupling in peptides,[30] tryptophan and histidine side chains,[31] the phenylalanine residue,[32] the dipolar tensors for the peptide bond in [1-^{13}C]glycyl[^{15}N]glycine·HCl·H_2O,[33] peptides of the form *N*-acetyl[1-^{13}C]glycyl[^{15}N]-X-amide where X = glycine, alanine, and tyrosine[34] and L[-^{13}C]alanyl-L-[^{15}N]alanine,[35] an analytical approach for the determination of the principal value σ_{33} of the amide ^{15}N chemical shift tensor element with respect to the molecular frame,[36] studies of the nitroso-groups in nitrobenzene and *p*-nitroso-N,N-dimethyl aniline (in which a very large CSA anisotropy of 1472 ppm was observed),[37] the two-dimensional PISEMA data on [1-^{15}N]-2′-deoxyguanosine,[38] the three-dimensional powder patterns of $^{15}N_{\varepsilon 1}$-tryptophan and $^{15}N_{\pi}$-hystidine side chains,[39] shift tensor values and orientation in the molecular frame in ^{13}C and ^{15}N labeled uracil.[40,41]

3.4 Dynamic Nuclear Polarization Experiments on Powders

Hu et al.[42,43] reported large ^{15}N DNP enhancement factors in benzamide (260, compared to CP data) and greater than 900 in carbazole and were able to compare the principal values of the shift tensors in powdered samples of these two molecules with those obtained by standard cross polarization and single pulse experimental techniques.

3.5 Two-Dimensional Experiments

A variety of two-dimensional experiments designed for separating the isotropic and anisotropic chemical shift information were instrumental in advancing resolution and data analysis of complex molecular systems.[44–50] The magic angle turning experiments, first conceived by Gan,[51] paved the way

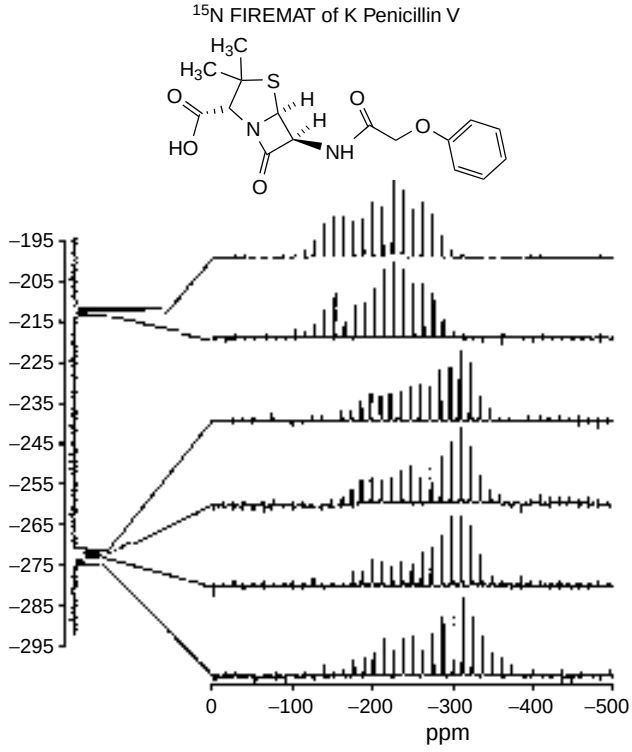

Figure 2 A two-dimensional natural abundance ^{15}N spectrum is shown in which the isotropic shift spectrum with no spinning side bands is plotted vertically on the left while the isolated spinning sideband patterns for the six resolved peaks are plotted on the right, connected to the corresponding isotropic peaks by guide lines

for development of experimental tools[12,13] that can reveal an amazing amount of detail regarding CSA in complex molecular systems. Recent modifications to the 5-π pulse experiments, FIREMAT[13] and 2D-PASS[14] have been particularly exciting in significantly expanding the range and complexity of molecules that can be studied. These two experiments, while related by virtue of a common 5-π pulse sequence for generating the two-D data set, possess important differences that are detailed in Ref.[10] Taking advantage of TIGER data processing in the FIREMAT experiment,[52] one is able to optimize S/N and resolution in the evolution dimension and obtain high quality ^{13}C data on molecules with more than 60 different tensors. The power of the FIREMAT experiment can be seen by examining the ^{15}N spectrum of penicillin V in Figure 2. Potassium penicillin V has two nitrogen atoms and, at ambient temperature, four molecules per asymmetric unit.[13] Conformational differences in these molecules split the NH nitrogen into the four peaks shown between −271.7 ppm and −275.3 ppm. The conformational differences do not affect the ring nitrogen to the same extent and three of the resonances are degenerate at −212.5 while the fourth is at −214.0 ppm. The FIREMAT experiment has also been used to obtain ^{15}N shift tensor data at the natural abundance level on nucleic acid bases,[15] purine,[53] and indolazines.[54]

4 RESULTS

4.1 Characteristics of Principal Values in Nitrogen Heterocycles

For convenience in consideration of ^{15}N shift tensors in organic molecules the discussion will be restricted to nitrogen heterocycles since this general class of compounds is ubiquitous in nature. The relatively simple five-and six-member heterocycles have been shown to provide the framework for understanding the shift tensor data in more complex heterocyclic structures including indolazines, the nucleic acid bases and related compounds. Consideration of ionic species also

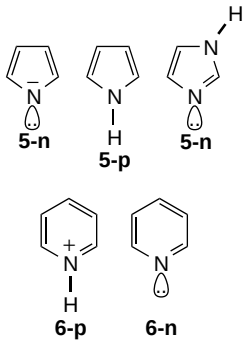

Figure 3 Definition of the different types of nitrogen atoms present in five-and six-member nitrogen heterocycles. The terms "n" and "p" represent non-bonded lone pair and protonated or bonded, lone pair, respectively

reflects the effects of hydrogen bonding interactions on the nitrogen shift tensors. This is especially interesting because of the lone pair of electrons. The structures portrayed in Figure 3 provide a useful framework from which to understand the experimental shift tensor data.

It is found that four different types of nitrogen tensors are present in simple nitrogen heterocycles. For convenience, the nitrogens with non-bonded lone electron pairs in five- and six-member rings shall be referred to as **5-n** and **6-n** types (such as pyrrole anion and the non-protonated nitrogens in imidazole and benzimidazole) and protonated **5-p** and **6-p** types (e.g., pyrrole, the protonated sites in imidazole and benzimidazole, the imidazolium cation, and the pyridinium cation).

Figure 4 presents a correlation diagram of the principal values of 12 simple heterocyclic structures. Quantum mechanical calculations were used to assign the orientation of the principal values to the molecular frame and to provide insight into the effects of electronic structure on the chemical shielding. These orientation assignments can be made with reasonable accuracy (estimated error of ±10 degrees based on work on uracil)[55] if

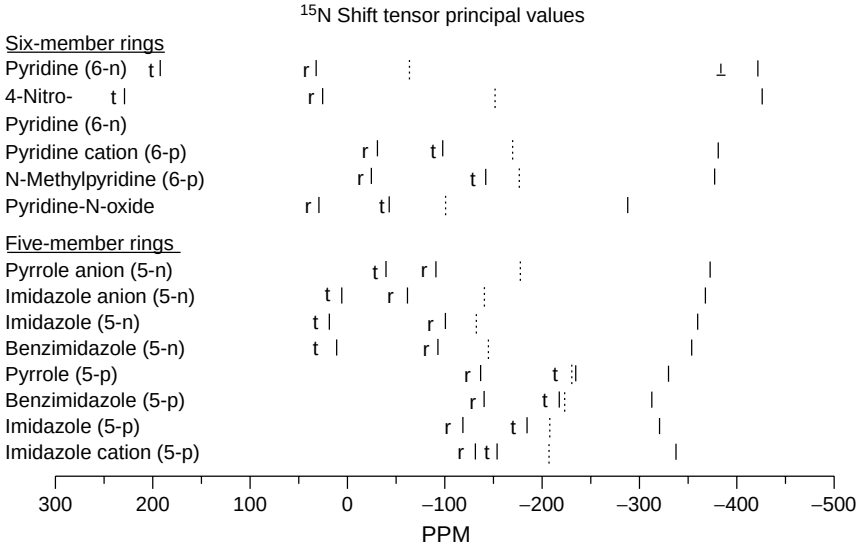

Figure 4 Correlation of the ^{15}N chemical shift principal values in 5-and 6-member heterocycles. The principal values are marked by solid lines, and the symbols indicate their approximate orientation in the molecular frames as described in Figure 5

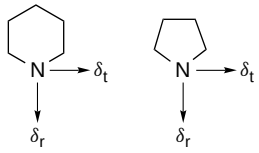

Figure 5 Orientation of the in-plane principal components in nitrogen heterocycles. δ_r and δ_t are depicted in the figure and lie in the plane of the ring approximately in the tangential and radial directions of the ring. $\delta_\perp$ is perpendicular to the ring. (*J. Am. Chem. Soc.*, published with permission)

sufficient structural data (e.g., crystal structure, bond length,) is available.[56,57]

A cursory inspection of Figure 4 illustrates the differences in the spans of the principal values of the nitrogen types. That the span of pyridine (622 ppm) is not unique as demonstrated by the span of 4-nitropyridine (674 ppm). In pyridine one observes that the δ_{11} shift component is oriented tangential to the ring, a direction that is also perpendicular to the lone pair (see Figure 6). When the hybridization of the nitrogen is changed from the **6-n** to the **6-p** type either by protonation, alkylation, or by *N*-oxide formation the tangential component crosses over the radial component, thus reducing the span of the shift tensor components by approximately 1/2 (to a range of 338−351 ppm). A similar affect is noted for the **5-n**/**5-p** case. The span in the pyrrole anion (333 ppm) is reduced to 192 ppm in pyrrole. Comparable effects are noted in each molecular pair studied. The data of Hoelger et al.[24] exhibit the same phenomena in the amine/imine pair of nitrogens in substituted pyrazoles.

The orientation of the shift tensor on the molecular frame of the compounds containing **5-n** type nitrogens corresponds to that found in pyridine (**6-n**). The span of the **5-n** tensor components is 337−374 ppm, a range that is nearly identical to that of the **6-p** nitrogens. In a manner similar to that noted for pyridine, protonation of the **5-n** loan pair inverts the order of the radial and tangential components and also significantly reduces (again, by approximately 1/2) the span of the **5-p** type nitrogens (to a range of 172−206 ppm). This reduction of span for the **5-n** and **5-p** species, compared to the respective **6-n** and **6-p** species, may be attributed to the larger degree of localization of the six π-electrons in five-member heterocycles compared with the six-member rings.[58] The increase of the localization of the π-electrons increases the electronic repulsion energy, thereby increasing the energy gaps corresponding to the $\sigma-\pi^*$ and $\pi-\sigma^*$ orbitals which dominate the paramagnetic contribution to the in-plane components. Thus, the paramagnetic contribution to the in-plane components of the shielding term decreases which reduces the shift tensor span.

The effects of interaction of the lone pair with neighboring atoms, whether bonded or non-bonded, is a matter of extreme interest and will be described in Section 4.3.

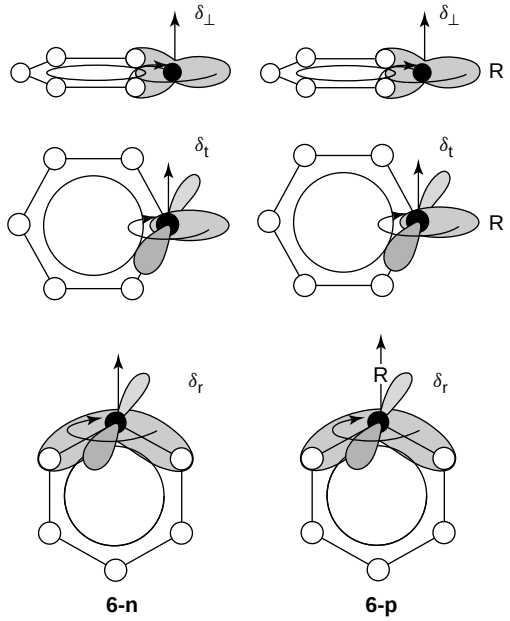

Figure 6 Electron orbitals making the largest contributions to the chemical shift principal components in pyridine. R corresponds to the lone pair in pyridine and R=H, O, or CH_3 in pyridine hydrochloride, pyridine-*N*-oxide, and *N*-methylpyridine. (*J. Am. Chem. Soc.*, published with permission)

4.2 The Nucleic Acid Bases

The simple nitrogen heterocycles can be used as a guide to understanding the electronic structure and intermolecular interactions in the nucleic acid bases. Employing a combination of two-dimensional experimental techniques (PHORMAT, TIGER data processing, and FIRMAT) that were dependent on the complexities of the ^{15}N spectra, the shift tensors were

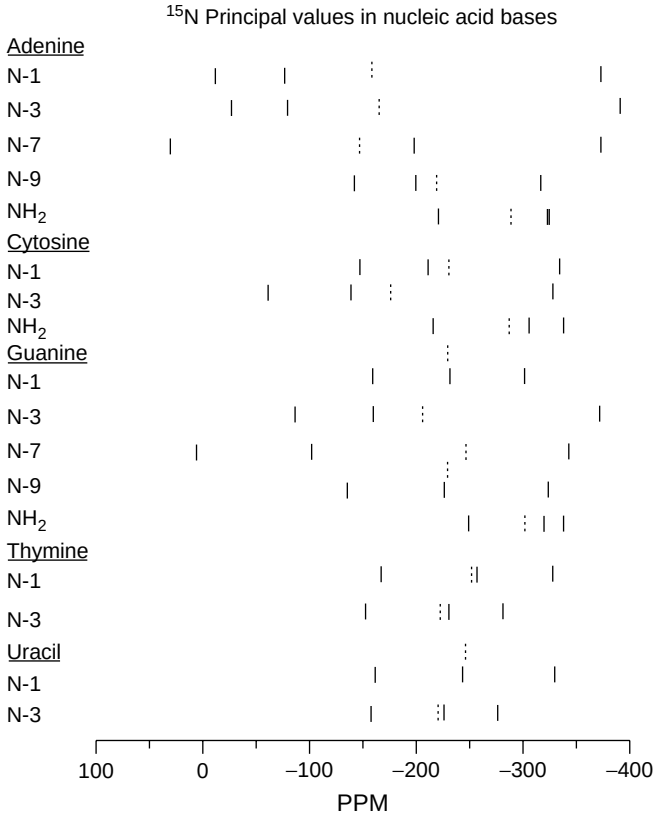

Figure 7 Correlation diagram of the ^{15}N shift tensor principal values in nucleic acid bases. Dashed lines are isotropic shift values

obtained on isotopically enriched adenine, and at natural abundance on thiamine, guanine, and cytosine.[15] The principal values obtained, together with data previously reported on uracil,[40] are presented as a bar graph in Figure 7 in order to visualize the relationship between the various shift tensor patterns.

The ^{13}C and ^{15}N shift tensor data obtained on purine[53] provides a useful model for interpreting the patterns observed in the nucleic acid bases. The purine data were obtained under separate sets of conditions and the position of the tautomeric proton could be definitely identified (by means of the ^{13}C isotropic shift data) as residing at either the N-7 or the N-9 position. The interpretation of the data is further confirmed by comparing the purine ^{15}N data with that of the simple nitrogen heterocycles previously described. In the five- and six-member heterocycles (Figure 4) the span ($\delta_{11}-\delta_{33}$) of the shift tensors of the **5/6-p** nitrogens are of the order of 1/2 that of the **5/6-n** nitrogens (compare, for example, the spans of N-1 and N-3 in benzimidazole in Figure 4). The N-7 and N-9 tautomeric structures in purine mirror this effect and, by comparing the spans of the N-7/9 positions in adenine and guanine (Figure 8), the position of the tautomeric proton is clearly evident in these two compounds. Furthermore, the spans of the N-1 and N-3 tensors in uracil and thiamine clearly indicate that the two labile protons occupy these sites while the cytosine data suggest that N-1 is the preferred site, in accordance with x-ray data. In the case of guanine the shift tensor data is consistent with the proton occupying the N-1 site.

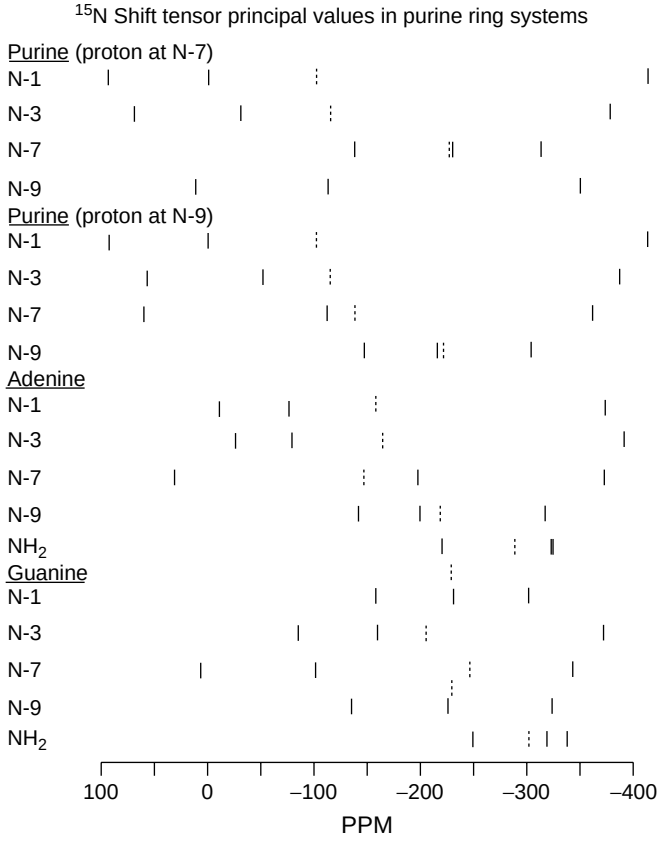

Figure 8 Comparison of shift tensor principal values in purine ring structures. The purine data is taken from Ref.[9] while the adenine and guanine data were taken from Ref.[15]

4.3 Effects of Hydrogen Bonding

The large changes in the shift tensor principal values provide a means for assessing hydrogen bonding in a wide range of heterocyclic ring systems. Using density functional theory (DFT) Facelli[3] simulated the shift tensor data in benzamide and these results, together with simulations of uracil,[40] highlighted the importance of including hydrogen bonding, and in general, intermolecular interactions in the calculation of ^{15}N chemical shift tensors. Further evidence for the importance of these intermolecular interactions in the calculation of ^{15}N chemical shift tensors can be found by analysis of these tensors in the series of heterocycles portrayed in Figure 4.

For these compounds the rms error between experimental and DFT calculated values, which did not include intermolecular effects, was approximately 30–40 ppm. This large scatter is approximately an order of magnitude greater than that found in simulated data on polyaromatic hydrocarbons.[56,57]

Utilizing the imidazole structural information obtained from neutron diffraction data it is possible to improve the chemical shift calculations and to examine the effects of hydrogen bonding on the ^{15}N shift principal values using a dimer model.[19] The correlation between experimental and calculated shift principal values in imidazole, with and without intermolecular interactions, is shown in Figure 9. The rms error of the predicted shift principal values is 40.9 ppm using an optimized geometry and is 13.8 ppm when the structural data includes the position of the hydrogens in the lattice structure along with the effects of hydrogen bonding.[19] Using the neutron diffraction data without including the intermolecular hydrogen bonding

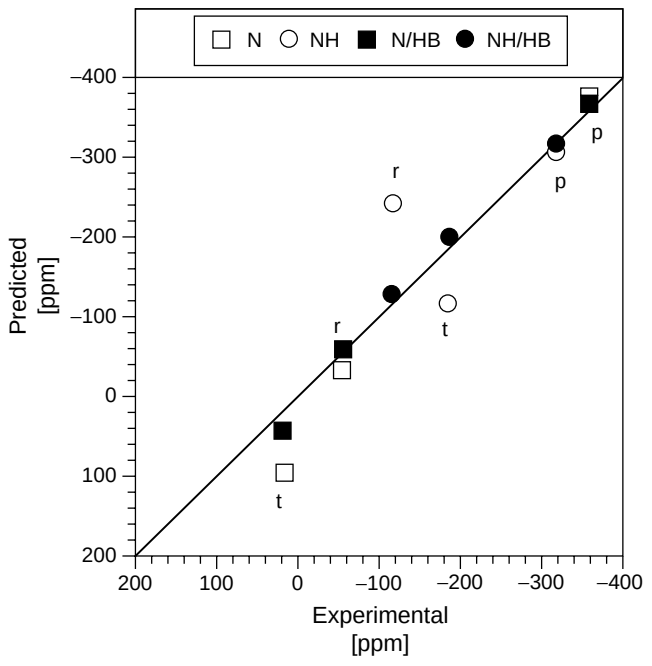

Figure 9 Experimental versus predicted chemical shift values for imidazole. The DFT method was used to calculate the ^{15}N shift tensor values using the neutron diffraction structure and including the effects of intermolecular interactions due to hydrogen bonding. The letters r, t, and p refer to the radial, tangential, and perpendicular components of the shift tensors. The legends N/HB and NH/HB designate predictions based on intermolecular interactions due to hydrogen bonding for the **5-n** and **5-p** nitrogens, respectively. (*J. Am. Chem. Soc.*, with permission)

effects produces only a modest improvement in the calculated values over those obtained with the optimized geometry. Introduction of intermolecular effects in the simulation of the nucleic acid bases plays a significant role in improving the correlation of experimental and theoretical result, reducing the rms error by a factor of two.[15] Given the 3–4 fold greater span of the nitrogen shift tensor, a rms error of 14 ppm in imidazole and 16 ppm for the nucleic acid bases compares favorably with the 3–5 ppm rms errors obtained in simulations of ^{13}C chemical shift tensors in polycyclic aromatic hydrocarbons based on x-ray structure data.[56,57]

5 CONCLUSIONS

^{15}N chemical shift tensors in heterocyclic compounds are very sensitive to the hybridization of the nitrogen atom and changes in the tangential component can vary from 200 ppm to as much as 340 ppm in five-and six-member rings, respectively, when the nitrogen lone-pair hybridization is changed. The changes in the magnitude of the in-plane components are so large that these effects may be useful in probing intermolecular interactions associated with hydrogen bonding in biological systems. It is possible to measure and spacially assign the principal components of the ^{15}N chemical shift tensors obtained from powder samples in heterocyclic compounds. The assignments of the chemical shift tensor components are critical for analyzing the relationship between the electronic structure and shift tensors. In all the compounds studied, the most deshielded component, δ_{11}, is in the plane of the ring and approximately perpendicular to the plane containing the bonding-antibonding or HOMO-LUMO pair of orbitals with the smallest energy gap. The most shielded component, δ_{33}, is always perpendicular to the plane of the ring, as in the ^{13}C tensors of aromatic compounds and is less sensitive to changes in the hybridization of the nitrogen atom than the principal components in the plane of the ring.

Employing modern instrumentation and experimental techniques that have been optimized for obtaining shift tensor data, it is now possible to study nucleic acid materials at the natural abundance level or with isotropic enrichment depending on the relaxation times and spectral complexity. The nucleic acid bases exhibit the same sensitivity to small changes in molecular geometry and environment noted for the five- and six-member heterocycles. Even for nitrogens with similar hybridization, differences as large as 50 ppm are found in corresponding principal shift components. Theoretical techniques now available enable the investigator to simulate the molecular environment with reasonable confidence. The agreement between experiment and theory is highly dependent on the molecular model used in the calculations, and molecular models that include the intermolecular interactions show superior correlation with the experimental values.

6 REFERENCES

1. M. Witanowski, L. Stefaniak, and G. A. Webb, in 'Annual Reports on NMR Spectroscopy', ed G. A. Webb, Academic Press: London, 1993, Vol. 25, p. 2 and reviews of these authors in this series.
2. J. Mason, in 'Encyclopedia of Nuclear Magnetic Resonance', eds D. M. Grant and R. K. Harris, Wiley: London, 1996, p. 3222.
3. J. C. Facelli, R. J. Pugmire, and D. M. Grant, *J. Am. Chem. Soc.*, 1996, **118**, 5488.
4. See for example: (a) Q. Teng, M. Iqbal, and T. A. Cross, *J. Am Chem. Soc.*, 1992, **114**, 5312; (b) A. Shoji, T. Ozaki, T. Fujito, K. Deguchi, I. Ando, and S. Ando, *J. Am. Chem. Soc.*, 1990, **112**, 4693; (c) H. Le and E. J. Oldfield, *J. Biomol. NMR*, 1994, **4**, 341; (d) C. J. Hartzell, T. K. Pratum, and G. Drobny, *J. Phys. Chem.*, 1987, **87**, 4324; (e) G. Harbison, J. Herzfeld, and R. G. Griffin, *J. Am. Chem. Soc.*, 1981, **103**, 4752; (f) G. A. Lorigan, R. McNamara, R. A. Jones, and S. J. Opella, *J. Magn. Reson.*, 1999, **140**, 315; (g) M. Hong, J. D. Gross, W. Hu, and R. G. Griffin, *J. Magn. Reson.*, 1998, **135**, 169; (h) Q. Teng and T. A. Cross, *J. Magn. Reson.*, 1989, **85**, 439; (i) K. T. Dayie and G. Wagner, *J. Am. Chem. Soc.*, 1999, **119**, 7797; (j) M. Ashikawa, A. Shoji, T. Ozaki, and I. Ando, *Macromolecules*, 1999, **32**, 2288; (k) J. R. Bender, D. M. Taylor, and A. Ramamoorthy, *J. Am. Chem. Soc.*, 2001, **123**, 914; (l) A. Ramamoorthy, C. H. Wu, and S. J. Opella, *J. Am. Chem. Soc.*, 1997, **119**, 10 479; (m) D. K. Lee, J. S. Santos, and A. Ramamoorthy, *Chem. Phys. Lett.*, 1999, **309**, 209; (n) K. G. Valentine, A. L. Rockwell, L. M. Gierasch, and S. J. Opella, *J. Magn. Reson.*, 1987, **73**, 519; (o) T. G. Oas, C. J. Hartzell, F. W. Dahlquist, and G. P. Drobny, *J. Am. Chem. Soc.*, 1987, **109**, 5962; (p) R. E. Stark, L. W. Jelinski, D. J. Ruben, D. A. Torchia, and R. G. Griffin, *J. Magn. Reson.*, 1983, **55**, 266; (q) G. S. Harbison, L. W. Jelinski, R. E. Stark, D. A. Torchia, J. Herzfeld, and R. G. Griffin, *J. Magn. Reson.*, 1984, **60**, 79; (r) J. F. Hinton, P. L. Guthrie, P. Pulay, K. Wilinski, and G. Fogarasi, *J. Magn. Reson.*, 1992, **96**, 154; (s) M. D. Lumsden, R. E. Wasylishen, K. Eichele, M. Schindler, G. H. Penner, W. P. Powell, and R. D. Curtis, *J. Am. Chem. Soc.*, 1994, **116**, 1403; (u) S. Kuroki, N. Asakawa, S. Ando, I. Ando, A. Shoji, and T. Ozaki, *J. Mol. Structure*, 1991, **245**, 69.
5. D. M. Grant, in 'Encyclopedia of Nuclear Magnetic Resonance', eds D. M. Grant and R. K. Harris, Wiley: London, 1996, p. 1298.
6. A. M. Orendt, in 'Encyclopedia of Nuclear Magnetic Resonance', eds D. M. Grant and R. K. Harris, Wiley: London, 1996, p. 1282.
7. M. H. Sherwood, in 'Encyclopedia of Nuclear Magnetic Resonance', eds D. M. Grant and R. K. Harris, Wiley: London, 1996, p. 1322.
8. J. C. Facelli, in 'Encyclopedia of Nuclear Magnetic Resonance', eds D. M. Grant and R. H. Harris, Wiley: London, 1996, p. 4327.
9. See, for instance, Modeling NMR Chemical Shift Tensors, Gaining Insights into Structure and Environment, ACS Symposium Series 732, eds J. C. Facelli and A. C. deDios, 1999.
10. D. M. Grant, in 'Encyclopedia of Nuclear Magnetic Resonance', eds D. M. Grant and R. K. Harris, Wiley: Chichester, 2002, Volume 9.
11. T. M. Duncan, 'A Compilation of Chemical Shift Anisotropies', 2nd edn, Farragut Press: Chicago, 1997.
12. J. Z. Hu, D. W. Alderman, C. Ye, R. J. Pugmire, and D. M. Grant, *J. Magn. Reson. A*, 1993, **105**, 82.
13. D. W. Alderman, G. McGeorge, J. Z. Hu, R. J. Pugmire, and D. M. Grant, *Mol. Phys.*, 1998, **95**, 1113.
14. O. N. Antzutkin, S. C. Shekar, and M. H. Levitt, *J. Magn. Reson.*, 1995, **115**, 7.
15. J. Z. Hu, J. C. Facelli, D. W. Alderman, R. J. Pugmire, and D. M. Grant, *J. Am. Chem. Soc.*, 1998, **120**, 9863.
16. G. Harbison, J. Herzfeld, and R. G. Griffin, *J. Am. Chem. Soc.*, 1981, **103**, 4752.
17. G. S. Harbison, L. W. Jelinski, R. E. Stark, D. A. Torchia, J. Herzfeld, and R. G. Griffin, *J. Magn. Reson.*, 1984, **60**, 79; R. E. Stark, L. W. Jelinski, D. J. Ruben, D. A. Trochia, and R. G. Griffin, *J. Magn. Reson.*, 1983, **55**, 266.
18. K. L. Anderson-Altmann and D. M. Grant, *J. Phys. Chem.*, 1993, **97**, 11 096.
19. M. S. Solum, K. L. Anderson, M. Strohmeier, D. A. Berges, Y. Zhang, J. C. Facelli, R. J. Pugmire, and D. M. Grant, *J. Am. Chem. Soc.*, 1997, **119**, 9804.

20. M. Strohmeier, A. M. Orendt, J. C. Facelli, M. S. Solum, R. J. Pugmire, R. W. Parry, and D. M. Grant, *J. Am. Chem. Soc.*, 1997, **119**, 7114.
21. F. Tian and T. A. Cross, *J. Magn. Reson.*, 1998, **135**, 535.
22. M. Sardashti and G. E. Maciel, *J. Phys. Chem.*, 1988, **92**, 4620.
23. R. Challoner, R. K. Harris, and J. A. Tossell, *J. Magn. Reson.*, 1997, **126**, 1.
24. E. G. Hoelger, F. Aguilar-Parrilla, J. Elguero, O. Weintraub, S. Vega, and H. H. Limbach, *J. Magn. Reson. Series A*, 1996, **120**, 46.
25. A. Shoji, T. Ozaki, T. Fujito, K. Deguchi, S. Ando, and I. Ando, *J. Am. Chem. Soc.*, 1990, **112**, 4693–4697.
26. M. Ashikawa, A. Shoji, T. Ozaki, and I. Ando, *Macromolecules*, 1999, **32**, 2288.
27. M. Sardashti and G. E. Maciel, *J. Phys. Chem.*, 1988, **92**, 4620.
28. M. D. Lumsden, R. E. Wasylishen, K. Eichele, M. Schindler, G. H. Penner, W. P. Power, and R. D. Curtis, *J. Am. Chem. Soc.*, 1994, **116**, 1403.
29. S. Kuroki, N. Asakawa, S. Ando, I. Ando, A. Shoji, and T. Ozaki, *J. Mol. Struct.*, 1991, **245**, 69.
30. M. Hong, J. D. Gross, W. Hu, and R. G. Griffin, *J. Magn. Reson.*, 1998, **135**, 169.
31. A. Ramamoorthy, C. H. Wu, and S. J. Opella, *J. Am. Chem. Soc.*, 1997, **119**, 10 479.
32. D. K. Lee, J. S. Santos, and A. Ramamoorthy, *Chem. Phys. Lett.*, 1999, **309**, 209.
33. G. S. Harbison, L. W. Jelinski, R. E. Stark, D. A. Torchia, J. Herzfeld, and R. G. Griffin, *J. Magn. Reson.*, 1984, **60**, 79.
34. T. G. Oas, C. J. Hartzell, F. W. Dahlquist, and G. P. Drobny, *J. Am. Chem. Soc.*, 1987, **109**, 5962.
35. C. J. Hartzell, M. Whitfield, T. B. Oas, and G. P. Drobny, *J. Am. Chem. Soc.*, 1987, **109**, 5966.
36. Q. Teng and T. A. Cross, *J. Magn. Reson.*, 1989, **85**, 439.
37. M. D. Lumsden, G. Wu, R. E. Wasylishen, and R. D. Curtis, *J. Am. Chem. Soc.*, 1993, **115**, 2825.
38. G. A. Lorigan, R. McNamara, R. A. Jones, and S. J. Opella, *J. Magn. Reson.*, 1999, **140**, 315.
39. A. Ramamoorthy, C. H. Wu, and S. J. Opella, *J. Am. Chem. Soc.*, 1997, **119**, 10 479.
40. K. L. Anderson-Altmann, Cu. G. Phung, S. Mavromoustakos, Z. Zheng, J. C. Facelli, C. D. Poulter, and D. M. Grant, *J. Phys. Chem.*, 1995, **99**, 10 454.
41. J. Leppert, B. Heise, and R. Ramachandran, *J. Magn. Reson.*, 2000, **145**, 307.
42. J. Z. Hu, J. Zhou, B. Yang, L. Li, J. Qui, C. Ye, M. S. Solum, R. A. Wind, R. J. Pugmire, and D. M. Grant, *Solid State NMR*, 1997, **8**, 129.
43. J. Z. Hu, M. S. Solum, R. A. Wind, B. L. Nilsson, M. A. Peterson, R. J. Pugmire, and D. M. Grant, *J. Phys. Chem., A*, 2000, **104**, 4413.
44. Y. Yarim-Agaev, P. M. Tutunjian, and J. S. Waugh, *J. Magn. Reson.*, 1982, **47**, 51.
45. A. Bax, N. M. Szeverenyi, and G. E. Maciel, *J. Magn. Reson.*, 1983, **51**, 400.
46. A. Bax, N. M. Szeverenyi, and G. E. Maciel, *J. Magn. Reson.*, 1983, **55**, 494.
47. R. Tycko, G. Dabbagh, and P. Mirau, *J. Magn. Reson.*, 1989, **85**, 265.
48. T. Terao, T. Fujii, T. Onodera, and A. Saiks, *Chem. Phys. Lett.*, 1984, **107**, 145.
49. L. Frydman, G. C. Chingas, Y. K. Lee, P. J. Grandinetti, M. A. Eastman, B. A. Barrall, and A. Pines, *J. Chem. Phys.*, 1992, **97**, 4800.
50. A. C. Kolbert and R. G. Griffin, *Chem. Phys. Lett.*, 1990, **166**, 87.
51. Z. Gan, *J. Am. Chem. Soc.*, 1992, **114**, 8307.
52. See discussion in Reference 10.
53. J. C. Facelli, J. Z. Hu, M. S. Solum, R. J. Pugmire, and D. M. Grant, in 'Modeling NMR Chemical Shift Tensors, Gaining Insights into Structure and Environment', ACS Symposium Series 732. eds J. C. Facelli and A. C. deDios, 1999, p. 162.
54. J. Z. Hu, D. Barich, R. J. Pugmire, and D. M. Grant, '^{15}N chemical Shift Tensors in Indolazines', in preparation.
55. K. L. Anderson-Altmann, C. G. Phung, S. Mavromoustakos, Z. Zheng, J. C. Facelli, C. D. Poulter, and D. M. Grant, *J. Phys. Chem.*, 1995, **99**, 10 454.
56. C. M. Carter, D. W. Alderman, J. C. Facelli, and D. M. Grant, *J. Am. Chem. Soc.*, 1987, **109**, 2639.
57. D. M. Grant, F. Liu, R. J. Iuliuci, C. G. Phung, J. C. Facelli, and D. W. Alderman, *Acta Crystallogr.*, 1995, **B51**, 540.
58. J. C. Facelli, R. H. Contreras, D. G. de Kowalewski, V. J. Kowalewski, and R. N. Piegaia, *J. Mol. Struct., Theochem*, 1983, **94**, 163.

Biographical Sketch

Ronald J. Pugmire, *b* 1937. B.S. 1959, Idaho State College; Ph.D., 1966, Chemistry, University of Utah, USA, where he was introduced to NMR by David M. Grant. Post Doctoral, 1966–68, University of Utah. Faculty in Chemical and Fuels Engineering and Chemistry (adjunct), and Associate Vice President for Research, University of Utah. Approximately 200 publications. Research specialties: carbon-13 and nitrogen-15 NMR, chemical shielding in solids, theoretical correlation of shielding tensors, coal chemistry, and applications of NMR spectroscopy to coal science and combustion science.

Oxygen-17 NMR: Applications in Biochemistry

John G. Pearson and Eric Oldfield

University of Illinois at Urbana-Champaign, IL, USA

1	Introduction	1
2	^{17}O NMR Parameters	1
3	Biophosphates	1
4	Amino Acids and Polypeptides	2
5	CO and O^2 in Hemoproteins	2
6	Summary and Prospects	2
7	Related Article	2
8	References	2

1 INTRODUCTION

^{17}O is the least utilized of the NMR active nuclei commonly found in biological systems. While oxygen atoms play an important role in the hydrogen bonding, electrostatics, and hydration of biomolecules, the very low natural abundance (0.037%) and quadrupolar nature ($I = \frac{5}{2}$) of ^{17}O nuclei have hindered the development of ^{17}O NMR as compared with ^{1}H, ^{13}C, ^{15}N, and ^{31}P NMR in biological systems. Over the last decade, however, the availability of both ^{17}O enriched materials and ever higher field FT NMR spectrometers have led to the utilization of ^{17}O nuclei as probes of biomolecular structure and function, some 40 years after the nucleus was first observed.[1]

It is the intention of this article to review the characteristic parameters governing the use of ^{17}O NMR in, and how the behavior of ^{17}O nuclear spin magnetization has been applied to, biological systems. The effects of ^{17}O quadrupolar relaxation on ^{31}P magnetization are also important, but are beyond the scope of this review.

2 ^{17}O NMR PARAMETERS

The detailed quantum chemical description of sites in biologically relevant molecules is, in general, extremely complex. The task is greatly simplified in NMR by modeling nuclear spin interactions as independent of the rest of the system, with time-dependent interactions between spins and the bulk (or lattice) being termed 'relaxation'. This, and other considerations, allows for the simplification of the ^{17}O NMR of biomolecules to the study of ^{17}O chemical shielding, ^{17}O relaxation (resulting from couplings between the nuclear quadrupole and its local environment), and ^{17}O quadrupole couplings.

The chemical shielding of a nucleus is a function of the electronic structure near the nucleus. ^{17}O nuclei are particularly sensitive to differences in chemical environment; for example, the two distinct oxygen sites in ozone are separated by 566 ppm.[2] Differences in chemical shift between sites in a molecule can be used to determine molecular structures, as well as to study dynamical processes in these structures, such as conformational changes, substrate binding, and hydrogen bonding. The ^{17}O chemical shift is commonly referenced to $H_2{}^{17}O$ in biological NMR studies.

All nuclei with $I > \frac{1}{2}$ have a nuclear quadrupole moment eQ. The interaction of eQ with an electric field gradient eq is quite strong, typically dominating the NMR spectrum of a quadrupolar nucleus. For most biomolecules, the interaction between the eQ of ^{17}O and eq is modulated by rotational motion, either molecular tumbling or internal rotations, making it an efficient relaxation mechanism. In the extreme narrowing limit (very fast motions on the NMR timescale), the nuclear quadrupole relaxation rate essentially determines the resonance linewidth L which can be expressed as

$$L \approx (12\pi/125)(1 + \eta^2/3)\chi^2\tau_r \qquad (1)$$

where $\chi = e^2qQ/h$ is the nuclear quadrupole coupling constant, η is the asymmetry parameter of the electric field gradient tensor, and τ_r is the rotational correlation time.[3] ^{17}O linewidths are therefore proportional to the square of the electric field gradient at the nucleus, and are generally inversely proportional to the molecular correlation time. This limits the applicability of ^{17}O NMR either to relatively small molecules or to sites in molecules where χ is much less than typically found for ^{17}O nuclei (about 10 MHz, see Kintzinger[4]). Within this limitation, ^{17}O relaxation can be used to measure differences in χ and τ_r for either two sites in the same molecule, or the same site under different conditions. For slow molecular motions ($\tau_r \gg 1/\nu_L$) relaxation is a weighted sum of three exponentials, resulting in deviations from Lorentzian lineshapes, and such effects have been observed experimentally for C^{17}O bound to heme proteins, where χ values are very small (about 1–2 MHz).[5]

3 BIOPHOSPHATES

Biophosphates are involved in many biological processes, such as energy transport and utilization, information storage and retrieval, and membrane structure and transport. Examples of such compounds are adenosine diphosphate (ADP), adenosine triphosphate (ATP), DNA, RNA, and phospholipids.

Tsai et al.[6] have demonstrated that bridging and phosphoryl ^{17}O resonances in biophosphates can be assigned from their relative linewidths, due to differences in χ between the various sites. Linewidths are all relatively broad, and several groups have demonstrated improved spectral resolution upon sample heating,[7–11] which decreases τ_r and thereby the ^{17}O linewidths, allowing for more accurate determination of ^{17}O chemical shifts and spin–spin coupling constants, $J(^{31}P, ^{17}O)$. Gerothanassis and Sheppard[11] also demonstrated the utility of using ^{17}O depleted water to minimize the background $H_2{}^{17}O$ solvent peak, which in aqueous samples frequently overwhelms the resonance from even an ^{17}O enriched sample.

The pH dependence of the ^{17}O chemical shift has been determined for phosphoryl oxygen atoms in several phosphates, including adenosine monophosphate (AMP), ADP, and

ATP,[9,10] demonstrating the effect of protonation upon the phosphoryl ^{17}O chemical shift.

The binding of several diamagnetic ions to ATP has been studied using ^{17}O relaxation rates.[12,13] The phosphoryl ^{17}O linewidth increases markedly upon ion binding, indicating the coordination sites for Mg(II), Co(III), Sc(III), La(III), and Lu(III) in $M \cdot ATP_n$ complexes.

The hydrogen bonding of uridine derivatives has been studied using ^{17}O NMR.[14] Equilibrium constants and interaction enthalpies of water–uridine hydrogen bond complexes were determined by observing changes in ^{17}O chemical shift as a function of water concentration, in acetonitrile.

^{17}O spectra of hemiacetal and aldehydic abasic sites in DNA of importance in DNA damage and repair have been studied,[15] demonstrating the ability to observe approximately 10 μM aldehyde signals in the presence of approximately 20 M solvent ^{17}O.

4 AMINO ACIDS AND POLYPEPTIDES

The tertiary structures of polypeptides and proteins in aqueous solution are strongly influenced by hydrogen bonding, both within the solute molecule and with the solvent, and ^{17}O NMR has been used to gain insights into these interactions.

The effects of proton exchange between peptide termini and water on ^{17}O chemical shifts have been used to probe the electronic structures of amino acids,[11,16] dipeptides,[17,18] and peptide carboxamides.[19] The ^{17}O chemical shift has also been used to monitor the presence of hydrogen bonding in peptide models,[20] dipeptides,[18] peptide carboxamide,[19] acylprolines (model β- and γ-turns),[21–23] and small polypeptides.[24]

The hydration and aggregation of peptides has been studied using ^{17}O relaxation measurements. ^{17}O linewidths of amino acids,[16,25] dipeptides,[18] peptide carboxamides,[19] and small polypeptides[24] have been determined in various solvents, locating hydration sites at carboxylate and carbonyl oxygen atoms, in addition to providing a method of monitoring peptide aggregation. In addition, a ^{17}O relaxation study of ATP binding to adenylate kinase[26] has been reported, demonstrating the feasibility of studying enzyme–substrate interactions via ^{17}O NMR, providing the ligand is not rigidly held.

^{17}O chemical shifts have also been found to be torsion-angle dependent in aryl carboxylic esters, acids, and amides,[27] and ^{17}O NMR promises to be a powerful technique for elucidating the structures of membrane peptides and proteins, using oriented samples.

5 CO AND O_2 IN HEMOPROTEINS

The nature of Fe–O_2 and Fe–CO bonding in heme proteins and model compounds has been studied using ^{17}O NMR. ^{17}O resonance frequencies and linewidths have been measured for O_2 bound to Vaska's compound,[28] O_2 bound to picket-fence and basket-handle porphyrin model compounds,[29–31] CO bound to peroxidases,[32] as well as other hemoproteins,[5,33] and O_2 bound to hemoproteins in the solid state.[31] Results were found to be in general agreement with Pauling's ideas of end-on bonding, with additional electrostatic field effects being proposed to take into account the chemical shift variation seen from protein to protein.[34] In Fe–O_2 systems, the chemical shift difference between the two oxygen nuclei has been found to be about 600 ppm,[29–31] comparable to that found in ozone, consistent with previous analogies between FeO_2 bonding and that found in O_3.

6 SUMMARY AND PROSPECTS

Given the central importance of oxygen in biochemical systems (lipids, proteins, nucleic acids and carbohydrates), there have been remarkably few studies of ^{17}O NMR chemical shifts, and even fewer studies aimed at detailed, quantum chemical analyses of chemical shifts and quadrupolar couplings. ^{17}O NMR in biochemistry is therefore still in its infancy. However, with the advent of 750 MHz spectrometers, the current development of 900–1000 MHz machines, as well as recent development in quantum chemical applications to macromolecules,[35] ^{17}O NMR can be expected to benefit enormously over the next few years. Thus, ^{17}O chemical shifts and quadrupole couplings can be exploited to analyze, for example, lipid headgroup and backbone orientations in membranes, sterol orientations and interactions, peptide/protein structures in condensed phases, carbohydrate conformations and interactions, as well as small DNA structures. For ^{17}O, only relatively low resolution magnets are required, thus the sensitivity gains possible with very high-field operation can be readily exploited. Indeed, most ^{17}O NMR studies of biochemical systems reported to date could have been obtained at about 1 ppm resolution only. With recent improvements in computer price/performance ratios, and much more efficient algorithms, theoretical analyses of ^{17}O shifts and χ values are also to be expected. Thus, ^{17}O NMR in biochemistry undoubtedly has an extremely bright future.

7 RELATED ARTICLES

Oxygen-17 NMR.

8 REFERENCES

1. F. Alder and F. C. Yu, *Phys. Rev.*, 1951, **81**, 1067.
2. I. J. Solomon, J. N. Keith, A. J. Kacmarek, and J. K. Raney, *J. Am. Chem. Soc.*, 1968, **90**, 5408.
3. A. Abragam, *The Principles of Nuclear Magnetism*, ed W. C. Marshall and D. H. Williamson, Oxford University, Oxford, 1961, pp. 297–305.
4. J.-P. Kintzinger and H. Marsmann, in *NMR Basic Principles and Progress*, ed. P. Diehl, E. Fluck, and R. Kosfeld, Springer, Berlin, 1981, Vol. 17, pp. 1–64.
5. H. C. Lee and E. Oldfield, *J. Am. Chem. Soc.*, 1989, **111**, 1584.
6. M.-D. Tsai, S. L. Huang, J. F. Kozlowski, and C. C. Chang, *Biochemistry*, 1980, **19**, 3531.
7. C. Rodger, N. Sheppard, H. C. E. McFarlane, and W. McFarlane, in *NMR and the Periodic Table*, ed. R. K. Harris and B. E. Mann, Academic, London, 1978, Chap. 12A.
8. H. M. Schwartz, M. MacCoss, and S. S. Danyluk, *Tetrahedron Lett.*, 1980, **21**, 3837.

9. J. A. Coderre, S. Mehdi, P. C. Demou, R. Weber, D. D. Traficante, and J. A. Gerlt, *J. Am. Chem. Soc.*, 1981, **103**, 1870.
10. J. A. Gerlt, P. C. Demou, and S. Mehdi, *J. Am. Chem. Soc.*, 1982, **104**, 2848.
11. I. P. Gerothanassis and N. Sheppard, *J. Magn. Res.*, 1982, **46**, 423; I. P. Gerothanassis, R. Hunston, and J. Lauterwein, *Helv. Chim. Acta*, 1982, **65**, 1764.
12. S. L. Huang and M.-D. Tsai, *Biochemistry*, 1982, **21**, 951.
13. Y.-J. Shyy, T.-C. Tsai, and M.-D. Tsai, *J. Am. Chem. Soc.*, 1985, **107**, 3478.
14. H. M. Schwartz, M. MacCoss, and S. S. Danyluk, *J. Am. Chem. Soc.*, 1983, **105**, 5901.
15. J. A. Wilde, P. H. Bolton, A. Mazumder, M. Manoharan, and J. A. Gerlt, *J. Am. Chem. Soc.*, 1989, **111**, 1894.
16. B. Valentine, T. St. Amour, R. Walter, and D. Fiat, *J. Magn. Reson.*, 1980, **38**, 413.
17. C. S. Irving and A. Lapidot, *J. Chem. Soc., Chem. Commun.*, 1976, 43.
18. B. Valentine, A. Steinschneider, D. Dhawan, M. I. Burgar, T. St. Amour, and D. Fiat, *Int. J. Peptide Protein Res.*, 1985, **25**, 56.
19. A. Steinschneider and D. Fiat, *Int. J. Peptide Protein Res.*, 1984, **23**, 591.
20. A. Steinschneider, M. I. Burgar, A. Buku, and D. Fiat, *Int. J. Peptide Protein Res.*, 1981, **18**, 324.
21. J. Lauterwein, I. P. Gerothanassis, and R. N. Hunston, *J. Chem. Soc., Chem. Commun.*, 1984, 367.
22. R. N. Hunston, I. P. Gerothanassis, and J. Lauterwein, *J. Am. Chem. Soc.*, 1985, **107**, 2654.
23. N. Birlirakis, I. P. Gerothanassis, C. Sakarellos, and M. Marraud, *J. Chem. Soc., Chem. Commun.*, 1989, 1122.
24. C. Sakarellos, I. P. Gerothanassis, N. Birlirakis, T. Karayannis, and M. Sakarellos-Daitsiotis, *Biopolymers*, 1989, **28**, 15.
25. J. Lauterwein, I. P. Gerothanassis, R. N. Hunston, and M. Schumacher, *J. Phys. Chem.*, 1991, **95**, 3804.
26. D. A. Wisner, C. A. Steginsky, Y.-J. Shyy, and M.-D. Tsai, *J. Am. Chem. Soc.*, 1985, **107**, 2814.
27. A. L. Baumstark, P. Balakrishnan, M. Dotrong, C. J. McCloskey, M. G. Oakley, and D. W. Boykin, *J. Am. Chem. Soc.*, 1987, **109**, 1059.
28. H. C. Lee and E. Oldfield, *J. Magn. Reson.*, 1986, **69**, 367.
29. I. P. Gerothanassis and M. Momenteau, *J. Am. Chem. Soc.*, 1987, **109**, 6944.
30. I. P. Gerothanassis, M. Momenteau, and B. Loock, *J. Am. Chem. Soc.*, 1989, **111**, 7006.
31. E. Oldfield, H. C. Lee, C. Coretsopoulos, F. Adebodun, K. D. Park, S. Yang, J. Chung, and B. Phillips, *J. Am. Chem. Soc.*, 1991, **113**, 8680.
32. H. C. Lee, K. Cummings, K. Hall, L. P. Hager, and E. Oldfield, *J. Biol. Chem.*, 1988, **263**, 16118.
33. K. D. Park, K. Guo, F. Adebodun, M. L. Chiu, S. G. Sligar, and E. Oldfield, *Biochemistry*, 1991, **30**, 2333.
34. J. D. Augspurger, C. E. Dykstra, and E. Oldfield, *J. Am. Chem. Soc.*, 1991, **113**, 2447.
35. A. C. de Dios, J. G. Pearson, and E. Oldfield, *Science*, 1993, **260**, 1491.

Acknowledgments

This work was supported by the United States Public Health Service (Grant HL-19481). J. G. P. was a USPHS Postdoctoral Fellow (grant GM-14545).

Biographical Sketches

John G. Pearson. *b* 1963. B.S., University of California at Santa Barbara; 1986; Ph.D., (Supervisor Alexander Pines), University of California at Berkeley, USA, 1991. Successively, postdoctoral work (with Eric Oldfield), postdoctoral research fellow, University of Illinois at Urbana–Champaign, 1991–present. Approx. 20 publications. Research specialties: protein chemical shifts and multiple quantum NMR.

Eric Oldfield. *b* 1948. B.Sc., 1969, University of Bristol, Ph.D., 1972 (supervisor Dennis Chapman), University of Sheffield, D.Sc., 1982, University of Bristol, UK. Postdoctoral work at Indiana University, Bloomington (with Adam Allerhand) and Massachusetts Institute of Technology, Cambridge (with John S. Waugh). Professor, University of Illinois at Urbana-Champaign, 1975–present. Approx. 200 publications. Research specialties: inorganic and biochemical applications, especially proteins, membranes, and heterogeneous catalysts.

Structural Analysis Enhancements for Natural Products

James K. Harper
Department of Chemistry, University of Utah, Salt Lake City, UT, USA

1	Introduction	1
2	Traditional Routes to Structure	1
3	Inadequate Structural Determinations	1
4	Conformational Analysis Using Solid-State NMR	3
5	Stereochemical Determination Using Solid-State NMR	6
6	Conclusions	8
7	Related Articles in this Volume	9
8	Related Articles in Volumes 1–8	9
9	References	9

1 INTRODUCTION

Natural products display remarkable structural diversity with many unusual bonding patterns and substituents commonly encountered. This structural variety makes general approaches to characterization challenging. NMR spectroscopy, with its extensive availability of pulse sequences, offers one of the best general solutions to these difficult structural problems and most molecular characterizations now include at least some NMR data. While relatively standard NMR approaches have developed, these techniques can, at times, allow for ambiguity in shift assignment, structure, conformation and stereochemistry. Fortunately, such NMR based characterizations continue to improve. The INADEQUATE experiment provides one of the best solutions for establishing bond connectivity but is seldom used because of intrinsic sensitivity problems. Herein an INADEQUATE approach is presented that relies on automated software analysis of data to greatly increase the sensitivity of the experiment and make more routine application feasible. Complementing the bond assembly information of INADEQUATE are conformational and stereochemical detail. While this information is typically obtained by solution NMR through proton-proton interactions, solid-state NMR offers access to more accurate characterizations. Therefore, recent investigations into the use of solid-state NMR shift tensors to extract such information are presented. Comparison to corresponding X-ray structures provides independent verification of these solid-state NMR approaches.

2 TRADITIONAL ROUTES TO STRUCTURE

Examination of the natural products literature reveals that NMR structural characterizations typically involve obtaining a molecular formula by mass spectroscopy, 1D ^{1}H and ^{13}C analyses, and other experiments usually including DEPT or APT, COSY, HSQC, and HMBC. Most analysts recognize the potential for ambiguity inherent to these approaches and rely heavily on analogy to previous studies of related molecules. Use of the INADEQUATE NMR analysis is less frequently encountered with only about 80 natural product structures being reported at natural abundance since the introduction of the method by Bax et al. in 1980.[1] The primary difficulty with INADEQUATE is a lack of sensitivity. However, the INADEQUATE directly establishes carbon skeletons and thus offers more rigor than more commonly used NMR experiments. This is perhaps best illustrated by those INADEQUATE studies that have reexamined previously proposed structures. Despite the limited published use of this approach, numerous structural and shift assignment corrections have been made with nearly 20% of published INADEQUATE natural products reports consisting of such revisions. With an average of only four INADEQUATE studies being reported annually, the uncertainty in typical structural assignments may be higher than realized. This potential for structural errors using currently adopted techniques is generally unappreciated.

The primary source of error in more conventional experiments appears to lie in their strong reliance on the presence of protons and their coupling to other nuclei in the molecule. Molecules lacking protons within 3 bonds or roughly 5 Å of a given carbon are at risk of being misassigned. Hence, even a locally hydrogen depleted region potentially leads to ambiguity in structural determination. In addition, three bond couplings (both $^{3}J_{HH}$ and $^{3}J_{HC}$) are predicted by the Karplus relationship to have magnitudes near zero for dihedral angles near 90° and 270°.[2] Hence, such conformations are missing from H–H and H–C correlation experiments. Further complicating the problem is the assumption, often made, that couplings of only 2 and 3 bonds are detectable in experiments. This can be particularly serious in long range C–H coupling experiments such as the HMBC. Strong couplings through more than 3 bonds are known to occur and can have surprising structural origins. Since the H–C correlation experiments show signals for coupled pairs, but give no information regarding magnitudes of the coupling, long range couplings are unidentifiable as such and can complicate the assignment process. The INADEQUATE approach to structure greatly eliminates the risk of error inherent in typical NMR studies.

3 INADEQUATE STRUCTURAL DETERMINATIONS

INADEQUATE has long been recognized as a powerful experiment, but requires the presence of 2 adjacent ^{13}Cs for detection.[1] At natural abundance, only 1 in approximately 10 000 carbon pairs satisfy this criterion and thus INADEQUATE is unusually insensitive. Typical expectations are that over a hundred milligrams of a moderate molecular weight molecule are needed for successful analysis. As most new natural materials are isolated in much smaller quantities, this experiment has largely been unavailable to natural product chemists. In the past decade Dunkel et al. have developed software for INADEQUATE data analysis that greatly increases sensitivity. A more complete description of this approach has been given elsewhere.[3] This analysis technique has the advantage of examining all quadrature phase components of the

dataset eliminating the need for phasing. For low signal-to-noise datasets corresponding manual phasing is nearly impossible and can cause peaks to be missed as only the real-real component of the 2D spectrum is typically examined. The software models second order coupling effects, providing the ability to differentiate such signals from noise at low signal intensities. In practice this software has provided the ability to characterize natural products using a little as 11 mg (30 μmoles) of material.[4] Such datasets are nearly impossible to analyze manually as seen in the INADEQUATE spectrum of the obscurinervidine (Figure 1). However, a software evaluation of the obscurinervidine data identified most bonds with high statistical confidence.[5] This greatly reduced demand for material makes it possible to apply the INADEQUATE on a

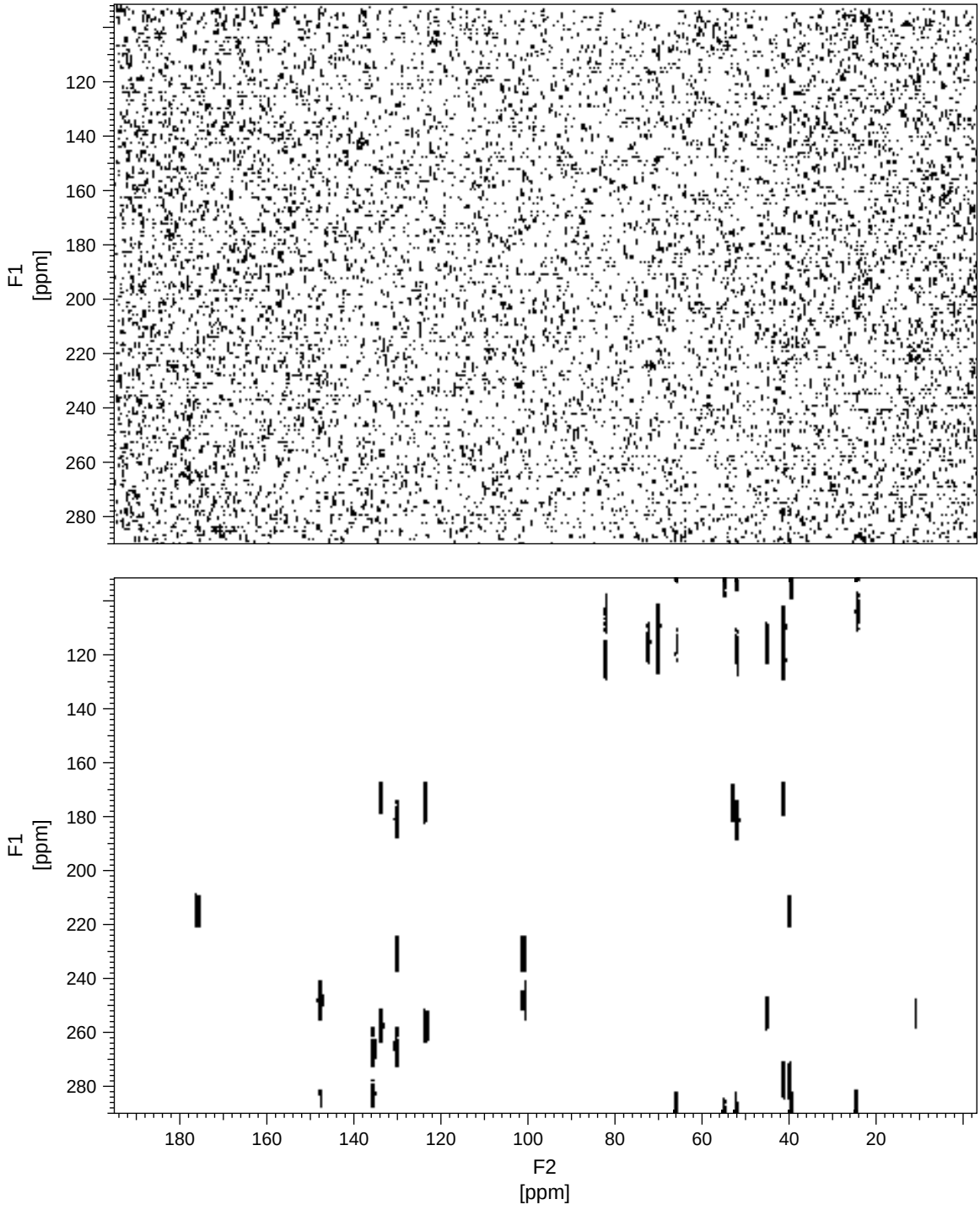

Figure 1 Comparison of the 2D INADEQUATE from the alkaloid, obscurinervidine, processed by standard techniques (top) and simulated from connections established by software analysis (bottom). Optimal phase parameters, determined by the computer analysis, were used to process the experimental data. The low signal-to-noise peaks observable in the upper right quadrant of the experimental spectrum are observable only after optimal phasing

more routine basis. The present version of the software fits anti-phase lineshapes in 2D INADEQUATE datasets. However, in principal, the software enhancements in sensitivity over manual analysis should also obtain for versions of the INADEQUATE displaying in-phase line shapes.[6]

Application of the INADEQUATE experiment is additionally complicated by the need to select an appropriate $^1J_{CC}$ value for use in the pulse delay, $[nJ_{CC}]^{-1}$, before the experiment begins. However, in natural products $^1J_{CC}$ values ranging from 35 to 80 Hz are common, making selection of a single correct value nearly impossible. While more recent versions of the pulse sequence are reasonably forgiving of this problem it remains a concern when the $^1J_{CC}$ values are inordinately different.[7] Fortunately, in practice, it is observed that setting the $^1J_{CC}$ value to match the largest anticipated value in the molecule often allows detection of almost all carbons present.[5] This apparently results from the strong dependence of the $^1J_{CC}$ value on carbon hybridization. Carbon-carbon bonds having small $^1J_{CC}$ values, typically sp^3–sp^3 bonds, involve carbons that carry more hydrogens and thus experience improved Overhauser enhancements. Since these signals are strongest, they can most afford to lose intensity because of a poor $^1J_{CC}$ selection and still remain detectable.

While carbon−carbon connectivity information from INADEQUATE is the primary goal, the $^1J_{CC}$ information obtained from the experiment is also of value. The $^1J_{CC}$ strongly reflects the % s character of a C–C bond (see Table 1) and thus can be important for identifying certain bonding arrangements.[8,9] In our lab this has proven useful in identifying the presence of epoxides in new natural materials. For three membered rings, such as epoxides, the % s character in the 'bent bonds' is anticipated to be smaller than the 25% expected from an sp^3–sp^3 bond.[10] Comparison of reported $^1J_{CC}$ values for a number of epoxides versus similarly substituted diols confirms this trend with $^1J_{CC}$ values of 30.1 ± 1.7 versus 41.5 ± 0.4 Hz observed, respectively.[9] This difference allows confident INADEQUATE identification of epoxides through examination of the $^1J_{CC}$ of adjacent carbons having shifts consistent with oxygen substitution.

Inclusion of the computerized INADEQUATE analysis suggests a more rigorous path to structural characterization than is typically used. Such an approach includes mass spectral analysis and NMR experiments including DEPT, INADEQUATE, HSQC and HMBC. The mass spectral analysis provides a molecular formula. The DEPT and INADEQUATE identify the carbon type (i.e., CH_3, CH_2, CH or quaternary) and all C–C connectivities, but cannot establish connectivity through heteroatoms. The heteronuclear correlation experiments, HSQC and HMBC, provide this final information giving the structure. This suggested approach relies on heteronuclear correlation experiments solely for establishing connections through heteroatoms and structures obtained are less prone to error. In addition, the suggested procedure directly and unambiguously determines the majority of an unknown structure, reducing the need for 'assignment by analogy'. However, structures determined by all of the procedures described still lack stereochemical and conformational information.

Table 1 Typical $^1J_{CC}$ values for carbon-carbon bonds

Compound	Hybridization	Percent s-character	$^1J_{CC}$ value
$\mathbf{C}H_3$–$\mathbf{C}H_3$	sp^3–sp^3	25	34.6
$\mathbf{C}H_3$–$\mathbf{C}H{=}CH_2$	sp^3–sp^2	29	41.9
$\mathbf{C}H_3$–$\mathbf{C}{\equiv}CH$, $H_2\mathbf{C}{=}\mathbf{C}H_2$	sp^3–sp, sp^2–sp^2	33	67.4, 67.6
$H_2\mathbf{C}{=}\mathbf{C}{=}CH_2$	sp^2–sp	40	98.7
$H\mathbf{C}{\equiv}\mathbf{C}H$	sp–sp	50	171.5

4 CONFORMATIONAL ANALYSIS USING SOLID-STATE NMR

Molecular conformation and stereochemistry are typically established by solution NMR or X-ray crystallography. NMR analyses usually rely on H–H interactions to establish either distances between protons through nuclear Overhauser enhancements or to find H–C–C–H dihedral angles through the $^3J_{HH}$ and the Karplus relationship.[2] Unfortunately, both methods are of limited use for hydrogen depleted substances. In such cases solid-state NMR offers a powerful alternative that is competitive even with X-ray when a hydrogen atom conformation is in question. The proposed approach involves comparing experimental shifts with ab initio computed values for model structures. Computed shifts can be obtained for any proposed conformation or stereochemistry by simply building the desired structure with a computer program, optimizing relevant geometry and calculating the corresponding shift tensors. A best fit of the experimental data to computed values establishes a best structure. Of particular interest is the use of chemical shift tensor principal values obtainable from solids from recently introduced techniques. In the work summarized here experimental principal values obtained either from the PHORMAT or FIREMAT techniques are employed.[11,12] Using these techniques three principal tensor values are obtained per nucleus rather than the average of these values provided by the liquid isotropic shift. Furthermore, principal values represent electronic shielding in characteristic directions for a given nucleus, making the correlation of shift and structure more direct than corresponding studies involving the isotropic shift. However, this comparison assumes the ability to compute shift tensors that accurately reproduce measured quantities. Fortunately, computational methods have greatly improved in the past decade.

Several chemical shift tensor computation methods are now commercially available. However, before these methods can be employed for structural analysis the magnitude of the errors must be established. Initial error analyses emphasized only the isotropic shift.[13] However, use of tensor values allows the origin of systematic computational errors to be more readily identified due to the association of specific tensor components with characteristic directions in a given moiety. A comparison was made for five methods (HF, BLYP, BPW91, B3LYP, and B3PW91) and 135 principal shift values obtained from caryophyllene oxide and parthenolide (Table 2).[14–19] All included computational methods compute sp^2 carbon tensors with less accuracy than corresponding sp^3 values due to electron correlation. Hence, errors for sp^2 and sp^3 carbons were determined separately in parthenolide where sufficient carbons of each type were available. For the compounds examined, the B3PW91 method gave the best results and provided all computed shift values reported herein. The quality of fit is graphically displayed in Figure 2. The relatively small overall

Table 2 Comparison of tensor computational methods for caryophyllene oxide and parthenolide[a]

	RMS error (ppm)		
	Caryophyllene oxide[b]	Parthenolide	
		sp^2	sp^3
HF	5.6	4.9	2.5
BLYP	4.5	4.7	2.4
BPW91	3.7	4.4	2.2
B3LYP	3.5	3.7	2.2
B3PW91	3.1	3.5	2.0

[a] Structures used for all calculations consisted of X-ray positions for heavy atoms and B3LYP/6-31G* refined hydrogen positions. The D95** basis set was used for all computed tensors.
[b] Caryophyllene oxide contains only two sp^2 carbons and thus does not allow for separate error analyses of sp^2 and sp^3 carbons.

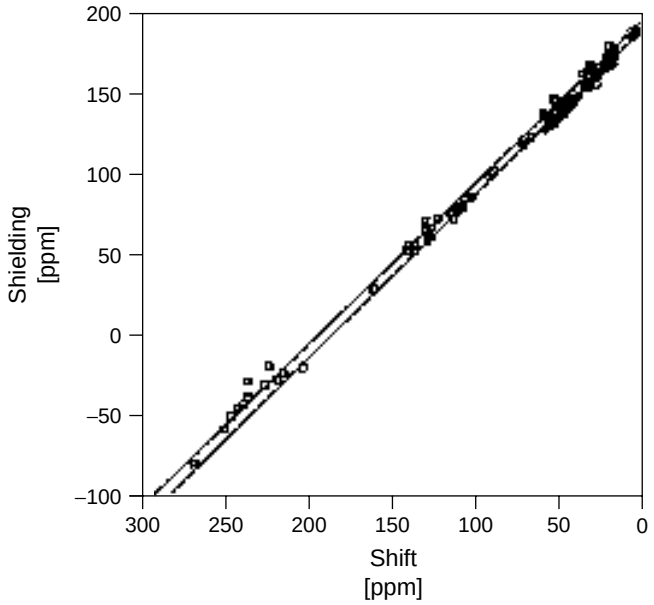

Figure 2 Correlation plot of shift versus shielding for 135 principal values obtained from the terpenes parthenolide and caryophyllene oxide. All shielding values were computed using the B3PW91 method using the D95** basis. Respective slope and intercept values of 1.006 and 194.933 were found for sp^2 carbons (□) while values of 1.031 and 190.325 were computed for sp^3 carbons (○)

error of 2.1 and 3.3 ppm for sp^3 and sp^2 carbons, respectively, suggests that structural investigations using computed tensors are feasible.

The sensitivity of computed tensors to structure was demonstrated in practice by the measured tensors for parthenolide (Figure 3).[19] Here, two geometrically distinct molecules are found in the crystallographic unit cell (i.e., two molecules per asymmetric unit). The two molecules are nearly identical (see Figure 4) differing by only 0.017 Å and 2.7° in bond lengths and dihedral angles, respectively, on average. However, the experimental isotropic spectrum differentiates the two molecules of the asymmetric unit with two lines observed for most molecular positions (Figure 5). Assignment of carbons to distinct molecules of the asymmetric unit is normally challenging as lines of a pair represent the same molecular position

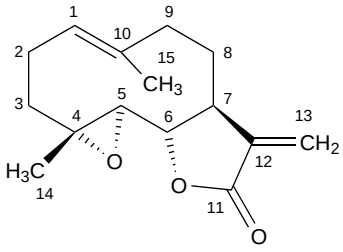

Figure 3 Structure of parthenolide

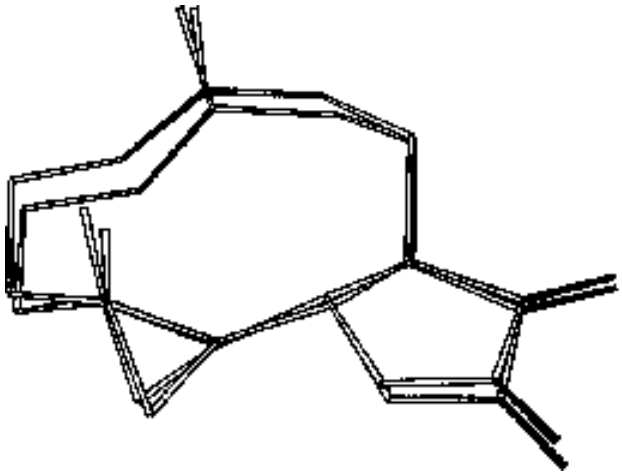

Figure 4 The two molecules of parthenolide present in the crystallographic asymmetric unit superimposed to show their similarities. Corresponding bond lengths and dihedral angles differ by only 0.017 Å and 2.7°, respectively, on average. Computed tensor principal values are sufficiently accurate to allow assignment of 10 of the 15 carbons to a specific molecule of the asymmetric unit

with only minor differences present in the local environments. Despite these similarities, computed tensors are sufficiently accurate to allow ten of the fifteen pairs of carbons in parthenolide to be assigned to a specific molecule of the asymmetric unit with reasonable statistical confidence as summarized in Table 3.

The small relative errors in the computed tensors also allow shift assignments to molecular position to be made. Correct assignments are crucial, as the correlation of structure to tensor values requires a correct identification of molecular positions. In the work summarized here, preliminary assignments were made by comparison of solid-state isotropic shifts to INADEQUATE determined solution isotropic values. Since differences in shift are known to occur between liquids and solids, solution assignments are considered reliable only when no other peaks are within ±10 ppm of a given line. The isotropic lines in the solid may then be differentiated by carbon type (i.e., CH_3, CH_2, CH, or quaternary) in a spectral editing procedure.[20] Remaining unassigned resonances within a given subgroup are then assigned by making all possible arrangements of computed tensors with experimental values. For each, an error is calculated and the best assignment identified. A statistical confidence in the assignment is provided by an F-test. This ability to confidently assign shifts and the demonstrated sensitivity of tensors to minor structural variation invites application to conformational analysis.

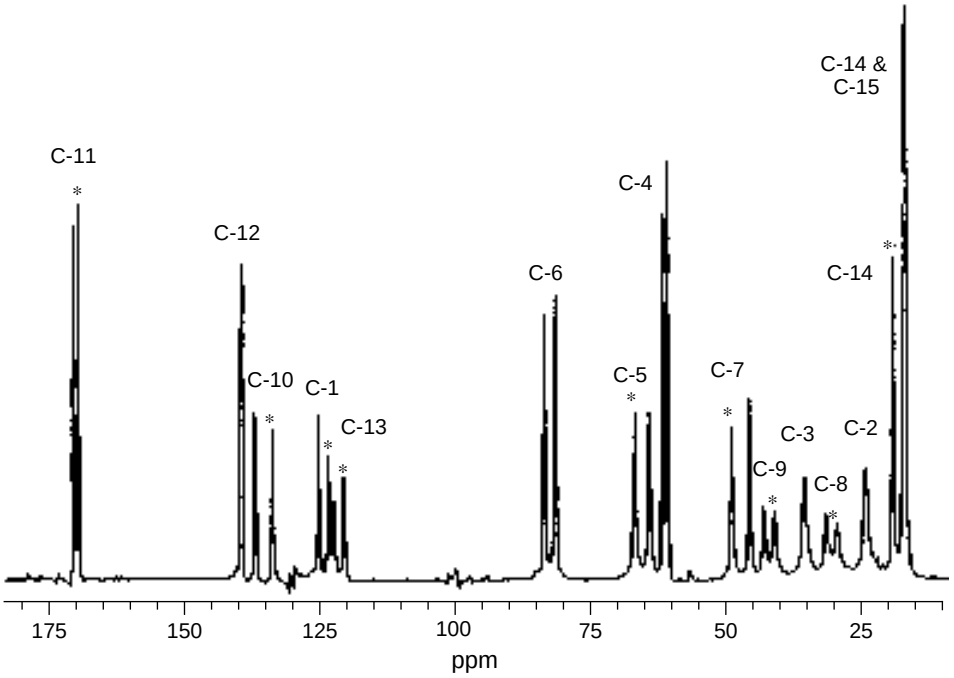

Figure 5 The isotropic spectrum of solid parthenolide showing the doubling of lines arising from minor geometric differences between the two molecules of the asymmetric unit. An asterisk denotes lines assigned to the same molecule of the asymmetric unit

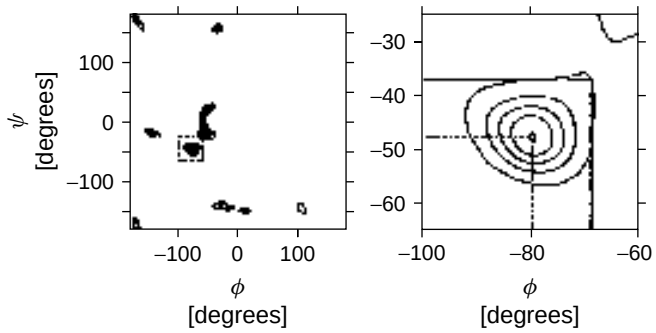

Figure 6 Probability surface for the C_α of alanine in G*AV. The Z-surface shown includes contributions to the fit from the isotropic shift, the span ($\delta_{11}-\delta_{33}$), and $\delta_{22}-\delta_{11}$. The boxed region contains the area of highest probability and is expanded in the right-hand plot

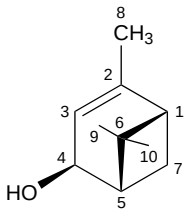

Figure 7 Structure of verbenol

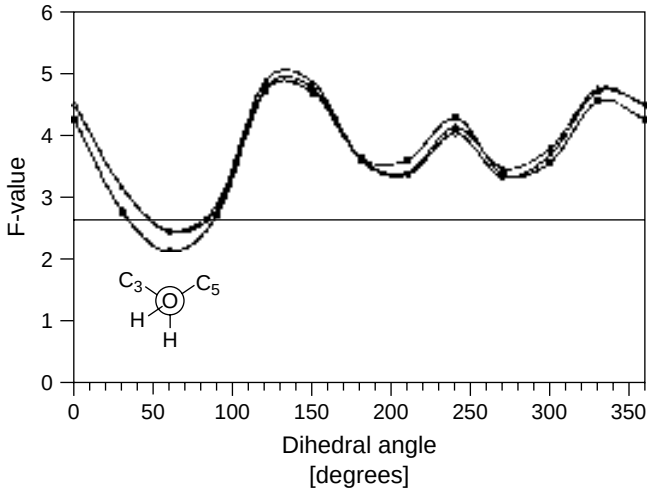

Figure 8 F-value versus dihedral angle for model conformations of verbenol. Tensors were computed at 30° intervals in the hydroxy dihedral angle (C3–C4–O–H) with extrapolated values used for intermediate angles. The 90% statistical confidence level is shown. Each curve shown corresponds to one of the three molecules of the asymmetric unit

Initial investigation of the sensitivity of principal values to molecular conformation were performed by Pines et al. using tripeptides which were ^{13}C labeled at the α-carbon of the central amino acid.[21] Comparisons of measured C_α principal values to corresponding ab initio computed values from conformationally varied model structures were performed using the Z-surface method, which gives the Bayesian probability that a given conformation (i.e., an ϕ/ψ pair) corresponds to experimental principal values.[22] The NMR analysis accurately predicted the X-ray determined conformation within $\pm 12°$ (Figure 6), validating the proposed approach. Further theoretical work by Oldfield et al. has demonstrated that the C_α principal values are especially sensitive to backbone conformation in several amino acids.[23] More recently, the introduction of improved experimental methods has eliminated the need to isotopically label materials and allows extensions of the methodology to less easily labeled materials like natural products.

Table 3 Principal values for parthenolide and corresponding theoretical values

	Chemical Shift. Experiment (Theory[a])				
Carbon #	δ_{11}	δ_{22}	δ_{33}	δ_{Iso}[b]	$\delta_{Solution}$[c]
Molecule 1					
1[d]	217.5 (222.9)	113.8 (117.0)	46.9 (50.1)	126.0 (130.0)	125.2
2	38.5 (42.5)	19.2 (21.3)	17.4 (16.1)	25.0 (26.6)	24.2
3	51.6 (55.9)	40.9 (44.6)	16.9 (19.7)	36.5 (40.1)	36.4
4	111.9 (108.4)	43.8 (42.8)	29.3 (26.3)	61.7 (59.2)	61.6
5	101.2 (102.1)	65.9 (65.5)	28.9 (23.7)	65.1 (63.8)	66.4
6	110.8 (111.0)	90.8 (87.0)	51.8 (46.1)	84.5 (81.4)	82.5
7	54.7 (55.6)	44.3 (46.9)	40.7 (44.0)	46.5 (48.8)	47.6
8	45.4 (50.3)	33.1 (32.8)	18.8 (17.2)	32.4 (33.4)	30.7
9	54.1 (53.6)	48.1 (51.0)	29.7 (30.7)	43.9 (45.1)	41.2
10[d]	241.3 (240.3)	140.4 (139.5)	31.7 (32.1)	137.7 (137.3)	134.7
11[d]	249.4 (254.3)	138.7 (136.5)	126.3 (126.7)	171.4 (172.5)	169.3
12[d]	235.6 (234.6)	128.3 (132.0)	57.3 (59.5)	140.4 (142.0)	139.3
13[d]	225.2 (226.2)	128.7 (126.7)	16.4 (15.2)	123.3 (122.7)	121.2
14	29.1 (27.8)	21.5 (21.1)	2.9 (-2.0)	17.8 (15.6)	17.3
15	31.6 (33.5)	16.3 (14.5)	5.1 (2.7)	17.6 (16.9)	17.0
Molecule 2					
1[d]	214.2 (218.6)	107.4 (113.6)	51.3 (50.7)	123.3 (127.6)	125.2
2	39.5 (43.5)	19.4 (19.5)	16.9 (16.3)	25.3 (26.4)	24.2
3	51.6 (49.5)	40.9 (41.7)	16.9 (17.6)	36.5 (36.3)	36.4
4	112.3 (114.8)	45.7 (42.7)	30.1 (31.8)	62.7 (63.1)	61.6
5	102.4 (101.8)	70.6 (66.3)	30.7 (35.2)	67.9 (67.8)	66.4
6	109.3 (107.7)	89.6 (85.8)	48.5 (46.2)	82.4 (79.9)	82.5
7	55.8 (57.7)	48.8 (49.3)	45.1 (45.6)	49.8 (50.9)	47.6
8	42.8 (47.8)	29.9 (32.5)	18.7 (16.2)	30.5 (32.2)	30.7
9	51.4 (55.0)	47.6 (50.5)	27.1 (28.7)	42.0 (44.7)	41.2
10[d]	238.1 (238.9)	135.6 (140.3)	30.5 (28.7)	134.7 (136.0)	134.7
11[d]	245.9 (246.6)	136.3 (136.4)	129.2 (122.2)	170.4 (168.4)	169.3
12[d]	235.9 (226.2)	126.1 (128.1)	58.6 (58.6)	140.1 (137.6)	139.3
13[d]	222.8 (215.2)	122.1 (118.6)	19.4 (14.6)	121.4 (116.1)	121.2
14	33.4 (30.0)	24.6 (23.6)	2.3 (-1.0)	20.0 (17.5)	17.3
15	32.4 (34.0)	16.3 (14.2)	5.5 (2.9)	18.1 (17.0)	17.0

[a] Theoretical tensor values, given in parentheses, calculated using the B3PW91 method and 6-31+G (2d, p) basis. Structure used consisted of X-ray positions for heavy atoms and B3LYP/6-31G** refined hydrogen positions.
[b] Isotropic experimental shifts obtained from a separate CP/MAS experiment. Theoretical isotropic values computed from the average of calculated principal values.
[c] Solution values obtained from 2D INADEQUATE.
[d] Principal values for these carbons were obtained from a FIREMAT analysis. All other values are derived from PHORMAT data.

The terpene verbenol (Figure 7) provides an ideal model to test the sensitivity of tensors to conformation in natural products.[24] Here the bicyclic ring system eliminates conformational flexibility from the majority of the molecule, with significant flexibility remaining only in the orientation of the hydroxy hydrogen. Relative orientation of the methyl groups is not considered as it is assumed that local steric factors accurately locate them. However, location of the hydroxy hydrogen often reflects lattice effects, making the characterization of orientation in isolated molecules difficult. To test the sensitivity of tensors to molecular conformation, twelve models were prepared in which the hydroxy hydrogen was rotated about the C–O axis in 30° increments. At each point the C–C–O–H dihedral angle was fixed and the remaining structure optimized via an energy minimization procedure. Computed tensors that displayed variation in tensors versus conformation larger than the anticipated error were used to characterize the best conformation. X-ray analysis of verbenol indicates that there are three molecules per asymmetric unit.[25] Hence up to three lines per carbon are observed in the isotropic spectrum. Comparison of computed tensors with experiment for all angles by an F-test provided a best fit at roughly $60° \pm 15°$ for each of the 3 distinct molecules of verbenol (Figure 8). This predicted conformation compares favorably with the X-ray determined angles of 55°, 69°, and 74°, validating the approach chosen.

5 STEREOCHEMICAL DETERMINATION USING SOLID-STATE NMR

The sensitivity of molecular conformation to tensors suggests that stereochemistry may also be predicted by principal values. Determination of stereochemistry in new natural products is an important and frequently encountered step. Characterization by solid-state NMR offers a solution in cases where X-ray or solution NMR fail as previously discussed. A comparison of experimental principal values with ab initio computed values for all possible diastereomers, analogous to

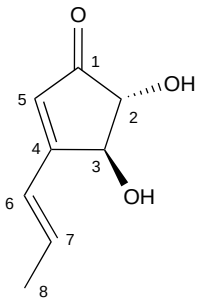

Figure 9 Structure of terrein

the approach proposed for conformational analysis, provides a solution.

The natural product, terrein, (Figure 9) has a relatively simple structure and the presence of only two stereocenters making it an ideal compound for investigating the sensitivity of tensors to stereochemistry. While absolute stereochemistry is unavailable from tensor data, principal values may potentially establish relative stereochemistry. Hence an analysis of terrein in which experimental principal values are compared with ab initio computed tensors for the 2R, 3S and 2S, 3S diastereomers is sufficient to establish relative stereochemistry.[26] Principal values cannot differentiate enantiomers, hence, comparisons involving any of the other three possible diastereomeric pairs (i.e., 2R, 3S and 2R, 3R or 2S, 3R and 2R, 3R or 2S, 3R and 2S, 3S) are equivalent as they involve only the exchange of one enantiomer for another and thus offer no additional information.

Conformational flexibility complicates the stereochemical analysis and must necessarily be included in the analysis. In terrein, a variety of conformations differing only in orientation of the hydroxy hydrogens at C2 and C3 were prepared for each diastereomer. Each conformation was then subjected to

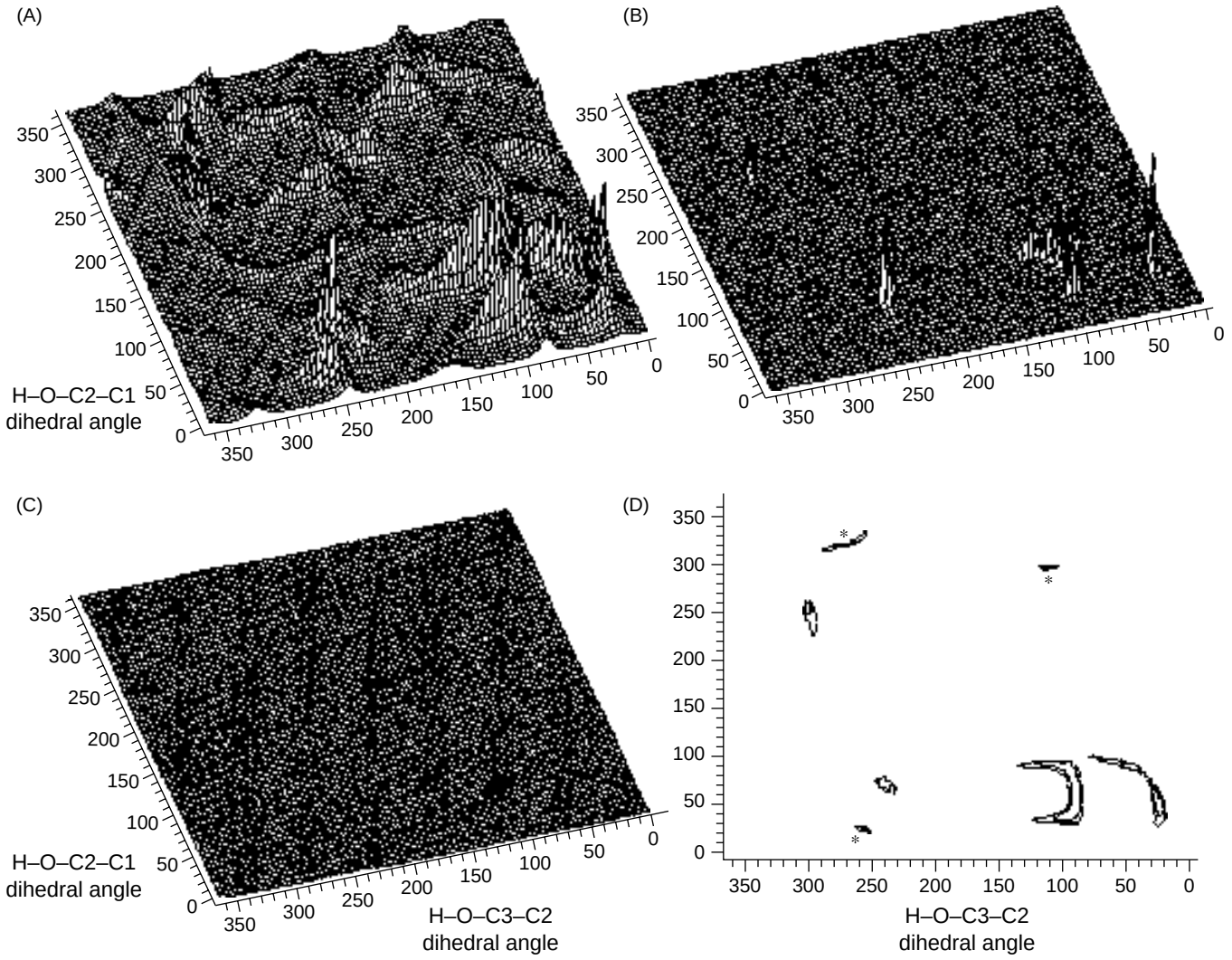

Figure 10 Probability surfaces illustrating the superior fit of the 2R, 3S stereoisomer (plot A) to the experimental data. In contrast, the 2S, 3S diastereomer (plot C) is a poor fit to experiment regardless of the chosen conformations. The 2R, 3S diastereomer can be differentiated from the best-matched 2S, 3S diastereomer with a high statistical probability of >99.5%. Plot B shows an alternative processing of the data from that in A. This Z-surface provides a more visually distinguishable local maxima for peaks of high probability but suppresses three marginally less probable peaks as denoted by the asterisks in plot D. The contour plot D lends statistical meaning to plots A and B by showing the 80% and 90% probability levels. The vertical scales in plots A and C are identical to allow direct comparison and represent the inverse F-value

a constrained geometry optimization and tensors computed. Tensor information from the stereocenters at carbons 2 and 3 are anticipated to provide the most sensitive information and initially are the only carbons included in the analysis.

Computed tensors for the two diastereomers of terrein differ significantly, allowing a confident assignment (>99.5% probability) of the stereochemistry as 2R*, 3S*. This is shown in a plot of probability versus hydroxy dihedral angles for the 2R, 3S and 2S, 3S diastereomers in Figure 10(A) and 10(C), respectively. Figure 10(B) shows the data from plot 10A processed using Oldfield's Z-surface technique for comparison to work shown in Figure 6.[22] Z-surfaces give more pleasing visual portrayal of areas of conformational best fit when compared to the corresponding surface of inverse F-values shown in the left-hand plots. However, Z-surfaces exponentially suppress peaks from marginally less probable conformations as seen in plot 10D where the 80% and 90% probability levels equally appropriate for both plots 10A and 10D are shown. The visually distinct peaks in the Z-surface are seen to correspond to roughly the 80% probability level. However, three additional regions are within 10% of the 80% probability level, as denoted by asterisks in plot 10D, but are completely unrecognized in the Z-surface of plot 10B. The conformations predicted in Figure 10 are from a limited sampling of the surface. More accurate predictions were obtained by greater sampling near regions of high probability.

Inclusion of additional data points near local maxima (H–O–C2–C1 = 50° and H–O–C3–C2 = 70°) provides most probable molecular conformations with an associated statistical significance. In terrein the region of conformational best fit for the hydroxy hydrogens corresponds with the X-ray determined orientations (see Figure 11).[27] The error in the NMR predicted H–O–C2–C1 angle was roughly the same (±20°) as that observed in the analysis of verbenol (top plot of Figure 11). However the error in the H–O–C3–C2 angle was nearly three times as large, suggesting a deficiency in the theoretical model or the presence of temporal fluctuations in the structure that is neglected in the shift model. Inclusion of conformational disorder in the model, performed by averaging tensor values for two different model conformations, resulted in a significant improvement in predicted conformation (see bottom plot of Figure 11). Final predicted conformations of 52° ± 12° and 58° ± 11° in the H–O–C2–C1 and H–O–C3–C2 angles, respectively, were made using the disordered model. Corresponding X-ray positions are 68° and 60°, supporting the NMR approach.

A corresponding prediction of stereochemistry and molecular conformation can be performed using only isotropic shift values. Isotropic shifts lack the directional information of the principal values but are more easily obtained. In terrein, a comparison of computed and experimental isotropic shifts correctly identifies the stereochemistry as 2R*, 3S*, but at a significantly reduced confidence (roughly 80% probability level compared to >99.5% from tensor shifts). Molecular conformations are likewise determined with much less confidence with nearly 80% of the potential conformations statistically indistinguishable from one another. Principal values thus appear to offer a superior assessment of both stereochemistry and molecular conformation than corresponding isotropic values.

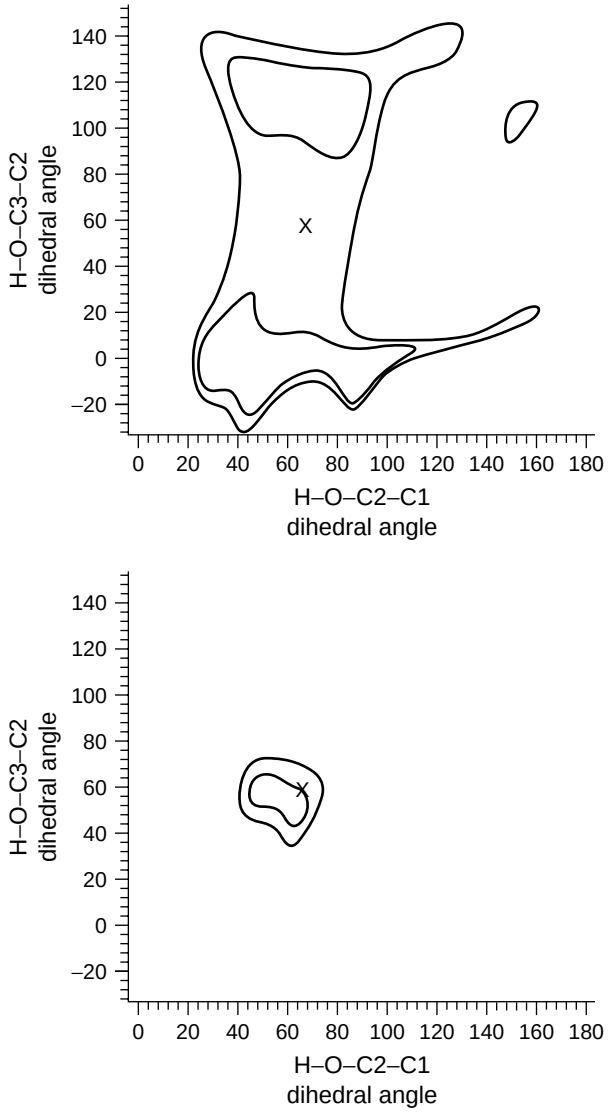

Figure 11 Contour maps showing selection of high probability dihedral angles in 2R, 3S terrein when additional data points near local maxima (H–O–C2–C1 = 35°–70°, H–O–C3–C2 = 10°–130°) are included. The top plot ignores motional disorder and displays contours at the 80% and 90% probability levels. In the lower plot, the effect of conformational disorder in the H–O–C2–C1 and H–O–C3–C2 angles is shown. Conformational averaging by ±20° and ±60°, respectively, about any given point were performed. The lower figure includes contours at one standard deviation and the 80% probability levels. The H–O–C2–C1 angle is defined such that 0° denotes the O–H eclipsing the C1–C2 bond with subsequent increases in angle indicating rotation towards the C2–H bond. The H–O–C3–C2 angle is likewise defined with the O–H eclipsing the C2–C3 bond at 0° and positive increments of angle denoting rotation towards the C3–C4 bond. The X-ray determined conformation is indicated with an X

6 CONCLUSIONS

Structural determination in natural products may be improved by a more routine use of the INADEQUATE experiment. Prior sensitivity concerns have been addressed by the introduction of a computer analysis technique coupled with improvements in available pulse sequences. In cases

where stereochemistry and molecular conformation are also of interest, solid-state NMR offers an alternative route to this information. The NMR approach complements presently available methodologies and appears to be especially useful for non-crystalline or hydrogen depleted materials. Presently, the proposed methods clearly characterize the stereochemistry and provide molecular conformations with reasonable errors. Assessment of conformational errors is presently limited by comparable errors in the corresponding X-ray determined hydrogen positions. Future extensions of the conformational analysis to systems involving non-hydrogen atoms should provide more accurate comparisons with X-ray values and thus establish the reliability of the NMR approach.

7 RELATED ARTICLES IN THIS VOLUME

Magic-angle Turning Spectra of Solids Involving 5π-pulse Sequences.

8 RELATED ARTICLES IN VOLUMES 1–8

Chemical Shift Tensors, Volume 2; Computer Assisted Structure Elucidation, Volume 2; INADEQUATE Experiment, Volume 4; Natural Products, Volume 5; Shielding Tensor Calculations, Volume 7.

9 REFERENCES

1. a. A. Bax, R. Freeman, and S. P. Kempsell, *J. Am. Chem. Soc.*, 1980, **102**, 4849; b. A. Bax, R. Freeman, and T. A. Frenkiel, *J. Am. Chem. Soc.*, 1981, **103**, 2102.
2. M. A. Karplus, *J. Am. Chem. Soc.*, 1963, **85**, 2870.
3. (a) R. Dunkel, C. L. Mayne, J. Curtis, R. J. Pugmire, and D. M. Grant, *J. Magn. Reson.*, 1990, **90**, 290; (b) R. Dunkel, C. L. Mayne, R. J. Pugmire, and D. M. Grant, *Anal. Chem.*, 1992, **62**, 3133.
4. D. C. Chauret, T. Durst, J. T. Arnason, P. Sanchez-Vindas, L. S. Roman, L. Poveda, and P. A. Keifer, *Tetrahedron Lett.*, 1996, **37**, 7875.
5. J. K. Harper, R. Dunkel, S. G. Wood, N. L. Owen, D. Li, R. G. Cates, and D. M. Grant, *J. Chem. Soc. Perkin Trans.*, 1995, **2**, 91.
6. T. Nakai and C. A. McDowell, *J. Magn. Reson.*, 1993, **104A**, 146.
7. (a) A. Torres, T. T. Nakashima, R. E. D. McClung, and D. R. Muhandiram, *J. Magn. Reson.*, 1992, **99**, 99; (b) N. C. Nielsen, H. Thogersen, and O. W. Sorensen, *J. Am. Chem. Soc.*, 1995, **117**, 11 365.
8. K. Frei and H. J. Bernstein, *J. Chem. Phys.*, 1963, **38**, 1216.
9. K. Kamienska-Trela, *Annu. Rep. NMR Spectrosc.*, 1995, **30**, 132–230.
10. A. Greenberg and J. F. Liebman, 'Strained Organic Molecules', Academic Press: New York, 1978, pp 31–34.
11. J. Z. Hu, W. Wang, F. Liu, M. S. Solum, D. W. Alderman, R. J. Pugmire, and D. M. Grant, *J. Magn. Reson.*, 1995, **113**, 210.
12. D. W. Alderman, G. McGeorge, J. Z. Hu, R. J. Pugmire, and D. M. Grant, *Mol. Phys.*, 1998, **95**, 1113.
13. (a) J. R. Cheeseman, G. W. Trucks, T. A. Keith, and M. J. Frisch, *J. Chem. Phys.*, 1996, **104**, 5497; (b) J. Gauss, *J. Chem. Phys.*, 1993, **99**, 3629.
14. A. D. Becke, *Phys. Rev.*, 1988, **38A**, 3098.
15. C. Lee, W. Yang, and R. G. Parr, *Phys. Rev.*, 1988, **37B**, 785.
16. J. P. Perdew and Y. Wang, *Phys. Rev.*, 1992, **45B**, 13 244.
17. A. D. Becke, *J. Chem. Phys.*, 1993, **98**, 5648.
18. J. K. Harper, G. McGeorge, and D. M. Grant, *Magn. Reson. Chem.*, 1998, **36**, S135.
19. J. K. Harper, G. McGeorge, and D. M. Grant, *J. Am. Chem. Soc.*, 1999, **121**, 6488.
20. J. Z. Hu, J. K. Harper, G. Taylor, R. J. Pugmire, and D. M. Grant, *J. Magn. Reson.*, 2000, **142**, 326.
21. J. Heller, D. D. Laws, M. Tomaselli, D. S. King, D. E. Wemmer, A. Pines, R. H. Havlin, and E. Oldfield, *J. Am. Chem. Soc.*, 1997, **119**, 7827.
22. H. Le, J. G. Pearson, A. C. de Dios, and E. Oldfield, *J. Am. Chem. Soc.*, 1995, **117**, 3800.
23. R. H. Havlin, H. Le, D. D. Laws, A. C. deDios, and E. Oldfield, *J. Am. Chem. Soc.*, 1997, **119**, 11 951.
24. J. K. Harper and D. M. Grant, *J. Am. Chem. Soc.*, 2000, **122**, 3708.
25. J. K. Harper, A. M. Arif, and D. M. Grant, *Acta Crystallogr. Sec. C: Cryst. Struct. Commun.*, 2000, **C56**, 451.
26. J. K. Harper, A. E. Mulgrew, J.-Y. Li, D. H. Barich, G. Strobel, and D. M. Grant, *J. Am. Chem. Soc.*, 2001, **123**, 9837.
27. J. K. Harper, A. M. Arif, J.-Y. Li, G. Strobel, and D. M. Grant, *Acta Crystallogr. Sec. C: Cryst. Struct. Commun.*, 2000, **C56**, e570.

Biographical Sketch

James K. Harper, *b* 1962, BS (1986) and MS (1993) at Brigham Young University, PhD (1999) at the University of Utah in physical-analytical chemistry. Introduced to natural products isolation and characterization at the Chemical Ecology Laboratory (Brigham Young University, 1986–1991) and during postdoctoral work with Gary Strobel (Montana State University, 1999–2000). Joint postdoctoral work at Montana State University and the University of Utah 1999–present. Approx. 15 publications. Research Interests: Correlation of shift tensors to structure and the NMR characterization of novel biologically active natural products.

Vitamin B_{12}

A. Ian Scott

Texas A&M University, College Station, TX, USA

1	Introduction	1
2	The First Methyltransferases, Their Specificities, and the Synthesis of Precorrin-2	1
3	From Precorrin-3 to Hydrogenobyrinic Acid	1
4	Related Articles	4
5	References	4

1 INTRODUCTION

The story of how Nature synthesizes the corrin structure of vitamin B_{12} began about 4×10^9 years ago, when archaebacteria first grew on our planet in an anaerobic atmosphere. (The subject has been reviewed by Scott, by Battersby, and by Leeper.[1]) Largely through the power of NMR spectroscopy, in combination with molecular biology and enzymology, the last 25 years have witnessed the elucidation of the pathway to hydrogenobyrinic acid (Scheme 1), which serves as the precursor to the vitamin via side-chain amidation, cobalt insertion, and addition of the nucleotide loop.

In 1968, at Yale, armed with a home-made FT NMR spectrometer, and liters of *Propionibacterium shermanii* cells, we were able to obtain 2–5% incorporations of the ^{13}C-enriched substrates aminolevulinic acid (ALA), porphobilinogen (PBG), and, most importantly, uro'gen III (Scheme 1) to observe ^{13}C signals above natural abundance (1.1%) in vitamin B_{12}, thus linking the porphyrin and corrin pathways. Later, with L. Siegel (Duke) and G. Müller (Stuttgart), we found and identified the structure of the intermediates precorrins-2 and -3 in their oxidized forms,[1] although the spectroscopy involved 11 days of continuous acquisition of ^{13}C at natural abundance. After this initial burst of success, the next decade was spent in the search for further intermediates during which a great deal was learned about enzymes 2, 3, and 4 (Scheme 1), but, apart from finding the sequence of C-methylation by $^{13}CH_3$-*S*-adenosyl methionine (SAM) in a 'pulsed' $^{13}C/^{12}C$ time course, the steps between precorrin-3 and the corrin structure remained cryptic until 1987, when Roth showed that *Salmonella typhimurium* makes B_{12} anaerobically, and provided the necessary plasmids *and* the DNA sequences of the corrin operon—the *cbi* genes—for overexpression in *E. coli*.[1]

The corresponding *cob* genes of *Pseudomonas denitrificans* (Rhone-Poulenc, Paris) now became accessible,[2] so that, by mid-1990, the complete repertoire of corrin-synthesizing enzymes for both the anaerobic and aerobic pathways was in hand. Now came the fascinating problem of matching each gene product to its function. Collaborative work in Paris and Cambridge[1] (A. R. Battersby) had established the pathway from precorrin-6x to the cobalt-free corrin, hydrogenobyrinic acid (see Scheme 1). Our strategy for deducing the function of the enzymes connecting precorrin-2 and -6x was to enrich precorrin-2 biosynthetically with ^{13}C, then watch the growth of new signals in the NMR spectrum when incubated with each of the gene products in turn, in the presence of $^{13}CH_3$-SAM. Space does not permit other than a brief summary of this complex pathway, but the following examples taken from our own work covering the central section of Scheme 1 typify the NMR techniques used.

2 THE FIRST METHYLTRANSFERASES, THEIR SPECIFICITIES, AND THE SYNTHESIS OF PRECORRIN-2

Uro'gen III (enriched from [5-^{13}C]ALA at the positions (■) shown in Scheme 2) was prepared by mixing the enzymes 1, 2, and 3 (dehydratase, deaminase, and uro'gen III synthase) and then incubating with the first methyltransferase, M-1 (enzyme 4), and [$^{13}CH_3$]SAM. The resultant spectrum of precorrin-2 revealed only one sp^3 enriched carbon (■) assigned to C-15, thereby locating the reduced center. By using a different set of ^{13}C labels (• from [^{13}C-3]ALA) and [$^{13}CH_3$]SAM the sp^2 carbons at C-12 and C-18 were located as well as the sp^3 centers coupled to the pendant ^{13}C-methyl groups at (*) C-2 and C-7. This result[3] confirms an earlier NMR analysis[4] of precorrin-2 isolated by careful anaerobic purification of the methyl ester, and shows that no further tautomerism takes place during the latter procedure. The two sets of experiments mutually reinforce the postulate that precorrins-1, -2, and -3 all exist as hexahydroporphinoids, and recent labeling experiments[5] have provided good evidence that precorrin-1 is discharged from the methylating enzyme (SUMT) as the species with the structure shown in Scheme 1.

However, prolonged incubation (2 h) of uro'gen III with M-1 provided a surprising result, for the UV and NMR changed dramatically from that of precorrin-2 (a dipyrrocorphin) to the chromophore of a pyrrocorphin, hitherto known only as a synthetic tautomer of hexahydroporphyrin. At first sight, this event seemed to signal a further tautomerism of a dipyrrocorphin to a pyrrocorphin catalyzed by the enzyme, but when $^{13}CH_3$-SAM was added to the incubation, it was found that a *third* methyl group signal appeared in the 19–21 ppm region of the NMR spectrum. When uro'gen III was provided with appropriate ^{13}C labels (•) (Scheme 2), three pairs of doublets appeared in the sp^3 region (δ = 50–55 ppm) of the pyrrocorphin product. The necessary pulse labeling experiments together with appropriate FAB MS data finally led to the structural proposal (Scheme 2)[6] for the novel trimethylpyrrocorphin produced by 'overmethylation' of the normal substrate, uro'gen III, in the presence of high concentration of enzyme. Thus, M-1 has been recruited to insert a ring C methyl and synthesize the long-sought 'natural' chromophore corresponding to that of the postulated precorrin-4, although in this case the regiospecificity is altered from ring D to ring C. Under physiological conditions, however, the next step catalyzed by enzyme 5 (M-2; Scheme 1) inserts the next SAM-derived methyl group at C-20 to reach precorrin-3.

3 FROM PRECORRIN-3 TO HYDROGENOBYRINIC ACID

Using ^{13}C NMR spectroscopy as a probe for the activity of all the overexpressed enzymes of the B_{12} pathway

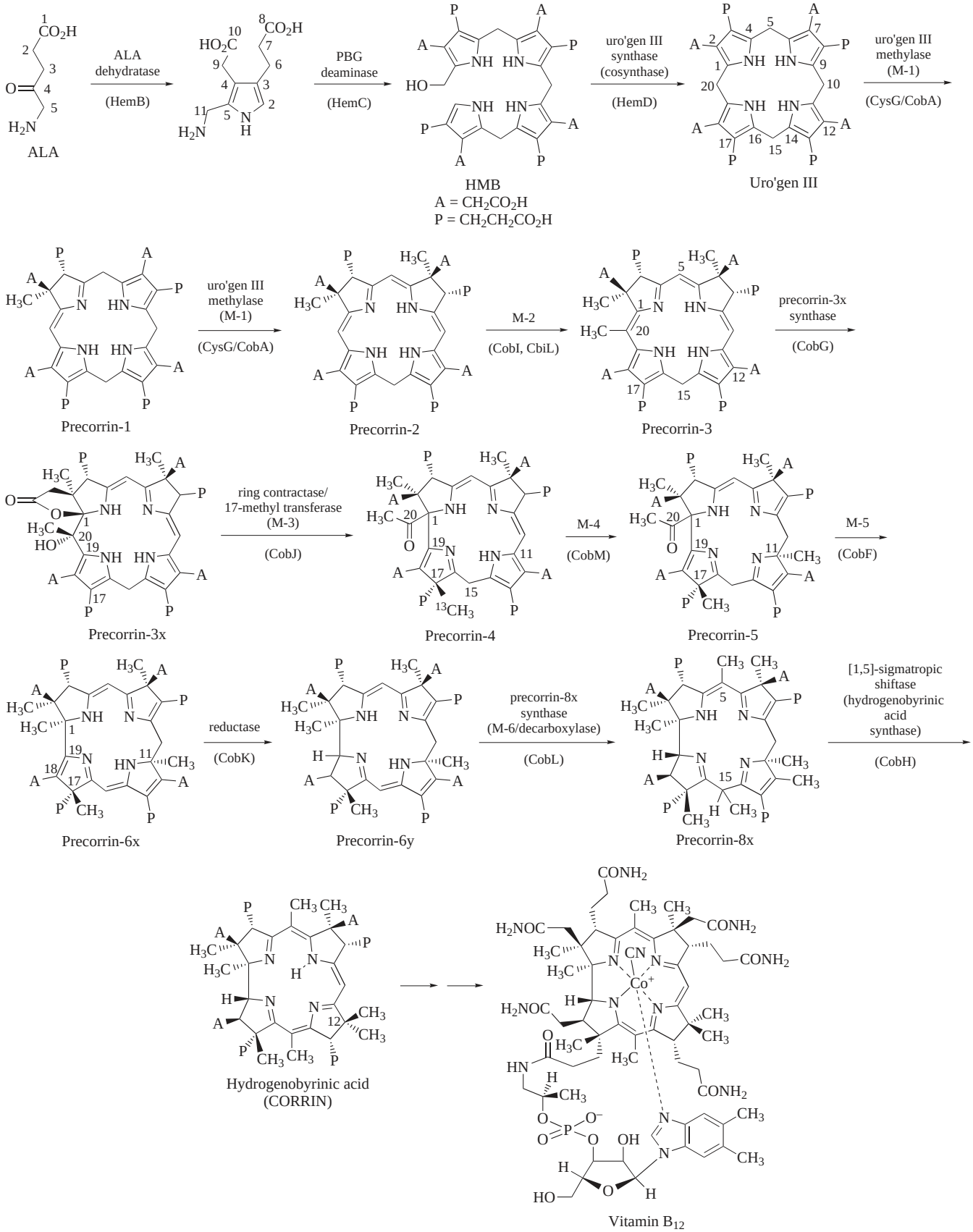
ALA
ALA dehydratase
(HemB)
PBG deaminase
(HemC)
HMB
A = CH2CO2H
P = CH2CH2CO2H
uro'gen III synthase (cosynthase)
(HemD)
Uro'gen III
uro'gen III methylase (M-1)
(CysG/CobA)
Precorrin-1
Precorrin-2
M-2
(CobI, CbiL)
Precorrin-3
precorrin-3x synthase
(CobG)
Precorrin-3x
ring contractase/ 17-methyl transferase (M-3)
(CobJ)
Precorrin-4
M-4
(CobM)
Precorrin-5
M-5
(CobF)
Precorrin-6x
reductase
(CobK)
Precorrin-6y
precorrin-8x synthase (M-6/decarboxylase)
(CobL)
Precorrin-8x
[1,5]-sigmatropic shiftase (hydrogenobyrinic acid synthase)
(CobH)
Hydrogenobyrinic acid (CORRIN)
Vitamin B12

Scheme 1

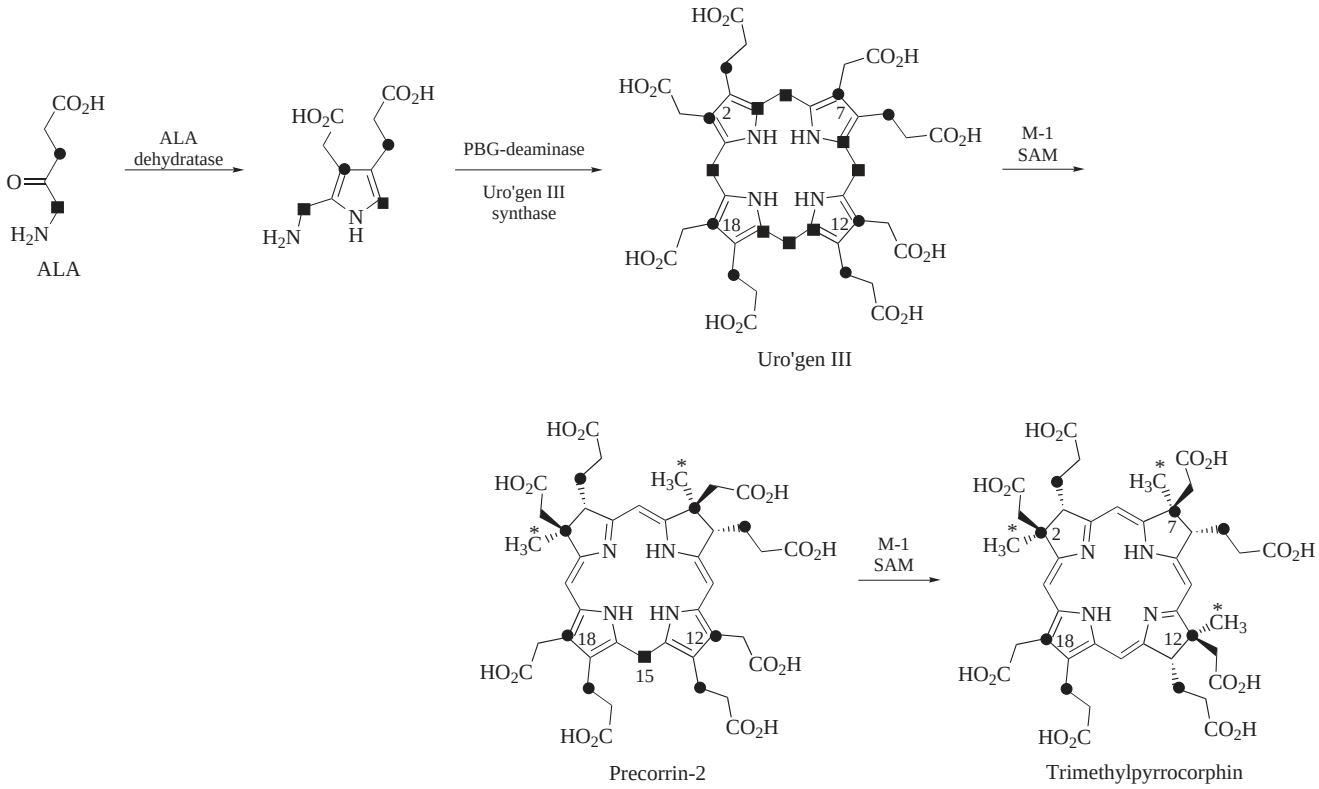

Scheme 2

in *P. denitrificans* each enzyme in turn was tested with precorrin-3 as substrate, and it was found that CobG[7] serves as an O_2-dependent enzyme whose role is to install oxygen-derived functionality at C-20, thus preparing the macrocycle for ring contraction. Remarkably, the resultant spring-loaded mechanism *does not operate until after the fourth C-methylation has occurred at C-17*, an event that is mediated by CobJ,[7] a SAM-requiring enzyme, thereby defining both the ring contraction and C-17 methylation sequences.

The NMR assays for the activities of CobG and J were developed as follows. First, precorrin-3 was prepared in two ^{13}C-isotopomeric versions—A, from [^{13}C-4](●)-, and B, from [^{13}C-5](■)-5-aminolevulinic acid, using the multienzyme synthesis described earlier,[8] as shown in Scheme 3. The reaction of isotopomer A (●) with CobG in the presence of O_2 and NADH resulted in a spectrum almost identical with that of the substrate except for the disappearance of the signal (●) for C-1 at δ = 146 ppm and the appearance of a peak (●) at δ = 106 ppm corresponding to sp^3 geometry and a new environment at C-1. When isotopomer B (■) served as substrate, the pattern of NMR signals remained constant, except for the resonance for C-20 (at δ = 103 ppm), which was replaced by a signal at δ = 78 ppm corresponding to oxygen insertion and resultant sp^3 hybridization at this center. In a separate experiment using precorrin-3 enriched at the C-20 methyl, the CH_3 signal (*) at C-20 (δ = 17.6 ppm) in precorrin-3 underwent a high-frequency shift to δ = 25 ppm during incubation with CobG. The above spectral changes are in accord with the addition of oxygen at both positions 1 and 20, and together with the observation by infrared spectroscopy of a γ-lactone (1799 cm^{-1}), lead to the structural proposal for the new product, precorrin-3x (Scheme 3), whose formation can be rationalized by epoxidation at C-1,20 by the O_2-dependent CobG enzyme, followed by participation of the ring A carboxylate in a lactonization-ring opening sequence. In the absence of O_2, no reaction of precorrin-3 with CobG was observed.[9]

Next, addition of SAM and, in turn, each of the remaining putative methyl transferases in the *P. denitrificans* repertoire (CobF, J, M) to precorrin-3x labeled from [4-^{13}C]ALA (●) resulted in a new signal for C-17 (δ = 66 ppm) corresponding to C-methylation at this center, *only when CobJ was present*. Confirmation that C-17 is indeed the site of the fourth methyl insertion came from double labeled incubation of isotopomer A (●) and $^{13}CH_3$-SAM (*) in the presence of *both* CobG and J. In this experiment, the new CH_3 signal (*) appearing at δ = 22.5 ppm was coupled (J = 37 Hz) to the C-17 resonance (●;δ = 66 ppm) (Scheme 3). Most significantly, the ^{13}C NMR spectrum of the new precorrin-4 also displays a pair of coupled carbons C-1, C-19 (δ = 82, 142 ppm, J = 52 Hz), showing that ring contraction occurs during incubation with CobJ. When the two-enzyme incubation was repeated using isotopomer B (■), the signal for C-20 in the product appeared at δ = 210 ppm, indicating that ring contraction is accompanied by the genesis of a new methyl ketone function pendant from C-1, by a process that corresponds formally to the pinacol-type rearrangement illustrated in Scheme 3. Analysis of the full set of spectral data (NMR, FAB MS, and FT IR) leaves no doubt that the new isolate is precorrin-4,[7,10] the long-sought tetramethylated intermediate of corrin biosynthesis.

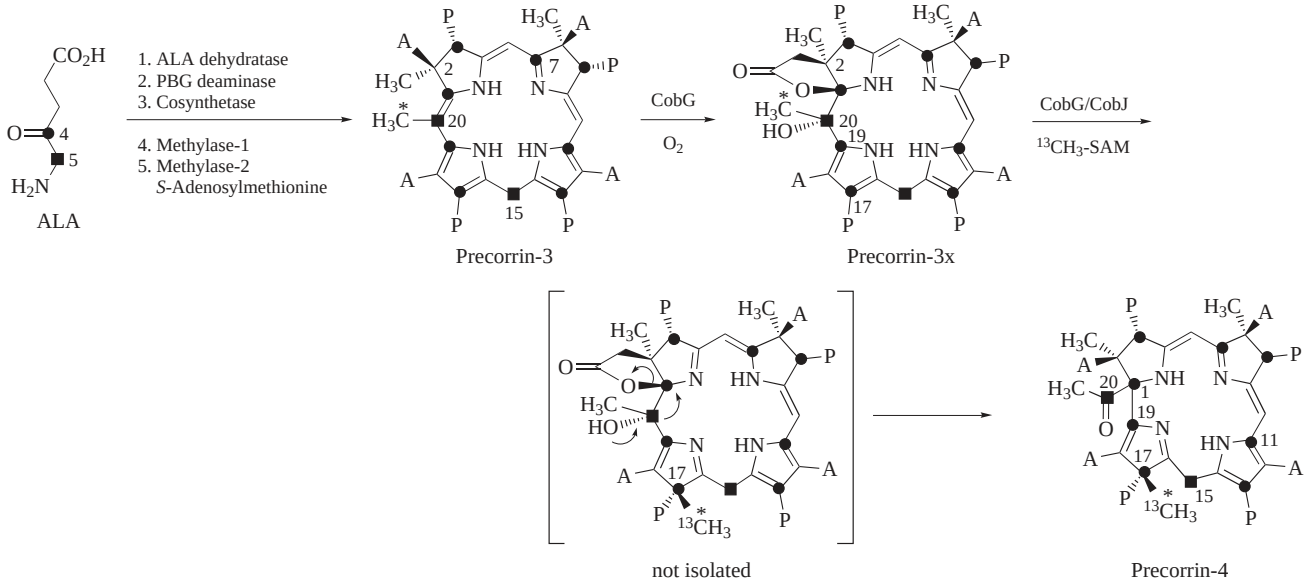

●■ = ^{13}C label (selected sites only shown for■)

Scheme 3

It is of considerable interest for the evolution of vitamin B_{12} synthesis that Nature should use both a 'modern' aerobic pathway (i.e., less than 2×10^9 years old) involving metal-free substrates for most of the way (Scheme 1), as well as the ancient, anaerobic sequence (dating to about 3.8×10^9 years) in which cobalt is inserted very early,[11] implying a corresponding dichotomy of the mechanism of ring contraction, in which O_2 is replaced in the metallo system by a two-electron valency change. Thus, the cobalt complex of precorrin-3x could be reached in the *Salmonella typhimurium* and *P. shermanii* series via internal redox of Co(III) → Co(I), which is formally equivalent to a two-electron oxidation of the ligand.

The discovery of the ring contractase system (CobG and CobJ) and the fourth methylating enzyme for C-17 (CobJ) (Scheme 3) reveals the way in which aerobic corrin biosynthesis uses an early oxidative ring contraction step concomitant with C-17 methylation on the β (upper) face of the substrate, precorrin-3x, leaving only the enzymes mediating the fifth (C-11) and sixth (C-1) C-methylation steps to be found. These have been identified recently[12] as CobM, which produces another new intermediate, precorrin-5 (step 8 in Scheme 1), and CobF (step 9), respectively. CobF was found to be the C-1 methyl transferase catalyzing both the insertion of the sixth methyl group in precorrin-5 and deacetylation at C-1 to reach precorrin-6x;. The route from precorrin-6x to (cobalt-free) hydrogenobyrinic acid (Scheme 1) has recently been described at the enzyme level,[13] so that almost every intermediate in the aerobic pathway has now been identified by NMR spectroscopy, and all of the functions necessary for corrin biosynthesis assigned in *P. denitrificans*. There now remains the experimentally challenging problem of analyzing the parallel, yet distinct, pathway in *S. typhimurium* and *P. shermanii*, for in these organisms the gene products are handling substrates in the form of cobalt complexes whose valency changes are believed to be at the heart of the mechanism of ring contraction in these anaerobic bacteria.[11]

It took an enormous international effort by Shemin, Scott (USA), Bykhovsky (Russia), Müller (Germany), Battersby (UK), and Arigoni (Switzerland) nearly 20 years to build the 'library' of the first seven intermediates,[1] yet, thanks to recombinant DNA technology, the remaining six structures (Scheme 1) have been discovered in the last three years—all of them determined by biosynthetic enrichment from ^{13}C-ALA and $^{13}CH_3$-SAM.

4 RELATED ARTICLES

Biosynthesis and Metabolic Pathways: Carbon-13 and Nitrogen-15 NMR; Enzymatic Transformations: Isotope Probes.

5 REFERENCES

1. A. I. Scott, *Acc. Chem. Res.*, 1990, **23**, 308; A. R. Battersby, *Acc. Chem. Res.*, 1993, **26**, 15; A. I. Scott, *Angew. Chem.*, 1993, **32**, 1223; F. J. Leeper, *Nat. Prod. Rep.*, 1989, **6**, 171.
2. J. Crouzet, B. Cameron, L. Cauchois, S. Rigault, M. Rouyez, F. Blanche, D. Thibaut, and L. Debussche, *J. Bacteriol.*, 1990, **172**, 5980.
3. M. J. Warren, N. J. Stolowich, P. J. Santander, C. A. Roessner, B. A. Sowa, and A. I. Scott, *FEBS Lett.*, 1990, **261**, 76.
4. W. M. Stork, M. G. Baker, P. R. Raithby, F. J. Leeper, and A. R. Battersby, *J. Chem. Soc., Chem. Commun.*, 1985, 1294.
5. R. D. Brunt, F. J. Leeper, I. Grgurina, and A. R. Battersby, *J. Chem. Soc., Chem. Commun.*, 1989, 428.
6. A. I. Scott, M. J. Warren, C. A. Roessner, N. J. Stolowich, and P. J. Santander, *J. Chem. Soc., Chem. Commun.*, 1990, 593.
7. A. I. Scott, C. A. Roessner, N. J. Stolowich, J. B. Spencer, C. Min, and S.-I. Ozaki, *FEBS Lett.*, 1993, **331**, 105.
8. M. J. Warren, C. A. Roessner, S.-I. Ozaki, N. J. Stolowich, P. J. Santander, and A. I. Scott, *Biochemistry*, 1992, **31**, 603.

9. J. B. Spencer, N. J. Stolowich, C. A. Roessner, C. Min, and A. I. Scott, *J. Am. Chem. Soc.*, 1993, **115**, 11 610.
10. D. Thibaut, L. Debussche, D. Frechet, F. Herman, M. Vuilhorgne, and F. Blanche, *J. Chem. Soc., Chem. Commun.*, 1993, 513.
11. G. Müller, F. Zipfel, K. Hlineny, E. Savvidis, R. Hertle, U. Traub-Eberhard, A. I. Scott, H. J. Williams, N. J. Stolowich, P. J. Santander, M. J. Warren, F. Blanche, and D. Thibaut, *J. Am. Chem. Soc.*, 1991, **113**, 9891.
12. C. Min, B. P. Atshaves, C. A. Roessner, N. J. Stolowich, J. B. Spencer, and A. I. Scott, *J. Am. Chem. Soc.*, 1993, **115**, 10 380.
13. D. Thibaut, F. Kiuchi, L. Debussche, F. J. Leeper, F. Blanche, and A. R. Battersby, *J. Chem. Soc., Chem. Commun.*, 1992, 139; D. Thibaut, M. Couder, A. Famechon, L. Debussche, B. Cameron, J. Crouzet, and F. Blanche, *J. Bacteriol*, 1992, **174**, 1043.

Biographical Sketch

A. Ian Scott. *b* 1928. B.Sc., 1949, Ph.D., 1952, D.Sc., 1963, M.A.(Hon.), Yale University, 1968. Lecturer, Glasgow University, 1957–62; Professor, University of British Columbia, 1962–65, University of Sussex, 1965–68, and Yale University, 1968–77. Davidson Professor of Science and Distinguished Professor of Chemistry and Biochemistry, Texas A&M University, 1981–present. Director of Center for Biological NMR, 1982–present. Three books, 1 patent, and approx. 320 publications. Research specialties: natural product bio-synthesis and NMR spectroscopy.

Accuracy Limitations on Internuclear Distances Measured by REDOR

Akira Naito

Yokohama National University, Yokohama, Japan

&

Hazime Saitô

Himeji Institute of Technology, Kamigori, Japan

1	Introduction	1
2	Theoretical Background of the REDOR Experiment	1
3	Rotational Echo Amplitude Calculated by the Density Operator Approach	2
4	Separation of S–I Distances from a S_m–I_n Multiple Spin System	2
5	Tips for Obtaining Accurate Interatomic Distances by REDOR Experiment	4
6	Natural Abundance ^{13}C REDOR Experiment	5
7	Accuracy Limit for REDOR Structure of Peptide and Proteins	6
8	Conclusions	8
9	Related Articles in Volumes 1–8	9
10	References	9

1 INTRODUCTION

In principle, accurate interatomic distances can be evaluated from careful analysis of specific dipolar interactions that were normally sacrificed under the condition of high power decoupling and magic angle spinning (MAS) techniques. A number of methods to recouple a single pair of dipolar interaction among homo and hetero nuclear spin pairs under the magic angle spinning condition have been proposed for determining the interatomic distances.[1–10] These distances have been used as constraints to determine the three-dimensional (3D) structure of peptides and proteins.[11–16] Rotational Echo DOuble Resonance (REDOR) was explored to recouple the relatively weak heteronuclear dipolar interactions under the MAS condition by applying a π pulse synchronously with the rotor period.[8,9] Consequently, the transverse magnetization cannot be refocused completely at the end of the rotor cycle, leading to a reduction of the echo amplitude. The extent of the reduction of the echo amplitude as a function of the number of rotor periods depends on the strength of the heteronuclear dipolar interaction. This method is extensively used to determine the relatively remote interatomic distance of 2–8 Å. When a number of isolated pairs are involved in a REDOR dephasing, the REDOR transformation could be useful in determining interatomic distances because it yields single peaks against distance axis for each heteronuclear coupling strength.[17,18] This approach is, however, not applicable for the case where the observed nuclei in REDOR are coupled with multiple nuclei.

It turned out that determination of accurate interatomic distances ($\pm$0.1 Å) is a prerequisite to arrive at a unique 3D structure of peptides and proteins.[15,16] It is emphasized that the distance measurement by REDOR is the only available means to satisfy this condition among the many kinds of proposed procedures mentioned above in view of the achieved accuracy and precision. Nevertheless, it is important to bear in mind that every possible effort to achieve the distance measurement with ultimate accuracy is essential to any possible applications. This is because any measurement based on the peak-intensity is susceptible to unexpected errors, which are not easy to check. After brief survey, tips to avoid this problem will be discussed in detail.

2 THEORETICAL BACKGROUND OF THE REDOR EXPERIMENT[8]

Transverse magnetization that precesses about the static magnetic field due to the dipolar interaction under the MAS condition moves back to the same direction at every rotor period because the integration of ω_D over one rotor period is zero. Consequently, the rotational echo signals are refocused at every rotor period. When a π pulse is applied to the I nucleus (Figure 1), which is coupled with the S nucleus, in one rotor period, this pulse plays a role to invert the precession direction of the magnetization of the observed S nucleus. Consequently, the magnetization vector of the S nucleus cannot move back to the same direction after one rotor period. Therefore the amplitude of the echo intensity decreases.

The extent of the reduction of the rotational echo amplitude yields the interatomic distances. To evaluate the REDOR echo amplitude theoretically, one has to consider the average precession frequency in the presence of the π pulse at the center of the rotor period over one rotor cycle as follows:

$$\overline{\omega_D(\alpha,\beta)} = \pm\frac{1}{Tr}\left[\int_0^{Tr/2}\omega_D dt - \int_{Tr/2}^{Tr}\omega_D dt\right] = \pm\frac{D}{\pi}\sqrt{2}\sin 2\beta\sin\alpha \quad (1)$$

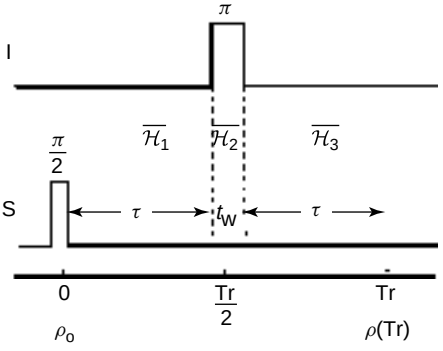

Figure 1 Pulse sequence and timing chart of REDOR experiment

where α is the azimuthal angle and β is the polar angle defined by the internuclear vector with respect to the rotor axis. Therefore, the phase angle, $\Delta\Phi(\alpha, \beta)$ for the Nc rotor cycle can be given by

$$\Delta\Phi(\alpha, \beta) = \overline{\omega_{\mathrm{D}}(\alpha, \beta)}\mathrm{NcTr} \tag{2}$$

where Tr is the rotor period. Finally, the echo amplitude can be obtained by averaging over every orientations as follows

$$S_{\mathrm{f}} = \frac{1}{4\pi}\int_{\alpha}\int_{\beta} cos[\Delta\varphi(\alpha, \beta)]\,\mathrm{d}\alpha \sin\beta\,\mathrm{d}\beta \tag{3}$$

Therefore, the normalized echo difference, $\Delta S/S_{\mathrm{o}}$, can be given by

$$\frac{\Delta S}{S_{\mathrm{o}}} = \frac{S_{\mathrm{o}} - S_{\mathrm{f}}}{S_{\mathrm{o}}} = 1 - S_{\mathrm{f}} \tag{4}$$

Experimentally, REDOR and full echo spectra are acquired for a variety of NcTr values and the respective REDOR (S_{f}) and full echo (S_{o}) amplitudes are evaluated.

3 ROTATIONAL ECHO AMPLITUDE CALCULATED BY THE DENSITY OPERATOR APPROACH[15]

The REDOR echo amplitude can be evaluated more rigorously by using density matrix operators and for the REDOR experiment. The time evolution of density operator, ρ_{o}, under the heteronuclear dipolar interaction during one rotor period, can be considered by taking the pulse length into account. The average Hamiltonian in the rotating frame over one rotor period can be given by

$$\begin{aligned}
\overline{\mathcal{H}} &= \frac{1}{\mathrm{Tr}}\left[\overline{\mathcal{H}_1(t)}\tau + \overline{\mathcal{H}_2(t)}\tau + \overline{\mathcal{H}_3(t)}\tau\right] \\
&= \frac{\mathrm{D}}{4\pi}\Big\{\sin^2\beta[\sin(2\alpha + \omega_{\mathrm{r}}t_{\mathrm{w}}) + \sin(2\alpha - \omega_{\mathrm{r}}t_{\mathrm{w}}) - 2\sin 2\alpha] \\
&\quad - 2\sqrt{2}\sin 2\beta\left[\sin\left(\alpha + \frac{1}{2}\omega_{\mathrm{r}}t_{\mathrm{w}}\right) + \sin\left(\alpha - \frac{1}{2}\omega_{\mathrm{r}}t_{\mathrm{w}}\right) + 2\sin 2\alpha\right] \\
&\quad - \sin^2\beta\,[\sin(2\alpha + \omega_{\mathrm{r}}t_{\mathrm{w}}) + \sin(2\alpha - \omega_{\mathrm{r}}t_{\mathrm{w}})]\,\frac{4\omega_{\mathrm{r}}^2 t_{\mathrm{w}}^2}{4\omega_{\mathrm{r}}^2 t_{\mathrm{w}}^2 - \pi^2} \\
&\quad + \sqrt{2}\sin 2\beta\left[\sin\left(\alpha + \frac{1}{2}\omega_{\mathrm{r}}t_{\mathrm{w}}\right) + \sin\left(\alpha - \frac{1}{2}\omega_{\mathrm{r}}t_{\mathrm{w}}\right)\right] \\
&\quad \times \frac{2\omega_{\mathrm{r}}^2 t_{\mathrm{w}}^2}{\omega_{\mathrm{r}}^2 t_{\mathrm{w}}^2 - \pi^2}\Big\}\hat{I}_Z\hat{S}_Z \\
&\quad + \frac{\mathrm{D}}{4\pi}\Big\{\sin^2\beta[\cos(2\alpha + \omega_{\mathrm{r}}t_{\mathrm{w}}) + \cos(2\alpha - \omega_{\mathrm{r}}t_{\mathrm{w}})] \\
&\quad \times \frac{2\pi\omega_{\mathrm{r}}t_{\mathrm{w}}}{4\omega_{\mathrm{r}}^2 t_{\mathrm{w}}^2 - \pi^2} \\
&\quad - \sqrt{2}\sin 2\beta\left[\cos\left(\alpha + \frac{1}{2}\omega_{\mathrm{r}}t_{\mathrm{w}}\right) + \cos\left(\alpha - \frac{1}{2}\omega_{\mathrm{r}}t_{\mathrm{w}}\right)\right] \\
&\quad \times \frac{2\pi\omega_{\mathrm{r}}t_{\mathrm{w}}}{\omega_{\mathrm{r}}^2 t_{\mathrm{w}}^2 - \pi^2}\Big\}\hat{I}_Z\hat{S}_Y \\
&= a\hat{I}_Z\hat{S}_Z + b\hat{I}_Z\hat{S}_Y
\end{aligned} \tag{5}$$

where ω_{r} is the angular velocity of the rotor and t_{w} is the duration of π pulse. $\overline{\mathcal{H}_1(t)}$, $\overline{\mathcal{H}_2(t)}$, and $\overline{\mathcal{H}_3(t)}$ are the average Hamiltonians corresponding to the period shown in Figure 1. Pulse length, t_{w}, is also considered in the calculations for the analysis of the REDOR results. The density operator, ρ (Tr), at Tr after evolution under the average Hamiltonian can be calculated as

$$\rho(\mathrm{Tr}) = \exp(-i\overline{\mathcal{H}}\mathrm{Tr})\rho_{\mathrm{o}}\exp(i\overline{\mathcal{H}}\mathrm{Tr}) \tag{6}$$

where ρ_{o} is considered to be $\hat{I}y$ after the contact pulse. Then finally the transverse magnetization at Tr can be given by

$$\begin{aligned}
\langle\hat{I}y(\mathrm{Tr})\rangle &= \mathrm{Tr}\{\rho(\mathrm{Tr})\hat{I}y\} \\
&= \cos\left(\frac{1}{2}\sqrt{a^2 + b^2}\mathrm{Tr}\right)
\end{aligned} \tag{7}$$

Echo amplitude in the powder sample can be calculated by averaging over every orientation as follows

$$S_{\mathrm{f}} = \frac{1}{4\pi}\int_{\alpha}\int_{\beta}\langle\hat{I}y(\mathrm{Tr})\rangle\sin\beta\,\mathrm{d}\beta\,\mathrm{d}\alpha \tag{8}$$

Therefore, the normalized echo difference, $\Delta S/S_{\mathrm{o}}$, can be given by equation (4). When the length of t_{w} is zero, equation (7) can be simplified as follows:

$$\langle\hat{I}y(\mathrm{Tr})\rangle = \cos\left(\frac{D}{\pi}\sqrt{2}\sin 2\beta\sin\alpha\mathrm{Tr}\right) \tag{9}$$

In this case, equation (8) is equivalent to equation (3) in the case of $\mathrm{Nc} = 1$.

4 SEPARATION OF S–I DISTANCES FROM A S_m–I_n MULTIPLE SPIN SYSTEM

It should be taken into account that a spin system for a doubly labeled sample should be generally treated as a multiple spin system (S–I_n system) as shown in Figure 2(a) in which S^* is the observed nuclei and the recoupling pulse is applied to the I^* nuclei. The ideal S–I system is available only when the doubly labeled preparation is infinitely diluted with unlabeled preparation. In contrast, uniformly and singly labeled preparations are treated as S_m–I_n and S–I_n systems, respectively (Figure 2b,c), although S^* in the latter is S nuclei of natural abundance. For this reason, it is advisable to utilize a variety of isotopically doubly labeled samples in order to obtain respective interatomic distances, although it is too laborious to make so many kinds of preparations. In fact, we made six kinds of doubly labeled preparations to determine the 3D structure of the pentapeptide, Leu-enkephalin.[16] In addition, it is essential to make certain that all such preparations take the same polymorphic structure, because crystalline peptides or proteins under consideration may take different kinds of polymorphs depending on condition for crystallization, pH, temperature, etc.[15,16] The most convenient way to check this problem is to use the conformation-dependent ^{13}C chemical shifts,

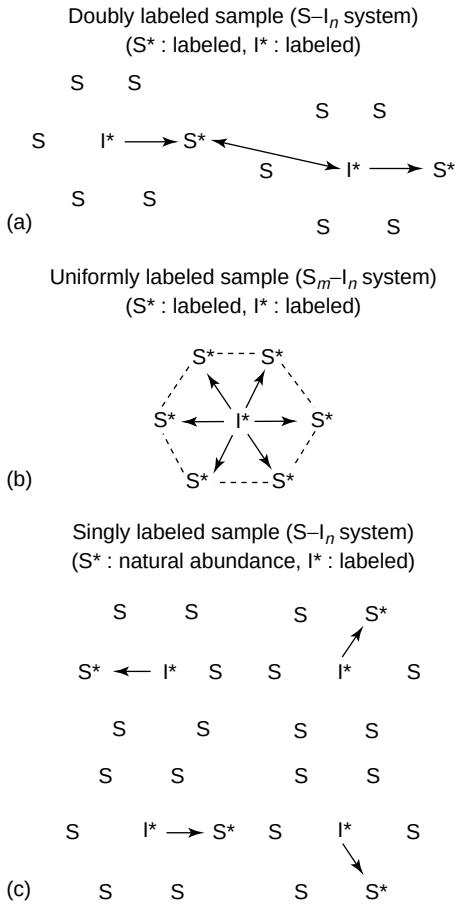

Figure 2 Schematic representation of multiple spin systems for (a) doubly labeled, (b) uniformly labeled and (c) singly labeled samples

which are very sensitive to the presence of such polymorphic structure.[15,16,19]

In this connection, use of a uniformly labeled sample seems to be more attractive both for the sample preparation and also to avoid the problem of polymorphs.[20] This view turned out to be not always true, however, because separation of a particular S–I interaction from S$_m$–I$_n$ spin systems, consisting of many homo- and heteronuclear dipolar and scalar interactions, is not always as straightforward as anticipated. In practice, all of the following conditions should be taken into account to determine the accurate interatomic distances of a particular spin pair from the uniformly labeled samples. First, J coupling among the observed S nuclei should be removed to reduce the phase twist due to the coherent evolution by J coupling, when its magnitude is comparable to the dipolar coupling, as illustrated for uniformly [^{15}N, ^{13}C]-labeled ammonium L-glutamate monohydrate at NcTr = 8 ms (Figure 3).[21,28] This phase twist can be removed by using a shaped pulse as a Z-filter instead of a π pulse at the center position of the REDOR evolution period.[21] Second, the linewidths of individual signals might be broadened due to strong homonuclear dipolar interaction with neighboring S nuclei, which should be eliminated by homonuclear decoupling pulses.[22] Thus, in the case of a uniformly labeled sample, combination of both homonuclear dipolar and scalar decoupling is required to simplify the S$_m$–I$_n$ to S–I$_n$ spin system. Third, relatively shortened transverse relaxation times (T_2), due to residual dipolar interactions, reduce the

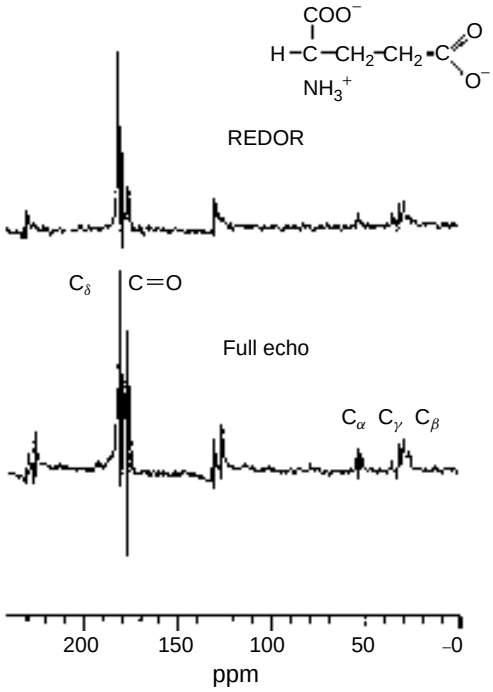

Figure 3 ^{13}C-REDOR and full echo spectra at NcTr = 8 ms for crystalline uniformly labeled ammonium [^{15}N]L-glutamate monohydrate

transverse magnetization during the dipolar recoupling period in REDOR experiments. This makes it difficult to observe the REDOR effect for the nuclei with relatively long internuclear distances, because it is required to measure relatively long evolution times to observe slow dephasing of the REDOR signals. Fourth, REDOR factors against the dipolar evolution time should be analyzed using multiply coupled S–I$_n$ spin systems rather than an isolated two-spin system under the condition of homonuclear decoupling.[23–26] Accordingly, the four kinds of obstacles mentioned above should be removed to determine a set of accurate interatomic distances simultaneously for a uniformly labeled sample.

Gullion et al.[27] proposed a θ-REDOR as an approach to determine the individual interatomic distance in a uniformly labeled sample by dividing S–I$_n$ spin system into 'n' number of isolated S–I two-spin systems. This makes the REDOR analysis simple and allows one to use the REDOR transformation to obtain the dipolar coupling frequencies of individual S–I spin couplings, although this method is not always easy to apply for measurement of a relatively long interatomic distance. Alternatively, homonuclear and scalar interactions are completely removed when natural abundant ^{13}C REDOR experiments were performed.[28] This approach provides an excellent means to determine the interatomic distances for a number of isolated spin pairs simultaneously under condition of high resolution (Figure 2c). Further, it is emphasized that this approach is free from the problem of the above-mentioned shortened T_2 values due to homonuclear ^{13}C spin interactions. However, a multiple coupled spin system, ^{13}C–^{15}N$_n$, has still to be explicitly considered, because the intermolecular dipolar interactions cannot be neglected for a small molecule. In practice, we have recently demonstrated that accurate interatomic distances can be determined by analyzing intramolecular and

intermolecular dipolar contributions based on root mean square deviation (RMSD) between the theoretically and experimentally obtained REDOR factors.[28]

5 TIPS FOR OBTAINING ACCURATE INTERATOMIC DISTANCES BY REDOR EXPERIMENT

It is emphasized that determination of interatomic distances accurate to 0.1 Å is a prerequisite to arrive at a unique solution of the three-dimensional structure of peptides, proteins, etc. A careful evaluation of the following points are the most important steps to obtain reliable interatomic distances by the REDOR experiment, although they have not always been seriously taken into account in a number of papers so far published.

5.1 The Finite Pulse Length and Fluctuation of RF Power

This effect is experimentally observed and calculated using equation (8) as shown in Figure 4. The REDOR parameter, $\Delta S/S_o$, as measured for 20% [1 − ^{13}C, ^{15}N]Gly($r_{CN} = 2.48$ Å) is plotted for the lengths of the ^{15}N π pulse of 13.0 μs for the experiment and 24.6 μs (chosen to satisfy 10% rotor cycle) as a function of NcTr with the calculated lines using the π pulse

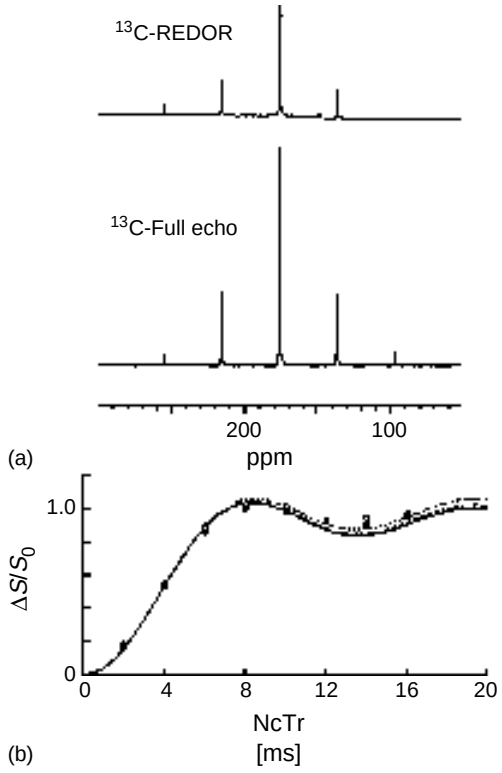

Figure 4 ^{13}C REDOR and full echo spectra of [1-^{13}C, ^{15}N]glycine as recorded by the rotor frequency of 4000 Hz and NcTr of 4 ms (a) and plots of the $\Delta S/S_o$ vs. NcTr (b). Solid and open circles denote the experimental points recorded using a ^{15}N π-pulse of 13.0 and 24.6 μs, respectively. Solid, broken and dotted lines are calculated using the π-pulses of δ, 13.0 and 24.6 μs, respectively, together with the C–N interatomic distance of 2.48 Å[15]

length and finite lengths (13.0 and 24.6 μs) of the π pulse. It turns out, however, that the finite length of the ^{15}N π pulse does not significantly affect the REDOR effect provided that the pulse length is less than 10% of the rotor cycle at the rotor frequency of 4000 Hz. This effect, however, should be seriously taken into account if fast MAS, e.g., 40 kHz is used.

For most spectrometers, it is difficult to be free from fluctuations of RF power during the acquisition of REDOR experiments. It is, therefore, critical that RF power be stabilized. If not, the π pulse will vary in length. Consequently, the REDOR factor is greatly decreased to yield relatively longer interatomic distances. Compensation of instability of such RF power, e.g., by approximate pulse sequence is, therefore, necessary to be free from long term fluctuations of amplifiers. xy-4 and xy-8 pulse sequences have been developed for this purpose. The xy-8 pulse is known to be the best sequence to compensate for the fluctuation of the RF power.[29]

5.2 Contribution from Natural Abundance Nuclei

Since the early stages of the REDOR experiment, contributions from natural abundance nuclei have been seriously considered as a major source of error in the distance measurement.[30] It appears that the observed dipolar interaction can be modified by the presence of such neighboring naturally abundant nuclei. This effect was originally taken into account by simply calculating the $\Delta S/S_o$ value for two isolated pairs and adding proportionally to the natural abundant fraction.[30] Careful analysis of the three-spin system, however, indicates that this sort of simple addition of the fraction of the two-spin system may result in a serious overestimate of the natural abundance effect, to yield shorter distances.[23] The most accurate way to consider the natural abundance effect is, therefore, to treat the whole spin system as a three-spin system by taking into account the neighboring carbons in addition to the labeled pair. In practice, contributions from naturally abundant nuclei can be ignored for ^{13}C REDOR but not for ^{15}N REDOR, because the proportion of naturally abundant ^{13}C nuclei is much higher than that of the ^{15}N nuclei.[23]

5.3 Sample Dilution

^{13}C, ^{15}N-doubly labeled samples are usually used in the REDOR experiment to determine the interatomic distances between the labeled nuclei. More importantly, the dipolar interaction with the labeled ^{15}N nuclei for the neighboring molecules should be taken into account as an additional factor to contribute to the dipolar interaction of the observed pair under consideration. This contribution could be serious when the observed distance is quite remote, because there are many contributions from nearby nuclei. This effect can be completely removed by diluting the labeled sample with a sample of naturally abundant molecules.[23] The sensitivity of the signals, however, has to be sacrificed if one wants to remove the effect completely as the sample must be diluted to 1/49 so that the signal intensity is reduced by a factor roughly 0.02.[11] Instead, it is advised to evaluate the REDOR factors at the infinitely diluted condition by extrapolating the data by stepwise dilution of the sample (i.e., 60%, 30%, etc.) without losing sensitivity, because a linear relationship between the REDOR factor and the dilution is ascertained by a theoretical consideration.[23] Alternatively, the observed plots of $\Delta S/S_o$ values against the

corresponding NcTr values for the sample without dilution can be fitted by a theoretical curve obtained from the dipolar interactions among three-spin systems, although the accuracy is not always improved to the level of the dilution experiment.

5.4 T_2 Effect

The transverse magnetization of the REDOR experiment decays as a function of the ^{1}H decoupling field.[31,32] Under appropriate conditions, molecular motion may interfere with dipolar decoupling. This occurs when molecular motion, if any, exists when the motional frequency is of the same order of magnitude as the decoupling field, and hence the transverse relaxation times (T_2) are significantly shortened. In fact, it was found that the T_2 values of the carbonyl carbons in crystalline Leu-enkephalin are relatively short because of the presence of backbone motion.[33] This is a serious problem for the REDOR experiment, especially for the long distance pairs, because the S/N ratio is significantly deteriorated. In this case, it is required to measure the ^{13}C REDOR signal under a sufficiently strong decoupling field to elongate the transverse relaxation times. It is also useful to perform measurements at low temperature so as to reduce the motional frequency. Note, however, that crystalline phase transitions might be associated together with the freezing of the solvent molecules. This effect has been observed in a variety of enkephalin samples.[34,35]

5.5 RF Inhomogeneity and Confinement of the Sample within RF Coil

In the commercial spectrometer, the rotor is designed to allow the sample volume to be as large as possible in order to gain better sensitivity. Obviously, this arrangement causes H_1 inhomogeneity, which results in a broad distribution of the lengths of the 90° pulses. This problem is serious for the REDOR experiment in which a number of π pulses are applied. As a result, the pulse error can accumulate during the acquisition to give serious error in the measurements of internuclear distances. Particularly, the samples located at the top or bottom part of the sample rotor feel quite a weak RF field. This causes a great reduction of the REDOR factor for a sample that is filled all the way along the sample rotor.[15] This effect should be seriously taken into account prior to experiments with a commercial spectrometer. It is, therefore, strongly recommended to fill the sample only in the central part of the coil just like a multiple pulse experiment to be able to acquire as accurate interatomic distances as possible in the REDOR experiment.

5.6 Standard Sample

All of the considerations mentioned above are essential to achieve accurate interatomic distances. Nevertheless, it is also possible that accuracy may deteriorate even if one of the conditions is not satisfied for every possible measurement. It is therefore advisable to determine the interatomic distances from a standard sample, in order to check that all the conditions are satisfied. More preferentially, use of two standard samples for short and long distances is recommended. In practice, it is recommended to use [1-^{13}C, ^{15}N]glycine as the former standard sample whose C–N interatomic distance is determined as 2.48 Å by a neutron diffraction study, and to check that all the instrumental conditions of a given spectrometer are satisfied prior to every new experiment. As a second standard sample for long distance, it is recommended to use [^{13}C, ^{15}N]*N*-acetyl-Pro-Gly-Phe (Table 1). This crystalline peptide is very stable with relatively long T_2 values, because it does not contain solvent molecules, and the presence of two polymorphic structures is well characterized.[15]

6 NATURAL ABUNDANCE ^{13}C REDOR EXPERIMENT[28]

As mentioned already, it is impossible to obtain meaningful interatomic distances from a uniformly labeled sample as far as the standard REDOR procedure is concerned. Instead, the natural abundance REDOR experiment is more preferable as a means free from both homonuclear dipolar and scalar interactions (Figure 3). This approach provides the interatomic distances for a number of isolated spin pairs simultaneously under high resolution conditions. Further, this approach is free from the problem of the shortened T_2 values due to homonuclear ^{13}C spin interactions. Figure 5 shows the REDOR and full echo spectra of natural abundance ^{13}C nuclei of singly ^{15}N labeled crystalline ammonium [^{15}N]L-glutamate monohydrate (I) at NcTr = 8 ms, in contrast to the twisted spectra from the same sample uniformly labeled (Figure 3). The assignment of peaks to the C_β, $C\gamma$, C_α, C=O and C_δ carbon nuclei, from high to low field, is also shown in Figure 5. The C=O (176.6 ppm) peak was distinguished from the C_δ (179.5 ppm) peak as a peak yielding a stronger REDOR effect as shown in Figure 5. Similarly, the peak at 56.0 ppm was assigned to the C_α carbon nucleus that give the strongest REDOR effect among the three aliphatic ^{13}C peaks. In a similar manner, the peak at 30.5 ppm showed a stronger REDOR effect compared

Table 1 C–N interatomic distances (Å) determined from REDOR experiments as compared with those by X-ray diffraction and MD[15]

Labeled peptides	Experimental			Calculated		
	REDOR	X-Ray		Energy-minimized[a]	MD	
	Orthorhombic	Orthorhombic	Monoclinic[b]		Orthorhombic	Monoclinic
I	3.24 ± 0.05 (3.43 ± 0.05)[c]	3.19	3.76	3.17	3.22 ± 0.10	3.63 ± 0.10
II	3.43 ± 0.05 (3.66 ± 0.05)	3.35	3.21	3.57	3.32 ± 0.10	3.33 ± 0.10
III	4.07 ± 0.05 (4.45 ± 0.05)	3.99	3.91	4.17	3.92 ± 0.10	3.83 ± 0.10

[a]Energy-minimized structure based on REDOR data.
[b]Ref.[36]
[c]Data from Ref.[23] based on fully packed 7.5 mm rotor systems.

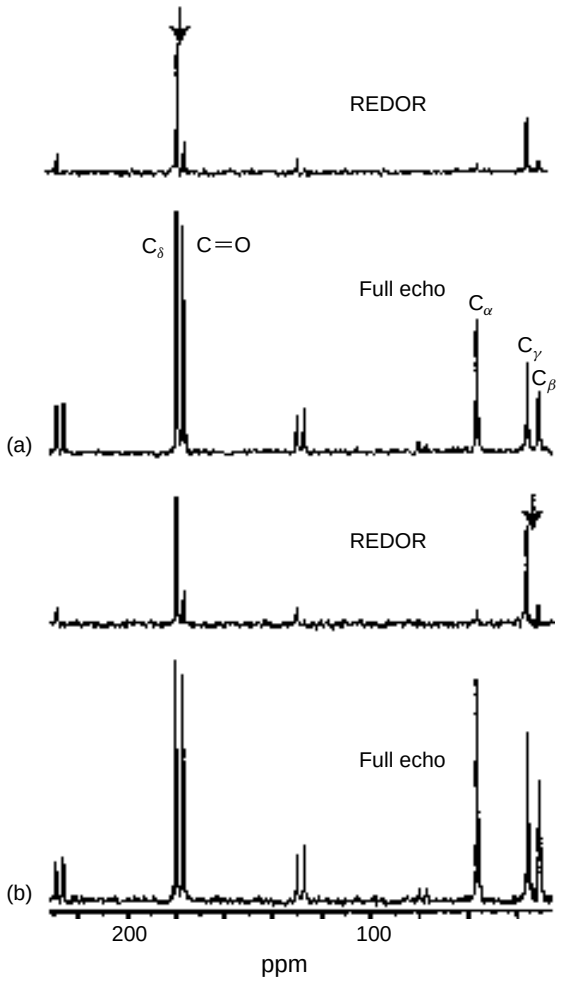

Figure 5 Naturally abundant ^{13}C-REDOR and full echo spectra at NcTr = 8 ms with two different carrier frequencies for crystalline ammonium [^{15}N]L-glutamate monohydrate. Arrows indicate carrier frequency positions at the center of (a) C=O and C_δ resonances; and (b) Cβ and C_γ resonances

with that at 35.2 ppm. Thus, the peaks at 35.2 and 30.5 ppm were assigned to the C_γ and C_β carbon nuclei, respectively.

The interatomic C–N distances between ^{15}N and ^{13}C=O, $^{13}C_\alpha$, $^{13}C_\beta$, $^{13}C_\gamma$, and $^{13}C_\delta$ carbon nuclei were determined with accuracy of 0.15 Å, after experimental conditions were carefully optimized. ^{13}C-REDOR factors for a three-spin system, $(\Delta S/S_o)_{CN1N2}$, and the sum of two isolated two-spin systems, $(\Delta S/S_o)^* = (\Delta S/S_o)_{CN1} + (\Delta S/S_o)_{CN2}$, were further evaluated by the REDOR measurements on isotopically diluted I in a controlled manner. Subsequently, the intramolecular and intermolecular C–N distances were separated by searching the minimum in the contour map of the root mean square deviation (RMSD) between the theoretically and experimentally obtained $(\Delta S/S_o)^*$ values against two interatomic distances, r_{C-N1} and r_{C-N2}. When the intramolecular C–N distance (r_{C-N1}) of the particular carbon nucleus is substantially shorter than the intermolecular distance (r_{C-N2}), C–N distances between the molecule in question and the nearest neighboring molecules can also be obtained, although accuracy is inevitably deteriorated. On the other hand, it was difficult to determine the interatomic distances in the same molecule when the intermolecular dipolar contribution is larger than the intramolecular one as in the case of the C_δ carbon nucleus.

7 ACCURACY LIMIT FOR REDOR STRUCTURE OF PEPTIDE AND PROTEINS

Naito et al.[15] systematically applied this technique to elucidate the three-dimensional structure of *N*-acetyl-Pro-Gly-Phe. They proposed that the carbonyl carbon of the (i-1)th residue and the amino nitrogen of the (i+1)th residue should be labeled with ^{13}C and ^{15}N, respectively. Namely, [1-^{13}C]*N*-acetyl-Pro-[^{15}N]Gly-Phe(I), *N*-acetyl-[1-^{13}C]Pro-Gly-[^{15}N]Phe(II) and [1-^{13}C]*N*-acetyl-Pro-Gly-[^{15}N]Phe(III) were synthesized and the resulting distances were determined to be 3.24 ± 0.05, 3.43 ± 0.05, and 4.07 ± 0.05 Å respectively, utilizing the REDOR factor obtained for the infinitely diluted state to prevent errors from the contributions of the neighboring labeled nuclei. No correction from the contribution of the naturally abundant nuclei turned out to be necessary. Surprisingly, these distances do not agree well with the values obtained from an X-ray diffraction study available when the initial part of this experiment was performed, showing the maximum discrepancy between them to be 0.5 Å.[36] This value seems to be much larger than the expected error as estimated from the precision of the REDOR experiment (±0.05 Å). The reason why the discrepancy is unexpectedly larger was explained by the fact that the crystal (orthorhombic) used for the REDOR experiments is different from that used in the X-ray diffraction study (monoclinic). To check the accuracy of the REDOR experiment, an X-ray diffraction study was performed on the same crystals used for the REDOR experiment. It was found that the distances from the new crystalline polymorph (orthorhombic) agree well between REDOR and X-ray diffraction, within an accuracy of 0.05 Å as shown in Table 1.

Conformational maps based on the possible combinations of the torsion angles of the Pro and Gly residues are calculated on the basis of the distance constraints thus obtained. Further, the difference of the chemical shifts between the C_β and C_γ carbons of the Pro residues $\Delta\beta\gamma$ was used as a constraint to determine the ψ value (−13°).[37] The φ angle of the Pro residue is in many instances restricted to −75° which shows the minimum energy in the residue. Therefore, the torsion angles of the Pro residue are uniquely determined to be (−75°, −28°). Using these torsion angles, conformational maps were again calculated. Finally two pairs of torsion angles were selected as (−112°, 48°) and (−112°, −48°). Minimization by a molecular mechanics calculation yielded the structure of the β-turn I structure, as shown in Figure 6(a). It is found that the three-dimensional structure of this peptide is well reproduced by a molecular dynamics simulation by taking into account all of the intermolecular interactions in the crystals, although a molecular dynamics calculation treating *single* molecular system does not always yield a correct picture as illustrated in Figure 6(b), unless otherwise all the molecules in a unit cell are correctly taken into account.[15,38]

Elucidation of the three dimensional structure of an opioid peptide Leu-enkephalin crystal, Tyr-Gly-Gly-Phe-Leu grown from MeOH/H_2O mixed solvent was performed by the REDOR method alone.[16] This seems to be an additional challenge for this technique to reveal the three-dimensional structure of more complicated systems. Six differently labeled

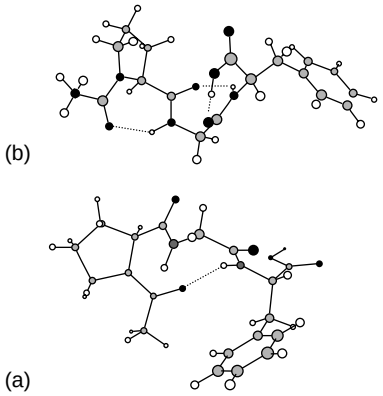

Figure 6 Optimized conformation of *N*-acetyl-Pro-Gly-Phe as obtained by the minimization of energy from the initial form as deduced from the REDOR experiment (a) and a snapshot of the conformation deduced by MD simulation in vacuo (at 100 K) (b)[15]

Leu-enkephaline molecules were synthesized and the resulting interatomic distances (Figure 7a) are accurately determined. It turns out, however, that an extremely careful experiment is required to avoid unexpected crystalline conversion among polymorphs either by dehydration from a tightly sealed rotor or a phase transition occurring at ambient temperature. In principle, pressure under MAS may shift a temperature of phase transition to some extent, because centrifugal force is proportional to the square of the spinning frequency. No significant effect, however, has been noted so far as a sample is spun at relatively low frequency such as 2−4 kHz but care might be taken when rotor is spun at a frequency one order of magnitude high as in 40 kHz.

This may be the reason why final refinement of X-ray diffraction data was abandoned in spite of the pioneering X-ray diffraction data as to the similarity of the tertiary structure between this opioid peptide and morphine.[39] Therefore, it is necessary to check whether the six differently labeled samples are all in the same crystalline polymorph by means of the ^{13}C chemical shifts. Otherwise, meaningless data can be obtained without this precaution. When the distance data are converted to yield the necessary numbers of torsion angles, a unique combination of torsion angles in the corresponding conformational map is determined sequentially as shown in Figure 7(b). It is emphasized that accuracy within 0.1 Å is essential to select unique torsion angles for each amino acid residue. Namely, if the error is larger than 0.41 Å, torsion angles can no longer be selected as shown in Figure 8.

It is also important to point out that the chemical shift data can be used as additional constraints. A three dimensional structure was thus determined as shown in Figure 9. However, this structure is not the same as that previously determined

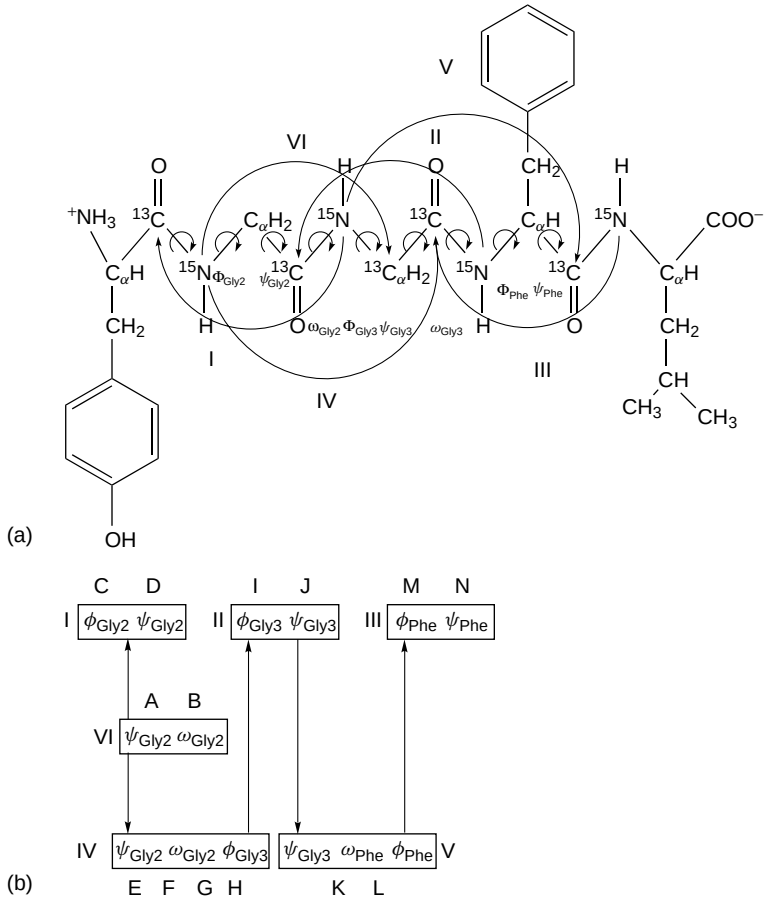

Figure 7 (a) Schematic representation between the sites of a variety of [^{13}C, ^{15}N]-doubly-labeled Leu-enkephalin dehydrates and their related torsion angles. (b) Block diagram to show how respective torsion angles are uniquely determined by the combined examinations of the conformation maps based on the distances of four-bonds apart (I, II, III and VI) and five-bonds apart (IV and V)[16]

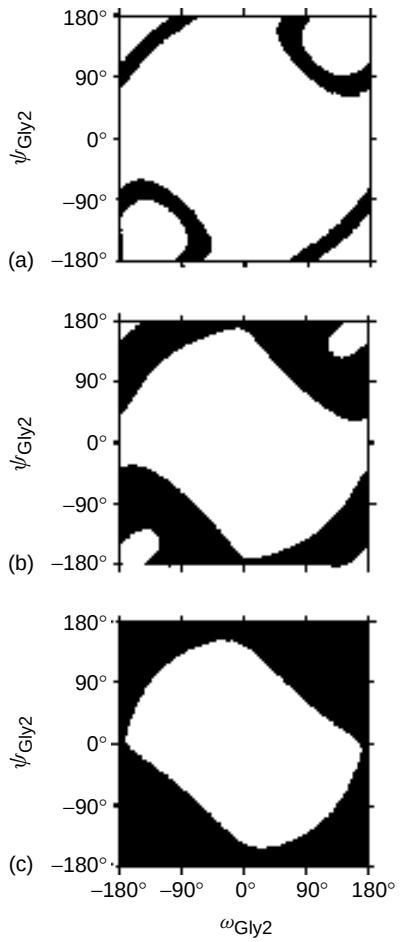

Figure 8 Conformation maps for (Ψ_{Gly2}, ω_{Gly2}) based on the interatomic distance of 4.55 Å with increased experimental errors: (a) ±0.10 Å, (b) ±0.20 Å, and (c) ±0.41 Å[16]

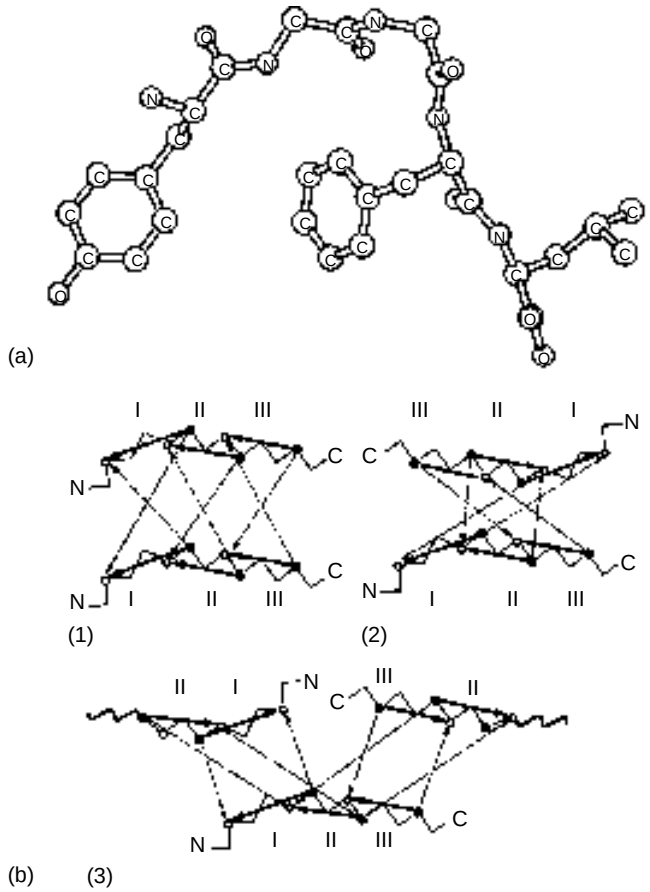

Figure 9 (a) Three-dimensional structure of Leu-enkephalin dihydrate determined uniquely by the successive application of the conformation maps as well as additional constraints of the conformation-dependent ^{13}C chemical shifts. (b) Three kinds of models for putative intermolecular packing as illustrated in the cartoons: (1) interaction through parallel β-sheet form; (2) interaction through an antiparallel β-sheet; and (3) interaction through interaction of three molecules. Solid and dotted arrows correspond with the dipolar interactions between intramolecular and intermolecular $^{13}C-^{15}N$ pairs, respectively[16]

by X-ray diffraction because one is dealing with a crystalline polymorph that is not fully explored. It is possible to figure out the molecular packing in the crystals by looking at the intermolecular dipolar contribution. Since the intermolecular dipolar contributions in I and III are larger than that of II, a β-sheet is formed as one peptide interacts with two peptides as an antiparallel β-sheet as shown in Figure 9(b).

Finally, it should be pointed out that, in order to isolate an S–I spin pair, it is essential to avoid any unnecessary errors from dipolar contributions of neighboring molecules from the overall $S-I_n$ spin system. This is generally encountered for a variety of peptides and the aforementioned dilution procedure turned out to be not required in the case of α-helical polypeptides as far as the measurement of the interatomic distance for $^{15}NH(i)\cdots O = {}^{13}C(i+4)$ is concerned.[40] This is because the interhelical dipolar contribution is found to be negligible in view of the mutual packing of α-helical chains or random mutual orientation between isotopically labeled atoms. Further, it was found that in helical peptides, due to the manner of chain packing, this kind of measurement is feasible to yield 4.5 ± 0.1 Å, without any assumptions, for a variety of transmembrane α-helical peptides in lipid bilayers to mimic a biomembrane at a temperature below liquid crystalline-gel phase transition at which rotation of such peptides about the α-helical axis turns out to be frozen, in spite of the presence of rotational motions of lipid molecules, as viewed from the observation of three principal components of ^{13}C and ^{31}P chemical shift tensors.[41] As is shown in this example, it is essential to ensure that molecular motion is reasonably ceased.

8 CONCLUSIONS

REDOR is one of the most powerful methods to determine accurate interatomic distances after taking into account a number of points in applying the method to a practical sample. Simultaneous measurement of interatomic distances using uniformly labeled samples can only be achieved by removing the homonuclear dipolar and scalar interactions. Alternatively, natural abundance ^{13}C REDOR measurements provide interatomic distances simultaneously free from homonuclear dipolar and scalar interactions. These accurate interatomic distances obtained from REDOR experiments can provide important information on structure and molecular packing of solid peptides and proteins.

9 RELATED ARTICLES IN VOLUMES 1–8

REDOR & TEDOR, Volume 6.

10 REFERENCES

1. D. P. Raleigh, M. H. Levitt, and R. G. Griffin, *Chem. Phys. Lett.*, 1988, **146**, 71.
2. M. H. Levitt, D. P. Raleigh, F. Creuzet, and R. G. Griffin, *J. Chem. Phys.*, 1990, **92**, 6347.
3. R. Tycko and G. Dabbagh, *Chem. Phys. Lett.*, 1990, **173**, 461.
4. B. -Q. Sun, P. R. Costa, D. Kocisko, P. T. Lansbury Jr., and R. G. Griffin, *J. Chem. Phys.*, 1995, **102**, 702.
5. T. Gullion and S. Vega, *Chem. Phys. Lett.*, 1992, **194**, 423.
6. A. E. Bennett, J. H. Ok, R. G. Griffin, and S. Vega, *J. Chem. Phys.*, 1992, **96**, 8624.
7. D. M. Gregory, D. J. Mitchell, J. A. Stringer, S. Kiihne, J. C. Shiels, J. Callahan, M. A. Mehta, and G. P. Drobny, *Chem. Phys. Lett.*, 1995, **246**, 654.
8. T. Gullion and J. Schaefer, *Adv. Magn. Reson.*, 1989, **13**, 57.
9. T. Gullion and J. Schaefer, *J. Magn. Reson.*, 1989, **81**, 196.
10. A. W. Hing, S. Vega, and J. Schaefer, *J. Magn. Reson.*, 1992, **96**, 205.
11. J. R. Garbow and C. A. McWherter, *J. Am. Chem. Soc.*, 1993, **115**, 238.
12. J. R. Garbow, M. Breslav, O. Antohi, and F. Naider, *Biochemistry*, 1994, **33**, 10 094.
13. A. W. Hing, N. Tjandra, P. F. Cottam, J. Schaefer, and C. Ho, *Biochemistry*, 1994, **33**, 8651.
14. R. C. Anderson, T. Gullion, J. M. Joers, M. Shapiro, E. B. Villhauer, and H. P. Weber, *J. Am. Chem. Soc.*, 1995, **117**, 10 546.
15. A. Naito, K. Nishimura, S. Kimura, S. Tuzi, M. Aida, N. Yasuoka, and H. Saitô, *J. Phys. Chem.*, 1996, **100**, 14 995.
16. K. Nishimura, A. Naito, S. Tuzi, H. Saitô, C. Hashimoto, and M. Aida, *J. Phys. Chem. B*, 1998, **102**, 7476.
17. K. T. Mueller, T. P. Jarvie, D. J. Aurentz, and B. W. Roberts, *Chem. Phys. Lett.*, 1995, **242**, 535.
18. T. P. Jarvie, G. T. Went, and K. T. Mueller, *J. Am. Chem. Soc.*, 1996, **118**, 5330.
19. H. Saitô, S. Tuzi, and A. Naito, *Annu. Rep. NMR Spectrosc.*, 1998, **38**, 79.
20. C. A. Michal and L. W. Jelinski, *J. Am Chem. Soc.*, 1997, **119**, 9059.
21. C. P. Jaroniec, B. A. Tounge, C. M. Rienstra, J. Herzfeld, and R. G. Griffin, *J. Am. Chem. Soc.*, 1999, **121**, 100–237.
22. J. Schaefer, *J. Magn. Reson.*, 1999, **137**, 272.
23. A. Naito, K. Nishimura, S. Tuzi, and H. Saitô, *Chem. Phys. Lett.*, 1994, **229**, 506.
24. K. Nishimura, A. Naito, S. Tuzi, and H. Saitô, *J. Phys. Chem. B*, 1999, **103**, 8398.
25. L. M. McDowell, C. A. Klug, D. D. Beusen, and J. Shaefer, *Biochemistry*, 1996, **35**, 5395.
26. J. M. Goetz and J. Schaefer, *J. Magn. Reson.*, 1997, **127**, 147.
27. T. Gullion and C. H. Pennington, *Chem. Phys. Lett.*, 1998, **290**, 88.
28. K. Nishimura, K. Ebisawa, E. Suzuki, H. Saito, and A. Naito, *J. Mol. Struct.*, 2001, **560**, 29.
29. T. Gullion and J. Schaefer, *J. Magn. Reson.*, 1991, **92**, 439.
30. Y. Pan, T. Gullion, and J. Schaefer, *J. Magn. Reson.*, 1990, **90**, 330.
31. D. Suwelack, W. P. Rothwell, and J. S. Waugh, *J. Chem. Phys.*, 1980, **73**, 2559.
32. W. P. Rothwell and J. S. Waugh, *J. Chem. Phys.*, 1981, **74**, 2721.
33. A. Naito, A. Fukutani, M. Uitdehaag, S. Tuzi, and H. Saitô, *J. Mol. Struct.*, 1998, **441**, 231.
34. M. Kamihira, A. Naito, K. Nishimura, S. Tuzi, and H. Saitô, *J. Phys. Chem. A*, 1998, **102**, 2826.
35. M. Kamihira, A. Naito, S. Tuzi, and H. Saitô, *J. Phys. Chem.*, 1999, **103**, 3356.
36. S. K. Brahmachari, T. N. Bhat, V. Sudhakar, M. Vijayan, R. S. Rapaka, R. S. Bhatnagar, and V. S. Aranthanarayanan, *J. Am. Chem. Soc.*, 1981, **103**, 1703.
37. von I. Z. Siemion, T. Wieland, and K. -H. Pook, *Angew. Chem.*, 1975, **87**, 712.
38. M. Aida, A. Naito, and H. Saitô, *J. Mol. Struct. Theochem.*, 1996, **388**, 187.
39. G. D. Smith and T. Blundel, *Science*, 1978, **199**, 1214.
40. S. Kimura, A. Naito, H. Saitô, K. Ogawa, and A. Shoji, *J. Mol. Struct.*, 2001, **157**, 562.
41. S. Kimura, A. Naito, S. Tuzi, and H. Saitô, *J. Mol. Struct.*, 2002, **125**, 602–603.

Biographical Sketches

Akira Naito, *b* 1949. B.Eng., 1973, Nagoya Institute of Technology. Ph.D., 1978, Kyoto University. Post Doctoral Fellow, University of British Columbia, 1978–1984. Assistant Professor, Kyoto University, 1984–1990. Associate Professor, Himeji Institute of Technology, 1990–2001. Professor, Yokohama National University, 2001–present. Approx. 110 publications. Current research specialty: development of solid-state NMR technique and its application to biological systems.

Hazime Saitô, *b* 1937. B.Sc., 1961, Ph.D., 1968, Kyoto University. Research Scientist, Basic Research Laboratories, Toray Industries, Inc., 1963–1975, Section head, Biophysics Division, National Cancer Center Research Institute, Tokyo, 1975–1990. Professor, Himeji Institute of Technology, 1990–present. Approx. 250 publications. Current research specialty: solid state NMR and its application to structural biology with emphasis on membrane proteins.

Chemical Shift Tensors in Single Crystals

Mark H. Sherwood

IBM Research Division, Almaden Research Center, San Jose, CA, USA

1	Introduction	1
2	Nuclear Shielding and the Chemical Shift Tensor	1
3	The Single Axis Rotation Method	3
4	Single Axis 2D Chemical Shift Tensor Correlation Spectroscopy	4
5	Multiple Axis 2D Chemical Shift Tensor Correlation Spectroscopy	6
6	Assignment Techniques	7
7	Related Articles	8
8	References	8

1 INTRODUCTION

Shortly after its first detection in condensed matter in 1945,[1,2] it became evident that NMR was an extremely sensitive probe of the local electronic environments of magnetic nuclei. Some of the first observations of NMR uncovered a chemical effect on the relative resonance frequencies of identical nuclear isotopes which has come to be known as the chemical shift, and because of this effect NMR has evolved into one of the premier spectroscopic techniques for chemical structure analysis. The primary use of NMR consists of measuring the isotropic chemical shifts of nuclei imbedded in molecules dissolved in solution; however, important information about the anisotropy of this interaction is available from the spectra of solids.[3–5]

Certain characteristics of the anisotropic chemical shift, the principal values of the chemical shift tensor for example, can be obtained from the spectra of powdered samples and, to a lesser extent, from molecules dissolved in liquid crystal solvents. Nevertheless, single crystal samples are preferred, when available, as they allow direct measurements of the complete chemical shift tensor. Single crystals are especially useful for studies of large molecules where the many overlapping powder patterns in traditional one-dimensional (1D) spectra are uninterpretable and where selectively labeling each individual site is impractical. Although progress has been made in extracting principal values from powdered samples of large molecules using two-dimensional (2D) NMR methods,[6] direct measurements of tensor orientations can be made only on single crystals.

This article is written as an introduction to the techniques that are available for measuring chemical shift tensors in single crystals. Although many aspects of the techniques are quite general, the emphasis here will be on measurements of ^{13}C chemical shift tensors in organic systems.

The first measurement of a ^{13}C chemical shift tensor was made in the very early days of ^{13}C NMR by Lauterbur[7] on the carbonate ion of single crystal calcite ($CaCO_3$). This particular sample proved to be ideal because all magnetic nuclei were at low abundance and thus the dipolar broadening was negligible. A few other systems were exploited where similar dilution occurred naturally or was introduced by substitution of ^{2}D for ^{1}H, but progress along these lines was limited. It was only after the introduction of the combined cross polarization and high-power dipolar decoupling techniques[8] that ^{13}C chemical shift tensor measurements became more generally applicable. One of the first demonstrations of these now widely used techniques was in the measurement of ^{13}C chemical shift tensors in single crystal durene (1,2,4,5-tetramethylbenzene).[9]

2 NUCLEAR SHIELDING AND THE CHEMICAL SHIFT TENSOR

The fundamental equation relating the NMR resonance frequency and the magnetic field strength is well known to all students of magnetic resonance

$$\nu_0 = |\gamma/2\pi| B_0 \tag{1}$$

For ^{13}C, this frequency corresponds to 50 MHz in a typical field of 4.7 T.

Due to the electronic circulation set up in a molecule by the applied magnetic field, the effective field experienced by a particular nucleus is not exactly equal to B_0. The electronic 'currents' induce a small shielding field $\boldsymbol{B}_s$ which must be added to $\boldsymbol{B}_0$ to obtain the effective field at the nucleus

$$\boldsymbol{B}_{\text{eff}} = \boldsymbol{B}_0 + \boldsymbol{B}_s \tag{2}$$

This vector addition is shown schematically in Figure 1.

Although $\boldsymbol{B}_s$ is called the shielding field, it does not necessarily oppose $\boldsymbol{B}_0$ and thus deshieldings or paramagnetic shifts are possible. In general, the direction of $\boldsymbol{B}_s$ is not parallel to $\boldsymbol{B}_0$ but the two are related through the shielding tensor which is represented as the 3×3 matrix $\boldsymbol{\sigma}$

$$\boldsymbol{B}_s = -\boldsymbol{\sigma} \cdot \boldsymbol{B}_0 \tag{3}$$

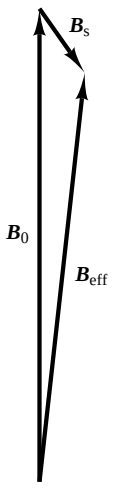

Figure 1 The relationship between the applied field $\boldsymbol{B}_0$, the shielding field $\boldsymbol{B}_s$ and the effective field $\boldsymbol{B}_{\text{eff}}$

The matrix $\boldsymbol{\sigma}$ is usually called a second rank Cartesian tensor although it also contains zeroth and first rank parts as well.

Since B_s is very small compared to B_0, equation (2) can be closely approximated by adding only the component of $\boldsymbol{B}_s$ that is either parallel or antiparallel to $\boldsymbol{B}_0$ to obtain

$$\boldsymbol{B}_{\text{eff}} = \boldsymbol{B}_0 - \frac{\boldsymbol{B}_0}{B_0} \cdot \boldsymbol{\sigma} \cdot \boldsymbol{B}_0 \tag{4}$$

The above approximation is equivalent to *truncation* or restriction to the *secular* terms of the chemical shift Hamiltonian in first-order perturbation theory. It should be pointed out that $\boldsymbol{\sigma}$ can be decomposed into a sum of second rank symmetric and first rank antisymmetric constituents

$$\boldsymbol{\sigma} = \boldsymbol{\sigma}^{\text{S}} + \boldsymbol{\sigma}^{\text{A}} \tag{5}$$

Since $\boldsymbol{\sigma}^{\text{A}}$ leads to components of $\boldsymbol{B}_s$ which are perpendicular to $\boldsymbol{B}_0$, it does not contribute to $\boldsymbol{B}_{\text{eff}}$ in first order and thus its effect on the resonance frequency of the nucleus can be ignored.

The effect of shielding is thus to change the precession frequency of the nucleus from ν_0 to the frequency given by

$$\nu = |\gamma/2\pi| B_{\text{eff}} \tag{6}$$

In practice, the frequency of the bare nucleus is not known, and measurements of the frequency ν are always made relative to a reference frequency ν_{ref}, which for ^{13}C is usually taken as the resonance of liquid tetramethylsilane (TMS). The frequency difference between sample and reference can be written as

$$\nu - \nu_{\text{ref}} = |\gamma/2\pi| \frac{\boldsymbol{B}_0}{B_0} \cdot (\boldsymbol{\sigma}^{\text{S}} - \sigma_{\text{ref}}\mathbf{1}) \cdot \boldsymbol{B}_0 \tag{7}$$

where σ_{ref} is the isotropic chemical shielding constant of the reference compound and $\mathbf{1}$ is the unit matrix. The symmetric difference matrix $(\boldsymbol{\sigma}^{\text{S}} - \sigma_{\text{ref}}\,\mathbf{1})$ is defined as the chemical shift tensor, and is assigned the symbol $\boldsymbol{\delta}$ in order to avoid its confusion with the shielding tensor $\boldsymbol{\sigma}$.

It is customary to report chemical shifts not as frequencies, since these always depend on B_0 which varies from one spectrometer to the next, but as fractions of ν_{ref}. If the chemical shift F is defined as $(\nu - \nu_{\text{ref}})/\nu_{\text{ref}}$, then

$$F = \frac{\boldsymbol{B}_0}{B_0} \cdot \boldsymbol{\delta} \cdot \frac{\boldsymbol{B}_0}{B_0} \tag{8}$$

Equation (8) is the master equation for the chemical shift in a single crystal, as it gives the observed shift in terms of the elements of $\boldsymbol{\delta}$ and the orientation of $\boldsymbol{B}_0$.

For elements with sufficiently low atomic numbers, the chemical shift tensor $\boldsymbol{\delta}$ can be represented in a Cartesian coordinate system as a 3×3 symmetric matrix

$$\boldsymbol{\delta} = \begin{bmatrix} \delta_{xx} & \delta_{xy} & \delta_{zx} \\ \delta_{xy} & \delta_{yy} & \delta_{yz} \\ \delta_{zx} & \delta_{yz} & \delta_{zz} \end{bmatrix} \tag{9}$$

The matrix $\boldsymbol{\delta}$ is called the Cartesian representation of the chemical shift tensor and is completely defined by six independent numbers. It will be seen below that other representations are possible.

The average value of $\boldsymbol{\delta}$ is known as the isotropic chemical shift

$$\delta_{\text{iso}} = \frac{1}{3}(\delta_{xx} + \delta_{yy} + \delta_{zz}) \tag{10}$$

and it is only this part of the chemical shift tensor which can be directly measured in solution samples due to rapid isotropic tumbling of the molecules. The isotropic chemical shift is also called the zeroth rank part of $\boldsymbol{\delta}$ since it transforms as a scalar quantity, i.e., it is invariant under rotation.

A Cartesian tensor can be expressed in a different coordinate system by performing a similarity transformation on the matrix $\boldsymbol{\delta}$

$$\boldsymbol{\delta}' = \mathbf{R}\boldsymbol{\delta}\mathbf{R}^{\text{T}} \tag{11}$$

where $\mathbf{R}$ is a unitary matrix. The element R_{ij} is given by the direction cosine of the ith new coordinate axis with respect to the jth old coordinate axis. For instance, $R_{12} = \cos \gamma_{x'y}$ where $\gamma_{x'y}$ is the angle between the new x axis and the old y axis.

A number of coordinate systems are necessary in single crystal work. The *laboratory frame* is a coordinate system whose z axis lies along the direction of the static magnetic field. Rather than working in the laboratory frame, it is usually more convenient to work in a coordinate system called the *sample frame* whose orientation is fixed with respect to the single crystal sample. The sample frame will always be the coordinate system in which tensors are measured. A third coordinate system is that defined by the symmetry elements of the crystal and this will be called the *crystal frame*. The orientation of the crystal frame relative to the sample frame can usually be found by diffraction methods. For molecules containing high symmetry, it is often useful to define a coordinate system based on molecule symmetry elements called the *molecular frame*. For molecules of low symmetry, coordinate systems can be defined based on the local symmetry of a particular nuclear site and these will be called *local frames*. Finally, there is an important coordinate system known as the *principal axis* system which is unique to each tensor. The principal axis system is discussed below.

The relationships between all of these reference frames, except for that between the sample frame and laboratory frame, are determined by the crystal and molecular structure, and therefore they are not under experimental control. It is clear from equation (11) that once the tensor is known in one of these reference frames, it can be expressed in any of the other frames provided the unitary matrix $\mathbf{R}$ is available.

For any symmetric second rank tensor such as the chemical shift tensor $\boldsymbol{\delta}$, there exists a unitary matrix $\mathbf{S}$ that transforms $\boldsymbol{\delta}$ into a coordinate system in which it is diagonal

$$\mathbf{S}\boldsymbol{\delta}\mathbf{S}^{\text{T}} = \boldsymbol{\Lambda} \tag{12}$$

where $\boldsymbol{\Lambda}$ is a diagonal matrix with elements λ_1, λ_2, and λ_3. This special coordinate system is called the principal axis system and the diagonal tensor elements are called the principal values. Multiplying both sides of equation (12) by $\mathbf{S}^{-1} = \mathbf{S}^{\text{T}}$ yields

$$\boldsymbol{\delta}\mathbf{S}^{\text{T}} = \mathbf{S}^{\text{T}}\boldsymbol{\Lambda} \tag{13}$$

Equation (13) is readily recognized as an algebraic eigenvalue equation and the eigenvalues (principal values) and eigenvectors (principal axes) can be found by solving the secular equation

$$|\boldsymbol{\delta} - \boldsymbol{\Lambda 1}| = \begin{vmatrix} \delta_{xx} - \lambda_1 & \delta_{xy} & \delta_{zx} \\ \delta_{xy} & \delta_{yy} - \lambda_2 & \delta_{yz} \\ \delta_{zx} & \delta_{yz} & \delta_{zz} - \lambda_3 \end{vmatrix} = 0 \qquad (14)$$

A convention for labeling the principal values is generally followed in which they are designated δ_{11}, δ_{22}, and δ_{33} in order of decreasing chemical shift. An alternative to the Cartesian representation of a chemical shift tensor is its representation as three principal values and the three Euler angles that orient the principal axis system with respect to one of the coordinate systems defined above. Other useful representations of the chemical shift tensor are described elsewhere.[10]

Recalling equation (8), the chemical shift F observed when the magnetic field is oriented with direction cosines cos γ_x, cos γ_y, and cos γ_z relative to the sample frame axes can be explicitly written as the quadratic form

$$F = [\cos(\gamma_x)\ \cos(\gamma_y)\ \cos(\gamma_z)] \begin{bmatrix} \delta_{xx} & \delta_{xy} & \delta_{zx} \\ \delta_{xy} & \delta_{yy} & \delta_{yz} \\ \delta_{zx} & \delta_{yz} & \delta_{zz} \end{bmatrix} \begin{bmatrix} \cos(\gamma_x) \\ \cos(\gamma_y) \\ \cos(\gamma_z) \end{bmatrix}$$

$$= \cos^2(\gamma_x)\,\delta_{xx} + \cos^2(\gamma_y)\,\delta_{yy} + \cos^2(\gamma_z)\,\delta_{zz} + 2\cos(\gamma_x)\ \cos,\ (\gamma_y)\delta_{xy} + 2\ \cos(\gamma_y)\ \cos(\gamma_z)\,\delta_{yz} + 2\ \cos(\gamma_z)\ \cos(\gamma_x)\,\delta_{zx} \qquad (15)$$

It is seen from equation (15) that if the chemical shift tensor $\boldsymbol{\delta}$ is known in the sample frame, the chemical shift can be calculated for any orientation of $\boldsymbol{B}_0$. Alternatively, if the chemical shift F is known for six suitably chosen directions of $\boldsymbol{B}_0$, the elements of $\boldsymbol{\delta}$ can be obtained by solving a system of linear equations.

Equation (15) takes on a particularly simple form when expressed in the principal axis system

$$F = \cos^2(\gamma_x)\delta_{11} + \cos^2(\gamma_y)\,\delta_{22} + \cos^2(\gamma_z)\,\delta_{33} \qquad (16)$$

Provided that the reference frequency is chosen such that the three principal values δ_{11}, δ_{22}, and δ_{33} are positive, a connection can be made between equation (16) and the equation of an ellipsoid with semiaxes a, b, and c

$$\frac{x^2}{a^2} + \frac{y^2}{b^2} + \frac{z^2}{c^2} = 1 \qquad (17)$$

The direction cosines of a radius vector $\boldsymbol{r}$ taken from the origin to a point on the surface of the ellipsoid are given by $\cos^2(\gamma_x) = x^2/r^2$, $\cos^2(\gamma_y) = y^2/r^2$, and $\cos^2(\gamma_z) = z^2/r^2$. Substituting these into equation (17) yields

$$\frac{r^2\cos^2(\gamma_x)}{a^2} + \frac{r^2\cos^2(\gamma_y)}{b^2} + \frac{r^2\cos^2(\gamma_z)}{c^2} = 1 \qquad (18)$$

Finally, by making the identities $a^2 = 1/\delta_{11}$, $b^2 = 1/\delta_{22}$, and $c^2 = 1/\delta_{33}$, equation (18) can be rearranged to give

$$\cos^2(\gamma_x)\,\delta_{11} + \cos^2(\gamma_y)\,\delta_{22} + \cos^2(\gamma_z)\,\delta_{33} = \frac{1}{r^2} \qquad (19)$$

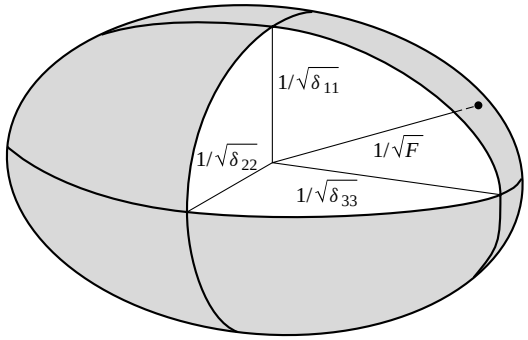

Figure 2 The chemical shift tensor representation ellipsoid

The surface described by equation (19) is called the representation ellipsoid[11] of the chemical shift tensor and is illustrated in Figure 2.

The semiaxes of the ellipsoid are given by $1/\sqrt{\delta_{11}}$, $1/\sqrt{\delta_{22}}$, and $1/\sqrt{\delta_{33}}$. Comparing equation (16) and (19), it is seen that when $\boldsymbol{B}_0$ is oriented along $\boldsymbol{r}$, the length of the radius vector is given by $r = 1/\sqrt{F}$.

The representation ellipsoid thus allows a geometrical interpretation of the chemical shift tensor, and the *mmm* (D_{2h}) symmetry of this object reflects the symmetry of the chemical shift interaction.

In order to understand the effect of crystallographic symmetry on the chemical shift, it is necessary to define some terminology. Nuclear sites related by the rotation or reflection symmetry operations of the space group of the crystal are called *crystallographically equivalent* sites. Those sites that are related by inversion or translation are called *magnetically equivalent* sites. This definition of magnetic equivalence is in contrast to that used in solution NMR where sites related by any symmetry element of the molecule are magnetically equivalent due to the rapid isotropic tumbling of the molecule. As the operations of either inversion or translation do not change the orientation of the representation ellipsoid, a set of magnetically equivalent sites gives rise to a single peak in the spectrum. On the other hand, the representation ellipsoids of crystallographically equivalent sites are oriented differently in the absence of accidental coincidence of the symmetry elements of the representation ellipsoid with those of the space group. Therefore, multiple peaks occur in the spectrum of a single crystal sample when the magnetic field is in a general orientation with respect to a lattice of crystallographically equivalent sites. Two tensors are said to be *congruent* if they are each associated with nuclear sites which are crystallographically equivalent. Congruent tensors have identical principal values, but differ in the orientations of their respective principal axes.

3 THE SINGLE AXIS ROTATION METHOD

In the case of a crystal containing only one set of magnetically equivalent nuclei, the measurement technique is straightforward since the spectrum of such a crystal contains a single peak in any orientation of the field. Six 1D spectra can be obtained with the magnetic field oriented along six different directions. The chemical shift derived from each spectrum, along with the corresponding direction cosines describing

the orientation of the magnetic field, is then substituted into equation (15) to obtain a set of six equations from which the tensor elements are extracted.

The spectrum of a sample containing multiple sets of magnetically equivalent nuclei has a corresponding multiplicity of peaks. In this case the six 1D spectra described above would be useless, since there would be no way to determine which peak in each of the spectra was from a particular set of magnetically equivalent nuclei. One solution to this problem is to acquire many 1D spectra which differ by small angle rotations of the crystal so that the paths of the lines can be traced from one spectrum to the next to form a *rotation pattern*.

Consider a rotation of the crystal about an axis that makes an angle β with the magnetic field $\boldsymbol{B}_0$. The arbitrary sample frame can be oriented such that the x axis is parallel to the rotation axis and the magnetic field $\boldsymbol{B}_0$ lies initially in the xy plane. If the crystal is rotated through an angle α, the direction cosines of the field with respect to the sample frame are given by

$$\cos(\gamma_x) = \cos(\beta) \tag{20}$$

$$\cos(\gamma_y) = \sin(\beta)\cos(\alpha) \tag{21}$$

$$\cos(\gamma_z) = \sin(\beta)\sin(\alpha) \tag{22}$$

It can easily be shown by substituting equations (20)–(22) into equation (15) that the chemical shift F is given by

$$F = A + B\cos(\alpha) + C\sin(\alpha) + D\cos(2\alpha) + E\sin(2\alpha) \tag{23}$$

where

$$A = \tfrac{1}{2}\sin^2(\beta)\,(\delta_{yy} + \delta_{zz}) + \cos^2(\beta)\,\delta_{xx} \tag{24a}$$

$$B = 2\sin(\beta)\cos(\beta)\,\delta_{xy} \tag{24b}$$

$$C = 2\sin(\beta)\cos(\beta)\,\delta_{zx} \tag{24c}$$

$$D = \tfrac{1}{2}\sin^2(\beta)\,(\delta_{yy} - \delta_{zz}) \tag{24d}$$

$$E = \sin^2(\beta)\,\delta_{yz} \tag{24e}$$

From equation (23) it is seen that if the chemical shift is observed at five different angles α, for a given angle β, the coefficients A, B, C, D, and E can be extracted. However, these five coefficients are insufficient to determine fully the six tensor elements and it is apparent that the complete chemical shift tensor cannot be measured from a single rotation pattern.

The most frequently used measurement technique is to obtain three patterns by rotating the crystal about a single axis perpendicular to $\boldsymbol{B}_0$ in the laboratory frame as depicted in Figure 3.

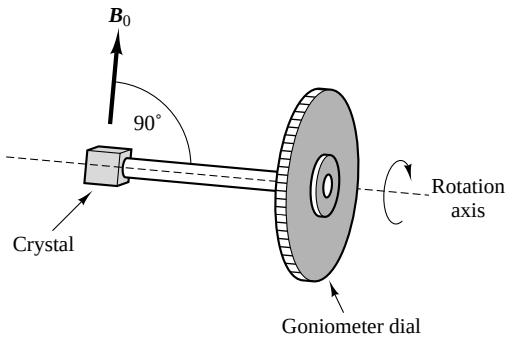

Figure 3 Schematic representation of a simple experimental set-up for obtaining single axis rotation patterns

The three rotation patterns are obtained first with the x, then the y, and finally the z sample frame axis along the rotation direction. The rotation pattern about the x axis is easily obtained from equations (23) and (24) by setting the angle β equal to $\pi/2$

$$F(\alpha_x) = \tfrac{1}{2}(\delta_{yy} + \delta_{zz}) + \tfrac{1}{2}(\delta_{yy} - \delta_{zz})\cos(2\alpha_x) + \delta_{yz}\sin(2\alpha_x) \tag{25}$$

The other two rotation patterns can be found by cyclic permutation of the sample axis labels x, y, and z

$$F(\alpha_y) = \tfrac{1}{2}(\delta_{zz} + \delta_{xx}) + \tfrac{1}{2}(\delta_{zz} - \delta_{xx})\cos(2\alpha_y) + \delta_{zx}\sin(2\alpha_y) \tag{26}$$

$$F(\alpha_z) = \tfrac{1}{2}(\delta_{xx} + \delta_{yy}) + \tfrac{1}{2}(\delta_{xx} - \delta_{yy})\cos(2\alpha_z) + \delta_{xy}\sin(2\alpha_z) \tag{27}$$

Although each rotation pattern is fully determined by measuring the chemical shift at only three different angles, the usual practice is to obtain spectra at many angles by stepping the goniometer from 0° to 180°, and to extract the tensor elements using least-squares methods. This allows a more accurate determination of the tensor and is a necessity if the spectrum of the crystal contains many peaks, since the path of a single peak can be traced only when the crystal is rotated in small angular increments. In order to obtain all six elements of the chemical shift tensor for a particular set of magnetically equivalent nuclei, the path of the corresponding peak must not only be traced within each rotation but must also be traced between rotations. This is accomplished by matching up the rotation patterns at the orientations where they intersect. Figure 4 shows three rotation patterns from which the ^{13}C chemical shift tensors of naphthalene can be obtained.

The rotation method has been successfully applied to many medium-sized molecules;[12] however, it fails when the peaks in the spectra become numerous and crowded since it becomes impossible to trace the paths of individual peaks through the three rotation patterns. Another drawback of the rotation method is the necessity of accurately mounting the crystal three times along the three orthogonal sample axes, but this problem has been overcome using a two-axis goniometer and a unique rf coil as demonstrated by Hauser et al.[13]

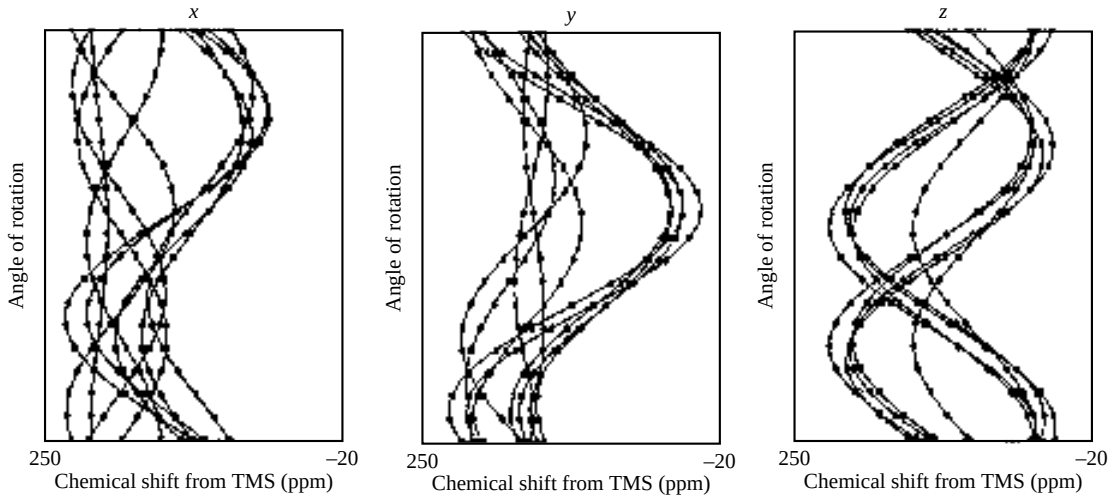

Figure 4 Rotation patterns through 180° about the x, y, and z sample axis sufficient to measure the 10 chemical shift tensors in single crystal naphthalene

4 SINGLE AXIS 2D CHEMICAL SHIFT TENSOR CORRELATION SPECTROSCOPY

The necessity of taking small angular increments in the rotation patterns can be eliminated using a 2D correlation method introduced by Carter et al.[14] This technique obtains 2D spectra in which a peak from a single set of magnetically equivalent nuclei is located by its resonant frequencies at two different orientations of the single crystal. Such spectra are obtained with the modified 2D chemical exchange[15] pulse sequence shown in Figure 5.

The preparation period of this sequence is identical to the usual cross-polarization experiment. During the evolution period, the spins precess at frequencies determined by their chemical shifts at the initial crystal orientation. The evolved magnetization is then stored along the z axis with the pulse labeled b and the crystal is reoriented during the mixing period. At the end of the mixing period, the stored magnetization is rotated back to the transverse plane with the pulse labeled a, and during the detection period the spins precess at frequencies determined by their chemical shifts at the final crystal orientation. An example of a 2D chemical shift tensor correlation spectrum is shown in Figure 6 where all 24 peaks in single crystal sucrose are resolved despite the severe crowding that exists in the corresponding 1D spectra.

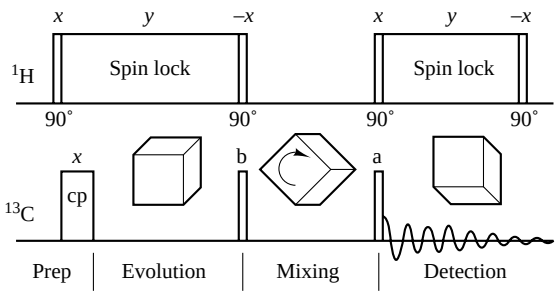

Figure 5 Modified chemical exchange sequence for 2D chemical shift tensor correlation spectroscopy. See text for details. (Reproduced by permission of Academic Press from M. H. Sherwood, D. W. Alderman, and D. M. Grant, *J. Magn. Reson.*, 1989, **84**, 466)

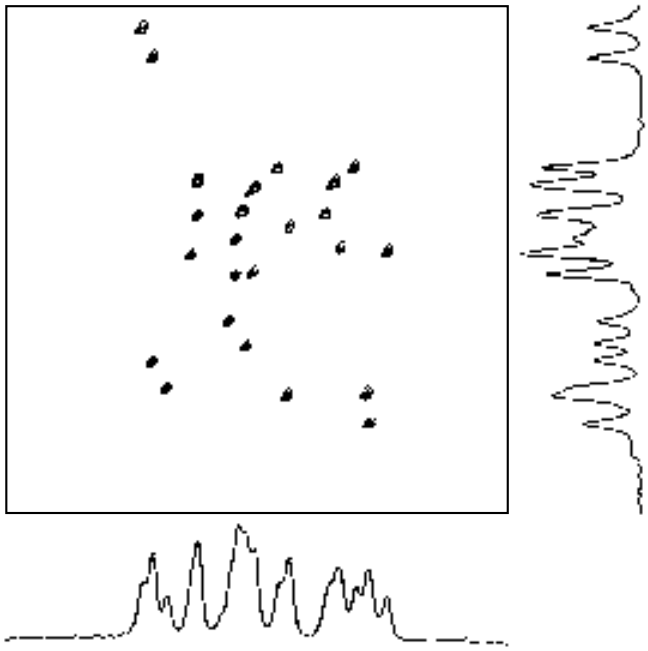

Figure 6 Two-dimensional absorption mode spectrum obtained from sucrose corresponding to a reorientation of $\boldsymbol{B}_0$ by 90° in the sample frame. The plotted spectral width is 5 kHz × 5 kHz (approximately 100 ppm × 100 ppm). The spectrum diagonal runs from upper left (high frequency) to lower right (low frequency). (Adapted by permission of Academic Press from M. H. Sherwood, D. W. Alderman, and D. M. Grant, *J. Magn. Reson.*, 1989, **84**, 466)

It has been shown that the information present in one rotation pattern can be obtained from four 2D spectra taken while stepping the sample from 0° to 45°, 45° to 90°, 90° to 135°, and 135° to 180° (equivalent to 0°).[16] The redundancy in this information permits a powerful square construction which resolves the uncertainties due to peak overlap within each rotation. However, this single axis 2D technique does

not address the problem of joining the three rotation patterns together when there are many overlapping lines in the spectra at the orientations where the patterns intersect. Thus the application of the single axis 2D method is limited to samples where the connections can be made by conventional means. As in the traditional 1D method, it is necessary to mount the sample accurately three times for the single axis 2D measurements.

5 MULTIPLE AXIS 2D CHEMICAL SHIFT TENSOR CORRELATION SPECTROSCOPY

The full power of the 2D technique can be realized by gathering data in such a way that all correlations between required crystal orientations are obtained with a single mounting of the crystal. This is accomplished with a multiple axis sample orienting mechanism which complements the 2D method to form an exceedingly powerful technique for measuring chemical shift tensors in complex single crystals.[17]

As mentioned above, the six independent elements of a chemical shift tensor, in principle, can be determined by measuring the chemical shift with the magnetic field oriented along six suitably chosen directions. Table 1 gives the orientations of six such directions in the sample frame.

Table 1 Six Magnetic Field Directions in the Sample Frame That can be Used to Measure a Chemical Shift Tensor

Magnetic field direction	$\cos(\gamma_X)$	$\cos(\gamma_Y)$	$\cos(\gamma_Z)$	Observed shift
X	1	0	0	F_X
XY	$1\sqrt{2}$	$1/\sqrt{2}$	0	F_{XY}
Y	0	1	0	F_Y
YZ	0	$1/\sqrt{2}$	$1/\sqrt{2}$	F_{YZ}
Z	0	0	1	F_Z
ZX	$1/\sqrt{2}$	0	$1/\sqrt{2}$	F_{ZX}

These directions lie on the surface of a trigonal pyramid and will be referred to here as the pyramidal directions. The observed chemical shifts F_X, F_{XY}, F_Y, F_{YZ}, F_Z, and F_{ZX} are easily calculated from equation (15), yielding the relationships

$$F_X = \delta_{xx} \tag{28a}$$

$$F_{XY} = \delta_{xy} + \delta_{xx}/2 + \delta_{yy}/2 \tag{28b}$$

$$F_Y = \delta_{yy} \tag{28c}$$

$$F_{YZ} = \delta_{yz} + \delta_{yy}/2 + \delta_{zz}/2 \tag{28d}$$

$$F_Z = \delta_{zz} \tag{28e}$$

$$F_{ZX} = \delta_{zx} + \delta_{zz}/2 + \delta_{xx}/2 \tag{28f}$$

which trivally invert to

$$\delta_{xx} = F_X \tag{29a}$$

$$\delta_{xy} = F_{XY} - F_X/2 - F_Y/2 \tag{29b}$$

$$\delta_{yy} = F_Y \tag{29c}$$

$$\delta_{yz} = F_{YZ} - F_Y/2 - F_Z/2 \tag{29d}$$

$$\delta_{zz} = F_Z \tag{29e}$$

$$\delta_{zx} = F_{ZX} - F_Z/2 - F_X/2 \tag{29f}$$

By obtaining the six 2D spectra corresponding to reorientation between the $X–XY$, $XY–Y$, $Y–YZ$, $YZ–Z$, $Z–ZX$, and $ZX–X$ direction pairs, the correlation data are sufficient to determine the complete chemical shift tensors for all of the sets of magnetically equivalent nuclei in the sample. Starting first with the $X–XY$ 2D spectrum, the chemical shifts of the X and XY directions are measured and correlated. Then the observed chemical shifts in the XY direction from the $X–XY$ spectrum are matched with those from the $XY–Y$ spectrum to advance the correlation of the chemical shift to the Y direction, and so forth through YZ, Z, ZX, and back to X. After completion of the full cycle of reorientations, the chemical shift is known for each set of magnetically equivalent nuclei at all six orientations and the tensor elements can be calculated from equations (29a)–(29f). The correlation of chemical shifts around the full cycle forms the closed path depicted in Figure 7(a).

It may be noted that the sense of the reorientation is unimportant. The same frequency information is obtained by reorienting from the X to the XY direction as is obtained by reorienting from XY to X. The only consequence is to interchange the F_1 and F_2 axes of the spectrum.

A powerful criterion, analogous to the square construction described for the single axis 2D approach, allows the correlation of peaks which have identical frequencies at one or more of the six magnetic field directions. It employs reorientations between other pairs of the six measurement directions. The full matrix of 36 possible 2D correlation spectra is shown in Figure 7(b). The 2D spectra that lie along the diagonal of this matrix correspond to trivial correlations between two identical orientations, and are thus of no experimental value. The spectra related by the transpose of this matrix differ only by the sense of the reorientation, and contain the same correlation information. Therefore, only 15 of the 36 possible spectra are necessary to obtain all of the available correlation and frequency information. The spectra matrix construction allows the chemical shifts of a single set of magnetically equivalent nuclei to be traced through all 15 possible 2D correlation spectra simply by connecting the peaks with horizontal and vertical lines as shown in Figure 7(b).

A mechanism which accomplishes the 15 flips has been described in detail elsewhere.[17] Briefly, it consists of an armature into which a glass tube containing the sample is

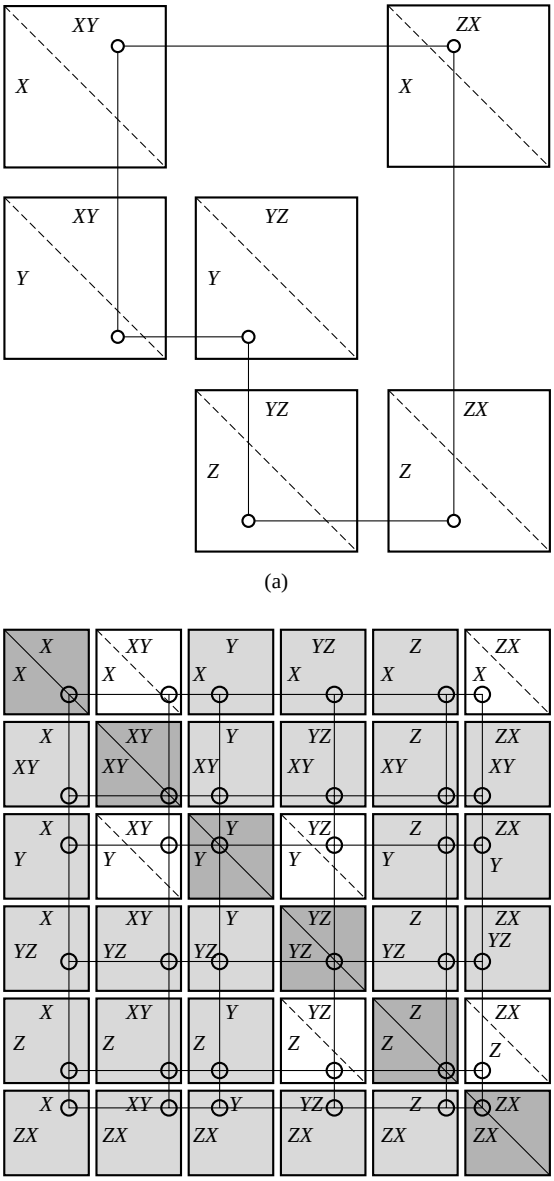

Figure 7 Matrix of 2D spectra. (a) Six 2D spectra corresponding to $XY-X$, $XY-Y$, $YZ-Y$, $YZ-Z$, $ZX-Z$, and $ZX-X$ reorientations. The relationship of the peaks in these spectra is shown for a single set of magnetically equivalent nuclei by the vertical and horizontal connecting lines. Dotted lines indicate the diagonals in the spectra. (b) All 36 possible 2D spectra. The relationship of the peaks in the spectra is shown for a single set of magnetically equivalent nuclei by the vertical and horizontal connecting lines. The six unshaded spectra with dotted diagonals correspond to those of Figure 7(a). The six darkly shaded spectra with solid diagonals are the trivial autocorrelation spectra with the peaks on the diagonals (Reproduced by permission of Academic Press from M. H. Sherwood, D. W. Alderman, and D. M. Grant, *J. Magn. Reson.*, 1989, **84**, 466)

mounted. The armature contains seven accurately drilled holes which define seven rotation axes in the sample frame. A stationary plate attached to the NMR probe contains five axle bearing holes which define five rotation axes in the laboratory frame. The mechanism is assembled by inserting an axle through one of the bearings in the stationary plate and into one of the holes in the armature. By selecting the appropriate combination of bearing and armature hole, each of the 15 possible flips can be performed. The angle of rotation is limited by a precise system of stops. One advantage of this mechanism is that the axis of the tube containing the sample changes by only 19.5° over all assemblies of the mechanism, so that a reasonably good filling factor can be achieved in the rf solenoid.

Although the pyramidal set of directions was used in the original demonstration of multiple axis 2D chemical shift tensor correlation spectroscopy, it should be realized that any set of six directions would suffice if when substituted into equation (15) they yield a system of linearly independent equations for the six chemical shifts. This restriction eliminates any set of directions that completely lie either in a plane or on the surface of a cone.

An important question that arises is how sensitive is the determination of a tensor given a particular set of measurement directions. To address this question, a variance-like figure of merit was developed[18] which quantifies the sensitivity of a given set of measurement directions. This figure of merit was evaluated for a variety of sets of measurement directions including the pyramidal set and the orthogonal rotation set. The most sensitive set of directions was found to be the six apolar directions defined by the vertices of an icosahedron. For this geometry, the figure of merit represents a significant decrease by a factor of 1.0/1.8 from that of the pyramidal directions. Therefore, it is worth considering the icosahedral direction set when designing future mechanisms. It should be noted that there is no further increase in sensitivity upon including more measurement directions than the six icosahedral directions. Another interesting result of this analysis is that the figure of merit for the orthogonal rotations set is only 1.2 times greater than that for the icosahedral directions set. This indicates that the sensitivity of the tensor measurements made using the traditional rotation method is nearly optimal.

The high symmetry of the icosahedron makes possible a very simple mechanism which rotates the crystal about a single laboratory axis inclined at an angle of 64.4° from the field. As can be seen in Figure 8, it will still be necessary to employ three rotation axes in the sample frame as specified by the three vertices labeled a, b, and c. Unfortunately the sample tube axis will reorient by 68.3° in this new mechanism, and a sacrifice in filling factor may be necessary when implementing this geometry.

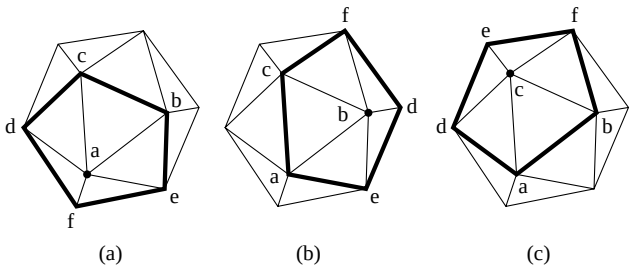

Figure 8 Icosahedra showing the vertex directions which can be aligned along the magnetic field by rotating around the a vertex (a), the b vertex (b), and the c vertex (c) (Reproduced by permission of Academic Press from D. W. Alderman, M. H. Sherwood, and D. M. Grant, *J. Magn. Reson.*, 1990, **86**, 60)

6 ASSIGNMENT TECHNIQUES

Before chemical shift tensors can be rationalized in terms of molecular structure, they must first be assigned to their respective nuclei in the unit cell. This can be a challenging step in the interpretation of the results, since the number of possible assignment permutations increases rapidly for larger molecules. The problem is compounded by the fact that most organic crystals contain two or more magnetically nonequivalent molecules in the unit cell. In order fully to exploit the power of the techniques described above, systematic methods of assignment have been developed based on local symmetry and dipolar spectroscopy. These methods have been described in detail in the literature and therefore will only be described qualitatively here.

Nearly all of the chemical shift tensor assignments made to date are based on the assumption that the symmetry elements of the representation ellipsoid should closely coincide with the actual or approximate local symmetry of its assigned nuclear site. For example, it is well established that the δ_{33} principal values of the ^{13}C chemical shift tensors orient perpendicular to the molecular plane in polycyclic aromatic hydrocarbons.[19] This fact is widely used to assign tensors to a particular molecule when there is more than one molecule in the unit cell. In more complicated molecules lacking any molecular symmetry, the approximate local symmetry established by the directly bonded atoms can be used to make assignments. For small molecules this procedure consists of manually comparing principal axis directions of the measured tensors with the approximate local symmetry elements determined from diffraction data until a reasonable match is found. As the number of measured tensors increases, it becomes more difficult to make all possible comparisons and their qualitative nature makes it difficult to distinguish between closely related assignments. In order to quantify such comparisons, the concept of a distance between two tensors was developed.[10] This distance concept has been combined with linear modeling in order to make possible an automated assignment technique which can explore all possible assignments of a reasonably large set of measured tensors to a corresponding set of chemically similar but magnetically nonequivalent nuclear sites.[10,20]

The orientational dependence of dipolar interactions has also been exploited in order to assign chemical shift tensors to specific nuclei in single crystal samples. Assignments made in this way are quite reliable since dipolar couplings can be calculated with a high degree of accuracy from the positions of the nuclei alone without resorting to molecular electronic theory. In many organic molecular crystals, the positions of all of the carbon and hydrogen nuclei in the unit cell are known from neutron diffraction studies and thus $^{13}C-^{1}H$ separated local field experiments[21,22] can be used in solving the assignment problem.

A simple extension of 2D chemical shift tensor correlation spectroscopy yields a 3D technique which allows detection of $^{13}C-^{1}H$ dipolar couplings for each of the magnetically nonequivalent sets of carbons in the sample.[20] The response of each spin is separated according to its chemical shifts at two different magnetic field orientations and a dipolar spectrum is displayed in the third dimension. This is accomplished by inserting a dipolar evolution period between the end of the mixing time and the beginning of the detection period of the previously described 2D experiment.

7 RELATED ARTICLES

Chemical Shift Tensor Measurement in Solids; Chemical Shift Tensors; Cross Polarization in Solids; Dipolar and Indirect Coupling Tensors in Solids; Multidimensional Spectroscopy: Concepts; Shielding Tensor Calculations; Two-Dimensional Powder Correlation Methods.

8 REFERENCES

1. F. Bloch, W. W. Hansen, and M. Packard, *Phys. Rev.*, 1946, **70**, 474.
2. E. M. Purcell, H. C. Torrey, and R. V. Pound, *Phys. Rev.*, 1946, **69**, 37.
3. M. Mehring, *Principles of High Resolution NMR in Solids*, Springer-Verlag, New York, 1983.
4. U. Haeberlen, *High Resolution NMR in Solids; Selective Averaging*, Academic Press, New York, 1976.
5. T. M. Duncan, *A Compilation of Chemical Shift Anisotropies*, Farragut Press, Chicago, IL, 1990.
6. J. Z. Hu, D. W. Alderman, C. Ye, R. J. Pugmire, and D. M. Grant, *J. Magn. Reson., Ser. A.* 1993, **105**, 82.
7. P. C. Lauterbur, *Phys. Rev. Lett.*, 1958, **1**, 343.
8. A. Pines, M. G. Gibbey, and J. S. Waugh, *J. Chem. Phys.*, 1973, **59**, 569.
9. S. Pausak, A. Pines, and J. S. Waugh, *J. Chem. Phys.*, 1973, **59**, 591.
10. D. W. Alderman, M. H. Sherwood, and D. M. Grant, *J. Magn. Reson. Ser. A.*, 1993, **101**, 188.
11. J. F. Nye, *Physical Properties of Crystals; Their Representation by Tensors and Matrices*, Oxford University Press, New York, 1985.
12. W. S. Veemann, *Prog. NMR Spectrosc.*, 1984, **16**, 193.
13. H. Hauser, C. Radloff, R. R. Ernst, S. Sundell, and I. Pascher, *J. Am. Chem. Soc.*, 1988, **110**, 1054.
14. C. M. Carter, D. W. Alderman, and D. M. Grant, *J. Magn. Reson.*, 1985, **65**, 183.
15. J. Jeener, B. H. Meier, P. Bachman, and R. R. Ernst, *J. Chem. Phys.*, 1979, **71**, 4546.
16. C. M. Carter, D. W. Alderman, and D. M. Grant, *J. Magn. Reson.*, 1987, **73**, 114.
17. M. H. Sherwood, D. W. Alderman, and D. M. Grant, *J. Magn. Reson.*, 1989, **84**, 466.
18. D. W. Alderman, M. H. Sherwood, and D. M. Grant, *J. Magn. Reson.*, 1990, **86**, 60.
19. M. H. Sherwood, J. C. Facelli, D. W. Alderman, and D. M. Grant, *J. Am. Chem. Soc.*, 1991, **113**, 750.
20. M. H. Sherwood, D. W. Alderman, and D. M. Grant, *J. Magn. Reson. Ser. A*, 1993, **104**, 132.
21. M. Mehring, *Principles of High Resolution NMR in Solids*, Springer-Verlag, New York, 1983, Chap. 5.
22. R. R. Ernst, G. Bodenhausen, and A. Wokaun, *Principles of Nuclear Magnetic Resonance in One and Two Dimensions*, Oxford University Press, New York, 1987, pp. 383–396.

Biographical Sketch

Mark H. Sherwood. *b* 1961. B.S., 1983, Colorado State University, where he was introduced to NMR by Gary E. Maciel, Ph.D., 1991, Chemistry, University of Utah, advisor David M. Grant. Visiting scientist, IBM Research Division, Almaden Research Center, 1991–present. Research specialties: carbon-13 and deuteron NMR in solids, NMR imaging at cryogenic temperatures.

Geometric Phases

Josef W. Zwanziger
Indiana University, Bloomington, IN, USA

1	Introduction	1
2	The Geometry of Quantum Evolution	1
3	Experimental Consequences of Geometric Phases	3
4	Summary	4
5	Related Articles	4
6	References	4

1 INTRODUCTION

The geometric phase of a quantum system is that portion of its total phase that is independent of the details of the system's temporal evolution. Thus, consider a quantum system prepared in an eigenstate $|\phi\rangle$ with energy E. The evolution of this system is just the familiar exp $(-\mathrm{i}Et/\hbar)|\phi\rangle$. The phase of the eigenstate, $-Et/\hbar$, is purely dynamic because it depends on the length of time t for which the system has evolved. It turns out, perhaps surprisingly, that in systems with sufficiently complex geometry there is an additional contribution to the total phase that is independent of time, but that does depend on the shape of the space through which the system evolves. This component of phase is thus termed geometric. As we illustrate below, even as simple a system as a spin in a moving magnetic field can acquire a geometric phase. Nevertheless, the existence of this effect was largely overlooked until Berry's seminal paper,[1] with some notable exceptions.[2,3] The history of the geometric phase has been outlined by Berry.[4] Since the publication of Berry's initial paper,[1] a wealth of primary and secondary literature has appeared (see, for example, Shapere and Wilczek[5] and Zwanziger et al.,[6] and references therein).

The geometric phase is a general phenomenon, and has been shown to be significant in a wide range of applications.[5,6] The exquisite control that magnetic resonance experiments can achieve has proven crucial in providing unambiguous tests of its existence and geometric properties.[7–10] Moreover, its description has stimulated a new way of thinking about a variety of NMR experiments that has led to the prediction of new phenomena.[8–11] Below we will briefly outline both the general theory of geometric phases, and NMR experiments that have verified the theory.

2 THE GEOMETRY OF QUANTUM EVOLUTION

2.1 The Aharonov–Anandan Phase

The geometric treatment of the general case of quantum evolution is due to Aharonov and Anandan,[12] and we follow their discussion here. Consider, for simplicity, a two-level system, assumed to be in a pure state. The state is completely characterized by its density operator $\hat{\rho}$, which is Hermitian ($\hat{\rho}^\dagger = \hat{\rho}$), idempotent ($\hat{\rho}^2 = \hat{\rho}$), and normalized such that it has unit trace. The set of all such operators spans a two-dimensional space that has the geometry of a sphere. The evolution of the two-level system can be viewed as a path on this sphere. We associate a wavefunction $|\psi\rangle$ with each density operator in this space, through $\hat{\rho} = |\psi\rangle\langle\psi|$; in fact, we can associate an infinite set of wavefunctions with each $\hat{\rho}$, since the overall phase of the wavefunction is irrelevant. Now suppose that the system is prepared initially in the state $|\psi(0)\rangle$, and that the system evolves along some closed path in the space of density operators during a time T. The system must return to its initial state, up to a phase, as shown in equation (1).

$$|\psi(T)\rangle = \mathrm{e}^{\mathrm{i}\alpha}|\psi(0)\rangle \tag{1}$$

In general, the phase α includes contributions from both the dynamic and geometric phases. Using $|\psi\rangle$, we define the ket $|\tilde{\psi}\rangle$ through equation (2).

$$|\tilde{\psi}(t)\rangle = \mathrm{e}^{-\mathrm{i}\phi(t)}|\psi(t)\rangle \tag{2}$$

Here ϕ is determined by the condition in equation (3)

$$\phi(T) - \phi(0) = \alpha \tag{3}$$

The reason for making this definition is that we have obtained a ket such that $|\tilde{\psi}(T)\rangle = |\tilde{\psi}(0)\rangle$. The original state $|\psi(t)\rangle$ obeys the Schrödinger equation

$$\mathrm{i}\hbar\frac{\mathrm{d}|\psi(t)\rangle}{\mathrm{d}t} = \hat{\mathcal{H}}(t)|\psi(t)\rangle \tag{4}$$

where $\hat{\mathcal{H}}(t)$ is the Hamiltonian of the system. By substituting the definition of $|\tilde{\psi}\rangle$ into equation (4), a differential equation for $\phi(t)$ can be obtained:

$$-\frac{\mathrm{d}\phi(t)}{\mathrm{d}t} = \frac{1}{\hbar}\langle\psi(t)|\hat{\mathcal{H}}(t)|\psi(t)\rangle - \langle\tilde{\psi}(t)|\mathrm{i}\frac{\mathrm{d}}{\mathrm{d}t}|\tilde{\psi}(t)\rangle \tag{5}$$

Integrating equation (5) shows that the total phase acquired by the system can be expressed in two parts. One part is dynamic, in the sense of depending in detail on the Hamiltonian, and is given in equation (6).

$$\alpha_{\mathrm{D}} = \frac{1}{\hbar}\int_0^T \langle\psi(t)|\hat{\mathcal{H}}(t)|\psi(t)\rangle\,\mathrm{d}t \tag{6}$$

The other portion of the phase is given in equation (7).

$$\gamma = \int_0^T \langle\tilde{\psi}(t)|\mathrm{i}\frac{\mathrm{d}}{\mathrm{d}t}|\tilde{\psi}(t)\rangle\,\mathrm{d}t \tag{7}$$

The phase γ is independent of the Hamiltonian, and in fact depends only on the path through the space of $\hat{\rho}$, and not at all on the mechanism that forces the system to traverse that particular path. Note that γ depends on $|\tilde{\psi}(t)\rangle$, not $|\psi(t)\rangle$. The functions $|\tilde{\psi}(t)\rangle$ were explicitly constructed to be free of phase factors, and so we can be sure that a phase generated by integrating the form $\mathrm{i}\langle\tilde{\psi}(t)|\mathrm{d}/\mathrm{d}t|\tilde{\psi}(t)\rangle$ is free of trivial (in the present context) contributions from energy factors and so forth.

Having derived a component of the overall phase of the system that depends only on the geometry and not the Hamiltonian, we can ask under what conditions this term is nonzero. Of particular interest is equation (7), evaluated along a closed loop in the space of density operators. Recognizing that the time t merely parameterizes the path (call the path C), we can rewrite the integral in terms of the path itself, as shown in equation (8).

$$\gamma(C) = \mathrm{i} \oint_C \langle \tilde{\psi} | \mathrm{d} | \tilde{\psi} \rangle \tag{8}$$

The phase $\gamma(C)$ is often called the Aharonov–Anandan phase (AA phase). Now at any given point on the path one could pick kets such that the integrand of equation (8) is zero there (this is probably why the geometric phase was overlooked for so long). But what is important is the integral around a finite path; it turns out that for spaces that are curved, such as spheres, or spaces with holes, such as the punctured plane, it is impossible to pick kets for which the integrand is *globally* zero. Then $\gamma(C)$ is, in general, nonzero. In NMR the experimentally relevant case is a spherical geometry, this being the shape of the space of density operators of a two-level system. The phase $\gamma(C)$ can be evaluated exactly in this case, yielding the beautifully compact formula shown in equation (9).

$$\gamma(C) = m\Omega(C) \tag{9}$$

Here m is the magnetic quantum number of the state being propagated, and $\Omega(C)$ is the solid angle subtended at the origin of the sphere by the path C. Examples of the geometric phase for different paths are shown in Figure 1.

2.2 The Adiabatic Limit: The Berry Phase

The AA phase described above arises from the geometry of the space of density operators; its generality is due to its independence of the details of the Hamiltonian associated with a given system. The discovery of the AA phase was actually preceded by the discovery by Berry of a geometric phase associated with adiabatic evolution;[1] this so-called Berry phase is a special case of the AA phase. The Berry phase arises from the geometry of the set of Hamiltonians associated with the slowly changing system; we sketch its derivation in this section.

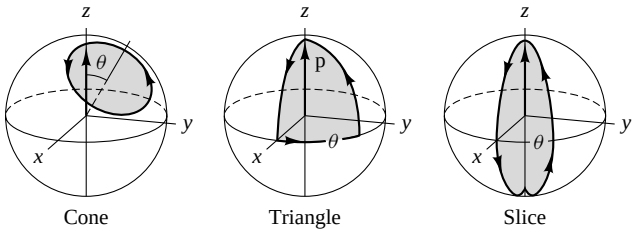

Figure 1 Paths in the space of density operators of a two-level system. The solid angle subtended at the origin is $2\pi(1 - \cos\theta)$ for the cone, θ for the triangle, and 2θ for the slice. (Reproduced by permission of the American Physical Society, from D. Suter, K. T. Mueller, and A. Pines, *Phys. Rev. Lett.*, 1988, **60**, 1218)

The calculation of the Berry phase begins by considering a Hamiltonian that depends on some set of parameters $\boldsymbol{R}$; for any given set $\boldsymbol{R}$ we solve the associated Schrödinger equation to find the energies and states of the system, conventionally indexed by the quantum number n, as shown in equation (10).

$$\hat{\mathcal{H}}(\boldsymbol{R})|n(\boldsymbol{R})\rangle = E_n(\boldsymbol{R})|n(\boldsymbol{R})\rangle \tag{10}$$

The time dependence of the problem is due to the time dependence of the parameters. If the Hamiltonian that drives the system varies slowly in time, compared with the natural precession period of the system, then the evolution can be accurately described in the adiabatic approximation.[13] In the adiabatic approximation, the state of the system at time t is

$$|\psi(t)\rangle = \mathrm{e}^{\mathrm{i}\gamma}\mathrm{e}^{-\mathrm{i}\int_0^t E_n[\boldsymbol{R}(t')]\,\mathrm{d}t'/\hbar}|n[\boldsymbol{R}(t)]\rangle \tag{11}$$

Here it is assumed that $|\psi(0)\rangle = |n[\boldsymbol{R}(0)]\rangle$. A differential equation for the phase γ can be obtained by using $|\psi(t)\rangle$ in the time-dependent Schrödinger equation, and acting with $\langle n(\boldsymbol{R})|$ on the left. The (integrated) result is summarized in equations (12) and (13).

$$\gamma = \mathrm{i}\int_0^T \langle n(\boldsymbol{R})|\frac{\mathrm{d}}{\mathrm{d}t}|n(\boldsymbol{R})\rangle\,\mathrm{d}t \tag{12}$$

$$= \mathrm{i}\oint_C \langle n(\boldsymbol{R})|\nabla_{\boldsymbol{R}}|n(\boldsymbol{R})\rangle\,\mathrm{d}\boldsymbol{R} \tag{13}$$

This phase is a special case of equation (8) above; we need merely to identify $|n(\boldsymbol{R})\rangle$ in the present case with $|\tilde{\psi}\rangle$. The natural interpretation is slightly different between the two cases; whereas we interpret the AA phase as arising from the geometry of the space of density operators, the Berry phase, equation (13), arises from the geometry of the parameter space as determined by the set $\boldsymbol{R}$.

A simple example of a nonzero Berry phase arises for a spin-J particle in a magnetic field of constant magnitude and time-dependent direction. The parameter space $\boldsymbol{R}$, here just the three components of the magnetic field, has again the geometry of a sphere. If the rate of change of the direction of the field is small compared with the precession rate of the spin around the field, then the adiabatic treatment outlined above holds, and we can expect the Berry phase shown in equation (14).

$$\gamma_n(C) = n\Omega(C) \tag{14}$$

This result is analogous to equation (9) above. This example appears in Berry's original paper,[1] and in more detail in the book by Bohm;[14] a rotating frame analog has been studied experimentally by Suter et al., and equation (14) verified.[15]

Although the Berry phase is a special case of the AA phase, more applications in NMR have made use of it, probably because the language describing it is somewhat more familiar. As noted above, whereas the AA phase arises from paths in density operator space, the Berry phase is best viewed as arising from the path followed by the Hamiltonian itself, or, more to the point, of the quantization axis of the system. A slowly varying quantization axis should always be suspected of giving rise to a Berry phase, which in many cases of interest is fairly simple to compute. The simplicity arises from the spherical geometry of the standard parameter space. For the

AA phase, however, while the two-level system yields a simple result, generalization to even a three-level system becomes significantly more complex.[16] The experimental examples of these phases to be discussed below also highlight the subtly different ways they affect real measurements.

3 EXPERIMENTAL CONSEQUENCES OF GEOMETRIC PHASES

3.1 Measurement of the Aharonov–Anandan Phase

A thorough investigation of the phase $\gamma(C)$ [equation (8)] has been carried out by Suter, Mueller, and Pines.[7] The primary obstacle that any experimental study of such a phase must overcome is that global phases associated with the density operator of an *isolated* system are in principle immeasurable. To see this, recall the invariance of $\hat{\rho}$ to phase changes; the density operator conveys all the information about the system, and the global phase is irrelevant. To measure the phase it is necessary to couple the system to its environment; since this is precisely what is done in any experiment, we see that phase shifts, even of density operators, can be expected to be important not only in theory but in practice as well.

The maximum amount of information about the phase of a system coupled to an environment is provided by an interferometric experiment, and this was the strategy pursued by Suter et al.[7] Using an approach similar to that employed by Vaughan and colleagues in a study of spinor behavior,[17] a pair of levels in a three-level system was used to provide the two-level density operator to be manipulated. Coherence to the third level provided the phase reference.

Call the phase reference level one and the two-level subsystem levels two and three. The experiment proceeds by applying a selective $\pi/2$ pulse to the $1-2$ transition, producing coherence. A time τ later a π pulse is applied to these levels, which will generate an echo. The phase of this echo provides the phase reference; it also has the advantage of refocusing all the dynamic evolution during the time τ. In a second experiment, during the refocusing period pulses are applied to the $2-3$ subsystem to drive the associated density operator through a cycle such as those shown in Figure 1. Because this subsystem has a level in common with the $1-2$ transition, the phase of the refocused $1-2$ coherence is sensitive to the phase of the $2-3$ state. In the work of Suter et al.,[7] this sequence was carried out for a variety of paths C of the $2-3$ subsystem, and the phase of the $1-2$ echo measured. The predicted phase shifts of these experiments are $\frac{1}{2}\Omega(C)$ [see equation (9)]; the experimental results and the theory are given in Figure 2. These results show that the phase $\gamma(C)$ does indeed depend on the solid angle in the way predicted; this experiment represents a complete and thorough test of the geometric evolution predicted in equation (8).

3.2 Measurement of the Berry Phase

Because any adiabatic reorientation of the quantization axis of a system can yield a geometric phase, there are a number of examples from NMR of this kind of geometric evolution. The most commonly occurring case is in solid state NMR at intermediate to low fields, where the spin degrees of freedom of the nuclei are not completely decoupled from the spatial degrees of freedom. In such a case, sample reorientations (for example, rotation) yield a slowly changing quantization axis, and hence a geometric phase.[8,9,11] The experiment of Tycko[8] is a particularly vivid example of this behavior.

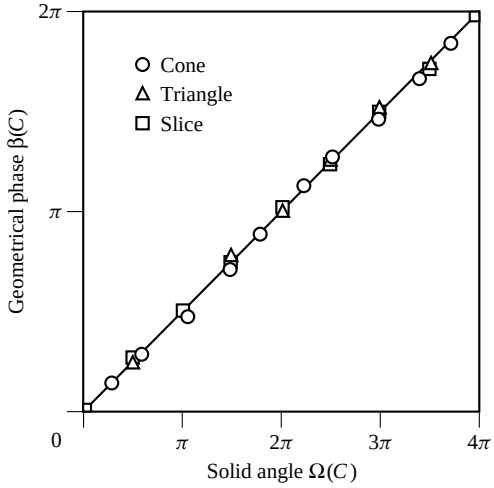

Figure 2 Experimentally determined values of $\gamma(C)$ as a function of solid angle $\Omega(C)$. The paths used are those shown in Figure 1. The solid line is theory [equation 9]. (Reproduced by permission of the American Physical Society, from D. Suter, K. T. Mueller, and A. Pines, *Phys. Rev. Lett.*, 1988, **60**, 1218)

Tycko performed a pure nuclear quadrupole resonance (NQR) experiment on the ^{35}Cl nuclei in a rotating single crystal of sodium chlorate ($NaClO_3$). In this material the quadrupolar interaction is dominant for the chlorine spins, yielding a transition frequency (in zero field) of some 30 MHz. The quantization axis for the chlorine is determined by the quadrupole principal axis system (PAS). By placing a single crystal of $NaClO_3$ in the tuned NQR detection coil, with the crystal c axis collinear with the coil axis, all four chlorine nuclei in the unit cell have equivalent orientations because the principal axis of each is at an angle of 54.74° with respect to the coil axis, and the quadrupolar interaction is axially symmetric ($\eta = 0$). Such an orientation, like any other, gives a single sharp NQR line. When the sample is made to rotate, however, the spectrum changes qualitatively. Rotating around the crystal c axis preserves the equivalence of the chlorine nuclei in the unit cell, but now the quantization axis of each one is time-dependent, tracing a circle around the coil axis (Figure 3).

Each spin state $|n\rangle$ acquires a geometric phase γ_n [see equation (13)] at a constant rate, and since the coupled partners in observable transitions ($|\frac{3}{2}\rangle \leftrightarrow |\frac{1}{2}\rangle$ and $|-\frac{3}{2}\rangle \leftrightarrow |-\frac{1}{2}\rangle$) pick up different phases, shifts of the resonance lines are observed in the spectrum. There is a subtlety in defining the spin states due to their degeneracy in zero field;[8,18,19] suffice it to say that the $|\pm\frac{3}{2}\rangle$ pair are unmixed by the rotation, and so yield good basis states, and that the superposition of the $|\pm\frac{1}{2}\rangle$ states with mixing angle arctan (2 tan θ), with θ being the angle between the quadrupole PAS and the coil axis, form good basis states. These states can be used in equation (13) to calculate the phase shift. The phase differences, modulo 2π, for the observable transitions are 0 and $\pm 2\sqrt{3}\pi$, which translate, in the frequency

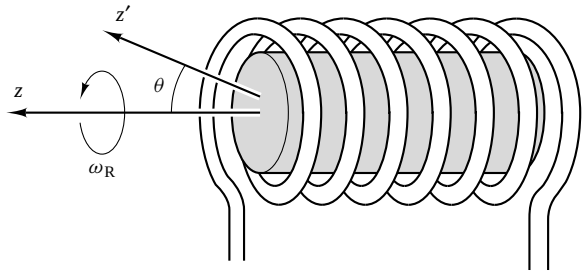

Figure 3 The experimental arrangement used in the pure NQR experiment of Tycko. The crystal *c* axis of $NaClO_3$ is oriented along the coil axis; the sample can be rotated around this axis. (Reproduced by permission of the American Physical Society, from R. Tycko, *Phys. Rev. Lett.*, 1987, **58**, 2281)

domain, into shifts at 0 and $\pm\sqrt{3}\omega_R/2\pi$ Hz (with $\omega_R/2\pi$ the rotation frequency). Note the difference between this result and the usual spinning sidebands of high field solid state NMR: here there are always four lines of constant relative intensity (two are degenerate at zero frequency shift) for all rotation speeds, and the splittings are irrationally related to the rotation frequency. Spectra, at different rotation frequencies, are shown in Figure 4. This very clean result clearly demonstrates the Berry phase, and also illustrates the primary regime in which geometric phases are important in NMR: intermediate to low field experiments, in which the quantization axis is time-dependent.

4 SUMMARY

While geometric methods have been important in relativistic quantum mechanics for some time, it is only recently that they have become used in the nonrelativistic case. The geometric phases discussed here are concrete realizations of the importance of geometry in even simple systems such as spins in magnetic fields. NMR has played a major role in demonstrating their properties, and in turn, geometric approaches are providing new insights and new predictive power into the design of magnetic resonance experiments.

5 RELATED ARTICLES

Phase Cycling; Quadrupolar Nuclei in Solids; Rotating Solids.

6 REFERENCES

1. M. V. Berry, *Proc. R. Soc. London, Ser. A*, 1984, **392**, 45.
2. S. Pancharatnam, *Proc. Indian Acad. Sci., Sect A*, 1956, **44**, 247 (reprinted in Ref. 5).
3. C. A. Mead and D. G. Truhlar, *J. Chem. Phys.*, 1979, **70**, 2284.
4. M. Berry, *Phys. Today*, 1990, **43**, 34.
5. A. Shapere and F. Wilczek (eds.), *Geometric Phases in Physics*, World Scientific, Singapore, 1989.
6. J. W. Zwanziger, M. Koenig, and A. Pines, *Annu. Rev. Phys. Chem.*, 1990, **41**, 601.

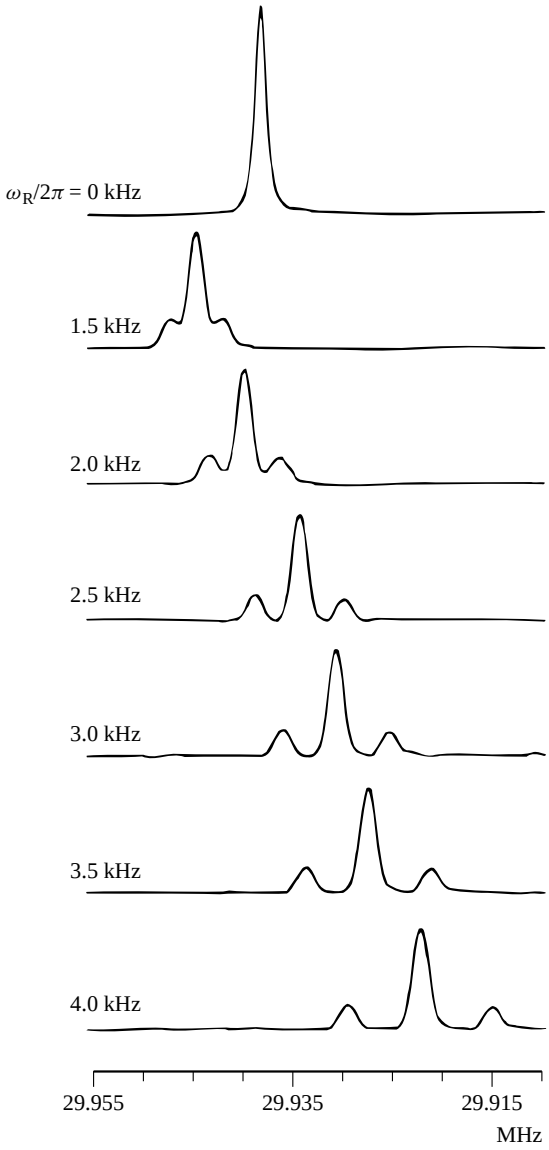

Figure 4 ^{35}Cl NQR spectra of a $NaClO_3$ single crystal in zero magnetic field at different rotation frequencies. The shift in the center of gravity is due to changing temperature. (Reproduced by permission of the American Physical Society, from R. Tycko, *Phys. Rev. Lett.*, 1987, **58**, 2281)

7. D. Suter, K. T. Mueller, and A. Pines, *Phys. Rev. Lett.*, 1988, **60**, 1218.
8. R. Tycko, *Phys. Rev. Lett.*, 1987, **58**, 2281.
9. J. W. Zwanziger, M. Koenig, and A. Pines, *Phys. Rev. A*, 1990, **42**, 1990, 3107.
10. J. W. Zwanziger, S. P. Rucker, and G. C. Chingas, *Phys. Rev. A*, 1991, **43**, 3232.
11. M. Goldman, P. J. Grandinetti, A. Llor, J. Sachleben, Z. Olejniczak, and J. W. Zwanziger, *J. Chem. Phys.*, 1992, **97**, 8947.
12. Y. Aharonov and J. Anandan, *Phys. Rev. Lett.*, 1987, **58**, 1593.
13. A. Messiah, *Quantum Mechanics*, Wiley, New York, 1958.
14. A. Bohm, *Quantum Mechanics: Foundations and Applications*, 3rd edn., Springer-Verlag, New York, 1993.

15. D. Suter, G. C. Chingas, R. Harris, and A. Pines, *Mol. Phys.*, 1987, **61**, 1327.
16. C. Bouchiat and G. W. Gibbons, *J. Phys. Paris*, 1988, **49**, 187.
17. M. E. Stoll, A. J. Vega, and R. W. Vaughan, *Phys. Rev. A*, 1977, **16**, 1521.
18. A. Zee, *Phys. Rev. A*, 1988, **38**, 1.
19. J. E. Avron, L. Sadun, J. Segert, and B. Simon, *Commun. Math. Phys.*, 1989, **124**, 595.

Biographical Sketches

Josef W. Zwanziger. *b* 1961. B.A., 1983, University of Chicago, M.S., 1985, Ph.D., 1988, Cornell University. Introduced to NMR as a postdoctoral associate with A. Pines. Faculty in Chemistry at Indiana, 1990–present. Approximately 35 publications. Research interests include the study of disordered solids with magnetic resonance, and the application of geometric methods to quantum mechanics.

Homonuclear Recoupling Schemes in MAS NMR

Janet M. Griffiths, Andrew E. Bennett and Robert G. Griffin

Massachusetts Institute of Technology, Cambridge, MA, USA

1	Introduction	1
2	Dipolar Hamiltonian Under Magic Angle Spinning	1
3	Rotor-Driven Homonuclear Recoupling	2
4	Homonuclear Recoupling Via Spin Echoes	3
5	Direct Recoupling Sequences: DRAMA and USEME	4
6	Emerging Techniques	4
7	Concluding Remarks	4
8	Related Articles	5
9	References	5

1 INTRODUCTION

Beginning in 1988, a number of developments have taken place in the design of NMR pulse sequences suitable for reintroducing homonuclear dipole–dipole couplings to magic angle spinning (MAS) experiments. These sequences utilize the direct coupling between nuclear magnetic dipoles to measure internuclear distances, thereby providing important constraints for the determination of molecular structure.[1] The motivation for utilizing solid state NMR stems from its ability to access polycrystalline and amorphous systems, including those with high molecular mass. Often, these systems are not amenable to study by crystallography or multidimensional solution NMR. The NMR methods described here offer resolution comparable with X-ray crystallography (0.005 to 0.02 nm for distances of $\leq$0.5 nm) and have been employed to investigate the structure of biomolecules and polymeric materials.[2,3]

In relatively rare circumstances, internuclear distance measurements can be made directly from well-resolved splittings in powder spectra.[4] A more common situation is for the shielding anisotropy and the multiplicity of homonuclear and heteronuclear couplings to obscure the splittings associated with coupled spins. It is therefore necessary to improve the spectral resolution using MAS, which attenuates these interactions, and to reintroduce the homonuclear dipolar couplings using a selectively engineered pulse sequence. Until quite recently, few MAS recoupling experiments had been proposed, in part due to the complexity of the theoretical analysis, which requires consideration of the time-dependent spin interactions during MAS. The complications arise because of the noncommutation of the flip-flop term of the homonuclear dipolar Hamiltonian with the chemical shift interactions.

This article describes several homonuclear MAS recoupling schemes. Rotational resonance (R^2)[5,6] relies on the mechanical motion of the sample rotor to recouple the spin system, while dipolar recovery at the magic angle (DRAMA),[7,8] unified spin echo and magic echo (USEME),[9,10] simple excitation for the dephasing of rotational echo amplitudes (SEDRA),[11] and rf-driven recoupling (RFDR),[12,13] employ multiple pulse sequences to interfere with the spatial averaging imposed by MAS. The coupled spin systems which are currently addressed with these schemes are comprised of 'magnetically dilute' spin$-\frac{1}{2}$ pairs, such as ^{13}C–^{13}C, ^{15}N–^{15}N, or ^{31}P–^{31}P. Typical ^{13}C dipolar strengths are $\sim$2 kHz for directly bonded spin pairs, and decrease to $<$50 Hz for distances $\sim$0.4 to 0.6 nm, which are of interest in structural problems. Owing to the small magnitude of these couplings, and also due to the low natural abundance of some nuclei (e.g. 1.1% for ^{13}C and 0.33% for ^{15}N), samples are prepared with selective or uniform labeling, and dipolar couplings are measured within the high-resolution environment afforded by MAS.

2 DIPOLAR HAMILTONIAN UNDER MAGIC ANGLE SPINNING

The dipolar Hamiltonian describes the coupling of nuclear magnetic moments in a high magnetic field, and can be expressed in the general form

$$\mathcal{H}_{\mathrm{D}}(t) = \sum_{i<j} \omega_{ij}^{\mathrm{D}}(t)[3I_{zi}I_{zj} - \boldsymbol{I}_i \cdot \boldsymbol{I}_j] \qquad (1)$$

Equation (1) is composed of two parts, the bilinear 'A' term, $2I_{zi}I_{zj}$, and the flip-flop 'B' term $-\frac{1}{2}[I_{-1}I_{+2} + I_{+1}I_{-2}]$. The coefficients, $\omega_{ij}^{\mathrm{D}}(t)$, are directly proportional to the magnitude of the dipole–dipole interaction between nuclei i and j according to equation (2), where r_{ij} is the internuclear distance, γ_i and γ_j are the gyromagnetic ratios of the two nuclei, and $\theta_{ij}(t)$ is the time-dependent angle between the static magnetic field and the internuclear vector:

$$\omega_{ij}^{\mathrm{D}}(t) = \frac{\mu_0}{4\pi}\frac{\gamma_i\gamma_j}{r_{ij}^3}\left(\frac{1-3\cos^2\theta_{ij}(t)}{2}\right) \qquad (2)$$

When the rotor axis is oriented at the magic angle, all terms of equation (2) become time-dependent.

For 'unlike' spins (i.e. possessing different γs), the flip-flop term in equation (1) is truncated, and the heteronuclear dipolar Hamiltonian reduces to the 'A' contribution. For 'like' spins, the flip-flop term is usually truncated when the difference in isotropic chemical shifts, $\Delta\omega = \omega_1 - \omega_2$, between the spins is relatively large compared with the dipole coupling, and the resulting Hamiltonian is similar to the heteronuclear case. This situation is frequently encountered for ^{13}C and ^{15}N spins. For ^{1}H pairs, the more common situation is $|\mathcal{H}_{\mathrm{D}}| \gg \Delta\omega$, and both terms in equation (1) are significant.

MAS imparts a time dependence to the chemical shift and dipolar coupling terms in the Hamiltonian. The chemical shift Hamiltonian ($\mathcal{H}_{\mathrm{CS}}$) consists of a time-independent isotropic contribution and oscillating terms due to the shielding anistropy, and it is efficiently averaged by MAS even if the rotation frequency, ω_{r} is less than the magnitude of $|\mathcal{H}_{\mathrm{CS}}|$, resulting in sharp spectral lines. The consequent MAS spectrum is comprised of a centerband at ω_{i}, flanked by a set of rotational sidebands spaced at integer multiples of ω_{r}. The 'inhomogeneous' dynamics of $\mathcal{H}_{\mathrm{CS}}$ arises from the fact that it is self-commuting at different times.[14] The heteronuclear coupling term is also inhomogeneous, and dipolar terms between weakly coupled spins are strongly attenuated at typical

MAS spinning speeds (3–12 kHz). In contrast, the homonuclear dipolar coupling behaves homogeneously in that sharp sidebands are not formed unless the rotation rate exceeds the coupling strength, $\omega_r \gg |\mathcal{H}_D|$. Under most conditions, the chemical shift difference also leads to truncation of the flip-flop term.

3 ROTOR-DRIVEN HOMONUCLEAR RECOUPLING

For homonuclear spin pairs, the energy mismatch created by the isotropic chemical shift difference limits the efficiency of magnetization exchange via the dipolar flip-flop term. An exception occurs when the sample rotation frequency satisfies the rotational resonance (R^2) condition, $\Delta\omega = n\omega_r$, where n is a small integer.[15] At R^2, the macroscopic sample spinning frequency matches the energy difference between two chemically shifted spins, and the dipolar flip-flop term again becomes significant. The reintroduction of the dipolar coupling permits energy to exchange between the spins at an enhanced rate which is governed by the coupling strength, and furthermore, induces spectral line broadening and splittings that are particularly prominent for strongly coupled spins.

In 1988, Raleigh et al. rediscovered the R^2 phenomenon and recognized that it could be exploited to measure weak homonuclear couplings.[5,6] The basis of this technique is a careful matching of spinning rate to the chemical shift difference ($\Delta\omega = n\omega_r$) and the detection of magnetization exchange between spin pairs. Figure 1 shows the pulse sequence used for measuring the distance between two chemically shifted spins I_{z1} and I_{z2}. A nonequilibrium population is established by inverting one of the resonance lines, and longitudinal exchange of the magnetization between coupled spins occurs during the mixing time, τ_m. The free induction decay signal is recorded for a number of discrete mixing times, and a plot of the difference polarization $\frac{1}{2}(I_{z1} - I_{z2})$ is compared with a numerical simulation of the exchange for the estimated dipolar coupling strength.

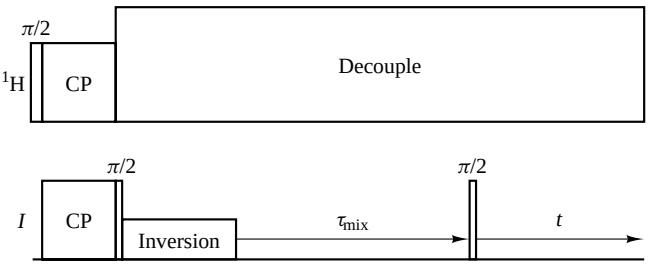

Figure 1 The R^2 pulse sequence. Initial transverse magnetization, generated with cross polarization, is placed along the z axis using a $\pi/2$ pulse. A population imbalance is created by inverting one resonance peak using a weak, selective pulse or DANTE sequence. Rotor-driven magnetization exchange takes place between coupled spins if the sample spinning rate is adjusted to match the difference in isotropic chemical shifts ($\Delta\omega_{iso} = n\omega_r$). After a variable mixing period, τ_m, a second ($\pi/2$) pulse returns the magnetization to the transverse plane and the remaining difference in signal intensities, $\frac{1}{2}(I_{z1} - I_{z2})$, is recorded as a free induction decay signal. A magnetization exchange curve is generated by recording this quantity for a number of discrete mixing times, usually between 0–30 ms. Strong proton decoupling reduces dephasing by abundant protons and helps to maintain a sharp R^2 condition

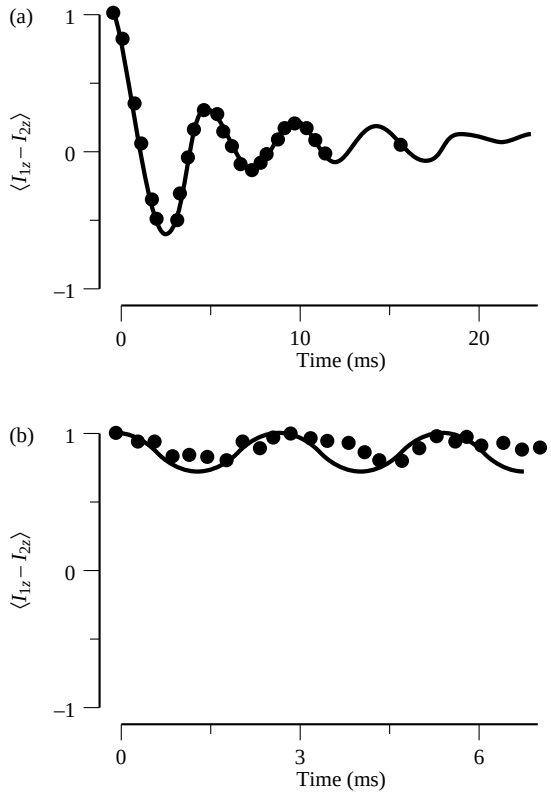

Figure 2 (a) Experimental (•) and simulated (–) magnetization exchange curve for double-^{13}C-labeled zinc acetate $Zn^{+2}(CH_3COO^-)_2.2H_2O$ recorded at the $n = 3R^2$ condition ($\omega_r/2\pi$ = 4.38 kHz). Experimental points represent the difference magnetization $\frac{1}{2}(I_{z1} - I_{z2})$ normalized to $\tau_m = 0$. (b) The magnetization exchange curve recorded at $\omega_r/2\pi$ = 4.26 kHz, corresponding to an off-R^2 condition. Simulation parameters for zinc acetate are found in Levitt et al.[6]

A demonstration of magnetization exchange at the $n = 3$ condition is shown in Figure 2(a) for 1,2-^{13}C-labeled zinc acetate $Zn^{2+}(CH_3COO^-)_2.2H_2O$, where oscillatory decay of the difference magnetization arises from exchange between these strongly coupled spins. A numerical simulation of the magnetization curve is also shown and corresponds to an internuclear distance of 0.151 ± 0.002 nm. Figure 2(b) shows the difference polarization recorded at a sample rotation rate which is set 120 Hz away from the $n = 3R^2$ condition. Model compound studies have demonstrated that internuclear distances ≤0.6 nm to a resolution of ±0.005 to ±0.02 nm are accessible via the R^2 method.

The theoretical aspects of magnetization exchange at the R^2 condition are treated in a number of works using Average Hamiltonian theory[6,16,17] and Floquet theory.[17–19] A fictitious field approach, wherein magnetization exchange is described within a $\{|2\rangle,|3\rangle\}$ subspace, provides a geometric description of resonant magnetization exchange.[6,13] The Floquet analysis leads to an expression for the effective Hamiltonian at sample rotation rates close to the R^2 condition $\Delta\omega \approx n\omega_r$ and which is valid for synchronous acquisition of the data:

$$\bar{\mathcal{H}}_{eff} = \tfrac{1}{2}(\Delta\omega - n\omega_r)[I_{z1} - I_{z2}] + \tfrac{1}{2}|\omega_{eff}^{D}(n)|[I_{+1}I_{-2} + I_{-1}I_{+2}] \quad (3)$$

The first term in equation (3) represents the offset from the R^2 condition. In general, the effective dipolar frequency $|\omega_{\text{eff}}^{\text{D}}(N)|$ appearing in the second term depends on both the coupling and the shielding anisotropies. However, in the case of small shielding anisotropy, it reduces to the magnitude of the nth Fourier coefficient $|\omega_n^{\text{D}}(\alpha, \beta)|$ of the time-dependent prefactor in equation (3), where (α, β) denote the orientation of the internuclear vector in a frame rotating with the rotor.

The exact time course of magnetization exchange at R^2 is determined by the magnitude of the homonuclear dipolar coupling, the principal values of the I_{z1} and I_{z2} chemical shift tensors, the relative orientations of the chemical shift and dipolar tensors, and the isotropic J coupling of the spin pair. Magnetization exchange rates are insensitive to molecular orientations for the $n = 1$ condition for a typical application, but have a stronger dependence for higher resonance orders.[20] In some circumstances, this sensitivity can be exploited to yield additional structural information, in the form of tensor orientations, from MAS spectra.

The R^2 analysis also requires an estimation of the zero quantum relaxation time, T_2^{ZQ} which is associated with the zero quantum coherence $(I_{x1}I_{y2} - I_{y1}I_{x2})$. Kubo and McDowell have shown that it can be approximated by the individual single quantum relaxation rates, T_2.[19] An estimate of $(T_2^{\text{ZQ}})^{-1}$ is therefore found by summing the inverse linewidths of resonance peaks (measured at an off-R^2 condition) after correction for magnet inhomogeneity. The zero quantum relaxation pathway competes with magnetization exchange at R^2 and is most significant when couplings are weak or resonance peaks are broad. Under these circumstances, the exchange processes is damped, and the magnetization exchange decays monotonically.

The R^2 technique has been applied to a variety of biological solid state systems. Examples include the investigation of the mechanism of inactivation in a ^{31}P-labeled enzyme bound inhibitor,[21] establishing the folding motif of membrane-bound peptides,[22] measuring retinal-to-protein distances in the 26 kDa integral membrane protein bacteriorhodopsin,[23,24] and describing the amide bond geometry of a fragment of the β-amyloid protein associated with Alzheimer's disease.[25]

4 HOMONUCLEAR RECOUPLING VIA SPIN ECHOES

RFDR (rf-driven dipolar recoupling) and SEDRA (simple excitation for the dephasing of rotational echo amplitudes) are two related approaches employing spin echoes to reintroduce homonuclear dipolar couplings to MAS spectra. In both experiments, recoupling is accomplished via the modulation of the dipolar Hamiltonian by the difference in chemical shifts between the coupled spins. Both schemes lead to an efficient reintroduction of the homonuclear dipolar interaction across a broad range of chemical shift differences and MAS spinning speeds.

The SEDRA experiment is based on the observation of transverse echo dephasing during a rotor-synchronized π pulse train. Dephasing due to shielding anisotropy and heteronuclear interactions is refocussed after each pair of spin echo π pulses, while a net dephasing arises from the homonuclear dipolar flip-flop term. A train of rotor-synchronized π pulses is also used

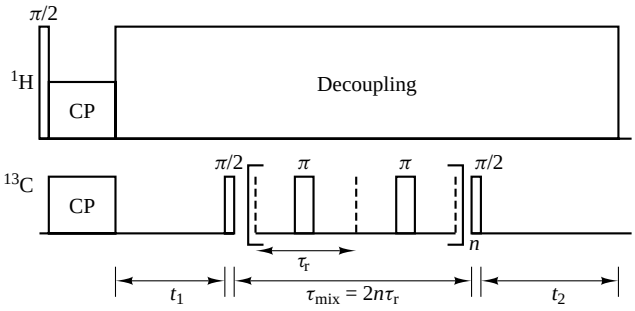

Figure 3 The RFDR pulse scheme for 2D homonuclear correlation spectroscopy. Following cross polarization to create transverse S spin magnetization (shown here for ^{13}C), spins evolve according to their chemical shifts during t_1. A nonselective $\pi/2$ pulse places the magnetization of one spin along the z axis. During a variable mixing time, τ_{m}, single π pulses (one per rotor period, τ_{r}) drive longitudinal magnetization exchange between coupled spins. A second nonselective $\pi/2$ pulse returns the magnetization to the transverse plane and S spin magnetization is recorded. The SEDRA sequence involves monitoring the dephasing with the same MAS spin echo sequence. Reprinted from Bennett et al.[12]

for RFDR, but the exchange of longitudinal magnetization among dipolar coupled spins is detected instead. Figure 3 shows a diagram of the RFDR pulse sequence. In the one-dimensional (1D) version, an inversion pulse is employed, and magnetization exchange between coupled spins is reported by the time course of the difference polarization. A 2D version of the experiment utilizes a t_1 evolution period, and the resulting chemical shift correlation spectra show cross peaks between dipole coupled sites.

The spin dynamics of the spin echo recoupling sequence can be approximated with average Hamiltonian theory[12] or Floquet theory.[11] The zeroth order result (neglecting shielding anisotropy) for a spin echo cycle of one π pulse per rotor period is an effective Hamiltonian containing only a dipolar flip-flop term:

$$\bar{\mathcal{H}}_{\text{eff}}^{(0)} = \tfrac{1}{2}\bar{\omega}_{\text{eff}}^{\text{D}}[I_{+1}I_{-2} + I_{+2}I_{-1}] \tag{4}$$

The dipolar frequency, $\bar{\omega}_{\text{eff}}^{\text{D}}$ depends on the spinning speed ω_{r} and $\Delta\omega$ as follows:

$$\bar{\omega}_{\text{eff}}^{\text{D}} = \frac{2}{\pi}\sum_{n=1,2}\text{Re}\{\omega_n^{\text{D}}(\alpha,\beta)\}\frac{\frac{\Delta\omega}{\omega_{\text{r}}}}{\left(\frac{\Delta\omega}{\omega_{\text{r}}}\right)^2 - n^2} \times(-1)^{n-1}\sin\left(n\pi\frac{\Delta\omega}{\omega_{\text{r}}}\right) \tag{5}$$

The dipolar frequency has maxima at the rotational resonance conditions, but significant recoupling is achieved over a broader range. The pulse sequence is particularly effective in recoupling under the condition $\omega_{\text{r}} \leq \Delta\omega \leq 2\omega_{\text{r}}$.

Simulation of the magnetization exchange during RFDR (monitored by 2D cross-peak intensities or 1D exchange curves) and dephasing during SEDRA experiments requires the measurement or reasonable estimation of relaxation parameters, and all relevant chemical shift and dipolar tensors parameters and orientations, as in the case of R^2.

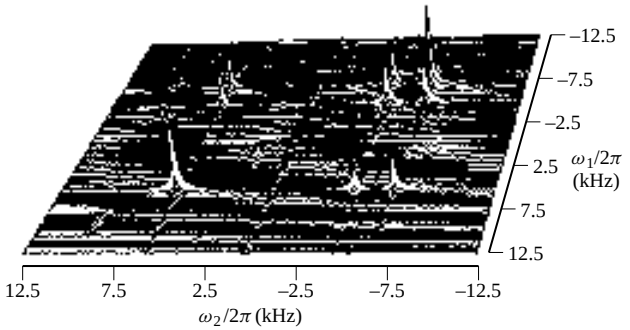

Figure 4 A stack plot of the 2D RFDR magnitude spectrum of uniformly ^{13}C-labeled alanine recorded with τ_m = 8.6 ms and $\omega_r/2\pi$ = 3.72 kHz. Cross peaks demonstrate the dipolar coupled spins. In this example, cross peaks from directly bonded ^{13}C nuclei appear in $\leq$ 2 ms. Reprinted from Bennett et al.[12]

SEDRA and RFDR are 'broadband' recoupling schemes that offer some important advantages over the R^2 technique in situations where spectral lines are inhomogeneously broadened, or when it is not feasible to match the rotation rate dictated by the R^2 condition. The RFDR technique and the recently introduced *t*-SEDRA experiment[26], are suitable for 2D homonuclear dipolar correlation spectroscopy, and may be used to map couplings between more than two coupled spins, if the exchange of magnetization between all coupled spins is traced. A demonstration of the 2D RFDR correlation experiment is given in Figure 4, for uniformly ^{13}C-labeled alanine, where cross peaks between all coupled ^{13}C sites are prominent after a mixing time of 8.6 ms. A similar 2D approach was adopted to examine the geometry of two conformers in the membrane protein bacteriorhodopsin.[27]

5 DIRECT RECOUPLING SEQUENCES: DRAMA AND USEME

A direct reintroduction of the homonuclear coupling is accomplished with rotor synchronized $\pi/2$ pulses in the DRAMA (dipolar recovery at the magic angle) experiment. This scheme, shown in Figure 5, relies on the interference between the RF modulation of the dipolar spin operators and the oscillations imposed on them by MAS. Chemical shift interactions are removed to zeroth order through the use of π pulses. The recoupling effect in DRAMA does not require the existence of chemical shift differences between the spins. However, it is most efficient when the chemical shift anisotropies and resonance offsets are small compared with ω_r since these interactions complicate the spin dynamics and lead to a loss of magnetization.

The effective Hamiltonian can be obtained with Floquet theory[28] or average Hamiltonian theory.[7,8] The latter analysis, equation (6) yields a nonzero dipolar term:

$$\bar{\mathcal{H}}^{(0)}_{\text{eff}} = \frac{4}{\pi}\text{Re}\left\{\omega^{\text{D}}_{n=1}(\alpha,\beta)\right\}\bar{\omega}^{\text{D}}_{\text{eff}}(I_{z1}I_{z2} - I_{y1}I_{y2}) \qquad (6)$$

DRAMA has also been extended to include double quantum filtering, which restricts the detected NMR signal to resonances from coupled spin pairs and therefore simplifies the spectra of

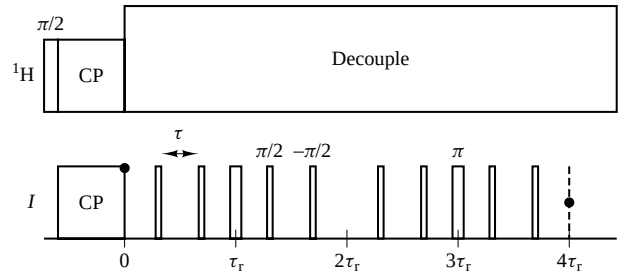

Figure 5 The DRAMA pulse sequence. The pulse cycle, consisting of 4 τ_r is comprised of a pair of $\pi/2$ pulses with alternating phase **X**, **X**, and two π pulses which are also alternated by **X**, $\bar{\mathbf{X}}$. The $\pi/2$ pulses interfere with dipolar refocussing by MAS

complex molecules.[8] This approach has been used to enhance selectively the signal of ^{13}C sites within a $\sim$0.5 nm radius of a selectively labeled site in an undecapeptide of molecular mass 1100.

Direct recoupling of the dipolar interaction is also achieved with a continuous rf field applied during the second half of each rotor cycle. This approach, called USEME (unified spin echo and magic echo) utilizes the partial cancellation of rotational echo refocussing via a combined spin echo and magic echo sequence to yields a scaled homonuclear coupling.[9,10]

6 EMERGING TECHNIQUES

Improvements in the efficiency of homonuclear recoupling schemes remains an important goal. Several recently introduced homonuclear recoupling sequences hold the promise of compensating for the complications introduced by large chemical shift differences in DRAMA-type experiments.[29,30] The MELODRAMA (melding of spin locking and DRAMA) method reintroduces the dipolar coupling in a spin-locking interaction frame by utilizing 90° rotor-synchronized phase shifts.[31] The recoupling effect is relatively insensitive to chemical shift and anisotropy, rendering the method suitable for 2D correlation spectroscopy. The double quantum filtering experiment called HORROR (homonuclear rotary resonance), utilizes a rotary resonance condition between the sample rotation frequency and the rf field to provide efficient double quantum transfer between coupled spin pairs.[32] A novel approach to homonuclear recoupling that combines angle switching and phase shifted π and $\pi/2$ pulses was recently reported by Tycko.[33] This experiment, called NASDY (normal angle spinning dipolar spectroscopy) takes advantage of the static contribution to the dipolar coupling by recovering this contribution at a sample rotation angle other than the magic angle.

7 CONCLUDING REMARKS

Solid state NMR experiments that restore dipolar couplings to MAS spectra are becoming increasingly important for investigating the molecular structure of polycrystalline and amorphous materials. These experiments provide geometric information by measuring precise distance measurements and establishing spatial connectivities. Selectivity is also offered

through the choice of nucleus and specific labeling scheme. Potential applications include distinguishing between various protein folding patterns, determining the bonding arrangements of molecules absorbed on surfaces, mapping the interface between two materials or phases such as polymer blends, and elucidating active site geometries in biomolecules.

A number of important challenges remain in the development of homonuclear recoupling schemes; these include improvements in sensitivity for the detection of weak couplings and extension of these methods to multiple spin environments in a manner analogous to multidimensional solution NMR. Such developments will vastly improve the efficiency of gathering structural information via solid state NMR.

8 RELATED ARTICLES

Average Hamiltonian Theory; Dipolar and Indirect Coupling Tensors in Solids; Magic Angle Spinning; REDOR and TEDOR; Rotational Resonance in Biology; Sideband Analysis in Magic Angle Spinning NMR of Solids.

9 REFERENCES

1. R. R. Ernst, G. Bodenhausen, and A. Wokaun, *Principles of Nuclear Magnetic Resonance in One and Two Dimensions*, Oxford University Press, Oxford, 1987.
2. J. M. Griffiths and R. G. Griffin, *Anal. Chim. Acta*, 1993. **283**, 1081.
3. A. E. Bennett, R. G. Griffin and S. Vega, in *NMR Basic Principles and Progress*, ed. B. Blümich, Springer-Verlag, Berlin, 1994, Vol. 32, p. 1.
4. G. E. Pake, *J. Chem. Phys.*, 1948 **16**, 327.
5. D. P. Raleigh, M. H. Levitt, and R. G. Griffin, *Chem. Phys. Lett.*, 1988, **146**, 71.
6. M. H. Levitt, D. P. Raleigh, F. Cruezet, and R. G. Griffin, *J. Chem. Phys.*, 1990, **92**, 6347.
7. R. Tycko and G. Dabbagh, *Chem. Phys. Lett.*, 1990, **173**, 461.
8. R. Tycko and S. O. Smith, *J. Chem. Phys.*, 1993, **98**, 932.
9. A. Ramamoorthy, T. Fujiwara and N. Nagayama, *J. Magn. Reson., Ser. A*, 1993, **104**, 366.
10. T. Fujiwara, A. Ramamoorthy, K. Nagayama, K. Hioka, and T. Fujito, *Chem. Phys. Lett.*, 1993, **212**, 81.
11. T. Gullion and S. Vega, *Chem. Phys. Lett.*, 1992, **194**, 423.
12. A. E. Bennett, J. H. Ok, and R. G. Griffin, *J. Chem. Phys.*, 1992, **96**, 8634.
13. D. K. Sodickson, M. H. Levitt, S. Vega, and R. G. Griffin, *J. Chem. Phys.*, 1993, **98**, 6742.
14. M. M. Maricq and J. S. Waugh, *J. Chem. Phys.*, 1979, **70**, 3300.
15. E. R. Andrew, A. Bradbury, R. G. Eades and V. T. Wynn, *Phys. Lett.*, 1963, **4**, 99.
16. Z. H. Gan and D. M. Grant, *Mol. Phys.*, 1989, **67**, 1419.
17. T. Nakai and C. A. McDowell, *Mol. Phys.*, 1992, **77**, 569.
18. A. Schmidt and S. Vega, *J. Chem. Phys.*, 1992, **4**, 2655.
19. A. Kubo and C. A. McDowell, *J. Chem. Soc., Faraday Trans.*, 1988, **84**, 3713.
20. F. Creuzet, D. P. Raleigh, M. H. Levitt, and R. G. Griffin, submitted 1994.
21. A. E. McDermott, F. Creuzet, R. G. Griffin, L. E. Zawadzke, Q. Ye, and C. T. Walsh, *Biochemistry*, 1990, **29**, 5767.
22. O. B. Peerson, S. Yoshimura, H. Hojo, S. Aimoto, and S. O. Smith, *J. Am. Chem. Soc.*, 1992, **114**, 4332.
23. L. M. Thompson, A. E. McDermott, J. Raap, C. M. van den Wielen, J. Lugtenburg, J. Herzfeld, and R. G. Griffin, *Biochemistry*, 1992, **31**, 7931.
24. K. V. Lakshmi, M. Auger, J. Raap, J. Lugtenburg, R. G. Griffin, and J. Herzfeld, *J. Am. Chem. Soc.*, 1993, **115**, 8515.
25. R. G. S. Spencer, K. J. Halverson, M. Auger, A. E. McDermott, R. Griffin, and P. T. Lansbury Jr., *Biochemistry*, 1991, **30**, 10 382.
26. O. Weintraub, S. Vega, C. Hoelger and H. H. Limbach, submitted, 1994.
27. J. M. Griffiths, K. V. Lakshmi, A. E. Bennett, J. Rapp, J. Lugtenburg, J. Herzfeld, and R. G. Griffin, *J. Am. Chem. Soc.*, 1994, **116**, 10 178.
28. O. Weintraub, and S. Vega, *J. Magn. Reson., Ser. A*, 1993, **105**, 245.
29. C. A. Klug, W. Zhu, M. E. Merritt and J. Schaefer, *J. Magn. Reson., Ser. A*, 1994, **109**, 134.
30. J. Callahan and G. Drobny, *Poster presentation at the Experimental Nuclear Magnetic Resonance Conference, CA, Asilomar, April 10-15, 1994*.
31. B. Sun, P. R. Costa, D. Kocisko, P. T. Lansbury, Jr., and R. G. Griffin, *J. Chem. Phys.*, 1995, **102**, 702.
32. N. C. Nielson, H. Bildsoe, H. J. Jakobsen, and M. H. Levitt, *Poster presentation at the Experimental Nuclear Magnetic Resonance Conference*, Asilomar, CA, April 10–15, 1994.
33. R. Tycko, *J. Am. Chem. Soc.*, 1994, **116**, 2217.

Acknowledgments

The authors acknowledge the support of the National Institutes of Health (GM-23403, GM-23289, GM-25505 and RR-00995). We wish to acknowledge P. R. Costa, F. Creuzet, M. H. Levitt, A. E. McDermott, D. P. Raleigh, D. K. Sodickson, B. Q. Sun, and S. Vega for stimulating discussions and for their contributions to the development of these NMR techniques.

Biographical Sketches

Janet M. Griffiths. *b* 1963. B.Sc. University of Cincinnati (Chemical Engineering), 1985; Ph.D., University of California, Berkeley (Chemical Engineering), 1992. American Cancer Society postdoctoral fellow, Department of Chemistry & Francis Bitter National Magnet Laboratory, Massachusetts Institute of Technology, 1992–1995. Research interests; the development and application of NMR techniques to investigate the structure of heterogeneous systems including catalytic surfaces and membrane proteins.

Andrew E. Bennett. *b* 1964. B.A., Wesleyan University (Chemistry), 1986; M.S., University of California, Berkeley (Physical Chemistry), 1990; Ph.D., Department of Chemistry & Francis Bitter National Magnet Laboratory, Massachusetts Institute of Technology, 1995. Research interest; the development of new methods for the measurement of dipolar couplings in solids.

Robert G. Griffin. *b* 1942. B.S., University of Arkansas, 1964; Ph.D., Washington University (St. Louis), 1969; postdoctoral fellow, Department of Chemistry, MIT 1969–72. Staff member Francis Bitter National Magnet Laboratory, MIT, 1972–1989; Professor of Chemistry, MIT 1989–current; Director, Francis Bitter National Magnet Laboratory, 1992–current. Approximately 190 publications. Research interests: development of new methods for performing high resolution NMR experiments in solids, high frequency EPR, and applications of these techniques to problems in biological, chemical, and physical systems.

Multiple Quantum Coherences in Extended Dipolar Coupled Spin Networks

Serge Lacelle
Université de Sherbrooke, Quebec, Canada

1	Background and Phenomenology	1
2	Ensemble Considerations	2
3	Quantum Mechanics of an N-Spin Subsystem	3
4	Quantum Statistical Mechanics of an Ensemble of N-Spin Subsystems	4
5	Development of Multiple Spin/Multiple Quantum Coherences in Dipolar Coupled Solids	5
6	Statistical Properties of Distributions of Dipolar Coupling Constants and Their Products in Large Spin Networks	7
7	Dynamical Scale Invariance in the Growth of Multiple Spin Correlations in Dipolar Coupled Solids	8
8	Related Articles	9
9	References	10

1 BACKGROUND AND PHENOMENOLOGY

In condensed matter, dipolar interactions among nuclear magnetic moments and their manipulation in multiple quantum (MQ) NMR experiments induce multiple spin correlations. The temporal and spatial development of these collective modes yield information about the structure and the dynamics of spin networks.[1–3] In this article, we examine the fundamental aspects of the growth of multiple spin/multiple quantum coherences in extended dipolar coupled spin networks driven by rf magnetic fields.

In MQ NMR, investigations of strongly dipolar coupled spin systems, such as rigid solids, the simplest relevant Hamiltonian needed to describe and understand experimental observations in a laboratory reference frame is given by

$$\hat{\mathcal{H}}(t) = \hat{\mathcal{H}}_{\mathrm{Z}} + \hat{\mathcal{H}}_{\mathrm{d}} + \hat{\mathcal{H}}_{\mathrm{rf}}(t) \tag{1}$$

The contributions to $\hat{\mathcal{H}}(t)$ in equation (1) include the interactions of the nuclear magnetic moments with a strong static magnetic field ($\hat{\mathcal{H}}_{\mathrm{Z}}$), with other nuclear magnetic moments through dipolar interactions ($\hat{\mathcal{H}}_{\mathrm{d}}$), and with time-dependent rf magnetic fields ($\hat{\mathcal{H}}_{\mathrm{rf}}$). Furthermore, $[\hat{\mathcal{H}}_{\mathrm{Z}}, \hat{\mathcal{H}}_{\mathrm{d}}] = 0$, and $[\hat{\mathcal{H}}_{\mathrm{Z}} + \hat{\mathcal{H}}_{\mathrm{d}}, \hat{\mathcal{H}}_{\mathrm{rf}}] \neq 0$.

In order to simplify the description and make connection with experiments, the Hamiltonian of equation (1) is transformed to a frame rotating about the z axis of the laboratory frame at the nuclear spin precession frequency. In this new reference frame, $\hat{\mathcal{H}}_{\mathrm{Z}}$ disappears. A further transformation to another noninertial frame, the rf toggling frame which 'follows' the directions of the rf fields during a pulse sequence, produces an effective Hamiltonian $\hat{\mathcal{H}}_{\mathrm{de}}(t)$. In this newest frame, $\hat{\mathcal{H}}_{\mathrm{de}}(t)$ results from the modulation of $\hat{\mathcal{H}}_{\mathrm{d}}$ by the time-dependent rf fields. The time average of $\hat{\mathcal{H}}_{\mathrm{de}}(t)$ over the period of a cycle of a multiple pulse excitation sequence yields, under appropriate conditions, a time-independent average Hamiltonian $\tilde{\hat{\mathcal{H}}}_{\mathrm{d}}$:

$$\tilde{\hat{\mathcal{H}}}_{\mathrm{d}} = \sum_{j>k} D_{jk}\, f(\hat{\boldsymbol{I}}_j, \hat{\boldsymbol{I}}_k) \tag{2}$$

where D_{jk} is a dipolar coupling constant between spins j and k

$$D_{jk} = \frac{\gamma^2\hbar^2(3\cos^2\theta_{jk} - 1)}{2r_{jk}^3} \tag{3}$$

and $f(\hat{\boldsymbol{I}}_j,\hat{\boldsymbol{I}}_k)$ is a function of bilinear operators involving the components of the spin angular momentum operators $\hat{\boldsymbol{I}}$, of spins j and k.

Formally, the geometrical interpretations of these transformations correspond to unitary transformations on the state of the spin system (i.e. the density operator) and its dynamical variables (i.e. the spin angular momentum and Hamiltonian operators). The resulting interaction pictures associate different parts of the time dependence of the physical system [i.e. the spins in the sample evolving under the Hamiltonian in equation (1)] to the state of the system and to the dynamical variables. This procedure is generic to all NMR experiments involving the manipulation of spin Hamiltonians. By a judicious choice of a reference frame, different portions of the Hamiltonian can be selected to appear to dominate the spin dynamics; hence, the possibility to discriminate among the various contributions in a spin Hamiltonian. Such an approach underlies the success of NMR spectroscopy. It is noteworthy that these transformations, from one frame to another, inertial or noninertial, do not necessarily preserve the invariance and conservation principles of physics. For example, spin energies measured in the laboratory frame are different from those measured in the rotating frame, while the spin quantum numbers, $I = \frac{1}{2}$ for protons, remain identical. However, observations restricted within a reference frame will be consistent with known laws of physics.

In pulsed NMR experiments, the evolution of the spin system is detected in the rotating frame. The time development of the spin system under $\tilde{\hat{\mathcal{H}}}_{\mathrm{d}}$ in the toggling frame is monitored directly, in multiple pulse line-narrowing sequences such as MREV-8, or indirectly, in MQ NMR, by stroboscopic observations when both the rotating and the toggling frames coincide.

A variety of rf multiple pulse sequences have been tailored to produce different average dipolar Hamiltonians $\tilde{\hat{\mathcal{H}}}_{\mathrm{d}}$. In MQ NMR experiments,[1–3] $[\hat{\mathcal{H}}_{\mathrm{Z}}, \tilde{\hat{\mathcal{H}}}_{\mathrm{d}}] \neq 0$. The spin portions [see equation (2)] $f(\hat{\boldsymbol{I}}_j,\hat{\boldsymbol{I}}_k)$ of these nonsecular average dipolar Hamiltonians include, among the bilinear spin operators, terms like $\hat{I}_{jz}\hat{I}_{k\pm}$, and $\hat{I}_{j\pm}\hat{I}_{k\pm}$, where $\hat{I}_+$ and $\hat{I}_-$ correspond to the raising and lowering (or ladder) spin angular momentum operators, respectively. These operators in $\tilde{\hat{\mathcal{H}}}_{\mathrm{d}}$ are responsible for the radiative coupling of Zeeman nuclear spin states with differing magnetic quantum numbers M_z by ±1 and ±2.

Evolution under $\bar{\mathcal{H}}_d$ for extended periods of time leads to nonstationary states with possibly larger differences in ΔM_z, as discussed in the next section. MQ NMR pulse excitation sequences for solids are specifically designed and optimized to generate multiple spin/multiple quantum coherences among the spins in a macroscopic sample.

The selection rules for the observation of transverse magnetization, or single spin/single quantum coherences, correspond to transitions with $\Delta M_z = \pm 1$. Thus, the creation and evolution of coherent superpositions of quantum states with $\Delta M_z \neq 1$ cannot be detected directly. Indirect piecewise mappings of multiple spin/multiple quantum coherences are accomplished through two-dimensional NMR methods as a function of the excitation and/or evolution times.[1–3] MQ NMR spectra obtained in this fashion reveal the presence of multiple spin/multiple quantum coherences with $\Delta M_z = n$, where n is the order of the coherences, in the sample during the excitation/evolution period (see Figure 1).

Figure 1 shows schematic MQ NMR spectra, obtained with time-resolved two-dimensional experiments, as a function of the excitation time. For a fixed excitation period, the spectral intensities decrease with increasing orders. With increasing excitation times, a redistribution of spectral intensities is observed to proceed or to 'flow' towards higher order coherences.

Understanding the behavior of the MQ NMR spectral intensity profiles of solids, as a function of order and excitation time, still poses an interesting challenge to NMR spectroscopists. Specifically, one would like to learn how the multiple spin dynamics depend on the lattice parameters and the space-filling properties of spin networks. Examples of the latter include spatial extent, morphologies, and effective dimensionalities of domain structures on mesoscopic length scales, i.e. in the range 1 nm to 1 μm, in condensed matter systems. More generally, the recognition of emergent properties, generic or universal behavior, amidst the complexities of this many-body problem with multiple scales, would deepen our understanding of the fundamental aspects of MQ NMR. These issues are addressed in the following sections, from the perspective of statistical mechanics.

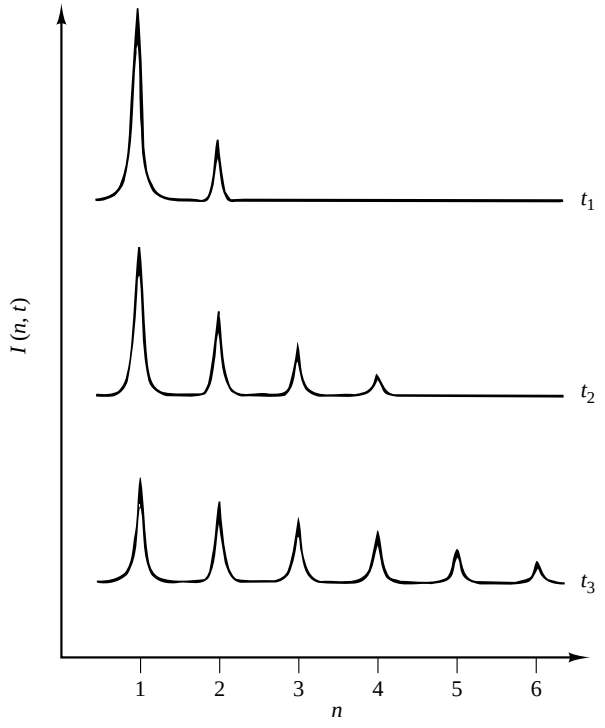

Figure 1 Typical MQ NMR spectra of a rigid solid: spectral intensities $I(n,t)$ as a function of order n and excitation time t, with $t_1 < t_2 < t_3$

2 ENSEMBLE CONSIDERATIONS

From a macroscopic point of view, in a MQ NMR experiment energy is pumped through rf magnetic fields produced by electronic devices into a solid sample residing in a strong static magnetic field. From a microscopic point of view, this injection of energy proceeds from individual nuclear magnetic moments, embedded in the lattice, to induce multiple spin correlations. Both the microscopic and macroscopic descriptions of the rf irradiation processes involve nonequilibrium driven systems: the macroscopic solid and the microscopic magnetic moments. As these experiments are performed in laboratories on a macroscopic scale, but interpreted microscopically, it is imperative to understand clearly how the macroscopic observables emerge from the numerous microscopic degrees of freedom.

A rigid solid is an aggregate of a large number of spatially fixed atoms. Various solids exist due to the nature of their constituents, which include atoms, ions, or molecules. In MQ NMR of rigid solids, ions and molecules lose their distinct identities on account of the through-space dipolar interactions among all magnetic moments. Hence, the spin network, consisting of the nuclear magnetic moments and their dipolar coupling constants, remains the only relevant and essential substratum onto which the microscopic degrees of freedom, the multiple spin coherences, evolve in MQ NMR experiments.

Solid samples used in MQ NMR investigations typically contain on the order of 10^{20} or more spins. The multiple spin correlations induced in spin networks by present-day MQ NMR methodologies involve coherences with up to possibly 10^2 spins. Consequently, the size difference between the sample and the multiple spin coherences suggests that the macroscopic observables, or responses, in MQ NMR experiments, arise from the random superposition of numerous multiple spin coherences. In other words, the sample could be viewed as an ensemble of loosely coupled subsystems.

Such a description of a macroscopic sample is certainly valid in liquid state NMR experiments, where under normal conditions, molecules behave as essentially independent subsystems. This outlook can also be extended to correlated molecular systems, as observed in critical fluctuations close to critical points.[4] For example, close to a consolute temperature, the intermolecular interactions among molecules in a critical binary fluid contrive and lead to composition fluctuations over length and timescales that can be quite large compared with those associated with the molecules, but still much smaller than those of the macroscopic sample. However, care must be exercised with such an analogy, since in critical phenomena systems are at equilibrium, while MQ NMR has to do with nonequilibrium driven systems. Possibly a more appropriate comparison for MQ NMR would be with the growth kinetics and processes of domain structures observed during phase

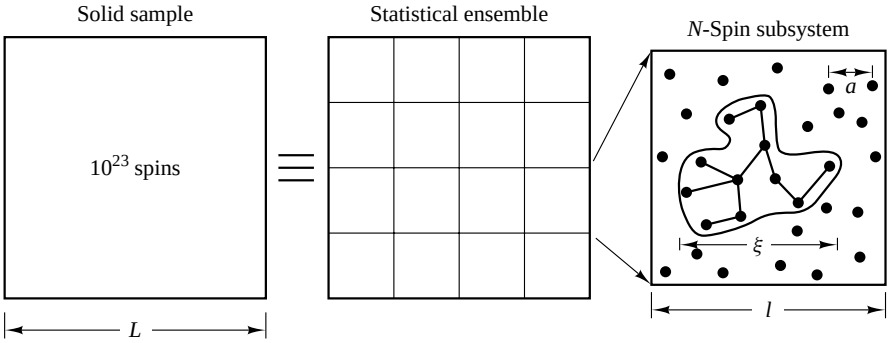

Figure 2 A macroscopic sample viewed as an ensemble of loosely coupled N-spin subsystems. Relevant length scales include: the lattice spacing a, the correlation length of a multiple spin coherence ξ, the extent of a subsystem l, and the sample size L, which satisfy $a < \xi < l \ll L$. Spins are denoted by •. An 11-spin coherence is also shown, with the lines representing the dipolar coupling constants appearing in the product, which multiplies the corresponding product operator term of the density operator

separation of binary fluids.[5] In this case, a similarity to critical phenomena exists; however, a richer behavior arises due to the nonequilibrium conditions and nonlinearity. In any event, the point at issue, that a macroscopic sample can be viewed, under certain conditions, as an ensemble of loosely coupled subsystems, where a subsystem can be one or several molecules, or even part of a spin network in a solid, would appear physically plausible.

Figure 2 shows a representation of a macroscopic sample as a statistical ensemble of N-spin subsystems. The number of spins N per subsystem is much smaller, by many orders of magnitude, than the total number of spins in the sample. The relevant length scales in this ensemble include the sample size L, the spatial extent of a subsystem l, the correlation length of the multiple spin coherences ξ, and the underlying lattice spacing a. This hierarchy of length scales satisfy the inequalities, $a < \xi < l \ll L$. Interaction energies between subsystems are assumed to be weak in comparison with interaction energies within the subsystems. This amounts to a neglect of surface effects for the MQ dynamics. Such approximation becomes more accurate in the limit when $\xi \ll l$. These effects are nevertheless necessary to achieve equilibrium or uniform spin temperature in the ensemble. The presence of the long-range dipolar interactions among the magnetic moments would appear to preclude or even invalidate this perspective of the sample as representing an ensemble of loosely coupled subsystems. However, as will be seen in Section 5, in time-resolved MQ NMR experiments, multiple spin coherences are 'weighted' by products of dipolar coupling constants. As it turns out, in spin networks, the distributions of dipolar coupling constants and their products are extremely wide. Since, at early excitation times, the MQ spin dynamics are dominated by the largest coupling constants and their products, the ensemble picture remains a good approximation for most experimental conditions. This approximation breaks down for mean field interpretations, e.g. MQ NMR experiments having infinite excitation periods.

Measurements performed over a short period of time on a macroscopic sample, made up of an ensemble of subsystems, correspond to averaging over the ensemble.[7] When a physical property of a macroscopic system is equal to this property averaged over the subsystems, spatial ergodicity exists. In statistical mechanics, the Gibbs canonical ensemble is composed of identical systems from the macroscopic point of view, i.e. they all have the same number of particles N, volume V, and temperature T. However, most systems are in different microscopic states. In the ensemble construction for a nonequilibrium driven macroscopic system, as described above, none of the subsystems need to be strictly identical. Instead, one assumes that statistical homogeneity is valid for the subsystems. On a subsystem scale, the statistical properties are stationary in space, i.e. a subsystem is statistically translationally invariant in space. Another feature of time-resolved MQ NMR measurements on such an ensemble, is the fact that, as the multiple spin coherences grow, so does their correlation length ξ. As the inequality $\xi < l$ must be satisfied for a consistent interpretation of the ensemble, this implies that the number of subsystems actually decreases as a function of time. This should be of no significant consequence, as long as $l \ll L$. Under present MQ NMR experimental conditions, these conditions are always satisfied, and the ensembles will consist of huge numbers of subsystems. Such ensembles yield asymptotic statistical states in experimental investigations.

Thus, a time-resolved MQ NMR measurement on a macroscopic solid is assumed to be equivalent to many independent measurements on the subsystems. Since the decomposition of the macroscopic sample into subsystems is not unique, the averaging process over the ensemble implied in a measurement is really a summation over the subsystems. As the spin dynamics are being probed on the scale of a subsystem, the response of the collective ensemble is taken to reflect the behavior of a typical subsystem. Underlying the spin dynamics are dipolar coupling constants and their products. Due to subtleties related to wide distributions and to averaging over products, the role of the couplings is more intricate than appears in the present discussion. For example, the distinction between average and typical behavior is very important in the MQ NMR of large spin networks.[6] We shall return to these issues in Section 6.

3 QUANTUM MECHANICS OF AN N-SPIN SUBSYSTEM

The focus on the spin dynamics within a subsystem and the subsequent averaging over a large collection of subsystems, yields a more tractable avenue to the understanding of

MQ NMR of solids, rather than treating a single spin system consisting of 10^{20} or more spins. Nevertheless, on the timescale of MQ NMR experiments, the spin dynamics within a subsystem still retain some of complexities of the many-body problem.

In a subsystem consisting of N spins I, there are $(2I + 1)^N$ stationary states of $\hat{\mathcal{H}}_Z$. For $I = \frac{1}{2}$, these 2^N energy levels can be classified according to the magnetic quantum numbers M_z given by

$$M_z = \sum_i^N m_{iz} \tag{4}$$

where m_{iz} is the eigenvalue ($m_z = \pm\frac{1}{2}$) of the ith spin. These Zeeman states, in the magnetic field $\boldsymbol{B}_0$, have corresponding energies

$$E_z = -\gamma\hbar B_0 M_z \tag{5}$$

and degeneracies

$$\Omega = \frac{N!}{(\frac{1}{2}N + M_z)!(\frac{1}{2}N - M_z)!} \tag{6}$$

The Zeeman manifolds are further broadened by homonuclear dipolar perturbations $\hat{\mathcal{H}}_d$. The resulting energy level diagram can be characterized, in principle, by the combined eigenvalues and eigenfunctions of $\hat{\mathcal{H}}_Z$ and $\hat{\mathcal{H}}_d$. However, due to the presence of bilinear spin operators in $\hat{\mathcal{H}}_d$, the combined eigenfunctions are constructed from direct products of $\hat{\mathcal{H}}_Z$ eigenfunctions. As a consequence, the m_{iz} eigenvalues are not good quantum numbers. In addition, the presence of large N rapidly makes this approach analytically intractable.

Therefore, as a first approximation, only the energy level diagram due to $\hat{\mathcal{H}}_Z$ is considered. This is justifiable, since the Zeeman splittings are usually of the order of tens to hundreds of megahertz as compared with tens of kilohertz for dipolar splittings. Radiative coupling of pairs of Zeeman levels leads to

$$\binom{2^N}{2} = 2^N(2^N - 1)/2 \tag{7}$$

possible transitions. The distinction between $+n$ and $-n$ coherences results in $2^N(2^N - 1)$ transitions. These transitions, or coherences, are classified according to their orders n. The number of coherences of order $n \neq 0$, Z_n, where $|n| \leq N$, is obtained from the constrained sum over the products of degeneracies of coupled Zeeman manifolds,

$$Z_n = \sum_{M_i - M_j = n} \binom{N}{\frac{1}{2}N + M_i}\binom{N}{\frac{1}{2}N + M_j} = \binom{2N}{N - n} \tag{8}$$

The number of coherences within a Zeeman manifold or with $n = 0$, Z_0, is given by

$$Z_0 \sum_{M_i = N/2+1}^{-N/2+1} \binom{N}{\frac{1}{2}N + M_i}\left[\binom{N}{\frac{1}{2}N + M_i} - 1\right] = \binom{2N}{N} - 2^N \tag{9}$$

Radiative coupling within a subsystem of N dipolar coupled spins $\frac{1}{2}$ can be rationalized, to a very good degree of approximation, on the basis of the possible $2^N(2^N - 1)$ transitions which connect the 2^N energy levels. The information content needed to describe this physical situation involves $2^N(2^N - 1)$ coherences and 2^N populations, or a total of 4^N parameters.

The 2^N eigenfunctions of $\hat{\mathcal{H}}_Z$, $|r\rangle$, for an N-spin-$\frac{1}{2}$ subsystem, constitute a complete basis set to characterize any spectroscopic experiments involving coherences and populations. As a consequence, any state $|\psi\rangle$ of a subsystem, can be expanded with the complete Zeeman basis set,

$$|\psi\rangle = \sum_{r=1}^{2^N} |r\rangle\langle r|\psi\rangle = \sum_{r=1}^{2^N} c_r|r\rangle \tag{10}$$

$$\langle r|\psi\rangle = c_r \tag{11}$$

Similarly, the observables or expectation values corresponding to any dynamical variables, such as the magnetization M_x, detected in a spectroscopic measurement on a subsystem, can be represented in this basis set with the corresponding operator $\hat{M}_x$ as,

$$\begin{aligned}\langle\psi|\hat{M}_x|\psi\rangle &= \sum_{r,s}\langle\psi|s\rangle\langle s|\hat{M}_x|r\rangle\langle r|\psi\rangle \\ &= \sum_{r,s} c_s^* c_r \langle s|\hat{M}_x|r\rangle\end{aligned} \tag{12}$$

where $c_r = \langle r|\psi\rangle$. The matrix elements $\langle s|\hat{M}_x|r\rangle$ are numbers related to the values of the dynamical variable M_x. The matrix elements, $c^*_s c_r$, are numbers describing the state $|\psi\rangle$ of the subsystem; there are 4^N such matrix elements. As a consequence, this matrix is isomorphic to, or has the same information content as, the description in terms of coherences and populations.[8,9] The diagonal elements are proportional to the probabilities of occupation of the energy levels, and consequently to the populations. The off-diagonal elements correspond to correlations between the values of the coefficients c_r. For time-dependent problems, as in spectroscopic measurements, these off-diagonal elements are related to coherent superpositions of the stationary states, i.e. coherences or transitions, present in a spin subsystem.

Different states $|\psi\rangle$ yield different values for the same observable, as can be seen from equation (12). The products, $c^*_s c_r$, vary according to the states $|\psi\rangle$, while the matrix elements $\langle s|\hat{M}_x|r\rangle$ remain invariant. It proves convenient to describe the state of the subsystem, with a projection operator for a single state, $\hat{P}_\psi = |\psi\rangle\langle\psi|$, in the Zeeman basis set:

$$\langle r|\hat{P}_\psi|s\rangle = c_s^* c_r \tag{13}$$

With this projection operator, the expectation value of $\hat{M}_x$ in a subsystem becomes [see equation (12)]:

$$\begin{aligned}\langle\hat{M}_x\rangle = \langle\psi|\hat{M}_x|\psi\rangle &= \sum_{r,s}\langle r|\hat{P}_\psi|s\rangle\langle s|\hat{M}_x|r\rangle \\ &= \mathrm{Tr}\{\hat{P}_\psi\hat{M}_x\}\end{aligned} \tag{14}$$

4 QUANTUM STATISTICAL MECHANICS OF AN ENSEMBLE OF N-SPIN SUBSYSTEMS

A measurement of M_x over an ensemble of subsystems is equivalent to averaging over $\langle \hat{M}_x \rangle$ in equation (14). As the state $|\psi\rangle$ or $c^*_s c_r$ of each subsystem will generally be different, while the dynamical variable will be identical, the averaging gives

$$\overline{\langle \hat{M}_x \rangle} = \sum_{r,s} \overline{\langle r|\hat{P}_\psi|s\rangle} \langle s|\hat{M}_x|r\rangle = \mathrm{Tr}\{\hat{\rho}\hat{M}_x\} \tag{15}$$

with $\hat{\rho}$, the density matrix of the ensemble,[8,9] defined as

$$\langle r|\hat{\rho}|s\rangle = \sum_\psi p_\psi \langle r|\hat{P}_\psi|s\rangle = \overline{\langle r|\hat{P}_\psi|s\rangle} = \overline{c^*_s c_r} \tag{16}$$

where p_ψ is the statistical weight of $|\psi\rangle$ in the ensemble.

For NMR experiments, the density matrix is represented by a density operator, corresponding to the Boltzmann weight of the canonical ensemble with the appropriate Hamiltonian operator defined with respect to some convenient reference frame,

$$\hat{\rho} = Q^{-1} \mathrm{e}^{-\hat{\mathcal{H}}/kT} \tag{17}$$

where Q is the ensemble partition function,

$$Q = \sum_{r=1}^{2^N} \langle r|\mathrm{e}^{-\hat{\mathcal{H}}/kT}|r\rangle \tag{18}$$

The description of any spectroscopic experiment will involve the time dependence, due to evolution under some Hamiltonian $\hat{\mathcal{H}}$ of $\hat{\rho}$ to characterize the ensemble, or $\hat{P}$ to represent a subsystem. In the Schrödinger picture, the time dependence is assigned to the state of the system, specifically, to the coefficients $c_r(t)$ of equation (11).[8,9] In MQ NMR experiments of solids, the relevant Hamiltonian corresponds to the time average of $\hat{\mathcal{H}}_\mathrm{d}$ in the rf toggling frame, $\tilde{\hat{\mathcal{H}}}_\mathrm{d}$ [see equation (2)], over a cycle of the rf excitation sequence. The equation of motion for $\hat{P}$ is obtained by inserting $|\psi\rangle$ into the time-dependent Schrödinger equation to yield[8,9]

$$\frac{\mathrm{d}\hat{P}}{\mathrm{d}t} = \frac{\mathrm{i}}{\hbar}[\hat{P}, \tilde{\hat{\mathcal{H}}}_\mathrm{d}] \tag{19}$$

The averaging of equation (19) over the ensemble of subsystems with identical $\tilde{\hat{\mathcal{H}}}_\mathrm{d}$ gives the equation of motion for $\hat{\rho}$:

$$\frac{\mathrm{d}\hat{\rho}}{\mathrm{d}t} = \frac{\mathrm{i}}{\hbar}[\hat{\rho}, \tilde{\hat{\mathcal{H}}}_\mathrm{d}] \tag{20}$$

Equation (20) is also known as the Liouville–von Neumann equation.

For a time independent average Hamiltonian, a formal solution to equation (20) is

$$\hat{\rho}(t) = \hat{U}\hat{\rho}(0)\hat{U}^{-1} \tag{21}$$

where the propagator $\hat{U}$ is defined as

$$\hat{U} = \exp\left(-\frac{\mathrm{i}}{\hbar}\tilde{\hat{\mathcal{H}}}_\mathrm{d} t\right) \tag{22}$$

The interpretation of equation (21) is of importance for understanding the development of multiple spin coherences in time resolved MQ NMR experiments. Insight in this many-body problem, as discussed in the next section, can be gained through a Taylor expansion of $\hat{\rho}(t)$ about $t = 0$:

$$\hat{\rho}(t) = \hat{\rho}(0) + \sum_{n=1}^{\infty} \frac{t^n}{n!} \frac{\mathrm{d}^n}{\mathrm{d}t^n} \hat{\rho}(t)|_{t=0} \tag{23}$$

From equations (21) and (22), one finds the derivatives of $\hat{\rho}(t)$, of which only the first two are given here:

$$\frac{\mathrm{d}\hat{\rho}(t)}{\mathrm{d}t} = \frac{\mathrm{i}}{\hbar}[\hat{\rho}(0), \tilde{\hat{\mathcal{H}}}_\mathrm{d}] \tag{24}$$

$$\frac{\mathrm{d}^2\hat{\rho}(t)}{\mathrm{d}t^2} = -\frac{1}{\hbar}[[\hat{\rho}(0), \tilde{\hat{\mathcal{H}}}_\mathrm{d}], \tilde{\hat{\mathcal{H}}}_\mathrm{d}] \tag{25}$$

Finally, by substituting equations (24) and (25) and all the other derivatives into equation (23), one obtains:

$$\hat{\rho}(t) = \hat{\rho}(0) + \frac{\mathrm{i}t}{\hbar}[\hat{\rho}(0), \tilde{\hat{\mathcal{H}}}_\mathrm{d}] - \frac{t^2}{2\hbar^2}[[\hat{\rho}(0), \tilde{\hat{\mathcal{H}}}_\mathrm{d}], \tilde{\hat{\mathcal{H}}}_\mathrm{d}] + \cdots \tag{26}$$

5 DEVELOPMENT OF MULTIPLE SPIN/MULTIPLE QUANTUM COHERENCES IN DIPOLAR COUPLED SOLIDS

The power series in time for $\hat{\rho}(t)$ in equation (26) describes the evolution of the spin dynamics in MQ NMR experiments. With the initial conditions corresponding to the spin system at equilibrium in a strong Zeeman field at a high temperature, equation (17) implies

$$\hat{\rho}(0) \propto \hat{I}_z = \sum_i \hat{I}_{zi} \tag{27}$$

As pointed out in Section 3, since $|\hat{\mathcal{H}}_\mathrm{Z}| \gg |\hat{\mathcal{H}}_\mathrm{d}|$, it is appropriate to neglect the contributions of $\hat{\mathcal{H}}_\mathrm{d}$ in the initial conditions. However, in the toggling reference frame, $\tilde{\hat{\mathcal{H}}}_\mathrm{d}$ is crucial for determining the evolution of the spin dynamics. By inserting $\hat{\rho}(0)$ and the nonsecular average Hamiltonian $\mathcal{H}_\mathrm{d}$ suitable for a particular MQ NMR experiment into equation (26), it is possible to examine the qualitative features of the growth of multiple spin/multiple quantum coherences in a solid.

With $\rho(0)$ corresponding to single-spin interactions and $\tilde{\hat{\mathcal{H}}}_\mathrm{d}$ to two-spin interactions, the ascending terms in the expansion of $\hat{\rho}(t)$ describe the sequential growth of multiple spin coherences due to the evolution under $\tilde{\hat{\mathcal{H}}}_\mathrm{d}$. In the first-order terms t^1, the commutators produces two-spin correlations of the form $\hat{I}_{i\alpha}\hat{I}_{j\beta}$, where the components α and β of the spin angular momentum operators are determined by the actual

details of $\hat{\mathcal{H}}_d$. The nested commutators in the second-order terms t^2 yield three-spin operators, $\hat{I}_{i\alpha}\hat{I}_{j\beta}\hat{I}_{k\gamma}$. The hierarchy of nested commutators from the higher order terms t^n generate $(n-1)$-spin operators. By introducing ladder (raising and lowering) operators in these product operators, the order n of the corresponding MQCs becomes explicit; the sum of raising operators minus the sum of the lowering operators in a product operator gives the order of the coherence. Thus, to observe an n quantum coherence it is necessary to have, at the minimum, a contribution of order t^{n+1}, implying the presence of an n-spin/n quantum operator in the expansion of $\hat{\rho}(t)$. Higher order terms can also produce n quantum coherences. The distinction between these different n quantum coherences comes from the number of spins participating in the correlations. Since multiple spin coherences contribute to equation (26) through the product of dipolar coupling constants (as discussed below and in Section 6), the lattice parameters r_{ij} and θ_{ij} will ultimately control and distinguish between the various n quantum coherences.

The interplay between the development of multiple spin coherences and the order of the resulting multiple quantum coherences depends on selection rules associated with the nature of $\hat{\mathcal{H}}_d$ and equation (26). With respect to the time development of the number of spins in multiple spin coherences, the bilinear spin operators of $\hat{\mathcal{H}}_d$ and the algebra of the nested commutators in equation (26) imply a cascade process in the growth of correlations. An n-spin coherence can only grow by sequentially incorporating one single spin at a time, one after another. The time development of multiple quantum coherences is constrained to pathways, in a K-spin/n quantum space, which depend uniquely on the nature of $\hat{\mathcal{H}}_d$.[2,10] The pulse excitation sequences for MQ NMR of solids produce generic classes of $\hat{\mathcal{H}}_d$ terms: 2-spin/0,2 quantum operators, 2-spin/1-quantum operators, and 2-spin/2 quantum operators. These excitation sequences achieve a redistribution of MQ NMR spectral intensities according to selections rules on ΔK and Δn. For example, with 2-spin/2 quantum operators in $\hat{\mathcal{H}}_d$, and an $\hat{I}_z$ initial condition, equation (26) and the selection rules $\Delta K = \pm 1$ and $\Delta n = \pm 2$, demonstrate that only even coherences develop; in addition, the evolution cannot generate 4-spin/4 quantum coherences. The redistribution of spectral intensities produced by the different $\hat{\mathcal{H}}_d$ terms is optimized according to the size or spatial distribution of the spins within a subsystem, e.g. for the detection of spin clusters, or extended spin networks.

One of the simplest models, the so-called statistical or Gaussian model,[1] used to interpret MQ NMR spectra of solids, consists of assuming that all the individual coherences possible in an N-spin subsystem have the same magnitudes with random phases, and that all have been excited at long excitation times in the sample or ensemble of subsystems. Time-reversal excitation produces transitions with identical phases within an order.[11] Hence, the assumption of a priori equal weight of the different coherences implies that the MQ NMR spectral intensities $I(n,t)$ are proportional to Z_n, [see equation (8)]. Stated differently, the distribution of coherences in the ensemble of subsystems is proportional to Z_n. For large N and small n, it is possible to transform Z_n in equation (8) with Stirling's approximation $y! \approx (2\pi y)^{\frac{1}{2}}\, y^y\, e^{-y}$ to give

$$Z_n \approx 4^N (\pi N)^{-\frac{1}{2}} e^{-n^2/N} \tag{28}$$

As a consequence, according to the statistical model, a MQ NMR spectral intensity profile as a function of order $I(n,t)$ should be Gaussian, as suggested by equation (28).

The time dependence of these profiles arises from the growth of the subsystem size $N(t)$. The variance $N(t)$ obtained from fitting $I(n,t)$ to a Gaussian function of n represents the effective number of dynamically coupled spins, in a typical subsystem, following an excitation period of duration t under $\hat{\mathcal{H}}_d$. In addition to spin counting with this variance, it has been suggested that the rate of change in $N(t)$ with time reflects on some of the space-filling properties, such as dimensionality effects, of spin networks.[1,1,12–14] Qualitatively, three generic classes of behavior have been observed for $N(t)$. Saturation in $N(t)$ implies the presence of isolated clusters of spins. Unbounded growth curves are observed in extended spin networks. Saturation behavior seen at early excitation times, followed by unbounded growth, indicates the occurrence of coupled clusters of spins.

The simplicity of the statistical model accounts for its widespread use in the MQ NMR literature of solids.[2,3] However, some questions have been raised concerning the validity of the assumption of the a priori equal weight of all coherences.[2,6] In addition, the convenience of the Gaussian model with the use of simple fitting procedures to analyze MQ NMR spectral intensity profiles is not successful with extended spin networks.[15] To appreciate the nature of these problems, and to understand the development of multiple spin/multiple quantum coherences in solids beyond the level of the statistical model, it is necessary to consider further fundamental aspects of the spin dynamics in MQ NMR.

As discussed in previous sections, the interpretation of MQ NMR experiments of solids relies on the spin dynamics within a subsystem, followed by averaging over an ensemble of subsystems. The density operator $\hat{\rho}$ in equation (17) and its equation of motion [equation (26)] reflect this two-fold averaging: a quantum mechanical averaging or the determination of expectation values in a subsystem [equation (14)], and a statistical averaging over the expectation values due to the distribution of subsystem states in the ensemble [equations (15) and (16)].

It is possible to construct a statistical ensemble of diagrams or graphs, including evolution, which is completely isomorphic with the density operator formalism used to describe MQ NMR.[2] This approach provides complementary physical insights into MQ NMR spin dynamics, averaging, and measurements. The diagrams include vertices corresponding to spins, and edges or links to delineate dipolar coupling constants between spins. The weight of an edge is proportional to the absolute value of the dipolar coupling constant. The state of a spin is represented by a color. For a spin $\frac{1}{2}$ there are three colors, $\hat{I}_x$, $\hat{I}_y$, and $\hat{I}_z$; generalization to higher spins is possible.

The decomposition of the density operator proceeds by examining an N-spin subsystem, under rigid lattice conditions and without any symmetry elements. In such an N-spin subsystem, the number of distinct subsets n_i each containing i spins is given by the binomial coefficient:

$$n_i = \binom{N}{i} \tag{29}$$

For example, the number of pairs of spins or dipolar coupling constants in a single subsystem is n_2. The subsets can range in size from $i = 1$ to N. The sum over all possible subsets is:

$$n_{\mathrm{T}} = \sum_{i=1}^{N} n_i = \sum_{i=1}^{N} \binom{N}{i} = 2^N - 1 \tag{30}$$

In equation (30), n_{T} is the sum of all possible spin correlations in the spin subsystem. By including the states of the spins or colors within the spin correlations, one obtains

$$n_{\mathrm{T}}^{\mathrm{c}} = \sum_{i=1}^{N} n_i 3^i = \sum_{i=1}^{N} \binom{N}{i} 3^i = 4^N - 1 \tag{31}$$

where $n_{\mathrm{T}}^{\mathrm{c}}$ is the total number of distinct colored subsets, and is equal to the number of elements (coherences and populations) of the normalized density operator in an N-spin-$\frac{1}{2}$ subsystem.

The growth of multiple spin/multiple quantum coherences is described by equation (26). From the interpretation of this equation, the coherences were seen to grow sequentially by adding one spin after another with increasing time. It is clear that this description is valid for the density operator, either in the product operator formalism or in the ensemble of colored spin correlations described above.

However, there is an essential feature related to the growth processes and the averaging over the subsystems, which becomes more obvious with the diagrams. Consider a generic term of $(n + 1)$th order in the Taylor expansion of equation (19) for the time dependence of the projection operator $\hat{P}_\psi$. The resulting equation is analogous to equation (26) with $\hat{P}_\psi$ replacing $\hat{\rho}$. The product of spin operators will include n-spin operators corresponding to different spins in the subsystem. As $\hat{\mathcal{H}}_{\mathrm{d}}$ is present in the nested commutators, there will also be products of $(n - 1)$ dipolar coupling constants which multiply the n-spin product operators. For example, a 3-spin coherence involving spins i, j, and k, will have a corresponding product operator of the form $\hat{I}_{i\alpha}\hat{I}_{j\beta}\hat{I}_{k\gamma}$, multiplied by a product of dipolar coupling constants $D_{ij}D_{jk}$. Hence, in general, the contributions or weights of n-spin coherences in the equation of motion are determined by products of $(n - 1)$ dipolar coupling constants. A diagram, consisting of n vertices connected with $(n - 1)$ edges is called a tree; no loops are permitted in such a graph. The number of ways to connect n vertices, with $(n - 1)$ edges chosen among $\binom{n}{2}$ distinct edges, corresponds to the number of distinct trees given by

$$n^{n-2} \tag{32}$$

Equation (32) also gives the number of products of n dipolar coupling constants for a particular n-spin coherence. In an N-spin subsystem, the total number of products of n dipolar coupling constants for n-spin coherences is

$$\binom{N}{n} n^{n-2} \tag{33}$$

The averaging over an ensemble of subsystems, in order to obtain $\hat{\rho}$, as discussed in Section 4 and in NMR texts,[8,9] proceeds by assuming that the Hamiltonians are identical for all subsystems [see equations (19) and (20)]. This is certainly true for a hypothetical representative ensemble, or approximately true for a sample viewed as an ensemble of loosely coupled subsystems, as presented in Section 2. However, when the averaging is done over a nonequilibrium ensemble for a finite sample, care must be taken to distinguish between the sum in the Hamiltonian [see equations (2), (19) and (20)] and the realizations of multiple spin correlations (with corresponding product operators) present in the ensemble. As an example, consider a 25-spin subsystem. In this subsystem, there is only a single MQ coherence of order 25 represented by a product operator consisting of 25 raising operators. According to equation (26), the 25-spin/25 quantum coherence is weighted by a product of 24 dipolar coupling constants. Among these spins, there are $\binom{25}{2} = 300$ distinct dipolar coupling constants. The number of distinct products of 24 dipolar coupling constants corresponds to the number of trees, in this case $25^{23} \approx 10^{32}$ realizations. It should be clear that a macroscopic sample consisting of 10^{20} spins will not have enough 25-spin subsystems to represent all trees or possible realizations of the 25-MQ coherence. An MQ NMR measurement on a macroscopic sample, consisting of an ensemble of subsystems, is really an average over the subsystems [see equation (16)]. The average over multiple spin coherences is really performed over the distribution of corresponding trees present in the ensemble, i.e. over products of dipolar coupling constants. To appreciate the intricacies of such a measurement or averaging procedure, we now examine the distributions of dipolar coupling constants and their products in spin networks.

6 STATISTICAL PROPERTIES OF DISTRIBUTIONS OF DIPOLAR COUPLING CONSTANTS AND THEIR PRODUCTS IN LARGE SPIN NETWORKS

Consideration of equation (26) demonstrated that different multiple spin coherences contribute to the evolution of ρ according to the values of the products of dipolar coupling constants. Thus, for a finite excitation time, coherences cannot be treated equally, as is assumed in the Gaussian statistical model.[1] Only in the limit of an infinite excitation time will all the coherences contribute equally to the spin dynamics.[6] The recognition that in spin networks the distributions of dipolar coupling constants and their products are characterized by asymmetry associated with extreme widths is important for understanding MQ NMR spin dynamics.[6] Difficulties encountered with the interpretation of equation (26), due to the presence of multiple length- and timescales, actually arise from these broad and peculiar distributions.

In three-dimensional solids, lattice sums of dipolar coupling constants can be replaced by a continuum approximation involving integrals such as

$$\sum_{i\rangle j}^{N} D_{ij} \propto \int_r (1/r^3) r^2 \, \mathrm{d}r \propto \ln r \tag{34}$$

For an infinite sample, the lattice sum diverges, while for finite spin networks the sum is conditionally convergent, i.e. it depends on the sample shape. Some approaches, such as the Ewald summation and the Lorentz cavity method, have

been devised to study these distributions in samples of general shapes.

In one-dimensional solids, the lattice sums can be performed analytically. Consider an infinite crystalline one-dimensional chain of spins with lattice parameter r oriented perpendicular to the Zeeman field. The average dipolar coupling constant per spin $\langle D \rangle_s$ is

$$\langle D \rangle_s = 2 \sum_{k=1}^{\infty} \tfrac{1}{2} \gamma^2 \hbar^2 (kr)^{-3} \approx 1.20 \gamma^2 \hbar^2 / r^3 \qquad (35)$$

In this case, 83% of the average is determined by the value of two nearest neighbor couplings out of an infinity of couplings!

Figure 3 shows a schematic distribution of the absolute values of dipolar coupling constants and their logarithms for a large spin subsystem. One should note that the distribution in Figure 3(a) is really a caricature, since in large networks the width essentially cannot be observed on linear scales.[6] Several statistical features are illustrated by Figure 3. The average $\langle |D| \rangle$ is determined by the coupling constants in the tail of the distribution, while the most probable value $|D|_{\mathrm{MPV}}$ is sensitive to the small and numerous long-range couplings. The transformation of the distribution on a logarithmic scale demonstrates the huge dynamic range of the distribution. For example in a two-dimensional square lattice of $10^2 \times 10^2$ spins, the distribution of coupling constants covers over 10 orders of magnitude. Differences between $\langle \ln |D| \rangle$ and $\ln \langle |D| \rangle$ are important to reconcile with measurements on an ensemble. The value of $\langle |D| \rangle$ is sensitive to the largest coupling constants, while $\langle \ln |D| \rangle$ is more sensitive to the details of the overall distribution. Such distinctions are significant in the physics of

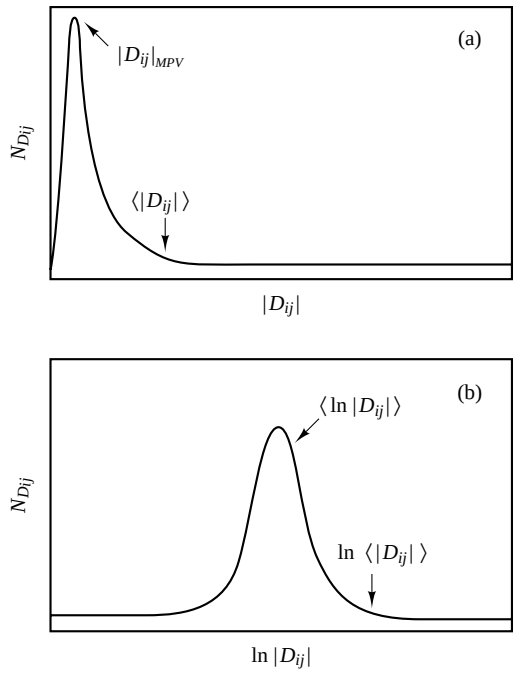

Figure 3 (a) Schematic distribution of the absolute values of dipolar coupling constants in an N-spin subsystem. (b) Schematic distribution of the logarithm of the absolute values of dipolar coupling constants in the same subsystem. Note the difference between $\langle \ln |D_{ij}| \rangle$ and $\ln \langle |D_{ij}| \rangle$. The analogous distributions, involving products of dipolar coupling constants, show similar behavior, but with wider distributions

disordered systems.[16,17] Products of dipolar coupling constants show similar features; however, the distributions are even wider.[6]

Probably the most interesting feature of these distributions arises from the scaling behavior of the statistical properties as a function of N, the number of spins. The relative fluctuations RF,

$$\mathrm{RF} = \frac{(\langle |D|^2 \rangle - \langle |D| \rangle^2)^{\frac{1}{2}}}{\langle |D| \rangle} \qquad (36)$$

measure the relative spread about the mean. In the limit of large spin networks,

$$\mathrm{RF} \propto N^{+\frac{1}{2}} \qquad (37)$$

This result implies that the distributions become wider as N increases, i.e. there is no self-averaging. The ratio of the most probable value to the first moment can be shown to scale as $N^{+\frac{3}{2}}$. The product of dipolar coupling constants shows a similar behavior with the same scaling exponents.[6] Such behavior is highly counterintuitive, since in random additive processes, within the central limit theorem, the relative fluctuations scale as $N^{-\frac{1}{2}}$, and the most probable value coincides with the first moment in the thermodynamic limit.

Some implications of these results for the growth of multiple spin coherences/multiple quantum coherences are beginning to emerge.[2,18] For example, anisotropy effects in the growth process should be determined by the products of the angular contributions of dipolar coupling constants. In a measurement on an ensemble of subsystems, the realizations of multiple spin coherences which are detected should be those with the largest products of dipolar coupling constants. However, these products are the least numerous but still dominate the dynamics due to their large weights. This last result would suggest that a single subsystem, where a multiple spin coherence with the largest possible product has been excited, could eventually dominate a macroscopic measurement. The statistical properties of the distributions of dipolar coupling constants and their products should also be relevant for other aspects of strongly dipolar coupled spin systems; examples include problems associated with FIDs[19] and the lineshapes,[20] spin diffusion,[21] and spin temperature.[22]

7 DYNAMICAL SCALE INVARIANCE IN THE GROWTH OF MULTIPLE SPIN CORRELATIONS IN DIPOLAR COUPLED SOLIDS

Dilation or scaling symmetry, observed under certain conditions in some physical systems, is a generalization of the concept of similarity among geometrical objects. In geometry, the properties of two circles with different radii are similar to one another by simple transformations of scales. In physical sciences, the practical aspects of scaling involve the determination of the relevant scaled variables to describe a phenomenon, such that all data acquired under a range of conditions collapse onto some single universal plot. Thus, scaling reveals an invariance or a kind of unification among the relevant scaled variables, which was not obvious

in the original unscaled variables. Understanding the physical reasons underlying scaling symmetry usually leads to deeper insights into the phenomenon.

Some scaling arguments have been applied to various aspects of the growth of multiple spin/multiple quantum coherences in solids.[1,2,15,23] In the context of the Gaussian statistical model, studies have focused on the behavior of the variance $N(t)$ in dilution effects[1] and power law growth[2] in spin networks, and dimensional analysis of growth curves.[23] A more elaborate scaling analysis of MQ NMR spectral intensity profiles, as a function of order and excitation time, demonstrated non-Gaussian behavior in extended spin networks.[15] These studies also provided additional support for the case of exponentially decaying intensity profiles. Behind these approaches lies the belief that the physics of the growth processes should be invariant or scale free, for some range of length- and timescales.

Baum et al.[1] have studied the effects of dilution of spin networks with MQ NMR. With increasing dilution, the growth curves $N(t)$ were shifted to longer excitation times. When the excitation time was multiplied by a scaling factor, all growth curves for the diluted systems could be collapsed onto the data of the undiluted or 'pure' spin network. In this case, the scaling symmetry demonstrates the invariance of the physics of the growth processes in the pure and diluted spin networks. A simple dilution in time relates these different systems. The scaling factor was observed to be a function of dilution; no serious attempts were made to understand this phenomenology.

Lacelle[2] has studied the growth curves $N(t)$ of a large variety of solid samples. All the data were seen to follow power law behavior,

$$N(t) \propto t^{\alpha} \tag{38}$$

where α is a growth exponent characteristic of the samples and the growth mechanism. The presence of power law growth indicates a scale invariant process, such that the functional

$$N(\lambda t) = \lambda^{\alpha} N(t) \tag{39}$$

exists for any values of the scaling factor λ. The solution of equation (39), i.e. equation (38), is obtained by setting $\lambda = 1/t$ in equation (39). In order to determine the physics behind the growth exponents, several models were considered. For example, in diffusive growth, the length scale ξ of the multiple spin correlations should follow

$$\xi \propto t^{\frac{1}{2}} \tag{40}$$

The space-filling properties of a homogeneously embedded solid in D dimensions imply that

$$N \propto \xi^{D} \tag{41}$$

Equations (40) and (41) yield

$$N \propto t^{D/2} \tag{42}$$

from which the growth exponent $\alpha = D/2$ is deduced for a diffusive growth mechanism. None of the models developed could account successfully for all the observed growth exponents. However, a classification of the spin networks could be achieved with the long time behavior of the growth rates

$$\frac{\mathrm{d}N}{\mathrm{d}t} \propto t^{\alpha-1} \tag{43}$$

When $\alpha < 1$, the growth rates converge to zero at long excitation times, implying the presence of clusters of spins. When $\alpha > 1$, a divergence in the growth rates should occur, which indicates the presence of an extended network. The case of $\alpha = 1$ corresponds to the threshold between these regimes. In a sense, α serves as a localization/delocalization criterion for multiple spin coherences.

Scruggs and Gleason[23] have examined the growth curves of different simple crystalline materials. By assuming that the growth processes were only determined by a relevant time-independent scale, the inverse of the square root of the second moment of the dipolar linewidths, the different growth curves collapsed onto a single universal curve for early excitation times. Their assumption for this empirical scaling is implicitly equivalent to assuming that the growth processes are dominated by nearest neighbor couplings, since Van Vleck's second moment is also dominated by such couplings.

One could argue about the quality and the quantitative aspects of the fitting procedures with the Gaussian approximation in these studies.[1,2,23] However, the value of such studies really lies in the efforts made to explore the possible facets of scaling in the growth processes of multiple spin/multiple quantum coherences. To ascertain any quantitative aspects of scaling, for example, growth exponents, under these circumstances it is clear that many more experiments involving high quality data will be required.

Lacelle et al.[15] have developed some scaling arguments in order to test the validity of the Gaussian statistical model. In particular, they strived to observe the scaling of MQ NMR spectra, as a function of order and excitation times, in extended spin networks. The Gaussian dependence suggested for the spectral intensity profiles $I(n,t)$ in equation (28) is actually a generalized homogeneous equation. With the time dependence of the variance $N(t)$ corresponding to a random walk model in product operator space,[1,10] the expected scaling, $I(n,t)/t^{-\frac{1}{2}}$ versus $n/t^{\frac{1}{2}}$, should have collapsed all MQ NMR spectra for a sample onto a single universal spectrum. The lack of scaling clearly demonstrated non-Gaussian behavior. Instead, consideration of the multiplicative nature of the coupling constants associated with product operators in equation (26) led to a heuristic argument predicting exponential decaying intensity profiles. The ensuing scaling analysis collapsed MQ NMR spectra, obtained at different excitation times, onto a single universal spectrum, thereby demonstrating dynamical scale invariance in the growth process of multiple spin/multiple quantum coherences. Such an approach reveals some aspects of the complexities, richness, and subtleness of multiple spin dynamics in MQ NMR of solids.

8 RELATED ARTICLES

Average Hamiltonian Theory; Double Quantum Coherence; Multiple Quantum Coherence in Spin-1/2 Dipolar Coupled Solids; Multiple Quantum NMR in Solids; Spin Diffusion in Solids.

9 REFERENCES

1. J. Baum, M. Munowitz, A. N. Garroway, and A. Pines, *J. Chem. Phys.*, 1985, **83**, 2015.
2. S. Lacelle, *Adv. Magn. Opt. Reson.*, 1991, **16**, 173.
3. K. K. Gleason, *Concepts Magn. Reson.*, 1993, **5**, 199.
4. H. E. Stanley, *Introduction to Phase Transitions and Critical Phenomena*, Oxford University Press, New York, 1971, Chap. 9
5. J. D. Gunton, M. San Miguel, and P. S. Sahni, in *Phase Transitions and Critical Phenomena*, ed. C. Domb and J. L. Lebowitz, Academic, London, 1983, Vol. 8, Chap. 3
6. S. Lacelle and L. Tremblay, *J. Chem. Phys.*, 1993, **98**, 3642.
7. D. Chandler, *Introduction to Modern Statistical Mechanics*, Oxford University Press, New York, 1987, Section 3.1.
8. C. P. Slichter, *Principles of Magnetic Resonance*, 3rd edn., Springer, Berlin, 1990, Section 5.4.
9. M. Goldman, *Quantum Description of High-Resolution NMR in Liquids*, Oxford University Press, New York, 1988, Section 4.1.
10. M. Munowitz, A. Pines, and M. Mehring, *J. Chem. Phys.*, 1987, **86**, 3172.
11. Y. S. Yen and A. Pines, *J. Chem. Phys.*, 1982, **78**, 3579.
12. D. H. Levy and K. K. Gleason, *J. Phys. Chem.*, 1992, **96**, 8125.
13. B. E. Scruggs and K. K. Gleason, *Chem. Phys.*, 1992, **166**, 367.
14. G. Cho and J. P. Yesinowski, *Chem. Phys. Lett.*, 1993, **205**, 1.
15. S. Lacelle, S. J. Hwang, and B. C. Gerstein, *J. Chem. Phys.*, 1993, **99**, 8407.
16. B. Derrida, *Phys. Rep.*, 1984, **103**, 29.
17. S. Redner, *Am. J. Phys.*, 1990, **58**, 267.
18. S. Lacelle and L. Tremblay, *Bull. Magn. Reson.*, 1994, in press.
19. I. J. Lowe and R. E. Norberg, *Phys. Rev.*, 1957, **107**, 46.
20. J. H. Van Vleck, *Phys. Rev.*, 1948, **74**, 1168.
21. N. Bloembergen, *Physica*, 1949, **15**, 386.
22. M. Goldman, *Spin Temperature and Nuclear Magnetic Resonance in Solids*, Clarendon, Oxford, 1970.
23. B. E. Scruggs and K. K. Gleason, *J. Magn. Reson.*, 1992, **99**, 149.

Biographical Sketch

Serge Lacelle. *b* 1955. B.Sc., Ottawa, 1978; Ph.D., Iowa State, 1984. Introduced to NMR by B. C. Gerstein. Faculty, Chimie Université de Sherbrooke, 1985–present. Research interests: the development and understanding of NMR methods to probe mesoscopic length scales (1 nm to 1 μm) in condensed matter; statistical mechanics of spin networks; multiple quantum NMR of solids; phase separation and critical phenomena; fluid mechanics; and pattern formation.

Polymorphism and Related Phenomena

Robin K. Harris
University of Durham, Durham, UK

1	Introduction	1
2	Applicability of NMR	1
3	Molecular Polymorphs	1
4	Polymorphism and Molecular Mobility	3
5	Macromolecular Polymorphs	4
6	Related Articles	6
7	References	6

1 INTRODUCTION

Polymorphism is ubiquitous in solid state chemistry, commonly occurring for a very wide range of materials. Polymorphs are different solid forms (usually crystalline) of a given compound. The differences lie in solid state structure, i.e. in the spatial arrangement of the atoms or molecules. They may be relatively minor (e.g. variations in mutual orientations of molecules) or major (leading, for instance, to substantially different atomic arrangements). Sometimes other terms are used for the phenomenon. Thus, when concerning different forms of the elements, the word allotrope is used, instead of polymorph. Also, polymorphs which have structures differing in the stacking sequence of layers (for example, in silicon carbide) are called polytypes.

A somewhat similar phenomenon is the ability of many compounds to incorporate solvent molecules in their structure during crystallization from solution. Thus compounds frequently exist in both anhydrous and hydrated forms, the crystal structures of which may be essentially identical or profoundly different. Other solvent molecules, such as acetone and chloroform, may be similarly incorporated. Ultimately this relates to the existence of clathrates, for which the structure may only be stable when both host and guest molecules are present. Sometimes hydrates lose water readily; on other occasions anhydrous forms may be hygroscopic. Although this article will concentrate on true polymorphism, the 'pseudopolymorphism' of solvates, which can carry similar NMR connotations, will be mentioned at times.

Of course, another closely-related topic is that of phase changes and phase diagrams, together with similar matters concerning the formation and interchange of polymorphic forms. These questions will be largely ignored in the present article. Under given conditions of temperature, pressure, etc., only one polymorph will clearly be favored by thermodynamic considerations. Frequently, however, kinetics of interconversions will be slow, and several forms will exist at ambient temperature and pressure for times in excess of the minimum required to obtain NMR spectra. Such metastable forms may be obtained, for instance, by crystallization from a solvent or by quenching from a temperature at which they are stable. The present article will concentrate on NMR data obtained under standard working conditions (atmospheric pressure and ambient temperature).

Cases of polymorphism and related phenomena may be divided into those involving molecular crystals and those relating to macromolecular structures (in one, two, or three dimensions). Of course, the bonding in the latter implies that interconversion between forms (e.g. between graphite and diamond) is extremely difficult. Indeed, it might be argued that cases of macromolecular structural differences, which require bond-breaking for interconversion (as for silicon carbide) are not properly labeled as polymorphic since they are more analogous to some types of isomerism in organic compounds. However, although interconversions between molecular polymorphs are usually relatively easy, it must not be assumed that intermolecular forces are negligible. Frequently they involve hydrogen bonding, with substantial energies.

Polymorphism is particularly important, and has been extensively investigated by NMR, for pharmaceutical compounds, for silicates and zeolites, for polymers (including naturally occurring materials such as cellulose and chitosan, as well as synthetic polymers), and for ceramic materials.

2 APPLICABILITY OF NMR

Since the electronic environments of corresponding atoms in different polymorphs of the same compound differ, the NMR chemical shifts will be in principle distinguishable. Indeed, the total NMR spectrum can clearly act as a fingerprint to identify polymorphic forms. Such differences are expected to be similar in magnitude to the crystallographic splittings observed when molecules or atomic groupings of the same chemical type are in locations in the unit cell unrelated by symmetry. The 'fingerprint' is of the crystallographic asymmetric unit, and simply counting the number of resonances may, on occasion, suffice to distinguish between polymorphs.

The techniques most commonly used to distinguish polymorphs are DSC, IR, and powder XRD, but all three have disadvantages. The DSC method is very crude, since it gives little or no chemical information. IR spectroscopy often suffers from lack of resolution and from difficulties in interpreting intensities. Powder XRD is often the preferred technique, but it is not sensitive to poorly crystalline or amorphous forms. NMR does not suffer from any of these problems, and the only drawback is the cost of the equipment.

Polymorphs often differ in molecular-level mobility, and hence in NMR relaxation times, but these are unlikely to be used as distinguishing features, except perhaps for polymeric systems.

3 MOLECULAR POLYMORPHS

The principal area of investigation of molecular polymorphism is that of pharmaceutical compounds. This is for very practical reasons: polymorphs sometimes show differing physiological activity (largely as a result of differences in rates of dissolution) and government regulations therefore require pharmaceutical companies to identify carefully the polymorphic form of their products. Moreover, very small changes in

conditions of preparation can readily result in a difference in polymorphic form, and scale-up can reveal problems not found in laboratory synthesis, so that an understanding of polymorphic variations is very important in pharmaceutical chemistry.

The first application of ^{13}C CP MAS NMR to pharmaceutical polymorphism appears to be that reported by Balimann et al.[1] in 1981, which featured spectra of two forms of Nolvadex (the ICI trade name for the generic tamoxifen). In the late 1980s and early 1990s the groups of Byrn[2,3] and of Harris[4–6] were particularly active in this area.

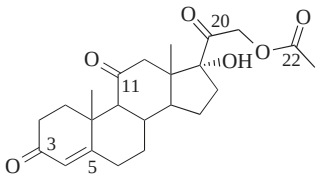

(1)

Steroids appear to be particularly prone to give rise to polymorphic forms. Cortisone acetate (**1**) is a typical example. A substantial number of polymorphs and solvated forms are known, and seven have been studied[4] by MAS NMR. Three of the polymorphs are anhydrous, and Figure 1 illustrates the ^{13}C CP MAS spectra for the high-frequency region (containing resonances from C-3, C-5, C-11, C-20 and C-22).

Immediately, two important conclusions can be made:

1. NMR readily distinguishes the three anhydrous forms (as it does the five hydrates and other solvates).
2. Whereas Forms I and II have asymmetric units consisting of a single molecule (since only five signals are seen in this region), Form III is more complex. In fact, expanded-scale spectra for all the carbon resonances show that Form III has three molecules in the asymmetric unit.

One can go further when peak assignments are firmly established. The apparent variation in the relative intensities of the two peaks on the right in Figure 1(a) and (b) arises from differing spinning sideband intensities. Complete analysis of the spinning sideband manifolds (at low spin rates) shows that C-5 and C-22 have distinguishable shielding anisotropies and asymmetries, which in turn indicates that the order of their isotropic chemical shifts is interchanged between Forms I and II. This variation can be correlated with hydrogen

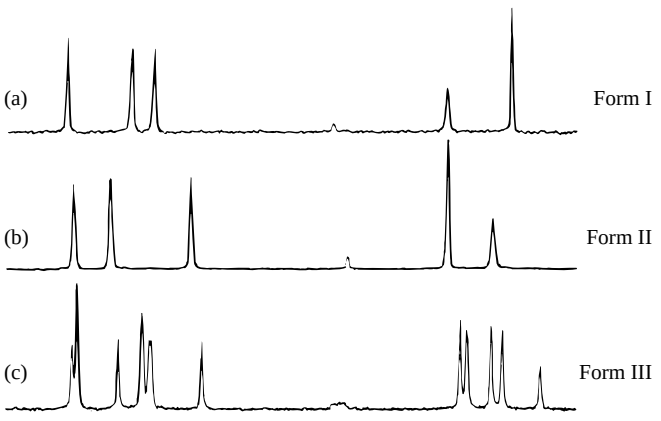

Figure 1 Carbon-13 CP MAS NMR spectra[4] (high-frequency region only) of three polymorphs of cortisone acetate (**1**) at 50.3 MHz

Table 1 Isotropic Chemical Shifts[a] for C-3, C-5, and C-22 of the Anhydrous Polymorphs of Cortisone Acetate

Carbon	Form I	Form II	Form III
C-3	202.8[b]	198.9	203.0[c], 203.0[c], 198.2
C-5	175.7	171.0	173.7, 173.7, 166.9
C-22	169.8	175.2[b]	174.3[c], 171.5, 170.3

[a]Given as δ_C (ppm).
[b]Shown by X-ray crystallography to be the acceptor site for hydrogen bonding.
[c]Concluded from the NMR evidence to be the acceptor site for hydrogen bonding.

bonding,[2,4] which causes an increase in chemical shift of 3–4 ppm at the acceptor carbonyl carbon resonance. Table 1 shows the assignments for carbons C-3, C-5 and C-22 for the three anhydrous forms, and indicates the known acceptor positions for hydrogen bonding. One can conclude that, of the three molecules in the asymmetric unit of Form III, two are hydrogen bonded at C-3 and the third, in contrast, at C-22. It may be noted that conjugation appears to relay the effect of hydrogen bonding on the chemical shift from C-3 to C-5.

This example illustrates how polymorphic form can affect chemical shifts. Unfortunately, matters are not often so simple. The differences in chemical shifts between analogous carbons for different polymorphs may arise either from *inter*molecular effects (packing, direct influence of neighboring molecules, hydrogen bonding, etc.) or *intra*molecular effects (variations in geometry and/or conformation). There is rarely any way that NMR can distinguish between the two influences. Of course, if crystal structures are known from X-ray studies, then knowledge of influences on chemical shifts obtained from solution state studies or by theory can be brought to bear. A case where intramolecular differences (but correlated with intermolecular differences!) are thought to be important is that of 4′-methyl-2′ nitroacetanilide (**2**), which exists in two forms (white and yellow), both of which have been subjected to study by single-crystal X-ray diffraction. In the white form, both the amide and nitro groups are in planes at a substantial angle (ca. 44°) to the plane of the aromatic ring, giving restricted conjugation and preventing intramolecular hydrogen bonding. On the other hand, the yellow form (with two molecules in the asymmetric unit) has more nearly coplanar groups (dihedral angles between 12° and 31°), allowing intramolecular hydrogen bonding between the amide NH and one of the nitro group oxygens. These facts suffice to explain the differences in chemical shifts between the polymorphs.[5] For example, the white form (C–NO_2 dihedral angle, 44.0°) has δ(C-2) = 144.1 ppm whereas the yellow form (C–NO_2 dihedral angles, 18.0° and 12.3°) gives δ(C-2) = 135.9 and 133.0 ppm (presumably respectively).

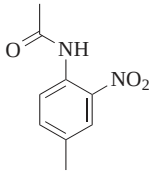

(2)

Certain simple but important measurements can be made of polymorphism via the fingerprinting ability. For example:

1. Mixtures of polymorphs can be readily studied and minor components can be quantified,[4] in favorable cases down to the 1% level.
2. NMR spectra can be used to monitor the polymorphic variations produced by different formation conditions (e.g. different rates of crystallization produced by cooling a solution quickly or slowly).[4]
3. Polymorphism can be studied directly in pharmaceutical tablets. Saindon et al.[3] have pointed out that the CP MAS technique can be used to discriminate against signals deriving from the excipient.

The combination of single-crystal XRD and CP MAS NMR for the study of polymorphism is particularly powerful. The former can give precise atomic positions but is frequently feasible for only some of the forms of a product (because of difficulties in growing suitable crystals). NMR, however, can almost always be relied upon to yield spectra of all polymorphs available in sufficient quantity, and interpretation is greatly aided by X-ray information on any one form. For example, of the two forms of fosinopril sodium, one was examined using single-crystal X-ray diffraction techniques, then both were studied[7] by CP MAS NMR of ^{13}C. The results provided by NMR enabled the conclusion to be drawn that the environment of the acetal side chain of fosinopril sodium differed in the two polymorphs. In this case ^{31}P CP MAS NMR was also used, and showed a significant chemical shift difference (2.2 ppm) between the forms.

It is possible to detect conformational disorder within polymorphs by CP MAS NMR. Thus Stoltz et al.[8] have shown that peak intensities for the monohydrate of oxyphenbutazone give a site ratio consistent with X-ray results in terms of sterically-favored isomers. However, it must be said that since CP MAS NMR spectra are obtained on microcrystalline or powdered material, it is not easy to differentiate between mixed crystals and disorder in a single type of crystal.

Differences in bonding between polymorphs can sometimes be quite startling but readily detectable by NMR. Thus, for 2-aminobenzoic acid (**3**), ^{13}C MAS NMR reveals[9] that Form I gives two signals each for C-1 and C-2. These are at chemical shifts which are characteristic of the normal and zwitterionic structures (**3**)A and (**3**)B, respectively, indicating that the unit cell contains equal proportions of each form. On the other hand, Forms II and III give spectra showing that each has an asymmetric unit containing one molecule of structure (**3**)A only.

A B

(3)

Interestingly, the ^{13}C spectra of Forms II and III are so similar as to be virtually indistinguishable. In these cases, it is necessary to turn to nuclei other than ^{13}C to differentiate. The proton CRAMP spectra of the two forms are, in fact, very different (Figure 2). Form II of the compound gives a strong signal at δ_H = 12.3 ppm, indicative of a hydrogen-bonded CO_2H group (in agreement with single-crystal X-ray results). This is not present for Form III (the crystal structure of which is unknown)—from which it can be deduced that hydrogen bonding is probably absent. However, the situation is complicated by the fact that there are proton-exchange processes occurring, involving amino and (in some cases) carboxylic acid protons, at a rate comparable with the NMR timescale, producing broad bands underlying the sharper aromatic proton signals at ambient probe temperature.

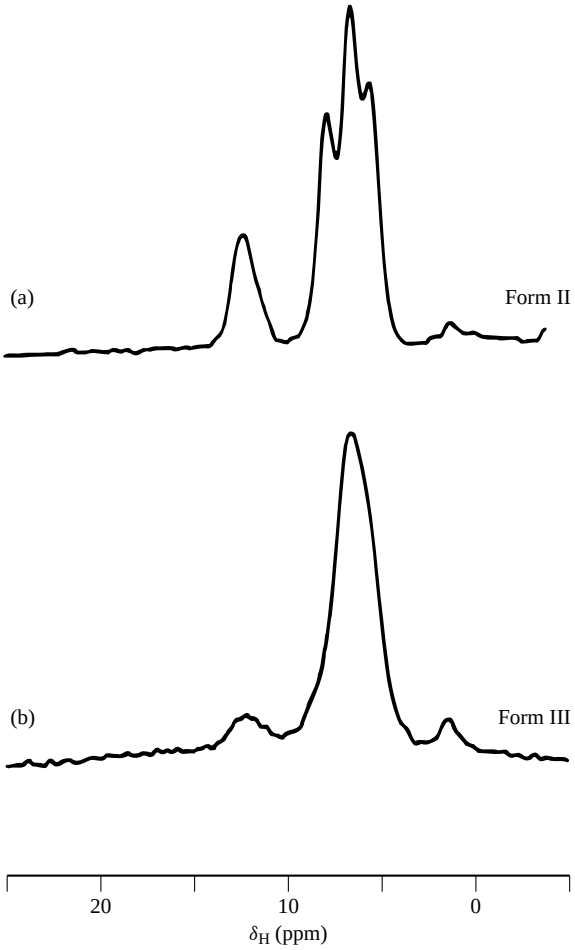

Figure 2 Proton CRAMP spectra[9] of two polymorphs of 2-aminobenzoic acid (**3**) at 200.13 MHz. The sample of Form III contains a small amount of Form II, which gives rise to the hydrogen-bonded peak at δ 12.3 ppm. The peak at $\delta \sim 1.5$ ppm in each spectrum is due to an impurity in the Kel-F rotors used. The broad line (assigned to NH_2 and CO_2H protons) underlying the spectrum of Form III is clearly visible

4 POLYMORPHISM AND MOLECULAR MOBILITY

In addition to the effects on chemical shifts arising from differences in intermolecular environment and intramolecular geometry between molecules of different polymorphs, variations in molecular level motion can often also be detected. A case in point is illustrated in Figure 3, which shows ambient probe temperature ^{13}C CP MAS spectra[10] of two forms

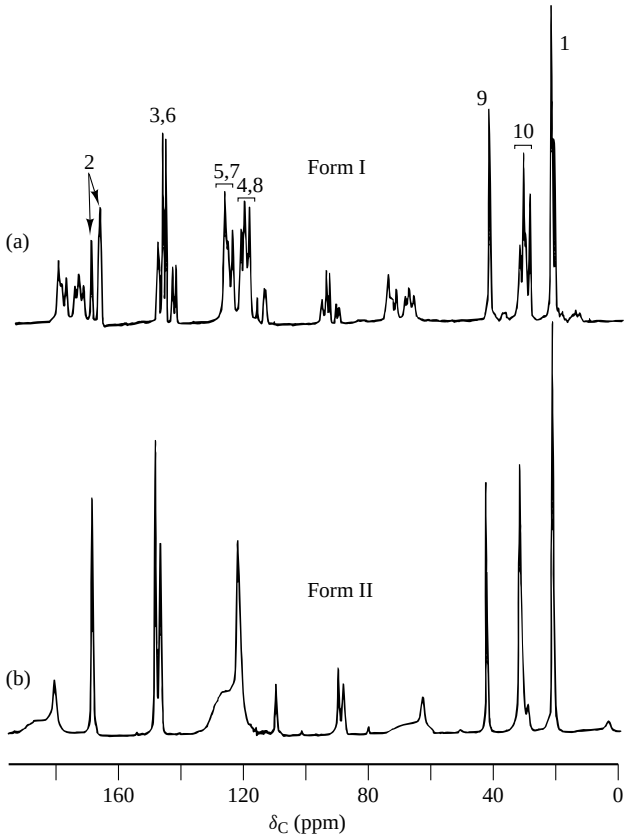

Figure 3 Carbon-13 CP MAS spectra[10] of two forms of bisphenol-A diacetate (**4**) at 50.3 MHz and ambient probe temperature. Signals not indicated by numbers in (a) [and corresponding peaks in (b)] are spinning sidebands

of bisphenol-A diacetate (**4**). Clearly, Form I gives a much more complex spectrum than Form II, as is consistent with the single-crystal X-ray results, which show that in the former case the asymmetric unit consists of two entire molecules. The second feature of importance is the breadth of the resonances for the aromatic CH carbons (C-4, C-5, C-7 and C-8) for Form II, which suggests there is substantial averaging, probably arising from 180° ring-flips of the phenylene rings (possibly by simultaneous motion of the two halves of the molecule). This suggestion is readily confirmed by variation of the temperature.

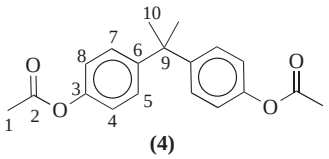

(4)

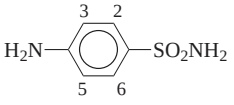

(5)

Such variable temperature ^{13}C CP MAS NMR experiments have been used[11] to study the motion of a phenylene ring about the *para* axis of one form of sulfanilamide, (**5**). Just below room temperature the C-3/C-5 resonance (but not the C-2/C-6 signal) is observably split because the SO_2NH_2 substituent is twisted with respect to the ring. An Arrhenius activation energy, E_a, of 63 ± 4 kJ mol^{-1} for the (assumed) 180° ring-flip was obtained. It should be noted that rapid motion of this type would not be detected by XRD.

An example from an entirely different area of chemistry concerns the polymorphism of phosphorus pentachloride, PCl_5. The stable form (Phase II) of this compound under normal conditions is ionic, with the structure PCl_4^+ PCl_6^-. Both ions are very mobile at ambient temperature, so that shielding anisotropy at the phosphorus nuclei is eliminated and the chlorine nuclei relax very rapidly. The latter effect causes self-decoupling of the chlorines and the net effect is that ^{31}P MAS spectra consist[12] of two sharp lines, one for each anion. However, Phase III, which can also be studied at ambient probe temperature, has the stoichiometry $[PCl_4]_2^+[PCl_6]^-Cl^-$. Since this form, like Phase II, contains PCl_4^+ and PCl_6^- ions, the ^{31}P MAS spectrum also consists of two bands, but at 81 MHz the resonances are broad and splittings arising from (Cl,P) coupling are seen at 36 MHz. Thus self-decoupling is substantially less efficient for Phase III than for Phase II, probably indicating more restricted rotational mobility for the ions in the former.

5 MACROMOLECULAR POLYMORPHS

Two types of example from widely different chemical areas should suffice to show some of the general features of polymorphism in macromolecular systems. Silicon carbide exemplifies the situation where the structure is three-dimensional so that interchange between forms is not feasible. The different polymorphs are essentially frozen-in at the time of preparation. All structures have alternating Si and C atoms, with all coordinations tetrahedral (though mostly not with the full symmetry). The structural differences between some of the forms can be appreciated from Figure 4, which shows a plane including the *c* crystallographic axis and alternating Si and C atoms in that plane for four forms of the material. It is evident that the detailed environments of all silicon atoms of the 2H form are equivalent, as is also the case for the β form (though β and 2H environments are not identical). However, the 4H form contains two types of Si and the 6H three types. The ^{29}Si spectra (Figure 5) show[13] the expected number of signals for the four forms. Similar considerations apply to the ^{13}C spectra. There is also a range of other forms. Assignment of the signals for the 4H and 6H polymorphs is not easy but has been made.[13,14] The separate signals have different relaxation times, probably as a result of the presence of impurities. Silicon carbide is a case where the amorphous material can also exist, without sizable domains of any of the potentially ordered structures. Such material gives rise to broad ^{29}Si and ^{13}C resonances, usually characterized by shorter values of T_1 than the crystalline material, probably because impurities tend to concentrate in amorphous regions.

Of course, silica provides the outstanding example of a compound with multiple polymorphs. Not only are there well-characterized crystalline forms (quartz, crystobalite, tridymite, etc.), together with the common amorphous glass, but it seems that many types of zeolites can be obtained with all aluminum atoms replaced by silicon so that they become silica polymorphs. Since zeolites are treated in other entries in this Encyclopedia they will not be discussed here. The book

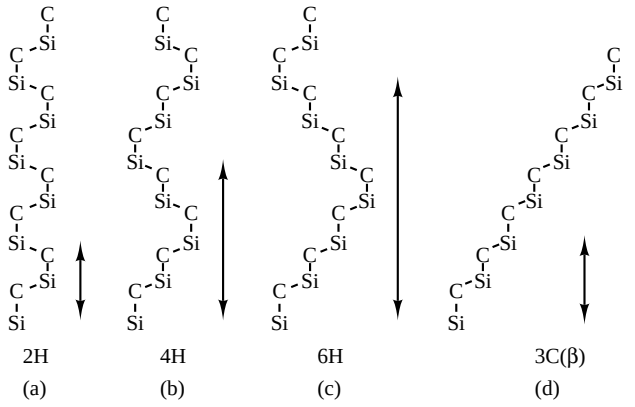

Figure 4 Schematic structures for silicon carbide polymorphs. The vertical arrows represent repeat distances

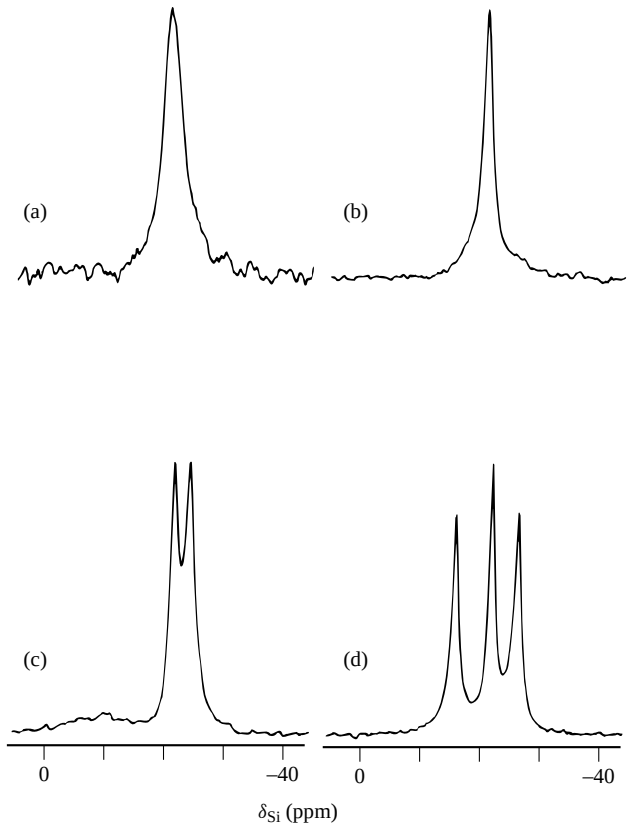

Figure 5 Silicon-29 MAS NMR spectra[13] of silicon carbide polymorphs at 59.58 MHz: (a) 3C (β); (b) 2H; (c) 4H; and (d) 6H

by Engelhardt and Michel[15] contains a useful discussion of NMR studies of nonzeolitic silica polymorphs (pp. 170–175). The ^{29}Si chemical shifts cover a wide range ($\delta_{Si} \sim -107$ to -121 ppm), the variation being attributed to differences in mean SiOSi bond angles, α, an increase in shielding resulting from widening SiOSi angles. A number of specific relationships have been proposed,[16] including (from theoretical considerations) $\delta_{Si} = -247.05\bar{\rho} + 2.19$, where $\rho = \cos\alpha/(\cos\alpha - 1)$. Of course, many of the silica polymorphs differ in the number of different crystallographic sites. Coesite, for instance, gives two widely-spaced ^{29}Si signals (δ_{Si} = 108.1 and 113.9 ppm), in accord with its structure.[16] In contrast to all the four-coordinate silica polymorphs, stishovite, which contains six-coordinate silicon, gives a signal at $\delta_{Si} = -191$ ppm.[16] As with silicon carbide, amorphous forms of silica (glass!) are well known.

Organic polymers may also show polymorphism. One of the early examples of CP MAS NMR related to the case of isotactic polypropene, which exists in several crystalline forms usually as domains separated by amorphous material. In effect, the chains constitute infinite one-dimensional bonded structures with weaker forces between the chains. The systems therefore are intermediate between the molecular polymorphs discussed in Section 3 and the infinite three-dimensional structures of SiC and SiO_2. The structure of the α form of polypropene is shown in Figure 6(a). The helical polymer units occur as pairs of interlocking chains with opposing handedness. This creates a situation where there are two distinct methyl sites, with two-thirds of the groups in a given helix facing the companion helix, and the remaining third facing outwards. Thus a 2:1 doublet is expected for the methyl carbons, and this is observed[17] in practice. A similar situation obtains for the CH carbons.

In contrast, the crystal structure of the β form contains separate groups of helices of the two types of handedness, with no pairing [Figure 6(b)]. The NMR spectrum therefore lacks the well-defined splitting shown by that of the α form.

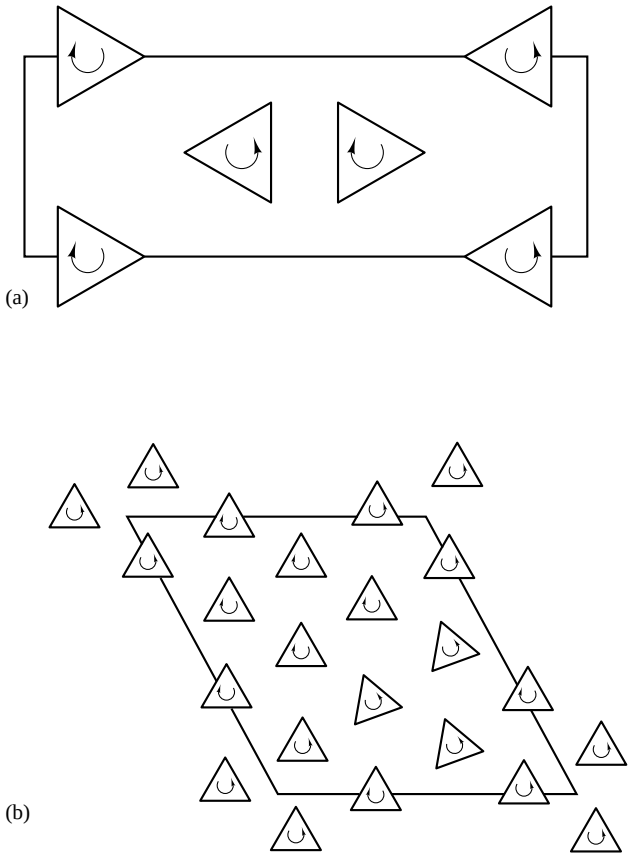

Figure 6 Diagrammatic crystal structures for two forms of isotactic polypropene: (a) α form; (b) β form. The figures show projections of the chains perpendicular to their axes, with the corners of the triangles indicating the positions of methyl groups. The arrows represent the handedness of the helices

Of course, isotactic polypropene also contains a significant proportion of amorphous material which, as usual, gives rise to somewhat broadened CP MAS ^{13}C lines. The differences between the α and β forms of isotactic polypropene arise from intermolecular packing of the polymer chains. Far greater differences occur, as expected, in NMR spectra[17,18] for polymer forms differing in tacticity (such as isotactic and syndiotactic polypropene). However, differences in tacticity are not normally classed under polymorphism.

Biochemical polymers such as cellulose and chitosan also give rise to polymorphism, which has been studied by solid state NMR methods.[19,20]

6 RELATED ARTICLES

Ceramics; Molecular Sieves: Crystalline Systems; Polysaccharide Solid State NMR; Silicon-29 NMR of Solid Silicates.

7 REFERENCES

1. G. E. Balimann, C. J. Groombridge, R. K. Harris, K. J. Packer, B. J. Say, and S. F. Tanner, *Philos. Trans. R. Soc. London, Ser. A*, 1981, **299**, 643.
2. S. R. Byrn, G. Gray, R. R. Pfeiffer, and J. Frye, *J. Pharm. Sci.*, 1985, **74**, 565; S. R. Byrn, P. A. Sutton, B. Tobias, J. Frye, and P. Main, *J. Am. Chem. Soc.*, 1988, **110**, 1609.
3. P. J. Saindon, N. S. Cauchon, P. A. Sutton, C.-J. Chang, G. E. Peck, and S. R. Byrn, *Pharm. Res.*, 1993, **10**, 197.
4. R. K. Harris, A. M. Kenwright, B. J. Say, R. R. Yeung, R. A. Fletton, R. W. Lancaster, and G. L. Hardgrove, *Spectrochim. Acta, Part A*, 1990, **46**, 927; E. A. Christopher, R. K. Harris, and R. A. Fletton, *Solid State NMR*, 1992, **1**, 93.
5. R. A. Fletton, R. W. Lancaster, R. K. Harris, A. M. Kenwright, K. J. Packer, D. N. Waters, and A. Yeadon, *J. Chem. Soc., Perkin Trans. 2*, 1986, 1705.
6. R. K. Harris, B. J. Say, R. R. Yeung, R. A. Fletton, and R. W. Lancaster, *Spectrochim. Acta, Part A*, 1989, **45**, 465; R. A. Fletton, R. K. Harris, A. M. Kenwright, R. W. Lancaster, K. J. Packer, and N. Sheppard, *Spectrochim. Acta, Part A*, 1987, **43**, 1111.
7. H. G. Brittain, K. R. Morris, D. E. Bugay, A. B. Thakur, and A. T. M. Serajuddin, *J. Pharm. Biomed. Anal.*, 1993, **11**, 1063.
8. M. Stoltz, D. W. Oliver, P. L. Wessels, and A. A. Chalmers, *J. Pharm. Sci.*, 1991, **80**, 357.
9. R. K. Harris and P. Jackson, *J. Phys. Chem. Solids*, 1987, **48**, 813.
10. D. Casarini, R. K. Harris, and A. M. Kenwright, *Magn. Reson. Chem.*, 1993, **31**, 540.
11. L. Frydman, A. C. Olivieri, L. E. Diaz, B. Frydman, A. Schmidt, and S. Vega, *Mol. Phys.*, 1990, **70**, 563.
12. E. R. Andrew, A. Bradbury, R. G. Eades, and G. J. Jenks, *Nature (London)*, 1960, **188**, 1096; R. K. Harris and A. Root, *Mol. Phys.*, 1989, **66**, 993.
13. D. C. Apperley, R. K. Harris, G. L. Marshall, and D. P. Thompson, *J. Am. Ceram. Soc.*, 1991, **74**, 777.
14. D. Guo, J. S. Hartman, and M. F. Richardson, *Can. J. Chem.*, 1992, **70**, 700; M. F. Richardson, J. S. Hartman, D. Guo, and B. G. Winsbarrow, *Chem. Mater.*, 1992, **4**, 318.
15. G. Engelhardt and D. Michel, *High-resolution Solid-state NMR of Silicates and Zeolites*, Wiley-Interscience, New York, 1987.
16. J. V. Smith and C. S. Blackwell, *Nature (London)*, 1983, **303**, 223; G. Engelhardt and R. Radeglia, *Chem. Phys. Lett.*, 1984, **108**, 271.
17. A. Bunn, M. E. A. Cudby, R. K. Harris, K. J. Packer, and B. J. Say, *Polymer*, 1982, **23**, 694; M. A. Gomez, H. Tanaka, and A. E. Tonelli, *Polymer*, 1987, **28**, 2227.
18. A. Bunn, M. E. A. Cudby, R. K. Harris, K. J. Packer, and B. J. Say, *J. Chem. Soc., Chem. Commun.*, 1981, 15.
19. R. H. Atalla, J. C. Gast, D. W. Sindorf, V. J. Bartuska, and G. E. Maciel, *J. Am. Chem. Soc.*, 1980, **102**, 3249; W. L. Earl and D. L. VanderHart, *J. Am. Chem. Soc.*, 1980, **102**, 3251.
20. H. Saito, R. Tabeta, and K. Ogawa, in *Industrial Polysaccharides: Genetic Engineering, Structure/Property Relations & Applications*, ed. M. Yalpani, Elsevier Science Publishers, Amsterdam, 1987, pp. 267–280.

Biographical Sketch

Robin K. Harris. *b* 1936. B.A. (Nat. Sci.), Ph.D. (supervisor Norman Sheppard), Sc.D., University of Cambridge, UK. Postdoctoral work at Mellon Institute, Pittsburgh, PA (with Aksel Bothner-By). Successively lecturer, senior lecturer, and professor, University of East Anglia, UK. Currently Professor of Chemistry, University of Durham, UK. Secretary-General of ISMAR, 1986–92. Approx. 350 publications. Current research specialty: solid state NMR and its applications in materials chemistry.

REDOR and TEDOR

Jacob Schaefer

Department of Chemistry, Washington University, St. Louis, MO, USA

1	Refocusing and Dephasing	1
2	REDOR Dephasing for Recrystallized Labeled Alanines	1
3	Long-Range Couplings and the Natural-Abundance Background	3
4	Coherence Transfer and Selectivity	5
5	Combination Experiments and Synchronous Detection	6
6	Related Articles	7
7	References	7

1 REFOCUSING AND DEPHASING

Rotational echo double resonance (REDOR) NMR is a new analytical spectroscopic technique for solids spinning at the magic angle which has been developed during the last 6 years.[1] REDOR provides a direct measure of heteronuclear dipolar coupling between isolated pairs of labeled nuclei. In a solid with a $^{13}C-^{15}N$ labeled pair, for example, the ^{13}C rotational echoes that form each rotor period following a $^{1}H-^{13}C$ cross polarization transfer can be prevented from reaching full intensity by insertion of a ^{15}N π pulse each half rotor period (Figure 1). The ^{15}N pulse in the middle of the evolution period is replaced by a ^{13}C pulse so that isotropic carbon chemical shifts are in phase at the beginning of data acquisition. The REDOR difference (the difference between a ^{13}C NMR spectrum obtained under these conditions and one obtained with no ^{15}N π pulses) has a strong dependence on the $^{13}C-^{15}N$ dipolar coupling and hence the $^{13}C-^{15}N$ internuclear distance.[2] REDOR is described as double resonance even though three radiofrequencies (typically ^{1}H, ^{13}C, and ^{15}N) are used because the protons are removed from the important evolution part of the experiment by resonant decoupling. The dephasing of magnetization in REDOR arises from a local dipolar $^{13}C-^{15}N$ field gradient and involves no polarization transfer. REDOR has no dependence on ^{13}C or ^{15}N chemical shift tensors and does not require resolution of a $^{13}C-^{15}N$ coupling in the chemical shift dimension.[2]

The evolution of observable S-spin magnetization for a single crystallite on resonance under magic angle spinning and an $I-S$ dipolar coupling is shown in Figure 2 (left). Each dot represents the result of evolution for an equal fraction of a rotor period, with a minor homogeneous decay superimposed for display purposes. At the beginning of the rotor cycle, the magnetization is the observable, $\langle\hat{S}_x\rangle$. Under sample rotation and $I-S$ dipolar coupling, the observable magnetization is transformed into nonobservable bilinear coherence, $\langle\hat{I}_z\hat{S}_y\rangle$, and then back into $\langle\hat{S}_x\rangle$. By the end of the rotor cycle the full observable magnetization has been recovered. For a collection of crystallites in a powder, individual phase accumulations (the product of resonance frequency and time) vary in size and sign depending on crystallite orientation in the magnetic field. This causes phase interference during the rotor cycle and an apparent decay of the observable signal for the powder. Nevertheless, because the magnetization from each crystallite refocuses completely, the dephasing for the powder is also refocused into a full rotational echo at the end of the rotor cycle.

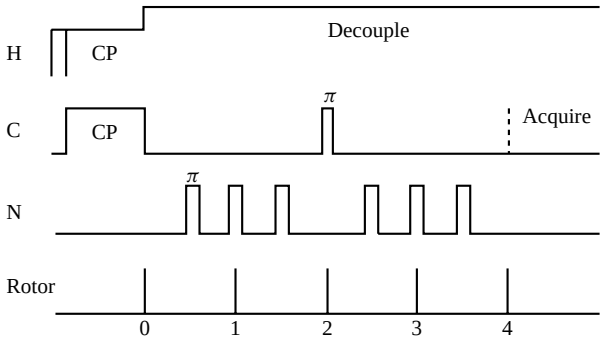

Figure 1 Pulse sequence for a version of REDOR ^{13}C NMR. Two equally spaced, ^{15}N 180° pulses per rotor period result in the dephasing of transverse carbon magnetization produced by a cross-polarization (CP) transfer from dipolar-coupled protons. Carbon–nitrogen dipolar coupling determines the extent of dephasing. A ^{13}C 180° pulse replaces the ^{15}N pulse in the middle of the dephasing period and refocuses isotropic ^{13}C chemical shift differences at the beginning of data acquisition. After the CP transfer, resonant decoupling removes the protons from the experiment. The illustration is for four rotor cycles

However, even for a single crystallite, the refocusing is incomplete in the presence of dephasing I-spin π pulses (Figure 2, right). Evolution for the crystallite is identical to that shown at the left of the figure between times '1' and '2'. The I-spin inverting π pulse, which ends at time '3', changes the sign of $\langle\hat{I}_z\hat{S}_y\rangle$. This process is repeated under the second I-spin π pulse which ends at time '5'. At the end of the rotor cycle (time '6'), the transformation of bilinear coherence created during the rotor cycle into observable magnetization is incomplete. For a powder, a rotational echo of diminished intensity is observed. The extent of the diminution depends on the $I-S$ coupling. The diminution is maximum for two dephasing pulses and is independent of their exact placement so long as the pulse spacing is one-half of the rotor period.[2]

2 REDOR DEPHASING FOR RECRYSTALLIZED LABELED ALANINES

The results of a REDOR experiment performed using the pulse sequence of Figure 1 on an equimolar, recrystallized mixture of L-[2-^{13}C,^{15}N]alanine and L-[1-^{13}C]alanine are shown in Figure 3.[3] The full echo ^{13}C NMR spectrum (S_0) after two rotor cycles with no dephasing is at the bottom of the Figure, and the REDOR difference ($\Delta S = S_0 - S$, where S is the spectrum with dephasing) as a function of the number of rotor cycles, is shown at the top of the Figure. The 900 Hz intramolecular $^{13}C-^{15}N$ coupling results in a sizeable ΔS for the methine carbon atom after only two rotor cycles; this ΔS reaches a maximum after four rotor cycles, and then oscillates in amplitude. The average 100 Hz intermolecular coupling produces a small carboxyl carbon atom ΔS after two rotor cycles, which increases monotonically with dephasing time.

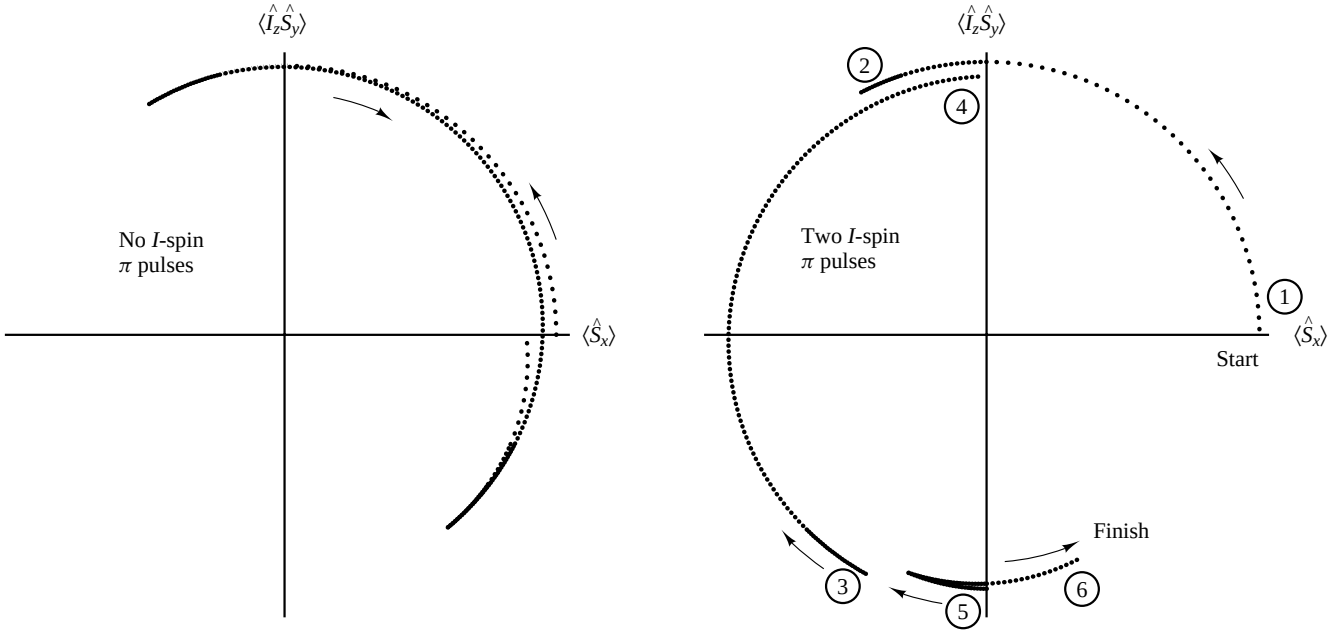

Figure 2 Schematic diagram of the evolution of the IS density matrix for a single crystal under magic angle spinning and $I-S$ dipolar coupling during a REDOR pulse sequence with no dephasing pulses (left) and with dephasing pulses (right)

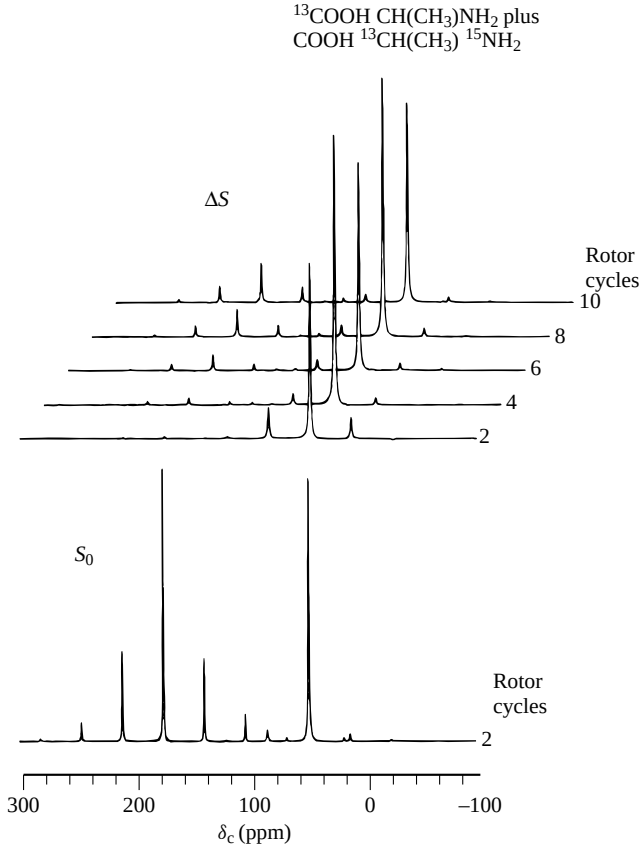

Figure 3 The 50.3-MHz REDOR ^{13}C NMR spectra of an equimolar, recrystallized mixture of L-[2-^{13}C,^{15}N]alanine and L-[1-^{13}C]alanine, as a function of the number of rotor cycles. A full echo spectrum (S_0) after two rotor cycles is shown at the bottom of the Figure and REDOR difference spectra (ΔS) at the top. Magic angle spinning was at 2702 Hz

The $\Delta S/S_0$ ratios for both carbon atoms have the same dependence on the dimensionless parameter, λ_D (Figure 4, solid circles and squares). The theoretical dependence (Figure 4, solid line) was calculated by performing an isotropic powder average over the dephasing for individual crystallites (Figure 2, right). Thus, the angular dependence of the dipolar interaction is suppressed. The resulting universal dephasing behavior needs to be calculated only once for all heteronuclear spin-1/2 pairs. (REDOR applications also include quadrupolar nuclei like ^{2}H, with either direct observation of deuterium or indirect observation through REDOR dephasing. Calculation of the theoretical $\Delta S/S_0$ behavior is slightly more complicated.)[4]

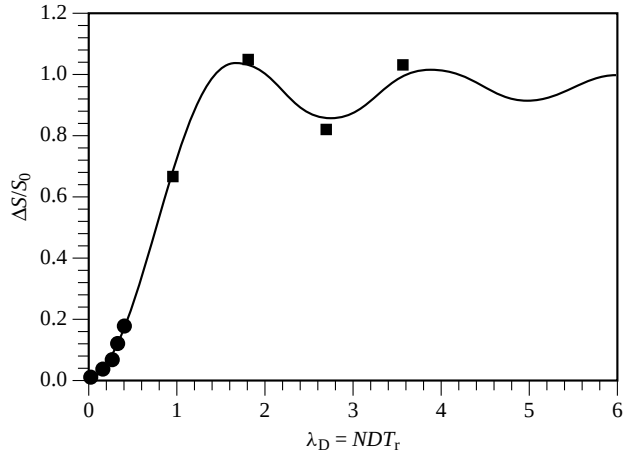

Figure 4 Observed dependence of $\Delta S/S_0$ on the universal parameter, λ_D, for the ^{13}C–^{15}N double-labeled alanine mixture of Figure 3. (N is the number of rotor cycles with dephasing, D is the dipolar coupling constant, and T_r is the rotor period)

A few experimental values of $\Delta S/S_0$ determine λ_D, which then establishes D since the total dephasing time (the product of the number of rotor cycles of dephasing and the rotor period) is known. Because $D = \gamma_I\gamma_S h/2\pi r^3_{IS}$, the observed dephasing can be translated into an internuclear distance directly. If $\Delta S/S_0$ and hence D are known experimentally to 10%, the distance is known with 2% accuracy. Weak dipolar couplings associated with large internuclear distances can be effectively amplified in REDOR by simply allowing the rotor to go around. The only practical problem is holding the echo train together. This depends on the technical difficulty of completely decoupling the protons, which may require low temperatures to suppress kHz regime molecular motions.[5] Translating dipolar couplings into distances in the presence of large-amplitude motions involves specifying a model for the motion.[6]

3 LONG-RANGE COUPLINGS AND THE NATURAL-ABUNDANCE BACKGROUND

In the early applications of REDOR to C–N distance determinations in peptides, relatively few dephasing pulses were used so that sometimes large natural-abundance corrections were necessary.[7] More recently, increased dephasing has been possible as a result of the development of phase routing schemes[8] (Figure 5) that eliminate the dependence of REDOR determinations on frequency offsets and pulse imperfections.[9]

For example, the ^{13}C signal for the label in the nine-residue emerimicin fragment, Ac-Phe-[1-^{13}C]MeA$_2$-MeA-MeA-Val-[^{15}N]Gly$_6$-Leu-MeA-MeA-*O*-Bzl, where Ac = acetyl, Phe = phenylalanine, MeA = methylalanine, Val = valine, Gly = glycine, Leu = leucine, Bzl = benzyl is not resolved from that of natural-abundance peptide carbonyl carbon atoms, which make a constant 7.7% contribution to the full echo signal, S_0. This correction can either be measured in a separate experiment on a natural-abundance sample, or calculated from the known structure.[10] In addition, the natural-abundance ^{13}C carbonyls of Val$_5$ and Gly$_6$ are, respectively, one and two bonds away from the ^{15}N label and so will make a contribution to ΔS that reaches a maximum value of 2% by about N_c = 16. The other natural-abundance carbonyl ^{13}C atoms are all farther away from the ^{15}N label than is the carbonyl label at MeA$_2$. Thus, for $N_c > 32$, the observed ΔS is dominated by the coupling of the ^{15}N–^{13}C labels and additional natural-abundance corrections are unimportant. By N_c = 96, $\Delta S/S_0$ is greater than 0.7 (Figure 6), consistent with a D value of 40 Hz, corresponding to a C–N distance of 4.2 ± 0.1 Å. The distance by X-ray analysis[11] is 4.16 Å. The natural-abundance correction to D is less than 2 Hz when N_c = 96, which means that less than a 0.05-Å correction for the C–N distance is required. The agreement between X-ray and REDOR determinations of the [1-^{13}C]MeA$_2$–[^{15}N]Gly$_6$ distance for this calibration sample for N_c = 8 to N_c = 112

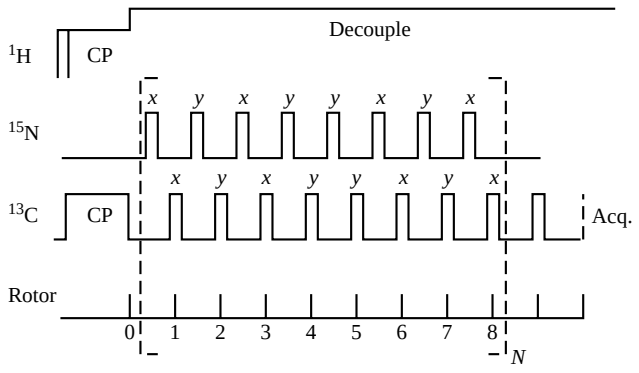

Figure 5 REDOR pulse sequence with dephasing π pulses on both the nitrogen and carbon channels. The pulses are applied using an *xy*-8 phase cycling scheme to eliminate offset effects and pulse imperfections. Signal acquisition begins two rotor cycles after the completion of a full 8*N* rotor cycles of dephasing. CP = cross polarization. Acq = acquisition

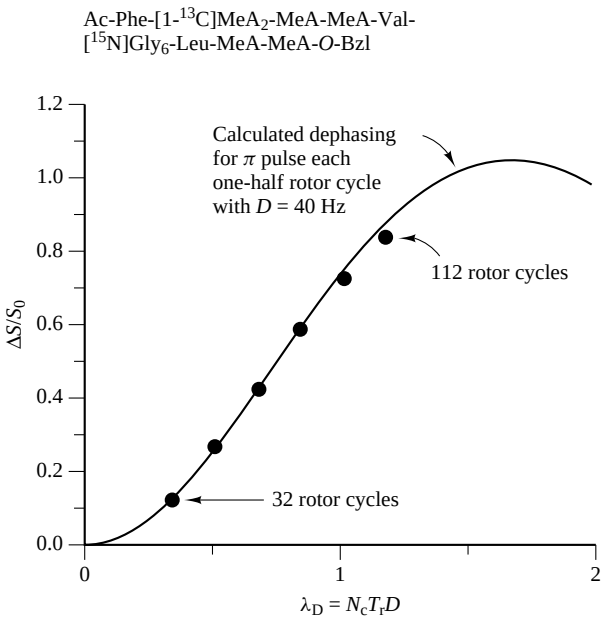

Figure 6 Observed dependence of $\Delta S/S_0$ on the universal parameter, λ_D, for a ^{13}C–^{15}N double-labeled fragment of emerimicin. The pulse sequence of Figure 5 was used. The experimental results (solid circles) are in agreement with calculation (solid line) assuming a ^{13}C–^{15}N dipolar coupling of 40 Hz corresponding to a C–N distance of 4.1 ± 0.1 Å. The natural-abundance correction to $\Delta S/S_0$ at N_c = 8 is 50% and at N_c = 100 is 4%

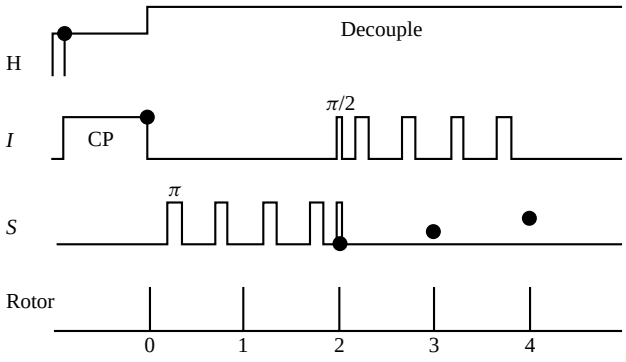

Figure 7 Pulse sequence for TEDOR *I*–*S* NMR. Following a cross-polarization (CP) transfer from abundant protons to generate initial *I*-spin magnetization, the effect of the protons is removed by resonant decoupling. The π pulses are shown separated by one-half rotor periods. The coherence transfer is achieved by simultaneous $\pi/2$ pulses in the middle of the evolution period. The solid circles represent observable magnetization

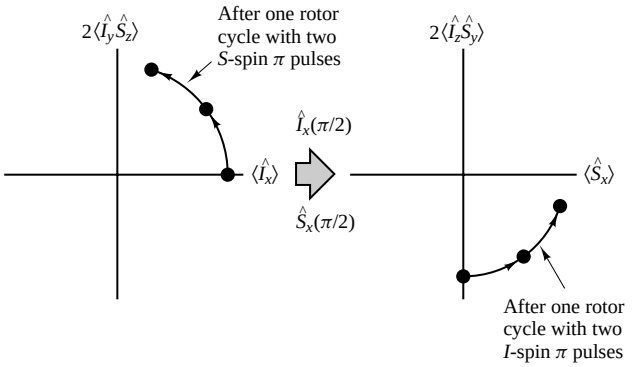

Figure 8 Schematic diagram of the evolution of the density matrix for a powder during the TEDOR pulse sequence of Figure 7 before the coherence transfer pulses (left) and after the application of the transfer pulses (right). The phase angle between $\langle\hat{I}_x\rangle$ and $\langle\hat{I}_y\hat{S}_z\rangle$ for each rotor cycle is indicated by the solid circles and is calculated using the technique illustrated in Figure 2 (right) together with a powder average. The effect of the 90° pulses is to permute I and S subscript indices

confirms that with the compensation of the *xy*-8 phase cycling scheme, hundreds of dephasing pulses can be used with no significant accumulation of error for a REDOR difference.[10] A few, accurate long range distance determinations are often sufficient to establish unambiguously the local conformation of a peptide or protein.[12]

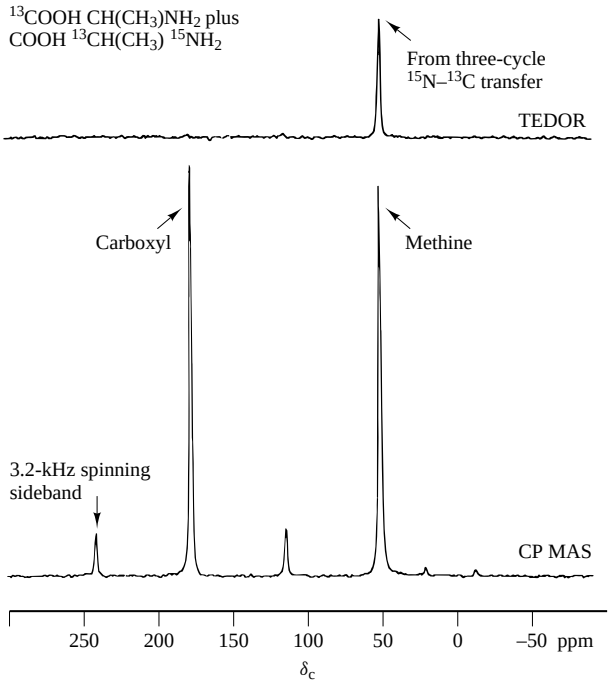

Figure 9 Transferred-echo double-resonance (top) and cross-polarization, magic angle spinning (CP MAS, bottom) ^{13}C NMR spectra of a recrystallized equimolar mixture of L-[2-^{13}C,^{15}N]alanine and L-[1-^{13}C]alanine. The TEDOR spectrum was obtained using three rotor cycles each of dephasing and refocusing. This is insufficient to generate significant carboxyl-carbon magnetization because the average intermolecular C–N dipolar coupling is weak

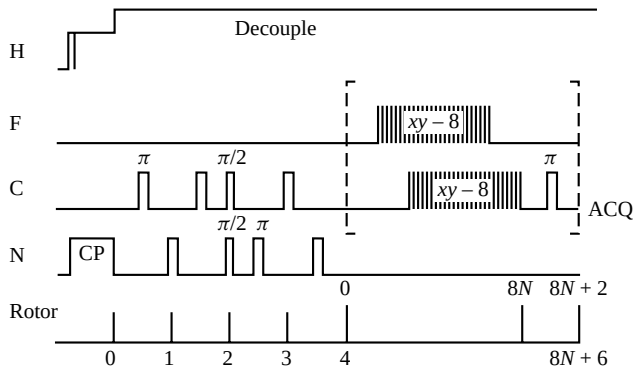

Figure 10 Pulse sequence for TEDOR combined with REDOR. The TEDOR part of the experiment (which for this illustration extends over the first four rotor cycles following the H–N cross polarization transfer) selects ^{13}C magnetization by a coherence transfer from ^{15}N. The REDOR part of the experiment (broken brackets) immediately follows the TEDOR preparation and measures dipolar coupling of the selected ^{13}C to ^{19}F. REDOR dephasing is performed using the phase-routing scheme illustrated in Figure 5. Two rotor cycles are added to the sequence so that the start of data acquisition is not coincident with a pulse

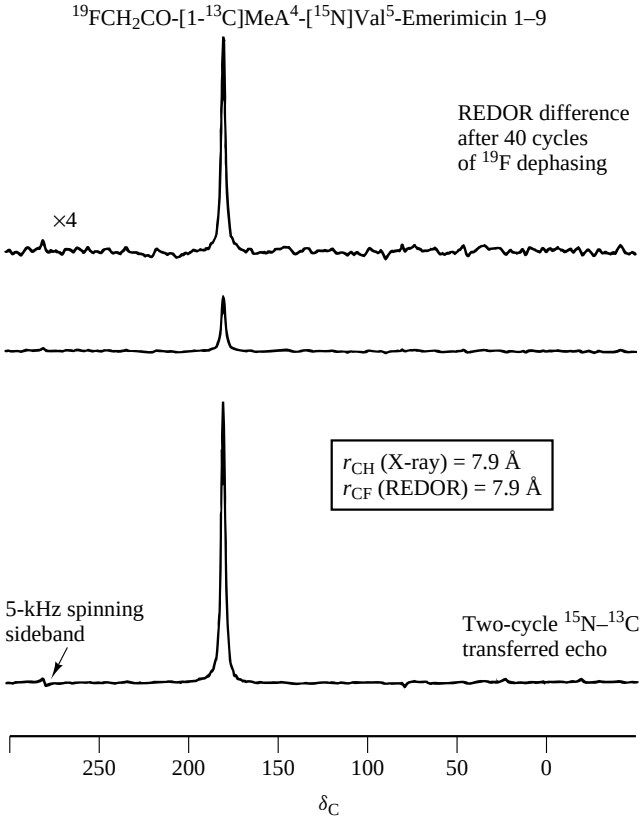

Figure 11 TEDOR–REDOR ^{13}C NMR spectra of a ^{19}F, ^{13}C, ^{15}N-labeled emerimicin (see Figure 6). The TEDOR spectrum (bottom) was obtained using an N–C coherence transfer as illustrated in Figure 7. The TEDOR–REDOR difference spectrum (the difference between TEDOR spectra with and without dephasing REDOR pulses) is shown at the top of the Figure. This spectrum was obtained by ^{19}F dephasing of the ^{15}N-TEDOR-selected ^{13}C magnetization over 40 rotor cycles

Background corrections for ^{13}C-observe ^{15}N-dephase REDOR are relatively simple to calculate because the ^{15}N natural abundance is low and γ_N is small. A measured value involves a separate sample with no ^{15}N label. The minor, observed $\Delta S/S_0$ for the single-labeled sample is then usually just subtracted from that for the double-labeled sample.[3] The correction is more involved for ^{13}C–^{31}P and ^{13}C–^{19}F pairs. For example, a ^{19}F-observe ^{13}C-dephase REDOR experiment designed to measure the dipolar coupling for a labeled ^{19}F–^{13}C pair separated by 10 Å must take into account the sizeable number of natural-abundance ^{13}C atoms within dephasing range of the ^{19}F. One way[13] to interpret the observed $\Delta S/S_0$ is to generate a model lattice with 1% randomly distributed ^{13}C. If all ^{13}C–^{13}C coupling is ignored, the ^{19}F-observed, ^{13}C-dephase REDOR ΔS can be interpreted in terms of a collection of independent, ^{19}F(label)-^{13}C(label)-^{13}C(natural abundance), three-spin clusters, whose dipolar-tensor orientations are known from the lattice parameters.

4 COHERENCE TRANSFER AND SELECTIVITY

Sometimes a natural-abundance background cannot be measured or calculated easily. In this situation, the dipolar-coupled spins can be selected from among the background of uncoupled spins by a coherence transfer from one spin of the heteronuclear pair to the other. The pulse sequence for this selection is shown in Figure 7. Transverse magnetization is first established in the I-spin system by a cross-polarization transfer from abundant protons. The dephasing of I-spin magnetization by dipolar-coupled S spins through rotor-synchronized S-spin π pulses leads to a bilinear coherence (Figure 8, left) that is transferred by an I,S pair of $\pi/2$ pulses (Figure 8, shaded arrow). These pulses occur together at the completion of a rotor cycle (Figure 7) and interchange the indices of the bilinear coherence. Finally, the transferred bilinear coherence is transformed into observable S-spin transverse magnetization by rotor-synchronized I-spin π pulses (Figure 8, right). The entire procedure is called transferred echo double resonance (TEDOR).[14] TEDOR is a rotor-synchronized solid state experiment which is based on some of the same coherence transfer principles as the INEPT solution state experiment.

The results of a TEDOR experiment using the pulse sequence of Figure 7 performed on the mixed double-labeled alanine sample discussed above are shown in Figure 9. Proton polarization is first transferred to nitrogen atoms. Then three rotor cycles are used to create bilinear ^{15}N–^{13}C coherence, and three more rotor cycles to produce observable methine carbon atom magnetization following the coherence transfer. The TEDOR theoretical transfer efficiency[14] is 50% compared with the observed 35% (Figure 9). Because TEDOR is not a difference experiment, TEDOR has the same theoretical sensitivity as REDOR. No sizeable carboxyl

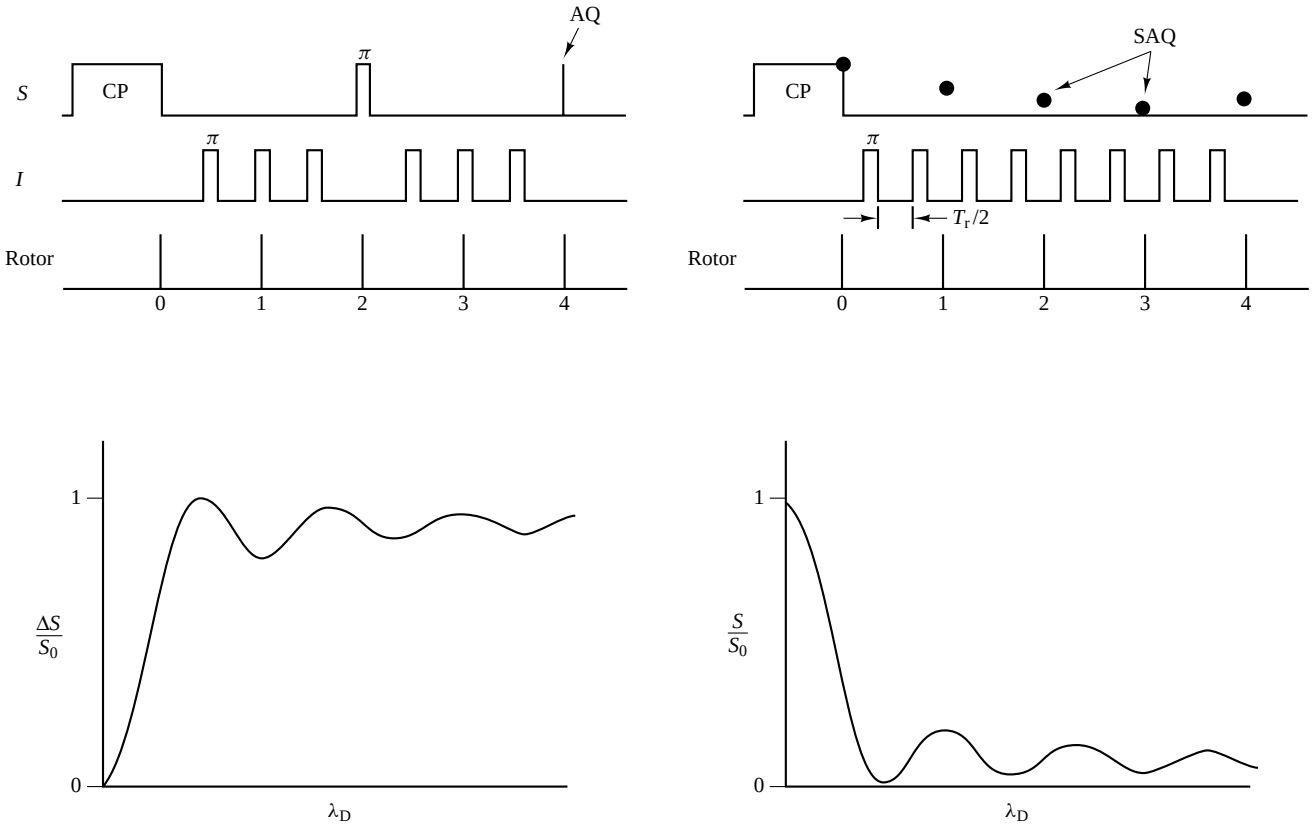

Figure 12 Two schemes for REDOR. (Left) Acquisition of a time domain signal follows evolution during which dephasing pulses diminish observable magnetization and create nonobservable $I-S$ bilinear coherence. This scheme is suitable for multiline spectra and a separate $\Delta S/S_0$ is measured for each line in the spectrum. The dependence on λ_D is determined by varying the number of rotor cycles. (Right) Synchronous detection of a time domain signal during evolution is suitable for a single-line spectrum. The observed S/S_0 is $1 - (\Delta S/S_0)$. AQ = acquisition; SAQ = synchronous acquisition

carbon magnetization is observed in Figure 9 because the short evolution time was insufficient for the weak intermolecular $^{15}N-^{13}C$ coupling to create significant bilinear coherence. If there had been a collection of nitrogen atoms all with comparable strong, couplings to carbon atoms, the TEDOR coherence transfer could still have been made selective by alternating the sign of the starting nitrogen magnetization for just one type of ^{15}N by DANTE inversion of the selected nitrogen atom signal every other scan.[15] The sign of the transferred bilinear coherence would then alternate, as would that of the observed carbon atom magnetization corresponding to the selected $^{15}N-^{13}C$ coupling. Data routing could then discriminate between carbon signals.

5 COMBINATION EXPERIMENTS AND SYNCHRONOUS DETECTION

TEDOR can be used alone or in combination to make highly selective TEDOR–TEDOR and TEDOR–REDOR experiments.[16] The pulse sequence for the latter is illustrated in Figure 10. A TEDOR sequence is tailored to select the carbonyl carbon atom signal of residue 4 of a ^{19}F, ^{13}C, ^{15}N triple-labeled emerimicin fragment (Figure 11). The $^{15}N-^{13}C$ selected magnetization is then dephased by REDOR ^{19}F π pulses resulting in the determination of a selected 8-Å C–F distance. This combination experiment involves four radiofrequencies in the same sequence which is possible using transmission-line probe technology.[17] The tuning elements in these probes are outside the magnet in a large, shielded box with isolation of all radiofrequencies, making high power on four channels practical.[18]

The observed signal in the TEDOR–REDOR experiment can be detected either as part of a two-dimensional experiment in which full S and S_0 spectra are obtained by normal acquisition starting with a rotor cycle (Figure 12, left), or synchronously with one sampling per rotor cycle (Figure 12, right). The former is used for complicated spectra with more than one resonance even after selection by TEDOR. The latter is used for the simple, one-line spectra that usually result from a TEDOR preparation. Synchronous detection[2] has the sensitivity advantage of generating the entire REDOR dephasing pattern in real time. The dipolar evolution dimension can be mapped by variation of the number of rotor cycles,[1] or variation of the position of the dephasing pulse within the rotor period.[2] The latter has a constant total dipolar evolution time which eliminates the echo-train lifetime from the analysis. In both of these two-dimensional methods, spins which contribute to the S-spin signal but have no $I-S$ coupling (a common situation for a natural-abundance background) do not interfere with the determination of the $I-S$ interaction.[16] Such spins produce a constant offset in the dipolar time domain and so a zero-frequency spike in the dipolar frequency domain. The $I-S$ coupling is determined by the width of the dipolar spectrum.[2]

Even an efficient TEDOR transfer does not result in observable magnetization associated with an isotropic powder. Thus, some crystallite orientations are discriminated against depending on the orientation of the *IS* and *SX* dipolar tensors in an $I-S-X$ three-spin TEDOR–REDOR experiment. Nevertheless, following an efficient $I-S$ TEDOR transfer, the *initial* S-observe, X-dephase REDOR behavior depends only on the size of the dipolar tensors and not on their orientation (Figure 13). Thus, interpretation of the 20% dephasing (Figure 14) in a TEDOR–REDOR experiment on the triple-labeled peptide of Figure 11 does not require knowledge of $^{15}N-^{13}C-^{19}F$ geometry in order to extract a C–F distance.[16] This will be the situation for most long-range distance determinations in general, simply because little dephasing is observed and determination of the dipolar coupling is based on the initial S/S_0 behavior. However, for systems with stronger couplings, Fourier transforms of the TEDOR–REDOR dipolar evolution offer the opportunity to establish geometry by comparisons with theoretical dipolar lineshapes (Figure 15).

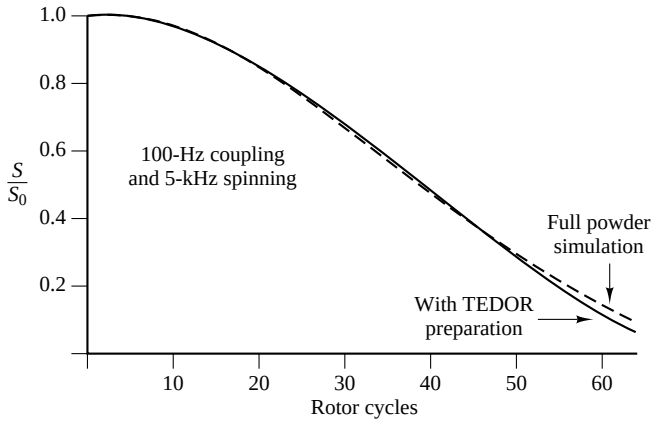

Figure 13 Simulation of X-spin REDOR dephasing of $I-S$ TEDOR-selected S-spin magnetization (solid line). The simulation assumed an $I-S$ coherence transfer after two rotor cycles of dephasing, followed by two rotor cycles of transformation of coherence into observable S-spin magnetization (see Figure 7). For $S/S_0 > 0.5$, the simulation is almost independent of orientation of $I-S$ and $S-X$ dipolar tensors (results not shown) and closely matches that for a full isotropic powder (dotted line). All simulations were performed assuming that the $I-S$ coupling was 1.2 kHz, the $S-X$ coupling was 100 Hz, and the magic angle spinning was 5 kHz

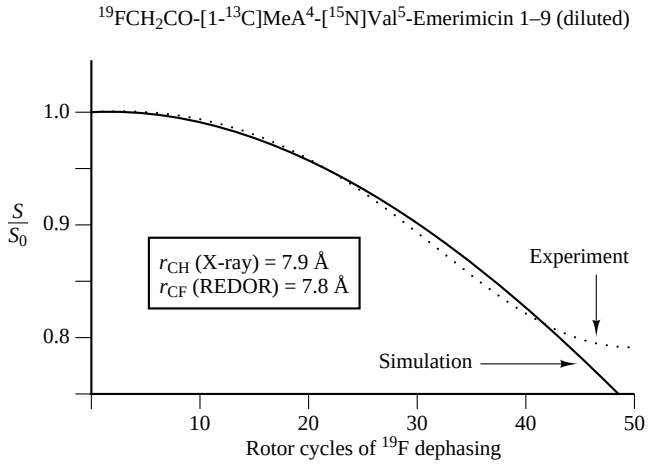

Figure 14 Synchronously sampled time domain ^{13}C signal of a ^{19}F, ^{15}N, ^{13}C-triple-labeled emerimicin diluted by natural-abundance peptide. The ^{15}N TEDOR-selected ^{13}C signal is sampled once each rotor period either with (S) or without (S_0) ^{19}F dephasing pulses. Magic angle spinning was at 5 kHz

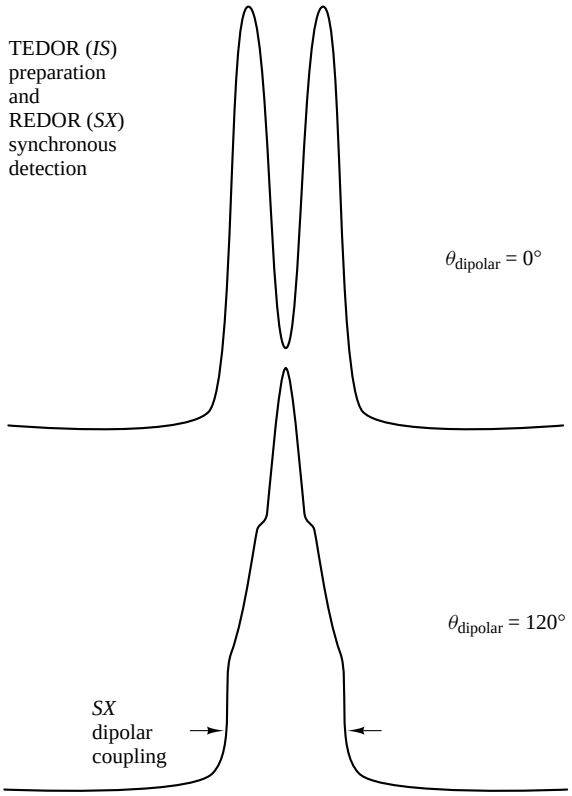

Figure 15 Dipolar spectra obtained by Fourier transforms of time domain simulations performed as described in the caption to Figure 13. The widths of both dipolar spectra are determined by the 100-Hz $S-X$ coupling. Details of the lineshape are determined by orientation of $I-S$ and $S-X$ dipolar tensors

6 RELATED ARTICLES

Cross Polarization in Solids; Electron– Nuclear Multiple Resonance Spectroscopy; INEPT; Magic Angle Spinning; Rotating Solids; Selective Excitation in MRI and MR Spectroscopy.

7 REFERENCES

1. T. Gullion and J. Schaefer, *J. Magn. Reson.*, 1989, **81**, 196.
2. T. Gullion and J. Schaefer, *Adv. Magn. Reson.*, 1989, **13**, 55.
3. Y. Pan, T. Gullion, and J. Schaefer, *J. Magn. Reson.*, 1990, **90**, 330.
4. A. Schmidt, R. A. McKay, and J. Schaefer, *J. Magn. Reson.*, 1992, **96**, 644.
5. B. A. Lewis, G. S. Harbison, J. Herzfeld, and R. G. Griffin, *Biochemistry*, 1985, **24**, 4671.
6. J. Schaefer, E. O. Stejskal, R. A. McKay, and W. T. Dixon, *Macromolecules*, 1984, **17**, 1479.
7. G. R. Marshall, D. D. Beusen, K. Kociolek, A. S. Redlinski, M. T. Leplawy, Y. Pan, and J. Schaefer, *J. Am. Chem. Soc.*, 1990, **112**, 963.
8. T. Gullion, D. B. Baker, and M. S. Conradi, *J. Magn. Reson.*, 1990, **89**, 479.
9. T. Gullion and J. Schaefer, *J. Magn. Reson.*, 1991, **92**, 439.
10. A. W. Hing, N. Tjandra, P. F. Cottam, J. Schaefer, and C. Ho, *Biochemistry*, 1994, **33**, 8651.
11. G. R. Marshall, E. E. Hodgkin, D. A. Langs, G. D. Smith, J. Zabrocki, and M. T. Leplawy, *Proc. Natl. Acad. Sci. U.S.A.*, 1990, **87**, 487.
12. A. M. Christensen and J. Schaefer, *Biochemistry*, 1993, **32**, 2868.
13. L. M. McDowell, C. A. Klug, D. D. Beusen, and J. Schaefer, *Biochemistry*, submitted.
14. A. W. Hing, S. Vega, and J. Schaefer, *J. Magn. Reson.*, 1992, **96**, 205.
15. D. D. Mueller, A. Schmidt, K. L. Papan, R. A. McKay, and J. Schaefer, 1995, **34**, 5597.
16. S. M. Holl, G. R. Marshall, D. D. Beusen, K. Kociolek, A. S. Redlinski, M. T. Leplawy, R. A. McKay, S. Vega, and J. Schaefer, *J. Am. Chem. Soc.*, 1992, **114**, 4830.
17. S. M. Holl, R. A. McKay, T. Gullion, and J. Schaefer, *J. Magn. Reson.*, 1990, **89**, 620.
18. R. A. McKay, US Patent 4446431, 1994.

Acknowledgments

This work was supported by NIH grant GM-40634.

Biographical Sketch

Jacob Schaefer, *b* 1938. B.S., 1960, Ph.D., 1964, physical chemistry, University of Minnesota, USA. Research scientist at Monsanto Company, St. Louis, 1964–1986; collaborated with E. O. Stejskal in 1976 to combine cross polarization with magic angle spinning. Faculty in Chemistry, Washington University in St. Louis, 1986–present. Approx. 200 publications. Research specialty: development of techniques for the NMR of polymeric and biological solids.

Three-dimensional Molecular Structures in Uniformly Labelled Solids Determined Using Rotational Resonance in the Tilted Rotating Frame

K. Takegoshi and Takehiko Terao

Department of Chemistry, Graduate School of Science, Kyoto University, Kyoto, Japan

1 Introduction 1
2 Theory 1
3 Method 2
4 Application to Glycylisoleucine 4
5 Concluding Remarks 10
6 References 10

1 INTRODUCTION

While solution NMR methods have been successfully applied for elucidating three dimensional (3D) structures of molecules including proteins (see **Biological Macromolecules: Structure Determination in Solution,** Volume 2), solid-state NMR has not attained such a stage. This review demonstrates the state of the art of structural determination of a whole molecule by solid state NMR, which should be complementary to solution NMR and irreplaceable for insoluble systems. In NMR of solids, measurements of dipolar interactions provide direct information on geometrical structures; they are most conveniently made under magic angle spinning (MAS) (see **Magic Angle Spinning,** Volume 5) with hidden potential of determining more than one distance using a single sample. However, most of the methods developed so far are of non-selective measurements of dipolar couplings, by which it is difficult to deduce quantitative structural information when more than two spins are involved. Hence, only one specific internuclear distance or dihedral angle is commonly determined by selectively isotope-labeling a particular pair of atoms. Then, many doubly-labeled samples must be prepared, if one tries to determine the 3D structure composed of sizable atoms by such non-selective approaches. On the other hand, if a specific dipolar interaction in a multiply or uniformly labeled system can selectively be recoupled, all the structural parameters necessary to determine the 3D structure can be obtained one by one using a single sample, significantly saving labor for sample preparation.

To achieve frequency-selective recoupling, it is required to remove all dipolar couplings at once, and recouple a specific pair. Using MAS, one can remove all the dipolar couplings together with chemical shift anisotropies under proton decoupling, and therefore the remaining problem is to achieve selective recoupling under MAS fast enough to remove all the other dipolar interactions simultaneously. For homonuclear dipolar interactions, rotational resonance (R^2)[1–8] has been developed as a simple selective recoupling method, and in fact, has been applied to biologically interesting molecules.[9] In the R^2 method, selection of a pair of spins is made by adjusting an integral multiple of the MAS frequency ν_R to the difference of the chemical shifts of the two spins. Therefore, R^2 is frequency-difference selective, and if more than one spin pair with the same separation exists, they are simultaneously recoupled. Further, when the chemical shift difference for the two spins is relatively small, the MAS frequency must be lowered, leading to imperfect decoupling of the other dipolar interactions.

Selective recoupling among homonuclear spins can also be achieved in a tilted rotating frame.[10] Under rf irradiation, the Zeeman interaction for a spin system can be written in a tilted rotating frame (X, Y, Z) as

$$\frac{\mathcal{H}}{\text{Hz}} = \sum_i \nu_{ei} \hat{I}_{Zi} \tag{1}$$

while the conventional Zeeman interaction in the rotating frame (x, y, z) is written as

$$\mathcal{H} = \sum_i \Delta\nu_i \hat{I}_{zi} \tag{2}$$

where ν_e denotes the effective field and $\Delta\nu$ is the resonance offset. By comparing these two equations, it may be expected that the R^2 condition in the rotating frame:

$$|\Delta\nu_1 - \Delta\nu_2| = n\nu_R \tag{3}$$

would be modified in the tilted rotating frame as

$$|\nu_{e1} - \nu_{e2}| = n\nu_R \tag{4}$$

In fact, this is one of the recoupling conditions in the tilted rotating frame. There are additional recoupling conditions, namely, $\nu_{e1} + \nu_{e2} = n\nu_R$ and $\nu_{eX} = n\nu_R$ ($X = I$ or S), as derived in the following section. These conditions are referred to as the R2TR (rotational resonance in the tilted rotating frame) conditions. There are three adjustable parameters to achieve one of the R2TR conditions, namely, the intensity ν_1 and the frequency ν of the rf irradiation and the MAS frequency ν_R. This diversity makes it possible to find an R2TR condition even for a pair of spins with a small chemical shift difference without relaxing the fast MAS condition necessary for decoupling all other dipolar couplings. Further, it should be pointed out here that, while R^2 is frequency-difference selective, R2TR is frequency selective. Hence, a particular dipolar coupling can be recoupled by properly choosing the experimental parameters even when more than two lines have equal chemical-shift differences.

2 THEORY

First, we briefly touch upon rotational resonance recoupling. A dipolar-coupled homonuclear two-spin $I - S$ system in a

rotating powdered sample is considered. For simplicity, the chemical shift anisotropies (CSAs) are neglected. The total spin Hamiltonian can be written as

$$\mathcal{H} = \Delta\nu_I \hat{I}_z + \Delta\nu_S \hat{S}_z + \mathcal{H}_D(t) \tag{5}$$

where $\mathcal{H}_D(t)$ is the homonuclear dipolar interaction

$$\mathcal{H}_D(t) = D(t)\left\{\hat{I}_z\hat{S}_z - \frac{1}{4}(\hat{I}_+\hat{S}_- + \hat{I}_-\hat{S}_+)\right\} \tag{6}$$

with the spatial part modulated by MAS

$$D(t) = \sum_{n=\pm1,\pm2} \nu_{Dn} \exp(in\nu_R t) \tag{7}$$

Here, ν_{Dn} is a function of the internuclear distance and the polar angles defining the direction of the $I-S$ vector in a rotor-fixed frame. $\mathcal{H}_D(t)$ is transferred into the frame of the Zeeman interaction by using the unitary operator

$$U(t) = \exp(i\Delta\nu_I \hat{I}_z t)\exp(i\Delta\nu_S \hat{S}_z t) \tag{8}$$

as

$$\begin{aligned}\widetilde{\mathcal{H}_D}(t) &= U(t)\mathcal{H}_D(t)U^{-1}(t)\\ &= \sum_{n=\pm1,\pm2} \nu_{Dn}\Big[\hat{I}_z\hat{S}_z\exp(in\nu_R t)\\ &\quad -\frac{1}{4}(\hat{I}_+\hat{S}_- + \hat{I}_-\hat{S}_+)\exp\{i(n\nu_R - \Delta)\}\Big]\end{aligned} \tag{9}$$

where Δ is the difference of the isotropic chemical shift: $\Delta = \nu_I - \nu_S$. This equation shows that the rotational resonance recoupling occurs at $\Delta = n\nu_R$ with $n = \pm1, \pm2$. If one takes account of the chemical shift anisotropies, one can prove that recoupling occurs even under higher-order ($|n| > 2$) conditions.[4]

Second, we examine the effect of continuous wave rf irradiation along the x-axis of the rotating frame for the two-spin system. The total Hamiltonian

$$\mathcal{H} = \Delta\nu_I \hat{I}_z + \Delta\nu_S \hat{S}_z + \nu_1(\hat{I}_x + \hat{S}_x) + \mathcal{H}_D(t) \tag{10}$$

is transformed into the tilted rotating frame (X, Y, Z) by the unitary transformation of

$$U_{TR} = \exp(i\beta_I \hat{I}_y)\exp(i\beta_S \hat{S}_y) \tag{11}$$

where β_X denotes the angle between the z-axis of the rotating frame (i.e., the direction of the static field) and the Z-axis of the tilted rotating frame (i.e., the direction of the effective field) for the X spin. The total spin Hamiltonian in the tilted rotating frame can be given by

$$\begin{aligned}\mathcal{H}^{TR} &= U_{TR}\mathcal{H}U_{TR}^{-1}\\ &= \nu_{eI}\hat{I}_Z + \nu_{eS}\hat{S}_Z + U_{TR}\mathcal{H}_D(t)U_{TR}^{-1}\end{aligned} \tag{12}$$

where ν_{eX} denotes the strength of the effective field for the X spin. This is further transferred into the interaction frame using the following unitary operator

$$U_{\text{eff}}(t) = \exp(i\nu_{eI}\hat{I}_Z t)\exp(i\nu_{eS}\hat{S}_Z t) \tag{13}$$

and the result is

$$\begin{aligned}\mathcal{H}_D^*(t) &= U_{\text{eff}}(t)U_{TR}\mathcal{H}_D(t)U_{TR}^{-1}U_{\text{eff}}^{-1}(t)\\ &= \sum_{n=\pm1,\pm2}\nu_{Dn}[A\hat{I}_Z\hat{S}_Z\exp(-in\nu_R t)\\ &\quad + B[\hat{I}_+\hat{S}_-\exp\{i(n\nu_R + \Delta_{\text{eff}})t\}\\ &\quad + \hat{I}_-\hat{S}_+\exp\{i(n\nu_R - \Delta_{\text{eff}})t\}]\\ &\quad + R[\hat{I}_Z\hat{S}_+\exp\{i(n\nu_R + \nu_{eS})t\}\\ &\quad + \hat{I}_Z\hat{S}_-\exp\{i(n\nu_R - \nu_{eS})t\}]\\ &\quad + S[\hat{I}_+\hat{S}_Z\exp\{i(n\nu_R + \nu_{eI})t\}\\ &\quad + \hat{I}_-\hat{S}_Z\exp\{i(n\nu_R - \nu_{eI})t\}]\\ &\quad + Q[\hat{I}_+\hat{S}_+\exp\{i(n\nu_R + \Sigma_{\text{eff}})t\}\\ &\quad + \hat{I}_-\hat{S}_-\exp\{i(n\nu_R - \Sigma_{\text{eff}})t\}]]\end{aligned} \tag{14}$$

where the coefficients A, B, R, S, and Q are functions of the angle β_X, whose explicit forms are found in Ref.[11]. It can be shown that the spatial part of $\mathcal{H}_D^*(t)$ is modulated by MAS with the spinning frequency ν_R and $2\nu_R$, while the spin part is modulated by the effective field with the frequencies of $\Sigma_{\text{eff}} = \nu_{eI} + \nu_{eS}$, $\Delta_{\text{eff}} = \nu_{eI} - \nu_{eS}$, ν_{eI}, and ν_{eS}. When any of the conditions Σ_{eff}, Δ_{eff}, ν_{eI}, or $\nu_{eS} = m\nu_R$ ($m = \pm1$ or ±2) is met, the time dependence of the spatial part and the spin part in $\mathcal{H}_D^*(t)$ is partially canceled with each other to give a static dipolar interaction $\overline{\mathcal{H}_D}^*$.

3 METHOD

Determination of the 3D structure of a multiply labeled molecule can be accomplished by obtaining all bond lengths, bond angles, and dihedral angles. For a peptide, however, one may use typical bond lengths and angles because they differ only slightly among peptides, and the peptide 3D structure can be constructed by determining dihedral angles.

Figure 1 illustrates the strategy. For a multiply $^{13}C/^{15}N$ labeled peptide, all dipolar interactions are removed uniformly by fast MAS and proton decoupling. Then, a specific three-bonds distant pair of spins is selectively recoupled by applying an rf field satisfying a proper R2TR condition. The time development of the magnetization of either of the paired spins is measured, from which the corresponding dihedral angle is deduced. This procedure is repeated for other spin pairs, until all the dihedral angles are determined.

The pulse sequence for the selective recoupling experiments is shown in Figure 2(a). During the recoupling period (t_m), the rf field satisfying a R2TR condition $\nu_{eI} + \nu_{eS} = \nu_R$ is applied to one of the paired spins concerned. This rf field also functions for spin-locking the magnetization. Then, the t_m dependence of the spin-locked magnetization is monitored after removing the possible small y component of the magnetization by applying a 90°_X pulse. The t_m dependence of the magnetization is also affected by $T_{1\rho}$ relaxation. Measuring $T_{1\rho}$ under the same irradiation condition but with a slightly ($\sim$500 Hz) different spinning frequency so as not to satisfy the DQ R2TR condition, we can remove the relaxation effect from the t_m dependence by multiplying it by $\exp(t_m/T_{1\rho})$.

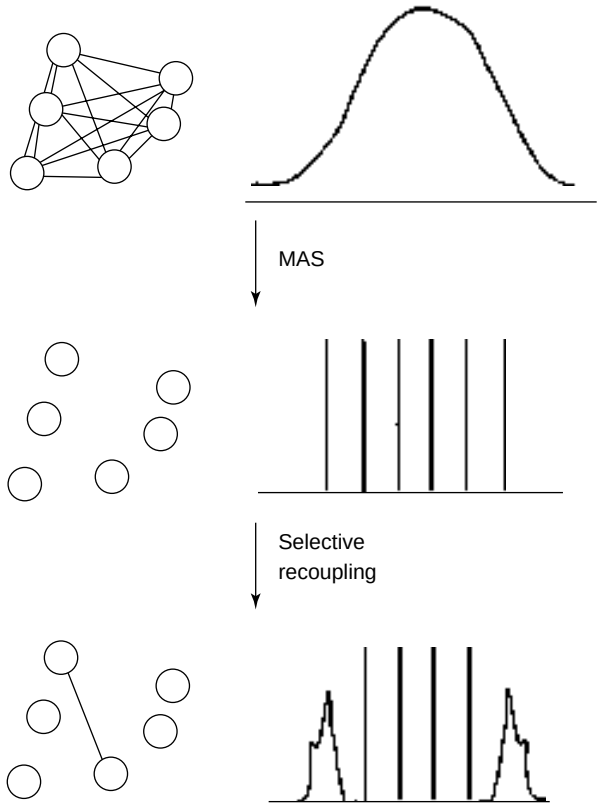

Figure 1 Schematic illustration of uniform decoupling by MAS and selective recoupling

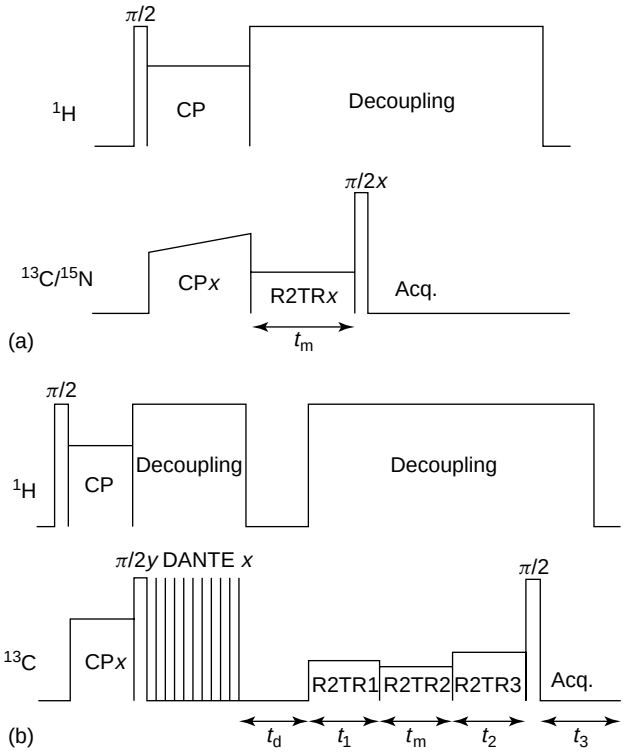

Figure 2 Pulse sequences to determine dihedral angles. (a) Dipolar recoupling experiment. After CP, a rf field satisfying a DQ condition for a particular pair of ^{13}C spins is applied on resonance to one of the spins for a recoupling time t_m. Then, the transverse magnetization of the spin is observed as a function of t_m. (b) 2D dipolar correlation experiment. After CP, the C magnetization in a four ^{13}C spin (A–B–C–D) system is suppressed by a DANTE pulse train. The A–B and the C–D dipolar interactions are selectively recovered in the t_1 and t_2 periods, respectively. These dipolar powder patterns are correlated by transferring magnetization from A or B to C or D in the mixing period. The AB/CD dipolar correlation spectrum is obtained by observing the C magnetization in the detection period t_3. (Reproduced from Nomura et al.[13] with kind permission from Kluwer Academic Publishers)

The other conditions of ZQ, SQ, and DQ ($n > 1$) are not suitable for the present experiments for the following reasons. First, to satisfy a ZQ condition, the chemical shift difference between a specific pair of spins must be larger than ν_R. However, chemical shift differences of ^{13}C or ^{15}N spin pairs at a common magnetic-field intensity are not so large as to satisfy a ZQ condition for ν_R fast enough to completely decouple the other dipolar couplings. Second, under a SQ condition, both chemical shift anisotropies (CSAs) of the relevant carbons are dominantly recovered, obscuring the effect of dipolar recoupling. Last, a DQ condition with $n > 1$, which requires a large rf-field intensity for ν_R fast enough to decouple the other dipolar couplings, lowers the selectivity of recoupling.

The influence of intermolecular dipolar couplings on the dipolar recoupling experiments was reduced by diluting a uniformly labeled sample (10%) with natural abundance material (90%). In the recoupling-time dependence experiments for the 10% uniformly labeled sample, 10% of the signal intensity at $t_m = 0$ was subtracted from the intensity observed at each recoupling time t_m, because it was found that the magnetization of the natural abundance material is kept almost constant during t_m.

An alternative approach to determine a dihedral angle is to measure mutual orientations of two or more anisotropic spin interactions. In the R2TR method, one can easily and quickly switch the dipolar interaction to be recoupled from one to another by changing ν and ν_1 under a constant spinning speed contrary to the normal R^2 method. This makes it possible to realize a 2D experiment which correlates the AB and CD dipolar powder patterns in an A–B–C–D ^{13}C spin system. Figure 2(b) shows the pulse sequence for the 2D dipolar correlation experiment. After cross polarization (CP), the C magnetization is suppressed by a selective 90° (DANTE) pulse followed by a dephasing period (t_d). In the first evolution period (t_1) the AB dipolar interaction is selectively recoupled, in the mixing period the A or B magnetization is selectively transferred to the C or D spin, and in the second evolution period (t_2) the C magnetization evolves under the selectively recoupled CD dipolar interaction. The AB/CD dipolar correlated 2D powder pattern is selectively obtained by observing the C spin in the detection period (t_3).

Recoupling may take place even in off-R2TR conditions to some extent, making the selectivity incomplete. The incompleteness of selectivity can be taken into account by including several spins into simulations in addition to the relevant two spins. To examine selectivity, we studied magnetization transfer in uniformly ^{13}C labeled L-alanine.[11] Figure 3(a) shows the ^{13}C 2D exchange NMR spectrum observed without applying any ^{13}C rf field during a mixing time of 4 ms under a MAS frequency of 5718 Hz. No conventional R^2 effects were observed at this spinning speed. The spectrum in Figure 3(b)

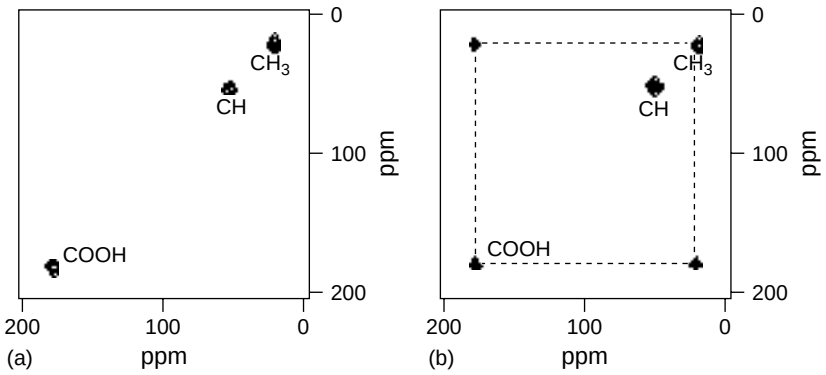

Figure 3 ^{13}C 2D exchange NMR spectra of uniformly ^{13}C labeled L-alanine. It was observed (a) without and (b) with applying a ^{13}C rf field during a mixing time of 4 ms under the MAS frequency of 5718 Hz. The rf field with the intensity of 4 kHz was applied at 296.7 ppm for the spectrum (b) to satisfy a R2TR condition $\Delta_{\text{eff}} = 2\nu_{\text{R}}$ for the carboxyl and the methyl carbons

was obtained at the same spinning speed while applying an rf field with the intensity of 4 kHz during the same mixing time to satisfy the ZQ R2TR condition $\Delta_{\text{eff}} = 2\nu_{\text{R}}$ for the carboxyl and methyl ^{13}C spins. Cross peaks appear between the carboxyl and methyl carbons, but no cross peaks can be seen between the carboxyl and methine carbons or between the methine and methyl carbons. This result confirms that the dipolar interaction between the carboxyl and the methyl carbons can be selectively recovered by the R2TR experiment, in spite of the fact that the recoupled dipolar coupling is below one fourth the other couplings. The stronger couplings remain completely decoupled by MAS.

Figure 4 shows the observed and the calculated mixing-time dependence of the individual ^{13}C magnetizations after saturation of the methyl carbon signal. The initial rapid oscillation of the carboxyl ^{13}C magnetization can be ascribed to the spinning sidebands in the tilted rotating frame,[11] which is damped quickly within a few milliseconds due to rf-field inhomogeneity. Hence, in the following, this oscillation in the simulation was damped to the same extent as the experimental data. Except for this initial oscillation and slight decay due to relaxation, the sum of the ^{13}C magnetizations of the carboxyl and the methyl carbons, $M_{0I} + M_{0S}$, is shown to be conserved. Further, the observed and the calculated curves for the methine carbon in Figure 4(b) again shows that the polarization transfer occurs selectively between the carboxyl and the methyl carbons, and further that a mixing time of 5 ms is enough for the polarization transfer between two carbons separated by 0.25 nm.

Further, to examine how large the chemical shift difference between non-relevant spins should be to achieve high selectivity, several isotropic chemical-shift values were assumed for the methine carbon, keeping its chemical shift anisotropy constant. Figure 5 shows the calculated mixing-time dependence of the methine ^{13}C magnetization for four chemical shift differences between the methyl and the methine carbons: 0, 500, 1000, and 2340 Hz. From Figure 5, it can be concluded that the chemical shift difference should be larger than 1000 Hz for selective transfer, leading to the following practical criteria of spins being added in simulations: For the selective recoupling experiment of A and D in a A–B–C–D ^{13}C system with observing the D magnetization, not only all the four spins, but also the following ^{13}C spin(s), if any: ^{13}C directly bonded to D (A), and ^{13}C within about 0.25 nm from D (A) with the ν_{e} difference between the ^{13}C and A (D) less than 1000 Hz.

4 APPLICATION TO GLYCYLISOLEUCINE

In the following, the complete 3D structure of a glycylisoleucine (Gly-Ile) molecule by R2TR is determined using a powder sample of uniformly ^{13}C,^{15}N-labeled Gly-Ile molecules, including all the positions of carbons, nitrogens, and oxygens in both main and side chains.[12,13] The 3D structure of a Gly-Ile molecule is obtained by measuring the six dihedral angles shown in Figure 6. In this study, ψ_{G}, ω_{G}, ϕ_{I}, χ_{I1}, and χ_{I2} are defined as dihedral angles N_{G}–$\text{C}^{\alpha}_{\text{G}}$–$\text{C}'_{\text{G}}$–$\text{N}_{\text{I}}$, $\text{C}^{\alpha}_{\text{G}}$–$\text{C}'_{\text{G}}$–$\text{N}_{\text{I}}$–$\text{C}^{\alpha}_{\text{I}}$, C'_{G}–N_{I}–$\text{C}^{\alpha}_{\text{I}}$–$\text{C}'_{\text{I}}$, C'_{I}–$\text{C}^{\alpha}_{\text{I}}$–$\text{C}^{\beta}_{\text{I}}$–$\text{C}^{\gamma 1}_{\text{I}}$, and $\text{C}^{\alpha}_{\text{I}}$–$\text{C}^{\beta}_{\text{I}}$–$\text{C}^{\gamma 1}_{\text{I}}$–$\text{C}^{\delta}_{\text{I}}$, respectively, by taking zero degrees for the *cis* conformation. ψ_{I} is defined as the angle between the N_{I}–$\text{C}^{\alpha}_{\text{I}}$ bond and the O^{1}_{I}–C'_{I}–O^{2}_{I} plane, being between 0 and 180°. ψ_{G}, ω_{G}, ϕ_{I}, and χ_{I1} were determined by performing the R2TR dipolar recouping experiment for a proper three or four-bonds distant spin pair, and χ_{I2} by a 2D dipolar correlation experiment because of the reason mentioned later, assuming the typical bond lengths and angles shown in Figure 6. The planar configuration of the peptide plane was also assumed.

Although the CSA interaction was neglected in Theory for simplicity, it does contribute to the results, and should thus be included into numerical calculations. Especially, the contribution of the CSA tensors for carbonyl carbons and amide nitrogens in the main chain are important owing to their large anisotropies (see **Chemical Shift Tensors,** Volume 2). However, the CSA tensors for carbonyl carbons are not very different from peptide to peptide. Hence, the mean values of δ and η for the carbonyl carbon tensors reported for some peptides are adopted (Table 1). For the directions of the principal axes, it is generally observed that the σ_{33} axis is perpendicular to the sp^2 plane.[14] On the other hand, the σ_{22} axis may make a small angle with the C=O bond direction. For C'_{G}, the σ_{33} axis is assumed to be perpendicular to the sp^2 plane and the σ_{22} axis makes the angle of 4.5° with the C'_{G}–O_{G} bond toward the C'_{G}–$\text{C}^{\alpha}_{\text{G}}$ bond.[15] For C'_{I}, the σ_{33} axis is perpendicular to the sp^2 plane and the σ_{11} axis is along the $\text{C}^{\alpha}_{\text{I}}$–$\text{C}'_{\text{I}}$ bond. The δ and η values for N_{I} and N_{G} were

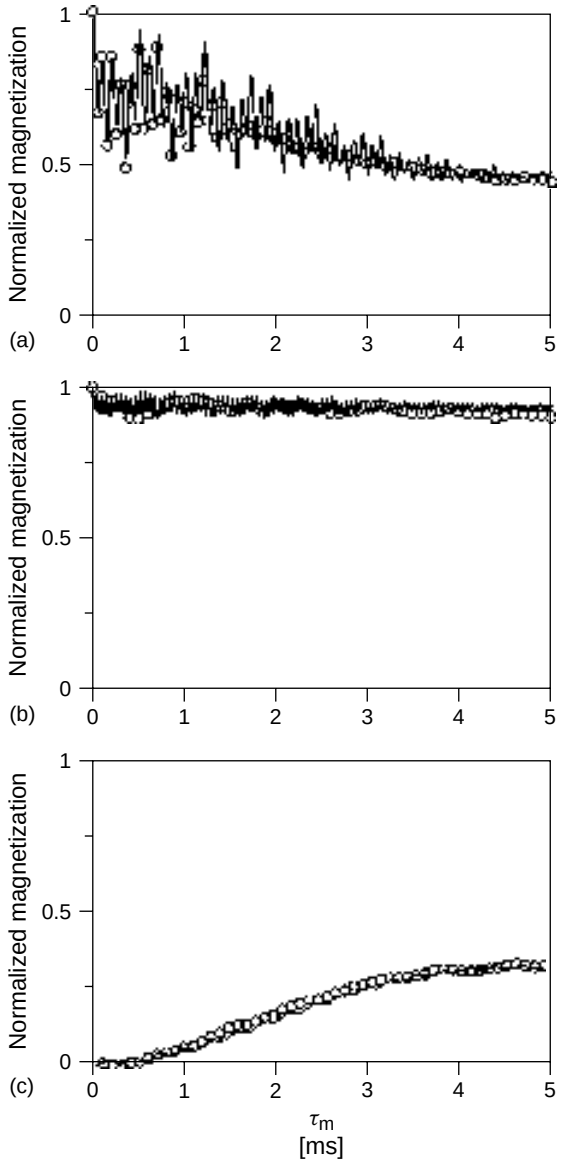

Figure 4 Experimental (○) and simulated (−) mixing-time dependence of the normalized magnetizations of (a) the carboxyl, (b) the methine, and (c) the methyl carbons under the condition $\Delta_{eff} = 2\nu_R$ satisfied between the carboxyl and the methyl carbons after saturation of the methyl carbon signal. The experiments were performed with the same parameters as described in the caption of Figure 3, excluding the initial magnetization for the methyl carbon. (Reproduced from Takegoshi et al.[11] with kind permission from Academic Press)

determined from spinning side bands observed at a low speed. The σ_{22} axis for N_I is assumed to be perpendicular to the peptide plane and the σ_{11} axis is along the N–C=O bond.[16] For N_G, the σ_{33} direction is along the N_G–C_G^α bond direction and the σ_{11} axis is perpendicular to the N_G–C_G^α–C'_G plane.[16] For the aliphatic carbons, it will be shown that the CSA interactions do not significantly affect simulated results. The ^{13}C and ^{15}N chemical shift parameters used for numerical simulations are collected in Table 1.

Figure 7 shows a ^{13}C COSY spectrum observed at $\nu_R = 17.5$ kHz under TPPM decoupling, presenting the connectivity between the observed eight signals (C_1–C_8) splitted by the

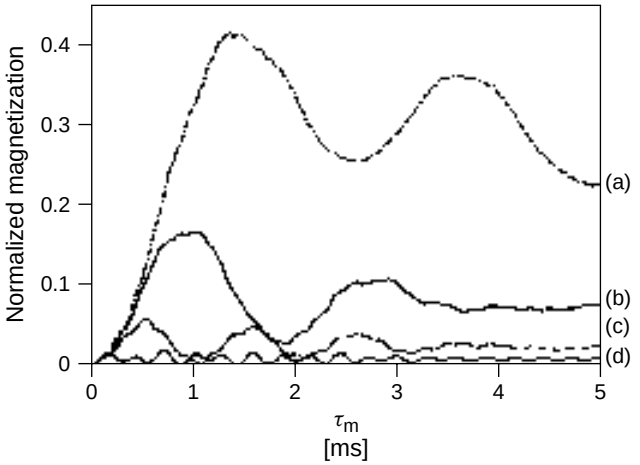

Figure 5 Simulated mixing-time dependence of the methine carbon magnetization under the same conditions as described in the caption of Figure 4, excluding the isotropic chemical shift of the methine carbon. The assumed chemical shift relative to the methyl carbon is: (a) 0 Hz, (b) 500 Hz, (c) 1000 Hz, and (d) 2340 Hz

^{13}C–^{13}C spin−spin couplings. From the connectivity and common knowledge of ^{13}C chemical shifts, all the signals can straightforwardly be assigned as $C_2 = C'_G$, $C_4 = C_G^\alpha$, $C_1 = C'_I$, $C_3 = C_I^\alpha$, $C_5 = C_I^\beta$, $C_6 = C_I^{\gamma 1}$, $C_7 = C_I^{\gamma 2}$, and $C_8 = C_I^\delta$. The observed isotropic chemical shifts are collected in Table 1.

Firstly, determination of the main-chain structure, which is described by dihedral angles conventionally named as ψ, ω, and ϕ (Figure 6), is discussed. ψ_G was determined by the selective-recoupling experiment of N_G and N_I. For the selective recoupling, an rf field with the intensity of 8300 Hz was applied on resonance to N_G, which satisfies a DQ condition under $\nu_R = 17.5$ kHz, and the recoupling-time dependence of the spin-locked magnetization of N_G was observed (Figure 8a). ψ_G was determined to be 180° from the root-mean-square deviation (RMSD) between the experimental data and the curves calculated for various ψ_G (Figure 8b). Let us examine to what extent the assumptions for the chemical shift tensors lead to error for determination of ψ_G. It was found that a deviation of 10° in the σ_{11} direction for N_I from the peptide bond direction to the N–C_α direction hardly changes the simulation curve. The deviation of 10° in the σ_{33} axis for N_G from the C_G^α–N_G bond direction does not change it either. The averages of the CSA parameters of the amide nitrogens[16] in $AcGlyGlyNH_2$, $AcGlyAlaNH_2$, $AcGlyTyrNH_2$, and GlyGly·HCl gives $(\delta, \eta) = (103.2\,\text{ppm}, 0.22)$, which are similar to the observed ones, leads to the same ψ_G value of 180° as above. It should be pointed out, however, that changing the observed CSA parameters of N_I to those for the amide nitrogen in $AcGlyTyrNH_2$ ($(\delta, \eta) = (96.4\,\text{ppm}, 0.26)$) or GlyGly·HCl ($(\delta, \eta) = (101.0\,\text{ppm}, 0.02)$)[16] results in the best-fit values of $\psi_G = \pm 154$ or $\pm 159°$, respectively. Such sensitivity of the recoupling-time dependence to the CSA parameters δ and η would be found particularly around $\psi = 180°$ at which the ^{15}N–^{15}N dipolar interaction becomes the weakest and thus insensitive to the dihedral angle. Nevertheless, the plot of $\Delta\chi^2$ shown in Figure 8(b) indicates that the 68% confidence interval ($\Delta\chi^2 < 1$) is still ±10°. For a better precision, it is desirable to measure the CSA parameters of amide nitrogens and use them in the simulations for determining ψ.

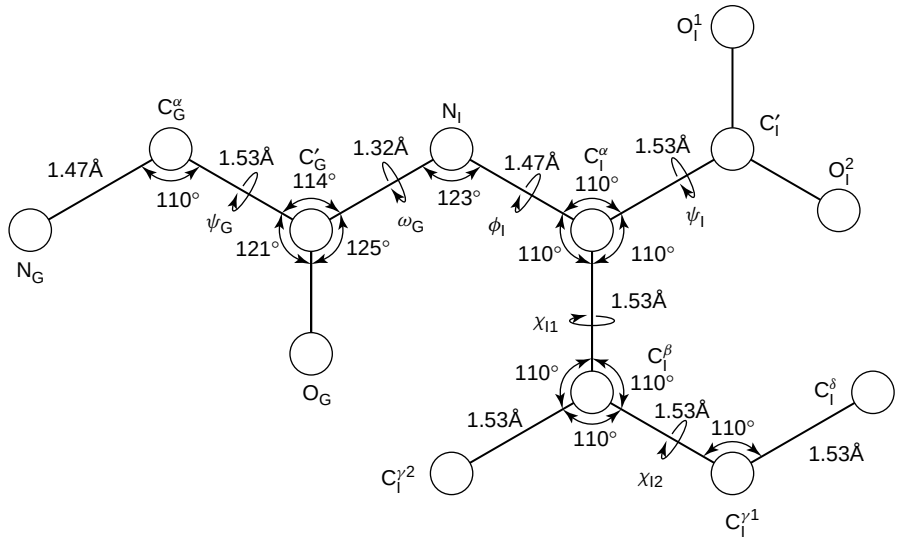

Figure 6 Schematic representation of a glycylisoleucine molecule. Typical values of the bond distances in Å and the bond angles in degrees are shown, which were used to simulate experimental results and construct the three dimensional structure of glycylisoleucine. The glycine carbonyl and C_α carbons are labeled as C'_G and C^α_G, and the isoleucine carboxyl, C_α, C_β, $C_{\gamma 1}$, $C_{\gamma 2}$, C_δ carbons are as C'_I, C^α_I, C^β_I, $C^{\gamma 1}_I$, $C^{\gamma 2}_I$, and C^δ_I, respectively. The glycine amine and the isoleucine amide nitrogens are labeled as N_G and N_I, respectively, and the glycine carbonyl oxygen as O_G, and the two isoleucine carboxyl oxygens as O^1_I and O^2_I. The dihedral angles ϕ_I, ω_G, ψ_G, ψ_I, χ_{I1}, and χ_{I2} are also shown. (Reproduced from Nomura et al.[13] with kind permission from Kluwer Academic Publishers)

Table 1 Chemical shift parameters used for the numerical simulations of the R2TR dipolar recoupling experiments in glycylisoleucine. (Reproduced by permission of Kluwer Academic Publishers from Nomura et al.[13])

	C'_I	C'_G	C^α_I	C^α_G	C^β_I	$C^{\gamma 1}_I$	$C^{\gamma 2}_I$	C^δ_I	N_I	N_G
δ_{iso}[a], ppm	178.9	169.3	64.0	40.3	36.3	26.7	17.0	12.4	120.9	23.1
δ[b], ppm	−71.0[c]	−79.3[d]	−19.7[e]	20.0[f]	6.67[g]	−12.3[h]	–	−13.9[i]	103.0[j]	19.5[j]
η[b]	0.84[c]	0.82[d]	0.44[e]	0.94[f]	0.60[g]	0.58[h]	–	0.32[i]	0.31[j]	0.68[j]

[a] ^{13}C and ^{15}N isotropic chemical shifts were obtained with respect to Me_4Si and liquid NH_3, respectively.
[b] The anisotropy δ and the asymmetry parameter η are defined as $\delta = \delta_{zz} - \delta_{iso}$ and $\eta = (\delta_{yy} - \delta_{xx})/\delta$, where δ_{iso} is the isotropic shift and $|\delta_{yy} - \delta_{iso}| \leq |\delta_{xx} - \delta_{iso}| \leq |\delta_{zz} - \delta_{iso}|$.
[c] Average of the values for the carboxyl carbons in glycine,[17] L-alanine,[18] L-serine,[19] L-threonine,[20] L-asparagine.[20]
[d] Average of the values for the carbonyl carbons in some peptides.[15]
[e] Values for the α carbon in L-alanine.[18]
[f] Values for the α carbon in glycine.[17]
[g] Values for the β carbon in isobutane.[22]
[h] Values for the α-methylene carbon in n-eicosane.[23]
[i] Values for the methyl carbon in n-eicosane.[23]
[j] Determined by the sideband analysis of a low-speed MAS spectrum.

To determine ϕ_I, the selective recoupling experiment was done for C'_G and C'_I, where an rf field with an intensity of 8500 Hz was applied on resonance to the C'_I carbon while spinning with $\nu_R = 17.054$ kHz. Figure 9(a) shows the observed recoupling-time dependence of the magnetization of C'_I. If only the dipolar interaction between C'_G and C'_I contributes to the result, only the absolute value of the dihedral angle ϕ_I can be determined from this experiment. In the present case, however, the large CSAs of both carbons and the relative orientations between the CSA tensors, and some dipolar tensors significantly affect the experimental result. Hence, there may be a good chance of determining not only ϕ_I but also ψ_I with the signs. Since peptide planes take the *trans* configuration except for cyclic peptides or peptides with proline, ω_G was assumed to be 180°. Therefore, the experimental curve was simulated, taking ϕ_I and ψ_I as adjustable parameters.

Figure 9(b) and (c) show the contour plots of RMSD between the experimental data and the curves calculated for various values of (ϕ_I, ψ_I) and $\Delta\chi^2$ around the global minimum of RMSD, respectively. These results provide the best-fit values of $(\phi_I, \psi_I) = (-76°, 147°)$ and the 68% confidence regions ($\Delta\chi^2 \sim 1$) of $(-1° \sim 1°)$ for ϕ_I and $(-9° \sim 6°)$ for ψ_I. Due to the imperfect selectivity of R2TR, C^α_G, C^α_I, and C^β_I in addition to C'_G and C'_I had to be included to best simulate the recoupling curve. This resolves the degeneracy for (ϕ_I, ψ_I) and $(-\phi_I, -\psi_I$ or $180 - \psi_I)$, which occurs if only C'_G and C'_I contribute to the recoupling curve. In fact, the $\Delta\chi^2$ value around $(\phi_I, \psi_I) = (76°, 33°)$ is relatively large (ca. 34). Hence, both ϕ_I and ψ_I could be uniquely determined. It should,

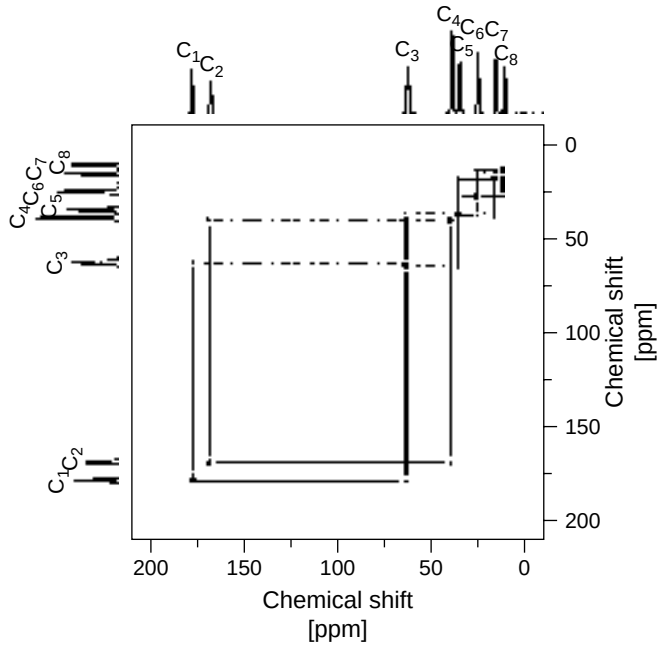

Figure 7 ^{13}C COSY spectrum of uniformly ^{13}C,^{15}N-labeled glycylisoleucine. It was obtained under the spinning speed of 17.5 kHz and TPPM decoupling. (Reproduced from Nomura et al.[13] with kind permission from Kluwer Academic Publishers)

however, be pointed out that ϕ_I is precisely determined but ψ_I is not. This is because the dipolar coupling directly contributes to the determination of ϕ_I, but ψ_I is obtained only through the relative orientation of the C'_I CSA tensor to the other tensors. Therefore, the validity of the use of the CSA tensors assumed for C'_G and C'_I in the above simulations should be examined.

First, as for C'_G, the experimental result was simulated using the CSA parameters and orientations determined for $AcGlyGlyNH_2$, $AcGlyAlaNH_2$, $AcGlyTyrNH_2$, and GlyGly·HCl.[15] The best-fit values of (ϕ_I, ψ_I) do not deviate significantly for the four sets of parameters ($-71° \sim -78°$, $139° \sim 148°$). As for the tensor orientation of C'_I, it was assumed that σ_{11} is parallel to the C^α_I–C'_I bond, while it may deviate from the bond direction by about 10°.[14] It was found that the 10° deviation leads to (ϕ_I, ψ_I) = ($-76°$, 138°). For the CSA parameters (δ, η), the values for glycine,[17] L-alanine,[18] L-serine,[19] L-threonine,[20] and L-asparagine[21] were used to find (ϕ_I, ψ_I) to be ($-75° \sim -76°$, $137° \sim 150°$).

These results show that the use of likely CSA tensors for C'_G and C'_I in the simulations causes only a small error in the determination of ϕ_I, but leads to a considerable error in ψ_I. This is also because the ϕ_I value is directly related to the distance, while the ψ_I value is related mainly to the relative orientations of the CSA tensors, being more sensitive to them. To obtain a more precise value for ψ_I, (δ, η) for C'_I should be measured by some method.

The present result of the recoupling experiment for C'_G and C'_I indicates that one dipolar recoupling experiment per amino acid residue is enough to determine dihedral angles (ψ, ω, ϕ) which provide the 3D backbone structure of a peptide. In the above, however, $\omega_G = 180°$ was assumed, while in cyclic peptides or peptides with proline, ω_G may be 0°. Hence, the possibility of determining whether $\omega_G = 0°$ or 180° was examined. The dotted line in Figure 9(a) shows

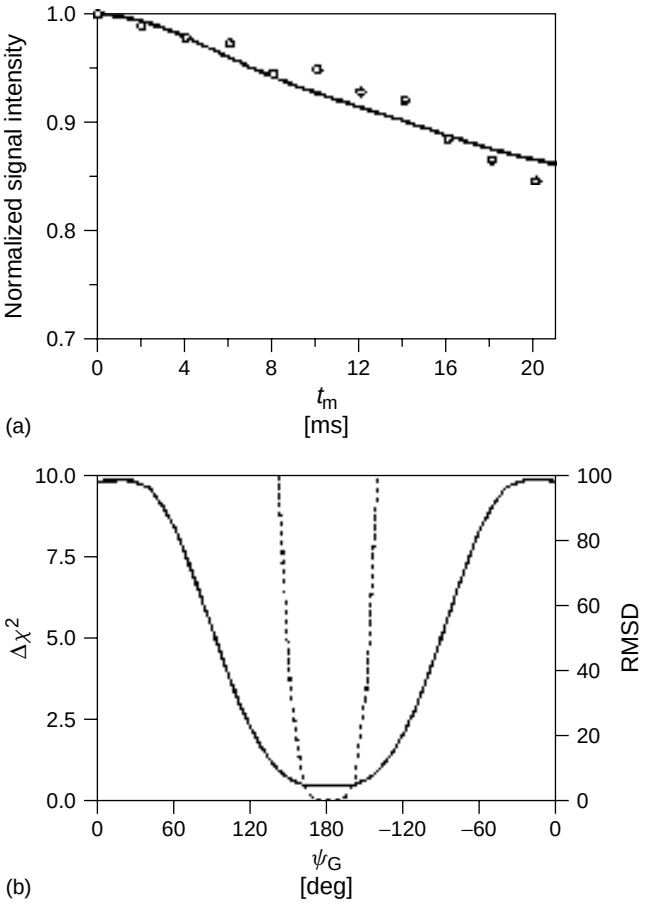

Figure 8 (a) Recoupling-time dependence of the normalized magnetization of N_G in 10% uniformly ^{13}C,^{15}N-labeled glycylisoleucine. The dipolar recoupling experiment was carried out using the pulse sequence in Figure 2(a) under a R2TR condition ($\nu_{eI} + \nu_{eS} = \nu_R$) satisfied for N_G and N_I by applying a rf field with the intensity of 8300 Hz on resonance to N_G under MAS with $\nu_R = 17.5$ kHz. Experimental points are shown by circles. The standard deviation for each point is ca. ±0.05. The curves are calculated for the dihedral angle ψ_G of 180°. $T_{1\rho}$ was determined to be 70 ms by an off-R2TR experiment, and used to remove the relaxation effect from the dipolar recoupling data. (b) Dihedral angle (ψ_G) dependence of RMSD (- - - - -) between the experimental (Figure 8a) and simulated data and of $\Delta\chi^2$ (———). (Reproduced from Nomura et al.[13] with kind permission from Kluwer Academic Publishers)

the curve simulated with $\omega_G = 0°$ and the best-fit values of (ϕ_I, ψ_I) = ($-86°$, 167°), showing that it is difficult to determine the difference between the two possibilities $\omega_G = 0°$ and $\omega_G = 180°$ by this experiment. Therefore, another recoupling experiment was made for C^α_G and C'_I, by applying an rf field with an intensity of 2800 Hz on resonance to the C'_I carbon which satisfies a DQ condition under spinning with $\nu_R = 17.03$ kHz. Figure 10 shows the recoupling-time dependence of the magnetization of C'_I together with the simulated curves obtained for the two sets of (ω_G, ϕ_I, ψ_I), namely, (180°, $-76°$, 147°) and (0°, $-86°$, 167°). Clearly, the former set reproduces the observation as expected. It indicates that even when one does not know whether $\omega = 0°$ or 180°, one can determine the three dihedral angles (ψ, ω, ϕ) by two dipolar recoupling experiments per amino acid residue.

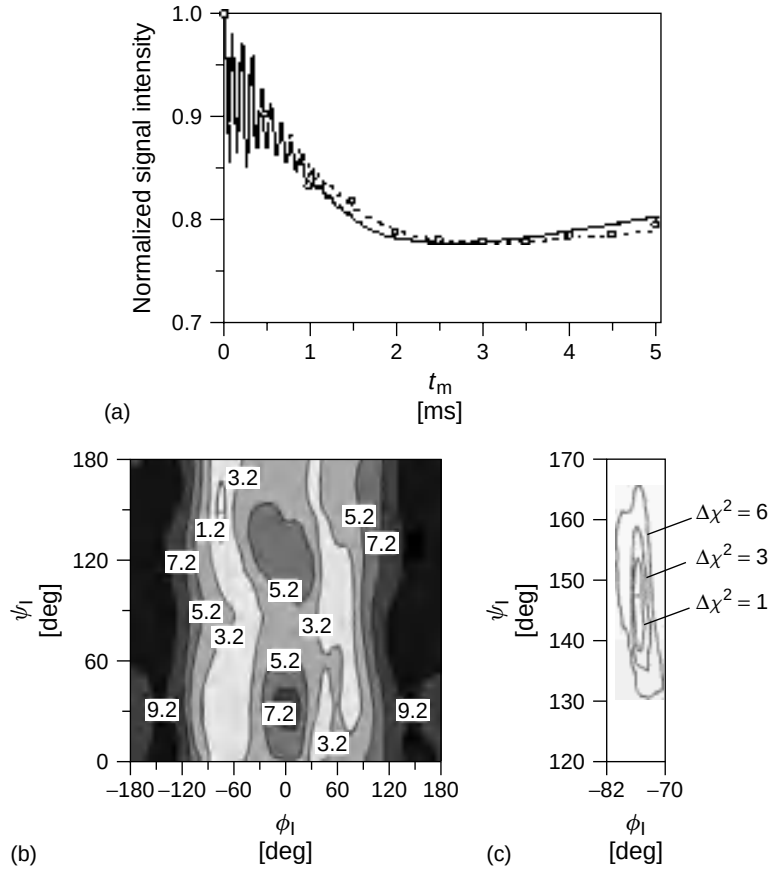

Figure 9 (a) Recoupling-time dependence of the normalized magnetization of C'_I in 10% uniformly ^{13}C,^{15}N-labeled glycylisoleucine. The dipolar recoupling experiment was carried out using the pulse sequence in Figure 2(a) under a R2TR condition ($\nu_{eI} + \nu_{eS} = \nu_R$) satisfied for C'_I and C'_G by applying a rf field with the intensity of 8500 Hz on resonance to the C'_I carbon under MAS with $\nu_R = 17.054$ kHz. Experimental points are shown by circles. The standard deviation for each point is ca. ± 0.03. The solid line is the curve calculated for the dihedral angles (ω_G, ϕ_I, ψ_I) = (180°, −76°, 147°), whereas the dotted line for (ω_G, ϕ_I, ψ_I) = (0°, −86°, 167°). $T_{1\rho}$ was determined to be 500 ms for C'_I in 10% uniformly ^{13}C,^{15}N-labeled glycylisoleucine, and used to correct the experimental data. (b) The contour plot of RMSD between the experimental spectrum (Figure 5a) and the simulations for various sets of (ϕ_I, ψ_I) and $\omega_G = 180°$. The global minimum is indicated by a dot. (c) Dihedral angles (ϕ_I and ψ_I) dependence of $\Delta\chi^2$ for $\omega_G = 180°$. (Reproduced from Nomura et al.[13] with kind permission from Kluwer Academic Publishers)

As exemplified here, the recoupling-time behavior in a general sp^2–sp^2 ^{13}C spin pair depends not only on the internuclear distance, but also on the relative orientations between the CSA tensors and the dipolar vector as well as the CSA parameters. Owing to the dependence caused by CSA, the magnitudes of not only ϕ but also ψ can be determined. Moreover, a few more carbons also contribute to the experimental result due to the incomplete selectivity; however, it provides the benefit of being able to determine the signs of ϕ and ψ. While the contribution of CSA tensors and other spins makes the simulation troublesome and somewhat reduces the accuracy in determination of dihedral angles, it provides information which cannot easily be obtained by other means.

As described above, the dihedral angles for the main chain were determined. The dihedral angles for the side chain in the isoleucine residue can also be determined in a similar manner. However, since their chemical-shift values are very similar to each other and moreover the atomic positions are close to each other, selective recoupling of one of these pairs is indeed difficult. In this sense, the isoleucine residue is one of the most demanding ones for the present approach.

The χ_{I1} angle was obtained by selective dipolar recoupling between C'_I and $C_I^{\gamma 1}$, which was attained by applying a rf field with the intensity of 2000 Hz on resonance to the C'_I carbon under MAS with $\nu_R = 17.46$ kHz. In the simulation, C_I^{α}, C_I^{β}, and C_I^{δ} besides C'_I and $C_I^{\gamma 1}$ were included, and χ_{I1} was determined to be 178°. The effect of the chemical shift tensors of C'_I on the χ_{I1} value were examined using the literature (δ, η) values of C′ in L-alanine, L-serine, L-threonine, and L-asparagine, and it was found that the best-fit values of χ_{I1} are virtually unaffected (175° ∼ 178°). Also, changing the CSA parameters for $C_I^{\gamma 1}$ to those determined for the α-methylene carbon of *n*-eicosane[23] provides essentially the same value of $\chi_{I1} = -176°$.

As exemplified by the present case, in a general sp^3–sp^2 ^{13}C spin pair, possible variations of the parameters and orientations of their CSA tensors barely affects the recoupling-time dependence. Thus, likely CSA parameters (δ, η) and tensor orientations for both carbons may be used safely.

To determine the χ_{I2} angle in the same way as above, it is necessary to selectively recouple C_I^{α} and C_I^{δ}, or $C_I^{\gamma 2}$ and C_I^{δ}. Due to the spectral congestion, it is difficult to find a R2TR

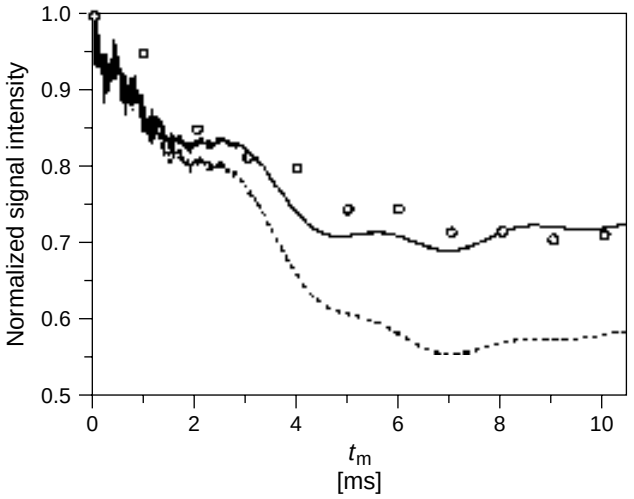

Figure 10 Recoupling-time dependence of the normalized magnetization of C'_I in 10% uniformly ^{13}C,^{15}N-labeled glycylisoleucine. The dipolar recoupling experiment was carried out using the pulse sequence in Figure 2(a) under a R2TR condition ($\nu_{eI} + \nu_{eS} = \nu_R$) satisfied for C'_I and C^{α}_G by applying a rf field with the intensity of 2800 Hz on resonance to the C'_I carbon under MAS with $\nu_R = 17.03$ kHz. Experimental points are shown by circles. The standard deviation for each point is ca. ± 0.04. The solid line is the curve calculated for the dihedral angles (ω_G, ϕ_I, ψ_I) = (180°, −76°, 147°), whereas the dotted line for (ω_G, ϕ_I, ψ_I) = (0°, −86°, 167°). $T_{1\rho}$ was determined to be 500 ms for C'_I in 10% ^{13}C,^{15}N-labeled glycylisoleucine, and used to correct the experimental data. (Reproduced from Nomura et al.[13] with kind permission from Kluwer Academic Publishers)

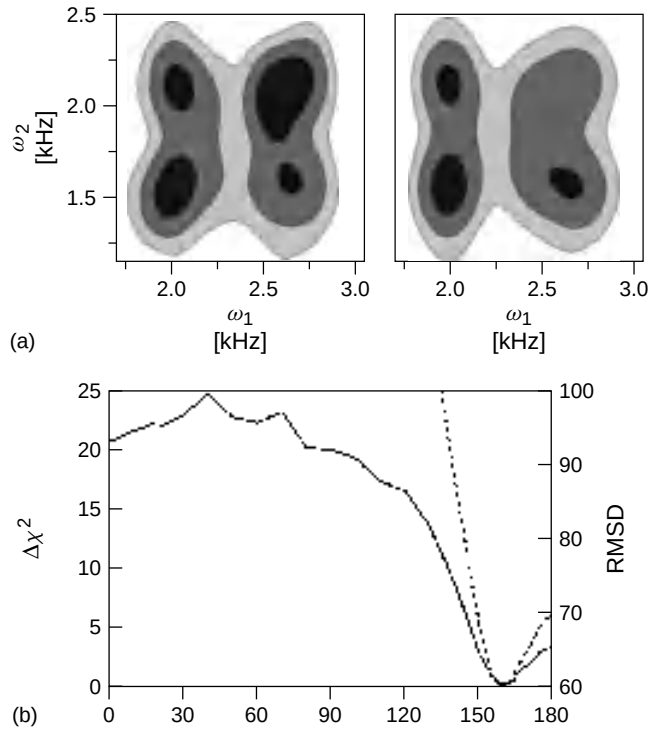

Figure 11 (a) The 2D C^{α}_I–C^{δ}_I/$C^{\gamma 2}_I$–C^{δ}_I dipolar correlation spectrum for uniformly ^{13}C,^{15}N-labeled glycylisoleucine. The experiment was performed using the pulse sequence in Figure 2(b). The spinning frequency ν_R is 5110 Hz. The ^{13}C rf-field intensities during the t_1 period, the mixing time, and the t_2 period are $\nu_1 = 2540$ (on resonance to the C^{δ}_I carbon), 0, and 1825 Hz (on resonance to the C^{α}_I carbon), respectively. (left) Experimental 2D spectrum. (right) Simulated 2D spectrum calculated for the $C^{\gamma 1}_I$–C^{δ}_I distance of 1.62 Å and the dihedral angle χ_{I2} of 160°. The contour lines are plotted at 65, 77, and 88% of the maximum intensity. (b) Dihedral angle (χ_{I2}) dependence of RMSD (- - - - -) between the experimental (Figure 11a) and simulated 2D dipolar correlation spectra and of $\Delta\chi^2$ (———). (Reproduced from Nomura et al.[13] with kind permission from Kluwer Academic Publishers)

condition suitable for these pairs. Therefore, a C^{α}_I–C^{β}_I/$C^{\gamma 1}_I$–C^{δ}_I dipolar correlation 2D powder pattern was observed using the sequence shown in Figure 2(b). In this experiment, a 100% uniformly labeled sample was used for obtaining a high signal-to-noise ratio. The use of the undiluted sample is justified, because the dipolar interactions recoupled in the t_1 and t_2 periods are of directly bonded ones, and thus much stronger than the intermolecular dipolar interactions.

The spinning speed ν_R was set to 5110 Hz, satisfying the R^2 condition for C^{δ}_I and C^{α}_I. In the t_1 period, a DQ condition is matched for $C^{\gamma 1}_I$ and C^{δ}_I by applying an rf field with an intensity of 2540 Hz on resonance to C^{δ}_I. During the mixing time t_m, the magnetization of C^{δ}_I is selectively transferred to C^{α}_I by R^2. In the t_2 period, a DQ condition is fulfilled for C^{α}_I and C^{β}_I by applying an rf field with an intensity of 1825 Hz on resonance to C^{α}_I. Figure 11(a) compares the experimental and the simulated 2D spectra, while Figure 11(b) shows the χ_{I2} dependence of RMSD between the experimental and calculated 2D spectra. Even though the agreement is not excellent, the $\Delta\chi^2$ plot in Figure 11(b) shows that the 68% confidence interval is ±5°, and χ_{I2} was determined to be 160°. The sign of χ_{I2} cannot be determined from this experiment. The dihedral angle ($C^{\gamma 2}_I$–C^{β}_I–$C^{\gamma 1}_I$–C^{δ}_I) was calculated to be 39° from $\chi_{I2} = -160°$, and to be 79° from $\chi_{I2} = 160°$; it suggests that the steric hindrance between the two methyl groups is smaller for the latter case. Therefore, the positive sign was preferred.

In the simulation, $C^{\gamma 2}_I$ in addition to C^{α}_I, C^{β}_I, $C^{\gamma 1}_I$, and C^{δ}_I were included, and a somewhat long $C^{\gamma 1}_I$–C^{δ}_I bond length of 1.62 Å had to be assumed for the best fitting. This unusual bond length was attributed to a thermal vibration of C^{δ}_I. It is worthy to be noted that with the existence of molecular motion, dihedral angles cannot be correctly determined from distance measurements. However, in a theoretical study of vibrational effects,[24] it has been proved that the dipolar 2D powder patterns provide correct dihedral angles even under the presence of molecular vibrations as long as the asymmetry of the vibration is negligible. It is a common problem for various methods of structure determination that we must pay attention to the presence of local motion.

In these simulations, chemical shift anisotropies are not included, but it was found that even if likely chemical shift tensors are included, the spectrum does not appreciably change, under the MAS frequency of ∼5 kHz. This is fortunate, because the CSA tensors of sp^3 carbons depend heavily on circumstances, so that it is very difficult to assume them appropriately for simulations. For a directly bonded sp^3–sp^3 ^{13}C spin pair, the effect of CSAs can indeed be neglected in comparison with the contribution of the dipolar coupling under MAS with a spinning speed a few times faster than $|\delta|$, according to

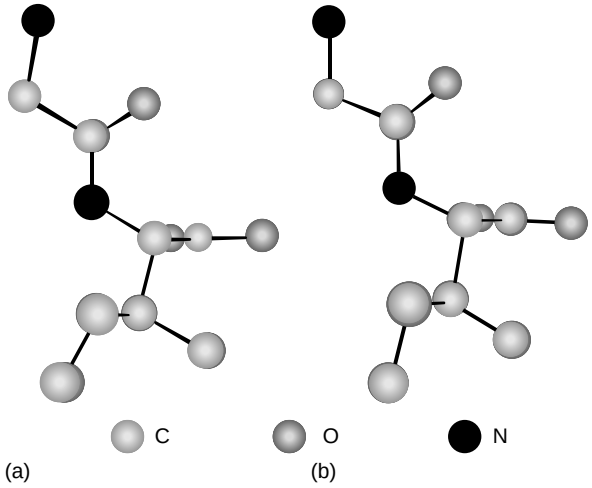

Figure 12 Three dimensional structure of glycylisoleucine. (a) NMR study; (b) X-ray crystallography. (Reproduced from Nomura et al.[13] with kind permission from Kluwer Academic Publishers)

our simulations. On the other hand, for a nonbonded, namely weakly dipolar coupled sp^3-sp^3 ^{13}C spin pair, the effect of the CSAs becomes more important than for a directly bonded pair. Therefore, the CSA effect must be reduced for accurate determination of dihedral angles by using a sufficiently fast spinning speed. Then large ν_1 is needed for satisfying a DQ recoupling condition, so that selectivity is declined. Therefore, when some other sp^3 carbons exist close to the relevant carbons, the dipolar recoupling experiment (Figure 2a) does not work well, and the 2D dipolar correlation experiment (Figure 2b) is recommended.

Figure 12 shows the 3D structure constructed from the dihedral angles determined by the R2TR experiments, and that determined by X-ray crystallography. The dihedral angles determined by NMR and X-ray are (ψ_G, ω_G, ϕ_I, ψ_I, χ_{I1}, χ_{I2}) = (180°, 180°, −76°, 147°, 178°, 160°) and (165°, 170°, −70°, 156°, 178°, 170°), respectively. Although of course the result by NMR includes errors, we note that the structure determined by X-ray diffraction is not very accurate either. Nevertheless, both structures are in good agreement, indicating that the present approach is useful for structure determination. Further, the X-ray diffraction showed that the thermal vibration parameters of C_I^{δ} are very large, agreeing with our observation by NMR.

5 CONCLUDING REMARKS

The complete 3D structure of a uniformly ^{13}C,^{15}N-labeled Gly-Ile molecule were determined using the R2TR method. All the dihedral angles were individually determined by selectively recoupling some dipolar interactions between three or four-bonds distant spins or observing a dipolar correlation 2D powder pattern. Choosing three adjustable parameters ν_1, ν_0, and ν_R properly, it was possible to find a R2TR condition suitable for selective recoupling of the pair of spins concerned. Furthermore, it is not always necessary that all resonances are resolved; it is possible to monitor the recoupling-time dependence if only one of the pair of the spins concerned is resolved well from the others.

The present approach can be applied to determine the 3D structure of a small molecule and also the structure of a restricted region important to the biological function of a large system using a sample in which the region is uniformly or multiply labeled. So far quantitative structural information obtained by solid state NMR has been almost limited to a single internuclear distance or dihedral angle. The present approach increases the obtainable quantity of structural information in a single powder sample.

6 REFERENCES

1. E. R. Andrew, S. Clough, L. F. Farnell, T. D. Gledhill, and I. Roberts, *Phys. Lett.*, 1966, **21**, 505.
2. D. P. Raleigh, G. S. Harbison, T. G. Neiss, J. E. Roberts, and R. G. Griffin, *Chem. Phys. Lett.*, 1987, **138**, 285.
3. B. H. Meier and W. L. Earl, *J. Am. Chem. Soc.*, 1987, **109**, 7937.
4. M. G. Colombo, B. H. Meier, and R. R. Ernst, *Chem. Phys. Lett.*, 1988, **146**, 189.
5. A. Kubo and C. A. McDowell, *J. Chem. Soc. Faraday Trans.*, 1988, **84**, 3713.
6. W. E. J. R. Maas and W. S. Veeman, *Chem. Phys. Lett.*, 1988, **149**, 170.
7. T. Nakai and C. A. McDowell, *J. Chem. Phys.*, 1992, **96**, 3452.
8. T. Nakai and C. A. McDowell, *Mol. Phys.*, 1996, **88**, 1263.
9. S. O. Smith, in 'Encyclopedia of NMR', eds D. M. Grant and R. K. Harris, Wiley: Chichester, 1996, Vol. 7, p. 4185.
10. K. Takegoshi, K. Nomura, and T. Terao, *Chem. Phys. Lett.*, 1995, **232**, 424.
11. K. Takegoshi, K. Nomura, and T. Terao, *J. Magn. Reson.*, 1997, **127**, 206.
12. K. Nomura, K. Takegoshi, T. Terao, K. Uchida, and M. Kaisnosho, *J. Am. Chem. Soc.*, 1999, **121**, 4064.
13. K. Nomura, K. Takegoshi, T. Terao, K. Uchida, and M. Kaisnosho, *J. Biol. NMR*, 2000, **17**, 111.
14. W. S. Veeman, *Prog. Nucl. Magn. Reson. Spectrosc.*, 1984, **16**, 193.
15. T. G. Oas, C. J. Hartzell, T. J. McMahon, G. P. Drobny, and F. W. Dahlquist, *J. Am. Chem. Soc.*, 1987, **109**, 5956.
16. T. G. Oas, C. J. Hartzell, F. W. Dahlquist, and G. P. Drobny, *J. Am. Chem. Soc.*, 1987, **109**, 5962.
17. R. A. Haberkorn, R. E. Stark, H. van Willigen, and R. G. Griffin, *J. Am. Chem. Soc.*, 1981, **103**, 2534.
18. A. Naito, S. Ganapathy, K. Akasaka, and C. A. McDowell, *J. Chem. Phys.*, 1981, **74**, 3190.
19. A. Naito, S. Ganapathy, P. Raghunathan, and C. A. McDowell, *J. Chem. Phys.*, 1983, **79**, 4173.
20. N. Janes, S. Ganapathy, and E. Oldfield, *J. Magn. Reson.*, 1983, **54**, 111.
21. A. Naito and C. A. McDowell, *J. Chem. Phys.*, 1984, **81**, 4795.
22. J. C. Facelli, A. M. Orendt, M. S. Solum, G. Depke, D. M. Grant, and J. Michl, *J. Am. Chem. Soc.*, 1986, **108**, 4268.
23. D. L. VanderHart, *J. Chem. Phys.*, 1976, **64**, 830.
24. Y. Ishii, T. Terao, and S. Hayashi, *J. Chem. Phys.*, 1997, **107**, 2760.

Biographical Sketches

K. Takegoshi, *b* 1956. B.Sc., 1979, Ph.D., 1984, Chemistry, Kyoto University, Japan. Postdoctoral Fellow at University of British Columbia (Canada) 1984–1986 and at University of California (Berkeley, USA) 1986–1987. Staff scientist at Foundation of Material Science and Technology of Japan 1987–1988. Assistant Professor at Hokkaido University 1988–1993. Associate Professor at Kyoto University 1993-present.

Takehiko Terao, *b* 1941. B.Sc., 1966, Ph.D., 1973, Physics, Kyoto University, Japan, where he was introduced to NMR by Tsuneo Hashi. Faculty of Science, Kyoto Sangyou University, 1971–75. Department of Chemistry, Graduate School of Science, Kyoto University, 1975-present. Research speciality: solid state NMR and its applications to chemistry and biology.

Carbanion Chemistry

John B. Grutzner

Purdue University, West Lafayette, IN, USA

1	Introduction	1
2	Chemical Shift	1
3	Coupling Constants	8
4	Kinetic Processes	11
5	Miscellaneous Methods	14
6	Related Articles in Volumes 1–8	15
7	References	15

1 INTRODUCTION

Carbanions are ubiquitous reagents for forming carbon–carbon bonds. This review will use the fundamental questions regarding the structure and a few reactions of carbanions to illustrate the repertoire of NMR tools available to chemists. But first, a caveat. Under common solution NMR conditions, almost all carbanions are not. In solids, a counter-ion is mandatory. In solution, carbanions exist as organometallic complexes with group I cations, e.g., $(CH_3Li)_4$, or their charge is delocalized onto electronegative heteroatoms commonly oxygen or nitrogen, e.g., acetylacetonate.[1–5] NMR is the best method for characterizing their structure, and for differentiating oligomers, solvated aggregates, contact ion pairs, solvent-separated ion pairs and free ions. The comprehensive review of organolithium compounds by Günther[1] provides many well illustrated examples of lithium nmr methods for studying these compounds. The present review focuses on carbon and provides an updated supplement to Guenther's report.

2 CHEMICAL SHIFT

The ^{13}C chemical shifts of some representative organolithiums/carbanions are shown in Figure 1.[6,7] Two scales are shown – the δ scale with $\delta = 0.0$ ppm for TMS, and the absolute shielding scale σ with $\sigma = 0$ ppm at $\delta = 185.6$ ppm.[8] The chemical shift range of carbanions is comparable to the range for neutral organics, so charge, per se, does not dominate shifts. A practical generalization is that, when Li^+ or another alkali metal cation replaces the proton, saturated carbons are shielded with respect to their parent hydrocarbons, whereas unsaturated centers show large deshielding effects.

The degree of aggregation, the counter-ion, and its solvation, modify the shielding at the anionic carbon and beyond. The results[9] for 3,5-di-t-butyl-phenyl lithium, **1**, are illustrative (Figure 2). Reich and coworkers[10] have provided a benchmark study of the power of nmr to characterize organolithium solutions. They studied the monomer/dimer/tetramer equilibria of phenyl lithium as a function of solvent and temperature. The temperature dependence of the ^{13}C and ^{6}Li spectra in ether is shown in Figure 3. Coupling patterns established the state of aggregation. At C_1 and C_2, δ increases as THF coordination increases while δ decreases at C_3 and C_4. As the changes in δ at each carbon are monotonic relative to the parent hydrocarbon, the shifts correlate with the strength of the interaction between the carbanion electron pair and its associated cation. The changes at the remote positions result from increased electron density. Similarly, on two electron reduction of aromatic hydrocarbons to form dianions, carbon is shielded by a total of ~135 ppm/electron.[11,12] Actual values depend significantly on the cation.

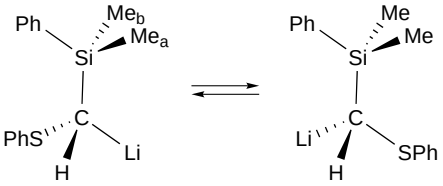

A detailed understanding of chemical shifts requires knowledge of the principal components of the chemical shift tensor (δ_{11}, δ_{22}, δ_{33}).[13,14] The shift observed in solution is the average of these three independent quantities. The measurement of shift tensors at individual sites is now practical through advances in solid state nmr methods,[15] but few have been reported for carbanions to date.

Chemical shifts are induced by electron circulation and the major contribution for carbon comes from the paramagnetic motion of the p electrons – the Ramsey term:[16]

$$\sigma^p_{\alpha\beta} = \frac{\mu_0 e^2}{8\pi m^2} \sum_\kappa{}' \frac{1}{E_0 - E_n} \left(\langle 0| \sum_k \frac{\hat{l}_{k\alpha}}{r_k^3} |n\rangle\langle n| \sum_k \hat{l}_{k\beta} |0\rangle + \langle 0| \sum_k \hat{l}_{k\beta} |n\rangle\langle n| \sum_k \frac{\hat{l}_{k\alpha}}{r_k^3} |0\rangle \right) \quad (1)$$

The induced magnetic field (paramagnetic deshielding for σ^p) is perpendicular to the preferred plane of electron circulation. The Ramsey term, which usually induces shifts to positive δ can be broken into three multiplicative factors for each electron pair and then summed over all the electrons. The terms are: $(\langle \phi_x / L_z / \phi_y \rangle \cdot \langle \phi_y^* / L_z / \phi_x^* \rangle; +C.C.)$, – the angular momentum (p character) and orbital symmetry term; $1/r^3$, the electron – nucleus radial term; and $1/(E_n - E_0)$, the electron excitation energy gap to allow circulation. Carbanion formation generates chemical shift changes from the differential motion between the carbanion electron pair and the C–H bonding pair. Within the framework of Ramsey theory, anion formation increases the effective electron–nucleus distance which reduces σ^p, while at the same time decreasing the electron energy gap which increases σ^p. The angular momentum factor will only change at second order. As the electronic factors change in opposite senses, qualitative predictions have limited utility, especially when the anion and its precursor have different geometries (e.g., propene and allyl anion). The severe problems of qualitative analysis are underlined by a consideration of the shift changes between benzene and phenyl

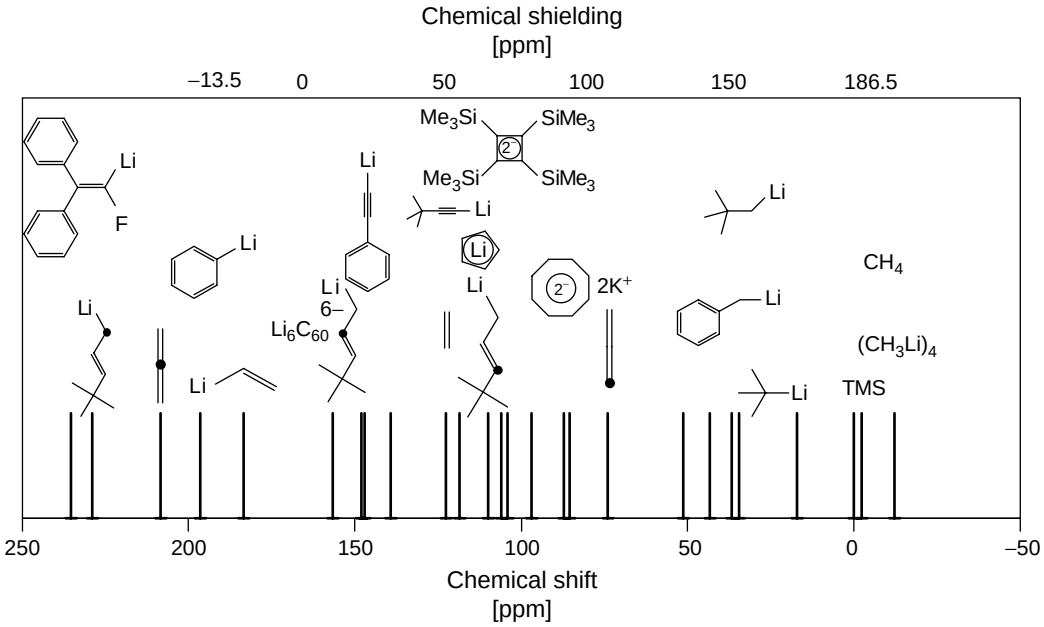

Figure 1 Carbon-13 Chemical Shifts and Shieldings of Organolithiums and Carbanions on the σ shielding scale (top) and δ shift scale (bottom)

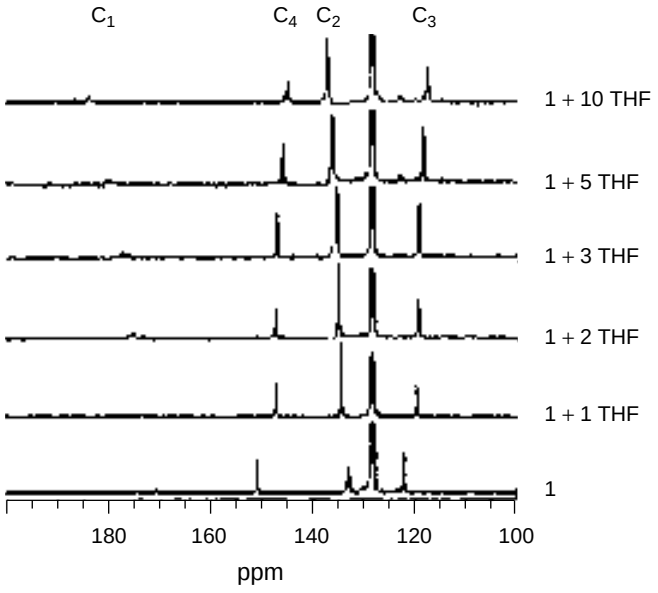

Figure 2 $^{13}C\{^1H\}$ NMR spectra of 3,5-di-t-butylphenyl lithium, **1**, with added THF in C_6D_6 at room temperature, which illustrate the conversion of tetramer (bottom) to dimer (top). (Reprinted with permission from Ref.[9] © (1997) American Chemical Society)

lithium (see below). Accurate molecular orbital calculations[17] are required to predict the shifts.

2.1 Chemical Shift and Charge Density

Chemists are naturally interested in charge density probes and it is often assumed that chemical shifts – especially carbon chemical shifts are such a probe. The contrary reality is nicely illustrated by the ^{13}C chemical shift of C_1 of phenyl lithium.[18] The isotropic δ value *increases* as C_1 becomes more negative (i.e., shielding *decreases* as the electron pair becomes less well bound). Each of the three principal values of the shielding tensor for C_1 changes significantly when its formal charge diminishes from 0 in benzene to −1 in phenyl lithium (Figure 4). The largest change occurs for the in plane shielding tensor perpendicular to the carbon–lithium bond δ_{11} where $\Delta\delta$ is +181 ppm relative to benzene. This large paramagnetic increase in δ is induced by circulation of the lone pair about the field axis in the molecular plane and involves n-π^* excitation. In marked contrast, δ_{33} decreases δ is −27 ppm – when the carbanion electron pair circulates about the field axis perpendicular to the molecular plane. n-σ^* excitation now induces an increase in shielding. Thus the same pair of electrons circulating about different axes induces shifts in opposite senses relative to benzene. The third tensor value δ_{22} shows the smallest change of +14 ppm as the electrons which induce this shift are not involved directly in the anion creation. Two of the three principal shift tensor values have increased δ values in striking opposition to the predictions of simple shift-charge correlations.

The chemical shift of C_1 *increases* as the carbon–Li bond length *decreases* from tetramer (174.0 ppm, 2.33 Å) to dimer (188.2 ppm, 2.24 Å) to monomer (196.4 ppm, 2.14 Å).[19] However, the C_1 shift in monomeric 2,4,6-tri-t-butylphenyl lithium in THF at −79° is 177 ppm.[20] Boersma and coworkers,[21] show a comparable sequence in an exemplary study of the solid-state and solution structure of 2-methoxyphenyl lithium:- tetramer (155.9 ppm), dimer (171.1 ppm) and monomer (175.6 ppm). Different aggregation states were generated by solvent changes and confirmed by ^6Li–^{13}C coupling patterns. A similar trend is seen for C_1 in vinyl lithium; tetramer (183.0 ppm, 2.26 Å)[22] to dimer (190.8 ppm, ?). Though the dimer structure has not yet been determined, the dimer bond lengths in α-styryl lithium are 2.36–2.42 Å[23] ($\delta_\alpha = 205.4$ ppm). A plausible explanation for the increase in δ with decrease in C–Li bond length is that there is a low lying covalent structure which has an even larger paramagnetic term than the ionic structure because of the $1/r^3$ factor. The location of the lithium ion may also be important

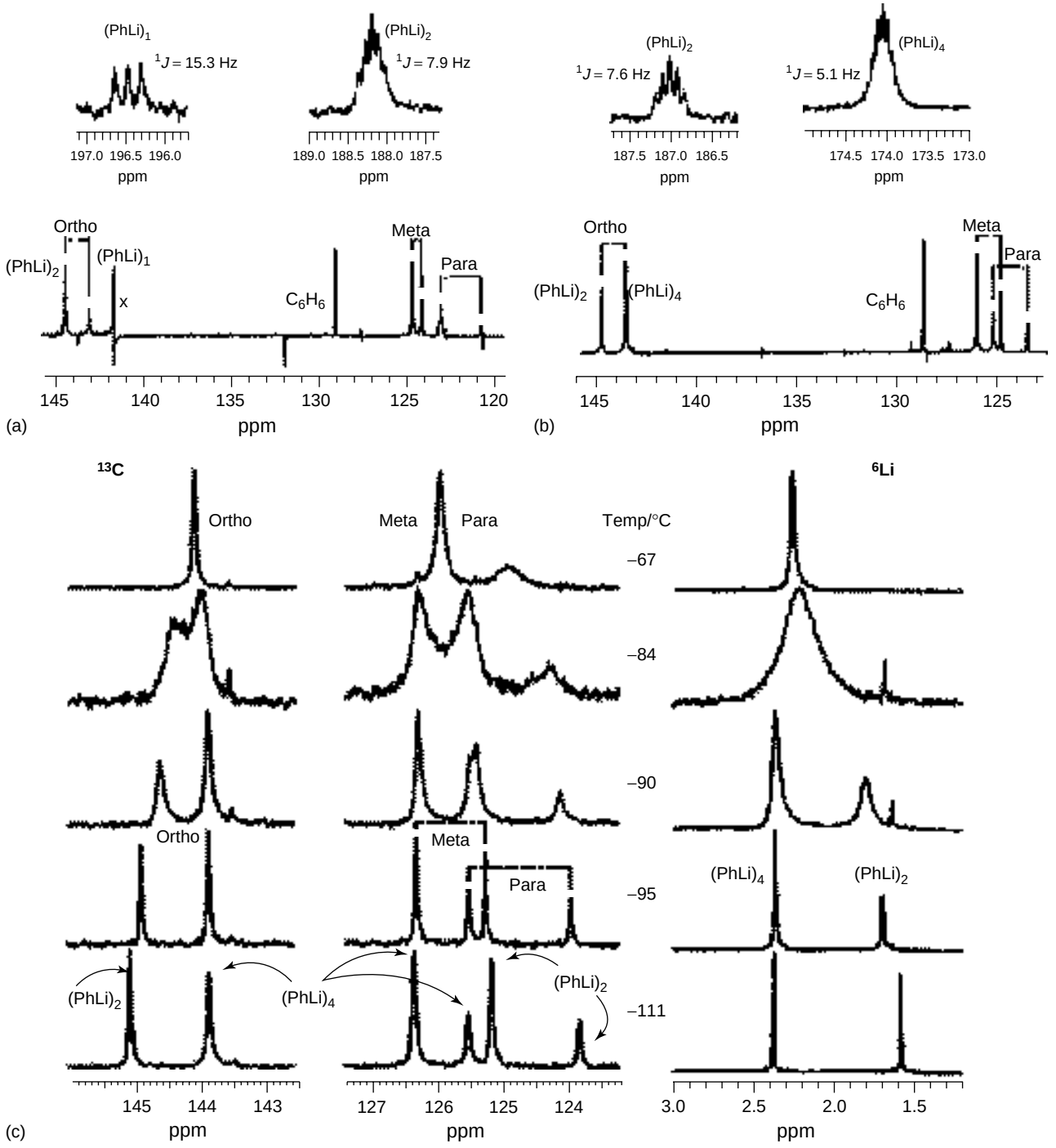

Figure 3 (a) ^{13}C NMR spectra of 0.08 M Ph ^{6}Li in THF at −111 C. (b) ^{13}C NMR spectra of 0.16 M Ph ^{6}Li in ether at −106 C. (c) Variable temperature ^{13}C and ^{6}Li NMR spectra of 0.08 M Ph ^{6}Li in ether. (Reprinted with permission from Ref.[10] © (1998) American Chemical Society)

as it is only in the monomer that the lithium is located in the plane of the ring. In the dimer, a pair, and in the tetramer, a trio of lithium ions is coordinated above and below the ring plane. Reich[24] illustrates how coordinating ligands and external agents can modify the structure and C_1 shifts in phenyl lithium (Figure 5).

Greater insight into carbanion chemical shifts requires measurement of more principal shielding values. At present, C_1 of phenyl lithium, and of lithium cyclopentadienide, are the only carbanion examples for which both experimental tensor values and high level theoretical calculations have been reported. The principal shift tensor values[25] in the series lithium cyclopentadienide, (182, 114, 21 ppm), benzene, (234, 146, 9 ppm), and tropylium tetrafluoroborate (280, 168, 22 ppm) again illustrate the Ramsey electron circulation model and the importance of orbital paramagnetism for shifts. Here the number of π electrons per carbon increases and the isotropic δ values decrease linearly. However, it is still the $\pi-\sigma^*$ and $\sigma-\pi^*$ circulation where the shift changes are generated (δ_{11} major, δ_{22} minor). The shift value perpendicular

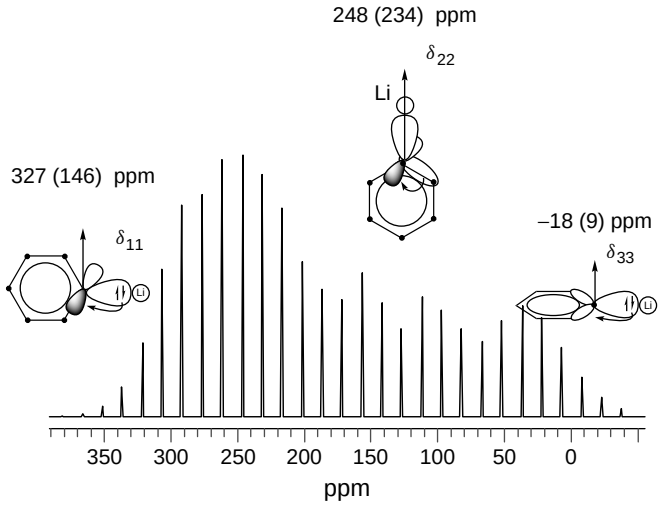

Figure 4 The simulated CP-MAS ^{13}C spectrum of 1-^{13}C phenyl lithium based on the data of Berger et al.[18] The principal values of the shift tensor are shown (values for benzene in parentheses) with the electron orbitals, and their associated electron circulations. (See also Ref.[14])

to the molecular plane (δ_{33}), which is induced by π electron circulation, is almost independent of charge. Wiberg and Zilm[26] reached similar conclusions from calculation of the shift differences between the methyl cation and anion – both axially symmetric. The isotropic value shifted by −480 ppm on addition of two electrons while δ_{33} only changed by 6 ppm. The calculated shift tensor, δ_{33} for methyl anion are close to the value calculated for the closed shell C^{4-} anion (−102 ppm).

The reduction of aromatic hydrocarbons to form dianions[11,12] and more highly reduced species provides additional insight into charge induced changes in the chemical shift and Ramsey circulation. Here the changes in charge occur predominantly in the π system and ring current (magnetic susceptibility) effects are observed. The experimental results show that the change in center of gravity of the ^{13}C signals per added electron varies widely from system to system. For example, acepleiadylene ($C_{16}H_{10}$) gives $\Delta\delta$/e of −2 ppm when reduced to the dianion but −32 ppm when reduced to the tetraanion.[11,27] As Zanasi[28] and coworkers calculated, there are dramatic differences in the π circulations between neutral acepleiadylene, and its dianion – a consequence of the change in HOMO-LUMO energy gap (Figure 6). Simple charge linearity models predict enhanced shielding–just the opposite from the observed trend. By contrast, the calculated (6-31G** basis set at the HF limit) shift values closely reproduce the experimental values, and provide a corrected assignment of the quaternary carbons. Both the paramagnetic vortex in the 7 membered ring and the large increases in δ are a consequence of small energy gaps in the π system of the dianion. Here again the Ramsey circulation accounts for the shifts, even when the charge density changes are localized in the π system. All three

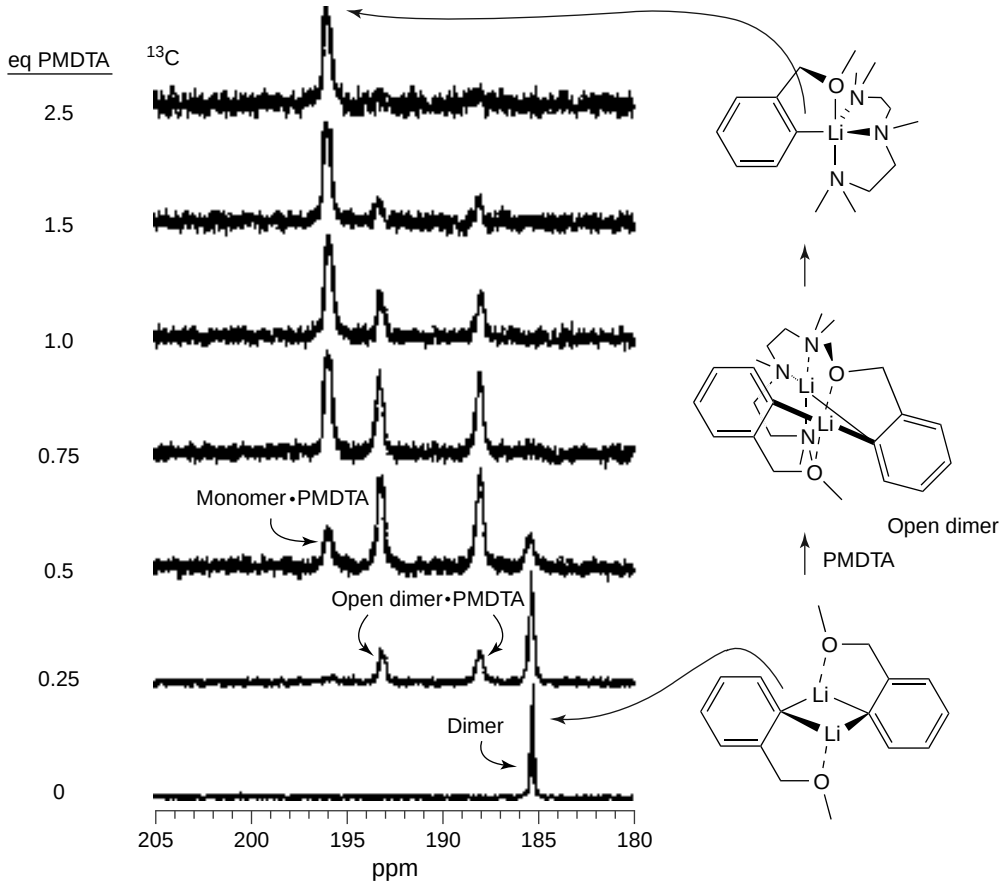

Figure 5 The effect of change in lithium coordination on the C_1 chemical shift of 2-methoxymethylphenyl lithium induced by coordination with pentamethyl-diethylenetriamine (PMDTA). (Spectrum kindly provided by A. W. Sanders and H. J. Reich)

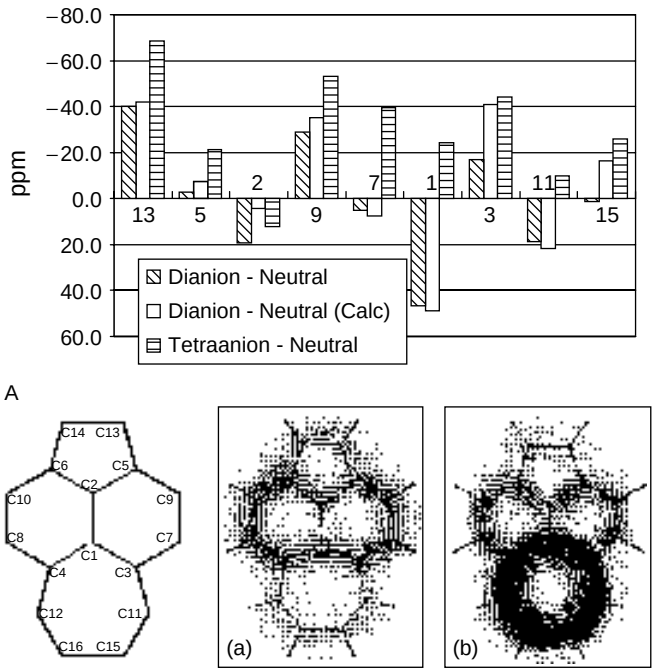

Figure 6 Comparison of the ^{13}C chemical shift changes ($\Delta\delta$) induced by reduction of acepleiadylene (A) to its dianion and tetraanion and the $\Delta\delta$ calculated in Ref.[28] The diatropic A, (a), and paratropic A^{-2}, (b), π electron circulations are shown at 1 bohr above the molecular plane. (Reprinted with permission from Ref.[28] © (1998) American Chemical Society)

Ramsey factors are involved. Clearly, high quality theoretical calculations are required for interpretation and charge linearity models fail. Eliasson, Edlund and Muller (EEM)[11] provided an interesting approach to disentangling charge factors alone from the orbital symmetry/energy gap contributions to chemical shift change. They recognized that the magnitude and sense of the ring current shifts induced by the π circulation are correlated with the π energy gaps. Since proton shifts can measure the ring current, an empirical linear correlation was found between $\Delta\delta$/e for carbon and the dia- or para-tropicity of the planar cyclic aromatic hydrocarbon. From the intercept, EEM deduced a shift of -134 ppm electron as the intrinsic charge contribution to carbon shielding for π anion formation in condensed aromatic hydrocarbons. The cyclophanes show the phenomenon and compound **2** is representative.[12] Proton shifts at each position in **2** are listed above and carbon shifts below (see **2**).

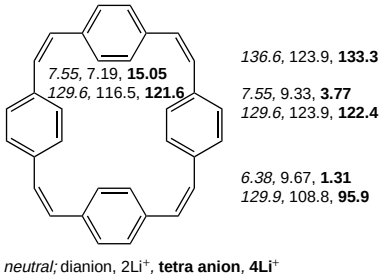

(2)

Dramatic shift differences are observed between the inside and outside protons as a consequence of the change in sense of magnetic anisotropy between 4n and 4n + 2 electron systems. The carbon shifts are less sensitive because anisotropy induced shifts are independent of nucleus. Also the carbons lie in a narrow range of distances, and when the carbons constitute the equivalent current loop the anisotropic shift is zero.

Reimers, Craw and Hush (RCH)[29] have performed the most detailed modern analysis of the semi-empirical correlation of charge density with carbon chemical shift. They employed Tolbert and Ogle's experimental data[30] for α,ω-diphenyl polyenyl anions as their test set and various charge density functions obtained from AM1 calculations. RCH concluded "Atomic charges are not uniquely defined, and it is possible to arrive at quite different results depending on the particular theoretical or experimental technique used for their determination. We have shown, however, that a major cause of this nonuniqueness arises from the way in which the polarization of the chemical bonds, the bond ionicity, is treated; consequently, comparison not of the atomic charges themselves, but rather of the average charges distributed about chemical bonds leads to very similar conclusions about the charge distribution *independently* of the technique used to determine it". Their best fit was obtained with a multiparameter correlation of observed shift with average π bond charges. They found different correlations for the polyene chain carbons ($\delta_i = 132.6 + 87.8\,(\pi q_i')$) and the phenyl termini ($\delta_i = 128.8 + 134.1\,(\pi q_i')$). It is intriguing that the $\Delta\delta$/e value for the polyene carbons is close to the 86.7 ppm value derived by Karplus and Pople[31] for an electron in a $2p$ orbital based simply on the $\langle 1/r^3\rangle_{2p}$ term and the average energy approximation. Likewise the phenyl value of $\Delta\delta$/e is very close to the EEM value. RCH also conclude "that families of compounds similar to the ones studied herein should also show Spiesecke-Schneider correlations with different coefficients to the (non-fundamental) coefficients used herein, as is observed". They attribute these familial differences to variation in bond polarization (or bond ionicities). In other words, the Ramsey circulation varies and semi-empirical correlations must be adjusted accordingly. Once this is done, experimental anion chemical shifts can provide chemically relevant parameters such as the width of a soliton – the original goal of the studies by both Tolbert and RCH.

One more striking example of the lack of correlation between carbon chemical shift and electron density is C_{60}. The addition of 10 electrons $\delta(C^{6+}) - \delta(C^{4-})$ causes a shift of only 28.5 ppm/electron as Ramsey paramagnetic shielding is zero for these ions by symmetry and simple Lamb diamagnetism determines the shifts. The formation of the hexa-anion, $C_{60}Li_6$, results in an *increase* in δ of 14 ppm.[32] Buhl[33] has reproduced this value theoretically, and calculates that the next 6 electrons will induce a decrease in δ by 32 ppm in $C_{60}Li_{12}$. This is a net change of -18 ppm for the 12 electrons distributed over 60 carbons and so $\Delta\delta/e = 90$ ppm/e.

As an example of the success of theory, Buhl et al.[17] applied Kutzelnigg's IGLO method to the calculation of isotropic chemical shifts in organolithium compounds. They found a very good correlation between experimental and calculated shifts for the majority of compounds shown in Figure 1. As part of this work, a linear correlation between p electron density and δ was found. However, it should be noted that in *all* compounds with $\delta > 110$ ppm, the p electron density in these *anions* was less than 1 – the exception being

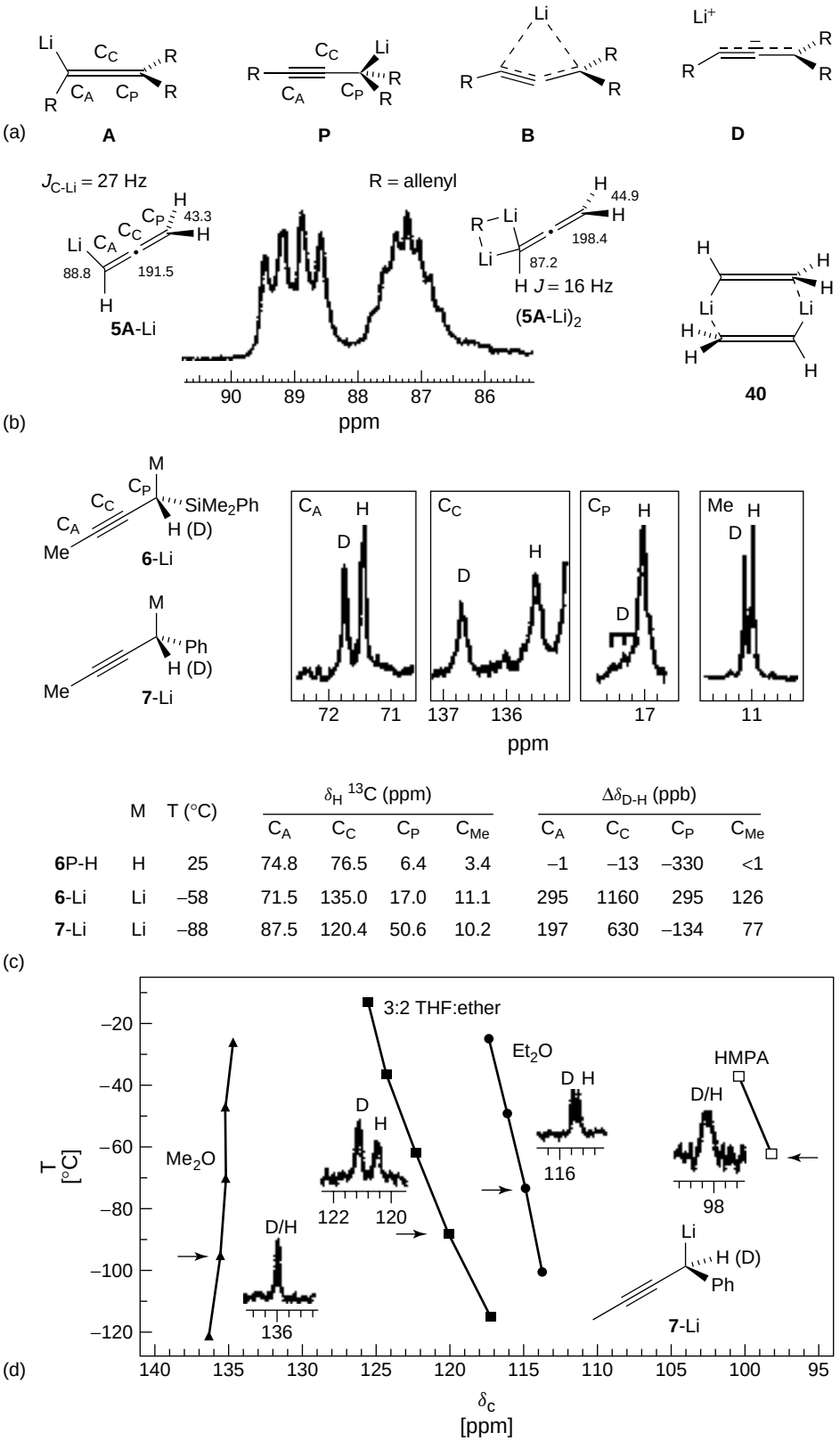

	M	T (°C)	δ_H ^{13}C (ppm)				$\Delta\delta_{D\text{-}H}$ (ppb)			
			C_A	C_C	C_P	C_{Me}	C_A	C_C	C_P	C_{Me}
6P-H	H	25	74.8	76.5	6.4	3.4	–1	–13	–330	<1
6-Li	Li	–58	71.5	135.0	17.0	11.1	295	1160	295	126
7-Li	Li	–88	87.5	120.4	50.6	10.2	197	630	–134	77

Figure 7 (a) Allenyl lithium isomeric forms (A) Allenyl, (P) Propargyl, (B) Bridged, (D) Delocalized. (b) C_1 of monomeric and dimeric allenyl lithium showing ^{13}C–^{7}Li coupling patterns. (c) D/H isotopic perturbation of ^{13}C chemical shifts of substituted allenyl lithiums showing equilibrating isomers; 90.56 MHz ^{13}C spectra of a 1.2 : 1 mixture of **6**-Li and D-**6**-Li at −58 C in 3 : 2 THF-ether: chemical shifts (for the protio compound) and ^{13}C isotope shifts of H/D labeled **6**-Li and **7**-Li and the precursor **6**P–H. (d) Temperature-dependent ^{13}C chemical shifts and 90.56 MHz ^{13}C spectra illustrating the isotope perturbation shifts observed for C_C of **7**-Li in several solvents. (Reprinted with permission from Ref.[37] © (2000) American Chemical Society)

the C_2 carbon of vinyl lithium where different levels of theory showed the greatest variation. Improvements in theoretical methods and more shielding tensor measurements can be expected to refine our knowledge of carbanion chemical shifts.

Despite the lack of a sound interpretive basis, chemical shift changes often provide useful guides to structures. Changes induced by solvation, degree of aggregation and temperature can be monitored and lead to meaningful structural results especially when anchored by coupling observations on limiting systems. Studies of the solvation of phenyl lithium from the relative shifts of the ring carbons provides an excellent example.[10] The Schade and Boche study[34] of solvation of a benzyl lithium discussed under 2D methods is another.

2.2 Chemical Shift and the Structure of Equilibrating Anions

Carbon chemical shifts provide a useful guide to carbanion structure and can distinguish between localized and delocalized valence isomers. The features of the highly variegated topology of the organolithium energy surface are discerned because of the sensitivity of chemical shift to structure. Subtle distinctions with substitution, aggregation and counter-ion are found in allyl,[35] benzyl[36] and allenyl[37] systems. Structural issues involving benzylic anions are addressed in the coupling constant and kinetics sections. In an insightful study, Reich[37] has used shifts as a discriminator in many systems which might formally be written as propargyl lithiums. He established that the allenyl structure is preferred over the propargyl structure as the ^{13}C shifts in the parent C_3H_3Li (C_1, 87.2; C_2, 196.4; C_3, 43.2 ppm) are clearly those of an allenic system. Figure 7 shows the resolved shifts of monomer and head-to-head dimer – also nicely illustrating ^{7}Li–^{13}C coupling patterns. Acetylenic valence tautomers are rare. Cyclopropyl substitution stabilizes the acetylenic tautomer and the shifts are representative (C_1, −7.5; C_2, 99.8; C_3, 68.3 ppm). The shift at the central carbon varies between the allenic (A) value, ca. 185 ppm, and the propargylic (P) value, ca. 95 ppm, as the A/P ratio changes with substituent, temperature and solvent. The A/P equilibrium constant is close to one, so minor perturbations are readily detected with this sensitive diagnostic tool. The Saunders isotopic method monitors the subtlest energy perturbations shown in the following section.

The allyl anion is a second system where different structures with similar energies may be distinguished by carbon nmr.[35] Limiting options include localized (L) and delocalized (D) π bonds; planar (Pl) and pyramidal (Py) lithiated centers; and syn (endo) and anti (exo) stereochemistries for substituents (Figure 8). The energetics of structural equilibration may often be determined by variable temperature studies of exchange by line broadening. For example 3-neopentylallyl lithium in cyclopentane was shown to be a mixture of syn and anti forms with lithium localized at the unsubstituted terminal carbon.[38] Addition of coordinating ligands for lithium initiates lithium exchange between allylic carbons C_1 and C_3. Choice of substituents modulates the C_1 vs C_3 preference for anionic localization. Substituents such as Ph,[39] $(CH_3)_3Si$–,[40] and PhS–[41] favor the C_1 position, while methyl prefers the C_3 position.[35(c)] Vicinal proton−proton coupling shows that relatively small substituents, including phenyl and methyl, prefer the syn conformation.[35(c),39] Balzer and Berger[42] used ^{1}H–^{1}H and ^{1}H–^{6}Li Overhauser effects to identify the endo and exo protons in 2-methyl-3-phenyl-allyl lithium as rotation around the C_{ipso}–C_3 bond was slow with an activation energy of 42 kJ mol^{-1}.

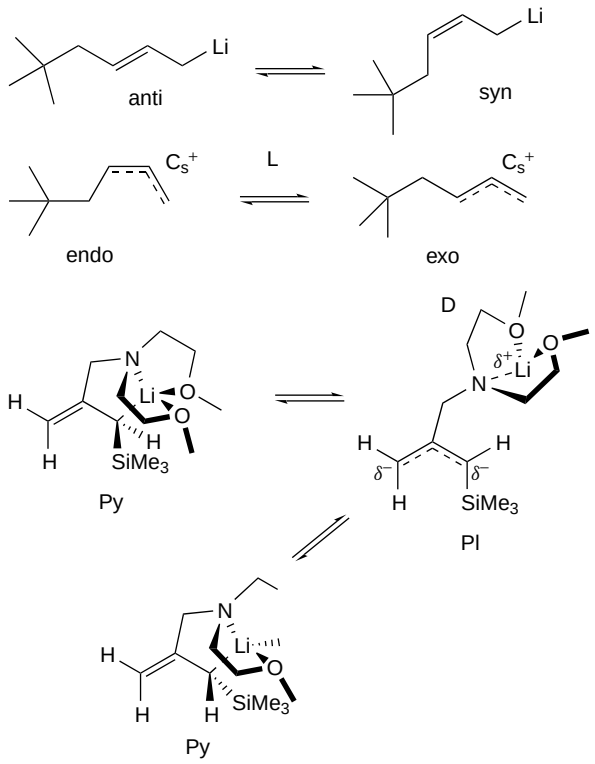

Figure 8 Structure of allyl anions modified from Refs.[35,40] (see text for definitions)

Fraenkel has crafted the properties of allylic[43] and benzylic[36(a)] systems by substitution with the lithium coordinating ligand, $–CH_2N(CH_2CH_2OCH_3)_2$. In combination with a dimethylphenylsilyl substituent he stabilized the twisted propenyl lithium structure in which the Li is located in the alkene plane and a localized double bond is preferred[35] (Figure 8). As a consequence, the first example of ^{6}Li–^{13}C coupling in an allylic lithium is detected. This unique form is thought to be the transition state (presumably pyramidal) for rotation about the C_1–C_2 bond. A low barrier exchange process is found which requires carbanion inversion accompanied by rotation around the C_1–C_2 bond. The rotation around the C_2–C_3 bond was too slow to be detected at 47 °C. Fraenkel selectively placed the coordinating ligand at positions 1[43] or 2,[35] and showed how lithium location influences structural isomerism. With the substituent at the central carbon C_2, the ligand arms are diastereotopic and show resolved resonances at low temperature. Line broadening techniques were used to identify three distinct processes – inversion of the tetrahedral lithiated carbon (from 2 site exchange broadening), dissociation of the carbon lithium bond (from ^{6}Li–^{13}C coupling collapse), and $C_1 \rightleftharpoons C_3$ allylic interchange (2 site exchange). With the substituent at the terminal carbon, C_1, the allylic system was induced to form both exo and endo isomers. The isomeric composition was established from 3 bond H–H coupling (endo 11.0, exo 16.2 Hz).[43] The activation energy for rotation around the allylic bond was determined by complex line shape fitting. Line broadening from the resolved

^{13}C signals of the diastereotopic arms of the ligand provided unique structural information about facial inversion. Measurably different barriers were found for exo–exo and endo–endo exchanges.

The structure of vinyl lithiums have been thoroughly elucidated by Bauer[44] and by Knorr.[23] The separate signals from the diastereomeric β protons in solution confirm the trigonal carbon character determined by X-ray. ^{1}H–^{6}Li HOESY spectra identify the syn and anti protons and the substantial barrier to carbanion inversion. Inversion was studied by exchange broadening of the syn and anti protons and follows first order kinetics ($t_{1/2} \sim 3$ min at 25 °C in toluene). The HOESY experiments further establish the intriguing structure of an α-lithiostyrene where the phenyl π system is overlapped with C–Li bond and is perpendicular to the carbon–carbon double bond.

2.3 Isotopic Perturbation of Chemical Shift

The Saunders isotope perturbation method[45] allows distinction between symmetrical single minimum systems and low barrier equilibrating species on a symmetric double (or higher) minimum energy surface. This is a common, but subtle, problem in carbanion chemistry where cation location is a ready source of symmetry breaking. The allyl carbanion was the first classic example studied, and Schlosser[46] showed that C_1 and C_3 were differentially shifted by 1.9 ppm when the allylic position was specifically di-deuterated in allyl magnesium bromide in THF. The deuterated carbon resonated at higher δ. In allyl lithium, an isotopic shift difference of 0.1 ppm was detected and subsequently resolved in work at higher magnetic field.[47] In monodeuterated allyl sodium and potassium, C_1 and C_3 were just resolved ($\Delta\delta \sim 0.1$ ppm) but now C_3 had the larger δ. These observations together establish that both allyl Grignard[48] and allyl lithium are a rapidly equilibrating pair of isomers while allyl sodium and potassium are delocalized. For observable distinction, the method requires that (i) the C–H bond vibrational frequencies differ in the two isomers (vinyl C–H, >alkyl C–H); (ii) there be a chemical shift difference between the carbons in the two isomers (δ vinyl > δ alkyl) – the larger the difference, the higher the resolving power of the method. Isotopic substitution breaks the symmetry of the energy surface, and the equilibrium shifts to favor the isomer with the deuterium on the carbon with the higher C–D vibrational frequencies. As the two isomers have different energies, the magnitude of the shift difference increases as the temperature is lowered. This temperature dependence is the third criterion to distinguish a delocalized single minimum structure with a large intrinsic isotope shift from an equilibrating system existing on a perturbed double minimum surface. For the single minimum cases of allyl sodium and potassium, lowering the temperature did not change the magnitude of the isotopic perturbation of chemical shifts. Schleyer[47] claimed that allyl lithium was an unsymmetrical dimer in THF. For a dimer, the isotope perturbation is the sum of contributions from head to head and head to tail forms, which should in principle, be resolvable if intra-aggregate lithium exchange can be slowed. Disubstitution at C_1 and C_3 with trimethylsilyl or phenyl substituents results in single minimum allyl lithiums.[49]

Reich and Thompson[37] have provided a notable example of the isotope perturbation method in their study of allenylpropargyl systems (Figure 7). Not only was the equilibrium perturbation observed at all three unsaturated carbons, but also the minute energy differences of 0–30 cal/mol (note small calories) were measured as the position of equilibrium was perturbed by changing solvent.

The isotope perturbation method has been applied to intermolecular exchange processes. Stevenson[50] has developed an isotope enrichment method based on electron exchange equilibria between aromatic hydrocarbons and their radical anions. The isotopic perturbation of the equilibrium is monitored by the chemical shift. One other example of isotopic perturbation of chemical shift is the elegant work of Guenther employing ^{6}Li shifts as a probe of aggregation.[51] A 50 : 50 mixture of protonated and perdeuterated substrates shows isotopic peak splitting with a Pascal triangle peak distribution – a monomer shows 2 equal peaks and an equilibrating tetramer a pentet.

3 COUPLING CONSTANTS

3.1 Coupling Constants, Aggregation and Solvation

Coupling to lithium is the Rosetta stone of organolithium chemistry. In early reports ^{7}Li–^{13}C coupling was used to enumerate aggregation and established the dynamic character of the carbon–lithium bond.[1] Wehrli[52] suggested that ^{6}Li was a superior partner because of its very small quadrupole coupling constant resulting in long relaxation times and sharp lines. Fraenkel and coworkers[53] quickly demonstrated its practical utility. The Guenther review[1] provides a detailed summary and many illustrative examples of the broad applicability of ^{6}Li–X coupling for the determination of solvation and aggregation. ^{6}Li has a nuclear spin of one and generates multiplets with $(2nI + 1)$ lines and intensity ratios of 1,1,1 for monomers; 1,2,3,2,1 for dimers and 1,3,6,7,6,3,1 for both trimers and the ubiquitous tetramers since only 3 of the 4 lithiums in the cube can be nearest neighbors in the absence of intra-aggregate exchange. Bond interchange processes involving inter and intra-aggregate exchange are readily distinguished as couplings are lost or averaged respectively. ^{7}Li–X coupling is found to be 2.641 times larger than ^{6}Li–X coupling – the magnetogyric ratio.

Solvation of aggregates is established via ^{7}Li–^{31}P couplings in HMPA[54,120] and ^{6}Li–^{15}N coupling in amine and amide systems[55] as exchange between solvates can be slowed to less than $10\,s^{-1}$. Discrete ^{31}P and ^{7}Li signals are resolved at low temperature for individual aggregates[56] (Figure 9). The coupling patterns provide a count of neighboring nuclei in different solvates and a range of solvate levels are generated by titration. Fluorenyl lithium[54] provides a textbook example where resolved signals are observed for 0–4 coordinated HMPA and also free HMPA. Jackman[57] showed the ^{6}Li–^{15}N coupling in lithium arylamides depended on aggregation (monomer 7.5 Hz, dimer 3.8 Hz). He noted that the ^{6}Li–^{15}N coupling in the monomeric anilide was in the ratio of γ_C/γ_{Li} to the ^{13}C–^{15}N coupling in the aniline precursor but was not related to the ^{1}H–^{15}N coupling.

Application of the magnitudes of coupling constants for structural interpretation has proved to be controversial. (See Ref.[35] and references therein). The appealing postulate[19] that a large J coupling between carbon and lithium is diagnostic of a covalent bond was withdrawn by its proponents as experimental data accumulated. A recent example is the 1.4 Hz

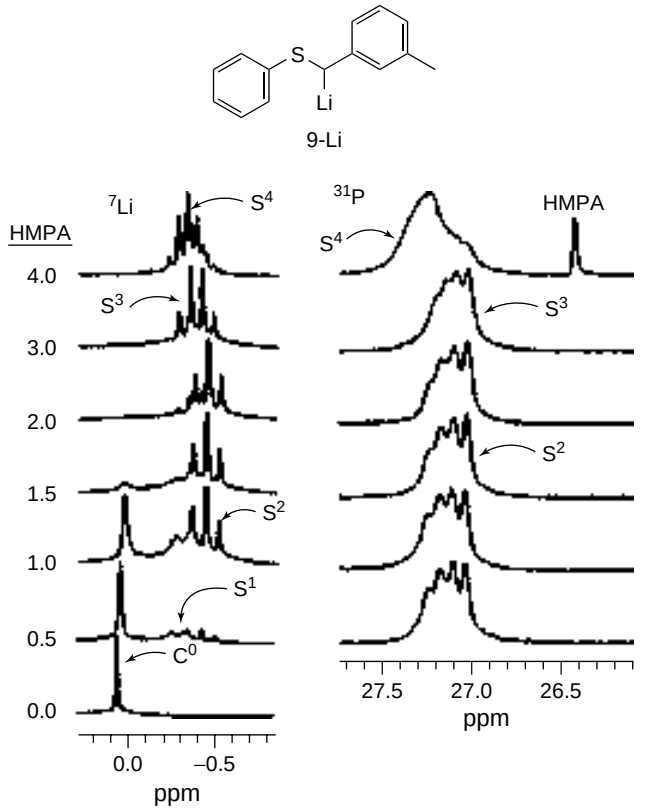

Figure 9 ^{7}Li and ^{31}P NMR spectra from an HMPA titration of 0.16 M phenylthio-(3-methyl)benzyl lithium in 3 : 2 THF/Et_2O at −129 °C. (Reprinted with permission from Ref.[56] © (1993) American Chemical Society)

^{13}C–^{6}Li coupling observed to both lithiums coordinated to the tetratrimethylsilyl cyclobutadiene dianion in THF (δ ^{13}C 104.1 ppm, δ ^{6}Li −5.07 ppm).[58] Bonding is ionic in this planar aromatic. The theoretical basis for large J coupling across ionic systems, such as methyl lithium, has recently been provided by Bartlett and del Bene.[59] They showed that coupling was dominated by the Fermi contact mechanism (<0.1 Hz from other sources). While the calculated J increased as the bond dipole moment decreased to zero – corresponding to pure covalency – J continued to increase monotonically as the electric dipole sense was inverted.

The next interesting proposition was that ^{13}C–Li coupling was diagnostic of the state of aggregation and that carbon hybridization was a minor perturbation.[19] Unfortunately, this conjecture of an approximately linear relationship between $J_{C–Li}$ and aggregation number is not supported by a broader data selection, including 7.4 Hz $J_{^{13}C–^{7}Li}$ for a monomeric benzyl lithium,[36(b)] and 6.0 Hz $J_{^{13}C–^{7}Li}$ for a monomeric allyl lithium.[35(b)]

Bauer and Griesinger[44] reported a complete coupling analysis for all 6 coupled nuclei in ^{6}Li labeled vinyl lithium which exists in dimeric and tetrameric forms in THF. A comprehensive analysis is given and small differences (1.8 Hz max.) between dimer and tetramer were detected in most couplings. The paper describes the FUCOUP method for determining the signs of active coupling constants.

The one bond carbon–hydrogen coupling has been invoked as a structural tool to infer geometry at benzylic sites. Correlations between the benzylic ^{13}C–^{1}H one bond J coupling, the benzylic carbon shift and the para proton and carbon chemical shifts generated a solvation order.[34] The major changes that can occur are shown in the series of $PhSCHXSiPh_2$ compounds[60] with values of 154 Hz (X = $Li(HMPA)_4$), 135 Hz (X = H), to 114 Hz (X = Li(THF)). The C–Si coupling varied in the same way, 95 Hz, 51 Hz, and 49 Hz. Change in heteroatom substituent can also induce major changes[61] – $PhCHLiSi(CH_3)_3$ 119 Hz; $PhCH_2Li$ 131 Hz; PhCHLiSPh 144 Hz; and $PhCHLiPO(OEt)_2$ 149.6 Hz. While the Fermi contact term has been clearly established as the major factor for coupling between first row elements,[62] correlations with hybridization/structure must still be treated circumspectly. Stevenson's example[63] of J_{CH} of 145.9 Hz in cyclo-octatetraene dianion versus 158.6 Hz in benzene while the one bond J_{CC} of 55.8 Hz remains the same, is a clear challenge for theoreticians and empiricists.

The observation by Bertz[64] of ^{13}C–^{13}C coupling (ca. 21 Hz) between ^{13}CN ligands in RCuLiCN (R = Ph, Et, Me) provided key proof of the coordination shell around copper.

3.2 2-D Methods

Coupling allows the generation of 2D spectra for definitive spectral assignment.

3.2.1 COSY[65]

This basic form of correlation spectroscopy, and its close relative TOCSY, provides atomic connectivity information via J coupling. Early and representative examples were given by Guenther[66] who applied ^{6}Li–^{13}C COSY to organolithiums soon after its development and noted the great advantage of incorporating ^{6}Li because of its sharp lines. In combination with a ^{6}Li–^{6}Li COSY[67] he demonstrated the power of the technique with the solution structure of dilithium tetramethylbutatriene. A recent example is shown in Figure 10 where Collum[68] used ^{6}Li–^{13}C COSY to unravel the complex catalytic mixture of chiral adducts generated from ephedrine and lithium cyclopropylacetylide.

3.2.2 HOESY[69]

^{1}H–^{6}Li HOESY (Heteronuclear Overhauser Effect Spectroscopy) is a very useful tool for establishing through-space connectivity in organolithiums. The observation of cross peaks in the two dimensional ^{1}H–^{6}Li correlation spectra establishes spatial proximity via the ^{1}H–^{6}Li dipole–dipole coupling constant. A cross peak shows that the lithium ion and proton of interest come, possibly transiently (see below), within 4 Å of each other on the time scale of the transfer interval (typically ∼1 s). Schade and Boche[34] illustrated the utility of the technique to investigate the solvation shell of α-phenylthiobenzyllithium in THF with added ethers and amines. They showed that one equivalent of triglyme was not sufficient to displace the THF solvation shell in the contact ion pair as cross peaks were present between lithium and protons at the benzylic and ortho positions, and the α and β THF protons, Figure 11. In a further example, Furstner et al.[70] established the perpendicular geometry of the dilithiated dianion of 1,2-diphenyl-1,2-bis(trimethysilyl)ethane with ^{1}H–^{6}Li

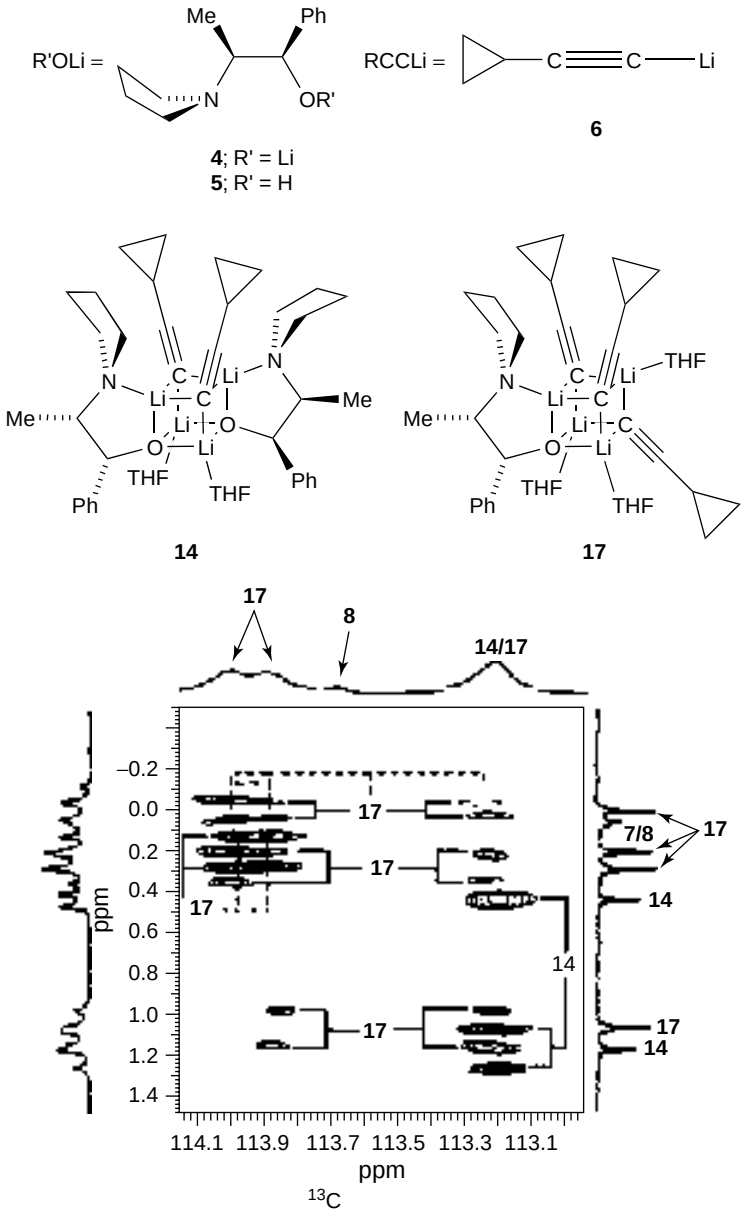

Figure 10 ^{6}Li, ^{13}C-HMQC spectrum of a sample containing 3 : 1 [^{6}Li,^{13}C]**6**/[^{6}Li]**4** (0.10 M total Li titer) in 1 : 1 THF/pentane at −125 C. The ^{6}Li NMR spectrum is on the left axis, the ^{6}Li{^{13}C} NMR spectrum appears on the right axis, and the ^{13}C{^{6}Li} NMR spectrum is displayed on top. (Reprinted with permission from Ref.[68] © (1998) American Chemical Society)

HOESY experiments. An attempt to specifically locate the lithium cation in THF solvated 1-^{13}C-benzyl lithium by a combination of quantitative ^{1}H and ^{13}C NOESY measurements and relaxation time data met with moderate success.[71] The HOESY study[72] of α-lithiomethoxy-allene in d_8-THF provides a useful cautionary example of how exchange can interfere with NOESY/HOESY experiments. The ^{6}Li–^{1}H distance of short lived forms may have small contact distances and give strong HOESY peaks. In this example, the sample contained 20% butyl lithium in fast exchange with the allenyl lithium so that a single lithium peak was observed. The strongest ^{6}Li–^{1}H HOESY peak was with the protons of butyl lithium although the butyl lithium peak, being the minor component in the mixture, gave the weakest peak in the direct proton spectrum.

The ^{7}Li–^{1}H HOESY experiment was introduced by Bauer[73] who showed the experimental advantages and requirements of the pulsed field gradient method with inverse detection using butyl lithium in hexane as a test sample. The PFG version of ^{6}Li–^{1}H HOESY has proved difficult to implement. Bauer[74] extended the HOESY technique to ^{133}Cs–^{1}H and established the composition of Lochmann's base prepared from triphenylmethyl lithium and a cesium alkoxide in THF. The HOESY cross peaks between ligand protons and lithium/cesium cations, and the 270 ppm change in Cs chemical shift on mixing, clearly showed that complete transmetallation had occurred on mixing. Bauer[75] has demonstrated that long-range ^{13}C–^{6}Li coupling can be used to distinguish dimers from trimers. The ^{6}Li{^{13}C} HMQC-TOCSY experiment generates 2 peaks for ^{13}C one-bond coupled to ^{6}Li in a dimer,

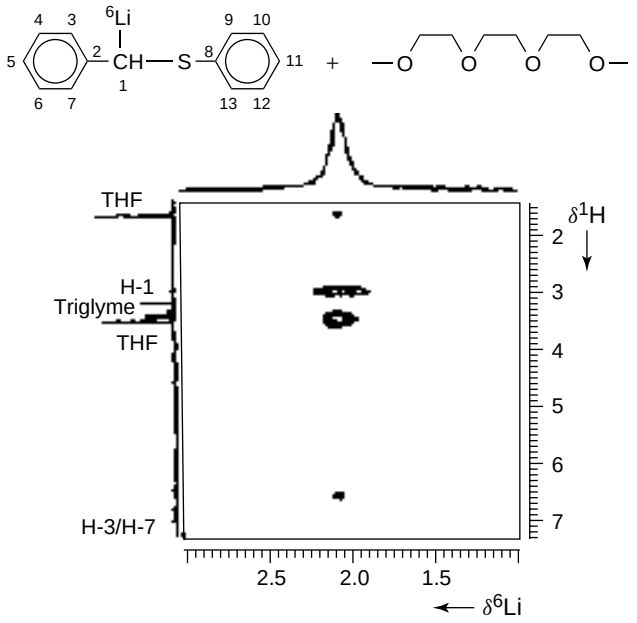

Figure 11 ^{1}H–^{6}Li HOESY spectrum of [^{6}Li] α-(phenylthio-)-benzyl lithium with 1 mol equivalent of triglyme in 1 : 1 THF/[D_8]THF at 25 °C. (Reproduced by permission of Elsevier from Ref.[34])

and 3 peaks for the trimer where one lithium ion is 3 bonds away from the observed carbon. Bauer carefully established the precautions necessary to optimize sensitivity and avoid erroneous conclusions from peaks created in exchange processes. This experiment is related to the Gilchrist and Collum[76] method for identifying ^{6}Li coupled and shared between ^{15}N ligands from the multiplicity of the zero quantum line.

3.2.3 Multiple Quantum Methods

Guenther[77] has generated a remarkable set of 1D and 2D experiments to establish the unsymmetrical dimeric structure of the dilithio compound (E)-2-lithio-1-(2 lithiophenyl)-l-pheny1pent-1-ene. This compound shows extensive ^{6}Li–^{1}H and ^{6}Li–^{13}C scalar couplings. Shift perturbation with D isotopic substitution was also employed. Guenther measured the ^{6}Li–^{6}Li coupling constant of 0.16 Hz in both an INADEQUATE and a DQF-COSY experiment together with ^{1}H–^{6}Li NOE and HOESY experiments to identify the lithiums. A detailed treatment of the INADEQUATE spectra of coupled spin 1 nuclei (e.g., ^{2}H, ^{6}Li, ^{14}N) was added subsequently.[78]

3.2.4 Multiple Quantum Methods in Solids ^{6}Li–^{13}C REDOR

The REDOR technique[79] has been used to measure carbon–lithium distances in lithium indenide[80] and fluorenide.[81] The ^{6}Li–^{13}C dipole–dipole coupling constant is 100 Hz at 3.5 Å and distances up to 4.2 Å were detected. In the TMEDA complex with lithium indenide the Li–C distances obtained from REDOR measurement were consistently larger by 0.1–0.4 Å than those obtained by X-ray. The bigger differences were at the longer distances as the accuracy of the REDOR fit diminished.

3.2.5 Lithium MQMAS and INADEQUATE

Stalke and coworkers[82] have demonstrated the power of triple quantum magic angle spinning methods (MQMAS) to resolve different ^{7}Li sites in the solid microporous aggregate of methyl lithium tetramer solvated by diethoxymethane. The multiple quantum experiment revealed the 3 : 1 ratio of lithiums in the face and cap of the lithium tetrahedra. This information was hidden within the linewidth of the simple MAS experiment. Interestingly, the lithium experiment succeeded where the ^{13}C CPMAS spectrum failed in the resolution of the different methyl sites, identified by X-ray.

4 KINETIC PROCESSES

NMR provides a wealth of kinetic information particularly for processes with time constants in the microsecond to second range ($k = 10^{6}\,s^{-1}$ to $1\,s^{-1}$). Examples include intra- and inter-molecular exchange between aggregates; bond rotation and anion inversion; electron and proton exchange; and degenerate rearrangements that are only detectable by NMR. A practical illustration is the use of multiplet coupling patterns to distinguish between intra- and inter-aggregate exchange processes in alkyl lithiums. In their classic work on ^{6}Li with 1-^{13}C propyl lithium in cyclopentane, Fraenkel and Henrichs[53] showed by line broadening techniques that interaggregate exchange rates were close to the same for carbon and lithium ($40\,s^{-1}$ at room temperature) and had a large negative entropy of activation. A recent version of this experiment[83] showed that butyl lithium forms a chiral tetramer when a chiral lithium pyrrolidide substitutes for one butyl ligand in the butyl lithium tetramer. The chiral substitution resolves the four non-equivalent Li sites into separate resonances as the temperature is lowered. The ^{6}Li singlet observed at room temperature resolves into 5 resonances at −81 °C – from the 4 sites in the chiral tetramer plus a peak for $[BuLi]_4$. A 2D exchange spectrum (EXSY, Figure 12) lacks cross peaks between the butyl lithium peak and the other sites providing clear demonstration that intra-aggregate exchange is much faster than inter-aggregate exchange. Closer inspection shows exchange cross peaks with different intensities indicating that intra-aggregate exchange occurs by a series of two site exchange processes each with a different rate.

4.1 Carbanion Inversion

One of the best examples of the power of NMR spectroscopy to reveal the subtlety of low barrier exchange processes is found in the area of carbanion inversion and stereochemistry. The rate of inversion of carbanions is important for the selectivity of organometallic reagents. Reich's study of inversion of a substituted cyclohexyl lithium[84] is illustrative and showed half-lives of 9 min at −78° in THF. The inversion rate was accelerated by added LiBr and strongly dependent on concentration. Lithium ligation with a coordinating polyamine slowed the inversion. Other definitive examples may be found in the work from the Fraenkel,[36(a)] Hoffman,[85] Boche,[34] and Reich[86] groups for heteroatom and phenyl stabilized carbanions and from the Knorr[23] group for vinyl systems. The detection of resolved peaks from diastereotopic substituents (e.g., Me_a and Me_b below) provides unambiguous

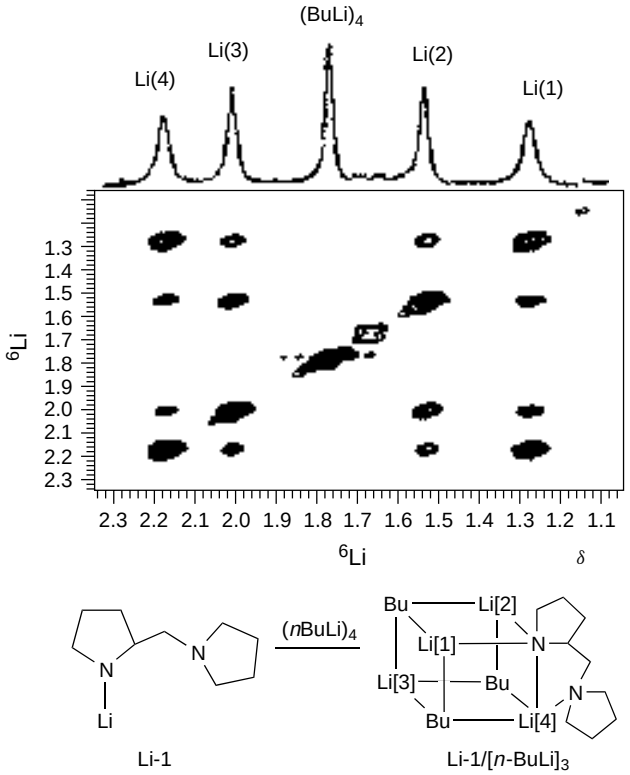

Figure 12 ^{6}Li–^{6}Li EXSY spectrum (τ_{mix} 0.45 s) of (S)-2-(1-pyrrolidinylmethyl)pyrrolidine-$^{6}Li_1$ (nBu[^{6}Li])$_3$ at −81.8 °C in [D_{10}]DEE. Note absence of cross peaks between the butyl lithium peak and the other sites showing intra-aggregate exchange is faster than inter-aggregate exchange. (Reproduced by permission of Wiley-VCH from Ref.[83])

proof of pyramidal carbanions. Reich and Dyksta[86] showed that inversion in the mono-HMPA solvated contact ion pair ($\Delta G^{\ddagger}$ 32.6 kJ mol^{-1}) of Ph(Me)$_2$Si-PhSCHLi is slightly faster than the unsolvated contact ion pair in THF/ether ($\Delta G^{\ddagger}$ 33.5 kJ mol^{-1}). The solvent separated ion pair was found to invert more slowly than the contact pair ($\Delta G^{\ddagger}$ 38.1 kJ mol^{-1}). A mechanism involving Li rotation around the carbon−sulfur bond (n-σ^* stabilizing interaction) was proposed to account for this intriguing counter-intuitive result. The solvation of the different ion pair forms was established from the coupling patterns found in the HMPA titration. In a simultaneous publication, Hoffmann and coworkers[87] confirmed the rotational character of the inversion process in a related compound by the absence of an isotope effect when the α-C–H was replaced with an α-C–D. A measurable isotope effect is expected for an inversion but not for a rotation process. They also found an increased barrier with increasing steric size of the rotating group. Clearly the heteroatom is playing a key role here. In another study of inversion at a benzylic center, Peoples[88] showed that solvation by ether solvents lowered the barrier to inversion in 7-phenylnorbornyl potassium. Solvent induced dissociation of the ion pair was the rate determining step.

4.2 Carbanion Rearrangments

Skeletal rearrangements of carbanions occur much less frequently than carbocation rearrangements.[89] Ring opening of the cyclopropylcarbinyl anion is an exception.[90] The degenerate scrambling of carbon in the bicyclo [3.2.2] nonatrienyl anion[91] has been examined by Ahlberg[92] employing specific ^{13}C and D labels. Label scrambling detected by NMR revealed this 'hidden' process. The lithium salt rearranged more rapidly than the potassium salt and the rearrangement was slower in the solid than DME solution. A ^{13}C–^{13}C coupling of 62.5 Hz was reported across the allylic bond. Stevenson[50] found an unchanged ^{13}C–^{13}C coupling of 55.8 Hz in the cyclo-octatetraene dianion-1,2-di ^{13}C after heating. This established the absence of carbon scrambling and showed that this aromatic dianion has higher thermal stability than benzene.

4.3 Kinetics of Proton Transfer

In a masterful study, Ahlberg and coworkers[93] measured the kinetics of proton transfer between carbanion sites in [1.1] ferrocenophanyl lithium, sodium and potassium. This is the first nmr measurement of the kinetics of reaction between a carbon acid and its conjugate base. It is better described as a proton/cation interchange as the rate determining step for the intramolecular first order rate process is strongly dependent on cation and solvent (K^+/Li^+ in THF/DEE = 4000).[94] This degenerate exchange is only detectable by NMR. The line broadening pattern is characteristic of an intramolecular proton transfer as the line broadening occurs for the 50% reaction where the spin coupled partners exchange α and β spin states (central lines) and broadening is absent for the 50% of the molecules where the spin states are conserved and α to α and β to β transfers occur (outer lines) (Figure 13). Under fast exchange conditions, the observed $J_{H–H}$ and $J_{C–H}$ splittings are half the J value for the static case and provide a diagnostic of the 'hidden' degenerate exchange reaction.

Klumpp and coworkers[95] have used nmr to establish the aggregation states of organolithiums in their detailed kinetic studies of the deprotonation of triphenylmethane.

4.4 Electron Exchange Processes

Rates of electron transfer processes have been extensively studied by epr methods.[96] Because of the high energetic cost of charge separation, especially in solvents with low dielectric constants, the electron transfer processes usually require coupled motion of the cation and solvent partners.[97] Rates change with cation and solvent. The electron/cation exchange rate for cyclo-octatetraene (COT) with its dianion is conveniently situated for nmr study by line-broadening ($t^{1/2} \sim 0.01–1\,s^{-1}$) and saturation transfer kinetics ($t^{1/2} \sim 1–100$ s).[98] The transfer rate in linked di-cyclo-octatetraenes has been 'tuned' to the nmr regime by the activation energy for flattening the COT tub – an energetic prerequisite for electron transfer. The linker between the neutral and dianion ring modulates the activation energy of the bond shift process (carbon π systems, 55.6 kJ mol^{-1}; Si(Me)$_2$, 69.5 kJ mol^{-1}). In the all carbon system with K^+, the ET process has a 21–24 kJ mol^{-1} higher barrier and the bond shift activation energy increases by 12 kJ mol^{-1}. In the silicon linked system the bond shift energy is almost unchanged between the neutral and dianion forms. The dianion shows an interesting cation dependent compensation of $\Delta H^{\ddagger}$ and $\Delta S^{\ddagger}$. The $\Delta H^{\ddagger}$ drops from 58.2 to 49.4 kJ mol^{-1} while $\Delta S^{\ddagger}$ becomes more negative

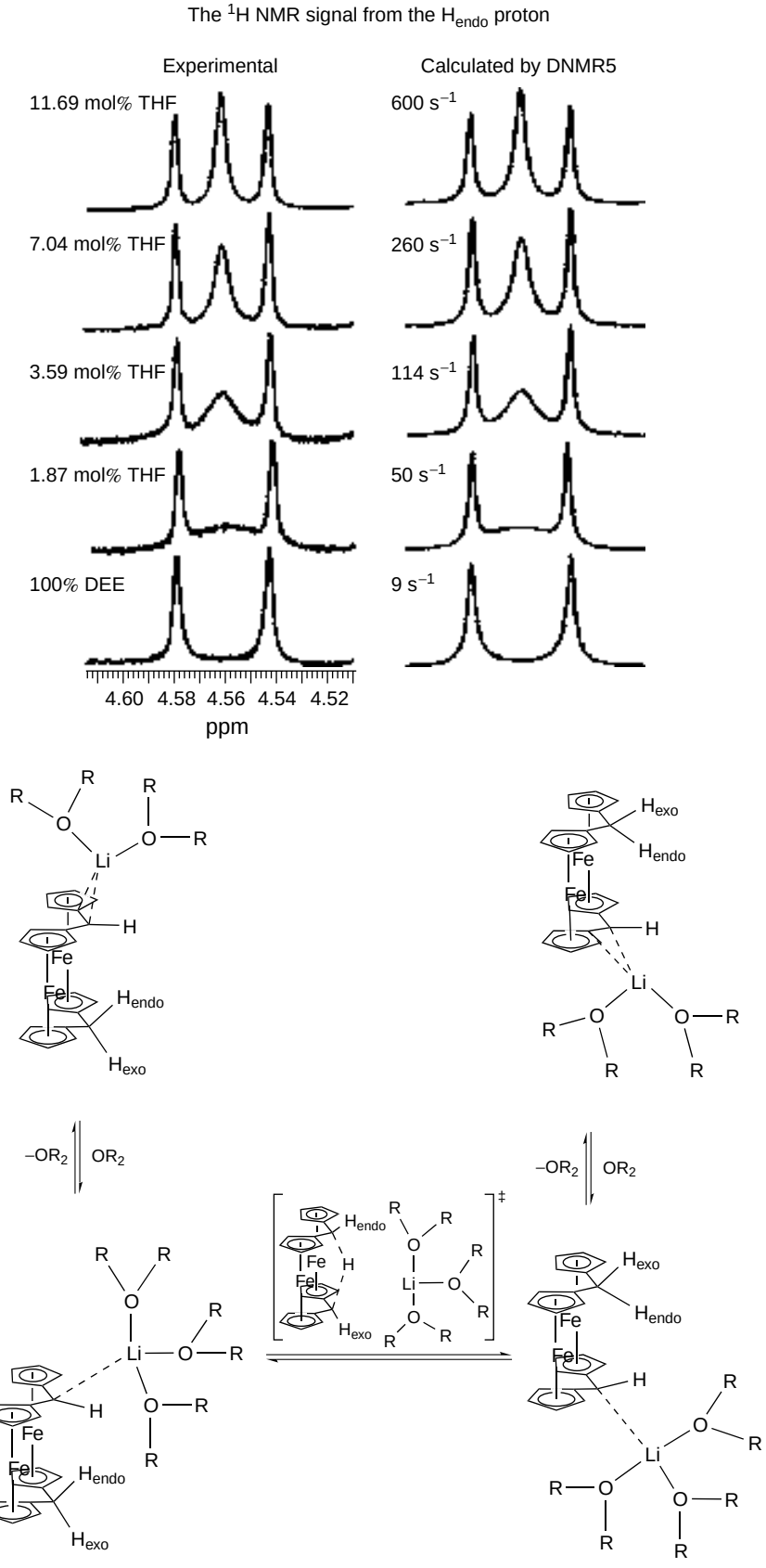

Figure 13 Partial ^{1}H NMR spectra (499.92 MHz) of 4 mM solutions of **1** at 27.0 C showing intramolecular exchange line-broadening in different mixtures of DEE-d_{10}/THF-d_8 and the corresponding calculated spectra using DNMR5. (Reprinted with permission from Ref.[93b] © (1997) American Chemical Society)

from -29.7 to $-56.1\,J\,mol^{-1}\,K^{-1}$ in the series Li^+, Na^+, K^+. The electron transfer process was too slow to measure by exchange line broadening for the sodium dianion with $\Delta G^{\ddagger} > 92\,kJ\,mol^{-1}$ and the lithium salt was faster than the potassium. Boman and Eliasson[99] also showed that the charged COT ring was rotating more slowly than the uncharged ring based on the ^{13}C T_1 relaxation times which differed by about a factor of two between the two rings of the salt.

Solutes with unpaired electrons may produce chemical shift changes through the hyperfine interaction in addition to shifts induced by changes in bulk magnetic susceptibility.[100] Separation of the two effects is achieved with the reference $Cr(AcAc)_3$ which gives the bulk susceptibility correction. The hyperfine shifts induced by electron–nucleus coupling in the radical anions reveal structural, energetic, and dynamic information about weak interactions with cations and their solvation shells. For example the ^7Li shift in lithium naphthalenide solutions was found to be inversely correlated with concentration while the THF peaks shifted linearly.[101] This revealed an ion pair exchange process with no change in the overall paramagnetism. Interpretation of the mechanism of electron–nucleus hyperfine coupling will require careful scrutiny akin to the discussion of J coupling in organolithiums.

4.5 Rapid Mixing Kinetics

McGarrity and Ogle[102] introduced rapid mixing techniques to nmr in their study of THF disruption of butyl lithium aggregates. More recently, Ogle[103] has applied the methodology to butyl lithium initiated polymerization reactions of styrene.

5 MISCELLANEOUS METHODS

5.1 A Carbon-13 Carbanion Thermometer

Variable temperature studies by NMR are always plagued by the problem of determining the actual sample temperature. Differences between the instrument set/indicator temperature and actual sample temperature can be substantial and vary with sample and gas flow. Reich[104] has found that tris(trimethylsilyl)methane can be used as an internal thermometer for carbanion solution studies as its chemical shift is solvent and temperature dependent. Calibration curves for different solvents are required, but available from Reich.

5.2 Relaxation

Nuclear spin lattice relaxation in solution requires molecular rotation and offers another approach to study aggregation. Carbon relaxes via dipole–dipole magnetic coupling, and the alkali metals, with the exception of ^6Li, relax via quadrupole coupling. Coupling fluctuates as a function of molecular tumbling with correlation time (τ_c). Molecular tumbling times and their anisotropy are controlled by the size of the tumbling particle, solvent viscosity, and temperature.[105] As τ_c is proportional to the third power of the tumbling radius, dimerization can give an order of magnitude change in relaxation time. Practically, the method is limited to species with radii up to 10 Å which are in the fast motion regime for dipolar relaxation. The DOSY technique (see below) is useful above this range. Anisotropic tumbling is readily detected and may reveal structural information.[106] Jackman's study[107] of ^{13}C relaxation in phenyllithium is a pioneering example of the information obtainable from the method. It illustrates the effects of both ^6Li–^7Li and of ^1H–^2D isotopic substitution on dipolar relaxation, and of applied magnetic field. At C_1, the contribution from chemical shift anisotropy increased from 34% at 2.35 T to 90% at 8.5 T. C-4 relaxed by dipole–dipole interaction alone.

Edlund and coworkers have studied the aggregation and ion pairing of the indenide[108] and fluorenide[109] ions by T_1 relaxation. They measured T_1 ratios between the lithium indenide and indane which ranged from 1.7 in DMF, through 2.4 in common ether solvents up to 10.9 in the poorer solvents butyl and propyl ether. These ratios were correlated with the combined molecular mass of the ion pair and its first solvation shell. The higher ratios were attributed to higher states of aggregation and included glyme-2 and glyme-3 suggestive of a solvent induced dimerization. The molecular mass correlation and T_1 averaging used here show how qualitative information can be obtained without a more accurate motional analysis.

5.3 Diffusion Studies

In principle, the size of a solvated aggregate may be determined from its diffusion coefficient and the Stokes–Einstein relationship. The DOSY technique[110] has been applied to carbanions derived from planar aromatic hydrocarbons.[111] The anthracenide dianion and its lithium counter ions gave the same diffusion coefficient in THF and in NH_3 showing that these ions migrate together.[112] This is expected for measurements on the millisecond timescale of the NMR experiment and the need to maintain local charge neutrality in solution. Differential ion motion would only be observable in the presence of swamping electrolyte. The salts migrated more slowly than their parent hydrocarbons. Williard[113] has used DOSY spectra to show that the dimeric aggregate of butyl lithium in THF at -84° diffuses 13% faster than its tetrameric aggregate consistent with their relative sizes.

5.4 Lithium Quadrupole Coupling Constants: (χ)

The ^7Li quadrupole coupling constant, (χ), have been measured directly in the solid state for a series of aryl lithium compounds.[114] The results confirm Jackman's observations[115] in solution that the coupling constant could be used to identify the degree of aggregation and the number and type of donor atoms in the coordination shell of the lithium cation. χ measures the electric field gradient at the lithium nucleus – the higher the symmetry of the coordination shell, the smaller the coupling. The largest couplings, above 400 kHz, are found for monomers. See Table 1. Guenther and coworkers[116] have found a linear relationship between the C–Li–C angle (Φ) and the ^7Li χ for a mixed series of aryl and alkyl organolithiums whose X-ray structures were known.

$$\chi = (3.9 \pm 0.4)\Phi_{CLC} - (215.2 \pm 55.6)$$

They found a similar relationship with a similar slope for lithium amides.[117] Solvent separated ion pairs show much smaller χ values than contact ion pairs because of the higher local symmetry of the solvation shell around the cation.

Penner[118] has reported the solid state ^6Li spectrum of 2,4,6-tri-isopropylphenyl lithium. In addition to the quadrupole

Table 1 ^{7}Li Quadrupole Coupling Constants (kHz) for Lithium Salts of Organic Carbon, Nitrogen and Oxygen Acids in Ethers and Tertiary Amines

Species	C (ethers)	(ethers)	N (3° amines)	(ethers)	O (3° amines)
$Li_4A_4S_4$	85			65	40
$Li_4A_4S_n$	116, 168			105	>51
$Li_2A_2S_4$	162	155		150	120
$Li_2A_2S_2$	>250	315	306		>184
$LiAS_3$		210		210	167
$LiAS_2$		>351			

splitting of 6.6 kHz, he determined the ^{6}Li chemical shielding from the asymmetry of the Pake doublet. An axially symmetric shielding tensor was derived with a surprisingly large span of 24 ± 4 ppm and $\delta_{\parallel} = -15$ and $\delta_{\perp} = 9$ ppm relative to aqueous LiCl. A smaller value would be anticipated from the small chemical shift range of less than 10 ppm found in most ^{6}Li and ^{7}Li spectra in the absence of ring currents. Significant asymmetry of the electron cloud around the lithium cation would be required to produce the necessary Ramsey paramagnetism. The method cannot be used for ^{7}Li because of its much larger quadrupole coupling constant.

6 RELATED ARTICLES IN VOLUMES 1–8

Brownian Motion & Correlation Times, Volume 2; Carbon-13 Relaxation Measurements: Organic Chemistry Applications, Volume 2; Carbon-13 Studies of Deuterium Labeled Compounds, Volume 2; Chemical Shift Scales on an Absolute Basis, Volume 2; Chemical Shift Tensor Measurement in Solids, Volume 2; Chemical Shift Tensors, Volume 2; COSY Two-Dimensional Experiments, Volume 3; Electric Field Effects on Shielding Constants, Volume 3; Isotope Effects on Chemical Shifts & Coupling Constants, Volume 4; Lithium NMR, Volume 5; Magic Angle Spinning, Volume 5; Nuclear Overhauser Effect, Volume 5; Organometallic Compounds, Volume 5; Quadrupolar Interactions, Volume 6; Quadrupolar Nuclei in Glasses, Volume 6; Quadrupolar Nuclei in Liquid Samples, Volume 6; Quadrupolar Nuclei in Solids, Volume 6; Relaxation: An Introduction, Volume 6; Relaxation Theory: Density Matrix Formulation, Volume 6; Shielding: Overview of Theoretical Methods, Volume 7; Shielding Tensor Calculations, Volume 7; Sodium-23 NMR, Volume 7; Two-Dimensional Carbon-Heteroelement Correlation, Volume 8; Two-Dimensional J-Resolved Spectroscopy, Volume 8.

7 REFERENCES

1. H. Guenther, in 'Encyclopedia of NMR', eds D. M. Grant and R. K. Harris, Wiley: Chichester, 1996, vol. 5, p 2807.
2. E. Buncel and T. Durst, 'Comprehensive Carbanion Chemistry', Elsevier: New York, 1980.
3. V. Snieckus, 'Advances in Carbanion Chemistry', JAI Press: 1992, Vol. 1.
4. L. D. McKeever, in 'Ions and Ion Pairs in Organic Reactions', ed M. Szwarc, Wiley Interscience: New York, 1972.
5. C. Lambert, P. von R. Schleyer, *Angew. Chem. Int. Ed. Engl.*, 1994, **33**, 1129.
6. J. P. C. M. van Dongen, H. W. D. van Dijkman, and M. J. A. de Bie, *Receuil.*, 1974, **93**, 29.
7. D. Seebach, R. Haassig, and J. Gabriel, *Helv. Chim. Acta*, 1983, **66**, 308.
8. A. K. Jameson and C. J. Jameson, *Chem. Phys. Lett.*, 1987, **134**, 461.
9. R. J. Wehmschulte and P. P. Power, *J. Am. Chem. Soc.*, 1997, **119**, 2847.
10. H. J. Reich, D. P. Green, M. A. Medina, W. S. Goldenberg, B. O. Gudmundsson, R. R. Dykstra, and N. H. Phillips, *J. Am. Chem. Soc.*, 1998, **120**, 7201.
11. B. Eliasson, U. Edlund, and K. Mullen, *J. Chem. Soc. Perk. Trans. 2*, 1986, 937.
12. E. Shabtai, O. Segev, R. Beust, and M. Rabinovitz, *J. Chem. Soc. Perk. Trans. 2*, 2000, **6**, 1233.
13. J. B. Grutzner, 'Recent Advances in Organic NMR Spectroscopy', Norell Press: Landisville, 1984, Chap. 2.
14. D. M. Grant, *Encyclopedia of NMR*, 1996, **2**, p 1298.
15. A. M. Orendt, J. C. Facelli, S. Bai, A. Rai, M. Gossett, L. T. Scott, J. Boerio-Goates, R. J. Pugmire, and D. M. Grant, *J. Phys. Chem. A.*, 2000, **104**, 149.
16. N. F. Ramsey, *Phys. Rev.*, 1950, **78**, 699; N. F. Ramsey, *Am. Scientist*, 1961, **49**, 509.
17. M. Buhl, N. J. R. van, E. Hommes, P. von R. Schleyer, U. Fleischer, and W. Kutzelnigg, *J. Am. Chem. Soc.*, 1991, **113**, 2459.
18. S. Berger, U. Fleischer, C. Geletneky, and J. C. W. Lohrenz, *Chem. Ber.*, 1995, **128**, 1183.
19. W. Bauer, W. R. Winchester, and P. von R. Schleyer, *Organometallics*, 1987, **6**, 2371.
20. G. Fraenkel, S. Subramanian, and A. Chow, *J. Am. Chem. Soc.*, 1995, **117**, 6300.
21. S. Harder, J. Boersma, L. Brandsma, G. P. M. Vanmier, and J. A. Kanters, *J. Organomet. Chem.*, 1989, **364**, 1.
22. W. Bauer and F. Hampel, *J. Chem. Soc. Chem. Commun.*, 1992, 903.
23. R. Knorr, C. Behringer, H. Noth, M. Schmidt, E. Lattke, and E. Rapple, *Chem. Ber.-Recueil.*, 1997, **130**, 585 and references therein.
24. H. J. Reich, W. S. Goldenburg, A. W. Sanders, and C. C. Tschucke, *Org. Lett.*, 2001, **3**, 33.
25. H. Strub, A. J. Beeler, D. M. Grant, J. Michl, P. W. Cutts, and K. W. Zilm, *J. Am. Chem. Soc.*, 1983, **105**, 3333.
26. K. B. Wiberg, J. D. Hammer, T. A. Keith, and K. Zilm, *Tetrahedron Lett.*, 1997, **38**, 323.
27. B. C. Becker, W. Huber, and K. Müllen, *J. Am. Chem. Soc.*, 1980, **102**, 7803.
28. P. W. Fowler, E. Steiner, B. Cadioli, and R. Zanasi, *J. Phys. Chem. A.*, 1998, **102**, 7297.
29. J. R. Reimers, J. S. Craw, and N. S. Hush, *J. Phys. Chem.*, 1993, **97**, 2778.
30. L. M. Tolbert and M. E. Ogle, *J. Am. Chem. Soc.*, 1990, **112**, 9519.
31. M. Karplus and J. A. Pople, *J. Chem. Phys.*, 1963, **38**, 2803.
32. J. W. Bausch, G. K. S. Prakash, and G. A. Olah, *J. Am. Chem. Soc.*, 1991, **113**, 3205.
33. M. Buhl, *Z. Anorg. Allg. Chem.*, 2000, **626**, 332.
34. S. Schade and G. Boche, *J. Organomet. Chem.*, 1998, **550**, 359; S. Schade and G. Boche, *J. Organomet. Chem.*, 1998, **550**, 381.
35. (a) G. Fraenkel and F. Qiu, *J. Am. Chem. Soc.*, 1997, **119**, 3571; (b) G. Fraenkel, J. H. Duncan, and J. H. Wang, *J. Am. Chem. Soc.*, 1999, **121**, 432; (c) G. Fraenkel and F. Qiu, *J. Am. Chem. Soc.*, 2000, **122**, 12 806; (d) G. Fraenkel, J. Cabral, C. Lanter, and J. H. Wang, *J. Org. Chem.*, 1999, **64**, 1302; (e) G. Fraenkel, A. Chow, and W. R. Winchester, *J. Am. Chem. Soc.*, 1990, **112**, 6190.
36. (a) G. Fraenkel, J. H. Duncan, K. Martin, and J. H. Wang, *J. Am. Chem. Soc.*, 1999, **121**, 10 538; (b) G. Fraenkel and F. Y. Qiu, *J. Am. Chem. Soc.*, 1996, **118**, 5828; (c) G. Fraenkel

and K. V. Martin, *J. Am. Chem. Soc.*, 1995, **117**, 10 336; (d) U. J. Bildmann and G. Muller, *Organomet.*, 2001, **20**, 1689.
37. H. J. Reich and J. L. Thompson, *Org. Lett.*, 2000, **2**, 783.
38. G. Fraenkel, A. F. Halasa, V. Mochel, R. Stumpe, and D. Tate, *J. Org. Chem.*, 1985, **50**, 4563.
39. H. Balzer and S. Berger, *Chem. Ber.-Recl.*, 1992, **125**, 733.
40. G. Fraenkel, A. Chow, and W. R. Winchester, *J. Am. Chem. Soc.*, 1990, **112**, 2582.
41. M. Piffl, J. Weston, W. Gunther, and E. Anders, *J. Org. Chem.*, 2000, **65**, 5942.
42. H. H. Balzer and S. Berger, *J. Phys. Org. Chem.*, 1997, **10**, 187.
43. G. Fraenkel and J. A. Cabral, *J. Am. Chem. Soc.*, 1993, **115**, 1551.
44. W. Bauer, C. Griesinger, *J. Am. Chem. Soc.*, 1993, **115**, 10 871.
45. M. Saunders, L. Telkowski, and M. R. Kates, *J. Am. Chem. Soc.*, 1977, **99**, 8070; M. Saunders and M. R. Kates, *J. Am. Chem. Soc.*, 1977, **99**, 8071.
46. M. Schlosser and M. Stahle, *Angew. Chem. Int. Edn.*, 1980, **19**, 487.
47. W. R. Winchester, W. Bauer, P. von R. Schleyer, *J. Chem. Soc. Chem. Commun.*, 1987, 177.
48. E. A. Hill, W. A. Boyd, H. Desai, A. Darki, and L. Bivens, *J. Organomet. Chem.*, 1996, **514**, 1.
49. G. Fraenkel, A. Chow, and W. R. Winchester, *J. Am. Chem. Soc.*, 1990, **112**, 1382.
50. C. D. Stevenson, D. J. McElheny, D. E. Kage, J. T. Ciszewski, and R. C. Reiter, *Anal. Chem.*, 1998, **70**, 3880.
51. H. Gunther, *J. Brazil Chem Soc.*, 1999, **10**, 241.
52. F. W. Wehrli, *J. Magn. Reson.*, 1978, **30**, 193.
53. G. Fraenkel, M. Henrichs, and J. M. Hewitt, *J. Am. Chem. Soc.*, 1980, **102**, 3345.
54. H. J. Reich, J. P. Borst, R. R. Dykstra, and D. P. Green, *J. Am. Chem. Soc.*, 1993, **115**, 8728.
55. (a) D. B. Collum, *Acc. Chem. Res.*, 1993, **26**, 227; (b) J. L. Rutherford and D. B. Collum, *J. Am. Chem. Soc.*, 1999, **121**, 10 198 and references therein.
56. H. J. Reich and W. H. Sikorski, *J. Org. Chem.*, 1999, **64**, 14.
57. L. M. Jackman and L. M. Scarmoutzos, *J. Am. Chem. Soc.*, 1987, **109**, 5348.
58. A. Sekiguchi, T. Matsuo, and H. Watanabe, *J. Am. Chem. Soc.*, 2000, **122**, 5652.
59. R. J. Bartlett, J. E. Del-Bene, and S. A. Perera, 'Proceedings of W. N. Lipscomb's 80th Birthday Symposium'. ACS Symposium Series, in press.
60. H. J. Reich and R. R. Dykstra, *J. Am. Chem. Soc.*, 1993, **115**, 7041.
61. T. Ruhland, R. W. Hoffmann, S. Schade, and G. Boche, *Chem. Ber.*, 1995, **128**, 551.
62. (a) J. Kaski, P. Lantto, J. Vaara, and J. Jokisaari, *J. Am. Chem. Soc.*, 1998, **120**, 3993; (b) R. D. Wigglesworth, W. T. Raynes, S. Kirpekar, J. Oddershede, and S. P. A. Sauer, *J. Chem. Phys.*, 2000, **112**, 3735.
63. E. C. Brown, R. M. Fico, R. C. Reiter, and C. D. Stevenson, *J. Org. Chem.*, 1998, **63**, 4444.
64. S. H. Bertz, *J. Am. Chem. Soc.*, 1991, **113**, 5470.
65. A. D. Bain, in 'Encyclopedia of NMR', eds D. M. Grant and R. K. Harris, Wiley: Chichester, 1996, vol. 3, p 1455; D. M. Doddrell, in 'Encyclopedia of NMR', eds D. M. Grant and R. K. Harris, Wiley: Chichester, 1996, vol. 3, p 1462.
66. H. Günther, D. Moskau, R. Dujardin, and A. Maercker, *Tetrahedron Lett.*, 1986, **27**, 2251.
67. D. Moskau, F. Brauers, H. Gunther, and A. Maercker, *J. Am. Chem. Soc.*, 1987, **109**, 5532.
68. A. Thompson, E. G. Corley, M. F. Huntington, E. J. J. Grabowski, J. F. Remenar, and D. B. Collum, *J. Am. Chem. Soc.*, 1998, **120**, 2028.
69. W. Bauer, G. Muller, R. Pi, P. von R. Schleyer, *Angew. Chem., Int. Edn.*, 1986, **25**, 1103.
70. A. Furstner, G. Seidel, H. E. Mons, and R. Mynott, *Eur. J. Inorg. Chem.*, 1998, 1771.
71. S. Berger, F. Muller, *Chem. Ber.*, 1995, **128**, 799.
72. C. Lambert, P. V. Schleyer, and E. U. Wurthwein, *J. Org. Chem.*, 1993, **58**, 6377.
73. W. Bauer, *Magn. Reson. Chem.*, 1996, **34**, 532.
74. W. Bauer and L. W. Lochmann, *J. Am. Chem. Soc.*, 1992, **114**, 7482.
75. W. Bauer, *J. Am. Chem. Soc.*, 1996, **118**, 5450.
76. J. H. Gilchrist and D. B. Collum, *J. Am. Chem. Soc.*, 1992, **114**, 794.
77. H. Gunther, O. Eppers, H. Hausmann, D. Huls, H. E. Mons, K. D. Klein, and A. Maercker, *Helv. Chim. Acta*, 1995, **78**, 1913.
78. N. Chandrakumar, H. E. Mons, D. Huls, and H. Gunther, *Magn. Reson. Chem.*, 1996, **34**, 715.
79. J. Schaefer, in 'Encyclopedia of NMR', eds D. M. Grant and R. K. Harris, Wiley: Chichester, 1996, vol. 6, p 3977.
80. A. Boman, U. Edlund, H. Forster, and D. Johnels, *Acta Chem. Scand.*, 1999, **53**, 699.
81. P. O. Quist, H. Forster, and D. Johnels, *J. Am. Chem. Soc.*, 1997, **119**, 5390.
82. B. Walfort, L. Lameyer, W. Weiss, R. Herbst-Irmer, R. Bertermann, J. Rocha, and D. Stalke, *Chem. Eur. J.*, 2001, **7**, 1417.
83. P. I. Arvidsson, P. Ahlberg, and G. Hilmersson, *Chem. Eur. J.*, 1999, **5**, 1348.
84. H. J. Reich, M. A. Medina, and M. D. Bowe, *J. Am. Chem. Soc.*, 1992, **114**, 11 003.
85. H. Ahlbrecht, J. Harbach, R. W. Hoffmann, and T. Ruhland, *Liebigs Annalen.*, 1995, 211.
86. (a) H. J. Reich and R. R. Dykstra, *Angew. Chem. Int. Edn. Engl.*, 1993, **32**, 1469; (b) H. J. Reich and K. J. Kulicke, *J. Am. Chem. Soc.*, 1996, **118**, 273.
87. T. Ruhland, R. Dress, and R. W. Hoffmann, *Angew. Chem. Int. Ed. Engl.*, 1993, **32**, 1467.
88. P. R. Peoples and J. B. Grutzner, *J. Am. Chem. Soc.*, 1980, **102**, 4709.
89. D. J. Cram, 'Fundamentals of Carbanion Chemistry', Academic Press: New York, 1965, Ch. VI; G. Boche, *Top. Curr. Chem.*, 1988, **146**, 1.
90. E. Grovenstein, K. W. Black, S. C. Goel, R. L. Hughes, J. H. Northrop, D. L. Streeter, and D. Vanderveer, *J. Org. Chem.*, 1989, **54**, 1671.
91. (a) J. B. Grutzner and S. Winstein, *J. Am. Chem. Soc.*, 1972, **94**, 2200; (b) M. V. Moncur, J. B. Grutzner, and A. Eisenstadt, *J. Org. Chem.*, 1974, **39**, 1604.
92. G. Jonsall and P. Ahlberg, *J. Chem. Soc. Perk. Trans. 2*, 1987, 461.
93. (a) P. Ahlberg, O. Davidsson, M. Lowendahl, G. Hilmersson, A. Karlsson, and M. Hakansson, *J. Am. Chem. Soc.*, 1997, **119**, 1745; (b) P. Ahlberg, A. Karlsson, O. Davidsson, G. Hilmersson, and M. Lowendahl, *J. Am. Chem. Soc.*, 1997, **119**, 1751.
94. A. Karlsson, G. Hilmersson, O. Davidsson, M. Lowendahl, and P. Ahlberg, *Acta Chem. Scand.*, 1999, **53**, 693.
95. (a) H. Luitjes, F. J. J. Dekanter, M. Schakel, R. F. Schmitz, and G. W. Klumpp, *J. Am. Chem. Soc.*, 1995, **117**, 4179; (b) W. Moene, M. Vos, M. Schakel, F. J. J. de Kanter, R. F. Schmitz, and G. W. Klumpp, *Chem. Eur. J.*, 2000, **6**, 225.
96. (a) F. Gerson, 'High-Resolution ESR Spectroscopy', Wiley and Verlag Chemie: New York and Weinheim, 1970; (b) E. Deboer, A. A. K. Klaassen, J. J. Mooij, and J. H. Noordik, *Pure Appl. Chem.*, 1979, **51**, 73; (c) Michael Szwarc ed, 'Ions and Ion Pairs in Organic Reactions', Wiley-Interscience: New York, 1972; (d) S. Mazur, V. M. Dixit, and F. Gerson, *J. Am. Chem. Soc.*, 1980, **102**, 5343.
97. R. A. Marcus, *J. Phys. Chem. B.*, 1998, **102**, 10 071 and references therein.
98. (a) P. Boman, B. Eliasson, R. A. Grimm, G. S. Martin, J. T. Strnad, and S. W. Staley, *J. Am. Chem. Soc.*, 1999, **121**, 1558;

(b) P. Boman, B. Eliasson, R. A. Grimm, and S. W. Staley, *J. Chem. Soc. Perkin Trans. 2*, 2001, 1130 and references therein.
99. P. Boman and B. Eliasson, *Acta Chem. Scand.*, 1996, **50**, 816.
100. (a) M. Micha-Screttas, G. A. Heropoulos, and B. R. Steele, *J. Chem. Soc. Perk. Trans. 2*, 1999, 2685; (b) C. G. Screttas, G. A. Heropoulos, B. R. Steele, and D. Bethell, *Magn. Reson. Chem.*, 1998, **36**, 656.
101. M. Micha-Screttas, G. A. Heropoulos, and B. R. Steele, *J. Chem. Soc. Perk. Trans. 2*, 1999, 1443.
102. (a) J. F. McGarrity and J. Prodolliet, *J. Org. Chem.*, 1984, **49**, 4465; (b) J. F. McGarrity, C. A. Ogle, Z. Brich, and H. R. Loosli, *J. Am. Chem. Soc.*, 1985, **107**, 1810.
103. C. A. Ogle, X. L. Wang, C. M. Carlin, F. H. Strickler, and B. Gordon, *J. Polym. Sci. Pol. Chem.*, 1999, **37**, 1157.
104. W. H. Sikorski, A. W. Sanders, and H. J. Reich, *Mag. Reson. Chem.*, 1998, **36**, S118.
105. R. T. Boere and R. G. Kidd, *Annu. Rep. NMR Spectrosc.*, 1982, **13**, 319.
106. (a) L. M. Jackman and C. W. Debrosse, *J. Am. Chem. Soc.*, 1983, **105**, 4177; (b) J. Q. Wen and J. B. Grutzner, *J. Org. Chem.*, 1986, **51**, 4220.
107. L. M. Jackman and L. M. Scarmoutzos, *J. Am. Chem. Soc.*, 1984, **106**, 4627.
108. T. Lejon and U. Edlund, *Acta Chem. Scand.*, 1989, **43**, 275.
109. I. Sethson, B. Eliasson, and U. Edlund, *Magn. Reson. Chem.*, 1991, **29**, 1012.
110. C. S. Johnson, in 'Encyclopedia of NMR', eds D. M. Grant and R. K. Harris, Wiley: Chichester, 1996, vol. 3, p 1626; C. S. Johnson, *Prog. NMR Spectrosc.*, 1999, **34**, 203.
111. Y. Cohen and A. Ayalon, *Angew. Chem. Int. Ed. Engl.*, 1995, **34**, 816.
112. R. E. Hoffman, E. Shabtai, M. Rabinovitz, V. S. Iyer, K. Mullen, A. K. Rai, E. Bayrd, and L. T. Scott, *J. Chem. Soc. Perkin Trans. 2*, 1998, 1659.
113. I. Keresztes and P. G. Williard, *J. Am. Chem. Soc.*, 2000, **122**, 10 228.
114. A. Boman and D. Johnels, *Magn. Reson. Chem.*, 2000, **38**, 853.
115. L. M. Jackman, L. M. Scarmoutzos, and C. W. DeBrosse, *J. Am. Chem. Soc.*, 1987, **109**, 5355.
116. A. Pepels, H. Gunther, J. P. Amoureux, and C. Fernandez, *J. Am. Chem. Soc.*, 2000, **122**, 9858.
117. M. Hartung, H. Gunther, J. P. Amoureux, and C. Fernandez, *Magn. Reson. Chem.*, 1998, **36**, S61.
118. G. H. Penner, *Chem. Phys. Letts.*, 1996, **261**, 665.

Biographical Sketch

John B. Grutzner, *b* 1941. B.Sc., 1962, Ph.D., 1967, University of Melbourne has been blessed to be an observer at several historical events in NMR. Jackman at Melbourne introduced me to the wonders of NMR and carbanions in the days when chemical shifts were determined by averaging field sweeps on the HA-60. I interviewed for a post-doc with Roberts at Caltech when Frank Weigert presented him with the natural abundance ^{13}C spectrum of cholesterol run on the DSP-60 – a revelation for an organicer. I spent a sabbatical with Freeman at Oxford drinking tea and reading Abragam, as Bodenhausen, Morris and Turner discovered the subtleties of 2D NMR on the CFT-20. Research interests: Molecular dynamics and NMR.

Carbon-13 Relaxation Measurements: Organic Chemistry Applications

George C. Levy and Deborah J. Kerwood

Informatrix Inc., Ann Arbor, MI, USA

1	Introduction	1
2	Measurements of ^{13}C Relaxation Parameters	5
3	Overview of Applications for ^{13}C Spin Relaxation Measurements	6
4	Summary	9
5	References	9

1 INTRODUCTION

Paralleling other developments in ^{13}C NMR,[1,2] interest in ^{13}C spin relaxation data increased greatly with the availability in the early 1970s of Fourier transform methods.[1–3] This interest initially arose for two reasons. First, it was necessary to have information about spin relaxation behavior in order to achieve sensitivity advantages approaching those theoretically possible in Fourier transform NMR experiments. Second, spin relaxation data can give chemical and dynamic molecular structural data that are either difficult or impossible to obtain from other kinds of measurements.

The ^{13}C nucleus is particularly well suited for spin relaxation studies for several reasons:

1. Since carbon atoms are usually found at the backbone of molecules, interpretation of ^{13}C relaxation behavior is generally not complicated by intermolecular relaxation processes, unlike the situation for ^{1}H and ^{19}F nuclei.
2. ^{13}C spectra are primarily observed under proton-decoupled conditions, where each carbon in the molecule is represented by a single spectral line whose spin–lattice (T_1) and spin–spin (T_2) relaxation times can be governed by single exponential time constants.[4]
3. The rather large chemical shift range of the ^{13}C nucleus makes it possible to resolve virtually all individual carbons, even in complex molecules. Thus, multiple sites are often available at which to probe a molecule's overall and internal motions.
4. Since ^{13}C is a rare spin (low natural abundance), consideration of ^{13}C–^{13}C dipolar interactions or of the phenomenon of spin diffusion[5] is usually not necessary. This greatly simplifies the interpretation of ^{13}C relaxation rates.

Carbon-13 relaxation times provide significant information in many areas of chemistry. Interpretation of ^{13}C relaxation data in terms of molecular dynamics (e.g. internal and overall molecular motions) provides the chemist with a unique and powerful probe into the detailed structure of organic molecular systems, and provides the theoretician with much needed motional data with which to test models for the microdynamic behavior of molecular systems. This potential for chemical insight, coupled with the ease of obtaining ^{13}C relaxation data on commercially available FT NMR spectrometers, argues for a basic understanding of NMR spin relaxation parameters by most chemists. This article considers the topic of ^{13}C spin relaxation in three overall parts: (1) a description of ^{13}C spin relaxation processes, (2) a short section outlining experimental methods, and (3) discussions of several types of applications in organic chemistry.

The magnetic resonance parameters that are relevant to molecular dynamics are the nuclear spin relaxation times T_1 and T_2 and (usually) for the ^{13}C nucleus, the ^{13}C–^{1}H nuclear Overhauser effect (NOE).

For a nucleus with a spin quantum number equal to $\frac{1}{2}$ (e.g., ^{1}H, ^{13}C, ^{19}F, ^{31}P, etc), there are two allowed orientations for each magnetic moment vector relative to an applied field, $\boldsymbol{B}_0$. If it is assumed that the spin system is in thermal contact with its environment and the nuclei do not strongly interact with one another, then in the absence of additional irradiation, a Boltzmann distribution of nuclei will be established among the two resultant energy states. The redistribution of populations arises from interactions of the nuclei with their surroundings. This interaction is the so-called spin–lattice relaxation process and is characterized by a relaxation time T_1, which represents the timescale for energy transfer between the spin system and the lattice or environment. (For a liquid, the term 'lattice' is taken essentially as the translational, rotational, and other degrees of freedom of the molecular system.)

The resonant condition in NMR is accomplished by imposing a radiofrequency field $\boldsymbol{B}_1$ at right angles to $\boldsymbol{B}_0$. When B_1 is equal to the nuclear Larmor frequency, two effects occur in the spin system. First, some nuclei in the lower energy state absorb energy from $\boldsymbol{B}_1$, which results in a transition to the upper energy state and a decrease in the net population difference between the states. This process decreases the value of M_z, the magnetization along the z axis coincident with $\boldsymbol{B}_0$. The second effect of B_1 is to generate a phase-coherent magnetization in the transverse plane, M_{xy}. After excitation, the nuclei tend to get out of phase again, thereby decreasing M_{xy}. The time constant for this process is the spin–spin relaxation time, T_2. Loss of phase coherence arises because fluctuating local magnetic fields augment or decrease $\boldsymbol{B}_0$, thus causing a spread of precessional frequencies among the individual nuclei and a corresponding loss of phase coherence. A second process tending to destroy the phase coherence arises from a mutual spin flip of two nuclei, if they are initially antiparallel and have precessing magnetic fields at the proper frequency. Although this interaction conserves the energy of the spin system, it does produce an uncertainty in the energy since it limits the lifetime of a state. The magnetization M_{xy} will decay to zero as the spins resume a random precession. When $M_{xy} = 0$, the net magnetization vector lies along the z direction; thus $\boldsymbol{M} = M_z$. However M_z may or may not at that moment equal $\boldsymbol{M}_0$. Simultaneous with the decay of M_{xy} is the restoration of M_z magnetization. The timescale for M_z to reassume the value $\boldsymbol{M}_0$ is determined by the spin–lattice relaxation time. From the above arguments, $T_1 \geq T_2$.

Bloch viewed both of the magnetic relaxation processes as first-order decays. The usual equations for describing these decays are

$$\frac{\mathrm{d}M_z}{\mathrm{d}t} = \frac{-(M_z - M_0)}{T_1} \qquad (1)$$

and

$$\frac{dM_{xy}}{dt} = \frac{-M_{xy}}{T_2} \tag{2}$$

These simple equations have been found to provide, in most cases, a good description of relaxation phenomena pertinent to much liquid-phase ^{13}C NMR.[6,7] The primary concern of this article will be the spin–lattice relaxation time, T_1, and the associated $^{13}C-^{1}H$ NOE; in general, it is more difficult to measure ^{13}C T_2 values accurately.

Unlike most molecular relaxation processes in liquids, the timescale for the spin–lattice relaxation process is relatively long because the nuclear spin system is only weakly coupled to the other motions of the system. Experimental values of ^{13}C T_1 values are correspondingly of the order of 10^{-2}–10^{2} s and are usually in the range of 0.1 s to several seconds for typical organic compounds as neat liquids or in solution[6,7] (provided the system is free of paramagnetic impurities). While this order of time constant indicates that the interactions governing the spin–lattice relaxation process are relatively inefficient, it is nevertheless only because of these weak interactions that nuclear spin relaxation occurs.

The coupling of the nuclear spin system to the lattice originates from the interaction of individual nuclear moments with fluctuating local magnetic fields, $\boldsymbol{B}_{loc}$, produced by the lattice at the nuclear site. If the various $\boldsymbol{B}_{loc}$ quantities have frequency components at values appropriate to the nuclear spin transition frequency, then energy can be transferred to the lattice and spin relaxation induced. The time dependence of the local fields arises from the overall and internal motions of the molecule, and other dynamic processes. To develop this link conceptually between $\boldsymbol{B}_{loc}$ and T_1, it is necessary to consider the origin and some of the properties of the lattice fields.

In fluids, typical sources of $\boldsymbol{B}_{loc}$ are nuclear and electromagnetic dipoles, electric quadrupoles (for nuclei with spin $I > \frac{1}{2}$), anisotropy of the chemical shielding tensor, modulation of scalar coupling, and rotation of the molecule or group itself (spin rotation). The efficiency of any one of these sources in causing relaxation depends on both the amplitude of the fluctuations in $\boldsymbol{B}_{loc}$ and the timescale of those fluctuations. The mathematical description of the interaction of the spin with $\boldsymbol{B}_{loc}$ is similar for each relaxation mechanism.

Since the interaction of a ^{13}C nucleus with the magnetic field arising from an attached proton ($^{13}C-^{1}H$ nuclear dipole–nuclear dipole interaction) is most often the pathway useful in broad applications of ^{13}C spin–lattice relaxation,[1,6,7] a brief account of the origin of the equation relating T_1 to this interaction is given immediately below.

1.1 The Dipole–Dipole Relaxation Mechanism

The prime source of ^{13}C spin relaxation in most diamagnetic liquids arises from the local magnetic fields produced by bonded or nearby protons. The instantaneous dipolar magnetic field (which may be as large as several gauss) that induces T_1 relaxation is proportional to the square of the magnetogyric ratios of both spins.

For a rigid system of intramolecular dipoles, molecular tumbling imparts the time-dependence to $\boldsymbol{B}_{loc}$ through the angle Θ between the through-space vector between the two dipoles, and $\boldsymbol{B}_0$ (for carbons with directly bonded protons, this vector is of course coincident with the C–H bond itself). For the intermolecular case, and for intramolecular relaxation in flexible molecules, both the angle Θ and the distance between the dipoles are time-dependent, owing to relative translation as well as rotational motion. Intermolecular interactions tend to be attenuated rapidly owing to the r^{-3} dependence of $\boldsymbol{B}_{loc}$ for the two spins and the consequent r^{-6} dependence for T_1 relaxation of the ^{13}C nucleus. This result has important consequences for ^{13}C relaxation.

Another case of dipolar interaction is where the relaxing field has its origin with an unpaired electronic spin rather than a nuclear spin: for example, from any paramagnetic species present in the sample. Since the magnetic moment of the electron is roughly three orders of magnitude greater than nuclear moments, the fields are correspondingly more intense. When modulated by molecular tumbling, such fields can then induce very efficient nuclear spin relaxation, even at low concentration in a sample.

1.1.1 Properties and Formal Description of $\boldsymbol{B}_{loc}$

By assuming that the molecules constituting the liquid can be described as particles undergoing Brownian motion, the local dipolar field then has the following properties:[8]

1. $\langle \boldsymbol{B}_{loc}(t_0) \rangle = 0$, where $\langle\ \rangle$ is an average over time.
2. $\langle \boldsymbol{B}_{loc}{}^{2}(t) \rangle \neq 0$; i.e., the mean of the square is nonzero.
3. $\langle \boldsymbol{B}_{loc}(t_0) \cdot \boldsymbol{B}_{loc}(t + \tau) \rangle = 0$, provided that τ is sufficiently long.

At long τ, the value of $\boldsymbol{B}_{loc}$ at time $t + \tau$ does not in any manner depend on the value at time t. If τ is sufficiently short, then the quantity is expected to have a nonzero value.

Mathematically, these characteristics are embodied in the so-called time-dependent correlation function $G(t)$ of $\boldsymbol{B}_{loc}$.[9] In a qualitative sense, such a function describes the persistence of a dynamical property of the system before being averaged out by molecular motions in the liquid, and is of particular value when two physical systems are weakly coupled, as is the case for the nuclear spin system and its lattice. The autocorrelation function of $\boldsymbol{B}_{loc}$ is given by the ensemble average

$$G(t) = \langle \boldsymbol{B}_{loc}(t_0) \cdot \boldsymbol{B}_{loc}(t_0 + \tau) \rangle_t \tag{3}$$

where the time-dependence is that produced by the molecular motion. The average is over an ensemble at the reference time t. Since $\langle \boldsymbol{B}_{loc}(t) \cdot \boldsymbol{B}_{loc}(t + \tau) \rangle$ is independent of the reference time, $G(t)$ is designated a correlation function of a stationary random process; $G(t)$ is independent of t_0 and is both a real and even function of τ.[9] If the time origin is taken as $t = 0$, then

$$G(\tau) = \langle \boldsymbol{B}_{loc}(0) \bullet \boldsymbol{B}_{loc}(\tau) \rangle_0 \tag{4}$$

and $G(\tau)$ then describes the timescale for the decay of inherent motional order in the system. Information on the molecular system is dependent on the existence of $G(\tau)$, and as $G(\tau)$ decays toward zero so does knowledge of the dynamical processes at the prior time.

The Fourier transform of $G(\tau)$, the spectral density function, $J(\omega)$ provides the means of characterizing the frequency distribution and magnitude of the fluctuations in $\boldsymbol{B}_{loc}$; $J(\omega)$

represents a transformation from the time to the frequency domain. It is given by

$$J(\omega) = \int_{-\infty}^{+\infty} G(\tau) e^{i\omega\tau} \, d\tau \tag{5}$$

and represents the power available at angular frequency ω to relax the spin system. Equation (5) indicates that, if $G(\tau)$ decays slowly, information [through $J(\omega)$] will persist for a long time and the spectral lines will be narrow. If $G(\tau)$ decays rapidly, information is lost quickly and the spectral peaks will be broad.

Evaluation of equation (5) requires a description of the decay of $G(\tau)$. For a liquid, assuming exponential decay for $G(\tau)$

$$G(\tau) = \langle B_{loc}^2(0) \rangle_0 e^{-\tau/\tau_e} \tag{6}$$

where τ_e is the characteristic exponential time constant (correlation time) in which it is assumed motional order decays out of the system. It can be further assumed that the different spatial components of $\boldsymbol{B}_{loc}$ are uncorrelated, i.e., $\langle \boldsymbol{B}_{loc}(x) \boldsymbol{B}_{loc}(y) \rangle = 0$ but for isotropic motion they share the same correlation time, τ_c. Substitution of equation (6) into equation (5) and integration results in

$$J(\omega) = \langle B_{loc}^2(0) \rangle \frac{2\tau_c}{1 + \omega^2 \tau_c^2} \tag{7}$$

From equation (7) it is evident that $J(\omega)$ is a maximum at $\omega = 0$ and is approximately constant over the range $\tau_c < \omega$; it decreases with increasing frequency as ω approaches $1/\tau_c$. The total spectral density, as a sort of probability distribution, is constant and independent of τ_c. Thus, variation in τ_c merely changes the distribution of 'spectral density' over the entire frequency spectrum.

This result indicates that T_1 goes through a minimum as a function of τ_c. Plots of T_1 versus τ_c as a function of spectrometer operating frequency are given in Figure 1. The left side of Figure 1, where T_1 is independent of spectrometer frequency, is called the region of motional narrowing. In this regime $J(\omega)$ is given by

$$J(\omega) = 2\langle B_{loc}^2(0) \rangle \tau_c \tag{8}$$

Liquids or solutions for which τ_c is within the motional narrowing limit include many organic molecules at or above room temperature. Use of increasing NMR magnetic field strengths, however, places more molecules outside the motional narrowing limit (see Figure 1). When the motional narrowing limit is valid, and when motion is isotropic, $^{13}C-^{1}H$ dipole–dipole relaxation is described by

$$\frac{1}{T_1} = \sum_{i=1}^{n} \frac{\gamma_C^2 \gamma_H^2 \hbar^2}{r_{CH}^6} \tau_c \tag{9}$$

where the summation is over all nearby protons, and the $r^6{}_{CH}$ values reflect the various ^{13}C,H internuclear distances.

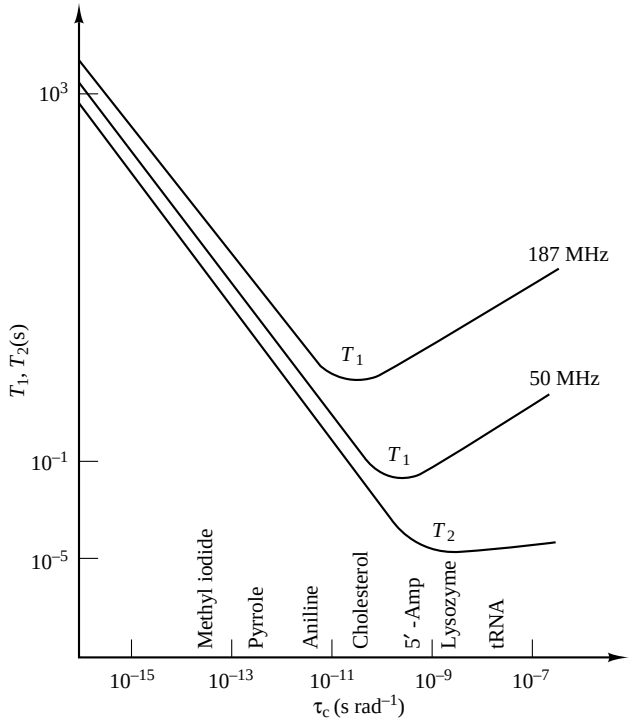

Figure 1 Spectral density $J(\omega)$ as a function of frequency for various values of the correlation time, τ_c (ω_0 corresponds to the nuclear Larmor frequency)

In the case of a ^{13}C nucleus that has one or more directly attached protons, longer range proton interactions can generally be ignored and equation (9) simplifies to:

$$\frac{1}{T_1} = \frac{N_H \hbar^2 \gamma_C^2 \gamma_H^2 \tau_c}{r_{CH}^6} \tag{10}$$

where N_H is the number of directly attached protons and $r_{CH}{}^{-6}$ is the C–H bond length. In those cases where the molecular tumbling is anisotropic or where internal motions are present, ^{13}C dipolar relaxation (T_1 and T_2) is described by more complex equations, described elsewhere.[8] Many applications can utilize equation (10), or approximate treatments that model motional anisotropy in terms of three orthogonal rotational diffusion constants (D_x, D_y, D_z).

1.2 Other ^{13}C Spin Relaxation Mechanisms

As described above, many carbons, particularly CH_x carbons, are relaxed completely by $^{13}C-^{1}H$ dipole–dipole interactions. However, at increasingly high magnetic fields, and for other selected cases, a given carbon's relaxation may be dominated by other mechanisms.[10] In applications of spin relaxation, it is of *paramount importance for the correct interpretation of results, that the investigator recognize all significant contributions to relaxation for the specific ^{13}C nuclei being examined.*

Briefly, the other ^{13}C spin relaxation mechanisms commonly encountered are: (a) dipolar interactions (DD) with other nuclides (e.g., ^{19}F, ^{31}P, sometimes ^{13}C, metal nuclei, etc.);

(b) dipolar interactions with unpaired electron spins (added paramagnetic agents, dissolved oxygen, etc.); (c) chemical shift anisotropy (CSA) relaxation of ^{13}C nuclei which occurs through the anisotropy of the ^{13}C shielding tensor; because CSA relaxation depends on $B_0{}^2$ as well as the square of the shielding anisotropy, it is significant, especially at higher $\boldsymbol{B}_0$, for sp^2 and sp carbons, and is often dominant at high $\boldsymbol{B}_0$ for those carbons not having directly attached protons; (d) ^{13}C relaxation through scalar interactions is common for spin–spin relaxation (linewidths), but the formalism restricts scalar T_1 relaxation to carbons scalar-coupled (SC) with nuclei having a closely similar resonance frequency and/or a very large scalar coupling constant; carbons bonded to bromine atoms, for example, can have highly efficient scalar relaxation to ^{79}Br, whose resonance frequency is only 0.3% different from ^{13}C (for ^{81}Br the Δ frequency is 7.4%); and (e) spin rotation (SR) relaxation, which in very small molecules or for freely rotating groups such as the methyl group of toluene, can dominate ^{13}C relaxation. This mechanism is more common for heavy nuclides.

1.3 Relationship of T_1 to Individual Relaxation Mechanisms

In a particular compound, all or any combination of the ^{13}C relaxation mechanisms discussed above may be of potential importance. However, only a single relaxation time is measured for each carbon. This is assumed to be related to the individual mechanisms via the reciprocal relationship:

$$\frac{1}{T_1^{\text{obs}}} = \frac{1}{T_1^{\text{DD}}} + \frac{1}{T_1^{\text{SR}}} + \frac{1}{T_1^{\text{CSA}}} + \frac{1}{T_1^{\text{SC}}} + \frac{1}{T_1^{\text{other}}} \qquad (11)$$

This equation ignores cross correlation between relaxation processes. Cross correlation relaxation can be important and useful.[4b,c] It can be significant particularly between CSA and dipolar processes, but there are experimental methods for separating these effects.[11] Extraction of the relevant molecular information from measured T_1 values requires evaluation of the contributions from individual relaxation mechanisms.

In 1973, Levy, Cargioli, and Anet published a paper[10] describing ^{13}C spin relaxation in benzene and a variety of substituted benzenoid compounds. In that early paper, evidence was found for different individual carbons having their spin relaxation controlled by each of the available spin relaxation mechanisms: dipole–dipole interactions, chemical shift anisotropy, spin rotation, and scalar interactions. It was seen that most carbons had their spin relaxation controlled by dipole–dipole interactions to attached or nearby hydrogens, except that for nonprotonated sp^2 carbons at (then) high fields (in 1973, 63 MHz operation for ^{13}C was considered high field) there were significant contributions from chemical shift anisotropy relaxation.

Another interesting exceptional case was found for the *ipso* ring carbon in bromobenzene, where the attached bromine was highly effective in producing scalar spin relaxation, at least for the ^{79}Br isotope. Because both ^{79}Br and ^{81}Br are present in roughly comparable amounts, the T_1 magnetization recovery was seen to be nonexponential (a combination of two dissimilar spin relaxation rates).[12]

In the 1973 paper on substituted benzenes,[10] there was an expansion on work from Grant and others on free methyl rotation. The methyl carbon in toluene was observed to have effective spin rotation relaxation, as confirmed by variable temperature measurements. The effect of dissolved oxygen from the air was noted for these benzenoid compounds. In the case of the smaller nonpolar compounds, and for nonprotonated carbons in some of the larger substituted benzenes, oxygen from the air contributed significantly to ^{13}C overall spin relaxation. In benzene itself, dissolved oxygen resulted in a contribution of approximately 25% to the ^{13}C relaxation rate at 38 °C, while spin rotation relaxation had a comparable contribution. Observation of several phenylacetylene compounds showed that chemical shift anisotropy relaxation was a major contributor for nonprotonated sp carbons, even at modest magnetic fields.

1.3.1 ^{13}C–^{1}H Dipole–Dipole Relaxation Outside of the Motional Narrowing Limit

For synthetic and biopolymers, where motion is slow and the $^{13}C-^{1}H$ dipolar T_1 (and NOE) becomes field-dependent, it is more difficult to quantify $^{13}C-^{1}H$ dipolar relaxation versus other contributors. However, especially for proton-bearing sp^3 carbons, it can usually be assumed that $^{13}C-^{1}H$ dipolar relaxation is the only significant operating mechanism.

In these cases, when dipolar T_1 and observed NOE show complex behavior as a function of the NMR observed frequency (magnetic field), it is possible to model molecular dynamics in terms of the complex overall and internal motions occurring at various frequencies and, in the case of internal motions, of varying angular amplitudes. A number of models have been proposed,[13] but many groups prefer to use a model-free description of complex dynamics initially proposed by Lipari and Szabo.[14] While the model-free approach does not explain specific conformational motions, it is quite useful for the assessment of local conformational mobility in synthetic and biopolymers.[15,16]

1.3.2 Complex Dynamics of Small Molecules; Nonexponential Decay of $G(\tau)$

In the mid-1970s it was recognized that, under a range of circumstances, the ^{13}C dipole–dipole T_1 values apparently indicative of motional narrowing in fact showed marked field-dependence.[17] This occurs when there are cooperative motions, as in some samples of aggregated molecules having relatively freely moving side chains. In the first ^{13}C study of this type, the ^{13}C dipolar T_1 values for all 10 carbons in 1,2-decanediol were found to have a strong field-dependence despite being fully due to $^{13}C-H$ dipolar interactions, and where lines were sharp and ^{13}C T_1 values were as long as 5 s (corresponding to a τ_c well within motional narrowing). The ^{13}C T_1 results of the 1,2-decanediol study[17] are summarized in Table 1, along with T_1 values for 1-decanol, which can be used for comparison purposes.

The important and unexpected thing to note in Table 1 is the large difference between the 22.6 MHz and 67.9 MHz ^{13}C T_1 values of decanediol. By contrast, the ^{13}C T_1 values of 1-decanol show no field dependence, in accordance with standard theories for molecules undergoing rapid reorientation

Table 1 ^{13}C Spin–Lattice Relaxation Data for 1,2-Decanediol and 1-Decanol

Compound[a]	Temp (° C)[b]	Frequency (MHz)	^{13}C T_1 values (s)[c]									
			C-1	C-2	C-3	C-4	C-5	C-6	C-7	C-8	C-9	C-10
1,2-Decanediol	54	22.6	0.27	0.41	0.3	0.37	0.3	0.4	0.5	0.95	1.5	3.4
	54	67.9	0.5	0.7	0.5	0.6	0.6	0.7	1.0	1.8	2.7	5.3
1-Decanol	36	22.6	0.7	0.7	0.7		~1.0[d]			1.5	2.4	3.9
	36	67.9	0.6	0.6	0.7		~1.0[d]			1.4	2.3	3.8

[a]Samples neat unless noted.
[b]Temperatures ±1 °C, measured directly before and after data collection.
[c]Maximum probable error ±5%–10%. Decanediol and decanol data, average of two to four runs.
[d]Peaks insufficiently resolved for individual T_1 assignment.

in solution. These results can be interpreted in terms of a distribution of τ values for overall motion [or, equivalently, a nonexponential autocorrelation function $G(\tau)$] at the H-bond restricted end of the diol, with effective transmission of this nonideality to all the other carbons along the alkyl chain, either by the inherent intramolecular characteristics[13b] of the chain segmented motion, or through intermolecular transmission from chain–chain entanglements.

1-Decanol is extensively hydrogen bonded in neat solution. The ^{13}C T_1 values of 1-decanol given in Table 1 do not show a significant field dependence. The two field T_1 data for decanol at 36 °C thus do not require invocation of a complex cooperative motional description as in 1,2-decanediol.

The type of effect observed for the end carbons (C_7–H_{10}) of 1,2-decanediol may be observed in organized molecules, e.g., micelles, etc, and it is characteristic of complex dynamics in large biological or synthetic polymers, where relatively freely moving side groups can continue to show marked field dependence. For these cases, multiple field (frequency) ^{13}C T_1, NOE and, where practical, T_2 measurements can provide an extremely sensitive probe of molecular dynamics, in favorable cases uniquely differentiating similar models for overall and internal dynamics.

2 MEASUREMENTS OF ^{13}C RELAXATION PARAMETERS

Pulsed Fourier transform NMR methods are available for accurately determining spin–lattice relaxation times and NOEs. In one-dimensional ^{13}C NMR, these methods have been used for over 25 years in order to determine simultaneously T_1 values for all carbons in the spectrum. Even though the measurements can be considered as routine on modern day spectrometers, there are many factors that can make the experimental values that are determined inaccurate.[18] These factors include: (i) the choice of measurement pulse sequence; (ii) stability and accuracy of pulses and the spectrometer stability as a whole; (iii) data processing method used for calculation of the time constants from the experimental data; (iv) the presence of sample impurities; (v) temperature or solvent variation between experiments to be compared; (vi) sample geometry; and (vii) unusual spin relaxation characteristics, e.g., nonexponential relaxation.

Measurement of nuclear Overhauser effects similarly depends on the control of variables such as sample state and temperature, the application of radiofrequency pulses and timing, and care in data processing. Further, both ^{13}C spin–lattice relaxation measurements and NOE experiments may become difficult for carbons having very long spin relaxation times, where the sample is limited in quantity, or where solubility is very low.

Various pulse sequences have been used to establish a nonequilibrium condition and monitor the magnetization as a function of the time variable τ, thereby measuring T_1. Several pulse sequences directly measure NOE values, and one version of this experiment can simultaneously measure T_1s and NOEs for all carbons (although the efficiency of this last experiment is not high). There are existing discussions of necessary precautions that should be taken in these measurements. Table 2 summarizes some of the experiments used for ^{13}C spin relaxation measurements.

Most of the experiments listed in Table 2 are straightforward; the experiments listed for the measurement of T_1 all produce a nonequilibrium magnetization with subsequent time recovery towards equilibrium being monitored by a 90° pulse. The IRFT[19] and the pulse sequences most commonly used are relatively forgiving, experimentally. However, IRFT experiments can be quite lengthy when one or more carbons that are being measured have one long T_1 value. In these cases the shorter FIRFT experiment is preferred. The progressive saturation method was used in the early days of ^{13}C NMR but it is not generally used today because the technique is not as accurate in the case of mis-set pulse angles. Both progressive saturation and saturation recovery techniques utilize in most cases homospoil pulses (z homospoil) (indicated as HS in Table 2). The saturation recovery technique avoids some of the experimental problems of progressive saturation but the magnetization change measured is only half that of full inversion–recovery technique, leading to the choice of the latter in most cases. One advantage of the FIRFT pulse sequence is that for different ^{13}C nuclei in the same sample, the magnetization change being monitored can range from full inversion–recovery to essentially half of that value for very long T_1 values.

NOE measurements for ^{13}C are easily performed in most cases. Care must be taken in high dielectric samples not to heat the sample differently during relaxation pulse intervals, and in some cases authors have utilized decoupling power at a constant level but have offset the frequency sufficiently such that the protons in the sample are not affected.

Pulse sequences have been proposed to improve IRFT-type measurements[24] and to remove the effects of cross correlation between dipolar and chemical shift anisotropy relaxation.[25] Use of indirect observation (through the ^1H channel) to

Table 2 Some Methods for Determining ^{13}C Spin Relaxation Data

Method	Pulse sequence[a]	Comments	References
(a) T_1 Measurements			
Inversion recovery (IRFT)	$(180^\circ, \tau, 90^\circ, \text{AT}, \text{PD})_n$	PD > 4 × longest T_1 to be measured	19
Fast inversion recovery (FIRFT)	$(180^\circ, \tau, 90^\circ, \text{AT}, \text{PD})_n$	PD > T_2* but short relative to T_1; first FID is discarded	20
Progressive saturation (PSFT)	$(90^\circ, \tau, 90^\circ, \text{HS})_n$		21
Saturation recovery	$(90^\circ, \text{HS}, \tau, 90^\circ, \text{AT}, \text{HS})_n$		22
(b) NOE Measurements			
Gated decoupling	$(90^\circ, \text{AT}, \text{PD})$	PD with and without decoupling	23
NOE build-up	$(\tau, 90^\circ, \text{AT}, \text{PD})$	Decoupling only during τ and AT. PD varies from 0 to >12-times T_1s of interest. Simultaneously measures T_1s for carbons having appreciable NOEs.	23

[a]AT = acquisition time; PD = pulse delay; HS = z homospoil pulse.

measure ^{13}C T_1 and T_2 values has been demonstrated.[26] New variations on direct T_2 pulse schemes have been proposed that improve their accuracy.[27]

3 OVERVIEW OF APPLICATIONS FOR ^{13}C SPIN RELAXATION MEASUREMENTS

Utilization of carbon-13 spin relaxation data for both structural and dynamic information has been widespread in the literature over the past 20 years. Molecular systems that have been examined range from one-carbon molecules to highly complex synthetic and biological macromolecules, as well as simple and complex organometallics. The theoretical underpinnings for these measurements have advanced over this time period, but the simplest theories of spin relaxation are still sufficient in many applications. This has not caused special difficulty, since cross correlation has shown the greatest effect in the simplest molecules, usually under conditions that are not pertinent to most experiments (for example, in experiments not utilizing proton decoupling). By contrast, learning the intimate details of complex molecular dynamics can require highly sophisticated treatment of relaxation data.

Use of ^{13}C spin relaxation data to obtain qualitative dynamic information is quite facile; quantitative interpretation requires more care in terms of both experiment and elucidation of the dynamics through model assumptions, even in the case of model-free approaches. For molecules that are highly associated, or that are large enough inherently to be outside the extreme spectral narrowing limit, proper interpretation of the data is best done utilizing spin relaxation data obtained across dispersed frequencies (utilizing spectrometers operating at several magnetic fields).

3.1 Structure Determination

Carbon-13 spin relaxation data can be used as primary or confirmatory evidence for the assignment of chemical structures. The inverse sixth power relationship between $^{13}C-^{1}H$ distances and the usual observed ^{13}C dipolar T_1 values can be converted into spectral assignment information, particularly for carbons not having directly attached hydrogens and yet dipolar-relaxed from protons on adjacent or nearby carbons, or from protons in the solvent. For carbons that have one or more directly attached hydrogens, the spin relaxation data may still be useful for spectral assignments, in many cases adding an independent check on assignments made by other methods. For molecules that are globular in shape and close to isotropic in tumbling behavior, the protonated carbon T_1 values often fall into three groups: CH_2 carbons with the shortest T_1s, CH carbons having T_1s approximately twice that of the CH_2 carbons (the relaxation rate is half because only one hydrogen contributes to the carbon's spin relaxation), and CH_3 T_1s ranging from 1.5-times shorter than those found for CH_2 (occasionally, for a methyl that is not rotating) to T_1 values that are longer than T_1 values observed for the CH carbons in that molecule (rapidly rotating CH_3 groups).

An early example of the use of ^{13}C T_1 values to differentiate carbons not having directly attached hydrogens, is the molecule mescaline (**1**). The three types of nonprotonated carbons on the benzene ring of mescaline have differing numbers of hydrogens in the *ortho* ring position, as shown in structure (**1**). The ^{13}C T_1s reflect this, the longest value belonging to the carbon having no adjacent ring *ortho* hydrogens. An example showing the ^{13}C T_1s of protonated carbons varying with the numbers of directly attached hydrogens is the molecule cholesterol (**2**). Cholesterol shows T_1 values around 0.3 s for CH_2 carbons of the steroid ring skeleton while CH ring carbons show ^{13}C T_1 values closer to 0.55 s and methyl carbons (in this case, with considerable internal mobility) have T_1 values of approximately 1 s.[28] In

cholesterol, group segmental motion is also demonstrated; the carbon T_1 values of the cholesterol side chain increase with removal from the fused four-ring structure. Note that the side-chain carbons close to the steroidal skeleton maintain the expected ^{13}C T_1 values but near the end of the chain the CH_2 and CH carbons have significantly longer T_1s, indicative of considerable group segmental motion. (The 1.6 s T_1 observed for the pendant methyl carbons results from combined segmental and methyl group internal rotation.)

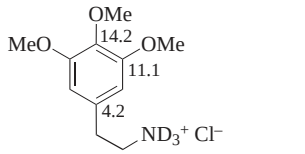

(1)

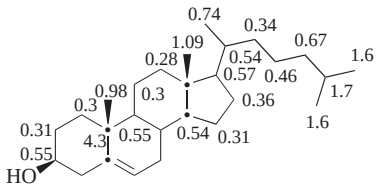

(2)

Another early example of the utilization of ^{13}C spin relaxation times to assist spectral assignments was the study of the tetrasaccharide stachyose (**3**).[29] Stachyose contains two galactose residues and the carbon lines were differentiated as a result of segmental motion increasing the T_1 values of the terminal galactose relative to the internal galactose residue.

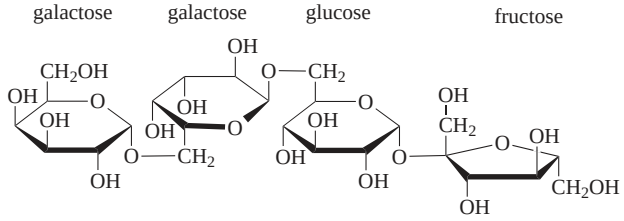

(3)

3.2 Dynamics of Small Molecules

Following pioneering work by the groups of David Grant[4] and Endel Lippmaa,[30] both examining ^{13}C spin relaxation in very small organic molecules, studies began on organic systems of moderate complexity, including examination of group internal mobility and steric effects, solvent effects and hydrogen bonding, ionization, and microphase changes, such as occur in micelles or other ordered phases.

One of the interesting results reported in the 1973 substituted-benzenes paper[10] related that preferred rotational motion around the axis coincident with the phenyl substituent was reflected in significantly shorter ^{13}C T_1 values for the protonated ring carbon *para* to the substituent, versus longer values for the carbons *ortho* and *meta* to the substituent. This effect was marked when the substituent was large or highly solvated, restricting motion through solvent–solute interactions or, in some cases, ion-pair formation. The 60° angular relationship for the *ortho* and *meta* CH vectors with respect to preferred overall rotation around the symmetry axis coincident with the substituent (or, equivalently from the point of view of the ^{13}C T_1s, for internal benzene ring spinning around the same axis), provides a sensitive probe of structure and solvation effects.[10] It was reported for the long molecule 1,4-diphenyldiacetylene that the ^{13}C T_1s for the *ortho* and *meta* carbons, approximately 5.3 s, were almost five-times longer than the ^{13}C T_1 values for the *para* carbon at 1.1 s. These results have some analogies to earlier work on methyl rotational rates, but the substituted-benzene structural unit allows for studies of a broader range of physical and chemical phenomena.

The 1973 paper also gave results for the phenol molecule, which when concentrated in solution is highly associated, giving shortened T_1s, reflecting slow overall motion of the molecule. Further, the anisotropy of tumbling was shown to be higher in these concentrated solutions, where aggregation was important. The aniline molecule was also studied, as a neat sample, in several solvents, and as the anilinium cation. In the latter case, motion was restricted by roughly an order of magnitude and the anisotropy of overall and internal phenyl ring motion approached that in diphenyldiacetylene.[10]

Another early paper giving information about group internal rotations for ring compounds was published in 1972.[31] In that study, two monosubstituted ferrocenes were examined. In both cases, ^{13}C T_1s of the substituted ring carbons were approximately half that of T_1 for the carbons of the unsubstituted ring. Most of this differential was considered to be due to free internal rotation of the unsubstituted planar five-membered aromatic ring, around the ring–Fe bond. One of the molecules, *n*-butylferrocene, also displayed chain segmental motion, where the γ-methylene and δ-methyl carbon T_1 values indicated increased mobility.

In other early work, alkyl chain mobility and steric effects were examined for amides and oximes[32] and in *n*-butylamine and the *n*-butylammonium ion.[33] In the study of several alkyl amides, differential effects were noted for group segmental motions *syn* and *anti* to the oxime function, and marked chain segmental motion was noted for *N,N*-di-*n*-butylacetamide, with ^{13}C T_1s for the four carbons being observed to be comparable to the last four carbons in the hydrogen-bonded molecule decanol. In the case of the acetamide, restriction of chain motion results from the molecular mass centered at the nitrogen and not from hydrogen-bonding interactions. In the *n*-butylammonium ion, ^{13}C T_1 values were observed to decrease by over an order of magnitude in changing from the relatively nonpolar amine to the protonated species, with associated counterion and strong solvation. In *n*-butylamine itself, methylene group segmental motion along the four carbon chain was masked by rapid overall molecular tumbling, but the data for the *n*-butylammonium ion showed ^{13}C T_1s comparable to those observed for the four carbon chain of *N,N*-di-*n*-butylacetamide, and also carbons 7 through 10 of 1-decanol.

3.3 Dynamics of Large Molecules

In the study of biological functions of macromolecules, it is essential to determine the nature and rate of internal motions of the molecule, as well as the overall average structure. Carbon-13 spin–lattice relaxation measurements, in conjunction with

NOE and when possible spin–spin relaxation measurements, have proven to be an important atomic probe of these internal motions. The relaxation of protonated ^{13}C nuclei is primarily dominated by the dipole–dipole interaction with the attached proton according to the following equation (valid inside or outside of the extreme narrowing limit):

$$\frac{1}{T_1} = R_1 = \frac{N_H}{20}\left(\frac{\mu_0\gamma_C\gamma_H\hbar}{4\pi r^3}\right)^2 \times [J(\omega_C - \omega_H) + 3J(\omega_C) + 6J(\omega_C + \omega_H)] \quad (12)$$

where N_H is the number of directly bonded hydrogens, r is the average C–H bond distance, and $J(\omega)$ is the spectral density function at the three indicated frequencies.

Relaxation parameters are related to the overall and internal motions of a molecule through their dependence on the spectral density functions. For large or aggregated molecules that reorient slowly compared with the extreme narrowing limit, the description of the function for a large molecule undergoing overall isotropic motion with fast internal motion is the model-free approach by Lipari and Szabo[14] in which the spectral density function is given by

$$J(\omega) = S^2\left(\frac{\tau_c}{1 + (\omega\tau_c)^2}\right) + (1 - S^2)\left(\frac{2\tau}{1 + (\omega\tau)^2}\right) \quad (13)$$

where S^2 is a generalized order parameter describing the amplitude of the internal motion and τ_c is the overall correlation time. The quantity τ is related to the overall and effective correlation time for the internal motion by $\tau^{-1} = \tau_c{}^{-1} + \tau_e{}^{-1}$. This two-parameter fit of the relaxation data has yielded good success in describing the internal motion of certain residues in macromolecules. Clore et al.[34] found it necessary to expand the above equation to include the internal motions of two uncoupled processes:

$$J(\omega) = S^2\left(\frac{\tau_c}{1 + (\omega\tau_c)^2}\right) + (1 - S_f^2)\left(\frac{2\tau_f}{1 + (\omega\tau_f)^2}\right) + (S^2 - S_f^2)\left(\frac{2\tau_s}{1 + (\omega\tau_s)^2}\right) \quad (14)$$

where 'f' refers to the fast motion and 's' to slower motion that may not be outside the extreme narrowing limit.

The motion of large molecules can also be complicated by overall molecular shape. For globular proteins or polynucleotides of the order of 5–7 base pairs (where the length of the chain is roughly equal to the diameter), the overall motion can be described as isotropic, but with molecules in which the shape is not close to spherical the molecule itself undergoes anisotropic motion. Equation (14) can also be used to describe anisotropic motion with internal motion. In addition to this model-free formalism, a number of different equations of spectral densities have been proposed for anisotropic motion,[35] multiple internal rotations and restricted diffusion,[36] and librational motions.[37]

Early work on the spin–lattice relaxation of carbon-13 of biological molecules provided a fragmentary analysis of internal motion. Instead of analyzing the relaxation data of a single ^{13}C resonance, usually composite ^{13}C resonances had to be studied. James[38] determined the internal motion of 23 Thr residues of chymotrypsinogen to 20 ns based on the combination of spin–lattice relaxation, NOE, and off-resonance rotating frame spin–lattice relaxation techniques. These findings suggested that, on the average, the rate of motion of the Thr residues is limited, possibly by steric hindrance or by interaction of the polar hydroxy with other polar groups. Levy et al.[39] looked at the relaxation data for the interaction of ethidium bromide with nucleosome core length DNA, of ca. 145 bp, and determined that the overall conformational dynamics were not altered by low to moderate levels of ethidium. In addition, the flexibility of the sugar rings was reduced when ethidium intercalated in DNA. Levy et al.[40] also found that the ^{13}C relaxation parameters of double-stranded DNA molecules of 100–300 bp were well fitted by a model which assumed that DNA undergoes rapid local motions such that the C–H vectors wobble inside a conic boundary with a half angle of 20–25°. In addition to these rapid local motions, slower overall axially symmetric rotation occurs. These are a few examples of early studies of ^{13}C relaxation in which qualitative or semiquantitative dynamic information could be ascertained from a combination of different relaxation techniques.

A comprehensive interpretation of ^{13}C relaxation data had been hampered by the inherent low sensitivity of the carbon-13 nucleus, the low natural abundance of carbon-13, and the low resolution of one-dimensional spectra. These problems have been alleviated to a certain extent by the development of proton-detected two-dimensional heteronuclear relaxation experiments,[41] which increase the sensitivity by approximately $(\gamma_H/\gamma_C)^{5/2}$ [42] and afford increased resolution by the addition of the second dimension. The pulse sequence consists of an initial DEPT sequence[43] to transfer the magnetization from protons to the carbon, a relaxation period T that is varied between the two-dimensional data sets, and the evolution time, followed by a second DEPT sequence in which the magnetization is transferred back from the carbon to the protons for detection. The intensities of the peaks, $I(T)$, are described by the usual T_1 equation of the inversion–recovery experiment.

Palmer et al.[44] have used this method, along with spin–spin relaxation and NOE studies, to characterize the intramolecular dynamics of Xfin-31, which is a 25-residue synthetic zinc finger peptide that is capable of binding nucleic acids and is recurrent in regulatory proteins. The studies suggest that the motion of the backbone carbons, excluding the terminal residues, are highly restricted, but with the residues forming a loop between the β-sheet and the helix showing slightly higher mobility. The motion of the side chains of the hydrophobic residues, Val and Leu, are also restricted, although they are more mobile than the backbone. These results suggest that the peptide is quite compact.

An additional development that has allowed comprehensive analysis of T_1 relaxation is site-specific ^{13}C enrichment. This has permitted certain sites in a macromolecule to be extensively studied. Nicholson et al.[45] have ^{13}C-enriched 11 leucine residues of the protein staphyloccal nuclease, which is a small enzyme of M_r = 16800. The leucines, which are nearly all buried within the closely packed interior, were studied with, and without, ligand binding by two-dimensional relaxation methods as described above. The parameters were fitted using the formalism of Lipari and Szabo[14] [equation (14)]. The results showed a rapid rotation of the methyl group

about the $C^{\gamma}-C^{\delta}$ bond, plus a slower motion associated with the reorientation of the $C^{\gamma}-C^{\delta}$ bond axis itself. A significant increase in the order parameter, S^2, was seen upon binding of the ligand to leucine in the vicinity of either Ca^{2+} or the pdTp heavy atoms, which indicates a localized restriction of motion in the vicinity of the ligand-binding sites.

Many groups have used relaxation data in order to characterize the motion of synthetic polymers.[46,47] Early on, Jacob Schaefer,[13a] using the results of carbon-13 spin–lattice relaxation times, linewidths, and NOE factors for isotactic polystyrene, *cis*-polyisoprene, and *cis*-polybutadiene, proposed a log χ^2 density function to describe the distribution of motion. The width of the distribution is a relative measure of the extent of cooperative segmental motion of the chain. In this 1973 study, it was shown that polybutadiene exhibits more long-range cooperative motions than the other two polymers studied.

3.4 Solvent Effects and Intermolecular Interactions

Unlike ^{15}N, in which intermolecular dipolar relaxation can contribute significantly to the nitrogen T_1 values carbon-13 intermolecular effects are usually negligible. Therefore, the use of ^{13}C spin–lattice relaxation to study intermolecular interactions, such as solvent effects hydrogen bonding, and ion–dipole pairing depends on the fact that the localized motions around the site of the interaction are restricted and the overall tumbling decreases due to the increased size of the complex. Both of these effects will result in a decrease in the ^{13}C spin–lattice relaxation times. These effects have been seen upon molecular association[48] and solute-solvent interactions[49] via hydrogen-bond formation.

In a study of molecular association, it was shown in 1971 by Alger, Grant, and Lyerla[48] that the carbon nuclei of formic and acetic acids have shorter T_1s, therefore relax faster, than the corresponding methyl esters. The carboxylic acid, which is dimerized by hydrogen bonding, rotates more slowly than the methyl esters. This behavior is seen in long- and branch-chain alcohol and acids, such as decanoic acid, decanol, and 3,7-dimethyloctanol, in which the hydrophobic end shows increased mobility, i.e. longer T_1s than the polar end which is hydrogen bonded and therefore less mobile. Other solvent effect studies had been discussed earlier.[10,17]

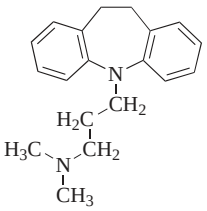

(4)

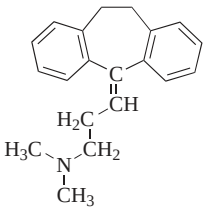

(5)

The intermolecular interaction of biological molecules in solution is of biological significance. Casarotto and Craik[50] looked at the interaction of tricyclic antidepressant drugs imipramine (**4**) and amitriptyline (**5**) with sodium dodecyl sulfate (SDS) (**6**) micelles. The ^{13}C relaxation parameters, including T_1 and NOE measurements at two different field strengths, were fitted to the model-free formalism of Lipari and Szabo.[14] The smallest T_1 value occurs in the middle of the aliphatic chain of neat SDS with a slight increase near the headgroup and a significant increase near the terminal methyl region. This corresponds to a low value for the order parameter for the terminal methyl, which reflects increased amplitude of mobility at the end. Upon addition of the drugs, there was a significant decrease in the T_1 values with an overall increase in the S^2 values. The aromatic carbons of the drugs showed the greatest change in T_1 upon association with the micelles. This indicated a marked decrease in overall tumbling rate. The rapid internal bridge flipping of the seven-membered ring is not significantly affected in the micelles. It was concluded from the relaxation studies that there is a notable increase in the micellar volume with a reduction of motion in the SDS alkyl chains. The drugs become extended in the micelles with the tricyclic moiety occupying the hydrophobic region of the micelle and the terminal dimethylammonium ion interacting at the micelle–water interface.

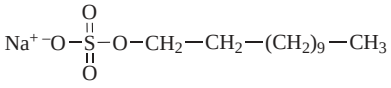

(6)

4 SUMMARY

Carbon-13 relaxation data provide unique insight into the structure and, especially, the structural dynamics of organic molecular systems, including complex biomolecules. The ability of these studies to probe molecules at each atomic site, and quantitatively to reflect dynamical information, is made especially useful by the central role of carbon atoms in these molecules and by the relatively simple mechanistic relaxation pathway for most ^{13}C nuclei. Carbon-13 relaxation complements other techniques in yielding to scientists the most basic structural secrets of complex molecules.

5 REFERENCES

1. G. C. Levy and G. L. Nelson, *Carbon-13 Nuclear Magnetic Resonance for Organic Chemists*, Wiley-Interscience, New York, 1972.
2. F. A. L. Anet and G. C. Levy, *Science*, 1973, **180**, 141.
3. R. R. Ernst and W. A. Anderson, *Rev. Sci. Instrum.*, 1966, **37**, 93.
4. (a) Early references: K. F. Kuhlmann, D. M. Grant, and R. K. Harris, *J. Chem. Phys.*, 1970, **52**, 3439; but see also (b) L. G. Werbelow and D. M. Grant, *Adv. Magn. Reson.*, 1977, **9**, 89; (c) D. M. Grant, C. L. Mayne, F. Liu, and T.-X. Xiang, *Chem. Rev.*, 1991, **91**, 1591.
5. R. Freeman, *A Handbook of Nuclear Magnetic Resonance*, Longman, Hanlow, UK, 1987, p. 147.
6. G. C. Levy, R. L. Lichter, and G. L. Nelson, *Carbon-13 Nuclear Magnetic Resonance Spectroscopy*, 2nd edn., Wiley-Interscience, New York, 1980.
7. H.-O. Kalinowski, S. Berger, and S. Braun, *Carbon-13 NMR Spectroscopy*, Wiley, Chichester, UK, 1988, Chap. 5

8. D. A. Wright, D. E. Axelson, and G. C. Levy, *Topics in Carbon-13 NMR Spectroscopy*, ed. G. C. Levy, Wiley, New York, 1979, Vol. 3, Chap. 2
9. A. Abragam, *The Principles of Nuclear Magnetism*, Oxford University Press, Oxford, UK, 1961.
10. G. C. Levy, J. D. Cargioli, and F. A. L. Anet, *J. Am. Chem. Soc.*, 1973, **95**, 1527.
11. L. E. Kay, L. K. Nicholson, F. Delaglio, A. Bax, and D. A. Torchia, *J. Magn. Reson.*, 1992, **97**, 359.
12. G. C. Levy, *J. Chem. Soc., Chem. Commun.*, **1972**, 352.
13. (a) J. Schaefer, *Macromolecules*, 1973, **6**, 882; (b) A. Kumar and G. C. Levy, *J. Chem. Phys.*, 1986, **85**, 485.
14. G. Lipari and A. Szabo, *J. Am. Chem. Soc.*, 1982, **104**, 4546, 4559.
15. L. M. Bull, D. G. Gillies, S. J. Matthews, L. H. Sutcliffe, and A. J. Williams, *Magn. Reson. Chem.*, 1991, **29**, 273.
16. P. N. Borer, S. R. LaPlante, A. Kumar, N. Zanatta, A. Martin, A. Hakkinen, and G. C. Levy, *Biochemistry*, 1994, **33**, 2441.
17. G. C. Levy, M. P. Cordes, J. S. Lewis, and D. E. Axelson, *J. Am. Chem. Soc.*, 1977, **99**, 5492.
18. G. C. Levy and I. R. Peat, *J. Magn. Reson.*, 1975, **18**, 500.
19. R. L. Vold, J. S. Waugh, M. P. Klein, and D. E. Phelps, *J. Chem. Phys.*, 1968, **48**, 3831.
20. D. Canet, G. C. Levy, and I. R. Peat, *J. Magn. Reson.*, 1975, **18**, 199.
21. R. Freeman and H. D. W. Hill, *J. Chem. Phys.*, 1971, **54**, 3367.
22. J. L. Markley, W. J. Horsley, and M. P. Klein, *J. Chem. Phys.*, 1971, **55**, 3604.
23. R. Freedman, H. D. Hill, and R. Kaptein, *J. Magn. Reson.*, 1972, **7**, 327.
24. A. Ejchart, P. Oleski, and K. Wroblewski, *J. Magn. Reson.*, 1986, **68**, 207.
25. L. E. Kay, L. K. Nicholson, F. Delaglio, A. Bax, and D. A. Torchia, *J. Magn. Reson.*, 1992, **97**, 359.
26. L. E. Kay, T. E. Bull, L. K. Nicholson, C. Griesinger, H. Schwable, A. Bax, and D. A. Torchia, *J. Magn. Reson.*, 1992, **100**, 538.
27. J. W. Peng, V. Thanabal, and G. Wagner, *J. Magn. Reson.*, 1991, **95**, 421.
28. H.-O. Kalinowski, S. Berger, and S. Braun, *Carbon-13 NMR Spectroscopy*, Wiley, Chichester, UK, 1988.
29. A. Allerhand and D. Doddrell, *J. Am. Chem. Soc.*, 1971, **93**, 2777.
30. (a) E. Lippmaa and M. Alla, *Eesti NSV Tead. Akad. Toim., Fuus., Mat., Tehnikatead. Seer.*, 1966, **3**, 473; (b) E. Lippmaa and M. Alla, *Eesti NSV Tead. Akad. Toim., Fuus., Mat.*, 1968, **17**, 117; (c) E. Lippmaa, M. Alla and A. Sugis, *Eesti NSV Tead. Akad. Toim., Fuus., Mat.*, 1967, **16**, 385.
31. G. C. Levy, *Tetrahedron Lett.*, 1972, 3709.
32. G. C. Levy and G. L. Nelson, *J. Am. Chem. Soc.*, 1972, **94**, 4897.
33. G. C. Levy, *J. Chem. Soc., Chem. Commun.*, 1972, 768.
34. G. M. Clore, A. Szabo, A. Bax, L. E. Kay, P. C. Driscoll, and A. M. Gronenborn, *J. Am. Chem. Soc.*, 1990, **112**, 4989.
35. D. E. Woessner, *J. Chem. Phys.*, 1962, **36**, 1.
36. (a) R. J. Wittebort and A. Szabo, *J. Chem. Phys.*, 1978, **69**, 1722; (b) R. E. London and J. Avitabile, *J. Am. Chem. Soc.*, 1978, **100**, 7159.
37. O. W. Howarth, *J. Chem. Soc., Faraday Trans. 2*, 1978, **74**, 1031.
38. T. L. James, *J. Magn. Reson.*, 1980, **39**, 141.
39. G. C. Levy, A. Ejchart, P. S. Marchetti, and R. L. Rill, *J. Magn. Reson.*, 1984, **57**, 130.
40. (a) G. C. Levy, P. R. Hillard, L. F. Levy, R. L. Rill, and R. Inners, *J. Biol. Chem.*, 1981, **256**, 9986; (b) P. R. Hillard, R. L. Rill, G. C. Levy, and L. F. Levy, in *ACS Symp. Ser. No. 191*, ed. G. C. Levy, Am. Chem. Soc., Washington, DC, 1982.
41. (a) V. Sklenar, D. Torchia, and A. Bax, *J. Magn. Reson.*, 1987, **73**, 375; (b) L. E. Kay, T. L. Jue, B. Bangerter, and P. C. Demon, *J. Magn. Reson.*, 1987, **73**, 558.
42. S. C. Kim and M. Garwood, *J. Magn. Reson.*, 1992, **99**, 660.
43. D. M. Doddrell, D. T. Pegg, and M. R. Bendall, *J. Magn. Reson.*, 1982, **48**, 323.
44. A. G. Palmer III, M. Rance, and P. E. Wright, *J. Am. Chem. Soc.*, 1991, **113**, 4372.
45. L. K. Nicholson, L. E. Kay, D. M. Baldisseri, J. Arango, P. E. Young, A. Bax, and D. A. Torchia, *Biochemistry*, 1992, **31**, 5253.
46. (a) G. C. Levy, *J. Am. Chem. Soc.*, 1973, **95**, 6117; (b) G. C. Levy, P. L. Rinaldi, J. J. Dechter, D. E. Axelson, and L. Mandelkern, *ACS Symp. Ser. No. 142* Am. Chem. Soc., Washington DC, 1980, p. 119; (c) G. C. Levy and D. Wang, *Macromolecules*, 1986, **19**, 1013.
47. (a) F. A. Bovey and L. W. Jelinski, *J. Phys. Chem.*, 1985, **89**, 571; (b) F. Heatley, *Prog. Nucl. Magn. Reson. Spectrosc.*, 1979, **13**, 47.
48. T. D. Alger, D. M. Grant, and J. R. Lyerla, *J. Phys. Chem.*, 1971, **75**, 2539.
49. R. E. Waysleshan and B. A. Pettitt, *Can. J. Chem.*, 1977, **55**, 2564.
50. M. G. Casarotto and D. J. Craik, *J. Phys. Chem.*, 1991, **95**, 7093.

Biographical Sketches

George C. Levy. *b* 1944. A.B., 1965, Ph.D., 1968, Chemistry, U.C.L.A., USA. General Electric Corporate R & D staff, 1968–73, Faculty member Florida State University, 1973–81. Faculty member and Science and Technology Professor, Syracuse University, 1981–94. In 1983, founded New Methods Research, Inc., the first company to develop and market NMR data processing and NMR laboratory networking software based on general purpose computers and workstations. Approximately 240 publications. Co-authored with Gordon Nelson the first published ^{13}C NMR book. Research specialties: ^{13}C NMR, data processing methods for one- and multidimensional NMR, utilization and commercialization of technology.

Deborah J. Kerwood, *b* 1959. B.S., 1981, Ph.D., 1986, Chemistry, Wesleyan University, USA. Postdoctoral research scientist, University of California at San Francisco, Research Scientist, Veterans Administration Hospital, San Francisco, NMR Laboratory Operational Manager, Syracuse University, 1992–present. Approx. 15 publications. Research specialties: structure determination via NMR techniques, ^{13}C-relaxation NMR.

Carbon-13 Studies of Deuterium Labeled Compounds

Stefan Berger
Philipps University, Marburg, Germany

1	Introduction and Definitions	1
2	Basic Theory	1
3	Deuterium Isotope Effects on Spin Coupling Constants	3
4	Deuterium Isotope Effects in Equilibrating Systems	4
5	Conclusions	4
6	Related Articles	5
7	References	5

1 INTRODUCTION AND DEFINITIONS

Whoever measures a ^{13}C NMR spectrum, detects, consciously or not, a deuterium isotope effect on the carbon chemical shift since, usually, ^{13}C spectra are recorded in deuterated solvents such as $CDCl_3$. As shown in Figure 1, the deuterium causes a splitting of the carbon resonance of this solvent into three lines due to its nuclear spin $I = 1$. The center of the triplet is, however, not at the same chemical shift position as the small signal stemming from the residue of undeuterated $CHCl_3$, but is displaced somewhat to lower frequency. Thus the definition of the deuterium isotope effect on the carbon chemical shift is given by equation (1), this sign convention being in accordance with the sign of the widely used substituent effects in ^{13}C NMR.

$$^{n}\Delta = \delta_{\text{deuterated}} - \delta_{\text{parent}} \tag{1}$$

The superscript n in equation (1) denotes the number of chemical bonds between the deuterium atom and the carbon atom in question. Thus one might observe isotope effects over one, two, and three bonds; furthermore, long-range isotope effects over up to 12 bonds are known.[1] The numerical values of the isotope effects are usually given in ppb instead of ppm, indicating that isotope effects are typically three orders of magnitude smaller than the effect of substituents.

The large interest in this field has prompted several review articles[2] which have collated large amounts of data[3] and provided the basis for the discussion of the theoretical[4] and physical organic aspects[5,6] of the effect.

2 BASIC THEORY

Isotope effects on chemical shifts are usually explained and calculated on the basis of vibrational theory. Within the Born–Oppenheimer approximation isotopes can be thought of as being electronically equivalent, thus deuterium should have the same electronegativity, etc. as hydrogen. However, due to its higher mass, the vibrational levels for deuterium within the electronic potential are lower than those of hydrogen, as shown in Figure 2. Due to the anharmonicity of the electronic potential, on average deuterium is closer to the carbon atom. This leads to a somewhat higher electron density at carbon and, hence, to a shielding effect of the heavier isotope.

The average shielding σ of a nucleus can be expressed by equation (2)

$$\langle\sigma\rangle = \sigma_e + \sum_i (\partial\sigma/\partial r_i)_e \langle\Delta r_i\rangle + \sum_{ij} (\partial^2\sigma/\partial r_i \partial r_j)_e \langle\Delta r_i \Delta r_j\rangle + \sum_{ij} (\partial\sigma/\partial\alpha_{ij})_e \langle\Delta\alpha_{ij}\rangle + \ldots \tag{2}$$

where the subscript e denotes the equilibrium values, r_i the distances to the neighboring nuclei, and α_{ij} the bond angles involved. Isotopic substitution affects the dynamic averages $\langle\Delta r_i\rangle$, $\langle\Delta r_i \Delta r_j\rangle$, and $\langle\Delta\alpha_{ij}\rangle$. For small molecules, this model can be used for quantitative calculations. For larger and asymmetric organic molecules, a complete vibrational analysis and the calculation of the first and second derivatives are difficult to obtain.

The common quantum chemical program packages are not capable of calculating isotope effects since, due to the Born–Oppenheimer approximation, they do not distinguish between isotopes, e.g. between hydrogen and deuterium. Model MO calculations have been carried out by varying the C,H distance to simulate the shorter C,D bond.[7,8] Although $^{1}\Delta$ values could be reproduced, the wrong sign for $^{2}\Delta$ was predicted.

2.1 $^{1}\Delta$ Isotope Effects on ^{13}C Chemical Shifts

In Table 1 some selected basic values for a series for simple compounds are given to provide an overview of the range of these $^{1}\Delta$ isotope effects.

By inspection of the few values in Table 1 several important conclusions can be drawn.

1. All $^{1}\Delta$ effects of deuterium on ^{13}C chemical shifts are negative, in accordance with vibrational theory.
2. Very good additivity is observed if more than one deuterium atom replaces hydrogen.
3. Primary, secondary, and tertiary carbon atoms in hydrocarbons show different isotope effects. There is, apparently, a dependence on the electronegativity of other substituents attached to the deuterated carbon atom. Substituents placed several bonds away can also influence the deuterium isotope effects.
4. There is a hybridization dependence and thus a bond length dependence of these isotope effects.
5. A positive charge increases, and complexation by transition metals decreases, the isotope effects.
6. A stereochemical dependence of deuterium isotope effects can be observed.

Conclusion 4 is exemplified in Figure 3. Since accurate measurements of C–H bond lengths of small organic compounds are rare, calculated values rather than experimental bond lengths were used to correlate the $^{1}\Delta$ deuterium isotope

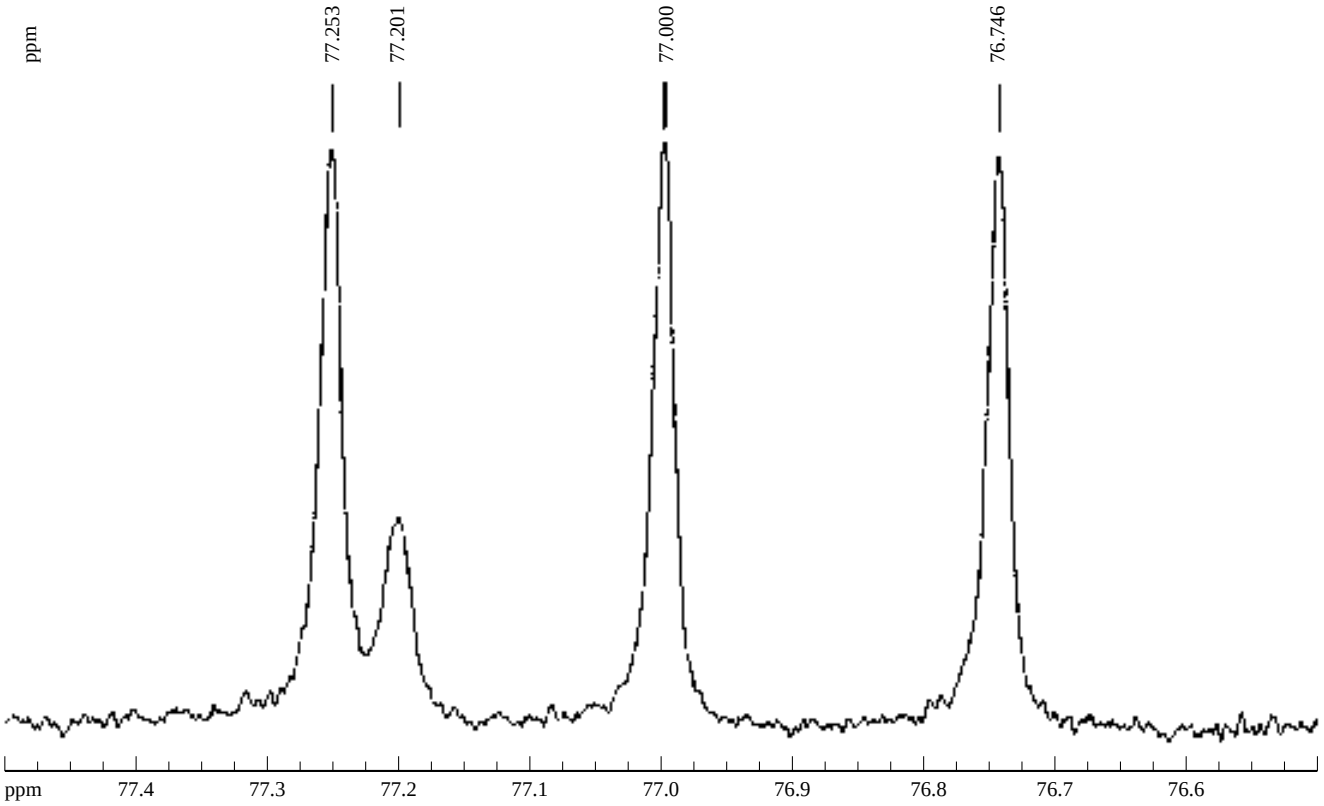

Figure 1 125 MHz ^{13}C NMR spectrum of neat $CDCl_3$

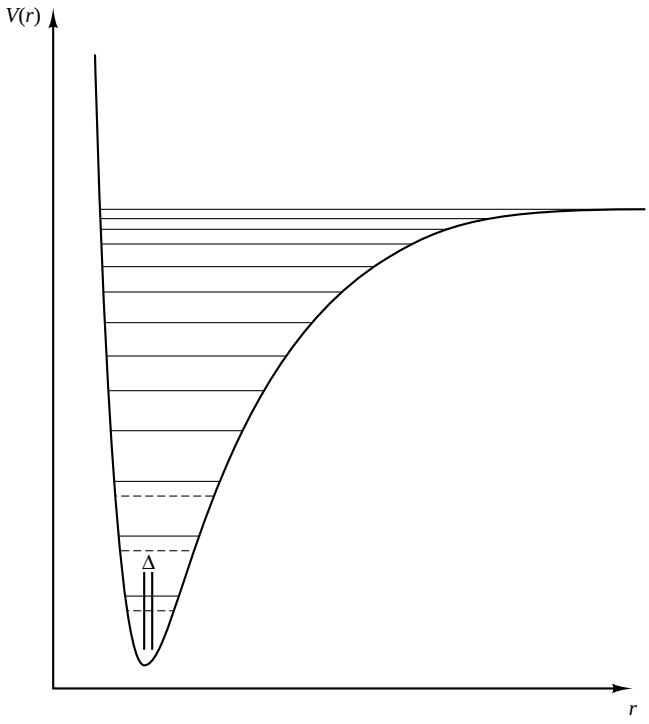

Figure 2 Vibrational levels of C–H and C–D vibrations within the electronic potential of a C–H bond

effects of a large variety of aromatic heterocycles.[9] The general outcome is that shorter bond lengths result in diminished isotope effects. Shorter bonds are believed to be less anharmonic and stronger, so that their fractional bond shortening caused by replacing hydrogen with deuterium is therefore less pronounced. Of course, such a correlation only holds in a series of closely related compounds; thus the slope of the straight line shown in Figure 3 is quite different from that obtained, for example by Günther et al., for the hydrocarbons ethane, ethene, and ethyne.[10]

Figure 4 shows the dependence of $^1\Delta$ isotope effects on the chemical shift in a series of *para*-substituted benzene derivatives. For such a series, it is well known that the chemical shift can be correlated with a large number of physical organic properties such as electron density, Hammett constants, or others. Apparently, the isotope effects display the same behavior as the chemical shifts, which resulted in the conclusion that deuterium isotope effects resemble all major influences on chemical shifts, simply on a very minor scale.[11]

2.2 $^2\Delta$ Isotope Effects on ^{13}C Chemical Shifts

Some selected values of $^2\Delta$ isotope effects are given in Table 1. As can be seen immediately, there are some unexpected sign changes of the isotope effect. Whereas these values behave 'normally' in hydrocarbons and aromatic compounds, with isotope effects in the order of -100 ppb, they change their sign when a carbonyl atom[12] or a cationic center[13] is the carbon atom in question. This led to the idea of correlating $^2\Delta$ values with the chemical shift of the corresponding carbon

Table 1 $^1\Delta$ and $^2\Delta$ Deuterium Isotope Effects on ^{13}C Chemical Shifts

Compound	$^1\Delta$(ppb)	$^2\Delta$(ppb)
CH_3D	−187	
CH_2D_2	−385	
CHD_3	−579	
CD_4	−774	
CD_3OD	−860	
CD_3NO_2	−690	
CD_3CN	−450	
CD_3Br	−430	
CD_3I	−130	
$C_6H_5CH_2D$	−275	−34
$(C_6H_5)_2CHD$	−342	−32
$(C_6H_5)_3CD$	−437	−49
CH_3CH_2D	−284	−93
$CH_3CH_2CH_2D$	−299	−90
CH_3CHDCH_3	−375	−113
$CH_3CD(CH_3)_2$	−472	−125
Cyclohexane-1-*d*	−418	−104
4-t-Butyl-cyclohexane-1-d_{eq}	−392	−106
4-t-Butyl-cyclohexane-1-d_{ax}	−442	−98
Adamantane-1-*d*	−482	−127
Adamantane-2-*d*	−436	−99
CH_3COCH_2D		+55
CD_3COOH	−664	+40
CH_2DCOF		+14
α-D-Glucose-2-*d*		−50 (C-3),−10 (C-1)
Ethene-1-*d*	−274	−131
Benzene-1-*d*	−283	−111
p-NO_2-C_6H_4D	−287	−107
p-$(CH_3)_2N$-C_6H_4D	−259	−111
Tropylium-ion-d_6	−408	−133
Tricarbonylchromobenzene-*d*	−198	
Ethyne-1-*d*	−226	−500
$CH_3C^+(CD_3)_2$		+800
$(CD_3)_3C^+$		+1400

atom.[14] Since it was found that normal substituent increments over two bonds are also dependent on the chemical shift of the affected carbon atom, this behavior of isotope effects can again be viewed as a further resemblance to substituent effects. In addition, an angular dependence of $^2\Delta$ isotope effects in bicyclic carbonyl compounds was demonstrated.[15]

2.3 $^3\Delta$ and Long-Range Isotope Effects on ^{13}C Chemical Shifts

For a series of norbornane derivatives, it was shown that $^3\Delta$ deuterium isotope effects display a Karplus-type behavior; thus the values are dependent on the dihedral angle between the C−D bond and the corresponding C−C bond.[16] CD_3 groups attached to aromatic systems exert $^3\Delta$ isotope effects which have been related to the π bond order of the corresponding C−C bond. This important result is shown in Figure 5 where both shielding and deshielding effects are observed. The correlation was interpreted in terms of hyperconjugation; compared with a CH_3 group, a CD_3 group should have a diminished hyperconjugative electron release.[17]

Deuterium isotope effects over more than three bonds are mainly found in extended π systems and, typically, display a sign variation along the carbon chain. Due to the many apparent similarities to substituent effects, the polar

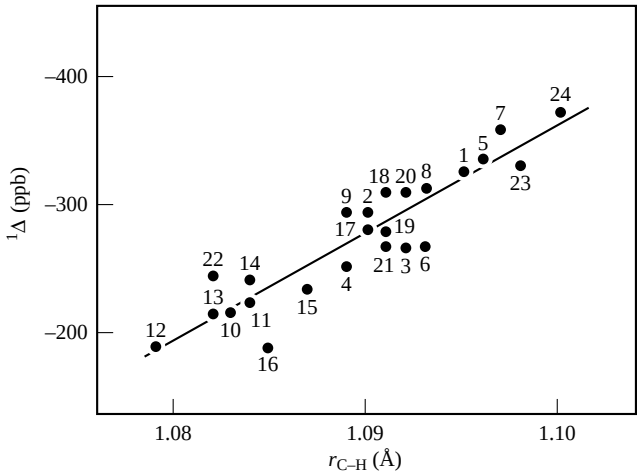

Figure 3 Correlation between $^1\Delta$ values and calculated r_{C-H} for a series of heterocyclic aromatic compounds (taken from Nakashima et al.[9])

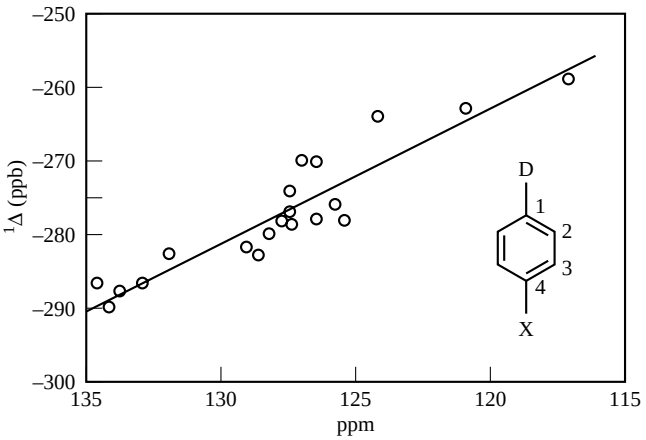

Figure 4 Correlation between $^1\Delta$ values and the ^{13}C chemical shift of C-1 in 1-deutero-4-X-benzenes (taken from Berger and Diehl[11])

substituent constants σ_I and σ_R have been calculated by correlation analysis for deuterium itself,[18] the CD_3 group, and the $C(CD_3)_3$ group.[19] These values are given in Table 2.

3 DEUTERIUM ISOTOPE EFFECTS ON SPIN COUPLING CONSTANTS

The study of deuterium isotope effects on C,H spin coupling constants is far more difficult than the study of isotope effects on chemical shifts. The topic was recently critically reviewed, and it was shown that most of the older data in the literature are unreliable.[20] The main reason for this is that C,H spin coupling

Table 2 Polar Substituent Constants for D, CD_3, and $C(CD_3)_3$

Group	σ_I	σ_R
D	−0.0021	−0.0003
CD_3	−0.0027	+0.0012
$C(CD_3)_3$	−0.0025	−0.0005

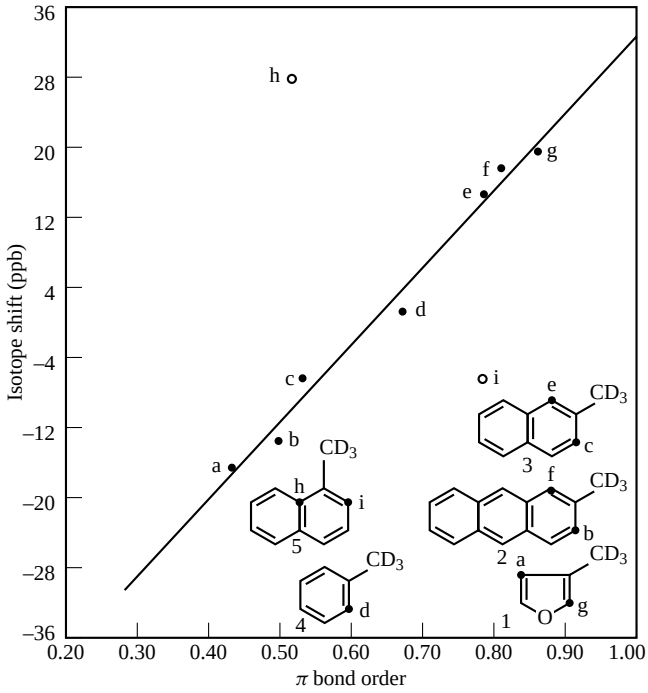

Figure 5 Correlation of $^{3}\Delta$ values and π bond orders for a series of deuteromethylated aromatic compounds (taken from Ernst et al.[17])

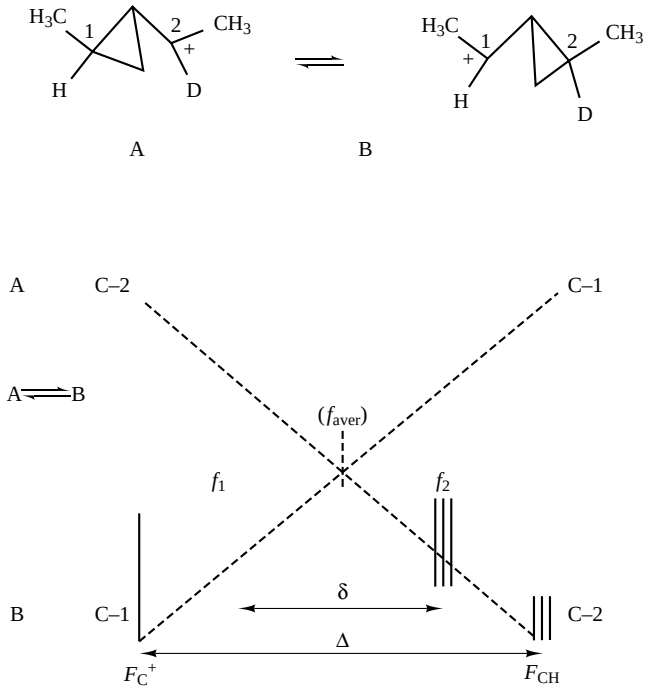

Figure 6 Schematic diagram for the explanation of the isotopic perturbation of equilibrium (taken from Siehl[21])

constants, as measured in ^{13}C NMR spectra, are usually seen as the X part of a complex spin system, which is most often of higher order. Thus, the extraction of exact C,H spin coupling constants requires careful computer simulation of high-quality spectra with excellent digital resolution. Equally good must be the measurement of the corresponding C,D spin coupling constants, where sometimes line broadening due to quadrupolar effects prohibits the evaluation in the required accuracy. From the C,D spin coupling constant, a virtual C,H spin coupling constant is calculated using the γ value of deuterium. For this calculation the best possible γ_D value of 6.514 399 178 $\times$ 10^7 T^{-1} s^{-1} rad should be used. The difference between the measured C,H coupling constant and this calculated value is the isotope effect. A survey of more modern, reliable data reveals that, at most, substitution of hydrogen by deuterium diminishes the C,H spin coupling constants by 0.1–0.3 Hz. There is no conclusive reason given in the literature why the shorter C–D bond length results in a diminished spin coupling constant.

4 DEUTERIUM ISOTOPE EFFECTS IN EQUILIBRATING SYSTEMS

The deuterium isotope effects discussed above can be classified as *intrinsic*, being observable in static molecules and solely dependent on their chemical structure. In addition to these *intrinsic* isotope effects there exists another class of isotope effects, which are usually significantly larger and which stem from the partition of deuterium or deuterated groups in chemical equilibria. This has been a particularly active branch of physical organic chemistry research in the last decade and was recently extensively reviewed.[21] Although the original finding stems from Baldry and Robinson,[22] the technique became most important in the field of carbocations and was named isotopic perturbation of equilibrium.[23] With this technique one can distinguish between systems which are rapidly equilibrating between two sites, and systems which have essentially a single minimum potential.

As seen from Figure 6, two rapidly equilibrating nondeuterated cations A and B would exist in equal concentrations, and C-1 and C-2 would resonate at the chemical shift position f_{aver}. Since the introduction of deuterium removes the degeneracy of the equilibrium, sites A and B are unequally populated and one observes, in addition to the *intrinsic* isotope effects, a large, temperature-dependent splitting, δ, from which the equilibrium constant can be calculated.

Another large area where deuterium takes part in chemical equilibria is the study of tautomeric systems, especially those with hydrogen bonds involved. Examples are the keto–enol equilibria of acetylacetonates, enaminoketones, ketohydrazones, and similar systems.[24]

5 CONCLUSIONS

It has been demonstrated in this article that deuterium isotope effects on chemical shifts resemble, on a minor scale, many properties of substituent effects for which a large body of data already exists. Substituent effects are, however, complicated due to the large chemical distortion they exert on a molecule. Thus the study of the small chemical shift displacements caused by deuterium, which is only a minor perturbation for the molecule, can lead to a better understanding of the chemical shift itself. Further theoretical developments are needed in order to provide predictions of these effects for medium-sized organic molecules. In systems with chemical

equilibria, the use of deuterium isotope effects has become a standard technique. As a whole, this field provides a link between physical organic chemistry and NMR spectroscopy.

6 RELATED ARTICLES

Indirect Coupling: Theory and Applications in Organic Chemistry; Isotope Effects in Carbocation Chemistry; Isotope Effects on Chemical Shifts and Coupling Constants

7 REFERENCES

1. S. Berger and H. Künzer, *Angew. Chem., Int. Ed. Engl.*, 1983, **22**, 321.
2. H. Batiz Hernandez and R. A. Bernheim, *Prog. NMR Spectrosc.*, 1967, **3**, 63.
3. P. E. Hansen, *Annu. Rep. NMR Spectrosc.*, 1983, **15**, 105; *Prog. NMR Spectrosc.*, 1988, **20**, 207.
4. C. J. Jameson and H. J. Osten, *Annu. Rep. NMR Spectrosc.*, 1986, **17**, 1; C. J. Jameson, in *Isotopes in the Physical and Biomedical Sciences, Isotopic Applications in NMR Studies*, ed. E. Buncel and J. R. Jones, Elsevier, Amsterdam, Vol. 2, 1991.
5. D. A. Forsyth, in *Isotopes in Organic Chemistry*, ed. E. Buncel and C. C. Lee, Elsevier, Amsterdam, 1984, Vol. 6.
6. S. Berger, in *NMR Basic Principles and Progress*, ed. P. Diehl, E. Fluck, H. Günther, R. Kosfeld, and J. Seelig, Springer, Berlin, 1990, Vol. 22, Chap. 1
7. S. Berger and H. Künzer, *Tetrahedron*, 1983, **39**, 1327.
8. K. L. Servis and R. L. Domenik, *J. Am. Chem. Soc.*, 1986, **108**, 2211.
9. Y. Nakashima, H. Kanada, M. Fukunaga, K. Suzuki, and K. Takahashi, *Bull. Chem. Soc. Jpn.*, 1992, **65**, 2894.
10. J. R. Wesener, D. Moskau, and H. Günther, *Tetrahedron Lett.*, **1985**, 1491.
11. S. Berger and B. W. K. Diehl, *Tetrahedron Lett.*, **1987**, 1243.
12. P. E. Hansen, F. M. Nicolaisen, and K. Schaumburg, *J. Am. Chem. Soc.*, 1986, **108**, 625.
13. K. L. Servis and F.-F. Shue, *J. Am. Chem. Soc.*, 1980, **102**, 7233.
14. C. H. Arrowsmith and A. J. Kresge, *J. Am. Chem. Soc.*, 1986, **108**, 7918.
15. S. Berger and B. W. K. Diehl, *J. Am. Chem. Soc.*, 1989, **111**, 1240.
16. R. Aydin, W. Frankmölle, D. Schmalz, and H. Günther, *Magn. Reson. Chem.*, 1988, **26**, 408.
17. L. Ernst, H. Hopf, and D. Wullbrandt, *J. Am. Chem. Soc.*, 1983, **104**, 4469.
18. H. Künzer and S. Berger, *J. Am. Chem. Soc.*, 1985, **107**, 2804.
19. S. Berger, B. W. K. Diehl, and H. Künzer, *Chem. Ber.*, 1987, **120**, 1059.
20. N. M. Sergeyev, in *NMR Basic Principles and Progress*, ed. P. Diehl, E. Fluck, H. Günther, R. Kosfeld, and J. Seelig, Springer, Berlin, 1990, Vol. 22, Chap. 2
21. H. U. Siehl, *Adv. Phys. Org. Chem.*, 1987, **23**, 63.
22. K. W. Baldry and M. J. T. Robinson, *Tetrahedron*, 1977, **33**, 1663; S. L. R. Ellison, M. J. T. Robinson, and J. G. Wright, *Tetrahedron Lett.*, **1985**, 2585.
23. M. Saunders, L. Telkowski, and M. R. Kates, *J. Am. Chem. Soc.*, 1977, **99**, 8070.
24. P. E. Hansen, *Magn. Reson. Chem.*, 1993, **31**, 23; P. E. Hansen, M. Christoffersen, and S. Bolvig, *ibid.*, 1993, **31**, 893.

Biographical Sketches

S. Berger. *b* 1946. Ph.D., 1973, University of Tübingen under supervision of Professor Dr. A. Rieker. Introduced to NMR by H. Suhr and A. Rieker, postdoctoral fellow with Professor J. D. Roberts, California Institute of Technology, 1973–74. University of Marburg, 1974–present. Approx. 100 publications. Current research interests: development of selective pulse methods and applications of NMR in the field of organometallic and bioorganic chemistry.

Combinatorial Chemistry

Michael J. Shapiro

Chemistry Research Technologies, Lilly Research Laboratories, Indianapolis, IN, USA

1 Introduction 1
2 Analysis in Solution 1
3 HPLC/NMR 1
4 On-flow NMR 1
5 Analysis on Solid Phase 1
6 Gel-Phase NMR 1
7 Magic Angle Spinning (MAS) NMR 2
8 Pins and Crowns 3
9 Peptides 4
10 Diffusion Weighted MAS-NMR 4
11 On-Resin Quantitation 4
12 Molecular Conformation On-Resin 5
13 Conclusions 5
14 References 6

1 INTRODUCTION

NMR spectroscopy is an analytical technique that provides information of both a qualitative and quantitative nature concerning purity and molecular constitution. NMR spectra can be obtained both in the liquid and solid phase, making it an ideal tool for combinatorial chemistry. This review focuses on the wealth of techniques and NMR methodologies applied to combinatorial chemistry problems. The use of NMR as library screening tool for biological activity is outside the scope of this article.[1–7]

2 ANALYSIS IN SOLUTION

Much of combinatorial chemistry is performed in solution or has a solution analysis aspect to it at some stage of development. The two main directions in the area of solution phase analysis involve HPLC/NMR and Flow NMR.

3 HPLC/NMR

Performing structure elucidation of compounds in mixtures or in a high-throughput manner is a fundamental aspect of combinatorial chemistry and the coupling of HPLC with NMR represents a powerful method to aid this analysis. While this technique has received general acceptance,[8] its routine use in combinatorial chemistry have been somewhat limited.[9,10] Commercially available equipment generally requires micrograms of material and in its current state, HPLC/NMR is not a high-throughput analytical tool. Specially designed probes capable of performing CE/NMR experiments on nanograms of compound have been described but as yet have not been commercialized.[11]

4 ON-FLOW NMR

Due to the potential of combinatorial chemistry producing large numbers of individual samples, the need for automated sample changing has taken on new emphasis. Very high-throughput data collection has been solved by the mass spectrometrists and a similar system using flow allows the analysis of NMR spectra about every 2 min has been introduced by the major NMR manufacturers. It is possible to obtain NMR data on 600–700 samples or about 6 times the throughput of current robotic sample changers in a 24-h period. Optimization of the volumes of these flow cells allow for NMR spectra to be obtained for samples in the low microgram range with the ability to obtain MS and NMR data simultaneously[12] as well as the ability to perform NMR on nano-scale samples.[11,13] Adequate solvent suppression is necessary for this tool to work effectively since most samples provided by chemists exist in protonated solvents. Fortunately, solvent suppression pulse sequences provide the solution to this troublesome experimental detail.[14] A large drawback of the flow NMR technology as it currently stands involves interspersing samples in different solvents, which creates problems with resolution and carryover.

The analysis of the overabundance of NMR information that can now be collected becomes rate limiting by interpretation of the spectra, which is still a slow process. The development of expert systems and automated data interpretation and will be needed to further spur the utility of this methodology. As a result, several new processing and display options have been presented that facilitate faster, easier, and more powerful analyses of the resulting NMR data. Unfortunately, at the time of this review, the analysis of individual spectra still must be made by hand although algorithms are currently in progress to alleviate this problem. The variety of display options now becoming routine, some of which are similar to the displays used for 2D-NMR data, are changing how chemists interact with NMR data.[15,16] Typical display characteristics of the flow NMR data are illustrated in Figures 1 and 2.

5 ANALYSIS ON SOLID PHASE

NMR is one of the most versatile tools for analysis of organic reactions and can now be used to obtain high quality spectra of compounds still attached to solid supports. Solid phase NMR analysis allows both quantitation and structure determination to be performed without the need to cleave compounds from the support and enables detection of intermediates and products unstable to cleavage conditions.

6 GEL-PHASE NMR

Early work by Manatt and coworkers[17] demonstrated that gel-phase NMR could be used to study reactions on solid

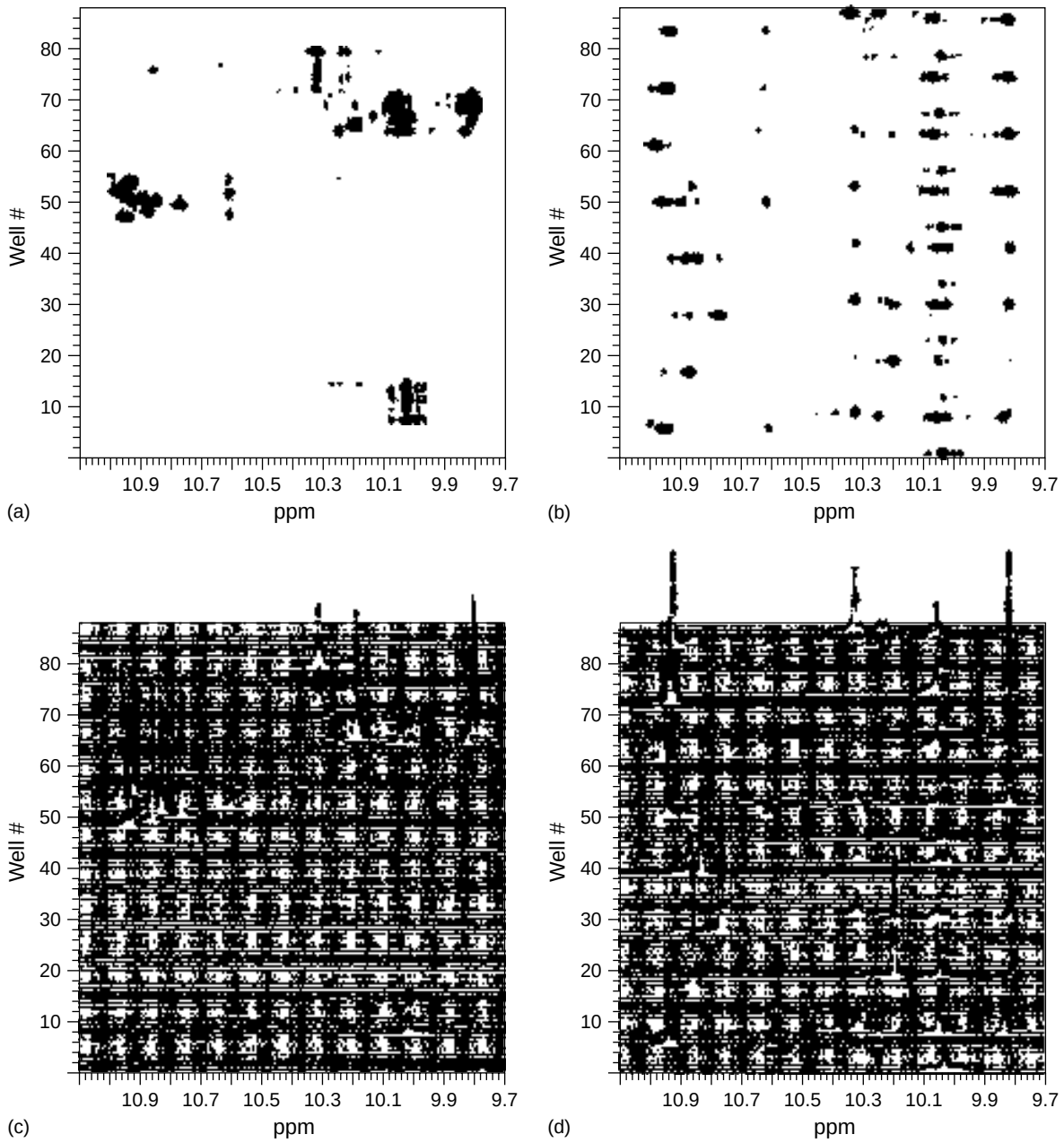

Figure 1 Four different representations of the same NMR data, acquired on the 88 library members in the 2.5 mM DMSO-h_6 plate. Each plot emphasizes different aspects of the data and allows different questions to be answered. The contour plots on the top (a and b) emphasize pattern relationships, while the stacked plots on the bottom (c and d) facilitate more quantitative comparisons. The plots on the left (a and c) were 'glued' in groups of eight along the short axis of the titer plate, while the plots on the right (b and d) were 'glued' in groups of 11 along the long axis of the plate. For clarity, only the NH region at 9.7–11.1 ppm is shown here

phase. The technique of gel-phase NMR requires only a routine NMR spectrometer system since the solid support is swollen in an appropriate solvent and placed into a standard NMR tube. Nuclei such as carbon-13, phosphorus-31, or fluorine-19 can be conveniently monitored. Gel-phase ^{1}H NMR spectra are too broad to be used for general purposes.

^{19}F NMR is particularly useful because ^{19}F chemical shifts have a large spectral dispersion. Structural modifications quite remote from the fluorine site can give rise to useful chemical shift changes.[18] High quality ^{19}F gel-phase NMR spectra can be obtained in only ten minutes on 50–200 mg of TentaGel resin. A large variety of fluorine containing building blocks and reagents are commercially available allowing the use of fluorine as a convenient NMR reporter element for ^{19}F gel-phase NMR without requiring the synthesis of special materials. In the case of gel-phase ^{15}N NMR one must resort to isotopically labeled ^{15}N materials.[19] The ^{15}N labeled amino acids are commercially available but most other compounds would require synthesis.

7 MAGIC ANGLE SPINNING (MAS) NMR

Magic angle spinning (MAS) NMR yields high quality proton and carbon NMR data on solvent swollen solid support.

	1	2	3	4	5	6	7	8	9	10	11	12
A	100	100	50	100	100	50	50	100	100	50	100	100
B	100	100	100	100	100	0	50	100	50	50	50	50
C	100	50	50	50	50	0	50	100	100	50	100	100
D	100	50	50	50	50	0	100	100	100	100	100	100
E	100	100	100	100	100	50	100	100	100	100	100	100
F	100	50	50	100	50	0	100	100	100	100	100	100
G	100	50	100	50	50	50	100	50	50	50	100	100
H	100	50	50	100	100	0	100	100	100	100	100	100

Figure 2 The ^{1}H NMR data were obtained using automated delivery of DMSO solutions of every library member from a 96-deep well microtiter plate to a flow probe-equipped NMR spectrometer. Plate view of scoring of ^{1}H NMR data of library compounds. Cells shaded in gray indicate reaction mixtures which do not contain the expected resonances of the products

Broadening due to dipolar coupling, which has a strong angular dependence in the form of $(3\cos^2\theta - 1)$, where θ is the angle between the dipolar-coupled spins and the static magnetic field[20] can be reduced to zero by rapidly spinning the sample about an axis at 54.7°, the magic angle, relative to the static magnetic field dipolar couplings (i.e., $\cos^2\theta - 1 = 0$). Sample spinning also averages the bulk magnetic susceptibility, substantially reducing line broadening due to this factor. Therefore NMR spectra approaching the quality of that of solution-phase samples can be obtained.[21–23] The resulting narrower line-widths also allow for increased sensitivity relative to gel-phase NMR, with the practical outcome being reduced acquisition times.

High-resolution MAS-NMR probes and the necessary hardware can readily be purchased for most high-field NMR spectrometers. Automated sample changing is available for MAS probes increasing the throughput. In general, the quality of MAS-NMR data is such that the method is amicable to a variety of two-dimensional NMR sequences. Thus making it is possible to obtain not only structural information on-resin but also conformational information as well. High-resolution MAS-NMR technology for combinatorial chemistry research is assessable for many laboratory situations. Because both quantitation and structure determination can be performed without the need to cleave compounds from the resin it is expected that MAS-NMR will take on a more significant role in the design of combinatorial chemistry libraries.

Most combinatorial chemistry has developed using resin beads as a primary format for the synthesis of non-peptide targets. Except for PEG derived solid state supports, the proton NMR spectra yield signals which are 6–10 Hz wide making it difficult to directly measure coupling constants. Since the coupling pattern and J-values are important for structure determination several strategies have been introduced to overcome this limitation[24] such as 2D E.COSY NMR, tilted and non-tilted two-dimensional J-resolved spectra, and 2D SECSY NMR data can also be used to obtain resolution enhanced spectra which rivals the appearance of solution NMR spectra.[25–28]

The role of solvent in determining the linewidth and utility of 1D NMR spectra has been described.[29,30] It has been found that the residual line broadening observed in the MAS-NMR spectra of swollen resins not averaged by MAS comes mainly from the anisotropic bulk magnetic susceptibility differences.

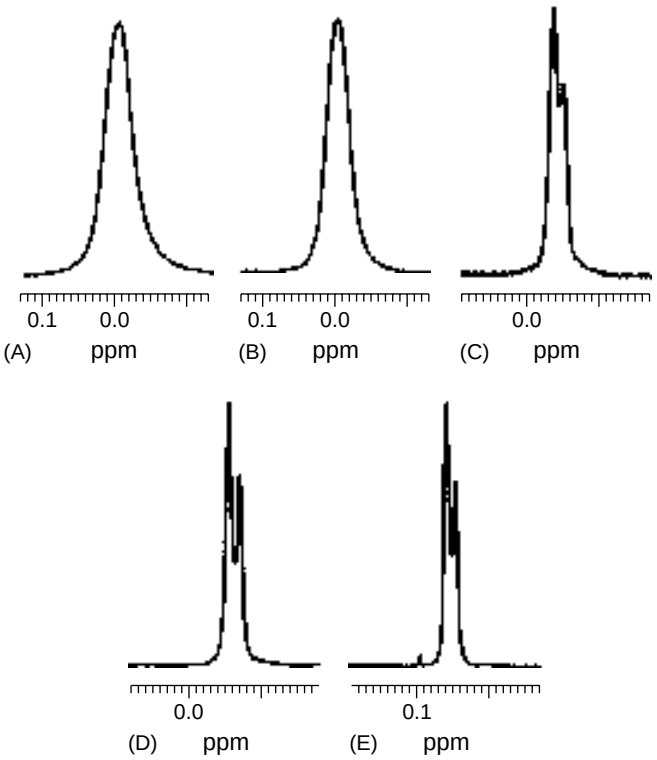

Figure 3 Partial 500 MHz ^{1}H HRMAS NMR spectra of resin-bound intermediates **5a** (A, Ellman's dihydropyran resin), **5b** (B, Wang resin), **5c** (C, NovaSyn TG resin), and **5d** (D, POEPOP resin) swollen in $CDCl_3$, and partial 400 MHz ^{1}H NMR spectrum of compound **11** (E, solution) in $CDCl_3$, showing the trimethylsilyl group chemical shift

It is most likely that this effect comes from the aromatic rings from the polystyrene resin.[31,32] With this in mind, a new resin that does not contain the aromatic rings has been developed.[33] These PEG-based resins give higher resolution spectra than the PEG grafted resins Tenta-Gel and Argo-Gel and all polystyrene based resins. The influence on resin type can be clearly seen in the data in Figure 3.

The introduction of a gradient MAS probe has been a significant advance in the ability to obtain artifact free data. The need for gradients is in fact more pronounced for MAS-NMR data sets, since sample spinning builds into the measurement an unavoidable modulation (primarily due to RF-intensity modulation and Q-modulation) giving rise to significant t_1-ridges.[34] The use of gradients allows the ability to obtain high quality HMQC and HMBC NMR spectra without the nuisance of artifactual noise stripes. The HMBC experiment is particularly important since it is one of the most powerful NMR structure determination tools.[35]

8 PINS AND CROWNS

The crown/pin system, where resin is grafted onto a base polymer carrier, is an alternate format to resin beads, and despite usefulness of the crown/pin system for solid-phase synthesis, there have been only a few of reports utilizing MAS NMR spectroscopy to analyze crown-based reaction products. It has been demonstrated that MAS-NMR offers

the additional benefit of allowing reaction progress to be monitored sequentially on the same crown, as the crown can be returned to the reaction apparatus until the desired transformation is complete.[36] There are no differences in obtaining data from this convenient solid phase chemistry system verses resin and all of the experiments that work on resin beads also work for crown/pin systems.[37]

For situations where spectral overlap exists between the compound of interest and the linker or resin, or in which the chemical transformation does not alter the number of protons, it would be expected that using MAS ^{13}C-NMR would facilitate monitoring reaction progression. Unfortunately, it has been found to be necessary to entirely fill the sample rotor with shaved surface material in order to acquire interpretable carbon spectra within 12 h.[38]

9 PEPTIDES

Peptide synthesis represents a significant area where solid phase synthesis has been applied for some time. The ability to obtain high quality spectra has played a major role in not only determining reaction products but also in understanding reaction kinetics. Step-by-step solid-phase synthesis of a ten-residue peptide was readily followed.[38] The full assignment of the peptide intermediates was accomplished by combined use of MAS TOCSY, MAS NOESY and MAS ^{1}H–^{13}C HMQC data sets. Line widths in peptide studies are directly related to chain mobility, and the lack of mobility due to aggregation is a potential source of synthesis difficulties. An eight-residue peptide attached to the POEPOP 1500 resin was readily analyzed using single resin bead MAS NMR.[33] The POEPOP resin has the advantage of yielding NMR spectra that are of higher quality than polystyrene based resins. It was found that it took only 20 min data acquisition for 1.6 nmol of peptide and that two-dimensional spectra could be obtained with only 6 nmol in an overnight data acquisition.

10 DIFFUSION WEIGHTED MAS-NMR

The ability to interpret MAS ^{1}H NMR data can be hampered by residual solvents, other impurities, and resin linker resonances. Compounds that are not attached to the solid phase matrix are typically small molecular weight compounds and exhibit relatively fast diffusion rates. By taking advantage of differences in the apparent diffusion coefficients between the compounds attached to the resin and compounds that are free in solution the analysis of solid phase synthesis reaction using MAS-NMR can been simplified. These experiments selectively attenuate the NMR signals of fast diffusing components simplifying spectral interpretation and has been demonstrated for DMF-d_7 swollen Fmoc-isoleucine on Wang resin.[39,40] The success of this experiment has been extended in the SPEEDY (Spin-Echo Enhanced Diffusion Filtered Spectroscopy) sequence to take advantage of the short T_2 relaxation times of the resin matrix.[41] This sequence incorporates both PFG diffusion-weighting and a CPMG spin-echo sequence to attenuate signals with short T_2 relaxation times (i.e., those of the resin matrix). The combination of the PFG diffusion-weighing and spin-echo sequences selects only the NMR signals that arise from molecules exhibiting slower self-diffusion rates and longer T_2 relaxation rates. Resonances in the resultant spectrum CAN then be interpreted as belonging to compounds that are attached to the resin.

11 ON-RESIN QUANTITATION

NMR spectra have even been obtained on a single bead[42,43] and, although the practical utility of this method is still to be proven, raises the possibility of using NMR as a decoding method for combinatorial mixture screening.

One of the aspects of on resin chemistry is to be able to tell when a reaction is over and what the yield might be, without cleaving the substances from the solid phase. Often this is best accomplished using a heteronuclear nucleus such as ^{19}F. Quantitation of on-resin chemical reactions using ^{19}F-NMR has been exemplified. The use of a fluorinated solvent (0.2% fluorobenzene) as an internal standard for quantifying the extent of resin loading using ^{19}F gel-phase NMR[44] has been demonstrated by comparing the ratio of the resonance intensities of the product to that of the solvent. Other reports using fluorinated linkers which are analogues of linkers commonly used in solid-phase peptide synthesis have been described. One of the linkers was used in combination with gel-phase ^{19}F NMR spectroscopy to develop conditions for solid-phase synthesis of chemical libraries. Attachment to and cleavage from the linker could be monitored based on the chemical shift of the fluorine atom of the linker. In addition, use of the linker as internal standard allowed quantification and optimization of reactions occurring further away from the linker when fluorinated building blocks were employed. For this method, high-quality ^{19}F NMR spectra were obtained for compounds linked to a TentaGel resin in a standard NMR tube using an ordinary NMR instrument.

A method for quantifying on-resin reaction yields using ^{19}F-NMR, which is more amenable for MAS has also been put forward.[45] This strategy incorporates into the resin a chemically stable fluorine moiety (4-fluorostyrene) to act as an internal standard. It was found that an internal standard (4-fluorostyrene) loading of $\sim$0.3 mmol F/g resin was sufficient to obtain a signal-to-noise ratio $\geq$15 using 50 mg of material in the gel-phase in a reasonable amount of spectrometer time (1 min at 470.15 MHz ^{19}F and 6 min at 188.23 MHz ^{19}F).

MAS ^{1}H-NMR can be used to quantitatively monitor solid phase reactions.[46] The kinetics of chemical reactions on solid support can be followed in situ in the NMR rotor itself. The potential applications for following synthetic chemistry on solid support are numerous and will definitely help in the acceleration of the optimization process of solid phase synthesis. The possibilities and limits of MAS NMR to detect and quantify side products during solid phase synthesis have also been evaluated. If well separated signals are available for the different molecules, reliable quantification and identification of impurities present in concentrations as low as 1% can be obtained when using a single pulse experiment on resins swollen in deuterated solvent. Using the PFG LED sequence to remove protonated solvent signals decreased sensitivity and showed differential losses of magnetization. Still, as all sample workup steps are eliminated, this technique will be helpful in detecting minority species in solid phase combinatorial chemistry, and its application at the different

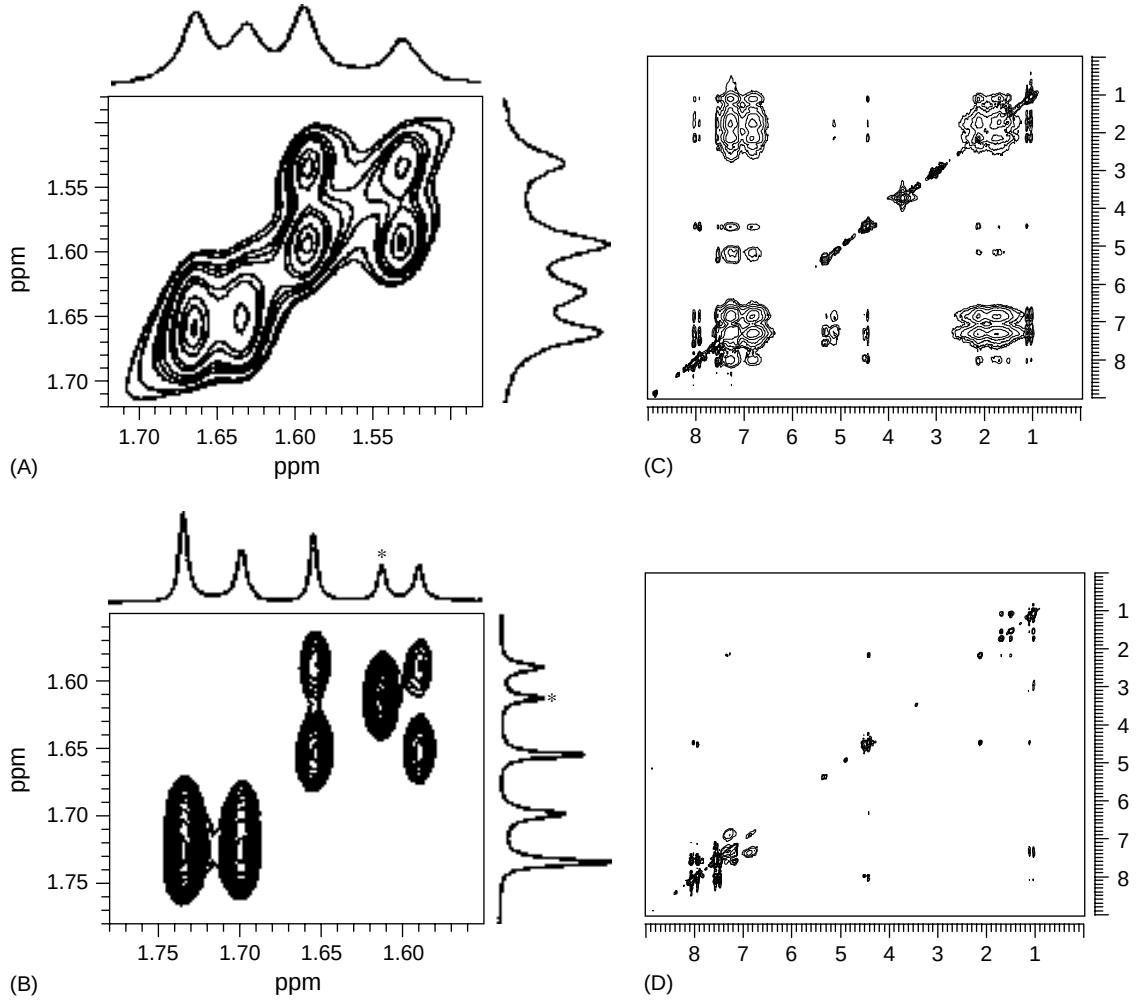

Figure 4 (A) Partial 500 MHz NOESY HRMAS NMR spectrum of POEPOP-bound intermediates (B) swollen in $CDCl_3$, and partial 400 MHz NOESY ($t_m = 650$ ms) NMR spectrum of compound **11** (top) in $CDCl_3$. Peak labeled with a star is due to water. (C) Fmoc-isoleucine Wang resin, DMF-d_7. NOESY spectrum $t_m = 650$ ms, ns = 16. (D) Bipolar STE-NOESY-CPMG spectra: $\delta = 2$ ms, $g = 48$ G cm^{-1}, $t_m = 650$ ms, ns = 64, $\tau_{cp} = 0.5$ ms, and $n = 70$

steps of the reaction might lead to the early detection of otherwise unidentifiable active components.

12 MOLECULAR CONFORMATION ON-RESIN

The on-resin conformation of a reaction intermediate can have a profound effect on chemical reactivity and the success of the reaction. Because the combination of MAS and resin swelling reduce to zero the dipolar interaction but does not affect dipolar relaxation, it is possible to collect NOE data from compounds on-resin. MAS-NOE(SY) experiments can be used to obtain a conformation-based understanding of chemical reactivity and the influence of the on-resin environment on molecular conformation providing valuable information during the design phase of a combinatorial library.

The majority of effort in studying on-resin molecular conformation has been directed towards peptides, although in our laboratory the conformations of a number of organic compounds have been studied (Michael Shapiro, unpublished results). 2D MAS NOESY experiments on the peptide GPGRAF bound to TentaGel resin suggested that the peptide adopted a biologically relevant conformation on the resin.[47–50] The possibility of observing molecular conformations on resin could play an important future role in the design phase of combinatorial chemistry as well as helping to understand compound reactivity and the influence of the linker on both chemical reactivity and binding events. The use of new resins and modern pulse sequences aids in the ability to obtain high quality NOESY data as shown in Figure 4.

13 CONCLUSIONS

Combinatorial chemistry has rapidly moved into the drug discovery arena and is playing a major role in the pharmaceutical industry. The ability to obtain structural data and reaction course information on solid supported reactions has inspired the development of new NMR methods for combinatorial chemistry. New solution NMR methods are useful for both solid phase and solution phase combinatorial chemistry and with greatly improved throughput could be used for quality control of libraries in the future. NMR methods will continue

to be developed and will find widespread utility in combinatorial chemistry. A significant advance in the ability to obtain relatively artifact free data has been the introduction of a gradient MAS probe having the same influence for MAS NMR that it has had on liquid NMR analysis.

14 REFERENCES

1. S. B. Shuker, P. J. Hajduk, R. P. Meadows, and S. W. Fesik, *Science*, 1996, **274**, 1531–1534.
2. M. Lin, M. J. Shapiro, and J. R. Wareing Jr, *J. Am. Chem. Soc.*, 1997, **119**, 5249–5250.
3. M. Mayer and B. Meyer, *Angew. Chem. Int. Ed.*, 1999, **38**, 1784–1788.
4. J. Klein, R. Meinecke, M. Mayer, and B. Meyer, *J. Am. Chem. Soc.*, 1999, **121**, 5336–5337.
5. A. Chen and M. J. Shapiro, *J. Am. Chem. Soc.*, 2000, **122**, 414–415.
6. J. M. Moore, *Anal. Biotechnol.*, 1999, **10**, 54–58.
7. M. J. Shapiro and J. R. Wareing, *Curr. Opin. Drug Disc.*, 1999, **2**, 396–400.
8. J. C. Lindon, J. K. Nicholson, and I. D. Wilson, *J. Chrom. B*, 2000, **748**, 233–258.
9. J. C. Lindon, J. K. Nicholson, and I. D. Wilson, *Prog. NMR*, 1996, **29**, 1–49.
10. J. C. Lindon, R. D. Farrant, P. N. Sanderson, P. M. Doyle, S. L. Goughg, M. Spraul, M. Hoffman, and J. K. Nicholson, *Magn. Reson. Chem.*, 1995, **33**, 857–863.
11. B. Behnke, G. Schlotterbeck, U. Tallarek, S. Strohschein, L. Tseng, T. Keller, K. Albert, and E. Bayer, *Anal. Chem.*, 1996, **68**, 1110–1115.
12. K. I. Burton, J. R. Everett, M. J. Newman, F. S. Pullen, D. S. Richards, and A. G. Swanson, *J. Pharmaceut. Biomed. Anal.*, 1997, **15**, 1903–1912.
13. D. L. Olson, T. L. Peck, A. G. Webb, and J. V. Sweedler, *Peptides: Chem. Struct. Biol.*, 1996, 730–731.
14. C. Dalvit and J. M. Bohlen, *Magn. Reson. Chem.*, 1996, **34**, 829–833.
15. P. A. Keifer, S. H. Smallcombe, E. H. Williams, K. E. Salomon, G. Mendez, J. L. Belletire, and C. D. Moore, *J. Comb. Chem.*, 2000, **2**, 151–171.
16. B. C. Hamper, D. M. Synderman, T. J. Owen, A. M. Scates, D. C. Owsley, A. S. Kesselring, and R. C. Chott, *J. Comb. Chem.*, 1999, **1**, 140–150.
17. S. L. Manatt, C. F. Amsden, C. A. Bettison, W. T. Frazer, J. T. Gudman, B. E. Lenk, J. F. Lubetich, E. A. McNelly, S. C. Smith, D. J. Templeton, and R. P. Pinnell, *Tetrahedron Lett.*, 1980, **21**, 1397.
18. A. Svensson, T. Fex, and J. Kihlberg, *Tetrahedron Lett.*, 1996, **37**, 7649–7652.
19. E. E. Swayze, *Tetrahedron Lett.*, 1997, **38**, 8643–8646.
20. G. E. Maciel, *Science*, 1984, **226**, 282.
21. H. D. Stöver and J. M. Fréchet, *Macromolecules*, 1989, **22**, 1574.
22. R. C. Anderson, M. A. Jarema, M. J. Shapiro, J. P. Stokes, and M. Ziliox, *J. Org. Chem.*, 1995, **60**, 2560.
23. W. L. Fitch, G. Detre, C. P. Holmes, J. N. Schoolery, and P. Keifer, *J. Org. Chem.*, 1994, **59**, 7955.
24. W. P. Aue, E. Bartholdi, and R. R. Ernst, *J. Chem. Phys.*, 1976, **64**, 2229.
25. A. Meissner, P. Bloch, E. Humpfer, M. Spraul, and O. Sorensen, *J. Am. Chem. Soc.*, 1997, **119**, 1787.
26. K. Nagayama, K. Wuthrich, and R. R. Ernst, *Biochem. Biophys. Res. Commun.*, 1979, **90**, 395.
27. J. A. Chin, B. Fell, S. Pochapsky, M. J. Shapiro, and J. R. Wareing, *J. Org. Chem.*, 1997, **62**, 1309.
28. M. J. Shapiro, J. Chin, R. E. Marti, and M. A. Jarosinski, *Tetrahedron Lett.*, 1997, **38**, 1333–1336.
29. P. Keifer, *J. Org. Chem.*, 1996, **61**, 1558.
30. C. F. Dhalluin, C. Boutillon, A. L. Tartar, and G. Lippens, *J. Am. Chem. Soc.*, 1997, **119**, 10 494.
31. K. Elbayed, M. Bourdonneau, J. Furrer, T. Richert, J. Raya., J. Hirschinger, and M. Piotto, *J. Magn. Reson.*, 1999, **136**, 127.
32. A. Bianco, J. Furrer, D. Limal, G. Guichard, K. E. Raya, M. Piotto, and J. P. Briand, *J. Comb. Chem.*, 2000, **2**, 681–690.
33. M. Grøtli, C. H. Grotfredsen, J. Rademann. J. Buchardt, A. J. Clark, J. Ø. Duus, and M. Meldal, *J. Comb. Chem.*, 2000, **2**, 108.
34. W. E. Maas, F. H. Laukien, and D. G. Cory, *J. Am. Chem. Soc.*, 1996, **118**, 13 085.
35. A. Bax and M. Summers, *J. Am. Chem. Soc.*, 1986, **108**, 2093–2094.
36. J. Chin, B. Fell, M. J. Shapiro, J. Tomesh, J. R. Wareing, and A. M. Bray, *J. Org. Chem.*, 1997, **62**, 538.
37. M. J. Shapiro and J. S. Gounarides, *Prog. Nucl. Magn. Reson. Spectrosc.*, 1999, **25**, 153.
38. A. M. Sefler and S. W. Gerritz, *J. Comb. Chem.*, 2000, **2**, 127.
39. M. J. Shapiro, J. Chin, A. Chen, J. R. Wareing, Q. Tang, R. A. Tommasi, and H. A. Marepalli, *Tetrahedron Lett.*, 1999, **40**, 6141.
40. J. Chin, A. Chen, and M. J. Shapiro, *Magn. Reson. Chem.*, 2000, **38**, 782.
41. J. A. Chin, A. Chen, and M. J. Shapiro, *J. Comb. Chem.*, 2000, **3**, 293.
42. S. K. Sarkar, G. R. Sarigipati, J. L. Adams, and P. A. Keifer, *J. Am. Chem. Soc.*, 1996, **118**, 2305–2306.
43. C. H. Gotfredson, M. Grotli, M. Willert, M. Meldal, and J. O. Duus, *J. Chem. Soc., Perkin 1*, 2000, 1167–1171.
44. M. Drew, E. Orton, P. Krolikowski, J. M. Salvino, and N. V. Kumar, *J. Comb. Chem.*, 2000, **2**, 8.
45. A. Svensson, T. Fex, and J. Kihlberg, *J. Comb. Chem.*, 2000, **2**, 736–748.
46. R. Warrass and G. Lippens, *J. Org. Chem.*, 2000, **65**, 2946.
47. R. Jelinek, A. P. Valente, K. G. Valentine, and S. J. Opella, *J. Magn. Reson.*, 1997, **125**, 185.
48. D. S. Wishart, B. D. Sykes, and F. M. Richards, *Biochemistry*, 1992, **31**, 1647.
49. B. C. Hamper, D. M. Synderman, T. J. Owen, A. M. Scates, D. C. Owsley, A. S. Kesselring, and R. C. Chott, *J. Comb. Chem.*, 1999, **1**, 140–150.
50. R. Warrass, J.-M. Wieruszeski, and G. Lippens, *J. Am. Chem. Soc.*, 1999, **121**, 3787–3788.

Biographical Sketch

Michael J. Shapiro, *b* 1947. 1969 B.S. Pennsylvania State University; 1974 Ph.D. Texas A&M University; 1977 Sandoz Inc.; 1998–2000 Novartis Research Institute, Novartis Leading Scientist, Principal Fellow and Novartis NMR Technology Expert; 2000–present Lilly Research Laboratories, Research Advisor Chemistry Research Technologies; Current interests: Utilization of NMR and Mass Spectrometry in drug discovery.

Coupling Through Space in Organic Chemistry

Frank B. Mallory
Bryn Mawr College, PA, USA
&
Clelia W. Mallory
University of Pennsylvania, Philadelphia, PA, USA

1	Introduction	1
2	FF Systems	2
3	NF and PF Systems	6
4	HF, CF, and CP Systems	7
5	HH Systems	8
6	F–F Coupling Through Nonbonded Interactions with an Intervening Orbital	9
7	Related Articles	9
8	References	9

1 INTRODUCTION

The concept that nuclear spin–spin coupling might occur by through-space as well as through-bond interactions was introduced many years ago to account for the observations that certain atoms which are crowded against one another intramolecularly exhibit unusually large coupling constants as measured by NMR spectroscopy.[1,2] The early work on through-space coupling was reviewed in 1975,[3] and a review of various theoretical treatments of the phenomenon appeared in 1985.[4]

This article is concerned only with spin–spin coupling between pairs of magnetic nuclei in molecules that are freely tumbling in fluid solution such that direct 'through-space' dipole–dipole interactions between the two nuclei are averaged to zero. The observed coupling arises instead from intramolecular Fermi contact and Hund interactions involving the nuclear spins and the spins of electrons in the molecule. Fermi contact interaction between a magnetic nucleus and an electron requires these two particles to be essentially coincident in space, which is possible only if the electron is in an orbital with s character at that nucleus. The system is lower in energy if the electron and the nucleus with which it is in intimate contact have antiparallel spins. Hund interactions are operative between two electrons that are contained in two different orbitals that have some spatial overlap of their electron densities. When an electron from one of the orbitals inhabits the same region of space as an electron from the other orbital the system has a lower energy if the two electrons have parallel spins.

The phenomenon of through-space coupling has been reported for spatially proximate pairs of nuclei of various types, including $^{19}F-^{19}F$, $^{1}H-^{19}F$, $^{13}C-^{19}F$, $^{1}H-^{1}H$, $^{15}N-^{19}F$, $^{31}P-^{19}F$, and $^{13}C-^{31}P$ systems. Some examples are shown in Figure 1.

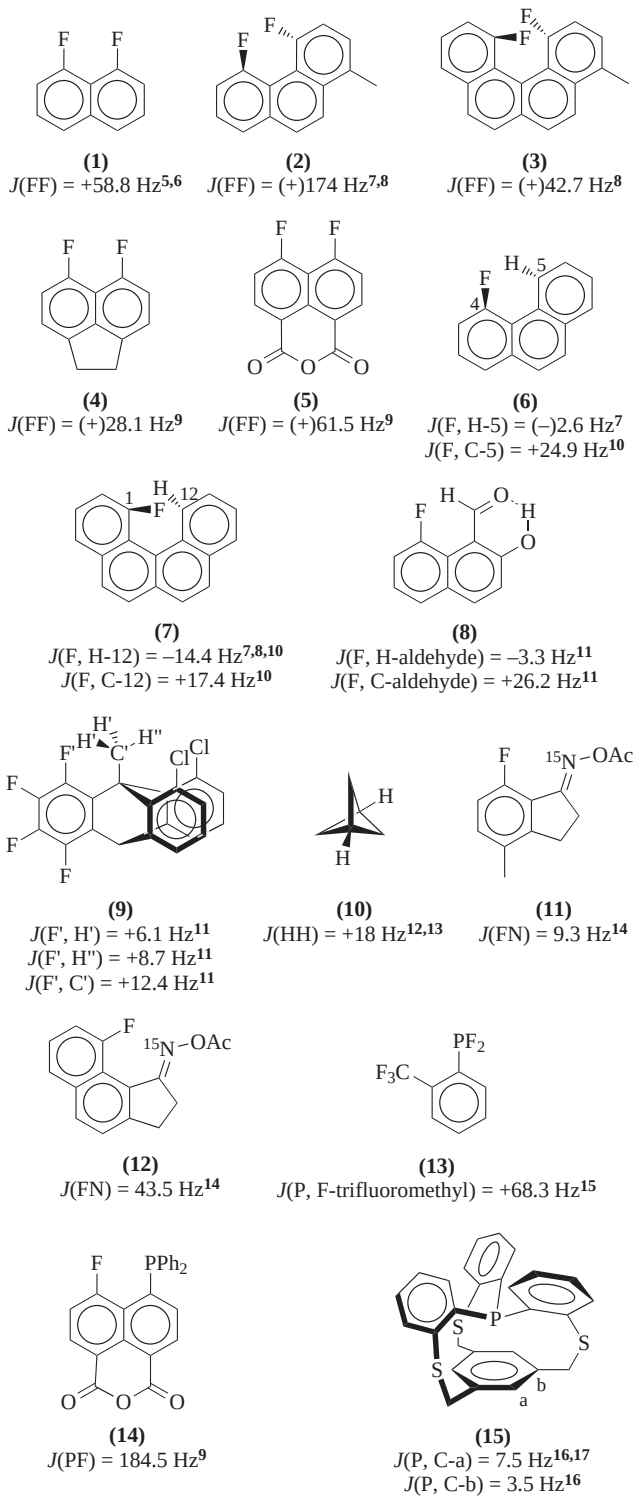

Figure 1 Examples of through-space coupling

Initially the proposals for the existence of a special through-space mode of coupling were greeted with some skepticism. For example, there seemed no convincing way to rule out the alternative possibility that the large coupling

constants observed for various molecules related to 1,8-difluoronaphthalene (**1**) result instead from peculiarly effective through-bond interactions in the U-shaped array of the four relevant bonds in the FCCCF fragment. The early history of the study of the through-space coupling phenomenon was marked by attempts to dispel this skepticism. One compeling piece of evidence in this context was the report that several disubstituted 4,5-difluorophenanthrenes, in which the shortest through-bond pathway is one bond longer than that in the 1,8-difluoronaphthalene system but the intramolecular crowding between the two fluorine atoms is greater, exhibited astonishingly large coupling constants in the range 167–170 Hz;[18] a value of 174 Hz was reported subsequently for the monosubstituted derivative (**2**).[7,8] Another convincing piece of evidence was provided by a study of the analog of the enzyme dihydrofolate reductase in which the four tryptophan residues in the native enzyme had been replaced biosynthetically by 6-fluorotryptophan residues.[19] It happens that the tertiary structure of this enzyme places two of these four tryptophan (or fluorotryptophan) residues, namely residues 133 and 158, in van der Waals contact with one another. The ^{19}F NMR spectrum of a fluorine-substituted enzyme shows four fluorine signals, two singlets and two doublets with a coupling constant of 17 Hz.[19] There is no reasonable way to attribute this F–F coupling to through-bond interactions, because the shortest through-bond pathway connecting the two spatially proximate fluorines is 89 bonds long!

Both through-space and through-bond interactions contribute to the observed coupling in molecules such as those shown in Figure 1. That is, the experimentally measured coupling constant J can be expressed as a sum of through-space and through-bond components, J^{TS} and J^{TB}, respectively:

$$J = J^{TS} + J^{TB} \quad (1)$$

Perhaps the central unsolved problem in the quest for a precise understanding of the dependence of through-space coupling on molecular structure is the lack of a reliable means of dissecting the observed coupling into its through-space and through-bond components. In a few atypical cases, such as the F–F coupling in the enzyme system discussed above, this dissection is easily made because it is clear that the through-bond component is zero. Although the experimentally determined values of J(FF) for molecules such as **(1)–(3)** are sufficiently large that it seems safe to conclude qualitatively that the through-space mode of coupling plays a dominant role, the actual magnitudes of the through-space components cannot be assessed quantitatively in any of these systems because there is no reliable way to determine experimentally the magnitudes of the accompanying through-bond contributions. At this time it appears that theoretical calculations offer the best, or perhaps the only, hope for evaluating the relative importance of the through-space and through-bond modes of coupling in particular molecules. Some computational methods currently under development appear promising in this context.[4,20,21]

In the early days of the study of through-space F–F coupling a conceptual view of the mechanism of this type of coupling was put forward by one of us based on the mixing of lone-pair orbitals through overlap interactions.[22] In the next section we present a modified version of this conceptual approach for various F–F systems, and then in subsequent sections we describe how this approach can be extended to account for through-space coupling between other kinds of magnetic nuclei, as exemplified in Figure 1. It should be acknowledged at the outset that various mathematically sophisticated and computationally oriented quantum mechanical theories of through-space F–F coupling have been presented in the past by other workers.[4] However, although quantum mechanical approaches are intrinsically superior to our conceptual approach, they have not yet proved wholly successful in giving theoretical values of F–F coupling constants that are in consistently good agreement with the experimentally observed values. Therefore we continue to think it useful to offer our orbital overlap description as a basis on which to consider the phenomenon of through-space coupling.

2 FF SYSTEMS

Through-space F–F coupling can be attributed to the overlap of a pair of nominally lone-pair orbitals, one from each of the two coupled fluorine atoms.[22] The situation for the particular intramolecular orientation found in the 1,8-difluoronaphthalene system (**1**), in which the C–F bonds are coplanar and approximately parallel to one another, is illustrated by the rough diagrams given in Figure 2. The relevant basis orbitals are the two in-plane one-center atomic lone-pair orbitals $p_{F\sigma}$ and $p'_{F\sigma}$ that would be characteristic of the fluorines if they were too far apart for these two orbitals to experience overlap interactions with each other. (For simplicity we neglect here the strong mixing of these $p_{F\sigma}$ and $p'_{F\sigma}$ orbitals with σ orbitals that are part of the carbon framework of the naphthalene system.) The F–F distance in (**1**), as measured by X-ray crystallography, is 0.2584 nm.[23] This is less than twice the 0.14 nm van der Waals radius of fluorine, so in fact the $p_{F\sigma}$ and $p'_{F\sigma}$ orbitals do overlap to a small extent. As shown schematically in Figure 2, this small F–F overlap transforms the pair of one-center atomic $p_{F\sigma}$ and $p'_{F\sigma}$ orbitals into a pair of two-center molecular orbitals, a weakly bonding orbital σ_{FF} and a weakly antibonding orbital σ^*_{FF}. Although

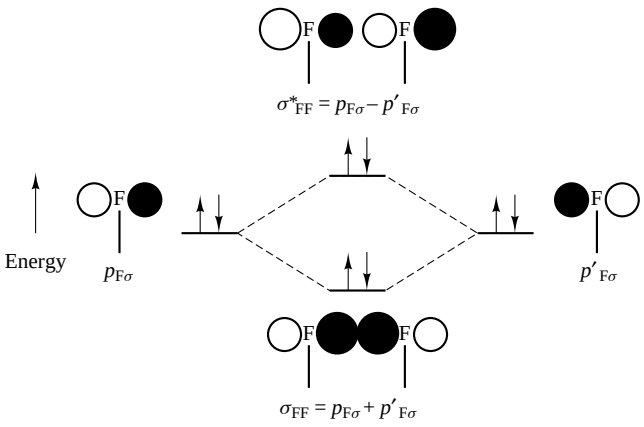

Figure 2 Schematic representations of the approximate shapes and relative energies of the bonding and antibonding molecular orbitals, σ_{FF} and σ^*_{FF}, that result from the overlap of the in-plane lone-pair orbitals, $p_{F\sigma}$ and $p'_{F\sigma}$, on two spatially proximate fluorine atoms oriented with their C–F bonds coplanar and essentially parallel, as in 1,8-difluoronaphthalene (**1**)

this combination of one filled bonding orbital and one filled antibonding orbital leads to no net chemical bonding between the two fluorine atoms, we believe it does provide a direct four-electron linkage that allows the transmittal of nuclear spin information between the two fluorine nuclei, and thereby gives rise to through-space F–F coupling.

In this lone-pair overlap theory through-space coupling is attributed to exactly the same kinds of interactions that are involved in through-bond coupling, namely Fermi contact interactions of the spins of the two magnetic nuclei with the spins of the surrounding electrons, electron correlation in accord with the Pauli principle for the two electrons within any given orbital, and Hund interactions between the spins of electrons in different orbitals. From this perspective the only distinction between through-space and through-bond coupling is a trivial one: through-space F–F coupling is transmitted by electrons that occupy weakly bonding and weakly antibonding orbitals, whereas through-bond coupling is transmitted by electrons that occupy strongly bonding orbitals. Given this picture, the term 'through-space coupling' can be seen as a misnomer. Perhaps this type of coupling would be more appropriately designated 'proximate coupling', 'direct coupling', or 'nonbonded coupling' but it seems unlikely that chemists will readily abandon the long-used term 'through-space coupling' and its juxtaposition with the term 'through-bond coupling'.

In principle, there are five different valence-level fluorine basis orbitals whose overlap interactions should be considered with regard to through-space F–F coupling: the 2*s* lone-pair orbital s_F; the in-plane 2*p* lone-pair orbital $p_{F\sigma}$; the out-of-plane 2*p* lone-pair orbital $p_{F\pi}$; the two-center bonding orbital σ_{CF}; and the empty two-center antibonding orbital σ^*_{CF}. The $p_{F\sigma}-p'_{F\sigma}$ interaction illustrated in Figure 2 is only one of 14 different pairwise overlap interactions whose potential role in through-space F–F coupling should be taken into account. We have chosen to begin our presentation with the 1,8-difluoronaphthalene system because of its relative simplicity; each of the other 13 overlap interactions in this system can be considered to be either nonexistent or negligibly small in magnitude for various reasons. For example, the $s_F-p'_{F\pi}$, $p_{F\sigma}-p'_{F\pi}$, $p_{F\pi}-\sigma'_{CF}$, and $p_{F\pi}-\sigma^*{}'_{CF}$ interactions are all zero by symmetry, as illustrated by the diagrams in Figure 3, and four other overlap interactions, $s_F-\sigma'_{CF}$, $s_F-\sigma^*{}'_{CF}$, $p_{F\sigma}-\sigma'_{CF}$, and $p_{F\sigma}-\sigma^*{}'_{CF}$, are nearly zero in magnitude because of local symmetry considerations as illustrated in Figure 4.

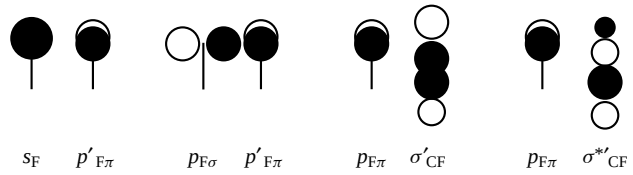

Figure 3 Schematic representations of F–F overlap interactions in the 1,8-difluoronaphthalene system (**1**) that are forbidden by symmetry

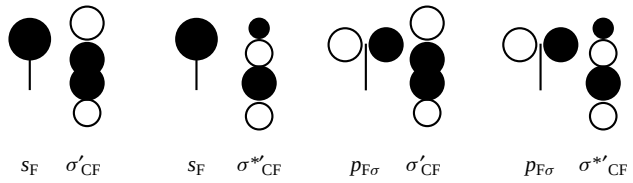

Figure 4 Schematic representation of overlap interactions in the 1,8-difluoronaphthalene system (**1**) that are nearly forbidden by symmetry

Furthermore, all of the pairwise orbital interactions other than $p_{F\sigma}-p'_{F\sigma}$ suffer from the fact that their spatial overlaps at the F–F distance of about 0.258 nm are small relative to the spatial overlap involved in the dominant $p_{F\sigma}-p'_{F\sigma}$ interaction. Finally, many of the orbital interactions are unfavorable because of a large mismatch in the energies of the interacting pairs of basis orbitals. This information is summarized in Table 1.

The σ_{FF} and σ^*_{FF} molecular orbitals shown in Figure 2 both have nodes at or very near each fluorine nucleus, so the four electrons in these two orbitals do not have significant Fermi contact with the fluorine nuclei. Instead, the Fermi contact that is relevant for the observed F–F coupling involves the electrons in the 2*s* lone-pair orbitals, s_F and s'_F. (For simplicity, the Fermi contact interactions involving the electrons in the 1*s* orbital at each fluorine nucleus are ignored here.) For a fluorine atom whose nucleus has a spin-up alignment, for example, Fermi contact interactions give rise to an enhanced probability of finding the spin-down s_F electron in the region of the s_F orbital closer to the fluorine nucleus and a correspondingly enhanced probability of finding the spin-up

Table 1 Evaluation of the Relative Magnitudes of 14 Different Types of Pairwise Orbital Overlap Interactions between the Two Fluorine Atoms in 1,8-Difluoronaphthalene (**1**)

Orbital	Orbital′	Interaction Magnitude	Explanation Regarding Magnitude (see text)
s_F	s'_F	Negligible	Long distance
	$p'_{F\sigma}$	Negligible	Long distance, energy mismatch
	$p'_{F\pi}$	Zero	Symmetry, long distance, energy mismatch
	σ'_{CF}	Negligible	Local symmetry, long distance, energy mismatch
	$\sigma^*{}'_{CF}$	Negligible	Local symmetry, long distance, energy mismatch
$p_{F\sigma}$	$p'_{F\sigma}$	Large	Good spatial overlap, perfect energy match
	$p'_{F\pi}$	Zero	Symmetry, long distance
	σ'_{CF}	Negligible	Local symmetry, long distance
	$\sigma^*{}'_{CF}$	Negligible	Local symmetry, long distance, energy mismatch
$p_{F\pi}$	$p'_{F\pi}$	Negligible	Long distance
	σ'_{CF}	Zero	Symmetry, long distance
	$\sigma^*{}'_{CF}$	Zero	Symmetry, long distance, energy mismatch
σ_{CF}	σ'_{CF}	Negligible	Long distance
	$\sigma^*{}'_{CF}$	Negligible	Long distance, energy mismatch

s_F electron in the region of the s_F orbital more remote from the fluorine nucleus. This phenomenon, in which the spin-up and spin-down electrons in a given orbital have different spatial distributions of their electron densities, is known as spin polarization. The transmission pathway for the communication of nuclear spin information between the two fluorine nuclei is completed by way of Hund interactions between the electrons in the spin-polarized s_F and s'_F orbitals and the electrons in the σ_{FF} and σ^*_{FF} orbitals. As background for our explanation about how these particular Hund interactions control through-space F–F coupling we first consider three simpler systems: an isolated fluorine atom, the hydrogen fluoride molecule, and a C–F bond.

Theoretical calculations for an isolated fluorine atom have shown that Hund interactions between the electron in the half-occupied 2*p* orbital and the electrons in the spin-polarized 2*s* orbital lead to a preference for this 2*p* electron to have its spin aligned parallel to the net electron spin density in the inner region of the 2*s* orbital (and therefore antiparallel to the spin of the nucleus) as shown in Figure 5(a).[24]

In the hydrogen fluoride molecule electron correlation effects cause one of the two electrons in the σ_{HF} bonding orbital to be closer to the fluorine nucleus and the other σ_{HF} electron to be closer to the hydrogen nucleus at a typical instant of time. This σ_{HF} orbital closely resembles a simple $2p_F$ orbital in the spatial distribution of its electron density, and as a consequence these two orbitals have analogous Hund interactions with their spin-polarized $2s_F$ orbitals. That is, the σ_{HF} electron that is closer to the fluorine nucleus prefers to have its spin aligned parallel to the electron spin density in the inner region of the spin-polarized fluorine 2*s* orbital. The net result is that a spin-up fluorine nucleus will cause the spin-down σ_{HF} electron to be located preferentially near the fluorine end of the hydrogen fluoride molecule as illustrated in Figure 5(b). As a consequence, the spin-up σ_{HF} electron will be located preferentially near the hydrogen end of the molecule. This spin-up σ_{HF} electron can experience direct Fermi contact interactions with the hydrogen nucleus, which means that there will be an energetic advantage if the hydrogen nucleus has a spin-down alignment as shown in Figure 5(b). This simple picture predicts that the fluorine and hydrogen nuclei will prefer to have antiparallel nuclear spins, which accounts for the fact that the one-bond J(FH) coupling constant for hydrogen fluoride molecule has been found to be positive in sign by both experimental and theoretical methods.[25]

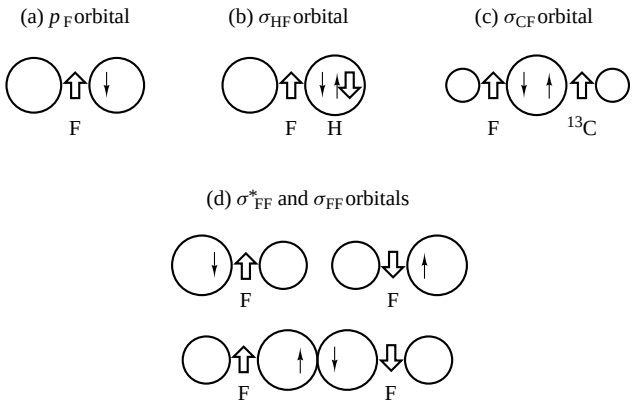

Figure 5 Schematic representations of the preferred electron and nuclear spin alignments for various systems: (a) the half-occupied 2*p* orbital of an isolated fluorine atom; (b) the σ_{HF} bonding orbital of the hydrogen fluoride molecule; (c) the σ_{CF} bonding orbital of a carbon–fluorine fragment; (d) the σ^*_{FF} antibonding and σ_{FF} bonding orbitals thought to be involved in through-space F–F coupling in a molecule such as (**1**)

In contrast, the one-bond J(FC) coupling constant for directly bonded carbon-13 and fluorine nuclei has been found to be negative in all known cases. Because of the usual electron correlation behavior the typical instantaneous configuration within the σ_{CF} orbital will have the two electrons located near opposite ends of the C–F bond. It has been argued earlier that the σ_{CF} electron that is located closer to the fluorine end of the bond experiences greater Hund interactions with the electron spin density in the outer region of the spin-polarized fluorine 2*s* orbital.[26] This reversal in the Hund behavior for the electrons in the C–F bond as compared with the H–F bond was attributed to the fact that the C–F bond is longer than the H–F bond.[26] The net result is a preference for the spin alignments shown in Figure 5(c), with the spin-up σ_{CF} electron located near the spin-up flourine nucleus and therefore with the spin-down σ_{CF} electron located near the carbon nucleus. This spin-down σ_{CF} electron can experience direct Fermi contact interaction with the carbon-13 nucleus, which means that there will be an energy advantage if the carbon-13 nucleus has a spin-up alignment as shown in Figure 5(c). This simple picture predicts that the carbon-13 and fluorine nuclei will prefer to have parallel nuclear spins, consistent with the experimentally observed negative signs for carbon-fluorine one-bond coupling constants.

We turn now to the σ_{FF} and σ^*_{FF} orbitals (Figure 2) that are of interest for through-space F–F coupling. As illustrated in Figure 5(d) the orbital amplitudes are such that the two electrons in the bonding σ_{FF} orbital will be located preferentially in the region between the two nuclei, whereas the two electrons in the antibonding σ_{FF}* orbital will be located preferentially in the two outer lobes of that orbital. As a consequence of electron correlation effects, one of the electrons in each orbital will be located preferentially near one of the fluorine nuclei while the other electron in each orbital will be located preferentially near the other fluorine nucleus. We hypothesize that because of the pronounced elongation of the bonding σ_{FF} orbital [the F–F distance of about 0.258 nm in a system such as (**1**) is considerably longer than the typical C–F bond distance of about 0.135 nm] the two σ_{FF} electrons experience Hund interactions preferentially with the outer regions of the spin-polarized s_F and s'_F orbitals, respectively, giving rise to a preference for the electron and nuclear spin alignments shown in Figure 5(d). This spin-polarization behavior is analogous to that noted for the C–F bond in Figure 5(c). We hypothesize further that the antibonding σ^*_{FF} orbital, which lacks the elongation of the σ_{FF} orbital because of the nodal plane at the midpoint of the line joining the two fluorine nuclei, shows spin-polarization behavior analogous to that of an isolated fluorine 2*p* orbital such that the two σ^*_{FF} electrons experience Hund interactions preferentially with the inner regions of the spin-polarized s_F and s'_F orbitals, respectively. This gives rise to a preference for the electron and nuclear spin alignments shown in Figure 5(d), which is analogous to the spin-polarization behavior noted for the F and HF systems in Figure 5(a) and (b). As a consequence of the cooperative effect

of all four electrons in the σ_{FF} and σ^*_{FF} orbitals there is an energetic advantage if the two fluorine nuclei have antiparallel spins rather than parallel spins. In this way we can account for the fact that in all of the cases in which the signs of the F–F coupling constants have been determined experimentally for molecules in which the through-space mode of F–F coupling is thought to predominate, these signs have been found to be positive.[6] Furthermore, the theory presented here leads to the conclusion that the magnitude of the through-space component of F–F coupling should depend on the extent to which the σ_{FF} and σ^*_{FF} orbitals are differentiated from one another in their electron densities in the region near the midpoint of the line connecting the two fluorine nuclei. This differentiation should depend in turn on the extent of overlap of the $p_{F\sigma}$ and $p'_{F\sigma}$ basis orbitals (see Figure 2), and this expectation leads to three experimentally testable predictions about the magnitude of $J(FF)^{TS}$: it should fall off exponentially with the distance between the two fluorine atoms, it should depend on orientation effects as well as distance effects, and it should not depend heavily on the π-electron withdrawing or π-electron supplying effects of any substituents that are located on the carbon framework that bears the two fluorine atoms. These implications are elaborated in the following paragraphs.

Many experimental studies have indicated that through-space F–F coupling has a very steep dependence on the distance between the coupled fluorine nuclei. One such study involves 15 compounds of types (**16**) and (**17**) (Figure 6) in which various peri substituents X and Y serve to perturb the F–F distance in predictable ways.[9,27] Systems (**16**) and (**17**) have the disadvantage that the through-bond components of the experimentally measured total F–F coupling may be large enough to muddle the interpretation of the results. But these systems have two advantages: there is no complication from out-of-plane distortions of the fluorines of the kind found, for example, in systems related to (**2**) and (**3**); and the molecules are relatively straightforward to synthesize. The experimental results for (**16**) and (**17**) are given in Table 2.

The total coupling constants $J(FF)$ were measured by ^{19}F NMR spectroscopy and the distances between the two fluorine nuclei d_{FF} were determined by averaging the results obtained by MM2 and AM1 computations. The values of $J(FF)$ cover a wide range: from 28.1 Hz for 5,6-difluoroacenaphthene,

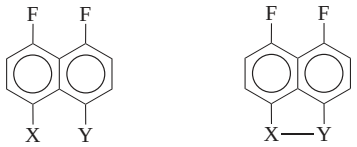

(16) **(17)**

Figure 6 The types of 1,8-difluoronaphthalene (**16**) and 5,6-difluoroacenaphthene (**17**) derivatives for which $J(FF)$ values are listed in Table 2 and plotted in Figure 7

in which the two fluorine atoms are splayed apart as a consequence of the distortions in the peri-angles caused by the strained five-membered ring, to 82.3 Hz for 4,5-dicyano-1,8-difluoronaphthalene, in which the two fluorine atoms are pushed together as a consequence of the distortions of the peri-angles in the opposite sense caused by van der Waals repulsion between the two cyano groups. A semilogarithmic plot of $J(FF)$ against d_{FF} is shown in Figure 7. The data appear to be well correlated by the straight line shown in Figure 7, which leads to the relationship:

$$J(FF) = (9.64 \times 10^5)e^{-3.78d_{FF}} \quad (2)$$

The average vertical deviation of points from the line in Figure 7 is ±2.6 Hz and the correlation coefficient is 0.99. [We did not include in Figure 7 the data of 5,6-difluoroacenaphthylene, which would have given a point about 9.6 Hz above the correlation line. The reason for this large discrepancy remains obscure, although we suspect that the –CH=CH– bridge might give rise to an enhanced through-bond component $J(FF)^{TB}$.]

Of course in order to use these data to provide a rigorous test of the validity of the lone-pair overlap theory one would need to plot not the total coupling constant $J(FF)$, but rather the through-space component $J(FF)^{TS}$, which is given by $J(FF) - J(FF)^{TB}$ where $J(FF)^{TB}$ is the through-bond component. Unfortunately, neither the magnitude nor the sign of $J(FF)^{TB}$ is known for any of the compounds in the series, although it seems likely from the large magnitudes of the observed coupling constants that the magnitude of $J(FF)^{TyB}$ is small relative to $J(FF)$. Granted that the interpretation of

Table 2 Values of the Measured F–F Coupling Constants $J(FF)$ and the Calculated F–F Distances d_{FF} for Various Molecules of Types (**16**) and (**17**), and the Amounts by which these Experimental Coupling Constants Deviate from the Linear Correlation Plotted in Figure 7 and Expressed by Equation (2)

System	Perisubstituents X and Y	d_{FF} (nm)	$J(FF)$ (Hz)	Deviation from plot (Hz)
17	$-CH_2-CH_2-$	0.2740	28.1	−2.2
17	–C(=NOH)–C(=NOH)–	0.2735	31.0	+0.1
17	–C(=O)–C(=O)–	0.2745	31.5	+1.8
17	Quinoxaline deriv. of diketone	0.2720	33.0	+0.3
16	–CH=CH–	0.2775	36.1	+9.6
16	H, H	0.2560	58.8	−1.0
16	–C(=O)–O–C(=O)–	0.2570	61.5	+3.9
16	H, NH_2	0.2520	61.8	−7.8
16	H, CH_3	0.2540	64.4	−0.1
16	H, $NHCOCH_3$	0.2525	64.6	−3.7
16	H, Cl	0.2530	65.7	−1.3
16	H, CN	0.2540	65.9	+1.4
16	H, Br	0.2525	67.4	−0.9
16	H, NO_2	0.2520	75.2	+5.6
16	CN, CN	0.2495	82.3	+5.8

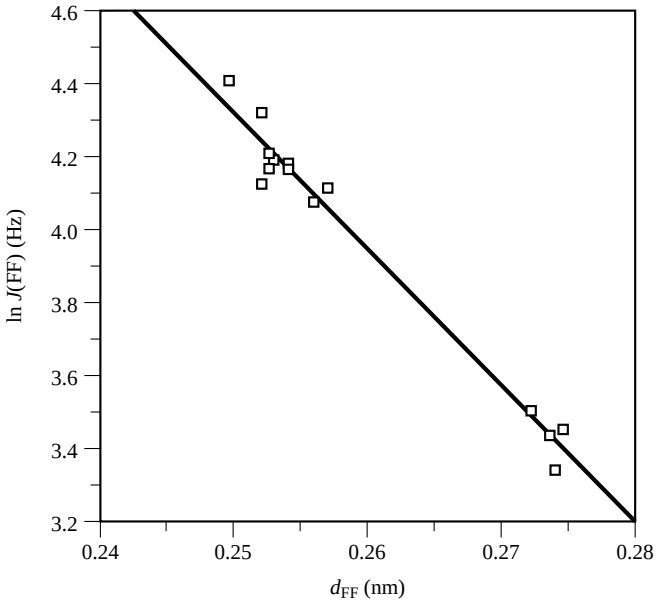

Figure 7 Semilogarithmic plot of J(FF) vs. d_{FF} for the derivatives of 1,8-difluoronaphthalene and 5,6-difluoroacenaphthene listed in Table 2 and pictured in Figure 6

the plot in Figure 7 is flawed by this uncertainty about the magnitude of the through-bond contribution to the observed J(FF) values, it nonetheless can be argued that the linear trend in this semilogarithmic plot provides at least qualitative support for the idea that through-space F–F coupling falls off exponentially with distance.

As an aside, an indication that there is a small through-bond component in the observed coupling constants in this series can be seen from the pattern exhibited by the small deviations of the experimental J(FF) values from the line plotted in Figure 7. The points for all seven of the compounds with π-acceptor substituents lie above the line: dicyano, +5.8; nitro, +5.6; anhydride, +3.9; diketone, +1.8; cyano, +1.4; quinoxaline, +0.3; and dioxime, +0.1 Hz. In contrast, the points for all six of the compounds with π-donor substituents lie below the line: methyl, −0.1; bromo, −0.9; chloro, −1.3; $-CH_2CH_2-$, −2.2; acetamido, −3.7; and amino, −7.8 Hz. The trend in these substituent effects is similar to the trend reported for the through-bond F–F coupling that takes place through the π-electron system in the 4-substituted-1,3-difluorobenzenes.[28] Relative to the F–F coupling constant of +6.6 Hz for 1,3-difluorobenzene itself, π-acceptor substituents at C-4 make J(FF) more positive and π-donor substituents at C-4 make J(FF) less positive by the following increments: nitro, +5.6; cyano, +4.3; chloro, −0.4; bromo, −0.5; methyl, −2.0; and amino, −8.7 Hz. It is perhaps not unreasonable to suspect that the 4-substituted-1,3-difluorobenzenes and the 4-substituted-1,8-difluoronaphthalenes may be analogous with respect to through-bond coupling through the π system because these two families of molecules share some common structural features; in each family the two fluorines are unconjugated with each other and separated by four bonds, and the substituent is *para* with respect to one of the fluorine atoms and also conjugated with the other fluorine atom.

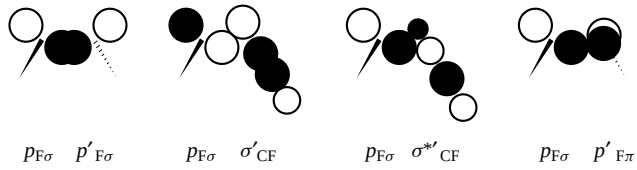

Figure 8 Schematic representations of several types of orbital overlap that may play a role in through-space F–F coupling in 4,5-difluorophenanthrene systems such as (**2**)

For 4,5-difluorophenanthrenes such as (**2**), the C–F bonds are neither parallel nor coplanar, which makes the orbital overlap picture of through-space F–F coupling more complicated than that described above for the 1,8-difluoronaphthalenes such as (**1**). As illustrated in Figure 8, the orientation of the two fluorine atoms in the 4,5-difluorophenanthrene system may allow contributions to through-space F–F coupling from overlap interactions of the $p_{F\sigma}-\sigma'_{CF}$, $p_{F\sigma}-\sigma^{*\prime}_{CF}$, and $p_{F\sigma}-p'_{F\pi}$ types in addition to the major contribution arising from overlap interaction of the $p_{F\sigma}-p'_{F\sigma}$ type. These additional modes of overlap may be responsible for the fact that the measured value of 174 Hz for the F–F coupling constant for 4,5-difluoro-1-methylphenanthrene (**2**) is so much larger than the value of 97 Hz that would have been predicted from the correlation line in Figure 7 for the F–F distance of 0.2434 nm found experimentally for (**2**).[29] One should be cautious, however, about attempting quantitative comparisons involving J(FF) values in different systems such as 1,8-difluoronaphthalenes and 4,5-difluorophenanthrenes because of the uncertainties about the magnitudes and the signs of the through-bond components.

Yet another spatial array that leads to through-space F–F coupling is found in 1,12-difluorobenzo[*c*]phenanthrenes such as (**3**). For steric reasons this ring system adopts a helical structure such that the dominant orbital overlap interaction leading to through-space coupling between the two fluorine atoms involves the 'out-of-plane' $p_{F\pi}$ and $p'_{F\pi}$ lone-pair orbitals as illustrated in Figure 9. (For simplicity in this conceptual presentation we have neglected the strong mixing of these $p_{F\pi}$ and $p'_{F\pi}$ orbitals with various π orbitals that are characteristic of the benzo[*c*]phenanthrene ring system.) For the particular example of 4-bromo-1,12-difluorobenzo[*c*]phenanthrene the F–F distance is 0.2535 nm and the value of J(FF) is 45 Hz.[8,29] At this F–F distance the correlation line for the 1,8-difluoronaphthalene system in Figure 7 would predict a significantly larger value of 66 Hz for J(FF). This discrepancy may reflect an orientation effect: the $p_{F\sigma}-p'_{F\sigma}$ overlap in the 1,8-difluoronaphthalene system is nearly optimum because the orbital axes are almost colinear, whereas the $p_{F\pi}-p'_{F\pi}$ overlap in the 1,12-difluorobenzo[*c*]phenanthrene system is less than optimum because of the significant departure of the orbital axes from colinearity, as shown in Figure 9. Once again, however, such comparisons between two different systems are risky because of our lack of knowledge of the through-bond contributions to the observed values of J(FF).

3 NF AND PF SYSTEMS

The lone-pair overlap theory presented here can be extended in a simple way to account for two other types of through-space coupling between spatially proximate atoms bearing lone

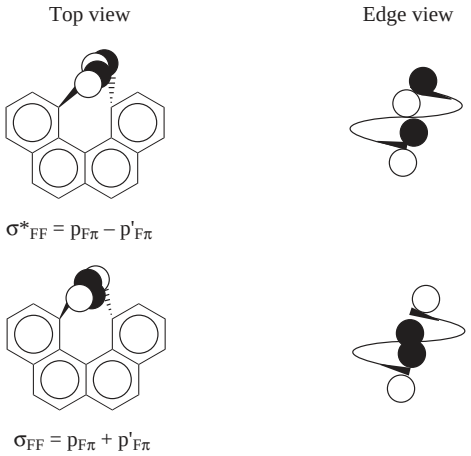

Figure 9 Schematic representations from two vantage points of the bonding and antibonding orbitals, σ_{FF} and σ^*_{FF}, resulting from the mutual overlap of the two 'out-of-plane' lone-pair orbitals, $p_{F\pi}$ and $p'_{F\pi}$, in 1,12-difluorobenzo[*c*]phenanthrene systems such as (**3**)

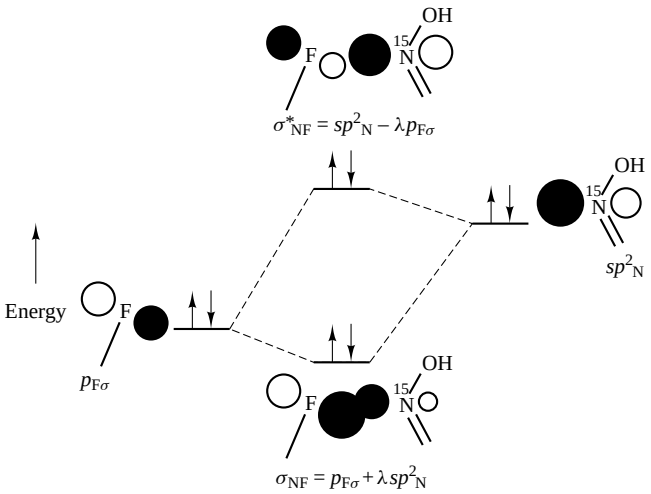

Figure 10 Schematic representations of the approximate shapes and relative energies of the bonding and antibonding molecular orbitals, σ_{NF} and σ^*_{NF}, that result from the overlap of an in-plane p_F lone-pair orbital and an $sp^2{}_N$ lone-pair orbital on spatially proximate fluorine and nitrogen atoms oriented as in oxime acetate (**12**)

pairs, namely N–F and P–F coupling. The lone-pair orbital overlap interactions thought to be important for through-space N–F coupling are illustrated in Figure 10 for a structural array similar to that in oxime acetate (**12**). Through-space P–F coupling in molecules such as (**14**) can be accounted for in an analogous fashion. The dependence of N–F and P–F through-space coupling on distance and orientation effects appears to be similar to the dependence on these two factors found for the much more thoroughly studied through-space coupling in F–F systems.[9,14,30]

4 HF, CF, AND CP SYSTEMS

The lone-pair overlap theory can be extended yet further by hypothesizing that through-space coupling can result from lone-pair–bond-pair overlap as well as from lone-pair–lone-pair overlap as considered above. Through-space H–F and C–F coupling has been extensively documented in a variety of molecules in which either the hydrogen end or the carbon-13 end of a C–H bond is in close spatial contact with a fluorine 2*p* lone pair. As illustrated in Figure 11 and Figure 12, respectively, this coupling can be attributed to the overlap of the fluorine lone-pair orbital with the CH bonding orbital, augmented by some overlap of the fluorine lone pair with the corresponding CH antibonding orbital. The orbital mixing that arises from this overlap of these three basis orbitals creates three three-center molecular orbitals in each case, a pair of filled bonding and antibonding orbitals that are involved in the through-space coupling, and also one high-energy antibonding orbital that is empty and therefore plays no role in coupling.

In the F ··· HC orientation, for which the two filled three-center orbitals σ_{FHC} and σ^*_{FHC} are depicted in Figure 11, the amplitudes of the wave functions are such that the electron density in the bonding σ_{FHC} orbital is concentrated mostly in the middle region of the three-atom array, whereas the electron density in the antibonding σ^*_{FHC} orbital is concentrated mostly at the ends of the three-atom array. The spin-polarization pattern of these two pairs of electrons that appears to lead overall to the most favorable combination of Hund and Fermi interactions in the F ··· HC system is shown in Figure 13(a). By analogy with the F–F system discussed in the preceding section, we believe that the σ_{FHC} electron will experience Hund interactions at the fluorine atom primarily with the outer region of the spin-polarized s_F orbital, and therefore will prefer to have its spin aligned parallel to the spin of the fluorine nucleus. Also by analogy with the F–F system discussed above, we believe that the σ^*_{FHC} electron will experience Hund interactions at the fluorine atom primarily with the inner region of the spin-polarized s_F orbital, and therefore will prefer to have its spin aligned antiparallel to

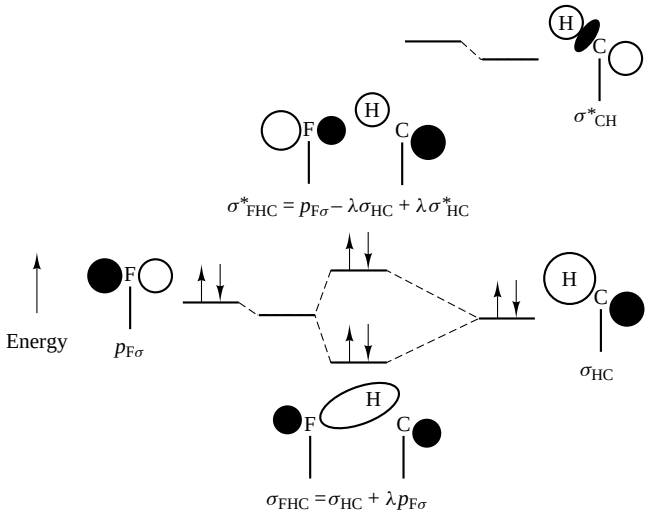

Figure 11 Schematic representations of the approximate shapes and relative energies of the three-center bonding and antibonding molecular orbitals, σ_{FHC} and σ^*_{FHC}, that result from the overlap of a $p_{F\sigma}$ lone-pair orbital with a σ_{HC} orbital and a σ^*_{HC} orbital in a system such as (**6**) or (**8**) in which the fluorine atom is crowded against the hydrogen end of the CH fragment

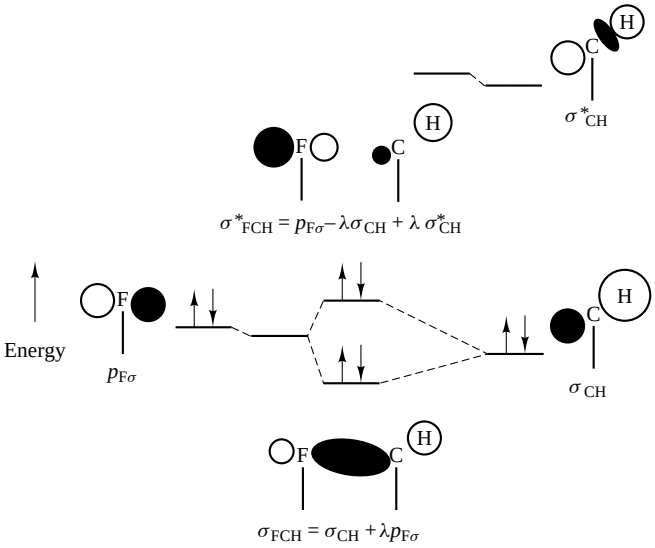

Figure 12 Schematic representations of the shapes and relative energies of the three-center bonding and antibonding molecular orbitals, σ_{FCH} and σ^*_{FCH}, that result from the overlap of a $p_{F\sigma}$ lone-pair orbital with a σ_{CH} orbital and a σ^*_{CH} orbital in a system such as (**9**) in which the fluorine atom is spatially proximate to the carbon end of the CH fragment

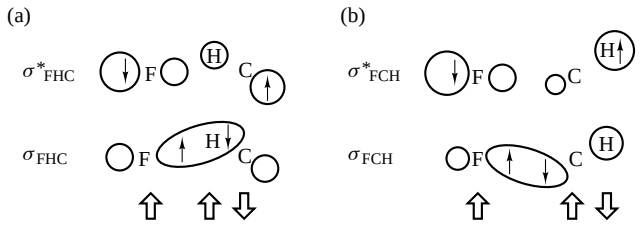

Figure 13 Schematic representations of the preferred relative alignments of electron spins and nuclear spins in two systems: (a) the F ··· HC system depicted in Figure 11, and (b) the F ··· CH system depicted in Figure 12

the spin of the fluorine nucleus. The hydrogen and carbon-13 nuclei in this system interact with the σ_{FHC} and σ^*_{FHC} electrons by direct Fermi contact, which results in a preference for an antiparallel alignment of nuclear and electron spins in the regions around each of these nuclei. This analysis leads to the overall prediction that with respect to the through-space components of the H–F and C–F coupling in this system the hydrogen and fluorine nuclei in the F ··· HC system will prefer to have parallel nuclear spins, while the carbon and fluorine nuclei and also the carbon and hydrogen nuclei will prefer to have antiparallel nuclear spins, as shown in Figure 13(a). This prediction is in accord with the experimental demonstrations in these F ··· HC systems that the H–F coupling constants are negative and the C–F and C–H coupling constants are positive.[10,11,31]

In the F ··· CH orientation, for which the two filled three-center orbitals σ_{FCH} and σ^*_{FCH} are depicted in Figure 12, the electron density in the bonding σ_{FCH} orbital is once again concentrated mostly in the middle region of the three-atom array while the electron density in the antibonding σ^*_{FCH} orbital is concentrated mostly at the ends of the three-atom array. The spin-polarization pattern of these two pairs of

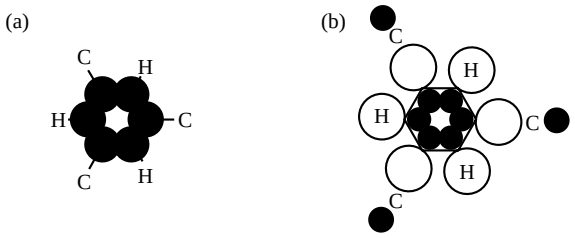

Figure 14 Top views of (a) the lowest-energy π orbital and (b) one of the σ orbitals of the basal trisubstituted benzene ring in phosphorus compound (**15**)

electrons that appears to lead overall to the most favorable combination of Hund and Fermi interactions in the F ··· CH system is shown in Figure 13(b). This analysis leads to the overall prediction that with respect to the through-space components of H–F and C–F coupling in this system the hydrogen and fluorine nuclei and also the carbon and hydrogen nuclei will prefer to have antiparallel nuclear spins, consistent with the experimental observations that the H–F and C–H coupling constants in these F ··· CH systems are each positive in sign. The pattern in Figure 13(b) also predicts that $J(FC)^{TS}$ in this system should be negative. In fact, the total coupling constant $J(FC)$ is found to be small and negative in a particular F ··· CH system similar to (**9**),[11] but in contrast $J(FC)$ is found to be positive in system (**9**) itself and other F ··· CH systems.[31] Perhaps this discrepancy arises because the through-bond component of the C–F coupling in molecules such as (**9**) is positive in sign and sufficiently large in magnitude to override the small negative through-space component of the C–F coupling that is predicted by the analysis shown in Figure 13(b). Alternatively, perhaps that analysis is simply not a reliable basis on which to predict the sign of $J(FC)$ in such systems.

The recently reported novel through-space coupling between phosphorus and carbon-13 nuclei in molecules such as (**15**) has been attributed to overlap interactions involving the lowest-energy π orbital of the basal trisubstituted benzene ring shown in Figure 14(a).[16,17] This π orbital has the proper symmetry to mix with the lone-pair orbital on the phosphorus atom to generate two new filled seven-center molecular orbitals, one bonding and the other antibonding in the region between the phosphorus atom and the benzene ring. As an alternative possibility for consideration we suggest that the observed P–C coupling in (**15**) might involve mixing of the phosphorus lone-pair orbital with the σ orbital of the basal benzene ring shown in Figure 14(b). This mixing would generate a bonding and antibonding pair of filled 13-center molecular orbitals.

5 HH SYSTEMS

Having considered above how through-space coupling can be viewed as arising mainly from overlap interactions between two lone pairs or between one lone pair and one bond pair, it remains to consider the through-space coupling that arises from overlap interactions between two bond pairs. The large 18 Hz coupling between the two bridgehead hydrogen atoms in bicyclo[1.1.1]pentane (**10**) can be attributed to such interactions.[12,13] As shown in Figure 15, the mutual overlap of the rear lobes of the two filled C–H bond orbitals σ_{CH} and

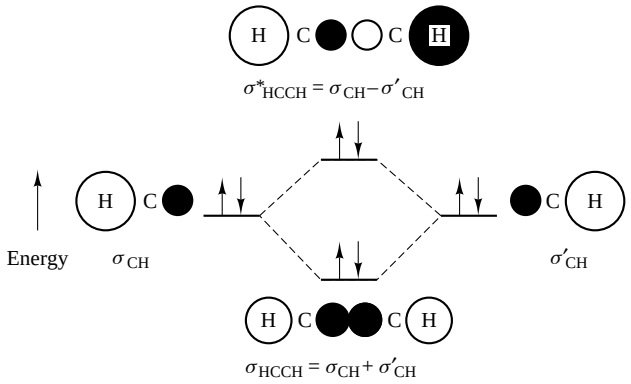

Figure 15 Schematic representations of the approximate shapes and relative energies of the four-center bonding and antibonding molecular orbitals, σ_{HCCH} and σ^*_{HCCH}, that result from the overlap of two filled CH bond-pair orbitals (with slight admixture of the corresponding two empty CH antibonding orbitals that are not shown explicitly here) oriented with their carbon ends spatially proximate as for the bridgehead C–H bonds in bicyclo[1.1.1]pentane (**10**)

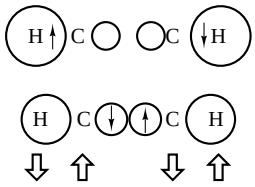

Figure 16 Schematic representations of the preferred relative alignments of electron spins and nuclear spins in the HC ··· CH system depicted in Figure 15

σ'_{CH}, modified slightly by overlap interactions of these filled orbitals with the empty antibonding orbitals σ^*_{CH} and $\sigma^{*\prime}_{CH}$, would give rise to two new four-center molecular orbitals, one bonding and the other antibonding. This orbital mixing creates a four-center four-electron HCCH linkage for the transmittal of nuclear spin information among the four nuclei. As illustrated in Figure 16, this analysis correctly predicts a positive sign for J(HH) in bicyclo[1.1.1]pentane (**10**).

One could imagine that through-space H–H coupling also might result when the hydrogen ends of two C–H bonds are brought into close proximity with one another. Many examples of through-space H–H couplings in this latter type of orientation have been reported, but they are very small in magnitude.

6 F–F COUPLING THROUGH NONBONDED INTERACTIONS WITH AN INTERVENING ORBITAL

Finally, the lone-pair overlap theory has proved itself to be useful by predicting the existence of a new type of through-space F–F coupling in which the two coupled fluorines are not crowded directly against one another but rather are each crowded in a nonbonding way against an intervening group X in molecules such as 1,8-difluoro-9-X-anthracenes.[32] For example, various 1,8-difluoro-9-phenylanthracenes show values of J(FF) in the range of 5–6 Hz as compared with

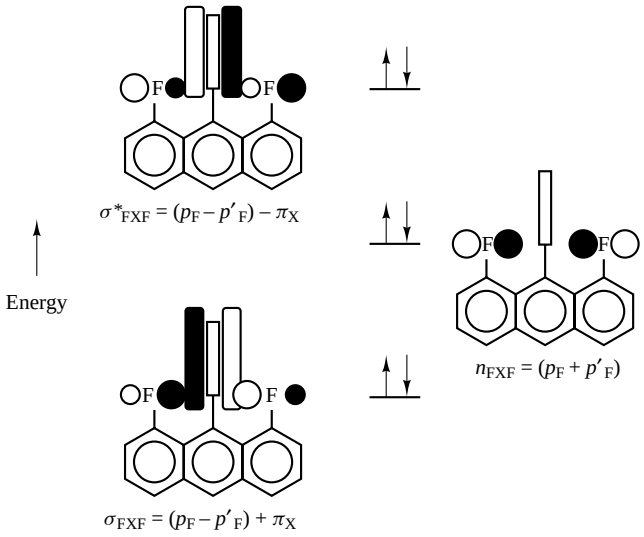

Figure 17 Schematic representations of the three mixed orbitals thought to be involved in through-space F–F coupling in the 1,8-difluoro-9-phenylanthracene system

J(FF) values of less than 1 Hz for the corresponding 1,8-difluoroanthracenes.[9,32] As a result of the steric demands in this system the phenyl group is oriented with its plane perpendicular to the plane of the anthracene ring. The pathway for the transmission of nuclear spin information in this system is believed to result from the overlap interactions of three basis orbitals, including two fluorine lone-pair orbitals and the lowest-energy filled π orbital on the intervening phenyl group. These interactions generate a set of three mixed orbitals, including one three-center bonding orbital σ_{FXF}, one three-center nonbonding orbital n_{FXF}, and one three-center antibonding orbital σ^*_{FXF} as in Figure 17. The lowest-energy π orbital is expected to have the most effective interactions here because ab initio molecular orbital calculations indicate that its energy is very close to that of the fluorine lone-pair orbitals.[9] In addition, however, other π and π^* orbitals on the phenyl that possess the correct symmetry for overlap with the fluorine orbitals also may play a role in the F–X–F coupling.

7 RELATED ARTICLES

NF153-Fluorine-19 NMR; NN303-Nuclear Spin Properties and Notation; NS465-Stereochemistry and Long Range Coupling Constants

8 REFERENCES

1. J. D. Roberts, D. R. Davies, and R. P. Lutz, *J. Am. Chem. Soc.*, 1961, **83**, 246.
2. L. Petrakis and C. H. Sederholm, *J. Chem. Phys.*, 1961, **35**, 1243.
3. J. Hilton and L. H. Sutcliffe, *Prog. NMR Spectrosc.*, 1975, **10**, 27.
4. R. H. Contreras, M. A. Natiello, and G. E. Scuseria, *Magn. Reson. Rev.*, 1985, **9**, 239.

5. S. L. Manatt, M. A. Cooper, C. W. Mallory, and F. B. Mallory, *J. Am. Chem. Soc.*, 1973, **95**, 975.
6. S. L. Manatt and M. A. Cooper, *J. Am. Chem. Soc.*, 1977, **99**, 4651.
7. F. B. Mallory, C. W. Mallory, and W. M. Ricker, *J. Am. Chem. Soc.*, 1975, **97**, 4770.
8. F. B. Mallory, C. W. Mallory, and W. M. Ricker, *J. Org. Chem.*, 1985, **50**, 457.
9. Some of the information in this article derives from unpublished experiments and calculations carried out at Bryn Mawr College in collaboration with: Eddie Luzik and Mercy Ramanjulu (graduate students); Laura Fredenburgh, Kelly Butler, Que Van, Mary Beth Lewis, Chandra Wray, Maia Whang, and Christine Hann (undergraduate students); and Michelle Francl, Maryellen Nerz-Stormes, and Lisa Chirlian (faculty colleagues).
10. L. C. Hsee and D. J. Sardella, *Magn. Reson. Chem.*, 1990, **28**, 688.
11. I. D. Rae, J. A. Weigold, R. H. Contreras, and G. Yamamoto, *Magn. Reson. Chem.*, 1992, **30**, 1047.
12. K. B. Wiberg, G. M. Lampman, R. P. Ciula, D. S. Connor, P. Schertler, and J. Lavanish, *Tetrahedron*, 1965, **21**, 2749.
13. M. Barfield, E. W. Della, P. E. Pigou, and S. R. Walter, *J. Am. Chem. Soc.*, 1982, **104**, 3549.
14. F. B. Mallory, E. D. Luzik, Jr, C. W. Mallory, and P. J. Carroll, *J. Org. Chem.*, 1992, **57**, 366.
15. T. Schaefer, K. Marat, A. Lemire, and A. F. Janzen, *Org. Magn. Reson.*, 1982, **18**, 90.
16. R. P. L'Esperance, A. P. West, Jr., D. Van Engen, and R. A. Pascal, Jr, *J. Am. Chem. Soc.*, 1991, **113**, 2672.
17. A. P. West, Jr, N. Smyth, C. M. Kraml, D. M. Ho, and R. A. Pascal, Jr, *J. Org. Chem.*, 1993, **58**, 3502.
18. K. L. Servis and K. Fang, *J. Am. Chem. Soc.*, 1968, **90**, 6712.
19. B. J. Kimber, J. Feeney, G. C. K. Roberts, B. Birdsall, D. V. Griffiths, A. S. V. Burgen, and B. D. Sykes, *Nature*, 1978, **271**, 184.
20. A. C. Diz, C. G. Giribet, M. C. Ruiz de Azua, and R. H. Contreras, *Int. J. Quantum Chem.*, 1990, **37**, 663.
21. M. C. Ruiz de Azua, A. C. Diz, C. G. Giribet, and R. H. Contreras, *Int. J. Quantum Chem.*, 1986, **S20**, 585.
22. F. B. Mallory, *J. Am. Chem. Soc.*, 1973, **95**, 7747.
23. A. Meresse, C. Courseille, F. Leroy, and N. B. Chanh, *Acta Crystallogr., Sect. B*, 1975, **31**, 1236.
24. D. A. Goodings, *Phys. Rev.*, 1961, **123**, 1706.
25. J. Kowalewski, *Prog. NMR Spectrosc.*, 1978, **11**, 1.
26. C. J. Jameson and H. S. Gutowsky, *J. Chem. Phys.*, 1969, **51**, 2790.
27. F. B. Mallory, C. W. Mallory, and M.-C. Fedarko, *J. Am. Chem. Soc.*, 1974, **96**, 3536.
28. R. J. Abraham, D. B. Macdonald, and E. S. Pepper, *J. Am. Chem. Soc.*, 1968, **90**, 147.
29. These F–F distances were determined through single-crystal X-ray diffraction studies carried out by P. J. Carroll at the University of Pennsylvania, PA, USA.
30. F. B. Mallory and C. W. Mallory, *J. Am. Chem. Soc.*, 1985, **107**, 4816.
31. M. Barfield, S. R. Walter, K. A. Clark, G. W. Gribble, K. W. Haden, W. J. Kelly, and C. S. Le Houllier, *Org. Magn. Reson.*, 1982, **20**, 92.
32. F. B. Mallory, C. W. Mallory, and M. B. Baker, *J. Am. Chem. Soc.*, 1990, **112**, 2577.

Biographical Sketches

Frank B. Mallory. *b* 1933. B.S., 1954, Chemistry, Yale University, USA, Ph.D., 1958, Chemistry, California Institute of Technology, USA. Faculty, Bryn Mawr College, USA, 1957–present. Currently W. Alton Jones Professor of Chemistry. Approx. 70 publications. Research specialties: ^{19}F NMR studies, photocyclizations of stilbenes, nuclear spin relaxation measurements of methyl rotation barriers in crystalline solids.

Clelia W. Mallory. *b* 1938. A.B., 1959, M.A., 1960, Ph.D., 1963, Chemistry, Bryn Mawr College, USA. Postdoctoral work at Bryn Mawr College, 1963–present. Faculty, Yale University, USA, 1977–80. Faculty, University of Pennsylvania, USA, 1980–present. Currently senior lecturer in Chemistry. Approx. 30 publications. Research specialties: ^{19}F NMR studies, photocyclizations of stilbenes.

Dynamics in Solid Organic Compounds: Intramolecular Motions

Frank G. Riddell

The University of St Andrews, St Andrews, UK

1 Introduction 1
2 Line Shape Methods 1
3 Spin Lattice Relaxation Time Methods 2
4 Maximum Dipolar Broadening 4
5 $T_{1\rho}$ Measurements 5
6 ^{2}H Quadrupolar Echo Methods 7
7 Measurement of Temperature in MAS Experiments 8
8 Related Articles in this Volume 8
9 Related Articles in Volumes 1–8 8
10 References 8

1 INTRODUCTION

Conventional crystallographic representations of molecules in solids give the impression that the molecules are held rigidly in place in the crystal as static motionless bodies. However, molecules and their component groups and atoms are certainly not motionless in solids. Molecules in solids are dynamic entities with a wide range of different molecular motion types.

Although most types of molecular motion are generally slower in solids than in liquids, they may have an important role in determining the macroscopic properties of solid materials. This applies to all solids irrespective of their degree of crystallinity. For example, the mechanical properties of important materials such as polymers are closely related to their microscopic structures and molecular motions. In addition, the conductivity of solid polymer electrolytes and the electrical properties of conducting polymers originate from motions at the molecular level. It becomes important, therefore, to gain an understanding of the nature of these motions in all types of solids and their relative rates and activation energies.

Several physical techniques can be employed to examine these molecular dynamics including the measurement and interpretation of anisotropic displacement parameters from diffraction techniques, Raman scattering, Brillouin scattering and dielectric relaxation. However, the most versatile technique is NMR spectroscopy. NMR is particularly powerful because by judicious choice of the nucleus to be observed and the NMR technique to be employed a wide range of time scales for molecular motions are available.[1] A general rule of thumb is that if the frequency, or time scale for a nuclear interaction is similar to that of the molecular process occurring, the molecular process will modulate the NMR interaction, which will give rise to an observable effect in most cases. Since many more NMR interactions are present in solids than in solution (where they are averaged to zero by rapid isotropic molecular tumbling) observation of molecular motions in solids is greatly facilitated. Moreover, both broad line (static samples) and high resolution (magic angle spinning) methods are available. Such processes have included, but are not restricted to, rotations or displacements of whole molecules; segmental motions in polymer chains; conformational dynamics in molecules such as bond rotations, ring inversions and pseudorotations; molecular rearrangements such as sigmatropic rearrangements and dynamic tautomerism; and hydrogen bond exchange processes.

An alternative way in which NMR can be used to measure the kinetics of molecular processes is to create a magnetic label at one site (chemical shift) and watch it being transferred to another. Such methods include inversion and saturation transfer and 2D EXSY spectroscopy. These measurements are made in real time and consequently their time scale is dependent on the nuclear relaxation times involved. This article reviews several diverse applications of solid-state NMR spectroscopy falling into the categories described above. Table 1 summarizes the major methods, their origins, and the typical rate ranges that they can be employed to study.

It is interesting to compare the kinetics of processes happening in the solid state with those observed in solution. In many cases involving conformational rate processes the rates in solids are considerably slower than those observed in solution. This is because of the additional constraints imposed upon such process by the neighboring molecules in the lattice. These constraints are not present in solution leading to lower energies of activation. This effect has been referred to as the principal of least distress.[3] On the other hand for intramolecular tautomerization processes in which hydrogen atoms travel short distances such effects are negligible.

2 LINE SHAPE METHODS

Line shape methods have been used extensively in high resolution solution state NMR for many years, and are also available in solids under conditions of magic angle spinning (MAS). In particular ^{13}C CP/MAS NMR has yielded much useful information. Line shape effects occur in the exchange region where the chemical shift difference between sites in a molecule is of the same order as the rate at which they are exchanging. The basic theory for these effects was given by McConnell,[2] and often the modified Bloch equations are used for line shape calculations. Many computer programs are available for line shape calculations.

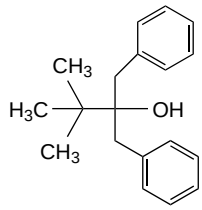

(1)

Table 1 Widely used methods for studying dynamic processes in solids

Method	Approximate rate range	Outcomes
T_1	Near Larmor frequency 10^6–10^9 Hz	Frequency of motion
$T_{1\rho}$	Near spin lock frequency 10^3–10^6 Hz	Frequency and often mode of motion
Line shape	Near chemical shift difference 10–10^4 Hz	Frequency of motion
2D EXSY	Near $1/T_1$ 10^{-2}–10 Hz	Frequency of motion
Magnetization transfer	Near $1/T_1$ 10^{-2}–10 Hz	Frequency of motion
^{2}H quadrupole echo spectra	Near quadrupole coupling constant 125– kHZ	Frequency and often mode of motion

Line shape changes due to dynamic effects in ^{13}C CP/MAS spectra are illustrated very simply in Figure 1.[3] The changes arise from the *t*-butyl group rotation in **(1)**. At low temperatures rotation of the *t*-butyl group is slow (i.e., rate of rotation is $\ll \delta\nu$(hz)) and three methyl resonances are seen. The coalescence of the three methyls into a single peak is observed at around 293 K ($\Delta G_c^{\neq} = $ ca 55 kJ mol^{-1}) The solution state coalescence takes place at approximately 183 K ($\Delta G_c^{\neq} = $ ca 38 kJ mol^{-1}). The lifting of the degeneracy of two of the methyl groups in solution is due to molecular dissymetry in the crystal lattice. The increase in the activation energy by around 17 kJ mol^{-1} is due to the additional constraints imposed upon the process in the solid by the neighboring molecules.

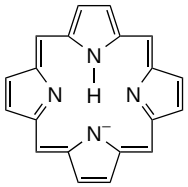

(2)

An alternative, both in the nucleus employed and the result obtained, is seen in Figure 2.[4] This shows the line shape changes in the ^{15}N CP/MAS spectra due to hydrogen exchange between the nitrogens in the porphyrin anion **(2)** encased in a solid matrix. In contrast to the example given above the degeneracy of the exchange seen in solution is not lifted in the solid state with only three ^{15}N resonances being observed. The rates of hydrogen transfer are very similar to those determined in solution. In this case there is no effect from neighboring molecules as the exchange is buried deep inside the molecule.

An example of six-membered ring inversion between two unequal sites is seen in Figure 3.[5] In this case the dynamic spectral effects arise from ring inversion of cyclohexanol encased in a thiourea inclusion compound and were obtained by a ^{13}C single pulse MAS technique not CP/MAS. The smaller set of peaks in the low temperature spectra arise from the axial conformation. The free energy of activation for the ring inversion process (51 kJ mol^{-1} (eq to ax)) and the free energy difference (ca. 2.5 kJ mol^{-1}) are close to those observed for the compound in non-hydrogen bonding solvents (50 kJ mol^{-1} (eq to ax)) and (ca. 2.1 kJ mol^{-1}). Interestingly for several other mono-substituted cyclohexanes in thiourea inclusion compounds very different conformational parameters are obtained from those of the molecules free in solution.

In the above examples there were no spinning side bands in the high resolution solid state ^{13}C spectra. Where there is a spinning sideband manifold, line shape analysis in principle requires consideration of the whole sideband pattern and not just the peaks at the isotropic chemical shifts. This is seen in a ^{13}C CP/MAS study of the sigmatropic Cope rearrangement of bullvalene in the solid state.[6,7] Because the crystal structure of bullvalene as determined by X-ray crystallography is very highly ordered it was originally thought that the Cope rearrangement was not taking place in the solid. However, NMR studies have shown that in the solid state the molecule of bullvalene undergoes a sigmatropic rearrangement followed by a reorientation to regain the original molecular orientation in the solid. This process is given the rate constant k_c. Accompanying this process is a 3-fold rotation of the molecules as a distinct process given the rate constant k_r. These processes are shown in Figure 4 and the observed CP/MAS spectra are shown in Figure 5.

If the rotation were the only process the resonance for C4 would remain unaffected. The fact that this line broadens less rapidly than the others as the temperature is increased indicates the existence of the two processes and the line shape patterns at varying temperatures can be fitted to a process involving the two rate constants k_c and k_r. It should be noted that the spinning sidebands are observed for the superimposed resonances of C2 and C3 and that these form part of the coalescence pattern. Extracted Arrhenius activation energies for the Cope rearrangement and the three-fold rotation are found to be 63 and 88 kJ mol^{-1} respectively.

3 SPIN LATTICE RELAXATION TIME METHODS

Spin lattice relaxation, designated by the relaxation time T_1, and relaxation in the rotating frame, designated by the relaxation time T_1 can form excellent probes for molecular motions in very different regions of molecular dynamics. The stimulation of NMR transitions at the heart of these relaxation processes occurs when the nucleus interacts with fluctuating fields inside the sample. There are two important fluctuating fields. The first is a fluctuating magnetic field that can interact with the nuclear magnetic moment. The second is a fluctuating electric field gradient (EFG) that can interact with the electric quadrupole moment of the nucleus (if it possesses one). Only quadrupolar nuclei ($I > 1/2$) have electric quadrupole moments. In all cases the frequency of the fluctuating field must be at or close to the field in which the nuclei are held. In addition, the exchange process to be studied must be the exclusive or principal cause of the nuclear relaxation.

For heteronuclei three cases can be identified: (i) static powders, (ii) powders being spun at the magic angle, and (iii) powders where longitudinal relaxation is isotropically

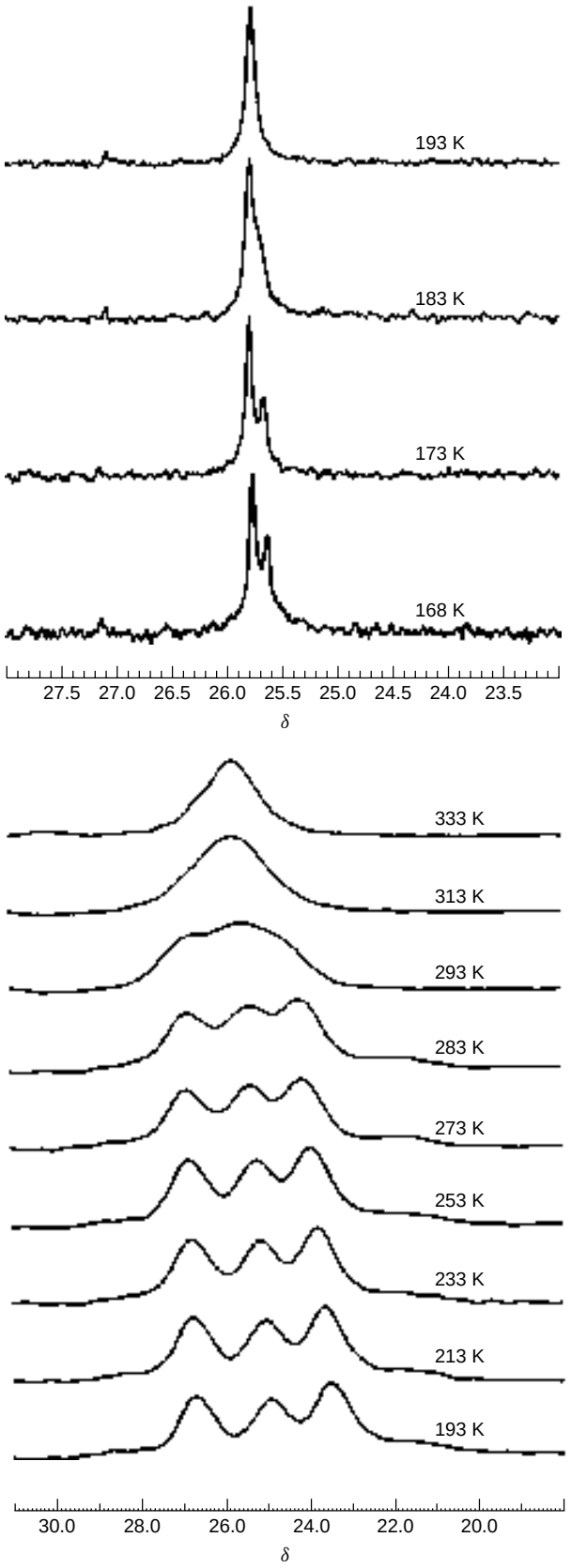

Figure 1 125.758 MHz ^{13}C line shape changes at variable temperature for **(1)** in the solid (CP/MAS) (lower set) and solution states. The changes are due rotation of the *tert*-butyl group. Reproduced with permission from Ref.[5]

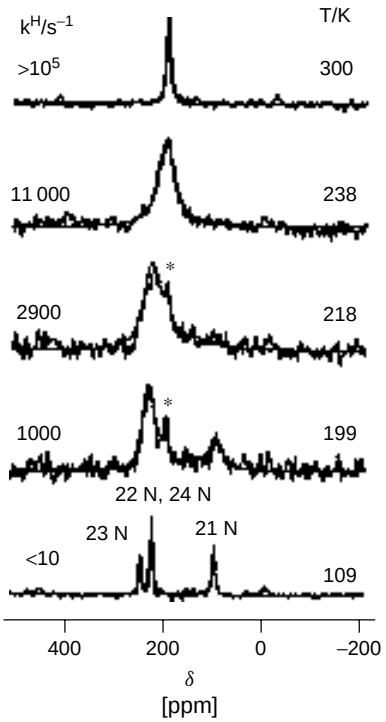

Figure 2 Line shape changes in the 9.12 MHz ^{15}N CP/MAS spectra of **(2)** at variable temperature. The changes are due to hydrogen exchange between the nitrogens in the porphyrin anion. Reproduced with permission from Figure 5 in Ref.[4]

averaged by magnetization transfer. In (i) relaxation is multiexponential and consequently difficult to evaluate. In (iii) relaxation is truly exponential with a single relaxation time T_1, which is related in a straightforward way to the dipolar interaction(s) and the equilibrium and rate constants, but this is experimentally very difficult to obtain. In contrast (ii) represents an ideal compromise – relaxation is quasi exponential and is governed to a good approximation by the dipolar interaction(s), rate and equilibrium constants. Rates of ultrafast exchanges can be measured by this technique. For example, this technique was employed by Hoelger et al.[8] to study the hydrogen exchange dynamics in ^{15}N labelled dimethyldibenzyltetraaza[14]annulene (see Figure 6).[8] The hydrogen transfer rates that were measured were in the range $10^6-10^8\ s^{-1}$.

Cross polarization is often used to generate the magnetization needed for T_1 measurements for ^{13}C or ^{15}N, for example. Under these circumstances the pulse sequence of Torchia is in widespread use.[9] In this sequence for ^{13}C the ^{13}C magnetization is generated in an enhanced form by a cross polarization sequence and then an inversion recovery type sequence is used to follow the recovery of the magnetization as a function of time. During the evolution period the ^{1}H nuclei are decoupled by continuous phase irradiation to avoid the possibility of their dephasing the ^{13}C magnetization. The FID is then collected accompanied by high power ^{1}H decoupling.

For ^{1}H in organic solids the spins are strongly coupled via a spin diffusion process and consequently all have the same T_1 value. Thus no information about specific sites can be obtained even if separate peaks for these sites can be seem by special spectral techniques, for example CRAMPS.

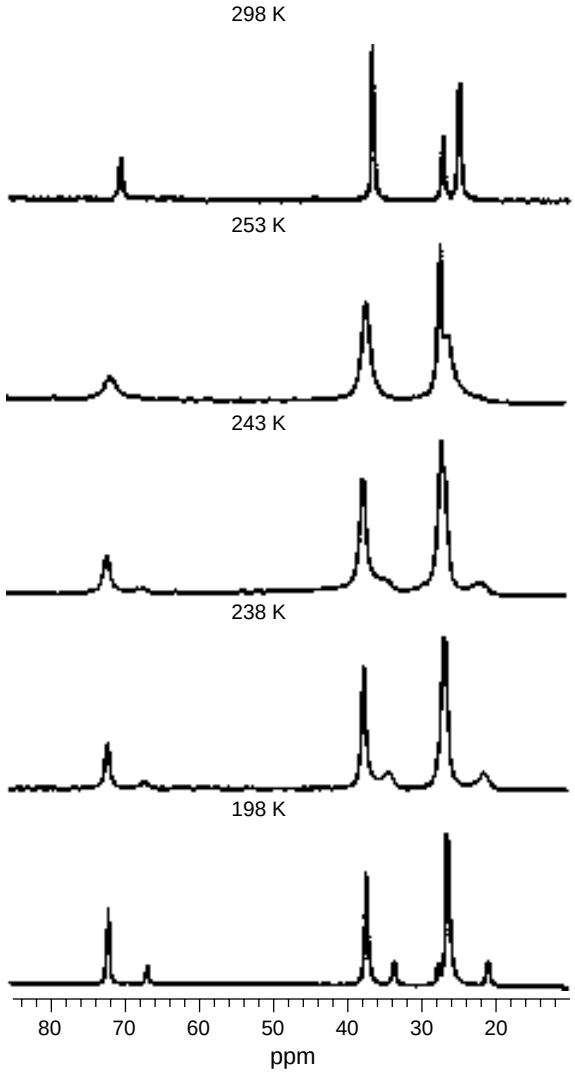

Figure 3 125.758 MHz ^{13}C line shape changes due to ring inversion of cyclohexanol in a thiourea inclusion complex (single pulse MAS spectra). Reproduced with permission from Figure 2 in Ref.[5]

This greatly decreases the utility of ^{1}H T_1 measurements for characterizing molecular motions. They have, however, been applied in simple cases in which all the protons are equivalent such as molecular rotation in benzene.

For ^{2}H T_1 is the most unambiguous relaxation time as it depends exclusively on molecular motion. The relaxation of quadrupolar nuclei such as ^{2}H depends upon the interaction between the quadrupole moment of the nucleus and the electric field gradient it experiences. Fluctuating electric field gradients produce spin lattice relaxation of the ^{2}H nucleus and the correlation time for molecular motion can be inferred if details of the quadrupole interaction are known. Modulation of the electric field gradient in molecular solids is usually produced by rotational or segmental motions. This technique has proved of particular value in chain-like structures, e.g., polymers or lipids where selective deuteriation along the chain can characterize the motion of different segments. Measurement of ^{2}H relaxation times for broad powder patterns can be troublesome and is often best achieved by a saturation recovery technique using the pulse sequence of Hirschinger et al.[10]

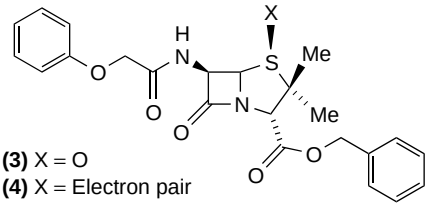

(3) X = O
(4) X = Electron pair

For powder samples, however, its interpretation is complicated by the anisotropy of T_1 because the relaxation time depends upon the orientation of the unique principal axis (C–D bond) with respect to the external magnetic field. This means that different parts of the sample relax with different rates. Fortunately, in general, this effect is small and the powder average T_1 often describes the relaxation process in the crystal satisfactorily.[11]

For the spin-lattice relaxation of ^{2}H the dependence of T_1 on the correlation time is given by

$$\frac{1}{T_1} = C\left\{\frac{\tau_c}{1+\omega_o^2\tau_c^2} + \frac{4\tau_c}{1+4\omega_o^2\tau_c^2}\right\} \tag{1}$$

Two regions occur depending on the magnitude of the correlation time. On the low temperature side of the T_1 minimum the rate of the molecular motion is slower than at the minimum, i.e., $\omega_o\tau_c \gg 1$. Combining equation (1) with the Arrhenius equation, it can be seen that the natural logarithm of the spin-lattice relaxation time depends on inverse temperature

$$\ln(T_1) = \frac{E_a}{RT} + \ln\left\{\frac{\omega_o^2 A}{2C}\right\} \tag{2}$$

On the high temperature side of the minimum the motion is faster than at the minimum, i.e., $\omega_o\tau_c \ll 1$

$$\ln(T_1) = \frac{E_a}{RT} - \ln(5CA) \tag{3}$$

Thus in both cases the Arrhenius activation energy (E_a) can be obtained from the slope of a plot of $\ln(T_1)$ vs $1/T$.

In certain cases, however, there is also a dependence of T_1 upon the amplitude of the motion. In these cases the parameter E_a is called the apparent activation energy.

4 MAXIMUM DIPOLAR BROADENING

In high resolution CP/MAS NMR, ^{1}H dipolar decoupling is extensively used to remove any remaining dipolar and J coupling from ^{1}H to heteronuclei. Invariably this is done by a single frequency placed near the centre of the ^{1}H resonance. Typical values for the dipolar decoupling field are in the region 50–100 kHz. If there is a molecular motion or exchange taking place at or near this frequency it can interfere with the efficiency of the decoupling and this causes an increase in the line widths of the affected resonances. This effect was first noted by Rothwell and Waugh.[12] In effect the frequency of the incoherent molecular motion is interfering with the coherent decoupling field reducing its efficiency and broadening the line. Maximum dipolar broadening is most often observed as an increase followed by a reduction in line width as the

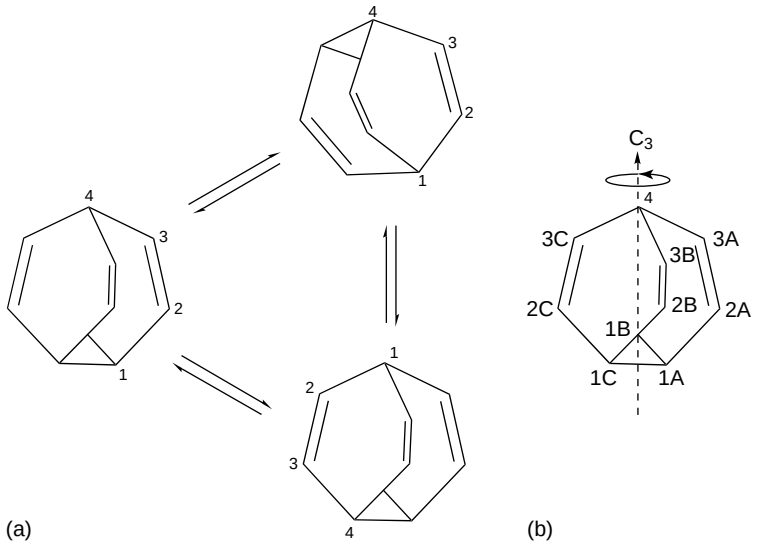

Figure 4 The sigmatropic rearrangement and rotational processes in solid bullvalene that give rise to the dynamic spectral changes seen in Figure 5. Reproduced with permission from Figure 1 in Ref.[6]

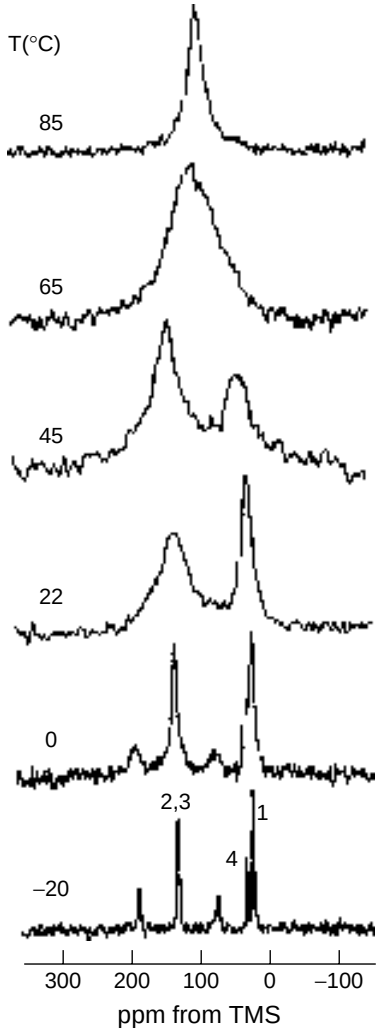

Figure 5 75.47 MHz ^{13}C CP/MAS spectra at variable temperature arising from the dynamic processes inside solid bullvalene illustrated in Figure 4. Reproduced with permission from Figure 2 in Ref.[6]

temperature is varied. A single rate constant at the temperature of maximum broadening may be extracted in the region $5-10 \times 10^4\ s^{-1}$.

An example of the use of maximum dynamic broadening may be found in work by Twyman and Dobson.[13] They showed that a combination of line shape analysis, maximum dipolar broadening and magnetization transfer could be used to study the phenyl rotation in the compounds **(3)** and **(4)** over a wide range of rates of rotation.

5 $T_{1\rho}$ MEASUREMENTS

Maximum dynamic broadening is, however, generally not the best way to study molecular motions in this frequency range in CP/MAS spectra. Measurements of $T_{1\rho}$ are generally superior.[14] In the $T_{1\rho}$ experiment the magnetization to be studied is flipped from equilibrium through 90° to take the magnetization into the x′y′ plane, where it is spin locked along a particular axis.[15] Thus a 90° +x′ pulse placing the magnetization onto the +y′ axis would be followed by a spin lock field (ω_1) (ca. 50–100 kHz) being applied along the y′ axis. The time course of the decay of the spin locked magnetization gives the relaxation rate in the rotating frame with time constant $T_{1\rho}$. In general the 90° pulse would be applied by a cross polarization sequence in which the ^{1}H and X nucleus fields are matched. The same fields would be used for spin locking (X) and for decoupling (^{1}H). This makes the $T_{1\rho}$ method sensitive in the same region as maximum dipolar broadening.

In principle the spin lock frequency can be varied to probe different rates of molecular motion. In practice dynamic information is more readily obtained by following the variation of $T_{1\rho}$ with temperature than by varying the spin lock field.

^{13}C $T_{1\rho}$ can be modulated both by molecular motions and by the ^{1}H spin diffusion process

$$\frac{1}{^{13}\mathrm{C}\,T_{1\rho}} = \frac{1}{^{13}\mathrm{C}\,T_{1\rho\,\mathrm{spin\ lattice}}} + \frac{1}{T_{\mathrm{CH}}(\mathrm{ADRF})} \qquad (4)$$

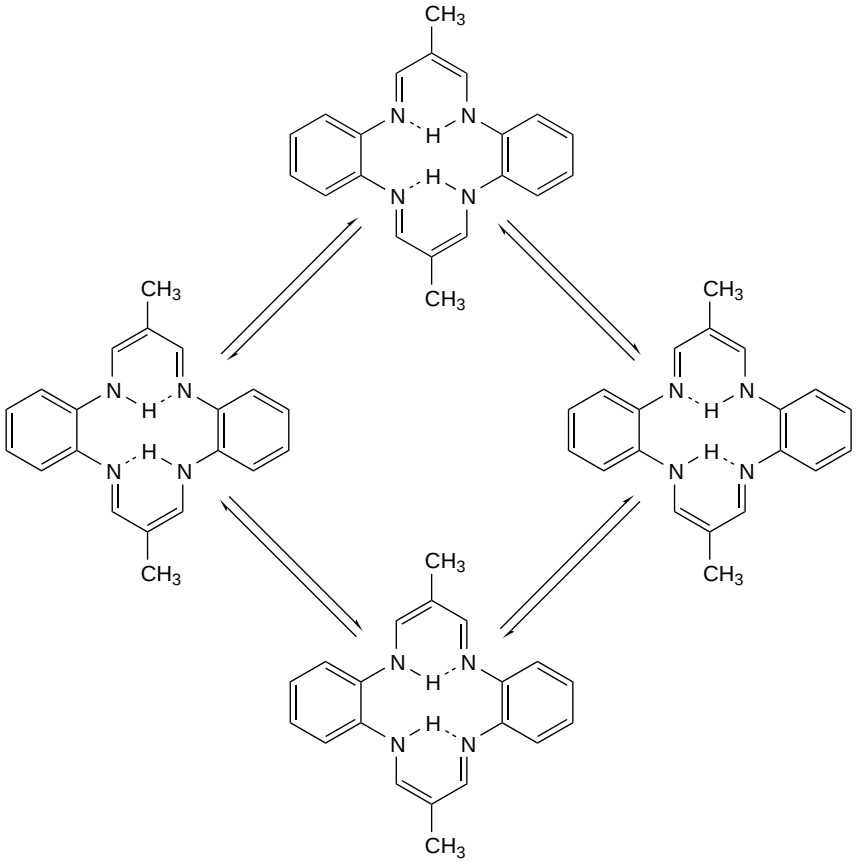

Figure 6 The ultrafast hydrogen bond exchanges in dimethyldibenzotetraaza[14]annulene studied by ^{15}N T_1 relaxation methods

^{13}C $T_{1\rho}$ spin lattice arises from modulation of the spin locking field by the molecular motion. T_{CH}(ADRF) comes from modulation of the dipolar interaction by the spontaneous rigid lattice proton fluctuations (spin diffusion). In practice the latter effects are generally found to be negligible with spin locking fields in excess of ca. 35 kHz. Also in practice $T_{1\rho}$ measurements in CP/MAS NMR are generally made with spin lock fields that are the same as those used for cross polarization and are 50 kHz or greater.

For a dipolar interaction between two unlike spins, e.g., ^{13}C and ^{1}H

$$\frac{1}{T_{1\rho}} = \frac{B^2\tau}{(1+\omega_1^2\tau^2)} \tag{5}$$

where ω_1 is the frequency of ^{13}C in the spin lock field, τ is the rotational correlation time for the molecular motion causing the relaxation (rotational correlation time), and B^2 is a measure of the ^{13}C–^{1}H dipolar interaction.[16] B^2 may be calculated for a particular model of motion and geometry from the equation given by Abragam.[17] The rate of the molecular motion will vary with temperature T and therefore $T_{1\rho}$ will have a temperature dependence. Equation (5) predicts that $T_{1\rho}$ will have a minimum at the temperature at which $\omega_1\tau = 1$.

Hence at the minimum value of $T_{1\rho}$, $\omega_1\tau = 1$ and B^2 conforms to

$$B^2 = \frac{2}{(T_{1\rho})_{\min}\tau} \tag{6}$$

Thus the minimum value of $T_{1\rho}$ allows an experimental determination of B^2. Two things follow from this. First the values of τ at each temperature may be extracted by solving the appropriate quadratic equation. Secondly the mode of motion may be checked by comparison of the calculated and experimental values of B^2.[18]

The use and validity of $T_{1\rho}$ methods is illustrated in a study of the rotation of both *tert*-butyl groups in **(5)**. Line shape analysis in the temperature range 202–233 K and $T_{1\rho}$ measurements in the temperature range 224–320 K were carried out.

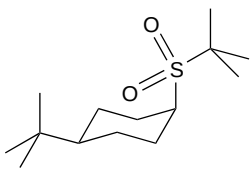

(5)

If the reductions in ^{13}C $T_{1\rho}$ in the *tert*-butyl groups arise from group rotations then four predictions can be made.

- Both the central and the methyl carbons in the same *tert*-butyl group should show $T_{1\rho}$ minima at the same temperature.
- For a constant geometry of *tert*-butyl groups the $T_{1\rho}$ minima should be the same for both groups.

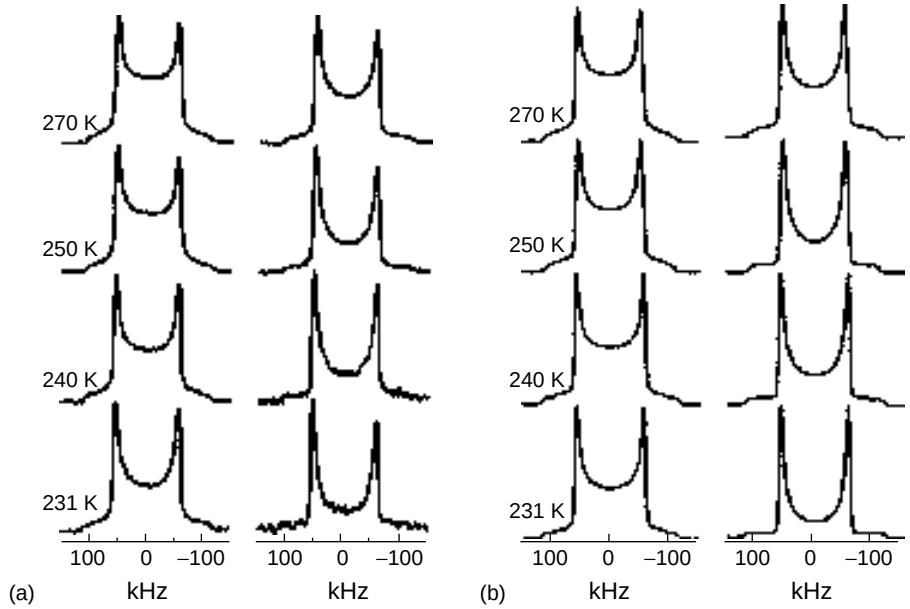

Figure 7 Observed (a) and calculated (b) 76.773 MHz ^{2}H quadrupole echo spectrum of 1,1,6,6-d_4-hexane-1,6-diyl bis(*p*-nitrobenzoate) at varying temperatures. The changes arise from librational motions of the CD_2 groups. Refocusing delays are 20 (a) and 120 μs (b). Reproduced with permission from Figure 6 in Ref.[20]

- Rate constants determined from the $T_{1\rho}$ data and the line shape analyses should fall on the same Eyring or Arrhenius plots.
- Experimentally determined B^2 values for the methyl and quaternary carbons should agree with those derived from calculation.

All four predictions are found to be correct.[16]

The same group went on to examine a wide variety of molecular motions in crystalline organic compounds including the related rotations of trimethylammonium and trimethylphosphonium groups. Interestingly and satisfyingly for the trimethylphosphonium group the data from the ^{13}C line shape changes, the ^{13}C $T_{1\rho}$ data and the ^{31}P $T_{1\rho}$ data all fitted the same activation plot.[19]

One further important point about $T_{1\rho}$ methods is that the measure of the dipolar interaction B^2 depends upon the geometry of the molecular motion.[17] In principle this allows differentiation between alternative models for the molecular motion. For example, in *trans*-1,2-cyclopentanediol this method allowed a differentiation to be made between a whole molecule rotation process and an internal ring pseudorotation process with the latter process being the more likely origin of the experimental measurements.[18]

6 ^{2}H QUADRUPOLAR ECHO METHODS

^{2}H quadrupolar echo line shape studies have been perhaps the widest used NMR technique for studying molecular motions in solids. Although ^{2}H incorporation in the molecule is required the technique has the compensation that information about both the frequency and geometry of the molecular motion can be obtained. Typically ^{2}H spectra of solids are a few hundred kilohertz wide. In the absence of molecular motions the spectrum is a Pake doublet with the horns of the pattern separated by the quadrupolar coupling constant. For a C–D bond this is ca. 125 kHz. As the frequencies of the molecular motions approach the value of the quadrupolar coupling constant the line shape changes. Figure 7 shows typical changes in the quadrupole echo spectra for 1,1,6,6-d_4-hexane-1,6-diyl bis(*p*-nitrobenzoate) **(6)**.[20] The line shape depends upon the motion of the C–D bond and can be calculated on the basis of frequency of the molecular motion and various possible geometric modes that are possible.[21] Conclusions can then be drawn.

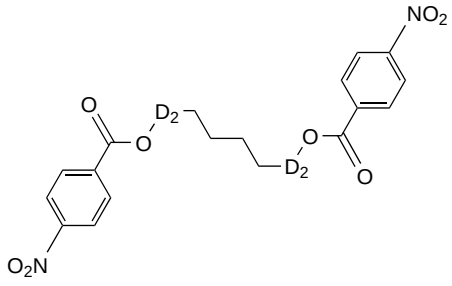

(6)

With line shapes of this width the free induction delays can be very short and some or all of the FID can be lost in the receiver dead time delay. This would lead to weak and distorted signals. To overcome this the quadrupole echo sequence is used in which a second $\pi/2$ pulse is applied in quadrature with the first at time τ. This results in refocussing of the magnetization and the formation of an echo at approximately 2τ after the first pulse.[22] By starting the FT at the echo maximum one does not need to worry about signal that has been lost during the receiver dead time and undistorted spectra may be obtained.

An additional complication is that artifacts can be caused by the finite length of the $\pi/2$ pulse width. This can lead to uneven excitation of the spectrum, to a feed through signal or to a virtual FID. Fortunately the program MXET1 that is most often used for the simulation of 2H quadrupolar echo spectra includes a correction factor for the $\pi/2$ pulse width meaning that correct spectra can be calculated.[23]

Finally, for a more certain assignment between different models of motion it is important that spectra are measured with different refocusing delays for comparison with simulated spectra. With longer delays more spectral intensity is lost and the measurement of quadrupole echo spectra in the intermediate exchange regime can become very time consuming for long refocusing delays since the echo intensity decays exponentially with the refocusing delay. In addition to the motional effects (T_2) in the intermediate exchange region the echo intensity is also decreased by dipolar couplings between deuterons and protons as the quadrupole echo sequence fails to refocus these couplings. Dipolar couplings also broaden the line shape and their effect can be taken into account by multiplying the free induction decay by a Gaussian broadening function that is a few kilohertz wide. Such a broadening has a fairly small effect on the line shape but the decrease in the echo intensity during the refocusing delay is considerable. For refocusing delays of 20 μs and 160 μs and an effective 2 kHz broadening it can be shown that the effect is an echo reduction of 0.67, and for an effective 3 kHz broadening the corresponding reduction would be 0.40. Thus, dipolar couplings reduce the echo intensity to about half its original intensity in addition to the T_2 effects in the intermediate exchange region. Thus for delays of 20 μs and 160 μs an echo reduction factor of ca. 0.5 is expected. If the echo reduction factor falls below this it is indicative of T_2 effects becoming important during the refocusing delay. If the echo reduction factor is greater than this it seems likely that the dipolar couplings between deuterons and protons are becoming less important. Either way an additional pointer is given to assist interpretation.[24] Figure 7 shows the effect of the echo reduction factor in the quadrupole echo spectra of 1,1,6,6-d_4-hexane-1,6-diyl bis(*p*-nitrobenzoate) **(6)**.

The angle of the C–D bond motion can be measured directly from a two-dimensional deuterium exchange experiment.[25] In the absence of molecular motion the 2D exchange spectrum consists of a Pake doublet along the diagonal. Molecular motions in the slow exchange regime where the correlation time is longer than a millisecond induce intensity off the diagonal. These off-diagonal ridges are very characteristic to motional modes and also in favourable cases allow direct measurements of the angle of the C–D bond motion to be made. Slowly moving deuterons, however, tend to relax very slowly and so in the absence of any additional relaxation modes these long relaxation times can make this technique very time-consuming.

7 MEASUREMENT OF TEMPERATURE IN MAS EXPERIMENTS

The establishment of temperatures in MAS NMR experiments is an important but difficult problem.[26] It is important because accurate temperatures are needed if activation parameters are to be determined for a particular process. It is difficult because it has been demonstrated by several groups that MAS causes the sample to heat. This heating is probably due to friction. It has been proposed and demonstrated that the heating varies with the square of the spinning speed.[26,27] Thus, at high spinning speeds careful temperature calibration becomes even more important. Several methods have been proposed for the measurement of sample temperatures. Probably the most reliable is to follow accurately known phase changes that show changes in the spectra through the transition.[26] Using this method it is possible to reliably calibrate a probe/temperature controller combination.

8 RELATED ARTICLES IN THIS VOLUME

Dynamics of Hydrogen Transfer in Liquids and Solids.

9 RELATED ARTICLES IN VOLUMES 1–8

Chemical Exchange Effects on Spectra, Volume 2; Cross Polarization in Rotating Solids: Spin-1/2 Nuclei, Volume 3; Deuterium NMR in Solids, Volume 3; Dynamic Nuclear Polarization & High-Resolution NMR of Solids, Volume 3; Magic Angle Spinning, Volume 5; Relaxation Effects of Chemical Exchange, Volume 6.

10 REFERENCES

1. K. D. M. Harris and A. E. Aliev, *Chem. Br.*, 1995, **31**, 132.
2. F. G. Riddell, S. Arumugam, and J. E. Anderson, *J. Chem. Soc., Chem. Commun.*, 1991, 1525–1527.
3. H. M. McConnell, *J. Chem. Phys.*, 1958, **28**, 430.
4. J. Braun, R. Schwesinger, P. G. Williams, H. Morimoto, D. E. Wemmer, and H. H. Limbach, *J. Am. Chem. Soc.*, 1996, **118**, 11 101–11 110.
5. A. E. Aliev and K. D. M. Harris, *J. Am. Chem. Soc.*, 1993, **115**, 6369.
6. J. J. Titman, Z. Luz, and H. W. Spiess, *J. Am. Chem. Soc.*, 1992, **114**, 3765.
7. Z. Luz, R. Poupko, and S. Alexander, *J. Chem. Phys.*, 1993, **99**, 7544.
8. C. G. Hoelger, B. Wehrle, H. Benedict, and H. H. Limbach, *J. Phys. Chem.*, 1994, **98**, 843–851.
9. D. A. Torchia, *J. Magn. Reson.*, 1978, **30**, 613–616.
10. J. Hirschinger, H. Miura, K. H. Gardner, and A. D. English, *Macromolecules*, 1990, **23**, 2153–2169.
11. D. A. Torchia and A. Szabo, *J. Magn. Reson.*, 1982, **49**, 107.
12. W. P. Rothwell and J. S. Waugh, *J. Chem. Phys.*, 1981, **74**, 2721.
13. J. M. Twyman and C. M. Dobson, *J. Chem. Soc., Chem. Commun.*, 1988, 786.
14. D. C. Ailon, in 'Encyclopedia of NMR', eds D. M. Grant and R. K. Harris, Wiley: Chichester, 1996, vol. 8, p. 4874.
15. A. J. Vega, *J. Magn. Reson.*, 1985, **65**, 252–267.
16. F. G. Riddell, S. Arumugam, K. D. M. Harris, M. Rogerson, and J. H. Strange, *J. Am. Chem. Soc.*, 1993, **115**, 1881.
17. A. Abragam, 'Principles of Nuclear Magnetism', Oxford University Press: Oxford, 1961.
18. F. G. Riddell, K. S. Cameron, S. A. Holmes, and J. H. Strange, *J. Am. Chem. Soc.*, 1997, **119**, 7555–7560.
19. F. G. Riddell, M. Rogerson, W. B. Turnbull, and F. Fülöp, *J. Chem. Soc. Perkin II*, 1997, 95.

20. J. K. Kujanpää and F. G. Riddell, *J. Chem. Soc. Perkin II*, 2000, 2225–2231.
21. A. K. Roy and P. T. Inglefield, *Prog. Nucl. Magn. Reson. Spectrosc.*, 1990, **22**, 569–603.
22. K. Müller, P. Meier, and G. Kothe, *Prog. Nucl. Magn. Reson. Spectrosc.*, 1985, **17**, 211–239.
23. M. S. Greenfield, A. D. Ronemus, R. L. Vold, R. R. Vold, P. D. Ellis, and T. E. Raidy, *J. Magn. Reson.*, 1987, **72**, 89–107.
24. For a more detailed description of the use of echo reduction factors see J. Kujanpää, PhD thesis, St Andrews, 1999.
25. H. W. Spiess, *Chem. Rev.*, 1991, **91**, 1321–1338.
26. F. G. Riddell, R. A. Spark, and G. V. Günther, *Magn. Reson. Chem.*, 1996, **34**, 824–828.
27. F. D. Doty and P. D. Ellis, *Rev. Sci. Instrum.*, 1981, **52**, 1868.

Biographical Sketch

Frank G. Riddell, *b* 1940. Studied chemistry at the University of Liverpool 1958–65, Ph.D., 1965, Liverpool, with M. J. T. Robinson. Ciba research fellow, Institut de Chimie, Université de Strasbourg, France with J. M. Lehn, 1965–67. Lecturer, Senior Lecturer and Reader, University of Stirling 1967–88. Reader, University of St Andrews since 1988. Approx. 150 publications nearly all involving the application of NMR spectroscopy to the solution of problems in organic and biological chemistry, particularly those related to molecular conformation, conformational dynamics and membrane transport.

Fluorine-19 NMR of Solids Containing Both Fluorine and Hydrogen

Shinji Ando

Department of Organic and Polymeric Materials, Tokyo Institute of Technology, Okayama, Tokyo, Japan

Robin K. Harris

Department of Chemistry, University of Durham, South Road, Durham, UK

&

Ulrich Scheler

Institut für Polymerforschung e.V., Dresden, Germany

1	Introduction: Special Problems	1
2	Special Techniques and Experimental Requirements	2
3	Cross Polarization Dynamics between ^{1}H and ^{19}F	4
4	Fluoropolymers	9
5	Fluorinated Organic Compounds	13
6	Fluorinated Organometallic and Metal Coordination Compounds	18
7	Fluorinated Inorganic Compounds	18
8	Concluding Remarks	18
9	References	19

1 INTRODUCTION: SPECIAL PROBLEMS

Since the early days of NMR, ^{19}F has been recognized as one of the most useful nuclei, and it has been widely studied for liquids and solutions. This is because it is present in 100% natural abundance, has a relatively high resonance frequency (near to that of the proton), and has a spin quantum number of 1/2. These properties convey very favorable sensitivity in the NMR experiment – the receptivity is 83.4% of that for ^{1}H and 4.90×10^{3} of that for ^{13}C. Moreover, the chemical shift range for ^{19}F is comparable to that of, say, ^{13}C and well over an order of magnitude greater than that for ^{1}H. It follows that, of the obvious nuclei used to examine fluorinated systems containing hydrogen by NMR, fluorine will often be preferred. However, although there have been a number of reports of ^{19}F relaxation parameters and broadline spectra of solids containing fluorine, the use of high-resolution ^{19}F spectra for studying such systems has been relatively limited. Indeed, until relatively recently the total amount of high-resolution ^{19}F NMR work on solids of all types was surprisingly small. It has been reviewed twice in the past decade.[1,2] This lack of reported work is particularly marked for systems containing both fluorine and hydrogen, which form the special topic of this article.

Paradoxically, the reasons for the relative lack of activity on ^{19}F are two of the major advantages of the nucleus, namely the 100% natural abundance and its high magnetic moment. These imply that dipolar interactions (both homonuclear and heteronuclear) are likely to be very strong. The present review will be largely limited to (^{19}F, ^{1}H) double resonance studies, usually involving ^{19}F magic-angle spinning (MAS) spectra obtained with proton decoupling. Associated relaxation time measurements, some related static experiments and some very-high speed MAS investigations will also be covered. Such experiments give improved quality of spectra for both static and magic-angle spinning experiments (especially yielding higher resolution for the latter), and also simplify the interpretation of relaxation data. Also, additional experiments become feasible from the $^{1}H \rightarrow {}^{19}F$ cross-polarization operation. However, the excitation bandwidth required for ^{19}F spectra, especially for high-field spectrometers, is a further source of experimental problems – for example, at 11 T, 100 ppm, which is insufficient for most spectra, is the equivalent of 47 kHz.

All the early ^{19}F NMR work on solid fluorinated systems that also contain hydrogen involved measurements of ^{19}F relaxation and broadline spectra, using what are now thought of as 'classical' NMR techniques.[3,4] Since proton decoupling was not generally employed, there are in principle complications in treating the experimental data which arise from cross-relaxation between ^{19}F and ^{1}H. This problem renders simple T_1 measurements (e.g., by inversion-recovery) intrinsically not single-exponential and raises questions about the influence of the nuclear Overhauser effect. Such issues were generally ignored in the early literature in this area, though they have been addressed by some authors.[5] Of course, all the relevant work before the advent[6] of the combined CPMAS suite of techniques in 1976 was based on low-resolution experiments. The data were interpreted in terms of dipolar interactions rather than chemical shifts and gave information on molecular-level mobility (and domain structure in polymers) rather than chemical structure.

However, there was a long delay following the development of CPMAS NMR before the new techniques were significantly employed for solid fluorinated materials which also contained hydrogen. This is because (^{19}F, ^{1}H) double-resonance experiments are significantly more difficult than analogous (^{13}C, ^{1}H) work, which is a result of the proximity of the resonance frequencies of ^{19}F and ^{1}H (within 6%). Since, for work on solids, decoupling protons from fluorines requires very high powers, there are obvious problems involving the efficiency of r.f. filtering, which inhibited developments. Moreover, without such filtering, $^{1}H \rightarrow {}^{19}F$ cross polarization is not feasible, thus preventing a wide range of informative experiments from taking place. However, the NMR community was in general, perhaps, too timid in this matter, since the first commercial $^{19}F-\{^{1}H\}$ probes suitable for solids were found to be very effective.[7–11] Recently, it has been shown (see below) that very-high-speed MAS is often an acceptable alternative to $^{19}F-\{^{1}H\}$ decoupling in moderate-speed MAS work.

Even with efficient ^{1}H decoupling, achieving high-resolution ^{19}F spectra of polyfluorinated systems presents difficulties because of the strong (^{19}F, ^{19}F) dipolar interactions, which require either multipulse homonuclear decoupling pulse

sequences (e.g., MREV 8) combined with modest-speed MAS (CRAMPS) or very fast (>20 kHz) MAS for their effective removal. Early work on both methods[12,13] was directed at perfluorinated systems. The technical difficulties involved meant that there was only very limited use of these techniques for hydrogen-fluorine systems until the mid-1990s. The next section will show how the experimental situation has now dramatically changed.

2 SPECIAL TECHNIQUES AND EXPERIMENTAL REQUIREMENTS

The origin of the attraction of ^{19}F as a probe nucleus for NMR also results in the majority of the experimental difficulties. Both the dipolar coupling and the chemical shift anisotropy are first-order anisotropic interactions, which are most conveniently averaged by magic-angle sample spinning (MAS). However, when spinning speeds are modest (<20 kHz), as has always been the case until very recently, it is also essential to effectively eliminate the influence of H,F dipolar coupling (for chemical systems containing both nuclei) by the usual heteronuclear double-resonance techniques. However, in the early days of high-resolution solid-state NMR this was thought to be a difficulty (see below) so that substantial work in this area only started in about 1992. In more recent years, the development of high-speed MAS systems, allowing for spinning speeds in excess of 30 kHz, has rendered the acquisition of high-resolution solid-state ^{19}F NMR spectra of compounds containing both abundant protons and fluorines possible without proton decoupling.[13–15]

However, MAS provides the same degree of line narrowing throughout the entire experiment, which is somewhat contrary to one of the major advantages of NMR, the possibility to manipulate and separate interactions. Therefore, even under high-speed MAS double-resonance experiments are desirable. Although proton decoupling leads to no significant resolution enhancement at such high speeds (though splittings arising from H,F isotropic indirect coupling are eliminated, resulting in some improvement), there is a general need for double-resonance experiments to manipulate the heteronuclear dipolar coupling for certain periods of the experiment. The application of high-speed (>20 kHz) MAS requires dedicated equipment that might not always be available. The low-volume rotors present possible difficulties for sample handling. For receptivity the small volume is not usually a problem (except for 'dilute' fluorine cases, such as compounds at interfaces), because the narrow lines from high-speed MAS result in good apparent signal-to-noise ratio. On the other hand, the small sample volume required in the high-speed MAS systems can be an advantage, when novel compounds, only obtainable in very small quantities, are investigated. The major advantage in the application of fast MAS, however, is the simultaneous averaging of the homonuclear fluorine–fluorine coupling, which can be strong in fluorine-rich systems (Figure 1). To follow the time development of any process (such as relaxation) in the experiment, rotor-synchronous detection is usually applied to exclude from the data analysis the additional time-dependence resulting from MAS.

The classical spectrometer design, based on an X channel, together with a proton channel mostly used for decoupling,

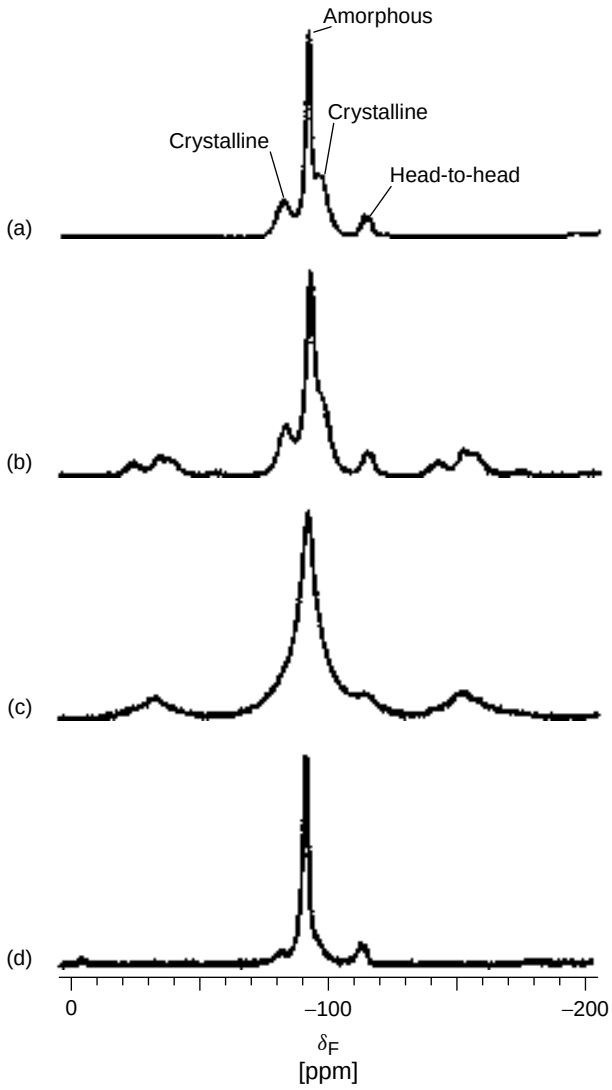

Figure 1 282 MHz fluorine-19 MAS NMR spectra of PVDF: (a) 32 kHz spin rate with no proton decoupling; (b) 16 kHz spin rate with proton decoupling; (c) 16 kHz spin rate with no proton decoupling; and (d) REDOR spectrum (mixing time 0.4 ms; 10 rotor cycles) with 32 kHz spin rate and proton decoupling

is inappropriate for proton–fluorine double-resonance experiments. Because the magnetogyric ratios of almost all X nuclei are lower than that of the proton by at least a factor of 0.4, the frequency range in the X channel of traditional spectrometers is limited. A flexible second channel is therefore needed for proton–fluorine double resonance. The same is true for the probe-head, since a typical H–X solid-state probe-head is based on a relatively large frequency separation. Usually, there is a high-frequency channel tunable to proton and fluorine, with an X channel that is also narrow-band but can be tuned to a wide range of frequencies. The separation/decoupling between the two RF channels is based on the large difference of the resonance frequencies of H and X.

The Larmor frequencies of proton and fluorine nuclei are separated by only 6%. Therefore, the standard double-resonance probe design is not applicable, so that a dedicated probe-head is required for proton–fluorine double resonance. The first reported proton-decoupled fluorine solid-state NMR

spectra were obtained[8–11,16] using dedicated double-resonance probes. Such probes are based on traditional technology, with oscillators and transmission lines. They are specially made for the two frequencies and do not allow more extended tuning. Another option is the use of an overcoupling network, introduced by Maas et al.[17] An additional oscillator inserted between the transmitter and the probe splits the high-frequency resonance of a traditional double-resonance probe symmetrically into two. While this setup was originally developed to achieve simultaneous proton and fluorine decoupling for ^{13}C-observe operation, it can also be applied for proton–fluorine double-resonance experiments. Appropriate external filtering also has to be employed. External RF filters are in any case needed to achieve the attenuation of more than 60 dB between the two channels that is necessary for the acquisition of any spectrum under high-power decoupling. Because the ^{19}F and ^{1}H frequencies are so close, filters of extremely narrow bandwidth have to be used. These filters may influence the rise and fall times of pulses.

The only known applications[18,19] of proton–fluorine double-resonance experiments where no bandpass filters were in use are multiple-pulse experiments. In those experiments no decoupling pulse is present during data acquisition. Omitting external RF filters allows shorter pulses, because there is no bandwidth limitation and no insertion loss. The usual multipulse sequences such as WAHUHA, MREV8 or BR24 are designed to average homonuclear dipolar coupling, which is bilinear in the spin operators. As a side effect they scale both the chemical shift and the heteronuclear dipolar coupling, which are each linear in the spin operators. Strong heteronuclear dipolar coupling (e.g., the coupling between protons and fluorine nuclei) results in an unacceptable linewidth. Therefore, heteronuclear decoupling has to be included, which is achieved by π pulses on the non-detected channel, synchronized with the multipulse sequence on the detection channel (Figure 2).

A minor additional problem appears in solid-state NMR probes dedicated to proton–fluorine double-resonance NMR: the question of probe background signals. Especially when variable-temperature experiments are required, there is little possibility to avoid both proton and fluorine-containing materials in capacitors and all structural materials in the sensitive part of the probe simultaneously. Therefore, usually one or the other has to be selected when designing/manufacturing the probe. Generally the acquisition of fluorine spectra is more desirable than that of proton spectra because of the information content in the larger chemical range of the former. However, in proton-detected experiments a background signal will then be present. The small chemical shift range of protons, however, permits detection at a small spectral width, where background signals from static solid material only show up as a minor baseline distortion.

Various experiments for background suppression have been proposed, such as composite pulses.[20] Another possibility is the excitation of fluorine magnetization via proton–fluorine cross polarization. Materials used in NMR probe manufacturing are usually perfluorinated and do not generate a ^{19}F signal from $^{1}\text{H} \rightarrow {}^{19}\text{F}$ CP. Similarly, background-free ^{1}H spectra can be obtained by $^{19}\text{F} \rightarrow {}^{1}\text{H}$ CP. However, both methods for background suppression introduce additional uncertainties for the experiment and usually inhibit quantitative analysis of the spectra, though they also allow additional useful measurements to be made. The preferable way is just to avoid the probe background signal for the experiment desired.

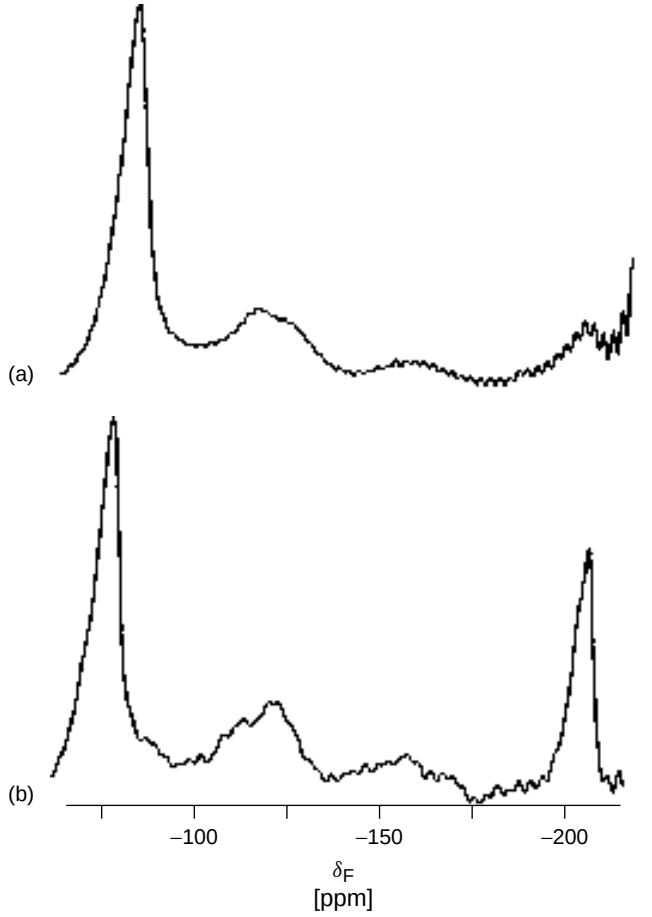

Figure 2 Combined rotational and multipulse experiments on a semifluorinated tetrapropyl-adamantane at 188.29 MHz: ^{19}F CRAMPS with synchronized pulses on the proton channel

Of course, most of the pulse sequences used traditionally for $^{1}\text{H} \rightarrow {}^{13}\text{C}$ CPMAS NMR (such as dipolar dephasing and two-dimensional HETCOR/EXSY) can be adapted to acquire $^{1}\text{H} \rightarrow {}^{19}\text{F}$ CPMAS spectra, starting with the simple CP sequence (Figure 3a). For instance, the WISE sequence[21] (Figure 3b) can be used[22] to obtain ^{1}H bandshapes with the chemical shift discrimination inherent in the ^{19}F spectrum. Usually the homonuclear F,F coupling requires fast MAS for resolution in the ^{19}F spectrum. Therefore, the ^{1}H band breaks up into spinning sidebands (ssb). The second moment of the ssb manifold contains valuable information on the residual dipolar coupling and can be used as a measure of mobility.[23] Moreover, various techniques can be applied[24,25] to discriminate between well-resolved ^{19}F subspectra of different domains in heterogeneous solids, such as use of a ^{1}H spin-lock ($T_{1\rho}^{H}$) or ^{1}H inversion recovery or T_2^H decay (delayed contact) prior to CP (Figure 3c). Similarly, a post-CP ^{19}F spin-lock ($T_{1\rho}^{F}$) or T_2^F decay (delayed acquisition) can be used, as can a one-dimensional (fixed mixing time) REDOR sequence, radiofrequency-driven recoupling (RFDR), a dipolar filter, or DIVAM.[26] The result of a REDOR selection for the amorphous region of the ^{19}F spectrum of poly(vinylidene fluoride), PVDF,

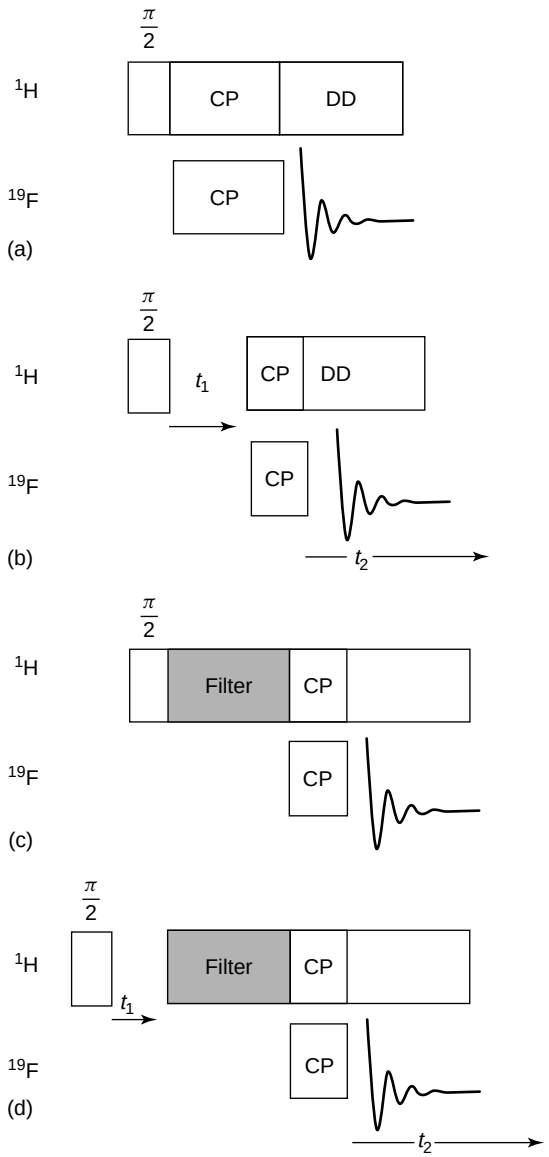

Figure 3 Pulse sequences used for proton–fluorine double-resonance experiments: (a) cross polarization; (b) wideline separation; (c) cross polarization after selection of a sub-ensemble of the proton spins based on proton relaxation times. Possible filters are: dipolar filter, $T_{1\rho}^{H}$ filter, T_1^H filter; (d) WISE experiment for a sub-ensemble after selection by a magnetization filter

is shown in Figure 1(d). Of course, the simple CPMAS sequence with variable contact time is itself discriminatory, especially when compared to single-pulse excitation (SPE) with MAS. Spin-diffusion can be studied[27] using the Goldman-Shen[28] type of sequence, with appropriate filtering, and the WISE experiment can be combined with various filtering arrangements (Figure 3d). The results of a number of filtering experiments on polymer spectra are discussed in Section 4.

Besides the thermodynamic analysis of the cross polarization dynamics for multiple spin baths, which will be described in the following section, there is the possibility to break the complicated multi-spin system experimentally into a superposition of spin pairs without diluting the sample. This idea makes use of the fact that in a spin-pair under cross polarization the magnetization oscillates between the two coupled spins (dipolar oscillation),[26,29,30] which has been reported for rare cases. However, usually such isolated spin pairs are not present in the sample and the dipolar oscillations are smeared out because the homonuclear dipolar coupling results in spin diffusion. The dipolar oscillations are often ignored for the thermodynamic treatment of the cross-polarization experiment.

Under a spin lock at the magic angle (Lee–Goldburg experiment) the homonuclear dipolar coupling is readily suppressed.[31] The heteronuclear dipolar coupling can be retained when simultaneously applying spin-lock fields at both frequencies to fulfil the Hartmann–Hahn condition.[32] The inherent beauty of this technique lies in the fact that a complex network of dipolar couplings can be broken down to a superposition of pairwise couplings, which are easily interpreted. While this approach has been applied to a case of proton-carbon cross polarization,[33] preliminary studies of proton–fluorine Lee–Goldburg cross polarization have been reported.[34] The complication here is that the homonuclear coupling in both spin baths has to be suppressed. This requires the application of spin-locking at the magic angle on both channels, resulting in a magnetization oriented at the magic angle (which requires an additional read-out pulse). The experiments can be simplified again under fast MAS, where the lines in the fluorine spectrum are well separated anyway. Because the homonuclear coupling is scaled by a factor of (−2) under the spin lock, this appears to be sufficient in many cases. For an example (5-fluoro-2 trifluorobenzoic acid), the signals for the CF and the CF_3 fluorines are well-resolved under MAS.[35] For each fluorine site the internuclear distances to the various neighboring protons have been determined. When the matching is on the first spinning sideband of the Hartmann–Hahn condition, the detected coupling (and thus the distance) is independent of the sample spinning frequency. Because the easiest data evaluation is performed from rotor-synchronized detection, the range of dipolar couplings is limited, so that the maximum coupling that can be characterized is determined by the spinning speed. The distances determined using this approach correspond within experimental error to those obtained from structural molecular simulations.

3 CROSS POLARIZATION DYNAMICS BETWEEN ^{1}H AND ^{19}F

A phenomenological spin thermodynamics[36–39] theory based on the spin-temperature hypothesis has been employed[39,40] to analyze the cross polarization (CP) dynamics between fluorine and proton in solids. The inverse spin temperature β, which is defined as $\hbar/kT$, is proportional to the magnitude of magnetization in the case that only the Zeeman interaction is considered. The variations with time of the inverse spin temperatures, β_H and β_F for the H and F spin baths, are described within this framework. The two spin baths can be in contact with each other and coupled with the lattice, which is suggested to have an infinitely high heat capacity at β_L as depicted in Figure 4.

The rate of the polarization transfer from H to F spin baths is characterized by a time constant T_{HF}. Under the spin-lock condition in the presence of simultaneous rf fields of B_{1F} for F and B_{1H} for H, each link between a spin bath

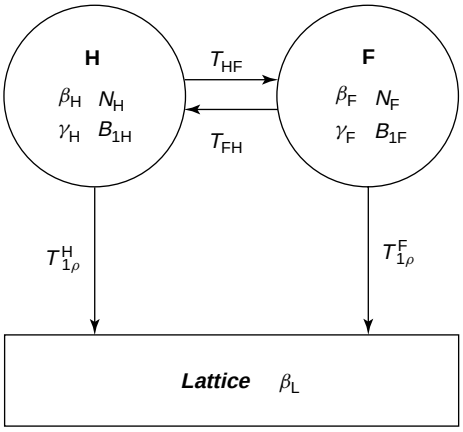

Figure 4 Schematic representation of an abundant ^{1}H spin bath and an abundant ^{19}F spin bath, which are spin-locked by RF irradiation and coupled to the lattice as expressed by their spin-lattice relaxation times in the rotating frame, $T^H_{1\rho}$ and $T^F_{1\rho}$ respectively. The rates of polarization transfer between the two spin baths are represented by the cross-relaxation times T_{HF} (H → F) and T_{FH} (F → H). β is the inverse spin temperature, N the density of spins, γ the gyromagnetic ratio, and B_1 the RF field for spin locking

and the lattice is characterized by a spin-lattice relaxation time in the rotating frame, $T^F_{1\rho}$ for F and $T^H_{1\rho}$ for H. When there is a difference between β_F and β_H, polarization transfer occurs between H and F spins during the contact time (t_{CP}) of cross-polarization (CP) and TORQUE[41] experiments. We assume that β in each spin bath is immediately equilibrated. Hence, oscillation of magnetization between H and F spins is neglected. Such phenomena can occur when there are strongly coupled H–F spin pairs. In addition, we consider only experimental situations where magic-angle spinning does not interfere with the CP process.

Assuming first-order kinetics, the variations of β_F and β_H under a cross-relaxation condition can be described by the coupled differential equations,

$$\frac{d}{dt}\beta_F = -\frac{1}{T_{HF}}(\beta_F - \beta_H) - \frac{1}{T^F_{1\rho}}\beta_F$$
$$\frac{d}{dt}\beta_H = -\frac{\varepsilon}{T_{HF}}(\beta_H - \beta_F) - \frac{1}{T^H_{1\rho}}\beta_H \quad (1)$$

where ε is defined as

$$\varepsilon = \frac{N_F(\gamma_F B_{1F})^2}{N_H(\gamma_H B_{1H})^2} \quad (2)$$

The N and the γ are the number of spins and the gyromagnetic ratio for the indicated nuclear type, respectively. When the Hartmann–Hahn condition

$$\gamma_H B_{1H} = \gamma_F B_{1F} \quad (3)$$

is achieved, ε is equal to N_F/N_H. In the case of H → F cross polarization, equation (1) can be straightforwardly solved under the initial conditions ($t_{CP} = 0$):

$$\beta_F = 0 \text{ and } \beta_H = \beta_{H0} \quad (4)$$

The dependence of β_F on t_{CP}, which corresponds to an evolution of F magnetization as a function of contact time in the standard CP experiment (which we will refer to as a CP curve), can be expressed as follows:

$$\left[\frac{\beta_F(t)}{\beta_{H0}}\right]_{CP} = \frac{1}{a_+ - a_-} \times \left[-\exp\left(-\frac{a_+}{T_{HF}}t_{CP}\right) + \exp\left(-\frac{a_-}{T_{HF}}t_{CP}\right)\right] \quad (5)$$

where
$$a_\pm = a_0 \pm \sqrt{a_0^2 - b} \quad (6)$$

with
$$a_0 = \frac{1}{2}\left(1 + \varepsilon + \frac{T_{HF}}{T^H_{1\rho}} + \frac{T_{HF}}{T^F_{1\rho}}\right) \quad (7)$$

and
$$b = \frac{T_{HF}}{T^H_{1\rho}}\left(1 + \frac{T_{HF}}{T^F_{1\rho}}\right) + \varepsilon\frac{T_{HF}}{T^F_{1\rho}} \quad (8)$$

In the same way, the dependence of β_F on t_{CP} in the H → F TORQUE experiments (which we will refer to as a TORQUE curve) can be expressed as

$$\left[\frac{\beta_F(t)}{\beta_{H0}}\right]_{TOR} = \exp\left(-\frac{t_{SL}}{T^H_{1\rho}}\right)\left[\frac{\beta_F(t)}{\beta_{H0}}\right]_{CP} \quad (9)$$

where t_{SL} is a spin-lock time for the H nuclei prior to the cross polarization to F nuclei.

Figure 5 shows[40] the calculated CP and TORQUE curves for $\varepsilon = 0.01$ and $\varepsilon = 1$. The constant spin-lock time for H spins, $t_{const} = t_{SL} + t_{CP}$, in the TORQUE curves is 5.0 ms, and the values of β_F are normalized at $t_{CP} = t_{const}$ in order to compare the shapes of the curves. T_{HF} was kept constant at 0.5 ms, and the relaxation parameters for the various curves used were: (A) $T^H_{1\rho} = 2.5$ ms, $T^F_{1\rho} = 100$ ms, (B) $T^H_{1\rho} = 2.5$ ms, $T^F_{1\rho} = 2.5$ ms, (C) $T^H_{1\rho} = 5.0$ ms, $T^F_{1\rho} = 5.0$ ms, (D) $T^H_{1\rho} = 100$ ms, $T^F_{1\rho} = 2.5$ ms. The CP curves for $\varepsilon = 0.01$ (Figure 5a) correspond to a typical case of ^{1}H → ^{13}C CP or to ^{1}H → ^{19}F CP for materials that are chemically dilute in fluorines but have abundant protons. In this case, it is well known that the decaying slope of the CP curves in a logarithmic scale is principally determined by $-1/T^H_{1\rho}$ in the region where $t_{CP} \gg T_{HF}$, and the influence of $1/T^F_{1\rho}$ on the slope is negligible. This indicates that different $T^H_{1\rho}$ s can be potentially discriminated from the decaying slope of CP curves when ε is much smaller than 1. When the number of fluorine atoms is much smaller than that of ^{1}H in organic molecules, there is no effective direct relaxation path from ^{19}F to the lattice under spin-locked conditions. As a result, the heat capacity of the ^{19}F spin bath is negligibly small, and $T^F_{1\rho}$ is generally much longer than $T^H_{1\rho}$.

On the other hand, the CP curves for $\varepsilon = 1$ (Figure 5b) correspond to a more typical case of ^{1}H → ^{19}F CP with both hydrogen and fluorine in high concentration, because ^{19}F has 100% natural abundance. For example, the N_F/N_H of one of the most popular fluoropolymers, poly(vinylidenefluoride), is 1. These curves show significantly different behavior from those in Figure 5(a). In particular, no difference was observed in the curves of A, C, and D in spite of the large differences in their values of $T^H_{1\rho}$ and $T^F_{1\rho}$. This can be explained by the fact that the decaying slope is principally determined

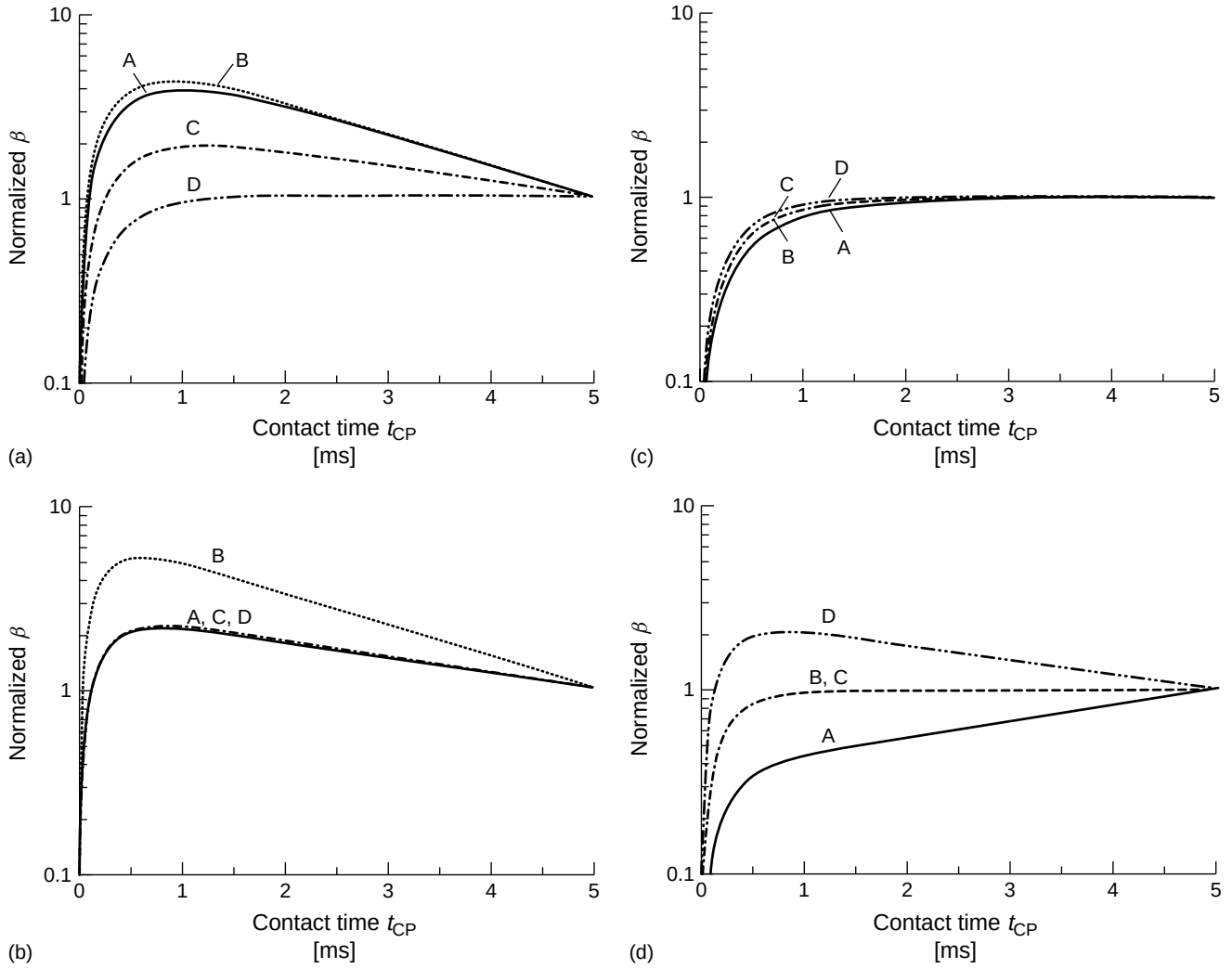

Figure 5 Evolution of the inverse spin temperature (β) for the F bath in the standard H → F CP experiment for (a) $\varepsilon = 0.01$ and (b) $\varepsilon = 1$ and in the H → F TORQUE experiment for (c) $\varepsilon = 0.01$ and (d) $\varepsilon = 1$. These curves were calculated according to equations (5) and (9) as a function of the contact time, t_{CP}, where t_{const} was chosen as 5 ms for TORQUE. All the curves were normalized at $t_{CP} = t_{const} = 5$ ms. T_{HF} was kept constant at 0.5 ms, and the relaxation parameters used, ($T_{1\rho}^{H}$, $T_{1\rho}^{F}$) were (A) (2.5, 100,), B (2.5, 2.5), C (5.0, 5.0) and (D) (100, 2.5), respectively, where the unit is ms. (Reproduced with permission from Ref.[40])

by $(1/T_{1\rho}^{H} + 1/T_{1\rho}^{F})/2$, not by $1/T_{1\rho}^{H}$, when $\varepsilon = 1$ and $1/T_{1\rho}^{F}$ is not negligibly small. The curves A, C, and D actually involve the same value of $(1/T_{1\rho}^{H} + 1/T_{1\rho}^{F})/2$. Consequently, a term involving $1/T_{1\rho}^{F}$ has to be explicitly incorporated into the analysis of CP dynamics between abundant nuclei. The high natural abundance of ^{19}F often makes $T_{1\rho}^{F}$ of the same order as $T_{1\rho}^{H}$. In addition, the heat capacity of the ^{19}F spin bath can be comparable to that of the ^{1}H spin bath when ε is close to 1. Figure 5(b) clearly indicates that CP curves can not discriminate between the three cases of $T_{1\rho}^{H} \ll T_{1\rho}^{F}$, $T_{1\rho}^{H} = T_{1\rho}^{F}$, and $T_{1\rho}^{H} \gg T_{1\rho}^{F}$. This is one of the major reasons that the conventional method can not be applied to analysis of ^{1}H → ^{19}F CP dynamics.

Furthermore, equation (5) can be approximated by the following

$$\left[\frac{\beta_F(t)}{\beta_{H0}}\right]_{CP} = A\left[-\exp\left(-\frac{t_{CP}}{T_{HF}^{*}}\right) + \exp\left(-\frac{t_{CP}}{T_{1\rho}^{*}}\right)\right] \qquad (10)$$

where A is a constant, and T_{HF}^{*} and $T_{1\rho}^{*}$ are effective time constants for the increase and decay of β_F. This indicates that any kind of CP curve for a homogeneous system can be well described by these two constants using the conventional expression. It is well-known that T_{HF}^{*} and $T_{1\rho}^{*}$ are analogous to T_{HF} and $T_{1\rho}^{H}$, respectively, when the following conditions are fulfilled: (1) F is a rare spin, (2) T_{HF} is considerably shorter than $T_{1\rho}^{H}$, and (3) $T_{1\rho}^{F}$ is considerably longer than $T_{1\rho}^{H}$. We will refer to this extreme situation ($\varepsilon \ll 1$ and $T_{HF} \ll T_{1\rho}^{H} \ll T_{1\rho}^{F}$) as the ideal CP condition. However, when ε is not negligibly small and $T_{1\rho}^{F}$ is comparable to $T_{1\rho}^{H}$ (as is frequently true for ^{1}H → ^{19}F CP), no simple relationship is expected between the effective parameters (T_{HF}^{*}, $T_{1\rho}^{*}$) and the true parameters for CP dynamics, T_{HF}, $T_{1\rho}^{H}$, and $T_{1\rho}^{F}$.

Figure 5(c) shows the TORQUE curves calculated for $\varepsilon = 0.01$. The decay of β_F is effectively suppressed in all the cases, indicating that it is mainly caused by $T_{1\rho}^{H}$. The shape of the curves is insensitive to the magnitude of $T_{1\rho}^{F}$. On the other

hand, the TORQUE curves calculated for $\varepsilon = 1$ (Figure 5d) show significantly different behavior from those in Figure 5(c). The decay of β_F can be suppressed only in the cases when $T_{1\rho}^H = T_{1\rho}^F$ (B and C). Otherwise, the slope at $t_{CP} = t_{const}$ is positive for $T_{1\rho}^H \ll T_{1\rho}^F$ (A) and negative for $T_{1\rho}^H \gg T_{1\rho}^F$ (D). This relationship can be mathematically verified.[40] Although the TORQUE sequence does not quench the relaxation process with $T_{1\rho}^H$ when ε is not negligibly small, the sign of the slope should be generally helpful in analyzing CP dynamics between abundant nuclei.

The contact-time dependence of β_H can also be obtained by solving equation (1) under the same initial conditions, giving:

$$\left[\frac{\beta_H(t)}{\beta_{H0}}\right]_{CP} = \frac{1}{a_+ - a_-}\left[-\left(1 + \frac{T_{HF}}{T_{1\rho}^F} - a_+\right)\exp\left(-\frac{a_+}{T_{HF}}t_{CP}\right) + \left(1 + \frac{T_{HF}}{T_{1\rho}^F} - a_-\right)\exp\left(-\frac{a_-}{T_{HF}}t_{CP}\right)\right] \quad (11)$$

This corresponds to the t_{CP} dependence of the residual H magnetization during the H → F CP experiment (which we will refer to as a CP-drain curve).[39] Equation (11) indicates that the residual proton magnetization decays with the same time constants of $-\frac{a_+}{T_{HF}}$ and $-\frac{a_-}{T_{HF}}$ as for the increase in F magnetization expressed by equation (5). The first of these time constants relates to the decrease in H magnetization caused by the polarization transfer to F spins, and the second time constant expresses the decrease caused by the relaxation to the lattice. Accordingly, at the ideal CP condition, the rates of the former and the latter processes are equal to $1/T_{HF}$ and $1/T_{1\rho}^H$.

When T_{HF} is much smaller than $T_{1\rho}^H$ and $T_{1\rho}^F$, the coefficient of the second term in equation (11) is expressed as

$$\frac{1}{a_+ - a_-}\left(1 + \frac{T_{HF}}{T_{1\rho}^F} - a_-\right) = \frac{1}{1+\varepsilon} \quad (12)$$

This indicates that, when the spin-lattice relaxation is very slow, the proportion of the residual magnetization in the H spin bath to the transferred magnetization to the F spin bath after CP is $1/(1+\varepsilon)$. In particular, this term becomes unity at the ideal CP condition.

Equation (11) can also be expressed in terms of effective values in the same way as equation (10). The corresponding equation for fitting CP-drain curves is

$$\left[\frac{\beta_H(t)}{\beta_{H0}}\right]_{CP} = (1-B)\cdot\exp\left(-\frac{t_{CP}}{T_{HF}^*}\right) + B\cdot\exp\left(-\frac{t_{CP}}{T_{1\rho}^*}\right) \quad (13)$$

It should be noted that the magnitude of the H magnetization can be normalized at $t_{CP} = 0$, which is a distinguishing feature of CP-drain curves. One may deduce additional information from the intensity of CP-drain curves, while only the shape of curves (slopes) can be examined for CP-curves. At the ideal CP condition, the decay of H magnetization is principally characterized by $-1/T_{1\rho}^H$ because $B = 1/(1+\varepsilon)$ is unity and $T_{1\rho}^* = T_{1\rho}^H$. When B takes a value between 0 and 1, this value is related to the proportion of the H magnetization that does not transfer to the F spin bath during H → F CP. As described above, when T_{HF} is much smaller than $T_{1\rho}^H$ and $T_{1\rho}^F$, B can be determined as the intercept of the slower decaying part of the CP-drain curve, which represents the relaxation to the lattice (time constant $= -1/T_{1\rho}^*$), to $t_{CP} = 0$, and this value should be equal to $1/(1+\varepsilon)$.

Furthermore, the comparison between equations (5) and (10) enables one to examine the relationship between T_{HF}^*, T_{HF}, $T_{1\rho}^*$ and $T_{1\rho}^H$ by introducing two parameters, f_1 and f_2.

$$T_{HF}^* = \frac{T_{HF}}{a_+} = \frac{T_{HF}}{a_0 + \sqrt{a_0^2 - b}} = f_1 \cdot T_{HF} \quad (14)$$

$$T_{1\rho}^* = \frac{T_{HF}}{a_-} = \frac{1}{a_0 - \sqrt{a_0^2 - b}}\frac{T_{HF}}{T_{1\rho}^H}\cdot T_{1\rho}^H = f_2 \cdot T_{1\rho}^H \quad (15)$$

The values of f_1 and f_2 can be calculated as functions of three parameters, namely ε, $T_{HF}/T_{1\rho}^H$ and $T_{HF}/T_{1\rho}^F$. At the ideal CP

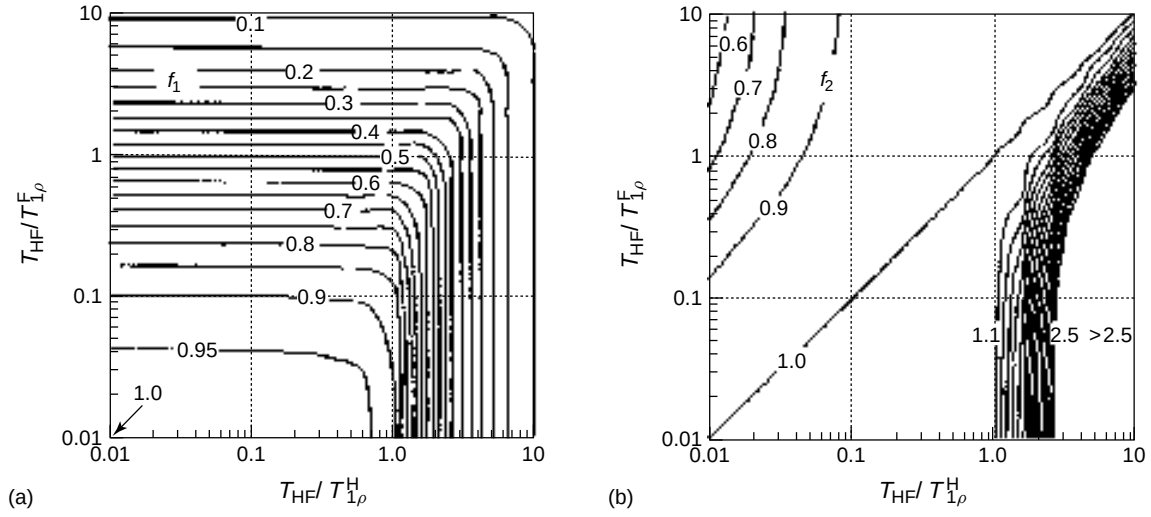

Figure 6 Contour maps of the two parameters f_1 (a) and f_2 (b) that were calculated according to equation (14) and equation (15) for $\varepsilon = 0.01$. These two factors are expressed as functions of $T_{HF}/T_{1\rho}^H$ and $T_{HF}/T_{1\rho}^F$. The limiting value of f_1 at $T_{HF}/T_{1\rho}^H \to 0$ and $T_{HF}/T_{1\rho}^F \to 0$ is 1.0. (Reproduced with permission from Ref.[39])

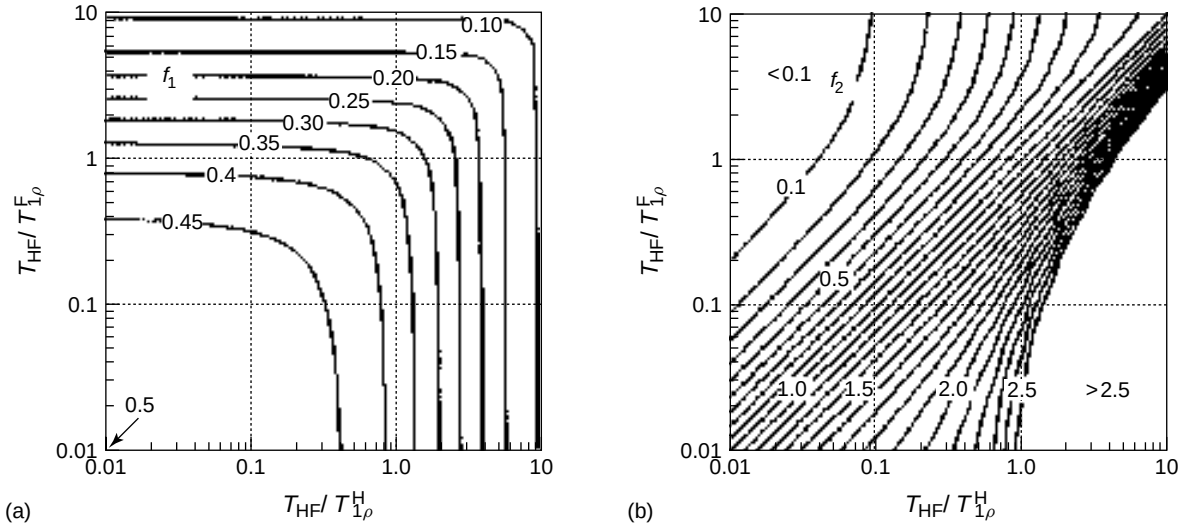

Figure 7 Contour maps of the two parameters f_1 (a) and f_2 (b) calculated for $\varepsilon = 1$. The limiting value of f_1 at $T_{HF}/T_{1\rho}^{H} \to 0$ and $T_{HF}/T_{1\rho}^{F} \to 0 = 0.5$. (Reproduced with permission from Ref.[39])

condition, f_1 and f_2 are unity (see below). Hence, f_1 and f_2 indicate the degree of deviation of the CP dynamics concerned from the ideal CP condition.

Figures 6(a) and 6(b) show the contour maps of f_1 and f_2 calculated using equations (6)–(8) when $\varepsilon = 0.01$, corresponding to the case of chemically dilute fluorines (or to the standard $^1H \to {}^{13}C$ situation). These two factors are expressed as functions of $T_{HF}/T_{1\rho}^{H}$ and $T_{HF}/T_{1\rho}^{F}$. Figure 6(a) indicates that, when $T_{HF}/T_{1\rho}^{H}$ and $T_{HF}/T_{1\rho}^{F}$ are smaller than 0.1, $T_{1\rho}^{*}$ and T_{HF}^{*} are analogous to $T_{1\rho}^{H}$ and T_{HF}, respectively, within an error of 10%. This condition is commonly fulfilled in semi-crystalline and amorphous polymers at temperatures lower than glass transition temperatures. Moreover, $T_{1\rho}^{*}$ has a similar value to $T_{1\rho}^{H}$ in a wide region of the map. These results support the use of the conventional method for the analysis of CP dynamics as long as the conditions described above are fulfilled, so that $T_{1\rho}^{*}$ and T_{HF}^{*} can be taken as $T_{1\rho}^{H}$ and T_{HF}, respectively. On the other hand, Figures 7(a) and 7(b) show the contour maps of f_1 and f_2 calculated when $\varepsilon = 1$, corresponding to many $^1H \to {}^{19}F$ CP situations.

These figures exhibit distinctly different features from those in Figure 6. Even when T_{HF} is one hundredth of $T_{1\rho}^{H}$ and $T_{1\rho}^{F}$, the effective T_{HF}^{*} is only half of T_{HF}. This indicates that the effective ('observed') T_{HF}^{*} is much shorter than the true value of T_{HF} when ε is not negligibly small. By using equation (14), it can be shown that T_{HF}^{*} is equal to $T_{HF}/(1+\varepsilon)$, when T_{HF} is much shorter than $T_{1\rho}^{H}$ and $T_{1\rho}^{F}$. This corresponds to the fact that the rates of the initial increase in the CP-curve and the fast decrease in the CP-drain curve are faster than the respective values of T_{HF}, as seen in Figure 6(b). In addition, f_2 is very sensitive to the variation in $T_{HF}/T_{1\rho}^{H}$ and $T_{HF}/T_{1\rho}^{F}$. This indicates that the $T_{1\rho}^{*}$ value determined from the slope of the experimental decay in the CP curve might not be similar to $T_{1\rho}^{H}$. This result can be explained by the decaying slope of the CP curve being principally determined by $(1/T_{1\rho}^{H} + 1/T_{1\rho}^{F})/2$, not by $1/T_{1\rho}^{H}$, when $\varepsilon = 1$, as described above. This corresponds to the decaying slopes of the CP and CP-drain curves being considerably different from the relevant vales of $T_{1\rho}^{H}$.

The approach described above can be generalized for any number of spin baths.[42] Typically, at modest MAS rates, a single proton spin bath but several fluorine spin baths will exist. This situation occurs when the proton spectrum is homogeneous whereas the relatively large chemical shift differences for ^{19}F ensure that separate signals are observed when proton-decoupling is employed. Under $^1H \to {}^{19}F$ CP conditions, spin exchange between the various ^{19}F spin baths can occur at varying rates (this will include a r.f.-driven CP-like component) (see Figure 8).

Simulations of multiple abundant spin-bath CP are based on a simple extension of the problem of two spin baths. Spins in separate baths, with inverse spin temperatures β_i, β_j etc., may be in contact with each other and with the lattice as seen in Figure 8. Invoking the constraints required by the conservation of energy in the rotation frame and the long-term equilibrium distribution of spin temperatures, the following differential equations can be derived, which are analogous to those in equation (1).

$$\begin{aligned}
\frac{d}{dt}\beta_A &= \frac{1}{T_{AB}}[\beta_B - \beta_A] + \frac{1}{T_{AC}}[\beta_C - \beta_A] + \cdots + \frac{1}{T_{AN}}[\beta_N - \beta_A] - \frac{1}{T_{1\rho}^{A}}\beta_A \\
\frac{d}{dt}\beta_B &= \frac{\varepsilon_{AB}}{T_{AB}}[\beta_A - \beta_B] + \frac{1}{T_{BC}}[\beta_C - \beta_B] + \cdots + \frac{1}{T_{2N}}[\beta_N - \beta_B] - \frac{1}{T_{1\rho}^{B}}\beta_B \\
\frac{d}{dt}\beta_C &= \frac{\varepsilon_{AC}}{T_{AC}}[\beta_A - \beta_C] + \frac{\varepsilon_{BC}}{T_{BC}}[\beta_B - \beta_C] + \cdots + \frac{1}{T_{2N}}[\beta_N - \beta_C] - \frac{1}{T_{1\rho}^{C}}\beta_C \\
&\vdots \qquad\qquad \vdots \qquad\qquad \vdots \qquad\qquad \vdots \qquad\qquad \vdots \\
\frac{d}{dt}\beta_N &= \frac{\varepsilon_{AN}}{T_{AN}}[\beta_A - \beta_N] + \frac{\varepsilon_{BN}}{T_{BN}}[\beta_B - \beta_N] + \cdots + \frac{\varepsilon_{N-1N}}{T_{N-1N}}[\beta_{N-1} - \beta_N] - \frac{1}{T_{1\rho}^{N}}\beta_N
\end{aligned} \tag{16}$$

In matrix form equation (16) is expressed as $\frac{d}{dt}\mathbf{B} = \mathbf{R}\cdot\mathbf{B}$, where $\mathbf{B} = [\beta_A, \beta_B, \beta_{C,\cdots}\beta_N]^T$. This system of equations can be solved as $\mathbf{B}(t) = \exp(\mathbf{M}t)\cdot\mathbf{B}(0)$ where $\mathbf{M}$ is the matrix shown in equation (17).

$$\begin{bmatrix} -\frac{1}{T_{AB}} - \frac{1}{T_{AC}} - \cdots & \frac{1}{T_{AB}} & \frac{1}{T_{AC}} & \cdots & \frac{1}{T_{AN}} \\ -\frac{1}{T_{AN}} - \frac{1}{T_{1\rho}^{A}} & & & & \\ \frac{\varepsilon_{AB}}{T_{AB}} & -\frac{\varepsilon_{AB}}{T_{AB}} - \frac{1}{T_{BC}} - \cdots & \frac{1}{T_{BC}} & \cdots & \frac{1}{T_{BN}} \\ & -\frac{1}{T_{BN}} - \frac{1}{T_{1\rho}^{B}} & & & \\ \frac{\varepsilon_{AC}}{T_{AC}} & \frac{\varepsilon_{BC}}{T_{BC}} & -\frac{\varepsilon_{AC}}{T_{AC}} - \frac{\varepsilon_{BC}}{T_{BC}} - \cdots & \cdots & \frac{1}{T_{CN}} \\ & & -\frac{1}{T_{CN}} - \frac{1}{T_{1\rho}^{C}} & & \\ \vdots & \vdots & \vdots & \ddots & \vdots \\ \frac{\varepsilon_{AN}}{T_{AN}} & \frac{\varepsilon_{BN}}{T_{BN}} & \frac{\varepsilon_{CN}}{T_{CN}} & \cdots & -\frac{\varepsilon_{AN}}{T_{AN}} - \frac{\varepsilon_{BN}}{T_{BN}} - \cdots \\ & & & & -\frac{\varepsilon_{N-1N}}{T_{N-1N}} - \frac{1}{T_{1\rho}^{N}} \end{bmatrix} \tag{17}$$

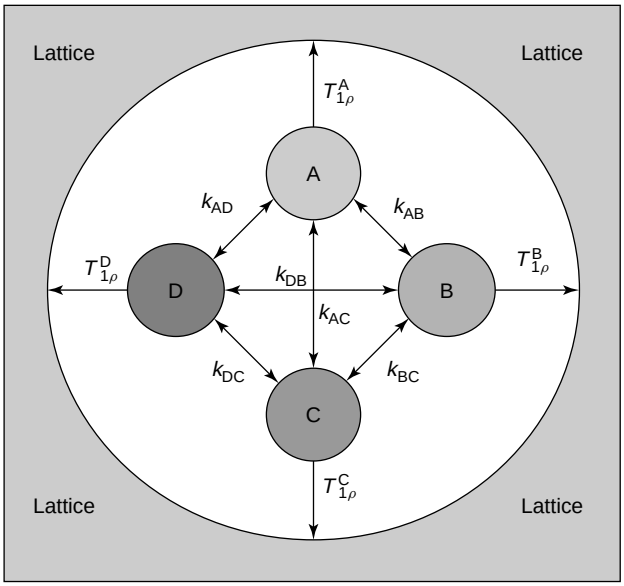

Figure 8 Diagrammatic view of cross-polarization dynamics for a system of four spin baths where one of them, A say, is initially produced in a non-equilibrium state by a 90° pulse. Each spin bath is characterized by an inverse spin temperature, β, and a relative population, ε

Exp(**M**) can be evaluated as $\boldsymbol{\Lambda}^{-1} \cdot \exp(\mathbf{D}) \cdot \boldsymbol{\Lambda}$ where **D** is the matrix of eigenvalues and $\boldsymbol{\Lambda}$ is the matrix of eigenvectors.

A computer program has been written,[42] using equation (17), to iteratively fit CP curves to yield values of characteristic inter-bath spin-exchange times (T_{HF} and T_{FF}), using separately measured values of $T_{1\rho}^{H}$ and $T_{1\rho}^{F}$ as part of the input.

4 FLUOROPOLYMERS

There have been four comprehensive reviews[1,2,43,44] in the last decade relating to the high-resolution ^{19}F NMR of fluoropolymers containing hydrogen. In 1987, a pioneering work on high-resolution ^{19}F MAS NMR at spin rates between 18 and 22 kHz was reported by Dec et al.[13] for copolymers of vinylidenefluoride (CF_2CH_2, VDF) and hexafluoropropylene (CF_3CFCF_2, HFP) and of VDF and chlorotrifluoroethylene (CF_3CFCl), and for terpolymers of VDF, HFP, and tetrafluoroethylene (CF_2CF_2, TFE). Structural assignments of chemical shifts in terms of pentad sequences were made on the basis of solution-state NMR. Recently, Isbester et al.[45] recorded ^{19}F NMR spectra for the same kinds of polymers by simultaneously using MAS rates up to 25 kHz and heating to 250 °C. Very high resolution was achieved at the higher temperatures,[46] and the peaks were assigned by comparison to results from solution-state NMR studies. Detailed monomer compositions of six polymers were quantitatively determined. The authors reported that equivalent resolution was observed for a copolymer if a spectrum acquired at a spin rate of 19 kHz is compared to the corresponding spectrum acquired at 4 kHz and a 50 °C higher temperature.

Harris and coworkers[22,24–27,30,39,40,47,49] have conducted a number of high-resolution ^{19}F NMR studies utilizing MAS, cross polarization (CP), and high-power proton/fluorine decoupling. In particular, several efforts have been devoted to poly(vinylidene fluoride) (PVDF) because of its interesting polymorphism and dielectric properties. The results from ^{19}F–pulsed, ^{19}F wideline, ^{19}F MAS and ^{1}H → ^{19}F CP/MAS NMR of PVDF, all with high-power proton decoupling, have been reviewed in detail.[2] Holstein et al.[24] have reported that, with ^{1}H decoupling, PVDF powder obtained from the melt shows, at ambient probe temperature, a major signal (peak I in Figure 9(c)), together with shoulders (on both high-frequency and low-frequency sides, II and III) and a weak doublet at lower frequency (peaks IV and V). The weak doublets were assigned to chain imperfections of *head-to-head* and *tail-to-tail* sequences, and the shoulders arise from crystalline regions.

The authors[24] showed that discrimination in favor of the crystalline regions can be obtained by spin-locking the protons prior to CP contact because $T_{1\rho}^{H}$ is substantially shorter for amorphous chains. On the other hand, discrimination in favor of the amorphous region was achieved by the dipolar dephasing pulse sequence because the hetero-nuclear dipolar interaction is substantially stronger for crystalline chains. Figure 9(b) shows a spectrum of the amorphous (mobile)

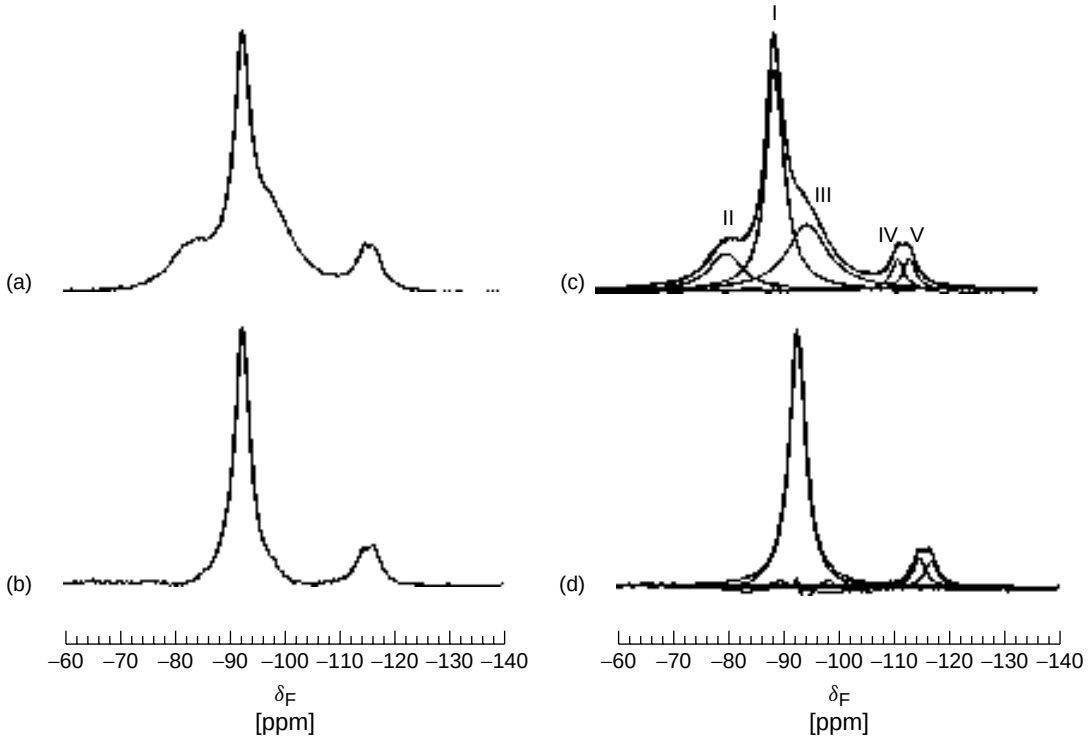

Figure 9 188.29 MHz ^{19}F spectra of solid PVDF powder using (a) $^{1}H \rightarrow {}^{19}F$ CP and (b) the DIVAM (discrimination induced by variable amplitude minipulses) pulse sequence, both obtained at a spin rate of 13.5 kHz with high-power ^{1}H decoupling. The DIVAM CP pulse sequence selectively observes the amorphous region. The spectra **c** and **d** show deconvolutions of **a** and **b** respectively, obtained using Lorentzian functions. For a discussion of the peaks I to V, see the text. (Reproduced with permission from Ref.[49])

domains obtained with an alternative pulse sequence.[49] This indicates that the imperfections are largely or wholly in the amorphous regions. Scheler et al.[22] have applied the two-dimensional (^{1}H and ^{19}F) wideline separation (WISE) sequence[21] to PVDF, both with and without ^{19}F–decoupling during the ^{1}H evolution time. The resulting spectra exemplify the mobility differences between the amorphous and α-crystalline chains. The signals from crystalline and amorphous regions were clearly distinguished in the proton lineshapes and the second moments of the lines. The selection of subspectra from the amorphous and crystalline parts of the polymer by dipolar and $T_{1\rho}$ filters, respectively, strongly supports the assignments.

There are two major crystalline forms, denoted α and β, in PVDF. The chains of the α-form have the $tg^{+}tg^{-}$ conformation, whereas those in the β-form have the all-*trans* conformation. Holstein et al.[25] have studied samples with partial conversion of the α-form to the β-form (obtained by uniaxial or biaxial drawing) and have shown that the β-form gives a single signal at $\delta_F = -98$ ppm whereas the α-form give two signals at $\delta_F = -82$ ppm (peak II) and -98 ppm (peak III), as described above. The immobile chains in the crystalline regions required the application of proton high-power decoupling to completely remove proton–fluorine interactions. The origin of the chemical shifts can be well understood in terms of the γ-gauche effect. Scheler[15] has shown that magic-angle spinning at 30 kHz or more adequately averages (H,F) as well as (F,F) dipolar interactions for PVDF giving high-resolution ^{19}F spectra. This removes the requirement for high-power proton decoupling. Scheler[15] also showed that the two-dimensional RFDR technique provides a simple test for the spatial proximity of different types of fluorines and thus enables the domain structure of PVDF to be explored. However, for the RFDR experiment proton decoupling is essential even at the highest spinning speeds because the recoupling pulses also recouple heteronuclear coupling.

Su and Tzou[48] have also examined the polymorphism of PVDF using fast MAS with spin speeds up to 35 kHz without ^{1}H decoupling. They were thus able to estimate the proportions of the crystalline region, amorphous region, and defect segments as 41%, 54%, and 5% respectively. The authors also analyzed spinning sideband manifolds in PVDF ^{19}F spectra obtained at very high magnetic fields (752.8 MHz frequency) to yield shielding tensor principal components for the different signals, though they do not seem to have taken into account any effects from (H,F) or (F,F) dipolar interactions on sideband intensities. They show that the two peaks assigned to crystalline regions have different shielding tensors, and that their shielding anisotropies are significantly larger than that of the amorphous peak, as commented earlier by Holstein et al.[25] Like Scheler,[15] Su and Tzou[48] used 2D spin-diffusion experiments to indicate proximity between the fluorine sites giving the crystalline-phase signals, and also between the fluorines in the defect structures and those of the amorphous regions. Ando et al.[49] have measured ^{19}F spin-lock, $^{1}H \rightarrow {}^{19}F$ CP, and $^{1}H \rightarrow {}^{19}F$ inversion recovery CP (IRCP) MAS spectra of PVDF to give proton and fluorine relaxation times ($T_{1\rho}^{F}$, $T_{1\rho}^{H}$) and effective parameters (T_{HF}^{*}, $T_{1\rho}^{*}$) relating to $^{1}H \rightarrow {}^{19}F$ CP (Figure 10).

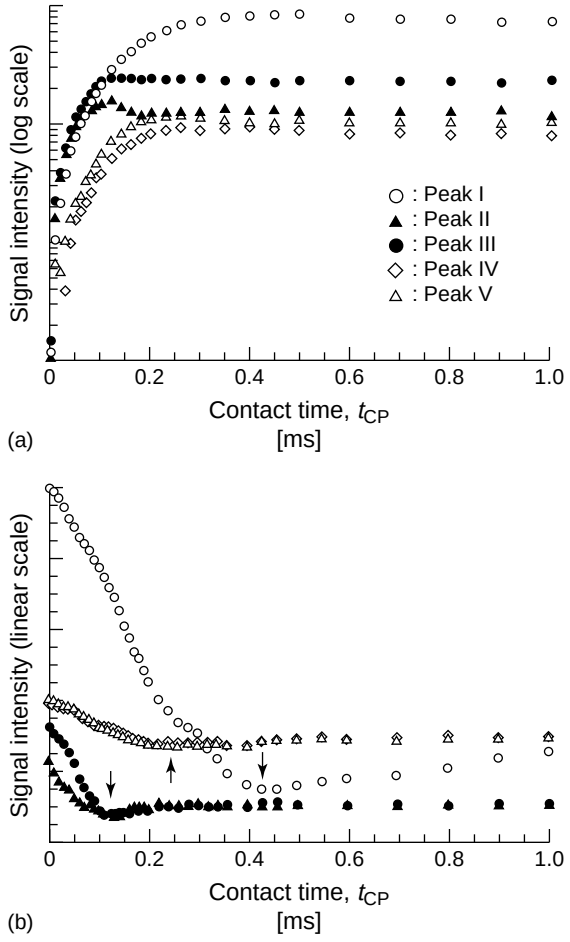

Figure 10 Dependence of the ^{19}F signal intensities for (a) $^{1}H \rightarrow {}^{19}F$ CP and (b) $^{1}H \rightarrow {}^{19}F$ IRCP experiments on PVDF at short contact times with MAS at 13.5 kHz and for $B_o = 4.7$ T. The pre-contact time of the IRCP was 0.2 ms, and the signal intensities of peaks II and III are displaced downwards in (b) to avoid overlap of symbols. The dips originating from the dipolar oscillation behavior are indicated by arrows. Reproduced with permission of Ref.[49]

The values of $T_{1\rho}^{F}$, $T_{1\rho}^{H}$ and $T_{1\rho}^{*}$ for peaks II and III in Figure 9 (crystalline region) are larger than those of peaks I, IV, and V (amorphous region), whereas the values of T_{HF}^{*} for the former pair of peaks are significantly shorter than those of the latter set of peaks. These facts coincide well with the stronger heteronuclear dipolar interactions in the crystalline region of PVDF. Although there is no difference in the spin dynamics between the CP and IRCP experiments, IRCP is superior to the standard CP in observing details of CP processes. The dipolar oscillations in the ^{19}F spectral intensities are clearly observed in the initial stage for IRCP not only for the crystalline peaks, but also for the amorphous peaks (Figure 10b). The first dips observed for peaks II and III are at 0.125 ms, while that for peak I is at 0.425 ms and those for peaks IV and V are around 0.25 ms. The effective average F–H bond distances calculated from these values are 2.2 Å, 3.3 Å, and 2.7 Å, respectively. The longer effective distances in the amorphous peaks are straightforwardly ascribed to molecular motion of the order of several tens of kHz. In addition, the authors[49] measured the $^{19}F \rightarrow {}^{1}H$ CP MAS spectrum of PVDF. The spinning sidebands originate from the residual dipolar interactions that are not averaged out by MAS at a spin rate of 13.5 kHz. Although the main peak and spinning sidebands can be fitted by single Lorentzian functions, the half-height width (hhw) of the former (900 Hz) is significantly smaller than those of the latter (ca. 3000 Hz). This suggests that the contribution of the amorphous signal is mostly limited to the main peak, while that of the crystalline signal is distributed to both the centreband and sidebands. The $^{19}F \rightarrow {}^{1}H$ CP dynamics (especially the effective parameter, T_{FH}^{*}) and the dipolar oscillation behavior, which is only observed for the sidebands, support this view. This phenomenon coincides well with the fact[27] that the spinning sidebands in a ^{1}H-decoupled ^{19}F MAS spectrum at a spin rate of 12 kHz contribute substantially to the spectra of the crystalline region.

Monti et al.[47] have investigated ^{19}F MAS and $^{1}H \rightarrow {}^{19}F$ CP/MAS NMR spectra of Viton-type fluoroelastomers (Figure 11), which are copolymers of VDF and HFP, and terpolymers containing TFE units also.

The $^{1}H \rightarrow {}^{19}F$ CP and TORQUE curves were well fitted by modified conventional equations, and different effective parameters were obtained for five separate peaks, which gave some insight into the CP dynamics between protons and fluorines, although the high abundance of fluorine atoms and efficient $T_{1\rho}^{F}$ process were not explicitly considered. Ando et al.[40] also measured $^{1}H \rightarrow {}^{19}F$ CP/MAS spectra of a Viton-type fluoroelastomer and reexamined the CP dynamics between ^{1}H and ^{19}F using the exact solutions of the equations for the spin thermodynamics. Simultaneous fitting of the evolution of magnetization in the standard CP and TORQUE experiments (Figure 12) gave unique sets of the parameters T_{HF}, $T_{1\rho}^{H}$, and $T_{1\rho}^{F}$ for the five separate peaks in the ^{19}F spectra.

The values of $T_{1\rho}^{H}$ and $T_{1\rho}^{F}$ are consistent with those independently measured by spin-locking experiments. The true values of T_{HF} are significantly larger (by a factor of ca. 4) than the values of T_{HF}^{*} derived from a simple two-parameter fit of the CP behavior with variable contact time.

Ando et al.[39] have also measured (Figure 13) ^{19}F MAS, $^{1}H \rightarrow {}^{19}F$ CP, and $^{1}H \rightarrow {}^{19}F$ CP-drain MAS spectra for a fluorinated polyimide, 6FDA/ODA. The CP dynamics between ^{1}H and ^{19}F for the polyimide (Figure 13) were analyzed

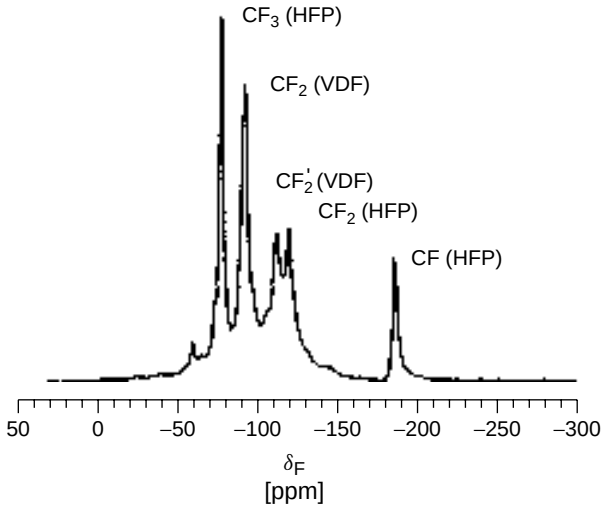

Figure 11 188.29 MHz fluorine-19 MAS spectrum of Viton obtained with proton decoupling, together with the assignments of the peaks

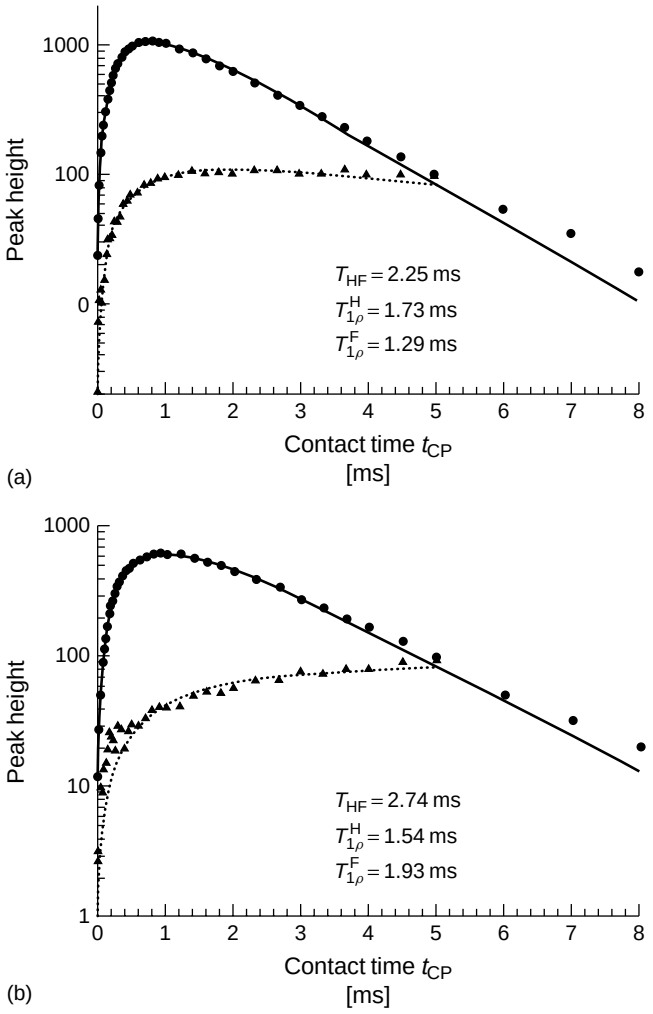

Figure 12 Simultaneous fitting of CP and TORQUE curves for CF_2 of VDF and CF of HFP units. Unique sets of three parameters (T_{HF}, $T_{1\rho}^{H}$, $T_{1\rho}^{F}$) were determined as shown in the figures. Filled circles and triangles represent the signal intensities obtained from the conventional CP and TORQUE experiments, respectively, and solid and dotted lines represent the fitted curves. (Reproduced with permission from Ref.[40])

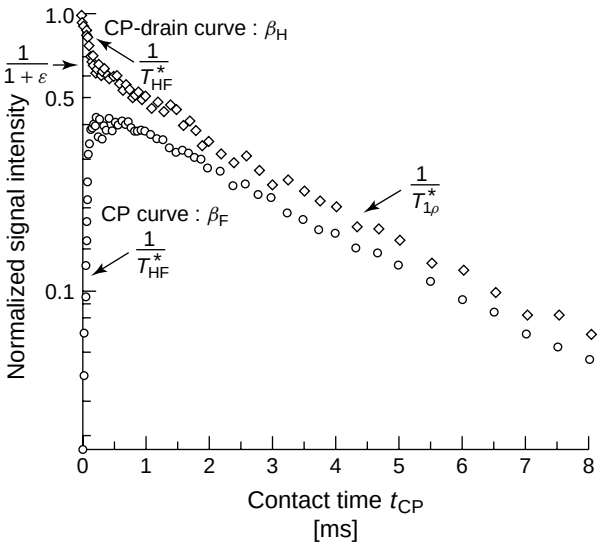

Figure 13 Contact time dependence of the ^1H signal intensity for the $^1H \rightarrow {}^{19}F$ CP (circles) and the $^1H \rightarrow {}^{19}F$ CP-drain (diamonds) experiments at $B_o = 4.7$ T on the fluorinated polyimide. They show the double-exponential behavior, and the value of ε ($=N_F/N_H$) can be calculated from the intercept of the slowly decaying line of the CP-drain curve to $t_{CP} = 0$

on the basis of the spin-thermodynamics theory described in the former section. The constant for polarization transfer (T_{HF}) was determined by the analysis using the effective CP parameters (T_{HF}^*, $T_{1\rho}^*$) together with independently measured values of $T_{1\rho}^{H}$ and $T_{1\rho}^{F}$. The CP-drain experiment, which can measure evolution of residual ^1H magnetization after $^1H \rightarrow {}^{19}F$ CP, was developed, and the value of ε thus obtained (0.49) was close to that determined from the chemical structure ($N_F/N_H = 0.43$) (Figure 13).

Reinsberg et al.[30] have examined ^{19}F MAS, $^1H \rightarrow {}^{19}F$, and $^1H \rightarrow {}^{13}C$ CP/MAS spectra of semi-crystalline poly(trifluoroethylene) (PTrFE). The ineffectiveness of the selection schemes between crystalline and amorphous regions ($T_{1\rho}$–filter and dipolar dephasing) indicates that relaxation parameters differ by less than an order of magnitude. The α-relaxation at ca. 50 °C was proved by a steep decrease of the $^1H \rightarrow {}^{19}F$ CP efficiency for the CF_2 fluorines. The dipolar oscillation frequencies in $^1H \rightarrow {}^{13}C$ CP curves were used to infer the motion of the polymer chain through effective bond distances, and it was concluded that the localized motion of the main chain is considerably hindered at −30 °C.

Ando et al.[26] have investigated $^1H \rightarrow {}^{19}F/{}^{19}F \rightarrow {}^1H$ CP/MAS and ^1H fast MAS spectra of semi-crystalline poly(vinylfluoride) (PVF). Significant differences in $T_{1\rho}^{F}$ and $T_{1\rho}^{H}$ were observed between the immobile and mobile regions, and the effective time constants, T_{HF}^* and $T_{1\rho}^*$ estimated from the $^1H \rightarrow {}^{19}F$ CP curves also clarify the difference in the strengths of dipolar interactions. The inverse $^{19}F \rightarrow {}^1H$ CP-MAS and $^1H \rightarrow {}^{19}F$ CP-drain MAS experiments also gave complementary information to the $^1H \rightarrow {}^{19}F$ CP-MAS spectra, although spinning at 35 kHz is necessary to separate the signals between CHF and CH_2 protons in the ^1H spectra. The dipolar oscillation frequency observed for a crystalline peak in the $^1H \rightarrow {}^{19}F$ CP spectrum correlates well with the H–F distance for a CHF group.

Mabboux and Gleason[50] have studied electron-beam-irradiated vinylidene fluoride/trifluoroethylene (VDF/TrFE) copolymers using high-speed (up to 25 kHz) high-temperature (up to 170 °C) MAS ^{19}F NMR in order to characterize the structure of the polymer. No peaks assigned to crosslinks were resolved, though the crosslinking was implied by linewidth effects. Lau and Gleason[51,52] have reported ^{19}F MAS NMR measurements of films obtained from pulsed plasma-enhanced chemical vapor deposition from hydrofluorocarbon gases, CHF_2CHF_2 and CH_2F_2 at a spin rate of 25 kHz and analyzed their chemical compositions. Various network sequences, namely three CF_3 (CF_3^*C, CF_3^*CF, $CF_3^*CF_2$), five CF_2 ($CF_2CF_2^*CF_2$, $CF_2CF_2^*CF_3$, $CF_2CF_2^*CHF_2$, $CF_2CF_2CF_2^*$, $CF_xCF_2^*CF_x$), and three CF (CF^*, CH_2F^*, $CF^*{=}C<$) segments, were identified in the spectra. Fluorine-19 spin-echo NMR measurements with long delay times (6 ms) were used for selective detection of the mobile region with slower transverse relaxation. In addition, the CF_2 peaks suffered significantly

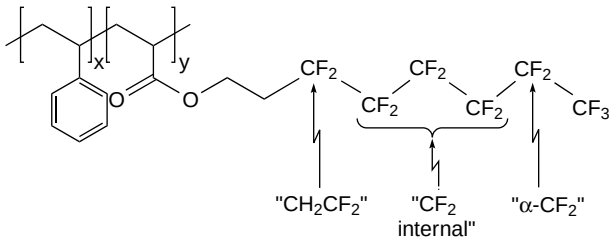

Figure 14 Schematic chemical structure of copoly, which has $x:y = 70:30$. The signals from the three CF_2 groups marked as 'internal' are unresolved, so these fluorines are treated as a single spin-bath

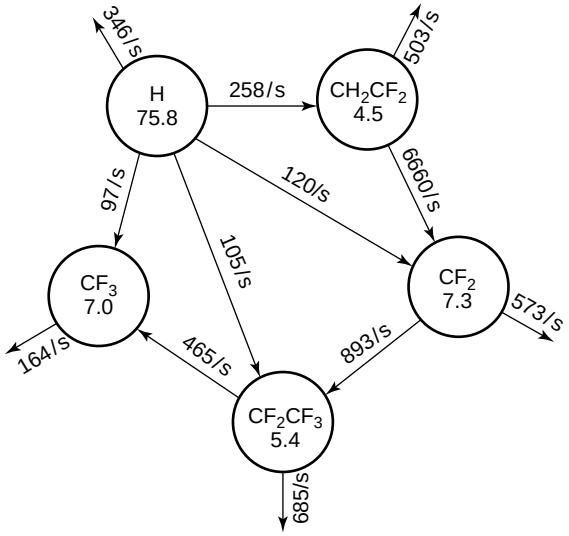

Figure 15 Diagram of the spin baths used for the copoly, with the values for the various rate constants obtained by simultaneously fitting the contact-time curves as shown in Figure 16. The spin-bath populations are also given (in %)

greater intensity loss by spin-echo experiments compared to the CF_3 and CHF peaks, which indicates that the latter groups are relatively more mobile.

The iterative fitting of a multiple spin-bath situation, as described in the previous section, has been applied[42] to the fluoropolymer shown in Figure 14 (which will be referred to as copoly). This system was treated as a problem involving five spin baths, as shown in Figure 15. The corresponding CP curves, Figure 16, were fitted using a program written in MATLAB. The various CP rate parameters, given in Figure 15 were optimized using the Levenberg-Marquardt non-linear least-squares routine.[53] Separately measured $T_{1\rho}$ values were used as constraints. The $^1H \rightarrow {}^{19}F$ CP rates are indicative of the structure of the fluorocarbon sidechain.

5 FLUORINATED ORGANIC COMPOUNDS

In addition to their practical importance, small organic molecules play an essential role as model systems to study NMR effects. Some examples of such use as models will be discussed below. Their major advantage is that they usually exhibit a high degree of crystallinity. On the other hand, the absence of significant motional averaging requires the application of all relevant line-narrowing techniques to obtain high-resolution solid-state spectra.

The large chemical shift range of ^{19}F results in a strong dependence of the Larmor frequency on the chemical environment. This implies the presence of information about both the chemical structure and the spatial arrangement. Therefore, fluorine chemical shifts appear to provide an appropriate tool to study polymorphism. It is also possible to use two-dimensional correlation techniques for the assignment of the signals of the respective forms.

The first applications of $^{19}F-\{^1H\}$ MAS NMR to monofluorinated organic solids were carried out by Hagaman.[7] However, this author reported no ^{19}F high-resolution spectra, but only ^{19}F transverse relaxation times for several different chemical types, including the dependence of T_2 on proton decoupling power. Contemporaneously and independently, Harris and co-workers[8,54] studied three solid fluorinated steroids by $^{19}F-\{^1H\}$ MAS NMR, including a system containing three non-equivalent fluorines. They showed that the technique offered considerable advantages over $^{13}C-\{^1H\}$ NMR for detection and study of polymorphism. The preliminary communication[8] was followed by a full article[10] discussing the methodology of the $^{19}F-\{^1H\}$ experiment, using the fluorinated steroids as examples, and discussing, inter alia, questions of decoupling efficiency, cross-polarization, ^{19}F shielding tensors, spin-lattice relaxation, spin diffusion, dipolar dephasing and rotational resonance. A further article by the same group reported results for a wider range of fluoro-organic systems.[9]

Vierkötter[11] recognized, for the first time, the significant influence (at low or moderate static magnetic fields) of the Bloch-Siegert effect on $^{19}F-\{^1H\}$ spectra of solids (not generally detectable for other solid-state experiments such as $^{13}C-\{^1H\}$). She showed that significant line-broadening of ^{19}F peaks arises from this effect if the sample is not confined to a small volume, because of inhomogeneities in B_1.

Further facets of solid-state $^{19}F-\{^1H\}$ NMR have been illustrated using urea or thiourea inclusion compounds containing fluoro-organic guests.[55–59] Thus, the rate of ring inversion of fluorocyclohexane was studied[55,56,58] by bandshape-fitting, selective polarization inversion, EXSY spectra and $T_{1\rho}$ measurements over a range of temperatures (Figure 17), yielding the thermodynamic parameters for the barrier.

Linear difluoroalkanes in urea inclusion compounds are disordered in the guest arrangements and $^{19}F-\{^1H\}$ NMR proves[56,57] to be a powerful technique to measure average intermolecular (F,F) distances because ideal isolated two-spin systems are involved.[56,57] Static MREV-8 and CPMG experiments yield separate information on dipolar coupling and shielding anisotropy, enabling the simple static pattern to be successfully simulated. The resulting data were used to discuss the distribution of end-group conformations in these systems, taking into account rapid molecular motion about the tunnel axis. MELODRAMA experiments gave[56,59] similar information about dipolar coupling constants for difluoroalkane-urea inclusion compounds.

In the MAS spectrum of 5-fluoro-2-trifluorobenzoic acid (Scheme 1) the signals of the CF and CF_3 fluorines are clearly distinguishable.[35] The existence of two different molecules in the asymmetric unit is shown by the appearance of two sets of lines for each of the CF and CF_3 groups, as depicted in

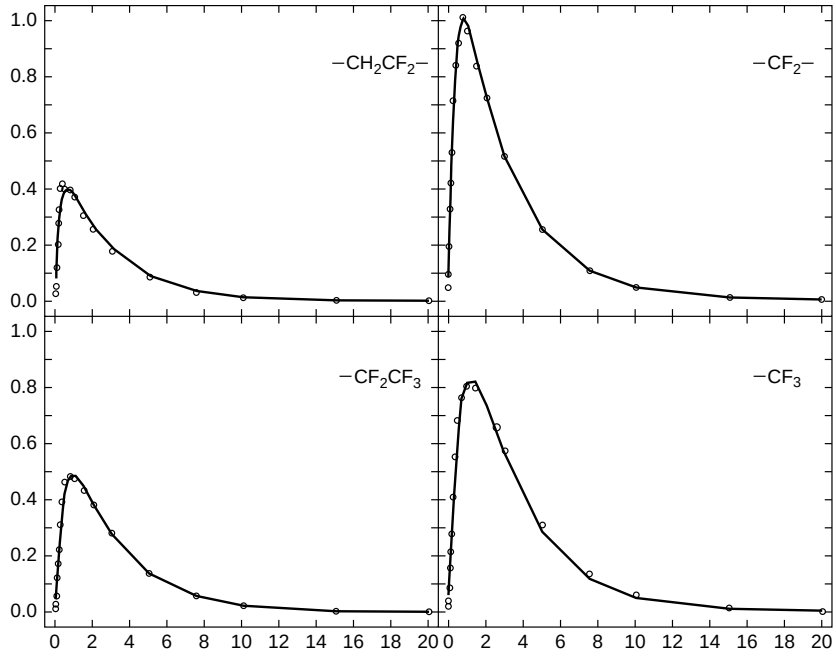

Figure 16 Fitted contact-time $^{1}H \rightarrow {}^{19}F$ CP curves for the four ^{19}F spin-baths of copoly, using the theory discussed in the text. (Reproduced from Ref.[42] by permission of the PCCP Owners Societies)

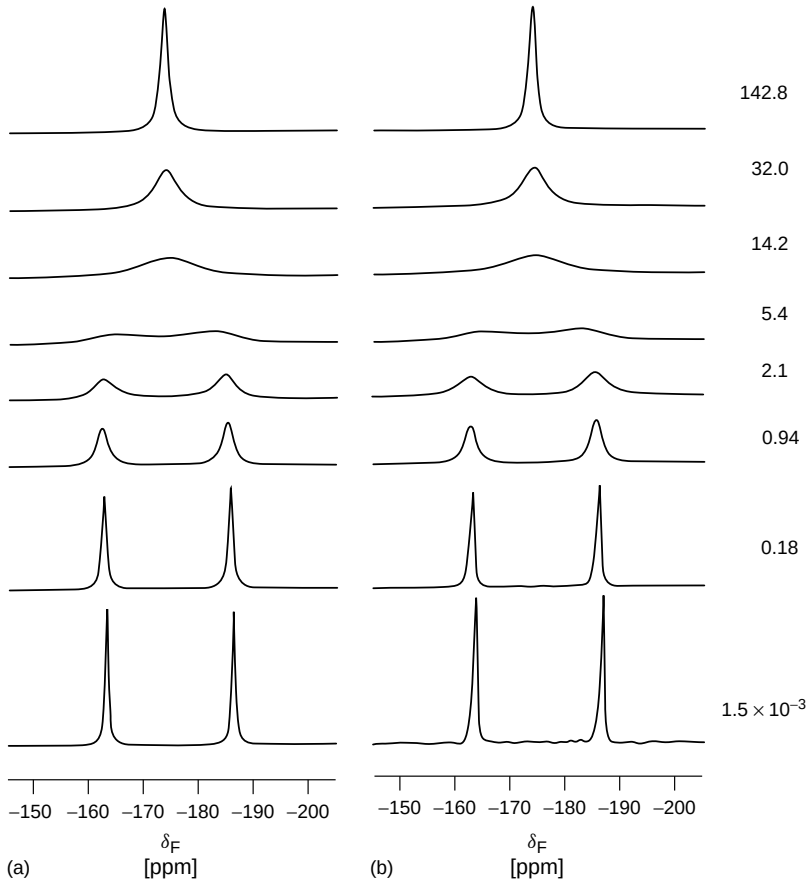

Figure 17 (a) Simulated and (b) experimental 188.29 MHz ^{19}F NMR spectra of fluorocyclohexane in its solid thiourea inclusion compound recorded at (from bottom to top) 177, 217, 237, 247, 258, 268, 278 and 300 K, with the average ring-inversion rate constants given in ms^{-1} down the right-hand side. The rate constants for 177 and 217 K were obtained using the SPI experiment. (Reproduced with permission from Ref.[58])

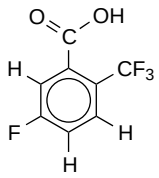

Scheme 1

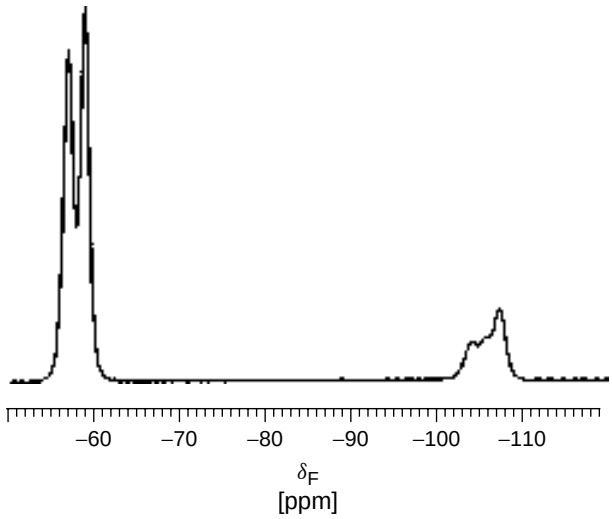

Figure 18 Fluorine-19 MAS NMR spectrum of 5-fluoro-2-(trifluoromethyl)benzoic acid acquired at a Larmor frequency of 282 MHz and a sample spinning frequency of 32 kHz

Figure 18. A possibility to assign the pairs of signals originating from the respective forms is by spin-exchange based on RFDR (radio-frequency driven recoupling).[60] This experiment probes spatial proximity by the distance-dependence of the direct dipolar coupling. Cross-peaks off the diagonal, as seen in Figure 19, are an indication of spin exchange during the mixing time, mediated by the direct dipolar coupling and thus spatial proximity. Normally this will link resonances for the same molecule of the asymmetric unit, though sometimes the intermolecular dipolar interactions may be sufficiently strong

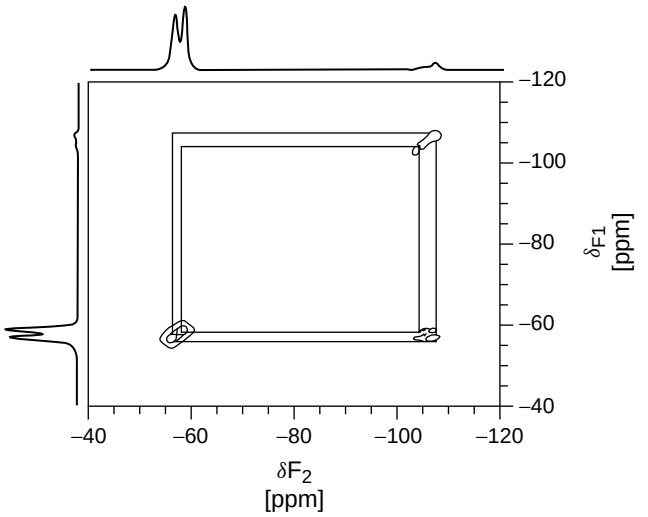

Figure 19 Fluorine-19 spin-exchange experiment under radio-frequency driven recoupling for 5-fluoro-2-(trifluoromethyl)benzoic acid, acquired at a Larmor frequency of 282 MHz with a sample spinning frequency of 32 kHz and a mixing time of 0.5 ms

to confuse matters, as is usual for any experiment exploiting the direct dipolar coupling. In this recoupling experiment proton decoupling during the mixing time is essential, because the recoupling would recouple the heteronuclear dipolar coupling as well, and thus suppress the total signal. The same type of information is available using double-quantum NMR[61] as depicted in Figure 20.[62] In these spectra the chemical shift in the single quantum, directly-detected, dimension is correlated with the double-quantum signal in the indirect dimension, in which the sum of the chemical shifts of the coupled nuclei appears. For double-quantum coherence in a spectrum of spin one-half nuclei, two spins must be coupled. Again, the coupling involved is the distance-dependent direct dipolar effect. The presence of double-quantum coherence is an indication of spatial and spectral proximity. The strength of the dipolar coupling and thus the distance between the coupled nuclei can be determined from a comparison of the spinning sideband pattern in the double-quantum dimension with simulations.

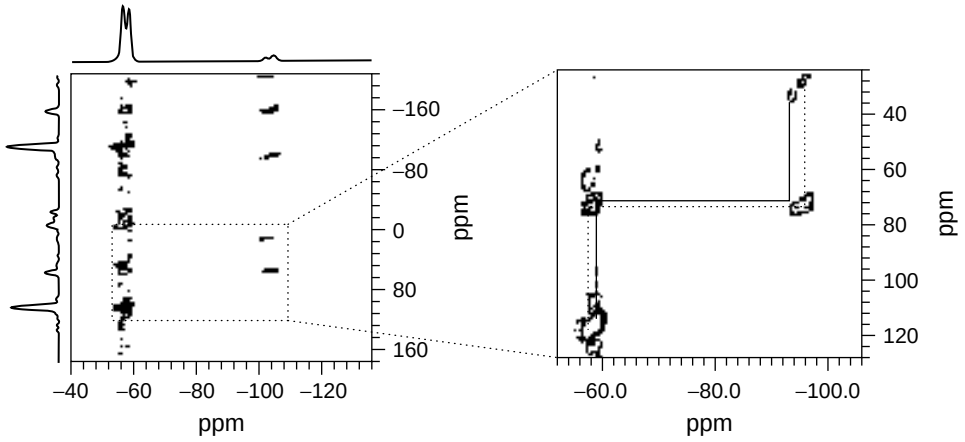

Figure 20 Fluorine-19 double-quantum experiment for 5-fluoro-2-(trifluoromethyl)benzoic acid, acquired at a Larmor frequency of 282 MHz with a sample spinning frequency of 32 kHz using back-to-back pulses with an excitation time of 15 μs. The extra lines in the expansion indicate the link between the CF and CF_3 signals

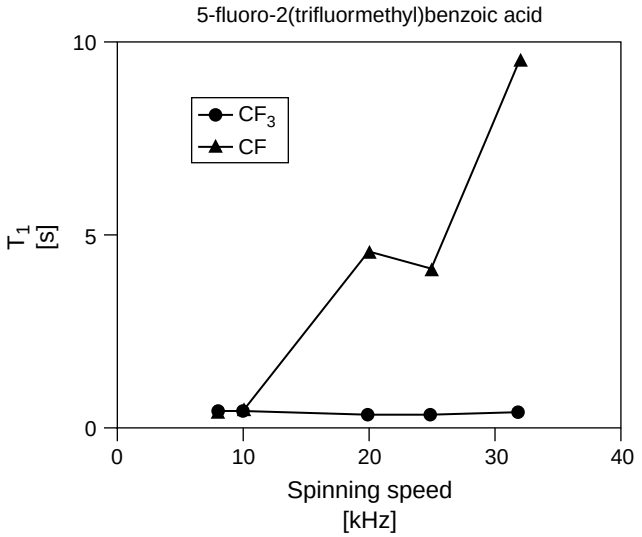

Figure 21 Fluorine-19 longitudinal relaxation times of the CF and CF_3 signals for 5-fluoro-2-(trifluoromethyl)benzoic acid as a function of the sample spinning frequency, obtained at a Larmor frequency of 282 MHz

Miyoshi et al. recently investigated[34] the dependence on MAS rate of T_1 in partially fluorinated derivatives of benzoic acid. In these systems, the fast rotation of a trifluoromethyl group provides an efficient relaxation sink for ^{19}F. At moderate sample spinning rates, there is sufficient overlap of the signals from the trifluoromethyl group and the single fluorine spin on the benzene ring to facilitate spin diffusion and thus fast T_1 relaxation of the isolated fluorine. At higher spinning speeds (Figure 21), there is considerable averaging of both the homonuclear and the heteronuclear dipolar coupling to achieve well-separated lines. This means spin flip-flops are no longer energy-conserving, and therefore spin diffusion is efficiently quenched by MAS. This results in a substantially longer T_1 for the isolated fluorine, which can be as large as 20 s. Although no proton decoupling was applied, it is understood that both homonuclear and heteronuclear coupling influence fluorine spin-diffusion. In most perfluorinated systems (such as fluoropolymers), which have a higher fluorine density, the same mono-exponential T_1 has been observed[63] for all resolved sites, even under high-speed MAS. This fact is attributed to spin-diffusion, which is rapid on the time scale of T_1. The same group of compounds has been used[34] to test and calibrate internuclear distance measurements using Lee–Goldburg cross-polarization between ^1H and ^{19}F. The results nicely correspond to the distances determined in molecular simulations.

Another example for monitoring fluorine spin diffusion is provided by spin-exchange in a partially fluorinated steroid (Scheme 2). Spin diffusion has been monitored[9,10] using spin-exchange spectroscopy based on an EXSY experiment (Figure 22). The rate of spin diffusion between protons is governed by the distance-dependent dipolar coupling only. Spin-diffusion between fluorine nuclei is also determined by the dipolar coupling. However, it can in addition be influenced by the spectral separation. In that case the elementary step in spin diffusion, the flip-flop between two coupled spins is no longer energy conserving. This has been investigated at moderate sample spinning rates with variations in the mixing time. Such moderate MAS rates, in conjunction with heteronuclear decoupling, provide sufficient line narrowing for the detection of highly resolved spectra. The heteronuclear coupling in this system is still significant at these spinning speeds. Therefore it is possible to effectively manipulate the dipolar coupling by RF pulses, e.g., during the mixing time, so as to investigate the various factors influencing fluorine spin diffusion. When no radio-frequency pulses are applied during mixing (Figure 22a), the spin-exchange rate reflects the spatial proximity of the fluorine nuclei in the molecule. If, however, the proton–fluorine dipolar coupling is suppressed during the EXSY mixing time, no exchange cross-peaks are visible between the CF and the CFH or the CFH_2 fluorine signals (Figure 22b) because suppression of the heteronuclear coupling leads to line narrowing, giving well-resolved, isolated lines in the spectrum. The spin-exchange process is no longer energy conserving and so is hindered. The opposite is true when the chemical shift difference is refocused and the line narrowing by MAS is stopped by rotor-synchronized π pulses during the mixing time (radio-frequency driven recoupling, RFDR). In such experiments (Figure 22c) the exchange rates are determined by the dipolar coupling strength and thus the internuclear distance only. In the case of RFDR, the exchange rate reflects the internuclear distance only when the chemical shift difference in the spectrum is refocused. Spin exchange is nearly suppressed when heteronuclear decoupling is applied. In the fully coupled spectra the exchange rate is influenced by the partial separation of the lines.

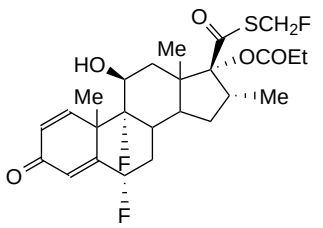

Scheme 2

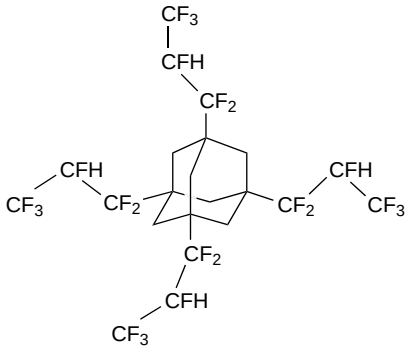

Scheme 3

The cross-polarization and relaxation behavior has been investigated[9,64] in a semifluorinated derivative of adamantane (Scheme 3). This molecule contains four identical sidechains

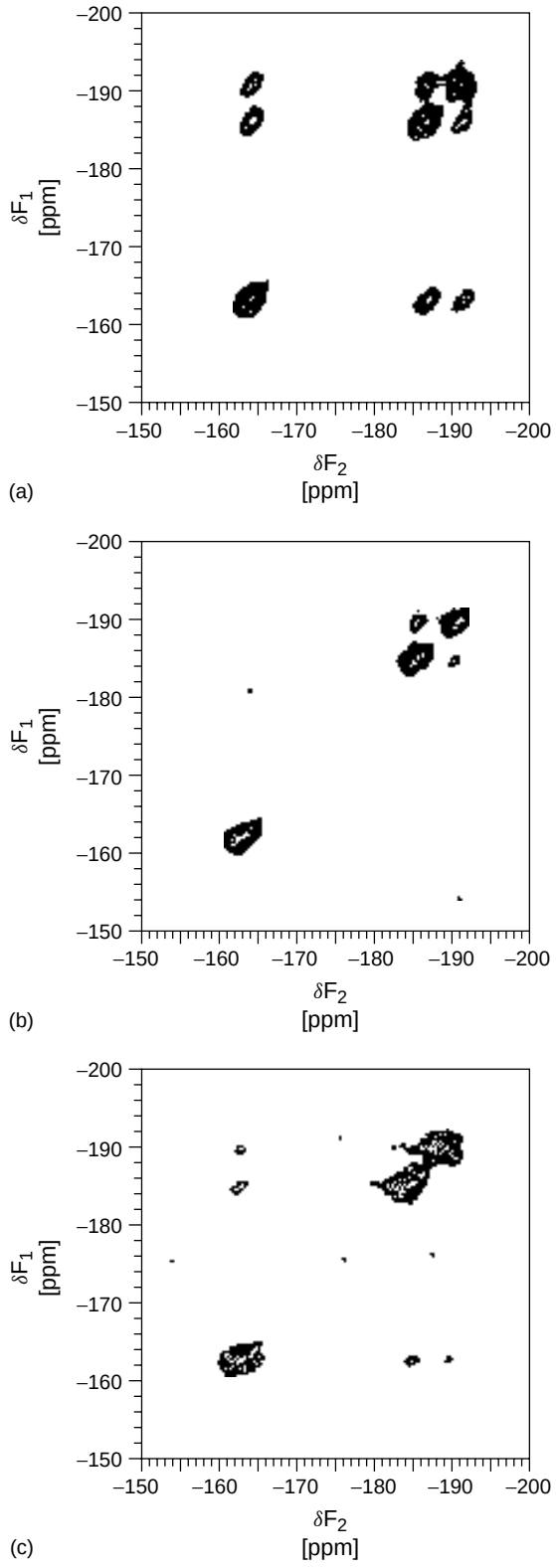

Figure 22 Two-dimensional 188.29 MHz ^{19}F CPMAS spin-exchange spectra of the fluorosteroid (Scheme 2): (a) without proton decoupling during the mixing time; (b) with proton decoupling during the mixing time; and (c) with RFDR during the mixing time. In all three cases the dwell time in both dimensions was 50 μs, the mixing time 5 ms, spinning rate 10 kHz, recycle delay 2 s, $\pi/2$ pulse duration 3 μs, contact time 2 ms, 32 transients per t_1 point and 128 slices in t_1

containing a CF_2, a CFH and a CF_3 group each. Different experimental methods for probing the dipolar coupling have been applied. By application of a variant of the DIPSHIFT experiment,[65] the heteronuclear dipolar coupling has been correlated with the fluorine chemical shift. Complementary information is obtained from a WISE (wideline separation experiment), where proton wideline information is correlated with the chemical shift of the neighboring fluorine nuclei. Both experiments can be utilized to probe local dynamics, which, via fluorine chemical shifts, can be attributed to chemical substructures. One-dimensional versions of the experiments, on the other hand, can be used as discriminating steps.

Brouwer et al.[66] have examined the supramolecular inclusion compound *p-tert* -butylcalix[4]arene-fluorobenzene, using $^1H \rightarrow {}^{19}F$ cross-polarization spectra to show that there must be considerable mobility of the guest fluorobenzene molecule in the host. Spectra of the static complex showed axially symmetric powder patterns with shielding anisotropy $\Delta\sigma = -42$ ppm, whereas solid fluorobenzene has an asymmetric shielding tensor[67] with $\Delta\sigma = -87$ ppm. The results[66] for the calixarene host-guest system are consistent with disorder in the crystal structure. Brouwer, Challoner and Harris[68] have studied a second *p-tert*-butylcalix[4]arene inclusion compound, with α, α, α-trifluorotoluene as a guest. The static $^{19}F-\{^1H\}$ spectra were analyzed (Figure 23) in terms of interplay between shielding anisotropy and F,F dipolar coupling to yield the 3 principal components of the shielding tensor and the F,F distances within the CF_3 group. Both shielding and dipolar tensors are strongly averaged by internal rotation about the $C-CF_3$ bond. The authors also studied the effect of magic-angle and off-angle spinning. The ^{19}F signal is narrow and very sensitive to the exact angle of the spinning axis. It is therefore proposed[68] that the compound be used to set the magic angle for ^{19}F spectra when proton decoupling is feasible.

Chisholm et al.[69] examined the $^{19}F-\{^1H\}$ MAS spectra of two monofluorinated pigment compounds and showed that in each case there is only one molecule in the asymmetric unit. Campbell et al.[70] examined two polymorphs of (3*S-trans*)-1-[3,4-dihydro-2,2-dimethyl-6-(pentafluoroethyl)-2*H*-1-benzo-pyran-4-yl]piperidin-2-one but found, somewhat unusually, that the $^1H \rightarrow {}^{19}F$ CP spectra did not distinguish very clearly between the forms, even though one (only) of them had more than one molecule in the crystallographic asymmetric unit. The ^{13}C spectra proved to be significantly more useful than the ^{19}F spectra.

Shapiro et al.[71] have shown that ^{19}F MAS NMR without proton decoupling gives high-resolution spectra for studying organic solid-phase reaction processes occurring on resin supports, using solvent-swelling (with benzene-d_6) to further decrease the linewidths. Specifically, they studied the reaction of 4-fluoro-3-nitrobenzamide, bonded to a polystyrene resin, with reagents causing an S_NAr displacement of the fluorine atom. The technique is complementary to gel-phase NMR and has the advantage of requiring less accumulation time. Grage et al.[72] applied a CPMG sequence to obtain pure dipolar spectra of flufenamic acid in a membrane (DMPC; 1,2-dimyristoyl-sn-glycero-3-phosphocholine) and, earlier,[73] diflucortolon-21-valerate in a fluorine-19-labelled DMPC; [1-myristoyl-2-(4,4-difluoro-

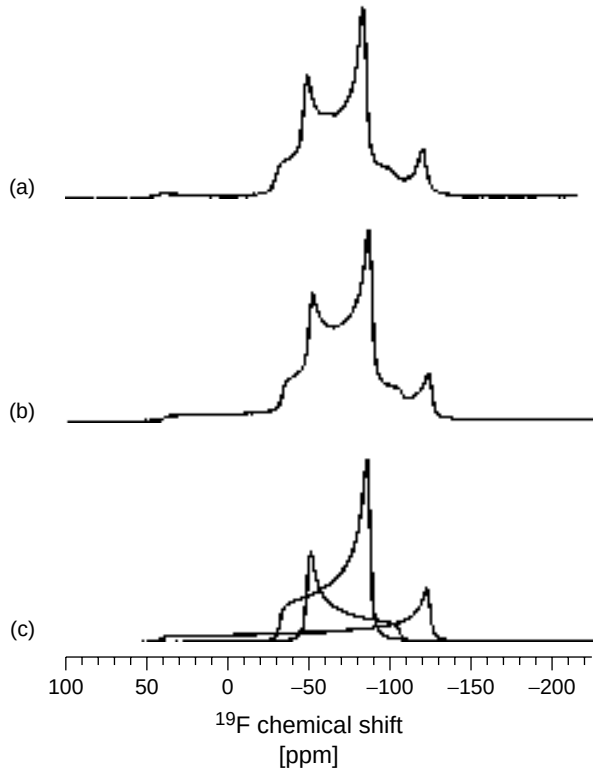

Figure 23 Experimental (a) and simulated (b) 188.297 MHz $^{1}H \rightarrow {}^{19}F\{H\}$ static NMR spectra of the *p-tert*-butylcalix[4]arene-α, α, α-trifluorotoluene inclusion compound. The three spectral components are depicted in (c). (Reproduced with permission from Ref.[68])

myristoyl)-sn-glycero-3-phosphocholine (DMPC-F_2)]. An investigation of the orientation dependence of the dipolar coupling strength in oriented membranes yields an order parameter. However, the axial rotation of the lipid molecules, which scales the dipolar couplings, has to be taken into account. With a two-dimensional version of the CPMG experiment, in which for each datapoint a full FID has been acquired, fluorine chemical shift resolution has been achieved under proton decoupling. A further report[74] on flufenamic acid in DMPC (but with the membrane named as dimyristoylphosphatidylcholine) was published by the same group later. In all three papers a range of NMR experiments (including Hahn echoes, CPMG pulse trains, and single-pulse excitation) was used, on static samples.

6 FLUORINATED ORGANOMETALLIC AND METAL COORDINATION COMPOUNDS

Surprisingly little work has been carried out in this area. Harris and co-workers[9,75] have used $^{19}F-\{^{1}H\}$ MAS NMR to study some organotin fluorides, R_3SnF. Spinning sideband analysis was carried out both on the main signals (arising from molecules containing spin-zero tin isotopes) and on the '$^{117/119}$Sn satellites' (Figure 24). Together with similar measurements on the $^{119}Sn-\{^{1}H\}$ spectra, the results enabled the authors to estimate the anisotropies in $^{1}J_{SnF}$, though with very large potential errors. In the case of Mes_3SnF (where Mes = mesityl) there are two molecules (with tetracoordinated

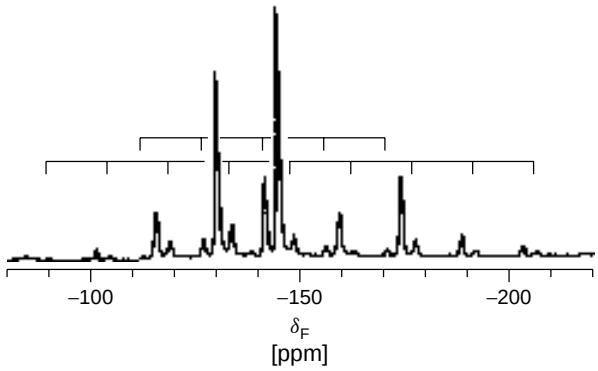

Figure 24 188.29 MHz fluorine-19 MAS spectrum of tri-*iso*butyltin fluoride, with the spinning sideband manifolds of the two 'tin satellite' resonances indicated separately. Experimental conditions: $\pi/2$ pulse duration 3.95 μs, spinning rate 2.7 kHz, 128 transients and 5 s recycle delay

tin) in the asymmetric unit and two-dimensional ^{119}Sn, ^{19}F HETCOR spectra enabled the ^{119}Sn and ^{19}F signals to be linked. The experiment was carried out with proton decoupling on both channels. The compound $^{n}Bu_3SnF$, on the other hand, contains pentacoordinate tin (involving Sn−F−Sn bridges), and the ^{19}F shielding anisotropy is substantially larger than for Mes_3SnF.

7 FLUORINATED INORGANIC COMPOUNDS

$^{1}H \rightarrow {}^{19}F$ cross-polarization and direct-polarization MAS spectra (along with ^{13}C and ^{31}P) have been obtained[76] for a solid chlorophosphane with aryl groups containing CF_3 substituents. Four signals were resolved throughout the temperature range −120 °C to +50 °C showing that local symmetry for the 2,6-$(CF_3)_2C_6H_3$ aromatic ring is lacking and that internal rotation about the relevant P−C bond is slow (which is not the situation in solution above ambient probe temperature). In contrast, the $^{19}F-\{^{1}H\}$ solid-state spectrum of a compound containing the 2,6-$(CF_3)_2C_6H_3PCl_2$ group as a ligand bonded to platinum shows[77] a single centreband signal at ambient temperature but a marked change to a more complex spectrum at low temperature. This suggests the slowing of a motional process (either rotation about the C−P bond or about the C−CF_3 bonds) as the temperature is lowered.

Fluorinated diazadiphosphetidines have been studied[78] by variable-temperature $^{19}F-\{^{1}H\}$ direct-polarization spectroscopy. At room temperature the fluorines in $(F_3PNPh)_2$ are all equivalent because of the existence of a rapid pseudorotation process. However, it was shown that at −106 °C this motion becomes slow on the NMR timescale.

8 CONCLUDING REMARKS

It is now clear that ^{19}F NMR has considerable potential for the study of molecular-level mobility and structure of solids across a wide range of chemistry. This is true for heterogeneous systems such as fluoropolymers, as well as for crystalline molecular and framework compounds, including biochemical situations. The considerable benefits from the

high natural abundance, strong magnetic dipole moment and substantial range of isotropic chemical shifts can now be routinely utilized because the technical problems of obtaining high-resolution ^{19}F spectra of excellent quality have now been overcome.

9 REFERENCES

1. R. K. Harris and P. Jackson, *Chem. Rev.*, 1991, **91**, 1427.
2. J. M. Miller, *Prog. NMR Spectrosc.*, 1996, **28**, 255.
3. V. J. McBrierty and K. J. Packer, 'Nuclear Magnetic Resonance in Solid Polymers', Cambridge University Press: Cambridge, 1993.
4. A. M. Kenwright and B. J. Say, in 'NMR Spectroscopy of Polymers', ed R. N. Ibben, Chapter 7, Chapman and Hall: London, 1993.
5. V. J. McBrierty and D. C. Douglass, *Macromolecules*, 1977, **10**, 855.
6. J. Schaefer and E. O. Stejskal, *J. Am. Chem. Soc.*, 1976, **98**, 1031.
7. E. W. Hagaman, *J. Magn. Reson.*, 1993, **104A**, 125.
8. S. A. Carss, R. K. Harris, P. Holstein, B. J. Say, and R. A. Fletton, *J. C. S. Chem. Commun.*, 1994, 2407.
9. R. K. Harris, S. A. Carss, R. D. Chambers, P. Holstein, A. P. Minoja, and U. Scheler, *Bull. Magn. Reson.*, 1995, **17**, 37.
10. S. A. Carss, U. Scheler, R. K. Harris, P. Holstein, and R. A. Fletton, *Magn. Reson. Chem.*, 1996, **34**, 63.
11. S. A. Vierkötter, *J. Magn. Reson.*, 1996, **118A**, 84.
12. B. C. Gerstein, R. G. Pembleton, R. C. Wilson, and L. M. Ryan, *J. Chem. Phys.*, 1977, **66**, 361.
13. S. F. Dec, R. A. Wind, G. E. Maciel, and F. E. Anthonio, *J. Magn. Reson.*, 1986, **70**, 355.
14. P. K. Isbester, T. A. Kestner, and E. J. Munson, *Macromolecules*, 1997, **30**, 2800.
15. U. Scheler, *Bull. Magn. Reson.*, 1999, **19**, 52.
16. R. D. Kendrick and C. S. Yannoni, *J. Magn. Reson.*, 1987, **75**, 506.
17. W. S. Veeman and W. E. J. R. Maas, *NMR Basic Principles Prog.*, 1994, **32**, 127.
18. P. van Hecke, H. W. Spiess, and U. Haeberlen, *J. Magn. Reson*, 1976, **22**, 103–116.
19. U. Scheler and R. K. Harris, *Chem. Phys. Lett.*, 1996, **262**, 137.
20. A. D. Bax, *J. Magn. Reson.*, 1985, **65**, 142–145.
21. (a) N. Zumbulyadis, *Phys. Rev.*, 1986, **33B**, 6495; (b) K. Schmidt-Rohr, J. Claus, and H. W. Spiess, *Macromolecules*, 1992, **25**, 3273.
22. U. Scheler and R. K. Harris, *Solid State NMR*, 1996, **7**, 11.
23. E. Brunner, D. Freude, B. C. Gerstein, and H. Pfeifer, *J. Magn. Reson.*, 1990, **90**, 90.
24. P. Holstein, R. K. Harris, and B. J. Say, *Solid State NMR*, 1997, **8**, 201.
25. P. Holstein, U. Scheler, and R. K. Harris, *Polymer*, 1998, **39**, 4937.
26. S. Ando, R. K. Harris, P. Holstein, S. A. Reinsberg, and K. Yamauchi, *Polymer*, 2001, **42**, 8137.
27. P. Holstein, G. A. Monti, and R. K. Harris, *Phys. Chem. Chem. Phys.*, 1999, **1**, 3549.
28. M. Goldman and L. Shen, *Phys. Rev.*, 1966, **144**, 321.
29. L. Müller, A. Kumar, T. Baumann, and R. R. Ernst, *Phys. Rev. Lett.*, 1974, **32**, 1402.
30. S. A. Reinsberg, S. Ando, and R. K. Harris, *Polymer*, 2000, **41**, 3729.
31. M. Lee and W. I. Goldburg, *Phys. Rev.*, 1965, **140A**, 1261.
32. S. R. Hartmann and E. L. Hahn, *Phys. Rev.*, 1962, **128**, 2042–2053.
33. B.-J. van Rossum, C. P. de Groot, V. Ladizhansky, S. Vega, and H. J. M. de Groot, *J. Am. Chem. Soc.*, 2000, **1222**, 3465.
34. T. Miyoshi and U. Scheler, to be published.
35. T. Miyoshi and U. Scheler, *Solid State NMR*, in preparation.
36. D. A. McArthur, E. L. Hahn, and R. E. Walstedt, *Phys. Rev.*, 1969, **188**, 609–638.
37. M. Mehring, 'Principles of High Resolution NMR in Solids', 'NMR – Basic Principles and Progress', 2nd edn., Vol. 11. Spinger: Berlin 1983.
38. D. Michel and F. Engelke, *NMR Basic Principles Prog.*, 1994, **32**, 69.
39. S. Ando, R. K. Harris, and S. A. Reinsberg, *J. Magn. Reson.*, 1999, **141**, 91.
40. S. Ando, R. K. Harris, G. A. Monti, and S. A. Reinsberg, *Magn. Reson. Chem.*, 1999, **37**, 709.
41. P. Tekely, V. Gerardy, P. Palmas, D. Canet, and A. Retournard, *Solid State NMR*, 1995, **4**, 361.
42. P. Hazendonk, R. K. Harris, G. Galli, and S. Pizzanelli, *Phys. Chem. Chem. Phys.*, 2002, **4**, 507.
43. R. K. Harris, G. A. Monti, and P. Holstein, 'Solid State NMR of Polymers.', eds I. Ando and T. Asakura, Elsevier Science: New York, 1998, ch 6.6, pp 253–266.
44. R. K. Harris, G. A. Monti, and P. Holstein, 'Solid State NMR of Polymers', eds I. Ando and T. Asakura, Elsevier Science: New York, 1998, ch 18, pp 667–712.
45. P. K. Isbester, J. L. Brandt, T. A. Kestner, and E. J. Munson, *Macromolecules*, 1998, **31**, 8192.
46. R. K. Harris, R. R. Yeung, P. Johncock, and D. A. Jones, *Polymer*, 1996, **37**, 721.
47. G. A. Monti and R. K. Harris, *Magn. Reson. Chem.*, 1998, **36**, 892.
48. T-.W. Su and D-.L. M. Tzou, *Polymer*, 2000, **41**, 7289.
49. S. Ando, R. K. Harris, and S. A. Reinsberg, *Magn. Reson. Chem.*, 2002, **40**, 97.
50. P.-Y. Mabboux and K. K. Gleason, *J. Fluorine Chem.*, 2002, **113**, 27.
51. K. K. S. Lau and K. K. Gleason, *J. Electrochem. Soc.*, 1999, **146**, 2652.
52. K. K. S. Lau and K. K. Gleason, *J. Fluorine Chem.*, 2000, **104**, 119.
53. W. H. Press, B. F. Flannery, S. A. Teukolsky, and W. T. Vetterling, 'Numerical Recipes: The Art of Science Computing', Cambridge University Press: Cambridge, 1987, ch 14, pp 523.
54. S. A. Carss, Ph.D. Thesis, University of Durham, 1995.
55. A. Nordon, R. K. Harris, L. Yeo, and K. D. M. Harris, *J. C. S. Chem. Commun.*, 1997, 961.
56. A. Nordon, Ph.D. Thesis, University of Durham, 1997.
57. A. Nordon, E. Hughes, R. K. Harris, L. Yeo, and K. D. M. Harris, *Chem. Phys. Lett.*, 1998, **298**, 25.
58. R. K. Harris, A. Nordon, and K. D. M. Harris, *Magn. Reson. Chem.*, 1999, **37**, 15.
59. R. K. Harris, 'Magnetic Resonance in Food Science: A View to the Future', eds G. A. Webb, P. S. Belton, A. M. Gil, and I. Delgadillo, Royal Society of Chemistry: London, 2001, ch. 3.
60. A. E. Bennett, J. H. Ok, and R. G. Griffin, *J. Chem. Phys.*, 1992, **96**, 8624.
61. I. Schnell, S. P. Brown, H. Y. Low, H. Ishida, and H. W. Spiess, *J. Am. Chem. Soc.*, 1998, **120**, 11 784.
62. U. Scheler, *Prog. NMR Spectrosc.*, in preparation.
63. B. Fuchs and U. Scheler, *Macromolecules*, 2000, **33**, 120.
64. R. K. Harris and U. Scheler, to be published.
65. M. G. Munowitz and R. G. Griffin, *J. Chem. Phys.*, 1982, **76**, 2848.
66. E. B. Brouwer, R. D. M. Gougeon, J. Hirschinger, K. A. Udachin, R. K. Harris, and J. A. Ripmeester, *Phys. Chem. Chem. Phys.*, 1999, **1**, 4043.
67. a. M. Mehring, H. Raber, and G. Sinning, *Proc. Congr. Ampére, 18th*, 1974, **1**, 35. b. U. Haeberlen, *Adv. Magn. Reson. Suppl.*, 1976, **1**, 142.
68. E. B. Brouwer, R. Challoner, and R. K. Harris, *Solid State NMR*, 2000, **18**, 37.

69. G. Chisholm, B. Hay, K. D. M. Harris, S. J. Kitchin, and K. M. Morgan, *Dyes & Pigments*, 1999, **42**, 159.
70. S. C. Campbell, R. K. Harris, M. J. Hardy, D. C. Lee, and D. J. Bushby, *J. Chem. Soc. Perkin Trans 2*, 1997, 1913.
71. M. J. Shapiro, G. Kumaravel, R. C. Petter, and R. Beveridge, *Tetrahedron Lett.*, 1996, **37**, 4671.
72. S. L. Grage and A. S. Ulrich, *J. Magn. Reson.*, 2000, **146**, 81.
73. S. L. Grage and A. S. Ulrich, *J. Magn. Reson.*, 1999, **138**, 98.
74. S. L. Grage, D. R. Gauger, C. Selle, W. Pohle, W. Richter, and A. S. Ulrich, *Phys. Chem. Chem Phys.*, 2000, **2**, 4574.
75. J. C. Cherryman and R. K. Harris, *J. Magn. Reson.*, 1997, **128**, 21.
76. A. S. Batsanov, S. M. Cornet, L. A. Crowe, K. B. Dillon, R. K. Harris, P. Hazendonk, and M. D. Roden, *Eur. J. Inorg. Chem.*, 2001, 1729.
77. (a) L. A. Crowe, K. B. Dillon, R. K. Harris, J. A. K. Howard, and M. D. Roden, to be published; (b) L. A. Crowe, Ph.D. Thesis, University of Durham, 2000.
78. R. K. Harris and L. A. Crowe, *J. Chem. Soc. Dalton*, 1999, 4315.

Acknowledgements

R. K. H. thanks the U.K. Engineering and Physical Sciences Research Council, which provided finances for the purchase of a spectrometer (research grant GR/J97557) and for staff (research grants GR/L02906 and GR/M73514). We are grateful to Dr. Paul Hazendonk for preliminary information on copoly. U.S. thanks the IPF for continuous support and the Deutsche Forschungsgemeinshaft for a fellowship (SCHE 524/1-1).

Biographical Sketches

Shinji Ando, *b* 1960. B.Eng., 1984, M.Eng.,1986, and Ph.D 1989, Tokyo Institute of Technology. Research Scientist at Nippon Telegraph and Telephone Corporation, 1989–1995. Associate Professor of the Department of Organic and Polymeric Materials at Tokyo Institute of Technology, 1995–present. Visiting Scientist of the Department of Chemistry, University of Durham, UK, 1998–1999. Research interests include characterization of fully aromatic polymers and fluoropolymers using solid-state NMR and optical spectroscopies.

Robin K. Harris, *b* 1936. B.A. (Nat. Sci.), Ph.D., (supervisor Norman Sheppard), Sc.D., University of Cambridge, UK. Postdoctoral work at Mellon Institute, Pittsburgh, PA (with Aksel Bothner-By). Successively lecturer, senior lecturer, and professor, University of East Anglia, UK. Currently Professor of Chemistry, University of Durham, UK. Secretary-General of ISMAR, 1986–92. Approx. 450 publications. Current research specialty: solid-state NMR and its applications in materials chemistry.

Ulrich Scheler, *b* 1964. Diploma in Physics 1991, Technical University of Dresden. Research student in the Max-Planck Institute for Polymer Research, Mainz (with H. W. Spiess), Ph.D. awarded 1994, University of Mainz. Postdoctoral Fellow, Department of Chemistry, University of Durham, U.K. (with R. K. Harris) 1994–1996. 1996–present: Institute for Polymer Research, Dresden, Germany, (1997–2000 fellowship from Deutsche Forschungsgemeinschaft, DFG). Currently head of the Surface Modification Department. Current Research interests: solid-state NMR based on high-speed MAS with a focus on ^{19}F, $^{1}H-^{19}F$ and $^{1}H-^{19}F-X$ NMR, fluoropolymers, polyelectrolytes, diffusion and electrophoresis NMR.

Fluorine-19 NMR

Wallace S. Brey and Mary Louise Brey
University of Florida, Gainesville, FL, USA

1	Introduction	1
2	Chemical Shifts	1
3	Indirect Spin–Spin Coupling	3
4	Relaxation; Nuclear Overhauser Effects	5
5	Applications to Biochemical Problems	6
6	Applications of Special Techniques	7
7	Related Articles	8
8	References	8

1 INTRODUCTION

1.1 Properties of Fluorine-19

Aside from carbon and hydrogen, fluorine-19 is possibly the most-studied nucleus. The reasons for this include both the properties of the nucleus and the practical importance of molecules containing this element. The nucleus ^{19}F has the advantage of 100% natural abundance and a high magnetogyric ratio, about 0.94 times that of ^{1}H. The chemical shift range is 20 or more times that of hydrogen, so that resonances of different fluorine nuclei are usually well separated. Furthermore, spectral positions are sensitive to the environments of fluorine atoms. The nuclear spin quantum number is $\frac{1}{2}$, and thus relaxation times are sufficiently long that spin–spin splittings may be resolved. Long-range spin–spin coupling constants have substantial magnitude; this has the advantage of providing extensive connectivity information but, for highly fluorinated molecules, it tends to create large spin systems and make resonances very complex and non-first-order.

Fluorinated molecules have achieved industrial prominence in the production of polymers, as surface active and lubricating materials, as refrigerants, and as anesthetics and drugs. Fluorine is particularly useful as a tracer in biological systems, as there is essentially no natural background, and it is often possible to substitute a single fluorine atom for a hydrogen atom without materially changing the properties of a molecule such as a protein.

Observation of ^{19}F in high-field spectrometers may present some problems, and care is required in selecting appropriate instrumentation. At a field of 11.75 T, corresponding to 500 MHz frequency for protons, the full spectral range for ^{19}F approaches 0.5 MHz. This requires appropriate high speeds for the analog-to-digital converter and wide bandwidths for the amplifiers, as well as large data arrays to afford good spectral resolution for narrow lines. Furthermore, uniform excitation over the whole spectrum requires quite short pulses from the transmitter.

1.2 Reviews and Compilations of Data

A small paperback volume by E. F. Mooney presents an introduction to ^{19}F NMR spectroscopy.[1] It includes a variety of typical spectra, as well as some representative NMR parameters for organic molecules, and it gives the reader an excellent feel for the field. Two full volumes have been devoted to compilations of chemical shifts,[2,3] one is devoted almost entirely to discussions and tables of spin–spin coupling constants,[4] and a database for C_xF_y compounds has been described.[5] A number of reviews covering publications on ^{19}F NMR over specific periods of 1 or 2 years have been included in the *Annual Reports on NMR Spectroscopy*.[6–12]

2 CHEMICAL SHIFTS

The shielding of fluorine nuclei varies quite widely, as illustrated in Table 1 for the range from XeF_6 at low fields to CH_3F at high fields. Several specific structure types will be discussed later. Compared with the situation for hydrogen, the effects of anisotropic magnetic fields, such as those generated by ring currents, are relatively much less important for fluorine, and the nature of the bonding of the atom has a much greater influence. The presence of unshared electron pairs leads to the existence of excited molecular states at relatively low energies, and these are mixed into the ground state as the result of a perturbation by the magnetic field of a spectrometer, producing an unshielding or 'paramagnetic' effect.

Table 1 Representative ^{19}F Chemical Shifts (in ppm to High Frequency of $CFCl_3$)

XeF_6	550	$CFBr_3$	7
F_2	430	CF_2Cl_2	−8
ReF_7	345	CF_3CH_3	−62
$ClF_{5,eq.}$	412	SiF_6^{2-}	−127
$ClF_{5,ax.}$	247	BF_3	−131
WF_6	166	$CF_2{=}CF_2$	−135
$C_6H_5SO_2F$	66	CH_3F	−272

2.1 References for Chemical Shift Measurements

Many early reports of ^{19}F shifts were based on the use of trifluoroacetic acid as an external reference. Because this is a hazardous and reactive material and because values based upon any external reference suffer from errors related to the magnetic susceptibility and geometry of the sample, it has been replaced by the internal reference fluorotrichloromethane, assigned a shift of zero. Under poor spectrometer resolution, the spectrum of this material has only a single peak, but in an instrument with good resolution this is resolved into four lines, corresponding in order, from low frequency to high frequency, to the presence of three, two, one, or no ^{37}Cl nuclei in the molecule. Thus a different result is obtained if the position of one of the individual lines is taken as reference rather than the center of gravity of the overall pattern. However, effects of medium and temperature on shifts are so large for fluorine that they are likely to lead to greater uncertainties than does the small isotope effect in the reference material.

Table 2 Chemical Shifts of Reference Compounds (in ppm to High Frequency of $CFCl_3$)

$CFCl_3$	0
$CFCl_2CF_2Cl$	−68.05
$CFCl_2CF_2Cl$	−72.2
CF_3CO_2H	−76.6
C_4F_8	−135.2
C_6F_6	−163

Since the resonance of $CFCl_3$ is well removed from those of most fluoroorganic molecules, and since many of these molecules require $CF_2ClCFCl_2$ in order to dissolve, it is often convenient to use one of the multiplets of this material as a reference for the sample peaks. The shift values for these two resonances compared with $CFCl_3$, along with the shifts of a few other materials which have sometimes been used as references, are given in Table 2.

By general agreement, the direction of the chemical shift is taken as positive in the direction of higher *resonance frequency* or lower magnetic field. This requires that the great majority of shift values for ^{19}F be negative with respect to $CFCl_3$. It is appropriate in discussing factors affecting *nuclear shielding* to follow the opposite convention: the greater the degree of shielding, the further to high field or *lower frequency* is the resonance.

2.2 Shifts of Fluorines Attached to Carbon

Some generalizations may be made about the ranges of shifts to be found in various environments in highly fluorinated organic molecules. First, we consider the effects of halogens or oxygen, along with other fluorine atoms in aliphatic molecules. In specifying the group in which the fluorine is found, the letter X will be used to represent either another fluorine atom, or an atom of chlorine, bromine, or oxygen. Thus $-CFX_2$ might be $-CF_3$, $-CF_2Br$, $-CFCl_2$, $-CF_2O-$, and so on, and $-CFX-$might be $-CFCl-$or $-CFBr-$.

The fluorine resonance in CF_3 in a saturated molecule appears at −75 to −82 ppm with respect to $CFCl_3$ and in other $-CFX_2$ units at −65 to −80 ppm. If the shift in $-CF_2Cl$ is compared with that in $-CF_3$, it is found that this chlorine substitution produces a high-frequency (*downfield*) shift or unshielding of about 10 ppm. However, the second substitution of a chlorine for a fluorine atom, giving $-CFCl_2$, has the opposite effect, so that the resonance is now more shielded than, and about 5 ppm upfield from, that of $-CF_2Cl$. The shifts of CF_3 attached to oxygen or to an alkenic carbon are in the region of −50 to −60 ppm.

The shifts of the fluorine in a −CFX group in a saturated molecule are observed at about −120 to −130 ppm, and here, in contrast to the $-CFX_2$ case, substitution of one fluorine by a chlorine, forming a CFCl group, causes an increased shielding of about 6–8 ppm. In a straight-chain fluorocarbon unit, the CF_2 group next to the terminating CF_3 can be identified because it is at −127 ppm, rather than at the −122 ppm characteristic of CF_2 fluorines flanked by other CF_2 groups.

The effect on nearby fluorine atoms of substitution of a chlorine for a fluorine atom in a highly fluorinated straight chain is an unshielding of about 6 ppm if the chlorine is on the adjoining carbon, and about 3 ppm if the chlorine is on a carbon atom one removed from the fluorine being observed. Calculations have been made to predict and correlate shifts in a wide variety of highly halogenated molecules.[13,14]

Shifts to lower field or to higher frequency, as for chlorine substitution, are produced by substitution of bromine on a vicinal carbon. The effect of chlorine or bromine has been attributed to a van der Waals interaction between the halogen and fluorine and termed ‘repulsive unshielding’. Similar unshielding is caused by crowding of a fluorine atom by a methyl group.[15]

Substitution of hydrogen for fluorine in either $-CF_2$ or $-CF_2X$ increases the shielding of the remaining fluorine. A tertiary fluorine atom is usually found at a relatively high field (about −160 to −180 ppm).

A carbonyl group in a perfluorinated chain typically causes unshielding of 2–5 ppm for fluorine atoms attached to the α carbon atoms, and an amine nitrogen in the chain produces an unshielding effect for α fluorine atoms of 5–10 ppm. A fluorine atom attached directly to a carbonyl carbon, in an acid fluoride unit, resonates at +30 to +50 ppm.

Fluorine atoms attached to an alkenic carbon atom appear anywhere in the range −50 to −220 ppm. In aromatic molecules, a fluorine substituent resonates anywhere from −100 to −180 ppm. The chemical shift difference produced by a second substituent in the *meta* or *para* position on a benzene ring correlates well with Hammett substituent parameters. If the substituent is *ortho* to the fluorine atom, substantial deviations appear, caused either by van der Waals forces or by electric field effects, and are experienced at the relatively short distances between the fluorine and the *ortho* substituent.

2.3 Shifts of Fluorine Atoms Attached to Other Nonmetals

Many fluorine atoms attached to nitrogen, oxygen, or sulfur resonate to low field or high frequency of $CFCl_3$ and thus are assigned positive shift values. In F–O–C units, the shift is often in the range 144–155 ppm,[16] but may vary as much as ±100 ppm from this region. In an NF_2 group, the shift is 15–20 ppm if the group is attached to CF_2, 20–30 ppm if attached to saturated −CF–, 50–60 ppm if attached to CH_2 in an aliphatic chain, and 30–45 ppm if attached to CH in an aliphatic chain. In an −NF–group the shifts are −80 to −120. In =NF, there is a very wide variation with the attached structure, from +55 to −67 ppm.[17]

Several compounds illustrate these shifts as well as shifts of fluorine attached to sulfur. In SF_5SO_3F, the fluorine atom attached to oxygen is at 46 ppm, the equatorial and axial fluorine atoms on sulfur are at 73 and 57 ppm, respectively. In FSO_3F, the OF is at 249 ppm and the SF is at 37 ppm.[18] In OF_2, the shift is 250 ppm, also far downfield. In SF_5NF_2, the NF_2 fluorine atoms are at 78 ppm, the equatorial fluorine atoms on sulfur are at 38 ppm, and the axial fluorine atom is at 50 ppm; with nitrogen attached to the sulfur, the equatorial–axial order is reversed from that when the octahedral sulfur atom is attached to another sulfur or to oxygen.

2.4 Isotope Effects on Shifts

Because fluorine is relatively sensitive to its environment, it exhibits considerable changes in chemical shift when

a nearby atom is replaced by an isotope. As mentioned above, the differential effect of ^{35}Cl versus ^{37}Cl attached to the carbon bearing the ^{19}F is readily resolved, and three-bond effects are also measurable. Studies of isotope shifts in several molecules show that they increase substantially with decreasing temperature, a behavior consistent with an explanation relating them to populations of vibrational energy levels.[19]

Replacement of ^{12}C by ^{13}C, either for the atom to which the fluorine is attached or for the carbon one removed, gives a quite measurable shift, usually to lower frequency. A consequence of the isotope effect is that ^{13}C satellites in a fluorine spectrum are not symmetrical about the $^{12}C-F$ resonance. Table 3 lists some carbon isotope effects on fluorine.

Table 3 Shifts of ^{19}F Resonance (in Hz to Lower Frequency in a Spectrometer at 94.1 MHz) on Substitution of ^{13}C for ^{12}C

Molecule	One-bond shift (Hz)	Two-bond shift (Hz)
$CF_2{=}CCl_2$	9.20	2.50
$CFCl{=}CCl_2$	10.28	2.61
$CF_3CCl{=}CCl_2$	12.31	0.95
CF_3CCl_3	11.70	1.20
CF_2ClCF_2Cl	13.05	1.46
$C\underline{F}_3CF_2CF_2CCl{=}O$	11.96	1.56
1,1,2,2-Tetrafluoro-3,3-dichlorocyclopropane	10.74	

Isotope shifts also result from the replacement of a nearby hydrogen atom by deuterium or by tritium.[20,21] Increased shielding of the fluorine in fluorobenzene is produced by substitution of ^{2}H at any ring position or by substitution for the three hydrogen atoms in a *para*-methyl group. If one is dealing with a nonrigid molecule, there is always the possibility that a change in chemical shift may arise in part from the effect of the isotope on a conformational equilibrium, as well as on an 'intrinsic' property of a specific geometrical structure. This seems to be the situation for trifluoromethylcyclohexane and may also be true for vicinal deuteration in monofluorocyclohexane.[22]

3 INDIRECT SPIN–SPIN COUPLING

Spin–spin coupling, usually represented by the symbol J, is an interaction transmitted from one nucleus which has a spin, through the electron cloud in a molecule, and then from the electrons to a second nucleus. The magnitude and sign of J is often characteristic of structural or geometrical relationships between the two nuclei involved, as well as of the nature of bonding of the nuclei. A number of attempts have been made to develop Karplus-type relationships for the angular dependence of coupling of ^{19}F to other nuclei, particularly ^{1}H or ^{13}C, but the difficulty of treating the effects of substituents, including that of fluorine itself, has led to only modest success for these relationships.

The value of J may be used as a test for the conformation of a fluorinated molecule which may exist in two structures. If the conformations are equilibrating rapidly, the observed J is a weighted average of the values in the two forms. The question then arises whether a change in conditions of temperature or solvent that affects the conformational equilibrium might also affect the values of J in the individual conformers. Experience indicates that the intrinsic values of J for interactions involving fluorine are more sensitive to conditions than are those for hydrogen, which are almost independent of circumstances.

In fluoropropenes, in which one would not expect conformational changes to occur, the J values in the vinyl moiety change by 1–2 Hz with a temperature change of 150 °C and by a few tenths of a hertz with a change in medium. In $CF_2{=}CFCF{=}O$, for which the two-bond constants are 4.0 and <1 Hz in the two conformational isomers frozen out at low temperature, the value at room temperature is 6.0 Hz, well outside the possible range for a weighted average.[23] Solvent and temperature effects have been shown to be appreciable for several types of coupling constant in fluorobenzene and 1,2-difluorobenzene.[24]

3.1 Trends in Homonuclear Coupling Constants

Coupling constants between fluorine atoms are usually relatively large compared with the homonuclear couplings of hydrogen atoms, and they extend over much longer distances than do those of hydrogen. Some ranges of values are given in Table 4, and J values for several perfluorinated molecules are shown in Figure 1.

Three-bond F–F couplings in substituted ethanes have been found to depend upon the sum of the electronegativities of the other four atoms or groups attached to the two carbon atoms. The higher the sum of the electronegativities, the smaller the magnitude, until for the highest possible value of the sum, corresponding to four fluorine atoms in hexafluoroethane, the value of J has gone through zero and changed sign. Calculations indicate that this behavior is the result of offsetting contributions of opposite sign from various pathways for transmission of spin information. The value of ^{3}J(F,F) for hexafluoroethane may be measured by observing the carbon-13 satellites for those molecules containing one carbon-13 atom, in which the fluorine atoms attached to that carbon atom are no longer equivalent to those attached to ^{12}C.

In the trifluorovinyl group, the values of $^{3}J_{trans}$ are surprisingly invariant, ranging only from about 106 to 130 Hz for a wide range of substituents. The values of $^{3}J_{cis}$, in

Table 4 Typical Values of Homonuclear Fluorine–Fluorine Coupling Constants

Structure	J (Hz)
Two-bond, F–C–F, aliphatic, noncyclic	170–220
Two-bond, three-carbon ring	150–180
Two-bond, four-carbon ring	190–230
Two-bond, epoxide ring	13–44
Two-bond, oxetane ring, on carbon next to oxygen	84–95
Two-bond, F–C–F, trifluorovinyl	5–100
Three-bond, F–C–C–F, aliphatic	0–30
Three-bond, alkene, *trans*	−106 to −127
Three-bond, alkene, *cis*	−24 to −65
Three-bond, aromatic	18–35
Four-bond, aromatic	0–15
Five-bond, aromatic	4–16

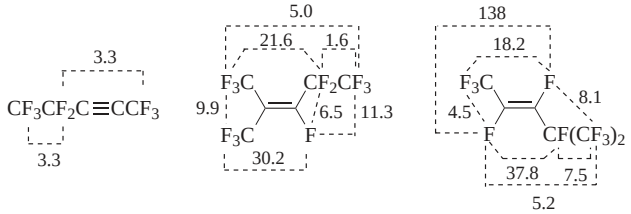

(1) **(2)** **(3)**

Figure 1 Homonuclear $^{19}F-^{19}F$ spin–spin coupling constants in three typical unsaturated fluorocarbon molecules. Values of J are given in hertz, adjoining the lines which link the two interacting nuclear types

contrast, vary from 24 to 65 Hz. The largest values are those where a halogen or an oxygen atom is bonded directly to the vinyl group, suggesting that it is the availability of lone-pair electrons that is significant.[25]

In contrast with proton–proton coupling across an ether oxygen atom, which is usually unresolvable, fluorine–fluorine coupling may be easily observed in a similar situation. Table 5 includes some values for J(F,F) in several simple ethers containing fluorine.

Table 5 Coupling Constants in Fluoroethers

Compound	^4J(F,F) (Hz)	^2J(F,H) (Hz)
CF_3OCF_3	8.2	
$CF_3OCF_2CF_3$	8.5	
CF_3OCHF_2	4.0	69
$CHF_2OCHFCl$	5	58, 70
CHF_2OCFCl_2	4	69
$CHFClOCF_2Cl$	4.5	59
$CF_3OCFClCHCl_2$	11	

3.2 Heteronuclear Coupling

3.2.1 Coupling to Hydrogen

Two-bond couplings through carbon are typically 40–60 Hz and are very characteristic in both ^{19}F and ^1H spectra for $-CF_2H$, $-CFH_2$, or $-CFH-$ groups. Table 5 illustrates the larger values, up to 80 Hz, found when the carbon is attached to an ether oxygen atom. Three-, four-, or five-bond coupling constants in aromatic compounds are about the same as the analogous H–H coupling constants. Three-bond (vicinal) couplings in aliphatic compounds range from very small values up to 15 Hz.

3.2.2 Coupling to Carbon-13

Multiplets produced by ^{19}F coupling in the ^{13}C spectrum of an organic molecule also containing many hydrogen atoms are easily resolved with the aid of proton broadband decoupling.

Values of ^1J(F,C) vary from 160 to 400 Hz in magnitude and are negative in sign, an exception to the general rule that one-bond couplings are positive. On comparison of the values in halo-substituted methanes with that in CF_4, it can be seen from Table 6 that substitution of other halogens for fluorine increases the value of the coupling constant substantially, whereas substitution of a hydrogen, except for the first one, reduces the value.

Table 6 Values (in Hz) of $^1J(^{19}F, ^{13}C)$ in Fluoromethanes

			CF_4	-259			
CHF_3	-274	CF_3Cl	-301	CF_3Br	-323	CF_3I	-344
CH_2F_2	-235	CF_2Cl_2	-325	CF_2Br_2	-352		
CH_3F	-158	$CFCl_3$	-337	$CFBr_3$	-372		

In alkenes, the values of ^1J(F,C) are about -300 Hz (our work); in the $=CF_2$ unit of an alkene which is unsymmetrically substituted, the values of the two coupling constants differ from one another. When a fluorine atom is attached to a carbonyl carbon, the value increases to about -370 Hz. In fluorinated aromatics, values lie between -260 for C_6F_6 and -245 for C_6H_5F when there is no other substituent; electron-withdrawing substituents on the ring increase J, while electron-releasing substituents decrease J. It is tempting to say that the former increase the π-electron donation of the fluorine atom to the ring system, whereas the electron-releasing substituents compete with the tendency for this donation.

The sign of ^2J(F,C) is positive, and values are typically 20–45 Hz. The value is about 20 Hz for a single fluorine atom in an aliphatic compound. The magnitude increases with substitution of electronegative groups. The value in alkenes depends upon the substitution pattern and is especially large when an electronegative substituent is *trans* to the fluorine. In benzenoid aromatics, the value is 15–25 Hz, except when the carbon bears a substituent, which is thus *ortho* to the fluorine. In cyclopropane rings, the values are small, between 5 and 15 Hz. An especially large value has been found for the two-bond coupling in the molecule CFBr=CFBr. Similarly, J between the fluorine attached to the carbonyl and the α carbon atom in (**4**) is 91 Hz, although ^2J between the carbonyl carbon and the α fluorine atom in (**4**) is only 31 Hz. Some other related molecules with very large values of ^2J are listed in Table 7.

Table 7 Molecules with Large Values of $^2J(^{19}F, ^{13}C)$

Compound	^2J between α-C and CFO (Hz)	^1J in CFO group (Hz)
$CF_3CF_2CF_2CF{=}O$	78	374
$(CF_3)_2CFCF{=}O$	66	369
$CF_2ICF_2OCF_2CF{=}O$	93	374
$O{=}CFCF_2OCF_2CF{=}O$	94	372
$(CF_3)_2C{=}CClCF{=}O$	85	355
$CF_3ClC{=}CClCF{=}O$	84	352

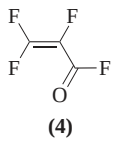

(4)

3.2.3 Coupling to Phosphorus and Nitrogen

The one-bond coupling constant to ^{31}P is negative and large. For units such as five-coordinate PF_4- or $XYPF_3$ or six-coordinate CH_3PF_5-, values range from about 700 to 1100 Hz.

Often the fluorine nuclei undergo a pseudorotation process which averages out values for the axial and equatorial positions, but if this process is sufficiently slow, a distinction can be made between the coupling constants for the two fluorine positions and the axial value is smaller, for some molecules by as much as 100–150 Hz, than the equatorial value. In five-coordinate compounds in which one ligand is a CF_3 group, ^2J(P,F) is 24–88 Hz for the axial position and 107–190 Hz for the equatorial position, providing sterochemical information about the complexes. The barrier to fluxional behavior in a number of complexes has been obtained from analysis of the NMR lineshapes.

The values for one-bond coupling to ^{15}N are usually between 110 and 160 Hz. In *cis*-N_2F_2, J is 203 Hz, in *trans*-N_2F_2 it is 190 Hz, but in the azide N_3F it is only 58 Hz.[26] There is an unusually large value of 53 Hz for ^2J(F,N) in 2-fluoropyridine, perhaps attributable to transmission via unshared electrons. No large couplings are found for adjacent substituents in benzene: in 2-fluoronitrobenzene, ^3J(F,N) is 2.66 Hz; and in 2-fluoroaniline, it is about 0.5 Hz. In 2-CF_3-aniline, ^4J(F,N) is 1.68 Hz. In 5-fluorouracil, the two values of ^3J are 1.12 and 1.66 Hz.

3.2.4 Coupling to Metals

Fluorine forms bonds to a wide variety of metals. In several binary compounds with nuclei having spin $\frac{1}{2}$ or small quadrupole moments, splittings can be resolved and values of J can be measured. Examples are TiF_6^{2-}, J = 34 Hz, and NbF_6^-, J = 335 Hz. Mercury compounds show positive two-bond couplings with magnitudes up to more than 2000 Hz and three-bond couplings as large as several hundred hertz. Some other examples are given in Table 8.

In TeF_6, $^1J(^{125}Te, ^{19}F)$ is 3746 Hz and in TeF_7^- it is 2876 Hz.[27] The smaller value in the latter has been attributed to weaker, more polar bonds. That there is only a single value of J and only a single shift for all six fluorine atoms indicates rapid exchange between axial and equatorial positions. It is interesting that the number of naturally occurring isotopes of tellurium leads to multiple, slightly shifted, fluorine resonances.

3.3 Long-Range Coupling

It has been proposed that many of the examples of coupling between two fluorine nuclei which are separated by a number of bonds (four, five, six or more) may result from overlap of electronic orbitals occupied by electrons which are unshared and therefore not involved in normal covalent bonding. The term applied to this effect, 'through space', is somewhat misleading, since only the anisotropic dipole–dipole interaction is effective through 'empty' space. All isotropic coupling is transmitted in some way by electrons, either in bonds or in unshared pairs.

Table 8 Fluorine–Metal Coupling Constants

Species	Solvent	Coupling Constant (magnitude) (Hz)
VOF_3	THF	110
VOF_4^-	CH_3CN	86
$VO(CF_3CO)_3F^-$	CH_3CN	80
VO_2ClF^-	CH_3CN	207
$VO_2F_2^-$	CH_3CN	272
$NbOF_4^-$	CH_3CN	410
$(CF_3)_2Hg$	CH_2Cl_2	1263

The idea of transmission of the indirect coupling through electrons not involved in bonds was proposed by Petrakis and Sederholm.[28] It has since been extended to systems involving nuclei other than fluorine.

Coupling via nonbonding electrons may be invoked to explain the temperature dependence of ^4J(F,F) in $CF_2ClCFClCFCl_2$ (**5**). As the temperature is lowered from room temperature to −100 °C, the value of the coupling between the fluorine atom in $CFCl_2$ and one of the fluorine atoms in the CF_2Cl unit increases from 17 to 28 Hz, whereas the other ^4J decreases from about 13 to 12 Hz. The large coupling at low temperature can be assigned to two fluorine atoms forced to be closer together by the increasing effects of steric repulsions with decreasing temperature, as represented in the diagram for (**5**).

(5)

Another example which can be explained by the 'through-space' mechanism involves coupling of the fluorine atoms in an oxetane ring with the *ortho* fluorine atoms in a pentaphenyl group substituted in the ring. The molecule (**6**) exists in two isomeric forms, differing in whether the pentafluorophenyl group and the chlorine atom are on the same side or on opposite sides of the ring. In one isomer, $J(F_A, F_D)$ is 1.3, $J(F_B, F_D)$ is 10.7, and $J(F_C, F_D)$ is 11.4 Hz. In the other isomer, $J(F_A, F_D)$ is 7.5, $J(F_B, F_D)$ is 1.4, and $J(F_C, F_D)$ is 0.9 Hz.

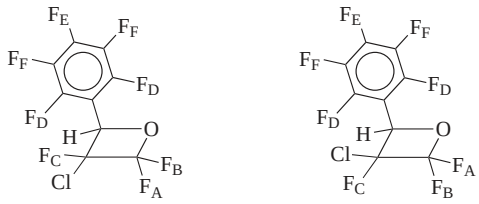

(6)

There are other examples of long-range coupling which cannot be explained by direct orbital overlap, but are probably associated with electron delocalization in π orbitals. Thus the stereochemistry of fluorinated alkenes and dienes is related to ^3J(F,C) in a way not fully explained by nuclear proximity.[29]

Outstanding among the interactions transmitted by π orbitals are those across aromatic ring systems. A number of these have been related to studies of molecular conformation. In 3,5-dichlorobenzyl fluoride, as an example, ^6J(F,H) is related to the rotational orientation of the $-CH_2F$ group with respect to the ring.[30] Long-range C–F coupling in derivatives of benzoic acid and benzoyl fluoride are related experimentally and theoretically to the dihedral twist angles of the substituent-to-ring C–C bond.[31] A study of fluorinated methyl phenyl sulfoxides showed that ^5J(F,H), ^4J(F,C), ^5J(F,C), and ^6J(F,C) are dependent upon the conformation about the sulfur atom.[32]

4 RELAXATION; NUCLEAR OVERHAUSER EFFECTS

Fluorine-19 nuclei may undergo spin–lattice relaxation by the direct dipolar mechanism, in much the same way as do protons. However, because of the presence of unshared electrons, spin–rotation (SR) and chemical shift anisotropy (CSA) mechanisms also contribute to the relaxation of ^{19}F. Because of the additional relaxation pathways, T_1 values are often substantially smaller than for protons in a similar environment.

Early workers reported that the CSA contribution is negligible and that spin rotation predominates. This is true for molecules such as CF_4 or SF_6, which are small and freely rotating, and for measurements at 2.4 T or lower magnetic field strength. Since the spin–rotation relaxation time decreases with increasing temperature, whereas the dipole–dipole relaxation time increases with increasing temperature, a maximum may be observed for T_1 as a function of temperature, as has been found, for example, for *o*-fluoroiodobenzene at about 110 °C.

Spin–rotation interaction constants can be calculated from the paramagnetic term of the NMR shielding constant.[33] They can also be measured by molecular beam methods, and the values for HF, F_2, SiF_5, CF_4, and CHF_3 show good agreement by the two methods. It should also be possible to calculate the spin–rotation constants from measured spin–lattice relaxation times, but this requires knowledge of the correlation time, and reasonable guesses for the latter give values of the constant too large by a factor of 2 to 3.

Rapid spin–spin relaxation is associated with broadening of spectral lines, such as is caused by inhibition of motion, as occurs with macromolecules. The extent of broadening is related to the anisotropy of the chemical shift, which is often large for ^{19}F. Since the CSA contribution increases with field, the broadening is greater at higher fields, often offsetting the improvement in sensitivity and resolution expected, such as by going to a frequency of 470 MHz. Since macromolecules do rotate more slowly, the SR contribution for the ^{19}F relaxation in them is small, except possibly for freely rotating CF_3 groups.

The nuclear Overhauser effect (NOE) of fluorine nuclei is much like that of protons. Most applications of the NOE to fluorine have been heteronuclear, where the close approach of one or more particular hydrogens atoms to a fluorine atom is monitored. In macromolecules, dipolar interactions are often the predominant T_1 relaxation mechanism, and saturation of protons should fully invert the normal ^{19}F intensities. Under circumstances where the T_1 of the ^{19}F nucleus is shorter than that of the ^1H, it is preferable in a one-dimensional NOE experiment to use the ^{19}F as the source of the Overhauser transfer so that irradiation maintains the nonequilibrium population.

Indirect Overhauser enhancements through ^{19}F from ^1H to ^1H or from ^1H to ^{13}C have been obtained for several cyclic compounds.[34] In NOE difference spectra, antiphase doublets were observed for protons undergoing simultaneous scalar coupling and dipolar relaxation with ^{19}F. The geometrical factors inherent in the three-spin NOE were utilized in conformational analysis. NOE measurements have also been used to confirm the proximity of hydrogen nuclei to fluorine nuclei in some tetrahydroindazole derivatives where long-range coupling between these nuclei was suspected of being the result of a 'through-space' interaction.[35]

It is interesting that pioneering work in the analysis of the NOE was the application by Solomon and Bloembergen[36] to the HF system. Because of the very large value of $^1J(F,H)$ in this molecule (more than 600 Hz), there is relaxation by interrupted scalar coupling, which produces a negative enhancement instead of the positive intensity change expected for the dipole–dipole mechanism.

5 APPLICATIONS TO BIOCHEMICAL PROBLEMS

By virtue of the circumstances that there is almost never any fluorine background in living systems and that fluorine shifts are quite sensitive to the environment, applications of ^{19}F NMR to biochemical problems have been extensive. Several reviews have appeared.[37,38]

Fluorine NMR has been applied in the investigations of several types of system, perhaps most extensively to proteins. Pioneer work in this field was that of Sykes and Hull,[39] who applied ^{19}F relaxation measurements to the study of motions of groups in proteins. Alkaline phosphatase was labeled with fluorotyrosine residues. Both overall rotation of the protein and internal rotation of the aromatic ring contribute to ^{19}F relaxation, which includes a substantial CSA component. Two of the tyrosine rings relax by chemical exchange, indicating that they are free to rotate, and one of the tyrosines relaxes faster in ^1H_2O than in ^2H_2O, indicating that it is exposed to the solvent.

In other systems, the nature of binding of small molecules to proteins has been studied. On binding of an inhibitor such as cytidine manophosphate (CMP) to ribonuclease S trifluoroacetylated at lysines-1 and -7, the fluorine resonance assigned to lysine-7 splits and becomes pH dependent.[40] This change could, of course, come either directly from contact of the inhibitor with the lysine or indirectly as a result of a conformational change of the protein caused by the inhibitor. A summary of the considerations involved in using fluorine as a tool in the investigation of ligand binding has been provided by Gerig.[41]

Several efforts have been made recently to provide a theoretical analysis of the effects of the environment on fluorine nuclei, and to explain the chemical shift effects of up to 20 ppm observed when a protein folds about the fluorine indicators.[42,43] The conclusion has been that the principal influence is via electrostatic interactions, and that this influence is effective in proportion to the magnitude of the paramagnetic term in the nuclear shielding expression.

Fluorine shifts and coupling constants are valuable in the conformational analysis of carbohydrates. Pioneering work in this area was that of Hall.[44] The spectrum of 6-deoxy-6-fluoro-D-glucose has been carefully analyzed in terms of the conformer population in various solvents; this analysis illustrates the very important point that, although the resonance frequency of ^{19}F is very far removed from that of ^1H, it may represent the X part of a non-first-order system, such as the ABCX system in this molecule, and a first-order interpretation is misleading.[45]

Fluorine-19 has been used as an indicator of the presence of various free ions in living systems. 5-Fluoro derivatives of

the molecule APTRA (*o*-aminophenol-*N*,*N*,*O*-triacetic acid) give separate resonances for free and magnesium-bound forms of the indicator, and knowledge of the equilibrium constants involved and the ratios of the two peaks permits evaluation of the free magnesium concentration. The 4-fluoro derivative of APTRA as well as fluorocitrate are in fast exchange with Mg^{2+}, giving a resonance which is at the weighted-average position of the free and magnesium-bound indicator resonances.[46] Chelators have also been employed to assess calcium concentrations. One, known as 5F RBAPTA, a 1,2-diphenoxyethane derivative, provides slow exchange with Ca^{2+}, and is designed to give rapid spin–lattice relaxation because it contains a *t*-butyl group adjacent to the fluorine.[47]

6 APPLICATIONS OF SPECIAL TECHNIQUES

Two- or three-dimensional ^{19}F correlation spectroscopy provides an attractive means of structure studies, especially for highly fluorinated materials. By firmly establishing coupling connections in a molecule which typically has a very complex spectrum, often with overlapping and non-first-order patterns, these techniques facilitate the relationship of resonances to structural features. COSY has been applied to the assignment of resonances and the study of microstructure of fluorinated polymers.[48]

Figure 2 shows an illustrative COSY spectrum of a mixture of three chlorofluorocarbon isomers. From the one-dimensional ^{19}F spectrum, it was not possible to assign the various multiplets unambiguously or even to be certain that the mixture did not contain some six-carbon as well as four-carbon components. Based on inspection of the off-diagonal correlations in the COSY spectrum, combined with consideration of the multiplets in the one-dimensional spectrum and the symmetries of possible components, definitive assignments of structure could be made.

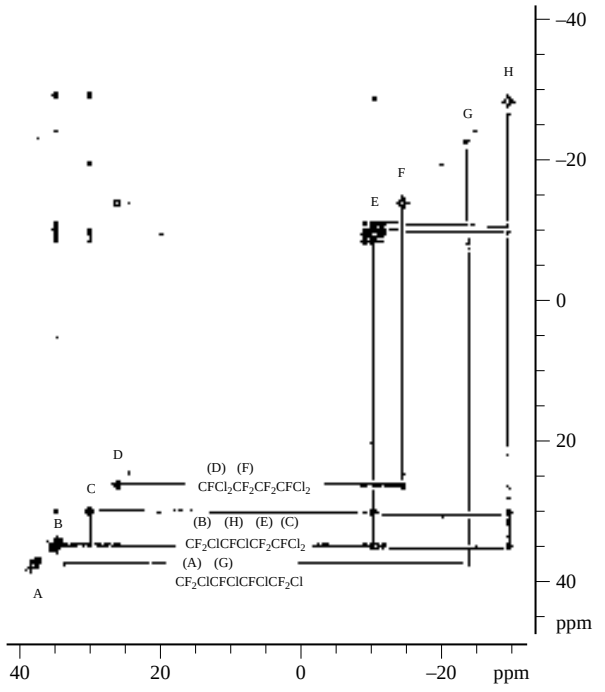

Figure 2 Homonuclear $^{19}F-^{19}F$ COSY (correlation spectroscopy) spectrum of a mixture of three isomers. Formulas of the three components of the mixture are shown and assignments of the resonances are indicated by letters. The spectrometer frequency was 282 MHz. The axes are labeled with arbitary scales based on the carrier frequency of the spectrometer

Because of the difficulties of chromatographic resolution of mixtures of isomers of compounds of this type, it is thus very helpful to be able to sort out the resonances belonging to each of the components in a mixture. Hartmann–Hahn-based experiments (HOHAHA or TOCSY) are difficult to apply to a typical fluorinated molecule, especially at the fields now in use, because of the difficulty of maintaining a spin lock over the very wide frequency range required, and a COSY or relayed COSY sequence may be more appropriate.[49] Even here, however, problems may arise from the spectral widths often encountered, because of the many data points in each dimension required to ensure adequate resolution. Thus selective excitation or selective polarization transfer, such as is possible with the pulse-shaping capabilities of modern instruments, is helpful in reducing the large size of the data arrays required.

By use of appropriate correlation experiments optimized for coupling constants of various magnitudes, it is also possible to determine the relative signs of coupling constants from the sense of the skew in the off-diagonal peaks.[50]

Two-dimensional heteronuclear NOE spectroscopy can be applied to structural studies of ^{19}F-labeled oligodeoxyribonucleotides. In macromolecules, chemical shift anisotropy dominates the spin–spin relaxation of ^{19}F, although T_1 relaxation is primarily dipolar in nature. As a result, the fluorine lines are broad, and small spin–spin couplings to hydrogen cannot be resolved. Since the Overhauser enhancement ratio for $^{19}F-\{^1H\}$ in a large molecule is -1, this technique affords a means of determining spatial adjacencies.[51]

In fluorine-labeled molecules such as steroids, there may be many proton spin–spin interactions with the label atom, and it is experimentally difficult to unravel the splittings in the fluorine spectrum by selective decoupling of protons. Two-dimensional heteronuclear correlation experiments, analogous to homonuclear COSY, can be used to establish long-range couplings, from which conformational information can be obtained.[52] In a number of steroids, small splittings caused by protons remained unresolved in the proton spectrum because of their number and the widths of the lines. In COSY, all interactions down to the limit imposed by the intrinsic linewidth can be resolved, and long-range couplings of 0.5 Hz or less are observable. Combining the information from the coupling constants with known effects on chemical shifts made it possible to assign the NMR spectra completely and to derive complete steroid structures.

As another means to establish connectivities, one might examine the proton spectrum with the fluorine decoupled; in the absence of a fluorine decoupler, this has been done by using the proton decoupler as the source of the observe signal and pulsing the fluorine signal from the transmitter between the acquisition intervals in the FID. Both COSY and one-dimensional experiments have been performed in this way.[53]

Finally, an alternative approach to unraveling complex fluorine–proton interactions involves the use of fluorine decoupling achieved by a spin-flip technique. The output of two channels of a dual-channel spectrometer is combined and

applied to the high-frequency coil in a probe. During the period of acquisition of the proton signals, pulses from the fluorine channel, applied in the empty time slots, are phase cycled according to an XY-4 or XY-32 scheme, spreading the irradiation frequency over the needed wide bandwidth.[54]

7 RELATED ARTICLES

Bilayer Membranes: Proton and Fluorine-19 NMR; Coupling Through Space in Organic Chemistry; Isotope Effects on Chemical Shifts and Coupling Constants; Nuclear Overhauser Effect.

8 REFERENCES

The data cited in this article come from so many sources, including the laboratory of the authors, that it is impracticable to list the sources individually. References for recent work are provided, and access to earlier results is usually possible through some of the reviews which are mentioned.

1. E. F. Mooney, *An Introduction to ^{19}F NMR Spectroscopy*, Heyden, London, 1970.
2. C. H. Dungan and J. R. Van Wazer, *Compilation of Reported F-19 NMR Chemical Shifts*, Wiley Interscience, New York, 1970.
3. J. W. Emsley and L. Phillips, *Prog. NMR Spectrosc.*, 1971, **7**, 1.
4. J. W. Emsley, L. Phillips, and V. Wray, *Prog. NMR Spectrosc.*, 1976, **10**, 83.
5. F. J. Weigert and K. J. Karel, *J. Fluorine Chem.*, 1987, **37**, 125.
6. E. F. Mooney and P. H. Winson, *Annu. Rev. NMR Spectrosc.*, 1968, **1**, 243.
7. K. Jones and E. F. Mooney, *Annu. Rep. NMR Spectrosc.*, 1970, **3**, 261.
8. K. Jones and E. F. Mooney, *Annu. Rep. NMR Spectrosc.*, 1971, **4**, 391.
9. R. Fields, *Annu. Rep. NMR Spectrosc.*, 1972, **5A**, 99.
10. L. Cavalli, *Annu. Rep. NMR Spectrosc.*, 1975, **6B**, 43.
11. R. Fields, *Annu. Rep. NMR Spectrosc.*, 1977, **7**, 1.
12. V. Wray, *Annu. Rep. NMR Spectrosc.*, 1983, **14**, 1.
13. A. Battais, G. Bauduin, B. Boutevin, and Y. Pietrasanta, *J. Fluorine Chem.*, 1986, **31**, 197.
14. T. Tanuma, K. Ohnishi, H. Okamoto, T. Miyajima, and S. Morikawa, *J. Fluorine Chem.*, 1992, **57**, 259.
15. G. W. Gribble, D. J. Keavy, E. R. Olson, I. D. Rae, A. Staffa, T. E. Herr, M. B. Ferraro, and R. H. Contreras, *Magn. Reson. Chem.*, 1991, **29**, 422.
16. C. J. Hoffman, *Fluorine Chem. Rev.*, 1968, **2**, 161.
17. W. S. Brey and J. B. Hynes, *Fluorine Chem. Rev.*, 1968, **2**, 111.
18. H. Willner, F. Mistry, and F. Aubke, *J. Fluorine Chem.*, 1992, **59**, 333.
19. W. S. Brey, K. H. Ladner, R. E. Block, and W. A. Tallon, *J. Magn. Reson.*, 1972, **8**, 406.
20. G. Angelini, G. Lilla, C. Sparapani, O. Ursini, E. Rossi, A. L. Segre, M. A. McAllister, and T. T. Tidwell, *Can. J. Chem.*, 1992, **70**, 1221.
21. S. Berger, in *NMR Basic Principles and Progress*, ed. P. Diehl, E. Fluck, H. Günther, R. Kosfeld, and J. Seelig, Springer, Berlin, 1990, Vol. 22, pp. 1–29.
22. J. B. Lambert and L. G. Greifenstein, *J. Am. Chem. Soc.*, 1974, **96**, 5120.
23. K. C. Ramey and W. S. Brey, *J. Chem. Phys.*, 1964, **40**, 2349.
24. S. Suntioinen, U. Weber, and R. Laatikainen, *Magn. Reson. Chem.*, 1993, **31**, 406.
25. C. G. Moreland and W. S. Brey, *J. Chem. Phys.*, 1966, **45**, 803.
26. G. Schatte, H. Willner, and M. Willert-Porada, *Magn. Reson. Chem.*, 1992, **30**, 118.
27. K. O. Christe, D. A. Dixon, J. C. P. Sanders, G. J. Schrobilgen, and W. W. Wilson, *J. Am. Chem. Soc.*, 1993, **115**, 9461.
28. L. Petrakis and C. H. Sederholm, *J. Chem. Phys.*, 1961, **35**, 1243.
29. M. P. Bosch, F. Camps, G. Fabrias, and A. Guerrero, *Magn. Reson. Chem.*, 1987, **25**, 347.
30. T. Schaefer, J. R. Mansfield, F. E. Hruska, and R. Sebastian, *Can. J. Chem.*, 1992, **70**, 1750.
31. P. E. Hansen, A. Berg, and K. Schaumburg, *Magn. Reson. Chem.*, 1987, **25**, 508.
32. R. Benassi, U. Folli, D. Iarossi, A. Mucci, L. Schenetti, and F. Taddei, *Magn. Reson. Chem.*, 1990, **28**, 702.
33. C. Deverell, *Mol. Phys.*, 1970, **18**, 319.
34. F. Sanchez-Ferrando and J. K. M. Sanders, *Magn. Reson. Chem.*, 1987, **25**, 539.
35. J. W. Lyga, R. N. Henrie, II, G. A. Meier, R. W. Creekmore, and R. M. Patera, *Magn. Reson. Chem.*, 1993, **31**, 323.
36. I. Solomon and N. Bloembergen, *J. Chem. Phys.*, 1956, **25**, 261.
37. J. T. Gerig, in *Biological Magnetic Resonance*, ed. L. J. Berliner and J. Reuben, Plenum, New York, 1978, Vol. 1, pp. 139–203.
38. B. D. Sykes and J. H. Weiner, in *Magnetic Resonance in Biology*, ed. J. S. Cohen, Wiley, New York, 1980, Vol. 1, pp. 171–196.
39. B. D. Sykes and W. E. Hull, *Methods Enzymol.*, 1978, **49**, 270.
40. W. H. Huestis and M. A. Raftery, *Biochemistry*, 1971, **10**, 1181.
41. J. T. Gerig, *Methods Enzymol.*, 1989, **177**, 3.
42. J. D. Augspurger and C. E. Dykstra, *J. Am. Chem. Soc.*, 1993, **115**, 12016.
43. J. G. Pearson, E. Oldfield, F. S. Lee, and A. Warshel, *J. Am. Chem. Soc.*, 1993, **115**, 6851.
44. L. D. Hall and J. F. Manville, *Can. J. Chem.*, 1969, **47**, 361.
45. R. J. Abraham, E. J. Chambers, and W. A. Thomas, *Magn. Reson. Chem.*, 1992, **30**, S60.
46. J. C. Veniero and R. K. Gupta, *Annu. Rep. NMR Spectrosc.*, 1992, **24**, 219.
47. L. A. Levy, E. Murphy, B. Raju, and R. E. London, *Magn. Reson. Chem.*, 1992, **30**, 723.
48. D. W. Ovenall and R. C. Ferguson, in *Pulse Methods in 1D and 2D Liquid-phase NMR*, ed. W. S. Brey, Academic, San Diego, 1988, pp. 489–505.
49. W. I. Bailey, A. L. Kotz, P. L. McDaniel, D. M. Parees, F. K. Schweighardt, H. J. Yue, and C. Anklin, *Anal. Chem.*, 1993, **65**, 752.
50. A. A. Ribeiro and M. J. Glen, *J. Magn. Reson. A*, 1994, **107**, 158.
51. W. J. Metzler, P. Leighton, and P. Lu, *J. Magn. Reson.*, 1988, **76**, 534.
52. D. W. Hughes, A. D. Bain, and V. J. Robinson, *Magn. Reson. Chem.*, 1991, **29**, 387.
53. S. H. Grode and R. W. Gillis, *J. Magn. Reson.*, 1989, **82**, 122.
54. J. J. Kotyk, *J. Magn. Reson.*, 1991, **95**, 632.

Biographical Sketches

Wallace S. Brey. *b* 1922. B.S., Ursinus, 1942, M.S., Pennsylvania, 1946, Ph.D., 1948. Faculty at DePauw Univ., 1948–49, St. Joseph's University, 1949–52; University of Florida, 1952 to date. Approximately

85 publications. Author of three textbooks in physical chemistry; Editor of the volume 'Pulse Methods in 1D and 2D Liquid-Phase NMR', 1987; Editor, Journal of Magnetic Resonance, 1969–present. Research specialties heterogeneous catalysis and adsorption, structure and interactions of proteins, ^{19}F, ^{27}Al, ^{29}Si, and ^{31}P NMR in liquids and solids.

Mary Louise Brey. *b* 1926. B.S., Florida Southern College, 1948, M.S., Florida, 1952, Ph.D., 1956. University of Florida, 1952–1955, 1957–1959. Research: synthesis of organic fluorine compounds and determination of their structure by IR and NMR spectroscopy, rates of oxidation of Zr–Nb alloys.

Fullerenes and Related Molecules as Studied by Solid State NMR

Anita M. Orendt

Center for High Performance Computing, University of Utah, Salt Lake City, UT, USA

1	Introduction	1
2	History of Fullerene Discovery	1
3	Studies on Pure C_{60}	1
4	Studies on Pure C_{70}	3
5	Studies on Pure Higher Fullerenes	4
6	Studies on Nanotubes	4
7	Studies on the Intercalation Complexes of Fullerenes	5
8	Concluding Remarks	6
9	References	7

1 INTRODUCTION

The fullerenes, which by definition are polyhedral, closed cages of n carbons having twelve pentagonal and $(n/2 - 10)$ hexagonal faces, have been proposed to be important constituents of soots and interstellar dust. In addition to the more common single-walled closed cage compounds such as C_{60} and C_{70}, multiple-walled cage structures are also known, with onion-like structures of up to twenty concentric layers having been demonstrated to exist. Among the related compounds are nanotubes, or elongated fullerenes; single-walled and multi-walled, capped or open-ended varieties exist. There also exist endohedral or *incar*-fullerenes that have atoms or small molecules trapped inside the cages. In addition, there are intercalation complexes of fullerenes with atoms or molecules held in the interstitial crystal sites. The intercalation complexes with alkali metal atoms have attracted much attention, especially A_3C_{60} species with A=K, Rb, or Cs, as they are superconductors with transition temperatures, T_c, above 30 K. Several books and reviews on the chemistry and physics of fullerenes are given in the references[1–5] to provide further information on this interesting class of compounds.

Solid state nuclear magnetic resonance, NMR, studies beyond simple MAS spectra (magic angle spinning) on this class of compounds have been mainly limited to studies on C_{60}, C_{70}, and intercalation complexes of C_{60}, mainly due to the sample requirements of solid state NMR. These studies have provided insight into the structure, phase transitions, dynamics, and electronic properties of these compounds. There has been one solid state NMR study of the dynamics of C_{76} as well as a recent study on nanotubes. This article will focus on these studies by solid state NMR and the information they have provided.

2 HISTORY OF FULLERENE DISCOVERY

Until relatively recently it was an accepted fact that pure carbon existed in one of two allotropic forms: graphite and diamond, both having extended structures, the first with sp^2-hybridized carbons and the second with sp^3-hybridized carbons. This changed in 1984 when the first spectroscopic evidence of a molecular form of carbon was published.[6]

A mass spectrum of laser vaporized graphite published by researchers at Exxon showed the existence of a number of carbon clusters with the maximum intensity being C_{60}. About a year later Harold Kroto's group at Sussex University in the UK found conditions where C_{60} was produced nearly exclusively.[7]

Richard Smalley of Rice University proposed the familiar truncated icosahedral or soccer ball structure for C_{60}, shown in Figure 1a, and the name buckminsterfullerene. This was not the first time such a structure had been suggested, however, as there had been a number of theoretical studies on the structure, stability, and properties of this C_{60} structure prior to 1984.[8–10]

The next advance in the study of C_{60} came in 1990 when Krätschmer, Fostiropoulos, and Huffman developed a method to make macroscopic quantities of C_{60} and obtained infrared, IR, and X-ray powder diffraction spectra that supported the predicted structure.[11] The subsequent work on the isolation and purification of C_{60} also led to the isolation of the first of the higher fullerenes, C_{70}, shown in Figure 1b, in which a band of ten carbons is added around the equator of the C_{60} structure. The confirmation of the C_{60} and C_{70} structures followed shortly thereafter, with ^{13}C solution NMR unambiguously confirming the proposed structure of both compounds. C_{60} showed the expected single line at 143 ppm for all 60 carbons while C_{70}, with D_{5h} symmetry, showed five lines between 130 and 150 ppm in a 10 : 20 : 10 : 20 : 10 ratio as expected.[12] The assignment of these resonances to the five groups of carbon atoms, labeled C_a through C_e in Figure 1b, was confirmed by a solution ^{13}C INADEQUATE spectrum (Incredible Natural Abundance DoublE QUantum Transfer Experiment).[13] Continuing work led to the isolation of a number of other fullerenes, both smaller and larger than the dominant C_{60} compound.

Richard Smalley and Robert Curl Jr. from Rice University in Houston, Texas along with Harold Kroto from Sussex University in England were awarded the 1996 Nobel Prize in Chemistry for their work on the discovery of fullerenes.

3 STUDIES ON PURE C_{60}

Before going into details on the NMR studies of pure C_{60}, some information on the crystal habitat is necessary. At room temperature C_{60} is known to exist as an orientationally disordered face-centered cubic (fcc) structure. There is a phase transition, observed by both differential scanning calorimetry and x-ray powder diffraction, at about 250 K to a simple cubic (sc) with orientational order.

Solid state NMR provided the first measure of the bond lengths of C_{60} through the $^{13}C–^{13}C$ dipolar coupling in

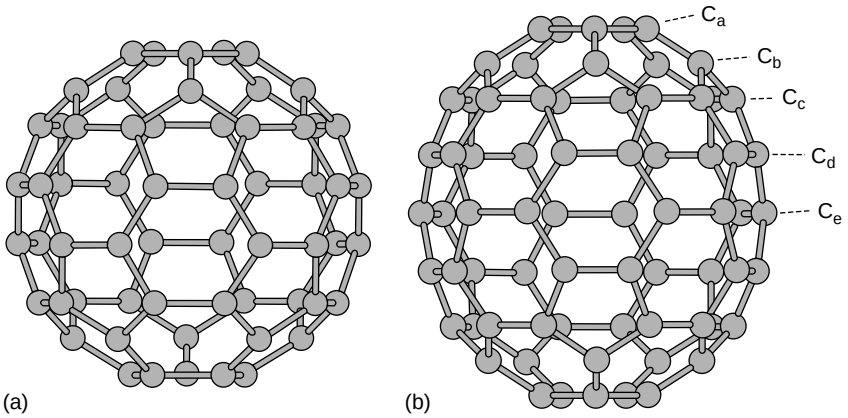

Figure 1 Structures of (a) C_{60} and (b) C_{70}. In C_{70}, carbons are labeled C_a–C_e, based on their chemical shifts

partially enriched C_{60}.[14] This was accomplished using the Carr-Purcell Meiboom-Gill pulse sequence, which selectively removes the chemical shift anistropy, CSA, while retaining the dipolar coupling. The measurement indicated that there were two different bond lengths, 1.45 Å and 1.40 Å, in a 2 : 1 ratio, consistent with the proposed structure. This result can be compared with a subsequent gas phase electron diffraction measurement of 1.458 Å for a bond joining two six-membered rings and 1.401 Å for the bond joining the five- and six-membered rings.[15] Similar distances have also been obtained by low temperature single crystal x-ray diffraction and by low temperature powder neutron diffraction.

In addition to the structural studies, work has been completed on the dynamics of C_{60}.[16,17] The static ^{13}C NMR powder patterns obtained as a function of temperature are shown in Figure 2. At room temperature a narrow line indicative of rapid, isotropic rotation is obtained. As the temperature is lowered a broad feature appears in the spectrum. Below 100 K the static spectrum is dominated with the broad anisotropic powder pattern characteristic of a molecule that is stationary on the NMR timescale, meaning that the correlation time for isotropic reorientation is large compared to the inverse of the static linewidth. There is no evidence of the 250 K phase transition from either the static or MAS spectrum. There is sometimes a small percentage of the material that is still motionally averaged as evidenced by the sharp peak superimposed on the broad CSA pattern. The intensity of this feature is a function of the purity of the sample and is believed to be due to molecules having low energy barriers to reorientation when they are near structural defects in the crystal structure due to the presence of impurities.

Additional information is obtained by looking at the T_1 relaxation times, generally obtained by saturation recovery methods, as a function of temperature, as shown in Figure 3.[17] In T_1 measurements a phase transition can be manifested as a discontinuity in the curve of T_1 versus temperature. This is the case in C_{60}. The T_1 data were fit to a model of going from essentially unhindered, rapid isotropic motion in the high temperature fcc phase to a reorientation restricted to jumping between symmetry related orientations in the low temperature sc form. Further analysis of the temperature dependence of the motion, using the fact that the dominant relaxation mechanism is the CSA, provided an activation barrier to rotation of about 5.9 J/mol in the fcc phase and from 17 to 25 J/mol in the sc form.

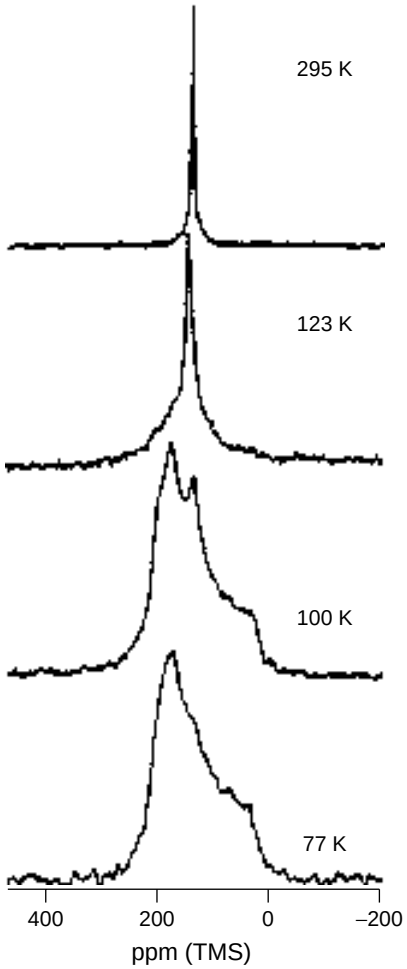

Figure 2 Static solid state ^{13}C NMR spectrum of C_{60} as a function of temperature. The spectra change from a lineshape indicative of rapid isotropic motion at 295 K to one of no molecular motion on the NMR timescale at 77 K. (Reproduced by permission of the American Chemical Society from Ref.[16])

The low temperature powder pattern also gives the principal components of the chemical shift tensor, which can be used to provide insight into the electronic structure. These have been measured to be 220, 186, and 40 ppm[16] (or 213, 182,

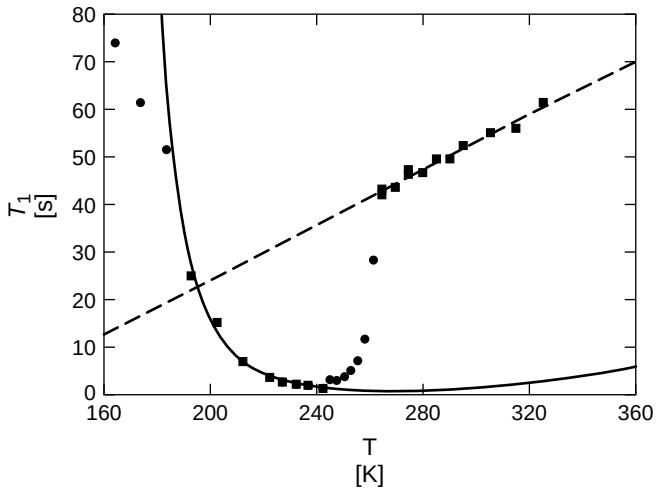

Figure 3 The temperature dependence of the ^{13}C T_1 relaxation time of solid C_{60} at a field strength of 9.39 T. The 260 K phase transition is responsible for the discontinuity in the curve. Squares are T_1 values obtained from a single exponential fit of the T_1 saturation recovery data; circles are the average of the two T_1 values obtained from a double exponential fitting. The solid line is the fit of the data for the sc phase between 193 and 243 K, based on a model of relaxation dominated by the CSA. The dashed line is the fit of the data above 263 K for the sample in the fcc phase. (Reproduced by permission of the American Physical Society from Ref.[17])

and 33 ppm).[17] These numbers are typical aromatic chemical shift tensor numbers with the δ_{33} component showing the characteristic shift to a higher value expected due to the strain of the five-membered rings. The principal values are similar to the values for the five-membered ring carbons in other aromatic systems, such as corannulene[18] (224, 177, and 6 ppm), acenaphthene[19] (213, 195, and 13 ppm), and pyracene[20] (202, 192, and 24 ppm). In contrast, the δ_{33} components for bridgehead carbons in six-membered ring compounds are usually less than 0 ppm, and in the case of coronene it is measured at −38 ppm for the innermost carbon.[18]

4 STUDIES ON PURE C_{70}

There are three solid state NMR studies, all published in 1993, that have measured the relaxation data, MAS spectra, and/or the static powder pattern as a function of temperature on samples of greater than 98% pure C_{70}.[21–23] While the basic dynamic interpretation of the spectra are consistent between these three reports, there are significant differences.

C_{70} has three known phases.[24] Above 330 K it exists in either an fcc or a hexagonal closed packed (hcp) structure with complete rotational disorder, similar to the room temperature phase of C_{60}. Between about 280 and 330 K the crystal structure is rhombohedral with the long axis directed essentially along the [111] crystal axis; rotational disorder exists perpendicular to this axis. A molecular dynamics simulation predicted that the motion in this phase is not pure uniaxial rotation about the long axis, but includes a precession of the long axis about this crystal axis.[25] Below 280 K the structure becomes monoclinic with orientational ordering; however, no details are known about the molecular orientation. It has also been determined that in order to obtain the equilibrium low temperature ordered phase, the crystal must be cooled extremely slowly (e.g., over a matter of many hours) from the high temperature phase through the lower temperature transition. If cooled quickly, as in sublimation, the two high temperature phases with their rotational freedom have been shown to persist until very low temperatures, even down to 10 K. Therefore, careful treatment of the sample is necessary to ensure knowledge of its phase.

NMR provides some evidence of the phase transitions. Upon increasing the temperature of a sample that has first been cooled slowly from 300 to 50 K, the MAS spectra as a function of temperature showed a small shift in the isotropic positions of several of the resonances at approximately 273 K and 323 K, consistent with the known phase transition temperatures.[24] The T_1 temperature dependence in one study[22] showed a deviation from the expected curve at about 280 K; in the other study[23] the T_1 measurements did not show any significant discontinuities at this phase transition temperatures.

There have been two static 1D NMR measurements as a function of temperature. In the first, by Blinc et al.,[21] the static lineshape was measured as a function of temperature from 450 to 50 K at a ^{13}C frequency of 67.89 MHz. There were two increases in the width of the static pattern as the temperature was lowered: from about 1 kHz above 300 K to nearly 3 kHz below 200 K with the full static linewidth of about 12 kHz being reached below 100 K. The spectra of the rhombohedral phase between 270 and 120 K were fit according to ordering of the sample along [111] crystallographic axis and the onset of uniaxial rotation with precession. Those between 120 and 50 K were fit as a gradual slowing of the uniaxial rotation, with the lowest temperature lineshape simulated as the overlap of five axially symmetric tensors. The lineshapes of these intermediate temperature spectra, however, were not the expected overlap of five axially symmetric patterns, and are not consistent, both in terms of spectral features and linewidths, with the experimental results of the other two studies. Maniwa et al.[22] also measured the 1D static powder pattern as a function of temperature between 340 and 77 K at a ^{13}C frequency of 65.5 MHz. From a single tensor fit of the 77 K spectrum the principal values were estimated to be 225, 200, and 25 ppm, values similar to those of C_{60}. The spectra at intermediate temperatures were simulated as five overlapping axially symmetric tensors using the above measured static principal values, adjusted to axial symmetry for the rotation about the long axis, and assuming the δ_{33} component is oriented perpendicular to the carbon cage. Therefore, the same tensor is averaged by a different angle, as the angle between the long axis and the δ_{33} component is different for each of the five inequivalent positions. There were no values for the measured anisotropy reported. The simulation was similar to the experiment, as can be seen in Figure 4, and differences were accounted for by the fact that the predicted precession of the long axis, which would lead to a further narrowing of the axially symmetric tensor, was not included in the simulation.

Tycko et al.[23] studied C_{70} with a slow spinning sideband intensity analysis between 320 and 230 K, a 2D MAS/CSA correlation experiment at 233 K, and a static 1D measurement

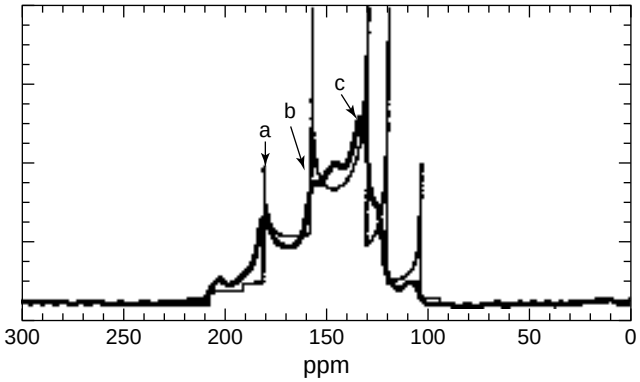

Figure 4 Observed (thick line) and simulated (thin line) ^{13}C static spectrum of C_{70} at 295 K at a frequency of 65.5 MHz. The simulation assumes five overlapping axially symmetric shift tensors based on static tensor components of 225, 200, 20 ppm, and angles of 38, 51, 78, 66, and 78° between the rotation axis and the δ_{33} component for carbons C_a–C_e, respectively. (Reproduced by permission of the Physical Society of Japan from Ref.[22])

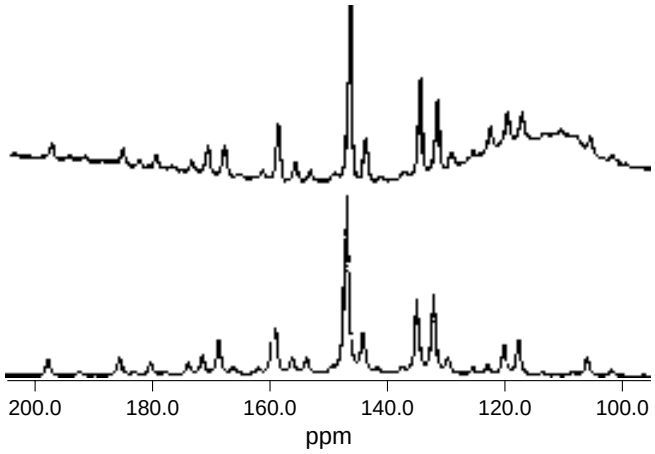

Figure 5 Slow spinning ^{13}C MAS NMR spectrum of C_{70} at 283 K and a spin rate of 1.2 KHz along with the simulated spectra using spinning sideband intensities from a Herzfeld-Berger analysis and information from a 2D MAS/CSA experiment. (Reproduced by permission of the American Institute of Physics from Ref.[23])

at 50 K. The 2D MAS/CSA experiment separates the individual powder patterns based in the 2D space by the isotropic chemical shift values. A representative spinning sideband pattern at 283 K, along with its simulation based on both a Herzfeld-Berger spinning sideband intensity analysis[26] and the values from the 2D experiment, are shown in Figure 5. From these simulations, the anisotropy (defined as $\Delta\sigma = \sigma_\perp - \sigma_\parallel$) of the five tensors at 230 K were reported as 162, 27, −42, −72, and −77 ppm for carbons C_a–C_e, respectively. In all cases the spectra are axially symmetric, indicative of the uniaxial rotation expected at this temperature. Based on a full anisotropy of 200 ppm for a static sample taken from the 50 K static pattern, the authors showed that the scaling of the anisotropy is consistent with that expected for uniaxial rotation about the long axis assuming the δ_{33} component is normal to the cage.

In summary, the variations in the ^{13}C NMR lineshape as a function of temperature from a sample of pure C_{70} are rich in information about the motional characteristics of the three known phases. The NMR studies give a consistent picture of the molecular motion first changing from anisotropic rotation to uniaxial rotation about the long axis, with a slight precession. This is followed by the transformation into the low temperature phase in which there is no molecular motion. However, the principal values of the five inequivalent carbons of C_{70} have not yet been obtained. Accurate tensor components for these five carbons should be obtainable from a 2D spectrum in which the CSA of individual carbons is separated by their isotropic values, provided that the experiment is performed below 100 K and that care is taken in the sample cooling procedure.

5 STUDIES ON PURE HIGHER FULLERENES

There is much less information, from any source, on the structure and dynamics of the larger fullerenes. For C_{76}, a single solid state NMR study exists.[27] The C_{76} molecule has a chiral D_2 structure calculated to have three distinct molecular axes of lengths 8.75, 7.50 and 6.54 Å. Solution NMR shows nineteen resonances in the range of 130–150 ppm. The solid state NMR lineshape gives evidence that at room temperature C_{76} also undergoes rapid, isotropic motion at room temperature, but as it is cooled there is no evidence of going first to uniaxial rotation as in C_{70}. Instead, the spectra indicate a relatively sharp transition between anisotropic rotation and a static molecule between approximately 170 and 135 K. The T_1 temperature dependence also showed a slight discontinuity in the range of 170 K; this may be evidence of a still unknown phase transition.

6 STUDIES ON NANOTUBES

Due to recent advancements in the procedures to make and purify nanotubes, samples of sufficient size and uniformity are now becoming available for study. The single walled nanotube (SWNT) structures can be thought of as a tube made from a single layer graphite sheet that has been rolled to form a tube; the ends can be open or closed with a semi-fullerene cap. Nanotubes are characterized by their diameters and their helicity, which is a measure of how the hexagons wind around the surface. Several representative structures of capped nanotubes with different helicities are given in Figure 6. Nanotubes can exhibit either semiconducting or metallic electronic properties depending on these two properties. The SWNT also self assemble into larger structures known as bundles or ropes; the manner of this assembly is also believed to affect the properties of the nanotube.

The first solid state NMR study of the CSA and T_1 relaxation behavior of a SWNT has very recently appeared in the literature.[28] Due to the manner of production of these structures, it is very important to either purify the samples to remove traces of paramagnetic metal catalysts that lead to extensive broadening of the powder pattern or to perform the synthesis with alternative catalysts. The reported static and MAS spectra of a SWNT sample with a diameter of 0.85 nm are given in Figure 7. The MAS has a single resolved peak at 124 ppm with a full width at half height of about

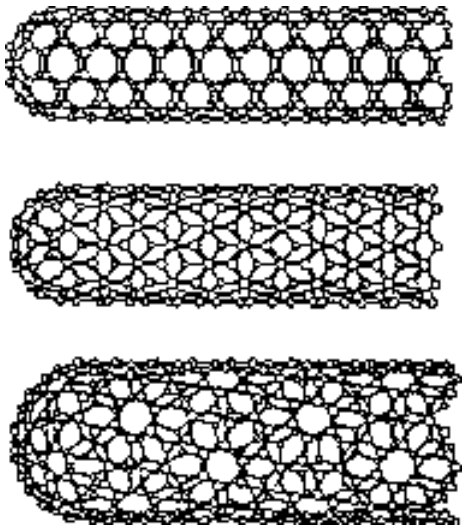

Figure 6 Sample structures of nanotubes of different diameters and helicity. (Reproduced by permission of Imperial College Press from Ref.[2], p. 33)

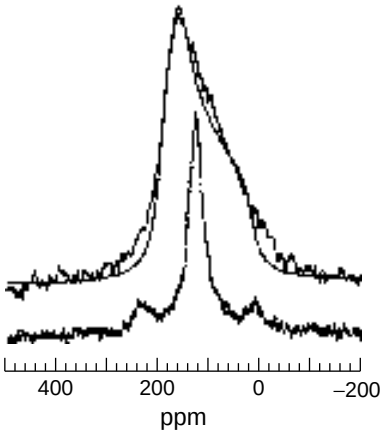

Figure 7 The static and MAS (at a spin rate of 11.7 KHz) solid state ^{13}C spectra of a nanotube of average diameter 0.85 nm. A fit of the static powder pattern to a single tensor is also shown. (Reproduced by permission of the American Association for the Advancement of Science from Ref.[28])

30 ppm; fitting the room temperature static pattern as a single tensor yielded the tensor principal values of 195, 160 and 17 ppm. These principal values again show the expected increase in the δ_{33} component associated with the strain of the non-planar environment. The T_1 relaxation behavior of this sample was best fit to a double exponential function with the slower relaxation component being attributed to tubes with metallic characteristics and the longer component due to tubes exhibiting semi-conducting behavior. However, both components showed the linear relationships with temperature expected for the Korringa relaxation (see discussion in next section) through the conducting electron band of metallic samples.

Further NMR studies on nanotubes should now follow as homogenous samples are becoming available in large enough quantities, allowing for a better understanding of the properties of these materials.

7 STUDIES ON THE INTERCALATION COMPLEXES OF FULLERENES

There are many examples of intercalation complexes of C_{60}. In the room temperature fcc structure of C_{60} there are two tetrahedral sites and one octahedral site per molecule with estimated radii of 1.1 and 2.1 Å, respectively. Both sites are large enough to hold most atoms and even small molecules.

The most widely studied group of intercalation complexes is the alkali fullerides, A_xC_{60}, ionic solids comprised of A^+ and C_{60}^{x-} ions. The $x = 1, 3, 4$, and 6 species have been isolated and characterized. Electronically, the lowest unoccupied molecular orbital (LUMO) of the parent C_{60} is triply degenerate. Therefore, both the neutral species with an empty LUMO and the C_{60}^{6-} ion with a full LUMO should be, and are, insulators. The others, with a partially full conduction band, are expected to have metallic behavior. However, no clear evidence of metallic behavior has been found in either the A_1 or A_4 species. The A_3 species have been shown to be conductors and superconductors,[29] with transition temperatures (T_c's) measured to be above 30 K.[30] These are among the highest T_c's known with the exception of the so-called "room temperature" copper oxide superconductors which have temperatures of about 150 K. For this reason the A_3C_{60} fullerides have attracted the most attention. A brief summary of the solid state NMR of A_3C_{60} follows; a more comprehensive treatment of the alkali fullerides, including details of the mechanisms of superconductivity, is referenced.[31]

Before going into details about the NMR results on these compounds, two effects of the conduction band on the NMR must be discussed. The first is the Knight shift, which is a shift in the resonance frequency observed in metals due to the hyperfine coupling of the nucleus to the conducting band electrons.[32] The measured resonance frequency is the sum of the chemical shift and the Knight shift. This electron-nuclear coupling also dominates the T_1 relaxation in these compounds. The linear relationship observed between the T_1 relaxation time and temperature in conducting systems is quantified by the Korringa[33] relationship, and is often reported as a plot of $(1/T_1T)$ versus T. Neither of these effects is observed in the superconducting state, leading to observable changes at T_c in plots of the temperature dependence of both the shift and the T_1 relaxation time.

The fcc structure of K_3C_{60}, as well as the other A_3C_{60} structures, is shown in Figure 8.[34] The most significant difference between this structure and that of pure C_{60} is that the C_{60} entities are no longer orientationally disordered, but are oriented with a hexagonal face directed towards the tetrahedral site, maximizing its size. A series of spectra of the A_3C_{60} compounds are shown in Figure 9. In the NMR of the alkali metal atoms, differentiation of the atoms in the tetrahedral and octahedral sites, as well as a splitting of the tetrahedral peak, is observed. The two tetrahedral peaks are believed to be due to crystal distortions and the splittings can be removed by going to higher temperatures. Diffraction studies have not shown any evidence of this distortion. The measured ^{13}C spectra show the effect of decreased motional freedom of the C_{60} ion as the size of the alkali metal increases (radii of the alkali ions are: K^+ 1.33 Å, Rb^+ 1.48 Å, Cs^+ 1.67 Å). In addition, the observed Knight shift is relatively small, with

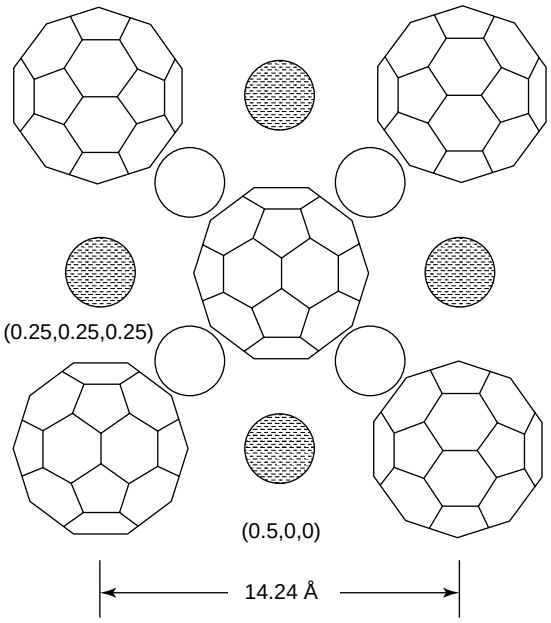

Figure 8 Structure of K_3C_{60} alkali fulleride. The open and hatched spheres represent the potassium at the tetrahedral and octahedral sites, respectively. (Reproduced by permission of the Nature Publishing Group from Ref.[34])

the sum of the Knight shift and any change in the chemical shift from neutral C_{60} being only 30–50 ppm. Most calculations of the expected Knight shift in these compounds are much larger. The temperature dependence of both the total shift (Knight and chemical) and the T_1 relaxation time are shown in Figure 10 for the case of Rb_2CsC_{60}, which has a T_c of about 30 K. All the plots show the expected changes at this temperature. Tycko et al.[35] has used the value of T_1T in the normal conducting state to make a rough estimation of the density of electronic states at the Fermi level (about 20 eV^{-1} per C_{60} ion). The Arrhenius behavior of the T_1 in the superconducting state was also used to obtain a measure of the electronic energy gap ($3T_c$ for K_3C_{60} and $4T_c$ for Rb_3C_{60}).

The above shows the important information on the structure and electronic properties of the alkali fullerides solid state NMR has provided. However, many questions about the structure and electronic properties remain unanswered. Also, contradictions in the experimental data still exist, and must be reconciled before the electronic behavior of this class of compounds can be understood.

8 CONCLUDING REMARKS

Solid state NMR has been shown to be a powerful tool in the study of the structure, phase transitions, dynamics, and electronic properties of the C_{60}, C_{70}, and several intercalation complexes of C_{60} and should continue to contribute to the study of these materials in the future. There still exist unresolved issues in the study of the alkali fullerides that solid state NMR can address. Higher fullerenes and nanotubes samples of sufficient size and purity (and uniformity in the case of nanotubes) are just now beginning to become available, and more solid state NMR studies probing into the structure and properties of these materials should follow. In addition, solution ^{3}He NMR studies of the endohedral or *incar*-fullerenes He@C_{60} and He@C_{70}, have shown how the helium atom can be used as a magnetic probe of the fullerene cage.[36] Variable temperature, solid state

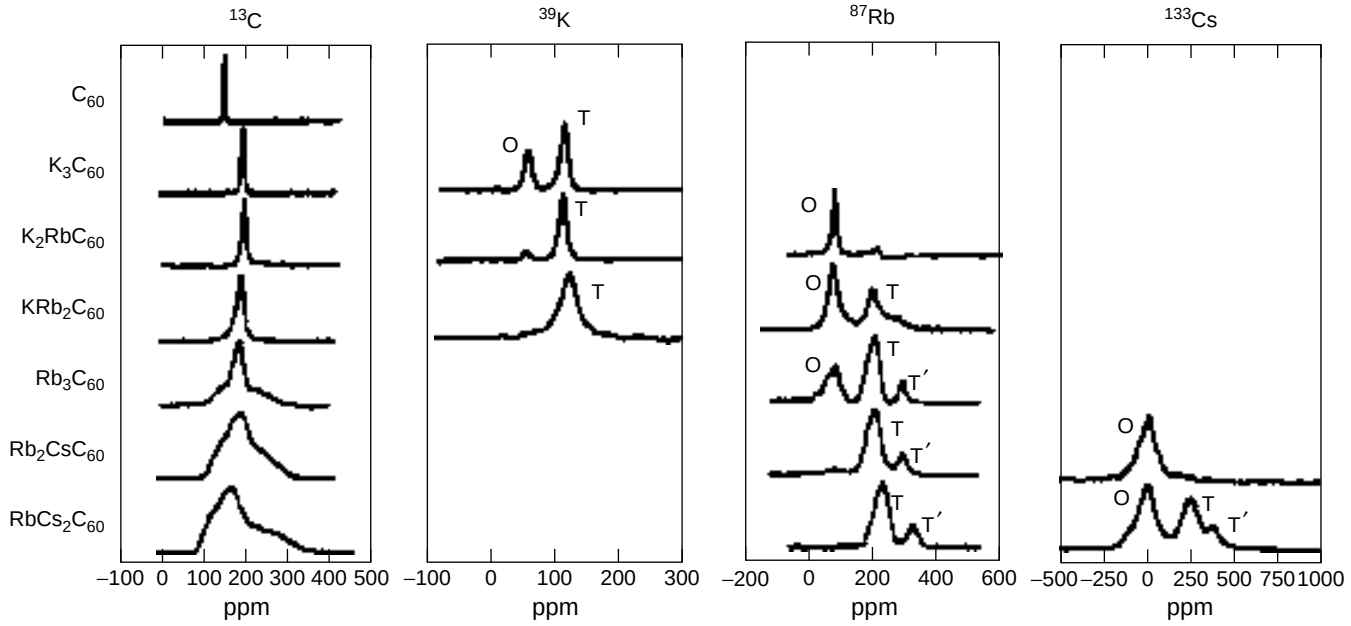

Figure 9 Static room temperature ^{13}C (referenced to TMS), ^{39}K, ^{87}Rb, and ^{133}Cs (all referenced to the free alkali ions) spectra for a series of A_3C_{60} compounds. Features of interest are the presence of multiple tetrahedral environments for the larger Rb and Cs ions, the anisotropy indicative of the lack of C_{60} rotation with the Cs ions, and the absence of a large Knight shift between C_{60} and any of the alkali fullerides. (Reproduced by permission of the American Physical Society from Ref.[31])

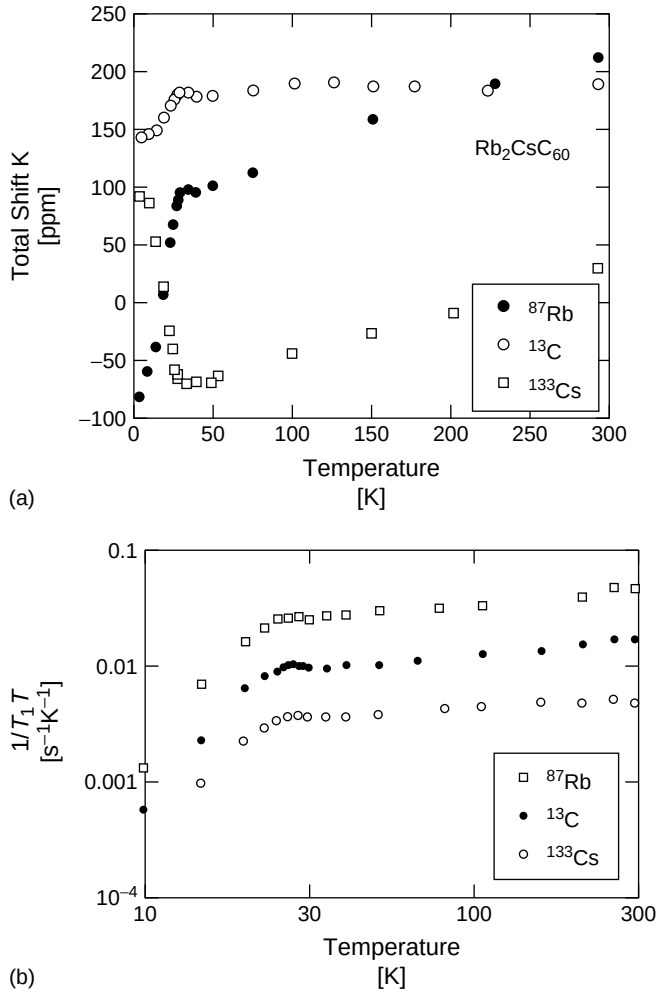

Figure 10 Knight shift (a) and T_1 (b) behavior as a function of temperature observed for Rb_2CsC_{60}, (T_c of about 30 K). All data is taken at a field strength of 8.8 T. The shifts for Rb in the figure are the center of mass of the two tetrahedral site resonances. The increasing chemical shift for Cs is believed to be due to a negative electron-nuclear hyperfine coupling. ((a) Reproduced by permission of the American Physical Society from Ref.[31]; and (b) Reproduced by permission of the American Physical Society from Ref.[37])

^{3}He NMR studies on these compounds should be of great interest.

9 REFERENCES

1. K. M. Kadish and R. S. Ruoff eds, 'Fullerenes Chemistry, Physics and Technology', Wiley-Interscience: New York, 2000.
2. R. Taylor, 'Lecture Notes on Fullerene Chemistry: A Handbook for Chemists', Imperial College Press: London, 1999.
3. H. Kuzmany, J. Fink, M. Mehring, and S. Roth eds, 'Physics and Chemistry of Fullerenes and Derivatives', World Scientific Publishing Co. Pte. Ltd.: New Jersey, 1995.
4. K. Prassides ed, 'Physics and Chemistry of the Fullerenes', NATO ASI Ser C., Vol. 443, Kluwer Academic Publishers: Boston, 1994.
5. G. S. Hammond and V. J. Kuck eds, 'Fullerenes: Synthesis, Properties, and Chemistry of Large Carbon Clusters', ACS Symposium Series 481, American Chemical Society: Washington, DC, 1992.
6. E. A. Rohlfing, D. M. Cox, and A. Kaldor, *J. Chem. Phys.*, 1984, **81**, 3322.
7. H. W. Kroto, J. R. Heath, S. C. O'Brien, R. F. Curl, and R. E. Smalley, *Nature*, 1985, **318**, 162.
8. E. Osawa, *Kagaku*, 1970, **25**, 854.
9. D. A. Bochvar and E. G. Gal'pern, *Proc. Acad. Sci., USSR*, 1973, **209**, 610.
10. R. A. Davidson, *Theor. Chim. Acta*, 1981, **58**, 193.
11. W. Krätschmer, L. D. Lamb, K. Fostiropoulos, and D. Huffman, *Nature*, 1990, **347**, 354.
12. R. Taylor, J. P. Hare, A. K. Abdul-Sada, and H. W. Kroto, *Chem. Commun.*, 1990, 1423.
13. R. D. Johnson, G. Meijer, J. R. Salem, and D. S. Bethune, *J. Am. Chem. Soc.*, 1991, **113**, 3619.
14. C. S. Yannoni, P. P. Bernier, D. S. Bethune, G. Meijer, and J. R. Salem, *J. Am. Chem. Soc.*, 1991, **113**, 3190.
15. K. Hedberg, L. Hedberg, D. S. Bethune, C. A. Brown, H. C. Dorn, R. D. Johnson, and M. deVries, *Science*, 1991, **254**, 410.
16. C. S. Yannoni, R. D. Johnson, G. Meijer, D. S. Bethune, and J. R. Salem, *J. Phys. Chem.*, 1991, **95**, 9.
17. R. Tycko, G. Dabbagh, R. M. Fleming, R. C. Haddon, A. V. Makhija, and S. M. Zahurak, *Phys. Rev. Lett.*, 1991, **67**, 1886.
18. A. M. Orendt, J. C. Facelli, S. Bai, A. Rai, M. Gossett, L. T. Scott, J. Boerio-Goates, R. J. Pugmire, and D. M. Grant, *J. Phys. Chem. A.*, 2000, **104**, 149.
19. R. J. Iuliucci, J. C. Facelli, D. W. Alderman, and D. M. Grant, *J. Am. Chem. Soc.*, 1995, **117**, 2336.
20. A. M. Orendt, N. K. Sethi, J. C. Facelli, W. J. Horton, R. J. Pugmire, and D. M. Grant, *J. Am. Chem. Soc.*, 1992, **114**, 2832.
21. R. Blinc, J. Dolinsek, J. Seliger, and D. Arcon, *Solid State Commun.*, 1993, **88**, 9.
22. Y. Maniwa, A. Ohi, K. Mizoguchi, K. Kume, K. Kikuchi, K. Saito, I. Ikemoto, S. Suzuki, and Y. Achiba, *J. Phys. Soc. Jpn.*, 1993, **62**, 1131.
23. R. Tycko, G. Dabbagh, G. B. M. Vaughan, P. A. Heiney, R. M. Strongin, M. A. Cichy, and A. B. Smith III, *J. Chem. Phys.*, 1993, **99**, 7554.
24. G. B. M. Vaughan, P. A. Heiney, D. E. Cox, J. E. Fischer, A. R. McGhie, A. L. Smith, R. M. Strongin, M. A. Cichy, and A. B. Smith III, *Chem. Phys.*, 1993, **178**, 599.
25. M. Sprik, A. L. Cheng, and M. L. Klein, *Phys. Rev. Lett.*, 1992, **69**, 1660.
26. J. Herzfeld and A. Berger, *J. Chem. Phys.*, 1980, **73**, 6021.
27. Y. Maniwa, K. Kume, K. Kikuchi, K. Saito, I. Ikemoto, S. Suzuki, and Y. Achiba, *Phys. Rev. B*, 1996, **53**, 14196.
28. X.-P. Tang, A. Kleinhammes, H. Shimoda, L. Fleming, K. Y. Bennoune, S. Sinha, C. Bower, O. Zhou, and Y. Wu, *Science*, 2000, **288**, 492.
29. A. F. Hebard, M. J. Rosseinsky, R. C. Haddon, D. W. Murphy, S. H. Glarum, T. T. M. Palstra, P. Ramirez, and A. R. Kortan, *Nature*, 1991, **350**, 600.
30. T. T. M. Palstra, O. Zhou, Y. Iwasa, P. E. Sulewski, R. M. Fleming, and B. R. Zegarski, *Solid State Commun.*, 1995, **93**, 327.
31. C. H. Pennington and V. A. Stenger, *Rev. Mod. Phys.*, 1996, **68**, 855.
32. W. D. Knight and S. Kobayashi, in 'Encyclopedia of Nuclear Magnetic Resonance', eds D. M. Grant and R. K. Harris, John Wiley & Sons: Chichester, 1996, Vol. 4, p. 2672.
33. C. P. Slichter, 'Principles of Magnetic Resonance', 3rd edition, Springer-Verlag: New York, 1992, page 151–157.
34. P. W. Stephens, L. Mihaly, P. L. Lee, R. L. Whetten, S.-M. Huang, R. Kaner, R. Deiderich, and K. Holczer, *Nature*, 1991, **351**, 632.

35. R. Tycko, G. Dabbagh, M. J. Rosseinsky, D. W. Murphy, A. P. Ramirez, and R. M. Fleming, *Phys. Rev. Lett.*, 1992, **68**, 1912.
36. M. Saunders, H. A. Jimenez-Vazquez, R. J. Cross, S. Mroczkowski, D. I. Freedburg, and F. A. L. Anet, *Nature*, 1994, **367**, 256.
37. V. A. Stenger, C. H. Pennington, D. R. Buffinger, and R. P. Ziebarth, *Phys. Rev. Lett.*, 1995, **74**, 1649.

Biographical Sketch

Anita M. Orendt, *b* 1958. B. S. 1980, Chemistry, University of Pittsburgh; Ph. D., 1987, Physical Chemistry, University of Utah. Postdoctoral work with Professor David M. Grant, University of Utah, 1987–1999. Assistant Professor of Chemistry (half-time), Westminster College of Salt Lake City, 1992–1994. Staff Scientist for Molecular Sciences, Center for High Performance Computing, University of Utah, 1999–present. Approximately 40 publications on measurement of chemical shift tensors. Research Interests: measurement and calculations of chemical shift tensors, especially in polycyclic aromatic hydrocarbons and in strained systems.

Heterocycles

Alan R. Katritzky
University of Florida, Gainesville, Florida, USA

James G. Keay and Ramiah Murugan
Reilly Industries, Inc., Indianapolis, IN, USA

1	Introduction	1
2	Three- and Four-Membered Rings	2
3	Heteroaromatic Five-Membered Rings	3
4	Saturated and Partially Unsaturated Five-Membered Rings	3
5	Heteroaromatic Six-Membered Rings	3
6	Saturated and Partially Unsaturated Six-Membered Rings	4
7	Seven-Membered and Larger Rings	4
8	Bibliography	5
9	Related Articles	6
10	References	6

1 INTRODUCTION

In general, the NMR properties of heterocyclic compounds are best understood by comparing them with ordinary organic compounds that do not contain heteroatoms. In this article the comparative aspects of heterocyclic compounds will be considered first, followed by a brief survey of the different classes of heterocyclic compounds, arranged according to the size and nature of the ring. The protons on the benzene ring experience a deshielding effect due to the aromatic ring current, which brings the chemical shift of the benzene protons to δ 7.24 ppm. The same ring current persists in the polyazabenzenes as in benzene itself.

Since 1955 magnetic resonance spectra have been indispensable to any serious study of heterocyclic chemistry. Proton resonance spectra, for example, yield information regarding the number of hydrogen atoms present in the molecule as well as their chemical environment and their relative orientation in space (Table 1).

Table 1 Chemical Shifts in Proton Resonance Spectra of Various Heterocycles (δ, ppm)

Compound	Chemical shift at position		
	2	3	4
Aziridine	1.48	–	–
Oxirane	2.54	–	–
Thiiran	2.27	–	–
Azetidine	3.58	2.32	–
Pyrrole	6.62	6.05	–
Furan	4.40	6.30	–
Thiophene	7.19	7.04	–
Pyridine	8.50	7.06	7.46
Pyridazine	–	9.17	7.68

Table 2 Chemical Shifts of Carbons of Some Heteroaromatic Compounds

Compound	^{13}C Chemical Shifts (δ, ppm)				
	C-2	C-3	C-4	C-5	C-6
Benzene	128.5	128.5	128.5	128.5	128.5
Pyridine	150.6	124.5	136.4	124.5	150.6
Pyridazine	–	152.8	127.6	127.6	152.8
Pyrimidine	159.5	–	157.5	122.1	157.5
Pyrazine	145.6	145.6	–	145.6	145.6
sym-Triazine	167.5	–	167.5	–	167.5
Pyrrole	118.5	108.2	108.2	118.5	–
Furan	142.6	109.6	109.6	142.6	–
Thiophene	125.4	127.2	127.2	125.4	–
Pyrazole	–	134.3	105.2	135.3	–
Imidazole	136.2	–	122.3	122.3	–

Compared with carbocyclic aromatic compounds the heteroaromatic compounds can basically be classified into two categories, those with π-deficient and those with π-excessive systems. This is experimentally demonstrated by the NMR chemical shifts of various nuclei. In the π-excessive systems the carbon atom resonances (Table 2) appear at much more shielded positions (δ 100–150 ppm) than do those of the carbons in π-deficient systems (δ 150–170 ppm).[1]

The ^{15}N chemical shifts of a number of heteroaromatic systems further demonstrate the electronic differences between π-deficient and π-excessive heteroaromatic compounds.[2] For example, the pyridine nitrogen (δ ^{15}N 312 ppm) is much more deshielded than the nitrogen in pyrrole (δ ^{15}N 149 ppm). The relative π-deficiency of a number of mono-, di-, and triazabenzenes is reflected by the ^{15}N chemical shifts given in Table 3. The most deshielded nitrogen of this series is pyridazine (δ_N 400 ppm), whereas the most shielded nitrogens are found in pyrimidine (δ_N 298 ppm). Thus the addition of nitrogen generally causes an increase in the π deficiency (pyrimidine being an apparent exception). In the π-excessive aza analogs of pyrrole, a similar trend is observed for the ^{15}N chemical shifts. Introduction of additional nitrogen atoms causes deshielding and thus decreases the π excessiveness of the ring systems.

Nitrogen compounds with three different substituents exist in enantiomeric forms. Usually, however, these cannot be separated as the molecule undergoes rapid inversion, sometimes referred to as 'umbrella-like' inversion. The barriers to inversion can be increased when the nitrogen atom is in a three-, four-, or six-membered ring. For example, in *N*-chloroaziridine the inversion is so strongly hindered that it is

Table 3 Chemical Shifts of Nitrogen of Some Heteroaromatic Compounds

Compound	^{15}N chemical shift (δ, ppm)
Pyridine	312
Pyridazine	400
Pyrimidine	298
Pyrazine	338
Pyrrole	149
Pyrazole	247
Imidazole	209

not possible to reach the coalescence temperature as decomposition occurs first ($T_c > 180\,^{\circ}C$).

2 THREE- AND FOUR-MEMBERED RINGS

The NMR spectra of three- and four-membered heterocycles display regularities of great value to structure determination. For protons on adjacent carbons the coupling constants J_{cis} seem to be always greater than J_{trans}. In three-membered rings J_{gem} is almost always smaller than J_{cis} and J_{trans}. The average values for aziridines are J_{gem} = 1.4, J_{trans} = 3.3, and J_{cis} = 6.4 Hz. The size of J_{gem} and of the vicinal C–H coupling constants seems to depend more on the number of nonbonding electron pairs at the heteroatom than on its electronegativity. In azetidine derivatives the proton-proton coupling constants J_{gem} on the carbons adjacent to nitrogen are 5–7.5 Hz, and J_{cis} is larger than J_{trans} (Table 4).

Nitrogen-15 NMR spectra of aziridines and azetidines have been measured. Relative to anhydrous ammonia the aziridine nitrogen absorbs at −8.5 ppm. *N*-Alkylation moves this shift to high frequency (downfield); for the N–Me derivative the signal is at 0.7 ppm, for N–$CHMe_2$ at 30.2 ppm, and for N–CMe_3 at 33.5 ppm. Aziridine ^{15}N shifts parallel the ^{13}C shifts—in a graph of ^{13}C versus ^{15}N shifts of aziridine derivatives the correlation coefficient was 0.953. Azetidine ^{15}N shifts are similar to those of the aziridines. Unsubstituted azetidine has its ^{15}N resonance, relative to anhydrous ammonia, at 25.3 ppm and *N*-*t*-butylazetidine shows the signal at 52 ppm.

In contrast to most cyclic and acyclic amines, the bonding constraints of the aziridine ring have the effect of retarding nitrogen inversion rates to extents where they are measurable by NMR spectroscopy. In fact, dynamic NMR spectroscopy has enabled the relatively easy determination of rates of nitrogen inversion through the measurement of resonance coalescence temperatures. Electron delocalizing substituents on a small-ring nitrogen lower the inversion barrier by lowering the energy of the transitional, 'flat' geometry in which three substituents of the nitrogen are all in the same plane. Substituents bearing unshared electron pairs raise the inversion barrier to levels at which enantiomers can be isolated. Pure invertomers have been obtained of *N*-haloaziridines and *N*-alkoxyaziridines. Observed coalescence temperatures of aziridines range from below −160 °C for *N*-acetylaziridine in vinyl chloride solution to above 145 °C for *N*-ethylaziridine in D_2O.

N-inversion in azetidine and azetidin-2-one is rapid, even at −77 and −40 °C, respectively. Again, halo substituents on nitrogen drastically slow the inversion rate, so that *N*-chloro-2-methylazetidine can be separated into two diastereomers. By and large, the *N*-inversion barrier of azetidines is 38 kJ mol^{-1} lower than that of similarly substituted aziridines.

Table 4 Chemical Shifts of Proton and Carbon of Three-membered Heterocyclic Systems and their Coupling Constants

Compound	δ^1H	J_{gem}	J_{cis}	J_{trans}	$\delta^{13}C$
Cyclopropane	0.22	−3–1	6–12	−4–8	−2.2
Aziridine	1.48	0.9–4	5–9	2–7	18–22
Oxirane	2.54	5–7	2–5	1–3	39.7
Thiirane	2.27	−14–1	6–7	5–6	18

Table 5 Some Oxirane δ and J Values

Compound	δ^1H (ppm)	$\delta^{13}C$ (ppm)	J_{gem} (Hz)	J_{cis} (Hz)	J_{trans} (Hz)
Oxirane	2.54	39.7	–	4.45	3.1
Oxiranes	–	–	4.5–6.3	2.2–4.5	1.4–3.1

Chemical shifts and coupling constants for oxiranes are summarized in Table 5. The configurations of chiral thiiranes and thiirane 1-oxides can be determined by ^1H NMR experiments in chiral solvents such as (*R*)-(−)-1-phenyl-2,2,2-trifluoroethanol. The protons α to sulfur are usually shifted to higher frequency for the (*S*) configuration than for the (*R*) configuration, all shifts being relative to the shifts in carbon tetrachloride. The *cis* and *trans* isomers of 2,3-diphenylthiirane can be distinguished easily by the difference in ^1H NMR shifts caused by shielding of the protons in the *trans* isomer by a phenyl group; other *cis*–*trans* isomers may be differentiated by the fact that the *cis* coupling constant is generally larger than the *trans*.

Extensive NMR studies of azetidines support a conformationally mobile, nonplanar structure in which rapid *N*-inversion occurs. The magnitude of the vicinal coupling constant ($J_{cis} \approx 7.5$ Hz, $J_{trans} \approx 3.0$ Hz) is widely used in the assignment of stereochemistry. Azetidin-2-ones or β-lactams have been studied extensively because of their structural similarity with that of antibiotics—cephalosporins and penicillins. In general, $J(3,4)_{cis} \approx 5.0–5.9$ Hz, while $J(3,4)_{trans} \approx 2.2–2.8$ Hz; this provides a simple method for determining the relative stereochemistry of 3,4-disubstituted β-lactams.

Support for the planarity of the 1-azetine ring comes from variable temperature NMR studies of 2-ethylthio-1-azetine. Vicinal coupling constants in 2-alkoxy- and 2-ethylthio-1-azetines are similar to those of analogous β-lactams, while geminal coupling constants in 3-substituted 1-azetines are of greater magnitude [$J(4,4) \approx -10$ Hz].

The NMR technique has been of great value in assigning oxetane structures, particularly because the α-protons in oxetanes have much higher chemical shift values than in any other class of ethers. For the parent compound the chemical shifts are at 4.73 and 2.72 ppm in deuterochloroform. ^1H NMR chemical shifts and coupling constants for a variety of thietane and thiete derivatives have been studied. In general, the α-protons of thietanes and their derivatives are deshielded relative to analogous derivatives with larger rings. Thus, the α-protons of thietane and thietane 1,1-dioxide absorb at δ 3.21 and 4.09 ppm, respectively, while the corresponding signals for the α-protons in thiolane and thiolane 1,1-dioxide are at δ 2.82 and 3.01 ppm, respectively. The α-proton chemical shifts of a series of cycloalkanes, oxacycloalkanes, azacycloalkanes, and cycloalkanones also show maximum deshielding at the four-membered ring.

An analysis of ^{13}C NMR chemical shift data for thietanes and thietes reveals that thietane 1,1-dioxides, thiete 1,1-dioxides, and thietane sulfoximines show unusual α-carbon deshielding and β-carbon shielding when compared with other thiacycloalkane 1,1-dioxides and acyclic counterparts. This has been referred to as the 'four-membered-ring sulfone effect'. Thus, the α-carbon shifts of thiolane and its 1-oxide

and 1,1-dioxide are at 31.7, 54.3, and 51.1 ppm while the corresponding α-carbon shifts for thietane and its *S*-oxides are at 26.1, 52.7, and 65.6 ppm.

3 HETEROAROMATIC FIVE-MEMBERED RINGS

The ^{1}H NMR spectra of the parent heterocycles (Table 6) each consist of two multiplets, of which the one at higher frequency is assigned to the α-hydrogens. Apart from pyrrole, the chemical shifts for the β-protons increase with decreasing electronegativity of the heteroatom. In contrast, the chemical shifts of the α-protons do not display any obvious regularity, probably due to paramagnetic shielding contributions which will become more important with increasing availability of d orbitals. The chemical shift of the pyrrole N–H is solvent dependent.

Table 6 ^{1}H NMR Spectral Data for Five-Membered Heteroaromatics

Compound	H-2	H-3	J(2,3)	J(2,4)	J(2,5)	J(3,4)
Pyrrole	6.68	6.22	2.70	1.44	1.87	3.35
Furan	7.29	6.24	1.75	0.85	1.40	3.30
Thiophene	7.18	6.99	4.90	1.04	2.84	3.50
Selenophene	7.88	7.22	5.40	1.46	2.34	3.74
Tellurophene	8.87	7.78	6.70	1.30	2.60	4.00

4 SATURATED AND PARTIALLY UNSATURATED FIVE-MEMBERED RINGS

The α-hydrogen resonances for the fully saturated monocycles occur at higher frequencies than the β-hydrogen resonances. The chemical shifts of the β-hydrogens vary systematically with the electronegativity of the heteroatom, but the chemical shifts of the α-hydrogens do not (Table 7). The spectra of 2,5-dihydrofuran and 2,5-dihydrothiophene are simple, showing two singlets at 4.51 and 5.85 ppm for the dihydrofuran, and 3.66 and 5.79 ppm for the sulfur analog; the lack of coupling is in accord with an almost planar conformation.

Carbon-13 NMR on partially and fully saturated heterocycles is much more limited, and is summarized in Figure 1. As would be expected, the high frequency shift of the α-carbon atom decreases with decreasing electronegativity of the heteroatom in the sequence O < NH < S < CH_2.

5 HETEROAROMATIC SIX-MEMBERED RINGS

In the aza derivatives of the aromatic hydrocarbons the nitrogen atoms exert a strong deshielding influence on the

Table 7 ^{1}H NMR Spectral Data (ppm) for Saturated Five-Membered Rings with One Heteroatom

Compound	H-2	H-3
Pyrrolidine	2.77	1.63
Tetrahydrofuran	3.62	1.79
Tetrahydrothiophene	2.75	1.92
Tetrahydroselenophene	2.79	1.96
Tetrahydrotellurophene	3.10	2.03

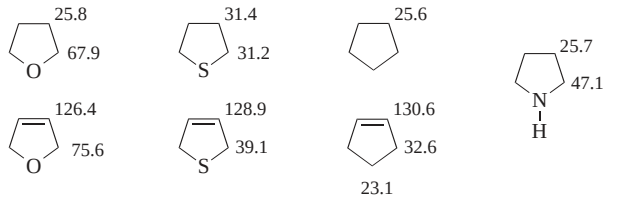

Figure 1 ^{13}C NMR chemical shifts of some partially and fully saturated heterocycles

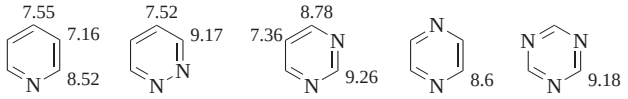

Figure 2 ^{1}H NMR chemical shifts of some heteroaromatic six-membered rings

α-hydrogen atoms, and a similar but smaller effect on the γ-hydrogens. The protons at the β positions in pyridine are in fact shifted slightly to lower frequencies than those of benzene (Figure 2). Further aza substitution produces similar effects, but strict additivity is not observed. For instance, two adjacent nitrogen atoms, as in pyridazine, exert a much larger deshielding effect on the α-protons than the sum of the α- and β-effects of a single nitrogen atom. Conversion of pyridine into the pyridinium cation causes a high-frequency shift of all the hydrogens, especially at the β and γ positions. The spectra of protonated polyaza heterocycles are frequently complicated by the occurrence of covalent hydration. This is more common with polycyclic systems, e.g. pteridine.

The extensive delocalization and aromatic character of pyridones, pyrones, etc., are shown by their chemical shift and coupling constant values (Figure 3). By contrast, pyrans and thiins show chemical shifts characteristic of alkenic systems (see below). For these and for rings containing only a single endocyclic double bond, ^{1}H NMR spectroscopy offers a most useful tool for structure determination. Solvent induced and lanthanide induced shifts are of great value in structure assignments in heterocyclic compounds, because cyclic nitrogen atoms, carbonyl groups, etc., undergo specific hydrogen bonding or coordination resulting in differential shifts of groups in different positions.

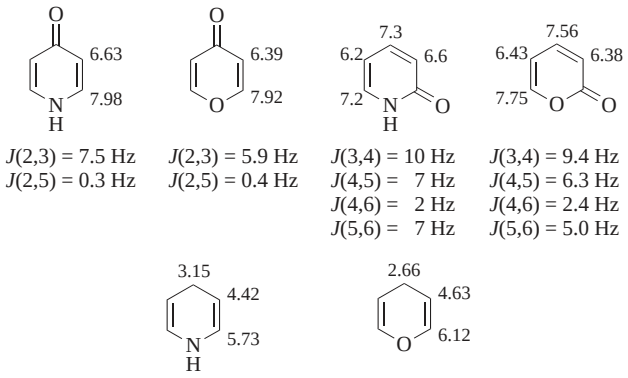

Figure 3 ^{1}H NMR chemical shifts and J values of some unsaturated six-membered rings

The normal pattern of coupling constants for aromatic six-membered rings is found in the heterocyclic aza systems, except that the *ortho* coupling to a proton α to a heterocyclic nitrogen is reduced from 7–8 to 4.5–6 Hz. The $J(2,3)$ value of pyrylium salts is still lower (about 3.5 Hz), but in pyridinium salts and pyridine *N*-oxide it is of intermediate value (about 6.5 Hz).

6 SATURATED AND PARTIALLY UNSATURATED SIX-MEMBERED RINGS

The chemical shifts of the α-, β- and γ-methylene carbon atoms of saturated six-membered ring systems are summarized in Table 8.

A nitrogen atom at X results in a variable high-frequency shift of the α-carbons, depending in its extent on what else is attached to the nitrogen. In piperidine the α-carbon signal is shifted by about 20 ppm to about δ 47.7 ppm, while in *N*-methylpiperidine it is at δ 56.7 ppm. Quaternization at nitrogen produces further effects similar to replacement of NH by an *N*-alkyl group, but simple protonation has only a small effect. *N*-Acylpiperidines show two distinct α-carbon atom signals because of restricted rotation about the amide bond. The chemical shift separation is about 6 ppm and the mean shift is close to that of the unsubstituted amine. The nitroso compound is similar, but the shift separation of the two α-carbons is somewhat greater (about 12 ppm). The signals of the β- and γ-carbon atoms of piperidines, *N*-acylpiperidines, and piperidinium salts are all to low frequency of the cyclohexane resonance, by 0–7 ppm.

7 SEVEN-MEMBERED AND LARGER RINGS

The NMR spectra of heterocyclic compounds with seven or more ring members are as diverse as the shape, size, and degree of unsaturation of the compounds. NMR is perhaps the most important physical method for ascertaining the structure, especially the conformational, statics, and dynamics, of large heterocycles. Proton–proton coupling constants provide a wealth of data on the shape of the molecules, while chemical shift data, heteroatom–proton coupling constants, and heteronuclear spectra give information on the electronic structure.

Historically, ^{1}H NMR spectroscopy was vital in determining the structure of the first azepines and has since proved to be invaluable in the conformational analysis of azepines and their benzologues, and in determining ring inversion activation energies of these conformationally mobile ring systems. Chemical shifts for the azepine ring protons, as might be anticipated from their nonplanar, polyene character, lie in the vinyl proton region (δ 4.5–6.8 ppm). Long-range couplings are evident in methyl-substituted 3*H*-azepines. For example, there is allylic coupling (J = 1 Hz) between the 7-Me and H-6, and between the 5-Me and H-4 (J = 1.5 Hz) in 2-ethoxy-3,5,7-trimethyl-3*H*-azepine.

Ring inversion of the azepine ring between the two stable boat forms has been studied extensively by ^{1}H NMR spectra. Work on 2-anilino-3*H*-azepine showed a coalescence temperature of −55 °C for the two conformers, and the barrier was calculated to be 42.7 kJ mol^{-1}. A feature of 1*H*-azepine chemistry that intrigued early researchers was the possibility of azepine-benzeneimine (or azanorcaradiene) valence isomerism akin to the oxepin-benzene oxide system. Variable temperature ^{1}H NMR evidence from simple azepines is overwhelmingly in favor of the azepine structure. For example, from low-temperature ^{1}H NMR studies on 1*H*-azepine it is concluded that the maximum amount of benzeneimine present at equilibrium must be <1%.

The ^{1}H NMR spectrum of oxepane is not particularly informative and consists of two broad bands at δ 1.7 and 3.7 ppm due to coupling of the ring protons and to the electronegativity effect of the oxygen atom. The ^{13}C NMR chemical shifts have been studied over a range of temperatures but showed no evidence of splitting due to individual conformers even at −150 °C, and suggested a low barrier to pseudorotation of about 17 kJ mol^{-1}. Benzannulation of the oxepane ring system leads to an increase in the barrier to ring inversion. Thus, variable temperature NMR spectra on 1,2,4,5-tetrahydro-3-benzoxepin suggested that a chair conformation was preferred with a barrier to ring inversion of about 39.7 kJ mol^{-1}.

NMR spectral studies have been used to investigate the oxepin-benzene oxide equilibrium. The ^{1}H NMR spectrum of oxepin at ambient temperature consisted of three multiplets of equal intensity centered at δ 6.1 (H-α), 5.7 (H-β), and 5.2 (H-γ) ppm due to the fast exchange process. At lower temperatures (−127 °C, CF_3Br/pentane) the rate of isomerization decreased until individual signals for the oxepin tautomer were observed. The α-, β-, and γ-proton signals in oxepin are in typical chemical shift positions for a range of monocyclic substituted oxepins. The oxepin and benzene oxide valence isomers were also distinguishable in the low temperature ^{13}C NMR spectrum (−134 °C, EtCl/$(CD_3)_2CO$). The spontaneous oxepin-benzene oxide isomerization proceeds in accord with the Woodward-Hoffmann rules of orbital symmetry control, and may thus be classified as an allowed thermal disrotatory electrocyclic reaction.

Table 8 ^{13}C NMR Chemical Shifts (δ, ppm) in Saturated Six-Membered Rings

(1)

X	2	3	4
CH_2	27.7	27.7	27.7
S	29.3	28.2	26.9
S-O (ax)	45.1	15.5	24.7
S-O (eq)	52.1	23.3	24.7
SO_2	52.6	25.1	24.3
NH	47.5	27.2	25.5
NMe	56.7	26.3	24.3
$NH_2^+I^-$	45.6	23.2	22.5
$NHMe^+I^-$	55.6	23.9	21.8
$NMe_2^+I^-$	63.5	20.6	21.0
NCOPh	42.8, 48.5	25.5, 26.3	24.4
N-NO	39.0, 50.8	25.5, 27.2	24.7
O	68.0	26.6	23.6

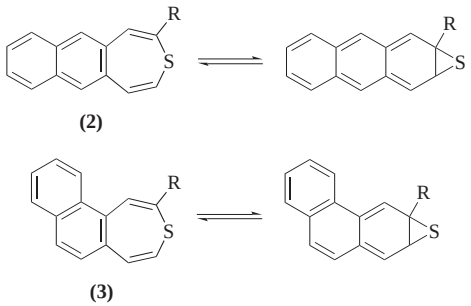

Figure 4 Tautomeric equilibrium in organosulfur heterocycles

The ^{1}H NMR spectrum of thiepane was similar to that of oxepane and showed only two broad signals at δ 2.5–2.8 (4H; H-2, H-7) and 1.5–2.1 (8H; H-3, H-4, H-5, H-6) ppm. NMR spectral analysis of monocyclic thiepins indicates that the thiepin ring system in solution generally prefers a nonplanar (boat) conformation. The boat conformation would be anticipated for a thiepin ring having a minimal degree of conjugation. Clear evidence for bond alternation is obtained from the NMR spectrum of thiepins where the chemical shifts of thiepin ring protons correlate well with those of appropriate substituted ethylenes. The ring inversion process in thiepins has been studied by low temperature NMR spectroscopy and a barrier of about 26.8 kJ mol^{-1} has been determined for 3-methyl-6-isopro-pylthiepin 1,1-dioxide.

NMR spectral evidence for the presence of the valence tautomeric thianorcaradiene (benzene episulfide) form (analogous to the arene oxide tautomer of an oxepin) has yet to be observed. The latter negative evidence, however, does not exclude the possibility of a rapid thiepin-thianorcaradiene equilibration since the number of monocyclic thiepins which have to date been synthesized is very small, and since the examples examined by NMR probably owe their stability to the very low proportion of benzene episulfide tautomer present.

As in the oxepin-arene oxide system, the resonance effect will also influence the position of equilibrium in the analogous organosulfur series (Figure 4). Compound (**2**) is much more stable than thiepin (**3**) since formation of the thianorcaradiene tautomers would be much more difficult in (**2**) where a total loss of aromaticity would be involved.

8 BIBLIOGRAPHY

8.1 Three and Four Rings

NMR spectra of three membered heterocyclic compounds. K. Michi and M. Ueyama, *Kagaku No Ryoiki, Zokan*, 1970, **92**, 1.

8.2 Five Ring

Carbon-13 NMR of pyrazoles. M. Begtrup, G. Boyer, P. Cabildo, C. Cativiela, R. M. Claramunt, J. Elguero, J. I. Garcia, C. Toiron, and P. Vedso, *Magn. Reson. Chem.*, 1993, **31**, 107.

Applications of nuclear magnetic resonance spectroscopy to heterocyclic chemistry. Indole and its derivatives. S. P. Hiremath and R. S. Hosmane, *Adv. Heterocycl. Chem.*, 1973, **15**, 2774.

Electronic structure, physical properties and reactivity of five-membered aromatic heterocycles. Review. I. A. Abronin and G. M. Shidomirov, *Khim. Geterotsikl. Soedin.*, 1977, **1**, 3.

8.3 Six Ring

Application of proton, carbon-13, and nitrogen-15 NMR in the chemistry of 1,4-diazines. O. N. Chupakhin, V. N. Charushin, and A. I. Chernyshev, *Prog. Nucl. Magn. Reson. Spectrosc.*, 1987, **20**, 95.

Stereochemistry of heterocycles. XI. Conformational analysis of 1,3-dioxanes and 1,3-dithianes. A. V. Bogatskii, *Vopr. Stereokhim.*, 1971, **1**, 3.

Carbon-13 NMR results in the field of nitrogen heterocycles; the detection of protonation sites. H. Günther, A. Gronenborn, U. Ewers, and H. Seel, *Jerusalem Symp. Quantum Chem. Biochem.*, 1978, **11**, 193.

8.4 Seven and Higher Rings

Large ring heterocyclic compounds. N. Goto and A. Ogawa, *Senryo To Yakuhin*, 1971, **16**, 264, 304.

8.5 Other Nuclei Heterocycles

Cyclic oxyphosphoranes. Phosphorus-31 chemical shift correlations. R. R. Holmes and T. K. Prakasha, *Phosphorus, Sulfur Silicon Relat. Elem.*, 1993, **80**, 1.

The chemical shift of two-coordinate phosphorus. II. Heterocycles. K. Karaghiosoff and A. Schmidapeter, *Phosphorus Sulfur*, 1988, **36**, 217.

Nuclear magnetic resonance of cyclophosphazenes. S. S. Krishnamurthy and M. Woods, *Annu. Rep. NMR Spectrosc.*, 1987, **19**, 175.

Applications of oxygen-17 NMR spectroscopy to structural problems in rigid, planar organic molecules. A. L. Baumstark and D. W. Boykin, *O-17 NMR Spectroscopy in Organic Chemistry*, ed. D. W. Boykin, CRC Press, Boca Raton, FL, 1991, p. 69.

C-Heterocyclic tin (IV) compounds: a review. V. G. Kumar Das, L. K. Mun, and S. Ng, *Main Group Met. Chem.*, 1988, **11**, 251.

Boron-11 NMR spectroscopy. A. R. Siedle, *Annu. Rep. NMR Spectrosc.*, 1988, **20**, 205.

Boron-11 NMR Spectroscopy. W. G. Henderson and E. F. Mooney, *Annu. Rev. NMR Spectrosc.*, 1969, **2**, 219.

NMR of Heteroatoms. Applications to Organic Chemistry. Y. Takeuchi and T. Harazono, *Yuki Gosei Kagaku Kyokaishi*, 1987, **45**, 583.

Fluorine-19 nuclear magnetic resonance spectroscopy. E. F. Mooney and P. H. Winson, *Annu. Rev. NMR Spectrosc.*, 1968, **1**, 243.

8.6 General Heterocyclic Chemistry

Use of physical methods in heterocyclic chemistry. I. Nuclear magnetic resonance spectroscopy. S. P. Hiremath and R. S. Hosmane, *J. Karnatak Univ. Sci.*, 1969, **14**, 202.

Nuclear magnetic resonance spectra. R. F. M. White and H. Williams, *Phys. Methods Heterocycl. Chem.*, 1971, **4**, 121.

Tautomerism studies using nuclear magnetic resonance spectra. A. I. Koltsov and G. M. Kheifets, *Usp. Khim.*, 1972, **41**, 877.

Wide-line NMR spectrometric studies. NMR of alicyclic and heteroalicyclic compounds. Determination of configuration and conformation with NMR spectroscopy. P. Ayras, *Tayden-nyskoulutuskurssi-Suom. Kem. Seura*, 1973, **18**, 148.

Proton nuclear magnetic resonance spectra of cyclic monoenes: hydrocarbons, ketones, heterocycles and benzo derivatives. H. Günther and G. Jikeli, *Chem. Rev.*, 1977, **77**, 599.

Use of NMR spectroscopy for studying the spatial structure of hydrogenated heterocycles. Y. Y. Samitov, *Khim. Geterotsikl. Soedin.*, 1978, **12**, 1587.

Carbon-13 NMR of nonaromatic heterocyclic compounds. E. L. Eliel and K. M. Pietrusiewicz, *Top. Carbon-13 NMR Spectrosc.*, 1979, **3**, 171.

Carbon-13 and proton NMR conformational studies of nitrogen heterocycles. H. Booth, *Kem.-Kemi*, 1980, **7**, 5.

Use of NMR spectroscopy to study the steric structure of hydrogenated heterocycles. II. Configuration and conformations of heterocycles. Y. Y. Samitov, *Khim. Geterotsikl. Soedin.*, 1980, **11**, 1443.

Nuclear magnetic resonance spectroscopy. M. D. Fenn, *Phys. Methods Heterocycl. Chem.*, ed. R. R. Gupta, Wiley, New York, 1984, 141.

Some applications of carbon-13 NMR spectroscopy in heterocyclic structure assignments. K. Nagarajan, *Proc. Indian Acad. Sci., Chem. Sci.*, 1985, **95**, 9.

T. J. Batterham, *NMR Spectra of Simple Heterocycles*, Krieger, New York, 1981.

9 RELATED ARTICLES

Boron NMR; Carbon-13 Relaxation Measurements: Organic Chemistry Applications; Coupling Constants Determined by ECOSY; Bacterial Chemotaxis Proteins: Fluorine-19 NMR; Nitrogen NMR; Optically Enhanced Magnetic Resonance; Oxygen-17 NMR; Phosphorus-31 NMR.

10 REFERENCES

1. G. C. Levy, R. L. Lichter and G. L. Nelson, *Carbon-13 Nuclear Magnetic Resonance for Organic Chemists*, Wiley-Interscience, New York, 1972.
2. G. C. Levy and R. L. Lichter, *Nitrogen-15 Nuclear Magnetic Resonance Spectroscopy*, Wiley, New York, 1979.

Biographical Sketches

Alan R. Katritzky. *b*. 1928. B.A. and B.Sc., 1952, M.A. and D.Phil., 1954, University of Oxford, UK; Ph.D., 1959, ScD., 1963, University of Cambridge, UK; 4 honorary doctorates from Spain, Poland and UK. Professor and Dean, University of East Anglia, UK, 1962–1980. Presently Kenan Professor and Director of Institute for Heterocyclic Compounds, University of Florida. Approx. 1500 publications. Research specialties: heterocyclic chemistry, synthetic methodology, QSPR.

Ramiah Murugan. *b*. 1955. B.Sc., 1975, M.Sc., 1977, Ph.D., 1987, Chemistry, University of Florida, Gainesville. After two years' postdoctoral work in aqueous organic chemistry (with Prof. A. R. Katritzky) joined Reilly Industries Inc as a Research Chemist and is currently a Research Associate. Approx. 40 publications. Research specialties: syntheses, transformations and spectral properties of heterocycles, specifically Pyridines.

James G. Keay. *b*. 1954. GRSC, 1976, PhD., 1982 (supervisor Alan Katritzky FRS), University of East Anglia, UK. Postdoctoral work at Texas Christian University, Fort Worth (with Manfred Reinecke). Successively Research Chemist, Group Leader, Section Head at Reilly Industries, Inc., Indianapolis. Currently, President, Morflex, Inc., Greensboro, NC, USA.

Hydrogen Bonding

Edwin D. Becker

National Institutes of Health, Bethesda, MD, USA

1	Introduction	1
2	Nature of the Hydrogen Bond	1
3	Effect of Hydrogen Bonding on ^{1}H Chemical Shifts	2
4	Chemical Shifts of Other Nuclei	4
5	Scalar Coupling	4
6	Relaxation Effects	4
7	Isotope Effects Resulting from Hydrogen Bonds	5
8	Magnetic Dipole and Electric Quadrupole Interactions in Solids	6
9	Related Articles	6
10	References	6

1 INTRODUCTION

The phenomenon of hydrogen bonding has been recognized in chemistry for over 70 years and has been studied by a variety of physical methods including NMR, a technique that can provide insight into a number of features of the hydrogen bond. This article reviews some of the salient features of the hydrogen bond and shows the ways in which hydrogen bonding influences the principal NMR parameters, such as chemical shifts, scalar coupling constants, and relaxation times. We provide a number of examples to illustrate the ways in which the study of these and other NMR parameters can be used to clarify some aspects of the phenomenon of hydrogen bonding, to elucidate molecular structures, and to study various processes of physical, chemical, and biological interest.

2 NATURE OF THE HYDROGEN BOND

Molecules are held together by chemical bonds between pairs of constituent atoms and are usually of the order of 200–500 kJ mol^{-1} in energy. At the other extreme, molecules interact with each other via van der Waals forces, which are typically of the order of 5 kJ mol^{-1} for small atoms. Intermediate between these are various types of more specific interactions (e.g. electric dipole–dipole interactions) which tend to produce clusters of molecular aggregates, often termed molecular complexes. In 1920 Latimer and Rodebush explained many of the physical properties of water by advancing the idea of a specific interaction, beyond the normal covalent bonds, involving the hydrogen atoms in water. Subsequent research identified hydrogen bonds in a vast array of molecules and refined the concept of hydrogen bonding.

Probably the most succinct definition of the hydrogen bond is an operational one, given by Pimentel and McClellan[1] in their classic treatise on the subject: *A hydrogen bond exists between a functional group A–H and an atom or a group of atoms B in the same or a different molecule when (a) there is evidence of bond formation (association or chelation), and (b) there is evidence that this new bond linking A–H and B specifically involves the hydrogen atom already bonded to A.* Criterion (b) differentiates hydrogen bonding from other types of association. Usually *B* is an electronegative atom or ion, such as oxygen, nitrogen or fluorine, and most often *A* is also such an electronegative atom. However, this definition of the hydrogen bond recognizes that interactions that might properly be termed hydrogen bonds can exist, for example, with certain C–H groups, such as that in chloroform, and that the hydrogen bond acceptor may be an electron-rich region in a molecule, such as π electrons in a double bond or an aromatic ring.

A hydrogen bond may be *intramolecular*, for example in salicylaldehyde (**1**), or *intermolecular*, as in the interaction between two methanol molecules (**2**) or between methanol and acetone (**3**). By the laws of mass action, the extent of intermolecular hydrogen bonding varies with the concentration of the constituents, whereas intramolecular hydrogen bonding may persist at low concentration in solution or in the gas phase at low pressure. Since the formation of a hydrogen bond is an exothermic reaction, the equilibrium constant for bond formation is expected to increase as the temperature decreases.

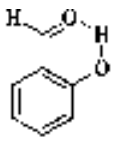

(1)

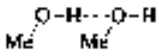

(2)

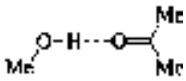

(3)

In addition to the thermodynamics, as expressed in the equilibrium constant, the *kinetics* of hydrogen bond making and breaking is a factor that is extremely important in NMR studies. Studies by ultrasonic absorption and dielectric relaxation have shown that many intermolecular hydrogen bonds in the liquid state are made and broken [equation (1)]

$$(A-H)\cdots B + (A-H)^{\#}\cdots B^{\#} \rightleftharpoons (A-H)\cdots B^{\#} + (A-H)^{\#}\cdots B \quad (1)$$

on a timescale (e.g. $\sim 10^{-5}$ s) that is fast relative to the difference in NMR frequencies between bonded and non-bonded forms. Thus, from the general theory of chemical exchange (see ***Chemical Exchange Effects on Spectra***), we would expect in these cases to observe only an average NMR property (e.g. chemical shift or relaxation rate) for two or more molecular species in hydrogen bond equilibrium. Moreover, in solvents with exchangeable hydrogen atoms (such as water or alcohols), there may be an actual exchange of protons between different molecular species [equation (2)].

$$A-H + A^{\#}-H^{\#} \rightleftharpoons A-H^{\#} + A^{\#}-H \quad (2)$$

Note that the two processes shown in equations (1) and (2) are different, the first involving making and breaking of only hydrogen bonds, the latter resulting from breaking of covalent chemical bonds (and usually hydrogen bonds as well).

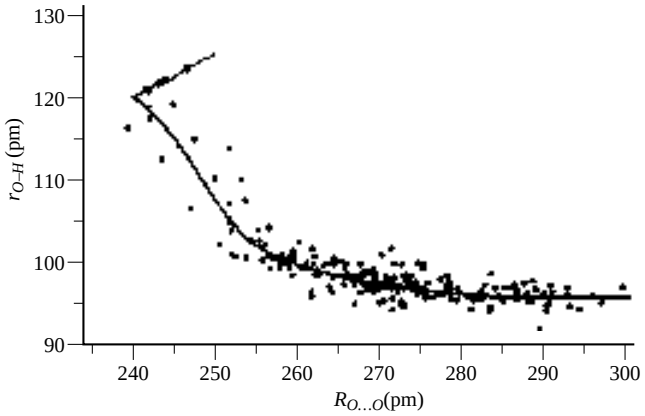

Figure 1 Variation of $R_{O\cdots O}$ and r_{O-H} for hydrogen bonds. (Reproduced by permission of Academic Press from Hibbert and Emsley[2])

The impact of these processes on NMR spectra is profound, as we shall see. At the opposite extreme of exchange rates are solids and some stable structures in solution, such as biopolymers, where hydrogen bonds are quite long lived, and the NMR results reflect a slow exchange limit. We shall discuss examples.

Several techniques, including X ray and neutron diffraction, as well as solid state NMR, provide detailed information on the geometry of hydrogen bonds. In general, an $A{-}H\cdots B$ hydrogen bond is usually close to linear in systems where bond angle constraints are not violated. For some intramolecular hydrogen bonds [e.g. (**1**)], on the other hand, distinctly nonlinear hydrogen bonds are formed in accord with normal chemical bond angles. The $A\cdots B$ distance R_{AB} is often taken to be an approximate measure of hydrogen bond strength, with shorter distances corresponding to stronger hydrogen bonds. (As we point out in later sections, it is really the $H\cdots B$ distance that should be considered, and a departure from linearity in the hydrogen bond weakens the correlation between bond strength and R_{AB}.) Figure 1 shows that the $A{-}H$ chemical bond distance r_{AH} is affected little for very weak hydrogen bonds but is invariably elongated when a hydrogen bond of moderate strength is formed.[2] The distance r_{AH} is still significantly less than r_{HB} except for strong hydrogen bonds ($R_{AB} < \sim 245$ pm), where equal $A{-}H$ and $H\cdots B$ distances correspond to a symmetric hydrogen bond, found in only a few instances, such as $[F\cdots H\cdots F]^-$.

Theoretical explanations for the energetics of hydrogen bonds have been postulated for 40 years. Although they differ in detail, there seems to be general agreement that electrostatic attraction between $A{-}H$ and B accounts for almost all the energy of weak hydrogen bonds ($R_{AB} > \sim 260$ pm), but as this distance decreases, the repulsive force from electron energy exchange largely cancels the electrostatic attraction. Other forces, such as (i) polarization of B to create an induced dipole, (ii) dispersion forces (induced $A{-}H$ and B dipoles), and (iii) electron delocalization, must then contribute. Many current theoretical approaches use ab initio molecular orbital treatments of the entire system without partitioning the various contributions. One question which can be addressed by NMR is the extent to which electron delocalization (i.e. incipient covalent bond formation) actually occurs. We shall come back to this point.

3 EFFECT OF HYDROGEN BONDING ON ^{1}H CHEMICAL SHIFTS

The first reported effect of hydrogen bonding on a ^{1}H chemical shift came soon after the discovery of the ^{1}H chemical shift itself in ethanol. Packard and Arnold[3] observed that the OH resonance, but not the CH_2 and CH_3 resonances, displayed a marked temperature dependence, an effect soon explained by Liddel and Ramsey[4] as resulting from hydrogen bonding. In fact, as was shown later[5] (Figure 2), the OH resonance of monomeric ethanol is at lower frequency (i.e. more shielded) than the CH_3 resonance, whereas in liquid ethanol at room temperature the OH resonance is about 5 ppm less shielded than that of the CH_3 protons. A vast amount of subsequent work has verified that hydrogen bonding to an electronegative atom always results in shifts to higher frequency for the $A{-}^1$H resonance, with a magnitude as large as $\sim$10–15 ppm. For some strong intramolecular hydrogen bonds in the enol form of β-diketones the observed chemical shifts are in the range of 20 ppm from the tetramethylsilane (TMS) reference. Likewise, in the solid state, carboxylic acids often have ^{1}H chemical shifts 12–14 ppm from TMS, but acid salts such as $KHCH_2(CO_2)_2$ show a chemical shift of about 19 ppm from the strong, symmetrical hydrogen bond.[6]

There is thought to be a qualitative correlation between the magnitude of the hydrogen bond shift and the strength of the hydrogen bond, but few hard thermodynamic data are available from solution studies. However, in the solid state the ^{1}H chemical shift correlates with R_{AB}, hence with the presumed strength of the hydrogen bond. For example, in maleic acid the ^{1}H signal from an intramolecularly bonded hydrogen is at 15.9 ppm, with $R_{O\cdots O}$ = 250.2 pm, while the hydrogen in an intermolecular bond of 264.3 pm length has a chemical shift of 13.2 ppm.[6,7] Moreover, an excellent linear correlation has been reported between the trace of the anisotropic ^{1}H chemical

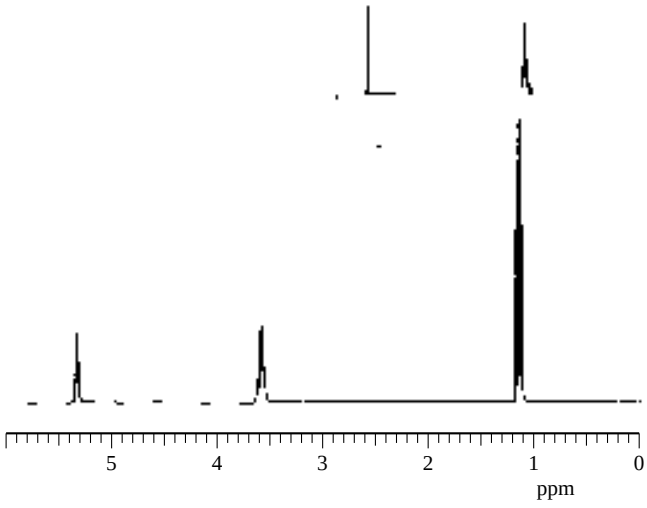

Figure 2 Proton NMR spectrum of ethanol at 300 MHz (room temperature). The full spectrum is for undiluted ethanol, while the insets show the OH resonance of ethanol in $CDCl_3$ at 1.0 and 0.001 M, the latter representing almost entirely the ethanol monomer. Note that the OH resonance is a single line in the neat liquid and the 1.0 M solution because rapid proton exchange prevents observation of scalar coupling to the methylene protons, whereas a triplet structure is observed in the 0.001 M solution

shift in about 20 crystalline solids and the $H\cdots O$ distance as measured by X-ray and neutron diffraction.[8] A slope of about -0.2 ppm per pm is found for r_{HO} from 130 to 190 pm.

The high frequency shift on hydrogen bonding is an important factor in interpreting ^{1}H NMR spectra, since OH and NH chemical shifts are often found to be solvent-dependent. In addition, the chemical shift of an OH or NH resonance can be of diagnostic value in structural elucidations when intramolecular hydrogen bonds are present. The shift to high frequency results from a decrease in diamagnetic shielding around the hydrogen nucleus, as demonstrated by molecular orbital calculations that show reduced electron density near the hydrogen. This redistribution of electrons in the $A\cdots H$ bond is probably brought about by repulsion from the nonbonding electrons in B.

A hydrogen bond to π electrons in aromatic rings leads to exactly the opposite observed shift, namely to low frequency. The reason is clear: the hydrogen atom bonds to the π-electron-rich face of the aromatic ring, where it is subject to a ring current effect that far outweighs any deshielding from the formation of the hydrogen bond itself. In this geometrical arrangement, then, the proton is subject to a net additional diamagnetic shielding, hence shifts to lower frequency.

NMR has been used to determine equilibrium constants and other thermodynamic properties for hydrogen-bonded systems. In most liquid phase systems there is rapid exchange between hydrogen-bonded and nonbonded molecular species, so that a single signal from the $A{-}H$ appears, as in the ethanol example. Then

$$\delta_{\text{obs}} = p_1\delta_1 + p_2\delta_2 + \cdots \tag{3}$$

where the p_i represent the fraction of $A{-}H$ in species i, with chemical shift δ_i. If there are thought to be only one or two hydrogen-bonded species, a number of data treatments can be used to permit the equilibrium constant(s) to be estimated from variation of δ_{obs} with concentration.

Two significant shortcomings to this determination by NMR are (i) the difficulty in obtaining an accurate measure of the chemical shift of the monomer and (ii) the problem of dealing with a multiparameter fit if several associated species are present. Reviews by Tucker and Lippert[9] and Limbach[10] give good summaries of the information that can be obtained and the limitations of these NMR methods. During the last 20 years there have been relatively few applications of NMR to determination of equilibria for hydrogen-bonded systems even though NMR techniques are now better able to provide data of adequate precision. Often it is preferable to utilize the NMR data only qualitatively and to derive equilibrium constants from other types of spectral data, such as infrared spectroscopy, where the time frame for exchange is such that bands for separate species can be identified.

In the situation described in equation (2), the hydrogen atom ionizes and exchanges rapidly with other species, such as water in an aqueous solution. When this condition obtains, quantitative evaluation of hydrogen bond equilibria generally becomes impossible.

If stable complexes are formed by hydrogen bonding (sometimes augmented by other factors, such as ionic or dispersion forces), the exchange rate may be sufficiently slow that separate signals can be observed for hydrogen-bonded and nonbonded species. A clear example is shown in Figure 3, where

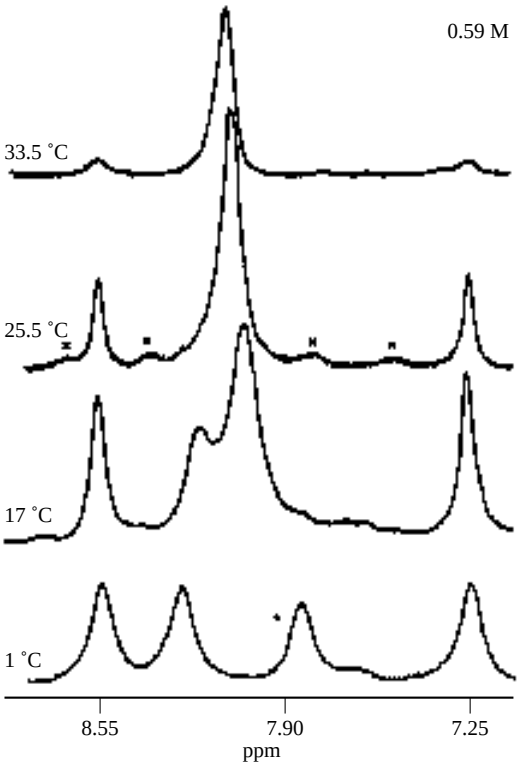

Figure 3 Temperature dependence of the H-8 resonance (220 MHz) of guanosine 5′-phosphate in D_2O at a concentration of 0.59 M.[11] The weak peaks marked × in the spectrum at 25.5 °C are artifacts

a complex of guanosine 5′-phosphate is believed to consist of two tetramers stacked above each other with a sodium ion in the center (Figure 4).[11] Here the association is observed not by the hydrogen-bonded protons themselves (which have been exchanged with deuterium in the solvent in this example) but by other protons on the guanosine rings. The temperature-dependent equilibrium can be followed from the relative intensities of the monomer and structurally nonequivalent protons in the hydrogen-bonded complex.

In many biopolymers and oligomers the hydrogen-bonded protons themselves can be observed. For example, in tRNAs hydrogen bonds between the purine and pyrimidine bases are quite strong, and exchange with protons in the aqueous

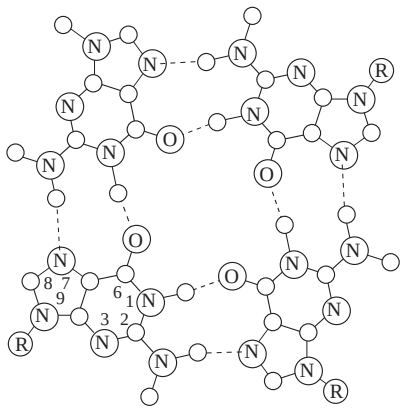

Figure 4 Guanosine 5′-phosphate complex

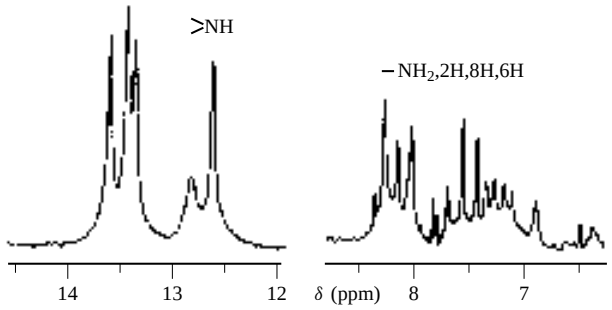

Figure 5 Proton NMR spectrum of a self-complementary decadeoxynucleotide, d(GCATTAATGC)$_2$, at 500 MHz in H_2O at 0.02 M[12]

solvent is suppressed. Figure 5 provides an illustration of a synthetic oligonucleotide in which the equilibrium so favors the hydrogen bonded form that no lines due to 'free' NHs are observed, while the bonded hydrogens show resonances at very high frequencies (~12–14 ppm). Likewise in native proteins, amide hydrogens are found in the 8–10 ppm range because of strong hydrogen bonding.[12] These ^{1}H resonances can usually be observed in an H_2O solvent because the hydrogen bond slows down proton exchange rates. NMR has become an indispensable technique for studying rates of H–D exchange when the protein is deuterated in order to provide information on secondary and tertiary protein structure and to investigate the mechanism of protein folding.[12]

4 CHEMICAL SHIFTS OF OTHER NUCLEI

In the $A–H\cdots B$ system the chemical shifts of both A and B are found to change on hydrogen bond formation. The magnitude of shifts on hydrogen bonding for an ^{17}O in a carbonyl group that serves as a hydrogen bond acceptor (B) can be as large as 50–60 ppm to lower frequency, while an oxygen in a single bond in B (such as an ether) displays a low frequency shift of only a few parts per million.[13] Oxygen-17 in the donor $A–H$, such as an alcohol or phenol, shifts ~5–20 ppm to higher frequency. Nitrogen-15 has been studied less extensively but shows somewhat similar behavior.[9,14] In proteins, ab initio computations of ^{15}N chemical shifts indicate that typical hydrogen bonding interactions ($N–H\cdots O$) cause deshielding of the ^{15}N of about 13 ppm.[15] Even ^{13}C in C=O groups is affected by hydrogen bonding, with shifts to high frequency of 2–40 ppm, depending partially on the strength of the hydrogen bond.[16] However, other factors, such as nearby electric charges, can be equally significant in determining the chemical shift.[17]

While these hydrogen bond shifts are quite significant, they nevertheless represent only a relatively small fraction of the total chemical shift range for these nuclei, in contrast to the situation for ^{1}H chemical shifts, where the hydrogen bond effect may be the dominant factor in determining a chemical shift.

5 SCALAR COUPLING

Because one-bond $X–H$ coupling constants are known to depend on s character, and hence on hybridization of electrons around X, it is expected that such couplings might be affected by hydrogen bonding with its accompanying redistribution of electron density in the $A–H$ bond. Only a few studies have been made of $^1J(X,\mathrm{H})$ for X = ^{13}C and ^{15}N, where generally the coupling is found to increase slightly (~5%) on hydrogen bonding.[14,18] Small changes in two- or three-bond couplings on hydrogen bonding have also been reported, but these primarily reflect conformational variations.

The question has been raised as to whether scalar coupling can be transmitted *through* a hydrogen bond. Such an effect would indicate that there is electron correlation, and hence covalent character, in the hydrogen bond. It is clear that such coupling could be observed only in a system such as an intramolecular hydrogen bond, where random exchange of group B does not occur through breaking of the hydrogen bond. Early attempts in our laboratory to demonstrate such coupling in intramolecular O–H$\cdots$^{15}N systems provided ambiguous results because of tautomerism between O–H$\cdots$^{15}N and O$\cdots$H–^{15}N forms. However, recently several ^{113}Cd–^{1}H and ^{199}Hg–^{1}H scalar couplings, of 0.3–3.9 Hz, have been observed in metal-substituted rubredoxin (a small protein), each of which seems to be mediated via a hydrogen bond between a backbone amide proton and sulfur in a cysteine residue that is coordinated to the metal ion.[19,20] Such three-bond couplings through the hydrogen bond provide strong evidence for covalent character in that bond.

The bifluoride ion HF_2^- has been of particular interest in theoretical investigations of hydrogen bonding, since it has a *symmetric* hydrogen bond, i.e. one in which the hydrogen is located halfway between the two electronegative centers. The NMR spectrum shows that the hydrogen is, in fact, equally coupled to the two ^{19}F nuclei, with $^1J(\mathrm{F,H})$ = 120.5 Hz, as compared with 476 Hz for HF. In a sense, this coupling goes 'through' the hydrogen bond, but it is a very unusual hydrogen bond.

6 RELAXATION EFFECTS

The theory of spin–lattice relaxation shows that the relaxation rate of a nuclear magnetic moment depends on the motions of the molecular system in which the nucleus resides (see ***Relaxation: An Introduction***). For spin-$\frac{1}{2}$ nuclei the predominant relaxation mechanism usually depends on magnetic dipole–dipole interactions, mediated by random molecular motions described in terms of one or more correlation times, τ_c. Since intermolecular hydrogen bonding causes the formation of a complex larger than the nonbonded species, which both rotates and translates more slowly, both intramolecular and intermolecular correlation times are expected to change. Thus, the study of T_1 as a function of concentration, temperature, or change of conditions such as solvent can provide information on the extent of hydrogen bonding.

If hydrogen bonds are made and broken rapidly, relaxation rates are averaged, in the same manner as chemical shifts, and interpretation of the data often suffers from similar problems of multiparameter fits. In addition, the presence of more than one relaxation mechanism or correlation time further complicates data analysis. Only a few studies of complex systems have been carried out in which these parameters have

been controlled, for example by studying ^{13}C relaxation in molecules where dipolar interaction with protons dominates relaxation. Usually a full interpretation requires the use of ancillary data, such as infrared spectra or vapor pressure determinations.[21]

For systems in slow exchange, where only one hydrogen bonded species is present, relaxation measurements can often be analyzed to provide information on molecular size, structure, or conformation. For example, in 1-hydroxyfluorenone (**4**) the location of the hydrogen atom in an intramolecular hydrogen bond has been estimated from its effect on the relaxation of three nearby ^{13}C nuclei.[22] Likewise, ^{13}C relaxation has been used to estimate the size and shape of molecular complexes such as that in Figure 4.[23]

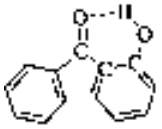

(4)

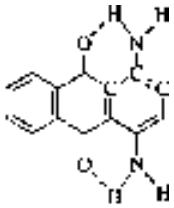

(5)

Extensive use has been made of ^{1}H NMR relaxation to explore hydrogen bonding and hydrogen exchange processes, especially in water. Because of the proximity of protons in adjacent molecules, intermolecular dipolar relaxation must be considered equally with intramolecular relaxation. Interpretation of the data is a rather complex process, discussed in detail by Hertz and Zeidler.[24]

7 ISOTOPE EFFECTS RESULTING FROM HYDROGEN BONDS

Substitution of one isotope for another is known to affect the chemical shift of the substituted nucleus (primary isotope effect) and of nearby magnetic nuclei (secondary isotope effects). Most studies of the isotope effect (see ***Isotope Effects on Chemical Shifts and Coupling Constants***) focus on the secondary isotope effect; indeed, in many instances the primary isotope effect is negligible. However, substitution of deuterium (or tritium) for hydrogen in a strong hydrogen bond causes a significant primary isotope effect, which provides information on the potential function for hydrogen bonding.

It is possible to define three types of hydrogen bond according to their strength—weak, strong, and very strong—and associated hydrogen bond length R_{AB}. As illustrated in Figure 6, the potential function is expected to vary as the two potential wells for the $A–H$ and $H\cdots B$ vibrational motions approach each other. For a weak hydrogen bond the occupied, zero-point level for the hydrogen stretching vibration in $A–H$ is well below the potential barrier, and that for deuterium in the isotopomer is, of course, still lower because of the mass effect. Thus, both H and D are essentially confined to the well as in an ordinary chemical bond, the existence of the hydrogen bond causes only a small perturbation, and the average r_{AH} is almost the same as r_{AD}, thereby leading to only a small primary isotope effect. However, as the hydrogen bond strengthens, the barrier eventually drops below the zero-point

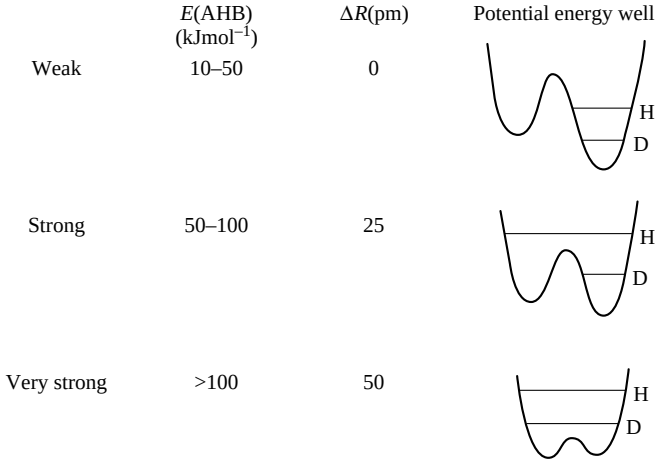

Figure 6 Potential energy wells for hydrogen bonds, illustrating the zero-point vibrational levels for hydrogen and deuterium and indicating typical shortenening of R_{AB} on formation of the hydrogen bond. (Reproduced by permission of Academic Press from Hibbert and Emsley[2])

level, first just for hydrogen, then for both hydrogen and deuterium. The average r_{AH} and r_{AD} may then differ sufficiently to cause a measurable primary isotope effect. The limiting potential function is one with a single minimum, believed to be applicable in HF_2^- and several other very short hydrogen bonds, in which the isotope effect is again small. These expectations are in accord with experimental observations of proton chemical shifts and primary deuterium isotope effects in a range of hydrogen-bonded systems.[2] The isotope effect becomes large for moderate strength hydrogen bonds but is small for FHF^-. In fact, negative values have been found for the isotope effects on both ^{2}H and ^{3}H substitution in the strong hydrogen bonds of the hydrogen maleate and hydrogen phthalate anions.[25]

Secondary isotope effects through two or more bonds are also useful in studying hydrogen bonds in a number of systems. One particularly interesting result occurs in (**5**), where the amino group rotation is slow enough to distinguish between the intramolecularly bonded and nonbonded hydrogens.[26] Deuterium isotope shifts ($^{n}\Delta$) for the three ^{13}C nuclei that are two or three bonds removed, as illustrated in (**5**), are approximately twice as large for substitution of the hydrogen-bonded proton as for substitution of the nonbonded hydrogen: $^{2}\Delta$ = 356 versus 145 ppb; $^{3}\Delta$ = 148 versus 74 ppb; $^{3}\Delta'$ = 136 versus 64 ppb.

Useful information on hydrogen bonding can also be obtained from measurement of the equilibrium distribution of deuterium relative to hydrogen at the hydrogen bond site, as compared with the corresponding distribution in the solvent or some other standard, a quantity expressed as the isotope fractionation factor ϕ. A growing body of experimental evidence suggests that there is an inverse correlation between ϕ and the strength of the hydrogen bond. Although ϕ does not involve NMR parameters per se, NMR usually provides the best method for obtaining the necessary data. For rapidly exchanging hydrogen, the variation in chemical shift on isotopic substitution can be used to estimate ϕ,[2] and for slow exchange the integrals of the separate signals usually give a precise measure of ϕ.[2] Proteins provide a particularly

interesting example, where ϕ has been found to vary over a very wide range (0.3–1.2) for different amino acid sites in staphylococcal nuclease.[27]

8 MAGNETIC DIPOLE AND ELECTRIC QUADRUPOLE INTERACTIONS IN SOLIDS

The estimation of interatomic distances in solids by analysis of magnetic dipolar interactions has been applied to the study of hydrogen bond distances and geometry. Early NMR results on the bifluoride ion and later on other strong hydrogen bonds indicated that the proton is centrosymmetric, but generally the NMR data could not exclude rapid exchange between a double minimum potential with a small barrier. Solid state NMR has also been used to investigate the geometry of water of hydration in various crystals in order to study the effect of hydrogen bonding.[28]

NMR has been used to investigate ferroelectric crystals, where, in some instances, the ferroelectric activity is believed to be related to changes in hydrogen position in a hydrogen bond: $O{-}H{\cdots}O \rightleftharpoons O{\cdots}H{-}O$. Deuteron NMR is particularly useful, since the nuclear quadrupole coupling constant (see ***Deuterium NMR in Solids***) provides a sensitive measure of the asymmetry of the surrounding electric field. Above the ferroelectric transition temperature, where the deuterium is moving rapidly between two potential wells, e^2Qq decreases abruptly.[28]

The deuterium quadrupole coupling constant, as determined from ^{2}H NMR or from pure nuclear quadrupole resonance, has been shown to vary significantly with hydrogen bond length. For example, excellent linear correlations have been found between e^2Qq for ^{2}H and $1/R^3$, where R is the $D{\cdots}O$ distance in bonds involving $O{-}D{\cdots}O$ or $N^+{-}D{\cdots}O$.[29] The correlations cover the range of weak hydrogen bonds, $R \approx 165{-}215$ pm, or R_{AB} (as defined previously) $\sim 260{-}310$ pm, with values of e^2Qq varying from 140 to 240 kHz.

9 RELATED ARTICLES

Biological Macromolecules: Structure Determination in Solution; Biological Macromolecules; Carbon-13 Relaxation Measurements: Organic Chemistry Applications; High-Pressure NMR; Nucleic Acids: Base Stacking and Base Pairing Interactions; Peptide and Protein Secondary Structural Elements; Protein Hydration; Synthetic Peptides.

10 REFERENCES

1. G. C. Pimentel and A. L. McClellan, *The Hydrogen Bond*, Freeman, San Francisco, 1960.
2. F. Hibbert and J. Emsley, *Adv. Phys. Org. Chem.*, 1990, **26**, 255.
3. M. E. Packard and J. T. Arnold, *Phys. Rev.*, 1951, **83**, 210.
4. U. Liddel and N. F. Ramsey, *J. Chem. Phys.*, 1951, **19**, 1608.
5. E. D. Becker, U. Liddel, and J. N. Shoolery, *J. Mol. Spectrosc.*, 1958, **2**, 1.
6. G. Scheler, U. Haubenreisser, and H. Rosenberger, *J. Magn. Reson.*, 1981, **44**, 134.
7. M. C. Etter, S. M. Reutzel, and G. M. Vojta, *J. Mol. Struct.*, 1990, **237**, 165.
8. G. A. Jeffrey and Y. Yeon, *Acta Crystallogr.*, 1986, **B42**, 410.
9. E. E. Tucker and E. Lippert, In: *The Hydrogen Bond*, ed P. Schuster, G. Zundel, and C. Sandorfy, North Holland, Amsterdam: 1976, p. 791.
10. H.-H. Limbach, *Stud. Phys. Theor. Chem.*, 1983, **26**, 410.
11. T. J. Pinnavaia, H. T. Miles, and E. D. Becker, *J. Am. Chem. Soc.*, 1975, **97**, 7198.
12. K. Wüthrich, *NMR of Proteins and Nucleic Acids*, Wiley, New York, 1986.
13. D. W. Boykin, *^{17}O NMR Spectroscopy in Organic Chemistry*, CRC Press, Boca Raton, 1990.
14. L. Paolillo and E. D. Becker, *J. Magn. Reson.*, 1970, **2**, 168.
15. A. C. de Dios, J. G. Pearson, and E. Oldfield, *Science*, 1993, **260**, 1491.
16. M. C. Etter and R. C. Hoye, *Trans. Am. Crystallogr. Assoc.*, 1986, **22**, 31.
17. S. Ando, I. Ando, A. Shoji, and T. Ozaki, *J. Am. Chem. Soc.*, 1988, **110**, 3380.
18. D. F. Evans, *J. Chem. Soc.*, 1963, 5575.
19. P. R. Blake, J.-B. Park, M. W. W. Adams, and M. F. Summers, *J. Am. Chem. Soc.*, 1992, **114**, 4931.
20. P. R. Blake, B. Lee, M. F. Summers, M. W. W. Adams, J.-B. Park, Z. H. Zhou, and A. Bax, *J. Biomol. NMR*, 1992, **2**, 527.
21. L. M. Sweeting and E. D. Becker, *J. Phys. Chem.*, 1984, **88**, 6075.
22. L. M. Jackman and J. C. Trewella, *J. Am. Chem. Soc.*, 1976, **98**, 5712.
23. C. L. Fisk, E. D. Becker, H. T. Miles, and T. J. Pinnavaia, *J. Am. Chem. Soc.*, 1982, **104**, 3307.
24. H. G. Hertz and M. D. Zeidler, In, *The Hydrogen Bond*, ed P. Schuster, G. Zundel, and C. Sandorfy, North Holland, Amsterdam, 1976.
25. L. J. Altman, D. Laungani, G. Gunnarsson, H. Wennerstrom, and S. Forsen, *J. Am. Chem. Soc.*, 1978, **100**, 8264.
26. P. E. Hansen, A. Kolonicny, and A. Lycka, *Magn. Reson. Chem.*, 1992, **30**, 786.
27. S. N. Loh and J. L. Markley, *Biochemistry*, 1994, **33**, 1029; J. L. Markley, W. M. Westler, A. S. Edison, and F. Weinhold, *International Society of Magnetic Resonance, Sydney, Australia, July 1995*, Abstract L-12.4.
28. W. C. Hamilton and J. A. Ibers, *Hydrogen Bonding in Solids*, Benjamin, New York, 1968.
29. M. J. Hunt and A. L. Mackay, *J. Magn. Reson.*, 1974, **15**, 402.

Biographical Sketch

Edwin D. Becker. *b* 1930. B.S., 1952, University of Rochester, Ph.D., 1955, Chemistry, University of California, Berkeley, USA. National Institutes of Health, 1955–present; Laboratory Chief (1972–80, 1988–); Associate Director for Research Services (1980–88). Concurrent position on Faculty, Georgetown University, 1959–present. Books on NMR. Research interests and publications: hydrogen bonding, molecular structure elucidation, technique development in NMR and other areas of molecular spectroscopy.

Inclusion Compounds

John A. Ripmeester, Christopher I. Ratcliffe and Eric B. Brouwer

National Research Council of Canada, Ottawa, Ontario, Canada

1	Introduction	1
2	Clathrate Hydrates	3
3	Metal Cyanide Inclusion Compounds	7
4	Calixarene Inclusion Compounds	11
5	Related Articles in this Volume	12
6	Related Articles in Volumes 1–8	12
7	References	12

1 INTRODUCTION

1.1 Definitions

Inclusion compounds belong to the class of guest-host materials where the host material provides a structural framework that contains void space that is occupied by a guest species. Such void space in inclusion compounds usually is classified as either a cage or a channel, although often the situation is more complex. In the case of well-defined cages, the materials are known as clathrates. In the case of layered materials, the void space is interlamellar and the materials are known as intercalation compounds. Some host frameworks are permanent, being composed of covalently bonded structural units such as the aluminosilicates known as zeolites and clays, but these will not be considered here. Instead, we will consider frameworks that can be classified as supramolecular, where the lattice is composed of building blocks that are assembled via van der Waals packing, hydrogen bonding or coordinate-covalent interactions. Examples of the first kind include inclusion compounds with cages or channels such as the cyclophosphazanes (Figure 1) and dibenzoylmethanates (Figure 2). The clathrate hydrates (Figure 3) and the β-quinols (Figure 4) are examples of hydrogen-bonded inclusion compounds, as are the channel inclusions of urea and thiourea. The coordination networks based on metal cyanides form an extremely versatile family of inclusion compounds with either cages or channels (see below). In many inclusion compounds more than a single type of bonding is present. For instance, in inclusions of Dianin's compound both van der Waals and hydrogen bonding are present, and the Werner clathrates pack according to van derWaals interactions, but since the building blocks bear a charge they require the presence of counterions (Figure 5). For a detailed presentation on structural and chemical aspects of inclusion compounds the series 'Comprehensive Supramolecular Chemistry'[1] (especially Volumes 6 and 7) will prove to be a valuable resource.

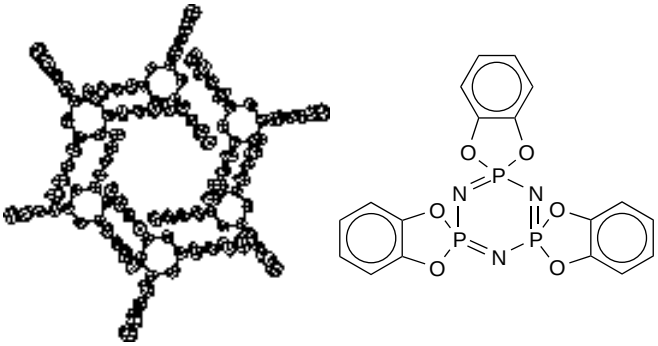

Figure 1 The host lattice of the channel inclusion compound of tris(*o*-phenylenedioxy)cyclotriphosphazene as formed by inclusions with benzene and xylene. A single host molecule is shown on the right. (H. R. Alcock, R. W. Allen, E. C. Bissell, L. A. Smeltz, and M. Teeter, *J. Am. Chem. Soc.*, 1976, **98**, 5120)

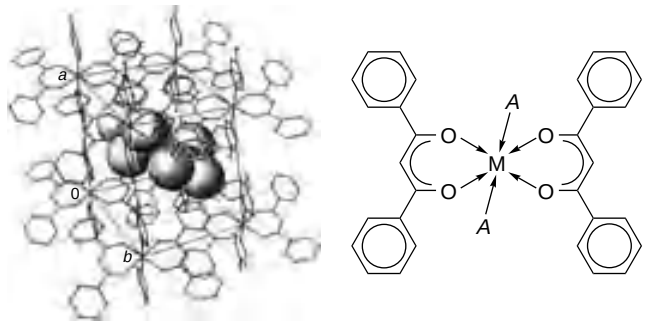

Figure 2 Cage inclusion compound of bis(4-vinylpyridine)nickel dibenzoylmethanate with a pair of carbon tetrachloride molecules in the cavity. On the right is the parent metal dibenzoylmethanate host molecule where A stands for the axially coordinating vinylpyridine; both the axial ligand (substituted pyridines) and the metal species can be varied to give a large variety of host species. (D. V. Soldatov and J. A. Ripmeester, *Chem. Eur. J.*, 2001, **7**, 2979)

1.2 NMR Spectroscopy and Inclusion Compounds: A Historical Perspective

The class of inclusion compounds known as clathrates had been under study for about 150 years before the structural basis for these materials became apparent. H. M. Powell[2] coined the term clathrate when he recognized the structure of a β-quinol inclusion compound as being a guest species encaged by a host without any specific chemical interactions. Structural studies of this nature became possible because of the development of single crystal X-ray diffraction to the stage where it could be used to decipher in atomic detail the molecular entrapment of guest species within a host lattice.

It is interesting to note that the experimental basis for nuclear magnetic resonance spectroscopy is just slightly older than the official birth of clathrate science, as the first successful experiments were reported in 1946.[3] In the middle 1960s, the group of C. A. MacDowell at the University of British Columbia was one of the first to apply the new methodology to inclusion compounds in a sustained manner. Urea channel inclusion compounds, clathrate hydrates and amine hydrates all were studied by moment analysis and/or relaxation methods. At the National Research Council of Canada, the Davidson group first used NMR spectroscopy in the middle sixties to

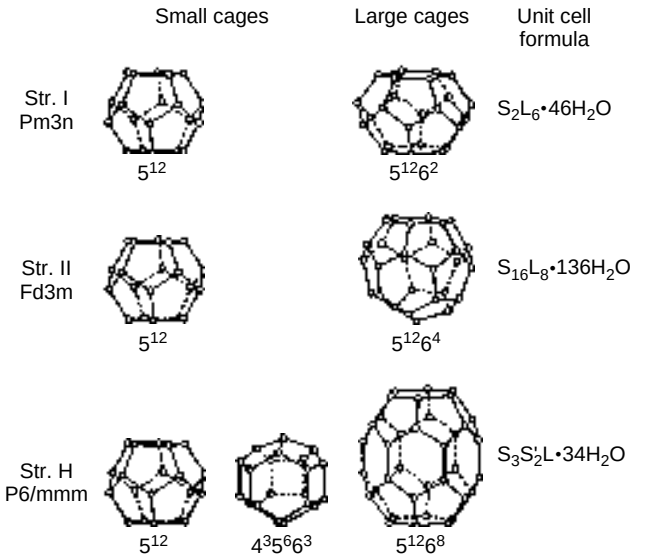

Figure 3 The polyhedral cages in the clathrate hydrate inclusions of structure I, structure II and structure H hydrates. The vertices represent the positions of the water molecule oxygens that are connected by hydrogen bonds. Also given are the space groups and the composition of the unit cells. S or S'stands for the small cages, L for large cage in each structure. The x^y descriptor denotes that a polyhedron consists of y polygons with x sides (Ref.[6])

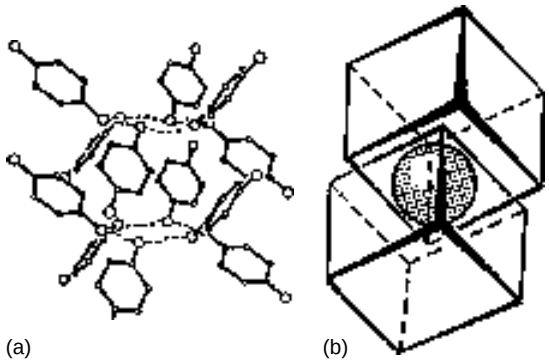

Figure 4 β-Quinol clathrate framework, showing the rings formed by 6 hydrogen bonded hydroquinone (1,4 benzenediol) host molecules (a), and a schematic representation of the mode of guest entrapment by the two independent but interpenetrating hydrogen bonded networks (b) of host molecules (T. C. W. Mak and B. R. F. Bracke, in 'Comprehensive Supramolecular Chemistry', eds J. L. Atwood, J. E. D. Davies, D. D. MacNicol, F. Vogtle, and J. M. Lehn, Elsevier: Oxford, 1996, Vol. 6, p. 23)

complement dielectric studies of guest and host dynamics of clathrate hydrates. The work by these pioneering groups has led to nearly 40 years during which NMR spectroscopy has become a tool of ever-increasing versatility in the unraveling of the complex interactions between guest and host in inclusion compounds. Over the years, the applications of NMR spectroscopy to the study of inclusion compounds have been reviewed a number of times.[4–7] Below, we will address several classes of inclusion compounds in more detail. Many of the early approaches to solid state NMR spectroscopy are conveniently reviewed in the book by Fyfe.[8]

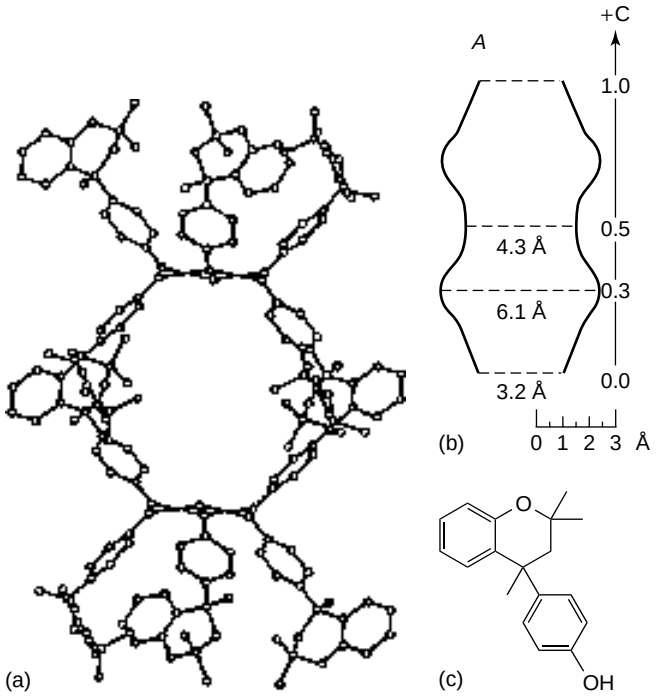

Figure 5 The empty host network of Dianin's compound clathrate (a). The top and bottom of the cage are formed by rings of 6 hydrogen-bonded host molecules, giving a double-sided 'egg-cup' structure. Stacks of 'egg-cups' give the double-sided cage held together by van der Waals interactions; (b) van derWaals' cross section through the double-sided cage; (c) the host molecule (From 'Inclusion Compounds', eds J. L. Atwood, J. E. D. Davies, and D. D. MacNicol, Academic Press, 1984, Vol. 2, p. 2, 16)

1.3 Problems Encountered in Inclusion Science

Two streams of thought contribute to modern concepts of inclusion chemistry. The first is classical and dates mainly from the statistical mechanical descriptions of inclusion compounds by van der Waals and Platteeuw[9] (see also Ref.[10]). The second derives from the development of supramolecular chemistry (chemistry beyond the molecule) as promoted by Lehn, Cram et al.,[1] where weak but specific and directional interactions play a more important role.

One of the main features of many inclusion compounds is that they are non-stoichiometric with a composition that depends on synthetic conditions. In such cases, the guest-host interactions are non-specific, and the empty host-lattice is unstable (it may be thermodynamically unstable, but persist because of slow kinetics). Such inclusion compounds exist as distinct phases only in the solid state, and arise when the components are brought together under the correct conditions of temperature (T) and pressure (P). They are described by the elegant 'solid-solution' formalism for clathrates.[9,10]

A second class of materials arises when a guest molecule binds to a receptor molecule in solution, and the solution complex crystallizes under suitable conditions to give a solid inclusion compound. Materials that belong to this class include the cyclodextrins (See Vol. 2 in Ref.[1]), native as well as modified (Figure 6), and the numerous versions of the versatile calixarenes.[11] Whether materials should be described as non-stoichiometric inclusions held together by non-specific interactions or as stoichiometric guest-host compounds with

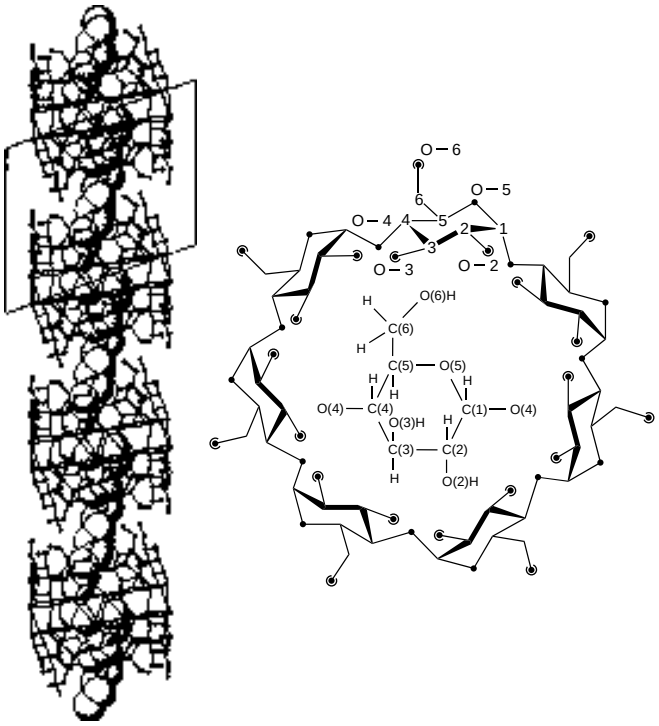

Figure 6 Inclusion compound of β-cyclodextrin with polyethylene glycol (left) Water molecules in the structure have been omitted for clarity. An inclusion compound where the guest threads through a host molecule is known as a rotaxane. On the right a hexameric molecule of β-cyclodextrin is shown, with a representation of the anhydroglucose monomer unit in its center. (K. A. Udachin and J. A. Ripmeester, *J. Am. Chem. Soc.*, 2000, **122**, 12 375)

specific binding often is not completely obvious, and it remains a key question in supramolecular science. In the former, only the simplest recognition principles apply (guest size, sometimes guest shape), in the latter some kind of specific (directional) interactions (H-bonding, $\pi-\pi$, C–H–π, etc.) should play a more important role, leading to the possibility of designing hosts for selective inclusion.

A very characteristic problem of many inclusion compounds is that often the guest and host sub-lattices have different symmetries. This introduces disorder, often dynamic, that involves especially the guest and sometimes the host. Thus, even though in many instances it is possible to obtain diffraction data, a good structural model requires a detailed understanding of the dynamic properties of the system. Thus, in a broad sense key issues involve the identification of new inclusion compounds, their structure, stoichiometry and dynamics, and the interplay amongst the latter. In well-developed areas of study such as the clathrate hydrates there also are compelling reasons to study kinetic processes such as formation and decomposition, thus posing new challenges for the study of transient structures, precursor phases, etc.

1.4 Scope

In this contribution we will outline the development of NMR spectroscopic applications to several classes of inclusion compounds, specifically, the clathrate hydrates, metal cyanides and calixarenes. A great variety of both organic and inorganic hosts and their guests are amenable to study by NMR spectroscopic techniques, but it is not possible to cover the field in a comprehensive manner as it has now so widely diversified. However, it should become completely clear that NMR has played a leading role in providing answers to important questions in inclusion science, and with the advent of ever-new approaches it should continue to do so. The opportunities for complementarity between long-range order techniques such as diffraction and local order techniques such as NMR spectroscopy certainly have come to full realization in applications to inclusion science.

2 CLATHRATE HYDRATES

2.1 Introduction

The cage inclusion compounds (Figures 3 and 7) known as clathrate hydrates have been recognized as a rather special state of matter, and much effort has been devoted to their understanding especially because they are found in nature. Because of their ability to hold vast quantities of gas such as methane and other small molecules, they can be expected to have an effect on human welfare that still is not fully understood.[12]

Clathrate hydrates, probably are the best-understood inclusion compounds. They have been under study for ~200 years, and by NMR spectroscopy steadily for about 35 years.[4–7] The field has benefited each time an innovation or new application in NMR spectroscopy has allowed the derivation of new types of information. Since clathrate hydrates also occur in natural and industrial settings there also is a considerable driving force not only for structural and compositional information,

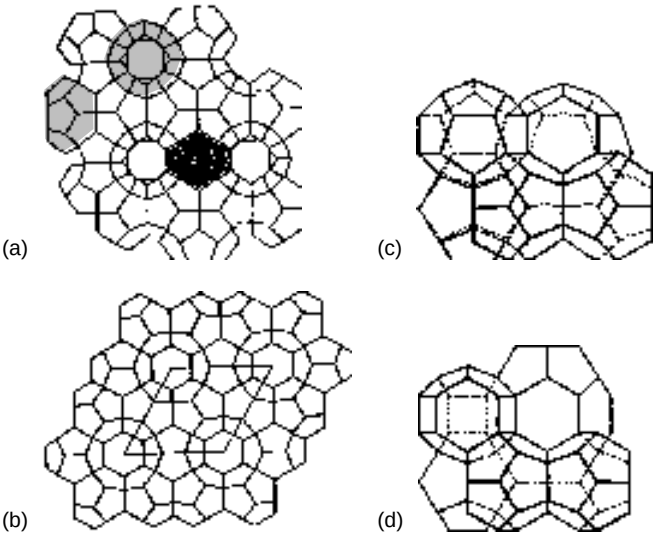

Figure 7 (a) Mode of assembly of polyhedra for str. I hydrate. There are stacks of $5^{12}6^2$ cages along each of the cubic axes. The remaining space consists of the 5^{12} cages; (b) layer of face-sharing 5^{12} polyhedra, the basic structural unit in str. II and str. H hydrates. (c) layer of 5^{12} polyhedra from the side, with 5^{12} and the $5^{12}6^4$ polyhedra that arise between layers stacked in the ABC*ABC* pattern for str. II. (d) layer of 5^{12} polyhedra from the side, with the $4^35^66^3$ and $5^{12}6^8$ polyhedra that arise between layers stacked in the AB*AB* pattern of str. H (J. A. Ripmeester, C. I. Ratcliffe, D. D. Klug, and J. S. Tse, *Ann. N. Y. Acad. Sci.*, 1994, **715**, 161)

but also for understanding formation and decomposition processes. Hence, significant challenges remain and there is much work to be done.

2.2 Early Studies: Dynamics and Hydrate Identification

Studies of dynamics in clathrate hydrates depended on the partial averaging of nuclear dipolar couplings in systems where the nucleus to be observed was of high natural abundance such as ^{1}H or ^{19}F. The mean square line widths (or second moments) of the resonance lines could be calculated exactly for static as well as dynamic models using the formalism of Van Vleck.[3] The motional rates as well as activation energies could be obtained by measuring the spin-lattice relaxation times as a function of temperature. It was also discovered early on that contributions from the guest and host could be isolated by isotopic substitution. Not only can the contribution from either guest or host be made to disappear from the spectrum, but the substitution of H by D also leads to a significant reduction in the nuclear dipolar interactions because of the lower gyromagnetic ratio of D as compared to H, thus resulting in line shapes with better resolution.

Several lessons were learned early on. One was that quality control had to be carried out on synthetic hydrate samples, eg phase identification by powder XRD, in order to ensure that meaningful data were obtained. Further, it became apparent that special care had to be taken to exclude oxygen during hydrate synthesis, as oxygen is far more soluble in the solid clathrates than in the solution with which the hydrate is in contact. Oxygen is an excellent guest for the D cages (Figures 3 and 7, Table 1) that are common to all the clathrate hydrate structures shown. Most of the early relaxation studies and some lineshape studies were affected by the presence of paramagnetic oxygen, either causing enhanced spin-lattice relaxation or line broadening, especially at low temperatures because of Curie law behavior of the oxygen magnetic dipole.

The great mobility of polar guest molecules in the hydrate cages was already known from dielectric studies,[4] and some models were presented that suggested hindrance to molecular motion arose from the interaction between molecular dipoles and electric fields in the hydrate cages. However, NMR experiments on non-polar molecules such as SF_6 showed that even these had a small but measurable barrier to rotation in the hydrate cages. In general, these results supported the 'cage' concept of clathrates as evident from the diffraction studies: a guest molecule physically entrapped in a host lattice with a great degree of reorientational freedom.

The main conclusions from early dynamics experiments can be summarized as follows. Reorientational processes can be studied quite easily with broadline NMR methods, however, as for dielectric experiments, the dynamic parameters always are dominated by the presence of distributed parameters.[4] This also illustrates one of the essential differences between NMR and diffraction, and it becomes of particular importance for the hydrates. Although one could conclude from diffraction results that each cage has a definite point group symmetry (Table 1), the NMR experiments show that this in fact is not necessarily so. The hydrate frameworks suffer from the same disorder as observed in many forms of ice, that is, hydrogen atoms are disordered over two sites in each O–O bond. Diffraction shows this as the presence of two half-hydrogens in each bond, however, NMR shows that this is due to space averaging over many distinct cage configurations at temperatures where water motions are frozen in. Each cage configuration leads to somewhat different sets of potential minima for the guest and therefore, distinct dynamic properties. Formally, the distributed motional parameters can be accounted for by incorporating a distribution function (Cole–Davidson, log-gaussian, etc.) into the line-narrowing or relaxation descriptions. Mean activation energies for reorientation determined from both dielectric and NMR experiments range from $\sim 100\,J\,m^{-1}$ to several $kJ\,m^{-1}$. For some simple guest molecules it was possible to distinguish several motional modes, such as reorientation of, as well as about, the polar axes of cyclobutanone and trifluoromethyl iodide guests. Quantum mechanical tunneling was seen to affect the line shapes of rotors with small moments of inertia such as CH_4[8] and $-CH_3$. Here, barriers to internal rotation of the methyl groups were seen to have a component contributed by the cage that is also affected by the H-bond disorder and gives rise to distributions in the dynamic parameters.

It was also observed that the NMR spectrum of guests in previously unknown hydrates could be used to confirm the clathrate nature of the material. The line width of the NMR signal of the guest in the clathrate is unique in the sense that it is much narrower than that expected for the same guest molecules in its pure bulk solid phase, and much broader than that expected for a liquid. A number of new hydrate-forming guests were identified this way before further

Table 1 Hydrate cages, cage sizes and ^{129}Xe and $^{13}CO_2$ chemical shift data

Structure	Cage type	Symmetry	Radius (Å)[a]	$\delta_{iso}{}^{Xe}$ (ppm)[b]	Δ^{Xe} (ppm)[c]	η^{Xe} [d]	$\delta_{iso}{}^{C}$ (ppm)[b]	Δ^{C} (ppm)[c]	η^{C} [d]
I	5^{12}(D)	$\underline{m}3$	2.50	242	0		128	0	
I	$5^{12}6^{2}$(T)	42m	2.93	152	21		128.2	−63.1	
II	5^{12}(D)	$\underline{3}$m	2.50	231	16		128.0	−53.0	
II	$5^{12}6^{2}$(H)	43m	3.28	80	0		128	0	
H	5^{12}(D)	mmm	2.45	231	13.7	0.701	128.5	+50	0.405
H	$4^{3}5^{6}6^{3}$(D′)	62m	2.40	212.4	31.4		128.5	−82.1	
H	$5^{12}6^{8}$(E)	6/mm	3.8	–	–		–	–	–

[a]Estimates for the cages roughly approximated as spheres from X-ray diffraction data.
[b]Isotropic chemical shift.
[c]$\Delta = \delta_{iso} - \delta_{zz}$ chemical shift anisotropy.
[d]Asymmetry parameter $\eta = (\delta_{yy} - \delta_{xx})/(\delta_{iso} - \delta_{zz})$; the δ_{ii} are the chemical shift tensor elements; the ^{129}Xe shifts are referenced to xenon gas at zero pressure, the ^{13}C shifts to tetramethylsilane. The error estimates on both δ_{iso} and Δ^{Xe} are ±1 ppm, ±2 ppm on Δ^{C}, ±0.04 on η^{Xe} and ±0.09 on η^{C}.

confirming the hydrate nature of the material by X-ray powder diffraction. In principle, the NMR signal even should reflect the cage symmetry, as the extent of motional averaging will depend quite markedly on the degree of asymmetry of the cage. If a guest forms more than one structure with guests in cages of different symmetries these can be distinguished quite readily.

The water molecules of the host lattice have been studied as well, and show dynamic properties closely related to those in ices.[4,7] Reorientation is thought to occur by means of a Bjerrum defect mechanism. Considerable differences in dynamic rates and activation energies have been attributed to the nature of the guest molecule. Both the dipole moment and the ability to interact with the host lattice by transient hydrogen bond formation are seen to be important factors. In return, the dynamic state of the host lattice also has a profound effect on the dynamics of the guest molecules. Sufficiently rapid reorientation of the water molecules averages the different cage configurations mentioned above, so that the cages actually attain the high symmetries apparent from diffraction. Thus, the hydrates are excellent examples of frameworks for which both space and time averaging are observed.

As noted earlier, the use of D_2O for the host leads to magnetic isolation of the guest. Guests with small numbers of spins (2,3,4,6) grouped together all give fine structure in their spectra that are characteristic of the geometric arrangement of the spins and, sometimes, the chemical shift tensors.

2.3 Chemical Shift and Quadrupolar Tensors: Structure, Composition and Dynamics

The advent of Fourier transform spectroscopy and the availability of broad-banded high power amplifiers and decouplers in the middle 1970s led to a revolution in the way that solid state NMR was carried out.[8] The first applications to clathrate hydrates date to ~1980 with a shift in emphasis on the nature of the information that became available.

One problem that is particular to clathrate hydrates is their non-stoichiometric nature. Therefore, in order for the complete structure to be defined, it is not only necessary to define the atomic positions of the guest and host, but also the cage occupancies. The van der Waals and Platteeuw[9] elegant statistical thermodynamical model mentioned earlier, often referred to as the 'solid solution theory', can be used to account for the variable cage occupancies. The model assumes that there is a hypothetical empty clathrate lattice with a chemical potential $\Delta\mu$ greater than the ice lattice. The fractional occupancies of the small and large cages, θ_S and θ_L, respectively, are related to the minimum partial pressure P_D of the guest under which the hydrate is stable by Langmuir absorption-like expressions:

$$P_D = \frac{\theta_i}{(1-\theta_i)C_i} \tag{1}$$

where C_i are Langmuir constants. Other assumptions are that the free energy difference is guest independent and that there are no guest–guest interactions. The chemical potential difference $\Delta\mu$ is then directly related to the absolute occupied cage fractions:

$$\Delta\mu = kT \sum_i \nu_i \ln(1-\theta_i) \tag{2}$$

Here ν_i is the number of cages of type i per water molecule. A converse of this is that for structure I hydrates the guest occupancy ratio determines directly the hydration number once $\Delta\mu$ is known. Although the theory had been used steadily with a great degree of success, it had never been tested at the molecular level. Testing of the theory for structure I hydrate where small guests occupy both kinds of cages requires a resolved signature from guests in the large T and small D cages (see Table 1, Figures 3 and 7). ^{129}Xe was chosen as the nuclide most likely to have the desired qualities: nuclear spin $I = 1/2$, a relatively large natural abundance ~26%, high gyromagnetic ratio (similar to ^{13}C), and a large polarizable electron cloud that was hoped to be sensitive to cage size and/or shape.[4–7] The results were extremely encouraging, showing a relationship between the isotropic chemical shift and cage size, and the anisotropic chemical shift and cage shape (Table 1). For a well-characterized xenon hydrate sample of known composition, the cage occupancy ratios led to the first completely experimentally determined value for $\Delta\mu$, $1297 \pm 110\,\mathrm{Jm^{-1}}$. This is in remarkable agreement with values derived from fitting vapor pressure data.[13]

Since the pioneering experiments on ^{129}Xe, similar cage-dependent chemical shift effects have been found for most other spin 1/2 nuclides, the chemical shift difference for the two sites scaling roughly with the atomic weight of the nuclide under study.[5–7] One of the more significant measurements was carried out on methane hydrate, where the ^{13}C chemical shift difference of a few ppm required the application of magic angle spinning at low temperature in order to resolve the contributions, but without decomposing the sample.[14] This laid the groundwork for using instrumental methods such as NMR to determine structure and composition of natural gas hydrates[15] from resolved cage contributions and experimental occupancy ratios. The chemical shift pattern is diagnostic of the structure of the hydrate, making the technique of great analytical utility in general. ^{129}Xe chemical shift tensors are now available for all of the cages (except E) in structures I, II and H (Figure 8, Table 1)

Since guest molecules are quite mobile in the clathrate cages, the chemical shift tensors associated with spin 1/2 nuclei present in the guest molecules also are averaged by the guest motions. The extent of motional averaging is strongly dependent on the symmetry of the hydrate cage, and it is possible to calculate averaged tensors and associated lineshapes for different motional models. For hydrates containing CO_2, the isotropic chemical shift shows little dependence on the size of the cage, nevertheless, the chemical shift tensor is completely diagnostic of the asymmetry of the cage (Figure 9, Table 1).[16]

Another feature that has proved to be extremely useful is the ability to contrast signals arising from solids from those of liquids. Cross-polarization methods, where magnetization is first generated on a nucleus such as ^{1}H and then transferred to a second nucleus such as ^{13}C or ^{129}Xe depends on the presence of dipolar coupling between these nuclei. Since these couplings are absent in liquids it is straightforward to distinguish guests trapped in hydrate cages from bulk liquid. Similarly, bulk xenon can be distinguished from xenon trapped in hydrate cages or xenon trapped next to water molecules.

The case for distinguishing hydrate cages based on guest dynamics extends to quadrupolar nuclei such as ^{2}H. A number of examples have been given in which guests in the D and T

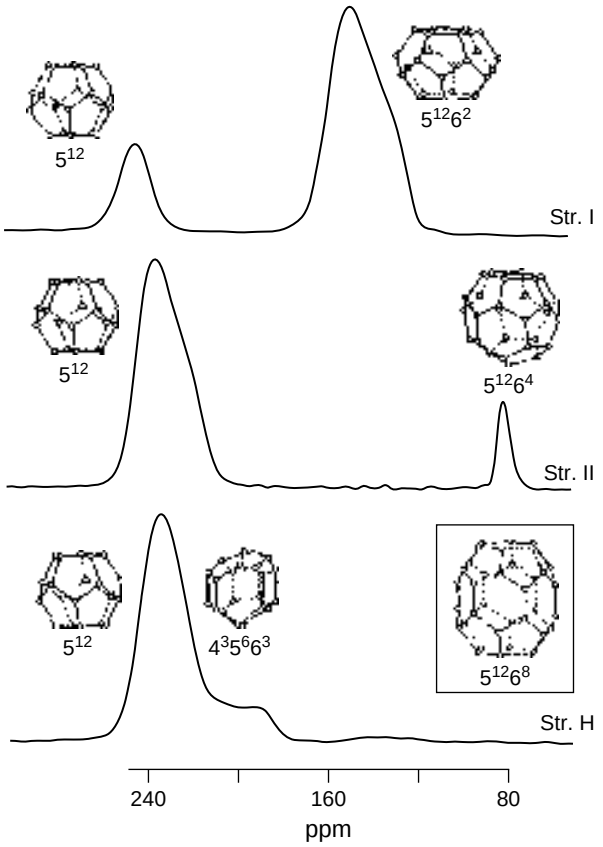

Figure 8 ^{129}Xe NMR spectra of str. I, II and H obtained with ^{1}H–^{129}Xe cross-polarization at 77 K. For Str. II most large cages contain a second guest, and for str. H all large cages are occupied by a second guest species (Ref.[6])

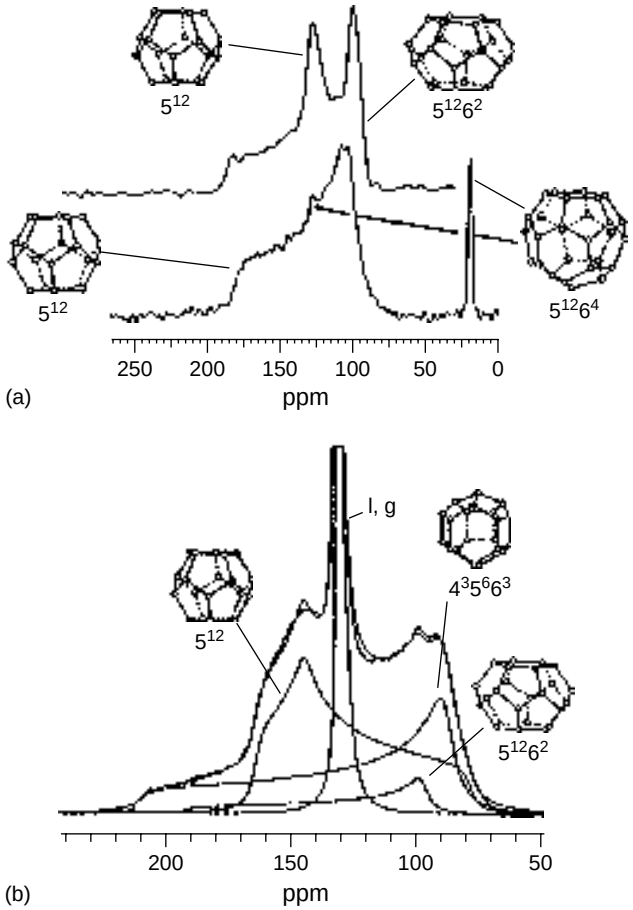

Figure 9 ^{13}C NMR powder pattern of CO_2 in hydrate polyhedra. (a, top spectrum) strI hydrate of $^{13}CO_2$ (a, lower spectrum) str. II hydrate of propane and $^{13}CO_2$ (line at ~17 ppm unresolved contributions from propane). Both patterns were determined using ^{1}H–^{13}C cross-polarization. (b) str. H hydrate of neopentane and $^{13}CO_2$, determined by ^{1}H decoupled, single pulse technique. (sharp line in center is from excess gas and liquid, there also is a str. I hydrate impurity, as marked). In each cage, the pattern is determined by the dynamics of the CO_2molecule in the cage, and illustrates the primary importance of cage symmetry. The 5^{12} cage in str. I and the $5^{12}6^4$ cage in str. II have cubic symmetry and hence give an isotropic spectrum, the other cages are asymmetric and give three structures have 5^{12} cages, although of different point group symmetries, and anisotropic spectra. It should also be noted that all hence they show different ^{13}C powder patterns (Ref.[16])

cages of structure I hydrate were distinguished and hydration numbers estimated from the occupancy ratios.[5–7]

In general, the chemical shift or quadrupolar tensors are more useful than dipolar couplings, as the latter require the evaluation of intra- and intermolecular lattice sums, whereas the former are essentially intramolecular in nature. Detailed models for the motion of the guest in the anisotropic cages are possible only when the cages take on their time-averaged symmetries.[5–7] As discussed above, the disordered cage configurations that result when water molecule motions freeze in cause distributed guest dynamics, as illustrated for CO_2 hydrate.[17]

At this stage, NMR spectroscopy presents us with the tools to study hydrates that are able to provide structure-specific and quantitative site-specific information. The applications of the NMR techniques described above played the major role in the discovery of structure H hydrate[18] and the subsequent exploration of suitable guests for this hydrate.[7]

2.4 The Study of Processes

One problem that has plagued NMR spectroscopy is its low sensitivity, thus often requiring significant data acquisition times in order to attain sufficient signal-to-noise ratios by signal averaging. The study of equilibrium properties such as structure and composition are well within the scope of NMR spectroscopy, as sufficient time can be taken to collect the data to give adequate signal-to-noise ratios. However, study of processes such as hydrate formation adds the need for time resolution. This means that the processes must be slow enough for the application of the standard spectroscopic techniques, or that new experimental approaches must be developed. In fact, both approaches have been explored for hydrates. The hope is that new information at the molecular level on the nucleation and kinetics of hydrate formation will lead to the development of useful models for the hydrate formation process. Specifically, this work will be of importance for the control of hydrate formation in pipelines, the possible recovery of gas from natural deposits, and industrial applications involving separation processes or gas storage.[19]

One approach has been to slow down the process of hydrate formation by going to low temperatures. In order to

eliminate mass transfer problems, it is necessary to prepare intimate amorphous mixtures of guest and host materials. Two methods are available for this: vapor co-deposition of water and the guest, and hyperquenching aqueous solutions of guest material by the extremely rapid cooling of micrometer-sized droplets.[20,21] In both cases the product appears amorphous to X-ray diffraction. Annealing by progressively warming the samples at higher temperatures initiates a number of processes that eventually lead to crystalline clathrate hydrates. The characterization of the processes and products is a complex procedure, requiring input from a number of techniques, again used in a complementary fashion. The THF-water system was studied in this fashion. Differential scanning calorimetry was used to map out the temperature regions of reactivity, powder XRD was used to monitor the samples for crystalline products, and NMR and Raman spectroscopy were used to follow changes in local order. For the case in question THF-d_8 and ^{2}H NMR were used. As described above, first of all ^{2}H NMR is sensitive to the dynamic state of the guest, and some striking differences were noted between vapor-deposited and hyperquenched materials. However, additional information was needed, and a new experiment was developed to probe nearest neighbour interactions. The QEDOR experiment[22] probes the guest-host interactions by monitoring the ^{1}H–^{2}H dipolar couplings. In a crystalline clathrate, such interactions are maximized as each deuterated guest is completely enclosed in a H_2O host cage. If there is phase separation in which clusters of deuteriated guest form, the ^{1}H–^{2}H dipolar couplings become minimal. Probing of such interactions during an annealing cycle therefore allows conclusions to be drawn about the degree of dispersion of the guest in the host lattice. The main conclusions are that vapor-deposited THF water mixtures transform directly to the clathrate hydrate, whereas the hyperquenched material first phase-separates into crystalline THF and Ice Ic before reacting further to form the clathrate.

The second approach, that of increasing the sensitivity of the NMR experiment has also been realized. In many ways, ^{129}Xe NMR spectroscopy is the ideal technique for the study of hydrate formation, as the signals for the gas, gas dissolved in water, and gas in the two hydrate cages are well resolved.[7] In principle it is possible to monitor the guest distribution quantitatively. However, the relaxation times of xenon are so long that time-dependent studies become impossible. The introduction of NMR techniques using hyperpolarized xenon have revolutionized Xe NMR spectroscopy, so that now it is indeed possible to carry out kinetic studies with hyperpolarized xenon.[23] Without going into details, the low sensitivity of traditional NMR spectroscopy arises from the small energy separation of the Zeeman levels in magnetic fields commonly available. The maximum signal that can be generated depends on the population difference between the levels, and at ordinary magnetic fields and temperatures this amounts to a few ppm. Hyperpolarized xenon is produced by spin exchange between the xenon nuclear states and rubidium that has polarized electron states produced by optical pumping, thus boosting the xenon population difference by a factor of 10^4–10^5. The lifetime of the hyperpolarized state is long enough so that hydrate formation experiments can be carried out on the surface of ice (Figure 10). It is expected that these experiments will lead to new molecular models for hydrate formation.

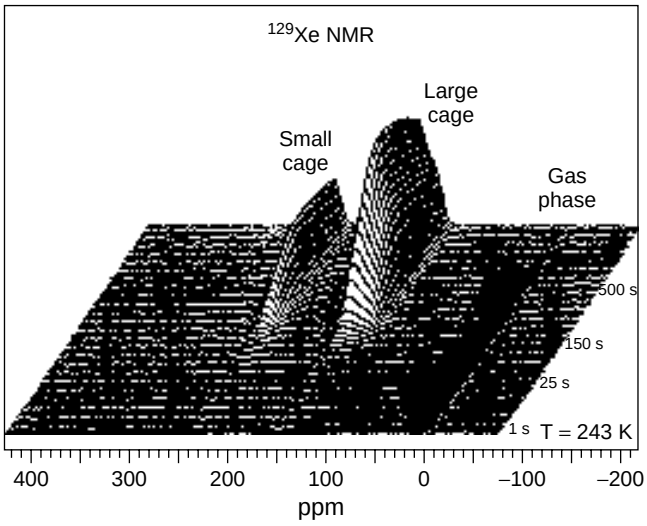

Figure 10 Time-resolved ^{129}Xe NMR spectra following the reaction of hyperpolarized xenon with the surface of powdered ice. Each spectrum is a single scan. The gas line is near ~0 ppm, the large and small cages in str. I hydrate near ~150 and 240 ppm (I. L. Moudrakovski, A. A. Sanchez, C. I. Ratcliffe, and J. A. Ripmeester, *J. Phys. Chem. B*, 2001, **105**, 12 338)

2.5 NMR Imaging and Spatially Resolved Spectroscopy

NMR imaging (MRI), and the related techniques of spatially resolved spectroscopy, are well-established diagnostic tools in medicine, and are now finding an increasing number of applications to materials science. These techniques also are likely to play a role in the science of clathrate hydrates. The decomposition of mineral gas hydrates from natural hydrate deposits as well as the formation and decomposition of hydrate plugs in pipelines are obvious applications where space resolved and time resolved imaging can contribute a great deal of information. Some initial work has been carried out to identify the melting of ice inside hydrate-coated ice particles.[24] Currently the technique is limited to distinguishing solids from liquids, as, except in very special cases, the signal decay times are too short to observe solid hydrate directly.

3 METAL CYANIDE INCLUSION COMPOUNDS

Solid state NMR has played a crucial role in the study of metal-cyanide inclusion compounds, with regard to structural problems involving disorder and to the dynamics of both guest and host molecules. In these materials the frameworks are constructed from metal centers, typically Ni, Pd, Pt, Zn, Cd, Hg, Cu and Ag, connected by coordinating cyanides, CN, sometimes together with other ligands, particularly with amine groups.[25] Most often these involve square planar, octahedral, tetrahedral and occasionally 5-coordinated metal centers in a rich variety of structures, with cavities or channels occupied by guest molecules and molecular ions.

3.1 Host Frameworks

The NMR of metal nuclei, in particular ^{113}Cd but also ^{63,65}Cu and ^{67}Zn together with the ^{13}C and ^{15}N NMR of specifically labelled ^{13}C^{15}N has helped determine local structures in

numerous systems, many of which are disordered and therefore incompletely determined by diffraction methods. Furthermore X-ray diffraction has some difficulty in distinguishing directly between Cu and Zn atoms, and between C and N atoms, though sometimes it is possible to suggest an orientation for the CN based on the distances to the metal atoms. (In-depth reviews of this area and original literature citations may be found in Refs.[5,7])

The most useful metal nucleus has been ^{113}Cd, which has spin 1/2, reasonable sensitivity and a sizeable chemical shift range. Furthermore, because of the presence of ^{1}H on many of the guest species it is often possible to carry out cross-polarisation and thus circumvent the often long T_1 of Cd itself. Early studies used CP/MAS spectra of several structurally ordered Hofmann-type and related inclusion compounds to determine the chemical shifts for Cd sites ranging from octahedral (Oh) CdN_6 or CdN_4O_2 to tetrahedral (Td) CdC_4. The range now extends from around 150 ppm to 682 ppm (referenced to solid $Cd(NO_3)_2{\cdot}4H_2O$). The chemical shifts illustrate the great sensitivity of the Cd atom to its environment, even for complexes with closely related structures. The complementarity of X-ray and NMR structural information can be illustrated nicely by two examples of $Cd(CN)_2$ inclusion compounds with different structures:

Pure $Cd(CN)_2$ has a cubic structure consisting of two interpenetrating frameworks of Cd coordinated tetrahedrally by linking CN groups. Removal of one of the frameworks leaves voids which can be occupied by certain guest molecules such as neopentane and cyclohexane and hence form clathrates. Early X-ray powder work on $Cd(CN)_2$ suggested it was ordered with CdC_4 and CdN_4 tetrahedral sites, whereas more recent single crystal work on the cyclohexane clathrate was unable to distinguish between C and N. ^{113}Cd MAS NMR of the cyclohexane clathrate $Cd(CN)_2{\cdot}C_6H_{12}$ (and of pure $Cd(CN)_2$) unequivocally shows that there is static disorder of the CN since there are 5 resonances from CdC_4, CdC_3N, CdC_2N_2, $CdCN_3$ and CdN_4, sites (Figure 11). This is quite distinct from an ordered structure which would have had only two equal lines from CdC_4 and CdN_4, or a structure with dynamically disordered CN where all the Cd would be equivalent on time average and therefore give a single resonance. The low field line can be assigned to CdC_4 progressing to CdN_4 at high field, based on comparisons of shifts with ordered materials and on the following finer details of the NMR spectra: (a) J-coupling to ^{14}N, probably of the order of 137–190 Hz (and possibly some residual dipolar coupling due to effects of the ^{14}N quadrupolar interaction) causes the widths of the lines to increase with the number of attached N atoms. (b) The chemical shift anisotropy for the CdC_4 and CdN_4 centers is vanishingly small since they have close to perfect Td symmetry, resulting in lines with no spinning sidebands in the MAS spectra. (c) Chemical shift anisotropies for the much less symmetrical CdC_3N, CdC_2N_2 and $CdCN_3$ centers give rise to lines with several sidebands. The relative populations determined from line intensities of the resonances also indicate that the distribution of the 5 species is not purely statistical; CdC_2N_2 seems to be more favored and CdC_4, CdN_4 least favored in these complexes.

Another interesting case is that of $Cd(CN)_2{\cdot}2/3H_2O{\cdot}Bu^tOH$, which has a unique honeycomb-like framework structure, with the guest Bu^tOH inside linear channels. The X-ray structural data were consistent with five different space groups, from which one (Amm2) was tentatively chosen on the basis

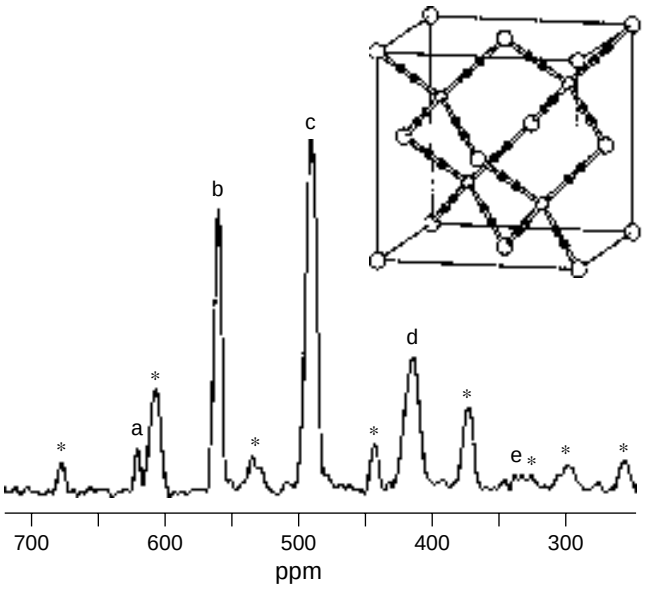

Figure 11 ^{113}Cd NMR MAS spectrum of $Cd(CN)_2{\cdot}C_6H_{12}$ at 39.35 MHz. (a) CdC_4; (b) CdC_3N; (c) CdC_2N_2; (d) $CdCN_3$; (e) CdN_4. $*$ = spinning sidebands. Inset: Cubic unit cell showing only the $Cd(CN)_2$ framework, disordered C/N atoms shaded (S. Nishikiori, C. I. Ratcliffe, and J. A. Ripmeester, *Can. J. Chem.*, 1990, **68**, 2270)

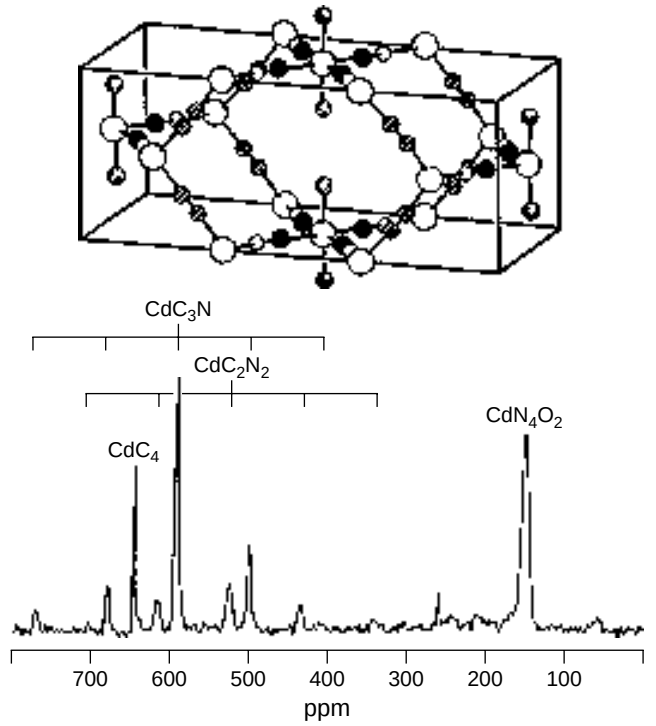

Figure 12 ^{113}Cd NMR CP/MAS spectrum of $Cd(CN)_2{\cdot}2/3H_2O{\cdot}Bu^tOH$ at 39.35 MHz. Spinning sideband manifolds are indicated for CdC_3N and CdC_2N_2. The unit cell above shows the framework with the NMR ordering scheme. Filled circles = N, small open circles = C, hatched circles = disordered C, N, shaded circles = O, large open circles = Cd (S. Nishikiori, C. I. Ratcliffe, and J. A. Ripmeester, *J. Chem. Soc. Chem. Commun.*, 1991, 735)

that it gave the lowest R factor. This X-ray scheme is completely ordered with $CdO_2C_2N_2$ (Oh, with two H_2O), CdC_4 (Td) and CdN_4 (Td) centers. ^{113}Cd NMR shows isotropic CdC_4 and anisotropic CdC_3N and CdC_2N_2 resonances in a 1 : 2 : 1 ratio, as well as one Oh Cd line. From this it can be determined that the CN groups bridging Td Cd atoms are randomly disordered and the CN groups linked to the octahedral center are ordered to give CdO_2N_4 (Figure 12). Thus space group Amm2 is untenable and the choice is narrowed to three of the original five: Ammm, A2mm or A222.

The picture which has emerged from the ^{113}Cd NMR results for Cd–(CN)–Cd linkages in these and other clathrates is that if the CN sits at an inversion center or symmetry axis which makes the two Cd crystallographically equivalent then the CN is statically disordered, 50% one way 50% the other, whereas CN linking inequivalent Cd can range from fully disordered 50 : 50 all the way through to fully ordered, 100 : 0. In some cases, provided the single crystal X-ray data is good enough, the atoms of ordered CN groups can be distinguished, but again the NMR can establish this unequivocally.

The use of doubly labelled cyanide, ^{13}C–^{15}N, provides another route to structural information from NMR, which can be particularly useful when the properties of the metal nuclei involved make them less amenable to study than Cd, for example quadrupolar nuclei such as Cu or Zn. This isotopic enrichment has been used to great advantage to study $NMe_4Cu^{I}Zn(CN)_4$ which has a framework structure very similar to that of the $Cd(CN)_2{\cdot}G$ clathrates with NMe_4^+ filling half of the cavities. The remaining cavities may be empty or filled with a neutral guest molecule. The cubic structure is retained for highly symmetrical guests such as CCl_4, but is distorted to trigonal for $CHBr_3$. For the empty clathrate an ordered structure with Cu–C–N–Zn linkages was surmised from X-ray diffraction work, based on interatomic distances, even though Cu/Zn and C/N centers were indistinguishable. The observation of single isotropic lines for both ^{65,63}Cu and ^{67}Zn NMR (all nuclei with large quadrupole moments) showed that these centers have quadrupole coupling constants of zero and hence perfect tetrahedral symmetry and no disorder of the CN links. The orientation of the CN, however, could not be determined unequivocally until ^{13}C^{15}N labelling was employed. Splittings in both the ^{65,63}Cu and ^{13}C MAS spectra from $J(^{13}C–^{65,63}Cu)$-coupling, confirm that the centers must be CuC_4 and ZnN_4. From the static ^{13}C NMR spectra of the enriched sample it was possible to derive values for the $^{13}C–^{65,63}Cu$ and $^{13}C–^{15}N$ dipolar couplings and bond lengths, which indicate that the CN has a moderately large amplitude librational motion. This motion reduces the dipolar coupling and leads to a long apparent CN bond length of 1.2 Å, whereas it also leads to a rather short apparent CN bond length in the X-ray diffraction study (Figure 13).

There are Cu/Cd analogs of this structure and the carbon tetrachloride clathrate, $NMe_4CuCd(CN)_4{\cdot}CCl_4$ presents a few puzzles. It shows a single isotropic ^{63}Cu resonance, with no quadrupole coupling, at almost the same shift as the Cu/Zn framework, which is assigned to CuC_4 centers.[8] However, although the ^{113}Cd spectrum shows an isotropic resonance from CdN_4 it also shows a second line with an axially symmetric chemical shift anisotropy (from a static spectrum),

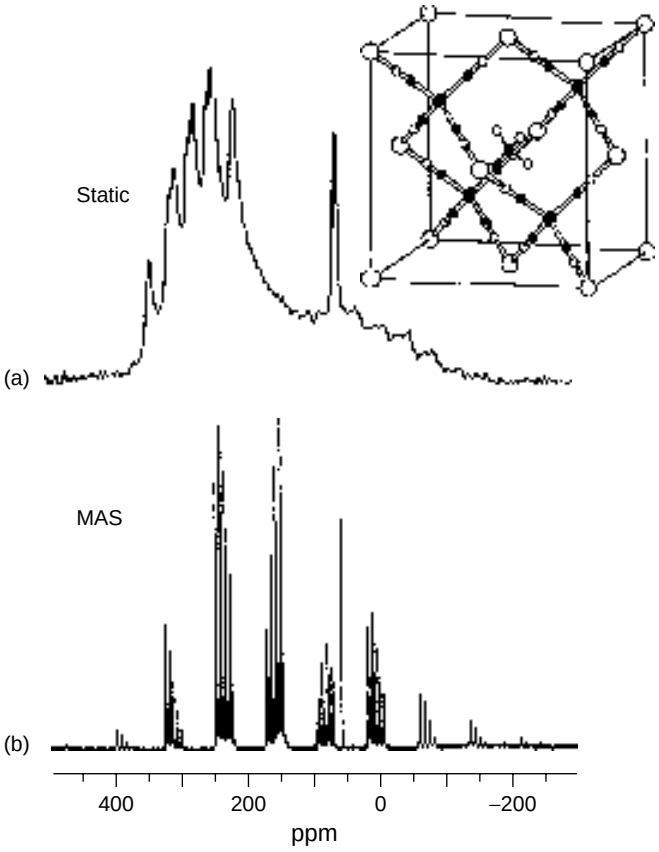

Figure 13 $^{13}C^{15}N$ labelled $NMe_4CuZn(CN)_4$ ^{13}C CP NMR spectra at 45.26 MHz: (a) static, showing features due to ^{13}C shielding anisotropy, dipolar coupling to ^{15}N and dipolar and J coupling to ^{63,65}Cu, any J anisotropy is indistinguishable from dipolar coupling; (b) MAS, showing quartets from $^{13}C–^{63,65}Cu$ J-coupling. The isolated sharp line is due to $N(CH_3)_4^+$. The inset shows the ordered structure with ZnN_4 and CuC_4 centers, N and Zn atoms in black (R. D. Curtis, C. I. Ratcliffe, and J. A. Ripmeester, *J. Chem. Soc. Chem. Commun.*, 1992, 1800)

with about 1/3 the intensity of the CdN_4 resonance, assignable to $CdCN_3$. Since there are equal numbers of Cu and Cd this implies that about 1/4 of the Cu must be CuC_3N centers. The absence of a resonance for CuC_3N in the ^{63}Cu spectra can be explained as an effect of an extremely large quadrupole coupling constant arising from the loss of Td symmetry. The ^{13}C CP/MAS spectrum of the $^{13}C^{15}N$ enriched material shows the same pattern of $J(^{13}C–^{65,63}Cu)$-coupled lines as in the Cu/Zn complex due to C in CuC_4, but beneath this there is a broader and more complex pattern which is due to C atoms attached to CuC_3N and $CdCN_3$ centers. The $CHBr_3$ clathrate has a similar but distorted framework with trigonal symmetry, however, it also shows the 1 : 3 ratio of Cd resonances. Consequently, from the NMR and diffraction data it appears that the small fraction of CN which are reversed are randomly distributed throughout the lattice, and that this is a property of CN linkages between Td Cu and Cd centers. The $NMe_4CuCd(CN)_4{\cdot}CHBr_3$ clathrate also shows a single ^{63}Cu MAS NMR resonance, but in this case displaying second order quadrupolar effects, which must be from CuC_4 centers whose symmetry has been slightly reduced from perfect Td (Figure 14).

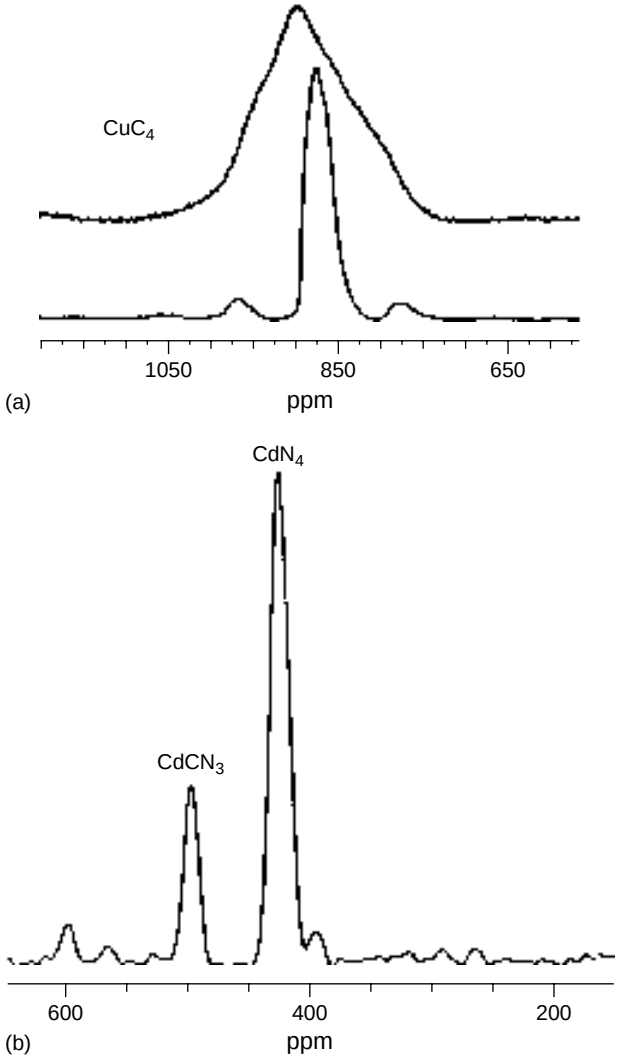

Figure 14 $NMe_4CuCd(CN)_4 \cdot CHBr_3$. (a) ^{63}Cu NMR at 79.5 MHz, static and MAS showing 2nd order quadrupolar effects. (b) ^{113}Cd CP/MAS NMR at 66.55 MHz showing anisotropic CdN_3C and isotropic CdN_4 resonances. (Ref.[7] and S. Nishikiori and C. I. Ratcliffe, unpublished results)

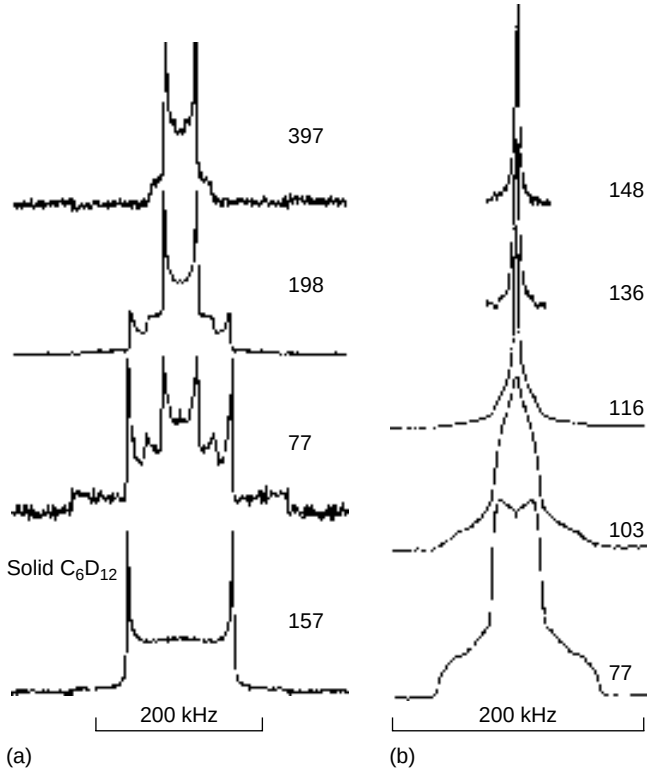

Figure 15 ^2H NMR spectra at 27.63 MHz as a function of temperature. (a) $Cd(mtn)Ni(CN)_4 \cdot 1/2C_6D_{12}$: The 198 K spectrum shows rapid reorientation about the molecular 3-fold axis and crystal 4-fold axis. This motion is considerably slower at 77 K. At 397 K there is also rapid inversion. (b) $Cd(CN)_2 \cdot 2C_6D_{12}$: The spectrum at 77 K is again characteristic of rapid reorientation about the molecular 3-fold axis, but the features are considerably broadened due to onset of new dynamics and CN disorder. There is rapid pseudo-isotropic motion by 148 K. The spectrum of the completely static C_6D_{12} in pure solid cyclohexane is shown at lower left for comparison (Ref.[7])

3.2 Guest Molecules

Guest species in metal cyanide inclusion compounds have largely been studied from the aspect of their dynamics and hence much use has been made of ^2H NMR and some ^1H T_1 as a function of temperature to determine the state of the motion and its activation energy, and how this relates to the symmetry and cavity shape and size. The effect of symmetry on the dynamics can be illustrated very elegantly by a comparison of cyclohexane C_6D_{12} in two complexes:

In $Cd(mtn)Ni(CN)_4 \cdot 1/2C_6D_{12}$ clathrate (mtn = *N*-methyl-1,3-diaminopropane) the cavity can be visualised as a square box and the cyclohexane fits into this with the 3-fold axis of its chair form along the 4-fold axis of the cavity. ^2H NMR (Figure 15) shows that *n*-fold (probably 12-fold) rotation about the cavity axis occurs at 77 K with an E_a estimated to be no more than 5.8 kJ mol^{-1}. This *n*-fold reorientation gives a characteristic lineshape consisting of broad and narrow doublets of equal intensity. This arises because the principal q_{zz} axis of the quadrupolar coupling tensor of each axial deuteron is parallel to the rotation axis and therefore does not change orientation. The equatorial deuterons on the other hand do change tensor orientation and are therefore averaged. This motion is rapid by about 117 K. Between 230 and 390 K the ^2H lineshapes undergo changes due to the inversion of the molecule, for which an E_a of 44.7 ± 1.0 kJ mol^{-1} was determined by comparison of simulated and observed lineshapes. The inversion motion also causes a reduction of intensity and broadening of the ^{13}C CP/MAS NMR cyclohexane resonance in the region of room temperature, due to the dipolar fade-out which occurs when there is interference between the coherent averaging of the decoupling field and the incoherent averaging of the motion.

In the $Cd(CN)_2 \cdot C_6D_{12}$ clathrate, whose cubic structure was described above, the cyclohexane sits within a cavity with tetrahedral symmetry. At 77 K the ^2H lineshapes[6] (Figure 15) show that the cyclohexane is already undergoing rapid reorientation, most probably about its 3-fold axis, but the lineshape is already showing some effects of a second motion which is rapid and pseudo-isotropic by 140 K. Reorientation of the 3-fold molecular axis among just the four tetrahedral axes of the cavity will produce a pseudo-isotropic lineshape. Another point of interest is that the features of the lowest temperature

lineshapes lack clarity. This is probably due to the disorder in the CN orientations of the framework, which effectively means that there are very many slightly different cages which brings about a slight distribution in the widths of the averaged lineshapes. A similar effect was described above for the clathrate hydrates.

It can be seen that motion in both compounds is determined by reorientation about the molecular axis at low temperature but by the cavity shapes at higher temperature, and that the cyclohexane has much more freedom in the $Cd(CN)_2$ clathrate.

4 CALIXARENE INCLUSION COMPOUNDS

Inclusion compounds formed with organic hosts form the third area of focus. The void space created by organic hosts may be intrinsic to the molecular structure (i.e., cavity-containing), or may be due to the long-range or collective assembly of host molecules in an ordered solid (i.e., cavity- and/or channel-forming). Examples of the former include cyclodextrins, crown ethers, Dianin's compound, while examples of the latter include tri-orthothymotides, cholic and deoxycholic acids and others.[7] Some inclusion compounds, like the calixarenes, form both molecular and supramolecular cavities; and thus calixarenes provide an ideal system to illustrate the general application of solid-state NMR studies of organic inclusion compounds. Calixarenes are synthetically versatile giving great control over the cavity geometry, selectivity and solubility properties.[11,26]

While calixarenes played a significant role in long-established phenolic polymers such as 'Bakelite', it was not until 1979 that X-ray diffraction established the nature of the molecular inclusion (Figure 16), and 1988 that the first solid-state NMR spectrum was collected.[27] The host is formed by four alkylphenols linked by methylene bridges to give a shallow cavity into which ions and small organic molecules are incorporated.

The ^{13}C CP-MAS NMR spectrum of t-butylcalix[4]arene•toluene at 20 °C (Figure 17b) shows two important structural features. First, each chemically-distinct carbon in the host t-butylphenol repeat unit has a single resonance, establishing the 4-fold (conical) symmetry of the structure. Second, the chemical shift value of the guest methyl carbon is deshielded relative to that in pure toluene solution. This complexation-induced chemical shift arises from the electron density of the host aromatic rings, and its value generally indicates the orientation of the guest molecule in the host cavity.[27,28] Thus in the case of toluene, the guest methyl group is situated

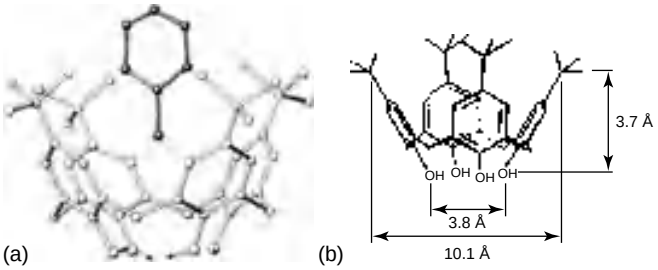

Figure 16 Guest-host unit of the 1 : 1 inclusion compound of *p-tert*-butylcalix[4]arene with toluene, from the crystal structure determination (a); chemical structure of host unit (b)

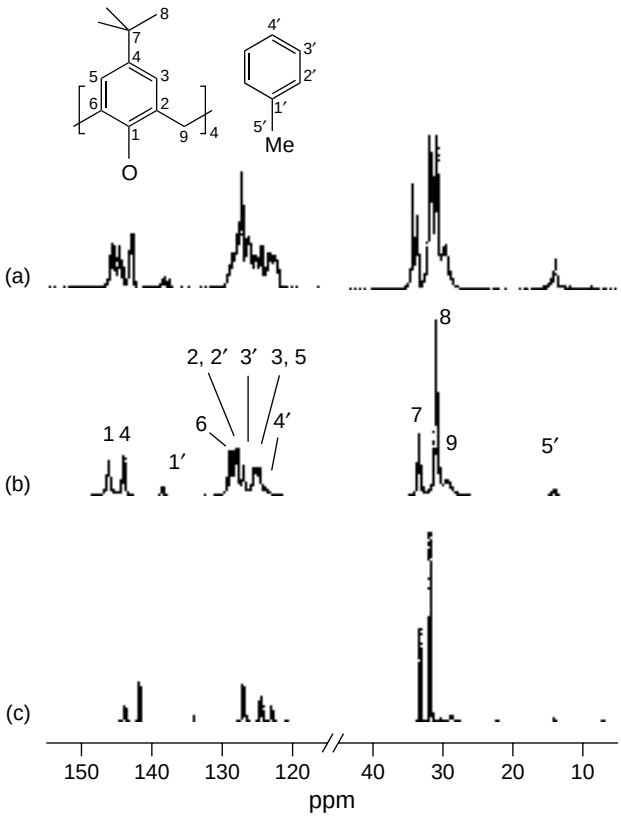

Figure 17 ^{13}C CP-MAS NMR spectra of the inclusion compound of *p-tert*-butylcalix[4]arene with toluene: (a) low temperature, (b) room temperature, (c) after conversion to 2 : 1 compound at ~150 C

deep in the host cavity. ^{13}C CP-MAS NMR spectroscopy has been used as a screening technique for both symmetry and orientation structural features with variations in the guest, and also in conjunction with complementary techniques such as TGA.[28,29]

Upon lowering the temperature below a phase transition at −20 °C, the signals in the ^{13}C CP-MAS NMR spectrum of t-butylcalix[4]arene•toluene increase in multiplicity, indicating that the symmetry is lowered (Figure 17a). Furthermore, an increase in temperature causes a structural change as 50% of the toluene molecules leave the solid; this too is reflected in changes in the ^{13}C CP-MAS NMR spectrum (Figure 17c).

With modification of the ^{13}C CP-MAS technique to allow the magnetization to be dephased briefly by ^{1}H–^{13}C dipolar interactions prior to acquisition under ^{1}H decoupling, the signals due to carbon nuclei with strong dipolar couplings to protons (rigidly held in the crystal lattice) disappear, while those of carbon nuclei with weaker couplings (quaternary carbons and proton-bearing carbons involved in molecular motion) persist. The disappearance of the toluene C_4 signal indicates that the C–H bond lies on an axis of molecular reorientation (Figure 17b).

^{2}H NMR is widely used to describe the motion of guest molecules in clathrates and inclusion compounds as temperature is varied. The toluene guest molecule re-orients in the t-butylcalix[4]arene cavity as a function of the cavity symmetry. Below −20 °C, the ^{2}H NMR lineshapes indicate a 2-fold reorientation (=180° jump) about the guest symmetry axis, whereas at higher temperatures, the lineshape indicates 4-fold

reorientation (=90° jump). Thus ^{2}H NMR spectra indicate that the local cavity has 2-fold symmetry at low temperatures, and 4-fold symmetry at high temperatures. Such information has been invaluable in resolving ambiguous diffraction data for the low-symmetry structure.[29] In general, inclusion compounds often possess significant molecular motion, and ^{2}H NMR is a unique tool to describe such 'soft' materials.

The structure and dynamics of inclusion compounds may also be investigated further with the use of ^{129}Xe NMR of inclusion compounds formed with xenon as guest, with t-butylcalix[4]arene•Xe as an example.[29] Xenon, with its large chemical shift range, is very sensitive to its local chemical environment, giving insight into symmetry and motion. The implementation of hyper-polarized ^{129}Xe NMR holds great promise as a technique to investigate organic inclusion compounds.

The relatively small size of the calixarene host lends itself to the application of NMR distance techniques based on the reintroduction of the dipolar interaction between two (or more) nuclei. A ^{19}F-containing guest has been used to determine the distance between host ^{13}C and the guest ^{19}F nuclei using REDOR.[30] However, such distance determinations are complicated by the need to describe any molecular motion prior to fitting the REDOR dephasing curves.

As the need for structural and dynamic information of inclusion compounds increases, the application of more complex NMR experiments such as REDOR and those using hyperpolarized ^{129}Xe will complement the wealth of information gained from the more routine ^{13}C CP-MAS NMR techniques.

5 RELATED ARTICLES IN THIS VOLUME

Dynamics in Solid Organic Compounds: Intramolecular Motions; Supramolecular Chemistry.

6 RELATED ARTICLES IN VOLUMES 1–8

Deuterium NMR in Solids, Volume 3; Imaging: A Historical Overview, Volume 4; Imaging Techniques for Solids and Quasi-solids, Volume 4; Intercalation Compounds, Volume 4; Microporous Materials & Xenon-129 NMR, Volume 5; Polarization of Noble Gas Nuclei with Optically Pumped Alkali Metal Vapors, Volume 6.

7 REFERENCES

1. J. L. Atwood, J. E. D. Davies, D. D. MacNicol, F. Vogtle, and J. M. Lehn eds, 'Comprehensive Supramolecular Chemistry', Elsevier: Oxford, 1996.
2. H. M. Powell, *J. Chem. Soc.*, 1948, 61.
3. F. Bloch, W. W. Hansen, and M. Packard, *Phys. Rev.*, 1946, **70**, 474; E. M. Purcell, H. C. Torrey, and R. V. Pound, *Phys. Rev.*, 1946, **69**, 37.
4. D. W. Davidson and J. A. Ripmeester, in 'Inclusion Compounds', eds J. L. Atwood, J. E. D. Davies, and D. D. MacNicol, Academic Press, 1984, Vol. 3, p. 69.
5. J. A. Ripmeester and C. I. Ratcliffe, in 'Spectroscopic and Computational Studies of Supramolecular Systems', ed J. E. D. Davies, Kluwer: Dordrecht, 1992, p. 1.
6. J. A. Ripmeester and C. I. Ratcliffe, in 'Inclusion Compounds', eds J. L. Atwood, J. E. D. Davies, and D. D. MacNicol, Oxford University Press: Oxford, 1992, Vol. 5, p. 37.
7. J. A. Ripmeester and C. I. Ratcliffe, in 'Comprehensive Supramolecular Chemistry, Physical Methods', eds J. L. Atwood, J. E. D. Davies, D. D. MacNicol, F. Vogtle, and J. M. Lehn, Elsevier: Oxford, 1996, Vol. 8, p. 323.
8. C. A. Fyfe, 'Solid State NMR for Chemists', CFC Press: Guelph, 1983.
9. J. H. van der Waals and J. C. Platteeuw, *Adv. Chem. Phys.*, 1959, **2**, 1.
10. N. G. Parsonage and L. A. K. Staveley, 'Disorder in Crystals', Clarenden Press: Oxford, 1978.
11. Z. Asfari, V. Boehmer, J. Harrowfield, and J. Vicens eds, 'Calixarenes 2001', Kluwer: Dordrecht, 2001.
12. K. A. Kvenvolden, *Proc. Natl. Acad. Sci. USA*, 1999, **96**, 3420.
13. D. W. Davidson, Y. P. Handa, and J. A. Ripmeester, *J. Phys. Chem.*, 1986, **90**, 6549.
14. J. A. Ripmeester and C. I. Ratcliffe, *J. Phys. Chem.*, 1988, **97**, 337.
15. D. W. Davidson, S. K. Garg, S. R. Gough, Y. P. Handa, C. I. Ratcliffe, J. A. Ripmeester, J. S. Tse, and W. F. Lawson, *Geochim. Cosmochim. Acta*, 1986, **50**, 619.
16. J. A. Ripmeester and C. I. Ratcliffe, *Energy Fuels*, 1998, **12**, 197.
17. C. I. Ratcliffe and J. A. Ripmeester, *J. Phys. Chem.*, 1986, **90**, 1259.
18. J. A. Ripmeester, J. S. Tse, C. I. Ratcliffe, and B. M. Powell, *Nature*, 1987, **325**, 135; K. A. Udachin, C. I. Ratcliffe, G. D. Enright, and J. A. Ripmeester, *Supramol. Chem.*, 1997, **8**, 173.
19. E. D. Sloan, 'Clathrate Hydrates of Natural Gas', 2nd edition, Marcel Dekker: New York, 1997.
20. C. A. Tulk, J. A. Ripmeester, and D. D. Klug, *Ann. N. Y. Acad. Sci.*, 2000, **912**, 859.
21. C. A. Tulk, Y. Ba, D. D. Klug, G. McLaurin, and J. A. Ripmeester, *J. Chem. Phys.*, 1999, **110**, 6475.
22. Y. Ba, C. I. Ratcliffe, and J. A. Ripmeester, *Chem. Phys. Lett.*, 1999, **299**, 201.
23. T. Pietrass, H. C. Gaede, A. Bifone, A. Pines, and J. A. Ripmeester, *J. Am. Chem. Soc.*, 1995, **117**, 7520.
24. I. L. Moudrakovski, C. I. Ratcliffe, G. MacLaurin, B. Simard, and J. A. Ripmeester, *J. Phys. Chem. A*, 1999, **103**, 4969.
25. T. Iwamoto, in 'Comprehensive Supramolecular Chemistry', eds J. L. Atwood, J. E. Davies, D. D. MacNicol, F. Vogtle, and J. M. Lehn, Elsevier: Oxford, 1996, Vol. 6, p. 643.
26. C. D. Gutsche, 'Calixarenes Revisited', RSC: Cambridge, 1998.
27. T. Komoto, I. Ando, Y. Nakamoto, and S. I. Ishida, *J. Chem. Soc., Chem. Commun.*, 1988, 135.
28. E. B. Brouwer, G. D. Enright, and J. A. Ripmeester, *J. Inclusion Phenom. Mol. Recogn. Chem.*, 1996, **24**, 1.
29. E. B. Brouwer and J. A. Ripmeester, *Adv. Supramol. Chem.*, 1999, **5**, 121.
30. E. B. Brouwer, R. D. M. Gougeon, J. Hirschinger, K. A. Udachin, R. K. Harris, and J. A. Ripmeester, *Phys. Chem. Chem. Phys.*, 1999, **1**, 4043.

Biographical Sketches

John A. Ripmeester, *b* 1944. B.Sc., 1965, Ph.D., 1970, University of British Columbia. Trained in solid state NMR in graduate school and during post-doctoral work (University of Illinois, Urbana), he joined the National Research Council of Canada in 1972 to study clathrate hydrate inclusions. Currently he leads a multidisciplinary group at NRC that synthesizes and characterizes functional materials. Approx. 370 papers; recent emphasis mainly on the characterization of supramolecular and mesoporous materials, with a heavy NMR component; 4 patents. Research interests: characterizing complex interactions in the solid state.

Christopher Ian Ratcliffe, *b* 1951. B.Sc., 1972, Ph.D., 1975, University of Durham, UK. Trained in solid state NMR during post-doctoral work (University of British Columbia), and as a Research Associate at the National Research Council of Canada. He joined NRC in 1982 where he is currently a Senior Research Officer in the Functional Materials Program. Approx. 170 papers. Current research focus: clusters and wires in zeolites and mesoporous materials, metal-silicon and related clathrates, applications of ^{129}Xe NMR, order/disorder and dynamics in solids.

Eric B. Brouwer, *b* 1967. B.Sc., 1990 Queen's University, M.Sc. 1992 University of British Columbia, Ph.D., 1996, Carleton University. Post-doctoral work with R. K. Harris at University of Durham in solid-state NMR. He is currently employed as a Research Scientist at i-STAT Corporation. Approx. 25 papers in supramolecular chemistry and NMR spectroscopy.

Indirect Coupling: Theory and Applications in Organic Chemistry

Michael Barfield

Department of Chemistry, University of Arizona, Tucson, AZ, USA

1	Introduction	1
2	Observations and Early Interpretations	1
3	Theoretical Formulations for Nuclear Spin–Spin Coupling	2
4	Applications to Specific Coupling Situations	9
5	References	11

1 INTRODUCTION

Nuclear spin−spin coupling theory has been the subject of several reviews[1−4] and it has been an annual topic in the Royal Society of Chemistry Reports since 1972.[5,6] In recent years there has been a renewed interest in the factors controlling heteronuclear spin−spin coupling constants. This is partially attributable to the emergence of multiple pulse techniques for spectral editing as these have produced a wealth of new data.

Like many other topics in NMR an exhaustive review of indirect nuclear spin−spin coupling theory would not be possible within the limitations of this review. Moreover, various aspects of J coupling will appear in other chapters of this monograph. Thus, the scope of this chapter is narrowed to reflect the author's interests in this topic for the past 30 years and to bring some coherence to this material. The coverage of the literature is fairly complete up until the early 1970s. It was at about this time that the FPT-INDO method [finite perturbation theory in the intermediate neglect of differential overlap approximation of self-consistent field molecular orbital (SCF-MO) theory] became generally available and was applied to an enormous number of problems.[7] In recent years high quality ab initio computations have appeared. These use large basis sets and include extensive correlation corrections applied to both Fermi contact and noncontact mechanisms.[8−15]

The spin−spin coupling phenomenon quickly emerged as a powerful tool for structural and conformational studies, in part, because of the general applicability of semiempirical methods in reproducing conformational and substituent trends. This is in marked contrast with chemical shielding where the data are even more abundant but semiempirical methods have not been as useful. The first part of this chapter will describe the observation and early interpretation of the spin−spin coupling phenomenon. The second part will present an overview of theoretical descriptions as expressed in density matrix notation and exemplified by semiempirical methods. The final section applies the theory to some organic structural aspects of J coupling, again emphasizing topics of interest to the author.

2 OBSERVATIONS AND EARLY INTERPRETATIONS

The early work in the observation of spin−spin coupling will be described elsewhere in this article and will only be described briefly here. In 1950 the application of spin echo methods to ethanol by Hahn[16] showed 'slow beats' in the echo. These were later shown to arise from nuclear spin−spin coupling. Using slow passage conditions, the fine structure in the ^{121}Sb resonance of a solution of $NaSbF_6$, which was observed by Proctor and Yu,[17] was thought to arise from the magnetic dipole interaction of the Sb nucleus with the surrounding F nuclei. Gutowsky and McCall[18] also observed fine structure in ^{31}P and ^{19}F spectra. In 1951 there were several other papers on this topic[19,20] and it was soon concluded that the interaction is independent of the external field but that it does depend on the product of the nuclear spin vectors,[21−23]

$$\Delta E_{\mathrm{NN}'} = h J_{\mathrm{NN}'} \boldsymbol{I}_{\mathrm{N}} \cdot \boldsymbol{I}_{\mathrm{N}'} \tag{1}$$

where $J_{\mathrm{NN}'}$ is the nuclear spin−spin coupling constant in hertz. The physical basis for these splittings was disputed until the appearance of papers by Ramsey and Purcell[24] and Ramsey.[25] They concluded that the interaction arises from 'the magnetic interaction between each nucleus and the electron spin of its own atom together with the exchange coupling of the electron spin with each other'. In the absence of a magnetic field the spin−spin coupling constant for H_2 is simply the energy difference in hertz between *ortho*- and *para*-hydrogen, e.g. in the absence of a magnetic field it is the difference between the triplet and singlet nuclear spin levels. This is depicted in Figure 1 for a pair of equivalent spin-$\frac{1}{2}$ nuclei. The nuclear Zeeman levels are plotted as a function of the magnetic induction B_0. The J coupling is taken to be of positive sign if the nuclear spin singlet energy is lower than the triplet energy. This is the case for H_2 because the Fermi contact mechanism (which is dominant) favors the antiparallel arrangement of electron and nuclear spins.

In his 1953 paper Ramsey developed a general formulation for nuclear spin−spin coupling. Equation (1) implies that coupling constant terms will occur in first order perturbation theory if the operators contain the product $\boldsymbol{I}_{\mathrm{N}} \cdot \boldsymbol{I}_{\mathrm{N}'}$, e.g. the one-electron or orbital diamagnetic term. Contributions will also arise in second order perturbation theory as products of operators ($\boldsymbol{A}_{\mathrm{N}} \cdot \boldsymbol{I}_{\mathrm{N}}$ and $\boldsymbol{A}_{\mathrm{N}'} \cdot \boldsymbol{I}_{\mathrm{N}'}$) containing the two nuclear spins. Ramsey identified three interaction terms of this form, those involving the electron orbital motion with the nuclear spin, the dipolar term involving the electronic spins and the nuclear spins, and the Fermi contact interaction associated with the electronic and the nuclear spins. Ramsey's expression for the (isotropic) Fermi contact term, which is of primary interest here, in Gaussian units is

$$J_{\mathrm{NN}'} = -(2/3h)\left(16\pi\beta\frac{\hbar}{3}\right)^2 \gamma_{\mathrm{N}}\gamma_{\mathrm{N}'} \sum_{\kappa} ({}^3E_\kappa - {}^1E_0)^{-1} \times \left\langle 0 \left| \sum_j \delta(r_{j\mathrm{N}}) S_j \right| \kappa \right\rangle \left\langle \kappa \left| \sum_k \delta(r_{k\mathrm{N}'}) S_k \right| 0 \right\rangle \tag{2}$$

where $J_{\mathrm{NN}'}$ denotes the isotropic coupling between nuclei N and N′ having magnetogyric ratios γ_{N} and $\gamma_{\mathrm{N}'}$, respectively. The first summation is over all triplets κ. In the Fermi contact

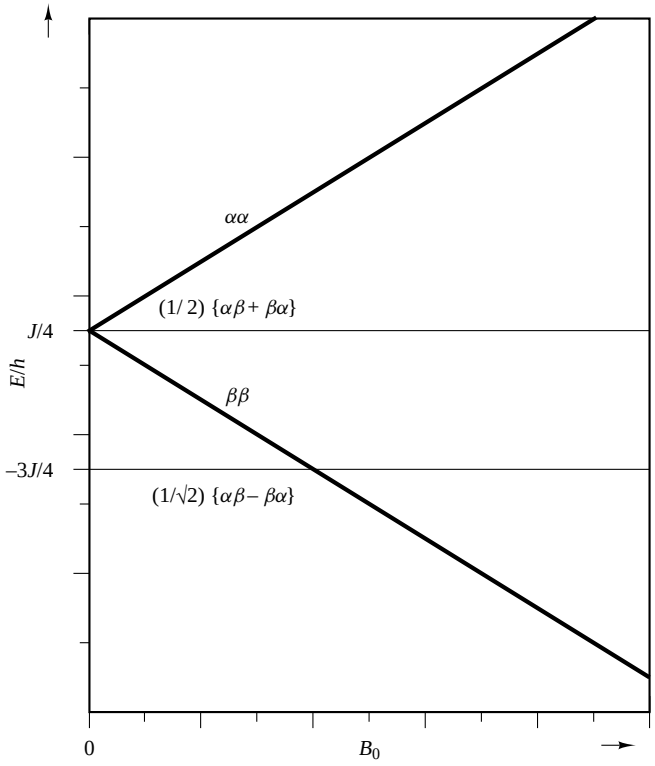

Figure 1 Energy level diagram for two equivalent spin-$\frac{1}{2}$ nuclei plotted as a function of the magnetic induction B_0. The coupling constant J is the separation between the nuclear spin singlet and the nuclear spin triplet

operators $\delta(r_{j\mathrm{N}})$, for example, denotes the Dirac delta function for electron j at nucleus N, S_j is the electron spin operator for the jth electron, and the summation is taken over all electrons j. Matrix elements connect the singlet states $\langle 0|$ having energy ${}^1E_0$ and triplet states $|\kappa\rangle$ having energies ${}^3E_\kappa$. Equation (2) is the starting point for most discussions of Fermi contact coupling. Ramsey also recognized the tensor nature of the J coupling but for the HD molecule only reported numerical estimates of the *isotropic* terms. Based on the James and Coolidge wavefunction, a value of 40 Hz for the Fermi contact term is in reasonable accord with the experimental value of 42.7 ± 0.7 Hz.[26] This also supported arguments for small contributions from noncontact mechanisms. Following speculation that the H–D spin–spin coupling constant had a negative sign,[27] Code and Ramsey used molecular beam methods to demonstrate[28] that the sign was indeed positive.

Ramsey also made the interesting observation that as the atoms of HD are pulled apart, the denominator in equation (2) approaches zero, a situation in which perturbation theory would not be applicable. Because of a possible relationship to long-range coupling, the dependence of the H–H nuclear spin–spin coupling on $r_{\mathrm{HH}'}$ was examined[29] using a variational method with Heitler–London wavefunctions including both the electron and nuclear spins. In the dissociation limit the splitting is the electron–nuclear hyperfine coupling. The total electronic spin S cannot be a good quantum number as the molecule dissociates as this would have the contradiction of nuclear spin–spin coupling being nonzero at infinite separation. In the simple Heitler–London picture for which the singlet and triplet energies are asymptotic as $R \rightarrow \infty$, the four basic product electron spin functions necessarily assume equal weights corresponding to two uncorrelated spins. Had effects as small as the indirect nuclear spin–spin coupling been of interest, these would have been implicit in the detailed work of the Wisconsin group on the H_2 hyperfine splitting.[30] The previous reviews[1–6] should be consulted for references to the many papers concerned with calculation of the HD coupling constant.

Before looking at specific molecular formulations, it will be convenient in the next section to transcribe the various expressions for (Fermi contact) nuclear spin–spin coupling constants into density matrix notation. These techniques will then be used in Sections 3.2–3.4 to discuss the specific quantum mechanical formulations.

3 THEORETICAL FORMULATIONS FOR NUCLEAR SPIN–SPIN COUPLING

3.1 Density Matrix Notation

The density matrix notation adopted here follows that introduced by McWeeny and co-workers.[31,32] This formalism was used extensively in these laboratories to investigate nuclear spin–spin coupling and a number of other types of NMR parameters. The one-electron *transition density matrix* associated with states Ψ_κ and Ψ_λ is given by

$$\rho_1(\kappa\lambda \mid 1; 1') = N \int \Psi_\kappa(1, 2, 3, \ldots, N)\Psi^*_\lambda \times \Psi_\lambda(1', 2, 3, \ldots, N)\ \mathrm{d}r_2\ \mathrm{d}r_3 \ldots\ \mathrm{d}r_N \quad (3)$$

where N is the number of electrons and the integrations are to be taken over the space and spin coordinates r_i of all but one electron. It is sometimes convenient to write the one-electron density matrix in terms of spinless components,

$$\rho_1(\kappa\lambda \mid 1; 1') = P_1(\kappa\lambda \mid \overset{\alpha}{1}; \overset{\alpha}{1'})\alpha(1)\alpha^*(1') + P_1\kappa\lambda \mid \overset{\beta}{1}; \overset{\beta}{1'})\beta(1)\beta^*(1') \quad (4)$$

from which it follows that for a given state ($\kappa = \lambda$) the diagonal element denotes the probability of finding an electron in volume element at point 1. *Transition spin densities* occur when spin operators are involved and these can be written in terms of the spinless components,

$$Q_1(\kappa\lambda \mid 1; 1') = P_1(\kappa\lambda \mid \overset{\alpha}{1}; \overset{\alpha}{1'}) - P_1(\kappa\lambda \mid \overset{\beta}{1}; \overset{\beta}{1'}) \quad (5)$$

For a given state ($\kappa = \lambda$) $Q_1(\kappa\kappa|1;1)$ is just a *spin density* for which integration over all space gives the number of unpaired spins.

From equations (2)–(5) the expression for the Fermi contact (FC) contribution to the isotropic spin–spin coupling is

$$J_{\mathrm{NN}'} = -(2h)^{-1}(16\pi\beta\hbar/3)^2\gamma_{\mathrm{N}}\gamma_{\mathrm{N}'}\sum_\kappa({}^3E_\kappa - {}^1E_0)^{-1} \times Q_1(0\kappa_0 \mid 1_{\mathrm{N}}; 1_{\mathrm{N}})Q_1(0\kappa_0 \mid 1_{\mathrm{N}'}; 1_{\mathrm{N}'}) \quad (6)$$

where $Q_1(0\kappa_0|1_N;1_N)$, for example, denotes the transition spin density evaluated at the position of nucleus N. The advantages of using density matrix notation rather than the integrals in equation (2) are the removal of the spin operators and the ease of writing general density matrix expressions. General density matrix expressions analogous to equation (6) can also easily be written for coupling constant contributions associated with the spin dipolar (SD), and orbital paramagnetic (OP) contributions, as well as the various cross terms.[33,34]

The initial theoretical work on J coupling invoked the so called 'average energy approximation' to simplify the second order expressions. This procedure invokes closure in the second order sum and replaces the excitation energies by an average value ΔE. Although it has long been clear that this procedure is not an approximation in the usual sense of the word,[35,36] it has led to some very important relationships between J couplings and molecular structures as well as some useful qualitative insights that have permitted correlations of many structural features. The 'average energy approximation' was particularly appealing in its very simple relationship to the electron correlation features in n-particle systems.[32,37,38] In density matrix notation the FC contribution to the spin–spin coupling between nuclei N and N′ at this level of theory is given by[32]

$$J_{NN'} = -(3h\Delta E)^{-1}(16\pi\beta\hbar/3)^2\gamma_N\gamma_{N'}Q_c(1_N, 2_{N'}; 1_N, 2_{N'}) \tag{7}$$

where $Q_c(1_N, 2_{N'}; 1_N, 2_{N'})$ denotes a two-electron spin density (or spin coupling matrix) evaluated at the positions of the coupled nuclei, and ΔE is an 'average excitation energy'. The usual state labels of density matrix notation are not used here because only the ground state wavefunction is involved. The two-electron spin density matrix is related to the two-electron spinless components of the density matrix,

$$Q_c(1, 2; 1', 2') = 3[P_2(\overset{\alpha}{1}, \overset{\alpha}{2}; \overset{\alpha}{1'}, \overset{\alpha}{2'}) - P_2(\overset{\alpha}{1}, \overset{\beta}{2}; \overset{\alpha}{1'}, \overset{\beta}{2'})] \tag{8}$$

where the first term on the right denotes the simultaneous probability of finding the two electrons with α spin in differential volume elements at points 1 and 2, and the second term denotes the corresponding probability for electrons of opposite spin. We now look at some important implications of these relationships. The spinless components in equation (8) are related to the one-particle spinless density matrix components in equation (4) and correlation functions for electrons of the same and opposite spins,

$$P_2(\overset{\alpha}{1}, \overset{\alpha}{2}; \overset{\alpha}{1}, \overset{\alpha}{2}) = P_1(\overset{\alpha}{1}; \overset{\alpha}{1})P_1(\overset{\alpha}{2}; \overset{\alpha}{2})[1 + f(\overset{\alpha}{1}, \overset{\alpha}{2})] \tag{9}$$

$$P_2[(\overset{\alpha}{1}, \overset{\beta}{2}; \overset{\alpha}{1}, \overset{\beta}{2})] = P_1(\overset{\alpha}{1}; \overset{\alpha}{1})P_1(\overset{\beta}{2}; \overset{\beta}{2})[1 + f(\overset{\alpha}{1}, \overset{\beta}{2})] \tag{10}$$

where $f(\overset{\alpha}{1}, \overset{\alpha}{2})$ and $f(\overset{\alpha}{1}, \overset{\beta}{2})$ denote correlation functions for electrons of the same and of opposite spins, respectively. The Pauli Exclusion Principle requires that as the coordinates of particle 2 approach those of particle 1,

$$f(\overset{\alpha}{1}, \overset{\alpha}{2}) \to -1 \quad \text{and} \quad f(\overset{\alpha}{1}, \overset{\beta}{2}) \to -1 \tag{10a}$$

corresponding to 100% negative correlation which prevents particles of like spin being found at the same point in space.[31]

Since essentially all of the molecules of interest are in singlet ground states

$$P_1(\overset{\alpha}{1}; \overset{\alpha}{1}) = P_1(\overset{\beta}{2}; \overset{\beta}{2}) = (\tfrac{1}{2})P_1(1; 1) \tag{11}$$

so that both the two-electron spin density matrix and the *nuclear spin–spin coupling are proportional to the differences in the correlation functions for electrons of the same and opposite spins*,

$$Q_c(1, 2; 1, 2) = (\tfrac{3}{4})P_1(1; 1)P_1(2; 2)[\, f(\overset{\alpha}{1}, \overset{\alpha}{2}) - f(\overset{\alpha}{1}, \overset{\beta}{2})] \tag{12}$$

At this level of theory the various bond orders provide estimates for the differences in the correlation functions in equation (12).

3.2 Early Theory

The recognition of the spin coupling phenomenon quickly led to theoretical discussion using the Heitler–London formulation.[39] It also provided an explanation for linewidths in solids which were larger than could be accounted for on the basis of the direct dipole–dipole interactions.[40,41]

3.2.1 Molecular Orbital Methods

In the period 1955–1957 McConnell considered the J coupling problem from several points of view including a molecular orbital description,[42] a Dirac vector model,[43] and a spin-exchange model.[44,45] The MO model was used by Saika[46] to investigate the J coupling in ammonia. On the basis of MO results in which interproton spin–spin coupling constants were proportional to the square of the MO bond order, McConnell speculated that interproton coupling constants were probably all positive in sign.[47] In the light of subsequent sign measurements, a formulation was used to rationalize the negative $J(H, H')$ in aromatic systems.[48] During this period Pople related the orbital contributions to nuclear spin–spin coupling to the anisotropy of the magnetic screening.[49]

In single determinant Hartree–Fock theory the correlation function for electrons of opposite spins in equation (12) vanishes identically, and assuming that the molecule has a singlet ground state,

$$Q_c(1, 2; 1, 2) = (\tfrac{3}{4})P_1(1; 1)P_1(2; 2)\, f(\overset{\alpha}{1}, \overset{\alpha}{2}) \tag{13}$$

which is negative because the correlation function $f(\overset{\alpha}{1}, \overset{\alpha}{2})$ is inherently negative (it is zero if the electrons are uncorrelated).

Expanding a Slater determinant via Laplace's development leads to an expression for the two-particle density matrix in terms of the Fock–Dirac density matrix $\rho_1(1;1')$,[32]

$$\rho_2(1, 2; 1', 2') = \rho_1(1; 1')\rho_1(2, 2') - \rho_1(1; 2')\rho_1(2; 1') \tag{14}$$

Rewriting the one-particle density matrices in terms of the spinless components provides an expression for the two-electron spinless components,

$$P_2(\overset{\alpha}{1},\overset{\alpha}{2};\overset{\alpha}{1'},\overset{\alpha}{2'}) = P_1(\overset{\alpha}{1};\overset{\alpha}{1'})P_1(\overset{\alpha}{2},\overset{\alpha}{2'}) - P_1(\overset{\alpha}{1};\overset{\alpha}{2'})P_1(\overset{\alpha}{2};\overset{\alpha}{1'}) \tag{15}$$

$$P_2(\overset{\alpha}{1},\overset{\beta}{2};\overset{\alpha}{1'},\overset{\beta}{2'}) = P_1(\overset{\alpha}{1};\overset{\alpha}{1'})P_1(\overset{\beta}{2};\overset{\beta}{2'}) \tag{16}$$

From equation (8) the spin coupling function can, therefore, be written in terms of the off-diagonal elements of the one-particle density matrix

$$Q_c(1,2;1,2) = -(\tfrac{3}{4})P_1(1;2)P_1(2;1) \tag{17}$$

where the off-diagonal elements of the one-particle density matrix can be written in terms of the molecular orbitals

$$P_1(1;2) = \sum_i n_i \chi_i(1)\chi_i^*(2) = \sum_{\mu\nu}\sum_i n_i c_{i\mu}c_{i\nu}^*\phi_\mu(1)\phi_\nu^*(2)$$
$$= \sum_{\mu\nu}\eta_{\mu\nu}\phi_\mu(1)\phi_\nu^*(2) \tag{18}$$

In the ith molecular orbital $c_{i\mu}$ and $c_{i\nu}$ are the coefficients of orbitals μ and ν, respectively, n_i is the occupation number, and $\eta_{\mu\nu}$ is the bond order between orbitals μ and ν as defined by Coulson and Longuet-Higgins,[50]

$$\eta_{\mu\nu} = \sum_i n_i c_{i\mu}c_{i\nu}^* \tag{19}$$

Substituting equation (18) into equation (17), one sees that at this level of MO theory the coupling constant is proportional to the square of the bond order. This is awkward, not only because of the single sign problem noted above, but also because this type of bond order vanishes for even alternant systems if orbitals μ and ν are in the same subset.[50] Of course, this result is not consistent with a large number of examples of sizable spin–spin coupling constants of either sign for atoms separated by an even number of bonds. These problems can be circumvented in alternant MO methods[38] in which both types of correlation are included in an easily visualized way. For the specific case of a molecule with two electrons, e.g. H_2 $P_2(\overset{\alpha}{1},\overset{\alpha}{2};\overset{\alpha}{1},\overset{\alpha}{2}) = 0$, so the coupling constant is proportional to

$$Q_c(\overset{\alpha}{1},\overset{\beta}{2};\overset{\alpha}{1},\overset{\beta}{2}) = -3P_2(\overset{\alpha}{1},\overset{\alpha}{2};\overset{\beta}{1},\overset{\beta}{2})$$
$$= -3P_1(1;1)P_1(2,2)[1 + f(\overset{\alpha}{1},\overset{\beta}{2})] \tag{20}$$

Since $f(\overset{\alpha}{1},\overset{\beta}{2}) = 0$ at the Hartree–Fock level, equation (13) becomes simply

$$Q_c(1,2;1,2) = -(\tfrac{3}{4})P_1(1;1)P_1(2,2) \tag{21}$$

For a two-electron system in terms of the occupied MO χ the diagonal element is simply

$$P_1(1;1) = 2\chi(1)\chi^*(1') \tag{22}$$

Taking χ to be a linear combination of atomic orbitals ϕ_μ and ϕ_ν, associated with nuclei N and N′, then

$$P_1(1;1') = \phi_\mu(1)\phi_\mu^*(1') + \phi_\nu(1)\phi_\nu^*(1')$$
$$+\phi_\mu(1)\phi_\nu^*(1') + \phi_\nu(1)\phi_\mu^*(1') \tag{23}$$

Neglecting terms like $\phi_\mu(1_N)\phi_\nu{}^*(1_N)$ in comparison with terms like $\phi_\mu{}^2(1_N)$, it then follows from equations (7) and (22) that the directly bonded coupling constant expression is

$$J_{NN'} = (h\Delta E)^{-1}(16\pi\beta\hbar/3)^2\gamma_N\gamma_{N'}\phi_\mu^2(1_N)\phi_\nu^2(1_{N'}) \tag{24}$$

Substitution of the form for a hybrid orbital for one or both of ϕ_μ and ϕ_ν where ϕ_μ is of the form

$$\phi_\mu = as_\mu + (1-a^2)^{1/2}p_{\sigma\mu} \tag{25}$$

where s_μ and $p_{\sigma\mu}$ denote 2s and 2p atomic orbitals on atom μ and a^2 is the s character. The resulting equation relates directly bonded, e.g. $^{13}C–H$ and $^{13}C–^{13}C$ coupling constants to the s characters at the carbon atoms.[51–53] Equation (25) neglects a factor of $(1 + S)^{-2}$, where S is the overlap integral between bonded orbitals ϕ_μ and ϕ_ν. By means of an alternant molecular orbital method it was noted[38] that *the neglect of overlap compensates to some extent for the neglect of electron correlation*!

3.2.2 Valence Bond (VB) Methods

These methods were used extensively in the early work in nuclear spin–spin coupling.[54–71] Certainly, the most widely known application is that for the angular dependence of the vicinal H–H coupling constants in ethane.[58] Since the VB method had an important impact on the development of spin–spin coupling theory, its application in conformational analyses, and some intuition regarding the electronic factors leading to the phenomenon, a brief review seems appropriate here. Even though VB concepts are closely tied to chemists' ideas of formulas, resonance, etc., the quantum mechanical methods are unfamiliar to many chemists. The derivation of VB coupling constant expressions demonstrates the simplicity provided by the density matrix formalism. In the simple VB method the singlet ground state wavefunction $^1\Psi_0$ is written as a linear combination of independent, nonpolar VB structures $^1\Phi_j$,[72]

$$^1\Psi_0 = \sum_j c_j\,{}^1\Phi_j \tag{26}$$

The $^1\Phi_j$ can be constructed formally by placing $2n$ points on the circumference of a circle and then drawing all possible structures which have all of the points connected, but in which no two lines cross. For example, depicted in Figure 2(a) are the two independent, singlet VB structures $^1\Phi_1$ and $^1\Phi_2$. These are useful for investigating geminal, vicinal, and long range H–H coupling as described simply by two C–H bonds as depicted in Figure 2(b). The perfect pairing structure is that in which there are covalent bonds between the carbon hybrid orbitals and the hydrogenic 1s atomic orbitals $c–h$ and $c'–h'$. The nonperfect pairing structure is of

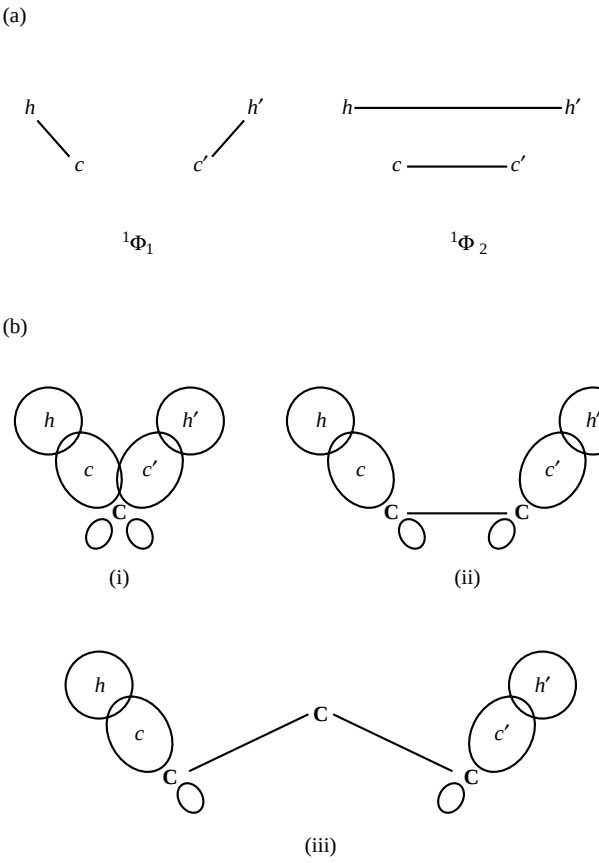

Figure 2 (a) Valence bond singlet structures for a system of four electrons associated with two C–H bonds. Structure $^1\Phi_1$ is the perfect pairing structure and $^1\Phi_2$ is the non-perfect pairing structure. (b) Schematic representations of four electron fragments for (i) geminal coupling in a CH_2 moiety, (ii) vicinal coupling in an ethanic moiety, and (iii) long-range coupling in a propanic moiety

higher energy since it involves breaking the two C–H bonds and forming bonds between h and h' and c and c'. In the VB formulation nonvanishing H–H coupling arises from the contributions of $^1\Phi_2$ to the ground state wavefunction. Matrix elements entering the secular determinant associated with equation (26) are constructed by superimposing the various structures.[73] The matrix elements are written as a sum of terms involving Coulomb and exchange integrals multiplied by a function which is determined by superimposing the VB structures. For a $2n$ electron system the coefficients of the Coulomb integrals are $(\frac{1}{2})^{n-i_{jl}}$ where i_{jl} is the number of islands (closed polygons) which occur in the superposition diagram of structures j and l. The coefficients of the exchange integrals are $(\frac{1}{2})^{n-i_{jl}} f_{jl}^{\mu\nu}$ where $f_{jl}{}^{\mu\nu}$ assumes the values 1, -2, and $-\frac{1}{2}$ depending on whether orbital μ and ν are in the same island separated by an odd number of bonds, or an even number of bonds, or are in different islands, respectively. The two-electron density matrix follows directly from the expression for the ground state energy,

$$P_2(1,2;1',2') = \sum_{j,l} c_j c_l (\tfrac{1}{2})^{n-i_{jl}} \sum_{\mu,\nu} [\phi_\mu(1)\phi_\nu(2)\phi_\mu(1')\phi_\nu(2') + f_{jl}^{\mu\nu}\phi_\mu(1)\phi_\nu(2)\phi_\nu(1')\phi_\mu(2')] \quad (27)$$

where c_j is the coefficient of the jth VB structure, and ϕ_μ and ϕ_ν are atomic orbitals. The spin–spin coupling function is obtained from equations (7) and (8) and the spinless components of $P_2(1, 2; 1', 2')$,[32,74]

$$Q_c(1,2;1',2') = -(\tfrac{1}{2}) \sum_{j,l} c_j c_l (\tfrac{1}{2})^{n-i_{jl}} \times \sum_{\mu,\nu} [(1 + 2f_{jl}^{\mu\nu})\phi_\mu(1)\phi_\nu(2)\phi_\mu(1')\phi_\nu(2') + (2 + f_{jl}^{\mu\nu})\phi_\mu(1)\phi_\nu(2)\phi_\nu(1')\phi_\mu(2')] \quad (28)$$

Equation (28) can immediately be rewritten in terms of the Penney–Dirac bond orders $p_{PD}(\mu, \nu)$,

$$Q_c(1,2;1',2') = -(\tfrac{3}{2}) \sum_{\mu\nu} \{p_{PD}(\mu,\nu)\phi_\mu(1)\phi_\nu(2)\phi_\mu \times(1')\phi_\nu(2') + (\tfrac{1}{2})[1 + p_{PD}(\mu,\nu)]\phi_\mu(1) \times\phi_\nu(2)\phi_\nu(1')\phi_\mu(2')\} \quad (29)$$

where[75]

$$p_{PD}(\mu,\nu) = (\tfrac{1}{3}) \sum_{j,l} c_j c_l (\tfrac{1}{2})^{n-i_{jl}} (1 + 2f_{jl}^{\mu\nu}) \quad (30)$$

Neglecting two-center overlap terms of the type $\phi_\mu(1_N)\phi_\nu(1_N)$ in equation (27) shows that the nuclear spin–spin (FC contribution) coupling is linearly related to the Penney–Dirac bond order $p_{PD}(\mu, \nu)$.[66] Consider several situations for H–H coupling represented by the two C–H bonds in Figure 2(b). Depending on whether the hybrid orbitals c and c' constitute (i) a geminal pair, (ii) a vicinal pair, or (iii) are hybrid carbon orbitals separated by two or more bonds, these structures provide a useful, but simplistic, representation of the corresponding coupling situations. Note that the PD bond order $p_{PD}(h, h')$ has no contribution from the perfect pairing structure [see Figure 2(a)] because $f_{11}{}^{hh'} = -\frac{1}{2}$ in equation (30). However, in the superposition diagram for $^1\Phi_1$ and $^1\Phi_2$, $f_{12}{}^{hh'} = 1$ leading to a nonvanishing contribution to $p_{PD}(h, h')$. Using perturbation theory $c_1 \approx 1$,[54,74] hence

$$c_2 \approx (\tfrac{1}{2}) \left[\frac{K(h,h') + K(c,c') - K(c,h') - K(c',h)}{K(c,h) + K(c',h') - K(c,c') - K(h,h')} \right] \quad (31)$$

where $K(\mu, \nu)$ is a two-center exchange integral associated with orbitals ϕ_μ and ϕ_ν,

$$K(\mu,\nu) = \int\int \phi_\mu(1)\phi_\nu(2)[(R_{ab})^{-1} + (r_{12})^{-1} - (r_{1b})^{-1} - (r_{2a})^{-1}]\phi_\nu(1)\phi_\mu(2)\ d\tau_1\ d\tau_2 \quad (32)$$

From equation (30) the PD bond order associated with the hydrogens is simply,

$$p_{PD}(h,h') = c_1c_2 + c_2^2 \approx c_1c_2 \approx c_2 \quad (33)$$

Since $c_2 \ll c_1 \approx 1$ for saturated systems, in this simple model the coupling constant is proportional to the contribution of the nonperfect pairing structure to the ground state wavefunctions,

and it related to the exchange integrals in equation (31). As the numerator and any one of the exchange integrals can be of either sign, the Penney–Dirac bond orders and coupling constants can be either positive or negative. This is a more plausible result than the quadratic dependence on the MO bond order, which occurs because of the very different ways in which electron correlation appears in these two methods! Because of the extreme importance of electron correlation effects for nuclear spin–spin coupling, the early successes of valence bond methods compared with simple MO methods should come as no surprise.

At an early stage in the development of NMR this simple VB theory qualitatively explained a number of aspects of interproton coupling: geminal H–H coupling is quite sensitive to exchange integral cancelation in the numerator of equation (31). In comparison with vicinal H–H coupling constants, geminal H–H coupling constants are very sensitive to H–C–H angles, substituent and solvent effects. The original VB calculations for vicinal H–H coupling constants in an ethanic fragment were based on a six-electron fragment for the ethane molecule. However, all of the important aspects are implicit in the four-electron model described herein. In the original paper[58] describing the dihedral angle dependence of vicinal H–H coupling constants, the only necessary nonbonded exchange integral was $K(c, c')$ occurring in the numerator of equation (29). The hybrid orbitals c and c' are depicted in Figure 2(b). The most general form of a, e.g., carbon hybrid orbital ϕ_μ can be written in terms of atomic s- and p-type atomic orbitals, the angle θ_μ that the hybrid orbital makes with the z axis, and the dihedral angle φ about the z axis,

$$\phi_\mu = a_\mu s_\mu + (1 - a_\mu^2)^{1/2}(\cos\varphi \sin\theta_\mu p_{x\mu} + \sin\varphi \sin\theta_\mu p_{y\mu} + \cos\theta_\mu p_{\sigma\mu}) \quad (34)$$

where s_μ, $p_{x\mu}$, $p_{y\mu}$, and $p_{\sigma\mu}$ denote the 2s and 2p atomic orbitals associated with the μth hybrid orbital, and a_μ is defined such that ${a_\mu}^2$ is the s character of the hybrid orbital. If equation (4) is specialized, for example, to tetrahedral hybrids with appropriate bond angles and a single dihedral angle φ, substitution of equation (34) into equation (32) gives the mathematical form for the vicinal exchange integral

$$K(c, c') = A\cos^2\varphi + B\cos\varphi + C \quad (35)$$

From equations (28)–(31), (33) and (7) this will also be the approximate form for dependence of vicinal coupling constants on dihedral angles.

This simple, qualitative VB model can be extended to systems which have more than four electrons by means of 'fragment' bond orders of the type given in equations (31) and (33). The fragment bond order $p^0(r, s)$ associated with bonds $r–r'$ and $s–s'$ is

$$p^0(r, s) = (\tfrac{1}{2})\left[\frac{K(r, s) + K(r', s') - K(r, s') - K(r', s)}{K(r, r') + K(s, s') - K(r, s) - K(r', s')}\right] \quad (36)$$

Consider the calculation of the PD bond order $p_{\mathrm{PD}}(h, h')$ for the molecular system depicted in Figure 3. In addition to the two C–H bonds there are N bond pairs $(t–t')_j$. The Penney–Dirac bond orders can be determined from the coefficients obtained by perturbation theory. Up to second order the bond order associated with the two hydrogens is written in terms of the fragment bond orders. An approximate expression is[74]

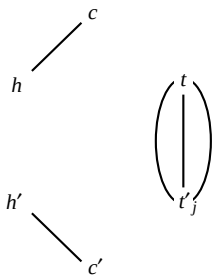

Figure 3 Schematic representations of a four-electron fragment plus n-bonds $(t–t')_j$

$$p_{\mathrm{PD}}(h, h') = p^0(h, h') + (\tfrac{3}{2})\sum_j p^0(h, t_j)p^0(t'_j, h') \quad (37)$$

where each of the fragment bond orders is of form of equation (36). The first term on the right hand side of equation (37) has been associated with a *direct* coupling mechanism and the second with the many possible *indirect* coupling mechanisms.[74] It seems likely that the widely but undefined terms 'through space' and 'through bond' have led to substantial confusion regarding the factors responsible for spin–spin coupling. Additional relationships among the bond order expressions are as follows:

$$p^0(h, h') = p^0(c, c') = -p^0(c, h') = -p^0(h, c') \quad (38)$$

These equations provide a basis for interrelating the various coupling constants and the simple VB bond order model provides a qualitative basis for interpreting a wide variety of substituent and conformational effects.[74,76–80]

3.3 Sum-Over-States Methods

3.3.1 Molecular Orbital Descriptions

Where the ground state wavefunction is given as an antisymmetrized product of molecular orbitals,

$${}^1\Psi_0 = \mathcal{A}[\chi_1(1)\overline{\chi_1(2)}\chi_2(3)\ldots\chi_i(k)\overline{\chi_i(k+1)}\ldots] \quad (39)$$

and triplet state wavefunctions are produced by exciting an electron from the ith occupied MO to the jth unoccupied MO,

$${}^3\Psi_{km} = \mathcal{A}[\chi_1(1)\overline{\chi_1(2)}\chi_2(3)\ldots\chi_i(k)\ldots\chi_j(k+1)\ldots] \quad (40)$$

In equation (40) electrons k and $k + 1$ have parallel spins and $m = +1$, 0, and -1. The transition density matrix associated with the ground state and $m = 0$ components of the triplet levels is given from equations (3), (32) and (33),

$$\rho_1(0\kappa_0 \mid 1; 1') = 2\int \chi_i(1)\chi_i(2)(1/\sqrt{2})[\alpha(1)\beta(2) - \beta(1)\alpha(2)] \times (1/\sqrt{2})[\chi_i^*(1')\chi_j^*(2) + \chi_j^*(1')\chi_i^*(2)] \times (1/\sqrt{2})[\alpha^*(1')\beta^*(2) + \beta^*(1')\alpha^*(2)]\ \mathrm{d}r_2 \quad (41)$$

Integration over the space and spin coordinates of electron 2 yields the transition density matrix

$$\rho_1(0\kappa_0 \mid 1; 1') = -(1/\sqrt{2})\chi_i(1)\chi_j^*(1')[\alpha(1)\alpha^*(1') - \beta(1)\beta^*(1')] \quad (42)$$

which defines the spinless components. These provide an expression for the transition spin density matrix

$$Q_1(0\kappa_0 \mid 1; 1') = -\sqrt{2}\chi_i(1)\chi_j^*(1') \quad (43)$$

Substituting equation (43) into equation (6) leads to an expression for the FC contribution

$$J_{\mathrm{NN}'} = -h^{-1}(16\pi\beta\hbar/3)^2\gamma_{\mathrm{N}}\gamma_{\mathrm{N}'}\sum_{i,j}(\epsilon_j - \epsilon_i)^{-1} \times \chi_i(1_{\mathrm{N}})\chi_j^*(1_{\mathrm{N}})\chi_i(1_{\mathrm{N}'})\chi_j^*(1_{\mathrm{N}'}) \quad (44)$$

where the sum is over the occupied and unoccupied MOs i and j, respectively. Expanding the MOs as a linear combination of atomic orbitals and neglecting contributions other than the s-type orbitals centered on atoms N and N′, this becomes

$$J_{\mathrm{NN}'} = -h^{-1}(16\pi\beta\hbar/3)^2\gamma_{\mathrm{N}}\gamma_{\mathrm{N}'}\sum_{i,j}(\epsilon_j - \epsilon_i)^{-1}c_{i\mu}c_{j\nu}c_{i\nu}c_{j\mu} \times \phi_\mu^2(1_{\mathrm{N}})\phi_\nu^2(1_{\mathrm{N}'}) \quad (45)$$

where orbitals ϕ_μ and ϕ_ν are associated with nucleus N and N′, respectively. Equation (44) is more conveniently written in the form

$$J_{\mathrm{NN}'} = -(4h)^{-1}(16\pi\beta\hbar/3)^2\gamma_{\mathrm{N}}\gamma_{\mathrm{N}'}\phi_\mu^2(1_{\mathrm{N}})\phi_\nu^2(1_{\mathrm{N}'})\pi_{\mu\nu} \quad (46)$$

where the mutual atom–atom polarizability $\pi_{\mu\nu}$ is given by[50]

$$\pi_{\mu\nu} = -4\sum_{i,j}(\epsilon_j - \epsilon_i)^{-1}c_{i\mu}c_{i\nu}c_{j\mu}c_{j\nu} \quad (47)$$

This equation has been used extensively to calculate contact contributions to spin–spin coupling constants and to rationalize substituent trends. Pople and Santry used this formulation and an independent electron MO model[81] to investigate spin–spin coupling constants in hydrocarbons. Perturbation theory was used to relate the mutual atom–atom polarizabilities in equation (47) to the off-diagonal elements of the Hamiltonian.[81] These techniques were extended by several groups to investigate J couplings in a variety of situations.[82–86] Murrell and Gil also used a perturbation approach but for hydrocarbons included the additional integrals which involve the hydrogens.[82] This formulation was also used with a variety of different types of approximate methods, including extended Hückel,[87–91] complete neglect of differential overlap (CNDO),[92] INDO,[93] and wavefunctions[94] based on a modified Mulliken approximation.[95]

The Pople–Santry sum-over-states formulation (usually with a modified denominator to account for triplet energies) or the finite perturbation theory (FPT) method described in the next section was used for ab initio calculations.[33,96–102] The results were unsatisfactory. For example, nonempirical results with SCF wavefunctions (with the exception of values for HFC=O) led to coupling constants which were 2–4 times too large in magnitude.[102]

In a number of cases molecular symmetry has been exploited in the sum-over-states formulation to provide elegant descriptions of substituent effects. These include geminal H–H,[103,104] long range H–H,[105,106] and coupling in ethylenic and aromatic systems.[107] The Pople–Santry method[81] was also used to investigate the importance of noncontact mechanisms, e.g. F–F coupling constants,[108,109] and ^{13}C–^{13}C coupling constants.[110]

Hiroike[111] noted that the simple VB and MO methods based on equation (46) without configuration interaction (CI) represent different contributions to the spin–spin coupling constant. In fact, for the case of long range H–H coupling over four bonds it was found that the sum of the two results gives a much better representation than either of the MO or VB results.[112]

3.3.2 *Valence Bond Sum-Over-Triplet Description*

In the VB sum-over-triplet level scheme from these laboratories,[113,114] the ground state wavefunction is written as before, and the wavefunctions for the manifold of triplets are written,

$$^3\Psi_\kappa = \sum_l c_{\kappa l}\,^3\Phi_l \quad (48)$$

where for a system of $2n$ electrons $^3\Phi_l$ denotes a set of $3[(2n)!/(n+2)!(n-1)!]$ linearly independent, nonpolar triplet canonical structures. These structures can most easily be obtained from the usual Rumer structures according to a scheme devised by McLachlan.[115] For the system of two c–h bonds these structures are depicted in Figure 4. The transition spin densities follow from equations (3)–(5), (26) and (48)

$$Q_1(0\kappa_0 \mid 1; 1') = \sum_{j,l} c_j c_{\kappa l}(\tfrac{1}{2})^{n-i_{jl}}\sum_\mu \phi_\mu(1)\phi_\mu^*(1')f_{jl}^\mu \quad (49)$$

where in the superposition diagrams of the singlet and triplet canonical structures, i_{jl} is the number of islands and $f_{jl}{}^\mu$ = +1 or −1 if orbital ϕ_μ is part of an island which contains a broken bond and is in the even or odd subset respectively.

The VB method with a sum-over-triplets has not been extensively applied. Even in its semiempirical form, a

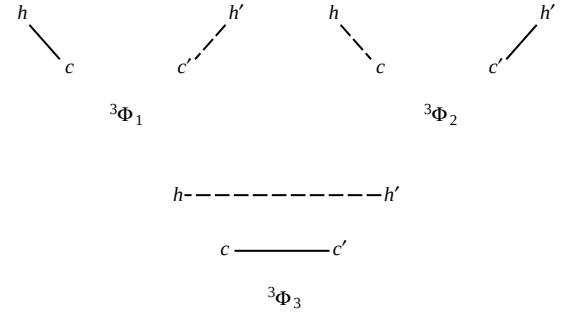

Figure 4 Valence bond triplet structures for a system of four electrons associated with two C–H bonds

molecule with $2n$ electrons requires the calculation of a ground state wavefunction having $[(2n!/n!(n+1)!]$ nonpolar singlet structures and $3[(2n)!/(n+2)!(n-1)!]$ nonpolar triplets. A general scheme for calculating coupling constants, which was developed within the framework of the generalized product approximation, permitted calculations of a large number of coupling constants via VB and other methods.[116–118] Since correlation effects are implicit in the ground state and triplet state VB functions, it is not surprising that it provides an excellent semiempirical description of nuclear spin–spin coupling.

3.3.3 *The Generalized Product Approximation with Intergroup Configuration Interaction*

This method provides a generalization of existing methods for FC spin–spin coupling in terms of the second order perturbation approaches of equations (2) and (6). The recognition of distinct groups in the molecule such as bonds and π-electron systems, permits a simplification of the discussion of many-electron systems.[32] However, for cases of more than one group, an adequate description of spin coupling requires intergroup CI. Group function methods have proved to be a convenient framework for investigating, e.g. long range coupling transmitted via the π-electron systems.[119–126] Although not originally cast in terms of density matrix notation, the various formulations for π-electron contributions to spin–spin coupling can conveniently be described by the generalized product approximation with intergroup CI.[127] For a molecular system in which distinct groups A, B, C, etc. are recognized, a single configuration wavefunction is of the form

$$^1\Phi_0 = \mathcal{A}[^1\phi_{A0}(1, 2, \ldots, N_A)\,{}^1\phi_{B0}(N_A+1, N_A+2, \ldots, N_A+N_B)\ldots] \quad (50)$$

where $\mathcal{A}$ is an operator which gives a normalized, antisymmetric wavefunction, and $^1\phi_{R_0}$ is the lowest energy singlet state wavefunction for the N_R electron group R. Triplet wavefunctions $^3\phi_{R_m}$ ($m = +1, 0, -1$) are obtained by exciting group R to the r_mth triplet state,

$$^3\Phi_{Rrm} = \mathcal{A}[^1\phi_{A0}\,{}^1\phi_{B0}\ldots{}^3\phi_{Rrm}\ldots] \quad (51)$$

In the single configuration approximation, transition spin densities between $^1\phi_0$ and $^3\phi_{R_m}$ only arise for group R,

$$Q_1(0\kappa_0 \mid 1; 1') = Q_1(0r_m \mid 1; 1') \quad (52)$$

Therefore, the only nonzero contributions to the nuclear spin coupling constant from equation (6) would be those for which electrons in group R have nonvanishing densities at nuclei N and N′. Presumably, this would only be the trivial situation in which there was only one group describable by the previous formulations. As a more interesting alternative, consider configurational mixing between the ground state and those singlets $^1\phi_{RS}$ produced by exciting two groups R and S to triplets and spin coupling to a singlet,

$$^1\Psi_0 = c_0\,{}^1\Phi_0 + \sum_{RS} c_{rs}\,{}^1\Phi_{RS} \quad (53)$$

where

$$^1\Phi_{RS} = 3^{-1/2}(\Phi_{Rr_{+1}\,Ss_{-1}} - \Phi_{Rr_0s_0} + \Phi_{Rr_{-1}r_{+1}}) \quad (54)$$

in which

$$\Phi_{Rr_{+1}Ss_{-1}} = \mathcal{A}(^3\phi_{Rr_{+1}}\,{}^3\phi_{Ss_{-1}}) \quad (55)$$

The summation in equation (53) is over all of the triplets. If one considers all possible coupling schemes, this would eventually produce all of the singlet, nonpolar VB structures. Furthermore, in the triplet manifold configurational mixing occurs, for example, between a given triplet and those obtained by exciting all the other groups to triplets,

$$^3\Psi_{\rho_0} = \sum_{r_0} c_{\rho_0 r_0}\,{}^3\Phi_{Rr_0} + \sum_{\rho_0 s_0} c_{\rho_0 s_0}\,{}^3\Phi_{Ss_0} \quad (56)$$

The transition spin densities which enter the FC coupling expression in equation (6) follow from equation (3), equations (53) and (56). The coefficients entering equations (53) and (56) and the energies appropriate to equation (6) can easily be obtained directly by solving the secular determinants[116–118] or by means of perturbation theory.[127,128]

3.4 Coupled Hartree–Fock/Finite Perturbation Descriptions

One of the most widely used methods for J coupling makes use of coupled Hartree–Fock theory. In coupled Hartree–Fock theory the nuclear perturbation of the electronic system is included in the Hamiltonian,

$$\mathcal{H} = \mathcal{H}_0 + \boldsymbol{A}_N \cdot \boldsymbol{\mu}_N + \boldsymbol{A}_{N'} \cdot \boldsymbol{\mu}_{N'} \quad (57)$$

and the Hartree–Fock equations are solved in the usual Roothaan type of formulation. Some of the previous equations, e.g. equation (44) conform to one type of uncoupling scheme for the Hartree–Fock equations.[129] There are several ways to perform calculations of J couplings that are equivalent to the coupled Hartree–Fock method. The most widely used is the FPT of Pople and co-workers.[7,130]

Expanding the energy in a Taylor's series over the magnetic moments, then the coupling constant is proportional to the second derivative of the energy,

$$J_{NN'} \propto \left[\frac{\partial^2 E(\mu_N, \mu_{N'})}{\partial\mu_N \partial\mu_{N'}}\right]_{\mu_N=\mu_{N'}=0} \quad (58)$$

From the Hellman–Feynman theorem the authors[7] further showed that

$$J_{NN'} \propto \left[\frac{\partial}{\partial\mu_{N'}}\langle\Psi(\mu_{N'})|A_N|\Psi(\mu_{N'})\rangle\right]_{\mu_{N'}=0} \quad (59)$$

where the matrix elements can be written in terms of the spin density matrix,

$$\rho = P_1(\overset{\alpha}{1}, \overset{\alpha}{1}) - P_1(\overset{\beta}{1}, \overset{\beta}{1}) \quad (60)$$

For FC coupling it follows from equation (59) that

$$\langle \Psi(\mu_{N'})|A_N|\Psi(\mu_{N'})\rangle = (8\pi\beta/3)\sum_{\mu\nu}\rho_{\mu\nu}(\mu_N)\langle\phi_\mu|\delta(r_N)|\phi_\nu\rangle \quad (61)$$

where μ and ν denote atomic orbitals and it is assumed as usual that matrix elements of $\delta(r_N)$ in equation (61) vanish except for s-type orbitals on N.

The self-consistent perturbation theory (SCPT) method was introduced by Blizzard and Santry[131] as a less computationally demanding alternative to the FPT approach. An alternative method makes use of the first-order polarization propagator (FOPPA).[132] This has been used extensively by Engelmann and Contreras[133] and co-workers. Applications of coupled Hartree–Fock methods including FPT, SCPT, and FOPPA formulations are far too numerous to be included here. Since noncontact mechanisms have not otherwise been emphasized here, mention should be made of the studies of ^1J(C,C)[134,135] coupling, those involving second row atoms,[135,136] and nonempirical calculations.[137–140] Within the semiempirical INDO framework, the FOPPA method (with respect to the inclusion of multicenter integrals)[141] leads to values of FC, OP, and SD contributions which are generally in accord with the nonempirical results.

A comparison of coupled Hartree–Fock methods with sum-over-states approaches indicated that the FPT method also introduces doubly excited states in a restricted way and should give quite different results when correlation is important for the unperturbed wavefunction.[142,143]

4 APPLICATIONS TO SPECIFIC COUPLING SITUATIONS

To examine the topic of scalar coupling from a qualitative point of view, it is often convenient to work with a simple VB bond order picture.[74] An alternative model, which leads to similar conclusions makes use of a MO model in which the MOs χ_i are written as a linear combination of hybrid type orbitals ϕ_μ (HTOs),

$$\chi_i = \sum_\mu c_{i\mu}\phi_\mu \quad (62)$$

where the ϕ_μ can be written in terms of atomic s- and p-type atomic orbitals as in equations (25) or (34). In the basis set of HTOs the expression for the FC contribution to $J_{NN'}$ is identical to the one obtained by Pople and Santry.[81] The nuclear spin–spin coupling constant is proportional to the mutual atom–atom polarizability in equations (46) and (47). For geminal, vicinal coupling, or long-range H–H coupling perturbation theory can be used to relate $\pi_{hh'}$ to the off-diagonal elements of the Hamiltonian,[81–86]

$$\pi_{hh'} = (-5\beta_{cc'}^2 - 2\beta_{hh'}^2 + 4\beta_{hc'}^2 + 2\beta_{cc'}\beta_{hh'})/(16\beta^3) \quad (63)$$

where $\beta_{cc'}$, for example, is the matrix element of the Hamiltonian operator between HTOs c and c', which are directed toward hydrogenic orbitals h and h' as in Figure 2(b).

$$\beta_{cc'} = \langle\phi_c|\mathcal{H}|\phi_{c'}\rangle \quad (64)$$

The off-diagonal element beta; in the denominator of equation (63) corresponds to an average of those between orbitals which are bonded in the primary valence structure. As a consequence of the assumptions which are implicit in the expressions for $\pi_{hh'}$, and others associated with the relation to the spin–spin coupling, this formulation is appropriate for *qualitative interpretations*. These methods will be used here to examine briefly some of the structural factors associated with geminal and vicinal H–H coupling constants.

4.1 Geminal Coupling Constants

Many features of geminal coupling can be rationalized by means of equations (46) and (63). Various terms in the numerator have opposite signs. Depending on the magnitudes of the various matrix elements, geminal H–H coupling constants could represent a delicate balance between terms of comparable magnitude but of opposite sign. The difficulty with early calculations of geminal coupling constants and the unusual sensitivity of geminal coupling constants to substituents and solvents would tend to support this view. Because of the renewed interest in the H–C–H angle dependence of ^2J(H,H′),[144,145] it may be useful to reexamine the proposed dependence of ^2J on the carbon hybridization. In equation (63) the most important term appears to be the geminal interaction integral $\beta_{cc'}$ since it is multiplied by 5. When expressed in terms of the diagonal matrix elements α_s and α_p in the s,p basis set, this term is proportional to the carbon s character a^2,

$$\beta_{cc'} = a^2(\alpha_s - \alpha_p) \quad (65)$$

If all of the integrals except this one could be neglected in the numerator of equation (63), the geminal coupling constants would be proportional to the products of the s character a^4 at the carbon atom. Therefore, the dependence of the coupling constants on the valence angle θ follows from the proportionality to a^4 and the relationship of a^2 to θ,

$$a^2 = -\cos\theta/(1-\cos\theta) \quad (66)$$

The slope of this function is 0.25 + 0.02 between θ = 102 and 129°.[144] Small variations of $\Delta\theta$ around both the tetrahedral and the trigonal interorbital angles should lead to approximately linear dependences of the geminal coupling constants on $\Delta\theta$. The recent ab initio MO data for ^2J(H,H′) of Geertsen et al.[145] indicate that this is the case. Their nonempirical results can also be fit to the expression

$$^2J(\mathrm{H,H'}) = 160.6a_C^4 - 24.6 \ \mathrm{Hz} \quad (67)$$

which has a standard deviation of only 0.2 Hz.

4.2 Vicinal Coupling Constants

Because of their sensitivity to variations of dihedral angles, vicinal H–H nuclear spin–spin coupling constants $^3J(H,H')$ have been used extensively for conformational studies. Much effort has been expended in specifying parameters for the torsion angle dependence for this type of coupling. Factors such as H–C–C internal angle dependence, C–C bond length dependence, and substituent electronegativity are also involved. Subsequent efforts have identified other factors, including substituent orientation and electronic contributions to $^3J(H,H')$ from other groups in the molecule. Based on either the VB bond order formulation, MO sum-over-states perturbation, or group function formulations, there can be important contributions to the nuclear spin–spin coupling constants arising from groups that are outside the coupling path. An interesting example of this is the nonequivalence of the *exo–exo* and *endo–endo* vicinal coupling constants in bicyclo[2.2.1]heptanes.[146]

4.2.1 Contributions from Remote Groups, e.g. Reasons for the Nonequivalence of Exo–Exo and Endo–Endo Coupling Constants

Attempts to refine the dihedral angle dependences of vicinal H–H coupling constants have demonstrated the importance of electronic factors outside the coupling path. An example of such an effect was the reason for the nonequivalence of the *exo–exo* and *endo–endo* coupling constants in the norbornane series.[146] In norbornanes it was observed that *exo–exo* coupling constants are several hertz larger than the *endo–endo* values even though both correspond to situations in which the dihedral angles are near 0°. These experimental trends were satisfactorily reproduced at the semiempirical (INDO-FPT) level. To investigate this nonequivalence a procedure was used in which certain nonbonded interactions between the ethanic bridge and other parts of the molecule were eliminated from the SCF procedure. Our first guess, that the most important interactions were between the two ethanic bridges of norbornane, turned out to be incorrect. Only on elimination of the interactions between the ethanic bridge and the methylene bridge did the two types of coupling become equivalent. These ideas have been incorporated into procedures for conformational analyses of 5-membered rings.[147,148] It is not our intent to minimize the practical applicability of the many empirical equations, but this provides one example of the reason that there can be no universal equations to describe the conformation dependences of nuclear spin–spin coupling constants.

4.2.2 Dependence on H–C–C Internal Angles as well as Dihedral Angles

Substantial deviations of internal H–C–C angles from the tetrahedral values are common in strained, multicyclic compounds. Because of their relative rigidity, such compounds are most appropriate for unambiguously relating spin–spin coupling constants to molecular structures. There are some interesting examples which clearly show the importance of internal angle change, e.g. the monotonic decrease of H–C=C–H coupling with decreasing ring size in cycloalkenes. The 5.3 Hz $^3J(H,H')$ in cubanes, which have C–C–H angles near 125°, is just about one-half of the value expected in molecules with tetrahedral angles.

An explicit expression was derived[149] for vicinal H–H coupling constants $^3J_{(H,H')}(\theta_1, \theta_2, \varphi)$ in terms of the two internal H–C–C angles θ_1 and θ_2 and the torsion angle φ. The resulting expression provides excellent correlations of most features of vicinal H–H coupling in ethanic (–CH–CH–), ethylenic (–CH=CH–), allylic (C=CH–CH–), and diene (C=CH–CH=C) moieties, and provide criteria for assessing the importance of internal angle changes. Because of the obvious extension of these equations to other spin–spin coupling situations, it is of interest to include a brief description of the results.

From equations (34) and (63) (and the proportionality of the matrix elements to overlap integrals in equation (64)) the vicinal coupling constants can be written in the form

$$^3J_{(H,H')}(\theta_1, \theta_2, \varphi) = c_a a(\theta_1, \theta_2)\cos^2\varphi + \sum_i c_{bi} b_i(\theta_1, \theta_2)\cos\varphi + C \quad (68a)$$

where

$$a(\theta_1, \theta_2) = (1 + \cos\theta_1)(1 + \cos\theta_2) \quad (68b)$$

$$b_1(\theta_1, \theta_2) = \cot(\theta_1/2)\ \cot(\theta_2/2)\cos\theta_1\cos\theta_2 \quad (68c)$$

$$b_2(\theta_1, \theta_2) = \cot(\theta_1/2)\ \cot(\theta_2/2)(\cos\theta_1\cos\theta_2)^{1/2} \quad (68d)$$

$$b_3(\theta_1, \theta_2) = \cot(\theta_1/2)\ \cot(\theta_2/2)[\cos\theta_2(-\cos\theta_1)^{1/2} + \cos\theta_1(-\cos\theta_2)^{1/2}] \quad (68e)$$

The C term is usually small in magnitude when $^3J(H,H')$ is written in the form of equation (35).[149] Equation (68) is an analytic expression but is subject to the many approximations that are implicit in the derivation.

In equations (68a)–(68e) the dependence of $^3J_{(H,H')}$ on C–C internuclear separations occurs in the overlap integrals, which are implicit in the coefficients c_a, c_{bi} and C. Therefore, there will be a set of coefficients for each value of r(C–C). In the spirit of semiempirical MO methods, where the β integrals are determined empirically, these coefficients were based on a least squares analysis of the available experimental data. In deriving this equation from equation (64) it was assumed that the $\beta_{cc'}$ term is dominant and that other integrals will have the effect of slightly modifying the empirically determined coefficients.

The term containing $\cos^2\varphi$ (the A term) in equation (68a) is the most important term controlling the vicinal coupling constants. The θ-dependence of the coefficient of this term [equation (68b)] is relatively simple when compared with the coefficients [equations (68c)–(68e)] of the cos φ term. Depicted in Figure 5 for ethanic coupling is a surface and contour plot of $^3J_{(H,H')}(\theta_1, \theta_2, \varphi)$ on the internal angles $\theta_1 = \theta_2$ and the dihedral angle φ. The decrease in the magnitude of the vicinal coupling constants with increasing H–C–C angle is substantial, especially for the *trans* coupling. Clearly, the usual tendency to neglect the effects of internal angle changes

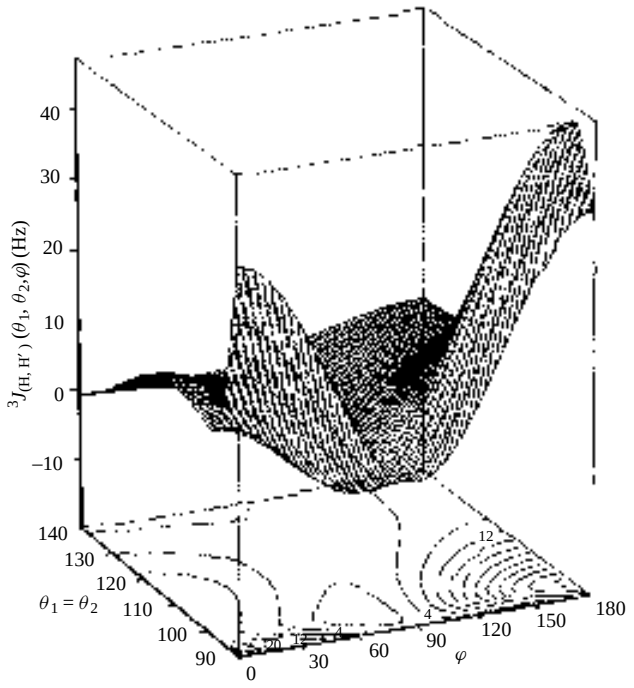

Figure 5 Surface and contour plots depicting the dependence of vicinal H–H coupling constants in an ethanic system as a function of the dihedral angle ϕ and the internal H–C–C angles θ_1=θ_2

cannot be justified in strained molecules or those with unusual bonding patterns.

5 REFERENCES

1. M. Barfield and D. M. Grant, *Adv. Magn. Reson.*, 1965, **1**, 149.
2. J. N. Murrell, *Prog. NMR Spectrosc.*, 1971, **6**, 1.
3. P. D. Ellis and R. Ditchfield, in *Topics in Carbon-13 NMR Spectroscopy*, ed. G. Levy, Wiley, New York, 1976, Vol. 2, p. 434.
4. J. Kowalewski, *Annu. Rep. NMR Spectrosc.*, 1982, **12**, 81.
5. H. Fukui, in *Nuclear Magnetic Resonance*, Specialist Periodical Reports, The Chemical Society, London, No. 22, 1993 and previous chapters in this series.
6. K. Kamienska-Trela, in *Nuclear Magnetic Resonance*, Specialist Periodical Reports, The Chemical Society, London, No. 22, 1993 and previous chapters in this series.
7. J. A. Pople, J. W. McIver, Jr., and N. S. Ostlund, *J. Chem. Phys.*, 1968, **49**, 2960, 2965.
8. J. Geertsen, J. Oddershede, W. T. Raynes, and G. E. Scuseria, *J. Magn. Reson.*, 1991, **93**, 458; W. T. Raynes, J. Geertsen, and J. Oddershede, *Chem. Phys. Lett.*, 1992, **197**, 516.
9. O. Vahtras, H. Ågren, P. Jorgensen, H. J. Aa. Jensen, S. B. Padkjaer, and T. Helgaker, *J. Chem. Phys.*, 1992, **96**, 6120; O. Vahtras, H. Ågren, P. Jorgensen, T. Helgaker, and H. J. Aa. Jensen, *Chem. Phys. Lett.*, 1993, **209**, 201.
10. H. Fukui, K. Miura, H. Matsuda, and T. Baba, *J. Chem. Phys.*, 1992, **97**, 2299; H. Fukui, K. Miura, and H. Matsuda, *J. Chem. Phys.*, 1991, **94**, 533.
11. I. Carmichael, *J. Phys. Chem.*, 1993, **97**, 1789.
12. I. Carmichael, D. M. Chipman, C. A. Podlasek, and A. S. Serianni, *J. Am. Chem. Soc.*, 1993, **115**, 10 863.
13. J. San-Fabián, J. Guilleme, E. Díez, P. Lazzeretti, M. Malagoli, and R. Zanasi, *Chem. Phys. Lett.*, 1993, **206**, 253.
14. A. S. Edison, J. L. Markley, and F. Weinhold, *J. Phys. Chem.*, 1993, **97**, 11 657.
15. G. A. Aucar and J. Oddershede, *Int. J. Quantum Chem.*, 1993, **47**, 425.
16. E. L. Hahn, *Phys. Rev.*, 1950, **80**, 580.
17. W. G. Proctor and F. C. Yu, *Phys. Rev.*, 1951, **81**, 20.
18. H. S. Gutowsky and D. W. McCall, *Phys. Rev.*, 1951, **82**, 748.
19. E. R. Andrew, *Phys. Rev.*, 1951, **82**, 443.
20. M. E. Packard and J. T. Arnold, *Phys. Rev.*, 1951, **83**, 210A.
21. H. S. Gutowsky, D. W. McCall, and C. P. Slichter, *Phys. Rev.*, 1951, **84**, 589.
22. E. B. McNeil, C. P. Slichter, and H. S. Gutowsky, *Phys. Rev.*, 1951, **84**, 1245.
23. E. L. Hahn and D. E. Maxwell, *Phys. Rev.*, 1951, **84**, 1246.
24. N. F. Ramsey and E. M. Purcell, *Phys. Rev.*, 1952, **85**, 143.
25. N. F. Ramsey, *Phys. Rev.*, 1953, **91**, 303.
26. T. F. Wimett, *Phys. Rev.*, 1953, **91**, 476A.
27. J. Musher, *Phys. Rev. Lett.*, 1965, **15**, 1015; 1966, **16**, 675E.
28. R. F. Code and N. F. Ramsey, *Phys. Rev. A*, 1971, **4**, 1945.
29. M. Barfield, unpublished results, 1967.
30. J. E. Harriman, M. Twerdochlib, M. B. Milleur, and J. O. Hirschfelder, *Proc. Natl. Acad. Sci. U.S.A.*, 1967, **57**, 1558; M. B. Milleur, L. A. Curtiss, M. Twerdochlib, and J. O. Hirschfelder, *J. Chem. Phys.*, 1968, **48**, 4261.
31. R. McWeeny, *Proc. R. Soc. London, Ser. A*, 1959, **253**, 242; R. McWeeny and Y. Mizuno, *Proc. R. Soc. London, Ser. A*, 1961, **259**, 554; R. McWeeny, *Rev. Mod. Phys.*, 1960, **32**, 335.
32. R. McWeeny and B. T. Sutcliffe, *Methods of Molecular Quantum Mechanics*, Academic Press, New York, 1969.
33. J. J. Reed, *Theoretical Studies of Nuclear Spin-Spin Coupling*, Ph.D. Thesis, University of Arizona, 1971.
34. M. Barfield, *Chem. Phys. Lett.*, 1970, **4**, 518.
35. A. D. McLachlan, *J. Chem. Phys.*, 1960, **32**, 1263.
36. M. Karplus, *J. Chem. Phys.*, 1960, **33**, 941.
37. J. A. Pople, W. G. Schneider, and H. J. Bernstein, *High Resolution Nuclear Magnetic Resonance*, McGraw-Hill, New York, 1959, p. 190.
38. M. Barfield, *J. Chem. Phys.*, 1966, **44**, 1836.
39. H. S. Gutowsky, D. W. McCall, and C. P. Slichter, *J. Chem. Phys.*, 1953, **21**, 279.
40. M. A. Ruderman and C. Kittel, *Phys. Rev.*, 1954, **96**, 99.
41. N. Bloembergen and J. T. Rowland, *Phys. Rev.*, 1955, **97**, 1679.
42. H. M. McConnell, *J. Chem. Phys.*, 1955, **23**, 760; 1956, **24**, 460.
43. H. M. McConnell, *J. Chem. Phys.*, 1955, **23**, 2454.
44. H. M. McConnell, *J. Mol. Spectrosc.*, 1957, **1**, 11.
45. A. D. McLachlan, *Mol. Phys.*, 1958, **1**, 233.
46. A. Saika, *Physica*, 1959, **25**, 51.
47. H. M. McConnell, *Annu. Rev. Phys. Chem.*, 1957, **8**, 105.
48. H. M. McConnell, *J. Chem. Phys.*, 1959, **30**, 126.
49. J. A. Pople, *Mol. Phys.*, 1958, **1**, 216.
50. C. A. Coulson and H. C. Longuet-Higgins, *Proc. R. Soc. London, Ser. A*, 1947, **191**, 39; 1947, **192**, 16; 1948, **193**, 447.
51. N. Muller and D. E. Pritchard, *J. Chem. Phys.*, 1959, **31**, 768.
52. J. N. Shoolery, *J. Chem. Phys.*, 1959, **31**, 1427.
53. H. S. Gutowsky and C. S. Juan, *J. Am. Chem. Soc.*, 1962, **84**, 307.
54. E. Aihara, *J. Chem. Phys.*, 1957, **26**, 1347.

55. M. Karplus, D. H. Anderson, T. C. Farrar, and H. S. Gutowsky, *J. Chem. Phys.*, 1957, **27**, 597.
56. M. J. Stephen, *Proc. R. Soc. London, Ser. A*, 1957, **243**, 274.
57. M. Karplus and D. H. Anderson, *J. Chem. Phys.*, 1959, **30**, 6.
58. M. Karplus, *J. Chem. Phys.*, 1959, **30**, 11; *J. Am. Chem. Soc.*, 1963, **85**, 2870.
59. H. S. Gutowsky, M. Karplus, and D. M. Grant, *J. Chem. Phys.*, 1959, **31**, 1278.
60. M. Karplus and D. M. Grant, *Proc. Natl. Acad. Sci. U.S.A.*, 1959, **45**, 1269.
61. E. Hiroike, *J. Phys. Soc. Jpn.*, 1960, **15**, 270; *Prog. Theor. Phys.*, 1961, **26**, 283.
62. S. Alexander, *J. Chem. Phys.*, 1961, **34**, 106.
63. J. Ranft, *Ann. Phys.*, 1961, **8**, 322; 1962, **9**, 124.
64. C. Juan and H. S. Gutowsky, *J. Chem. Phys.*, 1962, **37**, 2198; H. S. Gutowsky and C. Juan, *Discuss. Faraday Soc.*, 1962, **34**, 1.
65. M. Barfield and D. M. Grant, *J. Chem. Phys.*, 1962, **36**, 2054; *J. Am. Chem. Soc.*, 1963, **85**, 1899.
66. H. G. Hecht, *Theor. Chim. Acta*, 1963, **1**, 222.
67. S. Koide and E. Duval, *J. Chem. Phys.*, 1964, **41**, 315.
68. M. Barfield, *J. Chem. Phys.*, 1964, **41**, 3825.
69. P. Chandra and P. T. Narasimhan. *Mol. Phys.*, 1966, **11**, 189; 1967, **12**, 523.
70. E. Sackmann and H. Dreeskamp, *Spectrochim. Acta*, 1965, **21**, 2005.
71. R. A. Bernheim and T. P. Das, *J. Chem. Phys.*, 1960, **33**, 1813; T. P. Das and R. Bersohn, *Phys. Rev.*, 1959, **115**, 897.
72. G. Rumer, *Nachr. Ges. Wiss. Goettingen, Math. Phys. Kl, Fachgruppe 1*, 1932, 337.
73. L. Pauling and E. B. Wilson, Jr., *Introduction to Quantum Mechanics*, McGraw-Hill, New York, 1935, pp. 374–380.
74. M. Barfield and M. Karplus, *J. Am. Chem. Soc.*, 1969, **91**, 1.
75. W. G. Penney, *Proc. R. Soc. London, Ser. A*, 1937, **158**, 306.
76. S. Karplus and M. Karplus, *Proc. Natl. Acad. Sci. U.S.A.*, 1972, **69**, 3204.
77. D. Doddrell, M. Barfield, W. Adcock, M. Aurangzeb, and D. Jordan, *J. Chem. Soc., Perkin Trans. 2*, 1976, 402.
78. M. Barfield, S. A. Conn, J. L. Marshall, and D. E. Miiller, *J. Am. Chem. Soc.*, 1976, **98**, 6253.
79. M. Barfield, R. J. Spear, and S. Sternhell, *Chem. Rev.*, 1976, **76**, 593.
80. M. Barfield and S. R. Walter, *J. Am. Chem. Soc.*, 1983, **105**, 4191.
81. J. A. Pople and D. P. Santry, *Mol. Phys.*, 1964, **7**, 269; 1964, **8**, 1; 1965, **9**, 301, 311.
82. J. N. Murrell and V. M. S. Gil, *Theor. Chim. Acta*, 1966, **4**, 114.
83. F. B. van Duijneveldt, V. M. S. Gil, and J. N. Murrell, *Theor. Chim. Acta*, 1966, **4**, 85.
84. R. Ditchfield, G. T. Jones, and J. N. Murrell, *Theor. Chim. Acta*, 1968, **9**, 253.
85. V. M. S. Gil and J. J. C. Teixeira-Dias, *Mol. Phys.*, 1968, **15**, 47.
86. C. J. Jameson and H. S. Gutowsky, *J. Chem. Phys.*, 1969, **51**, 2790; C. J. Jameson and M. C. Damasco, *Mol. Phys.*, 1970, **18**, 491.
87. R. C. Fahey, G. C. Graham, and R. L. Piccioni, *J. Am. Chem. Soc.*, 1966, **88**, 193.
88. S. Polezzo, P. Cremaschi, and M. Simonetta, *Chem. Phys. Lett.*, 1967, **1**, 357.
89. W. H. de Jeu and G. P. Beneder, *Theor. Chim. Acta*, 1969, **13**, 349.
90. T. Yonezawa, I. Morishima, M. Fujii, and H. Kato, *Bull. Chem. Soc. Jpn.*, 1967, **40**, 487.
91. K. G. R. Pachler, *Tetrahedron Lett.*, **1970**, 1955.
92. R. Ditchfield and J. N. Murrell, *Mol. Phys.*, 1968, **14**, 481.
93. R. Ditchfield, *Mol. Phys.*, 1969, **17**, 33.
94. H. Frischleder and D. Klöpper, *Mol. Phys.*, 1970, **18**, 113.
95. M. D. Newton, F. P. Boer, and W. N. Lipscomb, *J. Am. Chem. Soc.*, 1966, **88**, 2353.
96. D. S. Bartow and J. W. Richardson, *J. Chem. Phys.*, 1965, **42**, 4018.
97. P. Loève and L. Salem, *J. Chem. Phys.*, 1965, **43**, 3402.
98. Y. Kato and A. Saika, *J. Chem. Phys.*, 1967, **46**, 1975.
99. E. A. G. Armour and A. J. Stone, *Proc. R. Soc. London, Ser. A*, 1967, **302**, 25.
100. E. A. G. Armour, *J. Chem. Phys.*, 1968, **49**, 5445.
101. N. S. Ostlund, M. D. Newton, J. W. McIver, Jr., and J. A. Pople, *J. Magn. Reson.*, 1969, **1**, 298.
102. Alan W. Douglas, *A Priori Calculations of Nuclear Spin Coupling Constants*, Ph.D. Thesis, State University of New York at Stony Brook, 1969.
103. J. A. Pople and A. A. Bothner-By, *J. Chem. Phys.*, 1965, **42**, 1339.
104. V. M. S. Gil and S. J. S. Formosinho-Simoes, *Mol. Phys.*, 1968, **15**, 639; V. M. S. Gil and C. F. G. C. Geraldes, *Rev. Port. Quim.*, 1970, **12**, 32.
105. M. Barfield and B. Chakrabarti, *Chem. Rev.*, 1969, **69**, 757.
106. M. Barfield, R. J. Spear, and S. Sternhell, *J. Am. Chem. Soc.*, 1971, **93**, 5322.
107. V. M. S. Gil, *Mol. Phys.*, 1968, **15**, 645.
108. H. Nakatsuji, I. Morishima, H. Kato, and T. Yonezawa, *Bull. Chem. Soc. Jpn.*, 1971, **44**, 2010; K. Hirao, H. Nakatsuji, H. Kato, and T. Yonezawa, *J. Am. Chem. Soc.*, 1972, **94**, 4078; K. Hirao, H. Nakatsuji, and H. Kato, *J. Am. Chem. Soc.*, 1973, **95**, 31.
109. A. D. C. Towl and K. Schaumburg, *Mol. Phys.*, 1971, **22**, 49; H. Jensen and K. Schaumburg, *Mol. Phys.*, 1971, **22**, 1041.
110. C. Barbier, H. Foucher, and G. Berthier, *Theor. Chim. Acta*, 1971, **21**, 105.
111. E. Hiroike, *J. Phys. Soc. Jpn.*, 1967, **22**, 379.
112. M. Barfield, A. M. Dean, C. J. Fallick, R. J. Spear, S. Sternhell, and P. W. Westerman, *J. Am. Chem. Soc.*, 1975, **97**, 1482.
113. M. Barfield, *J. Chem. Phys.*, 1967, **46**, 811; 1968, **49**, 4458.
114. M. Barfield, *J. Chem. Phys.*, 1968, **49**, 4463.
115. A. D. McLachlan, *J. Chem. Phys.*, 1960, **33**, 663.
116. M. Barfield, *J. Chem. Phys.*, 1968, **49**, 2145.
117. M. Barfield and J. J. Reed, *J. Chem. Phys.*, 1969, **51**, 3039.
118. M. Barfield and B. Chakrabarti, *J. Am. Chem. Soc.*, 1969, **91**, 4346.
119. M. Karplus, *J. Chem. Phys.*, 1960, **33**, 1842; *J. Am. Chem. Soc.*, 1960, **82**, 4431.
120. J. V. Acrivos, *Mol. Phys.*, 1962, **5**, 1.
121. A. V. Cunliffe and R. K. Harrris, *Mol. Phys.*, 1967, **13**, 269.
122. R. Ditchfield and J. N. Murrell, *Mol. Phys.*, 1968, **15**, 533.
123. A. V. Cunliffe, R. Grinter, and R. K. Harrris, *J. Magn. Reson.*, 1970, **3**, 299.
124. D. E. O'Reilly, *J. Chem. Phys.*, 1962, **36**, 274.
125. H. Frischleder and G. Bär, *Mol. Phys.*, 1966, **11**, 359.
126. T. Vladimiroff and E. R. Malinowski, *J. Chem. Phys.*, 1967, **46**, 1830.

127. W. J. van der Hart, *Mol. Phys.*, 1971, **20**, 385, 399, 407.
128. N. D. Chuvylkin, G. M. Zhidomirov, and R. B. Schastnev, *Mol. Phys.*, 1972, **23**, 639.
129. P. W. Langhoff, M. Karplus, and R. P. Hurst, *J. Chem. Phys.*, 1966, **44**, 505.
130. G. E. Maciel, J. W. McIver, Jr., N. S. Ostlund, and J. A. Pople, *J. Am. Chem. Soc.*, 1970, **92**, 1, 11, 4151, 4497, 4506.
131. A. C. Blizzard and D. P. Santry, *J. Chem. Phys.*, 1971, **55**, 950; 1973, **58**, 4714.
132. J. Linderberg and Y. Öhrn, *Propagators in Quantum Chemistry*, Academic Press, New York, 1973.
133. A. R. Engelmann and R. H. Contreras, *Int. J. Quantum Chem.*, 1983, **23**, 1033.
134. M. D. Newton and J. M. Schulman, *J. Am. Chem. Soc.*, 1972, **94**, 767, 773; M. D. Newton, J. M. Schulman, and M. M. Manus, *J. Am. Chem. Soc.*, 1974, **96**, 17; J. M. Schulman and M. D. Newton, *J. Am. Chem. Soc.*, 1974, **96**, 6295.
135. P. Lazzereti, F. Taddei, and R. Zanasi, *J. Am. Chem. Soc.*, 1976, **98**, 7989.
136. T. A. Albright, *Org. Magn. Reson.*, 1976, **8**, 489.
137. M. D. Beer and R. Grinter, *J. Magn. Reson.*, 1978, **31**, 187.
138. R. Ditchfield and L. C. Snyder, *J. Chem. Phys.*, 1972, **56**, 5823.
139. J. Oddershede, P. Jorgensen, and N. H. F. Beebe, *J. Chem. Phys.*, 1975, **63**, 2996.
140. M. F. Guest, V. R. Saunders, and R. E. Overill, *Mol. Phys.*, 1978, **35**, 427.
141. J. C. Facelli and M. Barfield, *J. Am. Chem. Soc.*, 1984, **106**, 3407; *J. Magn. Reson.*, 1984, **59**, 452.
142. R. Ditchfield, N. S. Ostlund, J. N. Murrell, and M. A. Turpin, *Mol. Phys.*, 1970, **18**, 433.
143. M. D. Johnston, Jr.and M. Barfield, *J. Chem. Phys.*, 1971, **54**, 3083.
144. M. Klessinger and M. Barfield, in *Modelling of Structure and Properties of Molecules*, ed. Z. B. Maksic, Ellis Horwood, Chichester, 1987, pp. 269–284.
145. J. Geertsen, J. Oddershede, and W. T. Raynes, *Magn. Reson. Chem.*, 1993, **31**, 722.
146. J. L. Marshall, S. R. Walter, M. Barfield, A. P. Marchand, N. W. Marchand, and A. L. Segre, *Tetrahedron*, 1976, **32**, 537.
147. A. Jaworski, I. Ekiel, and D. Shugar, *J. Am. Chem. Soc.*, 1978, **100**, 4357; A. Jaworski and I. Ekiel, *Int. J. Quantum Chem.*, 1979, **16**, 615.
148. C. A. G. Haasnoot, F. A. A. M. de Leeuw, and C. Altona, *Tetrahedron*, 1980, **36**, 2783; F. A. A. M. de Leeuw, C. Altona, H. Kessler, W. Bermel, A. Friedrich, G. Krack, and W. E. Hull, *J. Am. Chem. Soc.*, 1983, **105**, 2237; F. A. A. M. de Leeuw, A. A. van Beuzekom, and C. Altona, *J. Comput. Chem.*, 1983, **4**, 438.
149. M. Barfield and W. B. Smith, *J. Am. Chem. Soc.*, 1992, **114**, 1574; W. B. Smith and M. Barfield, *Magn. Reson. Chem.*, 1993, **31**, 696.

Biographical Sketch

Michael Barfield. *b* 1934. B.A., 1957, Ph.D., Chemistry, University of Utah, USA, 1962 (advisor David M. Grant). Postdoctoral Fellow, Harvard University, 1962–63 (with John D. Baldeschwieler). Assistant Professor, University of South Florida, 1963–65. Assistant Professor, Associate Professor, Professor, University of Arizona, 1965–present. Approx. 100 publications. Research specialties: studies of NMR parameters, especially nuclear spin–spin coupling and chemical shielding.

Intercalation Compounds

Werner Müller-Warmuth
Institut für Physikalische Chemie der Westfälischen Wilhelms-Universität, Münster, Germany

1 Introduction 1
2 Typical NMR Experiments with Intercalation Compounds 1
3 Structure and Motions of Hydrated Layered Chalcogenides 5
4 Structure and Dynamics of Guest Phases in Molybdenum Cluster Chalcogenides 7
5 Related Articles 9
6 References 9

1 INTRODUCTION

Intercalation compounds are formed by the reversible insertion of guest species into solid matrices which retain their structure except for certain lattice expansions. They may be considered as a subclass of inclusion compounds, a term that has been used for a larger group of materials consisting of host and guest species. For intercalation reactions an increasing number of host lattices with different structural dimensionality is nowadays available ranging from insulators such as layered silicates to semiconductors and metallic conductors, e.g. graphite, transition metal dichalcogenides, or molybdenum cluster compounds. The guest species include small atomic ions as well as solvated systems and larger molecular units. As far as the aspects of the materials, the preparation of the compounds, and other chemical and physical properties are concerned, we have to refer to review articles and monographs which cover a broader horizon and some specific aspects of the subject.[1] Applications of intercalation compounds comprise battery systems, electrochromic displays, catalysis, and sensors, as well as the employment as model systems for low-dimensional solids.

Solid state NMR studies have contributed substantially to the understanding of the structure and dynamics of intercalation compounds. The location of guest molecules, their orientation and bonding characteristics, guest–host interactions, the donation of electrons to the host, and motions of the intercalated species are some of the problems that have been addressed using NMR. Chemical shift, nuclear quadrupole, and dipole–dipole interactions, and relaxation rates have been utilized to obtain data on the structure and dynamics of intercalation compounds. High-resolution techniques such as MAS or multiple pulse methods were only applied in exceptional cases, since the information on the anisotropy is of major importance. Broadline spectra of compounds with reduced dimensionality are often distinguished by much better resolved structures than those of three-dimensional solids.

Among the materials that have been investigated using NMR techniques, characteristic differences exist between intercalation compounds with insulator host lattices and those which exhibit electronic conductivity. The most important groups of the first class of compounds are zeolites, pyrochlores, sheet silicates, and β-alumina, which are generally discussed in another context. We will concentrate on host lattices with electronic conductivity, which have attracted increased interest in recent years because of the large diversity of compounds. The intercalation in these materials can be described by the concept of reversible topotactic redox reactions, and is connected with the transfer of electrons entering or leaving the conduction band of the host matrix.

The most important classes of such systems are two-dimensional layered intercalation compounds with cationic or solvated ionic guest species or with intercalated molecules, and three-dimensional framework structures containing channels or cavities for the uptake of small guest species. Among the materials known for a long time, the graphite intercalation compounds belong to the layered systems, and hydrogen bronzes may be formed in both three- and two-dimensional structures.

Within this article it is of course not possible to present a survey of all the NMR results which contributed to the understanding of the structure of intercalation compounds or of the motions of guest species. For this the reader is referred to the literature, and especially to a recent, comprehensive review.[2] Here it is attempted to illustrate the potential of NMR for the examination of intercalation compounds by means of typical examples. To this aim, in the next section some example techniques and experiments using multinuclear magnetic resonance will be discussed as an introduction to the methods. Section 3 contains more recent NMR studies of some special layered chalcogenide systems, while Section 4 is devoted to molybdenum cluster sulfides, the class of intercalation compounds with a framework structure which was recently investigated in most detail.

2 TYPICAL NMR EXPERIMENTS WITH INTERCALATION COMPOUNDS

2.1 Powder Patterns or Oriented Samples

Optimum information is of course obtained if—in exceptional cases—single crystals are available. Figure 1 shows, as an example, the ^{1}H NMR spectrum of the metal–ammonia intercalation compound $Na_x(NH_3)_y[MoS_2]$ for the two limiting orientations, where the angle Θ between the crystalline c axis and the external field is either 0 or 90°. The angular dependence follows a $(3\cos^2\Theta - 1)$ law. The following information was obtained: (i) the large triplet splitting belongs to the dipolar proton–proton interaction in a rotating three-spin system; (ii) each component is split once more by the interaction with the nitrogen nucleus; (iii) the C_3 axes of NH_3 are oriented parallel to the layer planes; and (iv) there is an additional reorientational motion of the NH_3 molecules about an axis parallel to the hexagonal c axis and perpendicular to the direction of the C_3 axis; this motion becomes frozen at temperatures below about 100 K.

Most investigations refer to powder samples consisting of small crystallites of the material. In conducting layered compounds, as a consequence of the Pauli paramagnetic anisotropy, there is a tendency of the crystallites in sufficiently high magnetic fields to become aligned. Figure 2 shows as an example the ^{1}H NMR spectra of the hydrated system Na_x

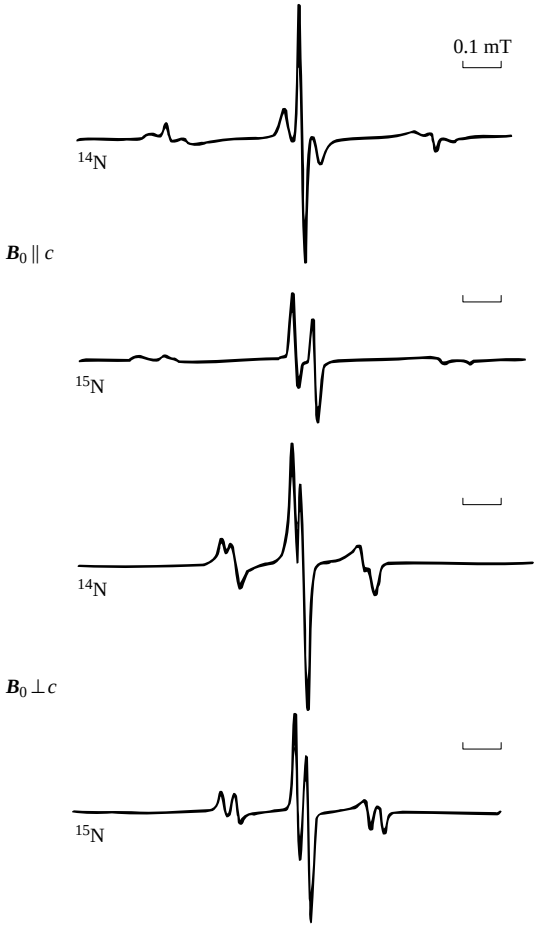

Figure 1 Proton NMR derivative spectra of an $Na_x(NH_3)_y[MoS_2]$ single crystal at 300 K for two orientations of the hexagonal *c* axis in a magnetic field of 0.19 T. Measurements were made for both intercalated $^{14}NH_3$ and $^{15}NH_3$. (Reproduced by permission of Oldenbourg Verlag from E. Wein, W. Müller-Warmuth, and R. Schöllhorn, *Z. Phys. Chem. (NF)*, 1987, **151**, 113)

$(H_2O)_y[NbS_2]$ for a loosely packed sample [Figure 2(a)], for a more compact sample [Figure 2(b)], and a sample where the small crystallites were embedded in Teflon powder and pressed into the ampule [Figure 2(c)]. The limiting spectra [Figure 2(a) and (c)] correspond to a normal powder pattern (Pake doublet with anisotropic chemical shift) and a situation where all the crystallites are completely oriented with their hexagonal *c* axes parallel to the external field.

The magnetic field induced orientation phenomena observed in many solid state NMR experiments of layered compounds can be explained in terms of the magnetic properties and depend on the density of states at the Fermi level of the transition metal chalcogenides or graphites.[3] Orientation or partial orientation may lead to misinterpretations of the spectra if not recognized, or we may profit from it by conducting experiments which are otherwise not possible. An example is given in Figure 3. The powder pattern of the ^{93}Nb NMR in the host lattice NbS_2 is broad and can be simulated by chemical shift and quadrupole interactions (δ_{iso} = 1350 ppm referred to niobium pentachloride, $\Delta\sigma$ = 4200 ppm, $\chi = e^2qQ/h$ = 61 MHz, $\eta_{CS} = \eta_Q = 0$). In a loosely packed sample, by contrast, only one narrow, central transition (CT) can be observed in the covered range. However, it is possible to detect

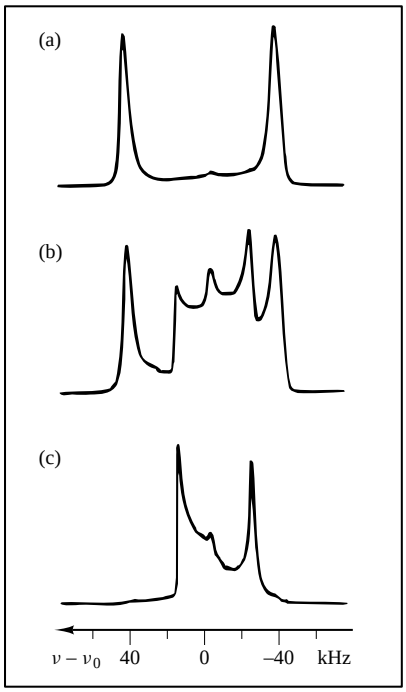

Figure 2 Proton NMR spectra of polycrystalline $Na_x(H_2O)_y[NbS_2]$ observed in a magnetic field of 7 T, whereby the density of the package of the sample was increased from top to bottom

all the eight satellite transitions (ST) of the spin-$\frac{9}{2}$ nucleus as well if the detection range is greatly expanded. The positions of these lines can be reproduced by spectrum simulation with first- and second-order quadrupole interactions, resulting in a very precise determination of the coupling constant.

Intercalation of copper produces a satellite spectrum of 18 lines [Figure 3(c)], which was explained by the superposition of two complete spectra with quadrupole coupling constants of 39.12 and 36.05 MHz instead of 60.02 MHz for the empty host. They belong to two distinct niobium environments in the host lattice with an occurrence ratio 1:1 caused by a well ordered arrangement of copper atoms in tetrahedral sites of the van der Waals gap.

Application of the magnetic field induced orientation effect is in many cases the only way at all to detect and to analyze NMR spectra in layered intercalation compounds. It is often possible to maintain the orientation in a sample by dispersing the crystallites in a resin, and curing the resin after a strong magnetic field had been applied to induce orientation. Angle-dependent measurements are then possible, as shown in Figure 4 for the ^{63}Cu NMR of $Cu_{0.5}[NbS_2]$.

2.2 Anisotropic Dynamics of an Intercalated Heteronuclear Four-Spin System

An instructive example from the NMR point of view is difluoromethane. In the presence of larger alkali cations it is possible to intercalate molecules with low solvating power such as CH_2F_2. Well structured ^{1}H and ^{19}F NMR spectra were observed (Figure 5) and could be simulated on the basis of a proper model.[4] They were calculated from the numerical solution of the eigenvalue problem of a Hamiltonian which

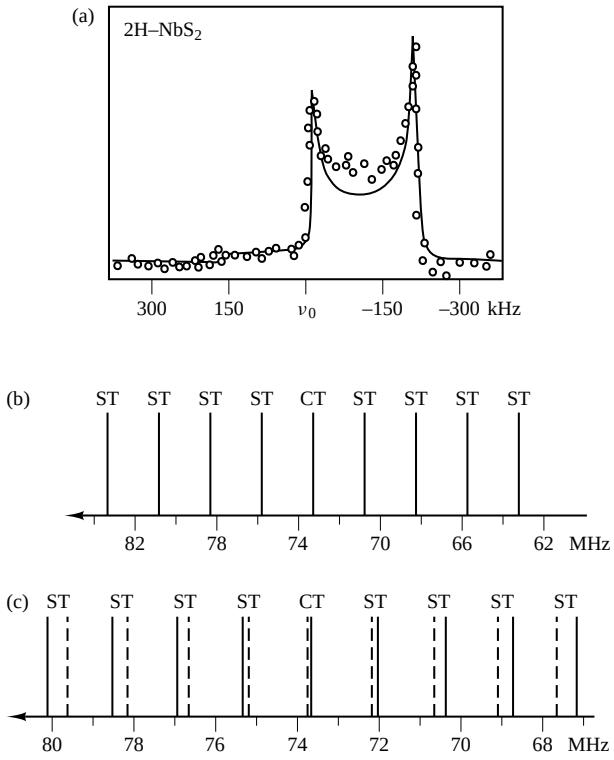

Figure 3 Niobium-93 NMR spectra of layered 2H−NbS_2 in a magnetic field of 7 T and 200 K. (a) The powder pattern (sample pressed in Teflon powder) was recorded at ν_0 = 73.41 MHz and superimposed of successively excited contributions (solid echo sequences with pulse lengths below 6 μs and delay times 15–40 μs). (b) For the loosely packed sample, where the crystallites appeared to be completely oriented in the external field, a central transition (CT) at 73.56 MHz and eight satellites (ST) were observed. (c) Upon intercalation, for $Cu_{0.5}[NbS_2]$ a spectrum of 18 lines was recorded (bottom). (Reproduced by permission of Elsevier Science Publishers from Janssen et al.[3])

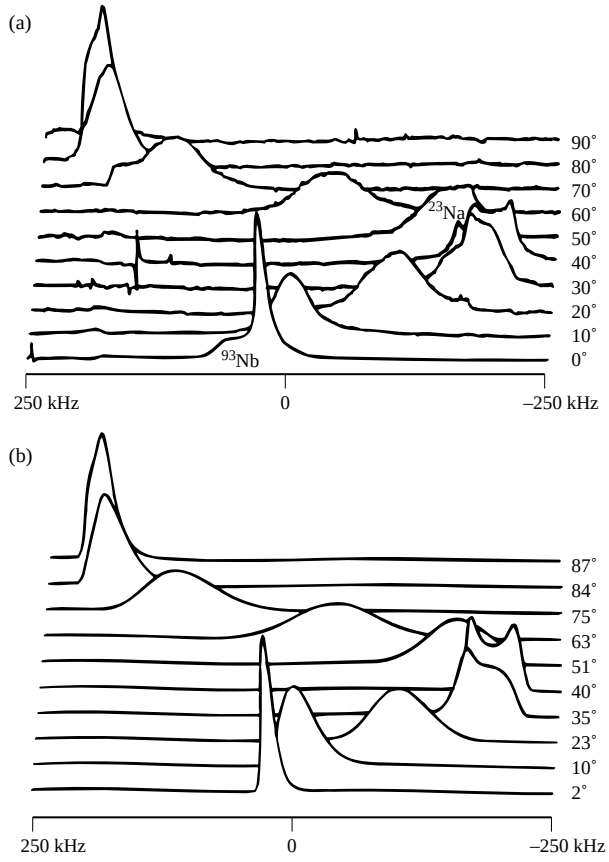

Figure 4 (a) Copper-63 NMR spectrum of $Cu_{0.5}[NbS_2]$ at 79.556 MHz and 210 K detected by the utilization of the field induced orientation of crystallites (solid echo sequences with pulse lengths 5 μs, delay 20 μs, repetition 0.1 s). The angles on the right-hand side indicate the angle between the c axis and $\boldsymbol{B}_0$. The satellites are not shown. (b) By computer simulation the following parameters were determined: δ_{iso} = 730 ppm (relative to CuCl), $\Delta\sigma = -600$ ppm, $\eta_{CS} = 0$, χ = 14.93 MHz, η_Q = 0.11; the principal axes of the CS and QF tensors coincide. Additional NMR signals arising from the ^{93}Nb nuclei and from ^{23}Na probe background are marked in the figure. (Reproduced by permission of Elsevier Science Publishers from Janssen et al.[3])

considers, in addition to the two Zeeman terms, 10 further interaction terms: the chemical shift of the four hydrogen and fluorine atoms [where the respective principal axis systems (PASs) are defined by the direction of the C−H and C−F bonds], the two homonuclear dipole−dipole interactions (PASs in the H−H and F−F directions), and the four heteronuclear dipole−dipole interactions (with the PASs given by the various H−F separation vectors).

In order to describe the orientation of a particular CH_2F_2 molecule with respect to the laboratory frame ($z \parallel \boldsymbol{B}_0$), a molecular fixed coordinate system was defined with its x' axis parallel to the F−F vector and the z' axis in the direction of the H−H vector of the tetrahedral molecule. In the further treatment, the transformation from the PASs of the various interactions to the laboratory frame was then replaced by the two successive transformations from the PASs to the molecular frame (Eulerian angles obtained from the geometry) and from the molecular to the laboratory frame (two Eulerian angles α' and β' appear in the result). Powder patterns result from spatially weighted sums over all possible orientations (α',β') of the CH_2F_2 molecules.

Theoretical NMR spectra were calculated for various chemical shift anisotropies and possible thermally activated reorientations about various axes. The obtained ^{1}H and ^{19}F NMR lineshapes were then compared with the experimental spectra such as those shown in Figure 5. In conclusion, intercalated difluoromethane appears to be oriented with its z' axis (H−H direction) perpendicular to the layer planes, and at 300 K it reorients rapidly about this axis. Another orientation of the intercalated molecules or another type of motion would result in quite different ^{1}H and ^{19}F NMR spectra.

2.3 NMR Spectra in the Presence of Various Interactions where the Principal Axes do not Coincide

Interpretation of solid state NMR spectra in the presence of dipole−dipole (DD), chemical shift (CS) and quadrupole (QF) interactions is straightforward if the principal axes of the CS and QF tensors coincide. Appropriate procedures and suitable computer programs have been developed. In two-dimensional intercalation compounds such a requirement is generally met (at least for the guest species), and the axis parallel to the layer planes is in most cases the principal axis for both the CS and QF tensors. The interpretation of the spectra shown in

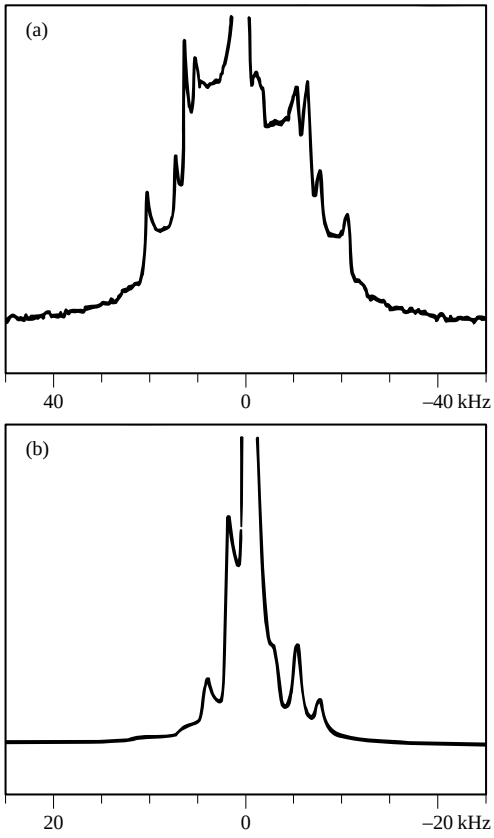

Figure 5 (a) Proton and (b) fluorine-19 NMR spectra of $Cs_x(CH_2F_2)_y[NbS_2]$ measured at 30 MHz and 295 K. The magnetic field was sufficiently low to rule out orientation effects of the crystallites. The intense central resonances belong to unreacted difluoromethane molecules in the sample. (Reproduced by permission of Academic Press from Möller et al.[4])

Figures 3 and 4 were examples of this behavior. Particularly in three-dimensional intercalation compounds, however, it may well be the case that the directions of the PASs do not coincide. An example is the broad and asymmetric ^{7}Li NMR spectra of the molybdenum cluster chalcogenides $Li_3Mo_6X_8$ (X = S, Se) shown in Figure 6.[5]

The lineshape was simulated by the following expression for the transition frequency from a state m to a state, $m-1$:

$$\begin{aligned}\omega = {} & \omega_0(1+\sigma_{\mathrm{iso}}) + \tfrac{1}{6}\omega_0\Delta\sigma \\ & \times\{3\sin^2\beta\sin^2\vartheta\cos 2\varphi - 3\sin 2\beta\sin 2\vartheta\cos\varphi \\ & +(3\cos^2\beta-1)(3\cos^2\vartheta-1) \\ & -\eta_{\mathrm{cs}}[\tfrac{1}{2}(1+\cos\beta)^2\sin^2\vartheta\cos 2(\varphi+\gamma) \\ & +\tfrac{1}{2}(1-\cos\beta)^2\sin^2\vartheta\cos 2(\varphi-\gamma) \\ & +(1+\cos\beta)\sin\beta\sin 2\vartheta\cos(\varphi+2\gamma) \\ & -(1-\cos\beta)\sin\beta\sin 2\vartheta\cos(\varphi-2\gamma) \\ & +\sin^2\beta\cos 2\gamma(3\cos^2\vartheta-1)]\} \\ & +\frac{3e^2qQ}{4I(2I-1)\hbar}(\tfrac{1}{2}-m)[3\cos^2\vartheta-1 \\ & -\eta_{\mathrm{Q}}\sin^2\vartheta\cos 2\varphi] \end{aligned} \quad (1)$$

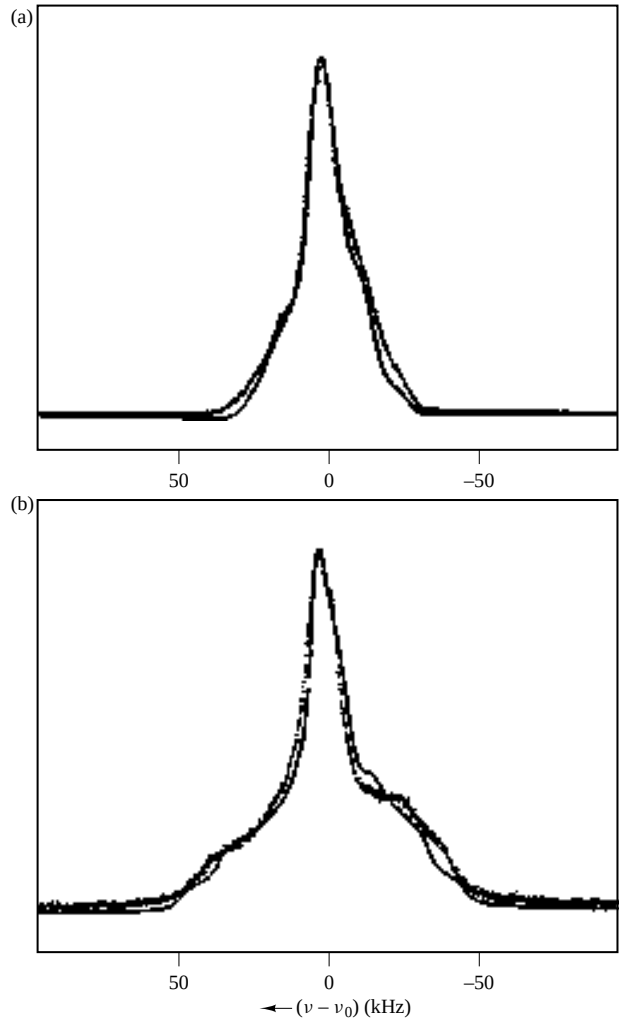

Figure 6 Lithium-7 NMR spectra of the molybdenum cluster chalcogenides (a) $Li_3Mo_6S_8$ and (b) $Li_3Mo_6Se_8$ obtained at 116.64 MHz and 100 K, and their simulations. (Reproduced by permission of the American Chemical Society from Prigge et al.[5])

The powder spectrum is obtained from a weighted integration over the angles ϑ and φ in equation (1) which describe the orientation of the PAS of the nuclear quadrupole interaction (QF) tensor with respect to the laboratory frame (determined by $\boldsymbol{B}_0$). The Eulerian angles β and γ can be determined from the experimental spectra by simulation using equation (1). β is the angle between the z axes of the QF and CS tensors. The projection of the z axis of the QF tensor on the azimuthal plane of the PAS of the CS tensor with the x axis of the latter makes the angle γ. For $\beta = \gamma = 0$, equation (1) changes into the well known formula for the transition frequencies if the PASs coincide. The other symbols have their usual meanings. Instead of the (negative) shielding constant σ_{iso}, the isotropic chemical shift δ = 94 (111) ppm relative to LiCl is given for $Li_3Mo_6S_8$ (in parentheses for $Li_3Mo_6Se_8$). The chemical shift anisotropy is $\Delta\sigma = -113$ (-90) ppm and the asymmetry factor $\eta_{\mathrm{cs}} = 0$. The quadrupole data thus obtained from the spectra are χ = 75 (95) kHz and η_{Q} = 0.25 (0.50). The angles turned out to be $\beta = 55^\circ$ and $\gamma = 90^\circ$ for both compounds. The DD interaction was taken into account by a Gaussian broadening with (full) width at halfheight of 8.2 (4.2) kHz. The results, and in

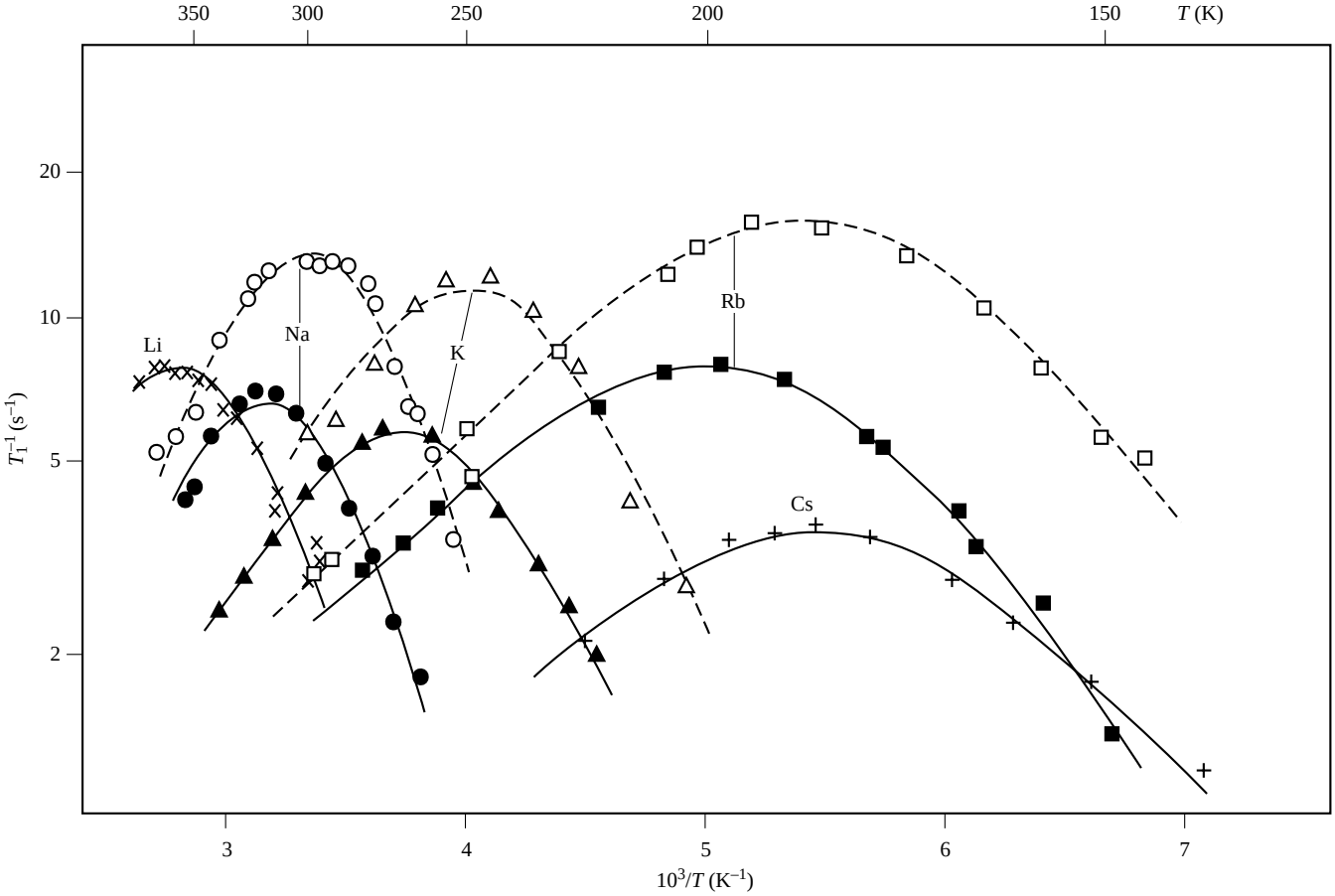

Figure 7 Dependence of the proton ^{1}H NMR spin–lattice relaxation rate upon reciprocal temperature for various hydrated chalcogenides $A_x(H_2O)_y[MS_2]$ with A = Li, Na, K, Rb, or Cs, and M = Nb or Ta, measured at 15 MHz (dotted lines) and 30 MHz (solid lines). (Reproduced by permission of the American Institute of Physics from Röder et al.[6])

particular the orientation of the PASs, can be well related to the structure, as will be shown in Section 4.

2.4 Molecular Motions

Molecular motions, the most important of which are those of the guest species, may either be studied from their influence on the spectra or by examining the relaxation behavior. An illustration of the first type of experiments was the example discussed in Section 2.2. If an intercalated molecule rotates, for instance, the Eulerian angles describing the orientation of the PAS (of the respective interaction) to $\boldsymbol{B}_0$ become time dependent and the spectra modified by partial averaging. In such cases it is useful to investigate the variation of the spectra with temperature.

Spin–lattice relaxation rates have been frequently used to explain details of the motional behavior. Two examples will be presented. Figure 7 shows $1/T_1$ versus reciprocal temperatures for hydrated transition metal disulfides with various alkali cations. The data depend strongly on the hydration enthalpy of the cations, and contain elements of low dimensionality. The fits were made on the basis of a model which included a logarithmic dependence on frequency, i.e. two-dimensional motions.[6] The second example refers to a material which will be discussed in a later section.

The relaxation rates of ^{7}Li in $Li_3Mo_6S_8$ (Figure 8) can be explained by the superposition of a BPP term due to diffusion and a term which is proportional to the temperature. The latter arises from the interaction of the lithium nuclei with conduction electrons.

Slow motions have also been investigated in intercalation compounds using standard techniques. An example is the proton exchange rate, i.e. the mean lifetimes τ_e in hydrated transition metal disulfides obtained via creation of spin alignment by the 'Jeener–Broekaert' pulse sequence. τ_e values between about 1 and 100 ms were thus determined (Figure 9). They display an Arrhenius behavior which could be extrapolated to lower temperatures (and shorter lifetimes) by lineshape analysis.

3 STRUCTURE AND MOTIONS OF HYDRATED LAYERED CHALCOGENIDES

A class of intercalation compounds that was studied in some detail by NMR and where NMR contributed substantially to the understanding of the structure and dynamics comprises the hydrated transition metal chalcogenides of the alkali and alkaline earth elements with the formula $A_x(H_2O)_y[MX_2]$, where M = Ti, V, Zr, Nb, Mo, Ta, or W and X = S or Se. These

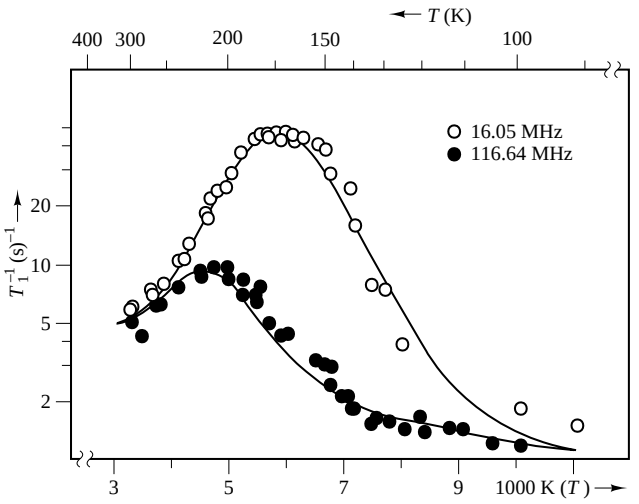

Figure 8 Lithium-7 NMR spin–lattice relaxation rate versus reciprocal temperature for the molybdenum cluster sulfide $Li_3Mo_6S_8$. The solid curve corresponds to the theoretical model description. (Reproduced by permission of the American Chemical Society from Prigge et al.[5])

compounds can be regarded as polyelectrolytes consisting of two-dimensional $[MX_2]^{x-}$ macroanions (host lattice) with monolayers of mobile hydrated cations in the van der Waals gap between the sheets (guest species). We shall present here only an outline of the most important NMR experiments to investigate the structure and dynamics.

3.1 Proton NMR Spectra

The ^{1}H NMR spectra of the guest species (Figures 2 and 10) display the influence of intra- and intermolecular dipole–dipole couplings as well as CSA interactions. Separation is possible either by studying the magnetic field dependence or by application of a multiple pulse sequence (cf. Figure 10). In a sufficiently low magnetic field, at ambient temperature a nearly perfect Pake doublet of isolated H_2O can be observed, since the intermolecular interactions are averaged out by hopping motions of the water molecules. However, there is an additional central signal which increases at elevated temperatures and which was explained by proton exchange in these two-dimensional hydrated systems. The fast motion process was further investigated by NMR T_1 measurements (cf. Figure 7), and the slower proton exchange by spin alignment techniques (cf. Figure 9).

As a final result of several ^{1}H NMR studies including the examination of single crystals and oriented crystallites, all the water molecules in the van der Waals gap appear to be aligned with their C_2 axes lying in the *a,b* planes defined by the chalcogenide layers and their H–H vectors parallel to the *c* axis (Figure 11). The proton–proton separations amount to 165 pm; they are not significantly different from those in water of crystallization (158 pm). Two-dimensional diffusion and/or reorientation about the *c* direction leaves the orientation of the water molecules unchanged. The activation energy for this motion varies from 9 kJ mol^{-1} (Cs^+) to 50 kJ mol^{-1} (Li^+) depending on the central cation which interacts immediately with the negatively polarized dipole ends of the H_2O molecules.

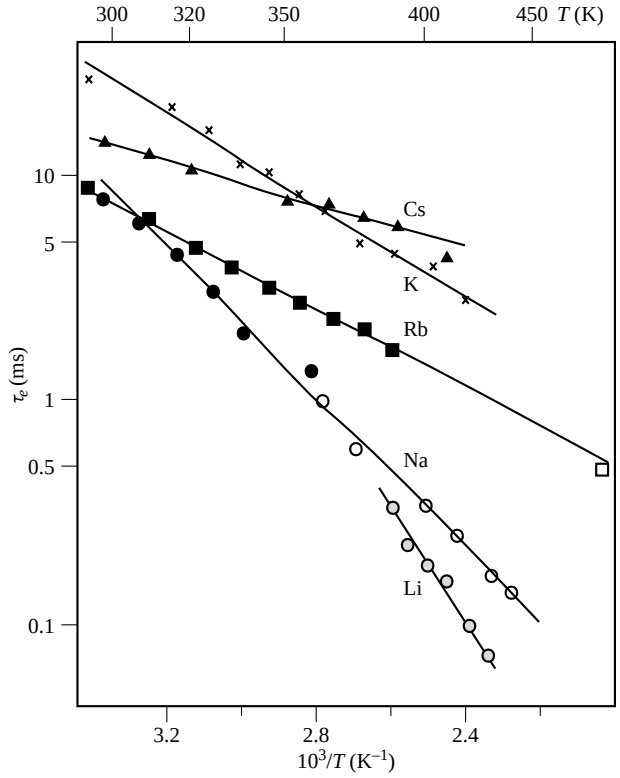

Figure 9 Proton mean lifetime versus reciprocal temperature for water in the chalcogenides $A_x(H_2O)_y[NbS_2]$ with A = Li, Na, K, Rb, or Cs derived from spin alignment measurements (solid symbols) and linewidth analysis (open symbols). (Reproduced by permission of VCH from E. Wein, W. Müller-Warmuth, and R. Schöllhorn, *Ber. Bunsenges. Phys. Chem.*, 1986, **90**, 158)

The diffusional motion of the water molecules explains also the axial symmetry of the chemical shift tensor derived from the spectra of Figure 10 (top). The PASs for the CS and DD interactions coincide. At lower temperature, the symmetry of the chemical shift disappears, and the intermolecular dipole interactions become important for broadening of the spectra (Figure 10) (bottom). The chemical shift anisotropy itself was found to depend greatly on the transition metal M. Going from W via Ta(1 T), Mo, Ta(2H), Ti, Nb to V, $\Delta\sigma$ increases from −11 to +69 ppm for fully intercalated compounds (x = 0.33). Upon increasing the degree of reduction x between 0.08 and 0.33, $\Delta\sigma$ increases from 8 to 17 ppm for M = Ti; it decreases, however, from 60 to 33 ppm for M = Nb.

The large range of chemical shift anisotropies cannot be interpreted in terms of the electronic proton shielding within the guest phase. This should lead to a contribution of only about −10 ppm, a value which was observed as a limit in two of the compounds. In all other cases the significant positive contribution from the host lattice has to be taken into account in addition. The effect was found to depend on the particular conduction band of the dichalcogenide material and its filling with electrons. In NbS_2 the lowest-lying energy level is the d_{z^2} band, which is half occupied and becomes further filled up during the course of intercalation. The density of states at the Fermi level $D(E_F)$ has its maximum, therefore, in the absence of any intercalant, and decreases as a function of x, if guest species are intercalated and s electrons donated. $\Delta\sigma$ appears to be proportional to $D(E_F)$.

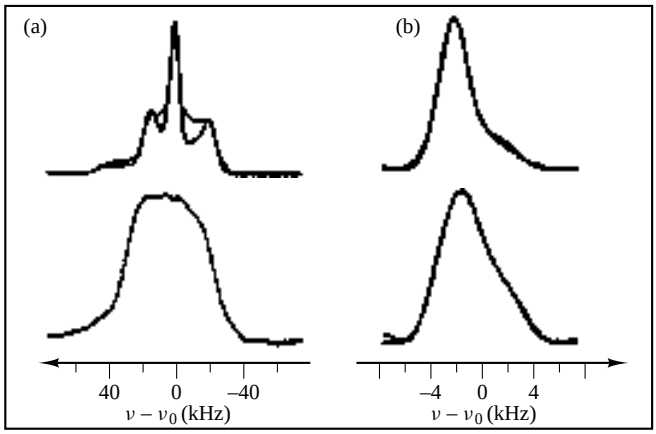

Figure 10 Proton NMR powder patterns of the hydrated layered compound $K_{0.25}(H_2O)_{0.75}[NbS_2]$ at two different temperatures (295 K, top and 150 K, bottom) measured in a magnetic field of 7 T. (a) Normal spectra. (b) Dipolar-decoupled spectra by MREV 8 multiple pulse sequences. The solid lines are computer simulations. (Reproduced by permission of VCH from M. Lobert, W. Müller-Warmuth, H. Katzke, and R. Schöllhorn, *Ber. Bunsenges. Phys. Chem.*, 1992, **96**, 1564)

This behavior was confirmed by the results for the compound $K_x(H_2O)_y[TiS_2]$. TiS_2 with the Group 4 element titanium has an empty d_{z^2} band, and, here, filling by progressive intercalation enhances both $D(E_F)$ and $\Delta\sigma$. Using the experimental data, the qualitative structure of the d_{z^2} band could be obtained for both compounds. The NMR results may be considered as a confirmation of the 'rigid band model', in which the only change to the electronic structure of the host is the increased d band filling. The proportionality between $\Delta\sigma$ and $D(E_F)$ was explained by the anisotropic Pauli paramagnetism; the magnetic susceptibility is also proportional to the density of states at the Fermi level.

3.2 Niobium-93 NMR Studies of the Intercalation

The process of intercalation from $x = 0$ to 0.33 could be studied in $K_x(H_2O)_y[NbS_2]$ and $K_x(H_2O)_y[NbSe_2]$ by observing the influence of the guest species on the ^{93}Nb NMR of the host lattice. The empty host lattices displayed spectra resembling those of Figures 3(a) and (b); the quadrupole coupling constants were determined with high accuracy, viz. 60.02 ± 0.02 MHz (60.05 ± 0.02 MHz) for 2H–NbS_2 (and 2H–$NbSe_2$). Intercalation of $K_x(H_2O)_y$ changes the mean local environment of niobium and reduces the coupling constant for a certain fraction of the ^{93}Nb NMR nuclei. For $x = 0.08$, 14% (11%) of the ^{93}Nb nuclei still have a coupling constant of 60 MHz, but 82% (89%) already one of 53 MHz, and 4% even one of 46 MHz. Upon increasing x further, the fractions with 60 MHz disappear in favor of the other two contributions. For $x = 0.33$ a coupling constant of 46 MHz (48 MHz) finally holds for 100% (41%) of the niobium sites in the NbS_2 ($NbSe_2$) host lattice. In $K_x(H_2O)_y[NbSe_2]$ the remaining 59% of ^{93}Nb nuclei experience the medium value of 53 MHz.

It is important to realize that there is no continuous variation of the NMR parameters with progressive intercalation, but there are three phases whose fractions change as a function of x. Structural variations are therefore responsible rather than electronic effects of the host. The three observed structures were attributed to local staging. For $x = 0$, the relatively large quadrupole coupling belongs to niobium atoms, which all 'see' on one side of the two-dimensional arrangement the empty van der Waals gap. Upon increasing x, two new environments occur, one with intercalated species on both sides (local ranges of first-stage character), the other one with intercalated species on one side only (second-stage character). The smaller coupling constant of the final compound ($x = 0.33$) was attributed to a homogenous occupation of the van der Waals gap ('first-stage compound').

3.3 Further NMR Studies of Layered Compounds

Among the materials that were studied in some detail by NMR and which cannot be discussed within the scope of this short article are metal–ammonia compounds with certain similarities to hydrated systems. Intercalated atoms or ions in dichalcogenides, such as hydrogen, lithium and copper, were examined as well as intercalated molecules, e.g. ammonia, amines, derivatives of methane, pyridine, and even larger intercalants. Layered compounds also include graphite intercalation compounds, where, in particular, ^{1}H, ^{7}Li and ^{13}C NMR was applied on a large scale by various authors. Some layered oxides were investigated as well. Further details can be found in the literature.[2]

4 STRUCTURE AND DYNAMICS OF GUEST PHASES IN MOLYBDENUM CLUSTER CHALCOGENIDES

Binary and ternary molybdenum cluster chalcogenides (Chevrel phases) with the compositions Mo_6X_8 and $A_xMo_6X_8$ (A = main group metal; X = S or Se) have attracted considerable interest because of their unusual structure (Figure 11) and remarkable physical properties. Using NMR, compounds with intercalated lithium, sodium and copper were investigated. The behavior of lithium as the intercalant was examined in particular, with the result that four distinct phases with $x = 1$, 3, 3.8, and 4 could be identified from the different isotropic chemical shifts, as shown in Figure 12 (at room temperature, narrow singlet lines or first-order quadrupole spectra were observed). From the δ_{iso} values it was concluded that lithium appears to be ionic in $Li_1Mo_6X_8$ and $Li_4Mo_6X_8$ whereas lithium clusters with partial metallic character are formed in $Li_3Mo_6X_8$ and $Li_{3.8}Mo_6X_8$. More details were obtained from broadline spectra at low temperatures and from relaxation measurements.[5,7]

In both $Li_1Mo_6X_8$ compounds the ^{7}Li NMR spectra display in addition to DD and CA interactions ($\Delta\sigma = -11$ ppm at 100 K for X = S, and -15 ppm for X = Se) well resolved quadrupole structures of first order ($\chi = 107$ kHz and 79 kHz, respectively). The chemical shift tensor is axially symmetric ($\eta_{cs} = 0$), but the quadrupole asymmetry factor η_Q varies from 0.24 (0.10 for X = Se) at 100 K to zero at 300 K upon increasing the temperature. Spectra simulations led to the conclusion that the intercalated Li^+ ions reside in one of the six equivalent inner tetrahedral sites Li_1 of Figure 11(b) (bottom). Hopping motions between these positions are thermally activated; the correlation times are of the order of 10^{-7}–10^{-3} s and follow an Arrhenius-type law (11 and 7 kJ mol^{-1}, respectively). In contrast to the other lithiated

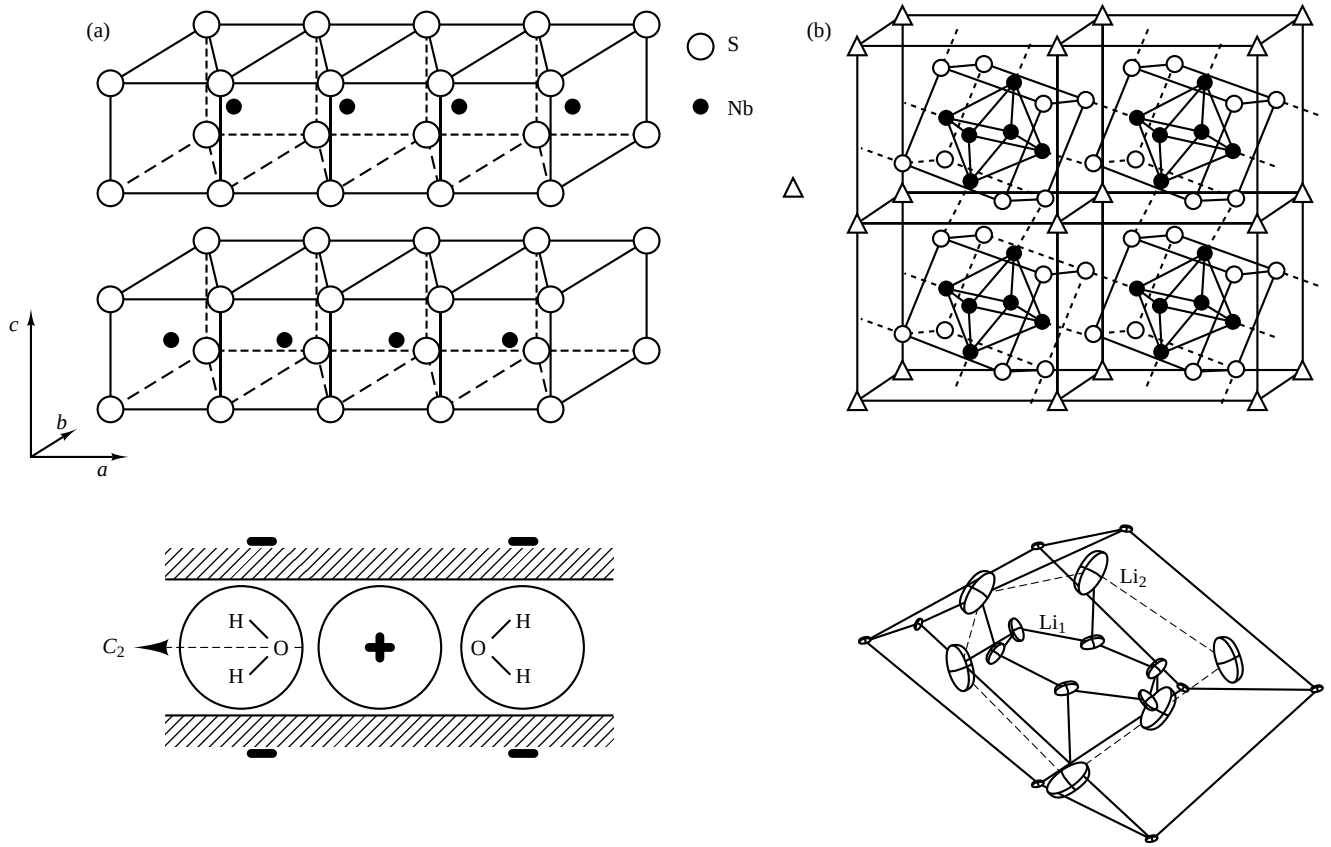

Figure 11 Schematic representation of the structure of the compounds discussed in Sections [3] and [4]. (a) Hydrated layered chalcogenides with the NbS_2 host lattice (top) and the arrangement of the H_2O molecules with the central cation (bottom). (b) Mo_6S_8 (● Mo, ○ S) structure with vacant channel positions (△) (top) and 2 × 6 potential lattice sites Li_1 (inner concentric ring) and Li_2 (outer ring) around the unit cell origin (bottom). The cavity is formed by sulfur atoms which belong to eight different Mo_6S_8 units

molybdenum cluster chalcogenides, at room temperature only this local motion is important; long range diffusion from cavity to cavity does not play a major role.

The extremely large δ_{iso} values of the $Li_3Mo_6X_8$ system were interpreted in terms of a Knight shift; the transfer of 2s electrons to the host lattice is incomplete, so that Li_3^{z+} clusters with $z < 3$ are formed. More detailed information was obtained from the ^{7}Li NMR spectra at low temperatures, which are governed by DD, CS, and QF interactions. The chemical shift tensor appears to be axially symmetric, with $\Delta\sigma$ being relatively large and negative (−113 and −90 ppm for the compounds containing S or Se, respectively). This was interpreted in terms of a symmetric arrangement of three lithium atoms on the potential sites of Figure 11(b) (bottom). The z principal axis of the CS tensor may thus be identified with the symmetry axis perpendicular to the plane of the two concentric rings of possible lithium positions; the residual 2s electron density at the intercalated lithium provides stronger screening in the plane.

The principal axes of the CS and QF tensors do not coincide as shown in Figure 6 and equation (1). The PAS of the QF (EFG) tensor seems to agree with the rhombohedral reference system of the structure [Figure 11(b) (top)]. Then the angles β and γ describing the relative positions of the noncoincident PASs of the CS and QF tensors should become 54.54 and 90°, respectively, as observed experimentally. The quadrupole coupling data are χ = 75 kHz, η_Q = 0.25 (X = S), and χ = 95 kHz, η_Q = 0.50 (Se).

The formation of lithium triclusters with short Li–Li distances and metal-like behavior is supported by spin–lattice relaxation measurements as in Figure 8. These contain in addition to a contribution from the lithium diffusion a term which is due to the interaction with conduction (2s) electrons and which fulfills the Korringa relation over a large range of temperatures. The diffusion of lithium species with activation energies of 13 and 19 kJ mol^{-1} corresponds to a high mobility of the translational motion from cavity to cavity. In contrast to $Li_1Mo_6X_8$, but in agreement with recent neutron diffraction studies,[8] for $Li_3Mo_6X_8$ the inner ring of lithium sites is enlarged and provides, together with the outer ring, a framework of symmetrically arranged potential sites. The distances between these sites are short and comparable, and are well suited as a diffusion pathway. Application of the van Vleck formula for the DD interaction leads to an estimate of 210 pm (370 pm) for the Li–Li separation in the triclusters of $Li_3Mo_6X_8$ ($Li_3Mo_6Se_8$).

In contrast to stoichiometries with $3 < x < 3.8$ where two ^{7}Li NMR signals appear, $Li_{3.8}Mo_6S_8$ is distinguished only by one NMR line, indicating a single-phase system. The chemical shift parameters (δ_{iso} = 39 ppm, $\Delta\sigma$ = −45 ppm)—though smaller than those of $Li_3Mo_6S_8$—and the other results, including relaxation, reveal that the lithium guest species possess metal-like properties as well. The Li–Li distances

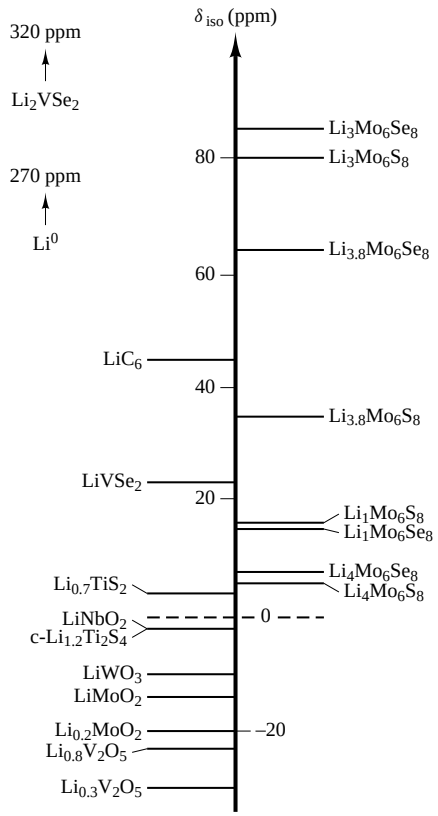

Figure 12 Lithium-7 NMR isotropic chemical shift values (related to LiCl in aqueous solution) for $Li_xMo_6X_8$ compounds (right). For the purpose of comparison, δ_{iso} values for various other lithium intercalation compounds and lithium metal are given (left)

are less and of the order of 330 pm, showing that the outer ring participates greatly in providing positions for the lithium atoms. The lithium mobility is again very high.

For the fully intercalated phases $Li_4Mo_6X_8$ there is no longer any Knight shift, and the chemical shift anisotropy is very small as well. Only the quadrupolar and dipolar data are of comparable orders of magnitude, but here the EFG values are somewhat distributed. The lithium mobility is much less as compared with the Li_3 and $Li_{3.8}$ compounds. The dramatic transition from Li_3 to Li_4, as observed by NMR and manifested by the macroscopic properties of the material, can be related to the electronic structure and to the arrangement of potential lithium sites. The inner ring is no longer enlarged, and there is a large separation between the Li1 and Li2 positions comparable to that in $Li_1Mo_6X_8$.

5 RELATED ARTICLES

Inorganic Solids; Lithium NMR; Magnetic Field Induced Alignment of Molecules; Quadrupolar Nuclei in Solids; Wide Lines for Nonquadrupolar Nuclei.

6 REFERENCES

1. R. Schöllhorn, in *Progress in Intercalation Research*, ed. W. Müller-Warmuth and R. Schöllhorn, Kluwer, Dordrecht 1994.
2. W. Müller-Warmuth, in *Progress in Intercalation Research*, ed. W. Müller-Warmuth and R. Schöllhorn, Kluwer, Dordrecht, 1994.
3. J. Janssen, M. Lobert, W. Müller-Warmuth, and W. Nonte, *Solid State NMR*, 1993, **2**, 201.
4. H. Möller, W. Müller-Warmuth, E. Wein, Z. T. Lalowicz, and R. Schöllhorn, *J. Magn. Reson.*, 1989, **83**, 1.
5. C. Prigge, W. Müller-Warmuth, E. Gocke, and R. Schöllhorn, *Chem. Mater.*, 1993, **5**, 1493.
6. U. Röder, W. Müller-Warmuth, H. W. Spiess, and R. Schöllhorn, *J. Chem. Phys.*, 1982, **77**, 4627.
7. C. Prigge, W. Müller-Warmuth, E. Gocke, and R. Schöllhorn, *Solid State Ionics*, 1993, **62**, 143.
8. C. Ritter, E. Gocke, E. Fischer, and R. Schöllhorn, *Mater. Res. Bull.*, 1992, **27**, 1217.

Biographical Sketch

Werner Müller-Warmuth. *b* 1929. Dr.phil.nat., 1955, Universität Frankfurt. Habilitation, 1961, Universität Mainz. Science collaborator Max Planck-Institut für Chemie, Mainz, 1955–65. Chief of Department, European Research Centre, Ispra (Italy), 1965–73. Professor of Physical Chemistry, Münster, 1973–present. Rector (president), Westfälische Wilhelms-Universität, 1978–82. Approx. 200 publications. Research interests include applications of solid state NMR (and other spectroscopic methods) to various classes of solid materials.

Isotope Effects in Carbocation Chemistry

David A. Forsyth
Northeastern University, Boston, MA, USA

1	Introduction	1
2	Hyperconjugation and the NMR Isotope Shift	1
3	Nonadditive NMR Isotope Shifts and Conformation	2
4	Isotope Shifts Associated with Motion along the Bridging Coordinate	3
5	Variation of NMR Isotope Shifts with Increasing Electron Demand	4
6	Related Articles	5
7	References	5

1 INTRODUCTION

Enormous progress in the understanding of the chemistry and structure of carbocations has come through the application of NMR techniques to long-lived carbocations in superacids.[1,2] The focus of this article is on the development of intrinsic NMR isotope shifts (see ***Carbon-13 Studies of Deuterium Labeled Compounds***; ***Isotope Effects on Chemical Shifts and Coupling Constants***) as a probe for elucidating structural features of carbocations. After the initial reports of intrinsic isotope effects on carbocation chemical shifts by Saunders that contrasted such effects with equilibrium isotope effects,[3,4] it has been clearly demonstrated that intrinsic NMR isotope shifts in themselves can reveal subtle features of carbocation structure that are not readily accessible by other means.

Substitution for hydrogen by deuterium in organic molecules produces small but measurable changes in ^{13}C NMR chemical shifts arising from perturbations of the motional averaging of nuclear shielding in a single molecular species due to changes in nuclear masses. A typical intrinsic isotope shift for a ^{13}C NMR signal, $^{n}\Delta$C(D), where n is the number of intervening bonds is a shielding of a few tenths of a ppm (part per million) at the carbon bearing the deuterium and smaller effects at the next carbon and more remote positions. Intrinsic NMR isotope shifts in carbocations are often larger than in typical organic molecules and very sensitive to structure. The sensitivity may arise in some cases from shallow energy surfaces for bending vibrations along the bridging coordinate, as well as chemical shifts that are highly dependent on the extent of bridging.[5] Patterns of chemical shift response to isotopic perturbation in carbocations have been established empirically that allow structural interpretation. For example, the direction and magnitude of the $^{2}\Delta$C(D) depends on the type of bonding involved in the carbocation, whether localized or π or σ delocalized.[6]

The first generalizations about the relation between structure and intrinsic isotope shifts were reached in the initial study by Servis and Shue.[6] In cases in which the carbocation may have a σ or π bridged structure, β deuteration produced unusually large shifts to lower frequency at the cationic center, for example -2.2 ppm in the 2-methyl-d_3-2-norbornyl cation (**1**), and -0.8 ppm in the 7-methyl-d_3-7-norbornenyl cation (**2**). For classical delocalized carbocations such as the 2-phenyl-2-propyl-1,1,1,3,3,3-d_6 cation (**3**), the isotope shifts at the cation center were nearly zero. Classical localized cations displayed isotope shifts to higher frequency at the cation center, such as the 1.4 ppm effect in the t-butyl-d_9 cation (**4**).

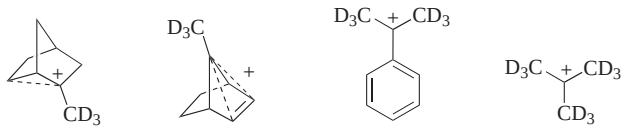

(1) **(2)** **(3)** **(4)**

Another source of structural insight is the nonadditivity of isotope shifts that occurs in some carbocations.[7] Typical NMR isotope shifts are additive, but nonadditivity may occur when C–H(D) bonds are conformationally mobile, because of the imposition of an equilibrium isotope effect on the population of conformers that may have different intrinsic NMR isotope shifts. Carbocations often have strong hyperconjugative interactions that lower the force constants of suitably aligned β C–H(D) bonds, so that a conformer will be favored if it has the β C–D bonds out of alignment with the p orbital of the cation center, i.e. in the more tightly bound position. The result is an average intrinsic isotope shift that differs from that expected in the absence of an equilibrium isotope effect on the conformer populations. The nonadditivity of intrinsic isotope shifts in conformationally mobile systems was exploited to particular advantage in the determination of the previously unknown conformation of cyclopentyl cations.[8]

2 HYPERCONJUGATION AND THE NMR ISOTOPE SHIFT

NMR isotope shifts to higher frequency occur at the cation center of simple carbenium ions (tricoordinated carbocations) upon deuterium substitution at an adjacent carbon atom (β C–D).[6] They also occur at more remote positions in π conjugated carbocations. The isotope shifts appear to result from isotopic perturbation of hyperconjugation, with the C–D bond behaving as a poorer hyperconjugative electron donor than a C–H bond. The effectiveness of the hyperconjugative interaction is perturbed through alteration of the portion of the electronic surface over which vibrational averaging occurs. The differences in vibrational averaging leads to small differences in electron distribution and accompanying changes in shielding. Theoretical modeling of a C–D bond by shortening a C–H bond in molecular orbital calculations supports this interpretation.[8–10]

Several lines of evidence indicate that the long range isotope effects on the ^{19}F chemical shift in p-fluorophenylcarbenium ions arise from perturbation of the hyperconjugative interactions of the alkyl groups and are transmitted via the π system.[7] For example, no isotope effect at ^{19}F is seen for the replacement of a nonhyperconjugating α hydrogen by deuterium in (**5**), ruling out an 'inductive' origin. The isotope effect in (**6**) rules out a 'steric' origin, wherein the coplanarity of the side chain and the ring would be altered by deuteration. Transmission via the π system is suggested by attenuation of the

effect between (**6**) and (**7**). The expected dependence on the dihedral angle between the β C–H(D) bond and the electron deficient p orbital of the cation center was established in the 2-(*p*-fluorophenyl)-2-bicyclo[2.2.2]octyl cation (**8**).[11] Precisely additive isotope shifts at ^{19}F of 0.143 and 0.286 ppm were found for (**8**)-3-*d* and (**8**)-3,3-d_2, respectively, but no measurable effect at ^{19}F was observed for deuteration at the bridgehead C-1 position in (**8**)-1-*d*.

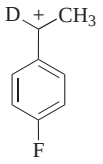

(5)

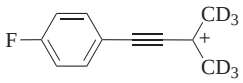

(6)

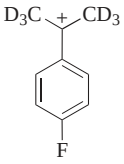

(7)

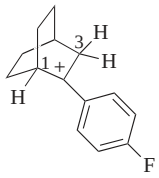

(8)

Upon deuteration of the methyl groups in the phenyldimethylcarbenium ion (**3**), long-range isotope shifts to higher frequency occur at the *ortho* (0.170 ppm) and *para* (0.222 ppm) carbons.[6,12] Similar alternation of the magnitude of isotope shifts occurs at the aryl carbons of the 2-(1′-naphthyl)-2-propyl (**9**), and 2-(2′-naphthyl)-2-propyl (**10**) cations. These shifts are clear evidence for transmission via the π system, and are consistent with isotopic perturbation of hyperconjugation to reduce slightly the supply of electrons to the carbenium center.

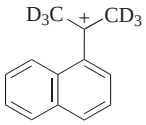

(9)

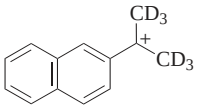

(10)

3 NONADDITIVE NMR ISOTOPE SHIFTS AND CONFORMATION

The association of isotope shifts arising from deuteration of β C–H bonds in carbocations with a hyperconjugative interaction affords possibilities for the study of conformation. If the angular dependence of the magnitude of a particular type of isotope shift were well enough understood to be predictable, it would be possible to assess structures of conformationally fixed systems simply by measuring the isotope shifts. The current capability to predict isotope shifts is insufficient to define conformations precisely, based simply on the magnitude of the shifts. However, the intrinsic isotope shift has provided qualitative information regarding conformation, especially via nonadditive behavior in conformationally mobile systems.

Nonadditivity was first noted in the isotope shift at ^{19}F due to deuteration of α-methyl groups in (*p*-fluorophenyl)carbenium ions.[7] The effects of substituting entire CD_3 groups for CH_3 groups are additive, i.e. in (**11**) and (**7**), but the effects of deuterium substitution within a methyl group are not additive. The isotope shift due to a single deuterium in the methyl group is less than one-third the isotope shift due to three deuteriums. The influence of two deuteriums is also less than the two-thirds effect expected from additivity. These findings can be explained by an isotope effect favoring methyl conformations with the C–D bonds out of alignment for hyperconjugation. No conformational equilibrium isotope effect can occur in the fully deuterated methyl group, so the full intrinsic effect is represented by the CD_3 effect. Thus, the intrinsic isotope effect on the chemical shift in partially deuterated species is diminished by the equilibrium isotope effect, because the favored conformers with C–D bonds poorly aligned for hyperconjugation have a smaller intrinsic effect on the chemical shifts.

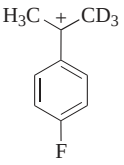

(11)

Cyclopentyl cations were shown to exist in twist (C_2) conformations rather than the possible planar (C_{2v}) or envelope (C_s) conformations through the nonadditive behavior of the intrinsic isotope shifts. The 1-(*p*-fluorophenyl)cyclopentyl cation (**12**), and the 1-methylcyclopentyl cation (**13**) display similar patterns of isotope shifts due to C-2 and C-5 deuteration.[8,13] Each monodeuterated ion has an isotope shift at $^{13}C^+$ (**13**) or ^{19}F (**12**) that is less than one-quarter and each trideuterated ion has an isotope shift that is less than three-quarters that of the tetradeuterated isotopomer (Figure 1). This nonadditivity indicates a perturbed conformational equilibrium in a nonplanar structure for the cyclopentyl ring. All four of the C-2 and C-5 C–H bonds would be equivalent in a planar structure, and additive isotope shifts would be expected.

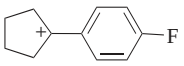

(12)

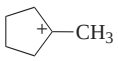

(13)

The key observation for identifying the nonplanar cyclopentyl structures is that the *trans*-2,5-d_2 isotopomers of (**12**) and (**13**) also exhibit isotope shifts that are smaller than expected on the basis of additivity, while the *cis*-2,5-d_2 and *geminally* labeled 2,2-d_2 isotopomers have isotope shifts at $^{13}C^+$ or ^{19}F that are additive, i.e. one-half the isotope shift of the 2,2,5,5-d_4 isotopomer. Clearly, *trans* dilabeling perturbs the conformational equilibrium while *cis* and *geminal* dilabeling do not. This combination is only possible if the cyclopentyl ring is rapidly equilibrating between two twist conformers, (**14**) and (**15**). The smaller isotope shift for the *trans*-2,5-d_2 case is due to an isotope effect on the conformational equilibrium that favors the conformer having

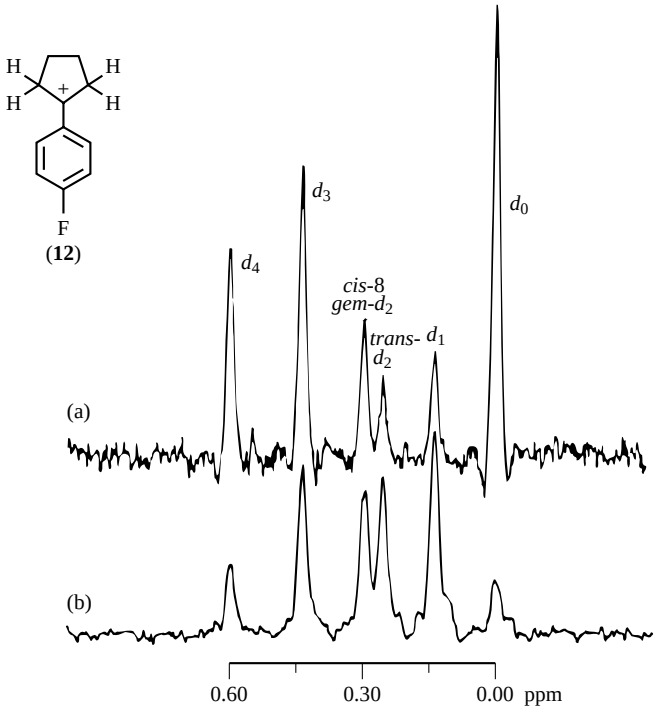

Figure 1 Proton decoupled 56.2 MHz ^{19}F NMR spectra, at about −75 °C, of the 1-(*p*-fluorophenyl)cyclopentyl cation as mixtures of isotopomers due to deuteration at C-2 and C-5. (a) Spectrum of a mixture of the unlabeled ion and a randomly labeled ion sample. (b) Spectrum of another mixture enriched in the *trans*-2,5-d_2 isotopomer. (Reproduced by permission of American Chemical Society from Forsyth and Botkin[13])

both C−D bonds in the pseudoequatorial positions and thus out of alignment with the p orbital at the cation center. The twist−twist equilibrium is not perturbed by *cis* or *geminal* dilabeling because then the twist conformers are degenerate, i.e. both have one pseudoaxial and one pseudoequatorial C−D bond. If the cyclopentyl ring had been an envelope structure, the *trans*-2,5-d_2 isotopomers would have had additive isotope shifts and the *cis*-2,5-d_2 isotopomers would have shown nonadditivity.

(14) **(15)**

4 ISOTOPE SHIFTS ASSOCIATED WITH MOTION ALONG THE BRIDGING COORDINATE

Isotope shifts for the ^{13}C signals in the 2-methyl-2-norbornyl cation (**1**), are truly remarkable.[5,6,14–16] As noted earlier, the cation center displays an unusually large isotope shift to low frequency of −2.26 ppm for the (**1**)-methyl-d_3 cation. This direction is opposite of the $^2\Delta$C(D) to high frequency attributed to isotopic perturbation of hyperconjugation in classical cations such as the *t*-butyl cation. A similar shift at C-2$^+$ of −2.51 ppm is seen for (**16**). Isotope shifts at C-2$^+$ are additive for labeling at C-3, with a $^2\Delta$C-2(*exo*-3-*d*) of

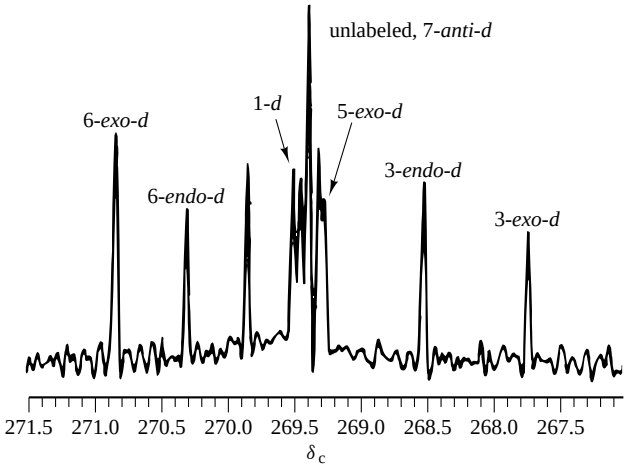

Figure 2 The C-2 region of a 75.4 MHz ^{13}C{^{1}H} NMR spectrum of all 10 possible singly deuterated positional isotopomers and the unlabeled 2-methyl-2-norbornyl cation. (Reproduced by permission of the Chemical Society from Forsyth and Panyachotipun[15])

−1.64 ppm and $^2\Delta$C-2(*endo*-3-*d*) of −0.87 ppm. Isotope shifts to high frequency occur for deuteration at some positions, most notably in a $^3\Delta$C-2(*exo*-6-*d*) of 1.45 ppm. Overall, changing the location of a single deuterium in the bicyclo[2.2.1]heptyl framework (Figure 2) can change the δ_C for the cation center of (**1**) by 3.1 ppm.

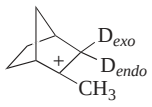

(16)

To place the large isotope shifts in context, C-3 deuteration in 2-norbornanone produces ΔC(D) values that are smaller than |0.10| ppm at all positions except the directly labeled C-3.[14] Upon comparison of isotope shifts in the 2-methyl-2-norbornyl cation with those for the 2-methyl-2-bicyclo[2.2.2]octyl cation (**17**), and the 2-methyl-2-bicyclo [2.1.1]hexyl cation (**18**), a similar pattern of isotope shifts emerges, namely that β deuteration at either the C-3 or methyl position produces isotope shifts to lower frequency at C-2, isotope shifts to higher frequency at C-1, and a shift to lower frequency at the remaining carbon (C-3 or methyl) directly attached to C-2. The isotope shifts are of similar magnitude in (**1**) and (**17**), and somewhat smaller in (**18**).

(17) **(18)**

A common origin for the isotope shifts in (**1**), (**17**), and (**18**) is likely, with similar force fields and shielding influences in all three ions. Perturbation of a σ delocalized bonding structure toward greater σ delocalization would increase electron density at C-2, decrease electron density at C-1, and decrease hyperconjugative involvement of the C-3 methylene and the

methyl group. However, this explanation must be elaborated because the C-2$^+$ chemical shift of 322 ppm for both (**17**) and (**18**) is in the range (320–340 ppm) considered typical of classical, nonbridged cations, while the more shielded C-2$^+$ in (**1**) (δ_C 269.5 ppm) has led to (**1**) being considered as a partially bridged cation.

Both the isotope shifts and chemical shifts of (**1**) and (**12**) show a small temperature dependence.[5] The magnitude of the isotope shifts at C-1, C-2, and C-3 in both structures decline slightly with temperature, e.g. from −2.26 ppm at −98 °C to −2.02 ppm at −38 °C for C-2 in (**1**)-methyl-d_3. A dynamic equilibrium between similar structures, namely an open nonbridged structure and a partially bridged structure, could account for the data in each case, but not an equilibrium between the classical tertiary and secondary forms of the cations.

A more likely explanation is that these ions have a relatively flat energy surface for the bending motion along the direction associated with bridging.[5] A broad energy surface would have low-lying vibrational excited states, so that not only isotope effects but temperature changes could easily perturb the vibrationally averaged geometry. Appropriately shaped anharmonic surfaces can account for the direction of the δ_C and ΔC(D) temperature dependences in each case. The large intrinsic isotope shifts may be diagnostic for the existence of the low energy bending motion associated with development of a three-center, two-electron (nonclassical) bond, but the isotope effects are not directly reflective of the extent of bridging. Since the shallow surface and large changes in shielding may occur even when bridging is not very extensive, the isotope shift may be a particularly sensitive probe for the onset of such bonding (see results for aryl-substituted ions below).

High level ab initio molecular orbital calculations support the idea of some distortion toward bridging accompanying bridging even in simple tertiary alkyl carbocations.[17] Theoretical ^{13}C chemical shifts calculated by the IGLO method for changes in the C$^+$–C–C angle in model cations show a very strong dependence of shielding of C$^+$ on the bridging angle once an angle of about 100° is reached. A change in the C$^+$–C–C angle of only 1° toward bridging results in ~6 ppm shielding of C$^+$. These calculations make it clear that a small isotope effect on the vibrationally averaged extent of bridging could produce large intrinsic isotope shifts of the type seen in (**1**), (**17**), and (**18**).

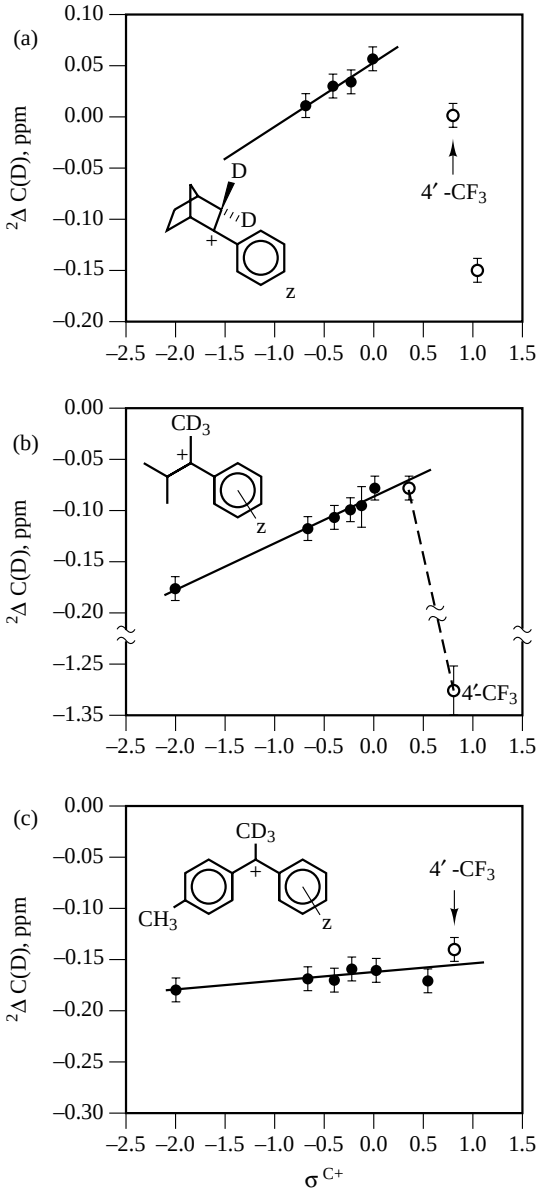

Figure 3 TIED plots of isotope shifts at the cation center, $^2\Delta$C(D) versus σ^{C+}: (a) 2-aryl-2-norbornyl cations, (b) 2-aryl-3-methyl-2-butyl cations, and (c) 1-aryl-1-tolylethyl cations. (Reproduced by permission of the American Chemical Society from Forsyth et al.[19])

5 VARIATION OF NMR ISOTOPE SHIFTS WITH INCREASING ELECTRON DEMAND

In aryl-substituted carbocations the dependence of the ^{13}C NMR chemical shifts of the cation centers on the aryl substituents has been used extensively to evaluate the electronic and structural characteristics of various carbocation types.[18] Deviations from linearity in plots of the chemical shifts at the cation center versus shifts in appropriate reference systems have been interpreted as indicating the onset of σ participation and other phenomena as electron demand increases. One of the difficulties in interpreting these 'tool of increasing electron demand' plots (referred to here as TIED plots) of chemical shifts is that the deviations from linearity are often rather similar in appearance in various systems despite different underlying causes for the deviant behavior. However, the use of NMR isotope shifts provides complementary data that can help differentiate between carbocations which show similar behavior in TIED plots of chemical shifts.[19]

Three carbocation series illustrate the use of isotope shifts: the 2-aryl-2-norbornyl-3,3-d_2 (**19**), 2-aryl-3-methyl-2-butyl-1,1,1-d_3 (**20**), and 1-aryl-1-tolylethyl-2,2,2-d_3 (**21**) cations.[19] All three systems give very similar chemical shift TIED plots for the δ_C at C$^+$. However, the isotope shift TIED plots (Figure 3) show quite different results for these three systems. The point for 4′-CF$_3$ in the 2-aryl-2-norbornyl case shows an unmistakable deviation of about −0.10 ppm toward a lower frequency isotope shift from the correlation line established for electron donating substituents. A much larger deviation of

−1.25 ppm is seen for the 4′-CF_3 point in the 2-aryl-3-methyl-2-butyl cation series, representing an isotope effect on a rapid equilibrium with a rearranged ion, a conclusion also supported by other evidence. On the other hand, the 4′-CF_3 point in the 1-aryl-1-tolylethyl cations deviates by only 0.02 ppm in the high-frequency direction. This latter deviation is in the same direction and of the same magnitude as in the reference system, the 2-aryl-2-propyl cations, so it likely indicates that there is no structural feature other than those also in the reference system that lends itself to perturbation of its vibrationally averaged character by deuterium substitution.

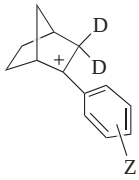

(19)

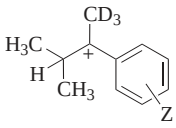

(20)

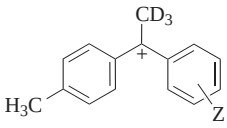

(21)

Isotope shifts in the 2-aryl-2-norbornyl series have been examined in considerable detail,[14,16] and, for electron withdrawing substituents, there is a clear resemblance to isotope shifts in the 2-methyl-2-norbornyl cation, although isotope shifts at C-2^+ are much smaller in the aryl series. The isotope shift TIED plots for this system as well as the 2-aryl-2-bicyclo[2.2.2]octyl, 2-aryl-2-bicyclo[2.1.1]hexyl, and 1-aryl-1-cyclopropylethyl cations could be explained by a lowering of the potential energy surface for motion of nuclei toward C−C bridging so that the vibrationally averaged structure becomes slightly bridged as electron demand increases.[19] Isotopic substitution may then alter the vibrationally averaged extent of bridging in the more electron deficient cations, thereby giving a different isotope shift than expected by extrapolation from the less electron deficient cations. The combination of the TIED with NMR isotope shifts appears to reveal the subtle transition from simple hyperconjugation to the point at which geometric distortion toward bridging has observable physical consequences.

6 RELATED ARTICLES

Carbon-13 Studies of Deuterium Labeled Compounds; Isotope Effects on Chemical Shifts and Coupling Constants.

7 REFERENCES

1. G. A. Olah, G. K. S. Prakash, and J. Sommer, *Superacids*, Wiley, New York, 1985.
2. M. Saunders and H. A. Jiménez-Vázquez, *Chem. Rev.*, 1991, **91**, 375.
3. M. Saunders and M. R. Kates, *J. Am. Chem. Soc.*, 1977, **99**, 8071.
4. M. Saunders, M. R. Kates, K. B. Wiberg, and W. Pratt, *J. Am. Chem. Soc.*, 1977, **99**, 8072.
5. D. A. Forsyth, J. H. Botkin, J. S. Puckace, K. L. Servis, and R. L. Domenick, *J. Am. Chem. Soc.*, 1987, **109**, 7270.
6. K. L. Servis and F. F. Shue, *J. Am. Chem. Soc.*, 1980, **102**, 7233.
7. D. A. Forsyth, P. Lucas, and R. M. Burk, *J. Am. Chem. Soc.*, 1982, **104**, 240.
8. J. H. Botkin, D. A. Forsyth, and D. J. Sardella, *J. Am. Chem. Soc.*, 1986, **108**, 2797.
9. D. A. Forsyth and J.-R. Yang, *J. Am. Chem. Soc.*, 1986, **108**, 2157.
10. K. L. Servis and and R. L. Domenick, *J. Am. Chem. Soc.*, 1986, **108**, 2211.
11. D. A. Forsyth, J. H. Botkin, and V. M. Osterman, *J. Am. Chem. Soc.*, 1984, **106**, 7663.
12. D. A. Forsyth and M. M. MacConnell, *J. Am. Chem. Soc.*, 1983, **105**, 5920.
13. D. A. Forsyth and J. H. Botkin, *J. Am. Chem. Soc.*, 1984, **106**, 4296.
14. K. L. Servis, R. L. Domenick, D. A. Forsyth, and Y. Pan, *J. Am. Chem. Soc.*, 1987, **109**, 7263.
15. D. A. Forsyth and C. Panyachotipun, *J. Chem. Soc., Chem. Commun.*, **1988**, 1564.
16. K. L. Servis, E. V. Koh, and P. Baine, *Croatica Chem. Acta*, 1992, **65**, 679.
17. P. v. R. Schleyer, J. W. de M. Carneiro, W. Koch, and D. A. Forsyth, *J. Am. Chem. Soc.*, 1991, **113**, 3990.
18. G. K. S. Prakash and P. S. Iyer, *Rev. Chem. Intermed.*, 1988, **9**, 65.
19. D. A. Forsyth, C. Panyachotipun, Y. Pan, A. M. Moussa, and A.-H. A. Youssef, *J. Org. Chem.*, 1990, **55**, 5375.

Biographical Sketch

David A. Forsyth. *b* 1948. B.S., 1969, Macalester College. Ph.D., 1973, University of California, Berkeley. Postdoctoral study with George A. Olah on NMR of carbocations. Faculty in Chemistry, Clarkson University, 1975−79, Northeastern University, 1979−present. Approx. 60 publications. Research interests include isotope effects in NMR, structure of electron-rich and electron-deficient organic species, molecular modeling.

Nitrogen NMR

Joan Mason

The Open University, Milton Keynes, UK

1	Introduction	1
2	Nitrogen-15 NMR Spectroscopy	3
3	Nitrogen-14 NMR Spectroscopy	6
4	Patterns of Nitrogen Shifts	9
5	Nitrogen Shielding Tensors	14
6	Patterns of Nitrogen Spin–Spin Couplings	19
7	Solid State Studies	23
8	Dynamics	24
9	Biomolecules	24
10	Related Articles	25
11	References	25

1 INTRODUCTION

Nitrogen has two useful nuclei for NMR spectroscopy, ^{14}N and ^{15}N, each with advantages and disadvantages. The drawbacks of these nuclei restricted the use of nitrogen NMR in the early decades of NMR spectroscopy, but Fourier transform spectroscopy, higher field magnets, larger samples, clever pulse techniques, and multidimensional spectroscopy have greatly expanded the use of nitrogen NMR.

The NMR properties of ^{14}N and ^{15}N are given in Table 1. Both nuclei have rather low magnetogyric ratios γ, so their sensitivity to NMR detection is rather low, relaxation processes are rather slow, coupling constants J(N,X) are small and J(N,N) values very small. Working at higher field (B_0) increases the accessibility, the signal intensity increasing as $\gamma^3 B_0^{\frac{3}{2}}$.

The spin-$\frac{1}{2}$ nucleus ^{15}N is now much used in high-resolution work, but its natural abundance is low, 0.36%. Another disadvantage is that $\gamma(^{15}\text{N})$ is negative, so NOE factors are negative, ^{15}N signals becoming more negative with proton decoupling. The maximal proton-induced NOE factor for ^{15}N is -4.93. A disadvantageous NOE can be removed by the use of paramagnetic additives such as [Cr(acac)$_3$].

Much work uses enrichment of ^{15}N, which may not be expensive if nitric acid, ammonium salts, or nitrites can be used as starting materials. With enrichment to 99% the NMR receptivity is six times that of ^{13}C in natural abundance. Sensitivity enhancement by polarization transfer, by INEPT or related methods, is helpful, particularly if there are protons directly attached to the ^{15}N. The gain compared with ^{13}C is now the greater, since $\gamma(^{15}\text{N})$ is smaller than $\gamma(^{13}\text{C})$.

The highly abundant nucleus ^{14}N (99.64%) has nearly six times the receptivity of ^{13}C in natural abundance (1%). Nitrogen-14, however, is quadrupolar (I = 1), so that ^{14}N NMR spectroscopy commonly suffers from line broadening and loss of spin–spin coupling due to too-fast relaxation. The ^{14}N quadrupole moment is relatively small, however, and if the local symmetry is high or the sample viscosity low ^{14}N work can be done in high resolution. This possibility is often overlooked nowadays, although the phenomenon of the chemical shift was uncovered very early on in ^{14}N resonance in an aqueous solution of ammonium nitrate NH_4NO_3, which gave two sharp lines.[1]

Quantitative work in ^{14}N or ^{15}N resonance is difficult because of the multiplicity of factors affecting the signal intensities, and in ^{14}N spectroscopy, the linewidth.

There is now a large volume of work in nitrogen resonance and only key or indicative references can be given. There have been two useful books on ^{15}N NMR spectroscopy.[2,3] The review literature includes the useful compendia of nitrogen NMR work published at intervals by Witanowski, Stefaniak, and Webb,[4–6] annual updates in appropriate chapters of the *Specialist Periodical Reports on Nuclear Magnetic Resonance*,[7] and several articles.[8–14] Experimental techniques are described in some detail in by Levy and Lichter,[2] Martin et al.,[3] and von Philipsborn and Müller,[13] and updates in Volumes 1–23 of *Specialist Periodical Reports on Nuclear Magnetic Resonance*.[7]

Nitrogen NMR spectroscopy affords a variety of information, with the choice of a spin $\frac{1}{2}$ or a quadrupolar nucleus, and an unusual variety of bond types, giving a range of 1350 ppm in chemical shift. Nitrogen forms bonds with all elements except those that are completely inert. Nitrogen can be found in nine stable oxidation states, with bond orders up to three, and coordination numbers up to six, the highest being in metal clusters. Moreover the shifts, coupling constants, and ^{14}N linewidths can be interpreted in terms of bond type, because of the characteristic influences of lone pair and π electrons associated with the observed nucleus, electrons which are of great importance to chemical structure and reactivity.

1.1 Nitrogen Referencing

Nitrogen NMR spectroscopy has suffered from a multiplicity of reference standards,[15] but consensus now favors the use of neat liquid nitromethane as external reference. Table 2 gives standards in the literature. Arguments in favor of nitromethane are that its ^{15}N signal is little affected by proton decoupling, the ^{14}N signal is sufficiently sharp, the neat liquid is accurately reproducible, and it can be obtained enriched with ^{15}N or ^{2}D with negligible effect on the chemical shift.

Nitrogen referencing should be by substitution. Internal referencing is unsatisfactory because of the magnitude and variety of medium effects for nitrogen (see Section 1.3 below). These are very large when nitrogen carries a lone pair, and can be quite large in the absence of lone-pair electrons if the nitrogen carries π electrons, as in nitromethane, as shown in Table 2. If [Cr(acac)$_3$] is used as a relaxation agent, a susceptibility correction, proportional to the concentration of the paramagnetic reagent, is necessary for precise work. The susceptibility shift in an electromagnet in which the field is perpendicular to the NMR tube is half the magnitude and opposite in sign to that in a superconducting magnet.

Ammonia is unsuitable as a reference substance since the nitrogen shift and the magnetic susceptibility are both highly sensitive to hydrogen bonding, and therefore to temperature, pressure, and to the presence of other substances. Ammonia is included in Table 2 as a 'theoretical' reference standard, since the spin–rotation determination of the nitrogen shielding (σ) in the isolated NH_3 molecule[16] forms the basis of an absolute scale for calculated values of σ.[17] Values of the shielding for

Table 1 NMR Properties of the Nitrogen Nuclei[a]

	^{14}N	^{15}N
Spin I	1	$\frac{1}{2}$
Natural abundance (%)	99.635	0.365
Magnetic moment μ (μ_N)	0.57099	−0.4903
Magnetogyric ratio γ (10^7 rad T^{-1} s^{-1})	1.9338	−2.712
Receptivity relative to that of ^{13}C	5.69	2.19×10^{-2}
Nuclear quadrupole moment Q (10^{-28} m^2)	1.99×10^{-2}	0
Linewidth factor l (10^{-59} m^4)[b]	2×10^{-3}	–
Reference standard	neat liquid CH_3NO_2/CD_3NO_2	
NMR frequency Ξ (MHz)	7.226329	10.136783

[a]I. Mills, T. Cvitas, K. Homann, N. Kally, and K. Kuchitsu, 'Quantities, Units and Symbols in Physical Chemistry', Blackwell (for IUPAC), Oxford, 1993, pp. 98–104.
[b]$l = Q^2(2I + 3)/I^2(2I - 1)$.

Table 2 Nitrogen Reference Standards

Substance	Concentration (M)	δ(N) (ppm)
Fluids[a]		
NH_3(equil. vap.), 302 K		−399.3[b]
NH_3(liq.), 300 K		−380.4[b]
NH_3(liq.), 223 K		−376.4[b]
NH_4NO_3(satd. aq.)	12.3	−359.6
NH_4Cl(satd. aq.)	5.64	−352.9
Me_4NCl(aq.)	0.30	−337.7
Me_4NCl(satd. aq.)	6.03	−336.7
CH_3CN(liq.)		−135.8
HNO_3(aq.)	10	−18.2
HNO_3(aq.)	7	−12.6
HNO_3(aq.)	1	−4.4
NH_4NO_3(in 2 M aq. HNO_3)	5	−4.6
NH_4NO_3(satd. aq.)	12.3	−4.0
$NaNO_3$(satd. aq.)	7.93	−3.7
$NaNO_3$ or KNO_3(aq.)	0.30	−3.5
CH_3NO_2 in CCl_4	0.30	−7.1
In $CHCl_3$	0.30	−3.8
Neat liquid	18.4	0.0
In D_2O	0.30	2.0
In DMSO	0.30	2.0
Solids[c]		
NH_4NO_3		−358.4
$(NH_4)_2SO_4$		−355.7
NH_4Cl		−341.0
NH_4NO_3		−5.0

[a]Shifts refer to 303 ± 2 K unless a temperature is specified, and are taken from Witanowski et al.[15] unless another source is given.
[b]Jameson et al.[17]
[c]Ratcliffe et al.[18]

other molecules are then obtained from the chemical shift (δ) by use of equation (1).

$$\sigma = -\delta - 135.8 \quad (1)$$

The use of ammonia or ammonium salts as reference material has been favored by those wishing to avoid negative shifts, as achieved by the use of TMS for ^1H, ^{13}C, or ^{29}Si. But ammonium salts are subject to medium effects, again because of hydrogen bonding. Table 2 shows that there is a difference of nearly 7 ppm from the nitrate to the chloride in saturated solutions. The use of Me_4NCl or Et_4NCl, which are less subject to medium effects, has not found favor. Nitrate ion, also, is susceptible to medium effects, which may be large in acidic solution because of equilibria involving nitric acid $HONO_2$.

Table 2 includes reference standards for solid state work. Ammonium chloride is commonly used for this, and should be the standard of choice.[18] There is a large variation in the NH_4^+ shift with different anions, particularly oxyanions, because of hydrogen bonding: Table 2 shows a difference of 17 ppm from the nitrate to the chloride.

The publications of Witanowski, Webb, and co-workers,[5,6] which use the nitromethane standard, give nitrogen shieldings (low frequency positive) rather than shifts (δ), maintaining consistency with their earlier reports when δ and σ had the same sign, before the IUPAC sign convention for δ was adopted in 1972.

1.2 Isotope Effects and Labeling

Nitrogen-14 and ^{15}N measurements are interchangeable, since primary isotope effects on nitrogen shifts are negligible. Bloch–Siegert shifts, arising from the negative magnetogyric ratio of ^{15}N, are detectable in double resonance experiments, and corrections may be needed in the determination of accurate values of chemical shifts by homonuclear decoupling experiments.[19]

Nearest-neighbor isotope effects are not uncommon. Normally a heavier isotopic substituent increases the nitrogen shielding, with some additivity for multiple substitution. Deuteration increases the nitrogen shielding by about 0.65 ppm per hydrogen replaced in NH_3, cf. 0.5–0.7 ppm in pyridinium ion, amines, or amides. The effects are smaller in NH_4^+, about 0.3 ppm per hydrogen.[20] Equilibrium isotope effects on the nitrogen shift have been reported, arising from the perturbation of tautomeric or hydrogen-bonding equilibria by deuteration.[21]

Neighbor effects of replacement of ^{16}O by ^{18}O are small, about 0.15 ppm per oxygen in nitrite ion, or 0.06 ppm in nitrate, but can be useful in mechanistic studies. In the oxidation of ammonia to nitrite by *Nitrosomonas europae*, or of nitrite to nitrate by *Nitrobacter vinogradsky*, the movement of the ^{18}O label has been monitored by ^{15}N NMR.[22]

Nitrogen-15 labeling for high-resolution NMR, particularly in biomolecules, has the added advantage that the isotope can

be used as a biological tracer. The most stable radioisotope, ^{13}N, has a half-life of only 10 min.

Equilibrium isotope effects can arise unexpectedly in studies of compounds partially enriched with ^{15}N. A doubling of the nitrogen line was observed for the five-coordinate dinitrosyl complex $[RuCl(NO)_2(PPh_3)_2]^+$, with 50% enrichment. This complex has one linear and one bent nitrosyl in the solid,[23] and shows bent linear fluxionality in solution.[24] ^{15}NO is slightly favored in the linear geometry in the $(^{14}NO)(^{15}NO)$ molecule, giving a slightly higher averaged shielding than the $(^{15}NO)_2$ molecule. Zero-point energies are generally small for nuclei as heavy as nitrogen. This isotope effect is observable because of large differences in stretching frequency and nitrogen shift in linear and bent nitrosyls, arising from the effects of the lone pair on the bent nitrogen.

1.3 Medium Effects

The NMR properties of nitrogen carrying a lone pair are very sensitive to changes of solvent, concentration, counterion, or pH. Nitrogen NMR spectroscopy is thus a useful probe of inter- and intramolecular influences and equilibria. Medium effects on the shielding may be pronounced if hydrogen bonding or acid–base interactions occur, as Table 2 indicates. The shifts are in the same direction as protonation shifts (Section 4.1), though smaller. Hydrogen bonding to a lone pair on nitrogen commonly decreases the nitrogen shielding in saturated groups such as ammonia and alkylamines,[25] with sizeable deshielding from gaseous to liquid NH_3, as from NH_3 to NH_4^+.[26] Nitrogen shielding is increased, however, by hydrogen bonding through hydrogen covalently bonded to nitrogen. The nitrogen shielding in NH_4^+ increases with an increase in the strength of the hydrogen bonding to the anion,[27] and is particularly high in anhydrous HF.[28] Corresponding results are observed for protonated amines.[26] Hydrogen-bonded systems, therefore, show complex behavior, including proton exchange.

For nitrogen in a π-bonded system, as in nitriles RCN, or aromatic azines such as pyridine, hydrogen bonding to a lone pair on nitrogen increases the nitrogen shielding. Again, the shifts are in the same direction as protonation shifts, but smaller in magnitude. Medium effects when the nitrogen carries π but not lone-pair electrons are illustrated by the 9 ppm range shown in Table 2 for the nitrogen shift in nitromethane in different solvents. Four-coordinate nitrogen not bonded directly to hydrogen is relatively insensitive to medium effects, as expected.

Medium effects are observable also in spin–spin couplings to nitrogen because of their sensitivity to the presence of lone pairs.

Nitrogen-14 Knight shifts have been used to study solutions of alkali metals in ammonia[29] or methylamine[30] which contain solvated electrons.

2 NITROGEN-15 NMR SPECTROSCOPY

Relaxation processes are important to the design of ^{15}N NMR experiments, because of the low natural abundance, one-third of that of ^{13}C, and low NMR sensitivity, one-fifteenth of that of ^{13}C, and because ^{15}N NOE factors are negative.

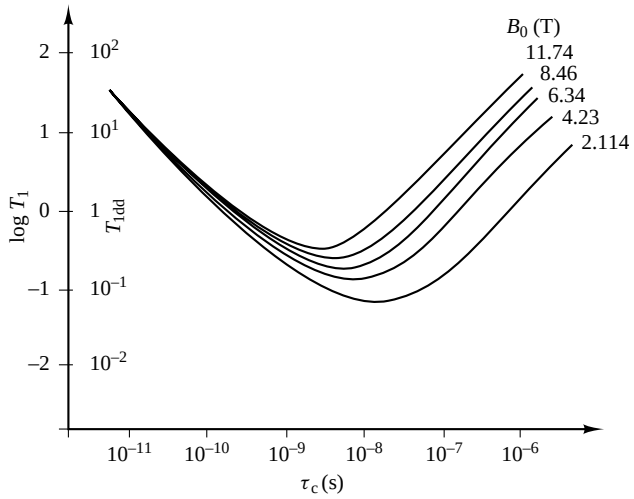

Figure 1 Dipolar spin–lattice relaxation times T_{1dd} as a function of the effective molecular correlation time τ_c for different field strengths B_0 (T). A field strength of 11.74 T for ^{15}N corresponds to 500 MHz for protons. Values of τ are given in Tables 3 and 4

2.1 Nitrogen-15 Relaxation[2–7,31,32]

Nitrogen-15 relaxation processes are qualitatively similar to those of ^{13}C in analogous environments, as in $>NH_2$ and $>CH_2$. The relative contributions of the possible mechanisms are usually different, because dipolar relaxation by protons is less efficient for ^{15}N than for ^{13}C, since $|\gamma(^{15}N)|$ is only 40% of $\gamma(^{13}C)$. This means that other relaxation mechanisms compete with the dipolar mechanism for ^{15}N. Representative values of relaxation times and NOE factors are given in Table 3, together with examples of particular relaxation mechanisms.

The dipole–dipole (dd) relaxation rate for nitrogen bonded to n_H hydrogens is given by equation (2). The relaxation time T_{1dd} depends on the changes in local fields as the molecule tumbles, and is proportional to $(1 + \omega^2\tau_c^2)$, where ω is the resonance frequency and τ_c is the 'correlation time'. This is the time the molecule takes to reorient itself in rotational motion, and may take an effective value in view of the complexity of tumbling motions in many molecules or groups, τ_c. Equation (2) assumes sufficient mobility that normal conditions of 'extreme narrowing' apply, with $\omega^2\tau_c \ll 1$.

$$1/T_{1dd} \approx \left(\frac{\mu_0}{4\pi}\right)^2 n_H(\gamma_N)^2(\gamma_H)^2 \left(\frac{\hbar^2}{r_{NH}^6}\right)\tau_c \qquad (2)$$

The contribution to the relaxation rate $(T_{1dd})^{-1}$ per hydrogen at a distance of 10 pm is then $5 \times 10^9\tau_c$. This corresponds to T_{1dd} values of 15–80 s for nitrogen with one attached hydrogen, in small-to-medium-sized molecules in common solvents. Liquid pyrrole has T_1 = 40 s[33] and aqueous acetamide T_1 = 14 s.[34]

As molecular tumbling slows down beyond the 'extreme narrowing' region, it reaches the Larmor precession frequency below which spin–lattice relaxation is less effective as τ_c increases.[35] The value of T_{1dd} falls to a minimum near $\omega\tau_c$ = 1 and then increases depending on the field strength B_0, as shown in Figure 1. There are concomitant changes in the NOE.

Such a decrease in T_{1dd} for longer correlation times is advantageous to the study of biomolecules such as lysozyme, a globular protein of molecular mass 14 600 Da, for which a

Table 3 Nitrogen-15 Spin–Lattice Relaxation Times (T_1), NOE Factors (η_{obs}), Correlation Times (τ_c), and Relaxation Mechanisms

Compound[a]	T_1(s)	B_0(T)	η_{obs}	τ_c (ps)[b]	Mechanism[c]
Gases					
NH_3(g)	0.3	6.35	0		sr
$^{14}N^{15}N$(g, 294 K)	0.8 (=T_2)	8.46	0		sc
Liquids					
$PhNO_2$(l)	450	1.41	−1.8	(τ_q = 10)	sr, dd
	170	7.42	−0.6	4	sa, sr
PhCN(l)	420	1.41	−1.6	(τ_q = 7.5)	dd, sr, e
NH_4NO_3(1:1 w/w in H_2O)	140	1.41	−0.9		sr
CH_3CN(l)	90	6.34			
CH_3CN(l) with 5×10^{-4} M [$Gd(pd)_3$]	53	6.34			e
Pyridine(l)	85	6.34	−0.4		sa, dd, sr
Pyridine(l) with 5×10^{-2} M [$Cr(pd)_3$]	3.7				e
n-$BuNH_2$	70	6.34	−3.9		dd
Pyrrolidine(l) (>NH)	58	6.34	−4.6	4	dd
trans-PhN=NPh (2.7 M in $CDCl_3$)	56	2.11			sr, dd, sa
Pyrrole(l) (aromatic >NH)	40	6.34	−4.3	5	dd
NH_4NO_3(1:1 w/w in H_2O)	37	1.41	−4.93		dd
n-BuONO(l)	24	2.11			sr(int)
$NaNO_2$ (0.7:1 w/w in H_2O)	23	1.41	−0.4		sr,sa
$NaNO_2$ (1.1 M in D_2O)	19.0	4.7			
	17.5	9.4			
KCN (1 M in 1:1 H_2O/D_2O, pH 12.5)	21	1.41	0		sa, sr
	14.5	4.23	0		sa, sr
CH_3CONH_2 (5.3 M in H_2O)	14.2	1.41	−5.1	7.5	dd
N_2(l, 77 K)	15	0.70		(τ_{sr} = 0.2)	sr
N_2(l, 126 K)	1.5	1.02		(τ_{sr} = 1)	sr
$TPPH_2^{2+}$	1.9	4.23	−4.93		dd
ZnTPP[d] (6×10^{-3} M in $CHCl_3$)	56	4.23	0		e, etc
Lysozyme (9.4×10^{-3} M in 0.1 M citrate, pH 5)		4.23			
(−C(O)−NH−)	0.16		−0.5	5000	dd
$>NH_2^+$	0.33		−3.5	3500	dd
Solids					
NH_4Cl		4	4.70	14	dd
TPP[d] (180 K) aromatic >NH	0.67	1.41	0.7		dd, pe
aromatic −N=	0.05	1.41	0.1		sa, dd, pe

[a]Measurements were made at ambient temperatures (300 ± 3 K) if no other temperature is given.
[b]Values of τ_c are in ps (10^{-12}s).
[c]Relaxation mechanisms are given in decreasing order of their contribution: dd = dipole–dipole (intra- or intermolecular), sr = spin–rotation, (int) = internal, sa = shielding anisotropy, e = electron–nuclear, sc = scalar coupling, pe = proton exchange.
[d]TPP is *meso*-tetraphenylporphin.

correlation time of 8.5×10^{-9} s was measured in aqueous solution. Lysozyme, hemoglobin, vitamin B_{12}, or transfer-ribonucleic acids could be studied in natural abundance of ^{15}N at 18.25 MHz (180 MHz for protons).[36] Internal motions, such as segmental rocking or spinning of a pendant group such as $-NH_3^+$, reduce the effective τ_c for the nitrogens concerned.

Working at higher fields is thus detrimental for biomolecules, since the T_{1dd} minima shift to smaller values of τ_c with an increase in B_0 (Figure 1).

Unlike T_1, the transverse (spin–spin) relaxation time T_2 decreases steadily with an increase in τ_c to a limiting value in the solid state determined by dipolar interactions. Uncertainty broadening may be a hazard, since T_{2dd} has an additional τ_c-dependence which is independent of ω. Deuteration was used to improve ^{15}N resolution in hemoglobin studies through the γ^2-dependence of the dipolar relaxation rate.[37]

The microviscosity η' is important, since the correlation time is proportional to η'/kT. In work with smaller molecules the relaxation rate may be doubled by the use of more viscous solvents such as dioxan or ethanol, rather than chloroform or acetone. Dipolar relaxation has been speeded up by the use of viscous additives, such as glycerol in aqueous solution, or polystyrene in toluene for organic-soluble molecules.[38] Higher macroviscosities are unlikely to broaden the lines by an increase in the transverse relaxation time T_2 since this depends on the microviscosity, which is smaller than the macroviscosity by a factor of six to seven.[33] Cooling is particularly effective as it increases the viscosity (depending exponentially on the temperature) and the sensitivity and the correlation time.

Relaxation times may be quite long in the absence of nearby hydrogen or of alternative mechanisms of relaxation. Neat liquid nitrobenzene and benzonitrile have T_1 values in excess of 400 s, compared with 140 s for aqueous nitrate (Table 3).[39] 'Exposed' nitrogen, as in a cyano group or in aromatic azines such as pyridine, experiences intermolecular dipolar relaxation

in which T_{1dd} is directly proportional to the distance of closest approach of the hydrogen.

Electron–nuclear relaxation, however, is likely to be present. This is promoted very efficiently by paramagnetic impurities, of iron or nickel for example, to which basic nitrogen is very sensitive. Rigorous purification is necessary for measurements of nitrogen relaxation times,[34] although the effects of dissolved oxygen are small.

Paramagnetic additives may be useful for quantitative studies, to quench dipolar relaxation and the NOE.[34] Susceptibility corrections may then be necessary for accurate shift measurement (Section 1.1). With [Cr(acac)$_3$] there is some hydrogen bonding between hydrogen attached to nitrogen and carbonyl groups in the ligand. Gadolinium complexes such as [Gd(acac)$_3$] interact quite strongly with basic nitrogen, and can be used for spin-labeling.

The spin–rotation (sr) mechanism is effective in the relaxation of ^{15}N in small molecules or ions, such as gaseous NH_3,[40] aqueous nitrate or nitrite ion,[40] or liquid dinitrogen; also in freely rotating substituents, nitro[40] or nitrite[41] for example (Table 3). The sr mechanism becomes more efficient at higher temperatures, the rate being proportional to kT.

Shielding anisotropy (sa) relaxation is important for linear groups such as $-C{\equiv}N$, as the aqueous ion CN^-,[42] in nitriles,[40] or as a ligand; the same applies to dinitrogen[43] (precise work with metal complexes is difficult because of the difficulty in excluding paramagnetic ions). This mechanism is efficient also in planar groups, such as nitro or nitrate, and azine nitrogen as in pyridine (Table 3). The rate is very sensitive to the shielding anisotropy $\Delta\sigma$, being proportional to $(\Delta\sigma)^2$; values of $\Delta\sigma$ are discussed in Section 5. This mechanism is very effective at higher fields, the rate being proportional to ${B_0}^2$. Table 3 shows the increase in relaxation rate with an increase in the applied field for the cyanide ion and nitrobenzene.[44]

In some molecules all three mechanisms (sa, dd, and sr) are operative, as for pyridine and *trans*-azobenzene. Another mechanism of importance for ^{15}N is afforded by proton exchange (pe) in hydrogen-bonded systems, magnetization being transferred by the migrating proton. Table 3 includes an example of the fast relaxation of ^{15}N by scalar coupling to fast-relaxing ^{14}N in $^{14}N^{15}N$ gas.[45]

In the solid state, the dipolar relaxation of ^{15}N is fast in NH_4Cl.[46] Relaxation is faster still in *meso*-tetraphenylporphin (TPP), in which two hydrogens exchange between the central four nitrogens, a process long known in solution. Studies of T_1 and NOE show that the unprotonated nitrogen relaxes by the sa mechanism, by dipolar interaction with the protons on the other nitrogens, and through proton exchange.[47]

2.2 Nitrogen-15 NOE Factors[48]

If ^{15}N is wholly relaxed by $^{15}N/^{1}H$ dipolar interactions, the NOE factor (η), with broadband proton decoupling, is given by equation (3):

$$\eta_{max} = \gamma(^1H)/2\gamma(^{15}N) = -4.93 \quad (3)$$

The negative sign corresponds to inversion of the signal. (Note the use of the symbol η for the NOE factor and also for the viscosity.) The net enhancement is then -3.93, better than the ^{13}C value of 2.99. There is a further gain in signal height from the collapse of multiplets.

The NOE factor observed depends on the proportion of the relaxation that takes place by $^{15}N/^{1}H$ dipolar interactions:

$$\eta_{obs} = (I - I_0)/I_0 = -4.93(T_1)_{obs}/T_{1dd} \quad (4)$$

If this proportion is small the signal intensity (I) is diminished and the signal vanishes if the proportion is 20% ($I = 0$, $\eta_{obs} = -1$).

Five mechanisms have been identified by which ^{15}N signals can be lost on proton decoupling.[49] The dipolar process diminishes when more efficient modes of relaxation are possible, as in the presence of paramagnetic compounds, or averaging by fast chemical exchange. Table 3 shows many molecules for which the full NOE factor -4.93 is not achieved under the conditions of the experiment.

The diminution in T_{1dd} as correlation times τ_c increase beyond the 'extreme narrowing' limit, illustrated in Figure 1, also diminishes the NOE, the more so at higher resonance frequencies ω. With large or highly associated molecules, the NOE may be unfavorable,[50] and working at higher fields disadvantageous. The maximal NOE factor shrinks from -4.93 to -0.12, and the signal is annulled for a correlation time of 1 ns at 11.7 T (500 MHz for protons). The NOE may be removed by gated decoupling or by paramagnetic additives, promoting electron–nuclear relaxation.

The NOE has various uses, i.e. as a measure of molecular mobility or dynamics, in spectral assignment, and to locate spin labels. A disadvantage is the difficulty in using signal intensities in quantitative work.

2.3 Nitrogen-15 Sensitivity Enhancement

Nitrogen-15 sensitivity is enhanced by the use of larger samples, higher fields, lower temperatures, and proton decoupling and the NOE, if favorable. Valuable enhancements are obtained by the use of special pulse sequences transferring polarization (magnetization) from a more sensitive nucleus, usually the proton, to which the ^{15}N nucleus is coupled. A 10-fold enhancement is given by the $\gamma(^1H)/\gamma(^{15}N)$ ratio, and the sign of γ is now immaterial. Further amplification may be gained by faster pulsing, allowed by the faster proton relaxation.

In the liquid phase magnetization can be transferred via spin–spin coupling to protons, if this is resolvable. Such methods have the advantage over NOE enhancement of not requiring the relaxation mechanism to be dipolar. They include J cross polarization (JCP), selective polarization transfer (SPT), 'insensitive nuclei enhanced by polarization transfer' (INEPT), 'distortionless enhancement by PT' (DEPT), and developments of these.[2,3,7,51] In >NH systems, as in bilirubins for example,[52] measurements may be made in this way in natural abundance of ^{15}N. Longer-range couplings also may be used in azaaromatic or peptide systems. The methods are used to determine coupling constants and their signs, to establish connectivities, to distinguish nitrogens bearing different numbers of hydrogens, to correlate signals of different nuclei, to investigate relaxation processes, and to measure relaxation times.

Multiple quantum methods involving a double transfer of magnetization, $^1H \rightarrow {}^{15}N \rightarrow {}^1H$, provide substantial improvements in ^{15}N sensitivity because of the detection in proton spectra. They are increasingly used to correlate ^{1}H and ^{15}N shifts in two-dimensional (2D) spectra through spin–spin

coupling pathways.[53] Polarization transfer from ^{15}N to ^{1}H decreases ^{1}H sensitivity, but has been used in 2D spectroscopy to assign all the ^{15}N signals of a labeled tRNA by heteronuclear decoupling difference spectroscopy.[54]

A variety of 2D, 3D, and even 4D experiments in correlation spectroscopy (COSY) are now being used to correlate ^{15}N, ^{13}C, and ^{1}H resonances.[55] A 3D experiment may correlate ^{15}N resonances with those of differently connected protons, as in $^{15}N^{1}H-C^{1}H$ groups in biological systems. 4D techniques are being used in protein research, as in the correlation of ^{1}H, ^{13}C, ^{15}N, and ^{13}CO resonances in calmodulin.[56]

Comparable experiments have been performed in which magnetization is transferred from ^{2}D, ^{19}F, or ^{31}P to ^{15}N. The faster relaxation of the deuteron, by the quadrupolar mechanism, compared with the proton, may outweigh the disadvantage of the relatively small magnetogyric ratio of ^{2}D. In the solid state, cross polarization (CP) is used to transfer magnetization via dipolar couplings. (See ***Organic Chemistry Applications***.)

3 NITROGEN-14 NMR SPECTROSCOPY

The ^{14}N quadrupole moment is relatively small ($Q = 0.0199 \times 10^{-28}\,m^2$) and a large volume of NMR work has been done in ^{14}N resonance, particularly when ^{15}N spectroscopy was less accessible. In some respects, ^{14}N work is coming into its own again as modern techniques turn the ^{14}N nuclear quadrupole interaction to advantage, to spread nitrogen spectra over a large range, more than compensating for quadrupolar line broadening.[57,58]

Nitrogen-14 linewidths vary quite widely, depending on the local electronic symmetry of the ^{14}N nucleus and its mobility. High-resolution spectroscopy is possible if the local electronic symmetry and the mobility are both high. Sharper lines may be obtained if the sample viscosity can be reduced by the use of higher temperatures or more mobile solvents (Section 3.2). Fast relaxation may be advantageous in allowing rapid pulsing. The variability of ^{14}N linewidths must be taken into account in quantitative work.[59]

^{14}N NMR is a useful probe of molecular dynamics, because of the sensitivity of the linewidth to local motions. Nitrogen-14 induced relaxation of protons in peptide ($-^{14}NH-CO-$) groups in protein backbones which exchange with water protons is of importance to proton NMR tomography.[60]

3.1 Nitrogen-14 Quadrupolar Relaxation[61]

The ^{14}N linewidth $W_{1/2}$, the width at halfheight of the (Lorentzian) line or component of a multiplet, is proportional to the relaxation rate and to the square of the nuclear quadrupole coupling constant (NQCC) χ [equation (5)]. The quadrupolar relaxation time T_q is equal to $T_1 = T_2$ in the extreme narrowing regime ($\omega^2\tau_c \ll 1$), i.e. for mobile species.

$$\pi W_{1/2} = 1/T_q = \tfrac{3}{8}\chi^2(1 + \eta^2/3)\tau_q \qquad (5)$$

where

$$\chi = e^2qQ/\hbar \text{ (in radians)} \qquad (6)$$

In equation (6), eq (or more precisely eq_z, where $|q_z| \geq |q_x| \geq |q_y|$) is the electric field gradient (efg) at the nucleus. The quantity η is now the asymmetry parameter, equal to $(q_x - q_y)/q_z$. Linewidths are very sensitive to χ but less sensitive to η, since $\eta \leq 1$ by definition. The quantity $\tau_q = \tau_c$ is the effective correlation or reorientation time of the ^{14}N quadrupole. NQCC values are obtained from the NQR spectroscopy of solids, from the microwave spectroscopy of gases, and by NMR methods.[62] Values of χ are usually similar in the liquid or solid phase of a particular species, and are about 15% greater in the gas phase.

The ^{14}N electric field gradient is largely determined by the disposition of the valence p electrons. In highly symmetric environments, in which there is no static efg, quadrupolar relaxation is mediated by collisional and vibrational distortion of molecules or ions.[63,64] Although the ^{14}N quadrupole moment is relatively small, relaxation of ^{14}N is almost invariably by the quadrupolar mechanism because of the χ^2-dependence of the rate. Even in the highly symmetric location in solid NH_4Cl, the dipolar relaxation mechanism is observed only below 220 K.[65] Above 220 K, rotation of the ammonium ion in the lattice switches the efg at the ^{14}N nucleus, so relaxing the nuclear electric quadrupole and the nuclear spin. In aqueous solution, ^{14}N in NH_4^+ shows zero NOE because of transient efgs arising from the buffeting by solvent dipoles.[66] In paramagnetic cyano complexes $K_3[M(CN)_6]$, where M = Cr, Mn, Fe, the ^{14}N relaxation was found to be wholly quadrupolar, even though the nitrogen shifts were determined by the contact interaction.[67]

3.2 Nitrogen-14 Linewidths

Table 4 lists the ^{14}N linewidths, relaxation times, NQCC values χ, and correlation times for a range of compound types, grouped by the coordination number of the nitrogen and in approximate order of increase in linewidth. Nitrogen-14 lines may be quite sharp, with χ values of 1 MHz or less, if the nitrogen is in a highly symmetrical location, as in NH_4^+,[61] NF_4^+ (tetrafluorammonium),[28] or tetraalkylammonium (R_4N^+) species.[68] Nitrogen-14 spectra were obtained in the first measurement of interstitial nitrogen, in the trigonal prismatic clusters of cobalt and rhodium[69] $[M_6N(CO)_{15}]^-$, before the ^{15}N lines were obtained with 97% enrichment. For the rhodium cluster there was some resolution of three lines of the septet, with $^{1}J(Rh,^{14}N) \approx 4$ Hz. The ^{14}N and ^{15}N lines were similar in width for the cobalt cluster because of line broadening by the ^{59}Co quadrupole and unresolved coupling.

Nitrogen-14 lines are sharp also if the nitrogen is centrally placed in linear groups such as the nitronium ion (NO_2^+)[6]a or azide ion (N_3^-),[70] or in trigonal planar groups such as nitrate ion,[71] all highly mobile in solution.

Linewidths may be small if the substituents on nitrogen do not differ greatly in electronegativity, as in the linear molecules NNO[72] and isonitriles RNC.[73,74] Compared with the nitrate ion, broader lines are observed for ethyl nitrate, nitromethane,[75,76] or NOF_2^+,[28] broader still for pyridine *N*-oxide,[77] $PhNO_2$,[78] or dimethylamide,[79] more bulky molecules. The line is very broad for the oxygenated nitrogen in azoxybenzene, which carries a π bond, a single bond, and a double bond.[80] The fluorammonium ion, NH_3F^+, with substituents of very different electronegativity, gives a broad

Table 4 Examples of ^{14}N Linewidths ($W_{1/2}$), Relaxation Times (T_q), Nuclear Quadrupole Coupling Constants (χ), and Correlation Times (τ_q)

Sample[a]	$W_{1/2}$[b] (Hz)	T_q (ms)	χ (MHz)	η[c] (cP)	τ_q[d] (ps)
Four-coordinate nitrogen					
Me_4NBr (1 M aq., 316 K)	0.1	10^4			
n-Bu_4NI (0.07 M aq., 316 K)	0.18	1800	0.04	0.45	20
n-Bu_4NI (0.07 M in benzene, 335 K)	3.7	85	0.23	0.39	15
NF_4AsF_6(HF)	3				
NH_4Cl (1 M aq., 316 K)		1600		1.08	5.9
NH_4Cl (1 M in D_2O, 316 K)		1200			7.2
NH_4Cl, ND_4Cl(s, 295 K)		700–800	0.016		20
n-HexylNMe_3Br (0.55 M in D_2O)		260	0.083		20
n-$C_{12}H_{25}NMe_3Cl$ (C_{12}TAC) (49% w/w in D_2O)		T_1 = 24	0.083		370 fast
		T_2 = 3.7			5×10^4 slow
n-$C_{16}H_{33}NMe_3Br$ (C_{16}TAB) (0.4 M aq.)		T_1 = 10	0.083		560 fast
		T_2 = 1			2×10^5 slow
Na[Co(*N*H_3)$_2$(NO_2)$_4$](aq.)	170		2.09		
(NH_3F)(CF_3SO_3)(HF) at 283 K	300				
at 233 K	550				
[Co(NH_3)$_6$]Cl_3(aq.)	370		3.62		10.3
[Co(NH_3)$_6$](ClO_4)$_3$ (0.24–0.5 M in DMSO-d_6)		0.29	3.3		20
[Co(en)$_3$]Cl_3(aq.)	600				22.1
Choline Me_3N headgroup of sphingomyelin (aq., 320 K)		T_1 = 37	0.135		
		T_2 = 2.0			
Six-coordinate nitrogen (see text)					
[Rh_6(μ_6-N)(CO)$_{15}$]$^-$(acetone-d_6)	20				
[Co_6(μ_6-N)(CO)$_{15}$]$^-$(acetone-d_6)	40				
Linear two-coordinate nitrogen					
N_2O (15 atm in hexane) (N*N*O)	0.45	2960	0.238		20
MeNC(*l*)	0.26	1220	0.27	0.35	30
t-BuNC(*l*)	1.6	180			
NO_2AsF_6(HF)	5				
PdCNBu^t complexes ($CDCl_3$)	4–12	30–80			
NaN_3 (1 M aq.) (N*N*N$^-$)		29.3	1.03		
[η^5-C_5H_5)Mo(CO)$_2$(NO)](CH_3CN)	30				
[Mo(NO)(S_2CNMe_2)$_3$](CH_2Cl_2)	40				
[Mo(NS)(S_2CNMe_2)$_3$](CH_2Cl_2)	150				
[Os(*N*Bu^t)O_3](CD_2Cl_2)	30				
[Ta(NHBu^t)$_2$(*N*$SiMe_3$)$_2${N($SiMe_3$)$_2$}] (CD_2Cl_2)	52				
[W(NBu^t)$_2$(OBu^t)$_2$](CD_2Cl_2)	185				
Terminal (one-coordinate) nitrogen					
N_2O (15 atm in hexane) (*N*NO)		280	0.792		
N_2(*l*, 126 K)		18.5	5.39		0.15
N_2 (*l*, 77 K)		1.7		0.074	0.2
$^{14}N^{15}N$(g, 294 K)		15.3			
NaN_3 (1 M aq.) (*N*NN$^-$)		7.4	1.79		
ClCN(*l*)		6	3.219		
MeCN (1% v/v in hexane)	53.5		3.74	0.29	0.82
MeCN(*l*)	78			0.34	0.67
$NO^+AsF_6^-$(HF)	95				
MeSCN(*l*)		2.0	3.75	0.72	2.4
HC–C≡C–CN (5 M in tol.-d_8)	189	1.7	4.14	0.45	2.36
NC–C≡C–CN (inf. diln. in hexane)	244		4.14	0.30	4.75
NC–C≡C–CN(*l*)	394			0.60	
CCl_3CN < *l*)		1.5	4.1	0.75	2.7
K_4[Fe(CN)$_6$] (0.2–0.8 M aq.)	550–650				
K_3[Co(CN)$_6$](aq.)	570		3.62		16.0
K_3[Fe(CN)$_6$] (0.2–1.0 M aq.)	780–1040				

Table 4 *Continued*

Sample[a]	$W_{1/2}$[b] (Hz)	T_q (ms)	χ (MHz)	η[c] (cP)	τ_q[d] (ps)
Planar three-coordinate nitrogen					
$NaNO_3$(s)		10^5	0.745		
$NaNO_3$ (1 M aq. 295 K)		85			$\tau_\perp$ = 1.43
$EtONO_2(l)$		45	0.9		2
$MeNO_2(l)$		22	1.7	0.6	1.03
$(NOF_2)AsF_6$(HF)	18				
Pyridine *N*-oxide (0.2 M in CCl_4)	28.3	11.2	1.1		3.4, 11.9, 2.9
$PhNO_2$ (1:1 v/v in hexane)		6.2	1.426	1.83	3.6, 11, 4.4
$PhNO_2(l)$		3.2		7.0, 21 6.3	
Pyrrole (17 mol% in pyridine)		4	2.12	1.2	12
Pyrrole(l)		2.0	2.06		8
$Me_2NCHO(l)$		2.0	3.6		
PhN = *N*(O)Ph(l, 284 K)	700		1.4		10
Pyramidal nitrogen					
$MeNH_2(l)$	30		3.98	0.18	0.55
$Me_3N(l)$	100		5.2	0.16	0.8
$Me_2NH(l)$	125		5.05	0.17	1.0
$(CH_2)_6N_4$ (0.1 M in hexane)	122	2.6	4.19	0.29	1.48
$(CH_2)_6N_4$ (0.1 M in CCl_4)	294		4.17	0.82	3.3
$(CH_2)_6N_4$ (0.1 M in $CDCl_3$)	1052		4.31	0.5	11.1
NF_3(l, 108 K)	318	1	7.07		1.35
$CH(CH_2CH_2)_3N$ (0.5 M in $CHCl_3$, 278 K)			5.4	0.51	$\tau_\parallel$ = 0.8, $\tau_\perp$ = 6.7
$N(CH_2CH_2)_3N$(s) at 415 K	484	T_2 = 0.658	4.925		4.23
$N(CH_2CH_2)_3N$(s) at 354 K	2100	T_2 = 0.152			18.4
Bent two-coordinate nitrogen					
$HNCO(C_6H_{12})$	20				
$MeNCO(l)$	35				
$EtONO(l)$		5.2	3.8		0.9
Pyridine(l)		1.65	4.58	0.89	1.95
i-C_5H_9 $ONO(l)$		1.6			3.0
$Na[Co(NH_3)_2(ONO)_4]$(aq.)	700		4.25		14.25

[a]Measurements were made at ambient temperatures (300 ± 3 K) if no other temperature is given.
[b]Observed linewidths may contain unresolved couplings.
[c]Viscosity.
[d]Values of τ_q are in ps (10^{-12} s); compare the values measured in ^{15}N resonance (Table 3). Where three values are given, these correspond to $\tau_{x,y,z}$, where the x direction is that of the axial bond to nitrogen and the y direction is in the molecular plane.

line[28] with some broadening being due to the hydrogen bonding in the HF solvent.

Long-chain tetraammonium species give very broad lines. The ^{14}N relaxation properties of Me_3N groups have been used to study reorientational motion. In the surfactants C_nTAC and C_nTAB, the two motions reported in Table 4 are rotation within a micelle and a slower diffusional motion.[81,82] In biomolecules, the choline Me_3N headgroup is a useful probe of orientation, as in studies demonstrating a phase transition in the phospholipid sphingomyelin, from bovine brain membrane,[83] or changes in phosphatidylcholine in the presence of anaesthetics.[84]

The efg and the linewidth are greatly increased by the presence of a lone pair on the nitrogen. This electronic charge is close to the nucleus, even closer if the substituents on the nitrogen are highly electronegative as in NF_3, in which the ^{14}N NQCC is very large.[28] Linewidths are sizeable generally for pyramidal nitrogen, as in amines,[85–88] and for bent (two-coordinate) nitrogen, as in organic isocyanates,[89] nitrites,[75] and pyridine.[90]

The lone pair on terminal (one-coordinate) nitrogen is less effective in line broadening because of the axial symmetry. Again, linewidths increase with an increase in electronegativity of the nearest neighbor, from dinitrogen[42,47] to nitrile species RCN[91–95] and to the nitrosyl ion NO^+.[28] In dinitrogen oxide, N_2O, the ratio of the linewidths for the two nitrogens in solution is as expected from the NQCCs determined by microwave spectroscopy in the gas phase.[73]

Similarly, protonation or coordination reduces NQCC values. They are reduced also by delocalization of a lone pair in conjugated systems, as in pyrrole,[96] and delocalization which flattens a pyramidal group, or increases the bond angle for two-coordinate nitrogen. The effects of bond-angle distortion are evident for nitrogen in three- to seven-membered rings.[69] Hydrogen bonding to a lone pair on nitrogen slightly reduces the NQCC, while hydrogen bonding of a lone pair on nitrogen has the opposite effect, as shown by pyrrole in pyridine.[96]

Certain ligands in metal complexes are usefully studied by ^{14}N NMR study, so long as the molecules are not too bulky or associated. Linear ligands may give sharp lines because of the axial symmetry at nitrogen. Sharp lines were observed for the imido (nitrene) ligand (=NR) in *trans*-$[WF_4(NMe)L]$ complexes,[97] and shifts were measurable for

the imido complexes of Ta, W, and Os, even with quite bulky R groups such as $SiMe_3$, helped by internal mobility.[98] Despite the ^{95}Mo quadrupole, ^{14}N lines were readily resolved in dialkyldithiocarbamato complexes of molybdenum with NO or NS coligands,[99] and ^{95}Mo–^{14}N couplings were resolved for η^5-cyclopentadienyl complexes with NO and CO ligands.[100] Quite sharp lines were observed in PdCN^{t}Bu complexes.[101] The kinetics of electron transfer reactions between ferricyanide and ferrocyanide ions in aqueous solution were studied by ^{14}N linewidth measurements.[102]

Otherwise, ^{14}N lines are usually broad for ligating nitrogen, whether with bulky (e.g. phosphine) coligands, of the difference in electronegativity of the nearest neighbors: examples in Table 4 are the ammine and ethylene diamine complexes of cobalt.[103,104]

There is a direct dependence of ^{14}N linewidth on the sample viscosity for a wide range of molecules. Linewidths may be halved by the use of diethyl ether solvent instead of chloroform, or acetone instead of water. Fluoronitrogen compounds are readily studied by ^{14}N NMR because of their high mobility.[28] Resolution of J couplings to quadrupolar nuclei has been achieved for super- or near-critical fluids in standard thick-walled tubes, including ^{14}N^{14}N and ^{14}N^{17}O couplings in liquid N_2O.[105]

Warming a sample is particularly helpful, the viscosity decreasing exponentially with increase in temperature. The rotational correlation time for a spherical molecule is given by the Stokes–Einstein–Debye theory as

$$\tau_c = V\eta/kT \tag{7}$$

where η is the viscosity and V is the molecular volume, equal to $4\pi r^3/3$.[33] equation (7) gives a correlation time of 1 ps for a molecule of radius 1 Å at 300 K for η = 1 cP. Observed rotational motions are faster by a factor of about 6, and a microviscosity η' that is one-sixth of the bulk viscosity is envisaged.

Direct dependence on viscosity breaks down for molecules that are small, linear, or flat, rotating or librating between neighboring molecules. Molecules rotating relatively freely in the liquid phase have a reduced temperature dependence of τ_c, according to equation (8), where I is a moment of inertia:

$$\tau_c = \tfrac{1}{2}(\pi I/3kT)^{1/2} \tag{8}$$

Quadrupolar relaxation in ionic solutions[67] is mediated by the rotations of ions and solvent dipoles, by collisions, and by molecular vibrations. In mobile solutions, with $\omega^2\tau_c \ll 1$, the relaxation rate is given approximately by equation (9):

$$\pi W_{1/2} = 1/T_q = 8\pi(\beta eqQ/\hbar)^2\left[\mu_s^2 c_s r_0^{-5}\tau_s + \sum_i z_i(3a_i^3)^{-1}c_i\tau_i\right] \tag{9}$$

Terms with the subscript s give the effects of solvent dipoles, and with the subscript i, the effects of ionic charges. The c terms are concentrations, r_0 and a_i are distances of closest approach, μ_s is the dipole moment, z_i are ionic charges, and τ_s, τ_i are the respective correlation times. Further terms are needed for hydrogen bonding or exchange processes. If D_2O replaces H_2O, the motions are slowed by the higher mass and stronger hydrogen bonds.

The electric field gradient is now amplified by a factor given by equation (10), as

$$\beta = P(1 - \gamma_\infty) \tag{10}$$

where $P = (2\epsilon + 3)/5\epsilon$ is the polarizability of the solvent, with dielectric constant ϵ. The quantity $(1 - \gamma_\infty)$ is the Sternheimer antishielding factor which represents the distortion of the inner electron shells by electric field gradients in the valence shell. Experimental determinations are rare: values of 9 and 22–26 have been determined for $(1 - \gamma_\infty)$ in solid NH_4Cl, compared with a calculated (ab initio) value of 6.8.[106]

4 PATTERNS OF NITROGEN SHIFTS

The large literature of nitrogen shifts is reviewed regularly.[6,7] Nitrogen shifts in diamagnetic compounds cover a range of 1350 ppm, over three times the carbon range. The comparison with carbon is helpful since carbon shielding patterns are well known. The greater range for nitrogen arises from its greater electronegativity, and its ability to carry lone-pair electrons with s character, which carbon does very rarely.

The major determinants of nuclear magnetic shielding are demonstrated by expressions such as equation (11) for the paramagnetic term σ_p, which dominates the nitrogen shift in diamagnetic compounds. The negative sign of σ_p (ppm) represents deshielding, so the shift δ increases with the absolute magnitude of σ_p.

$$\sigma_p \approx -\frac{\mu_0}{4\pi}\,\frac{e^2}{2m_e^2}\langle r^{-3}\rangle_{2p}\,\frac{\langle 0|\boldsymbol{L}^2|0\rangle}{\Delta E} \tag{11}$$

Equation (11) embodies an 'atom-in-a-molecule' approximation[107,108] in a simplified form. It does not give accurate results, but is useful in showing the three factors of importance to the shielding. The first is the radial term $\langle r^{-3}\rangle_{2p}$, where r represents the radius of the 2p electron on the observed atom. The value of the radial term for the free atom, which can be viewed as a scaling factor for the shifts of a particular nucleus, is twice as large for nitrogen (2.46 a.u.) as for carbon (1.23 a.u.);[109] the more electronegative atom holds its valence p electrons closer to the nucleus, giving a larger paramagnetic shift.

The second factor is the term in $\boldsymbol{L}^2$ representing the angular momentum which allows the electronic charge to circulate in a magnetic field, so as to reinforce the field. This paramagnetic circulation opposes the free diamagnetic circulation, which is fully realized only in the free atom or round the axis of a linear molecule. The paramagnetic circulation requires an asymmetry of charge in the valence shell of the observed atom, i.e. in the p orbitals of a second-row element such as carbon or nitrogen. The angular momentum term in equation (11) is analogous to the $\boldsymbol{Q}$ terms in the theory of Karplus and Pople, expressing imbalance of charge, or the $\boldsymbol{P}_u$ term in the theory of Jameson and Gutowsky.[109] Electronic asymmetries which potentiate the paramagnetic circulation are small in highly symmetric environments, as in CH_4 or NH_4^+, but may be large for two-coordinate nitrogen carrying a lone pair.

The third factor, ΔE, is an effective excitation energy for the paramagnetic circulation. This can be considered to arise from virtual excitations of p → p type, which may be $\pi \leftrightarrow \sigma$

(i.e., $\pi \rightarrow \sigma^*$ or $\sigma \rightarrow \pi^*$), $n \rightarrow \pi^*$, or $\sigma \rightarrow \sigma^*$ from one bond to another, as the magnetic field mixes into the ground state those excited states which allow circulation of charge. Excitation energies vary more widely for nitrogen than for carbon, since lone pair (n_N, or nonbonding) electrons afford a high lying HOMO, and LUMOs involving nitrogen are low lying because of the electronegativity of nitrogen. The frontier orbitals in question are those appropriate to charge rotation (e.g. $n_N \rightarrow \pi^*$, but not $\pi \rightarrow \pi^*$), and the terms HOMO and LUMO may represent more than one High lying Occupied MO, or Low lying Unoccupied MO, when more than one excitation contributes significantly to the deshielding. These magnetic-dipole-allowed excitations are normally forbidden in the electronic spectrum. They are weakly allowed in $n_N \rightarrow \pi^*$ excitations in which there is a component of the s $\rightarrow$ p type, giving the well-known long wavelength bands of the azo chromophore, for example. More precise formulations of equation (11) embody a summation over the magnetically active excitations.

Equation (11) shows that the deshielding (δ) is the greater the closer the paramagnetic circulation to the nucleus (the more electronegative the substituents), the smaller the energy ΔE of the virtual excitation (the HOMO–LUMO or frontier orbital gap for charge circulation), and the greater the imbalance of charge in the valence shell. All three factors are important when extremes of high or low shielding are observed.

In isoelectronic (isostructural) locations, the shieldings of nitrogen and carbon, indeed the shielding tensors, show similar shielding patterns, with scaling according to the radial factors. Similar patterns are evident in Figure 2, which compares nitrogen and carbon shift ranges for some standard bond types. Figure 3 gives nitrogen shift ranges for compounds formed with main group elements, and Figure 4 is a comparable chart for ligands in transition metal complexes.

4.1 Nitrogen Compared with Carbon

In Figure 2 the nitrogen and carbon charts are scaled by the 2:1 ratio of the radial terms $\langle r^{-3} \rangle_{2p}$ for the free atoms, to make the shifts readily comparable. A major difference between the nitrogen and carbon charts is the extension of the nitrogen range to lower shielding for π-bonded nitrogen carrying a lone pair of electrons, as in azo (diazene) groups RN=NR or nitroso compounds RNO.

High carbon or nitrogen shielding is observed in CH_4 or NH_4^+ because of the electropositive substituent hydrogen ($\langle r^{-3} \rangle_{2p}$ is small), the high electronic symmetry in the valence shell (the angular momentum term is small), and the high energy of the $\sigma \rightarrow \sigma^*$ excitations (ΔE is large).[110] The energy of the $n \rightarrow \sigma^*$ excitation is also high in ammonia, and the lower nitrogen shielding in NH_4^+ compared with NH_3 is largely attributable to the positive charge on the nitrogen, increasing the radial term and excitation energies. Nitrogen shifts are found to correlate with the atomic charges estimated for nitrogen in amines, nitro compounds, isonitriles, and azines.[111]

Nitrogen is strongly *de*shielded as an interstitial atom in the metal cluster carbonyls such as $[Rh_6N(CO)_{15}]^-$, a trigonal prism, and $[Ru_6N(CO)_{16}]^-$, which is octahedral.[70] The interstitial carbon in the corresponding clusters is even more strongly deshielded, as shown in Figure 2. The deshielding is unexpected in view of the high symmetry and the electropositive and heavy neighbors. Carbon in the corresponding clusters is even more strongly deshielded. Indeed, the deshielding increases with compression of the interstitial atom in the cluster, as observed in some other kinds of cages.[112]

The nitrogen shifts in alkylamines and hydrochlorides can be expressed by additive substituent parameters,[113] as for carbon in alkanes. For nitrogen shifts, as for carbon shifts, the increments for each C_α or C_β substituent arise from inductive effects, while the increments for C_γ substituents arise from steric and conformational effects. Substituent parameters have been developed for other compound types,[2,3] including peptides, but correlation spectroscopy is now used to assign nitrogen resonances.

Lower shielding is generally observed in multiply bonded compared with singly bonded compounds, because of the lower electronic symmetry of the observed atom when π and σ bonds are present and the lower energies of $\pi \leftrightarrow \sigma$ in comparison with $\sigma \rightarrow \sigma^*$ excitations. Figures 2–4 show that quite high shielding is observed for nitrogen as the central atom in a linear group, as in MeNC, N*N*O, or NO_2^+, or carbon in MeCN, NCO^-, or CO_2. The shielding is relatively high because of the free diamagnetic circulation about the axial direction, as in the noble gas compounds $RC{\equiv}N{-}XeF^+$, measured in ^{14}N resonance,[114] and $HC{\equiv}N{-}KrF$.[115]

The nitrogen shielding in comparable groups decreases with increasing electronegativity of the neighbor, or with an

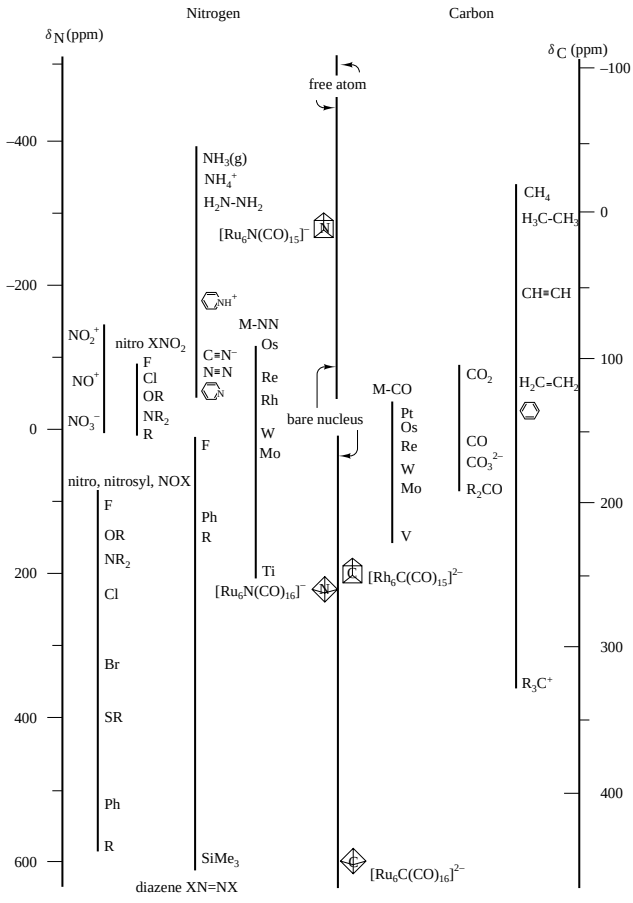

Figure 2 Comparison of nitrogen and carbon shifts

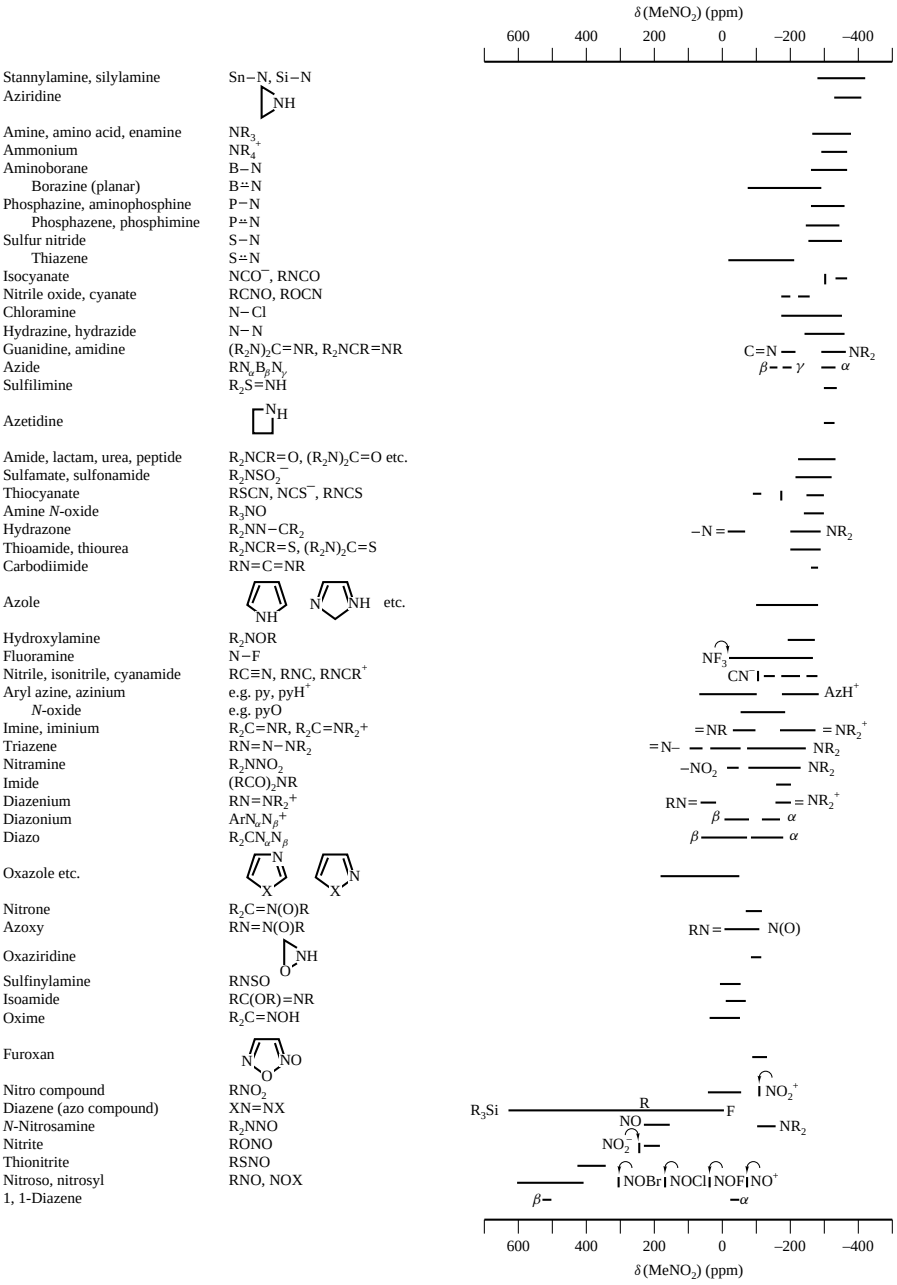

Figure 3 Ranges of nitrogen shifts in compounds with main group elements

increase in the positive charge on the ion. Lower shielding may be observed for terminal atoms in linear groups, as in MeCN > N_2 > NO^+, or MeNC > CN^- > CO.

Figure 2 shows the comparability of the carbon and the nitrogen shielding in isoelectronic pairs such as CH_4 and NH_4^+, CO (or CN^-) and NO^+, or CO_3^{2-} and NO_3^-, even for pairs which are not isostructural such as C_2H_6 and N_2H_4 since the lone-pair excitation energies in hydrazine are rather high. The shielding in comparable compounds decreases from single (e.g. $H_2N–NH_2$) to triple (N≡N) to double bonds (RN=NR) in nitrogen as in carbon resonance. This is the sequence of decrease in symmetry of the local electronic charge (and increase in the NQCC, as illustrated in Table 4) and of decreasing excitation energies.[116]

In the n → π* excitation, charge circulates from the p component of the lone pair into the π* orbital. The n → π* excitation energies are low for diazenes RN=NR, particularly in extended conjugated systems as in azo dyes.[117] The n → π* excitation energies and nitrogen shieldings are particularly low for nitroso compounds RNO and nitrosyls NOX. All three factors in equation (11) are operative: the bent nitrogen carrying a lone pair is highly anisotropic, $\langle r^{-3}\rangle_{2p}$ is large because of the electronegativity of oxygen, ΔE is very low since the π* LUMO is low (because of the electronegativity of oxygen), and the nitrogen lone pair HOMO is raised by the presence of lone-pair electrons on the oxygen.

When excitation energies are small, linear δ/λ correlations may be observed between the chemical shifts δ and the wavelength λ of the low-energy absorption band in the electronic

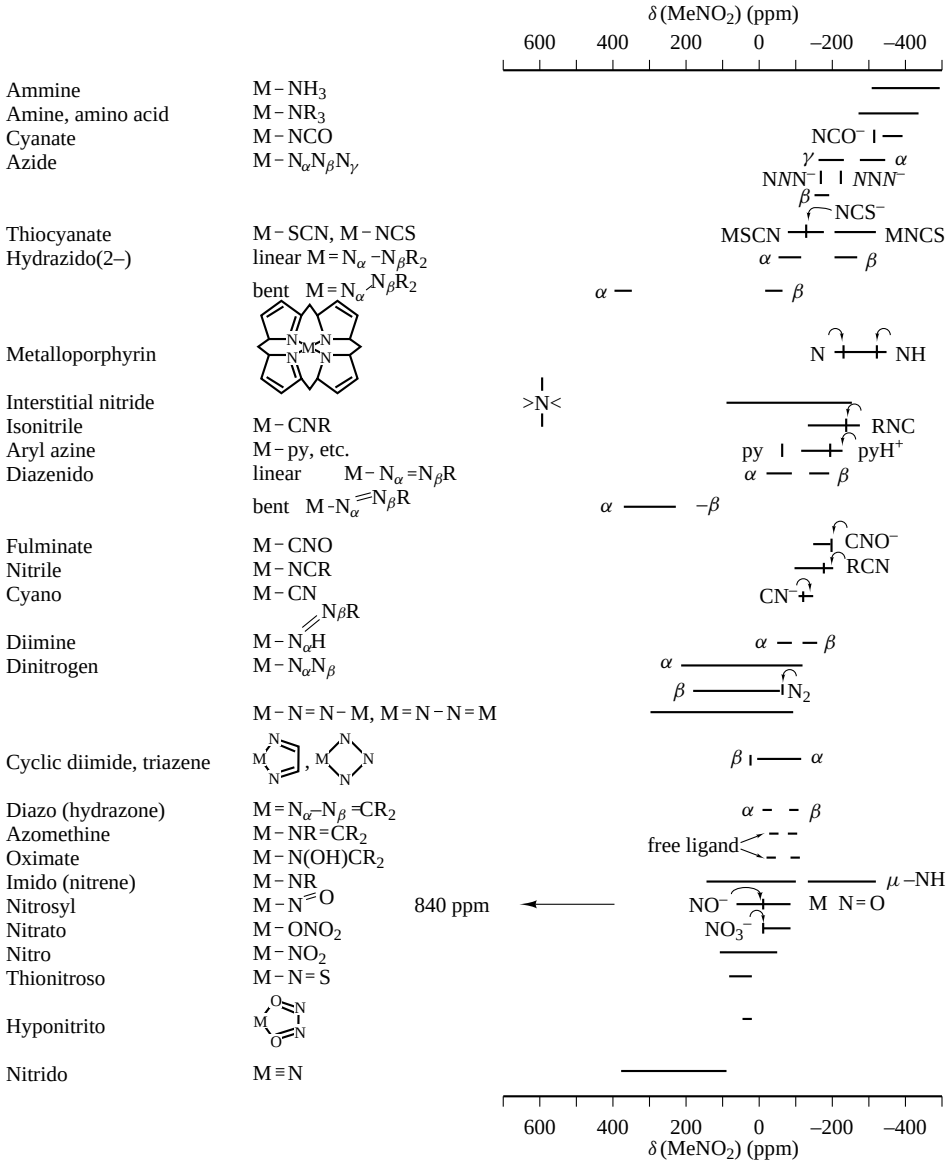

Figure 4 Ranges of nitrogen shifts in metal complexes

spectrum. Such correlations are well known for organic and inorganic compounds with $n_N \rightarrow \pi^*$ absorption: for carbonyl compounds RCHO or RCOR′ in carbon resonance, and in nitrogen resonance, for nitrosyl compounds NOX and RNO,[118] azo (diazene) compounds XN=NX and RN=NR,[119] diazo compounds YNN,[120] etc. The nitrogen shielding decreases as the $n_N \rightarrow \pi^*$ band moves to longer wavelengths, from the colorless oxo/fluoro compounds NOF, FNNF, etc., to the compounds with less electronegative substituents, such as PhNO, *t*-BuNO, or $Me_3SiN{=}NSiMe_3$ which are blue, and the 1,1-diazenes R_2NN which are purple.[121] In $n_N \rightarrow \pi^*$ chromophores, the nitrogen shift δ and $\lambda(n_N \rightarrow \pi^*)$ both increase in the sequence N=C < N=N < N=O of increase in the electronegativity of the partner in the double bond, lowering the π^* relative to the n_N orbital and increasing $\langle r^{-3} \rangle_{2p}$ for the nitrogen.

4.2 Protonation Shifts

Protonation of the singly bonded nitrogen in ammonia or amines deshields the nitrogen by up to 20 ppm. The deshielding is largest in ammonia in which the charge is strongly localized. Because of the relatively small protonation shifts in amines, there are similar shift relationships for amine nitrogen and alkane carbon in corresponding environments, depending on connectivity, although the groups are not isostructural. Amines which are branched at the α-carbon show small *in*creases in nitrogen shielding on protonation.

Since nitrogen is strongly deshielding by $n \rightarrow \pi^*$ circulations, the effects of protonation of nitrogen in a π-bonded system may be large. Protonation of pyridine increases the nitrogen shielding by about 100 ppm, as the lone-pair electrons on nitrogen are strongly stabilized by the formation of a bond to hydrogen. The radial term $\langle r^{-3} \rangle_{2p}$ is not greatly increased by the positive charge, which is delocalized. Large effects may be observed in metal complexes. Protonation of

dinitrogen attached to tungsten to form the (linear) diazenido ligand, and then the hydrazido(2-) ligand, increases the shielding of the β-nitrogen by 135 and then 55 ppm:[122] $W-N\equiv N \rightarrow W-N=NH \rightarrow W=N-NH_2$. Protonation shifts of 200 ppm are observed for the doubly bent diazenido group Pt(II)−N=NPh to give a hydrazido(1-) ligand, Pt−NH=NPh.[123]

An exception which proves the rule is the *de*shielding of nitrogen by ca. 100 ppm on protonation of the cyclic anion formed by deprotonation of 2,4,6-trimethylpyridine.[124]

4.3 Nitrogen NMR Criteria of Structure

The relationships illustrated in Figures 2–4 allow some generalizations on the structural determinants of nitrogen shieldings, in advance of more rigorous discussion of the shielding tensor.

1. In groups which may be bent or linear at nitrogen, the nitrogen is deshielded as the bond angle decreases. The deshielding on bending is the greater, the greater the deshielding in the linear group: thus, bent nitrogen in azides is still quite highly shielded.[125] Deshieldings are greater in aromatic azines and azoles, and may be greater still in triazenes, as in the $(Ts-NNN-Ts)^-$ ion (Ts = tosyl), in which the central nitrogen is deshielded by 286 ppm compared with the central nitrogen in azide ion, $N\mathit{N}N^-$.[126]
   The difference in nitrogen shift is small for linear and bent imido ligands M=NR,[127] but large in diazenido ligands M−N=NR which are bent at the ligating nitrogen.[124]
   The nitrosyl group shows large deshieldings. The bent nitrogen in the *N*-nitrosamine Me_2NNO is deshielded by 300 ppm compared with the central nitrogen in nitrous oxide, $N\mathit{N}O$, and the nitrogen is deshielded further if the group is distorted from planarity.[128] Deshieldings up to 800 ppm are reported for metal nitrosyls in the bent compared with the linear ligand,[129] with smaller shieldings for smaller MNO angles.[130]
   Reactions which involve the shift of a d-electron pair onto ligating nitrogen, allowing the metal to accept an incoming ligand and the nitrogen to coordinate a Lewis acid, are readily monitored by nitrogen NMR.]
2. In groups which may be pyramidal at nitrogen carrying a lone pair, or flat, with π delocalization of the lone-pair electrons, the nitrogen is deshielded the flatter the group, as noted early on in substituted anilines.[2,3] Planarity allows $\pi \leftrightarrow \sigma$ paramagnetic circulations of lower energy than $n_N \rightarrow \sigma^*$ circulations in the pyramidal group. In the planar hydrazido(2-) ligand $M=N-NH_2$, the nitrogen shift (ca. −230 ppm[131]) shows significant deshielding compared with hydrazines (ca. −320 ppm), being comparable with amide shifts (cf. −265 ppm for formamide).
3. Protonation and deprotonation shifts have considerable diagnostic value in structural studies. Hydrogen bonding to a lone pair on nitrogen leads to smaller shifts in the same sense. Hydrogen bonding of attached hydrogen gives nitrogen shifts in the opposite sense. Tautomeric and other acid–base systems involving nitrogen are thus well studied by nitrogen NMR methods, with the information from the shifts, ^{14}N linewidths, ^{15}N NOE, and couplings.
4. Coordination shifts may be comparable to protonation shifts. Thus, coordination of BH_3 or BMe_3 to ammonia or alkylamines deshields the nitrogen by a small amount, and coordination to π-bonded nitrogen increases the shielding markedly, as by 74 ppm when pyridine forms py · BH_3. Coordination to transition metals is a more complex question (Section 4.5).

4.4 Nitrogen Bonded to Heteroelements

Figures 3 and 4 show high shielding for carbon or nitrogen singly bonded to boron,[132] silicon, phosphorus,[133] etc., or to transition metals in ammine complexes. These elements are less electronegative than nitrogen. Nitrogen is strongly deshielded in singly-bonded compounds with fluoronitrogen compounds by 370 ppm for liquid NF_3 compared with NH_3, or 290 ppm for NF_4^+ compared with NH_4^+.[28] Because of the extreme electronegativity of fluorine, its effects as a substituent often have diagnostic value, and have been called (per)fluoro effects in photoelectron and electronic spectroscopy.

In a comparison of similar N–X compounds, the nitrogen shift ranges show periodic trends reflecting the inductive effects of the heteroelement. The nitrogen shielding decreases across the row of the heteroelement, e.g. from B–N to N–O and from Si–N to N–Cl, with an increase in the electronegativity of X; and increases down the group of the neighbor, with a decrease in the electronegativity of X, an increase in polarizability and relativistic effects, and with heavy atom neighbors.

Fluoro effects provide extreme examples, as in the σ-fluoro effects already described. These, and π-fluoro effects, are used in photoelectron and electronic spectroscopy for assignments to σ or π orbitals. Fluorination strongly stabilizes the σ-orbital manifold, of which the lone-pair orbital forms part. The stabilization is less for the π-orbital manifold, in part due to repulsion of π electrons by lone-pair electrons on fluorine. Although nitrogen is strongly deshielded in NF_3 and NF_4^+ compared with NH_3 and NH_4^+, nitrogen shielding is significantly increased on fluorination of azabenzenes and other planar species (cf. NOF, NO_2F, and N_2F_2).[134] π-Chloro effects are similar, and smaller.

4.5 Coordination Shifts in Metal Complexes

Coordination shifts from the free ligand to the complex are illustrated by a comparison of Figures 3 and 4, and in Figure 4 itself, since the shift for the free ligand is indicated.

Coordination shifts are usually small in the higher shielding ranges, and smaller for p-block than for d-block metals. On coordination to a transition metal, the nonbonding electrons on nitrogen are stabilized by bond formation, this tending to increase the nitrogen shielding, but low-lying orbitals may then become available to the paramagnetic circulation on ligating nitrogen.

Nitrogen NMR is a criterion of the mode of coordination of ambidentate ligands. Nitrogen is more shielded in M–NCS than in MSCN or in the free NCS^- ion.[135] Similarly, in the covalent azides $XN_\alpha N_\beta N_\gamma$, N_α is the most highly shielded nitrogen with N_β being buffered from the effects of coordination.[136]

Relatively low shielding is observed for ligating nitrogen in doubly bonded groups such as hydrazide(2−), $M=N-NH_2$, and for π-acceptor ligands such as NCMe, N_2, NO, NS, etc.

The importance of the ligand field splitting to the nitrogen shift is shown by the periodic dependence on the transition metal and by *trans* effects.[137] These influences are magnified if nitrogen is close to the metal, as in nitrido complexes,[133] and for bent or bridging nitrido or nitrosyl ligands.

Trans influences may parallel substituent effects in arenes, such as the increase in nitrogen shielding in anilines, pyridines, and benzonitriles with *para*-substituents which are π donors (and the deshielding if nitrogen with π acceptors). In linear nitrosyl or diazenido complexes, the shielding of ligating nitrogen is increased by *trans*-donors such as OH, and decreased by *trans*-acceptors such as CN or NCMe. The strength of binding of the *trans*-ligand is also significant, since the dσ-orbital splitting is larger with softer ligands for metals in low oxidation states. Such correlations include other physical properties such as IR stretching frequencies, reflecting back-bonding to acceptor ligands such as N_2, or redox potentials.

Interest in nitrogen fixation processes has stimulated the study of the dinitrogen ligand in complexes of molybdenum and related metals, and of ligands on the reduction pathway, diazenido, hydrazido, hydrazinium, imido, etc. Nitrogen NMR spectroscopy can usefully distinguish terminal and bridging, or linear and bent ligands, and monitor protonation reactions.

5 NITROGEN SHIELDING TENSORS

More rigorous consideration of the factors determining nitrogen NMR shifts requires a knowledge of the shielding tensor, preferably in conjunction with theoretical calculations. Shielding tensor components have been measured for a number of nitrogen bond types, including ligands in metal complexes. There has been much interest in groups of biological importance, in peptide or imino links for example, in which nitrogen shielding tensors give useful information on the effects of protonation and hydrogen bonding. Other articles discussing nitrogen shielding tensors in biomolecules are given at the end of this section.

Nitrogen tensors resemble those for carbon or phosphorus in isoelectronic and isostructural locations, with scaling by the respective radial factors $\langle r^{-3}\rangle_{np}$ which are in a 2:1 ratio for nitrogen and carbon, as discussed in Section 4.[109,110] Nitrogen shielding patterns are more closely related to those of phosphorus than of carbon, since the nitrogen and phosphorus valencies are closer, as are the scaling factors, since the ratio of $\langle r^{-3}\rangle_{2p}$(N) to $\langle r^{-3}\rangle_{3p}$(P) is 1:0.7.

A major factor for many nitrogen tensors is the presence of lone pair (n_N) electrons on the nitrogen which are strongly directional. The lone-pair axial direction then determines the principal axis system, and major deshieldings are observed for axes which mix n_N and π^* orbitals, following the arguments given in Section 4. Similarly, the nitrogen shielding tensor is a criterion for the bending of two-coordinate nitrogen and the flattening of three-coordinate nitrogen. Tensor measurements, combined with theoretical studies, can frequently throw light on the nature of the bonding.

5.1 Experimental Techniques

The spin–rotation interaction, measured as fine structure in the microwave spectra of gases, has given ^{14}N tensor information for NH_3,[16] N_2O,[142] HCN,[143] and PN[144] (Tables 5 and 6). Tensor measurements have been made on oriented single crystals of glycylglycine · HCl · H_2O[145,146] and L-histidine · HCl · H_2O in ^{15}N resonance, and some nitrates in ^{14}N resonance (Table 7). Most measurements, however, are made on powdered material by ^{15}N MAS or CP MAS techniques, and/or powder lineshape analysis on a static sample. Some anisotropies have been measured in liquid crystals (MeNC, MeCN, N_2O) and some by relaxation methods ($PhNO_2$, pyridine).

For some molecules or groups, the orientation of the shielding tensor in the molecular frame is obvious from the chemical structure, and for some it has been established by single crystal measurements. For some others, the orientation has been determined by concurrent measurement of dipolar interaction between ^{14}N or ^{15}N with ^{1}H, ^{2}H, ^{13}C, ^{31}P, or other nuclei.[140,145,147] Theoretical calculations, also, may help in the assignment of the axial directions.

Tables 5–7 give the principal components as absolute shieldings σ, with $\sigma_{33} > \sigma_{22} > \sigma_{11}$, and $\sigma_{iso} = \sigma_{tr} = (\sigma_{11} + \sigma_{22} + \sigma_{33})/3$. The shieldings are obtained from the chemical shift, δ, with neat liquid nitromethane as standard, according to equation (1), using the absolute scale[19] based on the spin–rotation measurement for NH_3, according to which nitrogen in neat liquid nitromethane has shielding $\sigma = -135.8$:

$$\sigma = -135.8 - \delta(MeNO_2) \qquad (12)$$

Some authors use a liquid ammonia standard, for which the nitrogen shieldings are 244.6 ppm at ambient temperatures and 240.6 at −50°C.[17] Some others use solid NH_4Cl as the reference material, with σ(N) = 202.5.

The tensor properties given in Tables 5–7 are the span $\Omega = \sigma_{33} - \sigma_{11}$ and the skew $\kappa = 3(\sigma_{22} - \sigma_{iso})/\Omega$.[148,149] For axial tensors, $\Omega = \sigma_{\parallel} \sim \sigma_{\perp}$ and $\kappa = \pm 1$. The parameters Ω and κ avoid ambiguities that have arisen with the traditional parameters,[150] the shielding anisotropy $\Delta\sigma$ and asymmetry η. For these, the ordering of the σ_{11}, σ_{22}, and σ_{33} axes depends on the ordering of the absolute values of the differences of the tensor elements from σ_{iso}. Some authors have followed the 'traditional' order σ_{33}, σ_{11}, and σ_{22},[145] while some use the numerical order σ_{33}, σ_{22}, and σ_{11}. In any case, the σ_{33} and σ_{11} axes have to be interchanged for those members of an extended series of compounds which have $\sigma_{22} < \sigma_{iso}$, as compared with those with $\sigma_{22} > \sigma_{iso}$. Such series include metal nitrosyls in nitrogen resonance, as described in Section 5.5, or organic carbonyl compounds in carbon resonance.[151]

Several authors[152] have used the relative magnitudes of the principal components to define the axes as here, rather than relative magnitudes of the absolute values of the differences from σ_{iso} as in the 'traditional' definition. The use of the skew parameter κ rather than the asymmetry parameter η preserves sign information, since on the traditional definition $0 \leq \eta \leq 1$ and $\eta = 0$ for axial symmetry whether $\sigma_{\parallel}$ is greater or less than $\sigma_{\perp}$. The skew κ, however, is +1 for $\sigma_{\parallel} > \sigma_{\perp}$ and −1 for $\sigma_{\parallel} < \sigma_{\perp}$.

5.2 Singly Bonded Nitrogen

Shielding tensors are given in Table 5 for nitrogen in ammonia and some derivatives. Although distortion of an oxyanion such as nitrate by hydrogen bonding to the

Table 5 Principal Components of Nitrogen Shielding Tensors in Ammonia, Ammines, and Ammonium

Compound	δ_{iso}	σ_{iso}	σ_{11}	σ_{22}	σ_{33}	Ω	κ	Reference
NH_3(g)	−400.3	263.5	237.7	278.0	278.0	40.3	1	Kukolich[16]
cis-[Pt($^{15}NH_3$)$_2$(SCN)$_2$]	−399.0	263.2	219.9	249.3	320.5	100.6	−0.41	Santos et al.[155]
(two crystal sites)	−386.0	250.2	212.5	244.1	294.1	81.6	−0.22	
$^{15}NH_4^+$ halides:								Ratcliffe et al.[153]
Cl^-	−338.1	202.3						
Br^-	−336.0	200.2						
I^-	−321.6	185.8						
$^{15}NH_4NCS$	−344.3	−171.9						Dickson et al.[154]

Table 6 Principal Components of Nitrogen Shielding Tensors in Linear and Near-Linear Groups

Compound	δ_{iso}	σ_{iso}	σ_{11}	σ_{22}	σ_{33}	Ω	κ	Reference
2,4,6-*t*Bu$_3$C$_6$H$_2$^{15}N≡P$^+$AlCl$_4^-$	−132	−3	−155	−121	266	421	−0.834	Curtis et al.[160]
4-MeC$_6$H$_4$C≡^{15}N	−126	−10	−151	−122	244	395	−0.851	Sardashti and Maciel[161]
MeN≡C	−266	130	10	10	370	360	−1	Yannoni[164]
*N*NO(g)	−240	105	−18	−18	349	367	−1	Casleton and Kukolish[142]
NH$_4$SC^{15}N	−169	34	−104	−104	311	415	−1	Dickson et al.[154]
MeC≡N	−157	21	−142	−142	346	488	−1	Kaplan et al.[159]
N*N*O(g)	−141	5	−174	−174	364	538	−1	Casleton and Kukolish[142]
HC≡N(g)	−109	−27	−215	−215	348	563	−1	Garvey and De Lucia[143]
N≡N(g)	−74	−62	−263	−263	340	603	−1	Ishol and Scott[162]
[Mo(dppe)$_2$(^{15}N$_2$)$_2$] N$_\beta$	−43.4	−92.2	−283	−283	289	572	−1	Groombridge et al.[165]
N$_\alpha$	−42.0	−93.6	−304	−304	327	631	−1	
P≡N(g)	213	−349	−698	−698	350	1048	−1	Raymonda and Klemperer[144]

Table 7 Principal Components of Nitrogen Shielding Tensors in Planar Groups

Compound	δ_{iso}	σ_{iso}	σ_{11}	σ_{22}	σ_{33}	Ω	κ	References
RC(O)^{15}NH$_2$·H$_2$O (asparagine)	−276.8	141.0	64.5	107.9	250.6	186	−0.53	Herzfeld et al.[166]
Nylon-6 (−CO^{15}NH−)	−268	132	34	154	209	175	0.37	Powell and Mathias[167]
Glycyl(^{13}C^{15}N)glycineHCl·H$_2$O	−267.4[a]	135.6	30.6	180.8	183.3	153	0.97	Hartzell et al.,[145] Harbison et al.[146]
L-Alanyl(^{13}C^{15}N)L-alanine	−256.8	121.0	25.1	162.5	175.3	150	0.83	Hartzell et al.[145]
Alanyl(^{13}C^{15}N)proline	−256	120	22	118	219	197	−0.030	Schweitzer and Spiess[172]
RCO^{15}NHR′ (peptides)	ca. −260	100–145	10–35	120–180	175–220			
L-Tryptophan·HCl		127.8	66.9	121.5	195	128	−0.15	Roberts et al.[157]
Tryptophan-26		126	70	116	185	115	−0.26	Cross and Opella[171]
L-Histidine·HCl·H$_2$O (π-^{15}N)		66.9	−19.8	35.6	184.9	205	−0.46	Roberts et al.[157]
Pyridine-^{15}N	−83	−53	−387	−168	395	782	−0.44	Schweitzer and Spiess[172]
Ph^{15}N(O)^{15}N(O)Ph		−66	−220	−43	65	285	0.24	Wasylishen[179]
PhCH=^{15}NPh	−48	−87	−365	−76	180	545	0.06	Curtis et al.[173]
PhCMe=^{15}NOH	−31.4	−104	−315	−83	85	400	0.16	Wasylishen et al.[174]
trans-RB (−CH=^{15}NH−)	−37.6	−97.8	−406.5	−92.5	205.6	612	0.026	de Groot et al.[180]
RBH$^+$Cl$^-$	−181.2	44.6	−79.2	22.5	189.8	269	−0.25	
RBH$^+$Br$^-$	−186.8	51.6	−69.5	33.8	190.4	260	−0.205	
RBH$^+$I$^-$	−198.5	62.5	−56.7	53.3	190.8	247	−0.11	
bR$_{568}$ (all-*trans*)	−209.3	73.6	−42.9	60.1	203.1	246	−0.165	
bR$_{548}$ (13-*cis*)	−202.3	66.5	−42.9	39.1	204.1	247	−0.33	
PhNO$_2$(soln.)	−2	−134	−399	−32	30	429	0.71	Friedrich and Wasylishen;[45] Stark et al.[78]
Nitrates:								
NH$_4$NO$_3$	−3.6	−132	−220	−189	11	231	−0.74	Delmotte et al.[226]
NaNO$_3$	−3	−133	−206	−206	16	222	−1	Barrie et al.[178]
KNO$_3$	−3	−133	−209	−207	17	226	−0.98	Bastow and Stuart[176]
AgNO$_3$		−142	−212	−206	−7	205	−0.94	Santos et al.[177]
Pb(NO$_3$)$_2$		−146	−220	−220	2	218	−1.02	Santos et al.[177]
Ba(NO$_3$)$_2$		−151	−227	−227	−0.5	226	−1.01	Santos et al.[177]
trans-Ph^{15}N=^{15}NPh	130	−267	−789	−146	136	925	0.39	Wasylishen et al.[175]
Na^{15}NO$_2$	245	−381	−915	−263	36	951	0.37	Wasylishen et al.,[140] Barrie et al.[178]
p-Me$_2$NC$_6$H$_4$^{15}NO	445	−581	−1457	−309	22	1479	0.55	Schweitzer and Spiess[172]

[a]Assumes glycine zwitterion reference has δ(N) −350 ppm.

ammonium ion has been observed in the nitrogen shielding tensor, the ammonium cation gives a symmetric tensor, as for near-tetrahedral symmetry and reorientational motion such as the switching in NH_4Cl (Section 3).

The shielding tensor for ammonia is unusual in having $\sigma_{\parallel} < \sigma_{\perp}$ ($\kappa = 1$) and a small span, 40.3 ppm.[16] Ammonia is unusual also in the substantial *decrease* in the nitrogen shielding on protonation, as discussed in Section 4. In ammonium salts, the NH_4^+ nitrogen shielding decreases with a decrease in strength of the hydrogen bond to the counteranion (i.e., with a decrease in the electronegativity of the anion), increasing the positive charge on nitrogen.[153,154] The deshielding is related to contraction of the 2p N orbitals from NH_3 to $NH_3 \cdots H^+$, with a strongly hydrogen-bonding anion, and then to NH_4^+, as the counterion hydrogen bonds more weakly.

Much smaller deshieldings are observed on the protonation of amines, in which cationic charge is less localized on the nitrogen. $R-NH_3^+$ tensors, of which a number have been measured in biomolecules such as histidine or glycine, have a very small span, about 10 ppm.

There is little change in the NH_3 isotropic shift on formation of ammine ligands in *cis*-[Pt($^{15}NH_3$)$_2$(SCN)$_2$], with weak bonding to the metal. There is some increase in span of the NH_3 tensor, but a considerable decrease in the skew, in this planar complex. The σ_{33} component is sensitive to a change in location in the crystal.[155]

Combined shielding tensor and dipolar shift measurements have been used to characterize NH protons and measure the bond distances in polycrystalline and amorphous solids of biological importance, in ^{14}N[156] and in ^{15}N[157] resonance. Protonated imine nitrogen is discussed under the heading of the parent compound.

5.3 Nitrogen in Linear Groups

The principal components of nitrogen shielding tensors for linear systems are given in Table 6. Maximal shielding is observed for the C_∞ axis with its largely diamagnetic circulation. Most values of the parallel shielding $\sigma_{\parallel}$ are in the range 300–370 ppm, resembling the (diamagnetic) shielding of atomic nitrogen, 325 ppm.[158]

The parallel shielding, 350 ppm in MeCN,[159] decreases by 80–100 ppm when the π electrons can delocalize into an aromatic ring, as in the iminophosphenium cation[160] and benzonitriles.[161] Interesting σ-inductive and π-conjugative effects of a 4-substituent in the benzene ring on the cyano-nitrogen shielding tensor have been monitored for benzonitriles 4-Y–C_6H_4–C≡^{15}N with Y = OMe, NMe_2, NO_2, CN, Cl, Br, F, Me, CMe_3, and NMe_3^+. Some of the largest changes in tensor components relative to Y = Me are produced by a positively charged substituent NMe_3^+, which decreases σ_{33} in the C≡N by 11 ppm (and σ_{11} and σ_{22} by 7 and 16 ppm, respectively). Similarly the parallel shieldings in dinitrogen N≡N[162] are reduced by 51 and 13 ppm on coordination to molybdenum.

The perpendicular tensor components arise from $\sigma \leftrightarrow \pi$ (i.e., $\sigma \rightarrow \pi^*$ and $\pi \rightarrow \sigma^*$) circulations, and for terminal nitrogen from $n_N \rightarrow \pi^*$ circulations also. The separation of the σ_{11} and σ_{22} components by around 30 ppm in the benzonitriles and iminophosphenium ion reflects conjugation with the aromatic ring. In the benzonitriles the separation is largest (41 ppm) with the π-donor Me_2N as the 4-substituent.

For terminal nitrogen in the linear groups the perpendicular shielding ($\sigma_{\perp}$) is highest in *N*NO and lowest for PN: the latter has the longest bond (so orbital splittings are smaller) and phosphorus is the least electronegative partner. For N_2O, ab initio calculations using the LORG method[163] show comparable (major) contributions to σ_p for the terminal nitrogen from its lone pair and the NN bond, and for the central nitrogen from the NN and NO bonds.

For two-coordinate nitrogen, the perpendicular shielding decreases from MeNC[164] to $ArNP^+$ and to [Mo(dppe)$_2$($^{15}N_2$)$_2$],[165] as the orbital splittings decrease.

5.4 Nitrogen in Planar Systems

Principal values for nitrogen tensors in planar systems are given in Table 7. The highest shielding and a small span are observed for three-coordinate nitrogen bound only to carbon and hydrogen, in amides or peptides, azinium nitrogen in the five-membered rings in tryptophan, and L-histidine · HCl · H_2O and iminium groups.

5.4.1 Peptides and Amides

Table 7 shows the similarities of the components in an amide, asparagine,[166] in which the σ_{33} axis bisects the NH_2 group, in Nylon-6,[167] and in peptides.[139–168] Concurrent observations of $^{13}C^{15}N$ and $^{15}N^{1}H$ dipolar interactions in L-(1-^{13}C)alanyl-L-(^{15}N)alanine confirmed earlier conclusions on the orientation of the nitrogen tensor.[142] The axis of lowest shielding σ_{11} is in the amide plane perpendicular to the CN bond, allowing relatively low-energy CN $\sigma \leftrightarrow \pi$ circulations. Unusually (in contrast to carbon tensors in peptides, and to carbon and nitrogen tensors in aromatic and other delocalized systems), the high-shielding axis σ_{33} is in-plane in the CN bond direction; the intermediate axis σ_{22} is perpendicular to the plane. These directions are approximate, varying somewhat in different peptides. In glycylglycine and related peptide links, there is, accidentally, near-axial symmetry, with $\kappa \approx +1$, and the σ_{11} axis is at 99° to the CN bond.

The σ_{11} component is the least variable because of constancy of the CN bond, although sensitive to the geometry of the hydrogen bonding, the σ_{11} axis being nearest to the N–H···O direction. The σ_{11} axis is smaller in an α-helix than in a β-sheet, and is sensitive also to the handedness of the helix. The out-of-plane component σ_{22} reflects the conformation and secondary structure, being larger in a β-sheet than in an α-helix.[169] The σ_{22} component is unusually low and σ_{33} unusually high ($\kappa = -0.3$) in the link to proline, in which the nitrogen is in a saturated five-membered ring, although the alanylalanine isotropic shift is maintained in alanylproline.[170] The importance of lattice effects is shown by differences of isotropic shifts in solution.

5.4.2 Azines, Azinium

Despite the chemical importance of aromatic azines, few of their nitrogen tensors have been studied to date. Table 7 includes ranges of principal components observed for protonated nitrogen in five-membered rings of biological interest, in tryptophan[159,171] and in histidine.[159] These components are comparable to the values for pyridine.[172] In delocalized ($p\pi$)

systems, the out-of-plane axis shows the highest shielding (σ_{33}) in carbon resonance, depending on the relatively high-energy $\sigma \rightarrow \sigma^*$ excitations in the plane. This is borne out in nitrogen resonance, as in the protonated imidazole ring in histidine hydrochloride: the σ_{33} axis is almost perpendicular to the ring and the σ_{11} axis almost along the NH bond. Similar components are observed for tryptophan, studied as the hydrochloride, and in vivo in a bacteriophage that orients in the magnetic field.

Comparison with pyridine shows the major increases in σ_{11} and σ_{22} on protonation. In pyridine, the σ_{11} axis is tangential to the ring, mixing n_N and π^* orbitals, and the σ_{22} axis radial, this shielding being mediated by $\sigma \leftrightarrow \pi$ circulations. The value of σ_{22} for pyridine resembles that of $\sigma_\perp$ in MeCN, rather than MeNC (Table 6).

5.4.3 Planar Systems with CN, NN, NP, and NO Bonds

The cyano and phosphenium groups in ArCN and ArN^+P can be described as planar, since conjugation with the aromatic system removes the axial symmetry of the CN and PN groups, although these bonds are triple and form the σ_{33} axis.

In the compounds with bent two-coordinate nitrogen, benzylideneaniline,[173] (*E*)-acetophenone oxime,[174] *trans*-azobenzene,[175] and 4-dimethylaminonitrosobenzene,[172] dipolar chemical shift measurements support the σ_{22} direction as bisecting the angle at nitrogen (effectively along the lone-pair axis). The σ_{11} axis is that of the $n_N \rightarrow \pi^*$ circulation. The nitrogen tensors show that the σ_{11} component in the planar groups becomes more strongly negative as the π^* LUMOs come down in energy relative to the n_N orbital, with increasing electronegativity of the partner in the double bond from C=N to N=N and to N=O. Very low shieldings are $\sigma_{11} = -789$ ppm for azobenzene (which is red–orange, with $n_N \rightarrow \pi^*$ absorption at 448 nm) and -1457 ppm for 1,4-dimethylaminonitrosobenzene[174] which is green.

In *trans*-azobenzene there are two molecular sites, differing in the span (925 and 880 ppm) and skew (0.392 and 0.325), while the isotropic shift is maintained. The azo group (CNNC) is effectively planar and centrosymmetric in both sites with the same N=N bond length, but the torsion angles NNCC are significantly different, 17° and <10°. (The low barrier to twisting of the phenyl group is shown by the torsion angle of 30° observed in the gas phase by electron diffraction.)

The nitrate ion is characterized by a small span.[176,177] The σ_{22} component is less negative in nitrobenzene because of the smaller paramagnetic contribution of the CN bond, and more negative when there is a lone pair on nitrogen in the plane as in the bent nitroso group in $Me_2NC_6H_4NO$. The nitrite ion is intermediate as expected.[178]

A sizeable (σ_{11}) deshielding is associated with the $n_N \rightarrow \pi^*$ circulation in bent nitrosyl groups, and to a lesser extent in NO_2^- for which LORG calculations[176] show that the contribution to $\sigma_{P_{iso}}$ of the n_N electrons on the symmetry axis exceeds that of the NO bonds. In contrast is the high shielding in the nitroso dimer PhN(O)N(O)Ph, which is a diazene bis-*N*-oxide: the σ_{11} and σ_{22} values match those in nitrobenzene, and σ_{33} matches $\sigma_\perp$ in the nitrate ion.[179]

The effects of protonation of π-bonded nitrogen, and of variations in the strength of hydrogen bonding to a counterion, have been studied in the Schiff base (aldimine) retinylidene-Bu^n-(^{15}N)imine, RB. This models the light-harvesting membrane protein bacteriorhodopsin (bR) which was measured with selective ^{15}N,^{13}C-enrichment. Protonation of bR with a strong acid (HCl) increases σ_{11} by 327 ppm and σ_{22} by 115 ppm (Table 7). From HCl to HBr to HI and to weak organic acids (carboxylic acids or phenols), σ_{11} and σ_{22} show small increases with strengthening of the $N-H^+$ bond (σ_{11} and σ_{22} being linearly related) while σ_{33} is little changed. The values for dark-adapted bR resemble those of RBH^+ when very weakly hydrogen bonded.[180]

The ^{15}N and ^{13}C studies demonstrate the major contribution of the counterion to the opsin shift in the photocycle. Color changes in the protein with pH correlate with changes in the ^{15}N shielding, which increases as the neutral purple membrane (568 nm) becomes the acid blue membrane (600 nm), reverting with the change to the acid purple membrane (565 nm); the weak hydrogen bond in the protein weakens in the blue form. The opsin-induced red shift, therefore, arises from interaction of an electronegative group in the protein with the Schiff base end of the chromophore, *cis–trans* isomerization being excluded by the comparison with the 13-*cis*,15-*syn*-bR_{548} tensor.

5.5 Linear and Bent Nitrosyls in Metal Complexes

The nitrogen shielding tensor is a useful criterion for the bending of the nitrosyl ligand, and many of the nitrosyls studied are unstable in solution. In five-coordinate $\{MNO\}^8$ complexes (i.e., with eight (d + n) electrons), the metal may have a trigonal pyramidal coordination sphere (d^8) with the nitrosyl linear (NO^+), or else a square-pyramidal coordination sphere (d^6) with bent apical nitrosyl (NO^-), and similarly for the diazenido ligand ($N{=}NR^+$ and $N{=}NR^-$). The first measurement of a nitrogen tensor in a metal complex was of $[RuCl(^{15}NO)_2(PPh_3)_2][BF_4]$,[23] which has one linear and one bent nitrosyl in the solid state and shows fast bent–linear fluxionality in solution.[24]

Table 8 lists the nitrogen tensor components for linear nitrosyl ligands, which may be compared with those of N*N*O and the bent nitrosyl in $[RuCl(^{15}NO)_2(PPh_3)_2]^+$ in Table 9. In the linear ligand, as in $[Fe(CO)_3(^{15}NO)]^-$,[181] the $\sigma_\parallel$ values are significantly more negative than is expected for the free ligand NO^+. This reflects greater back-bonding to the nitrosyl compared with the carbonyl ligand, which is a useful model with many ^{13}C tensors having been measured.[138] The perpendicular components in the nitrosyls are somewhat more negative than in N*N*O, and more negative in a bis-nitrosyl than in a mononitrosyl, for the same metal. Bis-nitrosyls are usually *cis* and the neighboring nitrosyls interact, to bend slightly. $[Fe(NO)_2$ (cystine)] is an example of a compound for which the nitrogen shielding tensor has given the structure: the solid is amorphous and insoluble, but the nitrogen tensors clearly show the nitrosyls to be linear and probably *cis*.[182]

The ruthenium complex with one bent and one linear nitrosyl shows that bending of the nitrosyl makes a large paramagnetic contribution to σ_{11} and a significant contribution also to σ_{33}. These effects can be seen to some degree in the bis-nitrosyls in Table 8, the adjacent linear ligands interacting to produce a small degree of bending.

Table 9 gives the tensor properties of bent nitrosyl ligands, and Figure 5 shows the structures of the complexes.[182–184] In some complexes the planarity of the basal ligand is maintained by chemical bonding or strong hydrogen bonding. In the

Table 8 Principal Components of ^{15}N Shielding Tensors in the Linear Nitrosyl Ligand[a]

Complex	δ_{iso}	σ_{iso}	$\sigma_{\perp}$	$\sigma_{\parallel}$	Ω	References
$[Fe(CO)_3(^{15}NO)]^-$	18	−154	−295	127	422	Laska and Root[181]
$[RuCl(^{15}NO)_2(PPh_3)_2][BF_4]$	26	−162	−309	133	442	Mason et al.[23]
$[Ru(^{15}NO)_2(PPh_3)_2]$	37	−173	−284	48	332	Mason et al.[23]
	40	−176	−281	35	316	
$[Fe(^{15}NO)_2$(cystine)]	40	−176	−337	145	482	Barrie et al.[182]

[a]All have $\kappa = -1$.

Table 9 Principal Components of ^{15}N Shielding Tensors in Bent Nitrosyl Ligands

Complex	<MNO (°)	δ_{iso}	σ_{iso}	σ_{11}	σ_{22}	σ_{33}	Ω	κ	$\delta_{soln.}$	Reference
$[RuCl(^{15}NO)_2(PPh_3)_2]^+$	136.0	303	−439	−994	−229	−94	900	0.700	flux.	Mason et al.[23]
$[CoCl_2(^{15}NO)(PPh_3)_2]$		531	−667	−1149	−550	−301	848	0.414	flux.	Barrie et al.[182]
$[Co(^{15}NO)(LL')_2]$:										
$LL' = (S_2CNMe_2)_2$	135.1	499	−535	−877	−672	−357	520	−0.790	501	Barrie et al.[182]
= (salen)	127	698	−835	−2050	−302	−151	1884	−0.85	725.4	Barrie et al.[182]
= (naphthen)		709	−875	−1819	−478	−226	1593	−0.898	n.o.	Barrie et al.[182]
= (benacen)	123	721	−857	−1536	−707	−327	1209	0.372	723.0	Barrie et al.[182]
= (amben)		721	−857	−1681	−576	−315	1366	0.617	734.3	Barrie et al.[182]
= (acacen)	122	723	−859	−1402	−850	−326	1076	0.025	714.3	Barrie et al.[182]
$= (phsal)_2$		720	−856	−1348	−740	−480	868	0.401	n.o.	Groombridge et al.[183]
$= (bzsal)_2$		722	−858	−2058	−427	−89	1969	0.657	530.2	Groombridge et al.[183]
$= (bsal)_2$		728	−864	−1398	−805	−390	1008	0.176	740.5	Groombridge et al.[183]
$= (msal)_2$		735	−871	−1273	−826	−510	763	0.177	n.o.	Groombridge et al.[183]
$= (esal)_2$	129	742	−878	−2095	−376	−162	1933	0.779	739.7	Groombridge et al.[183]
$= (ketox)_2$	126.3	781	−917	−1260	−1007	−484	776	−0.348	740.3	Groombridge et al.[183]
= (TPP) at 298 K	127	765	−901	−1062	−820	−820	242	1.0	770.7	Groombridge et al.[184]
at 220 K		758	−893	−1072	−804	−804	268	1.0		
at 200 K		757	−893	−1853	−626	−198	1655	0.484		
cf. $[Ru_3(CO)_{10}(\mu$-$^{15}NO)]^{-a}$		424	−560	−1160	−408	−112	1048	0.435	434	Laska and Root[181]

[a]Bridging NO.

others, the nitrogen tensor components are a useful proof of structure since all have the pyramidal structure, but not all the bis-chelate compounds are constrained to coplanarity. An example is the $[Co(NO)(rsal)_2]$ series, of which the parent complexes $[Co(rsal)_2]$ have tetrahedral coordination. For $[CoCl_2(^{15}NO)(PPh_3)_2]$, which is fluxional in solution, the tensor properties show the nitrosyl to be bent in the solid.

All three tensor components for bent nitrosyls show significant deshielding compared with those in linear nitrosyls. The σ_{11} values are strongly negative and very variable. The bridging nitrosyl in $[Ru_3(CO)_{16}(\mu_2$-NO)]$^-$ shows a relatively high σ_{11} shielding as the nitrogen is now three-coordinate, Ru_2NO; the σ_{33} shielding is unexpectedly high.

The apical nitrosyls show a remarkable variation in the span and skew, while the isotropic shift δ is maintained at 680−780 ppm, except for higher shielding with S_4 ligation of cobalt. All components reflect significant mixing of the nitrogen and the cobalt paramagnetic circulations (more precisely, the out-of-plane components of the ligand field circulations deshielding cobalt), as observed in solution studies showing some correlation of ^{15}N and ^{59}Co shifts.[129]

Because of the large effects of relatively small changes in small excitation energies, sensitivity may be expected to the internal MNO geometry and to the conformation of the nitrosyl relative to the ligators in the basal plane. The ligand field is also sensitive to the location of cobalt (usually above the plane), to the ligation, and to the bite of the chelate ligands. The nitrosyl oxygen may lie over a gap between two chelate ligands as in $[Co(NO)(ketox)_2]$ and $[Co(NO)(esal)_2]$, or over an electron acceptor such as a phosphine. It lies over the ethylene bridge in [Co(NO)(7-mesalen)] and [Co(NO)(salen)], over a linear nitrosyl in $[RuCl(^{15}NO)_2(PPh_3)_2]^+$, over sulfur in $[Co(NO)(S_2CNMe_2)_2]$, over oxygen in [Co(NO)(acacen)], and over nitrogen in [Co(NO)(benacen)].

The remarkable variation of the tensor components in Table 9 may involve the effects of the conformation of the nitrosyl relative to the ligand field of the coligands in the plane, and the small barrier to rotation of the nitrosyl which is disordered in many of the crystal structures. Torsional variation could account for compensatory effects in the tensor components, with σ_{22} and σ_{33} decreasing as σ_{11} increases, decreasing the span while maintaining the isotropic shift.

A low torsional barrier and the sensitivity of the projecting nitrosyl to intermolecular forces are shown by the unusual nitrogen tensors observed for $[Co(^{15}NO)(TPP)]$ at ambient temperatures, which demonstrate swinging or spinning of the nitrosyl in the solid state.[184] The isotropic shift is that of a bent nitrosyl, but from room temperature down to 220 K the tensor shows axial symmetry ($\kappa = 1$) and a small span, 242 ppm. The full span of 1655 ppm and nonaxial symmetry appeared when

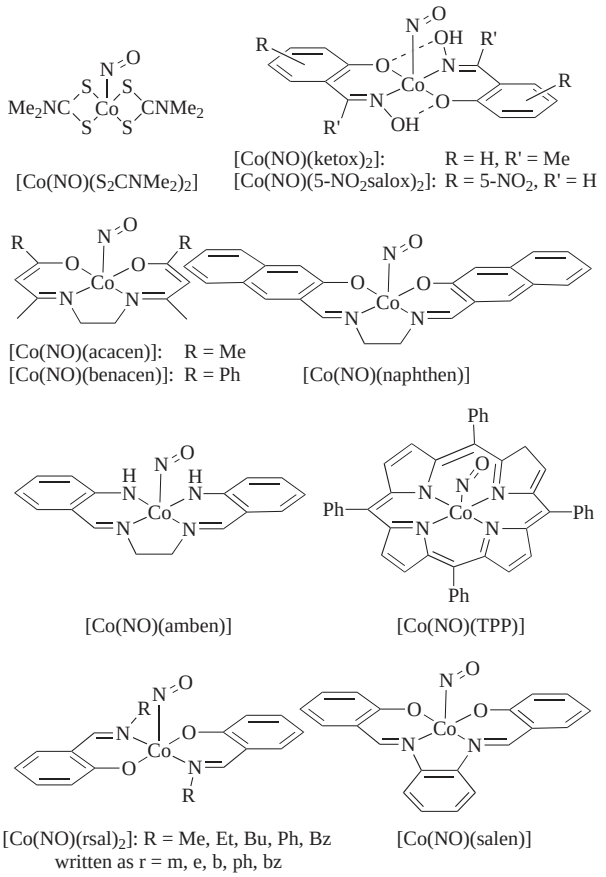

Figure 5 Structures of complexes with a bent apical nitrosyl ligand

the sample was cooled to 200 K, with little change in isotropic shift.

No intermediate rate behavior was observed and differential scanning calorimetry showed a phase transition in the solid at 206.7 K with ΔH = 649 J mol^{-1}. The lattice presumably relaxes at this temperature, allowing the nitrosyl to revolve about the C_4 axis at higher temperatures. A CoNO angle of 127° calculated from the tensor measurements agrees with the value of ≤128.5° estimated from the X-ray diffraction study at ambient temperatures.[185] This showed a fourfold disorder of the nitrosyl depicted in a many-headed 'hydra' diagram, the oxygen lying in the gap between two porphin nitrogens. This picture, therefore, is that of a swinging nitrosyl.

5.6 Theoretical Calculations of Nitrogen Shielding Tensors

Several ab initio methods are now being used with some success for the calculation of shielding tensors,[149] including the local-origin methods IGLO[186] and LORG.[187] Agreement with experiment is good for singly bonded molecules with high electronic excitation energies. It is less good when excitation energies are low, and for species with multiple bonds and lone pairs on the nucleus in question. This presents hazards in nitrogen studies, particularly in groups containing oxygen.

IGLO calculations[188] of nitrogen shieldings for a range of compounds have been analyzed in terms of the contributions from bonding electrons and lone pairs. The calculations show very small deshielding in NH_3, and greater deshielding on substitution of H by Me, then NH_2, OH, or F, with strong effects on the lone-pair contribution. The Cl and Ph groups behave as weakly electronegative substituents. Strong deshielding is found when the nitrogen is doubly bonded, with some exaggeration of the paramagnetic effect in the calculation. In aromatic azines, the calculations reflect the deshielding observed from pyrrole (with no n → π^* state) to pyridine and to pyridazine (with two adjacent nitrogens).

In molecules with low excitation energies the inclusion of electron correlation to second order, as in the SOLO (second-order LORG) method,[189] produces considerable improvement, as in a study of nitrite and nitrate ions.[178] There is further improvement with the inclusion of six surrounding cations for nitrite ion. The decrease in shielding with lengthening of the NO bonds, or, for nitrite, with an increase in the bond angle, shows that vibrational corrections are also significant.

6 PATTERNS OF NITROGEN SPIN–SPIN COUPLINGS

Figures 6–8 give ranges of one-bond J couplings between ^{15}N, ^{1}H, and ^{13}C in functional groups. Couplings to nitrogen are more commonly measured in ^{15}N than in ^{14}N resonance because of ^{14}N line broadening by quadrupolar relaxation. A large number of ^{14}N couplings have been measured, however, under favorable conditions of high local electronic symmetry and short correlation times (Section 3.2). All four ^{14}N couplings could be measured with accuracy in the linear cation RC≡NXeF$^+$.[114] More measurements of ^{14}N and other quadrupolar nuclei, such as the two ^{14}N^{17}O couplings measured in N_2O, are expected with the growing use of supercritical fluids.[105]

Values of $J(^{14}\text{N,X})$ are 30% smaller than $J(^{15}\text{N,X})$ values and opposite in sign, following the respective values of the magnetogyric ratios γ for ^{14}N and ^{15}N, as shown in equation (13):

$$-{}^{n}J(^{15}\text{N,X}) = 1.403\,{}^{n}J(^{14}\text{N,X}) = {}^{n}K(\text{N,X}) \times h\gamma_{\text{N}}\gamma_{\text{X}}/4\pi^2 \qquad (13)$$

Here K is the reduced coupling constant, which is independent of the nucleus, and n is the number of bonds through which the nuclei are coupled. The quantity J is in Hz and K is in N A^{-2} m^{-3}. Couplings to nitrogen are relatively small since the γ values are rather small. Couplings producing a 1:1 doublet in ^{15}N resonance produce a 1:1:1 triplet in ^{14}N resonance because of the three combinations of orientations for a nucleus with I = 1.

Figure 6 shows that ^{1}J(N,H) values are negative, becoming more negative with increasing s character in the N–H bonding orbital, from sp^3 hybridization of the nitrogen as in NH_4^+ or amines, to sp^2 as in the pyridinium ion pyH$^+$, and to sp as in the nitrilium ion RC≡NH$^+$. Linear equations have been given which relate the coupling to the percentage s character in the nitrogen orbital.[197–199] These equations, and a corresponding equation relating ^{1}K(C,N) to the product of the percentage s character in the nitrogen and carbon orbitals,[197] fail when there are lone pairs with s character on one or both of the coupled nuclei, and may fail in the presence of multiple bonding.

Values of ^{1}J(N,H) are reduced significantly in absolute magnitude by the presence of (s-type) lone pair electron density on nitrogen. The smallest couplings involve bent nitrogen in ketimines $R_2C{=}NH$ or diazenides M–N=NH,

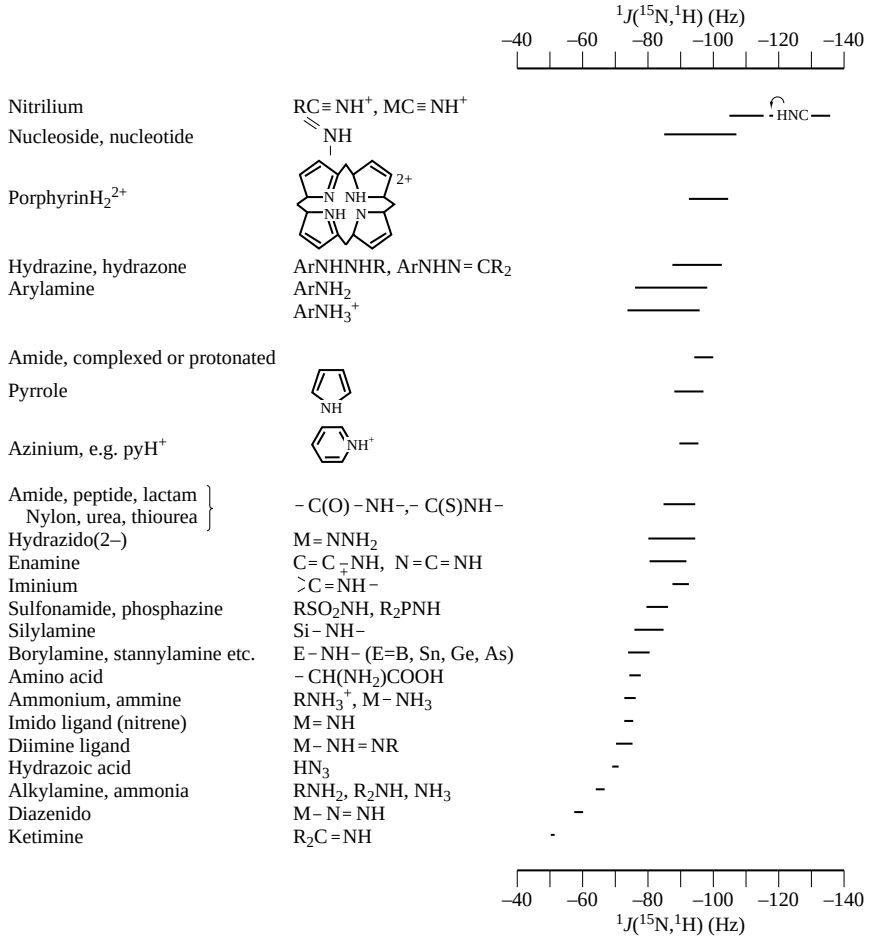

Figure 6 Ranges of $^1J(^{15}N,^1H)$ values

and those for amines or ammonia are small. Similarly, ^1J(N,H) values increase significantly in magnitude with the loss of lone pair electron density on nitrogen by coordination, delocalization (as in aniline), or protonation. They also increase with hydrogen bonding of the nitrogen, and may be solvent dependent. NH couplings may be lost through chemical exchange, and rigorous purification may be needed in order to observe them.

Couplings are increased in magnitude regardless of sign by the presence of more electronegative substituents on a coupled nucleus. Values of ^1J(N,H) are quite large in the –C(O)NH– link, present in peptides, amides, lactams, ureas, and Nylons. The values are larger if the proton is *trans* to oxygen but decrease with a departure from planarity at the nitrogen, with the development of a lone pair.

Signs reported for $^1J(^{15}N,^{13}C)$ are also normally negative, with some exceptional small positive values which change sign and increase in absolute magnitude on protonation. In pyridine $^1J(^{15}N,^{13}C)$ is +0.6 Hz, changing to −11.7 Hz on protonation and to −15.2 Hz in pyridine *N*-oxide.[200] Figure 7 shows that $^1J(^{15}N,^{13}C)$ values become more negative from azomethines $R_2{}^{13}C{=}{}^{15}NR$, with a lone pair on the nitrogen, to amines, and to ynamines $RC{\equiv}{}^{13}C{-}{}^{15}NR'_2$, in which there is no lone pair on the nitrogen. Such changes may thus be stereochemically diagnostic. In oximes $R_2C{=}NOH$, in which the nitrogen is pyramidal, the *Z* form is flatter than the *E* form thus reducing *cis* repulsions and, as expected, $^1J(^{15}N,C)$ is more negative for the *Z* than for the *E* form. Values of $^1J(^{15}N,C)$ are quite large in magnitude for pyrroles, in which the nitrogen 'lone pair' is of the p type.

Signs reported for $^1J(^{15}N,^{15}N)$ couplings are negative, but many are still unknown so the values in Figure 8 have been plotted regardless of sign. Values of $^1J(^{15}N,^{15}N)$ are generally small in magnitude when terminal nitrogen is involved, as in diazo compounds R_2N_2, N_2O, or dinitrogen ligands. Similarly in azides $RN_\alpha N_\beta N_\gamma$, which are bent at N_α, $^1J(^{15}N,^{15}N)$ couplings are much smaller for $N_\beta N_\gamma$ than for $N_\alpha N_\beta$. The couplings are very small, around 1 Hz, in arene-diazonium compounds $ArNN^+$. Many of these values are the result of complex effects of lone pairs and multiple bonds. Somewhat larger values are observed when the nitrogen is bonded to oxygen.[201]

Geminal couplings $^2J(^{15}N,H)$ and $^2J(^{15}N,C)$ are usually negative and relatively small. They become more negative if the nitrogen carries a *cis* or proximate lone pair, the more so if this lies in the NXH or NXC plane. Thus $^2J(^{15}N,H)$ is −3 Hz in pyH^+ but −11 Hz in pyridine. Such values are diagnostic of the geometry, and of protonation or coordination of the nitrogen. Couplings of the type $^2J(^{15}N,^{15}N)$, as observed in nucleotides for example, show similar lone-pair effects. Values of $^3J(^{15}N,H)$ also are increased in magnitude by a *cis* or proximate lone pair on the nitrogen as in oximes, and the magnitude increases with protonation of the nitrogen as

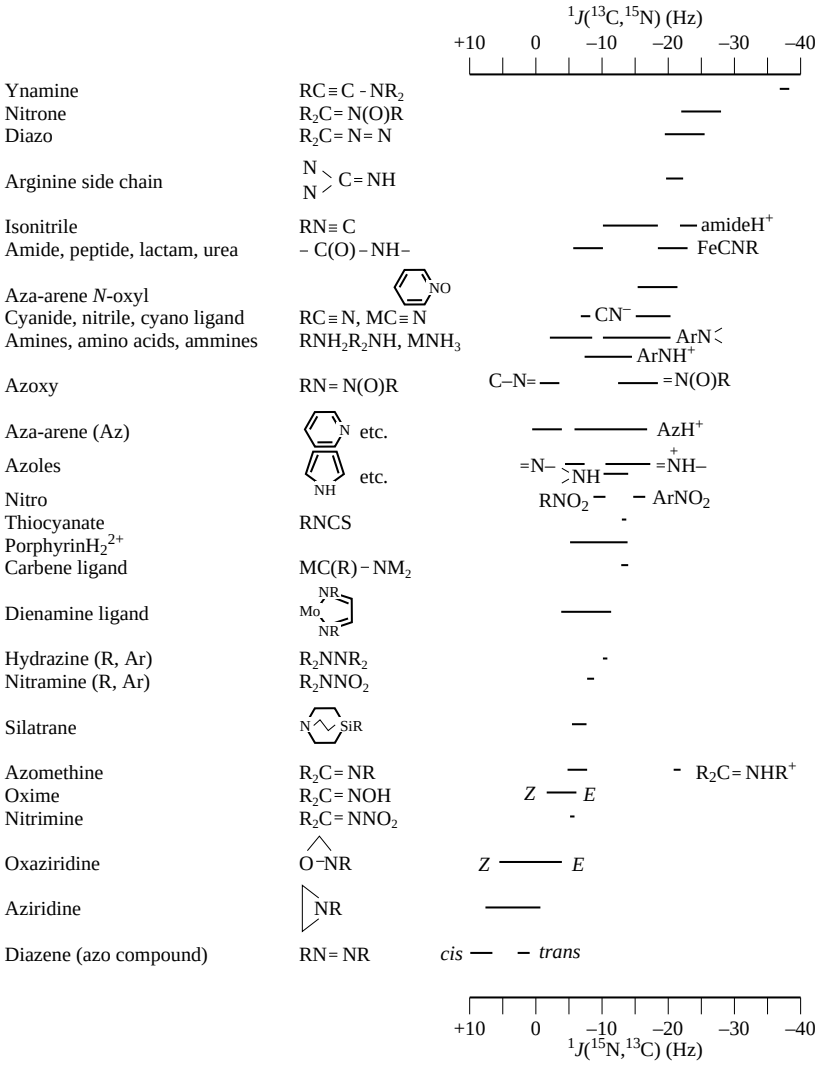

Figure 7 Ranges of $^1J(^{13}C,^{15}N)$ values

in pyridine. Values of $^3J(^{15}N,C,C,H)$ often show a Karplus-type dependence on the dihedral angles, and are of use in conformational studies of peptides in which the ^3J values may be larger than ^2J values of similar type.[202]

6.1 Contact, Orbital, and Spin–Dipolar Contributions to the Coupling[190,194,203–206]

Nitrogen couplings are sensitive to the s,p character of the bonding and to the presence and orientation of a lone pair with s character on the nitrogen, because the Fermi contact interaction of s electrons with the nucleus is usually the most important contribution to the coupling. The coupling patterns are usefully interpreted by means of the Dirac vector model[207] of the contact interaction (even though this model is incomplete, and sometimes misleading). Electrons in a bonding pair with antiparallel spins $\alpha\beta$ correlate their motions so that if the α spin is near one nucleus the β spin is near the other. For a nucleus with positive γ, the electron–nuclear configuration is more stable when the spins are antiparallel since $\gamma\epsilon$ is negative. The values of $^1J(X,Y)$, therefore, are normally positive, the difference hJ between the energy states with antiparallel and parallel spins being positive by definition. Corresponding values for $^1J(^{15}N,Y)$ are negative since $\gamma(^{15}N)$ is negative. The coupling increases in absolute magnitude with an increase in s character in the orbitals forming the bond between the coupled nuclei. Similarly, couplings are increased by the presence of more electronegative substituents on a coupled nucleus, since these demand greater p character, leaving more s character in the bond which is the coupling pathway.

Lone pair electron density on either or both of the coupled nuclei alters this picture. Figure 8 shows that if one of the coupled nuclei carries a lone pair, $^1J(N,C)$ diminishes in absolute magnitude by an amount that increases with the s character of the lone pair, e.g. from RNH_2, sp^3, to pyridine, sp^2 (though not to nitriles RCN, sp). As demonstrated in calculations of C–N and N–N couplings, the contribution to the Fermi contact term J^{fc} from the lone pair electrons is opposite in sign to that of the bonding electrons, since the nonbonding MO is antibonding with respect to the coupling pathway. Furthermore, the lone-pair contribution may be quite large, since the energy denominator is small for nonbonding

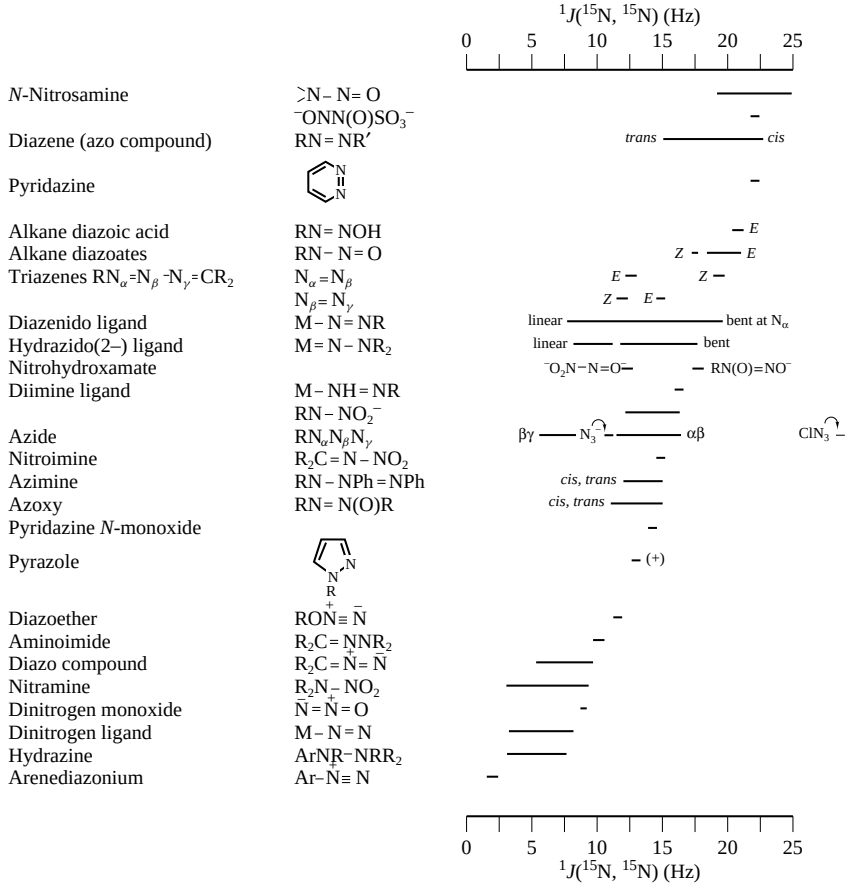

Figure 8 Ranges of $^1J(^{15}N,^{15}N)$ values

electrons. The most important energy term is that of the lowest singlet–triplet excitation, unpairing the electrons.

The changes in sign of $^1J(^{15}N,C)$ in Figure 8 can be understood in these terms. Thus, $^1J(^{15}N,C)$, which is commonly negative, becomes less negative and may become positive when the nitrogen carries a lone pair as in pyridine or *cis*-diazenes R–N=N–R. The value of $^1J(^{15}N,C)$ becomes negative again if the nitrogen is protonated.

Values of $J(^{15}N,^{15}N)$ may vary in a complex fashion if there is a lone pair on each of the nuclei. The coupling constant is very sensitive to the dihedral angle ϕ between the lone-pair orbitals, since they interact to give bonding and antibonding (HOMO) combinations. Calculations on hydrazine, N_2H_4, in which ϕ is near 90° show that $^1J(^{15}N,^{15}N)$ is negative and quite large for an N_2H_4 molecule with $\phi \approx 0°$, falling to zero for the geometry with ϕ = 115° and increasing to a large positive value for $\phi \approx 180°$.[207] Similarly, for planar systems such as diazenes as in azo compounds (RN=NR) or diazenido complexes (M–N=NR), $^1J(N,N)$ values are large and negative for *cis* compounds with $\phi \sim 0°$, but large and positive for *trans* compounds, with $\phi \approx 180°$. In longer range couplings, 'through-space' orbital overlap provides an additional route for the transmission of coupling information.

The contributions to the spin–spin coupling that are mediated by p,d,.. electrons are normally smaller than the contact contribution J^{fc}, and are very small for hydrogen, but may be sizeable if π bonding is present. The orbital term J^{o}(A,B) arising from the magnetic effect on nucleus B of the orbital motion of an electron on nucleus A, and the spin–dipolar term J^{sd}(A,B) arising from direct interaction of the spin of an electron on nucleus A with the spin (magnetic dipole) of nucleus B, increase in magnitude with the bond order. In the dinitrogen molecule N≡N with $^1J(^{15}N,^{15}N)$ = 2.5 Hz,[45] a theoretical study[208] found that the contact term made the smallest contribution, 0.82 Hz, compared with a dipolar contribution of −1.57 Hz and an orbital contribution of 3.35 Hz. Orbital and spin–dipolar contributions are large in the triply bonded molecules HCN, nitriles, and isonitriles.

The noncontact contributions, also, increase in magnitude when there are electronegative substituents on the coupled nuclei, because of a dependence on the radial term $\langle r^{-3}\rangle_{2p}$. Contact and noncontact contributions are all large in the benzonitrile *N*-oxide 2,4,6-$C_6Me_3H_2CNO$, giving an unusual overall value $^1J(^{15}N,^{13}C)$ = (−)77 Hz.[204]

6.2 Couplings to Other Nuclei

Nitrogen couplings to other nuclei are normally dominated by the contact interaction. They are sensitive to s character in the relevant bonding orbitals and to the presence of lone-pair electrons. Discussion of the signs is most usefully in terms of the reduced coupling constant K since $\gamma(^{15}N)$ is negative: thus, nitrogen couplings to fluorine are commonly measured in ^{14}N resonance as they are relatively large and the fluoro systems usually have low viscosity.

The periodic trends can be rationalized in terms of stabilization of bonding σ MOs and destabilization of nonbonding (lone pair) MOs with an increase in atomic number down the group or across the row of the Periodic Table. Amine–borane or aminoborane couplings ^1K are positive (and relatively small). Values of ^1K(C,N) and ^1K(Si,N) are normally positive, but ^1K(Sn,N) values may be of either sign and ^1K(Pb,N) values are negative. Couplings to transition metals are normally positive.

Couplings of the type ^1K(P,N) involving P(III) are negative as for ^1K(N,N), while couplings to P(V) may be of either sign. Couplings of the type ^2K(P,N) are usually small, but may be quite large for *trans* interactions in metal complexes.

Values of $^1K(^{19}F,N)$ are expected to be negative because of the lone-pair contribution. The largest value is $^1J(^{19}F,^{14}N)$ = 339 Hz in $FN{\equiv}NF^+$, corresponding to the maximal $^1J(^{15}N,H)$ = 135 Hz in the nitrilium ion $HC{\equiv}CNH^+$. The value of $^1J(^{19}F,^{14}N)$ is 231 Hz in $NF_4{}^+$ compared with 158 Hz in NF_3, another lone-pair effect.[28]

Ligating nitrogen is relatively low in the empirical series of *trans* influence, though above halides or alkoxy ligands. The *trans* influence measures the tendency of a ligand by forming a strong bond to the metal to weaken the *trans* bond in a metal complex, so reducing the magnitude of coupling constants involving the *trans* bond.

6.3 Couplings as Criteria of Structure

Nitrogen couplings may be diagnostic of *cis–trans* or *syn–anti* stereochemistry, conformation, hydrogen bonding, and related medium effects. The couplings are enhanced by protonation, alkylation, or coordination of the nitrogen, and so may be diagnostic of chelation or proton migration. The largest magnitudes of couplings are observed in linear systems. In ligands which may be bent or linear in their attachment to a metal, such as nitroso (–N=O), diazenido (–N=N–R), or hydrazido(2–) (=N–NR_2) ligands, M–N_α coupling constants are reduced on bending; the protonation of the bent α-nitrogen in $[PtCl(N{=}NPh)(PEt_3)_2]$ increases the $^1J(^{195}Pt,^{15}N)$ value from 157 to 510 Hz.[125] Couplings are also enhanced by flattening of a pyramidal group, delocalizing the s-type lone-pair electron density. Thus ^1J(N,H) values in the hydrazido(2–) ligand –N–NH_2 resemble those in amides rather than hydrazines, since the hydrazido(2–) ligand is flat.

Such relationships allow coupling constants to be estimated as required to optimize the experimental parameters. Equations relating ^1J values to percentage s character in the bond[197–199] can be used in this way if exceptional bond types are avoided.

7 SOLID STATE STUDIES[6,7,13,14]

The fast growth of nitrogen NMR studies in the solid state is documented in the annual reports of work on solid state techniques, macromolecules, natural and synthetic, and shielding tensors (Section 5).[7] Solid state NMR spectroscopy is increasingly being used in materials technology and for biological materials. Because of the volume of this work, reference can only be selective and directed towards new techniques or reviews.[209,210]

Molecular biology has seen a great increase in nitrogen NMR.[168,211,212] Peptide and protein backbones, planes, and side-chains can be studied with improved methods of orienting samples mechanically or magnetically. Ordered systems such as nucleoproteins or membrane–protein complexes[213] which are insufficiently soluble or mobile for solution studies, or insufficiently ordered for X-ray diffraction techniques, are becoming accessible to NMR study. Solid state NMR can provide spatial information which is lost by tumbling motions in solution, and can also monitor motions which are frozen or blurred in X-ray crystallographic studies.

For many systems, a combination of physical methods is needed; NMR to probe short-range interactions and X-ray crystallography methods showing long-range order.[214] Solid state NMR provides a useful link between X-ray crystallographic analysis and NMR solution studies, particularly as conformations may vary from solid to more fluid phases. Nitrogen spectra of biological material may be easier to interpret than carbon or proton spectra because of the relatively small number of nitrogens, characteristic shifts, and sizeable shielding range.

Nitrogen-14 properties measured in the solid state include electric field gradient (efg) tensors, quadrupole couplings, dipolar couplings, and spin diffusion[215] in studies of molecular structure and reorientation. Orientations of the ^{14}N efg tensors and carbonyl ^{13}C shielding tensors provide structural information in amino acids and peptides.[216] N–H bond lengths have been determined with high accuracy from dipolar interactions of ^{14}N or ^{15}N with ^1H.[217] Static ^{14}N powder spectra were used to study electric field gradients and reorientation in NH_4NCS.[218] Information on ^{14}N dipolar and quadrupolar couplings is also obtained by lineshape analysis of resonances of a bonded neighbor, whether ^{13}C,[219] ^{29}Si in nitrogen-containing ceramics,[220] ^{195}Pt in $K_2[Pt(CN)_4 \cdot 3H_2O]$,[221] etc.

Advantage can be taken of the high natural abundance of ^{14}N by using the ^{14}N nuclear quadrupole interaction to spread nitrogen spectra over a large range, more than compensating for quadrupolar line broadening. This method was used in ^{14}N and ^{13}C measurements of the CCN geometry and ^{14}N quadrupole coupling tensor in glycine single crystals.[57] The quadrupole interaction shifts the middle of the three ^{14}N energy levels (I = 1) relative to the other two, and produces a doublet splitting which is determined by the angular dependence of the first order quadrupole interaction. The second order quadrupole interaction, arising from the closeness of the Larmor and the quadrupole coupling frequencies, shifts the doublet somewhat and makes the overtone transition partially allowed. Information is thus available from the combination of the ^{14}N quadrupole splittings, second order ^{14}N quadrupole shifts, ^{14}N overtone frequencies, $^{14}N–^1H$ and $^{14}N–^{13}C$ dipolar splittings, and ^{13}C shielding tensor for determining orientations in a peptide plane in oriented samples. Cross polarization is very effective for ^{14}N spectra in amino acids, peptides, and proteins, because of strong NH coupling in the amido/peptide group. Peptide backbone conformations have been studied in this way by two-dimensional $^1H/^{14}N$ spectra and crystalline amino acids by $^{13}C/^{14}N$ spectra, with use also of $^1H/^{13}C/^{14}N$ triple resonance.[58,222]

Most nitrogen work in the solid state is done in ^{15}N resonance, using the techniques developed for ^{13}C of static powder patterns or CP MAS methods with high-power

proton dipolar decoupling. The principal components of the shielding tensors (Section 5) are obtained from powder pattern lineshapes, or from the intensities of spinning side-bands at slower spinning rates. The orientation of the principal axis system in the molecular frame is found by the use of oriented specimens or by the observation of dipolar interactions.[145,147]

Some solid state work has been done in natural abundance of ^{15}N, for example polymer studies of the α-helix and β-sheet components of homopolypeptides[223] and Nylons,[224] and of polyimines and the conducting polymers which they yield on oxidation.[225] Adsorption studies may be possible in natural abundance of ^{15}N, the occlusion of NPr_4^+ cations in zeolites[226] for example. Enrichment is usually necessary, however, and bioenrichment is particularly useful.

In a historic determination in 1972, the principal elements were reported for the nitrogen shielding tensor in the nitrate ion in ammonium nitrate, distorted by hydrogen bonding.[227] Recently, the principal values of the nitrate shielding tensors in five solid phases of NH_4NO_3, the phase transitions, crystal packing deformations, motional averaging at higher temperatures, and magnetic nonequivalence at low temperatures, have been examined by MAS and static NMR.[228] Section 5 discusses shielding tensors reported for nitrogen in ammonia and ammines, linear groups (iminophosphenium $RN{\equiv}P^+$, nitrile, isonitrile, N_2O, thiocyanate, N_2, the dinitrogen ligand, $P{\equiv}N$, linear NO), planar groups (amide, peptide, heterocycle, aldimine, ketimine, oxime, nitroso dimer, nitrobenzene, nitrates, nitrite ion, nitroso compounds, azo or diazene, nitrogen oxides), and metal nitrosyls, linear and bent.

The nitrogen tensor has been used as a criterion of bending of the nitrosyl ligand (Section 5),[183] and to investigate nitrosyl swinging in solid [Co(NO)TPP)],[184] and the bent–linear fluxionality of the five-coordinate complex $[RuCl(NO)_2(PPh_3)_2]BF_4$ in solution.[24]

Catalytic processes are usefully investigated by ^{15}N CP MAS NMR. Acid sites of the Brønsted or of Lewis type may be distinguished by nitrogen compounds of differing basicity, as in studies of γ-alumina and mordenites by the sorption of pyridine or ammonia,[229,230] and of zeolites by the sorption of ammonia[231] or trimethylamine,[232] cf. the interaction of pyridine with coals.[233] Some adsorption work can be done by conventional NMR techniques, as in the study of acetonitrile on zeolites.[234]

Double cross polarization in doubly labeled $^{13}C-^{15}N$ bonds, usually from ^1H to ^{13}C to ^{15}N, was developed to follow the progress of these bonds in vivo, in peptide and other linkages, an early application being to protein turnover in soybean leaves.[235]

The transferred echo double resonance (TEDOR) technique has been used to select a ^{13}C label by its dipolar coupling to ^{15}N, giving internuclear distances and geometries, in conjunction with the rotational echo double resonance (REDOR) technique measuring a dipolar coupling of the ^{13}C.[236]

Biological NMR studies using solid state techniques are discussed further in Section 9.

8 DYNAMICS[2–7,237,238]

Dynamic processes with a range of timescales have been monitored by nitrogen NMR. Fast motions such as the switching of the ammonium ion in the $^{14}NH_4Cl$ lattice are monitored by relaxation times (Section 3.1). Measurements of T_1 and NOE of the dipolar relaxation of ^{15}N by neighboring protons have been used to probe a variety of molecular motions, from segmental motions of large molecules to migrations of protons between nitrogens (Section 2). HH migrations between the nearby nitrogens, as in porphin or phthalocyanine molecules, were mentioned in Section 2.1, and a range of comparable systems has now been studied,[239] most recently, double, triple, and quadruple proton transfers in pyrazoles.[240]

Hindered motions about N–X bonds are studied by lineshape analysis, 2D spectroscopy, multicoalescence experiments, saturation transfer, or equilibration methods, or by methods involving longitudinal or transverse relaxation times. A large number of isomerization processes involving N–X bonds have been reviewed as to methods of investigation, dynamics, thermodynamics, and theoretical interpretation in terms of quantum mechanical treatments or empirical correlations.[241]

Examples of dynamic studies are fewer in inorganic chemistry. $^{14,15}N$ NMR spectroscopy has demonstrated kicking motions, as in the bent–linear fluxionality of the imido ligand M=NH in concert with a second imido or an alkoxy ligand in solution.[139] A corresponding fluxionality of nitrosyls in solution was observed for the five-coordinate complex $[RuCl(^{15}NO)_2(PPh_3)_2]^+$,[24] the averaged shift, the temperature dependence, and the equilibrium isotope effect with semienrichment suggesting that the trigonal bipyramidal form with two linear nitrosyls is present in dynamic equilibrium with the square-pyramidal form with one bent and one linear nitrosyl.[24] Swinging and spinning of the bent apical nitrosyl in solid $[Co(^{15}NO)(TPP)]$ was detected through changes in the nitrogen shielding tensor[184] (Section 5.5).

CIDNP enhancing absorption or emission in the NMR experiment, has been used in ^{15}N resonance to study a number of reactions in which radical pairs may be involved. The method is highly sensitive and species that give large signals may not be major intermediates. The contribution of radical pair mechanisms to the nitration of arenes by nitric and sulfuric acid mixtures is now thought to be small.[242] ^{15}N CIDNP has also been applied to the study of migrations of nitro groups,[243] azo coupling,[244] and the loss of dinitrogen from arene-diazonium salts.[245] Stable nitroxide radicals, also, are accessible to NMR spectroscopic study.[246]

9 BIOMOLECULES[2–7,9,13]

Biological applications of nitrogen NMR have increased in step with the development of NMR technology and have stimulated this development. Many examples of ^{14}N and ^{15}N NMR properties in biological materials have been given above together with the kinds of information now obtainable. Multidimensional correlation spectroscopy increasingly uses nitrogen as well as ^{13}C and ^1H.[6d,7] Other articles describing the use of nitrogen NMR in biomolecular and biological systems are listed at the end of this section.

Unique information can be obtained from nitrogen NMR on in vivo metabolism and cellular dynamics, as well as on protein (polypeptide) backbones, functional groups in enzymes, and DNA and RNA bases. Nitrogen-14 resonance may be used for material in which there is sufficient mobility for motional

averaging[247,248] and with solid state techniques making use of the quadrupolar interaction (Section 7). Bioenrichment of ^{15}N allows this to be used as a biological tracer in the absence of a stable radioisotope of nitrogen (^{13}N, the most stable, has a halflife of only 10 min). Highly selective bioenrichment can be obtained by supplying the organism with a ^{15}N-labeled nutrient, such as an amino acid. For ^{15}N work in the liquid phase, the dependence of the relaxation time T_{1dd} and the NOE on the molecular size has been discussed (Section 2.1).

Techniques and applications to biological systems have been described in a number of reviews[249] dealing with nucleic acids and nucleotides, enzyme systems, and intact cells,[250] amino sugars,[251] intermolecular interactions,[252] solid state peptide studies,[168] and work of pharmacological interest.[253,254] Nitrogen-15 spectra can resolve differences between diastereotopomers, as of 8-benzyl-5,6,7,8-tetrahydroquinoline in solutions of optically active carboxylic acids.[255]

In living cells, molecules that are sufficiently mobile can be studied by solution state techniques and bioenrichment of ^{15}N has been used to advantage. The first in vivo study was of a fungus *Ustilago sphaerogena* grow with ^{15}N-ammonium acetate as a nitrogen source, the resonances of small peptides being observed.[256] The mobilities of components of bacterial cell walls were estimated quite early on from ^{15}N NOE values, the observable resonances being those of mobile cross-linking groups.[257] The biosynthesis of amino acids from ^{15}N-ammonium salts and their intracellular environment was followed in the fungus *Neurospora crassa*[258] and in *Brevibacterium lactofermentum*.[259]

Nitrogen NMR is being used increasingly in metabolic studies using solid state techniques. In DNA from *E. coli* grown with $^{15}NH_4Cl$ as the source of nitrogen, 13 of the 14 nitrogens in the bases were distinguished by their dipolar coupling to protons.[260] This allowed the NH bond lengths to be measured, complementing the information available from X-ray and neutron diffraction.[261] DNA and protein spectra were obtained from the filamentous bacteriophage fd infecting the *E. coli*, and 2D spectra from oriented molecules of the virus.[262]

Solid state techniques have been developed for the study of nitrogen metabolism in growing plants using double cross polarization (DCP MAS) NMR (Section 8). This required double enrichment in vivo with $^{15}NH_4{}^{15}NO_3$ and pulsed $^{13}CO_2$ labeling, to form $^{13}C-^{15}N$ bonds, examined in intact or lyophilized material. Such DCP MAS NMR has been used to follow the metabolism of methionine[263] in soybean cotyledons, and also of allantoin[264] and alanine[265] in *Aerococcus viridans*.

Double labeling can establish biosynthetic pathways, such as cyclization to form the N–C(5) bond in isopenicillin N observed as a $^1J(^{15}N,^{13}C)$ coupling.[266]

With a variety of techniques, therefore, in vivo observation of components of appropriate mobility is now replacing the use of lyophilized (freeze-dried) tissue. Indeed, ^{15}N-labeled glycine has been detected by a probe implanted between the liver lobes, fixed to the abdominal wall, of a live rat.[267]

10 RELATED ARTICLES

Amino Acids, Peptides and Proteins: Chemical Shifts; Bacteriorhodopsin and Rhodopsin; Biosynthesis and Metabolic Pathways: Carbon-13 and Nitrogen-15 NMR; Carbon and Nitrogen Chemical Shifts of Solid State Enzymes; Shielding Calculations: LORG and SOLO Approaches; Chemical Shift Tensor Measurement in Solids; Chemical Shift Tensors; Chemical Shifts in Biochemical Systems; Chemically Induced Dynamic Nuclear Polarization; Coupling Through Space in Organic Chemistry; Dipolar and Indirect Coupling Tensors in Solids; Indirect Coupling: Semiempirical Calculations; Membrane Proteins; Nucleic Acid Structures in Solution: Sequence Dependence; Nucleic Acids: Chemical Shifts; Nucleic Acids: Spectra, Structures, and Dynamics; Organic Chemistry Applications; Overtone Spectroscopy of Quadrupolar Nuclei; Peptides and Polypeptides; Protein Dynamics from NMR Relaxation; Protein Dynamics from Solid State NMR; Protein Structures: Relaxation Matrix Refinement; Quadrupolar Nuclei in Glasses; Quadrupolar Nuclei in Solids; Ruby NMR Laser; Shielding Calculations: IGLO Method; Shielding: Overview of Theoretical Methods; Shielding in Small Molecules; Shielding Tensor Calculations; Shielding Theory: GIAO Method; Sideband Analysis in Magic Angle Spinning NMR of Solids; Solid Biopolymers; Solid Polymers: Shielding and Electronic States; Spin Diffusion in Solids; Structures of Larger Proteins, Protein-Ligand, and Protein-DNA Complexes by Multi-Dimensional Heteronuclear NMR; Synthetic Peptides.

11 REFERENCES

1. W. G. Proctor and F. C. Yu, *Phys. Rev.*, 1950, **77**, 717; W. G. Proctor and F. C. Yu, *Phys. Rev.*, 1951, **81**, 20.
2. G. C. Levy and R. L. Lichter, *^{15}N NMR Spectroscopy*, Wiley-Interscience, New York, 1979, pp. 1–221.
3. G. J. Martin, M. L. Martin, and J.-P. Gouesnard, *NMR Basic Principles Prog.*, 1981, **18**, 341.
4. M. Witanowski and G. A. Webb, *Annu. Rep. NMR Spectrosc.*, 1972, **5**, 395.
5. M. Witanowski and G. A. Webb (eds.), *Nitrogen NMR*, Plenum Press, London, 1973, pp. 1–403.
6. M. Witanowski, L. Stefaniak, and G. A. Webb, *Annu. Rep. NMR Spectrosc.*, 1977, **7**, 117; M. Witanowski, L. Stefaniak, and G. A. Webb, *Annu. Rep. NMR Spectrosc.*, 1981, **11B**, 1; M. Witanowski, L. Stefaniak, and G. A. Webb, *Annu. Rep. NMR Spectrosc.*, 1986, **18**, 1; M. Witanowski, L. Stefaniak, and G. A. Webb, *Annu. Rep. NMR Spectrosc.*, 1993, **25**, 1.
7. *Specialist Periodical Reports on Nuclear Magnetic Resonance*, Royal Society of Chemistry, London, UK, 1972–94, Vols. 1–23, et seq.
8. E. W. Randall and D. G. Gillies, *Prog. NMR Spectrosc.*, 1970, **6**, 119.
9. J. D. Roberts, in *Bloch Festschrift*, Rice University Press, Houston, TX, USA, 1980.
10. J. Mason, *Chem. Rev.*, 1981, **81**, 205.
11. R. L. Lichter, in *The Multinuclear Approach to NMR Spectroscopy*, eds. J. B. Lambert and F. G. Riddell, Reidel, Dordrecht, 1983, Chap. 10, pp. 207–244.
12. J. Mason, *Chem. Br.*, 1983, 654.
13. W. von Philipsborn and R. Müller, *Angew. Chem., Int. Ed. Engl.*, 1986, **25**, 383.
14. J. Mason, in *Multinuclear NMR*, ed. J. Mason, Plenum Press, New York, 1987, Chap. 12, pp. 335–367.
15. M. Witanowski, L. Stefaniak, S. Szymanski, and H. Januszewski, *J. Magn. Reson.*, 1977, **28**, 217 [compares reference standards; also see Witanowski et al.[6]a].

16. S. G. Kukolich, *J. Am. Chem. Soc.*, 1975, **97**, 5704.
17. A. K. Jameson, C. J. Jameson, D. Opposunggu, S. Wille, P. M. Burrell, and J. Mason, *J. Chem. Phys.*, 1981, **74**, 81; C. J. Jameson, A. K. Jameson, S. M. Cohen, H. Parker, D. Opposunggu, P. M. Burrell, and W. Wille, *J. Chem. Phys.*, 1981, **74**, 1608, give a value for (NH_3, liq.) at 223 K.
18. C. I. Ratcliffe, J. A. Ripmeester, and J. S. Tse, *Chem. Phys. Lett.*, 1983, **99**, 177; V. A. Pestunovich, B. Z. Shterenberg, E. T. Lippmaa, M. J. Miagi, M. A. Alla, S. N. Tandura, V. P. Baryshok, L. P. Petukhov, and M. G. Voronkov, *Dokl. Akad. Nauk SSSR*, 1981, **258**, 1410.
19. R. Freeman, *A Handbook of Nuclear Magnetic Resonance*, Longman, Harlow, 1987, pp. 14–16.
20. R. E. Wasylishen and J. O. Friedrich, *J. Chem. Phys.*, 1984, **80**, 585.
21. A. Lycka and P. E. Hansen, *Magn. Reson. Chem.*, 1985, **23**, 973.
22. J. M. Risley and L. van Etten, *Methods Enzymol.*, 1990, **117**, 376.
23. J. Mason, D. M. P. Mingos, J. Schaefer, D. Sherman, and E. O. Stejskal, *J. Chem. Soc., Chem. Commun.*, 1985, 444.
24. J. Mason, D. M. P. Mingos, D. Sherman, and R. W. M. Wardle, *J. Chem. Soc., Chem. Commun.*, 1984, 1223.
25. R. O. Duthaler and J. D. Roberts, *J. Magn. Reson.*, 1979, **34**, 129.
26. M. Alei, A. E. Florin, and W. M. Litchman, *J. Am. Chem. Soc.*, 1970, **92**, 4828, and refs. therein.
27. J. M. Briggs and E. W. Randall, *Mol. Phys.*, 1973, **26**, 699.
28. J. Mason and K. O. Christe, *Inorg. Chem.*, 1983, **22**, 1849.
29. M. Niibe and Y. Nakamura, *J. Phys. Chem.*, 1984, **88**, 5608.
30. D. M. Holton, P. P. Edwards, W. McFarlane, and B. Wood, *J. Am. Chem. Soc.*, 1983, **105**, 2104.
31. J. Kowalewski, *Annu. Rep. NMR Spectrosc.*, 1990, **22**, 307.
32. R. T. Boeré and R. G. Kidd, *Annu. Rep. NMR Spectrosc.*, 1982, **13**, 319.
33. G. C. Levy, J. J. Dechter, and J. Kowalewski, *J. Am. Chem. Soc.*, 1978, **100**, 2308.
34. D. D. Giannini, I. M. Armitage, H. Pearson, D. M. Grant, and J. D. Roberts, *J. Am. Chem. Soc.*, 1975, **97**, 3416.
35. N. Bloembergen, E. M. Purcell, and R. V. Pound, *Phys. Rev.*, 1948, **73**, 679.
36. D. Gust, R. B. Moon, and J. D. Roberts, *Proc. Natl. Acad. Sci. USA*, 1975, **72**, 4696; S. B. Dubin, N. A. Clark, and G. B. Benedek, *J. Chem. Phys.*, 1971, **54**, 5158.
37. A. Lapidot and C. S. Irving, *J. Am. Chem. Soc.*, 1977, **99**, 5488.
38. B. P. Bammel and R. F. Evilia, *Anal. Chem.*, 1982, **54**, 1318.
39. E. Lippmaa, T. Saluvere, and S. Laisaar, *Chem. Phys. Lett.*, 1971, **11**, 120.
40. A. D. H. Clague and J. P. C. M. van Dongen, personal communication.
41. J. B. Lambert and D. A. Netzel, *J. Magn. Reson.*, 1977, **25**, 531.
42. P. Loftus, W. H. Bearden, and J. D. Roberts, *Nouv. J. Chim.*, 1977, **1**, 283.
43. S. Donovan-Mtunzi, G. E. Hawkes, C. J. MacDonald, J. Mason, and R. L. Richards, *J. Chem. Soc., Dalton Trans.*, 1985, 2473.
44. D. Schweitzer and H. W. Spiess, *J. Magn. Reson.*, 1974, **16**, 243.
45. J. O. Friedrich and R. E. Wasylishen, *J. Chem. Phys.*, 1985, **83**, 3707.
46. B. K. Hunter and R. J. C. Brown, *J. Magn. Reson.*, 1982, **46**, 227.
47. J. Hennig and H.-H. Limbach, *J. Am. Chem. Soc.*, 1984, **106**, 292; H.-H. Limbach, J. Hennig, R. Kendrick, and C. S. Yannoni, *J. Am. Chem. Soc.*, 1984, **106**, 4059; H.-H. Limbach, D. Gerritzen, H. Rumpel, B. Wehrle, G. Otting, H. Zimmermann, R. Kendrick, and C. S. Yannoni, in *Photoreaktive Festkörper*, Karlsruhe, 1985.
48. J. H. Noggle and R. E. Schirmer, *The Nuclear Overhauser Effect*, Academic Press, New York, 1971; D. Neuhaus and M. Williamson, *The Nuclear Overhauser Effect in Structural and Conformational Analysis*, VCH Verlag, Berlin, 1989.
49. G. E. Hawkes, W. M. Litchman, and E. W. Randall, *J. Magn. Reson.*, 1975, **19**, 255.
50. C. S. Irving and A. Lapidot, *Biochim. Biophys. Acta*, 1977, **470**, 251.
51. R. Freeman, *A Handbook of Nuclear Magnetic Resonance*, Longman, Harlow, UK, 1987, pp. 157–163.
52. Y. Hiltunen, J. Jokisaari, J. Lounila, and A. Pulkkinen, *J. Am. Chem. Soc.*, 1989, **111**, 3217, and refs. therein.
53. A. Bax, R. H. Griffey, and B. L. Hawkins, *J. Magn. Reson.*, 1983, **55**, 301; L. Mueller, R. A. Schniksnis, and S. J. Opella, *J. Magn. Reson.*, 1986, **66**, 379.
54. S. Roy, M. Z. Papastavros, V. Sanchez, and A. G. Redfield, *Biochemistry*, 1984, **23**, 4395.
55. See, for example, Section 4.1 of Witanowski et al.[6]d
56. L. E. Kay, M. Ikura, G. Zhu, and A. Bax, *J. Magn. Reson.*, 1991, **91**, 422; M. Ikura, L. E. Kay, M. Krinks, and A. Bax, *Biochemistry*, 1991, **30**, 5498.
57. R. A. Haberkorn, R. E. Stark, H. van Willigen, and R. G. Griffin, *J. Am. Chem. Soc.*, 1981, **103**, 2534.
58. K. V. Ramanathan and S. J. Opella, *Trans. Am. Crystallogr. Assoc.*, 1988, **24**, 145; *J. Magn. Reson.*, 1990, **86**, 227, and refs. therein.
59. See, for example, Y. Seo and M. Murakami, *Proc. R. Soc. London, Ser. B*, 1991, **244**, 191.
60. S. H. Koenig, *Biophys. J.*, 1988, **53**, 91; S. H. Koenig, C. F. Beaulieu, R. D. Brown, III, and M. Spiller, *Biophys. J.*, 1990, **57**, 461.
61. J.-M. Lehn and J.-P. Kitzinger, *NMR Basic Principles Progr.*, 1981, **18**, 80.
62. E. A. C. Lucken, *Nuclear Quadrupole Coupling Constants*, Academic Press, London, 1969; J. A. S. Smith, *Chem. Soc. Rev.*, 1986, **15**, 225.
63. H. G. Hertz, *Ber. Bunsenges. Ges.*, 1973, **77**, 531, and refs. therein.
64. K. A. Valiyev, *Sov. Phys. JETP*, 1960, **10**, 77.
65. B. K. Hunter and R. J. C. Brown, *J. Magn. Reson.*, 1982, **46**, 227; D. F. Cooke and K. R. Jeffrey, *J. Magn. Reson.*, 1975, **18**, 455.
66. C. Deverell, *Prog. NMR Spectrosc.*, 1969, **4**, 235.
67. M. Shporer, G. Ron, and G. Navon, *Inorg. Chem.*, 1965, **4**, 358.
68. J.-P. Kintzinger and J.-M. Lehn, *Helv. Chim. Acta*, 1975, **58**, 905.
69. S. Martinengo, G. Ciani, A. Sironi, B. T. Heaton, and J. Mason, *J. Am. Chem. Soc.*, 1979, **101**, 7095.
70. A. Loewenstein, *J. Magn. Reson.*, 1982, **49**, 332.
71. M. Gourdji and L. Guibé, *C.R. Acad. Sci. Paris*, 1965, **260**, 1131; M. Gourdji, L. Guibé, and A. Peneau, *J. Phys.*, 1974, **35**, 497; A. M. de P. Nicholas and R. E. Wasylishen, *J. Phys. Chem.*, 1985, **89**, 5446.
72. A. Loewenstein and M. Brenman, *J. Magn. Reson.*, 1979, **34**, 193.
73. W. B. Moniz and C. F. Poranski, *J. Phys. Chem.*, 1969, **73**, 4145.

74. Y. Yamamoto and J. Uzawa, *Chem. Lett.*, 1978, 1213.
75. W. B. Moniz and H. S. Gutowsky, *J. Chem. Phys.*, 1963, **38**, 1155.
76. W. Suchanski and P. C. Canepa, *J. Magn. Reson.*, 1979, **33**, 389.
77. E. J. Pedersen, R. L. Vold, and R. R. Vold, *Mol. Phys.*, 1980, **41**, 811.
78. R. E. Stark, R. L. Vold, and R. R. Vold, *Chem. Phys.*, 1977, **20**, 337.
79. D. Wallach and W. T. Huntress, *J. Chem. Phys.*, 1969, **50**, 1219.
80. E. Lippmaa, T. Saluvere, and S. Laisaar, *Chem. Phys. Lett.*, 1971, **11**, 120.
81. P. O. Eriksson, A. Khan, and G. Lindblom, *J. Phys. Chem.*, 1982, **86**, 387.
82. U. Henriksson, L. Odberg, J. C. Eriksson, and L. Westman, *J. Phys. Chem.*, 1977, **81**, 76.
83. D. J. Siminovitch and K. R. Jeffrey, *Biochim. Biophys. Acta*, 1981, **645**, 270.
84. D. J. Siminovitch, M. F. Brown, and K. R. Jeffrey, *Biochemistry*, 1984, **23**, 2412.
85. A. Loewenstein and R. Waiman, *Mol. Phys.*, 1973, **25**, 49.
86. A. Maliniak, J. Kowalewski, and I. Panas, *J. Phys. Chem.*, 1984, **88**, 5628.
87. B. Ancian and B. Tiffon, *J. Chem. Soc., Faraday Trans. 2*, 1984, **80**, 1067.
88. R. E. Wasylishen, B. A. Pettit, and R. Y. Dong, *J. Chem. Soc., Faraday Trans. 2*, 1980, **76**, 571.
89. K. F. Chew, W. Derbyshire, N. Logan, A. H. Norbury, and A. I. P. Sinha, *J. Chem. Soc., Chem. Commun.*, 1970, 1708.
90. J.-M. Lehn and J.-P. Kintzinger, *Mol. Phys.*, 1971, **22**, 273.
91. N. M. Szeverenyi, R. R. Vold, and R. L. Vold, *Chem. Phys.*, 1976, **18**, **23**, 31.
92. K. T. Gillen and J. H. Noggle, *J. Chem. Phys.*, 1970, **52**, 4905.
93. B. Tiffon and B. Ancian, *J. Chem. Phys.*, 1982, **76**, 1212.
94. B. Lindman and S. Forsén, *NMR Basic Principles Prog.*, 1976, **12**.
95. R. R. Vold, R. L. Vold, and N. M. Szeverenyi, *J. Chem. Phys.*, 1979, **70**, 5213.
96. H. M. Ratajczak, J. A. Ladd, W. J. Orville-Thomas, and H. Ratajczak, *Mol. Phys.*, 1977, **34**, 1019.
97. O. R. Chambers, M. E. Harman, D. S. Rycroft, D. W. A. Sharp, and J. M. Winfield, *J. Chem. Res. (S)*, 1977, 150; *J. Chem. Res. (M)*, 1977, 1849.
98. D. C. Bradley, S. R. Hodge, J. D. Runnacles, M. Hughes, J. Mason, and R. L. Richards, *J. Chem. Soc., Dalton Trans.*, 1992, 1663.
99. M. Minelli, C. G. Young, and J. H. Enemark, *Inorg. Chem.*, 1985, **24**, 1111.
100. M. Minelli, J. L. Hubbard, K. A. Christensen, and J. H. Enemark, *Inorg. Chem.*, 1983, **22**, 2652.
101. Y. Yamamoto and J. Uzawa, *Chem. Lett.*, 1978, 1213.
102. M. Shporer, G. Ron, A. Loewenstein, and G. Navon, *Inorg. Chem.*, 1965, **4**, 361.
103. H. Hartmann and H. Sillescu, *Theor. Chim. Acta*, 1964, **2**, 371.
104. R. B. Jordan, *J. Magn. Reson.*, 1980, **30**, 287.
105. J. M. Robert and R. F. Evilia, *J. Am. Chem. Soc.*, 1985, **107**, 3733.
106. P. W. Fowler, H. M. Kelly, and R. J. C. Brown, *Chem. Phys. Lett.*, 1993, **216**, 200, and refs. therein.
107. C. J. Jameson and J. Mason, in *Multinuclear NMR*, ed. J. Mason, Plenum Press, New York, 1987, Chap. 3, p. 51.
108. J. Mason, *Adv. Inorg. Chem. Radiochem.*, 1979, **22**, 199; J. Mason, *Adv. Inorg. Chem. Radiochem.*, 1976, **18**, 197.
109. R. G. Barnes and W. V. Smith, *Phys. Rev.*, 1954, **93**, 95; T. A. Carlson, C. C. Lu, T. S. Tucker, W. W. Nestor, and F. B. Malik, *Eigenvalues, Radial Expectation Values, and Potentials for Free Atoms from Z = 2 to 126*, Oak Ridge National Laboratory, TN, USA, 1970.
110. M. B. Robin, *Higher Exited States of Polyatomic Molecules*, Academic Press, New York, Vol. I, 1974; Vol. II, 1975; and Vol. III, 1985.
111. M. Comeau, M. T. Béraldin, E. C. Vauthier, and S. Fliszar, *Can. J. Chem.*, 1985, **63**, 3226.
112. J. Mason, *J. Am. Chem. Soc.*, 1991, **113**, 6056.
113. R. O. Duthaler and J. D. Roberts, *J. Am. Chem. Soc.*, 1978, **100**, 3889; *J. Magn. Reson.*, 1979, **34**, 129.
114. A. A. A. Emara and G. J. Schrobilgen, *J. Chem. Soc., Chem. Commun.*, 1987, 1644.
115. G. J. Schrobilgen, *J. Chem. Soc., Chem. Commun.*, 1988, 863.
116. W. L. Jorgensen and L. Salem, *The Organic Chemist's Book of Orbitals*, Academic Press, New York, 1973.
117. A. Lyčka, *Ann. Rep. NMR Spectrosc.*, 1993, **24**, 247.
118. L.-O. Andersson, J. Mason, and W. van Bronswijk, *J. Chem. Soc. A*, 1970, 296.
119. J. Kroner, W. Schneid, N. Wiberg, B. Wrackmeyer, and G. Ziegleder, *J. Chem. Soc., Faraday Trans. 2*, 1978, **74**, 1909.
120. D. G. Morris and A. M. Murray, *J. Chem. Soc., Perkin Trans. 2*, 1976, 1579.
121. P. B. Dervan, M. E. Squillacote, P. M. Lahti, A. P. Sylwester, and J. D. Roberts, *J. Am. Chem. Soc.*, 1981, **103**, 1120.
122. A. Galindo, A. Hills, D. L. Hughes, M. Hughes, J. Mason, and R. L. Richards, *J. Chem. Soc., Dalton Trans.*, 1990, 283, and refs. therein.
123. B. L. Haymore, M. Hughes, J. Mason, and R. L. Richards, *J. Chem. Soc., Dalton Trans.*, 1988, 2935.
124. K. Konishi, A. Yoshino, M. Katoh, H. Matsumoto, K. Takahashi, and H. Iwamura, *Chem. Lett.*, 1982, 169.
125. R. D. Müller, J. D. Wallis, and W. von Philipsborn, *Angew. Chem. Int. Ed. Engl.*, 1985, **24**, 513.
126. C. Casewit and J. D. Roberts, *J. Am. Chem. Soc.*, 1980, **102**, 2364.
127. D. C. Bradley, S. R. Hodge, J. D. Runnacles, M. Hughes, J. Mason, and R. L. Richards, *J. Chem. Soc., Dalton Trans.*, 1992, 1663.
128. J. P. Gouesnard and G. Martin, *Org. Magn. Reson.*, 1979, **12**, 263.
129. P. A. Duffin, L. F. Larkworthy, J. Mason, A. N. Stephens, and R. M. Thompson, *Inorg. Chem.*, 1987, **26**, 2034.
130. D. H. Evans, D. M. P. Mingos, J. Mason, and A. Richards, *J. Organomet. Chem.*, 1983, **249**, 293.
131. S. Donovan-Mtunzi, J. Mason, and R. L. Richards, *J. Chem. Soc., Dalton Trans.*, 1984, 1329.
132. B. Wrackmeyer, *Annu. Rep. NMR Spectrosc.*, 1988, **20**, 175.
133. J. P. Gouesnard, J. Dorie, and G. J. Martin, *Can. J. Chem.*, 1980, **58**, 1295.
134. J. Mason, *J. Chem. Soc., Faraday Trans. 2*, 1982, **78**, 1539.
135. T. Yamaguchi, K. Yamamoto, and H. Ohtaki, *Bull. Chem. Soc. Jpn.*, 1985, **58**, 3235.
136. D. M. Kanjia, J. Mason, R. E. Banks, I. A. Stenhouse, and N. D. Venayak, *J. Chem. Soc., Perkin Trans. 2*, 1981, 975.
137. S. Donovan-Mtunzi, J. Mason, and R. L. Richards, *J. Chem. Soc., Dalton Trans.*, 1984, 469.

138. J. Mason, in *Nuclear Magnetic Shielding and Molecular Structure*, ed. J. A. Tossell, *NATO AST Series*, Kluwer, Dordrecht, 1993, p. 449.
139. T. M. Duncan, *A Compilation of Chemical Shift Anisotropies*, Farragut Press, 1990, Chicago, IL, USA, N1–9.
140. R. E. Wasylishen, R. D. Curtis, K. Eichele, M. D. Lumsden, G. H. Penner, W. P. Power, and G. Wu, in *Nuclear Magnetic Shielding and Molecular Structure*, ed. J. A. Tossell, *NATO AST Series*, Kluwer, Dordrecht, 1993, p. 297.
141. W. P. Power and R. E. Wasylishen, *Annu. Rep. NMR Spectrosc.*, 1991, **23**, 1.
142. K. H. Casleton and S. G. Kukolich, *J. Chem. Phys.*, 1975, **62**, 2696; P. K. Bhattacharyya and B. P. Dailey, *J. Chem. Phys.*, 1973, **59**, 5820.
143. R. M. Garvey and F. C. De Lucia, *J. Mol. Spectrosc.*, 1974, **50**, 38.
144. J. Raymonda and W. Klemperer, *J. Chem. Phys.*, 1971, **55**, 232.
145. T. G. Oas, C. J. Hartzell, T. J. McMahon, G. P. Drobny, and F. W. Dahlquist, *J. Am. Chem. Soc.*, 1987, **109**, 5956; C. J. Hartzell, T. K. Pratum, and G. Drobny, *J. Chem. Phys.*, 1987, **87**, 4324.
146. G. S. Harbison, L. W. Jelinski, R. E. Stark, D. A. Torchia, J. Herzfeld, and R. G. Griffin, *J. Magn. Reson.*, 1984, **60**, 79.
147. W. P. Power and R. E. Wasylishen, *Annu. Rep. NMR Spectrosc.*, 1991, **23**, 1.
148. J. Mason, *Solid State NMR*, 1993, **2**, 285 [proposals developed with A. E. Hansen, J. Herzfeld, and C. J. Jameson following discussions at the 1992 Workshop, see Tossell[149]].
149. J. A. Tossell (ed.), *Nuclear Magnetic Shielding and Molecular Structure*, *NATO ASI Series*, Kluwer, Dordrecht, 1993.
150. A. Abragam, *The Principles of Nuclear Magnetism*, Clarendon Press, Oxford, UK, 1961, et seq.; U. Haeberlen, *High Resolution NMR in Solids Supplement 1*, Academic Press, New York, 1976, p. 9.
151. R. G. Griffin, *Anal. Chem.*, 1977, **49**, 951A.
152. B. R. Appleman and B. P. Dailey, *Adv. Magn. Reson.*, 1974, **7**, 231; C. Fyfe, *Solid State NMR for Chemists*, CFC Press, Guelph, Ontario, Canada, 1983; B. C. Gerstein and C. R. Dybowski, *Transient Techniques in NMR of Solids*, Academic Press, Orlando, FL, USA, 1985.
153. C. I. Ratcliffe, J. A. Ripmeester, and J. S. Tse, *Chem. Phys. Lett.*, 1983, **99**, 177.
154. R. M. Dickson, M. S. McKinnon, J. F. Britten, and R. E. Wasylishen, *Can. J. Chem.*, 1987, **65**, 941.
155. R. A. Santos, W. J. Chien, and G. S. Harbison, *J. Magn. Reson.*, 1989, **84**, 357.
156. R. G. Griffin, G. Bodenhausen, R. A. Haberkorn, T. H. Huang, M. Munowitz, R. Osredkar, D. J. Ruben, R. E. Stark, and H. van Willigen, *Philos. Trans. R. Soc. London, Ser. A*, 1981, **299**, 547.
157. J. E. Roberts, G. S. Harbison, M. G. Munowitz, J. Herzfeld, and R. G. Griffin, *J. Am. Chem. Soc.*, 1987, **109**, 4163.
158. G. Malli and C. Froese, *Int. J. Quantum Chem.*, 1967, **1s**, 95.
159. S. Kaplan, A. Pines, R. G. Griffin, and J. S. Waugh, *Chem. Phys. Lett.*, 1974, **25**, 78; J. D. Kennedy and W. McFarlane, *Mol. Phys.*, 1975, **29**, 593.
160. R. D. Curtis, M. J. Schriver, and R. E. Wasylishen, *J. Am. Chem. Soc.*, 1991, **113**, 1493.
161. M. Sardashti and G. E. Maciel, *J. Phys. Chem.*, 1988, **92**, 4620.
162. L. M. Ishol and T. A. Scott, *J. Magn. Reson.*, 1977, **27**, 23.
163. E. A. Moore, in preparation.
164. C. S. Yannoni, *J. Chem. Phys.*, 1970, **52**, 2005.
165. C. J. Groombridge, J. Mason, and R. L. Richards, unpublished work.
166. J. Herzfeld, J. E. Roberts, and R. G. Griffin, *J. Chem. Phys.*, 1987, **86**, 597.
167. D. G. Powell and L. J. Mathias, *J. Am. Chem. Soc.*, 1990, **112**, 669.
168. A. Shoji, S. Ando, S. Kuroki, I. Ando, and G. A. Webb, *Annu. Rep. NMR Spectrosc.*, 1993, **25**, 55.
169. See, for example, A. Shoji, T. Ozaki, T. Fujito, K. Deguchi, S. Ando, and I. Ando, *J. Am. Chem. Soc.* 1990, **112**, 4693.
170. K. G. Valentine, A. L. Rockwell, M. Gierasch, and S. J. Opella, *J. Magn. Reson.*, 1987, **73**, 519.
171. T. A. Cross and S. J. Opella, *J. Am. Chem. Soc.*, 1983, **105**, 306.
172. D. Schweitzer and H. W. Spiess, *J. Magn. Reson.*, 1974, **15**, 529.
173. R. D. Curtis, G. H. Penner, W. P. Power, and R. E. Wasylishen, *J. Phys. Chem.* 1990, **94**, 4000.
174. R. E. Wasylishen, G. H. Penner, W. P. Power, and R. D. Curtis, *J. Am. Chem. Soc.*, 1989, **111**, 6082.
175. R. E. Wasylishen, W. P. Power, G. H. Penner, and R. D. Curtis, *Can. J. Chem.*, 1989, **67**, 1219.
176. T. J. Bastow and S. N. Stuart, *Chem. Phys. Lett.*, 1991, **180**, 305.
177. R. A. Santos, P. Tang, W.-J. Chien, S. Kwan, and G. S. Harbison, *J. Phys. Chem.*, 1990, **94**, 2717.
178. P. J. Barrie, C. J. Groombridge, J. Mason, and E. A. Moore, *Chem. Phys. Lett.*, 1994, **219**, 491.
179. R. E. Wasylishen, communication quoted in R. G. Griffin, *Anal. Chem.*, 1977, **49**, 951A.
180. H. J. M. de Groot, S. O. Smith, J. Courtin, E. van den Berg, C. Winkel, J. Lugtenburg, R. G. Griffin, and J. Herzfeld, *Biochemistry*, 1990, **29**, 6873, and refs. therein.
181. T. E. Laska and T. W. Root (1989), quoted in *Nuclear Magnetic Shielding and Molecular Structure*, ed. J. A. Tossell, *NATO ASI Series*, Kluwer, Dordrecht, 1993, p. N-4.
182. P. J. Barrie, C. J. Groombridge, L. F. Larkworthy, and J. Mason, in preparation.
183. C. J. Groombridge, L. F. Larkworthy, A. Marécaux, J. Mason, D. C. Povey, and G. W. Smith, *J. Chem. Soc., Dalton Trans.*, 1992, 3125.
184. C. J. Groombridge, L. F. Larkworthy, and J. Mason, *Inorg. Chem.*, 1993, **32**, 379.
185. W. R. Scheidt and J. L. Hoard, *J. Am. Chem. Soc.*, 1973, **95**, 8281.
186. W. Kutzelnigg, U. Fleischer, and M. Schindler, *NMR Basic Principles Prog.*, 1990, **23**, 165, and refs. therein.
187. Aa. E. Hansen and T. D. Bouman, *J. Chem. Phys.*, 1985, **82**, 5035.
188. M. Schindler, *J. Am. Chem. Soc.*, 1987, **109**, 5950; *Magn. Reson. Chem.*, 1988, **26**, 394; *J. Am. Chem. Soc.*, 1988, **110**, 6623.
189. T. D. Bouman and Aa. E. Hansen, *Chem. Phys. Lett.*, 1990, **175**, 292.
190. J. Kowalewski, *Annu. Rep. NMR. Spectrosc.*, 1982, **12**, 82; *Prog. NMR Spectrosc.*, 1977, **11**, 1.
191. W. Freyer, *Z. Chem.*, 1981, **21**, 47.
192. R. E. Wasylishen, in *NMR Spectroscopy of Nuclei Other than Protons*, eds. T. Axenrod and G. A. Webb, Wiley, New York, 1974, p. 105.
193. T. Axenrod, in *Nitrogen NMR*, ed. M. Witanowski and G. A. Webb, Plenum Press, London, 1973, p. 261.
194. R. E. Wasylishen, *Annu. Rep. NMR. Spectrosc.*, 1977, **7**, 262.
195. C. J. Jameson, in *Multinuclear NMR*, ed. J. Mason, Plenum, New York, 1987, Chap. 4, p. 89.
196. W. McFarlane, *Q. Rev. Chem. Soc.*, 1969, **23**, 187.
197. G. Binsch, J. B. Lambert, B. W. Roberts, and J. D. Roberts, *J. Am. Chem. Soc.*, 1964, **86**, 5564.

198. A. J. R. Bourn and E. W. Randall, *Mol. Phys.*, 1964, **8**, 567.
199. R. E. Wasylishen and T. Schaefer, *Can. J. Chem.*, 1971, **49**, 3627.
200. T. Bundgaard, H. J. Jakobsen, and E. J. Rahkamaa, *J. Magn. Reson.*, 1975, **19**, 345.
201. H. Schultheiss and E. Flück, *Z. Naturforsch.*, 1977, **32B**, 257.
202. S. Karplus and M. Karplus, *Proc. Natl. Acad. Sci. USA*, 1972, **69**, 3204.
203. J. M. Schulman and T. J. Venanzi, *J. Am. Chem. Soc.*, 1976, **98**, 4701.
204. J. M. Schulman and T. J. Venanzi, *J. Am. Chem. Soc.*, 1976, **98**, 6739; W. S. Lee and J. M. Schulman, *J. Am. Chem. Soc.*, 1979, **101**, 3182.
205. J. M. Schulman, J. Ruggio, and T. J. Venanzi, *J. Am. Chem. Soc.*, 1977, **99**, 2045.
206. J. Hilton and L. H. Sutcliffe, *Prog. NMR Spectrosc.*, 1975, **10**, 27; V. M. S. Gil and W. von Philipsborn, *Magn. Reson. Chem.*, 1989, **27**, 409; R. H. Contreras, M. A. Natiello, and G. E. Scuseria, *Magn. Reson. Rev.*, 1985, **9**, 239.
207. R. M. Lynden-Bell and R. K. Harris, *Nuclear Magnetic Resonance Spectroscopy*, Nelson, London, UK, 1969, p. 102.
208. J. Geertsen, J. Oddershede, and G. E. Scuseria, *J. Chem. Phys.*, 1987, **87**, 2138.
209. N. J. Clayden, *Annu. Rep. NMR Spectrosc.*, 1992, **24**, 1.
210. C. J. Groombridge, *Nucl. Magn. Reson.*, 1992, **21**, 201.
211. K. Wüthrich, *NMR of Proteins and Nucleic Acids*, Wiley, New York, 1986.
212. S. J. Opella, *Annu. Rev. Phys. Chem.*, 1982, **33**, 533; *Methods Enzymol.*, 1985, **17**, 327; S. J. Opella, P. L. Stewart, and K. G. Valentine, *Q. Rev. Biophys.*, 1987, **19**, 7.
213. K. J. Shon and S. J. Opella, *Biomed. Appl. Biotechnol.*, 1993, **1**, 87.
214. M. C. Etter (ed.), *NMR and X-ray Crystallography: Interfaces and Challenges*, Am. Crystallogr. Assoc, Washington, DC, 1988, Vol. 24.
215. D. Suter and R. R. Ernst, *Phys. Rev. B*, 1985, **32**, 5608.
216. Q. Teng, M. Iqbal, and T. A. Cross, *J. Am. Chem. Soc.*, 1992, **114**, 5312.
217. J. E. Roberts, G. S. Harbison, M. G. Munowitz, J. Herzfeld, and R. G. Griffin, *J. Am. Chem. Soc.*, 1987, **109**, 4163.
218. R. Blinc, J. Seliger, V. Zagar, T. Apih, J. Dolinsek, H. Warhanek, A. Fuith, and W. Schranz, *Phys. Rev. B*, 1990, **42**, 8125.
219. A. Naito, P. B. Barker, and C. A. McDowell, *J. Chem. Phys.*, 1984, **81**, 1583, and refs. therein.
220. A. C. Olivieri, *Z. Naturforsch.*, 1992, **47A**, 39.
221. A. J. Kim and L. G. Butler, *Concepts Magn. Reson.*, 1992, **4**, 205.
222. C. P. Grey and W. S. Veeman, *Chem. Phys. Lett.*, 1992, **192**, 379.
223. A. Shoji, T. Ozaki, T. Fujito, K. Deguchi, and I. Ando, *Macromolecules*, 1987, **20**, 2441.
224. L. J. Mathias and C. G. Johnson, *Macromolecules*, 1991, **24**, 6114, and refs. therein.
225. B. Chaloner-Gill, W. B. Euler, P. D. Mumbauer, and J. E. Roberts, *J. Am. Chem. Soc.*, 1991, **113**, 6831.
226. L. Delmotte, M. Soulard, and H. Kessler, *Chem. Lett.*, 1990, 1215.
227. M. G. Gibby, R. G. Griffin, A. Pines, and J. S. Waugh, *Chem. Phys. Lett.*, 1972, **17**, 80.
228. K. L. Anderson-Altmann and D. M. Grant, *J. Phys. Chem.*, 1993, **97**, 11 096; cf. S. Hayashi and K. Hayamizu, *Bull. Chem. Soc. Jpn.*, 1991, **64**, 688.
229. J. A. Ripmeester, *J. Am. Chem. Soc.*, 1983, **105**, 2925.
230. P. D. Majors and P. D. Ellis, *J. Am. Chem. Soc.*, 1987, **109**, 1648, and refs. therein.
231. D. Michel, A. Germanus, D. Scheller, and B. Thomas, *Z. Phys. Chem. (Leipzig)*, 1981, **262**, 113; D. Michel, A. Germanus, and H. Pfeifer, *J. Chem. Soc., Faraday Trans. 1*, 1982, **78**, 237.
232. W. L. Earl, P. O. Fritz, A. A. V. Gibson, and J. H. Lunsford, *J. Phys. Chem.*, 1987, **91**, 2091.
233. J. A. Ripmeester, R. E. Hawkins, J. A. MacPhee, and B. N. Nandi, *Fuel*, 1986, **65**, 740.
234. W. Meiler and T. Wutscherk, *Isotopenpraxis*, 1989, **25**, 41.
235. J. Schaefer, E. O. Stejskal, M. D. Sefcik, and R. A. McKay, *Philos. Trans. R. Soc. London, Ser. A*, 1981, **299**, 593; J. Schaefer, E. O. Stejskal, and R. A. McKay, *ACS Symp. Ser.*, 1982, **191**, 187; J. Schaefer, E. O. Stejskal, J. R. Garbow, and R. A. McKay, *J. Magn. Reson.*, 1984, **59**, 150.
236. S. M. Holl, G. R. Marshall, D. D. Beusen, K. Kociolek, A. S. Redlinski, M. T. Leplawy, R. A. McKay, S. Vega, and J. Schaefer, *J. Am. Chem. Soc.*, 1992, **114**, 4830.
237. M. L. Martin, G. J. Martin, and J.-J. Delpuech, *Practical NMR Spectroscopy*, Heyden, London, UK, 1980.
238. L. M. Jackman and F. A. Cotton (eds.), *Dynamic NMR Spectroscopy*, Academic Press, New York, 1975.
239. H. H. Limbach, *Intermol. Forces*, 1991, 281.
240. F. Aguilar-Parrilla, G. Scherer, H. H. Limbach, M. D. C. Foces-Foces, F. Hernandez Cano, J. A. S. Smith, C. Toiron, and J. Elguero, *J. Am. Chem. Soc.*, 1992, **114**, 9657.
241. M. L. Martin, X. Y. Sun, and G. J. Martin, *Annu. Rep. NMR Spectrosc.*, 1985, **16**, 188.
242. J. F. Johnston, J. H. Ridd, and J. P. B. Sandell, *J. Chem. Soc., Perkin Trans. 2*, 1991, 623, and refs. therein.
243. J. H. Ridd, S. Trevellick, and J. P. B. Sandall, *J. Chem. Soc., Perkin Trans. 2*, 1992, 1535.
244. N. N. Bubnov, K. A. Bilevitch, L. A. Poljakova, and O. Yu. Okhlobystin, *J. Chem. Soc., Chem. Commun.*, 1972, 1058.
245. E. L. Dreher, P. Niederer, A. Rieker, W. Schwarz, and H. Zollinger, *Helv. Chim. Acta*, 1981, **64**, 488.
246. I. A. Grigorev, L. B. Volodarsky, A. Z. Gogolev, and R. Z. Sagdeev, *Chem. Phys. Lett.*, 1985, **122**, 46.
247. D. J. Siminovitch, M. Rance, and K. R. Jeffrey, *FEBS Lett.*, 1980, **112**, 79.
248. T. M. Rothgeb and E. Oldfield, *J. Biol. Chem.*, 1981, **256**, 6004.
249. F. Blomberg and H. Rueterjans, *Biol. Magn. Reson.*, 1983, **5**, 21.
250. K. Kanamori and J. D. Roberts, *Acc. Chem. Res.*, 1983, **16**, 35.
251. B. Coxon, *Pure Appl. Chem.*, 1977, **49**, 1151.
252. Y. Kyogoku, *Appl. Spectrosc. Rev.*, 1982, **17**, 279.
253. E. Breitmaier, *Pharm. Unserer Zeit*, 1983, **12**, 161.
254. G. J. Martin, *Pharm. Weekbl.*, 1984, **119**, 5.
255. R. Dyllick-Brenzinger and J. D. Roberts, *J. Am. Chem. Soc.*, 1980, **102**, 1166.
256. M. Llinas, K. Wüthrich, W. Schwotzer, and W. von Philipsborn, *Nature (London)*, 1975, **257**, 817.
257. A. Lapidot and C. S. Irving, *Biochemistry*, 1979, **18**, 704, 1788.
258. K. Kanamori, T. L. Legerton, R. L. Weiss, and J. D. Roberts, *J. Biol. Chem.*, 1982, **257**, 4168, and refs. therein.
259. N. Haran, Z. E. Kahana, and A. Lapidot, *J. Biol. Chem.*, 1983, **258**, 2929.
260. T. A. Cross, J. A. Diverdi, and S. J. Opella, *J. Am. Chem. Soc.*, 1982, **104**, 1759.
261. J. A. DiVerdi and S. J. Opella, *J. Am. Chem. Soc.*, 1982, **104**, 1761.

262. T. A. Cross, P. Tsang, and S. J. Opella, *Biochemistry*, 1983, **22**, 721.
263. G. T. Coker, III, J. R. Garbow, and J. Schaefer, *Plant Physiol.*, 1987, **83**, 698.
264. G. T. Coker, III and J. Schaefer, *Plant Physiol.*, 1985, **77**, 129.
265. G. S. Jacob, J. Schaefer, and G. E. Wilson, Jr., *J. Biol. Chem.*, 1985, **260**, 2777.
266. R. L. Baxter, C. J. McGregor, G. A. Thomson, and A. I. Scott, *J. Chem. Soc., Perkin Trans. 1*, 1985, 369.
267. W. Gründer, P. Krumbiegel, K. Buchali, and H. J. Blesin, *Phys. Med. Biol.*, 1989, **34**, 457.

Biographical Sketch

Joan Mason. *b* 1923. B.A., 1944, M.A., 1947, Ph.D., 1950, Sc.D., 1982, Cambridge University. Introduced to fluorine and perfluoroalkyl chemistry by H. J. Emeléus at Cambridge, to boron chemistry by A. B. Burg at the University of Southern California, and to NO_x chemistry and bonding theory by C. K. Ingold at University College, London. Lecturer, senior lecturer, and Reader in Chemistry, the Open University, 1970–88. Research interests: nitrogen chemistry, nitrogen NMR, metal complexes, transition metal NMR.

Nitrogen-15 Chemical Shift Tensors and Organic Structure

Ronald J. Pugmire

Department of Chemical and Fuels Engineering, University of Utah, Salt Lake City, UT, USA

1 Introduction 1
2 Chemical Shielding 1
3 Experimental Techniques 3
4 Results 4
5 Conclusions 7
6 References 7

1 INTRODUCTION

During the past two decades solid state NMR spectroscopy and its applications have grown rapidly among the chemistry and biochemistry community. The availability of increasingly sophisticated instrumentation and software has created opportunities for conducting experiments in areas that have not previously been available to the general chemical community. These new opportunities have been especially helpful in the study of solids. While the majority of such solid state applications have utilized ^{13}C nuclei, a much broader range of interesting nuclei (e.g., ^{11}B, ^{14}N, ^{15}N, ^{17}O, ^{19}F, ^{23}Na, ^{27}Al, ^{29}Si, ^{31}P, ^{113}Cd, ^{209}Pb, etc.) has emerged for use by solid state scientists and engineers.

Interest in magnetic resonance studies of nitrogen has increased significantly in the past decade. The distribution of nitrogen containing substances in materials important to the chemical, biological, medical, agricultural, and environmental sciences is well documented. The ^{14}N nucleus (99.6% natural abundance, nuclear spin 1) is quadrupolar giving rise to a broad signal while the ^{15}N nucleus has spin 1/2. The relative sensitivity of both nuclei is approximately 1×10^{-3} compared to ^{1}H. Nitrogen NMR data have been extensively reviewed by Witanowski et al.[1] and by Mason.[2] Most of the literature describes liquid state isotropic shifts and their relationship to structure elucidation, the importance of solvent effects, and tautomeric equilibria. The combination of a large isotropic shift range, approximately 1350 ppm,[1] and sensitivity to electronic interactions involving the lone pair of electrons make ^{15}N shifts a very sensitive probe of both structural changes and intermolecular interaction.[3] These attractive features of the ^{15}N nucleus are off-set by the sensitivity challenges arising from a low natural abundance (0.365%), long relaxation times, small magnetogyric ratio, and a subsequent receptivity factor 2.19×10^{-2} relative to ^{13}C for an equivalent number of nuclei. Hence, much of the data reported has been obtained from ^{15}N labeled materials although modern high field spectrometers have proven their value in studies at the natural abundance level. A significant amount of attention has recently been focused on the role of nitrogen in biological structures[4] because of its sensitivity to both hydrogen bonding and intermolecular and long-range interactions. In this document the discussion will be restricted to the ^{15}N nucleus.

2 CHEMICAL SHIELDING

The well known relationship between magnetic field strength B_o(arbitrary orientation in the z direction), the magnetogyric ratio γ_I of nuclear spin I, and the NMR Larmor frequency ν_o (in frequency units, Hz) is given in equation (1)

$$\nu_o = \frac{\gamma_I B_o}{2\pi} \tag{1}$$

where ν_o is the difference in energy between any two of the allowed states. The magnetic inductive affect at the nucleus is equal to the vector sum of the static magnetic field and an induced magnetization vector arising from electronic currents that exist in the sample. The induced magnetization is proportional to B_o and the proportionality constant is the sum of the chemical shielding and the magnetic susceptibility of the material surrounding the nucleus of interest. In solids, where rapid motional averaging is absent, all intramolecular currents within the molecule of interest are assigned to chemical shielding. Electronic currents arising from neighboring molecules are assigned to magnetic susceptibility. A more detailed and very useful outline of these interactions is provided by Grant.[5]

The electronic circulation set up by the magnetic induction of the applied field perturbs the effects of B_o at the nucleus of interest. These electronic currents induce a shielding field, B_s, which may be either paramagnetic or diamagnetic (deshielding or shielding) and this induced field must be added to B_o in order to obtain the effective field, B_{eff}, experienced by the nucleus of interest (equation (2)).

$$B_{eff} = B_s + B_o \tag{2}$$

This effect is portrayed in vector form in Figure 1.

The shielding of the nuclear spin is a tensor quantity, described below, that depends on the electronic environment as well as the molecular orientation in the magnetic field. In solids the molecular orientation is locked into a powder pattern in which the nuclear resonance frequency is a function of the orientation of the microcrystalline particles. The random orientation of these particles leads to broad resonance patterns for each unique nuclear spin. The rich informational content of these powder patterns provides more information about electronic structure than the isotropic shifts observed in rapidly tumbling liquid molecules. Unfortunately, the diversity of the banding arising from multiple unique chemical environments in these broad powder patterns obscures the information content that is available in the isotropic chemical shift. However, the components of the shift tensor in the solid state reveal even more information regarding the subtle differences in electronic and geometrical structural characteristics and

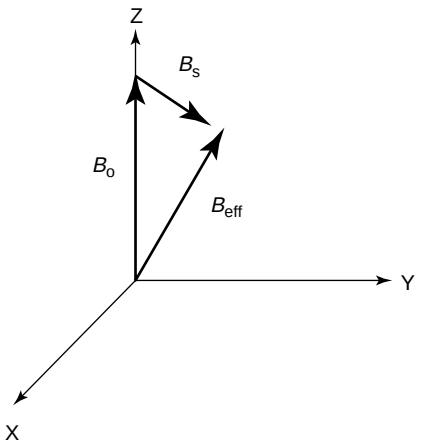

Figure 1 Relationship between the applied field, B_o, and the shielding field and effective fields (not drawn to scale) B_s and B_{eff}

the various experimental techniques employed to extract this information from solid samples is summarized in Section 3.

The shielding interaction with a nucleus is different for each unique chemical environment or symmetry position relative to the remainder of the lattice structure. Furthermore, the orientation dependence of the magnetic field to the screening currents induced around the nucleus presents an anisotropic environment that can be described by the chemical shift tensor. In principal, a different resonance frequency will be observed for each orientation of the nuclear spin with respect to the external magnetic field and the difference in this screening effect from that of a reference material is defined as the chemical shift. The reference that has emerged in the field is

$$\delta = \begin{bmatrix} \delta_{xx} & \delta_{xy} & \delta_{xz} \\ \delta_{yx} & \delta_{yy} & \delta_{yz} \\ \delta_{zx} & \delta_{zx} & \delta_{zz} \end{bmatrix} \tag{3}$$

external nitromethane ($\delta = 0$) with the convention of negative values for more shielded resonance positions. The chemical shift tensor δ in a general reference frame may be represented by a 3×3 Cartesian matrix that is called a second rank tensor (equation (3)) which can be decomposed into three individual tensors of rank zero, one, and two which are defined as the scalar isotropic chemical shift, the symmetric, and antisymmetric chemical shifts denoted (equation (4)) as

$$\delta = \delta_o + \delta_{sym} + \delta_{anti} \tag{4}$$

The isotropic shift, δ_o, of zeroeth rank, is the trace of the Cartesian tensor, e.g., $1/3(\delta_{xx} + \delta_{yy} + \delta_{zz})$, and is invariant to any rotational transformation of the coordinate frame. Hence, δ_o is the only part of the chemical shift tensor that can be measured in solution samples; this the result of rapid tumbling motion of the molecules. The antisymmetric (first rank) and symmetric (second rank,) chemical shifts are given in equations (5) and (6), respectively.

$$\delta_{ij}^{(a)} = \tfrac{1}{2}(\delta_{ij} - \delta_{ji}) \tag{5}$$

$$\delta_{ij}^{(s)} = \tfrac{1}{2}(\delta_{ij} + \delta_{ji}) \tag{6}$$

The absence of diagonal elements in the first rank tensor renders these second order infinitesimal shift frequencies immeasurable. The traceless second-rank symmetric matrix contains diagonal elements that can provide first-order anisotropic shifts that add to or subtract from the Zeeman frequencies and are measurable in the NMR spectrum of solids. In the symmetric matrix any change in orientation of the magnetic field in the molecular frame will still leave anisotropic shifts along the diagonal of the transformed second-rank matrix. Unlike the antisymmetric components, the off-diagonal shifts in the symmetric portion of the chemical shift tensor will affect the principal values under the transformations associated with matrix diagonalization.

There always exists some frame in which the matrix in equation (3) is diagonal, in which case the three diagonal elements of the chemical shift tensor are designated as the principal values, δ_{11}, δ_{22}, and δ_{33}. By convention the order of the principal values are given as $\delta_{11} \geq \delta_{22} \geq \delta_{33}$, with δ_{11} representing the highest frequency (least shielded) component. The axis system in which the symmetric chemical shift matrix is diagonal is designated the principal axis system (PAS). The diagonal components are the principle values in the PAS while the remaining three (off-diagonal) terms are the Euler angles which define the directions of these principal values in the molecular frame. Hence, the complete description of the chemical shift tensor requires six elements of the shift tensor. The breakpoints in a powder pattern provide the principal values of the chemical shift tensor. The off-diagonal terms can only be obtained experimentally by tracking the chemical shift of each unique nucleus as a molecule (e.g., a molecule in a single crystal) is rotated in the magnetic field. These data can then be transformed into any of a number of reference frames that can be used to determine the orientation of the tensor in the molecular frame. The details of these experiments and transformations are described in a general outline by Orendt[6] and in detail by Grant[5] and Sherwood.[7]

The difficulties associated with growing single crystals and then acquiring the necessary orientational data is daunting, time consuming, and complicated by the reality that acquiring a single crystal of sufficient size for NMR experiments is usually not practical. However, sufficient single crystal data, together with theoretical simulations of the shift tensors, have been acquired to demonstrate that quite good approximations can be obtained for the orientation of the shift tensor principal axis system on the molecular frame.[8,9] Hence, the various types of experiments that provide only the principal values of the shift tensor on powder samples[6,10] are sufficient, when combined with appropriate theoretical calculations, to describe the off-diagonal elements which fix the orientation in the molecular frame with reasonable accuracy (see Section 4.3). To date, the majority of chemical shift tensor data appearing in the literature has been restricted to the ^{13}C nucleus and the latest, but somewhat dated, compilation of these data together with available data on ^{15}N shift tensor principal values has been provided by Duncan.[11] The acquisition of shift tensor data on solid materials, however, has expanded considerably in the past 10–15 years as line narrowing methods and techniques have become available. A review has described these experimental advances[6] but additional major advances in multidimensional experiments have recently appeared[12–14] and are described in another article in this encyclopedia,

Magic-angle Turning Spectra of Solids Involving 5π-pulse Sequences.

Despite the challenges faced with obtaining shift tensor data, new experimental techniques now enable investigators to obtain high quality ^{13}C shift tensor data on molecules containing more than sixty unique carbon atoms[10] and ^{15}N shift tensors at the natural abundance level on molecules containing as many as five nitrogens (guanine)[15] and eight non-equivalent nitrogens in potassium penicillin V.[13]

3 EXPERIMENTAL TECHNIQUES

^{15}N chemical shift tensor data have been reported using five different types of experimental techniques: (1) single crystal studies; (2) analysis of static powder patterns and off-magic-angle spinning on simple ^{15}N enriched heterocycles; (3) analysis of powder patterns utilizing the dipolar interaction between ^{1}H–^{5}N or adjacent ^{13}C–^{15}N labeled pairs; (4) powder patterns obtained by means of dynamic nuclear polarization experiments; (5) two-dimensional experiments such as polarization inversion spin exchange at the magic angle (PISEMA), and the five-π pulse experiment five pi replicated magic angle turning (FIREMAT).

3.1 Single Crystals

A single crystal study of L-hystidine·HCl·H_2O[16] reported the full tensor of the two imidazole nitrogens in the amino acid while a single crystal study of [1-^{13}C]glycyl[^{15}N]glycine provided the principal values of the ^{15}N tensor and its orientation in the molecular frame.[17]

3.2 Static Powders and Off-Magic Angle Spinning

The major portion of the ^{15}N shift tensor data has been obtained by static powder pattern analysis. Illustrative examples of static experiments on ^{15}N-enriched materials include: studies of the various phases of NH_4NO_3,[18] protonated and non-protonated species in simple five- and six-member nitrogen heterocycles,[19] porphyrin complexes,[20] cation binding in a membrane-bound polypeptide,[21] substituted benzonitriles,[22] off-angle fast sample spinning of an isolated ^{15}N–^{15}N diazo system,[23] static and off-angle fast sample spinning of substituted pyrazoles,[24] secondary structure of peptides containing L-alanine[25] and poly(β-benzyl L-aspartate),[26] substituted benzonitriles,[27] the amide fragment of acetanilide and *N*-methylacetanilide,[28] and the relationship of the δ_{33} principal value to the hydrogen bond length in the glycine residue of some oligopeptides.[29]

3.3 Dipolar Interactions in Powders

^{15}N shift tensor principal values and their orientation in the molecular frame have been determined through the dipolar interaction between proton and nitrogen dipolar coupling in peptides,[30] tryptophan and histidine side chains,[31] the phenylalanine residue,[32] the dipolar tensors for the peptide bond in [1-^{13}C]glycyl[^{15}N]glycine·HCl·H_2O,[33] peptides of the form *N*-acetyl[1-^{13}C]glycyl[^{15}N]-X-amide where X = glycine, alanine, and tyrosine[34] and L[-^{13}C]alanyl-L-[^{15}N]alanine,[35] an analytical approach for the determination of the principal value σ_{33} of the amide ^{15}N chemical shift tensor element with respect to the molecular frame,[36] studies of the nitroso-groups in nitrobenzene and *p*-nitroso-N,N-dimethyl aniline (in which a very large CSA anisotropy of 1472 ppm was observed),[37] the two-dimensional PISEMA data on [1-^{15}N]-2′-deoxyguanosine,[38] the three-dimensional powder patterns of $^{15}N_{\varepsilon 1}$-tryptophan and $^{15}N_{\pi}$-hystidine side chains,[39] shift tensor values and orientation in the molecular frame in ^{13}C and ^{15}N labeled uracil.[40,41]

3.4 Dynamic Nuclear Polarization Experiments on Powders

Hu et al.[42,43] reported large ^{15}N DNP enhancement factors in benzamide (260, compared to CP data) and greater than 900 in carbazole and were able to compare the principal values of the shift tensors in powdered samples of these two molecules with those obtained by standard cross polarization and single pulse experimental techniques.

3.5 Two-Dimensional Experiments

A variety of two-dimensional experiments designed for separating the isotropic and anisotropic chemical shift information were instrumental in advancing resolution and data analysis of complex molecular systems.[44–50] The magic angle turning experiments, first conceived by Gan,[51] paved the way

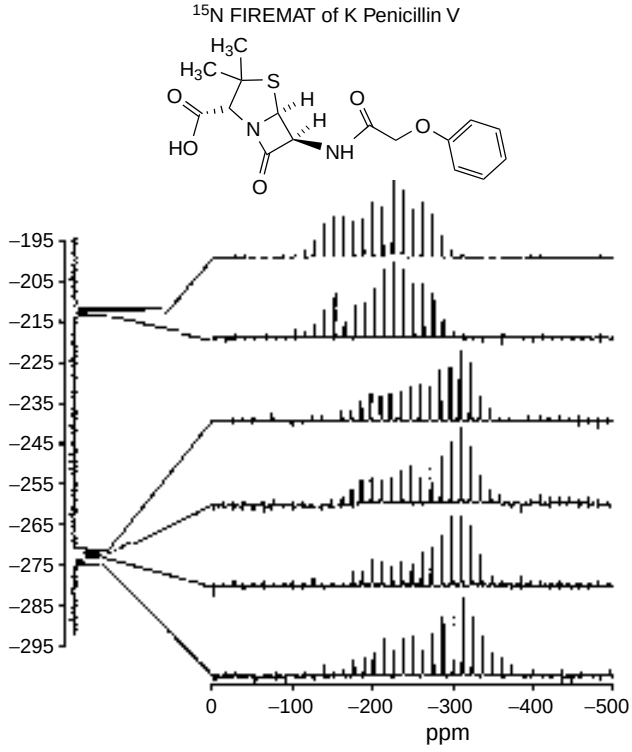

Figure 2 A two-dimensional natural abundance ^{15}N spectrum is shown in which the isotropic shift spectrum with no spinning side bands is plotted vertically on the left while the isolated spinning sideband patterns for the six resolved peaks are plotted on the right, connected to the corresponding isotropic peaks by guide lines

for development of experimental tools[12,13] that can reveal an amazing amount of detail regarding CSA in complex molecular systems. Recent modifications to the 5-π pulse experiments, FIREMAT[13] and 2D-PASS[14] have been particularly exciting in significantly expanding the range and complexity of molecules that can be studied. These two experiments, while related by virtue of a common 5-π pulse sequence for generating the two-D data set, possess important differences that are detailed in Ref.[10] Taking advantage of TIGER data processing in the FIREMAT experiment,[52] one is able to optimize S/N and resolution in the evolution dimension and obtain high quality ^{13}C data on molecules with more than 60 different tensors. The power of the FIREMAT experiment can be seen by examining the ^{15}N spectrum of penicillin V in Figure 2. Potassium penicillin V has two nitrogen atoms and, at ambient temperature, four molecules per asymmetric unit.[13] Conformational differences in these molecules split the NH nitrogen into the four peaks shown between −271.7 ppm and −275.3 ppm. The conformational differences do not affect the ring nitrogen to the same extent and three of the resonances are degenerate at −212.5 while the fourth is at −214.0 ppm. The FIREMAT experiment has also been used to obtain ^{15}N shift tensor data at the natural abundance level on nucleic acid bases,[15] purine,[53] and indolazines.[54]

4 RESULTS

4.1 Characteristics of Principal Values in Nitrogen Heterocycles

For convenience in consideration of ^{15}N shift tensors in organic molecules the discussion will be restricted to nitrogen heterocycles since this general class of compounds is ubiquitous in nature. The relatively simple five-and six-member heterocycles have been shown to provide the framework for understanding the shift tensor data in more complex heterocyclic structures including indolazines, the nucleic acid bases and related compounds. Consideration of ionic species also

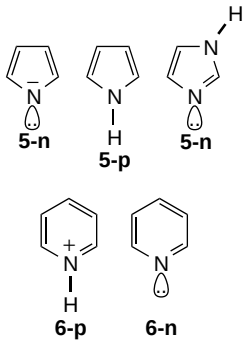

Figure 3 Definition of the different types of nitrogen atoms present in five-and six-member nitrogen heterocycles. The terms "n" and "p" represent non-bonded lone pair and protonated or bonded, lone pair, respectively

reflects the effects of hydrogen bonding interactions on the nitrogen shift tensors. This is especially interesting because of the lone pair of electrons. The structures portrayed in Figure 3 provide a useful framework from which to understand the experimental shift tensor data.

It is found that four different types of nitrogen tensors are present in simple nitrogen heterocycles. For convenience, the nitrogens with non-bonded lone electron pairs in five- and six-member rings shall be referred to as **5-n** and **6-n** types (such as pyrrole anion and the non-protonated nitrogens in imidazole and benzimidazole) and protonated **5-p** and **6-p** types (e.g., pyrrole, the protonated sites in imidazole and benzimidazole, the imidazolium cation, and the pyridinium cation).

Figure 4 presents a correlation diagram of the principal values of 12 simple heterocyclic structures. Quantum mechanical calculations were used to assign the orientation of the principal values to the molecular frame and to provide insight into the effects of electronic structure on the chemical shielding. These orientation assignments can be made with reasonable accuracy (estimated error of ±10 degrees based on work on uracil)[55] if

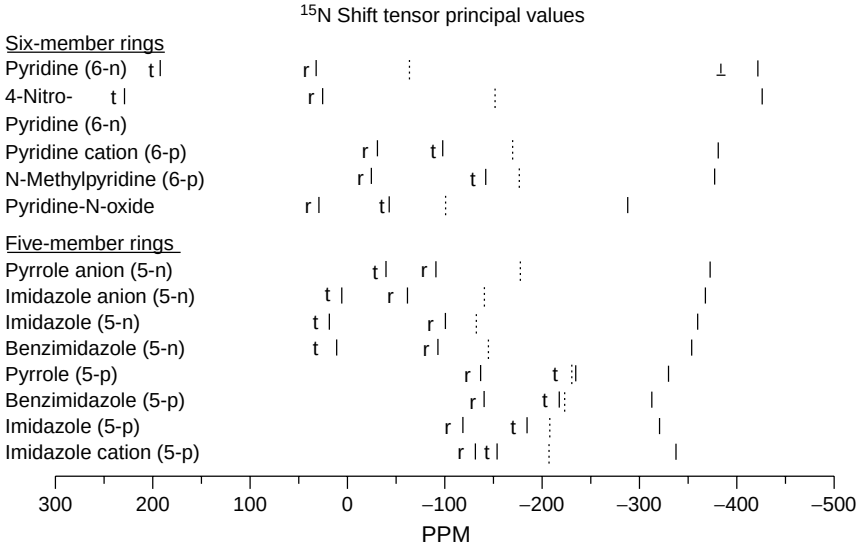

Figure 4 Correlation of the ^{15}N chemical shift principal values in 5-and 6-member heterocycles. The principal values are marked by solid lines, and the symbols indicate their approximate orientation in the molecular frames as described in Figure 5

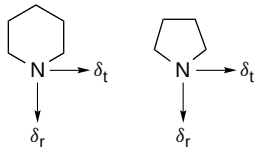

Figure 5 Orientation of the in-plane principal components in nitrogen heterocycles. δ_r and δ_t are depicted in the figure and lie in the plane of the ring approximately in the tangential and radial directions of the ring. $\delta_\perp$ is perpendicular to the ring. (*J. Am. Chem. Soc.*, published with permission)

sufficient structural data (e.g., crystal structure, bond length,) is available.[56,57]

A cursory inspection of Figure 4 illustrates the differences in the spans of the principal values of the nitrogen types. That the span of pyridine (622 ppm) is not unique as demonstrated by the span of 4-nitropyridine (674 ppm). In pyridine one observes that the δ_{11} shift component is oriented tangential to the ring, a direction that is also perpendicular to the lone pair (see Figure 6). When the hybridization of the nitrogen is changed from the **6-n** to the **6-p** type either by protonation, alkylation, or by *N*-oxide formation the tangential component crosses over the radial component, thus reducing the span of the shift tensor components by approximately 1/2 (to a range of 338−351 ppm). A similar affect is noted for the **5-n**/**5-p** case. The span in the pyrrole anion (333 ppm) is reduced to 192 ppm in pyrrole. Comparable effects are noted in each molecular pair studied. The data of Hoelger et al.[24] exhibit the same phenomena in the amine/imine pair of nitrogens in substituted pyrazoles.

The orientation of the shift tensor on the molecular frame of the compounds containing **5-n** type nitrogens corresponds to that found in pyridine (**6-n**). The span of the **5-n** tensor components is 337−374 ppm, a range that is nearly identical to that of the **6-p** nitrogens. In a manner similar to that noted for pyridine, protonation of the **5-n** loan pair inverts the order of the radial and tangential components and also significantly reduces (again, by approximately 1/2) the span of the **5-p** type nitrogens (to a range of 172−206 ppm). This reduction of span for the **5-n** and **5-p** species, compared to the respective **6-n** and **6-p** species, may be attributed to the larger degree of localization of the six π-electrons in five-member heterocycles compared with the six-member rings.[58] The increase of the localization of the π-electrons increases the electronic repulsion energy, thereby increasing the energy gaps corresponding to the $\sigma-\pi^*$ and $\pi-\sigma^*$ orbitals which dominate the paramagnetic contribution to the in-plane components. Thus, the paramagnetic contribution to the in-plane components of the shielding term decreases which reduces the shift tensor span.

The effects of interaction of the lone pair with neighboring atoms, whether bonded or non-bonded, is a matter of extreme interest and will be described in Section 4.3.

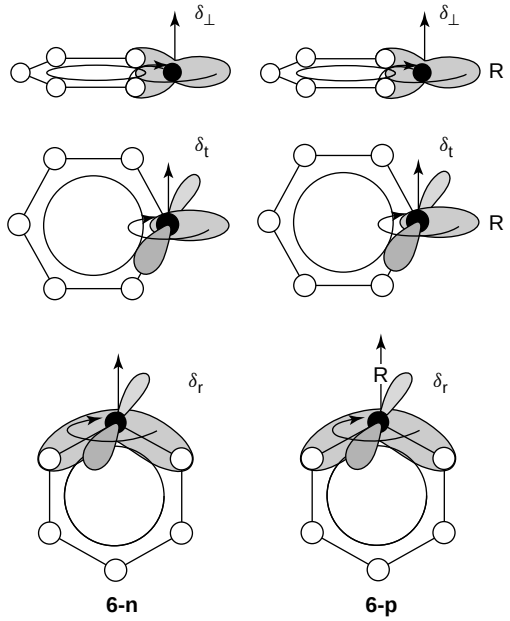

Figure 6 Electron orbitals making the largest contributions to the chemical shift principal components in pyridine. R corresponds to the lone pair in pyridine and R=H, O, or CH_3 in pyridine hydrochloride, pyridine-*N*-oxide, and *N*-methylpyridine. (*J. Am. Chem. Soc.*, published with permission)

4.2 The Nucleic Acid Bases

The simple nitrogen heterocycles can be used as a guide to understanding the electronic structure and intermolecular interactions in the nucleic acid bases. Employing a combination of two-dimensional experimental techniques (PHORMAT, TIGER data processing, and FIRMAT) that were dependent on the complexities of the ^{15}N spectra, the shift tensors were

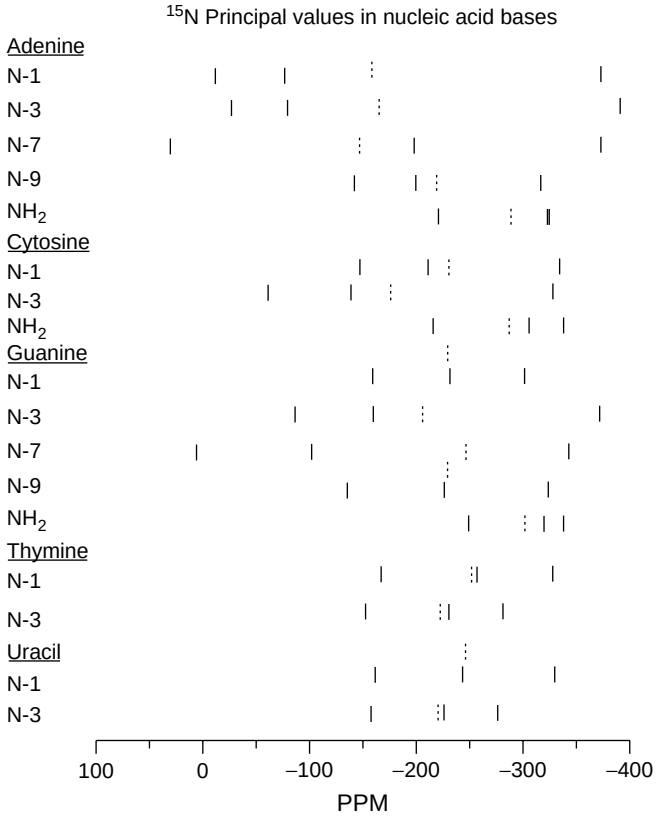

Figure 7 Correlation diagram of the ^{15}N shift tensor principal values in nucleic acid bases. Dashed lines are isotropic shift values

obtained on isotopically enriched adenine, and at natural abundance on thiamine, guanine, and cytosine.[15] The principal values obtained, together with data previously reported on uracil,[40] are presented as a bar graph in Figure 7 in order to visualize the relationship between the various shift tensor patterns.

The ^{13}C and ^{15}N shift tensor data obtained on purine[53] provides a useful model for interpreting the patterns observed in the nucleic acid bases. The purine data were obtained under separate sets of conditions and the position of the tautomeric proton could be definitely identified (by means of the ^{13}C isotropic shift data) as residing at either the N-7 or the N-9 position. The interpretation of the data is further confirmed by comparing the purine ^{15}N data with that of the simple nitrogen heterocycles previously described. In the five- and six-member heterocycles (Figure 4) the span ($\delta_{11}-\delta_{33}$) of the shift tensors of the **5/6-p** nitrogens are of the order of 1/2 that of the **5/6-n** nitrogens (compare, for example, the spans of N-1 and N-3 in benzimidazole in Figure 4). The N-7 and N-9 tautomeric structures in purine mirror this effect and, by comparing the spans of the N-7/9 positions in adenine and guanine (Figure 8), the position of the tautomeric proton is clearly evident in these two compounds. Furthermore, the spans of the N-1 and N-3 tensors in uracil and thiamine clearly indicate that the two labile protons occupy these sites while the cytosine data suggest that N-1 is the preferred site, in accordance with x-ray data. In the case of guanine the shift tensor data is consistent with the proton occupying the N-1 site.

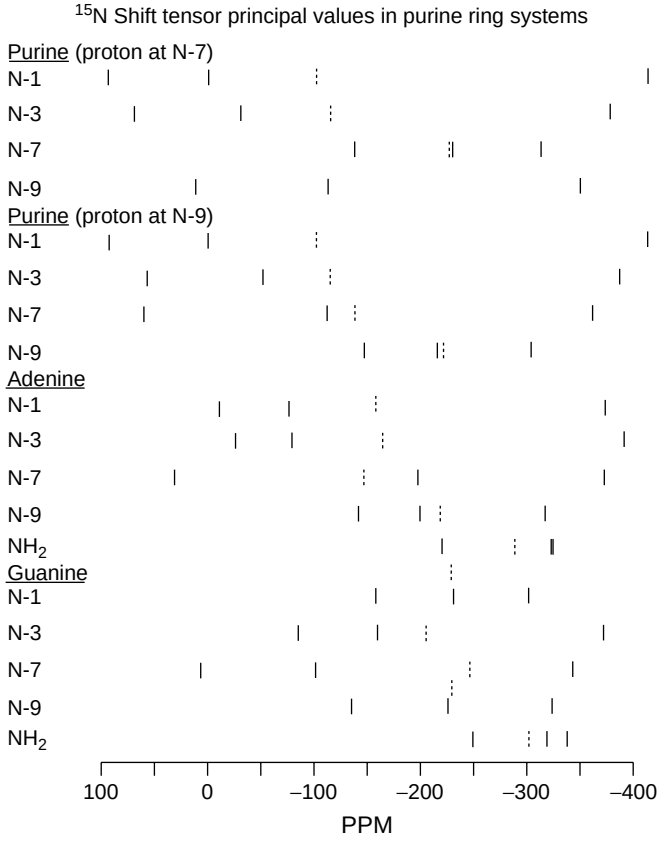

Figure 8 Comparison of shift tensor principal values in purine ring structures. The purine data is taken from Ref.[9] while the adenine and guanine data were taken from Ref.[15]

4.3 Effects of Hydrogen Bonding

The large changes in the shift tensor principal values provide a means for assessing hydrogen bonding in a wide range of heterocyclic ring systems. Using density functional theory (DFT) Facelli[3] simulated the shift tensor data in benzamide and these results, together with simulations of uracil,[40] highlighted the importance of including hydrogen bonding, and in general, intermolecular interactions in the calculation of ^{15}N chemical shift tensors. Further evidence for the importance of these intermolecular interactions in the calculation of ^{15}N chemical shift tensors can be found by analysis of these tensors in the series of heterocycles portrayed in Figure 4.

For these compounds the rms error between experimental and DFT calculated values, which did not include intermolecular effects, was approximately 30–40 ppm. This large scatter is approximately an order of magnitude greater than that found in simulated data on polyaromatic hydrocarbons.[56,57]

Utilizing the imidazole structural information obtained from neutron diffraction data it is possible to improve the chemical shift calculations and to examine the effects of hydrogen bonding on the ^{15}N shift principal values using a dimer model.[19] The correlation between experimental and calculated shift principal values in imidazole, with and without intermolecular interactions, is shown in Figure 9. The rms error of the predicted shift principal values is 40.9 ppm using an optimized geometry and is 13.8 ppm when the structural data includes the position of the hydrogens in the lattice structure along with the effects of hydrogen bonding.[19] Using the neutron diffraction data without including the intermolecular hydrogen bonding

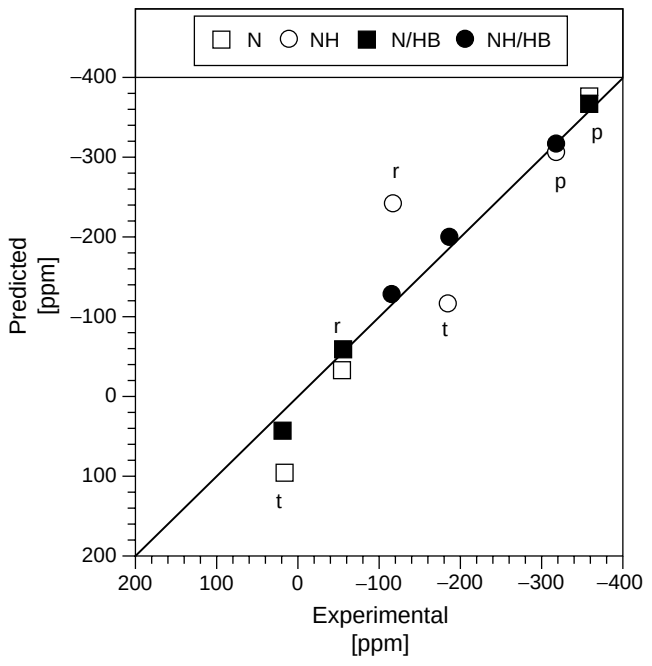

Figure 9 Experimental versus predicted chemical shift values for imidazole. The DFT method was used to calculate the ^{15}N shift tensor values using the neutron diffraction structure and including the effects of intermolecular interactions due to hydrogen bonding. The letters r, t, and p refer to the radial, tangential, and perpendicular components of the shift tensors. The legends N/HB and NH/HB designate predictions based on intermolecular interactions due to hydrogen bonding for the **5-n** and **5-p** nitrogens, respectively. (*J. Am. Chem. Soc.*, with permission)

effects produces only a modest improvement in the calculated values over those obtained with the optimized geometry. Introduction of intermolecular effects in the simulation of the nucleic acid bases plays a significant role in improving the correlation of experimental and theoretical result, reducing the rms error by a factor of two.[15] Given the 3–4 fold greater span of the nitrogen shift tensor, a rms error of 14 ppm in imidazole and 16 ppm for the nucleic acid bases compares favorably with the 3–5 ppm rms errors obtained in simulations of ^{13}C chemical shift tensors in polycyclic aromatic hydrocarbons based on x-ray structure data.[56,57]

5 CONCLUSIONS

^{15}N chemical shift tensors in heterocyclic compounds are very sensitive to the hybridization of the nitrogen atom and changes in the tangential component can vary from 200 ppm to as much as 340 ppm in five-and six-member rings, respectively, when the nitrogen lone-pair hybridization is changed. The changes in the magnitude of the in-plane components are so large that these effects may be useful in probing intermolecular interactions associated with hydrogen bonding in biological systems. It is possible to measure and spacially assign the principal components of the ^{15}N chemical shift tensors obtained from powder samples in heterocyclic compounds. The assignments of the chemical shift tensor components are critical for analyzing the relationship between the electronic structure and shift tensors. In all the compounds studied, the most deshielded component, δ_{11}, is in the plane of the ring and approximately perpendicular to the plane containing the bonding-antibonding or HOMO-LUMO pair of orbitals with the smallest energy gap. The most shielded component, δ_{33}, is always perpendicular to the plane of the ring, as in the ^{13}C tensors of aromatic compounds and is less sensitive to changes in the hybridization of the nitrogen atom than the principal components in the plane of the ring.

Employing modern instrumentation and experimental techniques that have been optimized for obtaining shift tensor data, it is now possible to study nucleic acid materials at the natural abundance level or with isotropic enrichment depending on the relaxation times and spectral complexity. The nucleic acid bases exhibit the same sensitivity to small changes in molecular geometry and environment noted for the five- and six-member heterocycles. Even for nitrogens with similar hybridization, differences as large as 50 ppm are found in corresponding principal shift components. Theoretical techniques now available enable the investigator to simulate the molecular environment with reasonable confidence. The agreement between experiment and theory is highly dependent on the molecular model used in the calculations, and molecular models that include the intermolecular interactions show superior correlation with the experimental values.

6 REFERENCES

1. M. Witanowski, L. Stefaniak, and G. A. Webb, in 'Annual Reports on NMR Spectroscopy', ed G. A. Webb, Academic Press: London, 1993, Vol. 25, p. 2 and reviews of these authors in this series.
2. J. Mason, in 'Encyclopedia of Nuclear Magnetic Resonance', eds D. M. Grant and R. K. Harris, Wiley: London, 1996, p. 3222.
3. J. C. Facelli, R. J. Pugmire, and D. M. Grant, *J. Am. Chem. Soc.*, 1996, **118**, 5488.
4. See for example: (a) Q. Teng, M. Iqbal, and T. A. Cross, *J. Am Chem. Soc.*, 1992, **114**, 5312; (b) A. Shoji, T. Ozaki, T. Fujito, K. Deguchi, I. Ando, and S. Ando, *J. Am. Chem. Soc.*, 1990, **112**, 4693; (c) H. Le and E. J. Oldfield, *J. Biomol. NMR*, 1994, **4**, 341; (d) C. J. Hartzell, T. K. Pratum, and G. Drobny, *J. Phys. Chem.*, 1987, **87**, 4324; (e) G. Harbison, J. Herzfeld, and R. G. Griffin, *J. Am. Chem. Soc.*, 1981, **103**, 4752; (f) G. A. Lorigan, R. McNamara, R. A. Jones, and S. J. Opella, *J. Magn. Reson.*, 1999, **140**, 315; (g) M. Hong, J. D. Gross, W. Hu, and R. G. Griffin, *J. Magn. Reson.*, 1998, **135**, 169; (h) Q. Teng and T. A. Cross, *J. Magn. Reson.*, 1989, **85**, 439; (i) K. T. Dayie and G. Wagner, *J. Am. Chem. Soc.*, 1999, **119**, 7797; (j) M. Ashikawa, A. Shoji, T. Ozaki, and I. Ando, *Macromolecules*, 1999, **32**, 2288; (k) J. R. Bender, D. M. Taylor, and A. Ramamoorthy, *J. Am. Chem. Soc.*, 2001, **123**, 914; (l) A. Ramamoorthy, C. H. Wu, and S. J. Opella, *J. Am. Chem. Soc.*, 1997, **119**, 10 479; (m) D. K. Lee, J. S. Santos, and A. Ramamoorthy, *Chem. Phys. Lett.*, 1999, **309**, 209; (n) K. G. Valentine, A. L. Rockwell, L. M. Gierasch, and S. J. Opella, *J. Magn. Reson.*, 1987, **73**, 519; (o) T. G. Oas, C. J. Hartzell, F. W. Dahlquist, and G. P. Drobny, *J. Am. Chem. Soc.*, 1987, **109**, 5962; (p) R. E. Stark, L. W. Jelinski, D. J. Ruben, D. A. Torchia, and R. G. Griffin, *J. Magn. Reson.*, 1983, **55**, 266; (q) G. S. Harbison, L. W. Jelinski, R. E. Stark, D. A. Torchia, J. Herzfeld, and R. G. Griffin, *J. Magn. Reson.*, 1984, **60**, 79; (r) J. F. Hinton, P. L. Guthrie, P. Pulay, K. Wilinski, and G. Fogarasi, *J. Magn. Reson.*, 1992, **96**, 154; (s) M. D. Lumsden, R. E. Wasylishen, K. Eichele, M. Schindler, G. H. Penner, W. P. Powell, and R. D. Curtis, *J. Am. Chem. Soc.*, 1994, **116**, 1403; (u) S. Kuroki, N. Asakawa, S. Ando, I. Ando, A. Shoji, and T. Ozaki, *J. Mol. Structure*, 1991, **245**, 69.
5. D. M. Grant, in 'Encyclopedia of Nuclear Magnetic Resonance', eds D. M. Grant and R. K. Harris, Wiley: London, 1996, p. 1298.
6. A. M. Orendt, in 'Encyclopedia of Nuclear Magnetic Resonance', eds D. M. Grant and R. K. Harris, Wiley: London, 1996, p. 1282.
7. M. H. Sherwood, in 'Encyclopedia of Nuclear Magnetic Resonance', eds D. M. Grant and R. K. Harris, Wiley: London, 1996, p. 1322.
8. J. C. Facelli, in 'Encyclopedia of Nuclear Magnetic Resonance', eds D. M. Grant and R. H. Harris, Wiley: London, 1996, p. 4327.
9. See, for instance, Modeling NMR Chemical Shift Tensors, Gaining Insights into Structure and Environment, ACS Symposium Series 732, eds J. C. Facelli and A. C. deDios, 1999.
10. D. M. Grant, in 'Encyclopedia of Nuclear Magnetic Resonance', eds D. M. Grant and R. K. Harris, Wiley: Chichester, 2002, Volume 9.
11. T. M. Duncan, 'A Compilation of Chemical Shift Anisotropies', 2nd edn, Farragut Press: Chicago, 1997.
12. J. Z. Hu, D. W. Alderman, C. Ye, R. J. Pugmire, and D. M. Grant, *J. Magn. Reson. A*, 1993, **105**, 82.
13. D. W. Alderman, G. McGeorge, J. Z. Hu, R. J. Pugmire, and D. M. Grant, *Mol. Phys.*, 1998, **95**, 1113.
14. O. N. Antzutkin, S. C. Shekar, and M. H. Levitt, *J. Magn. Reson.*, 1995, **115**, 7.
15. J. Z. Hu, J. C. Facelli, D. W. Alderman, R. J. Pugmire, and D. M. Grant, *J. Am. Chem. Soc.*, 1998, **120**, 9863.
16. G. Harbison, J. Herzfeld, and R. G. Griffin, *J. Am. Chem. Soc.*, 1981, **103**, 4752.
17. G. S. Harbison, L. W. Jelinski, R. E. Stark, D. A. Torchia, J. Herzfeld, and R. G. Griffin, *J. Magn. Reson.*, 1984, **60**, 79; R. E. Stark, L. W. Jelinski, D. J. Ruben, D. A. Trochia, and R. G. Griffin, *J. Magn. Reson.*, 1983, **55**, 266.
18. K. L. Anderson-Altmann and D. M. Grant, *J. Phys. Chem.*, 1993, **97**, 11 096.
19. M. S. Solum, K. L. Anderson, M. Strohmeier, D. A. Berges, Y. Zhang, J. C. Facelli, R. J. Pugmire, and D. M. Grant, *J. Am. Chem. Soc.*, 1997, **119**, 9804.

20. M. Strohmeier, A. M. Orendt, J. C. Facelli, M. S. Solum, R. J. Pugmire, R. W. Parry, and D. M. Grant, *J. Am. Chem. Soc.*, 1997, **119**, 7114.
21. F. Tian and T. A. Cross, *J. Magn. Reson.*, 1998, **135**, 535.
22. M. Sardashti and G. E. Maciel, *J. Phys. Chem.*, 1988, **92**, 4620.
23. R. Challoner, R. K. Harris, and J. A. Tossell, *J. Magn. Reson.*, 1997, **126**, 1.
24. E. G. Hoelger, F. Aguilar-Parrilla, J. Elguero, O. Weintraub, S. Vega, and H. H. Limbach, *J. Magn. Reson. Series A*, 1996, **120**, 46.
25. A. Shoji, T. Ozaki, T. Fujito, K. Deguchi, S. Ando, and I. Ando, *J. Am. Chem. Soc.*, 1990, **112**, 4693–4697.
26. M. Ashikawa, A. Shoji, T. Ozaki, and I. Ando, *Macromolecules*, 1999, **32**, 2288.
27. M. Sardashti and G. E. Maciel, *J. Phys. Chem.*, 1988, **92**, 4620.
28. M. D. Lumsden, R. E. Wasylishen, K. Eichele, M. Schindler, G. H. Penner, W. P. Power, and R. D. Curtis, *J. Am. Chem. Soc.*, 1994, **116**, 1403.
29. S. Kuroki, N. Asakawa, S. Ando, I. Ando, A. Shoji, and T. Ozaki, *J. Mol. Struct.*, 1991, **245**, 69.
30. M. Hong, J. D. Gross, W. Hu, and R. G. Griffin, *J. Magn. Reson.*, 1998, **135**, 169.
31. A. Ramamoorthy, C. H. Wu, and S. J. Opella, *J. Am. Chem. Soc.*, 1997, **119**, 10 479.
32. D. K. Lee, J. S. Santos, and A. Ramamoorthy, *Chem. Phys. Lett.*, 1999, **309**, 209.
33. G. S. Harbison, L. W. Jelinski, R. E. Stark, D. A. Torchia, J. Herzfeld, and R. G. Griffin, *J. Magn. Reson.*, 1984, **60**, 79.
34. T. G. Oas, C. J. Hartzell, F. W. Dahlquist, and G. P. Drobny, *J. Am. Chem. Soc.*, 1987, **109**, 5962.
35. C. J. Hartzell, M. Whitfield, T. B. Oas, and G. P. Drobny, *J. Am. Chem. Soc.*, 1987, **109**, 5966.
36. Q. Teng and T. A. Cross, *J. Magn. Reson.*, 1989, **85**, 439.
37. M. D. Lumsden, G. Wu, R. E. Wasylishen, and R. D. Curtis, *J. Am. Chem. Soc.*, 1993, **115**, 2825.
38. G. A. Lorigan, R. McNamara, R. A. Jones, and S. J. Opella, *J. Magn. Reson.*, 1999, **140**, 315.
39. A. Ramamoorthy, C. H. Wu, and S. J. Opella, *J. Am. Chem. Soc.*, 1997, **119**, 10 479.
40. K. L. Anderson-Altmann, Cu. G. Phung, S. Mavromoustakos, Z. Zheng, J. C. Facelli, C. D. Poulter, and D. M. Grant, *J. Phys. Chem.*, 1995, **99**, 10 454.
41. J. Leppert, B. Heise, and R. Ramachandran, *J. Magn. Reson.*, 2000, **145**, 307.
42. J. Z. Hu, J. Zhou, B. Yang, L. Li, J. Qui, C. Ye, M. S. Solum, R. A. Wind, R. J. Pugmire, and D. M. Grant, *Solid State NMR*, 1997, **8**, 129.
43. J. Z. Hu, M. S. Solum, R. A. Wind, B. L. Nilsson, M. A. Peterson, R. J. Pugmire, and D. M. Grant, *J. Phys. Chem., A*, 2000, **104**, 4413.
44. Y. Yarim-Agaev, P. M. Tutunjian, and J. S. Waugh, *J. Magn. Reson.*, 1982, **47**, 51.
45. A. Bax, N. M. Szeverenyi, and G. E. Maciel, *J. Magn. Reson.*, 1983, **51**, 400.
46. A. Bax, N. M. Szeverenyi, and G. E. Maciel, *J. Magn. Reson.*, 1983, **55**, 494.
47. R. Tycko, G. Dabbagh, and P. Mirau, *J. Magn. Reson.*, 1989, **85**, 265.
48. T. Terao, T. Fujii, T. Onodera, and A. Saiks, *Chem. Phys. Lett.*, 1984, **107**, 145.
49. L. Frydman, G. C. Chingas, Y. K. Lee, P. J. Grandinetti, M. A. Eastman, B. A. Barrall, and A. Pines, *J. Chem. Phys.*, 1992, **97**, 4800.
50. A. C. Kolbert and R. G. Griffin, *Chem. Phys. Lett.*, 1990, **166**, 87.
51. Z. Gan, *J. Am. Chem. Soc.*, 1992, **114**, 8307.
52. See discussion in Reference 10.
53. J. C. Facelli, J. Z. Hu, M. S. Solum, R. J. Pugmire, and D. M. Grant, in 'Modeling NMR Chemical Shift Tensors, Gaining Insights into Structure and Environment', ACS Symposium Series 732. eds J. C. Facelli and A. C. deDios, 1999, p. 162.
54. J. Z. Hu, D. Barich, R. J. Pugmire, and D. M. Grant, '^{15}N chemical Shift Tensors in Indolazines', in preparation.
55. K. L. Anderson-Altmann, C. G. Phung, S. Mavromoustakos, Z. Zheng, J. C. Facelli, C. D. Poulter, and D. M. Grant, *J. Phys. Chem.*, 1995, **99**, 10 454.
56. C. M. Carter, D. W. Alderman, J. C. Facelli, and D. M. Grant, *J. Am. Chem. Soc.*, 1987, **109**, 2639.
57. D. M. Grant, F. Liu, R. J. Iuliuci, C. G. Phung, J. C. Facelli, and D. W. Alderman, *Acta Crystallogr.*, 1995, **B51**, 540.
58. J. C. Facelli, R. H. Contreras, D. G. de Kowalewski, V. J. Kowalewski, and R. N. Piegaia, *J. Mol. Struct., Theochem*, 1983, **94**, 163.

Biographical Sketch

Ronald J. Pugmire, *b* 1937. B.S. 1959, Idaho State College; Ph.D., 1966, Chemistry, University of Utah, USA, where he was introduced to NMR by David M. Grant. Post Doctoral, 1966–68, University of Utah. Faculty in Chemical and Fuels Engineering and Chemistry (adjunct), and Associate Vice President for Research, University of Utah. Approximately 200 publications. Research specialties: carbon-13 and nitrogen-15 NMR, chemical shielding in solids, theoretical correlation of shielding tensors, coal chemistry, and applications of NMR spectroscopy to coal science and combustion science.

Organic Chemistry Applications

John D. Roberts

California Institute of Technology, Pasadena, CA, USA

1 Related Articles 14
2 References 14

Structures are at the heart of organic chemistry. The brains are in using structures and structural theory to achieve desired chemical transformations. Before the 1920s, the only way to determine the way that the constituent atoms in an organic molecule are bonded together was by degradation and synthesis. For complex molecules, the process of determining structures was often arduous, particularly when there were few functional groups as with many steroids. Nonetheless, extraordinary progress was made, even if slowly, by a combination of experimental and deductive skills.

After 1920, X-ray diffraction slowly became the definitive procedure for determining structures for substances that can be obtained in crystalline form and are otherwise amenable to diffraction techniques. In its earlier days, X-ray diffraction was decisive in structural studies of steroids, penicillin, vitamin B_{12} and, later, for many other important substances, often natural products, of which a recent triumph was of nitrogenase. The representations of structures so obtained are of necessity essentially static, although the root-mean-square amplitudes of thermal vibrations of the atoms in the crystal are usually determined.

For liquids or solutions, X-ray diffraction is not helpful, but considerable structural information is obtainable by infrared, Raman, ultraviolet, and mass spectroscopies. However, these alone do not often allow a complex structure to be determined. Applications of nuclear magnetic resonance spectroscopy to organic chemistry in the early 1950s provided an entirely new structural analysis tool that surely must rank as the most important advance in organic chemistry in the last 50 years, if not in the more than 100 years since the development of classical organic structural theory by Kekulé and Loschschmidt. This is a bold statement for which justification will be supplied in what follows. The practical details of running NMR spectra on organic compounds will not be covered here; there many excellent books for this purpose. Instead the focus will be on illustrative features of how NMR is used in organic chemistry.[1]

NMR spectra require samples containing atomic nuclei possessing magnetic moments and, fortunately, all of the kinds of atoms of general interest to organic chemists have one or more isotopes that have magnetic moments. Unfortunately, not all of these magnetic nuclei are equally capable of giving useful resonance signals and, furthermore, many have low natural isotopic abundances.

Of the atomic nuclei contained in the majority of organic compounds, an approximate order of importance for NMR spectroscopy is ^{1}H, ^{13}C, ^{15}N, ^{19}F, ^{31}P, ^{2}H, ^{14}N, ^{17}O, ^{3}H, and ^{33}S. It should be understood that NMR is not an especially sensitive spectroscopic procedure. For this reason, it is important that the magnetic moment of the nucleus and its natural abundance be reasonably large. It is also important that the linewidths of the nuclear resonances be narrow and this means that the magnetization induced in the nuclei should not decay away (relax) too quickly. An important contributor to the decay of induced nuclear magnetization arises when the nuclei have electric quadrupole moments and such quadrupole moments are associated with nuclei that have nuclear spins (I) greater than $\frac{1}{2}$. Consequently, it is advantageous to have the nuclear spin be $\frac{1}{2}$ and this is true for ^{1}H, ^{3}H, ^{13}C, ^{15}N, ^{19}F, and ^{31}P, but not for ^{2}H, ^{14}N, ^{17}O, ^{33}S, or for chlorine, bromine, and iodine. Except for fluorine, the halogens in organic compounds do not give useful NMR spectra. Hydrogen-3 is a superb nucleus for observation by NMR, with spin-$\frac{1}{2}$ and the largest known magnetic moment of any nucleus. However, it is radioactive with a halflife of $\sim$13 y, which means that to have observable quantities is to have a great deal of radioactivity, even in a small sample.

Proton NMR, besides having the advantage of $I = \frac{1}{2}$, benefits from both a large magnetic moment and high natural abundance, as well as being very common in organic compounds. Carbon NMR can only be achieved with ^{13}C which has $I = \frac{1}{2}$ but with a magnetic moment only one-fourth that of ^{1}H and a natural abundance of 1.1%. These factors make natural abundance carbon NMR more difficult to obtain than proton NMR by a factor of about 6000. Matters are still worse with natural abundance ^{15}N with a magnetic moment one-tenth of that of protons and an abundance of only 0.37%. These unfavorables translate to an increased difficulty of detection relative to protons by a factor of about 260 000.

Many organic molecules can exist in multiple conformations with different stabilities. X-Ray diffraction of organic crystals normally allows us not only to decide which atoms are bonded to one another, but also shows which conformation(s) exist in the crystals. Because most chemical transformations are carried out in solution, it is often vitally important to be able to determine which conformations exist in solution and it is well known that conformational preferences determined for crystals cannot be reliably extrapolated to the same material in solution. NMR has special importance for its ability to determine, at least qualitatively, conformational equilibria in solution and, in many cases, it is unique in its potential for measuring the rates of establishment of such equilibria. Further attention to this point will be given later.

The observables of NMR that apply with particular emphasis to organic chemistry are chemical shifts, spin−spin couplings, nuclear spin relaxation rates, signal intensities, and lineshapes. Lineshapes are particularly relevant when influenced by chemical kinetics of one kind or the other. For structural analyses, NMR spectroscopy is in many ways closely related to the classical degradation procedures. Degradation is used to break up molecules with the hope of being able to produce recognizable fragments with known bond connectivities. The structure is then deduced by fitting the pieces back together in the manner of a jigsaw puzzle. NMR operates to show the individual pieces of the puzzle while they are in place, and the structural analyst has to deduce the relationships of the pieces to one another to determine the connections between the atoms.

Differences in chemical shift of the resonances for a given kind of magnetic nucleus are the result of differences in the shielding of the nuclei by their electronic environments. Precise predictions of shieldings from first principles of quantum mechanics are difficult, but many useful qualitative generalizations are available. Proton (^{1}H) chemical shifts are customarily measured in Hz relative to the proton resonance of tetramethylsilane. Because the shifts so measured are strictly proportional to the strength of the magnetic field and NMR spectrometers operate at a variety of field strengths, it is convenient to divide measured shifts in frequency units by the spectrometer frequency and multiply by 10^6. Shifts are then expressed by ppm, dimensionless quantities, that allow immediate comparisons between measurements made at different field strengths. Spin–spin couplings are independent of field strength and should always be reported in Hz. Nuclear relaxation rates are commonly expressed in characteristic times, T_1 or T_2, and range over widely different values from μs to hours. The reciprocal of the characteristic time is the usual chemists' rate constant, k, that is most commonly expressed in s^{-1}. Integrals of line intensities, when properly measured, correspond to quite precise relative concentrations of the substances or groups corresponding to the lines integrated.

Some of the wealth of information obtainable by NMR can be illustrated by the very well-studied examples provided by ethanol and its one stable isomer, dimethyl ether. The ^{1}H spectrum of ethanol, by showing three chemically shifted groups of resonances with intensity ratios of 1:2:3 corresponding to HO, CH_2, and CH_3, distinguishes itself in an instant from that of dimethyl ether which displays only a single sharp ^{1}H resonance line for its two CH_3 groups. The single resonance for dimethyl ether might seem entirely obvious, but is not really so, because we would not expect all possible rotational angles about the C–O bond to be equally favorable. A possible conformation is shown by structure (**1**).

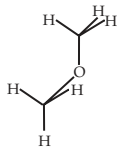

(1)

For a molecule having this structure and symmetry, it will be seen that there should be four hydrogens with the same chemical shift and two others with a different chemical shift. That only one shift can be observed at any magnetic field so far available is a consequence of very rapid rotation about the C–O bonds, whereby the different shifts are averaged to a single value over the lifetimes of the magnetic states of the hydrogen nuclei. Here, a confident judgment can be made that the rate of rotation is fast by simple inspection of the spectra. Infrared and Raman spectra can be used to reach similar conclusions, but not in any very simple way. It is expected that there will be at least some barrier to rotation of the methyl group about the C–O bond and that different proton chemical shifts would be observed at temperatures low enough that the interval between rotations is comparable or longer than the lifetimes of the magnetic states. However, for dimethyl ether, this temperature is lower than can be usefully achieved with present-day commercial NMR spectrometers. Nonetheless, if a CH_3 group is located in an environment where its rotation is restricted by virtue of severe steric crowding, and where different chemical shifts are predicted for the hydrogens by symmetry considerations, then it is possible to measure the rate of rotation as a function of temperature and determine the activation parameters for rotation. One example is provided by the molecule (**2**).

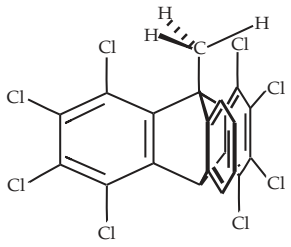

(2)

Here, steric hindrance is such that the barrier for rotation about the C–CH_3 bond is about 46 kJ mol^{-1} (11 kcal mol^{-1}) as compared to perhaps a 12 kJ mol^{-1} (3 kcal mol^{-1}) rotational barrier for the O–CH_3 bond of dimethyl ether.

Another lesson from dimethyl ether is that nuclei having the same resonance frequency do not show the phenomenon of spin–spin splitting. Viewed in the simplest way, spin–spin splitting arises because the resonance frequency of a given nucleus depends on the magnetic field that the nucleus is experiencing. Now, if another nucleus with a magnetic moment is in the same molecule, then the magnetic field that this second nucleus generates either augments or decreases the magnetic field at the first nucleus, depending on the magnetic quantum state of the second nucleus. In quantum terms, this means that the energy levels of the first nucleus depend on the magnetic quantum state of the second nucleus. Because the magnetic moment of the nucleus does not depend on the magnitude of the applied field it should be clear why the magnitudes of coupling constants are independent of the applied field.

The way of looking at the origin of spin–spin splitting that we have just described is incomplete, because the protons of the methyl groups of dimethyl ether might be expected to cause each other's resonances to be split but, as we have said, they are not split. The fact is that, while the protons of the methyl groups of dimethyl ether do have magnetic energy-level differences that correspond to spin–spin splittings, transitions between these levels are 'forbidden', so no splittings are observed. This behavior is rather general for protons with the same chemical shift.

Spin–spin splittings provide very valuable structural information and if for some reason it is desired to know the values of the J coupling constant between normally equivalent protons, as of the methyl groups of dimethyl ether, this can be achieved by replacing one or two (not three) of the hydrogens by deuterium. Because deuterium has a smaller resonance frequency than hydrogen by a factor of 6.5, the transitions that lead to spin–spin splitting of hydrogen by deuterium are now allowed and, with substitution of one deuterium, a 1:1:1 triplet with a spacing of 1.66 Hz is observed for the resonances of the two remaining and equivalent methyl group protons. The triplet is a consequence of the nuclear spin of deuterium being unity and its having magnetic quantum states of +1, 0, and

−1. The spacings of the triplet correspond to the ^2J(H,H) coupling divided by γ_D/γ_H and need to be corrected if ^2J(H,H) is desired. The value of ^2J(H,H) so obtained is 10.8 Hz and is not strictly equal to ^2J(H,H), because there will be a small isotope effect resulting from the substitution of D for H.

It is very useful to classify the magnetic nuclei in various kinds of molecules with regard to their potential patterns of spin–spin splittings. The protons of CH_4 will be in equivalent magnetic environments (unless the molecular symmetry is reduced by something like being adsorbed on a metal surface) and, furthermore, the ^2J(H,H) coupling constants between each of the four protons are expected to be equal. We categorize such a grouping as A_4. The situation for $CH_3–CH_3$ undergoing rapid rotation around its C–C bond is not the same, even though all six protons will have the same chemical shift. The difference here is that there are two different coupling constants, ^2J(H,H) for the protons in each methyl group and ^3J(H,H) between the methyl groups. The characterization is now $A_3A'_3$. With many of the possible arrangements of spin–spin splitting groups, the chemical shift difference is important to the line positions and intensities. Two coupled, spin-$\frac{1}{2}$, nuclei with the same magnetic moment and a shift difference large compared to the coupling constant J between them will give two doublets with all of the resonances having equal integrated intensities. Also, the spacing between the doublet centers will be equal to the chemical shift difference. If the chemical shift difference is comparable to the coupling then the outer lines of the doublet pair lose intensity while the inner lines get stronger. In addition, the spacing between the doublet centers is now not the shift difference δ, but instead $(\delta^2 + J^2)^{1/2}$. The first case, we designate as AX and the second as AB. Letters close together in the alphabet are used to represent shift differences comparable to couplings, those farther apart in the alphabet are used for large shift differences. The distinction can be blurred by which spectrometer is used. If a shift difference is 0.333 ppm and the coupling is 5 Hz, the separation between the doublet centers when observed with a spectrometer at 30 MHz will be $(100 + 25)^{1/2}$ or 11.18 Hz, a difference of 1.18 Hz (a 12% deviation) from what would be expected for an AX system. But at 600 MHz, the same separation will be $(40\,000 + 25)^{1/2}$ or 200.06 Hz, which is only 0.06 Hz (a deviation of 0.03%). Any ambiguity about whether chemical shifts are large with respect to the couplings is easily resolved when the shift units are in Hz rather than ppm. When there is more than one kind of nucleus in the spin system, the chemical shift difference in effect will be very large and so fluoroethane would be designated by A_3B_2X. This way of classifying spin systems is very widely used and helpful in understanding where spin–spin couplings are expected to be more complex than predicted by simple counting on one's fingers.

The oxygen NMR of dimethyl ether is only possible to observe for ^{17}O because neither ^{16}O nor ^{18}O has a nuclear magnetic moment and unfortunately ^{17}O has a very low natural abundance (0.037%). A further problem arises because the ^{17}O nucleus has a sizable electric quadrupole moment that normally makes the lifetimes of the states very short, thus usually giving broad featureless resonances for which chemical shifts, but seldom coupling constants, can be obtained.

The chemical shift of the naturally occurring ^{13}C in the carbons of dimethyl ether can be easily obtained at the natural abundance level, with, or without, proton decoupling. Without proton decoupling, the ^{13}C resonance will be split into a quartet by its three directly attached protons. The ^4J(H,H) couplings between the methyl hydrogens across the ether oxygen bridge will not correspond to allowed transitions if both carbons are ^{12}C, but if one is ^{13}C and ^4J(H,H) is large enough, then there will be a 1:3:3:1 quartet of transitions corresponding to spin–spin splittings, because now the frequencies of the methyl protons on one or the other carbon will be caused to differ by virtue of the $^1J(^{13}C,H)$ coupling. ^4J(H,H) couplings of this kind are usually small, 0.3–2 Hz.

To return to ethanol and its proton NMR spectrum. The shifts are in the order of increasing frequency from the usual standard, tetramethylsilane (TMS), the CH_3, the CH_2, and the OH protons. The usual rationalization of the sequence of these shifts (for pure liquid ethanol at 1.2, 3.7, and 5.3 ppm, respectively) is on the basis of electronegativity. The oxygen by virtue of its superior electronegativity attracts electrons from the OH hydrogen's valence shell, thus decreasing the diamagnetic shielding of that nucleus and causing its resonance to appear at higher frequency than TMS relative to the CH_2 or CH_3 protons. The shifts of the resonances of the CH_2 and CH_3 protons can be rationalized similarly, because the CH_2 carbon is attached to an oxygen while the CH_3 carbon is connected to another carbon. In general, this sort of reasoning has utility, as shown by the fact that there is a good linear relationship between the difference in proton shifts between the XCH_2 and CH_3 protons for XCH_2CH_3 and the Pauling electronegativities when X is halogen.

Matters are actually not nearly so simply related to electronegativity for the resonance of the OH proton, because its shift is very sensitive to intermolecular hydrogen bonding and, because, when such hydrogen bonding is decreased by dilution with a nonhydrogen bonding solvent like tetrachloromethane, the OH resonance moves toward that of TMS. At high dilution, the OH resonance is actually observed at a *lower* frequency than that of the CH_3 resonance, even though the OH proton is attached to a very electronegative atom. This is not an uncommon finding when hydrogen bonding is important and, in many proteins, strongly hydrogen-bonded protons are found at as much as 12–18 ppm from tetramethylsilane. Clearly, NMR provides a useful technique for the study of hydrogen bonding. Also, it should be remembered that the electronegativity of X in substances with X–H bonds is not necessarily a good predictor of the ^1H shifts in such substances.

Among the factors that influence ^1H shifts, besides electronegativity, is the aromatic ring-current effect. This effect arises because the π electrons in an aromatic ring are caused to circulate coherently through the π-orbital system under the influence of a magnetic field when the field axis is perpendicular to the plane of the ring. The effect is diamagnetic and diminishes the applied field in the center of the ring, but is paramagnetic and augments the applied field at the protons of the ring because they are in the return path of the magnetic lines of force [see structure (**3**)].

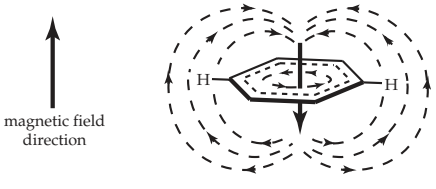

(3)

The ring-current effect makes the shift of protons attached to aromatic rings less shielded than those of protons attached to simple double bonds. One could argue that the otherwise well-known electronegativity of aromatic rings might produce the observed shifts, but this does not accord with the proton shifts of 18-annulene (**4**). This substance has a favorable 18 π-electron system and its molecular configuration is such that it has 12 *outside* and four *inside* protons attached to its carbons.

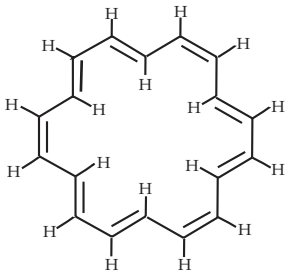

(4) 18-annulene

The *inside* protons, as expected from the ring-current effect, are strongly shielded and come into resonance at -1.9 ppm on the TMS scale. The *outside* protons are very deshielded and are observed at +8.8 ppm on the same scale. Thus, there is a difference of 10.7 ppm between the shifts of these protons.

We will have more to say about the chemical shifts of nuclei other than protons later.

Spin–spin couplings are observed between the several proton groups for ethanol, because they have different resonance frequencies. The coupling patterns are found to be variable because of the possibility of slow, or rapid, intermolecular exchange of the OH proton. With slow exchange, the OH proton is expected and found to be split into a 1:2:1 triplet by the CH_2 protons with ^3J(H,H) equal to 4.8 Hz. Our expectation of the 1:2:1 triplet is based on the concept that there are four different kinds of molecules as far as the CH_2 magnetic states are concerned. This means that the OH proton on any given individual ethanol molecule has a 25% probability of being attached to a CH_2 carbon with proton magnetic states of total quantum number +1 or -1 ($+\frac{1}{2}$, $+\frac{1}{2}$ and $-\frac{1}{2}$, $-\frac{1}{2}$), and a 50% probability of being on molecules with magnetic states having quantum numbers of zero ($+\frac{1}{2}$, $-\frac{1}{2}$ and $-\frac{1}{2}$, $+\frac{1}{2}$). Generally, as noted earlier, we expect the four-bond coupling, ^4J(H,H) to be small in most simple open-chain compounds, and for ethanol we can neglect the four-bond couplings. However, expectation that such couplings will invariably be small is not in accord with experience. The larger ^4J(H,H) couplings are often valuable in stereochemical studies. We will have more to say about the magnitudes of spin–spin couplings after taking a look at why the OH resonance in ethanol is not always observed to be split by the CH_2 protons.

Observation of the splitting of the OH resonance in ethanol depends on whether intermolecular exchange of the OH protons is rapid compared with the lifetime of the magnetic states involved. If exchange is rapid, then any given OH proton, as it goes from ethanol molecule to ethanol molecule, runs the gamut of CH_2 groups with different magnetic states. The result is that the given OH proton experiences the average of those CH_2 magnetic states. Because the average (+1, 0, 0, -1) is zero, no splitting is observed when exchange is fast compared with the lifetimes of the states. The lineshapes change between the extremes of slow and fast exchange and by analyzing those lineshapes it is possible to determine the rates of exchange as a function of solvent, exchange catalyst, or temperature with considerable precision over a range of rates amenable to exploration by few, if any, other techniques. A variant on the OH exchange studies of ethanol is to investigate the proton NMR of mixtures of ethanol with water. If a little water is added to pure ethanol, the OH resonances of the two substances are observed separately. As more water is added, OH exchange speeds up, the separate OH resonances merge and assume the weighted-average position determined by the shifts of the OH groups (if they could be determined separately for the mixture) and the relative concentrations of ethanol and water.

The proton–proton coupling patterns of ethanol under conditions of fast OH exchange are quite simple. There is a 1:2:1 group of resonances for the CH_3 group, reflecting the possible magnetic states of the two protons of the CH_2 group, and a 1:3:3:1 grouping for the CH_2 group arising from the possible magnetic states of three protons with the same resonance frequency ($+\frac{1}{2}$, $+\frac{1}{2}$, $+\frac{1}{2}$ and $+\frac{1}{2}$, $+\frac{1}{2}$, $-\frac{1}{2}$; $+\frac{1}{2}$, $-\frac{1}{2}$, $+\frac{1}{2}$; $-\frac{1}{2}$, $+\frac{1}{2}$, $+\frac{1}{2}$; and so on). The lines in each group are separated by 7.15 Hz which is the ^3J(H,H) coupling constant. If the chemical shift difference is comparable to the coupling constant, then smaller secondary splittings may be observed. As mentioned earlier, the secondary splittings are the result of quantum mechanical influences that are most often evident in the range of shifts between the extreme, where the transitions are forbidden, because even though the coupling constant may be large, the frequency difference is zero and the other extreme where the frequency difference is much greater than the chemical shift. However, it should be recognized that there are circumstances, such as for the so-called AA′XX′ nuclear spin systems, where the chemical shifts can be much larger than the couplings, but quantum effects override simple expectations of number of lines based on simply counting up the number of possible combinations of $+\frac{1}{2}$ and $-\frac{1}{2}$ nuclear magnetic states. With such systems, rather complex patterns of lines usually result.[2]

When OH exchange is slow, the CH_2 resonances of ethanol become complex because ^3J(H,H) involving the OH proton is 4.8 Hz and that involving the CH_3 protons is 7.15 Hz. In effect, each of the 1:3:3:1 quartet resonances observed when OH exchange is fast now becomes, with slow exchange, split into a doublet separated by 4.8 Hz, thus producing eight resonance peaks with unequal spacings.

Much can be done to simplify and analyze spin–spin coupling patterns by either selective proton decoupling or by substituting an isotope with a different, or no, magnetic moment. Selective proton decoupling achieves the same result that we have described for ethanol consequent to OH proton exchange. What decoupling means in this context is that if we irradiate the OH protons at their resonance frequency, under slow exchange conditions, those protons cycle rapidly between the $+\frac{1}{2}$ and $-\frac{1}{2}$ magnetic states, so that their magnetic effect on the CH_2 protons is averaged to zero and, as a result, we observe the same 1:3:3:1 quartet and 1:2:1 triplet as when OH exchange is fast. Selective irradiation of the CH_3 protons will lead to a 1:2:1 triplet for the OH protons and a 1:1 doublet for the CH_2 protons with the simple splitting of 4.8 Hz. Substitution of

deuterium for the OH hydrogen, with a consequent reduction of J by a factor of 6.5, can also simplify coupling patterns.

There are many ways in which spin–spin coupling patterns can be used to solve structural problems—some of astonishing simplicity. An example is provided by a supposed tetraazodibenzocyclooctatetraene (**5**).

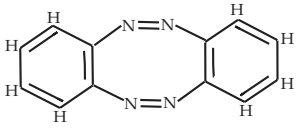

(5)

The hydrogens on each benzo group are expected to give NMR spectra of the AA′BB′ classification with respect to their coupling patterns. However, AA′BB′ patterns are always symmetrical, the resonances on the left side of the center being the mirror image of those on the right side. The problem with the supposed structure was that, in fact, the proton resonance pattern was not symmetrical and, furthermore, was too complex to be representative of AA′BB′. On this basis a different structure, shown in Scheme 1, was proposed. This is now of the ABCD type and expected to give an unsymmetrical coupling pattern.

From the description of spin–spin splitting given earlier, it might be inferred that the influence of the magnetic state of a particular nucleus on the magnetic field (and resonance frequency) of another in the same molecule is transmitted through space like an electrostatic effect. Magnetic influences of this kind are called dipolar effects and are quite large in some circumstances but, in fact, they do not contribute to spin–spin splittings for molecules in solution that are undergoing rapid tumbling. Such tumbling causes dipolar effects to be averaged to zero. What remains is the so-called scalar couplings that arise by magnetic polarization of the surrounding electrons of a magnetic nucleus and the transmission of that polarization effect through the molecule by electron delocalization in a manner analogous to the familiar resonance transmission of electrical effects.

One consequence of this mode of transmission of coupling information is to make qualitative predictions of the magnitudes of J values in many kinds of structural situations rather difficult. The one-bond coupling between the protons in dihydrogen can be calculated from the splittings in H–D and amounts to 280 Hz. A substantial amount of data is available for one-bond couplings, such as H–^{13}C, H–^{15}N, ^{13}C–^{13}C, and ^{13}C–^{15}N. The magnitudes of such splittings, particularly corresponding to ^1J(^{13}C,H) and ^1J(^{13}C,^{13}C), are valuable indicators of the hybridization of the carbons forming the bonds. The less p and the more s character to the C–H bond, the larger the coupling constant. An interesting and, in some other cases, important concern is for the signs of ^1J couplings. It is not obvious how a through-space magnetic influence of one magnetic moment in a particular magnetic quantum state could, on the one hand, reduce and, on the other, augment the field at another nucleus. But with electronic transmission of the coupling influence, it is not only possible, but common, for J couplings to have different signs. For one-bond couplings, indirect methods have to be used to establish the sign and, for ^1J(^{13}C,H), the sign turns out to be positive.

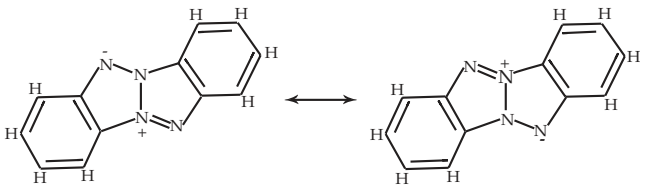

Scheme 1

Two-bond couplings, such as ^2J(H,H) of CH_2 groups, are unusually variable and dependent on the other attached groups to the carbon. Normally, ^2J(H,H) for an aliphatic or alicyclic CH_2 group will be negative and on the order of 10–12 Hz. However, when the CH_2 is part of a double bond, the coupling may be positive or negative, as well as large or small. Examples include CH_2O with ^2J(H,H) equal to +42 Hz.

Three-bond proton–proton couplings of the H–C–C–H variety are especially valuable for determination of the stereochemical relationships of groups. With protons on double bonds, the vicinal ^3J(H,H) couplings are usually much larger for *trans* relationships than for *cis* relationships. The same is also generally true for conformationally mobile systems, although the situation is much more complex; because, in principle, there is an essentially infinite range of rotational dihedral angles, θ, between the protons.

Because of its practical importance to the determination of stereochemical relationships, much theoretical and experimental research has been carried out on the relationship between ^3J(H,H) and θ in systems where the two carbons carrying the coupled protons are both saturated. Theoretical considerations suggested very early on that there should be an approximately cosine relationship between J and θ. One useful form of the equation is shown in equation (1) (see Figure 1).

$$^3J(\mathrm{H,\ H}) = 7.0 - 1.0\cos\theta + 5.0\cos 2\theta \qquad (1)$$

This curve, an example of the so-called Karplus curve, is quite satisfactory for qualitative correlations of coupling constants with stereochemistry. A variety of other relationships

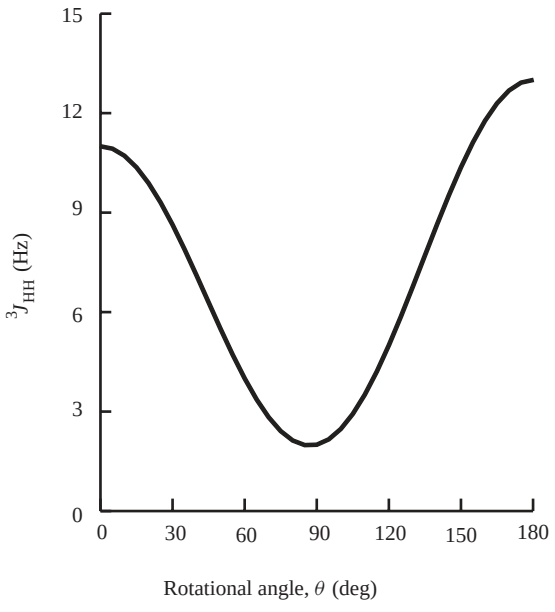

Figure 1 The Karplus curve corresponding to equation (1)

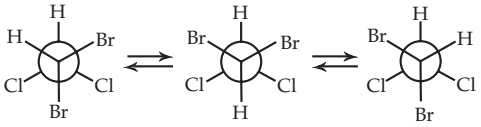

Scheme 2

have been proposed because there are clear effects of the electronegativities of the attached groups on ^3J(H,H). However, corrections for these effects still do not suffice for accurate calculations and adjustments have been offered for H−C−H and C−C−H bond angles, bond distances, and so on. Attempts to codify these couplings have led to multiparameter equations of accuracy probably not better than ±1 Hz and, often when these equations are tried for compounds of interest, it is found that some or all of the needed parameters are unavailable, or that the calculated values of ^3J(H,H) lead to inconsistent stereochemical results.

The areas of greatest interest in this connection are for the determination of the stereochemistry of conformationally mobile systems, of which the simplest examples are substituted ethanes. These substances are presumed to exist in more or less perfectly staggered *gauche* and *trans* conformations. A typical example might be the *gauche* and *trans* conformations of 1,1-dichloro-2,2-dibromoethane, shown in Scheme 2.

At room temperature, the rate of conformational equilibration of the respective rotamers is too fast to allow for observation of more than the averaged chemical shifts of the hydrogens. Because the chemical shift of the $HCCl_2$ proton is different from that of the $HCBr_2$ proton, a ^3J(H,H) coupling will be observed and if we assume, with conventional wisdom, that there are only three conformations, each most stable in the perfect staggered *gauche* and *trans* arrangements, then the experimental H−H coupling constant will depend on the equilibrium constant connecting the conformations. The system here is at its simplest because there is only one coupling constant of interest. Inspection of the conformations suggests that the one with the hydrogens *trans* to one another would seem to be the most favorable, because it has two *trans* and two *gauche* Br···Br interactions, while the other, with the hydrogens *gauche*, has one *trans* and three *gauche* Br···Br interactions.

The example of a simple Karplus curve shown in Figure 1 suggests that for $\theta = 60^\circ$ (*gauche*) the value of ^3J(H,H) should be about 4.0 Hz and for $\theta = 180^\circ$ (*trans*) about 11.5 Hz. The two *gauche* rotamers are enantiomers and, in the absence of a chiral environment, will have the same energy. A statistical equilibrium of the three forms would have the observed coupling $(2 \times 4.0 + 11.5)/3 = 6.5$ Hz. The experimental value is 3.0 Hz. Because this value is even smaller than that estimated for the *gauche* conformations exclusively, it is clear that something is amiss. One unknown is whether or not the conformations will assume perfectly staggered angles. If we solve equation (1) for the rotational angles that give 3.0 Hz for the H−H coupling constant, we get 68.2° and 105.6° as possible values. These angles can be seen to have the advantage of moving two pairs of halogens farther apart at the cost of bringing another pair closer together. The 68.2° rotational angle does this less extremely and intuition suggests that this is a possible solution to the conformational problem (Scheme 3).

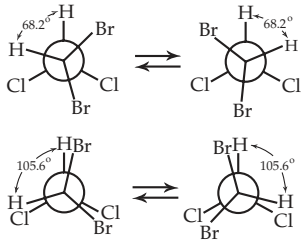

Scheme 3

However, we have alluded earlier to the need to correct the couplings for the electronegativity of substituent groups and, in general, strongly electronegative groups such as halogens make the couplings smaller. A multiparameter equation[3] that relates couplings to rotational angles and takes into account substituent electronegativities estimated by the Huggins procedure suggests that the *gauche* and *trans* couplings of the perfectly staggered conformations of 1,1-dichloro-2,2-dibromoethane should be 2.2 and 6.4 Hz, respectively. These figures suggest that the *gauche* form dominates to the extent of 81%. The overall level of uncertainty in the conformational analysis even for this very simple example is large, but at least the message is consistent that the *trans* conformation is not as favorable as the *gauche*.

Determination of the conformational equilibrium or stereochemical configuration for ethanes in general, or for other two-carbon fragments with more than two hydrogens, is often made difficult because of the need to perform a computer analysis to extract the vicinal coupling constants from complicated spin−spin coupling patterns. Such analyses can be carried out in several ways; one that has reasonably stood the test of time is the program LCN3, originally written in FORTRAN for IBM computers using punched-card input.[4] With this program, intuition and experience are called upon to input trial shift and coupling parameters that produce a sample spectrum to compare with the experimental spectrum. If there is reasonable correspondence, the user correlates and enters the experimental line positions with particular transitions calculated from the trial parameters. The computer program then attempts to find the best fit between parameters, the calculated and the experimental line positions for the given transition assignments. A second or third round of transition assignments is often required to give an rms fit between calculated and experimental line positions on the order of 0.2 Hz.

Consider now a 1,2-disubstituted ethane—once one has determined the coupling constants that correspond to its experimental proton spectrum, there is still the problem of obtaining a set of predicted couplings to compare them with to estimate the position of the conformational equilibria. Assuming only the conventional staggered conformations, it can be seen that there are two different vicinal couplings, J_t^g and J_t^t for the *trans* rotamer and four different vicinal couplings for the two energetically equivalent *gauche* rotamers, J_g^t, J_g^g, $J^{gg'}$, and $J_g^{g''}$ (see Scheme 4).

In this context, we use subscripts on the Js to denote the conformational family and superscripts to define the relationships between the coupling hydrogens. Matters become much more complex if X and Y are chiral groups, but we shall ignore that possibility here.

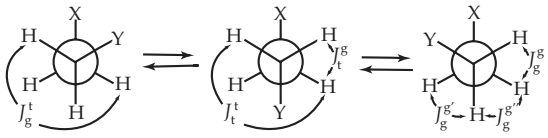

Scheme 4

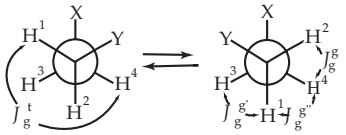

Scheme 5

Empirical relationships allow an estimation of all of these couplings and, in practice, rapid interconversion of the conformations averages some of these couplings for the *gauche* rotamers. If we number the hydrogens of the *gauche* rotamers, we will see that interconversion of these rotamers will cause $J(1,4)$ and $J(2,3)$ to be the average of J_g^t and $J_g^{g''}$. Similarly, $J(1,3)$ and $J(2,4)$ will be the average of J_g^g and $J_g^{g'}$ (see Scheme 5).

Unless the two-bond geminal H−H couplings are different, they will have no influence on the appearance of the spectra.

An illustrative and instructive example of the use of vicinal couplings in the conformational analysis of 1,2-disubstituted ethanes is for butanedioic acid, where X and Y are both carboxy groups. Having X and Y equivalent groups simplifies matters by making J_g^g and $J_g^{g'}$ equivalent, but also complicates them because now the chemical shift difference between the CH_2 groups disappears. With no chemical shift difference, the vicinal couplings become invisible. This part of the problem can be solved with the aid of ^{13}C labeling of one or both CH_2 groups, or by utilization of natural abundance ^{13}C, although this is only present to the extent of 1.11%. With a ^{13}C at one CH_2 group, the proton spin system becomes AA′BB′X and, with two ^{13}C atoms, it is AA′BB′XX′. In either case, the effect of the rather large $^1J(^{13}C,H)$ coupling (∼125 Hz) is to produce a complex proton spectrum from which the vicinal H−H couplings can be extracted.

The chemical interest in the conformational analysis and conformational preferences of butanedioic acid stems from the assessment they allow of the role of hydrogen bonding and electrostatic interactions between the carboxy groups as a function of pH, wherein by changing the pH we can have species with two $-CO_2H$, one $-CO_2H$ and one $-CO_2^-$, or two $-CO_2^-$ groups. Definition of the parameters of the system requires a substantial number of determinations of the changes in the vicinal couplings with pH, especially in the intermediate region where all three species exist in significant quantities. With these, it is possible to calculate the couplings of the monoanion, if it is reasonably assumed that the couplings of the unionized acidic and the dianionic species are invariant with pH and can be determined at low and high pH, respectively.

The results are interesting in that they indicate that the unionized acid prefers the *gauche* conformations to the extent of about 80%, the monoanion [perhaps expected to be highly internally hydrogen bonded and strongly favoring *gauche* (**6**)] exists actually somewhat less as the *gauche* rotamer (65%), and the dianion (where electrostatic repulsions might be expected to lead to a high percentage of the *trans* conformation) is only about 50% *gauche* and 50% *trans*.[5]

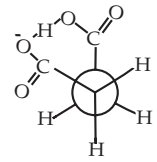

(6)

The type of procedures using vicinal coupling constants described here has very general utility in the determination of conformations and conformational equilibria in a wide variety of acyclic and alicyclic compounds. For complex molecules, the proton spectra may be so complicated that it is not easy or straightforward to determine which protons are coupled to which, much less analyze the coupling patterns. In such cases, two-dimensional spectra can be very helpful. It might seem that ordinary spectra are two dimensional in that we have one dimension of frequency and another of intensity. In NMR, what we call two-dimensional spectra are, in that sense, three dimensional—two dimensions of frequency and a third of intensity. But it is two dimensions of frequency, not of intensity, that we actually call attention to in the usual nomenclature. For the problems of sorting out H−H couplings, a technique called COSY (COrrelated SpectroscopY) is especially useful. It does not give the coupling constants itself, but does show which protons, or groups of protons, are coupled to each other. The usual presentation is a graph such as Figure 2, where the observed proton resonances are plotted along the horizontal and vertical axes and the chemical shifts are found along the diagonal. The coupling interactions between the protons show up as peaks,

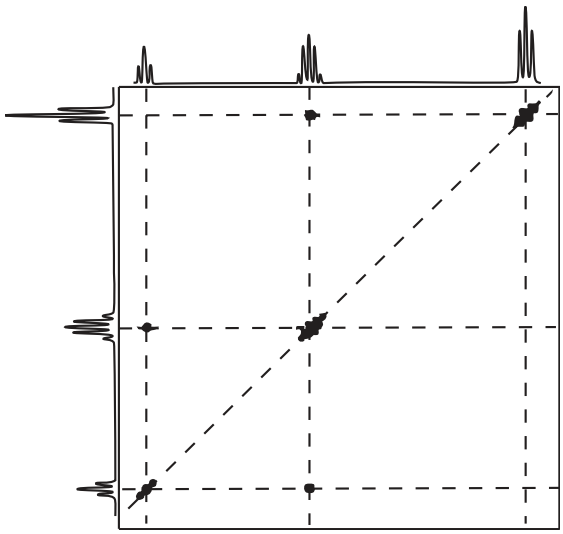

Figure 2 A two-dimensional COSY proton spectrum of ethanol. The purpose of the COSY spectrum is to show which proton groups are coupled to which other groups. Here we can see that the diagonal peaks correspond to the chemical shifts and the off-diagonal peaks to the spin−spin interactions of the OH and CH_2 protons, as well as to those of the CH_2 and CH_3 protons. The lack of coupling is also clear for the OH and CH_3 protons

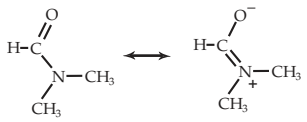

Scheme 6

or contours of peaks (depending on the plotting mode) off-diagonal, and can be correlated with the respective resonances plotted along the axes.

A very important use of NMR is for the measurement of rates of conformational equilibration and the classic case of the use of NMR for this purpose is *N*,*N*-dimethylmethanamide. Resonance theory suggests that this, and related, molecules are most stable with the planar amide configuration having a substantial measure of double-bond character to the C(O)–N bond (Scheme 6). The resonance stabilization energy calculated from bond energies and heats of combustion is usually about 79 kJ mol^{-1} (19 kcal mol^{-1}) and presumably all of this stabilization is lost at the midpoint of rotation about the C(O)–N bond.

N,*N*-Dimethylmethanamide shows two CH_3 proton resonances at room temperature, which demonstrates that rotation must be slow because rapid rotation would interchange the chemical shifts of the methyl groups. On heating, the separate methyl proton resonances first move closer together, because raising the temperature increases the rocking motion about the C(O)–N bond, and this decreases the chemical shift difference. Then, when the rate of surmounting the rotational barrier becomes great enough to affect the lineshapes, the methyl proton resonances broaden, coalesce, and finally narrow.[6] The actual temperature at which coalescence just occurs is called the *coalescence temperature* and the rotational rate which corresponds to it is given by equation (2), provided that one knows (normally by extrapolation) both the chemical shift difference, $\Delta\delta$, and the corresponding linewidths that protons would have at the temperature of the coalescence point, if rotation were slow.

$$k = \frac{\pi \Delta\delta}{\sqrt{2}} \qquad (2)$$

Equation (2) is not accurate if the linewidths are comparable to the shift difference. Clearly the coalescence temperature will change with the spectrometer frequency, because $\Delta\delta$ will change with the spectrometer frequency.

The activation energy, E_a, obtained from a number of studies of the changes in linewidth and coalescence of the methyl group resonances of *N*,*N*-dimethylmethanamide with temperature, was originally subject to large experimental errors, but is now agreed to be close to 83 kJ mol^{-1} (20 kcal mol^{-1}), in good agreement with the calculated loss of resonance energy at the midpoint of rotation about the C(O)–N bond.

In many studies, the chemical shift differences and linewidths are taken to be those measured at temperatures quite different from the coalescence point and this can lead to serious errors. There are other, and very useful techniques, for measuring rates of processes, such as restricted rotation by NMR.[7–9] In some cases, chemical shift differences are averaged; in other cases, coupling constants are averaged and, most often, both are involved. One excellent example of coupling constant averaging alone is provided by the hydroxy proton of ethanol as described earlier.

A quite different type is observed with 3,3-dimethylbutylmagnesium halides (**7**). Rotation is rapid, but the large *t*-butyl and MgX groups strongly prefer to be *trans* to one another. The two CH_2 groups are then expected to form an AA′XX′ spin system. However, at room temperature, one observes a typical triplet A_2X_2 spectrum. This is because the MgX group, by one mechanism or another, changes its configuration at C-1. The configurational change is accompanied, or followed, by a C–C bond rotation that causes the A and A′ protons to exchange positions. At −53 °C, a sharp AA′XX′ spectrum is observed and, from the spectral changes with temperature, it is possible to determine the activation energy, E_a, for the change in configuration at C-1.[10]

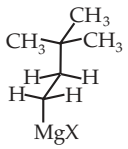

(7)

NMR has proved extraordinarily useful in determining the rates and positions of conformational equilibria in cyclic compounds of which cyclohexane (Scheme 7) is the prototype.

Unfortunately, cyclohexane itself, although giving only a single sharp proton resonance when equilibration is fast, provides a difficulty manageable complex splitting pattern when equilibration is slow. One elegant solution (Scheme 8) is to substitute deuterium for 11 of the hydrogens and remove the residual small H–D couplings by irradiating the deuteriums at their resonance frequencies.[11] This procedure leads to a sharp single proton line when interconversion is fast, and two chemically shifted lines, one for axial and one for equatorial protons, when interconversion is slow. An analogous, and also elegant, procedure is to label with tritium and irradiate the protons while observing the tritium spectrum. From the changes of lineshape with temperature, the activation energy for interconversion of the chair forms of cyclohexane has been found to be about 46 kJ mol^{-1} (11 kcal mol^{-1}). For many ring compounds, conformational equilibria can also be usefully studied by labeling with fluorine, which has 10–20-times larger chemical shift differences than protons when in comparable conformational situations but does not make much difference to the rates or activation parameters. Thus, changes in the ^{19}F spectrum of 1,1-difluorocyclohexane as a function of temperature give nearly the same E_a as with cyclohexane itself.[12]

Techniques such as these have been applied to a wide variety of mono- and polycyclic ring systems. They give information on such diverse situations as the degree of the flexing of cyclobutane rings to inversion barriers for cyclooctanes and for *cis*-decalins.

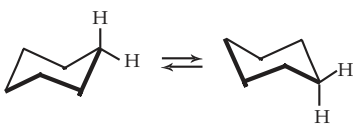

Scheme 7

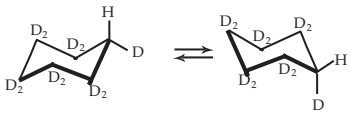

Scheme 8

Another and more subtle use of NMR in stereochemical analysis has to do with what are called *diastereotopic* atoms or groups. A simple example is afforded by diethyl sulfite (**8**).

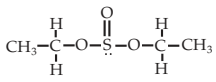

(8)

At first glance, this substance might be expected, like ethanol with rapidly exchanging OH protons, to give a 1:3:3:1 quartet for the CH_2 protons and 1:2:1 triplet for the CH_3 protons. The CH_3 protons, in fact, do show the expected 1:2:1 triplet, but the CH_2 protons give 16 resonances corresponding to four 1:3:3:1 quartets. The reason for this rather striking behavior is that the sulfite group is nonplanar and, as a result, the CH_2 protons on the same carbon are not equivalent by symmetry and are designated as diastereotopic. This phenomenon shows up in many kinds of compounds and can be used to determine the rates of conformational changes. One superb example is in the measurement of the inversion rates of a substituted cyclooctatetraene that exists most favorably as a 'tub' structure (Figure 3).

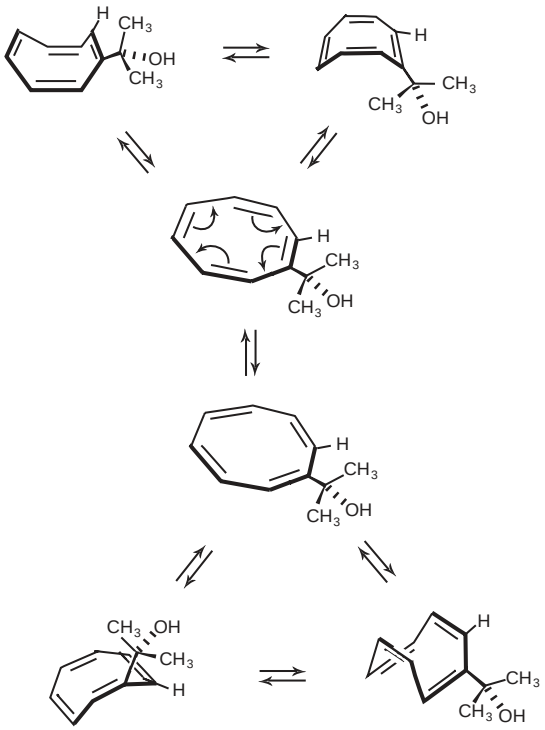

Figure 3 Interconversions of cyclooctatetraene conformations. At the top and bottom are shown the result of simple ring inversion without shift of the double bonds, while the vertical center equation represents inversion with bond shifts, as expected for something approximating a planar pseudoaromatic structure

It will be seen that the CH_3 groups are diastereotopic and if, as shown in Figure 3, the C_8 ring simply inverts, then the CH_3 groups interchange their positions. Thus, if inversion is fast in the NMR time sense, the methyl groups will be equivalent. Note, however, that this process makes no change in the status of any of the ring hydrogens relative to their neighbors. On the other hand, if the ring were to flatten and the double bonds shift, then the hydrogens next to the substituent group would change their relationship to the substituent. For the ring H shown in Figure 3, what is shown as a ring double bond between its carbon and the carbon carrying the dimethylhydroxymethyl group then becomes a single bond, so that there will be both chemical shift and coupling changes for this H. Analyses of the changes in lineshapes of the diastereotopic methyl groups, and of the ring hydrogens, provide a measure of the rates of both ring inversion and bond shifts. It turns out that both processes occur at roughly comparable rates.[13]

In the examples described here and earlier, it should be evident that NMR offers unique possibilities to probe processes that are of great theoretical and practical interest.

The NMR of other nuclei commonly found in organic compounds have also had an enormous impact on studies of organic structures and dynamic properties. Most prominent among these (all spin-$\frac{1}{2}$) nuclei are ^{13}C, ^{15}N, ^{19}F, and ^{31}P. Each of these nuclei has one important characteristic that is not shared with hydrogen. That is, their usual ranges of chemical shifts in ppm exceed those of hydrogen by a factor of 10 to 20. The reason for this is clearly connected to the fact that the elements corresponding to these nuclei form bonds to other atoms using p orbitals while hydrogen uses s orbitals. With p orbitals, the *second-order paramagnetic effect* becomes important whereby electron circulation through high-energy orbitals, mixed with the normal ground-state orbitals, is induced by an applied magnetic field to increase the ground-state stability and, at the same time, decrease the nuclear shielding. This effect, which acts to reduce the shielding at the nucleus of the oxygen of an alcohol, should operate to *increase* the shielding at the OH proton and thus allows rationalization of the substantial shielding observed of the OH proton when hydrogen bonding is decreased, as mentioned earlier.

We have alluded to the usefulness of ^{19}F as a label for hydrogen in conformational analysis and equilibration. This is a small benefit compared with the paramount importance of ^{19}F spectra through determination of shifts and couplings for the establishment of the structures of fluorocarbons and halofluorocarbons for which there are very few other useful techniques.

Phosphorus occurs much less commonly in organic compounds as a multiple substituent than do fluorines, but ^{31}P NMR has wide utility in the study of organophosphorus compounds and of organophosphorus ligands in metal complexes.

The NMRs of carbon and nitrogen are of special interest to organic chemistry in general, but unfortunately are not as easy to observe as those of ^{1}H, ^{19}F, and ^{31}P. The relevant isotopes are ^{13}C, ^{15}N, and ^{14}N. Of these, the last has a high natural abundance (99.63%) but a resonance frequency of about $\frac{1}{14}$ that of ^{1}H and, much worse, a spin of 1. The problem with nuclei having spins greater than $\frac{1}{2}$ is that they have electric quadrupole moments, in effect their nuclear changes are not spherically symmetrical. The result is that whenever the electron distribution around the nuclei is not spherically

symmetrical, rotational motions can create an electrostatic torque which causes the nuclei to change their magnetic orientation, i.e. to relax. This form of relaxation has a variable efficiency. It depends on the magnitude of the nuclear–electric quadrupole moment, on the degree of electrical dissymmetry, and also on the spectrum of rotational motions. For ^{14}N, the resultant of these factors is such that quadrupole relaxation is usually quite serious and the ^{14}N NMR linewidths may be more than 200 Hz wide. Because nitrogen has about a 900 ppm range of chemical shifts, which at 35 MHz (500 MHz for ^{1}H) amounts to 32 000 Hz, much can be done with ^{14}N NMR in terms of measuring chemical shifts, even with large linewidths.

There are important effects of ^{14}N on proton spectra. The coupling between ^{14}N and a directly attached (nonexchanging) proton is normally about 60 Hz. In the absence of fast relaxation, a 1:1:1 triplet with a 60 Hz splitting would be expected for a nonexchanging $^{14}N–H$ proton. Except for ammonium ion, which has a spherical symmetrical charge distribution, the lines making up these splittings are more or less broadened to the point of being unrecognizable. Of course, the relaxation rates of the ^{14}N nuclei that cause these effects are the same as those that cause broadening of the ^{14}N resonance signals themselves. Thus, for some substances such as pyrrole, their N–H proton resonances are often so broad that they can only be made clearly visible by integration.

Similar difficulties arising from rapid quadrupole-induced relaxation are usually encountered in the NMR of other nuclei with spins greater than $\frac{1}{2}$, such as ^{2}H, ^{7}Li, ^{11}B, ^{17}O, and ^{33}S. With some of these nuclei, particularly ^{17}O and ^{33}S, the difficulties are exacerbated by very low natural abundances and low availability of isotopically enriched materials.

For obvious reasons, carbon NMR has received much attention over the years. The abundant isotope ^{12}C (98.9%) has no spin, which can be regarded as a blessing because it avoids the complexities in proton spectra that would be associated with C–H and C–C couplings. The less-abundant ^{13}C (1.11%) has spin-$\frac{1}{2}$ and has a resonance frequency about one-fourth that of protons. In the initial days of NMR, ^{13}C could only be usefully observed with isotopically enriched samples. The first 'routine' ^{13}C spectra were taken by Lauterbur[14] using a special technique called 'adiabatic rapid passage' and these spectra, while lacking in resolution, made very clear the enormous potential importance of ^{13}C for structural analysis.

The next great step forward was made by Grant and co-workers[15] in which they demonstrated the utility of proton decoupling to simplify ^{13}C spectra and the importance of the nuclear Overhauser effect (NOE) attendant to proton decoupling to enhance the intensity of the decoupled signals.

Following on the heels of these advances came the introduction of stable enough NMR spectrometers to allow time averaging of signals, pulse Fourier transform procedures, and proton noise decoupling to simplify and enhance the spectra. The result was that only a few short years passed before ^{13}C NMR became a truly routine procedure for structural analysis.

The level of natural abundance of ^{13}C works to the advantage of the ^{13}C, as well as the ^{1}H, spectroscopist. If ^{13}C were highly abundant, $^{13}C–^{13}C$ couplings would enormously complicate the spectra and would require difficult homonuclear decoupling to simplify the peak patterns for structural analysis. With the probability of having two ^{13}C atoms per molecule being on the order of 0.01% in the absence of isotopic enrichment, it can be seen that $^{13}C–^{13}C$ couplings will not offer much complication of ^{13}C spectra. However, it is possible to detect such couplings by time averaging and they provide valuable structural information. Thus, the INADEQUATE procedure,[16] although requiring relatively larger amounts of sample than an ordinary ^{13}C spectrum, detects all of the one-bond $^{13}C–^{13}C$ couplings in a molecule and clearly shows which carbons are connected to which; in effect directing how the C–C bonds should be drawn. If, when using this procedure, a carbon resonance exhibits no $^{13}C–^{13}C$ coupling, it must be part of a CH_3O, CH_3N, or the like type of grouping.

One of the very useful characteristics of ^{13}C NMR is the sensitivity of carbon shifts to steric hindrance. An axial methyl group on a cyclohexane ring has a smaller shift relative to TMS than an equatorial methyl. Thus, for a methylcyclohexane (**9**) with a *cis* 4-R group that is larger than CH_3, a *t*-butyl group is excellent, the ^{13}C shift of the methyl, of C-1, and C-3, C-5 are on the order of 4–6 ppm more shielded than the corresponding carbons in the *trans* isomer.[17] This is a very general phenomenon and is vividly evident in the steroids, where there are usually multiple 1,3-diaxial interactions of the angular methyl groups with *trans* A,B and C,D ring junctions.

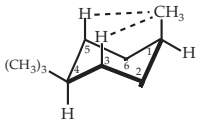

(9)

The sensitivity of ^{13}C shifts to steric interactions is a tremendous boon for the study of polymers. For example, solutions of the isotactic, syndiotactic, and atactic forms of polypropene give quite different ^{13}C spectra and it is very easy to determine the purity of isotactic polypropene by ^{13}C NMR.[18] Another characteristic of ^{13}C that is favorable for the study of polymers is that its large chemical shifts permit use of more viscous samples than is usually the case for ^{1}H spectra. Thus, natural rubber has sufficient molecular motion that its ^{13}C spectrum can be obtained without being dissolved in a solvent.

Another area where ^{13}C NMR has proved invaluable is in the study of the structures and dynamic interconversions of carbocations. In earlier days, the existence and properties of such ions were inferred from kinetics, stereochemical changes, and skeletal rearrangements. The exception was the triphenylmethyl (trityl) cation which could be studied spectroscopically (including by NMR) in concentrated sulfuric acid solutions. The reason that the trityl cation can be obtained in high concentration in strong enough acid is that this cation is stabilized sufficiently by resonance so that it does not react with the weakly nucleophilic HSO_4^- counterion. To form less stable carbocations requires solvent systems with still less nucleophilic counterions and this objective has been achieved by Olah with his 'magic acid' solutions concocted of mixtures of such substances as SbF_5, SO_2FCl, and SO_2F_2. In such media, stable carbocation solutions can be formed, usually at temperatures well below 0 °C that give excellent and enormously interesting NMR spectra.[19]

For example, the norbornyl cation (Scheme 9), whose structure has been the subject of vigorous debate for more than 40 years, shows only one ^{13}C resonance at room temperature.

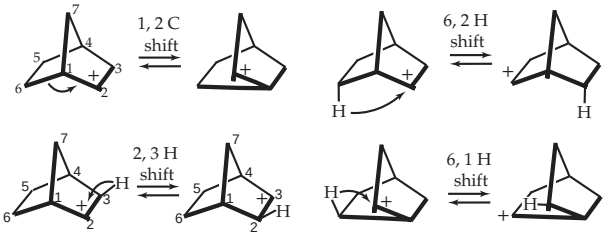

Figure 4 The upper left equation shows a 1,2-carbon shift of the Wagner–Meerwein type that would be expected for a simple 'classical' norbornyl cation. The rearranged cation is the mirror image of its precursor. If just these cations were in rapid equilibrium with each other, or had the nonclassical structure shown in Scheme 9, then the ^{13}C spectrum should show five different resonances in the ratio 1:1:1:2:2. That only one ^{13}C resonance is found at room temperature shows that there must be additional fast rearrangements involving 2,3-, 6,2-, and 6,1-H shifts. At $-70\,^{\circ}C$, the 2,3-H shifts are slow and at around $-140\,^{\circ}C$ the 6,2- and 6,1-H shifts become slow, so that only the 1,2-C shift operates or the structure shown in Scheme 9 is correct

To account for this result, on the basis of the classical structures shown in Figure 4, a primary contributor has to be very rapid 1,2-C shifts wherein C-6 changes from being bonded to C-1 to being bonded to C-2 and the reverse. Such shifts are examples of the well-studied Wagner–Meerwein carbocation rearrangements and, in this case, the original and rearranged cation have carbon skeletons that are mirror images of one another. If only 1,2-C shifts occurred, then one would expect five ^{13}C resonances in the ratio of 1:1:1:2:2 rather than the observed single resonance. So we have to call on somewhat less common hydride rearrangements from C-2 to C-3 and from C-6 to C-2 or C-6 to C-1 shown in Figure 4. If all of these hydrogen migrations and the 1,2-C shifts are fast, then only a single ^{13}C resonance is expected.[20]

Lowering the temperature to $-70\,^{\circ}C$ causes the 2,3-H shifts to slow down and then one observes the three ^{13}C resonances suggested by the combination of fast 1,2-C, 6,2-H, and 6,1-H shifts as shown in Figure 4. Further cooling to about $-140\,^{\circ}C$ causes the 6,2- and 6,1-H shifts to become slow.[20–22] Further cooling, even to liquid helium temperatures,[22] does not give seven ^{13}C resonances and there seems no question that the actual structure of the norbornyl cation is the bridged 'nonclassical' formulation (Scheme 9) postulated many years earlier from kinetic and product studies.

A very similar, but not as well-resolved, situation involves the $C_4H_7^+$ cation(s) that are intermediate in the carbocationic interconversion reactions of cyclopropylmethyl, cyclobutyl, and 3-butenyl derivatives.[19,23] Here, the ^{13}C NMR in 'super acid' solutions shows two ^{13}C resonances in the ratio 1:3. Lowering the temperature to $-132\,^{\circ}C$ causes changes in the shifts, but not in the multiplicity of lines, indicating that there is a fast equilibrium involving more than one cationic species.[24] On further cooling, Myhre and co-workers[25] have found that further ^{13}C spectral changes occur at about $-210\,^{\circ}C$ which

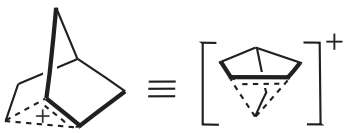

Scheme 9

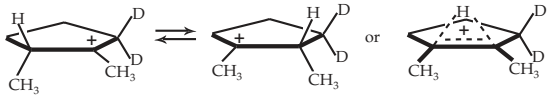

Scheme 10

correspond to slowing of the interconversion between the cationic species. Then, with continued cooling, the position of the equilibrium apparently shifts and, at liquid helium temperatures, there may well be only one nonclassical cationic species present with four nonequivalent carbons.

Another very interesting and potentially useful technique in the study of fast equilibria has been provided by the Saunders 'isotopic-perturbation' procedure.[26] In the study of carbocationic equilibria as described above for the norbornyl and $C_4H_7^+$ cations, there is always the question as to whether there is an equilibration between 'classical' structures or a stable 'nonclassical' intermediate. The formulas in Scheme 10 show a cation that involves either rapid 1,2-hydrogen shifts or has a hydrogen-bridged structure.

The ^{13}C resonances of C-1 and C-2 (Scheme 10) are equivalent in the absence of the deuterium labels and this means either that equilibration is very fast or that the bridged structure is stable. The Saunders technique involves substitution of just one of the methylene groups with deuterium as shown in Scheme 10. If there is fast equilibration and the bridged ion is unfavorable, then the deuterium should exert a sizable secondary isotope effect on the position of the equilibrium and thus change the relative C-1 and C-2 ^{13}C shifts. On the other hand, if the bridged ion is the important cationic intermediate, then there is little equilibration and the relative ^{13}C shifts changes with deuteration should be small. Experimentally, quite large changes in ^{13}C shifts are observed, but much smaller ones for the norbornyl and $C_4H_7^+$ examples discussed above.

Another very important use of ^{13}C NMR is for tracing biosynthetic pathways to aid in unraveling the mechanisms by which organisms achieve the myriad of transformations important to living systems. This can also be done with the radioactive isotope of carbon, ^{14}C, but to do so usually requires difficult and lengthy degradation procedures to determine specific positions of labeling. If the ^{13}C spectrum is known of the metabolite under investigation, ingestion of a suitable enriched ^{13}C precursor will result in greatly enhanced ^{13}C resonances, wherever the biosynthetic transformation puts a ^{13}C from the precursor into specific positions in the metabolite.

Another useful procedure in biosynthetic tracing is to use a precursor with adjacent doubly labeled ^{13}C positions where the level of enrichment is sufficiently high to make the ^{13}C–^{13}C coupling easy to detect. Now, if this labeled precursor is mixed with an unlabeled precursor, then it is possible to tell from the persistence or nonpersistence of the coupling whether or not the ^{13}C–^{13}C bond is broken apart and later reassembled with the possibility of formation of ^{13}C–^{12}C bonds, where the ^{12}C comes from the corresponding position in the unlabeled precursor.

Many of the ways of using ^{13}C are also adaptable to ^{15}N. The major problem with natural abundance ^{15}N NMR is that ^{15}N is present only to the extent of 0.37% in ordinary nitrogen. These numbers mean that ^{15}N is on the order of 2×10^5 times more difficult to obtain a useful signal than with ^{1}H.

This in no way means that natural abundance ^{15}N NMR is impossible. With the aid of time averaging and rather larger samples than are normally used with proton NMR, a substantial body of information on chemical shifts, couplings, relaxation times, and exchange rates has accumulated. At the natural abundance level with a modern high-field spectrometer, a reasonable spectrum can now be expected to be obtained in an hour or two in a 10-mm sample tube, if the nitrogen atoms of interest are present in 0.1 M concentration. Such expectations may not be realized because the T_1 relaxation times of ^{15}N, while highly variable, tend to be longer than those of ^{13}C and this can mean a substantial waiting time for the restoration of the Z-axis magnetization in taking time-averaged ^{15}N spectra. In some situations, it may be useful to add a small amount of a paramagnetic relaxing agent, such as the tris-chromium enolate salt of 2,4-pentadione, to shorten T_1 and to permit more rapid pulsing. However, shortening T_1 by adding a paramagnetic relaxing agent can be distinctly unhelpful, if it is hoped to develop a sizable NOE by proton decoupling. Development of a NOE by proton decoupling leads to positive enhancement of ^{13}C resonances. If the ^{13}C peak is split into a simple doublet by a single attached proton, decoupling of this proton will collapse the splitting making the signal twice as strong. The NOE then enhances the signal by another factor of three giving a total gain in peak height compared to one of the doublet peaks of a factor of six. This is a matter of great importance in the battle for higher sensitivity in the NMR detection of ^{13}C resonances.

The development of ^{13}C NOE by proton decoupling requires that the nucleus, whose resonance is being enhanced, relax by the T_1 path of so-called 'dipolar relaxation' involving the decoupled protons. Incursion of other relaxation modes, such as induced by paramagnetic ions, either diminishes or, if highly efficient, eliminates the NOE. With ^{13}C, the loss of NOE is serious but, at worse, the signal strength will be down by a factor of three to that expected for just removal of the splitting.

The situation with the NOE of ^{15}N is more complicated. The ^{15}N nucleus has a *negative* gyromagnetic ratio. This means that the ordering of the nuclear magnetic energy levels is different and the NOE is negative. A full NOE makes for an *emission* signal that is eight times more intense than either half of a doublet caused by a ^{1}H–^{15}N coupling. A partial NOE can turn out with ^{15}N to be worse than no NOE at all because, as one proceeds from a full NOE to no NOE, the negative signal becomes weaker, goes to zero, and then becomes positive. For this reason, a paramagnetic relaxing agent may well do more harm than good if the advantage of a ^{15}N NOE is desired.

It turns out that when molecular motions are slow, dipolar relaxation becomes inefficient compared with other mechanisms and this will cause the NOE to diminish or disappear. When ^{15}N spectra are taken of very large molecules, such as enzymes or tRNA, with proton decoupling, the resonances of the nitrogens on side chains that have substantial mobilities will be large and negative, while those in less mobile positions will show the effects of partial or no NOE. Raising the temperature to increase the rates of molecular motions then causes the nitrogen resonances of substances like these to increase, or decrease, in intensity depending on whether they were positive or negative before the increased NOE became effective.

There is a fine line to tread here with respect to long T_1 values and the loss of NOE. In general, large molecules have slower motions that lead to smaller T_1 values for ^{15}N than do small molecules with similar kinds of nitrogens. The shorter is T_1, the more efficiently one can perform time averaging. However, as mentioned, if the molecular motions become too slow, dipolar relaxation becomes inefficient and the NOE decreases. This combination of factors suggest that the ^{15}N T_1 of small molecules could be reduced and the efficiency of time averaging improved by any means that increases the viscosity of the solvent without losing NOE, until that point is reached where dipolar relaxation becomes inefficient.[27]

Nitrogen-15 NMR shifts of saturated amines closely parallel the ^{13}C shifts of analogously substituted carbon compounds. Thus, the ^{13}C resonance of a methyl group in 2,2-dimethylpropane correlates with the ^{15}N resonance of 2-amino-2-methylpropane. The ^{15}N shifts of primary, secondary, and tertiary amines fall on different linear correlation lines with the tertiary amines having the greatest scatter. Once unsaturation is introduced in the molecules, the correlation fails. Thus, the points for the ^{15}N shift of aminobenzene and the ^{13}C shift of the methyl in methylbenzene do not come close to the saturated primary amine correlation line.[28] The reason for this is that whereas the nitrogen lone pair can be delocalized into the unsaturated system, there is no electron lone pair available on the methyl group.

While there are many applications of ^{15}N NMR paralleling those of ^{1}H and ^{13}C, one rather special attribute of the chemical shifts of nitrogen is their sensitivity to hydrogen bonding and protonation, particularly if the nitrogen is part of a double bond or an aromatic ring. For example, the ^{15}N shift of azabenzene (pyridine) changes about 38 ppm in going from a poor hydrogen-bonding solvent (cyclohexane) to an excellent hydrogen-bonding solvent (trifluoroethanol). Outright protonation causes an overall shift of about 98 ppm.[29]

A very interesting aspect of both the hydrogen bonding and the protonation shifts is that they correspond to *increased* shielding of the unsaturated nitrogen. This is exactly opposite to what happens to the OH proton which experiences decreased shielding through being involved in hydrogen bonding. The explanation for this is through operation of the second-order paramagnetic effect mentioned earlier. The unprotonated or unhydrogen-bonded nitrogen has an unshared electron pair. In a magnetic field, the molecule gains some measure of stability through the paramagnetic circulation of one of those unshared electrons in an excited-state orbital. Hydrogen bonding or protonation is expected to diminish this paramagnetic circulation by making it electrostatically less favorable to promote one of the unshared electrons to a higher orbital.

An illustrative example of the use of ^{15}N NMR to study the state of molecules in solution is afforded by comparing the pH dependences of the ^{15}N spectra of the nitrogens of the imidazole rings of histidine[30] and the *cis* and *trans* isomers of urocanic acid (Scheme 11).[31]

Unprotonated imidazoles have two rapidly interconverting tautomeric forms and customarily, if there is a single substituent at C-4, that form is favored which has N-1 as an NH group (Scheme 12).

Because of the nature of the nitrogens, one being to a first approximation C=N– and the other being C–NH–, we expect and find a large ^{15}N chemical shift difference. However, the observed shift difference is expected to depend on the position of the tautomeric equilibrium. If the equilibrium constant is

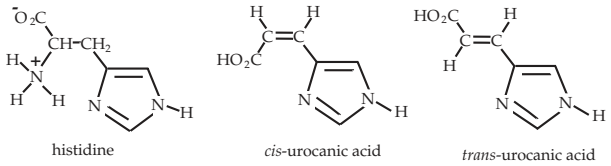

Scheme 11

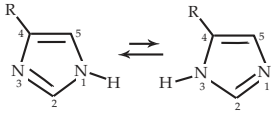

Scheme 12

near unity, then the difference will be small, if it is large then the shift difference should approach the difference in ^{15}N shifts of *N*-methylimidazole (83 ppm).[32] Thus, the shift difference can tell us something about the position of the equilibrium and the effect of R on it. 4-Methylimidazole shows a shift difference of 8.4 ppm and if we neglect the relatively small electrical effect of the methyl group on the individual shifts then we can calculate that the tautomer with N-1 as the NH is about 55%.

Figure 5 shows the pH dependences of the ^{15}N chemical shifts of the subject compounds. Histidine loses three protons over the pH range while the urocanic acid isomers lose two protons. The simplest case is of the *trans*-urocanic acid which at the lowest pH has the carboxy group unionized and the imidazole group protonated. It will be seen from Figure 5 that when both imidazole nitrogens are protonated there is little difference in their ^{15}N chemical shifts. The carboxy group being *trans* has no opportunity to flirt in an intramolecular fashion with the nitrogen of the imidazole ring and would not anyway when the carboxy group is unionized. When the pH is increased to about 4, the carboxy becomes ionized but the imidazole remains protonated. Here again, the carboxy

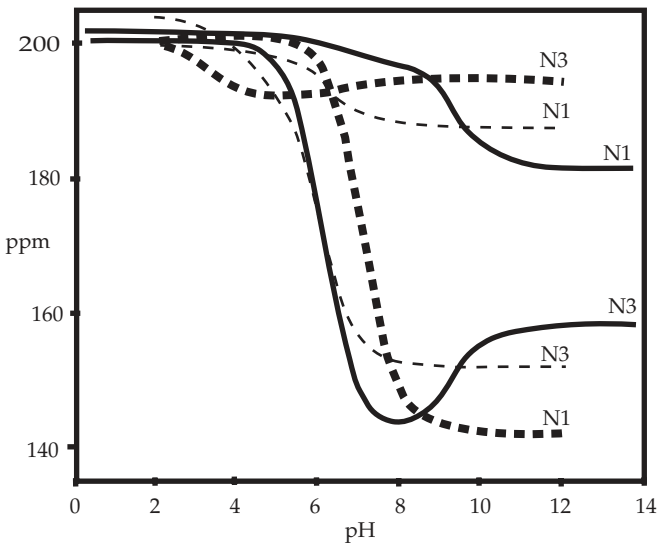

Figure 5 Changes of ^{15}N chemical shifts of *trans*-urocanic acid (----), *cis*-urocanic acid (– –), and histidine (—) as a function of pH. The numbering of the nitrogens follows Scheme 12

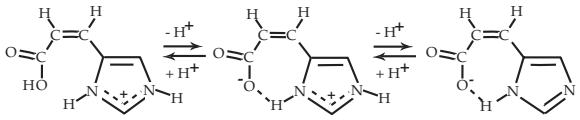

Figure 6 The principal structures of *cis*-urocanic acid expected, from left to right, in strong acid, neutral, and basic solutions, as well as the hydrogen bondings expected for the latter two which help to account for the ^{15}N shift changes seen in Figure 5

group is not positioned so as to be able to get close to and influence the nitrogens in the same molecule. There is little change in the ^{15}N chemical shifts until, between pH 4 and 8, the imidazolium cation loses its proton. At this point, the fast tautomeric equilibrium (Scheme 12) comes into play and the shift difference of 36 ppm at high pH suggests that the tautomer with N-1 as the NH amounts to 72%, larger than for 4-methylimidazole, but by a ΔG difference of only about 1.7 kJ mol^{-1} (0.4 kcal mol^{-1}).

The *cis* isomer behaves quite differently after the ionization of the carboxy group at about pH 4. Now, as shown in Figure 6, the *cis* orientation at the double bond allows the carboxylate group to swing around and hydrogen bond to the proton on N-3 of the imidazolium cation. This interaction causes the N-3 to become somewhat less shielded than N-1 and creates a moderate chemical shift difference. Further increase in pH causes the imidazolium cation to lose a proton and the carboxy group can now hydrogen bond with the tautomer having N-3 as the NH, thus moving the tautomeric equilibrium from its usual position favoring N-1 as the NH nitrogen. This has the effect of making N-1 the less shielded nitrogen and N-3 the more shielded nitrogen and, at the higher pH values, about 82% of the material has N-3 as the NH nitrogen. It is interesting that the electrostatic effect of the carboxylate group and/or its hydrogen bonding to the proton on N-3 makes the imidazole ring a stronger base by about 0.9 p*K* units.

The behavior of the ^{15}N shifts of *cis*-urocanic acid has a very close parallel in the behavior of the corresponding pH shifts of the ^{15}N resonances of the histidyl residue making up part of the 'catalytic triad' at the active site of α-lytic protease.[33] In this substance, the role of the urocanic carboxy group is taken by the free carboxy of an aspartate residue, which although many residues distant from the histidine, is held in close proximity by the folding of the peptide chains.

The pH dependences of the ^{15}N resonances of the imidazole nitrogens of histidine itself (see Figure 7) are more complicated because the α-amino group is not tied up in a peptide bond, as it is for the histidyl group at the active site of α-lytic protease. Further, free histidine has one more proton to ionize. In the low pH region, the N-1 and N-3 ^{15}N resonances are close together as before. When the carboxy ionizes, there are smaller, more subtle, changes in the shifts than for *cis*-urocanic acid. These can be rationalized on the basis that the positively charged ammonium group makes hydrogen bonding of the carboxylate group to the N-3 proton less favorable than for *cis*-urocanic acid. Furthermore, the loss of the imidazolium proton in the next step is more favorable than for *cis*-urocanic acid, because with the *cis* acid the proton is lost from a neutral entity while with histidine it is lost from a positive entity. However, when that proton is lost, there is a competition between the carboxylate hydrogen bonding to the tautomer with NH at N-3 and the ammonium group undergoing hydrogen bonding to

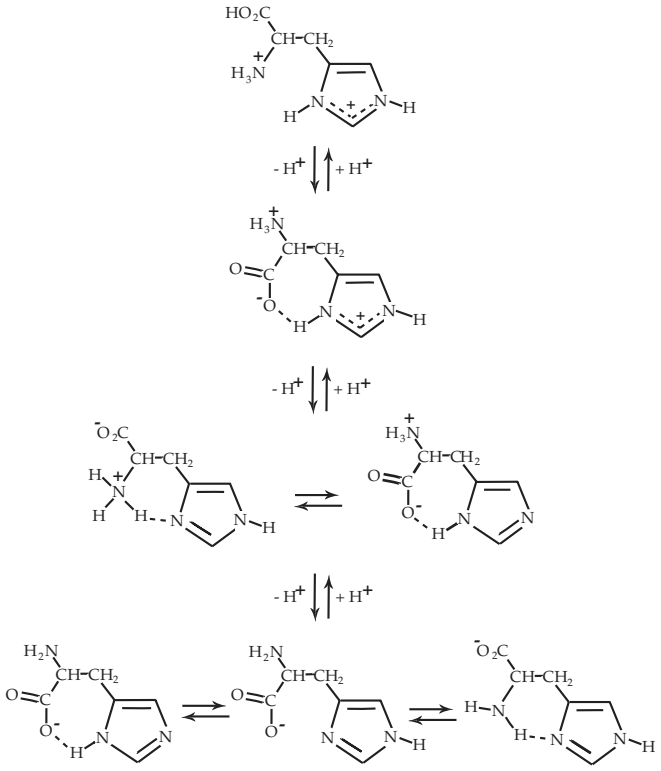

Figure 7 The tautomers and their hydrogen-bonded structures of histidine as a function of the protonation level

the tautomer with N-3 as C=N–. The ^{15}N shifts show that the latter possibility wins out, giving about 83% of the tautomer with N-1 as NH. Then, when the pH is increased further and the proton is removed from the ammonium group, there is a shift of equilibrium to about 64% of the tautomer with N-1 as NH. That this tautomer is favored, but the equilibrium is on the opposite side with *cis*-urocanic acid, can be understood in terms of the competing hydrogen-bonding arrangements and the fact that the more rigid *cis*-urocanic acid side chain will be better disposed for hydrogen bonding than the side chain of histidine from entropic considerations. That this entropic effect is likely to be important is shown by the fact that the pH dependences of the ^{15}N resonances of the imidazole nitrogens of the saturated analog of *cis*-urocanic acid, 3-(4-imidazoyl)propionic acid, are much more similar to those of *trans*-urocanic acid than to the *cis* isomer.[31]

These examples should show the power of ^{15}N NMR to elucidate structural features in solution that cannot be easily obtained in any other way.

1 RELATED ARTICLES

Amino Acids, Peptides and Proteins: Chemical Shifts; Biological Macromolecules: Structure Determination in Solution; Biological Macromolecules: NMR Parameters; Carbon-13 Relaxation Measurements: Organic Chemistry Applications; Chemical Shifts in Biochemical Systems; Enzymatic Transformations: Isotope Probes; Nucleic Acids: Chemical Shifts; Nucleic Acids: Phosphorus-31 NMR; Nucleic Acids: Spectra, Structures, and Dynamics; Oxygen-17 NMR: Applications in Biochemistry; Proton Chemical Shift Measurements in Biological Solids; Vicinal Coupling Constants and Conformation of Biomolecules; Vitamin B12.

2 REFERENCES

1. Two excellent books for this purpose are A. E. Derome, *Modern NMR Techniques for Chemistry Research*, *Vol. 6. of Organic Chemistry Series*, ed. J. E. Baldwin, Pergamon Press, New York, 1987, and J. K. M. Sanders and B. K. Hunter, *Modern NMR Spectroscopy, A Guide for Chemists*, 2nd edn., Oxford University Press, New York, 1993.
2. J. D. Roberts, *An Introduction to the Analysis of Spin–Spin Splitting in High-Resolution Nuclear Magnetic Resonance Spectra*, W. A. Benjamin, Inc., New York, 1961.
3. C. A. G. Haasnoot, F. A. A. M. de Leeuw, and C. Altona, *Tetrahedron*, 1980, **36**, 2783.
4. A. A. Bothner-By and S. M. Castellano, in *Computer Programs for Chemistry*, ed. D. F. DeTar, W. A. Benjamin, Inc., New York, 1968, Vol. 1, Chap. 3
5. E. S. Lit, F. Y. Mallon, H. Y. Tsai, and J. D. Roberts, *J. Am. Chem. Soc.*, 1993, **115**, 9563.
6. W. D. Phillips, *J. Chem. Phys.*, 1955, **23**, 1363.
7. S. Forsén and R. A. Hoffman, *J. Chem. Phys.*, 1963, **39**, 2892.
8. Z. Luz and S. Meiboom, *J. Chem. Phys.*, 1963, **39**, 366.
9. G. Wagner, G. Bodenhausen, N. Müller, M. Rance, O. W. Sørensen, R. Ernst, and K. Wüthrich, *J. Am. Chem. Soc.*, 1985, **107**, 6640.
10. G. M. Whitesides, M. Witanowski, and J. D. Roberts, *J. Am. Chem. Soc.*, 1965, **87**, 2854.
11. F. A. L. Anet, M. Ahmad, and L. D. Hall, *Proc. Chem. Soc.*, 1964, 145.
12. J. D. Roberts, *Chem. Br.*, 1966, **2**, 529.
13. F. A. L. Anet, A. J. R. Bourn, and Y. S. Lin, *J. Am. Chem. Soc.*, 1964, **86**, 3576.
14. P. C. Lauterbur, *J. Am. Chem. Soc.*, 1961, **83**, 1838.
15. E. G. Paul and D. M. Grant, *J. Am. Chem. Soc.*, 1964, **86**, 2977.
16. A. Bax, R. Freeman, T. A. Frankiel, and M. H. Levitt, *J. Magn. Reson.*, 1981, **43**, 478.
17. D. K. Dalling and D. M. Grant, *J. Am. Chem. Soc.*, 1967, **89**, 6612.
18. L. F. Johnson, F. Heatley, and F. A. Bovey, *Macromolecules*, 1970, **3**, 175.
19. G. A. Olah, D. P. Kelly, C. L. Jeull, and R. D. Porter, *J. Am. Chem. Soc.*, 1970, **92**, 2544.
20. G. A. Olah, A. M. White, J. R. DeMember, A. Commeyras, and C. Y. Lui, *J. Am. Chem. Soc.*, 1970, **92**, 4627.
21. C. S. Yannoni, V. Macho, and P. C. Myhre, *J. Am. Chem. Soc.*, 1982, **104**, 907.
22. P. C. Myhre, G. G. Webb, and C. S. Yannoni, *J. Am. Chem. Soc.*, 1990, **112**, 8991.
23. See for example, J. D. Roberts, *Proc. Robert A. Welch Foundation Conf. Chem. Res.*, 1990, **XXXIV**, 313.
24. J. S. Staral, I. Yavari, J. D. Roberts, G. K. S. Prakash, D. J. Donovan, and G. A. Olah, *J. Am. Chem. Soc.*, 1978, **100**, 8020.
25. P. C. Myhre, G. G. Webb, and C. S. Yannoni, *J. Am. Chem. Soc.*, 1990, **112**, 8992.
26. M. Saunders, L. Telkowski, and M. R. Cates, *J. Am. Chem. Soc.*, 1977, **99**, 8020.
27. A. Wei, undergraduate thesis, California Institute of Technology, 1989; M. K. Raymond, undergraduate thesis, Reed College, 1991.

28. R. L. Lichter and J. D. Roberts, *J. Am. Chem. Soc.*, 1972, **94**, 2495.
29. R. O. Duthaler and J. D. Roberts, *J. Am. Chem. Soc.*, 1978, **100**, 4969.
30. F. Blomberg, W. Maurer, and H. Rüterjans, *J. Am. Chem. Soc.*, 1977, **99**, 8149.
31. J. D. Roberts, Y. Chun, C. Flanagan, and T. R. Birdseye, *J. Am. Chem. Soc.*, 1982, **104**, 3945.
32. I. I. Schuster and J. D. Roberts, *J. Org. Chem.*, 1979, **44**, 3864.
33. W. W. Bachovchin and J. D. Roberts, *J. Am. Chem. Soc.*, 1978, **100**, 8041.

Biographical Sketch

John D. Roberts *b* 1918. B. A., 1941, Ph.D. 1944, UCLA. Introduced to NMR by W. D. Phillips and J. N. Shoolery. Faculty in Chemistry, Harvard University, 1945–46; MIT, 1946–53; California Institute of Technology, 1953–present. Approx. 485 publications and 5 books. Research interests include physical organic chemistry and applications of NMR to organic chemistry, particularly the determination of conformational equilibria and conformational equilibration, as well as of ^{15}N NMR to problems in biology and medicine.

Oxygen-17 NMR

Ioannis P. Gerothanassis
University of Ioannina, Greece

1	Introduction	1
2	Experimental Aspects	1
3	Characteristic Parameters	2
4	Selected Applications	6
5	Related Articles	9
6	References	9

1 INTRODUCTION

The structure and dynamics of oxygen-containing compounds is a subject of widespread significance. Compared with ^{1}H, ^{13}C, ^{31}P, and ^{19}F NMR, however, ^{17}O NMR has received little attention.[1–8] This neglect is not surprising since, of the naturally occurring oxygen isotopes, only ^{17}O possesses a nuclear spin ($I = \frac{5}{2}$). Due to its electric quadrupole moment ($Q_e = -2.6 \times 10^{-30}$ e m^2), its low natural abundance (0.037%), and the extremely low absolute sensitivity compared with that of ^{1}H (about 1.1×10^{-5}), the ^{17}O isotope is one of the more difficult nuclei to observe by NMR spectroscopy. It is, however, of great interest to use a nucleus such as oxygen that is located at strategic molecular sites and is directly involved in inter- and intramolecular interactions. The ^{17}O NMR parameters, i.e. isotropic shielding, principal elements of the ^{17}O shielding and electric field gradient tensors, and the transverse and longitudinal relaxation times, can be considered as excellent means of probing the structure, bonding, and dynamics of oxygen-containing compounds. Furthermore, recent advances in instrumentation, the extremely large chemical shift scale (which aids in the resolution of quadrupole broadened resonances), and the availability of ^{17}O enriched compounds have alleviated these difficulties; thus, an increased use of the ^{17}O NMR technique can be envisaged.[9–11]

2 EXPERIMENTAL ASPECTS

2.1 The Case of ^{17}O Enrichment

The stringent requirements in studies of compounds at natural abundance are the high concentrations (>0.1 M) and extensive signal averaging needed.[12] Recording of spectra can be greatly facilitated by the use of ^{17}O enriched samples (Figure 1). When using FT high field instruments and ^{17}O labeled compounds (^{17}O enrichment 10–40 atom %), concentrations of greater than 1 mM are desirable, depending on the linewidths. Synthesis involving oxygen isotopes tends to involve rather straightforward organic reactions. However, one caveat that should be kept in mind when contemplating the synthesis of an ^{17}O labeled compound is the expense of the starting reagents. Simple modifications of existing reactions are required. For example, $^{17}O_2$, C^{17}O, or C$^{17}O_2$, is added to evacuated systems, as opposed to more traditional procedures which involve bubbling through the reaction mixture. Recently, a comprehensive overview of ^{17}O enriched methods has been published.[14]

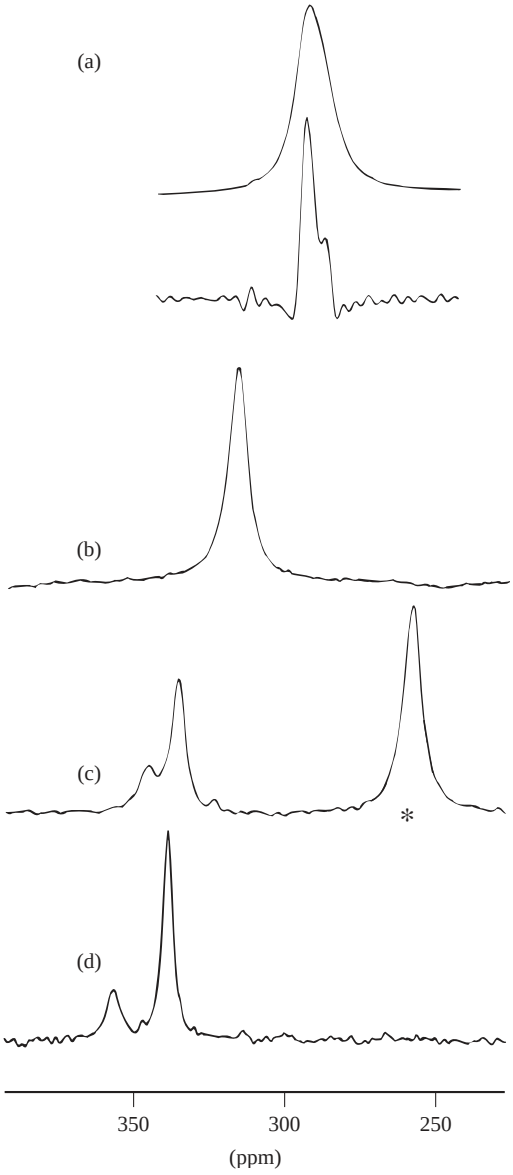

Figure 1 ^{17}O NMR spectra (48.8 MHz; 40 °C) of *N*-[^{17}O]acetyl-L-proline.[13] (a) 10% enrichment, 0.1 M in aqueous solution containing 1 M NaCl and 5×10^{-5} M EDTA; T_{acq} = 12 ms, NS = 300 000, total experimental time = 1 h: (upper trace) normal spectrum; (lower trace) after a Gaussian-exponential resolution enhancement. (b) 1% enrichment, 0.1 M in methanol, T_{acq} = 10 ms, NS = 200 000, total experimental time = 32 min, line broadening (LB) = 50 Hz. (c) 0.4 M natural abundance in acetone (the asterisk marks the carboxyl oxygen resonance); T_{acq} = 5 ms, number of scans (NS) = 1 900 000, total experimental time ≃10 h, LB = 50 Hz; (d) 1% enrichment, 0.1 M in acetone; T_{acq} = 10 ms, NS = 1 350 000, total experimental time ≃8 h, LB = 50 Hz. (Adapted by permission of The American Chemical Society from R. N. Hunston, I. P. Gerothanassis, and J. Lauterwein, *J. Am. Chem. Soc.*, 1985, **107**, 2654)

2.2 Referencing Techniques

As with many heteronuclei, a variety of reference compounds and referencing procedures (both internal and external) have been suggested for ^{17}O NMR. For diamagnetic solutions, an external standard in a combined use of two cylindrical cells has been recommended.[15] Using this technique, doubly distilled water or 1,4-dioxane can be used as external reference. Both compounds have chemical shifts which are indistinguishable at 30–40 °C and their magnetic susceptibility correction is small (<0.6 ppm) relative to common organic solvents. However, H_2O has the disadvantage that its chemical shift varies with temperature (−3 ppm between 27 and 90 °C) due to cleavage of intermolecular hydrogen bonds (the same applies for D_2O in addition to an isotopic effect of −3 ppm).

2.3 Solvent (H_2O) Suppression

Perhaps the most straightforward approach to solvent suppression is the use of ^{17}O depleted water, provided of course that rapid ^{17}O exchange does not occur between solvent and solute.[16] Further suppression can be achieved by exploiting the special relaxation properties of the solvent, by postexperiment data processing and by selectively exciting the whole spectrum apart from that of the solvent.[17] A critical note on the usefulness of the selective excitation pulse sequences in ^{17}O NMR has recently been published.[18]

2.4 Acoustic Ringing

Observation of very broad resonances in NMR is a potential problem due to baseline distortions. The most severe of the baseline artifacts is that due to the transient response of the NMR probe, often referred to as 'acoustic ringing', caused by the generation of ultrasonic waves from the action of the rf pulse. In the last decade, several pulse sequences designed for the suppression of acoustic ringing have been reported, and the reader should consult a relevant review article for details.[19] For experiments in solution, the extended spin echo sequence was found to be particularly useful, since it utilizes minimum pulse and preacquisition delay times. A closely related pulse sequence for experiments in the solid phase has also been suggested.[20]

3 CHARACTERISTIC PARAMETERS

3.1 Chemical Shifts

3.1.1 Experimental Shielding Ranges: Empirical Correlations

A general pattern of ^{17}O shielding is shown in Figure 2. For compounds containing oxygen bonded only to carbon and/or hydrogen there is a clear correlation between the C–O π bond order and a high frequency shift.[21] This type of correlation arises from the multiple bond term $\Sigma_{B\neq A}Q_{AB}$ in the Karplus–Pople equation.[22] For bridging oxygen atoms, a strong deshielding is observed when the substituents R are replaced by π-accepting acyl substituents which introduce π character into the C–O bond of the bridging oxygen. Thus, bridging oxygen resonances in carbonates and esters appear at high frequency relative to the corresponding resonances in alcohols, ethers, and acetals. An even greater high frequency shift is observed for anhydrides, where bridging oxygen atoms are bonded to two π acceptors. If chemical shifts are assumed to depend linearly on π bond order, the chemical shift of about 600 ppm for aliphatic aldehydes (π bond order of about 1) relative to water (π bond of 0) implies a chemical shift of about 200 ppm for CO_3^{2-} (π bond order of $\frac{1}{3}$). The observed shift of CO_3^{2-} (192 ppm) is in agreement with this crude prediction, further supporting the general correlation between π bond order and shielding discussed above.[2]

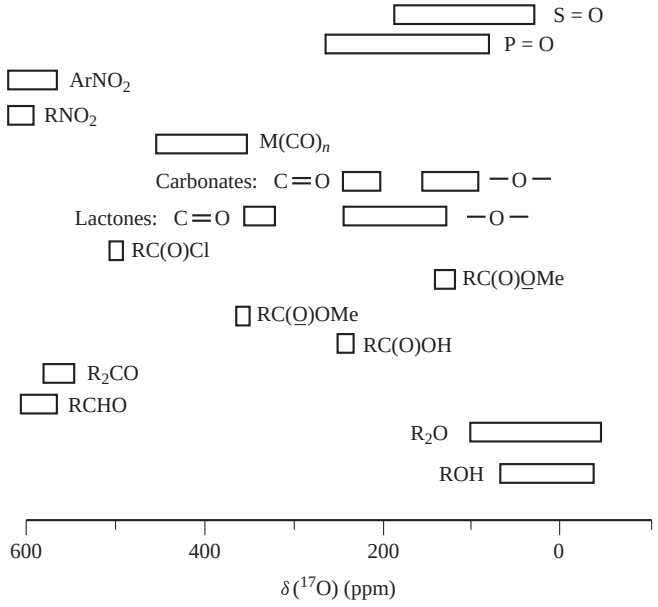

Figure 2 ^{17}O chemical shift ranges for different X–O bonds. (Adapted by permission of Plenum Press from W. McFarlane and H. C. E. McFarlane, in 'Multinuclear NMR', ed. J. Mason, 1987, Chap. 14)

In nitrogen-containing compounds, as in carbon compounds, chemical shift values are determined largely by π bonding effects.[23–25] Bridging oxygen resonances are observed at even higher frequency in nitrates, where π bonding is appreciable. A lesser, but nonetheless significant, effect is observed for bridging oxygen atoms in nitrates. The most striking feature of the ^{17}O shifts observed for P–O bonds is the small chemical shift range (20–260 ppm) which cannot be related to P–O bond order in a straightforward fashion. However, ^{17}O resonances for nonequivalent oxygen atoms in phosphates and polyphosphates can be resolved and have been used in stereochemical and binding site studies.[26–28] For S–O bonding, similar trends to those displayed by P–O bonds are observed. Modification of the π bond order in an X=O group due to substituents on X results in a decrease (or increase) in the net charge on X as the charge on oxygen increases (or decreases). The chemical shift variations experienced by the nuclei X and O are then opposite and roughly proportional to the ratio $\langle r^{-3}\rangle_{2p_X}/\langle r^{-3}\rangle_{2p_O}$.[24] For a series of oxyanions and a series of C=O and N=O compounds a linear correlation has been found between $\delta(^{17}O)$ and the variation in ΔE^{-1}.[29] A linear correlation exists between acetone chemical shifts and the first maximum of the $n \rightarrow \pi^*$ transition for acetone/water

solutions[30] and for acetone in different solvents.[31] Similar trends have also been observed in a variety of substituted acetophenones;[32] however, it was suggested that such trends may be fortuitous, since the transition energy depends upon the balance of several effects associated with both π donation and σ withdrawal.[33] From a study on a series of aliphatic ethers, a correlation between $\delta(^{17}O)$ and the first ionization potential has been suggested.[34]

Compounds containing oxygen–oxygen bonds and oxygen–fluorine bonds display large high-frequency shifts.[35–37] The ability, therefore, of ^{17}O NMR to distinguish unambiguously between nonequivalent oxygen atoms has found application in several structural and mechanistic studies. The same applies to oxygen bonded to transition metals (see below). Empirical correlations were extended to diamagnetic transition metal anions of the general formula MO_4^{n-}, and theoretical calculations were carried out to show that the absolute magnitude was reasonable.[29]

3.1.2 Theory of ^{17}O Chemical Shifts (see **Shielding: Overview of Theoretical Methods**)

3.1.2.1 Isolated Molecules. Ab initio calculations[38,39] of ^{17}O nuclear shielding tensors have been reported for a variety of simple molecules such as H_2O, CH_3OH, $(CH_3)_2O$, H_2CO, CH_3CHO, $HCONH_2$, and CO. The results are gauge dependent and in many cases vary considerably depending on the basis set used. Gauge independent ab initio results for H_2O and H_2CO indicate a ^{17}O shielding of 757.6, 860.3, or 858.8 ppm for H_2CO, with respect to H_2O, compared with the experimental result of 580–600 ppm. The calculated data represent a choice of three basis sets. Semiempirical INDO (intermediate neglect of differential overlap) calculations are numerically smaller than the experimental results, whereas the CNDO/S (complete neglect of differential overlap/S) calculations produce better overall agreement.[40–43] This probably reflects an insensitivity of the INDO orbital energies to changes in the environment of the oxygen. By omitting those molecules and ions which have nitrogen directly bonded to oxygen the CNDO/S results gave a standard deviation of 30.6 ppm and a correlation coefficient of 0.98 compared with the experimental values. Analysis of the CNDO/S results demonstrates that the ^{17}O shielding differences of some carbonyl compounds are dominated by the lowest energy $n \rightarrow \pi^*$ transition. For the linear species CO, CO_2, and NO_2^+, the largest contribution to the paramagnetic part σ_p of the ^{17}O shieldings arises from the lowest energy $\sigma \rightarrow \pi^*$ transition. Similarly, for the bent ion NO_2^- the lowest energy $\sigma \rightarrow \pi^*$ transitions are dominant for the in-plane components of the shielding tensor, while the out-of-plane contribution is controlled by $\sigma \rightarrow \sigma^*$ transitions. In general, these ^{17}O shieldings are in reasonable agreement with the available experimental data, and in some cases are an improvement upon ab initio results. Analogous calculations employing a basis set of gauge dependent atomic orbitals within the CNDO/2 framework have been reported for ^{17}O shieldings in electrolyte solutions.[44] For ozone,[45] the use of localized molecular orbitals within the IGLO method (see ***Shielding Calculations: IGLO Method***) allows the contributions to the total shielding to be partitioned into orbital contributions, so that the specific role played by the lone pairs on the atom in question and orbitals centered on neighboring atoms can be discerned.[46] The calculated shieldings for O_3 were found to be extremely large, highly anisotropic, and to differ from the experimental values by a factor of 2–3. The authors also noted that the paramagnetic contributions are mainly due to the lone pairs on the respective oxygen atoms, unlike the triatomic molecules CO_2 and FNO in which the paramagnetic contributions are mainly due to the bonds interacting with the antibonding π^* electrons and only to a limited extent to the lone pairs.

3.1.2.2 Solvent and medium effects. Recently, the effect of electrical polarization on the chemical shielding of carbon monoxide has been considered in detail.[47,48] In addition, the relationship between the vibrational frequency and the shieldings for three different types of electrical environments—a uniform field, a field gradient, and an axial point-charge dipole—together with experimental ^{13}C and ^{17}O isotropic shieldings and vibrational frequencies for a range of carbon monoxide derivatives of heme proteins has been described. For each type of environment, the shieldings vary linearly with the vibrational frequency for a relatively wide range of frequency shifts.[48] This shows, in agreement with experiment,[49] that there is a linear relationship that is opposite for ^{13}C and ^{17}O.[50]

The effects of solvents on the ^{17}O nuclear shielding of solute molecules may be categorized into hydrogen-bonding interactions and influences that arise from electronic interactions between the dipole moments of the solute and solvent molecules. Precise mathematical expressions are not available for many nonbonded interactions. Consequently, continuum models tend to be more popular for investigating solvent effects on NMR parameters. The most widely used of these, to date, is the solvaton model.[51] By means of this model the solute–solvent interaction can be included in the paramagnetic screening contribution, and the solvent induced shift is proportional to $(\epsilon - 1)/2\epsilon$, where ϵ is the dielectric constant of the medium. Some sum-over-states (SOS) and finite perturbation theory (FPT) calculations of oxygen nuclear shieldings of several organic functional groups, as obtained using the solvaton model, predict increases in shielding as ϵ increases.[50,52] An analysis of the various factors contributing to the paramagnetic term reveals that the increase in shielding arises from a concomitant decrease in $\langle r^{-3} \rangle_{2p}$ and an increase in the weighted average of the energies of the various transitions contributing to the paramagnetic term. The observed decrease in $\langle r^{-3} \rangle_{2p}$ is consistent with an increase in the average separation between the nucleus and its 2p electrons as the charge q increases. The increase in the weighted averaged of the transition energies is largely controlled by the increase in energy of the lowest $n \rightarrow \pi^*$ transition as the extent of solvation increases.

The shielding of the ^{17}O nuclei of several functional groups are quite sensitive to hydrogen-bonding interactions. From a theoretical standpoint the shielding may be considered by using the supermolecule approach. A good example is provided by formamide.[53] Ab initio calculations using GIAOs (gauge invariant atomic orbitals) within the FPT framework have been reported for formamide (FMA) in the presence of its first hydration shell. The ^{17}O shielding values reported for the complexes $FMA–(H_2O)_2$ show that the shift observed when the oxygen atom is directly involved in the hydrogen bond is much larger than the one occurring when the water molecules are bound to the NH group. The variation was calculated to be to low frequency in both cases. This is in agreement with

^{17}O NMR experimental data on FMA and several amides in different solvents.

3.2 Indirect Spin Coupling Constants

Because of the breadth of ^{17}O resonances, only relatively large coupling constants can be measured, and hence the majority of those recorded refer to couplings from directly bonded nuclei. ^{1}J(O,H) in water and alcohols has values close to 80 Hz.[54–56] The ^{1}J(P,O) couplings involving P=O groups cover a fairly wide range (145–210 Hz) and for a series of compounds of type OPX_3 (X = F or O in OMe, X = N in NMe_2, and X = C in Me) there is a consistent drop in coupling with decreasing electronegativity of X. This may be qualitatively attributed to the electronegative substituents removing electrons in outer orbitals from the phosphorus atom, leading to a greater effective atomic charge and hence stronger contact interaction between the phosphorus nucleus and the s orbitals. A finite perturbation theoretical treatment within the CNDO/2 formalism has reproduced the observed trends, but not the absolute values.[57] The oxygen atoms in P–OMe groups within phosphates give rise to a consistently smaller coupling constant, compared with P=O, of between 90 and 100 Hz; there is an indication of a considerably larger value for phosphites. The reduced coupling constants decrease with increasing atomic number of the central atoms along the isoelectronic sequence VO_4^{3-}, CrO_4^{2-}, and MnO_4^{-}.[58] The values of ^{17}O spin–spin couplings have been used to investigate H_3O^+ species.[59] The ^{17}O NMR spectrum revealed a perfect quartet with J(O,H) = 107 Hz. Furthermore, the effect of H/D substitution is evident in the ^{17}O NMR spectra of H_2O–D_2O in CH_2Cl_2. Thus, the species H_2O, HDO, and D_2O could be identified from coupling constants, without reference to chemical shift data.[60] ^{2}J couplings are normally about an order of magnitude smaller than the corresponding directly bonded couplings.[61] However, there seems to be a particularly favored coupling pathway from hydrogen to the 'ether' oxygen atom in HCOOR systems, which is probably associated with π bonding across the planar framework.

In some cases coupled resonances cannot be resolved into fine structure but exhibit a partially collapsed structure, depending on the rate of proton transfer. In such cases decoupling of the other nuclei can lead to reduced linewidths and information about coupling constants.

When a spin-$\frac{1}{2}$ nucleus is bonded directly to ^{17}O, the X nucleus will also be relaxed by virtue of its spin–spin coupling with ^{17}O. This has been termed 'scalar relaxation of the second kind'. Such a line-broadening effect for ^{17}O in ^{31}P NMR has been used to locate the position of the ^{17}O label and to calculate the percentage enrichment of ^{17}O. In addition, it has made possible analysis of the configuration of (^{16}O, ^{17}O, and ^{18}O) phosphate monoesters and (^{16}O, ^{17}O, and ^{18}O) thiophosphates by ^{31}P NMR.[62–64]

3.3 Nuclear Quadrupole Coupling Constants

The electrostatic interaction between the nuclear quadrupole electric moment Qe and the electric field gradient tensor eq_{ij} is the quadrupolar interaction. An appropriate reference axis system can be chosen to reduce this interaction to two values:[4] the main component

$$\chi = e^2 q_{zz} Q/h \tag{1}$$

and the asymmetry parameter (dimensionless)

$$\eta = (e^2 q_{xx} Q - e^2 q_{yy} Q)/e^2 q_{zz} Q \tag{2}$$

where $|e^2 q_{zz} Q| > |e^2 q_{yy} Q| > |e^2 q_{xx} Q|$.

The χ values for ^{17}O may be calculated by computing the field gradient from molecular wavefunctions and using the nuclear quadrupole moment Qe. Only relatively small molecules have been studied. Thus the calculated χ value for CO using the GAUSSIAN 88 program at the 6-31G* level[49] (3.1 MHz) was found to deviate from the experimental value (~4.4 MHz) (the value of 3.9 MHz obtained from ab initio calculations[47] is in better agreement with the experimental value). Furthermore, it was shown that hydrogen bonding to HF results in a significant decrease in χ of about 0.7 MHz for the linear species CO···HF.

Semiempirical methods of various degrees of sophistication have been used to compute electric field gradients. Within the framework of the Townes–Dailey theory, the three components of the field gradient can be related to the electronic populations in the orbitals describing the oxygen bonding and to eq, the field gradient created by an electron in a 2p atomic orbital (the contribution from the valence s electrons is neglected because of the spherical symmetry). More elaborate models incorporate hybridization of atomic orbitals into valence bonding and lone pair orbitals. Such studies include the determination of σ and π orbital populations for X–O bonds (X = C, N, P, or S).[65,66]

The majority of experimentally determined χ and η values have been obtained in the solid state by the use of NQR spectroscopy; however, some have been determined by NMR measurements on powders or single crystals, where χ is small with respect to the NMR frequency. Quadrupole coupling constants have also been derived from the splittings in the ^{17}O spectra of molecules partially oriented in an electric field[67] or dissolved in a nematic liquid crystal.[68,69] Detailed studies of polynuclear osmium carbonyl dynamics have been undertaken and together with ^{13}C measurements have provided estimates of the ^{17}O quadrupole coupling constants.[70] In molybdenum hexacarbonyl, the ^{95}Mo and ^{97}Mo linewidths gave the reorientational correlation time, which in turn made it possible to determine the χ values from the ^{17}O linewidth.[71]

Experimental χ values cover the range −8 to 17 MHz. The sign of χ is irrelevant to the NMR experiment, but from a theoretical point of view it gives information about the orientation of the field gradient. The experimental χ values for a series of compounds in the solid state that contain C=O, –O–, P–O, N–O, or S–O bonds show the following trends:[6]

1. For substituted nitrophenols, hydroxybenzaldehydes, and nitrobenzaldehydes, the χ values are nearly invariant with the electronic properties of the substituent, but are reduced by hydrogen bonding.
2. Strong hydrogen bonding reduces the χ values by as much as 2.6 MHz.

In summary, the following scale of χ values has been suggested:

O − O >	N − O >	NO_2 >	C = O >	P − OR ≃ S = O
16 − 17	16	13	11 − 9	9.5 − 9

ROH >	SO_2 >	P = O ≃ C = O >	XO_n^{m-}
9 − 8	6.7	4	1

The ^{17}O χ values for the terminal CO groups in metallocarbonyls were found to be 1–3 MHz, although values below 0.1 MHz have also been observed. It was suggested that increased dπ–pπ back-bonding from the metal will increase electron density perpendicular to the C–O axis and so reduce the χ values.[72]

3.4 Relaxation Properties (see *Relaxation Theory for Quadrupolar Nuclei*)

3.4.1 Relaxation in the Extreme Narrowing Condition

In isotropic systems and in the absence of chemical exchange, the T_1 and T_2 relaxation times are equal and are given by

$$1/T_1 = 1/T_2 = 3/125(1 + \eta^2/3)\chi^2 f(\omega,\ D) \qquad (3)$$

where χ is the nuclear quadrupole coupling constant. The asymmetry parameter η varies from 0 to 1 and describes the deviation of the electric field gradient from axial symmetry. $f(\omega,D)$ is the correlation function, which depends on the rotational diffusion constant D and its relative orientation with respect to the principal axes of the field gradient tensor. When isotropic reorientation is assumed, $f(\omega,D)$ reduces to the single correlation time τ_c. If the resonance absorption is a Lorentzian lineshape, the linewidth at halfheight $\Delta\nu_{\frac{1}{2}}$ is a direct measure of the relaxation time, provided that unresolved indirect spin coupling is not present and that chemical exchange phenomena do not take place. From equation (3) it is clear that the product $\chi^2(1 + \eta^2/3)$ can be obtained from ^{17}O relaxation times if the correlation time governing the relaxation is known. The Debye formula allows only the determination of the correct order of magnitude of τ_c. More precise values of τ_c could be obtained from the relaxation of other nuclei, such as ^{13}C or other quadrupolar nuclei; however, one should be aware of possible anisotropic reorientations due to molecular tumbling.[4]

3.4.2 Relaxation Outside the Extreme Narrowing Condition

In this case, the decay of the longitudinal (M_1) and transverse (M_2) magnetizations is no longer exponential but may be written as a weighted sum of $I + \frac{1}{2}$ exponentials:[73]

$$M_1(t) = M_1(\infty)\left\{1 - k\left[\sum_{i=1}^{I+1/2} C_{1,i}\ \exp\left(-R_{1,i}t\right)\right]\right\} \qquad (4)$$

$$M_2(t) = M_2(0)\left[\sum_{i=1}^{I+1/2} C_{2,i}\exp(-R_{2,i}t)\right] \qquad (5)$$

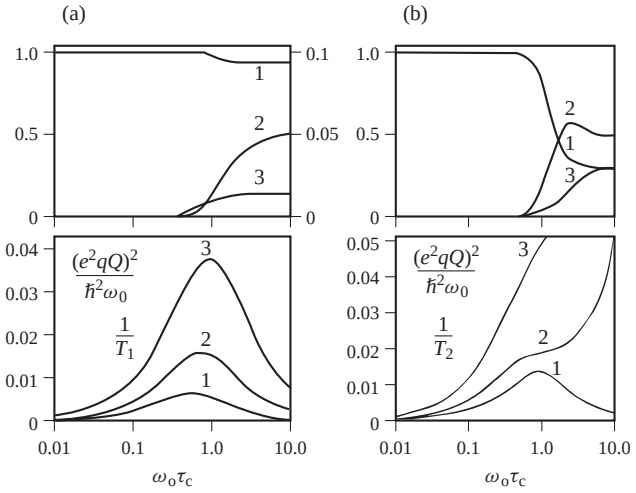

Figure 3 Longitudinal (a) and transverse (b) relaxation of spin-$\frac{5}{2}$ nuclei in the absence of chemical exchange. The upper plots show the normalized amplitudes $C_{1,i}$ and $C_{2,i}$ of the three exponential components as a function of $\omega_0\tau_c$ (coefficients 2 and 3 are plotted on the expanded scale given to the right). The lower plots show the relaxation rates as a function of the same parameter. (Adapted by permission of The American Institute of Physics from T. E. Bull, S. Forsen, and D. L. Turner, *J. Chem. Phys.*, 1979, **70**, 3106)

where $\sum_{i=1}^{I+1/2} C_{j,i}$ and $k = 2$ for an inversion–recovery experiment. Furthermore, although equation (4) is valid for the total magnetization, the decays of the individual components will normally not be exponential and will also depend on the length of the monitoring pulse. Equations (4) and (5) cannot be solved analytically, but must be solved numerically for each value of $\omega_0{}^2\tau_c{}^2$. Figure 3 illustrates the longitudinal and transverse relaxation of spin $I = \frac{5}{2}$ nuclei in the absence of chemical exchange. The longitudinal relaxation may be regarded as a single exponential, within the limits of experimental error, for all correlation times. Conversely, the transverse relaxation is governed by the three contributions and the weights of the different contributions have similar magnitudes for the longer correlation times. For values of $\omega_0{}^2\tau_c{}^2 \ll 1$, the transverse relaxation is approximately a single exponential. In the slow motion limit the rapid decay of the third component at longer correlation times may allow analysis in terms of just two exponential terms.

In addition to nonexponential relaxation for quadrupolar nuclei under conditions of nonextreme narrowing, the NMR signal will also be modified by shift changes which have been termed 'second-order dynamic frequency shifts' (see ***Quadrupolar Interactions*** and ***Dynamic Frequency Shift***). Although long recognized theoretically, the experimental demonstration of such a phenomenon is not straightforward, since the symmetry of the composite peak is in practice difficult to distinguish from small phase misadjustment and is thus usually overlooked. Furthermore, strongly relaxed transitions may decay so quickly as to be undetected if the instrument deadtime is too long. Expressions for the NMR bandshape for $I = \frac{5}{2}$ and $I = \frac{7}{2}$ nuclei have been derived, both in the presence and the absence of chemical exchange.[74] In the limit $\omega_0\tau_c \gg 1$, the $m = \frac{1}{2} \rightarrow m = -\frac{1}{2}$ component will dominate the spectrum because it is much narrower than the other components. This narrow signal will be shifted

towards lower frequency with a value proportional to χ^2/ω_0. Between these two limits the resonance will be more or less asymmetric, with an apparent shift to either high or low frequency depending on the values of ω_0, τ_c, and χ. The ratio of the dynamic shift to the linewidth $\Delta\omega_d/\Delta\omega_{\frac{1}{2}}$ in this region depends only on ω_0 and τ_c.

3.4.3 *Effects of Relaxation Mechanisms Other Than Quadrupolar*

It is evident from Figure 3 that the linewidth of the narrow component decreases as τ_c increases in the slow motion limit, while the linewidths of the intermediate and broad components increase. However, the linewidth of the narrow component does not necessarily decrease as τ_c increases if the chemical shift anisotropy is large. Such behavior has been observed in studies of the temperature and magnetic field strength dependence of ^{17}O NMR spectra of myoglobin MbC^{17}O samples.[75] For $\tau_c \simeq 14$ ns and $\sigma_{\parallel} - \sigma_{\perp} = 800$ ppm (which is the value for a model heme compound obtained from NMR studies in the solid state) a CSA contribution to the linewidth of about 100 Hz was obtained for the narrow components. This value is comparable to that of the pure quadrupolar contribution to the linewidth (about 96 Hz). The CSA contribution to T_1 was found to be negligible (about 170 ms).

4 SELECTED APPLICATIONS

4.1 Dynamic and Kinetic Studies

Numerous dynamic and kinetic studies have been performed using ^{17}O NMR. Lineshape analysis is not straightforward because the linewidth itself is temperature dependent. Nevertheless, it has been shown that dynamic ^{17}O NMR is a convenient alternative to ^{13}C NMR for studies of metal carbonyl compounds.[76] A solution of $HFeCO_3(CO)_{12}$ at $-89\,^{\circ}$C gives only two ^{13}CO signals in a ratio of 1:2 instead of the expected four signals with a 1:1:1:1 ratio. In ^{17}O NMR, the four signals are easily observed at $-11\,^{\circ}$C and a two-step exchange process averages all the sites, producing a single line at $108\,^{\circ}$C.

^{17}O NMR has been used to measure the rate of oxygen exchange in aldehydes and ketones,[77] cobaloximes,[78] and the periodate–water system.[79] It is possible to measure either the decay of a signal from a group enriched in ^{17}O or the growth of a signal that is undergoing exchange with ^{17}O labeled water.[3]

A substantial number of publications has been concerned primarily with studies of the hydration of ions in solution. The ^{17}O chemical shift of water molecules bound to Al^{3+} was found to be about 11 ppm to high frequency. Temperature dependence studies and lineshape analysis yielded the ^{17}O nuclear relaxation rates of the bound and free water molecules, the coordination number, and the rates of exchange between the bound and free water.[80] In addition, the thermodynamic parameters for activation characterizing the exchange reaction can be obtained. In cases where the chemical shift between 'bound' and 'free' water molecules is small, leading to overlapping of resonances, the resonance of the 'free' molecule can be shifted by adding small amounts of a paramagnetic salt. Estimates of 4, 6, and 6 for the hydration numbers of Be(II), Al(III), and Ga(III) were obtained from area measurements. An alternative method of determining hydration numbers, by evaluating the magnitude of the shift of the water resonances caused by the dissolved paramagnetic ion, has also been suggested.[80]

There is an extensive literature on ^{17}O NMR studies of the exchange rates of water molecules bound to paramagnetic ions.[81–84] In this case there is a much greater chance of observing separate resonances from ^{17}O nuclei in 'bound' water molecules in the solvation shells of paramagnetic cations than in the corresponding diamagnetic cations. The magnitudes and temperature dependences of the linewidths (or relaxation time measurements) of the 'bound' and 'free' resonances, and the chemical shift separations between these resonances, can in principle be used to derive information about the hyperfine splitting constant, a_N, the rate of the solvent interchange process, T_e, and the solvation number. However, because the shifted resonance of the solvated water molecules is also often very broad, it is rarely possible in practice to derive the hydration number of the paramagnetic cation from straightforward area measurements. In such cases the hydration numbers may be obtained by using the theory developed by Swift and Connick[85] who investigated a variety of systems. This type of work and the chemical significance of the results have been reviewed (see ***Paramagnetic Relaxation in Solution***).[86]

4.2 ^{17}O NMR and Torsion Angle Effects

^{17}O NMR spectroscopy is a powerful method for detecting steric effects in molecules in which the steric interactions are characterized by the rotation of functional groups about single bonds to relieve van der Waals interactions or in rigid systems in which the steric interactions are partially accommodated by bond angle and bond length distortions.[87] ^{17}O deshielding is expected when the rotation leads to greater double bond character or reduced electron density on oxygen (e.g. in an isolated carbonyl group). Shielding, however, is observed in the situation in which the carbonyl group assumes more single bond character or increased density on the oxygen atom. Studies of such steric effects have been done on aromatic and heteroaromatic nitro compounds, aryl ketones, aldehydes and 1,2-diketones, aromatic carboxylic acids, esters and amides.[88–91] For nitro aromatic compounds, a quantitative relationship was established between $\delta(^{17}O)$ of the nitro group and the torsional angle between the aromatic ring and the nitro group (Figure 4). It appears that the solid state conformational preference, and thus the angle, is in remarkably good agreement with the average angle determined in the solution state.

4.3 Hydrogen-Bonding Effects (see *Hydrogen Bonding*)

The use of ^{17}O NMR appears to be especially promising for studying hydrogen-bonding interactions, because of the large chemical shift range of the oxygen nucleus.[92–94] The dominance of intramolecular hydrogen-bonding effects over substituent effects has been clearly demonstrated in acetophenones, benzaldehydes, and hydroxynaphthoquinones.[32,95] In

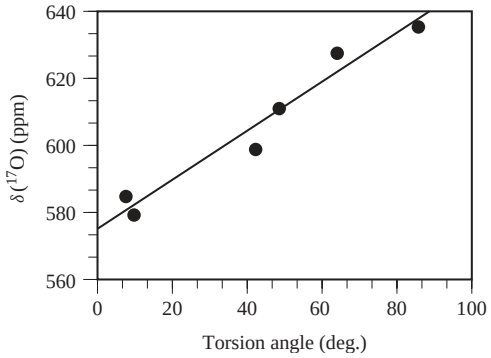

Figure 4 Plot of the torsion angles (X-ray) between aromatic rings and nitro groups versus ^{17}O chemical shift data.[87] (Reproduced by permission of CRC Press, Inc., from D. W. Boykin and A. L. Baumstark, in '^{17}O NMR Spectroscopy in Organic Chemistry', ed. D. W. Boykin, 1991, Chap. 3)

amides and peptides,[10,93,96–100] both long-range dipole–dipole interactions and specific hydrogen bonds at the amide oxygen atom induce significant and specific shielding of the ^{17}O nucleus. Thus the overall chemical shift change between an amide oxygen atom in the absence of hydrogen-bonding interactions in vacuum and one that is fully hydrated in aqueous solution is, very probably, over 95 ppm. There is a linear correlation between $\delta(^{17}O)$ and $\nu(CO)$, the infrared (IR) amide I stretching vibration, for different solvents which have varying dielectric constants and solvation abilities.[100] This demonstrates that both IR and ^{17}O NMR spectroscopy appear to be reflecting a similar type of electronic perturbation, i.e. hydrogen bonding and dipole–dipole solute–solvent interactions. Further studies include investigations of the hydration and intra- and intermolecular hydrogen bonding of the *cis*/*trans* peptide oxygen atoms in AcYOH and AcYNHMe (Y = Pro or Sar)[13,98] (Figure 1), protected dipeptides,[99] and peptide hormones.[101–103]

4.4 Oxygen Bonded to Transition Elements (Polyoxometalates)

^{17}O NMR has been employed frequently in stereochemical studies of polynuclear, anionic oxo complexes (polyoxoanions) of the early transition elements in a variety of oxidation states.[104–108] In spite of their structural complexity, these polyoxoanions often yield well resolved ^{17}O NMR spectra, since large chemical shifts are observed and samples may often be observed at elevated temperatures in nonviscous solvents. Furthermore, ^{17}O enrichment is easily obtained. A representative example is the $[V_{10}O_{28}]^{6-}$ species, the structure and spectrum of which are shown in Figure 5. Exchange of oxygen atoms in the complex ion with those of $H_2{}^{17}O$ in aqueous solution showed that all the different oxygen sites could be identified separately by their shieldings. If an oxygen atom attached to n vanadium atoms is designated as OV_n, then the observed chemical shifts are: OV $\simeq$1150; OV_2 (three different sites) $\simeq$ 900, 790 and 760; $OV_3 \simeq 390$; and $OV_4 \simeq 65$ ppm. It can be seen that there is a systematic reduction in $\delta(^{17}O)$ with an increase in the number of vanadium atoms to which the oxygen atom is bound. Other complex anions of the formula $[M_6O_{19}]^{n-}$, where M = Mo (n = 2), Nb

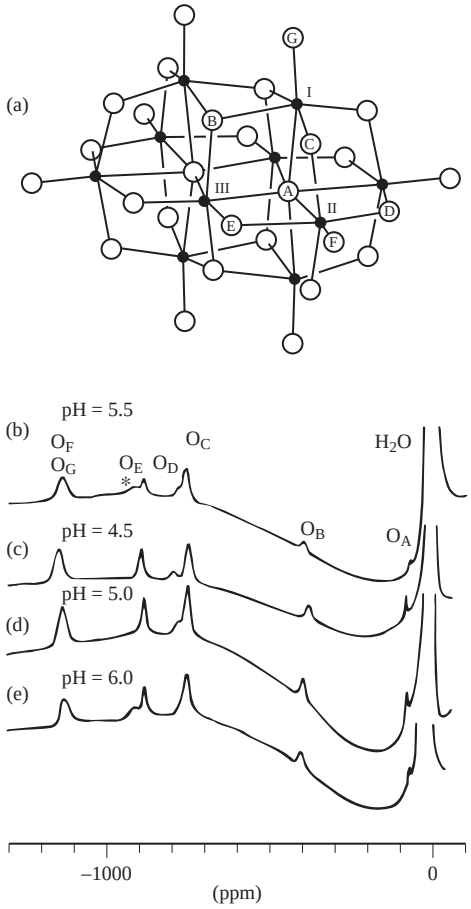

Figure 5 (a) The D_{2h} symmetrized structure of $V_{10}O_{28}{}^{6-}$. Small filled circles represent vanadium atoms and large open circles represent oxygen atoms. One member of each symmetry-equivalent set of atoms is labeled. (b–e) ^{17}O NMR spectra at 13.5 MHz of $V_{10}O_{28}{}^{6-}$ in H_2O. All spectra were measured at 25 °C with total vanadium concentrations of 1.5–1.8 M. The asterisk labels the metavanadate resonance. (Adapted by permission of The American Chemical Society from W. G. Klemperer and W. Shum, *J. Am. Chem. Soc.*, 1977, **99**, 3544)

(n = 8), or Ta (n = 8), show the same qualitative regularities in shielding, with OM > OM_2 > OM_6. These regularities have been interpreted as a correlation between increasing chemical shift and increasing π bonding from the metal to the oxygen in different sites. The regularities persist in the ^{17}O spectra of a variety of more complex anions of lower symmetry in which other metals or nonmetals are substituted within an $[M_xO_y]^{n-}$ framework. It should be noted that the resonances of oxygen nuclei in the highly symmetrical environments of the complex anions, e.g. OM_4 or OM_6, are relatively sharp. This is to be expected because the field gradient at these positions will be zero or very small; hence the normally dominant quadrupolar relaxation mechanism will be very weak and the relaxation times correspondingly long.

4.5 Heme Proteins and Model Compounds—Substrate Binding to Enzymes

The ^{17}O NMR spectra of several heme model compounds in solution have been reported.[11,109–111] Two signals at about

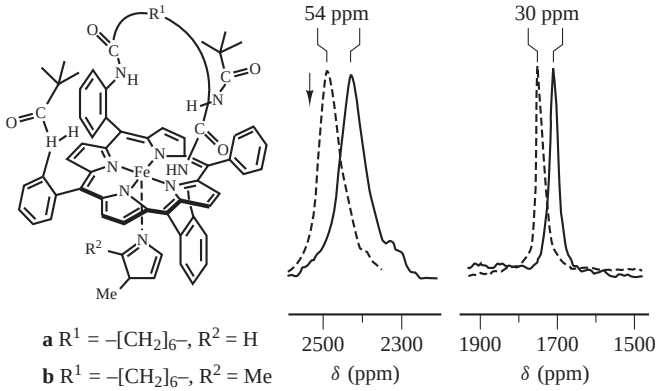

Figure 6 ^{17}O NMR spectra (54.2 MHz) of the oxygenated compounds **a**(- - - -) and **b** (—) with a preacquisition delay time Δt = 50 μs and recorded in two steps with the carrier frequency on the absorption resonances. Maximum concentration $\simeq 10^{-2}$ M in toluene solution. Concentration of 1,2-dimethylimidazole (1,2-Me_2Im) $\simeq 5.10^{-1}$ M, T = 297 K, NS = 1 080 000 (LB = 1 kHz) and 350 000 (LB = 500 Hz) for the high- and low-frequency resonances, respectively. The arrow denotes the region of the resonance position of the terminal oxygen atom of the picket-fence porphyrin model, with excess 1-MeIm, and ether models in which no hydrogen bonding interactions are expected. (Adapted by permission of the Royal Society of Chemistry from I. P. Gerothanassis, B. Look, and M. Momenteau, *J. Chem. Soc., Chem. Commun.*, 1992, 598)

1750 and 2500 ppm were observed for the FeO_2 linkage (Figure 6). The data were interpreted as ruling out sideways triangular bonding in favor of an end-on angular bonding arrangement. The data were explained in terms of bonding models in which the electrons of the FeO_2 moiety are totally paired.

Analysis of the ^{17}O relaxation and chemical shift data of $C^{17}O$ ligated hemoproteins has provided information on both the structural and the dynamic properties of the heme group.[49,75,112] Peroxidases are heme proteins with molecular weights of about 40–42 kDa that catalyze oxidations by hydrogen peroxide. They contain iron-protoporphyrin IX as a noncovalently bound prosthetic group. The ^{17}O NMR spectra of CO-horseradish peroxidase isoenzyme C (Figure 7) indicate a single hemoprotein $C^{17}O$ signal (at 358.3 ppm) below pH 10 and two separate signals at pH 10.5. The new signal, which was assigned with the alkaline form of CO-horseradish peroxidase isozyme C, is broader and at about 7 ppm to high frequency relative to that of the acidic form. A similar pH-dependent relationship of the chemical shift and linewidth was observed for CO-horseradish peroxidase isozyme A and CO-horseradish peroxidase isozyme C. It was concluded that CO-horseradish peroxidase isozyme C undergoes a transition between the acidic and alkaline forms.[112] However, unlike the case of CO-horseradish peroxidase isozyme A, the transition is slow on the NMR timescale (see ***Oxygen-17 NMR: Applications in Biochemistry***).

4.6 Hydration of Proteins: Water Orientation in Lyotropic Phases and Bilayers

Water plays a fundamental role in the conformation and activity of biological macromolecules (see ***Protein Hydration***).

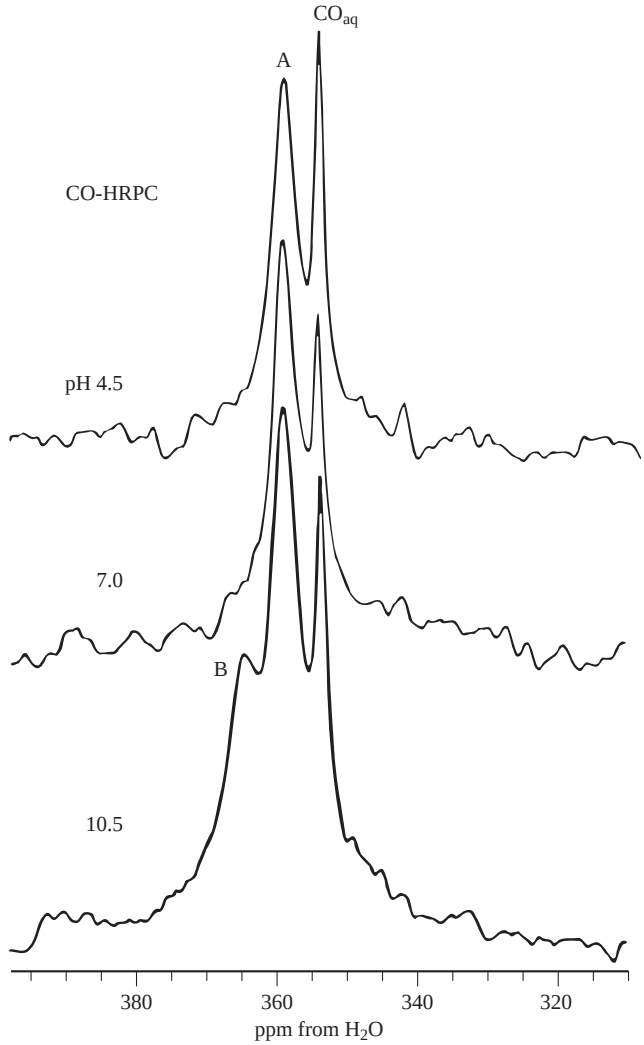

Figure 7 Oxygen-17 NMR spectra of CO-horseradish peroxidase isozyme C (CO-HRPC); concentration, 1 mM in 50 mM phosphate buffer at 11.7 T; NS = 50 000–250 000, recycle time 100–150 ms, pulse width 38 μs, LB = 100 Hz. A, B, and CO_{aq} denote the acidic form of CO-HRPC, the alkaline form of CO-HRPC, and free CO in solution, respectively. (Reprinted by permission of The American Society for Biochemistry and Molecular Biology from H. C. Lee, K. Cummings, K. Hall, L. P. Hager, and E. Oldfield, *J. Biol. Chem.*, 1988, **263**, 16 118)

^{17}O NMR studies have several advantages compared with ^{1}H and ^{2}H NMR for protein hydration:

1. The relaxation effect is large, permitting studies at low protein concentrations.
2. The ^{17}O relaxation in water is generally dominated by the quadrupolar mechanism.[113,114] The intramolecular origin of the electric field gradient makes the quadrupolar interaction virtually independent of the molecular environment.
3. The ^{17}O relaxation is not affected by proton (or deuteron) exchange with protic residues in the protein. Only T_2 can be affected by exchange within a narrow pH range near neutrality.
4. Cross relaxation that contributes to ^{1}H relaxation is unimportant for ^{17}O.[115,116]

Variable field T_1 and T_2 relaxation time measurements of several proteins[117] were interpreted in terms of two layers of

hydration having a reorientational correlation time of about 20 ps (about eight times slower than that of bulk water and independent of the nature of the protein). This rapid local motion has a small anisotropic component (corresponding to an order parameter of 0.06) which is averaged out by protein reorientation with a correlation time of the order of 10 ns.

Water molecules are important constituents of lyotropic phases and bilayers. In this case the molecular motions are strongly anisotropic and the quadrupolar interaction is not averaged out to zero and may be measured when it is small compared with the Zeeman interaction. Ordering of a water molecule results in a quadrupolar splitting which is related to the order parameter. It has been shown that important dynamic information can be obtained from ^{17}O linewidth data which complement the ordering results from ^{2}H NMR.[118] (see ***Amphiphilic Liquid Crystalline Samples: Nuclear Spin Relaxation*** and ***Liquid Crystalline Samples: Structure of Nonrigid Molecules***).

4.7 The Solid State

Under conditions of magic angle spinning (MAS) (see ***Magic Angle Spinning***), the $(\frac{1}{2}, -\frac{1}{2})$ transition of quadrupolar nuclei with nonintegral spin does not depend on first-order quadrupolar interactions or on the effects of θ (the angle between $\boldsymbol{B}_0$ and q_{zz}). The powder bandshapes depend upon second-order quadrupolar effects which do not eliminate the possibility of obtaining meaningful NMR spectra. In this case operation at very high magnetic fields will generally be most advantageous since the maximum second-order quadrupolar linewidth of the $(\frac{1}{2}, -\frac{1}{2})$ transition decreases linearly with the magnetic field.[119] Typical results are those obtained for a range of oxides, oxyanions and high temperature oxide superconductors.[120–122] For fosterite (Mg_2SiO_4), in which three crystallographically distinct oxygen sites were partly resolved, it was possible to determine the chemical shifts (61, 62, and 47 ppm), the quadrupole coupling constants (2.35, 2.35, and 2.7 MHz), and the electric field gradient tensor asymmetry parameters (0.2, 1.0, and 0.3) associated with each. From similar studies of silicate minerals and other compounds it was found that the χ values are related to the percentage ionic character of the bonds to oxygen.[120] It has also been found that VAS can be advantageous, especially for removing resonances arising from transitions other than $(\frac{1}{2}, -\frac{1}{2})$ (see ***Variable Angle Sample Spinning***). Furthermore, it has been demonstrated that ^{17}O spins can be polarized by the ^{1}H spin system, as is done for ^{13}C in CP MAS.[123]

^{17}O NMR studies on single crystals have the advantage, compared with studies on powders, that the complete principal components of the nuclear quadrupolar coupling constant and shielding tensors can be obtained and their orientation relative to the local molecular symmetry can be determined.[124]

5 RELATED ARTICLES

Amphiphilic Liquid Crystalline Samples: Nuclear Spin Relaxation; Dynamic Frequency Shift; Hydrogen Bonding; Liquid Crystalline Samples: Structure of Nonrigid Molecules; Magic Angle Spinning; Oxygen-17 NMR: Applications in Biochemistry; Paramagnetic Relaxation in Solution; Protein Hydration; Relaxation Theory for Quadrupolar Nuclei; Shielding Calculations: IGLO Method; Shielding: Overview of Theoretical Methods; Variable Angle Sample Spinning.

6 REFERENCES

1. C. Roger and N. Sheppard, in *NMR and the Periodic Table*, ed. R. K. Harris and B. E. Mann, Academic, New York, 1978, Chap. 12A.
2. W. G. Klemperer, *Angew. Chem., Int. Ed., Engl.*, 1978, **17**, 246.
3. T. St. Amour and D. Fiat, *Bull. Magn. Reson.*, 1980, **1**, 118.
4. J.-P. Kintzinger, in *NMR Basic Principles and Progress*, ed. P. Diehl, E. Fluck, and R. Kosfeld, Springer, Heidelberg, 1981, Vol. 17.
5. W. G. Klemperer, in *The Multinuclear Approach to NMR Spectroscopy*, ed. J. B. Lambert and F. G. Riddell, Reidel, Dordrecht, 1983, Chap. 11
6. J.-P. Kintzinger, in *NMR of Newly Accessible Nuclei*, ed. P. Laszlo, Academic, New York, 1983, Vol. 2.
7. M.-D. Tsai and K. Bruzik, in *Biological Magnetic Resonance*, ed. L. J. Berliner and J. Reuben, Plenum, New York, 1983, Vol. 5.
8. W. McFarlane and H. C. E. McFarlane, in *Multinuclear NMR*, ed. J. Mason, Plenum, New York, 1987, Chap. 14
9. D. W. Boykin (ed.), *^{17}O NMR Spectroscopy in Organic Chemistry*, CRC, Boston, 1991.
10. I. P. Gerothanassis, *Progr. NMR Spectrosc.*, 1994, **26**, 171.
11. I. P. Gerothanassis, *Progr. NMR Spectrosc.*, 1994, **26**, 239.
12. I. P. Gerothanassis, R. Hunston, and J. Lauterwein, *Helv. Chim. Acta*, 1982, **65**, 1764.
13. R. N. Hunston, I. P. Gerothanassis, and J. Lauterwein, *J. Am. Chem. Soc.*, 1985, **107**, 2654.
14. G. W. Kabalka, and N. M. Goudgaon, in *^{17}O NMR Spectroscopy in Organic Chemistry*, ed. D. W. Boykin, CRC, Boston, 1991, Chap. 1
15. I. P. Gerothanassis and J. Lauterwein, *Magn. Reson. Chem.*, 1986, **24**, 1034.
16. I. P. Gerothanassis, J. Lauterwein, and N. Sheppard, *J. Magn. Reson.*, 1982, **48**, 431.
17. J. Lauterwein and I. P. Gerothanassis, *J. Magn. Reson.*, 1983, **51**, 153.
18. J. Schulte and J. Lauterwein, *J. Magn. Reson., Ser. A*, 1993, **101**, 95.
19. I. P. Gerothanassis, *Progr. NMR Spectrosc.*, 1987, **19**, 267.
20. A. C. Kunwar, G. L. Turner, and E. Oldfield, *J. Magn. Reson.*, 1986, **69**, 124.
21. H. A. Christ, P. Diehl, H. R. Schneider, and H. Dahn, *Helv. Chim. Acta*, 1961, **44**, 865.
22. M. Karplus and J. A. Pople, *J. Chem. Phys.*, 1963, **38**, 2803.
23. H. A. Christ and P. Diehl, *Helv. Phys. Acta*, 1963, **36**, 170.
24. L.-O. Andersson and J. Mason, *J. Chem. Soc., Dalton Trans.*, 1974, 202.
25. E. Lippmaa, M. Magi, S. S. Novikov, L. I. Khmelnitski, A. S. Prihodko, O. V. Lebedev, and L. V. Epishina, *Org. Magn. Reson.*, 1972, **4**, 153.
26. J. A. Coderre, S. Mehdi, P. C. Demou, R. Weber, D. D. Traficante, and J. A. Gerlt, *J. Am. Chem. Soc.*, 1981, **103**, 1870.
27. I. P. Gerothanassis and N. Sheppard, *J. Magn. Reson.*, 1982, **46**, 423.
28. J. A. Gerlt, P. C. Demou, and S. Mehdi, *J. Am. Chem. Soc.*, 1982, **104**, 2848.

29. B. N. Figgis, R. G. Kidd, and R. S. Nyholm, *Proc. R. Soc. London, Ser. A*, 1962, **269**, 469.
30. W. H. De Jeu, *Mol. Phys.*, 1970, **18**, 31.
31. D. J. Sardella and J. B. Stothers, *Can. J. Chem.*, 1969, **47**, 3089.
32. T. E. St. Amour, M. I. Burgar, B. Valentine, and D. Fiat, *J. Am. Chem. Soc.*, 1981, **103**, 1128.
33. T. C. Brownlee, M. Sadek, and D. J. Craik, *Org. Magn. Reson.*, 1983, **21**, 616.
34. C. Delseth and J. P. Kintzinger, *Helv. Chim. Acta*, 1978, **61**, 1327.
35. I. J. Solomon, J. N. Keith, A. J. Kacmarek, and J. K. Raney, *J. Am. Chem. Soc.*, 1968, **90**, 5408.
36. I. J. Solomon, A. J. Kacmarek, and J. Raney, *Inorg. Chem.*, 1968, **7**, 1221.
37. I. J. Solomon, A. J. Kacmarek, W. K. Sumida, and J. K. Raney, *Inorg. Chem.*, 1972, **11**, 195.
38. R. Ditchfield, D. P. Miller, and J. A. Pople, *J. Chem. Phys.*, 1970, **53**, 613; 1971, **54**, 4186.
39. R. Ditchfield, *Mol. Phys.*, 1974, **27**, 789.
40. K. A. K. Ebraheem and G. A. Webb, *Progr. NMR Spectrosc.*, 1977, **11**, 149.
41. K. A. K. Ebraheem and G. A. Webb, *J. Magn. Reson.*, 1977, **25**, 399.
42. K. A. K. Ebraheem and G. A. Webb, *J. Magn. Reson.*, 1978, **30**, 211.
43. M. Jallali-Heravi and G. A. Webb, *J. Magn. Reson.*, 1978, **32**, 429.
44. J. Sadlej and A. J. Sadlej, *J. Magn. Reson.*, 1974, **14**, 97.
45. M. Schindler and W. Kutzelnigg, *Mol. Phys.*, 1983, **48**, 781.
46. C. J. Jameson, in *Nuclear Magnetic Resonance*, ed. G. A. Webb, Royal Society of Chemistry, London, 1985, Vol. 14, Chap. 1
47. J. D. Augspurger, C. E. Dykstra, and E. Oldfield, *J. Am. Chem. Soc.*, 1991, **113**, 2447.
48. J. D. Augspurger and C. E. Dykstra, *J. Phys. Chem.*, 1991, **95**, 9230.
49. K. D. Park, K. Guo, F. Adebodun, M. L. Chiu, S. G. Sligar, and E. Oldfield, *Biochemistry*, 1991, **30**, 2333.
50. I. Ando and G. A. Webb, *Org. Magn. Reson.*, 1981, **15**, 111.
51. G. Klopman, *Chem. Phys. Lett.*, 1967, **1**, 200.
52. M. Jallali-Heravi, B. Na Lamphun, G. A. Webb, I. Ando, M. Kondo, and S. Watanabe, *Org. Magn. Reson.*, 1980, **14**, 92.
53. F. R. Prado, C. Giessner-Prettre, A. Pullman, J. F. Hinton, D. Horspool, and K. R. Metz, *Theor. Chim. Acta*, 1981, **59**, 55.
54. Z. Luz and G. Yagil, *J. Phys. Chem.*, 1966, **70**, 554.
55. J. Reuben, A. Tzalmona, and D. Samuel, *Proc. Chem. Soc.*, 1962, 353.
56. H. Versmold, and C. Yoon, *Ber. Bunsenges. Phys. Chem.*, 1972, **76**, 1164.
57. G. A. Gray and T. A. Albright, *J. Am. Chem. Soc.*, 1977, **99**, 3243.
58. O. Lutz, W. Nepple, and A. Nolle, *Z. Naturforsch., Teil A*, 1976, **31**, 978, 1046.
59. G. D. Mateescu and G. M. Benedikt, *J. Am. Chem. Soc.*, 1979, **101**, 3959.
60. G. O. Mateescu, private communication.
61. W. L. Earl and W. Niederberger, *J. Magn. Reson.*, 1977, **27**, 351.
62. M.-D. Tsai, *Biochemistry*, 1979, **18**, 1468.
63. M.-D. Tsai, *Biochemistry*, 1980, **19**, 5310.
64. G. H. Reed and T. S. Leyh, *Biochemistry*, 1980, **19**, 5472.
65. C. P. Cheng and T. L. Brown, *J. Am. Chem. Soc.*, 1979, **101**, 2327.
66. C. P. Cheng and T. L. Brown, *J. Am. Chem. Soc.*, 1980, **102**, 6418.
67. B. H. Ruessink, and C. MacLean, *Mol. Phys.*, 1984, **53**, 421.
68. C. Chachaty and J. P. Quaegedeur, *Mol. Phys.*, 1984, **52**, 1081.
69. Y. Tricot and W. Niederberger, *Helv. Chim. Acta*, 1984, **67**, 1033.
70. G. E. Hawkes, E. W. Randall, S. Aime, and R. Gobetto, *J. Magn. Reson.*, 1986, **68**, 597.
71. R. T. C. Brownlee, M. J. O'Connor, B. P. Shehan, and A. G. Wedd, *J. Magn. Reson.*, 1985, **61**, 22.
72. S. Aime, R. Gobetto, D. Osella, G. E. Hawkes, and E. W. Randall, *J. Chem. Soc., Dalton Trans.*, 1984, 1863.
73. T. E. Bull, S. Forsen, and D. L. Turner, *J. Chem. Phys.*, 1979, **70**, 3106.
74. P. O. Westlund and H. Wennerstrom, *J. Magn. Reson.*, 1982, **50**, 451.
75. H. C. Lee and E. Oldfield, *J. Am. Chem. Soc.*, 1989, **111**, 1584.
76. S. Aime, D. Osella, L. Milone, G. E. Hawkes, and E. W. Randall, *J. Am. Chem. Soc.*, 1981, **103**, 5920.
77. P. Greenzaid, Z. Luz, and D. Samuel, *Trans. Faraday Soc.*, 1968, **64**, 2780, 2787.
78. E. H. Curzon, B. T. Golding, and A. K. Wong, *J. Chem. Soc., Chem. Commun.*, 1982, 63.
79. I. Pecht and Z. Luz, *J. Am. Chem. Soc.*, 1965, **87**, 4068.
80. J. A. Jackson, J. Lemons, and H. Taube, *J. Chem. Phys.*, 1960, **32**, 553.
81. R. E. Connick and D. N. Fiat, *J. Chem. Phys.*, 1963, **39**, 1349.
82. D. Fiat and R. E. Connick, *J. Am. Chem. Soc.*, 1966, **88**, 4754.
83. D. Fiat and A. M. Chmelnick, *J. Am. Chem. Soc.*, 1971, **93**, 2875.
84. R. E. Connick and D. Fiat, *J. Chem. Phys.*, 1966, **44**, 4103.
85. T. J. Swift and R. E. Connick, *J. Chem. Phys.*, 1962, **37**, 307; 1964, **41**, 2553.
86. J. P. Hunt, *Coord. Chem. Rev.*, 1971, **7**, 1.
87. D. W. Boykin and A. L. Baumstark, in *^{17}O NMR Spectroscopy in Organic Chemistry*, ed. D. W. Boykin, CRC, Boston, 1991, Chap. 3
88. M. G. Oakley and D. W. Boykin, *J. Chem. Soc., Chem. Commun.*, 1986, 439.
89. A. L. Baumstark, P. Balakrishnan, M. Dotrong, C. J. McCloskey, M. G. Oakley, and D. W. Boykin, *J. Am. Chem. Soc.*, 1987, **109**, 1059.
90. D. W. Boykin, G. H. Deadwyler, and A. L. Baumstark, *Magn. Reson. Chem.*, 1988, **26**, 19.
91. D. W. Boykin and A. L. Baumstark, *Tetrahedron*, 1989, **45**, 3613.
92. J. Reuben, *J. Am. Chem. Soc.*, 1969, **91**, 5725.
93. M. I. Burgar, T. E. St. Amour, and D. Fiat, *J. Phys. Chem.*, 1981, **85**, 502.
94. H. M. Schwartz, M. MacCoss, and S. S. Danyluk, *J. Am. Chem. Soc.*, 1983, **105**, 5901.
95. G. Jaccard and J. Lauterwein, *Helv. Chim. Acta*, 1986, **69**, 1469.
96. A. Steinschneider, M. I. Burgar, A. Buku, and D. Fiat, *Int. J. Peptide Protein Res.*, 1981, **18**, 324.
97. D. Fiat, *Bull. Magn. Reson.*, 1984, **6**, 30.
98. J. Lauterwein, I. P. Gerothanassis, and R. Hunston, *J. Chem. Soc., Chem. Commun.* 1984, 367.

99. N. Birlirakis, I. P. Gerothanassis, C. Sakarellos, and M. Marraud, *J. Chem. Soc., Chem. Commun.*, 1989, 1122.
100. I. P. Gerothanassis and C. Vakka, *J. Org. Chem.*, 1994, **59**, 2341.
101. H. Gilboa, A. Steinschneider, B. Valentine, D. Dhawan, and D. Fiat, *Biochim. Biophys. Acta*, 1984, **800**, 251.
102. C. Sakarellos, I. P. Gerothanassis, N. Birlirakis, T. Karayannis, M. Sakarellos-Daitsiotis, and M. Marraud, *Biopolymers*, 1989, **28**, 15.
103. I. P. Gerothanassis, N. Birlirakis, T. Karayannis, M. Sakarellos-Daitsiotis, C. Sakarellos, B. Vitoux, and M. Marraud, *Eur. J. Biochem.*, 1992, **210**, 693.
104. A. D. English, J. P. Jesson, W. G. Klemperer, T. Mamouneas, L. Messerle, W. Shum, and A. Tramontano, *J. Am. Chem. Soc.*, 1975, **97**, 4785.
105. M. Filowitz, W. G. Klemperer, L. Messerle, and W. Shum, *J. Am. Chem. Soc.*, 1976, **98**, 2345.
106. W. G. Klemperer and W. Shum, *J. Am. Chem. Soc.*, 1977, **99**, 3544.
107. M. Filowitz, R. K. C. Ho, W. G. Klemperer, and W. Shum, *Inorg. Chem.*, 1979, **18**, 93.
108. M. A. Freeman, F. A. Schultz, and C. N. Reilley, *Inorg. Chem.*, 1982, **21**, 567.
109. I. P. Gerothanassis and M. Momenteau, *J. Am. Chem. Soc.*, 1987, **109**, 6944.
110. I. P. Gerothanassis, M. Momenteau, and B. Loock, *J. Am. Chem. Soc.*, 1989, **111**, 7006.
111. I. P. Gerothanassis, B. Loock, and M. Momenteau, *J. Chem. Soc., Chem. Commun.*, 1992, 598.
112. H. C. Lee, K. Cummings, K. Hall, L. P. Hager, and E. Oldfield, *J. Biol. Chem.*, 1988, **263**, 16 118.
113. J. A. Glasel, *Proc. Natl. Acad. Sci. USA*, 1966, **55**, 479.
114. J. A. Glasel, *Nature*, 1968, **218**, 953.
115. S. H. Koenig, K. Hallenga, and M. Shporer, *Proc. Natl. Acad. Sci. USA*, 1975, **72**, 2667.
116. S. H. Koenig, R. G. Bryant, K. Hallenga, and G. S. Jacob, *Biochemistry*, 1978, **17**, 4348.
117. B. Halle, T. Andersson, S. Forsen, and B. Lindman, *J. Am. Chem. Soc.*, 1981, **103**, 500.
118. Y. Tricot and W. Niederberger, *Biophys. Chem.*, 1979, **9**, 195.
119. M. D. Meadows, K. A. Smith, R. A. Kinsey, T. M. Rothgelb, R. P. Skarjune, and E. Oldfield, *Proc. Natl. Acad. Sci. USA*, 1982, **79**, 1351.
120. S. Schramm and E. Oldfield, *J. Am. Chem. Soc.*, 1984, **106**, 2502.
121. S. Schramm, R. J. Kirkpatrick, and E. Oldfield, *J. Am. Chem. Soc.*, 1983, **105**, 2483.
122. E. Oldfield, C. Coretsopoulos, S. T. Yang, L. Reven, H. C. Lee, J. Shore, O. H. Han, E. Ramli, and D. Hinks, *Phys. Rev. B*, 1989, **40**, 6832.
123. T. H. Walter, G. L. Turner, and E. Oldfield, *J. Magn. Reson.*, 1988, **76**, 106.
124. W. Scheubel, H. Zimmermann, and U. Haeberlen, *J. Magn. Reson.*, 1985, **63**, 544.

Biographical Sketch

Ioannis P. Gerothanassis. *b* 1953. B.Sc., Aristotle University of Thessaloniki, 1974; M.Sc., School of Chemical Sciences, University of East Anglia, 1979; Ph.D. (supervisor Norman Sheppard, FRS), School of Chemical Sciences, University of East Anglia, 1981. Postdoctoral work at the Institut Chimie Organique, Universite de Lausanne. Successively, lecturer, assistant professor, and associate professor, Department of Chemistry, University of Ioannina, Greece. Approx. 60 publications. Current research specialties: multinuclear MR and multidimensional NMR and FT infrared studies of molecules of biological interest.

Phosphorus-31 NMR

Konstantin Karaghiosoff

Universität München, München, Germany

1	Introduction	1
2	Nuclear Properties and Standardization	1
3	Experimental Techniques	1
4	Chemical Shifts	2
5	Coupling Constants	3
6	Applications of ^{31}P NMR Spectroscopy	4
7	Related Articles	5
8	References	5

1 INTRODUCTION

With the discovery of the phenomenon of NMR in bulk samples in 1945, a new, powerful, analytical method became available to chemists. The ^{31}P nucleus was among the first nuclei to which NMR spectroscopy was applied. Phosphorus-31 spectroscopic data have been in the literature since 1951,[1,2] and their number increased rapidly in the following years. In 1967 the first comprehensive compilation of ^{31}P NMR data of simple phosphorus compounds, as well as a presentation of the current theory of phosphorus chemical shifts, was published.[3] Another publication[4] and a review[5] cover the literature up to 1969 and to mid-1982, respectively.

With the development of pulse Fourier transform NMR spectroscopy the sensitivity of the spectrometers improved and the ^{31}P NMR experiment became routine. As a consequence the amount of published ^{31}P NMR data increased dramatically. By 1987 it was estimated that more than 40 000 ^{31}P NMR data items were available in the literature. A 'Handbook of ^{31}P NMR Data' contains extensive compilations of representative data, including coupling constants, for all types of phosphorus compounds.[6] More data can be found in a series of books dedicated partially[7,8] or entirely[9–11] to ^{31}P NMR. A number of reviews[12–14] dealing with the application of ^{31}P NMR to transition metal complexes with phosphorus ligands, and a review[15] describing the main developments in ^{31}P NMR of transition metal–phosphine complexes in the period 1970–1977, are available.

With modern spectrometers and using all instrumental and relaxation aids phosphorus compounds at 200 ppm and even 5 ppm concentration levels can be detected by ^{31}P NMR.[9] Due to this capability, ^{31}P NMR spectroscopy has also gained importance as an analytical tool in biology and medicine. The work in this area is documented by a series of reviews[16–21] and books.[22,23]

2 NUCLEAR PROPERTIES AND STANDARDIZATION

The important properties of the ^{31}P nucleus for NMR spectroscopy are given in Table 1. Since phosphorus compounds are generally reactive, no suitable internal reference compound is available for general use. Phosphorus-31 chemical shifts are referenced to 85% aqueous H_3PO_4 as an external standard. According to the present sign convention shifts are given positive for signals appearing at higher frequency (lower field) with respect to that of the standard. Great care is recommended, however, when using data from the older literature, since there was a change in sign convention in the mid-1970s.

Table 1 Properties of the ^{31}P Nucleus[7,8,10]

Natural abundance, C (%)	100
Nuclear spin, I	$\frac{1}{2}$
Magnetic moment, μ (μ_N)	1.1316
Magnetogyric ratio γ (10^7 rad T^{-1} s^{-1})	10.8394
NMR frequency at 2.35 T (MHz)	40.480
Receptivity relative to that of ^{1}H, D^P	6.63×10^{-2}
Receptivity relative to that of ^{13}C D^C	3.77×10^2

A disadvantage of 85% H_3PO_4 as a standard is its broad resonance signal. A number of secondary external standards, giving much sharper signals, are therefore in use: P_4O_6 (δ^{31}P = 112.5), $P(OMe)_3$ (δ^{31}P = 140.4), $PO(OMe)_3$ (δ^{31}P = −2.4), $[P(OH)_4]ClO_4$ (δ^{31}P = −0.1), $Na_2[CH_2(PO_3H)_2]$ in D_2O (δ^{31}P = 16.7), $(NEt_4)_2HPO_4$ in H_2O (δ^{31}P = 2.1).[8,9] In some cases D_3PO_4 (δ^{31}P = 0.3) and $(CH_3)_3PO$ (δ^{31}P = 72.6) are used as internal standards.[8,9] Alternatively the ^{2}H internal lock signal can be used to obtain accurate chemical shifts referenced to $Si(CH_3)_4$ or to an idealized shift for 85% H_3PO_4. However, there is little agreement on Ξ for 85% H_3PO_4 with values ranging from 40 480 720 to 40 480 754 Hz.[7,9] An absolute ^{31}P shielding scale is based on gas phase measurements of PH_3.[24]

Normally the reported ^{31}P chemical shifts are not corrected for diamagnetic susceptibility. In addition temperature, solvent, and concentration dependence of δ^{31}P for both the reference compound and the compounds under study, may be important. Thus variations in reported chemical shifts for the same compound of up to ±10 units can be encountered in the literature.[7–10]

Measurements of the nuclear Overhauser enhancement show a wide variation extending from zero to the theoretical maximum of 124%.[8,10,25]

Spin–lattice relaxation times T_1 of phosphorus compounds vary mostly between 1 and 30 s and can depend strongly on solvent, temperature, and concentration. Compilations of T_1 data for simple phosphorus compounds are found in Mason,[8] Verkade and Quin,[9] and Berger et al.[10] Typical values are ∼1.3 s for RPH_2, 3–9 s for $P(OR)_3$, 3–6 s for PX_3 (X = halogen), 2–9 s for $[R_4P]X$, 10–31 s for R_3P, 6–30 s for $PO(OR)_3$, and 2–11 s for R_3PO.[9] For a number of three-coordinated phosphorus compounds the spin rotation mechanism has been shown to account for T_1 at ambient temperature, while at low temperatures dipolar contributions become important.[8] However, P_2t-Bu_4 relaxes by a dipolar mechanism even at ambient temperature. Going to four-coordination the relative contribution of the spin rotation mechanism decreases and is still important in the five-coordinated species PCl_nPh_{5-n} (n = 2–4) and the PF_6^- ion. A rare example, in which chemical shift anisotropy plays an important role in relaxation, is represented by Ph_3PO.[8]

3 EXPERIMENTAL TECHNIQUES

Due to its favorable nuclear properties (I = 1/2, high NMR frequency and high receptivity), the ^{31}P nucleus is easy to observe and no particular instrumental equipment is required. Early ^{31}P NMR spectra of solutions were recorded on continuous wave instruments and were often poorly resolved. Now practically all data are obtained with modern FT NMR spectrometers, equipped either with multinuclear probes or with separate pretuned probes for ^{31}P observation, yielding highly resolved spectra with $\Delta\nu_{1/2}$ often below 1.0 Hz. The optimum pulse duration depends on the relaxation time T_1 of the ^{31}P nucleus and the acquisition time T_{ac}. It has been recommended to set the pulse duration at $\cos^{-1}(e^{-T_{ac}/T_1})$.[26] Routine ^{31}P NMR spectra are obtained with broadband proton decoupling using a rapid pulse repetition (1 s) and a short pulse angle (30°).

A large number of special experimental NMR techniques have been applied to the ^{31}P nucleus including spin tickling,[9] selective[27] and broadband[9] ^{31}P decoupling, SPT,[9] COSY,[9] reverse shift heterocorrelated NMR spectroscopy,[9,28] homonuclear[9,29] and heteronuclear[9,30] J resolved two-dimensional NMR spectroscopy, EXSY,[31] and Hahn-echo extended pulse sequences.[32] The CP MAS technique is widely used to obtain solid state ^{31}P NMR spectra.[9,33] Liquid crystal ^{31}P NMR spectra of several cyclopolyphosphines $(RP)_n$ and of other trivalent and pentavalent phosphorus compounds have been reported.[9] In a few cases reactions of phosphorus compounds have been studied by CIDNP.[34]

For ^{31}P measurements at variable temperature a 0.1 M solution of triphenylphosphine and triphenylphosphine oxide in toluene-d_8 has been recommended as a shift thermometer. At an operating frequency of 40 MHz the change in δ^{31}P is 1.3 Hz per degree.[35]

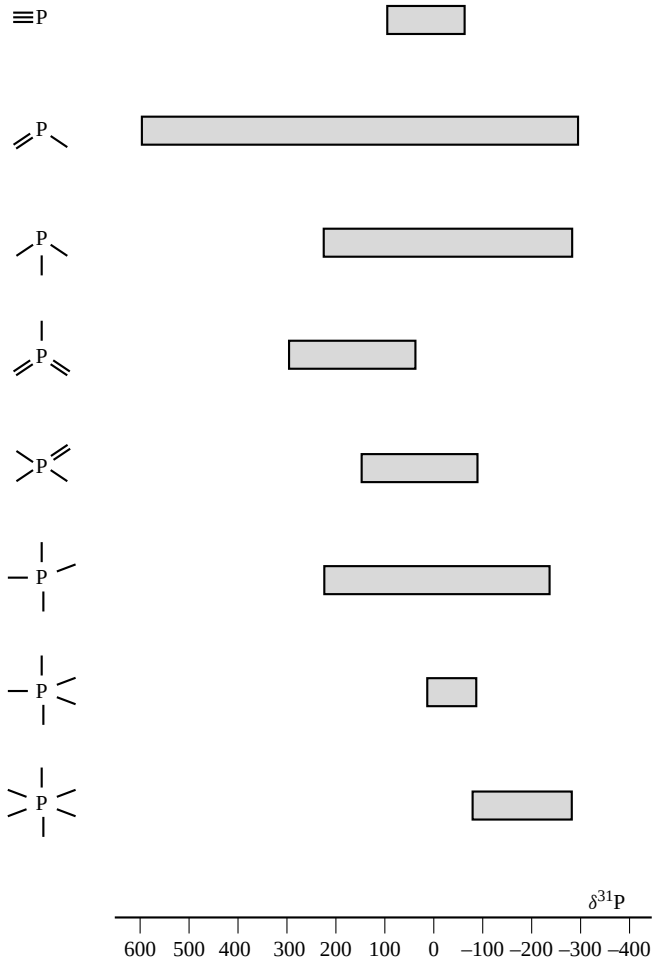

Figure 1 Typical ranges of δ^{31}P for differently coordinated phosphorus compounds

4 CHEMICAL SHIFTS

The range of ^{31}P chemical shifts for liquid, dissolved, or gaseous diamagnetic phosphorus compounds covers nearly 2000 ppm and extends from +1362 for t-BuP[Cr(CO)$_5$]$_2$ to −552 for gaseous P_4. If dissolved paramagnetic compounds are included, it widens to about 4700, with +3471 for the complex $[(C_4Me_4P)_2U(BH_4)]_2$ on the high-frequency side and −1219 for $OsCl_4(PBu_2Ph)_2$ on the low-frequency side.[9,10] The characteristic ranges of δ^{31}P for one- to six-coordinated phosphorus compounds are shown in Figure 1. For pentavalent phosphorus the shift ranges are relatively narrow, and shielding of the phosphorus nucleus increases as its coordination number increases from 3 to 6. No such dependence is found for the trivalent phosphorus and, except for one-coordinated phosphorus compounds, the shift ranges are much wider.[6,36] Detailed bar charts showing the dependence of δ^{31}P for individual classes of phosphorus compounds on the type of atoms bonded to phosphorus can be found in Tebby[6] and Mason.[8]

According to a semiempirical treatment proposed by Van Wazer and co-workers[3,37] phosphorus chemical shifts can be interpreted in terms of three contributions: the bond angles at the phosphorus atom, the electronegativity of the substituents, and the extent of π bonding. If only one parameter is being changed at a time, useful correlations within a class of compounds are obtained.[8,10] Thus for cyclopolyphosphines $(RP)_n$ the phosphorus chemical shift is almost linearly correlated with the average endocyclic PPP bond angles, and definite ranges can be established for n = 5 (δ^{31}P = +50 to −10), n = 4 (δ^{31}P = −50 to −80), and n = 3 (δ^{31}P = −30 to −180). The only known compound for n = 6, $(PhP)_6$, (δ^{31}P = −22) also fits this correlation.[8,10] Linear shift/bond angle correlations have also been reported for the basal phosphorus atoms in cage molecules of the series $P_4S_xSe_{3-x}$ (x = 0–3), $P_yAs_{4-y}S_3$, and $P_yAs_{4-y}Se_3$ (y = 0–4)[38] and for differently substituted cyclotriphosphines.[39] For δ^{31}P of *tert*-phosphines an additive relationship for the alkyl substituents is found; deshielding of phosphorus increases in the order Me < Et < i-Pr < t-Bu.[7] More additive relationships have been reported for δ^{31}P in polyphosphines P_nH_{n+2},[40] primary[41] and secondary phosphines,[42] and alkyl phosphonium salts.[42] Additive relationships often fail, however, when π bonding or electronegative substituents are involved.[7,8,10]

Theoretical calculations of ^{31}P chemical shifts for a series of simple phosphorus compounds by semiempirical methods and for PH_3 by ab initio methods have been reviewed.[9] Using the IGLO method, ab initio calculations of δ^{31}P for larger molecules have also been performed.[43]

Isotope effects on ^{31}P nuclear shielding caused by ^{2}H, ^{13}C, ^{15}N, ^{18}O, ^{34,36}S, ^{35,37}Cl, and ^{79,81}Br have been observed.[44,45]

In 2-amino-1,3,2-dioxaphosphorinane 2-chalcogenides the isotopic effect of ^{15}N on $\delta^{31}P$ is larger for the shorter equatorial than for the longer axial P–N bond.[44]

4.1 One-Coordinate Phosphorus

The range of ^{31}P chemical shifts for one-coordinated phosphorus compounds (phosphaalkynes R–C≡P[6,36,46,47] and [2,4,6-*t*-$Bu_3C_6H_2$–N≡P][$AlCl_4$][48]) extends mainly from +96 to −70. Depending on R, shielding of the phosphorus nucleus in phosphaalkynes increases generally in the order $(CH_3)_3Si$ < aryl,H < alkyl < amino < F.[36,46] A linear relationship results for $\delta^{31}P$ and δN of identically substituted phosphaalkynes and nitriles.[36] Phosphorus-31 solid state NMR investigations of 2,4,6-*t*-$Bu_3C_6H_2$–C≡P[49] and [2,4,6-*t*-$Bu_3C_6H_2$–N≡P][$AlCl_4$][50] have been published.

4.2 Two-Coordinate Phosphorus

Compilations of $\delta^{31}P$ are available for the large number of two-coordinated phosphorus compounds.[6,51–53] Values of $\delta^{31}P$ extend from +954 to −363 with most of them between +600 and −300. This wide shift range corresponds to a variation of phosphorus character from a phosphenium type with a high-frequency chemical shift to a phosphide type with a low-frequency chemical shift. The overall charge of the molecule seems not to be important.[6,51] Values of $\delta^{31}P$ of fully unsaturated phosphorus heterocycles extend from +495 to −5 with most of the shifts between +300 and +50.[6,36,52,53]

Linear correlations are found for $\delta^{31}P$ in aryl-substituted phosphaalkenes with Hammett constants and for $\delta^{31}P$ in iminophosphines with the $n \rightarrow \pi^*$ transition energies. Values of $\delta^{31}P$ of =PR in various acyclic compounds and $\delta^{13}C$ and $\delta^{77}Se$ of the corresponding $=CH_2$ and =Se compounds also give fair linear correlations. More linear correlations are found for the exchange of =P– for =N– in both acyclic and heterocyclic compounds and for =CH– in otherwise identical heterocycles.[36]

Solid state ^{31}P NMR spectra of a diphosphene,[54] a phosphaalkene,[49] and benzo-anellated heterophospholes[55] have been reported.

4.3 Three-Coordinate Phosphorus

The ^{31}P chemical shifts of three-coordinate tervalent phosphorus cover a wide range from +282 to −461 with most of the shifts between +220 and −290.[6] Ranges of $\delta^{31}P$ for individual types of P (III) compounds are found in Tebby,[6] Mason,[8] and Berger et al.[10] Values of $\delta^{31}P$ of conformationally mobile di- and polyphosphines are likely to be temperature-dependent. In alkenic-substituted phosphines the ^{31}P nucleus is more shielded in the *Z*- compared with the *E*-isomer (effect of steric compression). A nearly linear correlation is found between $\delta^{31}P$ in Ph_2P–R and $\delta^{13}C$ in CH_3–R.[8–10]

For three-coordinate pentavalent phosphorus $\delta^{31}P$ ranges (excluding extreme values) essentially from +300 to +40 and is thus found at higher frequency than $\delta^{31}P$ of higher-coordinated phosphorus(V).[6,36,56] In σ^3-phosphoranes of the type R–PXY, depending on the double bonded substituents X and Y, phosphorus shielding generally increases in the order ML_n < S < Se < CR_2 < NR < O.[36,56]

4.4 Four-Coordinate Phosphorus

The ^{31}P chemical shift range of pentavalent tetracoordinate phosphorus extends essentially between +140 and −90 with a few extreme values for phosphonium compounds of up to −308.[6] Shift ranges for individual classes of compounds can be found in Tebby,[6] Mason,[8] and Berger et al.[10]

A number of phosphonic and phosphinic acids, inorganic phosphates, and polyphosphates have been investigated by solid state ^{31}P NMR spectroscopy.[10] In the case of polyphosphates, the different $\delta^{31}P$ values of the terminal and bridging phosphate groups have been interpreted in terms of the electronegativity difference between terminal and bridging oxygen atoms (estimated at 0.4) and the difference in π-bonding order.[57] A linear relationship results between $\delta^{31}P$ and the P–O bond strength in inorganic phosphates.[58]

In phosphates and phosphate esters, as well as in their thio derivatives a clear dependence of $\delta^{31}P$ on the XPX angle (X = O,S) is observed. In phosphoric and phosphonic acids, and in mono- and dinucleotides the ^{31}P chemical shift shows a dependence on pH. Good linear Hammett correlations and a linear $\delta^{31}P/\delta^{13}C$ relationship for [Ph_3PR]X and CH_3–R have been reported.[10]

In contrast to the tetracoordinate phosphorus(V), the ^{31}P chemical shift range for the tetracoordinate tervalent phosphorus (phosphoranide-type phosphorus) is much larger and extends from +222 to −242.[6]

4.5 Five-Coordinate Phosphorus

The chemical shift of five-coordinate phosphorus covers a range between +31 and −195 with the majority of shifts between 0 and −80.[6] A temperature dependence of the NMR spectra is often encountered, due to intermolecular[9,59] or intramolecular (pseudorotation)[9,60] ligand exchange or to hindered rotation.[9,61]

4.6 Six-Coordinate Phosphorus

The chemical shifts of six-coordinate phosphorus are found between −57 and −441 with most of the shifts between −80 and −290.[6] The major factors determining the chemical shifts are electronegativity and anisotropic effects of the substituents. Increasing the overall charge of the species from +1 through zero to −1 shifts $\delta^{31}P$ to lower frequency, while incorporation of the phosphorus in a five-membered ring results in a shift of $\delta^{31}P$ in the opposite direction.[6,9]

5 COUPLING CONSTANTS

Scalar spin–spin couplings of phosphorus to almost all elements of the Periodic Table are known, and remarkably large coupling constants up to 17000 Hz (!) have been observed. Compilations of phosphorus–element coupling constants can be found in several books.[7–10,62] Representative values are contained in most of the compilations of ^{31}P chemical shift data.[4–6,51–53] Specialized reviews on phosphorus–phosphorus,[63] phosphorus–hydrogen,[64] and phosphorus–carbon[65,66] coupling constants are available.

Table 2 Observed Phosphorus–Phosphorus Coupling Constants

Coupling constant	J (Hz)	References
$^{1}J(P^{III},P^{III})$	−55 to −670	8–10,51–53,63
$^{1}J(P^{III},P^{V})$	−157 to −684	8–10,63
$^{1}J(P^{V},P^{V})$	−67 to +766	8–10,63
$^{2}J(P^{III},P^{III})$	−35 to +665	8–10,63
$^{2}J(P^{III},P^{V})$	−28 to +150	8–10,63
$^{2}J(P^{V},P^{V})$	11 to 210	8–10,63
^{3}J(P,P)	0 to 227	8–10,63
^{4}J(P,P)	2 to 35	9, 10, 63
^{5}J(P,P)	5 to 9	67
^{6}J(P,P)	3 to 12	67, 68
^{7}J(P,P)	1 to 8	67
^{8}J(P,P)	1 to 2	67
^{9}J(P,P)	4	67

More information on specific phosphorus–element coupling constants can be found in the references in Tables 2 and 3.

It is generally observed, that the values of the reduced coupling constants ^{n}K(P,X) decrease in the order $^{1}K(P,X) \gg {}^{3}K(P,X) > {}^{2}K(P,X) > {}^{4}K(P,X)$.[9] In many cases, however, the order of ^{3}K(P,X) and ^{2}K(P,X) is reversed, due to structural factors. Coupling constants over more than four bonds are normally two or more orders of magnitude smaller than ^{1}K(P,X). In special cases and particularly in compounds with a delocalized π system long-range coupling constants ^{n}J(P,P) for $n = 5–9$[67,68] and $^{n}J(^{31}P,^{13}C)$ up to $n = 7$[69] have been observed.

The presence of a lone pair of electrons at the phosphorus atom or at the atom coupled with it seems to be associated with a negative one-bond reduced coupling constant ^{1}K(P,X). An exception is provided by $^{1}K(^{31}P,^{1}H)$, however, which is positive. The magnitude of ^{1}K(P,X) increases with increasing electronegativity of the substituents regardless of its sign. Linear relationships have been found between ^{1}K(P,X) and the sum of the electronegativity of the substituents at the phosphorus atom for $^{1}K(^{183}W,^{31}P)$, $^{1}K(^{77}Se,^{31}P)$, $^{1}K(^{95}Mo,^{31}P)$, $^{1}K(^{31}P,^{31}P)$, $^{1}K(^{31}P,^{13}C)$, and $^{1}K(^{31}P,^{1}H)$.[9,10,70]

In molecules with a trigonal bipyramidal geometry ^{1}K(P,X) through the shorter equatorial bond is larger than through the longer axial bond.[9,10,71] In transition metal–phosphine complexes the one-bond phosphorus–metal coupling constant is found to increase with decreasing *trans*-effect of the ligand in the *trans*-position to the phosphorus atom in the order $MePh_2Si > Ph > Me \gg R_3P > (PhO)_3P$, $CN > Et_3As > NO_2 >$ amine, NCO, NCS > Cl, Br, I > $ONO_2 > F$.[9,10] A bond angle and dihedral angle dependence of ^{1}K(P,X) has also been discussed.[5,9,72,73]

Geminal coupling constants ^{2}K(P,X) show, in principle, the same dependences as ^{1}K(P,X); the signs are often reversed, however. For the three-coordinate trivalent phosphorus there is a dependence of ^{2}K(P,X) on the dihedral angle between the phosphorus lone pair and the X nucleus,[73] which has been investigated for $^{2}J(^{31}P,^{31}P)$, $^{2}J(^{31}P,^{13}C)$, and $^{2}J(^{31}P,^{1}H)$. For tetracoordinate phosphorus a similar dependence is found with an electronegative substituent in place of the lone pair.[9]

Of general importance is the dependence of vicinal reduced coupling constants ^{3}K(P,X) on the dihedral angle between the phosphorus and the X nucleus (Karplus relationship), which has been investigated for a number of compounds. In all cases a minimum near 90° and maxima at 0° and 180° are observed.[9,10,74]

5.1 Phosphorus–Phosphorus Coupling Constants

Typical ranges for P,P coupling constants are given in Table 2. The value of $^{1}J(^{31}P,^{31}P)$ is negative between trivalent phosphorus atoms and, where the sign is known, also between trivalent and pentavalent phosphorus atoms. Between pentavalent phosphorus atoms $^{1}J(^{31}P,^{31}P)$ is often positive. One-bond phosphorus–phosphorus coupling constants show a large stereochemical dependence on rotation about the P–P bond, especially when there are lone pairs at the phosphorus atoms.[8–10]

Geminal P(III), P(III) coupling constants are mostly positive and extend up to +665 Hz. In acyclic compounds geminal P(III), P(V) couplings range mainly between +50 Hz and +150 Hz, whereas for cyclic compounds smaller and negative values are found. The value of $^{2}J(^{31}P,^{31}P)$ between pentavalent phosphorus atoms in acyclic compounds is generally small (11–43 Hz), but can assume large values up to +210 Hz in cyclic compounds.[8]

5.2 Phosphorus Couplings to Other Nuclei

Typical ranges for the coupling constants of phosphorus to other elements of the Periodic Table are given in Table 3. The signs of the coupling constants, where known, have also been included. The value of $^{1}J(^{31}P,^{1}H)$ tends to increase with increasing oxidation state and coordination number of phosphorus; the individual ranges overlap considerably, however.[70] One-bond phosphorus–fluorine coupling constants show the opposite trend, in accord with the opposite signs of $^{1}J(^{31}P,^{1}H)$ and $^{1}J(^{31}P,^{19}F)$.[9,10] An isotope effect of ^{2}H on $^{1}J(^{31}P,^{1}H)$ has been reported.[103] The $^{1}J(^{31}P,^{15}N)$ value is positive (+24 to +105 Hz) in trivalent, generally positive (−44 to +60 Hz) in tetracovalent, and negative (−40 to −80 Hz) in pentacovalent phosphorus compounds. The $^{1}J(^{77}Se,^{31}P)$ value is larger for a phosphorus–selenium double bond (−500 to −1200 Hz) than for a single bond (−100 to −500 Hz). Similarly $^{1}J(^{125}Te,^{31}P)$ is larger for P=Te (1324–2290 Hz) than for P–Te (80–996 Hz).[8,9] Exceptionally large values, reaching orders of magnitude of the corresponding one-bond coupling constants, are observed for $^{2}J(^{77}Se,^{31}P)$,[92] $^{2}J(^{119}Sn,^{31}P)$,[10] $^{2}J(^{205}T1,^{31}P)$,[102] and $^{2}J(^{207}Pb,^{31}P)$[104] in transition metal complexes.

6 APPLICATIONS OF ^{31}P NMR SPECTROSCOPY

Phosphorus-31 NMR spectroscopy has been used to monitor the progress of chemical reactions and exchange equilibria since its early days. Today ^{31}P NMR spectroscopy is a powerful diagnostic tool in practically all areas of preparative chemistry where phosphorus is present. Alone, or in combination with the NMR spectroscopy of other nuclei, it is mostly used for the identification and structure elucidation of phosphorus compounds. The enantiomeric purity of chiral alcohols, thiols (via the corresponding phosphites and thiophosphonates), and phosphines is conveniently checked by ^{31}P NMR. Based on

Table 3 Observed Coupling Constants of Phosphorus to Other Nuclei

Coupling constant	J (Hz)	Sign	References
$^{1}J(^{31}P,^{1}H)$	110 to 1200	+	9, 10, 64
$^{2}J(^{31}P,^{1}H)$	0 to 205	±	9, 10, 36
$^{3}J(^{31}P,^{1}H)$	0 to 51	±	9, 10, 36
$^{4}J(^{31}P,^{1}H)$	0 to 18		9, 10, 75
$^{5}J(^{31}P,^{1}H)$	0 to 12		10, 75
$^{1}J(^{31}P,^{2}H)$	30 to 112		76
$^{2}J(^{31}P,^{2}H)$	6 to 10		77, 78
$^{1}J(^{31}P,^{7}Li)$	33 to 55		9, 10, 79
$^{2}J(^{31}P,^{7}Li)$	2		80
$^{2}J(^{31}P,^{9}Be)$	2 to 6		8
$^{1}J(^{31}P,^{10}B)$	9		10
$^{1}J(^{31}P,^{11}B)$	10 to 217	+	8, 9, 81
$^{1}J(^{31}P,^{13}C)$	−40 to +500	±	9, 10, 65
$^{2}J(^{31}P,^{13}C)$	−20 to +90	±	9, 10, 65
$^{3}J(^{31}P,^{13}C)$	0 to 26	+	9, 10, 65
$^{4}J(^{31}P,^{13}C)$	0 to 7		10, 69
$^{5}J(^{31}P,^{13}C)$	0 to 26		10, 69
$^{6}J(^{31}P,^{13}C)$	0 to 2		69
$^{7}J(^{31}P,^{13}C)$	0 to 2		69
$^{1}J(^{31}P,^{15}N)$	−80 to +105	±	9, 10, 36, 82, 83
$^{2}J(^{31}P,^{15}N)$	0 to 55	+	30, 82
$^{3}J(^{31}P,^{15}N)$	4 to 9		82
$^{1}J(^{31}P,^{17}O)$	48 to 220	+	8–10,84
$^{1}J(^{31}P,^{19}F)$	463 to 1555	−	4, 9, 10
$^{2}J(^{31}P,^{19}F)$	2 to 700	+	4, 10, 36
$^{3}J(^{31}P,^{19}F)$	0 to 313	+	4, 10
$^{4}J(^{31}P,^{19}F)$	6 to 64		4, 10
$^{5}J(^{31}P,^{19}F)$	4 to 33		10
$^{1}J(^{31}P,^{27}Al)$	90 to 290		8–10
$^{2}J(^{31}P,^{27}Al)$	11 to 30		8, 85
$^{1}J(^{31}P,^{29}Si)$	7 to 154	−	10, 36, 86
$^{2}J(^{31}P,^{29}Si)$	1 to 59	−	10, 36, 87
$^{3}J(^{31}P,^{29}Si)$	3 to 6		10
$^{1}J(^{35}Cl,^{31}P)$	105 to 127		88
$^{1}J(^{37}Cl,^{31}P)$	100		88
$^{2}J(^{45}Sc,^{31}P)$	30 to 40		8
$^{1}J(^{51}V,^{31}P)$	110 to 510		8, 10
$^{1}J(^{53}Cr,^{31}P)$	105 to 153		8, 89
$^{1}J(^{55}Mn,^{31}P)$	140 to 405		8
$^{1}J(^{57}Fe,^{31}P)$	10 to 149		8, 10, 77, 90
$^{1}J(^{59}Co,^{31}P)$	375 to 1222		8–10
$^{1}J(^{61}Ni,^{31}P)$	161 to 482		8–10,77
$^{1}J(^{63}Cu,^{31}P)$	1109 to 1458	+	8–10
$^{1}J(^{65}Cu,^{31}P)$	1275 to 1302		8–10
$^{2}J(^{71}Ga,^{31}P)$	38		8
$^{1}J(^{77}Se,^{31}P)$	100 to 1200	−	8–10,91
$^{2}J(^{77}Se,^{31}P)$	0 to 140		91, 92
$^{3}J(^{77}Se,^{31}P)$	0 to 18	±	91
$^{4}J(^{77}Se,^{31}P)$	0 to 1		91
$^{1}J(^{79}Br,^{31}P)$	296 to 350		88
$^{1}J(^{81}Br,^{31}P)$	315 to 380		88
$^{1}J(^{89}Y,^{31}P)$	5 to 52		90
$^{2}J(^{89}Y,^{31}P)$	5		8
$^{1}J(^{93}Nb,^{31}P)$	1050		9
$^{1}J(^{95}Mo,^{31}P)$	90 to 284		8, 9
$^{1}J(^{97}Mo,^{31}P)$	254		8
$^{1}J(^{99}Tc,^{31}P)$	400 to 909		10
$^{1}J(^{103}Rh,^{31}P)$	8 to 374	−	9, 10, 90
$^{2}J(^{103}Rh,^{31}P)$	0 to 34		9, 10
$^{3}J(^{103}Rh,^{31}P)$	1 to 24	−	9, 10
$^{1}J(^{107}Ag,^{31}P)$	212 to 1118		9, 10
$^{1}J(^{109}Ag,^{31}P)$	220 to 1217		8, 90
$^{2}J(^{109}Ag,^{31}P)$	9 to 10		8
$^{1}J(^{111}Cd,^{31}P)$	1091 − 2443		9, 93, 94
$^{1}J(^{113}Cd,^{31}P)$	1142 − 2240	−	8, 94
$^{2}J(^{113}Cd,^{31}P)$	2 − 80		8
$^{1}J(^{117}Sn,^{31}P)$	76 − 2260	+	7, 10, 95
$^{1}J(^{119}Sn,^{31}P)$	50 − 3125	+	4, 9, 10, 95, 96
$^{2}J(^{119}Sn,^{31}P)$	83 − 4269		10, 96
$^{1}J(^{125}Te,^{31}P)$	84 − 2290	+	8–10
$^{2}J(^{125}Te,^{31}P)$	11		10
$^{1}J(^{183}W,^{31}P)$	80 − 847	+	8–10,90
$^{2}J(^{183}W,^{31}P)$	2 − 24		8, 10
$^{1}J(^{187}Os,^{31}P)$	149 − 492	+	10, 90, 97
$^{1}J(^{195}Pt,^{31}P)$	62 − 9150	+	8–10
$^{2}J(^{195}Pt,^{31}P)$	36 − 1977	±	8–10,98
$^{3}J(^{195}Pt,^{31}P)$	6 − 245	−	9, 10, 99
$^{4}J(^{195}Pt,^{31}P)$	34		9
$^{1}J(^{199}Hg,^{31}P)$	143 − 17528	+	8–10,100
$^{2}J(^{199}Hg,^{31}P)$	40 − 160	−	8, 99
$^{1}J(^{203,205}Tl,^{31}P)$	3144,3203		101, 102
$^{2}J(^{205}Tl,^{31}P)$	1056 − 1202		8, 10, 102
$^{1}J(^{207}Pb,^{31}P)$	1100 − 2452	−	9, 104
$^{2}J(^{207}Pb,^{31}P)$	28 − 3460		104

the pH dependence of δ^{31}P, the pK_a values of phosphoric acids have been determined. Phosphorus-31 NMR is also extensively used for the investigation of dynamic processes.[9,10]

In biochemistry and medicine in vivo ^{31}P NMR and ^{31}P NMR imaging gain increasingly in importance.[8,105,106] Oxygen-18 isotope effects on ^{31}P nuclear shielding are extensively used to study the chirality of phosphorus compounds and the stereospecificity of enzymatic reactions.[44]

7 RELATED ARTICLES

Brain Neoplasms in Humans Studied by Phosphorus-31 NMR Spectroscopy; Inorganic Chemistry Applications; Membranes: Phosphorus-31 NMR; Nucleic Acids: Phosphorus-31 NMR; Phosphorus-31 Magnetization Transfer Studies In Vivo; Proton Decoupling During In Vivo Whole Body Phosphorus MRS; Single Voxel Whole Body Phosphorus MRS; Tissue Behavior Measurements Using Phosphorus-31 NMR.

8 REFERENCES

1. W. C. Dickinson, *Phys. Rev.*, 1951, **81**, 717.
2. H. S. Gutowsky, D. W. McCall, and C. P. Slichter, *Phys. Rev.*, 1951, **84**, 589.
3. M. M. Crutchfield, C. H. Dungan, and J. R. Van Wazer, *Top. Phosphorus Chem.*, 1967, **5**, 1.
4. G. Mavel, *Annu. Rep. NMR Spectrosc.*, 1973, **5B**, 1.
5. D. G. Gorenstein, *Prog. NMR Spectrosc.*, 1983, **16**, 1.
6. J. C. Tebby (ed.), *Handbook of Phosphorus-31 Nuclear Magnetic Resonance Data*, CRC Press, Boca Raton, FL, 1991.
7. R. K. Harris and B. E. Mann (eds.), *NMR and the Periodic Table*, Academic Press, London, 1978.
8. J. Mason (ed.), *Multinuclear NMR*, Plenum Press, New York, 1987.
9. J. G. Verkade and L. D. Quin (eds.), *Phosphorus-31 NMR Spectroscopy in Stereochemical Analysis*, VCH, Deerfield Beach, FL, 1987.

10. S. Berger, S. Braun (eds.), and H.-O. Kalinowski, *NMR-Spektroskopie von Nichtmetallen*, *Vol. 3* ^{31}*P-NMR Spektroskopie*, Thieme, Stuttgart, 1993.
11. L. D. Quin and J. Verkade (eds.), *Phosphorus-31 NMR Special Properties in Compound Characterization and Structural Analysis*, VCH, Deerfield Beach, FL, 1994.
12. J. F. Nixon and A. Pidcock, *Annu. Rep. NMR Spectrosc.*, 1969, **2**, 346.
13. P. E. Garrou, *Chem. Rev.*, 1981, **81**, 229.
14. A. Pidcock, *Adv. Chem. Ser.*, 1982, **196**, 1.
15. P. S. Pregosin and R. W. Kunz, *NMR Basic Principles Progr.*, 1979, **16**, 1.
16. C. T. Burt and A. M. Wyrwicz, *Trends Biochem. Sci.*, 1979, **4**, 244.
17. D. G. Gadian, G. K. Radda, R. E. Richards, and P. J. Seeley, in *Biological Applications of Magnetic Resonance*, ed. R. G. Schulman, Academic Press, New York, 1979, p. 463.
18. I. K. O'Neil and C. P. Richards, *Annu. Rep. NMR Spectrosc.*, 1980, **10A**, 133.
19. D. P. Hollis, in *Biological Magnetic Resonance*, eds. L. J. Berliner and J. Rouben, Plenum Press, New York, 1980, Vol. 2, p. 1.
20. E. M. Bradbury, G. K. Radda, and P. S. Allen, *Ann. Intern. Med.*, 1983, **98**, 514.
21. D. E. Gadian, *Spec. Publ. R. Soc. Chem.*, 1984, **47**, 58.
22. D. G. Gorenstein, *Phosphorus-31 NMR, Principles and Applications*, Academic Press, New York, 1984.
23. B. C. Tyler, *Phosphorus NMR in Biology*, CRC Press, Boca Raton, FL, 1987.
24. C. J. Jameson, A. De Dios, and A. K. Jameson, *Chem. Phys. Lett.*, 1990, **167**, 575.
25. P. L. Yeagle, W. C. Hutton, and R. B. Martin, *J. Am. Chem. Soc.*, 1975, **97**, 7175.
26. M. L. Martin, J. J. Delpuech, and G. J. Martin, *Practical NMR Spectroscopy*, Heyden, London, 1980.
27. I. J. Colquhoun, W. McFarlane, S. O. Grim, J. D. Mitchell, and P. H. Smith, *Inorg. Chem.*, 1981, **20**, 2516.
28. S. J. Berners-Price, P. J. Sadler, and Ch. Brevard, *Magn. Reson. Chem.*, 1990, **28**, 145.
29. C. J. Turner and P. B. Garlick, *J. Magn. Reson.*, 1984, **57**, 221.
30. P. H. Bolton and G. Bodenhausen, *J. Magn. Reson.*, 1982, **46**, 306.
31. K. G. Orrell and V. Sik, *Annu. Rep. NMR Spectrosc.*, 1993, **27**, 103.
32. B. Wrackmeyer, E. Kupce, and A. Schmidpeter, *Magn. Reson. Chem.*, 1991, **29**, 1045.
33. A. Yamasaki, *Coord. Chem. Rev.*, 1991, **109**, 107.
34. L. Jacobson, *J. Magn. Reson.*, 1982, **49**, 522.
35. F. L. Dickert and S. W. Hellmann, *JEOL (Jpn. Electron Opt. Lab.) News (Ser.) Anal. Instrum.*, 1982, **18A**, 57.
36. K. Karaghiosoff, in *Multiple Bonds and Low Coordination in Phosphorus Chemistry*, eds. M. Regitz and O. J. Scherer, Thieme, Stuttgart, 1990, p. 463.
37. J. H. Letcher and J. R. Van Wazer, *J. Chem. Phys.*, 1966, **44**, 815.
38. R. Blachnik, U. Wickel, and P. Schmitt, *Z. Naturforsch., Teil B*, 1984, **39**, 1135.
39. J. Hahn, M. Baudler, C. Krüger, and Y. H. Tsay, *Z. Naturforsch., Teil B*, 1982, **37**, 797.
40. M. Baudler, *Angew. Chem.*, 1987, **99**, 429; *Angew. Chem., Int. Ed. Engl.*, 1987, **26**, 419.
41. L. Maier, *Helv. Chim. Acta*, 1966, **49**, 1718.
42. L. D. Quin and J. J. Breen, *Org. Magn. Reson.*, 1973, **5**, 17.
43. W. Kutzelnigg, U. Fleischer, and M. Schindler, *NMR Basic Principles Progr.*, 1990, **23**, 165.
44. P. E. Hansen, *Prog. NMR Spectrosc.*, 1988, **20**, 207.
45. W. Buchner, W. Ries, and W. Malisch, *Magn. Reson. Chem.*, 1990, **28**, 515.
46. M. Regitz, in *Multiple Bonds and Low Coordination in Phosphorus Chemistry*, eds. M. Regitz and O. J. Scherer, Thieme, Stuttgart, 1990, p. 58.
47. J. Grobe, D. Le Van, B. Lüth, and M. Hegemann, *Chem. Ber.*, 1990, **123**, 2317.
48. E. Niecke, M. Nieger, and F. Reichert, *Angew. Chem.*, 1988, **100**, 1781; *Angew. Chem. Int. Ed. Engl.*, 1988, **27**, 1715.
49. J. C. Duchamp, M. Pakulski, A. H. Cowley, and K. W. Zilm, *J. Am. Chem. Soc.*, 1990, **112**, 6803.
50. R. D. Kurtis, M. J. Schriver, and R. E. Wasylishen, *J. Am. Chem. Soc.*, 1991, **113**, 1493.
51. S. Lochschmidt and A. Schmidpeter, *Phosphorus Sulfur*, 1986, **29**, 73.
52. K. Karaghiosoff and A. Schmidpeter, *Phosphorus Sulfur*, 1988, **36**, 217.
53. R. K. Bansal, K. Karaghiosoff, and A. Schmidpeter, *Tetrahedron*, 1994, **50**, 7675.
54. K. W. Zilm, G. G. Webb, A. H. Cowley, M. Pakulski, and A. Orendt, *J. Am. Chem. Soc.*, 1988, **110**, 2032.
55. R. D. Curtis, B. W. Royan, R. E. Wasylishen, M. D. Lumsden, and N. Burford, *Inorg. Chem.*, 1992, **31**, 3386.
56. H. Germa and J. Navech, *Phosphorus Sulfur*, 1986, **26**, 327.
57. U. Haubenreisser, G. Scheler, and A. R. Grimmer, *Z. Anorg. Allg. Chem.*, 1986, **532**, 157.
58. A. K. Cheetham, N. J. Clayden, C. M. Dobson, and R. J.B. Jakeman, *J. Chem. Soc., Chem. Commun.*, **1986**, 195.
59. D. Robert, C. Demay, and J. G. Riess, *Inorg. Chem.*, 1982, **21**, 1805.
60. I. Ruppert, *Z. Anorg. Allg. Chem.*, 1981, **477**, 59.
61. A. Connelly and R. K. Harris, *J. Chem. Soc., Dalton Trans.*, 1984, 1547.
62. M. Regitz and O. J. Scherer (eds.), *Multiple Bonds and Low Coordination in Phosphorus Chemistry*, Thieme, Stuttgart, 1990.
63. E. G. Finer and R. K. Harris, *Prog. NMR Spectrosc.*, 1971, **6**, 61.
64. J. F. Brazier, D. Houalla, M. Loenig, and R. Wolf, *Top. Phosphorus Chem.*, 1976, **8**, 99.
65. J. R. Llinas, E.-J. Vincent, and G. Peiffer, *Bull. Soc. Chim. Fr.*, 1973, 3209.
66. L. D. Quin, *The Heterocyclic Chemistry of Phosphorus*, Wiley, New York, 1981, Chap. 6
67. L. Ernst, *J. Chem. Soc., Chem. Commun.*, 1977, 375.
68. G. Szalontai, J. Bakos, I. Toth, and B. Heil, *Magn. Reson. Chem.*, 1987, **25**, 761.
69. L. Ernst, *Org. Magn. Reson.*, 1977, **9**, 35.
70. A. Schmidpeter, J. Ebeling, H. Stary, and C. Weingand, *Z. Anorg. Allg. Chem.*, 1972, **394**, 171.
71. J. W. Emsley, L. Phillips, and V. Wray, *Prog. NMR. Spectrosc.*, 1975, **10**, 83.
72. C. A. Tolman, *Chem. Rev.*, 1977, **77**, 313.
73. V. M. S. Gil and W. von Philipsborn, *Magn. Reson. Chem.*, 1989, **27**, 409.
74. G. Grossmann, R. Lang, G. Ohms, and D. Scheller, *Magn. Reson. Chem.*, 1990, **28**, 500.

75. M.-P. Simonnin and C. Charrier, *Org. Magn. Reson.*, 1969, **1**, 27.
76. H. H. Mantsch, H. Saito, and I. C. P. Smith, *Prog. NMR Spectrosc.*, 1977, **11**, 211.
77. R. Benn and A. Rufinska, *Magn. Reson. Chem.*, 1988, **26**, 895.
78. S. Kerschl, B. Wrackmeyer, A. Willhalm, and A. Schmidpeter, *J. Organomet. Chem.*, 1987, **319**, 49.
79. A. Zschunke, M. Riemer, E. Leissring, and K. Issleib, *Z. Anorg. Allg. Chem.*, 1985, **525**, 35.
80. P. R. Rubini, L. Rodehüser, and J.-J. Delpuech, *Inorg. Chem.*, 1979, **18**, 2962.
81. B. Wrackmeyer, *Annu. Rep. NMR. Spectrosc.*, 1988, **20**, 61.
82. M. Witanowski, L. Stefaniak, and G. A. Webb, *Annu. Rep. NMR Spectrosc.*, 1993, **25**, 1.
83. B. W. Tattershall, *J. Chem. Soc., Chem. Commun.*, 1989, 216.
84. E. L. Eliel, S. Chandrasekaran, L. E. Carpenter II, and J. G. Verkade, *J. Am. Chem. Soc.*, 1986, **108**, 6651.
85. J. W. Akitt, *Prog. NMR Spectrosc.*, 1989, **21**, 1.
86. E. A. Williams, *Annu. Rep. NMR Spectrosc.*, 1983, **15**, 235.
87. E. Niecke and W. Flick, *Angew. Chem.*, 1974, **86**, 128; *Angew. Chem., Int. Ed. Engl.*, 1974, **13**, 134.
88. V. Mlynarik, *Prog. NMR Spectrosc.*, 1986, **18**, 277.
89. M. F. A. Dove, E. M. L. Jones, and R. J. Clark, *Magn. Reson. Chem.*, 1989, **27**, 973.
90. B. E. Mann, *Annu. Rep. NMR Spectrosc.*, 1991, **23**, 141.
91. I. J. Colquhoun, H. C. E. McFarlane, W. McFarlane, J. A. Nash, R. Keat, D. R. Rycroft, and D. G. Thompson, *Org. Magn. Reson.*, 1979, **12**, 473.
92. T. Chivers, D. D. Doxsee, and R. W. Hilts, *Inorg. Chem.*, 1993, **32**, 3244.
93. P. A. W. Dean, N. C. Payne, J. J. Vittal, and Y. Wu, *Inorg. Chem.*, 1993, **32**, 4632.
94. J. S. Casas, M. S. Garcia-Tasende, A. Sanchez, J. Sordo, E. M. Vazquez-Lopez, E. E. Castellano, and J. Zukerman-Schpector, *Inorg. Chim. Acta*, 1993, **209**, 137.
95. D. Hänssgen, E. Stahlhut, H. Aldenhoven, and A. Dörr, *J. Organomet. Chem.*, 1992, **425**, 19.
96. R. Colton and D. Dakternieks, *Inorg. Chim. Acta*, 1988, **143**, 151.
97. R. Benn, H. Brenneke, E. Joussen, H. Lehmkuhl, and F. L. Ortiz, *Organometallics*, 1990, **9**, 756.
98. A. Zschunke, H. Meyer, I. Heidlas, B. Messbauer, B. Walther, and H.-D. Schädler, *Z. Anorg. Allg. Chem.*, 1983, **504**, 117.
99. P. G. Pringle and B. L. Shaw, *J. Chem. Soc., Chem. Commun.*, 1982, 81.
100. B. Wrackmeyer and R. Contreras, *Annu. Rep. NMR Spectrosc.*, 1992, **24**, 267.
101. J. F. Hinton, K. R. Metz, and R. W. Briggs, *Annu. Rep. NMR Spectrosc.*, 1982, **13**, 211.
102. J. F. Hinton, *Magn. Reson. Chem.*, 1987, **25**, 659.
103. N. M. Sergeyev, *NMR Basic Principles Progr.*, 1990, **22**, 31.
104. B. Wrackmeyer and K. Horchler, *Annu. Rep. NMR Spectrosc.*, 1990, **22**, 249.
105. G. Navon, T. Kushnir, N. Askenasy, and O. Kaplan, *NMR Basic Principles Progr.*, 1992, **27**, 237.
106. M. Rudin and A. Sauter, *NMR Basic Principles Progr.*, 1992, **28**, 161.

Biographical Sketch

Konstantin Karaghiosoff. *b* 1956. Ph. D., 1986, University of Munich. Introduced to NMR by A. Schmidpeter. Inorganic Chemistry, University of Munich, 1980–present. Approx. 50 publications. Research interests include synthesis and reactions of monocyclic and anellated heterophospholes, phosphorus–sulfur and phosphorus–selenium rings and cages, ^{31}P and ^{77}Se NMR spectroscopy, analysis and simulation of high-order spin systems.

Polymorphism and Related Phenomena

Robin K. Harris
University of Durham, Durham, UK

1	Introduction	1
2	Applicability of NMR	1
3	Molecular Polymorphs	1
4	Polymorphism and Molecular Mobility	3
5	Macromolecular Polymorphs	4
6	Related Articles	6
7	References	6

1 INTRODUCTION

Polymorphism is ubiquitous in solid state chemistry, commonly occurring for a very wide range of materials. Polymorphs are different solid forms (usually crystalline) of a given compound. The differences lie in solid state structure, i.e. in the spatial arrangement of the atoms or molecules. They may be relatively minor (e.g. variations in mutual orientations of molecules) or major (leading, for instance, to substantially different atomic arrangements). Sometimes other terms are used for the phenomenon. Thus, when concerning different forms of the elements, the word allotrope is used, instead of polymorph. Also, polymorphs which have structures differing in the stacking sequence of layers (for example, in silicon carbide) are called polytypes.

A somewhat similar phenomenon is the ability of many compounds to incorporate solvent molecules in their structure during crystallization from solution. Thus compounds frequently exist in both anhydrous and hydrated forms, the crystal structures of which may be essentially identical or profoundly different. Other solvent molecules, such as acetone and chloroform, may be similarly incorporated. Ultimately this relates to the existence of clathrates, for which the structure may only be stable when both host and guest molecules are present. Sometimes hydrates lose water readily; on other occasions anhydrous forms may be hygroscopic. Although this article will concentrate on true polymorphism, the 'pseudopolymorphism' of solvates, which can carry similar NMR connotations, will be mentioned at times.

Of course, another closely-related topic is that of phase changes and phase diagrams, together with similar matters concerning the formation and interchange of polymorphic forms. These questions will be largely ignored in the present article. Under given conditions of temperature, pressure, etc., only one polymorph will clearly be favored by thermodynamic considerations. Frequently, however, kinetics of interconversions will be slow, and several forms will exist at ambient temperature and pressure for times in excess of the minimum required to obtain NMR spectra. Such metastable forms may be obtained, for instance, by crystallization from a solvent or by quenching from a temperature at which they are stable. The present article will concentrate on NMR data obtained under standard working conditions (atmospheric pressure and ambient temperature).

Cases of polymorphism and related phenomena may be divided into those involving molecular crystals and those relating to macromolecular structures (in one, two, or three dimensions). Of course, the bonding in the latter implies that interconversion between forms (e.g. between graphite and diamond) is extremely difficult. Indeed, it might be argued that cases of macromolecular structural differences, which require bond-breaking for interconversion (as for silicon carbide) are not properly labeled as polymorphic since they are more analogous to some types of isomerism in organic compounds. However, although interconversions between molecular polymorphs are usually relatively easy, it must not be assumed that intermolecular forces are negligible. Frequently they involve hydrogen bonding, with substantial energies.

Polymorphism is particularly important, and has been extensively investigated by NMR, for pharmaceutical compounds, for silicates and zeolites, for polymers (including naturally occurring materials such as cellulose and chitosan, as well as synthetic polymers), and for ceramic materials.

2 APPLICABILITY OF NMR

Since the electronic environments of corresponding atoms in different polymorphs of the same compound differ, the NMR chemical shifts will be in principle distinguishable. Indeed, the total NMR spectrum can clearly act as a fingerprint to identify polymorphic forms. Such differences are expected to be similar in magnitude to the crystallographic splittings observed when molecules or atomic groupings of the same chemical type are in locations in the unit cell unrelated by symmetry. The 'fingerprint' is of the crystallographic asymmetric unit, and simply counting the number of resonances may, on occasion, suffice to distinguish between polymorphs.

The techniques most commonly used to distinguish polymorphs are DSC, IR, and powder XRD, but all three have disadvantages. The DSC method is very crude, since it gives little or no chemical information. IR spectroscopy often suffers from lack of resolution and from difficulties in interpreting intensities. Powder XRD is often the preferred technique, but it is not sensitive to poorly crystalline or amorphous forms. NMR does not suffer from any of these problems, and the only drawback is the cost of the equipment.

Polymorphs often differ in molecular-level mobility, and hence in NMR relaxation times, but these are unlikely to be used as distinguishing features, except perhaps for polymeric systems.

3 MOLECULAR POLYMORPHS

The principal area of investigation of molecular polymorphism is that of pharmaceutical compounds. This is for very practical reasons: polymorphs sometimes show differing physiological activity (largely as a result of differences in rates of dissolution) and government regulations therefore require pharmaceutical companies to identify carefully the polymorphic form of their products. Moreover, very small changes in

conditions of preparation can readily result in a difference in polymorphic form, and scale-up can reveal problems not found in laboratory synthesis, so that an understanding of polymorphic variations is very important in pharmaceutical chemistry.

The first application of ^{13}C CP MAS NMR to pharmaceutical polymorphism appears to be that reported by Balimann et al.[1] in 1981, which featured spectra of two forms of Nolvadex (the ICI trade name for the generic tamoxifen). In the late 1980s and early 1990s the groups of Byrn[2,3] and of Harris[4–6] were particularly active in this area.

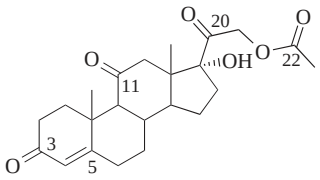

(1)

Steroids appear to be particularly prone to give rise to polymorphic forms. Cortisone acetate (**1**) is a typical example. A substantial number of polymorphs and solvated forms are known, and seven have been studied[4] by MAS NMR. Three of the polymorphs are anhydrous, and Figure 1 illustrates the ^{13}C CP MAS spectra for the high-frequency region (containing resonances from C-3, C-5, C-11, C-20 and C-22).

Immediately, two important conclusions can be made:

1. NMR readily distinguishes the three anhydrous forms (as it does the five hydrates and other solvates).
2. Whereas Forms I and II have asymmetric units consisting of a single molecule (since only five signals are seen in this region), Form III is more complex. In fact, expanded-scale spectra for all the carbon resonances show that Form III has three molecules in the asymmetric unit.

One can go further when peak assignments are firmly established. The apparent variation in the relative intensities of the two peaks on the right in Figure 1(a) and (b) arises from differing spinning sideband intensities. Complete analysis of the spinning sideband manifolds (at low spin rates) shows that C-5 and C-22 have distinguishable shielding anisotropies and asymmetries, which in turn indicates that the order of their isotropic chemical shifts is interchanged between Forms I and II. This variation can be correlated with hydrogen

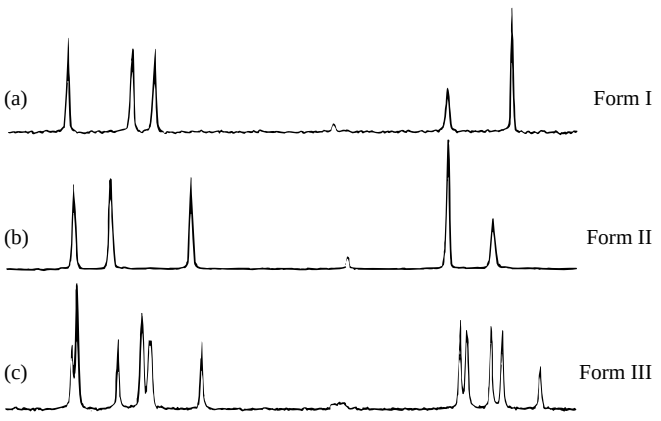

Figure 1 Carbon-13 CP MAS NMR spectra[4] (high-frequency region only) of three polymorphs of cortisone acetate (**1**) at 50.3 MHz

Table 1 Isotropic Chemical Shifts[a] for C-3, C-5, and C-22 of the Anhydrous Polymorphs of Cortisone Acetate

Carbon	Form I	Form II	Form III
C-3	202.8[b]	198.9	203.0[c], 203.0[c], 198.2
C-5	175.7	171.0	173.7, 173.7, 166.9
C-22	169.8	175.2[b]	174.3[c], 171.5, 170.3

[a]Given as δ_C (ppm).
[b]Shown by X-ray crystallography to be the acceptor site for hydrogen bonding.
[c]Concluded from the NMR evidence to be the acceptor site for hydrogen bonding.

bonding,[2,4] which causes an increase in chemical shift of 3–4 ppm at the acceptor carbonyl carbon resonance. Table 1 shows the assignments for carbons C-3, C-5 and C-22 for the three anhydrous forms, and indicates the known acceptor positions for hydrogen bonding. One can conclude that, of the three molecules in the asymmetric unit of Form III, two are hydrogen bonded at C-3 and the third, in contrast, at C-22. It may be noted that conjugation appears to relay the effect of hydrogen bonding on the chemical shift from C-3 to C-5.

This example illustrates how polymorphic form can affect chemical shifts. Unfortunately, matters are not often so simple. The differences in chemical shifts between analogous carbons for different polymorphs may arise either from *inter*molecular effects (packing, direct influence of neighboring molecules, hydrogen bonding, etc.) or *intra*molecular effects (variations in geometry and/or conformation). There is rarely any way that NMR can distinguish between the two influences. Of course, if crystal structures are known from X-ray studies, then knowledge of influences on chemical shifts obtained from solution state studies or by theory can be brought to bear. A case where intramolecular differences (but correlated with intermolecular differences!) are thought to be important is that of 4′-methyl-2′ nitroacetanilide (**2**), which exists in two forms (white and yellow), both of which have been subjected to study by single-crystal X-ray diffraction. In the white form, both the amide and nitro groups are in planes at a substantial angle (ca. 44°) to the plane of the aromatic ring, giving restricted conjugation and preventing intramolecular hydrogen bonding. On the other hand, the yellow form (with two molecules in the asymmetric unit) has more nearly coplanar groups (dihedral angles between 12° and 31°), allowing intramolecular hydrogen bonding between the amide NH and one of the nitro group oxygens. These facts suffice to explain the differences in chemical shifts between the polymorphs.[5] For example, the white form (C–NO_2 dihedral angle, 44.0°) has δ(C-2) = 144.1 ppm whereas the yellow form (C–NO_2 dihedral angles, 18.0° and 12.3°) gives δ(C-2) = 135.9 and 133.0 ppm (presumably respectively).

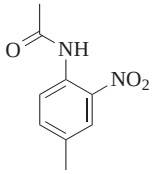

(2)

Certain simple but important measurements can be made of polymorphism via the fingerprinting ability. For example:

1. Mixtures of polymorphs can be readily studied and minor components can be quantified,[4] in favorable cases down to the 1% level.
2. NMR spectra can be used to monitor the polymorphic variations produced by different formation conditions (e.g. different rates of crystallization produced by cooling a solution quickly or slowly).[4]
3. Polymorphism can be studied directly in pharmaceutical tablets. Saindon et al.[3] have pointed out that the CP MAS technique can be used to discriminate against signals deriving from the excipient.

The combination of single-crystal XRD and CP MAS NMR for the study of polymorphism is particularly powerful. The former can give precise atomic positions but is frequently feasible for only some of the forms of a product (because of difficulties in growing suitable crystals). NMR, however, can almost always be relied upon to yield spectra of all polymorphs available in sufficient quantity, and interpretation is greatly aided by X-ray information on any one form. For example, of the two forms of fosinopril sodium, one was examined using single-crystal X-ray diffraction techniques, then both were studied[7] by CP MAS NMR of ^{13}C. The results provided by NMR enabled the conclusion to be drawn that the environment of the acetal side chain of fosinopril sodium differed in the two polymorphs. In this case ^{31}P CP MAS NMR was also used, and showed a significant chemical shift difference (2.2 ppm) between the forms.

It is possible to detect conformational disorder within polymorphs by CP MAS NMR. Thus Stoltz et al.[8] have shown that peak intensities for the monohydrate of oxyphenbutazone give a site ratio consistent with X-ray results in terms of sterically-favored isomers. However, it must be said that since CP MAS NMR spectra are obtained on microcrystalline or powdered material, it is not easy to differentiate between mixed crystals and disorder in a single type of crystal.

Differences in bonding between polymorphs can sometimes be quite startling but readily detectable by NMR. Thus, for 2-aminobenzoic acid (**3**), ^{13}C MAS NMR reveals[9] that Form I gives two signals each for C-1 and C-2. These are at chemical shifts which are characteristic of the normal and zwitterionic structures (**3**)A and (**3**)B, respectively, indicating that the unit cell contains equal proportions of each form. On the other hand, Forms II and III give spectra showing that each has an asymmetric unit containing one molecule of structure (**3**)A only.

A B

(3)

Interestingly, the ^{13}C spectra of Forms II and III are so similar as to be virtually indistinguishable. In these cases, it is necessary to turn to nuclei other than ^{13}C to differentiate. The proton CRAMP spectra of the two forms are, in fact, very different (Figure 2). Form II of the compound gives a strong signal at δ_H = 12.3 ppm, indicative of a hydrogen-bonded CO_2H group (in agreement with single-crystal X-ray results). This is not present for Form III (the crystal structure of which is unknown)—from which it can be deduced that hydrogen bonding is probably absent. However, the situation is complicated by the fact that there are proton-exchange processes occurring, involving amino and (in some cases) carboxylic acid protons, at a rate comparable with the NMR timescale, producing broad bands underlying the sharper aromatic proton signals at ambient probe temperature.

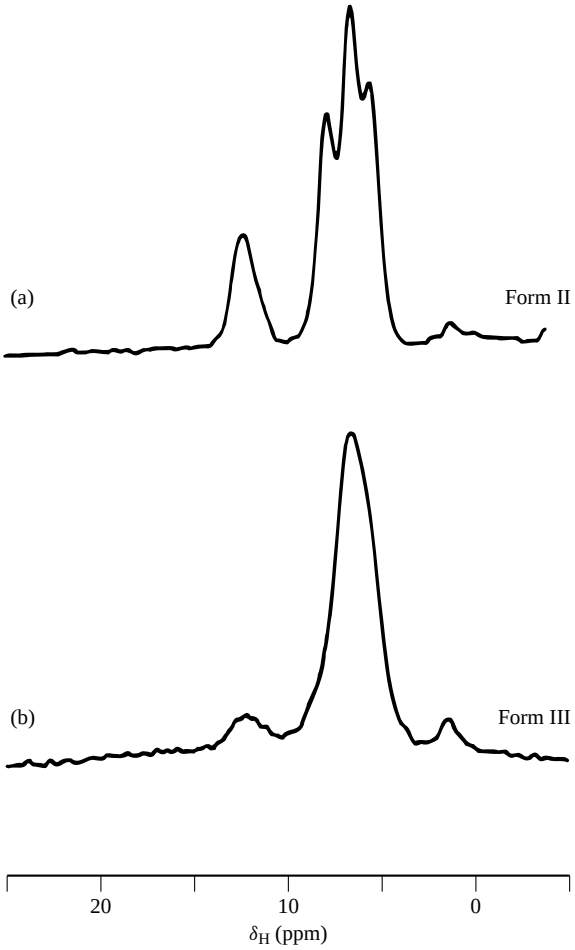

Figure 2 Proton CRAMP spectra[9] of two polymorphs of 2-aminobenzoic acid (**3**) at 200.13 MHz. The sample of Form III contains a small amount of Form II, which gives rise to the hydrogen-bonded peak at δ 12.3 ppm. The peak at $\delta \sim 1.5$ ppm in each spectrum is due to an impurity in the Kel-F rotors used. The broad line (assigned to NH_2 and CO_2H protons) underlying the spectrum of Form III is clearly visible

4 POLYMORPHISM AND MOLECULAR MOBILITY

In addition to the effects on chemical shifts arising from differences in intermolecular environment and intramolecular geometry between molecules of different polymorphs, variations in molecular level motion can often also be detected. A case in point is illustrated in Figure 3, which shows ambient probe temperature ^{13}C CP MAS spectra[10] of two forms

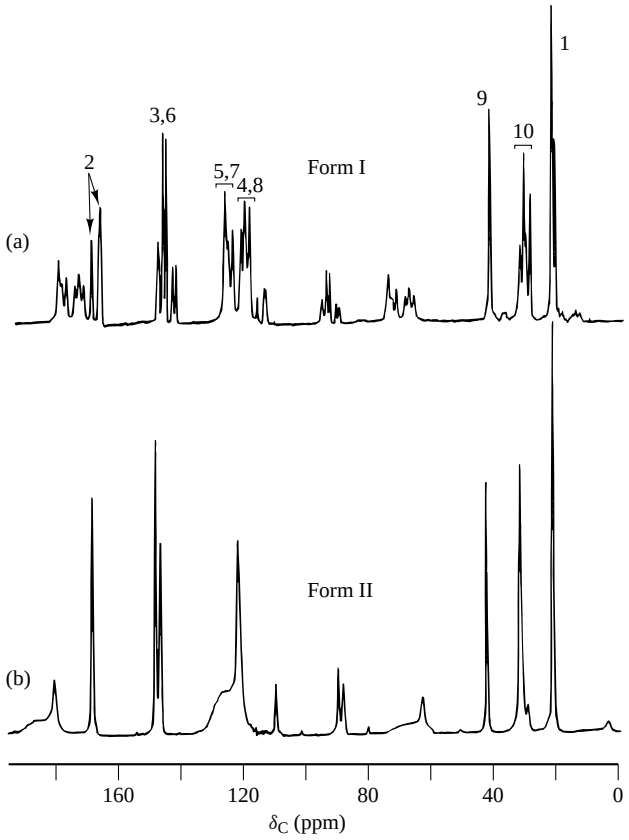

Figure 3 Carbon-13 CP MAS spectra[10] of two forms of bisphenol-A diacetate (**4**) at 50.3 MHz and ambient probe temperature. Signals not indicated by numbers in (a) [and corresponding peaks in (b)] are spinning sidebands

of bisphenol-A diacetate (**4**). Clearly, Form I gives a much more complex spectrum than Form II, as is consistent with the single-crystal X-ray results, which show that in the former case the asymmetric unit consists of two entire molecules. The second feature of importance is the breadth of the resonances for the aromatic CH carbons (C-4, C-5, C-7 and C-8) for Form II, which suggests there is substantial averaging, probably arising from 180° ring-flips of the phenylene rings (possibly by simultaneous motion of the two halves of the molecule). This suggestion is readily confirmed by variation of the temperature.

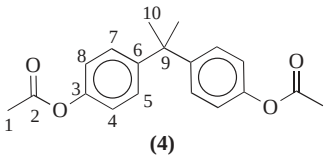

(4)

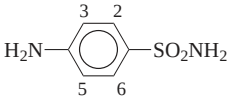

(5)

Such variable temperature ^{13}C CP MAS NMR experiments have been used[11] to study the motion of a phenylene ring about the *para* axis of one form of sulfanilamide, (**5**). Just below room temperature the C-3/C-5 resonance (but not the C-2/C-6 signal) is observably split because the SO_2NH_2 substituent is twisted with respect to the ring. An Arrhenius activation energy, E_a, of 63 ± 4 kJ mol^{-1} for the (assumed) 180° ring-flip was obtained. It should be noted that rapid motion of this type would not be detected by XRD.

An example from an entirely different area of chemistry concerns the polymorphism of phosphorus pentachloride, PCl_5. The stable form (Phase II) of this compound under normal conditions is ionic, with the structure PCl_4^+ PCl_6^-. Both ions are very mobile at ambient temperature, so that shielding anisotropy at the phosphorus nuclei is eliminated and the chlorine nuclei relax very rapidly. The latter effect causes self-decoupling of the chlorines and the net effect is that ^{31}P MAS spectra consist[12] of two sharp lines, one for each anion. However, Phase III, which can also be studied at ambient probe temperature, has the stoichiometry $[PCl_4]_2^+[PCl_6]^-Cl^-$. Since this form, like Phase II, contains PCl_4^+ and PCl_6^- ions, the ^{31}P MAS spectrum also consists of two bands, but at 81 MHz the resonances are broad and splittings arising from (Cl,P) coupling are seen at 36 MHz. Thus self-decoupling is substantially less efficient for Phase III than for Phase II, probably indicating more restricted rotational mobility for the ions in the former.

5 MACROMOLECULAR POLYMORPHS

Two types of example from widely different chemical areas should suffice to show some of the general features of polymorphism in macromolecular systems. Silicon carbide exemplifies the situation where the structure is three-dimensional so that interchange between forms is not feasible. The different polymorphs are essentially frozen-in at the time of preparation. All structures have alternating Si and C atoms, with all coordinations tetrahedral (though mostly not with the full symmetry). The structural differences between some of the forms can be appreciated from Figure 4, which shows a plane including the *c* crystallographic axis and alternating Si and C atoms in that plane for four forms of the material. It is evident that the detailed environments of all silicon atoms of the 2H form are equivalent, as is also the case for the β form (though β and 2H environments are not identical). However, the 4H form contains two types of Si and the 6H three types. The ^{29}Si spectra (Figure 5) show[13] the expected number of signals for the four forms. Similar considerations apply to the ^{13}C spectra. There is also a range of other forms. Assignment of the signals for the 4H and 6H polymorphs is not easy but has been made.[13,14] The separate signals have different relaxation times, probably as a result of the presence of impurities. Silicon carbide is a case where the amorphous material can also exist, without sizable domains of any of the potentially ordered structures. Such material gives rise to broad ^{29}Si and ^{13}C resonances, usually characterized by shorter values of T_1 than the crystalline material, probably because impurities tend to concentrate in amorphous regions.

Of course, silica provides the outstanding example of a compound with multiple polymorphs. Not only are there well-characterized crystalline forms (quartz, crystobalite, tridymite, etc.), together with the common amorphous glass, but it seems that many types of zeolites can be obtained with all aluminum atoms replaced by silicon so that they become silica polymorphs. Since zeolites are treated in other entries in this Encyclopedia they will not be discussed here. The book

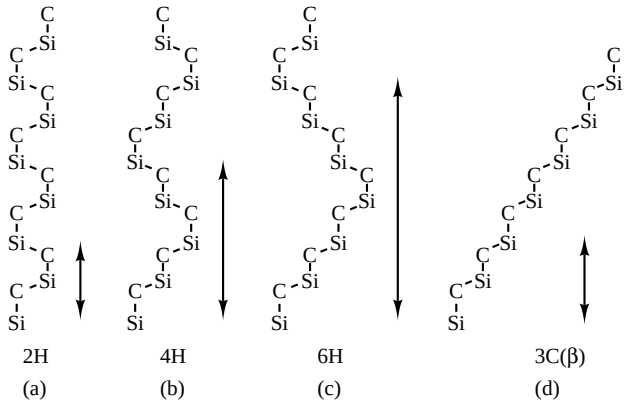

Figure 4 Schematic structures for silicon carbide polymorphs. The vertical arrows represent repeat distances

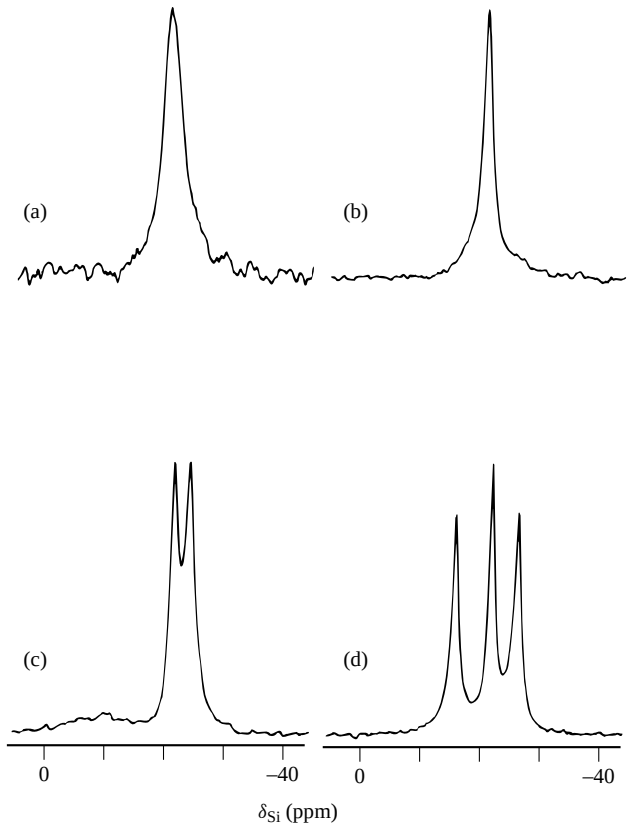

Figure 5 Silicon-29 MAS NMR spectra[13] of silicon carbide polymorphs at 59.58 MHz: (a) 3C (β); (b) 2H; (c) 4H; and (d) 6H

by Engelhardt and Michel[15] contains a useful discussion of NMR studies of nonzeolitic silica polymorphs (pp. 170–175). The ^{29}Si chemical shifts cover a wide range ($\delta_{Si} \sim -107$ to -121 ppm), the variation being attributed to differences in mean SiOSi bond angles, α, an increase in shielding resulting from widening SiOSi angles. A number of specific relationships have been proposed,[16] including (from theoretical considerations) $\delta_{Si} = -247.05\bar{\rho} + 2.19$, where $\rho = \cos\alpha/(\cos\alpha - 1)$. Of course, many of the silica polymorphs differ in the number of different crystallographic sites. Coesite, for instance, gives two widely-spaced ^{29}Si signals (δ_{Si} = 108.1 and 113.9 ppm), in accord with its structure.[16] In contrast to all the four-coordinate silica polymorphs, stishovite, which contains six-coordinate silicon, gives a signal at $\delta_{Si} = -191$ ppm.[16] As with silicon carbide, amorphous forms of silica (glass!) are well known.

Organic polymers may also show polymorphism. One of the early examples of CP MAS NMR related to the case of isotactic polypropene, which exists in several crystalline forms usually as domains separated by amorphous material. In effect, the chains constitute infinite one-dimensional bonded structures with weaker forces between the chains. The systems therefore are intermediate between the molecular polymorphs discussed in Section 3 and the infinite three-dimensional structures of SiC and SiO_2. The structure of the α form of polypropene is shown in Figure 6(a). The helical polymer units occur as pairs of interlocking chains with opposing handedness. This creates a situation where there are two distinct methyl sites, with two-thirds of the groups in a given helix facing the companion helix, and the remaining third facing outwards. Thus a 2:1 doublet is expected for the methyl carbons, and this is observed[17] in practice. A similar situation obtains for the CH carbons.

In contrast, the crystal structure of the β form contains separate groups of helices of the two types of handedness, with no pairing [Figure 6(b)]. The NMR spectrum therefore lacks the well-defined splitting shown by that of the α form.

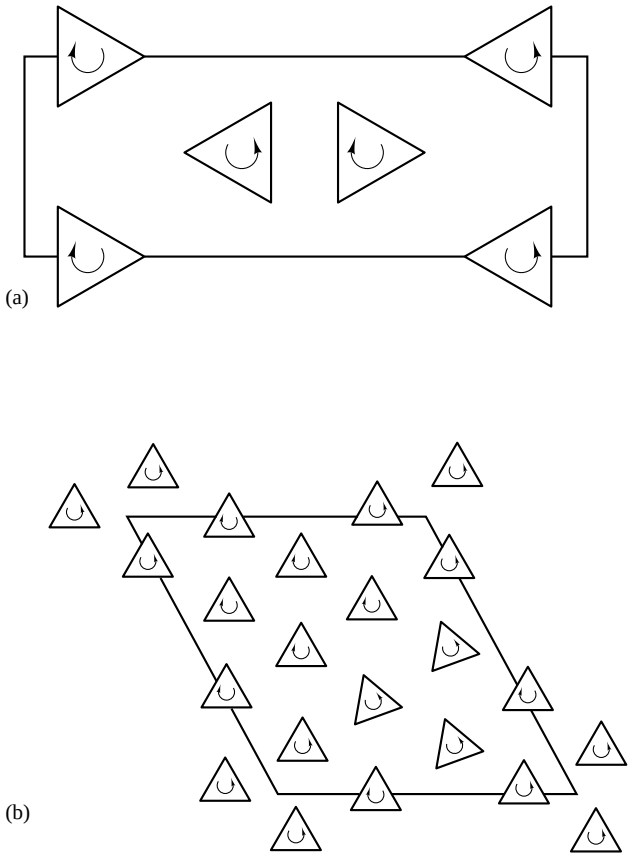

Figure 6 Diagrammatic crystal structures for two forms of isotactic polypropene: (a) α form; (b) β form. The figures show projections of the chains perpendicular to their axes, with the corners of the triangles indicating the positions of methyl groups. The arrows represent the handedness of the helices

Of course, isotactic polypropene also contains a significant proportion of amorphous material which, as usual, gives rise to somewhat broadened CP MAS ^{13}C lines. The differences between the α and β forms of isotactic polypropene arise from intermolecular packing of the polymer chains. Far greater differences occur, as expected, in NMR spectra[17,18] for polymer forms differing in tacticity (such as isotactic and syndiotactic polypropene). However, differences in tacticity are not normally classed under polymorphism.

Biochemical polymers such as cellulose and chitosan also give rise to polymorphism, which has been studied by solid state NMR methods.[19,20]

6 RELATED ARTICLES

Ceramics; Molecular Sieves: Crystalline Systems; Polysaccharide Solid State NMR; Silicon-29 NMR of Solid Silicates.

7 REFERENCES

1. G. E. Balimann, C. J. Groombridge, R. K. Harris, K. J. Packer, B. J. Say, and S. F. Tanner, *Philos. Trans. R. Soc. London, Ser. A*, 1981, **299**, 643.
2. S. R. Byrn, G. Gray, R. R. Pfeiffer, and J. Frye, *J. Pharm. Sci.*, 1985, **74**, 565; S. R. Byrn, P. A. Sutton, B. Tobias, J. Frye, and P. Main, *J. Am. Chem. Soc.*, 1988, **110**, 1609.
3. P. J. Saindon, N. S. Cauchon, P. A. Sutton, C.-J. Chang, G. E. Peck, and S. R. Byrn, *Pharm. Res.*, 1993, **10**, 197.
4. R. K. Harris, A. M. Kenwright, B. J. Say, R. R. Yeung, R. A. Fletton, R. W. Lancaster, and G. L. Hardgrove, *Spectrochim. Acta, Part A*, 1990, **46**, 927; E. A. Christopher, R. K. Harris, and R. A. Fletton, *Solid State NMR*, 1992, **1**, 93.
5. R. A. Fletton, R. W. Lancaster, R. K. Harris, A. M. Kenwright, K. J. Packer, D. N. Waters, and A. Yeadon, *J. Chem. Soc., Perkin Trans. 2*, 1986, 1705.
6. R. K. Harris, B. J. Say, R. R. Yeung, R. A. Fletton, and R. W. Lancaster, *Spectrochim. Acta, Part A*, 1989, **45**, 465; R. A. Fletton, R. K. Harris, A. M. Kenwright, R. W. Lancaster, K. J. Packer, and N. Sheppard, *Spectrochim. Acta, Part A*, 1987, **43**, 1111.
7. H. G. Brittain, K. R. Morris, D. E. Bugay, A. B. Thakur, and A. T. M. Serajuddin, *J. Pharm. Biomed. Anal.*, 1993, **11**, 1063.
8. M. Stoltz, D. W. Oliver, P. L. Wessels, and A. A. Chalmers, *J. Pharm. Sci.*, 1991, **80**, 357.
9. R. K. Harris and P. Jackson, *J. Phys. Chem. Solids*, 1987, **48**, 813.
10. D. Casarini, R. K. Harris, and A. M. Kenwright, *Magn. Reson. Chem.*, 1993, **31**, 540.
11. L. Frydman, A. C. Olivieri, L. E. Diaz, B. Frydman, A. Schmidt, and S. Vega, *Mol. Phys.*, 1990, **70**, 563.
12. E. R. Andrew, A. Bradbury, R. G. Eades, and G. J. Jenks, *Nature (London)*, 1960, **188**, 1096; R. K. Harris and A. Root, *Mol. Phys.*, 1989, **66**, 993.
13. D. C. Apperley, R. K. Harris, G. L. Marshall, and D. P. Thompson, *J. Am. Ceram. Soc.*, 1991, **74**, 777.
14. D. Guo, J. S. Hartman, and M. F. Richardson, *Can. J. Chem.*, 1992, **70**, 700; M. F. Richardson, J. S. Hartman, D. Guo, and B. G. Winsbarrow, *Chem. Mater.*, 1992, **4**, 318.
15. G. Engelhardt and D. Michel, *High-resolution Solid-state NMR of Silicates and Zeolites*, Wiley-Interscience, New York, 1987.
16. J. V. Smith and C. S. Blackwell, *Nature (London)*, 1983, **303**, 223; G. Engelhardt and R. Radeglia, *Chem. Phys. Lett.*, 1984, **108**, 271.
17. A. Bunn, M. E. A. Cudby, R. K. Harris, K. J. Packer, and B. J. Say, *Polymer*, 1982, **23**, 694; M. A. Gomez, H. Tanaka, and A. E. Tonelli, *Polymer*, 1987, **28**, 2227.
18. A. Bunn, M. E. A. Cudby, R. K. Harris, K. J. Packer, and B. J. Say, *J. Chem. Soc., Chem. Commun.*, 1981, 15.
19. R. H. Atalla, J. C. Gast, D. W. Sindorf, V. J. Bartuska, and G. E. Maciel, *J. Am. Chem. Soc.*, 1980, **102**, 3249; W. L. Earl and D. L. VanderHart, *J. Am. Chem. Soc.*, 1980, **102**, 3251.
20. H. Saito, R. Tabeta, and K. Ogawa, in *Industrial Polysaccharides: Genetic Engineering, Structure/Property Relations & Applications*, ed. M. Yalpani, Elsevier Science Publishers, Amsterdam, 1987, pp. 267–280.

Biographical Sketch

Robin K. Harris. *b* 1936. B.A. (Nat. Sci.), Ph.D. (supervisor Norman Sheppard), Sc.D., University of Cambridge, UK. Postdoctoral work at Mellon Institute, Pittsburgh, PA (with Aksel Bothner-By). Successively lecturer, senior lecturer, and professor, University of East Anglia, UK. Currently Professor of Chemistry, University of Durham, UK. Secretary-General of ISMAR, 1986–92. Approx. 350 publications. Current research specialty: solid state NMR and its applications in materials chemistry.

Spectral Editing Techniques: Hydrocarbon Solids

Kurt W. Zilm

Yale University, New Haven, CT, USA

1	Introduction	1
2	Background on Spectral Editing of Liquids	1
3	Challenges Posed by Solids	1
4	Experimental Considerations and Caveats	5
5	Summary	6
6	Related Articles	6
7	References	6

1 INTRODUCTION

Spectral editing techniques in NMR in general are methods that aid the spectroscopist in assigning or simplifying complex high-resolution spectra. Most approaches to spectral editing have been developed in the context of NMR of ^{13}C where the emphasis has been on separating ^{13}C resonances on the basis of their multiplicity, i.e. the number of directly attached ^{1}Hs. This type of information, when combined with the analysis of ^{13}C chemical shifts, is very often sufficient for determining the chemical structure of rather complex organic molecules. As such, spectral editing of solution NMR finds wide application in industry for the structural characterization of polymers, drugs, and petroleum based products. Development of similar methods which are applicable to solid samples has been motivated by a large number of important applications to geochemical and material science.

This article deals with spectral editing approaches developed specifically for high-resolution solid state NMR of ^{13}C. Many different strategies have been applied to this problem, and the space provided here unfortunately does not permit covering every aspect of this subfield. Most of the relevant literature is cited in two recent papers,[1,2] and the interested reader may find more extensive citations contained therein.

2 BACKGROUND ON SPECTRAL EDITING OF LIQUIDS

The high information content of ^{13}C NMR spectra of liquids is well known. It follows directly from the large dispersion of the ^{13}C chemical shift and the remarkably tight correlation of ^{13}C chemical shifts with structure. The beautiful stick-spectrum simplicity of ^{13}C spectra is made possible by ^{1}H decoupling and the low natural abundance of ^{13}C which eliminates complications from ^{13}C–^{13}C J couplings. Their information content is greatly increased if the multiplicity of the ^{13}C resonances can be determined.

Editing techniques for ^{13}C NMR of liquids rely on the fairly narrow range of values for $^{1}J(^{13}\mathrm{C},^{1}\mathrm{H})$. This permits one to devise pulse sequences in which the evolution of the ^{13}C magnetization can be made to depend principally upon the number n of directly attached ^{1}Hs in CH_n groups. The attached proton test (APT) is the simplest example. In its most basic form, a $\pi/2$, τ, π, τ, acquire echo sequence is applied to the ^{13}C with ^{1}H decoupling during acquisition. A π pulse is also applied to the ^{1}Hs after the first τ, resulting in J modulation of the ^{13}C spin echo. During the 2τ evolution period the dephasings of the ^{13}C chemical shifts are refocused, while those due to $^{1}J(^{13}\mathrm{C},^{1}\mathrm{H})$ accumulate. Setting τ to $\frac{1}{2}J$ produces a spectrum in which the CH_3 and CH_1 resonances are inverted, while the CH_2 and CH_0 resonances are absorptive.

For complex ^{13}C spectra, more powerful methods are required, but all rely upon J couplings in some manner. In editing protocols based on INEPT, J modulation is used to label the ^{1}H magnetization which is then transferred to the ^{13}C (see ***INEPT***). The various CH_n groups can be amplitude modulated in distinct ways depending upon the length of the time evolution due to J coupling. On this basis schemes can be devised in which linear combinations of a few different experiments produce CH_3-only, CH_2-only, CH_1-only, and CH_0-only spectra. Techniques utilizing DEPT provide some improvement in selectivity, as the differentiation of CH_n groups depends upon a pulse flip angle rather than a period τ of free evolution under $^{1}J(^{13}\mathrm{C},^{1}\mathrm{H})$. Especially clean separation of CH_n subspectra has been achieved using multiple quantum coherence among the J-coupled spins. This *s*ubspectral *e*diting using a *mu*ltiple-quantum *t*rap (SEMUT) has the advantage of being relatively insensitive to the value of $^{1}J(^{13}\mathrm{C},^{1}\mathrm{H})$.

3 CHALLENGES POSED BY SOLIDS

As discussed elsewhere in the Encyclopedia, obtaining high-resolution ^{13}C spectra of organic solids requires both magic angle spinning (MAS) and high-power decoupling of the protons. These techniques are usually combined with cross polarization (CP) in a CP MAS experiment. The need to remove broadening associated with chemical shift anisotropy and ^{13}C–^{1}H dipolar couplings presents a new set of problems in the design of methods for spectral editing. Over the last 20 years of development in high-resolution NMR of solids three basic strategies have been applied to this problem. The first has been to design pulse sequences which produce J-modulated signals in solids, and thereby directly adapt the techniques just discussed to solids. The others use ^{13}C–^{1}H dipolar couplings as the basis for selection of CH_n. Some of these methods use the relative strengths of dipolar couplings or rates of CP to differentiate ^{13}C signals of different multiplicities. Others rely upon the establishment of quasi-equilibrium states in the CP process and thus differentiate the ^{13}C multiplicities on the basis of the ratio of the inverse rotating frame spin temperature of the ^{13}C to that for its directly bonded protons.

3.1 *J* Modulation in Solids

Observing resolved $^{1}J(^{13}\mathrm{C},^{1}\mathrm{H})$-coupled multiplets in CP MAS ^{13}C spectra of solids is made difficult by the strong

$^1H-^1H$ and $^1H-^{13}C$ dipolar couplings. In the absence of strong on-resonance ^1H decoupling, CP MAS spectra of typical rigid samples are broad and relatively featureless. The $^1H-^{13}C$ dipolar broadening is by itself inhomogeneous, and should therefore be suppressed by MAS. However the spin-exchange mediated by the $^1H-^1H$ dipolar couplings is faster than typical rates of MAS. Therefore the spin states of ^1H can change several times during a MAS cycle, and the average of the $^1H-^{13}C$ dipolar interaction is then no longer zero. In a simplified picture one can consider this to be a lifetime broadening of the ^{13}C resonances due to the short lifetime of the spin states of the directly attached protons. Terao and co-workers[3] first demonstrated that suppression of the $^1H-^1H$ dipolar couplings could make it possible to observe $^1J(^{13}C,^1H)$-coupled multiplets in solids. In their work, ^1H decoupling at the magic angle in the rotating frame was first used. Subsequently a number of homonuclear sequences such as MREV-8 have been applied as homonuclear multiple pulse decoupling (MPD) for this purpose. For systems such as plastic crystals where molecular motion has already appreciably averaged the dipolar couplings, MPD produces CP MAS spectra with well-resolved $^1J(^{13}C,^1H)$ coupled multiplets. The couplings observed are reduced by the scaling factor appropriate to the particular MPD sequence used.

This approach has been extended to editing schemes that most resemble those used in liquids. The basic approach is to insert MPD sequences in the periods of free evolution under $^1J(^{13}C,^1H)$. APT-type spectra of motionally narrowed solids have been acquired in this fashion, but in the general case the MPD does not produce sufficient narrowing of the proton NMR spectra to permit sustained J modulation. Terao and co-workers[4] have investigated the limitations of this approach most extensively for rigid solids. One sequence they have successfully used in producing J modulation for rigid solids consists of CP followed by a J-modulated rotor synchronized echo. During the first half of the echo, magnetization of the ^{13}C nuclei evolves under proton homonuclear decoupling. This period, t_1, is adjusted to be equal to one rotor cycle. Over the course of the rotor period J modulation accumulates, but any modulation by the $^{13}C-^1H$ dipolar coupling and the ^{13}C CSA is refocused. After the π pulse, high-power dipolar decoupling is applied for another period t_1. This second interval refocuses the isotropic chemical shift and effects of any bulk susceptibility broadening that accumulated during the first t_1 period. FIDs taken as a function of t_1 then are largely only modulated by $^1J(^{13}C,^1H)$. In this manner a 2D heteronuclear J-resolved spectrum can be obtained with multiplets in the ω_1 dimension. However this approach still does not yield clean multiplets. For instance, the outer lines in quartets for CH_3 groups are very much broader than the central pair, and they are barely resolved.

At the moment, J modulation based editing techniques for solids will remain useful only for systems with significant motional narrowing. Advances in the efficiency of homonuclear decoupling, especially under conditions of MAS, are needed before such techniques can become widely applicable. Problems also remain in combining these homonuclear decoupling requirements with the typical hardware used for CP MAS NMR. While the approach has been proven in principle, development of generally applicable methods for solids along these lines remains a challenge for the future.

3.2 Dipolar Dephasing and Related Schemes

The most generally applicable editing techniques for solids take advantage of the strong dipolar couplings inherent in solids, rather than treating them as a nuisance to be eliminated. The simplest approach to spectral editing in CP MAS NMR of organic solids is the venerable technique[5] of dipolar dephasing (DD) or interrupted decoupling. After CP, the ^1H decoupler is turned off for $\sim 50\,\mu s$. This is a sufficient time for the $^{13}C-^1H$ dipolar coupling to dephase the transverse magnetization for any ^{13}C with a directly bonded ^1H, as long as the dipolar coupling is not motionally averaged. Therefore the lines for rigid CH_1 and CH_2 groups are effectively suppressed. Rapid rotation of CH_3 groups at room temperature leads to different behavior for these protonated carbons. This rotation renders the three $^{13}C-^1H$ dipolar couplings equal, and reduces them to one-third of their static value. Depending upon the spin state of the protons, the ^{13}C in a CH_3 group can experience one of two possible dipolar fields. Whenever the three protons are in the same state ($\alpha\alpha\alpha$ or $\beta\beta\beta$), the three couplings reinforce one another, and the ^{13}C experiences the field of a single full $^{13}C-^1H$ dipolar coupling. However, three-quarters of the time the ^1Hs are in a state such as $\alpha\alpha\beta$ or $\beta\beta\alpha$. In this instance the fields due to two of the couplings will exactly cancel. The net dipolar field then is usually only one-third of a single $^{13}C-^1H$ dipolar coupling, and this is similar to that often experienced through nonbonded contacts by a CH_0. Thus, in most instances, methyl groups at room temperature behave like nonprotonated carbons under dipolar dephasing. The DD spectrum then consists of slightly attenuated resonances for just the CH_0 and CH_3 groups. Comparison with a fully polarized CP MAS spectrum provides a simple qualitative method for categorizing resonances as either CH_3 + CH_0 or CH_2 + CH_1. In many instances, a simple CP MAS spectrum can be fully assigned using this approach in combination with information from linewidth or chemical shifts.

Several approaches have been taken to improve on the basic DD technique. In some instances the dephasing interval leads to an unacceptable linear phase correction due to the delayed acquisition. A π pulse may be inserted in the interrupted decoupling interval to alleviate this to some degree. However, as first pointed out by Munowitz and Griffin,[6] the π pulse should be applied only after a full rotor period to ensure that both the isotropic and anisotropic portions of the ^{13}C chemical shift are refocused. Other groups have investigated the spin dynamics of the DD experiment with the desire to separate CH_n resonances more completely or quantitatively.[7] The approach has been to fit the dephasing of the ^{13}C resonances as a function of the dephasing time, τ_D, to some type of model dephasing function. Since it can be argued the different CH_n groups may have characteristic dephasing characteristics, this approach would seem to have some validity. In this manner one can then extrapolate back in dephasing time to recover the initial intensities of the CH_3 and CH_0 resonances.

The best way to view the DD experiment is actually as a low-resolution 1D version of separated local field (SLF) spectroscopy under MAS conditions. During τ_D the ^{13}C FID is dominated by the $^{13}C-^1H$ dipolar couplings, and is damped by the $^1H-^1H$ dipolar interactions. An isolated CH_1 group then has a decay profile that is essentially a damped Pake doublet FID, that for a CH_2, i.e. a Pake 'triplet'. Since the local structure of isolated CH_n groups of a given n does not

vary appreciably in organic solids, these decays would be quite characteristic were it not for the $^1H-^1H$ dipolar couplings. This complication can be removed by applying MPD during the dephasing interval. In this manner the number of dipolar couplings is determined from a spectral pattern, i.e. sideband intensities, rather than from a less structure-specific average dephasing rate.

The first proposal for this type of MAS SLF spectroscopy was by Munowitz and Griffin[6] as a means of measuring C–H distances. Webb and the author[8] later investigated using the spinning sideband patterns characteristic of the different CH_n groups for spectral editing. The proposed 2D experiment consists of CP followed by MPD (usually MREV-8) for t_1 to produce dipolar evolution in the first frequency dimension. This is followed by a $\pi/2(\phi_i)$, τ, $\pi/2(x)$ sequence to selectively project the ^{13}C magnetization onto one axis of the rotating frame. The period, τ, is a few hundred μs and is used to dephase magnetization not placed along z by the $\pi/2(\phi_i)$ pulse. Following the $\pi/2(x)$ pulse, the normal dipolar decoupled ^{13}C FID is acquired during time period t_2. Cycling the phase ϕ_i in a time proportional phase incrementation scheme avoids the need to acquire a quadrature data set in t_1. The sideband patterns generated this way in the ω_1 dimension retain both dipolar and CSA effects. However, at low-to-moderate field strengths the patterns are so dominated by the $^{13}C-^1H$ dipolar couplings that they can still be easily deconvolved into their CH_n components. Since CH_2 groups have two dipolar couplings, they have nearly twice as many sidebands, and are readily distinguished from CH_1 groups by this technique. Decomposition of complex CP MAS spectra with many overlapping lines has been demonstrated using this approach. At higher fields the same deconvolution methods can be applied using Munowitz and Griffin's rotor-synchronized sequence to eliminate the complications due to CSA. The requirement for delaying acquisition to several rotor periods after the initial CP interval, however, can result in substantial losses in sensitivity. A further simplification has been proposed by Sethi.[9] Since the temporal evolution during t_1 in the MAS SLF experiments is well understood, only a few special times t_1 need be acquired. Using this approach Sethi has introduced 1D editing schemes that also can be used to separate CH_1 and CH_2 resonances.

3.3 Schemes Using CP Dynamics

The previous methods rely upon the relative strengths of $^{13}C-^1H$ dipolar couplings or the different numbers of dipolar couplings to discriminate between different CH_n groups. The dipolar couplings are used essentially to dephase or modulate the ^{13}C resonances in a predictable manner. Another strategy is to use the ways in which these differences in the dipolar coupling network result in differences in the CP dynamics between the CH_n groups.

The simplest description of the CP process considers the transfer as a first-order kinetic process with a time constant T_{CH}. However, it is well known that this description is only qualitatively correct, and only phenomenologically describes the long-time behavior ($t \gg T_2$). At short CP times the Hartmann–Hahn transfer is dominated by the details of the dipolar coupling network between a ^{13}C and its directly bonded ^1Hs. In single crystals, one even observes transient oscillations in the polarization transfer. For powdered samples under moderate MAS, the transient effect manifests itself as a rapid initial period of CP transfer in which the ^{13}C and its attached ^1Hs come into a quasi-equilibrium. Spin diffusion to the more distant protons transports polarization more slowly to these ^1Hs coupled to the ^{13}C. This slower process determines the rate at which the ^{13}C reaches its final fully polarized state. In the quasi-equilibrium state, the initially unpolarized ^{13}C nuclei share the polarization equally with their directly attached protons. CH_1 and CH_2 groups then polarize to one-half and two-thirds of their full intensity, respectively, on the short timescale. Because of their motionally averaged dipolar field, CH_3 groups behave similarly to nonprotonated carbons. Both the CH_0 and CH_3 groups then polarize more slowly, with the polarization bottleneck to full enhancement usually being the rate of $^1H-^1H$ spin diffusion. As long as the transfer of transient polarization among the closely coupled spins is faster than the $^1H-^1H$ spin diffusion and direct transfer from more distant protons, it can be put to good use in spectral editing schemes.

One particularly useful approach for distinguishing the signals of $CH_1 + CH_2$ from those of $CH_0 + CH_3$ based on the previous ideas is the depolarization (DEP) technique.[10] After a several ms CP interval, the spin locked ^1H magnetization is allowed to dephase by turning off the ^1H rf for several hundred μs, while keeping the ^{13}C spin locked. Turning the ^1H rf back on reestablishes the CP contact, and the ^{13}C magnetization can be used to repolarize the depolarized ^1Hs. If the phase of the ^1H rf is switched 90° every 25–50 μs over a total period of a few hundred μs, there will be no net buildup in the ^1H magnetization, only a net drain from the ^{13}C. Since only the $CH_1 + CH_2$ carbons polarize on this timescale, their signals are fully depleted after the depolarization, while the $CH_0 + CH_3$ signals are attenuated only slightly. The resulting DEP spectrum is much like a DD spectrum. However since the ^{13}C are spin locked until the depolarization is finished, there are no problems with linear phase errors as in DD.

Polarization inversion (PI) can also be used in a similar fashion.[11] In this technique the ^{13}C are first fully polarized by CP, and the phase of the rf in the ^1H channel suddenly inverted. Since the ^1H spin temperature has now been inverted, the ^{13}C will try to follow. Those ^{13}C with strong $^{13}C-^1H$ dipolar couplings first quickly depolarize, and then repolarize in the opposite direction. Since the zero crossings for CH_1 and CH_2 groups are different, they can be used in some instances to distinguish resonances. Nulling of resonances in this manner has also been referred to as cross depolarization[12] (CPD). A further variant adds a final short polarization period onto the CPD sequence.[13] The depolarization and repolarization periods in this cross-depolarization–repolarization technique (CPDR) can be adjusted so as simultaneously to null the CH_1 and CH_2 groups. This is not in general possible with the cross-depolarization interval alone.

Sangill et al.[2] have presented a thorough study of the use of CPD and CPDR in spectral editing. Their analysis focused on using optimized combinations of CPD and CPDR spectra to produce CH_n-only spectra, $n = 0–3$, while maintaining good sensitivity. By paying careful attention to the CP dynamics, they were able successfully to separate complex CP MAS spectra into their CH_n subspectral components.

Burum and Bielecki[14] have introduced a particularly clever method based on CP dynamics for selectively detecting CH_2

groups in CP MAS NMR. Their method, WIMSE (*w*indowless *i*sotropic *m*ixing for *s*pectral *e*diting), starts with a CP interval under a multiple pulse cycle which eliminates the $^1H-^1H$ dipolar couplings during the CP step while maintaining the $^{13}C-^1H$ couplings. Over a MAS rotor period under these conditions, no net polarization is transferred to ^{13}C nuclei in CH groups. Instead, whatever magnetization is transferred at the start of the rotor cycle 'echoes' back from the ^{13}C to the ^1H at the end. However, the presence of two dipolar couplings in a CH_2 group defeats this 'rotational polarization echo' effect. The resulting spectrum then consists solely of the CH_2 component in a complex CP MAS spectrum. CH_3 and CH_0 lines do not appear as their CP rates are too slow.

3.4 Techniques Using Quasi-Equilibrium States

Another successful method based on differences in CP dynamics between the different CH_n groups is the solid state attached proton test, or SSAPT method. Initially the ^{13}C are fully polarized using a 2–3 ms CP interval. Immediately following this, a short PI period is applied, typically on the order of 50 μs. At the beginning of the PI time the ^{13}C and their directly attached ^1Hs are equally polarized. Upon reversal of the phase in the ^1H spin locking rf, this equilibrium is broken, and the spins try to reequilibrate. Since the CH_3 and CH_0 groups polarize slowly, they are relatively unaffected by this short PI interval. The CH_2 and CH_1 groups, on the other hand, have sufficient time to reach a quasi-equilibrium state through a rapid transient CP transfer. In the case of the CH_1 group, the ^{13}C and the ^1H have equal but opposite polarizations at the start of the PI. During the short PI time these magnetizations cancel, and the signal for the CH_1 carbons is very effectively nulled. The ^{13}C nuclei in the CH_2 groups carry 1 unit of polarization as opposed to the -2 units in the ^1Hs at the beginning of the PI interval. This results in -1 unit of total polarization to be shared among the three spins in the quasi-equilibrium state. At the end of the PI period, the CH_2 signal is then inverted with an intensity of $-\frac{1}{3}$ of its fully polarized signal. The SSAPT spectrum then has CH_3 + CH_0 signals nearly fully polarized and positive, CH signals nulled, and CH_2 signals inverted at one-third intensity. In many instances this provides a very straightforward means of separating the contributions from the different CH_n groups to a ^{13}C CP MAS spectrum.[15,16]

This approach has been extended to a complete spectral editing protocol by Wu, Burns, and the author.[1] Since the establishment of the quasi-equilibrium state depends upon the ratio of the inverse rotating frame spin temperatures of the ^{13}C and its directly bonded ^1Hs, this technique is less sensitive to the CP rates. In this sense it is a relatively robust editing procedure.

The complete spectral editing procedure due to Wu et al. uses four basic experiments (see Figure 1). One begins by acquiring a CH_2-only spectrum. The sequence used starts with a short CP contact which polarizes the CH and CH_2 groups to their quasi-equilibrium intensities of $\frac{1}{2}$ and $\frac{2}{3}$ respectively. This is followed by a short PI interval of roughly the same length. During PI the CH signals null, as does any small CH_3 or CH_0 polarization built up during the CP step. The CH_2 ^{13}C magnetization goes to $-\frac{1}{3}$ of its initial value, resulting in a spectrum with $-\frac{2}{9}$ the intensity for these carbons. This

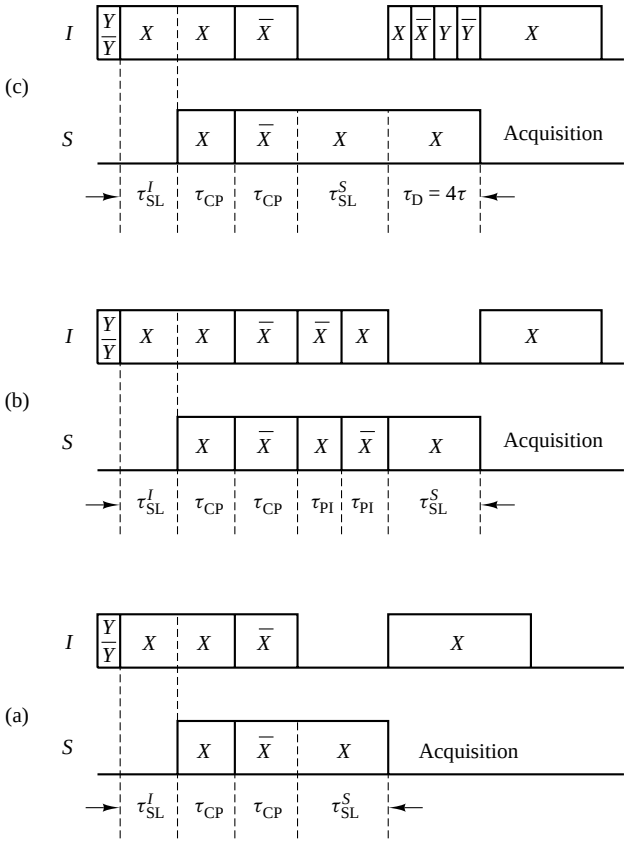

Figure 1 Sequences used in the editing protocol of Wu et al. All employ simultaneous phase inversion to alleviate problems with Hartmann–Hahn mismatches. (a) CP sequence. The additional spin locking delay τ_{SL}^S is used to make the total ^{13}C spin locking time the same in all of the sequences. (b) SCPPI sequence used to acquire CH_2-only spectra. (c) Depolarization sequence. The time τ_{SL}^I is added in these sequences mainly to minimize distortions from ^1H rotating frame relaxation

short CP polarization inversion (SCPPI) spectrum then has contributions from only the CH_2 groups.

The second experiment is a short contact CP (SCP). This will have intensity principally from the CH and CH_2 carbons. Another short CP spectrum with a depolarization interval is also acquired (SCPD). The SCPD spectrum can be used to subtract out the contamination of the SCP data from CH_3 and CH_0 groups. Unfortunately the CH_3 and CH_0 carbons have sufficiently different CP dynamics that they are differentially attenuated, and this subtraction alone is insufficient. In most instances, however, the shift ranges for CH_3 and CH_0 groups are adequately separated so that a dividing line on the ^{13}C chemical shift scale can be chosen to separate these groups. Different weighting factors can then be applied to the upfield (CH_3) and downfield (CH_0) regions for this purpose. The result of this procedure is a relatively clean CH-only spectrum.

To acquire semiquantitatively correct CH_0 and CH_3 spectra, a long CP depolarization spectrum is acquired (LCPD). This spectrum is again split into CH_0 and CH_3 regions, and each part corrected for the differential signal loss of the two types of groups in the depolarization step.

The cleanest and most quantitative results are obtained with this method if the intensity factors for spectral decomposition are determined experimentally on a known model system.

Table 1 Typical Intensities for CH_n Resonances in Pulse Sequences Used for Spectral Editing

	CH_n			
Experiment	CH_0	CH_1	CH_2	CH_3
LCP	100	100	100	100
SCP	10.5	57.5	68	22.6
SCPPI	0	0	−22	0
SCPD	7.2	0	0	10.4
LCPD	82.5	0	0	57.5

Using the set of sequences shown in Figure 1, the intensity matrix in Table 1 is found to be typical. LCP is used to denote a standard (long) CP experiment which is used as the 100% intensity reference.

As the entries demonstrate, the CH and CH_2 group intensities in the SCPPI and SCP experiments are quite close to those expected from the quasi-equilibrium description of the CP dynamics.

Figure 2 compares the four spectra acquired in the editing protocol for cholesteryl acetate to the normal CP MAS spectrum. In the solid state there are two molecules in the unit cell producing a doubling of the lines. Furthermore, changes in conformation lead to significant shifts in many resonances. Using the intensity matrix in Table 1, the CH_n, $n = 0-3$, only spectra can be reconstructed from these data. The results of this data manipulation are shown in Figure 3, clearly demonstrating the simplifications made possible by this spectral editing approach. As a check on this editing protocol, one may sum the CH_n subspectra to produce a synthetic CP MAS spectrum. This is compared with the normal CP MAS spectrum in Figure 4, along with the difference of the two. The small differences observed indicate the reliability of the approach used.

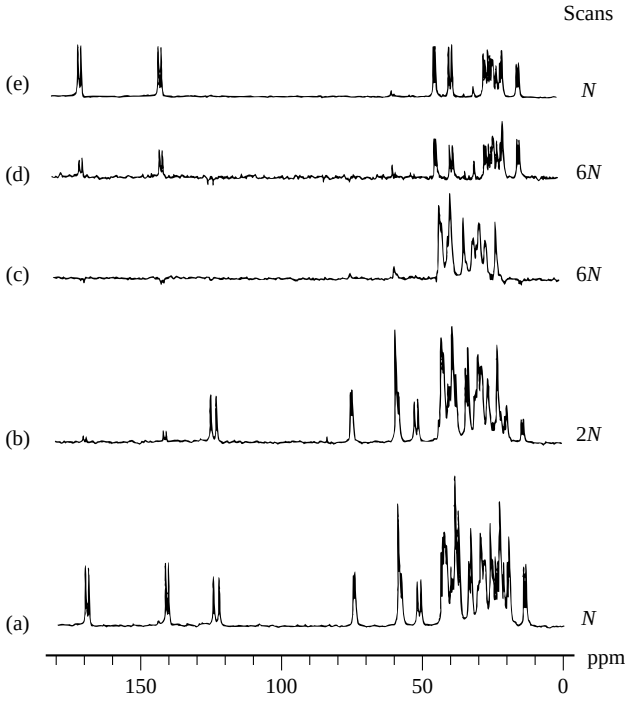

Figure 2 Data from a spectral editing experiment on cholesteryl acetate. (a) Normal CP spectrum for comparison. (b) SCP spectrum. (c) SCPPI spectrum. (d) SCPD spectrum. (e) LCPD spectrum. In practice larger numbers of scans are acquired for the lower signal-to-noise experiments as indicated in the figure

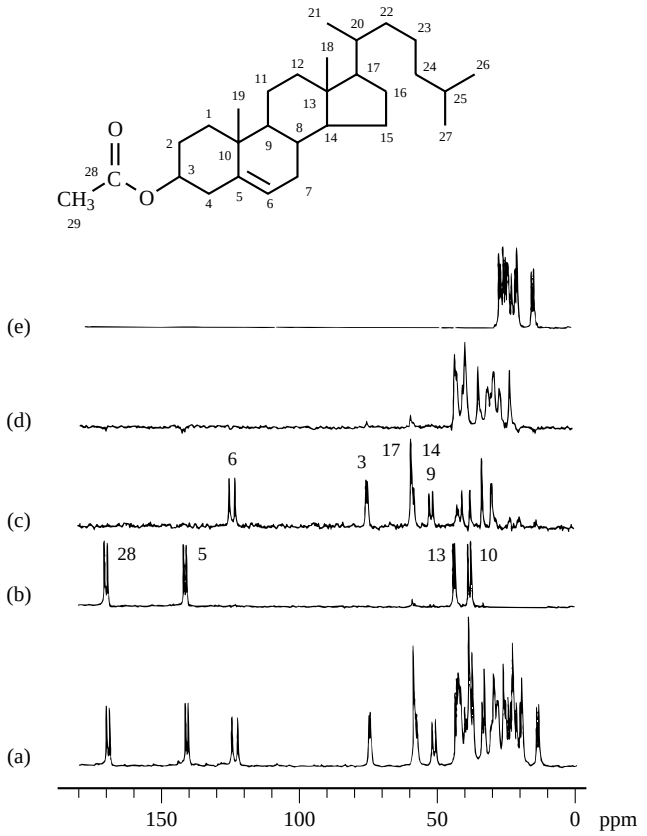

Figure 3 Subspectra constructed from the data in Figure 2. (a) Normal CP MAS spectrum again for comparison. (b) CH_0-only. (c) CH_1-only. (d) CH_2-only. (e) CH_3-only. Some of the assignments made possible by the editing technique are given in the inset

4 EXPERIMENTAL CONSIDERATIONS AND CAVEATS

Except for the simplest approaches to spectral editing in solids, one must pay some extra attention to the experimental setup. In particular, very high MAS spin rates and rf inhomogeneity can adversely affect the CP dynamics relied upon in most methods. The sharpening of the Hartmann–Hahn condition, and the need to match typically on a sideband condition, $\omega_1 = \omega_2 + \omega_r$, makes a homogeneous rf field more important than in a standard CP MAS experiment. Good experimental practice requires stable rf levels, restricting the sample to well within the rf coil, and a stable spin rate. For experiments utilizing short CP, PI, or depolarization periods, additional modifications that make the matching condition less sensitive are needed. Our group has found the simultaneous phase inversion method[1,14,15] easy to incorporate in editing schemes. The pulse sequences in Figure 1 utilize this approach to make the results much less sensitive to how well the matching condition is set and maintained throughout the experiment.

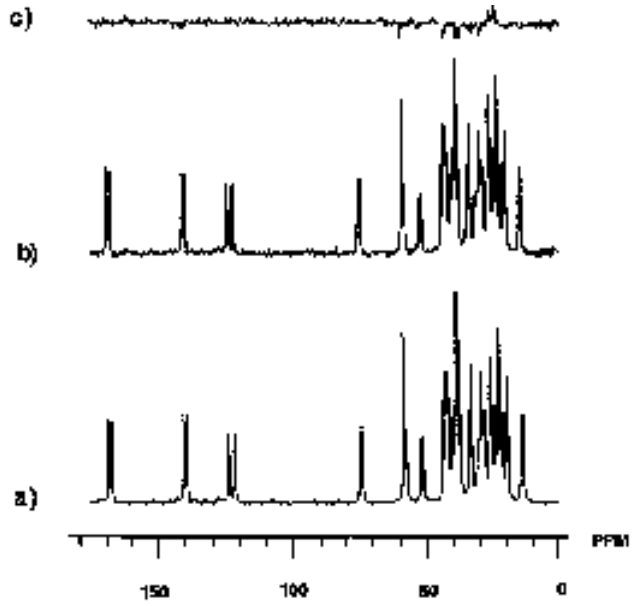

Figure 4 Comparison of the (a) normal CP MAS spectrum and (b) the synthetic one produced by direct summation of the subspectra in Figure 3(b)–(e). (c) The difference between the normal and synthetic CP MAS spectra

When spectra are to be combined in an editing procedure, it is also important to consider rf heating, droop in the rf levels, and $T_{1\rho}$ relaxation. Whenever possible, it is a good practice then to keep the rf fields on for comparable periods of time in the different experiments to be combined. The sequences in Figure 1 have been constructed to take these additional complications into account. Table 2 gives the set of delays in reference to Figure 1 that have been found to give optimal performance in editing applications on rigid solids at moderate fields and MAS rates. These parameters have been used and tested in applications to many coals and polymers as well as on model systems.

Methods which employ homonuclear decoupling sequences require additional care in spectrometer alignment. For these methods one must more carefully adjust all rf levels, and pay especial attention to rf homogeneity. In practice one must follow the same procedures as used to prepare for a ^{1}H CRAMPS experiment. Similar complications from the interaction of the MAS and the MPD also occur as found in CRAMPS.

The majority of the methods that have been discussed here rely on differences in the dipolar coupling networks found between the various CH_n groups. These are washed out when there is significant motional averaging, and as such all of these methods have limitations. On the other hand, such motional narrowing has many signatures which are easy to recognize, and provides another means of discriminating between resonances in a complex spectrum. When very fast MAS rates are employed, the spin dynamics also change.[17] Most methods presented here work best at low to moderate MAS rates (5 kHz or below). Additional complications can arise at high fields because of the CSA spinning sidebands. Since different molecular orientations with respect to the rotor contribute more intensity to some sidebands than others, the inhomogeneous nature of the CP dynamics can be accentuated. Under many editing schemes the center and sidebands can then behave differently, complicating analysis. In the light of these difficulties, most applications to complex systems have employed low field operation ($B_0 < 4$ T). Additional work is needed to delineate how high-field and high-speed MAS operation can be accommodated with the majority of these methods.

Table 2 Delay Parameters for Spectral Editing

	Delay (μs)				
Experiment	$\tau_{SL}{}^I$	$2\tau_{CP}$	$2\tau_{PI}$	$\tau_{SL}{}^S$	τ_D
LCP	140	1500	0	400	0
SCP	1600	40	0	400	0
SCPPI	1600	40	35	365	0
SCPD	1600	40	0	300	100
LCPD	140	1500	0	300	100

5 SUMMARY

At present there are many methods available for distinguishing CH_3 + CH_0 groups from CH and CH_2 centers in CP MAS spectra. A number of reliable approaches for separating CH and CH_2 groups have also appeared, and some of these have been combined in complete spectral editing protocols which separate resonances by multiplicity. These methods have many applications in organic geochemistry and polymer science. Further advances are required before most of these techniques can be combined with operation at the highest available field strengths and spin rates.

6 RELATED ARTICLES

CRAMPS; Cross Polarization in Rotating Solids: Spin-1/2 Nuclei; Cross Polarization in Solids; Fossil Fuels; Heteronuclear Assignment Techniques; INEPT; Magic Angle Spinning; Quantitative Measurements; Rotating Solids; Solid State Probe Design; Spin Echo Spectroscopy of Liquid Samples.

7 REFERENCES

1. X. Wu, S. T. Burns, and K. W. Zilm, *J. Magn. Reson. Ser. A*, 1994, **107**, in press.
2. R. Sangill, N. Rastrup-Andersen, H. Bildsøe, H. J. Jakobsen, and N. C. Neilsen, *J. Magn. Reson. Ser. A*, 1994, **107**, 67.
3. T. Terao, H. Miura, and A. Saika, *J. Chem. Phys.*, 1981, **75**, 1573.
4. H. Miura, T. Terao, and A. Saika, *J. Chem. Phys.*, 1986, **85**, 2458.
5. M. Alla and E. Lippmaa, *Chem. Phys. Lett.*, 1976, **37**, 260.
6. M. G. Munowitz and R. G. Griffin, *J. Chem. Phys.*, 1982, **76**, 2848.
7. L. B. Alemany, D. M. Grant, R. J. Pugmire, T. D. Alger, and K. W. Zilm, *J. Am. Chem. Soc.*, 1983, **105**, 2133.
8. G. W. Webb and K. W. Zilm, *J. Am. Chem. Soc.*, 1989, **111**, 2455.
9. N. K. Sethi, *J. Magn. Reson.*, 1991, **93**, 265.

10. X. Wu, S. Zhang, and X. Wu, *Chem Phys. Lett.*, 1989, **162**, 321.
11. X. Wu, S. Zhang, and X. Wu, *J. Magn. Reson.*, 1988, **77**, 343.
12. M. T. Melchior, *22nd Exp. NMR Conf., Asilomar, CA, March 1991*, poster B-29.
13. J. S. Hartman and J. A. Ripmeester, *Chem. Phys. Lett.*, 1990, **168**, 219.
14. D. P. Burum and A. Bielecki, *J. Magn. Reson.*, 1991, **95**, 184.
15. X. Wu and K. W. Zilm, *J. Magn. Reson., Ser. A*, 1993, **104**, 119.
16. X. Wu and K. W. Zilm, *J. Magn. Reson., Ser. A*, 1993, **102**, 205.
17. X. Wu and K. W. Zilm, *J. Magn. Reson., Ser. A*, 1993, **104**, 154.

Acknowledgments

I wish to acknowledge the especially important contributions of two of my colleagues in this field. The first is Dr Gretchen Webb, my first graduate student, who was instrumental in working out 2D MAS SLF methods for editing, as well as developing much of the hardware that still makes these experiments work so well in our laboratory. The second is Dr Xiaoling Wu, my long-time associate, collaborator, and friend. It is because of Xiaoling's experimental acumen and theoretical insight that our laboratory has been able to contribute so successfully to the development of spectral editing methods for solids.

Biographical Sketch

Kurt W. Zilm. *b* 1955. B.S., 1976, Ph.D., 1981, University of Utah. Introduced to NMR by D. M. Grant. Faculty in Chemistry Yale University, 1983–present. Approx. 80 publications. Research interests: theory and development of NMR techniques for solving problems of chemical interest, studies of transition metal polyhydrides, supported metal catalysts, matrix-isolated organic intermediates and metal clusters, applications of optical pumping in gas phase NMR, tunneling in NMR, dipolar demagnetizing field effects in NMR and development of new solids NMR techniques for structural studies in polymers and organic geochemistry.

Stereochemistry and Long Range Coupling Constants

Ted Schaefer

University of Manitoba, Winnipeg, MB, Canada

1	Introduction	1
2	Stereochemistry	1
3	The Coupling Constant Between Nuclei	2
4	$^nJ(n \geq 4)$ in Saturated Molecules	4
5	$^nJ(n \geq 4)$ in Unsaturated Molecules	5
6	Aromatic Molecules	7
7	Proximate Long Range Coupling Constants	9
8	The Future of Long Range Coupling Constants	10
9	Related Articles	10
10	References	10

1 INTRODUCTION

Stereochemistry (from the Greek *stereos*, meaning 'solid'), the three-dimensional architecture of molecules at the atomic level, underlies our world of appearances, from the grit of grains of sand to the intricacies of an infant's hand. It is a tenet that the macroscopic properties of solids are a consequence of this architecture. It is also thought that the myriad of chemical transformations depends in a subtle way on stereochemistry; the living cell, a microscopic center for the chemical reactions essential to life, depends on stereochemistry for the 'recognition' of one molecule by another during the initiation of reactions which, in turn, produce molecules whose biological utility again has an exquisite dependence on their architecture. Such are the working hypotheses at the root of an enormous effort to establish the stereochemistry of animate and inanimate materials.

NMR is playing an important role in this quest—witness the ubiquity of NMR spectrometers in chemical laboratories. One stereosensitive property of a molecule is the scalar interaction between magnetic nuclei ^nJ, in which n represents the number of intervening chemical bonds; n can run from unity, in all molecules, to at least 14 in some molecules (see ***Indirect Coupling: Theory and Applications in Organic Chemistry***). For $n \geq 4$, ^nJ is often relatively small. As the resolution of NMR spectra improved, the presence of such long range coupling constants became clear and their relationship to stereochemistry became a subject of study. Among the earliest theoretical and experimental investigators of this topic were F. A. L. Anet, M. Barfield, A. A. Bothner-By, D. M. Grant, H. Günther, R. A. Hoffman, H. S. Gutowsky, G. J. Karabatsos, M. Karplus, J. Meinwald, and H. M. McConnell. Barfield has been particularly active over a long period in providing theoretical stimulation to experimentalists. A number of extensive reviews[1–8] of the theory of long range coupling constants and their stereochemical applications are recommended.

The aim of this article is to provide an overview of the utility of long range coupling constants in stereochemical analysis. A very brief discussion is given of stereochemical concepts, followed by a heuristic description of the origins of ^nJ, which is elaborated by specific examples drawn mainly from organic chemistry. This choice is dictated by the available space and is also colored by personal taste. Apologies are in order to those authors whose work may well have been cited. Only a few of the thousands of long range coupling constants can be included; even if only the more familiar NMR-active nuclei (^{1}H, ^{13}C, ^{19}F, and ^{31}P) were included for $4 \leq n \leq 12$, then the variety of chemical bonding patterns would require a substantial book for an adequate discussion.

2 STEREOCHEMISTRY

The electrons in a molecule move with speeds near a million meters per second and therefore traverse the space of a moderately sized molecule about a thousand million million times in one second. In so doing, the electrons tie the very small but relatively massive nuclei into a floppy, pulsating, rotating object, which is stable at ambient temperatures. At certain distances between the nuclei, the Coulombic forces of attraction between the nuclei and electrons outweigh those of repulsion between nuclei and between electrons. For nearest-neighbor nuclei these distances are called 'bond lengths'; intuition is correct in suggesting that the electrons tend to concentrate in the regions between neighboring nuclei. If two electrons undergo this concentration one has a single bond, if four, a double bond, and so forth.

The diversity of molecular size and shape is breathtaking. The diatomic oxygen molecule, so necessary to our very existence, contains two nuclei and sixteen electrons. A small diamond, also thought necessary by some, is a single molecule containing some 10^{22} nuclei and six times as many electrons. When diamond burns in oxygen, one obtains the linear, triatomic molecule, carbon dioxide, which is considered obnoxious, yet is essential for photosynthesis. One of the aims of modern experimental and theoretical chemistry is the elucidation of the detailed shapes of these various three-dimensional objects, i.e. their stereochemistry.

Consider a tetra-atomic molecule ABCD. In (**1**), the four different nuclei are connected in a unique way: A is attached to B by a single bond and not to C, and so forth. This connection scheme defines the *connectivity* or *constitution* of the molecule and represents the first step in the stereochemical description. The angles between the internuclear vectors, A–B and B–C, for example, are called 'bond angles'. An important angle θ, the torsion or dihedral angle between the two planes containing ABC and BCD, defines the *configuration* or the *conformation* of the molecule. If a very large energy input is needed to interconvert (**1**) and (**3**), i.e. if the thermal kinetic energy (motion of the molecules through space may lead to a collision in which one molecule receives energy from another) is small compared to the energy needed to twist (**1**) into (**3**), or vice versa, then one may speak of two configurations of the molecule, or of *configurational isomers*. If you have configuration (**1**) and, some time later, say days, (**1**) has not turned even partially into (**3**), even under heat, then you may speak of configuration. Often, such a situation requires a double bond between C and D, indicated by two strokes (double bond), and one refers to 'breaking the double bond' during configurational isomerization. If the energy needed

to interconvert (**1**) and (**3**) is not large compared to the thermal energies, then the sample of the substance ABCD may well contain appreciable amounts of (**1**) to (**3**). One has an equilibrium among conformational isomers or *conformers*. The relative amounts, or populations, of the conformers usually change as the temperature changes.

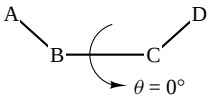

(**1**)

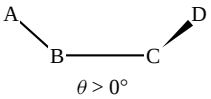

(**2**)

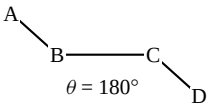

(**3**)

The two terms 'configuration' and 'conformation' relate to the human timescale. Near absolute zero in temperature, there would be little need for both terms; one would suffice in most instances. It all depends on the flexibility or floppiness of the molecule. A certain care is therefore needed in the description of the stereochemistry of a molecule. If the energy barrier to interconversion among (**1**) to (**3**) is small, then ABCD takes on all conformations, defined by θ, with similar probabilities. All angles from 0° to 180° are then significantly represented in the sample (ensemble). A molecule's reactivity, how it combines with other molecules to form one or more product molecules, and how rapidly it does so, can depend strongly on its conformation/configuration; this is one reason for the study of stereochemistry.

A complete stereochemical description requires precise values of bond lengths and bond and torsion angles, preferably with a potential function describing the energy of a molecule as a function of θ. Furthermore, because the molecule vibrates (pulsates), a knowledge of all the other vibrational motions, such as bond stretches and bond angle deformations, together with their frequencies and amplitudes, is desirable. Finally, a map of the electron density, at least up to distances of 10^{-9} m from the molecular periphery, is also needed.

Needless to say, a variety of experimental and theoretical techniques is necessary for these purposes. Most techniques utilize the fact that rotational, vibrational and electronic energies of molecules are quantized and directly related to the stereochemical properties. The energies, or at least their differences, can be ascertained by stimulating transitions between the various states of different energies with the photons available from electromagnetic radiation. Other methods scatter the photons from the molecule in the gas or solid and, from interference patterns formed by the scattered photons, deduce electron densities and, by inference, the sites of the nuclei.

NMR techniques, by way of contrast, use the magnetic properties of nuclei and their magnetic interactions with other nuclei and/or electrons to deduce molecular stereochemistry. The magnetic interactions between the nuclei and electrons in molecules are about a million times smaller than the electrostatic interactions which actually determine the stereochemistry. Therefore, at first sight it appears unreasonable to focus on the magnetic interactions as a source of stereochemical information. After all, the magnetic dipole moment of the nucleus is only weakly coupled to the very forces which mould the molecular shape. Paradoxically, it is this fact which allows NMR to be perhaps the single most general tool for stereochemical analysis. The magnetic field $\boldsymbol{B}_0$ of the NMR spectrometer penetrates the molecular space almost unaltered and orients the magnet moment of the nucleus into certain definite directions. Under certain conditions the magnetic interactions between the nuclei and between the nuclei and the electrons appear as perturbations of the interaction between $\boldsymbol{B}_0$ and the nuclei. As a consequence, the NMR spectrum, whose basic frequency represents the $\boldsymbol{B}_0$/nucleus energy, is somewhat shifted and split into a number of peaks or frequencies. These shifts and splittings, the latter being related to the J values, can be interpreted in terms of stereochemistry.

3 THE COUPLING CONSTANT BETWEEN NUCLEI

The scalar spin–spin interaction energy between two nuclei is represented by $hJ\hat{I}_i \cdot \hat{I}_j$, where $\hat{I}_i$ is the spin angular momentum vector operator of nucleus i. Because the magnetic moment μ is proportional to $\hat{I}$, J is also proportional to the product of the two nuclear moments (see ***Nuclear Spin Properties and Notation***). In this article, J is given in units of hertz. The dot, or scalar, product in the expression above applies to molecules in the isotropic liquid or gaseous states. It depends on the relative orientations of the two spins, not on their positions in space. Therefore J is unchanged by molecular reorientations, unlike the dipolar interactions which average to zero during such reorientations (see ***Dipolar and Indirect Coupling Tensors in Solids***). The directions of the nuclear spins are only very slightly coupled to the orientation of the molecule in space, but are coupled to $\boldsymbol{B}_0$. The scalar interaction modifies this latter coupling by definite amounts, proportional to J, and hence appears in the fine structure of the NMR spectrum. Figure 1 shows the ^{1}H NMR spectrum of the methyl protons of 1-phenylpropyne (**4**). In the absence of J only a single peak would occur; instead there exist many peaks arising from $^{6,7,8}J$, long range proton–proton coupling constants, over six, seven and eight formal bonds (n = 6, 7, 8). The long range coupling constants can be extracted by standard procedures (see ***Analysis of High-Resolution Solution State Spectra***).

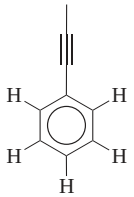

(**4**)

How does J come about? Consider a hydrogen atom. In addition to the electrostatic attraction between the electron and the proton, an energy of 13.6 eV, there exists a magnetic interaction of 6.0×10^{-6} eV (the hyperfine interaction, that is, very small), which aligns the spins of the proton and

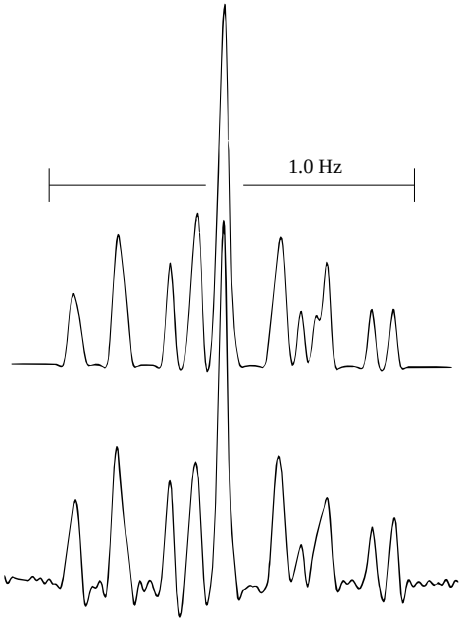

Figure 1 The ^{1}H NMR spectrum at 300 MHz of the methyl protons of 1-phenylpropyne ($C_6H_5C{\equiv}CCH_3$) as a dilute solution in acetone-d_6 at 300 K, has a linewidth at halfheight of somewhat less than 0.03 Hz. The upper, theoretical, spectrum comes from a precise spectral analysis and has the long range coupling constants ^6J(**H**,C**H**$_3$), ^7J(**H**,C**H**$_3$), and ^8J(**H**,C**H**$_3$) of −0.298(1), 0.145(1), and −0.254(1) Hz, respectively. (Reproduced with permission of The National Research Council of Canada from T. Schaefer, R. Sebastian, and R. W. Schurko, *Can. J. Chem.*, 1992, **70**, 2365)

electron in an antiparallel fashion, as in (**5**). Mutual flips of these alignments give rise to radiation at 1420 MHz which is detectable in radioastronomy, exemplifying the underlying unity of the natural sciences. The hyperfine interaction operates when the electron is very near the proton (the contact interaction).

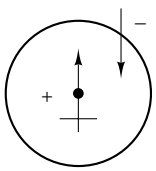

(**5**)

3.1 A Model of ^1J

Now consider the hydrogen molecule (**6**). Because the electrostatic energies ensure the antiparallel spin alignment of the two electrons (paired off, singlet state), a consequence of the quantum properties of small particles, the contact interaction favors the overall spin orientations shown in (**6**). The nuclear spin is said to 'spin polarize' the electrons in the sense that—although the net electron spin in the bond, 'down' minus 'up', is zero when averaged over the space of the bond—at the left of the bond in (**6**) there occurs more 'down' than 'up' spin, and vice versa on the right. The net result is that an antiparallel arrangement, defining a positive J, of the proton spins (crossed arrows) is favored by about 10^{-12} eV. This magnetic energy is tiny compared with the electrostatic energies yet, paradoxically, is easily measured by NMR. In the hydrogen molecule, J is 280 Hz or 1.1×10^{-3} kJ mol^{-1}, which is miniscule compared with the bond energy of 460 kJ mol^{-1}. It is clear that J, transmitted via the electrons, is proportional, at each end of the coupling path, to the size of the magnetic moment of the nucleus and, therefore, to the product of the two nuclear magnetic moments.

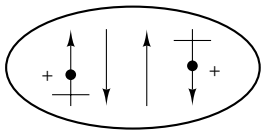

(**6**)

J is a second-order property of the molecule in the sense that it results from the product of two first-order interactions; here, two contact interactions. In another sense, because that contact interaction perturbs the ground state molecular wavefunction, the theoretical computation of J must take this perturbation into account; it does so by mixing electronically excited states into the ground state in a complicated fashion. Hence the quantitative computation of J from first principles is not easy (see ***Indirect Coupling: Theory and Applications in Organic Chemistry***). In the present article, qualitative models of ^nJ, $n \geq 4$, which nevertheless can be made semiquantitative, are used to illustrate its stereochemical applications. As will be seen, the torsional dependence of J can sometimes be ascertained by empirical methods which allow rather precise stereochemical conclusions.

3.2 Models of ^2J and ^3J

In (**7**), a pair of protons separated by two formal bonds, as in a CH_2 fragment of a molecule, is indicated to have a negative ^2J. The coupling mechanism favors a parallel orientation of the proton spin vectors. This is so because the two electrons, in different bonds but near carbon, have a lower electrostatic energy if their spins are parallel than if they are antiparallel. The lower energy, an illustration of Hund's rule, is probably a consequence of the fact that these two electrons move in such a way that they are attracted more strongly by the carbon nucleus when their spins are parallel—the spin serves as a sort of traffic policeman, one electron tending not to get between the other electron and the nucleus. The picture in (**7**) is called the 'Dirac vector model' of ^2J, predicting a negative value, for example, in methane, where ^2J is indeed −12.4 Hz. However, ^2J(H,H) is positive in some molecules. This failure of the model is shared by another kind of model, which is now illustrated for ^3J.

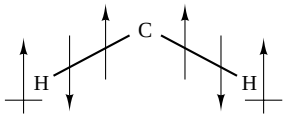

(**7**)

The HCCH or ethanic fragment in (**8**) is the prototype of an important class of vicinal or ^3J interactions (***Vicinal Coupling Constants and Conformation of Biomolecules***). The Dirac vector model correctly predicts a positive ^3J, but it cannot account for its dependence on the torsion angle θ in (**9**). In fact, it is a direct interaction (not a dipolar interaction, which is also sometimes called 'direct') between the electrons in the two C–H bonds which is important in correlating the electron, and hence the proton, spins. The direct interaction, proportional to valence bond exchange integrals, is minimal when the two C–H bonds lie in mutually perpendicular planes ($\theta = 90^\circ$). An acquaintance with trigonometry, together with the constraint that ^3J be positive, suggests that the θ dependence between 0° and 180° is mainly on $\cos^2\theta$, and perhaps slightly on $\cos\theta$. This is indeed true. The stereochemical significance is obvious. Note that the 'through bond' mechanism, as in (**8**), is relatively unimportant.

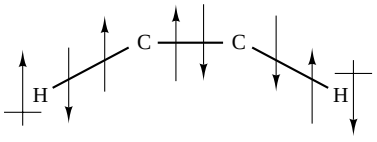

(**8**)

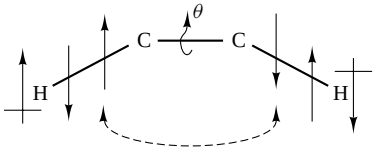

(**9**)

This manner of argument implies that geminal spin correlations, as in (**7**), could combine with vicinal spin correlations, as in (**9**), to yield long range coupling constants ^nJ ($n \geq 4$) in larger molecular fragments and is therefore related to their geometrically extended stereochemistry. This is also true. One drawback concerns the magnitude of long range coupling constants. Generally speaking, for saturated fragments (single bonds) the magnitude decreases as n increases, simply because ^nJ arises either from the product of small interactions of the kind shown in (**8**) and (**9**), or because the direct interaction between bonds decreases with their separation; the bond exchange integrals (interactions) giving rise to spin correlation between electrons in different bonds depend on interelectronic distances in these structures. In (**9**), ^3J is of the order of 10 Hz at $\theta = 0^\circ$ or 180°, whereas ^4J has a magnitude of about 1 Hz in the propanic fragment below. Note that at least some deviation from perfect pairing is necessary for a finite J. However, for unsaturated molecules, in which extensive electron delocalization occurs, ^nJ can be sizeable and does not necessarily drop off monotonically as n increases. As an extreme example,[10] ^{14}J(F,F) in (**10**) is 0.2 Hz in magnitude.

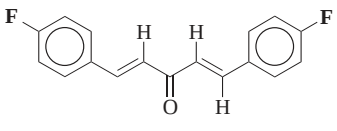

(**10**)

4 $^nJ(n \geq 4)$ IN SATURATED MOLECULES

In the propanic fragment (**11**) to (**14**), direct and indirect mechanisms can contribute to ^4J(H,H). The direct mechanisms are important[11] in conformations (**12**) and (**13**). In (**12**), the two C–H bonds are proximate in space and $1 \rightarrow 3$ interactions are important. Coupling constants arising in this way are often called 'through space', which is a misnomer because the molecule itself is largely empty space; perhaps, 'proximate' ^nJ would be a better name. In (**13**), an all-*trans* or zig-zag conformer, there is a direct interaction between the orbitals on the carbon atoms (rear lobes) to which the coupled protons are bonded, resulting in a relatively large positive ^4J(H,H). Indirect mechanisms are associated with $1 \rightarrow 2'' \rightarrow 3$ and $1 \rightarrow 2''' \rightarrow 3$, vicinal–vicinal, and with $1 \rightarrow 2 \rightarrow 3$ or $1 \rightarrow 2' \rightarrow 3$, geminal–vicinal, interactions in (**11**); the latter are difficult to evaluate. The indirect mechanisms can contribute to ^4J(H,H) with either sign, so that ^4J(H,H) can be positive or negative,[11] depending on the dihedral angles θ and $z\theta'$. In (**14**), the value of ^4J(H,CH_3) is large, corresponding to $\theta = 180^\circ$.

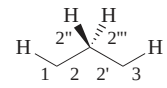

(**11**)

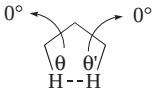

(**12**)

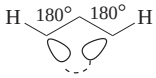

(**13**)

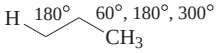

(**14**)

A recent analysis (Schaefer et al., 1993) of the ^{1}H NMR spectrum of 2-phenyl-1,3-dithiane, (**15**), illustrates the stereochemical dependence of ^4J(H,H). The approximate torsion (dihedral) angles are given in (**15**). Note the positive shift of ^4J(H,H) as HCSCH, containing the heteroatom, sulfur, replaces the propanic fragment. A heteroatom attached to the propanic fragment can also alter ^4J. Such substituent perturbations complicate stereochemical assignments and present challenges to the theorist [in fact, the positive shift noted for (**15**) can be reproduced with the INDO MO FPT formalism,[12] which takes a number of coupling mechanisms into account]. In principle, ^4J(H,H) is useful in the stereochemical analysis of other six-membered alicyclic rings which can occur in sugars and steroids, for example. Another example is provided[13] by the five-membered ring in the anhydronucleoside (**16**). The signs and magnitudes of ^4J(H,H) are related to torsion angles[14] in the furanose ring. Also, coupling constants over five bonds exist between H-1′ and the methylene protons in (**16**).

As the molecular mass increases, the ^{1}H NMR spectra become very complex and the peak widths also increase due to unresolved long range coupling constants and to shorter relaxation times. Nevertheless, the presence of ^4J(P,H), as in the nucleotide (**17**) and whose magnitude is determined[15] by the geometry of the P–O–C-5′–C-4′ fragment, allows[15] the assessment of ^3J(H-4′,H-5′) and ^3J(H-4′,H-5″) in a double-helical dodecanucleotide (a DNA fragment). The vicinal coupling constants help in fixing the torsion angle in the fragment O–C-5′–C-4′–C-3′.

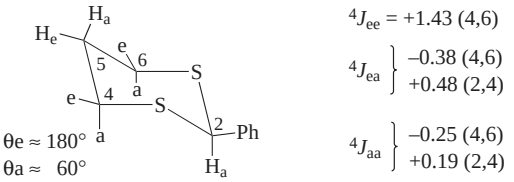

(15)

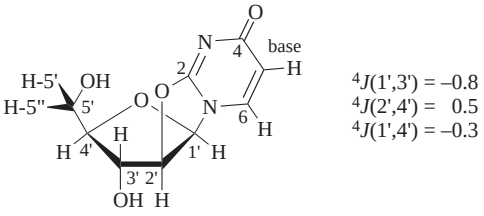

(16)

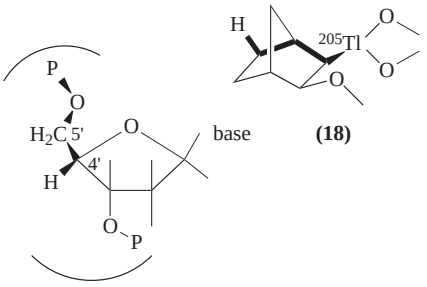

(17)

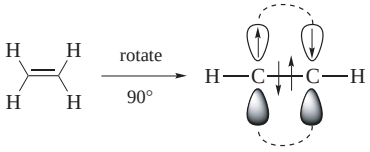

(19)

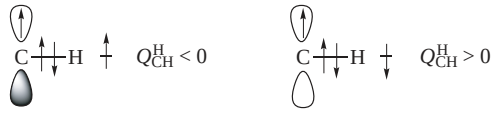

(20) **(21)**

In rigid bicyclic systems,[5] extended or multiple, all-*trans*, coupling pathways can exist, so that $^{4,5,6}J$(H,H) can be large [propanic (**11**), butanic, and pentanic paths]. Furthermore, C–H, F–H, P–H, F–F, Tl–H, and C–C long range couplings are known in such molecules; some of these are large for conformations analogous[16] to (**12**) (proximate couplings). Many are tens of hertz in magnitude, or even as large[17] as 820 Hz as in (**18**), a norbornane derivative; the electron density at the thallium nucleus is very large for this nucleus of atomic number 81.

5 $^nJ(n \geq 4)$ IN UNSATURATED MOLECULES

5.1 Alkenes and Acetylenes: σ, π Model

In unsaturated molecules such as alkenes and acetylenes the valence electrons are usually considered to be of two different types: σ and π electrons. Thus, in planar ethylene (**19**), the double bond between the carbon atoms is thought of as a single σ bond and a single π bond; the latter is formed from electrons in p orbitals on the carbon atoms and yields maximum electron density above and below the plane of the molecule (the six nuclei lie in a plane in the most stable state of the molecule). This σ, π model has been very successful in the description of long range coupling constants although, again, it is a topic of critical discussion.[18]

The σ, π model of ^nJ begins with the recognition that the contact contribution depends on the probability that the electrons, involved in the transmission of ^nJ, are found at the sites of the coupled nuclei; the protons in ethylene, for example. However, electrons in π orbitals have a zero probability of being found at the nuclear sites—p orbitals have nodes in the plane of the nuclei.

This conundrum is resolved by the invocation of a σ, π spin polarization mechanism, rather similar to that involving the σ electrons in (**7**). The single p or π electron in (**20**) and (**21**) spin polarizes the σ electrons in the C–H bond and leads to an 'up' or a 'down' arrangement of the proton spin (crossed arrow). By Hund's rule, (**20**) is energetically favored. This fact is represented by the σ, π hyperfine interaction parameter $Q^{\mathrm{H}}_{\mathrm{CH}} < 0$ (in the subscript the first symbol represents the atom carrying the unpaired spin, the two subscripts together indicate the bond being spin polarized, and the superscript designates the nucleus coupled to the unpaired electron). $Q^{\mathrm{H}}_{\mathrm{CH}}$ is negative by definition—the p electron and the proton spins are parallel. Consolidation of this fact with the bonding in ethene (**22**) where the π electrons are spin correlated (paired off), leads to a π electron spin coupling pathway as shown, in addition to that through the σ bond. It is then found that $^3J^{\pi} \propto Q^{\mathrm{H}}_{\mathrm{CH}} \times Q^{\mathrm{H}}_{\mathrm{CH}}$, yielding about +1.5 Hz, which adds to $^3J^{\sigma}$ which is an order of magnitude larger, to give $^3J^{\pi} + {}^3J^{\sigma}$.

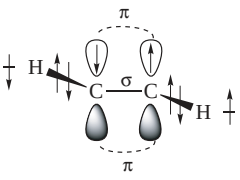

(22)

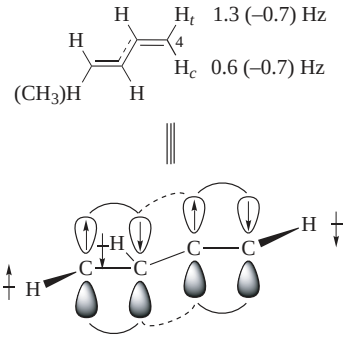

(23)

Now, consider butadiene (**23**). The bond between the middle carbon atoms is not a single bond but has considerable 'double-bond character'; it is said to have a mobile bond order between zero and one, a result of the relatively easy delocalization of π electrons (unlike σ electrons). The magnitude of $^5J^{\pi}$ depends on how strongly the p electrons at the central carbon atoms [dashed lines in (**23**)] are spin correlated. The

hyperfine interaction at each end of the coupling pathway provides the link between the σ and π electron systems. Note that $^5J^\pi > 0$, the proton spins in (**23**) being antiparallel, even though $Q^{\mathrm{H}}_{\mathrm{CH}} < 0$. The sign of J^π depends on the number of intervening bonds, being positive for n odd and negative for n even. Note also that this mechanism implies equal ^5J(H,H) values in (**23**), i.e. the values are independent of the configuration at C-4. The observation that ^5J_t is 1.3 Hz whereas ^5J_c is 0.6 Hz implies a contribution to ^5J_t from the σ electrons, $^5J^\sigma$. The coupling mechanisms discussed above for ^4J(H,H) allow for two vicinal–vicinal interactions involving the central C–C bond in each and thus are expected to contribute most efficiently for an all-*trans* arrangement of the intervening bonds [extend structure (**13**)].

An estimate of $^5J^\pi$ can be made using the 'methyl group replacement technique', the use of which involves the following argument. In (**24**), a proton in one C–H bond of a methyl group has a positive hyperfine interaction $Q^{\mathrm{H}}_{\mathrm{CCH}} \rangle 0$ with the electron in the p orbital on the neighboring carbon atom [a so-called β-interaction, contrasting with the α-interaction in (**20**)]. Furthermore, $Q^{\mathrm{H}}_{\mathrm{CCH}} \propto \sin^2\theta$ so that $Q^{\mathrm{H}}_{\mathrm{CCH}}$ is largest when the sigma C–H bond lies in the plane containing the p orbital (best overlap). For a rotating methyl group, with three C–H bonds, $\sin^2\theta$ has an average value of 0.5.

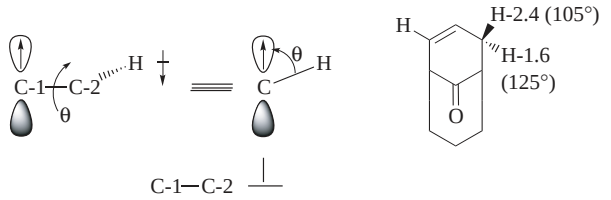

(24) **(26)**

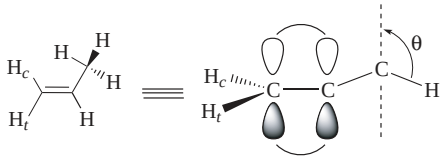

(25)

It then turns out that $Q^{\mathrm{H}}_{\mathrm{CCH}} \approx -Q^{\mathrm{H}}_{\mathrm{CH}}$, with the consequence that $^6J^\pi$(H,CH_3) $\approx -\ ^5J^\pi$(H,H). From the data on (**23**) it follows that $^5J^\pi \approx 0.7$ Hz and $^5J^\sigma \approx 0.6$ Hz. The model is not exact, of course, but has been used to estimate π electron contributions to ^nJ in a variety of molecules, including cumulenes ($CH_2{=}C_n{=}CH_2$) and acetylenes [HC–$(C{\equiv}C)_n$–CH]. In such molecules, the extended spin correlation of the π electrons is relatively high,[2] leading to significant ^nJ for n as large as 9. Note that, as the mobile bond order of the central C–C bond in (**23**) decreases (dashed lines), $^5J^\pi$ will also decrease in magnitude. In this sense $^nJ^\pi$ is a measure of π electron delocalization: the mobile bond order in ethene (**22**) is unity, is about 0.4 for the central C–C bond in (**23**), and is less than unity for the other two C–C bonds. The use of ^nJ(H, CH_3) in testing the extent of delocalization in various molecules is described in a later section of this article.

5.2 Allylic and Homoallylic Couplings: ^4J(H,H) and ^5J(H,H)

The $\sin^2\theta$ dependence of $Q^{\mathrm{H}}_{\mathrm{CCH}}$ has many stereochemical applications, only two examples of which can be given here. ^4J_c(H,CH_3) $\equiv\ ^4J_c$ and ^4J_t(H,CH_3) $\equiv\ ^4J_t$ in propene (**25**) are called 'allylic coupling constants' and have values of -1.7 and -1.3 Hz, respectively. If the σ component of ^4J were to vanish and the conformation of the methyl group was exactly the same as that in (**25**), but with rapid interconversion so that each C–H bond sampled each of the three values of θ (namely 0°, 120°, and 240°), then $\langle\sin^2\theta\rangle$, the average value of $\sin^2\theta$, would be 0.5. Actually, for free rotation of the methyl group, $\langle\sin^2\theta\rangle$ is also 0.5, a consequence of the three-fold symmetry of a methyl group (a CH_2X group has lower symmetry, with important consequences for the derivation of internal rotational potentials, as described below). It would follow that ^4J is a measure of the magnitude of $^3J^\pi$ in ethene ($Q^{\mathrm{H}}_{\mathrm{CH}} \approx -Q^{\mathrm{H}}_{\mathrm{CCH}}$).

However, because in (**25**) $^4J_c \neq\ ^4J_t$, the argument is only semiquantitative. The inequality may be attributable to the presence of $^4J^\sigma$. Thus, if the all-*trans* arrangement [see (**13**)] is most effective for $^4J^\sigma$, giving a positive contribution to ^4J_t, a rough assessment of $^3J^\pi$ in ethene would be +1.7 Hz. The true situation is more complex;[11] nevertheless, large negative ^4J values are expected and observed for $\theta \approx 90°$. An example in which $^4J \propto \sin^2\theta$ is (**26**), where the ratio of the two coupling constants is 1.5, as compared with a ratio of 1.4 for the corresponding values of $\sin^2\theta$. To within the combined errors of the J values and the two angles, the relationship is very likely satisfied.

Homoallylic coupling constants ^5J(H,H) arise from protons in C–H bonds flanking the double bond at both ends. Hence ^5J(H,H) $\propto Q^{\mathrm{H}}_{\mathrm{CCH}} Q^{\mathrm{H}}_{\mathrm{CCH}} \propto \sin^2\theta \sin^2\theta'$, where the two torsional angles θ and θ' are analogous to those in (**25**).

A somewhat subtle stereochemical problem involves the degree of nonplanarity of 1,4-dihydrobenzene (**27a**)–(**27c**). If the equivalent (isoenergetic), nonplanar conformers (**27a**) and (**27c**) are the most stable ones, they may interconvert via the planar conformer (**27b**). The molecule is then said to undergo 'conformational isomerization by inversion'. The potential energy function opposing inversion has two minima, as indicated; the speed of inversion depends on how the available thermal energy compares to the potential hindering the inversion. Alternatively, the most stable conformer may be (**27b**). Then the internal potential has a single minimum; nonplanar conformers occur with decreasing probabilities as the bending angle α deviates increasingly from 180°.

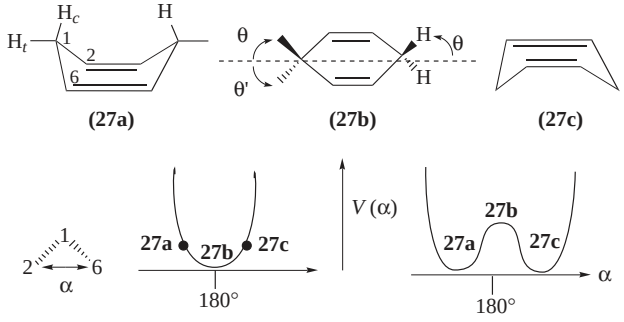

(27a) **(27b)** **(27c)**

In (**27b**), the angles θ and θ' are 60° for an idealized geometry, but are not equal in (**27a**). Hence ${}^5J_c = J_t$ in (**27b**), but ${}^5J_c \neq {}^5J_t$ in (**27a**). In solution ${}^5J_c = 1.2\ {}^5J_t$, from which it might be deduced[19] that α is about 172°. The derivation of α assumes two rigid forms (**27a**) and (**27c**), a so-called 'two-site analysis' in which the measured values of ${}^5J_c$ and ${}^5J_t$ are simple averages of their values in these conformers. However, another interpretation holds that torsion about the C–C bonds of a stable, planar (**27b**), producing nonplanar conformers, would also cause the inequality ${}^5J_c > {}^5J_t$, so that either potential curve could correspond to observation. In fact, today the available evidence from various sources is that (**27b**) is the stable form.

6 AROMATIC MOLECULES

6.1 Some Coupling Mechanisms

In benzene (**28**) the indicated ${}^{3,4,5}J$(H,H) are of obvious use in assigning substitution sites in derivatives of (**28**). ${}^4J$(H,H), corresponding to an all-*trans* arrangement, has only a small π component. The ${}^6J$(**H**,C**H**$_3$) value of −0.60 Hz in toluene (**29**) indicates that ${}^5J$(H,H) in (**28**) is mainly J^π, while the ${}^7J$(C**H**$_3$,C**H**$_3$) value of −0.60 Hz in (**30**) implies $Q^{\mathrm{H}}_{\mathrm{CH}} = -Q^{\mathrm{H}}_{\mathrm{CCH}}$ in these compounds. Furthermore,[20] in (**31**), which represents derivatives of anisole (X = O), thioanisole (X = S), and ethylbenzene (X = CH_2), it is true that ${}^5J$(C,C) = −1.50 ${}^6J$(C,H) + 0.02 and ${}^6J$(C,C) = −0.37 ${}^5J$(C,C) + 0.02. The signs and relative magnitudes of the corresponding hyperfine interaction parameters near C-4, as in (**32**), are then $Q^{\mathrm{H}}_{\mathrm{CH}} = -Q^{\mathrm{H}}_{\mathrm{CCH}}$, $Q^{\mathrm{C}}_{\mathrm{CH}} = -1.50\,Q^{\mathrm{H}}_{\mathrm{CH}}$, and $Q^{\mathrm{C}}_{\mathrm{CC}} = 0.56\,Q^{\mathrm{H}}_{\mathrm{CH}}$. Such relationships also hold for other nuclei in the side chain, such as ^{19}F, typified by (**33**), showing that the π-electron mechanism is dominant for the indicated ${}^{5,6,7}J$ couplings and that they depend on $\sin^2\theta$.

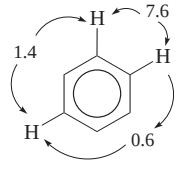

(28)

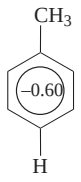

(29)

(30)

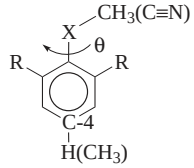

X = O, S, CH_2
R = H, F, Cl, Br

(31)

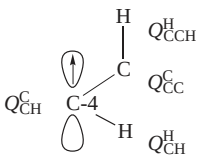

(32)

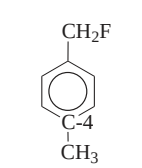

^7J(F, H) = 2.1$_5$
^6J(F, C) = 1.1$_5$
^5J(F, C) = 3.1$_5$

(33)

6.2 Internal Rotational Potentials from Long-Range Coupling Constants

When conformations are well defined, that is when the barrier to interconversion between conformers is large compared to the thermal energies (see Section 1), the angle dependence of a long-range coupling constant is a good indicator of conformation. An example from aromatic chemistry is a benzaldehyde derivative (**34**). ${}^5J$(**H**,C**H**O) is apparently a ${}^5J^\sigma$ and, as such, is large for the all-*trans* pathway. If the indicated J values are correct, then measurement of ^{5}J(**H**,C**H**O) yields the populations of (**34a**) and (**34b**) by simple proportion. This simple strategy works well because nonplanar conformers are negligible at ambient temperatures.

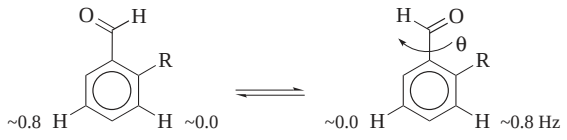

(34a) **(34b)**

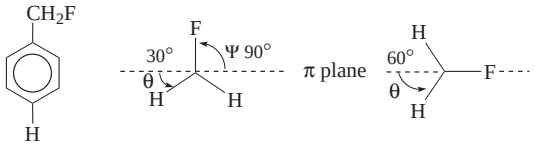

(35a) **(35b)** **(35c)**

Suppose, however, that the barrier to rotation about the ring–CHO bond were very small compared with thermal energies. In such circumstances the idea of one or a few conformations would lose utility because many angles θ would be of similar probability. In the limit of a zero barrier, an infinite number of conformations (all values of θ) would be present.

When the barrier to internal rotation about a bond is small, it is advantageous to discuss stereochemical problems in terms of the internal rotational potential $V(\theta)$, which gives the relative energy of the molecule at each value of θ. Can long range coupling constants be used to determine $V(\theta)$? In some instances, certainly. These statements are best illustrated with one of the many examples available.

Consider benzyl fluoride (**35**) and the potential hindering rotation about the exocyclic C–C bond. If (**35b**) and (**35c**) represent extrema in the potential, the barrier $V(\psi)$ [or $V(\theta)$] is said to be two-fold because it repeats itself twice between 0° and 360° [see (**36**)]. The barrier turns out to be solvent dependent,[21] which is an advantage in the following logic. One has ${}^6J$(F,H) = ${}^6J^{\mathrm{F}}_{90}\langle\sin^2\psi\rangle$ and ${}^6J$(H,H) = ${}^6J^{\mathrm{H}}_{90}\langle\sin^2\theta\rangle$; here ${}^6J_{90}$ is the value when C–F or C–H lies 90° out of the benzene ring plane, and the angle brackets indicate an average over the internal motion controlled by the potential. The roughly tetrahedral geometry at the carbon atom of the CH_2F group implies $\langle\sin^2\theta\rangle = 0.75 - 0.5\langle\sin^2\psi\rangle$. It follows that measurements of the two coupling constants in two different solvents yield both the ${}^6J_{90}$ values as well as $\langle\sin^2\psi\rangle$ and $\langle\sin^2\theta\rangle$ in each solvent. The latter can be calculated[22] by quantum mechanical or classical methods as a function of the internal potential, V_2. A comparison between the theoretical $\langle\sin^2\psi\rangle$, say, and its experimental values yields V_2 in the two solvents. Together with measurements of ${}^5J$(F,C), also a J^π, one finds that V_2 is 3.2 kJ mol^{-1} in very polar solvents and 0.7 kJ mol^{-1} in nonpolar solvents. Curve (a) in Figure 2 describes the potential form. Extrapolation to the vapor phase implies that the potential is now as in curve

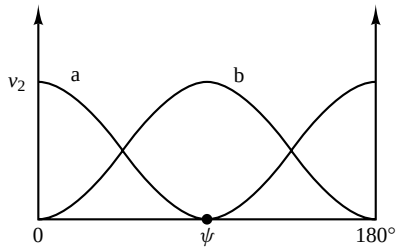

Figure 2 Twofold internal rotational potential, as applicable to (**35b**)

(b) in Figure 2, which is qualitatively confirmed by high-level molecular orbital computations on the free molecule. The change in phase of the potential is of interest in the theory of solutions. A phase change can also be induced by substituents on the ring. Each derivative will possess its own, distinctive, solvent dependent, internal rotational potential, the determinations of which present as yet unmet challenges for the various spectroscopic and theoretical methods (***Liquid Crystalline Samples: Structure of Nonrigid Molecules***).

6.3 Stereospecific Long Range Coupling Constants in Extended Aromatic Molecules

Examples of ^nJ with n as large as 11 are provided by ^nJ(F,F) and ^nJ(F,C) in (**36**) and (**37**). It is known that the torsion angle θ in (**37**) is effectively 90°, the two benzene planes being perpendicular, and that it is near 45° in (**36**). Note that $^{7,8}J$(F,C) and ^9J(F,F) vanish when $\theta \approx 90°$, indicating that π electron spin correlation has been broken across the central C-4–C-5 bond; there is no π electron conjugation or delocalization between the two aromatic moieties in (**37**). The finite values of these ^nJ can be related[23] to $\cos^2\theta$ in (**36**), as can ^{11}J(F,F) when the fluorine atoms in (**36**) are replaced[24] by CH_2F groups. Of course, ^{11}J(F,F) will, in addition, be proportional to $\sin^2\psi$, where ψ is the angle by which the C–F bond turns out of the benzene plane, as in (**35b**); thus $^{11}J(\text{F,F}) \propto \sin^2\psi\cos^2\theta$.

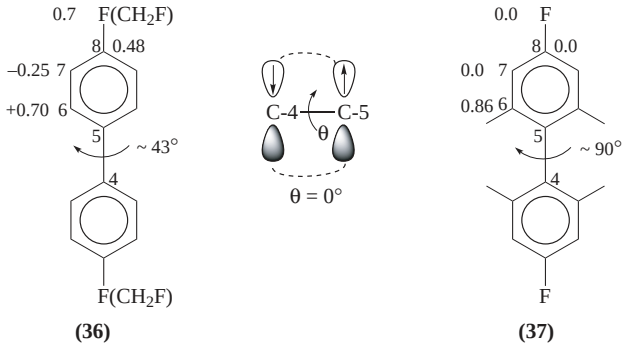

(36) **(37)**

A composite mechanism must also operate for ^6J(F,C) at site 6 in (**36**) and (**37**) because it is larger in (**37**). The C-5–C-6 bond undergoes a hyperfine interaction with the π electron at C-4, characterized by $Q^{\text{C}}_{\text{CCC}}$ and analogous to $Q^{\text{H}}_{\text{CCH}}$ in (**32**), which is maximal in (**37**) and hence varies as $\sin^2\theta$. The other part of the mechanism varies as $\cos^2\theta$, just as for $^{7,8}J$(F,C); hence $^6J(\text{F,C}) = A\sin^2\theta + B\cos^2\theta$. Such composite mechanisms also occur in other conjugated systems, an excellent example being styrene,[25] where an alkenic group is bonded to an aromatic system.

6.4 Electron Delocalization and Long Range Coupling Constants

Aromaticity is related to the delocalization of π electrons, leading to mobile bond orders. The structure and reactivity of a molecule are sensitive to the extent of delocalization. There are various definitions of mobile bond order, but all agree that the bond order is zero for a C–C bond, unity in ethene (**19**) or propene (**25**) and 2 for a triple bond, as in (**4**). Clearly, the allylic $^4J(\text{H,CH}_3)$ in (**25**) depends on the π electrons. If delocalization were to decrease the mobile bond order, then the magnitude of $^4J(\text{H,CH}_3)$ would also decrease. This idea has been exploited, particularly by Sternhell and co-workers,[26] to determine the mobile bond orders in aromatic systems; however, in this case ^4J is called a 'benzylic J'. In (**38**)–(**45**), the degree of delocalization is evident from the indicated ^4J. If -0.70 Hz in (**41**) is a measure of the delocalization of the π electrons in the prototypical aromatic molecule, benzene, then in (**42**), for example, some localization (double bond fixation) has been induced by the strong conjugation between the hydroxyl and nitro groups. In the cyclophane (**45**) the benzene moiety is strongly nonplanar, yet delocalization of the π electrons is still substantial.

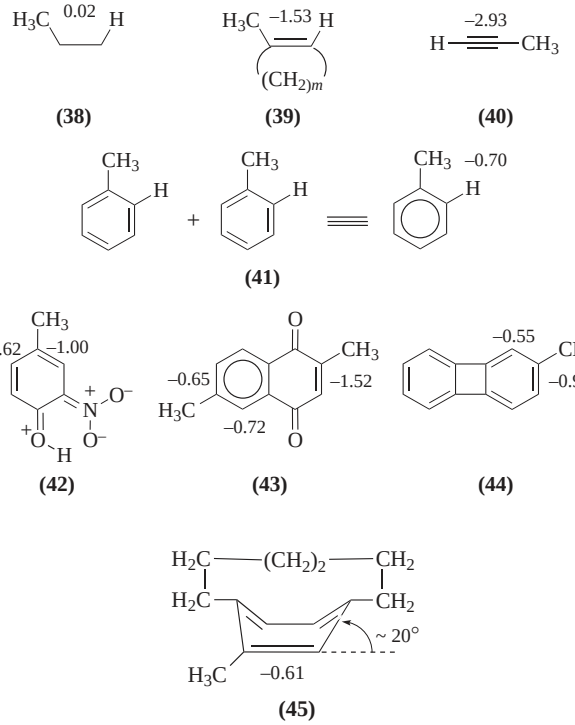

(38) **(39)** **(40)**

(41)

(42) **(43)** **(44)**

(45)

Of course, $^7J(\text{CH}_3,\text{CH}_3) \equiv {}^7J = 0.60$ Hz in 1,4-dimethylbenzene (**30**) is also a measure of delocalization of π electrons. The pyridine derivatives (**46**)–(**48**) are delocalized, whereas the benzoquinone (**49**) and the borazine (**50**) are not. Borazine itself is isoelectronic and isostructural with benzene and is sometimes considered as an inorganic analog of benzene.

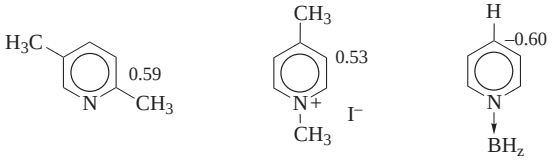

(46) **(47)** **(48)**

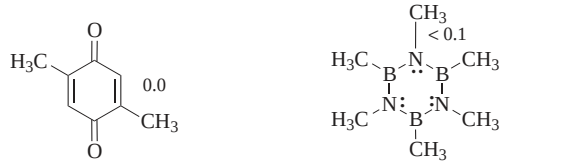

(49) **(50)**

6.5 ^4J(C,C) in Some Condensed Aromatics

^4J(C,C) in condensed aromatics such as (**51**)–(**54**) are thought[27] to be transmitted mainly via the π electrons, which are delocalized to a large extent. ^4J(C,C) was measured by enriching with ^{13}C at the position marked by an asterisk; the sign of ^4J(C,C) is known only in the case where it is given in the structures. The generalized mobile bond order between the coupled sites vanishes for these even alternant hydrocarbons,[28] which suggests very little spin correlation of the electrons at these sites. Furthermore, the atom–atom polarizabilities, which might in this connection be thought of as indicating how the π electron at the second site responds to a perturbation at the first site, are also very small for the indicated atoms. However, the atom–atom polarizability involving the penultimate site in the shortest coupling path, indicated by solid triangles in (**51**) and (**52**), is relatively large except for the ^4J of 0.3 Hz in (**53**) and that of 0.0 Hz in (**54**). This observation may represent an accidental coincidence; it has not been discussed in the scientific literature, but may be worth further study. It may be noted that $Q^{\mathrm{C}}_{\mathrm{C'C}}$ is sizeable and negative, and contributes to a negative ^4J(C,C) because it measures the hyperfine interaction of a π electron at the nearest carbon atom (solid spade) with the ^{13}C nucleus at the coupled site (solid circle). In this connection it would be useful to have many more ^nJ(C,C) values. There now exist methods[29] for finding ^nJ for unenriched molecules.

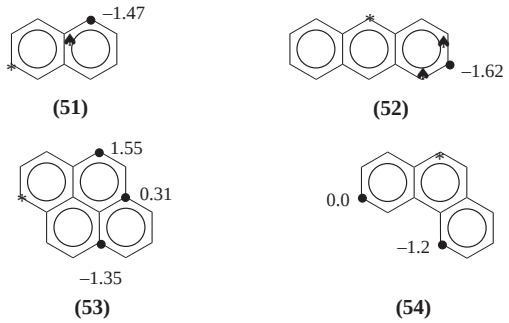

(51) **(52)** **(53)** **(54)**

6.6 A Unique Conformation Determined from ^nJ(H,H)

Were a chemist asked to predict the conformation of 2-hydroxythiophenol (**55**) in solution, he or she might well suggest an equilibrium among three planar structures, HS···OH, HS···HO, and SH···OH. This suggestion depends on the knowledge that conjugation of the lone pairs of electrons on oxygen or sulfur with the aromatic π electrons creates a mobile bond order, C···S and C···O (partial double bonds), leading to planar structures with concomitant barriers to rotation about the exocyclic bonds. A more sophisticated chemist might also suggest that the HS···HO structure would be most stable because the electrically polar $O^- - H^+$ bond would seek the lone pair on sulfur, forming an intramolecular hydrogen bond, thereby stabilizing this structure. Indeed, the vibrational spectrum of (**55**) in CCl_4 solution has been interpreted in terms of an equilibrium among three planar forms.

^5J(OH, SH), –0.14; ^5J(SH, H-3), 0.36;
^4J(OH, H-3), –0.11; ^5J(SH, H-5), 0.39

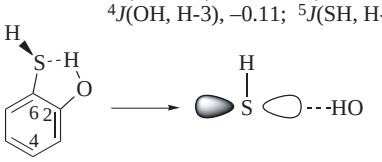

^6J(OH, H-5), 0.00; ^4J(SH, H-6), –1.07;
^5J(OH, H-4), 0.42; ^6J(SH, H-4), –0.96;
^5J(OH, H-6), 0.00

(55)

On analysis,[30] the ^{1}H NMR spectrum of such a solution yields nine ^nJ(H,H) ($4 \leq n \leq 6$) for protons in the side chains. These demonstrate unequivocally that the perpendicular conformation depicted in (**55**) is dominant. In view of the previous discussions, the large magnitudes of ^nJ(SH,H) and the stereospecific ^5J(OH,H-4) are consistent only with the indicated conformation, the one in which the S–H bond lies in a plane roughly perpendicular to that of the rest of the molecule. The polar O–H bond twists the 3p lone pair into the molecular plane, forming a hydrogen bond, and the S–H bond must therefore twist out of that plane. The formal ^5J(OH,SH) is an example of one kind of proximate J, in this case most probably being transmitted via the hydrogen bond.

7 PROXIMATE LONG RANGE COUPLING CONSTANTS

The stereochemistry of a molecule may be such that two of its fragments, while separated by many formal bonds, may still be proximate. Couplings between nuclei in the different fragments[6,31] are called 'proximate' (originally, 'through space'). An example is the ^5J(F,F) of 174 Hz in (**56**),[32] which is thought to be transmitted by the interaction of the lone pair electrons on the two fluorine atoms. The internuclear distance is well within the sum of the van der Waals radii of the atoms. Another example is (**57**) where the proximity mechanism is relayed via an H–F overlap to yield a ^4J(F,C) the magnitude of which decays exponentially with the H–F distance.[33] The scientific literature abounds with examples of proximate coupling constants between many different pairs of nuclei. Their stereochemical use is obvious. (See also ***Coupling Through Space in Organic Chemistry***)

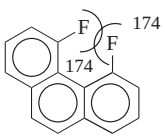

(56)

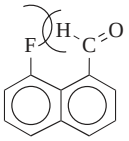

(57)

The most striking example[34] is a J of about 17 Hz between fluorine nuclei of 5-fluorotryptophan residues placed in the enzyme dihydrofolate reductase. The fluorine atoms are separated by dozens (n) of covalent bonds, yet must approach each other to within about 0.3 nm, a consequence of the folding pattern of the protein. The value of n may well be a record.

8 THE FUTURE OF LONG RANGE COUPLING CONSTANTS

One of the goals of mathematical chemistry is the computation of accurate stereochemical properties of molecules. Great progress has been made towards this goal, particularly for molecules for which the accurate measurement of small ^nJ values is feasible. As computers become faster, the general computation of ^nJ for reliable theoretical stereochemistries may also become a reliable procedure. Until then, measurements of ^nJ will likely retain their empirical utility. Furthermore, ^nJ values are normally measured in solution, in which perturbations by solvent molecules of conformational equilibria can be large; the ^nJ values may serve as checks of the theoretical descriptions or models of such perturbations.

9 RELATED ARTICLES

Analysis of High-Resolution Solution State Spectra; Analysis of Spectra: Automatic Methods; Coupling Through Space in Organic Chemistry; Double Resonance; Electron–Nuclear Hyperfine Interactions; Fluxional Motion; Hydrogen Bonding; Indirect Coupling: Intermolecular and Solvent Effects; Indirect Coupling: Theory and Applications in Organic Chemistry; Magnetic Equivalence; Organic Chemistry Applications; Quantitative Measurements; Recording One-Dimensional High Resolution Spectra; Vicinal ^{1}H, ^{1}H Coupling Constants in Cyclic π-Systems.

10 REFERENCES

1. L. M. Jackman and S. Sternhell, *Nuclear Magnetic Resonance Spectroscopy in Organic Chemistry*, 2nd edn, Pergamon, Oxford, 1969.
2. M. Barfield and B. Chakrabarti, *Chem. Rev.*, 1969, **69**, 757.
3. J. Kowalewski, *Prog. NMR Spectrosc.*, 1977, **11**, 1; *Ann. Rep. NMR Spectrosc.*, 1982, **12**, 81.
4. P. E. Hansen, *Prog. NMR Spectrosc.*, 1981, **14**, 175.
5. A. P. Marchand, *Stereochemical Applications of NMR Studies in Rigid Bicyclic Systems*, Verlag Chemie, Deerfield Beach, FL, 1982.
6. R. H. Contreras, M. A. Natiello, and G. E. Scuseria, *Magn. Reson. Rev.* 1985, **9**, 239.
7. L. B. Krivdin and E. W. Della, *Prog. NMR Spectrosc.*, 1991, **23**, 301.
8. R. H. Contreras, M. C. Ruiz de Azúa, C. G. Giribet, G. A. Aucar, and R. Lobayan de Bonczok, *J. Mol. Struct. (Theochem)*, 1993, **284**, 249.
9. M. Barfield and M. Karplus, *J. Am. Chem. Soc.*, 1969, **91**, 1.
10. P. J. Mitchell, L. Phillips, S. J. Roberts, and V. Wray, *Org. Magn. Reson.*, 1974, **6**, 127.
11. M. Barfield, A. M. Dean, C. J. Fallick, R. J. Spear, S. Sternhell, and P. W. Westerman, *J. Am. Chem. Soc.*, 1975, **97**, 1482.
12. J. A. Pople and D. L. Beveridge, *Approximate Molecular Orbital Theory*, McGraw-Hill, New York, 1970.
13. F. E. Hruska, J. G. Dalton, and M. Remin, *Can. J. Chem.*, 1979, **57**, 2191.
14. D. B. Davies, *Prog. NMR Spectrosc.*, 1978, **12**, 135.
15. R. H. Sarma, R. J. Mynott, D. J. Wood, and F. E. Hruska, *J. Am. Chem. Soc.*, 1973, **95**, 6457.
16. K. V. R. Chary, V. K. Rastogl, and G. Govil, *J. Magn. Reson., Ser. B*, 1993, **102**, 81.
17. F. A. L. Anet, *Tetrahedron Lett.*, **1964**, 3399.
18. P. A. Schultz and R. P. Messmer, *J. Am. Chem. Soc.*, 1993, **115**, 10 925; 10 938; 10 943.
19. E. W. Garbisch, Jr, and M. G. Griffith, *J. Am. Chem. Soc.*, 1968, **90**, 3590.
20. T. Schaefer and G. H. Penner, *Can. J. Chem.*, 1988, **66**, 1229.
21. T. Schaefer, C. Beaulieu, R. Sebastian, and G. H. Penner, *Can. J. Chem.*, 1990, **68**, 581.
22. W. J. E. Parr and T. Schaefer, *Acc. Chem. Res.*, 1980, **13**, 400.
23. T. Schaefer, J. Peeling, and G. H. Penner, *Can. J. Chem.*, 1986, **64**, 2162.
24. L. Ernst and S. Pulmann, *Org. Magn. Reson.*, 1981, **16**, 63.
25. M. Barfield, C. J. Macdonald, I. R. Peat, and W. F. Reynolds, *J. Am. Chem. Soc.*, 1971, **93**, 4195.
26. J. E. Gready, T. W. Hambley, K. Kakiuchi, K. Kobiro, S. Sternhell, C. W. Tansey, and Y. Tobe, *J. Am. Chem. Soc.*, 1990, **112**, 7537.
27. J. L. Marshall, *Carbon–Carbon and Carbon–Proton NMR Couplings: Applications to Organic Stereochemistry and Conformational Analysis*, Verlag Chemie, Deerfield Beach, FL, 1983.
28. C. A. Coulson and A. Streitwieser, Jr, *Dictionary of π Electron Calculations*, W. H. Freeman, San Francisco, 1965.
29. É. Kupče and R. Freeman, *J. Magn. Reson., Ser. A*, 1993, **104**, 234.
30. T. Schaefer, T. A. Wildman, and S. R. Salman, *J. Am. Chem. Soc.*, 1980, **102**, 107.
31. J. Hilton and L. H. Sutcliffe, *Prog. NMR Spectrosc.*, 1975, **10**, 27.
32. F. B. Mallory, E. D. Luzik, Jr, C. W. Mallory, and R. J. Carroll, *J. Org. Chem.*, 1992, **57**, 366.
33. I. D. Rae, A. Staffa, A. C. Diz, C. A. Giribet, M. C. Ruiz de Azúa, and R. H. Contreras, *Austr. J. Chem.*, 1987, **40**, 1923.
34. B. J. Kimber, J. Feeney, G. C. K. Roberts, B. Birdsall, D. V. Griffiths, A. S. V. Burgen, and B. D. Sykes, *Nature*, 1978, **271**, 184.

Biographical Sketch

Theodore P. Schaefer. *b* 1933. B.Sc., 1954, M.Sc., 1955, chemistry, University of Manitoba, Canada, D. Phil, 1958, University of Oxford, (supervisor, R. E. Richards). Faculty in Chemistry, University of Manitoba, 1958–present. Approx. 300 publications. Research interests: very high resolution NMR yielding precise long-range spin–spin coupling constants and their relationship to conformation and internal motions in highly flexible molecules.

Supramolecular Chemistry

Miquel Pons and Pau Bernadó

Departament de Química Orgànica, Universitat de Barcelona, Spain

1	Introduction	1
2	Detection of Supramolecular Interactions by NMR Methods	1
3	Dynamic of Supramolecular Complexes	6
4	Concluding Remarks	10
5	Related Articles in this Volume	10
6	Related Articles in Volumes 1–8	10
7	References	11

1 INTRODUCTION

The subject of supramolecular chemistry is the design, preparation and study of discrete chemical systems composed of several units linked by non-covalent bonds to form a well-defined structure under thermodynamic control.[1–4] This definition is sometimes applied loosely to include species formed by several molecular entities that are not in equilibrium with the separate components or are non-discrete. The first situation applies to complexes that have very large energy barriers to dissociation. The second includes polymeric materials or solid-state systems in which one of the components forms a crystalline lattice that can accommodate the other component.

NMR has been the most important analytical tool for the study of supramolecular systems in solution and it has also been applied extensively, along with X-ray and other techniques, to solid systems. The success of NMR in this field is due to its ability to (i) study complex chemical systems in equilibrium, (ii) report about their symmetry properties, (iii) determine the conformation of the individual components and their mutual interactions and (iv) characterize the dynamic behavior of the system in a wide range of time scales. The role of NMR in supramolecular chemistry has been recently reviewed.[5,6]

In this review we shall give an overview of the structural and dynamic problems encountered in supramolecular chemistry and of the methods that are used to address them.

2 DETECTION OF SUPRAMOLECULAR INTERACTIONS BY NMR METHODS

2.1 Supramolecular Complexes Involving Several Components

Intermolecular interactions can affect all the NMR observables. Perturbations in the environment of the different nuclei are reflected in chemical shift changes. Differences in the size and shape of the complex, compared to the isolated molecules, result in differences in diffusion and relaxation experiments.

Because of their easy availability, changes in chemical shifts are extensively used to detect the formation of supramolecular complexes. The association constants and the stoichiometry of the process can be extracted by fitting titration curves to the equations that describe the binding.

Binding is a chemical exchange process and its effect on the observed NMR spectra depends on the lifetime of the complex. When it is long, compared to the reciprocal of the frequency difference with respect to the uncomplexed form, the complex contributes a new set of signals and the equilibrium concentrations of the complex and free forms can be determined by integration. When exchange is fast, average signals are observed at chemical shifts that are the weighted average of those of all the species that participate in the equilibrium. Intermediate exchange rates affect the line shape in a well-determined way and kinetic information can be extracted.

Rate constants are temperature sensitive and experimental conditions, for which the process of interest is either in the fast or slow exchange regime, can usually be found.

The book by Connors discusses NMR methods for determining binding constants.[7]

For a 1 : 1 ($A-B$) complex the binding isotherm is given by

$$\delta_{\text{obs}} - \delta_{\text{free}} = \delta_{\text{complex}} - \delta_{\text{free}} \frac{(K[B])}{(1 + K[B])} \tag{1}$$

where δ_{obs} is the observed chemical shift of a nucleus in species A. δ_{free} and δ_{complex} are the chemical shifts of A in the free state and in the complex. K is the association constant with ligand B and $[B]$ is the concentration of free ligand. $[B]$ can be replaced by the total concentration of B if $K[A] \ll 1$, where $[A]$ is the concentration of free A. This condition is fulfilled when B is in large excess with respect to A or when binding is weak (K small).

The concentration range explored during a titration has to cover a substantial fraction of the binding curve in order to determine the binding constant meaningfully. It has been suggested that experimental conditions covering 20% to 80% of the maximum possible concentration of the complex have to be examined. This is achieved when the concentration of the observed component (A) is maintained at about one tenth of the dissociation constant (K^{-1}) and the added ligand B is varied from this concentration to about ten times the dissociation constant.[8]

When binding is strong, the dissociation constant is very small and the optimal concentration of the observed species would be very low, causing sensitivity problems. In this case a dilution protocol may be used. In this type of experiment, an equimolar solution of A and B is prepared and spectra are observed after successive dilution steps. Obviously, dilution is the only available possibility to study self-association, i.e., when $A = B$.

The stoichiometry of the complex can be determined using Job's method of continuous variation. In this method the ratio of the two species A and B is varied, while keeping the total concentration, $[A]_{\text{o}} + [B]_{\text{o}}$, constant. The concentration of the complex will be maximal when $[A]_{\text{o}} = [B]_{\text{o}}$ for an AB complex but when $[A]_{\text{o}} = 2[B]_{\text{o}}$ for an A_2B complex.

The observed chemical shift δ_{obs} is related to the concentration of the complex and the total concentration of A, $[A]_{\text{o}}$, by

$$\frac{(\delta_{\text{obs}} - \delta_{\text{free}})}{(\delta_{\text{complex}} - \delta_{\text{free}})} = \frac{[\text{complex}]}{[A]_{\text{o}}} \tag{2}$$

If the sum of the concentrations of A and B are constant, $[A]_o$ is proportional to X_A and a plot of $(\delta_{obs} - \delta_{free})X_A$ versus X_A has a maximum at a value of $X_A = n/(n+1)$ for a complex A_nB.

Other NMR parameters that have different values for a molecule free in solution or when forming part of a complex can be used to derive binding constants.

In the fast exchange limit, the observed relaxation rate constant R is a weighted average of the relaxation rate constants of the free molecule (R_{free}) and the complex ($R_{complex}$). In complete analogy with the chemical shift situation, the binding isotherm for 1 : 1 binding is given by

$$R_{obs} - R_{free} = R_{complex} - R_{free}\frac{(K[B])}{(1 + K[B])} \qquad (3)$$

Changes of the relaxation rates in complexes are associated to changes in correlation time, related to the size and shape of the molecule, or to changes in relaxation mechanisms. However, application of equation (3) is independent of the mechanistic details.

Diffusion coefficients can also been used to obtain binding constants. Diffusion coefficients depend on the size and shape of the molecule. When the two interacting species are very different in size, the diffusion coefficient of the complex can usually be assumed to be equal to that of the larger molecule.

Correlation times and diffusion are very sensitive to the viscosity of the solution, and relaxation time and diffusion coefficient measurements have to be corrected for changes in viscosity of the solution during the titration.

2.2 High Symmetry Supramolecular Complexes between Identical Molecules

When complexes between identical molecules are formed with large association constants, the NMR spectra of the isolated component may not be available under the experimental conditions (solvent, temperature) that promote complex formation. Detecting and characterizing the formation of supramolecular complexes by NMR is then a non-trivial task.

Supramolecular complexes between identical molecules are earmarked by their symmetry and this is faithfully reflected in their NMR spectra.[9] Most of the examples that can be found in the very extensive literature about characterization of specific supramolecular species can be classified according to Box 1.

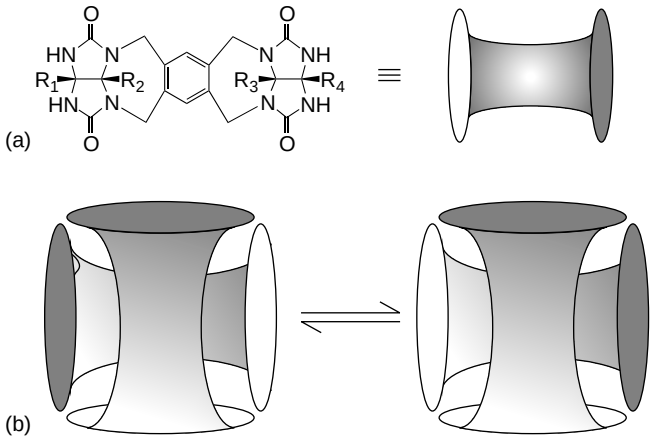

Figure 1 (a) Chemical structure of the precursor of the 'tennis ball'. When $R_1 \neq R_4$ and $R_2 \neq R_3$ the monomer has a plane of symmetry but the dimeric capsule is chiral and the two NH groups in each glycouril are not equivalent. (b) Dissociation and reassociation of the dimer leads to racemization. (Reproduced with permission from Ref.[6] from Elsevier Science © 2001)

A few examples will clarify the scenarios presented in Box 1. These examples will also serve to introduce some of the most extensively studied supramolecular families. The 'tennis ball' capsule illustrates the situation 1(a) of Box 1. The 'tennis ball' is a high symmetry dimer held together by intermolecular hydrogen bonds that define an interface with a shape reminiscent of the seam in a tennis ball.[10] The monomer is a curved molecule based on two glycoluril groups and a durene spacer (Figure 1). The assembly has D_{2d} symmetry and the NMR spectra obtained in benzene-d_6 or $CDCl_3$ reflects the two symmetry planes expected for the isolated molecule. Early evidence for the formation of this capsule was derived from the chemical shifts of the NH protons, suggesting hydrogen bonding, and the observation of strongly shielded signals from small hosts, like methane or xenon, that were included in the capsule.

The introduction of two differently substituted glycoluril groups on the durene spacer reduces the symmetry of the monomer to C_s. However, the dimer, a chiral (C_2) capsule, has no symmetry planes and the two NH groups in each glycoluril unit are not equivalent. This is the situation indicated in point 2(a) of Box 1.

Box 1 Detection of complex formation between identical molecules by comparing the observed NMR spectrum with that expected from the isolated component

1. The number of NMR signals reflects an apparent symmetry equal to that of the isolated component.
   (a) In a rigid system, this implies that the components are symmetry related. Chemical shift arguments are the only evidence for complex formation.
   (b) The symmetry of the complex results from fast average of lower symmetry arrangements. NMR spectra at low temperature may show signal splitting.
2. The number of signals in the NMR spectrum of the complex increases, reflecting a lower local symmetry.
   (a) The relative disposition of the components destroys symmetry elements present in the isolated components.
   (b) A fast local internal motion, which resulted in average signals in the isolated component, is slowed down as a result of complex formation.
   (c) The interacting molecules become fixed in a low symmetry conformation in the complex.
3. Multiple sets of signals are observed.
   (a) The subunits, although constitutionally identical, are not related by symmetry in the complex. The integration of the NMR signals reflects the complex stoichiometry.
   (b) Isomeric complexes, possibly of different symmetry, are formed. Integration reflects the relative populations.

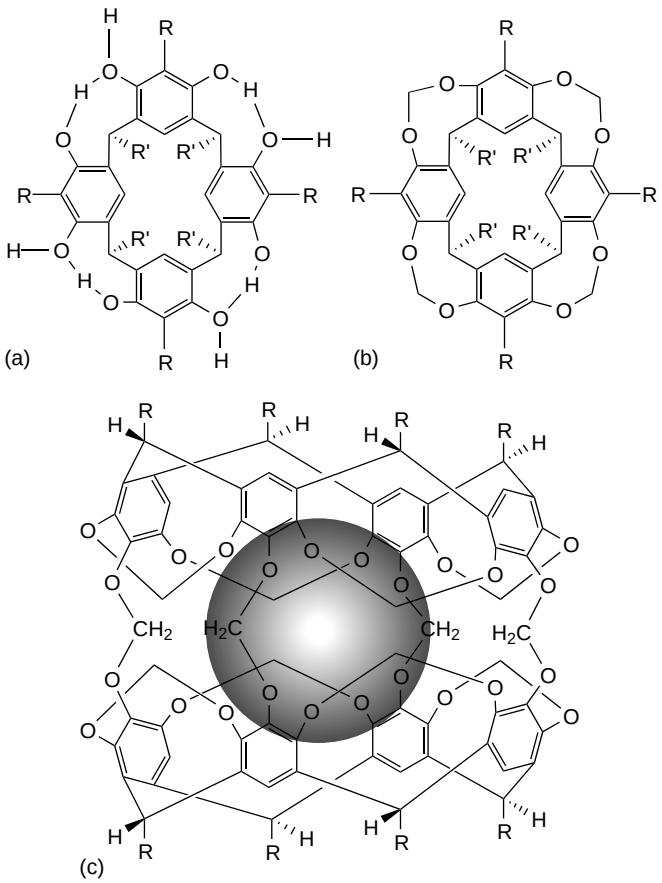

Figure 2 Resorcin[4]arene building blocks. (a) Parent resorcin[4]arenes have free OH groups than can participate in intra- and intermolecular hydrogen bonds. (b) Bridged resorcin[4]arene are known as cavitands. (c) Carcerands are covalent dimers of cavitands. A carcerand with an irreversibly trapped guest is called a carceplex. (Reproduced with permission from Ref.[6] from Elsevier Science © 2001)

Bowl-shaped cyclic molecules can define a cavity by face-to-face dimerization. This is the case of cavitands, that contain a resorcin[4]arene skeleton (Figure 2).[11] Cavitand-based non-covalent dimer capsules, stabilized by intermolecular hydrogen bonds, and covalent dimers, with linkers between the two moieties, share a number of structural characteristics, including their ability to incorporate molecules in the internal cavity. Molecules incorporated in the covalent dimer during their preparation are permanently trapped. Appropriately, the covalent dimers are called carcerands and their complexes with small molecules are called carceplexes. The X-ray structures of different carceplexes or non-covalent capsules show inter-bowl twists of 13–21°. The solution NMR spectra suggest that resorcinarene capsules and carcerands are highly symmetric achiral structures, compatible with a D_{4h} symmetry. This is the result of fast interconversion between dimers differing in the sign of the relative twist between the two halves of the dimer. These two forms have been called twistomers. At low temperature, interconversion between twistomers is slow and the dimer loses all symmetry planes. The D_{4h} symmetry is then reduced to D_4 (Figure 3). This symmetry reduction is not reflected in the NMR spectra under achiral conditions but leads to signal duplication when the carceplex contains a chiral guest. The observation of signal splitting at low temperature was listed as situation 1(b) in Box 1.

A different family of bowl-shaped molecules, the calix[4]arenes,[12] can be modified to form capsules by introducing urea substituents in one of the rims (Figure 4).[13,14] Urea groups from two different molecules are interdigitated and form a cyclic array of hydrogen bonds. Under conditions in which capsules are not formed, e.g., in the presence of solvents that can compete for the formation of hydrogen bonds, fast rotation about the C–N bond linking the urea group to the calixarene results in a symmetrical species in which the macrocyclic aromatic protons are all equivalent. In the dimer, reorientation of the urea group is not possible, as it requires breaking the cyclic hydrogen bond array.

As a consequence, formation of the capsule can be determined by NMR from the observation of the splitting of the signal of the aromatic protons of the calixarene into two *meta* coupled doublets, an example of the situation indicated in point 2(b) of Box 1. When the symmetry of the precursor calix[4]arene is lowered from C_{4v} to C_{2v} by placing two different substituents in alternate positions, the symmetry of the dimer is reduced to C_2. This is a consequence of the directionality of the hydrogen bond array and the interdigitation of the urea groups (cf. Figure 7 below). In this dimer, the two calixarenes are non-equivalent and duplicated signals are observed, as prescribed in point 3(a) of Box 1.

Helicates are discrete supramolecular complexes formed by one or more covalent organic strands wrapped about and coordinated to a series of ions.[15] The ions define a helical axis. The otherwise flexible organic strand becomes fixed in a helical structure that is intrinsically chiral (Figure 5). This situation, listed as point 2(c) in Box 1, is reflected in the NMR spectra of methylene groups that are rendered diastereotopic.[16] This allows double stranded helicates to be easily distinguished from isomeric non-helical side-by-side complexes, a possibility contemplated as point 3(b) of Box 1.

The same line of thought can be applied to the analysis of higher order supramolecular complexes involving different types of molecules. For example, the melamine-cyanuric acid rosettes studied by Whitesides and coworkers are discrete aggregates composed of four molecules: one

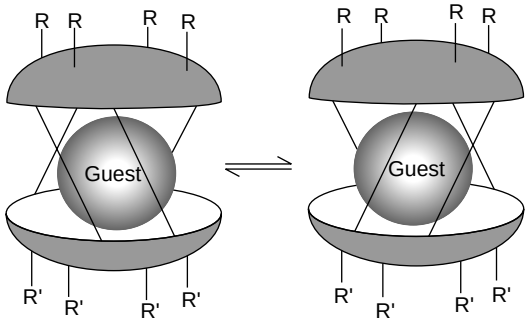

Figure 3 Due to the relative twisting of the two moieties, the minimum energy conformations of cavitands have no symmetry plane, even R = R′. At low temperature interconversion of the two enantiomers (called 'twistomers') is slow. Under these conditions, enantiotopic groups in the included guest may become diastereotopic. (Reproduced by permission of the American Chemical Society © 1999)

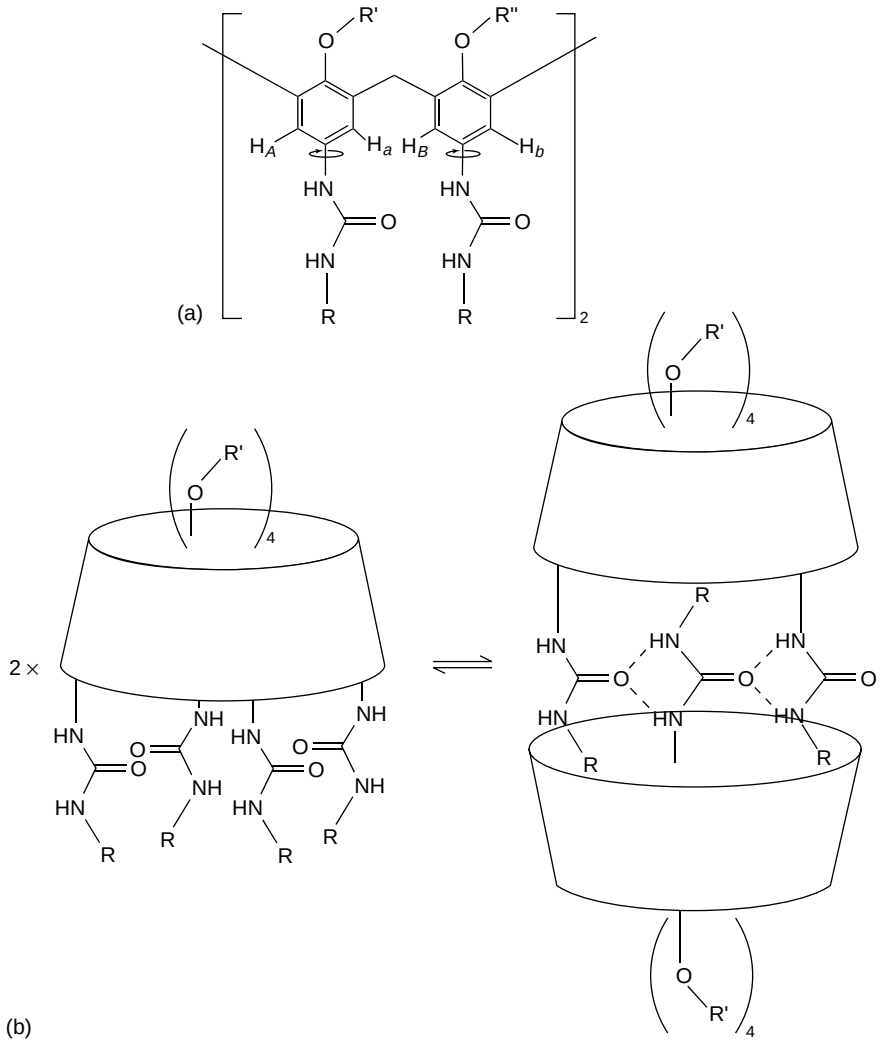

Figure 4 (a) A urea substituted calix[4]arene. (b) Schematic representation of the dimerization of tetra urea calix[4]arenes, interdigitated urea groups form the array of hydrogen bonds. Exchange between *A* and *a* or *B* and *b* reflects the rotation of the urea group that is slowed down dramatically when the capsule is formed. In the cone conformation adopted by the calix[4]arene in the capsule, protons from neighbor aromatic rings (e.g., a and *B* or *b* and *A*) show strong NOEs. When $R' = R''$, $A \equiv B$, $a \equiv b$ and the NOESY (e.g., *a*-*B*) and exchange (e.g., *a*-*A*) cross-peaks overlap. (Reproduced with permission from Ref.[6] from Elsevier Science © 2001)

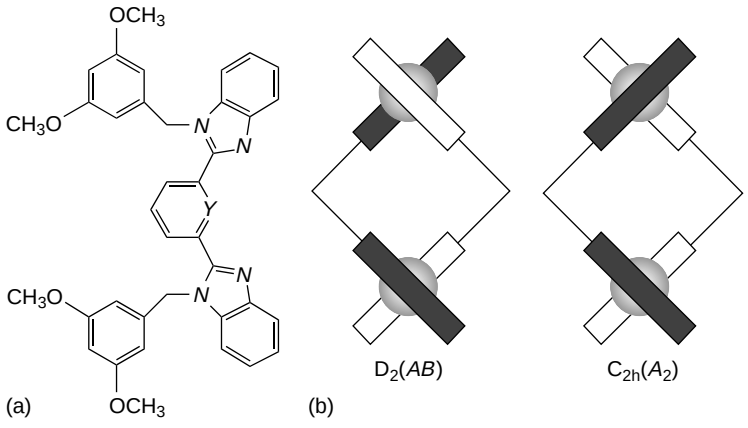

Figure 5 (a) Chemical structure of an organic ligand that can form helicates with Cu^+. (b) Schematic representation of two double stranded complexes $[Cu_2L_2]^{2+}$. When $Y = N$ a helicate with D_2 symmetry is formed and the methylene groups in the ligand give *AB* type spectra. When $Y = CH$ a side-by-side complex with C_{2h} symmetry is formed and the methylene groups appear as A_2 singlets. (Reproduced with permission from Ref.[6] from Elsevier Science © 2001)

tris-melamine, Hub(M)$_3$, and three isocyanuric acid, CA, molecules (Figure 6).[17] Aggregates of two different symmetries, C_3 and C_1, are substantially populated and the imide proton region of the ^{1}H–NMR spectra of some of the rosettes show eight signals, two from the C_3 isomer and six from the C_1 isomer. This is an example of the situation 3(b) of Box 1 applied to systems with two components.

2.3 Supramolecular Complexes between a Large and a Small Molecule

Formation of supramolecular complexes between molecules of different sizes causes substantial changes in the hydrodynamic properties of the smaller component that can be detected by NMR methods. Both translational and rotational diffusion coefficients are affected.

Translational diffusion coefficients are determined by NMR using pulsed field gradient spin-echo (PFGSE) experiments.[18] After initial excitation, magnetization from molecules in different positions within the sample acquires different phases by the application of a pulsed field gradient. As a result, the net magnetization from the complete sample becomes zero. If the position of the molecules does not change, application of a second gradient pulse causes refocusing of the magnetization. However, diffusion of the molecule during the interval between the two gradient pulses results in an attenuated signal.

Quantitative determination of the translational diffusion coefficient can be achieved by fitting the signal intensity of a

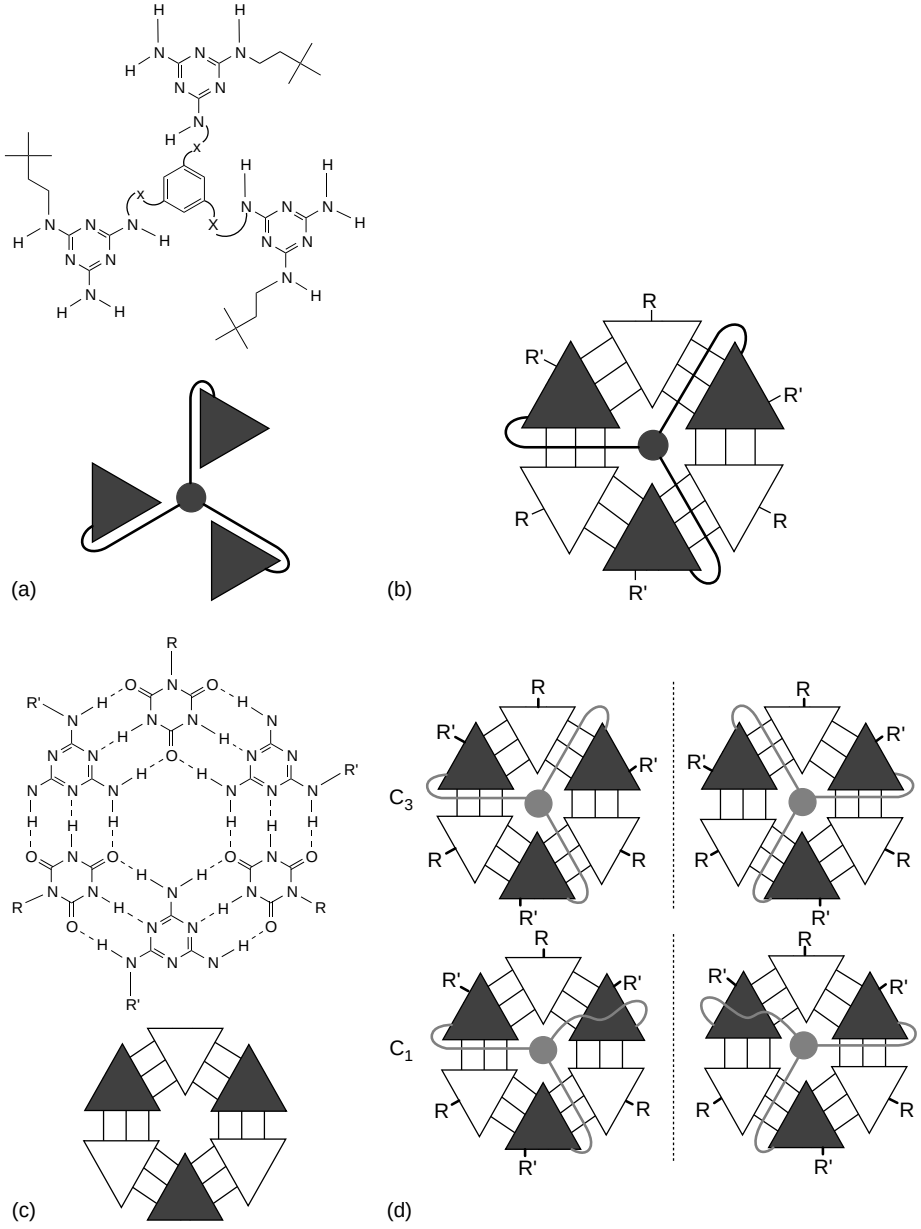

Figure 6 (a) Tris-melamine Hub(M)$_3$ and its schematic representation, where X is a rigid spacer. (b) Schematic representation of a Hub(M)$_3$: CA$_3$ aggregate. (c) Chemical structure and schematic representation of a melamine-cianuric acid (CA) hydrogen bond array to form a rosette. (d) The four possible isomers for the complex Hub(M)$_3$: CA$_3$. The two enantiomers shown on top present C_3 symmetry, the enantiomers on bottom do not have elements of symmetry (C_1). (Reproduced by permission of the American Chemical Society © 1993)

series of PFGSE experiments with different gradient strengths to the Stejskal–Tanner[19] equation:

$$I(\Delta, \delta, G) = I_o \exp\left(-\gamma^2 G^2 \delta^2 \left(\Delta - \left(\frac{\delta}{3}\right)\right)\right) D \qquad (4)$$

where D is the translational diffusion coefficient, Δ corresponds to the delay between gradients, δ is the gradient duration, G is the gradient strength and γ is the gyromagnetic ratio.

Translational diffusion coefficients are related to the size and shape of the molecule. For a spherical object the diffusion coefficient can be calculated from

$$D = \frac{k_B T}{6\pi\eta r} \qquad (5)$$

where, η is the solvent viscosity and r is the radius of the sphere. Similar analytical equations exist for ellipsoids and cylinders.[20] Methods to calculate translational and rotational diffusion coefficients for rigid molecules of arbitrary shape have been described.[21,22]

Affinity NMR makes use of the large differences between the translational diffusion coefficients of small ligands and macromolecules. In this experiment, small, uncomplexed molecules are attenuated beyond detection by a PFGSE sequence. However, molecules that interact with the slowly diffusing large component are still observable and therefore can be identified, usually from a mixture of candidate ligands.

Association of small molecules can also be characterized sometimes by diffusion based experiments specially when the association involves a large number of components and leads to large polyhedral assemblies.[23]

Rotational diffusion coefficients determine the relaxation rates. Transverse relaxation is fast in macromolecules resulting in broad lines that may even prevent the observation of the macromolecule or the complex. Cross-relaxation rates in the macromolecule and in the complex are also much faster than in the free small component. The intramolecular NOE (nuclear Overhauser effect) generated in the complex can be measured in the free molecule if the off-rate is large enough. Thus, the formation of the complex can be detected by the observation of intramolecular negative NOE values, typical of large molecules, in small molecules studied in the presence of a macromolecule with which they can interact. This effect is the well-known transferred NOE.[24,25] Transferred NOE experiments provide information about the conformation of flexible ligands in the complex.

Interpretation of transferred NOE requires caution, because of fast spin diffusion involving spins in both the ligand and the macromolecule.

Intermolecular cross-relaxation is used constructively to detect ligand binding to macromolecules by the methods of NOE pumping and saturation transfer difference (STD).[26,27] In NOE pumping experiments, a diffusion filter eliminates signals from all small molecules and those from the bound ligands are recovered by intermolecular NOE from the macromolecule. In the STD experiment, protons in the complex, including those from any bound ligand, are saturated by strong radiofrequency irradiation at a frequency where only signals from the macromolecule are absorbing, even if they are too broad to be observed. Fast spin diffusion transfers the saturation to the complete ensemble of protons in the complex. Saturation is maintained after dissociation of the complex and results in a smaller intensity in the signals from molecules that can bind to the macromolecule. Thus ligands can be detected in a difference experiment.

3 DYNAMIC OF SUPRAMOLECULAR COMPLEXES

3.1 Interference between Exchange and Cross-Relaxation

Dynamic processes are an inherent part of the chemistry of supramolecular complexes. The definition of supramolecular complexes includes the fact that these entities are in equilibrium with their separated components implying that the processes of formation and dissociation have to be fast. In addition, other dynamic processes involving changes in the relative arrangement of the subunits in the complex can also take place. NMR methods are especially useful to study dynamic processes in equilibrium if they involve a change in the environment of NMR-active nuclei. This includes many degenerate processes that involve the interconversion between symmetry related forms of the same complex.

A typical situation involves the formation of a (racemic) chiral complex from achiral components. Enantiotopic groups in the isolated molecules become diastereotopic in the complex, and therefore NMR-distinguishable if the dissociation–reassociation process is slow with respect to the reciprocal of the chemical shift difference. Dissociation and random reassociation yields the starting isomer and its enantiomer with 50% probability and, when the rate is large enough, leads to coalescence of the signals from enantiotopic groups. The racemization rate is half the dissociation rate. The dissociation kinetics of the asymmetric tennis ball was determined by this method.[28]

Racemization of chiral supramolecular complexes is not always associated to dissociation processes. This is the case, for example, of some helicates that can change the configuration around the different metal centers without dissociation. An experimental proof of intramolecular inversion of chirality is obtained by observing the coalescence of diastereotopic groups in the complex in the presence of excess ligand and showing that the signals from the free ligand are not affected.

Dynamic processes that are slow in the chemical shift time scale but faster than the relevant relaxation rates can be studied by 1D or 2D magnetization exchange techniques.

Chemical exchange and cross-relaxation have very similar effects on NMR spectroscopy. In fact, the same pulse sequence is used in EXSY (exchange spectroscopy) or NOESY (NOE spectroscopy) and the two experiments differ on whether the conditions chosen avoid cross-relaxation and emphasize chemical exchange or if cross-relaxation is the dominant effect.

Supramolecular complexes contain extensive intermolecular contacts and have long correlation times that makes cross-relaxation very efficient. In addition, composite cross-relaxation exchange pathways can transfer magnetization between distant sites. As a consequence, spin diffusion effects complicate the interpretation of NOESY/EXSY experiments in supramolecular complexes.

When cross-relaxation and exchange contribute to different cross-peaks, the process that is mainly responsible for the appearance of each cross-peak in NOESY spectra can be determined using ROESY (rotating frame Overhauser enhancement

spectroscopy) spectra, in which cross-relaxation and exchange peaks have opposite signs. Off-resonance effects and TOCSY (total correlation spectroscopy) coherence transfer complicate quantification of ROESY spectra.

Off-resonance ROESY uses an off-resonance spin-locking field forming an angle θ with the transverse plane. For small values of θ, off-resonance ROESY is similar to ROESY and for angles close to 90°, it gives results similar to those of NOESY spectra. For intermediate values of θ, the cross-relaxation contribution can be made to vanish, resulting in a pure exchange spectrum.

Figure 7 shows expansions of NOESY, ROESY and off-resonance ROESY spectra of a dimer of a urea-substituted, low-symmetry calix[4]arene in d_6-benzene.[29] Notice that the two calixarene units are non-equivalent. The sense of rotation of the hydrogen bond array is what defines the 'top' and 'bottom' units. When the direction of the hydrogen bonds is reversed, the top and bottom units are exchanged. Separation of cross-relaxation and exchange is facilitated by the use of different substituents in adjacent aromatic rings.

Separate quantification of exchange and cross-relaxation rates from NOESY spectra is best carried out by a

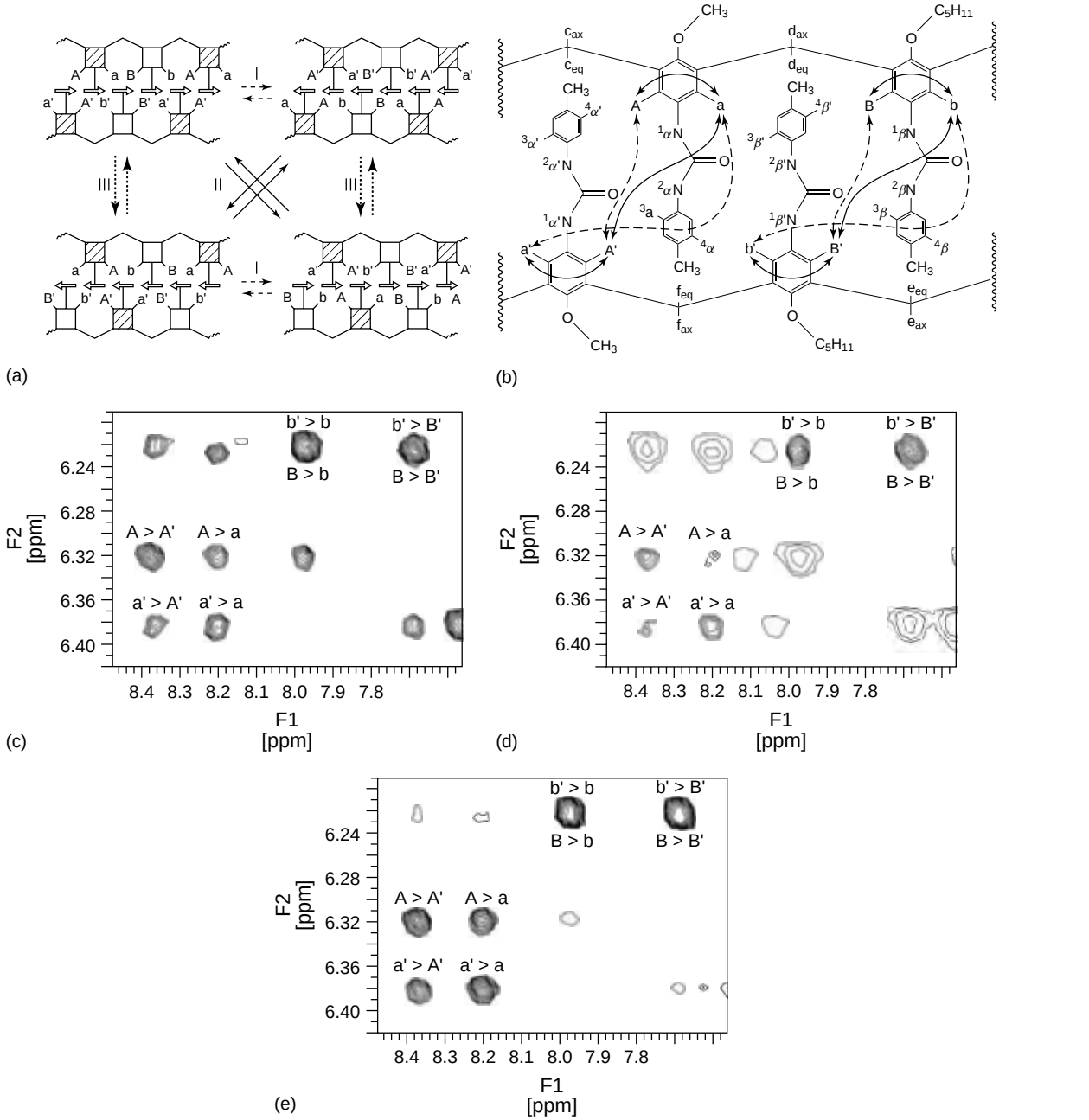

Figure 7 (a) Schematic representation of the homomerization pathways for a low symmetry calix[4]arene. (b) Observed exchange cross-peaks in the EXSY experiment are indicated by arrows in a schematic formula of the dimer. (c–e) Partial 2D NMR spectra of the low symmetry calix[4]arene in d_6-benzene (500 MHz, 298 K, $\tau_m = 300$ ms): (c) NOESY, (d) ROESY, (e) off-resonance ROESY ($\theta = 35.6°$). Negative cross-peaks in (d) arising from cross-relaxation are plotted with a reduced number of contours. (Reproduced by permission of the American Chemical Society © 1997)

relaxation-plus-exchange matrix approach.[30] The intensity matrix (**I**) is related to the kinetic plus relaxation matrix (**L**), the relative population of the sites (**P**) and the mixing time τ_m by

$$I = \exp(\mathbf{L} \cdot \tau_m) \cdot \mathbf{P} \tag{6}$$

Matrix **L** can be obtained directly from the normalized experimental intensity **A** by taking the logarithm of **A** and dividing by the mixing time. This involves diagonalization of **A** as indicated in the following equations:

$$\mathbf{A} = \mathbf{I} \cdot \mathbf{P}^{-1} \tag{7}$$

$$\mathbf{A} = \mathbf{X} \cdot \boldsymbol{\Lambda} \cdot \mathbf{X}^{-1} \tag{8}$$

$$\mathbf{L} = \ln \frac{\mathbf{A}}{\tau_m} = \frac{\mathbf{X} \cdot (\ln \Lambda)}{\tau_m \cdot \mathbf{X}^{-1}} \tag{9}$$

This procedure has the advantage that spin diffusion is corrected for, allowing the use of longer mixing times. In particular, interference from composite exchange cross-relaxation pathways is minimized.

A more complicated situation arises when separate exchange and cross-relaxation processes involve the same pair of nuclei (cf. Figure 4, $R' = R''$). Direct analysis of the 2D spectra can only provide a composite rate constant. In order to separate the contributions, the different temperature dependencies of cross-relaxation and exchange processes can be used. As an alternative, EXSY spectra measured at different magnetic fields but at the same temperature will have different contributions from cross-relaxation but the same exchange effects. Finally, in some instances in which the geometry of the system is fixed and well known (e.g., pairs of methylene protons) the cross-relaxation rate can be calculated from independent measurements of the correlation time of the complex.

3.2 Dynamics of Hosts: Catenanes and Rotaxanes

The especially rich dynamic behavior found in catenanes and rotaxanes has been studied extensively by NMR.[31,32] Strictly speaking, catenanes and rotaxanes are not supramolecular complexes but true molecules formed by several interlocked components. Catenanes have different topology to the separate components and are said to possess 'topological bonds'. Rotaxanes are held together by steric or other kinds of hindrance to dethreading of a cyclic component from a linear one.

Both catenanes and rotaxanes can be prepared efficiently by making use of self-assembly processes between the precursors. These interactions are still present in the final product and, as a consequence, only a discrete number of low energy conformations and co-conformations are possible and the interconversion processes are well defined.

Figure 8 shows the eight possible supramolecular dynamic processes that take place in a [2]catenane with two stations. The NMR characterization of the different processes has been addressed by dynamic NMR methods using derivatives of lower symmetry, e.g., by introducing elements of planar chirality in the spacers X1, X2, A1 or A2.

The conceptually simplest dynamic process in rotaxanes is the translation of the ring along the axle, although additional motions of the cyclic component – analogous to those observed in catenanes – are also observed (Figure 9).

Polyrotaxanes contain several threaded macrocycles. In pseudo-polyrotaxanes, there are no steric barriers to prevent dethreading and the macrocyclic components can equilibrate with the free form. However, macrocycles cannot pass each other on their way to the end of the linear chain and dethreading.

Pseudo-polyrotaxanes display complex dynamic processes involving interference between translational motion, dethreading and steric effects between different macrocycles threaded by the same linear component. These specific supermolecular dynamic problems give rise to unusual dynamic NMR situations. The NMR spectra of a system formed by a polymeric thread, alternating electron rich 1,5-dioxonaphthalene and 1,4-dioxobenzene, and an electron-poor cyclophane displays two sets of signals in slow exchange.[33] However, the site-hopping rate was independently determined to be fast in the NMR

Process	Rotation of ...	Through/Around ...
1	Crown ether	Cyclophane
2	Cyclophane	Crown ether
3	A1 ring	O----------O axis
4	A2 ring	O----------O axis
5	X1 ring	C----------C axis
6	X2 ring	C----------C axis
7	Bipyridinium	N----------N axis
8	Crown ether, Cyclophane	Dihedral axis defined by the two mean planes

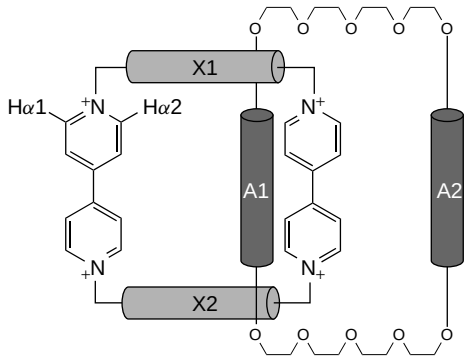

Figure 8 Description of eight possible supramolecular dynamic processes in a [2]catenane. (Reproduced with permission from Ref.[6] from Elsevier Science © 2001)

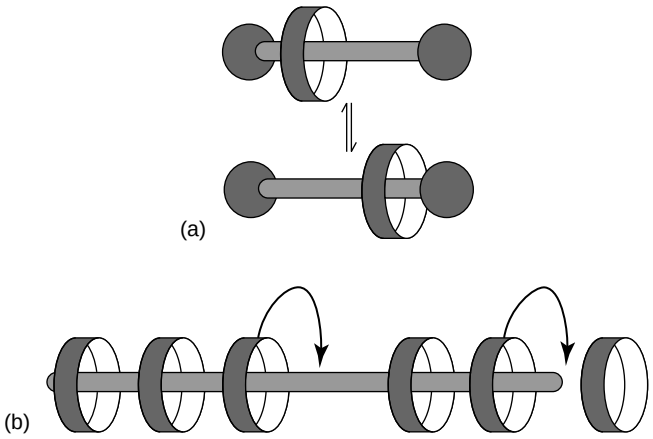

Figure 9 Shuttling in rotaxanes and pseudo-polyrotaxanes. (a) The translation process in a two-station rotaxane. (b) Translation and dethreading of macrocycles in a pseudo-polyrotaxane

chemical shift time scale. The two signals arise from fast average between different populations: one of them comprises the free form and those macrocycles that can escape rapidly from the thread. The second population includes all macrocyclic rings that exchange slowly with the free form because of the presence of another ring along the thread that prevents them from reaching the end of the polymer. The 'membership' in one of the two populations is therefore defined by the fulfillment or not of the fast exchange condition with the free form. At constant temperature, the population of each site depends on the observation frequency and therefore the average chemical shift that characterizes each site is also field dependent.

3.3 Dynamics of Guests: Guest Exchange

NMR methods are well suited to study the kinetics of exchange of small guests in and out of the cavities determined by their hosts. Exhaustive recompilations of kinetic and thermodynamic data for macrocyclic hosts and a variety of guests have been published.[34–36]

Exchange contributes to line broadening by modulating the chemical shift or the quadrupolar interaction in the guest. In the well-studied alkali metal ions, quadrupolar relaxation is usually substantially enhanced in the complexes because of their lower symmetry, compared with the solvated species. On the other hand, the alkali metal chemical shift differences between the complexed and solvated forms are smaller than the line-widths and the signals overlap.

The lifetime of the solvated state, τ_a, in the intermediate exchange regime is given by

$$\frac{1}{\tau_a} = (R_{av} - P_a R_a - P_b R_{obs}) \frac{(R_{obs} - R_a)}{(R_{av} - R_{obs})} \qquad (10)$$

where P_a and R_a are the population and transverse relaxation rate of the solvated ion in the absence of exchange and P_b, R_b are the corresponding values for the complexed form. R_{obs} is the observed transverse relaxation rate and $R_{av} = P_a R_a + P_b R_b$.[37]

When the relaxation rates of the complexed and free forms are comparable, i.e., $(\omega_a - \omega_b)^2 \gg (R_a - R_b)^2$, the exchange contribution to transverse relaxation provides an estimation of the exchange lifetime, τ, which has contributions from the lifetimes of both the solvated and the complexed forms, through

$$\frac{1}{\tau} = \frac{1}{\tau_a} + \frac{1}{\tau_b} = P_a P_b (\omega_a - \omega_b)^2 R_{ex}^{-1} \qquad (11)$$

In the slow exchange regime, separate signals are observed and exchange rates can be obtained by EXSY or 1D magnetization transfer experiments.

3.4 Dynamic Coupling between Host and Guest

The mobility of guests molecules is restricted to different degrees by their hosts. Kitzinger et al.[38] suggested that the dynamic coupling between molecular motions of the components should be one of the three defining parameters for supramolecular complexes, in addition to their thermodynamic stability and dissociation kinetics.

Dynamic coupling coefficient in the nano-picosecond time scale is defined as the ratio of the correlation times of the host and the guest. Correlation times are derived from heteronuclear NMR relaxation rate measurements. Size and shape matching and the existence of multiple specific binding points between host and guest have a strong influence in the dynamic coupling between host and guest.

Signal splitting in a symmetrical host may also be caused by the inclusion of a low symmetry guest that undergoes restricted reorientation inside the host's cavity. This is the case of a D_2 symmetrical tetrameric capsule that can accommodate large hosts. When the host is 2-adamantanone, the symmetry of the complex is reduced from D_2 to C_2 and signal splitting is observed (analogous to situation 2(a) in Box 1). On the other hand, with 2,6-adamantanedione the D_2 symmetry is maintained and no signal splitting is observed (Figure 10).[39]

Restricted reorientation of an asymmetric guest can also cause the appearance of isomeric complexes (cf. situation 3(b)

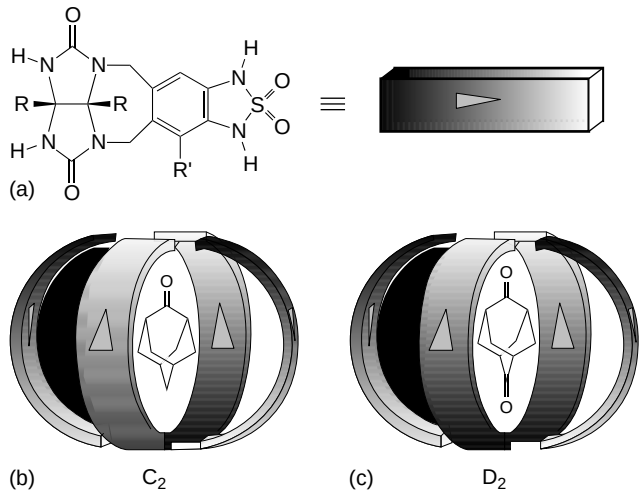

Figure 10 Symmetry reduction by the enclosed guest. The structure shown in (a) can form a large tetrameric capsule. When $R' \neq H$ the capsule has no symmetry planes. Inclusion of adamantanone leads to signal splitting as the 'top' and 'bottom' parts of the capsule become non-equivalent. This is not observed when the guest is more symmetrical

of Box 1). Carcerands formed by linking two different bowl-shaped molecules and containing a low symmetry guest can exist as a mixture of two carceplexes that differ only by the orientation of the guest inside the cavity. These isomers have been called 'carceromers'.[40]

Guest molecules trapped inside cavities may show different conformational preferences and different activation energies to the interconversion between isomers. The inversion of six member ring systems (cyclohexane, 1,4-dioxane, 1,4-thioxane, fluorocyclohexane, chlorocyclohexane, bromocyclohexane) have been measured in different supramolecular complexes, either in solution or in the solid state as urea inclusion compounds.

Interestingly, the increase in the interconversion barriers, if it exists, is small and seems to depend more on specific interactions between host and guest than on steric hindrance by the host walls. In particular, the inversion of 1,4-dioxane and 1,4-thioxane in a covalently linked carcerand or in a structurally related non-covalent capsule have the same barriers.[41] Also, the inversion barrier of fluorocyclohexane in solution is identical, within experimental error, to that measured in solid thiourea-fluorocyclohexane inclusion compounds by three different techniques: line shape analysis, $T_{1\rho}$ measurement and selective polarization inversion. On the other hand, substantial differences are observed in the rate of rotation of the amide bond in dimethylformamide or dimethylacetamide in carceplexes and are interpreted as a combination of steric and solvation effects.

3.5 Solid State NMR Studies of Guest Reorientation

Solid state NMR techniques can be applied to the study of the motions of guest inside host's cavities. Two types of supramolecular systems can be considered. On the one hand, there are 'molecular' host-guest systems that can exist as discrete entities in solution. On the other hand guests can be included in cavities that only exist in a crystalline arrangement of the host and, therefore, can only be studied in the solid-state.

Solid state studies are useful for 'molecular' host-guest systems, as the mobility of the host is strongly restricted. In addition, NMR can be used to differentiate static from dynamic disorder in X-ray structures.[42]

Solid hosts can have cavities of different sizes and topology, including linear channels, cages, networks and planes. Hosts can be inorganic, such as aluminosilicates (zeolites and clay materials) or organic solids, such as urea, and thiourea. See **Inclusion Compounds**.

^{2}H-NMR is the method of choice to study guest mobility in the solid state. ^{2}H-NMR is dominated by the nuclear quadrupole coupling. This arises from the interaction of the nuclear quadrupole moment with the electric field gradient, a tensorial quantity. For deuterium ($I = 1$) quadrupole coupling gives rise to two lines. A powder line shape is obtained by the summation of the contributions of randomly oriented crystallites. Pairs of singularities (edges, shoulders and peaks) in the spectrum are separated by frequencies that are proportional to the magnitudes of the principal values of the effective quadrupole coupling tensor. Reorientation of the guest at intermediate rates ($>10^4\ s^{-1}$) changes the ^{2}H-NMR line shape. By comparison with simulations, specific motional models can be proved. In the fast motion limit ($>10^7\ s^{-1}$) the line shape corresponds to an average effective tensor, which is obtained by adding the weighted contributions from all the sites visited during the motion.

Dynamic information can equally be obtained from the averaging of other tensorial quantities such as the shielding tensors.

Under cross-polarization magic angle spinning conditions (CP-MAS) indications about mobility can be obtained from the averaging of dipolar interactions. Rigid C–H fragments, with large dipolar couplings, show strong signal attenuation by dipolar dephasing when a short delay is introduced before acquisition.[43] Mobile C–H fragments show enhanced sensitivity, due to the NOE, under pulse saturation techniques.[44]

4 CONCLUDING REMARKS

Dynamic processes are inherent to species stabilized by non-covalent bonds and changes in experimental conditions may cause substantial changes in the geometry or the nature of supramolecular species. The relative dynamics of guest and host can also have a substantial effect on the spectroscopic and chemical properties of supramolecular inclusion compounds. NMR spectroscopy is unique among the spectroscopic and analytical tools in its capability to capture the complex static and dynamic stereochemistry properties of supramolecular complexes. In these efforts, the design and study of species of reduced symmetry is often an essential part in the characterization of supramolecular systems. Spectroscopic, stereochemical and synthetic chemical knowledge have to be integrated.

In the rapidly evolving field of supramolecular chemistry, NMR is expected to keep playing a central role, but supramolecular chemistry is also expected to contribute to the development of NMR techniques. This is especially evident in the light of the renewed interest in liquid crystalline systems, in the use of paramagnetic tags to induce orientation in proteins, the use of micellar systems to reduce the correlation times of large molecules by using low viscosity solvents, or the screening of ligand libraries. All these are basically supramolecular phenomena that forecast an even stronger connection between supramolecular chemistry and NMR.

5 RELATED ARTICLES IN THIS VOLUME

Chemical Exchange Effects in Biological Macromolecules; Combinatorial Chemistry; Diffusion-Based Studies of Aggregation, Binding and Conformation of Biomolecules: Theory and Practice; Inclusion Compounds; Liquid Crystalline Samples: Application to Macromolecular Structure Determination.

6 RELATED ARTICLES IN VOLUMES 1–8

Carbon-13 Relaxation Measurements: Organic Chemistry Applications, Volume 2; Chemical Exchange Effects on Spectra, Volume 2; Deuterium NMR in Solids, Volume 3; Diffusion Measurements by Magnetic Field Gradient Methods, Volume 3; Inorganic Chemistry Applications, Volume 4; NOESY, Volume 5; Nuclear Overhauser Effect, Volume 5;

Organic Chemistry Applications, Volume 5; Protein Structures: Relaxation Matrix Refinement, Volume 6; Relaxation: An Introduction, Volume 6; Relaxation Effects of Chemical Exchange, Volume 6; ROESY, Volume 7; Rotating Frame Spin-Lattice Relaxation Off-Resonance, Volume 7; Structure of Rigid Molecules Dissolved in Liquid Crystalline Solvents, Volume 7.

7 REFERENCES

1. J.-M. Lehn, 'Supramolecular Chemistry. Concepts and Perspectives', VCH: Weinheim, 1995.
2. J. L. Atwood, J. E. D. Davies, D. D. MacNicol, F. Vögtle, and J.-M. Lehn, eds, 'Comprehensive Supramolecular Chemistry', Pergamon: New York, 1996.
3. R. Ungaro and E. Dalcanale, eds, 'Supramolecular Chemistry: Where it is and Where it is Going', Kluwer: Dordrecht, 1999.
4. J. W. Steed and J. L. Atwood, 'Supramolecular Chemistry. A Concise Introduction', Wiley: Chichester, 2000.
5. M. Pons, ed, 'NMR in Supramolecular Chemistry', Kluwer: Dordrecht, 1999.
6. M. Pons and O. Millet, *Prog. Nucl. Magn. Reson. Spectrosc.*, 2001, **38**, 267.
7. K. A. Connors, 'Binding Constants. The Measurement of Molecular Complex Stability', Wiley-Interscience: New York, 1987, Chapter 5.
8. G. Weber, in 'Molecular Biophysics', eds B. Pullman and M. Weissbluth, Academic Press: New York, 1965.
9. L. R. MacGillivray and J. L. Atwood, *Angew. Chem. Int. Edn. Engl.*, 1999, **38**, 1018.
10. R. Wyler, J. De Mendoza, and J. Rebek, Jr, *Angew. Chem. Int. Edn. Engl.*, 1993, **32**, 1699.
11. A. Jasat and J. C. Sherman, *Chem. Rev.*, 1999, **99**, 931.
12. C. D. Gutsche, in 'Calixarenes Revisited. Monographs in Supramolecular Chemistry', ed J. Stoddart, The Royal Society of Chemistry: Cambridge, 1998.
13. K. D. Shimizu and J. Rebek, Jr, *Proc. Natl. Acad. Sci. USA.*, 1995, **92**, 12 403.
14. O. Mogck, V. Böhmer, and W. Vogt, *Tetrahedron*, 1996, **52**, 8489.
15. C. Piguet, G. Bernardinelli, and G. Hopfgartner, *Chem. Rev.*, 1997, **97**, 2005.
16. S. Rüttimann, C. Piguet, G. Bernardinelli, B. Bocquet, and A. F. Williams, *J. Am. Chem. Soc.*, 1992, **114**, 4230.
17. G. M. Whitesides, E. E. Simanek, J. P. Mathias, C. T. Seto, D. N. Chin, M. Mammen, and D. M. Gordon, *Acc. Chem. Res.*, 1995, **28**, 37.
18. A. R. Waldeck, P. W. Kuchel, A. J. Lennon, and B. E. Chapman, *Prog. Nucl. Magn. Reson. Spectrosc.*, 1993, **25**, 507.
19. E. O. Stejskal and J. E. Tanner, *J. Chem. Phys.*, 1965, **42**, 288.
20. E. G. Richards, 'An Introduction to Physical Properties of Large Molecules in Solution', Cambridge University Press: Cambridge, 1980.
21. J. García de la Torre and V. A. Bloomfield, *Biopolymers*, 1977, **16**, 1747.
22. J. García de la Torre, M. L. Huertas, and B. Carrasco, *J. Magn. Reson.*, 2000, **147**, 138.
23. B. Olenyuk, M. D. Levin, J. A. Whiteford, J. E. Shield, and P. J. Stang, *J. Am. Chem. Soc.*, 1999, **121**, 10 434.
24. F. Ni, *Prog. Nucl. Magn. Reson. Spectrosc.*, 1994, **26**, 517.
25. D. Neuhaus and M. Williamson, 'The Nuclear Overhauser Effect in Structural and Conformational Analysis', 2nd edn., Wiley-VCH: New York, 2000.
26. A. Chen and M. J. Shapiro, *J. Am. Chem. Soc.*, 1998, **120**, 10 258.
27. M. Mayer and B. Mayer, *Angew. Chem. Int. Edn. Engl.*, 1999, **38**, 1784.
28. T. Szabo, G. Hilmerson, and J. Rebek, Jr, *J. Am. Chem. Soc.*, 1998, **120**, 1485.
29. O. Mogck, M. Pons, V. Böhmer, and W. Vogt, *J. Am. Chem. Soc.*, 1997, **119**, 5706.
30. C. L. Perrin and T. Dwyer, *Chem. Rev.*, 1990, **90**, 935.
31. S. A. Nepogodiev and J. F. Stoddart, *Chem. Rev.*, 1998, **98**, 1959.
32. R. Jäger and F. Vögtle, *Angew. Chem. Int. Edn. Engl.*, 1997, **36**, 930.
33. P. E. Mason, I. W. Parsons, and M. S. Tolley, *Angew. Chem. Int. Edn. Engl.*, 1996, **35**, 2238.
34. R. M. Izatt, K. Pawlak, J. S. Bradshaw, and R. L. Bruening, *Chem. Rev.*, 1991, **91**, 1721.
35. R. M. Izatt, J. S. Bradshaw, K. Pawlak, R. L. Bruening, and B. J. J. Tarbet, *Chem. Rev.*, 1992, **92**, 1261.
36. R. M. Izatt, K. Pawlak, J. S. Bradshaw, and R. L. Bruening, *Chem. Rev.*, 1995, **95**, 2529.
37. E. Shchori, J. Jagur-Grodzinski, Z. Luz, and M. Shporer, *J. Am. Chem. Soc.*, 1971, **93**, 7133.
38. J. P. Kitzinger, F. Kotzyba-Hibert, J.-M. Lehn, A. Pagelot, and K. Saigo, *J. Chem. Soc. Chem. Commun.*, 1981, 833.
39. C. Nuckolls, F. Hof, T. Martin, and J. Rebek, Jr, *J. Am. Chem. Soc.*, 1999, **121**, 10 281.
40. P. Timmerman, W. Verboom, F. C. J. M. van Veggel, J. P. M. van Duynhoven, and D. N. Reinhoudt, *Angew. Chem. Int. Edn. Engl.*, 1994, **33**, 2345.
41. R. G. Chapman and J. C. Sherman, *J. Org. Chem.*, 2000, **65**, 513.
42. E. B. Brouwer and J. A. Ripmeester, *Adv. Supramol. Chem.*, 1999, **5**, 121.
43. S. J. Opella and M. H. Frey, *J. Am. Chem. Soc.*, 1979, **101**, 5854.
44. T. Yamanobe, I. Nakamura, K. Hibino, T. Komoto, H. Kurosu, I. Ando, Y. Nakamoto, and S.-I. Ishida, *J. Mol. Struct.*, 1995, **335**, 15.

Biographical Sketches

Miquel Pons, *b* 1956. Lic. Química, 1979, Barcelona, Lic. Biologia, 1986, Barcelona, Ph.D., 1983, London. Interested in structural and dynamic aspects of intermolecular association. From the NMR point of view his interests include the study of relaxation and exchange and the development of anisotropic systems. Approx. 100 papers.

Pau Bernadó, *b* 1974. Lic. Química, 1997, Barcelona. He is currently doing postgraduate studies in the University of Barcelona under the supervision of Prof. Pons. His research is related to the study of relaxation, hydrodynamics and orienting systems.

Thioredoxin and Glutaredoxin

H. Jane Dyson

The Scripps Research Institute, La Jolla, CA, USA

1	Introduction	1
2	NMR of *Escherichia coli* Thioredoxin	1
3	NMR of Human Thioredoxin	3
4	NMR of *Escherichia coli* Glutaredoxin	4
5	Related Articles	6
6	References	6

1 INTRODUCTION

Thioredoxins and glutaredoxins are ubiquitous small proteins involved in redox reactions in cells and viruses, including ribonucleotide reduction, sulfate metabolism, and both oxidative and reductive thiol−disulfide reactions with proteins.[1,2] Recent work implicates thioredoxin in cellular redox control mechanisms and also in mammalian virus systems, with possible applications in therapeutics.[3] The active sites of thioredoxin and glutaredoxin are similar, consisting of two cysteine (Cys) residues which are separated by two other residues and which are present as a disulfide in the oxidized protein and as a dithiol in the reduced protein. The active-site sequence in thioredoxin is -Cys-Gly-Pro-Cys- (where Gly = glycinexs, Pro = proline) and in glutaredoxin is -Cys-Pro-Tyr-Cys- (where Tyr = tyrosine).[2]

NMR spectra of *Escherichia coli* thioredoxin were reported as early as 1976,[4] but extensive NMR studies on these proteins were not made until the advent of high-field spectrometers in the 1980s. The NMR spectrum of a protein gives information on the three-dimensional (3D) structure (see ***Structures of Larger Proteins, Protein-Ligand, and Protein-DNA Complexes by Multi-Dimensional Heteronuclear NMR***). Structure determination has provided a major impetus in the study of thioredoxins and glutaredoxins by NMR, since, with the exception of the well-known X-ray crystal structure of the oxidized form of *E. coli* thioredoxin,[5] X-ray crystallography could not be used to derive structures because crystals were not formed. Oxidized *E. coli* thioredoxin was crystallized in the presence of Cu^{2+};[6] crystals of reduced *E. coli* thioredoxin have not been found under the same conditions due to the redox reaction between the copper ions and the protein dithiol. Its 3D structure has therefore been solved by NMR spectroscopy,[7] and a recent high-resolution structure determination by NMR for both oxidized and reduced *E. coli* thioredoxin[8] has allowed direct comparison of the two forms of the protein under identical conditions.

The structure of reduced human thioredoxin cloned from T-lymphocytes and overexpressed in *E. coli* has also been solved by NMR,[9] and the structures of both oxidized and reduced forms of a mutant protein have recently been published.[10] Although the glutaredoxin from T4 bacteriophage has been crystallized and its structure determined by X-ray crystallography,[11] *E. coli* glutaredoxin has not been crystallized; the structures of both oxidized and reduced glutaredoxin have recently been determined by NMR.[12,13]

The NMR spectrum of a protein also gives a great deal of useful site-specific information, and can be used to probe enzyme mechanism and function and ligand binding. A number of such studies have been performed for thioredoxins and glutaredoxins and are summarized in this article, together with work on the structures of these proteins.

2 NMR OF ESCHERICHIA COLI THIOREDOXIN

2.1 Solution Conditions for NMR

The stability and small size of *E. coli* thioredoxin (108 amino acids, M_r 11 700) make it a suitable candidate for NMR spectroscopy. Both the oxidized and reduced forms are soluble to approximately 4 mM at pH 5.7 in 100 mM phosphate buffer[4,14] and to 5−8 mM in 150 mM NaCl/20 mM phosphate, pH 5.7.[15] Dithiothreitol (DTT)-free reduced thioredoxin is prepared from the oxidized form of the protein by the addition of DTT and subsequent passage of the solution through a short column of Sephadex G25 equilibrated under argon.[16] The NMR spectrum is well dispersed with narrow resonance lines under these conditions. At pH values below 5.5 broadening of resonances in the NMR spectrum is observed, indicating the onset of aggregation, which occurs as the pI ($\sim$ 4) is approached.[4] The NMR spectrum as a whole is unaffected by pH changes up to pH 10, indicating that the structure of the protein is largely unaffected by pH in this range.[17] Certain resonances shift with pH due to the titrations of the N-terminal amine, the single histidine residue, and a buried aspartate near the active site in both oxidized and reduced thioredoxins, and by the titrations of the two thiol groups in reduced thioredoxin.[17]

2.2 Resonance Assignments and Structure Determination

A number of methods have been used for resonance assignment of *E. coli* thioredoxin. Pioneering studies in the use of isotope labeling were performed with oxidized thioredoxin, including the development of random fractional deuteration as a means of spectrum simulation and stereospecific assignment,[15,18,19] and specific labeling of amino acids as a means of sequential resonance assignment.[20,21] Backbone and C-β,H ^{1}H resonance assignments of the oxidized form of *E. coli* thioredoxin were largely completed using these methods combined with conventional ^{1}H two-dimensional (2D) spectroscopy.[15] Proton-only 2D NMR was used to obtain complete ^{1}H assignments for both oxidized and reduced *E. coli* thioredoxin,[16] and these assignments were used as a basis for the calculation of the solution structure of reduced *E. coli* thioredoxin using distance and dihedral angle restraints from ^{1}H 2D NOESY and COSY spectra.[7] The NMR spectra of reduced and oxidized *E. coli* thioredoxin are very similar, differing only in the region of the active site,[14,16] and the NMR solution structure of reduced thioredoxin is virtually identical to the X-ray crystal structure of oxidized thioredoxin.[5] Even

in the active site region where the NMR spectra of the two forms are different, the backbone conformations of the two forms of the protein are superimposable, and there are only the most subtle differences in the disposition of the side chains in this region. A total of 853 interresidue and 391 intraresidue distance constraints and 43 dihedral angle constraints were used in the calculation of the structure using the program DISGEO, and the resulting structures were refined with molecular dynamics (AMBER), for a final average rms deviation from the average structure of 0.564 for backbone heavy atoms of residues 3–108.[7]

The NMR solution structure of reduced *E. coli* thioredoxin represents probably one of the largest that has been calculated using ^{1}H 2D methods alone. Resonance overlap and the resulting ambiguities in estimates of internuclear distance lower the number of available distance and dihedral angle restraints, and hence the potential resolution of the structure. The additional resolution provided by the use of protein uniformly labeled with ^{13}C and ^{15}N[22,23] allows the addition of a significantly greater number of restraints to the calculation, resulting in a higher resolution structure. High-resolution structures have recently been calculated, using the program DIANA followed by refinement with molecular dynamics (AMBER), for both oxidized and reduced *E. coli* thioredoxin[8] using 2846 (reduced) and 2710 (oxidized) NOE distance restraints from 3D ^{13}C and ^{15}N heteronuclear NOESY spectra and 131 (reduced) and 136 (oxidized) dihedral angle restraints obtained from coupling constants. Final backbone average rms deviations from the average structure of 0.29 Å and 0.35 Å were obtained for the well-defined residues (4–107) of 30 reduced and oxidized thioredoxin structures respectively.[8] A superposition of 20 of each of the calculated structures is shown in Figure 1.

2.3 Nitrogen-15 Relaxation and Polypeptide Backbone Dynamics

The backbone and tryptophan side-chain dynamics of oxidized and reduced thioredoxin have been estimated using uniformly ^{15}N-labeled protein,[24] and show a number of regions, especially in turns and loops, where backbone flexibility is high compared with that of the polypeptide present in ordered secondary structure. The rather low proportion of flexible regions in thioredoxin is consistent with the exceptionally high thermal stability of this protein in either oxidation state.[25] The active site loop is also apparently flexible, but measurements are hampered because the sequence contains Gly and Pro, for which the ^{15}N relaxation parameters are not measurable. Differences in the flexibility of loops adjacent to the active site occur between the oxidized and reduced forms of the protein (see Section 2.5).

2.4 pH-Dependence of the Mechanism of Thioredoxin Dithiol–Disulfide Exchange

The mechanism of reduction by thioredoxin is thought to proceed via nucleophilic attack by a thiolate anion belonging to Cys-32, with formation of a mixed disulfide.[26] Control of the pH in the active site region is therefore likely to be crucial to the reaction. The pK_a for deprotonation of Cys-32 was shown in chemical modification studies to be considerably lowered from normal, to a value of about 6.7,[26] consistent with its postulated role as primary nucleophile. However, the mechanism is apparently quite complex, as shown by an NMR study of reduced and oxidized thioredoxin as a function of pH between 5.7 and 10.[17] pK_a values of 7.1 and 8.4 were obtained

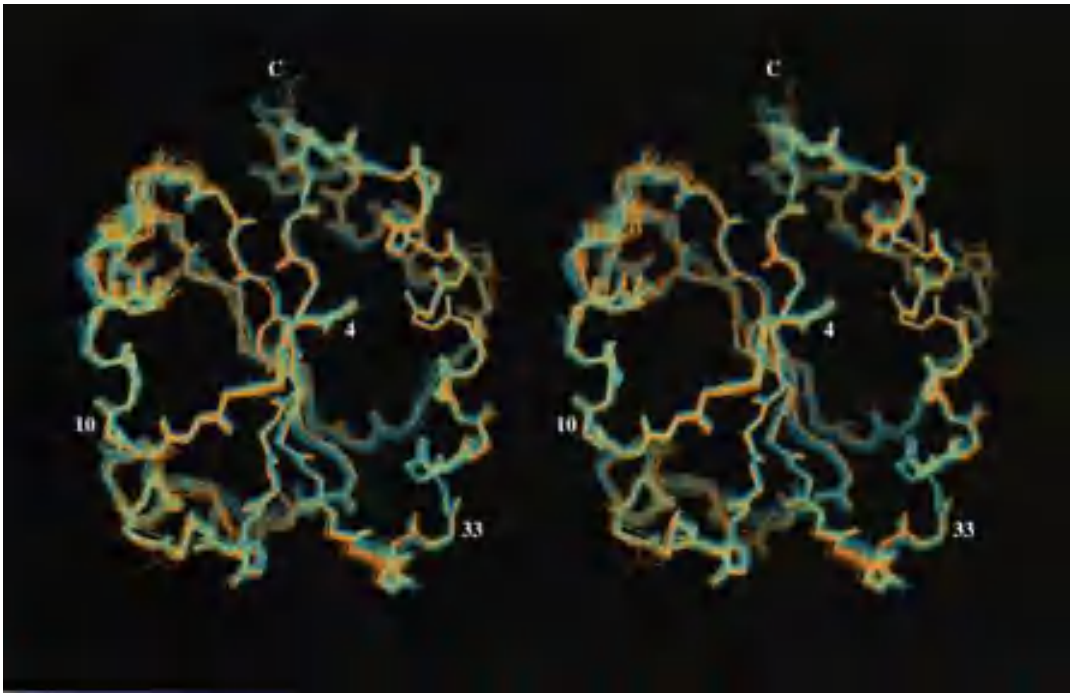

Figure 1 Stereo view showing the best-fit superposition for residues 4–107 of 20 NMR solution structures of reduced *E. coli* thioredoxin (yellow) and oxidized thioredoxin (blue) obtained using the distance geometry program DIANA followed by molecular dynamics refinement with AMBER. The active site (residues 32–35) is at the bottom right of the structure. (Reproduced by permission from Jeng et al.[8])

for two groups titrating in the active site region of reduced thioredoxin, consistent with the values previously obtained for the two active site thiols.[26] However, a third group also titrates in the active site region, giving a pK_a of 7.5 in oxidized thioredoxin and ∼7.1 in reduced thioredoxin. Mutant studies by NMR[27] and other methods[28,29] indicate that this titrating group is most likely the buried carboxyl group of aspartic acid (Asp)-26, which is thus revealed as an important factor in the pH control of the mechanism of *E. coli* thioredoxin.

2.5 Structural and Functional Differences between Oxidized and Reduced Thioredoxin

There are a number of functional differences between oxidized and reduced thioredoxin that are not due entirely to the presence or absence of thiol groups. Reduced thioredoxin is required for the assembly of filamentous bacteriophages[30,31] and is an essential subunit of the DNA polymerase induced by T7 phage.[32] Oxidized thioredoxin does not function in these systems. Mutants where one or both Cys residues are replaced with serine (Ser) or alanine (Ala) are partially functional,[31,33] suggesting some structural or conformational difference between the two forms that can be differentiated in the phage systems. The extremely small structural differences between the two forms of thioredoxin is illustrated in Figure 1. Indeed, the only significant difference appears to be a slight change in the backbone configuration at the active site due to the change in position of the reduced sulfur of Cys-32,[8] as shown in Figure 2. In the absence of a strongly marked change in the structure, the difference may lie in the relative mobility of the polypeptide chain in the vicinity of the active site. Backbone dynamics of both oxidized and reduced thioredoxin were studied using ^{15}N relaxation[24] and revealed a significant difference in the local flexibility of several of the loops that abut the active site. In particular, the sequence that precedes the highly conserved *cis*-Pro at position 76 is more flexible in reduced thioredoxin, suggesting that certain structural states may be kinetically accessible to reduced thioredoxin but not to the oxidized form due to the constraint imposed by the disulfide bond. This interpretation is borne out by a comparison of the rates of amide proton hydrogen exchange in the two forms of the protein,[34] which indicate a significantly greater protection in the active site region in oxidized thioredoxin, consistent with lower flexibility of the polypeptide chain. If one or more of these low-energy states was required for thioredoxin function in the filamentous and T7 phage systems, then reduced thioredoxin would be functional and the oxidized form would not. A recent NMR study of a double Cys-to-Ser mutant of *E. coli* thioredoxin[27] revealed that its behavior most closely resembled reduced rather than oxidized thioredoxin, consistent with these ideas and with previous functional studies of mutants.[31]

3 NMR OF HUMAN THIOREDOXIN

3.1 Solution Conditions for NMR

The thioredoxin cloned from human T-lymphocytes (105 amino acids) is approximately 25% homologous with the *E. coli* protein, mainly in the active site region.[35] Reduced human thioredoxin is soluble to at least 2 mM and solutions prepared

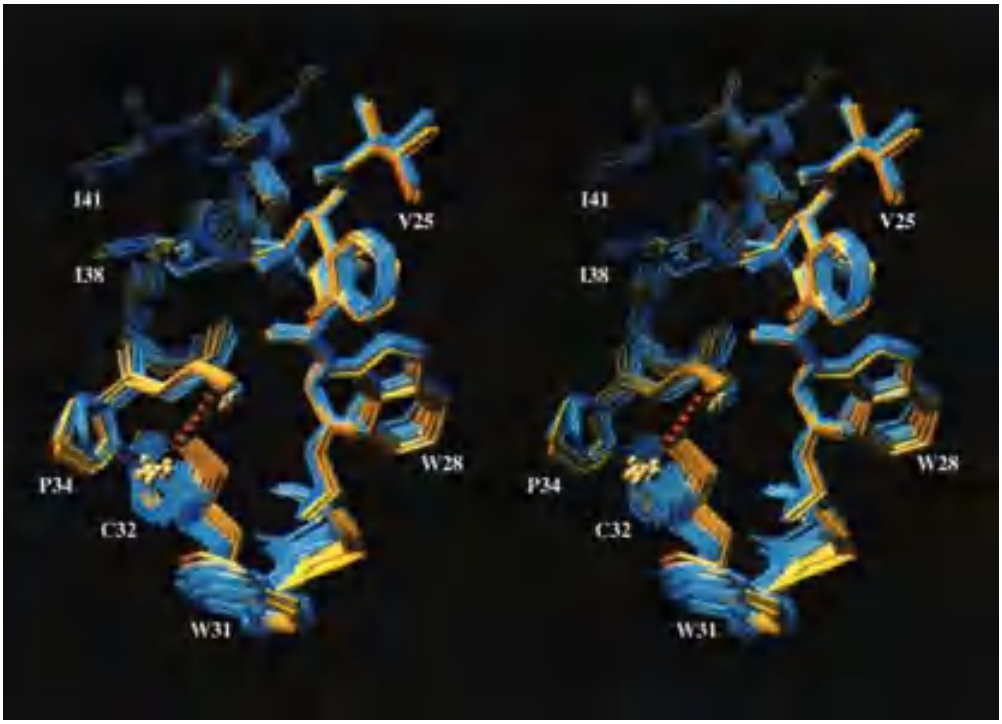

Figure 2 Stereo superposition (on the backbone of the entire molecule, residues 4–107, as in Figure 1) of the active site, including selected side chains, for 20 structures each of reduced (yellow) and oxidized (blue) thioredoxin. The disulfide bond is indicated by the hatched red and black bars, and the positions of the Cys sulfur atoms in reduced thioredoxin are shown by yellow spheres. (Reproduced by permission from Jeng et al.[8])

in 100–150 mM phosphate buffer containing 0.2 mM DTT under argon appear to be stable at pH 7.0 or 5.5 for at least 2 months, over a temperature range of 4–50 °C.[36] Solubility is reduced at pH values below 5.6.[37] Only the reduced form of unmodified human thioredoxin has so far been studied by NMR, because of the presence of three Cys residues in addition to the two in the active site. The presence of these additional thiol groups causes problems with aggregation of the protein upon oxidation. The recombinant human thioredoxin isolated from an *E. coli* expression system is heterogeneous at the N-terminus, with about 30% of the protein containing an extra methionine residue,[36] although the N-terminal methionine is processed more efficiently during bacterial growth in minimal media.[38] A triple Cys-to-Ala mutant of human thioredoxin has been constructed to allow NMR studies of both oxidation states of human thioredoxin.[39]

3.2 Resonance Assignments and Structure Determination

The ^{1}H resonances of reduced human thioredoxin were initially assigned and a description of the secondary structure was obtained using ^{1}H 2D methods.[36] Extensive ^{15}N assignments and coupling constant measurements have been made for reduced human thioredoxin,[38] and a high-resolution structure has been calculated.[9] A family of NMR solution structures of reduced human thioredoxin (Figure 3) were calculated using a hybrid distance geometry–simulated annealing method[9] with 1294 interresidue and 689 intraresidue distance restraints obtained from NOESY and ^{15}N heteronuclear multiple quantum coherence (HMQC)–NOESY experiments and 241 torsion angle restraints obtained from coupling constants. Proton and ^{15}N resonance assignments have also been made for the reduced form of a triple mutant of human thioredoxin, in which the three Cys residues other than those in the active site have been mutated to Ala residues,[39] and structures have been calculated for the oxidized and reduced forms of this mutant[10] using 2571 distance restraints, 273 torsion angle restraints, and 89 ^{3}J(HN-α) coupling constant restraints for the reduced form, and 2649 distance restraints, 278 torsion angle restraints, and 91 ^{3}J(HN-α) coupling constant restraints for the oxidized form. The backbone atomic rms deviations from the mean structure were 0.19 Å and 0.18 Å respectively for 40 structures of reduced and oxidized mutant thioredoxin.[10] The structure consists of a 5-stranded twisted β-sheet surrounded by four α-helices and the overall structure is similar to those of *E. coli* thioredoxins.[5,7] The major differences between the thioredoxins from these two different sources is in helices α_1 and α_3, which are longer and more regular in human thioredoxin. The active site conformations are all very similar, as would be expected from the high degree of sequence homology in this region.

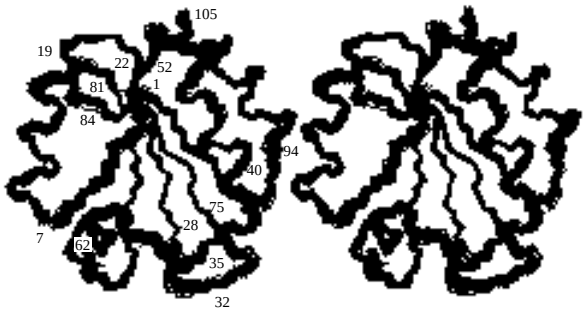

Figure 3 Stereo view (approximately the same view as Figure 1) showing the best-fit superpositions of the backbone (N, C-α, and C) atoms of 33 NMR solution structures of reduced human thioredoxin obtained by a distance geometry–simulated annealing method. (Reproduced by permission from Forman-Kay et al.9)

3.3 Bound Water Molecules in the Structure of Human Thioredoxin

The positions of relatively tightly bound water molecules in the structure of reduced human thioredoxin have been determined using 3D ^{1}H–^{15}N ROESY–HMQC spectroscopy.[40] A number of backbone amide protons are in close proximity to a total of four best-fit bound water molecules in structures recalculated to include them. Two of the water molecules could be located in fairly tight families, one in the β-bulge between strands 4 and 5 of the β-sheet and one associated with the C-terminal ends of the α_2 and α_4 helices. Of the other two water molecules, one occupies two positions near the loop between α_1 and β_2 and the other occupies two positions close to the N-terminus of α_2, near the active site. Several of the positions found for the bound water molecules in the solution structure of reduced human thioredoxin[40] are similar to those found in the X-ray crystal structure of oxidized *E. coli* thioredoxin.[5]

3.4 Electrostatics and Redox Function in Human Thioredoxin

An extensive study of the pH-dependent behavior of reduced human thioredoxin was made using ^{1}H and ^{15}N NMR spectroscopy.[37] Inclusion of measurements on solutions of pH lower than 5.6 allowed determination of the pK_a values of aspartate and glutamate side chains, although many of the titration curves exhibit complex behavior due to the effects of interacting titrating groups. Unlike *E. coli* thioredoxin,[17] no clear-cut effect of the titration of the buried carboxyl side chain of Asp-26 was observed, and the pK_a of the thiol of Cys-32 was measured to be 6.3, lower than the value for *E. coli* thioredoxin. The anomalously low pK_a for the Cys-32 thiol was attributed[37] to an interaction of the S-γ atom of Cys-32 with the amide group of Cys-35 seen in the solution structure of reduced human thioredoxin.[9]

4 NMR OF *ESCHERICHIA COLI* GLUTAREDOXIN

4.1 Solution Conditions for NMR

E. coli glutaredoxin (85 residues, M_r ~10 000) is a heat-stable acidic protein which reacts with glutathione and is responsible for mediating many glutathione-dependent redox functions in the cell. There is very little sequence homology between *E. coli* glutaredoxin and thioredoxin, although both contain an active site disulfide/dithiol group. The solution conditions required for NMR studies of glutaredoxin are less than optimal for structure determination.[41] Oxidized

glutaredoxin is insoluble at pH values below 5.5 and the NMR spectrum shows evidence of aggregation at pH 6.0. The protein appears to be stable and monomeric at pH 7.0 and 28 °C, at a concentration of 2.5 mM in 50 mM phosphate buffer. Reduced glutaredoxin is prepared from the oxidized form of the protein at 4 °C by the addition of DTT followed by buffer exchange in an ultrafiltration cell.[12] Final solution conditions were 3 mM protein in 50 mM phosphate, pH 7.0, 28 °C.

4.2 Resonance Assignments and Structure Determination

Nearly complete resonance assignments have been made for oxidized[41] and reduced[12] *E. coli* glutaredoxin, using mainly ^{1}H 2D methods, with the addition of 3D ^{15}N NOESY spectra for the resolution of ambiguities in NOE assignments and for measurement of ^{3}J(HN-α) coupling constants. Initial NMR spectra showed some heterogeneity, as glutaredoxin is apparently susceptible to proteolysis; this problem was overcome by the use of protease inhibitors.[41] Additional heterogeneity in the NMR spectra of oxidized glutaredoxin was also due to the presence of about 10% of a form elongated at the N-terminus or to conformational isomerism.[41] No conformational heterogeneity was reported for reduced glutaredoxin.[12] Three-dimensional structures were calculated for both forms of glutaredoxin using the program DIANA followed by simulated annealing. For oxidized glutaredoxin, 563 interresidue and 219 intraresidue distance constraints and 74 dihedral angle constraints were used.[13] For reduced glutaredoxin, 402 interresidue and 221 intraresidue distance constraints and 191 dihedral angle constraints were used.[12] The structure of glutaredoxin, shown in Figure 4, consists of a 4-stranded β-sheet and three helices, and is very similar in both oxidized and reduced forms of the protein.[13] Exchange rates of slowly exchanging amide protons are similar, indicating similar hydrogen-bonding patterns, but

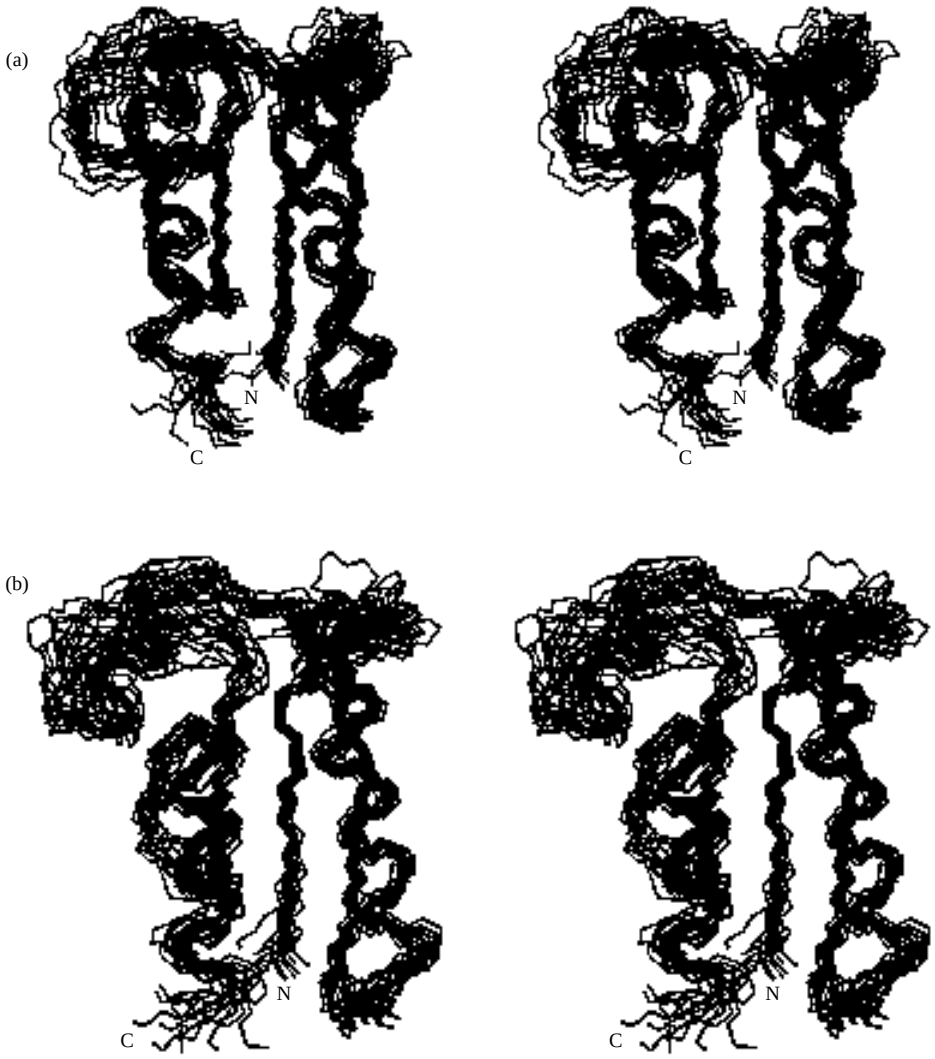

Figure 4 Stereo views of the 20 conformers used to represent the solution structure of (a) reduced and (b) oxidized *E. coli* glutaredoxin obtained using the program DIANA followed by simulated annealing. The complete polypeptide backbone from residues 1 to 85 is shown. The conformers 2–20 were superimposed with conformer 1 (which has the smallest residual violations) for pairwise minimal rms deviation of the backbone atoms N, C-α, and C′ of residues 1–8, 13–43, and 60–83. The active site (residues 11–14) is at the top right of the structure. (Reproduced by permission from (a) Sodano et al.[12] and (b) Xia et al.[13])

differences in local dynamics are evident near the active site and the C-terminal α-helix.[13] A comparison of Figures 1–4 shows that, despite the low sequence homology between glutaredoxin and thioredoxin, the overall folds of thioredoxin and glutaredoxin are quite similar.

4.3 Structure of a Mixed Disulfide Complex of Glutathione and Glutaredoxin

As for thioredoxin, the mechanism of thiol–disulfide exchange of glutaredoxin was thought to proceed via a mixed disulfide intermediate between one of the active site thiols and a molecule of glutathione.[42] In order to probe the structure of such an intermediate, a mutant glutaredoxin was prepared with one of the active site cysteines, Cys-14, substituted by Ser. The physiological substrate, glutathione, could then be bound to the remaining cysteine, Cys-11, forming a mixed disulfide which ought to have the same structure as that of the wild-type, but which is stable since reaction of the second thiol (now a Ser) with a second molecule of glutathione and release of the oxidized glutathione dimer is not possible. The C14 $\rightarrow$ S glutaredoxin mutant and the mixed disulfide complex with glutathione have been prepared and characterized by NMR,[42] and the structure of the complex has recently been reported.[43] Nitrogen-15 NMR studies[42] confirmed that the glutathione molecule is attached via a disulfide bond to Cys-11, and the structure shows that it lies along a shallow cleft in the protein that includes a number of hydrophobic residues.[43]

5 RELATED ARTICLES

Amino Acids, Peptides and Proteins: Chemical Shifts; Biological Macromolecules: Structure Determination in Solution; Enzymatic Transformations: Isotope Probes; Motional Effects on Protein Structure: Acyl Carriers; Peptides and Polypeptides; Protein Dynamics from NMR Relaxation; Protein Hydration; Structures of Larger Proteins, Protein-Ligand, and Protein-DNA Complexes by Multi-Dimensional Heteronuclear NMR; Three- and Four-Dimensional Heteronuclear Magnetic Resonance.

6 REFERENCES

1. A. Holmgren, *Annu. Rev. Biochem.*, 1985, **54**, 237.
2. A. Holmgren, *J. Biol. Chem.*, 1989, **264**, 13 963.
3. J. Yodoi and T. Tursz, *Adv. Cancer Res.*, 1991, **57**, 381.
4. A. Holmgren and G. Roberts, *FEBS Lett.*, 1976, **71**, 261.
5. S. K. Katti, D. M. LeMaster, and H. Eklund, *J. Mol. Biol.*, 1990, **212**, 167.
6. A. Holmgren and B.-O. Söderberg, *J. Mol. Biol.*, 1970, **54**, 387.
7. H. J. Dyson, G. P. Gippert, D. A. Case, A. Holmgren, and P. E. Wright, *Biochemistry*, 1990, **29**, 4129.
8. M.-F. Jeng, A. P. Campbell, T. Begley, A. Holmgren, D. A. Case, P. E. Wright, and H. J. Dyson, *Structure*, 1994, **2**, 853.
9. J. D. Forman-Kay, G. M. Clore, P. T. Wingfield, and A. M. Gronenborn, *Biochemistry*, 1991, **30**, 2685.
10. J. Qin, G. M. Clore, and A. M. Gronenborn, *Structure*, 1994, **2**, 503.
11. B.-O. Söderberg, B.-M. Sjöberg, U. Sonnerstam, and C.-I. Brändén, *Proc. Natl. Acad. Sci. U.S.A.*, 1978, **75**, 5827.
12. P. Sodano, T.-H. Xia, J. H. Bushweller, O. Björnborg, A. Holmgren, M. Billeter, and K. Wüthrich, *J. Mol. Biol.*, 1991, **221**, 1311.
13. T.-H. Xia, J. H. Bushweller, P. Sodano, M. Billeter, O. Björnberg, A. Holmgren, and K. Wüthrich, *Protein Sci.*, 1992, **1**, 310.
14. H. J. Dyson, A. Holmgren, and P. E. Wright, *FEBS Lett.*, 1988, **228**, 254.
15. D. M. LeMaster and F. M. Richards, *Biochemistry*, 1988, **27**, 142.
16. H. J. Dyson, A. Holmgren, and P. E. Wright, *Biochemistry*, 1989, **28**, 7074.
17. H. J. Dyson, L. L. Tennant, and A. Holmgren, *Biochemistry*, 1991, **30**, 4262.
18. D. M. LeMaster, *FEBS Lett.*, 1987, **223**, 191.
19. D. M. LeMaster, *FEBS Lett.*, 1988, **233**, 326.
20. D. M. LeMaster and F. M. Richards, *Biochemistry*, 1985, **24**, 7263.
21. D. M. LeMaster and F. M. Richards, in *Thioredoxin and Glutaredoxin Systems: Structure and Function*, eds. A. Holmgren, C.-I. Brändén, H. Jörnvall, and B.-M. Sjöberg, Raven Press, New York, 1986, p. 67.
22. K. Chandrasekhar, G. Krause, A. Holmgren, and H. J. Dyson, *FEBS Lett.*, 1991, **284**, 178.
23. K. Chandrasekhar, A. P. Campbell, M.-F. Jeng, A. Holmgren, and H. J. Dyson, *J. Biomol. NMR*, 1994, **4**, 411.
24. M. J. Stone, K. Chandrasekhar, A. Holmgren, P. E. Wright, and H. J. Dyson, *Biochemistry*, 1993, **32**, 426.
25. T. Hiraoki, S. B. Brown, K. J. Stevenson, and H. J. Vogel, *Biochemistry*, 1988, **27**, 5000.
26. G. B. Kallis and A. Holmgren, *J. Biol. Chem.*, 1980, **255**, 10 261.
27. H. J. Dyson, M.-F. Jeng, P. Model, and A. Holmgren, *FEBS Lett.*, 1994, **339**, 11.
28. K. Langsetmo, J. A. Fuchs, and C. Woodward, *Biochemistry*, 1991, **30**, 7603.
29. K. Langsetmo, J. A. Fuchs, C. Woodward, and K. A. Sharp, *Biochemistry*, 1991, **30**, 7609.
30. M. Russel and P. Model, *Proc. Natl. Acad. Sci. U.S.A.*, 1985, **82**, 29.
31. M. Russel and P. Model, *J. Biol. Chem.*, 1986, **261**, 14 997.
32. S. Adler and P. Modrich, *J. Biol. Chem.*, 1983, **258**, 6956.
33. H. E. Huber, M. Russel, P. Model, and C. C. Richardson, *J. Biol. Chem.*, 1986, **261**, 15 006.
34. M.-F. Jeng and H. J. Dyson, *Biochemistry*, 1995, **34**, 10 101.
35. H. Eklund, F. K. Gleason, and A. Holmgren, *Proteins*, 1991, **11**, 13.
36. J. D. Forman-Kay, G. M. Clore, P. C. Driscoll, P. Wingfield, F. M. Richards, and A. M. Gronenborn, *Biochemistry*, 1989, **28**, 7088.
37. J. D. Forman-Kay, G. M. Clore, and A. M. Gronenborn, *Biochemistry*, 1992, **31**, 3442.
38. J. D. Forman-Kay, A. M. Gronenborn, L. E. Kay, P. T. Wingfield, and G. M. Clore, *Biochemistry*, 1990, **29**, 1566.
39. J. D. Forman-Kay, G. M. Clore, S. J. Stahl, and A. M. Gronenborn, *J. Biomol. NMR*, 1992, **2**, 431.
40. J. D. Forman-Kay, A. M. Gronenborn, P. T. Wingfield, and G. M. Clore, *J. Mol. Biol.*, 1991, **220**, 209.
41. P. Sodano, K. V. R. Chary, O. Björnberg, A. Holmgren, B. Kren, J. A. Fuchs, and K. Wüthrich, *Eur. J. Biochem.*, 1991, **200**, 369.
42. J. H. Bushweller, F. Åslund, K. Wüthrich, and A. Holmgren, *Biochemistry*, 1992, **31**, 9288.

43. J. H. Bushweller, M. Billeter, A. Holmgren, and K. Wüthrich, *J. Mol. Biol.*, 1994, **235**, 1585.

Acknowledgments

I wish to acknowledge Dr Peter Wright for helpful discussions and a critical reading of the manuscript and Dr Mei-Fen Jeng for preparing Figures 1 and 2. This work was supported by grant GM43238 from the National Institutes of Health.

Biographical Sketch

H. Jane Dyson. *b* 1951. B.Sc.(hons), 1973; Ph.D. 1977, Sydney. Postdoctoral in Biology, MIT, 1977–78, Chemistry faculty, University of New South Wales, 1979–1984. NMR work begun in earnest at Scripps Clinic in 1984 in collaboration with Peter Wright; faculty at Scripps 1984–present. Approx. 50 publications. Research interests in the conformation of short peptides and in structure–function studies of proteins including thioredoxin.

Tritium NMR

Mark G. Kubinec and Philip G. Williams

Lawrence Berkeley National Laboratory, Berkeley, CA, USA

1	Background	1
2	Safety	1
3	Features and Parameters	2
4	Applications	5
5	Conclusion	11
6	Related Articles	11
7	References	11

1 BACKGROUND

The fundamental magnetic properties of tritium (^{3}H) were first reported in 1947[1–3] in a series of NMR measurements which demonstrated the triton to be a spin-$\frac{1}{2}$ nucleus, with a positive magnetic moment about 6.66% larger than that of the proton. Despite the fact that these measurements established tritium as the most sensitive NMR-active nucleus, very little research was conducted over the next two decades. In short, we have found only 24 reports of tritium spectra in the first 30 years, and 14 of those were published in the period 1974–76. The lack of activity in the early years of tritium NMR development is readily rationalized—tritium is a radioactive nucleus and, with the limited sensitivity of early spectrometers, the quantities required to make the 1947 measurements were enormous. [No specific details of sample sizes were given, but 50 μL of HTO with 50% abundance of ^{3}H contains ca. 3000 GBq of radioactivity, and we estimate that the samples must have been of this order, i.e. 1850–18 500 GBq (50–500 Ci).] Hence, applications were limited to US National Laboratories, where facilities existed for obtaining and handling large quantities of tritium.

The first liquids ^{3}H NMR spectrum other than HTO was described in 1964,[4] and set several important precedents for the newly developing field: (i) samples required large amounts of tritium (ca. 370 GBq in this instance); (ii) instrumental modification for ^{3}H detection was simple; (iii) proton–tritium couplings were obvious and readily measured; and (iv) the labeling pattern (or percentage of ^{3}H in various positions) was accessible from the spectrum. The sample used in this experiment was ethylbenzene prepared by metal-catalyzed reduction of phenylacetylene with tritium gas, and interestingly, the integrated ratio of methylene to methyl tritium was 1:1.5, not 1:1 as predicted. This result established high-resolution ^{3}H NMR as the tool of choice for analysis of tritiated products. The 'nontextbook' labeling pattern would have been difficult to detect and almost certainly overlooked using the conventional methods of the time, and incorrect assumptions about the labeling pattern would have affected downstream uses of the product. Indeed, biochemical applications of tritium have been slow to recover from the poorly characterized materials used in the 1950s and 1960s, when ^{3}H NMR was not available for product analysis.

Such demonstrations of the power of ^{3}H NMR spectroscopy led to a renewed interest in technical development in the late 1960s and early 1970s. Fortunately, the resurgence coincided with advances in instrumentation that allowed many other low abundance and/or low sensitivity nuclei to be routinely observed. This revolution in NMR spectrometer sensitivity was crucial. Since tritium sensitivity is $>$ 75-times that of ^{13}C, the ability to collect ^{13}C spectra at natural abundance clearly implies that tritium spectra could be obtained at the very low ^{3}H concentrations necessary to ensure the technique is safe and accessible to laboratories around the world. During this period, the sample requirement of 370–3700 GBq was drastically reduced to the range of 3.7–3700 MBq, depending on the complexity of the signals and the S/N level required. Of course, tritium detection by NMR still suffers from the inherent insensitivity of the technique, and some perspective can be gained from the fact that liquid scintillation counting (LSC) techniques can detect tritium at a level 10^{-7} lower than the highest field spectrometers of today. Yet, the detailed information which NMR yields about the chemical and magnetic environment of the nuclei makes this loss of sensitivity easy to justify.

The most influential force in the promotion of ^{3}H NMR spectroscopy as a routine research tool came from a fruitful collaboration between the University of Surrey and Amersham International. The early published work (1971–76) concentrated on methodology and proof of principle, and in the late 1970s a host of applications were reported. A number of other groups adopted the ^{3}H NMR approach, and by 1985 the Surrey group was able to publish an excellent compilation of techniques and results, describing a mature field.[5] In this article, we will discuss the major features of ^{3}H NMR spectroscopy, and address the more recent, popular, and significant chemical applications.

2 SAFETY

Tritium is the very rare, but naturally occurring, radioactive isotope of hydrogen. It is a pure β-emitter and its 12.4 year halflife is convenient for most chemical or biological experiments. In Table 1 we list a variety of chemical and physical properties of tritium and elementary tritiated compounds.

As mentioned above, the large amounts of tritium necessary for early experiments made containment of tritiated NMR samples a point of major concern, and a number of convenient containment systems have evolved.[5] Since tritium is a 'soft' β emitter, i.e. the energy of the β particle associated with its radioactive decay has very little penetrating power (Table 1, $E_{\max}$ = 18.6 keV, 6 μm range in water), it is readily contained by a thin surface of plastic, Teflon, or glass. The major hazard is from ingestion, so care should be taken to keep samples sealed and clean on the exterior. We favor a double encapsulation approach using either a 3-mm glass tube inside a regular NMR tube, or a capped Teflon liner inside a sealed glass tube. These components are all commercially available.

Since the number of tritium nuclei needed for NMR detection exceeds that required for liquid scintillation counting by a factor of ca. 10^7, the monitoring of equipment or personnel for contamination is readily accomplished by standard radiochemical techniques. At the minimum level readily detectable by liquid scintillation counting (LSC) (37 Bq L^{-1}) in a conventional urine analysis, the radiation exposure for an individual is less than 0.001 mSv y^{-1}. The sensitivity

Table 1 General Physical and Chemical Data for Tritium, and Common Radioactivity Units[a]

Production	^{6}Li(n, α)^{3}H
Radiation	β(100%); range = 4.5–6 mm in air, 6 μm in H_2O
β Energy	E_{max} = 18.6 keV, E_{mean} = 5.7 keV
Radioactive halflife	12.43 y (4540 d)
Biological halflife	ca. 10 d
Decay product	^{3}He
Maximum specific activity	1064 GBq milliatom^{-1} (28.76 Ci milliatom^{-1})
Detection limit (in 24 h): LSC	0.037 Bq = 2.09 $\times$ 10^7 atoms (ca. 0.1 fmol)
NMR	1064 kBq = 6.02 $\times$ 10^{14} atoms (ca. 1 nmol)
Diameter of tritium atom (approx.)	1.1 Å
Volume of 37 GBq (1 Ci) of tritium gas at standard temperature and pressure	0.385 mL
Radiation produced by 37 MBq (1 mCi) in a man (70 kg = 40 L, i.e. 25 μCi L^{-1})	0.044 mSv d^{-1} (= 4.4 mrem d^{-1}, or 1.6 rem y^{-1})
Density, triple point, and boiling point of	H_2O: 1.000 g mL^{-1}; 0.01°C; 100.00°C
isotopic water molecules	D_2O: 1.106 g mL^{-1}; 3.82°C; 101.42°C
	T_2O: 1.214 g mL^{-1}; 4.49°C; 101.51°C
Tritium content of pure T_2O at STP	117.4 TBq mL^{-1} (3173 Ci mL^{-1})
	96.7 TBq g^{-1} (2614 Ci g^{-1})

[a]37 gigabecquerels (GBq) = 1 curie (Ci) = 3.7 $\times$ 10^{10} disintegrations per second; 1 gray (Gy) = 10 000 erg g^{-1} = 100 rad (units of absorbed dose); 1 sievert (Sv) = 100 rem (units of radiation exposure).

of LSC thus provides a level of detection well below the average exposure from background, medical, and terrestrial sources (3 mSv y^{-1}) or the current recommendation for a US Department of Energy radiation worker (<20 mSv y^{-1}). In addition, tritium uptake in the body is cleared as tritiated water (HTO) with a 10 day biological halflife, and this period can be drastically reduced by increasing fluid intake or by diuretics (e.g. water, beer, or coffee).

The hazards associated with analyzing ^{3}H samples are real, but have been grossly overemphasized in the past. A rational assessment of the risks involved is in order. Tritium is readily contained and is physiologically benign at the levels used in most high-resolution NMR experiments. When making a benefit/hazard judgement of conducting research on a 2220 MBq (60 mCi) sample contained as described above, it is reasonable to remember that safety lights in aircraft contain up to 370 GBq (10 Ci) of tritium, a marine compass may have as much as 28 GBq (0.75 Ci), and commonly available night sights for rifles contain 2 GBq (50 mCi) of tritium. The spectroscopist may be at greater risk from the lock solvent or other chemical entity in the sample than from the radioactivity, e.g. in a 0.25 mL sample containing 2220 MBq of a tritiated compound in C_6D_6, there are 2 μmol of ^{3}H but 2.75 mmol of benzene. It is clearly less hazardous to handle a well-contained tritium sample than milligram quantities of neurotoxins and other biologically active compounds routinely analyzed in normal glass NMR tubes in many laboratories.

In summary, the handling and health physics of analyzing tritiated samples is an important but trivially solved consideration, allowing ^{3}H NMR spectroscopy to be readily executed in most laboratories having a pulsed Fourier transform NMR spectrometer.

3 FEATURES AND PARAMETERS

The characteristics of ^{3}H are compared with other common NMR active nuclei in Table 2. Tritium enjoys all the spectral advantages normally associated with spin-$\frac{1}{2}$ nuclei of high γ: narrow lines, high sensitivity, and good dispersion. A brief perusal of Table 2 indicates the strong similarity between triton and proton magnetic properties, with tritium having slightly higher sensitivity and dispersion, and similar relaxation characteristics. The similarity between nuclei extends to chemical shifts, allowing one to use the extensive library of proton chemical shifts when making tritium resonance assignments. Since tritium also has extremely low natural abundance, spectra are free of background signals and this, combined with the a priori knowledge of chemical shifts from analogous protons, makes assignment of tritium spectra particularly straightforward.

Many of the favorable properties of tritium are illustrated in the spectra in Figure 1, where a comparison of proton, deuterium, and tritium NMR spectra of labeled glucose is shown. The superior resolution and dispersion of tritium over deuterium, a spin-1 nucleus, is obvious. Note that this labeled molecule is low molecular weight, and the line broadening of deuterium signals for larger molecules is even more striking, hence eliminating deuterium NMR as a useful technique for the structural analysis of large molecules in solution. In addition, since the dominant relaxation mechanism for deuterium is quadrupolar, NOE determinations are impossible, and sensitivity in saturation transfer is reduced due to rapid spin–lattice relaxation. In contrast, tritium analysis greatly simplifies the proton spectrum in Figure 1(a), particularly around the solvent where a less fortuitous proton chemical shift (or sample temperature) would have completely obscured one of the glucose signals under the HDO peak. Even in H_2O, tritium spectra require no solvent suppression and are much more easily assigned than the generally more crowded proton analog.

To understand the quantities involved in a tritium NMR experiment, one must be aware of the common units and conversion factors which are listed in Table 1. One of the most important benchmarks is that complete replacement of hydrogen by tritium in one position of a molecule gives a specific activity (*SA*) of 1064 GBq mmol^{-1} (28.76 Ci mmol^{-1}). Obviously, for lower percentages of tritium replacement the *SA* value is proportionately reduced and this relationship,

Table 2 NMR Properties of ^{3}H and Common NMR Nuclei[a]

Nucleus	Natural abundance	Spin	γ	Resonant frequency	Relative sensitivity[b]
^{1}H	99.984	$\frac{1}{2}$	26.7510	300.13	1.00
^{2}H	0.0156	1	4.1064	46.07	9.65×10^{-3}
^{3}H	$<$**10^{-16}**	$\frac{1}{2}$	**28.5335**	**320.13**	**1.21**
^{13}C	1.10	$\frac{1}{2}$	6.7263	75.46	1.59×10^{-2}
^{15}N	0.37	$\frac{1}{2}$	-2.7116	30.40	1.04×10^{-3}
^{19}F	100	$\frac{1}{2}$	25.1665	282.23	0.83
^{31}P	100	$\frac{1}{2}$	10.8289	121.43	6.63×10^{-2}

Chemical shift (δ) range:	20 ppm
Isotope effects:	^{3}H primary, $1^\circ \approx 0.028$ ppm; 9.0 Hz at 7.1 T
	^{3}H secondary, $2^\circ \approx 0.013$ ppm; 4.2 Hz at 7.1 T
	^{2}H primary, $1^\circ \approx 0.020$ ppm; 6.7 Hz at 7.1 T
Coupling constant (J) range:	0–20 Hz
	$J(\mathrm{T,H}) = J(\mathrm{H,H}) \times \gamma_\mathrm{T}/\gamma_\mathrm{H}$
	$J(\mathrm{T,T}) = J(\mathrm{H,H}) \times (\gamma_\mathrm{T})^2 \times (1/\gamma_\mathrm{H})^2$
T_1	0–10 s
T_2	0–10 s

[a]7.1 T field.
[b]Sensitivity given for equal numbers of nuclei in the same field.

combined with a knowledge of the total number of millimoles of labeled substrate, readily yields the amount of radioactivity involved in the experiment.

3.1 Chemical Shifts and Referencing

Early measurements established that the ratios of nuclear screenings among the hydrogen isotopes was very close to unity. This implies that the chemical shift for a triton is essentially identical to that of a proton or deuteron in the analogous molecular environment. Thus tritium spectra can be referenced to, say, monotritiated TMS and chemical shifts will be nearly identical to proton chemical shifts. Since the tritium/proton Larmor frequency ratio is very well determined for TMS[6] (1.066 639 739 $\pm$ 2 $\times$ 10^{-9}), in practice it is not necessary to add a tritiated reference material to a sample to achieve accurate referencing. Instead, a simple measurement of the *proton* frequency of a reference material and multiplication by the figure above gives the tritium resonance frequency for the reference. This procedure is known as ghost referencing. Some care must be taken in very precise work when using ghost referencing because more careful studies of the Larmor frequency ratio for a variety of tritium-labeled materials[6,7] have shown that nuclear screenings are not identical, but vary slightly with carbon–hydrogen (tritium) bond hybridization. Thus, when referencing tritiated methyl groups a TMS ghost may be appropriate, but a tritiated phenyl position is more accurately referenced by a phenyl proton and a slightly different Larmor frequency ratio. These differences are usually so small that they do not interfere with routine analysis, and are not discerned in a wide display (0–6 ppm), such as that in Figure 1.

3.2 Coupling Constants and Isotope Effects

Coupling constants between tritium and other nuclei may be calculated from the analogous proton coupling constants. In particular, J(T,T) and J(T,H) are given by the relationships in Table 2, i.e. tritium–proton spin–spin coupling constants may be calculated as ca. 6.664% larger than the analogous proton constant. There is a small isotope effect on the coupling constant,[8] and measurements have been reported for tritium coupled to a number of other nuclei besides protons including carbon, tin, silicon, and boron.

Although there are isotope effects, measurement of a J(T,H) value is still an accurate way of predicting a proton–proton coupling constant, since the calculation involves division by 1.06664 rather than multiplication by 6.5144, as required by prediction from J(D,H). For isochronous protons (e.g. methyl protons having degenerate chemical shifts), measurement of the J(T,H) value readily yields a usually 'invisible' coupling constant (see Figure 2, below).

Besides the small isotope effects on nuclear screening and on coupling constants discussed above, there are also more commonly observed isotope effects on tritium chemical shifts caused by substitution of a heavy isotope in place of a proton. These are largest and therefore most easily observed when a geminal proton is replaced by a triton. This effect was first reported in analyses of highly tritiated methyl groups,[9] where the R–CT_3 singlet was resolved from the R–CT_2H doublet in the proton coupled tritium spectrum. The proton-decoupled spectrum was used to show that this primary isotope effect is ca. 0.025 ppm (i.e. 2.4 Hz at 96 MHz).

Figure 2 illustrates tritium isotope effects on chemical shifts and demonstrates how the methyl J(H,H) may be calculated from measured J(T,H) values, as discussed above. A sample of *m*-xylene was tritium-labeled by Raney nickel catalyzed exchange with T_2, which is known to give almost exclusive methyl tritiation. All three tritio-methyl species are produced, as shown in the proton-decoupled tritium spectrum in Figure 2(a), where these species are separated by the primary isotope effect ($\Delta\delta$) on the tritium chemical shift. At 320 MHz, tritium signals from methyl groups have a proton–tritium coupling constant which is double $\Delta\delta$, so that the proton-coupled tritium spectrum in Figure 2(b) has a deceptively simple

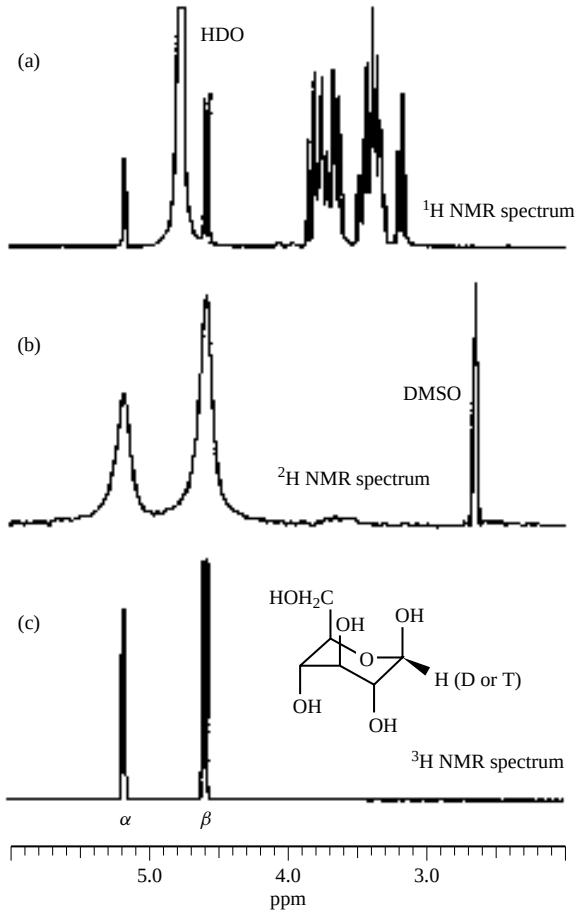

Figure 1 Hydrogen NMR spectra of D-glucose in water. (a) Proton spectrum of C-1 tritiated D-glucose; the large peak is due to HDO. (b) Proton decoupled deuterium NMR spectrum of C-1 deuterated glucose; DMSO is an integration marker. (c) Proton-coupled tritium spectrum of C-1 tritiated glucose, labeled by the same catalytic technique as in (b)

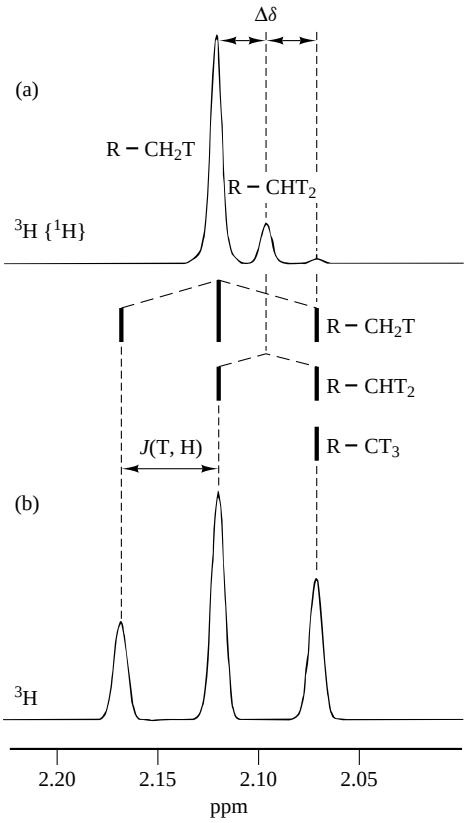

Figure 2 Deceptively simple tritium NMR spectra in C_6D_6 of *m*-xylene labeled by T_2 gas exchange over Raney nickel catalyst. (a) Proton-decoupled tritium spectrum showing peaks for R−CH_2T, R−CHT_2, and R−CT_3 species separated by $\Delta\delta = 0.025 \pm 0.001$ ppm (7.89 ± 0.21 Hz at 7.1 T). (b) Proton-coupled spectrum showing overlapped tritium multiplets separated by J(H,T) = 15.58 ± 0.21 Hz

appearance. The splitting patterns are shown on the figure, and our assignments are readily verified by integration of the signals in each of the spectra. The methyl J(H,H) for *m*-xylene methyl groups may be calculated from the observed J(T,H) value.

Secondary tritium isotope effects on chemical shifts have also been well quantified,[10] and the primary deuterium isotope effect on tritium chemical shifts is also easily measured (Table 2).

3.3 Tritium NMR Intensity and the NOE

One of the major advantages of tritium NMR spectroscopy is that the labeling pattern in a sample may be determined without the time-consuming and laborious degradative determinations previously required.[11] Indeed, a tritium spectrum gives nondestructive, quantitative information on relative tritium abundance at different sites in a molecule. Of course, care must be exercised in any measurement of NMR peak intensities so that accumulation of the data does not *differentially* affect the various peaks. When proton decoupling is used, for example, the tritium intensities will be affected by the Nuclear Overhauser Effect (NOE). Because of the frequent use of proton decoupling in tritium experiments, the importance of this effect has been the subject of several studies and discussions.[12] While the maximum theoretical NOE enhancement to tritons from proton irradiation is 47%, the observed enhancements vary from 10−35%. More importantly, there are situations where differential NOEs may prejudice tritium spectral intensities, such as a labeled molecule with a high abundance of tritium in a position without neighboring protons and a second tritiated position which has many relaxation partners, and integrals should only be compared when these issues have been considered.

3.4 Relaxation

The similarity of tritium and proton nuclei means that their pathways for relaxation are nearly identical. A feature of tritium NMR is that the simple spectra allow straightforward relaxation measurements. The analogous measurements in proton spectra can be difficult due to spectral crowding, solvent suppression, or the complexity of the physical system. Hence tritium relaxation can be the more useful probe of molecular interactions. A classic example is the use of proton and tritium relaxation measurements combined with homo- and heteronuclear saturation transfer experiments to study the relaxation of water molecules in the presence of a macromolecular suspension.[13] A rather simple suspension was created

by the formation of egg phosphatidylcholine/cholesterol lipid bilayers in solution. In a lipid suspension the water can exist in two distinct environments, a 'free' state exhibiting bulk water properties, and a motionally hindered or 'bound' state that is associated with the lipid in a hydration shell. Nuclei in these populations relax differently. The free water has the familiar characteristics of small rapidly tumbling molecules in solution, while the bound water has an additional slow component of tumbling due to its association with the lipid. This lipid-induced hydrodynamic effect causes a more rapid relaxation in the bound state and the presence of two water populations with different relaxation rates makes the overall relaxation behavior of the water signal complex. In general, it will depend on a combination of processes including the hydrodynamic effect, chemical exchange between free and bound environments, and the dipolar interaction (cross relaxation).

In the investigation of these processes, tritium doped water was used to separate the exchange contribution from other relaxation processes in the heteronuclear tritium–proton experiments. The measurements made on this rather complicated system were thus simplified to an analysis of several single-line spectra using inversion–recovery and saturation transfer experiments. The results indicated that the dipolar interaction (in the spin diffusion limit) dominates the relaxation of the water, and two models of this limit were proposed which accurately predicted the results, including a rigid and dynamic description of the lattice in the lipid solution. A complete model of the relaxation behavior of water is very desirable since the difference in relaxation properties of free and bound water populations is the basis for contrast and tissue characterization techniques in magnetic resonance imaging.

4 APPLICATIONS

We will limit the discussion here to chemical applications: (i) analysis of labeled materials for chemical and radiochemical purity; (ii) reaction mechanisms and tritium NMR techniques; (iii) specific activity measurements; (iv) solution conformation, stereochemistry, and optical purity; (v) proton exchange studies; and (vi) miscellaneous tritium NMR studies. Biological applications of ^{3}H NMR, e.g. ligand binding, metabolism studies, etc., are discussed elsewhere (see ***Tritium NMR in Biology***).

4.1 Analysis of Labeled Materials

The vast majority of reports involving ^{3}H NMR spectroscopy describe the products of tritium-labeling reactions, and in this application the technique is invaluable. Tritium NMR has been used extensively for the investigation of many tritium exchange techniques, including radiation-induced and acid-, base-, metal-, or zeolite-catalyzed reactions.[14] In general, these techniques rely on the replacement of a hydrogen atom by a tritium (i.e. exchange) in the native structure, and give low specific activity products which may contain tritium in one of several distinct sites.

In contrast, high level tritium labeling usually involves a synthetic transformation such as dehalogenation, hydrogenation, or hydride reduction of a suitable precursor. Dehalogenation reactions are an attractive method for introducing tritium into a compound, but surprisingly these reactions rarely give quantitative replacement of halogen by tritium, even when 100% T_2 gas is used. Our experience is that 10–30% of product molecules will incorporate adventitious hydrogen (^{1}H) rather than ^{3}H. In general, the shorter the reaction time, the less hydrogen incorporated (i.e. the higher the *SA* value obtained), and it is advisable to use an iodo derivative as the substrate since the facility of halogen removal is I > Br > Cl > F. Also, 1 equiv. of organic base (e.g. triethylamine) enhances the reaction rate and neutralizes the acid formed.

The power of tritium NMR in the analysis of a tritiodehalogenation reaction product is best illustrated by an example. Figure 3(a)–(e) show a full proton and ^{3}H NMR analysis of a peptide labeled by catalytic dehalogenation of the analogous 3,5-diiodotyrosyl peptide. The aromatic portion of the proton spectrum of the tritiated material [Figure 3(a)] shows ca. 15% proton intensity at the tyrosine 3 & 5 chemical shift, with the usual tyrosine 2 & 6 and Phe aromatic signals. Note that the splitting of the tyrosine 2 & 6 doublet reflects J(T,H), not coupling to the 3 & 5 protons. The proton-coupled tritium spectrum in Figure 3(b) shows a clean doublet at the tyrosine 3 & 5 chemical shift for the incorporated tritium. Broadband decoupling of the protons yields the singlet tritium signal in Figure 3(c), as expected. Selective irradiation at the tritium tyrosine 3 & 5 frequency causes the tyrosine 2 & 6 doublet to collapse, as shown in the proton spectrum in Figure 3(d) [cf. Figure 3(a)]. Similarly, selective ^{1}H decoupling at the tyrosine 2 & 6 frequency yields a singlet tritium signal at the tyrosine 3 & 5 chemical shift [Figure 3(e)]. These experiments are readily performed and characterize the product beyond any doubt.

The other most common method for introducing high levels of tritium is catalytic hydrogenation of an unsaturated site on a suitable precursor. Interestingly, heterogeneous metal-catalyzed hydrogenation reactions often do not yield 'textbook' results, and it is remarkable that so few researchers are aware of these details, despite their repeated demonstration.[5] Two effects contribute to the complicated mixture of isotopomers obtained from these reactions:[10] (i) there is an inventory of hydrogen ($^1H_1$) in the catalyst, solvent, substrate, and reaction vessel which serves to **decrease** the maximum level of tritium which may be incorporated into the labeled material; and (ii) vinylic and allylic protons may undergo metal-catalyzed exchange prior to saturation of the multiple bond, thus leading to **increased** specific activity.[15] As a result, the products of a hydrogenation reaction often have (a) lower than theoretical incorporation of tritium, (b) tritium in positions remote from the original site of unsaturation, and (c) unequal amounts of tritium on each side of the original multiple bond.

When ^{3}H NMR is used to analyze the products of both heterogeneous and homogeneous catalysis of an identical reduction, the complexities of heterogeneous catalysis are clear. Such a comparison of tritiation techniques for the labeling of an unsaturated phospholipid molecule is shown in Figure 4. All the problems described above for heterogeneous catalysis complicate the spectrum shown in Figure 4(a), including small amounts of tritium incorporated at the positions adjacent to the double bond. In contrast, the product of the homogeneous tritiation using Wilkinson's catalyst [Figure 4(b)] shows clean addition of tritium, with a 1:1 ratio at the C-7 and C-8 positions. A ^{3}H–^{3}H COSY analysis of this product [Figure 4(c)] showed that the two

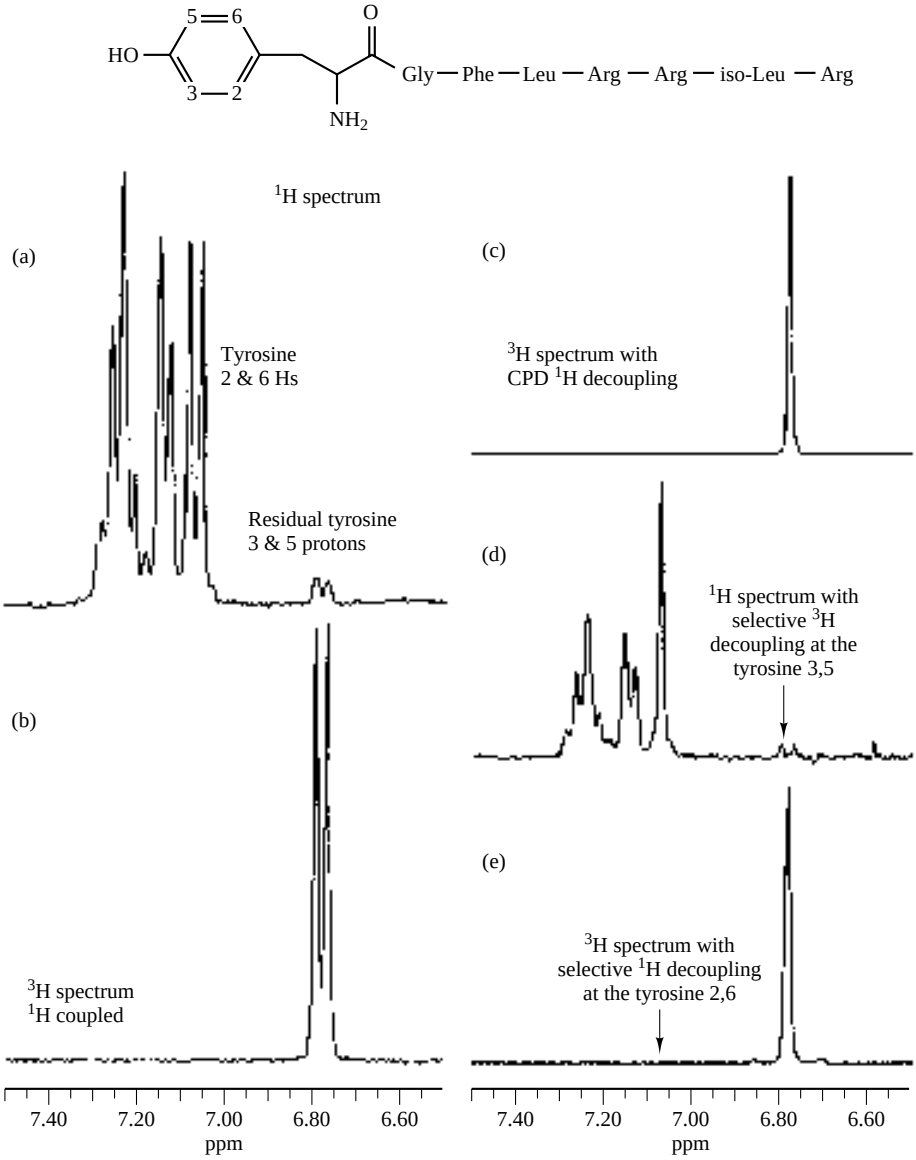

Figure 3 Proton and tritium NMR spectra in D_2O of a peptide labeled by catalytic tritio-dehalogenation of the appropriate diiodotyrosyl peptide. (a) Aromatic region of the proton spectrum showing signals from the phenylalanine residue and a clean doublet from the tyrosine 2 and 6 protons. Residual proton signals are obvious from the tyrosine 3 and 5 position. (b) Tritium spectrum showing the doublet of the tyrosine 3 and 5 tritons coupled to the 2/6 protons. (c) Proton-decoupled tritium spectrum showing the tritium singlet from the 3 & 5 tritium atoms. (d) Selectively tritium-decoupled proton spectrum: comparison with the spectrum in (a) shows the collapse of the tyrosine 2 & 6 doublet. (e) Selectively proton decoupled tritium spectrum, with irradiation only at the tyrosine 2 & 6 doublet

expected diastereotopic products were obtained, in a 1:1 ratio.[16] Although this tritium analysis shows that Wilkinson's catalyst gives a very clean product, it is not applicable in all circumstances. Such mundane issues as sample solubility and recovery of the labeled material from the reaction mixture often affect the decision of which catalyst is used. Heterogeneous catalysts have the advantages that they are tolerant of a variety of solvent systems and are easily filtered away after the reaction. Wilkinson's catalyst is usually employed as a benzene solution and may not perform well in a binary mixture if the substrate is insoluble in benzene. In addition, Wilkinson's catalyst is designed to form an intimate mixture with the substrate, and postreaction separation steps need to be optimized for each new substrate.

4.2 Reaction Mechanisms and Tritium NMR Techniques

Tritium spectra are almost always simple, hence there has been no strong drive to apply more sophisticated NMR techniques to tritium analyses. However, the subtleties of exchange effects in heterogeneous catalysis and the complex products from enzymatic reactions often require careful interpretation, and such studies may be greatly enhanced by the use of modern multipulse approaches.

The following techniques have been applied to tritium analyses over the past decade: double quantum filtering, DEPT, 2D homonuclear COSY, 2D tritium/proton correlation, 2D *J*-resolved, and 2D NOESY and EXSY experiments. The NOESY and EXSY approaches have been used for macromolecular structure studies and are discussed elsewhere

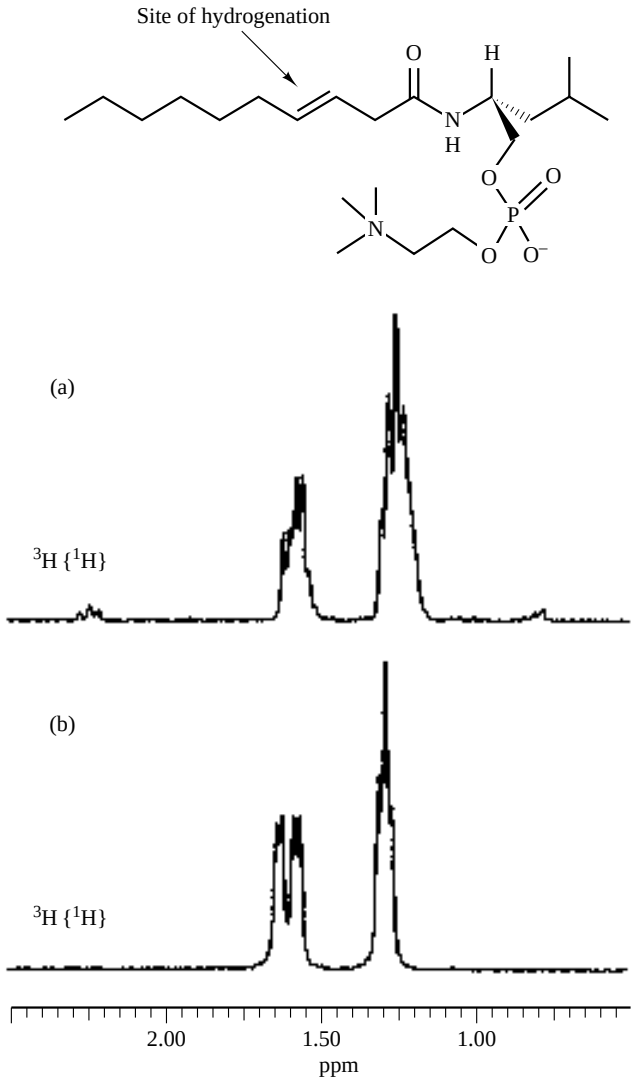

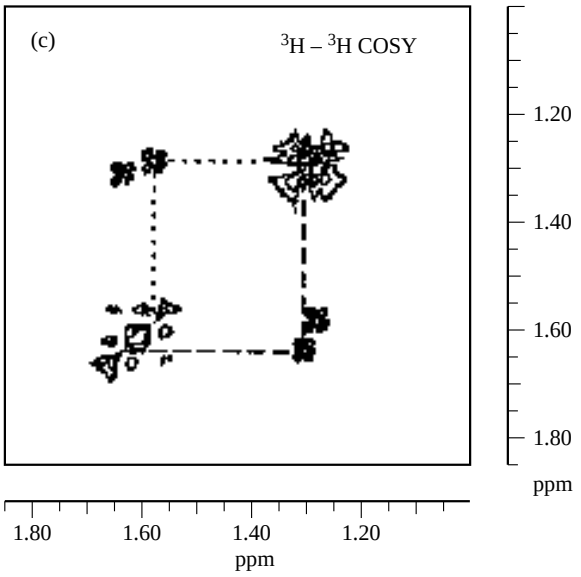

Figure 4 Proton-decoupled tritium NMR spectra of a labeled phospholipid in D_2O. (a) Product of a heterogeneous catalytic hydrogenation reaction. (b) Product from catalytic hydrogenation in the presence of Wilkinson's catalyst. (c) {^{1}H} ^{3}H–^{3}H COSY of the product in (b)

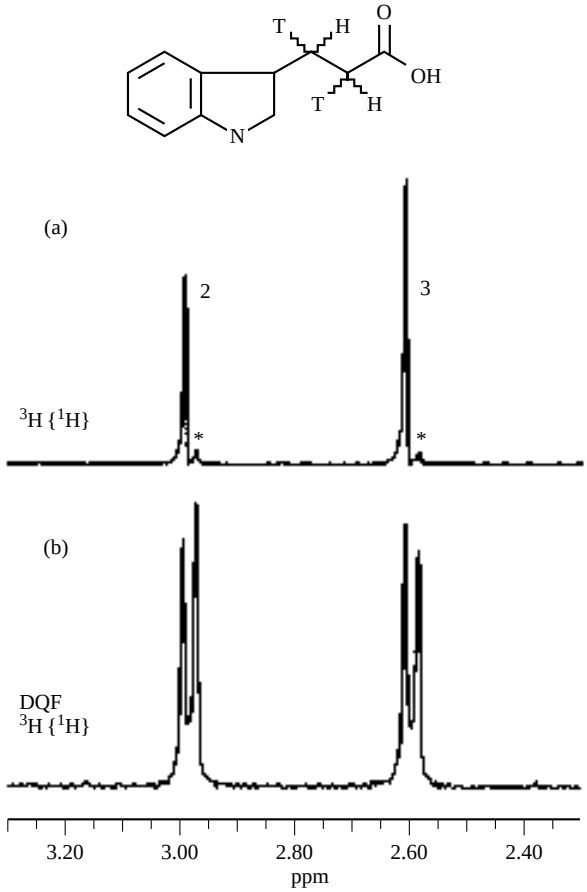

Figure 5 Tritium NMR spectra of tritiated 3-indolepropionic acid in CD_3OD. (a) Proton-decoupled tritium spectrum of the product of a heterogeneous catalytic hydrogenation reaction using 15% T/H. (b) Double quantum filtered proton-decoupled tritium spectrum of the same product as shown in (a). The observed J(T,T) = 7.32 ± 0.12 Hz, suggesting a J(H,H) value of ca. 6.4 Hz

(see ***Tritium NMR in Biology***). The pulse sequences we regard as most useful for analytical applications are the DQF and 2D J-resolved experiments. These have been used for detailed investigation of the 'nontextbook' results typically encountered in tritiation reactions, which are usually invisible in the corresponding reaction with $^1H_2$. Hence tritiation and tritium NMR spectroscopy provide an excellent approach for investigation of these imperfectly understood reaction mechanisms, as discussed below.

The research staff at Berkeley routinely use a mixture of 5–15% T_2 in H_2 for exploratory labeling reactions and in a training program. In the hydrogenation of 3-indoleacrylic acid using a 10% Pd/C catalyst and 15% T_2 in H_2 gas, simple statistics predict that 2.25% of labeled 3-indolepropionic acid product molecules will contain two ^{3}H atoms, 25.5% will have a tritium at one carbon or the other, and 72.25% will contain no tritium. The ^{1}H-decoupled tritium NMR spectrum in Figure 5(a) shows several features: (i) the large singlet signals arise from molecules containing one tritium atom, and it is obvious that unequal amounts of ^{3}H are incorporated across the double bond, and (ii) one signal from a small doublet can be discerned at the base of each singlet (asterisked), presumably arising from the doubly tritiated species. The unequal substitution pattern in the singly tritiated species is thought to arise from

exchange at those carbons prior to saturation of the double bond, and tritium NMR represents the best method for the further study of the mechanism of such exchange.[15] The doubly tritiated species can be observed simply and directly by the application of a familiar multiple pulse technique, a double quantum filtered (DQF) experiment. The results of the DQF experiment on this molecule are remarkably clean, as shown in Figure 5(b). The spectrum is simple because the doubly tritiated species is the only one present with tritium homonuclear double quantum transitions, and is further simplified because all couplings to protons are heteronuclear and have been removed by broadband decoupling. This result has tremendous potential for the study of the mechanism of this type of addition and would not have been possible without the use of tritium NMR. Clearly this unique ability to separate labeled species and perform careful analysis of complex mixtures of isotopomers resulting from a theoretically simple tritiation reaction is essential for understanding the mechanism of these reactions.

Two-dimensional *J*-resolved ^{3}H NMR[10] can be an even more powerful tool for the analysis of complex isotopic mixtures. β-Methylstyrene was tritiated by catalytic reduction with 100% T_2 over 5% Pd/C catalyst, to give highly tritiated *n*-propylbenzene with ca. 40% of the tritium on the α-methylene carbon, 50% on the β-methylene, and 10% in the methyl group. In addition, all of the multiplets for these tritiated positions showed a complex structure, not at all like the simple doublet of doublets which might have been proposed assuming clean addition of a tritium atom to each end of the double bond.

The methyl region of the proton-decoupled tritium *J*-resolved analysis of this sample (Figure 6) provided most insight into the species giving rise to the various signals. There is a repeating and slightly overlapped singlet–doublet–triplet pattern, with each repetition moved successively to lower frequency by ^{3}H isotope effects. These first of these patterns (group A, Figure 6) is due to the species X–CH_2–CH_2T, singlet; X–CHT–CH_2T, doublet; and X–CT_2–CH_2T, triplet (species 1, 2, and 3), and the small change in chemical shift between these signals is the secondary tritium isotope effect induced by addition of a T at the β-CH_2. There are similar patterns for the –CHT_2 (B) and –CT_3 (C) methyl species, successively moved to lower frequency by the primary tritium isotope effect on the methyl chemical shift. Inspection of several slices along the ω_2 dimension (submatrix, or .smx plots shown in Figure 6) show the relative abundance of each species in this mixture, and analysis of ω_1 slices allows us to extract all the ^{3}H–^{3}H coupling constants. Similar detailed analysis of the α-CH_2 and β-CH_2 regions of the *J*-resolved spectrum is also possible, and evidence was found for almost all of the 35 statistically possible, tritium-containing isotopomers. While the theoretical product, Ph–CHT–CHT–CH_3, was the most abundant species, the presence of another 34 tritiated isotopomers makes it clear that the mechanism of heterogeneous metal-catalyzed hydrogenation reactions is not as simple as commonly thought.

4.3 Specific Activity Measurements

The molar specific activity (i.e. radioactivity per unit weight) of tritium-labeled molecules is an important property, and tritium NMR may be used to determine this quantity.[5] This approach is essential when the labeled material has no UV

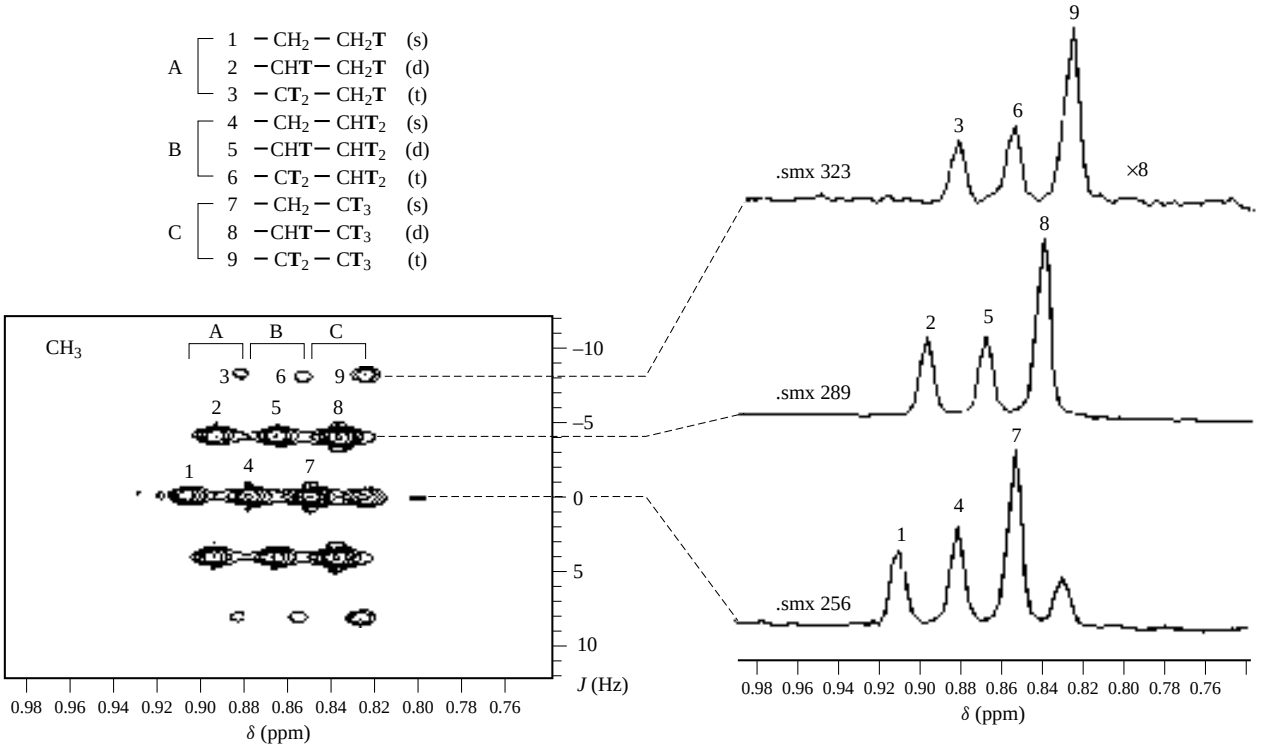

Figure 6 The methyl section (0.68–0.93 ppm) of the contour plot of the proton-decoupled tritium *J*-resolved spectrum of *n*-propylbenzene, labeled by catalytic tritiation of β-methylstyrene. Sine-bell window functions were applied in both dimensions, 2k × 512 W transform, with magnitude calculation of peak intensities. The data were 'tilted' and 'symmetrized'

spectrum, or the high specific activity precludes weighing to determine sample concentration. An example of the latter was the determination of the *SA* value for a series of $NaBT_4$ preparations.[17] Boron has two NMR active isotopes (^{10}B, 20%, $I = 3$ and ^{11}B, 80%, $I = \frac{3}{2}$), so the proton spectrum of sodium borohydride in basic CD_3OD shows a large quartet ($Na^{11}BH_4$, $\delta = -0.168$ ppm, $J = 80.6$ Hz) and a small septet ($Na^{10}BH_4$, $\delta = -0.166$ ppm, $J = 26.98$ Hz). The proton-decoupled tritium spectrum of exchange labeled $NaBH(T)_4$ shows a similar spectrum for each isotopomer, i.e. $NaBH_3T$, $NaBH_2T_2$, $NaBHT_3$, $NaBT_4$, shifted to lower frequency for each additional T. The multiplicity (redundancy) of the peaks is useful since peak overlap does not occur for all the species, and the isotopomer ratios may be compared between large quartet signals and the smaller septets. The amount of unlabeled ($NaBH_4$) material present was estimated by comparison with $NaBH_3T$ signals in the proton spectrum. Knowing the mole ratio of all the isotopomers yields the *SA* value, and this property was compared for several production 'lots' of tritiated borohydride.

Even when determination of *SA* by UV spectroscopy and LSC counting, or by mass spectrometry, is possible, the NMR technique provides a useful cross check. In comparison to the sodium borohydride case above, a very simple example of using ^3H and ^1H NMR to determine specific activity is given in Figure 7. Pinoline (6-methoxy-1,2,3,4-tetrahydro-9*H*-pyrido[3,4-*b*]indole) was labeled by catalytic hydrogenation of the unsaturated 3,4-dihydro analog. The product consisted of a mixture of three isotopomers containing zero, one, or two tritium atoms per molecule. Obviously, at the chemical shift of the C-1-methylene, one of these species has only a proton spectrum, one has a tritium spectrum, and one [R–CHT, δ = 4.39 ppm, Figure 7(a) and (b)] has both a tritium and a proton NMR spectrum. In this case, the use of selective tritium [Figure 7(a)] or proton [Figure 7(b)] decoupling allows the observation of single lines for each of the isotopomers in the proton or tritium spectrum. Since the R–CHT signal occurs in both spectra, the molar ratio of the three species may be extracted from these spectra and the specific activity calculated.

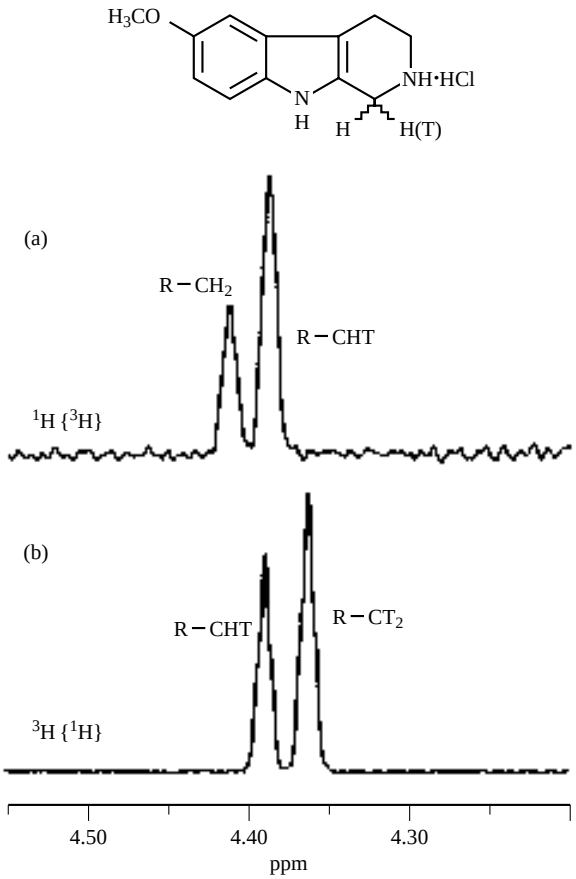

Figure 7 Proton and tritium NMR spectra of tritiated pinoline in CD_3OD. (a) Selectively tritium-decoupled proton spectrum. (b) Selectively proton-decoupled tritium spectrum

4.4 Solution Conformation, Stereochemistry, and Optical Purity

Tritium NMR has been used to obtain the axial–equatorial conformational preference of tritium in [^3H]cyclohexane.[18] Tritium has the advantage of giving sharp and well-separated peaks that are well suited for high-accuracy integration at low temperatures, i.e. the peak separation in these experiments was ca. 150 Hz at 7.1 T, whereas the analogous deuterium experiment at 11.7 T gave a separation of only 36 Hz. [^3H]Cyclohexane was made from cyclohexylmagnesium chloride in diethyl ether by the addition of HTO (5% tritium) followed by distillation of the tritiated product. A sample (ca. 0.9 GBq, 33 mCi) in CS_2 containing some CD_2Cl_2 for lock purposes was transferred into a standard thin-wall glass 5-mm NMR tube and ^3H {^1H} NMR spectra were obtained at 320 MHz (300-MHz ^1H frequency). Narrow lines (ca. 2 Hz at halfheight) with good lineshapes were obtained at $-88\,^\circ C$ by using the tritium FID as well as the ^2H lock signal for shimming. For accurate integration it is essential that the base of the peaks be narrow and symmetrical, and that the baseline is flat. A number of data sets, each consisting of the sum of 512 FIDs were acquired, several with the carrier at a higher frequency than the sample signals, some with the carrier at a lower frequency, and others with the carrier centered between the signals. The ^{13}C satellites of both the axial and equatorial ^3H signals ($\delta\nu = 0.471$ ppm) were visible in each set of spectra and gave $J(^{13}C,^3H_{ax}) = 131.1$ Hz and $J(^{13}C,^3H_{eq}) = 135.2$ Hz. Integration of the spectra showed that tritium prefers the equatorial over the axial site by about 46.9 J mol^{-1} and a ^3H EXSY experiment showed that the axial and equatorial tritium atoms are undergoing (slow) exchange at $-88\,^\circ C$. Conformational analysis by ^3H NMR relaxation has also been used in enzyme ligand studies (see NT497-***Tritium NMR in Biology***).

The absolute stereochemistry of a tritium atom on a carbon may be determined by tritium NMR if there is another chiral center in the molecule. If this is not the case on the parent molecule, it can often be created by esterification or some other derivatization. This feature was exploited in analysis of tritiated ethanol produced by enzymatic oxidation of 'chiral ethane', i.e. $CH_3–CHDT$, as part of a study of the mechanism of methane monooxygenase.[19] Tritium NMR analysis of the methylene region of the ethanol product showed signals from $CH_3–CHT–OH$ and $CH_3–CDT–OH$, separated by the ^2H isotope effect on the tritium chemical shift [Figure 8(a)]. Whereas this spectrum gives information on the relative rate of removal of an H or D atom in the oxidation process, it gives no stereochemical data. A simple derivatization with

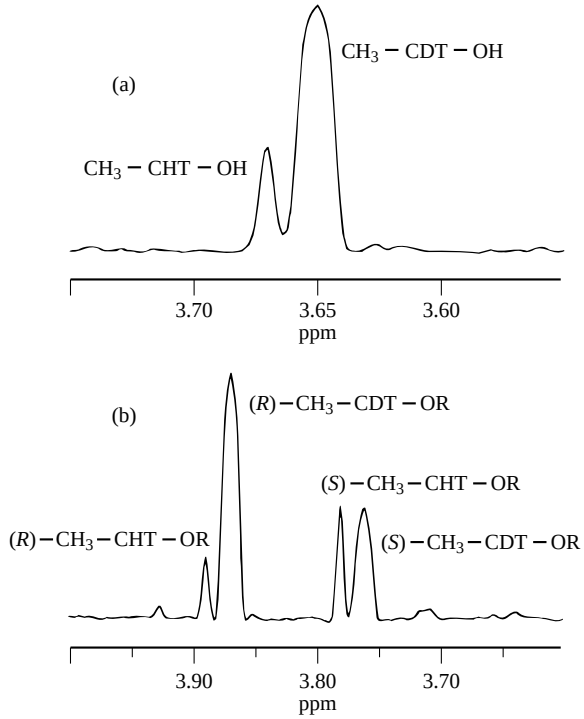

Figure 8 Proton-decoupled tritium NMR spectra of the products from enzymatic oxidation of chiral ethane. (a) Ethanol in H_2O. (b) Derivatized ethanol in C_6D_6, where R = (2*R*)-2-acetoxy-2-phenylethanoic acid

(2*R*)-2-acetoxy-2-phenylethanoic (mandelic) acid yields ethyl mandelate, and the four possible species can be readily separated and quantitated by ^3H $\{^1H\}$ NMR, as shown in Figure 8(b). The *absolute* stereochemistry was previously established by a known synthesis of the deuterium-substituted molecules and proton NMR analysis.

Tritium NMR has been used to determine the optical purity of labeled materials. The use of a lanthanide shift reagent[20] or Pirkle's alcohol[21] is a more general technique than the careful stereochemical determinations discussed above, and does not require the presence of an alcohol or amine functionality for derivatization to the appropriate ester or amide. This general approach is especially important for materials labeled at low tritium abundance because the optical properties of the bulk material may not be the same as the small subpopulation of labeled molecules.

4.5 Proton Exchange Studies

The NMR properties of tritium make it particularly well suited for in situ measurements of acid- and base-catalyzed proton exchange kinetics using tritium NMR spectroscopy.[22] Despite the great sensitivity and simplicity of this approach,[5] previous tritium NMR mechanistic studies of proton exchange have been confined to a static approach, i.e. the analysis of aliquots of a kinetic experiment.[23] In most circumstances, it is desirable to perform one-tube, accurate, kinetic experiments, especially for compounds which are only available in small amounts or have several exchanging positions with similar rates. Use of deuterium NMR spectroscopy, hampered by its low sensitivity and resolution, is inherently limited to initial rates,[24] and if several positions are measured simultaneously, relative rates for the positions must lie within a small range. In contrast, tritium NMR spectroscopy allows one to measure the proton exchange kinetics of several compounds which may have similar rates or vary by a factor of 1000. Since tritium is a highly sensitive nucleus, the sample need not contain high levels of tritium for detection (especially compared with deuterium) and tritium therefore functions as a true tracer in the reaction kinetics. Only 20–180 MBq (0.5–5 mCi) per position (1.5×10^{-5}% incorporation) is necessary for an adequate S/N ratio. This low tritium concentration also ensures the absence of tritium–tritium coupling, and the high γ and excellent relaxation characteristics of the nucleus lead to sharp resonance lines. The integrity of the reactant mixture may be monitored by proton NMR spectroscopy at any stage of the experiment. An inverse-gated proton-decoupling scheme may be used to ensure that single peaks are observed for each magnetic environment and that the relative peak integrals are not affected by NOE build-up. The quality of the kinetic data obtained by this technique suggests that it may be readily applied to other chemical proton-transfer systems.

As an example, this technique has been applied to the measurement of detritiation rates for the characterization of isotope effects. The Swain–Schaad relationship predicts that the deuterium and tritium isotope effects on the rate of a reaction are related as follows: $(k_H/k_D)^x = k_H/k_T$. Theoretical calculations put x in the range 1.33–1.58, and a simple zero-point energy formulation of isotope effects gives x = 1.44. Deviations from this range have recently been used as evidence of tunneling in enzyme-catalyzed reactions, so the accuracy of experimental results in simple chemical systems is important. Such a simple system is the hydroxide ion-catalyzed enolization of acetone (a prototype ketone ionization reaction), but the originally published measurements give an anomalously low exponent, x = 1.08.[25] This exponent was based upon rates of detritiation of labeled acetone, which were determined by a technique that involved a difficult separation of acetone from water.

This reaction was reinvestigated[26] using tritium NMR to monitor the exchange of tritium between acetone and water in situ,[22] thus avoiding the troublesome acetone–water separation. In NMR experiments using a range of base concentrations, the tritium signal from the acetone at δ = 2.1 ppm was seen to decay while another resonance at δ = 4.7 ppm, attributable to HTO, appeared (Figure 9). Least-squares fitting of the observed exponential rise and decay gave first-order rate constants that agreed well with each other.

When the NMR result was combined with k_H and a literature value of k_D determined by mass spectrometric measurements, it yielded k_H/k_D = 7.2 and k_H/k_T = 19.2. These isotope effects provide the Swain–Schaad exponent x = 1.49 $\pm$ 0.07, which is in complete agreement with theory. Thus, tritium NMR provided a simple method for the measurement of an important exchange rate which was essentially inaccessible by chemical techniques.

4.6 Miscellaneous

Tritium NMR spectroscopy has been used in a number of other very specific chemical and physical investigations, most of which have been comprehensively reviewed elsewhere.[5]

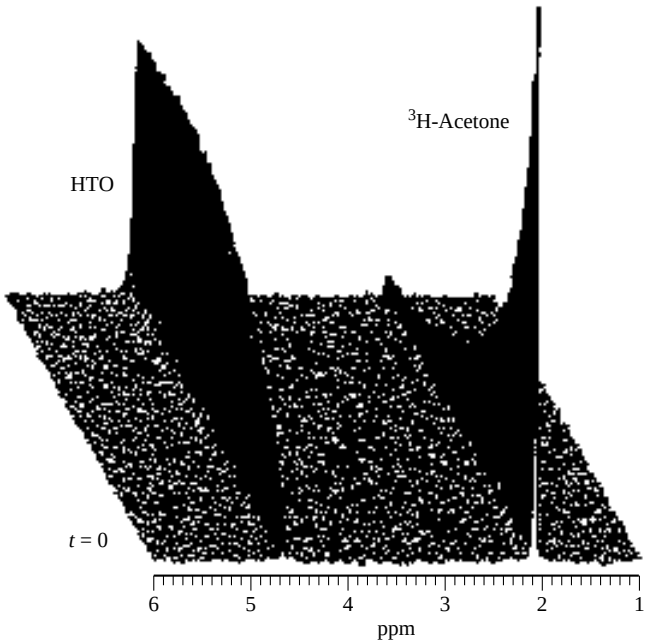

Figure 9 A stacked plot of the proton-decoupled tritium NMR spectra of the base-catalyzed detritiation of acetone (δ = 2.1 ppm) with exchange into the solvent (HTO, 4.7 ppm). The experimental parameters were: 500 μL, 0.04 M, NaOH; 5 μL, ^{3}H-acetone; T = 298 K; 120 transients; 100 experiments over 10.5 h (ca. 4-min interval for the first 50, then 8-min interval); spectrometer unlocked; t = 0 when the acetone was added, and the first spectrum was finished at t = 20 min. Seventy-seven spectra are plotted

These applications have included: (i) the observation of hydrogen-bonding effects on the chemical shift of proton versus tritium NMR signals; (ii) determination of solvent isotope effects and fractionation factors; (iii) aspects of radiation chemistry including sample radiolysis, studies of DNA hydration, and in situ production of labeled carbocations; (iv) investigations of labeled molecules in a liquid crystal environment; (v) solids tritium NMR and characterization of trapped gases in irradiated lithium hydride (tritide) samples;[27] and (vi) study of the origin of an anomalously large proton–proton coupling in transition metal polyhydrides.[28]

5 CONCLUSION

We have discussed a wide range of applications where the use of tritium NMR has been useful, and some instances where it was essential. The similarity in NMR properties between protons and tritons means that many systems may be studied using either nucleus. Moreover, when proton systems become too complex, the spectral simplification of tritium spectroscopy suggests that tritium NMR should be considered. Radioactivity is the only issue hindering the universal application of tritium in many more general NMR studies.

6 RELATED ARTICLES

Enzymatic Transformations: Isotope Probes; Multidimensional Spectroscopy: Concepts; Tritium NMR in Biology.

7 REFERENCES

1. H. L. Anderson and A. Novick, *Phys. Rev.*, 1947, **71**, 372.
2. F. Bloch, A. C. Graves, M. Packard, and R. W. Spence, *Phys. Rev.*, 1947, **71**, 373.
3. F. Bloch, A. C. Graves, M. Packard, and R. W. Spence, *Phys. Rev.*, 1947, **71**, 551.
4. G. V. D. Tiers, C. A. Brown, R. A. Jackson, and T. N. Lahr, *J. Am. Chem. Soc.*, 1964, **86**, 2526.
5. E. A. Evans, D. C. Warrell, J. A. Elvidge, and J. R. Jones, *Handbook of Tritium NMR Spectroscopy and Applications*, Wiley, Chichester, 1985, pp. 1–249.
6. J. P. Bloxsidge, J. A. Elvidge, J. R. Jones, R. B. Mane, and M. Saljoughian, *Org. Magn. Reson.*, 1979, **12**, 574.
7. J. M. A. Al-Rawi, J. P. Bloxsidge, C. O'Brien, D. E. Caddy, J. A. Elvidge, J. R. Jones, and E. A. Evans, *J. Chem. Soc., Perkin Trans. 2*, 1974, 1635.
8. J. M. A. Al-Rawi, J. A. Elvidge, J. R. Jones, and E. A. Evans, *J. Chem. Soc., Perkin Trans. 2*, **1975**, 449.
9. J. P. Bloxsidge, J. A. Elvidge, J. R. Jones, E. A. Evans, J. P. Kitcher, and D. C. Warrell, *Org. Magn. Reson.*, 1981, **15**, 214.
10. P. G. Williams, H. Morimoto, and D. E. Wemmer, *J. Am. Chem. Soc.*, 1988, **110**, 8038.
11. J. M. A. Al-Rawi, J. P. Bloxsidge, J. A. Elvidge, J. R. Jones, V. E. M. Chambers, V. M. A. Chambers, and E. A. Evans, *Steroids*, 1976, **28**, 359.
12. F. M. Kaspersen, C. W. Funke, E. M. G. Sperling, and G. N. Wagenaars, *J. Labelled Compds. Radiopharm.*, 1987, **24**, 219.
13. T. L. Ceckler and R. S. Balaban, *J. Magn. Reson.*, 1991, **93**, 572.
14. P. G. Williams, in *Isotopes in the Physical and Biomedical Sciences*, ed. E. Buncel and J. R. Jones, Elsevier, Amsterdam, 1991, Vol. 2, p. 55.
15. J. A. Elvidge, J. R. Jones, R. M. Lenk, Y. S. Tang, E. A. Evans, G. L. Guilford, and D. C. Warrell, *J. Chem. Res. (S)*, 1982, 82.
16. A. S. Culf, Ph.D. Thesis, University of Surrey, UK, 1994.
17. L. J. Altman and L. Thomas, *Anal. Chem.*, 1980, **52**, 992.
18. F. A. L. Anet, D. J. O'Leary, and P. G. Williams, *J. Chem. Soc., Chem. Commun.*, 1990, 1427.
19. N. D. Priestley, H. G. Floss, W. A. Froland, J. D. Lipscomb, P. G. Williams, and H. Morimoto, *J. Am. Chem. Soc.*, 1992, **114**, 7561.
20. J. A. Elvidge, E. A. Evans, J. R. Jones, and L. M. Zhang, *Synth. Appl. Isot. Labeled Compd., Proc. 2nd Int. Symp.*, ed. R. R. Muccino, Elsevier, Amsterdam, 1986, p. 401.
21. F. M. Kaspersen, C. W. Funke, E. M. G. Sperling, F. A. M. Van Rooy, and G. N. Wagenaars, *J. Chem. Soc., Perkin Trans. 2*, 1986, 585.
22. R. E. Dixon, P. G. Williams, M. Saljoughian, M. A. Long, and A. Streitwieser, *Magn. Reson. Chem.*, 1991, **29**, 509.
23. E. Buncel, J. P. Davey, G. J. Buist, J. R. Jones, and K. D. Perring, *J. Chem. Soc., Perkin Trans. 2*, 1990, 169.
24. D. W. Boerth, and A. Streitwieser, Jr., *J. Am. Chem. Soc.*, 1981, **103**, 6443.
25. J. R. Jones, *Trans. Faraday Soc.*, 1969, **65**, 2138.
26. Y. Chiang, A. J. Kresge, H. Morimoto, and P. G. Williams, *J. Am. Chem. Soc.*, 1992, **114**, 3981.
27. R. C. Bowman, Jr., A. Attalla, P. C. Souers, C. L. Folkers, T. McCreary, G. D. Snider, F. Vanderhoofven, and R. T. Tsugawa, *J. Nucl. Mater.*, 1988, **154**, 318.
28. K. W. Zilm, D. M. Heinekey, J. M. Millar, N. G. Payne, and P. Demou, *J. Am. Chem. Soc.*, 1989, **111**, 3088.

Acknowledgments

M.G.K. is supported by the Office of Energy Research, Office of Health and Environmental Research, Health Effects Research Division of the US Department of Energy under Contract DE-AC03-76SF00098, and through Instrumentation Grants from the US Department of Energy, DE FG05-86ER75281, and the National Science Foundation, DMB 86-09035. P.G.W. is supported by the Biomedical Research Technology Program, National Center for Research Resources, US National Institutes of Health, under Grant P41 RR01237, through Contract DE-AC03-76SF00098 with the US Department of Energy.

Biographical Sketches

Mark G. Kubinec. *b* 1964. B.S., 1986, biochemistry, B.S., 1987, chemistry, Michigan State University, USA, Ph.D., 1994, Chemistry, University of California, Berkeley, USA. Postdoctoral fellow, Lawrence Berkeley National Laboratory, 1995–present.

Philip G. Williams. *b* 1956. B.Sc., 1980, chemistry, Ph.D., 1984, chemistry, University of New South Wales, Australia. Research Fellow, Ludwig Institute for Cancer Research, Sydney, Australia, 1984–85; staff scientist, Lawrence Berkeley National Laboratory, USA, 1986–present. Approx. 70 publications Current research specialties: tritium labeling, tritium NMR.

Vicinal ^{1}H,^{1}H Coupling Constants in Cyclic π-Systems

Harald Günther

University of Siegen, Germany

1	Discussion	1
2	Related Articles	2
3	References	3

1 DISCUSSION

According to the Karplus theory of vicinal ^{1}H,^{1}H coupling constants, i.e. $^3J(^1\mathrm{H},^1\mathrm{H})$, such parameters depend on the structural features of the corresponding HC–CH fragment (dihedral angle Φ, bond length R_{cc}, and HCC valence angles) as well as on the electronic effects of substituents.[1,2] These results form the basis for numerous applications of ^{1}H NMR spectroscopy in organic, bio-organic, and organometallic chemistry.

While the dihedral angle dependence of $^3J(^1\mathrm{H},^1\mathrm{H})$—the well-known *Karplus curve*—is one of the major tools in conformational analysis,[3] structural research in the field of cyclic π-systems profits from the R_{cc} and valence angle dependence which dominates $^3J(^1\mathrm{H},^1\mathrm{H})$ values in planar unsaturated hydrocarbons, where $\Phi = 0^\circ$ for a *cis*-HC$_\mu$⋯C$_\nu$H arrangement and where substitutents are absent. This aspect was first highlighted as a linear dependence between $^3J(^1\mathrm{H},^1\mathrm{H})_{cis}$ and the Hückel (HMO) π-bond order, $P_{\mu\nu}$, of the C$_\mu$⋯C$_\nu$ bond was found for benzenoid aromatics[4] and later extended to olefinic systems.[5,6] At the same time, related correlations between $^3J(^1\mathrm{H},^1\mathrm{H})$ and the CC bond length $R_{\mu\nu}$ were established for aromatics[7] and polyenes.[8] An early application of $^3J(^1\mathrm{H},^1\mathrm{H})$ data for the analysis of the bonding situation in a cyclic π system was the detection of partial π-bond fixation in biphenylene (**1**),[9] which in terms of resonance theory demonstrated the preference for Kekulé structures with exocyclic double bonds at the central four-membered ring. Later, the olefinic nature of tropone (**2**) was established from its $^3J(^1\mathrm{H},^1\mathrm{H})$ values,[10] partial bond fixation in heterocyclic compounds was detected,[11,12] and the characteristic $^3J(^1\mathrm{H},^1\mathrm{H})$ data measured for cyclic dienes and trienes were recognized as important tools for the structural analysis of cyclic diene–triene isomers like norcaradienes and cycloheptatrienes.[13]

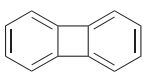

(1)

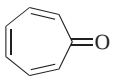

(2)

A detailed investigation of the $^3J(^1\mathrm{H},^1\mathrm{H})_{cis}/R_{\mu\nu}$ and $P_{\mu\nu}$ relations in unsaturated six-membered rings of various benzenoid aromatics and other hydrocarbons,[14,15] where the magnitude of these constants ranges between 5 and 9 Hz (and—as for other $^3J(^1\mathrm{H},^1\mathrm{H})$ values—a positive sign is found[16]), finally led to equations (1) and (2) which can be used to derive bond length and π-bond order information from experimental $^3J(^1\mathrm{H},^1\mathrm{H})_{cis}$ data:

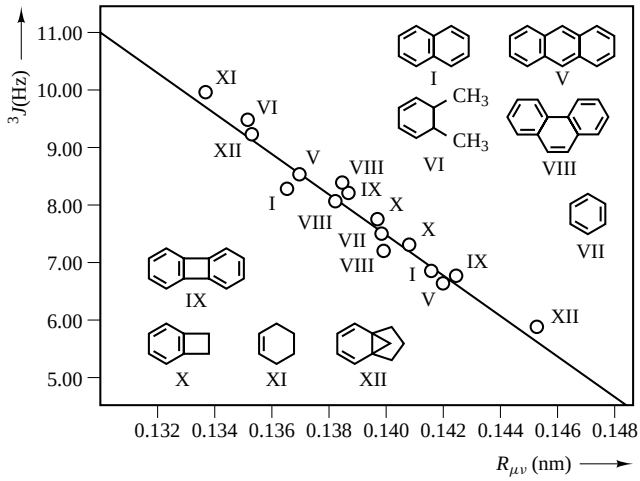

Figure 1 Dependence of $^3J(^1\mathrm{H},^1\mathrm{H})_{cis}$ on the CC bond length in the HC⋯CH fragment of six-membered rings [equation (1)]. (Reproduced with permission from H. Günther, 'NMR Spectroscopy', 2nd edn., Wiley, Chichester, 1995)

$$^3J(^1\mathrm{H},^1\mathrm{H})_{cis} = -351.0R_{\mu\nu}(\mathrm{nm}) + 56.65 \quad (1)$$

$$^3J(^1\mathrm{H},^1\mathrm{H})_{cis} = 12.47P_{\mu\nu}(\mathrm{HMO}) - 0.71 \quad (2)$$

The sensitivity of $^3J(^1\mathrm{H},^1\mathrm{H})_{cis}$ for bond length changes is high (Figure 1) and provides a valuable probe for the bonding situation in various cyclic π systems and annulenes. Steric compression and strain effects may cause deviations from equation (1) if changes of the HCC valence angles are induced.[17,18] This becomes apparent if one compares the data for 1,4-di-*t*-butylnaphthalene[18] with those of naphthalene[15] or data for *o*-di-*t*-butylbenzene[19] and the highly strained benzocyclopropene[17] with those of the unstrained 9,10-dihydroanthracene[17] (Figure 2).

Strain and steric compression are frequently encountered in fused ring systems where these factors cause a decrease in $^3J(1,2)$ and an increase in $^3J(2,3)$ if a small ring ($n < 6$) is fused to a large ring (**3**). The reverse trend—an increase of $^3J(1,2)$ and a decrease of $^3J(2,3)$—is found if a larger ring is fused to a smaller one (**4**).[20]

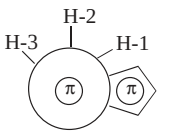

(3)

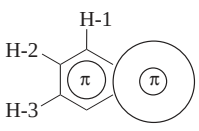

(4)

More drastic changes of the HCC valence angles are induced in π systems of different ring size and modified correlations have been derived for these cases:

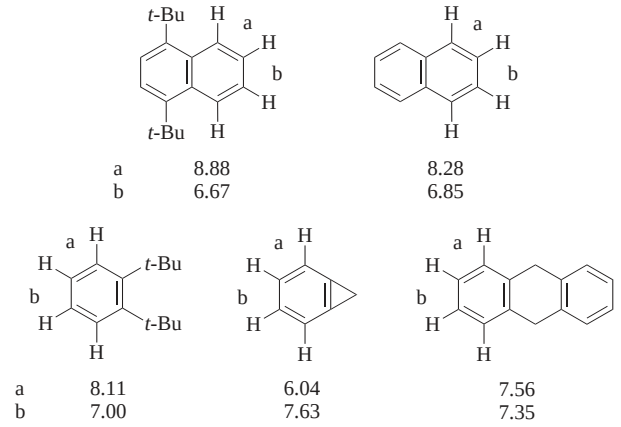

Figure 2 The effect of steric compression and strain on $^3J(^1H,^1H)_{cis}$ values (in Hz) of various HC⎓CH fragments (a, b)

Table 1 The Ring Size Dependence of $^3J(^1H,^1H)_{cis}$ Values

Cycloalkene ring size	^3J(Hz)
3[28]	1.3
4[29]	2.85
5[27]	5.57
6[27]	10.11
7[27]	11.02
8[27]	10.41

Five -membered rings:[5,21]

$$^3J(^1H,^1H)_{cis} = -322.6R_{\mu\nu}(\text{nm}) + 48.45 \quad (3)$$

$$^3J(^1H,^1H)_{cis} = 7.12P_{\mu\nu}(\text{HMO}) - 1.18 \quad (4)$$

Seven-membered rings:[20,22]

$$^3J(^1H,^1H)_{cis} = -367.4R_{\mu\nu}(\text{nm}) + 60.68 \quad (5)$$

$$^3J(^1H,^1H)_{cis} = 21.91P_{\mu\nu}(\text{HMO}) - 3.85 \quad (6)$$

The ring size dependence of the HCC valence angles is a consequence of the changes in internal CCC valence angles for the respective perimeters and a linear correlation of ∢CCC with $^3J(^1H,^1H)_{cis}$ is thus not unexpected. Using five-, six-, seven-, and eight-membered ring systems, an increment of 0.29 Hz per degree was found after correcting for different π-bond orders.[23] Similar relations were established for the long-range ^{1}H,^{1}H couplings ^4J and ^5J.[23] For isolated double bonds, the effect of HCC valence angle changes is most clearly seen by the ring size dependence of $^3J(^1H,^1H)_{cis}$ in cycloalkenes,[24–27] as shown in Table 1.

A systematic study of $^3J(^1H,^1H)_{cis}$ for benzo-annelated annulenes[30] has shown that in addition to steric effects the electronic nature of the annulenes, i.e. the number of π electrons and the degree of delocalization, influences the $^3J(^1H,^1H)_{cis}$ data in the annelated benzene ring in a characteristic way. Thus, the π-electron structure of annulenes can be monitored by the $^3J(^1H,^1H)_{cis}$ data for the benzene ring in the corresponding benzoannulene. The π-bond orders P_{12} and P_{23} are determined from the measured coupling constants according to equation (7), which is based on PPP–SCF π-electron calculations,[31,32]

$$P_{\mu\nu}(\text{SCF}) = 0.104^3J(^1H,^1H)_{cis} - 0.120 \quad (7)$$

a Q value being defined as $Q = P_{12}/P_{23}$. The magnitude of Q is related to the bonding situation in the annulene: $Q < 1.00$ for antiaromatic ($4n$) π systems, $Q > 1.10$ for aromatic ($4n + 2$) π systems, and $1.00 < Q > 1.10$ for olefinic systems. Typical examples are found with the benztropylium ion (**5**)[23] and benzocycloheptatriene-id (**6**)[33] or the two dehydroannulenes (**7**) and (**8**).[34]

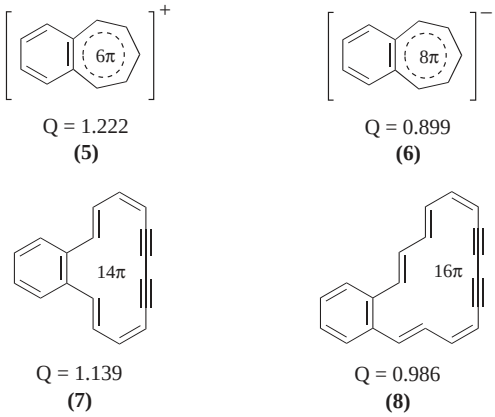

Substituent effects have mostly been studied with substituted benzenes, where a careful determination of the $^3J(^1H,^1H)$ values[35] has established the effect of electronegativity: ^3J(a,b) increases in the (X)C–CH_a–CH_b–CH_c–fragment if X is more electronegative than hydrogen, while a small decrease is found for the coupling ^3J(b,c).

;Vicinal ^{1}H,^{1}H coupling via a *trans*-HC–CH fragment, $^3J(^1H,^1H)_{trans}$, is found only in larger annulene rings which tolerate *trans* double bonds. As a consequence of the different dihedral angle $\Phi = 180°$, such couplings are larger than the *cis* values, as the data reported for [18]annulene [$^3J(^1H,^1H)_{cis}$ = 8.0 and $^3J(^1H,^1H)_{trans}$ = 15.5 Hz][36] demonstrate. Other values have been collected in the literature,[34,37] but a detailed analysis of these data was not attempted. For bridged annulenes, various steric requirements imposed on the perimeter geometry by the bridging group usually lead to a loss of coplanarity of all HC–CH fragments and the magnitude of the vicinal ^{1}H,^{1}H coupling constants is subject to additional factors such as varying dihedral angles.[38–40] Early theoretical calculations for $^3J(^1H,^1H)_{cis}$ have been reviewed.[41]

In conclusion, vicinal ^{1}H,^{1}H coupling constants provide the basis for detailed insights into the electronic structure of annulenes and other cyclic π systems and complement the information obtained from shielding properties such as, for example, ring current effects.

2 RELATED ARTICLES

Heterocycles; Indirect Coupling: Theory and Applications in Organic Chemistry.

3 REFERENCES

1. M. Karplus, *J. Chem. Phys.*, 1959, **30**, 11.
2. M. Karplus, *J. Am. Chem. Soc.*, 1963, **85**, 2870.
3. H. Booth, *Prog. Nucl. Magn. Reson. Spectrosc.*, 1969, **5**, 149; C. Altona, J. H. Ippel, A. J. A. W. Hoekzema, C. Erkelenz, M. Groesbeek, and L. A. Donders, *Magn. Reson. Chem.*, 1989, **27**, 564.
4. N. Jonathan, S. Gordon, and B. P. Dailey, *J. Chem. Phys.*, 1962, **36**, 2443.
5. W. B. Smith, W. H. Watson, and S. Chiranjeevi, *J. Am. Chem. Soc.*, 1967, **89**, 1438.
6. H. Günther, *Tetrahedron Lett.*, 1967, 2967.
7. D. R. Eaton, A. D. Josey, W. D. Phillips, and R. E. Benson, *J. Chem. Phys.*, 1963, **39**, 3513.
8. G. Scheibe, W. Seiffert, G. Hohlneicher, C. Jutz, and H. J. Springer, *Tetrahedron Lett.*, 1966, 5053.
9. A. R. Katritzky and R. E. Reavill, *Recl. Trav. Chim. Pays-Bas*, 1964, **83**, 1230.
10. D. J. Bertelli, T. G. Andrews, Jr., and P. O. Crews, *J. Am. Chem. Soc.*, 1969, **91**, 5286.
11. N. M. D. Brown and P. Bladon, *Spectrochim. Acta*, 1968, **24A**, 1869.
12. A. J. Boulton, P. J. Halls, and A. R. Katritzky, *Org. Magn. Reson.*, 1969, **1**, 311.
13. H. Günther and H. H. Hinrichs, *Tetrahedron Lett.*, 1966, 787.
14. M. A. Cooper and S. L. Manatt, *J. Am. Chem. Soc.*, 1969, **91**, 6325.
15. J. B. Pawliczek and H. Günther, *Tetrahedron*, 1970, **26**, 1755.
16. P. C. Lauterbur and R. J. Kurland, *J. Am. Chem. Soc.*, 1962, **84**, 3405.
17. M. A. Cooper and S. L. Manatt, *J. Am. Chem. Soc.*, 1970, **92**, 1605.
18. M. A. Cooper and S. L. Manatt, *J. Am. Chem. Soc.*, 1970, **92**, 4646.
19. S. Castellano and R. Kostelnik, *Tetrahedron Lett.*, 1967, 5211.
20. H. Günther, H. Schmickler, M.-E. Günther, and D. Cremer, *Org. Magn. Reson.*, 1977, **9**, 420.
21. H. L. Ammon and G. L. Wheeler, *J. Am. Chem. Soc.*, 1975, **97**, 2326.
22. S. Braun and J. Kinkeldei, *Tetrahedron*, 1977, **33**, 3127.
23. H. Günther, A. Shyoukh, D. Cremer, and K.-H. Frisch, *Liebigs Ann. Chem.*, 1978, 150.
24. O. L. Chapman, *J. Am. Chem. Soc.*, 1963, **85**, 2014.
25. G. V. Smith and H. Kriloff, *J. Am. Chem. Soc.*, 1963, **85**, 2016.
26. P. Laszlo and P. v. R. Schleyer, *J. Am. Chem. Soc.*, 1963, **85**, 2017.
27. M. A. Cooper and S. L. Manatt, *Org. Magn. Reson.*, 1970, **2**, 511.
28. J. B. Lambert, A. P. Iovanovich, and W. I. Oliver, *J. Phys. Chem.* 1970, **74**, 2221.
29. E. A. Hill and J. D. Roberts, *J. Am. Chem. Soc.*, 1967, **89**, 2047.
30. H. Günther and D. Cremer, *Justus Liebigs Ann. Chem.*, 1972, **763**, 87.
31. R. Pariser and R. G. Parr, *J. Chem. Phys.*, 1953, **21**, 466.
32. J. A. Pople, *Trans. Faraday Soc.*, 1953, **49**, 1375.
33. S. W. Staley and A. W. Orvedal, *J. Am. Chem. Soc.*, 1973, **95**, 3384.
34. H. Günther, M.-E. Günther, D. Mondeshka, H. Schmickler, F. Sondheimer, N. Darby, and T. M. Cresp, *Chem. Ber.*, 1979, **112**, 71.
35. S. Castellano and C. Sun, *J. Am. Chem. Soc.*, 1966, **88**, 4741.
36. J. F. M. Oth, *Pure Appl. Chem.*, 1971, **25**, 573.
37. R. C. Haddon, V. R. Haddon, and L. M. Jackman, *Topics Curr. Chem.*, 1971, **16**, 103.
38. H. Günther, *Z. Naturforsch.*, 1969, **24B**, 680.
39. H. Günther and H.-H. Hinrichs, *Tetrahedron*, 1968, **24**, 7033.
40. A. Alscher, W. Bremser, D. Cremer, H. Günther, H. Schmickler, W. Sturm, and E. Vogel, *Chem. Ber.*, 1975, **108**, 640.
41. J. Kowalewski, *Prog. Nucl. Magn. Reson. Spectrosc.*, 1977, **11**, 1.

Biographical Sketch

Harald Günther, *b* 1935. Studied chemistry at the Universities of Stuttgart and Heidelberg, Ph. D., 1961, Heidelberg with G. Wittig. Research fellow at Mellon-Institute, Pittsburgh 1961–63; introduced to NMR by A. A. Bothner-By. 1963–77 Staff member at the Institute of Organic Chemistry, University of Cologne; Habilitation 1968 with E. Vogel; Associate Professor 1970; since 1977 Full Professor at the University of Siegen. 1973 Chemistry Award of the Academy of Sciences, Göttingen; 1973 Award of the Fonds der Chemischen Industrie, Frankfurt; ca. 200 publications; author of NMR textbook (German, English, Russian, Polish, French editions). Editor-in-Chief of *Magnetic Resonance in Chemistry* since 1992. Research interests include applications of high-resolution and solid state NMR in organic and organometallic chemistry.

Amorphous Materials

Hellmut Eckert

University of California, Santa Barbara, CA, USA

1	Introduction	1
2	Historical Background	1
3	Silicate Glasses	2
4	Borate Glasses	13
5	Phosphate Glasses	16
6	Chalcogenide Glasses	17
7	Amorphous Semiconductors	21
8	References	21

1 INTRODUCTION

The term 'amorphous' describes a state of matter that possesses most of the macroscopic and thermodynamic properties of the solid state, while displaying the structural disorder and isotropic behavior typical of a liquid or gas. This lack of microscopic periodicity implies that it is not possible to describe the structure by a definite set of atomic coordinates and symmetry relations. Structural questions in amorphous systems concern distribution functions rather than fixed values of geometrical parameters. Furthermore, the structure can be influenced by the mode of preparation, thermal history, and by compositional variations. The following topics are of interest in the structural description of an amorphous solid: nearest-neighbor atomic connectivities ('short-range order'); second and third-nearest neighbors and higher-order correlations ('intermediate-range order'); topological disorder, i.e. the distribution of specific geometrical parameters; kinetic aspects, including the presence of restricted atomic or molecular motion below the glass transition temperature, T_g, and the motional processes associated with the glass transition; general thermodynamic and other macroscopic aspects, concerning the chemical equilibria and phase relationships involved, and the connection between glass structure and physical properties.

Techniques of solid state NMR are uniquely well suited for studying questions of this kind. Since NMR selectively probes the local environment of a chosen nuclear species, it easily lends itself to applications to disordered and compositionally complex systems. The direct proportionality of the signal intensity to the number of nuclei makes NMR the method of choice for quantitative applications in the bulk. The structural information arises from terms in the spin Hamiltonian that describe the internal interactions of the magnetic nuclei with their electronic and magnetic local environments. These terms, which are incorporated in the theoretical treatment by means of standard perturbation theory, are: direct (through-space) nuclear dipole–dipole coupling, $\hat{\mathcal{H}}_d$, indirect nuclear spin–spin coupling, $\hat{\mathcal{H}}_J$, chemical shielding, $\hat{\mathcal{H}}_{\mathrm{CS}}$, and, for nuclei with spin quantum numbers $>\frac{1}{2}$, nuclear electric quadrupole coupling, $\hat{\mathcal{H}}_Q$. All of the internal interactions are anisotropic, and $\hat{\mathcal{H}}_J$ and $\hat{\mathcal{H}}_{\mathrm{CS}}$ also contain an isotropic part. Furthermore, $\hat{\mathcal{H}}_d$ and $\hat{\mathcal{H}}_J$ have homonuclear and heteronuclear contributions with intrinsically different transformation properties.

The NMR spectroscopist addressing structural questions in solids thus faces a dual task: (i) to evaluate accurately the parameters (and their distribution functions) characterizing the Hamiltonians of these internal interactions, and (ii) to uncover the structural significance of the numerical values or distribution functions thus obtained.

The most successful strategy for meeting the first task is to simplify the effective spin Hamiltonian by 'selective averaging' experiments. A combination of several such experiments often results in a wealth of complementary information. The second task involves finding a physical relationship between an interaction parameter and local geometries. In the case of $\hat{\mathcal{H}}_d$ there is a straightforward dependence on internuclear distances. In the case of other interactions one often takes recourse to empirical correlations established with crystalline model compounds or ab initio calculations on simple molecular models mimicking the nearest-neighbor environments. In systems where the composition is variable, the detailed dependence of chemical shifts or quadrupolar couplings on the composition of the material offers important structural insights. On occasion, structural information on an amorphous material has also been inferred from the detailed temperature dependence of the NMR chemical shifts in the liquid state.

Overall there are well over 3000 publications dealing with NMR studies of amorphous materials, more than 1000 of which deal with the structure of inorganic systems. Since space limitations preclude a comprehensive treatise of this work, the present review will focus on the work deemed most influential, representative, and/or best exemplifying the potential of solid state NMR in glass science. These choices are certainly based on the highly subjective tastes of the author, who wishes to apologize in advance for omitting any important work that should have been cited.

2 HISTORICAL BACKGROUND

NMR measurements on glasses began to appear in the 1950s;[1] however, the CW NMR study of ^{11}B in borate glasses in 1958 by Silver and Bray was really the first one to provide any insight into glass structure.[2] Borate glasses contain variable amounts of three- and four-coordinate boron sites, which are easily discriminated by low-field CW NMR, because of their large difference in the magnitude of the nuclear electric quadrupolar coupling constant. While the exploration of borate glasses using low-field CW NMR (and more recently NQR) techniques continues to the present date, such studies of other nuclei were generally plagued by low detection sensitivities, saturation effects, and limited chemical shift dispersion due to the use of low field strengths.

The nearly simultaneous publication in 1982 of several pulsed, high-field Fourier transform NMR studies,[3–6] using line narrowing by MAS constituted a major breakthrough. This technique made it possible to resolve (and thereby quantify) distinct local structures present in silicate glasses and to provide unambiguous information about the coordination number of aluminum and other important glass constituents. Although MAS has remained the mainstay of NMR applications to amorphous materials to the present date, during the past decade

new third-generation experiments have emerged, whose applications to glasses have recently produced insights of amazing detail. Many of these newer techniques utilize the inherent advantages of multifrequency irradiation and multidimensional data processing, providing correlation and enhanced resolution, and quantitative specification in more than one interaction domain.

Several recent reviews have been given on the subject of NMR of amorphous materials.[7–10] While these articles are by now slightly out of date due to the rapid development of this field, they are still valuable sources of information, because in the field of glass science the use of improved NMR technology has only rarely resulted in a major reevaluation of previous work and/or dramatic changes in the mode of thinking. More commonly, the progress over the years has been the resolution of more and more detail, in many cases reinforcing and providing new rationales to earlier interpretations.

3 SILICATE GLASSES

The majority of modern NMR studies conducted on amorphous materials during the past 10 years has been in the area of silicate glasses. The great interest in these systems arises from their importance as structural and optical materials, and from the pivotal role of molten silicates in the earth sciences. Figure 1 summarizes the principal questions studied in this area. Specifically, the NMR studies have been devoted to (i) the Si–O–Si bond angle distribution, (ii) the distribution of nonbridging oxygen atoms introduced by network modifiers, (iii) the spatial distribution of alkali and alkaline earth metal cations, (iv) the structural role and the distribution of intermediate oxides such as Al_2O_3, (v) anion substitution effects (F, C, N), (vi) the speciation and structural role of water and other volatiles, (vii) the effect of high pressures, and (viii) the influence of sol–gel processing upon the structure of these glasses.

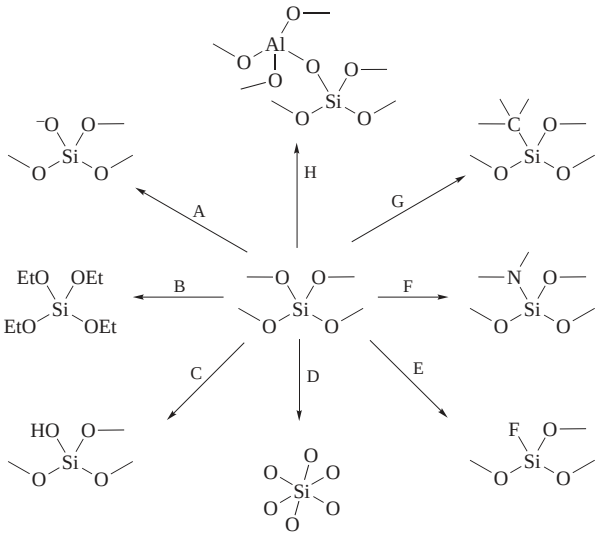

Figure 1 Structural and chemical issues in the area of silicate glasses studied by ^{29}Si NMR spectroscopy. A, network modification by alkali ions; B, glass synthesis by the sol–gel method; C, hydrolysis; D, coordination change at high pressures; E, F, G, nearest-neighbor substitution with fluorine, nitrogen, and carbon; H, next-nearest neighbor substitution by alumina and other network-forming oxides (Reproduced by permission of Pergamon Press from H. Eckert, *Prog. Nucl. Magn. Reson*, 1992, **24**, 159)

3.1 Bond Angle Distribution in Vitreous SiO_2 and Alkali Silicate Glasses

While glassy silica retains the local structure based on corner-shared $SiO_{4/2}$ tetrahedra present in all of the ambient-pressure polymorphs of silica, the intrinsic disorder in this material is attributed to a large variability in the Si–O–Si bond angle. This view is supported by theoretical calculations, which show a very broad energy minimum in the Si–O–Si bond angle distribution F_α(Si–O–Si).[11] In principle, this distribution function can be probed by NMR, because ^{29}Si chemical shifts are correlated empirically with the mean Si–O–Si bond angle. A variety of physical correlations have been proposed, and have been critically reviewed and compared with each other in the literature.[12,13]

The ^{29}Si MAS NMR spectrum of vitreous silica has an approximately Gaussian shape centered at -112 ppm with a full width at halfheight of 11.5 ppm.[14] Under the usual MAS conditions (3–5 kHz) in samples containing ^{29}Si at natural abundance, the lineshape is entirely governed by a distribution of isotropic chemical shifts. Thus, using one of the correlations proposed, Si–O–Si bond angle distribution functions can be inferred. The results (Figure 2) suggest a most probable Si–O–Si bond angle of between 142° and 151° (depending on which empirical correlation is used) and a narrower distribution function than deduced from X-ray diffraction.

A fundamental difficulty of this procedure arises from the fact that the measured chemical shift reflects the composite effect of four Si–O–Si bond angles. This difficulty has been overcome by ^{17}O NMR studies of the bridging oxygen sites. Ab initio calculations carried out on the model molecule $H_3Si–O–SiH_3$ have shown that the ^{17}O nuclear electric quadrupolar coupling parameters χ and η depend on the intertetrahedral bond angles α.[15] Indeed, these calculations reflect the same trend as predicted by a simple oxygen sp hybridization model:

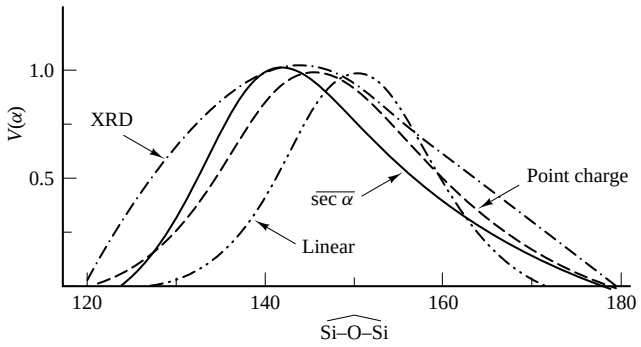

Figure 2 Various Si–O–Si bond angle distribution functions derived from ^{29}Si chemical shift data, using four different empirical correlations. Details are discussed elsewhere[12,13] (Reproduced by permission of Elsevier Science Publishers BV from R. F. Pettifer, R. Dupree, I. Farnan, and U. Sternberg, *J. Noncryst. Solids*, 1988, **106**, 408)

$$\chi \sim \cos\alpha/(1-\cos\alpha) \quad (1)$$

$$\eta = 1+\cos\alpha \quad (2)$$

Thus, with increasing α values, χ increases, whereas η decreases, approaching the value of zero for the cylindrically symmetric environment when α = 180°. These correlations have been qualitatively confirmed by experimental ^{17}O NMR measurements on model compounds. Obtaining a distribution of Si–O–Si bond angles α then requires that the distribution functions of χ and/or η be determined in an accurate fashion. Farnan et al. have accomplished this feat for glassy $K_2Si_4O_9$, using 2D DAS NMR.[16] The experiment yields a completely isotropic spectrum in the projection on the ω_1 axis, correlated with lineshapes perturbed by the electric field gradient in the anisotropic ω_2 dimension. Figure 3 reveals a systematic variation of the magnitude and asymmetry of the electric field gradient across the isotropic lineshape in the ω_1 domain: progressing from low to high values of ω_1, χ decreases while η increases, in good agreement with the predictions made by eqs. (1) and (2). The distribution function of α derived on the basis of this 2D correlation is shown as the solid circles in Figure 4(c). This analysis can be extended further to derive a more complete distribution function (open circles in Figure 5) if the entire lineshape in the ω_1 domain is transformed into the distribution of ^{17}O second-order nuclear electric quadrupolar shifts. Characteristically, the bond angle distribution is significantly narrower than that obtained by X-ray diffraction on glassy silica.[17] It is also at variance with recent molecular dynamics simulations on compositionally related sodium silicate glasses[18] (see Figure 6).

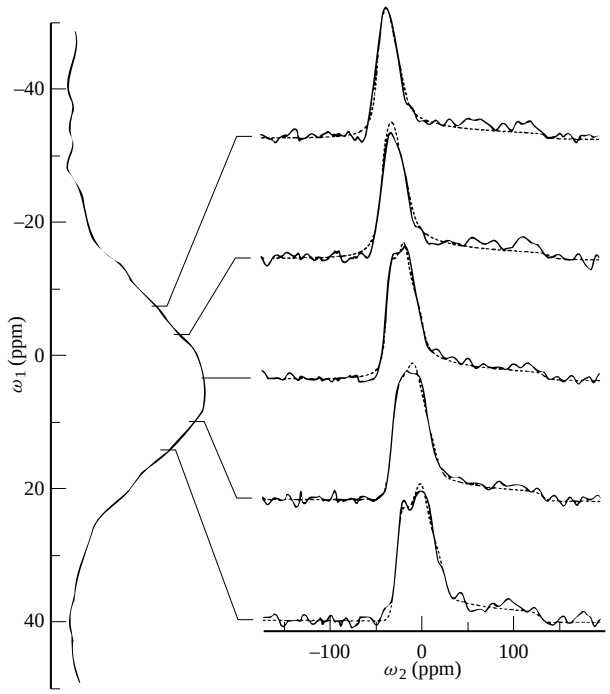

Figure 3 Oxygen-17 DAS NMR results on glassy $K_2Si_4O_9$. Indicated are the individual anisotropic slices for various points across the broadened DAS spectrum in the isotropic dimension. Note the systematic change in the asymmetry parameter. Dashed curves are simulated spectra. (Reproduced with permission of Macmillan Magazines Ltd. from I. Farnan, P. J. Grandinetti, J. H. Baltisberger, J. F. Stebbins, U. Werner, M. A. Eastman, and A. Pines, *Nature (London)*, 1992, **358**, 31)

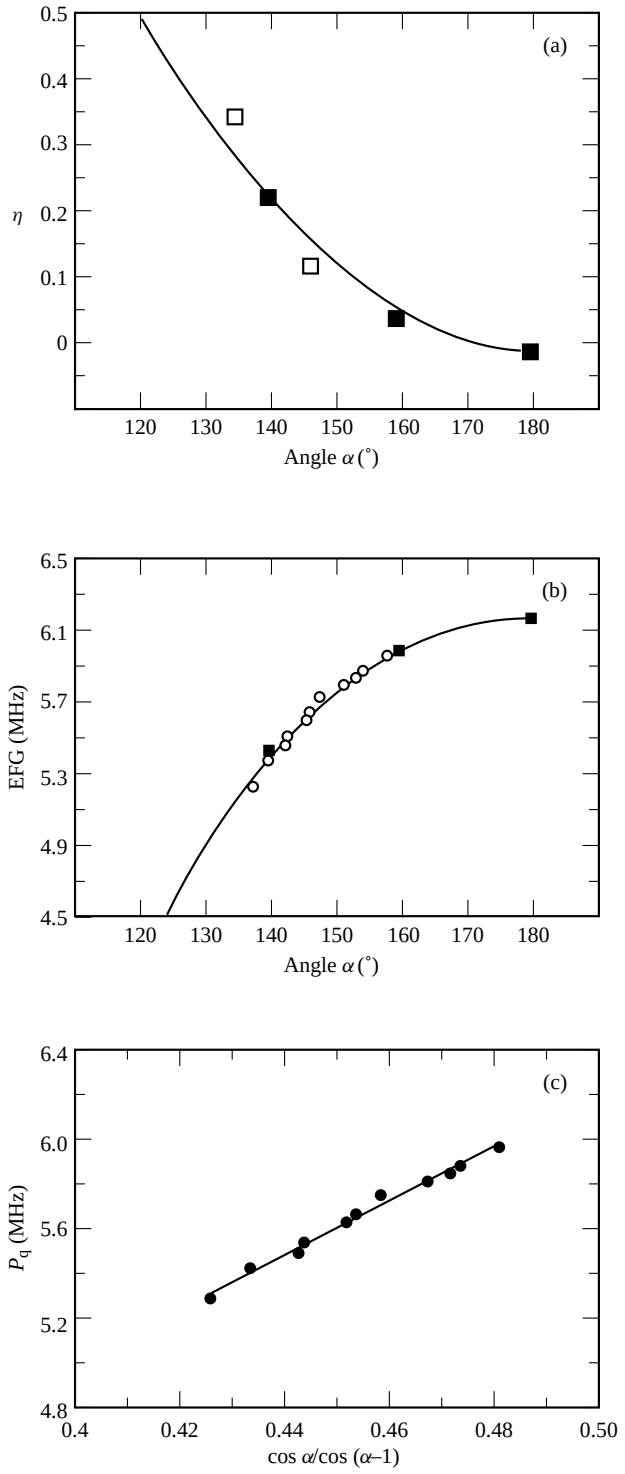

Figure 4 Variation of (a) the ^{17}O asymmetry parameter, (b) the electric field gradient, and (c) the quadrupolar product P_q with various functions relating to the Si–O–Si bond angle α. Solid squares are results from ab initio calculations. Other details are given in Farnan et al.[16] (Reproduced by permission of Macmillan Magazines Ltd. from I. Farnan, P. J. Grandinetti, J. H. Baltisberger, J. F. Stebbins, U. Werner, M. A. Eastman, and A. Pines, *Nature (London)*, 1992, **358**, 31)

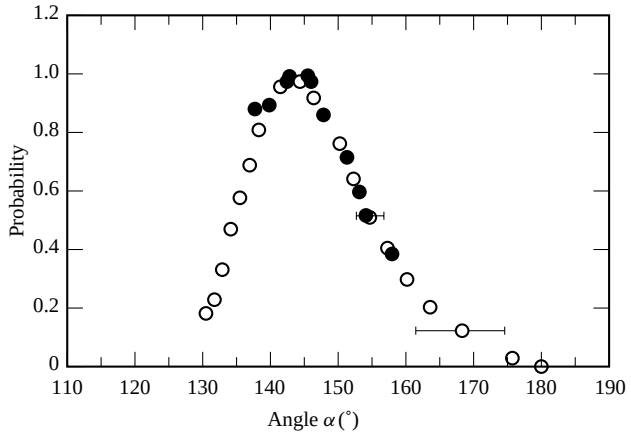

Figure 5 Si–O–Si bond angle distribution function derived from the DAS NMR data (○) from the fitted *h* values and the correlation in Figure 16(a). •, using the procedure described in the text. (Reproduced with permission of Macmillan Magazines Ltd. from I. Farnan, P. J. Grandinetti, J. H. Baltisberger, J. F. Stebbins, U. Werner, M. A. Eastman, and A. Pines, *Nature (London)*, 1992, **358**, 31)[16]

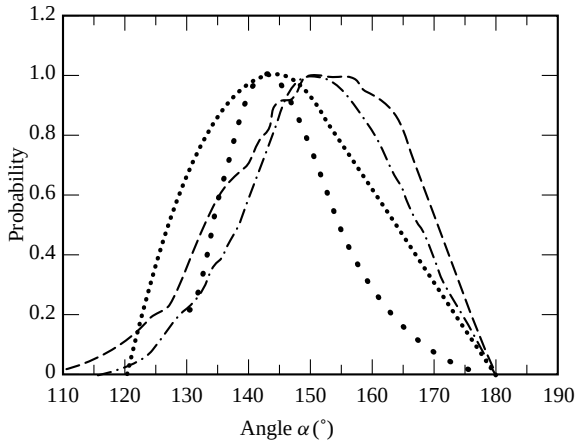

Figure 6 Comparison of the bond angle distribution function derived from ^{17}O DAS NMR for glassy $K_2Si_4O_9$ (circles) with the respective function derived from X-ray data on glassy SiO_2 (dots) and various molecular dynamics simulations (dashed curves). (Reproduced with permission of Macmillan Magazines Ltd. from I. Farnan, P. J. Grandinetti, J. H. Baltisberger, J. F. Stebbins, U. Werner, M. A. Eastman, and A. Pines, *Nature (London)*, 1992, **358**, 31)

3.2 Network Structure of Silicate Glasses

3.2.1 Analysis of $Si^{(n)}$ Sites by ^{29}Si NMR.

Incorporation of alkali and alkaline earth oxides into glassy silica leads to depolymerization with formation of nonbridging oxygen atoms. As a result, silicate glasses generally contain the five distinct silicon microstructures ($Si^{(n)}$) species (also labeled $Q^{(n)}$ species in the literature) shown in Figure 7. Benchmark data on crystalline model compounds reveal that each type of $Si^{(n)}$ unit is distinguished by a unique isotropic ^{29}Si chemical shift range,[19] and chemical shift anisotropy powder pattern: specifically, the isotropic environments of $Si^{(4)}$ and $Si^{(0)}$ species result in sharp static ^{29}Si NMR spectra, which are easily distinguished from the anisotropically broadened $Si^{(1)}$, $Si^{(2)}$, and $Si^{(3)}$ resonances. Furthermore, the latter three species differ in the sign of the anisotropy and in the asymmetry of the shielding tensor.

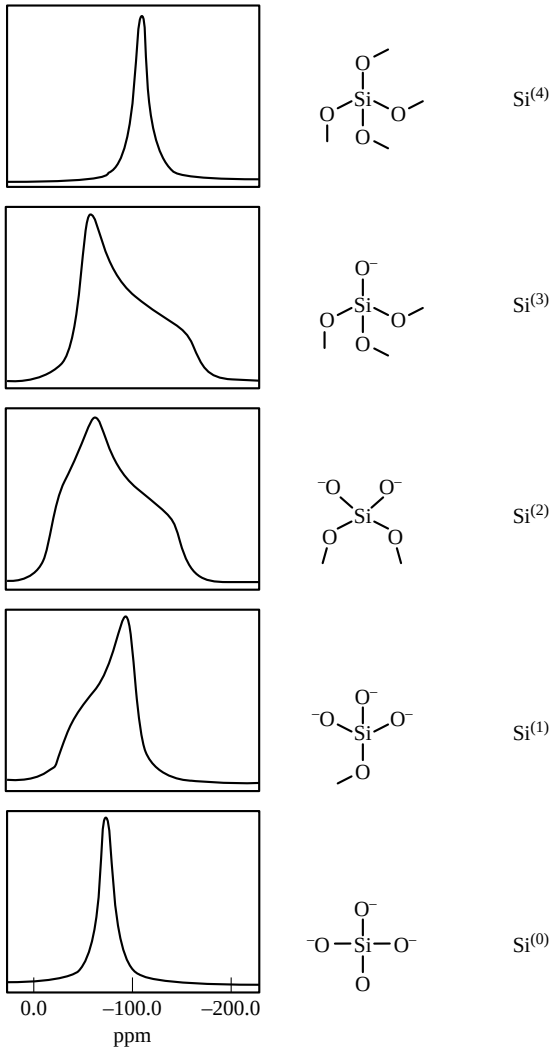

Figure 7 $Si^{(n)}$ (also labeled $Q^{(n)}$ in the literature) species in alkali silicate glasses and their ^{29}Si chemical shift powder patterns (Reproduced by permission of Pergamon Press from H. Eckert, *Prog. Nucl. Magn. Reson*, 1992, **24**, 159)

The MAS NMR spectra of ^{29}Si in alkali silicate glasses yield partially resolved resonances for the various $Si^{(n)}$ species, which are usually deconvoluted into Gaussians [Figure 8(a)]. In most cases, the $Si^{(n)}$ species distributions thus obtained are quantitatively compatible with the amount of nonbridging oxygen introduced with the network modifier.[20] Small concentrations of $Si^{(4)}$ and $Si^{(0)}$ are most favorably detected by static NMR.[21]

3.2.2 $Si^{(n)}$ Species Distribution in Binary Silicate Glasses

The quantitative distribution of $Si^{(n)}$ units in alkali silicate glasses has been discussed in terms of two possible schemes: in the 'binary' model the glass structure contains only those $Si^{(n)}$ species that are present in the bordering stoichiometric crystalline phases, while in the statistical model all sites are present, their contributions calculable from binomial statistics.

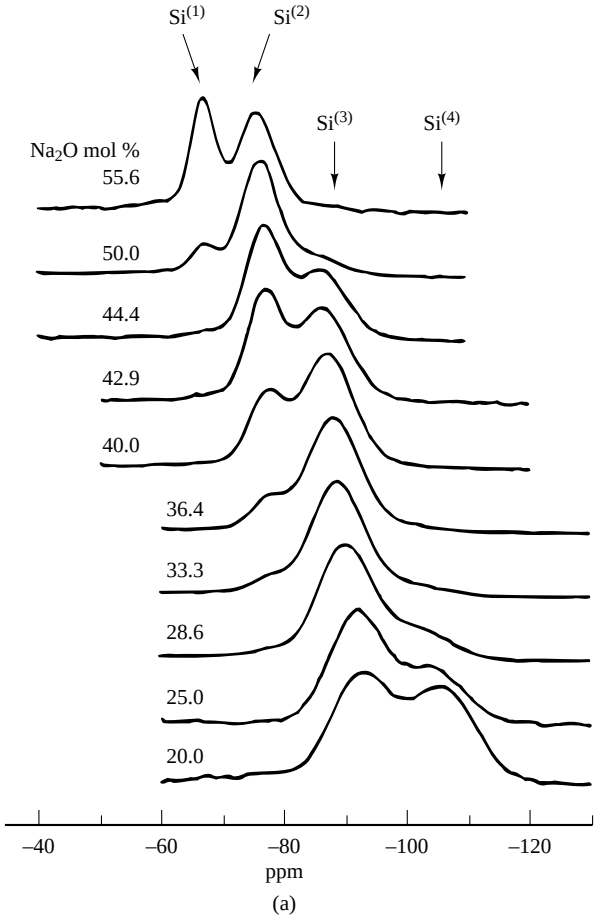

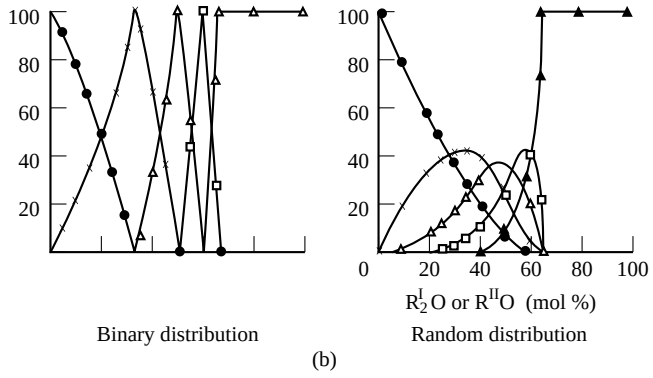

Figure 8 (a) Compositional dependence of the ^{29}Si MAS NMR spectra in the glass system $Na_2O–SiO_2$. Peak assignments are indicated. (Reproduced with permission of The Society of Glass Technology and Elsevier Science Publishers BV from H. Maekawa, T. Maekawa, K. Kawamura, and T. Yokokawa, *J. Noncryst. Solids*, 1991, **127**, 53). (b) Quantitative predictions for the ^{29}Si species distributions in the binary and the random model. ▲, $Q^{(0)}$; □, $Q^{(1)}$; △, $Q^{(2)}$; × , $Q^{(3)}$; •, $Q^{(4)}$. (Reproduced with permission of The Society of Glass Technology and Elsevier Science Publishers BV from R. Dupree, N. Ford, and D. Holland, *Phys. Chem. Glasses*, 1987, **28**, 78)

Figure 8(b) contrasts the quantitative predictions made by the two different models. The experimental results reported in more recent studies[20] in most cases detect clear deviations from the binary distribution; however, the $Si^{(n)}$ distribution is far from random. This intermediate situation can be modeled by assuming melt equilibria of the kind[22]

$$\underset{(a)}{Si^{(3)} \rightleftharpoons Si^{(2)} + Si^{(4)}} \quad \underset{(b)}{Si^{(2)} \rightleftharpoons Si^{(3)} + Si^{(1)}}$$

$$\underset{(c)}{Si^{(1)} \rightleftharpoons Si^{(2)} + Si^{(0)}} \qquad (3)$$

characterized by equilibrium constants K_3, K_2, and K_1, respectively. $K_i = 0$ corresponds to the binary model, $K_i = 1$ to the random situation, and $K_i >> 1$ to phase segregation and/or crystallization. K_i tends to increase with increasing ionic potential Z/r of the cation in the glass. Thus, lithium silicate glasses show the highest tendency toward site randomization, whereas in potassium silicate glasses K_i is so small that the distribution approaches that predicted by the binary model.[23] Furthermore, in general $K_1 > K_2 > K_3$. The effect of the alkali ions upon the silicon site distribution may reflect changes in the electronic properties of the Si–O bonds, as suggested by recent ab initio MO calculations.[24]

The relevant temperature for these equilibrium constants K_i is the glass transition temperature T_g, at which all bond-breaking and bond-making processes are frozen in. By varying T_g over a range of 80 K (using different quenching rates), Brandriss and Stebbins showed that for $Na_2Si_2O_5$ glass, K_1 for the reaction (3a) increases with increasing temperature. From this temperature dependence, ΔH is estimated at 30 ± 15 kJ mol^{-1}.[25] Similar effects are observed in a mixed $Na_2O–CaO–$silicate glass.

3.2.3 Spatial Distribution and Intermediate Range Order

As known from the structure of metasilicates and other crystalline model compounds, nonbridging oxygen atoms tend to aggregate around modifier cations and vice versa, resulting in a cation distribution that resembles clustering at least at low modifier concentrations. The cation distribution is closely linked with the spatial distribution of the various $Si^{(n)}$ units. Are they statistically linked within a single extended network or do they form separated islands? Direct evidence for $Si^{(n)}–O–Si^{(n-1)}$ connectivity has come from 2D COSY–MAS NMR studies (Figure 9) on two ^{29}Si-enriched sodium silicate glasses with Na_2O contents of 20 and 41 mol%, respectively.[26] The cross peaks seen in Figure 9 between the $Si^{(3)}$ and $Si^{(4)}$ resonances arise from coherence transfer via two-bond scalar coupling, thus providing direct evidence for such links. Participation in a $Si^{(n)}–O–Si^{(n-1)}$ linkage appears to shift the $Si^{(n)}$ resonance to lower frequency and the $Si^{(n-1)}$ resonance to higher frequency compared with respective majority sites. This finding probably signifies bond angle redistributions that may be unique to such site connections. The results thus support the description of these glasses as continuous networks, although the 2D experiments indicate only that such links exist in principle; their exact quantification requires further work.

3.2.4 Si^n Species Distribution in Alkaline Earth Silicate Glasses and Related Systems

Silicon-29 MAS NMR spectra of silicate glasses modified by divalent cations show no clear site resolution, indicating that the spread of chemical shifts due to bond angle variations is comparable to the effect of the nonbridging oxygen.[27]

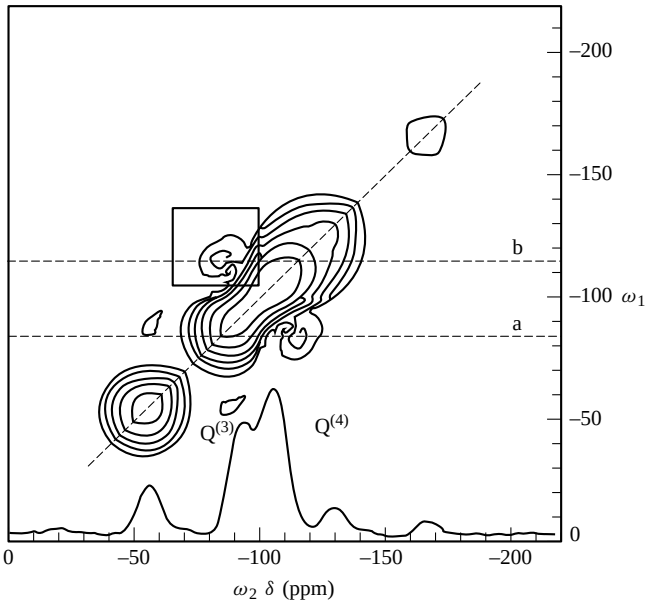

Figure 9 2D ^{29}Si COSY of a glass with the composition $Na_2Si_4O_9$. The $Si^{(3)}-Si^{(4)}$ connectivities are revealed by the cross peaks b and a. (Reproduced with permission of Elsevier Science Publishers BV from C. T. G. Knight, R. J. Kirkpatrick, and E. Oldfield, *J. Noncryst. Solids*, 1990, **116**, 140)

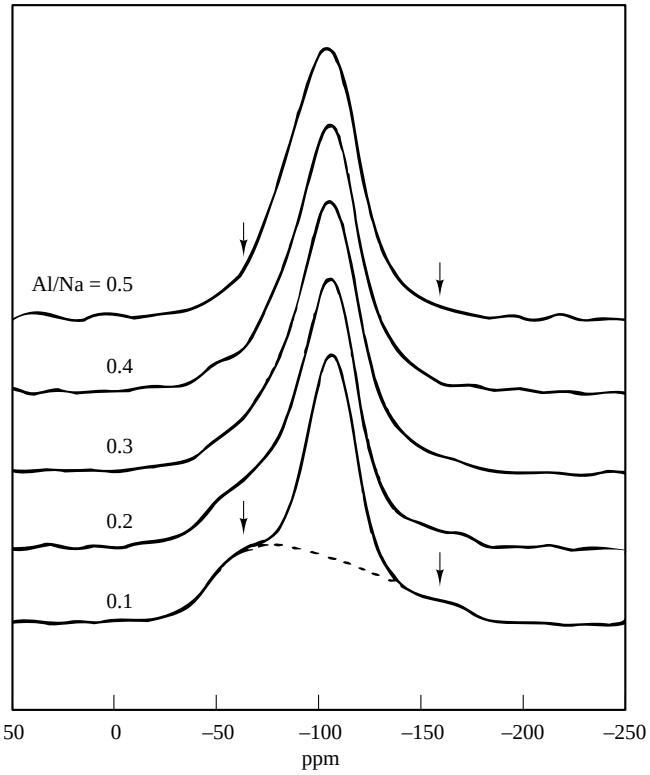

Figure 10 Wideline ^{29}Si NMR in aluminosilicate glasses along the compositional series $(1-x)Na_2O{\cdot}xA1_2O_3{\cdot}4SiO_2$. Note the emergence of an $Si^{(3)}$ powder pattern (chemical shift principal components indicated by arrows) at low Al/Na ratios. (Reproduced with permission of The American Chemical Society from H. Maekawa, T. Maekawa, K. Kawamura, and T. Yokokawa, *J. Phys. Chem.*, 1991, **95**, 6822)

Significantly better resolution is observed in the system $PbO-SiO_2$. Here, the statistical $Si^{(n)}$ distribution seems to be favored,[28] in sharp contrast to alkali silicate glasses. Pb_2SiO_4 glass (66.6 mol% PbO) appears to be an interesting example where the $Si^{(n)}$ speciation differs from that expected from the composition.[29] Several crystalline Pb_2SiO_4 polymorphs are known, none of which has $Si^{(0)}$ sites, in spite of the orthosilicate stoichiometry. The structure of the glass resembles that of the low-temperature polymorph, which contains dimeric $Si^{(1)}$ environments. This, in turn, implies that the glass must contain Pb–O–Pb bonds, a view indeed supported by some very early ^{207}Pb NMR work.[30]

3.3 Aluminosilicate Glasses

3.3.1 General Aspects and Spectroscopic Approaches

Introduction of Al_2O_3 into alkali silicate glasses enhances their thermal, mechanical, and chemical stability to a considerable extent, resulting in widespread practical applications. Structural questions associated with these effects include (i) the influence of aluminum on the $Si^{(n)}$ distribution, (ii) the distribution of Si–O–Si and Si–O–Al linkages, and (iii) the coordination number of aluminum and its structural role in the network. The spectroscopic approaches to these questions have been largely traditional, namely ^{29}Si MAS NMR (which is of limited benefit) and ^{27}Al MAS NMR, which affords a straightforward assignment of aluminum coordination number.

The structure of aluminosilicate glasses can be discussed in terms of 15 different $Si_m^{(n)}$ units, corresponding to SiO_4 tetrahedra with all possible permutations of n bridging oxygen atoms and m aluminum next-nearest neighbors ($m \leq n$). Studies of crystalline model compounds show that the presence of aluminum next-nearest neighbors has a strong effect on δ_{iso} (^{29}Si). Unfortunately, however, changes in m as well as in n by one unit lead to chemical shift effects of comparable magnitude, generally resulting in poorly resolved spectra whose interpretation is highly ambiguous. In contrast, ^{27}Al MAS NMR offers a fairly easy distinction in chemical shift between four-coordinate aluminum (Al^{IV}, 40 ppm $\leq \delta_{iso} \leq$ 80 ppm), five-coordinate aluminum (Al^{V}, 20 ppm $\leq \delta \leq$ 40 ppm), and six-coordinate aluminum (Al^{VI}, -20 ppm $\leq \delta_{iso} \leq$ 20 ppm). Quantitative interpretations are often complicated by signal loss due to second-order quadrupolar broadening effects, and careful spin-counting studies on weighed samples are mandatory.

The structures of alkali or alkaline earth silicate glasses (general formula $M_{(2)}O-Al_2O_3-SiO_2$) depend critically on the Si/Al and the M/Al molar ratios, and show common features within each of the following four groups:

Region A: $Al_2O_3/SiO_2 \leq 0.5$ and $M_{(2)}O/Al_2O_3 = 1$.
Region B: $Al_2O_3/SiO_2 \leq 0.5$ and $M_{(2)}O/Al_2O_3 > 1$.
Region C: $Al_2O_3/SiO_2 > 0.5$ and $M_{(2)}O/Al_2O_3 \geq 1$.
Region D: $M_{(2)}O/Al_2O_3 < 1$.

3.3.2 Region A: Fully Polymerized Aluminosilicate Networks

Most ^{29}Si and ^{27}Al MAS NMR studies have supported the preexisting view that such glasses are fully polymerized networks comprised of $Si^{(4)}$ units and $MAlO_2$ fragments

($AlO_{4/2}^-$ tetrahedra balanced by cationic charges).[7,31,32] The ^{29}Si MAS NMR spectra of such glasses are poorly resolved and the center of gravity is shifted to higher frequency, from −110 to −86 ppm with an increasing ratio of Al_2O_3/SiO_2, reflecting the successive replacement of Si−O−Si bonds by Si−O−Al linkages. Similar trends in chemical shifts have been observed experimentally in zeolites. All of these results are consistent with the Lowenstein rule,[33] according to which Al^{IV}−O−Al^{IV} linkages, which represent an energetically unfavorable accumulation of charge in the network, are being avoided.

Recently, unusual behavior was found in rapidly quenched slightly peraluminous samples along the $MgAl_2O_4$−SiO_2 join, indicating substantial amounts of five- and six-coordinate aluminum atoms.[34] This result requires further examination.

3.3.3 Region B: Modified Aluminosilicate Networks

These glass compositions have excess modifier oxide, which in principle could create nonbridging oxygen atoms coordinated with either the silicon or the aluminum sites. Wide-line NMR studies of the system $4SiO_2$−$(Na_2O)_{1-x}$−$(Al_2O_3)_x$ ($0 \leq x \leq 0.5$) strongly favor the former possibility. Figure 10 shows that as the Al/Na ratio is decreased from 0.5 to 0.1, the axially symmetric chemical shift pattern of $Si^{(3)}$ units (not bonded to aluminum) emerges with its quantitatively expected contribution.[35] Figure 11 shows the number of nonbridging oxygen atoms per tetrahedral atom (obtained by NMR peak area analysis) as a function of N_{Al} = 4 [Al]/([Al + [Si]) in this glass system. These data are compared with (i) a model assuming that the excess sodium oxide modifies the Si−O−Si bonds excessively (solid lines) and (ii) a model assuming random association of Na_2O with nonbridging oxygen atoms attached to both silicon and aluminum atoms. Clearly the data favor model (i), revealing that the nonbridging oxygen atoms are directed towards the silicon atoms.[35] This result is expected, since attachment of a nonbridging oxygen to a negatively charged AlO_4^- unit is electrostatically less favorable than its attachment to an uncharged silicon unit.

3.3.4 Region C: Alumina-Rich Charge-Balanced Aluminosilicate Glasses

The region of glass formation in the system $CaO-Al_2O_3-SiO_2$ extends all the way to glassy $CaAl_2O_4$. This material is of interest for applications to long-wavelength optical fibers. The aluminum atoms are tetrahedrally coordinated as found in crystalline $CaAl_2O_4$. The corresponding magnesium compound has six-coordinated aluminum atoms and is impossible to vitrify. Ultrahigh-temperature NMR studies reveal a large chemical shift difference between both liquids, indicating differences in the average coordination numbers. [36] Addition of small amounts of SiO_2 to molten $CaAl_2O_4$ results in glasses that are more stable toward recrystallization. The ^{29}Si chemical shifts in these silica-poor glasses lie between −75 and −78 ppm, consistent with either $Si^{(4)}(OAl)_{4/2}$ units or with depolymerized $Si^{(2)}$ groups.[37] If part of the CaO were indeed used to generate nonbridging oxygen atoms associated with $Si^{(2)}$, not enough CaO would be available to charge balance the AlO_4^- groups, and thus aluminum in higher coordination numbers should be observed. NMR results for sodium and calcium aluminosilicate glasses are contradictory with regard to this question; particularly concerning the structure of $CaAl_2SiO_6$ glass.[38,39]

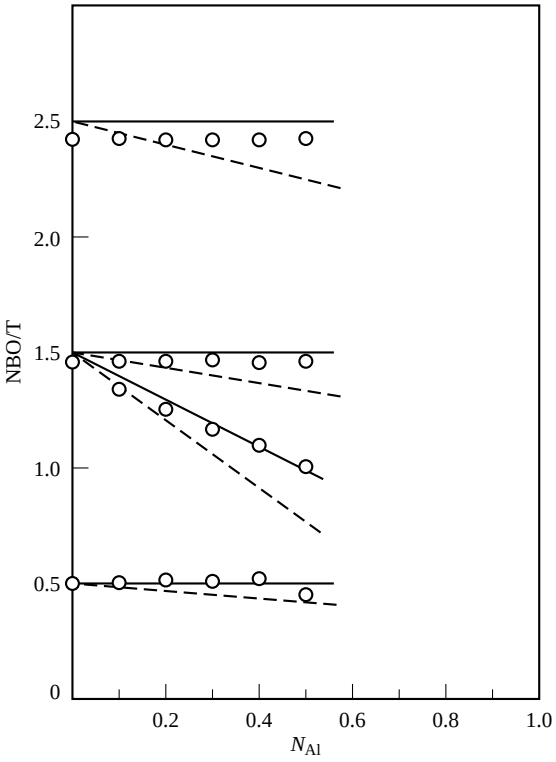

Figure 11 Numbers of nonbridging oxygen atoms per tetrahedral atom (aluminum and silicon) obtained from NMR peak area analysis (circles) in sodium aluminosilicate glasses. Solid line: calculated number assuming that nonbridging oxygen atoms are exclusively associated with silicon atoms. Dashed line: calculated number assuming that nonbridging oxygen atoms are associated with both silicon and aluminum atoms. (Reproduced with permission of The American Chemical Society from H. Maekawa, T. Maekawa, K. Kawamura, and T. Yokokawa, *J. Phys. Chem.*, 1991, **95**, 6822)

3.3.5 Region D: Peraluminous Aluminosilicate Glasses

Aluminosilicate glasses in which the $M_{(2)}O/Al_2O_3$ ratio is below 1, lack the cations necessary to balance the negative charge associated with the Al^{IV} sites. Consequently, not all of the aluminum atoms can be present in this form. Considerations of this kind have led to the proposal of charge-neutral $Al(AlO_2)_3$ 'triclusters';[40] other possibilities include extended phase segregation, or a network-modifier role of the aluminum atoms. In general support with such proposals, ^{27}Al NMR studies reveal that in all peraluminous glasses a significant fraction of the aluminum atoms are five- and six-coordinate.[31,38] Typical results are shown in Figure 12. On the other hand, the NMR data are not sufficiently informative to advocate specific structural proposals for these glasses.

3.3.6 Binary SiO_2−Al_2O_3 Glasses

The binary system $SiO_2-Al_2O_3$ shows a region of metastable liquid−liquid immiscibility, resulting in glasses whose structures show a strong dependence on quenching

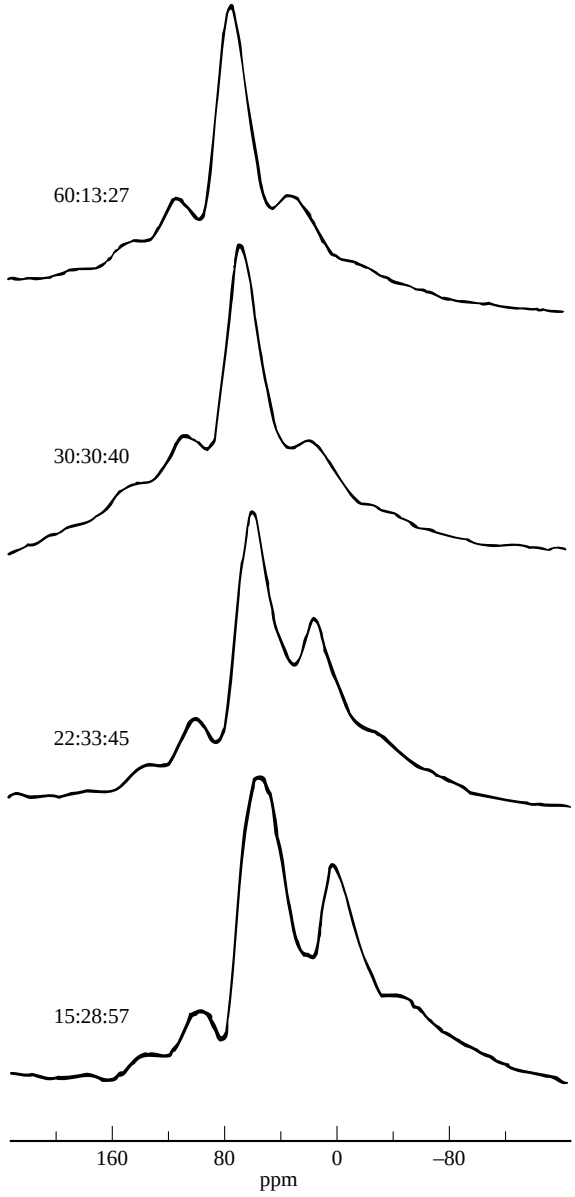

Figure 12 Typical ^{27}Al MAS NMR spectra of various calcium aluminosilicate glasses. The numerals indicate the molar ratios of $CaO:Al_2O_3:SiO_2$. (Reproduced with permission of The Society of Glass Technology and Elsevier Science Publishers BV from G. Engelhard, M. Nofz, K. Forkel, F. G. Wihsmann, M. Magi, A. Samoson, and E. Lippmaa, *Phys. Chem. Glasses*, 1985, **26**, 157)

rate. Apparently homogeneous glasses, obtained either by "superquenching" (rates of 10^5 °C s^{-1}) or by sol–gel technology show aluminum to be present in four, five, and six-fold coordination, whereas for the phase-separated glasses the NMR spectra reveal primarily Al^{IV} and Al^{VI}. Spin-counting studies and comparison with reference standards reveal further that in the superquenched samples only ~70–85% of aluminum atoms are observable, whereas in slower quenched samples the detection is quantitative.[41] There are also large differences in the ^{29}Si NMR spectra: in the phase-separated samples the silicon environments resemble those in glassy SiO_2, whereas in the superquenched samples, signal contributions at higher frequencies indicate either nonbridging oxygen

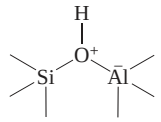

Figure 13 A structural motif of amorphous silica-aluminas with a low-to-moderate aluminum content

atoms or Si–O–Al connectivities.[41] Apparently the ordering that accompanies the unmixing of the two liquid phases disfavors the formation of Al^V and possibly of other highly distorted sites.

3.3.7 Amorphous Silica-Aluminas

Amorphous silica-aluminas are high surface area materials that can be prepared by coprecipitation or sol–gel techniques from solutions containing sodium silicate and sodium aluminate. Owing to their high surface acidities they are potent hydrocarbon-cracking catalysts, but their activity is strongly dependent on the silica/alumina ratio and on the method of preparation. It is possible to generate both single-phase and diphasic materials. Diphasic materials are prepared by mixing sols of silica and boehmite, and studies by MAS NMR of ^{27}Al and ^{29}Si confirm that the resulting powders can be viewed as intimate mixtures of amorphous silica and γ-alumina. In contrast, preparation from solutions containing both sodium silicate and sodium aluminate results in monophasic materials over a wide compositional region. For low-to-moderate aluminum contents, aluminum is thought to substitute into the silica network. Protons balance the resulting negative charge on the network, giving rise to sites of the type shown in Figure 13 which possess high Brønsted acidities. Charge balancing is also accomplished by partially hydrolyzed Al^{3+} cations in octahedral environments, and phase separation occurs for Al/Al + Si ratios above 0.8, with the formation of crystalline γ–alumina.[42] In general, ^{27}Al MAS NMR spectra show that the fraction of Al^{VI} sites can be highly variable, but increases with increasing Al/(Al + Si) ratio. In samples with high alumina contents the signal is indistinguishable from that of γ–alumina. The spectra are also greatly affected by the state of hydration[43] and by the details of sample preparation.

3.4 Anion Substitution in Silicate Glasses

Partial replacement of oxide by fluoride, nitride, or carbide ions influences both the optical and mechanical properties of silicate glasses. NMR studies have helped understand these features on a structural basis. Duncan et al. have studied the atomic distribution of small amounts of fluoride in glassy silica.[44] In principle, the incorporation of fluorine could generate $SiO_{3/2}F$, $SiO_{2/2}F_2$, $SiO_{1/2}F_3$, and SiF_4 coordination environments, which are easily distinguishable on the basis of the homonuclear $^{19}F–^{19}F$ dipolar coupling. Spin echo spectroscopy of a glass containing 1.03 wt.% fluorine reveals that only the first two units are present. The $SiO_{2/2}F_2$ units, which contain two closely spaced fluorine atoms, are responsible for a fast-decaying component at short evolution times ($2t_1 < 0.2$ ms), whereas the less strongly coupled fluorine atoms in the $SiO_{3/2}F$ units give rise to a much slower spin echo decay component at longer evolution times.

Comparison of the experimental data with simulations reveals that the fraction of $SiO_{2/2}F_2$ units is substantially enhanced over the statistical probability.

Fluorine containing aluminosilicate glasses are important model systems for geological glasses, since fluorine is a frequent volatile component in natural magmas. Similarly to water, the presence of fluorine reduces the melt viscosity and increases the diffusion coefficients, even at small concentrations. The location of the fluorine species in geologically relevant aluminosilicate glasses has been addressed recently by multinuclear MAS MR.[45,46] Cross polarization from ^{19}F dramatically enhances the spectral contribution from five- and six-coordinate aluminum sites,[45] hence suggesting that fluorine preferentially coordinates with aluminum. In support of this conclusion, $^{19}F \rightarrow {}^{29}Si$ CP MAS experiments give no evidence for Si–F bonds.[46] The effect of fluoride on the melt viscosity is attributed to a depolymerization process resulting in the formation of AlF_5^{2-} and AlF_6^{3-} species. Ab initio calculations of the ^{27}Al nuclear electric quadrupolar coupling constants suggest that the five-coordinate species are actually $AlF_3(OH)_2$ sites with D_{3h} symmetry.[47]

In silicon oxynitride glasses, Si–O bonds are partially substituted by Si–N bonds, resulting in a more rigid network due to an increased average coordination number. Compared with regular $Si^{(4)}$ sites, nitrogen-bonded $Si^{(4)}$-type species resonate at higher frequencies, and NMR chemical shift analysis can be used to estimate the average number of Si–N bonds. In nitrided aluminosilicate glasses, nitrogen shows a distinct preference for silicon over aluminum.[48] Amorphous oxycarbide materials can be realized from sol–gel chemistry, followed by pyrolysis. These materials contain mixed $SiO_{4-n}C_n$ local environments, which are well resolved by ^{29}Si MAS NMR.[49]

3.5 Silicate Glass and Melt Structure at High Temperatures and Pressures

An important feature of glassy materials as contrasted to other crystalline or amorphous solids is the phenomenon of structural relaxation, associated with long-range molecular mobility activated above the glass transition temperature T_g. NMR spectroscopy affords techniques for the study of glass and melt dynamics over a wide range of timescales. Very slow atomic motions (timescale ~1 s) are sensitively detected by 1D or 2D chemical shift exchange spectroscopy. NMR lineshape parameters are affected by motions with correlation times in the millisecond region, whereas the spin–lattice relaxation times are most sensitive to motions on the timescale of nuclear precession periods, i.e. 10^{-8} s.

High-temperature studies of silicate glasses reveal an essentially rigid structure on the NMR timescale at temperatures below T_g. 2D ^{29}Si chemical exchange spectroscopy has shown that in glassy $K_2Si_4O_9$ the glass transition at 500 °C is probably associated with a slow $Si^{(4)} \rightarrow Si^{(3)}$ site exchange process.[50] Figure 14 shows a typical result, obtained at 571 °C. Site exchange manifests itself as a cross peak (−106 ppm, −55 ppm) corresponding to the peak maxima of the static powder patterns of $Si^{(4)}$ and $Si^{(3)}$, respectively. $Si^{(4)} \rightarrow Si^{(3)}$ site exchange is very slow at this temperature, and thus has no effect on the static NMR lineshapes. Nevertheless, these results establish a direct link between the glass transition

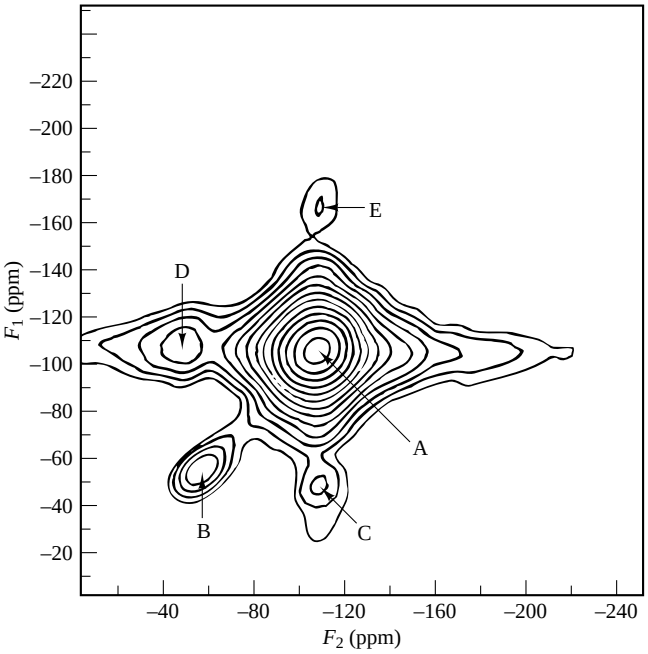

Figure 14 Contour plot of the 2D chemical exchange ^{29}Si NMR spectrum of $K_2Si_4O_9$ glass at 571°C. The cross peaks C and D reveal that the $Si^{(3)}$ and $Si^{(4)}$ species are in chemical exchange. Feature E possibly reflects a five-coordinated species in equilibrium with $Si^{(4)}$. (Reproduced with permission of Elsevier Science Publishers BV from I. Farnan and J. F. Stebbins, *J. Noncryst. Solids*, 1990, **124**, 207)

and the Si–O bond-breaking/bond-making processes resulting in chemical exchange phenomena, and explain why fibers quenched during rapid shearing of liquids produce no local alignment.[51] Since the Si–O bonds are so labile at temperatures as low as T_g, shearing cannot produce cooperative flow.

Figure 15 shows that the $Si^{(3)}$ and $Si^{(4)}$ powder patterns persist up to temperatures of 700 °C, ~200 °C above T_g, before being affected simultaneously by site exchange and motional narrowing. Above 1000 °C, the fast exchange limit is reached, and sharp 'liquid-like' spectra are observed. Although rather complex, it is possible to simulate the chemical exchange effect on the lineshape, and derive approximate exchange rates at different temperatures (Figure 15).[52] The Arrhenius plot of exchange rate versus temperature yields an activation energy of 179.4 ± 5.4 kJ mol^{-1}. Furthermore, from back-extrapolation of this line it is predicted that the exchange rate at T_g amounts to ~9 Hz.[52] Because of the availability of empty d orbitals on the silicon atom, it is reasonable to speculate that the site interchange mechanism is based on an addition/elimination mechanism, involving a higher-coordinate silicon intermediate. Indeed, the ^{29}Si silicon NMR spectra of various $M_2Si_4O_9$ glasses show a weak peak (comprising ~0.06–0.10% of the total ^{29}Si signal) around −150 ppm.[53,54] This chemical shift appears approximately halfway between those measured for four- and six-coordinate silicon sites and is therefore assigned to five-coordinate silicon atoms (Si^V). Substantial amounts of Si^V and Si^{VI} are present in analogous $Na_2Si_4O_9$ glasses quenched from elevated pressures (>6 GPa), hence further supporting the above peak assignment (Figure 16).[55] The structural behavior of silicate melts at high pressures is of central importance for the understanding of many geological processes occurring in the Earth's interior. The

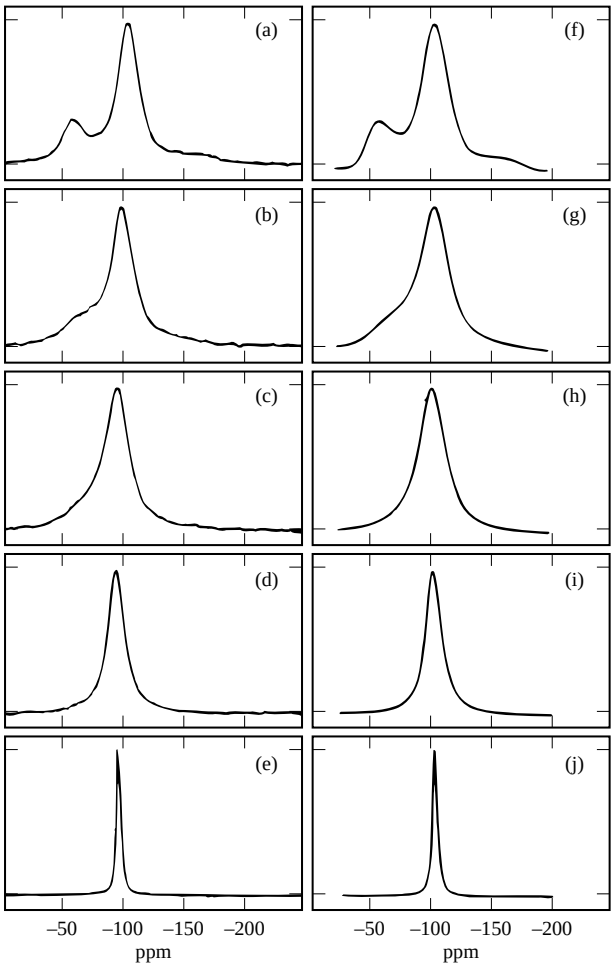

Figure 15 (a)–(e) Variable-temperature ^{29}Si NMR spectra of $K_2Si_4O_9$ glass and (f)–(j) corresponding simulations based on chemical exchange between $Si^{(3)}$ and $Si^{(4)}$ units. Temperatures and exchange rates are: (a) 697°C, (b) 774°C, (c) 800°C, (d) 847°C, (e) 997°C, (f) 2000 Hz, (g) 10 000 Hz, (h) 25 000 Hz, (i) 50 000 Hz, (j) 500 000 Hz. (Reproduced with permission of The American Chemical Society from I. Farnan and J. F. Stebbins, *J. Am. Chem. Soc*, 1990, **112**, 32)

gradual change in silicon coordination number is illustrated in Figure 16 for $Na_2Si_4O_9$ glasses quenched at different external pressures and decompressed at room temperature. In contrast, no coordination change appears for albite melts in a similar pressure range.[56]

3.6 The Interaction of Water with Silicate Melts and Glasses

Silicate melts are known to dissolve considerable amounts of water at elevated temperatures and pressure, resulting in dramatic effects on the physical and optical properties of the glasses. From a structural point of view, water is thought to depolymerize the silicate network, according to the reaction

$$Si{-}O{-}Si + H_2O \rightarrow 2Si{-}OH \qquad (4)$$

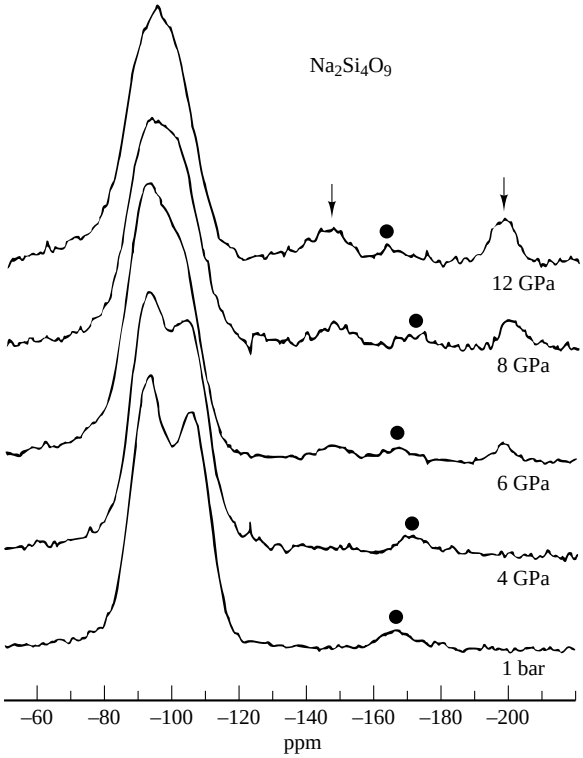

Figure 16 Silicon-29 MAS NMR spectra of glassy $Na_2Si_4O_9$ samples quenched from high temperatures and different pressures (listed in the figure) and decompressed at room temperature. The formation of Si^V and Si^{VI} is indicated by the gradual emergence of peaks at −150 and −210 ppm (arrows) as the pressure is increased. The solid circles denote spinning sidebands. (Reproduced with permission of The Mineralogical Society of America from X. Xue, J. F. Stebbins, M. Kanzaki, P. F. McMillan, and B. Poe, *Am. Miner.*, 1991, **76**, 8)

This hypothesis has been confirmed for amorphous silica using ^{29}Si CP MAS NMR.[57] Since CP requires the presence of ^{1}H–^{29}Si dipole couplings, only those silicon atoms that are near a hydrogen atom are detected, resulting in selective amplification of the signal due to Si–OH groups. The spectra obtained are consistent with a model in which the reaction of water with the silica melt produces mostly Si–OH and only few $Si(OH)_2$ units.[57] In sharp contrast, CP MAS NMR studies fail to detect any Si–OH groups in albite glasses, suggesting that reaction (4) is not applicable to this network.[58] The presence of water perturbs the ^{23}Na resonance significantly, suggesting that there are strong OHNa interactions.[58]

Complementary information on the hydrous species has been obtained using ^{1}H NMR. Static spectra appear to be superpositions of a broad Pake doublet attributed to molecular H_2O and a sharper Gaussian component assigned to OH groups.[59–62] The relative amounts of OH and molecular H_2O species have been determined by ^{1}H MAS NMR for a series of aluminosilicate glasses with water contents ranging from 0.5 to 8 wt.% H_2O.[60] Typical spectra are shown in Figure 17. At spinning speeds around 8 kHz, the OH groups yield a strong MAS NMR central line, because all the interactions affecting the static spectrum of the OH groups are effectively averaged by MAS. In contrast, 8 kHz MAS is unable to average the strong intramolecular dipolar interaction between the two hydrogen atoms in the water molecule. Theory predicts that the homonuclear dipolar interaction within

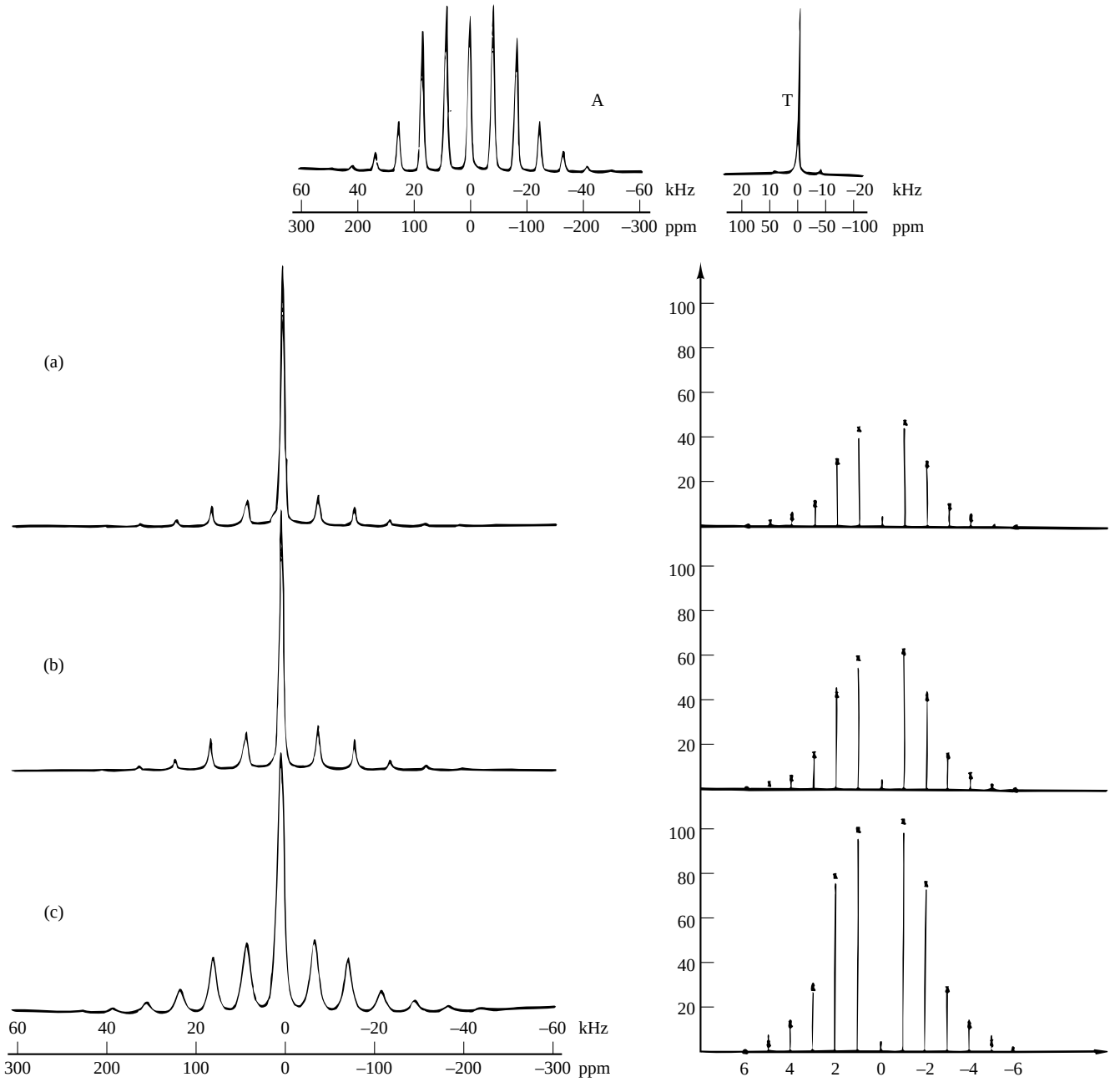

Figure 17 Proton MAS NMR spectra of hydrous aluminosilicate glasses containing (a) 1.5 wt.%, (b) 2.7 wt.%, and (c) 7.9 wt.% H_2O. Top: experimental spectra obtained from tremolite (T; isolated OH groups) and analcite (A; isolated H_2O molecules). Left side: experimental spectra at 8 kHz spinning speed. Right side: spinning sideband heights for the same glasses. Solid lines are experimental results, crosses are heights predicted by additive superposition of the experimental spectra of analcite and tremolite, in a ratio such that identical heights for the center bands (not shown here) result. (Reproduced with permission of The American Chemical Society from H. Eckert, J. P. Yesinowski, E. M. Stolper, and L. A. Silver, *J. Phys. Chem.*, 1988, **92**, 2055)

an isolated pair of two spins is inhomogeneous, resulting in well-defined spinning sideband patterns upon MAS. The fact that this behavior is observed experimentally suggests that the H_2O molecules in these glasses are structurally fairly isolated, and that MAS succeeds in averaging the intermolecular dipolar interactions among OH and H_2O species. The OH/H_2O ratio can then be determined from the intensity of the sidebands relative to the center band. Figure 18 summarizes the resulting NMR-derived water speciation for various aluminosilicate glasses.[60] At low overall water contents, most of the hydrous species are present in the form of OH groups. As the water concentration increases, the OH species concentrations level off at 2–3 wt.% H_2O, and the concentration of molecular water species increases steeply.

Another question of interest is the strength of the interaction between the hydrous species and the silica network, i.e. the hydrogen bond strength characteristics. Proton chemical shifts are known to be sensitive to hydrogen-bonding effects. As a convenient measure of the hydrogen-bonding strength, one may take the O–HO distance of the hydrogen bond.

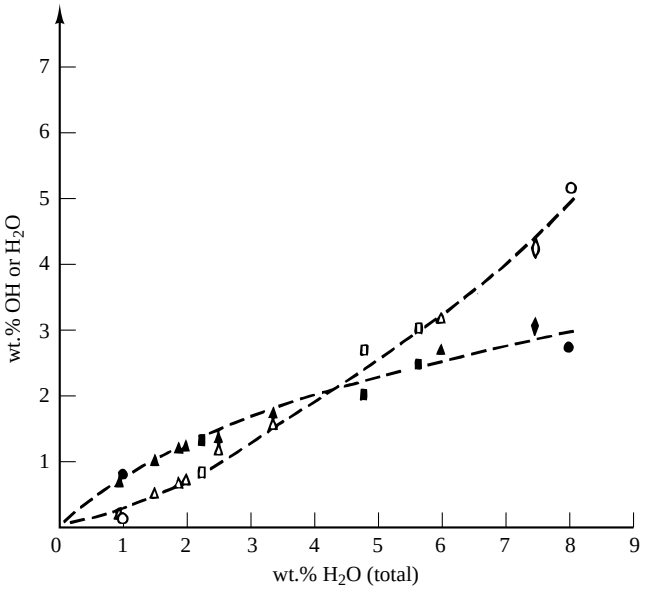

Figure 18 Speciation of water in various aluminosilicate glasses. Open symbols: H_2O contents; closed symbols: OH contents. △, ▲, orthoclase; □, ■, albite, ◇, ◆, albite–orthoclase; ○, ●, anorthite–silica–wollastonite. (Reproduced with permission of Elsevier Science Publishers BV from H. Eckert, J. P. Yesinowski, and E. M. Stolper, *Solid State Ionics*, 1989, **32/33**, 298)

Regression analysis of the ^1H chemical shift database on crystalline model compounds, for which those distances are well known, then allows one to estimate average hydrogen-bonding lengths in a variety of water-bearing silicate glasses. In albitic glasses the distribution is more or less uniformly centered around $d(O–HO) = 0.29\,nm$.[59,60] This result has been confirmed independently by measurements of the average ^2H quadrupolar coupling constant of D_2O-bearing glasses on the basis of a similar empirical correlation with O–DO distances.[63] In contrast, ^1H MAS NMR spectra obtained on hydrous alkali silicate glasses reveal a decidedly bimodal behavior including rather short (0.26 nm) and longer (0.29 nm) distances.[64] The appearance of short hydrogen bonds is believed to be due to a strong association of OH groups with the nonbridging oxygen atoms in these glasses.

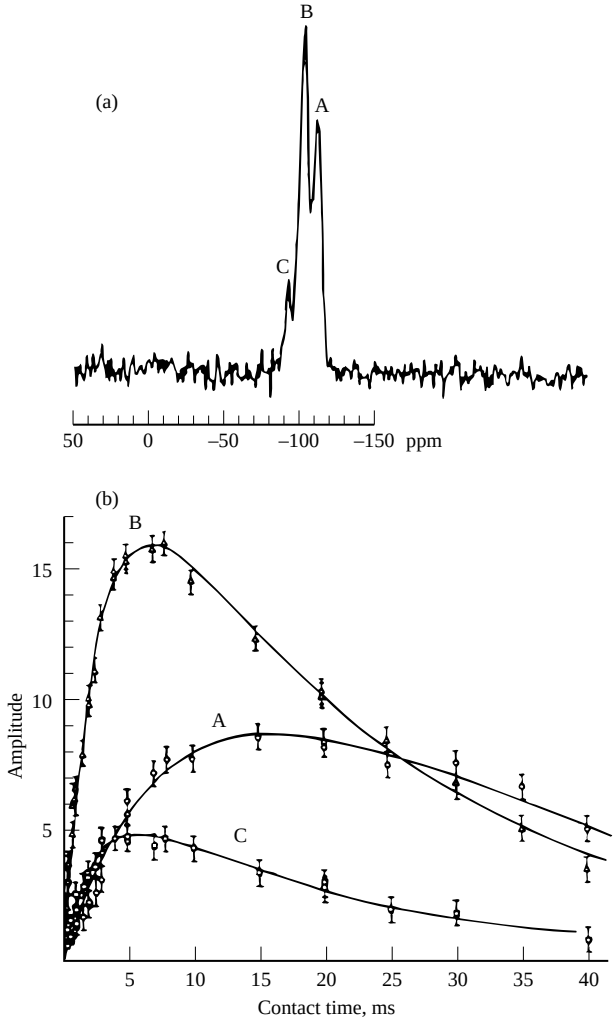

Figure 19 (a) Silicon-29 CP MAS NMR spectrum of silica gel. (b) Silicon-29 signal amplitude versus CP MAS contact time. Peaks A, B, and C correspond to $SiO_{4/2}$, $SiO_{3/2}OH$, and $SiO_{2/2}(OH)_2$ groups, respectively. Note in particular the different CP dynamics for these three species. (Reproduced with permission of The American Chemical Society from G. E. Maciel and D. W. Sindorf, *J. Am. Chem. Soc.*, 1980, **102**, 7606)

3.7 Sol–Gel-Prepared Glasses and Amorphous Silicas

The 'sol–gel' process used in the synthesis of oxide glasses is based upon the hydrolysis of tetraethyl orthosilicate (TEOS) or other suitable monomeric precursor species. The hydrolysis product, $Si(OH)_4$, subsequently undergoes polycondensation, resulting in a heavily hydrated 'gel'. Dehydration at elevated temperatures results in densification and formation of bulk glassy material.

$$\text{Hydrolysis: } Si(OEt)_4 + 4H_2O \rightarrow Si(OH)_4 + 4EtOH \quad (5a)$$

$$\text{Condensation: } nSi(OH)_4 \rightarrow [SiO_x(OH)_{4-2x}]_n + xnH_2O \quad (5b)$$

$$\text{Dehydration: } [SiO_x(OH)_{4-2x}]_n \rightarrow n'SiO_2{}' + n(4-2x)/2H_2O \quad (5c)$$

The processes summarized in equations (5a)–(5c) proceed via many steps. Substitution of OEt by OH occurs one moiety at a time, and the polymerization of the resulting $Si^{(0)}$ species yields more highly condensed $Si^{(n)}$ species, i.e. $Si^{(1)}$ (end groups), $Si^{(2)}$ (middle groups), $Si^{(3)}$ (2D branching groups), and $Si^{(4)}$ (3D branching groups). These species are analogous to those introduced in Section 3.1, except that they are terminated by OH rather than O^-.

NMR has proven to be an excellent method for monitoring the various stages of the sol–gel process. Since the hydrolysis and the initial stages of polymerization of the hydrolysis products occur in homogeneous solution, they can be easily followed by standard liquid state ^{29}Si NMR.[65] In contrast, studies of the dried and dehydrated gels require solid state NMR methodology. Figure 19(a) demonstrates that ^{29}Si chemical shifts differentiate generally quite well between $SiO_{4/2}$, $Si(OH)O_{3/2}$, and $Si(OH)_2O_{2/2}$ species (peaks A, B, and C, respectively).[66] The peak assignments are based on the

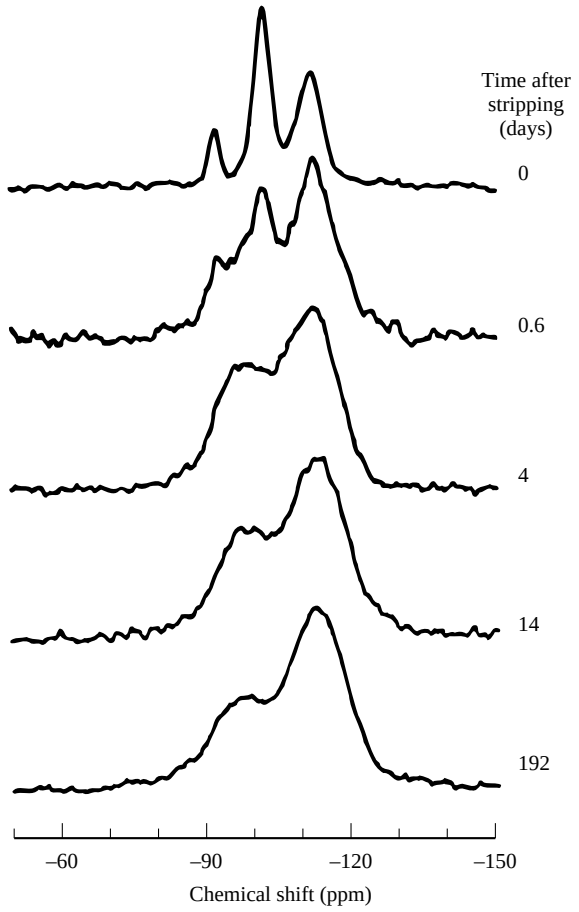

Figure 20 Static ^{29}Si NMR spectra of an aging gel kept in a closed vial at room temperature after refluxing for 3 h and stripping to 1.1 g ml^{-1}, as a function of aging time. The molar composition of the parent solution was TEOS/H_2O/ethanol/HCl = 1/16/4.0/0.01. (Reproduced with permission of Elsevier Science Publishers BV from A. J. Vega and G. W. Scherer, *J. Noncryst. Solids*, 1989, **111**, 153)

different CP dynamics of the silanol groups compared with those of silicon atoms more removed from hydrogen. This is demonstrated by the variable contact time experiments in Figure 19(b) CP MAS experiments with short contact times tend to enhance the signals of the hydroxyl-bound silicon atoms, whereas ^{29}Si MAS NMR studies result in quantitatively representative spectra.

The influence of specific experimental conditions on the network structure and the fate of residual hydrous species during the various stages of the gel–glass transition have been studied in detail by Vega and Scherer.[67] Figure 20 shows an experiment monitoring the aging process of an SiO_2 gel over a period of several months. The spectra show three peaks, assigned to $Si^{(2)}$, $Si^{(3)}$, and $Si^{(4)}$ species. The speciation changes remarkably little upon aging and syneresis, indicating that the polymerization is to a large degree arrested at the gelation stage. The peak deconvolution on the final glass samples attained after prolonged aging shows $Si^{(4)}$ and $Si^{(3)}$ in roughly equal proportions and a small amount (<5%) of $Si^{(2)}$ species. This corresponds to a final OH content of 0.5 to 0.6 units per silicon. This conclusion is confirmed by complementary ^{1}H NMR studies, which also serve to characterize the motional properties of the hydrous species.[67]

4 BORATE GLASSES

While technologically of less interest, borate glasses have been the subject of intense structural investigations during the past three decades. Specific topics of study have been (i) structural implications of the Lewis acid character of boron oxide, resulting in increased polymerization by basic oxides, (ii) the description of borate glasses in terms of molecular cluster units known from the crystal chemistry of borates, and (iii) the interaction of boron oxide with other network formers and intermediate oxides in borosilicate, borophosphate, and boroaluminate glasses. Much of the early NMR work on glasses (prior to the early 1970s) concentrated on borate systems, where the only technique widely available then, low-field CW NMR, proved to be an ideal structural tool for probing short-range order. In spite of the availability of more modern techniques, this remains true to the present date.

4.1 Site Distribution in Glassy Boron Oxide

The structure of glassy B_2O_3 is generally viewed to consist largely of six-membered boroxol rings in addition to loose BO_3 units. While previous CW NMR studies of ^{11}B and ^{10}B were unable to resolve distinct resonances for these sites, this has been accomplished recently using pure NQR. As shown in Figure 21(a), the NQR spectrum reveals two distinct boron sites with quadrupolar frequencies (χ/2) of 1358

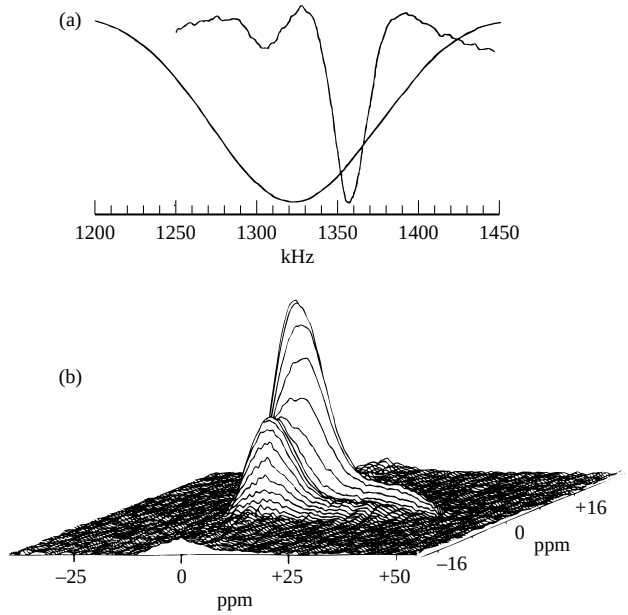

Figure 21 Two recent experimental ^{11}B NQR/NMR results relating to the structure of glassy B_2O_3. (a) CW ^{11}B NQR, both experimental and predicted based on previous ^{11}B NMR studies. (Reproduced with permission of Elsevier Science Publishers BV from S. J. Gravina, P. J. Bray, and G. L. Petersen, *J. Noncryst. Solids*, 1990, **123**, 165). (b) 2D ^{11}B DAS NMR, carried out on an isotopically depleted sample. (Reproduced with permission of Elsevier Science Publishers BV from R. E. Youngman and J. W. Zwanziger, *J. Noncryst. Solids*, 1994, **168**, 293). The NQR and DAS methods detect two different types of boron sites, assigned to boron atoms within boroxol rings (majority site) and loose BO_3 groups (minority site)

and 1305 kHz, which are assigned to boron atoms inside of and outside of boroxol rings, respectively.[68] The peak ratio suggests that 85% of all boron atoms are contained within boroxol rings. Very similar results have been obtained most recently using the ^{11}B DAS NMR technique [Figure 21(b)].[69] The nuclear electric quadrupole coupling constants obtained for these sites from the anisotropic dimension in the DAS experiment are in excellent agreement with the values obtained from pure NQR.

4.2 Binary Alkali and Alkaline Earth Borate Glasses

4.2.1 Spectroscopic Approaches

Introduction of alkali oxide into glassy B_2O_3 results in the formation of four-coordinate boron atoms (B^{IV} units), as well as three-coordinate boron atoms associated with one to three nonbridging oxygen atoms ($B^{III(0-2)}$ units). Low-field CW NMR techniques have been very effective in differentiating quantitatively between these principal types of boron nearest-neighbor environments, exploiting differences in the magnitude and symmetry of the nuclear electric field gradient at the boron sites. These differences are summarized in Figure 22. Symmetric-trigonal $BO_{3/2}$ (B^{IIIs}) groups with D_{3h} symmetry are characterized by χ around 2.6 MHz and an asymmetry parameter near zero. Asymmetric-trigonal $BO_{2/2}O^-$ or $BO_{1/2}(O^-)_2$ (B^{IIIa}) groups have χ around 2.6 MHz and $\eta \sim 0.6$, while four-coordinate $BO_{4/2}{}^-$ (B^{IV}) groups are characterized by substantially smaller electric field gradients. At low field strengths, both types of three-coordinate boron sites show well-defined powder patterns due to second-order quadrupolar perturbations, whereas four-coordinate $BO_{4/2}{}^-$ groups yield sharp lines with little evidence of quadrupolar broadening.[70]

Additional structural insights into the conversion of the B_2O_3 network by alkaline oxides have recently been obtained by the CW NQR method,[71] revealing the successive destruction of boroxol groups upon addition of alkali oxide network modifiers, and their virtually complete elimination near 20 mol% alkaline oxide. For individually resolved sites, it appears that the distribution functions of the quadrupole coupling parameters are substantially narrower than previously believed, suggesting the presence of some intermediate-range order. This result confirms the general view held that alkali borate glasses comprise statistical assemblies of various ring structures present in crystalline borates.

While the quantitative distinction between the various boron sites shown in Figure 22 has been accomplished well by ^{11}B CW NMR, this method suffers from low intrinsic detection sensitivity. An additional problem is the increasing lack of availability of such spectrometers. Standard FT wideline experiments at higher fields have generally given less satisfactory results. With increasing field strength, the width of the B^{III} resonance decreases (due to diminished second-order quadrupolar effects), while that of the B^{IV} resonance increases (due to increased chemical shift dispersion), hence making the spectral separation more difficult. Even with high-field, high-speed MAS NMR one observes substantial peak overlap, because the isotropic chemical shift difference between the B^{III} and the B^{IV} units ($\sim$15–20 ppm) is largely canceled by their respective difference in $\delta^{(2)}$, which has opposite sign.

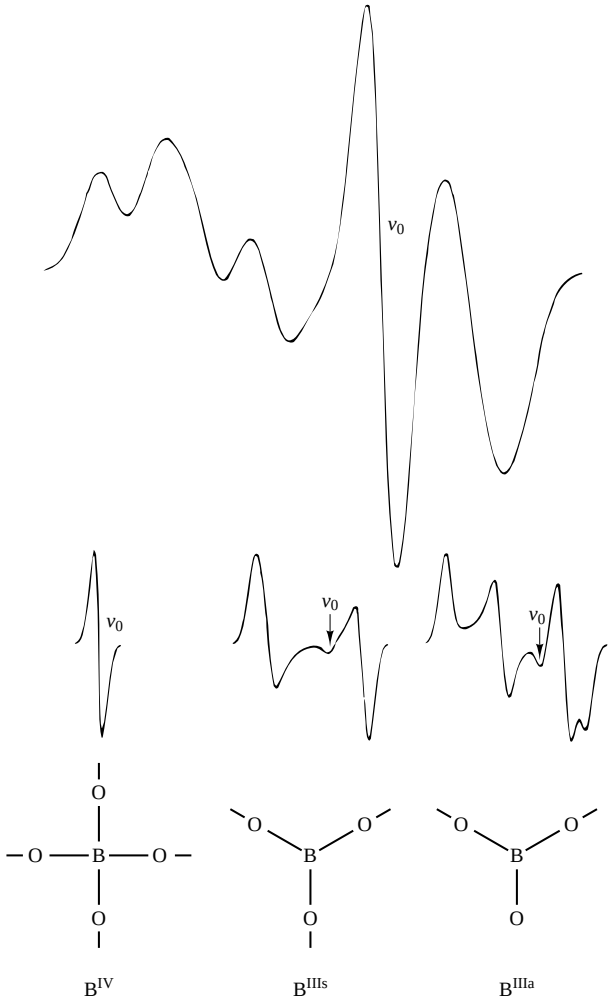

Figure 22 Boron sites in borate glasses and their derivative ^{11}B NMR spectra as detected by CW wideline NMR (Reproduced by permission of Pergamon Press from H. Eckert, *Prog. Nucl. Magn. Reson.*, 1992, **24**, 159)

This problem has been recently addressed successfully by focusing the attention on the first-order satellite transitions (SATRAS NMR). From theory it is known that for spin-$\frac{3}{2}$ nuclei the second-order shifts associated with the first-order quadrupolar satellites are twice as large as those for the central transition, and, furthermore, have positive sign.[72] An important consequence is that the spectral resolution between B^{III} and B^{IV} units is enhanced for the satellite transitions because the differences in δ_{iso} and $\delta^{(2)}$ now possess the same sign. Important new results demonstrating this resolution improvement are shown in Figure 23[73] Besides quantitative reliability, the SATRAS method affords accurate chemical shift and quadrupolar coupling information on the various types of boron sites.

4.2.2 Experimental Results on Binary Systems

Using NMR strategies outlined above, quantitative site ratios B^{IIIs}:B^{IIIa}:B^{IV} have been determined systematically for a huge number of binary and ternary borate glass systems. Typically, the fraction N_4 of four-coordinate boron atoms is plotted as a function of R, the molar ratio of network modifier

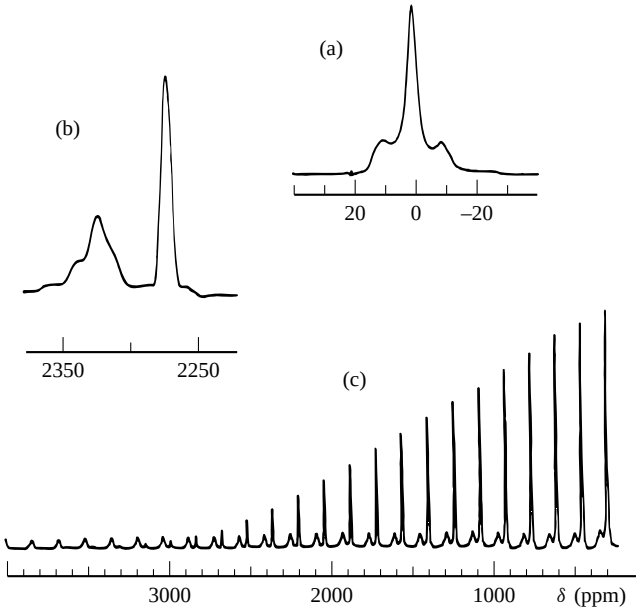

Figure 23 Boron-11 SATRAS NMR results on a glass containing 33 mol% Li_2O and 67 mol% B_2O_3. (a) Central transition, (b) 13th sideband (to high frequency) of the satellite transition, (c) higher frequency part of the satellite transition spinning sideband spectrum. (Reproduced with permission of Elsevier Science Publishers BV from L. Van Wüllen and W. Müller-Warmuth, *Solid State NMR*, 1993, **2**, 279)

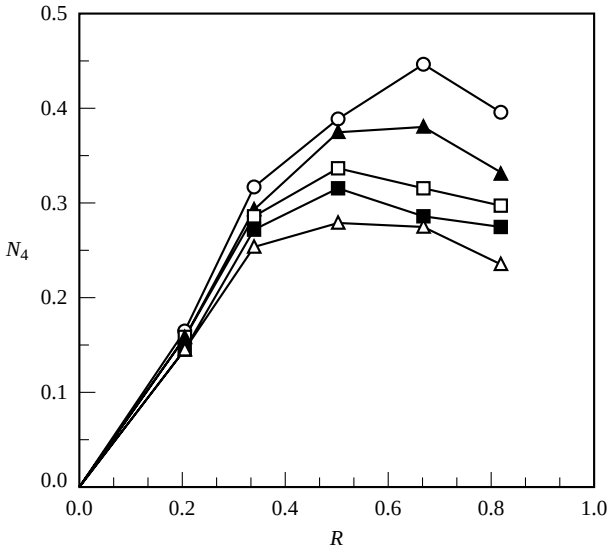

Figure 24 Dependence of N_4 on R as a function of the alkali ion in alkali borate glasses. ○, lithium borate; ▲, sodium borate; □, potassium borate; ■, rubidium borate; △, cesium borate glasses. (Reproduced with permission of Elsevier Science Publishers BV from J. Zhong and P. J. Bray, *J. Noncryst. Solids*, 1989, **111**, 67)

to network former. At low network modifier concentrations ($R \leq 0.5$), $N_4 = R$, i.e. each oxide ion introduced into the borate network converts two boron atoms from threefold to fourfold. At higher values of R, N_4 decreases again, and the successive growth of signal components due to B^{IIIa} units marks the increasing production of nonbridging oxygen species. Recent studies, using improved lineshape deconvolution procedures, suggest special cation effects for alkali borate glasses.[74] Figure 24 suggests that N_4 for a given R value decreases with increasing cation size. In addition, mixed alkali glasses show systematically reduced N_4 values, indicating that B^{IIIa} units compete more successfully with B^{IV} units.[74]

4.2.3 Experimental Results on Ternary Systems

The presence of additional network formers or of intermediate oxides has a profound influence on the boron speciation, and such effects have been widely documented by ^{11}B CW NMR for many ternary systems, including borophosphate,[75] borosilicate,[76] and borovanadate[77] glasses. A simple phase diagram scheme has been proposed to rationalize the experimental results.[78,79] In essence, this scheme uses the lever rule to predict N_4 for a given glass from the experimental N_4 values of certain 'standard' glasses, whose compositions correspond to those of congruently melting compounds in the ternary phase diagram. If the phase diagram is not well known, however, additional assumptions have to be introduced with regard to the composition of such 'standard' glasses. Whether or not such choices can always be rationalized in a plausible way, the predictive schemes developed by these authors appear to work well for a variety of ternary borate glasses and can serve as an alternative for the (less general) empirical relations used previously, particularly in the borosilicate systems[76] for describing the dependence of N_4 on composition.

Aluminoborate glasses of the composition $M_{(2)}O–Al_2O_3–B_2O_3$ (M = alkali or alkaline earth metal) have been studied in particular detail. Incorporation of aluminum into alkali and alkaline earth borate glasses at constant R leads to a considerable reduction in N_4.[80,81] This observation indicates that part of the cations are associated with four-coordinate AlO_4^- units, at the expense of the boron conversion process. Not all of the alkaline oxide is directed towards aluminum, however, because even in glasses with an $M_{(2)}O/Al_2O_3$ ratio of unity, a substantial fraction of the boron atoms remain four-coordinate. This finding is consistent with ^{27}Al MAS NMR data, which show that a sizable fraction of the aluminum atoms are present as Al^V and Al^{VI}.[82] In interpreting the aluminum speciations, Brow and co-workers estimate the stability of various oxygen nearest-neighbor environments on the basis of bond valence considerations.[83] Maximum stability is expected if the bond valence sums (charge divided by coordination number) of the cations next to an oxygen site are close to +2 for a neutral oxygen site, and +1 for a nonbridging oxygen site. Such considerations show, for instance, that $B^{IV}–O–B^{IV}$ and $Al^{IV}–O–A^{IV}$ connectivities are less stable than $B^{III}–O–Al^{IV}$ linkages, and that three-coordinate oxygen atoms must exist to explain the presence of Al^V and Al^{VI}. As shown in Figure 25 the bond valence concept is also useful for explaining chemical shift trends for the Al^{IV} site. The shift values observed experimentally (55–60 ppm) are much more consistent with $Al^{IV}–O–B^{III}$ linkages than with the $Al^{IV}–O–B^{IV}$, $Al^{IV}–O–Al^{IV}$, and $Al^{IV}–O–Al^{VI}$ linkages previously proposed. These conclusions are also in agreement with the stability arguments outlined above. Most recently, SATRAS NMR has allowed a much cleaner distinction between the three aluminum sites in aluminoborate glasses.[84] This is expected from theory, predicting that second-order

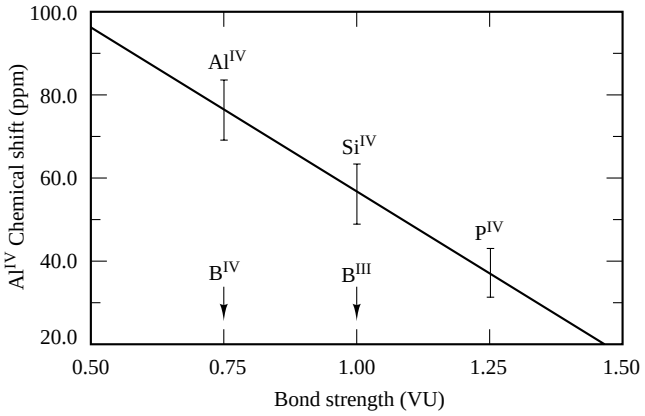

Figure 25 Correlation of the ^{27}Al chemical shift ranges observed for Al^{IV} in framework structure crystalline model compounds (four network next-nearest neighbors) with the bond valence sum ('bond strength') of the next-nearest neighbor cation. From this plot it is predicted that an Al^{IV} species linked to four B^{IV} or to four B^{III} species should resonate at 75 and 55 ppm, respectively. (Reproduced with permission of The American Ceramic Society from B. C. Bunker, R. J. Kirkpatrick, R. K. Brow, G. L. Turner, and C. Nelson, *J. Am. Ceram. Soc.*, 1991, **74**, 1430)

quadrupolar broadening effects are greatly reduced for the $\pm\frac{1}{2} \rightarrow \pm\frac{3}{2}$ satellite transitions of spin $I = \frac{5}{2}$ nuclei.[72]

5 PHOSPHATE GLASSES

The local order in phosphate glasses is described, in a manner very similar to silicate glasses, in terms of four individual $P^{(n)}$ sites ($n \leq 3$), varying in the number of bridging oxygen atoms. As illustrated in Figure 26, these sites are easily distinguished by ^{31}P isotropic and anisotropic chemical shift parameters. Quantitative deconvolution of the ^{31}P MAS NMR spectra reveal that in binary alkali and silver phosphate glasses[85,86] and in alkaline earth phosphate glasses[87] the $P^{(n)}$ site distribution follows the binary model. Since water acts as a network modifier in these hygroscopic glasses, a precise analysis of NMR spectra of these glasses requires the exact water content to be known. Most recently, the binary model has been confirmed for alkali phosphate glasses prepared and stored under rigorously anhydrous conditions.[88] The binary model is also substantiated in the fast ionic conductors based on Ag_2O–AgI–P_2O_5 glasses, which show excellent chemical shift resolution for the various $P^{(n)}$ species. Here, the AgI component does not participate in the network modification, but is dispersed throughout the glass structure.[86]

Zwanziger and co-workers have utilized the VACSY technique to correlate specific isotropic chemical shifts with the corresponding anisotropic chemical shift information in ionically conducting silver phosphate glasses.[89] Figure 27 shows an interesting result for a glass with the composition $(Ag_2O)_{41}(AgI)_{39}(P_2O_5)_{20}$. The MAS NMR spectrum shows a low-intensity peak at 23.6 ppm, assigned to PO_4^{3-} ($P^{(0)}$) groups, and a dominant resonance centered around 3 ppm, assigned to $P_2O_7^{4-}$ ($P^{(1)}$) groups. Both peaks are broadened by a distribution of isotropic chemical shifts, reflecting the inherent disorder in the glass. As intended, VACSY is able to recover the individual CSA information for these two

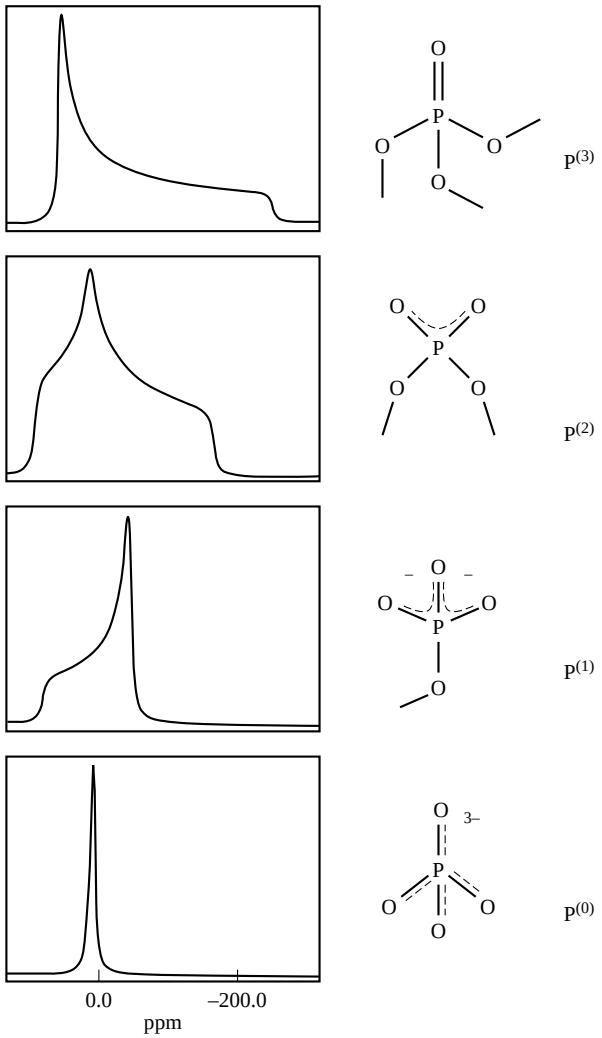

Figure 26 Phosphorus sites in alkali phosphate glasses and their wideline ^{31}P NMR anisotropic chemical shift powder patterns. The terminology used here is analogous to that defined in Figure 7(a) (Reproduced by permission of Pergamon Press from H. Eckert, *Prog. Nucl. Magn. Reson.*, 1992, **24**, 159)

distinct sites. Furthermore, the chemical shift tensor elements for the $P^{(1)}$ resonance depend on the exact position within the isotropic chemical shift distribution. The low-frequency shoulder of the $P^{(1)}$ resonance is correlated with a nonaxially symmetric chemical shift tensor, revealing the presence of distinct, more distorted pyrophosphate groups. The ability of VACSY to enhance the resolution between sites whose MAS NMR centerbands overlap makes it a potentially very powerful tool for the investigation of many other spin-$\frac{1}{2}$ nuclei in glasses and other disordered materials that give rise to very poorly resolved MAS NMR spectra.

Excellent site resolution has been observed by ^{31}P MAS NMR in borophosphate and (to a lesser extent) aluminophosphate glasses.[90–93] Considering next nearest-neighbor environments, these glasses may contain (depending on composition) up to 11 $P_m^{(n)}$ sites, where m is the number of boron or aluminum next-nearest neighbors ($m \leq n$). Among these sites, features not known for binary alkali phosphate glasses are the tetrahedral, fully bridging $P_4^{(4)}$ sites, well known in crystalline BPO_4 and $AlPO_4$. The ^{31}P MAS NMR spectra of silver

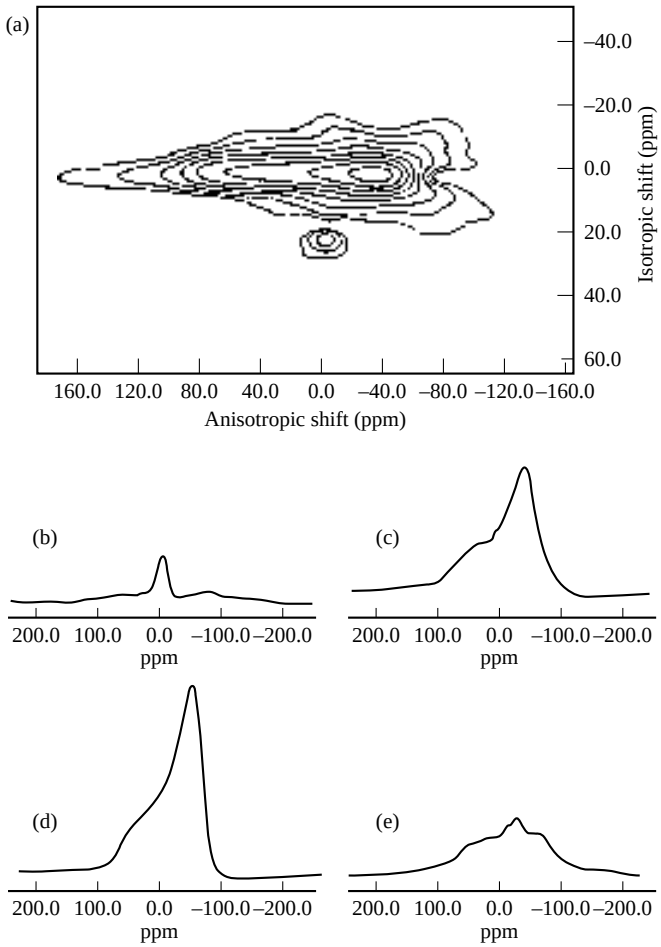

Figure 27 Phosphorus-31 VACSY NMR results obtained on a glass containing 41 mol% Ag_2O, 39 mol% AgI, and 20 mol% P_2O_5. (a) Overall contour plot. (b)–(e) Slices through the VACSY spectrum at isotropic shifts of (b) 23.6 ppm, (c) 8.1 ppm, (d) 3.3 ppm, and (e) −7.3 ppm. (Reproduced with permission from J. W. Zwanziger, K. K. Olsen, and S. L. Tagg, *Phys. Rev. B*, 1993, **47**, 14618)

borophosphate glasses were found to be exceptionally well resolved,[90] permitting a quantitative distinction between various of these sites. In contrast, only partial site resolution is observed for sodium aluminophosphate glasses.[91–93] For the sodium aluminophosphate glasses, bond valence arguments predict that the interaction of a $P^{(2)}$ (metaphosphate) site is more favorable with Al^{VI} than with Al^{IV}.[93] The compositional dependence of the average aluminum coordination number is summarized in Figure 28, revealing a distinct influence of the total oxygen/phosphorus ratio. Contrary to previous assumptions, the ^{27}Al NMR spectra indicate that the majority of aluminum sites are six-coordinate in most of the materials within the glass-forming region. Four-coordinate $AlPO_4$-like sites are only observed at the highest oxygen/phosphorus ratios.

6 CHALCOGENIDE GLASSES

6.1 Binary Silicon Chalcogenide Glasses

Glassy SiS_2 and $SiSe_2$ form structures based on $SiX_{4/2}$ tetrahedra interconnected by both corner- and edge-sharing, in violation of the traditional continuous random network model, which explicitly excludes any connectivities different from corner-sharing. The ^{29}Si MAS NMR spectra show three broad peaks, which can be assigned to silicon tetrahedra sharing edges with no, one, or two adjacent tetrahedral units. These sites have been denoted $E^{(0)}$, $E^{(1)}$, and $E^{(2)}$, respectively.[94] Similar kinds of materials can be prepared by plasma-enhanced chemical vapor deposition (PECVD) from SiH_4 and H_2S. Compared with the bulk glass, the PECVD samples possess higher concentrations of $E^{(0)}$, and reduced concentrations of $E^{(2)}$ species. This structural speciation is critically influenced by the H_2S/SiH_4 flow rate ratio under synthesis conditions. Thus, PECVD offers the opportunity of controlling the ratio of corner-shared to edge-shared $SiS_{4/2}$ tetrahedra in the final product.[95] This is not possible in molten state synthesis, where changes in the silicon/sulfur melt composition just produce different relative amounts of segregated phases consisting of glassy SiS_2 and elemental sulfur.[96]

The structure of glassy $SiSe_2$ closely resembles that of a low-temperature crystalline $SiSe_2$ phase stable near 500 °C, close to the temperature where molten $SiSe_2$ undergoes its glass transition.[97] Si–Se glasses with higher selenium contents and $SiSe_2$–P_2Se_5 glasses show increased fractions of the $E^{(0)}$ component, whereas the $E^{(2)}$ component is essentially absent.[98] These results indicate a continuous distribution of silicon microstructures, including the presence of Si–Se–Se and Si–Se–P linkages.

6.2 Lithium Thiosilicate and Selenosilicate Glasses

Glasses in the system $(Li_2S)_x$–$(SiS_2)_{1-x}$ ($0.4 \leq x \leq 0.6$) are interesting because of their high ionic conductivities. These systems have been studied as interesting test cases on whether the compositional analogy of these glasses to binary alkali silicate systems translates into structural analogy as well. The NMR results show that introduction of Li_2S into glassy SiS_2 initially reduces the extent of edge-sharing markedly, and the $E^{(2)}$ species have disappeared for the composition $x = 0.30$. Figure 29 illustrates the network modification scheme developed on the basis of the NMR data.[99] The destruction of edge-sharing units by Li_2S (represented by diagonal arrows) results in the formation of nonbridging sulfur atoms. In the compositional region where the most stable glasses form ($0.38 < x < 0.6$) the $E^{(n)}$ distribution remains approximately constant, with an $E^{(0)}/E^{(1)}$ ratio of ~2.5:1. Extension of these investigations to the system Li_2Se–$SiSe_2$ reveals qualitatively many of the same features, except that the chemical shift discrimination between various $Si^{(n)}$ units is markedly improved here, and semiquantititative species concentrations can be derived from the ^{29}Si MAS NMR spectra.[100] Parallel studies of crystallized samples reveal that with an increasing number of bridging selenium atoms in the $Si^{(n)}$ notation the chemical shifts become less negative, the opposite trend as observed in the silicates.

6.3 The Phosphorus–Selenium System

The phosphorus–selenium system is characterized by a pronounced tendency toward vitrification. Glasses are formed over a wide compositional region, from 0–52 and 62–80 mol%

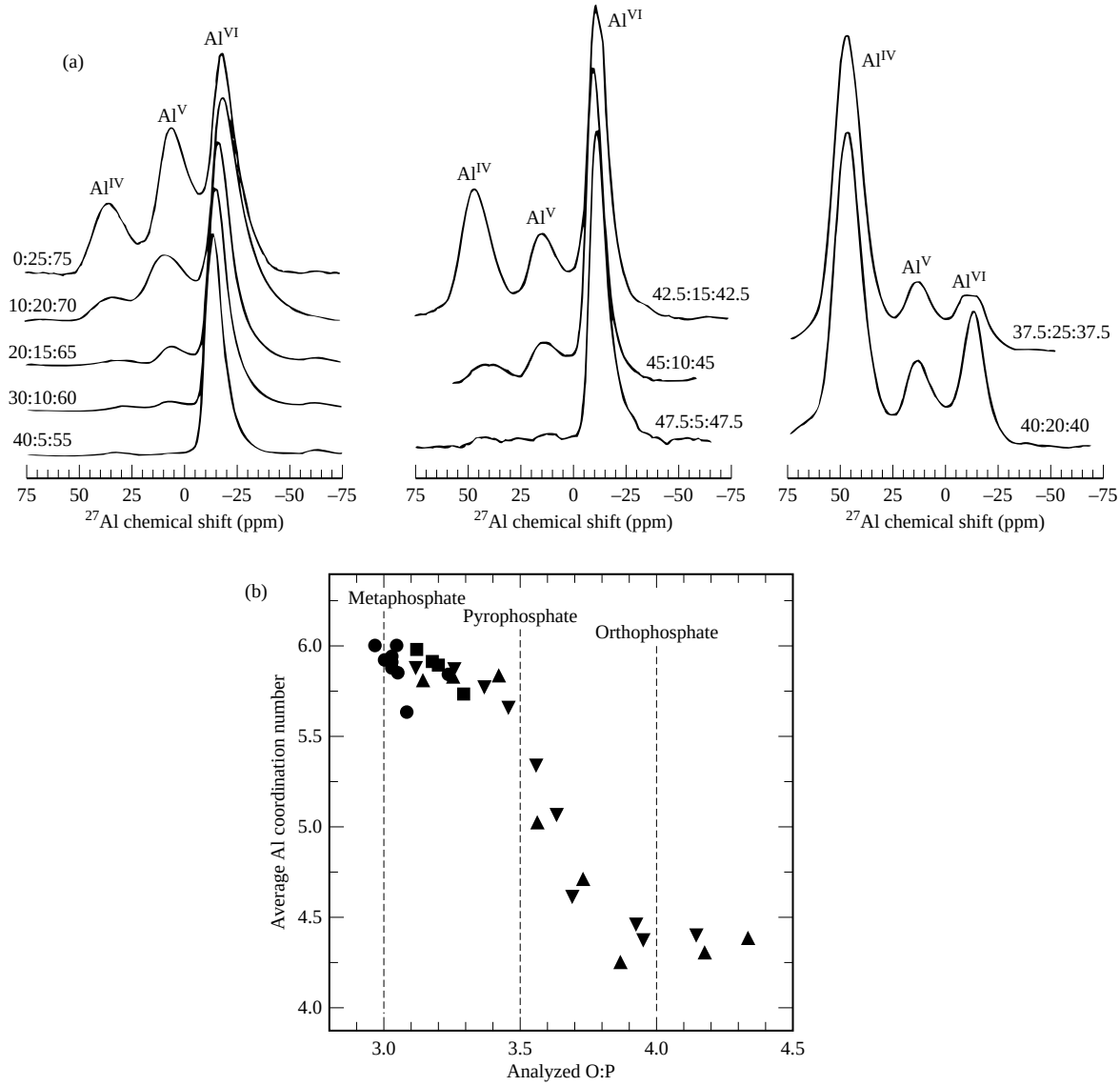

Figure 28 (a) Typical ^{27}Al MAS NMR spectra of sodium aluminophosphate glasses. Compositions are denoted by the molar ratio of Na_2O:Al_2O_3:P_2O_5. (b) Dependence of the average aluminum coordination number on the O:P ratio in these glasses. (Reproduced with permission of The American Ceramic Society from R. K. Brow, R. J. Kirkpatrick, and G. L. Turner, *J. Am. Ceram. Soc.*, 1993, **76**, 919)

P. MAS NMR chemical shifts clearly distinguish between Se=$PSe_{3/2}$ and three-coordinate phosphorus atoms; however, they do not allow one to identify the number of phosphorus or selenium nearest neighbors unambiguously.[101]

The above problem has been successfully addressed by a detailed analysis of the spin echo decay. Due to the substantial difference in the strength of the homonuclear dipole–dipole interactions, the spin echo decays for phosphorus atoms coordinated to selenium only and those for the phosphorus atoms with a phosphorus nearest neighbor are distinctly different. The experimental results indicate that P–P bonds contribute to the glass structure above 25 at.% P, and their contribution can be quantitatively evaluated. The combined analysis of ^{31}P spin echo and MAS NMR results then yields the final phosphorus speciation shown in Figure 30.[102] There is a definite preference toward formation of P–Se over P–P bonds. It is important to realize that all of the above structural findings, obtained on melt-quenched glasses, reflect molten state chemical equilibria that are frozen in at the glass transition temperature, T_g. To understand these speciations further, and to predict the influence of quenching rates on glass structures, it is important to characterize these equilibria and the thermodynamic parameters involved. Consider, for instance, the compositional dependence of the P^{IV} mole fraction, i.e. the fraction of Se=$PSe_{3/2}$ groups in the phosphorus–selenium system, replotted in Figure 31. The data can be consistently described assuming a melt equilibrium model of the form (6)

$$PSe_{3/2} + Se \rightleftharpoons Se{-}PSe_{3/2} \qquad (6)$$

with an equilibrium constant K_1 around 0.8 (at. fraction)$^{-1}$. Recent in situ high-temperature NMR studies have shown that in the melt K_1 consistently decreases with increasing temperature.[103] The associated reaction enthalpies and entropies have been determined as -5 kJ mol^{-1} and -17 J

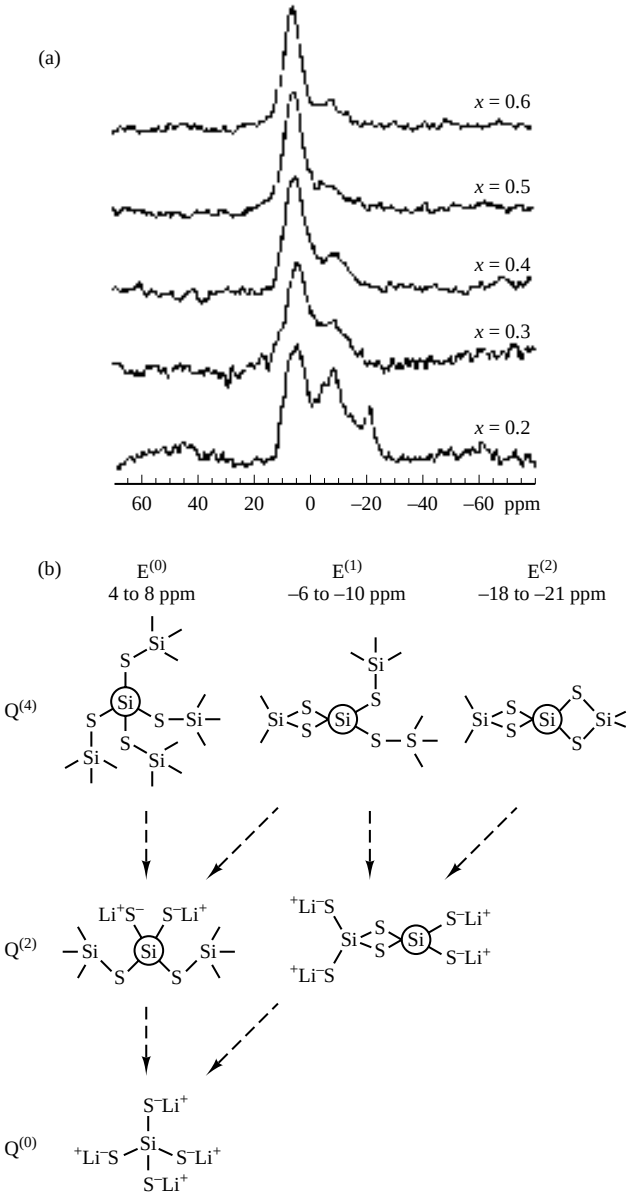

Figure 29 (a) Silicon-29 MAS NMR spectra and (b) network modification scheme developed for lithium thiosilicate glasses. (Reproduced with permission of Elsevier Science Publishers BV from H. Eckert, J. H. Kennedy, A. Pradel, and M. Ribes, *J. Noncryst. Solids*, 1989, **113**, 287)

mol^{-1} K^{-1}, respectively. A second temperature-dependent chemical equilibrium is apparent in glasses containing $\geq$ 40 at.% P, resulting in the appearance of molecular P_4Se_3 cluster units, whose spectral contribution grows with increasing temperature. This depolymerization reaction has been modeled in terms of scheme (7)

$$3Se_{2/2}P{-}PSe_{2/2} \rightarrow P_4Se_3 + 2PSe_{3/2} \qquad (7)$$

The temperature dependence of the associated equilibrium constant indicates a reaction enthalpy of 50 kJ mol^{-1}.[103]

Complementary thermodynamic and kinetic data have been obtained using variable-temperature ^{77}Se NMR studies, the results of which are shown in Figure 32.[103] At low

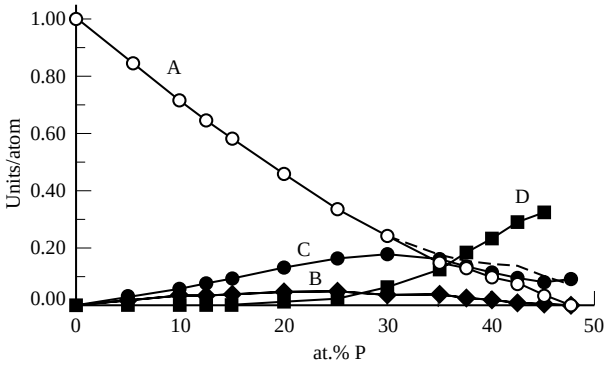

Figure 30 Site speciation in phosphorus–selenium glasses, as deduced from the combined analysis of spin echo and MAS NMR investigations. A, Se–Se bonds; B, $PSe_{3/2}$ units; C, Se=$PSe_{3/2}$ units; D, P–P bonded units. (Reproduced with permission from D. Lathrop and H. Eckert, *Phys. Rev. B*, 1991, **43**, 7279)

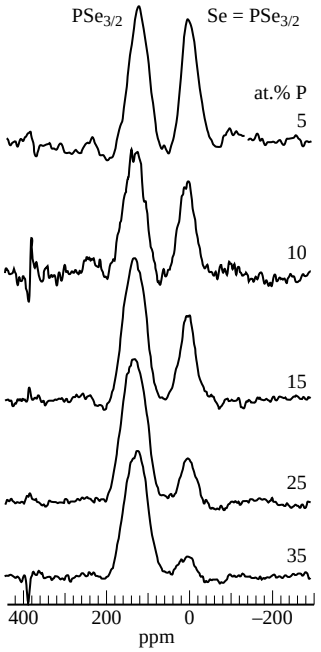

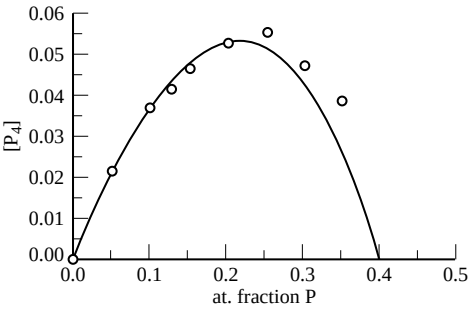

Figure 31 Concentration of four-coordinate Se=$PSe_{3/2}$ units in binary phosphorus–selenium glasses. The solid curve is calculated assuming an equilibrium of the kind $PSe_{3/2}$+ Se $\rightleftarrows$ Se=$PSe_{3/2}$ with an equilibrium constant K_1 of 0.83 (at. fraction)$^{-1}$ (Reproduced by permission of Pergamon Press from H. Eckert, *Prog. Nucl. Magn. Reson.*, 1992, **24**, 159)

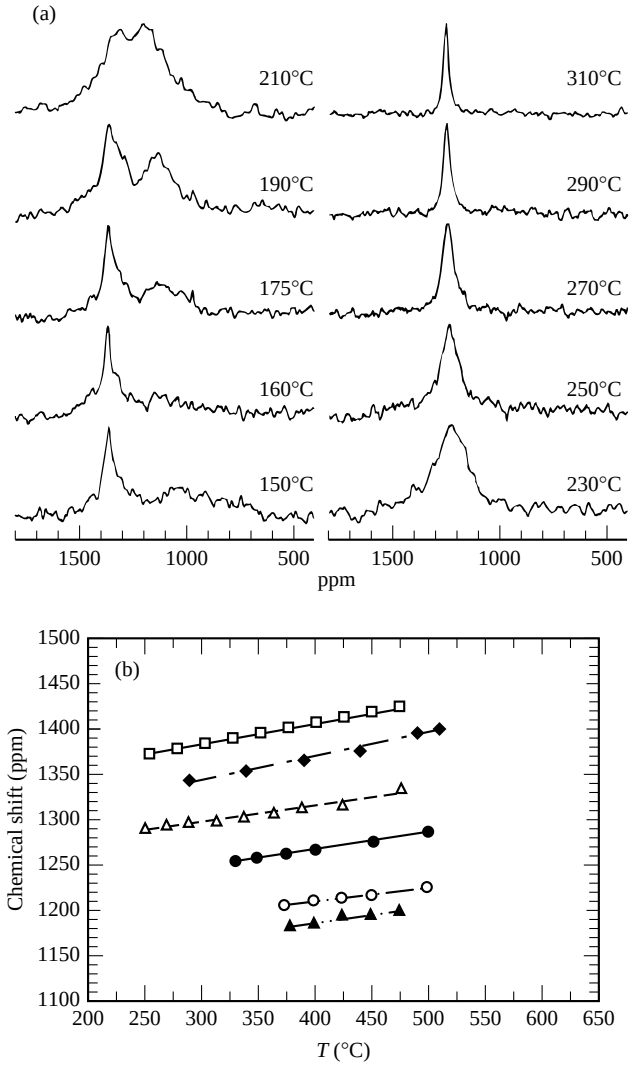

Figure 32 (a) Temperature-dependent ^{77}Se NMR spectra of a phosphorus–selenium glass containing 20 at.% P. The resonances observed at low temperatures near 1380 and 1150 ppm correspond to selenium-only and phosphorus-bonded selenium atoms, respectively. (b) Temperature dependence of ^{77}Se chemical shifts in various phosphorus–selenium melts. □, liquid selenium; ♦, 5 at.% P glass; △, 13 at.% P glass; •, 20 at.% P glass; ○, 32 at.% P glass; ▲, 40 at.% P glass (Reproduced with permission of The American Chemical Society from R. Maxwell and H. Eckert, *J. Am. Chem. Soc.*, 1994, **116**, 682)

temperatures, distinct resonances for phosphorus-bonded and selenium-only bonded selenium atoms can be resolved, which coalesce approximately 100 K above T_g into a single resonance due to chemical exchange on the NMR timescale. The average ^{77}Se chemical shift measured in the fast exchange limit reflects the quantitative distribution of Se–Se versus Se–P bonding in the glass; the same information previously also obtained (albeit with lower accuracy) by ^{31}P–^{77}Se spin echo double resonance NMR.[104] When combined with the phosphorus speciations from ^{31}P NMR, these data allow important conclusions about intermediate-range order. Figure 33 illustrates that the data are most compatible with a glass structure model in which PSe_n units and Se–Se units are randomly linked, with a slight preference for P–Se–P bridges.[105] The data also clearly rule out previous structural

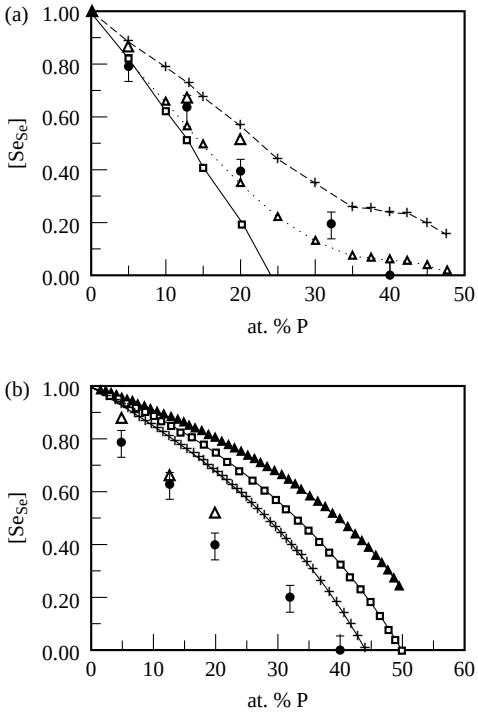

Figure 33 Experimentally determined fraction [Se_{Se}] of selenium-only bonded selenium atoms in phosphorus–selenium glasses, and comparisons with the predictions made from various atomic distribution models. (a) Isolated phosphorus sites, corresponding to a homogeneous phosphorus distribution, formation of domains with preferred P–Se–P linkages, and random linkage between PSe_n and Se units. (□, isolation model; +, domain model; ▲, random model; △, SEDOR; •, high-temperature NMR). (b) P_4Se_n clusters dispersed in a selenium matrix as suggested by Price et al.[106] (+ P_4Se_5; □, P_4Se_4; ▲, P_4Se_3; △, SEDOR; •, high-temperature NMR). (Reproduced with permission of Elsevier Science Publishers BV from R. Maxwell, D. Lathrop, and H. Eckert, *J. Noncryst. Solids*, 1995, **180**, 244)

models[106] based on P_4Se_n clusters embedded in a selenium-rich matrix.

6.4 Ternary Metal Thiophosphate Glasses

Phosphorus-31 MAS NMR studies have been undertaken ona variety of ionically conductive glasses derived from the pseudobinary systems $Li_2S–P_2S_5$[107] and $Ag_2S–P_2S_5$.[108] In many of these glasses, large chemical shift differences between crystalline and glassy phases are observed, indicating substantial differences in short-range order.

Glass with the composition $Li_4P_2S_7$, for example, disproportionates on crystallization, undergoing the transformation from a pyrothiophosphate to a hexahypothiodiphosphate with a phosphorus–phosphorus bond.

$$Li_4P_2S_7(\text{glass}) \rightarrow Li_4P_2S_6(\text{crystalline}) + S \qquad (8)$$

Also, the crystalline phases $Ag_2P_2S_6$ and $Li_2P_2S_6$ form dimers of edge-sharing $PS_{4/2}$ tetrahedra, which do not appear to be represented in the glassy state. The structural conclusions are summarized in Figure 34. Local environments of glassy thiophosphates generally resemble those present in

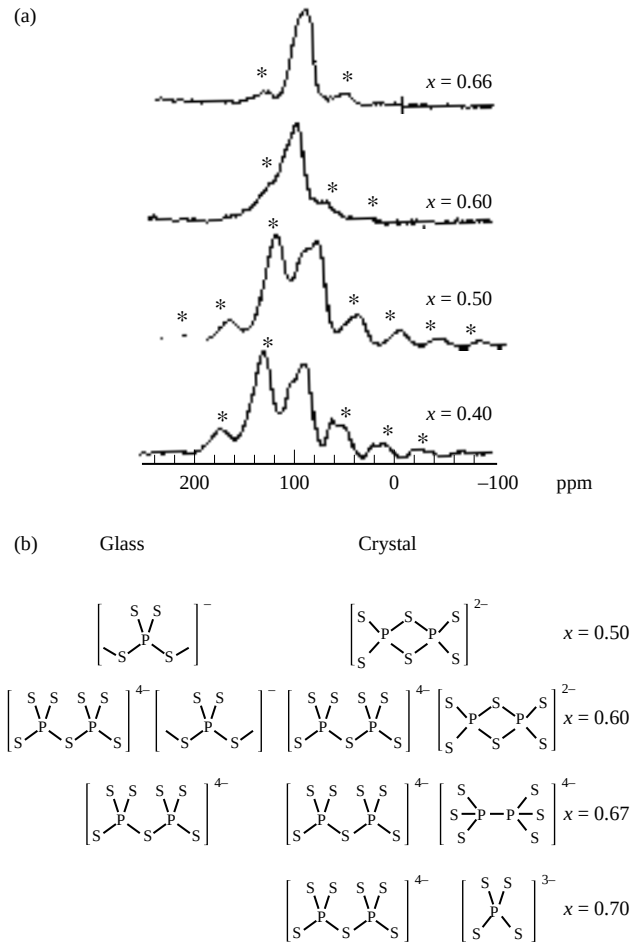

Figure 34 (a) Phosphorus-31 MAS NMR spectra and (b) structural interpretations for glasses in the system $(Ag_2S)_x-(P_2S_5)_{1-x}$. (Reproduced with permission of The American Chemical Society from Z. Zhang, J. H Kennedy, and H. Eckert, *J. Am. Chem. Soc.*, 1992, **114**, 5775)

phosphate glasses, whereas there are large differences in the local environments between crystalline thiophosphates and crystalline phosphates.

7 AMORPHOUS SEMICONDUCTORS

The issue of glass formation in amorphous semiconductors, where all of the atoms are tetrahedrally coordinated, has been the subject of considerable research activity. Molecular modeling has been used to 'amorphize' the cubic silicon lattice by the introduction of random bond switches, which alter the ring statistics of the original lattice and newly introduces five- and seven-membered rings.[109] Unfortunately, it has been impossible to detect such structural defects by solid state NMR. The ^{29}Si NMR spectra of amorphous silicon materials are largely dominated by hydrogen doping effects, and ^{1}H NMR has been used extensively to study the spatial arrangements of the hydrogen atoms[110] (see also ***Amorphous Silicon Alloys***).

For heteropolar structures such as III–V or II–IV–V_2 lattices, the presence of such odd-membered rings necessarily implies the formation of homopolar (such as V–V) bonds. Past attempts to identify such 'wrong bonds' in amorphous GaAs by ^{69,71}Ga and ^{75}As NMR have only met with limited success, because the lineshapes perturbed by the quadrupolar interaction for these nuclei are difficult to interpret.[111] However, there are several related glass-forming systems, most notably $CdGeAs_2$, $CdGeP_2$, and their corresponding alloys, where this question can be examined. In their crystalline forms, these materials arrange themselves in the chalcopyrite structure, a simple superstructure of the silicon lattice. For these materials, the question of homopolar bond formation has been studied by measuring ^{31}P–^{31}P dipole–dipole couplings, which are very sensitive to the formation of P–P and P–Cd bonds. Figure 35 shows the comparison of the experimental ^{31}P spin echo decay data with simulations for a chemically ordered chalcopyrite structure, a random distribution of phosphorus atoms over all the lattice sites, and an additive superposition of both. The experimental results are quantitatively consistent with the occurrence of P–P bonds in glassy $CdGeP_2$, albeit at a substatistical level.[112,113] The formation of pnictogen–pnictogen bonds in the glassy state of $CdGeP_2$ and $CdGeAs_2$ is facilitated by the high electronegativity of germanium. In contrast, glass formation is strongly inhibited in the analogous systems based on silicon and tin, which have significantly lower electronegativities and thus form more polar bonds with pnicogens.

8 REFERENCES

1. P. J. Bray and A. H. Silver, in *Modern Aspects of the Vitreous State*, ed. J. D. Mackenzie, Butterworth, London, 1960, p. 92, and references therein.
2. A. H. Silver and P. J. Bray, *J. Chem. Phys.*, 1958, **29**, 984.
3. A. R. Grimmer, P. Starke, and W. Wieker, *Z. Chem.*, 1982, **22**, 44
4. E. Lippmaa, A. Samoson, M. Magi, R. Teeaar, J. Schraml, and J. Gotz, *J. Noncryst. Solids*, 1982, **50**, 215.
5. W. Schiller, D. Muller, and G. Scheler, *Z. Chem.*, 1982, **22**, 44.
6. S. Schramm and E. Oldfield, *J. Chem. Soc., Chem. Commun.*, **1982**, 980.
7. H. Eckert, *Prog. Nucl. Magn. Reson. Spectrosc.*, 1992, **24**, 159.
8. P. J. Bray, S. J. Gravina, D. H. Hintenlang, and R. V. Mulkern, *Magn. Reson. Rev.*, 1988, **13**, 263.
9. A. R. Grimmer, *Exp. Tech. Phys.*, 1988, **36**, 81.
10. P. J. Bray, J. F. Emerson, D. Lee, S. A. Feller, D. L. Bain, and D. A. Feil, *J. Noncryst. Solids*, 1991, **129**, 240.
11. A. Navrotsky, K. L. Geisinger, P. McMillan, and G. V. Gibbs, *Phys. Chem. Miner.*, 1985, **11**, 284.
12. R. F. Pettifer, R. Dupree, I. Farnan, and U. Sternberg, *J. Noncryst. Solids*, 1988, **106**, 408.
13. R. Dupree, S. C. Kohn, C. M. B. Henderson, and A. M. T. Bell, in *Nuclear Magnetic Shieldings and Molecular Structure*, ed. J. A. Tossell, Kluwer, Dordrecht, 1993, p. 421.
14. L. F. Gladden, T. A. Carpenter, and S. R. Elliott, *Philos. Mag.*, 1986, **B53**, L81
15. J. A. Tossell and P. Lazzeretti, *Phys. Chem. Miner.*, 1988, **15**, 564.
16. I. Farnan, P. J. Grandinetti, J. H. Baltisberger, J. F. Stebbins, U. Werner, M. A. Eastman, and A. Pines, *Nature (London)*, 1992, **358**, 31.

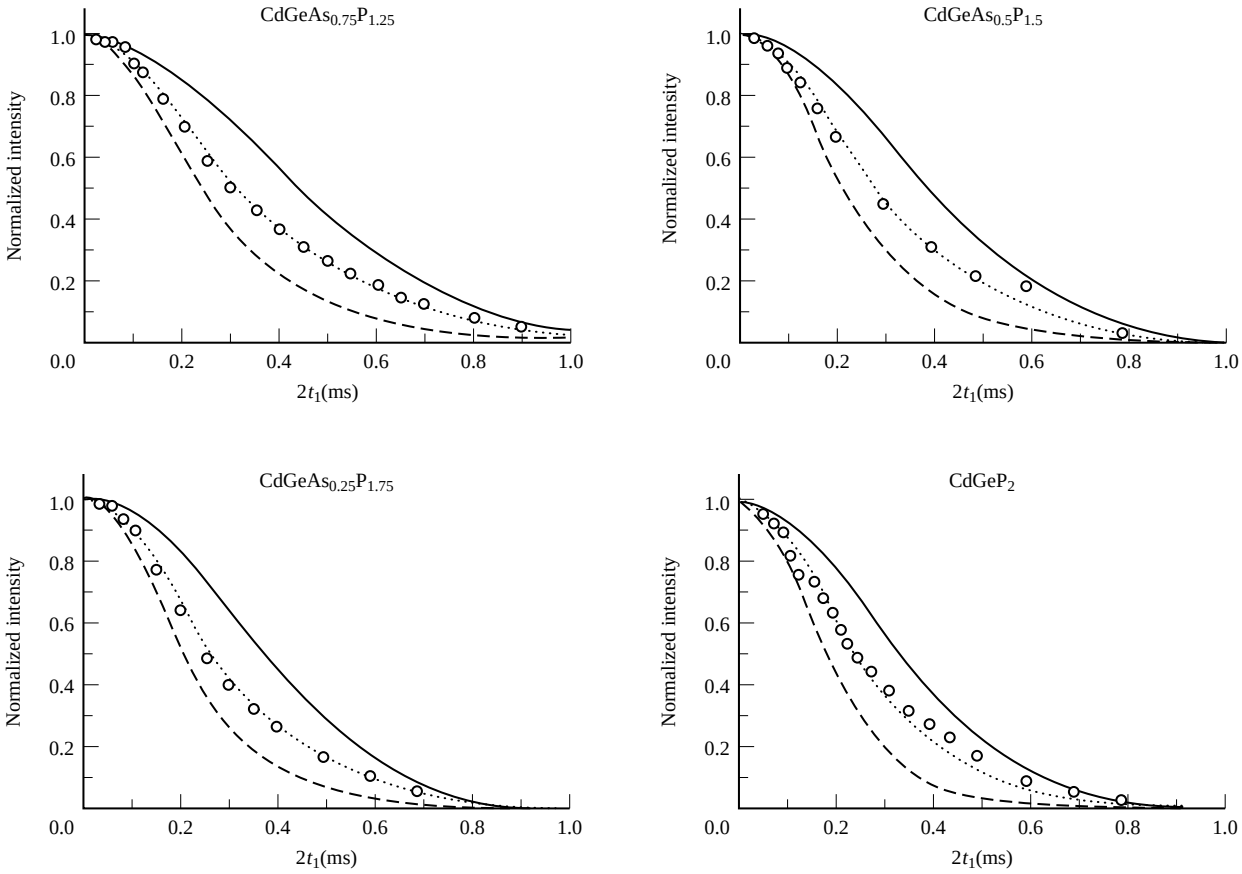

Figure 35 Phosphorus-31 spin echo NMR results in $CdGeAs_{2-x}P_x$ glasses. The experimental data are compared with simulations corresponding to a random distribution of phosphorus and arsenic atoms over the anionic sites of the chalcopyrite lattice ('ordered model', solid curves), and to a random distribution of phosphorus and arsenic over all sites of a zincblende lattice ('random model', dashed curves). The dotted curves show the linear combination of both models (0.45 ordered +0.55 random) that reproduces best the experimental data (○). (Reproduced with permission from D. Franke, R. Maxwell, D. Lathrop, K. Banks, and H. Eckert, *Phys Rev. B*, 1992, **46**, 8109)

17. R. L. Mozzi and B. E. Warren, *J. Appl. Crystallogr.*, 1969, **2**, 164
18. H. Melman and S. H. Garofalini, *J. Noncryst. Solids*, 1991, **134**, 107.
19. E. Lippmaa, M. Mägi, A. Samoson, G. Engelhardt, and A. R. Grimmer, *J. Am. Chem. Soc.*, 1980, **102**, 4889.
20. H. Maekawa, T. Maekawa, K. Kawamura, and T. Yokokawa, *J. Noncryst. Solids*, 1991, **127**, 53.
21. J. F. Stebbins, *J. Noncryst. Solids*, 1988, **106**, 359.
22. S. J. Gurman, *J. Noncryst. Solids*, 1990, **125**, 151.
23. A. R. Grimmer and W. Muller, *Monatsh. Chem.*, 1986, **117**, 799.
24. T. Uchino, T. Sakka, Y. Ogata, and M. Iwasaki, *J. Phys. Chem.*, 1992, **96**, 2455.
25. M. E. Brandriss and J. F. Stebbins, *Geochim. Cosmochim. Acta*, 1988, **52**, 2659.
26. C. T. G. Knight, R. J. Kirkpatrick, and E. Oldfield, *J. Noncryst. Solids*, 1990, **116**, 140.
27. J. B. Murdoch, J. F. Stebbins, and I. S. E. Carmichael, *Am. Mineral*, 1985, **70**, 332.
28. R. Dupree, N. Ford, and D. Holland, *Phys. Chem. Glasses*, 1987, **28**, 78.
29. R. J. Kirkpatrick, T. Dunn, S. Schramm, K. A. Smith, R. Oestrike, and G. L. Turner, *Structure and Bonding of Non-Crystalline Solids*, Ed. G. Walrafen and A. G. Revesz, 1986, p. 303.
30. M. Leventhal and P. J. Bray, *Phys. Chem. Glasses*, 1965, **6**, 113.
31. C. I. Merzbacher, B. L. Sherriff, J. S. Hartmann, and W. B. White, *J. Noncryst. Solids*, 1990, **124**, 194.
32. R. K. Sato, P. F. McMillan, P. Dennison, and R. Dupree *Phys. Chem. Glasses*, 1991, **32**, 149.
33. W. Loewenstein, *Am. Mineral*, 1954, **39**, 92.
34. P. F. McMillan and R. J. Kirkpatrick, *Am. Mineral*, 1992, **77**, 898.
35. H. Maekawa, T. Maekawa, K. Kawamura, and T. Yokokawa, *J. Phys. Chem.*, 1991, **95**, 6822.
36. B. T. Poe, P. F. McMillan, B. Cote, D. Massiot, and J. P. Coutures, *Science*, (Washington, D.C.), 1993, **259**, 786.
37. C. I. Merzbacher, K. J. McGrath, and P. L. Higby, *J. Noncryst. Solids*, 1991, **136**, 249.
38. R. J. Kirkpatrick, R. Oestrike, C. A. Weiss, Jr., K. A. Smith, and E. Oldfield, *Am. Mineral*, 1986, **71**, 701.
39. G. Engelhard, M. Nofz, K. Forkel, F. G. Wihsmann, M. Magi, A. Samoson, and E. Lippmaa, *Phys. Chem. Glasses*, 1985, **26**, 157.
40. E. D. Lacy, *Phys. Chem. Glasses*, 1963, **4**, 234.
41. R. K. Sato, P. F. McMillan, P. Dennison, and R. Dupree, *J. Phys. Chem.*, 1991, **95**, 4483.
42. P. Cloos, A. J. Leonard, J. P. Moreau, A. Herbillon, and J. J. Fripiat, *Clays Clay Mineral*, 1969, **17**, 279.

43. A. P. M. Kentgens, K. F. M. G. J. Scholle, and W. S. Veeman, *J. Phys. Chem.*, 1983, **87**, 4357.
44. T. M. Duncan, D. C. Douglass, R. Csencsits, and K. L. Walker, *J. Appl. Phys.*, 1986, **60**, 130
45. S. C. Kohn, R. Dupree, M. G. Mortuza, and C. M. B. Henderson, *Am. Mineral*, 1991, **76**, 309.
46. T. Schaller, D. B. Dingwell, H. Keppler, W. Knöller, L. Merwin, and A. Sebald, *Geochim. Cosmochim. Acta*, 1992, **56**, 701.
47. J. A. Tossell, *Am. Mineral*, 1993, **78**, 16.
48. W. Hater, W. Müller-Warmuth, B. Steffesthun, and G. H. Frischat, *Glastechn. Ber.*, 1990, **63**, 32.
49. H. Zhang and C. G. Pantano, *J. Am. Ceram. Soc.*, 1990, **73**, 958.
50. I. Farnan and J. F. Stebbins, *J. Noncryst. Solids*, 1990, **124**, 207.
51. J. F. Stebbins, D. R. Spearing, and I. Farnan, *J. Noncryst. Solids*, 1989, **110**, 1.
52. I. Farnan and J. F. Stebbins, *J. Am. Chem. Soc.*, 1990, **112**, 32.
53. J. F. Stebbins, *Nature (London)*, 1991, **351**, 638.
54. J. F. Stebbins and P. McMillan, *J. Noncryst. Solids*, 1993, **160**, 116.
55. X. Xue, J. F. Stebbins, M. Kanzaki, P. F. McMillan, and B. Poe, *Am. Mineral*, 1991, **76**, 8.
56. J. F. Stebbins and D. Sykes, *Am. Mineral*, 1990, **75**, 965.
57. I. Farnan, S. C. Kohn, and R. Dupree, *Geochim. Cosmochim. Acta*, 1987, **51**, 2869.
58. S. C. Kohn, R. Dupree, and M. Smith, *Geochim. Cosmochim. Acta*, 1989, **53**, 2925.
59. H. Eckert, J. P. Yesinowski, E. M. Stolper, and L. A. Silver, *J. Phys. Chem.*, 1988, **92**, 2055.
60. H. Eckert, J. P. Yesinowski, and E. M. Stolper, *Solid State Ionics*, 1989, **32/33**, 298.
61. R. F. Bartholomew and J. H. Schreurs, *J. Noncryst. Solids*, 1980, **38/39**, 679.
62. N. I. Bezmen, V. A. Zharikov, M. B. Epelbaum, V. O. Zavelsky, Y. P. Dikov, N. I. Suk, and S. K. Koshemchuk, *Contrib. Mineral Petrol.*, 1991, **109**, 89.
63. H. Eckert, J. P. Yesinowski, E. M. Stolper, T. R. Stanton and J. Holloway, *J. Noncryst. Solids*, 1987, **93**, 93.
64. (a) S. C. Kohn, R. Dupree, and M. E. Smith, *Nature (London)*, 1989, **337**, 539; (b) J. Kummerlen, L. H. Merwin, A. Sebald, and H. Keppler, *J. Phys. Chem.*, 1992, **96**, 6405.
65. L. W. Kelts, N. J. Effinger, and S. M. Melpolder, *J. Noncryst. Solids*, 1986, **83**, 353.
66. G. E. Maciel and D. W. Sindorf, *J. Am. Chem. Soc.*, 1980, **102**, 7606.
67. A. J. Vega and G. W. Scherer, *J. Noncryst. Solids*, 1989, **111**, 153.
68. S. J. Gravina and P. J. Bray, *J. Magn. Reson.*, 1990, **89**, 515.
69. R. E. Youngman and J. W. Zwanziger, *J. Noncryst. Solids*, 1994, **168**, 293
70. P. J. Bray, *J. Noncryst. Solids*, 1985, **75**, 29.
71. S. J. Gravina, P. J. Bray, and G. L. Petersen, *J. Noncryst. Solids*, 1990, **123**, 165.
72. A. Samoson, *Chem. Phys. Lett.*, 1985, **119**, 29.
73. L. Van Wüllen and W. Müller-Warmuth, *Solid State NMR*, 1993, **2**, 279.
74. J. Zhong and P. J. Bray, *J. Noncryst. Solids*, 1989, **111**, 67.
75. Y. H. Yun and P. J. Bray, *J. Noncryst. Solids*, 1978, **30**, 45.
76. W. J. Dell, P. J. Bray, and S. Xiao, *J. Noncryst. Solids*, 1983, **58**, 1.
77. R. N. Pletnev, A. D. Galaktionov, and A. A. Fotiev, *Izv. Akad. Nauk SSSR, Neorg. Mater.*, 1974, **10**, 133.
78. J. Zhonghong and T. Yongxing, *J. Noncryst. Solids*, 1992, **146**, 57.
79. T. Yongxing, J. Zhonghong, and S. Xiuyu, *J. Noncryst. Solids*, 1989, **112**, 131.
80. S. G. Bishop and P. J. Bray, *Phys. Chem. Glasses*, 1966, **7**, 73.
81. R. Gresch, W. Müller-Warmuth, and H. Dutz, *J. Noncryst. Solids*, 1976, **21**, 31.
82. R. Dupree, D. Holland, and D. S. Williams, *Phys. Chem. Glasses*, 1985, **26**, 50.
83. B. C. Bunker, R. J. Kirkpatrick, R. K. Brow, G. L. Turner, and C. Nelson, *J. Am. Ceram. Soc.*, 1991, **74**, 1430.
84. C. Jäger, W. Müller-Warmuth, L. Mundus, and L. Van Wüllen, *J. Noncryst. Solids*, 1992, **149**, 209.
85. R. K. Brow, R. J. Kirkpatrick, and G. L. Turner, *J. Noncryst. Solids*, 1990, **116**, 39.
86. S. Hayashi and K. Hayamizu, *J. Solid State Chem.*, 1989, **80**, 195.
87. P. Losso, B. Schnabel, C. Jäger, U. Sternberg, D. Stachel, and D. O. Smith, *J. Noncryst. Solids*, 1992, **143**, 265.
88. R. K. Brow, Personal communication (to be published).
89. J. W. Zwanziger, K. K. Olsen, and S. L. Tagg, *Phys. Rev. B*, 1993, **47**, 14618.
90. M. Villa, M. Scagliotti, and G. Chiodelli, *J. Noncryst. Solids*, 1987, **94**, 101.
91. D. Muller, G. Berger, I. Grunze, G. Ladwig, E. Hallas, and U. Haubenreisser, *Phys. Chem. Glasses*, 1983, **24**, 37.
92. A. V. Dmitriev, Yu. F. Zhuravlev, R. N. Pletnev, and V. K. Slepukhim, *Fiz. Khim. Stekla*, 1986, **12**, 636.
93. R. K. Brow, R. J. Kirkpatrick, and G. L. Turner, *J. Am. Ceram. Soc.*, 1993, **76**, 919.
94. M. Tenhover, R. D. Boyer, R. S. Henderson, T. E. Hammond, and G. A. Shreve, *Solid State Commun.*, 1988, **65**, 1517.
95. R. K. Shibao, M. Hay, V. Srdanov, and H. Eckert, *Chem. Mater.*, 1994, **6**, 306.
96. M. Tenhover, R. S. Henderson, M. A. Hazle, D. Lukco, and R. K. Grasselli, in *Design of New Material*, ed. D. L. Cocke, and A. Clearfield, Plenum, New York, p. 329.
97. A. Pradel, V. Michel-Lledos, M. Ribes, and H. Eckert, *Chem. Mater.*, 1993, **5**, 377.
98. K. L. Moran, R. K. Shibao, and H. Eckert, *Hyperfine Int.*, 1990, **62**, 55.
99. H. Eckert, J. H. Kennedy, A. Pradel, and M. Ribes, *J. Noncryst. Solids*, 1989, **113**, 287.
100. A. Pradel, V. Michel-Lledos, M. Ribes, and H. Eckert, *Solid State Ionics*, 1992, **53–56**, 1187.
101. D. Lathrop and H. Eckert, *J. Phys. Chem.*, 1989, **93**, 7895.
102. D. Lathrop and H. Eckert, *Phys. Rev. B*, 1991, **43**, 7279.
103. R. Maxwell and H. Eckert, *J. Am. Chem. Soc.*, 1994, **116**, 682
104. D. Lathrop and H. Eckert, *J. Am. Chem. Soc.*, 1990, **112**, 9017.
105. R. Maxwell, D. Lathrop, and H. Eckert, *J. Noncryst. Solids*, 1995, **180**, 244.
106. D. L. Price, M. Misawa, S. Susman, T. I. Morrison, G. K. Shenoy, and M. Grimsditch, *J. Noncryst. Solids*, 1984, **66**, 443.
107. H. Eckert, Z. Zhang, and J. H. Kennedy, *Chem. Mater.*, 1990, **2**, 273.
108. Z. Zhang, J. H. Kennedy, and H. Eckert, *J. Am. Chem. Soc.*, 1992, **114**, 5775.
109. J. Wejchert, D. Weaire, and F. Wooten, *J. Noncryst. Solids*, 1990, **122**, 241.
110. S. R. Elliott, *J. Noncryst. Solids*, 1990, **123**, 149.

111. S. G. Greenbaum, R. A. Marino, K. J. Adamic, and C. Case, *J. Noncryst. Solids*, 1985, **77/78**, 1285.
112. D. Franke, R. Maxwell, D. Lathrop, and H. Eckert, *J. Am. Chem. Soc.*, 1991, **13**, 4822.
113. D. Franke, R. Maxwell, D. Lathrop, K. Banks, and H. Eckert, *Phys. Rev. B*, 1992, **46**, 8109.

Acknowledgments

I would like to thank my past and present graduate students, Dr. Nandini Das, Dr. Delphine Davis, Dr. Deanna Franke, Becky Gee, Christopher Hudalla, Dr. David Lathrop, Dr. Carri Lyda, Dr. Robert Maxwell, Dr. Kelly Moran, Dr. Robert Shibao, and Yin Xia for all the contributions they have made to the work partly reviewed here. This review contains excerpts of their Ph.D. dissertations. I would like to thank further the numerous undergraduates who have worked in our laboratory, and my collaborators, Dr. Annie Pradel and Dr. Michel Ribes (University of Montpellier), Dr. J. H. Kennedy (Professor Emeritus, UCSB), Dr. Galen Stucky (UCSB), Dr. James Yesinowski (Naval Research Laboratory), and Dr. Edward Stolper (California Institute of Technology) for their contributions to joint work that is discussed and cited here. Our research program is supported by the National Science Foundation, grants DMR 89-13738 and 92-21197. This support is gratefully acknowledged.

Biographical Sketches

Hellmut Eckert, *b* 1956. Diplom, 1978, University of Münster, Germany, Ph.D., 1982, University of Münster, Germany. Introduced to NMR by W. Müller-Warmuth. Postdoctoral research associate, Rutgers University, USA (with R. H. Herbert, 1982–84, staff scientist, California Institute of Technology 1984–87 (with S. I. Chan and J. P. Yesinowski), Faculty in Chemistry, University of California, Santa Barbara, USA 1987–present. Approx. 130 publications. Research specialties: the experimental development of heteronuclear X–Y solid state NMR techniques and the application of solid state NMR techniques to inorganic disordered materials, including glasses, ceramics, and semiconductors.

Amorphous Silicon Alloys

Mark A. Petrich

Northwestern University, Evanston, IL, USA

1	Introduction	1
2	Hydrogen- and Deuterium-Related Microstructure (^{1}H, ^{2}D)	1
3	Lattice Structure (^{29}Si, ^{13}C)	7
4	Dopant Atoms (^{11}B, ^{31}P)	8
5	Related Articles	10
6	References	10

1 INTRODUCTION

Amorphous semiconductors are used extensively in electronic and optoelectronic devices. While properties of amorphous semiconductors such as carrier lifetime are usually inferior to those of crystalline semiconductors, several unique characteristics make amorphous semiconductors the materials of choice for applications such as solar cells, large area image sensors, and thin-film transistors for liquid crystal displays. Amorphous semiconductors can be deposited over large areas using plasma-enhanced chemical vapor deposition, their photoconductivities are many orders of magnitude higher than their dark conductivities, and their properties can be tailored by doping and alloying. Amorphous hydrogenated silicon (a-Si:H) is the most studied amorphous hydrogenated semiconductor. Electronic device-quality material has an optical band gap of $\sim$1.75 electron volts (eV), and a paramagnetic defect density of less than $10^{16}\,\mathrm{cm}^{-3}$. A particularly attractive feature of a-Si:H is its high photoconductivity-to-dark conductivity ratio, which is often greater than 10^5. The technological applications of a-Si:H range from thin film transistors to solar photovoltaic devices.[1]

Amorphous hydrogenated semiconductors are heterogeneous. To the eye, or even with the aid of an optical microscope, thin films of a-Si:H appear smooth and homogeneous. However, as the scale of observation decreases to less than 1 μm an inhomogeneous structure becomes evident. Transmission and scanning electron microscopy have revealed lamellar structures, columns, and voids in amorphous hydrogenated semiconductors.[2] Even 'device-quality' amorphous silicon has a heterogeneous microstructure.[3]

Many of the technological applications of amorphous silicon are restricted by light-induced metastable defects. In fact, the highest quality materials tend to exhibit the greatest changes upon light exposure. Understanding these light-induced changes, and reducing or exploiting them, has been the object of a significant fraction of the research on amorphous silicon and its alloys. Current opinion links these light-induced defects with the microstructural features of a-Si:H.

This article presents examples of the use of nuclear magnetic resonance to investigate technological and scientific issues concerning amorphous hydrogenated silicon and its alloys. Nuclear magnetic resonance (NMR) has been an important tool in characterizing the microstructure of a-Si:H and related materials, and its application has been discussed in several earlier reviews.[2–7]

2 HYDROGEN- AND DEUTERIUM-RELATED MICROSTRUCTURE (^{1}H, ^{2}D)

From the first preparation of a-Si:H thin films, certain issues have attracted attention. It was found that a-Si (no hydrogen), prepared by evaporation or sputtering techniques, was of little interest as an electronic material. However, when a-Si:H was prepared by the glow-discharge decomposition of silane gas, a much improved material was obtained. NMR experiments helped to answer questions about hydrogen content and distribution, and the effects of materials production conditions on hydrogen in a-Si:H. The current consensus is that a-Si:H can contain as much as 50 at.% hydrogen, but that 8–18% is typical for high electronic quality materials. The hydrogen is distributed in three environments: a dilute 'phase' consisting of silicon monohydride groups greater than three or four lattice spacings apart, a clustered 'phase' in which hydrogen nuclei bonded as silicon mono-, di-, or trihydride are close enough together to produce ^{1}H NMR linewidths of 20–30 kHz, and a small amount of trapped molecular hydrogen.

^{19}F NMR studies of fluorinated amorphous silicon have been discussed in an earlier review.[5]

2.1 ^{1}H NMR

2.1.1 Free Induction Decay Spectra

Most NMR experiments have studied hydrogen because of the large magnetic moment and near 100% natural abundance of the ^{1}H isotope. ^{1}H NMR free induction decay spectra can be used to determine hydrogen contents and distributions in a-Si:H in a quantitative, nondestructive manner.

The most recognizable characteristic of the ^{1}H NMR spectra of a-Si:H obtained at room temperature is the two-component lineshape illustrated by Figure 1.[8–10] The overlapping broad and narrow lineshapes indicate that two different spin–spin relaxation time constants (T_2) are involved. The fast-relaxing component has a Gaussian shape and is typically 25–30 kHz wide. This lineshape and width are indicative of homonuclear dipole coupling among hydrogen nuclei, leading to the conclusion that the broad component represents 'clustered' hydrogen, or a hydrogen-rich environment. The slow-relaxing component has a Lorentzian shape and is typically 1–5 kHz wide. This lineshape and width are indicative of nuclei which relax by mechanisms other than dipolar coupling, leading to the assignment of this component to isolated hydrogen nuclei, or silicon monohydride groups. The T_2 values for the two environments can be estimated from the linewidths. The hydrogen-rich phase has $T_2 \approx 20\ \mu$s while the hydrogen-poor phase has $T_2 \approx 60\,\mu$s. The extent of the hydrogen-poor phase may be as large as 88% of the

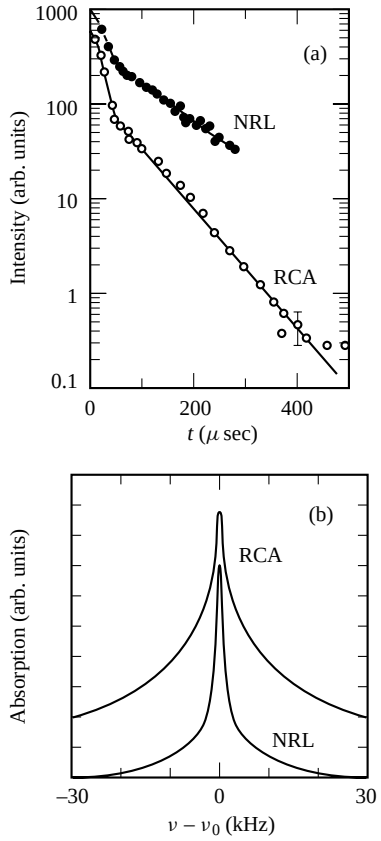

Figure 1 ^{1}H free induction decays (top) and the corresponding Fourier-transformed spectra (bottom) for two a-Si:H samples. The two-component nature of the ^{1}H NMR spectrum is clearly demonstrated. (Reproduced by permission of the authors and The American Physical Society from W. E. Carlos and P. C. Taylor, *Phys. Rev. B*, 1982, **26**, 3605)

material volume, depending upon the amount of hydrogen clustering.[11]

2.1.2 Investigations of the Broad Line

The assignment of the broad line to dipole-coupled hydrogen nuclei was confirmed by a hole-burning experiment.[10] A saturation pulse applied at a frequency well-displaced from the line center only saturated the broad line. This result showed that the hydrogen nuclei in the broad line were dipole-coupled to each other, but not to the hydrogen nuclei represented by the narrow line. Solid echo experiments confirmed that the clustered and dilute hydrogen phases are separated from each other by at least 500 pm.[8] Additional echo experiments that exploit the 'quasiquadrupolar' nature of small groups of spin-$\frac{1}{2}$ particles suggested that *isolated* $-SiH_2$ or $-SiH_3$ groups are atypical features in a-Si:H, but did not preclude the existence of clustered di- and trihydrides.

Despite the wide range of processing conditions and material properties, all ^{1}H NMR observations of a-Si:H are remarkably similar. While the relative intensities of the two components in the lineshape vary with deposition conditions and hydrogen content, component shapes and linewidths are essentially invariant. Calculations of the dipolar linewidths show that certain configurations cannot be present in a-Si:H. For example, hydrogen-passivated mono- and divacancies, containing four and six hydrogen atoms respectively, would yield ^{1}H NMR linewidths (full width at half-maximum, FWHM) of 90 and 69 kHz, which are far greater than those observed in a-Si:H. Simpler configurations such as $-SiH_2$, $-SiH_3$, and $(-SiH_2)_n$ yield ^{1}H NMR linewidths less than 20 kHz.[10]

2.1.3 Investigations of the Narrow Line

The content of the hydrogen giving rise to the narrow line in a-Si:H never exceeds 12 at.%, despite variations in total hydrogen content between 2 and 32 at.%.[2,4,5,12] A precise description of the environment of this species has not been established, but it is known that the narrow component of the ^{1}H NMR spectrum is too broad for the hydrogen to be distributed randomly.[8–10]

The content of hydrogen in this species correlates inversely with the density of paramagnetic spins in a-Si:H. A decrease in ESR-measured spin density with increasing content of hydrogen giving rise to the narrow line has been observed in studies of the deposition of a-Si:H from silane (SiH_4) and from disilane (Si_2H_6) plasmas.[13] While it is tempting to suggest that the narrow-line hydrogen is 'good hydrogen' and the broad-line hydrogen is 'bad hydrogen', the accumulated results of over 10 years of ^{1}H NMR experiments show that all a-Si:H films contain the clustered hydrogen phase. The relative amounts of each phase vary as a function of material preparation conditions, but the narrow line contributes at most 60% of the signal intensity in normally deposited films.

2.2 Deuterium Magnetic Resonance

The substitution of deuterium for hydrogen allows one to use the quadrupolar interaction to determine additional information about the hydrogen (deuterium) distribution in a-Si:(D,H). The deuterium magnetic resonance (^{2}D NMR) spectrum of a-Si:(D,H) is rich in structure. ^{2}D NMR experiments provide an interesting contrast to ^{1}H NMR work, since the results, while not contradicting each other, do not seem to coincide directly. Some of these disagreements may be ascribed to chemical differences between hydrogen and deuterium which have manifested themselves in deposition chemistry studies of amorphous silicon.[6]

2.2.1 Typical ^{2}D NMR Spectra

Typically, three components are observed in ^{2}D NMR spectra such as those shown in Figure 2. First, there is a quadrupolar doublet that is remarkably invariant with sample preparation conditions, always having a splitting of 66 $\pm$ 1 kHz. This doublet is assigned to tightly-bound deuterium in SiD and SiD_2 configurations located in regions of a-Si:(D,H) that are far away from microvoids and have very small bond angle distortions.[14,15] Second, there is a broad central feature with approximately 27 kHz linewidth that is independent of temperature between 4 and 70 K, but narrows by a factor of five between 70 and 300 K. This

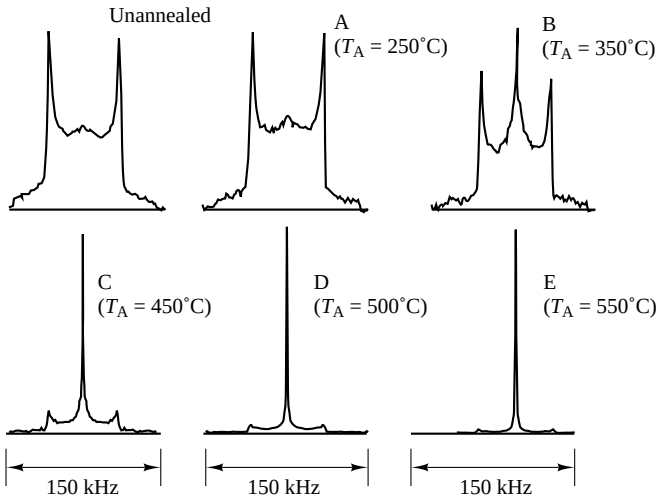

Figure 2 ^{2}D NMR spectra as a function of annealing temperature (T_A) for an a-Si:D sample, plasma-deposited at 230 °C. (Reproduced by permission of the authors and The American Physical Society from V. P. Bork, P. A. Fedders, D. J. Leopold, R. E. Norberg, J. B. Boyce, and J. C. Knights, *Phys. Rev. B*, 1987, **36**, 9351)

broad central line is assigned to weakly-bound deuterium associated with strained bonds in distorted regions near microvoids and to relatively immobile trapped D_2 and HD.[16] The T_1 of ^{2}D giving rise to this feature is much shorter than that of the T_1 of tightly-bound deuterium.[14,17] Third, there is a temperature-dependent narrow central feature indicative of trapped molecular D_2 or HD species.[15] This line actually has a two-component shape, as revealed by hole-burning experiments.[14,17] The narrow (300 Hz) component becomes more narrow with additional annealing, and is probably associated with mobile, dense, molecular deuterium in the microvoids. The broader component narrows from 13 kHz at 18 K to 1 kHz at 300 K, and is probably associated with molecular deuterium adsorbed on microvoid surfaces.

2.2.2 Relationship between ^{2}D NMR and Infrared Spectroscopy

The stretching force constant for the Si–D bond can be calculated from parameters of the ^{2}D NMR spectrum.[15] The predicted value is in good agreement with those observed in a-Si:H and a-Si:D using infrared absorption spectroscopy.

2.2.3 Relationship between ^{2}D NMR and Optoelectronic Quality

The structural information provided by NMR and the electronic properties of a-Si:H have been connected in, at best, an indirect manner. Although NMR studies have certainly contributed to the level of understanding of a-Si:H growth and structure, the connections to electronic applications of the material have not been obvious. Fortunately, this situation is changing. It has been found that the ratio of tightly-bound deuterium (TBD) to molecular deuterium (or HD) in samples of amorphous germanium and amorphous silicon correlates extremely well with the photoresponse ($\eta\mu\tau$) over five orders of magnitude in $\eta\mu\tau$.[18] Higher values of TBD relative to molecular deuterium correlate with higher photoresponses.

The spin–lattice relaxation of deuterium in a-Si:D and a–Ge:D samples has been described by an error function, indicative of extremely inhomogeneous line broadening.[18] The reciprocal rate parameter in the error function expression correlates well with electronic quality (again measured as the photoresponse, $\eta\mu\tau$). The longer the spin–lattice relaxation time for the ^{2}D NMR spectral components, the larger the $\eta\mu\tau$ value. These correlations between NMR observables and properties relevant to applications of a-Si:H are extremely significant findings.

2.3 Hydrogen and Deuterium Diffusion in Amorphous Silicon

2.3.1 ^{1}H NMR Lineshape Measurements

Changes in the ^{1}H NMR lineshape with annealing, as shown in Figure 3, have been used to infer changes in hydrogen distribution, and to measure the activation energy for hydrogen diffusion.[19]

The narrow component linewidth in the ^{1}H NMR spectra of room-temperature deposited a-Si:H decreases with thermal annealing, presumably because of hydrogen diffusion.[19] It is important to note that since the paramagnetic defect density decreases simultaneously with the diffusion of hydrogen to a less clustered state, this experiment provides direct evidence for the role of hydrogen in defect passivation. This study also determined that the hydrogen that evolves from a-Si:H at temperatures below 400 °C comes exclusively from the clustered environments.[19] Another annealing study that used a sample deposited at 330 °C did not find this decrease in narrow-component linewidth, nor

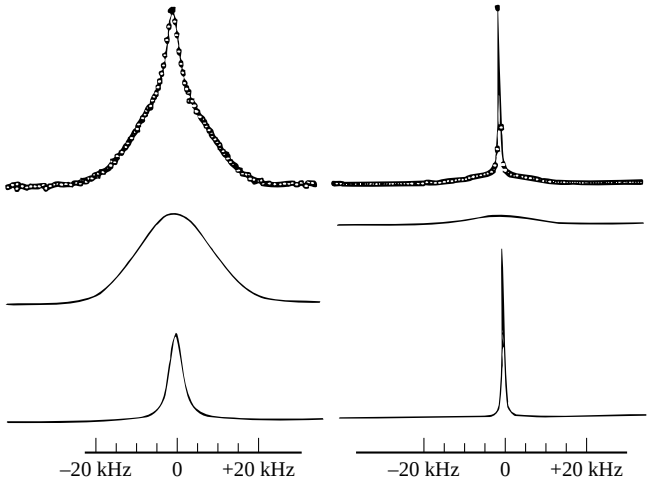

Figure 3 ^{1}H NMR spectra of a-Si:H before (left) and after (right) annealing at 400 °C. Top spectra are data fitted by the sum of broad (middle) and narrow (bottom) components. Notice the loss of the broad line and the narrowing of the narrow line with annealing. (Reproduced by permission of the authors and Pergamon Press, from J. A. Reimer, R. W. Vaughan, and J. C. Knights *Solid State Commun.*, 1981, **37**, 161)

was a redistribution of hydrogen from the broad to narrow lines observed.[8] Both studies find a decrease in total hydrogen content above roughly 400 °C, although the study with the room-temperature material also observed a significant loss of hydrogen at temperatures between 300 and 400 °C.

2.3.2 Activation Energy Measurements

An activation energy for diffusion can be calculated from the narrow-component linewidth data as a function of temperature,[19] from the increase in spin–lattice relaxation rate with temperature,[8] or from the dipolar spin–lattice relaxation time.[20] The calculated values, ranging from 0.2–0.31 eV, are much smaller than values determined by secondary ion mass spectrometry (SIMS) studies and hydrogen-evolution experiments which are typically between 1.0 and 1.5 eV. The significance of the NMR-measured activation energy for diffusion is still not known.[6]

2.3.3 Molecular Hydrogen Evolution

A pronounced increase in trapped molecular hydrogen accompanying the evolution of hydrogen at a-Si:H annealing temperatures above 400 °C has been studied with ^{1}H NMR. This molecular hydrogen causes the minimum in the spin–lattice relaxation of ^{1}H in the sample to shift from roughly 54 K to 23 K. A comparison of the molecular hydrogen content measured by spectral intensity[21] and the H_2 content inferred from analysis of the behavior of T_1 shows that there is much more H_2 in the annealed samples than is predicted from the relaxation experiments. The conclusions are that the microvoids grow with annealing from a radius of approximately 2500 to 5000 pm, and that only those hydrogen molecules on the void surfaces participate in the spin–lattice relaxation process.[22]

2.3.4 Microstructure and Hydrogen Diffusion

The relationship between microvoids and molecular hydrogen content has been studied via ^{1}H T_1 measurements for sputtered a-Si:H prepared with high and low microvoid densities.[23] Hydrogen diffuses very slowly in the high microvoid density sample, and diffuses rapidly in the low microvoid density sample. Although the sample with more microvoids initially has a lower value of T_1 (presumably because of a greater concentration of trapped molecular H_2), the difference in the values of T_1 disappears after moderate annealing drives the molecular hydrogen content of both samples to the same level.

2.3.5 Deuterium Magnetic Resonance Studies of Thermal Annealing Effects

Deuterium magnetic resonance lineshapes for a high quality a-Si:D sample as a function of annealing temperature are shown in Figure 2.[14] Data were acquired at 11 K after anneals at the temperatures shown on the figure. The tightly-bound deuterium (TBD) 66 kHz doublet is clearly observed in all of the spectra, although its intensity diminishes considerably above 350 °C. The narrow central line, indicative of molecular deuterium, is clearly observed at 350 °C and above. The feature assigned to weakly-bound deuterium (WBD) is a 27 kHz broad central line that is not observed after the 350 °C anneal.[17] This deuterium may account for the observed gas evolution at this annealing temperature. Note that the lineshape is virtually unchanged during the 250 °C anneal (20 °C above the deposition temperature), but that dramatic changes are observed as the annealing temperature exceeds the sample deposition temperature by more than 100 °C.

NMR studies of the annealing behavior of amorphous silicon alloys have been discussed in more detail in an earlier review.[6]

2.4 Multiple Quantum NMR Studies

Multiple quantum NMR has been extremely helpful in understanding the structure of the clustered hydrogen environment, and has provided important information about microstructural changes in a-Si:H caused by doping and annealing.

2.4.1 How Many Hydrogen Atoms are in a Cluster?

^{1}H NMR experiments have provided overwhelming support for the hydrogenated microvoid picture of the clustered hydrogen environment, with multiple quantum NMR (MQNMR) being especially valuable.[12, 24, 25] MQNMR is a multiple pulse technique which examines the behavior of dipole-coupled spin systems (***Multiple Quantum NMR in Solids***). It is actually possible to 'count' the number of spins which are involved in a particular isolated system. MQNMR data from spin systems which interact with one another through intercluster couplings can be analyzed to determine the individual cluster sizes. ^{1}H MQNMR has been used to determined the size of coupled ^{1}H spin systems in samples of a-Si:H with hydrogen contents from 8–50 at.%, prepared in several laboratories.[24] As shown in Figure 4, the sample with the lowest hydrogen content (∼8%) displayed an MQNMR response expected for isolated, small (5–7 atoms) clusters of spins. As the hydrogen content of the samples increased, the small intracluster signal persisted, although there was evidence of an increasing amount of intercluster coupling. At the very highest hydrogen content, the isolated cluster signal was not observed. Once again, there is the temptation to assign the broad ^{1}H NMR line to a hydrogenated divacancy in the silicon lattice but, as has already been discussed, this would be inconsistent with the observed ^{1}H NMR linewidth. Based on the NMR and MQNMR results, the broad-line hydrogen is most likely to be located at the surfaces of small microstructural features, or microvoids, and these microvoids must be larger than a divacancy.

2.4.2 The Effect of Deposition Conditions on Microstructure

MQNMR has been used to observe the effects of substrate temperature during deposition on the hydrogen microstructure of plasma-deposited a-Si:H.[12] The definition of the hydrogen clusters decreases with substrate temperature, with the highest temperature materials having the

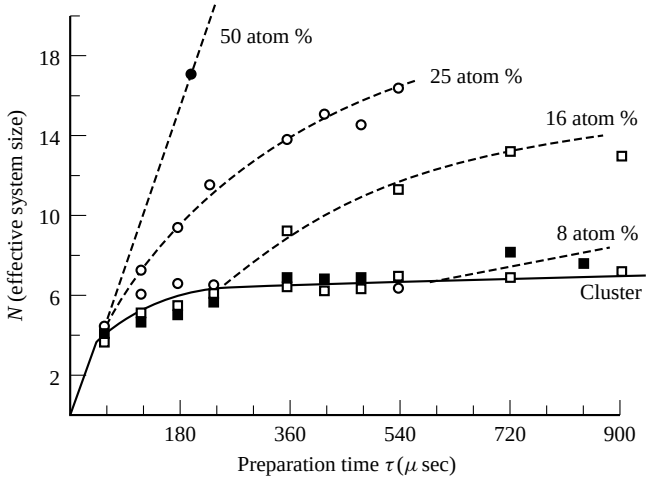

Figure 4 Multiple quantum NMR results for four a-Si:H samples with different hydrogen contents. In this plot, τ is the time that the experimenter has allowed for spins to interact with each other and N is the number that have interacted during this time. The solid line indicates the effective cluster size, $N_c(\tau)$, which is virtually identical to the effective system size, $N(\tau)$, for the 8 at.% hydrogen sample, while $N_c(\tau)$ and $N(\tau)$ are the width parameters of two Gaussians used to fit the data. The value of $N(\tau)$ increases for the 16 and 25 at.% hydrogen samples, while $N_c(\tau)$ remains at roughly six spins. The sample with 50 at. % hydrogen shows no clustering, but behaves as a uniform distribution of spins with N increasing continuously with τ. (Reproduced by permission of the authors and The American Physical Society from J. Baum, K. K. Gleason, A. Pines, A. N. Garroway, and J. A. Reimer, *Phys. Rev. Lett.*, 1986, **56**, 1377)

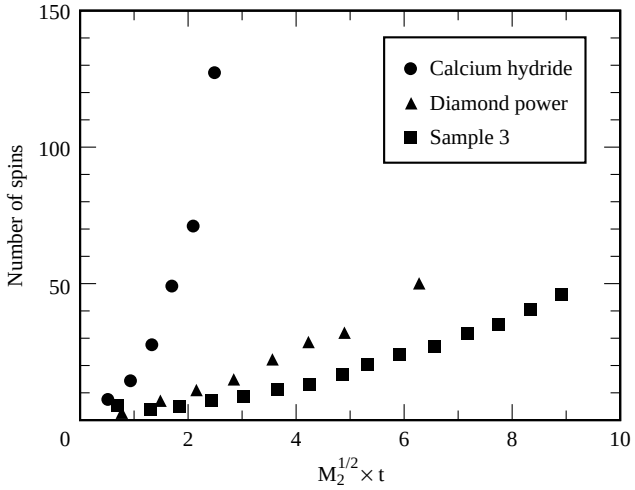

Figure 5 Growth rate of hydrogen multiple quantum coherence in an a-Si:H sample (sample 3) compared with behavior expected for three-dimensional (calcium hydride) and two-dimensional (diamond powder) hydrogen distributions. The slower growth rate in the a-Si:H sample suggests that the hydrogen is in columnar microvoids or a similar environment. (Reproduced by permission of the authors and The American Physical Society from S. Mitra, K. K. Gleason, H. Jia, and J. Shinar, *Phys. Rev. B*, 1993, **48**, 2175)

relatively isolated, 5–7 hydrogen nuclei clusters observed for high-quality films in the earlier study.[24] As the substrate temperature decreases, the isolated clusters appear to come closer together, with a larger intercluster coupling observed.

The geometry of the clustered hydrogen in sputtered a-Si:H film has been studied by analysis of MQNMR data (see ***Multiple Quantum NMR in Solids***) as shown in Figure 5. The slope of the plotted data represents the dimensionality of the hydrogen atom distribution in the sample. Calcium hydride presents a three-dimensional (bulk) distribution, while diamond powder presents a two-dimensional (surface) distribution. The a-Si:H data on the plot indicate a dimensionality less than two, suggesting that the clustered hydrogen in this undoped sample is distributed on the inner surfaces of columnar voids.[25]

2.4.3 Effects of Doping on Hydrogen Microstructure

MQNMR studies of hydrogen demonstrate the effects of dopant atoms on the microstructure of a-Si:H. Doping a-Si:H with phosphorus leads to an increase in hydrogen clustering as observed with ^{1}H NMR[10] and ^{1}H MQNMR.[12] Boron doping results in a highly segregated hydrogen microstructure.[25] This segregation is observed in data similar to those shown in Figure 5, where data from boron-doped a-Si:H have an even smaller slope than the undoped material. This slow growth rate in the number of correlated spins is good evidence that the clusters of hydrogen are small and well separated.

2.4.4 Multiple Quantum NMR Studies of Annealing

MQNMR is an excellent monitor of microstructural changes caused by annealing. Samples of a-Si:H, plasma-deposited at temperatures ranging from 113–324 °C, were studied with MQNMR as a function of postdeposition annealing temperature.[12] The annealing study demonstrated that there are massive rearrangements of the hydrogen microstructure at temperatures well below those required to cause hydrogen evolution ($T < 350$ °C). Even high-quality films, deposited at temperatures near 300 °C, show considerable rearrangements of hydrogen during annealing. The ill defined hydrogen microstructure in a-Si:H deposited at low substrate temperatures can be driven toward better defined clusters of hydrogen. However, these low-temperature films do not attain the same structure as the better ones.

2.5 Trapped Molecular Hydrogen

Below 10 K, the ^{1}H NMR spectrum consists of three components. In addition to the broad Gaussian and narrow Lorentzian absorptions observed at room temperature, a Pake doublet with a splitting of 175 $\pm$ 10 kHz is seen in low-temperature spectra.[21] This feature is ascribed to trapped molecular hydrogen.

The concentration of molecular hydrogen is usually 0.1 at.% or lower for high-quality a-Si:H. Based on this fact, and experimental studies of the broad and narrow components of the ^{1}H NMR spectrum, it is very unlikely that trapped molecular hydrogen accounts for any significant portion of the narrow Lorentzian component in the

^{1}H NMR spectrum.[26] However, molecular hydrogen does play an important role in a-Si:H NMR studies, since it turns out to provide the predominant spin–lattice relaxation mechanism for bonded hydrogen. NMR of trapped molecular hydrogen and deuterium in a-Si:(D,H) has provided important data for comparison with theories of molecular behavior in porous media and low-temperature phenomena.[27] The highly developed level of understanding of the role of trapped molecular hydrogen in ^{1}H spin–lattice relaxation has been valuable in discovering the structural changes induced in a-Si:(D,H) by thermal annealing. In addition, recent studies have shown that trapped molecular deuterium is a useful probe for observing light-induced defects in a-Si:(D,H).[18]

2.5.1 Spin–Lattice Relaxation of Hydrogen in a-Si:H

The characteristic low-temperature minimum in the T_1 of ^{1}H as illustrated in Figure 6 was initially postulated to arise from the relaxation of hydrogen nuclei by hydrogen-associated disorder modes or 'tunneling' modes.[28] However, theoretical calculations showed that the number of hydrogen-associated disorder modes that are required to account for the magnitude of the observed ^{1}H T_1 is too large to be reasonable. This result was later confirmed experimentally.[29]

It was later proposed that the ^{1}H in a-Si:H relax via spin diffusion to trapped *ortho*-hydrogen molecules in microvoids. These *ortho*-H_2 serve as spin–lattice relaxation centers.[30] The role of spin diffusion in the relaxation process was shown in a series of experiments that used partially deuterated a-Si:H samples and employed a technique allowing the determination of T_1 in the absence of homonuclear dipolar interactions.[31] The presence of molecular hydrogen in a-Si:H was confirmed by the detection of the conversion of *ortho*- to *para*-hydrogen at 4.2 K,[32] and by the previously mentioned direct observation of a Pake doublet from solid hydrogen in ^{1}H NMR spectra at temperatures below 10 K.[21] Deuterium magnetic resonance experiments showed that deuterium molecules trapped in microvoids of a-Si:(D,H) serve as spin–lattice relaxation centers for deuterons.[15]

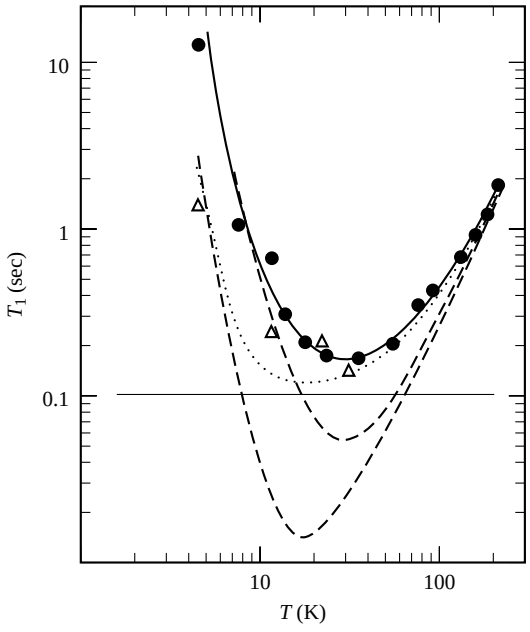

Figure 6 Data which clearly show the temperature minimum in ^{1}H T_1. Data were acquired at 42.3 MHz (solid dots) and 12.3 MHz (triangles). The solid and dot-dashed lines are fits to the data using a relaxation model that incorporates the effects of spin diffusion. The dashed lines are model predictions without considering spin diffusion. The horizontal line marks the spin diffusion-limited T_1 minimum of 0.16 s. (Reproduced by permission of the authors and The American Physical Society from M. S. Conradi and R. E. Norberg, *Phys. Rev. B*, 1981, **24**, 2285)

2.5.2 Modeling the Spin–Lattice Relaxation of Hydrogen

Theoretical calculations have been helpful in understanding the relaxation process in intrinsic (undoped) a-Si:H.[27,33] A 'spin diffusion bottleneck' term is required to model accurately the T_1 versus temperature observations as shown in Figure 6[27,30] This term represents the transfer of magnetization from bonded hydrogen in the bulk of a-Si:H to the microvoid regions (where trapped molecular hydrogen resides) by spin diffusion. Note that the bottleneck term is most significant near the T_1 minimum, and is not important in room-temperature measurements of T_1.

Hydrogen in doped a-Si:H relaxes via a slightly different mechanism. For example, spin–lattice relaxation measurements versus temperature in boron-doped a-Si:H do not show a well-defined minimum. The boron in the material affects the microstructure in such a way that the importance of the spin diffusion bottleneck term is significantly enhanced.[34]

Condensed molecular hydrogen has been observed in a-Si:H by a variety of methods.[21,33] However, the temperature-dependence of the ^{1}H T_1 in a-Si:H seems to indicate a coupling to *dilute ortho*-H_2 molecules. The spin–lattice relaxation of condensed H_2 does not show the characteristic minimum between 25–55 K, magnetic field dependence, or relaxation rates that are typical of ^{1}H in a-Si:H that are presumably relaxed by coupling to trapped molecular hydrogen.[33] This apparent paradox may be resolved by considering that the *ortho*-H_2 molecules responsible for relaxation of bonded hydrogen are adsorbed on the internal surfaces of microvoids. These molecules are then 'effectively dilute', because their intermolecular electric quadrupole–quadrupole interactions are quenched by their interaction with the silicon surface.[27] This prevents the adsorbed *ortho*-H_2 from interacting with the bulk, condensed H_2 in the microvoid. This model can also account for the observation that the concentrations of molecular hydrogen determined from spectral areas of the Pake doublet are always larger than those inferred from ^{1}H T_1 measurements. Only that fraction of the trapped hydrogen molecules adsorbed on the void surfaces in a-Si:H are relaxation centers for hydrogen atoms bonded to silicon.[21]

2.5.3 Trapped Molecular Hydrogen and Microvoid Structure

A particularly interesting conclusion of these studies, which is complemented by recent studies of microvoids and hydrogen clustering in a-Si:H, is that the trapped molecules

reside in well-defined sites.[32] The spin–lattice relaxation behavior of several a-Si:H samples was modeled with various assumptions made about the symmetry of the electric field gradient (EFG) at the *ortho*-H_2 molecule. It was found that the EFG has, at most, axial symmetry and this symmetry is only observed in certain samples. The sites with axial symmetry are *ortho*-H_2 located in small voids of ~500 pm diameter, and the sites with no (or low) symmetry are larger voids in which the *ortho*-H_2 are adsorbed at the surface.[27]

2.5.4 ^{2}D NMR Observation of Light-Induced Defects

^{2}D NMR spectra have been observed before and after light-soaking a-Si:D samples.[18] All of the features discussed above for typical ^{2}D spectra are observed in both spectra, with the tightly-bound deuterium doublet and the narrow central line unchanged. However, the broad central component does change. Approximately 0.5% of the deuterium atoms in the sample are affected by light exposure, most probably because they are in the vicinity of a light-induced paramagnetic defect. These deuterium atoms are those that are either nanovoid-trapped HD and D_2, or weakly-bound deuterium involved in distorted silicon-deuterium bonds. Based on the change in paramagnetic centers measured with electron spin resonance, roughly 500 deuterium atoms are affected by each light-induced defect.

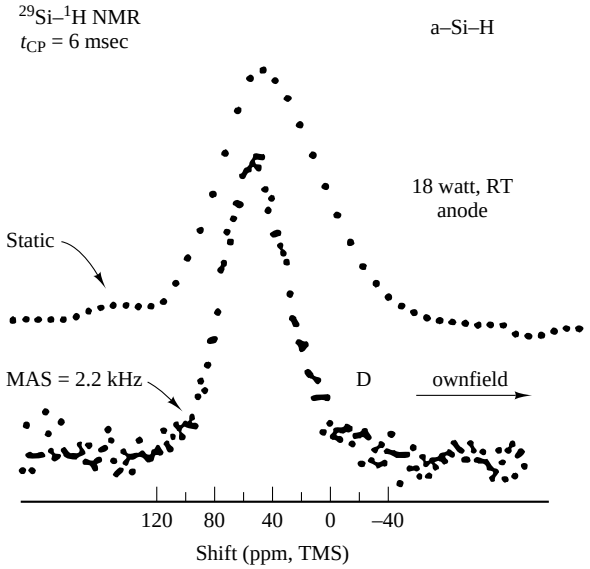

Figure 7 ^{29}Si NMR spectra for a-Si:H acquired with (bottom) and without (top) 2.2 kHz magic angle spinning (MAS). Although the spectrum narrows with MAS, the narrowing is much less than expected if chemical shift anisotropy were responsible for the line broadening. (Reproduced by permission of the authors and The American Institute of Physics from J. A. Reimer, P. Dubois Murphy, B. C. Gerstein, and J. C. Knights, *J. Chem. Phys.*, 1981, **74**, 1501)

3 LATTICE STRUCTURE (^{29}Si, ^{13}C)

The concepts of disorder and randomness are common themes in discussions of amorphous materials. NMR studies of the silicon network itself in a-Si:H have been used to learn more about the order that does exist amidst the long-range aperiodicity. NMR studies of alloyant atoms in amorphous hydrogenated silicon alloys have been helpful in studying the structural differences between a-Si:H and related alloys.[3]

3.1 ^{29}Si NMR of a-Si:H

3.1.1 Cross-Polarization Experiments

The low natural abundance of ^{29}Si (4.7%), relatively low resonance frequency, and long spin–lattice relaxation times make ^{29}Si NMR experiments difficult.[6] Cross polarization techniques are the most common NMR experiments used to study silicon in a-Si:H because of the ^{29}Si sensitivity enhancement, and because signal averaging is dependent only on the ^{1}H T_1[35–37] (see ***Cross Polarization in Solids***).

The results of initial ^{29}Si NMR studies of plasma-deposited a-Si:H films were disappointing.[37] Cross-polarization experiments with high-power hydrogen decoupling during data acquisition, with and without magic angle spinning, yielded extremely broad lines whose width far exceeded the chemical shift range expected for silicon–hydrogen environments. The modest narrowing induced by magic angle spinning is illustrated in Figure 7. These observations suggested that neither the dipolar interaction nor chemical shift anisotropy was responsible for the ^{29}Si NMR linewidth. The insensitivity of linewidth to magic angle spinning, and the elimination of other line-broadening interactions as factors, led to the conclusion that the silicon NMR line is inhomogeneously broadened by the variation in silicon bonding environments in a-Si:H (see ***Magic Angle Spinning***).

The large residual linewidths were predicted using a model of a-Si which included large charge-density fluctuations in the lattice, leading to large chemical shift dispersions. The results of the calculations were in excellent agreement with the observed ^{29}Si linewidths of sputtered a-Si:H samples.[36]

There is a correlation between the average chemical shift of ^{29}Si and the fraction of the hydrogen NMR signal represented by the narrow line (see Section 2).[35] This change in the ^{29}Si chemical shift also correlates well with the 'amount of microstructure' parameter derived from IR measurements, suggesting that the local environment beyond nearest-neighbor bonding can be inferred from ^{29}Si NMR measurements.[38]

Variations on the cross polarization pulse sequence have been used to probe the relationship between silicon and hydrogen, and to resolve the overlapping signals from environments with different hydrogenation.[39] In the most straightforward experiment, it was confirmed that molecular hydrogen was a negligible contributor to the intensity of the ^{1}H NMR narrow line, and that the broad- and narrow-line hydrogen in a-Si:H are spatially separated. This experiment and a related study using cross depolarization have been discussed in detail in an earlier review.[6]

The dynamic nuclear polarization (DNP) technique has been used to enhance ^{29}Si NMR signals, and to study selectively regions of samples near paramagnetic defects in nonhydrogenated a-Si.[40] DNP is a double resonance experiment that uses the unpaired electron as the source of

magnetization to transfer to the ^{29}Si (see ***Dynamic Nuclear Polarization and High-Resolution NMR of Solids***).

3.1.2 Free Induction Decay Measurements

Recently, ^{29}Si has been studied in a-Si:H[38,41] and a-Si[42] by acquiring free induction decays. This experiment allows the observation of both hydrogenated and nonhydrogenated silicon atoms, and the measurement of relaxation time constants. Although it is the most basic pulsed NMR technique, this experiment is challenging because of the long spin–lattice relaxation times of ^{29}Si in a-Si:H. Spin–lattice relaxation times were determined to be on the order of 100 min for high-quality samples. These long relaxation times can be modeled by a paramagnetic center relaxation mechanism, and results for samples prepared under different conditions can be interpreted in terms of the distribution of paramagnetic defects in the material. High-quality samples show a single relaxation time (T_1), while samples of lower quality (with demonstrably worse electronic properties) show at least two distinct relaxation times. These observations suggest that paramagnetic dangling-bond defects are distributed randomly in high-quality a-Si:H, whereas in lower grade a-Si:H the defects tend to cluster. This interpretation is reminiscent of just about every other measurement of a-Si:H microstructure, and provides yet another bit of support for the view that these materials are heterogeneous rather than random.[41]

The effects of thermal annealing on the local order of the silicon lattice in sputtered, nonhydrogenated a-Si have been studied with silicon NMR and correlated with Raman spectroscopy measurements.[42] There is a gradual decrease in ^{29}Si NMR linewidth with annealing temperature above 400 °C, while the line position is essentially constant until the temperature exceeds 600 °C. At this point the sample begins to crystallize, and a narrow feature typical of crystalline silicon appears in the spectra at −79.9 ppm. Note that none of these changes is due to hydrogen diffusion, since these samples are not hydrogenated. Rather, these changes reflect rearrangements of the silicon lattice with concomitant changes in the short-range order.

3.2 ^{13}C NMR of Amorphous Silicon Carbide (a-SiC:H)

NMR studies of 'backbone' atoms in amorphous silicon alloys have been reviewed previously.[3] An example of these studies is provided by the spectra depicted in Figure 8. Carbon-13 NMR spectra of a-SiC:H were acquired as free induction decays with and without high-power proton decoupling. Two major pieces of information were obtained from the data: carbon exists in both sp^3 and sp^2 configurations in a-SiC:H, and the sp^2 carbons are not hydrogenated.[43] Prior to this work, it was common to assume that carbon was incorporated into the a-Si:H lattice substitutionally, and behaved similarly to silicon.

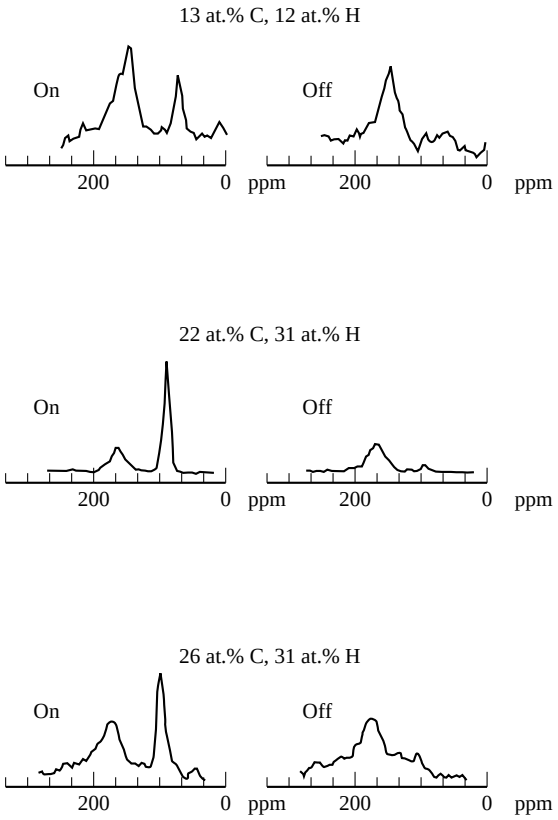

Figure 8 Carbon-13 NMR spectra of three a-SiC:H samples. 'On' and 'Off' indicate proton decoupling and no proton decoupling, respectively. The left peak is sp^2 carbon; the right peak is sp^3 carbon. Notice the negligible change in the sp^2 peak with proton decoupling. The disappearance of the sp^3 peak in the spectra without decoupling indicates that the sp^3 carbon environments are hydrogenated. (Reproduced by permission of the authors and The American Physical Society from M. A. Petrich, K. K. Gleason, and J. A. Reimer, *Phys. Rev. B*, 1987, **36**, 9722)

4 DOPANT ATOMS (^{11}B, ^{31}P)

Phosphorus and boron are the most commonly used dopants in a-Si:H. Phosphorus doping results in an n-type, or electron rich, material, while boron doping leads to a p-type, or electron deficient (hole-rich) material. Phosphorus doping provides additional electron energy states near the conduction band; boron doping provides additional states near the valence band.[1] These nuclei have been observed in simple NMR experiments,[44–48] their relaxation behavior has been studied,[44,47,48] and their spatial relationship to hydrogen has been probed with double-resonance experiments.[44]

4.1 ^{31}P NMR

The doping efficiency of amorphous silicon is quite low compared with crystalline silicon. In order to be an active dopant, phosphorus atoms must be bonded in fourfold-coordinated configurations. However, several ^{31}P NMR studies have shown that the large majority of phosphorus atoms in a-Si:H are in threefold-coordinated bonding configurations.[44,48,49] Spectra were determined to consist of two overlapping resonance bands by acquiring ^{31}P NMR data with both free induction decay and spin echo measurements. The two resonances have been assigned to threefold- and fourfold-coordinated phosphorus by comparison with phosphorus reference compounds.[48]

The spin–spin relaxation time (T_2) for threefold-coordinated phosphorus in a-Si:H(P) can be modeled by considering only the homonuclear dipole coupling. The interaction between hydrogen and phosphorus does not have to be included in computations of the dipolar linewidths, which is consistent with the experimental observation that hydrogen contributes negligibly to ^{31}P spin–spin relaxation.[48] Samples prepared with different hydrogen contents, or with the hydrogen removed by thermal annealing, have virtually identical ^{31}P spin–spin relaxation times (T_2 = 1.0–1.5 ms). Experiments using heteronuclear dipolar decoupling also show no appreciable coupling between hydrogen and phosphorus.[46,47] It is also interesting to note that, below 2 at.% the phosphorus concentration has little effect on the magnitude of T_2 of ^{31}P. Samples with 2% and 0.5% phosphorus have essentially the same values of T_2 leading to the conclusion that phosphorus does not distribute homogeneously in a-Si:H(P) but is located in regions of constant *local* concentration.[44] In samples with higher phosphorus concentrations, local concentrations of phosphorus will increase, leading to shorter values, of T_2. A sample with 21 at.% phosphorus, for example, had T_2 = 460 μs.[47]

The fourfold-coordinated phosphorus configuration has only been observed in two studies,[48,49] one of which showed the light-induced conversion of fourfold-coordinated sites to threefold-coordinated sites. That experiment is described below. Other studies which did not detect evidence for the fourfold-coordinated sites probably involved light-soaked materials,[44,46,47] as has been suggested by one of the authors.[44] Spin–spin relaxation of the fourfold-coordinated phosphorus is considerably different from the threefold-coordinated phosphorus. The relaxation is much faster (T_2 < 0.2 ms), and coupling to hydrogen is an important relaxation mechanism. In fact, these fourfold-coordinated phosphorus atoms must be located near the environment of the clustered hydrogen or else the coupling to hydrogen would be an ineffective mechanism for relaxation.[44,48] The exact relationship between the phosphorus and hydrogen environments is not known, but it is estimated that the fourfold-coordinated phosphorus sites are located within 500 pm of the hydrogenated microvoids, and may actually be at the surface of the voids.[48]

The phosphorus spin–lattice relaxation time (T_1) varies from several minutes to less than 1 min depending upon sample preparation conditions and phosphorus content. Compensated samples [a-Si:H(P,B)] have much longer $^{31}PT_1$ values (18.3 min) than similarly prepared singly-doped material (1.5 min).[44] The relaxation mechanism provides additional information about the sample. The values of T_1 are so large that it is unlikely that interaction of phosphorus nuclei with conduction electrons (Knight shift) is important. Also, the large shifts in resonance frequency typical of Knight shifts are not observed[49] (see ***Internal Spin Interactions and Rotations in Solids***).

4.1.1 *Observation of Metastable Bonding Configurations of ^{31}P*

The effects of light exposure on the bonding configurations of phosphorus in a-Si:H were dramatically revealed by ^{31}P NMR as shown in Figure 9.[49] These studies showed that as deposited, phosphorus-doped a-Si:H contains only threefold-coordinated phosphorus, with a single broad resonance observed at 170 ppm (relative to phosphoric acid). Exposing this material to light had no effect on the phosphorus bonding. However, annealing the samples at 100 °C in the dark for 2 h induced a transformation of 20% of the threefold-coordinated phosphorus to the fourfold-coordinated form, as indicated by overlapping broad resonances at 80 and 170 ppm. Subsequent exposure to light reversed the effect of annealing, and the sample again contained only threefold-coordinated phosphorus. All of these changes were well within the sensitivity of the spectrometer used. This experiment was the first to elucidate the structural changes involved in a metastable response of a-Si:H to light exposure and thermal annealing.

The location of the metastable phosphorus relative to hydrogen was determined by using the Hahn spin echo technique. When a delay of 250 μs was used between the initial pulse and the echo pulse, the observed lineshape only showed threefold-coordinated phosphorus. This result suggested that the fourfold-coordinated phosphorus nuclei are in close proximity to clustered hydrogen nuclei that promote rapid relaxation of the phosphorus magnetization.[49]

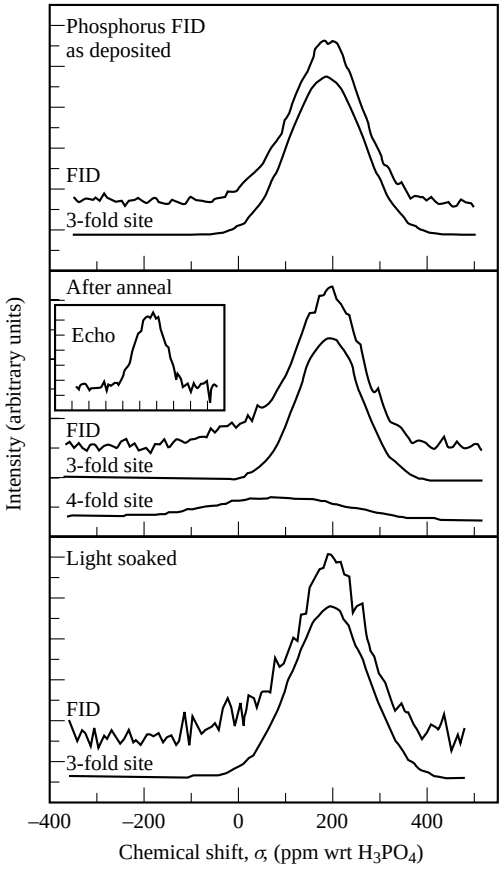

Figure 9 ^{31}P NMR spectra from n-type a-Si:H as deposited (top), after annealing in the dark (middle), and then after light soaking (bottom). Because the as deposited sample can be assumed to be light-soaked, these spectra show the metastable formation of fourfold coordinated phosphorus bonding sites. (Reproduced by permission of the authors and The American Physical Society from M. J. McCarthy and J. A. Reimer, *Phys. Rev. B*, 1987, **36**, 4525)

4.2 ^{11}B NMR

NMR studies of ^{11}B in a-Si:H have provided additional information about why doping efficiencies are so poor.[34,44,45,50] Spin echo linewidths ($1/T_2$*) can be used to determine nuclear quadrupole coupling constants for ^{11}B, which are extremely sensitive to local bonding coordination. In samples ranging from 0.7–10 at.% boron, the boron atoms are overwhelmingly in threefold configurations. There are no detectable fourfold-coordinated boron atoms.[50] Films with the lowest boron levels contain singly or doubly hydrogenated boron, but when boron concentrations are large the films also contain boron atoms which are bonded to three silicon atoms. Measurements of spin–spin relaxation (T_2) via the spin echo technique demonstrate that neither B–B bonds nor B_2H_6 molecules exist in greater than trace amounts in boron-doped a-Si:H. The T_2 values are too large. However, the T_2 values are too small to support a picture of randomly distributed boron atoms even in the 0.7 at.% boron materials. There are significant variations in the local concentration of boron atoms, but these variations do not include boron atoms directly bonded to each other.[45]

In compensated materials [a-Si:H(P,B)] approximately 25% of the boron atoms bond in a fourfold-coordinated fashion.[44] These are identified by their very narrow linewidths (<2 kHz) which are comparable to the observed ^{11}B NMR linewidths in p-type crystalline silicon. Despite this high fraction of boron in the supposedly desired fourfold-coordinated environment, the doping efficiency in these materials is still quite low. As described below, it is known that the boron–phosphorus clustering occurs to a high degree in compensated a-Si:H, so these fourfold-coordinated boron atoms are most likely in $BPSi_3$ units or similar configurations. The presence of boron and phosphorus in close proximity obviates the doping effect from either atom.

4.3 Spin Echo Double Resonance Experiments

Spin echo double resonance (SEDOR) experiments have been used to measure the distances between phosphorus and boron atoms in compensated a-Si:H, and to measure the distance between hydrogen atoms and either phosphorus or boron in both compensated and singly-doped films.[44] The SEDOR pulse sequence consists of a standard spin echo experiment (e.g. 90°, τ, 180°, τ, echo) with an additional 180° pulse applied at a different resonance frequency simultaneously with the 180° pulse in the sequence. The additional pulse flips the heteronuclear spins, changing the local field at the observed nuclei. Since the local field depends upon the distance between the two nuclei, comparisons of the spin echo with and without the 'extra' pulse provide the information needed to calculate the distance between two different nuclei, or to establish the parameters of a distribution of nuclei around the observed nucleus.

The SEDOR data shown in Figure 10 demonstrate the clustering of boron and phosphorus that occurs in compensated a-Si:H films. The figure also shows the results of calculations for situations where the boron and phosphorus are totally clustered, arranged completely at random, and when they are arranged in a CsCl-type lattice. None of these situations is representative of the real situation. The data are fitted by two

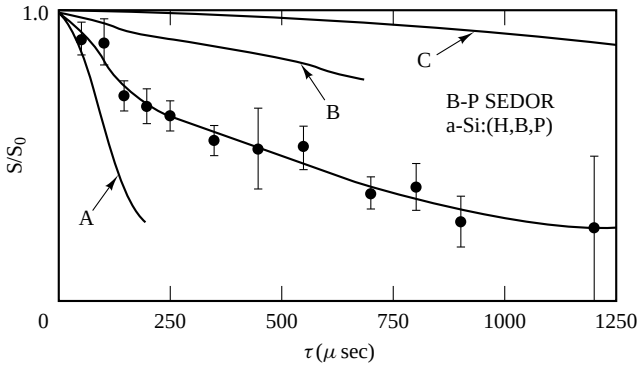

Figure 10 Boron–phosphorus SEDOR decay data for compensated a-Si:H. The sample contains 2 at.% B and 2 at.% P. Three models fail to explain the observed data. Curve A comes from assuming that each B is bonded to a P, curve B is based on a random distribution of B–P pairings, and curve C is based on B and P being arranged on a CsCl-type lattice. (Reproduced by permission of the authors and The American Physical Society from J. B. Boyce and S. E. Ready, *Phys. Rev. B*, 1988, **38**, 11 008)

Gaussian curves whose parameters indicate that B–P units with a bond length of 210 pm account for roughly 40% of the boron in the film, and that the other 60% of the boron atoms have phosphorus atoms roughly 380 pm away. In this film, with 2 at.% boron and 2 at.% phosphorus, a random distribution of dopants would have 8% of the boron atoms bonded in B–P units. The observed 40% is far in excess of the random value, showing that boron and phosphorus have a strong chemical affinity for each other in a-Si:H. This helps to explain the poor doping efficiency of compensated materials.[44]

5 RELATED ARTICLES

Amorphous Materials; Cross Polarization in Solids; Diamond Thin Films; Dynamic Nuclear Polarization and High-Resolution NMR of Solids; Internal Spin Interactions and Rotations in Solids; Magic Angle Spinning; Multiple Quantum NMR in Solids; Silicon-29 NMR

6 REFERENCES

1. R. A. Street, *Hydrogenated Amorphous Silicon*, Cambridge University Press, 1991.
2. S. R. Elliott, *Adv. Phys.*, 1989, **38**, 1.
3. J. A. Reimer and M. A. Petrich, in *Advances in Amorphous Semiconductors*, ed. H. Fritzsche, World Scientific Publishing Co., New York, 1989, p. 3.
4. J. A. Reimer, *J. de Physique C*, 1981, **42**, C4.
5. P. C. Taylor, in *Semiconductors and Semimetals*, ed. J. I. Pankove, Academic Press, Orlando, 1984, Vol. 21C, 99.
6. M. A. Petrich, *Magn. Reson. Rev.*, 1993, **16**, 183.
7. H. Eckert, *Prog. NMR Spectrosc.*, 1992, **24**, 159.
8. W. E. Carlos and P. C. Taylor, *Phys. Rev. B*, 1982, **26**, 3605.
9. J. A. Reimer, R. W. Vaughan, and J. C. Knights, *Phys. Rev. Lett.*, 1980, **44**, 193.
10. J. A. Reimer, R. W. Vaughan, and J. C. Knights, *Phys. Rev. B*, 1981, **24**, 3360.

11. F. R. Jeffrey and M. E. Lowry, *J. Appl. Phys.*, 1981, **52**, 5529.
12. K. K. Gleason, M. A. Petrich, and J. A. Reimer, *Phys. Rev. B*, 1987, **36**, 3259.
13. M. Kumeda, H. Komatsu, T. Shimizu, N. Fukuda, and N. Kitagawa, *Jpn. J. Appl. Phys.*, 1985, **24**, L495.
14. V. P. Bork, P. A. Fedders, D. J. Leopold, R. E. Norberg, J. B. Boyce, and J. C. Knights, *Phys. Rev. B*, 1987, **36**, 9351.
15. D. J. Leopold, P. A. Fedders, R. E. Norberg, J. B. Boyce, and J. C. Knights, *Phys. Rev. B*, 1985, **31**, 5642.
16. M. P. Volz, P. Santos-Filho, M. S. Conradi, P. A. Fedders, R. E. Norberg, W. Turner, and W. Paul, *Phys. Rev. Lett.*, 1989, **63**, 2582.
17. P. A. Fedders, V. P. Bork, D. J. Leopold, R. E. Norberg, J. B. Boyce, and J. C. Knights, *J. Non-Cryst. Solids*, 1987, **97/98**, 357.
18. R. E. Norberg, P. A. Fedders, J. Bodart, R. Corey, W. Paul, W. Turner, and S. Jones, *J. Non-Cryst. Solids*, 1991, **137/138**, 71.
19. J. A. Reimer, R. W. Vaughan, and J. C. Knights, *Solid State Commun.*, 1981, **37**, 161.
20. P. Hari, P. C. Taylor, and R. A. Street, *Mater. Res. Soc. Symp. Proc.*, 1992, **258**, 293.
21. J. B. Boyce and M. Stutzmann, *Phys. Rev. Lett.*, 1985, **54**, 562.
22. J. B. Boyce, S. E. Ready, M. Stutzmann, and R. E. Norberg, *J. Non-Cryst. Solids*, 1989, **114**, 211.
23. M. Zheng, E. J. Vanderheiden, P. C. Taylor, R. Shinar, S. Mitra, and J. Shinar, *Mater. Res. Soc. Symp. Proc.*, 1990, **192**, 657.
24. J. Baum, K. K. Gleason, A. Pines, A. N. Garroway, and J. A. Reimer, *Phys. Rev. Lett.*, 1986, **56**, 1377.
25. S. Mitra, K. K. Gleason, H. Jia, and J. Shinar, *Phys. Rev. B*, 1993, **48**, 2175.
26. W. E. Carlos, J. A. Reimer, and P. C. Taylor, *Phys. Rev. Lett.*, 1985, **54**, 1205.
27. R. E. Norberg, *Phys. Rev. B*, 1985, **31**, 7925.
28. W. E. Carlos and P. C. Taylor, *Phys. Rev. Lett.*, 1980, **45**, 358.
29. J. B. Boyce, M. Stutzmann, and S. E. Ready, *Phys. Rev. B*, 1985, **32**, 6062.
30. M. S. Conradi and R. E. Norberg, *Phys. Rev. B*, 1981, **24**, 2285.
31. J. A. Reimer, R. W. Vaughan, and J. C. Knights, *Phys. Rev. B*, 1981, **23**, 2567.
32. W. E. Carlos and P. C. Taylor, *Phys. Rev. B*, 1982, **25**, 1435.
33. P. A. Fedders, R. Fisch, and R. E. Norberg, *Phys. Rev. B*, 1985, **31**, 6887.
34. S. G. Greenbaum, W. E. Carlos, and P. C. Taylor, *Physica (The Hague)*, 1983, **117B/118B**, 886.
35. S. Hayashi, K. Hayamizu, S. Yamasaki, A. Matsuda, and K. Tanaka, *Phys. Rev. B*, 1987, **35**, 4581.
36. F. R. Jeffrey, P. Dubois Murphy, and B. C. Gerstein, *Phys. Rev. B*, 1981, **23**, 2099.
37. J. A. Reimer, P. Dubois Murphy, B. C. Gerstein, and J. C. Knights, *J. Chem. Phys.*, 1981, **74**, 1501.
38. M. K. Cheung and M. A. Petrich, *J. Appl. Phys.*, 1993, **73**, 3237.
39. N. Zumbulyadis, *Phys. Rev. B*, 1986, **33**, 6495.
40. H. Lock, R. A. Wind, G. E. Maciel, and N. Zumbulyadis, *Solid State Commun.*, 1987, **64**, 41.
41. M. K. Cheung and M. A. Petrich, *Phys. Rev. B*, 1992, **45**, 9006.
42. W. L. Shao, J. Shinar, B. C. Gerstein, F. Li, and J. S. Lannin, *Phys. Rev. B*, 1990, **41**, 9491.
43. M. A. Petrich, K. K. Gleason, and J. A. Reimer, *Phys. Rev. B*, 1987, **36**, 9722.
44. J. B. Boyce and S. E. Ready, *Phys. Rev. B*, 1988, **38**, 11 008.
45. S. G. Greenbaum, W. E. Carlos, and P. C. Taylor, *J. Appl. Phys.*, 1984, **56**, 1874.
46. S. Hayashi, K. Hayamizu, S. Yamasaki, A. Matsuda, and K. Tanaka, *Phys. Rev. B*, 1988, **38**, 31.
47. S. Hayashi, K. Hayamizu, S. Yamasaki, A. Matsuda, and K. Tanaka, *Jpn. J. Appl. Phys.*, 1987, **26L**, 2041.
48. J. A. Reimer and T. M. Duncan, *Phys. Rev. B*, 1983, **27**, 4895.
49. M. J. McCarthy and J. A. Reimer, *Phys. Rev. B*, 1987, **36**, 4525.
50. S. G. Greenbaum, W. E. Carlos, and P. C. Taylor, *Solid State Commun.*, 1982, **43**, 663.

Biographical Sketches

Mark A. Petrich. *b* 1961. B.S., 1982, Washington University, Ph.D., 1987, University of California, Berkeley. Introduced to NMR by Jeff Reimer. Faculty in Chemical Engineering at Northwestern University, 1987–94. Senior chemical engineer with Merck and Co., Inc., 1994–present. Approx. 40 publications. Research interests include powder formation and characterization, plasma-deposited materials, and polymer recycling.

Colloidal Systems

Terence Cosgrove and Timothy M. Obey
University of Bristol, UK

1	Introduction	1
2	Special Considerations	1
3	Interactions of Small Molecules with Colloidal Particles	2
4	Interaction of Surfactants with Colloidal Particles	3
5	Interaction of Polymers with Colloidal Particles	4
6	Polymer–Surfactant Interactions	5
7	Particle/Emulsion Characterization	6
8	References	6

1 INTRODUCTION

The physicochemical diversity of multiphase and multicomponent systems inevitably poses a great many difficulties to the experimentalist. NMR allows investigation of these systems by a combination of direct structural information, obtained through lineshape analysis and chemical shift data, and indirect information from dynamic measurements of spin relaxation and diffusion. In this article we focus on a specific subset, i.e. dispersions of colloidal particles in fluids. In particular, we describe how NMR methods can be used to investigate the interfacial properties of the system under study and help to shed light on the structure of the adsorbed layer (e.g. solvent, polymer, etc.) at the particle surface. Colloidal dispersions are of considerable importance industrially and are also of intrinsic scientific interest themselves. Specific examples of their use include such diverse applications as additives for toothpaste, engine oils, paints, and cements, to name but a few. These systems generally consist of solid particles dispersed in a liquid phase (e.g. polystyrene latex, silica sol). Colloidal systems such as foams (gas dispersed in a liquid phase) and aerosols (liquid or solid dispersed in a gas phase) will not be discussed. Polymer–surfactant interactions and emulsions (one liquid phase dispersed in another liquid phase) are briefly discussed; however, a detailed review of these systems will not be presented. For more specific references the reader is referred to other articles within the Encyclopedia dealing with these subject areas.

The present article is divided into sections focusing on the interactions of the colloidal particle with either the dispersion medium itself, or with other small molecules, surfactants, polymers, or proteins also present in the dispersion medium. It is not intended that the current article provide an extensive review, rather we seek to highlight, by example, a small number of the numerous and varied applications of NMR within this area.

2 SPECIAL CONSIDERATIONS

NMR spectroscopy, by virtue of its operating frequency and the limitations imposed by the Boltzmann distribution, is not a sensitive spectroscopic technique, though major advances (albeit in rather specific situations) such as the PASADENA (*para*-hydrogen and synthesis allow dramatically enhanced nuclear alignment)[1,2] experiment seek to alleviate these problems. Nevertheless, at high field and with suitable sample volumes, it is relatively easy to obtain spectra of interfacial species specifically. Several factors determine this sensitivity, and as these are different from the more usual NMR considerations we will discuss them in some detail.

2.1 Surface Area

In any interfacial study of adsorbed species, two important considerations are the adsorption isotherm and the total surface area available for adsorption. For a nonaggregated substrate consisting of monodisperse spherical particles at a given volume fraction, the surface area is inversely proportional to the particle radius. Hence, particles in the colloid size regime (ca. 10–500 nm) are ideally suited to provide a well-defined system with a high surface area per gram of substrate. A high volume fraction of the substrate is desirable in order to improve the signal-to-noise ratio of the NMR spectrum. However, the consequences of interparticle interactions at these high concentrations and their effects on the structure and stability of the colloidal system must be considered during sample preparation.

2.2 Stability

The stability of the dispersion is closely related to its surface area. Aggregation/flocculation of the colloidal particles can dramatically reduce the available area to adsorbing species such as solvent or polymer. For charged particles in aqueous dispersions, this problem can often be neglected during the timescale of an NMR experiment, though settling might be problematical if the density of the particles is considerably greater than that of the surrounding dispersion medium. In nonaqueous dispersions it is essential that the particles are stabilized in some fashion since a charge stabilization mechanism is usually inoperative in the low dielectric constant media used in these formulations. In these cases, stabilization may be achieved by matching the Hamaker constant[3] of the particle with that of the dispersion medium, or by adding a suitable polymeric stabilizer or surfactant.[3]

The reduction in surface area is not the only problem brought about by destabilization (i.e. aggregation/flocculation) of the colloidal system, since the adsorbed surface layer can become compressed, desorbed, or otherwise modified by the (now) high degree of particle packing. This effect is particularly noticeable with measurements of the linewidths of the adsorbed species, since the surface species may now have a considerably reduced mobility dependent on the exact nature of the aggregates formed.[4]

2.3 Exchange

In many colloidal dispersions the continuous phase (e.g. water) will be in dynamic exchange between the bulk and the surface. In the fast exchange limit the average relaxation

rate of the solvent will depend on the accessible surface area and its residence time/interaction mechanism at the particle surface. The residence time of the solvent will also be sensitive to competitive solutes such as surfactants and polymers. Examples of these measurements will be given in later sections. In cases where the lifetime of the adsorbed species is very long or where the exchange rate is limited by strong surface interactions or physical barriers, then complex exchange equations must be employed.[5] Direct observation of spectra from surface species that are not in fast exchange can also be used to probe both the surface orientation and the dynamics of the adsorbed species.

2.4 Susceptibility/Homogeneity/Anisotropy

In any multiphase system there will be abrupt changes in magnetic susceptibility upon passing from one phase into another. This may have severe consequences for conventional high-resolution NMR studies in terms of resolving and interpreting the chemical shifts or (in solid state studies) chemical shift tensors. In such systems, however, these exchange-broadened resonance lines may be the only route to obtain any useful information. In extreme cases it may be impossible to obtain spectra from the surface layers.

The anisotropic nature of the mobility of the adsorbed species must also be considered. If such motion occurs, detailed quadrupolar relaxation measurements can be used rather effectively to probe the dynamics of the surface layer. In many systems a lack of mobility of the surface-adsorbed phase means that it is impossible to obtain spectra from that phase directly using conventional high-resolution spectrometers, and thus solid state techniques are required. However, both methods have associated problems, such as the centrifugation of the colloidal dispersion during magic angle spinning and the shortening of rotating frame relaxation times on adsorption. The resulting consequence is that some cross polarization experiments become difficult.

2.5 Techniques

In colloidal dispersions the full panoply of NMR methods can, in principle, be used to some advantage though, generally, the more conventional methods of relaxation analysis, diffusion and high-resolution/solid state chemical shift measurements have been employed most extensively. Other approaches such as imaging have a role to play, although by their very nature colloidal particles are too small for the spatial resolution currently possible, and thus a detailed structural analysis is not possible. Techniques that operate on the molecular length scale (e.g. relaxation) are often more appropriate in such cases. Combined electrophoresis and NMR self-diffusion techniques may have significant roles to play, though at present these methods are not widely available (see ***Electrophoretic NMR***.). One interesting facet of the study of particulate colloidal dispersions by NMR is the spectrum that arises from the substrate itself. The methods and techniques that can be used to study the substrate directly rely on dipolar decoupling (discussed extensively in other articles within this Encyclopedia); however, below a certain size (ca. 1–2 nm) the rotational diffusion of the particle itself may be sufficient to narrow the resonance line.

3 INTERACTIONS OF SMALL MOLECULES WITH COLLOIDAL PARTICLES

As mentioned before, the average relaxation time (rate) of solvent molecules in colloidal dispersions consisting of particulate matter is a source of direct information on the particle structure and affinity of the surface for the solvent molecule. Figure 1 shows a set of water spin–spin relaxation

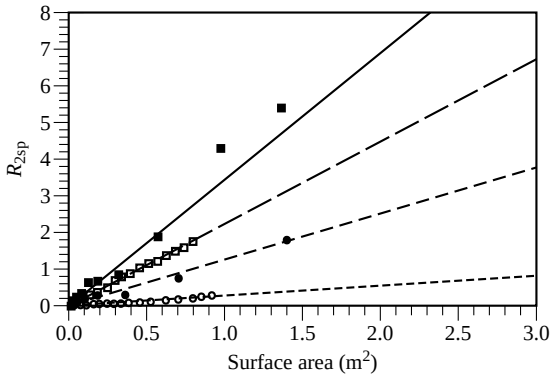

Figure 1 Normalized specific solvent (water) relaxation rates for hydrophobic and hydrophilic surfaces as a function of surface area: (■) alumina; (□) silica; (●) positive polystyrene latex; (○) negative polystyrene latex

data expressed as a specific relaxation rate, $R_{2sp} = (R_{2d} - R_{2s})/R_{2s}$, where d relates to the overall colloidal dispersion and s to the pure solvent. Several interesting features can be seen in these data. Firstly, data taken from different sized particles of the same substrate (e.g. silica sols) fall on the same line, demonstrating that NMR can be used to monitor the total available surface area in a dispersion in situ, which is not straightforward to achieve by other means. Secondly, and possibly of more general interest, is the gradient and nature of each line: the straight line dependencies indicate that the samples satisfy the fast exchange limit and the gradients are related to the relative affinity of the particles, both in a magnetic and chemical sense, for the solvent. Comparison of the silica and alumina data show a stronger solvent–surface interaction for the latter. Care must, however, be taken when interpreting these data since paramagnetic impurities may be present in the sols and these may artificially (in this case) enhance the relaxation rate. Comparing the two polystyrene latex samples with the inorganic sols demonstrates the more hydrophobic nature of the polymer particles and, in the case of the negatively charged polystyrene latex, its lower surface charge density. In mixed particulate dispersions the specific relaxation rates are additive, and these simple measurements can be used to monitor heteroflocculation and competitive solvation. For example, competitive solvation has been investigated in the system comprising water, dimethylformamide, and silica, using relaxation rate measurements.[6] More detailed studies of the structure of the solvent layer (water) can be made using ^{17}O and ^{2}H relaxation which are sensitive to changes in intramolecular motion.[7] These studies make it possible to distinguish effects such as proton exchange with surface hydroxyl groups and the role of anisotropic surface mobility

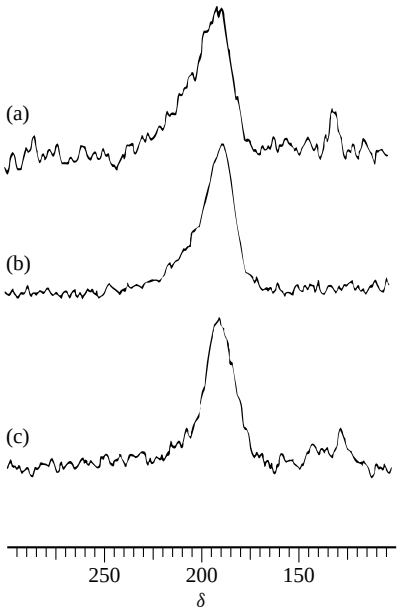

Figure 2 Variable temperature 75 MHz ^{13}C NMR spectra of CO adsorbed on colloidal palladium (ca. 1% in methylcyclohexane) at: (a) 220 K (364 transients); (b) 298 K (8000 transients); (c) 333 K (50 000 transients). Spectra are proton decoupled

of adsorbed solvent. The extension of these methods to other colloidal systems (micelles, vesicles, microemulsions, etc.) is well established,[8] as is the use of paramagnetic probes as relaxation-rate enhancers.[9]

Several recent studies have focused on the adsorption of small molecules (as distinct from solvent) from solution onto colloidal particles. One interesting example is the use of ^{13}C NMR to follow the adsorption of carbon monoxide onto colloidal platinum, a system of commercial interest in the automotive industry.[10]

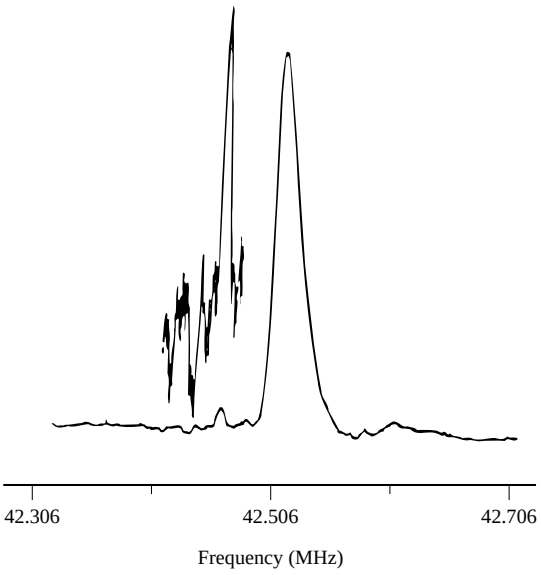

Figure 3 ^{195}Pt NMR spectrum obtained from platinum colloid after bubbling with CO gas for 30 min. Resonance at 42.460 MHz [full width at half maximum (FWHM) of 8 kHz] due to platinum surface atoms bound to CO

Figure 2 shows a 75 MHz ^{13}C spectrum of 2 nm diameter particles stabilized by poly(vinyl pyrrolidone) dispersed in methylcyclohexane. A standard high-resolution spectrometer was used to obtain the data. The adsorbed CO resonance occurs at 200 ppm but shows no Knight shift. This latter observation was explained by the particle being of insufficient size to have metallic character. In a later paper,[11] the authors presented indirect evidence which indicated that larger particles did indeed show such a shift. The effects of exchange with CO in the bulk, of course, must be allowed for when interpreting these chemical shifts. The adsorption of CO onto colloidal platinum[12] can also be seen by direct observation of the ^{195}Pt spectrum, as shown in Figure 3 where a shoulder appears to the left of the main peak. These two examples indicate the complementary nature of multinuclear MR in surface studies of this type.

4 INTERACTION OF SURFACTANTS WITH COLLOIDAL PARTICLES

There are two approaches to monitoring the structure of adsorbed surfactants in colloidal dispersions. Firstly, if the added surfactant alters the exchange rate of the solvent, then a measure of the exchange-averaged relaxation rate of the solvent will give information on the surfactant, provided that any bulk solvent–surfactant interaction is taken into account. One system where this approach has proven itself useful is in the study of the adsorption of nonionic surfactants onto silica.[13] Figure 4(a) shows the solvent relaxation enhancement $R_{2sp} = (R_{2d} - R_{2p})/R_{2p}$ (where d represents the total colloidal dispersion, and p is a 'bare' particle dispersion at the same solids concentration) for the nonionic, dodecylpoly(ethylene oxide) surfactant $C_{12}EO_6$ as a function of the solution equilibrium concentration. The results show a sharp increase in the solvent relaxation rate enhancement at a solution concentration of ca. 0.8 mmol dm^{-3} [approximately equal to the critical micelle concentration (CMC) of the surfactant] which then becomes independent of solution concentration. These changes follow the adsorption isotherm rather closely. In the 'plateau' region of the adsorption isotherm, $C_{12}EO_6$ forms a bilayer. In Figure 4(b) we show data for two other poly(ethylene oxides): an EO_{22} homopolymer and a $C_{12}EO_{25}$ copolymer. In the latter case the solvent relaxation rate enhancement is slightly lower than that for $C_{12}EO_6$, and the sharp increase is slightly less pronounced. Again, the changes follow the adsorption isotherm, this time forming surface aggregates (or a 'broken bilayer') at the silica surface. The single layer formed by the poly(ethylene oxide) homopolymer E_{22} shows only a very weak relaxation rate enhancement, suggesting that the bilayer formed by $C_{12}E_6$ and the surface aggregates formed by $C_{12}EO_{25}$ immobilize much more water at the silica–water interface.

The second approach is to study the adsorbed layer directly with a quadrupolar nucleus such as ^{2}H. This has been carried out in a study of the adsorption of sodium 4-(1′-heptylnonyl)benzenesulfonate (SHBS) (a double-tailed surfactant) at pH 4 onto γ-alumina.[14] Figure 5 shows a series of spectra obtained at an operating frequency of 30.7 MHz using a quadrupolar echo sequence and 20 000 transients. Data at two coverages are shown, together with the spectra for

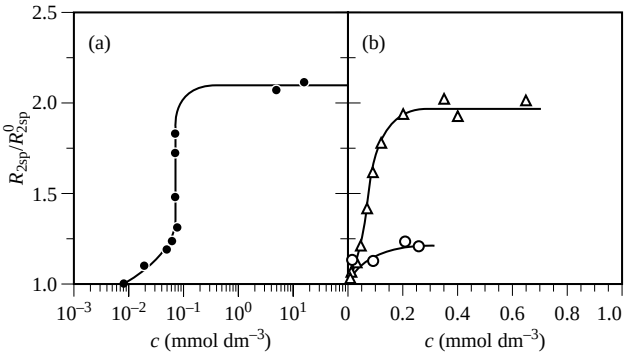

Figure 4 Normalized specific solvent relaxation rates of surfactant/water/silica systems as a function of surfactant equilibrium concentration. (a) $C_{12}(EO)_6$. (b) $C_{12}(EO)_{25}$ (Δ) and $(EO)_{22}$ (○)

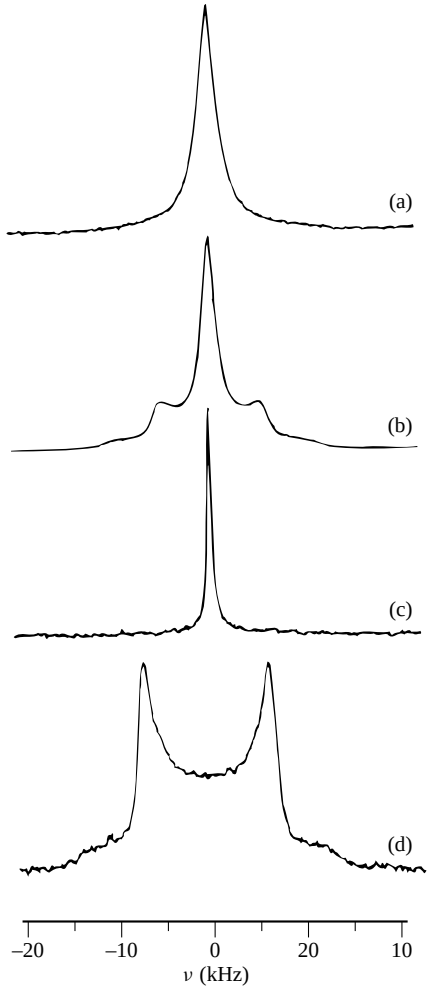

Figure 5 ^{2}H spectra of SHBS-d_4 at 25 °C: (a) adsorbed on γ-alumina at low surface coverage; (b) adsorbed at high coverage; (c) in a 2% (w/w) water solution; (d) in liquid crystals with water

the same molecule in solution and in a liquid crystal. At low surface coverage (a) the spectrum consists of a single broad line [in comparison with the molecule in a 2% (w/w) solution (c)]. Given that a proportion of the signal must come from free surfactant the observed spectrum (a) must be exchange broadened. The absence of any quadrupolar splitting suggests that the sample motion is not completely anisotropic. At high coverage (b), a distinct Pake doublet and a sharp central line appear. This can be compared with (d) which shows the same surfactant dissolved in a liquid crystal where the motion is very anisotropic. According to the authors, these strongly suggest that there are now two environments: an inner ordered layer, and a more mobile outer layer which is in fast exchange with the bulk. It is also likely that there will be slow exchange between the two domains. In other words, the authors suggest the formation of a surfactant bilayer at the alumina–water interface. They were unable, however, to indicate more precisely the exact nature of this bilayer. The spectral detail that results from this study again indicates the complementary nature of the two approaches.

An elegant technique developed by Macdonald et al.[15–18] uses the quadrupolar splitting observed in the ^{2}H spectra of an adsorbed surfactant [deuterium-labeled hexadecylphosphocholine (HDPC)] to monitor the surface charge of the substrate or changes in the surface charge upon adsorption of another species, say, a polyelectrolyte. If an external force alters the conformation of HPDC then a change in the quadrupolar splitting in its ^{2}H NMR spectrum will be observed. Clearly though, some assumptions have to be made regarding the structure of the mixed layer if species other than HPDC are present at the particle surface. Nevertheless, this technique offers great potential for studies of surface electrostatics in colloid science.

5 INTERACTION OF POLYMERS WITH COLLOIDAL PARTICLES

Polymers are used in a multitude of colloidal formulations to modify the properties of both the substrate and the dispersion medium. The addition of polymer can increase the viscosity of the dispersion medium and hence increase the stability to settling. Alternatively, they can be added to promote or discourage stabilization via adsorption onto the colloidal particles. The properties that the adsorbing polymers impart to the substrate are directly related to the structure and dynamics of the adsorbed polymer layer. These relationships have been discussed in detail in a recent text.[19] The NMR techniques available to monitor these adsorbed, polymeric structures are solvent relaxation and diffusion, adsorbed polymer relaxation, multiple pulse, and cross polarization; each of these will be discussed briefly.

The first observation of polymer adsorption using NMR found that the spectrum arising from the adsorbed layer disappeared at low polymer coverages.[20] This was interpreted as the adsorbed chains lying flat at the interfacial plane and being sufficiently dipolar broadened that they were not visible in a normal high-resolution spectrum. This led to the idea that, by making quantitative measurements of signal intensity, and knowing the adsorption isotherm, it should be possible to determine the fraction of polymer segments immobilized at the interface (p) as a function of the adsorbed amount.[21] The data derived from multiple pulse experiments of both solid and liquid echoes are shown in Figure 6. In this instance, p is defined as the height of the solid echo divided by the height of the solid and liquid echoes combined. The results show that as the surface occupancy increases the chains become more extended and a smaller proportion of

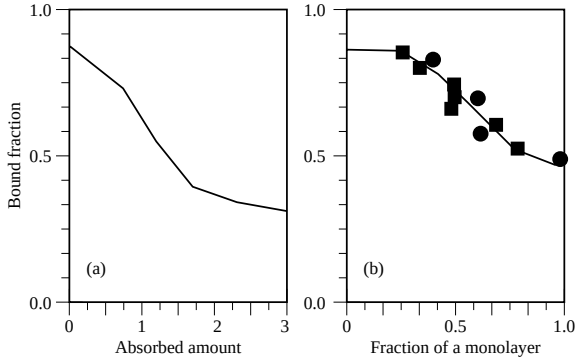

Figure 6 (a) Scheutjens–Fleer lattice model calculation for the polymer bound fraction as a function of adsorbed amount. (b) Experimental data as a function of surface coverage: (•) NMR; (■) ESR

the segments is immobilized. For comparison, ESR data on the same system are shown, as is a theoretical lattice model calculation based on the Scheutjens–Fleer theory of polymer adsorption.[19] The agreement between the two experimental methods is rather pleasing and shows the consistency in using a mobility criterion to distinguish different parts of the adsorbed chain. The qualitative agreement with a theoretical model is also rather good.

More detailed experiments focusing on the relaxation time of the adsorbed segments are also possible, and a range of CPMG experiments on adsorbed terminally grafted poly(ethylene oxide) chains on polystyrene latex have been reported.[22] As strongly dipolar-coupled spins are not visible in these experiments, the results reflect the mobility of segments that are part of the anchored chains but are not in direct contact with the particle surface. The mobility of the polymer segments is complex and anisotropic, though some qualitative description of the dynamics is possible, since the major contribution to the relaxation process is the segmental dynamics. The results show that as the surface-grafted amount increases, the average spin–spin relaxation time decreases, corresponding to increased intermolecular interaction. On increasing the chain length the average relaxation time increases, because the longer chains have more mobility, especially at the ends far from the interface. These changes reflect the change in overall mobility of the so-called 'loops' and 'tails' of the adsorbed polymer layer.

In more complex systems consisting of block copolymers of vinyl pyridine and styrene, both high-resolution ^{13}C and ^{2}H methods have been successfully employed to detect the binding and mobility of the adsorbed blocks.[23] This work showed that the vinyl pyridine groups of the copolymer were preferentially bound to the surface. The unadsorbed styrene segments were found to have a different mobility to the same segments when free in an equivalent concentrated solution. It was suggested that the strongly adsorbed vinyl pyridine segments restricted some of the motional modes of the adsorbed styrene.

Cross polarization between ^{29}Si atoms in the substrate and adsorbed poly(vinyl alcohol) has also been used to view surface and near-surface polymer segments selectively and to estimate the distance ratios of the hydroxyl groups and the polymer backbone to the silica surface.[24]

The solvent relaxation method can also be applied to adsorbed polymers and the results show that the observed

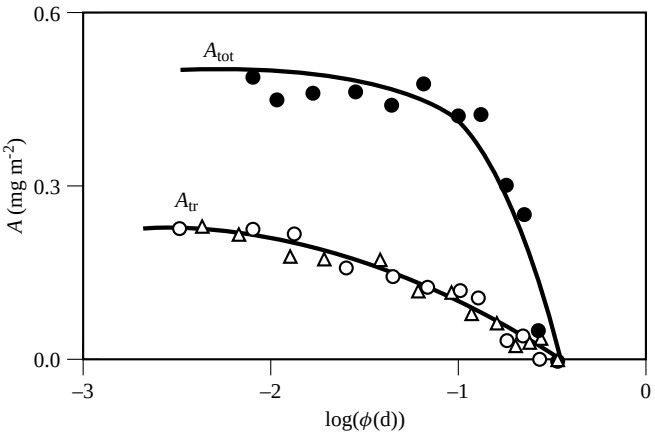

Figure 7 Poly(ethylene oxide) (PEO) (molecular weight 20 kDa) desorption from silica by increasing the volume fraction of displacer ϕ(d): (○) adsorbed amount train segments for dimethylformamide as displacer; (•) total adsorbed amount for dimethylformamide as displacer; (Δ) adsorbed amount train segments for dimethyl sulfoxide as displacer

relaxation rate enhancement is due to adsorbed polymer segments in close proximity to the surface.[25,26] One very useful application of this method is to find the critical displacement condition. This may be carried out by measuring the relaxation enhancement as a function of displacer concentration (in this case dimethylformamide). Figure 7 shows such a plot, clearly indicating the point when all the polymer has been desorbed and the relaxation rate reverts to that associated with the bare particles.

NMR relaxation methods have been applied extensively to investigate the structure and dynamics of polymer melts near particle surfaces. Several zones have now been identified where the bulk polymer mobility has been slowed by interacting either directly with the particle surface, or indirectly through entanglement with the surface-adsorbed chains.[27] The detailed analysis of the relaxation times originating from these different regions is complex, and thus far only a qualitative description has been given. A full description of these systems is beyond the scope of the present article.

6 POLYMER–SURFACTANT INTERACTIONS

NMR is an ideal technique for investigating polymer–surfactant interactions, and many reports appear in the literature which describe the use of these methods to good effect. We shall cite two recent examples of the detail that can be elicited from NMR measurements of these systems.

The interactions of surfactants with gelatine is of commercial importance to the photographic industry, and hence a detailed understanding of how the surfactant binds to the protein under different solution conditions (pH and ionic strength) is of continuing interest. High-resolution ^{13}C chemical shift data show that for sodium dodecyl sulfate (SDS) only the two carbon atoms nearest the headgroup are affected by interactions with gelatine.[28] Table 1 shows these data and compares them with SDS–poly(vinyl pyrrolidone) interactions.

The low-frequency shifts seen for both polymers are likely to be caused by desolvation of the headgroup water by the

Table 1 ^{13}C Chemical Shifts of SDS Relative to *p*-Dioxane

Carbon No.	1% SDS/Hz	1% SDS + 5% gelatine/Hz	Δ (SDS-gelatine)/Hz	Δ (SDS-PVP)/Hz
1	5222	5182	−40	−94
3	1906	1923	+17	+60
10	2387	2392	+5	+54

polymer. The high-frequency shifts may be associated with the fact that more SDS micelles are present in the system as the gelatine (or, more specifically, its associated counterions) lowers the CMC of the SDS by nearly an order of magnitude. The spectrum of the gelatine itself is also quite revealing, showing that specific resonances (e.g. the aspartic and glutamic acid groups) are unaffected by SDS, but that the linewidths associated with the cationic residues and the hydrophobic groups become progressively broader with increasing SDS concentration.

In another ^{13}C study,[29] the interaction of SDS with poly(ethylene oxide) has been investigated as a function of surfactant concentration. When the polymer is saturated with SDS (above its CMC) the NMR relaxation results indicate a dramatic slowing down of the motion of the polymer segments attached to the micelles, even though these represent only a small fraction of the total number of segments. However, the whole system is dynamic, and fast exchange occurs between free monomer and free and adsorbed micelles.

7 PARTICLE/EMULSION CHARACTERIZATION

In any colloidal dispersion it is essential to know the surface area and dispersed state of the system. For particle systems we have seen that the relaxation rate enhancement provides a monitor of the aggregation state (available surface area), but other NMR methods can be used. For example, the flow of solvent through a suspension can be used to infer the volume fraction of particles in the colloidal dispersion. In particular, NMR diffusion experiments have shown that the average diffusion coefficient of the solvent depends on the particle concentration and also on the structure of any adsorbed layer present.[30] Effectively the diffusion path is lengthened by the obstacle.

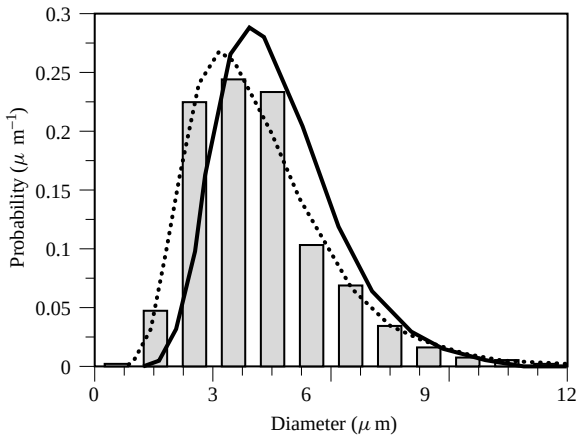

Figure 8 Size distribution curve obtained with a microscope for an emulsion containing 10% water. (- - - -) The best fit of the data with a log−normal size distribution; (—) the size distribution obtained by NMR

For emulsions, where it is difficult to measure the size and/or volume fraction, NMR diffusion offers many advantages over more conventional methods such as light scattering where the sample must be diluted. Recently, NMR diffusion has been extended to obtaining particle size distributions by choosing a specific distribution function to interpret the attenuation data.[31] Figure 8 shows data obtained from an NMR analysis, assuming a log−normal distribution and results from optical microscopy. The two approaches are in reasonable agreement, but of course the NMR approach can be used in many systems which are inaccessible to microscopy or any other optical technique

8 REFERENCES

1. C. R. Bowers and D. P. Weitkamp, *Phys. Rev. Lett.*, 1986, **57**, 2645.
2. C. R. Bowers, D. H. Jones, N.D. Kurur, J. A. Labinger, M. G. Pravica, and D. P. Weitkamp, *Adv. Magn. Reson.*, 1990, **14**, 249.
3. R. R. Hunter, *Foundations of Colloid Science*, Clarendon, Oxford, 1989, Vol. 1, p. 181.
4. E. Söderlind and P. Stilbs, *Langmuir*, 1993, **9**, 2024.
5. A. Carrington and A. D. McLachlan, *Introduction to Magnetic Resonance*, Harper & Row, New York, 1967, Chap. 12
6. T. Cosgrove, unpublished data.
7. L. Piculell, *J. Chem. Soc., Faraday Trans. 1*, 1986, **82**, 387.
8. J. B. Nagy, *Colloid. Surf.*, 1989, **35**, 201.
9. Y. E. Shapiro, *Usp. Khim.*, 1988, **57**, 1253.
10. J. S. Bradley, J. Millar, E. W. Hill, and M. Melchior, *J. Chem. Soc., Chem. Commun.*, 1990, 705.
11. J. S. Bradley, J. M. Millar, and E. W. Hill, *J. Am. Chem. Soc.*, 1991, **113**, 4016.
12. R. D. Newmark, M. Fleischmann, and B. S. Pons, *J. Electroanal. Chem.*, 1988, **255**, 325.
13. M. R. Böhmer, L. K. Koopal, R. Janssen, E. M. Lee, R. K. Thomas, and A. R. Rennie, *Langmuir*, 1992, **8**, 2228.
14. E. H. Söderlind and F. D. Blum, *J. Colloid Interface. Sci.*, 1993, **157**, 172.
15. Y. Yue, J. R. Rydall, and P. M. Macdonald, *Langmuir*, 1992, **8**, 390.
16. S. C. Kuebler and P. M. Macdonald, *Langmuir*, 1992, **8**, 397.
17. P. M. Macdonald, D. Staring, and Y. Yue, *Langmuir*, 1993, **9** 381.
18. P. M. Macdonald and Y. Yue, *Langmuir*, 1993, **9**, 1206.
19. G. J. Fleer, M. A. Cohen Stuart, J. M. H. Scheutjens, T. Cosgrove, and B. Vincent, *Polymers at Interfaces*, Chapman & Hall, London, 1993.
20. T. Miyamoto and H. J. Cantow, *Makromol. Chem.*, 1972, **162**, 43.
21. K. G. Barnett, T. Cosgrove, M. Cohen Stuart, D. S. Sissons, and B. Vincent, *Macromolecules*, 1981, **14**, 1018.

22. T. Cosgrove and K. Ryan, *Langmuir*, 1990, **6**, 136.
23. F. D. Blum, *Colloid. Surf.*, 1990, **45**, 361.
24. N. Zumbulyadis, J. M. O'Reilly, and D. M. Teegarden, *Macromolecules*, 1992, **25**, 3317.
25. G. P. van der Beek, M. A. Cohen Stuart, and T. Cosgrove, *Langmuir*, 1991, **7**, 327.
26. T. Cosgrove, T. M. Obey, and M. Taylor, *Colloid. Surf.*, 1992, **64**, 311.
27. J. P. Cohen Addad and A. Viallat, *Polymer*, 1986, **27**, 1855.
28. D. D. Miller, W. Lenhart, B. J. Antalek, A. J. Williams, and J. M. Hewitt, *Langmuir*, 1994, **10**, 68.
29. K. Chari, B. Antalek, M. Y. Lin, and S. K. Sinha, *J. Chem. Phys.*, 1994, **100**, 5294.
30. T. Cosgrove and P. C. Griffiths, *Colloid. Surf.*, 1994, in press.
31. B. Balinov, O. Urdahl, O. Soderman, and J. Sjoblom, *Colloid. Surf. Sec. A*, 1994, **82**, 173.

Biographical Sketches

Terence Cosgrove. *b* 1948. B.Sc., M.Sc., 1971, Ph.D., 1973, University of Manchester. D.Sc., 1991, University of Bristol. Junior fellow, 1973–75, lecturer, 1975–92, reader, 1992–present, University of Bristol UK. Approx. 101 publications. Research specialties: NMR relaxation and diffusion of polymers and surfactants in colloidal dispersions. Neutron scattering and reflection and Monte Carlo simulation in colloidal applications.

Timothy M. Obey. *b* 1961. B.Sc., 1982, University of Leeds. Ph.D., 1987, University of Bristol. Currently, senior research associate working with Dr T. Cosgrove, University of Bristol.

Ceramics

Raymond Dupree

University of Warwick, Coventry, UK

1	Introduction	1
2	Ceramics of SiC and Si_3N_4	1
3	Oxynitride Ceramics	1
4	Zirconia Ceramics	3
5	Related Articles	4
6	References	4

1 INTRODUCTION

Whilst most people have some idea of what constitutes a metal or a polymer, 'ceramic' is a less certain term. Dictionaries define ceramics in terms of pottery and earthenware; however, a more scientific definition is 'nonmetallic, inorganic materials that are made or used at high temperatures'. The range of ceramics is very broad and covers both very old and very new materials. This article will be mostly concerned with what might be termed advanced structural ceramics, since it is for these materials that NMR has been most useful in characterization and in providing structural information. (The ceramic superconductors are covered in ***High Temperature Superconductors***, and will not be discussed here.) These engineering ceramics are typically based on oxides or low-density covalently bonded materials such as silicon nitride or carbide. They are often compositionally complex and, in addition, many ceramics contain atoms of similar X-ray scattering factors such as silicon and aluminum, oxygen and nitrogen, or carbon and nitrogen, so that X-ray scattering techniques are of limited value for obtaining structural information. NMR is a particularly valuable investigative tool for ceramics because it is element- and site-specific. The chemical shift, which is the most often used NMR parameter to obtain structural information in these systems, is most sensitive to the local environment around the atom under investigation, i.e. the nature, number, and position of nearest-neighbor atoms with some sensitivity to the next neighbor shell but very little sensitivity to the structure beyond the fourth coordination sphere. Hence, NMR can be used to characterize poorly crystallized or glassy (see ***Amorphous Materials***) samples and to study the formation of the crystalline phase from the amorphous precursor. Many practical ceramics are solid solutions of different compounds and thus, at least in principle, compositionally disordered (i.e. a particular site can be occupied by, say, either a silicon or an aluminum atom); the distinct shifts observed for each 'local' configuration are very useful in determining this local order.

2 CERAMICS OF SIC AND SI_3N_4

The sensitivity of NMR to small structural changes in these systems is illustrated by the ^{29}Si, ^{13}C, and ^{15}N shifts of two important ceramic materials, Si_3N_4 (using ^{15}N-enriched samples for Si_3N_4) and SiC, given in Table 1. The different polymorphs of Si_3N_4 and polytypes of SiC all have readily distinguishable shifts (except the 6H and 15R polytypes, which differ only slightly in the stacking order). It can be seen that ^{15}N is a particularly sensitive probe: each nitrogen is bonded to three silicon atoms, [NSi_3], yet the different sites have shifts which cover ∼20 ppm in both Si_3N_4 polymorphs compared with only 2.1 ppm for the two silicon sites in α-Si_3N_4.[1–6]

Table 1 The ^{29}Si, ^{13}C, and ^{15}N Shifts of the Different Polytypes of SiC and Polymorphs of Si_3N_4[10]

β-SiC	4H SiC	6H SiC	15R SiC	α-Si_3N_4	β-Si_3N_4
δSi/ppm					
−17.2	−19.7	−14.3	−14.6	−49.0	−48.5
	−22.5	−20.4	−20.5	−47.1	
		−24.9	−24.9		
δC/ppm					
23.7	14.7	15.2	16.0		
	21.5	20.2	20.7		
		22.7	22.7		
δN/ppm				51.6	50.9
				53.4	68.4
				64	
				74.6	

Because of the differences in spectra of the different polymorphs and polytypes, the phase purity of a particular material (often very important in determining the final product of a reaction) can be readily determined. Figure 1 shows, as an example, the ^{29}Si resonance of two samples of Si_3N_4 which differed only slightly in preparation conditions. Whilst both spectra show two lines indicative of the presence of α-Si_3N_4, in the upper spectrum the lines are of unequal intensity, and careful inspection shows that the right-hand line is slightly shifted from the value expected for pure α-Si_3N_4, indicating that some β-Si_3N_4 is present. The amount can be estimated by subtraction to an accuracy of order 1%, which is difficult to achieve using other techniques. However, one problem with NMR investigations of spin $I = \frac{1}{2}$ nuclei in ceramic materials is their very long spin−lattice relaxation times, T_1, which can make experiments fairly time-consuming or difficult. Typically, in pure samples, T_1 of ^{29}Si, ^{13}C, and ^{15}N can all be >1000 s, and in fact in one experiment on SiC[4] no signal was observed even after allowing the sample to polarize in the magnet field for 96 h! For samples with more than one site it is therefore important for quantitative results to make sure that possible differences in T_1 of the different sites have been investigated.

3 OXYNITRIDE CERAMICS

A number of oxynitride ceramics, particularly the 'sialons', have practical applications as high-temperature engineering components. The simplest (in the compositional sense) of these 'sialons' are those based upon the β-Si_3N_4 structure into which alumina has been substituted. These β'-sialons have the general formula $Si_{3-x}Al_xO_xN_{4-x}$ ($0 \leq x \leq 2$). The ^{29}Si spectrum changes very little with alumina substitution even for $x = 2$, which seems to indicate that silicon is always surrounded by nitrogen.[1] If this is the case, then aluminum will have a range of tetrahedral AlO_yN_{1-y} ($y = 0, \ldots, 4$)

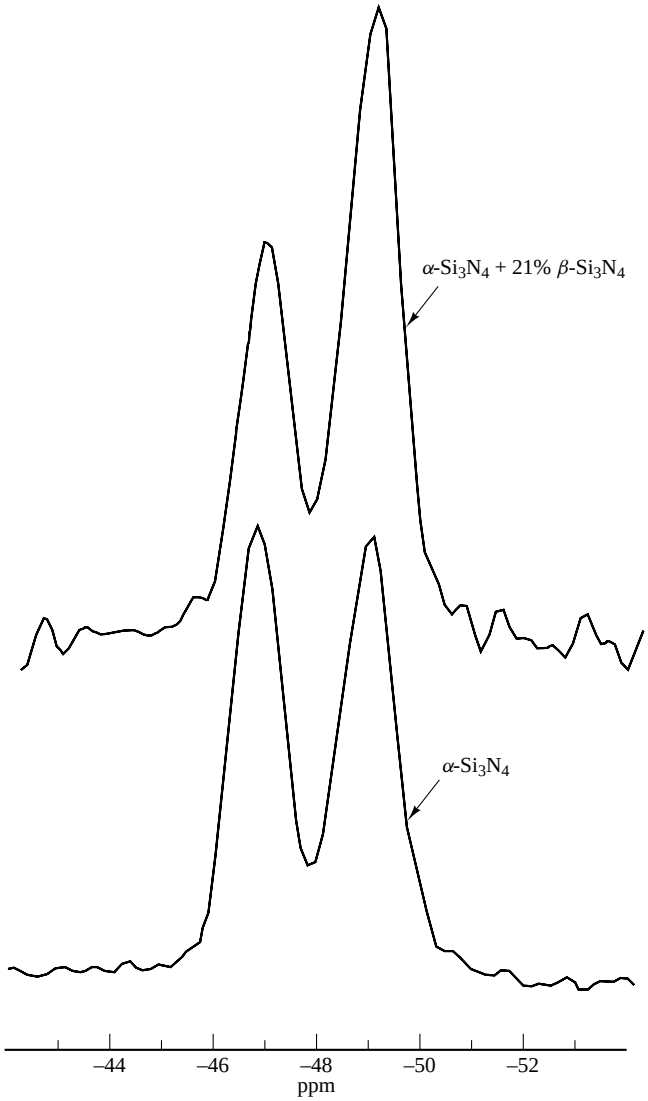

Figure 1 The ^{29}Si spectrum of two samples of Si_3N_4. The lower spectrum is pure α-Si_3N_4, while the upper is from a sample with 79% α-Si_3N_4 and 21% β-Si_3N_4

environments. In the case of mixed AlON tetrahedra, one can expect there to be a very large electric field gradient (EFG) at the aluminum site; furthermore, because of the different possibilities for the arrangement of the oxygen and nitrogen around the aluminum, there will be several different EFGs associated with each possibility. Thus, very broad ^{27}Al lines are to be expected. In fact in early experiments at 8.45 T it was found that because of the extreme breadth of the line only a small fraction of the ^{27}Al was being observed, the fraction increasing with oxygen content because more AlO_4 tetrahedra which have relatively smaller EFGs are formed.[7] Later work at 11.7 T using a probe with a short ($\sim$2 μs) dead time and fast (16 kHz) spinning was able to observe more of the aluminum present. A broad line from AlO_4 tetrahedra at 68 ppm for $x = 2$ ($SiAl_2O_2N_2$) shifts to $\sim$75 ppm, and further broadens as x decreases. The peak at $\sim$75 ppm was assigned to AlO_3N.[8] A small shoulder at 89 ppm, probably from AlO_2N_2, is also visible for all samples. It should be noted that if the aluminum and silicon were randomly distributed, then AlO_4

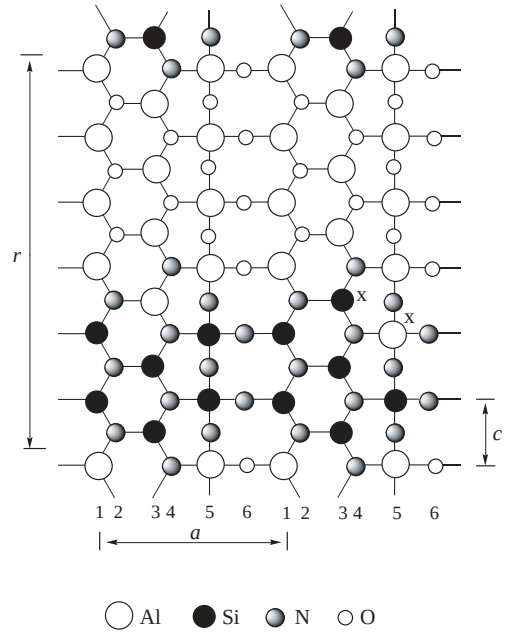

Figure 2 Schematic representation of the local structure of β'-sialon with $x = 2$ (i.e. Si_{3-x} $AI_xO_xN_{4-x}$ or $SiAl_2O_2N_2$). The atoms in columns 1, 4, and 6 are above the plane of the paper, those in column 3 below, with columns 2 and 5 in the plane. The repeat unit along c is between the lines r. x are defects within the layers. (Adapted from Dupree et al.[7])

would not be dominant even at $x = 2$, and mixed tetrahedra for ^{29}Si would be expected. When combined with the ^{29}Si data the ^{27}Al results strongly indicate a 'microdomain' type of structure in this material. A schematic diagram of this is shown in Figure 2. For small x the thickness of the AlO_4 'block' is reduced, leading to a rapidly increasing amount of mixed AlON tetrahedra.

Many practical oxynitride ceramics require sintering aids in their manufacture, and these react with the SiO_2 found on the surface of the Si_3N_4 grains, forming glassy intergranular phases. Study of these phases and their crystallization products is important in achieving an understanding of the limiting factors which determine the high-temperature properties of these ceramics. One popular aid in sintering is Y_2O_3, and a number of compounds formed in the Y–Si–Al–O–N have been studied by NMR, as has the crystallization behavior of the glasses formed in this system. Initial measurements on ^{29}Si in this and related systems have determined the shifts of the various compounds, such as Y_2SiAlO_5N, $YSiO_2N$, etc., which are formed and helped to delineate the shift ranges of the SiO_xN_{1-x} ($0 \leq x \leq 2$) tetrahedra shown in Figure 3.[9,10] Note that, as with SiO_4 tetrahedra where there are different numbers of bridging oxygens, there is considerable overlap in the shift range of each local structural unit so that the number of oxygen and nitrogen neighbors cannot be unambiguously determined by the shift position alone. For a proper understanding of the local structure, full multinuclear studies are needed, and ^{15}N on enriched samples has been quite helpful in clarifying several issues. In general, it is found that when nitrogen is coordinated to three silicon atoms, [NSi_3], the shifts are typically 40–80 ppm, whereas when coordinated to two silicon atoms, [NSi_2], it resonates in the range 90–160 ppm.[5] When a glass of the composition

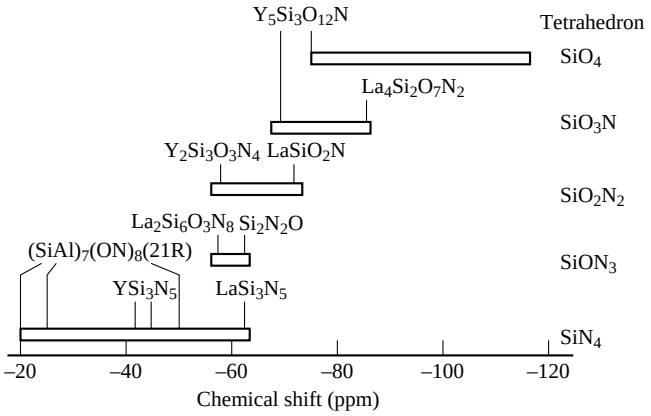

Figure 3 Silicon-29 shift ranges in oxynitrides showing the effect of differing numbers of oxygen neighbors. (Adapted from Dupree et al.[10])

$Y_{1.04}Si_{1.27}Al_{1.27}O_{4.8}N_{0.8}$ was crystallized at 1100°C the ^{29}Si spectrum showed that six different compounds containing silicon were present including β'-sialon and Si_2N_2O, both of which are also evident in the ^{15}N spectrum. The ^{15}N spectrum also showed a broad peak at ∼148 ppm and a sharp peak at 285 ppm. The former was shown to be from metastable Y_2SiAlO_5N, where nitrogen coordination would be either $[NSi_2]$ or [NSiAl], by annealing at 1250°C when both the ^{29}Si signal from this phase and the ^{15}N line at 148 ppm were markedly reduced. The peak at 285 ppm was identified as nitrogen substituted into yttrium aluminum garnet, $Y_3Al_5O_{12}$ (YAG), which is a major phase present. Analysis with TEM-EDAX showed that in the crystalline YAG approximately 14% of the aluminum was replaced by silicon, and it is likely that nitrogen will concurrently substitute for oxygen to maintain charge balance. The shift of this peak is much larger than for $[NSi_2]$ sites, so the most likely local environment is a nitrogen coordinated to a single silicon atom at the tetrahedral site in YAG and a vacancy at the octahedral aluminum site, i.e. [NSi*].

4 ZIRCONIA CERAMICS

Zirconia (ZrO_2) is an important high-toughness engineering ceramic which in its practical form is usually a mixture of several different crystallographic phases and/or is stabilized by some substituent such as yttrium or magnesium. Neither ^{91}Zr nor ^{17}O (unless enriched) can be regarded as ideal NMR probes, both have spin $I = \frac{5}{2}$, and whilst the natural abundance of ^{91}Zr at 11.2% is enough for NMR experiments (the sensitivity is 2.9 times ^{29}Si) the quadrupole moment is quite large such that in noncubic environments the linewidth is much too great for narrowing techniques such as MAS or DOR to be effective. Oxygen-17 has a much smaller (10^{-2}) quadrupole moment than ^{91}Zr, such that in an ionic environment such as ZrO_2 the EFG is quite small, the quadrupole coupling constant χ ($= e^2qQ/h$) being less than 3 MHz. In this case, despite the natural abundance of ^{17}O being only 0.037%, it is possible (with considerable averaging) to obtain spectra from unenriched materials that clearly distinguish between the tetragonal phase with one oxygen site ($\delta \approx 380$ ppm), the monoclinic phase with two sites ($\delta \approx 325$ and 401 ppm), and the cubic phase with a broad line at ∼375 ppm from the disorder due to vacancies in the structure.[11] Natural abundance ^{17}O experiments are time-consuming, however, and of limited practicality for day-to-day examination of these materials.

The phases of ZrO_2 zirconium have either seven (orthorhombic and monoclinic) or eight (cubic and tetragonal) oxygen neighbors, and thus the ^{91}Zr chemical shift difference between these phases is likely to be small. However, because of differences in local symmetry the ^{91}Zr EFG and the asymmetry parameter, η, are likely to be very different, and thus the phases can be distinguished by their quadrupolar lineshapes. The very large linewidth (∼500 kHz in a 9.4 T field) means that the spectrum is best acquired on a static sample point by point. An advantage of a static NMR experiment is that the sample does not have to be powdered, which on this type of material may change the relative phase content via the phase transformation (tetragonal → monoclinic, tetragonal → orthorhombic). The spectra of cubic, monoclinic, and a fired, partially stabilized zirconia (PSZ), acquired at 25 kHz intervals using a spin echo sequence, are shown in Figure 4.[12] In the cubic phase (which contains ∼13.5 mol% MgO for stabilization) the presence of

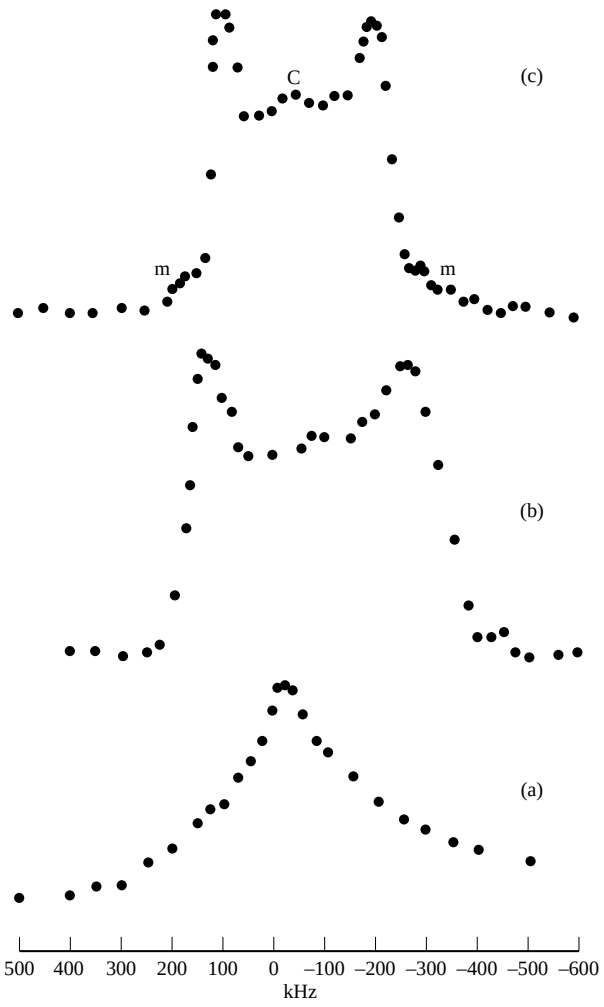

Figure 4 The ^{91}Zr spectra of several forms of ZrO_2. (a) Magnesia-stabilized cubic zirconia (13.5 mol% MgO), (b) monoclinic ZrO_2, and (c) tetragonal ZrO_2 (MS grade MgPSZ). The minor peaks are from residual monoclinic (m) and cubic (c) phases. (Adopted from Bastow et al.[12])

oxygen vacancies, needed for charge balance, means that there will be a distribution of quadrupolar coupling constants; thus, a broad featureless line is observed and any structure is lost. The monoclinic phase is well fitted by a line with χ = 23.1 MHz and η = 0.1, whilst the spectrum of MS grade PSZ is narrower (χ = 19.1 MHz, η = 0), showing that it is mostly tetragonal with some monoclinic and cubic phase material present.

5 RELATED ARTICLES

Amorphous Materials; Inorganic Solids.

6 REFERENCES

1. R. Dupree, M. H. Lewis, G. Leng-Ward, and D. S. Williams, *J. Mater. Sci. Lett.*, 1985, **4**, 393.
2. G. R. Finlay, J. S. Hartmann, M. F. Richardson, and B. L. Williams, *J. Chem. Soc. Chem. Commun.*, 1985, 159.
3. J. R. Guth and W. T. Petuskey, *J. Phys. Chem.*, 1987, **91**, 5361.
4. J. S. Hartman, M. F. Richardson, B. L. Sherriff, and B. G. Winsbarrow, *J. Am. Chem. Soc.*, 1987, **109**, 6059.
5. R. K. Harris, M. J. Leach and D. P. Thompson, *Chem. Mater.*, 1990, **2**, 320.
6. D. Kruppa, R. Dupree, and M. H. Lewis, *Mater. Letts.*, 1991, **11**, 195.
7. R. Dupree, M. H. Lewis, and M. E. Smith, *J. Appl. Cryst.*, 1988, **21**, 109.
8. M. E. Smith, *J. Phys. Chem.*, 1992, **96**, 1444.
9. R. Dupree, M. H. Lewis, and M. E. Smith, *J. Am. Chem. Soc.*, 1988, **110**, 1083.
10. R. Dupree, S. C. Kohn, C. M. B. Henderson, and A. M. T. Bell, *NATO ASI Ser.*, 1992, **386**, 421.
11. T. J. Bastow, M. E. Smith, and S. N. Stuart, *Chem. Phys. Lett.*, 1992, **191**, 125.
12. T. J. Bastow and M. E. Smith, *Solid State NMR*, 1992, **1**, 165.

Biographical Sketch

Raymond Dupree. *b* 1937. B.Sc., Ph.D., University of Exeter, UK. Assistant lecturer, University of Exeter, 1963–66, lecturer and currently Professor, University of Warwick, UK, 1966–present. Sabbaticals at AT&T Bell Laboratories, USA, Oregon State University, USA, University of California at Berkeley, USA, and University of California at Santa Barbara, USA. Approx. 140 publications. Current research specialties: the application of NMR to structurally and compositionally disordered materials, including glasses, ceramics, and minerals, NMR in oxide superconductors.

Ceramics Imaging

David G. Cory

Massachusetts Institute of Technology, Cambridge, MA, USA

1	Introduction	1
2	An Overview of Imaging Methods	2
3	Imaging of Green-State Ceramics	3
4	Imaging of Sintered Ceramics	3
5	Imaging of Fluids in Ceramics	4
6	Local Measurements	4
7	Conclusions	4
8	Related Articles	5
9	References	5

1 INTRODUCTION

NMR imaging of ceramics provides a wide range of opportunities for microscopic imaging of both liquids[1–3] (***Image Formation Methods***) and solids[4–6] (***Imaging Techniques for Solids and Quasi-Solids***). Techniques for imaging macroscopic samples of liquids are well developed and finding wide application in medical imaging. Techniques that are appropriate at the microscopic scale and for solid objects are only now being developed, however. Part of the reason these areas lag behind medical imaging is due to difficulties associated with the broad linewidth of solids, the low sensitivity of small samples (see also ***NMR Microscopy: Resolution***), the large signal attenuation from molecular diffusion in a strong magnetic field gradient[7] (see also ***Diffusion and Perfusion in MRI***), and the susceptibility shifts from small heterogeneities within a sample[8] (see also ***Susceptibility and Diffusion Effects in NMR Microscopy***). The underlying cause, however, is the widespread realization that many of the most pressing imaging applications are in the medical arena. This difference is apparent in the way new techniques are being developed; most techniques for medical imaging are developed for specific applications, while many of the developments in solid state imaging and microscopy are focused on a challenging NMR problem. Structural ceramics, however, present a set of important real-world problems in processing that require imaging techniques, both to characterize the general processing conditions and for nondestructive evaluation (NDE) of critical components.[9,11]

Although high performance structural ceramics possess superior mechanical and chemical properties, they are subject to catastrophic failure, and it is this failure mechanism that limits their applicability. These failures arise from defects in the sintered ceramic. A goal of ceramic imaging is to detect those defects that are larger than a critical size of approximately 100 μm. It is interesting to contrast ceramics to polymers, where imaging is primarily directed towards characterizing conditions of processing. Even though most imaging studies of solids are of organic polymers (see also ***Polymer MRI***), there are extremely few applications where the costs of MRI NDE methods could be supported by a polymer product. In ceramics, however, a piece can be costly to manufacture and it may be critical that it does not fail. Under these conditions, it is reasonable to consider using MRI as a method for NDE.

Ceramics are formed by complex thermal and chemical processing. First, ceramic powder is combined with an organic binder, which is mixed to form a solid green-state ceramic. These green-state ceramics can then be shaped prior to sintering. Often the sintered ceramic is nearly the finished product, and only a final finishing or machining step is required. The binder, or mixture of binder and plasticizer, has as its primary component a waxy organic polymer. These materials have T_2 values for ^{1}H of a few to 10 ms at room temperature and T_1 values of a few hundred milliseconds. The green-state ceramic can therefore be easily characterized by NMR techniques that, while not of high resolution, are certainly not in the solid state regime. After the sample is sintered, the ^{1}H content of the ceramic is minimal, and heteronuclear solid state techniques must be employed (see also ***Ceramics***).

The successful manufacture of a structural ceramic requires that the inevitable flaw content be controlled. These flaws include cracks, voids, inclusions, and density variations. The idea of NDE in ceramic processing is to intercept defective pieces early in the manufacturing process, since each successive stage tends to be more costly. A green-state ceramic is relatively inexpensive and easily formed, but the energy costs of densification and sintering the material are quite significant. Finally, the labor costs associated with finishing a complex part can be very high. Ideally then there should be at least two NDE steps, one of the green-state material and a second of the sintered material. Since the NMR properties of the ceramic are very different in these two states, the imaging methods will also vary.[12]

An obvious question is why employ NMR to characterize the sintered material rather than X-ray computed tomography (CT) methods? The sintered sample is a complex mixture; in addition to the ceramic matrix there may be ceramic fibers, or whiskers added to the material to improve the strength and prevent catastrophic failure, and one needs to distinguish between sintered ceramic and agglomerates of additives, as well as detecting voids and variations in density. The material is therefore too complex for simple analysis by X-ray CT. Energy selected X-ray techniques are applicable, but these methods are not widely available. With NMR there is a great potential for chemical selectivity, particularly with regard to many of the quadrupolar nuclei that are used in ceramics, and it is the information content that drives the continuing development of NMR materials-imaging techniques.

Imaging techniques are not restricted to observing the ceramic matrix directly since the ceramics contain voids (both in the sintered and in the green state), and these voids may be filled with fluids which are observable via liquid state techniques.[13–15] Additionally, the binder in the green state can be swelled by a solvent that then facilitates the imaging of the binder distribution, by reducing its linewidth, or can be observed itself. There are similarities between imaging liquids in ceramics and oil core imaging (see also ***Oil Reservoir Rocks Examined by MRI*** and ***Well Logging***), but ceramics have the benefit of magnetic purity, while oil cores often suffer from large concentrations of magnetic material.

Instead of measuring an image to obtain the absolute concentration of a species throughout the sample, it is occasionally

desired to record statistical information regarding the entire sample, such as the porosity, the pore size distribution, or the tortuosity.[16] These quantities and others can be measured via a variety of diffusive scattering techniques (see also ***Diffusion in Porous Media***). Since these measurements are average properties of the entire sample, the sensitivity is good, and spatial information may be obtained at much finer resolution than is possible with imaging methods.

One difficulty that has yet to be adequately addressed in ceramic imaging (or in materials imaging in general) is that of sample size. For solid state methods, it is usually the case that the rf field needs to be sufficiently large to dominate the variation of the local field across the sample. Therefore the samples tend to be small, and almost all solid state imaging has been performed on samples of less than 1 cm in diameter. A similar problem is encountered in microscopy where the sample is constrained to be sufficiently small that effective magnetic coupling of the spin response and the receiver is maintained. However, the critical size of defects does not scale with the sample size, and so, regardless of the size of the piece, image resolution needs to be at the sub-100 μm scale.

Not all ceramics are synthetic; bone and teeth have many properties in common with the synthetic structural ceramics discussed here, and these have also been studied.[17,18]

2 AN OVERVIEW OF IMAGING METHODS

Much of the power of NMR spectroscopy and imaging arises from the flexibility to tailor an experiment to the sample and the information desired. Therefore, there is a broad spectrum of methods that may be chosen to optimize the resolution, sensitivity, and contrast of an image (see also ***Image Formation Methods***). Here the various methods used in imaging ceramics will be introduced. Ceramic samples range from liquids in porous materials through waxy solids to rigid solids, and the techniques used in imaging are similarly diverse.

Nearly all imaging experiments involve a precession period in the presence of a magnetic field gradient. Since the normally dominant Zeeman interaction is directly proportional to the magnetic field strength, this precession labels the spins according to their location within the gradient field. It is useful to distinguish between encoding by phase and by frequency. Data are not acquired until the end of the phase encoding period, and so it is only the overall phase angle of spin precession that is observable. In frequency encoding, data are acquired continuously, and the periodicity of data acquisition allows the frequency of spin precession to be determined. The criteria for resolution and sensitivity are different for these two approaches. For frequency encoding, the resulting image is a convolution of the spin density and the NMR spectrum, so the NMR linewidth acts as the system point-spread function and limits the obtainable resolution, the resolution being given by the linewidth divided by the gradient strength. If the gradient is increased to obtain a higher resolution, the frequency spread of the resolution element is broadened and the experimental sensitivity is correspondingly reduced. In phase encoding (which we will limit here to constant-time methods),[19] the NMR linewidth is decoupled from the image representation, and a true spin density can be measured. This result is a consequence of being at high field where the internal spin Hamiltonians and the gradient Hamiltonian commute. The overall spin evolution is then simply the sum of the evolution due to the internal interactions and that due to the gradient. In a constant-time experiment the internal Hamiltonians are constant and the spin evolution due to them is reproducible. The linewidth still limits the sensitivity, however, since the NMR signal decays over the time period of the spatial encoding.

One approach to obtaining higher resolution is to increase the gradient strength and accept the loss in sensitivity. An appealing alternative is to use line-narrowing methods that can recover both sensitivity and resolution[20] (see also ***Line Narrowing Methods in Solids Imaging of Wide-Band Systems by Line-Narrowing Methods***). A good line-narrowing method may reduce the linewidth by a factor on the order of 1000, while preserving the full sensitivity. For an imaging experiment, the resolution is increased as the reduction in the linewidth, and the sensitivity also increases due to the reduction in the bandwidth.

There are two general classes of coherent averaging techniques for reducing the NMR linewidth: those that manipulate the spin state of the system through a series of rf pulses (see also ***Average Hamiltonian Theory***); and those that manipulate the spatial orientation of the spin system so as to average anisotropic contributions to the linewidth (see also ***Magic Angle Spinning***). The two approaches may also be applied simultaneously (see also ***CRAMPS***). All three methods have been applied to solid state imaging.[5] These coherent averaging techniques are, however, often complex to apply, and the result is somewhat sample dependent. Coherent averaging of internal interactions reduces the linewidth by modulating effective spin interactions such that the time average is either reduced or zero. The success of these methods depends on the accuracy of the modulation scheme and on the absence of competing modulations (particularly those from random molecular motions). Coherent averaging is very useful where there is little molecular motion (such as for engineering plastics, where these methods have been widely applied), or where there is high-frequency motion of limited angular displacements (such as in elastomers). One can expect that imaging of sintered ceramics will greatly benefit from line narrowing,[21,22] but the case is not so clear for the waxy binder of green-state ceramics.

There are a variety of contributions to the solid state linewidth (see also ***Internal Spin Interactions and Rotations in Solids***). Most coherent averaging methods have aimed at removing homonuclear dipolar coupling (particularly for ^{1}H imaging), chemical shift anisotropies, inhomogeneous interactions, and all of the above via time-suspension cycles. Heteronuclear line narrowing experiments have also been performed with broadband ^{1}H decoupling. In the special case of half-integer quadrupolar nuclei, which have $m = -\frac{1}{2}$ to $m = +\frac{1}{2}$ transitions, the same methods that sharpen homonuclear dipolar couplings will remove the second-order quadrupolar broadening.[22] The first-order quadrupolar terms do not broaden this transition (see also ***Quadrupolar Nuclei in Solids***).

Nearly every ceramic imaging study requires some specialized instrumentation, either in the form of strong gradients, or as a setup for coherent averaging methods. Magnetic field gradients of a few tesla per meter are difficult to achieve over large volumes, typically have long switching times and large induced

eddy currents, as well as being difficult to contain mechanically, and to cool. For these reasons back-projection methods are often used to avoid the necessity of gradient switching (see also ***Projection–Reconstruction in MRI***). The stray field imaging experiment[23] is a variation of the large gradient back-projection method where each one-dimensional projection of the spin density is mapped out successively while translating the sample through the strong gradient which exists in the fringe field of a high field magnet. The resolution is dependent on the excitation bandwidth of the experiment and can be quite high, although the sensitivity of the experiment is generally low. This is an incoherent, constant-time imaging technique. Line-narrowing techniques typically require only very modest gradient strengths, but often need better than average rf control and setup, and for optimal results extremely short (5 μs) gradient pulses.[24] Since the spin state of the system is being modulated, the gradient Hamiltonian no longer commutes with the effective internal Hamiltonians. Therefore, the gradient must be carefully applied to avoid the gradient interfering with the line narrowing.

3 IMAGING OF GREEN-STATE CERAMICS

NMR imaging techniques are being actively developed in the area of nondestructive evaluation of green-state ceramics.[25–28] The goal of the method would be to acquire a correct spin density image of the binder distribution throughout a modest sized sample to help detect any nonuniformity in the binder distribution and to locate cracks, voids, and other defects.

For the purposes of ^{1}H NMR, green-state ceramics are waxy solids, and far from ideal samples. They have too little motion to exhibit sharp resonances, and yet sufficient motions that coherent averaging schemes tend to fail. Examples of binder material include low-molecular-weight poly(ethylene oxide), poly(vinyl alcohol), and poly(ethylene terephthalate). Although waxy materials are often compared to elastomeric materials, there is a large difference in the NMR properties. Elastomers tend to have restricted molecular motions, which are fast on the NMR timescale. Modulation rates in coherent averaging methods tend to be in the region of kilohertz to a few tens of kilohertz. Molecular motions in elastomers are significantly faster than this. Waxy materials tend to have less well-defined motions that have a broad frequency spectrum with significant contributions in the appropriate range for coherent averaging. The residual linewidth in an elastomer arises from an incomplete averaging of internal Hamiltonians based on fast but restricted motions. The linewidth in waxy materials arises from an incomplete averaging based on both restricted motions and slower motions. Elastomers are therefore easily line narrowed since in the NMR experiment the residual Hamiltonians from the fast motions are static and of modest size. Waxes are more difficult to line narrow since the residual interactions are time dependent.

There are three apparent options to recording high-resolution images of green-state ceramics:

1. Use large magnetic field gradients with the sample at room temperature to achieve the desired resolution at a sacrifice of sensitivity.
2. Heat the sample until the line sharpens and use liquid state techniques.
3. Cool the sample to freeze out molecular motions and then use solid state techniques.

The use of large gradients has the advantage of least impact on the sample, as well as of avoiding artifacts. Heating the sample must be performed with care to stay below the temperature where sample integrity is lost. Reducing the linewidth increases the sensitivity, but note that the entire binder may not narrow. Perhaps only a fraction (such as a plasticizer, or the low-molecular-weight cut) will narrow, and then the image will not yield a true representation of the spin density. Cooling the sample and employing solid state techniques has the advantage of preserving the true spin density; however, the spin–lattice relaxation time is also dependent on molecular motions and may lengthen appreciably. Also care must be taken to ensure that the binder does not phase separate or crystallize.

To date the preferred methods have been to employ modestly strong gradients, but the resolutions required for NDE applications have not been achieved. The progress in this area has been recently reviewed.[9] Some examples are two-dimensional (2D) images of a 2.54 cm diameter green-state ceramic with both Fourier imaging and constant-time techniques.[25] The sample contained 15.5% by weight of binder, and using a gradient of 0.033 T m^{-1} with an encoding time of 1.98 ms; a resolution of 552 μm was achieved in the Fourier imaging experiment and of 326 μm in the constant-time experiment. The Fourier image was acquired in 25 min and, as expected, the constant-time experiment took much longer, requiring 220 min. Back-projection techniques were employed[11] to acquire images of a 2.5% by weight green-state ceramic with 0.35 T m^{-1} gradients at a resolution of 175 μm.[3] However, the data required a collection time of 18 h. These experiments do as much to point out the remaining difficulties as they do to show the promise of the method. Clearly, much work is still required to increase both the resolution and the sensitivity of the methods.

4 IMAGING OF SINTERED CERAMICS

Probably the most underexplored area of ceramic imaging is of the final sintered piece. Since the proton content of the sintered ceramic is extremely low, many of the methods for solid state imaging that have been developed for proton-rich solid polymers are not directly applicable. To characterize the sample by direct observation of the solid ceramic matrix, the available nuclei are predominantly Al, Si, B, N, and P. It is expected that the sensitivity will be lower than seen in ^{1}H images of bulk solid polymers due to a combination of low spin concentration, low magnetogyric ratios, and quadrupolar interactions. For now, both Si and N can be excluded on sensitivity grounds: ^{29}Si has low abundance and has unacceptably long T_1 values in the solid state, and ^{15}N has low abundance and a low magnetogyric ratio. While ^{14}N is reasonably abundant, it has spin = 1 with an appreciable quadrupole coupling constant and a large chemical shift anisotropy.

The other three nuclei, ^{27}Al, ^{11}B, and ^{31}P, are all reasonable candidates for solid state imaging experiments, and some preliminary results have been reported for each.[29,30]

Phosphorus-31 is 100% abundant with spin = $\frac{1}{2}$, so where it is present in the ceramic the imaging approach is reasonably

straightforward. The linewidth is dominated by homonuclear dipole–dipole couplings and chemical shift anistropy, so here techniques very similar to those used for multiple-pulse proton imaging will apply. Phosphorus-31 images have been recorded of biologically significant solid calcium phosphates where there was an appreciable proton content.[29] The ^{31}P linewidth was dominated by ^{1}H dipolar interactions, a facet which was used to increase the sensitivity via cross polarization and then decoupled during acquisition to reduce the linewidth. An important feature of the cross polarization experiment is that the recycle time is dependent on the T_1 of ^{1}H and not on the longer T_1 of ^{31}P.

Aluminum-27 and ^{11}B are both half-integer quadrupolar nuclei and hence both have an $m = -\frac{1}{2}$ to $m = +\frac{1}{2}$ transition which can be conveniently observed. These are attractive nuclei for imaging since the central transition is not broad compared to the spectral width of broadcast and receive channels of solid state spectrometers, and can be further sharpened by multiple pulse methods.[22] Another virtue of the quadrupole interaction is that it leads to short T_1 values, so the experiment can be efficient in terms of data acquisition. Strong gradient methods have been used to record images of phantoms using both of these nuclei,[30] including a 2D ^{11}B image of a borosilicate glass sample (6 mm field of view) at a resolution of 520 μm using a gradient of 1.55 T m^{-1} and an experimental time of 133 min. For a similar phantom composed of γ-alumina, an image of ^{27}Al was obtained at the same resolution in 90 min with a gradient of 2.25 T m^{-1}.

The apparent nutation frequency of the central transition of half-integer quadrupole nuclei is dependent on the strength of the quadrupole coupling constant (see also ***Nutation Spectroscopy of Quadrupolar Nuclei***), and hence the nutation frequency can be used to introduce contrast into an image. In this way pure images of the alumina and aluminate fractions were obtained from a composite phantom.[30]

5 IMAGING OF FLUIDS IN CERAMICS

Fluids can be introduced into either sintered ceramics or green ceramics. In the case of sintered materials the fluid may be vacuum impregnated and the fluid imaged to look for defects. In the case of green ceramics, the fluid can either swell the binder, or be introduced into the pore structure of the material. It has been suggested that the fluid can be removed for NDE, although this addition of extra processing steps is undesirable. The spin density image allows one to characterize the porosity of the material and to easily find defects into which the fluid can flow. A perhaps surprising result is that the image of the fluid can provide information about defects that are inaccessible to the fluid, based on local variations in the bulk magnetic susceptibility (see also ***Susceptibility and Diffusion Effects in NMR Microscopy***). The variation in the bulk magnetic susceptibility throughout a heterogenous sample implies that, when placed in a magnetic field, the magnetic field inside the sample will be spatially varying. The result is a complex local distortion of the magnetic field in the vicinity of boundaries. If a defect in a ceramic material has a susceptibility that is significantly different than that of the bulk of the sample, the presence of the defect will appear as a resonance shift for spins that are adjacent but not in direct contact with the defect. In this fashion voids that are not filled with fluid can still be detected via liquid state imaging. In favorable cases even agglomerates of fibers or other fillers may be detected.

Areas of susceptibility variations introduce distinct image distortions that are readily identifiable. It is also quite straightforward to test for their presence either by reorienting the sample in the field and repeating the experiment, or by employing an imaging experiment that is insensitive to susceptibility artifacts, such as constant-time imaging and refocused gradient imaging experiments.

Liquid state imaging methods have been used to follow the drying of slipcasting, and the uniformity of the resulting compact.[31] Benzene that was vacuum impregnated into a green ceramic has been imaged in a matter of a few minutes at a resolution of 380 μm $\times$ 350 μm for a 2 mm thick slice.[12] From these images the overall porosity could be observed along with some rather large defects that were intentionally introduced into the sample. These are relatively early results that have not been revisited and the low resolution was a result of the small gradient strengths employed at that time.

6 LOCAL MEASUREMENTS

Imaging allows the absolute spatial properties of a selected spin system to be recorded at a resolution of up to approximately 10 μm by spreading the resonance line with a sufficiently strong gradient such that each volume element is resolved from its neighbors. Much below about 10 μm, diffusional losses and the limited number of spins in a selected cubic volume element greatly reduce the signal intensity. Therefore, absolute spatial information is not, presently, available at this and higher resolutions. Average local geometries may be characterized, however, by observing the temporal evolution of spin transport of all spatially distributed mobile spins simultaneously, thus avoiding the signal-to-noise limit on resolution. The resolution limits of these studies are only dependent on the gradient strength, the diffusion coefficient and relaxation times. For many samples the lower limit to resolution may be extended a factor of 100 below that of imaging methods. Some examples of the types of information that are available from these spin transport studies include: (1) self-diffusion constants, (2) compartment sizes and distributions, (3) eccentricities and volumes of compartments, (4) fluxes through semipermeable membranes, and (5) the existence and nature of wall relaxation. These quantities may be of interest in characterizing the packing of ceramic powders[16] (see also ***Diffusion in Porous Media***).

7 CONCLUSIONS

While much work still remains to be done, high performance structural ceramics is an area that can clearly benefit from techniques of high resolution NMR imaging. The problems that remain are to devise methods that increase the sensitivity and resolution for waxy solids, and to devise methods of studying relatively large solid samples while preserving high resolution.

8 RELATED ARTICLES

Average Hamiltonian Theory; Ceramics; CRAMPS; Diffusion and Perfusion in MRI; Diffusion in Porous Media; Image Formation Methods; Imaging Techniques for Solids and Quasi-Solids; Internal Spin Interactions and Rotations in Solids; Line Narrowing Methods in Solids; Imaging of Wide-Band Systems by Line-Narrowing Methods; Magic Angle Spinning; NMR Microscopy: Resolution; Nutation Spectroscopy of Quadrupolar Nuclei; Oil Reservoir Rocks Examined by MRI; Polymer MRI; Projection–Reconstruction in MRI; Quadrupolar Nuclei in Solids.

9 REFERENCES

1. P. T. Callaghan *Principles of NMR Microscopy*, Clarendon, Press, Oxford, 1991.
2. P. Mansfield and E. L. Hahn, *NMR Imaging*, The Royal Society, London, 1990.
3. B. Blümich and W. Kuhn (ed.), *Magnetic Resonance Microscopy*, VCH, Weinheim, 1992.
4. P. Jezzard, J. J. Attard, T. A. Carpenter, and L. D. Hall, *Prog. NMR Spectrosc.*, 1991, **23**, 1.
5. D. G. Cory, *Annu. Rep. NMR Spectrosc.*, 1992, **24**, 88.
6. P. Blümler and B. Blümich, *NMR Basic Principles Prog.*, 1993, **30**, 209.
7. C. D. Eccles and P. T. Callaghan, *J. Magn. Reson.*, 1986, **68**, 393.
8. P. T. Callaghan and C. D. Eccles, *J. Magn. Reson.*, 1987, **71**, 426.
9. W. A. Ellingson, P. S. Wong, S. L. Dieckman, J. L. Ackerman, and L. Garrido, *Ceram. Bull.*, 1989, **68**, 1180.
10. J. L. Ackerman, L. Garrido, J. R. Moore, B. Pfleiderer, and Y. Wu, in *Magnetic Resonance Microscopy*, ed. B. Blümich and W. Kuhn, VCH, Weinheim, 1992, p 237.
11. N. Gopalsami, S. L. Dieckman, W. A. Ellingson, R. E. Botto, P. S. Wong, H. C. Yeh, and J. P. Pollinger, Nuclear Magnetic Resonance Imaging of Green-State Ceramics Report ANL-90/27, Argonne National Laboratory, Argonne, IL 1990.
12. J. L. Ackerman and W. A. Ellingson, Advanced Tomographic Imaging Methods for the Analysis of Materials, *Materials Research Society Symposium Proceedings*, Materials Research Society, Pittsburgh, 1991, Vol. 217.
13. K. Hayashi, K. Kawashima, K. Kose, and T. Inouye, *J. Phys. D.*, 1988, **21**, 1037.
14. W. A. Ellingson, J. L. Ackerman, L. Garrido, J. D. Weyand, and R. A. DiMilia, *Ceram. Eng. Sci. Proc.*, 1987, **8**, 503.
15. J. L. Ackerman, L. Garrido, W. A. Ellingson, and J. D. Weyand, in *Proceedings of the Joint Conference on Nondestructive Testing of High Performance Ceramics, Boston, MA, 25–27 August 1987*, ed. A. Vary and J. Snyder, American Ceramic Society, p. 88.
16. L. Garrido, J. L. Ackerman, and B. Pfleiderer, *Ceram. Eng. Sci. Proc.*, 1991, **12**, 2042.
17. J. L. Ackerman, Personal communications, MGH, 1994.
18. K. Zick, Personal communications, Bruker Instruments, Inc., 1993.
19. S. Emid and J. Creyghton, *Physica*, 1985, **125B**, 81.
20. P. Mansfield and P. Grannel, *Phys. Rev. B.*, 1975, **12**, 3618.
21. M. S. Conradi, *J. Magn. Reson.*, 1991, **93**, 419.
22. J. Listerud, S. W. Sinton, and G. P. Drobny, *Anal. Chem.*, 1989, **61**, 23.
23. A. Samoilenko, D. Yu Artemov, and L. Sibel'dina, Russ, *J. Phys. Chem.*, 1987, **61**, 1623.
24. J. B. Miller, D. G. Cory, and A. N. Garroway, *Chem. Phys. Lett.*, 1989, **164**, 1.
25. L. Garrido, J. Ackerman, and W. A. Ellingson, *J. Magn. Reson.*, 1990, **88**, 340.
26. S. L. Dieckman, P. Rizo, N. Gopalsami, and R. Botto, in *Materials Research Society Symposium Proceedings*, 1991, Vol. **217**, p. 169.
27. N. Gopalsami, S. L. Dieckman, W. A. Ellingson, R. E. Botto, and H. Yeh, in *Review of Progress in Quantitative NDE*, ed. D. O. Thompson and D. E. Chimenti, Plenum, New York, 1990, Vol. 10B, p. 1215.
28. L. Garrido, J. Ackerman, W. Ellingson, and J. D. Weyand, *Ceram. Eng. Sci. Proc.*, 1988, **9**, 1465.
29. J. L. Ackerman, D. P. Raleigh, and M. J. Glimcher, *Magn. Reson. Med.*, 1992, **25**, 1.
30. J. R. Moore, L. Garrido, and J. Ackerman, *Ceram. Eng. Sci. Proc.*, 1990, **11**, 1302.
31. K. Hayashi, K. Kawashima, K. Kose, and T. Inouye, *J. Phys. D.*, 1988, **21**, 1037.

Biographical Sketch

David G. Cory. *b* 1958. B.A., Ph.D. (supervisor William M. Ritchey), Chemistry, Case Western Reserve University. Postdoctoral work at the University of Nijmegen, The Netherlands (with Wiebren Veeman), and at the Naval Research Laboratory, Washington, DC (with Al Garroway and Joel Miller), followed by a period as a senior research and development scientist with Bruker Instruments, Inc., Billerica, MA. Currently Assistant Professor of Nuclear Engineering, Massachusetts Institute of Technology, Cambridge. Approx. 55 publications. Research interests: new NMR methodologies and instrumentation. Current projects include: solid state imaging, rf gradient spectroscopy, and diffusive scattering methods.

Agriculture and Soils

Roger H. Newman

Industrial Research Limited, Lower Hutt, New Zealand

1	Introduction	1
2	Sample Preparation	1
3	Signal Assignments for ^{13}C	1
4	Signal Assignments for Other Nuclei	2
5	Reliability of NMR Results	3
6	Applications	3
7	Separating Overlapping Signals	4
8	References	4

1 INTRODUCTION

Soils are heterogeneous mixtures of organic substances, minerals and organomineral complexes. The organic substances include macromolecules lacking well-defined structures or repeating units. The minerals include poorly ordered or amorphous matter. These difficulties have hindered scientific studies of soil, leaving fundamental questions of structural chemistry open to debate until recent years. NMR spectroscopic studies have provided some convincing answers that broaden our understanding of the origins of soil characteristics, the influences of land management on soil fertility, and the fate of agrochemicals.

Soil organic substances were extracted, methylated, and dissolved in deuterated solvents for the earliest ^{1}H and ^{13}C NMR studies of soil chemistry.[1–3] These studies provided little worthwhile information. Much more detail emerged from a 1976 paper describing ^{13}C NMR spectra of soil organic substances in alkaline aqueous solution.[4] The first ^{13}C CP MAS NMR spectrum of whole soil was published in 1981.[5] The publication rate has now risen to an average of about one paper per month describing ^{13}C CP MAS NMR studies of humic substances. Solution ^{13}C NMR spectroscopy is used on occasions, and several other nuclei provide useful spectra.

This article is not intended as a comprehensive review. More complete references to relatively early work can be found in two books published in 1987.[6,7]

2 SAMPLE PREPARATION

Soil organic substances are commonly separated into three fractions defined in terms of solubility. 'Humic acids' are not soluble in water under acid conditions, but are soluble under alkaline conditions. 'Fulvic acids' are soluble under all pH conditions. 'Humins' are not soluble under any pH conditions.

Humic acids generally account for the major part of soil organic matter. They have been characterized by CP MAS NMR or dissolved in aqueous alkali for solution NMR, the two procedures yielding similar patterns of signal intensities.[8,9] Fulvic acids are hygroscopic and yield poor CP MAS NMR spectra unless they are carefully dried.[10]

Differences between ^{13}C CP MAS NMR spectra of humic acids and the corresponding humins are not as pronounced as might be expected for separation based on differences in chemical properties.[11,12] It appears that differences in solubility are rather caused by differences in physical accessibility of the organic matter.[11] The NMR spectra of fulvic acids are usually distinctly different from the corresponding humic acids or humins,[11,12] so humic acids are not representative of the organic matter in the complete soil.

Soil extracts can be used for NMR studies without fractionation into humic and fulvic acids. This procedure is particularly advisable in preparing samples for ^{31}P NMR,[13] since phosphate esters could be hydrolyzed under the acidic conditions required for precipitation of the humic acid fraction. Sequential extraction procedures have been developed to remove over 80% of organic phosphorus from soils for solution NMR characterization.[14]

Removal of paramagnetic species such as Fe^{3+} can improve ^{13}C CP MAS NMR spectra of solid soils and humins.[15–17] As a general rule, the ratio C:Fe;>>1 is required for a good spectrum.[15] Pretreatment by a mixture of HCl and HF has the added advantage of removing inorganic substances and therefore concentrating the organic matter.[17]

3 SIGNAL ASSIGNMENTS FOR ^{13}C

A typical CP MAS NMR spectrum of whole soil (Figure 1) shows overlapping signals that are grouped in four chemical shift ranges for discussion here.

Signals in the range δ = 10–50 are assigned to alkyl carbon, including side chains in amino acids, structures derived from higher-plant polymers such as cutins and suberins, and structures formed by cross-linking between polyunsaturated

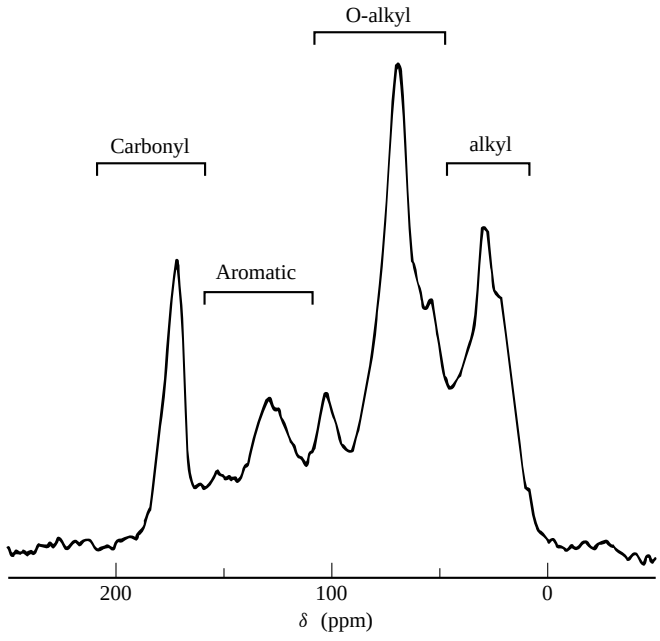

Figure 1 Carbon-13 CP MAS NMR spectrum (50.3 MHz) of Taupo Soil, A horizon: 7 mm diameter cylindrical rotor spun at 5.0 kHz, 1 ms contact time, 15 ms data acquisition time, 300 ms pulse delay, 10.6 h of data accumulation

microbial lipids.[18] Input from microbial activity has been demonstrated by incubating soil with ^{13}C-labeled glucose.[19] A signal near δ = 31 is sometimes relatively strong in spectra of soil fractions sieved to select particles with dimensions less than 2 μm.[20–22] This signal has been assigned to polymethylene chains, including organo-clay complexes.[20]

Signals in the range δ = 50–110 are assigned primarily to *O*-alkyl carbon, i.e. oxygen-substituted carbon in alcohols and ethers, including plant carbohydrates and their degradation products. These substances are relatively abundant in fractions sieved to select coarse particle sizes,[22] and are particularly well preserved in cold climates.[23] This chemical shift range includes signals between δ = 50 and 60 assigned to *N*-substituted carbon in amino acids.[4]

Signals in the range δ = 110–160 are assigned primarily to aromatic carbon. The question of whether aromatic substances form a major or minor component of soil organic matter has been debated as recently as 1985.[24,25] Perhaps the best answer is that considerable variation has been observed. A band centered on δ = 130 is particularly prominent in NMR spectra of organic matter found in soils that have been affected by fire.[26,27] Signals in the range δ = 150–160 have been assigned to oxygen-substituted aromatic carbon. The degree of oxygen substitution shows a strong negative correlation with soil development, perhaps as a result of selective degradation of the more highly substituted structures.[28]

Signals in the range δ = 160–210 are assigned to carbonyl carbon.[29] This region is usually dominated by a peak in the region δ = 170–180, assigned primarily to carboxylic acids. Secondary amides can also contribute to the peak.[30] The signal strength is usually stronger than would be expected from chemical analyses for carboxylic functional groups, and nitrogen contents fail to account for the discrepancies. Schnitzer and Preston concluded that 'it is possible that chemical methods do not react stoichiometrically with materials of high molecular weight, such as humic substances, because of steric factors.'[29]

4 SIGNAL ASSIGNMENTS FOR OTHER NUCLEI

Poor signal dispersion has discouraged widespread use of ^{1}H NMR in soil science. Bands of partly resolved signals have been observed in the ranges δ = 0.8–2.5 (alkyl), 3.3–3.8 (*O*-alkyl), and 6–8 (aromatic).[31] Features within these bands have been assigned to more specific chemical structures.[32] Aromatic protons can exchange with deuterons in solvent, resulting in underestimation of aromaticity.[33]

After ^{13}C, ^{31}P is the nucleus most commonly used in NMR studies of soil. Some generalized signal assignments are shown in Figure 2. The sample was chosen for the diversity of chemical species. The orthophosphate monoesters include choline phosphate (δ = 3.5) and inositol hexaphosphate (four signals).[13] Orthophosphate diesters include phospholipids. Phosphonates are clearly distinguished by the chemical shift range characteristic of a direct carbon–phosphorus bond. This category includes phosphonolipids (δ = 20) and their degradation products (δ = 18).[13] Many ^{31}P NMR spectra of pasture soil extracts show only a dominant signal near δ = 5, assigned to inorganic orthophosphate, with a weaker band across the range δ = 3–5, assigned to orthophosphate monoesters.[34] Some spectra of soil extracts include a signal near δ = – 21, assigned to polyphosphate chain units.[13]

The natural abundance of ^{15}N is so low that isotopic enrichment is necessary. Soil organic matter matures over periods of centuries, so only the first steps of humification can be studied by monitoring the fate of ^{15}N-enriched additives. At least three different chemical shift scales have been used in studies relevant to agriculture. The chemical shifts mentioned here are expressed in parts per million to high frequency from ammonia. Typical values are δ = 30–70 for amine nitrogen, 90–120 for amide nitrogen, and δ > 120 for heterocyclic nitrogen.[35] Chemical shifts have been reported for a number of specific substances considered relevant to the chemistry of humic substances.[35] When a soil humic acid was incubated with ^{15}N-enriched $NaNO_3$, the ^{15}N CP MAS NMR spectrum of the product was dominated by a broad band at δ = 119, assigned to secondary amides, e.g. in proteins.[36] The ^{15}N CP MAS NMR spectra of composts prepared with ^{15}N-enriched plant material are dominated by a peak assigned to proteins, with weaker signals at 83 and 71 ppm assigned to nucleic acids.[37]

NMR is not normally the technique of choice for studies of inorganic matter in soil, but there have been exceptions.

Most soil silicates contribute ^{29}Si NMR signals in a broad band across the region δ = – 80 to –115.[38] Fractionation of a soil into particle size ranges has been used to demonstrate the predominance of quartz (δ = – 113) in a coarse fraction, and layered aluminosilicates (δ = – 92) in a fine fraction.[39] One of the hydrated aluminosilicates, imogolite, contributes a relatively narrow peak at a distinctive chemical shift of δ = – 78.[38] Therefore, ^{29}Si NMR can be used to estimate the imogolite content of soil.

Solution NMR methods have been used to characterize aqueous ^{27}Al in plugs of soil.[40] Most of the signal strength was

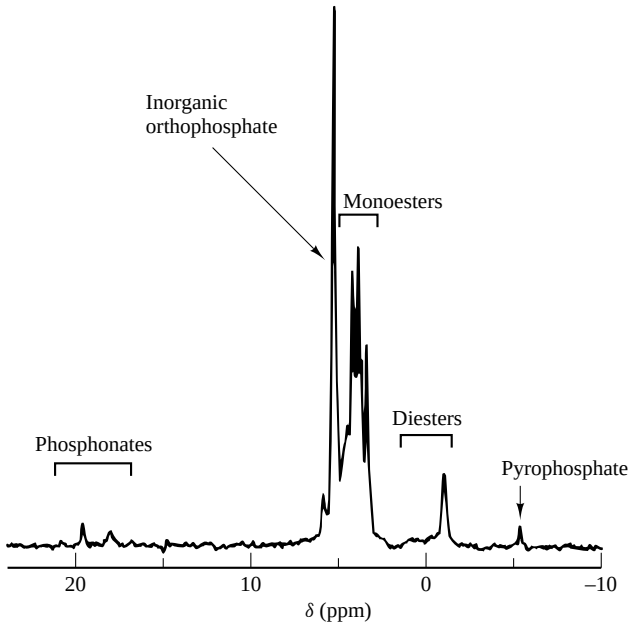

Figure 2 Phosphorus-31 NMR spectrum (32.2 MHz) of an aqueous NaOH extract from Carrick tussock-grassland soil. Sample mixed with D_2O in a 10 mm tube; 12 μs pulse width, 0.8 s data acquisition time with proton decoupling, 5.0 s pulse delay without proton decoupling, 79 h of data accumulation. The soil properties are described elsewhere[43]

found in a band from $\delta = -9$ to 12. This band was assigned to species with octahedral coordination, including complexes with humic substances. A relatively sharp peak at $\delta = 63.5$ was assigned to a polynuclear cation, believed to be more toxic to plants than the mononuclear cation.[40]

5 RELIABILITY OF NMR RESULTS

Patterns of relative signal areas have been compared for ^{13}C NMR spectra of extracted humic substances run as solids and as solutions.[8,9,41] The overall similarities have been encouraging, but sources of errors have been identified in both techniques.

In the case of solution NMR spectroscopy, it is necessary to choose a pulse delay that is adequate for both T_1 relaxation and suppression of NOEs. Preston and Blackwell drew attention to the need to consider magnetic field strength in selecting a suitable pulse spacing.[8] Values of $T_1 < 0.2$ s have been reported for protonated carbon in solutions of humic substances run at a field strength of 1.87 T,[42] but values in the range 0.2–0.8 s have been reported for experiments at 5.6 T.[8] These observations are consistent with molecular motion including components with correlation times longer than required for the T_1 minimum. Values of NOEs are particularly low and values of T_1 are particularly long for carboxyl carbon, so the content of this chemical functional group can be underestimated unless the decoupler output is gated off during the pulse delay.[8,42] A dramatic improvement in the strength of these signals has been reported for pulse delays increased from 0.5 to 5.0 s.[41] A pulse delay of 2 s has been suggested for solution ^{13}C NMR at 63 MHz.[8] Pulse delays as long as 20 s have been found necessary in ^{31}P NMR of soil extracts.[43]

The choice of magnetic field strength should be considered in ^{13}C CP MAS NMR also. Fründ and Lüdemann reported T_1(H) values in the range 3–6 ms for humic matter run at 2.35 T, rising to the range 10–20 ms for the same sample run at 7.05 T.[41] These values are fortunately all so short that the pulse spacing is more likely to be determined by the duty cycle of the spectrometer. It is important that the contact time should be long enough for adequate cross polarization, yet short enough to avoid the effects of variations in $T_{1\rho}$(H) between chemical functional groups. These two criteria conflict for most humic substances. On one hand, contact times as long as 1 ms are needed to achieve maximum signal strength for nonprotonated carbon, e.g. carboxylic carbon.[8] On the other hand, values of $T_{1\rho}$(H) can vary between chemical functional groups, because of the heterogeneous nature of soil organic matter. This was particularly evident in a clay fraction, where values of $T_{1\rho}$(H) ranged from 2.0 ms for *O*-alkyl carbon to 6.2 ms for *O*-substituted aromatic carbon.[44] Variations in $T_{1\rho}$(H) can arise, e.g. from selective binding of metal ions to specific chemical structures.[45] A contact time of 1 ms seems to provide a reasonable compromise.[45]

Paramagnetic ions such as Fe^{3+} can shorten values of $T_{1\rho}$(H) until organic matter in the immediate vicinity of each ion no longer responds to CP MAS NMR.[46] Interference from organic free radicals is not as important, as shown by a 'spin counting' experiment in which 97% of carbon in a solid ash-free fulvic acid responded to CP MAS NMR, despite the presence of organic free radicals.[46]

6 APPLICATIONS

Soils are often classified according to their color, so studies of the origin of color can provide a fundamental basis for classification schemes. NMR experiments have shown that the more intensely colored humic and fulvic acids contain relatively high proportions of aromatic carbon.[26,47] Humic substances in general display strong absorbance in the UV, tailing off across the visible region. Absorptivity at 272 nm has been found to be highly correlated ($r = 0.94$) with the strength of ^{13}C NMR signals assigned to aromatic carbon in humic acids.[48] Weaker correlations have been reported for fulvic acids.[49]

CP MAS NMR has been used to demonstrate a correlation ($r = 0.997$) between the aromatic carbon content of humic acids and the partition coefficient for binding of pyrene.[50] This suggests that the chemical structure of humic material should be considered in any attempts to model the transport or fate of organic pollutants. Carbon-13 NMR has been used to demonstrate formation of covalent bonds between ^{13}C-labeled 2,4-dichlorophenol and humic acid.[51] Decreased herbicide activity in tilled soil has been attributed to the organic matter being in a more reactive state than in soil that was not tilled.[52] The ^{13}C NMR spectrum of humic acid from the tilled soil showed a relatively strong band assigned to aromatic carbon, but the authors advised caution in the interpretation of the results, in view of the small magnitude of the observed differences and the small number of samples tested.[52]

A combination of ^{1}H, ^{13}C, and ^{31}P NMR has been used to monitor degradation of a herbicide, glyphosate (*N*-phosphonomethylglycine), in soil.[53]

Fecal fibre is rich in carbohydrates, particularly crystalline cellulose, contributing relatively sharp ^{13}C NMR signals across the region assigned to *O*-alkyl carbon.[54] These signals become weaker when feces are composted. In the case of composts formed from cattle manure, the relative signal area of the O-alkyl band dropped from 59% to 33% over a period of 147 days of composting.[55] CP MAS NMR has been described as the 'most quantitative procedure' of those tested for use in characterizing compost maturity.[56]

Intensive land management practices are known to cause long-term decreases in soil organic matter. Carbon-13 NMR has been used in attempts at characterizing the residual organic matter. Divergent results indicate a complex dependence on the nature of the initial material and details of the management regime. Oades et al. found relatively high aromaticity in a red–brown earth cultivated for 60 years, compared with undisturbed soil.[57] On the other hand, Schulten et al. found relatively low aromaticity in soils cultivated for periods up to 35 years.[58] Schulten et al. found lowest concentrations of residual organic matter in soils treated with high doses of mineral fertilizers. It is possible that their results reflect the influence of fertilizers rather than the influence of crops. Preston et al. observed a decrease in the area of the O-alkyl band and a corresponding increase in the area of the alkyl band in CP MAS NMR spectra of peat cultivated for periods up to 15 years.[59] These changes may reflect the influence of plowing, exposing organic matter to biological oxidation. Skjemstad et al. studied soils cultivated for periods up to 45 years.[60] They found no detectable changes in relative signal areas across CP MAS NMR spectra, but the signals became broadened in the spectra of soils with the lowest concentrations of residual

organic matter. They suggested that a major mechanism for the relative stability of persistent soil organic matter may be a physical association with the inorganic component. The effects of cultivation are also evident in ^{31}P NMR spectra of soil extracts, the diversity of chemical species being greater in uncultivated soils than in corresponding samples of cultivated soils.[61]

Several authors have studied the influence of climate and vegetation on soil properties. A negative correlation ($r = -0.998$) has been found between rainfall and the strength of ^{13}C signals assigned to aromatic carbon in humic acids.[62] The ^{31}P NMR spectra of soil extracts show a particularly wide diversity of chemical species for sites with high annual precipitation.[43] No correlations were found in a study of vegetation and its influence on the chemical structure of soil.[63]

7 SEPARATING OVERLAPPING SIGNALS

The applications sketched above have been hindered by problems with overlapping signals, particularly in solid state ^{13}C NMR. Most authors describe soil organic matter in very general terms, e.g. distinguishing 'aromatic' or 'aliphatic' carbon. Some spectra show hints of variations in details within one or more of the bands. Several strategies have been suggested for separating these overlapping signals.

Dipolar dephasing suppresses CP MAS NMR signals from most CH and CH_2 groups, leaving signals assigned to nonprotonated carbon or protonated carbon in functional groups with some freedom for internal motion. This technique has been used to demonstrate differences between the degrees of aromatic substitution in different humic acids.[64]

Proton spin relaxation editing exploits the heterogeneous nature of soil.[65] A proton inversion–recovery pulse sequence is combined with ^{13}C CP MAS NMR. Linear combinations of partly relaxed and fully relaxed spectra are generated to separate subspectra assigned to distinctly different forms of organic matter with distinctly different values of T_1(H). This procedure has been used to separate subspectra from the CP MAS NMR spectrum of a humic acid, suggesting that material extracted from clays may differ from material extracted from other soil fractions.[28] Variations in $T_{1\rho}$(H), mentioned above, could also be used for separation of subspectra.

2D NMR techniques show some promise for separation of overlapping signals. A ^{1}H–^{13}C heteronuclear chemical shift correlation experiment has been used to construct a 2D NMR plot for a sample of fulvic acid, with the ^{1}H CRAMP spectrum on one axis and the ^{13}C CP MAS spectrum on the other.[66] This showed that a broad band in the CRAMP spectrum could be assigned to a mixture of contributions from alkyl and *O*-alkyl structures, with the latter offset to slightly higher chemical shifts.

Despite this progress, the problem of separating overlapping signals remains one of the greatest challenges in NMR studies of agricultural and soil samples.

8 REFERENCES

1. D. H. R. Barton and M. Schnitzer, *Nature*, 1963, **198**, 217.
2. H.-D. Lüdemann and H. Nimz, *Biochem. Biophys. Res. Commun*., 1973, **52**, 1162.
3. J. A. Neyroud and M. Schnitzer, *Can. J. Chem.*, 1974, **52**, 4123.
4. F. J. Gonzalez Vila, H. Lentz, and H.-D. Lüdemann, *Biochem. Biophys. Res. Commun.*, 1976, **72**, 1063.
5. P. F. Barron and M. A. Wilson, *Nature*, 1981, **289**, 275.
6. R. L. Wershaw and M. A. Mikita (eds.), *NMR of Humic Substances and Coal*, Lewis, Chelsea, MI, 1987.
7. M. A. Wilson, *NMR Techniques and Applications in Geochemistry and Soil Chemistry*, Pergamon Press, Oxford, 1987.
8. C. M. Preston and B. A. Blackwell, *Soil Sci.*, 1985, **139**, 88.
9. R. Fründ and H.-D. Lüdemann, *Sci. Total Environ.*, 1989, **81/82**, 157.
10. P. G. Hatcher and M. A. Wilson, *Org. Geochem*., 1991, **17**, 293.
11. R. Fründ and H.-D. Lüdemann, *Z. Naturforsch*., 1991, **46c**, 982.
12. C. Saiz-Jimenez, B. L. Hawkins, and G. E. Maciel, *Org. Geochem*., 1986, **9**, 277.
13. R. H. Newman and K. R. Tate, *Commun. Soil Sci. Plant Anal*., 1980, **11**, 835.
14. L. M. Condron, K. M. Goh, and R. H. Newman, *J. Soil Sci*., 1985, **36**, 199.
15. M. A. Arshad, J. A. Ripmeester, and M. Schnitzer, *Can. J. Soil Sci*., 1988, **68**, 593.
16. M. Oades, A. M. Vassallo, A. G. Waters, and M. A. Wilson, *Aust. J. Soil Res*., 1987, **25**, 71.
17. C. M. Preston, M. Schnitzer, and J. A. Ripmeester, *Soil Sci. Soc. Am. J.*, 1989, **53**, 1442.
18. G. Almendros, J. Sanz, F. J. González-Vila, and F. Martín, *Naturwissenschaften*, 1991, **78**, 359.
19. J. A. Baldock, J. M. Oades, A. M. Vassallo, and M. A. Wilson, *Environ. Sci. Technol*., 1990, **24**, 527.
20. B. K. G. Theng, G. J. Churchman, and R. H. Newman, *Soil Sci*., 1986, **142**, 262.
21. J. A. Baldock, J. M. Oades, A. G. Waters, X. Peng, A. M. Vassallo, and M. A. Wilson, *Biogeochem*., 1992, **16**, 1.
22. G. Catroux and M. Schnitzer, *Soil Sci. Soc. Am. J*, 1987, **51**, 1200.
23. M. A. Wilson, K. M. Goh, P. J. Collin, and L. G. Greenfield, *Org. Geochem.*, 1986, **9**, 225.
24. M. Ghosal and E. S. K. Chian, *Soil Sci. Soc. Am. J*., 1985, **49**, 616.
25. V. C. Farmer and D. L. Pisaniello, *Nature*, 1985, **313**, 474.
26. K. R. Tate, K. Yamamoto, G. J. Churchman, R. Meinhold, and R. H. Newman, *Soil Sci. Plant Nutr*., 1990, **36**, 611.
27. G. Almendros, F.-J. González-Villa, F. Martín, R. Fründ, and H.-D. Lüdemann, *Sci. Total Environ.*, 1992, **117/118**, 63.
28. R. H. Newman and K. R. Tate, *J. Soil Sci*., 1991, **42**, 39.
29. M. Schnitzer and C. M. Preston, *Soil Sci. Soc. Am. J.*, 1986, **50**, 326.
30. R. H. Newman, B. K. G. Theng, and Z. Filip, *Sci. Total Environ*, 1987, **65**, 69.
31. M. A. Wilson, A. J. Jones, and B. Williamson, *Nature*, 1978, **276**, 487.
32. M. A. Wilson, *J. Soil Sci*., 1981, **32**, 167.
33. P. Ruggiero, F. S. Interesse, and O. Sciacovelli, *Soil Biol. Biochem*., 1980, **12**, 297.
34. G. E. Hawkes, D. S. Powlson, E. W. Randall, and K. R. Tate, *J. Soil Sci*., 1984, **35**, 35.
35. K. A. Thorn and M. A. Mikita, *Sci. Total Environ*., 1992, **113**, 67.
36. L. Benzing-Purdie, J. A. Ripmeester, and C. M. Preston, *J. Agric. Food Chem*., 1983, **31**, 913.
37. G. Almendros, R. Fründ, F. J. Gonzalez-Vila, K. M. Haider, and

H.-D. Lüdemann, *FEBS Lett.*, 1991, **282**, 119.

38. P. F. Barron, M. A. Wilson, A. S. Campbell, and R. L. Frost, *Nature*, 1982, **299**, 616.
39. M. A. Wilson, in *Soil Analysis: Modern Instrumental Techniques*, ed. K. A. Smith, Dekker, New York, 1991, Chap. 14, p. 601.
40. D. Hunter and D. S. Ross, *Science*, 1991, **251**, 1056.
41. R. Fründ, F. J. Gonzalez-Vila, H.-D. Lüdemann, and F. Martin, *Z. Naturforsch*., 1987, **42c**, 205.
42. R. H. Newman and K. R. Tate, *J. Soil Sci*., 1984, **35**, 47.
43. K. R. Tate and R. H. Newman, *Soil Biol. Biochem*., 1982, **14**, 191.
44. J. A. Baldock, J. M. Oades, A. M. Vassallo, and M. A. Wilson, *Aust. J. Soil Res*., 1990, **28**, 193.
45. C. M. Preston, R. L. Dudley, C. A. Fyfe, and S. P. Mathur, *Geoderma*, 1984, **33**, 245.
46. A. M. Vassallo, M. A. Wilson, P. J. Collin, J. Malcolm Oades, A. G. Waters, and R. L. Malcolm, *Anal. Chem*., 1987, **59**, 558.
47. S. Dou, E. Chen, X. Xu, S. Tan, S. Hua, and T. Zhu, *Turang Tongbao*, 1989, **20**, 263 (*Chem. Abstr*., 1990, **112**, 177 449k).
48. S. J. Traina, J. Novak, and N. E. Smeck, *J. Environ. Qual*., 1990, **19**, 151.
49. J. M. Novak, G. L. Mills, and P. M. Bertsch, *J. Environ. Qual*., 1992, **21**, 144.
50. T. D. Gauthier, W. R Seitz, and C. L. Grant, *Environ. Sci. Technol*., 1987, **21**, 243.
51. P. G. Hatcher, J. M. Bortiatynski, R. D. Minard, J. Dec, and J. M. Bollag, *Environ. Sci. Technol*., 1993, **27**, 2098.
52. G. K. Stearman, R. J. Lewis, L. J. Tortorelli, and D. D. Tyler, *Soil Sci. Soc. Am. J.*, 1989, **53**, 1690.
53. M. L. Rueppel, B. B. Brightwell, J. Schaefer, and J. T. Marvel, *J. Agric. Food Chem.*, 1977, **25**, 517.
54. R. M. Elofson, J. A. Ripmeester, N. Cyr, L. P. Milligan, and G. Mathison, *Can. J. Anim. Sci.*, 1984, **64**, 93.
55. Y. Inbar, Y. Chen, and Y. Hadar, *Soil Sci. Soc. Am. J.*, 1989, **53**, 1695.
56. Y. Inbar, Y. Chen, Y. Hadar, and H. A. J. Hoitink, *BioCycle*, 1990, **31**, 64.
57. J. M. Oades, A. G. Waters, A. M. Vassallo, M. A. Wilson, and G. P. Jones, *Aust. J. Soil Res.*, 1988, **26**, 289.
58. H.-R. Schulten, R. Hempfling, K. Haider, F. F. Gröblinghoff, H.-D. Lüdemann, and R. Fründ, *Z. Pflanzenernähr. Bodenk.*, 1990, **153**, 97.
59. C. M. Preston, S.-E. Shipitalo, R. L. Dudley, C. A. Fyfe, S. P. Mathur, and M. Levesque, *Can. J. Soil Sci.*, 1987, **67**, 187.
60. J. O. Skjemstad, R. C. Dalal, and P. F. Barron, *Soil Sci. Soc. Am. J.*, 1986, **50**, 354.
61. L. M. Condron, E. Frossard, H. Tiessen, R. H. Newman, and J. W. B. Stewart, *J. Soil Sci.*, 1990, **41**, 41.
62. M. A. Arshad, and M. Schnitzer, *Z. Pflanzenernähr. Bodenk.*, 1989, **152**, 11.
63. M. Krosshavn, J. O. Bjørgum, J. Krane, and E. Steinnes, *J. Soil Sci.*, 1990, **41**, 371.
64. P. G. Hatcher, M. Schnitzer, A. M. Vassallo, and M. A. Wilson, *Geochim. Cosmochim. Acta*, 1989, **53**, 125.
65. C. M. Preston and R. H. Newman, *Can. J. Soil Sci*, 1992, **72**, 13.
66. C. E. Bronnimann, C. F. Ridenour, D. R. Kinney, and G. E. Maciel, *J. Magn. Reson.*, 1992, **97**, 522.

Biographical Sketch

Roger H. Newman. *b* 1949. B.Sc.(Hons.), 1970, University of Canterbury, NZ. Ph.D. (supervisor Robin Harris), 1976, University of East Anglia, UK. NMR spectroscopist for the New Zealand DSIR, 1970–73 and 1976–92, and for Industrial Research Limited, 1992–present. Approx. 70 publications. Research specialty: applying solid state NMR to characterize heterogeneous organic solids.

Coal Structure from Solid State NMR

Ronald J. Pugmire
University of Utah, Salt Lake City, UT, USA

1	Introduction	1
2	Experimental Techniques	1
3	Description and Constituents	4
4	Applications to Coal Science	5
5	Note	9
6	References	9

1 INTRODUCTION

Coal has been used as an important source of fuel for thousands of years, but it is a complex, heterogeneous fuel which is difficult to burn or process without serious environmental implications. Coals can vary significantly among different geographic areas in important properties such as rank, ash, sulfur and nitrogen content, mineral impurities, and maceral constituents. Substantial worldwide attention is being focused on more efficient and cleaner methods for utilization of this important energy resource.

The wide heterogeneity of coal has made it difficult to characterize and to correlate its structure. Evidence exists that differences in geological histories and maceral constituents affect coal chemistry and technological applications of coals, since coals of the same apparent rank but of different geological history can exhibit a variety of physical and chemical properties. Coal structure varies with recognizable geological and geochemical features which affect its reactivity. The variations in the geochemical history and the complexities of the macromolecular structure of coal further confound a clear understanding of the complex nature and interrelationships among coals.[1]

Our understanding of the details of coal structure has improved markedly over the last decade. Coal is now believed to be a heterogeneous mixture composed of a macromolecular network of varying degrees of cross-linking within the macromolecular phase with a smaller molecular phase imbibed or associated with this network. A major portion of the credit for the present state of knowledge of the general characteristics of coal structure can be traced to studies that employed NMR spectroscopy. It is interesting to observe that NMR was first applied to the study of coals in 1955,[2] only nine years following the discovery of the NMR phenomenon in bulk matter. These first NMR observations employed broadline ^{1}H techniques which, in the absence of means to reduce the large proton dipole–dipole interactions, produced very broad bands in fossil fuel related materials. In 1968 Haeberlen and Waugh[3] demonstrated that the hydrogen dipole–dipole interaction could be significantly reduced by averaging in spin space via a multiple pulse approach[4] rather than attempting to spin the sample mechanically at very high MAS rates in order to achieve the same results. In the mid-1970s Schnable[5] and Gerstein et al.[6,7] demonstrated that if the sample is spun simultaneously about the magic angle then the chemical shift anisotropy (CSA) as well as the inhomogeneous heteronuclear dipolar interactions are simultaneously averaged. Hence, much narrower peaks are obtained with this experiment which Gerstein named CRAMPS. The proton CRAMPS experiment was first applied to coals by Gerstein in 1981.[8] The CRAMPS experiments have been especially useful as a probe to study the 'mobile phase' present in coal structure wherein solvents such as perdeuterated pyridine are imbibed into the parent coal.[9–13] The reduction in proton NMR linewidths is attributed to motional narrowing and to reduction of bulk and molecular susceptibility anisotropies by partial mobilization of certain structural moieties in coal caused by disruption of hydrogen bonds and other noncovalently bonded structural units.

As early as 1966 the first ^{13}C NMR spectra appeared of materials derived from coal.[14] Broadline ^{13}C NMR spectroscopy was first applied to whole coals in 1971 to confirm the high aromaticity of anthracite.[15] Significant improvements in resolution began to emerge five years later[16] with the application of the cross polarization technique followed by applications of magic angle spinning to coal.[17] In 1979 Opella and Frey[18] introduced the concept of the dipolar dephasing experiment which discriminates between nonprotonated and protonated carbons by means of the effective C–H dipole–dipole interaction. Alemany et al. studied the characteristics of the dipolar dephasing experiment on model compounds[19] and then demonstrated the utility of this experiment in a careful study of an Illinois No. 6 coal.[20] Work by Wilson,[21] Murphy,[22] and Gerstein[23] and their co-workers has verified the value of dipolar dephasing experiments in the study of coal. The data derived from the techniques described, together with others to be described in subsequent sections, have been extremely valuable in probing the general structural features of coals and have greatly enhanced the usable knowledge base for improved coal utilization.

2 EXPERIMENTAL TECHNIQUES

Since the organic constituents of coal are composed primarily of hydrogen and carbon with smaller amounts of oxygen, nitrogen, and sulfur (typical elemental compositions of a lignite, high volatile bituminous, and anthracite coal are $C_{100}H_{78.9}N_{1.4}S_{0.4}O_{22.7}$, $C_{100}H_{76.2}N_{1.7}S_{0.4}O_{6.1}$, and $C_{100}H_{17.5}N_{0.7}S_{0.2}O_{1.5}$, for the Beulah-Zap, Pittsburgh No. 8, and Buck Mountain, respectively) (see Section 5), NMR experiments have focused primarily on ^{1}H and ^{13}C applications. While ^{1}H NMR experiments (particularly the CRAMPS applications) have added valuable insight for coal structural studies, the major area of interest has been in the elucidation of the carbon skeletal structure since many of the questions regarding the physical and chemical properties can be addressed from a clear understanding of the details of the carbon backbone and associated functional groups. Carbon-13 NMR spectroscopy has become one of the premier tools in organic structure analysis due to the relationship between the local electronic environment of the carbon nucleus and the ^{13}C chemical shift and, hence, the use of ^{13}C NMR techniques has become essential for the study of solid carbonaceous materials such as coal chars, pitches, and geochemical materials in general.

2.1 CP MAS and Isotropic Shifts

The combination of cross polarization and magic angle spinning has been used to obtain high-resolution NMR spectra from solids for many years. Magic angle sample spinning at a rate greater than the chemical shielding anisotropy (CSA) of the carbon nuclei will average the principal values of the chemical shift tensor (δ_{11}, δ_{22}, δ_{33}) to the isotropic chemical shift value. Linewidths obtained by CP MAS experiments are typically of the order of 1–2 ppm in simple organic compounds but relaxation effects (T_2), anisotropy in bulk susceptibility, crystallinity, and solid state effects can considerably broaden the individual spectral lines. In some cases one may observe multiple lines due to lattice structures that contain multiple structures per unit cell or crystal lattice effects that impose a preferred conformation which breaks the local symmetry. In general, the solid state isotropic chemical shifts are similar to those in solution and the appropriate chemical shift/structure relationships developed in solution studies may be used to interpret solid state CP MAS spectra.

The Utah group[24,25] illustrated the relationship between isotropic chemical shifts and the CP MAS spectra of coals. While coal spectra are characterized by banded structures in the aliphatic and aromatic regions, it is evident from the bandshapes and shoulders on these bands that structural information is available beyond that obtained from aromaticity considerations only. Gerstein demonstrated that isotropic chemical shifts could be used to look .. 'beyond just aromaticity; chemical functionality'.[26] An example of the diversity of the ^{13}C NMR spectra of coals is presented in Figure 1 for a series of coals of ranks ranging from lignite through anthracite.

Solum et al.[27,28] have used a rather detailed isotropic chemical shift distribution together with dipolar dephasing data to obtain 12 structural parameters for the coals contained in the Argonne Premium Coal Sample Bank. Wilson et al.[29] and Hatcher et al.[30] have used isotropic ^{13}C NMR data to propose chemical transformation pathways for coal precursors, while Hatcher et al.[31] have used such data to construct a three-dimensional computer simulation of coal formation from components of plant precursors. Hence, CP MAS chemical shift data have had a major impact in geochemical applications in general and fossil fuels in particular.

2.2 Shielding Tensors and 2D Methods

The CSA is a reflection of the interaction of the electronic environment of the nuclei with the external magnetic field. Depending on the orientation of a given molecule in the field, a different value of the chemical shift is observed. If the sample simultaneously exists in all possible orientations (as in the case of a powder sample), a superposition of all the possible shift values for the nuclei in the molecule is observed. The frequencies obtained from the breakpoints or discontinuities of this powder pattern are the principal values of the chemical shift tensor. For a ^{13}C nucleus in an anisotropic environment, three distinct values are observed, and these values correspond to the three elements (δ_{11}, δ_{22}, δ_{33}) found as the diagonal elements of the chemical shift tensor. From the study of single crystals, both the principal values of the shift tensor and their orientation in the molecular framework can be determined.

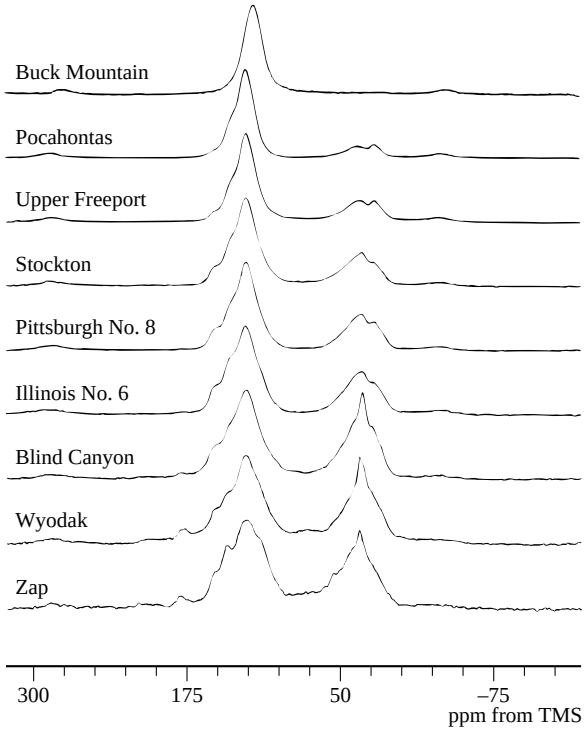

Figure 1 CP MAS spectra of the Argonne Premium Coals plus the Buck Mountain anthracite (PSOC-1468). The data were acquired as described by Solum et al.[27,28] Coal rank increases from bottom to top in the figure

Single crystal studies of aromatic compounds show that δ_{33} is always perpendicular to the plane of the aromatic ring[32] and its value in the aliphatic region reflects its independence of the π system. The other two tensor components, δ_{11} and δ_{22}, are oriented in the plane of the aromatic system. Theoretical studies have placed δ_{11} nearly perpendicular to the C–C bond with the largest π-bond order in all of the polycondensed aromatic hydrocarbons studied.[32]

Orendt et al.[33] have provided a brief description of experimental methods for studying chemical shift tensors in model compounds and coals. Extracting principal values from powders is extremely difficult due to the inherent low resolution of the experiment. Hence, principal values can normally be obtained only for very simple compounds or compounds of high symmetry containing only two to three tensors. The variable angle sample spinning (VASS) technique improves the resolving capacity to only three to four tensors.[34] Yet the information provided by CSA data is very valuable in the study of small molecules and even relatively large systems such as naphthalene, pyrene, hexahydropyrene, pyracene, and coals.[33,35] The data obtained on such systems have demonstrated that the shape of the tensor patterns can be used to distinguish different types of carbons in an environment where spectral overlap might preclude identification based on isotropic chemical shift information. This is particularly advantageous for coal due to spectral overlap in both the aromatic and aliphatic regions. Due to the large range in the principal values of the chemical shift tensors in aromatic carbons, an effort to obtain such data on coals is most fruitful since the carbon backbone of coals is dominated by aromatic species.

Table 1 Average Chemical Shift Tensor Values for Aromatic Carbons[a]

Carbon type	δ_{11}	δ_{22}	δ_{33}	δ_{av}
Protonated (75)	207 ± 22	146 ± 19	18 ± 12	124 ± 11
Substituted (21)	226 ± 11	165 ± 15	23 ± 14	138 ± 8
Phenolic (16)	227 ± 16	163 ± 9	72 ± 3	154 ± 6
Condensed (7)	205 ± 2	195 ± 2	−72 ± 5	133 ± 2

[a]The numbers in parentheses following the carbon type are the number of measurements considered in the analysis. Errors represent standard deviations of available data. All values are given in parts per million. The first three lines of data are from T.M. Duncan, 'A Compilation of Chemical Shift Anisotropies', Farragut Press, Chicago, IL, 1990, p. C-5. The data on condensed carbons come from data obtained at the University of Utah.

For convenience, the aromatic carbons in coal can be grouped into four categories: protonated, substituted (having an alkyl group substituent), phenolic (having a hydroxy or ether substituent), and bridgehead or condensed. Presently available chemical shift tensor data on these types of carbons are summarized in Table 1 while Figure 2 portrays the ideal lineshapes for the four types of carbon of interest. These ideal lineshapes were obtained by tabulating literature values for the shift tensor components for aromatic carbons in simple organic compounds measured by a variety of methods.[32–37] These data have been used to study the aromatic structure in a fusinite maceral, two anthracite, and three bituminous coals.[33,35]

A detailed description of methods for obtaining chemical shift tensors is contained elsewhere (see ***Chemical Shift Tensors***.). Hughes et al.[33] have used a static chemical shift–chemical shift correlation spectroscopy experiment (referred to as the 2D flipper experiment) to examine the chemical shift tensor patterns in a medium volatile and a low volatile bituminous coal. In a conventional 1D static solid state spectrum of coal, a large degree of overlap between aromatic and aliphatic signals occurs, whereas the 2D chemical shift–chemical shift correlation spectrum clearly separates the two spectral regions and exhibits the presence of multiple overlapping chemical shift tensors in both the aromatic and aliphatic regions of both samples. Furthermore, this separation of spectral regions allows for the determination of the aromaticity from a non-MAS spectrum. The aromaticity values (f_a) are 0.78 for the Upper Freeport and 0.87 for the Pocahontas No. 3 coals compared with values of 0.81 and 0.86 determined by CP MAS experiments.[27,28]

In an effort to address the problem of spectral overlap many 2D techniques have been developed to obtain a spectrum with an isotropic shift along one axis and a stationary or slow-spinning sideband powder pattern along the other. One such technique, the triple echo magic angle turning (triple echo MAT) experiment (see ***Magic Angle Turning and Hopping***), has proven to be especially effective for studying model compounds and has been used to examine a number of coals, including those in the Argonne Premium Coal Sample Bank,[38] a naphthalene-derived pitch, a semi-anthracite, and an anthracite coal.[39] The chemical shift tensor patterns taken at various isotropic shift values in coals clearly exhibit the presence of the characteristic shapes of the chemical shift tensors of protonated, substituted, phenolic, or bridgehead carbons and, hence, one is able to distinguish different types of carbons in broad spectral regions where it is impossible to distinguish individual lines. An example of the deconvolution of overlapping lines is given in Figure 3, where the slice taken at an isotropic chemical shift value of 124 ppm is shown for Pocahontas No. 3 low volatile bituminous coal.[40]

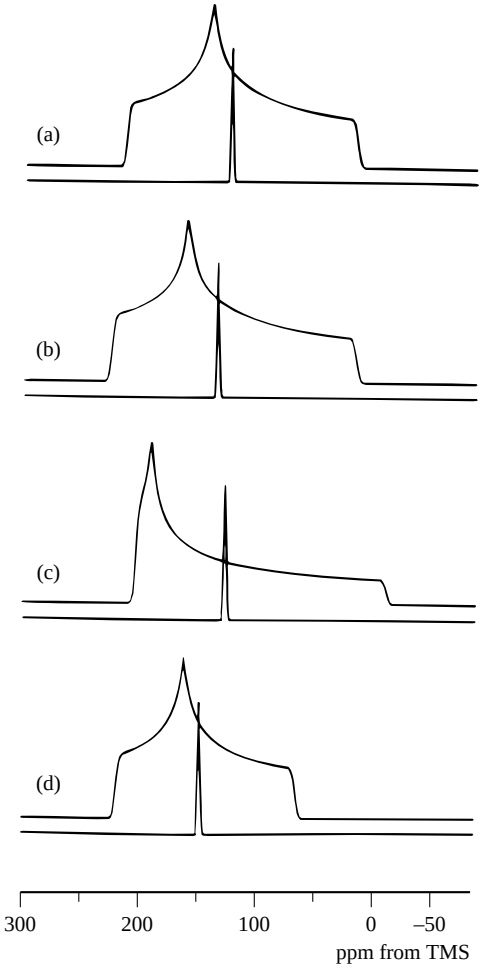

Figure 2 Ideal tensor patterns and average isotropic shifts for the four types of aromatic carbons in coal: (a) protonated, (b) alkyl substituted, (c) condensed or bridgehead, and (d) phenolic

The simulation of the individual powder patterns for an axially symmetric aromatic tensor and an overlapping protonated tensor are compared with the experimental data in Figure 3. A modified version of the triple echo MAT experiment called PHORMAT (see ***Magic Angle Turning and Hopping***), which incorporates rotor pulse synchronization, has been used in a blind comparison of the tensor principal values obtained from single crystal data in methyl α-D-glucopyranoside.[41] The principal values for the six carbons in this model compound have an rms average distance of 0.57 ppm from the tensors determined from the single crystal data, while the estimated variation in the principal values of the tensors studied with the triple echo MAT experiment vary by approximately 2 ppm.[40] Hence, the principal values reported by the Utah group have been shown to represent faithfully the single crystal data within 2 ppm when the triple echo MAT experiment is used, and an error of 0.5–1 ppm is expected if the more precise rotor pulse synchronized PHORMAT experiment is used. A remarkably good correlation is also obtained between the carbon aromaticities (ratio of

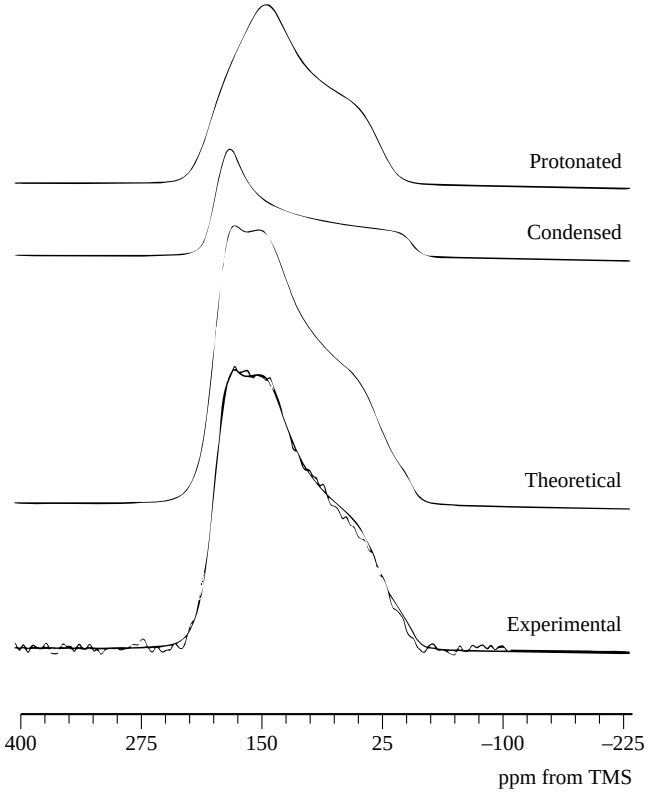

Figure 3 Spectral slice taken at an isotropic chemical shift of 124.5 ppm from the triple echo MAT experiment on Pocahontas No. 3 coal obtained from the Argonne Premium Coal Sample Bank. The experimental data were simulated as the superposition of protonated and condensed (bridgehead) aromatic carbon tensor patterns, labeled theoretical, which is overlaid on the experimental trace

aromatic to aromatic plus aliphatic carbons) determined from variable contact time CP MAS data and the triple echo MAT experiment. This relationship is shown in Figure 4 for the coals in the Argonne Premium Coal Sample Bank, two anthracites and a methylnapthalene-derived pitch (correlation coefficient $R^2 = 0.991$), demonstrating that the slow spinning triple echo MAT experiment does not lead to any apparent distortions of the structural components in coals.

3 DESCRIPTION AND CONSTITUENTS

3.1 General Nature of Coals and NMR Parameters

Coal is a complex sedimentary rock derived from plant remains. During the coalification process the accumulated plant material underwent differing degrees of chemical decomposition and depolymerization. These degradation processes formed peat which was subsequently transformed into coal of different ranks and properties based on sedimentary input, local environment, depth of burial, and local geological history. These various local conditions combined to produce a material that can be quite variable in terms of elemental composition and the nature of the inorganic materials incorporated into the coal material either as mineral inclusions or as chemically bound species. The elemental composition (particularly

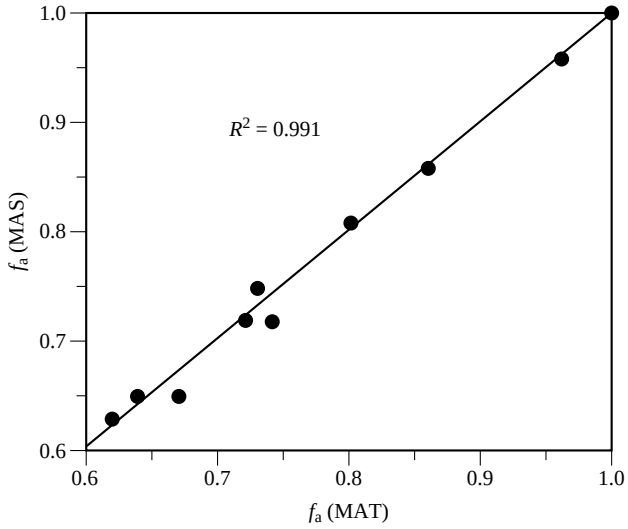

Figure 4 Comparison of aromaticity values for the Argonne Premium Coals, two anthracite coals (PSOC-867 and PSOC-628), and a methylnaphthalene-derived pitch. The CP MAS data were obtained as described by Solum et al.[27,28] while the MAT values were obtained from the triple echo MAT experiment (see ***Magic Angle Turning & Hopping***)

hydrogen, oxygen, and carbon) of the organic material can be used in a general classification scheme for describing the rank of a coal which, in increasing order, is given as peat, lignite, subbituminous, high volatile bituminous, medium volatile bituminous, low volatile bituminous, semianthracite, anthracite, and meta-anthracite. This rank progression exhibits a general order where the atomic ratios H/C and O/C decrease with increasing rank.

The most uniform microscopic constituents of coal, whose morphologically preserved or repolymerized materials retain distinct characteristics, are known as macerals. A large number of macerals have been identified and named. All macerals, however, can be conveniently grouped into three major subdivisions; liptinite, vitrinite, and inertinite. The vitrinite group of macerals are thought to be derived from plant cell wall material and make up the majority (50–90%) of most North American coals. The liptinite group of macerals is derived from algae and/or the resinous and waxy parts of plants such as resin, spores, pollen, and cuticules. These materials make up 5–15% of most North American coals but can be considerably higher in other coals and in coals derived from unique depositional environments. These macerals are the most aliphatic and hydrogen-rich of all the maceral groups. The inertinite group of macerals is derived from degraded woody tissue, making up 5–40% of most North American coals, but in western Canada and all southern hemisphere coals the percentage can be considerably higher.

The carbon aromaticity, f_a, is an important parameter in the study of coal and coal-derived materials and is the most widely used NMR parameter for coal studies. The first serious applications of ^{13}C NMR experiments to coal were directed at determining the carbon aromaticity. While several investigators studied a wide range of coals, Maciel et al.[42] and Gerstein et al.[23a] were the first investigators to investigate systematically the aromaticity/rank relationship. Gerstein et al. compared ^{13}C NMR-derived aromaticities with those obtained

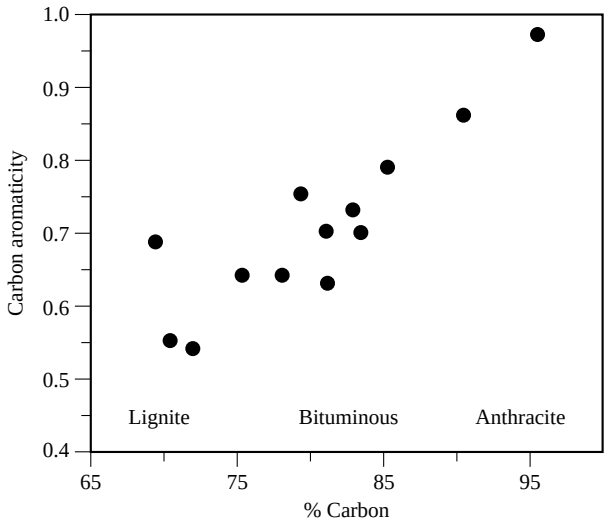

Figure 5 Carbon aromaticity, f_a, as a function of carbon content on a dry, ash-free basis

indirectly from graphical densities. The relationship between carbon aromaticity and rank (as derived from % carbon) is given in Figure 5. In NMR studies of macerals, the general trend in f_a values is liptinite < vitrinite < inertinite. Early studies by Maciel et al.[43] and Zilm et al.[44] helped to define the variations in aromaticity in the different maceral groups as well as the apparent differences is chemical functionality arising from differences noted in the isotropic shift/intensity distributions. More detailed NMR studies of maceral groups helped to refine the range of variations in aromaticities and chemical functionality.[25,45,46]

The quantitative accuracy of the f_a values derived from CP MAS experiments has been questioned and this controversy is addressed by Botto et al.[47] (see ***Fossil Fuels***). Orendt and co-workers have demonstrated that quantitative accuracy is obtainable if the CP MAS data are taken carefully with a variable contact time experiment and the data fitted to the proper model.[28]

3.2 Structural Components

The description of coal as a macromolecular network is credited to van Krevelen[48] who proposed a gel/sol model. The tools of polymer chemistry have been applied to study coal and advanced characterization techniques such as ^{13}C NMR have assisted in defining the parameters of the macromolecular structure of coals. The current model for coal structure consists of clusters of aromatic and hydroaromatic ring systems that are cross-linked such that domains exist which can, in some cases, undergo rapid reorientational motion. The argument that supports a cross-linked macromolecular network, other than the fact that the bulk of coals are not soluble in common solvents, is that coals swell by as much as 250% when brought into contact with appropriate solvents. The degree of reversibility is also consistent with a covalently cross-linked structure and rules out entanglements as the only associative force. Coals also display viscoelastic properties which are consistent with a macromolecular structure.

The type and characteristic of the second phase or component of coal is not as well defined as the macromolecular network, and has been the subject of extensive debate.[49] The 'mobile components' observed in proton NMR experiments have been shown to be complex and their relationship to a trapped molecular phase is yet to be completely resolved. Two views have been taken regarding the 'mobile protons' observed in ^{1}H NMR experiments. The first is that these protons can be attributed to molecules that are free to rotate in cages of the macromolecular network, and the second is that the mobile protons are associated with fragments of the macromolecular network capable of rotation due to single C–C or C–O bonds linking such fragments to the network. Jurkiewicz et al.[12,50] have used proton CRAMPS techniques to examine carefully the nature of the mobile protons in coal by comparing the native Argonne Premium Coals with those imbibed with pyridine-d_5. In pyridine-saturated coals the aliphatic and aromatic protons are better resolved and more structural details are evident. In addition, imbibing the samples with pyridine dramatically changes the structural or dynamic characteristics of a coal. The CRAMPS data provide a rough correlation between proton mobilities and the extractable components of coal. Employing a careful pyridine extraction study, Fletcher et al.[51] have studied the ^{13}C NMR structural components of the extracts and residues from the Argonne Premium Coals and contrasted the subtle differences between the extractable and residual components in terms of cross-linking between aromatic clusters.

An excellent review of the molecular structure, chemistry, and existing structural models of coal (up to 1986) is given by Davidson.[52] The early coal structure models proposed by Given and Weiser[53] and further refined by Shinn and Solomon[53] were based, in part, on available NMR data. From these models investigators attempted to construct an average or representative macromolecular structure of coal. In general, the information used for assembling a coal structure is molecular weight, aromatic cluster size, linkages between aromatic units, carbon aromaticity, elemental composition, as well as experimental results from chemical and thermal reactions. In order to explain the physical properties of coal and the thermal and chemical behavior of coal, network models have recently emerged[54–57] and solid state NMR data have become indispensable in constructing models that describe coal behavior.[51,54–57]

4 APPLICATIONS TO COAL SCIENCE

4.1 Refinements in Structural Detail

Gerstein suggested that ^{13}C NMR spectroscopy could provide more information on coal structure than just aromaticity and demonstrated that one could use dipolar dephasing techniques to examine functional groups and estimate aromatic cluster size.[22] Alemany et al.[19–21] refined the functionality studies employing painstakingly acquired dipolar dephasing data. Solum et al.[27,28] carefully employed a variety of experiments (i.e. dipolar dephasing, variable contact time experiments, and integrations of the ^{13}C spectra over selected chemical shift ranges) to derive 12 structural parameters for the eight

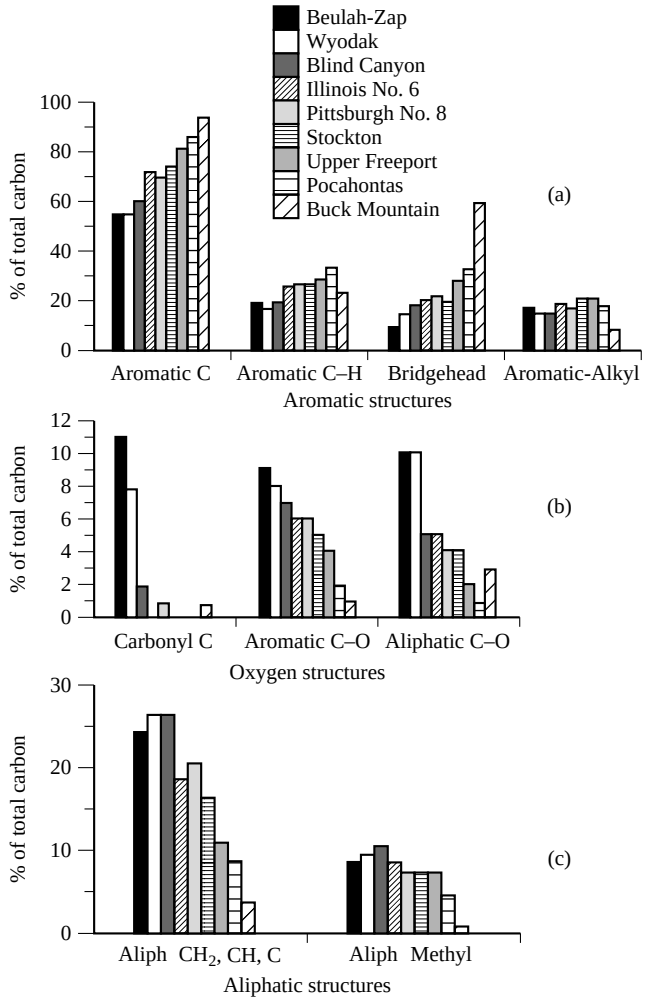

Figure 6 (a) Aromatic carbon structure distribution of the Argonne Premium Coals; (b) structural distribution of carbons associated with oxygen in the Argonne Premium Coals; and (c) carbon distribution of the aliphatic region of the Argonne Premium Coals

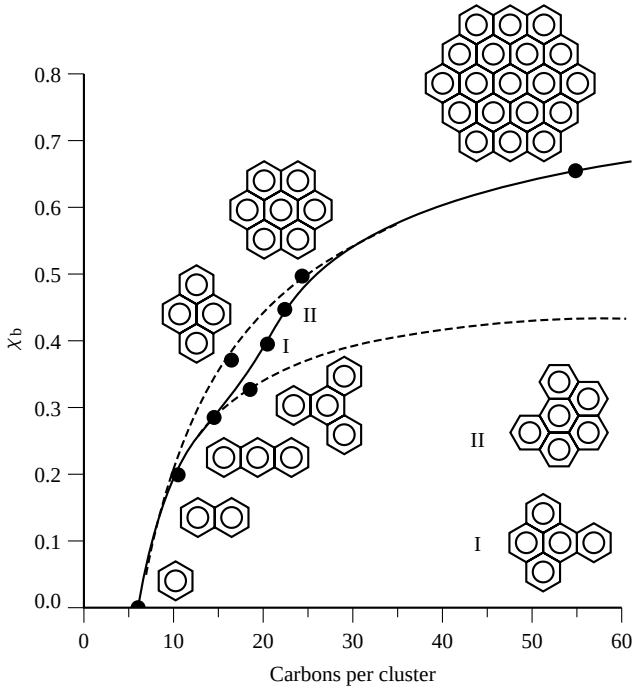

Figure 7 Plot of the mole fraction of bridgehead carbons, χ_b, versus C where C is the number of carbon atoms per aromatic cluster. The solid curve is for the combined model, the upper dashed curve is for the circular catenation model, and the lower dashed curve is for the primary catenation mode. (See Solum et al.[27] for details)

Argonne Premium Coals as well as a large variety of other coals and coal-derived chars.[51,56,57] The traditionally defined carbon aromaticity, f_a, is a sum of the contributions of all sp^2 carbons to an NMR spectrum. In coal samples it is assumed that ethylene groups are not present in any significant quantity. Hence, the f_a values are assumed to consist of aromatic plus carbonyl groups and these parameters have been redefined as f_a' and f_a^C, respectively. Employing lengthy dipolar dephasing experiments, the relative contributions of protonated and nonprotonated aromatic carbons can be estimated as f_a^H and f_a^N, respectively. The nonprotonated aromatic carbons, f_a^N, consist of contributions from alkyl-substituted, oxygen-substituted (phenols and phenolic ethers), and bridgehead carbons, defined as f_a^S, f_a^P, and f_a^B, respectively. The aliphatic groups have been segregated by chemical shift ranges which can be used to approximate the contributions from methyl groups, f_{al}*, oxygen-substituted alkyl carbons, f_{al}^O, and f_{al}^H, which is defined as the sum of all CH, CH_2, and nonprotonated aliphatic carbons. While these parameters are derived from chemical shift ranges that are known to contain some overlap with other functional groups, these approximations are reasonable and can be used to develop approximate model structures that are consistent with other analytical data. The major structural parameters derived from the coals in the Argonne Premium Coal Sample Bank plus Buck Mountain anthracite are given in Figure 6. From a knowledge of the relative number of peripheral and bridgehead carbons, it is possible to estimate the average aromatic cluster size of coal samples.[27] The average cluster size model for coal is shown in Figure 7 and the range of average number of aromatic carbons per cluster (AC/Cl) is given in Figure 8. This parameter has proven extremely useful in analyzing changes that occur during conversion and combustion processes.

If one defines the total number of ring attachments as the number of alkyl and oxygen substituents on the average aromatic cluster, it is possible to estimate the number of attachments per cluster. This number is between three and six for all coals studied but small variations in this parameter, defined as the cluster coordination number (σ + 1), are very important in explaining phenomena associated with coal structure, physical properties, and combustion behavior. The cluster coordination numbers for the coals previously described are given in Table 2.

4.2 Applications to Combustion and Pyrolysis Modeling

As previously discussed, the present model for coal structure is based on a network consisting of aromatic clusters of varying size connected by various types of bridging groups, and a simple schematic of the major types of structural elements that can by derived from NMR data is shown in Figure 9.

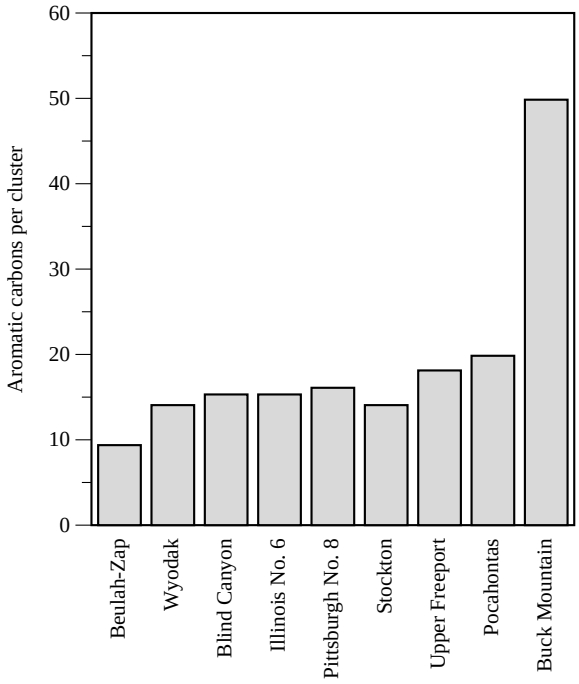

Figure 8 Aromatic cluster size of the Argonne Premium Coals and Buck Mountain anthracite, PSOC-1468

Table 2 Average Cluster Descriptions for ACERC Coals[a]

Coal	AC/Cl	(σ + 1)	P_o	*BL*	*MW*	m_δ
Beulah-Zap[b]	9	4.1	0.64	2.6	269	40
Wyodak	14	5.6	0.55	3.1	408	42
Blind Canyon	15	5.1	0.49	2.5	366	36
Illinois No. 6	15	5.0	0.63	3.2	322	27
Pittsburgh No. 8[b]	16	4.7	0.64	3.0	330	24
Stockton	14	4.8	0.69	3.3	272	20
Upper Freeport	18	5.3	0.67	3.6	312	17
Pocahontas No. 3	20	4.4	0.74	3.3	307	14
PSOC-1443	10	4.8	0.59	2.8	297	36
PSOC-1488	11	4.7	0.54	2.5	310	37
PSOC-1468	50	4.7	0.89	4.2	656	12

[a]The Advanced Combustion Engineering Research Center (ACERC) selected a set of standard coals for characterization and combustion testing and modeling. The 11 coals consist of the eight coals contained in the Argonne Premium Coal Sample Bank and three additional coals obtained from the Penn State Coal Sample Bank. Column headings are defined in the text.
[b]Averaged over two or more sample vials.

A number of investigators have applied statistical methods to predict how such a network would behave when subjected to thermally induced bridge-breaking cross-linking and mass transport processes. The geometry of a network is described by its degree of branching. An unbranched linear network will have one bridge per ring cluster attaching it to the next cluster. Thus, each cluster has two attachments and is said to have a coordination number (σ + 1) of two. A highly branched network would have several bridges attached to it and a higher coordination number. When coal is heated, the connecting bridges can break and new bridges can form. The objectives of network models of coals are, given the geometry

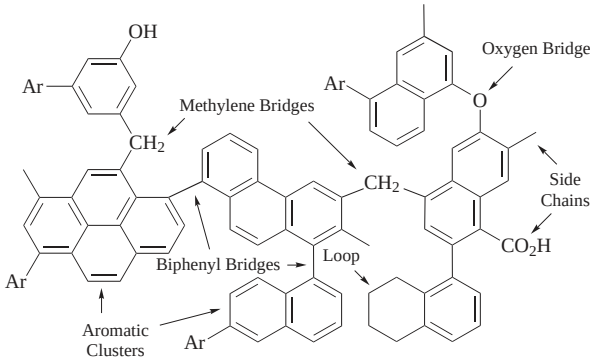

Figure 9 Representative chemical structural units identified in ^{13}C NMR analysis of coal and coal chars

of the macromolecular network, to predict the concentrations of individual aromatic ring clusters (monomers) and linked clusters (oligomers of *n* clusters, '*n*-mers') that are completely detached from the totally linked network, as a function of the number of unbroken bridges. By assigning an average or distribution of molecular weights to the ring clusters, the amounts of tar, extractables, liquids, or char can then be defined from the distribution of oligomer sizes. The application of network models appears to unify many observations of coal pyrolysis, including tar formation, extract formation, metaplast formation, fluidity, and solvent swelling behavior.[54]

A major challenge to all network models is the acquisition of analytical data that describe the network with sufficient detail that the investigator is not required to make guesses or fit the experimental data in order to derive critical network parameters. Grant et al.[55] have demonstrated that the coal macromolecular structure can be modeled as a Bethe lattice and that this lattice structure can explain the nonlinear behavior associated with devolatilization processes of coals. The coordination number of the Bethe lattice, σ + 1, is a key element in predicting the lattice behavior, and this parameter is determined directly from NMR data as the average number of substituents on an average aromatic cluster. Four other essential parameters, P_o, *BL*, *MW*, and m_δ, can be derived from the NMR data of coals.

The fraction of intact bridges between clusters, P_o is calculated with the assumption that all nonbridging cluster substituents are terminated by a methyl group and can be estimated as

$$P_o = [(\text{attachments}/100\text{C}) - f_{al}^*]/(\text{attachments}/100\text{C}) \quad (1)$$

While it is recognized that aryl–aryl bridges and phenolic groups are present in relatively small amounts in most coals, these structural units cannot be easily derived from NMR data and, hence, this approximation neglects hydroxy and aryl groups as possible chain terminators. The remaining cluster attachments must be either aliphatic or ether bridges between different clusters or aliphatic loops between two adjacent carbons in the same aromatic cluster, i.e. a hydroaromatic structure such as exists in tetralin. The number of bridges and loops, *BL*, on a cluster is defined as

$$BL = P_o \times (\sigma + 1) \quad (2)$$

The mechanical properties of the network will be related to this parameter because *BL* is related to the cross-link density of the macromolecular structure. The average cluster molecular weight (*MW*), and the total mass of the attachments to the aromatic cluster (m_δ) are

$$MW = (\text{aromatic carbons/cluster} \times 12.011)/(f_{a'} \times \%C) \quad (3)$$

$$m_\delta = (MW - C_{\text{clust}} \times 12.011)/(\sigma + 1) \quad (4)$$

where C_{clust} is the average number of carbons per cluster. While these parameters fall within certain ranges (see Table 2), each coal is unique and must be modeled separately.

During coal devolatilization, both tar (defined as volatiles, other than water, that condense at room temperature) and gas (CH_4, CO, CO_2, H_2O, light hydrocarbons, etc.) are released and a residual char remains. Employing the NMR-derived parameters needed to model the macromolecular network of each coal, it is possible to predict the tar and total mass loss (tar plus gas) of a set of coals with reasonable accuracy, as seen in Figure 10, without the necessity of invoking fitting parameters.

The mass of attachments to the aromatic ring is directly related to the amount of gas liberated during coal devolatilization through thermal cracking of the side chains.[57] During the pyrolysis process the physical and chemical properties of the residual char are continually changing. Solum et al.[56] were able to follow the details of the release of tar and gas together with the evolution of char structure from a lignite (Beulah-Zap) and a high volatile bituminous (Illinois No. 6) coal during devolatilization. The NMR data were used to track the lattice parameters associated with average cluster size and cross-linking reactions. Under rapid heating conditions (10^4 K s^{-1}), the data demonstrate that Zap coal undergoes early cross-linking behavior due to the loss of carboxy groups whereas Illinois No. 6 exhibits a slower overall rate of cross-linking. It was further noted from the NMR data that the number of cluster attachments remained constant during mass release during rapid pyrolysis at a temperature of 1250 K. However, near the end of the mass release the number of bridges and loops increased, suggesting that the coal lattice had begun to cross-link as tar release was terminated but as gas release continued. Under rapid heating but short resident time conditions in the reactor employed, the data exhibited little evidence of cluster size growth in the macromolecular structure. These data suggest that near the end of the devolatilization process cross-linking occurs at the same time as aliphatic carbons are released and the graphitization process does not occur under the conditions of the experiments performed. In the Illinois No. 6 coal, most of the mass loss occurred before the onset of significant changes in aromaticity. For the Zap coal, the changes in aromaticity occurred much earlier than for Illinois No. 6. The carbon skeletal structure of the final chars are similar for these two coals and Fletcher et al.[57] have reported similar results on a number of other chars even though the structure of the initial coals are quite different.

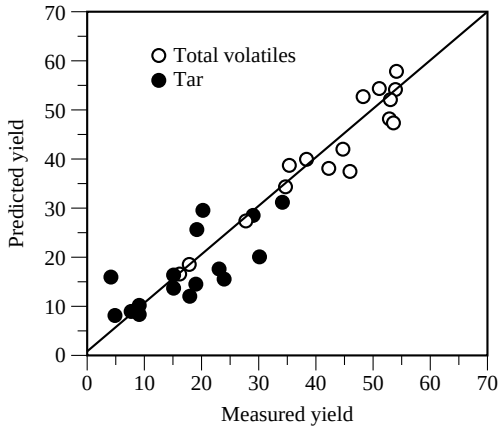

Figure 10 Comparison of predicted and measured tar and total volatiles yields for a wide range of coals. Data are for coals from the Argonne Premium Coal Sample Bank and from the Penn State Sample Bank for which NMR and pyrolysis data are available. (See Solum et al.[56] for details)

The physical properties of the macromolecular structure are related to the extent of cross-linking present. The NMR-derived bridges and loops parameter can be used estimate the degree of cross-linking that exists in coals and chars. An NMR cross-link index can be defined as

$$\text{NMR index} = (M_\infty - M_T)/(M_\infty - M_o) \quad (5)$$

where M_T is the number of bridges and loops per cluster at temperature T and the o and ∞ subscripts refer to the parent coal and the fully pyrolyzed char respectively.

Figure 11 compares the cross-link density obtained from the ^{13}C NMR data with that obtained from solvent swelling experiments.[57] These data clearly demonstrate that the functional form of the NMR cross-linking index is consistent with the normalized volumetric swelling index commonly used to study the cross-link structure in polymers. In the Beulah-Zap lignite, the number of bridges and loops increase with temperature, indicating that initial cross-linking has occurred at a relatively low temperature ($\sim$ 500 K) and progressive cross-linking occurs as the temperature increases. In the case of the Pittsburgh No. 8 coal, the NMR data suggest that the initial solvent swelling behavior is due to the breaking of labile bridges at moderate temperatures (500–600 K), which permits increased flexibility of the macromolecular network. At higher temperatures (>700 K), the number of bridges begins to increase as the swelling of the coal decreases. Such behavior would be expected as a more rigidly cross-linked network developed. The NMR data confirm that low-temperature cross-linking occurs in low-rank coals and that cross-linking at moderate temperatures is observed in both bituminous and low-rank coals.

The preceding examples demonstrate that NMR spectroscopy provides a great deal of information on coal structure and is perhaps the premier analytical tool in coal studies despite the inherent difficulties in carrying out experiments and interpreting the quantitative nature of the data. Even so, data carefully taken can be used to assess differences that occur in coals and follow many processes associated with coal utilization. Ambiguity exists in extracting information from overlapping spectral bands in both the aromatic and aliphatic regions. However, promising new experiments, such as the triple echo MAT and PHORMAT, that take advantage of the information contained in the chemical shift tensors, will probably resolve

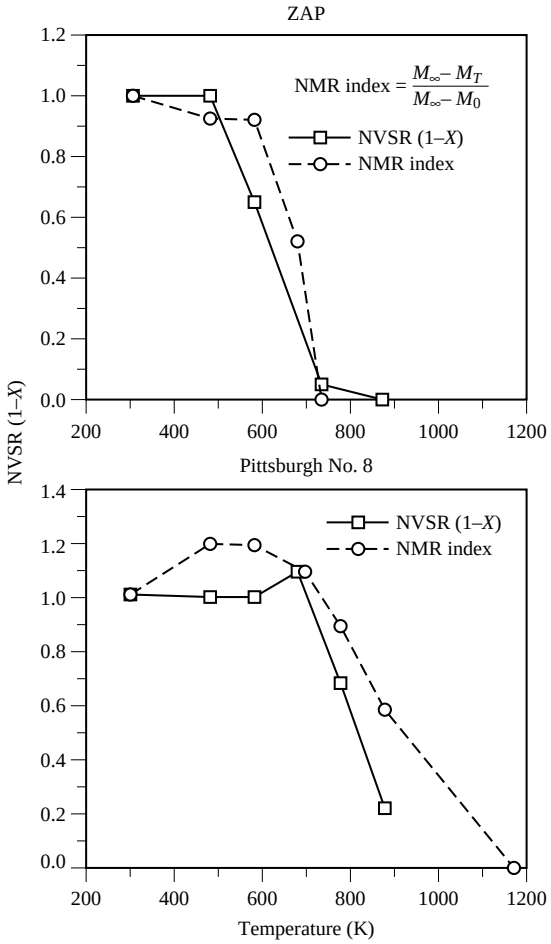

Figure 11 Comparison of the normalized volumetric swelling ratio (NVSR) for Beulah-Zap lignite and Pittsburgh No. 8 with the ^{13}C NMR index derived from the number of bridges and loops present in the parent coals and the pyrolysis chars. (See Solomon et al.[54] for details)

some of these ambiguities, particularly those associated with the aromatic region of the spectra.

5 NOTE

Beulah-Zap and Pittsburgh No. 8 are from the Argonne Premium Coal Sample Bank, while the Buck Mountain anthracite is available from the Penn State Sample Bank as PSOC-1468.

6 REFERENCES

1. K. L. Smith, L. D. Smoot, T. H. Fletcher, and R. J. Pugmire, *The Structure and Reaction Processes of Coal*, Plenum Press, New York, 1994, pp. 1–2.
2. P. C. Newman, L. Pratt, and R. E. Richards, *Nature (London)*, 1955, **175**, 645.
3. U. Haeberlen and J. S. Waugh, *Phys. Rev.*, 1968, **175**, 453.
4. J. S. Waugh, L. M. Huber, and U. Haeberlen, *Phys. Rev. Lett.*, 1968, **20**, 180.
5. B. Schnabel, U. Haubenreisser, G. Scheler, and R. Muller, *Proc. 19th Congr. AMPERE (Heidelberg), 1976*, 441.
6. B. C. Gerstein, R. G. Pembleton, R. D. Wison, and L. J. Ryan, *J. Chem. Phys.*, 1977, **66**, 361.
7. B. C. Gerstein, C. Chou, R. G. Pembleton, and R. C. Wilson, *J. Phys. Chem.*, 1977, **81**, 565.
8. B. C. Gerstein, *Philos. Trans. R. Soc. London*, 1981, **A299**, 521.
9. G. E. Maciel, D. E. Bronninmann, and C. F. Ridenour, in *Magnetic Resonance of Carbonaceous Solids*, eds. R. E. Botto and Y. Sanada, *Adv. Chem. Ser. No. 229*, Am. Chem. Soc., Washington, DC, 1993, Chap. 2
10. C. E. Bronnimann and G. E. Maciel, *Org. Geochem.*, 1989, **14**, 189.
11. M. F. Davis, G. R. Quinting, C. E. Bronnimann, and G. E. Maciel, *Fuel*, 1989, **68**, 763.
12. A. Jurkiewicz, C. E. Bronnimann, and G. E. Maciel, *Fuel*, 1989, **68**, 872.
13. A. Jurkiewicz, C. E. Bonnimann, and G. E. Maciel, *Fuel*, 1990, **69**, 804.
14. R. A. Friedel and H. L. Retcofsky, *Chem. Ind. (London)*, 1966, 455.
15. H. L. Retcofsky and R. A. Friedel, *Anal. Chem.*, 1971, **43**, 485.
16. D. L. VanderHart and H. L. Retcofsky, *Fuel*, 1976, **55**, 202.
17. V. J. Bartuska, G. E. Maciel, J. Schaefer, and E. O. Stejskal, *Fuel*, 1977, **56**, 354.
18. S. J. Opella and M. H. Frey, *J. Am. Chem. Soc.*, 1979, **101**, 5854.
19. L. B. Alemany, D. M. Grant, T. D. Alger, and R. J. Pugmire, *J. Am. Chem. Soc.*, 1983, **105**, 6697.
20. L. B. Alemany, D. M. Grant, R. J. Pugmire, and L. M. Stock, *Fuel*, 1984, **63**, 513.
21. M. A. Wilson, A. M. Vassalo, P. J. Connin, and H. Rottendorf, *Anal. Chem.*, 1984, **56**, 433; M. A. Wilson, R. J. Pugmire, J. Karas, L. B. Alemany, W. R. Woolfenden, P. H. Given, and D. M. Grant, *Anal. Chem.*, 1984, **56**, 933.
22. P. D. Murphy, T.J. Cassady, and B. C. Gerstein, *Fuel*, 1982, **61**, 1233; P. D. Murphy, B. C. Gerstein, V. L. Weinberg, and T. L. Yen, *Anal. Chem.*, 1982, **54**, 522.
23. (a) B. C. Gerstein, P. D. Murphy, and L. M. Ryan, in *Coal Structure*, Ed. R. A. Meyers, Academic Press, New York, 1982, Chap. 4; (b) P. DuBois, T. J. Cassady, and B. C. Gerstein, 1982, *Fuel*, **61**, 1233.
24. K. W. Zilm, R. J. Pugmire, D. M. Grant, R. E. Wood, and W. H. Weiser, *Fuel*, 1979, **58**, 11.
25. R. J. Pugmire, K. W. Zilm, D. M. Grant, S. R. Larter, J. Allen, J. T. Senftle, A. Davis, and W. Spackman, in *New Approaches in Coal Chemistry*, eds. B. D. Blaustein, B. C. Bockrath, and S. Friedman, *ACS Symp. Ser. No. 169*, Am. Chem. Soc., Washington, DC, 1981.
26. B. C. Gerstein, P. D. Murphy, and L. M. Ryan, in *Coal Structure*, ed. R. A. Meyers, Academic Press, New York, 1982, p. 120.
27. M. S. Solum, R. J. Pugmire, and D. M. Grant, *Energy Fuels*, 1989, **3**, 187.
28. A. M. Orendt, M. S. Solum, N. K. Sethi, R. J. Pugmire, and D. M. Grant, in *Advances in Coal Spectroscopy*, ed. H. L. C. Meuzelaar, Plenum Press, New York, 1992.
29. M. A. Wilson, J. V. Hanna, P. A. Cole-Clark, P. F. Greenwood, and G. D. Willett, *Fuel*, 1992, **71**, 1097; M. A. Wilson, J. V. Hanna, P. A. Cole-Clark, G. D. Willett, and P. F. Greenwood, *Org. Geochem.*, 1992, **18**, 555.
30. P. G. Hatcher, *Org. Geochem.*, 1990, **16**, 959; P. G. Hatcher, K. A. Wenzel, and J.-L. Faulon, *Am. Chem. Soc., Div. Fuel Chem., Prepr.*, 1993, **38**, 1270.

31. D. J. Clifford, J. P. Mathews, J.-L. Faulon, and P.G. Hatcher, *Am. Chem. Soc., Div. Fuel Chem., Prepr.*, 1994, **39**, 198.
32. J. C. Facelli, D. G. Grant, and J. Michl, *Acc. Chem. Res.*, 1987, **20**, 152; J. C. Facelli and D. M. Grant, *Theor. Chim. Acta*, 1987, **71**, 277; A. M. Orendt, N. K. Sethi, J. C. Facelli, W. J. Horton, R. J. Pugmire, and D. M. Grant, *J. Am. Chem. Soc.*, 1992, **114**, 2832.
33. A. M. Orendt, M. S. Solum, N. K. Sethi, C. D. Hughes, R. J. Pugmire, and D. M. Grant, in *Magnetic Resonance of Carbonaceous Solids*, eds. R. E. Botto and Y. Sanada, *Adv. Chem. Ser. No. 229*, Am. Chem. Soc., Washington, DC, 1993, Chap. 22
34. N. K. Sethi, D. M. Grant, and R. J. Pugmire, *J. Magn. Reson.*, 1987, **71**, 476.
35. N. K. Sethi, R. J. Pugmire, J. C. Facelli, and D. M. Grant, *Anal. Chem.*, 1988, **60**, 1574; A. M. Orendt, N. K. Sethi, J. C. Facelli, W. J. Horton, R. J. Pugmire, and D. M. Grant, *J. Am. Chem. Soc.*, 1992, **114**, 2832.
36. M. H. Sherwood, J. C. Facelli, D. W. Alderman, and D. M. Grant, *J. Am. Chem. Soc.*, 1991, **113**, 750; C. M. Carter, D. W. Alderman, J. C. Facelli, and D. M. Grant, *J. Am. Chem. Soc.*, 1987, **109**, 2639.
37. J. Z. Hu, A.M. Orendt, D. W. Alderman, C. Ye, R. J. Pugmire, and D. M. Grant, *Solid State Nucl. Magn. Reson.*, 1993, **2**, 235.
38. R. J. Pugmire, J. Z. Hu, D. W. Alderman, A. M. Orendt, C. Ye, and D. M. Grant, *Int. Conf. Coal Sci., Banff, Canada, September 12–17, 1993*, p. 485.
39. J. Z. Hu, M. S. Solum, D. W. Alderman, R. J. Pugmire, C. Ye, and D. M. Grant, *Energy Fuels*, 1995, **9**, 717.
40. J. Z. Hu, A. M. Orendt, D. W. Alderman, R. J. Pugmire, C. Ye, and D. M. Grant, *Solid State Nucl. Magn. Reson.*, 1994, **3**.
41. J. Z. Hu, W. Wang, F. Liu, M. S. Solum, D. W. Alderman, R. J. Pugmire, and D. M. Grant, *J. Magn. Reson.*, 1995, **A113**, 210.
42. F. P. Miknis, M. Sullivan, V. J. Bartuska, and G. E. Maciel, *Org. Geochem.*, 1981, **3**, 19.
43. G. E. Maciel, V. J. Bartuska, L. Petrakis, and D. W. Grandy, *Fuel*, 1982, **61**, 411.
44. K. W. Zilm, R. J. Pugmire, S. R. Larter, J. Allen, and D. M. Grant, *Fuel*, 1981, **60**, 717.
45. R. J. Pugmire, W. R. Woolfenden, C. L. Mayne, J. Karas, and D. M. Grant, in *Chemistry and Characterization of Coal Macerals*, eds. R. E. Winans and J. C. Crelling, *ACS Symp. Ser. No. 252*, Am. Chem. Soc., Washington, DC, 1984, Chap. 6
46. M. A. Wilson, R. J. Pugmire, J. Karas, L. B. Alemany, W. R. Woolfenden, P. H. Given, and D. M. Grant, *Anal. Chem.*, 1984, **56**, 933.
47. R. A. Wind, G. E. Maciel, and R. E. Botto, in *Magnetic Resonance of Carbonaceous Solids*, eds. R. E. Botto and Y. Sanada, *Adv. Chem. Ser. No. 229*, Am. Chem. Soc., Washington, DC, 1993, Chap. 1
48. D. W. van Krevelen, *Coal Science and Technology 3: Coal*, Elsevier, New York, 1981.
49. F. Derbyshire, A. Marzec, H-R. Schulten, M.A. Wilson, A. Davis, P. Tekely, J-J. Delpuech, A. Jurkiewicz, C. E. Bronnimann, R. A. Wind, G. E. Maciel, R. Narayan, K. Bartle, and C. Snape, *Fuel*, 1989, **68**, 1091.
50. A. Jurkiewicz, C. E. Bronnimann, and G. E. Maciel, in *Magnetic Resonance of Carbonaceous Solids*, eds. R.E. Botto and Y. Sanada, *Adv. Chem. Ser. No. 229*, Am. Chem. Soc., Washington, DC, 1993, Chap. 21
51. T.H. Fletcher, S. Bai, R. J. Pugmire, M. S. Solum, S. Wood, and D. M. Grant, *Energy Fuels*, 1993, **7**, 734.
52. R. M. Davidson, in *Coal Science*, eds. M. L. Gorbaty, J. W. Larsen, and I. Wender, Academic Press, New York, 1982, Vol. 1, p. 83; R. M. Davidson, Nuclear Magnetic Resonance Studies of Coal, Rep. No. ICTIS/TR32, January 1986, IEA Coal Research, London.
53. K. L. Smith, L. D. Smoot, T. H. Fletcher, and R. J. Pugmire, *The Structure and Reaction Processes of Coal*, Plenum Press, New York, 1994, Chap. 3
54. P. R. Solomon, T. H. Fletcher, and R. J. Pugmire, *Fuel*, 1993, **72**, 587.
55. (a) D. M. Grant, R. J. Pugmire, T. H. Fletcher, and A. R. Kerstein, *Energy Fuels*, 1989, **3**, 175; (b) T. H. Fletcher, A. R. Kerstein, R. J. Pugmire, and D. M. Grant, *Energy Fuels*, 1990, **4**, 54; (c) T. H. Fletcher, A. R. Kerstein, R. J. Pugmire, and D. M. Grant, *Energy Fuels*, 1992, **6**, 414.
56. R.J. Pugmire, M. S. Solum, D. M. Grant, S. Critchfield, and T. H. Fletcher, *Fuel*, 1991, **70**, 414.
57. T. H. Fletcher, M. S. Solum, D. M. Grant, and R. J. Pugmire, *Energy Fuels*, 1992, **6**, 643.

Biographical Sketch

R. J. Pugmire. *b* 1937. B.S., 1959, Idaho State College, Ph.D., 1966, Chemistry, University of Utah, USA, where he was introduced to NMR by David M. Grant. Postdoctoral research, University of Utah, 1966–68. Faculty in Chemical and Fuels Engineering, and Associate Vice President for Research, University of Utah, 1968–present. Approx. 140 publications. Research specialties: carbon-13 NMR, chemical shielding in liquids and solids, coal chemistry and applications of NMR spectroscopy to coal science.

Fossil Fuels

Robert E. Botto

Argonne National Laboratory, Argonne, IL , USA

1	Introduction	1
2	Applications to Coal Science	1
3	Applications to Shale Oil Research	12
4	Other Fuels	14
5	Related Articles	15
6	References	15

1 INTRODUCTION

Energy[1] is an important commodity because it affects our lives in many ways. In the past, a direct relationship had been drawn between energy consumption and economic growth. Advancement in economic growth was shown to have a favorable impact on the quality of life in economically advanced societies by fostering better health and educational services, a robust industrial base with which to sustain future development, and various forms of labor-saving devices for common use. Often concerns about the negative impacts from economic growth, such as pollution, overpopulation, and crime have been neglected by nations striving to improve their economic status.

In the rapidly changing world of the last 20 years, however, there have been escalating demands placed on global energy resources. An ever-increasing number of developing countries have competed for the existing energy supply. Environmental issues have become the highest priority in guiding the utilization of global resources. While traditional 'old-world' fuels such as wood, agricultural products, and animal dung are still in use around the globe, they remain effective sources of energy only for less developed societies. Alternative energy resources in the form of geothermal and hydroelectric power are limited throughout the world, while renewable resources such as solar, wind, and tidal have been slow to develop on a large commercial scale. Development of nuclear energy, once heralded as the answer to meet the future global energy demands into the next millennium, has been severely curtailed because of apprehension about radioactive release into the environment and problems in storage of high level radioactive wastes. Consequently, a greater burden of world energy demands over the past 20 years has centered on fossil fuels. With increasing demands on supplies worldwide, fuel quality has diminished significantly. In addition, utilization of fossil fuels as a carbon source for the production of bulk and specialty chemicals, and of high technology polymer blends and composites may be almost as important economically as their use as an energy source.

Fossil fuel energy resources include coal, peat, petroleum, oil shale, tar sands, and natural gas. Total world resources of coal are 15.1×10^{12} ton; total world production is estimated to be 3.0×10^{9} ton per year. The importance of coal as a resource is that, despite having greater problems with production, transportation and utilization compared with oil and gas, it represents a vast resource to meet energy demands well into the future (for more than 1000 years). World resources of peat, being far less utilized than the other fuels, is estimated to be only 0.2×10^{12} ton. Estimates of the reserves and resources of petroleum, having received considerable attention because of concern over their eminent depletion globally, are on the order of 0.3×10^{12} ton, of which about 0.1×10^{12} ton are proven reserves. Worldwide oil production is about 4×10^{9} ton per year. Enhanced oil recovery strategies have added approximately an additional 0.1×10^{12} ton to the estimate of total recoverable resources of petroleum. Tar sands are fairly localized throughout the world, with estimated reserves of only 0.03×10^{12} ton. On the other hand, oil shale deposits are widely distributed geographically and represent a potentially enormous resource, with estimates ranging between 100×10^{12} and 500×10^{12} ton of potential oil. Limitations for the commercialization of this vast energy resource are the large-scale operations required for production and hence prohibitive investment costs, and the severe environmental problems that would be created by the massive excavation of natural lands and subsequent disposal of enormous quantities of solid waste. Natural gas, with proven reserves similar in energy equivalence to those of petroleum, has the advantage of being the cleanest of the fossil fuels; however, transportation costs of this commodity between continents are high unless supplies can be reached economically via pipeline.

Applications of NMR spectroscopy to the study of fossil fuels have experienced extraordinary growth since the inception of the technique in 1946.[2,3] Early experiments focused on the application of broadline ^{1}H NMR spectroscopy to petroleum, oil shale, and coal research. High-resolution liquid state ^{1}H NMR proved to be an extremely useful structure elucidation tool for fuel extracts and solubilized conversion products in subsequent years. However, NMR did not flourish as a celebrated technique for fossil fuel characterization until the 1970s. The growth of the technique was brought about by several factors: (1) integration of computers with instrumentation in the late 1960s enhanced data acquisition capabilities considerably; (2) introduction of Fourier transform methods paved the way for the development of pulsed NMR spectroscopy, which made detection of less sensitive nuclei more routine, and spawned a wide variety of pulsed techniques for sensitivity enhancement, relaxation measurements and multidimensional NMR studies; and (3) the oil embargo of 1973–74 and the Organization of Petroleum Exporting Countries (OPEC) incident in 1979 catalyzed abrupt increases in the price of petroleum, reversing the trend of cheap and abundant energy supplies that had lasted over the past 100 years. This incident prompted general concern over the availability of energy resources in the future and, as a consequence, stimulated growth of basic and applied research in the area of fossil fuels to seek alternate forms of energy. Nearly two decades of intensive research in NMR characterization of fossil fuels ensued.

2 APPLICATIONS TO COAL SCIENCE

Coal[4] is considered to be a heterogeneous organic rock and is typically black in color, although geologically younger deposits can range in color from brown to brownish red. It is formed by the accumulation of plant debris which has been

altered over geological time by the action of biological, chemical, and physical (heat and pressure) degradation processes. The relative quantities of remaining plant parts, and the degree of their thermal maturation and degradation result in coals with varied properties. Coals may be classified as banded (humic coals) or nonbanded (cannel or boghead coals), are hard or soft, or can vary in rank from brown coal, through lignite, subbituminous, bituminous to anthracite. The degree of thermal maturation of plant matter, or coalification, is referred to as *rank*.

The evolution of coal, the enormous variation found in its composition, its microheterogeneity, and its differentiation toward chemical reactions suggest that coal is a complex mixture of compounds. While this is true, however, there is some order to its inherent, overall structure. There are microscopically discrete, optically homogeneous aggregates of organic materials derived from various plant parts that constitute coal. These individual domains are referred to as *macerals*.[5,6] There are three major maceral groups, each having their own distinct set of properties and selective chemistries. The most abundant of the macerals found in US coals is *vitrinite*, which is derived from woody tissue of plants and is a largely lignin based polymer. The group of macerals called *liptinite* may be derived either from waxy leaf cutin, parts of spores and pollen, or algal bodies. This group of macerals tend to be composed of highly aliphatic material. The last maceral group, *inertinite*, named for its relative unreactivity in most chemical reactions, is thought to be derived from material that has undergone extensive oxidation or that is a form of fossilized charcoal derived from primordial forest fires. The inertinite macerals have a high degree of aromatic character.

Apart from the organic components, there may be substantial quantities of water and mineral matter present in coal. The minerals can be varied and also rather complex in composition; hydrated aluminosilicates, clay minerals, quartz, sulfides, sulfates, pyrite and carbonates have been identified, to name a few. The main elemental constituents of coals, therefore, are carbon, hydrogen and oxygen, with varying amounts of nitrogen and sulfur, and lesser amounts of silicon, calcium, aluminum, iron, magnesium, sodium, and other trace elements. Given this diversity of chemistry and elemental composition, coals have been a rich source for study by NMR techniques.

2.1 Structure Characterization

2.1.1 Liquid State NMR

The first published account of high-resolution ^{1}H NMR of a coal liquid, or soluble reaction product, appeared in 1959.[7] This first ^{1}H spectrum (Figure 1) of a coal asphaltene recorded in carbon disulfide at 125 °C demonstrated that the technique could readily distinguish three magnetically inequivalent types of proton nuclei in the sample, and confirmed that few polynuclear aromatic structures were present. This was the first definitive structural information obtained on a fossil fuel material. Two years later, the first liquid state ^{1}H NMR spectrum of a coal extract was reported. Since that time, numerous workers have reported on similar studies involving

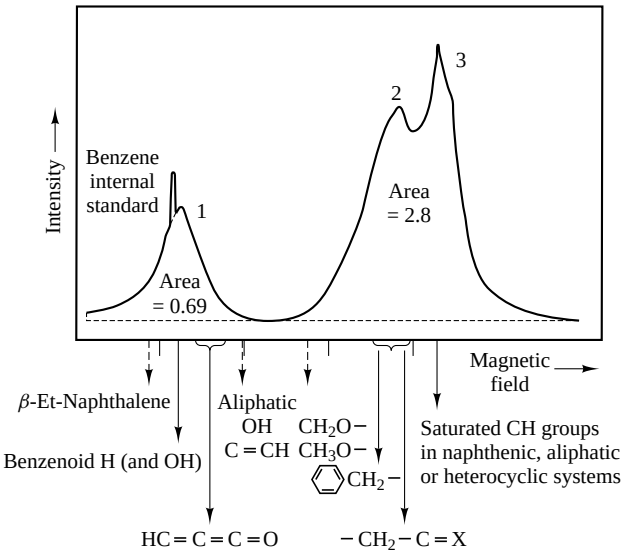

Figure 1 The first proton NMR spectrum of an asphaltene in carbon disulfide at 125 °C. Recorded by J. N. Shoolery, H. E. Weaver, and R. C. Jones at Varian Associates

coal extracts and have demonstrated the utility of the technique for analyzing the hydrogen distributions in these materials.[8]

In 1960, Brown and Ladner[9] were the first to demonstrate that the hydrogen distribution in carbonaceous fuels determined by ^{1}H NMR could be used to infer information about the carbon skeleton. Initial experiments were performed on a series of vacuum carbonization products from coals. The method used information from the ^{1}H NMR spectrum and carbon and hydrogen elemental analysis to determine several important structural parameters, including the fraction of aromatic carbon (f_a) of the sample. The fraction of carbon aromaticity was defined as that fraction of the total number of carbon atoms which are aromatic, $f_a = C_{ar}/C_{tot}$. The normalized intensities of the types of hydrogen were determined from integration of the proton spectrum to calculate the carbon aromaticity using the equation:

$$f_a = \left[(C/H) - (H_\alpha/x) - \frac{(H_\gamma + H_\beta)}{y} \right] \Big/ (C/H) \qquad (1)$$

where C/H is the atomic ratio of carbon to hydrogen from elemental analysis data; x and y are the average number of hydrogen atoms per α-alkyl group to an aromatic ring and the remaining alkyl groups, respectively; and H_α and $(H_\gamma + H_\beta)$ represent the normalized integrated intensities of the α-alkyl hydrogen atoms and other hydrogen atoms, respectively. From this basic equation can be deduced other key structural parameters, such as the degree of aromatic ring substitution, i.e. that fraction of peripheral aromatic carbon atoms bearing substituent groups, and the atomic H/C ratio for the hypothetical aromatic ring system, which provides an estimate of the average size of the polycondensed aromatic rings.

In subsequent years, numerous researchers applied the Brown–Ladner equation to a wide variety of coal-derived liquids, including coal extracts, autoclave asphaltenes, carbonization oils, solvent-refined coals, coal tar pitches, and coal liquefaction products. However, there were several assumptions which had to be made in the application of the

Brown–Ladner equation, and the results obtained often depended on assumed values for x and y. For most fossil fuels, x and y were assumed to be 2, which was the same as suggesting that the average aliphatic carbon structure in these materials represented a methylene group. There was also the problem with accurate integration of the H_α and (H_γ + H_β) protons because of severe overlap of the resonance lines. Derivation of the remaining parameters from the Brown–Ladner approach necessitated accurate deconvolution of the phenolic protons from aromatic protons, which was not always possible because of solvent-induced shifts of the hydroxyl resonances. Nevertheless, the approach was used to estimate the chemical structure parameters for many fossil fuels prior to the advent of high-resolution ^{13}C NMR.

The first high-resolution ^{13}C NMR spectrum of liquid products was published as early as 1966 using computer-assisted techniques. However, it was not until the mid-1970s, after the development of Fourier transform methods, that ^{13}C NMR of liquid and soluble materials from coal became routine.[9] The first studies focused on comparing aromaticity data obtained directly by ^{13}C NMR with those estimated from the Brown–Ladner treatment of the corresponding ^{1}H NMR spectra. Several laboratories reported generally good agreement; for example, one correlation of ^{1}H and ^{13}C NMR data for five coals of different rank, coal tar pitches, coal carbonization oils, coal-derived asphaltenes, and products from five different liquefaction processes is presented in Figure 2.[10] For the case of low boiling coal-derived oils, poor agreement was found because these materials tended to have shorter aliphatic chains, and hence the estimate for the ratio of aliphatic hydrogen to carbon (y in the Brown–Ladner equation) should have been greater than 2. Similar arguments were made for highly aromatic pyrolyzate products, in which there were high amounts of methyl substituents.

Later work focused on the assignment of chemical shift values to ^{13}C spectra of coal liquids. Efforts were made not only to assign chemical shifts to various carbon functional groups in samples, but also to estimate the relative abundances of these groups. Inference was made for a relationship between ^{1}H and ^{13}C NMR data on the same sample, leading to the idea that complementary information from both techniques could lead to detailed structural characterization of complex, multicomponent fractions of coal liquids. Thereafter, numerous separation methods and other spectroscopic techniques were combined with characterization by ^{1}H and ^{13}C NMR to provide detailed structural profiles of individual components in complex coal mixtures.

One of the cornerstones of structural analysis methods has been the information provided by NMR, and there have been many practices of presenting the data. Three approaches that have frequently been used are: characterization by the formulation of structural parameters; characterization by the construction of average, or representative, molecular structures; and characterization by functional group analysis.[11] The first approach is considered by many to be limited because estimation of numerous parameters often relies on assumptions about molecular structure, and the average parameters calculated are not guaranteed to represent actual structures in fuel liquids. The use of an average structure, or model, to represent the system is flawed by the latter drawback. The advantage of the functional group analysis approach is that, by definition, it is chemical functionalities that govern the overall chemical and physical behavior of these complex molecular systems.

Functional group analysis has been applied in several laboratories to describe coal extracts and soluble reaction products.[11] The initial step in the process was to propose a set of functional groups that described the structure of the complex mixture. The concentrations of this selected set of functional groups were subsequently related to experimental data through a sequence of equations, where the effects of known stoichiometry are taken into account. In general, a set of equations can be written:

$$\sum_{j=1}^{n} A_{ij}|y_j| = b_i \ (i = 1, \ldots, m) \qquad (2)$$

where y_j (j = 1, ... , n) represents the unknown functional group concentrations, b_i (i = 1, ... , m) represents quantities from experimental data, and A_{ij} represents the stoichiometric coefficients. The summation defined a range of possible solutions and a best fit was selected computationally through a minimization procedure by assuming that the distribution of atomic species among the functional groups is equally probable.

These methods have been tested on known mixtures and were subsequently used to characterize complex coal liquids. Utilizing data from NMR and elemental analysis gave fair estimates of molecular composition; incorporating data from mass spectrometry improved the results considerably. Characterization of separated fractions of coal asphaltenes derived from solvent-refined coal heavy distillate and supercritical gas extracts from two different coals provided information on the hydroaromatic content, distribution of heteroatomic functional groups, and nature of the polycondensed aromatic rings structures. In addition, these same methods have been used to reliably predict the thermophysical properties of liquid fuels,

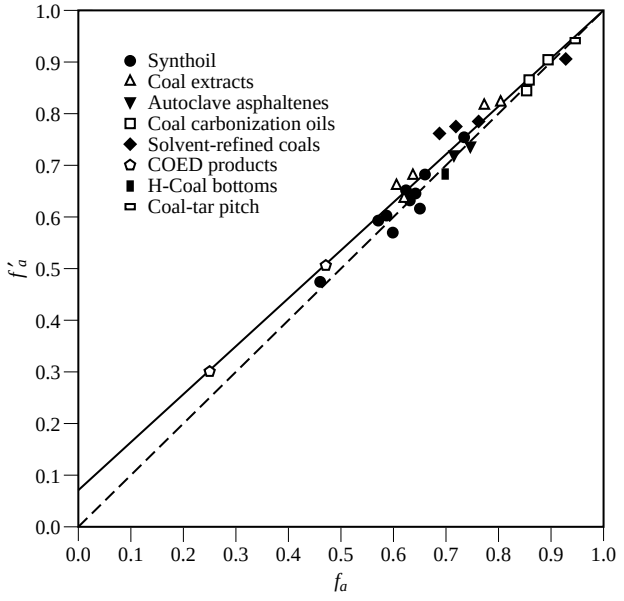

Figure 2 Comparison of proton (f'_a) and carbon (f_a) aromaticities for materials derived from coal; H-coal, solvent-refined coals, COED, and Synthoil are liquefaction processes

by utilizing group additivity principles and the idea of continuous thermodynamics.

Numerous studies have centered on the use of conventional solution state NMR techniques to study the heteroatomic functional groups in coal-derived liquids, principally those containing oxygen, nitrogen and sulfur.[12] Regions within the ^{13}C NMR spectra of coal asphaltenes and coal-derived oils were examined and assigned to carbonyl groups, aromatic ethers and phenols, aliphatic ether groups, and nitrogen groups. Other investigations have employed derivatization methods to specifically 'tag' functional groups in combination with NMR analysis. Several approaches have been attempted. These include: either acetylation or reductive alkylation followed by ^{13}C NMR; trimethylsilylation with analysis by ^{1}H, ^{13}C and ^{29}Si NMR (see Figure 3); hexafluoroacetone adduction which can be analyzed by ^{19}F NMR; and phosphorylation followed by ^{31}P NMR. Direct analysis by ^{17}O NMR has facilitated examination of some fractions of coal liquids, leading to the identification of oxygen functional groups on the basis of their chemical shifts: for instance, alcohols, phenols and ethers; furans and carboxylic acids; esters; and ketones and aldehydes.

Given the complicated nature of the ^{13}C spectra of coal-derived liquids, several multipulse techniques based on the spin echo method were developed which allowed the selective examination of different carbon types.[11,12] The gated spin echo (GASPE) or partially coupled spin echo (PCSE) pulse sequences were used to differentiate between aliphatic quaternary C and CH_2, as one phase-related spin group, and CH and CH_3 as the other. The same techniques were also applied to obtain edited aromatic carbon spectra, for which the distinction between quaternary and tertiary aromatic carbon atoms could readily be made. The spin echo broadband off-resonance decoupling (SEBBORD) technique was used to differentiate further between quaternary and CH resonances on the basis of broadening of the CH resonances. Later, with the development of polarization transfer pulse methods, the use of either INEPT or DEPT sequences allowed separation of the entire carbon spectrum, into quaternary C, CH, CH_2 and CH_3 resonances. Utilization of two-dimensional *J*-resolved and ^{1}H-^{13}C COSY experiments on coal liquids, however, has met with limited success.

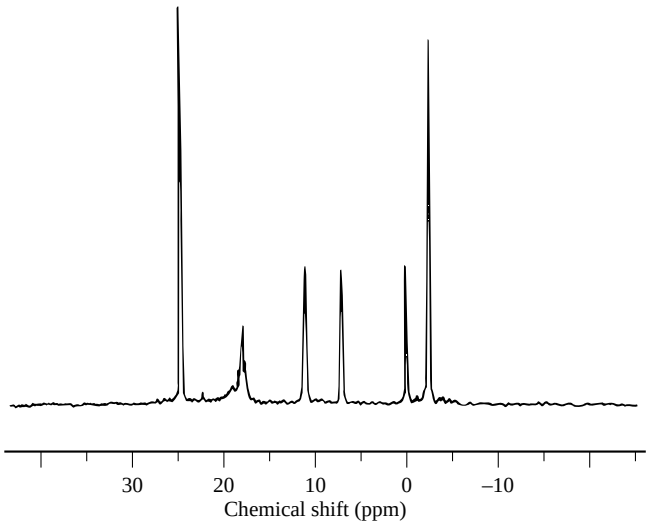

Figure 3 A typical ^{29}Si NMR spectrum of a coal liquid derivatized with trimethylsilyl chloride

2.1.2 Solid State NMR

The earliest report on the use of broadline ^{1}H NMR in coal research was published in 1955 by Newman et al.[13] However, apart from demonstrating that the NMR experiment was feasible on such materials, little chemical information was gleaned from this original work. It was more than 20 years later, in 1976, when the first solid state ^{13}C NMR spectra appeared in the literature,[14] utilizing then recently developed CP methods for sensitivity enhancement together with strong proton decoupling.[15] These initial ^{13}C spectra, recorded for four coal samples of different rank, are shown in Figure 4. It was the first time that coal structure was determined by a direct method for whole coals in their native state. Less than a year later, MAS with respect to the static magnetic field was used in combination with CP and proton decoupling to produce the first high-resolution solid ^{13}C CP MAS spectra of coal.[16] This constituted a major breakthrough in the field; removing broadening effects arising from both CSA and $^{1}H-^{13}C$ dipolar interactions produced isotropic resonance lines and facilitated the analysis of different carbon functional groups in coals. Also during 1977, MAS was combined with multiple pulse methods to produce the first high-resolution ^{1}H CRAMP spectra of whole coal samples.[17] The technique facilitated analysis of aromatic and aliphatic proton distributions of coals in their native state.

Applications of solid ^{13}C CP MAS and ^{1}H CRAMP spectroscopy in coal structure determination have been reviewed extensively.[12,18–22] Early ^{13}C CP spectra of coals (see Figure 4) exhibited two broad, overlapping resonance bands

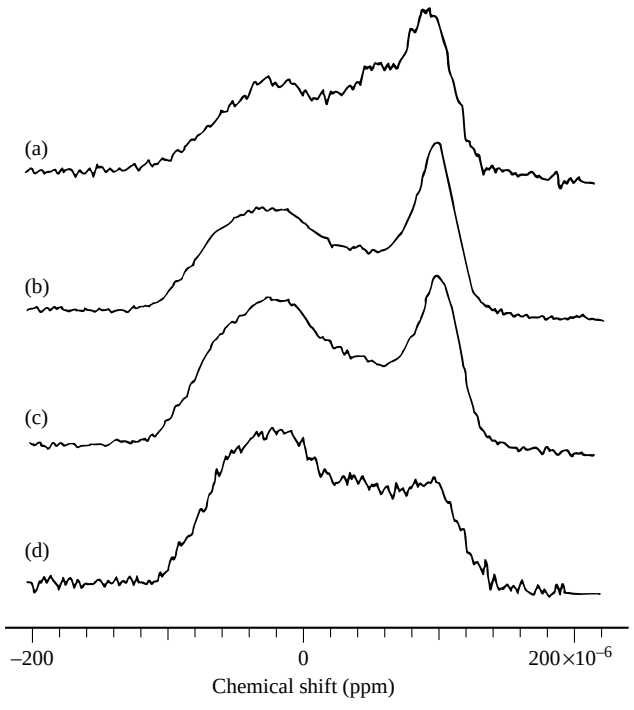

Figure 4 CP ^{13}C NMR spectra of coals of increasing rank

that could be assigned to regions of aliphatic (0–60 ppm) and aromatic (30–250 ppm) carbon atoms. From these spectra, the fractional carbon aromaticities (f_a) were estimated by employing peak deconvolution methods. The results supported the classical view that coals were highly aromatic materials and that the aromaticity of coals increased with increasing rank as calculated on the basis of their carbon content. Comparing ^{13}C CSA lineshapes of coals and model compounds allowed identification of regions of polycondensed aromatic ring structures, simple aromatic systems, aliphatic structures, and also aliphatic ether linkages. However, it was difficult to obtain estimates of these different functionalities with any degree of reliability because of lack of resolution in the spectra.

This situation changed dramatically with the introduction of MAS in the experiment to remove CSA. Narrowing of the resonances to their isotropic chemical shift values facilitated the assignment of a host of carbon functional groups, including aromatic and alkenic carbons, carboxylic acids and other carbonyl groups, phenolic and furanyl carbon atoms, carbon-substituted aromatic carbon atoms, oxygen-substituted carbon atoms (including methoxyl groups), as well as methylene and methyl carbon atoms. Assignments for a typical high-resolution solid ^{13}C spectrum of a whole coal is shown in Figure 5. First and second moments of the aromatic carbon resonance band were shown to vary as a function of the carbon content of coals ranging in rank from lignite to anthracite. The first moments were found to increase with increasing rank, which was in accord with estimates derived from models for the increase in the aromatic ring condensation index. The second moments decreased with rank, implying that the dispersion of chemical shifts in the aromatic region was decreasing, or becoming more homogeneous with increasing carbon content of the coal.

Structural parameters were derived from solid ^{13}C and ^{1}H NMR data of whole coals and maceral concentrates during subsequent years, leading to a greater understanding of coal structure. Carbon and proton aromaticities were found to increase with increasing rank of the coal; and for macerals, in the order liptinite < vitrinite < inertinite. Carbon and hydrogen aromaticities were used to estimate the aromatic and aliphatic hydrogen-to-carbon mole ratios, and given the weight per cent of carbon and hydrogen derived from elemental analysis, it was possible to approximate the average size of the polycondensed aromatic clusters in coals as a function of rank. Estimates of the aromatic cluster size ranged from 1 to 2 rings for low-rank coals, 2 to 6 rings for bituminous coals, and approached 30 rings for anthracite.

As the state of the art progressed, greater emphasis was placed on obtaining specific, detailed information on the chemical functionality of coals and coal macerals. Several approaches were implemented to enhance the resolution of ^{13}C CP MAS spectra so that greater structural information could be obtained.[12,17,18]

The first, and still most utilized, spectral editing technique developed for spectral simplification of coal spectra was the interrupted decoupling (or dipolar dephasing) experiment[23] which was originally proposed by Alla and Lippmaa.[24] The basic approach distinguished between carbon atoms on the basis of dissimilarities in transverse relaxation times between protonated and nonprotonated carbon atoms, owing to differences in the magnitudes of their $^{1}H-^{13}C$ dipolar couplings. In the absence of a strong proton decoupling field, which is turned off during a finite period of time during the course of the experiment, the protonated carbon magnetization decays at a significantly faster rate than that of nonprotonated carbons. Methyl carbon atoms exhibit intermediate decay rates due to fast molecular motion. In principle, this allowed signals from these four types of carbon to be separated quantitatively, provided that the appropriate mathematical solutions had been performed to calculate initial signal intensities (at $\tau = 0$) from experimental decay rates in a series of variable interrupted decoupling time experiments.

The interrupted decoupling experiment has been applied to the study of whole coals, isolated macerals, coal-derived asphaltenes, and coal oxidation products and pyrolysis chars. From the results of these experiments, it has been possible to

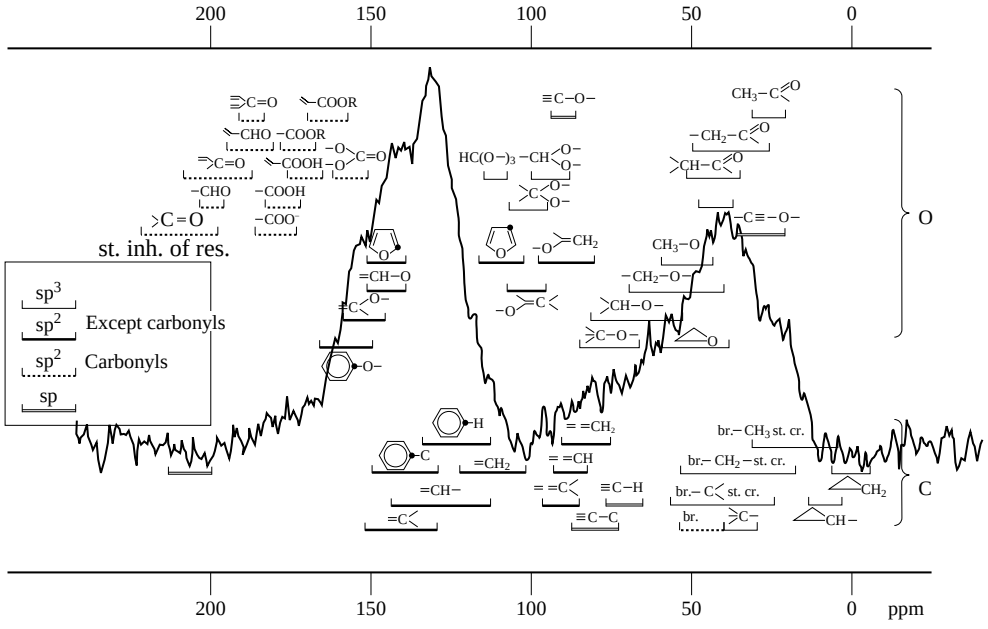

Figure 5 CP MAS spectrum of a whole coal with the NMR chemical shift correlation chart

estimate the fraction of substituted and bridgehead aromatic carbon atoms (f_{s+b}), and the number of quaternary aliphatic carbon atoms in these systems. Attempts to estimate the average cluster size of the aromatic rings from these data has had the caveat that it has been impossible to assign aromatic substituted and bridgehead carbon atoms with confidence because of severe overlap of the resonances. Nevertheless, interrupted decoupling solid state NMR has provided valuable insight into the nature of coal as a macromolecular material, and the technique has been used to explain some of the chemistry occurring upon its treatment under a variety of conditions.

Interrupted decoupling has also been employed with detection by CRAMPS to enhance the resolution of solid state proton spectra of carbonaceous materials.[22] Analogous to the carbon version of the experiment in CP MAS spectroscopy, a dephasing period is inserted between the initial $\pi/2$ pulse that places the proton magnetization in the transverse plane and initiation of the multipulse decoupling sequence used for detection. The technique has been used on pyridine-sorbed coals and has provided selectivity of protons on the basis of molecular mobility.[22]

Mathematical manipulation has been employed to enhance the resolution of solid NMR coal spectra.[18] The several methods that have been implemented include: (1) convolution difference spectroscopy, which uses a filtering function composed of two exponentials and an adjustable weighting constant; (2) Gaussian multiplication, which has been used to improve resolution on the basis of lineshape modification; and (3) a variety of curve and Fourier deconvolution methods, for which the usual practice has been to fit mathematically a broad band of unresolved resonances to a series of peaks that are varied according to frequency position, lineshape, linewidth, and intensity.

Resolution enhancement in these systems has also been achieved based on carbon and proton relaxation time differences in CP MAS experiments.[12] Differentiation of carbon atoms in coals has been accomplished on the basis of differences in $^{1}H-^{13}C$ polarization transfer rates R_{CH}, proton rotating frame spin–lattice relaxation rates $R_{1\rho}{}^{H}$, and carbon spin–lattice relaxation rates $R_1{}^{C}$.

Chemical derivatization techniques in conjunction with solid state ^{13}C NMR have been used to highlight the reactive oxygen functional groups, such as phenols, aliphatic alcohols and carboxylic acids. Acetylation[12] was employed to target specifically hydroxyl groups in coals and could be monitored by the introduction of additional carbonyl and methyl resonances in the solid reaction products. Comparing integrated signal intensities of the introduced acetyl resonances with those of native C–O gave estimates on the amounts of hydroxyl versus ether groups. The combined use of selective alkylation with ^{13}C-enriched methyl iodide and solid state ^{13}C NMR has also facilitated the assignment of methyl carboxylates, unhindered aryl methyl ethers, and hindered aryl methyl ethers in coals[25,26] and isolated coal macerals.[27]

Solid state NMR spectroscopy has seen limited applications to the study of mineral phases in coals. The first application focused on the use of ^{29}Si and ^{27}Al NMR to characterize mineral concentrates obtained by low temperature ashing of coals in order to obtain information on their mineralogy.[28] Silicon spectra allowed the identification of silicate resonances from quartz and clays, while aluminum spectra provided information on the tetrahedral and octahedral coordination sites which allowed discrimination between kaolinite and illite clays that were present in the concentrates. A subsequent study[29] on mineral residues obtained from coal flash pyrolysis indicated that ^{29}Si and ^{27}Al spectra were broad because of the presence of paramagnetic species; however, the spectra were sufficiently resolved to detect the thermal transformation of kaolinite to quartz and mullite with increasing pyrolysis temperature. Characterization of the layer silicate minerals in the suite of Argonne Premium coals was carried out by using sink-float techniques to isolate mineral concentrates in combination with ^{29}Si and ^{27}Al NMR.[30] CP MAS and VAS techniques were employed to distinguish between the various clay minerals; quartz, kaolinite and smectite clays could readily be identified. Tetrahedral/octahedral aluminum ratios were determined for the coals, and the observation of increasing tetrahedral aluminum content with coal rank indicated there was a parallel between the diagenesis of the organic and inorganic matter in the coals.

2.1.3 Determination of Physical Structure

Solid state NMR spectroscopy has been applied extensively to the study of complex molecular dynamics in synthetic polymers. However, such investigations of coals have been limited. Work in this area has been hampered by the complex nature of coal. Interpretation of nuclear relaxation, which underlies the study of molecular motion, is complicated by the existence of discrete heterogeneous domains in coals and by relatively large quantities of paramagnetic centers which are present either in the form of paramagnetic inorganic ions or as organic free radicals.

To date, an overwhelming majority of papers dealing with relaxation measurements on coals has focused on the study of ^{1}H NMR spin–lattice relaxation times both in laboratory (T_1) and rotating ($T_{1\rho}$) reference frames. Early ^{1}H NMR measurements[31–34] indicated that proton T_1 times in coals can either display single exponential or nonexponential relaxation behavior. The observation by Yokono et al.[33] that $T_1{}^{H}$ varied linearly with the square root of resonance frequency for several bituminous coals was consistent with diffusion-limited relaxation to paramagnetic centers. Several laboratories[34–37] later demonstrated similar behavior for a wide variety of evacuated coal samples. The work indicated that spin–lattice relaxation may be a fundamental property of coals themselves, and be independent of either their oxygen or moisture content. In two specific papers,[37,38] the authors independently proposed that proton relaxation in bituminous coals was influenced by differences in molecular mobilities rather than by the relative concentrations of paramagnetic species.

A difficulty with the interpretation of spin–lattice relaxation of abundant proton spins in coals rests with the development of an experimental strategy to separate contributions from molecular mobility from spin diffusion of the magnetization to paramagnetic centers within different phase (maceral) boundaries. Three thorough investigations of ^{1}H NMR spin–lattice relaxation in coals[39–41] have attempted to address this issue. The authors independently concluded that simple correlations of proton relaxation with other coal parameters was not easily realized. The presence of residual amounts of molecular oxygen in evacuated samples and the effects of different concentrations of unpaired electrons within different domains in

coals were thought to have a profound, yet undeterminable, influence on the relaxation times. Others[42] have reported proton relaxation data for eight Argonne Premium coals and three oxidized coals and have shown that oxidized samples have shorter $T_1{}^H$ values. Finally, in careful $T_1{}^H$ and ESR studies of Argonne coals, various chemical treatments established that the important proton relaxation mechanism in lignite and subbituminous coals was due to the presence of paramagnetic mineral ions, whereas that in the higher rank coals is due to organic free radicals.[43]

The problems were not confined to measurements of $T_1{}^H$. An early paper[44] reported proton $T_{1\rho}$ values for a pitch and three Canadian coals and had emphasized the effects of paramagnetic species, including oxygen, on the experimental results. Other studies indicated a general trend, but lack of any definitive correlation, between $T_{1\rho}{}^H$ values and radical concentrations for a series of 'more homogeneous' maceral concentrates.[45] It was concluded that the $T_{1\rho}{}^H$ values for macerals are clearly complicated by having two competing mechanisms for relaxation, i.e. molecular motion and heterogeneous spin diffusion to paramagnetic centers. Without knowledge of the relative contributions of each to the overall relaxation times in the individual samples, any meaningful interpretation of the data was impossible. In the case of a homogeneous resinite sample doped with increasing amounts of a stable organic radical, however, an excellent correlation of $T_{1\rho}{}^H$ with radical concentration could be established.

In contrast with proton relaxation, relatively little work has been done on the measurement of ^{13}C relaxation times in coals. Carbon-13 spin–lattice relaxation measurements have been carried out on a bituminous coal from the Powhatan No. 5 mine.[46,47] It was established that aromatic resonances in this sample decayed with a single time constant, while the aliphatic resonances could be separated into two distinct regions having markedly different time constants for decay. Differences observed in the $T_1{}^C$ values for different spectral regions were interpreted in terms of molecular motion, although the contribution of free radicals to spin relaxation were acknowledged as being important as well. Other researchers[48] investigated the effect of static field strength on the $T_1{}^C$ relaxation parameters of five Argonne Premium coals and five Canadian coals, and correlated the relaxation times with various coal properties.

In a recent study,[49] eight Argonne Premium coals and three weathered Argonne coal samples were investigated and the proton and carbon spin–lattice relaxation times were reported for aromatic and aliphatic carbon atoms. In general, the proton and carbon spin–lattice relaxation data could be evaluated as the sum of two exponential decays. The longer components of carbon relaxation times in the laboratory and rotating reference frames were found to vary in a systematic way with coal rank, and the trends were explained in terms of motional properties of the coals and the presence of paramagnetic species. Marked increases in the carbon $T_{1\rho}$ values observed between pristine and weathered coals were interpreted to indicate a decrease in molecular mobility resulting from increased cross-linking as a result of oxidation.

2.1.4 Advanced Characterization Techniques

Several NMR methods have appeared in the recent literature on coal which deserve particular attention. They often incorporate special pulse sequences for solids aimed at sensitivity enhancement, spectral simplification or resolution enhancement, and multidimensional NMR spectroscopy and imaging.

The first two-dimensional $^1H-^{13}C$ COSY experiment on a coal was demonstrated in the mid-1980s.[50] By dispersing the carbon and proton spectral information over two dimensions (see Figure 6), the proton resonances became separated such that the aromatic, methylene and methyl protons could be resolved and their abundances estimated. Similar methods were applied to the analysis of the proton content of macerals.[51] Overlapping carbon functional groups have been estimated from two-dimensional dipolar shift (DIPSHIFT) techniques.[52] In the latter experiment, isotropic chemical shifts were plotted on a frequency axis facing dipolar shift sideband spectra on a second axis. Multiplicity of individual sideband patterns in the aliphatic region were then used to assign resonances in the isotropic spectrum on the basis of the number of protons attached to each carbon atom.

Dynamic nuclear polarization has been used with some success for the analysis of a wide range of coals of varying rank.[53] By polarizing carbon spins via the electron spins directly, or by CP techniques through the protons, large signal enhancements have been possible.[54] The technique has allowed the analysis of coals in short measuring times; however, because polarization is transferred from electron spins that reside predominantly within aromatic structures, the technique has generally overestimated the carbon aromaticity values in these systems.

Determination of the principal values of carbon CSA in anthracite coals and fusinite macerals through lineshape analysis has led to the quantitative analysis of the different carbon bonding types in these systems.[55] Using powder pattern lineshapes, three different bands due to aromatic condensed bridgehead and inner carbon atoms, and substituted carbon atoms were readily distinguished. The mole fractions of the condensed aromatic carbon atoms were then used to estimate the average cluster size of the polycondensed aromatic hydrocarbons in the coals. Later, VAS experiments were

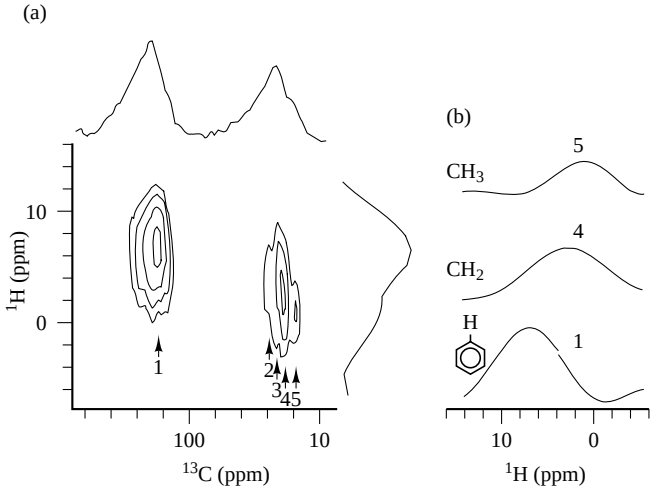

Figure 6 (a) The heteronuclear shift correlation spectra of Illinois No. 6 coal with three fully resolved contours (1, 4, and 5) and two partially resolved contours (2 and 3) observed. (b) Proton spectra from slices at 1, 4, and 5

carried out in conjunction with powder pattern analysis in order to unscramble overlapping shielding tensors in coals and macerals.[56] A review of possible methods for obtaining carbon shielding tensor information on coals has recently appeared;[57] methods for separating individual CSA patterns in complex spectra include VAS, slow MAS, chemical shift correlation spectroscopy, magic angle hopping (MAH), stop-and-go (STAG) methods, DAS, and MAS with synchronized pulsing.

The first direct magnetic resonance imaging (MRI) experiment on solid coal and maceral specimens appeared in 1989.[58] These initial studies (see Figure 7) demonstrated the potential of MRI spatially to map proton distributions in whole coals. Individual macerals within the coals were readily distinguished by image contrast based on differences in proton density or spin–lattice relaxation. A subsequent MRI investigation focused on elucidating changes in the physical structure and on determining solvent accessibility parameters in solvent swollen coals.[59] Other researchers have utilized MRI to determine the distribution of water in coalified woods and low-rank coals.[60] Correlation of proton spin distributions determined by MRI with the void spaces from other techniques allowed analysis of porosity and permeability in the specimens. Transient MRI studies of solvent penetration into solid coal and polymer specimens has led to a detailed understanding of transport phenomena for systems in which the glass transition is induced by solvent; the data have led to the development of a new model for anomalous transport behavior in coals and other glassy polymer systems.[61]

2.2 Conversion Processes

The combined use of ^{1}H and ^{13}C NMR has been employed to examine the chemical behavior of coal, in reactions such as oxidation which may be undesirable, in thermolysis and pyrolysis reactions, and in upgrading reactions for its conversion into clean, high quality liquid fuels, and chemical feedstocks.[62] Studies in the liquid state have provided information on the liquefied products, while solid state NMR has been used to characterize the original coal material as well as the chars and cokes produced in these reactions.

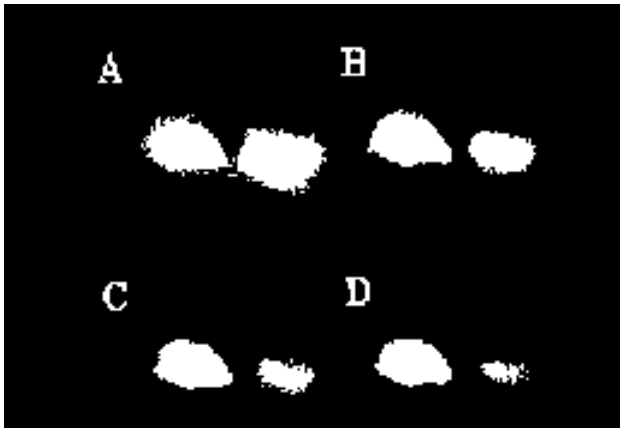

Figure 7 Two-dimensional *xy* images of resinite (left) and vitrinite (right) macerals using rotational gradients and MREV-8 back-projection reconstruction protocol with 90 projections about 180°, and 512 averages per projection. The recycle delays used in A–D were 235, 585, 1085, and 1585 ms, respectively

Several researchers have focused their efforts on characterization of coal oxidation. Early proton relaxation time measurements have been used to explore oxidation of cokes in air at elevated temperatures. The data were compared with changes in the optical texture of the coke, and a correlation between the appearance of an isotropic phase and the T_1 minimum was found. T_2 experiments indicated that the mobile phase becomes more rigid, which was interpreted to reflect an increase in the degree of cross-linking. Structural studies carried out with ^{13}C CP MAS showed that a decrease in aromaticity accompanied oxidation of coals in air at elevated temperatures. Independent studies indicated that oxidation caused a loss of specific functional groups in the aliphatic region; an increase in carbon aromaticity was observed, contradicting previous results. Conflicting evidence was also reported in the literature concerning either the appearance or disappearance of certain aromatic structures, with specific reference to phenolic structures.

Other researchers have focused on elucidating structural changes after low-temperature oxidation, or weathering, of coals of different rank. Little change in the aromatic carbon content was noticed; however, the amount of the aliphatic CH_2 was found to decrease significantly after weathering. Dipolar dephasing studies were also in conflict with earlier elevated temperature experiments. Consequently, the entire body of evidence in the NMR literature has been inconclusive regarding specific structural changes that accompany oxidation. Investigations[49,63] involving oxidation or prolonged weathering of Argonne Premium coals later established that changes in free radical content significantly affect pertinent relaxation times in CP MAS and dipolar dephasing experiments. These relaxation effects may in fact account for the discrepancies found in previous comparisons of NMR data between native and oxidized coal samples, ultimately leading to conflicting results on different coals.

The use of NMR for characterizing coal liquids derived from liquefaction processes began as early as 1975.[64] Proton NMR, and in several instances ^{13}C NMR methods, including CP and CP MAS, have been applied to study coal liquefaction under different conditions to produce solvent refined coals, H-coals and Synthoil products.[10–12,65,66] NMR has played an important role in coal liquefaction research because it has been the only method able to characterize the complement of materials involved in the process, including the original coal feedstocks, liquid products, solid residues and products, catalyst materials, and solvent systems. The functional group analysis approach has been widely used to examine the structural changes in coal liquefaction and has led to the following general conclusions concerning the overall process in tetralin: (1) hydroaromatic structures are partially or completely dehydrogenated, while others are cleaved during the reactions; (2) alkyl groups in the products result from cleavage of the hydroaromatic ring structures; and (3) aromatic structures are formed via dehydrogenation reactions.

With the advent of ^{13}C CP MAS spectroscopy, not only liquid products but also the solid residues from liquefaction became amenable to analysis by NMR. The chars formed after prolonged reaction times at higher temperatures tended to have extremely high aromatic carbon content, (f_a up to 0.96). In general, it was found that the aliphatic content of

the chars decreased with increasing hydrogenation time while the composition of the liquid products remained relatively constant. Also observed was a marked decrease in the number of polar functional groups. The general conclusions drawn from the NMR results suggested a mechanism involving the decomposition of hydroaromatic structures, whereby under higher temperature reaction conditions an increasing proportion of aliphatic structures was converted into aromatic material and/or gaseous products. Furthermore, the increase in the polycyclic aromatic content meant that hydroaromatic systems were decomposing via retrogressive condensation reactions. Most recently, coal liquefaction residues were characterized by solid state CP MAS techniques.[67]

Other researchers[62] have focused on the use of CP MAS to study coking deposition on coal liquefaction catalysts, which was thought to be one of the principal causes of catalyst deactivation. Several studies[62] have compared liquefaction behavior in the presence of different catalysts or with no catalyst at all, and have compiled results on the reaction yields and quality of liquid products. Both ^{13}C and ^{1}H NMR have been used to monitor the hydrogen donor solvent employed in liquefaction. The results demonstrated that loss of hydrogen in the solvent occurs primarily via aromatization of hydroaromatic structures. By estimating the concentration of donatable hydrogen of the liquefaction solvent through chemical shift assignments, hydrogen donor values of various solvents were independently derived.

Labeling studies employing deuterated tetralin have been used with great success to study hydrogen transfer processes during liquefaction and to follow the incorporation of deuterium into liquid products.[62] A combination of ^{1}H, ^{2}H, and ^{13}C NMR and separation methods such as gel permeation chromatography was employed to study the evolution of coal liquefaction products in d_4-tetralin.[68] Later on GASPE, INEPT, and two-dimensional J-resolved NMR were used to obtain more detailed structural information on exchange mechanisms of hydrogen and deuterium.[11,69,70] The majority of studies on a wide variety of coals and catalyst systems led to a common conclusion: the distribution of deuterium in liquefaction products was found to be reasonably representative of the fate of hydrogen incorporation into coal tars. While there was some total scrambling of hydrogen, for the most part hydrogen was incorporated into aromatic residues and at α- and β-carbon atoms preferentially attached to aromatic structures.

The ability of NMR methods to provide reasonably quantitative information on the distribution of hydrogen in both the starting coals, liquid and solid reaction products, and solvents has made it possible to account for the total hydrogen consumption in liquefaction.[62] A mass balance equation for the total consumption of hydrogen in liquefaction has been derived:

$$\Delta H = \Delta f_a + \Delta(C - C) + \Delta NOS \qquad (3)$$

where ΔH is the net change in hydrogen between the original coal and all liquefaction products, Δf_a is the corresponding change in total aromaticity, $\Delta(C-C)$ is the total number of carbon–carbon bonds ruptured via hydrogenolysis, and ΔNOS is the composite loss of nitrogen, oxygen, and sulfur atoms. The NMR data combined with information from elemental analysis were used to estimate the fate of total hydrogen utilized in hydrogenation processes leading to reduction, carbon–carbon bond-breaking reactions which generate either light gases or liquid products, and for removal of heteroatoms. The NMR approach of using the concept of total aromaticity as a means to assess the mass balance of consumed hydrogen has been an important step in evaluating the performance of liquefaction processes and has offered some of the best insights into coal liquefaction chemistry to date.

Numerous investigations have also been concerned with developing an understanding of the fundamental chemical processes involved during coal pyrolysis and carbonization.[62] NMR has been used to study the response of coals to heating, by comparing data on solid and liquid products with the data obtained on the original solid coals. Researchers have developed comprehensive models based on the changes in functional groups during pyrolysis. Specific information on changes in aromaticity, degree of substitution on aromatic structures, types of aliphatic functional groups, and aromatic ring condensation have been compiled by both ^{13}C NMR, and ^{1}H NMR using the approach of Brown and Ladner, together with compiled data on the yields of aromatic hydrogen and carbon as a function of temperature during pyrolysis. General conclusions have been summarized on the basis of the results: (1) only the weakest coal bonds fragmented at temperatures below 600 °C; (2) maximum yields were obtained at temperatures of 600–700 °C with little change observed in the aromatic structures and marked changes in the aliphatic components, suggesting that significant decomposition in the aliphatic substituents had occurred; and (3) at temperatures above 700 °C the less condensed aromatic structures began to decompose into gaseous products.

The nature of flash pyrolysis tars produced from a wide variety of coals throughout the world has been investigated by NMR techniques in several laboratories.[62] In general, it was found that larger polycyclic aromatic ring structures were produced at higher pyrolysis temperatures. However, results compiled from a survey of many pyrolysis experiments suggest that the nature of the coal and the method of pyrolysis rather than the final pyrolysis temperature were most important in determining tar structure. Alkenes in the tars were correlated with the decomposition of polymethylene chains, while ^{13}C NMR suggested that a large proportion of the alkyl carbon atoms were part of long-chain alkyl groups. NMR analysis of chars produced in variable temperature flash pyrolysis experiments showed that the aliphatic peak decreased with increasing pyrolysis temperature, while the aromatic band remained unchanged, suggesting that the aromatic content in the char was relatively constant. Furthermore, NMR studies demonstrated that the carbon aromaticity of the original coal, (f_a), or the amount of methylene structures present in the tars were linearly correlated with tar yields in coals ranging from bituminous to semianthracite; lignite tar yields, however, did not correlate well. Based on these results, it was concluded that aliphatic carbon atoms in coals, in particular the methylene groups, were essential to the production of pyrolysis tars. Later studies employing NMR considered correlating pyrolysis yields with the loss of specific regions of chemical shift within the aliphatic and aromatic resonance bands. The production of gases was consistent with decreases in the CH_2 resonance at 30 ppm. On the other hand, high tar yields correlated well with the loss of the remaining aliphatic groups in the region 13–47 ppm, i.e. consistent with the loss of hydroaromatic

structures in the coals. In addition, coal aromaticities correlated well with char production.

In general, the majority of coal processing technologies involve heating, and it is in this area that NMR has played a unique role in understanding the physical behavior of coal at the elevated temperatures typically employed in hydroliquefaction and other catalytic upgrading processes. Wideline ^{1}H NMR has been used to study changes in the molecular mobility or viscosity of coals during heating to temperatures as high as 875 K.[62,71,72] Early studies measured changes in $\Delta H_{\frac{1}{2}}$. However, later on the use of second moment (M_2) analysis of the solid echo signal led to a more accurate representation of average molecular mobility. Variations in M_2 with temperature were consistent with a depolymerization of the coal structure followed by recondensation. The concurrence of temperatures for M_2 minima and bulk fluidity from Giesler plastometry suggested that there was a significant molecular basis to the thermoplasticity of coal. In general, a strong correlation was found between hydrogen content, and perhaps high sulfur content, with coal fusibility.

2.3 The Quest for Quantitation

^{1}H and ^{13}C NMR spectroscopy have been applied with great utility to the analysis of hydrogen and carbon functional group distributions in a wide variety of liquid and solid fuels and their reaction products. The increasingly important role over the past three decades of NMR as a characterization tool for fuels has led to a significant advance in our understanding of their structure, origin, and evolution. The enormous impact that NMR has made in the area of fuel research has been a direct consequence of its utility as a quantitative tool. In principle, NMR of spin-$\frac{1}{2}$ nuclei is unique as a spectroscopic method in that the transition probabilities of each and every isochromat in the absorption spectrum is the same, or unity. Notwithstanding this unique capability, from the outset concerns about the quantitative reliability of ^{13}C NMR spectroscopy has placed the general utility of the method in question. Carbon-13 NMR in liquids was perceived in this way until the mid-1970s, when its usefulness as an analytical technique was demonstrated by the judicious implementation of the proper pulse techniques and recycle delay times, sometimes with the aid of relaxation reagents to shorten spin–lattice relaxation times and to suppress the nuclear Overhauser effect. For ^{13}C analysis of solid coal samples, the issues regarding quantitation were not resolved until the late 1980s because of the enormous complexities involved.

With the advent of ^{1}H decoupling,[15] CP[15] and MAS,[73] which have made it possible to obtain high-resolution ^{13}C NMR spectra in solids in a relatively short measuring time, CP MAS techniques have been applied extensively in coal research.[12,14,18,42,74–78] In fact, ^{13}C CP MAS NMR has become one of the most widely used methods for investigating coal. However, there has been growing concern during the past decade about the quantitative reliability of CP MAS spectroscopy for coal analyses. In the very first ^{13}C CP NMR study of coal,[14] it was estimated that only about 50% of the total carbon spins could be detected via this technique. Since then the issue of quantitation in NMR analyses of coal and related materials has been a topic of much debate.[14,44,45,47,75,79–85] Although the quantity of observable carbon atoms for coals and their macerals have been shown to vary widely, the general consensus was that, for reasons which can be related to both specific coal properties and the applied NMR techniques, a substantial fraction of the carbon atoms was not observed.

It was known that coal is one of the most complex carbonaceous materials known. It was by nature an extremely heterogeneous solid composed of a number of distinct organic phases termed macerals, and to a lesser extent, of an inorganic mineral phase. Each maceral and mineral phase exhibited a unique set of physical and chemical properties that contributed to the overall behavior of coal. The macerals typically ranged in size from micrometers upwards, and pure bands were commonly found in coal seams up to meters in thickness. Consequently, maceral dimensions were sufficiently large to expect that nuclear spin diffusion across maceral boundaries would be incomplete on the NMR timescale, typically on the order of 1000–2000 pm and 10^4 to 2×10^4 pm in the limits of proton relaxation in the rotating frame and laboratory frame, respectively. This meant that nuclei within different maceral phases acted as isolated spin reservoirs with very different magnetic properties.

There were additional factors to consider as well. Individual macerals were in many instances intimately associated with inorganic minerals, some of which may contain paramagnetic ions. Moreover, the macerals contained different concentrations of organic free radicals, causing relaxation time differences that would ultimately govern the evolution of magnetization within these isolated domains. The presence of paramagnetic centers raised the possibility that significant portions of the carbons were sufficiently broadened or shifted outside the spectral range to render them invisible in the NMR experiment. Moreover, variations in free-radical content among these isolated phases was shown to lead to serious distortions in the carbon signal measured for the entire coal sample.

Thus, complexities in the organic, inorganic, and physical structures of coal limited the quantitative reliability of solid ^{13}C NMR measurements. The inherent limitations associated with measuring a complex solid such as coal were unavoidable. However, a fundamental understanding of these complexities was necessary in order to establish confidence limits for the measurements so that meaningful parameters could be obtained from the data.

A comprehensive review on the subject of quantitation in solid NMR analysis of coals has recently appeared.[86] In that review, several factors limiting quantitation in both single pulse and cross polarization experiments were discussed along with possible remedies. Important aspects to the problem of quantitation included in that discussion were: the nature of the unpaired electron spin interactions; interference between molecular motions and the proton decoupling field; insufficient MAS rotation; interference between molecular motions and MAS; consequences of long spin–lattice relaxation times; dependence of the Hartmann–Hahn matching condition; modulation of C–H coupling due to MAS; and complexities involving CP spin dynamics.

Finally, resolution of the issues concerning the quantitative reliability of solid ^{13}C measurements was made possible by the establishment of a standard, homogeneous suite of coal samples. As in other disciplines of fuel science, the complex nature of carbonaceous fuels together with the diversity of

samples chosen for study has made comparisons between published results difficult. With the inception of the Argonne Premium Coal Sample Program,[87] NMR results on a common suite of pristine coal samples spanning a diverse rank range could be compared.[88] Thus, valid comparisons between data measured using different experimental techniques and under a variety of different experimental conditions had become feasible for the first time.

A comparison has been made of data obtained from experiments which were carried out at static field strengths ranging from 1.4 to 9.4 T (corresponding to carbon resonant frequencies of 15–100 MHz) and using a variety of methods, including CP MAS, single pulse excitation (SPE) with MAS, MAS with TOSS, and DNP CP without MAS. Carbon aromaticities were determined from CP experiments employing contact times generally between 1–2 ms and, in certain instances, by mathematically fitting signal intensities derived from variable contact-time experiments. Proton decoupling field strengths employed were typically 40–82 kHz; MAS frequencies varied from 3 to 13 kHz. Recycle delay times ranged from 1–3 s in CP experiments to 60 s in SPE experiments.

For bituminous coals, mean carbon aromaticity values that were determined for three data sets (CP MAS, CP MAS at 2.3 T, and SPE) were found to be the same within the limits of the standard deviations. The results indicated that the variability in carbon aromaticities reported by different laboratories for the coals was greater than the differences observed between experimental techniques, i.e. CP and SPE experiments. However, the mean values from SPE experiments always tended to be on the high end of the range of CP values.

Differences in mean carbon aromaticity values for CP and SPE experiments were found to be significant for the two low-rank sub-bituminous and lignite coals samples. Their mean SPE carbon aromaticities were clearly higher by approximately 10% and 20%, respectively. The differences were accounted for by complications arising from paramagnetic transition metal ions intimately associated with the coal organic phase. The presence of paramagnetic metal ions in these coals was shown adversely to affect their spin–lattice relaxation properties,[48] and these factors were invoked to explain lower derived CP MAS aromaticity values resulting from reduced CP efficiencies.

Comparing mean CP and SPE aromaticity values for Argonne coals with aromaticities obtained by other pulse techniques showed the expected trends. While carbon aromaticities obtained using the TOSS pulse sequence in one laboratory were in reasonable agreement with the mean, those reported by other laboratories turned out to be significantly lower than mean CP or SPE aromaticity values. The disparity of the TOSS results illustrated the severe demands that are placed on proper implementation of the TOSS pulse sequence for quantitative analysis. On the other hand, aromaticity values obtained from DNP CP experiments tended to be high, which was entirely consistent with signal enhancement via electron–nuclear polarization from free radical centers that reside within aromatic coal structures.

The principal conclusion gleaned from the interlaboratory study was that SPE methods generally gave the most reliable results. Proper sample handling techniques to prevent oxidation or weathering of samples was also thought to be an important factor in the analysis of coals.

2.4 Origin of Coal and its Evolution

From the beginning of its deposition at the surface of the Earth and throughout its burial, sedimentary organic plant debris underwent progressive changes in composition and structure; when the process involved has related specifically to the metamorphosis of coal, it has been generally referred to as 'coalification'.[89] The nature of metamorphic processes of coal has changed significantly at different stages of its evolution. At the earliest stages, coalification was dominated by microbial reactions and physical processes such as maceration and compaction. Later stages of coalification were governed predominantly by abiogenic chemical reactions such as dehydration, dehydrogenation, and aromatization, as well as polymerization and depolymerization reactions. The final stages involved graphitization processes, leading eventually to the formation of anthracite.

During the past three decades, there have been numerous investigations concerned with elucidating the important chemical processes responsible for the transformation of plant biopolymers into the specific organic macerals that compose coals.[89] During the 1980s, numerous studies employing NMR techniques sought to uncover the chemistry involved in the transformation of woody tissue, obtained from both natural and synthetic sources, into the maceral vitrinite. Often, NMR studies were carried out in parallel with analysis by mass spectrometry. The structural evolution of vitrinite was studied through detailed characterization of naturally occurring coalified log specimens which spanned the entire coalification range.[90–94] In independent studies, laboratory simulated coalification experiments were carried out on lignin samples isolated from modern wood, in the presence of clay catalysts at relatively low temperatures (150 °C).[95] Subsequent simulated coalification investigations[96,97] focused on solid state ^{13}C and ^{1}H NMR analyses of synthetically prepared ^{13}C-labeled lignins[98] and model compounds to monitor abiogenic evolution pathways. The remarkable parallels found between solid state ^{13}C spectra of artificial coals and naturally occurring coalified specimens of similar maturation level laid the framework which revolutionized modern thinking on the process of coalification.

Previous views of coalification held that in early stages of diagenesis plant biopolymers (predominantly lignin) were degraded and depolymerized through microbial transformation into low molecular weight humic substances, and these materials subsequently repolymerized to form the macromolecular building blocks that became coals. The bulk of recent results from studies by NMR has not validated this paradigm of coalification. Rather, evidence has mounted indicating that coalification of woody tissue proceeded primarily by selective preservation of lignin structures, as biochemical processes removed carbohydrates preferentially, followed by a subtle thermal alteration of lignin directly into the macromolecules found in coal. There was little evidence to suggest that any major disruption in lignin structure had taken place; consequently, humic acids were no longer considered major intermediates in the formation of coal.

From investigations of coalification of both natural and synthesized precursors, evolutionary changes in the chemical structure of vitrinite were clearly delineated throughout the principal stages of coalification, and detailed mechanisms leading to its transformation could be sketched. It was shown that

initial biochemical stages of coalification involved the complete loss of hemicellulose structures, as well as a significant loss in cellulose from woody tissue, with minimal alteration of lignin. Later diagenetic stages leading to the formation of lignite coals resulted in complete loss of all the carbohydrates and some modification of lignin structure. The changes observed were predominantly rearrangement reactions of the aryl–ether bonds that formed linkages between the 3-methoxyphenol subunits; concomitant with these processes was demethylation of methoxyl groups followed by concerted methylation of the aromatic rings to produce methylcatechol structures. The final stages involving transformation into bituminous coals were characterized by reactions that resulted in complete demethylation of the aromatic methoxyl groups and subsequent reductive elimination of the 3-hydroxyl groups to form predominantly phenol-like building blocks. Progression to the higher rank bituminous coals was distinguished by the continued loss of oxygen functionalities along with ring condensation reactions leading to the formation of increased amounts of polycyclic aromatic structures.

3 APPLICATIONS TO SHALE OIL RESEARCH

Oil shales[99] are fine-grained sedimentary rocks that contain complex organic polymers ranging in molecular weight. There are two fractions of organic matter present: bitumen constitutes the fraction that is soluble in common organic solvents and kerogen constitutes the major portion of organic matter that is insoluble in organic solvents. The organic kerogen fraction is thought to be a cross-linked, three-dimensional macromolecular network of high molecular weight. Oil shale deposits were formed throughout geological time by the slow deposition of organic and inorganic residues in ancient lakes and inland seas. As the bodies of water stagnated and evaporated to dryness, the organic and inorganic matter compacted into sedimentary rock. The structure and composition of the inorganic and organic kerogen components of oil shale vary significantly with the location and the history of the sedimentary basin. If the organic portion originated from a land-based plant source, the kerogen fractions are similar in composition to coal, tend to be highly aromatic materials with hydrogen contents of about 5 wt%, and yield little oil on pyrolysis. On the other hand, kerogen fractions derived from marine aquatic sources tend to have high hydrogen contents ranging from 10 to 12 wt% and are good sources of oil.

Because oil shale kerogen was completely insoluble in common solvents, direct structural and compositional data were difficult to obtain without first performing time-consuming isolation and preparation procedures to produce kerogen concentrates that would be amenable to analysis. As was the case for coal, solid state NMR techniques fostered a resurgence of research devoted to characterization of oil shale in its native state. With the application of high-resolution proton CRAMP and carbon CP MAS spectroscopy, a great deal of fundamental information was obtained about the carbon and proton structure of these materials, about which there was little direct structural information known previously.

3.1 Structure Studies

The first application of NMR to the study of oil shales was reported in 1971, and this initial investigation was focused on the use of broadline ^{1}H NMR as a quantitative approach to predict oil yields that was less time consuming than Fischer assay methods.[100] Three years later, a more comprehensive study was reported in which pulsed ^{1}H NMR techniques were employed for oil shale characterization.[101]

Analyses of oil shale components by high-resolution ^{1}H and ^{13}C NMR have been carried out on samples from the Green River formation that were thermally fractionated into naphtha, light distillate, heavy distillate and residue fractions.[102] Resonances in the spectra were assigned to normal alkanes, and to methyl- and dimethyl-branched alkanes, and the compositions of the various fractions were reported. Relaxation time experiments were correlated to the intermolecular segmental motion of the carbon chains in separate fractions. Solution NMR studies that followed have focused on applications of NMR to oil shale processing.[103,104] Two-dimensional NMR techniques have been applied to the characterization of shale oils.[105] Carbon and hydrogen functional group distributions for oils, obtained from eastern and western oil shales within the USA, were determined using DEPT and quaternary-only (QUAT) pulse methods for editing carbon spectra.[106]

The first solid state ^{13}C NMR spectra using CP enhancement techniques on native oil shales were reported in 1976;[107] however, the authors mentioned that the spectra were quite disappointing because of the lack of resolution between a broad aliphatic resonance band and a weak, partially resolved aromatic band. Later studies extended the CP measurements to include wide variety of oil shales.[108] Resing et al.[109] were the first to report CP MAS measurements on the aromaticity of a Colorado oil shale, the value of which was in basic agreement with that obtained by chemical degradation methods. In subsequent investigations, several laboratories performed CP MAS measurements in order to classify oil shale kerogens of varied origins and depositional environments throughout the globe.[110–113]

Early studies were also concerned with interference from mineral matter, particularly carbonate minerals, with the signals arising from the organic carbon in shales.[109,114] The general consensus reached was that spectra exhibited little interference from carbonates because of the long spin–lattice relaxation times of the minerals. For detailed investigations of the carbon structure of the organic fraction, NMR analyses were carried out on the kerogen concentrates that were prepared by removing the mineral matter by acid treatment (HCl or HF). Spectra of the kerogen concentrates were always found to be better resolved than those obtained from the raw shales, and even simple washing with HCl improved the quality of the spectra.[111,115] The question remained, however, whether the preparation of concentrates by acid treatment had altered the chemical structure of the kerogen in the raw oil shale. A detailed study was carried out to address this issue, employing CP MAS techniques to characterize the organic carbon distributions in six oil shales and their isolated kerogen concentrates.[116] It was determined that the raw shales and their corresponding kerogen concentrates had similar gross compositional features, e.g. carbon aromaticities, indicating that acid extraction did not significantly alter the chemical structure of the organic kerogen material. However,

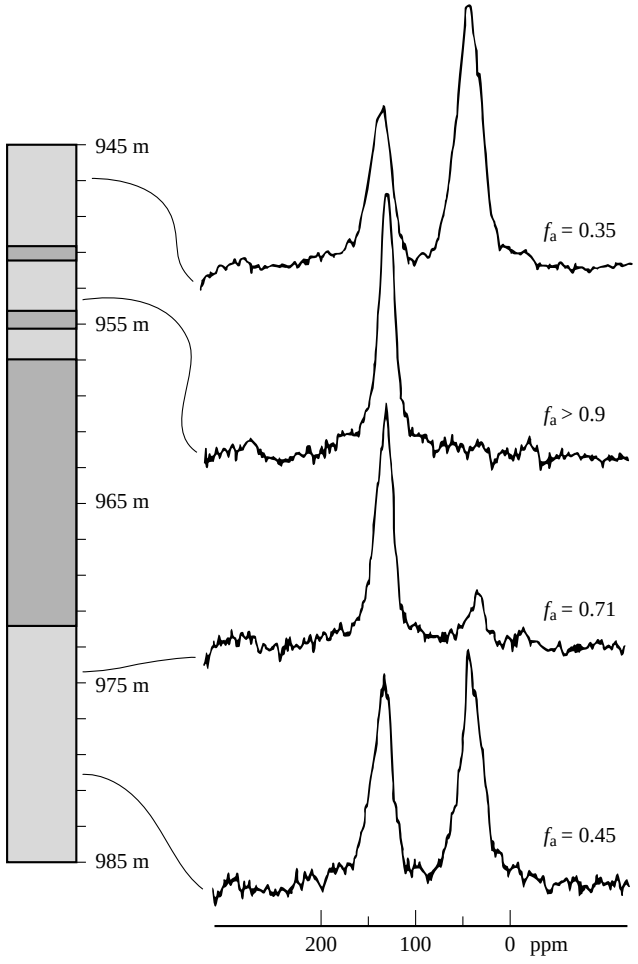

Figure 8 CP MAS ^{13}C NMR spectra and f_a values of oil shale samples at various depths in the vicinity of a basaltic intrusion. Dark areas indicate regions of intrusion

carbohydrate structures if present in the original oil shales, were removed during acid extraction.

The utility of CP MAS NMR as a chemical elucidation method was demonstrated on a series of samples from a section of core taken from the Atlantic ocean, where a basaltic intrusion of magma had permeated the sediment during the Miocene period (see Figure 8).[117] The thermal effects on the organic fraction were clearly visible in the spectra; samples closest to the basaltic intrusion zone clearly showed higher aromaticity values as a result of thermal cracking and subsequent loss of their long-chain aliphatic structures. Aromaticities derived from NMR were compared with results from more traditional vitrinite reflectance measurements, and it was concluded that NMR aromaticities were more sensitive and more quantitative to thermal changes in the kerogen structure.

NMR spectral editing using dipolar dephasing techniques has been applied to derive structural parameters for three oil shales from Colorado, Tennessee and Kentucky;[118] measurements were obtained on the native shales. Differences in carbon structure between the three shales were provided by the DD data, including the distribution of primary through quaternary aliphatic structures, protonated and nonprotonated aromatic groups, the number of methyl groups per aromatic ring, the number of substituted or bridgehead carbon atoms per aromatic ring, and the minimum aliphatic chain length. A later investigation employed curve fitting procedures in conjunction with DD techniques to determine the distribution of carbon bonding types in a kerogen from the Green River Formation.[119] Fourteen representative carbon functional groups were analyzed and these were used to derive an average structure for the kerogen. Analysis of the data indicated that the kerogen was composed of long-chain aliphatic residues as well as alicyclic ring structures, although relative proportions of each were not totally quantifiable on the basis of NMR results.

3.2 Resource Evaluation

The quality of the organic matter in oil shale has traditionally been used as the standard for its potential for bearing oil on heating. Conventional pulsed ^1H NMR has been employed as a rapid method of analysis for oil shale evaluation.[108,120–122] The method relies on the measurement of the amplitude of the free induction decay to assess the overall hydrogen content of the shale. In actuality, the measurement was simply a measure of the quantity of kerogen in the sample. To date, ^1H CRAMPS has not been employed for the analysis of oil shales.

With the development of ^{13}C CP MAS spectroscopy, a new method was introduced which has played a significant role in oil shale resource evaluation because it provides a direct means of analyzing aliphatic/aromatic carbon distributions in these systems, and thereby manifests an immediate relationship to yields of saturated oil products. Aliphatic structures tend to be hydrogen rich; thus oil shales having greater aliphatic carbon content were known to produce higher fractions of liquids than those more aromatic in nature.

The first CP MAS studies to establish a correlation between the aliphatic carbon content of oil shales and oil yields determined by traditional Fischer assay methods were performed by Maciel et al.[123,124] Several additional CP MAS studies followed on a wide range of kerogens and oil shales.[125–128] The correlation between aliphatic carbon and oil yields was determined to be linear for samples spanning a diverse range of geological time periods, geographic locations and depositional environments. The excellent correlation between genetic potential, or the amount of oil and gas that an oil shale kerogen is able to generate, and fraction of aliphatic carbon has since been documented in several laboratories.[129–133] Conversely, the aromatic carbon content has been shown to correlate with the carbon residue remaining after pyrolysis.[115,132–134] Solid state ^{13}C NMR has since been considered the paradigm for resource evaluation in the field, because the method relies on structure parameters that are closely identified with fuel yields. Moreover, the information is independent of the total kerogen content in the oil shale, which is often a misleading parameter for oil generation.

3.3 Oil Shale Conversion

Solid and liquid state NMR, in combination with elemental analysis and mass spectrometry, have provided valuable insight into the chemistry of oil shale conversion throughout the last two decades. From the perspective of processing, NMR has been attractive because it is capable of measuring directly

the changes associated with the carbon bonding distributions that occur as a function of temperature and other retorting parameters. Early studies involved liquid-state ^{1}H and ^{13}C NMR on oils produced from pyrolysis and hydropyrolysis of shales from eastern and western USA; a comprehensive set of average molecular structure parameters were derived for the hydrocarbon mixtures.[135] Research performed in several laboratories[115,136–141] has combined CP MAS NMR measurements with data from elemental analysis to determine the degree of aromatization during oil shale pyrolysis.

Hershkowitz et al.[136] were the first to quantify the increase in aromatic carbon formed in pyrolysis of Colorado oil shale. Their experiments were carried out at a slow heating rate up to a temperature of 600 °C under high pressure (2600 kPa) N_2 or H_2. The net increase in total aromatic carbon for the oil and residue products over that of the starting shale oil was determined by solution state and CP MAS ^{13}C NMR. The increase was rationalized in terms of aromatization of the aliphatic carbon functional groups and the associated evolution of light gases and oils that were composed of hydrogen-rich aliphatic species. Similar trends were observed in the pyrolysis studies of Green River and Kentucky oil shales,[137,138] where increases in aromatic carbon content of 29% and 17% were reported, respectively. Consequently, it had been shown that aromatization of aliphatic structures in oil shales was indeed a facile thermal reaction, and that only by carefully controlling the pyrolysis temperature was it possible to minimize aromatization reactions responsible for oil loss.

4 OTHER FUELS

4.1 Petroleum

The earliest high-resolution ^{1}H NMR spectra of petroleum fractions, obtained at a frequency of 30 MHz, were reported in 1957.[142–144] Two practical uses of the application of ^{1}H NMR in the petroleum industry appeared 2 years later, in 1959. A paper[145] was published which described NMR as a technique to evaluate the elemental hydrogen content of petroleum, and a patent[146] was issued in the same year concerning NMR as a method for process control for determining fuel quality on the basis of the degree of branching of alkylated aromatic hydrocarbons.

Although high-resolution ^{1}H NMR had proved to be valuable in the characterization of petroleum and petroleum fractions, the introduction of ^{13}C NMR in 1967 as a quantitative tool using time-averaged slow passage techniques[147] provided a prelude of what was soon to become a powerful analytical method. Nine years later, the first detailed ^{13}C NMR investigation of crude oils and petroleum fractions appeared using FT methods.[148] Replacement of continuous wave techniques by FT made the ^{13}C NMR characterization of crude oils and petroleum products more or less routine. Several conference proceedings and reviews have appeared in the literature which summarize much of the information that has been derived from NMR about the chemistry and structure of heavy crude oils and petroleum, including the use of NMR in petroleum exploration and as an oil logging tool.[149–151]

Several fundamental advances have been realized in the elucidation of heavy oils by NMR. In 1981, Gillet et al.[152] presented and discussed numerous criteria necessary for obtaining quantitatively reliable structural parameters from NMR experiments. One year later, NMR was used to provide a 'fingerprint' of various crude oils.[153] SEBBORD pulse methods were used for spectral editing of carbon spectra of petroleum fractions, facilitating the discrimination of the different bonding schemes of aliphatic carbon structures, i.e. between CH, CH_2, and CH_3 groups.[154,155] The analysis provided sufficient information such that average structural parameters could be derived for these complex mixtures. Carbon chemical shifts and spin–lattice relaxation times were later used to characterize oil products.[156] Nitrogen compounds in crude oils have also been examined and identified with ^{13}C NMR.[157]

The use of ^{33}S NMR as a tool for the characterization of petroleum oils[158] and an oxidized petroleum asphaltene[159] have been reported. The technique has met with limited success because of the considerable quadrupolar linewidths of sulfur combined with the large number of sulfur species present in these complex mixtures.

4.2 Peat

Humic substances have been described as the predominant fraction of the organic matter found in peat. Peat was formed in depositional environments where water had flowed near the surface of the peat profile, slowly but continually inundating the peat subsurface, and where anerobic conditions prevailed within the subsurface layers. These conditions led to the preservation, from oxidative and microbial processes, of the organic matter in peat which has always been thought to be derived from lignin from vascular plants.

An excellent treatise[160] on the use of ^{13}C CP MAS NMR as a structural tool for the investigation of sedimentary humic substances has appeared. The review covers the relevant literature concerning early liquid state and solid state NMR studies of aquatic and terrestrial sediments, and describes in detail recent CP MAS experiments on peat fractions from various geographical locations.

Early studies[161] on humic acids and humins from holocene sediments were the first to suggest that CP MAS NMR can be used to distinguish between humic acids from terrestrial and aquatic environments on the basis of their carbon aromaticities. Source materials for the two sediments were entirely different: terrestrial sediments were based on lignin-derived material that was highly aromatic, whereas aquatic sediments were formed from primarily algal or microbial remains. In a subsequent paper,[162] the same authors attributed the presence of aliphatic structures in marine humic acids to an algal source, and in terrestrial humic acids to lipid material. These initial observations provided the basis for understanding later NMR investigations on humic acids derived from peats.

In those subsequent studies,[160] CP MAS measurements were performed on isolated fractions of fulvic acid, humic acid, and humin from peats obtained from Minnesota, Okefenokee, and the Everglades. Absolute quantities of the aromatic and paraffinic structures, carboxyl, carbonyl and ether functional groups, and carbohydrates were determined and compared for individual fractions from the different peat samples. The data were used to determine the chemical composition of the varied structural components within peat samples from different

depositional environments, and the information was used to develop a model for the transformation of plant residues into humic substances. An investigation[163] published one year later focused on the use of ^{13}C CP MAS spectroscopy, among other techniques, to identify structural changes that occur in humic acids during coalification through the stages of peat, lignite, and sub-bituminous coal.

4.3 Tar Sands

Tar sands are composed of complex mixtures of minerals containing aliphatic, heteroaromatic, and polycyclic aromatic compounds. Because of the strong intermolecular associations between molecules, organic matter in tar sands is often considerably viscous. Bitumen and heavy oil fractions of tar sands from different geographical locations differ widely in chemical composition and physical properties.

To date, there have been few published reports on the use of NMR for characterizing tar sands. Two early studies have attempted to characterize organic–inorganic interactions directly in heavy oil/bitumen-derived solids using ^{13}C CP MAS NMR.[164,165] A subsequent investigation[166] used ^{1}H CRAMPS to provide information on the types of hydrogen functionality that were present at the surface of tar sand residues. The data indicated that hydroaromatic structures were bound more strongly to the mineral surfaces, and that residues of tar sands after pyrolysis became highly aromatic in nature. Relaxation time (T_1) measurements[167] were used to determine the rates of intermolecular association of a tar sand bitumen after its thermally induced dissociation. Separate studies were carried out whereby viscosities of tar sand bitumens could be calculated from T_2 relaxation time measurements performed at room temperature.[168] Viscosities of bitumens from three US tar sands were correlated to weighted T_2 relaxation rates for semiliquid, mobile solid-like and rigid phases.

5 RELATED ARTICLES

Chemical Shift Tensors; Coal Structure from Solid State NMR; Cokes; CRAMPS; Cross Polarization in Rotating Solids: Spin-1/2 Nuclei; Cross Polarization in Solids; Dynamic Nuclear Polarization and High-Resolution NMR of Solids; Geological Applications; Heteronuclear Assignment Techniques; Magnetic Resonance Imaging: A Historical Overview; Magic Angle Spinning; Magic Angle Turning and Hopping; Paramagnetic Relaxation in Solution; Polymers: Regio-Irregular Structure; Rotating Solids; Selective Excitation in MRI and MR Spectroscopy; Variable Angle Sample Spinning; Well Logging; Wood and Wood Chars.

6 REFERENCES

1. H. Perry, in *Kirk–Othmer Encyclopedia of Chemical Technology*, 3rd edn, Wiley, New York, 1978, Vol. 11.
2. E. M. Purcell, H. C. Torrey, and R. V. Pound, *Phys. Rev.*, 1946, **69**, 37.
3. F. Bloch, W. W. Hansen, and M. Packard, *Phys. Rev.*, 1946, **69**, 127.
4. K. S. Vorres, in *Kirk–Othmer Encyclopedia of Chemical Technology*, 4th edn, Wiley, New York, 1993, Vol. 6.
5. E. Stach and co-workers, *Stach's Textbook of Coal Petrology*, 3rd edn, Gebruder Bornstraeger, Berlin, 1982.
6. R. E. Winans and J. C. Crelling, *Chemistry and Characterization of Coal Macerals*, *American Chemical Society Symposium Series No. 252*, ACS, Washington, DC, 1984.
7. R. A. Friedel, *J. Chem. Phys.*, 1959, **31**, 280.
8. H. L. Retcofsky and R. A. Freidel, in *Spectrometry of Fuels*, Plenum, New York, 1970, Chap. 6
9. H. L. Retcofsky and R. A. Friedel, in *Spectrometry of Fuels*, Plenum, New York, 1970, Chap. 8
10. H. L. Retcofsky and T. A. Link, in *Analytical Methods for Coal and Coal Products*, Academic, San Diego, 1978, Vol. II, Chap. 24
11. L. Petrakis and D. Allen, *NMR of Liquid Fossil Fuels*, Elsevier, Amsterdam, 1987, Analytical Spectroscopy Library, Vol. 1.
12. R. M. Davidson, Nuclear Magnetic Resonance Studies of Coal, IEA Coal Research Report No. ICTIS/TR32, IEA Coal Research, London, 1986.
13. P. C. Newman, L. Pratt, and R. E. Richards, *Nature (London)*, 1955, **125**, 645.
14. D. L. Vanderhart and H. L. Retcofsky, *Fuel*, 1976, **55**, 202.
15. A. Pines, M. G. Gibby, and J. S. Waugh, *J. Chem. Phys.*, 1972, **15**, 1776; 1973, **59**, 596.
16. V. J. Bartuska, G. E. Maciel, J. Schaefer, and E. O. Stejskal, *Fuel*, 1977, **56**, 354.
17. B. C. Gerstein, C. Chow, R. G. Pembleton, and R. C. Wilson, *J. Phys. Chem.*, 1977, **81**, 565.
18. D. E. Axelson, Solid State Nuclear Magnetic Resonance of Fossil Fuels, Multiscience, 1985.
19. B. C. Gerstein, P. D. Murphy, and L. M. Ryan, in *Coal Structure*, ed. R. A. Meyers, Academic, New York, 1982, Chap. 4
20. H. Schmiers, *Konstitutionaufklarung von Kohlen und verwandten Produkten*, Freiberger Forshungshefte, VEB Deutscher Verlag fur Grundstoffindustrie, 1986.
21. H Rosenberger and K.-H. Rentrop, Strukturuntersuchungen an Kohlen und kohlestammigen Verbindungen mittels hochflosender ^{1}H- und ^{13}C-NMR in Festkorpern, Vortrag auf der Arbeitstagung *Moderne Methoden und Ergebnisse der Festkorper-NMR-Spektroskopie* ed. H. Rosenberger, Eisenach-Wartburg, Freiberg, 1982.
22. G. E. Maciel, C. E. Bronnomiann, and C. F. Ridenour, in *Magnetic Resonance of Carbonaceous Solids*, ed. R. E. Botto and Y. Sanada, *American Chemical Society Advances in Chemistry Series No. 229*, ACS, Washington, DC, 1992, Chap. 2
23. P. D. Murphy, B. C. Gerstein, V. L. Weinberg, and T. F. Yen, *Anal. Chem.*, 1982, **54**, 522.
24. M. Alla and E. Lippmaa, *Chem. Phys. Lett.*, 1976, **37**, 260.
25. R. Liotta, and G. J. Brons, *J. Am. Chem. Soc.*, 1981, **103**, 1735.
26. R. R. Chambers, Jr., E. W. Hagaman, M. C. Woody, K. E. Smith, and D. R. McKamey, *Fuel*, 1982, **61**, 53.
27. C.-Y. Choi, J. V. Muntean, A. R. Thompson, and R. E. Botto, *Energy Fuel.*, 1989, **3**, 528.
28. J. R. Barnes, A. D. H. Clague, N. J. Claydent, C. M. Dobson, and R. B. Jones, *Fuel*, 1986, **65**, 437.
29. M. A. Wilson, B. C. Young, and K. M. Scott, *Fuel*, 1986, **65**, 1584.
30. A. R. Thompson and R. E. Botto, *Preprint, ACS Division Fuel Chem.*, 1987, **32**, 280.
31. H. L. Retcofsky and R. A. Friedel, *Fuel*, 1968, **47**, 391.
32. B. C. Gerstein, C. Chow, R. G. Pembleton, and R. C. Wilson, *J. Phys. Chem.*, 1977, **81**, 565.

33. T. Yokono, K. Miyazawa, Y. Sanada, and H. Marsh, *Fuel*, 1979, **58**, 896.
34. L. J. Lynch and D. S. Webster, *J. Magn. Reson.*, 1980, **40**, 259.
35. D. S. Webster and L. J. Lynch, *Fuel*, 1981, **60**, 549.
36. J. A. Ripmeester, C Couture, J. A. MacPhee, and J. A. Nandi, *Fuel*, 1984, **63**, 522.
37. R. A. Wind, M. J. Duijvestijn, C. van der Lugt, J. Smidt, and H. Vriend, *Fuel*, 1987, **66**, 876.
38. M. J. Sullivan, N. M. Szeverenyi, G. E. Maciel, L. Petrakis, and D. W. Grandy, in *Magnetic Resonance: Introduction, Advanced Topics and Applications to Fossil Energy*, ed. L. Petrakis, J. P. Fraissard, *NATO ASI Series C124*, Reidel, Dordrecht, 1984, p. 607.
39. W. A. Barton and L. J. Lynch, *Energy Fuel.*, 1989, **3**, 402.
40. R. A. Wind, A. Jurkiewicz, and G. E. Maciel, *Fuel*, 1989, **68**, 1189.
41. L. dela Rosa, M. Pruski, D. Lang, B. Gerstein, and P. Solomon, *Energy Fuel.*, 1992, **6**, 460.
42. M. S. Solum, R. J. Pugmire, and D. M. Grant, *Energy Fuel.*, 1989, **3**, 187.
43. K. Hayamizu, S. Hayashi, K. Kamiya, and M. Kawamura, in *Magnetic Resonance of Carbonaceous Solids*, ed. R. E. Botto and Y. Sanada, *American Chemical Society Advances in Chemistry Series No. 229*, ACS, Washington, DC, 1992, Chap. 15
44. R. L. Dudley and C. A. Fyfe, *Fuel*, 1982, **61**, 651.
45. R. E. Botto, R. Wilson, and R. E. Winans, *Energy Fuel.*, 1987, **7**, 173.
46. C. E. Snape, D. E. Axelson, R. E. Botto, J. J. Delpuech, P. Tekely, B. C. Gerstein, M. Pruski, G. E. Maciel, and M. E. Wilson, *Fuel*, 1989, **68**, 547.
47. M. J. Sullivan and G. E. Maciel, *Anal. Chem.*, 1982, **54**, 1606, 1615.
48. R. E. Botto and D. E. Axelson, *Preprint, ACS Division Fuel Chem.*, 1988, **33**, 50.
49. C. Tsiao and R. E. Botto, in *Magnetic Resonance of Carbonaceous Solids*, ed. R. E. Botto and Y. Sanada, *American Chemical Society Advances in Chemistry Series No. 229*, ACS, Washington, DC, 1992, Chap. 18
50. K. W. Zilm and G. G. Webb, *Fuel*, 1986, **65**, 721.
51. M. Wilson, J. Hanna, K. B. Anderson, and R. E. Botto, *Org. Geochem.*, 1993, **20**, 985.
52. K. W. Zilm and G. G. Webb, *Preprints, ACS Division Fuel Chem.*, 1986, **31**, 230.
53. R. A. Wind, M. J. Duijvestijn, C. van der Lugt, J. Smidt, and H. Vriend, *Fuel*, 1987, **66**, 876.
54. R. A. Wind, R. Lewis, H. Lock, and G. E. Maciel, in *Magnetic Resonance of Carbonaceous Solids*, ed. R. E. Botto and Y. Sanada, *American Chemical Society Advances in Chemistry Series No. 229*, ACS, Washington, DC, 1992, Chap. 3
55. N. K. Sethi, R. J. Pugmire, J. C. Facelli, and D. M. Grant, *Anal. Chem.*, 1988, **60**, 1574.
56. N. K. Sethi, R. J. Pugmire, and D. M. Grant, in *1987 International Conference on Coal Science*, ed. J. A. Moulijn, and H. A. Chermin, Elsevier, Amsterdam, 1987, p. 41.
57. A. M. Orendt, M. S. Solum, N. K. Sethi, C. D. Hughes, R. J. Pugmire, and D. M. Grant, in *Magnetic Resonance of Carbonaceous Solids*, ed. R. E. Botto and Y. Sanada, *American Chemical Society Advances in Chemistry Series No. 229*, ACS, Washington, DC, 1992, Chap. 22
58. S. L. Dieckman, N. Gopalsami, and R. E. Botto, *Energy Fuel.*, 1990, **4**, 417.
59. D. C. French, S. L. Dieckman, and R. E. Botto, *Energy Fuel.*, 1993, **7**, 90.
60. L. Hou, G. D. Cody, P. G. Hatcher, S. Gravina, and M. A. Mattingly, *Fuel*, 1994, **73**, 199.
61. G. D. Cody and R. E. Botto, *Energy Fuel.*, 1993, **7**, 561.
62. R. M. Davidson, Nuclear Magnetic Resonance Studies of Coal, IEA Coal Research Report No. ICTIS/TR32, IEA Coal Research, London, 1986, Chap. 10
63. J. A. McPhee, H. Kawashima, Y. Yamashita, and Y. Yamada, in *Magnetic Resonance of Carbonaceous Solids*, ed. R. E. Botto and Y. Sanada, *American Chemical Society Advances in Chemistry Series No. 229*, ACS, Washington, DC, 1992, Chap. 17
64. H. Z. Sternberg, R. Raymond, and F. K. Schweighardt, *Science*, 1975, Apr., 49.
65. R. J. Pugmire, D. M. Grant, K. W. Zilm, L. L. Anderson, A. G. Oblad, and R. E. Wood, *Fuel*, 1977, **56**, 295.
66. J. W. Stadelhofer, K. D. Bartle, and R. S. Matthews, *Erdol Kohle-Erdgas-Petrochem. vereinigt Brennstoff-Chem.*, 1981, **34**, 71.
67. N. Cyr and N. O. Egiebor, in *Magnetic Resonance of Carbonaceous Solids*, ed. R. E. Botto and Y. Sanada, *American Chemical Society Advances in Chemistry Series No. 229*, ACS, Washington, DC, 1992, Chap. 14
68. J. Franz, *Fuel*, 1979, **58**, 405.
69. D. K. Dalling, G. Haider, R. J. Pugmire, J. Shabtai, and W. E. Hull, *Fuel*, 1983, **62**, 587.
70. P. J. Collin and M. A. Wilson, *Fuel*, 1983, **62**, 1243.
71. R. Sakurovs, L. J. Lynch, and W. A. Barton, in *Magnetic Resonance of Carbonaceous Solids*, ed. R. E. Botto and Y. Sanada, *American Chemical Society Advances in Chemistry Series No. 229*, ACS, Washington, DC, 1992, Chap. 11
72. Y. Sanada and L. J. Lynch, in *Magnetic Resonance of Carbonaceous Solids*, ed. R. E. Botto and Y. Sanada, *American Chemical Society Advances in Chemistry Series No. 229*, ACS, Washington, DC, 1992, Chap. 7
73. E. O. Stejskal, J. Schaefer, and R. A. McKay, *J. Magn. Reson.*, 1977, **25**, 569.
74. G. E. Maciel, V. J. Bartuska, and F. P. Miknis, *Fuel*, 1979, **58**, 391.
75. F. P Miknis, M. J. Sullivan, V. J. Bartuska, and G. E. Maciel, *Org. Geochim.*, 1981, **3**, 19.
76. K. W. Zilm, R. J. Pugmire, D. M. Grant, S. R. Larter, and J. Allen, *Fuel.*, 1981, **60**, 717.
77. R. E. Botto and R. E. Winans, *Fuel*, 1983, **62**, 271.
78. R. A. Wind, M. J. Duijvestijn, C. van der Lugt, J. Smidt, and J. Vriend, *Fuel*, 1987, **66**, 876.
79. M. S. Solum, R. J. Pugmire, and D. M. Grant, *Energy Fuel.*, 1989, **3**, 187.
80. D. E. Wemmer, A. Pines, and D. D. Whitehurst, *Phil. Trans. R. Soc. London, Ser. A*, 1981, **300**, 15.
81. E. W. Hagaman and M. C. Woody, *Proceedings of the International Conference on Coal Science*, Glueckauf, Essen, 1981, 807.
82. P. D. Murphy, T. J. Cassady, and B. C. Gerstein, *Fuel*, 1981, **61**, 1233.
83. M. A. Wilson, R. J. Pugmire, J. Karas, L. B. Alemany, W. R. Woolfenden, D. M. Grant, and P. H. Given, *Anal. Chem.*, 1984, **56**, 933.
84. J. M. Dereppe, in *Magnetic Resonance: Introduction, Advanced Topics and Applications to Fossil Energy*, ed. L. Petrakis and J. P. Fraissard, Reidel, Dordecht, 1984, p. 585.
85. C. E. Snape, D. E. Axelson, R. E. Botto, J. J. Delpuech, P. Tekely, B. C. Gerstein, M. Pruski, G. E. Maciel, and M. A. Wilson, *Fuel*, 1989, **68**, 547.

86. R. A. Wind, G. E. Maciel, and R. E. Botto, in *Magnetic Resonance of Carbonaceous Solids*, ed. R. E. Botto and Y. Sanada, *American Chemical Society Advances in Chemistry Series No. 229*, ACS, Washington, DC, 1992, Chap. 14
87. K. S. Vorres, *Energy Fuel.*, 1990, **4**, 420.
88. B. G. Silbernagel and R. E. Botto, in *Magnetic Resonance of Carbonaceous Solids*, ed. R. E. Botto and Y. Sanada, *American Chemical Society Advances in Chemistry Series No. 229*, ACS, Washington, DC, 1992, Chap. 33
89. J. R. Levine, in *Hydrocarbons from Coal*, ed. B. E. Rice and D. D. Law, *American Association of Petroleum Geologists Studies in Geology Series No. 38*, AAPG, 1993, Chap. 3
90. P. G. Hatcher, I. A. Breger, and W. L. Earl, *Org. Geochem.*, 1981, **3**, 49.
91. P. G. Hatcher, I. A. Breger, N. Szeverenyi, and G. E. Maciel, *Int. J. Coal Geol.*, 1989, **13**, 99.
92. P. G. Hatcher, M. A. Wilson, and A. M. Vassalo, *Int. J. Coal Geol.*, 1989, **13**, 99.
93. P. G. Hatcher, H. E. Lerch, and T. V. Verheyen, *Int. J. Coal Geol.*, 1989, **13**, 65.
94. P. G. Hatcher, *Org. Geochem.*, 1990, **16**, 959.
95. R. Hayatsu, R. L. McBeth, R. G. Scott, R. E. Botto, and R. E. Winans, *Org. Geochem.*, 1984, **6**, 463.
96. R. E. Botto, *Energy Fuel.*, 1987, **1**, 228.
97. R. E. Botto, R. Hayatsu, K. A. Carrado, and R. E. Winans, *'Proceedings of the International Conference on Coal Science', Tokyo, Japan, 23–27 October 1989*, New Energy and Industrial Technology Development Organisation, p. 1.
98. R. E. Botto, *Macromolecules*, 1988, **21**, 1246.
99. T. F. Yen and G. V. Chilingarian (eds), *Oil Shale*, Elsevier, New York, 1976.
100. A. W. Decora, F. McDonald, and G. Cook, United States Bureau of Mines Report of Investigation 7523, USBMR, 1971.
101. F. Miknis, A. Decora, and G. Cook, United States Bureau of Mines Report of Investigation 7984, USBMR, 1974.
102. D. A. Netzel, D. R. McKay, R. A. Heppner, F. D. Guffey, S. D. Cooke, D. L. Varie, and D. E. Linn, *Fuel*, 1981, **60**, 307.
103. F. P. Miknis, *Proc. Intersoc. Convers. Eng. Conf.*, 1982, **17**, 935.
104. D. E. Lambert and M. A. Wilson, *Preprint, ACS Division Fuel Chem.*, 1985, **30**, 256.
105. W. T. Sobol, L. J. Schreiner, L. Miljkovic, M. E. Marcondes-Helene, L. W. Reeves, and M. M. Pintar, *Fuel*, 1985, **64**, 583.
106. A. D. Netzel, *Anal. Chem.*, 1987, **59**, 1775.
107. F. P. Miknis and D. A. Netzel, in *Magnetic Resonance in Colloid and Interface Science*, ed. H. A. Resing and C. G. Wade, *American Chemical Society Symposium Series No. 34*, ACS, Washington, DC, 1976, Chap. 16
108. D. Vitorovic, D. Vucelic, M. J. Gasic, N. Juranic, and S. Macura, *Org. Geochem.*, 1978, **1**, 89.
109. H. A. Resing, A. N. Garroway, and R. N. Hazlett, *Fuel*, 1978, **57**, 450.
110. D. Vucelic, N. Juranic, and D. Vitorovic, *Fuel*, 1979, **58**, 759.
111. F. P. Miknis, G. E. Maciel, and V. J. Bartuska, *Org. Geochem.*, 1979, **1**, 169.
112. F. P. Miknis, A. W. Lindner, A. J. Gannon, M. F. Davis, and G. E. Maciel, *Org. Geochem.*, 1984, **7**, 239.
113. F. P. Miknis and J. W. Smith, *Org. Geochem.*, 1984, **5**, 193.
114. F. P. Miknis, J. Jhou, D. B. MacGowan, and R. C. Surdam, *Org. Geochem.*, 1993, **20**, 339.
115. F. P. Miknis, *Fuel*, 1993, **71**, 731.
116. G. E. Maciel and L. W. Dennis, *Org. Geochem.*, 1982, **3**, 105.
117. L. W. Dennis, G. E. Maciel, P. G. Hatcher, and B. R. T. Simoneit, *Geochim. Cosmochim. Acta*, 1982, **46**, 901.
118. K. D. Schmitt and E. W. Sheppard, *Fuel*, 1984, **63**, 1241.
119. M. J. Trewhella, I. J. F. Poplet, and A. Grint, *Fuel*, 1986, **65**, 541.
120. F. P. Miknis, A. W. Decora, and G. L. Cook, United States Bureau of Mines Report of Investigation 7984, USBMR, 1974.
121. F. P. Miknis, A. W. Decora, and G. L. Cook, in *Science and Technology of Oil Shale* ed. T. F. Yen, Ann Arbor Science, Ann Arbor, MI, 1976.
122. R. D. Sydansk, *Fuel*, 1978, **57**, 66.
123. G. E. Maciel, V. J. Bartuska, and F. P. Miknis, *Fuel*, 1978, **57**, 505.
124. G. E. Maciel, V. J. Bartuska, and F. P. Miknis, *Fuel*, 1979, **58**, 155.
125. F. P. Miknis and G. E. Maciel, in *Nuclear Magnetic Resonance*, ed. R. H. Filby, B. S. Carpenter, and R. C. Ragaini, Plenum, New York, 1982.
126. F. P. Miknis, D. A. Netzel, J. W. Smith, M. A. Mast, and G. E. Maciel, *Geochim. Cosmochim. Acta*, 1982, **46**, 977.
127. F. P. Miknis and G. E. Maciel, in *Magnetic Resonance. Introduction, Advanced Topics and Applications to Fossil Energy*, ed. L. Petrakis and J. P. Fraissard, Reidel, Dordrecht, 1984.
128. F. P. Miknis, J. W. Smith, E. K. Maughan, and G. E. Maciel, *Am. Assoc. Petrol. Geol. Bull.*, 1982, **66**, 1396.
129. G. E. Maciel, V. J. Bartuska, and F. P. Miknis, *Fuel*, 1978, **57**, 505.
130. E. W. Hagaman, F. M. Schell, and D. C. Cronauer, *Fuel*, 1984, **63**, 915.
131. E. Evans, B. Batts, and N. Cant, *Fuel*, 1987, **66**, 326.
132. F. P. Miknis and P. J. Conn, *Fuel*, 1986, **65**, 248.
133. S. Sato, M. Enomoto, and S. Takahashi, *Fuel Proc. Technol.*, 1988, **18**, 305.
134. K. Qin, D. Chen, and Z. Li, *Org. Geochem.*, 1991, **17**, 856.
135. D. A. Netzel and F. P. Miknis, *Fuel*, 1982, **61**, 1101.
136. F. Hershkowitz, W. N. Olmstead, R. P. Rhodes, and K. D. Rose, in *Geochemistry and Chemistry of Oil Shales*, ed. F. P. Miknis and J. F. McKay, *American Chemical Society Symposium Series No. 230*, ACS, Washington, DC, 1983, Chap. 15
137. A. K. Burnham, and J. A. Happe, *Fuel*, 1984, **63**, 1353.
138. F. P. Miknis and P. J. Conn, *Fuel*, 1986, **65**, 248.
139. F. P. Miknis, N. M. Szeverenyi, and G. E. Maciel, *Fuel*, 1982, **61**, 341.
140. G. E. Maciel, V. J. Bantuska, and F. P. Miknis, *Fuel*, 1978, **57**, 505.
141. F. P. Miknis, T. F. Turner, L. W. Ennen, and D. A. Netzel, *Fuel*, 1988, **67**, 1568.
142. R. B. Williams, ASTM Special Technical Publication No. 224, American Society for Testing Materials Philadelphia, 1957, p. 168.
143. J. R. Zimmerman and J. A. Lasater, ASTM Special Technical Publication No. 224, American Society for Testing Materials, Philadelphia, 1957, p. 195.
144. S. H. Hastings, B. H. Johnson, H. E. Lumpkin, and R. B. Williams, ASTM Special Technical Publication No. 224, American Society for Testing Materials, Philadelphia, 1957, p. 250.
145. R. B. Williams, *Spectrochim. Acta*, 1959, **14**, 24.
146. R. B. Williams, US Patent No. 2 871 443, January 1959.
147. S. A. Knight, *Chem. Ind.*, 1967, 1920.
148. J. N. Shoolery and W. L. Budde, *Anal. Chem.*, 1976, **48**, 1458.

149. H. L. Retcofsky and K. D. Rose, *Preprint, ACS Division Petrol. Chem.*, 1985, **30**, 232.
150. L. Petrakis and E. Edelheit, *Appl. Spectros. Rev.*, 1979, **15**, 195.
151. J. Speight, *Liquid Fuel. Technol.*, 1984, **2**, 211.
152. S. Gillet, P. Rubini, J. J. Delpuech, J. C. Encalier, and P. Valentin, *Fuel*, 1981, **60**, 221.
153. M. Bouquet and A. Bailleul, *Proc. Inst. Pet., London, 1982*, 2, 394.
154. D. F. Cookson and B. E. Smith, *Fuel*, 1983, **62**, 34.
155. D. F. Cookson and B. E. Smith, *Fuel*, 1983, **62**, 39.
156. T. A. Holak, D. W. Aksnes, and M. Stocker, *Anal. Chem.*, 1984, **56**, 725.
157. I. A. Khan, Z. A. K. Al-Asadi, F. S. Muttawalli, and A. H. Tameesh, *J. Petr. Res.*, 1982, **1**, 58.
158. M. B. Ngassoum, R. Faure, J. M. Ruiz, L. Lena, E. J. Vincent, and B. Neff, *Fuel*, 1986, **65**, 142.
159. D. D. McIntyre and O. P. Strausz, *Magn. Reson. Chem.*, 1987, **25**, 36.
160. P. G. Hatcher, I. A. Breger, L. W. Dennis, and G. E. Maciel, in *Aquatic and Terrestrial Humic Materials*, ed. R. F. Christman and E. T. Gjessing, Ann Arbor Science, Ann Arbor, MI, Chap. 3, 1983.
161. P. G. Hatcher, D. L. VanderHart, and W. L. Earl, *Org. Geochem.*, 1980, **2**, 87.
162. P. G. Hatcher, G. E. Maciel, and L. W. Dennis, *Org. Geochem.*, 1981, **3**, 43.
163. J. V. Ibarra and R. Juan, *Fuel*, 1985, **64**, 650.
164. A. Majid, J. A. Ripmeester, and D. W. Davidson, NRC Report No. C1095-825, Ottawa, Ontario, 1982.
165. D. E. Axelson, *Fuel*, 1987, **66**, 40.
166. D. A. Netzel, P. T. Coover, and C. E. Bronnimann, *Fuel*, 1990, **69**, 429.
167. D. A. Netzel and P. T. Coover, *Energy Fuel.*, 1989, **3**, 259.
168. D. A. Netzel and T. F. Turner, *Fuel Sci. Technol. Int.*, 1990, **8**, 379.

Biographical Sketch

Robert E. Botto. *b* 1946. A.B., Rutgers College, New Brunswick, 1968; M.S., Michigan State University, 1970; US Army Science and Engineering Corps, 1970–72; Ph.D. (supervisor Donald G. Farnum), Michigan State University, 1975. Postdoctoral work at California Institute of Technology (with John D. Roberts). Successively, visiting professor at University of Southern California; NRC fellow at National Bureau of Standards; chemist at Argonne National Laboratory. Approx. 90 publications. Research specialties: solid state NMR spectroscopy and imaging of fossil fuels, polymers, catalysts, and advanced materials.

Geological Applications

R. James Kirkpatrick
University of Illinois, Urbana, IL, USA

1	Introduction	1
2	Historical Development	1
3	Al,Si Order in Aluminosilicate Minerals and Chemical Shift Correlations	1
4	Alkali Sites in Aluminosilicate Minerals	3
5	Structural Phase Transitions in Minerals	3
6	High-Pressure Minerals	4
7	Exchangeable Water and Cations in Clay Minerals	4
8	Thermal Decomposition of Phyllosilicate Minerals	6
9	NMR of Less Abundant Elements: ^{31}P, ^{11}B	6
10	^{17}O NMR of Minerals	7
11	Natural Organic Materials	7
12	Natural Glasses and Melts	7
13	Related Articles	7
14	References	8

1 INTRODUCTION

The Earth and planets are complex systems which contain a wide range of chemical and physical environments. In and on the Earth, for instance, temperatures range from ca. $-50\,^{\circ}$C at the polar regions to at least 4000 K in the core, and pressures range from zero at the surface to ca. 3.6 Mbar at the center. In detail the chemical environments of the Earth are extraordinarily diverse, but can be thought of as varying from near-surface hydrous conditions at relatively low temperatures and pressures (e.g., weathering and hydrothermal environments) to hydrous or anhydrous conditions at higher pressures and temperatures in the interior (e.g., partial melting conditions that produce magma in the mantle and lower crust and molten and solid metal outer and inner cores). The 90 natural elements are all of geochemical interest, although the bulk of the Earth is composed of about 10 elements, of which O and S are the most important anions and Si, Al, Fe, Mg, Ca, Na, Ti, K, C, and P are the most important cations. Most of the minerals in the crust and mantle (surface to a depth of ca. 2900 km) are silicates or aluminosilicates, and thus these materials (along with the economically important natural organic materials) are the focus of most NMR investigations relevant to geoscience.

NMR methods provide data and insight relevant to a wide range of geological problems that go far beyond simply characterizing the structures of minerals and natural organic and inorganic species. They have for instance, helped to obtain an understanding of the structure and dynamics of silicate and aluminosilicate glasses and melts (magma and lava), the structure and dynamics of water molecules and cations in clays and zeolites, reactions at mineral–water interfaces, the thermodynamics of homogeneous equilibrium in minerals, and the structural and dynamical changes which occur at phase transitions in minerals. Additionally, most products used by modern society start as natural materials, and NMR has helped elucidate the mechanisms by which natural materials are converted to these products (e.g., clays to ceramics).

This article deals primarily with inorganic minerals and their reactions and briefly touches on natural organic materials and glasses. There are other chapters in this Encyclopedia concerning zeolites, amorphous materials, high-temperature NMR, and a variety of natural organic materials and products obtained from them that are relevant to geochemistry and geology.

2 HISTORICAL DEVELOPMENT

NMR investigations of minerals began soon after the discovery of NMR in 1945. The earliest study was the ^{1}H study of single crystal and powdered gypsum ($CaSO_4{\cdot}2H_2O$) by Pake[1] in 1948. This paper was an early example of how NMR methods can be applied to solids and paved the way to understanding the relationships between the structure and NMR behavior of water, and by implication other constituents of solids. Other early papers include work in the 1950s on ^{27}Al in Li-pyroxene (spodumine, $LiAlSi_2O_6$)[2] and ^{1}H in portlandite [$Ca(OH)_2$].[3]

During the 1960s and 1970s most work on natural inorganic compounds used single crystal methods for ^{27}Al and alkali cations to investigate Al,Si order in the tetrahedral sites of aluminosilicates, to determine the relationships between the overall crystal symmetry and local site symmetry, to investigate structural phase transitions (SPTs), and to investigate the nature of the bonding in these materials.[4,5] This work provided significant information complementary to the X-ray diffraction structural studies of these materials being undertaken at that time, but were limited by the need for ca. 1 cm^3-sized single crystals. Investigation of the structure and dynamics of water molecules in minerals (especially clays) also grew rapidly during this time.[6,7]

NMR applications to both organic and inorganic natural materials expanded rapidly beginning in about 1980, as the use of high-field superconducting magnets, the pulse Fourier transform method of data collection, and magic angle spinning (MAS) became common. To date there have been more than 1000 papers focusing specifically on geochemical and mineralogical problems and using these methods. The seminal papers were those of Lippmaa and his coworkers on the ^{29}Si MAS NMR of first silicates with a variety of structural types, and then zeolites.[8,9] These were followed soon after by papers on ^{29}Si of the silica polymorphs and silicate and aluminosilicate minerals.[10,11] The ability to examine quadrupolar nuclide via the $\frac{1}{2}$, $-\frac{1}{2}$ transition assumed great significance,[12,13] because of the important natural nuclides only ^{1}H, ^{13}C, ^{29}Si, and ^{31}P have spin $I = \frac{1}{2}$. Work on natural organic compounds (e.g., coal and its precursors and derivatives, oil shale, and plants and their weathering products) also grew rapidly during this time.[14]

3 Al,Si ORDER IN ALUMINOSILICATE MINERALS AND CHEMICAL SHIFT CORRELATIONS

One of the most important applications of MAS NMR in the geosciences has been the investigation of Al,Si order

in aluminosilicate minerals. This work has used primarily ^{29}Si and to a lesser extent ^{27}Al, and has paralleled similar developments for synthetic zeolite catalysts and molecular sieves. This problem is of significance because silicates and aluminosilicates are the most abundant minerals in the Earth, and diffraction methods cannot effectively probe the state of local Al,Si order on tetrahedral sites if the Al and Si are not ordered onto crystallographically different sites.[15,16] This local state of order can have a significant effect on the thermodynamic properties of the minerals, because of the relatively high energy of the tetrahedral Al–O–Al linkage and because of entropic effects. The concentration of tetrahedral Al–O–Al linkages is usually minimized (the 'aluminum avoidance' or 'Loewenstein's' rule). This issue is of most significance for framework and sheet silicates (Q^4 and Q^3 polymerizations) and to a lesser extent for chain silicates (Q^2 polymerization), because Al does not often enter the tetrahedral sites of less polymerized structures.

The classic demonstration of the capabilities of NMR to investigate tetrahedral Al,Si order is the ^{29}Si investigation of the increase in Al,Si order in the framework structure of corderite ($Mg_2Al_4Si_5O_{10}$) with high-temperature annealing, and the relationship of the local state of order to the observed decrease from hexagonal through modulated to monoclinic symmetry.[17] The results for corderite are clearer than for other aluminosilicates because the ^{29}Si peaks for Si on the two tetrahedral sites are better resolved. The most important results of this study are that corderite is always quite well-ordered (number of Al–O–Al linkages is always <1.5 per formula unit), that the number of Al–O–Al linkages decreases with increasing annealing time at temperatures between 1185 and 1400 °C, and that although the transition from modulated to monoclinic corderite is strongly first order as observed by X-ray diffraction (the average structure), the local Al,Si order as observed by NMR varies continuously and shows no discontinuity. Quantitative analysis of the NMR and thermochemical data indicate that the enthalpy of the ordering reaction Si–O–Si + Al–O–Al = 2(Si–O–Al) is about $-34\,kJ\ mol^{-1}$, comparable to values determined for other aluminosilicate phases using similar methods.[18]

The ^{29}Si MAS NMR spectra of most framework aluminosilicates with more than one crystallographic tetrahedral site are not as well resolved as those of corderite because of overlap of the peaks from Si on different sites with different numbers of Al next-nearest neighbors (NNN), but in some cases analysis of the first and second moments of the spectra can provide useful information about the state of order.[18]

Analysis of the ^{29}Si MAS NMR spectra of sheet silicates (clays and micas) has also proven to be very fruitful, in large part because peak overlap is often not a problem due to the presence of only one tetrahedral site, over which Al and Si are distributed.[19] Comparison of the observed NMR spectra and the results of Monte Carlo computer simulations of the Al,Si order in these materials shows that the short-range Al,Si order is greater than expected just by the absence of Al–O–Al linkages, and can be well described by the so-called homogeneous distribution of charge model. This model is based on the idea that the Al atoms distribute themselves in the way that most effectively balances the charges of the cations which occupy the interlayers between the aluminosilicate sheets. Site interaction energies for sheet silicates appear to be comparable to those of framework silicates, and configurational entropies calculated via cluster variation methods based on these models are such that long range Al,Si order is not expected.[19]

^{27}Al NMR has wide application to minerals but has proven less useful in probing Al,Si order than ^{29}Si, because of the increased peak width due to unaveraged second-order quadrupole broadening under MAS. For oxide materials, octahedral ^{27}Al resonates near 0 ppm, whereas tetrahedral ^{27}Al resonates between 50 and 80 ppm. Thus, under MAS, peaks for these types of sites can normally be resolved, although quantitation of sites occupancies cannot always be assured. For tetrahedral Al, the chemical shifts generally become more positive with decreasing polymerization (paralleling the behavior of ^{29}Si).[15] Unfortunately, in MAS spectra it is rare to be able to resolve peaks for Al on separate sites in Al,Si disordered phases, but in some cases analysis of the spinning sidebands of the satellite $\frac{1}{2}$, $\frac{3}{2}$ transitions can be useful.[20]

One important feature of the NMR data for aluminosilicate materials is that there are several well-understood empirical relationships between ^{29}Si and ^{27}Al chemical shifts and structural and chemical parameters. These can be understood from quantum chemical principles, although computer capabilities still limit quantitative calculations.[21] The most significant effects are due to nearest-neighbor (NN) coordination, with the chemical shift becoming more negative (more shielded) with increasing coordination. For ^{29}Si, the chemical shifts range from ca. -60 to -129 ppm for tetrahedral coordination and from ca. -180 to -210 ppm for octahedral coordination. Five-coordinate Si resonates near -150 ppm. For ^{27}Al the isotropic chemical shifts range from ca. +55 to +85 ppm for tetrahedral coordination, from ca. +30 to +41 ppm for five-coordination, and from near 0 to ca. 15 ppm for octahedral coordination.[22]

The following are some of the most important correlations for tetrahedrally coordinated ^{29}Si (see also Kirkpatrick[15] and Stebbins,[22] and references therein).

1. For the SiO_2 phases, the ^{29}Si chemical shift becomes more negative with increasing mean Si–O–Si bond angle and mean Si–Si distance per tetrahedron, although the best functional forms are not well understood.[23]
2. For silicates, the ^{29}Si and ^{27}Al chemical shifts become more positive with decreasing polymerization, although due to other structural effects there is considerable overlap of the chemical shift ranges.
3. For aluminosilicates with the same polymerization (e.g., Q^4), the ^{29}Si chemical shift becomes less negative as the number of tetrahedral Al next-nearest neighbors (NNN) increases, again with considerable overlap of the ranges.
4. For all aluminosilicates, the ^{29}Si chemical shift becomes more negative as the sum of the strengths of the NN and NNN bonds and the local group electronegativity increase.
5. For all aluminosilicates, the relationships with bond strength, NNN composition, interatomic distance, and interatomic angle can be accounted for by a single model involving these parameters.[24]

There are also quite good empirical correlations between the ^{29}Si chemical shift of six-coordinate Si and various structural parameters. The best of these involves a parameter related to the bond strengths of the nearest neighbor cations and the angle of the Si–O–M bond.[25] Qualitatively, Si(6) chemical shifts become less shielded as the bond strengths of the nearest-neighbor cations decrease.

For tetrahedral ^{27}Al, the chemical shift correlations are less clear, but they generally become more positive with increasing Al/Si ratio, and framework (Q^4) structures generally yield less positive values than less polymerized phases.[22] For both ^{29}Si and ^{27}Al, coordination to P causes less positive or more negative chemical shifts compared with similar sites coordinated to Si.

Aluminum-27 quadrupole coupling constants (QCCs) generally increase as the local site symmetry decreases,[4,22] although there is no well-developed quantitative understanding of the relative effects of local symmetry and long range symmetry on their magnitudes.

4 ALKALI SITES IN ALUMINOSILICATE MINERALS

Many aluminosilicate phases, especially those with framework and sheet structures, compensate the charge imbalance caused by tetrahedral Al for Si substitution by the incorporation of alkali or alkaline earth cations in relatively large sites within the framework or between the sheets. In many cases the large cations are disordered because of a distribution of two or more species (e.g., Na and K) over one or more crystallographic sites, or because there are fewer cations per formula unit than available sites in the structure. In many cases the nearest-neighbor (NN) coordination of the large cation is poorly defined, with oxygens occurring at a range of interatomic distances. In some cases the cations are in rapid exchange among the various sites. In all of these cases, diffraction methods are insufficient to define adequately the distribution and behavior of the large cations, and NMR methods have proven useful. Most investigations of large cations in aluminosilicates have focused on the alkalis (primarily ^{23}Na), because the NMR-active alkaline earth nuclides have large quadrupole moments and thus typically yield broad peaks. NMR investigation of alkali cations began with single crystal work in the early 1960s[26] and greatly expanded after about 1982 with the advent of the pulse Fourier transform method and high-field superconducting magnets.[15]

An important example of the problem of defining the nature of the alkali site in framework aluminosilicates is the Na site of the feldspar albite ($NaAlSi_3O_8$). This site is quite distorted (its NN coordination could be considered to be any value from five to nine), and early structure refinements based on X-ray diffraction data used a so-called split site model in which the Na atoms are distributed over two positions in the same general site. Single crystal ^{23}Na NMR showed that this model is not correct and that in fact there is only one, well-defined but anisotropic, Na site.[26] Later MAS NMR work at higher field confirmed this result.[27] Sodium-23 MAS NMR of mixed Na,K feldspars shows that the Na site becomes larger and more symmetrical with increasing K/Na ratio, as demonstrated by progressively more negative isotropic chemical shifts and smaller QCCs. This observation demonstrates that the strain caused by K for Na substitution is quite long range (more than a unit cell) and affects not only the individual sites occupied by K but also those occupied by Na.[20] For Al,Si disordered phases, the singularities in the ^{23}Na peaks due to quadrupolar effects are usually poorly defined, probably due to a range of isotropic chemical shifts, quadrupole coupling constants, and asymmetry parameters caused by differences in the local Al,Si distribution.

Alkali cations in many framework aluminosilicates often have quite large diffusion coefficients at only moderate temperatures (a few hundred °C), and it is likely that the motion of the alkali cations in them can be examined by high-temperature NMR. The Na behavior in the framework mineral nepheline (actual composition of the sample = $Na_{0.95}K_{0.05}AlSiO_4$) is an excellent example.[28] In this mineral Na is partitioned between two sites, which yield well-resolved ^{23}Na MAS NMR peaks. At ca. 300 °C these peaks begin to merge, and at 500 °C there is only a single peak. High-temperature X-ray structure refinements do not indicate the presence of structural distortions sufficient to cause the ^{23}Na signal for the two sites to become similar, and the best interpretation of these data is that above ca. 500 °C the Na is in exchange between these sites at frequencies greater than ca. 2 kHz. These frequencies are in good agreement with diffusion coefficients of about 10^{-12} cm^2 s^{-1} for similar materials estimated from electrical conductivity.

Recent work shows that there are well-defined relationships between the ^{23}Na chemical shifts of aluminosilicates and their polymerization and NN Na coordination.[29] There has been less systematic study of the other alkali cations, and little systematic study of the alkaline earth cations, although ^{25}Mg, ^{87}Sr, and ^{137}Ba are observable for some materials.

5 STRUCTURAL PHASE TRANSITIONS IN MINERALS

Minerals, like all crystalline compounds, change their structure with changing environmental conditions (P, T, PH_2O, etc.). Many of these changes involve reconstruction of the crystal structure and occur via ordinary chemical reactions (e.g., solid state or solution–reprecipitation). Many minerals, however, undergo so-called structural phase transitions (SPTs) which involve adjustments of the structure but not destruction and formation of strong chemical bonds. Ferromagnetic and ferroelectric transitions are technologically important examples, and the $\alpha-\beta$ transition of quartz is the best known mineralogical example. SPTs can have significant effects on the thermodynamic and mechanical properties of materials in which they occur and thus can be of considerable geological importance.[30,31]

The first geologically important SPT to be investigated by NMR was the $P\bar{1}$–$I\bar{1}$ transition in the Ca-feldspar anorthite ($CaAl_2Si_2O_8$). This phase is the end-member of the Ca–Na plagioclase feldspar series, which is the most abundant mineral in the Earth's crust. In the 1960s and 1970s there had been considerable controversy about the existence of this transition, and single crystal ^{27}Al NMR results demonstrated that the number of Al sites in anorthite is reduced from eight to four with increasing temperature at ca. 240 °C.[5] Recent ^{29}Si MAS NMR work confirms this result and demonstrates that the number of Si sites is likewise reduced from eight to four at the transition.[31]

The SPTs of the SiO_2 polymorphs, quartz, cristobalite, and tridymite, and their $AlPO_4$ analogs have been the focus of extensive recent NMR investigation.[32–34] These SiO_2 phases are important both naturally and technologically, and their $AlPO_4$ analogs, which have similar SPTs, allow investigation of the structural changes through the quadrupole interaction

of ^{27}Al, as well as through the chemical shifts and ^{17}O quadrupolar interaction. Data for these phases are also an essential base from which to investigate the SPTs of the wide range of minerals and synthetic compounds with stuffed quartz, cristobalite, and tridymite structures (e.g, nepheline, eucryptite).

For the SPTs of these materials, the chemical shifts, relaxation rates, and ^{17}O and ^{27}Al QCCs provide clear probes of the temperatures, extent, and hysteresis of the transitions, and also provide information about the local structural changes which occur. For instance for SiO_2-cristobalite, changes in the ^{29}Si MAS NMR spectra clearly reflect the changes in the mean Si−O−Si bond angle per tetrahedron with temperature in the low-temperature phase and the discontinuous change in this parameter at the SPT. The T_1 relaxation rates also change discontinuously.[32,33] X-ray diffraction indicates that the low-temperature phase is tetragonal and that the average structure of the high-temperature phase is cubic. ^{27}Al NMR results also indicate that the Al site of the high-temperature $AlPO_4$ cristobalite phase has cubic symmetry on timescales longer than about 1 μs.[33] The SPT is associated with the onset of diffuse streaking in electron diffraction patterns, indicating disorder in the high-temperature phase. However, the mean Si−O−Si bond angle in the high-temperature phase determined from empirical correlations is about 152.5 $\pm$ 1°, inconsistent with the value of 180° required by cubic symmetry. The only explanation consistent with all these observations is that the oxygen atoms in the high-temperature phase are dynamically disordered on positions located on an annulus around the mean oxygen position, and that the average structure as observed by X-ray diffraction is a dynamical average of structures that instantaneously are not cubic. The high-temperature phases of tridymite appear to behave in a similar way,[34] and similar dynamical disordering is likely to occur in many materials with relatively open structures. NMR will be an important tool in investigating such materials.

6 HIGH-PRESSURE MINERALS

The structures of silicate and aluminosilicate materials normally change less with increasing pressure than, for example, organic compounds or alkali halides. Nonetheless, the pressures in planetary interiors are extremely large, and the minerals present are denser and have different structures than those present at and near the surfaces. One of the most dramatic changes in the Earth's structure occurs in the depth range 400 to 650 km (P = ca. 130 to 220 kbar). In this region, the so-called transition zone of the mantle, the densities and sound velocities as observed by geophysical techniques increase dramatically (ca. 15−20%). High-pressure and -temperature laboratory experiments indicate that the structures of the major minerals of the upper mantle (olivine, pyroxenes, and garnets) transform to denser phases in this pressure range. Thus, although there is considerable controversy about whether there is a change in the bulk composition of the Earth at this depth, there is no controversy about the fact that structural changes in the minerals present contribute significantly to the observed changes in properties.

The most significant aspect of the structures of these high-pressure minerals is that they contain octahedrally coordinated Si [Si(6)], as opposed to the tetrahedrally coordinated Si [Si(4)] of lower pressure phases. NMR of quenched samples has played a useful role in understanding the structures of these high-pressure phases.[25] Unfortunately, in situ high-pressure/high-temperature NMR probes with sufficient sensitivity and resolution to probe oxide materials usefully do not appear to be on the horizon.

An example of the ability of NMR to address structural questions concerning high-pressure phases is a recent study of Mg,Si disorder on the six-coordinate sites of $MgSiO_3$-garnet.[35] At low pressures this composition has a pyroxene (chain silicate) structure in which all the Si is four-coordinate and connected in single chains (Q^2 polymerization). Between ca. 170 and 220 kbar, depending on the temperature, it has a garnet structure consisting of isolated Si tetrahedra (Q^0 polymerization) connected by octahedra occupied by Mg and Si. At pressures above about 220 kbar, it has a well-ordered perovskite structure with all the Si in six-coordination. The garnet phase has two crystallographically distinct octahedral sites and three crystallographically distinct tetrahedral sites. All of the tetrahedral sites are fully occupied by Si, and X-ray diffraction indicates that one of the octahedral sites is occupied primarily but not completely by Si and the other primarily but not completely by Mg. ^{29}Si MAS NMR spectra readily resolve not only Si(4) and Si(6), but multiple Si(4) sites.[35] Calculations based on simulations of this spectrum indicate that in fact one of the octahedral sites is 0.88 Mg and 0.12 Si, and the other is 0.88 Si and 0.12 Mg. Similar garnet samples with some Al for (Mg + Si) substitution have cubic structures with only one octahedral site. For these samples, ^{27}Al and ^{29}Si NMR shows that all of the Al and Mg and part of the Si enters the octahedra site, that the remainder of the Si fills the tetrahedral sites, and that the Al, Mg, and Si on the octahedral sites are essentially randomly distributed.[35,36] High-pressure minerals are difficult to synthesize because large and complex pressure vessels are needed to generate the simultaneous high pressures and temperatures (ca. 1000−2000 °C). Most samples are quite small (a few mg), and the best results are obtained with ^{29}Si-enriched material.

Future NMR work on high-pressure phases is likely to focus considerably on ^{1}H and ^{2}H, because hydrogen (primarily as OH groups and water molecules) plays an important role in controlling the physical properties of the upper mantle and in the formation of magma and lava. It appears that hydrous aluminosilicate minerals are the dominant reservoir of H in the mantle, but the structures and physical and chemical behavior of these phases are poorly known.

High pressures are also generated at meteor impacts, and NMR has also proven useful for characterizing the materials resulting from both natural meteor impacts and laboratory experiments simulating impact conditions. It is possible, for instance, to determine readily the presence of high-pressure SiO_2 phases such as coesite and stishovite, to characterize the amorphous phases sometimes created during shocking.[37]

7 EXCHANGEABLE WATER AND CATIONS IN CLAY MINERALS

Clay minerals are stable and nearly ubiquitous at low pressures at or near the Earth's surface, at the opposite end of the spectrum of physical conditions from the dense

aluminosilicates just described. There is a bewildering variety of clay minerals, but most have structures containing parallel sheets of octahedral and tetrahedral sites, with the tetrahedral sites having Q^3 polymerization. Cation substitution in both types of sites [e.g., Al(4) for Si(4), Mg(6) for Al(6), and Li(6) for Mg(6)] is common and causes a net negative charge on the aluminosilicate sheets, leading to the incorporation of mono- and divalent cations and water molecules between the sheets in the so-called interlayer. Organic cations and neutral molecules are also readily incorporated into clay interlayers.

The behavior of the cations and water in and on clays is critical in many important geochemical and biological processes, including such diverse phenomena as plant growth, adsorption and release of agricultural fertilizers, the stabilization of road beds, the movement of organic and inorganic pollutants and radionuclides in the environment, and the migration of petroleum in the subsurface. Because single crystal X-ray diffraction is not possible for most clays due their small grain sizes, NMR spectroscopy has played a key role in understanding the structural environments and dynamical behavior of cations and molecules in clay interlayers.

In addition, because clay minerals have such large surface areas, they have proven to be excellent materials with which to study the fundamental behavior of water near surfaces. NMR investigation of water, inorganic cations, and organic molecules on clays began in the late 1960s and has continued to the present.

A clay grain presents primarily planes of protonated or nonprotonated oxygen atoms to water molecules, ions, or other species with which it is in contact. The presence of this surface changes the structural arrangements and dynamical behavior of these molecules and ions within about three molecular layers of the surface. These effects can be observed as changes in NMR relaxation rate, chemical shift, and quadrupole coupling.[7,38]

Most NMR investigations of mineral surfaces up to the 1980s focused on the structural environments and dynamical behavior of water and used ^{1}H and ^{2}H as the primary probes. Two types of samples have been investigated. One type (low hydrated) has a relatively low water content, with most of the water contained in the interlayers of collapsed clays. In this case the bulk of the signal comes from species near or at the surface. The other type of sample has a large water/solid ratio (high hydrated), and the bulk of the signal comes from molecules not near the surface. In this case, the surface and bulk species are in rapid exchange, and the effects of the surface are observed as changes in, for example, the ^{2}H quadrupole coupling with changing water/solid ratio.

High hydrated systems yield quadrupole doublets for ^2H_2O and Pake doublets for ^1H_2O.[6,39,40] The splittings normalized for surface area are remarkably similar for all clays examined, suggesting that the presence of the surface but not the composition of the clay dominates the reduction of the reorientation rate and the increase of the anisotropy of the reorientation due to the surface. Theoretical work supports this idea.[41] ^{2}H T_1 relaxation rates for such systems indicate that reorientational correlation times are of the order of 10^{-10} s near the surface, compared with 10^{-12} s in bulk ^2H_2O, with only a small pressure effect up to 5 kbar.[42] The peak splittings and relaxation rates clearly show that the effects of the surface on the electric field gradient and rates of reorientational motion extend to only approximately three molecular layers from the surface.

Additional ^{2}H and ^{17}O results suggest that the charge of the counterion significantly affects the axis of rotation of water molecules at the surface.[40] If the counterion is Na, the water molecules bond relatively weakly to it and relatively more strongly to the oxygens of the surface via hydrogen bonds. In this case the molecule rotates predominantly around the hydrogen bond. If the counterion is Ca, however, the M–O bond is stronger, the hydrogen bond to the surface is relatively weaker (although absolutely stronger), and the axis of rotation is the metal–oxygen bond. This change is consistent with increased polarization of the water molecule in the presence of a higher charge cation and with the observed increased Brönsted acidity under these conditions.

Low hydrated clay/water systems can be investigated in more detail, in large part because it is possible to undertake experiments with partially oriented samples in addition to those with random particle orientations. Partially oriented samples are made by sedimenting clay flakes from water such that their C^* axes are subparallel. Directions perpendicular to C^* are not oriented. The C^* axis is perpendicular to the aluminosilicate layers. Clay particles typically have diameters of ca. $1-2\,\mu$m and thicknesses of a few tens of Å.

The most well-understood low hydrated system is the two-layer hydrate of Na-exchanged vermiculite.[43] Vermiculite has a relatively large negative charge on the aluminosilicate structure due to Al for Si substitution in the tetrahedral sites, and thus accepts relatively large concentrations of exchangeable interlayer cations and their associated shells of hydration water. The interlayer structure of vermiculite is much more ordered than those of most other clays, because of the proximity of the negative charge deficit to the interlayer. Most montmorillonites, on the other hand, have quite disordered interlayers because they develop their negative charges by substitution in the octahedral layers and their net layer charges are smaller than those of vermiculites. In the Na two-layer hydrate of vermiculite, each Na has six water molecules in its hydration shell. Analysis of ^{2}H and ^{1}H NMR lineshapes and T_1 relaxation data for oriented aggregates of this material leads to the following conclusions:

1. The threefold (C_3) axis of the $Na{\cdot}6H_2O$ cluster is parallel to the C^* axis, and the entire hydration shell rotates around the C_3 axis at frequencies greater than ca. 23 kHz.
2. Each water molecule is rotating at frequencies of about 10^{10} s^{-1} around the Na–O vector. This vector is perpendicular to the H–H vector of the molecule and at an angle of about 65° to the C^* axis.
3. Proton exchange appears to be occurring between the molecules of the cluster at frequencies of 10^4-10^5 Hz, 10–100-times faster than in bulk water.

The presence of a cation near the surface appears to be necessary to cause the preferential orientations of the water molecules observed for most clay interlayers.[44] ^{1}H and ^{2}H lineshape, T_2, and T_1 results for water on halloysite show no preferred orientation of the molecules but do show an anisotropy of the molecular motion, with the rate of rotation around the C_2 axis of the water molecule being more than two orders of magnitude greater than the rate of rotation perpendicular to this axis. Unlike most other clay minerals, halloysite has no net charge on its aluminosilicate layers and thus no essential exchangeable cations.

Other low hydrated systems in which the behavior of the water molecules has been investigated include one-layer

hydrates of vermiculite with various exchanged cations, and various montmorillonites.[7] For the one-layer hydrate of Li-exchanged hectorite, the Li is apparently coordinated by only three water molecules, with the remainder of their coordination shells made up of basal oxygens of the aluminosilicate layers.

The advent of high-field spectrometers has made it possible to use NMR methods to investigate not just the structure and dynamical behavior of water molecules in clays, but also the same properties of the interlayer cations. To date, interlayer ^{7}Li, ^{23}Na, ^{39}K, ^{133}Cs, and ^{111}Cd have been observed (see Kloprogge et al.,[45] and references therein).

For instance, the behavior of ^{133}Cs in the clay interlayer shows extremely complex behavior depending on temperature, concentration, and partial pressure of water.[46] Under water-saturated conditions (the typical state below the water table), the room-temperature ^{133}Cs MAS NMR spectrum of Cs-exchanged hectorite (an Li-smectite) consists of two narrow peaks. One of these is for Cs in the aqueous phase and the other is for Cs in the clay interlayer. With decreasing temperature the peak for Cs in the interlayer splits into two, and below ca. $-60\,^{\circ}$C there are two well-resolved peaks. Simulation of the spectra show that the room-temperature (RT) peak for interlayer Cs is due to dynamical averaging of the signal from Cs on the two sites represented by the two low-temperature peaks at frequencies greater than ca. 10 kHz. One of the observed sites is probably Cs in inner-sphere complexes relatively tightly bound to the basal oxygens of the silica tetrahedra, and the other is probably Cs in outer sphere complexes not tightly bound to the basal oxygens. Similar behavior is observed at 100% RH with no bulk liquid phase present. Under fully dehydrated conditions, however, the Cs chemical shifts are very different, and RT site exchange does not occur. There are two interlayer Cs sites with greatly different NN coordinations, possibly nine and 12.

Hectorite develops its layer charge in the octahedral sites, which are separated from the interlayer by a layer of Si tetrahedra. The interlayer Cs is, thus, bound relatively weakly to the silicate structure and can move relatively easily. This contrasts with the behavior of Cs in vermiculite, which develops its layer charge by Al for Si substitution in the tetrahedral sites. In vermiculite there appears to be no detectable motion of the Cs and the chemical shift does not change with changing hydration state.[46,47] The difference is probably due to relatively tight bonding of the Cs to the basal oxygens of the tetrahedral sheets.

For vermiculite the ^{23}Na and ^{111}Cd NMR spectra are quite well resolved and are generally in agreement with the results concerning the behavior of water molecules in vermiculite interlayers described above.[47] For ^{23}Na and ^{111}Cd, the two-layer hydrates, one-layer hydrates, and dehydrated phases (which are produced at different relative humidities) yield different chemical shifts for the exchangeable cations, with the shielding increasing with progressive dehydration (more negative chemical shifts).

Potassium-39 is difficult to observe in solids due to its large quadrupole moment and low resonance frequency, but spin echo pulse sequences and high fields yield useful static spectra of powder and oriented aggregates of clay minerals.[48] For montmorillonite, signals for K in collapsed and uncollapsed interlayers can be resolved, providing evidence for increased interlayer collapse with an increasing number of wetting and drying cycles.

Many organic cations and neutral molecules can be readily incorporated into clay interlayers, and their structural environments and dynamical behavior can be observed by ^{1}H, ^{2}H, and ^{13}C NMR. Nuclides of other elements that are often part of organic molecules (e.g., ^{14}N, ^{15}N, ^{31}P) could also be observed. There have been few studies of the structure and dynamics of organic molecules and cations in clay interlayers, but the available results suggest that such work has considerable promise. For benzene in the interlayers of an oriented sample of hectorite, ^{13}C NMR shows that at room temperature the benzene molecules have their hexad axes approximately parallel to the planes of the clay layers and that the molecules are in rapid rotation about the hexad axis.[49]

It is likely that there will be considerable future efforts to use NMR methods to understand clay interlayer behavior because of the significance of adsorption on clays to environmental concerns. The discussion in this section has focused on NMR investigation of water molecules and interlayer cations, but as noted above ^{27}Al and ^{29}Si are useful probes of the aluminosilicate portion of clays.[19,50,51]

8 THERMAL DECOMPOSITION OF PHYLLOSILICATE MINERALS

The decomposition of phyllosilicates and other fine-grained hydrous aluminosilicates by heating is a common route for producing ceramic materials such as catalyst supports and mullite. ^{29}Si and ^{27}Al NMR provide useful insight into the mechanisms by which such reactions take place.[52,53] Decomposition of the 1:1 phyllosilicate kaolinite [$Al_2Si_2O_5(OH)_4$] is the best studied, and proceeds from crystalline kaolinite through a poorly crystalline compound called metakaolinite at ca. $500-550\,^{\circ}$C to a mixture of γ-alumina, mullite (often poorly crystalline), and amorphous silica at ca. $1000\,^{\circ}$C.[53–56] NMR has been instrumental in demonstrating that the actual reactions are much more complicated than previously thought based on XRD data. In particular, metakaolinite appears to be a complex mixture of ill-defined regions with three-dimensional silica-rich volumes in which Q^4 units dominate, aluminosilicate regions, residual kaolinite-like regions, and alumina-rich regions with little silica. Five-coordinate Al appears to be an important species, although its structural role is not fully understood.

9 NMR OF LESS ABUNDANT ELEMENTS: ^{31}P, ^{11}B

Although most natural inorganic compounds in the Earth are aluminosilicates, there are also a great many other kinds of compounds. Borate and phosphate minerals are common and have been investigated by NMR, especially via ^{11}B and ^{31}P. Results for these phases are described below. Carbonates are also common, but their range of ^{13}C chemical shifts is small.[57] Ferric oxides and oxyhydroxides and sulfides of many types are very common, but have not been usefully investigated by NMR. NMR investigation of many other elements, perhaps most notably the alkaline earths, is limited by technical limitations due primarily to low frequencies, large quadrupole moments, long relaxation times, or large chemical

shift anisotropies. Other elements are normally limited by very low concentrations in most minerals (e.g., the rare earths).

Borate minerals are most abundant in unusual near-surface geochemical environments in which B is concentrated by aqueous transport and precipitation. Otherwise, B occurs in borosilicate minerals or at trace levels in many minerals. Both wideline and pulse Fourier transform MAS ^{11}B NMR can distinguish tetrahedrally coordinated B [B(4)], asymmetrical trigonal B [B(3)], and symmetrical trigonal B.[58,59] The ^{11}B chemical shift is also useful for distinguishing B(4) sites linked to other B(3) or B(4) sites (values near 0 ppm) from those linked to Si tetrahedra in a borosilicate environment (values near -2 ppm).[59]

Phosphate minerals occur in many geochemical environments, and almost all are orthophosphates. There is a relatively large ^{31}P chemical shift range of ca. 30 ppm due to different nearest-neighbor linkages.[60,61] Alkali and alkaline earth phosphates commonly have chemical shifts that are positive or near 0 ppm, whereas aluminophosphates typically have more negative chemical shifts. The $AlPO_4$ analogs of the SiO_2 phases quartz, cristobalite, and tridymite have ^{31}P chemical shifts between -25 and -30 ppm. Synthetic compounds have an even larger range. The results for phosphate minerals with known structures have provided references with which to interpret data for phosphate, aluminophosphate, and phosphosilicate glasses, and for understanding the structural environments of phosphate adsorbed on mineral surfaces.[62]

10 ^{17}O NMR OF MINERALS

Oxygen is the most abundant anion in the Earth and is thus a major component of most minerals. The only NMR-active oxygen nuclide is ^{17}O, which has a natural abundance of only 0.37% and, thus, for solids can only be observed in synthetically-enriched samples. For the most part, NMR work on ^{17}O in minerals and mineral analogs has been limited to the investigation of materials with known structures.[63,64] The database for model compounds is now large enough that recent studies have used it effectively as a probe of less well-understood materials and structural phase transitions.[32]

For oxide materials, the ^{17}O chemical shifts are mostly positive relative to water and range from nearly +1200 ppm for Ag_2O to -227 ppm for Cu_2O. For silicates and aluminosilicates, most chemical shifts fall in the range +170 to near 0 ppm, with the values for nonbridging oxygen sites having a wider range than bridging oxygen sites.[22] Oxygen-17 quadrupole coupling constants for simple oxides are typically quite small (<ca. 2.5 MHz, and often less than 1 MHz), due to the high symmetry of most of these materials. For silicates and aluminosilicates, the QCCs are typically >2.5 MHz, with bridging oxygen sites typically having values >4.0 MHz. Oxygens in OH linkages appear typically to have the largest values (>6.0 MHz). Most silicates and aluminosilicates have orthorhombic, monoclinic, or triclinic symmetry, and thus significant electric field gradients at their O sites.

The use of dynamic angle spinning (DAS) to investigate ^{17}O in solids is a recent and potentially very productive approach. Under MAS conditions there is often extensive peak overlap due to unaveraged second-order quadrupole interactions which limits spectral resolution. DAS resolves, for example, signals for the nine O sites in wollastonite ($CaSiO_3$) with only some peak overlap.[64]

High-temperature ^{17}O NMR has also been useful in investigating the dynamics of silicate melts.[65] In particular, these results demonstrate conversion between bridging and nonbridging oxygen sites and provide support for a model of viscous flow of these materials involving the formation and destruction of five-coordinated Si sites. Silicon-29 NMR has demonstrated the presence of such sites in some glasses.[66]

11 NATURAL ORGANIC MATERIALS

Naturally occurring organic compounds are not abundant in the Earth overall, but are common near the surface and are essential for the existence of life on this planet and for crop production and most energy used by humans. There is an extensive literature concerning NMR investigation of natural organic compounds of many kinds [plants, the weathering products of plants (humic and fulvic acids), peat and coal, oil shale, and petroleum]. Much of this literature is reviewed in the articles in this Encyclopedia on fossil fuels, cokes, rock porosity and petroleum flow, and wood. Articles by Wilson[14] and Hayes et al.[67] provide introductions to applications of NMR for understanding the structures of these materials.

12 NATURAL GLASSES AND MELTS

Natural glasses are formed most commonly by quenching natural aluminosilicate melts (magma below ground and lava above). Thus their structures and properties are quite similar to those of synthetic glasses. Motivations for studying the structures of natural glasses include understanding the crystallization and fluid flow properties of natural melts,[65,68] understanding the effects of water and CO_2 on these properties, and understanding the hydration and dissolution behavior of natural and synthetic glasses (including nuclear waste glasses).[69–73] There is extensive overlap of the literature concerning natural and synthetic glasses, and these results are discussed in the articles on ***Amorphous Materials*** and ***Quadrupolar Nuclei in Glasses*** in this Encyclopedia and in recent reviews.[65,74]

13 RELATED ARTICLES

Adsorbed Species: Spectroscopy and Dynamics; Agriculture and Soils; Amorphous Materials; Boron NMR; Brønsted Acidity of Solids; Brownian Motion and Correlation Times; Ceramics; Coal Structure from Solid State NMR; Cokes; Colloidal Systems; Diffusion in Porous Media; Diffusion in Solids; Ferroelectrics and Proton Glasses; Fossil Fuels; High-Pressure NMR; Imaging Techniques for Solids and Quasi-Solids; Incommensurate Systems; Inorganic Solids; Magic Angle Spinning; Microporous Materials and Xenon-129 NMR; Molecular Sieves: Crystalline Systems; Molten Salts; Natural Products; Oil Reservoir Rocks Examined by MRI; Oxygen-17 NMR; Phase Transitions and Critical Phenomena in Solids; Phosphorus-31 NMR; Quadrupolar Nuclei in Glasses; Quadrupolar Nuclei in Solids; Reactions in Zeolites; Silica

Surfaces: Characterization; Silicon-29 NMR; Silicon-29 NMR of Solid Silicates; Sodium-23 NMR; Terrestrial Magnetic Field NMR; Ultraslow Motions in Solids; Well Logging; Wood and Wood Chars.

14 REFERENCES

1. G. E. Pake, *J. Chem. Phys.*, 1948, **16**, 327.
2. H. E. Petch, N. G. Cranna, and G. M. Volkoff, *Can. J. Phys.*, 1953, **31**, 837.
3. D. M. Henderson and H. S. Gutowsky, *Am. Mineral.*, 1962, **47**, 1231.
4. S. Ghose and T. Tsang, *Am. Mineral.*, 1973, **58**, 748.
5. J. L. Staehli and D. Drinkmann, *Z. Kristallogr. Mineral.*, 1974, **140**, 360.
6. D. E. Woessner and B. S. Snowden, *J. Chem. Phys.*, 1969, **50**, 1516.
7. J. J. Fripiat, in *Advanced Chemical Methods for Soil and Clay Mineral Research*, eds. J. W. Stucki and W. L. Banwart, D. Reidel Publishing, London, 1980, Chap. 5
8. E. Lippmaa, M. Mägi, A. Samoson, A. R. Grimmer and G. Engelhardt, *J. Am. Chem. Soc.*, 1980. **102**, 4889.
9. E. Lippmaa, M. Mägi, A. Samoson, M. Tarmak, and G. Engelhardt, *J. Am. Chem. Soc.*, 1981, **103**, 4992.
10. J. V. Smith and C. S. Blackwell, *Nature (London)*, 1983, **303**, 223.
11. K. A. Smith, R. J. Kirkpatrick, E. Oldfield, and D. M. Henderson, *Am. Mineral.*, 1983, **68**, 1206.
12. M. D. Meadows, K. A. Smith, R. A. Kinsey, T. M. Rothgeb, R. P. Skarjune, and E. Oldfield, *Proc. Natl. Acad. Sci. USA.*, 1982, **79**, 1351.
13. E. Oldfield and R. J. Kirkpatrick, *Science*, 1985, **227**, 1537.
14. M. A. Wilson, *NMR Techniques and Applications in Geochemistry and Soil Chemistry*, Pergamon Press, Oxford, 1987, 353pp.
15. R. J. Kirkpatrick, in *Spectroscopic Methods in Mineralogy and Geology*, ed. F. C. Hawthorne, Mineral. Soc. Am., Washington, DC, 1988, Chap. 9
16. J. F. Stebbins, in *Spectroscopic Methods in Mineralogy and Geology*, ed. F. C. Hawthorne, Mineral. Soc. Am., Washington, DC, 1988, Chap. 10; J. F. Stebbins and I. Farnan, *Science*, 1989, **245**, 257.
17. A. Putnis, E. Salje, S. A. T. Redfern, C. A. Fyfe, and H. Strobl, *Phys. Chem. Minerals*, 1987, **14**, 446.
18. B. L. Phillips, R. J. Kirkpatrick, and M. A. Carpenter, *Am. Mineral.*, 1992, **77**, 484.
19. C. P. Herrero and J. Sanz, *J. Phys. Chem. Solids*, 1991, **52**, 1129.
20. B. L. Phillips, R. J. Kirkpatrick, and G. L. Hovis, *Phys. Chem. Minerals*, 1988, **16**, 262.
21. J. A. Tossell (ed.), *Nuclear Magnetic Shieldings and Molecular Structure*, Kluwer Academic Publishers, Dordrecht, *NATO ASI Series C, No. 386*, 1993, p. 584.
22. J. F. Stebbins, in *Handbook of Physical Constants*, ed. T. Ahrens, Am. Geophys. Union, Washington, DC, in press.
23. R. F. Pettifer, R. Dupree, I. Farnan, and U. Sternberg, *J. Non-Cryst. Solids*, 1988, **106**, 408.
24. B. Sherriff, H. D. Grundy, and J. S. Hartman, *Eur. J. Mineral.*, 1991, **3**, 751.
25. J. F. Stebbins and M. Kanzaki, *Science*, 1991, **251**, 294.
26. E. Brun, S. Hafner, and P. Hartmann, *C. R. Soc. Suisse Phys.*, 1960, **33**, 495.
27. R. J. Kirkpatrick, R. A. Kinsey, K. A. Smith, D. M. Henderson, and E. Oldfield, *Am. Mineral.*, 1985, **70**, 106.
28. J. F. Stebbins, I. Farnan, E. H. Williams, and J. Roux, *Phys. Chem. Minerals*, 1989, **16**, 763.
29. X. Y. Xue and J. F. Stebbins, *Phys. Chem. Minerals*, 1993, **20**, 297.
30. E. K. H. Salje (ed.), *Physical Properties and Thermodynamic Behavior of Minerals*, D. Reidel, Dordrecht, *NATO ASI Series C, No. 225*, 1988, p. 707.
31. B. L. Phillips, R. J. Kirkpatrick, and J. G. Thompson, in *Nuclear Magnetic Shieldings and Molecular Structure*, ed. J. A. Tossell, Kluwer, Dordrecht, *NATO ASI Series C, No. 386*, 1993, p. 584.
32. D. R. Spearing, I. Farnan, and J. F. Stebbins, *Phys. Chem. Minerals*, 1992, **19**, 307.
33. B. L. Phillips, J. G. Thompson, Y. H. Xiao, and R. J. Kirkpatrick, *Phys. Chem. Minerals*, 1993, **20**, 341.
34. Y. H. Xiao, R. J. Kirkpatrick, and Y. J. Kim, *Am. Mineral.*, 1993, **78**, 241.
35. B. L. Phillips, D. A. Howell, R. J. Kirkpatrick, and T. Gasparik, *Am. Mineral.*, 1992, **77**, 704.
36. P. McMillan, M. Akaogi, E. Ohtani, Q. Williams, R. Nieman, and R. Sato, *Phys. Chem. Minerals*, 1989, **16**, 428.
37. M. B. Boslough, R. T. Cygan, and R. J. Kirkpatrick, *Proc. Lunar Planet. Sci.*, 1993, **24**, 127.
38. W. W. W. Stone, in *Advanced Techniques for Clay Mineral Analysis, Developments in Sedimentology 34*, ed. J. J. Fripiat, Elsevier, Amsterdam, 1982, Chap. 4
39. D. E. Woessner, *J. Magn. Reson.*, 1980, **39**, 297.
40. J. Grandjean and P. Laszlo, *Clays Clay Miner.*, 1989, **37**, 403.
41. R. H. Walmsley and M. Shporer, *J. Chem. Phys.*, 1978, **68**, 2584.
42. J. Jonas, D. Brown, and J. J. Fripiat, *J. Colloid Interface Sci.*, 1982, **89**, 374.
43. J. Hougardy, W. E. E. Stone, and J. J. Fripiat, *J. Chem. Phys.*, 1976, **64**, 3840.
44. M. I. Cruz, M. Letellier, and J. J. Fripiat, *J. Chem. Phys.*, 1978, **69**, 2018.
45. J. T. Kloprogge, J. B. H. Jansen, R. D. Schuiling, and J. W. Gues, *Clays Clay Miner.*, 1992, **40**, 561.
46. C. A. Weiss, R. J. Kirkpatrick, and S. P. Altaner, *Geochim. Cosmochim. Acta*, 1990, **54**, 1655.
47. V. Laperche, J. F. Lambert, R. Prost, and J. J. Fripiat, *J. Phys. Chem.*, 1990, **94**, 8821.
48. J. F. Lambert, R. Prost, and M. E. Smith, *Clays Clay Miner.*, 1992, **40**, 253.
49. H. A. Resing and D. Slotfeldt-Ellingsen, *J. Magn. Reson.*, 1980, **38**, 401.
50. R. A. Kinsey, R. J. Kirkpatrick, J. Hower, K. A. Smith, and E. Oldfield, *Am. Mineral.*, 1985, **70**, 537.
51. D. E. Woessner, *Am. Mineral.*, 1989, **74**, 203.
52. R. L. Frost and P. F. Barron, *J. Phys. Chem.*, 1984, **88**, 6206.
53. R. H. Meinhold, K. J. D. MacKenzie, and I. W. M. Brown, *J. Mater. Sci. Lett.*, 1985, **4**, 163.
54. J. Sanz, A. Madani, J. M. Serratosa, J. S. Moya, and S. Aza, *J. Am. Ceram. Soc.*, 1988, **71**, C-418.
55. J. F. Lambert, W. S. Millman, and J. J. Fripiat, *J. Am. Chem. Soc.*, 1989, **111**, 3517.
56. J. Rocha and J. Klinowski, *Phys. Chem. Minerals*, 1990, **17**, 179.
57. H. W. Papenguth, R. J. Kirkpatrick, B. Montez, and P. A. Sandberg, *Am. Mineral.*, 1989, **74**, 1152.
58. P. J. Bray, F. Bucholtz, A. E. Geissberger, and I. A. Harris, *Nucl. Instrum. Methods*, 1982, **199**, 1.

59. G. L. Turner, K. A. Smith, R. J. Kirkpatrick, and E. Oldfield, *J. Magn. Reson.*, 1986, **67**, 544.
60. D. Müller, E. Jahn, G. Ladwig, and U. Haubereisser, *Chem. Phys. Lett.*, 1984, **109**, 332.
61. G. L. Turner, K. A. Smith, R. J. Kirkpatrick, and E. Oldfield, *J. Magn. Reson.*, 1986, **70**, 408.
62. W. F. Bleam, P. E. Pfeffer, S. Goldberg, R. W. Taylor, and R. Dudley, *Langmuir*, 1991, **7**, 1702.
63. H. K. C. Timken, S. E. Schramm, R. J. Kirkpatrick, and E. Oldfield, *J. Phys. Chem.*, 1987, **91**, 1054.
64. K. T. Mueller, J. H. Baltisberger, E. W. Wooten, and A. Pines, *J. Phys. Chem.*, 1992, **96**, 7001.
65. J. F. Stebbins, I. Farnan, and X. Y. Xue, *Chem. Geol.*, 1992, **96**, 371.
66. J. F. Stebbins and P. McMillan, *Am. Mineral.*, 1989, **74**, 965.
67. M. H. B. Hayes, P. MacCarthy, R. L. Malcolm, and R. S. Swift (eds.), *Humic Substances II, In Search of Structure*, John Wiley and Sons, Chichester, p. 764.
68. S. C. Kohn, R. A. Brooker, and R. Dupree, *Geochim. Cosmochim. Acta*, 1991, **55**, 3879.
69. H. Eckert, J. P. Yesinowski, E. M. Stolper, T. R. Stanton, and J. Holloway, *J. Non-Cryst. Solids*, 1987, **93**, 93.
70. H. Eckert, J. P. Yesinowski, L. A. Silver, and E. M. Stolper, *J. Phys. Chem.*, 1988, **92**, 2055.
71. B. C. Bunker, D. R. Tallant, T. J. Headley, G. L. Turner, and R. J. Kirkpatrick, *Phys. Chem. Glasses*, 1988, **29**, 106.
72. W. H. A. Yang and R. J. Kirkpatrick, *Geochim. Cosmochim. Acta*, 1989, **53**, 805.
73. S. C. Kohn, R. Dupree, and M. G. Mortuza, *Chem. Geol.*, 1992, **96**, 399.
74. H. Eckert, *Prog. NMR Spectrosc.*, 1992, **24**, 159.

Biographical Sketch

R. James Kirkpatrick. *b* 1946. A.B., 1968, Cornell University, Ph.D. 1972, University of Illinois. Postdoctoral fellow in Geophysics, Harvard University, 1973–1976; asst. res. geologist, Scripps Institution of Oceanography, 1976–1978; Progressively Assistant Professor, Associate Professor, Professor and Head of Geology, University of Illinois, 1978–present. Approx. 125 publications. Research interests include the application of solid state NMR to the investigation of the structure, dynamical behavior, and chemical reactivity of minerals, ceramics, glasses, and cements.

Oil Reservoir Rocks Examined by MRI

Ken J. Packer

University of Nottingham, Nottingham, UK

1	Introduction	1
2	NMR of Fluids in Rocks	1
3	Imaging of Rocks Containing a Single Fluid Phase	3
4	Imaging of Two-Phase Fluids in Rocks	6
5	Imaging of Oil Industry Processes	9
6	Summary	10
7	Related Articles	11
8	References	11

1 INTRODUCTION

The production of hydrocarbons involves, inter alia, drilling wells into oil-bearing rock strata at selected locations and utilizing a number of production strategies, often referred to as primary, secondary, etc., where primary, for example, refers to the fluid production consequent on the release of the naturally occurring internal pressures of the reservoir, with secondary implying some form of pressurization of the reservoir through the injection of water, gas, or some similar combination. Wells are expensive and the choice of where to place them for optimum production relies on assessments based on a wide range of information. Part of this assessment utilizes samples of rock, referred to as 'cores' taken at various depths whilst drilling wells, usually at the appraisal stage of determining a reservoir's potential. This article is concerned with the use of NMR imaging to investigate and characterize the properties of such core samples. These have traditionally been subjected to laboratory measurements of the basic properties of porosity, ϕ, and permeabilities, κ, the first being the fraction of the rock volume available to contain the reservoir fluids, comprising one or more of gas and liquid hydrocarbon and aqueous phases, and the second a measure of the ability of these fluids to flow through the rock under given fluid composition, pressure gradient and temperature conditions. NMR and NMR imaging have the potential both to support the evaluation of production strategies in a given reservoir and to advance the understanding of the underlying fluid dynamic processes. In neither case has NMR yet made the impact it could. An important issue is the nature of the samples studied and the degree to which they are representative of the conditions in the reservoir. This is a more subtle issue than just a matter of temperature and pressure. On retrieving core material it may be recovered in a 'preserved' state where attempts are made to retain the fluid saturations which existed in the reservoir. Releasing the pressure and lowering the temperature will alter these and can also affect the surface characteristics or wettability of the rock surface. However, this is not uniquely a problem for NMR studies, but is a generic issue for all such studies on cores. Many measurements are made on cleaned samples where the reservoir fluids have been removed by flushing/solvent extraction followed by resaturation with chosen fluids to allow the characterization of the required properties.

NMR has had a long history of application to the problem of characterizing fluids contained within porous rocks and other solids. Many of the relevant details may be found in other articles in this Encyclopedia, in particular ***Well Logging***, ***Imaging Techniques for Solids and Quasi-Solids***, and ***Diffusion and Flow in Fluids***. This article is concerned solely with imaging of rock–fluid systems and will restrict discussion of the NMR properties of such systems to those required to understand the strengths and limitations of such investigations. No description of imaging principles is given and, again, relevant details will be found in the many articles in this Encyclopedia and in the referenced papers. Section 2 summarizes the basic NMR of fluids in rocks, whilst Sections 3 and 4 discuss the imaging of rocks saturated with one and two fluid phases, respectively. Section 5 outlines the application of NMRI to processes of importance to the oil industry.

2 NMR OF FLUIDS IN ROCKS

Most NMR studies of fluids in rocks have been carried out using ^{1}H nuclei and, unless otherwise indicated, this will be assumed. Oil reservoir rocks are of two main types: sandstones and limestones. Sandstones are predominantly comprised of silica grains which have often been considerably changed and cemented through diagenetic geological processes, such that they present a porosity which is usually less than 0.3. In addition, they may often contain many other mineral types and, in particular, clays which may be distributed within the basic silica-based porosity. There may also be a range of transition metal species present, particularly iron, and these can significantly affect the NMR response of fluids contained within the pore spaces. In sandstones, the pore spaces tend to be in the range of $0.1-100\,\mu$m, determined by the original silica grain size and the subsequent modification by geological processes. Limestones are predominantly calcium carbonate and the pore space can cover a wider range of scales, reflecting the biological origins and processes responsible for their formation. In particular, they may have some pore spaces which are as large as 1 mm in scale arising, for example, from the fossilization/dissolution of the shells of larger species trapped in the original matrix.

NMR imaging of oil reservoir rocks is carried out using the signals from the fluid phases and, to that extent, is similar to biomedical imaging. The differences lie mainly in the degree to which the solid matrix in which the fluids reside and move, together with the multiphase character of the fluids, affect their NMR properties. In addition, the fluid content is usually less than 30% of the sample by volume, which is smaller by a considerable margin than that of typical tissues imaged in biomedical studies. As a consequence, in most cases, the time required to achieve good signal-to-noise ratios will be longer. However, as long as the samples are not undergoing changes on the relevant timescale this is not a problem as rocks, unlike patients, are not concerned with how long they spend in the imaging system! The NMR properties which may be used for generating useful contrast in NMR images of fluid-filled porous rocks are, spin density, resonance frequency, spin relaxation processes, and the fluid transport processes of diffusion and flow. All of these

have been used, separately and in combination, to generate images of these systems. In the most general case, the fluids comprise gas, oil, and aqueous phases. The naturally occurring aqueous phases, usually referred to as 'formation water', have a significant ionic salt concentration which is reservoir-dependent. Typically, imaging experiments which require a replacement aqueous phase will use 3% NaCl brine. These aqueous ionic solutions can influence the tuning and quality factors of the rf coil systems and lead to rf attenuation effects within the samples. These effects should be taken into account when quantitative measurements are the goal.[1]

2.1 Magnetic Susceptibility Broadening

The principal difficulty presented by fluid/rock systems in terms of NMR imaging is that, for many such materials, the transverse relaxation of the contained fluids can be strongly affected by magnetic susceptibility variations on the scale of the pore dimensions. This, combined with diffusion of molecules through these internal gradients, may lead to very rapid transverse relaxation for the spins in the contained fluids.[2] This effect is a strong function of the magnetic field strength of the NMR system used, in the worst case giving a T_2 value which varies as ${B_0}^{-2}$. As a consequence, the specifications required of the imaging spectrometer in order to achieve a representative signal reflecting all fluid present in the rock depend on the choice of operating field and can often exceed those which are readily accessible. Thus, there are a significant fraction of sandstones in particular for which quantitative measurements will prove impossible with conventional imaging techniques. Typically, when using the slice-selected 2D Fourier transform spin echo imaging sequence, for example, an echo time of 1 ms or less can be desirable and this places demanding requirements on the switching and settling times of the gradient systems, as well as on their maximum amplitude. Even with such short echo times, for some systems, only a fraction of the fluid will be detected. The reason that this is of concern is that, unlike some aspects of medical imaging, quantitative information is the ultimate goal when studying reservoir rocks.

The choice of magnetic field strength for imaging studies of fluid-saturated rocks is a compromise between the sensitivity and resolution required and the performance needed to overcome, as much as possible, the field-dependent T_2 effects referred to above. Many imaging studies of rocks have used a field strength of 2 T, corresponding to a ^{1}H resonance frequency of 85 MHz, and excellent quality images are achieved at this frequency. It is important, however, to recognize that these may reflect the properties of only a fraction of the fluid present and, for quantitative studies, this issue must be addressed directly. A further effect of these susceptibility contributions to the linewidth is to make chemical shift based discrimination of oil and water phases increasingly difficult as they get larger.

2.2 Surface-Enhanced Relaxation

In addition to the susceptibility effects, fluids contained within the pore space of reservoir rocks often show complex spin relaxation behavior (longitudinal and transverse), which arises from enhanced relaxation when molecules find themselves at the rock–fluid interface. Diffusion is the usual process which brings molecules of a surface-wetting phase to this interface and the effect of this process is to make the relaxation times reflect the size scale of the pore space in which they are contained,[3,4] see also ***Well Logging***. The dependence of the relaxation times on this size can vary between linear and quadratic. In most sandstone rock systems it has been established that, for saturation with an aqueous phase alone, the so-called fast-diffusion limit applies[5] making the contribution of this surface-mediated relaxation have the form

$$R_1 = (T_1)^{-1} \sim \rho(S/V) \sim \rho/a \qquad (1)$$

where S/V is the surface-to-volume ratio of the pore space, a its linear dimension, and ρ the surface relaxation strength which has the units of m s^{-1}. The key relationship is that T_1 relates directly to pore size within this model. In most natural rock systems there exists a distribution of size scales within the fluid-containing space. As a consequence, the contributions of this mechanism of relaxation, particularly to spin–lattice relaxation for which it is usually dominant, generate a multiple exponential process. This can be treated in a number of ways, the choice of which will depend on the relationship between voxel size and the heterogeneity scale of the pore size distribution. At one extreme, when a voxel contains the full range of pore sizes, then if signal-to-noise (S/N) is sufficient, a regularized inversion to give a distribution of relaxation times (directly mapping onto a pore size distribution) could be used.[6] For poorer S/N ratios, a fit to a stretched exponential is an alternative.[7] At the other extreme then a single exponential fit may be appropriate, with the histogram of voxel relaxation times then revealing the distribution.

2.3 Fluid Transport

Both diffusion and flow are important processes for fluid transport within oil reservoir rocks and both can be used to generate contrast in NMR images of fluid-saturated rocks. The principles and practice of measuring diffusion effects and flow velocities may be found in a number of other articles in this Encylopedia and the interested reader should consult these for the details,[8] see, for example, ***Diffusion and Flow in Fluids***. There are two main approaches to studying these processes. The main one is to use magnetic field gradient pulses to monitor the displacement of spins in the direction of the gradients. The range of timescales over which these displacements may be observed are dictated by the relaxation properties of the spins, while the amplitude of gradients available determine the spatial scales accessed. A second approach is to image the movement of an incoming or penetrating front which may be distinguished through some distinctive NMR property either present naturally or induced (see Section 2.4). These time-of-flight methods do not reveal the microscopic details of the process but can be simpler to implement.

2.4 Phase Discrimination

Imaging of two or more phases, present together within a porous rock, requires means of discriminating the signals from

those phases and there are a number of possible approaches. The choice available depends on the detailed characteristics of both the fluids and the containing rock. The principal methods are based on chemical shift or relaxation time differences, and can be either intrinsic or introduced. The chemical shift imaging methods used to discriminate water from fat in medical applications can be used to discriminate water and oil in rocks provided that the intrinsic transverse relaxation processes do not broaden the lines significantly beyond the shift difference and the oil phase is of low viscosity. Many crude oils have high viscosity and intrinsic linewidths which prohibit chemical shift imaging although, of course, a large difference in T_2 between the oil and aqueous phase will allow the aqueous phase to be detected uniquely. An extreme example of chemical shift imaging is the use of a substitute fluid which does not contain resonant spins, such as D_2O in place of H_2O, and, say, a fluorinated oil in place of normal oil. Spin–lattice relaxation-based discrimination is possible when the two phases have well-separated relaxation time characteristics. This can usually be achieved for water-wet rocks containing either light oil or heavy oil, which tend to give relaxation times longer and shorter, respectively, than the aqueous phase. If the spin–lattice relaxation characteristics of the two phases are too similar, then one or other may be changed by the introduction of relaxation agents, e.g. Mn^{2+}, in the aqueous phase or an oil-soluble molecule containing a nitroxide radical for the oil phase. Few of these approaches have been taken in practice in other than one-off investigations, so they cannot be regarded as well-established routines.

3 IMAGING OF ROCKS CONTAINING A SINGLE FLUID PHASE

With the development of actively shielded gradient coils[9] almost all imaging of fluids in rocks has been carried out using slice-selected 2D or direct 3D imaging techniques, although some early work utilized projection–reconstruction methods.[10] Usually, these are implemented on systems with 31-cm horizontal bore magnets with gradient coil sets and rf coils which allow for samples between core plug size (2.5–4 cm diameter) and whole core (up to 10 cm diameter). Preparation and containment of samples depends on the goal of the experiment. For simple porosity/T_1 imaging, samples may be encapsulated, after saturation under vacuum/pressure treatments, with epoxy resin[11] or other plastic film coatings[12] to prevent fluid loss during imaging. Experiments which aim to study cores under dynamic or steady-state flow conditions, or under controlled temperature/pressure regimes, require the construction of core holders which can be inserted into the rf coils and, at the same time, allow the creation of the required flow/saturation conditions. Again, there is no universal design and these vary from resin-encapsulation to contain and constrain the fluid pressures and flow to more sophisticated designs employing radial hydrostatic pressure applied via a cylindrical sleeve in a so-called Hassler cell arrangement to achieve the same requirements.[13]

3.1 Imaging of Fluid Saturation/Porosity

The measurement of the spatial distribution of fluid saturation for a single phase requires the use of porosity standards as described by Edelstein et al.[14] These workers used Cu^{2+}-doped H_2O/D_2O agarose gels as standards, allowing control of the volume concentration of ^1H spins, T_1 and T_2, as required. Using slice-selected 2D spin echo imaging, with echo times between 3 and 12 ms, they showed that they could determine the spatial distribution of fluid-filled porosity by extrapolation of the image intensities back to zero time. Figure 1 shows the resulting images for four samples together with a porosity standard and a gray-scale porosity reference scale. The only real check on the quantitative accuracy of such porosity images is to integrate the data over the image slices and compare the result with bulk measurements of the NMR porosity, calibrated by an independent determination of porosity using standard laboratory methods. Chen et al.[11] extended this T_2-extrapolation approach to obtaining quantitative porosities/fluid saturations. Using as many as 15 different echo times, covering a range which gave signal attenuations greater than a decade, they investigated the use of a number of models of the transverse relaxation process, including single and multiexponential, and the stretched exponential, to perform the required extrapolation. They found, for the small number of samples they studied, that the best agreement with porosities determined gravimetrically was obtained using a double exponential model for the transverse relaxation of each voxel. There are, of course, significant time penalties to be paid to carry out such detailed multiimage extrapolations. However, if truly quantitative measurements are required, then an element of such calibration of the systems under investigation will be necessary in most cases. The use of a double exponential model was also endorsed by Fordham et al.[15]

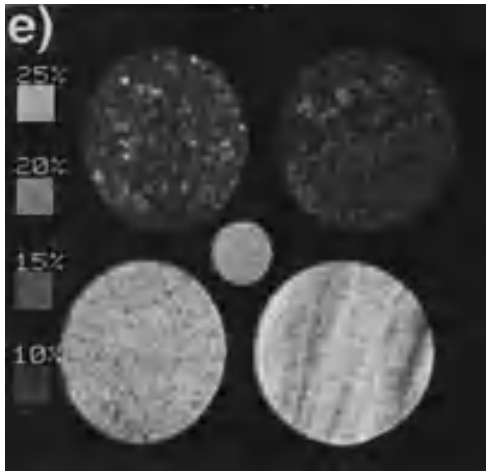

Figure 1 Porosity images of a cluster of four rock samples determined by extrapolation to zero time of a series of T_2-weighted images. Slice thickness was 3 mm. A 20% porosity standard is imaged at the center with a porosity gray scale defined at the left-hand side. (Reproduced by permission of the Society of Petroleum Engineers from Edelstein et al.[14])

Figure 2(a) is a cut-away view of a 3D porosity image of a North Sea sandstone saturated with 3% NaCl brine. This was obtained with an echo time of 1 ms and voxel dimensions of 0.3 mm. Figure 2(b) is a histogram of the distribution of porosity derived from the image in Figure 2(a) using a calibrated porosity standard without extrapolation. The mean of the distribution is 0.23 which is close to the value measured

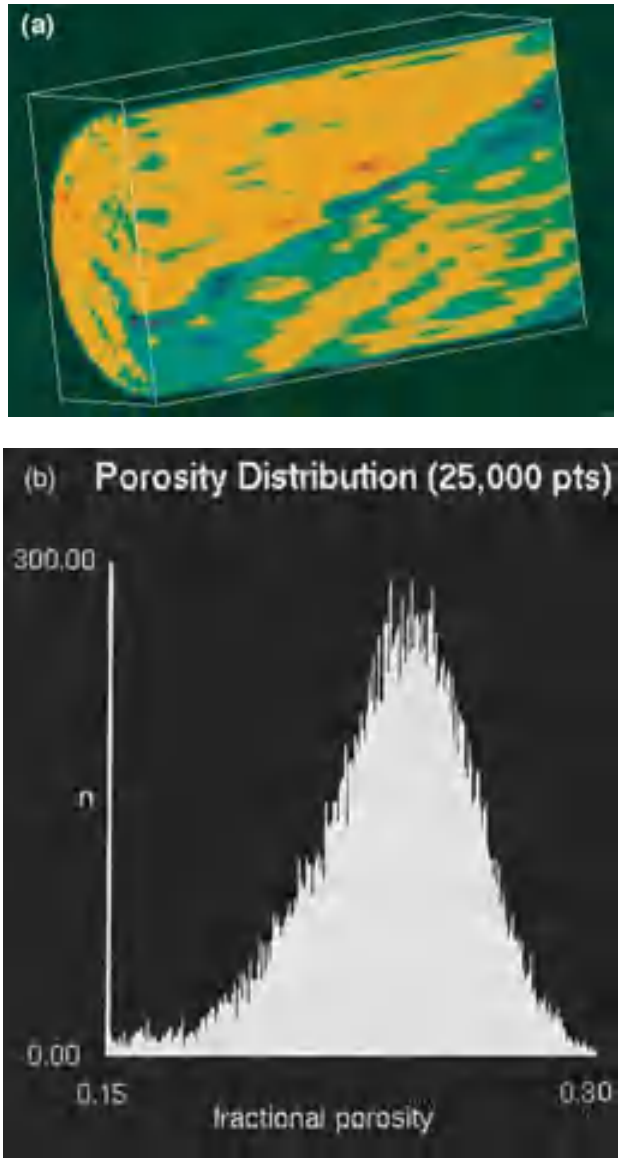

Figure 2 (a) A cut-away view of a 3D porosity image of a brine-saturated North Sea sandstone together with (b) the calibrated porosity histogram derived from the complete image. The independently-determined porosity of this sample was 23%, which agrees closely with the mean of the histogram. (Data supplied and reproduced by kind permission of A. Hardwick and D. R. Roberts, BP Research and Engineering Centre, Sunbury-on-Thames, UK)

using conventional techniques. For this sample, then, the NMR methods used are seeing essentially all the aqueous fluid contained within the rock. As already mentioned, this is by no means always the case. The histogram of Figure 2(b) gives a useful, if limited, statistical view of the nature of the spatial porosity distribution. However, as pointed out elsewhere,[16] there is a considerable amount of such information contained in the data set, of which Figure 2(a) is an example, which is not captured in any quantitative manner by these displays. A clear challenge for the future will be to characterize these complex structures, revealed by such fluid saturation spatial distributions and other image contrast mechanisms, using more sophisticated statistical treatments. The examples given in Figures 1 and 2 were of brine-saturated sandstones. Figure 3

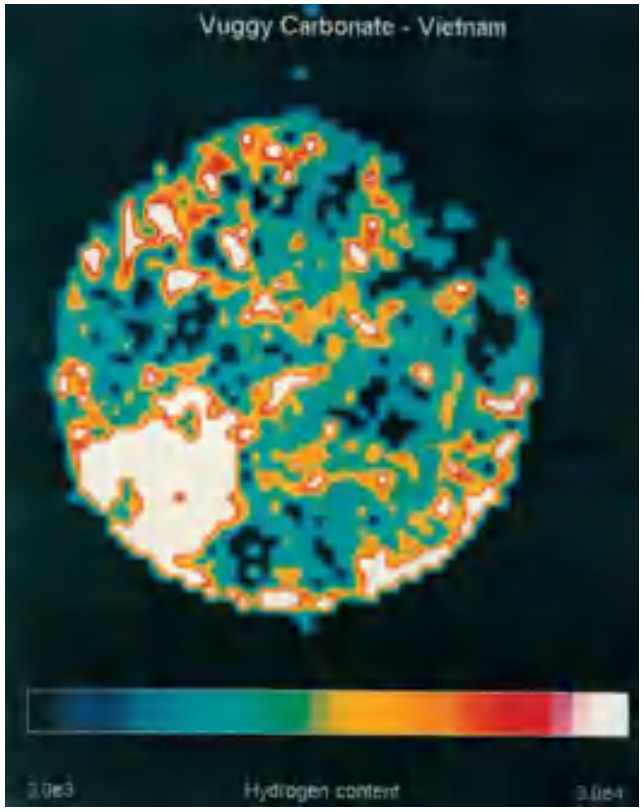

Figure 3 A 2D slice-selected ^{1}H density image of a brine-saturated carbonate rock which has a wide range of porosity, some of which is comprised of pores considerably larger than the image resolution. The porosity scale covered by this image is between 1–100%. The image resolution is 3 × 0.5 × 0.5 mm. (Data supplied and reproduced by kind permission of A. Hardwick and D. R. Roberts, BP Research and Engineering Centre, Sunbury-on-Thames, UK)

shows a porosity image of a brine-saturated carbonate. This shows very clearly the considerably greater porosity range encountered in such rock types in comparison with sandstones. The voxels in this image show porosities spanning the range 1–100%. The latter are represented by the large white areas of the image and arise from the presence of so-called vugs. A further example of imaging of larger-scale porosity in limestones is illustrated in Figure 4.[17] In this case, a 3D image data set is displayed using a computer program which enables the porosity to be viewed from different angles. On the basis of this investigation it was concluded that there was only one connected path through this particular sample, an observation which was borne out by imaging fluid flow (see Section 3.3). It should be remembered that these measurements only yield this information because, for these limestone systems, the imaging resolution can be made less than some of the pore sizes.

3.2 T_1 Imaging

The imaging of spin–lattice relaxation is of value because of the relationship between T_1 and pore size, as discussed above. The T_1 images are usually obtained by prefacing the imaging pulse sequence with either an inversion–recovery or a saturation–recovery sequence, with images being determined as a function of the recovery interval. The data for each voxel

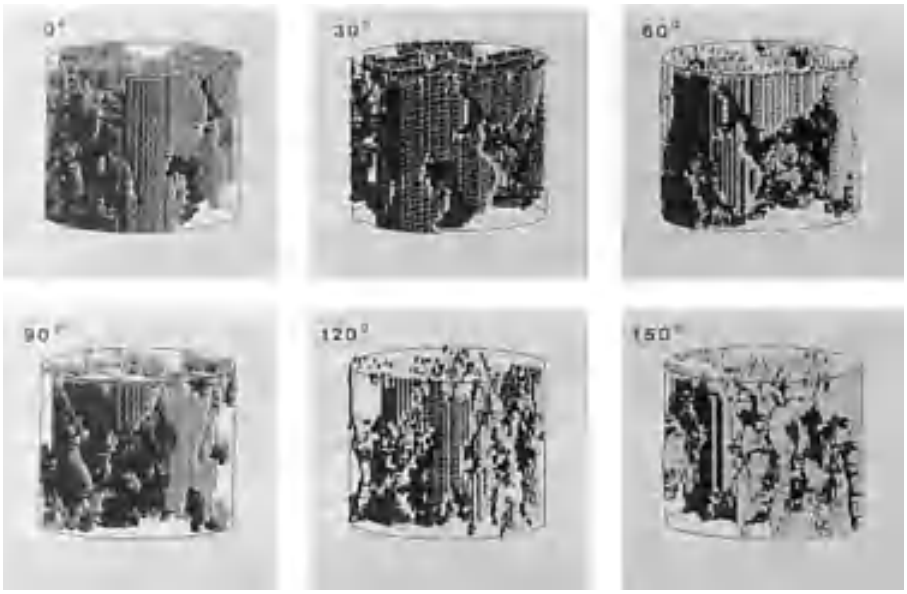

Figure 4 A 3D reconstruction of the porosity distribution inside a water-saturated limestone. Each image is of the same data but viewed from different angles by the rotations indicated. The 3D data set was constructed from a series of adjacent 2D slices. (Reproduced by permission of the publisher from Gleeson and Woessner.[17] © 1991 by Elsevier Science Inc.)

in the image can then be fitted to an appropriate model for the spin–lattice relaxation process (see Section 2.2). Figure 5(a) and (b) show corresponding T_1 and porosity images for the same brine-saturated sandstone for which the full 3D porosity image was given in Figure 2. In this case, the experimental data for each voxel have been fitted to a single exponential recovery and lead to both a T_1 and an extrapolated M_0 (porosity) value for each voxel. These images are of a central slice of the cylindrical rock sample with a slice thickness of 3 mm and an in-plane resolution of 0.5 mm. This sample has a shale band running diagonally from near 10 o'clock to around 4 o'clock and it is clear that the T_1 image reveals this with more contrast than the M_0 image. This is because the shale bed, whilst having significant porosity, has a smaller pore size on average than the other porosity. This means that although there is significant fluid content in this bed, the T_1 value is considerably reduced. Similar differences in contrast are seen in the lower left parts of these images. As indicated above, the amount of information available in such images has yet to be fully exploited in even a semiquantitative manner.[16] (The images shown in Figure 5(c) and (d) are discussed later—Sections 3.3 and 4.3.)

3.3 Diffusion and Flow Imaging

As already indicated, there are two basic approaches to the characterization of transport processes,[18] see also ***Diffusion and Flow in Fluids***. The first of these are time-of-flight methods which measure the appearance or disappearance, in a particular spatial location, of fluid spins which have been selected or saturated elsewhere. An example of this is the study of such flow-weighted imaging in a limestone.[17] Figure 6 shows the normal and flow-weighted images of the same water-saturated limestone plug. The flow-weighted image was obtained using a 2D method which saturates stationary spins and generates signal only from spins flowing into the imaged region on the repetition timescale of the sequence. It is clear from these images that only one of the several regions of significant porosity apparent from the porosity image (see Figure 4) contributes to fluid transport through this particular core plug.

Imaging of fluid velocity can, of course, be achieved directly using pulsed magnetic field gradient techniques to encode the displacements of the spins and coupling this with a suitable imaging procedure,[18] see also ***Diffusion and Flow in Fluids***. Typical results of such investigations are shown in Figure 5(c). This is a slice-selected image, obtained with a 2D FT technique incorporating two gradient pulses to encode the flow along the axis of the cylindrical rock sample, of the same sample used to generate the images of Figure 5(a) and (b). Whilst such 'velocity' images are relatively easy to measure, there are still a number of important issues which need to be addressed before quantitative data can be guaranteed. These issues are similar to those involved in the imaging of perfusion in medical applications[19–21] and relate to the time variation of velocity brought about by changes in pore size and direction of flow relative to the gradient direction. It is important to remember that this approach to characterizing fluid transport actually measures displacements (see ***Diffusion and Flow in Fluids***) with the velocity being a derived quantity. It is only in the limit that the velocity remains constant over the flow-encoding period that an unambiguous interpretation in terms of velocity can be given. These questions have been summarized by Nesbitt et al.[22] That said, the image shown in Figure 5(c) illustrates the strong heterogeneity in flow paths within this sandstone rock core and can be compared with the corresponding images in Figure 5(a) and (b). Strong similarities are apparent with both the M_0 and T_1 images, although some significant differences can be seen, particularly in the region between 7 and 9 o'clock. It should be recalled that the M_0 image reflects porosity within a voxel, while T_1 reflects pore size. Flow would be expected to reflect both of these, in that larger and connected pores will have a high conductance

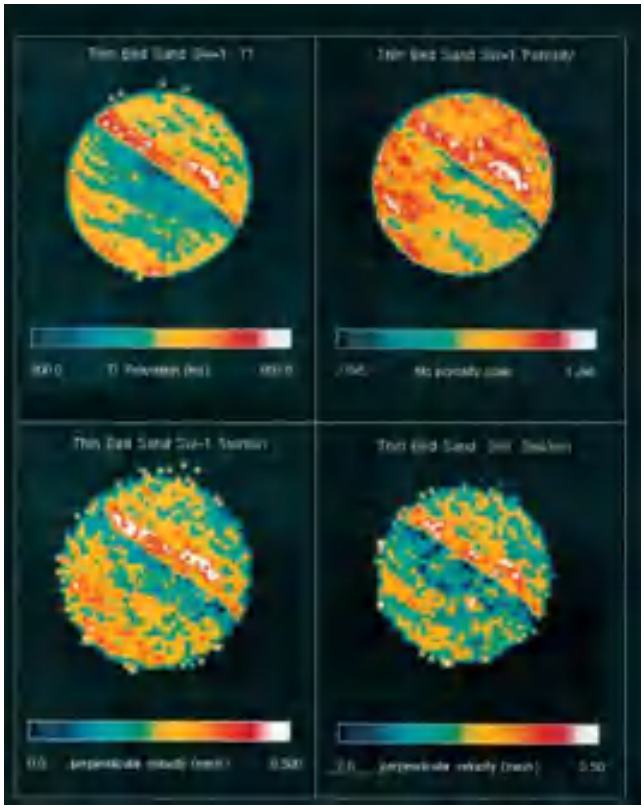

Figure 5 Images of the central slice (3-mm thick; in-plane resolution, 0.5×0.5 mm) of the brine-saturated sandstone also illustrated in Figure 2: (a) (top left) and (b) (top right) are spin–lattice relaxation time and porosity maps, respectively. These two images are constructed from a fit of each voxel magnetization recovery, measured using a saturation–recovery T_1 imaging experiment, to a single exponential process. While similar rock structures are revealed in both images, the marked differences arise because of the dependence of the T_1 value on pore size, as discussed in the text. (c) (bottom left) and (d) (bottom right) are velocity images of fluid flow in the same rock under conditions of (c) $S_w = 1$ and (d) S_{wi} (irreversible water saturation; the fractional porosity left occupied by the brine phase when displacement of this by an oil phase, under given flow conditions, has reached a steady state). The velocity is encoded along the cylindrical axis of the sample (perpendicular to the page) and was achieved by flowing the fluid at a constant rate of 5 mL min^{-1}. For (c) the fluid was the normal brine solution. For (d) the flowing fluid is a model oil, kerosene, and the signal in this case is predominantly from the oil phase. It can be seen that oil flow as visualized by comparison of these two images is less extensive, which is consistent with the presence of the residual aqueous phase. In addition, the strong similarity of (d) with (a), the T_1 image, is consistent with the water-wet characteristics of this rock which would confine the oil to larger pores. Images (c) and (d) are discussed in Sections **3.3** and **4.3**. (Data supplied and reproduced by kind permission of A. Hardwick and D. R. Roberts, BP Research and Engineering Centre, Sunbury-on-Thames, UK)

for fluid while small pores, corresponding to the shorter T_1 values, even if having similar total porosities in a voxel, are likely to have a lower fluid conductance.

The flow rates present in producing reservoirs are very low, corresponding to fluid velocities sometimes as low as 10^{-2}–10^{-1} mm s^{-1}. The measurement of such low flow rates in the presence of internal magnetic field gradients, caused by the magnetic susceptibility heterogeneities, can require special sequences of rf and gradient pulses. This can be illustrated by the use of echo planar imaging (EPI) methods to characterize the slow flow of water through porous rocks.[23] In this approach, velocity-encoding of the image for the slow fluid flow through the rock was achieved using a combination of a Carr–Purcell/Gill–Meiboom echo sequence with an applied gradient pulse sequence which allowed the build up of a cumulative phase shift of the transverse magnetization because of the flow in the applied gradients. This sequence is illustrated in Figure 7. At the same time as maximizing the phase accumulation from flow, this sequence significantly reduces the contribution to T_2 of diffusion through the internal gradients by keeping the pulse spacing small. The overall sequence for flow imaging concludes with an EPI sequence utilizing 180° rf pulses instead of the more usual gradient reversal echoes. This is required to overcome the significantly inhomogeneous nature of the lineshape. Figure 8 shows the results of the use of this sequence to image the flow of water flowing through a clean sandstone, Bentheimer.[23] In a further development of this study, Mansfield and Issa[24] have investigated the quantitative behavior of the flow velocity distributions generated as a function of the pressure difference driving the flow. They have proposed a model to explain the observed behavior which, inter alia, suggests an explanation for their observations that the precise flow pattern seen in an image slice perpendicular to the main flow direction is not reproduced in detail on stopping and restarting the flow.

Despite the importance of diffusion, and the well-documented ability of NMR to characterize both structure and transport via its effects (see ***Diffusion and Flow in Fluids***), imaging studies of fluid-saturated rocks using diffusion effects for contrast have been limited. Gibbs et al.[25] determined self-diffusion coefficient images for two brine-saturated cores (one sandstone and one limestone). They interpreted their results in terms of a reduction in the diffusion coefficient brought about by hindrance of the molecular displacements by the pore surfaces. The difficulty with diffusion imaging is that to take full advantage of the potential of the pulsed field gradient methods requires a wider range of gradient strengths than are usually found on imaging systems. This is particularly true when the intrinsic relaxation processes of the fluid spins are efficient.

4 IMAGING OF TWO-PHASE FLUIDS IN ROCKS

There are a number of approaches to obtaining spatially-resolved information from rocks containing more than one fluid phase. As already discussed, the essential discrimination methods which allow the images from the different fluid components to be separated are usually chemical shift or relaxation time differences, or some method of introducing such contrast via use of dopants or substitute fluids which, for example, give no signal.

4.1 Chemical Shift Resolved Imaging

In general, the line broadening found in rocks precludes the use of simple chemical shift imaging, although in favored cases it is possible.[14,26] Figure 9 shows oil and water images for a carbonate rock, containing both oil and water phases, obtained using standard chemical shift imaging methods.[27] It shows the

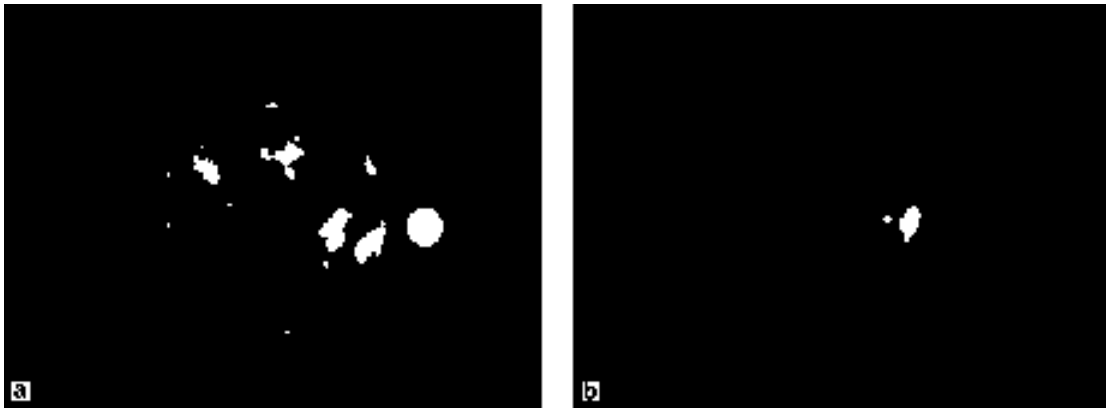

Figure 6 NMR images of the same slice of a limestone sample saturated with water showing (a) the porosity distribution and (b) the fraction of the fluid-saturated porosity which can flow under applied pressure. The method used to detect the movable fluid involved saturation of the NMR signal so that only regions of fluid receiving magnetization from outside the saturated volume on the timescale of the experiment would give a signal. (Reproduced by permission of the Society of Petroleum Engineers from Gleeson et al., *SPE Form. Eval.*, 1993, 123)

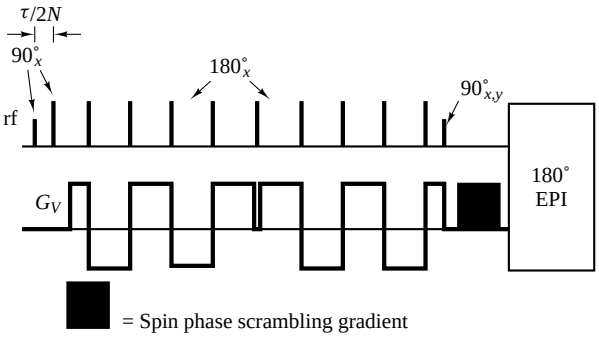

Figure 7 The flow-encoding pulse sequence used, together with an echo planar imaging sequence based on 180° rf pulses, to generate the flow image shown in Figure 8. The combination of field gradient pulse sign alternation and reflection symmetry around the midpoint, together with even echo selection in the Carr–Purcell/Gill–Meiboom rf pulse sequence, maximizes the phase shifts produced by flow through the applied gradients, eliminates phase shifts arising from flow through internal field gradients, and minimizes the effects of diffusion through the same internal field gradients. These latter are caused by the magnetic susceptibility differences within the fluid/rock system. (Reproduced with permission of Academic Press from Guilfoyle et al.[23])

presence of a large fracture which, in this case, is not cemented and hence contains fluid, predominantly water. The largely complementary nature of the two images is readily apparent. In cases such as this, chemical shift resolved imaging should be a powerful tool for characterizing the spatial distributions of both immiscible fluid saturations and, via relaxation and transport-contrast methods, the quantitative details of the pore sizes accessed by the different phases and the various displacement processes, such as imbibition, drainage, and pressure-driven flow.

In general, however, chemical shift imaging has not found extensive use because of the limitations of spectral resolution. However, a method developed by Horsfield et al.[26] has extended the scope of this approach by using a model of the line-broadening mechanism, based on the magnetic susceptibility and shape of the sample, together with an assumed form for the underlying spectrum, to estimate the best values for the separate chemically shifted images. Their method utilizes a set of images obtained for a range of free precession times (see Figure 10) which, at their extreme, produce a phase shift of 180° between the assumed oil and water resonance frequencies. Figure 11 shows a set of images reconstructed using these principles and for which the corresponding spectra were considerably overlapped.

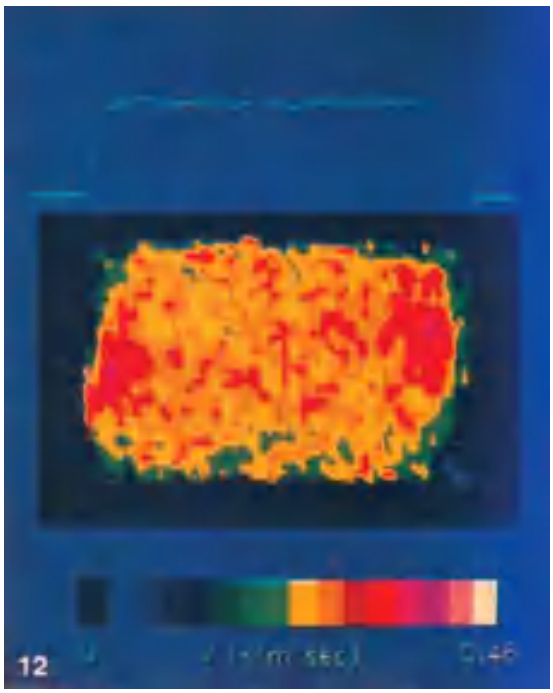

Figure 8 The fluid velocity image for a longitudinal slice (flow direction from left to right) through a cylindrical sample of Bentheimer sandstone. The saturating/flowing fluid was water. Slice thickness was 10 mm with in-plane resolution of 3 × 3 mm. The image is the result of 16 averages of the sequence shown in Figure 7 with a flow-encoding time of 42 ms. The integrated flow at each point along the image axis is shown above the image. While this is constant, significant variations are seen in the image. In particular, regions of higher velocity are seen at the either end of the sample consistent with the single entrance/exit points of the flow cell used. (Reproduced by permission of Academic Press from Guilfoyle et al.[23])

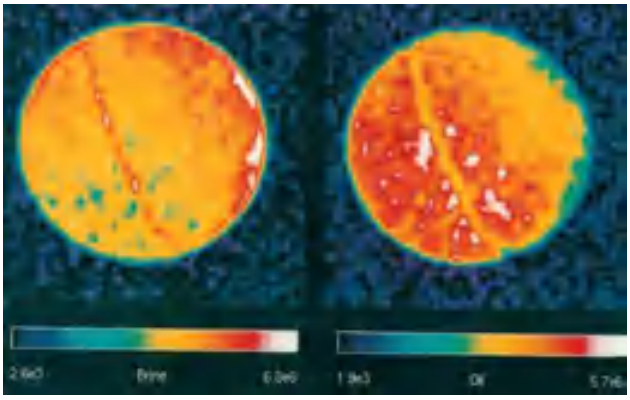

Figure 9 Chemical shift resolved images of the brine and oil phase distributions within a preserved carbonate rock core. The large fault running from top left to bottom right is shown to contain largely the aqueous phase with the smaller porosity in the rest of the sample having complementary phase contents, i.e. large oil content is associated with low water content and vice versa. (Reproduced by permission of the publisher from Davies et al.[27] © 1994 Elsevier Science Inc.)

4.2 Phase Discrimination via Spin–Lattice Relaxation

For most rock–fluid systems, the voxel size employed in imaging of core-size samples is considerably larger than the underlying pore sizes. In these circumstances, the NMR signal from each voxel, for systems saturated with two immiscible fluids, will contain contributions from each fluid. In order to separate these contributions using the spin–lattice relaxation properties, these have to be sufficiently different. In practice this means they must differ by at least a factor of three in relaxation time. Crude oils can vary very significantly in their intrinsic spin–lattice relaxation properties[28] and the aqueous phase can show a wide variation in its relaxation behavior dependent on the pore sizes, whether the rock surface is water-wet, and on the relative saturations in the rock of each phase.[29] As a consequence it is not possible to offer a general prescription and each case has to be treated individually. In some cases a clear and quantitative separation is possible and Figure 12 shows a set of spin–lattice relaxation-resolved images for the same preserved carbonate core which was used to generate the chemical shift images shown in Figure 9.[27] This sample had oil and water saturations of 0.43 and 0.56, respectively. In this case, the relaxation times of the oil and aqueous phases differ by an order of magnitude and the saturation–recovery data for each voxel were fitted to a double exponential process to extract the relaxation times for each phase. The images show clearly the considerable variation of the oil and brine saturations along the core plug. The slice shown in Figure 9 corresponds to the first slices in the middle rows of the image sets in Figure 12. It can be seen that the same features may be distinguished in both shift-resolved and relaxation-resolved images.

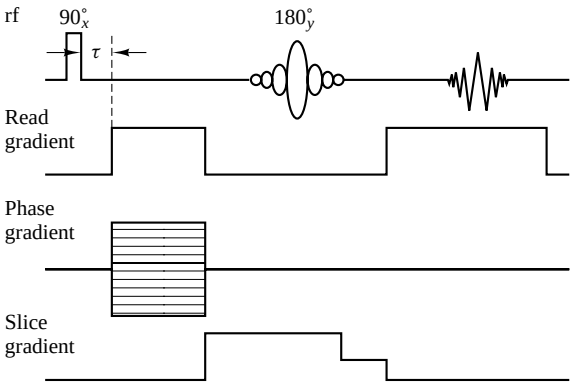

Figure 10 The pulse sequence for phase-encoded chemical shift imaging. The time interval τ allows the development of a phase shift between different precession frequencies. (Reproduced by permission of Academic Press from Horsfield et al.[26])

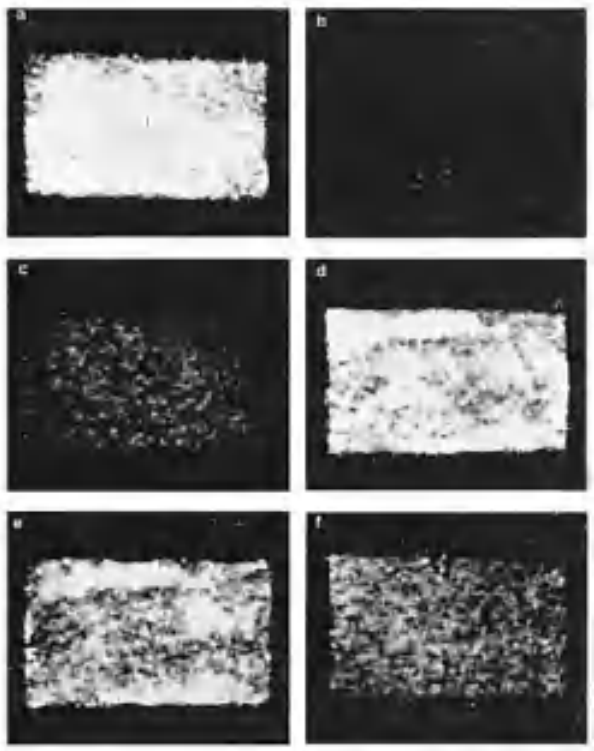

Figure 11 A series of chemical shift resolved images of a sandstone in different states of saturation, the saturating fluids being water and dodecane. The images were obtained with the sequence illustrated in Figure 10 using the modeling technique of Horsfield et al.[26] for systems with strongly overlapped spectra. Images on the left-hand side of the Figure are of the aqueous phase protons; those on the right of the dodecane protons; (a) and (b) are of the rock in its fully water-saturated state, (c) and (d) following displacement with dodecane, and (e) and (f) following further displacement with KCl solution. (Reproduced by permission of Academic Press from Horsfield et al.[26])

4.3 Flow Imaging with Two Immiscible Phases

The direct imaging of fluid displacements/velocities when two fluid phases are present requires, in principle, that separation of signals from the two phases be achieved using either of the techniques discussed in Sections 4.1 and 4.2, or the deliberate removal of the signal from one of the phases via doping with relaxation-enhancing agents or nonresonant spins. If the latter approach is adopted then this reduces the imaging experiment to effectively a single-phase measurement. Figure 5(d) is a velocity image of the same slice of the same rock used for the other images in Figure 5. In this case, the rock

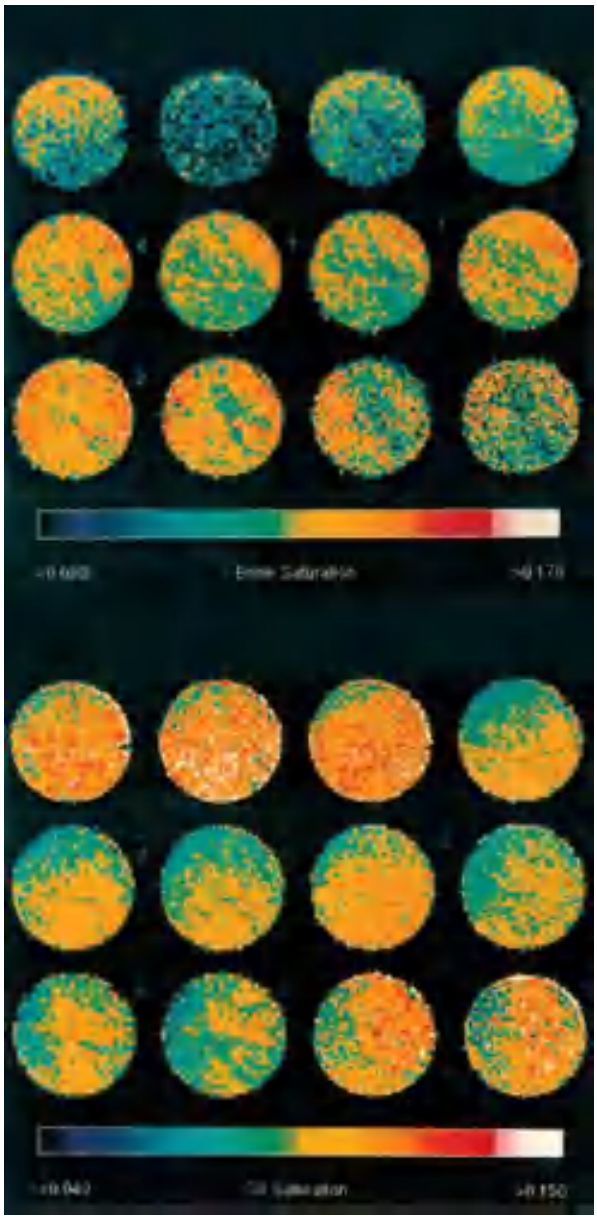

Figure 12 NMR images of oil and aqueous phase distributions in the same carbonate core sample used for Figure 9. In this case the separation of the signals from the two phases was achieved through the differences in their spin–lattice relaxation behaviors. A saturation–recovery spin–lattice relaxation imaging experiment was used to acquire the data, with the magnetization recovery for each voxel being fitted to a double exponential process. The amplitudes of these two processes can be identified with the amounts of the two phases present and are used to generate the images shown. These are a succession of transverse slices along the cylindrical sample axis. The images shown in Figure 9 correspond to the first (left-hand side) image in the middle rows of the two sets shown in this figure. (Reproduced by permission of the publisher from Davies et al.[27] © Elsevier Science Inc.)

(initially saturated with brine) has been flooded with an oil to achieve a state of irreducible water saturation (S_{wi}) at the flow rate used, 5 mL min^{-1}, which is the same flow rate used for the single-phase flow image of Figure 5(c). At S_{wi} the flowing oil has removed all the water it can and, because this is a water-wet rock, the remaining water occupies the smaller pores and will not be moving. Because of these factors this image is of the oil-phase flow only. Comparison of this image with that of Figure 5(c) shows that the oil flow is not as extensive as that of the water at $S_w = 1$ (complete saturation with brine). In addition, the oil-flow image has clear similarities with Figure 5(a), the T_1 image. This would be expected as the oil occupies, and flows through, the larger pore spaces and it is these which have the larger T_1 values.

5 IMAGING OF OIL INDUSTRY PROCESSES

In this section examples will be given of how the imaging capabilities outlined above have been used to investigate a number of processes which are utilized or encountered in oil industry operations. The industry has not, in general, taken a significant and coherent approach to the use of NMRI and the examples given in this section are the result of small groups of researchers in both industry and academic institutions who have attempted to demonstrate the ability of NMR to address phenomena and processes of importance.

5.1 Fluid Displacement

The central feature of hydrocarbon production is, of course, the relative movement of the oil and aqueous phases through the rock. This is a complex process and takes place under a range of conditions, either naturally occurring or engineered. In general, both phases coexist on a microscopic spatial scale as well as on a reservoir scale. The 'Holy Grail' for production is to move out all the oil and none of the water at very low cost! Clearly this is not an attainable goal. The processes involved in the production thus require the stimulation of the flow of the fluids and this can be driven by a natural pressure drop, or by externally applied pressures generated, for example, by pumping water and/or gas into the reservoir. The processes occurring in fluid displacement are usually characterized as being drainage or imbibition, the former being when the invading phase is nonwetting and the latter when it is the wetting phase.

Chen et al.[11] have studied both primary imbibition and drainage using a combination of 1D longitudinal profile images and 1D projections of thin-slice images, for both limestone and sandstone rocks. For a limestone core, saturated initially with the oil phase, displacement with D_2O (imbibition) was followed via measurement of longitudinal 1D projections to determine the variation with time, and the volume of injected D_2O, of the oil saturation along the displacement direction. A key observation arising from this study is that the transverse relaxation characteristics of the signal, in this case arising solely from the oil phase, depend on the oil saturation to a significant degree. This could arise from the introduction of further magnetic susceptibility inhomogeneity at the pore scale.[30] The effect is estimated to lead to a reduction in derived saturations if not properly accounted for. Figure 13 shows a set of 1D profile images obtained by projecting the signal from a thin slice perpendicular to the fluid displacement direction onto an axis in the slice plane parallel with the main bedding planes of the laminated structure of this rock. The profiles represent the oil saturations at different times in the process of imbibition of D_2O into this, originally, fully oil-saturated

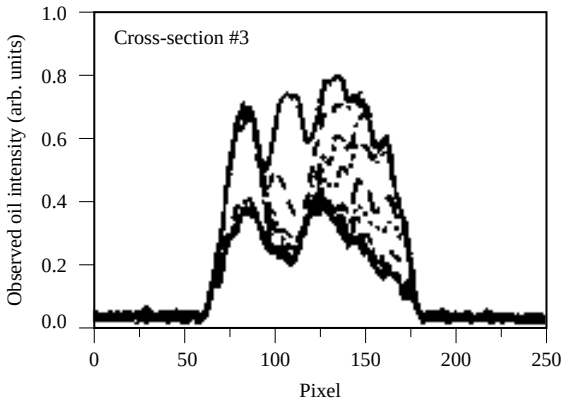

Figure 13 The evolution of 1D projection images of a laminated sandstone undergoing imbibition in which the oil phase, which gives rise to the signal, is spontaneously replaced by the wetting phase, water (D_2O). The signal decreases as the D_2O enters the slice and, because of the choice of orientation of the sample with respect to the gradient, the differential rates of transport in the different bedding planes can be discerned. The timescale spanned by the different curves is 192 min from the start of water injection. (Reproduced by permission of the Society of Petroleum Engineers from Chen et al.[11])

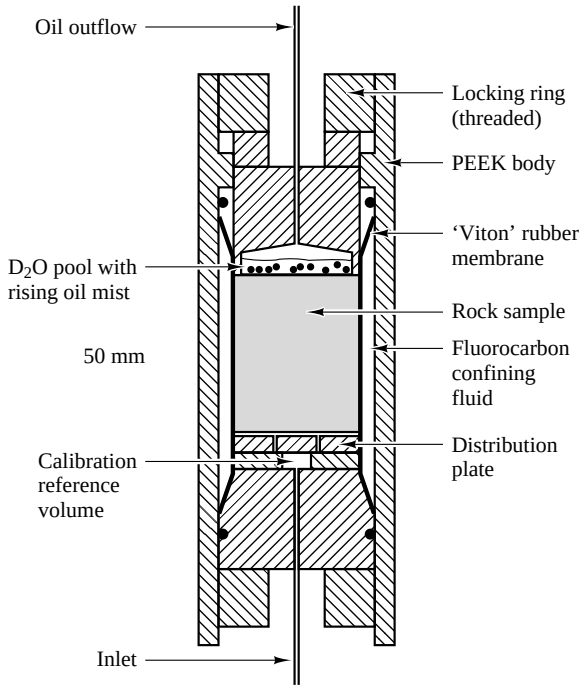

Figure 14 The sample cell used by Fordham et al.[15] to study the drainage process in a sandstone rock. The wetting phase (D_2O) is displaced by oil with the end of the sample held at $S_w = 1$. In this case the sample axis was mounted vertically within the horizontal magnet bore. The diagram shows clearly the arrangements for the generation of a reference signal, the lateral pressurized fluid containment, and the maintenance of the condition $S_w = 1$. (Reproduced by permission of the American Institute of Chemical Engineers from Fordham et al.[15] © AIChE 1993. All rights reserved)

sandstone. Analysis of the set of images from slices along the full length of the core indicated that fluid is displaced at significantly different rates in the different layers, which was interpreted as indicating significant permeability variations in the different planes of the structure. Similar slice-profile images, taken under different steady-state flow conditions, showed that for the imbibition process all the mobile oil was displaced at the lowest flow rate whereas, for the subsequent drainage process in which oil is used to displace D_2O, the oil saturation continued to increase with flow rate throughout the range investigated. It was deduced, also, that there was no significant variation of wetting behavior across the laminated structure of this sandstone.

Related investigations of fluid displacements have been carried out by other groups[12,13,15,32] and, whilst it is clear that these processes can be probed using the versatility of NMR imaging experiments, there remain the problems of signal-to-noise ratio/resolution, fast transverse relaxation, and the variation of this with saturation. These offer a considerable challenge to the NMRI/petrophysics communities if they are to capture the full potential of this combination in a quantitative manner.

A study by Fordham et al.[15] goes a long way towards meeting that challenge and, to a degree, extends the approaches of Chen et al.[11] and Enwere and Archer.[32] These workers again use D_2O together with an oil phase (*n*-dodecane) to make a quantitative study of oil saturation variations along the length of a core. In this case the displacement of the wetting phase, D_2O, by the oil phase (drainage) was investigated under the conditions that the outflow end of the rock was held at $S_w = 1$. The cell used, which was mounted vertically in the horizontal magnet bore, is shown in Figure 14 while the derived spatial variation of oil saturations and T_2 values as a function of flow rate are given in Figure 15. This study was aimed at validating a method which had been proposed for the study of two-phase flow under these conditions, which it succeeded in doing. This is probably the only example where a strong and quantitative link has been established between the complex fields of NMRI and petrophysics.

5.2 Drilling Mud Invasion/Depth Filtration

Drilling muds may contain particulates such as clays which are small enough to penetrate the rock formation being drilled. The timescale and extent of such penetration is of interest and NMRI has been used to investigate this phenomenon.[33,34] The basis of the approach is that the T_1 value of the fluid contained within the rock is reduced by the addition of fine clay particles. An earlier study of filtration[35] established the relationship between an average measure of the spin–lattice relaxation time and the local 'concentration' of the filtered solid particles. In one study[33] penetration of bentonite particles into rocks of different pore size and permeabilities were imaged and it was shown that the T_1 profiles reflected the presence of the clay and the extent of its penetration. In a further study[34] the same process was observed dynamically using a fast imaging method called 'prefocused FLASH'. Figure 16 shows a series of such images showing the time course of the penetration of the clay into the rock. The main changes occur over a time interval of 15 s and these images illustrate the potential of NMRI for the investigation of the dynamics of such processes.

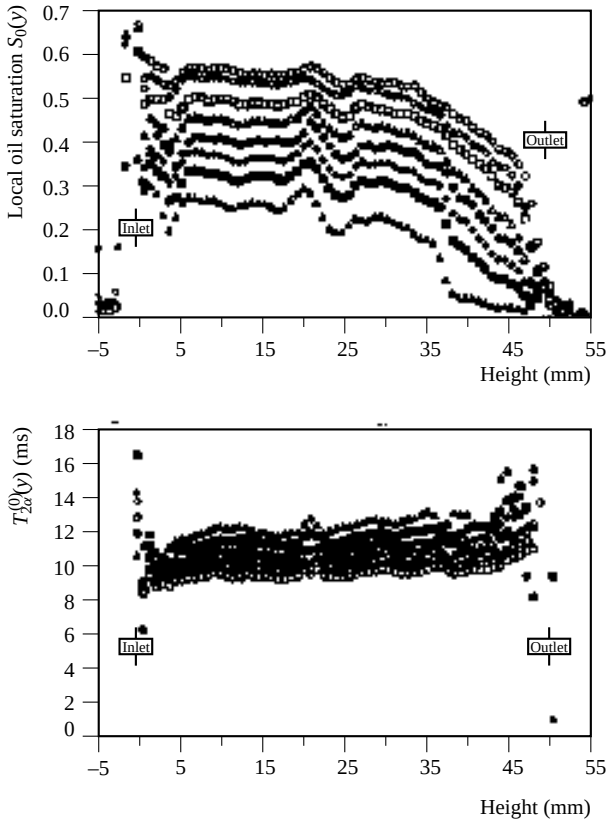

Figure 15 The 1D image profiles for the drainage process referred to in the text and in Figure 14. The upper set of profiles are the oil saturation along the length of the rock core while the lower set are of the corresponding T_2 values, each data set corresponding to different volumetric flow rates. An important observation from these data is the clear variation of T_2 of the oil phase with saturation. (Reproduced by permission of the American Institute of Chemical Engineers from Fordham et al.[15] © AIChE 1993. All rights reserved)

6 SUMMARY

NMRI studies of fluids in porous oil reservoir rocks are at a stage of development where, to a large extent, the measurement techniques with their attendant strengths and limitations have been explored and the underlying NMR physics defined in many aspects. This, coupled with studies on model and related systems,[22,36,37] will only make a real contribution to oil industry problems through a dedicated and collaborative effort between NMRI specialists and reservoir engineers and petrophysicists.

7 RELATED ARTICLES

Agriculture and Soils; Anisotropically Restricted Diffusion in MRI; Chemical Shift Imaging; Contrast Agents in Whole Body Magnetic Resonance: An Overview; Diffusion and Flow in Fluids; Diffusion Measurements by Magnetic Field Gradient Methods; Diffusion and Perfusion in MRI; Diffusion in Porous Media; Echo-Planar Imaging; Field Gradients and Their Application; Whole Body Magnetic Resonance Angiography; Imaging Techniques for Solids and Quasi-Solids; Indirect Coupling: Semiempirical Calculations; Lung and Mediastinum: A Discussion of the Relevant NMR Physics; Microporous Materials and Xenon-129 NMR; Quantitation in In Vivo MRS; Relaxation Measurements in Imaging Studies; Relaxation Measurements in Whole Body MRI: Clinical Utility; Spin Warp Data Acquisition; Susceptibility and Diffusion Effects in NMR Microscopy; Susceptibility Effects in Whole Body Experiments.

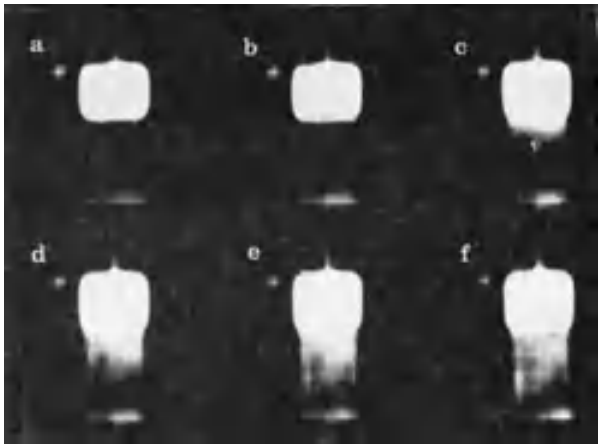

Figure 16 Rapidly acquired NMR images showing the time course of the penetration of clay particles into a rock sample. The times, from the start of the filtration process, corresponding to the successive images (a)–(f) were 7.6, 9.5, 11.4, 13.3, 15.2, and 119.7 s, respectively. The pulse sequence used was prefocused FLASH, which generates the images rapidly but at the expense of a unique image contrast mechanism, thus limiting its quantitative application in terms of local clay and fluid phase concentrations. (Reproduced by permission of the American Institute of Chemical Engineers from Fordham et al.[34] © AIChE 1991. All rights reserved)

8 REFERENCES

1. M. A. Robinson, *J. Magn. Reson.*, 1991, **95**, 574.
2. R. L. Kleinberg and M. A. Horsfield, *J. Magn. Reson.*, 1990, **88**, 9.
3. S. J. Davies and K. J. Packer, *J. Appl. Phys.*, 1990, **67**, 3163.
4. R. L. Kleinberg, *Magn. Reson. Imag.*, 1994, **12**, 271.
5. L. L. Latour, R. L. Kleinberg, and A. Sezginer, *J. Colloid Interface Sci.*, 1992, **150**, 535.
6. J. J. Howard, W. E. Kenyon, and C. Straley, *Proc. 65th Annu. Tech. Conf. Soc. Pet. Eng., 1990*, 733.
7. W. E. Kenyon, P. I. Day, C. Straley, and J. F. Willemsen, *Proc. 61st Annu. Tech. Conf. Soc. Pet. Eng., 1986*, 1.
8. P. T. Callaghan, *Principles of NMR Microscopy*, Clarendon Press, Oxford, UK, 1991.
9. P. Mansfield and B. Chapman, *J. Magn. Reson.*, 1986, **66**, 573.
10. W. P. Rothwell and H. J. Vinegar, *Appl. Opt.*, 1985, **24**, 3969.
11. S. Chen, F. Qin, K.-H. Kim, and A. T. Watson, *Proc. 67th Annu. Tech. Conf. Soc. Pet. Eng.*, 1992, 1013.
12. B. A. Baldwin and W. S. Yamanashi, *Magn. Reson. Imag.*, 1988, **6**, 493.
13. E. J. Fordham, M. A. Horsfield, C. Hall, and L. D. Hall, *Magn. Reson. Imag.*, 1991, **9**, 803.
14. W. A. Edelstein, H. J. Vinegar, P. N. Tutunjian, P. B. Roemer, and O. M. Mueller, *Proc. 63rd Annu. Tech. Conf. Soc. Pet. Eng., 1988*, 101.

15. E. J. Fordham, L. D. Hall, T. S. Ramakrishnan, M. R. Sharpe, and C. Hall, *AIChE J.*, 1993, **39**, 1431.
16. P. A. Osment, K. J. Packer, M. J. Taylor, J. J. Attard, T. A. Carpenter, L. D. Hall, N. J. Herrod, and S. J. Doran, *Philos. Trans. R. Soc. London, Ser. A*, 1990, **333**, 441.
17. J. W. Gleeson and D. E. Woessner, *Magn. Reson. Imag.*, 1991, **9**, 879.
18. A. Caprihan and E. Fukushima, *Phys. Rep.*, 1990, **198**, 195.
19. D. LeBihan, E. Breton, D. Lallemand, P. Grenier, E. A. Cabanis, and M. Laval-Jeantet, *Radiology*, 1986, **161**, 401.
20. R. Turner, in *Cerebral Blood Flow*, eds. A. Rescigno and A. Boicelli, Plenum Press, New York, 1988, p. 245.
21. R. Turner and P. Keller, *Prog. NMR Spectrosc.*, 1991, **23**, 94.
22. G. J. Nesbitt, T. W. Fens, J. S. van den Brink, and N. Roberts, in *Magnetic Resonance Microscopy*, eds. B. Blumich and W. Kuhn, VCH, Wienheim, 1992, p. 287.
23. D. Guilfoyle, P. Mansfield, and K. J. Packer, *J. Magn. Reson.*, 1992, **97**, 342.
24. P. Mansfield and B. Issa, *Magn. Reson. Imag.*, 1994, **12**, 275.
25. S. J. Gibbs, J. J. Attard, and L. D. Hall, *AIChE J.*, 1993, **39**, 689.
26. M. A. Horsfield, C. Hall, and L. D. Hall, *J. Magn. Reson.*, 1990, **87**, 319.
27. S. Davies, A. Hardwick, D. Roberts, K. Spowage, and K. J. Packer, *Magn. Reson. Imag.*, 1994, **12**, 349.
28. H. J. Vinegar, P. N. Tutunjian, W. A. Edelstein, and P. B. Roemer, *Proc. 64th Annu. Tech. Conf. Soc. Pet. Eng., 1989*, 1.
29. W. E. Kenyon, *Nucl. Geophys.*, 1992, **6**, 153.
30. S. Chen, H. K. Liaw, and A. T. Watson, *Magn. Reson. Imag.*, 1994, **12**, 201.
31. B. A. Baldwin and W. S. Yamanashi, *The Log Analyst*, 1989, 45.
32. M. P. Enwere and J. S. Archer, *Proc. 8th SPE/DOE Symp. Enhanced Oil Recovery*, 1992, 99.
33. E. J. Fordham, M. A. Horsfield, L. D. Hall, and G. C. Maitland, *J. Colloid Interface Sci.*, 1993, **156**, 253.
34. E. J. Fordham, T. P. L. Roberts, T. A. Carpenter, L. D. Hall, and C. Hall, *AIChE J.*, 1991, **37**, 1900.
35. M. A. Horsfield, E. J. Fordham, C. Hall, and L. D. Hall, *J. Magn. Reson.*, 1989, **81**, 593.
36. G. J. Nesbitt, A. de Groot, T. W. Fens, and J. H. M. Bonnie, *Magn. Reson. Imag.*, 1991, **9**, 779.
37. J.-D. Chen, M. M. Dias, S. Patz, and L. M. Schwartz, *Phys. Rev. Lett.*, 1988, **61**, 1489.

Biographical Sketch

Ken J. Packer. *b* 1938. B.Sc., 1959, Chemistry, Imperial College, London, Ph.D., 1962, Cambridge University. Introduced to NMR by making a new compound and collaborating with fellow graduate student (Robin Harris) in the analysis of its spectrum. Reinforced by a postdoctoral year with Earl Muetterties at the duPont Experimental Station, Wilmington. 1963–84, School of Chemical Sciences, University of East Anglia; 1984–93, BP Research, Chief Research Associate in Spectroscopy and latterly Chief Scientist. Currently, Research Professor in Chemistry, Department of Chemistry, University of Nottingham. Approx 120 publications including book NMR of Solid Polymers with V. J. McBrierty. Current research interests: NMR/MRI applied to heterogeneous catalysts, solid polymers, and fluid transport processes in porous solids.

Terrestrial Magnetic Field NMR

Georges J. Béné
Université de Genève, Genève, Switzerland

1 Introduction 1
2 The Character of NMR in the Terrestrial Magnetic Field (See ***Zero Field NMR***) 1
3 Utility of Terrestrial Field NMR at the Fundamental Level 2
4 Applications of NMR in the Terrestrial Field 4
5 Related Articles 5
6 References 5

1 INTRODUCTION

Nuclear magnetic resonance in weak $\boldsymbol{B}_0$ fields (of the order of magnitude of the terrestrial magnetic field $\boldsymbol{B}_\mathrm{T}$) has only a modest place in this area of nuclear magnetism. One sometimes imagines that such experiments are without any real specific interest; our objective here is to state the interest these experiments have as precisely as possible. Sometimes they are simpler or more efficient than experiments with strong fields and in some cases strong field experiments cannot be performed at all.

After having compared these areas of application of NMR we will recall the important results obtained with weak fields, both on the fundamental level and in applications.

2 THE CHARACTER OF NMR IN THE TERRESTRIAL MAGNETIC FIELD (SEE)

2.1 The Field B_0

2.1.1 The Terrestrial Magnetic Field B_T[1]

The terrestrial magnetic field is dipolar, its direction in our neighborhood varying by only a few degrees from the geographic N–S. It is of weak amplitude, between 2.5×10^{-5} and 7.5×10^{-5} T, and about 5×10^{-5} T in temperate regions. Its interest lies in its large homogeneity and slow diurnal and secular variation for suitably chosen sites, this allowing measurement at a precision of 10^{-10} T.

2.1.2 Additional Fields

The use of the terrestrial magnetic field does not usually allow one to avoid superposing either an additional positive or negative field to change ω_0 or a gradient. Such a gradient can be obtained, for example, by supplying two identical, parallel, coaxial coils wound in opposite senses with a continuous current i. Variation of i allows one to vary the homogeneity at the center of symmetry of the system in a calculable way. (See ***Field Gradients and Their Application***.)

2.2 Lack of Information

2.2.1 Weak Field Strength

The small amplitude of the terrestrial magnetic field implies a weak nuclear polarization. For a nucleus with magnetic moment μ placed in the terrestrial field $\boldsymbol{B}_\mathrm{T}$ at absolute ambient temperature T, the ratio between the number of dipoles parallel to the field and those antiparallel is given approximately by the expression $1 + 2(\mu B_\mathrm{T}/kT)$, which has a value of about $1 + 3 \times 10^{-10}$ (k = Boltzmann constant). Here we understand why NMR was discovered with fields in the range 0.2–0.7 T and why the fields used these days can attain or surpass 17 T. One often overcomes the handicap of a weak amplitude by prepolarizing the nuclei with a strong field.

2.2.2 Exploration Restricted to Narrow Lines

$\boldsymbol{B}_\mathrm{T}$ not being greater, on average, than 5×10^{-5} T, one can only easily observe and study lines of a width less than 10^{-7} T. However, this condition is not sufficient as one must choose nuclei with a large gyromagnetic ratio γ, which are of spin-$\frac{1}{2}$ (to avoid quadrupole broadening) and which are present in a large density in the sample. This excludes notably solids, paramagnetic media, and liquids trapped in porous media that are too fine.

2.2.3 Lack of a High Homonuclear Resolution

This resolution is governed by the chemical shift δ and the indirect interaction constant J between the nuclei. If the nuclei are all the same, then δ tends to zero for a weak field as does the amplitude of the satellites due to J. For example, ethanol has only one spectral line in $\boldsymbol{B}_\mathrm{T}$ whose width depends only on the relaxation times T_1 and T_2.[1] Everyone knows the complicated spectrum of this compound in a high field.

2.3 Positive Aspects

2.3.1 Measurement and Study of the Terrestrial Magnetic Field

The first spectrometers were built with the measurement of $\boldsymbol{B}_\mathrm{T}$ in view. This approach seems to have been abandoned these days.

2.3.2 Samples Not Readily Accessible or of Large Volume

One of the applications of NMR in the terrestrial field is the geophysical exploitation of underground deposits: either by spectrometric investigation of bore holes or with spectrometers resting at ground level used to search for underground water reserves.

2.3.3 Study of Fundamental Phenomena in NMR Not Easily Accessible at High Field

It is relatively simple to study separately the diverse parameters which characterize NMR and the effects of a change in these parameters:

- Amplitude and homogeneity of $\boldsymbol{B}_0$;

- Speed of crossing resonance, modulation of $\boldsymbol{B}_0$;
- Nonlinear effects (when $\boldsymbol{B}_1$ is not orthogonal to $\boldsymbol{B}_0$);
- Application of a nonresonant rf field $\boldsymbol{B}_1$;
- Separate study of the two rotating components of $\boldsymbol{B}_1$ both at and away from resonance.

2.4 Terrestrial Field Spectrometers

One can use both spectrometers of the same type as those employed for high fields, adapted for low frequencies, and apparatus using a different principle (with prepolarization). Special techniques have also been used for particular problems.

2.4.1 Conventional Spectrometers

The first observations of proton NMR in the terrestrial magnetic field were made either with a crossed coil spectrometer (the need for a large S/N ratio requires that particular care be taken with the receiver coil having a 2 L volume) or with a single coil (useful volume, 8 L).[2]

The working frequency was in the neighborhood of 2 kHz, the coil surrounding the sample having a large number of turns: care must be taken to reduce the interlayer capacitance to a minimum.

One must note an original type of spectrometer brought into operation by a Russian–Australian collaboration.[3] Here the sample is an underground permeable layer filled with water, either stagnant or flowing. One lays a circular coil of large diameter on the ground linked to a powerful high-frequency generator or a detector tuned to the Larmor frequency ω_T of protons in the local terrestrial field.

Knowing the value of $\boldsymbol{B}_T$, a strong $\boldsymbol{B}_1$ field pulse at the frequency ω_T is sent by the coil. This has the effect of aligning the magnetic moment $\boldsymbol{M}_T$ in the plane perpendicular to $\boldsymbol{B}_1$. After the pulse is finished, the vector $\boldsymbol{M}_T$ precesses around the direction $\boldsymbol{B}_T$ at the frequency ω_T. The same coil serves to receive the signal.

According to the authors, one can detect water at a depth of the order of magnitude of the coil diameter (at present around 200 m). The telluric currents are the main cause of noise.

2.4.2 Spectrometers Using Prepolarization

2.4.2.1 Permanent regime. The sample, a liquid circulating around a closed circuit, passes first through an intense magnetic field $\boldsymbol{B}_P$, where the nuclei are strongly polarized. It then arrives in the field $\boldsymbol{B}_T$, where the NMR signal is observed. For this system to be useful one must suppose that the time t spent in the field $\boldsymbol{B}_P$ is long enough ($\approx T_1$) and that spent between $\boldsymbol{B}_P$ and $\boldsymbol{B}_T$ is smaller than the effective relaxation time T'_2 of the nucleus studied.

2.4.2.2 Dynamic regime. The sample is placed in a coil B whose axis is perpendicular to the direction of the terrestrial field $\boldsymbol{B}_T$. The measurement is made in two stages:

1. The coil is supplied with a continuous current i_P strong enough to give an $\boldsymbol{M}_P$ polarization proportional to i_P and directed along the coil axis. A large polarization will result if the polarization time t is of the order of magnitude of T_1.
2. The current i_P is suddenly cut and the coil linked to a receiver tuned to the frequency ω_T. A decreasing signal is detected:
   - whose initial amplitude is proportional to $\boldsymbol{M}_P$,
   - whose frequency is ω_T,
   - whose decay allows the measurement of T_2 in $\boldsymbol{B}_T$ if the field is sufficiently homogeneous.

2.4.3 Special Techniques

2.4.3.1 Study of nuclear magnetism away from resonance. Such a study is relatively easy using the technique of prepolarization before free precession. It suffices to apply a permanent rf field perpendicular to the direction of the terrestrial field after removing the polarizing field.

2.4.3.2 Inversion of reference system without resonant impulsion[10]. Spin echoes, discovered by E. Hahn and much studied since, are normally obtained using rf pulses at Larmor frequency with a suitably chosen length, periodicity, and phase, and directed along an axis perpendicular to $\boldsymbol{B}_0$. The effect of these pulses is always to produce artificial 'time reversal', which is the origin of the resetting in the phase of the nuclei and the resulting echoes.

In the constant and homogeneous terrestrial field it is easy to superpose a gradient whose inversion can be equivalent to a resonant pulse π.

2.4.3.3 Relaxometry[4] *(see* ***Field Cycling Experiments****).* The essential aim of this technique is to measure the size of the relaxation times T_1, $T_{1\rho}$, and T_2 in a field $\boldsymbol{B}_R$ of different amplitude to the field $\boldsymbol{B}_0$ for which one observes resonance, in order to measure the correlation times τ_c at the origin of the relaxation. When $\omega_0{}^{-1} \approx \tau_c$ one has variations of the relaxation times as a function of the applied field $\boldsymbol{B}_R$. It is better to evaluate $T_1(\boldsymbol{B}_R)$ because T_1 only depends on those τ_c values longer than $\omega_0{}^{-1}$, whereas T_2 and $T_{1\rho}$ are conditioned by all the τ_c values characterizing the explored medium. (See ***Brownian Motion and Correlation Times***.)

Moreover, one finds that in many aqueous solutions, notably protein solutions and physiological fluids, T_1 is the most sensitive relaxation time in the range 10^{-2} to 10^{-7} T for B_R. Such small values for B_R may be larger or smaller than the terrestrial field B_T and it is a very simple matter to describe the curve $T_1(\boldsymbol{B}_R)$ which consists of:

1. polarizing the nuclei of the sample in the field $\boldsymbol{B}_P$ to obtain the polarization $\boldsymbol{M}_P$.
2. measuring $T_1(\boldsymbol{B}_R)$ by submitting the sample to the field $\boldsymbol{B}_R$ for a variable length of time. The decrease of $\boldsymbol{M}_P(B_R < B_P)$ with increasing time during which the sample is subjected to the field $\boldsymbol{B}_R$ allows one to observe, at the cutoff of $\boldsymbol{B}_R$, the free precession of the magnetization $\boldsymbol{M}_P$: the initial amplitude of this signal allows the calculation of $T_1(\boldsymbol{B}_R)$ and its exponential decay allows the evaluation of T_2 in the terrestrial field.
3. making the measurements for a series of values of $\boldsymbol{B}_R$ with the aid of an additional field superposed with $\boldsymbol{B}_T$ and either parallel or antiparallel to it.

3 UTILITY OF TERRESTRIAL FIELD NMR AT THE FUNDAMENTAL LEVEL

3.1 Historical Digression: Negative Results[2]

We will not insist on the questions that were usually asked during the first years following the discovery of NMR, but

Figure 1 Benzene dispersion with $B_1 \approx 1.5 \times 10^{-10}$ T

which were then found to be without interest. The relation $\omega_0 = B_0\gamma$ is verified even for very weak fields. There is no particular interaction between the spins of the dipoles of an electromagnet and nuclear spins. The indirect interactions J between spins are as simply explained in weak fields as in strong ones.

3.2 The Width of the Narrowest Resonance Lines

As soon as proton resonance was observed in the terrestrial field $\boldsymbol{B}_T$, the homogeneity and constancy of this field in suitable locations was exploited to investigate the natural width of the narrowest spectral lines. The measurement of the proton relaxation time in benzene allowed the prediction of a linewidth not exceeding 2.4×10^{-10} T. Figure 1 shows the experimental result of G. Hochstrasser.[11]

3.3 Perturbations due to $\boldsymbol{B_0}$

3.3.1 Line Broadening by Inhomogeneity

The precise calculation of the inhomogeneity of the field $\boldsymbol{B}_0$ over the sample volume, when this field is produced by two Helmholtz coils and one moves the sample along the axis starting from the symmetry center of the system, allows the precise evaluation of the influence of inhomogeneity on the resonant linewidth.[2]

3.3.2 Modulation Effects

The field $\boldsymbol{B}_0$ is often superposed with a swept alternating field of frequency Ω and amplitude $\boldsymbol{B}_M$. Rocard[5] precisely analyzed the effects of such modulation when $B_0 = 2 \times 10^{-4}$ or 7×10^{-5} T. The spins 'see' the frequency spectrum $\omega \pm k\Omega$ and therefore the transitions $\omega \pm k\Omega = \gamma B_0$. The relative phase of $\boldsymbol{B}_1$ and $\boldsymbol{B}_M$ gives a large variation in the shape of the resonant signal.

3.3.3 Time-Varying Inhomogeneity: Spin Echoes Without Resonant Pulses[2]

Reference frame reversal by inversion of the field $\boldsymbol{B}_0$ or its inhomogeneity can be simply realized by supplying the generating coil with a 'pure gradient' by an alternating field. In the free precession after the prepolarization technique, the cutting of the polarizing field $\boldsymbol{B}_P$ is equivalent to a resonant $\pi/2$ pulse. Inverting the gradient of the field $\boldsymbol{B}_T$ (by inverting the current direction in the coils) is equivalent to a π pulse in the usual spin echo technique. It is much simpler to study the gradient-generating coils with an alternating current: here the reference frame inversion is achieved by time-dependent pulsation (Figure 2).

Figure 2 Spin echoes in an alternating gradient

3.4 Perturbations to the Rf Field $\boldsymbol{B_1}$

3.4.1 Resonant Linewidth Broadening

The homogeneity of the terrestrial magnetic field allowed Hochstrasser[1] to evaluate precisely the influence of the amplitude of $\boldsymbol{B}_1$ on the width and form of the proton resonance: he showed that this perturbation did not affect the form (Lorentzian central part) but determined the linewidth.

3.4.2 Nonlinear Effects[12]

Pommier and Benoit studied the influence of angles θ (between $\boldsymbol{B}_0$ and $\boldsymbol{B}_1$) different from $\pi/2$ at $\omega_0 = 3$ kHz. Application of the Bloch equations predicts resonances for $\omega_0 = n\omega$, which translates at first order to the Bloch–Siegert shift and generation of harmonics as well as sidebands $[\omega_0 = (n \pm 1)\omega]$.

3.4.3 Effect of a Nonresonant Field B_1[2]

Using the technique described in Section 2.4.3.1, after removing the polarizing field $\boldsymbol{B}_P$ the magnetization $\boldsymbol{M}_P$ is subjected to the field $\boldsymbol{B}_T$ which is superposed with a perpendicular nonresonant field $\boldsymbol{B}_1$ of frequency ω, which is either rotating or alternating. In each case one determines the pulsations of the free precession phenomenon observed in $\boldsymbol{B}_T$. If one has a rotating field [either in the same sense as the nuclear precession (+) or in the opposite (−)] one has three solutions

$$(+)\ \omega,\ \omega \pm \sqrt{(\omega_0 + \omega)^2 + \omega_1^2}$$

$$(-)\ \omega,\ \omega \pm \sqrt{(\omega_0 - \omega)^2 + \omega_1^2}$$

where $\omega_1 = \gamma B_1$. With $\omega_0 = 2$ kHz, ω was varied between 500 and 4000 Hz. Figure 3 shows that the first-order effect of an alternating field reduces to the superposition of two rotating fields. For a sufficient intensity of the field $\boldsymbol{B}_1$ one observes higher-order effects, notably transitions involving 3 quanta.

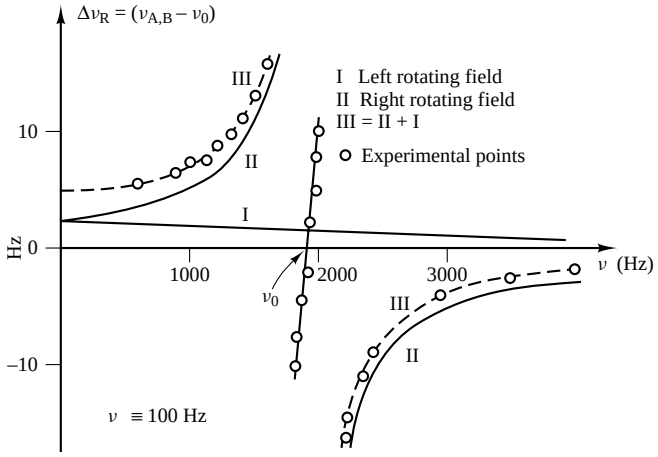

Figure 3 The nonresonant dispersion shift, in rotating and alternating excitation

3.5 Determination of Intra- and Intermolecular Parameters

3.5.1 Indirect Spin–Spin Interactions in Weak Fields[2] *(See **Analysis of High-Resolution Solution State Spectra**)*

As recalled above, only interactions between nuclei of different type are observed.

3.5.1.1 Nuclei of adjacent spin-$\frac{1}{2}$ atoms. Extending the work of Roux[13] to weak fields, Erbeia[14] analyzed the $J(^{31}P,^{1}H)$ interaction in a field $B_0 = 1.4 \times 10^{-4}$ T by the observation of a proton doublet in phosphoric acid (AB type spectrum) (see ***Phosphorus-31 NMR***). The same author studied the AB_2 multiplet obtained in hypophosphoric acid. Our group has observed $^{13}C-^{1}H$ and even $^{15}N-^{1}H$ multiplets in the Earth's field and at natural concentration, in the latter case by using electronic dynamic polarization of ammonium ions. Figure 4 shows the quadruplet resulting from the $^{13}C-^{1}H$ interaction in methanol and the corresponding theoretical spectrum.

3.5.1.2 Nuclei of spin different to $\frac{1}{2}$ adjacent to protons. The Paris (F) group studied the $^{2}D-^{1}H$ coupling in a current of prepolarized HD liquid. A transition at $\nu_0 = 54$ Hz was observed in a field $B_0 < 3 \times 10^{-6}$ T: the smallest Larmor frequency observed in condensed matter. The weak field interaction between ^{14}N ($I = 1$) and ^{1}H in the ammonium ion was first studied by J. M. Rocard[15] at $B_0 = 2 \times 10^{-4}$. Merck[15] demonstrated the second-order quadrupole $[J^2_{AB}/(\Delta_A - \Delta_B)]$ of 1.35 Hz (the first order corresponding to $J = 52.55$ Hz). (See ***Overtone Spectroscopy of Quadrupolar Nuclei***.)

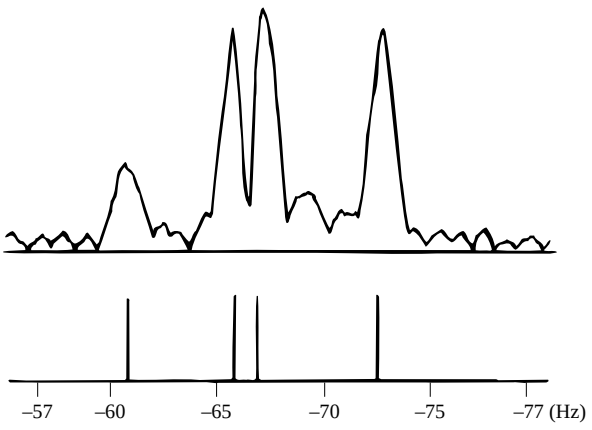

Figure 4 Proton quadruplet resulting from $^{13}C-^{1}H$ interaction in methyl alcohol at the natural concentration of ^{13}C

3.5.1.3 Nonadjacent spin-$\frac{1}{2}$ nuclei. E. Duval has studied the $^{31}P-^{1}H$ interactions in triethyl phosphate and triethyl phosphite in the positions P–O–C–H-α and P–O–C–C–H-β. He observed that the complex multiplet obtained allowed the evaluation of the interaction constants J(P,H-α) = 8.4 Hz and J(P,H-β) = 0.84 Hz and was sensitive to the relative signs of these two coupling constants. (See ***Indirect Coupling: Semiempirical Calculations***.)

*3.5.2 Relaxation Dispersion of Proton Nuclei (See **Protein Dynamics from NMR Relaxation**)*

It is well known that the relaxation time in mobile liquids depends essentially on the correlation times τ_c [or the correlation frequencies $\nu_c = (2\pi\tau_c)^{-1}$] defined by microscopic molecular motion or the lifetime of molecular structures in a given configuration.

It was found that, in water and many diamagnetic aqueous solutions of proteins or other organic molecules, the dynamics of these solutes appear as a correlation frequency spectrum covering the range 10^2-10^7 Hz. These correlation times can be directly studied by measuring the relaxation time of the solvent water, and in particular by measuring T_1 in the range of B_0 corresponding to $\nu_0 \approx \nu_c$. More precisely, if ν_0 is much greater than the largest ν_c then $T_1 = \infty$ or more simply $T_1^{-1} = 0$, whereas if ν_0 is much less than the smallest ν_c then $T_1 = T_2$. In the intermediate region T_1 changes more or less rapidly each time B_0 crosses a region where ν_0 is of the order of the magnitude of ν_c.

The relaxometry technique described above in Section 2.4.3.3 allows B_0 to be varied between 10^{-7} and 10^{-2} T. It has notably allowed the observation for the first time of the dispersion in T_1 due to the lifetime of H^+ and OH^- ions in water, without having to use ^{17}O enrichment (see ***Oxygen-17 NMR***). On the same lines we have measured the dispersion of the proton relaxation time in diverse types of amides in solution (see ***Relaxation Effects of Chemical Exchange***).

Finally, the study of proteins or other organic macromolecular solutions has shown an important dispersion of T_1 in the range 10^3-10^6 Hz. This dispersion is often a characteristic of the studied medium, whether it would be simple or complex, in solution or gel. Figure 5 shows the dispersion curve of an aqueous solution of human fibrinogen.[4,6] This gives the possibility of application to medical diagnostics, as we will show later.

4 APPLICATIONS OF NMR IN THE TERRESTRIAL FIELD

4.1 Measurement of B_T

This application, which was largely developed in the 15 or so years following the first publication (1954), allowed the

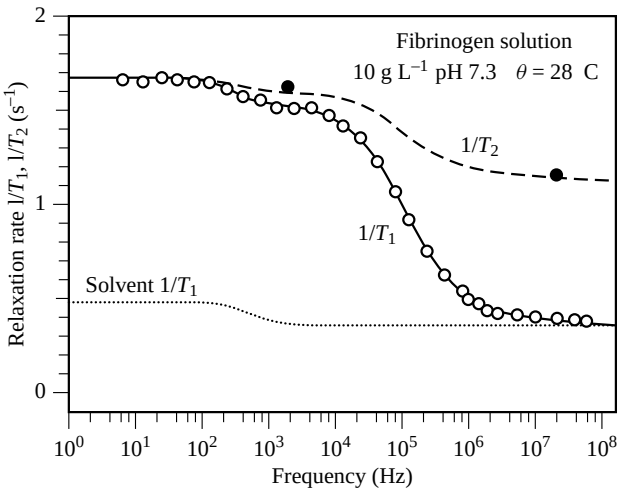

Figure 5 Experimental and theoretical frequency dependences of $T_1{}^{-1}$ (open circles) and $T_2{}^{-1}$ (filled circles) in a fibrinogen solution

measurement of either the amplitude of the vector $\boldsymbol{B}_T$ or its gradient. It was then abandoned in favor of other techniques independent of NMR.

4.2 Search and Study of Underground Liquids (See *Geological Applications*)

NMR in the terrestrial field is studied for two types of application:

- In bore holes, by introducing a spectrometer which recognizes the crossing of layers rich in water or petrol (and in some cases allows the description of the fluid encountered and its environment with a certain precision) (see ***Coal Structure from Solid State NMR***).
- From the surface, the spectrometer described in Section 2.4.1 (hydroscope) was used for layers at depths of up to 200 m, allowing the determination of the depth, thickness, and richness in free water of the layer. This technique is the subject of current research.[3]

4.3 Applications to Medical Diagnostics (See *Body Fluids*)

4.3.1 Measurement of Relaxation Times[4] *(See **Relaxometry of Tissue**)*

Relaxometry allows the construction and comparison of the dispersion curves for the relaxation time T_1 of macromolecular solutions. As an example, the human body contains such solutions at different points, e.g. blood in the circulatory system, urine in the kidneys and bladder, ascite liquid, and the amniotic fluid of pregnant women. A pathological change in one of these liquids is sometimes indicated in a strong way in their T_1 dispersion curves.

We have undertaken such a study using prepolarization and free precession and shown, in situ, a change in the amniotic fluid when it is contaminated. Such a measurement was realized by placing the exploratory coil directly on the patient's abdomen. Clearly one chooses an optimum value of $\boldsymbol{B}_R$ which, in this case, is not critical.

*4.3.2 Weak Field Imaging (See **Image Formation Methods** and **Low-Field Whole Body Systems**)*

The university research groups of Lyon (F) and Ljubljana (SLO) have presented results on imaging: an apparatus using prepolarization, which is nearly ready for applied use, has been prepared by the latter. The images of phantoms exhibit a spatial resolution close to 2 mm.[7] Self-diffusion and flow imaging were also successfully investigated[8] (see ***Diffusion Measurements by Magnetic Field Gradient Methods*** and ***Flow NMR***). Relaxation imaging, in which T_1 is measured in the polarizing field, and T_1 and T_2 in the Earth's field, is able to give better contrast than in high-field imaging[9] (see ***Relaxation Measurements in Imaging Studies***).

5 RELATED ARTICLES

Analysis of High-Resolution Solution State Spectra; Body Fluids; Brownian Motion and Correlation Times; Carbon-13 Relaxation Measurements: Organic Chemistry Applications; Diffusion Measurements by Magnetic Field Gradient Methods; Field Cycling Experiments; Field Gradients and Their Application; Flow NMR; Geological Applications; Image Formation Methods; Indirect Coupling: Semiempirical Calculations; Low-Field Whole Body Systems; Overtone Spectroscopy of Quadrupolar Nuclei; Oxygen-17 NMR; Phosphorus-31 NMR; Protein Dynamics from NMR Relaxation; Relaxation Effects of Chemical Exchange; Relaxation Measurements in Imaging Studies; Relaxometry of Tissue; Zero Field NMR.

6 REFERENCES

1. G. Hochstrasser, *Helv. Phys. Acta*, 1961, **34**, 189.
2. G. J. Béné, *Phys. Rep.*, 1980, **58**, 213.
3. M. Schirov, A. Legchenko, and G. Creer, *Explor. Geophys. (Oxford)*, 1991, **22**, 333.
4. F. Noack, *NMR Principles Prog.*, 1971, **3**, 84.
5. J. M. Rocard, *Arch. Sci.*, 1957, **10**, 377. See also ref. [2].
6. S. Conti, *Mol. Phys.*, 1986, **59**, 449.
7. J. Stepisnik, M. Kos, G. Planinsic, and V. Erzen, *Phys. Med.*, 1990, **VI**, 235.
8. J. Stepisnik, M. Kos, G. Planinsic, and V. Erzen, *J. Magn. Reson.*, 1994, **A107**, 167.
9. J. Stepisnik, V. Erzen, and M. Kos, *Magn. Reson. Med.*, 1990, **15**, 386.
10. Ref 2, p. 248.
11. Ref 2, p. 241.
12. Ref 2, p. 250.
13. Ref 2, p. 357.
14. Ref 2, p. 256.
15. Ref 2, p. 261.

Biographical Sketch

Georges-J. Béné. *b* 1919. Dr.Sc. 1951, University of Paris (F). Successively Attaché, Chargé, Maître de Recherches CNRS (F), 1948–1957; Professeur Associé, Extraordinaire, Ordinaire, University of Geneva (CH), 1956–1989. President Physics Section of

Geneva Univ., 1969–1977. General Secretary (1956–89) and President (1970–72) of the Ampère Group; Member of the Steering Committee (1966–68) and of the Council (1968–89) of the European Physical Society. Approx. 250 publications. Retired (Honorary Professor) since 1989.

Well Logging

Robert L. Kleinberg

Schlumberger-Doll Research, Ridgefield, CT, USA

1	Introduction	1
2	NMR Relaxation Processes in Rocks	1
3	Practical Importance of NMR Measurements	4
4	Instrumentation for Well Logging	5
5	Related Articles	9
6	References	9

1 INTRODUCTION

Well logging is the means by which physical properties of subsurface earth formations are measured in situ. The most important, and the most technically challenging, application of well logging is to the characterization of hydrocarbon reservoirs. Oil and gas are found up to 10 km underground in beds of sedimentary or other porous rock. Only a part of a typical sedimentary rock is solid mineral matter. The pore space, which accounts for up to 30% of the volume, can be filled by combinations of oil, water, or natural gas. Well logging is directed toward understanding these fluids and their relationship to the solid mineral matrix. A large variety of electromagnetic, acoustic, and nuclear borehole instruments are used for various purposes. Each technique has drawbacks and limitations, and no one logging device ('tool') is adequate to give a complete description of an earth formation.[1,2]

Measuring properties of earth formations in situ by NMR obviously requires apparatus very different than that commonly used in the laboratory. Instead of placing the sample inside the apparatus, the apparatus is placed inside the 'sample', which is in fact the earth. Thus 'inside-out' NMR equipment is required: large static magnetic fields and high-frequency oscillatory magnetic fields must be projected outside of the apparatus and into the surrounding rock formations. Moreover, the apparatus is normally in motion during the measurement.

The amplitude of the proton NMR signal is proportional to the fluid content of the rock, and relaxation times give information on the pore size distribution and, under favorable conditions, the amount and type of oil. These measurements are used by the oil industry to estimate the quantity of hydrocarbon in a reservoir and the rate at which it can be economically extracted. The application of NMR to well logging is the subject of an extensive bibliography, covering 1946–1990, compiled by Jackson and Mathews.[3] The reader also is referred to review articles[4,5] and proceedings of international conferences.[6]

Owing to limitations of signal-to-noise ratio, the only nucleus accessible to borehole NMR is hydrogen. Throughout this article, all statements refer to proton NMR. Nonuniformity of the static magnetic field precludes the acquisition of chemical shift spectra.

2 NMR RELAXATION PROCESSES IN ROCKS

2.1 Surface-Limited and Diffusion-Limited Regimes

NMR relaxation rates of fluids in porous media are enhanced by relaxation at the pore–grain interface.[7,8] Fluid molecules diffuse, eventually reaching a grain surface, where they have a finite probability of being relaxed. The rate-limiting step can either be the relaxation process at the surface or the transport of unrelaxed spins to the surface.

If the rate-limiting step is relaxation at the surface, the nuclear magnetization in a pore is uniform. Therefore the magnetization decay in the pore is monoexponential and does not depend on pore shape but only on the surface-to-volume ratio of the pore. This is referred to as the 'fast diffusion' or 'surface-limited' regime.[9]

In the opposite case, magnetic relaxation occurs at the grain surface, but the decay of macroscopic magnetization is controlled by the transport of molecules to the surface. This is possible when pores are relatively large and/or surface relaxation is strong. This is called the 'slow diffusion' or 'diffusion-limited' regime. In this regime, magnetization in the pore is not uniform. This gives rise to a magnetization decay, which, in each pore, has multiexponential character, and which depends on the shape of the pore.[10]

Support for the surface-limited hypothesis comes from measurements of the temperature dependence of relaxation times in rocks.[11] Remarkably, T_1 and T_2 are nearly independent of temperature over the range 25–175 °C, at least for the modest number of rock samples studied. If NMR relaxation were in the diffusion-limited regime, the relaxation time would depend on the diffusion coefficient of the pore fluid, which is very temperature-dependent. The lack of temperature dependence is a mark of the surface-limited regime.

2.2 Surface Relaxation Mechanisms

The basic principles of NMR relaxation of fluids at solid surfaces in porous media were established by Korringa, Seevers, and Torrey (KST).[12] Two surface processes were identified. One occurs at all sites on the surface and the other is associated with dilute paramagnetic metal ion impurities on the surface. The relaxation process associated with nonmagnetic sites is much too weak to account for the observed relaxation of water in rocks.[13] Paramagnetic ions, such as iron, manganese, nickel, and chromium, are particularly powerful relaxers, and tend to control the rate of relaxation whenever they are present. Rocks primarily composed of silica (sandstones) generally have an iron content of about 1%, and also frequently contain manganese in significant concentrations; these ions make fluid proton relaxation fairly efficient. Occasionally, sandstones contain grains of magnetic minerals such as magnetite (Fe_3O_4), which are sites of relaxation. In carbonate rocks, which are composed of calcite ($CaCO_3$) and related minerals, the rate of fluid relaxation tends to be lower than in sandstones.

Considering only relaxation by dilute paramagnetic ions, the KST equations for surface relaxation in a single pore reduce to

$$\frac{1}{T_1} = \frac{Sh}{V}\frac{n_M}{T_{1M}} = \rho_1 \left(\frac{S}{V}\right)_{pore} \tag{1}$$

where S and V are the surface area and volume of the pore, h is the thickness of the surface layer within which relaxation can take place, n_M is the proportion of surface sites occupied by paramagnetic metal ions, and T_{1M} is the relaxation time of protons in molecules coordinated with paramagnetic ions. All material constants are included in the surface relaxivity parameter ρ_1, which has dimensions of m s^{-1}.

KST do not discuss T_2 in porous media. T_2 is shortened by > molecular diffusion in the inhomogeneous magnetic field arising from the magnetic susceptibility contrast between grains and pore fluid (see Section 2.3), which is unrelated to surface relaxation. However, for proton Larmor frequencies below 5 MHz and for Carr–Purcell echo spacings less than about one millisecond, the enhancement of T_2 decay coming from diffusion in inhomogeneous local fields is often negligible compared with the surface relaxation mechanism. Then[14]

$$\frac{1}{T_2} = \frac{Sh}{V}\frac{n_M}{T_{2M}} = \rho_2\left(\frac{S}{V}\right)_{pore} \tag{2}$$

The surface relaxation mechanism is treated in detail by Kleinberg, Kenyon, and Mitra.[14] Briefly, the relaxation of fluid protons at paramagnetic ion sites on the surface of rock grains is controlled by the dipolar and scalar interactions between the ion and nuclear moments. Among other things, the theory explains why T_1 and T_2 are correlated at low frequency: $T_1 \approx 1.6\ T_2$.

2.3 Molecular Diffusion in Magnetic Field Gradients

A second contribution to transverse relaxation is the diffusion of spins in static magnetic field gradients. In a uniform B_0 gradient, the contribution of this mechanism is

$$\left(\frac{1}{T_2}\right)_D = \tfrac{1}{12}D(\gamma G T_E)^2 \tag{3}$$

where D is the molecular diffusion coefficient, γ is the gyromagnetic ratio of the proton, G is the gradient strength in T m^{-1}, and T_E is the Carr–Parcell echo spacing. This equation is applicable to bulk liquids, for which the diffusion coefficient is a constant. In porous media, the diffusion coefficient is time-dependent,[15] and equation (3) must be modified.

A further complication is the presence of local magnetic field gradients, which result from the magnetic susceptibility contrast between grain material and pore fluid. Rocks typically have paramagnetic ion contents of about 1%, and grain volumetric susceptibilities (SI dimensionless) are typically $\chi_g = +10^{-4}$; grain susceptibilities of the magnetic minerals are much higher. Pore fluids are usually diamagnetic. The internal gradient is proportional to B_0. It also depends on the details of the pore geometry, and therefore varies from point to point within the pore space; some realistic models have been developed.[16,17]

The Carr–Purcell–Meiboom–Gill (CPMG) method mitigates the effect of diffusion in a magnetic field gradient. Keeping both the CPMG echo spacing and the applied magnetic field to a minimum reduces the contribution of diffusion to T_2 relaxation. At low values of B_0 typical of borehole logging tools, in the absence of an applied field gradient, and for closely spaced pulses in the CPMG measurement sequence, T_2 is dominated by surface relaxation. Diffusion effects become important when substantial field gradients are applied, and/or longer pulse spacings are used.

2.4 Bulk Fluid Processes

The last relaxation process is that of the bulk fluid itself. This occurs in the absence of grain surfaces and internal field gradients, and is unaffected by them. Bulk relaxation often can be neglected, but it is important when fluid is in very large pores and therefore is little affected by a surface. Bulk relaxation can also be important for very viscous fluids, such as heavy oils, and also can be the dominant process when the pore fluid has a high concentration of paramagnetic ions. For example, chromium lignosulfonate is a common additive in drilling fluids; chromium ion that enters the pore fluid from the borehole can dramatically reduce the observed relaxation time.

Fine particulates from the borehole can also enter the pore space. When in suspension they also reduce the fluid relaxation time, by making 'floating' solid surface area available for fluid molecules to encounter. However, it has been shown, using a novel NMR imaging technique, that this is not likely to be a problem for NMR logging tools.[18]

2.5 Pore Size Distributions and Distributions of Relaxation Times

Rocks tend to have very broad distributions of pore sizes, and therefore magnetization decays of fluids in rocks are nonexponential. In early work,[19] NMR data were analyzed in terms of two- or three-exponential decays. Later, magnetization decays of water in rock were fitted to stretched exponentials,[20] which assumes a particular form of pore size distribution. The most general way to analyze relaxation data is with a distribution (spectrum) of relaxation times: a plot of signal intensity versus relaxation time. In the following discussion, we assume that the transverse relaxation is controlled by the surface relaxation mechanism and that relaxation is surface-limited. The magnetization decay in an individual pore is then monoexponential, and does not depend on pore shape but only on the surface-to-volume ratio:

$$M(t) = M_0 \exp\left(-\frac{t}{T_2}\right) = M_0 \exp\left[-\rho_2\left(\frac{S}{V}\right)_{pore} t\right] \tag{4}$$

The time evolution of the magnetization of a sample having a distribution of pore sizes can be expressed as a sum of exponential decays:

$$M(t) = \sum_i m_i \exp\left(-\frac{t}{T_{2i}}\right) = \sum_i m_i \exp\left[-\rho_2\left(\frac{S}{V}\right)_i t\right] \tag{5}$$

where m_i is proportional to the volume of fluid relaxing at the rate $1/T_{2i}$. The sum of the volumes is proportional to the porosity ϕ:

$$M_0 = \sum_i m_i \propto \phi \tag{6}$$

Thus, in this model, there is a direct mapping from the spectrum of pore sizes, or more precisely the spectrum of surface-to-volume ratios, to the spectrum of relaxation times.

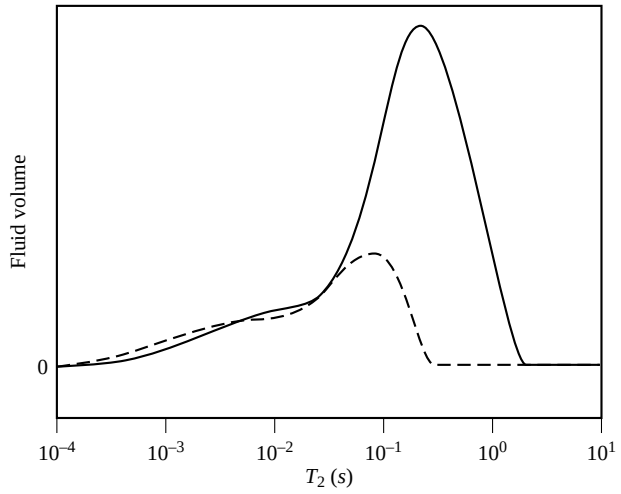

Figure 1 Distribution of relaxation times for a sedimentary rock. The spectrum is a plot of fluid volume as a function of relaxation time. Solid curve: rock fully saturated with water. Dashed curve: the same rock after centrifuging. Centrifugation drains the largest pores, and the corresponding part of the relaxation time distribution disappears. Fluid content before and after centrifuging is directly proportional to the area under the respective curve

Implicit in this discussion is the assumption that pores exist as identifiable entities. On the basis of steady state measurements such as hydraulic permeability and electrical conductivity, it is known that the pore space in rocks is well connected. However, pulse NMR is not a steady state measurement. Molecules only sample a limited volume of pore space before they are relaxed.[21] The radius of the volume sampled is approximately the root mean square distance the molecule diffuses in the NMR relaxation time, $\sqrt{6DT_1}$, the diffusion coefficient, is itself a function of observation time in porous media.[15] If there is significant coupling of pores of different sizes, the relaxation time distributions will be narrowed.[22]

A confirmation of the connection between pore size and NMR relaxation time was provided by Straley et al.[23] Rock specimens were fully saturated with water, and the spectrum of longitudinal relaxation times was determined. Then each rock was centrifuged at a number of rotor speeds. At successively higher speeds, water was progressively expelled from the samples as the centrifugal pressure overcame the capillary pressure of successively smaller pore spaces. At each step, the NMR relaxation spectrum was remeasured. At low centrifuge speed, the components with the longest T_1 disappeared from the spectrum, while the short-T_1 components were unaffected, indicating that only the largest pores had drained. As the centrifuge speed was increased, smaller pores drained and shorter components disappeared. A typical result of a similar T_2 measurement is shown in Figure 1.

The extraction of the values of m_i from the measurement data $M(t)$ poses significant mathematical problems. The inversion is not unique when $M(t)$ is noisy or when the mathematical computation has finite precision. In the past, either the number of terms in equation (5) was limited to two or three—a sparse spectrum indeed—or many terms were used, resulting in spiky, unphysical spectra. This problem can be solved by the use of regularization.[24] Regularization has the effect of smoothing the spectrum, which removes spikes and makes the inversions reproducible. The obvious disadvantages are that the distributions are artificially broadened and that real, narrow features can be filtered out of the results. To avoid problems of arbitrary smoothing, it is essential to use an algorithm that selects the regularization parameter in a data-dependent but objective manner. One such algorithm is that of Butler, Reeds, and Dawson.[25] This automatically selects a regularization parameter based on the signal-to-noise ratio of the measurement data to obtain a minimally broadened, but reproducible, inversion.

2.6 Determination of Surface Relaxivity

To relate quantitatively the NMR relaxation rate spectrum to the pore size spectrum, it is necessary to know the coefficient ρ in equations (1) and (2). Determination of the strength of the surface relaxation has proved to be elusive, because it is difficult to obtain independent information on pore size distributions of sedimentary rock.

The first problem is that the connection between a surface-to-volume distribution and a pore size distribution is poorly defined for rocks. The pore space of rocks has been modeled as spheres connected by throats, an interconnected network of tubes, and an interconnected network of sheets. None of these models has universal applicability. Thus the term 'pore size' should be understood to mean a quantity inversely proportional to the surface-to-volume ratio of a locality in the pore space.

Even more importantly, grain surfaces can have fractal character.[26] That is, the apparent surface area depends on the characteristic scale length η of the measurement. Relaxation time measurements also have characteristic scale lengths: the distance a molecule can diffuse in the shortest recovery time of an inversion-recovery measurement of T_1, or before the first spin echo of a CPMG determination of T_2.

Surface area determinations based on low-temperature adsorption of gas, e.g., the BET method,[27] probe the surface at molecular scale and are dominated by the finest features of grain surfaces. Optical microscopy of thin sections has a resolution of about $\eta = 5\,\mu$m: large pores appear to have smooth surfaces and small pores are invisible. It is not unusual to find that the surface-to-volume ratio determined by a combination of BET and buoyancy porosity methods is orders of magnitude larger than that determined by optical imaging measurements. An interesting new technique measures the surface-to-volume ratio by pulsed field gradient NMR measurements of diffusion.[28] The scale length is determined by the distance fluid molecules diffuse during the finite-length gradient pulses that tag the spins; in recent experiments,[29] $\eta = 2\,\mu$m.

The ambiguity in the determination of surface-to-volume ratio results in an ambiguity in the determination of ρ_1 and ρ_2. When the BET method is used to measure surface area and the relaxation time is determined by the initial slope method, for which $\eta < 1\,\mu$m,[21] ρ_1 is found to be in the range $0.1–0.8\,\mu$m s^{-1}. The pulsed field gradient diffusion measurements[29] yield ρ_1 in the range $3–40\,\mu$m s^{-1}. From optical imaging,[30] ρ_1 is $30–300\,\mu$m s^{-1}.

Yet another technique for determining ρ is based on capillary pressure measurements.[27,31] Differential mercury intrusion porosimetry measures a pore size distribution, on the assumption that the pore space is composed of a well-connected network of tubes of various diameters. For many

sandstones, the pore size distribution deduced from mercury porosimetry overlays the NMR relaxation time distribution.[32] These comparisons indicate that $\rho_1 = 4\,\mu\text{m s}^{-1}$ and $\rho_2 = 7\,\mu\text{m s}^{-1}$.

The relatively high values of ρ_1 found using the optical microscopy, PFG NMR, and capillary pressure methods reflect the fact that they measure not $(S/V)_{\text{pore}}$ but pore size, from which are calculated *effective* relaxivities. Sandstones can have significant amounts of clay or microporosity, which have large surface areas. BET measurements include this surface area while other methods miss it. Since large pore spaces are the dominant passages for fluid flow, the effective relaxivity ρ_{eff} is the appropriate quantity to use to convert relaxation times to pore sizes for many petrophysical applications.

3 PRACTICAL IMPORTANCE OF NMR MEASUREMENTS

3.1 T_1 versus T_2

Relaxation measurements can provide valuable information about rock formations. Unfortunately, measurements of T_1 and T_2 both have serious problems, though the problems are of very different natures. T_2 of fluids in rocks is dominated by molecular diffusion in random internal magnetic field gradients when the Larmor frequency is 10 MHz and above. This makes 'high-field' T_2 difficult to interpret. In contrast, T_1 is generally controlled by the surface relaxation mechanism, because it is unaffected by diffusion in gradients; thus interpretation of T_1 measurements is usually straightforward. However, determination of the longitudinal decay curve requires a time-consuming series of inversion–recovery measurements. For practical reasons, the time available for NMR measurements in an oil well is very limited (see Section 4.1). A CPMG determination of T_2 is much faster, and is therefore preferred.

Fortuitously, the borehole tools are not able to generate high static magnetic fields, and therefore do not generate large internal magnetic field gradients. Static field gradients are either known apparatus constants or are negligible (see Section 4). Under these conditions, transverse relaxation times are readily interpretable. Therefore, most recent work related to borehole NMR has focused on T_2 at frequencies of 2 MHz and below.

3.2 Porosity

Porosity, defined as the fraction of rock volume that can be occupied by fluid, is one of the most important parameters characterizing a hydrocarbon reservoir. In economically significant reservoirs, porosities generally range from 5% to 30%. There are many ways of measuring porosity in situ.[1,2] The speed of compressional sound waves, the scattering of neutrons, and the scattering of gamma rays are commonly measured for this purpose. However, these techniques require knowledge of the mineralogy of the solid matrix to make a determination of porosity.

NMR has the unique capability of measuring fluid-filled porosity without the need to know anything about the solid matrix. The amplitude of a proton NMR measurement is directly proportional to the amount of hydrogen in the material investigated. Protons are present in both oil and water (in approximately equal concentrations), in water associated with clay minerals, and in some matrix minerals such as gypsum (calcium sulfate hydrate). T_2 is sufficiently short in solid matrix materials, on the order of 10 μs, that the signal from protons in the matrix is lost in the deadtime of the borehole instruments. Protons in clay-bound water relax in a millisecond or less, so these generally are lost in the noise of the first one or two CPMG echoes of the borehole tools. On the other hand, relaxation times of protons in the fluids are usually greater than 10 ms, so these protons contribute significantly to the long echo trains collected by the downhole apparatus.

Pore fluids can be further subdivided into capillary-bound fluid and producible fluid. The partition depends on the pressure difference that drives fluids from the rock formation to the wellbore. This pressure is commonly around 0.7 MPa. It has been found that centrifuging sandstones at a differential pressure of 0.7 MPa depletes them of all water protons with $T_1 > 50$ ms.[23] Thus protons with $T_1 > 50$ ms (or $T_2 > 30$ ms) are associated with large pores containing 'unbound' or 'free' fluid. Although the total porosity measurement is independent of rock type, the 50 ms partition between bound and free fluid is merely typical, and depends on the surface relaxivity (see Section 2.2). Nonetheless, the estimation of producible fluid is a unique and valuable capability of NMR logging tools.

3.3 Permeability to Fluid Flow

Hydraulic permeability is one of the most difficult rock properties to estimate, because it depends sensitively on pore sizes and connectivities, which are themselves hard to measure. In simple models of porous media, the permeability is inversely proportional to the square of the surface-to-volume ratio and therefore directly proportional to the square of the NMR relaxation times, a hypothesis that has been substantiated by a large body of laboratory experiments on water-saturated sandstones.[20,33] The correlation between hydraulic permeability and NMR relaxation time appears to depend on limited variability of the surface relaxivity. Attempts to establish similar correlations for carbonates have been less successful, probably because their microgeometry is much more diverse than that of sandstones.

3.4 Measurement of Oil Content

Oil and water are generally found together in reservoir rocks. Many factors affect the NMR response of oil and water mixed in porous media:

1. the relative amounts of each phase;
2. the wettability of the grain surfaces;
3. the surface relaxivity;
4. the bulk relaxation times of each phase;
5. the extent to which the original formation fluids have been replaced by borehole fluid filtrate.

When magnetic field gradients are present (see Section 4.5), the restricted diffusion coefficients of the phases are also a factor.

The water–oil interface does not assist relaxation, so if a fluid is not in contact with grain surface, it relaxes at its

bulk liquid relaxation rate. The bulk relaxation time of oil depends on its viscosity, while the bulk relaxation time of water depends primarily on the concentration of paramagnetic ions. The proton density of an oil is generally within 10% of that of water, so its contribution to the relaxation time distribution is simply weighted by concentration.

Most reservoir rocks are thought to be hydrophilic. In such cases, droplets of oil sit in the center of pores and are unaffected by the surface. Therefore they relax at their bulk liquid relaxation time, which can be rather long if the oil has a low viscosity. In many cases, the water in contact with the grains will relax considerably faster, and there can be two distinct peaks in the relaxation time spectrum.[23] Then the amount of oil in the rock can be determined quantitatively.

When the oil is very viscous, its bulk relaxation time is shorter than the tool deadtime, and it will not be detected. Then the NMR porosity is just the water-filled porosity.[34] By subtracting the NMR porosity from a porosity measurement that is insensitive to the material properties of the oil, the quantity of oil can be obtained.

Borehole NMR measurements probe the formation to depths of 10 cm or less. In many cases, original formation fluids are flushed away from the rock near the well bore and replaced by borehole fluids ('invasion' by 'mud filtrate'). In these cases, NMR does not give information about the quantity of original oil in place. It can, however, estimate the amount of oil that will be retained in the formation after the usual recovery processes: water floods that, in fact, resemble invasion by mud filtrate, but on a larger scale. This information is useful in planning enhanced oil recovery projects.

4 INSTRUMENTATION FOR WELL LOGGING

4.1 The Borehole Environment and Field Operations

The borehole environment is unusually harsh. Boreholes drilled to extract oil are typically 20 cm in diameter and 1–10 km deep. The geothermal gradient of the Earth can give rise to temperatures of 175 °C or more, and pressures range to 140 MPa. Borehole logging tools must not only survive but must make quantitative measurements under these conditions. The requirements on electronic components exceed military specifications by a wide margin.

Borehole NMR tools must be rugged enough to survive transport in arctic, tropical, desert, and marine environments, and then a 1 m drop onto a steel surface, which typically produces a shock of $500g$. They must survive the abrasion resulting from being dragged over kilometers of rough rock face in the well bore. They must comply with laws regulating transport by aircraft and helicopter, which is of particular significance for NMR equipment containing strong permanent magnets. The conditions and space constraints are in many respects more severe than those encountered in the exploration of outer space or the ocean bottom.

During well logging operations, the drilling rig is idle. Since rig charges can be $10 000 to $100 000 per day, oil companies wish to minimize logging time. This poses a significant constraint on practical logging operations. Typically, data might be required over a depth interval of 300 m or more, with a vertical resolution of 50 cm. To be economically viable, the NMR apparatus must move continuously past the formation at a rate of 300 m h^{-1}. This means that it is necessary to measure signal amplitude and a distribution of relaxation times in 6 s, while the sample and apparatus are in motion relative to each other, at low field, and with an unprecedentedly small coil filling factor.

Skilled NMR specialists are not available for logging operations. The borehole NMR tool must be maintained, set up, and operated by field engineers, who also are responsible for other electromagnetic, acoustic, and nuclear radiation instruments that are being run simultaneously. Thus there is a large premium on instruments that can operate autonomously under conditions of continuously changing environmental conditions, including radical excursions in temperature. The NMR and electromagnetic properties of the materials presented to the apparatus also vary radically, on a timescale of seconds.

Logging tools are generally transported to the wellsite on a truck, which also carries 10 km of 7-conductor armored cable ('wireline') used to lower a string of several tools into the borehole. In present practice, the cable carries nothing but 1 kW of power and 500 kilobits s^{-1} of digital telemetry. The power budget for an individual tool is normally around 100 W, which for an NMR tool must be apportioned among transmitter, receiver, auxiliary sensors, and a downhole computer.

Laboratory NMR apparatus consists of a magnet that provides a strong, steady magnetic field that is as uniform as possible, and a radiofrequency coil that produces an oscillating magnetic field perpendicular to the static field direction. A relatively small, compact sample (which may be a human being) is placed inside the coil. It requires a leap of imagination to see how NMR measurements can be made 'inside-out' on a sample external to the apparatus.

4.2 Early Work

It was recognized at an early date that nuclear magnetic resonance could contribute to the in situ investigation of earth formations. Laboratory NMR studies of fluids in rocks, of clays, and in other porous media started in the 1950s at a number of oil company research laboratories, most notably those of Chevron and Mobil. More than three dozen patent applications for borehole NMR devices were filed between 1950 and 1960, representing work sponsored by Chevron, Schlumberger, Mobil, Texaco, and Varian. Efforts accelerated in the 1960s and 1970s. A chronological bibliography[3] is an excellent guide to the early patents and publications.

4.3 Chevron Tool

The first practical NMR borehole logging device did not use magnets and an rf coil, but instead employed free precession in the Earth's magnetic field. It was invented at the Chevron research laboratory,[35] and was subsequently commercialized by Schlumberger as the Nuclear Magnetism Tool (NMT). The NMT contains a large coil of 1000 turns of wire energized by 1 kW direct current; the power consumption prevents other tools from being used at the same time as the NMT. The current produces a spatially inhomogeneous magnetic field in the formation. The current is left on for several seconds, long enough to polarize the proton spins of the formation fluids. The

magnetization varies in magnitude and direction from point to point in the earth formation, but over a large volume the polarization is substantially greater than that associated with the Earth's field alone.

The coil current is then turned off rapidly, and the spins precess around the Earth's field direction.[36] A signal is coupled into the same coil used to polarize the spins. A bandpass filter selects the signal from hydrogen, which in any event is by far the largest signal of nuclear origin. The proton Larmor frequency in the Earth's magnetic field varies considerably with geographical location: 2.6 kHz in Canada and 1.0 kHz in Argentina. The free induction decay is often controlled by the T_2 of the rock. It can also be affected by small perturbations in the local Earth's field, such as might be caused by grains of magnetic minerals in the formation.

The deadtime of the NMT, controlled by the decay of coil current after the polarizing pulse, is about 25 ms. Most of the signal from clay-bound and capillary-bound fluid has decayed by then, so the amplitude of the remaining signal, extrapolated back to the turn-off time, is directly proportional to the producible fluid porosity ('free fluid index'). The formation response is spatially weighted and decreases rapidly with distance from the coil. Therefore the tool is calibrated in a large tank of water-saturated sand, representing a uniform formation of known porosity.

The borehole is always full of water or oil. In the absence of precautions, the received signal would be dominated by protons in the borehole, which are both closer and more numerous than those in the surrounding rock formation. To solve this problem, the borehole is 'doped' with magnetite (Fe_3O_4) grains. The magnetic grains rapidly relax protons in the wellbore. Since the grains cannot enter the formation, relaxation of protons in the pore fluid is unaffected.

The tool can make neither continuous wave nor pulsed NMR measurements. Neither T_2* not T_2 is measured with this device. T_1 can be measured by varying the polarization time, and measuring the signal amplitude at subsequent field turn-offs.

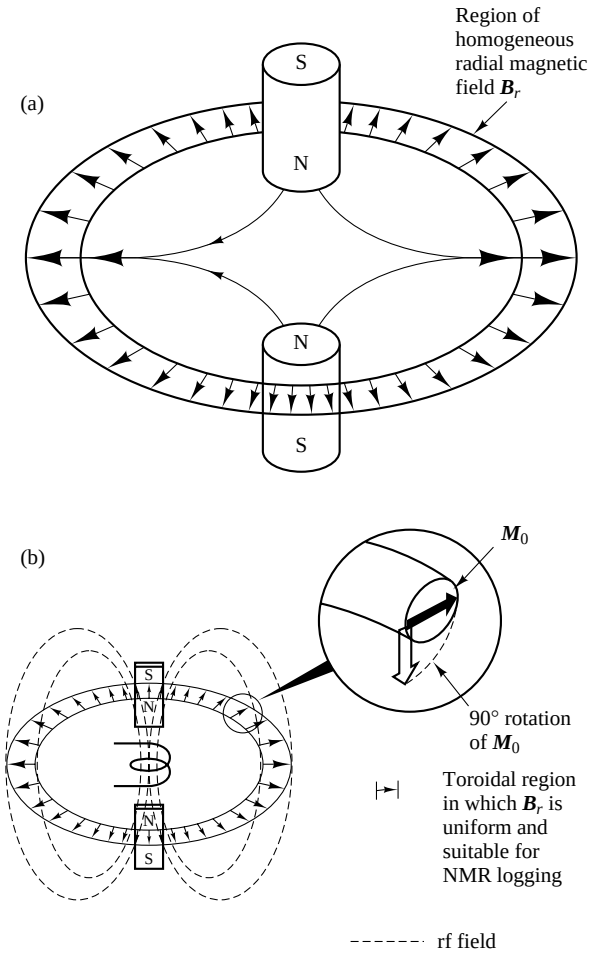

Figure 2 Schematic views of Los Alamos NMR well logging tool. (a) Static field generation. (b) rf field generation. The inset shows a cross section of the toroidal resonance region, where $\boldsymbol{B}_0$ is perpendicular to $\boldsymbol{B}_1$. (Reproduced by permission of Academic Press from J. A. Jackson et al., *J. Magn. Reson.*, 1980, **41**, 411)

4.4 Los Alamos Tool

An 'inside-out NMR' device was designed and built at Los Alamos National Laboratory (LANL);[37] the basic idea is illustrated in Figure 2. The apparatus contains two axially magnetized cylindrical bar magnets. These are placed with like poles facing each other in a cylindrical housing ('sonde'). The radial magnetic field in the transverse symmetry plane is a maximum at a distance from the sonde axis that depends on the radius and spacing of the magnets. A toroidal region of relatively uniform static magnetic field strength is created. A prototype instrument generated a static field of 12 mT in a toroid having a major diameter of 28 cm.

A radiofrequency coil is placed between the magnets, and irradiates the resonance region. In the resonance region, the rf field is perpendicular to the static magnetic field. When driven by 1 kW peak power, the coil generates an oscillating magnetic field of 0.1 mT in the resonance region. The same coil detects the NMR response of the earth formation.

Unlike the field turn-off scheme of the NMT, the LANL tool is capable of performing a variety of pulsed NMR measurements. Both inversion–recovery and Carr–Purcell–Meiboom–Gill measurements are easy to implement. Pulse lengths are comparable to those of laboratory instruments, and the 200 μs deadtime achieved at Los Alamos is adequate for relaxation measurements on rock formations.

Although the Los Alamos design was never commercialized, it attracted considerable interest in the geophysical community, and was an inspiration for a number of other tool design efforts.

4.5 NUMAR Tool

Shtrickman and Taicher invented another NMR borehole logging tool,[38] and a small company (NUMAR) commercialized the technology. A cylindrical ferrite magnet roughly 1 m long is magnetized perpendicular to its long axis. A cross-sectional view is shown in Figure 3. The field outside the magnet is purely dipolar in the transverse plane; thus the magnitude of $\boldsymbol{B}_0$ is independent of azimuth and depends only on radius.

The radiofrequency field $\boldsymbol{B}_1$ is provided by a coil wound longitudinally around the magnet, so that $\boldsymbol{B}_1$ is also transverse to the tool's long axis. Whereas a metallic magnet would

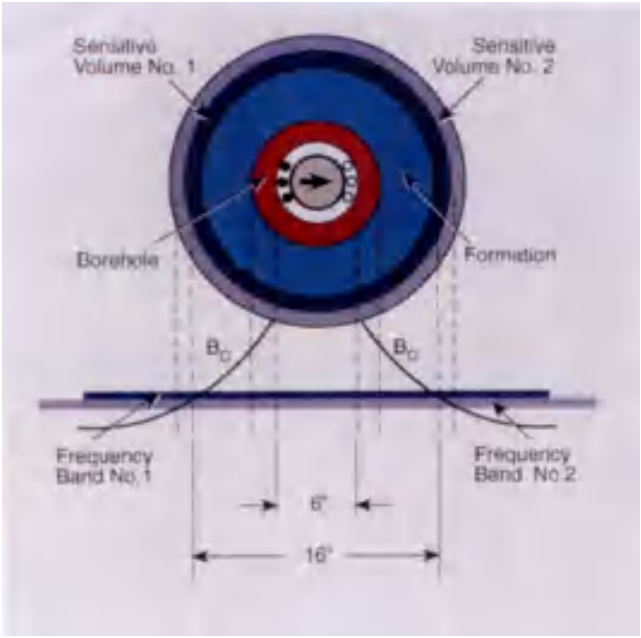

Figure 3 Cross-sectional view of the NUMAR tool. The permanent magnet is magnetized in the direction of the arrow. The tool is centered in the borehole, and the resonance region is a thin cylindrical shell. $\boldsymbol{B}_0$ is perpendicular to $\boldsymbol{B}_1$ everywhere in space. (Courtesy of NUMAR Corp.)

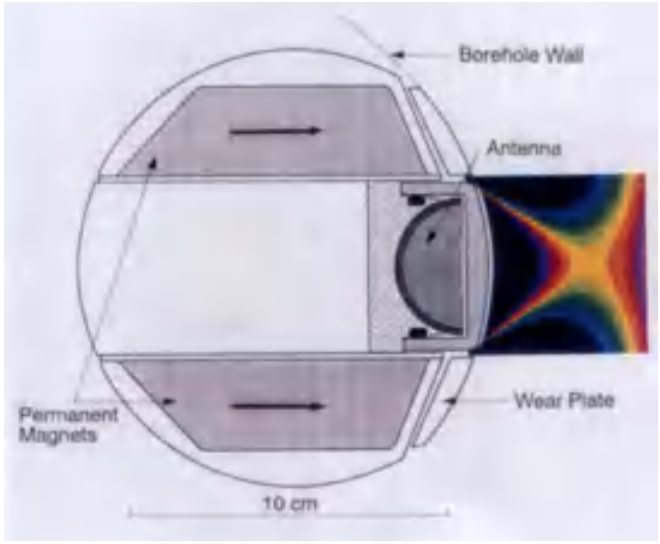

Figure 4 Cross-sectional view of the Schlumberger tool. The permanent magnets are magnetized in the direction of the arrows. The sonde is pressed against the borehole wall, and $\boldsymbol{B}_0$ is directed radially into the formation. A region of relatively homogeneous magnetic field is located inside the formation. Colors code for static field strengths: the resonance region is coded in yellow, stronger fields are coded in greens, weaker fields in reds. The antenna is in a semicircular cavity under a nonmetallic wear plate

exclude the rf field from its interior, the ferrite magnet allows free penetration of the field, improving efficiency in both transmission and reception. The windings are spaced so as to produce a dipolar field, and so, like $\boldsymbol{B}_0$, the magnitude of $\boldsymbol{B}_1$ is independent of azimuth. Because the dipoles are perpendicular to each other, $\boldsymbol{B}_1$ is perpendicular to $\boldsymbol{B}_0$ at every point in space.

The NUMAR tool is unusual in that it does not produce a region of uniform static magnetic field; to be more precise, there is no place outside the magnet where all spatial derivatives of $\boldsymbol{B}_0$ vanish. The coil may be energized at any frequency: selecting a frequency selects a thin cylindrical shell on which the resonance condition is satisfied. The cylindrical resonant shell has thickness because spin tipping is effective where $B_1 > |\boldsymbol{B}_0(r) - \boldsymbol{B}_0(r_0)|$, where $\boldsymbol{B}_0(r)$ is the static magnetic field at radius r, and r_0 is the radius at which the resonance condition is exactly satisfied. Thus, the larger the B_1, the thicker the shell from which signal is obtained. The resonance frequency is selected to be between 0.5 and 1 MHz, with resonant shell radii $r_0 = 0.23$ and 0.18 m, respectively. $\mathrm{d}B_0(r_0)/\mathrm{d}r = 0.25\,\mathrm{T\ m^{-1}}$, and the shell is 2.5 mm thick. Volume selection allows CPMG sequences to be collected continuously without waiting for longitudinal recovery: the tool hops between two or more frequencies, resonating separate shells during successive sequences.

The applied gradient of $0.25\,\mathrm{T\ m^{-1}}$ is considerably larger than typical internal gradients due to magnetic susceptibility contrast between grains and pore fluids of rocks. Diffusion in the magnetic field gradient is an important contribution to transverse relaxation, and must be taken into account explicitly in understanding the measurements. Since the magnetic field gradient is known, an effective diffusion coefficient can be estimated by varying the CPMG pulse spacing. Extrapolating the pulse spacing to zero allows estimation of the part of T_2 that is due to surface relaxation.

4.6 Schlumberger Tool

Schlumberger has developed a novel tool design for NMR logging.[39] Unlike the other tools, the sonde is pressed against the borehole wall; the length of the wall-engaging section is about 40 cm. A cross sectional view of the Schlumberger logging sonde is shown in Figure 4. Two samarium cobalt magnets are magnetized in the same direction, transverse to the sonde axis. The static magnetic field is predominantly radial into the formation. The figure shows a contour plot of the total field strength in the plane transverse to the borehole axis. The field has a saddle point about 25 mm inside the formation; at this location, all three spatial derivatives of $\boldsymbol{B}_0$ are zero. The field strength in the resonant region is 55 mT, so the Larmor frequency is 2.3 MHz.

The antenna used to radiate the formation at the resonance frequency is placed in a semicircular cylindrical cavity on the face of the sonde. The antenna is essentially a half coaxial cable 15 cm long that irradiates the formation with a field transverse to the static field. It is loaded with ferrite and has a high Q, which is desirable for the reception of weak signals from the nuclear spin system. The field produced by the antenna is not particularly homogeneous over the resonance region; inhomogeneity of $\boldsymbol{B}_1$ is acceptable, so long as error-correcting pulse sequences such as the Carr–Purcell–Meiboom–Gill sequence are used. The antenna resides underneath a wear plate, which is the only nonmetallic surface on an otherwise all-metal sonde. Magnetoacoustic ringing of metal structures, which would increase the deadtime of the instrument, is suppressed.

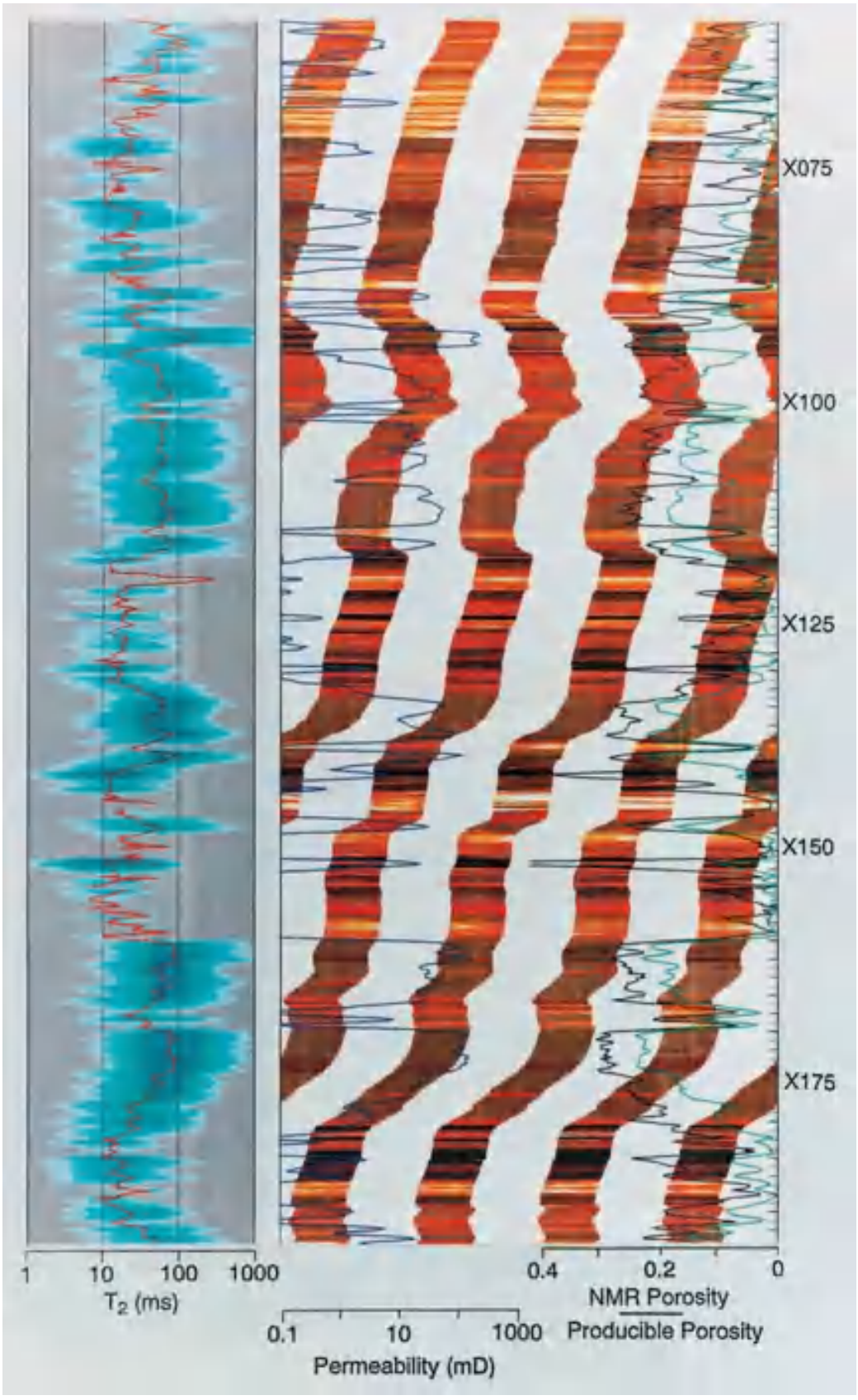

Figure 5 NMR well log. Left panel: A log of the transverse relaxation time distribution is shown in blue, darker color indicating higher amplitude. The red line is the logarithmic mean of T_2. Right panel: The variegated orange and brown background is an unwrapped electrical image of the borehole wall, showing fine statigraphic features. NMR porosity is shown as a black curve, producible fluid porosity is shown as a green curve, and permeability to fluid flow is shown as a blue curve. The curves are explained fully in the text. The depth scale is in feet; the most significant figure has been replaced by X (Reproduced by courtesy of Schlumberger)

4.7 Log Example

A well log consists of the readings of one or more borehole logging tools plotted as a function of depth. Figure 5 is an example of an NMR well log. The vertical scale is depth, marked in feet. The left panel is a presentation of the spectrum of transverse relaxation times; the horizontal scale is T_2 in milliseconds. Higher amplitude is coded as darker color. This is an indicator of pore size distribution: for example, high amplitude at short relaxation times indicates a formation with relatively small pores. The red line is the logarithmic mean of T_2, $T_{2\mathrm{LM}}$:

$$T_{2\mathrm{LM}} = \exp\langle \log T_2 \rangle = \exp\left(\frac{\sum_i m_i \log T_{2i}}{\sum_i m_i} \right) \tag{7}$$

On the right panel is an electrical image of the borehole created by the Formation Microscanner (FMS). The FMS measures the local electrical conductivity using a number of small electrodes placed in contact with the borehole wall by retracting arms. Darker colors indicate high electrical conductivity, usually associated with the presence of saline water or clay. Lighter colors indicate low conductivity, and suggest low porosity or the presence of oil. The resulting electrical image of the borehole is unwrapped: the 0° azimuth is at the left edge of the panel and the 360° azimuth is at the right. The blank stripes represent areas of the borehole wall that are not in contact with the four arms of the tool. The stripes change azimuth slowly because the tool rotates as it is pulled up.

The NMR logs overlay the FMS image. By convention, porosity is plotted on the right-hand side of the panel and increases to the left, while hydraulic permeability is plotted on the left-hand side of the panel and increases to the right. The total NMR porosity is shown in black and the producible fraction of the porosity in green. Zones with small pores have low producible porosity, even when the total porosity is high. The permeability to fluid flow (measured in millidarcies, mD) is computed using the empirical equation

$$k = (2.25 \times 10^6 \text{ mD s}^{-2})\phi^4 T_{2\mathrm{LM}}^2 \tag{8}$$

where ϕ is the porosity. The permeability is plotted on a logarithmic scale, and changes by orders of magnitude from one zone to the next. In this powerful combination of measurements, the FMS gives a high-resolution stratigraphic image of the subsurface, while NMR provides quantitative producibility information.

5 RELATED ARTICLES

Diffusion in Porous Media; Microporous Materials and Xenon-129 NMR; Oil Reservoir Rocks Examined by MRI; Terrestrial Magnetic Field NMR.

6 REFERENCES

1. J. R. Hearst and P. H. Nelson, *Well Logging for Physical Properties*, McGraw-Hill, New York, 1985.
2. D. V. Ellis, *Well Logging for Earth Scientists*, Elsevier, New York, 1987.
3. J. A. Jackson and M. Mathews, *Log Anal.*, 1993, **34**(3), 35.
4. C. Chardaire-Riviere and J.C. Roussel, *Rev. Inst. Fr. Pet.*, 1992, **47**, 503.
5. W. E. Kenyon, *Nucl. Geophys.*, 1992, **6**, 153.
6. *Magn. Reson. Imaging*, 1991, **9**(5), entire issue; *Magn. Reson. Imaging*, 1994, **12**(2), entire issue.
7. F. Bloch, *Phys. Rev.*, 1951, **83**, 1062.
8. R. J. S. Brown and I. Fatt, *Petrol. Trans. AIME*, 1956, **207**, 262.
9. M. H. Cohen and K. S. Mendelson, *J. Appl. Phys.*, 1982, **53**, 1127.
10. K. R. Brownstein and C. E. Tarr, *Phys. Rev. A*, 1979, **19**, 2446.
11. L. L. Latour, R. L. Kleinberg, and A. Sezginer, *J. Colloid Interface Sci.*, 1992, **150**, 535.
12. J. Korringa, D. O. Seevers, and H. C. Torrey, *Phys. Rev.*, 1962, **127**, 1143.
13. F. D'Orazio, S. Bhattacharja, W. P. Halperin, K. Eguchi, and T. Mizusaki, *Phys. Rev. B*, 1990, **42**, 9810.
14. R. L. Kleinberg, W. E. Kenyon, and P. P. Mitra, *J. Magn. Reson., Ser. A*, 1994, **108**, 206.
15. L. L. Latour, P. P. Mitra, R. L. Kleinberg, and C. H. Sotak, *J. Magn. Reson., Ser. A*, 1993, **101**, 342.
16. P. Le Doussal and P. N. Sen, *Phys. Rev. B*, 1992, **46**, 3465.
17. R. J. S. Brown and P. Fantazzini, *Phys. Rev. B*, 1993, **47**, 14 823.
18. E. J. Fordham, A. Sezginer, and L. D. Hall, *J. Magn. Reson., Ser. A*, 1995, **113**, 139.
19. A. Timur, *J. Petrol. Tech.*, 1969, **21**, 775.
20. W. E. Kenyon, P. I. Day, C. Straley, and J. F. Willemsen, *Soc. Petrol. Eng. Form. Eval.*, 1988, **3**, 622; erratum: *Soc. Petrol. Eng. Form. Eval.*, 1989, **4**, 8.
21. W. P. Halperin, F. D'Orazio, S. Bhattacharja, and J. C. Tarczon, in *Molecular Dynamics in Restricted Geometries*, eds. J. Klafter and J. M. Drake, Wiley, New York, 1989, Chap. 11
22. K. R. McCall, D. L. Johnson, and R. A., Guyer, *Phys. Rev. B*, 1991, **44**, 7344.
23. C. Straley, C. E. Morriss, W. E. Kenyon, and J. J. Howard, in *Transactions of the SPWLA 32nd Annual Logging Symposium, 1991*, Paper CC.
24. D. P. Gallegos and D. M. Smith, *J. Colloid Interface Sci.*, 1988, **122**, 143.
25. J. P. Butler, J. A. Reeds, and S. V. Dawson, *SIAM J. Numer. Anal.*, 1981, **18**, 381.
26. A. H. Thompson, *Annu. Rev. Earth Planet. Sci.*, 1991, **19**, 237.
27. S. Lowell and J. E. Shields, *Powder Surface Area and Porosity*, Chapman and Hall, New York, 1984.
28. P. P. Mitra, P. N. Sen, L. M. Schwartz, and P. Le Doussal, *Phys. Rev. Lett.*, 1992, **68**, 3555.
29. M. D. Hurlimann, K. G. Helmer, L. L. Latour, and C. H. Sotak, *J. Magn. Reson. Ser. A*, 1994, **111**, 169.
30. J. J. Howard, W. E. Kenyon, and C. Straley, *Soc. Petrol. Eng. Form. Eval.*, 1993, **8**, 194.
31. J. D. Loren and J. D. Robinson, *Soc. Petrol. Eng. J.*, 1970, **10**, 268.
32. C. E. Morriss, J. MacInnis, R. Freedman, J. Smaardyk, C. Straley, W. E. Kenyon, H. J. Vinegar, and P. N. Tutunjian, in *Transactions of the SPWLA 34th Annual Logging Symposium, 1993*, Paper GGG.
33. G. C. Borgia, G. Brighenti, P. Fantazzini, G. D. Fanti, and E. Mesini, *Soc. Petrol. Eng. Form. Eval.*, 1992, **7**, 206.
34. C. H. Neuman and R. J. S. Brown, *J. Petrol. Tech.*, 1982, **34**, 2853.
35. R. J. S. Brown and B. W. Gamson, *Petrol. Trans. AIME*, 1960, **219**, 199.

36. A. Abragam, *Principles of Nuclear Magnetism*, Clarendon Press, Oxford, 1961, p. 64–65.
37. R. K. Cooper and J. A. Jackson, *J. Magn. Reson.*, 1980, **41**, 400; L. J. Burnett and J. A. Jackson, *J. Magn. Reson.*, 1980, **41**, 406; J. A. Jackson, L. J. Burnett, and J. F. Harmon, *J. Magn. Reson.*, 1980, **41**, 411.
38. Z. Taicher, G. Coates, Y. Gitartz, and L. Berman, *Magn. Reson. Imaging*, 1994, **12**, 285.
39. R. L. Kleinberg, A. Sezginer, D. D. Griffin, and M. Fukuhara, *J. Magn. Reson.*, 1992, **97**, 466.

Biographical Sketch

Robert L. Kleinberg. *b* 1949. B.S., 1971, chemistry, University of California, Berkeley. Ph.D., 1978, physics, University of California, San Diego. Postdoctoral physicist, Exxon Research, 1978–80. Schlumberger-Doll Research, 1980–present. Approx. 50 publications, 10 US patents. Research specialties: borehole instrumentation (ultrasonics, electrical resistivity, nuclear magnetic resonance, gravimetry) and NMR properties of rocks and other porous media.

Ferroelectrics and Proton Glasses

Robert Blinc

University of Ljubljana, Ljubljana, Slovenia

1	Introduction	1
2	Inhomogeneous Ferroelectrics and Proton Glasses	1
3	NMR in Homogeneous Ferroelectrics and Antiferroelectrics in the Fast Motion Regime	3
4	NMR in the Slow and Intermediate Motion Regime	8
5	NMR in Proton and Deuteron Glasses	9
6	NMR Determination of Order Parameters in Inhomogeneous Ferroelectrics	12
7	Related Articles	13
8	References	13

1 INTRODUCTION

Conventional methods of crystal structure determination such as X-ray and neutron scattering yield the unit cell structure averaged over space and time. While the knowledge of such a space and time averaged structure is sufficient in most systems this is not the case in inhomogeneous- or order–disorder-type ferroelectrics and proton glasses where local deviations from the averaged structure determine the specific properties of these systems. 1D and 2D NMR of nuclei with a nonzero quadrupole coupling or chemical shift tensor interaction as well as NQR provide here a unique tool for the determination of the local atomic structure and dynamics which is unobtainable by other techniques.

In the fast motion regime, $\omega\tau \ll 1$, the nucleus at site i 'sees' the time averaged value of the quadrupole coupling or chemical shift tensor interaction so that[1]

$$\omega_i = \omega_0 + \omega_1\langle\eta_i\rangle;\ \langle\eta_i\rangle \neq 0 \quad T < T_c \tag{1a}$$

whereas

$$\omega_i = \omega_0;\ \langle\eta_i\rangle = 0 \quad T > T_c \tag{1b}$$

Here $\langle\eta_i\rangle$ is the time averaged value of the long-range order parameter at site i. It is $\langle\eta_i\rangle$ which is zero above T_c and non-zero below T_c.

Close to the phase transition temperature T_c, the spin-lattice relaxation rate will be determined by the order parameter fluctuations[1]

$$T_1^{-1} \propto \sum_{\boldsymbol{q}} \int_{-\infty}^{\infty} \langle\delta\eta(\boldsymbol{q}, 0)\delta\eta(\boldsymbol{q}, t)e^{i\omega t}\, dt \tag{2a}$$

where $\delta\eta(\boldsymbol{q}, t) = \eta(\boldsymbol{q}, t) - \langle\eta(\boldsymbol{q}, t)\rangle$ and $\langle \ldots \rangle$ denotes the ensemble average.

Applying the fluctuation dissipation theorem, equation (3) can be rewritten as[1]

$$T_1^{-1} \propto \sum_{\boldsymbol{q}} \frac{\chi(\boldsymbol{q}, 0)\tau(\boldsymbol{q})}{1 + \omega^2\tau(\boldsymbol{q})^2} \tag{2b}$$

where $\chi(\boldsymbol{q}, 0)$ is the wave vector dependent static susceptibility of the order parameter and $\tau(\boldsymbol{q})$ is the corresponding wave vector dependent correlation time.[1] For the Ising model one finds

$$\chi(\boldsymbol{q}) = \frac{\chi(\boldsymbol{q} = 0, 0)}{1 + \boldsymbol{q}^2\xi^2} \tag{3a}$$

and

$$\tau(\boldsymbol{q}) = \frac{\tau(\boldsymbol{q} = 0)}{1 + \boldsymbol{q}^2\xi^2} \tag{3b}$$

where

$$\tau(\boldsymbol{q} = 0) \propto \chi(\boldsymbol{q} = 0) \propto \frac{C}{T - T_c}; \quad T > T_c \tag{3c}$$

and ξ is the correlation length, which diverges at T_c. In the limit $\omega\tau \ll 1$ T_1^{-1} thus exhibits a critical behavior near T_c, while for $\omega\tau \gg 1$ T_1^{-1} should stay nearly constant. Another point to be stressed is that in the slow motion regime the nucleus 'sees' the instantaneous value of the order parameter and not the time averaged value.

2 INHOMOGENEOUS FERROELECTRICS AND PROTON GLASSES

Ferroelectric and antiferroelectric phase transitions[1] are characterized by:

1. the breaking of a discrete symmetry group at the paraelectric to ferroelectric or antiferroelectric transition;
2. the appearance of a long-range order parameter below T_c—the spontaneous polarization P in ferroelectrics or the sublattice polarization $P_a = -P_b$ in antiferroelectrics;
3. the critical slowing down of the order parameter dynamics $\tau(\boldsymbol{q}_{crit}) \to \infty$ as $T \to T_c$ from above or below.

The breaking of the symmetry of the high temperature paraelectric phase is the result of the condensation of a polar soft phonon or a—usually overdamped—soft pseudospin wave mode, the frequency of which increases with decreasing temperature in the high-temperature phase and vanishes at T_c. The frozen out eigenvector of the soft mode represents the order parameter of the transition. In ferroelectrics the condensation of the soft mode occurs at the Brillouin zone center, whereas it occurs in antiferroelectrics at the Brillouin zone boundary.

The free energy of a ferroelectric with a one-component order parameter has a single minimum at $P = 0$ at $T > T_c$ and two minima at $+P$ and $-P$ below T_c corresponding to oppositely polarized domains [Figure 1(a)].

Solid solutions of ferroelectric (FE) and antiferroelectric (AFE) crystals form in the intermediate concentration range $x_{FE} \leq x \leq x_{AFE}$ (Figure 2) a pseudospin-like dipolar glassy phase where no macroscopic symmetry breaking takes place

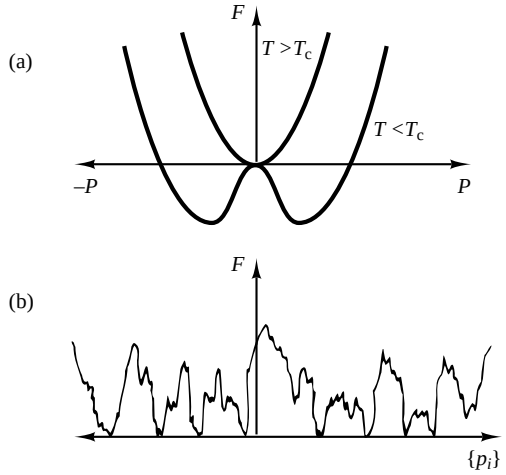

Figure 1 Free energy surface in (a) a homogeneous ferroelectric and (b) a deuteron pseudospin glass

at any temperature and no long range order parameter appears. Instead we have a random local freeze-out of the dipoles and possibly an ergodic–nonergodic transition. The existence of the glassy phase is due to randomly competing ferroelectric and antiferroelectric interactions and the resulting random frustration of the system. The free energy surface of such a system is rough and fractal-like and exhibits a large number of nearly degenerate minima separated by high potential barriers[2] [Figure 1(b)]

In the concentration range $0 \leq x \leq x_{\mathrm{FE}}$ and $x_{\mathrm{AFE}} \leq x \leq 1$ (Figure 2) we have an inhomogeneous ferroelectric and antiferroelectric phase, respectively, where long range order and glassy order coexist at $T \neq 0$.

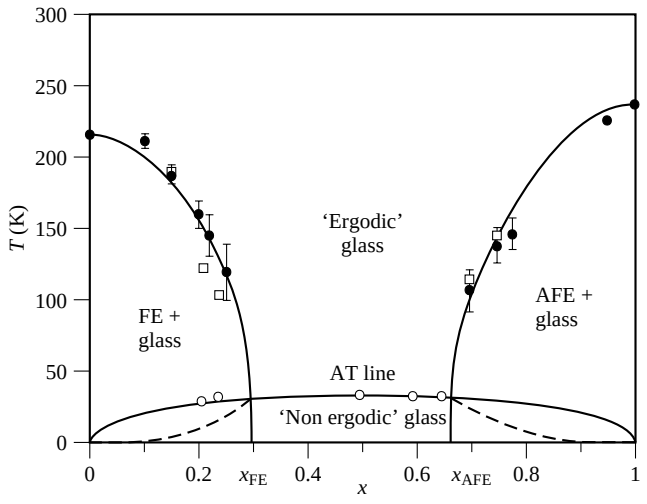

Figure 2 Phase diagram[5] of the ferroelectric solid solution $Rb_{1-x}(ND_4)_xD_2PO_4$ which forms a deuteron glass in the intermediate concentration range $x_{\mathrm{FE}} \leq x \leq x_{\mathrm{AFE}}$. Also shown are the inhomogeneous ferroelectric and inhomogeneous antiferroelectric regions for $0 \leq x \leq x_{\mathrm{FE}}$ and $x_{\mathrm{AFE}} \leq x \leq 1$. The solid lines are calculated from the random bond–random field pseudospin Ising model. Also shown is the Almeida–Thouless (AT) line separating the ergodic from the nonergodic glassy phase

The local dipolar structure of the above phases can be characterized by a local polarization distribution function,[3]

$$W(p) = \frac{1}{N}\sum_i \delta(p - \langle S^z\rangle_i) \tag{4}$$

where the pseudospin $S_i^z = \pm 1$ describes the two orientational states of the dipole at site i, and the brackets $\langle \ldots \rangle$ stand for the thermal average. In a homogeneous ferroelectric the first moment of $W(p)$,

$$P = \int W(p)p\,\mathrm{d}p \neq 0 \quad T < T_{\mathrm{c}} \tag{5a}$$

$$P = 0 \quad T > T_{\mathrm{c}} \tag{5b}$$

is the spontaneous polarization

$$P = \frac{1}{N}\sum_i \langle S_i^z\rangle \tag{5c}$$

which is different from zero for $T < T_{\mathrm{c}}$ and zero for $T > T_{\mathrm{c}}$.

In a homogeneous ferroelectric

$$W(p) = \delta(p - P) \tag{5d}$$

and the second moment of $W(p)$ is zero,

$$\tilde{q} = q - P^2 = \int W(p)p^2\,\mathrm{d}p - P^2 = 0 \tag{5e}$$

In a proton or deuteron dipolar glass the first moment of $W(p)$ is zero as there is no long range order,

$$P = \int W(p)p\,\mathrm{d}p = 0 \tag{6a}$$

but the second moment of $W(p)$ is different from zero,

$$q = \int W(p)p^2\,\mathrm{d}p \neq 0 \tag{6b}$$

Here, q is just the well known Edwards–Anderson glass order parameter which is also defined[2] as

$$q = \lim_{t\to\infty}\lim_{N\to\infty}\frac{1}{N}\sum_i \langle S_i^z(0)S_i^z(t)\rangle \tag{6c}$$

If there are no random fields present, we have a paraelectric–glass transition[3] at T_{g}:

$$q = 0 \quad T > T_{\mathrm{g}} \tag{7a}$$

$$q \neq 0 \quad T < T_{\mathrm{g}} \tag{7b}$$

In the presence of a random field, which is conjugate to this glass order parameter, $q \neq 0$ at all temperatures.[3,4] We have, however, at lower temperatures an ergodic–nonergodic transition below the Almeida–Thouless line in the random field variance–temperature plane where the pseudospin glass susceptibility, as well as the longest glass relaxation time,

diverge.[2,5] Here the replica symmetry of the 'ergodic' glassy phase is broken[2] and instead of a single order parameter q we have an infinite number of order parameters represented by the order parameter function[2] $q(x)$.

In an inhomogeneous ferroelectric, on the other hand, both

$$P \neq 0 \tag{8a}$$

and

$$\tilde{q} = q - P^2 \neq 0 \tag{8b}$$

The local polarization distribution function $W(p)$ is reflected in the inhomogeneous NMR frequency spectrum $f(\omega)$ via

$$f(\omega)\,\mathrm{d}\omega = W(p)\,\mathrm{d}p \tag{9}$$

A knowledge of the inhomogeneous NMR frequency spectrum $f(\omega)$, obtainable by 2D 'separation of interactions' NMR, and the relationship $\omega = \omega(p)$ thus enables one to determine $W(p)$ and all its moments. This is of crucial importance in glasses and inhomogeneous ferroelectrics and antiferroelectrics.

3 NMR IN HOMOGENEOUS FERROELECTRICS AND ANTIFERROELECTRICS IN THE FAST MOTION REGIME

3.1 Deuteron NMR and Relaxation

In hydrogen-bonded ferroelectrics and antiferroelectrics the O–H···O bonds are of the double-well type (Figure 3) and are the main reversible dipoles in the structure. The two positions of the proton ($I = \frac{1}{2}$) or respectively deuteron ($I = 1$) in this limit can be represented by a pseudospin $S^z = \pm 1$. The quadrupole perturbed NMR frequency of the deuteron ω_i changes when the deuteron is transferred from the 'left' to the 'right' position, O–H···O ↔ O···H–O, in the double-well potential:

$$\omega_i = \omega_0 + \omega_1 S_i^z(t) \tag{10a}$$

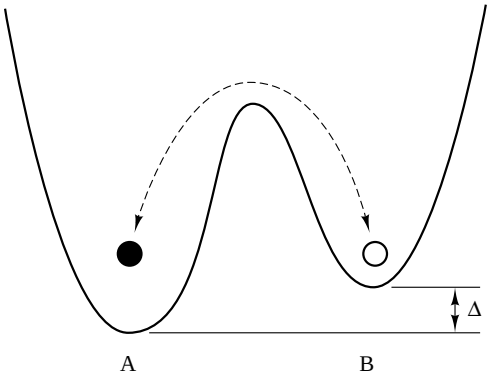

Figure 3 Double-well O–H···O hydrogen bond potential in hydrogen-bonded ferroelectrics. The two positions of the proton or deuteron in this potential can be described by a pseudospin $S^z = \pm 1$

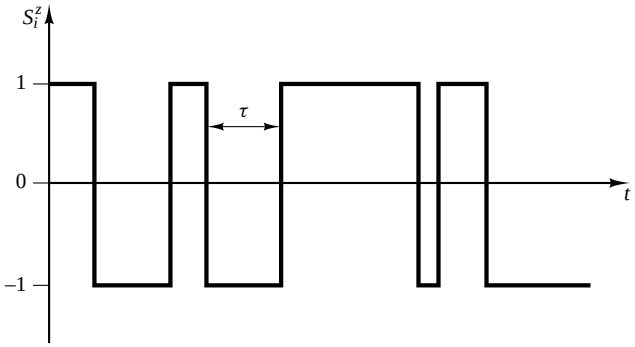

Figure 4 Time dependence of the pseudospin variable $S^z(t)$ reflecting the deuteron motion between the two equilibrium sites in the O–H···O bond

In the 'fast motion' limit, where $\tau \ll \tau_{\mathrm{NMR}} = 1/2\omega_1$ (Figure 4) the nucleus 'sees' just the time averaged value of $S_i^z(t)$ so that equation (10a) becomes

$$\omega_i = \omega_0 + \omega_1 p_i \tag{10b}$$

where $p_i = \langle S_i^z(t) \rangle$ is the local polarization. In a homogeneous ferroelectric, where equation (5d) holds, $p_i = p_j = p = P$, so that ^{2}H NMR provides a method for a microscopic measurement of the long range order parameter P as well as yielding direct information about the deuteron order–disorder transition at T_c in KD_2PO_4-type crystals.[1] As it can be seen from Figure 5, $\langle S^z(t) \rangle = 0$ above T_c and $\langle S^z(t) \rangle \neq 0$ below T_c. The deuterons are dynamically disordered between the two equilibrium sites above T_c and order into one of the two positions below T_c.[6] The T dependence of $p = P$ is equal to the one determined by macroscopic polarization measurements.

The fluctuating part of the local polarization $p_i = p + \delta p_i(t)$ and the related part of the quadrupole coupling Hamiltonian $\hat{\mathcal{H}}_{\mathrm{Q}}^{(1)}(t)$,

$$\hat{\mathcal{H}}_{\mathrm{Q}}(t) = \langle \hat{\mathcal{H}}_{\mathrm{Q}} \rangle + \hat{\mathcal{H}}_{\mathrm{Q}}^{(1)}(t) \tag{11a}$$

produces, in agreement with equations (2) and (3), a characteristic dip in T_1 at T_c (Figure 6). The form of the T_1^{-1} anomaly

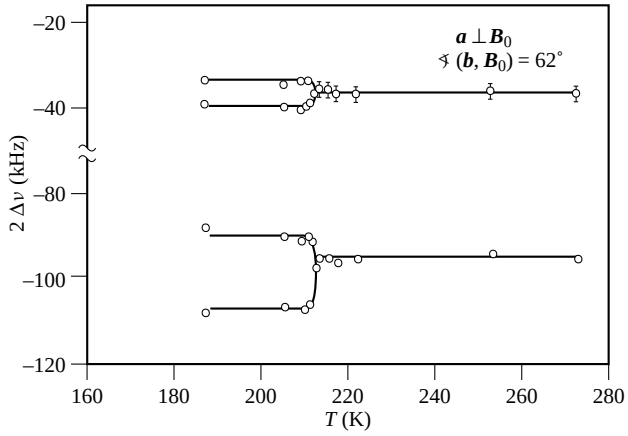

Figure 5 Temperature dependence of the quadrupole splitting of the deuteron NMR lines in CsD_2AsO_4

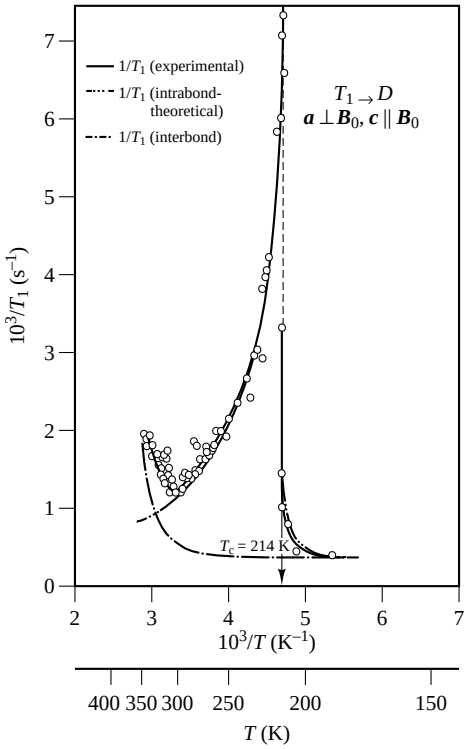

Figure 6 Temperature dependence of the deuteron spin–lattice relaxation rate in KD_2PO_4 at $\boldsymbol{B}_0$ = 1.65 T

is the one expected[1] for the condensation of an overdamped soft pseudospin wave mode:

$$T_1^{-1} \propto \ln \frac{T - T_c}{T_c} + \text{constant} \quad T > T_c \tag{11b}$$

$$T_1^{-1} \propto 1 - p^2 \quad T < T_c \tag{11c}$$

From the above data the noninteracting deuteron correlation time, i.e. the time the deuteron stays at a given site before it jumps to the other site in the O–D$\cdots$O potential, is determined as $\tau_0 = 2.7 \times 10^{-13}$ s at room temperature. This justifies the fast motion approximation. Similar results were obtained in other hydrogen bonded ferroelectrics.[1,7]

3.2 Oxygen-17–Proton Nuclear Quadrupole Double Resonance

In view of the 'geometrical' isotope effect[8] and the resulting expansion and changes in the shape of the hydrogen bond potential on deuteration one cannot simply transfer the conclusions obtained for deuterated crystals to the undeuterated ones. Since the distance between the two equilibrium sites of the hydrogen in short O–H$\cdots$O bonds ($R_{O-O} \leq 2.49$ Å) may be 0.35 Å or less, it is difficult to determine by neutron diffraction whether the proton is located in the center of the hydrogen bond or dynamically disordered between two separate, off-center equilibrium sites. For $T > T_c$ a single peaked proton density distribution in the center of the hydrogen bond is usually observed by neutron scattering. Below T_c the diffraction data show an off-center position of the proton.

The answer is provided by ^{17}O–^{1}H quadrupole double resonance spectroscopy and the direct determination of the ^{17}O–^{1}H distance from the magnetic dipole–dipole fine structure of the ^{17}O NQR lines.[9]

As an example let us consider[7] RbH_2PO_4, which is isomorphous with KH_2PO_4 and has all O–H$\cdots$O bonds equivalent. In this system the PO_4 groups are linked by O–H$\cdots$O bonds. In view of the low natural abundance of ^{17}O (0.037%) there is at most one ^{17}O nucleus ($I = \frac{5}{2}$) per O–H$\cdots$O bond.

The energies of the three doubly degenerate ($|\pm\frac{1}{2}\rangle, |\pm\frac{3}{2}\rangle, |\pm\frac{5}{2}\rangle$) ^{17}O quadrupole energy levels $E = x\,A$, $A = e^2qQ/4I(2I-1)$, $eq = V_{zz}$ can be obtained from

$$x^3 - 7(3+\eta^2)x - 20(1-\eta^2) = 0 \tag{12}$$

where $\eta = (V_{xx} - V_{zz})/V_{zz}$ is the asymmetry parameter of the EFG tensor and where $V_{zz} \geq V_{yy} \geq V_{xx}$. For small η we have

$$\nu_{1/2\rightarrow 3/2} = \frac{3e^2qQ}{20h}\left(1 + \frac{59}{54}\eta^2\right) \tag{13a}$$

$$\nu_{1/2\rightarrow 5/2} = \frac{3e^2qQ}{10h}\left(1 - \frac{11}{54}\eta^2\right) \tag{13b}$$

and $\nu_{1/2\rightarrow 5/2} = \nu_{1/2\rightarrow 3/2} + \nu_{3/2\rightarrow 5/2}$.

If the proton is centrally located we expect just one set of ^{17}O NQR lines ($\nu_{1/2\rightarrow 3/2}$, $\nu_{3/2\rightarrow 5/2}$, $\nu_{1/2\rightarrow 5/2}$) per ^{17}O–H$\cdots$O bond. If the proton is located in an 'off-center' site we expect, in view of the random occurrence of the ^{17}O isotope, two sets of ^{17}O NQR lines per O–H$\cdots$O bond. One of them would correspond to the proton in the 'close' position, i.e. ^{17}O–H$\cdots$O, and the other to the proton in the 'far' position, i.e. ^{17}O$\cdots$H–O. If the protons are dynamically disordered between the two 'off'-center sites, the observed ^{17}O EFG tensor should be an average of the tensors for the two separate 'off'-center sites, the 'far' and the 'close' one. It should be noted that the ^{17}O quadrupole coupling constant increases with decreasing O–H bond distance,[8] thus allowing for a discrimination between 'close' and 'far' sites.

The ^{17}O nuclear quadrupole double resonance results for RbH_2PO_4 are shown in Figure 7. Above T_c only three ^{17}O lines ($\nu_{1/2\rightarrow 3/2}$, $\nu_{3/2\rightarrow 5/2}$, $\nu_{1/2\rightarrow 5/2}$) are observed, demonstrating that all PO_4 oxygen sites are equivalent on the NQR timescale. Below T_c each line splits symmetrically into two components, demonstrating that we are dealing with dynamic disorder between two equivalent sites above T_c. The average value of the two components is constant while the difference is proportional to the order parameter p and measures the time averaged asymmetry in the hydrogen bond potential below T_c. We thus have

$$\begin{aligned}\langle \boldsymbol{\nu}\,(^{17}\text{O-H})\rangle &= \langle \boldsymbol{\nu}\,(^{17}\text{O}\cdots\text{H})\rangle \\ &= \tfrac{1}{2}[\boldsymbol{\nu}\,(^{17}\text{O-H}) \\ &\quad + \boldsymbol{\nu}\,(^{17}\text{O}\cdots\text{H})] \quad T > T_c\end{aligned} \tag{14a}$$

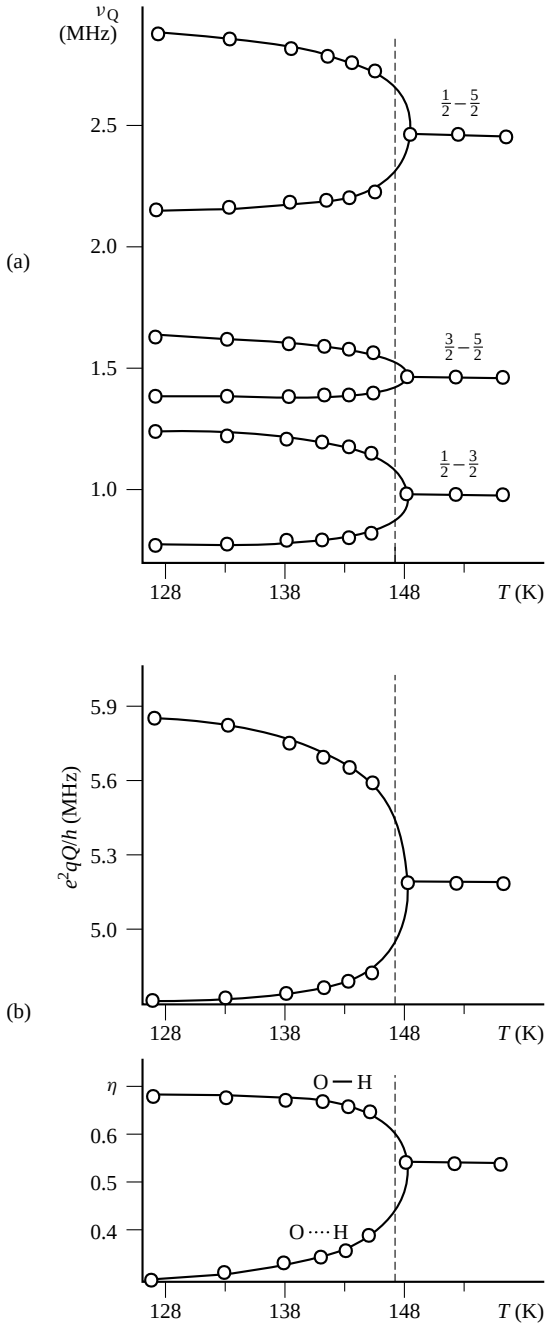

Figure 7 Temperature dependence of (a) the ^{17}O NQR transition frequencies in RbH_2PO_4 and (b) the quadrupole coupling constant and asymmetry parameter

and

$$\langle \boldsymbol{\nu}\,(^{17}\text{O-H})\rangle = \frac{1+p}{2}\boldsymbol{\nu}\,(^{17}\text{O-H}) + \frac{1-p}{2}\boldsymbol{\nu}\,(^{17}\text{O}\cdots\text{H}) \quad T < T_c \quad (14b)$$

$$\langle \boldsymbol{\nu}\,(^{17}\text{O}\cdot\text{H})\rangle = \frac{1-p}{2}\boldsymbol{\nu}\,(^{17}\text{O-H}) + \frac{1+p}{2}\boldsymbol{\nu}\,(^{17}\text{O}\cdots\text{H}) \quad T < T_c \quad (14c)$$

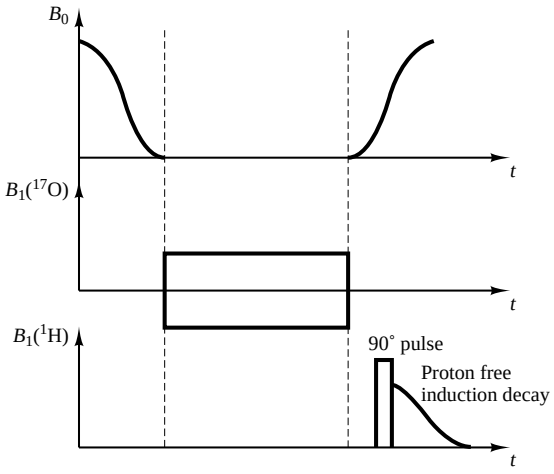

Figure 8 Field sequence for the ^{17}O–H double resonance in the laboratory frame experiment

The difference

$$\langle \boldsymbol{\nu}\,(^{17}\text{O-H})\rangle - \langle \boldsymbol{\nu}\,(^{17}\text{O..H})\rangle = p[\boldsymbol{\nu}\,(^{17}\text{O-H}) \times -\boldsymbol{\nu}\,(^{17}\text{O}\cdots\text{H})] \quad (14d)$$

is here indeed proportional to p and allows for a measurement of the local asymmetry of the hydrogen bond potential in frequency units.

The corresponding measuring sequence for the ^{17}O–^{1}H double resonance experiment in the laboratory frame is schematically shown in Figure 8.

An independent confirmation of the above results is provided by the proton magnetic dipolar fine structure of the ^{17}O lines obtained with a double frequency irradiation technique.[9] For $\eta = 0$, $E_{\pm 5/2}$ and $E_{\pm 3/2}$ split up into two doubly degenerate energy levels,

$$E_{\pm 5/2} = \frac{e^2qQ}{4} \pm \tfrac{5}{2}K\sqrt{1+3\cos^2\theta} \quad (15a)$$

$$E_{\pm 3/2} = -\frac{e^2qQ}{20} \pm \tfrac{3}{2}K\sqrt{1+3\cos^2\theta} \quad (15b)$$

whereas $E_{\pm 1/2}$ splits into four levels,

$$E_{\pm 1/2} = -\frac{e^2qQ}{5} + \frac{K}{2}[3 \pm \sqrt{37-12\cos 2\theta}] \quad (15c)$$

$$E_{\pm 1/2} = -\frac{e^2qQ}{5} + \frac{K}{2}[-3 \pm \sqrt{13-12\cos 2\theta}] \quad (15d)$$

Here $K/\hbar = 8.16\,\text{kHz}/R_{0-H}^3$ (angstroms), $\hbar$ is Planck's constant, and θ is the angle between the largest principal axis of the axially symmetric ($\eta = 0$) ^{17}O EFG tensor and the ^{17}O–H bond direction.

The effective dipolar splitting of the ^{17}O NQR lines is determined by

$$\langle R^{-3}\rangle = \frac{1+p}{2}R_{\text{O-H}}^{-3} + \frac{1-p}{2}R_{\text{O}\cdots\text{H}}^{-3} \quad T < T_c \quad (16a)$$

where p can be determined from the temperature dependence of the ^{17}O lines. The ^{17}O–H distance for the 'close' proton

site is here obtained as $R_{O-H} = 1.06 \pm 0.01$ Å at $T = 138$ K, i.e. well below T_c. The result agrees with the one obtained by neutron scattering.

Above T_c the proton spends an equal amount of time at the 'close' ($R_{O-H} = 1.06$ Å) and 'far' ($R_{O\cdots H} = 1.45$ Å) equilibrium site so that the dipolar splitting is characterized by an 'apparent' $^{17}O-H$ distance

$$\langle R^{-3} \rangle = \tfrac{1}{2}[R_{O-H}^{-3} + R_{O\cdots H}^{-3}] \quad T > T_c \tag{16b}$$

yielding $R = 1.18$ Å. If, on the other hand, the proton is above T_c, situated in the center of the O–H–O bond, the effective O–H distance obtained from the dipolar fine structure would be

$$R_{\text{symm}}(\text{O-H}) = 1.225\text{Å} \quad T > T_c \tag{16c}$$

which would contradict the experimental data. The ^{17}O quadrupole coupling as well as the $^{17}O-H$ magnetic dipolar fine structure thus provide direct evidence for the proton intra-$^{17}O-H\cdots O \leftrightarrow {}^{17}O\cdots H-O$ motion between the two sites and the dynamic order–disorder nature of the phase transition in RbH_2PO_4.

Similar results were obtained for KH_2PO_4, CsH_2PO_4, TlH_2PO_4, $PbHPO_4$, as well as squaric acid ($C_4H_2O_2$) and $KH_3(SeO_3)_2$.[7,10] In partially deuterated $RbH_{2x}D_{2(1-x)}PO_4$ the results show that the O–H$\cdots$O bonds are practically identical to the ones in pure RbH_2PO_4 whereas the O–D$\cdots$O bonds expand and show a nearly 25% higher spontaneous asymmetry below T_c than the O–H$\cdots$O bonds.[7]

3.3 Proton Chemical Shift Tensors

For protons ($I = \frac{1}{2}$) in solids, the chemical shift term $\hat{\mathcal{H}}_\sigma$ in the spin Hamiltonian

$$\hat{\mathcal{H}} = \hat{\mathcal{H}}_Z + \hat{\mathcal{H}}_D + \hat{\mathcal{H}}_\sigma \tag{17a}$$

$$\hat{\mathcal{H}}_\sigma = \gamma \sum_i \hat{\boldsymbol{I}}_i \cdot \boldsymbol{\sigma}_i \cdot \boldsymbol{B}_0 \tag{17b}$$

is usually much smaller than the dipolar term so that proton chemical shifts are lost in the dipolar width of the NMR line. Using high-resolution NMR-in-solids techniques like the WAHUHA sequence,[11]

$$(\tau, P_x, 2\tau, P_{-x}, \tau, P_y, 2\tau, P_{-y})$$

the homonuclear dipolar broadening can be eliminated while the chemical shifts are reduced by $\sqrt{3}$. This allows for a determination of the proton chemical shift tensors $\boldsymbol{\sigma}$ from the angular dependence of the spectra. Such measurements were performed in KH_2PO_4 and other hydrogen bonded systems.[12] The information obtained is in principle similar to that obtained from the deuteron quadrupole coupling data but the experiments are more tedious and the resolution is lower.

3.4 Phosphorus-31 Chemical Shift Tensors

Whereas ^{17}O NQR and deuteron quadrupole perturbed NMR measure the single-particle intra-hydrogen bond dynamics, the ^{31}P chemical shift tensor $\boldsymbol{\sigma}$ interaction in KH_2PO_4-type crystals measures the local arrangement of the four O–H$\cdots$O bonded protons in the hydrogen bonds linking a given PO_4 group to its neighbors. The chemical shift term is

$$\hat{\mathcal{H}}_\sigma = \gamma \sum_i \hat{\boldsymbol{I}}_i \cdot \boldsymbol{\sigma}_i \cdot \boldsymbol{B}_0 \tag{18a}$$

where

$$\boldsymbol{\sigma} = \boldsymbol{\sigma}(p_1, p_2, p_3, p_4) \tag{18b}$$

The temperature dependence of the ^{31}P chemical shift on going through T_c in KD_2PO_4 is shown[7,10] in Figure 9(a). There are four ^{31}P nuclei per unit cell of KH_2PO_4 both above and below T_c. The edges of two PO_4 tetrahedra are rotated by $+13^\circ$ with respect to the orthorhombic a, b axes (A sites) whereas the other two are rotated by -13° (B sites). Above T_c all ^{31}P sites in the unit cell are chemically and physically equivalent due to dynamic proton disorder in the O–H$\cdots$O bonds. The ^{31}P chemical shift tensor is axially symmetric around the fourfold c axis which passes through

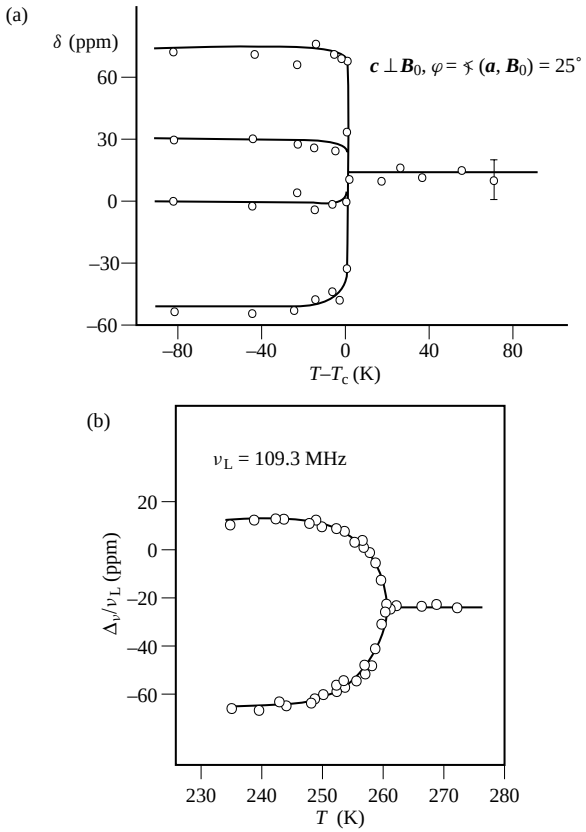

Figure 9 (a) Temperature dependence of the ^{31}P chemical shift on cooling through T_c in KD_2PO_4. (b) Splitting of the ^{31}P NMR line[11] in pseudo-1D CsD_2PO_4 where the O–H(1)$\cdots$O bonds are ordered above and below T_c whereas the O–H(2)$\cdots$O bonds are disordered above T_c and ordered below T_c and where $\sigma_{T>Tc} = \frac{1}{2}(\sigma_1+\sigma_2)_{T<Tc}$

the phosphorus sites. Below T_c there are four physically nonequivalent ^{31}P sites, which are all chemically equivalent and which reflect the ordering of the four protons into two 'close' and two 'far' sites in the O–H···O bonds: $\boldsymbol{\sigma}_1 = \boldsymbol{\sigma}_A(+\boldsymbol{P})$, $\sigma_2 = \sigma_A(-\boldsymbol{P})$, $\sigma_3 = \sigma_B(+\boldsymbol{P})$, $\sigma_4 = \sigma_B(-\boldsymbol{P})$. The paraelectric σ tensor is the average of the four ferroelectric ones.[7,10] This confirms that the phase transition in KH_2PO_4 is a protonic order–disorder one and is not driven by electronic instabilities.

The largest principal axes of the ^{31}P chemical shift tensor is nearly exactly parallel to the line connecting the two PO_4 oxygens to which the protons are directly attached. A change in the H_2PO_4 proton 'arrangement' from the 'top' to the 'bottom' oxygens, as viewed along the c axis, results in a polarization reversal ($\boldsymbol{P} \rightarrow -\boldsymbol{P}$) and in a rotation of the two largest principal axes of the ^{31}P $\boldsymbol{\sigma}$ tensor by 90°. The ^{31}P $\boldsymbol{\sigma}$ tensor is thus a very sensitive indicator of the arrangement of the four protons around a given PO_4 group in KH_2PO_4 crystals.

Similar results were also obtained in pseudo-1D CsD_2PO_4[13] [Figure 9(b)] and $PbHPO_4$[14] using high-resolution NMR-in-solids techniques.

3.5 Arsenic-75 Quadrupolar Coupling

Information similar to that from the ^{31}P chemical shift tensor can be obtained from the ^{75}As quadrupole coupling tensor in KH_2AsO_4-type arsenates.

Here, however, the resolution of the experiment is much larger as the ^{75}As NQR frequency changes[10] from ≈3.5 MHz at $T > T_c$ to ≈35 MHz at $T < T_c$ (Figure 10). The ^{75}As EFG tensor as well depends on the arrangement of the four protons around a given AsO_4 group:

$$\boldsymbol{V} = \boldsymbol{V}(p_1, p_2, p_3, p_4) \tag{19}$$

The direction of the largest principal axis (V_{zz}) of this tensor is parallel to the line connecting the two oxygens in the AsO_4 group to which the two protons are directly attached, whereas the smallest principal axis (V_{xx}) is parallel to the direction of the electric dipole moment of the H_2AsO_4 group.

The ^{75}As EFG tensors determined[1,7,10,15] in ferroelectric KH_2AsO_4 and antiferroelectric $NH_4H_2AsO_4$ could be thus assigned to the six Slater[16] H_2AsO_4 configurations predicted by the Slater–Nagamiya model[16] of the phase transition in KH_2PO_4. In ferroelectric KH_2AsO_4 both 'close' hydrogens are either attached to the 'upper' ($\boldsymbol{V}^{(1)}$) or to the 'lower' two H_2AsO_4 oxygens ($\boldsymbol{V}^{(2)}$) as viewed along the c axis,

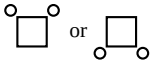

so that the dipole moment points along $\pm c$. In antiferroelectric $NH_4H_2AsO_4$ on the other hand, one hydrogen is attached to the 'upper' and one to the 'lower' oxygen,

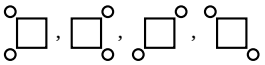

resulting in four 'antiferroelectric' H_2AsO_4 arrangements—($\boldsymbol{V}^{(3)}$, $\boldsymbol{V}^{(4)}$, $\boldsymbol{V}^{(5)}$, $\boldsymbol{V}^{(6)}$)—with dipole moments along the $\pm b$ and $\pm a$ crystal axes. In the antiferroelectric domain, where the sublattice polarization $\overleftrightarrow{P}$ ∥[100] is along the $\pm a$ axis, one sublattice corresponds to $\boldsymbol{V}^{(3)}$ and the other to $\boldsymbol{V}^{(4)}$, whereas for $\overleftrightarrow{P}$ ∥[010] the corresponding EFG tensors are $\boldsymbol{V}^{(5)}$ and $\boldsymbol{V}^{(6)}$. These results represented the first direct proof that the antiferroelectric proton ordering suggested by Nagamiya[16] is correct.

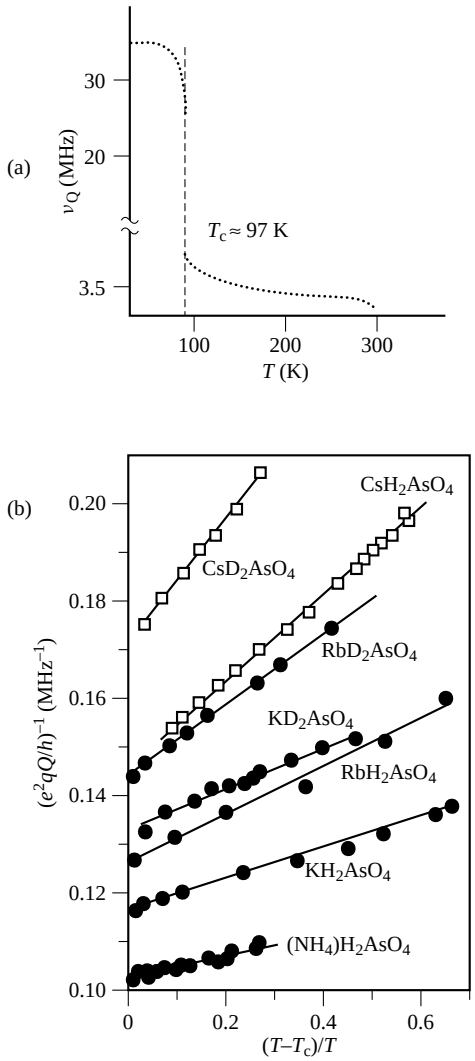

Figure 10 (a) Temperature dependence of the ^{75}As NQR frequency ν_Q in KH_2AsO_4 on cooling through T_c. (b) Dependence of the inverse ^{75}As quadrupole coupling constant $(e^2qQ/h)^{-1}$ on $(T - T_c)/T_c$ in KH_2AsO_4-type crystals above T_c

In the paraelectric phase each H_2AsO_4 group fluctuates between the six Slater configurations. The fluctuations result in a time averaging of the EFG tensors and in an anomalous increase in the ^{75}As spin–lattice relaxation rate as $T \rightarrow T_c$[19] (Figure 11). The ^{75}As T_1^{-1} has been measured by the proton–arsenic cross-relaxation technique in the dipolar frame.[17]

3.6 Fluctuations at Cationic Sites

In contrast to the nuclei discussed so far which were all covalently bonded, the EFG tensor at the K, Cs or Rb sites in

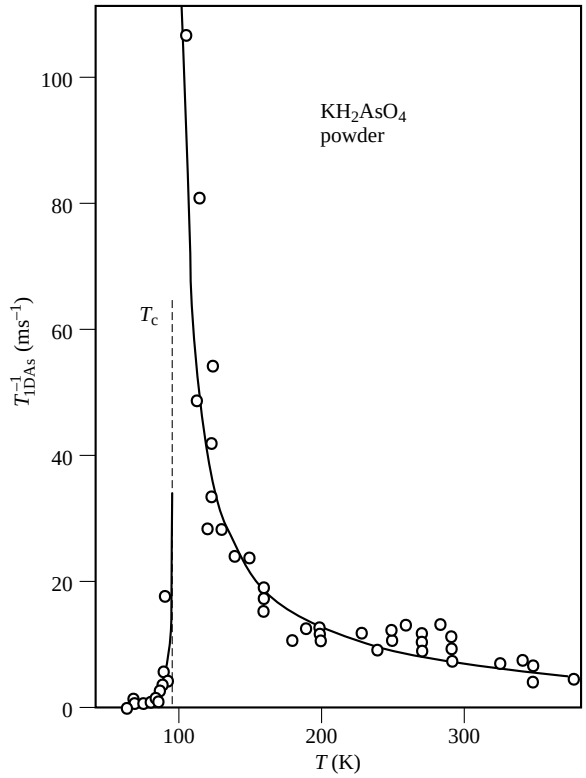

Figure 11 Temperature dependence of the arsenic spin–lattice relaxation rate in the dipolar (rotating) frame as determined by proton–arsenic cross relaxation

KH_2PO_4-type ferroelectrics is of ionic character. These nuclei are thus nonlocal probes which measure the charge distribution and order on a scale of 40–50 unit cells (i.e. more than 10^2 O–H$\cdots$O bonds). Here

$$\boldsymbol{V}_i = \boldsymbol{V}_i(p_1, p_2, \ldots, p_L) \tag{20a}$$

The temperature dependence of the ^{133}Cs ($I = \frac{7}{2}$) quadrupole coupling constant in CsH_2AsO_4, for instance[7] can be described above T_c by

$$\langle \boldsymbol{V}_i \rangle = \boldsymbol{V}_0 \quad T > T_c \tag{20b}$$

if the mean square fluctuations in the order parameter can be neglected. Below T_c, on the other hand, one finds

$$\langle \boldsymbol{V}_i \rangle = \boldsymbol{V}_0 + \boldsymbol{A}p + \boldsymbol{B}p^2 \quad T < T_c \tag{20c}$$

where the forms of the $\boldsymbol{V}_0$, $\boldsymbol{A}$, and $\boldsymbol{B}$ tensors are determined by crystal symmetry.[7,18] Similar results are obtained for the ^{39}K and ^{87}Rb quadrupole coupling tensors in other KH_2PO_4-type crystals.[1]

3.7 NMR in Perovskite Ferroelectrics

The local properties of phase transitions in perovskite-type ferroelectrics and antiferroelectrics have been extensively studied by NMR.[21] Cotts and Knight[21] and Hewitt[21] were the first to study electric quadrupole interactions in perovskites. Hewitt[21] in particular measured the temperature dependence of the EFG tensor at the ^{93}Nb sites in $KNbO_3$. The spin–lattice relaxation studies of $NaNbO_3$[21] gave important information on the softening of the collective rotations of the oxygen tetrahedra at the M point, $\boldsymbol{q} = (\frac{1}{2}, \frac{1}{2}, 0)$—of the Brillouin zone.

4 NMR IN THE SLOW AND INTERMEDIATE MOTION REGIME

4.1 Dynamic Symmetry Breaking and NMR in KSCN, RbSCN, and NH_4SCN Antiferroelectrics

The second-order quadrupole shifts[19] of the ^{39}K or ^{87}Rb $\frac{1}{2} \rightarrow -\frac{1}{2}$ NMR transitions in tetragonal KSCN and RbSCN show the effects of dynamic symmetry breaking on the NMR timescale.[19,20] The symmetry of the angular rotation pattern in the high-temperature paraelectric tetragonal phase is lower than the K or Rb site symmetry as determined by X-ray scattering[19] [Figure 12(a) and (b)]. At the same time the ^{39}K and ^{87}Rb 'site' and '90° domain' doublet splittings which are proportional to the long range order parameter vanish above T_c [Figure 12(c)] as expected from equations (1a) and (1b).

The above systems undergo at T_c antiferroelectric–paraelectric phase transitions connected with a head–tail ordering of the SCN^- groups. These groups are dynamically disordered above T_c and order in an antiparallel arrangement below T_c, resulting in a doubling of the unit cell size and the formation of 0, 90, 180, and 270° orthorhombic domains. The shift of the K^+ or Rb^+ ions from their position on the fourfold rotation axis is linearly coupled to the orientational degrees of freedom of the SCN^- ions.

The NMR results[19] show that for the second-order shifts and corresponding lineshapes the time fluctuating quadrupolar perturbation $\hat{\mathcal{H}}_Q^{(1)}(t)$, connected with the flipping of the SCN^- groups, averages out in two steps.[20] This is because both diagonal and off-diagonal matrix elements—in the representation of eigenstates of the main Hamiltonian—are important. A resonance line is a doublet with a splitting $4A$ at very long correlation times ($A\tau \gg 1$) where the spectrum is the same as in the case of two static Hamiltonians

$$\hat{\mathcal{H}}_A = \hat{\mathcal{H}}_Z + \langle \hat{\mathcal{H}}_Q^{(0)} \rangle + \hat{\mathcal{H}}_Q^{(1)} \tag{21a}$$

and

$$\hat{\mathcal{H}}_B = \hat{\mathcal{H}}_Z + \langle \hat{\mathcal{H}}_Q^{(0)} \rangle - \hat{\mathcal{H}}_Q^{(1)} \tag{21b}$$

It becomes a singlet when τ^{-1} exceeds the doublet splitting, i.e. when $A\tau \ll 1$. The second-order shift of the resonance line caused by the off-diagonal matrix element of the quadrupolar perturbation $\hat{\mathcal{H}}_Q^{(1)}(t)$ vanishes, however, only when τ^{-1} exceeds the resonance frequencies ω_L of the main Hamiltonian, $\hat{\mathcal{H}}_Z + \langle \hat{\mathcal{H}}_Q^{(0)} \rangle$. For $A\tau \ll 1$, $\omega_L\tau \gg 1$ we are thus in the intermediate motion limit and have a partial motional averaging. The doublet splitting induced by $\hat{\mathcal{H}}_Q^{(1)}(t)$ is averaged

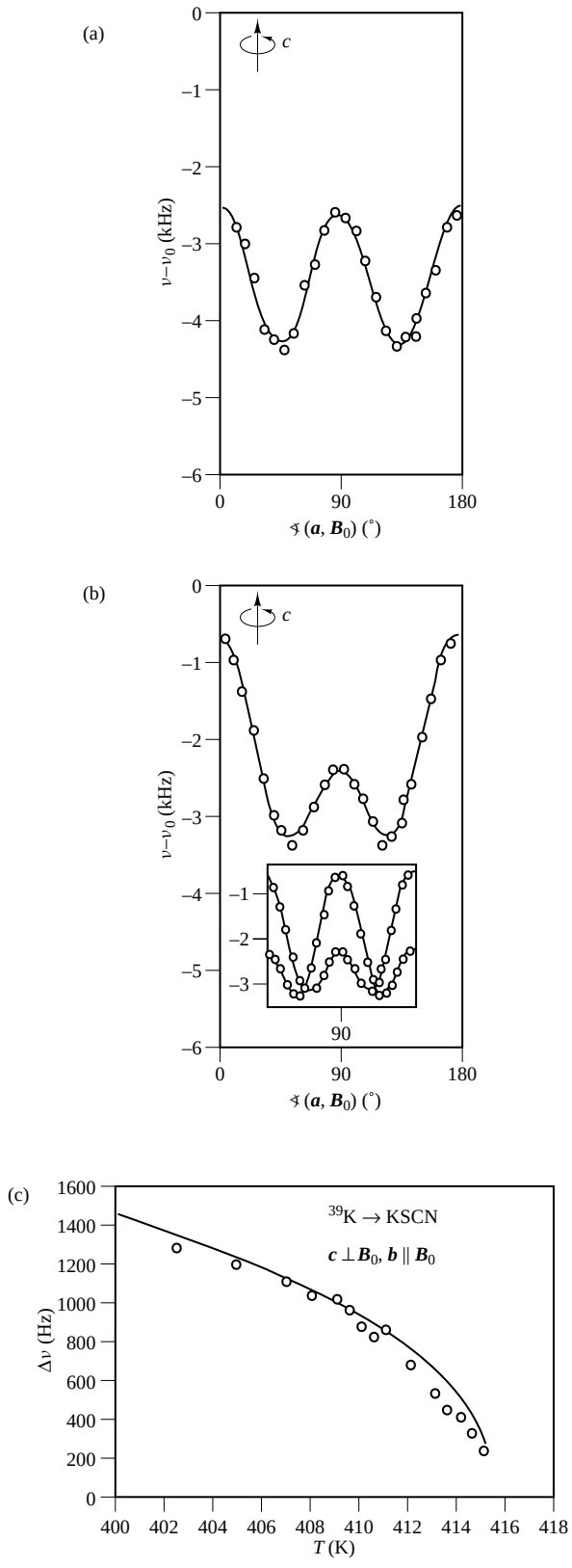

Figure 12 (a) Temperature dependence of the ^{39}K angular rotation pattern in KSCN for the c rotation above T_c and (b) below T_c. The domain splitting seen below T_c [inset to (b)] disappears above T_c whereas the angular dependence observed above T_c is incompatible with the tetragonal symmetry of the phase. (c) Temperature dependence of domain splitting

out, but the second-order quadrupolar shift induced by $\hat{\mathcal{H}}_Q^{(1)}(t)$ is still nonzero:

$$\Delta\omega_{1/2\rightarrow -1/2}(\tau) = \Delta\omega^{(0)}_{1/2\rightarrow -1/2} + \Delta\omega^{(1)}_{1/2\rightarrow -1/2}(\tau) \qquad (22a)$$

where

$$\Delta\omega^{(1)}_{1/2\rightarrow -1/2}(\tau) \propto \frac{(\omega_L\tau)^2}{1+(\omega_L\tau)^2} \qquad (22b)$$

It is only in the fast motion limit, $\omega_L\tau \ll 1$, that $\Delta\omega_{1/2\rightarrow -1/2}{}^{(1)}(\tau) \rightarrow 0$ and the angular dependence of the second-order quadrupolar shift is $\Delta\omega_{1/2\rightarrow -1/2}{}^{(0)}$, i.e. it is determined by the time averaged Hamiltonian $\langle\hat{\mathcal{H}}_Q^{(0)}\rangle$.

In agreement with this model and equations (2a)–(3c), the ^{39}K and ^{87}Rb spin–lattice relaxation rates show no anomaly at T_c as all critical factors in equation (2b) cancel (Figure 13). T_1 is proportional to $\omega_L{}^2\tau_0$, and continues to decrease with increasing temperature as the crystal is heated above T_c since τ_0 is thermally activated.

The dynamic symmetry breaking effects are not seen in the ^{14}N (I = 1) NMR in NH_4SCN,[19] as here first-order quadrupole splittings were studied where off-diagonal matrix elements are not important.

4.2 Dynamic Symmetry Breaking in KH_2AsO_4

In addition to the broad paraelectric arsenic lines, sharp 'ferroelectric' arsenic $\frac{1}{2} \rightarrow -\frac{1}{2}$ lines have been observed in KH_2AsO_4 well above T_c.[15] The angular dependence of these lines shows that here the symmetry of the paraelectric phase is also broken on the timescale of the NMR Larmor frequency. In contrast to KSCN and RbSCN where—in view of the large moment of inertia of the SCN group and the correlations between the flips of different SCN^- groups induced by the small available space for single ion reorientations—the intrinsic dynamics are very slow, we have in KH_2AsO_4 a high frequency soft mode similarly as in KH_2PO_4. The formation of nearly static polar clusters above T_c and the resulting dynamic symmetry breaking may thus be, in contrast to KSCN and RbSCN, induced here by defects.

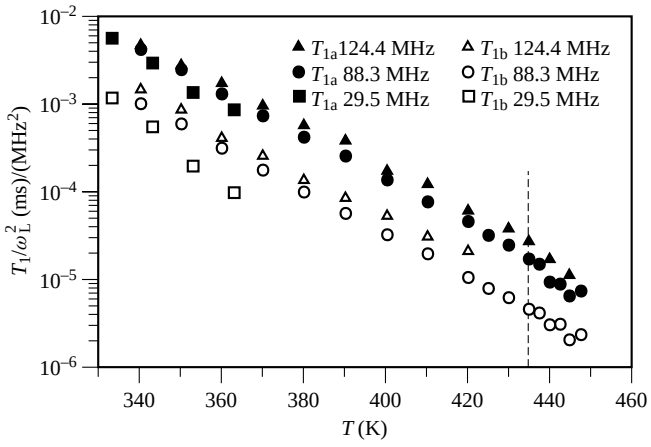

Figure 13 Temperature dependence of the normalized ^{87}Rb NMR T_1 components in RbSCN

5 NMR IN PROTON AND DEUTERON GLASSES

5.1 Determination of the Edwards–Anderson Order Parameter q_{EA} in the Fast Motion Limit

Solid solutions $Rb_{1-x}(ND_4)_xD_2PO_4$ (RADP) of ferroelectric RbH_2PO_4 and antiferroelectric $ND_4D_2PO_4$ represent a randomly frustrated hydrogen-bonded system with competing ferroelectric and antiferroelectric interactions. For $0.22 \leq x \leq 0.78$ the system forms a deuteron glass[21] with no macroscopic symmetry breaking and no spontaneous polarization at any temperature. Here too the O–D$\cdots$O bond represents a two-position reorientable dipole (see Figure 3) which can be described by an Ising pseudospin, $S^z = \pm 1$. In contrast to magnetic spin glasses where we deal with random bond interactions, proton and deuteron glasses are characterized by the presence of both random bonds and random fields[22]

$$\hat{\mathcal{H}} = -\sum_{i<j} J_{ij} S_i^z S_j^z - \sum_i f_i S_i^z \tag{23}$$

Here the J_{ij} are quenched random interactions and f_i are quenched random fields characterized by their second cumulants $[J_{ij}^2]_{AV} = J^2/N$ and $[f_i f_j]_{AV} = \delta_{ij}\Delta$. The random bond distribution is assumed to be Gaussian and centered around a mean value $J_0 = J_{AFE}x + J_{FE}(1-x)$ where x represents the NH_4 concentration. J^2 and Δ, on the other hand, are proportional to $x(1-x)$ and vanish for $x \to 0$ and $x \to 1$. For $|J_0| < J$ the system forms a glass phase without long range order whereas for $|J_0| > J$ a long range ordered inhomogeneous ferroelectric or antiferroelectric phase is predicted to occur.

The basic question in deuteron glasses is how to measure the Edwards–Anderson order parameter[2]

$$q_{EA} = \frac{1}{N}\sum_i \langle S_i^z \rangle^2 \tag{24}$$

as there is no macroscopic conjugate field attached to it. The answer is provided by NMR. In the fast motion limit NMR also allows for a direct determination of the local polarization distribution function $W(p)$, the second moment of which is q_{EA}.

In the simplest case the local NMR frequency ω_i of the deuteron in an O–D$\cdots$O bond is in the fast motion limit $[\omega_{AB}\tau \ll 1, \omega_{AB} = \omega_A - \omega_B]$ linearly related to the pseudospin polarization $\langle S_i^z \rangle = p_i$ of this bond:

$$\omega_i = \omega_0 + \omega_1 \langle S_i^z \rangle = \omega_0 + \omega_1 p_i \tag{25}$$

O–D$\cdots$O bonds with different local polarizations p_i will thus have different NMR frequencies resulting in an inhomogeneous broadening of the NMR line. The resulting frequency distribution,

$$f(\omega) = \frac{1}{N}\sum_i \delta(\omega - \omega_i) = [\delta(\omega - \omega_i)]_{AV} \tag{26}$$

is related to the local polarization distribution $W(p)$ [equation (4)] via

$$f(\omega)\,\mathrm{d}\omega = W(p)\,\mathrm{d}p \tag{27}$$

A measurement of $f(\omega)$ thus allows for a determination of $W(p)$ and its second moment q_{EA} if the relation between ω_i and p_i [equation (25)] is known from experiments on pure systems. q_{EA} in particular is obtained from

$$M_2[f(\omega)] = \int \mathrm{d}\omega\, f(\omega)(\omega - \omega_0)^2 = \omega_1^2 q_{EA} \tag{28}$$

Such experiments have been indeed performed,[4] and the results can be well described by the random bond–random field model.[4,22] The temperature dependence of q_{EA} (Figure 14) in particular demonstrates that in contrast to magnetic spin glass, random fields are present in addition to random bonds. From the shape of the deuteron NMR spectrum [Figure 15(a)] the temperature dependence of $W(p)$ can be determined [Figure 15(b)]. $W(p)$ is here symmetric around $p = 0$ and changes from a single-peaked to double-peaked form with decreasing temperature.

At lower temperatures where the pseudospin fluctuations are no longer very fast as compared to the rigid lattice quadrupole splittings ω_{AB}, we have to take into account the additional broadening due to the slowing down of the fluctuations by convoluting $W(p)$ with the well known dynamic lineshape $I(\omega, p, \tau)$ for exchange in an asymmetric two-site potential. Equation (26) now becomes

$$f(\omega) = \int I(\omega, p, \tau) W(p)\,\mathrm{d}p \tag{29}$$

When the fluctuations become too slow, $\omega_{AB}\tau \geq 1$, the second moment of the lineshape is no longer proportional to q_{EA} but

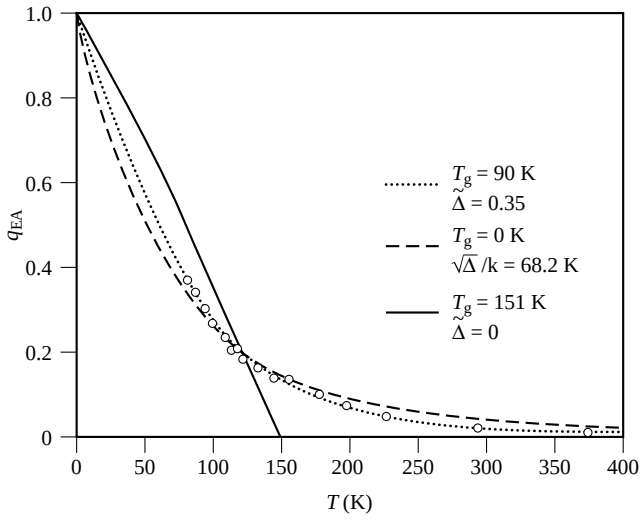

Figure 14 Temperature dependence of q_{EA} as determined from the second moment of the ^{87}Rb $\frac{1}{2} \to -\frac{1}{2}$ NMR spectra in $Rb_{0.56}(ND_4)_{0.44}D_2PO_4$. The dotted line represents the fit to the random bond–random field model with $\Delta/J^2 = 0.35$, $T_g = J/k = 90$ K, whereas the dashed line represents the best fit for the pure random field model where $T_g = 0$ K and $\sqrt{\Delta}/k = 68$ K. The solid line represents the fit to the pure random bond model with $T_g = 151$ K and $\sqrt{\Delta}/k = 0$ K

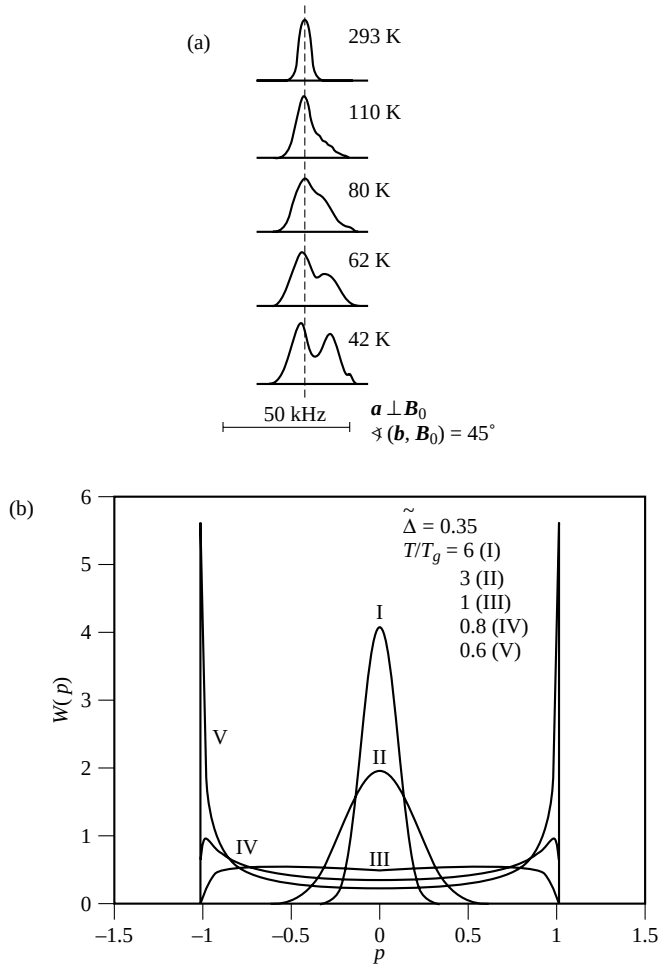

Figure 15 (a) O–D···O deuteron NMR spectrum in $Rb_{0.56}(ND_4)_{0.44}D_2PO_4$ at various temperatures. (b) Temperature dependence of the local polarization distribution function W(p) for $Rb_{0.56}(ND_4)_{0.44}D_2PO_4$ where $\Delta/J^2 = 0.35$

approaches a constant value determined by $I(\omega, p, \tau = \infty)$. Here 1D NMR cannot be used for a determination of q.

5.2 Determination of the Glass Order Parameter q in the Slow Motion Limit

In the slow motion limit where $\omega_{AB}\tau \gg 1$ the nucleus 'sees' the instantaneous value of the Hamiltonian corresponding to $S^z = \pm 1$. The NMR spectrum of the O–D···O bond deuteron will thus consist of two lines,

$$\omega_A = \omega_0 + \omega_1 \tag{30a}$$

and

$$\omega_B = \omega_0 - \omega_1 \tag{30b}$$

corresponding to the 'left' and 'right' position of the deuterons in the double-minimum hydrogen bond potentials. 2D 'exchange' NMR spectroscopy[23] can be used here to determine the glass order parameter q as well as the intrabond deuteron jump rate. The corresponding pulse sequence

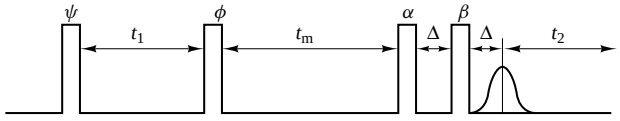

Figure 16 2D exchange NMR pulse sequence[24]

(Figure 16) developed by Spiess et al.[24] selects the signal of the form

$$\begin{aligned} F(t_1, t_2, t_m) = \exp(-t_m/T_1)\exp[-(t_1+t_2)/T_2] \\ \times[a_{AA}(t_m)\cos(\omega_A t_1)\cos(\omega_A t_2) \\ + a_{BB}(t_m)\cos(\omega_B t_1)\cos(\omega_B t_2) \\ + a_{AB}(t_m)\cos(\omega_A t_1)\cos(\omega_B t_2) \\ + a_{BA}(t_m)\cos(\omega_B t_1)\cos(\omega_A t_2)] \end{aligned} \tag{31}$$

After a Fourier transformation with respect to t_1 and t_2 the results are presented in the $\omega_1 - \omega_2$ plane. If no intrabond deuteron exchange, A $\leftrightarrow$ B, has taken place the absorption peaks lie on the diagonal of the $\omega_1 - \omega_2$ plane at (ω_A, ω_A) and (ω_B, ω_B). If intrabond deuteron transfer has taken place between the two physically nonequivalent sites A and B, we also find cross peaks at (ω_A, ω_B) and (ω_B, ω_A). The intensities of the cross peaks (Figure 17) are proportional to the fraction of nuclei that have undergone exchange in the time t_m. Since

$$a_{AA}(\infty) = \frac{1}{N}\sum_i W_{Ai}^2 \tag{32a}$$

$$a_{BB}(\infty) = \frac{1}{N}\sum_i W_{Bi}^2 \tag{32b}$$

and

$$a_{AB}(\infty) = a_{BA}(\infty) = \frac{1}{N}\sum_i W_{Ai} W_{Bi} \tag{32c}$$

where W_{Ai} is the probability of finding the deuteron of the i th O–D···O bond in site A, etc., we get for the ratio of the intensities of the cross peaks to the diagonal peaks in the limit $t_m \to \infty$ the expression

$$R(t_m \to \infty) = \frac{a_{AB}(\infty)}{a_{AA}(\infty)} = \frac{\sum_i W_{Ai} W_{Bi}}{\sum_i W_{Ai}^2} \tag{33a}$$

Using $\langle S_i^z \rangle = W_{Ai} - W_{Bi}$ and

$$q = \frac{1}{N}\sum_i \langle S_i^z \rangle^2 = \frac{1}{N}\sum_i (W_{Ai} - W_{Bi})^2 \tag{33b}$$

as well as

$$\frac{1}{N}\sum_i \langle W_{Ai} + W_{Bi})^2 = 1 \tag{33c}$$

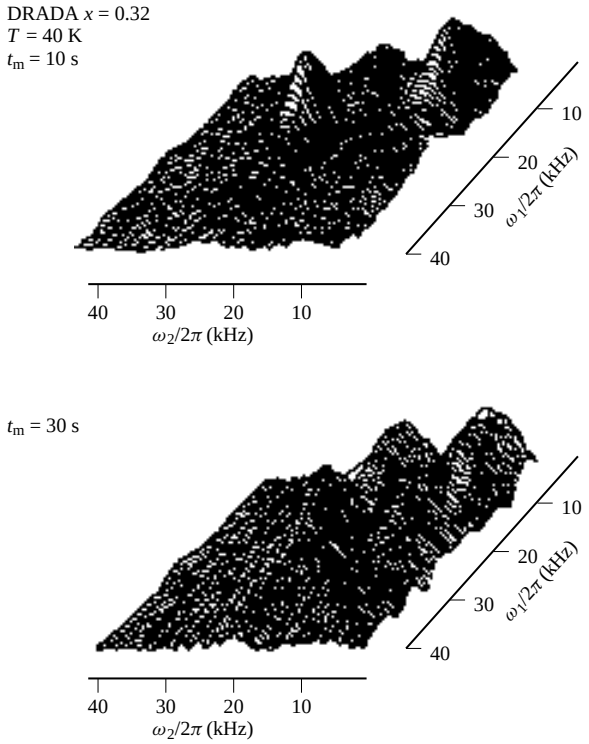

Figure 17 2D O–D···O intrabond deuteron 'exchange' NMR spectra of $Rb_{0.68}(ND_4)_{0.32}D_2AsO_4$ for $\boldsymbol{a} \perp \boldsymbol{B}_0, \sphericalangle\ (\boldsymbol{b}, \boldsymbol{B}_0) = 45^\circ$ at T = 40 K showing the gradual appearance of cross peaks with increasing mixing time

and $a_{AA} = a_{BB}$, equation (33a) can be rewritten as

$$R(t_m \to \infty) = \frac{1-q}{1+q} \tag{34}$$

A measurement of $R(t_m \to \infty)$ thus allows for a determination of q in the slow motion limit.[23]

The time evolution of $R(t_m) = a_{BA} / a_{AA}$, on the other hand (Figure 18), allows for a direct site specific measurement of

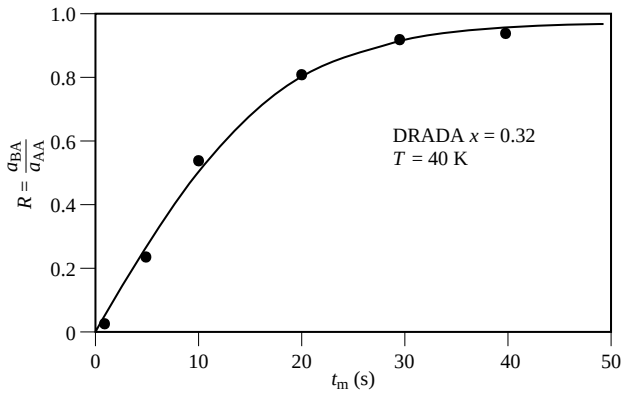

Figure 18 Ratio of cross peak to diagonal peak intensity R as a function of the mixing time t_m at T = 40 K. The same curve is obtained for different crystal orientations with different ω_{AB} splittings so that spin diffusion is excluded

the deuteron intra-hydrogen bond exchange rates, A → B:

$$R(x) = \tanh x \quad x = t_m/\tau \tag{35}$$

The observed intra-hydrogen bond deuteron exchange times[23] vary from 14.4 s at T = 45 K to 235 s at T = 24 K. The motion is thermally activated with E_a = 12.8 meV and τ_0 = 0.43 *s*, showing that phonon assisted deuteron tunneling may be important.

6 NMR DETERMINATION OF ORDER PARAMETERS IN INHOMOGENEOUS FERROELECTRICS

For $0 \le x < x_{FE}$ or $x_{AFE} \le x \le 1$ (see Figure 2) where $|J_0| > J$ a long-range ordered inhomogeneous ferroelectric or antiferroelectric phase exists below T_c. Here long-range and glassy order should coexist below T_c. Above T_c, long-range order vanishes whereas glassy order should persist. The glassy state is characterized above T_c by the Edwards–Andersson parameter q_{EA} and below T_c by $\tilde{q}_{EA} = q_{EA} - P^2$, i.e. by the difference between the EA order parameter and the square of spontaneous polarization P^2. Both $\tilde{q}_{EA}$ and q_{EA} have been determined[25] by ^{75}As NQR ($T < T_c$) and quadrupole perturbed NMR ($T > T_c$) in $Rb_{1-x}(NH_4)_xH_2AsO_4$ for x = 0.01 and x = 0.02.

In pure RbH_2AsO_4 the experimentally measured temperature dependences of the spontaneous polarization $P = P(T)$ and the ^{75}As NQR frequency $\nu_Q(T)$ determine the relationship $\nu_Q = \nu_Q(P)$. In a mixed crystal in the weak disorder limit $x \to 0$ the $\nu_Q = \nu_Q(P)$ relation for the mean NQR frequency is the same as in the pure crystal. In the general case we replace the reduced spontaneous polarization $\tilde{P} = P/P(T=0)$ by the local polarization p. We thus have

$$\omega_Q = \omega_0 + \omega_2 p^2 + \omega_4 p^4 \tag{36}$$

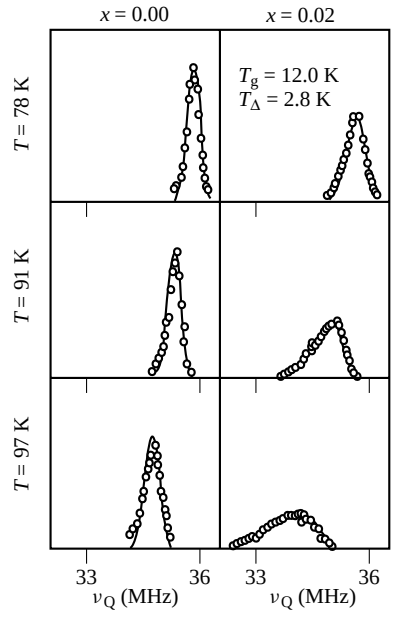

Figure 19 Experimental and theoretical ^{75}As NQR lineshapes[25] in $Rb_{1-x}(NH_4)_xH_2PO_4$ for x = 0.00 and x = 0.02 for $T < T_c$

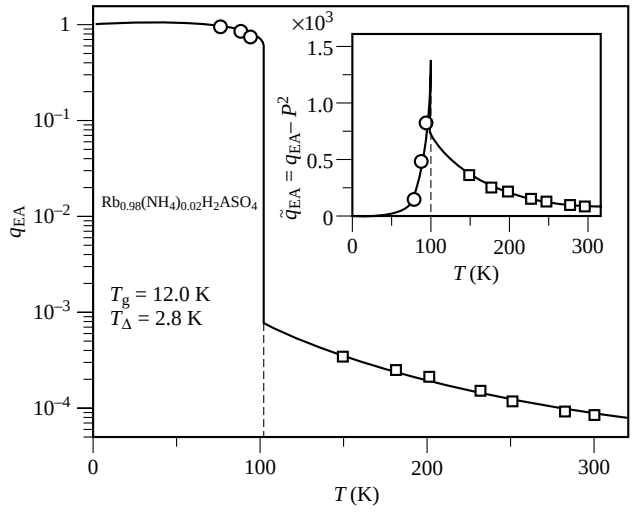

Figure 20 Temperature dependence[25] of q_{EA} and $\tilde{q}_{EA} = q_{EA} - P^2$ in $Rb_{1-x}(NH_4)_xH_2AsO_4$ for x = 0.02. Theoretical fits are shown as solid lines

as the ^{75}As NQR frequency is invariant with respect to the sign reversal of p. The temperature dependence of the mean ^{75}As NQR frequency thus yields the long-range order parameter P whereas the inhomogeneous ^{75}As NQR lineshape yields the local polarization distribution function $W(p)$, and its second moment q_{EA}, via

$$f(\omega) = W(p)|\mathrm{d}\omega/\mathrm{d}p|^{-1} \tag{37}$$

The ^{75}As pure NQR lineshapes of $Rb_{1-x}(NH_4)_xH_2AsO_4$ for $T < T_c$ are shown in Figure 19 for x = 0.00 and x = 0.02 together with the theoretical fits obtained from the compressible random bond–random field pseudospin Ising model.[25] In contrast to the case of proton and deuteron glasses ($| J_0 | < J$) the local polarization distribution function $W(p)$ is asymmetric with respect to p = 0 here.

The temperature dependence of q_{EA} and $\tilde{q}_{EA} = q_{EA} - P^2$ for x = 0.02 is shown in Figure 20. The theoretical fits are shown as solid lines. The jump in q_{EA} at T_c demonstrates the occurrence of a first-order phase transition.

Theoretical fits demonstrate that random bond effects dominate random field effects thus proving the existence of a collective glassy state in inhomogeneous ferroelectrics even in the weak substitutional disorder limit.

7 RELATED ARTICLES

Incommensurate Systems; Phase Transitions and Critical Phenomena in Solids.

8 REFERENCES

1. R. Blinc and B. Zeks, *Soft Modes in Ferroelectrics and Antiferroelectrics*, North Holland, Amsterdam, 1974.
2. K. Binder and A. P. Young, *Rev. Mod. Phys.*, 1986, **58**, 801 and R. Pirc, B. Tadić, and R. Blinc, *Physica A*, 1992, **185**, 322.
3. R. Pirc, B. Tadić, and R. Blinc, *Phys. Rev. B*, 1987, **36**, 8607.
4. R. Blinc, J. Dolinsek, R. Pirc, B. Tadić, B. Zalar, R. Kind, and O. Liechti, *Phys. Rev. Lett.*, 1989, **63**, 2248; J. Dolinšek, *J. Magn. Reson*, 1991, **92**, 312.
5. A. Levstik, C. Filipic, Z. Kutnjak, I. Levstik, R. Pirc, B. Tadić, and R. Blinc, *Phys. Rev. Lett.*, 1991, **66**, 2368.
6. J. L. Bjorkstam, *Adv. Magn. Reson.*, 1974, **7**, 1; J. L. Bjorkstam and E. A. Uehling, *Phys. Rev.*, 1959, **114**, 961; V. H. Schmidt and E. A. Uehling, *Phys. Rev.*, 1962, **126**, 447.
7. R. Blinc, in *Magnetic Resonance of Phase Transitions*, ed. F. J. Owens, C. P. Poole, and H. A. Farach, Academic Press, London, 1979, p. 247.
8. E. Matsushita and T. Matsubara, *Prog. Theor. Phys.*, 1982, **67**, 1.
9. J. Seliger, V. Žagar, R. Blinc, and V. H. Schmidt, *Phys. Rev. B*, 1990, **42**, 3881; S. G. P. Brosnan and D. T. Edmonds, *J. Magn. Reson.*, 1980, **38**, 47; D. T. Edmonds, *Phys. Rep.*, 1977, **29**, 233.
10. R. Blinc, *Ferroelectrics*, 1977, **16**, 33.
11. J. S. Waugh, L. Huber, and U. Haeberlen, *Phys. Rev. Lett.*, 1968, **20**, 180.
12. B. Schröter, H. Rosenberger, and D. Hadži, *J. Mol. Struct.*, 1983, **96**, 301.
13. R. Blinc, I. Zupančič, G. Lahajnar, J. Slak, V. Rutar, M. Verbec, and S. Žumer, *J. Chem. Phys.*, 1980, **72**, 3626.
14. F. Ermark, B. Topić, U. Haeberlen, and R. Blinc, *J. Phys.: Cond. Matter*, 1989, **1**, 5489.
15. R. Blinc and J. L. Bjorkstam, *Phys. Rev. Lett.*, 1969, **23**, 788; J. L. Bjorkstam, *J. Phys. Soc. Jpn. Suppl.*, 1970, **28**, S101.
16. J. C. Slater, *J. Chem. Phys.*, 1941, **9**, 16; *Phys. Rev.*, 1950, **78**, 748; T. Nagamiya, *Prog. Theor. Phys.*, 1952, **7**, 275.
17. R. Blinc and S. Žumer, *J. Chem. Phys.*, 1975, **62**, 3118; R. Blinc, in *Nuclear Magnetic Resonance in Solids*, ed. L. Van Gerven, Plenum, New York, 1977, p. 303.
18. R. Blinc, M. Mali, J. Slak, J. Stepišnik, and S. Žumer, *J. Chem. Phys.*, 1972, **56**, 3566.
19. R. Blinc, J. Seliger, T. Apih, J. Dolinšek, I. Zupančič, O. Plyush, A. Fuith, W. Schranz, and H. Warhanek, *Phys. Rev. B*, 1991, **43**, 569; R. Blinc, J. Seliger, V. Žagar, T. Apih, J. Dolinšek, H. Warhanek, A. Fuith, and W. Schranz, *Phys. Rev. B*, 1990, **42**, 8125; B. Topić, U. Haeberlen, R. Blinc, A. Fuith, and H. Warhanek, *Solid State Commun.*, 1989, **72**, 151.
20. J. Seliger, *J. Magn. Reson. A*, 1993, **103**, 175; J. L. Bjorkstam and M. Villa, *Phys. Rev. B*, 1980, **22**, 5025.
21. K. A. Müller (ed.), *Local Properties at Phase Transitions*, North Holland, Amsterdam, 1976; R. M. Cotts and N. D. Knight, *Phys. Rev.*, 1954, **96**, 1285; R. R. Hewitt, *Phys. Rev.*, 1961, **121**, 45; G. F. Bonera, F. Borsa, and A. Rigamonti, *Rev. Nuovo Cim.*, 1972, **2**, 325.
22. E. Courtens, *J. Phys. (Paris) Lett.*, 1982, **43**, 199; R. Blinc, J. Dolinšek, and S. Žumer, *J. Non-Crystalline Solids*, 1991, **131–133**, 125.
23. J. Dolinšek, B. Zalar, and R. Blinc, *Europhys. Lett.*, 1993, **23**, 289.
24. K. Schmidt-Rohr and H. W. Spiess, *Phys. Rev. Lett.*, 1991, **66**, 3020.
25. G. Papantopoulos, G. Papavassiliou, F. Milia, V. H. Schmidt, J. E. Drumheller, N. J. Pinto, R. Blinc, and B. Zalar, *Phys. Rev. Lett.*, 194, **73**, 276.

Biographical Sketch

Robert Blinc. *b* 1933. Ph.D., 1959, Physics, University of Ljubljana, Postdoctoral work with J. S. Waugh, MIT, Cambridge, Mass. Faculty

member (currently Professor of Physics), University of Ljubljana, J. Stefan Institute, 1969–present. President of AMPERE Society 1988–94. Member of Slovenian, Croatian, Polish, Saxon and European Academies of Sciences. Member of Academy of Athens and Academia Europea. Approx. 450 publications and, with B. Zeks, the book 'Soft Modes in Ferroelectrics and Antiferroelectrics'. ISMAR prize 1977. Research interests include NMR of phase transitions and disordered condensed matter.

Oxygen-17 NMR

Ioannis P. Gerothanassis
University of Ioannina, Greece

1	Introduction	1
2	Experimental Aspects	1
3	Characteristic Parameters	2
4	Selected Applications	6
5	Related Articles	9
6	References	9

1 INTRODUCTION

The structure and dynamics of oxygen-containing compounds is a subject of widespread significance. Compared with ^{1}H, ^{13}C, ^{31}P, and ^{19}F NMR, however, ^{17}O NMR has received little attention.[1–8] This neglect is not surprising since, of the naturally occurring oxygen isotopes, only ^{17}O possesses a nuclear spin ($I = \frac{5}{2}$). Due to its electric quadrupole moment ($Q_e = -2.6 \times 10^{-30}$ e m^2), its low natural abundance (0.037%), and the extremely low absolute sensitivity compared with that of ^{1}H (about 1.1×10^{-5}), the ^{17}O isotope is one of the more difficult nuclei to observe by NMR spectroscopy. It is, however, of great interest to use a nucleus such as oxygen that is located at strategic molecular sites and is directly involved in inter- and intramolecular interactions. The ^{17}O NMR parameters, i.e. isotropic shielding, principal elements of the ^{17}O shielding and electric field gradient tensors, and the transverse and longitudinal relaxation times, can be considered as excellent means of probing the structure, bonding, and dynamics of oxygen-containing compounds. Furthermore, recent advances in instrumentation, the extremely large chemical shift scale (which aids in the resolution of quadrupole broadened resonances), and the availability of ^{17}O enriched compounds have alleviated these difficulties; thus, an increased use of the ^{17}O NMR technique can be envisaged.[9–11]

2 EXPERIMENTAL ASPECTS

2.1 The Case of ^{17}O Enrichment

The stringent requirements in studies of compounds at natural abundance are the high concentrations (>0.1 M) and extensive signal averaging needed.[12] Recording of spectra can be greatly facilitated by the use of ^{17}O enriched samples (Figure 1). When using FT high field instruments and ^{17}O labeled compounds (^{17}O enrichment 10–40 atom %), concentrations of greater than 1 mM are desirable, depending on the linewidths. Synthesis involving oxygen isotopes tends to involve rather straightforward organic reactions. However, one caveat that should be kept in mind when contemplating the synthesis of an ^{17}O labeled compound is the expense of the starting reagents. Simple modifications of existing reactions are required. For example, $^{17}O_2$, C^{17}O, or C$^{17}O_2$, is added to evacuated systems, as opposed to more traditional procedures which involve bubbling through the reaction mixture. Recently, a comprehensive overview of ^{17}O enriched methods has been published.[14]

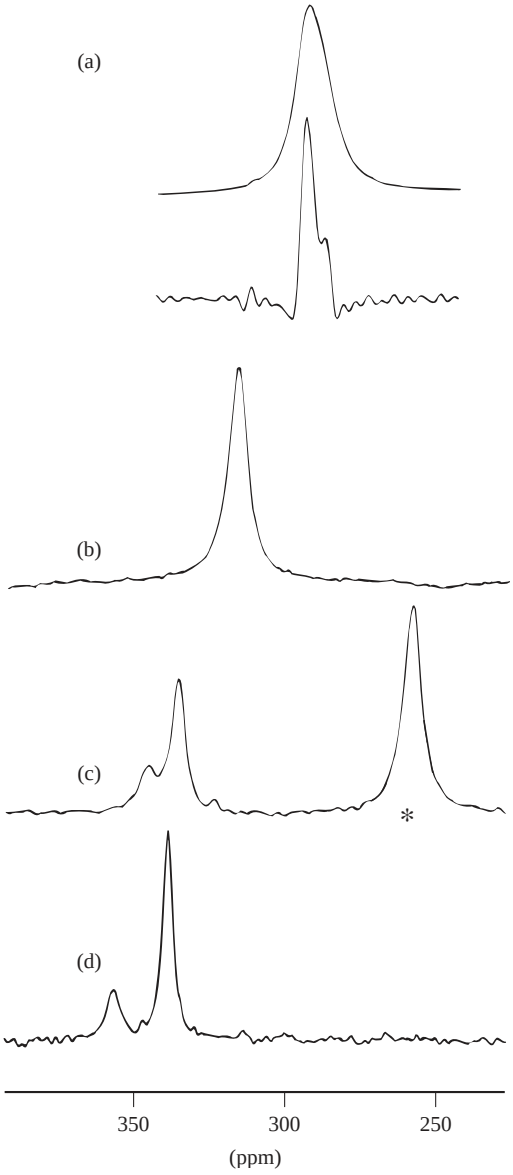

Figure 1 ^{17}O NMR spectra (48.8 MHz; 40 °C) of *N*-[^{17}O]acetyl-L-proline.[13] (a) 10% enrichment, 0.1 M in aqueous solution containing 1 M NaCl and 5×10^{-5} M EDTA; T_{acq} = 12 ms, NS = 300 000, total experimental time = 1 h: (upper trace) normal spectrum; (lower trace) after a Gaussian-exponential resolution enhancement. (b) 1% enrichment, 0.1 M in methanol, T_{acq} = 10 ms, NS = 200 000, total experimental time = 32 min, line broadening (LB) = 50 Hz. (c) 0.4 M natural abundance in acetone (the asterisk marks the carboxyl oxygen resonance); T_{acq} = 5 ms, number of scans (NS) = 1 900 000, total experimental time ≃10 h, LB = 50 Hz; (d) 1% enrichment, 0.1 M in acetone; T_{acq} = 10 ms, NS = 1 350 000, total experimental time ≃8 h, LB = 50 Hz. (Adapted by permission of The American Chemical Society from R. N. Hunston, I. P. Gerothanassis, and J. Lauterwein, *J. Am. Chem. Soc.*, 1985, **107**, 2654)

2.2 Referencing Techniques

As with many heteronuclei, a variety of reference compounds and referencing procedures (both internal and external) have been suggested for ^{17}O NMR. For diamagnetic solutions, an external standard in a combined use of two cylindrical cells has been recommended.[15] Using this technique, doubly distilled water or 1,4-dioxane can be used as external reference. Both compounds have chemical shifts which are indistinguishable at 30–40 °C and their magnetic susceptibility correction is small (<0.6 ppm) relative to common organic solvents. However, H_2O has the disadvantage that its chemical shift varies with temperature (−3 ppm between 27 and 90 °C) due to cleavage of intermolecular hydrogen bonds (the same applies for D_2O in addition to an isotopic effect of −3 ppm).

2.3 Solvent (H_2O) Suppression

Perhaps the most straightforward approach to solvent suppression is the use of ^{17}O depleted water, provided of course that rapid ^{17}O exchange does not occur between solvent and solute.[16] Further suppression can be achieved by exploiting the special relaxation properties of the solvent, by postexperiment data processing and by selectively exciting the whole spectrum apart from that of the solvent.[17] A critical note on the usefulness of the selective excitation pulse sequences in ^{17}O NMR has recently been published.[18]

2.4 Acoustic Ringing

Observation of very broad resonances in NMR is a potential problem due to baseline distortions. The most severe of the baseline artifacts is that due to the transient response of the NMR probe, often referred to as 'acoustic ringing', caused by the generation of ultrasonic waves from the action of the rf pulse. In the last decade, several pulse sequences designed for the suppression of acoustic ringing have been reported, and the reader should consult a relevant review article for details.[19] For experiments in solution, the extended spin echo sequence was found to be particularly useful, since it utilizes minimum pulse and preacquisition delay times. A closely related pulse sequence for experiments in the solid phase has also been suggested.[20]

3 CHARACTERISTIC PARAMETERS

3.1 Chemical Shifts

3.1.1 Experimental Shielding Ranges: Empirical Correlations

A general pattern of ^{17}O shielding is shown in Figure 2. For compounds containing oxygen bonded only to carbon and/or hydrogen there is a clear correlation between the C–O π bond order and a high frequency shift.[21] This type of correlation arises from the multiple bond term $\Sigma_{B\neq A}Q_{AB}$ in the Karplus–Pople equation.[22] For bridging oxygen atoms, a strong deshielding is observed when the substituents R are replaced by π-accepting acyl substituents which introduce π character into the C–O bond of the bridging oxygen. Thus, bridging oxygen resonances in carbonates and esters appear at high frequency relative to the corresponding resonances in alcohols, ethers, and acetals. An even greater high frequency shift is observed for anhydrides, where bridging oxygen atoms are bonded to two π acceptors. If chemical shifts are assumed to depend linearly on π bond order, the chemical shift of about 600 ppm for aliphatic aldehydes (π bond order of about 1) relative to water (π bond of 0) implies a chemical shift of about 200 ppm for CO_3^{2-} (π bond order of $\frac{1}{3}$). The observed shift of CO_3^{2-} (192 ppm) is in agreement with this crude prediction, further supporting the general correlation between π bond order and shielding discussed above.[2]

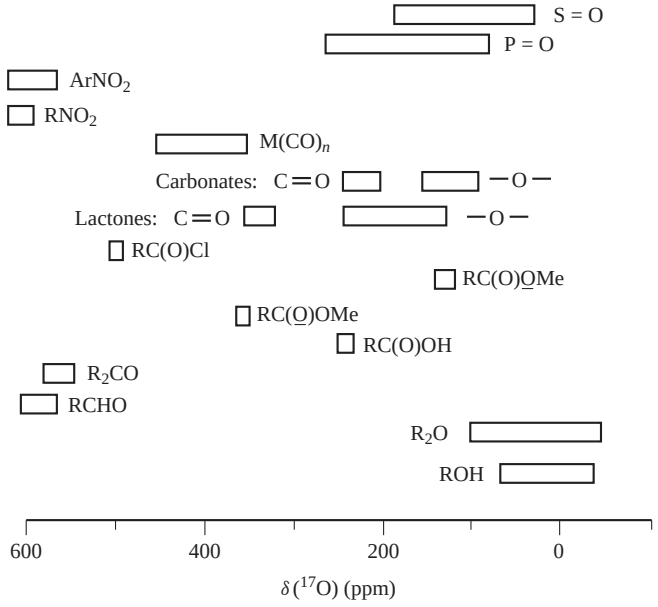

Figure 2 ^{17}O chemical shift ranges for different X–O bonds. (Adapted by permission of Plenum Press from W. McFarlane and H. C. E. McFarlane, in 'Multinuclear NMR', ed. J. Mason, 1987, Chap. 14)

In nitrogen-containing compounds, as in carbon compounds, chemical shift values are determined largely by π bonding effects.[23–25] Bridging oxygen resonances are observed at even higher frequency in nitrates, where π bonding is appreciable. A lesser, but nonetheless significant, effect is observed for bridging oxygen atoms in nitrates. The most striking feature of the ^{17}O shifts observed for P–O bonds is the small chemical shift range (20–260 ppm) which cannot be related to P–O bond order in a straightforward fashion. However, ^{17}O resonances for nonequivalent oxygen atoms in phosphates and polyphosphates can be resolved and have been used in stereochemical and binding site studies.[26–28] For S–O bonding, similar trends to those displayed by P–O bonds are observed. Modification of the π bond order in an X=O group due to substituents on X results in a decrease (or increase) in the net charge on X as the charge on oxygen increases (or decreases). The chemical shift variations experienced by the nuclei X and O are then opposite and roughly proportional to the ratio $\langle r^{-3}\rangle_{2p_X}/\langle r^{-3}\rangle_{2p_O}$.[24] For a series of oxyanions and a series of C=O and N=O compounds a linear correlation has been found between $\delta(^{17}O)$ and the variation in ΔE^{-1}.[29] A linear correlation exists between acetone chemical shifts and the first maximum of the $n \rightarrow \pi^*$ transition for acetone/water

solutions[30] and for acetone in different solvents.[31] Similar trends have also been observed in a variety of substituted acetophenones;[32] however, it was suggested that such trends may be fortuitous, since the transition energy depends upon the balance of several effects associated with both π donation and σ withdrawal.[33] From a study on a series of aliphatic ethers, a correlation between $\delta(^{17}O)$ and the first ionization potential has been suggested.[34]

Compounds containing oxygen–oxygen bonds and oxygen–fluorine bonds display large high-frequency shifts.[35–37] The ability, therefore, of ^{17}O NMR to distinguish unambiguously between nonequivalent oxygen atoms has found application in several structural and mechanistic studies. The same applies to oxygen bonded to transition metals (see below). Empirical correlations were extended to diamagnetic transition metal anions of the general formula MO_4^{n-}, and theoretical calculations were carried out to show that the absolute magnitude was reasonable.[29]

3.1.2 Theory of ^{17}O Chemical Shifts (see **Shielding: Overview of Theoretical Methods**)

3.1.2.1 Isolated Molecules. Ab initio calculations[38,39] of ^{17}O nuclear shielding tensors have been reported for a variety of simple molecules such as H_2O, CH_3OH, $(CH_3)_2O$, H_2CO, CH_3CHO, $HCONH_2$, and CO. The results are gauge dependent and in many cases vary considerably depending on the basis set used. Gauge independent ab initio results for H_2O and H_2CO indicate a ^{17}O shielding of 757.6, 860.3, or 858.8 ppm for H_2CO, with respect to H_2O, compared with the experimental result of 580–600 ppm. The calculated data represent a choice of three basis sets. Semiempirical INDO (intermediate neglect of differential overlap) calculations are numerically smaller than the experimental results, whereas the CNDO/S (complete neglect of differential overlap/S) calculations produce better overall agreement.[40–43] This probably reflects an insensitivity of the INDO orbital energies to changes in the environment of the oxygen. By omitting those molecules and ions which have nitrogen directly bonded to oxygen the CNDO/S results gave a standard deviation of 30.6 ppm and a correlation coefficient of 0.98 compared with the experimental values. Analysis of the CNDO/S results demonstrates that the ^{17}O shielding differences of some carbonyl compounds are dominated by the lowest energy $n \rightarrow \pi^*$ transition. For the linear species CO, CO_2, and NO_2^+, the largest contribution to the paramagnetic part σ_p of the ^{17}O shieldings arises from the lowest energy $\sigma \rightarrow \pi^*$ transition. Similarly, for the bent ion NO_2^- the lowest energy $\sigma \rightarrow \pi^*$ transitions are dominant for the in-plane components of the shielding tensor, while the out-of-plane contribution is controlled by $\sigma \rightarrow \sigma^*$ transitions. In general, these ^{17}O shieldings are in reasonable agreement with the available experimental data, and in some cases are an improvement upon ab initio results. Analogous calculations employing a basis set of gauge dependent atomic orbitals within the CNDO/2 framework have been reported for ^{17}O shieldings in electrolyte solutions.[44] For ozone,[45] the use of localized molecular orbitals within the IGLO method (see ***Shielding Calculations: IGLO Method***) allows the contributions to the total shielding to be partitioned into orbital contributions, so that the specific role played by the lone pairs on the atom in question and orbitals centered on neighboring atoms can be discerned.[46] The calculated shieldings for O_3 were found to be extremely large, highly anisotropic, and to differ from the experimental values by a factor of 2–3. The authors also noted that the paramagnetic contributions are mainly due to the lone pairs on the respective oxygen atoms, unlike the triatomic molecules CO_2 and FNO in which the paramagnetic contributions are mainly due to the bonds interacting with the antibonding π^* electrons and only to a limited extent to the lone pairs.

3.1.2.2 Solvent and medium effects. Recently, the effect of electrical polarization on the chemical shielding of carbon monoxide has been considered in detail.[47,48] In addition, the relationship between the vibrational frequency and the shieldings for three different types of electrical environments—a uniform field, a field gradient, and an axial point-charge dipole—together with experimental ^{13}C and ^{17}O isotropic shieldings and vibrational frequencies for a range of carbon monoxide derivatives of heme proteins has been described. For each type of environment, the shieldings vary linearly with the vibrational frequency for a relatively wide range of frequency shifts.[48] This shows, in agreement with experiment,[49] that there is a linear relationship that is opposite for ^{13}C and ^{17}O.[50]

The effects of solvents on the ^{17}O nuclear shielding of solute molecules may be categorized into hydrogen-bonding interactions and influences that arise from electronic interactions between the dipole moments of the solute and solvent molecules. Precise mathematical expressions are not available for many nonbonded interactions. Consequently, continuum models tend to be more popular for investigating solvent effects on NMR parameters. The most widely used of these, to date, is the solvaton model.[51] By means of this model the solute–solvent interaction can be included in the paramagnetic screening contribution, and the solvent induced shift is proportional to $(\epsilon - 1)/2\epsilon$, where ϵ is the dielectric constant of the medium. Some sum-over-states (SOS) and finite perturbation theory (FPT) calculations of oxygen nuclear shieldings of several organic functional groups, as obtained using the solvaton model, predict increases in shielding as ϵ increases.[50,52] An analysis of the various factors contributing to the paramagnetic term reveals that the increase in shielding arises from a concomitant decrease in $\langle r^{-3} \rangle_{2p}$ and an increase in the weighted average of the energies of the various transitions contributing to the paramagnetic term. The observed decrease in $\langle r^{-3} \rangle_{2p}$ is consistent with an increase in the average separation between the nucleus and its 2p electrons as the charge q increases. The increase in the weighted averaged of the transition energies is largely controlled by the increase in energy of the lowest $n \rightarrow \pi^*$ transition as the extent of solvation increases.

The shielding of the ^{17}O nuclei of several functional groups are quite sensitive to hydrogen-bonding interactions. From a theoretical standpoint the shielding may be considered by using the supermolecule approach. A good example is provided by formamide.[53] Ab initio calculations using GIAOs (gauge invariant atomic orbitals) within the FPT framework have been reported for formamide (FMA) in the presence of its first hydration shell. The ^{17}O shielding values reported for the complexes $FMA–(H_2O)_2$ show that the shift observed when the oxygen atom is directly involved in the hydrogen bond is much larger than the one occurring when the water molecules are bound to the NH group. The variation was calculated to be to low frequency in both cases. This is in agreement with

^{17}O NMR experimental data on FMA and several amides in different solvents.

3.2 Indirect Spin Coupling Constants

Because of the breadth of ^{17}O resonances, only relatively large coupling constants can be measured, and hence the majority of those recorded refer to couplings from directly bonded nuclei. ^{1}J(O,H) in water and alcohols has values close to 80 Hz.[54–56] The ^{1}J(P,O) couplings involving P=O groups cover a fairly wide range (145–210 Hz) and for a series of compounds of type OPX_3 (X = F or O in OMe, X = N in NMe_2, and X = C in Me) there is a consistent drop in coupling with decreasing electronegativity of X. This may be qualitatively attributed to the electronegative substituents removing electrons in outer orbitals from the phosphorus atom, leading to a greater effective atomic charge and hence stronger contact interaction between the phosphorus nucleus and the s orbitals. A finite perturbation theoretical treatment within the CNDO/2 formalism has reproduced the observed trends, but not the absolute values.[57] The oxygen atoms in P–OMe groups within phosphates give rise to a consistently smaller coupling constant, compared with P=O, of between 90 and 100 Hz; there is an indication of a considerably larger value for phosphites. The reduced coupling constants decrease with increasing atomic number of the central atoms along the isoelectronic sequence VO_4^{3-}, CrO_4^{2-}, and MnO_4^{-}.[58] The values of ^{17}O spin–spin couplings have been used to investigate H_3O^+ species.[59] The ^{17}O NMR spectrum revealed a perfect quartet with J(O,H) = 107 Hz. Furthermore, the effect of H/D substitution is evident in the ^{17}O NMR spectra of H_2O–D_2O in CH_2Cl_2. Thus, the species H_2O, HDO, and D_2O could be identified from coupling constants, without reference to chemical shift data.[60] ^{2}J couplings are normally about an order of magnitude smaller than the corresponding directly bonded couplings.[61] However, there seems to be a particularly favored coupling pathway from hydrogen to the 'ether' oxygen atom in HCOOR systems, which is probably associated with π bonding across the planar framework.

In some cases coupled resonances cannot be resolved into fine structure but exhibit a partially collapsed structure, depending on the rate of proton transfer. In such cases decoupling of the other nuclei can lead to reduced linewidths and information about coupling constants.

When a spin-$\frac{1}{2}$ nucleus is bonded directly to ^{17}O, the X nucleus will also be relaxed by virtue of its spin–spin coupling with ^{17}O. This has been termed 'scalar relaxation of the second kind'. Such a line-broadening effect for ^{17}O in ^{31}P NMR has been used to locate the position of the ^{17}O label and to calculate the percentage enrichment of ^{17}O. In addition, it has made possible analysis of the configuration of (^{16}O, ^{17}O, and ^{18}O) phosphate monoesters and (^{16}O, ^{17}O, and ^{18}O) thiophosphates by ^{31}P NMR.[62–64]

3.3 Nuclear Quadrupole Coupling Constants

The electrostatic interaction between the nuclear quadrupole electric moment Qe and the electric field gradient tensor eq_{ij} is the quadrupolar interaction. An appropriate reference axis system can be chosen to reduce this interaction to two values:[4] the main component

$$\chi = e^2 q_{zz} Q/h \tag{1}$$

and the asymmetry parameter (dimensionless)

$$\eta = (e^2 q_{xx} Q - e^2 q_{yy} Q)/e^2 q_{zz} Q \tag{2}$$

where $|e^2 q_{zz} Q| > |e^2 q_{yy} Q| > |e^2 q_{xx} Q|$.

The χ values for ^{17}O may be calculated by computing the field gradient from molecular wavefunctions and using the nuclear quadrupole moment Qe. Only relatively small molecules have been studied. Thus the calculated χ value for CO using the GAUSSIAN 88 program at the 6-31G* level[49] (3.1 MHz) was found to deviate from the experimental value (~4.4 MHz) (the value of 3.9 MHz obtained from ab initio calculations[47] is in better agreement with the experimental value). Furthermore, it was shown that hydrogen bonding to HF results in a significant decrease in χ of about 0.7 MHz for the linear species CO···HF.

Semiempirical methods of various degrees of sophistication have been used to compute electric field gradients. Within the framework of the Townes–Dailey theory, the three components of the field gradient can be related to the electronic populations in the orbitals describing the oxygen bonding and to eq, the field gradient created by an electron in a 2p atomic orbital (the contribution from the valence s electrons is neglected because of the spherical symmetry). More elaborate models incorporate hybridization of atomic orbitals into valence bonding and lone pair orbitals. Such studies include the determination of σ and π orbital populations for X–O bonds (X = C, N, P, or S).[65,66]

The majority of experimentally determined χ and η values have been obtained in the solid state by the use of NQR spectroscopy; however, some have been determined by NMR measurements on powders or single crystals, where χ is small with respect to the NMR frequency. Quadrupole coupling constants have also been derived from the splittings in the ^{17}O spectra of molecules partially oriented in an electric field[67] or dissolved in a nematic liquid crystal.[68,69] Detailed studies of polynuclear osmium carbonyl dynamics have been undertaken and together with ^{13}C measurements have provided estimates of the ^{17}O quadrupole coupling constants.[70] In molybdenum hexacarbonyl, the ^{95}Mo and ^{97}Mo linewidths gave the reorientational correlation time, which in turn made it possible to determine the χ values from the ^{17}O linewidth.[71]

Experimental χ values cover the range −8 to 17 MHz. The sign of χ is irrelevant to the NMR experiment, but from a theoretical point of view it gives information about the orientation of the field gradient. The experimental χ values for a series of compounds in the solid state that contain C=O, –O–, P–O, N–O, or S–O bonds show the following trends:[6]

1. For substituted nitrophenols, hydroxybenzaldehydes, and nitrobenzaldehydes, the χ values are nearly invariant with the electronic properties of the substituent, but are reduced by hydrogen bonding.
2. Strong hydrogen bonding reduces the χ values by as much as 2.6 MHz.

In summary, the following scale of χ values has been suggested:

O − O >	N − O >	NO_2 >	C = O >	P − OR ≃ S = O
16 − 17	16	13	11 − 9	9.5 − 9

ROH >	SO_2 >	P = O ≃ C = O >	XO_n^{m-}
9 − 8	6.7	4	1

The ^{17}O χ values for the terminal CO groups in metallocarbonyls were found to be 1–3 MHz, although values below 0.1 MHz have also been observed. It was suggested that increased dπ–pπ back-bonding from the metal will increase electron density perpendicular to the C–O axis and so reduce the χ values.[72]

3.4 Relaxation Properties (see *Relaxation Theory for Quadrupolar Nuclei*)

3.4.1 Relaxation in the Extreme Narrowing Condition

In isotropic systems and in the absence of chemical exchange, the T_1 and T_2 relaxation times are equal and are given by

$$1/T_1 = 1/T_2 = 3/125(1 + \eta^2/3)\chi^2 f(\omega,\ D) \qquad (3)$$

where χ is the nuclear quadrupole coupling constant. The asymmetry parameter η varies from 0 to 1 and describes the deviation of the electric field gradient from axial symmetry. $f(\omega,D)$ is the correlation function, which depends on the rotational diffusion constant D and its relative orientation with respect to the principal axes of the field gradient tensor. When isotropic reorientation is assumed, $f(\omega,D)$ reduces to the single correlation time τ_c. If the resonance absorption is a Lorentzian lineshape, the linewidth at halfheight $\Delta\nu_{\frac{1}{2}}$ is a direct measure of the relaxation time, provided that unresolved indirect spin coupling is not present and that chemical exchange phenomena do not take place. From equation (3) it is clear that the product $\chi^2(1 + \eta^2/3)$ can be obtained from ^{17}O relaxation times if the correlation time governing the relaxation is known. The Debye formula allows only the determination of the correct order of magnitude of τ_c. More precise values of τ_c could be obtained from the relaxation of other nuclei, such as ^{13}C or other quadrupolar nuclei; however, one should be aware of possible anisotropic reorientations due to molecular tumbling.[4]

3.4.2 Relaxation Outside the Extreme Narrowing Condition

In this case, the decay of the longitudinal (M_1) and transverse (M_2) magnetizations is no longer exponential but may be written as a weighted sum of $I + \frac{1}{2}$ exponentials:[73]

$$M_1(t) = M_1(\infty)\left\{1 - k\left[\sum_{i=1}^{I+1/2} C_{1,i}\ \exp\left(-R_{1,i}t\right)\right]\right\} \qquad (4)$$

$$M_2(t) = M_2(0)\left[\sum_{i=1}^{I+1/2} C_{2,i}\exp(-R_{2,i}t)\right] \qquad (5)$$

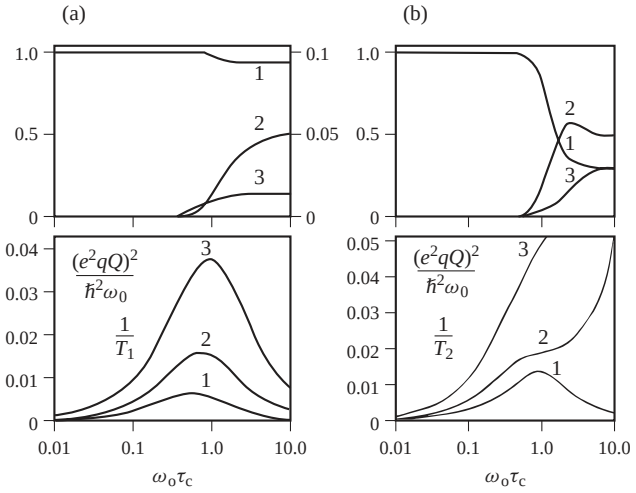

Figure 3 Longitudinal (a) and transverse (b) relaxation of spin-$\frac{5}{2}$ nuclei in the absence of chemical exchange. The upper plots show the normalized amplitudes $C_{1,i}$ and $C_{2,i}$ of the three exponential components as a function of $\omega_0\tau_c$ (coefficients 2 and 3 are plotted on the expanded scale given to the right). The lower plots show the relaxation rates as a function of the same parameter. (Adapted by permission of The American Institute of Physics from T. E. Bull, S. Forsen, and D. L. Turner, *J. Chem. Phys.*, 1979, **70**, 3106)

where $\sum_{i=1}^{I+1/2} C_{j,i}$ and $k = 2$ for an inversion–recovery experiment. Furthermore, although equation (4) is valid for the total magnetization, the decays of the individual components will normally not be exponential and will also depend on the length of the monitoring pulse. Equations (4) and (5) cannot be solved analytically, but must be solved numerically for each value of $\omega_0{}^2\tau_c{}^2$. Figure 3 illustrates the longitudinal and transverse relaxation of spin $I = \frac{5}{2}$ nuclei in the absence of chemical exchange. The longitudinal relaxation may be regarded as a single exponential, within the limits of experimental error, for all correlation times. Conversely, the transverse relaxation is governed by the three contributions and the weights of the different contributions have similar magnitudes for the longer correlation times. For values of $\omega_0{}^2\tau_c{}^2 \ll 1$, the transverse relaxation is approximately a single exponential. In the slow motion limit the rapid decay of the third component at longer correlation times may allow analysis in terms of just two exponential terms.

In addition to nonexponential relaxation for quadrupolar nuclei under conditions of nonextreme narrowing, the NMR signal will also be modified by shift changes which have been termed 'second-order dynamic frequency shifts' (see ***Quadrupolar Interactions*** and ***Dynamic Frequency Shift***). Although long recognized theoretically, the experimental demonstration of such a phenomenon is not straightforward, since the symmetry of the composite peak is in practice difficult to distinguish from small phase misadjustment and is thus usually overlooked. Furthermore, strongly relaxed transitions may decay so quickly as to be undetected if the instrument deadtime is too long. Expressions for the NMR bandshape for $I = \frac{5}{2}$ and $I = \frac{7}{2}$ nuclei have been derived, both in the presence and the absence of chemical exchange.[74] In the limit $\omega_0\tau_c \gg 1$, the $m = \frac{1}{2} \rightarrow m = -\frac{1}{2}$ component will dominate the spectrum because it is much narrower than the other components. This narrow signal will be shifted

towards lower frequency with a value proportional to χ^2/ω_0. Between these two limits the resonance will be more or less asymmetric, with an apparent shift to either high or low frequency depending on the values of ω_0, τ_c, and χ. The ratio of the dynamic shift to the linewidth $\Delta\omega_d/\Delta\omega_{\frac{1}{2}}$ in this region depends only on ω_0 and τ_c.

3.4.3 *Effects of Relaxation Mechanisms Other Than Quadrupolar*

It is evident from Figure 3 that the linewidth of the narrow component decreases as τ_c increases in the slow motion limit, while the linewidths of the intermediate and broad components increase. However, the linewidth of the narrow component does not necessarily decrease as τ_c increases if the chemical shift anisotropy is large. Such behavior has been observed in studies of the temperature and magnetic field strength dependence of ^{17}O NMR spectra of myoglobin MbC^{17}O samples.[75] For $\tau_c \simeq 14$ ns and $\sigma_{\parallel} - \sigma_{\perp} = 800$ ppm (which is the value for a model heme compound obtained from NMR studies in the solid state) a CSA contribution to the linewidth of about 100 Hz was obtained for the narrow components. This value is comparable to that of the pure quadrupolar contribution to the linewidth (about 96 Hz). The CSA contribution to T_1 was found to be negligible (about 170 ms).

4 SELECTED APPLICATIONS

4.1 Dynamic and Kinetic Studies

Numerous dynamic and kinetic studies have been performed using ^{17}O NMR. Lineshape analysis is not straightforward because the linewidth itself is temperature dependent. Nevertheless, it has been shown that dynamic ^{17}O NMR is a convenient alternative to ^{13}C NMR for studies of metal carbonyl compounds.[76] A solution of $HFeCO_3(CO)_{12}$ at $-89\,^{\circ}$C gives only two ^{13}CO signals in a ratio of 1:2 instead of the expected four signals with a 1:1:1:1 ratio. In ^{17}O NMR, the four signals are easily observed at $-11\,^{\circ}$C and a two-step exchange process averages all the sites, producing a single line at $108\,^{\circ}$C.

^{17}O NMR has been used to measure the rate of oxygen exchange in aldehydes and ketones,[77] cobaloximes,[78] and the periodate–water system.[79] It is possible to measure either the decay of a signal from a group enriched in ^{17}O or the growth of a signal that is undergoing exchange with ^{17}O labeled water.[3]

A substantial number of publications has been concerned primarily with studies of the hydration of ions in solution. The ^{17}O chemical shift of water molecules bound to Al^{3+} was found to be about 11 ppm to high frequency. Temperature dependence studies and lineshape analysis yielded the ^{17}O nuclear relaxation rates of the bound and free water molecules, the coordination number, and the rates of exchange between the bound and free water.[80] In addition, the thermodynamic parameters for activation characterizing the exchange reaction can be obtained. In cases where the chemical shift between 'bound' and 'free' water molecules is small, leading to overlapping of resonances, the resonance of the 'free' molecule can be shifted by adding small amounts of a paramagnetic salt. Estimates of 4, 6, and 6 for the hydration numbers of Be(II), Al(III), and Ga(III) were obtained from area measurements. An alternative method of determining hydration numbers, by evaluating the magnitude of the shift of the water resonances caused by the dissolved paramagnetic ion, has also been suggested.[80]

There is an extensive literature on ^{17}O NMR studies of the exchange rates of water molecules bound to paramagnetic ions.[81–84] In this case there is a much greater chance of observing separate resonances from ^{17}O nuclei in 'bound' water molecules in the solvation shells of paramagnetic cations than in the corresponding diamagnetic cations. The magnitudes and temperature dependences of the linewidths (or relaxation time measurements) of the 'bound' and 'free' resonances, and the chemical shift separations between these resonances, can in principle be used to derive information about the hyperfine splitting constant, a_N, the rate of the solvent interchange process, T_e, and the solvation number. However, because the shifted resonance of the solvated water molecules is also often very broad, it is rarely possible in practice to derive the hydration number of the paramagnetic cation from straightforward area measurements. In such cases the hydration numbers may be obtained by using the theory developed by Swift and Connick[85] who investigated a variety of systems. This type of work and the chemical significance of the results have been reviewed (see ***Paramagnetic Relaxation in Solution***).[86]

4.2 ^{17}O NMR and Torsion Angle Effects

^{17}O NMR spectroscopy is a powerful method for detecting steric effects in molecules in which the steric interactions are characterized by the rotation of functional groups about single bonds to relieve van der Waals interactions or in rigid systems in which the steric interactions are partially accommodated by bond angle and bond length distortions.[87] ^{17}O deshielding is expected when the rotation leads to greater double bond character or reduced electron density on oxygen (e.g. in an isolated carbonyl group). Shielding, however, is observed in the situation in which the carbonyl group assumes more single bond character or increased density on the oxygen atom. Studies of such steric effects have been done on aromatic and heteroaromatic nitro compounds, aryl ketones, aldehydes and 1,2-diketones, aromatic carboxylic acids, esters and amides.[88–91] For nitro aromatic compounds, a quantitative relationship was established between $\delta(^{17}O)$ of the nitro group and the torsional angle between the aromatic ring and the nitro group (Figure 4). It appears that the solid state conformational preference, and thus the angle, is in remarkably good agreement with the average angle determined in the solution state.

4.3 Hydrogen-Bonding Effects (see *Hydrogen Bonding*)

The use of ^{17}O NMR appears to be especially promising for studying hydrogen-bonding interactions, because of the large chemical shift range of the oxygen nucleus.[92–94] The dominance of intramolecular hydrogen-bonding effects over substituent effects has been clearly demonstrated in acetophenones, benzaldehydes, and hydroxynaphthoquinones.[32,95] In

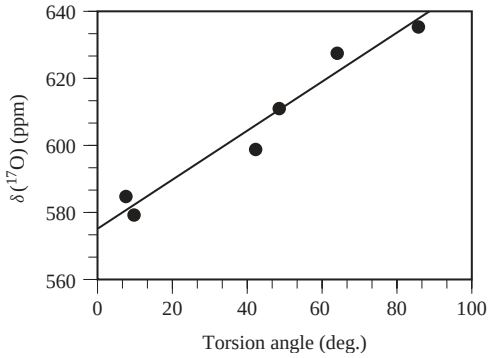

Figure 4 Plot of the torsion angles (X-ray) between aromatic rings and nitro groups versus ^{17}O chemical shift data.[87] (Reproduced by permission of CRC Press, Inc., from D. W. Boykin and A. L. Baumstark, in '^{17}O NMR Spectroscopy in Organic Chemistry', ed. D. W. Boykin, 1991, Chap. 3)

amides and peptides,[10,93,96–100] both long-range dipole–dipole interactions and specific hydrogen bonds at the amide oxygen atom induce significant and specific shielding of the ^{17}O nucleus. Thus the overall chemical shift change between an amide oxygen atom in the absence of hydrogen-bonding interactions in vacuum and one that is fully hydrated in aqueous solution is, very probably, over 95 ppm. There is a linear correlation between $\delta(^{17}O)$ and $\nu(CO)$, the infrared (IR) amide I stretching vibration, for different solvents which have varying dielectric constants and solvation abilities.[100] This demonstrates that both IR and ^{17}O NMR spectroscopy appear to be reflecting a similar type of electronic perturbation, i.e. hydrogen bonding and dipole–dipole solute–solvent interactions. Further studies include investigations of the hydration and intra- and intermolecular hydrogen bonding of the *cis*/*trans* peptide oxygen atoms in AcYOH and AcYNHMe (Y = Pro or Sar)[13,98] (Figure 1), protected dipeptides,[99] and peptide hormones.[101–103]

4.4 Oxygen Bonded to Transition Elements (Polyoxometalates)

^{17}O NMR has been employed frequently in stereochemical studies of polynuclear, anionic oxo complexes (polyoxoanions) of the early transition elements in a variety of oxidation states.[104–108] In spite of their structural complexity, these polyoxoanions often yield well resolved ^{17}O NMR spectra, since large chemical shifts are observed and samples may often be observed at elevated temperatures in nonviscous solvents. Furthermore, ^{17}O enrichment is easily obtained. A representative example is the $[V_{10}O_{28}]^{6-}$ species, the structure and spectrum of which are shown in Figure 5. Exchange of oxygen atoms in the complex ion with those of $H_2{}^{17}O$ in aqueous solution showed that all the different oxygen sites could be identified separately by their shieldings. If an oxygen atom attached to n vanadium atoms is designated as OV_n, then the observed chemical shifts are: OV $\simeq$1150; OV_2 (three different sites) $\simeq$ 900, 790 and 760; $OV_3 \simeq 390$; and $OV_4 \simeq 65$ ppm. It can be seen that there is a systematic reduction in $\delta(^{17}O)$ with an increase in the number of vanadium atoms to which the oxygen atom is bound. Other complex anions of the formula $[M_6O_{19}]^{n-}$, where M = Mo (n = 2), Nb

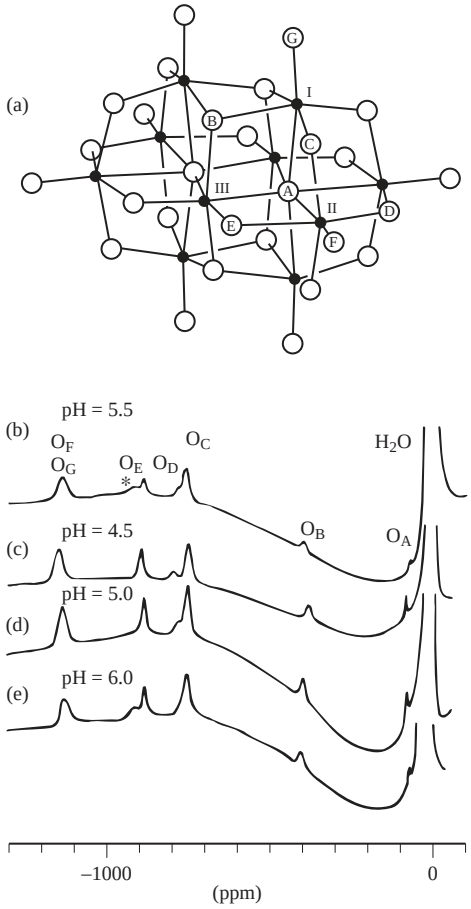

Figure 5 (a) The D_{2h} symmetrized structure of $V_{10}O_{28}{}^{6-}$. Small filled circles represent vanadium atoms and large open circles represent oxygen atoms. One member of each symmetry-equivalent set of atoms is labeled. (b–e) ^{17}O NMR spectra at 13.5 MHz of $V_{10}O_{28}{}^{6-}$ in H_2O. All spectra were measured at 25 °C with total vanadium concentrations of 1.5–1.8 M. The asterisk labels the metavanadate resonance. (Adapted by permission of The American Chemical Society from W. G. Klemperer and W. Shum, *J. Am. Chem. Soc.*, 1977, **99**, 3544)

(n = 8), or Ta (n = 8), show the same qualitative regularities in shielding, with OM > OM_2 > OM_6. These regularities have been interpreted as a correlation between increasing chemical shift and increasing π bonding from the metal to the oxygen in different sites. The regularities persist in the ^{17}O spectra of a variety of more complex anions of lower symmetry in which other metals or nonmetals are substituted within an $[M_xO_y]^{n-}$ framework. It should be noted that the resonances of oxygen nuclei in the highly symmetrical environments of the complex anions, e.g. OM_4 or OM_6, are relatively sharp. This is to be expected because the field gradient at these positions will be zero or very small; hence the normally dominant quadrupolar relaxation mechanism will be very weak and the relaxation times correspondingly long.

4.5 Heme Proteins and Model Compounds—Substrate Binding to Enzymes

The ^{17}O NMR spectra of several heme model compounds in solution have been reported.[11,109–111] Two signals at about

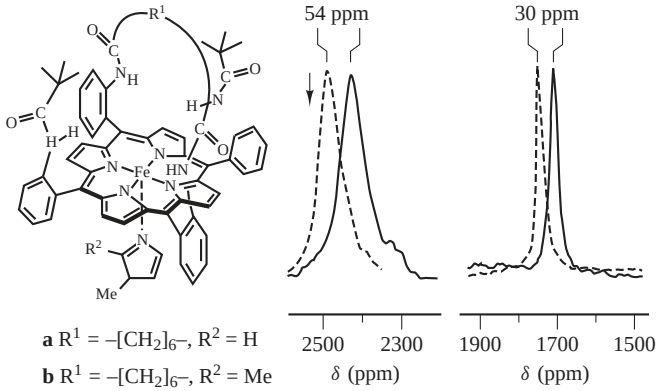

Figure 6 ^{17}O NMR spectra (54.2 MHz) of the oxygenated compounds **a**(- - - -) and **b** (—) with a preacquisition delay time Δt = 50 μs and recorded in two steps with the carrier frequency on the absorption resonances. Maximum concentration $\simeq 10^{-2}$ M in toluene solution. Concentration of 1,2-dimethylimidazole (1,2-Me_2Im) $\simeq 5.10^{-1}$ M, T = 297 K, NS = 1 080 000 (LB = 1 kHz) and 350 000 (LB = 500 Hz) for the high- and low-frequency resonances, respectively. The arrow denotes the region of the resonance position of the terminal oxygen atom of the picket-fence porphyrin model, with excess 1-MeIm, and ether models in which no hydrogen bonding interactions are expected. (Adapted by permission of the Royal Society of Chemistry from I. P. Gerothanassis, B. Look, and M. Momenteau, *J. Chem. Soc., Chem. Commun.*, 1992, 598)

1750 and 2500 ppm were observed for the FeO_2 linkage (Figure 6). The data were interpreted as ruling out sideways triangular bonding in favor of an end-on angular bonding arrangement. The data were explained in terms of bonding models in which the electrons of the FeO_2 moiety are totally paired.

Analysis of the ^{17}O relaxation and chemical shift data of $C^{17}O$ ligated hemoproteins has provided information on both the structural and the dynamic properties of the heme group.[49,75,112] Peroxidases are heme proteins with molecular weights of about 40–42 kDa that catalyze oxidations by hydrogen peroxide. They contain iron-protoporphyrin IX as a noncovalently bound prosthetic group. The ^{17}O NMR spectra of CO-horseradish peroxidase isoenzyme C (Figure 7) indicate a single hemoprotein $C^{17}O$ signal (at 358.3 ppm) below pH 10 and two separate signals at pH 10.5. The new signal, which was assigned with the alkaline form of CO-horseradish peroxidase isozyme C, is broader and at about 7 ppm to high frequency relative to that of the acidic form. A similar pH-dependent relationship of the chemical shift and linewidth was observed for CO-horseradish peroxidase isozyme A and CO-horseradish peroxidase isozyme C. It was concluded that CO-horseradish peroxidase isozyme C undergoes a transition between the acidic and alkaline forms.[112] However, unlike the case of CO-horseradish peroxidase isozyme A, the transition is slow on the NMR timescale (see ***Oxygen-17 NMR: Applications in Biochemistry***).

4.6 Hydration of Proteins: Water Orientation in Lyotropic Phases and Bilayers

Water plays a fundamental role in the conformation and activity of biological macromolecules (see ***Protein Hydration***).

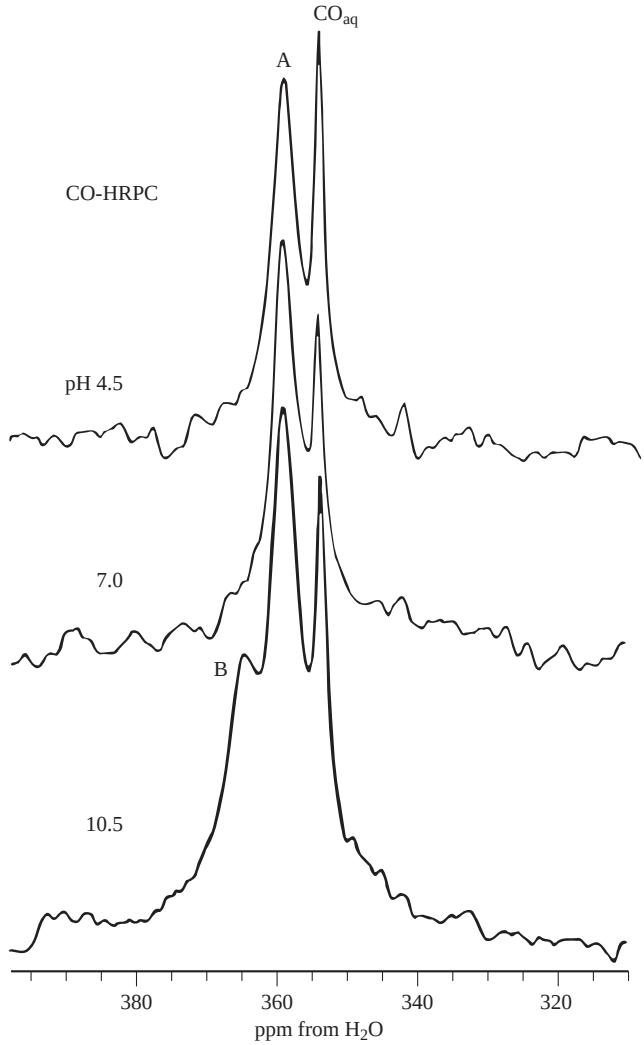

Figure 7 Oxygen-17 NMR spectra of CO-horseradish peroxidase isozyme C (CO-HRPC); concentration, 1 mM in 50 mM phosphate buffer at 11.7 T; NS = 50 000–250 000, recycle time 100–150 ms, pulse width 38 μs, LB = 100 Hz. A, B, and CO_{aq} denote the acidic form of CO-HRPC, the alkaline form of CO-HRPC, and free CO in solution, respectively. (Reprinted by permission of The American Society for Biochemistry and Molecular Biology from H. C. Lee, K. Cummings, K. Hall, L. P. Hager, and E. Oldfield, *J. Biol. Chem.*, 1988, **263**, 16 118)

^{17}O NMR studies have several advantages compared with ^{1}H and ^{2}H NMR for protein hydration:

1. The relaxation effect is large, permitting studies at low protein concentrations.
2. The ^{17}O relaxation in water is generally dominated by the quadrupolar mechanism.[113,114] The intramolecular origin of the electric field gradient makes the quadrupolar interaction virtually independent of the molecular environment.
3. The ^{17}O relaxation is not affected by proton (or deuteron) exchange with protic residues in the protein. Only T_2 can be affected by exchange within a narrow pH range near neutrality.
4. Cross relaxation that contributes to ^{1}H relaxation is unimportant for ^{17}O.[115,116]

Variable field T_1 and T_2 relaxation time measurements of several proteins[117] were interpreted in terms of two layers of

hydration having a reorientational correlation time of about 20 ps (about eight times slower than that of bulk water and independent of the nature of the protein). This rapid local motion has a small anisotropic component (corresponding to an order parameter of 0.06) which is averaged out by protein reorientation with a correlation time of the order of 10 ns.

Water molecules are important constituents of lyotropic phases and bilayers. In this case the molecular motions are strongly anisotropic and the quadrupolar interaction is not averaged out to zero and may be measured when it is small compared with the Zeeman interaction. Ordering of a water molecule results in a quadrupolar splitting which is related to the order parameter. It has been shown that important dynamic information can be obtained from ^{17}O linewidth data which complement the ordering results from ^{2}H NMR.[118] (see ***Amphiphilic Liquid Crystalline Samples: Nuclear Spin Relaxation*** and ***Liquid Crystalline Samples: Structure of Nonrigid Molecules***).

4.7 The Solid State

Under conditions of magic angle spinning (MAS) (see ***Magic Angle Spinning***), the $(\frac{1}{2}, -\frac{1}{2})$ transition of quadrupolar nuclei with nonintegral spin does not depend on first-order quadrupolar interactions or on the effects of θ (the angle between $\boldsymbol{B}_0$ and q_{zz}). The powder bandshapes depend upon second-order quadrupolar effects which do not eliminate the possibility of obtaining meaningful NMR spectra. In this case operation at very high magnetic fields will generally be most advantageous since the maximum second-order quadrupolar linewidth of the $(\frac{1}{2}, -\frac{1}{2})$ transition decreases linearly with the magnetic field.[119] Typical results are those obtained for a range of oxides, oxyanions and high temperature oxide superconductors.[120–122] For fosterite (Mg_2SiO_4), in which three crystallographically distinct oxygen sites were partly resolved, it was possible to determine the chemical shifts (61, 62, and 47 ppm), the quadrupole coupling constants (2.35, 2.35, and 2.7 MHz), and the electric field gradient tensor asymmetry parameters (0.2, 1.0, and 0.3) associated with each. From similar studies of silicate minerals and other compounds it was found that the χ values are related to the percentage ionic character of the bonds to oxygen.[120] It has also been found that VAS can be advantageous, especially for removing resonances arising from transitions other than $(\frac{1}{2}, -\frac{1}{2})$ (see ***Variable Angle Sample Spinning***). Furthermore, it has been demonstrated that ^{17}O spins can be polarized by the ^{1}H spin system, as is done for ^{13}C in CP MAS.[123]

^{17}O NMR studies on single crystals have the advantage, compared with studies on powders, that the complete principal components of the nuclear quadrupolar coupling constant and shielding tensors can be obtained and their orientation relative to the local molecular symmetry can be determined.[124]

5 RELATED ARTICLES

Amphiphilic Liquid Crystalline Samples: Nuclear Spin Relaxation; Dynamic Frequency Shift; Hydrogen Bonding; Liquid Crystalline Samples: Structure of Nonrigid Molecules; Magic Angle Spinning; Oxygen-17 NMR: Applications in Biochemistry; Paramagnetic Relaxation in Solution; Protein Hydration; Relaxation Theory for Quadrupolar Nuclei; Shielding Calculations: IGLO Method; Shielding: Overview of Theoretical Methods; Variable Angle Sample Spinning.

6 REFERENCES

1. C. Roger and N. Sheppard, in *NMR and the Periodic Table*, ed. R. K. Harris and B. E. Mann, Academic, New York, 1978, Chap. 12A.
2. W. G. Klemperer, *Angew. Chem., Int. Ed., Engl.*, 1978, **17**, 246.
3. T. St. Amour and D. Fiat, *Bull. Magn. Reson.*, 1980, **1**, 118.
4. J.-P. Kintzinger, in *NMR Basic Principles and Progress*, ed. P. Diehl, E. Fluck, and R. Kosfeld, Springer, Heidelberg, 1981, Vol. 17.
5. W. G. Klemperer, in *The Multinuclear Approach to NMR Spectroscopy*, ed. J. B. Lambert and F. G. Riddell, Reidel, Dordrecht, 1983, Chap. 11
6. J.-P. Kintzinger, in *NMR of Newly Accessible Nuclei*, ed. P. Laszlo, Academic, New York, 1983, Vol. 2.
7. M.-D. Tsai and K. Bruzik, in *Biological Magnetic Resonance*, ed. L. J. Berliner and J. Reuben, Plenum, New York, 1983, Vol. 5.
8. W. McFarlane and H. C. E. McFarlane, in *Multinuclear NMR*, ed. J. Mason, Plenum, New York, 1987, Chap. 14
9. D. W. Boykin (ed.), *^{17}O NMR Spectroscopy in Organic Chemistry*, CRC, Boston, 1991.
10. I. P. Gerothanassis, *Progr. NMR Spectrosc.*, 1994, **26**, 171.
11. I. P. Gerothanassis, *Progr. NMR Spectrosc.*, 1994, **26**, 239.
12. I. P. Gerothanassis, R. Hunston, and J. Lauterwein, *Helv. Chim. Acta*, 1982, **65**, 1764.
13. R. N. Hunston, I. P. Gerothanassis, and J. Lauterwein, *J. Am. Chem. Soc.*, 1985, **107**, 2654.
14. G. W. Kabalka, and N. M. Goudgaon, in *^{17}O NMR Spectroscopy in Organic Chemistry*, ed. D. W. Boykin, CRC, Boston, 1991, Chap. 1
15. I. P. Gerothanassis and J. Lauterwein, *Magn. Reson. Chem.*, 1986, **24**, 1034.
16. I. P. Gerothanassis, J. Lauterwein, and N. Sheppard, *J. Magn. Reson.*, 1982, **48**, 431.
17. J. Lauterwein and I. P. Gerothanassis, *J. Magn. Reson.*, 1983, **51**, 153.
18. J. Schulte and J. Lauterwein, *J. Magn. Reson., Ser. A*, 1993, **101**, 95.
19. I. P. Gerothanassis, *Progr. NMR Spectrosc.*, 1987, **19**, 267.
20. A. C. Kunwar, G. L. Turner, and E. Oldfield, *J. Magn. Reson.*, 1986, **69**, 124.
21. H. A. Christ, P. Diehl, H. R. Schneider, and H. Dahn, *Helv. Chim. Acta*, 1961, **44**, 865.
22. M. Karplus and J. A. Pople, *J. Chem. Phys.*, 1963, **38**, 2803.
23. H. A. Christ and P. Diehl, *Helv. Phys. Acta*, 1963, **36**, 170.
24. L.-O. Andersson and J. Mason, *J. Chem. Soc., Dalton Trans.*, 1974, 202.
25. E. Lippmaa, M. Magi, S. S. Novikov, L. I. Khmelnitski, A. S. Prihodko, O. V. Lebedev, and L. V. Epishina, *Org. Magn. Reson.*, 1972, **4**, 153.
26. J. A. Coderre, S. Mehdi, P. C. Demou, R. Weber, D. D. Traficante, and J. A. Gerlt, *J. Am. Chem. Soc.*, 1981, **103**, 1870.
27. I. P. Gerothanassis and N. Sheppard, *J. Magn. Reson.*, 1982, **46**, 423.
28. J. A. Gerlt, P. C. Demou, and S. Mehdi, *J. Am. Chem. Soc.*, 1982, **104**, 2848.

29. B. N. Figgis, R. G. Kidd, and R. S. Nyholm, *Proc. R. Soc. London, Ser. A*, 1962, **269**, 469.
30. W. H. De Jeu, *Mol. Phys.*, 1970, **18**, 31.
31. D. J. Sardella and J. B. Stothers, *Can. J. Chem.*, 1969, **47**, 3089.
32. T. E. St. Amour, M. I. Burgar, B. Valentine, and D. Fiat, *J. Am. Chem. Soc.*, 1981, **103**, 1128.
33. T. C. Brownlee, M. Sadek, and D. J. Craik, *Org. Magn. Reson.*, 1983, **21**, 616.
34. C. Delseth and J. P. Kintzinger, *Helv. Chim. Acta*, 1978, **61**, 1327.
35. I. J. Solomon, J. N. Keith, A. J. Kacmarek, and J. K. Raney, *J. Am. Chem. Soc.*, 1968, **90**, 5408.
36. I. J. Solomon, A. J. Kacmarek, and J. Raney, *Inorg. Chem.*, 1968, **7**, 1221.
37. I. J. Solomon, A. J. Kacmarek, W. K. Sumida, and J. K. Raney, *Inorg. Chem.*, 1972, **11**, 195.
38. R. Ditchfield, D. P. Miller, and J. A. Pople, *J. Chem. Phys.*, 1970, **53**, 613; 1971, **54**, 4186.
39. R. Ditchfield, *Mol. Phys.*, 1974, **27**, 789.
40. K. A. K. Ebraheem and G. A. Webb, *Progr. NMR Spectrosc.*, 1977, **11**, 149.
41. K. A. K. Ebraheem and G. A. Webb, *J. Magn. Reson.*, 1977, **25**, 399.
42. K. A. K. Ebraheem and G. A. Webb, *J. Magn. Reson.*, 1978, **30**, 211.
43. M. Jallali-Heravi and G. A. Webb, *J. Magn. Reson.*, 1978, **32**, 429.
44. J. Sadlej and A. J. Sadlej, *J. Magn. Reson.*, 1974, **14**, 97.
45. M. Schindler and W. Kutzelnigg, *Mol. Phys.*, 1983, **48**, 781.
46. C. J. Jameson, in *Nuclear Magnetic Resonance*, ed. G. A. Webb, Royal Society of Chemistry, London, 1985, Vol. 14, Chap. 1
47. J. D. Augspurger, C. E. Dykstra, and E. Oldfield, *J. Am. Chem. Soc.*, 1991, **113**, 2447.
48. J. D. Augspurger and C. E. Dykstra, *J. Phys. Chem.*, 1991, **95**, 9230.
49. K. D. Park, K. Guo, F. Adebodun, M. L. Chiu, S. G. Sligar, and E. Oldfield, *Biochemistry*, 1991, **30**, 2333.
50. I. Ando and G. A. Webb, *Org. Magn. Reson.*, 1981, **15**, 111.
51. G. Klopman, *Chem. Phys. Lett.*, 1967, **1**, 200.
52. M. Jallali-Heravi, B. Na Lamphun, G. A. Webb, I. Ando, M. Kondo, and S. Watanabe, *Org. Magn. Reson.*, 1980, **14**, 92.
53. F. R. Prado, C. Giessner-Prettre, A. Pullman, J. F. Hinton, D. Horspool, and K. R. Metz, *Theor. Chim. Acta*, 1981, **59**, 55.
54. Z. Luz and G. Yagil, *J. Phys. Chem.*, 1966, **70**, 554.
55. J. Reuben, A. Tzalmona, and D. Samuel, *Proc. Chem. Soc.*, 1962, 353.
56. H. Versmold, and C. Yoon, *Ber. Bunsenges. Phys. Chem.*, 1972, **76**, 1164.
57. G. A. Gray and T. A. Albright, *J. Am. Chem. Soc.*, 1977, **99**, 3243.
58. O. Lutz, W. Nepple, and A. Nolle, *Z. Naturforsch., Teil A*, 1976, **31**, 978, 1046.
59. G. D. Mateescu and G. M. Benedikt, *J. Am. Chem. Soc.*, 1979, **101**, 3959.
60. G. O. Mateescu, private communication.
61. W. L. Earl and W. Niederberger, *J. Magn. Reson.*, 1977, **27**, 351.
62. M.-D. Tsai, *Biochemistry*, 1979, **18**, 1468.
63. M.-D. Tsai, *Biochemistry*, 1980, **19**, 5310.
64. G. H. Reed and T. S. Leyh, *Biochemistry*, 1980, **19**, 5472.
65. C. P. Cheng and T. L. Brown, *J. Am. Chem. Soc.*, 1979, **101**, 2327.
66. C. P. Cheng and T. L. Brown, *J. Am. Chem. Soc.*, 1980, **102**, 6418.
67. B. H. Ruessink, and C. MacLean, *Mol. Phys.*, 1984, **53**, 421.
68. C. Chachaty and J. P. Quaegedeur, *Mol. Phys.*, 1984, **52**, 1081.
69. Y. Tricot and W. Niederberger, *Helv. Chim. Acta*, 1984, **67**, 1033.
70. G. E. Hawkes, E. W. Randall, S. Aime, and R. Gobetto, *J. Magn. Reson.*, 1986, **68**, 597.
71. R. T. C. Brownlee, M. J. O'Connor, B. P. Shehan, and A. G. Wedd, *J. Magn. Reson.*, 1985, **61**, 22.
72. S. Aime, R. Gobetto, D. Osella, G. E. Hawkes, and E. W. Randall, *J. Chem. Soc., Dalton Trans.*, 1984, 1863.
73. T. E. Bull, S. Forsen, and D. L. Turner, *J. Chem. Phys.*, 1979, **70**, 3106.
74. P. O. Westlund and H. Wennerstrom, *J. Magn. Reson.*, 1982, **50**, 451.
75. H. C. Lee and E. Oldfield, *J. Am. Chem. Soc.*, 1989, **111**, 1584.
76. S. Aime, D. Osella, L. Milone, G. E. Hawkes, and E. W. Randall, *J. Am. Chem. Soc.*, 1981, **103**, 5920.
77. P. Greenzaid, Z. Luz, and D. Samuel, *Trans. Faraday Soc.*, 1968, **64**, 2780, 2787.
78. E. H. Curzon, B. T. Golding, and A. K. Wong, *J. Chem. Soc., Chem. Commun.*, 1982, 63.
79. I. Pecht and Z. Luz, *J. Am. Chem. Soc.*, 1965, **87**, 4068.
80. J. A. Jackson, J. Lemons, and H. Taube, *J. Chem. Phys.*, 1960, **32**, 553.
81. R. E. Connick and D. N. Fiat, *J. Chem. Phys.*, 1963, **39**, 1349.
82. D. Fiat and R. E. Connick, *J. Am. Chem. Soc.*, 1966, **88**, 4754.
83. D. Fiat and A. M. Chmelnick, *J. Am. Chem. Soc.*, 1971, **93**, 2875.
84. R. E. Connick and D. Fiat, *J. Chem. Phys.*, 1966, **44**, 4103.
85. T. J. Swift and R. E. Connick, *J. Chem. Phys.*, 1962, **37**, 307; 1964, **41**, 2553.
86. J. P. Hunt, *Coord. Chem. Rev.*, 1971, **7**, 1.
87. D. W. Boykin and A. L. Baumstark, in *^{17}O NMR Spectroscopy in Organic Chemistry*, ed. D. W. Boykin, CRC, Boston, 1991, Chap. 3
88. M. G. Oakley and D. W. Boykin, *J. Chem. Soc., Chem. Commun.*, 1986, 439.
89. A. L. Baumstark, P. Balakrishnan, M. Dotrong, C. J. McCloskey, M. G. Oakley, and D. W. Boykin, *J. Am. Chem. Soc.*, 1987, **109**, 1059.
90. D. W. Boykin, G. H. Deadwyler, and A. L. Baumstark, *Magn. Reson. Chem.*, 1988, **26**, 19.
91. D. W. Boykin and A. L. Baumstark, *Tetrahedron*, 1989, **45**, 3613.
92. J. Reuben, *J. Am. Chem. Soc.*, 1969, **91**, 5725.
93. M. I. Burgar, T. E. St. Amour, and D. Fiat, *J. Phys. Chem.*, 1981, **85**, 502.
94. H. M. Schwartz, M. MacCoss, and S. S. Danyluk, *J. Am. Chem. Soc.*, 1983, **105**, 5901.
95. G. Jaccard and J. Lauterwein, *Helv. Chim. Acta*, 1986, **69**, 1469.
96. A. Steinschneider, M. I. Burgar, A. Buku, and D. Fiat, *Int. J. Peptide Protein Res.*, 1981, **18**, 324.
97. D. Fiat, *Bull. Magn. Reson.*, 1984, **6**, 30.
98. J. Lauterwein, I. P. Gerothanassis, and R. Hunston, *J. Chem. Soc., Chem. Commun.* 1984, 367.

99. N. Birlirakis, I. P. Gerothanassis, C. Sakarellos, and M. Marraud, *J. Chem. Soc., Chem. Commun.*, 1989, 1122.
100. I. P. Gerothanassis and C. Vakka, *J. Org. Chem.*, 1994, **59**, 2341.
101. H. Gilboa, A. Steinschneider, B. Valentine, D. Dhawan, and D. Fiat, *Biochim. Biophys. Acta*, 1984, **800**, 251.
102. C. Sakarellos, I. P. Gerothanassis, N. Birlirakis, T. Karayannis, M. Sakarellos-Daitsiotis, and M. Marraud, *Biopolymers*, 1989, **28**, 15.
103. I. P. Gerothanassis, N. Birlirakis, T. Karayannis, M. Sakarellos-Daitsiotis, C. Sakarellos, B. Vitoux, and M. Marraud, *Eur. J. Biochem.*, 1992, **210**, 693.
104. A. D. English, J. P. Jesson, W. G. Klemperer, T. Mamouneas, L. Messerle, W. Shum, and A. Tramontano, *J. Am. Chem. Soc.*, 1975, **97**, 4785.
105. M. Filowitz, W. G. Klemperer, L. Messerle, and W. Shum, *J. Am. Chem. Soc.*, 1976, **98**, 2345.
106. W. G. Klemperer and W. Shum, *J. Am. Chem. Soc.*, 1977, **99**, 3544.
107. M. Filowitz, R. K. C. Ho, W. G. Klemperer, and W. Shum, *Inorg. Chem.*, 1979, **18**, 93.
108. M. A. Freeman, F. A. Schultz, and C. N. Reilley, *Inorg. Chem.*, 1982, **21**, 567.
109. I. P. Gerothanassis and M. Momenteau, *J. Am. Chem. Soc.*, 1987, **109**, 6944.
110. I. P. Gerothanassis, M. Momenteau, and B. Loock, *J. Am. Chem. Soc.*, 1989, **111**, 7006.
111. I. P. Gerothanassis, B. Loock, and M. Momenteau, *J. Chem. Soc., Chem. Commun.*, 1992, 598.
112. H. C. Lee, K. Cummings, K. Hall, L. P. Hager, and E. Oldfield, *J. Biol. Chem.*, 1988, **263**, 16 118.
113. J. A. Glasel, *Proc. Natl. Acad. Sci. USA*, 1966, **55**, 479.
114. J. A. Glasel, *Nature*, 1968, **218**, 953.
115. S. H. Koenig, K. Hallenga, and M. Shporer, *Proc. Natl. Acad. Sci. USA*, 1975, **72**, 2667.
116. S. H. Koenig, R. G. Bryant, K. Hallenga, and G. S. Jacob, *Biochemistry*, 1978, **17**, 4348.
117. B. Halle, T. Andersson, S. Forsen, and B. Lindman, *J. Am. Chem. Soc.*, 1981, **103**, 500.
118. Y. Tricot and W. Niederberger, *Biophys. Chem.*, 1979, **9**, 195.
119. M. D. Meadows, K. A. Smith, R. A. Kinsey, T. M. Rothgelb, R. P. Skarjune, and E. Oldfield, *Proc. Natl. Acad. Sci. USA*, 1982, **79**, 1351.
120. S. Schramm and E. Oldfield, *J. Am. Chem. Soc.*, 1984, **106**, 2502.
121. S. Schramm, R. J. Kirkpatrick, and E. Oldfield, *J. Am. Chem. Soc.*, 1983, **105**, 2483.
122. E. Oldfield, C. Coretsopoulos, S. T. Yang, L. Reven, H. C. Lee, J. Shore, O. H. Han, E. Ramli, and D. Hinks, *Phys. Rev. B*, 1989, **40**, 6832.
123. T. H. Walter, G. L. Turner, and E. Oldfield, *J. Magn. Reson.*, 1988, **76**, 106.
124. W. Scheubel, H. Zimmermann, and U. Haeberlen, *J. Magn. Reson.*, 1985, **63**, 544.

Biographical Sketch

Ioannis P. Gerothanassis. *b* 1953. B.Sc., Aristotle University of Thessaloniki, 1974; M.Sc., School of Chemical Sciences, University of East Anglia, 1979; Ph.D. (supervisor Norman Sheppard, FRS), School of Chemical Sciences, University of East Anglia, 1981. Postdoctoral work at the Institut Chimie Organique, Universite de Lausanne. Successively, lecturer, assistant professor, and associate professor, Department of Chemistry, University of Ioannina, Greece. Approx. 60 publications. Current research specialties: multinuclear MR and multidimensional NMR and FT infrared studies of molecules of biological interest.

Polymer Conformations in Glassy Solutions as Studied by Off-resonance Radiation

Jacques-François Jacquinot and Maurice Goldman

CEA Saclay, Gif-sur-Yvette Cedex, France

1 Introduction 1
2 Basics of Relaxation by Fixed Paramagnetic Centers 2
3 The Model Structure of Linear Polymers 4
4 Experimental Methods – Validation on a 3-D System 4
5 Results for Polymer Solutions 5
6 The Problem of Spin Diffusion 7
7 Conclusion and Perspectives 8
8 References 9

1 INTRODUCTION

The statistical structure of linear polymers in dilute or semi-dilute solution, whose main characteristic is its fractal dimension, has been the subject of extensive studies in modern times, on both theoretical and experimental levels. The interest it raised in physics is because, as a branch of theoretical statistical physics, it is amenable to extremely clean and elaborate treatments making use of sophisticated mathematical techniques.[1–3] It also offered an ample field for experimentation. One of the most sensitive and most extensively used tools for these polymer studies is small angle neutron scattering (SANS), which yields the Fourier transform of the average space correlation of pairs of nuclei. This kind of approach corresponds to an exploration of the reciprocal or k space of the polymers.

NMR has been largely absent so far from this class of problems; there are a few exceptions. The numerous NMR studies of polymers (for example, see the articles on polymers in the *Encyclopedia of NMR*) are centered on different properties of these systems. The first exception is the use of dynamic polarization in partly protoned and partly deuterated polymers in solid glassy solutions, in connection with SANS, whose unique quality is that it enables one to change continuously the neutron scattering *amplitude* by the polarized nuclei, an enormous advantage for disentangling the various contributions to the neutron scattered intensity.[4,5] The second exception is mentioned later.

The approach described is to study the influence of the average polymer structure on the characteristics of spin-lattice relaxation.[6,7] More precisely, we study nuclear relaxation without spin diffusion, under the influence of paramagnetic centers, in polymers in solution in a solid glass. The advantage of this is that, since the various spins relax independently of one another, we can see the sum of the individual magnetization evolutions, which is an additive phenomenon. Therefore, the bulk evolution under relaxation of the NMR signal reflects the statistical structural distribution of the polymers. This statistical sensitivity to the environment is well known in ordinary 3D solids, as is discussed later.

Several conditions are required for this study of polymers.

1. The polymers must be static, that is embedded in a solid, which must be a glass, so as not to strain their structure with respect to that in liquid solution. This constraint does not exist in standard SANS, because the high energy of the neutrons (by comparison with the kinetic energy of the atoms or molecules), the polymer motions in a liquid are completely unnoticed by them: for neutrons, a liquid is as 'static' as a solid.
2. Only the nuclei of the polymer must have a large nuclear moment, and not those of the solvent, to investigate the structure of the polymer itself, without contributing to relaxation from the solvent nuclei. The obvious choice is that of protonated polymers in a deuterated solvent. The latter must be a good solvent down to the glassy transition, so as to preserve the structure of the polymers and to avoid their segregation.
3. The only sufficiently tractable case is that when the paramagnetic centers are located on the polymer itself, and not in the solvent. For usual protonated polymers, the choice is most often limited to nitroso radicals. Furthermore, these radicals must be easily grafted to the polymers.
4. The electronic relaxation time, which in practice is the correlation time for the nuclear relaxation, must have an adequate value which imposes that the sample temperature be in the liquid nitrogen range.
5. In order for the time required for nuclear relaxation to remain within a reasonable range, it is necessary for the concentration of paramagnetic centers relative to the relaxing nuclei not to be too small. In the case when only one center is grafted on each polymer, this imposes in practice a maximum size for the polymers.

An experiment of diffusion-free nuclear relaxation by impurities on fractal systems has already been done. (This is the second exception to non-NMR studies to polymer-like fractal structure.) It was performed on ^{29}Si by Devreux et al. in silica aerogels.[8] These have a network structure characterized by a fractal dimension D slightly in excess of two. Using an angular average for the individual relaxation rates, the authors showed that the initial variation of the nuclear polarization was proportional to $t^{D/6}$. This was tentatively extended to an exponential law of the form

$$\langle p(t) - p_{eq} \rangle \propto \exp\left[-\left(\frac{t}{\tau_1} \right)^{D/6} \right] \tag{1}$$

Experimentally, spin diffusion was quenched by averaging the dipole-dipole interactions between ^{29}Si nuclei to zero by

sample spinning at the magic angle $\theta = \text{acos}(1/\sqrt{3})$, and the results correlated well with theory.

In this article, diffusion-free relaxation is investigated in the absence of irradiation, or under off-resonance nuclear irradiation as a function of the angle between the effective field in the rotating frame and the steady field. The measurements concern both the rate of evolution of the bulk nuclear magnetization along the effective field and its steady-state limit. Two types of systems were studied: the paramagnetic centers are grafted at random positions on the polymer; or only one center is grafted on each polymer in a well defined position, usually at one end. For the results to be interpretable, the polymers are monodispersed.

The article is organized in the following sections:

1. A review of the basic facts of nuclear relaxation by dipolar coupling with paramagnetic centers.
2. Description of the experimental procedure and its validation in a 3D solid.
3. Statistical properties of linear polymers in dilute or semi-dilute solution, as results from theory backed by neutron scattering experiments.
4. Description of the investigation of several systems and comparison with theory.
5. Discussion of the problem of spin 'diffusion'.
6. Conclusion and perspectives.

2 BASICS OF RELAXATION BY FIXED PARAMAGNETIC CENTERS

This section is essentially a short summary of well-known facts of NMR.

It has been known since 1949[9] that in insulating solids, the relaxation of nuclear spins 1/2 proceeds from the combination of two processes: direct relaxation by paramagnetic centers, usually present at low concentration, combined with homogenization of the polarization throughout the sample via dipolar-induced flip-flops among the nuclear spins, described by a diffusion equation, leading to an exponential decay of the bulk polarization. The situation is changed when the flip-flops are quenched by a decrease of the effective dipolar interactions, for instance through a strong off-resonance rf irradiation so as to orient the effective field in the rotating frame at the magic angle from the external field.[10–12] Then, one observes the independent direct relaxation of the individual spins. Even when the dipolar interactions are not completely averaged to zero, it is generally possible to observe the diffusion-free relaxation at the beginning of the nuclear magnetization evolution. These are the conditions used in the present study.

2.1 Nuclear Spins Subjected to Strong rf Irradiation

A system of nuclear spins I in a steady magnetic field is subjected to a strong rf field B_1 rotating at a frequency ω at a value $\Delta = \omega_0 - \omega$ from the Larmor frequency. In a frame rotating at frequency ω, the spins are subjected to a steady magnetic field B_{eff} of components $-\Delta/\gamma$ and B_1 along the axes Oz and Ox respectively, that is oriented along an axis OZ tilted by the angle $\theta = \text{atan}\,(B_1/(-\Delta/\gamma))$ Oz (see Figure 1). The effective Hamiltonian has the form

$$\mathcal{H}_{\text{eff}} = \Delta I_z + \omega_1 I_x + \mathcal{H}'_{Dz} = \Omega I_Z + \mathcal{H}'_{Dz} \tag{2}$$

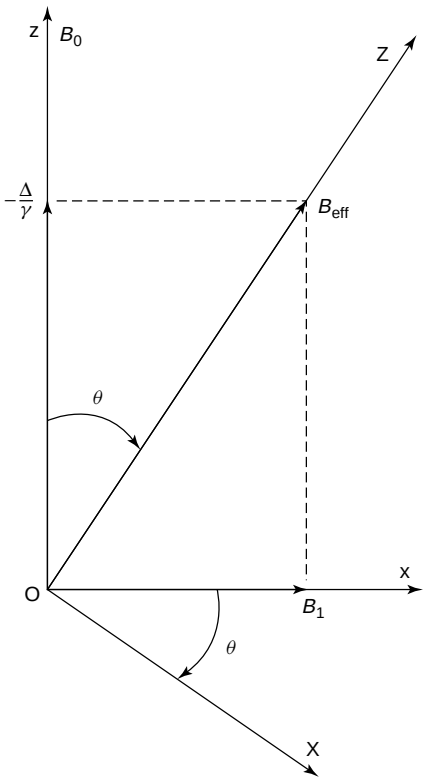

Figure 1 Effective field in the rotating frame under off-resonance irradiation

where, in the last term on the right-hand side, we express the effective Zeeman interaction with respect to the orientation OZ of the effective field (see Figure 1), and $\mathcal{H}'_{Dz}$ is the secular dipolar interaction in the rotating frame, commuting with the operator I_z.

If as we assume, the effective Zeeman interaction is much larger than the dipolar one, the latter has to be truncated so as to retain only its part which commutes with the effective Zeeman interaction, that is with the spin operator I_Z. This is done by rewriting the dipolar Hamiltonian in the system of axes OXYZ and rejecting all terms which differ from $\mathcal{H}'_{Dz}$, of the same form as $\mathcal{H}'_{Dz}$ but expressed in the new system of axes. The corresponding coefficient is equal to $1/2(3\cos^2\theta - 1)$, a standard result recalled in Tabti et al. and discussed at length in Blumberg, Tse and Hartmann, and Lin and Hartmann.[7,9–11] It is easily recovered by an elementary calculation The new effective dipolar interaction is then

$$\mathcal{H}''_{Dz} = \frac{1}{2}(3\cos^2\theta - 1)\mathcal{H}'_{Dz} \tag{3}$$

The magnitude $1/2|3\cos^2\theta - 1|$ can be modified at will within limits by adjusting the angle θ. If we use a second rotating frame, of frequency Ω around OZ, the evolution of the spin system is governed by the effective dipolar interaction $\mathcal{H}''_{Dz}$.

2.2 Local Nuclear Relaxation by a Paramagnetic Center

We consider a paramagnetic spin S at the origin and a nuclear spin I with polar coordinates (r, α, β) Under rf irradiation, the orientation of the spin I is locked along the

direction OZ of its effective field in the rotating frame. Its relaxation through its dipolar coupling with the spin S is calculated through a combination of the methods of Abragam and Tomita.[13,14] The spin S components fluctuate randomly under the effect of its own spin-lattice relaxation, with a longitudinal time T_{1e}. We assume that $\omega_e T_{1e} \gg 1$, where ω_e is the electronic Larmor frequency, so that the only effective S spin component contributing to the nuclear relaxation is S_z, and the correlation time of the random $I - S$ coupling is $\tau_c = T_{1e}$. The relaxing Hamiltonian is of the form

$$\mathcal{H}_{IS}(t) = AS_z(t)I_z + \{BS_z(t)[I_x + iI_y] + h.c.\} \tag{4}$$

with

$$A = \frac{\gamma_I \gamma_S \hbar}{r^6}(1 - 3\cos^2\alpha),$$
$$B = -\frac{3}{2}\frac{\gamma_I \gamma_S \hbar}{r^6}\sin\alpha\cos\alpha\exp(-i\beta) \tag{5}$$

In the hypothesis, often realistic, that $\Omega\tau_c \ll 1$, the relaxation evolution of the component I_Z is a weighted average of those of I_z and I_x. It corresponds to the equation

$$\frac{d}{dt}\langle I_Z\rangle = -\frac{1}{T_1}[\langle I_Z\rangle - \langle I_Z\rangle_{st}] \tag{6}$$

where a standard relaxation calculation yields

$$\frac{1}{T_1} = \frac{S(S+1)}{3}[A^2\sin^2\theta\, J(0) + 2|B|^2(1+\cos^2\theta)J(\omega)] \tag{7}$$

The spectral densities are of the usual form

$$J(\omega) = \frac{\tau_c}{1+\omega^2\tau_c^2} \tag{8}$$

The relaxation rate, equation (7), can be written under the general form

$$\frac{1}{T_1}(\alpha, r) = \frac{C(\alpha)}{r^6} \tag{9}$$

where $C(\alpha)$, which depends on the angle α between the direction of the vector SI and the external field through the square of its sine or cosine, also depends on the angle θ between effective and external fields.

Equation (7) agrees with the relaxation rates derived for the z and x components

$$\frac{1}{T_{1z}} = \frac{1}{T_1}(\theta = 0); \quad \frac{1}{T_{1x}} = \frac{1}{T_1}(\theta = 90^\circ) \tag{10}$$

As for the steady-state value towards which $\langle I_Z\rangle$ evolves, it corresponds to a compromise between the tendency of $\langle I_z\rangle$ to evolve towards the thermal equilibrium value I_0 and that of $\langle I_x\rangle$ to evolve towards 0. The result is

$$\langle I_Z\rangle_{st} = I_0\frac{\cos\theta}{\cos^2\theta + (T_{1z}/T_{1x})\sin^2\theta} \tag{11}$$

All these results can be cleanly derived, and they can be extended to the case when the condition $\Omega\tau_c \ll 1$ is not fulfilled: one must simply replace $J(0)$ with $J(\Omega)$ in equation (7).[15]

2.3 The Steady-State Polarization in a Bulk Sample

The steady-state polarization for a single spin I given in equation (11) depends on the polar angle α through the dependence of T_{1z} and T_{1x} on this angle. In a bulk sample, flip-flop processes, when given enough time to take place, homogenize these steady-state values. The final result is a bulk steady-state polarization of the form

$$\frac{\langle I_Z\rangle_{st}}{I_0} = \frac{\cos\theta}{\cos^2\theta + f(\tau_c)\sin^2\theta}, \tag{12}$$

where the factor $f(\tau_c)$ is equal to a ratio of average relaxation rates

$$f(\tau_c) = \overline{\left(\frac{1}{T_{1x}}\right)}\Big/\overline{\left(\frac{1}{T_{1z}}\right)} \tag{13}$$

Its formal expression is

$$f(\tau_c) = \frac{1}{2} + \frac{2}{3}\omega^2\tau_c^2 \tag{14}$$

The importance of equations (12) and (14) is that by merely measuring the steady-state NMR signal as a function of the angle θ between effective and external field, one obtains an accurate determination of the correlation time τ_c, that is the spin-lattice relaxation time of the paramagnetic centers, irrespective of whether the EPR linewidth is homogeneous or inhomogeneously broadened. This very general result, independent of the structure of the system, may be considered a by-product of some value of the present study.

2.4 Diffusion-Free Relaxation in a Bulk Sample

We give here but an outline of the way of handling the problem of determining the shape of the relaxation evolution of the bulk polarization towards its steady-state value.

The problem is essentially of statistical nature. The magnetization of each individual nuclear spin evolves according to the equation

$$\langle I_Z^i\rangle(t) = \langle I_Z^i\rangle_{st} + (\langle I_Z^i\rangle(0) - \langle I_Z^i\rangle_{st})\exp\left(\frac{-t}{T_1^i}\right) \tag{15}$$

One must sum over all spins, or else consider a 'typical' spin and calculate its average evolution through the probability distribution of relaxation times and steady-state limits

$$\langle I_Z\rangle(t) = \overline{\langle I_Z\rangle_{st}} + \langle I_Z\rangle(0)\overline{\exp\left(\frac{-t}{T_1}\right)} - \overline{\langle I_Z\rangle_{st}\exp\left(\frac{-t}{T_1}\right)} \tag{16}$$

Where the overbar means a bulk statistical average, whereas the brackets correspond as usual to quantum-mechanical expectation values.

As a general rule, all initial magnetizations are equal, which is why the second average on the right-hand side of equation (16) is only on the time-dependent term. This average is relatively easy to calculate. This is not the case for the last joint average, because both the individual $\langle I_Z^i\rangle_{st}$ and T_1^i produced by a single paramagnetic center depend on the polar angle α. This is not too severe when the paramagnetic centers are distributed at random, because most spins will be relaxed by several centers, and the local $\langle I_Z^i\rangle_{st}$ will not differ much from the average. The problem might arise in the case of dilute polymers with only one center grafted on each, that is when

all nuclear spins are relaxed only by one center. However, in all cases studied so far, one always had $\omega\tau_c \gg 1$, so that except in a very small domain of angles α around the magic value, one has $T_{1z}^i/T_{1x}^i \gg 1$ and $\langle I_Z^i\rangle_{st}$ is small compared with $\langle I_Z\rangle(0)$, so that its exact value is of little importance over most of the evolution.

The methods used for calculating the average $\overline{\exp(-t/T_1^i)}$ will not be detailed here, and we will only give and briefly comment on the results for the various cases under study.

3 THE MODEL STRUCTURE OF LINEAR POLYMERS

Although the experimental study was made with finite and relatively short polymers, we describe them by the same model as that derived theoretically in the limit of very long polymers.[1–3]

Linear polymers in dilute solution, that is at a concentration c smaller than the overlap concentration c^*, to be defined later, are independent of each other. Being flexible, they can be present under a variety of configurations. One can define a mean statistical structure by performing an average of all possible configurations. This structure is of spherical symmetry and is characterized by a fractal dimension D. What is meant by this is that around any point of the polymer the number of monomers (or the number of nuclei) present in a sphere of radius r is of the form

$$n_n(r) = \lambda r^D \tag{17}$$

from which we can define an average nuclear density $\rho(r)$ through

$$\frac{d}{dr} n_n(r) = D\lambda r^{D-1} = 4\pi r^2 \rho(r) \tag{18}$$

that is

$$\rho(r) = \frac{1}{4\pi} D\lambda r^{D-3} \tag{19}$$

For linear polymers in solution in a good solvent, this dimension is equal to $D = 1.7$.

We define an effective radius R as that of a sphere that contains all the nuclei N_n of the polymer

$$R = \left(\frac{N_n}{\lambda}\right)^{1/D} \tag{20}$$

and we assume that the density $\rho(r)$ is of the form shown in equation (19) up to $r = R$ and vanishes at larger values. This is obviously an oversimplification, but it will turn out to be convenient.

Among other kinds of radii used in the study of polymers there is the so-called gyration radius R_G defined through

$$R_G^2 = \frac{1}{2(N+1)^2} \sum_{i,j} (\mathbf{r}_i - \mathbf{r}_j)^2 \tag{21}$$

where N is the number of monomers and $\mathbf{r}_i - \mathbf{r}_i$ is the vector joining the monomers i and j. Its value is experimentally derived by small angle neutron scattering.

Another radius, called R_F, equal to the r.m.s. end-to-end distance of the polymer, is theoretically related to R_G through $R_F = 2.51\, R_G$. The vector R of equation (20) is likely to be of an order of magnitude that is similar to these radii.

Among several different definitions of the polymer overlap concentration c^*, the simplest one in the present case is

$$4\pi R^3 c^* = 1 \tag{22}$$

The polymers are said to be in semi-dilute solution when their concentration c is somewhat larger than the concentration c^*, so that they partly overlap. In this case, all points of the polymer are still statistically equivalent: in a sphere of radius ξ around a 'typical' point, the fractal dimension has the same value $D = 1.7$ as in dilute solution, and beyond this distance, the dimension is the same as that of the host medium, that is $D = d = 3$.

The knowledge of the fractal dimension is sufficient to determine the shape of the signal evolution at short time, when only those nuclei close to a paramagnetic center are substantially relaxed. The centers are at low concentration, so that these nuclei are only relaxed by one impurity. The centers being grafted on the polymers, the density of nuclei around them corresponds to the same fractal dimension as the polymers. Starting from zero initial saturation, the evolution of the nuclei at a polar angle α with respect to the center is approximately of the form

$$\langle I_Z\rangle(\alpha; t) \propto \langle I_Z\rangle_{st} \int_{r=b_0}^{\infty} \left[1 - \exp\left(\frac{-C(\alpha)t}{r^6}\right)\right] d(r^D) \tag{23}$$

where b_0 is the barrier within which the nuclei, of frequency shifted by the average electronic dipolar field, are not observed. For $ct/b_0^6 \gg 1$, and by using the notation

$$x = \frac{C(\alpha)t}{r^6} \tag{24}$$

we obtain a result of the form

$$\langle I_Z\rangle(\alpha; t) = \langle I_Z\rangle_{st}(1 - \zeta t^{D/6}) \tag{25}$$

This form remains true when integrating over the angle α. As for the complete form of the evolution, it requires a more elaborate calculation, and it depends on the distribution of the relaxing centers around the nuclei.

4 EXPERIMENTAL METHODS – VALIDATION ON A 3-D SYSTEM

4.1 Experimental Procedure

Within an electromagnet producing a horizontal field, the sample is cooled in a cryostat by flowing cooled nitrogen gas around it. A resistor is used to adjust the gas temperature to within 0.5 K between liquid nitrogen and room temperatures. The sample temperature was as a rule around 100 K. The pulsed spectrometer operates at a frequency around 100 MHz. The field B_1 is of the order of 1 mT, rotating component, that is much larger than the local field of the compounds used, about 0.2 to 0.3 mT. The rf field can be applied up to 9 s without problems.

The measuring sequence goes as follows: the thermal equilibrium magnetization is spin-locked along the direction OZ of the effective field; after an evolution time t, the

magnetization is as a rule realigned with the steady field and then subjected to a $\pi/2$ pulse, and the FID amplitude is measured. The manipulations of the magnetization directions are performed by appropriate pulses and evolution periods.

4.2 Validation on a 3-D Solid: Protonated *O*-Terphenyl

The sample was protonated *o*-terphenyl (OTP) doped with the radical 4-hydroxyl TEMPO (tetramethyl-2,2,6,6 piperidinol-4 oxyle-1) at a concentration of $4.3 \times 10^{19}\,\mathrm{cm}^{-3}$. It was degassed and cooled at 143 K. The centers were then randomly distributed. The relaxation time without rf irradiation was 0.78 s.

For randomly distributed relaxing centers, the theoretical evolution of the nuclear magnetization is an exponential function of $\sqrt{t}$, in accordance with the initial law (see equation (25)).[6,7,10–12,16]

$$\langle I_Z\rangle(t) - \langle I_Z\rangle_{st} = (\langle I_Z\rangle(0) - \langle I_Z\rangle_{st}) \exp\left[-\left(\frac{t}{\tau_1}\right)^{1/2}\right] \quad (26)$$

This law is deduced from a statistical analysis of the paramagnetic center random distribution, and from the fact that, when 'seeing' several paramagnetic centers, the relaxation rate of a given nucleus is the sum of those due to the individual centers.

The expressions for the relaxation rates and steady-state magnetizations as a function of the angle θ between external and effective fields are given in Tabti and Tabti et al. with only two adjustable parameters: the correlation time $\tau_c = T_{1e}$ and the concentration of the relaxing centers. The variation of the steady-state reduced magnetization as a function of the angle θ is shown in Figure 2, together with a best-fit theoretical curve corresponding to

$$\tau_c = 6.5 \pm 0.2 \times 10^{-8}\,\mathrm{s}. \quad (27)$$

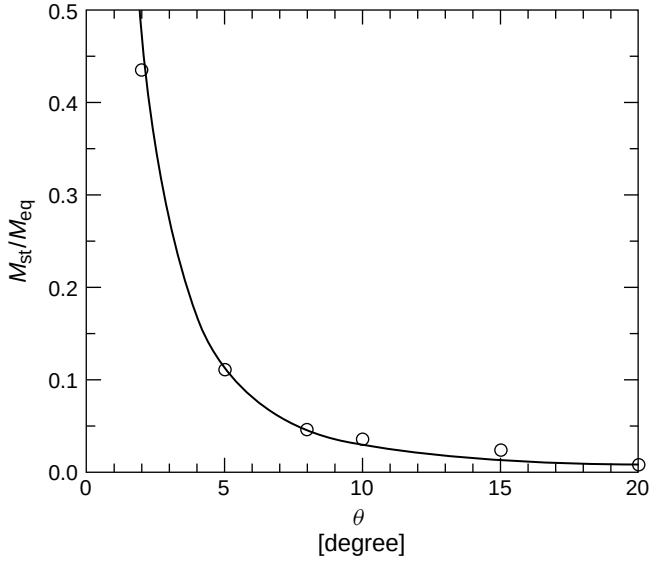

Figure 2 Reduced steady-state magnetization as a function of the angle θ between external and effective field in protonated OTP, together with a best-fit theoretical curve with $\tau_c = 6.5 \pm 0.2 \times 10^{-8}$ s

As for the time-decaying part, it consists of three parts: an initial plateau due to the non-observation of the nuclei close to the centers, an exponential function of $\sqrt{t}$ of the form shown in equation (26), and a final exponential decay as a function of t, when spin diffusion becomes faster than direct relaxation. For the part evolving according to equation (26), the variation of $\tau_{1/2}$ as a function of the angle θ is shown in Figure 3 together with a best-fit curve.

Using the preceding value of τ_c, it yields the concentration of paramagnetic centers

$$N_p = 6.4 \pm 0.1 \times 10^{19}\,\mathrm{cm}^{-3} \quad (28)$$

The fact that this concentration is larger than the nominal one is attributed to the evaporation of some OTP during the degassing process.

These results constitute a validation of the experimental procedure, and provide in addition two pieces of information: the electronic relaxation time and the concentration of the centers.

5 RESULTS FOR POLYMER SOLUTIONS

5.1 Polymers with Randomly Distributed Paramagnetic Centers

The only system studied consisted of poly 2-vinyl pyridine (P_2VP) of average molecular mass $2 \times 10^5\,\mathrm{g\,mole}^{-1}$ on which paramagnetic vanadyl sulphate $VOSO_4$ was grafted at random. It was in semi-dilute solution ($c = 0.05\,\mathrm{g\,cm}^{-3}$) in deuterated glycerol. This system, studied only for illustration purposes, did not use rf irradiation, and it concerns only the longitudinal relaxation.

For polymers of fractal dimension D with random relaxing centers grafted on them, a statistical calculation analogous to that use for 3-D solids yields an evolution law of the magnetization of the form

$$\langle I_Z\rangle(t) - \langle I_Z\rangle_{st} = (\langle I_Z\rangle(0) - \langle I_Z\rangle_{st}) \exp\left[-\left(\frac{t}{\tau_1}\right)^{D/6}\right] \quad (29)$$

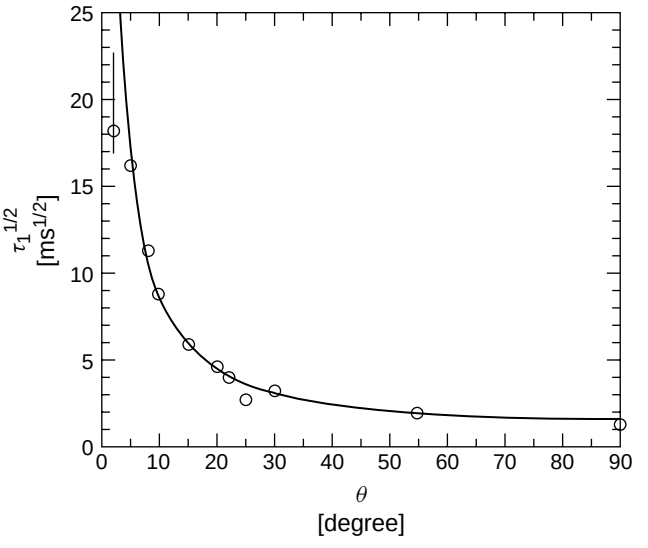

Figure 3 Variation of $\tau_1^{1/2}$ as a function of the angle θ in protonated OTP, together with a best-fit curve with $N_p = 6.4 \pm 0.1 \times 10^{19}\,\mathrm{cm}^{-3}$

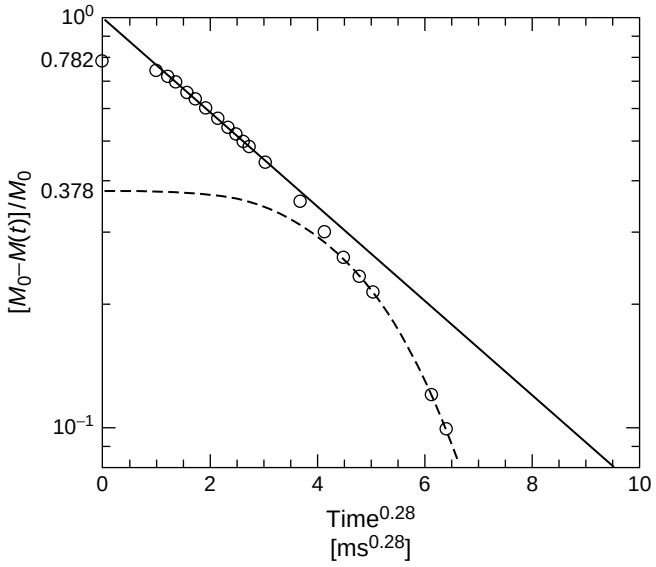

Figure 4 Longitudinal relaxation curve for a semi-dilute solution of P_2VP. The initial decay, an exponential function of $t^{D/6} = t^{0.28}$ (solid line), is followed by an exponential function of time (dashed curve)

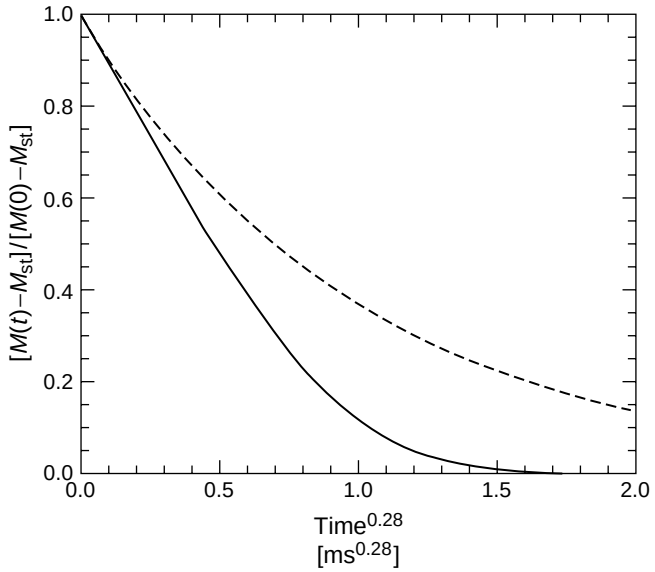

Figure 5 Theoretical variation of the reduced magnetization as a function of $t^{0.28}$ in a dilute solution of polymers with one relaxation center at one end (solid curve). For comparison, the dashed curve is an exponential with the same initial slope

The experimental magnetization evolution, shown in Figure 4, does indeed display such an initial behavior, followed at longer times by an exponential variation, when spin diffusion takes over.

5.2 Polymers with One Paramagnetic Center at One End

The situation for relaxation is markedly different from the preceding one. Indeed, for dilute solution, the relaxation of the nuclei of a polymer is essentially produced by only one center, the one located on the polymer. What the statistical calculation predicts is that over a substantial range, the evolution of the magnetization is a *linear* function of $t^{D/6}$

$$\langle I_Z\rangle(t) - \langle I_Z\rangle_{st} = (\langle I_Z\rangle(0) - \langle I_Z\rangle_{st})\left(1 - \left(\frac{t}{\tau_1}\right)^{D/6}\right) \quad (30)$$

The theoretical curve for the model used is shown in Figure 5, together with an exponential of equal initial slope for comparison. The expected variation for the polymer is indeed linear from initial value 1 down to about 0.4–0.3. We come now to the experimental investigation.

The polymer used is polystyrene of molecular mass of about 8000 (i.e., corresponding to 80 monomers) at the end of which was grafted the radical tetramethyl-2,2,5,5 carboxy-3 pyrrolinyl oxyle-1 (commercial name 3-carboxy PROXYL), diluted in deuterated OTP and then cooled to 120 K The overlap concentration c^* is estimated to about $0.25\,\mathrm{g\,cm^{-3}}$. Experiments were performed on dilute and semi-dilute solutions.

From a study of the steady-state reduced polarization as a function of the angle θ, shown in Figure 6, the best-fit value for the correlation time is

$$\tau_c = 2.6 \pm 0.4 \times 10^{-8}\,\mathrm{s}. \quad (31)$$

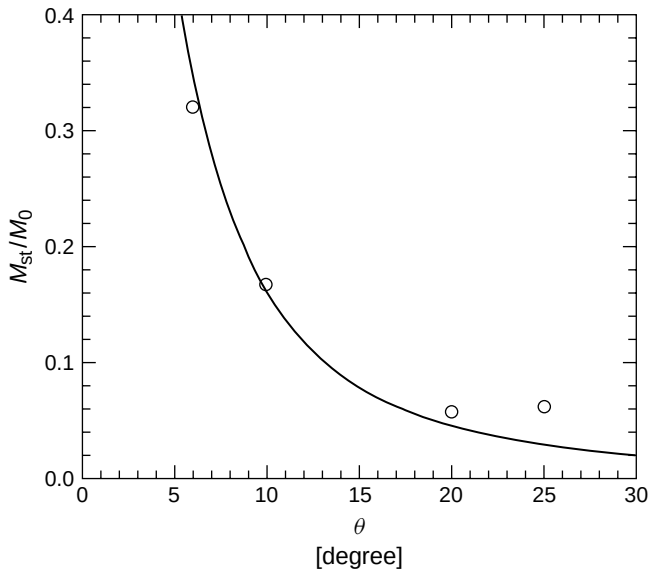

Figure 6 Dilute solution of polystyrene with one relaxing center at one end. Reduced steady-state magnetization as a function of the angle θ, together with a best-fit theoretical curve with $\tau_c = 2.5 \pm 0.4 \times 10^{-8}\,\mathrm{s}$

5.2.1 Dilute Solution

The polystyrene concentration was $0.05\,\mathrm{g\,cm^{-3}}$. A typical evolution curve, for the magic angle $\theta = \mathrm{acos}(1/\sqrt{3})$, is shown in Figure 7.

One observes indeed a linear variation, but down to about 0.1, that is beyond theoretical expectation. This may be due to the crude structure model used: a sudden drop of the nuclear concentration beyond R, or to the interaction with the other polymers. In the absence of any firm theoretical model for the concentration variation of the nuclear density at the largest

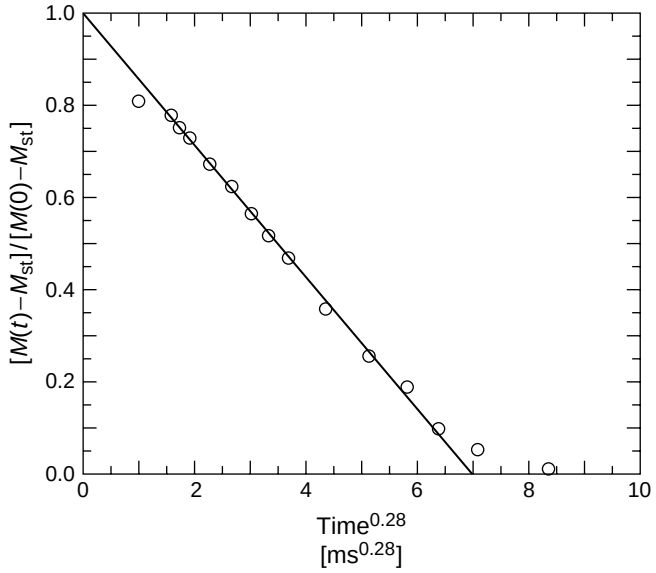

Figure 7 Dilute solution of polystyrene with one relaxing center at one end. Relaxation along an effective field at the magic angle from the external field. Linear reduced magnetization as a function of $t^{0.28}$

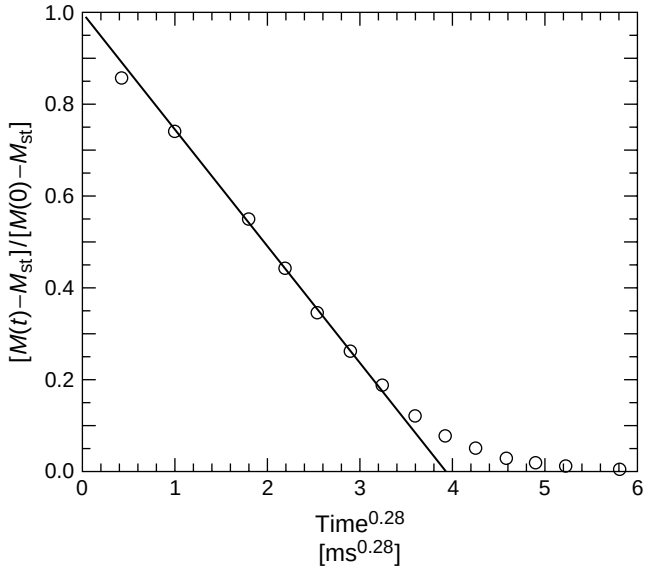

Figure 8 Semi-dilute solution of polystyrene with one relaxing center at one end, under irradiation at resonance. Linear reduced magnetization as a function of $t^{0.28}$

distances, we did not investigate this matter further. Knowing τ_c from the steady-state variation, it is possible to determine the radius R from the evolution with angle θ of the value of τ_1 in equation (30). The best fit value is:

$$R = 3.1 \pm 0.15\,\text{nm}, \tag{32}$$

to be compared with the neutron-scattering-measured value $R_G = 2.1\,\text{nm}$ and the corresponding $R_F = 5.2\,\text{nm}$ All three radii are indeed of the same order of magnitude.

5.2.2 Semi-dilute Solution

The same polystyrene polymers were used at a concentration of $0.30\,\text{g cm}^{-3}$, slightly above the overlap concentration $c^* = 0.25\,\text{g cm}^{-3}$. The experimental relaxation evolution is shown in Figures 8 and 9 for $\theta = 90°$. In Figure 8, the signal is plotted as a function of $t^{D/6}$ and it exhibits the same linear variation as for the dilute solution. In Figure 9, the signal is plotted as a function of $t^{1/2}$ on a logarithmic scale, showing that in the end the signal varies as an exponential function of $\sqrt{t}$. All these features agree qualitatively with the model of semi-dilute solutions of polymers: a region of fractal dimension 1.7 with at most one impurity, surrounded by a homogeneous medium with randomly distributed paramagnetic centers.

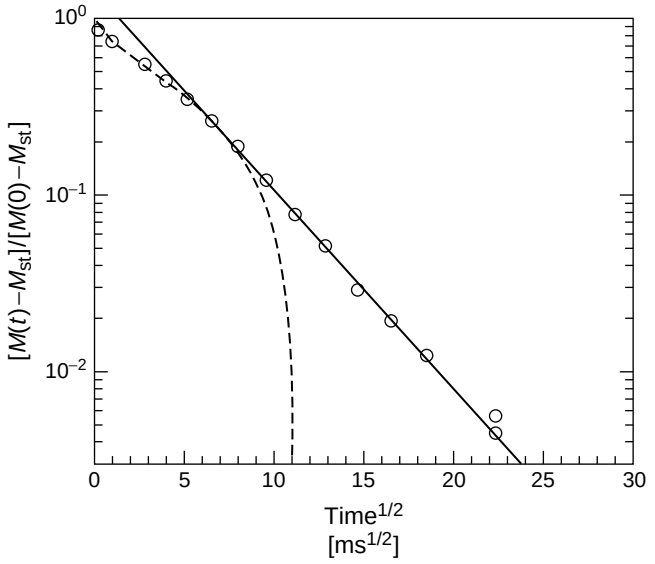

Figure 9 Same as Figure 8, but with different scales: Logarithm of the reduced magnetization as a function of $t^{1/2}$ (solid line), and its variation as a function of $t^{0.28}$ (dashed curve)

6 THE PROBLEM OF SPIN DIFFUSION

This topic, which is not directly connected with the NMR investigation of the polymer structure, will be given a schematic discussion only.

When the angle between the effective and external fields is different from the magic angle, i.e., when the effective secular dipolar interactions do not vanish, the end of evolution of the signal is an exponential function of time. This is brought about by the homogenization of the polarization through flip-flop processes under the influence of the secular dipole-dipole interactions. In usual 3-D solids, this nuclear polarization transfer through space is tentatively described by a diffusion equation, and referred to as spin diffusion. All experimental results on nuclear relaxation by paramagnetic centers in non-conducting solids are in good agreement with this description.

Besides more or less complicated and approximate theoretical treatments of this problem, a particularly enlightening picture of spin-diffusion-induced exponential evolution is that of Blumberg. We summarize it for the so-called diffusion-limited case, in a spherical system of radius R with a relaxing center at the origin, and neglect the angular dependence of the

coefficient C, in equation (9), as well as that of the diffusion coefficient D. The time necessary for direct relaxation to reach the distance r is of the order of $t_r = r^6/C$, whereas the corresponding time for diffusion is of the order of $t_d = r^2/D$. Both times are equal at a distance

$$b \approx \left(\frac{C}{D}\right)^{1/4} \tag{33}$$

Up to this distance, relaxation acts independently on the nuclei, and beyond it diffusion homogenizes the polarization. The relaxation of this part is exponential, with a relaxation rate equal to the average of the individual rates. If ρ is the nuclear density, we obtain

$$\frac{1}{T_1} \approx \frac{C\int_b^R \rho r^{-4}\,dr}{\int_b^R \rho r^2\,dr} \tag{34}$$

which, for a 3-D solid where the density is constant and for $b \ll R$, yields

$$\frac{1}{T_1} \approx \frac{C}{R^3 b^3} \tag{35}$$

a result equal, within a numerical factor of order unity, to that predicted by more sophisticated methods, and in agreement with experiment for randomly distributed centers at low concentration, with R equal to the average distance between centers. We can compare it with the time τ necessary for diffusion to travel the distance R

$$\tau \approx \frac{R^2}{D} \tag{36}$$

We obtain from equations (33) and (35)

$$\frac{\tau}{T_1} \approx \frac{(C/D)R^2}{R^3 b^3} \approx \frac{b}{R} \ll 1 \tag{37}$$

which validates the coherence of the model.

This approach is not adapted to dilute polymers of fractal dimension $D = 1.7$, for two reasons. First, and contrary to direct relaxation, it is hardly justified to use an 'average' polymer, since the dipolar-induced transport of polarization is likely to depend critically on the spatial structure of each polymer. In particular, linear polymers make loops, and there is at present no clean theory of the relative importance of polarization transport along the polymer and through monomers well separated in the linear polymer but accidentally close in space. It is even not known whether this transport can be described by a diffusion equation, nor if the average square distance over which polarization is transported is proportional to time. The second reason why the Blumberg approach fails is that it would yield unphysical predictions even if we could use an average polymer structure and a diffusion equation. We see this briefly. Let us assume that in a polymer both equations (33) and (34) are valid. With a density $\rho \propto r^{D-3}$, we obtain for $b \ll R$, and after a little algebra

$$\frac{1}{T_1} \approx \frac{C}{R^D b^{6-D}} \text{ and } \frac{\tau}{T_1} \approx \left(\frac{b}{R}\right)^{D-2} \tag{38}$$

For $D < 2$, the last ratio is larger than unity! This is in contradiction with the hypotheses of the model. The conclusion is that for a system of low dimensionality, diffusion can take over direct relaxation only at distance substantially larger than b as given by equation (33). This conclusion is confirmed by the experimental results on dilute and semi-dilute solutions of polystyrene. As an example, for an angle $\theta = 25°$ between effective and external fields in a dilute solution of polystyrene, the exponential part of the signal corresponds approximately to 30 per cent of the total signal. The distance r_1 beyond which the polarization is homogenized by diffusion corresponds to $(r_1/R)^D \simeq 0.7$ that is $(r_1/R \simeq 0.8)$. We use this value in equation (34), with the integrations between r_1 and R for calculating T_1. As for the diffusion time, it has to be taken from r_1 to $R : \tau \approx (R - r_1)^2/D$. We obtain finally, with the help of equation (33)

$$\frac{\tau}{T_1} \approx 0.03\left(\frac{b}{R}\right)^4 \ll 1, \tag{39}$$

which lifts the inconsistency.

It would be pointless to extend the discussion further, both because of the doubtful validity of a spin diffusion equation for a collection of polymers and because it is at distances close to R that the model for the variation of the nuclear density with distance should cease to be strictly valid.

7 CONCLUSION AND PERSPECTIVES

The study of direct spin-lattice relaxation of polymers by fixed paramagnetic centers grafted on the polymers turns out to be indeed a useful complement to their investigation by small angle neutron scattering, in particular for confirming their fractal structure. At the present experimental stage, it cannot be claimed that NMR by itself can actually determine the fractal dimension with great accuracy, but it confirms the findings of SANS from a very different type of approach.

However, NMR has potential capabilities that might go beyond those of SANS. An example provided by the experiments on dilute solutions of polystyrene is the shape of the relaxation decay, distinctly different in its last part from theoretical expectation, which hints at the possibility of refining the form of nuclear density near the edge of the polymer. We list a number of openings for which NMR could equally well provide information essentially unavailable by other means:

- placing the paramagnetic centers in the solvent rather than on the polymers, which could provide information on the space excluded by the presence of the polymers and its shape.
- use of a polycrystalline host in order to reveal whether this has an influence on the polymer shape. This possibility is forbidden to SANS, since the grain boundaries would cause a neutron scattering far larger than that due to the polymers.
- use of partly deuterated polymers, so as to have access to the position of given parts of the polymer relative to the end where the relaxing center is grafted.
- consider other polymer configurations. A general but still preliminary study has in fact been made on the relaxation characteristics of polymers close to a surface where paramagnetic centers are located, either grafted to the surface

or adsorbed by the surface, as a function of the surface density of the polymers with respect to their length.[16] This study also envisioned the interest of using partly deuterated polymers.

8 REFERENCES

1. P. Flory, 'Statistical Mechanics of Chain Molecules', reprinted edn., Hanser Publishers: Munich, 1989.
2. P. G. de Gennes, 'Scaling Concepts in Polymer Physics', Cornell University Press: Ithaca and London, 1979.
3. J. des Cloizeaux and G. Jannink, 'Polymers in Solution: Their Modelling and Structure', Clarendon Press: Oxford, 1990.
4. M. G. D. Van der Grinten, H. Glättli, C. Fermon, M. Eisenkremer, and M. Pinot, *Nucl. Instrum. Methods Phys. Res.*, 1995, **A356**, 422–431.
5. H. B. Stuhrmann, *Physica*, 1999, **B267–268**, 92.
6. T. Tabti, *Thèse de Doctorat*, Université de Paris XI, 1995, No. 3699.
7. T. Tabti, M. Goldman, J.-F. Jacquinot, C. Fermon, and G. Le Goff, *J. Chem. Phys.*, 1997, **107**, 9239.
8. F. Devreux, J.-P. Boilot, F. Chaput, and B. Sapoval, *Phys. Rev. Lett.*, 1990, **65**, 614.
9. N. Bloembergen, *Physica*, 1949, **15**, 386.
10. W. E. Blumberg, *Phys. Rev.*, 1960, **119**, 79.
11. D. Tse and S. R. Hartmann, *Phys. Rev. Lett.*, 1968, **21**, 511.
12. N. A. Lin and S. R. Hartmann, *Phys. Rev.*, 1973, **B8**, 4079.
13. A. Abragam, 'The Principles of Nuclear Magnetism', Oxford University Press: Oxford, 1961.
14. K. Tomita, *Prog. Theor. Phys.*, 1958, **19**, 541.
15. M. Goldman, *J. Magn. Reson.*, 2001, **149**, 160–187.
16. T. Tabti, J. Chikina, J.-F. Jacquinot, and M. Daoud, *Phys. Rev. E*, 1999, **60**, 645.

Biographical Sketches

Jacques-François Jacquinot, *b* 1946. Studied at Ecole Normale Supérieure de Saint Cloud. Senior Physicist at Commissariat à l'Energie Atomique (CEA) 1974–present. Research specialties: spin temperature, nuclear magnetic ordering, relaxation in solids, solid state NMR, spin dynamics in rotating samples.

Maurice Goldman, *b* 1933. Diplôme d'Ingénieur Chimiste ESPCI, 1955; Doctorat d'Etat, 1967, University of Paris. Physicist, Commissariat à l'Energie Atomique (CEA), 1955–69 and 1984–89. Vice-Director, Collège de France, 1969–83. Research Director, CEA, 1989–93. Scientific Advisor, CEA, 1993–present. Vice-President, President, Past-President of ISMAR, 1992–present. Approx.130 publications, including three books. Research specialties: spin temperature and thermodynamics, dynamic nuclear polarization, nuclear magnetic ordering, relaxation in liquids and solids, and quantum theory of high-resolution NMR.

Quadrupolar Nuclei in Glasses

Philip J. Bray
Brown University, Providence, RI, USA

1	Introduction	1
2	NMR With a Quadrupolar Perturbation	1
3	Pure Nuclear Quadrupole Resonance (NQR) Studies	5
4	NQR With a Zeeman Perturbation	8
5	Related Articles	10
6	References	10

1 INTRODUCTION

The first use of nuclear magnetic resonance (NMR) to study glass structure using nuclei having electric quadrupole moments was reported by Silver and Bray in 1958.[1] In that work, the interaction between the nuclear electrical quadrupole moment (possessed by all nuclei having a spin $I > \frac{1}{2}$) and the electric field gradient at the nuclear site is small in comparison with the Zeeman interaction of the nuclear magnetic dipole moment with an externally applied magnetic field. The energy levels and transition frequencies can be calculated[2] using the quadrupolar interaction as a perturbation of the Zeeman interaction.

It is this case that is discussed and illustrated with specific examples in the following section. Extensive studies of this type have been summarized and referenced in a number of reviews of NMR studies of glasses.[3–7] (Note that the review by Eckert[3] contains, on p. 163, a table of 39 earlier reviews, listing their main topics.) Succeeding sections of this article contain discussions of the cases in which the magnetic field is absent [i.e., pure nuclear quadrupole resonance (NQR) studies], and cases in which the Zeeman interaction is present but sufficiently small to be treated as a perturbation of the quadrupolar interaction.

There will necessarily be some overlap between the material presented in this article and in other portions of the Encyclopedia. Cross references to pertinent subjects are given at the end of the article.

2 NMR WITH A QUADRUPOLAR PERTURBATION

Figure 1 displays the energy levels for the case of the pure Zeeman interaction (i.e. no quadrupolar interaction present), and the shifting of those levels when a relatively small quadrupolar interaction is present. The shifts depend on the coupling of the nuclear electrical quadrupole moment eQ with the components of the electric field gradient (EFG) tensor at the nuclear site. These are V_{xx}, V_{yy}, and V_{zz} in the system of principal axes for the EFG. Here V is the electrical potential at the nuclear site arising from charges outside the nucleus, and $V_{xx} = \partial^2 V/\partial x^2$, etc. The shifts also depend on the angles θ and ϕ that specify the orientation of the magnetic field $\boldsymbol{B}$ with respect to the principal axes of the EFG. Since all angles θ and ϕ are equally probable in a finely divided polycrystalline powder or a glass, the NMR spectra for those cases will be the envelope of responses observed for a single crystal as it is placed in all possible orientations in the magnetic field. The resulting theoretical 'powder pattern' for a quadrupolar interaction that is sufficiently small to be treated with first-order perturbation theory is displayed in Figure 2 for the case of a nuclear spin $I = \frac{3}{2}$. (No dipolar or other broadening mechanisms have been taken into account.) Here $\chi = e^2qQ = e^2V_{zz}Q$ is the quadrupole coupling constant that measures the strength of the quadrupolar interaction, and $\eta = (V_{xx} - V_{yy})/V_{zz}$ is the asymmetry parameter that measures the departure of the EFG from axial symmetry. (With $|V_{zz}| \geq |V_{yy}| \geq |V_{xx}|$, one finds that $0 \leq \eta \leq 1$.) Note that the 'central' transition ($m = +\frac{1}{2} \leftrightarrow -\frac{1}{2}$) is unaffected at first-order, and remains at the Larmor frequency ν_0, while the 'satellite' transitions ($m = +\frac{3}{2} \leftrightarrow +\frac{1}{2}$ and $m = -\frac{3}{2} \leftrightarrow -\frac{1}{2}$) are spread out into the 'powder patterns'.

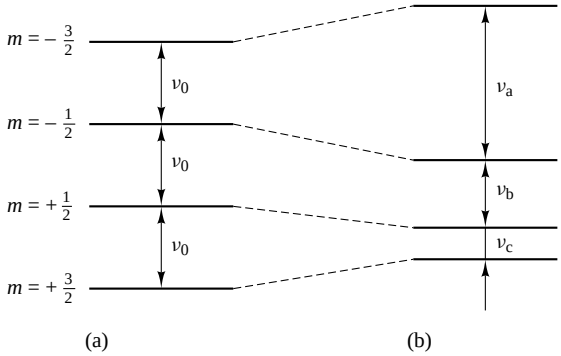

Figure 1 Energy levels arising from the interaction of the nuclear magnetic dipole moment with a magnetic field: (a) no electrical quadrupolar interaction; (b) small quadrupolar interaction present (the levels shown are appropriate for the ^{11}B nucleus)

Broadening mechanisms (e.g., dipolar interactions, and distributions in the EFG components) smooth the divergences in the theoretical powder pattern, and give breadth to the central transition peak. This is exemplified in Figure 3 for the particular case of $\eta = 0$. When use is made of older

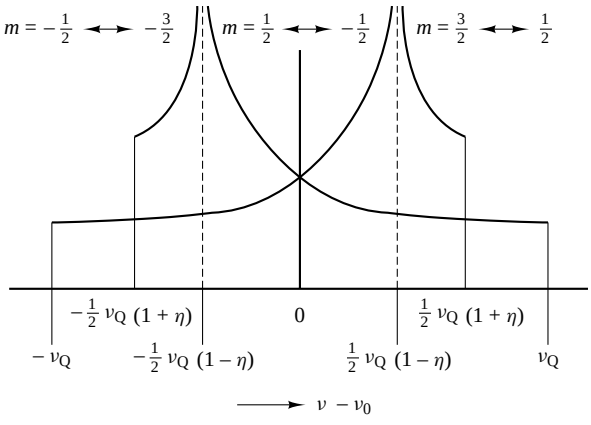

Figure 2 First-order quadrupolar spectrum for $I = \frac{3}{2}$ nuclei in a powder or glass. Here $\nu_Q = 3\chi/2I(2I - 1)$

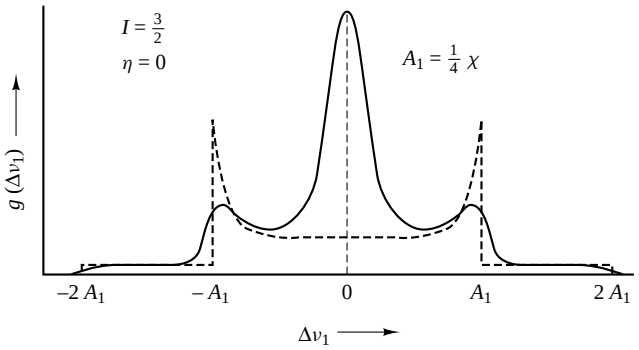

Figure 3 Resonance lineshape (solid curve) predicted for a nucleus such as ^{11}B with a small quadrupolar interaction in a glass or polycrystalline powder. This is the $\eta = 0$ case

CW NMR spectrometers, the recorded resonance is usually the first derivative of the absorption curve. This is displayed in Figure 4 for the ^{11}B ($I = \frac{3}{2}$) response in polycrystalline boron phosphate (BPO_4), for which the value of $\chi = 50.4$ kHz if η is assumed to be zero.[8] (The boron atom is at the center of a BO_4 tetrahedron that is only slightly distorted, so the components of the EFG are quite small. The EFG vanishes for perfect tetrahedral and octahedral symmetry.)

Figure 5 displays[9] the derivative response for ^7Li ($I = \frac{3}{2}$) in a glass containing 25 mol% Li_2O and 75 mol% B_2O_3. If $\eta = 0$ then $\chi \approx 185$ kHz. (The electrical quadrupole moment Q for ^7Li is relatively small.) The partial 'smearing' of the divergences in the powder pattern arises from the distribution in the EFG components caused by the disorder of the vitreous state. See Krämer et al.[10] for other examples of ^7Li NMR spectra for glasses.

When the quadrupolar interaction is larger (but still treatable as a perturbation of the Zeeman interaction), the central ($m = \frac{1}{2} \leftrightarrow -\frac{1}{2}$) transition is affected at second order. Figure 6 displays the theoretical pattern for this case, both for $\eta < \frac{1}{3}$ and $\eta > \frac{1}{3}$. The particular case of small or zero η is illustrated in Figure 7

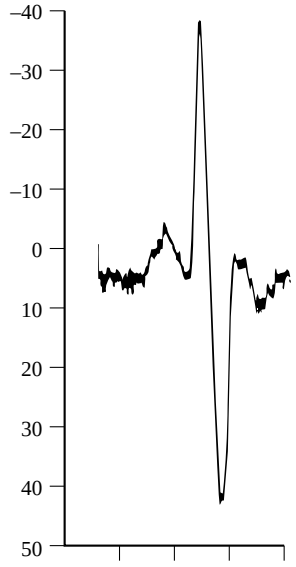

Figure 4 ^{11}B NMR spectrum in boron phosphate (BPO_4); $\nu_0 = 7.177$ MHz

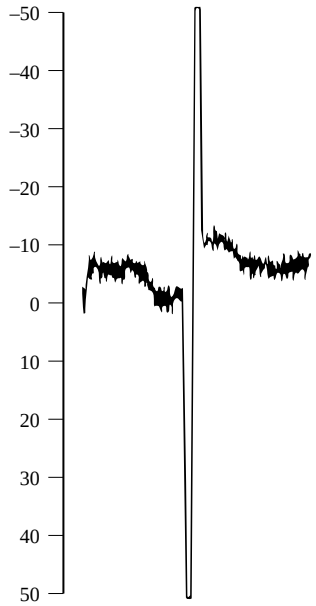

Figure 5 ^7Li NMR spectrum of glass of composition $Li_2O{\cdot}3B_2O_3$

where the dashed lines indicate the theoretical pattern without broadening and the solid line indicates the expected lineshape when broadening is included.

This transition[11a] for ^{11}B in vitreous boron oxide (B_2O_3) is displayed in Figure 8. In this case, in which all of the boron atoms are at the center of planar triangles of oxygens (i.e., BO_3 units) and all of the oxygens are bridging (i.e., bonded to two borons), one finds $\chi = 2.76$ MHz and $\eta = 0.10$. The departure from perfect trigonal symmetry about the axis perpendicular to the BO_3 units and passing through the boron is small or moderate. One finds for such BO_3 units

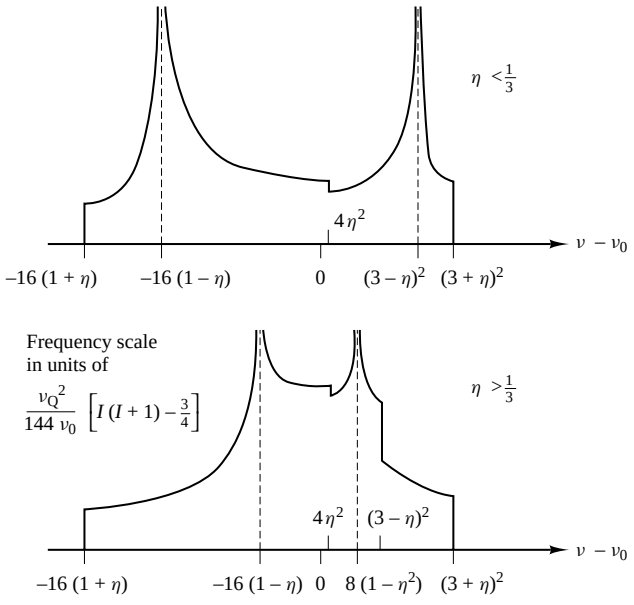

Figure 6 Powder patterns for the central transition ($m = -\frac{1}{2} \leftrightarrow m = +\frac{1}{2}$) of half-integer spin nuclei in the presence of second-order quadrupolar interactions for two regimes: $\eta < \frac{1}{3}$ and $\eta > \frac{1}{3}$. Here $\nu_Q = 3\chi/2I(2I-1)$ and ν_0 is the Larmor frequency

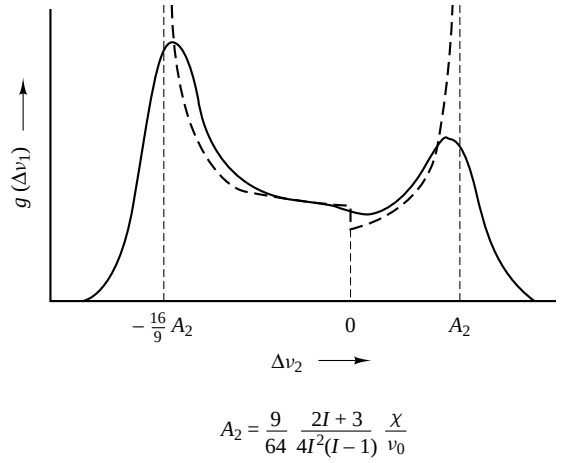

Figure 7 Resonance lineshape (solid curve) for a nucleus with a large quadrupole interaction in a glass or polycrystalline powder. This is the $\eta = 0$ case

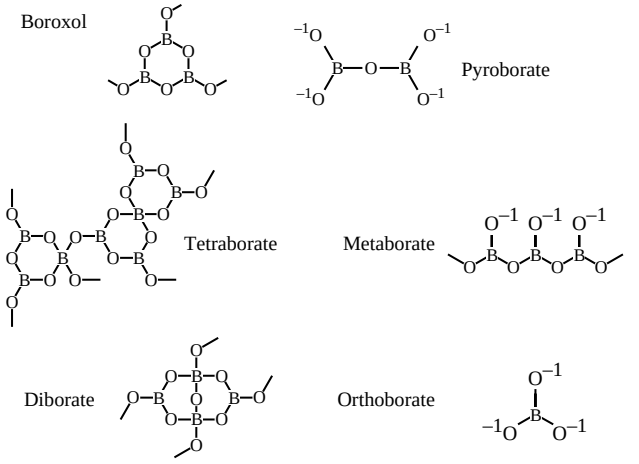

Figure 9 Structural groupings found in alkali borate compounds and glasses

that 2.4 MHz $\leq \chi \leq$ 2.9 MHz and $0 \leq \eta \leq 0.2$. (In the case of vitreous B_2O_3, the BO_3 units are portions of the boroxol structural groupings depicted in Figure 9, but they occur also in other borate structural groupings shown there.)

In alkali borate compounds of 50 mol% or more of alkali oxide, one finds BO_3 units that have one or more nonbridging oxygens (NBO) (i.e., the oxygen is bonded to only one boron and is negatively charged). If the BO_3 unit has one or two of these, the trigonal symmetry noted above is lost, and the asymmetry parameter has been found from NMR spectra to rise into the range $0.4 \leq \eta \leq 0.9$. An example is calcium metaborate ($CaO{\cdot}B_2O_3$), whose chain structure is depicted in Figure 9. The NMR spectrum[11a] of this material is displayed in Figure 10. These asymmetric BO_3 units, and the BO_4 and symmetric BO_3 units, are all present in many borate glasses. Responses from all three units are present in the ^{11}B NMR spectrum[11a] displayed in Figure 11, where the narrow structureless line from BO_4 units is off scale and the symmetric BO_3 units give rise to the middle positive peak on the left and part of one of the negative peaks on the right. The fraction of each type of unit present in the glass can be obtained from the intensity of the corresponding NMR responses, as illustrated in Figure 12 for a low-alkali glass where N_4 is the fraction of four-coordinated borons (i.e. in BO_4 tetrahedra). Figure 13 displays N_4 as a function of the molar fraction x of alkali oxide in alkali borate glasses.[12] With the composition $x\,Na_2O(1 - x)B_2O_3$, N_4 is $x/(1 - x)$ if each oxygen added as Na_2O converts two borons from three- to four-coordination.

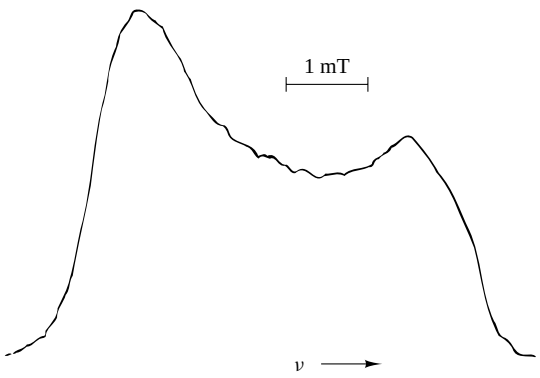

Figure 8 ^{11}B NMR spectrum of vitreous B_2O_3 at 16 MHz[11b]

Kirkpatrick and Oldfield and co-workers[13] have demonstrated that the ^{11}B NMR responses from BO_3 and BO_4 configurations can be separated using magic angle sample spinning (MAS) with high spinning speeds at high magnetic fields. Figure 14 displays the BO_3 and BO_4 responses for polycrystalline $Li_2O{\cdot}2B_2O_3$ and Pyrex glass. (For the Pyrex glass, they conclude that two BO_3 and two BO_4 sites are present. χ for the BO_3 units can be determined to perhaps two significant figures if η is assumed to be zero.)

Quadrupolar effects, then, clearly identify the various boron–oxygen bonding configurations in glasses. That information makes possible the development and validation of structural models for binary,[14] ternary,[15] and more complex glasses containing boron oxide.

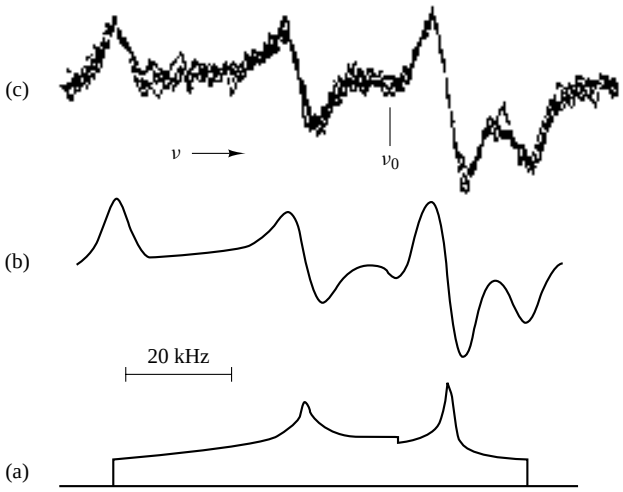

Figure 10 (a) Theoretical powder pattern for the transition ($m = +\frac{1}{2} \leftrightarrow m = -\frac{1}{2}$), with $I = \frac{3}{2}$, $\nu_0 = 16$ MHz, $\chi = 2.56$ MHz, and $\eta = 0.54$. (b) First derivative of the theoretical powder pattern after convolution with a Gaussian curve of linewidth $2\sigma = 5$ kHz. (c) Superposition of four experimental traces for ^{11}B in polycrystalline calcium metaborate, at a resonant frequency of 16 MHz[11b]

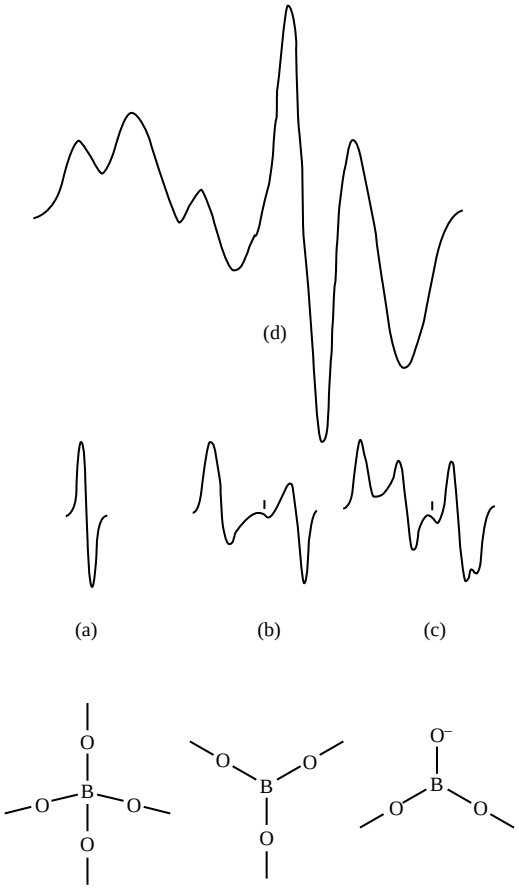

Figure 11 ^{11}B NMR spectrum of (a) a BO_4 unit, (b) a BO_3 unit, (c) a BO_3^- unit (with one NBO), and (d) a sample containing all three units[11b]

Müller-Warmuth and colleagues[16] have improved the resolution and accuracy, and obtained values of χ for the BO_4 units, using very high speed (e.g. 15 kHz) spinning rates and satellite transition spectroscopy (SATRAS). Very short excitation pulses (e.g., 0.5 μs) are used to excite large spectral ranges. Figure 15 displays ^{11}B spectra for a glass of composition (mol%) $33Li_2O{-}67B_2O_3$. Values of χ can be determined from the extent of the spinning sidebands or locations of the centers of gravity of the central and satellite transitions, and (for BO_3) computer simulation of the central transition lineshape as narrowed by the MAS procedure.[17] For the glass of Figure 15, the values of quadrupolar parameters found are 2.6 MHz and 0.3 for BO_3, and 0.80 MHz for BO_4. (The isotropic chemical shifts for BO_3 and BO_4 can also be determined.)

^{27}Al NMR has been extensively employed to study glass structure. Static NMR investigations have generally revealed only structureless, but asymmetric, lines. But utilization of MAS MMR spectroscopy by D. Müller,[18] Samoson and Lippmaa,[19] Kirkpatrick,[20] and Dupree[21] and their colleagues has yielded separation of Al responses from different sites in glasses due to different chemical shifts (and quadrupolar parameters). Kirkpatrick and co-workers[20] clearly identified four-, five-, and six-coordinated aluminum sites in $SiO_2{-}Al_2O_3$ glasses. Those studies have generally been focused on the chemical shifts, but Müller-Warmuth

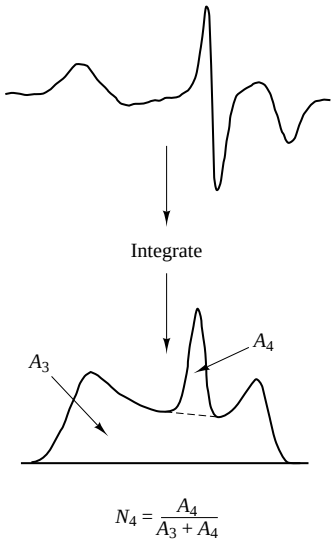

Figure 12 Method for determining N_4 in a ^{11}B NMR spectrum. The experimental spectrum at the top is the first derivative of the absorption curve

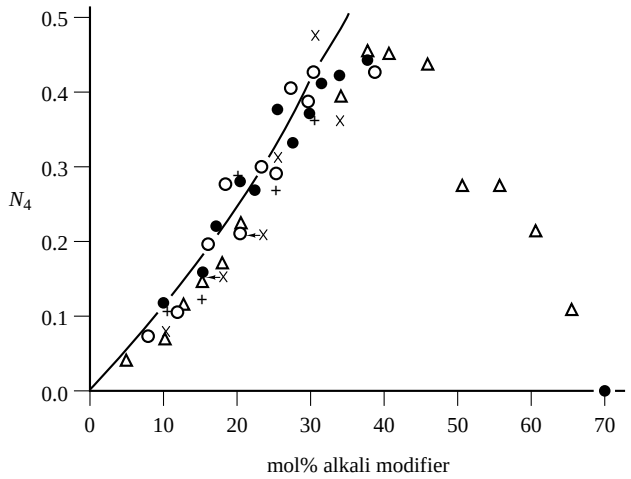

Figure 13 The fraction N_4 of boron atoms in BO_4 configurations in alkali borate glasses plotted against the molar percentage of alkali oxide: •, Na_2O; ○, K_2O; Δ, Li_2O; +, Rb_2O; ×, Cs_2O

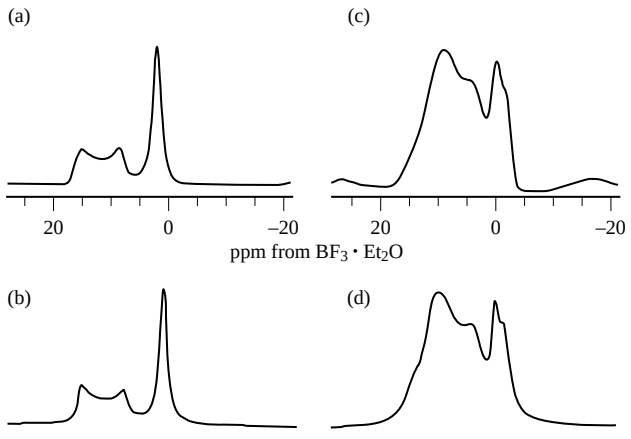

Figure 14 ^{11}B NMR spectra at 11.7 T: (a) $Li_2O{\cdot}2B_2O_3$ at a 6 kHz spinning rate; (c) commercial Pyrex glass at a 4.2 kHz spinning rate; (b) and (d) are the respective computer simulations (see Turner et al.[13])

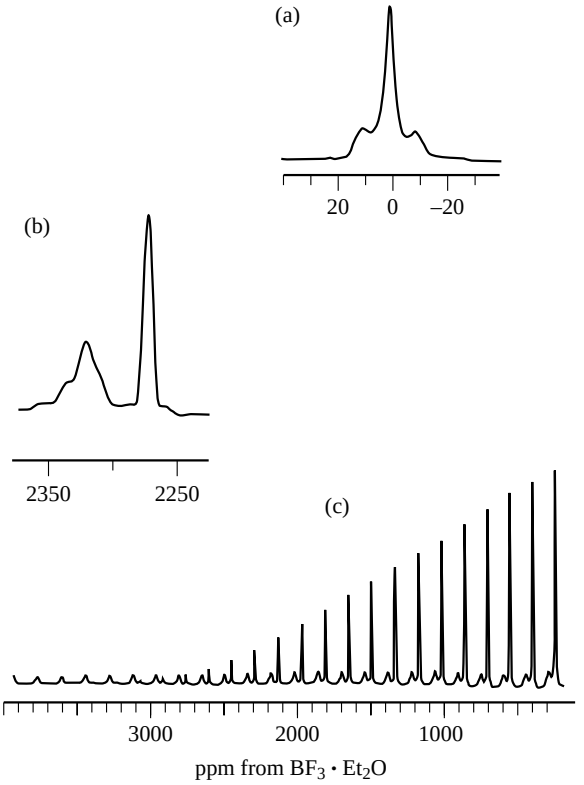

Figure 15 ^{11}B MAS–SATRAS spectrum of glass of composition (mol%) $33Li_2O–67B_2O_3$: (a) central transition; (b) 13th sideband of the satellite transition (ST); (c) part of the ST rotational sideband spectrum. The frequency of rotation is 15 kHz (see van Wüllen and Müller-Warmuth[16])

and associates[22] have used the high-field, high-spinning-rate SATRAS procedure to obtain both the isotropic chemical shifts and the values of χ for a number of ternary glasses. The value of η was not determined, and χ values are therefore limited to an accuracy of about 14%.

Oxygen bonding in vitreous SiO_2 [23] and B_2O_3 [24] has been studied using samples substantially enriched in the ^{17}O ($I = \frac{5}{2}$) isotope from the natural abundance of 0.037%. The ^{17}O spectrum in SiO_2 was simulated by only one oxygen site using the parameters χ = 5.17 MHz and η = 0.2. Changing the value of η or the width of the distributions in χ and η by as much as 30% still yielded an acceptable fit to the experimental spectrum, but the central value (5.17 MHz) of χ could be changed by only 1%. These results can be related to a distribution in the Si–O–Si bond angle between 130° and 180°, which is consistent with an earlier X-ray investigation of SiO_2 glass.

The ^{17}O NMR spectrum for vitreous B_2O_3, shown in Figure 16, required a two-site fit. Quadrupolar parameters for the two sites are χ = 4.69 MHz, η = 0.58 and 5.75 MHz, 0.40. The first site has only small distributions in χ and η, and is assigned to an oxygen in the boroxol ring (see Figure 9). The second site also has a small distribution of χ but a broad distribution in η, and arises from the oxygens connecting boroxol rings. About 83% of the borons in the glass are in boroxol rings. Kirkpatrick and co-workers[25] have extended ^{17}O NMR studies to high fields, and have succeeded in assigning features of the quadrupolar induced structure

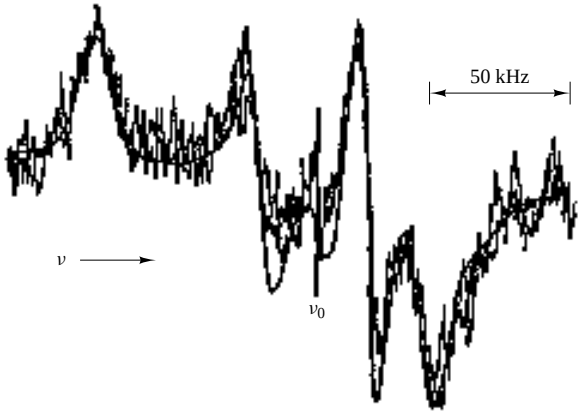

Figure 16 Two superimposed ^{17}O spectra from B_2O_3 glass and a computer simulation using the quadrupolar parameters given in the text

to oxygens in various bonding arrangements (e.g., Si–O–Si, Na–O–Si, and B–O–B).

Segel and Creel[26] prepared vitreous potassium metavanadate and found that the ^{51}V NMR response is the typical ($m = +\frac{1}{2} \leftrightarrow -\frac{1}{2}$) transaction displaying second-order quadrupolar effects. The quadrupolar parameters at 300 K are approximately 3.35 MHz and 0.47. These values are in line with those for the crystalline metavanadates,[26,27] in which each vanadium is enclosed in a tetrahedron of oxygens. In vanadium phosphate glasses[28] and crystalline V_2O_5,[29] in which the vanadiums are five-coordinated to oxygens in VO_5 units, the values of χ are found by NMR to be lower. The value[29] in crystalline V_2O_5 is 805 kHz (with η = 0.04), and rough estimates of χ for the vanadium phosphate glasses are in the 1.0–1.5 MHz range.[28]

The reader is directed to the review by Eckert[3] for summaries of, and references for, similar works on boron-doped amorphous silicon, boron in metal–metalloid glasses, gallium and arsenic studies of GaAs and GaP amorphous semiconductors, deuteron studies of 'water' in glasses, glasses based on B_2S_3, B_2Se_3, Ga_2O_3, and BeF_2, glasses containing Na_2O and Cs_2O, and other quadrupolar nuclei in glasses.

3 PURE NUCLEAR QUADRUPOLE RESONANCE (NQR) STUDIES

Since the quadrupolar interaction generates a set of energy levels in the absence of a magnetic field, transitions between these levels will yield resonance spectra if the spectrometers employed are sufficiently sensitive in the relevant frequency regions. These zero field NMR studies are labeled pure nuclear quadrupole resonance (NQR) spectroscopy.

Pure NQR spectra in solids were first detected by Dehmelt and Kruger in 1950.[30] A large body of NQR studies of chemical bonding and atomic arrangements in crystalline solids, using quadrupolar nuclei, has followed from that discovery and continues to expand (see, e.g., the summaries by Lucken,[31] Schempp and Bray,[32] Semin et al.,[33] and Rubenstein and Taylor[34,35]). The following sections summarize the application of NQR to glass studies employing particular nuclei.

3.1 ^{75}As NQR

The first detection of NQR in a glass was reported by Rubenstein and Taylor in 1972[34] and extended by Taylor and colleagues.[35,36] Rubenstein and Taylor[34] employed the spin $I = \frac{3}{2}$ nucleus ^{75}As in vitreous arsenic trisulfide (As_2S_3). The extended studies[35,36] also encompassed vitreous arsenic telluride and elemental arsenic.

The Hamiltonian for the pure quadrupolar interaction is[37]

$$\hat{\mathcal{H}} = \frac{\chi}{4I(2I-1)}[3\hat{I}_z^2 - I(I+1) + \tfrac{1}{2}\eta(\hat{I}_+^2 + \hat{I}_-^2)] \qquad (1)$$

where $\hat{I}_\pm = \hat{I}_z \pm \hat{I}_y$. When $I = \frac{3}{2}$, the secular equation (with E in units of $\frac{1}{4}\chi$) is

$$E^2 - (1 + \tfrac{1}{3}\eta^2) = 0 \qquad (2)$$

and the frequency ν_0 of the single allowed transition between the m $= \pm\frac{3}{2}$ and m $= \pm\frac{1}{2}$ states, both of which are degenerate in the absence of a magnetic field, is

$$\nu_0 = \tfrac{1}{2}\chi\sqrt{1 + \tfrac{1}{3}\eta^2} \qquad (3)$$

(Clearly, the values of χ and η cannot be independently extracted from this one transition. Methods to determine η, and thus χ, independently are discussed later in this article.)

The transition at frequency ν_0 given in equation (3) was observed by Rubenstein and Taylor[34] for crystalline (orpiment) and vitreous As_2S_3 at 4.2 K using a variable frequency pulsed NQR/NMR spectrometer and observing the frequency dependence of the spin echo amplitude. Figure 17 displays the data points and fitted Gaussian curve for the glass; the two narrower lines in the 70–73 MHz region are data for crystalline As_2S_3. The latter resonances occur at 70.38 and 72.86 MHz with respective halfwidths at half-maximum amplitude (HWHM) of 87 and 44 kHz. (There are two inequivalent As sites in the known structure of orpiment.)

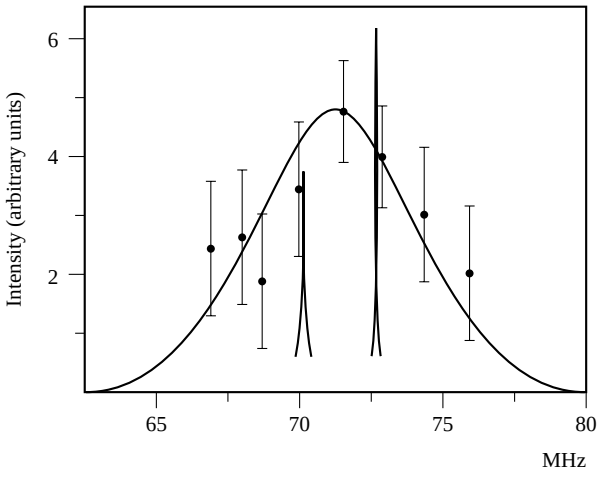

Figure 17 ^{75}As NQR in glassy and crystalline As_2S_3 at 4.2 K. The solid circles are experimental points for the glass through which a Gaussian curve has been drawn. The two narrow lines are data for crystalline As_2S_3 (see Rubenstein and Taylor[34])

But the glass yields only one very broad response centered at 71.6 MHz and having an HWHM of 3.5 MHz.

Orpiment has a layer structure in which each As atom is bonded to three S atoms in a triangular pyramidal arrangement with an As atom at the apex and three S atoms at the base. Rubenstein and Taylor[34] assumed that the large breadth of the lineshape in the As_2S_3 glasses arises from a distribution of distortions in the apex angles α. Since a difference of 1.3° between the α values for the two sites in orpiment produces a difference of 3.48 MHz between the NQR responses, a distribution of apex bonding angles α with a halfwidth of 2° will produce a distribution of frequencies with the observed halfwidth of 3.5 MHz for the glass. (The analysis assumes that the sites present in orpiment, and yielding the observed NQR frequencies, are present in the As_2S_3 glass. This has been placed in question by the work of Szeftel and Alloul that is discussed later in this article.)

In a later study, Rubenstein and Taylor[35] detected and analyzed the pure NQR spectra for crystalline and vitreous As_2Se_3 and obtained a better-resolved spectrum for vitreous As_2S_3. They also measured the spin–lattice relaxation time T_1 at various temperatures. From the near equality of the As_2S_3 crystalline and amorphous initial relaxation behavior, they concluded that the near-neighbor environments of As atoms in the crystal and the glass are quite similar (i.e., the two sites in orpiment, and two-dimensional correlations between As_2S_3 pyramidal units in the layer-structured crystalline phase, are retained in the glass).

Application of a small magnetic field at a series of orientations of an orpiment single crystal yielded data that, based on calculations by Bersohn[37] and Dean,[38] yielded values of the asymmetry parameter for the two sites in the crystal that Rubenstein and Taylor concluded are also present in the glass. This case of a Zeeman perturbation of an NQR spectrum is discussed in the next section. The values of η for the two sites are 0.343 and 0.374.

Jellison, Petersen, and Taylor[36] reported in 1980 an NQR study of amorphous, orthorhombic, and rhombohedral arsenic. Figure 18 displays the highly asymmetric response for the arsenic glass, and the much narrower line for orthorhombic arsenic. Jellison et al. found that the asymmetric pattern obtained for the glass could be reproduced in a calculation by varying the dihedral angle using distributions in the angle

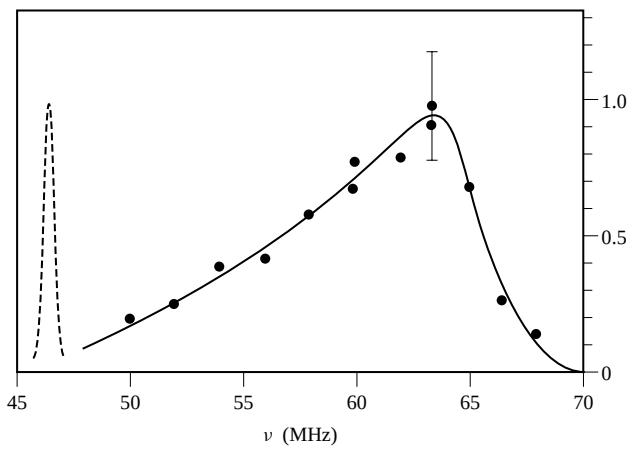

Figure 18 NQR absorption in amorphous As (circles and solid line) and orthorhombic As (dashed line) at 4.2 K (see Jellison et al.[36])

suggested in the literature. (The dihedral angle is the angle of rotation along the As–As bond required to bring the pair into an eclipsed position.) The temperature dependence of the NQR frequencies for the crystalline forms of arsenic were obtained, and could be well fitted by the customary Bayer model,[39] but the NQR lineshape for the arsenic glass is too broad for observation of shifts in the peak frequency with temperature.

In more recent studies,[40] Taylor and colleagues have used ^{75}As NQR and ^{63}Cu NMR spectroscopy to study chalcogenide glasses in the systems Cu–As–S and Cu–As–Se.

3.2 ^{11}B and ^{10}B NQR

The NQR resonance frequencies, predicted from the quadrupolar effects observed in NMR studies, for many other quadrupolar nuclei in glasses (e.g., ^{7}Li, ^{10}B, ^{11}B, ^{14}N, ^{17}O, ^{23}Na, ^{27}Al, ^{39}K, and ^{51}V) lie below 10 MHz and even below 1 MHz. Sufficient signal-to-noise (S/N) values for detection of those responses can be very difficult to achieve. However, a modified Robinson circuit,[41] placing the entire inductive-capacitive tank circuit at 77 K and utilizing state-of-the-art solid state components and Zeeman modulation, has achieved high S/N at low frequencies. Figure 19 from Gravina and Bray,[42] displays the ^{11}B NQR spectrum for crystalline boron oxide (B_2O_3). (^{11}B has spin $I = \frac{3}{2}$, and equation (3) predicts the NQR frequency.) A S/N value between 100 and 200 is easily obtained at this frequency of 1.358 MHz. Figure 20 displays a vertically expanded version of Figure 19 in which the highest frequency of 13 allowed ^{10}B transitions is seen in full detail. (^{10}B is 18.8% and ^{11}B 81.2% abundant in nature.)

In light of the extreme width of the ^{75}As NQR spectra in amorphous As and vitreous As_2S_3 and As_2Se_3, one might anticipate failure in seeking the ^{11}B NQR spectrum in borate glasses near 1.35 MHz. But, if those widths of some megahertz are caused by distributions in the EFG components, they will scale with the resonance frequency. Figure 21 displays the ^{11}B NQR spectrum for vitreous B_2O_3. The full width at half-maximum (FWHM) is 21 kHz. This is only a moderate increase in width from the FWHM of 15 kHz, arising from dipolar broadening, in crystalline B_2O_3. The larger response in Figure 21 must arise from borons in the boroxol groups that predominate[24] in the glass (see Figure 9). The site for the borons yielding the lower-frequency response in Figure 21 has not yet been identified.

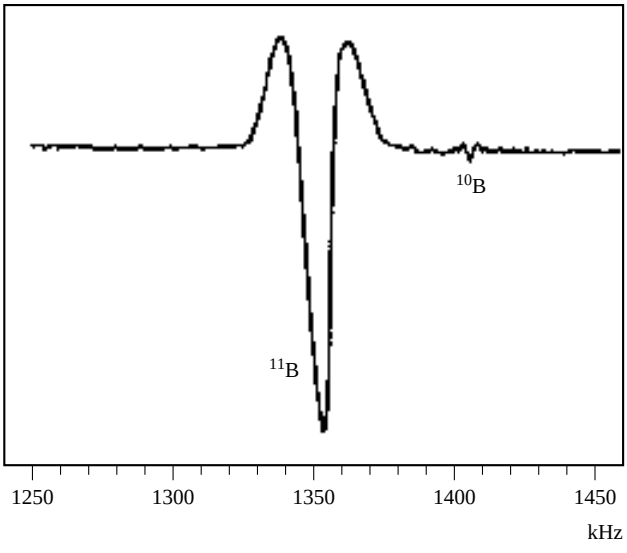

Figure 19 Boron NQR spectrum of crystalline B_2O_3

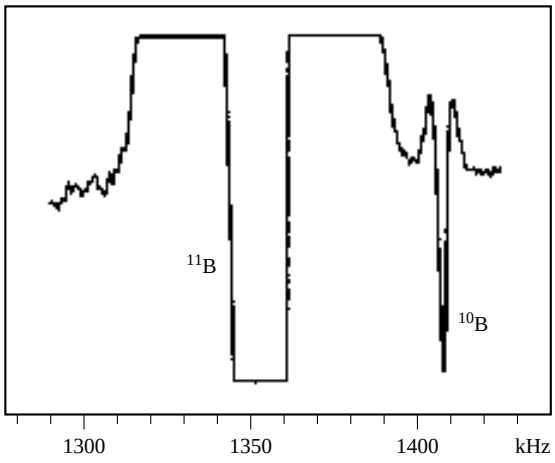

Figure 20 The features of Figure 19 displayed with a greatly expanded vertical scale

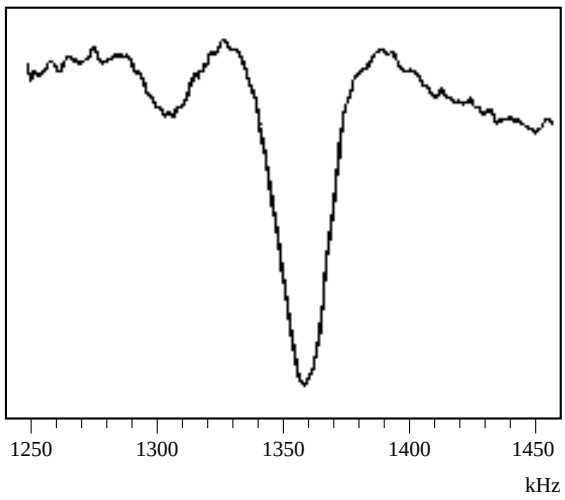

Figure 21 ^{11}B responses from vitreous B_2O_3

Some work has been completed in ^{11}B NQR studies of structural arrangements and chemical bondings in alkali borate glasses. According to the model proposed by Krogh-Moe[43] and supported (but not proved) by the ^{11}B and ^{10}B NMR studies of Bray and co-workers,[44] those glasses should be composed of mixtures of the structural groupings presented in Figure 9. As an indication of the sensitivity of the ^{11}B NQR resonance frequency to the particular structural grouping in which the BO_3 or BO_4 units are located, it is instructive to study Figure 22. The sample under study was prepared as polycrystalline sodium tetraborate ($Na_2O{\cdot}4B_2O_3$), but X-ray diffraction showed the material to be a mixture of sodium borate compounds. ^{11}B NQR responses from at least six sites are resolved in the spectrum displayed in Figure 22, and they span a range of some 150 kHz. There is hope, then, of identifying the particular structural groupings present in any

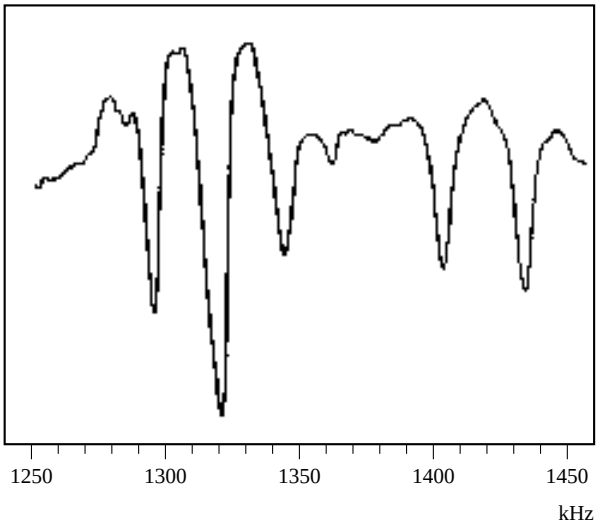

Figure 22 ^{11}B responses from a polycrystalline sample having the sodium tetraborate composition ($Na_2O{\cdot}4B_2O_3$)

borate glass, and even gaining a measure of the amount of each grouping present.

An example of the degree of correspondence between the ^{11}B NQR spectra for crystal and glass is displayed in Figure 23. The spectrum in (a) is for polycrystalline sodium diborate ($Na_2O{\cdot}2B_2O_3$), and the spectrum for the glass is in (b). The crystal is known from X-ray diffraction studies to consist of sodium ions and diborate groupings (see Figure 9). Figure 24 shows the ^{11}B NQR spectrum for a glass of molar composition $0.15\,Na_2O{-}0.85B_2O_3$, with the spectrum for vitreous B_2O_3 superposed. It is clear that there are at least three different structural groupings present in the sodium borate glass, and that one of them is probably the boroxol unit found in vitreous B_2O_3. On the basis that the structural groupings from the crystalline compounds nearest in composition to the glass should predominate, the other responses may arise from the tetraborate group or the pentaborate and triborate groups that can join to form the tetraborate structural grouping (see Figure 9).

3.3 ^{27}Al NQR

The Robinson-type CW spectrometer has been used successfully[45] to detect ^{27}Al NQR spectra in polycrystalline powders and glasses at relatively low frequencies. ^{27}Al has spin $I = \frac{5}{2}$, and the secular equation for the energy values E (with E in units of $\frac{1}{20}\chi$) is

$$E^3 - 7(3 + \eta^2)E - 20(1 - \eta^2) = 0 \qquad (4)$$

Numerical solution via a computer program yields the values of E and the transition frequencies for any set of values of χ and η.

Figure 25 displays the two NQR responses for ^{27}Al in a glass of composition (mol%) of $16.8Al_2O_3{-}83.2TeO_2$ at 77 K. The frequencies are 490.1 and 853.3 kHz and the widths (FWHM) are approximately 15 kHz. Values of χ = 2.909 ± 0.014 MHz and η = 0.346 ± 0.014 were obtained from the

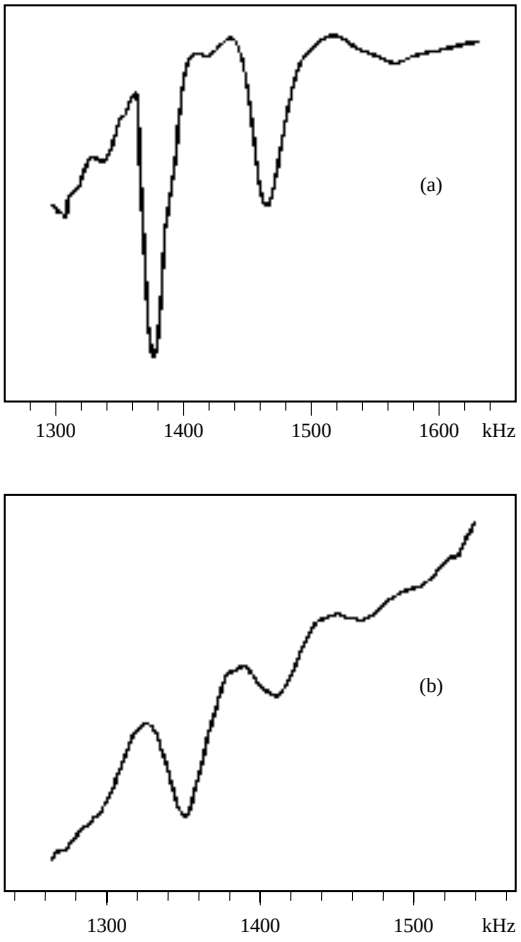

Figure 23 ^{11}B NQR spectra of (a) crystalline and (b) vitreous $Na_2O{\cdot}2B_2O_3$

data. An NMR measurement yielded an isotropic chemical shift of 36.7 ppm, which identifies a pentahedrally coordinated aluminum site.

It is clear that NQR studies of aluminum in four-, five-, and six-coordination in glasses are feasible and very accurate in measurements of the quadrupolar parameters.

4 NQR WITH A ZEEMAN PERTURBATION

We now survey the case in which a small magnetic field is present during the NQR experiment. This Zeeman splitting of a pure NQR spectrum was first treated by Bersohn[37] using a perturbation procedure. Dean[38] subsequently treated the theory of Zeeman splitting rigorously, and discussed the case of nuclear spin $I = \frac{3}{2}$ in detail. The applied field lifts the degeneracy of the $m = \pm\frac{3}{2}$ and $m = \pm\frac{1}{2}$ states, yielding the energies[46] and transition frequencies displayed in Figure 26.

Rubenstein and Taylor[35] applied the expressions for the four transition frequencies $\omega_i = \nu_i$, i = 1, ... , 4 to rotations about the a, b, and c axes of a single crystal (orpiment) of As_2S_3, using a magnetic field of about 87.5 mT. (The Zeeman interaction in this field would be 638 kHz, whereas the NQR frequencies are in the 70–72 MHz range. A first-order perturbation treatment of the Zeeman interaction is adequate.)

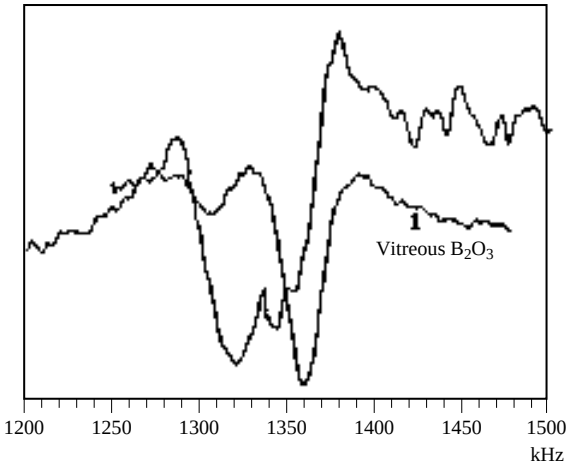

Figure 24 ^{11}B NQR spectrum of a glass of composition $0.15\,Na_2O{-}0.85B_2O_3$ referenced to vitreous B_2O_3

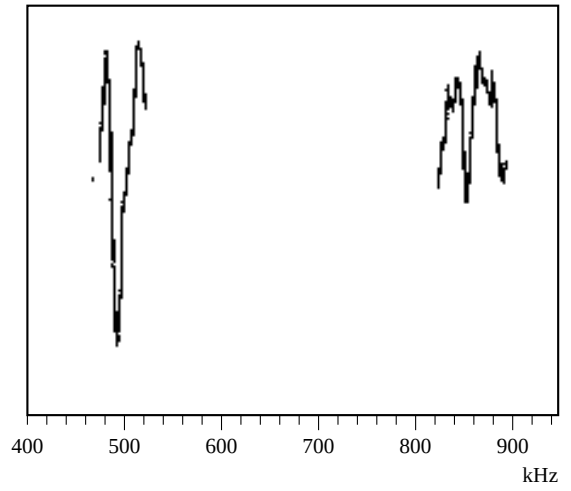

Figure 25 The two ^{27}Al NQR responses for vitreous $16.8Al_2O_3{-}83.2TeO_2$ (mol%)

The values of η extracted for the two inequivalent As sites in orpiment are 0.343 and 0.374.

Szeftel and Alloul[47] employed the frequency Ω_1 in Figure 26 to determine the value of the asymmetry parameter for ^{75}As in several vitreous chalcogenides. (In theory, Ω_3 could also be used, but the transition probability is lower than for Ω_1. No response was detected[47] at Ω_3.) The frequency Ω_1 is given by

$$\Omega_1 = \Omega\left[\left(1-\frac{2}{\rho}\right)^2\cos^2\theta + \left[\left(1+\frac{1}{\rho}\right)^2 + \frac{\eta^2}{\rho^2} - 2\frac{\eta}{\rho}\left(1+\frac{1}{\rho}\right)\cos 2\phi\right]\sin^2\theta\right]^{1/2} \quad (5)$$

where $\Omega = \gamma B$, γ is the gyromagnetic ratio, and $\rho = 1 + \frac{1}{3}\eta^2$. Since equation (4) does not include the quadrupolar coupling constant χ, this transition can be used to obtain the value of η quite decoupled from that of χ.

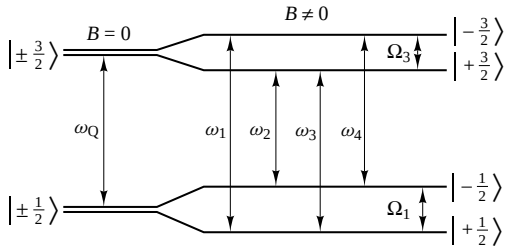

Figure 26 Energy level diagram for a nuclear spin $I = \frac{3}{2}$ in the presence of a strong quadrupolar coupling and, respectively, zero and nonzero Zeeman perturbation (see Szeftel and Alloul[47])

Prediction of the observable lineshape for a polycrystalline powder or glass requires averaging over all θ and ϕ, including the dependence of the state functions and transition probabilities on those angles. Figure 27 displays the calculated lineshapes for two values of η. The parameter $r = \Omega/\nu = \gamma H_0/\nu$, where ν is the frequency of the spectrometer, has the limits $r_m \leq r \leq r_M$, and a logarithmic divergence occurs at r_p, where

$$\left.\begin{aligned} r_m &= \left[1+\frac{1+\eta}{\rho}\right]^{-1}, \quad r_M = \left(\frac{2}{\rho}-1\right)^{-1} \\ r_p &= \left[1+\frac{1-\eta}{\rho}\right]^{-1} \end{aligned}\right\} \quad (6)$$

The ^{75}As spectra obtained at 4.2 K for four vitreous chalcogenides are displayed in Figure 28. Analysis of the spectra was carried out using Gaussian distributions in η about the value determined at the logarithmic divergence (τ_p). For vitreous As_2S_3 and As_2Se_3, it was found necessary to include the contributions from two As sites with distinctly different values of η. These were determined as 0.12 and 0.36 for vitreous As_2S_3, whereas the values for crystalline orpiment found by Rubenstein and Taylor[35] using a single crystal are 0.343 and 0.374. The site with $\eta = 0.12$ is clearly not present in orpiment, and is a site not considered by Rubenstein and Taylor[35] in their discussions of the ^{75}As NQR spectrum for vitreous As_2S_3. For vitreous As_2Se_3, the values of η were determined by Szeftel and Alloul[47] to be 0.14 ± 0.02 and 0.45.

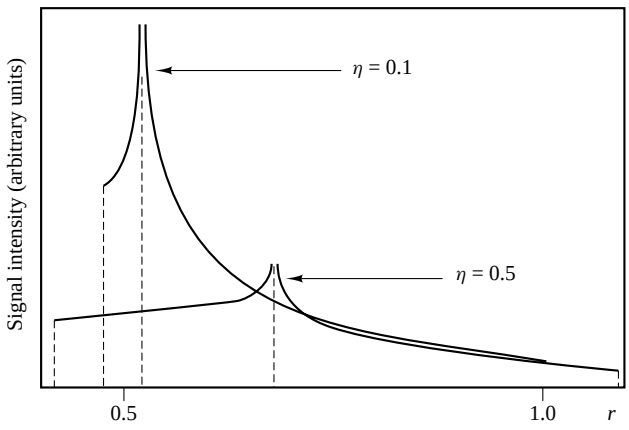

Figure 27 Spectra (solid lines) calculated for two values of η (see Szeftel and Alloul[47])

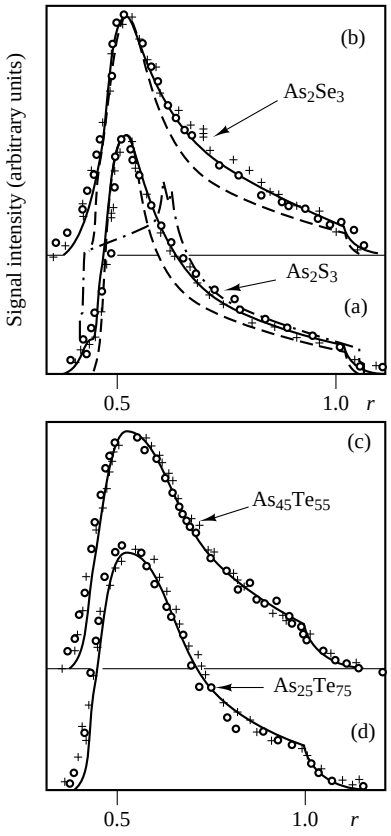

Figure 28 ^{75}As spectra recorded in four vitreous chalcogenides at 5.9 MHz (circles) and 10.3 MHz (crosses). The powder spectrum calculated with the η values of orpiment is plotted as dash-dotted lines. Solid lines indicate the best fit. When two Gaussian distributions are needed to obtain the best fit, the contribution of the distribution of higher weight is plotted as a dashed line (see Szeftel and Alloul[47])

5 RELATED ARTICLES

Amorphous Materials; Boron NMR; Ceramics; Deuterium NMR in Solids; High Speed MAS of Half-Integer Quadrupolar Nuclei in Solids; Lithium NMR; Oxygen-17 NMR; Quadrupolar Interactions; Quadrupolar Nuclei in Solids; Relaxation Theory for Quadrupolar Nuclei; Sodium-23 NMR; SQUIDs; Zero Field NMR.

6 REFERENCES

1. A. H. Silver and P. J. Bray, *J. Chem. Phys.*, 1958, **29**, 984.
2. M. H. Cohen and F. Reif, in *Solid State Physics*, eds. F. Seitz and D. Turnbull, Academic Press, New York, 1958, Vol. 5, p. 321.
3. H. Eckert, in *Progress in Nuclear Magnetic Resonance Spectroscopy*, eds. J. W. Emsley, J. Feeney, and L. N. Sutcliffe, Pergamon Press, Oxford, 1992, Vol. 24, p. 159.
4. P. E. Stallworth and P. J. Bray, *Glass Sci. Technol.*, 1990, **4**, 77.
5. A. R. Grimmer, *Exp. Tech. Phys.*, 1988, **36**, 81.
6. P. J. Bray, S. J. Gravina, D. H. Hintenlang, and R. V. Mulkern, *Magn. Reson. Rev.*, 1988, **13**, 263.
7. P. J. Bray, *J. Non-Cryst. Solids*, 1987, **95/96**, 45.
8. P. J. Bray, J. O. Edwards, J. G. O'Keefe, V. F. Ross, and I. Tatsuzaki, *J. Chem. Phys.*, 1961, **35**, 435.
9. P. J. Bray, *Classe des Mémoirs, de l'Académie Royale de Belgique, Sciences XXXIII*, 1961, **3**, 37.
10. F. Krämer, W. Müller-Warmuth, J. Scheerer, and H. Dutz, *Z. Naturforsch. A.*, 1973, **28**, 1338.
11. (a) P. J. Bray, in *Interaction of Radiation with Solids*, ed. A. Bishay, Plenum Press, New York, 1970, p. 11; (b) S. G. Bishop, Ph.D. Thesis, Brown University, 1969.
12. P. J. Bray and J. G. O'Keefe, *Phys, Chem. Glasses*, 1963, **4**, 37; J. Zhong and P. J. Bray, *J. Non-Cryst. Solids*, 1989, **111**, 67.
13. G. L. Turner, K. A. Smith, R. J. Kirkpatrick, and E. Oldfield, *J. Magn. Reson.*, 1986, **67**, 544; G. L. Turner, R. J. Kirkpatrick, S. H. Risbud, and E. Oldfield, *Am. Ceram. Soc. Bull.*, 1987, **66**, 656.
14. G. E. Jellison, Jr., and P. J. Bray, *Solid State Commun.*, 1976, **29**, 517; *J. Non-Cryst. Solids*, 1978, **29**, 187.
15. P. J. Bray and W. J. Dell, *J. Phys. (Orsay, Fr.)*, 1982, **43**, C9-131; W. J. Dell, P. J. Bray, and X. Z. Xiao, *J. Non-Cryst. Solids*, 1983, **58**, 1.
16. L. van Wüllen and W. Müller-Warmuth, *Solid State Nucl. Magn. Reson.*, 1993, **2**, 279.
17. D. Müller, *Ann. Phys. (Leipzig)*, 1982, **39**, 451.
18. D. Müller, G. Berger, I. Grunze, G. Ludwig, E. Hallas, and V. Haubenreisser, *Phys. Chem. Glasses*, 1983, **24**, 37.
19. G. Engelhardt, M. Nofz, K. Forkel, F. G. Wihsmann, M. Mägi, A. Samoson, and E. Lippmaa, *Phys. Chem. Glasses*, 1985, **26**, 157.
20. S. H. Risbud, R. J. Kirkpatrick, A. P. Taglialavore, and B. Montez, *J. Am. Ceram. Soc.*, 1987, **70**, C-10.
21. R. K. Sato, P. F. McMillan, P. Dennison, and R. Dupree, *J. Phys. Chem.*, 1991, **95**, 4483.
22. W. Müller-Warmuth, C. Mundus, and L. van Wüllen, *J. Non.-Cryst. Solids*, 1992, **149**, 209.
23. A. E. Geissberger and P. J. Bray, *J. Non-Cryst. Solids*, 1983, **54**, 121.
24. G. E. Jellison, Jr., L. W. Panek, P. J. Bray, and G. B. Rouse, Jr., *J. Chem. Phys.*, 1977, **66**, 802.
25. B. C. Bunker, D. R. Tallant, R. J. Kirkpatrick, and G. L. Turner, *Phys. Chem. Glasses*, 1990, **31**, 30.
26. S. L. Segel and R. B. Creel, *Can. J. Phys.*, 1970, **48**, 2673.
27. D. Mao, P. J. Bray, and G. L. Petersen, *J. Am. Chem. Soc.*, 1991, **113**, 6812.
28. F. R. Landsberger and P. J. Bray, *J. Chem. Phys.*, 1970, **53**, 2757.
29. S. D. Gornostansky and C. V. Stager, *J. Chem. Phys.*, 1967, **46**, 4959.
30. H. G. Dehmelt and H. Kruger, *Naturwissenschaften*, 1950, **37**, 111; 1951, **38**, 921.
31. E. A. C. Lucken, *Nuclear Quadrupole Coupling Constants*, Academic Press, New York, 1969.
32. E. Schempp and P. J. Bray, in *Physical Chemistry, an Advanced Treatise*, eds. H. Eyring, D. Henderson, and W. Jost, Academic Press, New York, 1970, Vol. 4, p. 521.
33. G. K. Semin, T. A. Babushkina, and G. G. Yakobson, *Nuclear Quadrupole Resonance in Chemistry*, Wiley, New York, 1975.
34. M. Rubenstein and P. C. Taylor, *Phys. Rev. Lett.*, 1972, **29**, 119.
35. M. Rubenstein and P. C. Taylor, *Phys. Rev. B*, 1974, **9**, 4258.
36. G. E. Jellison, Jr., G. L. Petersen, and P. C. Taylor, *Phys. Rev. B*, 1980, **22**, 3903.
37. R. Bersohn, *J. Chem. Phys.*, 1952, **20**, 1505.
38. C. Dean, *Phys., Rev.*, 1952, **96**, 1053.
39. H. Bayer, *Z. Phys.*, 1951, **130**, 227.
40. Z. M. Saleh, G. A. Williams, and P. C. Taylor, *Phys. Rev. B*, 1989, **46**, 10 557.

41. F. N. H. Robinson, *J. Phys. E: Sci. Instrum.*, 1980, **13**, 861; 1982, **15**, 814.
42. S. J. Gravina and P. J. Bray, *J. Magn. Reson.*, 1990, **89**, 515.
43. J. Krogh-Moe, *Phys. Chem. Glasses*, 1962, **3**, 101.
44. P. J. Bray, *J. Non-Cryst. Solids*, 1985, **75**, 29, and references therein.
45. D. Lee and P. J. Bray, *J. Magn. Reson.*, 1991, **94**, 51.
46. T. P. Das and E. L. Hahn, in *Solid State Physics*, eds. F. Seitz and D. Turnbull, Academic Press, New York, 1958, Suppl. 1.
47. J. Szeftel and H. Alloul, *Phys. Rev. Lett.*, 1979, **42**, 1691.

Biographical Sketch

Philip J. Bray. *b* 1925. B.S., 1948, Brown University, U.S.A.; Ph D. (supervisor Norman Ramsey), 1953, physics, Harvard University. Currently Hazard Professor of Physics, Emeritus, Brown University. Approx. 270 publications. Current research specialties: NMR and NQR studies of glass structure, and NQR of organic compounds and glasses.

Amphiphilic Liquid Crystalline Samples: Nuclear Spin Relaxation

Bertil Halle

Lund University, Lund, Sweden

1	Introduction	1
2	Relaxation Mechanisms and Experimental Methods	1
3	Order and Dynamics at the Molecular Level	4
4	Microstructure and Diffusion	5
5	Long-Wavelength Director Fluctuations	6
6	Related Articles	7
7	References	8

1 INTRODUCTION

Amphiphilic molecules (surfactants) consist of a polar, often charged, headgroup linked to one or two hydrocarbon, usually alkyl, chains. In the presence of water and possibly additional components, such as long-chain alcohols, alkanes, or simple electrolytes, surfactants spontaneously assemble into finite aggregates (micelles) or build up structures that extend indefinitely in one, two, or three dimensions. This gives rise to numerous liquid crystalline phases, differing in their macroscopic translational and rotational symmetries and displaying a fascinating geometrical and topological variety in their self-assembled microstructure.[1–6] The structural and dynamic characterization of these phases and the rationalization of their microstructure and phase behavior in terms of intermolecular and interaggregate forces is a challenging task. The importance of amphiphilic liquid crystals derives partly from their biological significance and diverse technical applications. In a more general context, amphiphilic liquid crystals are prime examples of complex fluids (soft matter) and their study has proven to be a rich source of fundamental knowledge.

Nuclear magnetic resonance has contributed more than any other technique to the understanding of amphiphilic liquid crystals. The NMR experiments used in this field are basically of three kinds: lineshape, diffusion, and relaxation studies. Spectral lineshapes from powder samples are now used routinely to distinguish among cubic, uniaxial, and biaxial phases (see ***Lyotropic Liquid Crystalline Samples***). Pulsed field gradient spin echo experiments can, under favorable conditions, provide the principal components of the macroscopic diffusion tensor for various molecular components (see ***Liquid Crystalline Samples: Diffusion***). Nuclear spin relaxation can provide detailed information about structure and dynamics on a wide range of length and time scales. As compared with lineshapes and diffusion, spin relaxation is a less direct source of information and therefore requires a more elaborate theoretical framework for its interpretation. On the other hand, liquid crystals can yield a large amount of relaxation data, including a variety of spin relaxation rates associated with high-rank polarization modes, and their dependence on Larmor frequency and sample orientation.

The first spin relaxation studies of amphiphilic liquid crystals appeared in the late 1960s. In a seminal contribution from the early years, Charvolin and Rigny[7] identified the three main sources of spin relaxation as: (i) local, orientationally restricted motions (rotational isomerization in the case of surfactant chains); (ii) molecular diffusion over curved interfaces; and (iii) collective director fluctuations. It was not until the 1980s, however, that improved instrumental capabilities, new pulse techniques, and advances in relaxation theory established nuclear spin relaxation as a major source of quantitative information about amphiphilic liquid crystals.[8,9] This is a highly interdisciplinary field of study where ideas and methods are continuously exchanged with several related fields, most notably molecular (thermotropic) liquid crystals and phospholipid bilayers (see Related Articles in Section 6).

2 RELAXATION MECHANISMS AND EXPERIMENTAL METHODS

2.1 General Considerations

The proton is not an ideal nucleus for relaxation studies of amphiphilic liquid crystals due to the complex relaxation behavior of the strongly coupled aliphatic chain protons, the rapid exchange of labile headgroup protons, and the contribution from intermolecular dipole–dipole couplings. Fortunately, there are several other nuclei more suitable for relaxation studies, e.g. ^{2}H or ^{13}C in surfactant chains, and ^{2}H or ^{17}O in water. For studies of microstructure, the choice is restricted to nuclei that are effectively confined to the interface, i.e. surfactant headgroup nuclei (e.g. ^{14}N), counterion nuclei (e.g. ^{23}Na), or ^{2}H nuclei in the α-position of the surfactant chain.

Despite important advances in recent years, the complex spin-dynamical behavior of quadrupolar nuclei and coupled spin-$\frac{1}{2}$ nuclei (such as $^{13}C^1H_2$) in liquid crystals has not yet been fully explored. Since most of the relevant nuclei have spin $I > \frac{1}{2}$, we emphasize quadrupolar relaxation. With the exception of $I \geq \frac{3}{2}$ nuclei, most pulse techniques for relaxation studies of anisotropic systems have been developed in other fields (see ***Deuteron Relaxation Rates in Liquid Crystalline Samples: Experimental Methods***); only a brief discussion is included here.

2.2 Quadrupolar Relaxation

Nuclei with $I \geq 1$ are coupled to the molecular degrees of freedom via the interaction of their electric quadrupole moment with the electric field gradient (EFG) generated by the surrounding charge distribution (see ***Quadrupolar Interactions***). The first-order effect of the quadrupole coupling is to split the resonance into $2I$ equidistant lines (see ***Quadrupolar Nuclei in Solids***). The quadrupole splitting occurs in all noncubic phases and contains information about the orientational order in the phase. In all but the simplest cases, however, the quadrupole splitting yields a product of order parameters, associated with different orientational

degrees of freedom, which cannot be separated without recourse to additional (e.g. relaxation) data.

The principal second-order effect of the quadrupole coupling is to induce spin relaxation (see ***Relaxation Theory for Quadrupolar Nuclei***). All information about liquid crystal structure and dynamics that can be derived from quadrupolar relaxation rates is contained in the three lab-frame spectral densities (LFSDs) $J^{\mathrm{L}}_{kk}(k\omega_0; \Omega)$ with $k = 0, 1, 2$:

$$J^{\mathrm{L}}_{kk}(k\omega_0; \Omega) = \int_0^\infty \mathrm{d}\tau \cos(k\omega_0\tau)[\langle V^{\mathrm{L}*}_k(0) V^{\mathrm{L}}_k(\tau)\rangle - |\langle V^{\mathrm{L}}_k\rangle|^2] \quad (1)$$

which are functions of the magnitude $B_0 = \omega_0/\gamma$ and orientation Ω (with respect to the liquid crystal) of the external magnetic field. The quantity within brackets in equation (1) is the time autocorrelation function of the kth spherical component V^{L}_k (in the lab frame) of the EFG tensor. The secular ($k = 0$) spectral density contains information about motions on all timescales (within the motional narrowing regime), while the nonsecular ($k = 1, 2$) spectral densities are affected only by motions on the timescale $1/\omega_0$ or faster. To determine the three individual LFSDs at a given magnetic field, one needs to measure at least three independent relaxation rates.

A system of spin I nuclei admits nonequilibrium states with magnetic tensor polarization of rank $k = 1, 2, \ldots 2I$ and coherence order $q = 0, \pm 1, \ldots \pm k$. The spin system can thus be described in terms of $(2I + 1)^2 - 1$ state multipoles[10] of rank k and projection index q. The axial ($q = 0$) multipole components, referred to as polarizations or alignments, are the generalizations of longitudinal magnetization ($k = 1$, $q = 0$). The remaining ($q \neq 0$) multipole components, referred to as q quantum coherences, are the generalizations of transverse magnetization ($k = 1$, $q = \pm 1$). The effect of hard radiofrequency pulses is simply to rotate the state multipoles, i.e. to mix the quantum order q without affecting the tensor rank k, whereas evolution under the (fluctuating) quadrupolar Hamiltonian mixes the rank without affecting the quantum order.[11]

In noncubic liquid crystals, the evolution of the polarizations involves $2I$ generalized longitudinal relaxation rates which depend on the two nonsecular LFSDs. (This dependence is linear for $I = 1$ and $I = \frac{3}{2}$, but nonlinear for $I \geq \frac{5}{2}$). The principal longitudinal relaxation experiments are the classical inversion–recovery and Jeener–Broekaert experiments[12] and their generalizations.[13]

The evolution of the coherences involves $I(2I + 1)$ generalized transverse relaxation rates, some of which may be degenerate. The homogeneous linewidths of satellite peaks, i.e. spectral lines that exhibit a first-order quadrupolar shift, are linear combinations of all three LFSDs, whereas the widths of the unshifted central peaks are linear combinations of the two nonsecular LFSDs. (This linear dependence of the linewidths on the LFSDs holds only if the quadrupole splitting is large compared with the nonsecular linewidth.)

Accurate measurements of homogeneous linewidths require echo experiments to refocus dephasing due to spatial inhomogeneities in the magnetic field and in the (static) quadrupole coupling (usually due to imperfect alignment). Whereas either 1D or 2D experiments can be performed on $I = 1$ nuclei, 2D experiments are indispensible for $I \geq \frac{3}{2}$ nuclei. The nonsecular central linewidths, associated with the $-q/2 \leftrightarrow q/2$ transitions, are obtained from 2D spin echo experiments, while the secular satellite linewidths are obtained from 2D quadrupolar echo experiments.[14–16] Table 1 lists the number of distinct relaxation rates that can be measured for different quadrupolar nuclei.

Table 1 Number of Independent Spin Relaxation Rates for Quadrupolar Nuclei in Non-Cubic Liquid Crystals

Relaxation rate	$I = 1$	$I = \frac{3}{2}$	$I = \frac{5}{2}$	$I = \frac{7}{2}$
Longitudinal	2	3	5	7
Transverse[a]	2	2	6	10
secular	1	1	3	6
nonsecular	1	1	3	4

[a]From homogeneous linewidths only.

2.3 Dipolar Relaxation

For studies of local surfactant dynamics one can use the ^{13}C nuclei in the alkyl chain, which are relaxed by the dipole–dipole coupling to directly bonded protons. The relaxation behavior of a weakly coupled AX_2 spin system such as $^{13}C^1H_2$ is complicated by $^{13}C-^1H$ cross relaxation, which is the basis of the nuclear Overhauser effect (NOE), and by cross correlation (interference) between the two C–H pairs which leads to the formation of high-rank polarization (three-spin order).[17] The ^{13}C longitudinal relaxation becomes effectively exponential, however, if the protons are decoupled by strong irradiation and if relaxation within the (strongly coupled) proton spin system quenches the development of high-rank polarization.[18] The ^{13}C inversion–recovery and steady-state NOE are then determined by the three LFSDs $J^{\mathrm{L}}_{kk}(\omega_{\mathrm{C}} + (k - 1)\omega_{\mathrm{H}}; \Omega)$ with $k = 0, 1, 2$, defined as in equation (1) but with V^{L}_k now denoting the spherical components of the $^{13}C-^1H$ dipole–dipole interaction tensor.

2.4 Relaxation Anisotropy and Phase Symmetry

For a system as complex as an amphiphilic liquid crystal, the LFSDs obtained from spin relaxation experiments are usually not amenable to direct physical interpretation without recourse to detailed structural and dynamic models. However, by transforming the lab-frame components V^{L}_k of the interaction tensor to a crystal-fixed frame, the LFSDs can be decomposed as

$$J^{\mathrm{L}}_{kk}(\omega_k; \Omega) = \sum_{n,p} F_{knp}(\Omega) J^{\mathrm{C}}_{np}(\omega_k) \quad (2)$$

where $\omega_k = k\omega_0$ for quadrupolar relaxation and $\omega_k = \omega_{\mathrm{A}} + (k - 1)\omega_{\mathrm{X}}$ for longitudinal dipolar relaxation of nucleus A coupled to nucleus X. When the time reversal invariance present in all dynamic models of interest has been taken into account there are 15 crystal-frame spectral densities (CFSDs) $J^{\mathrm{C}}_{np}(\omega_k)$, defined in analogy with equation (1). Depending on the rotational symmetry of the liquid crystal, some of these CFSDs

Table 2 Number of Independent Crystal-frame Spectral Density Functions (N) and Second-rank Order Parameters (n_2) for Different Crystallographic Point Groups

Phase	Point group	N	n_2
Isotropic fluid	K_h	1	0
Cubic	O_h	2	0
Lamellar, nematic U, hexagonal	$D_{\infty h}$, D_{6h}	3	1
Tetragonal, rhombohedral	D_{4h}, D_{3d}	4	1
Rectangular, orthorhombic, nematic B	D_{2h}	6	2
Oblique	C_{2h}	9	3
Monoclinic	C_i	15	5

may vanish or be linearly dependent. Taking the rotational symmetry into account, equation (2) can be expressed as[19]

$$J^{\mathrm{L}}_{kk}(\omega_k;\Omega) = \sum_{\lambda} F_{k\lambda}(\Omega) J^{\mathrm{C}}_{\lambda}(\omega_k) \tag{3}$$

with the composite index $\lambda = (\alpha,\mu,\mu')$ labeling the irreducible representations α of the liquid crystal point group and the independent subspaces μ of α. The irreducible CFSDs $J^{\mathrm{C}}_{\lambda}(\omega_k)$, constructed from symmetry-adapted tensor components, constitute the complete model-independent information content of a fixed-field spin relaxation study of a liquid crystal.[19] The number N of independent CFSD functions is given in Table 2 for liquid crystals of different symmetry. By measuring three linearly independent spin relaxation rates at N different orientations Ω of the (homeotropically aligned) liquid crystal, one can thus determine the $3N$ quantities $J^{\mathrm{C}}_{\lambda}(\omega_k)$. This relative wealth of model-independent information (as compared to isotropic fluids) imposes severe constraints on models of structure and dynamics.

In isotropic powder samples, the relaxation of the central peak ($-q/2 \leftrightarrow q/2$ transition) for noncubic phases and of the single peak for cubic phases is governed by the isotropically averaged (by interdomain exchange) LFSD:[19]

$$J^{\mathrm{L}}_{\mathrm{iso}}(\omega_k) = \frac{1}{5}\sum_{\alpha} d_{\alpha} \sum_{\mu} J^{\mathrm{C}}_{\alpha\mu\mu}(\omega_k) \tag{4}$$

with d_{α} being the dimension of the irreducible representation α.

While the rotational symmetry of a liquid crystal is determined by its crystallographic point group, the observable manifestations of this symmetry depend on the tensor rank of the measured physical property. The powder lineshape, being determined by the (motionally averaged) second-rank EFG tensor, can only distinguish between effectively isotropic, uniaxial, and biaxial symmetries. This is reflected in the number n_2 of independent second-rank order parameters (see Table 2). The CFSDs, involving products of two components V^{L}_k of a second-rank tensor, can be decomposed into terms transforming as tensors of rank 0, 2, and 4; hence there are $N = 1 + n_2 + n_4$ independent CFSDs.[19] Phases with the same 'second-rank symmetry' can thus have different relaxation behavior (see Table 2). On the other hand, since spin relaxation does not involve a higher tensor rank than 4, the relaxation anisotropy is of the same form for hexagonal phases (sixfold symmetry) as for lamellar and uniaxial nematic phases (full cylindrical symmetry). Since the second-rank spherical components V_n transform according to the

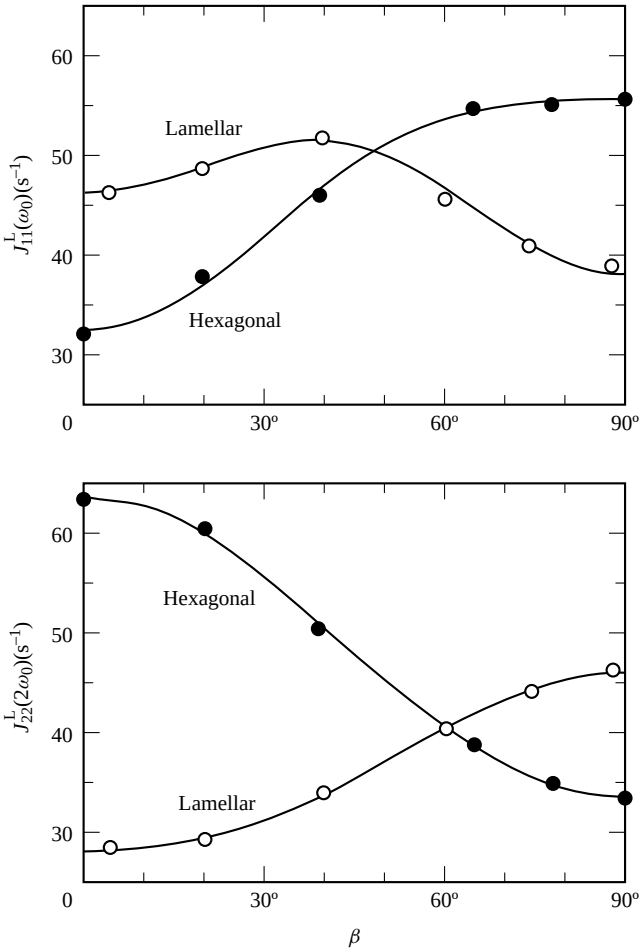

Figure 1 Anisotropy of the nonsecular lab-frame spectral densities obtained from the counterion ^{23}Na relaxation in the hexagonal[20] and (nonclassical) lamellar[21] phases of the sodium dodecyl sulfate/decanol/water system at 25 °C. The curves are fits according to equation (5)

irreducible representations (A_1, E_1, and E_2) of the point group $D_{\infty\mathrm{h}}$, the relaxation anisotropy for these phases takes the form:

$$J^{\mathrm{L}}_{kk}(\omega_k;\beta) = \sum_{n=0}^{2}(1-\delta_{n0}/2)\{[d^2_{kn}(\beta)]^2 + [d^2_{k-n}(\beta)]^2\} J^{\mathrm{C}}_{nn}(\omega_k) \tag{5}$$

where the $d^2_{kn}(\beta)$ are reduced Wigner functions and β is the angle between the magnetic field and the symmetry axis of the phase. Figure 1 shows the nonsecular ^{23}Na relaxation anisotropy of counterions in a hexagonal phase[20] and in a lamellar phase with disrupted bilayers.[21] In each case, the fit of equation (5) to the LFSD data yields the six model-independent CFSDs $J^{\mathrm{C}}_{nn}(k\omega_0)$ with $k = 1, 2$ and $n = 0, 1, 2$.

2.5 Relaxation Dispersion and Low-Frequency Dynamics

The dynamic processes responsible for spin relaxation in amphiphilic liquid crystals take place mainly on three time scales: local, restricted motions (1–100 ps), molecular

diffusion over curved interfaces (1–10 ns), and collective processes (> 100 ns). While the local motions are usually in the extreme narrowing limit, the dispersion of the surface diffusion contribution to the nonsecular spectral densities is in the frequency range ($\omega_0/2\pi \approx 1$–100 MHz) accessible by conventional relaxation experiments. While the secular spectral density $J^{\mathrm{L}}_{00}(0)$ reflects motions on all timescales, special techniques are required to investigate the low-frequency dispersion associated with collective processes.

Two methods are available for probing the secular LFSD $J^{\mathrm{L}}_{00}(\omega)$ in the kHz frequency range. For $I = 1$ nuclei, the quadrupolar echo train $(\pi/2)_x - [\tau - (\pi/2)_y - \tau]_n$ yields an effective spectral density[22]

$$\frac{8}{\pi^2}\sum_{n=0}^{\infty}(2n+1)^{-2}J^{\mathrm{L}}_{00}\left((2n+1)\frac{\pi}{2}\omega_{\mathrm{p}}\right) = J^{\mathrm{L}}_{00}(0)\left[1-\omega_{\mathrm{p}}\tau_{\mathrm{c}}\tanh\left(\frac{1}{\omega_{\mathrm{p}}\tau_{\mathrm{c}}}\right)\right] \quad (6)$$

with $\omega_{\mathrm{p}} = 1/\tau$ the pulse train frequency. The second form in equation (6) holds only if $J^{\mathrm{L}}_{00}(\omega)$ is Lorentzian, with correlation time τ_{c}. Relaxation in the presence of a spin lock field B_1 yields, in a $T_{1\rho}$ experiment on $I = 1$ nuclei, an effective spectral density given approximately by[23]

$$\frac{(2\Omega_1)^2}{\omega_Q^2+(2\Omega_1)^2}J^{\mathrm{L}}_{00}\left(\sqrt{\omega_Q^2+(2\Omega_1)^2}\right) \quad (7)$$

with $\Omega_1 = \gamma B_1$ and ω_{Q} the static (residual) quadrupole frequency. If $J^{\mathrm{L}}_{00}(\omega)$ is Lorentzian, equation (7) has a maximum of $J^{\mathrm{L}}_{00}(0)(\sqrt{1+x^2}+x)^{-2}$ at $\Omega_1 = (\omega_Q/2)(1 + x^{-2})^{1/4}$, with $x = \omega_Q\tau_{\mathrm{c}}$

A much wider frequency range, from the conventional MHz range down to ca. 100 Hz, can be explored by the field cycling technique[24] (see ***Field Cycling Experiments***). Unfortunately, this technique is not applicable to rapidly relaxing quadrupolar nuclei; so far only ^{1}H field cycling studies of amphiphilic liquid crystals have been reported. As seen from Figure 2, the entire dispersion due to collective processes can be obtained in this way.[25]

3 ORDER AND DYNAMICS AT THE MOLECULAR LEVEL

3.1 Water and Counterions

Amphiphilic interfaces induce only small and short-ranged perturbations of the strongly hydrogen-bonded network in liquid water. Since the surface-induced orientational order and reorientational anisotropy are weak, the three LFSDs are equal, $J^{\mathrm{L}}_{kk}(\omega_k) = J^{\mathrm{L}}_{00}(0)$, and the spin relaxation exhibits neither anisotropy nor dispersion. Water reorientation in the first molecular 'layer' is typically slowed down by a factor of two to three, and there is no evidence for long (> 100 ps) water residence times in any amphiphilic system. Water ^{2}H and ^{17}O relaxation rates thus report essentially on the fast, local water dynamics, which are insensitive to variations in microstructure.[26,27]

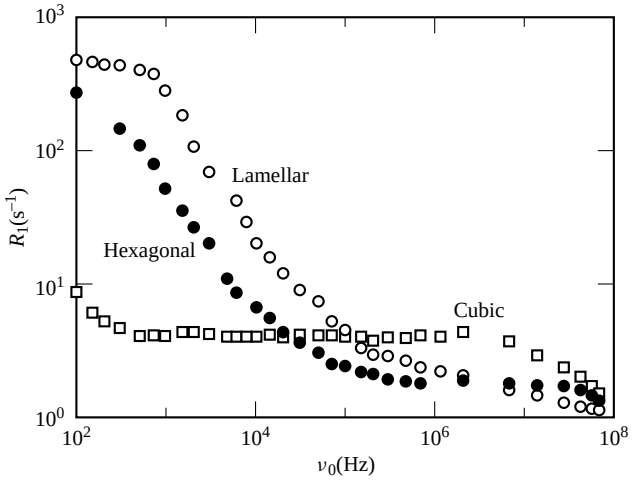

Figure 2 Dispersion of the longitudinal relaxation rate R_1 of surfactant chain protons in powder samples of the lamellar, hexagonal, and cubic phases of the potassium dodecanoate/D_2O system at 70 °C[25]

Counterion relaxation rates reflect fast, local motions as well as slower motions, e.g. diffusion over curved interfaces. The relative contributions from fast and slow motions can be estimated[26] as $\langle\chi^2\rangle\tau_{\mathrm{f}}$ and $\langle\chi\rangle^2\tau_{\mathrm{s}}$, respectively, where $\langle\chi^2\rangle$ is the mean square quadrupole coupling constant (QCC), $\langle\chi\rangle$ the residual QCC (averaged by the fast motions), and τ_{f} and τ_{s} the effective correlation times. As in the case of water, the residual anisotropy is weak ($\langle\chi\rangle^2 \ll \langle\chi\rangle^2$), and the fast-motion contribution to the LFSDs is independent of orientation and frequency.[20] However, the ratio $\tau_{\mathrm{s}}/\tau_{\mathrm{f}}$ is typically (in the presence of curved interfaces) an order of magnitude larger for counterions than for water, making the fast and slow contributions comparable. For atomic counterions, where the EFG is of intermolecular origin, the local motion contribution $\langle\chi^2\rangle\tau_{\mathrm{f}}$ and the residual QCC $\langle\chi\rangle$ depend markedly on the molecular details of the interface region, but in a way that is not readily captured by simple models.

3.2 Surfactant Molecules

Rotational isomerization in surfactant alkyl chains is too fast (< 10 ps) to produce a dispersion in the ^{2}H or ^{13}C relaxation.[8,28] This introduces a certain model dependence in the interpretation,[28–30] although constraints are imposed by the individual bond order parameters deduced from static dipole or quadrupole couplings.[8] On a longer timescale (typically, 0.1–1 ns), the conformationally averaged surfactant molecule undergoes restricted reorientation within the aggregate. This motion can produce a high-field dispersion in the ^{13}C relaxation (which involves the Larmor frequency of ^{1}H), whereas the ^{2}H relaxation is usually in the extreme narrowing limit.[28] The relaxation anisotropy is expected to be weak for alkyl chain nuclei, but can be substantial for headgroup nuclei in double-chain surfactants.[28] The overall motion of surfactants is usually modeled as rotational diffusion of a symmetric top in a uniaxial potential of mean torque (see ***Liquid Crystalline Samples: Relaxation Mechanisms***).

The relaxation of a surfactant nucleus induced by the intermolecular dipole coupling with a nuclear or electron spin in a counterion can, in certain cases, provide information about

Table 3 Relaxation Processes in Amphiphilic Liquid Crystals

Dynamics	Order fluctuations	Director fluctuations
Single-molecule	Diffusion in order gradient	Diffusion on curved interface
		Diffusion in nematic director field
Collective	Critical fluctuations	Micelle reorientation
		Nematic director fluctuations
		Interface shape fluctuations

the spatial distribution of the surfactant nucleus with respect to the interface.[8,31] The interpretation of such relaxation data is, however, strongly model dependent.[32]

4 MICROSTRUCTURE AND DIFFUSION

4.1 Fluctuating Local Anisotropy

Much of the intricate spin relaxation behavior of complex fluids such as amphiphilic liquid crystals can be rationalized in terms of a unifying concept: the fluctuating local anisotropy. On longer timescales, the net effect of the fast, local motions (see Section 3) is to project the quadrupole (or dipole–dipole) interaction tensor onto an axis, the (local) director, which usually coincides with the local interface normal. The motionally averaged, or projected, interaction tensor is proportional to the second-rank ordering tensor $\boldsymbol{S}$, with three independent components in the usual case of local uniaxial symmetry. In the director frame, $\boldsymbol{S}$ is diagonal and the three independent variables are the principal order parameter S and the set Ω of two angles that specify the director orientation (with respect to the crystal axes).

All relaxation processes, apart from the local motions, can be classified as either local order fluctuations, which modulate the order parameter $S(t)$, or local director fluctuations, which modulate the director orientation $\Omega(t)$. Each of these classes can be further subdivided according to whether the fluctuations are due to single-molecule dynamics (translational diffusion) or to collective processes, involving many molecules. Among the relaxation processes listed in Table 3, those in the director fluctuation class are generally most important. Diffusion of water or counterions between interface ($S \neq 0$) and bulk ($S = 0$) regions[33] is usually an inefficient relaxation process,[21,34] and critical order fluctuations[35] occur only near phase transitions.

4.2 Diffusion on Curved Interfaces

All amphiphilic liquid crystalline phases, save the lamellar one, are built from curved interfaces, over which surfactants and counterions diffuse freely. (The long-range Coulomb interaction effectively reduces the dimensionality of the diffusion space for counterions to two.[21,33,34]) This constitutes an efficient relaxation process of the director fluctuation type, which can yield quantitative information about the interface geometry (microstructure) and the surface diffusion coefficient, D_s. Typically, the microstructure involves radii of curvature of the order 1–2 nm, while $D_s \approx (0.1\text{–}1) \times 10^{-9}\,\mathrm{m^2\ s^{-1}}$. The associated correlation times are thus in the 1–10 ns range, which places the relaxation dispersion in the conventional MHz range of Larmor frequencies. We now consider how surface diffusion induced quadrupolar spin relaxation can be exploited in the various phases.

4.3 Hexagonal Phases

The normal hexagonal phase is built from cylindrical surfactant aggregates of indefinite length, arranged on a two-dimensional hexagonal lattice. Since the director, i.e. the cylinder surface normal, is everywhere perpendicular to the sixfold symmetry axis of the phase, surface diffusion around the cylinder contributes to only one of the three CFSDs, i.e.

$$J^{C}_{nn}(k\omega_0) = J_{loc} + \delta_{n2}\langle\chi\rangle^2 \frac{3}{8}\frac{\tau_s}{1+(k\omega_0\tau_s)^2} \qquad (8)$$

with the correlation time $\tau_s = R^2/(4D_s)$, and R the diffusion radius. In addition, the adiabatic ($k = 0$) CFSDs have contributions from long-wavelength cylinder undulations.

With R obtained from the X-ray Bragg spacing, the surface diffusion coefficients D_s of surfactants and counterions can be accurately ($\pm$ 10%) determined from the nonadiabatic ($k = 1$, 2) CFSDs obtained from the nonsecular relaxation anisotropy (see Figure 1) at a single magnetic field.[20,36] In reversed hexagonal phases, the radius of the aqueous cylinders can be varied in a controlled way, allowing a direct verification of the R^2 scaling of the correlation time.[34]

4.4 Lamellar Phases

In a classical lamellar phase, with periodically stacked, planar surfactant bilayers of indefinite lateral extent, one expects neither anisotropy nor dispersion in the nonsecular LFSDs, since in the absence of interface curvature, $J^{C}_{nn}(k\omega_0) = J_{1oc}$ for $k = 1$, 2. (The secular LFSD, however, should exhibit anisotropy due to long-wavelength bilayer undulations; see Section 5.3). Spin relaxation is therefore a sensitive curvature probe for lamellar phases; any deviation from the classical microstructure is unambiguously revealed by the relaxation anisotropy and dispersion produced by molecular diffusion over curved interfaces.

In the lamellar phase of the sodium dodecyl sulfate/decanol /water system, the ^{23}Na relaxation (see Figure 1) provides direct evidence for a highly curved interface at low decanol content,[21] whereas at higher decanol content the microstructure is classical. The relaxation behavior is consistent with a microstructure of ribbon-like aggregates, arranged on the smectic planes so as to preserve the uniaxial symmetry of the lamellar phase. The three CFSD functions $J^{C}_{nn}(\omega)$ can then be related to two irreducible (D_{2h}) ribbon-frame spectral density functions associated with surface diffusion around the ribbon-like aggregate.

4.5 Uniaxial Nematic Phases

Two types of uniaxial nematic phase occur in amphiphilic systems:[4] the calamitic (N_C) and discotic (N_D) phases, built from orientationally ordered nonspherical micellar aggregates of approximately prolate and oblate spheroidal shape, respectively. To understand these phases, one needs to quantify the size of the micelles and their long-range orientational order.

Nuclear spin relaxation studies can, in principle, yield the micelle dimensions as well as the second-rank nematic order parameter.[37] Two difficulties are encountered, however. First, the fast magnetic alignment of nematic fluids precludes relaxation anisotropy measurements with conventional methods. This experimental problem can be partly overcome by sample spinning techniques (see ***Spinning Liquid Crystalline Samples***). The second difficulty is intrinsic: spin relaxation is induced not only by molecular diffusion over the micelle surface, but also by rotation of the micelle around its symmetry axis and restricted tumbling of this axis. While the three CFSDs associated with spheroidal surface diffusion and single-micelle reorientation (in a uniaxial potential of mean torque) can be accurately calculated,[38] it is more difficult to describe the cooperative reorientation modes in the transition zone between the single-micelle and viscoelastic continuum behaviors (see Section 5.2). However, in the frequency range (typically > 10 MHz) where the cooperative modes are unimportant, quadrupolar relaxation of counterion and surfactant nuclei can yield useful, albeit somewhat model-dependent, information about micelle size and nematic order.[37,39]

4.6 Cubic Phases

According to the topology of their microstructure, amphiphilic cubic phases are either of the micellar type with a three-dimensional periodic arrangement of nonspherical surfactant aggregates, or of the bicontinuous type with both aqueous and nonpolar regions connected over macroscopic distances in all three dimensions.[5] In both types of cubic phase, surface diffusion is the major relaxation process. For micellar cubic phases, the spectral densities can be calculated as for nematic phases, also including molecular exchange between differently oriented micelles.[40]

The microstructure of bicontinuous cubic phases is usually modeled in terms of certain triply periodic minimal surfaces. Due to the high symmetry of these surfaces, the surface-diffusion spectral densities should be nearly Lorentzian (as for diffusion on a sphere). The effective correlation times can then be expressed as[41]

$$\tau_s = -\frac{1 - cQ}{6D_s\langle K\rangle} \tag{9}$$

with c a numerical constant, Q the fourth-rank cubic order parameter, and $\langle K\rangle$ the (negative) average Gaussian curvature of the minimal surface, related via the Gauss–Bonnet theorem to the unit cell surface area and topology (Euler–Poincaré characteristic). The correlation time τ_s decreases strongly with increasing topological complexity and can therefore, in contrast to X-ray diffraction, distinguish among different microstructures that belong to the same crystallographic space group.[41]

The quadrupolar relaxation dispersion of surfactant chain and headgroup nuclei has been used to determine micelle dimensions in cubic phases.[42,43] Since only powder samples of cubic phases have been studied so far,[25,42,43] the full model-independent information content of the relaxation has not been extracted. Although sometimes referred to as the 'viscous isotropic phase', the cubic phase has an inherently anisotropic relaxation behavior (see Section 2.4) and the two irreducible CFSDs can be determined from single crystal relaxation data.[40]

4.7 Low-Symmetry Phases

Although attractive with regard to their rich model-independent information content (see Table 2), amphiphilic phases of lower than hexagonal symmetry have not yet been subjected to spin relaxation studies. The four irreducible CFSDs from triply periodic tetragonal and rhombohedral phases might be analyzed in terms of surface diffusion on minimal surfaces, as for bicontinuous cubic phases. For two-dimensional rectangular phases, the ribbon-frame spectral densities discussed in Section 4.4 should be appropriate. Biaxial nematic phases pose a greater challenge however, in view of the large number of model parameters needed to describe surface diffusion on biaxial micelles undergoing asymmetric-top reorientation in a biaxial potential of mean torque.

5 LONG-WAVELENGTH DIRECTOR FLUCTUATIONS

5.1 General Considerations

For noncubic phases, spin relaxation in the sub-MHz frequency range is usually dominated by slow director fluctuations. The actual dynamic process inducing spin relaxation can be either long-range molecular diffusion or the intrinsic dynamics of collective modes. The theory of spin relaxation due to such processes is based on a phenomenological continuum description of liquid crystal mechanics, carried to second order in the elastic deformations.[44] The relaxation theory has so far been developed only for the uniaxial nematic and lamellar phases. Information about long-wavelength director fluctuations is contained in the anisotropic, secular LFSD $J^L_{00}(0;\beta)$ and in the low-frequency relaxation dispersion accessible by field cycling, echo train, and spin lock techniques (see Section 2.5).

5.2 Uniaxial Nematic Phases

The orientational state of a uniaxial nematic phase is specified at the continuum level by the director field $\boldsymbol{n}(\boldsymbol{r})$, where $\boldsymbol{n}$ is the unit vector along the principal axis of the micelle ordering tensor averaged over a macroscopically small volume of order λ_c^3 around the point $\boldsymbol{r}$. The three CFSDs involve time correlation functions of the transverse director components $\boldsymbol{n}_\perp = (n_x, n_y)$, which measure the orientational deviation of the director from the symmetry axis of the phase.

The CFSD $J^{C}_{11}(\omega_0)$, which is of second order in $n_\perp$, has a complicated dispersion with three regimes (equations (10a)–(10c)):

$$J^{C}_{11}(\omega_0) = \alpha_N \frac{\xi_m}{D_e}\left[1 - \left(\frac{\omega_0}{2\omega_m}\right)^{1/2}\right], \quad \omega_0 \ll \omega_m \qquad (10a)$$

$$J^{C}_{11}(\omega_0) = \frac{\alpha_N}{(2D_e\omega_0)^{1/2}}, \quad \omega_m \ll \omega_0 \ll \omega_c \qquad (10b)$$

$$J^{C}_{11}(\omega_0) = \alpha_N \frac{(4\pi)^2 D_e}{\lambda_c^3 \omega_0^2}, \quad \omega_c \ll \omega_0 \qquad (10c)$$

with $\alpha_N = \frac{3}{4}\pi \langle\chi\rangle^2 k_B T/K$, $D_e = D + K/\eta$, K and η the effective curvature-elasticity and viscosity of the nematic fluid,[44] and D the long-range diffusion coefficient of the spin-bearing species. Further, $\omega_c = D_e (2\pi/\lambda_c)^2$ and $\omega_m = D_e/\xi^2_m$, with $\xi_m = \sqrt{\mu_0 K \Delta\chi}\ /B_0$ the magnetic coherence length.[44] Since, in amphiphilic nematic phases, $\omega_c/2\pi$ is typically of order 1 MHz, the classical[45] $1/\sqrt{\omega_0}$ dispersion regime in equation (10b) is accessible only with special techniques such as field cycling. In the conventional MHz range, only the high-frequency $1/\omega_0^2$ tail contributes to the relaxation (at $<$ 10 MHz). In this frequency range, however, the theory may be inaccurate since short-wavelength (of order λ_c) continuum modes and single-micelle restricted tumbling modes make comparable contributions.

In the presence of a magnetic field, a stationary nematic sample (of thickness $\gg \xi_m$) adopts either a parallel or a perpendicular phase orientation with respect to the field. According to equation (5), the secular LFSD then involves only the CFSDs $J^{C}_{00}(0)$ and $J^{C}_{22}(0)$. Since these are of fourth order in $n_\perp$, the rates of molecular diffusion (D) and viscoelastic mode relaxation (K/η) are no longer additive.[46] For the case $D \gg K/\eta$ which usually applies to counterions, the result is[46]

$$J^{C}_{00}(0) = 3J^{C}_{22}(0) = \langle\chi\rangle^2 \left(\frac{3k_B T}{4\pi K}\right)^2 \frac{1}{D}[\ln(2\pi\xi_m/\lambda_c) - 1.119] \qquad (11)$$

The secular LFSD can thus be used to determine either the curvature-elasticity K or the long-range diffusion coefficient D.[46]

The second-order adiabatic CFSD $J^{C}_{11}(0)$ in equation (10) can be obtained from relaxation studies at oblique phase orientations, achievable by sample spinning techniques. Two complications then arise. First, the magnetic field breaks the intrinsic uniaxial symmetry of the nematic phase, thus altering the low-frequency ($\omega_0 < \omega_m$) relaxation behavior.[47] Due to the orientation-dependent magnetic quenching of long-wavelength elastic fluctuation modes, the relaxation anisotropy involves CFSDs $J^{C}_{np}(0)$ with $n \neq p$, and hence no longer obeys equation (5).[47] (equation (10a) and equation (11) are strictly valid only for parallel alignment.) Second, since $J^{C}_{11}(0)$ exceeds $J^{C}_{00}(0)$ by a factor $\xi_m K/k_B T$ of order 10^3, the conventional perturbation theory of spin relaxation may break down.

5.3 Lamellar Phases

Due to its layered microstructure, the lamellar phase differs fundamentally from a nematic fluid in its mechanical properties. Since the orientation of the bilayer normal (the director) is coupled to the position of the bilayer, director fluctuations in lamellar phases are suppressed not only by the bending rigidity of the bilayers but also by the (osmotic) forces that maintain the bilayer spacing. The continuum-mechanical description of the lamellar phase thus involves two elastic constants:[44] the splay-curvature modulus K_1 and the osmotic compression modulus $\overline{B}$. These are related to the average bilayer spacing d, the bilayer bending rigidity κ, and the curvature $V''(d)$ of the bilayer interaction as: $K_1 = \kappa/d$ and $\overline{B} = d\ V''(d)$. The lateral orientational correlation length $\xi_p = (d^2 K_1/\overline{B})^{1/4}$, also called the patch length, defines the crossover from a short-wavelength regime with independent bilayer fluctuations to a long-wavelength regime with highly coupled bilayer fluctuations. Since interbilayer forces limit the amplitude of long-wavelength fluctuation modes, magnetic quenching is unimportant in lamellar phases.

As in the nematic case, the dispersion of the second-order CFSD $J^{C}_{11}(\omega_0)$ exhibits three regimes (equations (12a)–(12c)):[48]

$$J^{C}_{11}(\omega_0) = \alpha_L \frac{\xi_p^2}{D_e}\left[\ln\left(\frac{d}{L_z} + \frac{\omega_0}{\omega_p}\right)^{-1} + \frac{\omega_0}{\omega_p}\right], \quad \omega_0 \ll \omega_p \qquad (12a)$$

$$J^{C}_{11}(\omega_0) = \alpha_L \frac{\pi}{\omega_0}, \quad \omega_p \ll \omega_0 \ll \omega_a \qquad (12b)$$

$$J^{C}_{11}(\omega_0) = \alpha_L \frac{2\pi^2 D_e}{a^2 \omega_0^2}, \quad \omega_a \ll \omega_0 \qquad (12c)$$

with $\alpha_L = (3/16\pi)\langle\chi\rangle^2 k_B T/\kappa$, $D_e = D_\perp + K_1/\eta$, $\omega_a = D_e(\pi/a)^2$, and $\omega_p = D_e\pi/\xi_p^2$. Further, L_z is the sample thickness and a is a lateral cut-off length, with a^2 of the order of the surfactant cross-section.

The adiabatic CFSD $J^{C}_{11}(0)$ is proportional to $\langle u^2\rangle$, with u the vertical bilayer displacement, and hence exhibits a logarithmic divergence with sample size, characteristic of one-dimensional crystals.[44] At frequencies $\omega_0 \gg \omega_p$, $J^{C}_{11}(\omega_0)$ reflects independent bilayer fluctuations and the range $\omega_p \ll \omega_0 \ll \omega_a$ corresponds to the classical $1/\omega_0$ dispersion regime,[49] where $J^{C}_{11}(\omega_0)$ depends neither on the inter-bilayer forces (ξ_p) nor on the fluctuation rate (D_e). Since ξ_p is generally of the same order as the bilayer spacing d, $\omega_p/2\pi$ is of order 10 MHz for typical lamellar phases (but lower for very dilute samples). The experimentally accessible low-frequency dispersion (see Section 2.5) then reflects coupled bilayer fluctuations and can thus, like the adiabatic CFSD $J^{C}_{11}(0)$, provide information about inter-bilayer forces.

6 RELATED ARTICLES

Bilayer Membranes: Deuterium and Carbon-13 NMR; Bilayer Membranes: Proton and Fluorine-19 NMR; Deuteron Relaxation Rates in Liquid Crystalline Samples: Experimental

Methods; Liquid Crystalline Samples: Deuterium NMR; Liquid Crystalline Samples: Relaxation Mechanisms; Lyotropic Liquid Crystalline Samples; Membranes: Deuterium NMR; Micellar Solutions and Microemulsions; Relaxation Theory for Quadrupolar Nuclei.

7 REFERENCES

1. V. Luzzati, in *Biological Membranes*, ed. D. Chapman, Academic Press, New York, 1968, Vol. 1, p. 71
2. P. Ekwall, in *Advances in Liquid Crystals*, ed. G. H. Brown, Academic Press, New York, 1975, Vol. 1, p. 1.
3. G. J. T. Tiddy, *Phys. Rep.*, 1980, **57**, 1.
4. B. J. Forrest and L. W. Reeves, *Chem. Rev.*, 1981, **81**, 1.
5. K. Fontell, *Colloid Polym. Sci.*, 1990, **268**, 264.
6. J. Charvolin, *Contemp. Phys.*, 1990, **31**, 1.
7. J. Charvolin and P. Rigny, *J. Chem. Phys.*, 1973, **58**, 3999.
8. C. Chachaty, *Mol. Eng.*, 1992, **2**, 65.
9. B. Halle, P.-O. Quist, and I. Furó, *Liq. Cryst.*, 1993, **14**, 227.
10. K. Blum, *Density Matrix Theory and Applications*, Plenum Press, New York, 1981.
11. B. C. Sanctuary and T. K. Halstead, *Adv. Magn. Opt. Reson.*, 1990, **15**, 79.
12. R. R. Vold, in *Nuclear Magnetic Resonance of Liquid Crystals*, ed. J. W. Emsley, Reidel, Dordrecht, 1985, p. 253.
13. I. Furó and B. Halle, *J. Chem. Phys.*, 1989, **91**, 42.
14. I. Furó, B. Halle, and T. C. Wong, *J. Chem. Phys.*, 1988, **89**, 5382.
15. I. Furó and B. Halle, *J. Magn. Reson.*, 1992, **98**, 388.
16. I. Furó and B. Halle, *Mol. Phys.*, 1992, **76**, 1169.
17. L. G. Werbelow and D. M. Grant, *Adv. Magn. Reson.*, 1977, **9**, 189.
18. D. Canet, *Prog. NMR Spectrosc.*, 1989, **21**, 237.
19. S. Gustafsson and B. Halle, *Mol. Phys.*, 1993, **80**, 549.
20. P.-O. Quist, I. Blom, and B. Halle, *J. Magn. Reson.*, 1992, **100**, 267.
21. P.-O. Quist and B. Halle, *Phys. Rev. E*, 1993, **47**, 3374.
22. J. S. Blicharski, *Can. J. Phys.*, 1986, **64**, 733.
23. J. R. C. van der Maarel, *J. Chem. Phys.*, 1993, **99**, 6546.
24. F. Noack, *Prog. NMR Spectrosc.*, 1986, **18**, 171.
25. W. Kühner, E. Rommel, F. Noack, and P. Meier, *Z. Naturforsch.*, 1987, **42a**, 127.
26. B. Halle and H. Wennerström, *J. Chem. Phys.*, 1981, **75**, 1928.
27. M. P. Bozonnet-Frenot, J. P. Marchal, and D. Canet, *J. Phys. Chem.*, 1987, **91**, 89.
28. C. Chachaty and T. Bredel, *J. Phys. Chem.*, 1991, **95**, 5335.
29. A. Ferrarini, G. J. Moro, and P. L. Nordio, *Liq. Cryst.*, 1990, **8**, 593.
30. R. Y. Dong, *Phys. Rev. A*, 1991, **43**, 4310.
31. Ph. Brûlet and H. McConnell, *Proc. Natl. Acad. Sci. USA*, 1975, **72**, 1451.
32. J. P. Korb, Th. Bredel, C. Chachaty, and J. R. C. van der Maarel, *J. Chem. Phys.*, 1990, **93**, 1964.
33. B. Halle, *Mol. Phys.*, 1984, **53**, 1427; 1987, **60**, 319.
34. I. Furó, B. Halle, P. O. Quist, and T. C. Wong, *J. Phys. Chem.*, 1990, **94**, 2600.
35. J. H. Freed, *J. Chem. Phys.*, 1992, **96**, 3901.
36. P. O. Quist, B. Halle, and I. Furo, *J. Chem. Phys.*, 1991, **95**, 6945.
37. P. O. Quist, B. Halle, and I. Furo, *J. Chem. Phys.*, 1992, **96**, 3875.
38. B. Halle, *J. Chem. Phys.*, 1991, **94**, 3150.
39. I. Furó and B. Halle, *Phys. Rev. E*, 1995, **51**, 466.
40. B. Halle, *Liq. Cryst.*, 1992, **12**, 625.
41. B. Halle, S. Ljunggren, and S. Lidin, *J. Chem. Phys.*, 1992, **97**, 1401.
42. O. Söderman, H. Walderhaug, U. Henriksson, and P. Stilbs, *J. Phys. Chem.*, 1985, **89**, 3693.
43. O. Söderman and U. Henriksson, *J. Chem. Soc., Faraday Trans. 1*, 1987, **83**, 1515.
44. P. G. de Gennes, *The Physics of Liquid Crystals*, Clarendon Press, Oxford, 1974.
45. P. Pincus, *Solid State Commun.*, 1969, **7**, 415.
46. B. Halle, P. O. Quist, and I. Furo, *Phys. Rev. A*, 1992, **45**, 3763.
47. B. Halle, *Liq. Cryst.*, 1994, **17**, 759.
48. B. Halle, *Phys. Rev. E*, 1994, **50**, R2415.
49. J. A. Marqusee, M. Warner, and K. A. Dill, *J. Chem. Phys.*, 1984, **81**, 6404.

Biographical Sketches

Bertil Halle. *b* 1951. M.Sc. (Civilingenjör), 1977, Ph.D., 1981, Physical Chemistry, Lund University, Sweden. Postdoctoral work in Department of Applied Mathematics, Australian National University, Canberra, 1982–84. Faculty of Physical Chemistry, Lund University, 1984–present. Approx. 75 publications. Research specialties: theory of nuclear spin relaxation, physics of complex fluids (especially amphiphilic liquid crystals), hydration and dynamics of biomolecules.

Anisotropy of Shielding and Coupling in Liquid Crystalline Solutions

Jukka Jokisaari

Department of Physics, University of Oulu, FIN-90570 Oulu, Finland

1	Introduction	1
2	Liquid Crystals	1
3	The Hamiltonian Operator and Observables	2
4	Shielding Anisotropy	2
5	Spin–Spin Coupling Anisotropy	7
6	Related Articles	9

1 INTRODUCTION

In the beginning of the 1960s, NMR spectroscopists started to look for means to orient molecules with a particular goal in mind, i.e. to find a situation where the intermolecular direct dipolar couplings would average out whereas the corresponding intramolecular couplings would average to a nonzero value. Various methods were tried until, in 1963, Saupe and Englert[1] proposed that the sought-after properties can be reached by using liquid crystals as solvents.

The anisotropic orientational distribution of solute molecules in liquid crystals makes it possible to use the NMR observables (anisotropic couplings including both the direct dipole–dipole couplings and a contribution from the anisotropy of the indirect spin–spin coupling tensor, chemical shifts, and nuclear quadrupole splittings) for the determination of molecular structures, the anisotropies of nuclear shielding and spin–spin couplings, and quadrupole couplings for nuclei with spin ≥ 1. In principle, the method is quite straightforward but in practice some complications may appear. In particular, the determination of molecular structures necessitates the introduction of the vibrational[2] and deformational[3–5] corrections (see ***Structure of Rigid Molecules Dissolved in Liquid Crystalline Solvents***). Since the anisotropic contribution of the spin–spin coupling tensor can only be separated from the experimental coupling when the direct dipole–dipole coupling is known, the corresponding effects have also to be considered here. To obtain reliable shielding anisotropies for protons and for nuclei with small anisotropy in general, various disturbing effects on the experimentally determined chemical shifts, such as local anisotropy due to solvent molecules, have to be taken into account.

A comprehensive review on the anisotropies of shielding and spin–spin coupling tensors determined using liquid crystalline solvents appeared in 1982.[6] Since then, however, remarkable progress has taken place. This concerns spin–spin coupling anisotropy, in particular, where the inclusion of the deformational corrections leads to unambiguous, solvent independent results.

The NMR spectra observable from the spin-$\frac{1}{2}$ nuclei in molecules dissolved in liquid crystals resemble those in isotropic liquids; relatively sharp, well resolved lines can be detected. Hence, analyses of spectra taken in the two phases are, in principle, similar (see ***Liquid Crystalline Samples: Spectral Analysis***, and ***Analysis of High-Resolution Solution State Spectra***). There are, however, also a few basic differences. Firstly, the anisotropic couplings between magnetically and chemically equivalent nuclei affect the structure of the spectrum. Thus, for example, the ^{1}H NMR spectrum of three methyl protons is a triplet and the six benzene protons give a spectrum very rich in resonance lines. Secondly, the dipole–dipole coupling constants are often large, of the order of kHz, and consequently the first-order approximation can usually be carried out only when the coupled nuclei are of different species.

2 LIQUID CRYSTALS

The liquid crystals most applicable in NMR spectroscopy are the thermotropic ones which have mesophases within certain temperature ranges.[7] In a few cases, lyotropic liquid crystals have also been used. They are formed by mixing, for example, alkyl sulfates and the corresponding alcohols, sodium sulfate, and water.[8]

Thermotropic liquid crystals which are mainly used as solvents in NMR spectroscopy, can be classified into two main categories; nematic (N) and smectic (S). In the nematic phases, the molecules have only a short range positional order. However, if the liquid crystals consist of elongated molecules, as those used in the applications described in this context usually do, they tend to align with their long axes parallel to a common axis which defines the director (often called also the optic axis), $\boldsymbol{n}$, of the liquid crystal. The nematic phases are almost in all known cases uniaxial (rotational symmetry exists around the director) and apolar (the directions $\boldsymbol{n}$ and $-\boldsymbol{n}$ are equivalent). In the smectic phases the liquid crystal molecules possess long range order. A specific feature of smectic phases is the appearance of one-dimensional density waves or, as often called, layered structures. Smectic phases are divided into subgroups of which the smectic A phase (S_A) is the one used in the present applications. In this phase, the director coincides with the normal of the layer, and $\boldsymbol{n}$ and $-\boldsymbol{n}$ are equivalent. The structures of the nematic and smectic A phases are shown in Figure 1.

When a liquid crystalline sample is placed in an external magnetic field $\boldsymbol{B}$, the sample is magnetized so that the magnetization $\boldsymbol{M}$ is given by

$$M_\alpha = \mu_0^{-1} \chi_{\alpha\beta} B_\beta \tag{1}$$

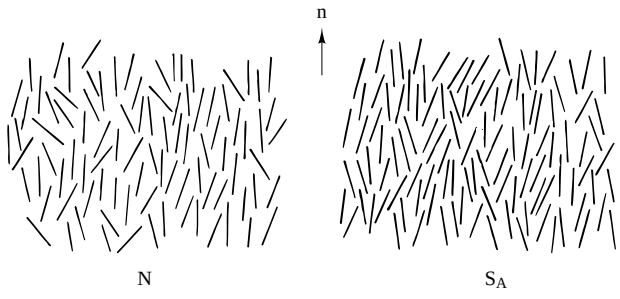

Figure 1 Structures of thermotropic nematic (N) and smectic A (S_A) liquid crystalline phases. The direction of the director is shown by **n**

where μ_0 is the permeability in vacuo and the $\chi_{\alpha\beta'}$s are elements of the diamagnetic (volume) susceptibility tensor, χ_{m}, which is diagonal in uniaxial phases.

The energy density, ρ_{B}, due to the magnetization $\boldsymbol{M}$ is:

$$\rho_B = -\int_0^B M \cdot \mathrm{d}B = -\frac{B^2}{2\mu_0}\left[\chi_{\mathrm{m}} + \frac{2}{3}\Delta\chi_{\mathrm{m}} P_2(\cos\theta)\right] \tag{2}$$

where $\chi_{\mathrm{m}} = \frac{1}{3}\,\mathrm{Tr}\chi_{\mathrm{m}}$ is the isotropic susceptibility, $\Delta\chi_{\mathrm{m}}$ is the anisotropy of the susceptibility tensor, and $P_2(\cos\theta) = \frac{1}{2}(3\cos^2\theta - 1)$ is the second Legendre polynomial (θ being the angle between $\boldsymbol{B}$ and $\boldsymbol{n}$). Considering the condition of minimum energy density, one can conclude the following:

1. When $\Delta\chi_{\mathrm{m}}$ is positive, ρ_{B} reaches a minimum with $P_2(\cos\theta) = 1$, i.e. the director is oriented parallel with the external magnetic field.
2. When $\Delta\chi_{\mathrm{m}}$ is negative, ρ_{B} reaches a minimum with $P_2(\cos\theta) = -\frac{1}{2}$, i.e. when the director is oriented perpendicular to the external field.

Both types of thermotropic liquid crystals exist and have been used in studies of the properties of solute molecules. Furthermore, proper mixtures of liquid crystals with opposite signs of diamagnetic anisotropies have been utilized. (See ***Liquid Crystals: Mixed Magnetic Susceptibility Solvents***.)

3 THE HAMILTONIAN OPERATOR AND OBSERVABLES

When considering the NMR spectra of spin-$\frac{1}{2}$ nuclei in molecules partially oriented in liquid crystals, the transition frequencies are dependent upon the nuclear shielding tensor, σ_i, the indirect spin–spin coupling tensor, $\boldsymbol{J}_{ij}$, and the direct dipole–dipole coupling tensor, $\boldsymbol{D}_{ij}$ (see ***Liquid Crystals: General Considerations***). Then the total Hamiltonian operator is (in energy units):

$$\hat{\mathcal{H}} = -\hbar\sum_i \gamma_i \hat{\boldsymbol{I}}_i \cdot (\boldsymbol{1} - \boldsymbol{\sigma}_i)\cdot B + h\sum_{i<j} \hat{\boldsymbol{I}}_i \cdot (\boldsymbol{J}_{ij} + \boldsymbol{D}_{ij})\cdot \hat{\boldsymbol{I}}_j \tag{3}$$

where $\hbar$ is Planck's constant divided by 2π, γ_{i} is the magnetogyric ratio of nucleus i, and $\boldsymbol{1}$ is the unit tensor. On the basis of perturbation theory one can conclude that the terms of the Hamiltonian operator which do not commute with the total spin component, $\hat{I}_z$,in the direction of $\boldsymbol{B}$ (defined as the z direction of the laboratory frame) can be safely neglected. Furthermore, taking the time average of the observables over the anisotropic molecular tumbling, the operator shown in equation (3) can be approximated by:

$$\begin{aligned}\hat{\mathcal{H}} = &-\hbar\sum_i \gamma_i(1-\sigma_i)B\hat{I}_{iz} \\ &+ h\sum_{i<j} J_{ij}\left[\hat{I}_{iz}\hat{I}_{jz} + \frac{1}{2}(\hat{I}_{i+}\hat{I}_{j-} + \hat{I}_{i-}\hat{I}_{j+})\right] \\ &+ h\sum_{i<j}(2D_{ij} + J_{ij}^{\mathrm{aniso}})\left[\hat{I}_{iz}\hat{I}_{jz} - \frac{1}{4}(\hat{I}_{i+}\hat{I}_{j-} + \hat{I}_{i-}\hat{I}_{j+})\right]\end{aligned} \tag{4}$$

In the operator shown in equation (4), the shielding is represented as

$$\begin{aligned}\sigma_i = \langle\sigma_{izz}\rangle &= \frac{1}{3}\sum_\alpha \sigma_{i\alpha\alpha} + \frac{2}{3}\left(\sum_{\alpha,\beta} S_{\alpha\beta}\sigma_{i\alpha\beta}\right)P_2(\cos\theta) \\ &= \sigma_i^{\mathrm{iso}} + \sigma_i^{\mathrm{aniso}}\end{aligned} \tag{5}$$

The isotropic spin–spin coupling constant, J_{ij}, and the anisotropic contribution, $J_{\mathrm{ij}}^{\mathrm{aniso}}$, are

$$J_{ij} = \frac{1}{3}\sum_\alpha J_{ij\alpha\alpha} \tag{6}$$

and

$$J_{ij}^{\mathrm{aniso}} = \left(\frac{2}{3}\sum_{\alpha,\beta} S_{\alpha\beta}J_{ij\alpha\beta}\right)P_2(\cos\theta) \tag{7}$$

In equations (5)–(7), $\sigma_{\mathrm{i}\alpha\beta}$ and $J_{\mathrm{ij}\alpha\beta}$ are the elements of the shielding and spin–spin coupling tensor, respectively, in the molecule fixed coordinate system while the $S_{\alpha\beta}$ terms in turn, are the elements of the Saupe ordering tensor[9] which are defined as

$$S_{\alpha\beta} = \frac{1}{2}\langle 3\cos\theta_{\alpha n}\cos\theta_{\beta n} - \delta_{\alpha\beta}\rangle \tag{8}$$

where $\theta_{\alpha n}$ is the angle between the director $\boldsymbol{n}$ and the α axis of the coordinate system, the $\langle\ \rangle$ brackets indicate a time average, and $\delta_{\alpha\beta}$ is the Kronecker delta. The dipole–dipole coupling constant, D_{ij}, appearing in the operator shown in equation (4) is defined (when the correlation of the molecular reorientational and vibrational motions is neglected) as

$$D_{ij} = -\frac{\mu_0\hbar\gamma_i\gamma_j}{8\pi^2 r_{ij}^3}S_{ij} \tag{9}$$

where r_{ij} is the internuclear distance, and

$$S_{ij} = \frac{1}{2}\langle 3\cos^2\theta_{ijB} - 1\rangle \tag{10}$$

is called the order parameter (with respect to the external magnetic field) of the axis passing through i and j, and θ_{ijB} is the angle between the ij direction and the magnetic field. Since the order tensor is traceless and symmetric, it consists of five independent elements which are usually chosen as S_{cc}, $(S_{\mathrm{aa}} - S_{\mathrm{bb}})$, S_{ab}, S_{ac}, and S_{bc} (a, b and c are the axes of the molecule fixed coordinate system). Utilizing the coordinate transformation equation

$$S_{ij} = \sum_{\alpha,\beta}\cos\theta_{ij\alpha}\cos\theta_{ij\beta}\ S_{\alpha\beta} \tag{11}$$

S_{ij} can be written as:

$$\begin{aligned}S_{ij} = \Big[&\frac{1}{2}S_{cc}(3\cos^2\theta_{ijc} - 1) + \frac{1}{2}(S_{aa} - S_{bb})(\cos^2\theta_{ija} - \cos^2\theta_{ijb}) \\ &+ 2S_{ab}\cos^2\theta_{ija}\cos^2\theta_{ijb} + 2S_{ac}\cos^2\theta_{ija}\cos^2\theta_{ijc} \\ &+ 2S_{bc}\cos^2\theta_{ijb}\cos^2\theta_{ijc}\Big]P_2(\cos\theta)\end{aligned} \tag{12}$$

The number of the independent elements of the order tensor can be reduced by taking into account molecular symmetry. The values of the order tensor elements are obtained from the dipole–dipole coupling constants provided that at least one internuclear distance is known.

4 SHIELDING ANISOTROPY

For a moment let us forget the complications that may occur particularly when determining small anisotropies of nuclear shieldings, and concentrate on the principles of how the shielding anisotropy is obtained from an NMR spectrum of a molecule partially oriented in a liquid crystal. Let us choose as an example a molecule possessing at least a

threefold symmetry axis, e.g. acetonitrile (CH_3CN). In such a case, the molecular orientation is completely determined by one order tensor element. Thus the experimental chemical shift, δ^{exp}, can be expressed in the form (note that δ increases to high frequency whereas σ increases to low frequency; for simplifying notations the subscript i will be omitted):

$$\begin{aligned}\delta^{exp} &= \delta^{iso} - \frac{2}{3}\left[\sigma_{zz} - \frac{1}{2}(\sigma_{xx} + \sigma_{yy})\right] SP_2(\cos\theta) \\ &\equiv \delta^{iso} - \frac{2}{3}\Delta\sigma SP_2(\cos\theta)\end{aligned} \tag{13}$$

where $\sigma_{zz} - \frac{1}{2}(\sigma_{xx} + \sigma_{yy}) \equiv \Delta\sigma$ is the anisotropy of the shielding tensor [(x, y, z) is a molecule fixed coordinate system] and S is the order parameter of the molecular symmetry axis (which in the case of acetonitrile lies along the $-C-C\equiv N$ direction). Equation (13) contains two unknown parameters δ^{iso} and $\Delta\sigma$; the order parameter S is obtained from the experimental dipole–dipole couplings [defined in equation (9)] which do not contain an anisotropic contribution, J_{ij}^{aniso}, and are corrected for harmonic vibrations and preferably also for deformational contributions. Usually couplings of the type D_{HX} with ^1H as a coupling partner (D_{HH} in CH_3CN) are a safe choice.

The shielding anisotropy can be determined by changing either S or $P_2(\cos\theta)$. There exist several possibilities for both. They are described below.

4.1 Use of Isotropic–Nematic Phase Transitions

In this method, $\delta^{iso} = \delta^{exp}$(isotropic) is determined in the liquid crystal heated to the isotropic state (when $S \equiv 0$) and assumed not to be affected by the change of phase. Then the sample is cooled to the nematic state and δ^{exp}(nem.) is measured. Consequently,

$$\Delta\sigma = -\frac{3}{2}\left[\frac{\delta^{exp}(\text{nem.}) - \delta^{exp}(\text{isotropic})}{SP_2(\cos\theta)}\right] \tag{14}$$

4.2 Gradient Method

One disadvantage of the previous method is that the experiments have to be carried out at two different phases, isotropic and nematic. This can be avoided by working exclusively in a nematic or smectic phase and changing the molecular degree of order, i.e. the order parameter S. This is achieved by changing the temperature or concentration of the sample. When δ^{exp} is expressed graphically as a function of $SP_2(\cos\theta)$, the slope of the resulting straight line gives $\Delta\sigma$ and the intercept δ^{iso}.

4.3 Use of Smectic Phases

The smectic A phases of thermotropic liquid crystals often possess the property that once oriented in a magnetic field they keep the orientation for a long time. This makes it possible to change in a very straightforward way the angle between the director $\boldsymbol{n}$ and the magnetic field $\boldsymbol{B}$, i.e. the factor $P_2(\cos\theta)$ in equation (13), while S remains unchanged.[10] The shielding anisotropy is then obtained without changing solvent properties.

When the liquid crystal is heated to the isotropic state and then cooled in the magnetic field to the smectic state, the director orients (when $\Delta\chi_m > 0$) along the magnetic field and $\theta = 0$. Thus

$$\delta^{exp}(0) = \delta^{iso} - \frac{2}{3}\Delta\sigma S \tag{15}$$

The rotation of the sample (in a conventional electromagnet) around the tube axis by 90° [generally, the rotation angle is obtained from the ratio of the dipolar couplings: $D_{ij}(\theta)/D_{ij}(0) = P_2(\cos\theta)$] gives:

$$\delta^{exp}(90) = \delta^{iso} + \frac{1}{3}\Delta\sigma\ S \tag{16}$$

and consequently,

$$\Delta\sigma = \frac{\delta^{exp}(90) - \delta^{exp}(0)}{S} \tag{17}$$

In the smectic phases the degree of solute molecular orientation is usually high, when both S and the chemical shift difference [nominator in equation (17)] are large, leading to a good relative precision in $\Delta\sigma$. Figure 2, which shows the ^{199}Hg NMR spectrum of dimethylmercury $(CH_3)_2Hg$ at the orientation described above, illustrates the method.

4.4 Use of Mixtures of Thermotropic Nematic Liquid Crystals

4.4.1 Liquid Crystals with Opposite Diamagnetic Anisotropy

This method, called NEMIX, is comparable with the one described in Section 4.3. When two thermotropic nematic liquid crystals possessing opposite anisotropies of diamagnetic susceptibility, $\Delta\chi_m$, are mixed at a certain critical concentration ratio ($\Delta\chi_m$ of the critical mixture is equal to 0), the 90°

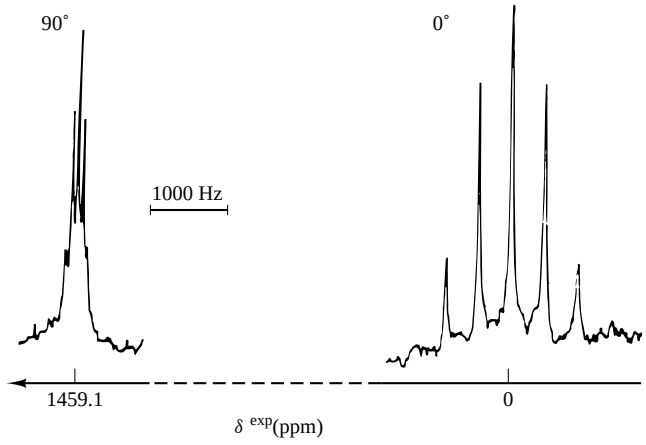

Figure 2 ^{199}Hg NMR spectrum of dimethylmercury [$(CH_3)_2Hg$] in the smectic A phase of HAB: 0°, director parallel with the external magnetic field, 90°, director perpendicular to the external magnetic field. (Reproduced with permission of Heyden & Sons from J. Jokisaari and P. Diehl[26])

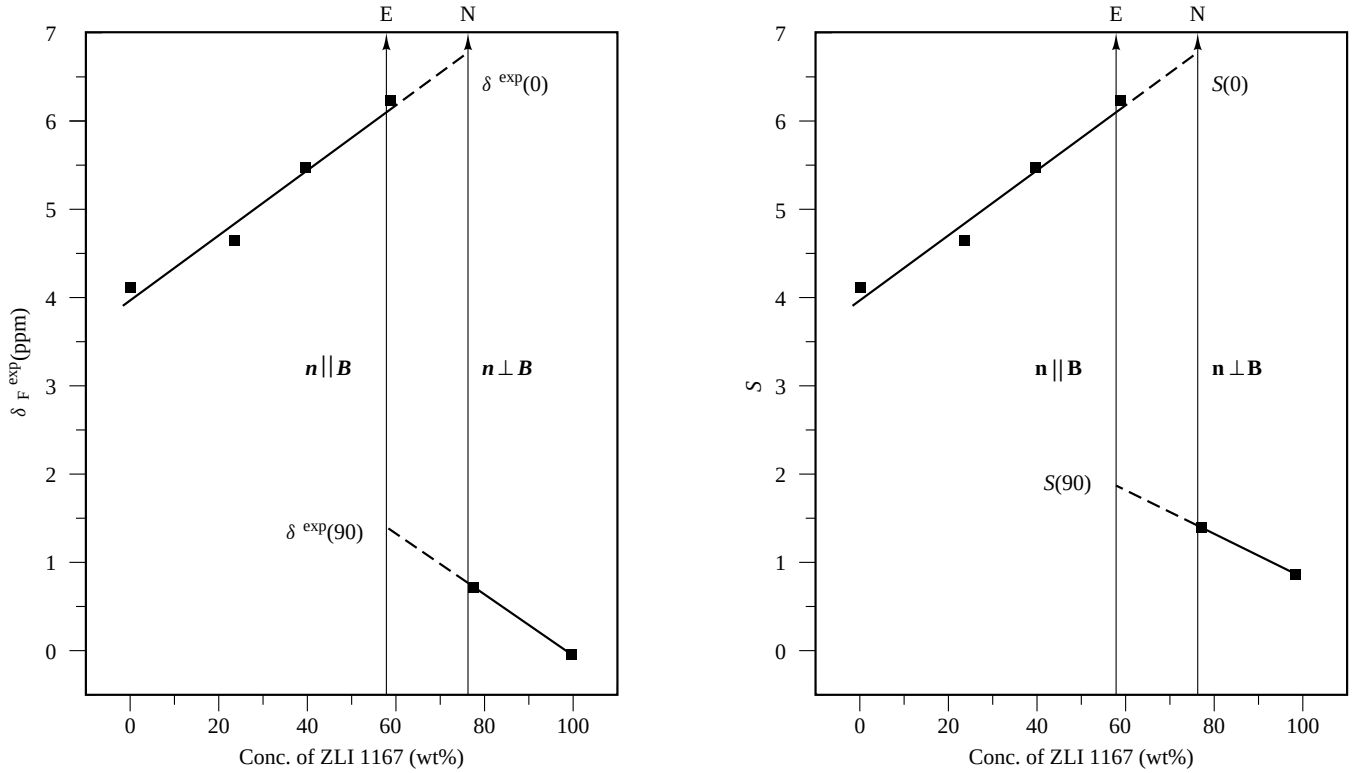

Figure 3 The experimental chemical shift, $\delta_F{}^{exp}$, of the ^{19}F nucleus and the order parameter of the C_3 symmetry axis, S, for methyl fluoride (CH_3F) as a function of the liquid crystal composition in mixtures of ZLI 1167 and EBBA. The mixtures used in the NEMIX and ENEMIX methods are indicated by N and E, respectively

rotation of the liquid crystal director is achieved by changing the sign of $\Delta\chi_m$ with the aid of a slight temperature change or a small temperature gradient over the sample volume (see ***Liquid Crystals: Mixed Magnetic Susceptibility Solvents***). In the latter case, the NMR spectra corresponding to the two director orientations can be detected simultaneously.[11,12] The shielding anisotropy can be calculated from equation (17). Figure 3 shows how the method works.

4.4.2 Liquid Crystals with Opposite Deformational Effects on Molecular Structure

The anisotropic forces that cause the orientation of solute molecules at the same time deform their structure leading to the solvent dependence of structure. It has appeared that ^{13}C-enriched methane ($^{13}CH_4$) is a convenient and practical reference, not only for chemical shifts but also for structural deformations. It has been found that in certain mixtures of thermotropic liquid crystals the methane molecule is not deformed.[13] The components of the mixture may be selected so that they possess opposite diamagnetic anisotropies and, consequently, parallel and perpendicular orientations of the director with respect to the external magnetic field can be produced in a similar way to that discussed above. Figure 3 also demonstrates this method, which is called ENEMIX. In contrast to the NEMIX method and the method based on the utilization of smectic liquid crystals, the ratio of the S parameters corresponding to the two director orientations may not exactly equal -2, whence

$$\Delta\sigma = -\frac{3}{2}\left[\frac{\delta^{exp}(0) - \delta^{exp}(90)}{S(0) - S(90)}\right] \tag{18}$$

4.5 Use of Sample Spinning

4.5.1 Sample Tube Axis Perpendicular to the Magnetic Field

As discussed above, the liquid crystals director orients either along the external magnetic field or perpendicular to it depending upon the sign of the diamagnetic anisotropy. In a conventional electromagnet, the director orients perpendicular to the tube axis (when $\Delta\chi_m > 0$; if $\Delta\chi_m < 0$ the director orients along the tube axis and no change in the orientation can be achieved by spinning the sample tube). When the sample is spinning around the tube axis the liquid crystal experiences a viscous torque

$$N_v = \lambda_1\Omega \tag{19}$$

where Ω is the angular speed and λ_1 a coefficient proportional to the viscosity of the solution. The magnetic torque opposes the viscous torque, and in equilibrium $N_B = N_v$. Thus the angle θ_0 between the magnetic field and the director is determined by

$$\sin 2\theta_0 = -\frac{2\mu_0\lambda_1}{B^2\Delta\chi_m}\Omega \tag{20}$$

The value of $SP_2(\cos\theta_0)$ can be determined from the dipolar coupling constants and the shielding anisotropy calculated as in the previous method. On the other hand, θ_0 can be varied by varying the angular speed Ω. There is, however, an upper limit for Ω, the so-called critical speed, $\Omega_c = -B_2\Delta\chi_m/2\,\mu_0\lambda_1$, above which no equilibrium state can be reached but the director rotates with the tube. When the experimental chemical shift is plotted as a function of $SP_2(\cos\theta_0)$, the shielding

anisotropy is obtained from the slope of the resulting straight line.

4.5.2 *Variable Angle Spinning*

Let us consider a general case where the spinning axis of a sample tube forms an angle β with the magnetic field. Transforming the susceptibility tensor into the principal axis system rotating around the magnetic field direction and taking a time average,[14] the magnetic energy density can be represented in the form

$$\langle \rho_B \rangle = -\frac{B^2}{2\mu_0}\left[\chi_m + \frac{2}{3}\Delta\chi_m P_2(\cos\beta)P_2(\cos\delta)\right] \quad (21)$$

where δ is the angle between the spinning axis and the liquid crystal director. From the condition of minimum energy density, one can conclude the following: (a) when $\Delta\chi_m > 0$ and $0 \leq \beta < \beta_m$ (β_m is the magic angle, 54.7°), the liquid crystal director orients parallel with the spinning axis, i.e. the angle between the director and the magnetic field equals β; (b) when $\Delta\chi_m > 0$ and $\beta_m < \beta \leq \pi/2$, the directors are equally distributed in the plane perpendicular to the spinning axis; (c) when $\Delta\chi_m < 0$ and $0 \leq \beta < \beta_m$, the situation is similar to (b); and (d) when $\Delta\chi_m < 0$ and $\beta_m < \beta \leq \pi/2$, the situation is similar to (a).

The slope of the resulting straight line obtained by plotting the experimental chemical shift as a function of $SP_2(\cos\beta)$, or as a function of a dipolar coupling constant as shown in Figure 4, gives the shielding anisotropy.

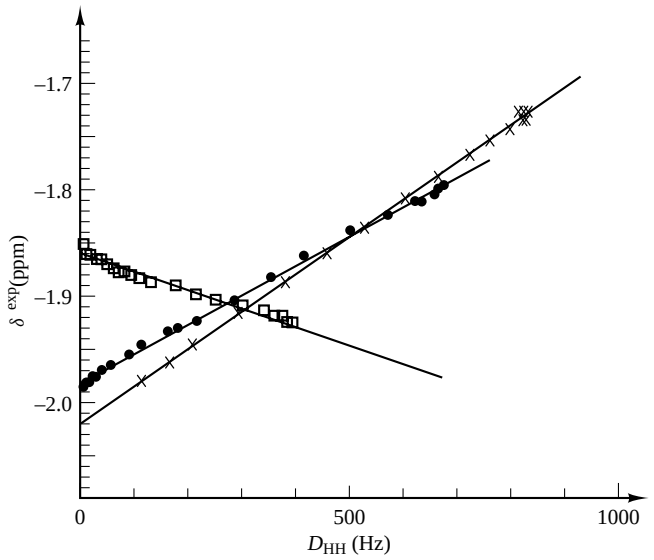

Figure 4 Plot of δ^{exp} for the ^{1}H nucleus (referenced to internal TMS) as a function of D_{HH} for methyl iodide (CH_3I) in three liquid crystals: phase 4 (□); ZLI 1167 (39.1%)/phase 4 (60.9%) (•); and ZLI 1167 (57.6%)/phase 4 (42.4%) (x). The data were produced on a VAS system by varying the angle between the spinning axis and the external magnetic field. The slope, κ, of the straight line yields the proton shielding anisotropy $\delta\sigma_H = (3/4)\,(K_{HH}/r^3_{HH})\kappa$, where $K_{HH} = \mu_0\hbar{\gamma_H}^2/8\pi^2$. (Reproduced with permission of Academic Press from T. Väänänen, J. Jokisaari, and M. Seläntaus[33]). Note: the δ scale is opposite to the one used in the present text

4.6 Examples and Reliability of Results

4.6.1 *Molecules Whose Orientation Can Be Described by One Order Parameter*

Tables (1)-(3) show $\Delta\sigma$ values determined by applying various liquid crystals and methods described above. The examples are chosen so that they cover a wide range of values, and consequently yield the weaknesses on the one hand and the reliability on the other hand of liquid crystal NMR spectroscopy as applied to the determination of shielding anisotropies. Table 1 lists the proton shielding anisotropy values measured for acetonitrile (CH_3CN). As can be seen, they vary over a relatively wide range, and both positive and negative values have been reported. The $\Delta\sigma_H$ value seems to depend upon the method used, liquid crystal solvent, and reference method and substance. This is due to the fact that the measured shielding is affected by three different anisotropic contributions:

$$\sigma^{exp} = \sigma^{mol} + \sigma^{local} + \sigma^{bulk} \quad (22)$$

where σ^{mol} (the quantity of interest) arises from the electron distribution in the molecule, σ^{local} (the local effect) from the nearest neighbor molecules, and σ^{bulk} (the bulk effect) from the other parts of the sample. The greatest problem is caused by the local effects; obviously the solute and reference molecules do not probe exactly the same local fields, leading to an erroneous $\Delta\sigma$. Local effects in a smectic liquid crystal, and in mixtures of thermotropic nematic liquid crystals with opposite diamagnetic anisotropies, have been studied by using globular solutes (which do not orient in liquid crystals, i.e. $S - 0$) and found to be from -0.2 to -0.5 ppm for protons.[15–17] These experiments and the earlier ones[18,19] mean that the anisotropic contribution of the local effects may be of the same magnitude as σ^{aniso} for protons, but also for other nuclei if their shielding anisotropy is not very large.

The first column of Table 2 shows that the shielding anisotropy of the methyl carbon, $\Delta\sigma CH_3$ in acetonitrile, being of the order of 20 ppm, also depends markedly on the applied experimental method and liquid crystal solvent. On the contrary, the shielding anisotropies measured for the $-C{\equiv}N$ carbon, $\Delta\sigma_{CN}$, in acetonitrile as well as those for the ^{199}Hg nucleus in dimethylmercury [$(CH_3)Hg$] (see Table 3) are virtually insensitive to all these factors. The small scatter arises from the internuclear distance chosen as a basis in calculating the order parameter S and from whether vibrational corrections are taken into account or not.

The experiments carried out until now and comparisons made with the values produced by other techniques or theoretical calculations provide strong support for the modified ENEMIX method giving the most reliable estimates for small $\Delta\sigma$s.[21]

4.6.2 *Molecules Whose Orientation Can Be Described by Two Order Parameters*

In cases where molecules possess two perpendicular planes of symmetry as, for example, monosubstituted benzenes and heteroatomic five-membered rings, the experimental chemical shift can be represented in the form:

$$\delta^{exp} = \delta^{iso} - \frac{2}{3}\left\{S_{zz}\left[\sigma_{zz} - \frac{1}{2}(\sigma_{xx} + \sigma_{yy})\right] + \frac{1}{2}(S_{xx} - S_{yy})(\sigma_{xx} - \sigma_{yy})\right\} P_2(\cos\theta) \quad (23)$$

Table 1 Proton Shielding Anisotropy of Acetonitrile Determined by Various Methods in Different Liquid Crystals

$\Delta\sigma_H$ (ppm)	Method	Liquid crystal	Chemical shift reference[a]
+3.9 ± 0.2	Gradient method[20]	ZLI 1167	$^{13}CH_4$
+2.3 ± 0.1	Gradient method[20]	ZLI 1167	TMS
+2.1	Modified ENEMIX[21]	ZLI 1167/Phase 4	$^{13}CH_4$
+0.30 ± 0.08 to +1.06 ± 0.8	NEMIX[20]	Various LCs mixed with ZLI 1167	TMS
−2.7 ± 0.1	Smectic phase[20]	HAB	$^{13}CH_4$
−4.5 ± 0.8	Gradient method[20]	EBBA	$^{13}CH_4$
−4.7 ± 0.1	Smectic phase[20]	HAB	TMS

[a]Internal reference.

Table 2 ^{13}C Shielding Anisotropies in Acetonitrile Determined by Various Methods in Different Liquid Crystals. For Comparison, Theoretical Values are Also Included

$\Delta\sigma CH_3$ (ppm)	$\Delta\sigma_{CN}$ (ppm)	Method	Liquid crystal	Chemical shift reference[a]
22.9	324.6	Modified ENEMIX[21]	ZLI 1167/phase 4	$^{13}CH_4$
20.5 ± 0.7	328 ± 8	Gradient[20]	ZLI 1167	$^{13}CH_4$
15.7 ± 1.5		Smectic phase[20]	HAB	$^{13}CH_4$
13.6 ± 0.6	311 ± 6	Gradient[20]	EBBA	$^{13}CH_4$
	304 ± 5	Gradient[22]	MIX	ext. $^{13}CS_2$
	307 ± 4	I–N phase transition[23]	EBBA	^{1}H reson. of CH_3CN
	299 ± 5	I–N phase transition[22]	MIX	ext. $^{13}CS_2$
21, 15	340, 348	Theory[24b]		

[a]Internal reference if not otherwise indicated.
[b]IGLO method with two different basis sets. Large basis set results on the right.

The shielding anisotropy, $\Delta\sigma = \sigma_{zz} - \frac{1}{2}(\sigma_{xx} + \sigma_{yy})$, and the difference $(\sigma_{xx} - \sigma_{yy})$ are obtained separately only if the ratio $(S_{xx} - S_{yy})/S_{zz}$ can be varied. Consequently, none of the methods described above which are based on the change of direction of the liquid crystal director with respect to the external magnetic field, i.e. the variation of the $P_2(\cos\theta)$ factor, is applicable here. The variation of the ratio $(S_{xx} - S_{yy})/S_{zz}$ may be produced by changing the sample temperature or by using different liquid crystal solvents. Then one has to assume that the shielding tensor elements are not affected by the experimental conditions.

The determination of the ^{13}C shielding anisotropies in molecules which are large in the liquid crystal NMR scale (when the number of magnetic nuclei increases, the NMR spectrum of an oriented molecule becomes very complex; in practice the upper limit for the number of active, interacting nuclei is 10–12), and contain several carbon atoms and ^{13}C in natural abundance, is usually at least very cumbersome if not impossible from the proton coupled spectra. Therefore, a method has been proposed which uses a spin echo sequence $[90^\circ - \tau - 180^\circ - 2\tau - 180^\circ - \tau - \text{acquisition}]$ and phase-alternated broadband decoupling.[30] The echo sequence cancels the possible overlap of the solute signals by the solvent signals.

Table 3 ^{199}Hg Shielding Anisotropy in Dimethylmercury Determined by Various Methods in Different Liquid Crystals. For Comparison, Results obtained from Spin–Lattice Relaxation Time Measurements are also Included

$\Delta\sigma^{199}Hg$ (ppm)	Method	Liquid crystal	Comments
7475 ± 80	Gradient[25]	EBBA	No vibr. corr.
7799 ± 55	Smectic phase[26]	HAB	No vibr. corr.
7325 ± 55	Smectic phase[26]	HAB	D_{ij}s corrected for harm. vibr.
7260 ± 90	ENEMIX[27]	ZLI 1167	D_{ij}s corrected for harm. vibr.
4600 ± 1000	T_1[28]		Saturation-recovery method
5820 ± 10%	T_1[28]		Inversion–recovery method

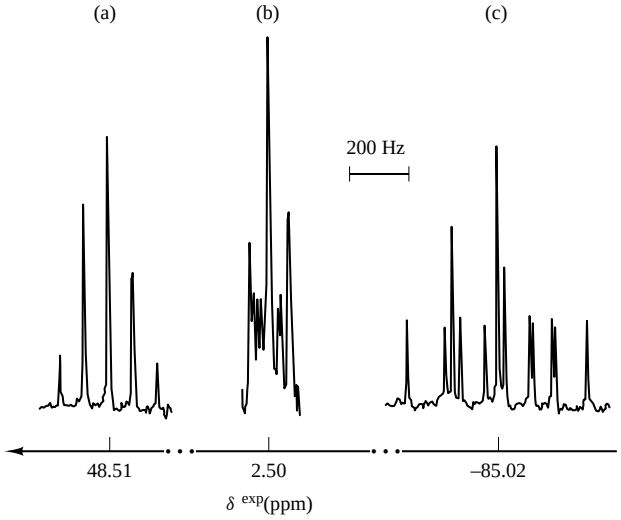

Figure 5 The ^{125}Te NMR spectrum of tellurophene (C_4H_4Te) in (a) ZLI 1167 (58%)/phase 4(42%), (b) EBBA and (c) ZLI 1167. (Reproduced with permission of Taylor & Francis from J. Jokisaari and T. Väänänen[31])

The ^{13}C NMR spectrum yields the chemical shifts whereas the order parameters appearing in equation (23) are obtained from the ^{1}H spectrum.

The NMR spectroscopy of solute molecules in liquid crystals has not been applied very much to the investigations of shielding anisotropies of the so-called heavy nuclei. Most of the studies deal with the ^{1}H, ^{13}C, ^{19}F, and ^{31}P nuclei, and highly symmetrical molecules.[6] This is somewhat surprising because the method is best when the shielding anisotropy is fairly large. There has been, however, some work carried out for ^{111}Cd, ^{113}Cd, and ^{199}Hg in molecules with C_3 symmetry, and one work for the ^{125}Te nucleus in a C_{2v} symmetric molecule, tellurophene (C_4H_4Te).[31] The ^{125}Te NMR spectra of tellurophene in three liquid crystals are shown in Figure 5.

Equation (23) can be rewritten in the form

$$-\frac{3}{2}\left[\frac{\delta^{\text{exp}}-\delta^{\text{iso}}}{S_{zz}}\right]=\left[\sigma_{zz}-\frac{1}{2}(\sigma_{xx}+\sigma_{yy})\right]+\frac{\sigma_{xx}-\sigma_{yy}}{2}\,\frac{S_{xx}-S_{yy}}{S_{zz}} \quad (24)$$

The intercept of the straight line obtained by plotting the left hand side of equation (24) as a function of $(S_{xx} - S_{yy})/S_{zz}$ yields $[\sigma_{zz} - \frac{1}{2}(\sigma_{xx} + \sigma_{yy})]$ whereas the slope gives $(\sigma_{xx} - \sigma_{yy})$. The results derived for ^{125}Te in tellurophene are collected in Table 4.

5 SPIN–SPIN COUPLING ANISOTROPY

The determination of reliable anisotropies, ΔJ_{ij}, of the spin–spin coupling tensors using NMR spectroscopy of molecules dissolved in liquid crystals may be a fairly difficult task. This is due to the fact that the experimental couplings, D_{ij}^{exp}, are dominated by the direct dipole–dipole coupling tensor elements, and moreover, in real molecules the dipole–dipole as well as spin–spin coupling tensors are averages over intramolecular motions. However, when performing proper analyses of data (sets of D_{ij}^{exp} values) preferably (often necessarily) produced in many liquid crystal solvents, most reliable and accurate ΔJ_{ij} values can be determined.

5.1 Quantitative Determination of *J* Anisotropy

The experimentally available couplings D_{ij}^{exp} can be expressed as a sum of several contributions (***Structure of Rigid Molecules Dissolved in Liquid Crystalline Solvents***):

$$D_{ij}^{\text{exp}}=D_{ij}^{\text{e}}+D_{ij}^{\text{ah}}+D_{ij}^{\text{h}}+D_{ij}^{\text{d}}+\frac{1}{2}J_{ij}^{\text{aniso}} \quad (25)$$

In equation (25), the first four terms on the right-hand side constitute the direct dipolar part of the coupling: D_{ij}^{c} is the dipole–dipole coupling corresponding to the equilibrium structure of the molecule; D_{ij}^{aff} is the contribution from the anharmonicity of the vibrational potential (the sum of these terms $D_{ij}^{\text{e}} + D_{ij}^{\text{ah}} = D_{ij}^{\alpha}$ is the dipole–dipole coupling corresponding to the so-called r_α structure of the molecule; the anharmonic force constants are often not available and thus only the r_α structure can be determined); D_{ij}^{h} is the contribution from the harmonic vibrations; and D_{ij}^{d} (the so-called deformational contribution which is responsible for the solvent dependence of structure) from the correlation between

Table 4 The Results of the ^{125}Te NMR Study of Tellurophene Dissolved in three Liquid Crystals.[31] The Signs of δ^{exp} and δ^{iso} are Opposite to those in the Original Paper due to the Different Definition of the δ scale

Liquid crystal	δ^{exp} (ppm)	δ^{iso} (ppm)[a]	$S_{xx} - S_{yy}/S_{zz}$	S_{zz}[b]
EBBA	2.41	1.55	0.5033	0.1563
ZLI 1167/phase 4	48.51	−2.18	1.7478	0.1954
ZLI 1167	−85.02	15.65	1.9992	−0.0592

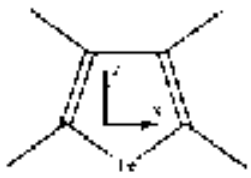

$\Delta\sigma = \sigma_{zz} - \frac{1}{2}(\sigma_{xx} + \sigma_{yy}) = 1560 \pm 21$ ppm

$\sigma_{xx} - \sigma_{yy} = 307 \pm 36$ ppm

[a] Assumed to be a simple hexagonal benzenic state.
[b] Determined from the ^{13}C–^{125}Te dipolar coupling constants assuming the corresponding J^{aniso} to be negligible.
[c] With respect to the external magnetic field.

vibrational and reorientational motions (time averages of S_{ij} and r_{ij}^{-3} appearing in the definition of the dipole–dipole coupling, equation (9), cannot be taken independently).

In order to get a reliable value for J_{ij}^{aniso} (which is normally small and in many cases comparable in magnitude with the vibrational and deformational correction terms), the molecular structure should be determined as completely as possible with the aid of the D_{ij}^{exp} values. This necessarily means a full analysis of data taking into account the interactions (the anisotropic forces that tend to orient molecules) between the solute and solvent molecules. In such an analysis the number of unknown parameters often exceeds the number of D_{ij}^{exp} values obtainable from one experiment, i.e. the problem becomes underdetermined. This increasing number of parameters is a consequence of the deformational effects. For example, in order to be able to calculate deformational corrections to J^{aniso}, one should know the derivatives of the spin–spin coupling tensor with respect to the vibrational normal coordinates. These are not available, and consequently must be used as adjustable parameters.[32] The problem of underdetermination can, however, be overcome by carrying out experiments in several liquid crystalline solvents.

Another uncertainty in the determination of J_{ij}^{aniso} may appear in cases of spin systems consisting of different nuclear species, for instance I and S spins. Thus, the NMR spectrum yields only the sum $|2D_{is}^{exp} + J_{is}|$. If the spin–spin coupling constant, J_{IS}, cannot be determined under the same experimental conditions (the same solvent, temperature, concentration, etc.) as the sum, an additional uncertainty is introduced into D_{IS}^{exp}, and consequently, also into J_{IS}^{aniso}. In principle, J_{IS} can be determined in liquid crystalline phases by performing, for instance, VAS (Variable Angle Spinning) experiments.[33]

Let us consider the determination of the anisotropy of the $^{13}C-^{19}F$ spin–spin coupling in the methyl fluoride (CH_3F) molecule. Due to the C_3 symmetry of the molecule, its orientation can be described by one order parameter, S, of the symmetry axis. Then the anisotropic contribution to the experimental coupling $D_{CF}{}^{exp}$ can be expressed in the form:

$$J_{CF}^{aniso} = \frac{2}{3}\Delta J_{CF} S P_2(\cos\theta) \tag{26}$$

where $\Delta J_{CF} = J_{CFzz} - \frac{1}{2}(J_{CFxx} + J_{CFyy})$ is the anisotropy of the coupling tensor $\boldsymbol{J}_{CF}$. When the experimental dipolar couplings are corrected for harmonic vibrations but the deformational corrections are neglected, ΔJ_{CF} appears to be solvent dependent to a very great extent, as shown in Table 5. This large scatter of results is removed when all the dipolar couplings and J_{CF}^{aniso} are corrected for deformational effects and a joint analysis of nine experiments (44 couplings, D_{CF}^{exp} in one liquid crystal could not be obtained, and 23 parameters) is carried out. This analysis results in $\Delta J_{CF} = 404 \pm 31$ Hz. The relative anisotropy, $\Delta J_{CF}/J_{CF}$, is -2.50 ± 0.20 (J_{CF} appears to be slightly dependent upon the liquid crystal solvent, its average value is -161.43 Hz) and should be compared with -2.70 obtained by Hartree–Fock theory (ab initio) and by a semiempirical finite perturbation method at the INDO MO level of approximation.[34] The first-order polarization propagator approach has led to the ΔJ_{CF} value of 296.41 Hz.[35] Consequently, the experimental results of a joint analysis and the theoretical results are in fair agreement.

Reinforcement for the workability of the method is provided by the studies on acetonitrile (CH_3CN) and methyl isocyanide (CH_3NC). Table 6 clearly shows that when the harmonic vibrational and deformational effects are taken into account in the experimental dipolar couplings, the ΔJ values are in nice accord with the theoretical ones.

Table 5 The Anisotropy ΔJ_{CF} of the $^{13}C-^{19}F$ Spin–Spin Coupling Tensor for Methyl Fluoride ($^{13}CH_3F$) in Various Liquid Crystals. The Dipolar Couplings are Corrected for Harmonic Vibrations but not for Deformational Effects. The Result of the Joint Analysis (which takes into account also the Deformational Effects) of Nine Sets of D_{ij}^{exp} Values (44 Couplings and 23 Parameters) is also given for Comparison[32]

ΔJ_{CF} (Hz)	Liquid crystal solvent[a]
690 ± 60	ZLI 1167
646 ± 46	ZLI 1167 (78.4)/EBBA (21.6)
390 ± 82	ZLI 1167 (58.7)/EBBA (41.3)
49 ± 49	ZLI 1167 (40.1)/EBBA (59.9)
-653 ± 103	ZLI 1167 (23.6)/EBBA (76.4)
-4955 ± 260	EBBA
-1365 ± 72	Phase 4
546 ± 14	Phase 1221
404 ± 31[b]	
296[c]	

[a]The figures in parentheses show the concentration (in wt.%) of the component in the mixture.
[b]Results of the joint analysis. For details, see text.
[c]Theoretical value obtained by first-order polarization propagator approach.[35]

5.2 Qualitative Revelation of J Anisotropy

Molecular symmetry can place very restrictive conditions for the ratios of dipolar coupling constants. Consequently, this can be used to reveal whether D^{exp} includes a contribution from J^{aniso} or not. If the examination of the ratios $D_{ij}{}^{exp}/D_{kl}{}^{exp}$ shows that they differ from the corresponding ratios of direct dipolar couplings ($D^{dir} = D^{exp} - \frac{1}{2}J^{aniso} = D^{e} + D^{ah} + D^{h} + D^{d}$, see equation (26)), they (or at least some of them) may be affected by J^{aniso}.

Benzene is a good example of a molecule in which symmetry completely fixes the ratios of the dipolar couplings. The order parameter of each ij direction equals $-\frac{1}{2}S$ (S is the order parameter of the sixfold symmetry axis) and consequently the following equation is valid:

$$\frac{D_{ij}^{dir}}{D_{kl}^{dir}} = \frac{\gamma_i\gamma_j}{\gamma_k\gamma_l}\left(\frac{r_{kl}}{r_{ij}}\right)^3 \tag{27}$$

It follows from the hexagonal symmetry of benzene that $r_m = \sqrt{3}r_o$ and $r_p = 2r_o$ (o = *ortho*, m = *meta*, p = *para*). Thus for the nuclei of same isotopic species, $D_o/D_m/D_p = 1 : \sqrt{3}/9 : 1/8 \sim 1 : 0.1925 : 0.1250$. It has been found that the $^1H-^1H$ couplings in benzene indeed fulfil these ratios (in particular, when the experimental couplings are corrected for harmonic vibrational and deformational effects) and thus the $J_{HH}{}^{aniso}$ values are obviously negligible.[4] In contrast, remarkable deviations have been detected for the $^{13}C-^{13}C$ couplings (corrected for harmonic vibrations).[39]

Equation (27) is not only valid for benzene but more generally. Thus, if S_{ij} for the nuclei i and j is the same as S_{kl} for the nuclei k and l, in other words the axes passing through

Table 6 Anisotropies of the $^{13}C-^{13}C$ and $^{13}C-^{15}N$ Spin–Spin Coupling Tensors in Acetonitrile (CH_3CN) and Methyl Isocyanide (CH_3NC)

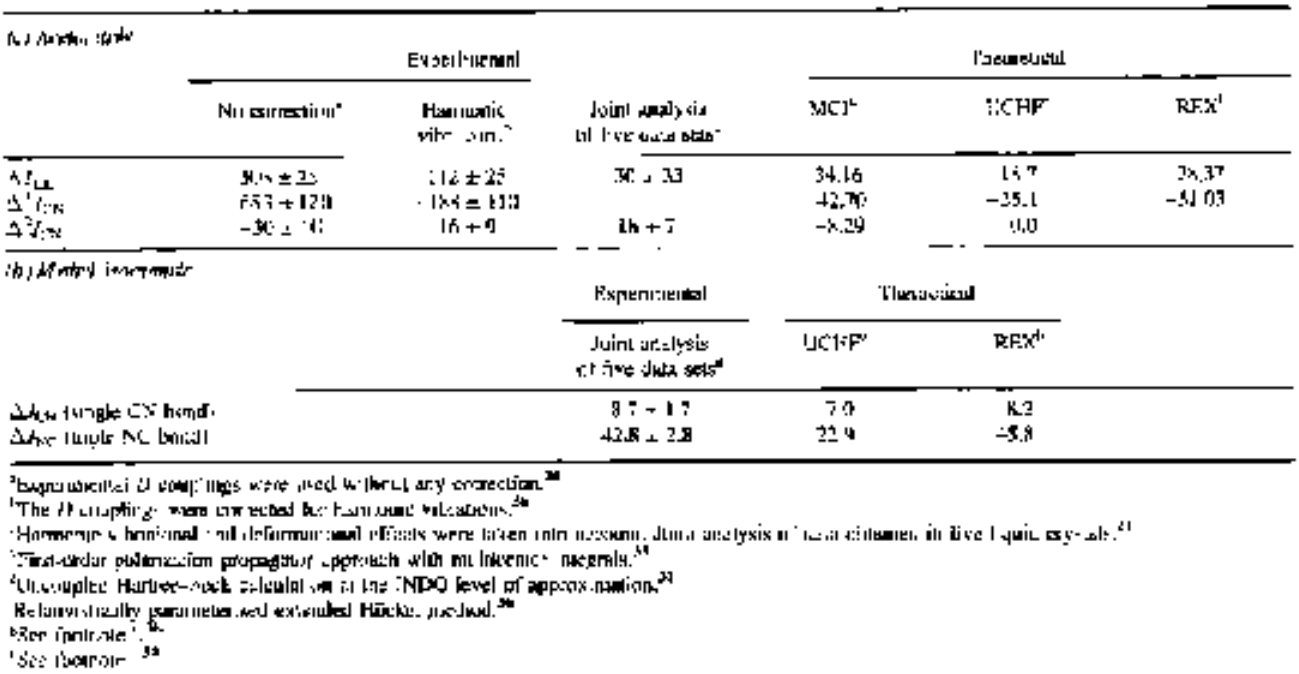

Table 7 Code Names and Compositions of the Liquid Crystals Mentioned in the Text

Code name[a]	Composition
ZLI 1167 ($\Delta\chi_m < 0$)	Mixture of 4-propyl-*trans*,*trans*-bicyclohexyl-4′-carbonitrile (36%), 4-pentyl-*trans*,*trans*-bicyclohexyl-4′-carbonitrile (34%), and 4-heptyl-*trans*,*trans*-bicyclohexyl-4′-carbonitrile (30%)
Phase 4 ($\Delta\chi_m > 0$)	Eutectic mixture of *p*-methoxy-*p*′-butylazoxybenzenes
HAB ($\Delta\chi_m > 0$)	*p*,*p*′-diheptylazoxybenzene
EBBA ($\Delta\chi_m > 0$)	(*p*-Ethoxybenzylidene)-*p*-butylaniline
ZLI 1132 ($\Delta\chi_m > 0$)	Mixture of *trans*-4-propyl-(4-cyanophenyl)cyclohexane (24%), *trans*-4-pentyl-(4-cyanophenyl)cyclohexane (36%), *trans*-4-heptyl-(4-cyanophenyl)cyclohexane (25%), and *trans*-4-pentyl-(4′-cyanobiphenyl-4)cyclohexane (15%)
Phase 1221 ($\Delta\chi_m > 0$)	Mixture of phenylcyclohexanes, biphenylcyclohexane, and phenylcyclohexane esters
MIX ($\Delta\chi_m > 0$)	Mixture of butyl-*p*-(*p*-ethoxyphenoxycarbonyl)phenyl carbonate (75%) and *p*-capronyloxy-*p*′-ethoxyazoxybenzene (25%)

[a]The sign of the anisotropy of diamagnetic susceptibility is shown below; when $\Delta\chi_m > 0$ the liquid crystal director orients along, and when $\Delta\chi_m < 0$ the director orients perpendicular to the external magnetic field.

the nuclear pairs *ij* and *kl* are parallel, the ratio $D_{ij}^{dir} : D_{kl}^{dir}$ is independent of the orientation. If the corresponding ratio of the experimental couplings is found to vary, it suggests anisotropic contribution at least in one of the couplings.[40,41] The code names and compositions of the liquid crystals mentioned above are defined in Table 7.

6 RELATED ARTICLES

Average Hamiltonian Theory; Chemical Shift Tensor Measurement in Solids; Chemical Shift Tensors; Dipolar and Indirect Coupling Tensors in Solids; Indirect Coupling: Semiempirical Calculations; Liquid Crystalline Samples: Spectral Analysis; Liquid Crystals: General Considerations; Liquid Crystals: Mixed Magnetic Susceptibility Solvents; Shielding Calculations: IGLO Method; Shielding Calculations: Perturbation Methods; Spinning Liquid Crystalline Samples; Structure of Rigid Molecules Dissolved in Liquid Crystalline Solvents.

7 REFERENCES

1. A. Saupe and G. Englert, *Phys. Rev. Lett.*, 1963, **11**, 462.
2. S. Sýkora, J. Vogt, H. Bösiger, and P. Diehl, *J. Magn. Reson.*, 1979, **36**, 53.
3. J. Lounila and P. Diehl, *J. Magn. Reson.*, 1984, **56**, 254.

4. J. Lounila and P. Diehl, *Mol. Phys.*, 1984, **52**, 827.
5. J. Lounila, *Mol. Phys.*, 1986, **58**, 897.
6. J. Lounila and J. Jokisaari, *Prog. NMR Spectrosc.*, 1982, **15**, 249.
7. A. J. Leadbetter, in *Thermotropic Liquid Crystals*, ed. G. W. Gray, John Wiley & Sons, Guildford, 1987, Chap. 1
8. C. L. Khetrapal, A. C. Kunwar, A. S. Tracey, and P. Diehl, in *NMR Basic Principles and Progress*, eds. P. Diehl, E. Fluck, and R. Kosfeld, Springer-Verlag, Heidelberg, 1975, Vol. 9.
9. A. Saupe, *Z. Naturforsch.*, 1964, **19a**, 161.
10. A. J. Montana and B. P. Dailey, *Mol. Phys.*, 1975, **30**, 1521.
11. C. L. Khetrapal and A. C. Kunwar, *Mol. Cryst. Liq. Cryst.*, 1981, **72**, 13.
12. C. L. Khetrapal and A. C. Kunwar, *Chem. Phys. Lett.*, 1981, **82**, 170.
13. J. Jokisaari and Y. Hiltunen, *Mol. Phys.*, 1983, **50**, 1013.
14. R. Teeäär, M. Alla, and E. Lippmaa, *Org. Magn. Reson.*, 1982, **19**, 134.
15. P. Diehl, J. Jokisaari, F. Moia, and J. Lounila, *Mol. Cryst. Liq. Cryst.*, 1982, **87**, 319.
16. Y. Hiltunen and J. Jokisaari, *J. Magn. Reson.*, 1987, **75**, 213.
17. E. E. Burnell and C. A. de Lange, *Chem. Phys. Lett.*, 1987, **136**, 87.
18. R. A. Bernheim and T. R. Krugh, *J. Am. Chem. Soc.*, 1967, **89**, 6784.
19. A. D. Buckingham, E. E. Burnell, and C. A. de Lange, *J. Am. Chem. Soc.*, 1968, **90**, 2972.
20. P. Diehl, J. Jokisaari, and F. Moia, *J. Magn. Reson.*, 1982, **49**, 498.
21. J. Lounila, M. Ala-Korpela, and J. Jokisaari, *J. Chem. Phys.*, 1990, **93**, 8514.
22. P. K. Bhattacharyya and B. P. Dailey, *Chem. Phys. Lett.*, 1975, **32**, 305.
23. J. D. Kennedy and W. McFarlane, *Mol. Phys.*, 1975, **29**, 593.
24. M. Schindler, *J. Am. Chem. Soc.*, 1987, **109**, 5950.
25. J. D. Kennedy and W. McFarlane, *J. Chem. Soc., Faraday Trans. 2*, 1976, **72**, 1653.
26. J. Jokisaari and P. Diehl, *Org. Magn. Reson.*, 1980, **13**, 359.
27. A. Pulkkinen, Y. Hiltunen, and J. Jokisaari, *Liq. Cryst.*, 1988, **3**, 737.
28. C. R. Lassigne and E. J. Wells, *Can. J. Chem.*, 1977, **55**, 1303.
29. R. E. Wasylishen, R. E. Lenkinski, and C. Rodger, *Can. J. Chem.*, 1982, **60**, 2113.
30. B. M. Fung, *J. Am. Chem. Soc.*, 1983, **105**, 5713.
31. J. Jokisaari and T. Väänänen, *Mol. Phys.*, 1986, **58**, 959.
32. J. Jokisaari, Y. Hiltunen, and J. Lounila, *J. Chem. Phys.*, 1986, **85**, 3198.
33. T. Väänänen, J. Jokisaari, and M. Seläntaus, *J. Magn. Reson.*, 1987, **72**, 414.
34. H. Nakatsuji, K. Hirao, H. Kato, and T. Yonezawa, *Chem. Phys. Lett.*, 1970, **6**, 541.
35. J. C. Facelli and M. Barfield, *J. Magn. Reson.*, 1984, **59**, 452.
36. P. Diehl, J. Jokisaari, J. Amrein, T. Väänänen, and P. Pyykkö, *J. Magn. Reson.*, 1982, **48**, 495.
37. H. Nakatsuji, I. Morishima, H. Kato, and T. Yonezawa, *Bull. Chem. Soc. Jpn.*, 1971, **44**, 2010.
38. Y. Hiltunen, J. Jokisaari, J. Lounila, and A. Pulkkinen, *J. Am. Chem. Soc.*, 1989, **111**, 3217.
39. P. Diehl, H. Bösiger, and J. Jokisaari, *Org. Magn. Reson.*, 1979, **12**, 282.
40. J. Gerritsen and C. MacLean, *J. Magn. Reson.*, 1971, **5**, 44.
41. J. Gerritsen and C. MacLean, *Mol. Cryst. Liq. Cryst.*, 1971, **12**, 97.

Biographical Sketches

Jukka P. Jokisaari. *b* 1944. M.S., 1968, Ph.D., 1974, University of Oulu, Finland; Postdoctoral work at University of Basel, Switzerland (with Peter Diehl). Professor of Physics (Atomic and Molecular Spectroscopy), University of Oulu, Finland. Approx. 100 publications. Current research specialty: NMR of small molecules and noble gases in liquid crystals.

Deuteron Relaxation Rates in Liquid Crystalline Samples: Experimental Methods

Gina L. Hoatson and Robert L. Vold
College of William and Mary, Williamsburg, VA, USA

1	Introduction	1
2	Spin Dynamics	1
3	Experimental Design	3
4	Site Specific Spectral Densities	7
5	Sample Rotation Experiments	9
6	Conclusions	10
7	Related Articles	10
8	References	11

1 INTRODUCTION

Deuteron NMR spectroscopy (^{2}H NMR) is an extremely powerful technique for investigating molecular order and dynamics. The usefulness and uniqueness of this method lies in the wide range of timescales that are accessible for quantitative investigation. Fast molecular motion, with correlation times in the picosecond range, can be investigated by using relaxation rates to determine the orientation and temperature dependence of individual spectral density functions.[1] In the intermediate regime, processes with correlation times in the range $\tau_c \approx 10^{-4}$–10^{-8} s are characterized by motional narrowing effects on quadrupole echo lineshapes.[2] For slow motions, decay of quadrupolar order,[3] selective inversion,[4] or 2D exchange spectroscopy[5] permit investigation of rotational dynamics with correlation times approaching the spin–lattice relaxation time, which can vary from milliseconds to several hundred seconds. This article is focused on describing ^{2}H NMR experiments which can be used to measure specific relaxation times, T_j, in oriented media. The primary motivation is to provide information which is essential to improving the understanding of molecular motion in thermotropic liquid crystals. Many experiments have been developed to measure different relaxation rates ($R_j = 1/T_j$); these will be summarized and their sensitivity to random and systematic errors will be considered.

The utility of ^{2}H NMR is enhanced by the fact that the dominant quadrupole interaction is both small enough to permit recording of undistorted spectra and sufficiently large to be a sensitive probe of local structure and dynamics. Dipolar interactions and associated many-body complications are usually negligible, and the interaction between the nuclear quadrupole moment and the local electric field gradient (EFG) tensor is described by a one-particle Hamiltonian. As a result the spin dynamics of deuterons, in realistically complicated systems, is simple enough to allow rigorous density matrix analysis of multiple pulse sequences and relaxation behavior. This greatly facilitates the development of new NMR techniques and simplifies the interpretation of relaxation behavior, thereby providing stringent tests of theoretical descriptions of ordering and dynamics.

In discussing motion in ordered environments, it is necessary to distinguish between studies on nonmesogenic solutes dissolved in anisotropic fluids, and studies of the liquid crystal molecules themselves. Measurements of spin relaxation of small, rigid solute molecules can be interpreted without the uncertain approximations inherent in descriptions of internal motion, and provide useful tests for general theories of how an ordering potential affects the dynamic processes of small solutes. However, the weak ordering and fast motion of solutes make them unreliable probes of liquid crystal dynamics. An understanding of the basic physics of liquid crystals is better achieved through direct investigations of carefully chosen liquid crystalline materials.

In the nematic phase, the motion of liquid crystal molecules is assumed to be fast enough to be in the motional narrowing regime. Thus, the fluctuating Hamiltonian $\hat{\mathcal{H}}'(t)$ responsible for relaxation varies rapidly compared with precession under the static Hamiltonian $\hat{\mathcal{H}}_0$, i.e. the motion is fast compared with the rigid lattice linewidth. Under these circumstances, Redfield theory[6] can be used to express the measured relaxation rates in terms of spectral densities of motion. The long-range order, which leads to a nonzero average value of the anisotropic quadrupole interaction, has profound effects on the motional spectral densities which govern spin relaxation. It is now well established that in the nematic phase, contributions to nuclear spin relaxation are made by restricted reorientation of individual molecules, internal rotations within the molecule, and by long-range quasi-coherent hydrodynamic modes such as order director fluctuations (ODFs).

In the more ordered liquid crystal phases, including smectics, lyotropics, and discotics, there is more uncertainty about the dominant motional processes. Spin relaxation studies can be used to help clarify the details of molecular dynamics in these systems. Throughout this article, Redfield theory will be used to describe the effects of molecular reorientation on spin relaxation. It should be appreciated that such motional narrowing approximations may not remain valid for these more complicated mesophases. For ultraslow motions, the concept of spectral densities is not sufficiently general to describe spin relaxation, and more rigorous approaches based on the stochastic Liouville equation must be used.

2 SPIN DYNAMICS

The time-independent Hamiltonian for a deuteron in an anisotropic environment is given by

$$\hat{\mathcal{H}}_0 = -\omega_0 \hat{I}_Z + \tfrac{1}{3}\omega_Q(3\hat{I}_Z^2 - \hat{\boldsymbol{I}} \cdot \hat{\boldsymbol{I}}) \qquad (1)$$

Here $\omega_0 = 2\pi\nu_0$ is the Larmor frequency (in radians per second), $2\omega_Q = 4\pi\nu_Q$ is the quadrupole splitting, and $\hat{\boldsymbol{I}}_Z$ is the operator for spin angular momentum about the space-fixed Z axis. Energy levels and transition frequencies associated with this Hamiltonian are illustrated in Figure 1. In isotropic liquids, where $\nu_Q = 0$, the two transitions are degenerate and occur at the Larmor frequency. In an oriented medium the quadrupolar

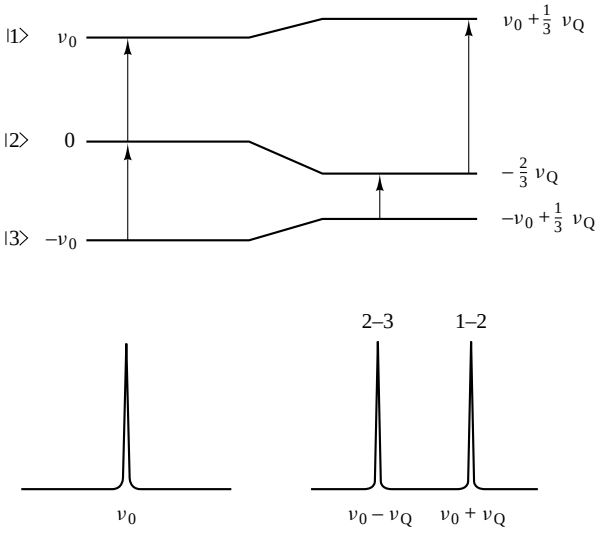

Figure 1 The energy level diagram for a spin-1 deuteron in a static magnetic field (left), and including the first-order quadrupolar interaction (right). Single quantum transition frequencies are indicated by vertical arrows on the diagram, and the corresponding NMR spectra are sketched

splitting between the $1 \rightarrow 2$ and $2 \rightarrow 3$ transitions ($2\nu_Q$) depends on the order parameters. Detailed discussions of the effects of orientational order on the NMR spectra of liquid crystals are available in the literature.[7,8]

Relaxation of deuterons in an ordered medium is best described using density matrix formalism. In the Redfield limit, in the absence of rf irradiation, the spin density matrix element, $\rho_{ij}(t)$, for an ensemble of deuterons evolves according to the equation

$$\frac{\partial \rho_{ij}(t)}{\partial t} = \mathrm{i}\omega_{ij}\rho_{ij} + \sum_{kl} R_{ijkl}[\rho_{kl}(t) - \rho_{kl}(\infty)] \qquad (2)$$

Here $\omega_{ij} = (\omega_j - \omega_i)$ is the transition frequency between the eigenstates $|i\rangle$ and $|j\rangle$ of the time-independent spin Hamiltonian, the R_{ijkl} are elements of the Redfield relaxation supermatrix, and $\rho_{kl}(\infty)$ is element kl of the thermal equilibrium density matrix. There are two fundamentally different types of states of the density matrix: diagonal elements ($i = j$), which correspond to populations of the eigenstates, and coherences ($i \neq j$), which correspond to phase coherence in the wavefunctions of the eigenstates. For a single deuteron the off-diagonal density matrix elements include two single quantum coherences $\rho_{12}(t)$ and $\rho_{23}(t)$ with precession frequencies $\nu_{12} = (\Delta + \nu_Q)$ and $\nu_{23} = (\Delta - \nu_Q)$, respectively, and one double quantum coherence $\rho_{13}(t)$ with precession frequency 2Δ. In this notation, Δ is the offset from resonance. The precession frequencies of the single quantum coherences correspond to the transition frequencies illustrated in Figure 1. Diagonal density matrix elements can be used to construct two linearly independent combinations of eigenstate populations: $(\rho_{11} - \rho_{33}) = \langle \hat{I}_Z \rangle$ is the expectation value of Zeeman polarization, and $(\rho_{11} - 2\rho_{22} + \rho_{33}) = \langle \hat{Q}_Z \rangle$ is the expectation value of quadrupole order. Theoretical expressions for the relaxation behavior of the five independent density matrix elements are easy to calculate in terms of the Redfield elements R_{ijkl}, which are in turn expressed in terms of spectral densities for molecular motion using the equations

$$R_{ijkl} = \int_0^\infty \exp[\mathrm{i}\tau(\omega_{ik} - \omega_{jl})]\langle \mathrm{i}|\hat{\mathcal{H}}'(t)|\ j\ \rangle \times \langle k|\hat{\mathcal{H}}'(t+\tau)|l\rangle^*\,\mathrm{d}\tau \qquad (3)$$

$$\hat{\mathcal{H}}'(t) = \sum_{m=-2}^{2} (-1)^m A^{(2)}_{-m} \sum_{k=-2}^{2} [D^{(2)*}_{mk}(t) - \langle D^{(2)*}_{mk}(0)\rangle] T^{(2)}_k(\mathrm{PAS}) \qquad (4)$$

Here the $A^{(2)}_{-m}$ are second rank spherical tensor spin operators, the $D^{(2)}_{mk}(t)$ are the time-dependent Wigner rotation matrix elements, the $T_k{}^{(2)}(\mathrm{PAS})$ are spherical components of the quadrupole coupling tensor, expressed in its principal axis system (PAS), and the angular brackets $\langle\ \rangle$ denote an ensemble average. The $D^{(2)}_{mk}(t)$ depend on Euler angles, $\alpha(t)$, $\beta(t)$, and $\gamma(t)$, which define the time-dependent orientation of the PAS relative to a laboratory-fixed frame. The inclusion of the term $\langle D^{(2)*}_{mk}(0)\rangle$ is necessary to ensure that the relaxation Hamiltonian fluctuates about a mean value of zero, so that the Fourier transform, defined in equation (3), is convergent. In isotropic liquids the $\langle D^{(2)*}_{mk}(0)\rangle$ are zero, but in liquid crystals they define characteristic order parameters of the anisotropic phase.

Without further analysis, several implications of the theory embodied in equations (2)–(4) are apparent. First of all, since $\mathcal{H}'(t)$ gains its time dependence exclusively through orientational variables, deuteron relaxation is sensitive only to rotational motion. This implies that the spatial order characteristic of complex mesophases is not directly probed by deuteron relaxation measurements. Instead, it is necessary to rely on theories which approximate the coupling between translation and rotation. Partially for this reason, most detailed interpretations of deuteron relaxation have been confined to the nematic phase, where translational order is unimportant. Secondly, the appearance of order parameters in the fluctuating Hamiltonian leads ultimately to expressions for measurable relaxation rates which also depend on the orientational order. This implies that the spectral density functions for motion in ordered environments are fundamentally different from those for isotropic liquids. Finally, since the Redfield relaxation matrix elements depend on the average of the product of elements of $\mathcal{H}'(t)$, they include higher-rank order parameters of the form $\langle D^{(2)*}_{mk}(0) D^{(2)*}_{mk}(0)\rangle$. In principle such quantities can be derived from relaxation studies, but they do not influence the equilibrium spectra.

In oriented nematic phases the observed quadrupole splitting is proportional to $\frac{1}{2}(3\cos^2\beta_{\mathrm{MP}} - 1)$, where β_{MP} is the angle between the largest component of the electric field gradient (EFG) tensor, q_{zz}, and the molecule fixed Z axis. Typically, in organic molecules, deuteron quadrupole coupling tensors have the largest component coincident with the C–D bond direction. Hence, C–D bonds which make different angles with the molecular Z axis give rise to resolved quadrupolar doublets, whose relaxation behavior can be determined independently. This provides a uniquely powerful way to investigate rotational anisotropy, but requires that the relaxation rates for each

deuteron be expressed in terms of spectral densities for the overall rotation of the molecule-fixed coordinate system. Thus, it is useful to decompose the Euler rotation from laboratory to PAS frames, Ω_{LP}, into separate transformations: a time-dependent transformation from laboratory to molecule-fixed coordinates [$\alpha_{LM}(t)$, $\beta_{LM}(t)$, $\gamma_{LM}(t)$], followed by a time-independent transformation to the PAS of each individual deuterated site (α_{MP}, β_{MP}, γ_{MP}). It can be shown[1] that there are then just three distinct spectral density functions, given by the equations

$$J_m(m\omega_0) = \frac{1}{(T_0^{(2)})^2} \sum_{k=-2}^{2} \sum_{k'=-2}^{2} \sum_{n=-2}^{2} \sum_{n'=-2}^{2} T_n^{(2)} T_{n'}^{(2)*} \times D_{kn}^{(2)}(\Omega_{MP})\, D_{k'n'}^{(2)*}(\Omega_{MP})\, J_{mkk'}(m\omega_0) \quad (5)$$

where m = 0, 1, or 2, and

$$T_0^{(2)} = \frac{\sqrt{6}}{4} \frac{e^2 q_{zz} Q}{\hbar} \quad (6a)$$

$$T_{\pm 1}^{(2)} = 0 \quad (6b)$$

$$T_{\pm 2}^{(2)} = \frac{\eta}{4} \frac{e^2 q_{zz} Q}{\hbar} \quad (6c)$$

Here $\eta = (q_{xx} - q_{yy})/q_{zz}$ is the asymmetry parameter of the deuteron EFG tensor. In most cases, η is small enough to ignore, and this greatly simplifies the evaluation of equation (5). Molecular motion appears in this expression through the Fourier transforms of correlation functions of time-dependent Wigner rotation matrix elements:

$$J_{mkk'}(m\omega_0) = \int_0^\infty \exp(-\mathrm{i}m\omega_0\tau) C_{mkmk'}(\tau)\, \mathrm{d}\tau \quad (7a)$$

$$C_{mkmk'}(\tau) = \langle E_{mk}^{(2)*}[\Omega_{LM}(t)) E_{mk'}^{(2)}(\Omega_{LM}(t+\tau))] \rangle \quad (7b)$$

$$E_{mk}^{(2)}[\Omega_{LM}(t)] = D_{mk}^{(2)}[\Omega_{LM}(t)] - \langle D_{mk}^{(2)}[\Omega_{LM}(0)] \rangle \quad (7c)$$

In essence, the spectral densities, J_m $(m\omega_0)$ are Fourier transforms of certain correlation functions which relate the orientation of a molecule at time t to the orientation at a later time $t + \tau$. The key idea is that by the appropriate selection of relaxation experiments, the different spectral densities for individual deuterons can be determined as a function of temperature, Larmor frequency ω_0 (magnetic field strength), and orientation with respect to the static field (for sufficiently rigid mesophases). This constitutes the maximum amount of information available from deuteron relaxation experiments.

It is implicit in the formalism presented here that relaxation during rf pulses can be ignored. When this is not the case, for example in spin lock measurements in the rotating frame ($T_{1\rho}$), the same spectral densities arise but some must be evaluated at the rf field amplitude, ω_1, rather than integer multiples of the Larmor frequency.[9]

3 EXPERIMENTAL DESIGN

Designing experiments to determine spectral densities amounts to choosing a particular state of the density matrix, calculating its relaxation rate in terms of spectral densities, designing a rf pulse sequence that creates the desired state, and measuring the relaxation time. Pulse sequences that are currently being used to create specific population distributions or coherences are summarized in Table 1. Strategies for using combinations of experiments to determine the individual spectral densities from these measurements will be described in this section. Salient practical aspects will also be discussed: which techniques give the most reliable results and where potential problems in implementation are anticipated. To a certain extent this depends on the details of the spin system, i.e. the number and relative order of magnitude of quadrupolar splittings, and the degree of orientational order of the liquid crystal, S_{zz} and $(S_{xx} - S_{yy})$.

To date, most relaxation experiments have focused on determining $J_1(\omega_0)$ and $J_2(2\omega_0)$ from the recovery of nonequilibrium population distributions. These are the simplest, most reliable and accurate experiments. In principle, $J_1(\omega_0)$ and $J_2(2\omega_0)$ can be obtained from any two relaxation experiments which depend on linearly independent combinations of these two spectral densities. These include nonselective and selective inversion recovery measurements of Zeeman polarization, conventional (JB) and broadband (BBJB) Jeener–Broekaert excitation of quadrupole order, and two-dimensional measurements of the decay rate of double quantum coherence. In practice, the accuracy of selective inversion recovery experiments is limited because the recovery curves are biexponential. The formulae given in Table 1 refer to the initial slope of the recovery, but this is difficult to measure without introducing systematic errors. Nonselective inversion recovery with quadrupolar echo detection (IRQE) does not suffer from this disadvantage, and is the method of choice for measuring T_{1Z}. Because deuteron relaxation times in liquid crystals are short there is no need to resort to inherently less accurate methods such as saturation recovery or progressive saturation.

For studies of thermotropic liquid crystals two potentially serious instrumental problems arise. The first is temperature control: the quadrupole splitting is directly proportional to order parameters which can be strongly temperature dependent. Close to the nematic–isotropic phase transition, where the order parameter changes most rapidly, temperature coefficients as large as 5 kHz K^{-1} have been observed.[10] Temperature drifts, gradients and instabilities as small as a few millidegrees can then lead to severe line broadening. Moreover, in frequency-selective preparation sequences, such as the conventional two-pulse JB sequence, a temperature drift translates into irreproducible changes in the amount of quadrupole order created. In general, accurate measurements of T_{1Z} and T_{1Q} require temperature control and gradients to less than 0.1 K, preferably to within 0.01 K. Secondly, in nematic liquid crystals, quadrupolar splittings approaching 100 kHz are common. In order to achieve uniform inversion over such large spectral widths, rf field strengths of $\nu_1 \approx 150$ kHz are required (typical 90° pulse lengths of 1.5–2.0 μs in a 5 mm coil). Thus, high-power amplifiers similar to those required for solid state ^{2}H NMR are essential. Fortunately, instrumentation with the necessary capabilities is now commercially available.

It has been shown[11] that the best procedure for determining $J_1(\omega_0)$ and $J_2(2\omega_0)$ is not the conventional JB experiment designed to retain both quadrupole and Zeeman order. Rather, two separate IRQE and BBJB experiments are performed which can be optimized independently for maximum

Table 1 Relaxation Experiments and Measured Spectral Densities

	Spectral Density[a]
Populations	
Nonselective T_{1Z} (IRQE)	
$180-T^{b}-90_x-\tau-90_y$	$2J_1(\omega_0) + 8J_2(2\omega_0)$
Broadband T_{1Q} (BBJB)	
$(90_x-2\tau-67.5_{-y}-2\tau-45_y-\tau-45_y-)-T-45_x-t-90_x-$	$6J_1\ (\omega_0)$
Conventional Jeener–Broekaert (JB)	
$90_x-\tau-45_y-T-45_y$	Sum: $2J_1(\omega_0) + 8J_2(2\omega_0)$ Difference: $6J_1(\omega_0)$
Selective T_{1Z}[c]	
$180_x^{A}-T-90^{A}$	$5J_1(\omega_0) + 2J_2(2\omega_0)$
Coherences	
Quadrupolar echo T_{2e}	
90_x-T-90_y	$3J_0\ (0) + 3J_1(\omega_0) + 2J_2(2\omega_0)$
Multipulse quadrupolar echo T_2 (MQE)	
$90_x-\tau-(90_y-2\tau-)_n$	Short τ: $3J_0(0) + 5J_1\ (\omega_0) + 2J_2(2\omega_0)$
$(T = 2n\tau)$	Long τ: $3J_0(0) + 3J_1(\omega_0) + 2J_2(2\omega_0)$
Selective single quantum T_2[c]	
$90_x^{A}-T/2-180^{A}-T/2-$	$3J_0(0) + 3J_1(\omega_0) + 2J_2(2\omega_0)$
Double quantum T_{DQ}	
$90_x-\tau-90_x-T/2-180-T/2-90$	$2J_1(\omega_0) + 4J_2(2\omega_0)$

[a]Units of $(3\pi^2/4)(e^2q_{zz}Q/\hbar)^2$.
[b]T denotes the relaxation delay.
[c]The superscript A indicates that the pulse is applied selectively at the frequency of peak A.

precision and accuracy. In particular, the use of broadband (frequency-independent) procedures for exciting quadrupole order, combined with echo detection to avoid pulse recovery problems, was shown to increase greatly the accuracy with which T_{1Q} can be determined.[11] This is important because small uncertainties in measured values of the relaxation times propagate into larger errors in determining $J_2(2\omega_0)$.

Figure 2 illustrates the difference between conventional (JB) and broadband (BBJB) excitation of quadrupole order. The sample is pure 4-*n*-pentyl-4′-cyanobiphenyl selectively deuterated (5CB-d_6) in the 1,4- and 5-positions of the alkyl chain. Figure 2(a) shows the pulse sequence, spectrum, and quadrupolar order excitation profile for the conventional JB pulse pair, $90_x-\tau-45_y$. This sequence is inherently frequency selective, with efficiency proportional to $\sin \nu_Q\tau$. The excitation delay of $\tau = 46\,\mu$s is a particularly unfortunate choice: the spectrum shows that the sign of the quadrupole order is opposite for the C-1 and C-2 methylene deuterons and there is little excitation of quadrupole order for the methyl deuterons (C-5). It is impossible to achieve full excitation of quadrupole order for all the transitions with any single τ value. The BBJB sequence does not suffer from this limitation. Figure 2(b) shows that uniform excitation is achieved by this sequence, with total excitation time $5\tau = 46\,\mu$s. Thus, for materials with several different quadrupole splittings, broadband procedures for exciting quadrupole order are definitely preferable to the simple JB pulse pair. In practice, the choice of τ in the BBJB sequence is not very critical. It is usually sufficient to use a small enough value to excite full quadrupole order for the largest splitting, and this ensures that all others will be uniformly excited. However, it must be noted that all methods of exciting quadrupole order fail as the quadrupole splitting tends to zero. For splittings less than a few kilohertz, the BBJB sequence described here is somewhat less efficient than the simple two-pulse (JB) excitation sequence. This is demonstrated by the excitation profiles shown for the JB and BBJB sequences in the lower traces of Figures 2(a) and 2(b), respectively. Computer-optimized broadband sequences have now been developed to deal with this problem.[12] In summary, the BBJB experiment has many advantages and is rapidly superseding the conventional JB experiment as the method of choice for measuring T_{1Q}. Moreover, since this technique can be applied successfully to powder patterns (which have a continuous distribution of quadrupolar splittings), it will be useful for measuring the orientation dependence of T_{1Q} in smectic and lyotropic mesophases.

To demonstrate procedures for determining individual spectral densities measurements of relaxation times of a liquid crystal mixture, consisting of 25 mol% of perdeuterated 4-methyl-4′-cyanobiphenyl (1CB-d_{11}) and 75 mol% 5CB-d_6, will be outlined as a case study.[13] 5CB-d_6 is selectively deuterated on the alkyl chain carbon at positions C-1, C-4 and C-5, as shown in the molecular structure. Figure 3 illustrates the measurement of T_{1Z} using a nonselective inversion pulse followed by quadrupole echo detection. The bottom trace is an equilibrium spectrum, and spectral assignments for each of the quadrupolar doublets are indicated. Dipolar fine structure is apparent on the 1CB transitions, but it can be shown that this does not interfere with the T_{1Z} measurements.

The top trace in Figure 3 shows a partially relaxed spectrum with relaxation delay $T = 1$ ms, and all the transitions are inverted. After 10 ms the aromatic doublet of 1CB (peak 5) has recovered substantially while the other lines remain inverted. After 45 ms, the 1CB methyl lines (peak 2) are nulled while the methyl (C-5) deuterons of 5CB (peak 4), which have the longest T_{1Z}, are still inverted. In order to obtain accurate T_{1Z} values from these data, it is necessary to choose a set

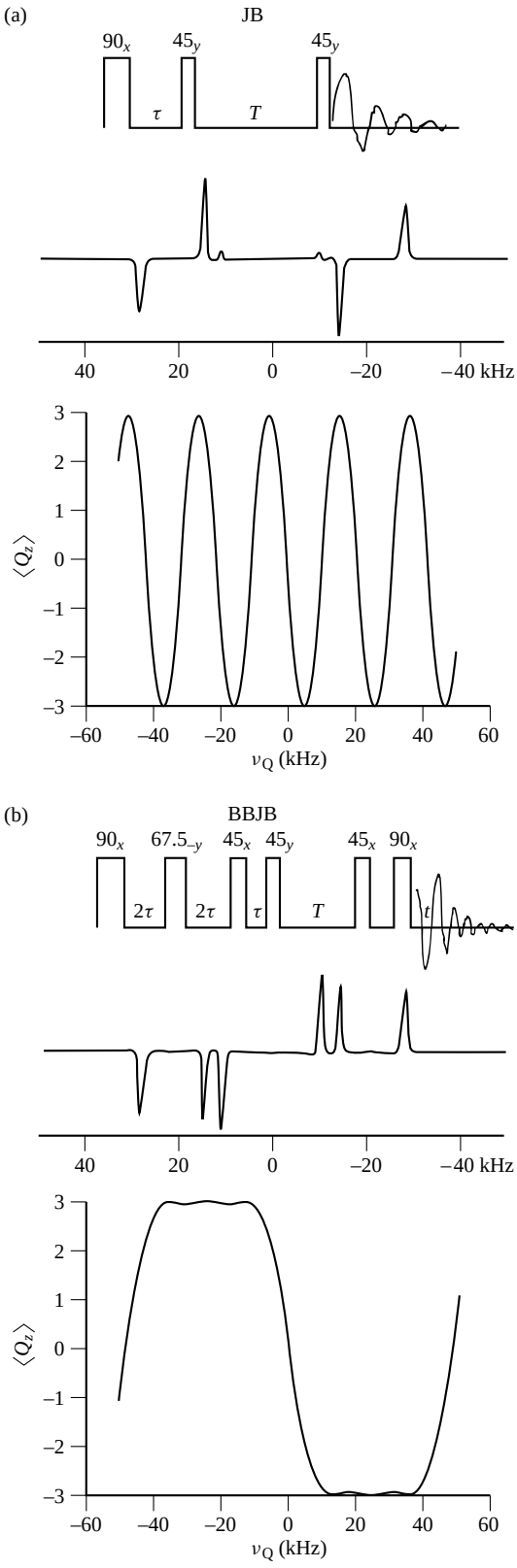

Figure 2 Pulse sequences, 5CB-d_6 spectra, and quadrupolar order excitation profiles for (a) the conventional JB pulse pair and (b) the BBJB sequence. For (a) the pulse delay was τ = 46 μs, and in (b) the total excitation time 5τ = 46 μs. The simulated quadrupolar order excitation profiles include the effects of finite pulse lengths (90° pulse width of 1.6 μs). The spectra were recorded at 46.06 MHz

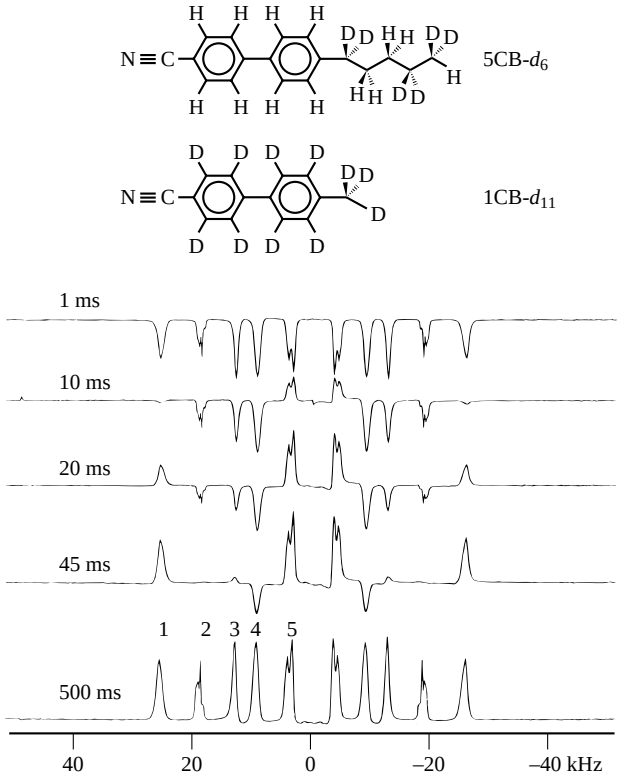

Figure 3 Molecular structures of the binary mixture of 1CB-d_{11} (25 mol%) and 5CB-d_6. Partially relaxed spectra at 46.06 MHz from the inversion–recovery experiment with quadrupolar echo detection (IRQE) were taken in the nematic phase at 28.2°C. Relaxation delay times are indicated on the left of each trace. Spectral assignments for the labeled peaks in the equilibrium spectrum, shown in the bottom trace, are: (1) deuterons on the first methylene carbon on the alkyl chain of 5CB; (2) methyl deuterons of 1CB; (3) deuterons on the fourth alkyl chain carbon of 5CB; (4) methyl deuterons of 5CB; and (5) aromatic ring deuterons of 1CB

of relaxation delays which span at least one full decade of recovery for every line. T_{1Z} for each deuteron is then obtained by fitting to the equation

$$M(\infty) - M(T) = [M(\infty) - M(0)] \exp(-T/T_{1Z}) \quad (8)$$

Here $M(T)$ is the sum intensity of the quadrupolar doublet at time T, $M(\infty)$ is its thermal equilibrium value, and $M(0)$ is the intensity immediately after inversion. In principle, perfect inversion should give $M(0) = -M(\infty)$. However, erroneous T_{1Z} values are obtained if this is assumed and the data are fitted to a two-parameter equation. A nonlinear fit in which $M(0)$, $M(\infty)$, and T_{1Z} are simultaneously adjusted is more reliable. Typically, 10 or more T values are needed for accurate results.

In the 1CB/5CB mixture, at 28.2 °C, T_{1Z} ranges from 9.8 ms for the 1CB aromatic deuterons to 209 ms for the 5CB methyl deuterons. Thus, it is not possible to construct one set of relaxation delays which is appropriate for every transition. Instead, the list must be expanded to include T values which are appropriate for all the relaxation times. In practice, this requires a few preliminary experiments to establish the approximate range of T_{1Z} values, and when the range is large, as many as 20–30 delays may be required. A common source of error in this type of experiment is failure

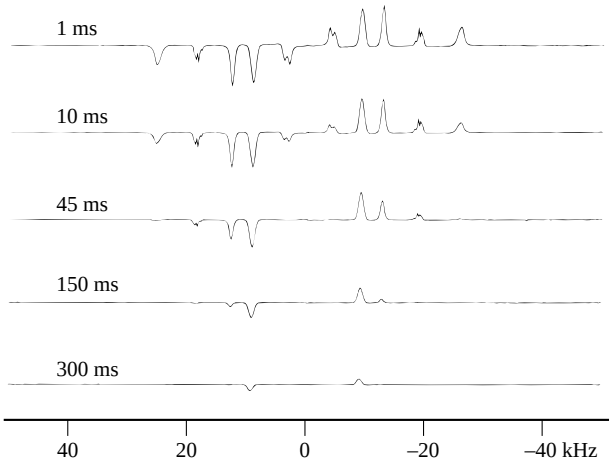

Figure 4 Partially relaxed spectra at 46.06 MHz from a BBJB experiment on the nematic phase of the binary mixture of 1CB-d_{11} (25 mol%) and 5CB-d_6 at 28.2°C. Relaxation delay times are indicated on the left of each trace. Spectral assignments are identical to those given in Figure 3

to wait for full equilibrium between successive scans: it is essential to wait at least five times the longest T_{1Z} value if systematic errors are to be avoided. Thus for the 1CB/5CB mixture, where 2048 scans were accumulated for each of 20 T values, the recycle delay was 1 s and the total experiment time was approximately 12 h.

Next, the BBJB sequence is used to excite quadrupole order uniformly. The relaxation time T_{1Q} can be measured by monitoring the decay of the difference magnetization for each doublet. Typical partially relaxed spectra for the 1CB/5CB binary mixture are shown in Figure 4. Since the difference magnetization for each doublet decays rigorously toward zero, the exponential decay function can be fitted with just two adjustable parameters (the initial intensity and T_{1Q}). Construction of an appropriate list of relaxation delays is as important as for T_{1Z} measurements, and the total experimental time is usually comparable.

Spectral densities may be calculated from the relationships

$$J_1(\omega_0) = \frac{2R_{1Q}}{9\pi^2(e^2q_{zz}Q/h)^2} \tag{9}$$

and

$$J_2(2\omega_0) = \frac{1}{18\pi^2(e^2q_{zz}Q/h)^2}(3R_{1Z} - R_{1Q}) \tag{10}$$

Here $e^2q_{zz}Q/h$ is the quadrupole coupling constant in hertz. When proper precautions are taken, and the signal-to-noise ratio is favorable, it is possible to determine the relaxation rates, $R_{1Z} = 1/T_{1Z}$ and $R_{1Q} = 1/T_{1Q}$, with a precision of 2–5%. This is sufficiently accurate that the use of approximate values for the quadrupole coupling constant should be avoided. Estimated values, from data reported for more or less similar materials, can lead to significant uncertainty in the spectral densities. Wherever possible, low-temperature quadrupole echo lineshapes should be analyzed to determine static values of the relevant quadrupole coupling constants.

While numerous measurements of $J_1(\omega_0)$ and $J_2(2\omega_0)$ have been reported, determinations of $J_0(0)$ are relatively scarce. Potential dynamic information inherent in this spectral density is very important in the study of liquid crystals. In particular, the spectral density at zero frequency should be exquisitely sensitive to long-wavelength modes of order director fluctuations. Even though this small-angle process contributes in first order only to $J_1(\omega_0)$, higher order calculations[14] reveal contributions to $J_0(\omega)$ which can be large as ω tends to zero.

All methods for determining $J_0(0)$ rely on measuring the dephasing rate of one quantum coherence, and subtracting contributions from $J_1(\omega_0)$ and $J_2(2\omega_0)$. For example, making use of the spectral densities listed in Table 1, it can be shown that $J_0(0)$ is given by

$$J_0(0) = \frac{1}{9\pi^2(e^2q_{zz}Q/h)^2}(4R_2^0 - 2R_{1Z} - 3R_{1Q}) \tag{11}$$

where $R_2{}^0$ is the limiting decay rate obtained in a multiple-pulse quadrupole echo sequence in the limit of zero pulse spacing ($2\tau \rightarrow 0$), much smaller than $(e^2q_{zz}Q/h)^{-1}$.[15] Alternatively, if the transverse relaxation rate R_2(sel) of one line of the quadrupolar doublet is measured using a selective Carr–Purcell sequence, $J_0(0)$ is given by

$$J_0(0) = \frac{1}{27\pi^2(e^2q_{zz}Q/h)^2}[12R_2(\text{sel}) - 3R_{1Z} - 5R_{1Q}] \tag{12}$$

To date, there is no single method that is successful for measuring T_2 in all liquid crystalline systems. Figure 5 illustrates an efficient 2D procedure appropriate for spectra with many lines. The sample is perdeuterated fluorene dissolved in the nematic phase of 5CB. In this experiment a train of n equally spaced 90_y° refocusing pulses are applied during the evolution period and the acquisition is started at the top of the last echo. The evolution time must therefore be incremented in integral multiples of the echo spacing. For the 2D spectrum shown in Figure 5, the spacing was $2\tau = 300\,\mu$s, and every fifth echo was recorded (n = 1, 6, 11, ... , 76). Thus the spectral width in the f_1 frequency domain is $\pm 1/(20\tau) = \pm 333$ Hz. The ordinary spectrum is recovered as a slice along $f_1 = 0$, and is displayed at the right edge of the contour plot (spectral assignments are indicated). Each peak has a Lorenztian profile in f_1, and its T_2 can be determined simply from the linewidth at half maximum. However, before relying on these T_2 values to determine $J_0(0)$ it is necessary to consider the pulse spacing dependence of the relaxation time,[15] and potential sources of systematic errors. In some cases, T_2 may be so short that only a few echoes can be observed, and the digital resolution in f_1 is then insufficient for accurate linewidth measurements. It is encouraging that the T_2 values determined in the frequency domain, from the 2D linewidths, are found to agree (within experimental error) with those determined in the time domain by fitting the line intensities as a function of relaxation delay.

Unresolved dipolar interactions are a potentially serious source of error in multiple pulse quadrupolar echo measurements of T_2 in liquid crystals. Dipolar precession is not refocused by the nonselective 90_y° pulses, and unresolved dipolar couplings produce apparent dephasing which can be confused with a true T_2 process. This problem is also unavoidable in nonselective two-pulse procedures where the echo amplitude

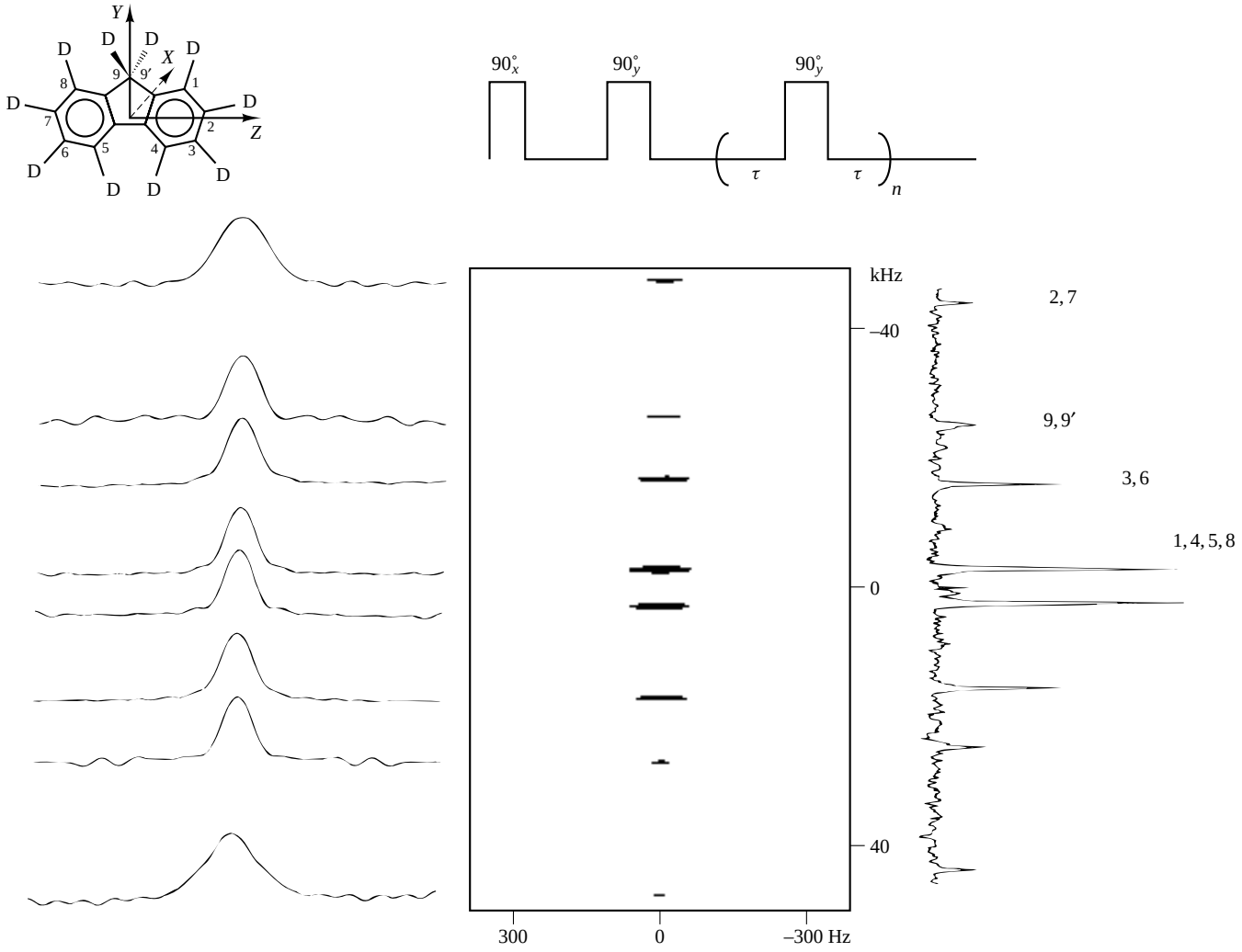

Figure 5 A 2D method for determining T_2s in a multiline spectrum. The sample is perdeuterated fluorene-d_{10} in the nematic phase of 5CB. The normal ^{2}H NMR spectra (46.06 MHz) is obtained from the $f_1 = 0$ slice through the data matrix, and is shown to the right of the contour plot. T_2 of each line is obtained from the full width at half maximum of the Lorenztian lineshape for the corresponding slice in f_2, as shown on the left. The pulse sequence for this experiment is shown, and for this data set the pulse spacing was $2\tau = 300\,\mu$s, and every fifth echo was recorded

is monitored as a function of pulse spacing to give T_{2e}. The use of selective pulses, designed to monitor spin echoes from one-half of the quadrupolar doublet, circumvents this difficulty. However, in samples with small quadrupolar splittings and many lines it may not be possible to achieve adequately selective pulses. Alternatively, all precession of the transverse magnetization can be suppressed by using the multiple quadrupolar echo experiment with closely spaced 90_y° pulses. This achieves effective spin locking when the pulse spacing is smaller than the inverse of the largest quadrupole splitting. In practice, this procedure requires a very robust temperature controller to avoid overheating the sample. A general, accurate method of measuring $J_0(0)$ in liquid crystals remains to be established, and this continues to be a topic of current research.

The decay rate of double quantum coherence for a single deuteron depends exclusively on $J_1(\omega_0)$ and $J_2(2\omega_0)$. Thus there is no additional information to be gained by measuring this relaxation rate that cannot be obtained more accurately from simple measurements of T_{1Z} and T_{1Q}. In a few carefully chosen systems, with well-resolved deuteron dipolar coupling, it has been possible to create and monitor the decay of both double- (R_{1313}) and four-quantum (R_{1414}) coherences.[16] This permitted determination of the cross-correlation terms in the motion of two different quadrupole coupling tensors, and provided insight into rotational anisotropy of small rigid solutes in liquid crystalline solvents. Unfortunately, this method cannot be readily extended to typical liquid crystal molecules because of extensive dipolar couplings, which are usually too small to be resolved and thus contribute to the apparent multiple-quantum linewidth.

4 SITE SPECIFIC SPECTRAL DENSITIES

Deuteron relaxation in liquid crystals gains much of its utility from the unambiguous way in which the spectral densities depend on the orientation of the EFG tensor with respect to molecule-fixed coordinates. By measuring spectral densities for deuterons with several different orientations, it is possible to obtain a very stringent test of models of rotational motion. The general orientation dependence, expressed in

equation (5), can be quite complex, and it is useful to consider the special case of a linear molecule. In this case, the EFG tensor has zero asymmetry parameter, and the largest component is collinear with the molecule-fixed Z axis ($\beta_{MP} = 0$). The fourfold summation in equation (5) then collapses to a single term:

$$J_m(m\omega_0) = J_{m00}(m\omega_0) \tag{13}$$

It can be shown that the spectral densities $J_{m00}(m\omega_0)$ are determined exclusively by processes which reorient the long molecular axis. These include order director fluctuations, which make a large contribution only to $J_{100}(\omega_0)$, and molecular reorientation which contributes to both $J_{100}(\omega_0)$ and $J_{200}(2\omega_0)$. Illustrative data for cyanoacetylene-*d* dissolved in a commercial nematic liquid crystal mixture (Merck Phase V)[17] are shown in Figure 6. $J_1(\omega_0)$ clearly includes a frequency-dependent contribution which is absent from $J_2(2\omega_0)$. Numerous investigations of the deuteron relaxation of small rigid solutes in nematic phases have made use of this frequency dispersion to isolate the contributions from director fluctuations.

Measurements[18] have demonstrated that director fluctuations do not play a major role in the deuteron relaxation of the liquid crystal molecules themselves. The rotational motion of typical nematogens is apparently slow enough to occur on approximately the same timescale as director fluctuations. It can then be shown that cross-correlation effects act to quench the contribution of director fluctuations, so that the spectral densities can be interpreted exclusively in terms of single-molecule rotation.[19]

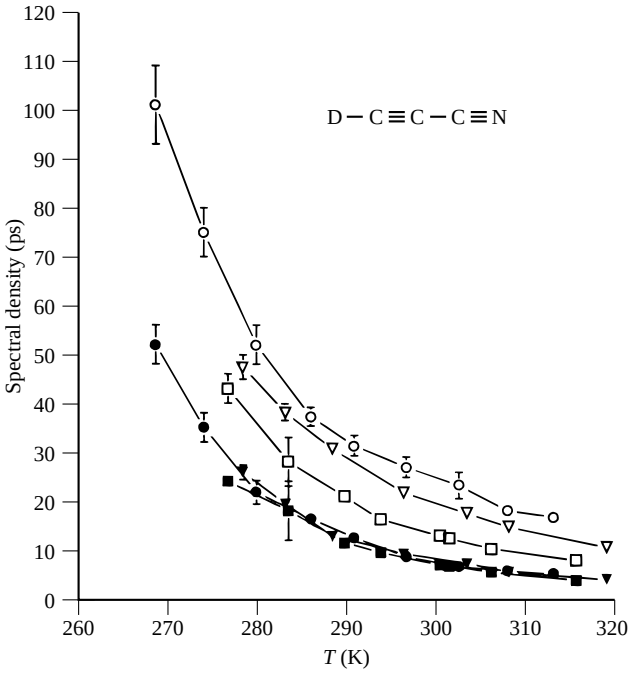

Figure 6 Spectral densities $J_1(\omega_0)$ (open symbols) and $J_2(2\omega_0)$ (solid symbols) for cyanoacetylene-*d* in nematic Merck Phase V.[17] Data were acquired at several Larmor frequencies: triangles, ν_0 = 4.6 MHz; circles, ν_0 = 9.2 MHz; squares, ν_0 = 38.4 MHz. The experimental points are joined by lines to guide the eye. For reasons discussed in the text, $J_1(\omega_0)$ depends on the Larmor frequency while $J_2(2\omega_0)$ does not

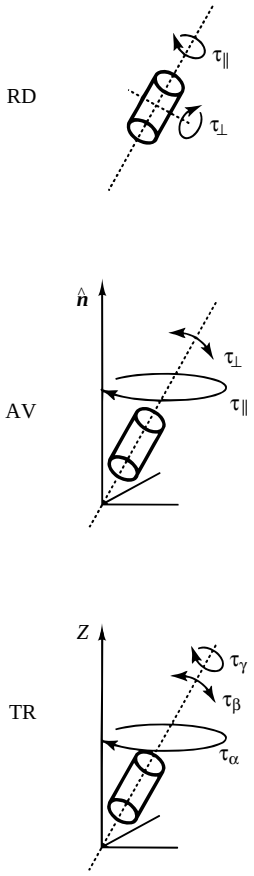

Figure 7 Models used to describe molecular motion in oriented environments. (a) rotational diffusion (RD), (b) anisotropic viscosity (AV) and (c) the 'third rate' (TR) model

While a full discussion of molecular motion is beyond the scope of this article, three popular rotational models are illustrated in Figure 7: rotational diffusion (RD),[20] anisotropic viscosity (AV),[21] and the 'third rate' (TR) model.[22]

Small-step rotational diffusion of a symmetric rotor is fully characterized by two correlation times, $\tau_\perp = 1/(6D_\perp)$ and $\tau_\parallel = 1/(6D_\parallel)$, where $D_\perp$ and $D_\parallel$ are rotational diffusion constants. If the diffusion tensor is assumed to be diagonal in laboratory-fixed coordinates, where its principal components are related to anisotropic viscosity coefficients, the relevant correlation times for this 'anisotropic viscosity' model are still labeled $\tau_\perp$ and $\tau_\parallel$ but their physical meaning is different. Assuming that the nematic director remains parallel to the magnetic field, τ_β and τ_α in the TR model have the same physical significance as $\tau_\perp$ and $\tau_\parallel$ (respectively) in the AV model. The third rate is characterized by a correlation time τ_γ for rotation about the long molecular axis, which can occur in steps of arbitrary size as specified by a collision parameter p, where $0 \leq p \leq 1$.

The nematogen 2-fluorenyl 4′-tetradecyloxybenzoate-d_9 (FLOC$_{14}$-d_9) provides an excellent example of how spectral densities can be used to test these rotational models. Figure 8 shows the molecular structures and the assigned NMR spectrum in the nematic phase of a binary mixture of FLOC$_{14}$-d_9 and *p*-xylene-d_{10} (~10 mol%). The temperature dependence of the spectra gives the orientational order parameters of both molecules.[23] By measuring and analyzing T_{1Z} and T_{1Q} for all

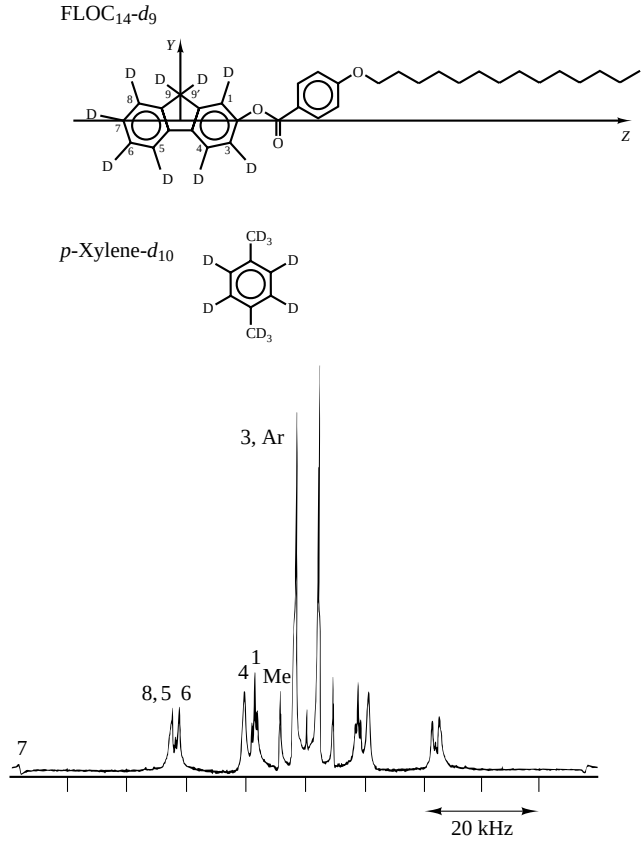

Figure 8 Quadrupole echo spectrum at 32.8 MHz with spectral assignments for a binary mixture of $FLOC_{14}$-d_9 and *p*-xylene-d_{10} in the nematic phase. Analysis of relaxation data for this sample using the TR model provided correlation times for both the rigid solute and the flexible liquid crystal molecule[24]

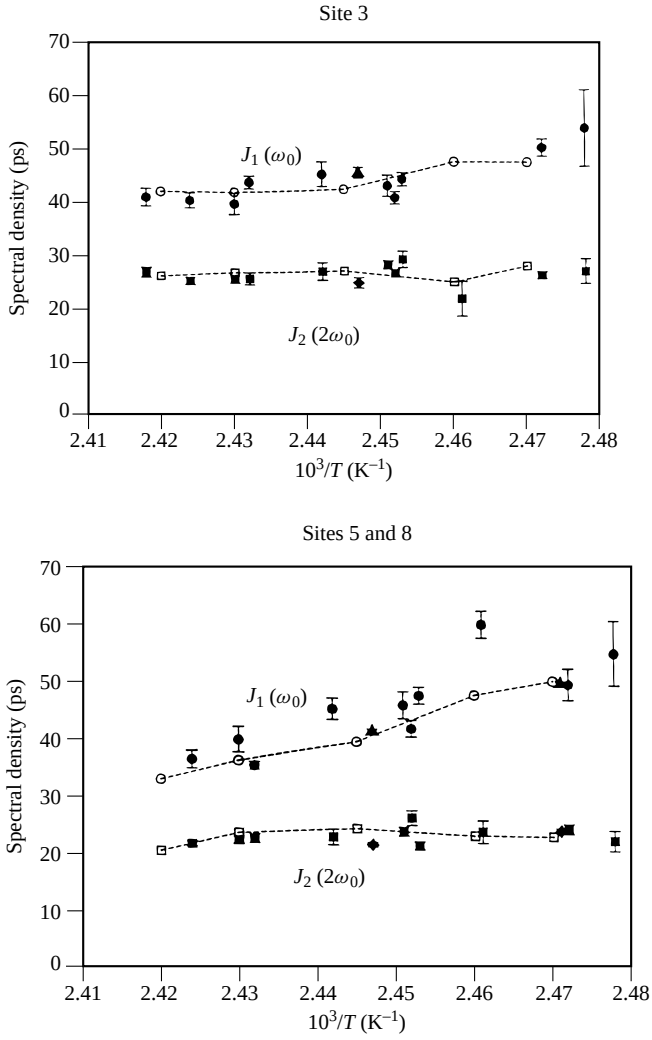

Figure 9 Individual spectral densities, $J_1(\omega_0)$ and $J_2(2\omega_0)$, for positions 3 and 5,8 of $FLOC_{14}$-d_9, as a function of inverse temperature. Closed circles are $J_1(\omega_0)$ measured at 46 MHz, closed triangles are $J_1(\omega_0)$ at 38.4 MHz, closed squares are $J_2(2\omega_0)$ at 46 MHz and closed diamonds are $J_2(2\omega_0)$ at 38.4 MHz. The open symbols, which are connected by dotted lines to guide the eye, are fits of the 46 MHz data, from all positions, to the third rate model of molecular reorientation. (Adapted from Goetz et al.[18])

the lines as a function of temperature, it was possible to determine rotational correlation times for both components of the mixture.[24]

Measurements on pure $FLOC_{14}$-d_9, which has deuterons at five different orientations of the EFG tensor, yielded 10 independent spectral densities at each temperature.[18] A representative selection of the extensive data is shown in Figure 9 which gives the spectral densities for two molecular sites—the 3 (β_{MP} = 54.65°) and 5,8 (β_{MP} = 78.15°) positions. The points are experimental spectral densities, and the lines represent a nonlinear least-squares fit of the data from all positions to the TR model.

The problem of fitting the spectral densities to the various motional models is highly overdetermined, and the quality of the fit can be used to assess the validity of each model. Not surprisingly, it was found that no two-parameter model was capable of simultaneously fitting the spectral density data for all the sites. The TR model, with four independently adjustable parameters, provided by far the best fit. Figure 10(a) shows a 3D minimum $\Delta\chi^2$ surface (68% confidence boundaries) in the correlation time phase space (τ_α, τ_β, τ_γ), for $FLOC_{14}$-d_9 at 135.7 °C.[18] At this temperature the order parameter S_{zz} = 0.523, and the correlation times are τ_α = 610 ± 300 ps, τ_β = 1050 ± 250 ps, and τ_γ = 266 ± 20 ps. Measuring the temperature dependence of the correlation times allowed activation energies for the three independent rotations to be determined.

5 SAMPLE ROTATION EXPERIMENTS

When a liquid crystal sample is rotated in a magnetic field, the diamagnetic susceptibility anisotropy results in a torque on the director which tends to align it either parallel or perpendicular to the field. In nematic mesophases, the opposing viscous forces are too weak, and spontaneous realignment of the director occurs. This is unfortunate, because when the director can be rotated, profound changes are observed in both the NMR spectrum and relaxation times. Deuteron spectra with well-resolved doublets are observed only when the director is aligned with respect to the field. If it is not so aligned, the distribution of molecular orientations about the director

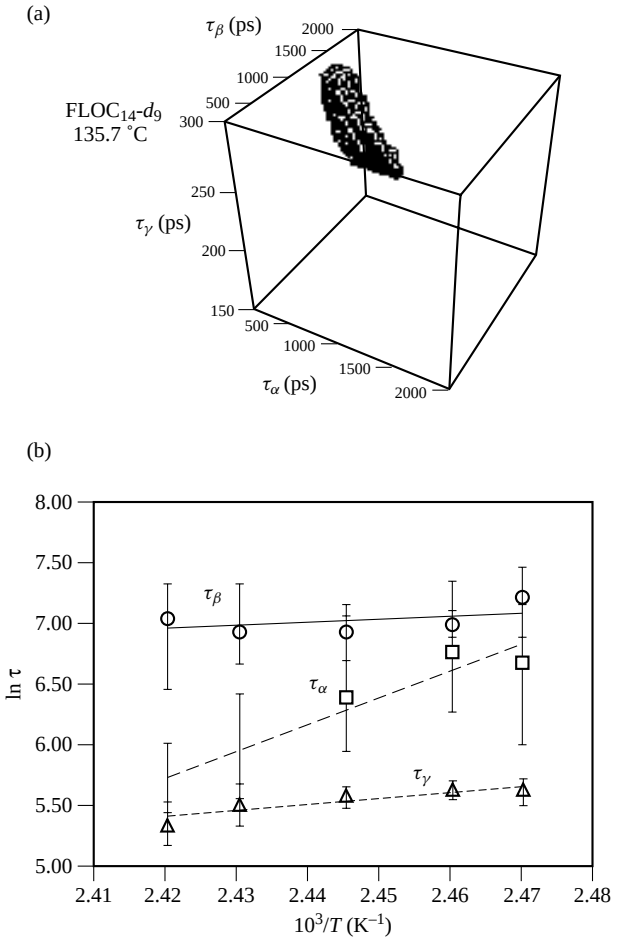

Figure 10 TR model parameters for pure FLOC$_{14}$-d_9 in the nematic phase at 135.7°C. (a) Constant $\Delta\chi^2$ boundary of 68% confidence in the 3D parameter space of the TR model, (τ_α, τ_β, τ_γ). (b) Arrhenius plots of the temperature dependence of the motional correlation times; τ_α data are shown as squares, τ_β as circles, and τ_γ as triangles. The error bars correspond to the 68% confidence boundaries, and the lines are least squares fits of the data which give the activation energies. (Adapted from Goetz et al.[18])

produces a distribution of doublet splittings, and the resulting characteristic spectra are reminiscent of the powder patterns observed in solid state ^{2}H NMR. Analysis of these lineshapes and rotation patterns can provide a wealth of information about the orientational distribution function. This technique has been especially successful in elucidating structure and organization in a magneto-aligned chiral smectic C phase, S_C*.[25]

Relaxation measurements as a function of sample orientation are relatively scarce, in part because methods for obtaining individual spectral densities from complex powder patterns have only been devised in the 1990s.[26] The information available from such experiments can be appreciated by considering the simple case of a uniaxial phase, such as smectic A or hexatic smectic B. It can then be shown[27] that the spectral densities are given by

$$J_0(\beta, 0) = \tfrac{1}{4}(1 - 3\cos^2\beta)^2 J_0(0) + 3\cos^2\beta \times \sin^2\beta\, J_1(0) + \tfrac{3}{4}(1 - \cos^2\beta)^2 J_2(0) \quad (14a)$$

$$J_1(\beta, \omega_0) = \tfrac{3}{2}\cos^2\beta \sin^2\beta\, J_0(\omega_0) + \tfrac{1}{2}(1 - 3\cos^2\beta + \cos^4\beta) J_1(\omega_0) + \tfrac{1}{2}(1 - \cos^4\beta) J_2(\omega_0) \quad (14b)$$

$$J_2(\beta, 2\omega_0) = \tfrac{3}{8}(1 - \cos^2\beta)^2 J_0(2\omega_0) + \tfrac{1}{2}(1 - \cos^4\beta) \times J_1(2\omega_0) + \tfrac{1}{8}(1 + 6\cos^2\beta + \cos^4\beta) J_2(2\omega_0) \quad (14c)$$

If T_{1Z} and T_{1Q} are analyzed to yield $J_1(\beta, \omega_0)$ and $J_2(\beta, 2\omega_0)$ as functions of sample rotation angle β, inversion of equations (14b) and (14c) will yield six spectral densities: $J_0(\omega_0)$, $J_1(\omega_0)$, $J_2(\omega_0)$, $J_0(2\omega_0)$, $J_1(2\omega_0)$, and $J_2(2\omega_0)$. It must be noted that these results are applicable only for uniaxial phases, and most phases which are rigid enough to support sample rotation have more complicated, biaxial symmetry. While this further complicates the orientation dependence of the spectral densities, it should not preclude using them to test motional models.

6 CONCLUSIONS

This article has discussed and summarized the existing experimental methods which are used to measure various deuteron relaxation times in liquid crystals. Accurate determination of appropriate combinations of relaxation rates allows the derivation of the individual spectral density functions $J_1(\omega_0)$, $J_2(2\omega_0)$, and, occasionally, $J_0(0)$. These spectral densities are Fourier transforms of rotational correlation functions and can be interpreted in terms of models of molecular motion. Currently, when appropriate precautions are taken, it is possible to measure spectral densities with an accuracy of 2–5%. This places very tight constraints on acceptable theoretical descriptions of molecular dynamics. In the nematic phase of thermotropic liquid crystals, performing these experiments as a function of temperature and magnetic field strength (ω_0) provides a rigorous test for models of molecular motion in the presence of an orientating potential. Extension of the measurements to more complex ordered smectic, lyotropic, and discotic mesophases offers the possibility of determining the orientation dependence of the relaxation rates, and represents a dramatic increase in the available information.

In conclusion, measuring ^{2}H NMR relaxation rates is a powerful and important method for investigating and understanding molecular dynamics in liquid crystal samples.

7 RELATED ARTICLES

Amphiphilic Liquid Crystalline Samples: Nuclear Spin Relaxation; Bilayer Membranes: Deuterium and Carbon-13 NMR; Brownian Motion and Correlation Times; Deuterium NMR in Solids; Double Quantum Coherence; Dynamic NMR in Liquid Crystalline Solvents; Echoes in Solids; Field Cycling

Experiments; Liouville Equation of Motion; Liquid Crystalline Samples: Carbon-13 NMR; Liquid Crystalline Samples: Deuterium NMR; Liquid Crystalline Samples: Diffusion; Liquid Crystalline Samples: Relaxation Mechanisms; Liquid Crystalline Samples: Structure of Nonrigid Molecules; Liquid Crystals: General Considerations; Lyotropic Liquid Crystalline Samples; Membranes: Deuterium NMR; Molecular Motions: T_1 Frequency Dispersion in Biological Systems; Multiple Quantum Spectroscopy in Liquid Crystalline Solvents; Polymer Dispersed Liquid Crystals; Protein Dynamics from NMR Relaxation; Relaxation of Coupled Spins from Rotational Diffusion; Relaxation Processes in Coupled-Spin Systems; Relaxation Processes: Cross Correlation and Interference Terms; Relaxation Theory: Density Matrix Formulation; Relaxation Theory for Quadrupolar Nuclei; Two-Dimensional NMR of Molecules Oriented in Liquid Crystalline Phases.

8 REFERENCES

1. R. R. Vold and R. L. Vold, *Adv. Magn. Opt. Reson.*, 1991, **16**, 85.
2. H. W. Spiess and H. Sillescu, *J. Magn. Reson.*, 1981, **42**, 381.
3. H. W. Spiess, *J. Chem. Phys.*, 1980, **72**, 6755.
4. T. M. Duncan, A. M. Thayer, and T. W. Root, *J. Chem. Phys.*, 1990, **92**, 2663.
5. C. Schmidt, B. Blümich, S. Wefing, S. Kaufmann, and H. W. Spiess, *Ber. Bunsenges. Phys. Chem.*, 1987, **91**, 1141.
6. A. G. Redfield, *Adv. Magn. Reson.*, 1965, **1**, 1.
7. J. W. Emsley and L. C. Lindon, *NMR Spectroscopy Using Liquid Crystal Solvents*, Pergamon Press, New York, 1975.
8. C. A. Veracini, in *NMR of Liquid Crystals*, ed. J. W. Emsley, D. Reidel, Boston, 1985, p. 99.
9. J. R. C. van der Maarel, *J. Chem. Phys.*, 1984, **80**, 5646.
10. L. S. Selwyn, R. L. Vold, and R. R. Vold, *J. Chem. Phys.*, 1984, **80**, 5418.
11. G. L. Hoatson, *J. Magn. Reson.*, 1991, **94**, 152.
12. G. P. Drobny, *J. Magn. Reson.*, 1993, **103**, 313.
13. G. L. Hoatson, T. Y. Tse, and R. L. Vold, *J. Magn. Reson.*, 1992, **98**, 342.
14. R. L. Vold, R. R. Vold, and M. Warner, *J. Chem. Soc. Faraday Trans.*, 1988, **84**, 997.
15. S. B. Ahmad and K. J. Packer, *Mol. Phys.*, 1979, **37**, 47.
16. D. Jaffe, R. R. Vold, and R. L. Vold, *J. Magn. Reson.*, 1982, **46**, 475.
17. R. R. Vold, R. L. Vold, and N. M. Szeverenyl, *J. Phys. Chem.*, 1981, **85**, 1934.
18. J. M. Goetz, G. L. Hoatson, and R. L. Vold, *J. Chem. Phys.*, 1992, **97**, 1306.
19. B. J. Gertner and K. Lindenberg, *J. Chem. Phys.*, 1991, **94**, 5143.
20. P. L. Nordio, G. Rigatti, and U. Segre, *J. Chem. Phys.*, 1972, **56**, 2117.
21. J. H. Freed, *J. Chem. Phys.*, 1977, **66**, 4183.
22. R. R. Vold and R. L. Vold, *J. Chem. Phys.*, 1988, **88**, 1443.
23. G. L. Hoatson and J. M. Goetz, *J. Chem. Phys.*, 1991, **94**, 3885.
24. J. M. Goetz, Ph.D. Thesis, College of William and Mary, 1993.
25. B.-G. Wu and J. W. Doane, *J. Magn. Reson.*, 1987, **75**, 39.
26. G. L. Hoatson, R. L. Vold, and T. Y. Tse, *J. Chem. Phys.*, 1994, **100**, 4756.
27. T. M. Barbara, R. R. Vold, and R. L. Vold, *J. Chem. Phys.*, 1983, **79**, 6338.

Biographical Sketches

Gina L. Hoatson. *b* 1955. B.Sc., 1977, Ph.D., 1980 (supervisor K. J. Packer), University of East Anglia, UK. Postdoctoral work: Iowa State University, USA (B. C. Gerstein), 1981–82, and University of British Columbia, USA (M. Bloom and E. E. Burnell), 1982–86. Assistant and Associate Professor of Physics, College of William and Mary, USA, 1986–present. Current research specialty: NMR studies of order and dynamics in solids and liquid crystals.

Robert L. Vold. *b* 1942. B.Sc., 1963, University of California, Berkeley, Ph.D. (supervisor H. S. Gutowsky), 1966, University of Illinois, USA. Postdoctoral work at Massachusetts Institute of Technology, 1966–67 (J. S. Waugh). Assistant, associate, and full professor of Chemistry, University of California, San Diego, 1968–91; Program Officer, National Science Foundation, 1992; National Research Council Fellow, NASA Langley Research Center, 1993; Professor of Applied Science and Physics, College of William and Mary, Virginia, 1994–present. Current research specialty: NMR studies of order and dynamics in solids.

Dynamic NMR in Liquid Crystalline Solvents

Raphy Poupko and Zeev Luz

Weizmann Institute of Science, Rehovot, Israel

1	Introduction	1
2	Dynamic NMR LineShapes in Liquid Crystalline Solutions	1
3	Experimental Aspects	3
4	Applications to Spin $I = \frac{1}{2}$ Nuclei	3
5	Multiple Quantum Dynamic NMR for Spin $I = \frac{1}{2}$ Nuclei	6
6	Dynamic NMR for Spin $I = 1$ Nuclei	7
7	Two-Dimensional Exchange NMR Spectroscopy for Spin $I = 1$ Nuclei	9
8	Dynamic Echo Train Experiments	12
9	Related Articles	13
10	References	14

1 INTRODUCTION

The effect of dynamic processes on high-resolution NMR spectra in liquids was first observed[1] in 1953 soon after the discovery of the chemical shift[2] and spin–spin coupling phenomena.[1,3] Since then the effect has been extensively used to study a wide range of dynamic processes in liquids including protolysis, solvation, hindered rotation, bond shift tautomerism, and a variety of other isomerization reactions.[4,5] The effect of dynamic processes on the high-resolution spectra is manifested in line broadening, coalescence, and eventual line narrowing, yielding motionally averaged spectra with average magnetic parameters. The effect on the lineshape is most pronounced when the exchange rate is of the order of the magnetic interactions. For protons these range from several hertz to several kilohertz, while for ^{13}C the range is an order of magnitude larger. Quantitative studies can generally be made within the range where the lifetime broadening or the exchange-narrowed linewidth exceeds that of the natural width, i.e. $1–10^6$ s^{-1} for protons and one to two orders of magnitude faster for carbon-13.

Proton or carbon-13 high-resolution spectra of molecules dissolved in liquid crystalline solvents usually exhibit more complicated structures than in normal (isotropic) liquids and often span a wider frequency range.[6] This is so because in anisotropic solvents, in addition to the scalar spin–spin coupling and isotropic chemical shift, anisotropic interactions also affect the spectrum. These include intramolecular dipole–dipole interactions, anisotropic indirect spin–spin couplings, anisotropic chemical shifts, and, for $I > \frac{1}{2}$ nuclei, also quadrupolar interactions. The fast anisotropic motion of the molecules reduces these interactions, but unlike in isotropic liquids their averages are, in general, not zero and depend on the ordering characteristics of the molecules in the liquid crystals. If the number of magnetic nuclei in the molecule is not too large (say below 10) a well-resolved high-resolution spectrum can usually be observed, but for more nuclei the number of lines becomes exceedingly large and the spectrum unresolved. It should be emphasized that the fast translational diffusion completely averages out the intermolecular dipolar interactions. Otherwise a featureless spectrum as in solids would always be observed.

When the solute molecules dissolved in liquid crystals undergo dynamic processes, lineshape changes similar to those observed in isotropic liquids take place.[7] We refer to this phenomenon as 'dynamic NMR in liquid crystalline solvents' and in the present article we outline its basic theory and review some applications. Because of the more complex structure of the spectra in liquid crystalline solutions the interpretation is more complicated, but the basic principles are the same as in isotropic liquids. On the other hand, due to the larger interactions involved, the dynamic range over which kinetic parameters can be measured is much wider. Nuclei with spins $I > \frac{1}{2}$ usually exhibit splittings due to quadrupole interactions which are often much larger than the dipolar or chemical shift interactions. The structure of the spectrum is then predominantly determined by the quadrupole splittings with the other interactions often within the experimental linewidth.

We start the review by extending the theory of dynamic lineshape in isotropic liquids to the liquid crystalline case by adding anisotropic terms to the spin Hamiltonian (Section 2). After a short section (3) dealing with some experimental aspects, we review applications (Section 4) for spin $I = \frac{1}{2}$ nuclei (^{1}H and ^{13}C), including the use of multiple quantum spectroscopy (Section 5). In Sections 6 and 7 we discuss applications of one- and two-dimensional dynamic NMR to deuterium and in Section 8 we briefly describe a dynamic deuterium study using quadrupole echo pulse trains.

2 DYNAMIC NMR LINESHAPES IN LIQUID CRYSTALLINE SOLUTIONS

The theory of dynamic NMR lineshapes in anisotropic liquids is, in principle, identical to that for isotropic liquids.[1,5,8–12] However, since dipolar interactions involve essentially all magnetic nuclei in the molecule, and for homonuclei cases these interactions are usually larger than the chemical shifts, the NMR spectra always correspond to combination transitions. The simple Bloch–McConnell type treatment[8] is therefore not adequate for the analysis of the dynamic lineshapes and the more general density matrix formalism must be used.[9–13] We shall restrict ourselves to intramolecular rearrangement kinetics because higher order processes involving two or more molecules[10] have not been applied so far in liquid crystalline solutions. The equation of motion of the density matrix, $\hat{\rho}(t)$, during free induction decay, is then:

$$\frac{\mathrm{d}\hat{\rho}(t)}{\mathrm{d}t} = -\mathrm{i}[\hat{\mathcal{H}}, \hat{\rho}(t)] + k[\hat{R}\hat{\rho}(t)\hat{R}^{-1} - \hat{\rho}(t)] - \hat{\rho}_{\mathrm{od}}(t)/T_2 - [\hat{\rho}_0 - \hat{\rho}_{\mathrm{dg}}(t)]/T_1 \quad (1)$$

where $\hat{R}$ is an operator describing the exchange process, k the rate constant for the reaction, $\hat{\rho}_0$ the equilibrium density

matrix, and $\hat{\rho}_{\rm dg}(t)$ and $\hat{\rho}_{\rm od}(t)$ the diagonal and off-diagonal parts of $\hat{\rho}(t)$ which are assumed to relax by respectively single longitudinal and transverse modes. Limiting ourselves to the homonuclei case the Hamiltonian, $\hat{\mathcal{H}}$, in the rotating coordinate system includes both single and binuclear terms,

$$\hat{\mathcal{H}} = \hat{\mathcal{H}}_Z + \hat{\mathcal{H}}_Q + \hat{\mathcal{H}}_S \tag{2}$$

where

$$\hat{\mathcal{H}}_Z = -\sum_i \omega_0(1-\sigma_i)\hat{I}_{iz} = \sum_i \omega_i \hat{I}_{iz} \tag{3a}$$

$$\hat{\mathcal{H}}_Q = \sum_i \omega_{Qi}[(\hat{I}_{iz})^2 - \hat{I}_i(\hat{I}_i+1)/3] \tag{3b}$$

$$\hat{\mathcal{H}}_S = \sum_{i<j}\{2(D_{ij}+J^{\rm a}_{ij})[\hat{I}_{iz}\hat{I}_{jz} - (\hat{I}_{i+}\hat{I}_{j-}+\hat{I}_{i-}\hat{I}_{j+})/4] + J_{ij}[\hat{I}_{iz}\hat{I}_{jz} - (\hat{I}_{i+}\hat{I}_{j-}+\hat{I}_{i-}\hat{I}_{j+})/2]\} \tag{3c}$$

In these equations ω_0 and ω_i are the reference and resonance frequencies in the rotating frame, σ_i the motionally averaged chemical shift, ω_{Qi} the average quadrupole interaction, D_{ij} the average direct dipole–dipole interaction, and $J^{\rm a}_{ij}$ and J_{ij} are respectively the average anisotropic and scalar spin–spin couplings. The sum is over all magnetic nuclei in the molecule assumed to belong to the same isotope (homonuclei). The averaged anisotropic parameters, $T = \sigma_i$, ω_{Qi}, D_{ij}, $J^{\rm a}_{ij}$, are related to their static tensorial components, $T_{\alpha\beta}$, in the molecular-fixed frame $\alpha, \beta = x, y, z$ via the so-called motional constants, C^2_α.[14,15] The liquid crystal is assumed to have a nonpolar cylindrical symmetry defined by a director which aligns parallel to the magnetic field. The molecular orientation distribution function can then be expanded in even orders of the (real) spherical harmonic functions

$$P(\theta,\phi) = \frac{1}{4\pi} + C^2_{3z^2-r^2}D^2_{3z^2-r^2} + C^2_{x^2-y^2}D^2_{x^2-y^2} + C^2_{xz}D^2_{xz} + C^2_{yz}D^2_{yz} + C^2_{xy}D^2_{xy} + \mathrm{O}(D^4) \tag{4}$$

where the D^2_αs are normalized so that $\int_0^{2\pi}\int_0^{\pi} D^2_\alpha D^2_{\alpha'} \sin\theta \, \mathrm{d}\theta \, \mathrm{d}\phi = (1/4\pi)\delta_{\alpha\alpha'}$

$$\left.\begin{aligned} D^2_{3z^2-r^2} &= \left(\frac{\sqrt{5}}{4\pi}\right)\tfrac{1}{2}(3\cos^2\theta - 1) \\ D^2_{x^2-y^2} &= \left(\frac{\sqrt{15}}{4\pi}\right)\tfrac{1}{2}(\sin^2\theta\cos 2\phi) \\ D^2_{xy} &= \left(\frac{\sqrt{15}}{4\pi}\right)\tfrac{1}{2}(\sin^2\theta\sin 2\phi) \\ D^2_{xz} &= \left(\frac{\sqrt{15}}{4\pi}\right)(\sin\theta\cos\theta\cos\phi) \\ D^2_{yz} &= \left(\frac{\sqrt{15}}{4\pi}\right)(\sin\theta\cos\theta\sin\phi) \end{aligned}\right\} \tag{5}$$

and $C^2_\alpha = 4\pi \int_0^{2\pi}\int_0^{\pi} P(\theta,\phi) D^2_\alpha \sin\theta \, \mathrm{d}\theta \, \mathrm{d}\phi$. The averages of the anisotropic interactions are given by

$$T = \frac{1}{\sqrt{15}}\left\{C^2_{3z^2-r^2}\frac{2}{\sqrt{3}}[T_{zz} - \tfrac{1}{2}(T_{xx}+T_{yy})] + C^2_{x^2-y^2}(T_{xx}-T_{yy}) + C^2_{xz}(T_{xz}+T_{zx}) + C^2_{yz}(T_{yz}+T_{zy}) + C^2_{xy}(T_{xy}+T_{yx})\right\} \tag{6}$$

Molecular symmetry will reduce the number of nonzero motional constants by choosing the appropriate molecular coordinates x, y, and z.[15]

To calculate the time domain signal it is necessary to compute the expectation value of the transverse magnetization

$$M_+(t) = \mathrm{Tr}(\hat{\rho}(t)\hat{I}_+) = \sum_{k,\ell}\rho_{k\ell}(t)(I_+)_{\ell k} \tag{7}$$

which upon Fourier transformation yields the frequency spectrum

$$I(\omega) = \mathrm{Re}\int M_+(t)\exp(-\mathrm{i}\omega t)\,\mathrm{d}t \tag{8}$$

As $(I_+)_{lk} \propto \delta_{k,l-1}$ we only need off-diagonal elements of the density matrix of the type $\rho_{k,k+1}(t)$. Consequently, since the Hamiltonian is secular and the exchange operators only mix states of the same total azimuthal quantum number, m_l we extract from equation (1) those blocks of equations which couple between m_k and m_{k-1} states. For a spin system with N nuclei of spin $I = \frac{1}{2}$, there are N such blocks with dimensions

$$(N!)^2/[(N/2-m)!(N/2+m)!(N/2+1-m)!(N/2-1+m)!] \tag{9}$$

The largest blocks are the $0 \rightarrow \pm 1$ transitions for N even and the $-\frac{1}{2} \rightarrow +\frac{1}{2}$ transitions for N odd with dimensions

$$\frac{N}{N+2}\frac{(N!)^2}{[(N/2)!]^4} \quad \text{and} \quad \left(\frac{(N+1)}{2}\right)^2\frac{(N!)^2}{[((N+1)/2)!]^4} \tag{10}$$

respectively. The general equation for the $m_k \rightarrow m_l$ manifold becomes

$$\frac{\mathrm{d}}{\mathrm{d}t}\rho_{kl}(t) = \mathrm{i}\left[\sum_r \rho_{kr}(t)H_{rl} - \sum_i H_{ki}\rho_{il}(t)\right] + k\left[\sum R_{kn}\rho_{nm}(t)(R^{-1})_{ml} - \rho_{kl}(t)\right] - \frac{\rho_{kl}}{T_2}(t) \tag{11}$$

These equations can be cast into the following matrix form

$$\frac{\mathrm{d}}{\mathrm{d}t}\boldsymbol{\rho}(t) = \mathbf{L}\boldsymbol{\rho}(t) \tag{12}$$

where $\boldsymbol{\rho}(t)$ is the vector of the $\rho_{kl}(t)$ quantities. The formal solution of $\boldsymbol{\rho}(t)$ then becomes

$$\boldsymbol{\rho}(t) = \exp(\mathbf{L}t)\boldsymbol{\rho}(0) = \mathbf{T}\exp(\Lambda t)\mathbf{T}^{-1}\boldsymbol{\rho}(0) \qquad (13)$$

where Λ is the diagonal matrix of the eigenvalues of $\mathbf{L}$ and $\mathbf{T}$ the matrix of its eigenvectors. From equation (10), it follows that the dimensions of the blocks corresponding to the $m = 0$ to $m = \pm 1$ or $m = \frac{1}{2}$ to $m = -\frac{1}{2}$ transitions for $N = 6$, 7, and 8 become 300, 1225, and 3920, respectively, rendering the calculation of such spectra rather time-consuming and prone to roundoff errors even on large mainframe computers.

Symmetry considerations can often be helpful in factorizing the blocks.[16,17] To do so, the $\rho_{kl}(t)$ terms are calculated in bases of symmetry adapted linear combinations of spin product functions belonging to irreducible representations of the symmetry group of the static molecule.[18] This reduces the dimension of the blocks to just the number of allowed transitions which depending on the symmetry of the molecule can be considerably smaller than given by equation (10). Further factorization is provided by the fact that the exchange operator usually couples only between a limited number of representations, in fact only between those representations that induce the same irreducible representation of the symmetry group of the exchange-averaged Hamiltonian.[16] They can readily be determined by correlation diagrams relating the symmetries of the two groups. These symmetry considerations have in many cases very effectively reduced the size of the matrices that need be solved. For example, in the case of the bondshift reaction of cyclooctatetraene, the largest matrix that need be diagonalized in order to calculate the proton NMR spectrum in a liquid crystalline solution is 3920×3920, while when symmetry considerations are included it reduces to 224×224.

3 EXPERIMENTAL ASPECTS

3.1 Liquid Crystalline Solvents

So far only thermotropic nematic phases with positive anisotropic magnetic susceptibility, $\Delta\chi > 0$, i.e. which align with their director parallel to the magnetic field, have been used as solvents for dynamic NMR studies. The nematic phase is usually very fluid and consequently yields sharp-line spectra for dissolved solute molecules. The samples are contained in long cylindrical tubes as for high-resolution NMR of isotropic liquids. If a permanent magnet or an electromagnet with the magnetic field perpendicular to the tube axis is used, it is not allowed to spin the sample because the spinning smears out the director orientation and causes broadening of the spectrum. However, for superconducting magnets where the magnetic field is parallel to the sample axis, spinning usually sharpens the lines and increases the spectral resolution. The choice of solvent depends on the solubility of the solute, its degree of ordering, and the desired temperature range for the measurements. The solute concentrations range between 1–10 wt.%. Addition of solute usually reduces the clearing temperature but on the other hand it also often facilitates supercooling. Table 1 lists some common liquid crystals used in dynamic NMR studies with their nematic ranges.

For proton (and ^{13}C), NMR background signal may also be a consideration in the choice of solvent. For certain solutes, such as polar or hydroxylic compounds, lyotropic nematic phases may be the preferred choice as a solvent, but these have so far not been used for dynamic studies. Compounds exhibiting the uniaxial smectic A phase may also serve as adequate solvents. This phase, once aligned, for example, by cooling from a nematic or an isotropic phase within a magnetic field, will remain aligned in the sample holder even if rotated with respect to the field.[19] This allows reduction of the frequency range of the spectrum if a small sweep width is desired. Smectic phases are however usually more viscous than nematic and in the presence of solutes often undergo phase separation.

3.2 NMR Measurements

Most dynamic NMR studies in liquid crystalline solvents have been performed on protons, carbon-13, and deuterons.[20–38] The proton spectra are dominated by dipolar interactions and usually span several kHz. Carbon-13 dynamic studies have so far only been made[24,25] under proton decoupling so that the spectrum depends on the chemical shift anisotropy which is of the same order as that of the isotropic shift in normal liquids. For deuterium NMR the dominant effect on the spectrum is due to the quadrupole interaction, which depending on the motional constants of the solute may extend up to several tens of kHz.

When the frequency range does not exceed about 5–10 kHz, adequate spectra can be obtained by single pulse experiments. For wider frequency ranges, echo experiments are required. This is particularly true for deuterium NMR, where the method of choice is that of quadrupole echo.[39] In such experiments the observed lineshape will depend on the time intervals between the pulses in the sequence. This is taken into account[40] in the simulation by repeated application of equation (13) for the time intervals, where the magnetization evolves freely and performing proper transformations of the density operators representing the rf pulses.

Temperature stability and homogeneity are crucial for obtaining high-resolution spectra. Because of the sensitivity of the orientational order to temperature, small gradients may cause excessive line broadening and corresponding loss of resolution. Imperfect alignment may also be a source for loss of resolution. This is caused by the fact that different domains have slightly different orientations and accordingly slightly different splittings. The effect is often manifested by progressive line broadening for peaks which are further removed from the spectrum center.

4 APPLICATIONS TO SPIN I = $\frac{1}{2}$ NUCLEI

Several applications of high-resolution proton NMR in liquid crystalline solutions have been published and here we describe two such cases. Dynamic ^{13}C spectra recorded under proton decoupling will also be reviewed. The emphasis is on systems for which kinetic information was derived from a lineshape analysis, rather than on dynamic equilibria between species in the extreme fast regime.

Table 1 Nematic Liquid Crystals Used as Solvents for NMR Studies of Solute Molecules

Brand name or acronym	Chemical name and/or composition	Nematic range (°C)
DHAB	4,4′-dihexyloxyazoxybenzene	84–127
TBBA	terephthalaldehyde-bis(4-*n*-butylaniline)	199–233
S 1131 BCH	*trans*-4-pentyl-1-(4′-cyanobiphenylyl-4)-cyclohexane	96–222
10836	*p*-(*p*-ethoxyphenylazo)phenyl crotonate	109–194
Phase V	eutectic mixture of (two isomers each): *p*-ethoxy-*p*′-butyloxyazoxybenzene *p*-methoxy-*p*′-butyloxyazoxybenzene	5–75
ZLI 2452	mixture of derivatives of cyanophenylcyclohexane, cyanobiphenylcyclohexane, and unspecified esters	−40–110
ZLI 2142	—	−40–85
1565 TNC	mixture of derivatives of phenylcyclohexane and biphenylcyclohexane	−20–85
E8	mixture of derivatives of cyanobiphenyls	−12–72
Nematic mixture	several undisclosed mixtures by Kodak	5–105

4.1 Ring Inversion of *s*-Trioxan

The rate of the ring inversion of *s*-trioxan (Scheme 1) was studied by proton NMR in isotropic solutions.[41] The chemical shift difference between the axial and equatorial protons and their spin–spin coupling are quite small (0.093 ppm and 6.3 Hz, respectively), while the rate of the process at room temperature is rather high. It was therefore necessary to cool the solutions to below −50 °C to obtain dynamic spectra. When the compound is dissolved in a nematic solvent the spectrum is dominated by the dipolar interactions and its spectral width is considerably larger. Above about 70 °C it exhibits sharp peaks with splittings corresponding to the average dipolar interaction of the two conformations.[42] However on cooling to room temperature and below, the lines broaden because the exchange rate becomes of the order of the dipolar interactions.[22] Examples of spectra are shown in Figure 1. Note that the spectra were recorded in two different nematic solvents which give different background signals. The

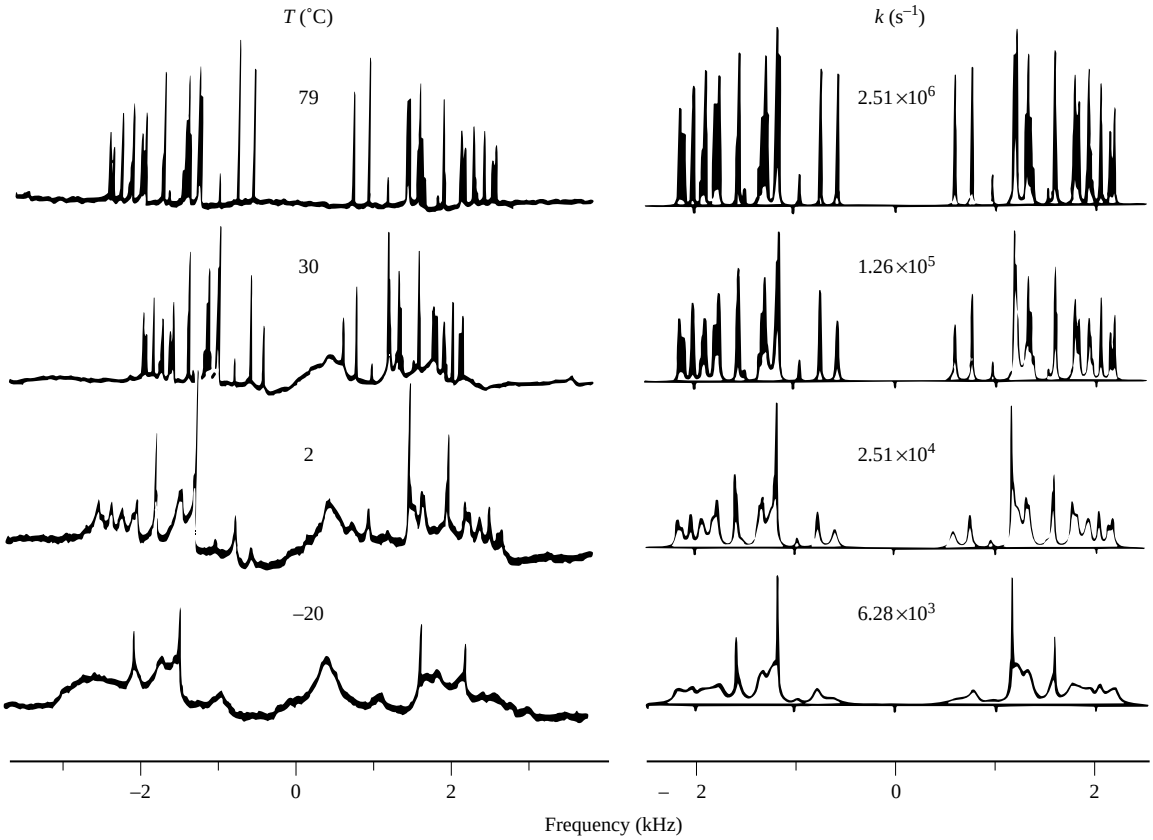

Figure 1 Left: Experimental proton NMR spectra of solutions of *s*-trioxan in liquid crystalline solvents at various temperatures. The solvent used was phase V (2.8 wt.%), except for the 79 °C spectrum which corresponds to a 2.0 wt.% solution in DHAB. Note the different background signals for the two liquid crystal solvents. Right: Corresponding simulated spectra, calculated using the indicated rate constants and the magnetic parameters given in Table 2 with a fixed motional constant $C^2_{3z^2-r^2} = -0.2$

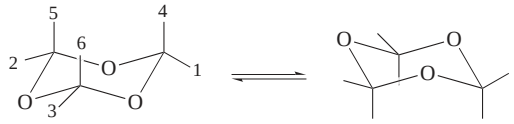

Scheme 1

Table 2 Parameters Used in the Simulation of the *s*-Trioxan Spectra in Figure 1

J_{14} = 6.3 Hz	$D_{12} = D_{13} = D_{23} = C^2_{3z^2-r^2}$ 3941.6 Hz
σ_{ae} = 0.093 ppm	$D_{14} = D_{25} = D_{36} = C^2_{3z^2-r^2}$ (−9651.26) Hz
	$D_{45} = D_{56} = D_{46} = C^2_{3z^2-r^2}$ 775.59 Hz
$D_{15} = D_{16} = D_{24} = D_{26} = D_{34} = D_{35} = C^2_{3z^2-r^2}$ 499.28 Hz	

spectra were simulated using equation (11) with magnetic and kinetic parameters as given in Table 2 and in Figure 1. For simplicity a fixed motional constant was used for displaying the calculated spectra. The dipole–dipole, indirect spin–spin, and chemical shift interactions were determined from low-temperature spectra in isotropic solutions and high-temperature spectra in liquid crystalline solvents. The anisotropic chemical shift and the anisotropic indirect spin–spin coupling were neglected. Since the molecule has threefold symmetry only one motional constant, $C^2_{3z^2-r^2}$, is required. Its value can be obtained from the line splittings, in particular from the so-called dynamically invariant lines, i.e. lines that remain sharp throughout the dynamic range. These lines correspond to transitions that are not modulated (or nearly not modulated) by the dynamic process. Such lines are the two $\pm 1 \rightarrow 0$ pairs of A_2 symmetry clearly seen in the low-temperature spectra of Figure 1. Inspection of the eigenfunctions[22] between which these transitions occur shows that the exchange-induced permutation of nuclei does not change the dipolar interactions of either the initial or final states. The chemical shift on the other hand is modulated by the exchange, but the effect is small and is averaged out already at much lower temperatures than those for which spectra are depicted in Figure 1.

The derived rate constants for the ring inversion reaction are plotted in Figure 2. The figure demonstrates one of the main advantages of the method, i.e. the large dynamic range over which measurements can be made. The lower bound of the dynamic range (10^4 s^{-1}) in this experiment was set by the lack (at the time) of suitable nematic liquids for high-resolution measurements below −20 °C. Also depicted in Figure 2 are the results obtained in an isotropic solvent. These correspond to rates which are orders of magnitude slower than those obtained in the nematic solvent and span a much smaller dynamic range. It may be seen however that both sets of data fit a single Arrhenius line. This indicates that within the accuracy of the experiment the kinetic parameters for the reaction are not very sensitive to the solvent, not even on going from an isotropic to a nematic solvent. This is not surprising for a ring-inversion process, since its rate is predominantly determined by the internal coordinates of the molecule. In other cases, where solute–solvent interactions play a role or for bimolecular reactions where ordering effects are important, the situation may be different.

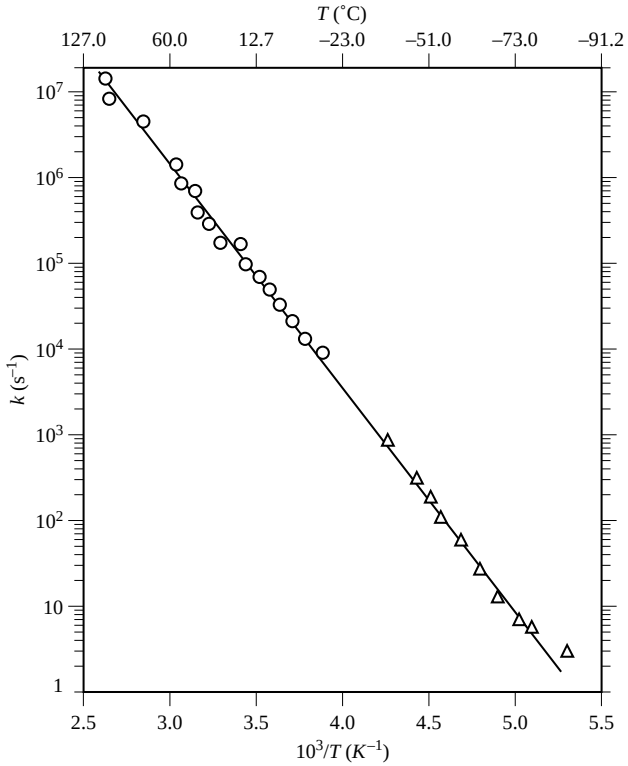

Figure 2 Arrhenius plot of the rate constant for the ring inversion of *s*-trioxan in liquid crystalline (circles) and isotropic (triangles) (Freon) solvents. The circles above 60 °C correspond to solvent DHAB while those below to phase V

4.2 Bond Shift in Cyclooctatetraene (COT)

As a second example we consider the bond shift process in COT (Scheme 2). This molecule has D_{2d} symmetry rendering all eight protons of the molecule equivalent. Consequently the proton NMR spectrum in an isotropic solvent consists of a single line and is not useful for dynamic measurements. The bond shift reaction could therefore only be studied in substituted molecules and in a qualitative manner from the ^{13}C spectrum.[43,44] The proton NMR spectrum of COT in a liquid crystalline solvent on the other hand is highly structured, reflecting the dipolar interactions between all protons in the molecule and exhibits dynamic effects as the temperature is raised from below −20 °C to well above 100 °C.[21] Examples of spectra are depicted in Figure 3. The 'static' spectrum at −25 °C could readily be interpreted with the parameters summarized in Table 3. On heating to above −25 °C line broadening sets in and at room temperature only a number of invariant (or almost invariant) lines are observed. Above 100 °C the spectrum coalesces yielding at 170 °C a pattern corresponding to the averaged dipolar interactions. Simulation of such dynamic spectra would require, without the use of

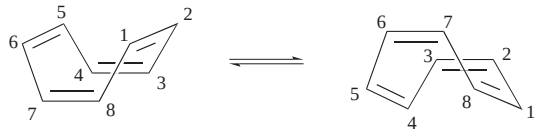

Scheme 2

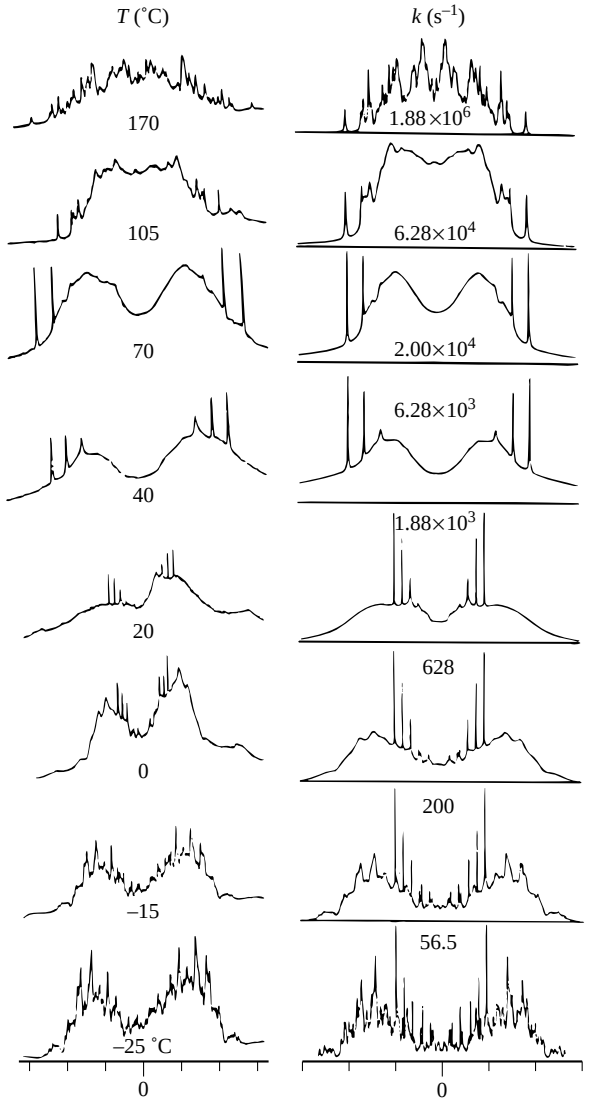

Figure 3 Left: Experimental proton NMR spectra of COT in liquid crystalline solvents at different temperatures. The solvents were: for −25 °C to 20 °C, phase V; for 40 °C, 'Nematic Mixture'; 70 °C and 105 °C, DHAB; and for 170 °C, TBBA. Right: Simulated spectra calculated with the indicated rate constants and the magnetic parameters given in Table 3. A fixed motional constant was used for all the simulated spectra. The spacings between the markers on the left are 500 Hz for the bottom four spectra, 250 Hz for the next three and 125 Hz for the topmost one. On the right, the spacings are 1000 Hz for the bottom four traces and 500 Hz for the four upper ones

symmetry, the diagonalization of matrices as large as 3920 × 3920. When symmetry considerations are included[16] and group theoretical methods are applied to factorize the matrices, the largest block becomes 224 × 224. This in fact made the problem solvable in practice,[23] as shown by the simulated spectra in the right column of Figure 3.

In the original work on the NMR spectrum of COT in liquid crystalline solutions[21] dynamic information was derived from proton spectra of almost but not completely deuterated COT. The isotopic mixture contained a relatively large fraction of $C_8D_6H_2$ isotopomers, each yielding at slow exchange a single doublet. From the initial broadening of the peaks and from the width of the lines in the fast exchange region, estimates

Table 3 Magnetic Parameters of COT used in the Simulation of the Dynamic Spectra Depicted in Figure 3

D_{12}	−1620.3
$D_{13} = D_{17}$	−103.8
D_{14}	−84.5
D_{15}	−147.5
D_{16}	−206.3
D_{18}	+960.9
J_{12}	11.8

of the rate parameters for the bond shift process were derived. The use of such incompletely deuterated samples to obtain simplified proton spectra was found helpful in many structural studies of solute molecules.[45–48] To eliminate broadening due to dipolar interactions with the deuterons, a special decoupling technique was designed involving saturation of the deuterium double quantum transition.[45,46] This requires much less rf power and eliminates sample heating problems.

4.3 Hindered Rotation Measurements

Dynamic NMR has also been applied to natural-abundant ^{13}C of solute molecules dissolved in liquid crystals as demonstrated by Fung et al.[24] Since such spectra are extremely weak and are often masked by the more intense solvent peaks, they were recorded under proton decoupling conditions. The spectra are then essentially identical to those in isotropic solutions except that the chemical shift is modified by the solute ordering. To reduce the interference effect of the solvent signals, special spin echo sequences were used to take advantage of the shorter T_1 values of the nematic solvent carbons, but even then special solvents with ^{13}C windows at the solute frequencies had to be used.

Further simplification may be achieved by using magic angle spinning.[25] For $\Delta\chi > 0$ solvents the director aligns along the spinning axis and the spectrum becomes identical to that in an isotropic solvent. Under these conditions, there is no advantage in using a liquid crystalline solvent, unless of course one wishes to study the effect of ordering on the dynamic process. The method was applied to several systems exhibiting hindered rotations; 4-(dimethylamino)pyrimidine and 6-(dialkylamino)fulvenes. The main conclusion of the work confirms that within the experimental accuracy the ordering by the nematic solvent does not affect the kinetic parameters of the process.

5 MULTIPLE QUANTUM DYNAMIC NMR FOR SPIN $I = \frac{1}{2}$ NUCLEI

The proton NMR spectra in liquid crystalline solvents for molecules with 10 or more hydrogens are so rich in lines that they become structureless with few features that can be used for quantitative analysis. The difficulty can partially be resolved by employing the method of multiple quantum spectroscopy. In such experiments one displays $\Delta m > 1$ spectra which involve less transitions than the corresponding ordinary $\Delta m = 1$ spectra, and are therefore better resolved and more convenient for comparison with calculations.[49] As for

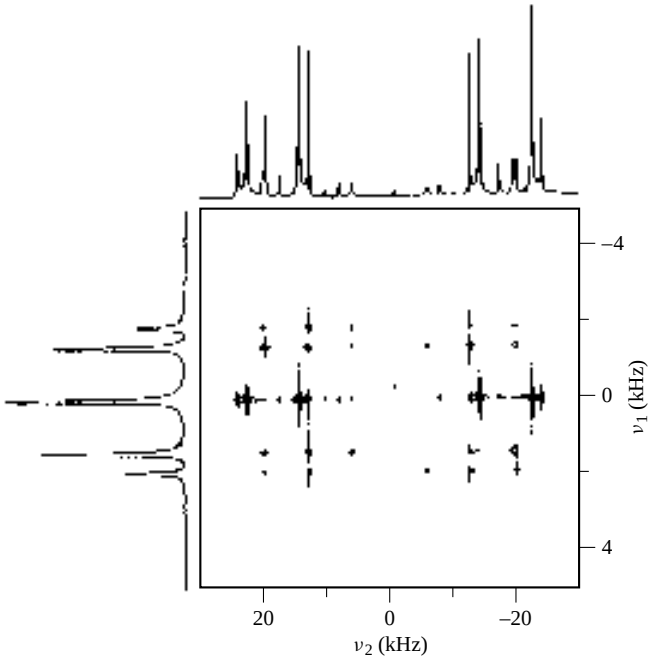

Figure 4 Experimental 2D fourth quantum order contour plot for a solution of *s*-trioxan (2.7 wt.%) in phase V at 17 °C using the SMQ experiment. The one-dimensional spectra along ν_1 and ν_2 are skyline projections and correspond respectively to fourth and single quantum order transitions

single quantum spectra these also exhibit line broadening and coalescence effects. They cannot be detected by ordinary pulse NMR, but can be obtained by several indirect ways which usually involve 2D methods. Two methods were considered for dynamic proton NMR in liquid crystalline solvents. The time proportional phase increment (TPPI) sequence[50] was employed for simulating[26] dynamic multiple quantum spectra and, subsequently, a simpler version[51] which allows recording a particular single multiple quantum (SMQ) spectrum was used.[27] We refer to the literature[26,27] for the theoretical background and confine ourselves here to briefly reviewing experimental results obtained in liquid crystalline solutions.

In Figure 4 a 2D plot of the proton SMQ spectrum of a solution of *s*-trioxan recorded at 17 °C is displayed[27] together with skyline projections along ν_1 (the evolution coordinate) and ν_2 (the detection coordinate). The latter is a $\Delta m = 1$ spectrum but the much simpler ν_1 projection corresponds to the fourth quantum order. Similar fourth quantum projection spectra recorded at different temperatures are presented in Figure 5. These are compared with simulated spectra which were computed by two methods; exact calculation employing the full density matrix formalism and approximate methods. The latter are the density matrix analogs for the slow (bottom trace) and fast (all other traces) exchange regimes. No adjustable parameters were used in the calculations (except for the order parameter), rather the known rate constants and magnetic parameters from earlier studies were adopted. As may be seen, the fit of the experimental and simulated spectra is quite satisfactory. It should be noted however that despite the simple appearance of the MQ spectra their simulations are as complicated as those for the single quantum spectra. This is so because for the calculations it is necessary to follow the evolution of a multitude of coherences. Fortunately, approximate methods exist[26] that are much simpler and as may be seen in Figure 5 they result in spectra very similar to those calculated by the exact method.

6 DYNAMIC NMR FOR SPIN I = 1 NUCLEI

Of the nuclei with spin I = 1, deuterium is the most important for dynamic NMR studies in nematic solvents. However due to its low natural abundance it is necessary to work with isotopically enriched samples. This might require special skills, but techniques are available that allow complete or selective deuteration of many compounds.[52] The method has several advantages; the spectrum is free of background signals and is usually very simple. The dipolar interactions between the deuterons or with other nuclei (protons) are usually within the linewidths, and the structure of the spectrum is predominantly due to the much larger quadrupole interaction. For spin I = 1 nuclei, this corresponds to a single doublet for each type of nucleus, and thus the deuteron spectrum of a deuterated solute in a nematic solvent consists of a number of doublets according to the number of inequivalent deuterons in the molecule. The simulation of dynamic spectra then requires only the solution of Bloch–McConnell type equations rather than the full density matrix equations. In the absence of chemical shift effects, the spectrum of the $m = -1$ to $m = 0$ manifold is the mirror image about the center frequency of the $m = 0$ to $m = +1$ manifold. A third advantage is the large dynamic range that can be studied by deuterium NMR. Since the splitting can be as high as several dozens of kHz, the upper limit of the dynamic range may be considerably higher than that for protons.

6.1 Ring Inversion in Cyclohexane and *p*-Dioxan

As a simple example where the advantages of dynamic deuterium NMR in nematic solvents are well demonstrated, consider the ring inversion process in cyclohexane-d_{12} (C_6D_{12}) (Scheme 3). Experimental spectra[28] are depicted in the left column in Figure 6. At low temperatures the spectrum consists of two doublets due to the axial (outer doublet) and equatorial (inner doublet) deuterons with a relative splitting of ~3. The quadrupole interaction for aliphatic deuterons are nearly constant at $\nu_Q^s \approx 125$ kHz (as compared to ~140 kHz for aromatic deuterons) with cylindrical symmetry about the C–D bond. Accordingly the average quadrupole splitting for a molecule with threefold symmetry, such as cyclohexane, will be proportional to $\nu_Q^s \frac{1}{2}(3\cos^2\beta - 1)$ where β is the angle between the C–D bond and the molecular symmetry axis. For the axial and equatorial deuterons in cyclohexane, this corresponds to $\langle\nu_Q{}^{ax}\rangle/\langle\nu_Q{}^{eq}\rangle \sim -3$ as observed experimentally. In the dynamic spectra the opposite signs of the $\langle\nu_Q\rangle$ quantities is reflected in the mixing of the high-frequency axial

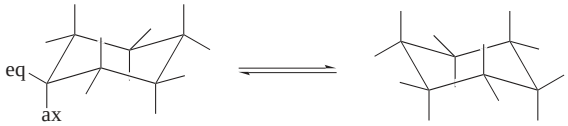

Scheme 3

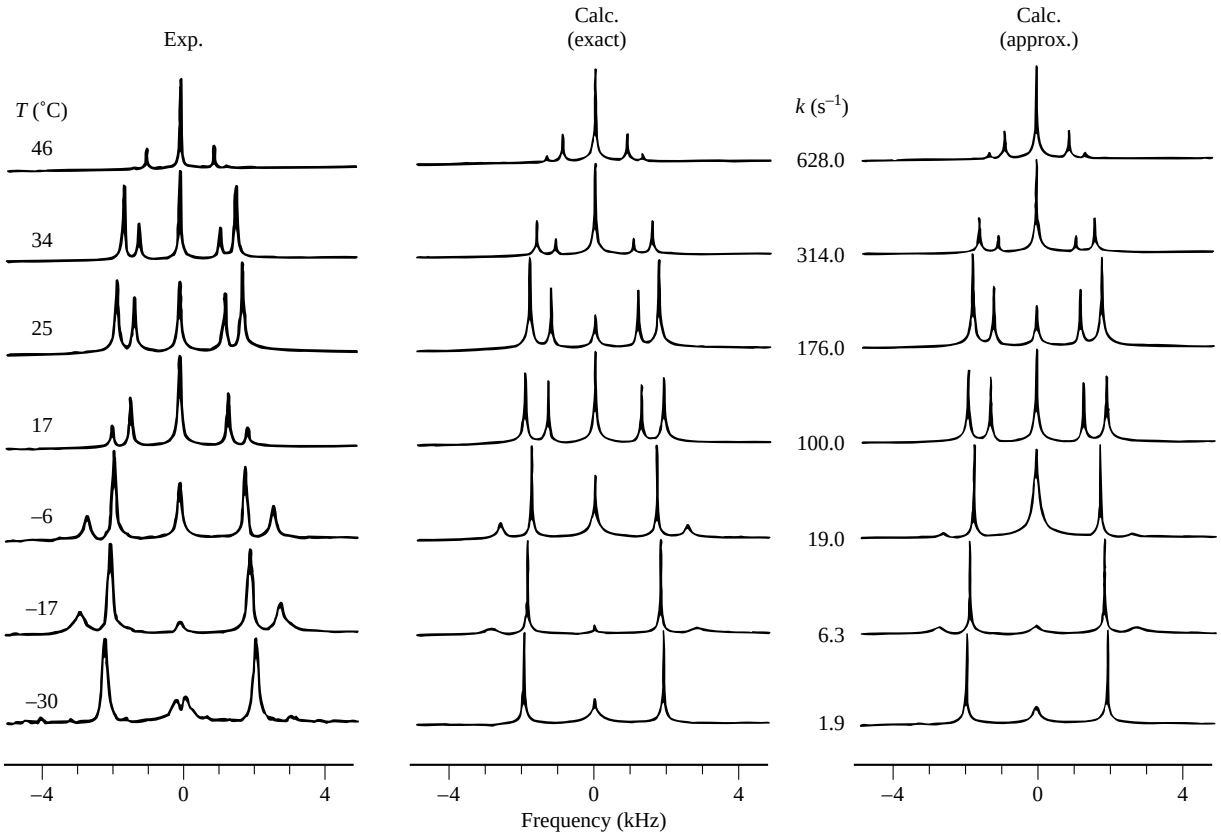

Figure 5 Experimental (left) and calculated (center and right) fourth order quantum spectra of *s*-trioxan solutions in phase V. The experimental spectra were obtained as in Figure 4, the spectra in the middle column were calculated by the exact density matrix formalism, those in the right column were calculated by approximate methods

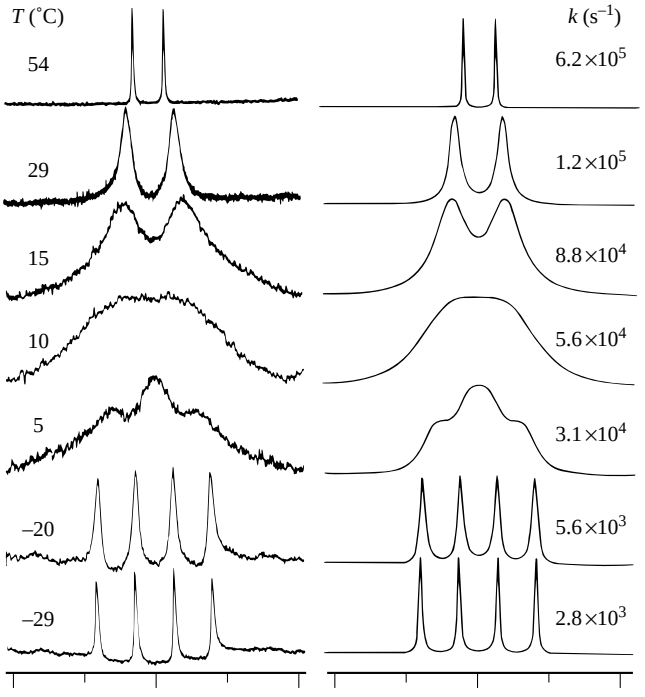

Figure 6 Experimental (left) and simulated (right) deuterium NMR spectra of cyclohexane-d_{12} (3.6 wt.%) in phase V. The overall frequency range corresponds to 83.3 kHz for the lowest three traces and 50.0 kHz for the upper four

peak with the low-frequency equatorial peak and vice versa. This is clearly observed in the experimental spectra depicted in Figure 6 and in the corresponding simulated traces. The spectra correspond to inversion rates ranging from $10^3\,s^{-1}$ to almost $10^6\ s^{-1}$, and when semilogarithmically plotted as a function of the inverse absolute temperature a straight Arrhenius line is obtained which extrapolates perfectly through the results obtained in isotropic liquids at much lower temperatures.[53] In the simulation of the spectra the order parameter, $C^2_{3z^2-r^2}$, must be known. In the low- and high-temperature regions, where sharp peaks are observed, this parameter can be calculated from the line splitting and by interpolation the values at the intermediate range can be derived.[28]

As a second example we consider the case of *p*-dioxan (Scheme 4). This molecule has C_{2h} symmetry and therefore three motional constants are required to describe its orientation in a liquid crystalline solvent. The average quadrupole splitting is given by

$$\langle \nu_Q^i \rangle = \nu_Q^s \sqrt{\frac{3}{5}} \left[\frac{1}{\sqrt{3}} C^2_{3z^2-r^2} \tfrac{1}{2} (3\cos^2\beta^i - 1) + C^2_{x^2-y^2} \tfrac{1}{2} \sin^2\beta^i \cos 2\alpha^i - C^2_{xy} \tfrac{1}{2} \sin^2\beta^i \sin 2\alpha^i \right] \quad (14)$$

where β^i and α^i are the polar and azimuthal angles of the C–D^i bond in the molecular coordinate system x, y, z with

Scheme 4

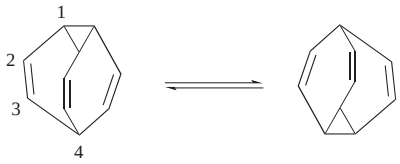

Scheme 5

z perpendicular to the symmetry plane of the molecule. The motional constants are independent and their ratios vary with temperature and from solvent to solvent. Therefore there is no a priori relation between the quadrupole splittings of the axial and equatorial deuterons as is in cyclohexane. In particular their relative sign can be both positive and negative.

The *p*-dioxan molecule undergoes ring inversion in a similar fashion to cyclohexane[53] and the reaction was studied by deuterium dynamic NMR in two nematic solvents, phase V and 1565 TNC.[29] Experimental spectra are shown in the left columns of Figure 7. As may be seen, their evolution with temperature is quite different and this has been interpreted as due to different relative signs of the axial and equatorial quadrupole interactions (same signs in phase V and opposite signs in 1565 TNC). When this effect is taken into account, satisfactory simulation of both sets of spectra are obtained as shown in the right columns of Figure 7. The derived rate constants for the ring-inversion process were found to be identical in both solvents.

The spectra shown above for C_6D_{12} and $C_4O_2D_8$ (Figures 6 and 7) were recorded by single pulses and are therefore distorted due to the dead-time effect. In subsequent works this problem was resolved by using the quadrupole echo method. The spectrum is then also a function of the time interval between the pulses and this must be included in the simulation.[55]

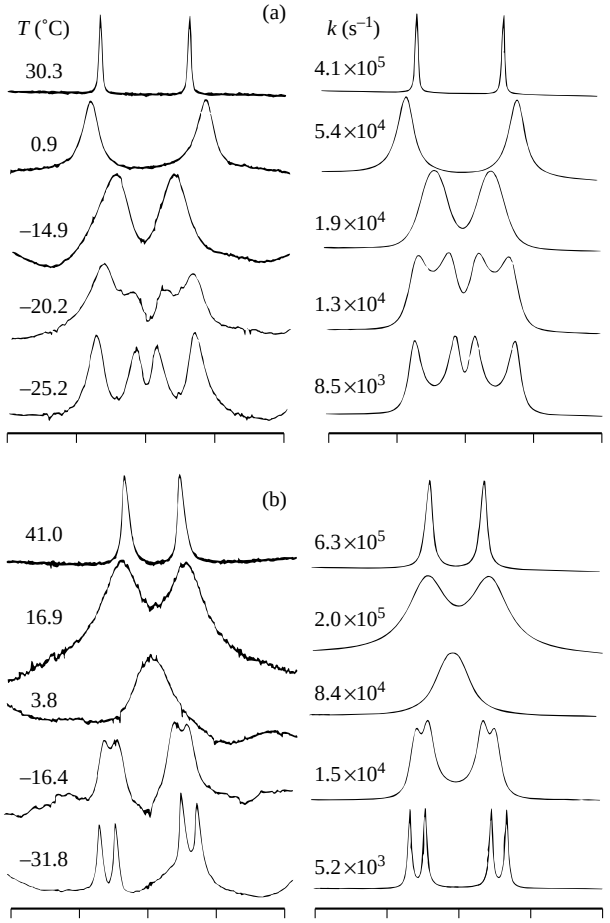

Figure 7 (a) Experimental and simulated deuterium NMR spectra of *p*-dioxan-d_8 dissolved in phase V. The overall frequency scale is 50 kHz for the bottom three spectra and 20 kHz for the top two. In the simulation identical signs of the quadrupole interactions were assumed for the axial and equatorial deuterons. (b) Same as in (a) but for a solution in 1565 TNC. The overall scale is 100 kHz for the bottom three traces and 20 kHz for the top two. In the simulation, opposite signs for the axial and equatorial deuterons were assumed

6.2 Cope Rearrangement in Bullvalene

Bullvalene undergoes fast Cope rearrangement (Scheme 5) and this process has been extensively studied by ^{1}H and ^{13}C NMR in isotropic solutions.[54] The reaction is highly degenerate and results in complete equivalence of all the carbons and all the hydrogens in the molecule. Proton spectra of bullvalene dissolved in a nematic solvent were also recorded[56] but only at high temperatures where they correspond to the fast exchange limit. More extensive studies involving liquid crystalline solutions were made by deuterium NMR.[30] At low temperatures the spectrum consists of four doublets with relative intensities 3:3:3:1 [see Figure 8(a)]. The identification of the outer peaks with deuteron number 4 is straightforward while the other peaks were identified from the known structure of the molecule. The spectrum shows a small asymmetry which is due to the fact that the olefinic deuterons have a slight high-frequency shift relative to the aliphatic ones. At high temperatures [upper trace in Figure 8(a)] the spectrum coalesces into a single doublet, reflecting the fact that all deuterons become equivalent. In the intermediate temperature range typical dynamic spectra are observed, Figure 8(b), that could readily be simulated as shown in Figure 8(c). The deuterium quadrupolar couplings, ν_Q^i, used for the simulation of the dynamic spectra are listed in Table 4 in units of the largest splitting, ν_Q^4. The good fit between the experimental and simulated spectra confirms the high degeneracy of the Cope rearrangement. A more direct confirmation of the kinetic pathway was obtained by the two-dimensional exchange method described in the next section.[33]

Table 4 Deuterium Quadrupolar Couplings, ν_Q^i, Used in the Simulation of the Dynamic Spectra of Bullvalene [Figure 8(b)], in Units of the Largest Splitting, ν_Q^4

i	1	2	3	4
ν_Q^i/ν_Q^4	0.727	−0.401	0.271	1.0

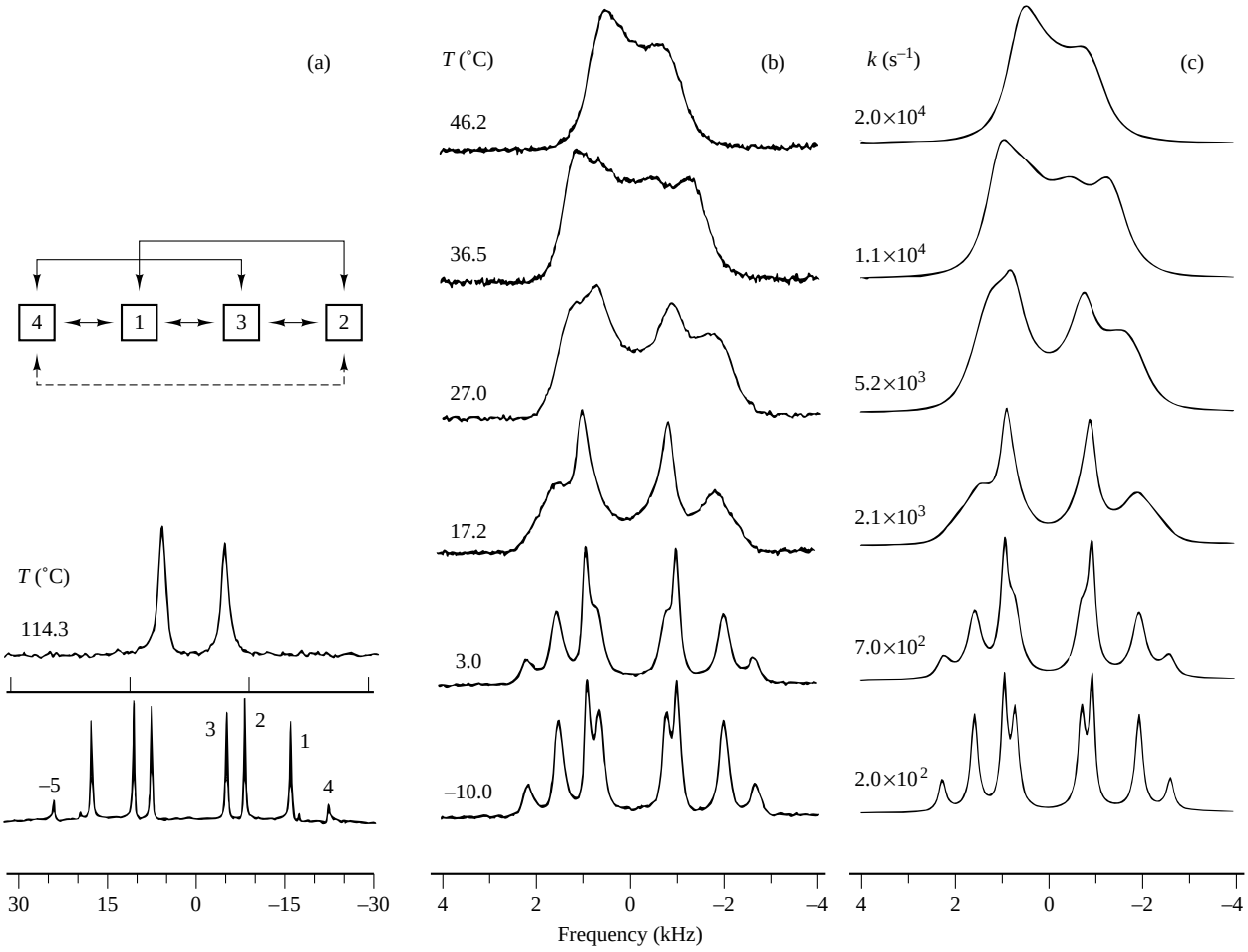

Figure 8 (a) Experimental deuterium NMR spectra of bullvalene-d_{10} dissolved in ZLI 2452 (3.8 wt.%) at $-5\,^{\circ}$C (lower trace) and in DHAB (4.7 wt.%) at 114.3 °C (upper trace). The diagram at the top indicates the different orders of exchange by the Cope rearrangement. Double arrow, full line, and dashed line correspond to first-, second-, and third-order exchanges. (b) Experimental dynamic NMR spectra of bullvalene-d_{10} in phase V (5.7 wt.%) at the indicated temperatures. (c) Simulated dynamic spectra calculated using the indicated rate constants and the relative quadrupole interactions given in Table 4. For each spectrum, a suitable motional constant was chosen[30]

7 TWO-DIMENSIONAL EXCHANGE NMR SPECTROSCOPY FOR SPIN I = 1 NUCLEI

Two-dimensional (2D) exchange NMR was introduced by Jeener et al. to study slow exchange processes for spin $I = \frac{1}{2}$ nuclei.[57] The method was subsequently extended to deuterons (I = 1) in solids and ordered systems in general by Spiess and collaborators.[58–60] It is most useful in the dynamic window for which $1/T_1 \lesssim k < 1/T_2$ and has also found interesting application in liquid crystalline solutions of deuterated solutes. Some of these will be described below.

The basic scheme of the experiment consists of three pulses (Scheme 6).[31] Following the first 90° pulse (P_1) which takes the magnetization to the transverse plane, the various nuclei precess according to their quadrupole interactions and are thus phase-encoded. A second θ pulse (P_2) then produces either Zeeman or quadrupole order depending on the relative phases ($\phi_1 - \phi_2$) of the two pulses. These longitudinal magnetizations are allowed to undergo exchange during a preset mixing time, τ_m, following which a third pulse (P_3) takes them back to the transverse plane and the signal is detected as a function of the detection period t_2. To obtain pure 2D exchange spectra, signals from Zeeman and quadrupole order experiments are combined with appropriate relative intensities, so as to eliminate nonexchange off-diagonal peaks. Two-dimensional Fourier transformation then produces a 2D map with peaks corresponding to the one-dimensional spectrum along the main diagonal and exchange cross peaks off the main diagonal. These cross peaks link between sites i, j which interchange by the exchange process. Their intensity is proportional to

$$I_{ij} = P_i[\exp(kK\tau_m)]_{ij}\ \exp(-\tau_m/T_1) \qquad (15)$$

where P_i is the equilibrium population of site i, and k and K are respectively the rate constant and the exchange matrix for the process. The experiment has several important advantages; measurements can be made in a dynamic range inaccessible by the lineshape method; the cross peaks directly identify the interchanging sites and thus the mechanistic pathway of the process; the cross peaks provide information on the relative signs of the quadrupole interactions of the interchanging sites, and from their evolution with τ_m kinetic parameters may be derived.

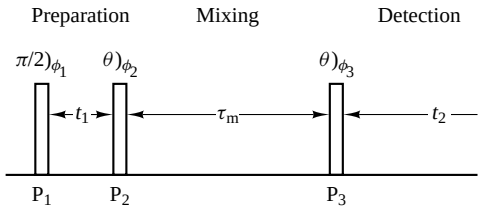

Scheme 6

7.1 Peak Assignment and Relative Signs of Quadrupole Interactions

An example where some of the points mentioned in the last paragraph are demonstrated is that of *p*-dioxan-d_8 already discussed[29] in Section 6.1. It was pointed out there that the signs of the quadrupole interactions of the axial and equatorial deuterons are the same when *p*-dioxan is dissolved in phase V and the opposite in 1565 TNC. This is clearly seen in the exchange 2D spectra[31] in Figure 9, where for phase V the cross peaks link separately the high-field and the low-field signals of the axial and equatorial deuterons, while in 1565 TNC a low-field axial peak is linked with a high-field equatorial peak and vice versa.

An application of the 2D exchange method which was essential for the peak assignment, is that of perdeuterated *cis*-decalin.[34] The molecule undergoes ring inversion (Scheme 7)[61] and in liquid crystalline solutions exhibits temperature dependent dynamic spectra as shown in the left column of Figure 10. To simulate the spectra it is necessary to identify the peaks with particular deuterons in the molecule, or at least to identify the interchanging pairs of peaks. This can readily be done for deuterons 1,1′ which are bonded to the tertiary carbons and remain invariant to the dynamic process. However for all other lines the assignment is not trivial. Since the molecule has C_2 symmetry, three motional constants are required to describe the ordering of the molecules [equation (14)] and the assignment cannot be made simply from a knowledge of the molecular structure. The problem was resolved by 2D exchange spectroscopy.[34] A 2D spectrum recorded at $-5\,^{\circ}C$ is shown in Figure 11 where cross peaks linking pairs of diagonal signals are clearly observed. Although this does not completely assign the peaks, it does identify the signals which interchange by the ring-inversion process. Using this information, dynamic spectra could be simulated which satisfactorily reproduce the experiments as shown in the right-hand column of Figure 10. Other examples where 2D exchange provided assignment and even identified hidden peaks masked by strong signals include 1,1- and 1,4-dimethylcyclohexane.[38]

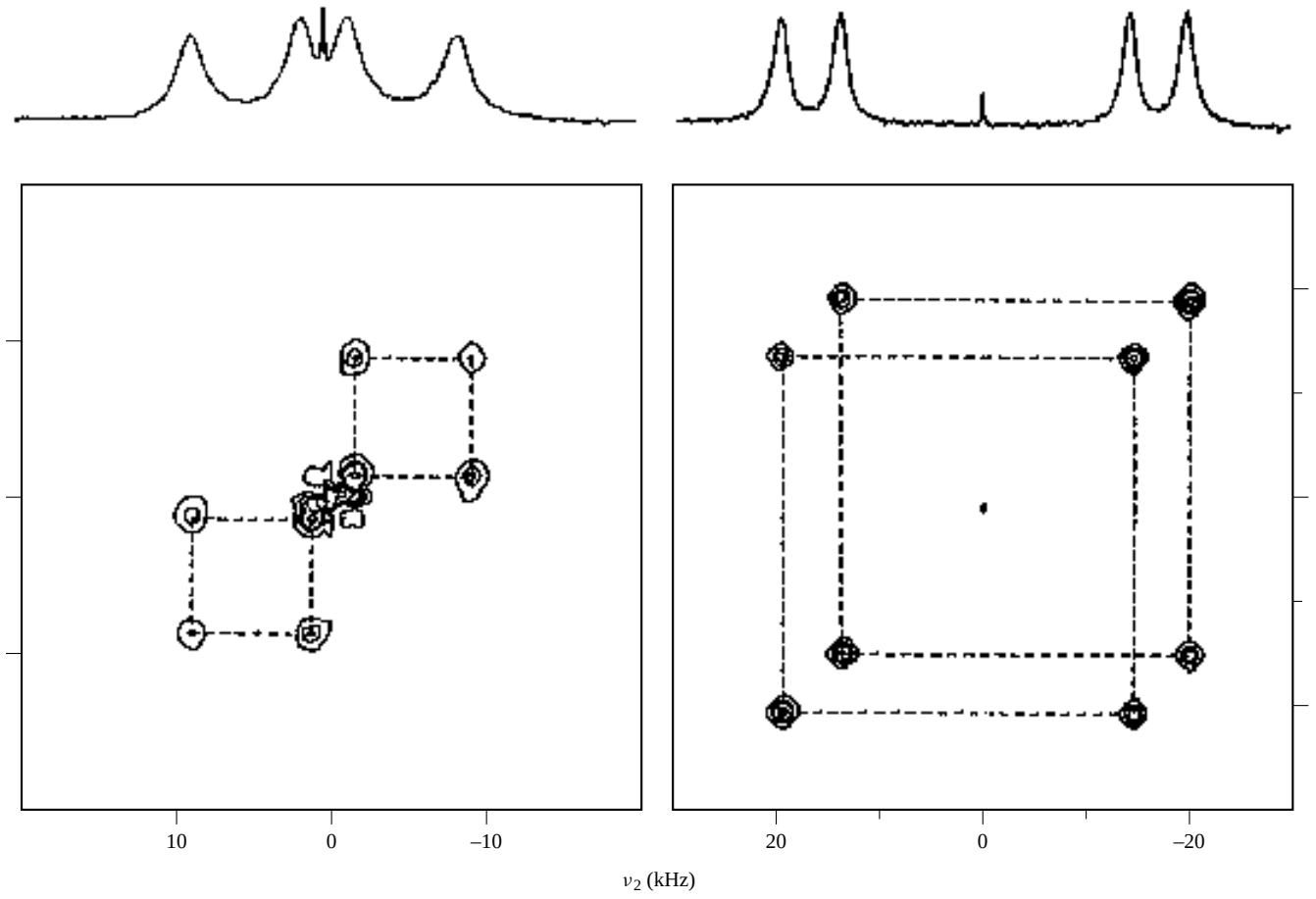

Figure 9 Two-dimensional deuterium exchange spectra on solutions of *p*-dioxan-d_8 dissolved in phase V (left) and 1565 TNC (right). The spectra were taken at $-43\,^{\circ}C$ with a mixing time τ_m = 1 ms. Note that the signs of the quadrupole interactions of the two exchanging deuterons is the same in phase V and the opposite in 1565 TNC

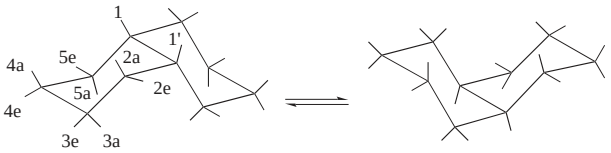

Scheme 7

7.2 Cope Rearrangement In Bullvalene: Higher Order Cross Peaks

Most examples of monomolecular exchange phenomena involve twofold degeneracy, i.e. interchange between two configurations. In the 2D exchange spectrum this is manifested by cross peaks linking separate pairs of lines. The bullvalene molecule provides an example of a high degree of degeneracy where a diagonal peak can be linked by the exchange to more than one other signal. Consequently at longer mixing times, when two or more exchange steps occur, higher order cross peaks between signals not directly connected by the exchange process may show up.

This is demonstrated[33] in the 2D exchange spectra of bullvalene depicted in Figure 12. For a mixing time of 2 ms only first-order cross peaks are observed [see diagram in Figure 8(a)], i.e. between peaks directly linked by a single Cope rearrangement. At 5 ms an additional second order cross peak appears $(1, \bar{2})$ which is linked by two successive rearrangement steps, while at 10 ms even a third-order cross peak (4, 2) may

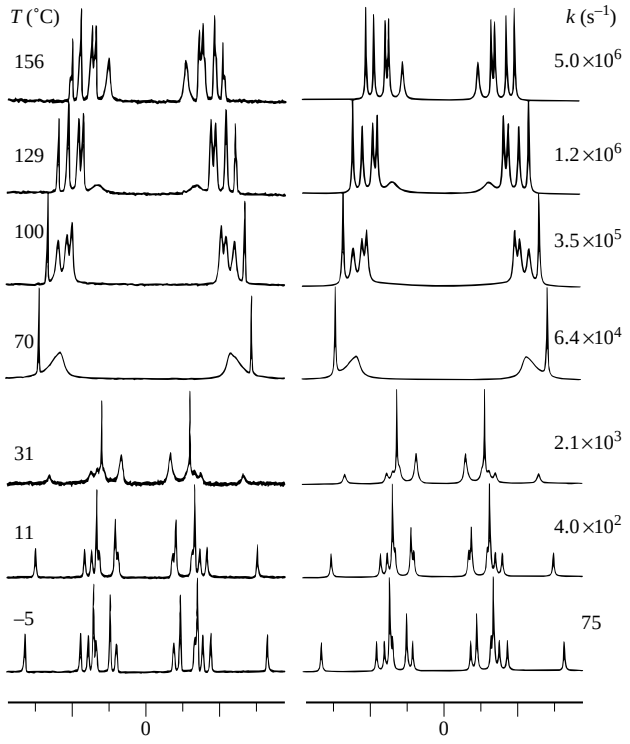

Figure 10 Experimental (left) and simulated (right) deuterium spectra of *cis*-decalin-d_{18} in liquid crystalline solvents. The bottom three traces correspond to the solvent ZLI 2452 while the upper four to S 1131 BCH. The separation between the frequency markers corresponds to 10 kHz for the bottom three traces and to 5 kHz for the top four

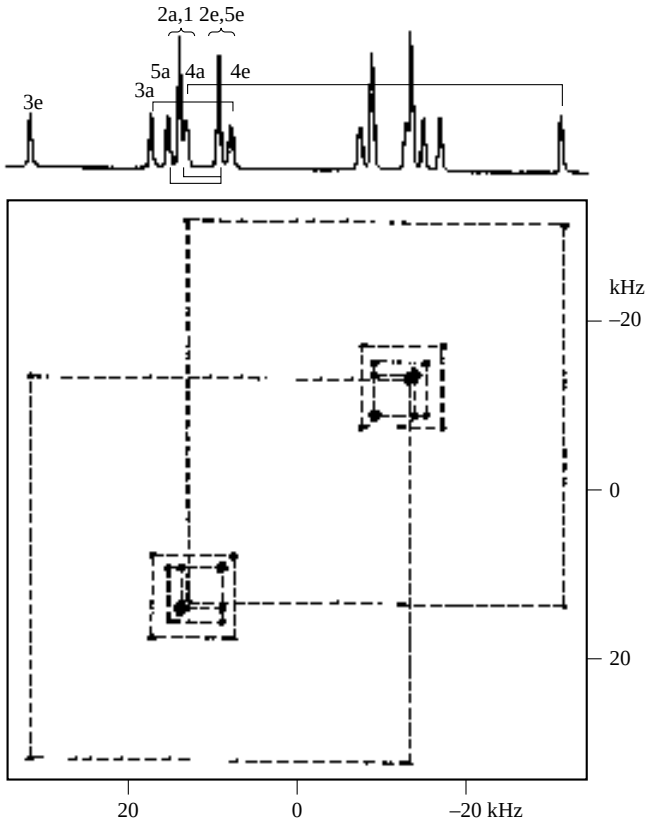

Figure 11 A two-dimensional deuterium-exchange spectrum of a solution of *cis*-decalin-d_{18} in ZLI 2452 at −5 °C. The dashed lines identify the interchanging peaks due to ring inversion. The assignment of the peaks based on the 2D spectra and other considerations are indicated on the 1D spectrum above

be identified. Expanding equation (15) in powers of τ_m gives

$$I_{ij} = P_i[\delta_{ij} + k\boldsymbol{K}\tau_m + \tfrac{1}{2}k^2\boldsymbol{K}^2\tau_m^2 + \tfrac{1}{6}k^3\boldsymbol{K}^3\tau^3 + \ldots]_{ij} \quad (16)$$

where for the case of bullvalene

$$\boldsymbol{K} = \begin{bmatrix} -1 & 0 & 2/3 & 1/3 \\ 0 & -1/3 & 1/3 & 0 \\ 2/3 & 1/3 & -1 & 0 \\ 1 & 0 & 0 & -1 \end{bmatrix} \quad (17)$$

Computation of $\boldsymbol{K}^2$ and $\boldsymbol{K}^3$ shows that indeed the element $\underline{1}, \bar{2}$ which is zero in $\boldsymbol{K}$ is nonzero in $\boldsymbol{K}^2$ while an entry at 4, 2 appears only at $\boldsymbol{K}^3$ and higher powers of K. In the short τ_m approximation, second- and third-order peaks should therefore increase as ${\tau_m}^2$ and ${\tau_m}^3$, while first-order cross peaks (and the diagonal peaks) should increase (decrease) linearly. This is indeed confirmed experimentally.

8 DYNAMIC ECHO TRAIN EXPERIMENTS

In some cases dynamic spectra can only be obtained in the fast exchange regime, e.g. when the rate is fast and the activation energy too low to reduce it effectively to the intermediate and slow-exchange limit by cooling. Kinetic data can then be obtained by transverse relaxation studies but the

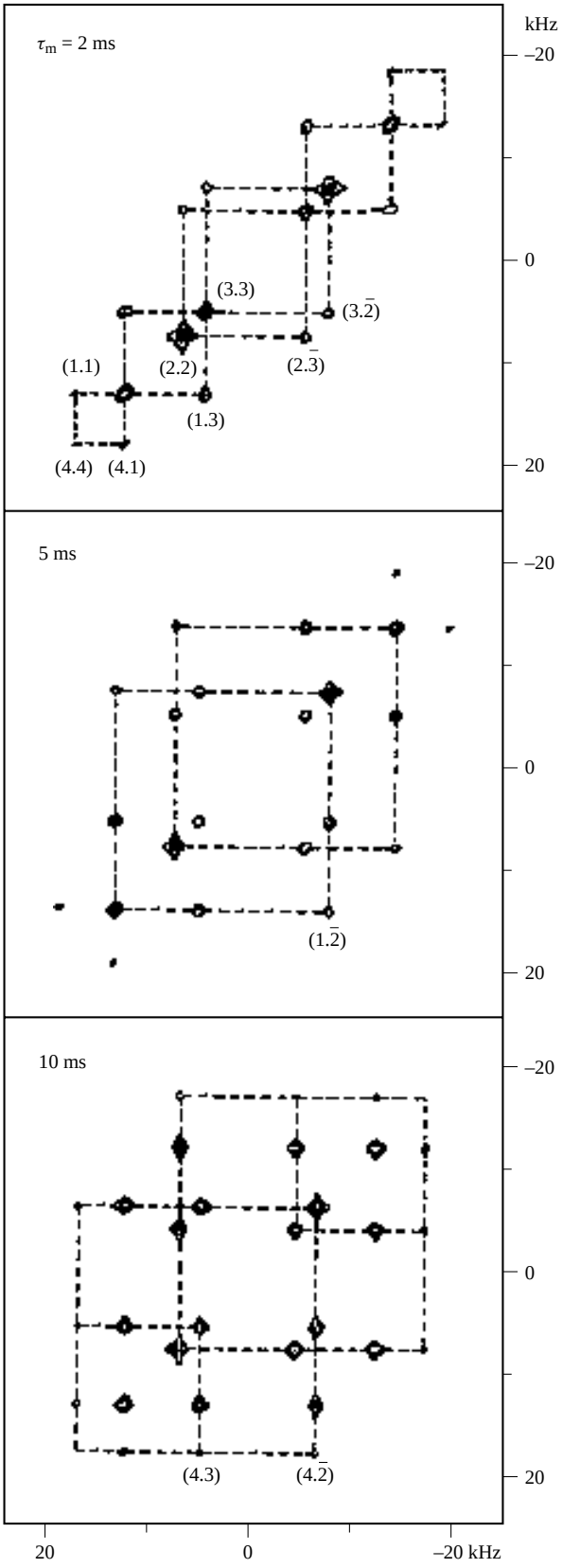

Figure 12 Two-dimensional deuterium exchange spectra of bullvalene-d_{10} dissolved in ZLI 2452 at 5 °C for several mixing times as indicated in the figure. The dashed lines connect first-, second-, and third-order cross peaks in respectively the upper, middle and bottom spectra

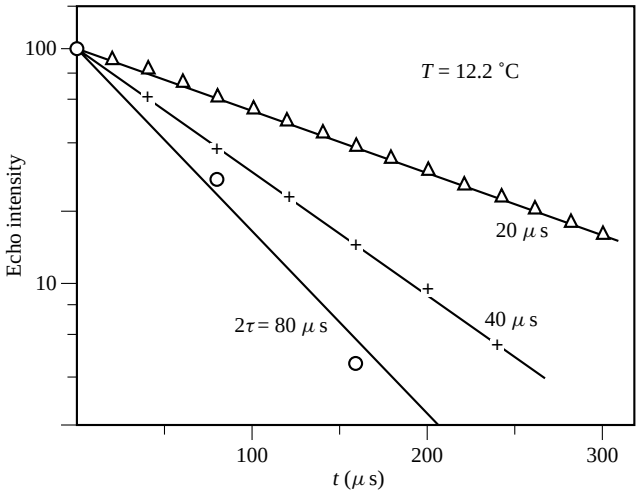

Figure 13 Semilog plots of the echo intensity versus time in quadrupole echo train experiments performed on a solution of C_6D_{12} in phase V (7 wt.%) at 12.2 °C for different pulse repetition rates as indicated

calculation requires knowledge of the magnetic interactions. When these are not known, ordinary relaxation data are not very useful. However when the transverse relaxation is measured by the Carr–Purcell sequence, or for spin $I = 1$ in liquid crystalline solvents by its quadrupole echo train analog, a determination of the rate constant can still be made if the time interval, τ, between the pulses is of the order of the mean lifetime between exchanges. In the fast-exchange regime, the transverse relaxation rate, as measured by the echo decay, is then also a function of the ratio of the exchange and pulse repetition rates.[62] For deuterons jumping between two sites of equal populations the contribution to the decay rate of the echoes in a quadrupole echo train experiment becomes[32,35]

$$\frac{1}{T_{2\epsilon}} = \frac{(\Delta\omega_Q)^2}{8k}\left[1 - \frac{\tanh(2k\tau)}{2k\tau}\right] \qquad (18)$$

where $\Delta\omega_Q = \omega_Q{}^A - \omega_Q{}^B$ is the difference between the quadrupole splittings of the nuclei at the two sites.

The method was demonstrated[32] for the case of ring inversion of C_6D_{12} in the nematic phase V between 0 °C and the clearing temperature. Experimental echo intensities at 12.2 °C for different time intervals between pulses are depicted in Figure 13 and the dependence of the decay rate, $1/T_{2\epsilon}$ on the pulse repetition rate, $1/\tau$, is plotted in Figure 14 for several temperatures. Analysis of these data in terms of equation (18) yields results for k that are in good agreement with those derived from the ordinary lineshape analysis.

The method was subsequently extended to the intermediate and slow-exchange regime[35] and although not very often used it has been successfully applied to study the self-diffusion in the plastic phase of succinonitrile.[63]

9 RELATED ARTICLES

Anisotropy of Shielding and Coupling in Liquid Crystalline Solutions; Deuteron Relaxation Rates in Liquid Crystalline Samples: Experimental Methods; Liouville Equation of

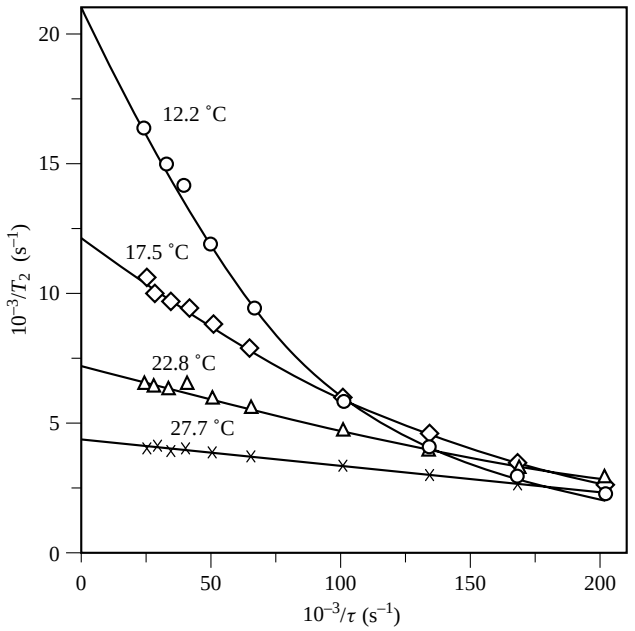

Figure 14 Plots of $1/T_{2\epsilon}$ as function of the pulse repetition rate obtained from the same solution as in Figure 13 for different temperatures. The lines are calculated using equation [18]

Motion; Liquid Crystalline Samples: Carbon-13 NMR; Liquid Crystalline Samples: Deuterium NMR; Liquid Crystalline Samples: Diffusion; Liquid Crystalline Samples: Relaxation Mechanisms; Liquid Crystalline Samples: Spectral Analysis; Liquid Crystalline Samples: Structure of Nonrigid Molecules; Liquid Crystals: General Considerations; Multiple Quantum Spectroscopy in Liquid Crystalline Solvents; Relaxation Effects of Chemical Exchange; Structure of Rigid Molecules Dissolved in Liquid Crystalline Solvents; Two-Dimensional NMR of Molecules Oriented in Liquid Crystalline Phases.

10 REFERENCES

1. H. S. Gutowsky, D. W. McCall, and C. P. Slichter, *J. Chem. Phys.*, 1953, **21**, 279.
2. W. G. Proctor and F. C. Yu, *Phys. Rev.*, 1950, **77**, 717; W. C. Dickenson, *Phys. Rev.*, 1950, **77**, 736.
3. E. L. Hahn and D. E. Maxwell, *Phys. Rev.*, 1952, **88**, 1070.
4. L. M. Jackman and F. A. Cotton (eds.), *Dynamic Nuclear Magnetic Resonance Spectroscopy*, Academic Press, New York, 1975.
5. C. S. Johnson, Jr., *Advances in Magnetic Resonance*, ed. J. S. Waugh, Academic Press, New York, 1965, Vol. 1, p. 33.
6. J. W. Emsley and J. C. Lindon, *NMR Spectroscopy Using Liquid Crystal Solvents*, Pergamon Press, Oxford, 1975.
7. Z. Luz, *Isr. J. Chem.*, 1983, **23**, 305.
8. H. M. McConnell, *J. Chem. Phys.*, 1958, **28**, 430.
9. S. Alexander, *J. Chem. Phys.*, 1962, **37**, 967.
10. S. Alexander, *J. Chem. Phys.*, 1962, **37**, 974.
11. J. I. Kaplan and G. Fraenkel, *NMR of Chemically Exchanging Systems*, Academic Press, New York, 1980.
12. G. Binsch, *J. Am. Chem. Soc.*, 1969, **91**, 1304.
13. J. Kaplan, *J. Chem. Phys.*, 1958, **28**, 278; ibid., 1958, **29**, 462.
14. A. Saupe, *Z. Naturforsch.*, 1964, **19a**, 161.
15. L. C. Snyder, *J. Chem. Phys.*, 1965, **43**, 4041.
16. Z. Luz and R. Naor, *Mol. Phys.*, 1982, **46**, 891.
17. D. Gamliel, Z. Luz, and S. Vega, *J. Chem. Phys.*, 1986, **85**, 2516.
18. P. L. Corio, *Structure of High Resolution NMR Spectra*, Academic Press, New York, 1966.
19. Z. Luz and S. Meiboom, *J. Chem. Phys.*, 1973, **59**, 275.
20. J. M. Anderson and A. C.-F. Lee, *J. Magn. Reson.*, 1970, **3**, 427.
21. Z. Luz and S. Meiboom, *J. Chem. Phys.*, 1973, **59**, 1077.
22. Z. Luz, R. Naor, and E. Meirovitch, *J. Chem. Phys.*, 1981, **74**, 6621.
23. R. Naor and Z. Luz, *J. Chem. Phys.*, 1982, **76**, 5662.
24. B. M. Fung, R. V. Sigh, and M. M. Alcock, *J. Am. Chem. Soc.*, 1984, **106**, 7301.
25. J. Afzal and B. M. Fung, *J. Chem. Phys.*, 1986, **84**, 6119.
26. D. Gamliel, Z. Luz, and S. Vega, *J. Chem. Phys.*, 1988, **88**, 25.
27. D. Gamliel, Z. Luz, A. Maliniak, R. Poupko, and A. J. Vega, *J. Chem. Phys.*, 1990, **93**, 5379.
28. R. Poupko and Z. Luz, *J. Chem. Phys.*, 1981, **75**, 1675.
29. M. E. Moseley, R. Poupko, and Z. Luz, *J. Magn. Reson.*, 1982, **48**, 354.
30. R. Poupko, H. Zimmermann, and Z. Luz, *J. Am. Chem. Soc.*, 1984, **106**, 5391.
31. C. Boeffel, Z. Luz, R. Poupko, and A. J. Vega, *Isr. J. Chem.*, 1988, **28**, 283.
32. A. J. Vega, R. Poupko, and Z. Luz, *J. Magn. Reson.*, 1989, **83**, 111.
33. C. Boeffel, Z. Luz, R. Poupko, and H. Zimmermann, *J. Magn. Reson.*, 1989, **85**, 329.
34. C. Boeffel, Z. Luz, R. Poupko, and H. Zimmermann, *J. Am. Chem. Soc.*, 1990, **112**, 7158.
35. K. Müller, R. Poupko, and Z. Luz, *J. Magn. Reson.*, 1990, **90**, 19.
36. E. Gelerinter, Z. Luz, R. Poupko, and H. Zimmermann, *J. Phys. Chem.*, 1990, **94**, 8845.
37. K. Müller, R. Poupko, and Z. Luz, *J. Magn. Reson.*, 1991, **93**, 291.
38. K. Müller, Z. Luz, R. Poupko, and H. Zimmermann, *Liq. Cryst.*, 1992, **11**, 547.
39. J. H. Davis, K. R. Jeffrey, M. Bloom, and M. I. Valic, *Chem. Phys. Lett.*, 1976, **42**, 390.
40. A. J. Vega and Z. Luz, *J. Chem. Phys.*, 1987, **86**, 1803.
41. B. Pedersen and J. Schaug, *Acta Chem. Scand.*, 1968, **22**, 1705.
42. M. Cocivera, *J. Chem. Phys.*, 1967, **47**, 3061.
43. F. A. L. Anet, A. J. R. Bourn, and Y. S. Lin, *J. Am. Chem. Soc.*, 1964, **86**, 3576.
44. F. A. L. Anet, *J. Am. Chem. Soc.*, 1962, **84**, 671.
45. R. C. Hewitt, S. Meiboom, and L. C. Snyder, *J. Chem. Phys.*, 1973, **58**, 5089.
46. L. C. Snyder and S. Meiboom, *J. Chem. Phys.*, 1973, **58**, 5096.
47. S. Meiboom, R. C. Hewitt, and Z. Luz, *J. Chem. Phys.*, 1977, **66**, 4041.
48. R. Poupko, Z. Luz, and H. Zimmermann, *J. Am. Chem. Soc.*, 1982, **104**, 5307.
49. W. S. Warren, D. P. Weitekamp, and A. Pines, *J. Chem. Phys.*, 1980, **73**, 2084.
50. G. Drobny, A. Pines, S. Sinton, D. P. Weitekamp, and D. Wemmer, *Faraday Symp. Chem. Soc.*, 1978, **13**, 49.
51. A. Wokaun and R. R. Ernst, *Chem. Phys. Lett.*, 1977, **52**, 407.
52. H. Zimmermann, *Liq. Cryst.*, 1989, **4**, 591.
53. Reference 4, Chap. 14.

54. J. F. M. Oth, K. Müllen, J.-M. Gilles, and G. Schröder, *Helv. Chim. Acta*, 1974, **57**, 1415.
55. R. Poupko, Z. Luz, A. J. Vega, and H. Zimmermann, *J. Chem. Phys.*, 1987, **86**, 5358.
56. C. S. Yannoni, *J. Am. Chem. Soc.*, 1970, **92**, 5237.
57. J. Jeener, B. H. Meier, P. Bachmann, and R. R. Ernst, *J. Chem. Phys.*, 1979, **71**, 4546.
58. C. Schmidt, S. Wefing, B. Blümich, and H. W. Spiess, *Chem. Phys. Lett.*, 1986, **130**, 84.
59. C. Schmidt, B. Blümich, and H. W. Spiess, *J. Magn. Reson.*, 1988, **79**, 269.
60. C. Schmidt, B. Blümich, S. Wefing, S. Kaufmann, and H. W. Spiess, *Ber. Bunsenges. Phys. Chem.*, 1987, **91**, 1141.
61. D. K. Dalling, D. M. Grant, and L. F. Johnson, *J. Am. Chem. Soc.*, 1971, **93**, 3678.
62. Z. Luz and S. Meiboom, *J. Chem. Phys.*, 1963, **39**, 366.
63. A. Golemme, S. Zamir, R. Poupko, H. Zimmermann, and Z. Luz, *Mol. Phys.*, 1994, **81**, 569.

Biographical Sketches

Raphy Poupko. *b* 1936. B.Sc., 1963, M.Sc., 1965, D.Sc. 1969, Technion—Israel Institute of Technology. Senior research fellow, Weizmann Institute of Science, 1970–present. Postdoctoral training at Southampton University (with G. Luckhurst), 1973–1974; UCSD, San-Diego, 1977–78; University of Paris, Orsay, 1987; M.P.I. für Medizinische Forschung, AG. Molekülkristalle, Heidelberg, 1993. Research activities: dynamic NMR, liquid crystals, solid state.

Zeev Luz. *b* 1932. M.Sc., 1957, Hebrew University, Jerusalem, Ph.D., 1961, The Weizmann Institute of Science, Rehovot. Postdoctoral training at Bell Telephone Laboratories (with Saul Meiboom), 1961–64. Since 1964, at The Weizmann Institute of Science. Successively scientist, senior scientist, associate, and full professor. Oxford University, 1966–67; Bell Laboratories, Murray Hill, 1971–72; University of California, Berkeley, 1976–77; DuPont, Wilmington, 1984–85; MPI f. Poly. Research, Mainz, 1990–91. Approx. 220 publications. Research specialties: dynamic NMR, liquid crystals, solid state.

Liquid Crystalline Samples: Carbon-13 NMR

Bing M. Fung

University of Oklahoma, Norman, OK, USA

1	Introduction	1
2	Anisotropic ^{13}C Chemical Shifts in Liquid Crystals	1
3	MAS and VAS	1
4	The Effect of the Local Dipolar Field	2
5	Study of ^{13}C–^{1}H Dipolar Couplings with VAS	4
6	Applications Combining Measurements of Chemical Shifts and Dipolar Couplings	5
7	Relaxation	6
8	Conclusions	6
9	Related Articles	6
10	References	7

1 INTRODUCTION

Because of the ubiquitous presence of the carbon atom in organic compounds, ^{13}C NMR has been widely used to study liquid, liquid crystalline, and solid samples. The application of ^{13}C NMR to study liquid crystals offers important information that complements that obtained from proton and deuterium NMR experiments. The most important parameters obtained in ^{13}C NMR studies of liquid crystals are anisotropic ^{13}C chemical shifts, ^{1}H–^{13}C dipolar coupling constants, and ^{13}C relaxation times. They will be reviewed in this article.

2 ANISOTROPIC ^{13}C CHEMICAL SHIFTS IN LIQUID CRYSTALS

For macroscopically oriented liquid crystal samples, the major advantage of ^{13}C NMR is the simplicity of the spectra. With broadband proton decoupling, the ^{13}C spectra of liquid crystals usually show resolvable peaks which can be assigned to individual carbon atoms, similar to the case of isotropic samples. However, because of the presence of ^{13}C chemical shift anisotropy, the chemical shifts of the observed signals (δ^{obs}) are often considerably different from those in the isotropic state (δ^{iso}):

$$\begin{aligned}\delta^{\text{obs}} &= \delta^{\text{iso}} + \delta^{\text{aniso}} \\ &= \delta^{\text{iso}} + \tfrac{2}{3}S_{zz}[\sigma_{zz} - \tfrac{1}{2}(\sigma_{xx} + \sigma_{yy})] \\ &\quad + \tfrac{1}{3}(S_{xx} - S_{yy})(\sigma_{xx} - \sigma_{yy}) \\ &\quad + \tfrac{2}{3}S_{xy}\sigma_{xy} + \tfrac{2}{3}S_{xz}\sigma_{xz} + \tfrac{2}{3}S_{yz}\sigma_{yz} \qquad (1)\end{aligned}$$

where the S_{ij} are components of the order parameter matrix, and the δ_{ij} are components of the chemical shift tensor, both being in the same axis system.

The first report on the ^{13}C NMR of liquid crystals was given by Yannoni and Whipple, who studied ^{13}C-enriched CH_3I dissolved in a liquid crystalline solvent.[1] They determined the order parameter S_{zz} of the molecule from its proton spectrum (the other components of the order parameter matrix are zero), and calculated the ^{13}C chemical shift anisotropy $\delta_{zz} - (\delta_{xx} + \delta_{yy})/2$ according to equation (1). Subsequently, similar studies of other small solute molecules have been made, using either enriched or naturally abundant compounds. Examples include acetonitrile,[2,3] hydrogen cyanide,[4] benzene,[5,6] acetylene,[7] chloroform,[3] methyl halides,[3] methanol,[3] a further study of CH_3I,[8] benzonitrile,[9] halobenzenes,[10] pyridine,[11] and diazenes.[11] Details of the determination of ^{13}C chemical shift anisotropy using liquid crystalline solvents are discussed by Jokisaari (see ***Anisotropy of Shielding and Coupling in Liquid Crystalline Solutions***), and will not be repeated here.

A much more general application of ^{13}C NMR is the investigation of bulk liquid crystals in their natural abundance. The first work of this type was reported by Pines and co-workers, who studied the ^{13}C chemical shifts of 4,4′-azoxyanisole,[12] 4-methoxybenzylidene-4′-*n*-butylaniline (MBBA)[13] and 4-alkoxyazoxybenzenes[14] as a function of temperature. Fyfe, Lyerla, and Yanonni also demonstrated the significant effect of orientational ordering on the ^{13}C chemical shifts of MBBA, 4,4′-di-*n*-hexyldiphenyldiacetylene, and 4-*n*-octyl-4′-cyanobiphenyl (8CB).[15] By using model compounds to estimate the components of the chemical shift tensors in the molecular axis system, Pines and co-workers calculated the order parameter S_{zz} of the liquid crystals from equation (1), omitting other terms.[12–14] The method of employing ^{13}C chemical shifts to estimate the order parameters of liquid crystals is rather simple and straightforward, and studies have been made on other systems. Examples include a eutectic mixture of MBBA and 4-ethoxybenzylidene-4′-*n*-butylaniline (EBBA),[16] several chiral smectic C (SmC*) compounds,[17,18] and 4-cyanobenzylidene-4′-*n*-octyloxyaniline.[19] However, because the ^{13}C chemical shift tensors are highly dependent upon the molecular structure and the nature of substituents, and their principal axis systems do not always coincide with the molecular axis system used to define the order parameters, the values obtained from model compounds may not be very accurate. Thus, the order parameters calculated are only approximations. On the other hand, calculations made by combining the ^{13}C chemical shift data with dipolar and quadrupolar splittings[20] give more reliable results.

If a liquid crystal sample is not macroscopically oriented, the ^{13}C spectrum would be a superposition of peaks, showing a ‘powder pattern’; if the sample is partially oriented, such as cholesteric or SmC* phases with the helical axes aligned along the magnetic field, the spectra exhibit ‘partial powder patterns’. In these cases, information obtained from the ^{13}C spectra is rather limited. An attempt has been made to calculate diffusion constants of two cholesteric mixtures from the lineshapes of their ^{13}C spectra,[21] but it depends on a number of assumptions and is less reliable than the pulsed field gradient method, which is discussed by Lindblom (see ***Liquid Crystalline Samples: Diffusion***).

3 MAS AND VAS

To obtain resolvable peaks in the ^{13}C spectra of liquid crystals, broadband proton decoupling must be used.[12–15] Because the proton spectra of liquid crystals have wide spectral windows, the decoupler power applied must be considerably larger than that for liquid samples. Excessive decoupler power, however, leads to rf heating, which is an extremely undesirable effect[22] because the orientational ordering of liquid crystals is very sensitive to temperature. To alleviate this problem, the MAS (magic angle spinning) and VAS (variable angle spinning) techniques can be used.

With MAS, the ^{13}C linewidths of liquid crystal samples can be greatly reduced even with rather nominal decoupler power.[23] The MAS method has been employed to investigate the conformation of liquid crystal molecules,[24–26] phase transition,[18,27] the rate process of dissolved solute molecules,[28] and lipid systems.[29–32] It should be noted that, because of the fast motions in liquid crystals, cross polarization is effective for static samples,[12–14] but much less so with MAS.[23] MAS also removes the anisotropic chemical shifts and dipolar couplings, which are often the most interesting aspects of the ^{13}C NMR of liquid crystals.

Like MAS, the VAS technique results in sharp ^{13}C peaks for bulk liquid crystals.[16,33] In addition, part of the anisotropic interactions are preserved, offering an advantage over MAS. The principles of the VAS technique are reviewed in a recent article[34] and discussed by Courtieu (see ***Spinning Liquid Crystalline Samples***). Here, the essential features pertinent to ^{13}C NMR are briefly outlined for the convenience of discussion.

Solid samples with VAS show residual 'powder patterns' in the proton-decoupled ^{13}C spectra, because the chemical shift anisotropy is not averaged to zero. On the other hand, even though residual chemical shift anisotropy is present in nematic liquid crystal samples with VAS, the ^{13}C spectra show sharp peaks due to macroscopic alignment of the director.[16,33] For a nematic liquid crystal being spun along an axis forming an angle η with respect to the magnetic field $\boldsymbol{B}_0$, the macroscopic orientation of the director is determined by a competition between the magnetic torque and the viscous torque. If the spinning rate is high enough, the nematic director of liquid crystals with a positive anisotropy of the magnetic susceptibility ($\Delta\chi > 0$) aligns along the spinning axis for $0^\circ < \eta < 54^\circ 44'$, and aligns perpendicular to the spinning axis for $54^\circ 44' < \eta < 90^\circ$. The alignment with respect to the spinning axis for liquid crystals with $\Delta\chi < 0$ is opposite to liquid crystals with $\Delta\chi > 0$.[16,33] Smectic liquid crystals can also be aligned similarly, provided that they are cooled down from the nematic phase while the sample is being spun rapidly.[23]

The macroscopic alignment of the director gives sharp peaks in the ^{13}C spectra, with scaled anisotropic chemical shifts expressed by

$$\delta^{\text{obs}} = \delta^{\text{iso}} + \frac{3\cos^2\eta - 1}{2}\delta^{\text{aniso}} \tag{2}$$

for parallel alignment, and by

$$\delta^{\text{obs}} = \delta^{\text{iso}} - \frac{3\cos^2\eta - 1}{4}\delta^{\text{aniso}} \tag{3}$$

for perpendicular alignment, where δ^{aniso} is the anisotropic part of the chemical shift, which is given in equation (1).

The spectra in Figure 1 illustrate the effect of VAS on the proton-decoupled ^{13}C NMR of 4-*n*-pentyl-4′-cyanobiphenyl (5CB). With the normal condition of $\eta = 0$, the ^{13}C peaks show large shifts [Figure 1(c)] from their isotropic values [Figure 1(a)], and the changes in the chemical shifts of different carbons are related to the corresponding chemical shift tensors. However, the peaks are not very sharp due to incomplete proton decoupling. On the other hand, the proton–proton dipolar interactions are reduced in a VAS experiment, so that much better decoupling can be achieved with a reasonable decoupler power (20–25 kHz). Thus, sharp ^{13}C peaks can be observed, with the anisotropic part of the chemical shifts scaled by the factor $(3\cos^2\eta - 1)/2$ [Figure 1(b)].

By taking advantage of the changes in ^{13}C chemical shifts with the alignment of the director, the dynamics of the realignment process of liquid crystals in a magnetic field can be studied with ^{13}C NMR. When the spinning sample is suddenly stopped, the action of the magnetic torque causes the director to realign from being parallel to the spinning axis to being parallel to the magnetic field. Consequently, the ^{13}C spectrum gradually changes from that in Figure 1(b) to Figure 1(c). The chemical shift is related to the angle β formed between the director and the magnetic field by an equation similar to equation (2) for the angle η. The time dependence of β is governed by the relationship[35,36]

$$\beta = \tan^{-1}[(\tan\eta)\,e^{-t/\tau}] \tag{4}$$

where τ is the time constant for the reorientation of the nematic director in the magnetic field. Thus, by using a least-squares fitting of the chemical shift data as a function of time after the rotor stops, the value of τ can be determined.[37] Actually, equation (4) is strictly applicable to rigid rods only. However, liquid crystal molecules are flexible and the order parameters of individual molecular segments differ along the long axis. Because the hydrodynamic behavior of liquid crystals is related to their order parameters, the reorientation times for different parts of the molecule need not be the same. For 5CB at room temperature, it was found that $\tau = 8.7$ ms for the aromatic rings and 11 ms for the methyl group.[37] The smectic A compound 8CB is much more viscous, and the corresponding τ values are about 300 times longer, being 2.4 and 3.2 s, respectively.[37]

In the application of VAS to study liquid crystals, a sufficiently high spinning rate must be used to induce macroscopic alignment with respect to the spinning axis (~1 kHz at $B_0 = 7$ T for most liquid crystals), and the critical spinning rate is proportional to the square of the magnetic field.[33,34] However, the inertial torque tends to oppose the viscous torque and the magnetic torque, and would destroy the alignment at very high spinning rates.[34] Therefore, one must be careful to balance the different torques to obtain the desired macroscopic orientation of the liquid crystalline samples.

4 THE EFFECT OF THE LOCAL DIPOLAR FIELD

In Section 2, it was pointed out that in most cases it is difficult to evaluate accurately the order parameters from ^{13}C chemical shifts because the use of equation (1) requires a

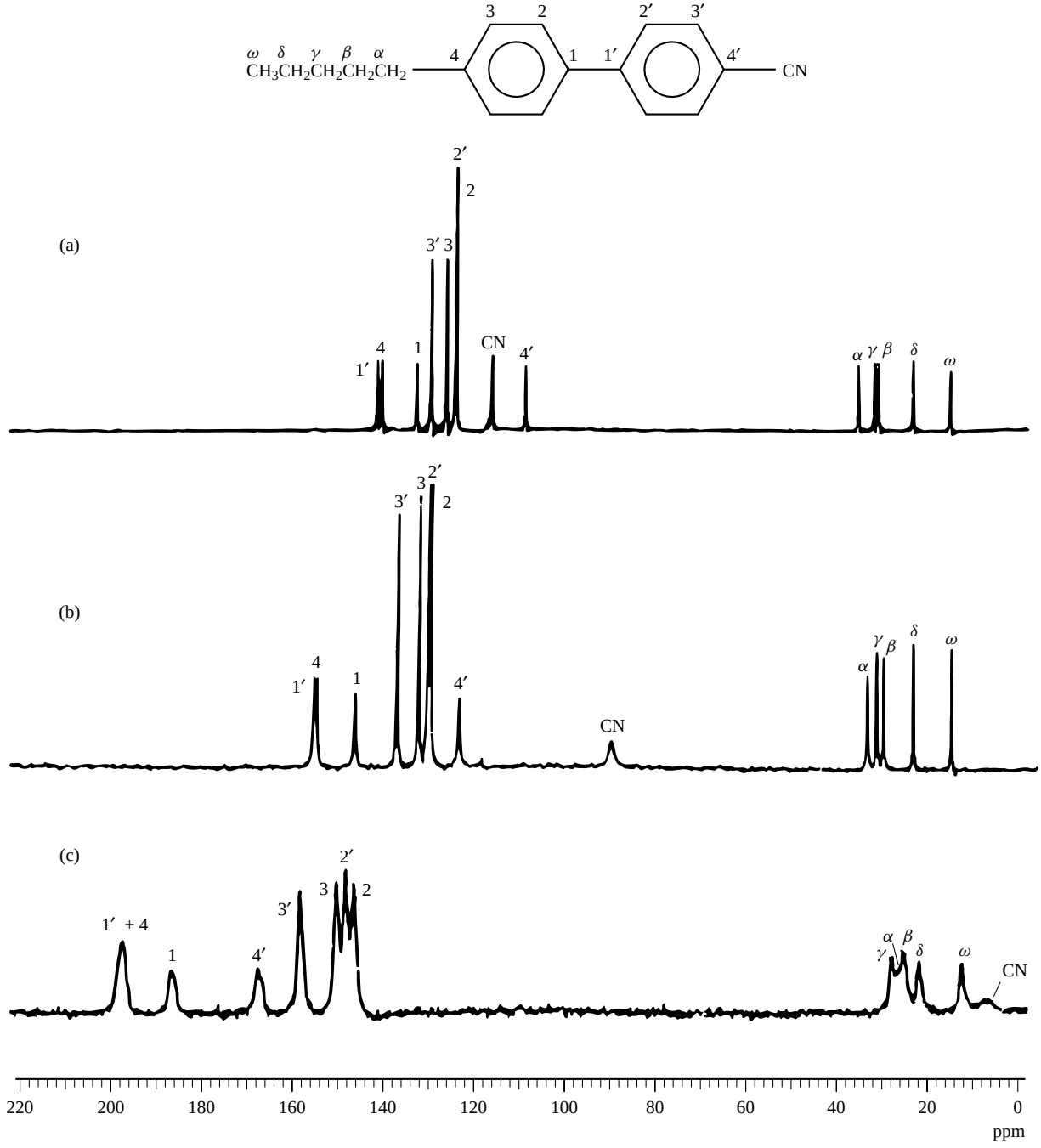

Figure 1 Proton-decoupled ^{13}C NMR spectra of 5CB at 75.43 MHz. (a) Isotropic spectrum at 37°C. (b) Anisotropic spectrum at 26°C, with a spinning angle of $\eta = 44.6°$ and a spinning rate of 1.1 kHz. (c) Anisotropic spectrum at 26°C, nonspinning

knowledge of the components of the chemical shift tensors in the molecular frame defining the ordering matrix. On the other hand, dipolar coupling constants can be used to calculate the order parameters of liquid crystals without relying on parameters estimated from model compounds. With broadband proton decoupling, dipolar coupling constants (D) between ^{13}C and ^{15}N,[38] between ^{13}C and ^{19}F,[39] and between two ^{13}C nuclei[40] can often be determined directly from the ^{13}C spectra, because the pairwise splittings are expressed by

$$\Delta\nu = 2D + J \tag{5}$$

where J is the scalar coupling constant, the anisotropy of which is usually small compared with the value of D and can be neglected. On the other hand, except for perdeuterated compounds,[41] it is less straightforward to determine $^{13}C-^{1}H$ dipolar coupling constants from the ^{13}C spectra.

To discuss this, let us first consider the example of benzene dissolved in a liquid crystalline solvent. With broadband ^{1}H decoupling, there is only a single sharp ^{13}C peak for benzene. On the other hand, the proton-coupled ^{13}C spectrum is complicated [Figure 2(a)] because the ^{13}C nucleus is coupled to six protons, which are in turn strongly coupled to each other. Although the spectrum can be analyzed exactly by

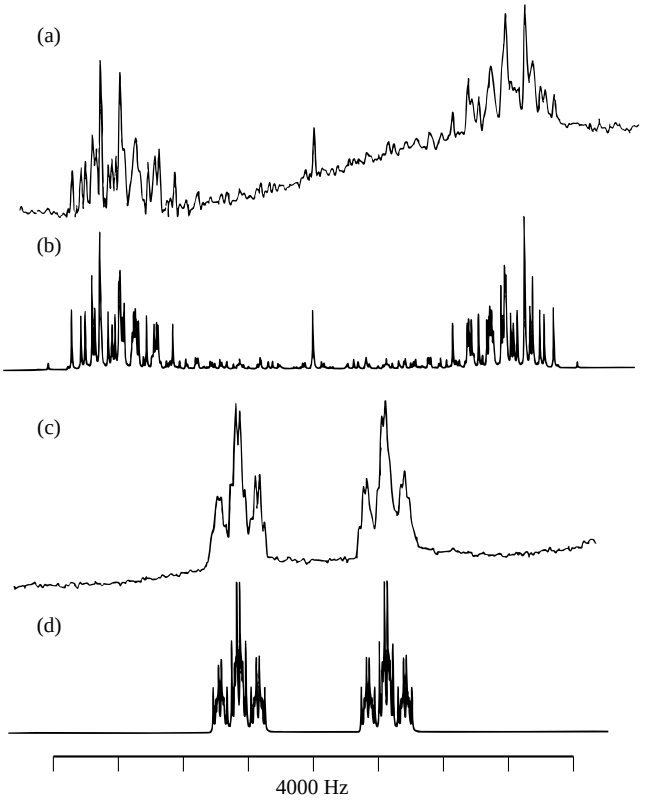

Figure 2 Carbon-13 NMR spectra of benzene dissolved in the liquid crystalline solvent ZLI 1167 at 75.43 MHz and 25°C. (a) Experimental spectrum without decoupling; the baseline is due to the solvent. (b) Calculated spectrum with complete $^1H-^1H$ and $^1H-^{13}C$ coupling. (c) Experimental spectrum with BLEW-48 decoupling and a decoupler power of 14 kHz. (d) Spectrum calculated by scaling the $^1H-^{13}C$ coupling constants obtained from case (b) and setting the $^1H-^1H$ dipolar coupling constants to zero

computer simulation [Figure 2(b)] due to the high symmetry of benzene, the spectral analyses for more complex molecules are practically intractable. This problem can be overcome by applying a special decoupling sequence to remove the $^1H-^1H$ dipolar coupling, so that the ^{13}C spectrum becomes first order in terms of $^{13}C-^1H$ coupling [Figure 2(c) and (d)].[42] Among several well known dipolar decoupling sequences introduced for the study of solids, it was found that the so-called 'BLEW-48' sequence[43] is the most effective one for liquid crystal systems.[44] The first-order splittings resulting from using a dipolar decoupling sequence is given by[45]

$$\Delta\nu = f[(3\cos^2\eta - 1)D + J] \qquad (6)$$

where f is a scaling factor determined by the $^1H-^1H$ dipolar decoupling sequence. For BLEW-48, the theoretical value is $f = 0.424$;[43] experimentally, the scaling factor varies slightly with the decoupler offset, and the best average value is $f = 0.420$.[42] Although the sign of $\Delta\nu$ cannot be determined from the spectra, several different possibilities can be distinguished by a consideration of the molecular geometry and the macroscopic orientation of the liquid crystal in the magnetic field. Thus, for the spectrum shown in Figure 2(c), the values of $\Delta\nu$ for the directly bonded and the *ortho* C–H pairs can be measured directly from the first-order splittings without computer simulation, and the corresponding values of D can be easily calculated by the use of equation (6). These values are the same as those obtained from a computer simulation of the spectrum [Figure 2(d)] within experimental error. This method is particularly useful for compounds with more complex structures, for which the completely coupled ^{13}C spectra are practically intractable by computer simulation.

For the ^{13}C spectra of bulk liquid crystals, there are many peaks in the spectra, and the $^{13}C-^1H$ splittings overlap with each other. To resolve the splitting pattern of each ^{13}C peak unambiguously, a two-dimensional (2D) method called separated local field (SLF) spectroscopy[46–49] can be applied. Like the MAS technique, the SLF method was first developed for solid state NMR. In this 2D method, the spin system is allowed to evolve with $^{13}C-^1H$ coupling and $^1H-^1H$ dipolar decoupling in the evolution period, so that information on dipolar coupling constants can be obtained from the ω_1 dimension. In the acquisition period, complete proton decoupling is applied, so that resolved peaks for individual carbon atoms can be obtained from the ω_2 dimension. Thus, 'slices' of the 2D spectra give clear splitting patterns for each chemically distinct ^{13}C peak, in the same way as the 'heteronuclear 2D J-resolved' method (see ***Two-Dimensional J-Resolved Spectroscopy***).

The first application of the SLF method to liquid crystals was the study of EBBA with the director aligned along the magnetic field.[38] However, because of the presence of large $^1H-^1H$ dipolar couplings which were not completely removed, the ^{13}C peaks in the ω_2 dimension were rather broad, and the splittings in the ω_1 dimension did not yield accurate $^{13}C-^1H$ dipolar coupling constants. Later on, the application of the SLF method to study a static sample of an SmC* liquid crystal was also reported,[50] and a similar problem was encountered. In principle, increasing the decoupling power would alleviate this problem. However, it would create excessive rf heating and a large temperature gradient, which is not acceptable for liquid crystals.[22]

5 STUDY OF $^{13}C-^1H$ DIPOLAR COUPLINGS WITH VAS

Because the use of VAS can reduce dipolar couplings by a factor of $(3\cos^2\eta - 1)/2$ [equation (2)] or $-(3\cos^2\eta - 1)/4$ [equation (3)], a combination of VAS with the SLF method solves the problem of incomplete proton dipolar decoupling. For example, $(3\cos^2\eta - 1)/2 = 0.2$ for $\eta = 46.91°$, and a nominal decoupler power (20–25 kHz) is sufficient to obtain good $^1H-^1H$ dipolar decoupling with the use of the BLEW-48 sequence. It was shown that, for the application of the SLF method to EBBA, the use of VAS[51] yielded much better first-order spectra in the ω_1 dimension than the use of a static sample.[38]

As an example of the ^{13}C spectra obtained from the VAS/SLF technique, the spectra of 4-*n*-heptyl-4′-cyanobiphenyl (7CB) at 75 MHz and 31°C are shown in Figure 3.[52] It can be seen that all seven peaks in the aliphatic chain and all nine peaks in the mesogenic core are resolved in the ω_2 dimension. The spectra in the ω_1 dimension show first-order $^{13}C-^1H$ splittings. The CH_3 group exhibits a clear quartet, and each of the CH_2 groups exhibits a triplet, with discernible

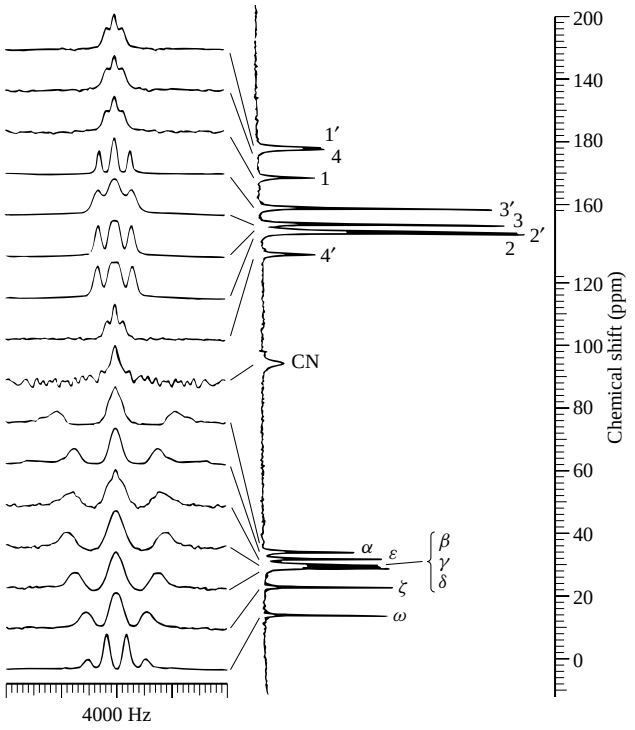

Figure 3 2D ^{13}C NMR spectra of 7CB at 75.43 MHz and 31°C obtained by the SLF/VAS method. The spectra were obtained with variable angle spinning at $\eta = 45.6°$. The spectra in the ω_1 dimension are shown on the left, and the first spectrum in the ω_2 dimension is shown on the right. (Reproduced by permission of the Royal Society of Chemistry from Foster and Fung[52])

long range splittings for the α- and β-carbons. Each peak for the quaternary carbons (1, 4, 1′, and 4′) in the phenyl rings is split into a triplet by the *ortho* protons, and each peak for the protonated carbons (2, 3, 2′, and 3′) is split into a doublet of doublets by the directly bonded and the *ortho* protons, respectively. Some of the peaks overlap slightly, but the values of $\Delta\nu$ can be readily obtained by least-squares analysis of the spectra. Then, the ^{13}C–^{1}H dipolar coupling constants can be evaluated by the use of equation (6), and the order parameters for the corresponding molecular segments can be calculated. The procedure for the calculation is briefly summarized in the following discussion.

In the nematic phase, each phenyl ring has an effective D_2 symmetry because it undergoes rapid jumps between four equilibrium positions. Therefore, two order parameters, S_{zz} and $S_{xx} - S_{yy}$, are sufficient to describe the orientational ordering of each ring. These order parameters are related to the dipolar coupling constant of each C–H pair in the ring by

$$D_{ij} = -\frac{\gamma_i \gamma_j h}{8\pi^2 r_{ij}^3}[(3\cos^2\theta_{ijz} - 1)S_{zz} + (\cos^2\theta_{ijx} - \cos^2\theta_{ijy}) \times (S_{xx} - S_{yy})] \quad (7)$$

where r_{ij} is the internuclear distance and $\theta_{ij\alpha}$ is the angle between r_{ij} and the molecular axis α. The twofold axis of the phenyl ring is taken as the z axis, and the axis perpendicular to the plane of the phenyl ring is taken as the y axis. Assuming that $r_{CC} = 0.140$ nm and $r_{CH} = 0.108$ nm, the order parameters and the bond angles can be calculated from least-squares fitting of a set of D values to equation (7). This procedure has been used to determine the order parameters of the phenyl rings in many liquid crystals.[45,52–67]

The situation is more complicated for phenyl rings with lateral substituents or compounds containing cyclohexyl rings, and more order parameters are needed to describe the orientational ordering of the rings. The cyclohexyl ring in a liquid crystal has a C_s symmetry, and an additional order parameter S_{xy} is needed to describe the orientational ordering of the ring. Unfortunately, the ^{13}C peaks in the ω_1 dimension are quite broad due to unresolved long range couplings.[55,56,66] Therefore, only approximate values of S_{zz} and $S_{xx} - S_{yy}$ were obtained by assuming $S_{xy} \approx 0$. A laterally substituted phenyl ring or a substituted cyclohexyl ring has no symmetry, and all five order parameters are nonzero.

The aliphatic chain has a large number of segmental motions, and it is difficult to define the order parameters for the whole chain. A simplified treatment can be made to define a C–H bond order parameter for each aliphatic segment, considering the C–H bond as having an approximate axial symmetry. Then, the order parameter for the C–H bond is related to the corresponding C–H dipolar coupling constant by

$$D = -\frac{\gamma_C \gamma_H h}{4\pi^2 r_{CH}^3} S_{CH} \quad (8)$$

in which the value of r_{CH} is generally assumed to be 0.110 nm.

The results for studying the orientational ordering of 5CB using the VAS/SLF technique have been compared with those obtained from deuterium NMR.[45] A good agreement was obtained, establishing the validity of the VAS/SLF method. This method has been further applied to investigate the orientational ordering of a large number of liquid crystals, including 4-*n*-alkyl-4′-cyanobiphenyls (*k*CBs, where *k* is the number of carbon atoms in the alkyl chain),[45,53,59,60] 4-*n*-alkoxy-4′-cyanobiphenyls (*k*OCBs),[54] phenylcyclohexanes,[52,55,56] bicyclohexylnitriles,[66] ferroelectric liquid crystals of the α-chloroesters of 4-alkoxy-4′-hydroxybiphenyls[57,61] and of 4′-hydroxyphenyl-4-alkoxythiobenzoates,[58] 4′-cyanophenyl-4-alkylcarboxylates,[62] 4-*n*-alkoxybenzylidene-4′-*n*-alkylanilines (*n*O.*m*s),[63] nematic compounds with four-unit links between two phenyl rings,[64,65] and liquid crystals with lateral substituents.[67]

6 APPLICATIONS COMBINING MEASUREMENTS OF CHEMICAL SHIFTS AND DIPOLAR COUPLINGS

It was mentioned in the Introduction that the use of equation (1) to determine the order parameters from anisotropic ^{13}C chemical shifts requires the knowledge of the components of the chemical shifts tensors in the axis system defining the ordering matrix. To avoid this difficulty but still take advantage of the simplicity and accuracy in the chemical shift measurement, an empirical approach has been suggested.[60] The method involves a determination of the order parameters of a liquid crystal at several temperatures by using the VAS/SLF technique as described in the previous section, and

a measurement of the ^{13}C chemical shifts for the same sample with slow spinning at $\eta = 0^\circ$. The order parameter S_{zz} for the phenyl rings or S_{CH} for the aliphatic chains is plotted against the corresponding ^{13}C chemical shifts, and it has been found that they are linearly related:

$$\delta^{obs} - \delta^{iso} = aS + b \quad (9)$$

where a and b are constants.[60] Although equation (9) is a result of equation (1), it is only an empirical relationship for the following reasons. A strict theoretical correspondence between the two equations implies that $a = 2[\sigma_{zz} - (\sigma_{xx} + \sigma_{yy})/2]/3$ and that the other order parameters are independent of temperature. The first condition requires the major axis of the chemical shift tensor to coincide with the z axis of the ring or the C–H axis in the chain. Although this is approximately true for the carbon atoms lying on the z axis of the phenyl rings, it is not necessarily so for other carbon atoms. Usually the second condition is approximately fulfilled because the values of $S_{xx} - S_{yy}$ are very small and vary randomly with temperature within experimental error, and S_{xy}, S_{xz}, and S_{yz} are zero for phenyl rings without lateral substituents. These approximations make equation (9) a semiempirical relationship; nevertheless, it has been found to work surprisingly well for many types of compounds.[60,62–65,67]

After the constants a and b in equation (9) have been determined from the experimental VAS/SLF data at several temperatures, the order parameter S at other temperatures can be calculated from the ^{13}C chemical shifts without the use of approximate values of the shift tensors estimated from model compounds. This method has several advantages. First, the chemical shifts can be obtained from 1D experiments, which require much less spectrometer and processing time than the 2D VAS/SLF method. Second, the chemical shifts can be determined more accurately than the dipolar coupling constants, and their systematic changes with temperature are less subjected to random experimental uncertainties. Third, investigators who do not have the VAS/SLF facility can obtain order parameters directly from ^{13}C chemical shifts using published values of a and b for other homologous compounds. Thus, although the order parameters determined from ^{13}C chemical shifts via the use of equation (9) is an indirect method, the study of their temperature dependence is greatly facilitated. Problems such as the effect of various solutes on the orientational ordering of liquid crystal solvents,[54] the order of phase transitions,[63] and the temperature dependence of the position of the major axis of the mesogenic core[64,65] can be studied more conveniently by this method.

7 RELAXATION

Because of the presence of orientational ordering, the translational and rotational motions of liquid crystals are highly anisotropic. As a result, their relaxation behavior is very different from that of isotropic liquids. Details of relaxation in liquid crystals are discussed in the articles by Hoatson (see ***Deuteron Relaxation Rates in Liquid Crystalline Samples: Experimental Methods***) and Nordio (see ***Liquid Crystalline Samples: Relaxation Mechanisms***). Examples of the study of ^{13}C relaxation are summarized below.

The earliest ^{13}C spin–lattice relaxation time (T_1) measurements reported were for 4,4′-azoxyanisole[68,69] and MBBA.[70] More recently, a comprehensive investigation of ^{13}C T_1 and nuclear Overhauser enhancement (NOE) of 4-*n*-alkyl-4′-cyanobiphenyls (*k*CBs; k = 5, 6, 7, and 8) as functions of temperature and at different resonance frequencies has been made by Lewis, Tomchuk, and co-workers.[71–73] They analyzed the results by considering angular fluctuations as well as director fluctuations, and concluded that at high fields the contribution of ^{13}C chemical shift anisotropy to relaxation is important, but cautioned that the quantitative analysis is not straightforward.

A better understanding of the dynamic behavior of liquid crystals can be obtained by investigating the relaxation of several kinds of nuclei in the same molecule. A small probe molecule, CH_3CN with ^{13}C enrichment, was used for such study by two groups of investigators.[74–78] Grant and co-workers measured the relaxation of ^1H and ^{13}C with non-, semi-, and completely selective excitation of individual spectral lines.[76,77] Later on, Luyten et al. carried out similar measurements, plus ^{14}N relaxation, at six different field strengths, and calculated the contributions of rotational anisotropy, random local field, and director fluctuation to the relaxation process.[78]

Multinuclei relaxation measurements including ^{13}C and other nuclei have also been made for lyotropic liquid crystal systems,[79] phospholipids,[29–31] and lead carboxylates.[80] The ^{13}C relaxation of an SmC* compound has been reported recently.[18]

8 CONCLUSIONS

In applying ^{13}C NMR to study liquid crystals, the major parameters of interest are anisotropic chemical shifts, $^{13}C–^1H$ dipolar coupling constants, and ^{13}C relaxation times. The advantages of ^{13}C NMR are its high resolution with regard to the chemical structure of the liquid crystal molecules, and the use of naturally abundant compounds without the need for special isotope substitution. However, macroscopic sample orientation is required to obtain resolvable ^{13}C peaks unless MAS is used. Therefore, ^{13}C NMR is not very informative for the study of unaligned samples generally found for higher smectic phases, discotic phases, and liquid crystal polymers. Furthermore, ^{13}C relaxation measurements do not offer as much information on relaxation mechanisms as ^2H relaxation measurements. Therefore, ^{13}C NMR and ^2H NMR complement each other, and both offer more detailed information than ^1H NMR in the study of liquid crystals.

9 RELATED ARTICLES

Anisotropy of Shielding and Coupling in Liquid Crystalline Solutions; Carbon and Nitrogen Chemical Shifts of Solid State Enzymes; Carbon-13 Relaxation Measurements: Organic Chemistry Applications; Complex Radiofrequency Pulses; Deuteron Relaxation Rates in Liquid Crystalline Samples: Experimental Methods; Liquid Crystalline Samples: Deuterium NMR; Liquid Crystalline Samples: Relaxation Mechanisms; Liquid Crystals: General Considerations; Membranes: Carbon-13 NMR; Shielding Tensor Calculations; Spinning Liquid Crystalline Samples.

10 REFERENCES

1. C. S. Yannoni and E. B. Whipple, *J. Chem. Phys.*, 1967, **47**, 2508.
2. I. Morishima, A. Mizuno, and T. Yonezawa, *Chem. Phys. Lett.*, 1970, **7**, 633.
3. B. R. Appleman and B. P. Dailey, *Adv. Magn. Reson.*, 1974, **7**, 231.
4. F. Millett and B. P. Dailey, *J. Chem. Phys.*, 1971, **54**, 5434.
5. G. Englert, *Z. Naturforsch. A*, 1972, **27**, 715.
6. B. M. Fung and P. Parhami, *J. Magn. Reson.*, 1985, **63**, 168.
7. S. Mohanty, *Chem. Phys. Lett.*, 1973, **18**, 581.
8. T. Väänänen, J. Jokisaari, and M. Seläntaus, *J. Magn. Reson.*, 1987, **72**, 414.
9. B. M. Fung, *J. Am. Chem. Soc.*, 1983, **105**, 5713.
10. B. M. Fung and C. F. Kong, *J. Am. Chem. Soc.*, 1984, **106**, 6193.
11. P. Parhami and B. M. Fung, *J. Am. Chem. Soc.*, 1985, **107**, 7304.
12. A. Pines and J. J. Chang, *J. Am. Chem. Soc.*, 1974, **96**, 5590.
13. A. Pines and J. J. Chang, *Phys. Rev. A*, 1974, **10**, 946.
14. A. Pines, D. J. Ruben, and S. Allison, *Phys. Rev. Lett.*, 1974, **33**, 1002.
15. C. A. Fyfe, J. R. Lyerla, and C. S. Yannoni, *J. Magn. Reson.*, 1978, **31**, 315.
16. R. Teeäär, M. Alla, and E. Lippmaa, *Org. Magn. Reson.*, 1982, **19**, 134.
17. M. Luzar, V. Rutar, J. Seliger, and R. Blinc, *Ferroelectrics*, 1984, **58**, 115.
18. A. Yoshizawa, A. Yokoyama, H. Kikuzaki, and T. Hirai, *Liq. Cryst.*, 1993, **14**, 513.
19. R. J. Wittebort, R. Subramanian, N. P. Kulshreshtha, and D. B. DuPré, *J. Chem. Phys.*, 1985, **83**, 2457.
20. F. Separovic, R. Pax, and B. Cornell, *Mol. Phys.*, 1993, **78**, 357.
21. R. Stannarius and H. Schmiedel, *J. Magn. Reson.*, 1985, **65**, 1.
22. B. M. Fung, *J. Magn. Reson.*, 1990, **86**, 160.
23. B. M. Fung and M. Gangoda, *J. Chem. Phys.*, 1985, **83**, 3285.
24. K. Hayamizu, M. Yanagisawa, and O. Yamamoto, *Chem. Phys. Lett.*, 1986, **127**, 566.
25. T. Kato and T. Uryu, *Mol. Cryst. Liq. Cryst. Lett.*, 1987, **5**, 17.
26. K. Hayamizu, M. Yanagisawa, and O. Yamamoto, *Liq. Cryst.*, 1989, **4**, 273.
27. M. Bose and S. Sanyal, *Mol. Cryst. Liq. Cryst.*, 1990, **185**, 115.
28. J. Afzal and B. M. Fung, *J. Chem. Phys.*, 1986, **84**, 6119.
29. J. Forbes, J. Bowers, X. Shan, L. Moran, E. Oldfield, and M. A. Moscarello, *J. Chem. Soc., Faraday Trans. 1*, 1988, **84**, 3821.
30. E. Oldfield, F. Adebodun, J. Chung, B. Montez, K. D. Park, H. B. Le, and B. Phillips, *Biochemistry*, 1991, **30**, 11025.
31. F. Adebodun, J. Chung, B. Montez, E. Oldfield, and X. Shan, *Biochemistry*, 1992, **31**, 4502.
32. K. L. Li, C. A. Tihal, M. Guyo, and R. E. Stark, *Biochemistry*, 1993, **32**, 9926.
33. J. Courtieu, D. W. Alderman, D. M. Grant, and J. P. Bayle, *J. Chem. Phys.*, 1982, **77**, 723.
34. J. Courtieu, J. P. Bayle, and B. M. Fung, *Prog. Nucl. Magn. Reson. Spectrosc.*, 1994, **26**, 141.
35. R. A. Wise, A. Olah, and J. W. Doane, *J. Phys. (Paris) Colloq.*, **1975**, 117.
36. R. Y. Dong, *Mol. Cryst. Liq. Cryst.*, 1981, **72**, 59.
37. M. L. Magnuson and B. M. Fung, *J. Chem. Phys.*, 1994, **100**, 1470.
38. A. Höhener, L. Muller, and R. R. Ernst, *Mol. Phys.*, 1979, **38**, 909.
39. M. L. Magunson and B. M. Fung, *Liq. Cryst.*, 1994, **16**, 857.
40. C. R. Sanders II and J. H. Prestegard, *J. Am. Chem. Soc.*, 1991, **113**, 1987; D. Sandström, K. T. Summanen, and M. H. Levitt, *J. Am. Chem. Soc.*, 1994, **116**, 9357.
41. E. J. Delikatny and E. E. Burnell, *Mol. Phys.*, 1989, **67**, 757.
42. B. M. Fung, *J. Magn. Reson.*, 1986, **66**, 525.
43. D. P. Burum, N. Linder, and R. R. Ernst, *J. Magn. Reson.*, 1981, **44**, 173.
44. B. M. Fung, *J. Magn. Reson.*, 1987, **72**, 353.
45. B. M. Fung, J. Afzal, T. Foss, and M.-H. Chau, *J. Chem. Phys.*, 1986, **85**, 4808.
46. J. S. Waugh, *Proc. Natl. Acad. Sci. USA*, 1976, **73**, 1394.
47. R. K. Hester, J. L. Ackerman, B. L. Neff, and J. S. Waugh, *Phys. Rev. Lett.*, 1976, **36**, 1081.
48. J. S. Waugh and S. J. Opella, *J. Chem. Phys.*, 1977, **66**, 4919.
49. E. R. Rybaczewski, B. L. Neff, J. S. Waugh, and J. S. Sherfinsky, *J. Chem. Phys.*, 1977, **67**, 1231.
50. C. D. Poon and B. M. Fung, *Liq. Cryst.*, 1989, **5**, 1159.
51. B. M. Fung and J. Afzal, *J. Am. Chem. Soc.*, 1986, **108**, 1107.
52. P. Foster and B. M. Fung, *J. Chem. Soc., Faraday Trans. 2*, 1988, **84**, 1083.
53. B. M. Fung, C. D. Poon, M. Gangoda, E. L. Enwall, T. A. D. Diep, and C. Bui, *Mol. Cryst. Liq. Cryst.*, 1986, **141**, 267.
54. C. D. Poon, C. M. Wooldridge, and B. M. Fung, *Mol. Cryst. Liq. Cryst.*, 1988, **157**, 303.
55. C. B. Frech, B. M. Fung, and M. Schadt, *Liq. Cryst.*, 1988, **3**, 713.
56. C. B. Frech, B. M. Fung, and M. Schadt, 1989, *SPIE Proc.*, 1989, **1080**, 215.
57. C. D. Poon and B. M. Fung, *J. Chem. Phys.*, 1989, **91**, 7392.
58. W. Richter, D. Reimer, B. M. Fung, R. J. Twieg, and K. Betterton, *Liq. Cryst.*, 1990, **8**, 687.
59. W. Guo and B. M. Fung, *Liq. Cryst.*, 1991, **9**, 117.
60. W. Guo and B. M. Fung, *J. Chem. Phys.*, 1991, **95**, 3917.
61. M.-S. Ho, B. M. Fung, M. Wand, and R. T. Vohra, *Ferroelectrics*, 1993, **138**, 51.
62. N. S. Balakrishnan, J. P. Bayle, M.-S. Ho, S. C. Pham, and B. M. Fung, *Liq. Cryst.*, 1993, **14**, 591.
63. B. M. Fung, M. L. Magnuson, T.-H. Tong, and M.-S. Ho, *Liq. Cryst.*, 1993, **14**, 1495.
64. J. P. Bayle, M.-S. Ho, and B. M. Fung, *New J. Chem. (Paris)*, 1993, **17**, 345.
65. J. P. Bayle and B. M. Fung, *Liq. Cryst.*, 1993, **15**, 87.
66. W. Richter, B. M. Fung, and M. Schadt, *Liq. Cryst.*, 1990, **8**, 63.
67. J. P. Bayle, P. Berdagné, M.-S. Ho, and B. M. Fung, *New J. Chem. (Paris)*, 1994, **18**, 715.
68. M. Schwartz, P. E. Fagerness, C. H. Wang, and D. M. Grant, *J. Chem. Phys.*, 1974, **60**, 5066.
69. K. Hayamizu and O. Yamamoto, *Bull. Chem. Soc. Jpn.*, 1977, **50**, 1295.
70. H. Hutton, E. Bock, E. Tomchuk, and R. Dong, *J. Chem. Phys.*, 1978, **68**, 940.
71. J. S. Lewis, J. Peeling, E. Tomchuk, W. Danchura, J. Bozek, H. M. Hutton, and E. Bock, *Mol. Cryst. Liq. Cryst.*, 1987, **144**, 57.
72. J. S. Lewis, E. Tomchuk, and E. Bock, *Liq. Cryst.*, 1989, **5**, 1033.
73. J. S. Lewis, E. Tomchuk, and E. Bock, *Liq. Cryst.*, 1993, **14**, 1507.
74. H. A. L. Cardozo, J. Bulthuis, and C. MacLean, *J. Magn. Reson.* 1979, **33**, 27.
75. H. A. L. Cardozo, J. Bulthuis, J. H. Freed, and W. M. M. J. Bovée, *Chem. Phys. Lett.*, 1979, **60**, 335.

76. J. Courtieu, N. T. Lai, C. L. Mayne, J. M. Bernassau, and D. M. Grant, *J. Chem. Phys.*, 1982, **76**, 257.
77. E. P. Black, J. M. Bernassau, C. L. Mayne, and D. M. Grant, *J. Chem. Phys.*, 1982, **76**, 265.
78. P. R. Luyten, J. Bulthuis, W. M. M. J. Bovée, and L. Plomp, *J. Chem. Phys.*, 1983, **78**, 1712.
79. O. Söderman, H. Walderhaug, U. Henriksson, and P. Stilbs, *J. Phys. Chem.*, 1985, **89**, 3693.
80. G. Feio, H. D. Burrows, C. F. G. C. Geraldes, and T. J. T. Pinheiro, *Liq. Cryst.*, 1991, **9**, 417.

Biographical Sketch

Bing M. Fung. *b* 1939. 1963, Diploma, Chung Chi College (now Chinese University of Hong Kong). Ph.D., 1967, California Institute of Technology. Faculty at the University of Oklahoma, 1972–present. Approx. 160 publications. Research interests include NMR study and synthesis of liquid crystals.

Liquid Crystalline Samples: Application to Macromolecular Structure Determination

Ad Bax, James J. Chou, and Benjamin E. Ramirez

Laboratory of Chemical Physics, National Institute of Diabetes, and Digestive and Kidney Diseases, National Institutes of Health, Bethesda, MD, USA

1	Introduction	1
2	Theoretical Considerations	1
3	Measurement of Dipolar Couplings	3
4	Alignment Media for Macromolecules	6
5	Relation between Alignment and Shape	9
6	Structure Validation	10
7	Concluding Remarks	11
8	Related Articles in Volumes 1–8	11
9	References	11

1 INTRODUCTION

NMR spectra of small molecules dissolved in organic liquid crystalline media permit measurement of large numbers of intramolecular dipolar couplings that carry very precise information on molecular structure.[1,2] However, for molecules with more than half a dozen protons, the strong degree of solute alignment obtained in such media typically results in a vast number of large, non-first-order splittings that make these spectra difficult to analyze. On the other hand, very weak alignment, caused by a molecule's own magnetic susceptibility anisotropy, also gives rise to measurable dipolar couplings.[3,4] However, typically only the largest couplings are detectable and manifest themselves as small, field-dependent changes in the corresponding J splittings. The advantages of such ultra-weak alignment are that the NMR spectrum retains its regular high-resolution simplicity and that, owing to the extremely weak magnetic forces involved, it does not perturb the structure of the molecule.

Tolman et al.[5] demonstrated that small dipolar couplings, on the order of a few hertz, could be measured for the backbone amides in paramagnetic myoglobin, and that these data correlate well with values expected on the basis of its crystal structure. Tjandra et al. subsequently measured a substantial number of very small ^{15}N–^{1}H and ^{13}C$^{\alpha}$–^{1}H$^{\alpha}$ dipolar couplings in a diamagnetic protein-DNA complex and demonstrated that incorporation of these data as restraints in the structure calculation yields a remarkable improvement in both local and global geometry.[6] In particular, by defining the relative orientation of structural elements in a macromolecule with few interconnecting NOEs, these dipolar restraints solve a long-standing problem.

General applicability of the weak alignment approach greatly increased when the suitability of very dilute liquid crystalline media for this purpose was discovered.[7–14] The macromolecules are dispersed in the aqueous phase that separates the highly ordered liquid crystalline particles, which have a spacing much larger than the diameter of the molecule under study. Despite the typically rather large macroscopic viscosity of such samples, the ordered particles are spaced by essentially pure water, and usually no adverse effect on rotational diffusion is therefore observed.[7] However, exceptions to this rule can occur in cases where alignment is dominated by attractive electrostatic interactions between the nematogen and the solute.[15] As discussed in Section 4.6, an alternate way for inducing weak alignment relies on axially compressed or stretched polyacrylamide gels. From a theoretical perspective, alignment in gels and in dilute lyotropic liquid crystalline suspensions are very similar.

The ability to tune the degree of macromolecular alignment over more than an order of magnitude, usually in the range from 3×10^{-4} to 3×10^{-3}, makes it possible to measure a whole plethora of short-range dipolar interactions, including those between directly bonded ^{1}H–^{13}C, ^{1}H–^{15}N, ^{13}C–^{13}C and ^{13}C–^{15}N pairs, and also between spatially proximate nonbonded ^{1}H–^{1}H, ^{1}H–^{13}C and ^{1}H–^{15}N spin pairs.[8,16–18] The measurement and application of dipolar couplings and CSA effects in weakly oriented macromolecules has already proven to be extremely useful in biomolecular structural studies. Several reviews have appeared on various aspects of this work,[19–22] and further developments in this area of research are occurring at a very rapid pace. Even at present, a comprehensive review of this area would fill hundreds of pages, and is therefore well beyond the scope of this article. Instead, the relation between this work and conventional liquid crystal NMR will be highlighted, as well as illustrating some of the advantageous features of the weak ordering approach.

2 THEORETICAL CONSIDERATIONS

Although standard theory described for liquid crystals elsewhere in this encyclopedia is directly applicable to the case of very weakly ordered macromolecules, the early applications of the weak ordering technology derive from the magnetic-susceptibility induced alignment. As a result, the terminology differs somewhat and will be briefly reviewed below.

2.1 Dipolar Couplings in Aligned Macromolecules

The relation between the internuclear vector and the dipolar coupling between two spins, A and B can be found in numerous textbooks. For the purpose of deriving the resonance frequencies (i.e., dipolar splittings) only the z component of the local field of one nuclear dipole at the position of the second nucleus is relevant (secular approximation):

$$H_{dd} = D_{\max}^{AB} \langle I_{Az} I_{Bz} (3\cos^2 \zeta - 1) \rangle \qquad (1a)$$

where the $\langle\rangle$ brackets refer to the time or ensemble average, which are equivalent for isotropic and liquid crystalline

solutions, ζ is the angle between the $A - B$ internuclear vector and the magnetic field, and

$$D^{AB}_{\max} = \frac{-\mu_o(H/2\pi)\gamma_A\gamma_B}{(4\pi^2 r^3_{AB})} \tag{1b}$$

is the static dipolar coupling in SI units (21.7 kHz for H–N pairs, assuming an internuclear distance $r_{NH} = 1.04$ Å. The constant, $-\mu_o$, is the magnetic permittivity of vacuum, h is Planck's constant, γ_X is the magnetogyric ratio of spin X, and r_{AB} is the distance between nuclei A and B. The residual dipolar splitting between spins A and B equals

$$D^{AB} = D^{AB}_{\max}\langle P_2(\cos\zeta)\rangle \tag{1c}$$

with $P_2(x) = (3x^2 - 1)/2$. Note that some texts differ in the definition of the dipolar coupling, D_{AB}, by a factor two.

If the molecule is rigid, the orientation of the internuclear vector, r_{AB}, in an arbitrary molecular coordinate system can be described by the angles α_x, α_y, and α_z between the vector and the x, y, and z axis of the coordinate system. The $P_2(\cos\zeta)$ term can be expressed as

$$\langle P_2(\cos\zeta)\rangle = \sum_{i,j=\{x,y,z\}} S_{ij}\cos\alpha_i\cos\alpha_j \tag{2}$$

where S is a traceless symmetric 3×3 matrix, commonly referred to as the Saupe matrix, the Saupe order matrix, or simply the order matrix.

If the structure of the molecule is known, i.e., $\cos\alpha_i$ factors in equation (2) are known, the five independent elements of S generally can be solved provided that dipolar couplings for at least five internuclear vectors are available. However, if any pair of internuclear vectors is parallel, and for other special cases such as a set that includes three mutually orthogonal interactions, more measured couplings are required. For macromolecules, many more dipolar couplings are frequently measured, and S is overdetermined. The Saupe matrix elements are then best determined using singular value decomposition.[23]

The order matrix is real and symmetric, and it therefore is always possible to define a molecular axis system where S becomes diagonal. In a number of applications it can be advantageous to work in this principal axis frame, where D^{AB} now can be expressed in terms of the polar coordinates of the $A-B$ internuclear vector:

$$D^{AB}(\theta,\phi) = \frac{3}{2}D^{AB}_{\max}[\cos^2\theta A_{zz} + \sin^2\theta\cos^2\phi A_{xx} + \sin^2\theta\sin^2\phi A_{yy}] \tag{3a}$$

where A is the diagonalized alignment tensor, with $|A_{zz}| > |A_{yy}| > |A_{xx}|$. This frequently is rewritten as

$$D^{AB}(\theta,\phi) = D^{AB}_{\max}\left[P_2(\cos\theta)A_a + \frac{3}{4}A_r\sin^2\theta\cos 2\phi\right] \tag{3b}$$

where $A_a = 3A_{zz}/2$ is the axial component of the alignment tensor, and $A_r = (A_{xx} - A_{yy})$ is referred to as its rhombic component.

Note that the maximum value for A_a equals one when the z axis of the principal alignment tensor is fully aligned with the static field. In practice, the dilute liquid crystal work discussed in this article concerns A_a values on the order of 10^{-3}. Equation (3b) is sometimes rewritten as

$$D^{AB}(\theta,\phi) = D^{AB}_a\left[(3\cos^2\theta - 1) + \frac{3}{2}R\sin^2\theta\cos 2\phi\right] \tag{3c}$$

where $D^{AB}_a = 1/2A_aD^{AB}_{\max}$ is referred to as the magnitude of the dipolar coupling tensor, frequently normalized to the N–H dipolar interaction, and $R = A_r/A_a$ is the rhombicity. Note that $0 \le R \le 2/3$.

2.2 Estimate for Alignment Tensor in Case of Unknown Structure

When working with a molecule of unknown structure, the above-described singular value decomposition approach for determining the order matrix is not applicable. However, as briefly discussed below, a reasonable estimate for the principal components of the alignment tensor can be obtained from the range and distribution of observed dipolar couplings.

First, it is convenient to normalize all observed one-bond and two-bond dipolar couplings to, for example, the N–H dipolar coupling, by multiplying the observed $P - Q$ dipolar coupling by $(\gamma_N\gamma_H r^3_{PQ})/(\gamma_P\gamma_Q r^3_{NH})$. Empirically determined optimum scaling factors are listed in Table 1. In the absence of measurement error in the dipolar couplings, the bond vector with the largest absolute value for the normalized dipolar coupling provides a lower limit for $2D^{NH}_a$ in equation (3c). Similarly, an estimate for the rhombicity R in equation (3c) can be obtained from the dipolar coupling value, D_{opposite}, with the other extreme value (negative for $D^{NH}_a > 0$; positive for $D^{NH}_a < 0$). The value of R itself, defined in this manner, is always positive and follows from $D_{\text{opposite}} = -D^{NH}_a\,[1 + 3/2R]$, or

$$R = -\frac{2}{3}\left[1 + \left(\frac{D_{\text{opposite}}}{D^{NH}_a}\right)\right] \tag{4}$$

This approach only uses the extreme values of the distribution of observed dipolar couplings. A more robust approach plots the histogram of the entire ensemble of normalized dipolar couplings.[24] Figure 1 shows an example of such histograms for the two globular domains of Ca^{2+}-ligated calmodulin. The histograms have been compiled from nearly complete sets of ${}^1D_{NH}$, ${}^1D_{C\alpha H\alpha}$, ${}^1D_{C'N}$, ${}^2D_{C'H\alpha}$ and ${}^1D_{C'C\alpha}$ couplings, recorded in a medium of filamentous phage *Pf1*.

Table 1 Magnitude of dipolar couplings relative to ${}^1D_{NH}$

	NMR[a]	X-ray[b]
${}^1D_{C\alpha H\alpha}$	2.08	2.02
${}^1D_{C\alpha C'}$	0.198	0.198
${}^1D_{C'N}$	0.120	0.121
${}^2D_{C'HN}$	0.300	0.319
${}^1D_{CH3}$	0.628	0.628

[a]Values that result in the lowest energy NMR structure of ubiquitin and yield best fit to ${}^{13}C'$ CSA.[74]
[b]Optimized by fitting experimental couplings to the ubiquitin X-ray structure.[16]

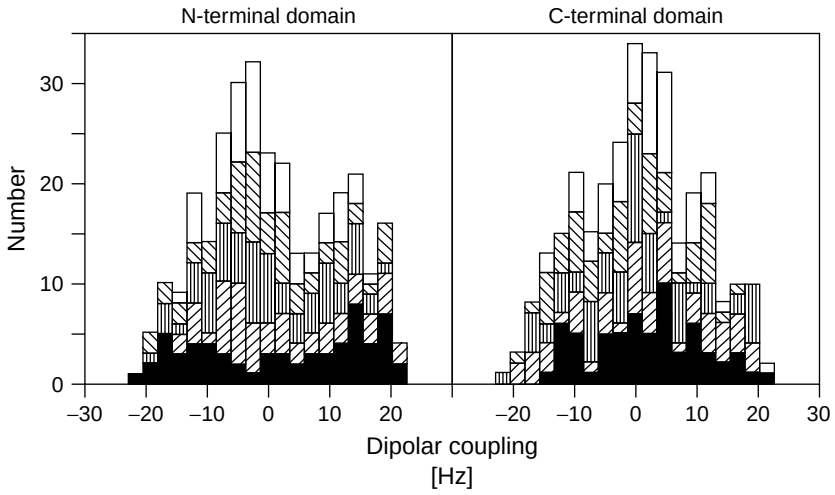

Figure 1 Histogram of normalized dipolar couplings measured in the N- and C-terminal domains of Ca^{2+}-ligated calmodulin, dissolved in a liquid crystalline medium containing 15 mg Pf1/ml and 10 mM KCl. Dipolar couplings are normalized relative to the one-bond ^{15}N–^{1}H interaction. SVD fits to the crystal structure and the use of a freely floating alignment tensor during structure calculation[77] both yield $D_a^{NH} = 11.0$ Hz; $R = 0.38$ and $D_a^{NH} = 10.1$ Hz; $R = 0.66$ for the N- and C-terminal domains, respectively. Note that even while the two histograms cover the same width, they have considerably different asymmetries (rhombicity, R). A dearth of bond vectors parallel to the z-axis of the alignment tensor causes the absence of dipolar couplings >22 Hz for the N-terminal domain. Different types of dipolar couplings are shaded separately in the histograms: $^{1}D_{NH}$ – solid; $^{1}D_{C\alpha H\alpha}$ – shaded (///); $^{1}D_{C'N}$ – shaded (\\\); $^{1}D_{C'C\alpha}$ – shaded (|||); $^{2}D_{C'H\alpha}$ – blank

It can be shown that for a uniform distribution of bond vectors, such a histogram will resemble the solid state powder pattern observed for chemical shift anisotropy.[25] In the present case, the singularities in the powder pattern correspond to D_{zz}^{NH}, D_{xx}^{NH} and D_{yy}^{NH}, with the condition that $D_{zz}^{NH} + D_{xx}^{NH} + D_{yy}^{NH} = 0$. The relation between the powder pattern singularities D_{zz}^{NH}, D_{xx}^{NH}, D_{yy}^{NH} and the parameters D_a^{NH} and R is given by:[24]

$$D_{zz}^{NH} = 2D_a^{NH} \tag{5a}$$

$$D_{yy}^{NH} = -D_a^{NH}(1 + 1.5R) \tag{5b}$$

$$D_{xx}^{NH} = -D_a^{NH}(1 - 1.5R) \tag{5c}$$

If outliers appear to be present in the histogram, it is worth while checking the origin of these extreme dipolar couplings. They may correspond to $^{1}D_{C'N}$, $^{2}D_{C'H\alpha}$ or $^{1}D_{C'C\alpha}$ couplings derived from weak or partially overlapping correlations, and critical visual inspection of the raw data may be needed before including them.

3 MEASUREMENT OF DIPOLAR COUPLINGS

To date, measurement of dipolar couplings has focused primarily on one-bond interactions, which as a result of their known internuclear distance, are readily interpreted in terms of orientation. Also, they are generally the easiest to measure. Two-bond interactions also have the benefit of a fixed internuclear distance, but owing to their larger separation, they can be more difficult to measure at the same level of relative accuracy. New analysis schemes promise to make measurement of ^{1}H–^{1}H dipolar couplings more straightforward, and they may also become popular as structural restraints. Except for geminal ^{1}H–^{1}H interactions and pairs of protons in structural elements of fixed geometry, the interproton distance is an additional parameter influencing the dipolar coupling. This therefore results in a less direct relation between the value of the coupling and the orientation of the corresponding vector. However, structure calculation programs such as CNS[26] can readily deal with this additional complexity.[27]

So far, most measurements of dipolar couplings have focused on the one-bond and two-bond couplings along the polypeptide backbone in proteins (Figure 2), but dipolar couplings within and between sidechains are becoming increasingly used. Below, some of the most widely used techniques for measuring the various types of couplings are briefly discussed, with particular emphasis on ^{15}N–^{13}C labeled proteins. With the exception of couplings between protons separated by more than three bonds, where the J coupling is usually negligible, the coupling observed in the liquid crystalline phase represents the sum of the scalar and dipolar contributions. Considerable variation in the scalar couplings frequently exists,

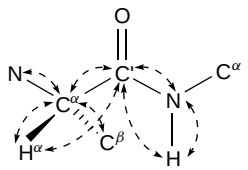

Figure 2 Protein backbone fragment, with dipolar interactions that can readily be measured marked by dashed lines. Although $D_{NC\alpha}$ can be measured experimentally, its relative accuracy tends to be lower, and for *trans*-peptide bonds its normalized value is very similar to that of $^{1}D_{C'C\alpha}$ of the preceding residue. $^{1}D_{C\alpha C\beta}$ is most useful in perdeuterated proteins, where no value for $^{1}D_{C\alpha H\alpha}$ can be measured and where the slow transverse relaxation of the deuterated $^{13}C^{\alpha}$ permits its accurate measurement

making it necessary to measure the couplings both in the isotropic and aligned environment.

Two conceptually different approaches can be used for measurement of J or dipolar splittings. First, the splitting can be measured directly from a two- or three-dimensional spectrum recorded in the absence of decoupling of the interaction of interest. Frequently, an E.COSY,[28] S^3E,[29] or IPAP version[30] of the multi-dimensional experiment is used in order to reduce overlap. Second, in a so-called quantitative-J correlation experiment,[31] the size of the splitting can be derived from the intensity of a given resonance relative to that of a reference.

3.1 Accuracy of Measured Splitting

For splittings measured from relative peak displacements in the multi-dimensional NMR spectrum, the accuracy of a peak position is directly proportional to its signal-to-noise ratio, and inversely related to its line width. Although the accuracy also depends on the method used for peak position determination and on the digital resolution, a reasonable approximation for the root-mean-square uncertainty, ΔJ, in a measured splitting for a well resolved, undistorted, pure phase or pure antiphase doublet is given by:

$$\Delta J = \frac{LW}{SN} \tag{6}$$

where LW is the line width at half height (in the dimension where the splitting is being measured), and SN is the signal-to-noise ratio. Note that equation (6) provides a lower limit for the true accuracy of the measurement, because other distortions such as partial overlap or imperfect phasing can contribute to the error in a reproducible manner.

3.2 Measurement of $^1J_{HN}$

One-bond $^1D_{NH}$ dipolar coupling were the first ones to be measured in a weakly oriented protein, simply by recording a ^1H–^{15}N HSQC spectrum without the regular ^1H 180° decoupling pulse applied at the midpoint of the t_1 evolution period. Transverse relaxation is considerably slower in the ^{15}N dimension compared to the ^1H dimension, and measurement in the indirect ^{15}N dimension is therefore preferred over measurement in the ^1H dimension. However, the spectral crowding doubles when HSQC spectra are recorded without decoupling, typically resulting in an unacceptable degree of resonance overlap.

A conceptually very simple method for measuring $^1J_{NH}$ separates the F_1-coupled HSQC into two separate subspectra, containing only the upfield or downfield components of the F_1 ^{15}N–{^1H} doublets. This is done by interleaving two experiments: one where the F_1 ^{15}N–{^1H} doublets are in phase, and one where they are exactly antiphase. The sum of the antiphase and the in-phase spectra yields a spectrum containing only the downfield components, whereas the difference yields the upfield components (Figure 3). This approach is referred to as IPAP (for in-phase and anti-phase)[32] and is easily extended to higher dimensionality experiments.

A small region of the two-dimensional ^1H–^{15}N IPAP-HSQC spectrum of calmodulin is shown in Figure 3. Isotropic ^1H–^{15}N J splittings are ca. 93 Hz, and the large deviations

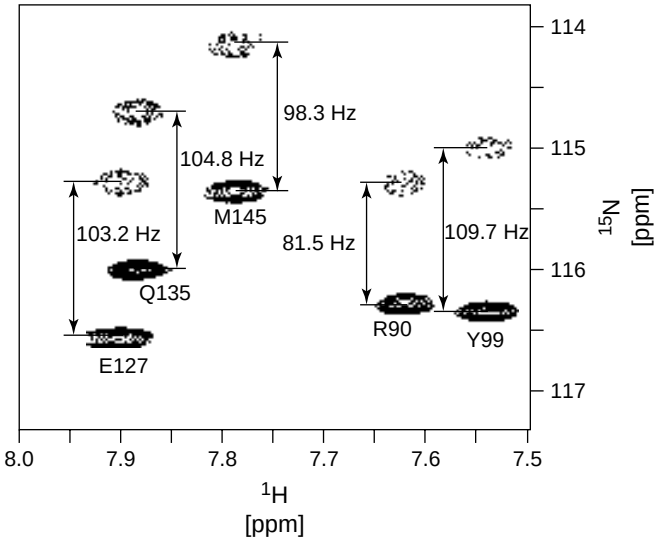

Figure 3 Small region of the IPAP ^{15}N–^1H HSQC spectrum of Ca^{2+}-ligated calmodulin in *Pf1* medium. The solid and dashed contours correspond to the downfield and upfield ^{15}N–{^1H} doublet components, which are separated into two two-dimensional subspectra. These subspectra are superimposed in this plot for visual simplicity, as none of the resonances overlap one another in the displayed region of the spectrum. The size of the splittings are marked in the figure and correspond to $|^1J_{NH} + {}^1D_{NH}|$

from this value correspond to the dipolar contributions to these splittings. So, both the sign and the magnitude of the dipolar coupling are obtained from such spectra.

3.3 Measurement of $^1J_{C'C\alpha}$

Due to the longer internuclear distance, and the lower product of the gyromagnetic ratios involved, the $^1D_{C'C\alpha}$ coupling is inherently five times smaller than the one-bond ^1H–^{15}N coupling (Table 1). In order to obtain meaningful information, it therefore is necessary to measure this coupling at high accuracy. There are two ways to measure $^1J_{C'C\alpha}$: observation of the C^α or of the C' resonance in the absence of decoupling the non-observed spin. For protonated proteins at moderate field strengths ($\leq$14 T), the $C'T_2$ is invariably much longer than the $C^\alpha T_2$, favoring detection of C' for most accurate measurement of $^1J_{C'C\alpha}$. For perdeuterated proteins, detection of $^{13}C^\alpha$ in the presence of ^2H and $^{13}C^\beta$ decoupling yields narrower ^{13}C resonances, particularly at higher fields.

Usually, the most accurate method for measurement of $^1J_{C'C\alpha}$ is to simply record a 3D HNCO spectrum where the C^α pulse, normally applied at the midpoint of the $^{13}C'$ evolution period, is omitted.[33] The HNCO experiment yields among the best resolved triple resonance spectra and the two-fold increase in the number of resonances relative to the $^{13}C^\alpha$-decoupled spectrum is generally not much of a problem. The $^{13}C'$ transverse relaxation rate is dominated by its chemical shift anisotropy, and $^{13}C'$ line widths at 600 MHz are about 30% larger than at 500 MHz ^1H frequency. It is therefore preferable to measure the $^1J_{C'C\alpha}$ splitting at a relatively low magnetic field strength.

3.4 Measurement of $^1J_{C'N}$ and $^2J_{C'HN}$

Dipolar couplings across the peptide bond between $^{15}N_i$ and $^{13}C'_{i-1}$ are inherently 8.3 times weaker than $^1D_{NH}$ (Table 1). Therefore, accuracy of their measurement is critical for making optimal use of these small couplings in structure determination. Owing to the favorable relaxation properties of ^{15}N, especially when selecting the downfield ^{15}N–{^1H} doublet component, the $^1J_{C'N}$ coupling is detected through the ^{15}N and not the $^{13}C'$ nucleus. The simplest method just records a two-dimensional HSQC on the $^{13}C/^{15}N$ doubly labeled protein, and inserts a $^{13}C^\alpha$ but not a $^{13}C'$ 180° decoupling pulse at the mid-point of ^{15}N evolution.[34] The resulting doublet in the ^{15}N dimension corresponds to $^1J_{C'N}$. Interestingly, the detected amide proton is also coupled to $^{13}C'$ (which has not changed its spin state during or after ^{15}N evolution). Therefore, the two doublet components are also displaced relative to one another by the $^2J_{C'HN}$ coupling in the $^1H^N$ dimension. Although normally this splitting would be very difficult to resolve because the $^1H^N$ line width is typically much larger than the $^2J_{C'HN}$ coupling, the E.COSY principle[28] effectively separates the two $^1H^N$–{$^{13}C'$} doublet components (Figure 4).

An interesting alternative approach, based on the principle of quantitative J correlation, derives $^1J_{C'N}$ from the relative intensities of two interleaved 3D TROSY-HNCO spectra.[35] In one experiment (reference spectrum) the pulse scheme uses optimal one-bond ^{15}N–{$^{13}C'$} dephasing of 33 ms, whereas in the second experiment (attenuated spectrum) the dephasing delay is set near the null condition (66 ms). Any deviation from $^1J_{C'N} + {}^1D_{C'N} = (66\,\text{ms})^{-1}$ results in non-zero intensity in the second spectrum. The relative intensities of these two spectra then give a very precise measure for $^1J_{C'N}$, and permit

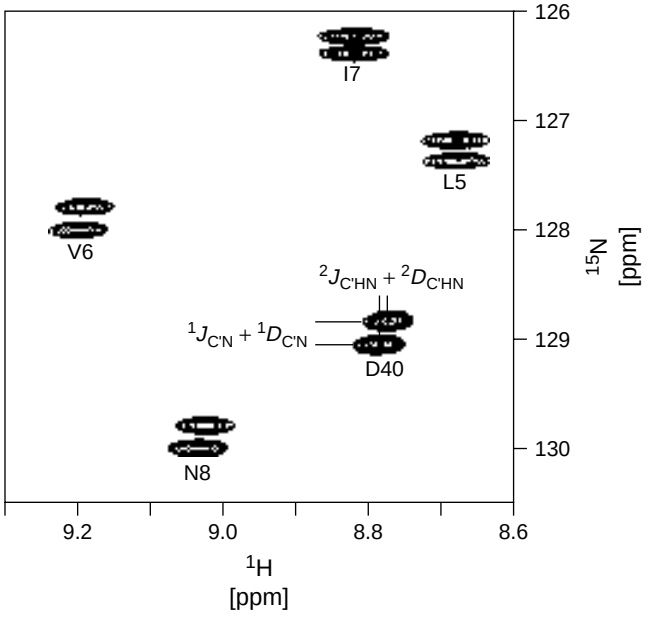

Figure 4 Small region of the ^{15}N–^1H HSQC spectrum of the first immunoglobulin binding domain of protein G, recorded in the absence of $^{13}C'$ decoupling in *Pf1* liquid crystal (11 mg ml^{-1}). The vertical and horizontal displacements within each doublet correspond to $|^1J_{C'N} + {}^1D_{C'N}|$ and $|^2J_{C'HN} + {}^2D_{C'HN}|$, respectively. Doublets are labeled by their one-letter residue type and number

$^1D_{C'N}$ to be derived at an accuracy that is a fraction of a hertz, provided the signal to noise in the reference spectrum exceeds 20 : 1.

3.5 Measurement of $^1J_{C\alpha H\alpha}$ and $^1J_{C\alpha C\beta}$

Although, in principle, $^1J_{C\alpha H\alpha}$ can be measured from a ^1H–^{13}C two-dimensional correlation spectrum, recorded in the absence of heteronuclear decoupling in either the F_1 or F_2 dimension, the increase in spectral crowding frequently leads to unacceptable overlap for all but the smallest proteins. In practice, therefore, $^1J_{C\alpha H\alpha}$ is most commonly measured either from a series of J_{CH}-modulated HSQC spectra, simultaneous to measurement of sidechain J_{CH} couplings (see below), or from a H^α-coupled HN(CO)CA or (HA)CA(CO)NH spectrum. This latter experiment makes it easy to decouple the $^1J_{C\alpha C\beta}$ coupling by using a constant-time C^α evolution period, and is therefore preferred when dealing with small or medium-size proteins. Its pulse sequence is identical to a scheme previously used for measuring relaxation interference between the $^{13}C^\alpha$ CSA tensor and the $^{13}C^\alpha - {}^1H^\alpha$ dipolar interaction,[36] but now it is the splitting itself rather than the difference in doublet intensities that is the focus of the measurement.

In perdeuterated proteins, $^1J_{C\alpha H\alpha}$ is inaccessible, but the long $^{13}C^\alpha$ transverse relaxation time permits measurement of $^1J_{C\alpha C\beta}$ from a regular HNCA experiment, recorded in the presence of ^2H decoupling during $^{13}C^\alpha$ evolution.[37]

3.6 Measurement of Sidechain $^1J_{CH}$ Couplings

To date, most attention has focused on measurement of backbone-related dipolar couplings. Nevertheless, dipolar couplings also are starting to become used for studying sidechain conformations. However, a significant fraction of the sidechains may be subject to rotameric averaging, which reduces the dipolar coupling relative to a static, single conformation. If the smaller dipolar coupling is imposed during structure calculation as if it were rigid, this can result in distorted sidechain conformations with high energy. A way around this is to impose the observed dipolar coupling as a lower bound for the true dipolar coupling.[38] An even better way would be to evaluate for each site separately what the degree of sidechain mobility is by conducting the requisite relaxation experiments.

For small and medium-size proteins, an accurate way for extracting both backbone $^1J_{C\alpha H\alpha}$ and sidechain $^1J_{CH}$ couplings is the recording of a set of CT-HSQC spectra, in which the ^1H 180° decoupling pulse is systematically shifted. The intensity modulation pattern observed in the fully decoupled CT-HSQC spectrum then provides an accurate measure for $^1J_{CH}$. For methylene groups, the modulation frequency corresponds to the sum of the two $^1J_{CH}$ couplings. Methyl group intensities are modulated by $^1J_{CH}$ and by $3 \times {}^1J_{CH}$, with amplitudes of the modulation having a ratio of approximately 1 : 3. As a result of the rapid three-fold rotation about the three-fold symmetry axis of the methyl group, the $^1D_{CH}$ dipolar coupling is scaled down by -0.31 relative to its static value.[39] Figure 5 compares the $^1D_{CH}$ and $^1D_{CC}$ dipolar couplings for methyl groups in ubiquitin. The tight correlation seen in this figure testifies to the precision at which these dipolar couplings can be measured. As suggested by this figure, for structure calculation

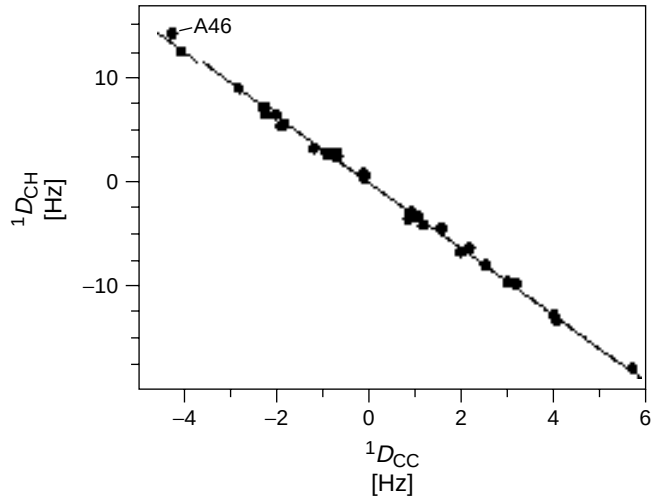

Figure 5 Plot of $^1D_{CH}$ versus $^1D_{CC}$ residual dipolar couplings of methyl groups in the protein ubiquitin, dissolved in a liquid crystalline medium containing 5% (w/v) bicelles. The solid line represents the best fit of the data by linear regression, with a slope of -3.17 ± 0.03. The outlier, labeled A46, corresponds to an alanine residue with a positive ϕ angle, for which there is a steric clash between the methyl group and a backbone carbonyl oxygen. (Reprinted, with permission, from Ottiger et al.[39])

purposes the methyl group $^1D_{CH}$ value may be converted into $^1D_{CC}$, thereby restraining the C–C(H_3) orientation.

For larger proteins, the lower sensitivity and increased spectral overlap in a CT-HSQC spectrum frequently result in a relatively small fraction of residues for which the $^1J_{CH}$ coupling can be measured. As an alternative, spectra recorded with CCH-COSY or HCCH-COSY, without decoupling in the detected dimension may be used for measurement of J_{CH}. An additional benefit of this approach is that for the case of non-equivalent methylene protons, both J_{CH} couplings can be measured separately. In favorable cases, the ^{1}H–^{1}H multiplet structure in such spectra also permits measurement of $^2J_{HH}$.[40]

3.7 Measurement of ^{1}H–^{1}H Couplings

The history of measuring ^{1}H–^{1}H J couplings is particularly rich and has been reviewed in numerous places. The E.COSY approach, applied in either a homo- or heteronuclear manner has proven particularly useful in this respect.[28] However, few of these methods are suitable for measurement of ^{1}H–^{1}H dipolar couplings. When oriented, ^{1}H–^{1}H multiplet structure tends to become very complex as a result of the multitude of coupling partners any given proton experiences. Fortunately, in heteronuclear type E.COSY spectra this does not pose a serious problem, and the utility of triple resonance experiments for measurement of both the sign and magnitude of intraresidue and sequential $J_{H\alpha HN}$ couplings has been demonstrated in oriented media.[41] Nevertheless, with some exceptions,[42,43] such experiments tend to be less suitable for measurement of dipolar couplings that are spatially proximate but far apart in the covalent bond network. Alternatively, the popular HNHA experiment can be used for measuring ^{1}H–^{1}H dipolar couplings that involve an amide proton.[6,44] In this experiment, the magnitude of $|J_{HH} + D_{HH}|$ is derived from the diagonal to cross peak intensity ratio. So, except for the intraresidue H^N–H^α interaction, where there also is a significant scalar contribution to the interaction, the sign of D_{HH} is not available from this experiment.

4 ALIGNMENT MEDIA FOR MACROMOLECULES

A prerequisite for studying macromolecules in a liquid crystalline phase is that the order imposed on the macromolecule is very small, typically less than 0.002. The order of the liquid crystal particles themselves is invariably much higher, in the 0.5–0.85 range. Clearly, for achieving such a weak solute alignment in the strongly oriented liquid crystalline medium, interaction between the macromolecule and the liquid crystal must be very weak. The medium must also be aqueous, such that the proteins or nucleic acids remain in their natural environment. An efficient way to satisfy these conditions is the use of a very dilute ($\leq$10% (w/v)) lyotropic nematic liquid crystalline suspension, where the nematogenic unit itself is a large particle. In a liquid crystalline phase, the weak steric and electrostatic interactions between liquid crystal particles cause their cooperative alignment. There is a lower limit for the nematogen concentration, c_n, required to form a stable liquid crystalline phase. If the sample is diluted below this threshold, it separates into an isotropic phase with concentration c_i and a nematic phase, with the c_n being 5–20% higher than c_i. The aspect ratio of the nematogenic particle is a critical determinant for the lowest concentration at which liquid crystalline ordering occurs. The time needed for formation of a homogeneous liquid crystalline phase strongly depends on the nematogen concentration, and can be very long for concentrated samples, but also for samples that are close to the threshold concentration, where separation between microscopic aligned and isotropic domains takes place.

All liquid crystalline media that have proven to be useful for weak ordering of proteins and nucleic acids consist of large (>1000 Å), water-soluble particles, with relatively low surface charge densities ($\leq 0.5\, e\, nm^{-2}$). The interaction between the liquid crystal particles results in increased macroscopic viscosity relative to pure water. However, rotational diffusion of the macromolecule itself is virtually unchanged, unless it has a weak affinity for the liquid crystal particle. In the latter case, the degree of order typically is much too large and therefore is of little practical interest. For all lyotropic liquid crystals discussed below, the degree of order imposed on the solute can be adjusted by changing the concentration of the liquid crystal itself over the range where it yields an ordered phase. There is not yet a single, ideal liquid crystal. For example, phospholipases without inhibitors cannot be studied in bicelles as they break down the phospholipids; active proteases can destroy phage-based liquid crystals; other proteins may stick to phospholipids, or the surface charge distribution of the liquid crystal may cause too strong an electrostatic interaction with the solute. Also, liquid crystals require some degree of surface charge to keep their order and may fail to remain liquid crystalline at high salt concentrations. Below, several of the most widely used systems are briefly discussed.

4.1 Bicelles

Bicelles were the first liquid crystalline medium used for weak alignment of proteins and DNA.[7,8] These are planar

bilayered particles that usually consist of regular saturated phospholipids. Most commonly, a mixture of dimyristoyl phosphatidyl choline (DMPC) and dihexanoyl phosphatidyl choline (DHPC) is used. DMPC makes up the bilayer, which constitutes the plane of the bicelle, and the DHPC detergent protects the long DMPC alkyl chains at the rims of the bilayer from exposure to solvent. Bicellar liquid crystals were originally developed by Prestegard, Sanders and co-workers for the purpose of studying lipophilic molecules, anchored in these highly ordered membranes.[45,46] The DMPC/DHPC combination was found to be particularly robust. When raising the temperature above 25 °C, the system switches from isotropic to a nematic liquid crystalline phase.[47] This temperature corresponds to the melting temperature of DMPC, i.e., the temperature at which the saturated alkane chains of DMPC melt from a crystalline or gel state, in which the alkane chains are all *trans*, to a flexible, liquid crystalline phase. Near this transition temperature, the sample has high macroscopic viscosity and tends to be slightly opaque. Below 25 °C the solution remains clear and unordered and both small angle neutron scattering and NMR diffusion experiments indicate the bicelles to be disk-shaped bilayers in this unordered phase.[48,49]

The phase diagram of the DMPC/DHPC mixture is very complex and depends on a large number of variables, including the absolute concentration, the molar ratio [DMPC]/[DHPC] = q, temperature, ionic strength, and on the presence of charged amphiphilic molecules such as sodium dodecyl sulfate (SDS) or cetyl trimethylammonium bromide (CTAB). Bicelles were long believed to remain disk-shaped above the DMPC melting temperature, with a diameter determined by q. However, the diameters predicted by such a model are incompatible with the very dilute concentrations (down to $\leq$2% (v/v)) at which the sample remains liquid crystalline. Recent tracer diffusion obstruction and neutron scattering data indicate the liquid crystalline phase to consist of highly porous bilayers, presumably with the detergent covering the rims of the pores.[49,50]

Intrinsically, DMPC/DHPC bicelles can form a liquid crystalline phase over the temperature range of 25–45 °C. However, near the lower end of this range (25–30 °C), dilute samples tend to be unstable and they frequently separate into an aligned and an isotropic phase. This can be prevented by addition of a small molar fraction (typically 1–3%, relative to DMPC) of charged amphiphiles, such as CTAB (positive) or SDS (negative).[51] Alternatively, charged phospholipids such as dimyristoyl phosphatidylserine (negative), or dimyristoyl trimethylammonium propane (positive) can be used. Charging the bicelles in this manner helps prevent phase separation and widens the part of the phase diagram over which the liquid crystalline phase remains stable. The electrostatic potential repels and attracts oppositely charged groups on the solute, and generally causes a change in both the orientation and magnitude of the alignment tensor. This can be a highly beneficial side effect, as it permits measurement of dipolar couplings under multiple orientations of the protein (Figure 6).[52] Usually, this change in orientation is approximately linear with charge. So, if more than two different samples are prepared in this manner, they simply yield alignment tensors that are linear combinations of one another.[53]

Regular phospholipids are subject to acid- and base-catalyzed hydrolysis of the carboxyester linkage between the alkyl chain and the glycerol backbone. The rate of hydrolysis is minimal at pH 6.5, but rapidly increases once the pH differs by more than one unit from this value.[54] Use of ether lipids, where the carboxyester bond is replaced by an ether linker can prevent this hydrolysis and such samples can be stable over a very wide range of pH[55,56] for periods of several years.

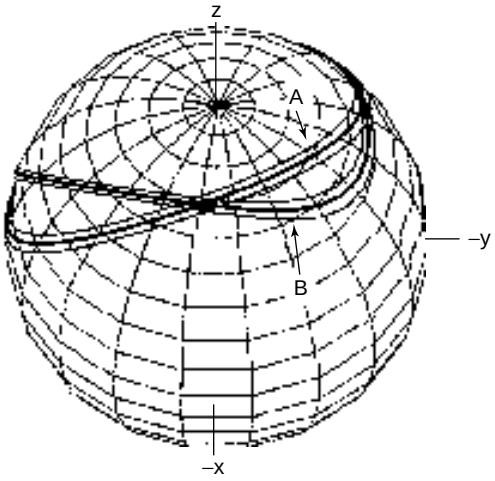

Figure 6 Orientations of the Gln[40] N–H vector in ubiquitin compatible with the ^{15}N–^{1}H one bond dipolar coupling measured in undoped bicelles (band A) and in positively charged bicelles (band B). Orientations are given in the coordinate frame of the X-ray structure of this protein. Heavy lines correspond to the measured dipolar couplings; thinner lines correspond to orientations if D_{NH} is increased or decreased by 1 Hz. The solid dot marks the orientation of the N–H vector when the protons are model-built into the crystal structure, assuming H^N is located on the line bisecting the C′–N–C$^\alpha$ angle. (Adapted, with permission, from Ramirez and Bax[52])

The temperature range over which the bicelles are liquid crystalline can be extended either by introducing a small fraction of mono-unsaturated DMPC, which lowers the melting temperature of the alkane chain,[54] or by using shorter alkane chains. Use of shorter alkane chain phospholipids, such as dilauroyl PC (12-C chains)[57] or ditridecanoyl PC (13-C chains)[55] lowers the transition temperature by about 12 and 6 °C, respectively, and increases the upper temperature limit as well. However, the macroscopic viscosity of these solutions below the transition temperature tends to be much higher than for DMPC/DHPC bicelles, such that preparation of the sample can be more cumbersome, particularly when using a microcell.

4.2 Filamentous Phage

Use of a liquid crystalline solution consisting of filamentous phages for aligning macromolecules was introduced in 1998.[9,10,58] Clore et al. used a medium based on the filamentous phage fd, and also demonstrated the potential of tobacco mosaic virus (TMV). The Pardi group demonstrated the utility of the phage *Pf1*, which is similar to *fd*, but which at a contour length of ca. 2 μm is nearly twice as long. Both phages have a diameter of 6.5 nm, and are quite rigid, with a persistence length of ca. 1 μm. As a result of the high aspect ratios of these particles, solutions can remain liquid crystalline down to very low concentrations, as low as a

few $mg\,ml^{-1}$. Although it was suggested that liquid crystallinity is independent of ionic strength, we find this to be true only at higher phage concentrations,[15] whereas at lower concentrations ($\sim 13\,mg\,ml^{-1}$ for *Pf1*) the degree of alignment becomes sensitive to ionic strength, and at very high salt concentrations the samples become isotropic. In contrast to *fd*, *Pf1* solutions tend to remain homogeneous when their concentration is lowered below the nematic threshold concentration, c_n. However, below this threshold, the degree of both phage and solute alignment becomes a function of the magnetic field strength, characteristic of a so-called paranematic phase.[15]

The negative surface charge (ca. $0.5\,e\,nm^{-2}$) is necessary to maintain a uniform suspension of these large particles. When lowering the pH below 6, partial protonation of the glutamate and aspartyl sidechains of the phage coat protein reduces the net charge of the virus particle and the phage precipitates. However, *fd* has been shown to be soluble and liquid crystalline when the pH is reduced further, to ca. 3.[59]

As highlighted by Clore et al. for an immunoglobulin-binding domain of Streptococcal protein G, the alignment tensor in the phage medium can be very different from that in the bicelle medium.[10] This is advantageous as it permits measurement of dipolar couplings relative to two independent axis systems, thereby resolving much of the degeneracy that occurs in interpreting a dipolar coupling in terms of two orientational variables, θ and ϕ in equation (3c). The phage particles are aligned with their long axis parallel to the magnetic field. Therefore, if the alignment of solute macromolecules were caused exclusively by steric interaction, the alignment tensor would be very similar to that in the bicelle medium. In practice, the alignment tensors in phage and bicelle media tend to be quite different as there usually are relatively strong electrostatic interactions between the phage and the solute (see also Section 5).

4.3 Alkyl-poly(ethylene glycol) Based Media

A lyotropic liquid crystal consisting of a mixture of alkyl-poly(ethylene glycol) and hexanol is another very useful medium for protein and nucleic acid alignment.[14] Alkyl-poly(ethylene glycol) type compounds generally do not tend to bind to proteins, making this an attractive medium for a wide range of biological systems. In contrast to bicelles, the liquid crystal is not subject to hydrolysis and it can remain stable for years, provided the concentration of hexanol does not decrease as a result of slow evaporation. The medium remains liquid crystalline over a wide pH range and a considerable temperature range of 10–40 °C, which is tunable by varying the type of alkyl-poly(ethylene glycol) and the chain length of the alcohol.[14]

The different alkyl-poly(ethylene glycol) compounds are referred to as C*m*E*n*, where *m* is the number of carbons in the alkyl group, and *n* is the number of ethylene glycol units. Typically, a hexanol to $C_{12}E_5$ molar ratio of 0.96 (5 wt.% $C_{12}E_5$ in H_2O) is used yielding a particularly stable liquid crystal that is easy to prepare, but the medium is relatively tolerant to changes in the absolute and relative concentrations. $C_{12}E_5$ is commercially available at low cost. In many cases, the sample can simply be recovered from the liquid crystal by extensive dialysis.

4.4 Other Liquid Crystals

Ternary mixtures of cetylpyridinium chloride (CPCl) or bromide (CPBr), hexanol, and NaCl or NaBr in water can form stable liquid crystalline phases over a wide range of conditions. Prosser et al.[11] demonstrated that the CPCl version yielded alignment for the protein ubiquitin, and Barrientos et al.[12] described the use of the CPBr based medium. Remarkable differences were found between the CPBr and CPCl based liquid crystals, with CPBr being more suitable for low ionic strength measurements (10–40 mM NaBr) and the CPCl system requiring higher salt concentrations (200–500 mM NaCl).[12]

Dilute suspensions of natural cellulose fibers, derived either from wood pulp or from filter paper by careful sulfuric acid hydrolysis, also can form a liquid crystalline phase suitable for macromolecular ordering.[60] Although negatively charged, the net surface charge density is lower than for filamentous phage, making it a useful complement to the other media, mentioned above. However, the lower surface charge and the smaller aspect ratio relative to filamentous phage result in a higher minimal threshold concentration for liquid crystal formation.

A suspension of purple membrane (PM) fragments has also been shown suitable for inducing a weak degree of macromolecular order.[53,61] These fragments consist primarily (75% (w/w)) of bacteriorhodopsin, an integral membrane protein with seven transmembrane helices. The PM fragments have an average diameter of about 1 μm. This is sufficiently large that the total magnetic susceptibility anisotropy of such a particle causes it to align nearly 100% when placed in a strong magnetic field ($\geq$11 T), with the membrane plane orthogonal to the direction of the magnetic field.[62] So, in contrast to the bicelle, phage and CPBr systems, PM does not need to form a liquid crystalline phase for obtaining alignment.

The strong net negative surface charge of PM causes very weak transient binding of solute proteins that carry clusters of positively charged groups on their surfaces, and thereby can result in net alignment.[53,61] The electrostatic interactions are typically weak enough not to distort the structure of globular proteins. However, as is the case with all liquid crystal studies in this chapter, when studying flexible regions in a protein, care must be taken when interpreting the dipolar coupling data as the protein only transiently interacts with the liquid crystal. Interaction with the nematogen may be favored when the flexible region temporarily adopts a given shape, whereas other, non-binding conformations of the flexible region may not be sampled.

4.5 Polyacrylamide Gel

In order to prevent sedimentation, suspensions of large particles such as phages, bicelles, and cellulose require a repelling interaction, i.e., a net surface charge. These local electrostatic fields generally result in stronger solute alignment, which then may become too strong for facile dipolar coupling measurement. In other cases, solutes may cause the liquid crystal particles to aggregate and precipitate. For example, no stable liquid crystal has yet been described that is suitable for detergent-solubilized proteins. So, although the above mentioned liquid crystalline systems will cover the majority of systems of interest, there remain exceptions.

Recently, a very useful alternative method for inducing weak alignment has been developed that is known as strain-induced alignment in a gel (SAG).[63,64] This method relies on anisotropically compressed polyacrylamide gel, which forms an extremely stable and inert aqueous matrix for solute proteins, and even permits their study under partially or fully denaturing conditions.[65] The gels may either be compressed or stretched in the axial direction,[64] with stretching generally yielding stronger alignment.[66] The robustness of such a medium makes it particularly useful for challenging applications such as detergent-solubilized systems.[66] The solutes may either be diffused into the gel, or they may be included in the medium before polymerization of the hydrogel is induced.

Compression of the gel can simply be achieved by first casting it in a narrow diameter (3–3.5 mm) cylinder. Then, after soaking in the solute of interest, it is transferred to a regular 4.2-mm inner diameter (ID) NMR sample tube, followed by axial compression by a susceptibility-matched plunger. Stretching can be achieved by radial compression, using a funnel-like device to squeeze a larger diameter gel (5–7 mm) into a regular 4.2-mm ID NMR sample tube.[66] Polyacrylamide gels appear to yield the most widely applicable method for inducing weak macromolecular alignment as the system is very inert and stable. Their principal disadvantage is a potential decrease in rotational diffusion rate of the solute, resulting in line broadening.[64,67] This latter effect can be minimized by using gel concentrations as low as possible ($\leq$5%) combined with high degrees of stretching, and by using low cross-linking ratios ($\leq$1 : 40).

4.6 Use of Multiple Alignment Media

As discussed in Section 5, solute alignment is defined by both steric and electrostatic interaction. So, by using nearly neutral liquid crystals, such as bicelles or the alkyl poly(ethylene-glycol) medium, and a charged medium such as phage or the cetyl-pyridinium based phase, a single molecule can be studied using two or more independent alignment tensors. As illustrated in Figure 6, this removes much of the degeneracy in the relation between dipolar coupling and internuclear vector orientation.[52] A dipolar coupling measured in a given medium defines the internuclear vector to be on one of two oppositely oriented cones. The alignment tensor in a second medium will generally be oriented differently relative to the molecular frame and a dipolar coupling defines the same vector to be situated on a different cone. The true internuclear vector orientation then must be located on one of the intersections between the two sets of cones (Figure 6). In the general case of a non-axially symmetric (rhombic) alignment tensor there are up to eight intersections. If a third, independent alignment tensor can be obtained, this degeneracy may be reduced to two-fold. The true orientation and its inverse can never be distinguished from measurements on a single dipolar interaction, and two-fold degeneracy is therefore the best that can be achieved for a single vector.

Besides changing the liquid crystal medium, the alignment tensor may also be altered by subtly changing the protein. For example, when the pH is altered such that the surface charge distribution becomes different, this will affect the alignment tensor in the charged liquid crystalline media. Similarly, if protein preparations are available with and without a His-tag tail, their alignment tensors will generally be different, although not necessarily by a large amount. Also, for a protein with a His-tag, a relatively small change in pH from 6 to 7.5 can significantly alter the alignment tensor.

If one-bond dipolar couplings are measured for a set of non-collinear interactions in a fragment of known secondary structure, such as an α-helix, there are four different ways to orient the fragment relative to the alignment tensor. Dipolar couplings measured in a second, independent medium, can lift this degeneracy, defining its orientation uniquely.[68]

5 RELATION BETWEEN ALIGNMENT AND SHAPE

Tjandra et al. demonstrated that in a bicelle medium the principal axes of the molecular alignment tensor closely coincide with those of the rotational diffusion tensor.[8,69] This shows that in this nearly neutral medium, alignment is defined by the solute's shape. As mentioned above, the alignment tensor can be modified by adding a net charge to the bicelles, by doping them with either CTAB (+) or SDS (−). This demonstrates that electrostatic interactions also play a role. In fact, for an oriented medium of strongly negatively charged, rod-shaped viral particles, or oriented PM fragments, electrostatic interactions usually dominate alignment of solute proteins.

A simple steric model has been proposed that quantitatively describes the relation between the solute's shape and its alignment in the type of lyotropic liquid crystals described in this article.[70] So far, it has only been demonstrated for the case of (nearly) neutral particles, such as bicelles, but preliminary results indicate that the method can be extended to account for the effect of charge.

In the so-called steric-obstruction model, the solute sample can be simulated as a collection of randomly oriented, uniformly distributed molecules, from which the fraction that sterically clashes with the ordered array of liquid crystal particles is removed. For example, for a lamellar phase such as bicelles or $C_{12}E_5$, a larger fraction of molecules oriented orthogonal to the bilayer will be obstructed than molecules parallel to the surface, resulting in net ordering of the remaining, non-obstructed molecules. For each non-obstructed molecule a Saupe order matrix is calculated, using equation (2). Averaging of the Saupe matrices for all non-obstructed proteins than yields the sterically predicted alignment tensor.[70] In an extension of this method that accounts also for the effect of electrostatics, different weighting factors are given to each of the non-obstructed solute molecules, depending on the Boltzmann factor calculated when taking the electrostatic potential into account (M. Zweckstetter, unpublished results).

Figure 7 shows the correlation between the ^{15}N–^{1}H dipolar couplings measured for the Ig binding domain of Streptococcal protein G, and that predicted from its 1.0 Å crystal structure, using an alignment tensor that is not best-fitted to the data, but calculated on the basis of its shape.[69] When ignoring electrostatics, the predicted alignment tensors for bicelle and phage media are very similar. However, the experimentally observed dipolar couplings in the two media are very different and, as expected, good agreement is only observed for the bicelle medium (Figure 7). When electrostatic terms are included in the calculations for the phage medium, the

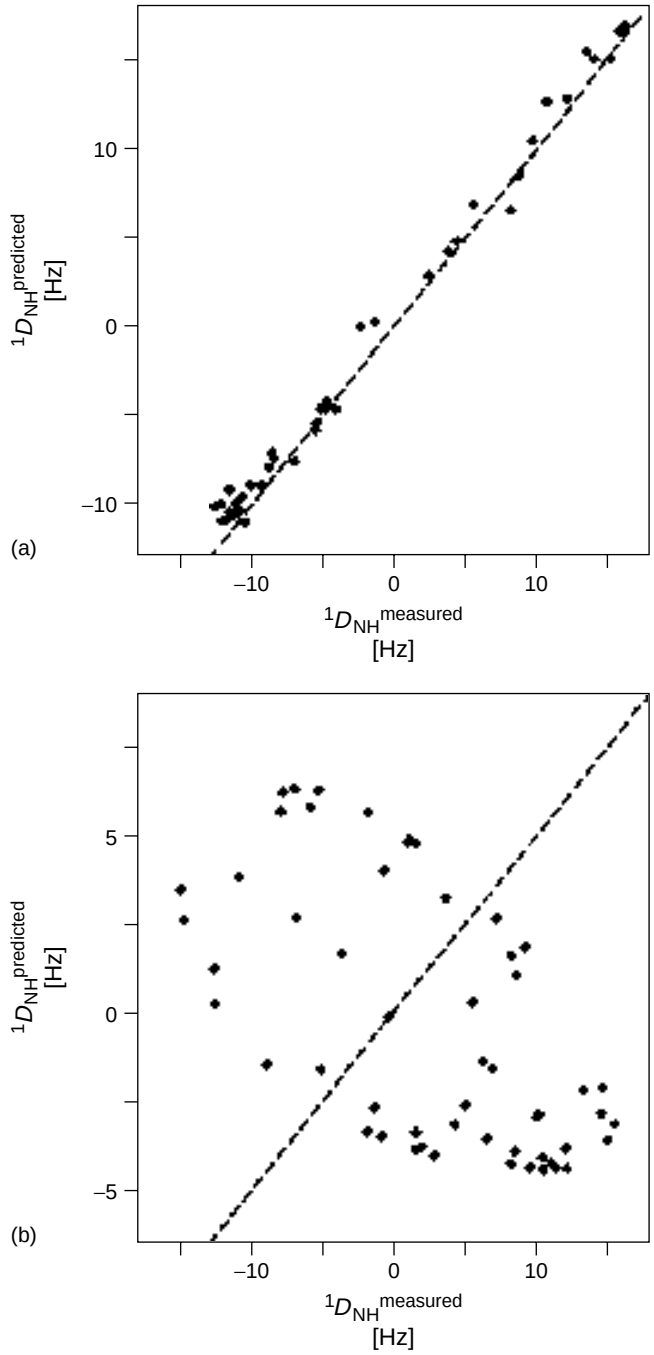

Figure 7 Correlations between experimental $^1D_{NH}$ values and values calculated from the shape-predicted alignment tensor of the third immunoglobulin binding domain of protein G in (a) 5% (w/v) bicelle medium, and (b) 28 mg ml^{-1} *fd* medium. Dashed lines correspond to $y = x$. The poor correlation in (b) indicates that in phage medium the protein alignment is dominated by electrostatic interactions, which are ignored in the alignment tensor prediction, and not by steric interaction. (Adapted, with permission, from Zweckstetter and Bax[15])

agreement becomes nearly as good as for the neutral bicelle medium. Note that in contrast to the results of an SVD fit, the data shown in Figure 7 do not include any adjustable parameters. So, the alignment tensor orientation and magnitude are calculated on the basis of the protein's shape, and subsequently dipolar couplings are predicted on the basis of the orientation of the internuclear vector relative to this alignment tensor.

6 STRUCTURE VALIDATION

One particularly attractive feature of dipolar couplings is that they can be used in a very direct manner to evaluate the accuracy of any given structure: the more accurate the structure, the better the agreement is between experimental dipolar couplings and this structure. In order to evaluate this agreement, one first needs to determine the alignment tensor or Saupe matrix. As mentioned earlier, there are two conceptually different ways to do this. One can either predict the alignment on the basis of the molecule's shape and charge distribution, or one can determine the Saupe matrix elements of equation (2) simply by singular value decomposition. There are five independent elements in the Saupe matrix. If the number of experimentally measured independent (i.e., non-collinear) dipolar interactions is much larger than five, the SVD approach is preferred as it eliminates the effect of errors in the shape-predicted alignment tensor. Clearly, for effective validation it is necessary that the number of observables (dipolar couplings) is much larger than the number of variables in the SVD fit. If this condition is not met, corrections can be made for the significance of the correlation in terms of F statistics. For proteins, typically the number of observed dipolar couplings is much larger than five, and the goodness of the fit provides a direct measure for the accuracy of the structure.

Figure 8 shows a typical example of the correlation between measured dipolar couplings and those predicted by two structures of the C-terminal domain of Ca^{2+}-calmodulin (after best fitting the Saupe matrix to the experimental couplings). The first correlation (Figure 8a) is calculated by using the 1.0-Å X-ray crystal structure of Paramecium tetraurelia calmodulin to fit the data measured for the highly homologous mammalian protein. It yields a Pearson's correlation coefficient, R^P, of 0.95. The second structure was calculated on the basis of N–H, C′–N, H^α–C^α and C′–C^α dipolar couplings, and the H^α–C′ couplings are best-fit to this structure. Clearly, the NMR structure ($R^P = 0.98$) predicts the experimental H^α–C′ couplings better than the X-ray structure, which is related to a slight rearrangement of relative helix orientations in solution relative to the crystalline state.[71]

When accurate experimental dipolar couplings are available, it is always advantageous to incorporate them into the structure calculation process. However, once this is done, they no longer are useful for validation purposes. A way around this is to compare the observed and predicted changes in chemical shift between isotropic and aligned samples for a type of nucleus with a well-defined chemical shift anisotropy. The first application of this idea was for the change in ^{15}N chemical shift with field strength in a small protein-DNA complex,[72] caused by the anisotropy of the magnetic susceptibility of this complex. Although the changes were minute ($\leq$5 ppb), a clear improvement in the correlation was observed upon incorporation of dipolar couplings in the structure calculation process. Subsequently, comparison of much larger ^{13}C′ chemical shift changes between a protein in isotropic and aligned bicellar medium also showed an excellent correlation with structure.[73]

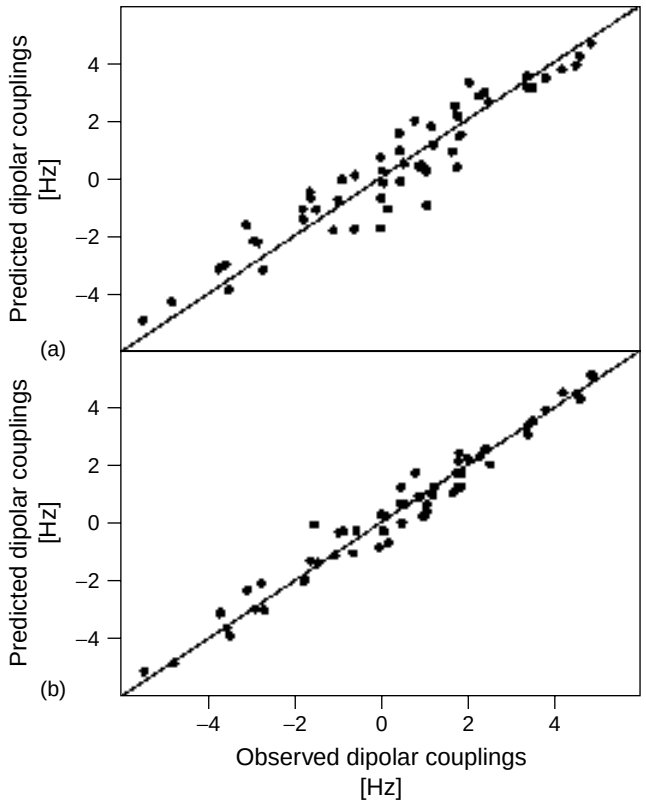

Figure 8 Correlation between measured, normalized $^2D_{C'H\alpha}$ dipolar couplings and those predicted by the 1.0-Å X-ray crystal structure (a), and by the NMR structures of the C-terminal domain of Ca^{2+}-calmodulin, calculated without $^2D_{C'H\alpha}$ couplings (b). The slightly better fit to the NMR structure is caused by a small rearrangement of the relative helix orientations in solution relative to those observed in the crystalline state of this protein[71]

7 CONCLUDING REMARKS

The introduction of methods for generating tunable, very weak alignment of macromolecules makes it possible to measure the one-bond and other short range dipolar couplings with a remarkable degree of accuracy. Even while the splittings are reduced by about three orders of magnitude relative to their static values, the narrow line widths and relatively high signal-to-noise ratio attainable in high resolution NMR more than compensate for the low degree of order. For example, one-bond ^{15}N–^{1}H dipolar couplings typically can be measured with an accuracy of ca. 0.1 Hz, whereas their range covers up to 50 Hz. Even for the intrinsically much smaller interactions, such as the one-bond ^{15}N–$^{13}C'$ dipolar coupling, the error typically is smaller by up to two orders of magnitude relative to the range of couplings observed. Similarly, chemical shift effects can be measured at a relative accuracy that rivals that attainable in solid state NMR, but the problem of resonance overlap is much less severe because isotropic shifts in solution are more effective at dispersing NMR spectra. Experimental correlations between $^{13}C'$, ^{15}N, and $^{1}H^{N}$ CSA tensors and secondary structure in proteins could be clearly established from such data.[74]

Dipolar couplings are not very sensitive to small amplitude oscillations about an average orientation. Conversely, relatively small discrepancies between observed and predicted magnitudes of dipolar couplings require rather large amplitude angular fluctuations if this discrepancy is entirely attributed to dynamic effects.[75,76] Nevertheless, because averaging of the observed dipolar interactions is sensitive to motions that cover the entire time scale from milliseconds to femtoseconds, it can potentially provide a powerful complement for the study of dynamic processes.

Measurement of tensorial interactions in macromolecules is a new and rapidly expanding area in structural biology. It offers numerous new opportunities, including rapid determination of backbone folds, rapid structure determination, refinement of conventional NMR structures, and the study of relative orientations of components in multi-molecular complexes. It is likely that a further marriage between conventional solid-state NMR techniques and the weak alignment approach may expand these areas even further.

8 RELATED ARTICLES IN VOLUMES 1–8

Biological Macromolecules: Structure Determination in Solution, Volume 2; Liquid Crystals: General Considerations, Volume 4; Liquid Crystals: Mixed Magnetic Susceptibility Solvents, Volume 4; Two-Dimensional NMR of Molecules Oriented in Liquid Crystalline Phases, Volume 8.

9 REFERENCES

1. A. Saupe and G. Englert, *Phys. Rev. Lett.*, 1963, **11**, 462–464.
2. J. W. Emsley in 'Encyclopedia of NMR', eds D. M. Grant and R. K. Harris, Wiley: Chichester, 1996, Vol. 4, pp 2788–2799.
3. E. W. Bastiaan, C. Maclean, P. C. M. vanZijl, and A. A. Bothner-By, *Annu. Rep. NMR Spectrosc.*, 1987, **19**, 35–77.
4. A. A. Bothner-By, in 'Encyclopedia of NMR', eds D. M. Grant and R. K. Harris, Wiley: Chichester, 1996, Vol. 5, pp 2932–2938.
5. J. R. Tolman, J. M. Flanagan, M. A. Kennedy, and J. H. Prestegard, *Proc. Natl. Acad. Sci. USA*, 1995, **92**, 9279–9283.
6. N. Tjandra, J. G. Omichinski, A. M. Gronenborn, G. M. Clore, and A. Bax, *Nature Struct. Biol.*, 1997, **4**, 732–738.
7. A. Bax and N. Tjandra, *J. Biomol. NMR*, 1997, **10**, 289–292.
8. N. Tjandra and A. Bax, *Science*, 1997, **278**, 1111–1114.
9. M. R. Hansen, L. Mueller, and A. Pardi, *Nature Struct. Biol.*, 1998, **5**, 1065–1074.
10. G. M. Clore, M. R. Starich, and A. M. Gronenborn, *J. Am. Chem. Soc.*, 1998, **120**, 10 571–10 572.
11. R. S. Prosser, J. A. Losonczi, and I. V. Shiyanovskaya, *J. Am. Chem. Soc.*, 1998, **120**, 11 010–11 011.
12. L. G. Barrientos, C. Dolan, and A. M. Gronenborn, *J. Biomol. NMR*, 2000, **16**, 329–337.
13. K. Fleming, D. Gray, S. Prasannan, and S. Matthews, *J. Am. Chem. Soc.*, 2000, **122**, 5224–5225.
14. M. Ruckert and G. Otting, *J. Am. Chem. Soc.*, 2000, **122**, 7793–7797.
15. M. Zweckstetter and A. Bax, *J. Biomol. NMR*, 2001, **20**, 365–377.
16. M. Ottiger and A. Bax, *J. Am. Chem. Soc.*, 1998, **120**, 12 334–12 341.
17. D. W. Yang, R. A. Venters, G. A. Mueller, W. Y. Choy, and L. E. Kay, *J. Biomol. NMR*, 1999, **14**, 333–343.
18. P. Permi, P. R. Rosevear, and A. Annila, *J. Biomol. NMR*, 2000, **17**, 43–54.
19. J. H. Prestegard, *Nature Struct. Biol.*, 1998, **5**, 517–522.
20. N. Tjandra, *Struct. Fold. Des.*, 1999, **7**, R205–R211.

21. A. Bax, G. Kontaxis, and N. Tjandra, *Methods Enzymol.*, 2001, **339**, 127–174.
22. E. Brunner, *Concepts Magn. Reson.*, 2001, **13**, 238–259.
23. J. A. Losonczi, M. Andrec, M. W. F. Fischer, and J. H. Prestegard, *J. Magn. Reson.*, 1999, **138**, 334–342.
24. G. M. Clore, A. M. Gronenborn, and A. Bax, *J. Magn. Reson.*, 1998, **133**, 216–221.
25. D. M. Grant, in 'Encyclopedia of NMR', eds D. M. Grant and R. K. Harris, Wiley: Chichester, 1996, Vol. 2, pp 1298–1321.
26. A. T. Brunger, P. D. Adams, G. M. Clore, W. L. DeLano, P. Gros, R. W. Grosse-Kunstleve, J. S. Jiang, J. Kuszewski, M. Nilges, N. S. Pannu, R. J. Read, L. M. Rice, T. Simonson, and G. L. Warren, *Acta Crystallogr. Sec. D-Biol. Crystallogr.*, 1998, **54**, 905–921.
27. N. Tjandra, J. Marquardt, and G. M. Clore, *J. Magn. Reson.*, 2000, **142**, 393–396.
28. C. Griesinger, O. W. Sørensen, and R. R. Ernst, *J. Magn. Reson.*, 1987, **75**, 474–492.
29. A. Meissner, J. O. Duus, and O. W. Sorensen, *J. Biomol. NMR*, 1997, **10**, 89–94.
30. M. Ottiger, F. Delaglio, and A. Bax, *J. Magn. Reson.*, 1998, **131**, 373–378.
31. A. Bax, G. W. Vuister, S. Grzesiek, F. Delaglio, A. C. Wang, R. Tschudin, and G. Zhu, *Methods Enzymol.*, 1994, **239**, 79–105.
32. M. Ottiger, F. Delaglio, and A. Bax, *J. Magn. Reson.*, 1998, **131**, 373–378.
33. S. Grzesiek and A. Bax, *J. Magn. Reson.*, 1992, **96**, 432–440.
34. F. Delaglio, D. A. Torchia, and A. Bax, *J. Biomol. NMR*, 1991, **1**, 439–446.
35. J. J. Chou and A. Bax, *J. Biomol. NMR*, 2000, **18**, 101–105.
36. N. Tjandra and A. Bax, *J. Am. Chem. Soc.*, 1997, **119**, 9576–9577.
37. J. Evenas, A. Mittermaier, D. W. Yang, and L. E. Kay, *J. Am. Chem. Soc.*, 2001, **123**, 2858–2864.
38. M. Ottiger, F. Delaglio, J. L. Marquardt, N. Tjandra, and A. Bax, *J. Magn. Reson.*, 1998, **134**, 365–369.
39. M. Ottiger and A. Bax, *J. Am. Chem. Soc.*, 1999, **121**, 4690–4695.
40. E. T. Olejniczak, R. P. Meadows, H. Wang, M. L. Cai, D. G. Nettesheim, and S. W. Fesik, *J. Am. Chem. Soc.*, 1999, **121**, 9249–9250.
41. M. L. Cai, H. Wang, E. T. Olejniczak, R. P. Meadows, A. H. Gunasekera, N. Xu, and S. W. Fesik, *J. Magn. Reson.*, 1999, **139**, 451–453.
42. G. Otting, M. Ruckert, M. H. Levitt, and A. Moshref, *J. Biomol. NMR*, 2000, **16**, 343–346.
43. W. Peti and C. Griesinger, *J. Am. Chem. Soc.*, 2000, **122**, 3975–3976.
44. G. W. Vuister and A. Bax, *J. Am. Chem. Soc.*, 1993, **115**, 7772–7777.
45. C. R. Sanders and J. H. Prestegard, *Biophys. J.*, 1990, **58**, 447–460.
46. C. R. Sanders and J. H. Prestegard, *J. Am. Chem. Soc.*, 1991, **113**, 1987–1996.
47. C. R. Sanders and J. P. Schwonek, *Biochemistry*, 1992, **31**, 8898–8905.
48. P. A. Luchette, T. N. Vetman, R. S. Prosser, R. E. W. Hancock, M. P. Nieh, C. J. Glinka, S. Krueger, and J. Katsaras, *Biochim. Biophys. Acta–Biomembranes*, 2001, **1513**, 83–94.
49. S. Gaemers and A. Bax, *J. Am. Chem. Soc.*, 2001, in press.
50. M. P. Nieh, C. J. Glinka, S. Krueger, R. S. Prosser, and J. Katsaras, *Langmuir*, 2001, **17**, 2629–2638.
51. J. A. Losonczi and J. H. Prestegard, *J. Biomol. NMR*, 1998, **12**, 447–451.
52. B. E. Ramirez and A. Bax, *J. Am. Chem. Soc.*, 1998, **120**, 9106–9107.
53. J. Sass, F. Cordier, A. Hoffmann, A. Cousin, J. G. Omichinski, H. Lowen, and S. Grzesiek, *J. Am. Chem. Soc.*, 1999, **121**, 2047–2055.
54. M. Ottiger and A. Bax, *J. Biomol. NMR*, 1998, **12**, 361–372.
55. M. Ottiger and A. Bax, *J. Biomol. NMR*, 1999, **13**, 187–191.
56. S. Cavagnero, H. J. Dyson, and P. E. Wright, *J. Biomol. NMR*, 1999, **13**, 387–391.
57. H. Wang, M. Eberstadt, E. T. Olejniczak, R. P. Meadows, and S. W. Fesik, *J. Biomol. NMR*, 1998, **12**, 443–446.
58. M. R. Hansen, M. Rance, and A. Pardi, *J. Am. Chem. Soc.*, 1998, **120**, 11 210–11 211.
59. L. G. Barrientos, J. M. Louis, and A. M. Gronenborn, *J. Magn. Reson.*, 2001, **149**, 154–158.
60. K. Fleming, D. Gray, S. Prasannan, and S. Matthews, *J. Am. Chem. Soc.*, 2000, **122**, 5224–5225.
61. B. W. Koenig, J. S. Hu, M. Ottiger, S. Bose, R. W. Hendler, and A. Bax, *J. Am. Chem. Soc.*, 1999, **121**, 1385–1386.
62. B. A. Lewis, C. Rosenblatt, R. G. Griffin, J. Courtemanche, and J. Herzfeld, *Biophys. J.*, 1985, **47**, 143–150.
63. R. Tycko, F. J. Blanco, and Y. Ishii, *J. Am. Chem. Soc.*, 2000, **122**, 9340–9341.
64. H. J. Sass, G. Musco, S. J. Stahl, P. T. Wingfield, and S. Grzesiek, *J. Biomol. NMR*, 2000, **18**, 303–309.
65. D. Shortle and M. S. Ackerman, *Science*, 2001, **293**, 487–489.
66. J. J. Chou, S. Gaemers, B. Howder, J. M. Louis, and A. Bax, *J. Biomol. NMR*, 2001, **21**, 377–382.
67. Y. Ishii, M. A. Markus, and R. Tycko, *J. Biomol. NMR*, 2001, **21**, 141–151.
68. H. M. Al-Hashimi, H. Valafar, M. Terrell, E. R. Zartler, M. K. Eidsness, and J. H. Prestegard, *J. Magn. Reson.*, 2000, **143**, 402–406.
69. E. de Alba, J. L. Baber, and N. Tjandra, *J. Am. Chem. Soc.*, 1999, **121**, 4282–4283.
70. M. Zweckstetter and A. Bax, *J. Am. Chem. Soc.*, 2000, **122**, 3791–3792.
71. J. J. Chou, S. Li, C. B. Klee, and A. Bax, *Nature Struct. Biol.*, 2001, **8**, 990–997.
72. M. Ottiger, N. Tjandra, and A. Bax, *J. Am. Chem. Soc.*, 1997, **119**, 9825–9830.
73. G. Cornilescu, J. L. Marquardt, M. Ottiger, and A. Bax, *J. Am. Chem. Soc.*, 1998, **120**, 6836–6837.
74. G. Cornilescu and A. Bax, *J. Am. Chem. Soc.*, 2000, **122**, 10 143–10 154.
75. J. R. Tolman, J. M. Flanagan, M. A. Kennedy, and J. H. Prestegard, *Nature Struct. Biol.*, 1997, **4**, 292–297.
76. J. Meiler, J. J. Prompers, W. Peti, C. Griesinger, and R. Bruschweiler, *J. Am. Chem. Soc.*, 2001, **123**, 6098–6107.
77. S. Moltke and S. Grzesiek, *J. Biomol. NMR*, 1999, **15**, 77–82.

Biographical Sketch

Ad Bax, *b* 1956. Ph.D. 1981 Applied Physics, Delft University of Technology, The Netherlands. Research associate, Colorado State University, 1982–83; National Institutes of Health, Visiting Scientist, NMR Section, Laboratory of Chemical Physics, NIDDK, 1983–88. National Institutes of Health, Chief, Biophysical NMR Spectroscopy Section, 1988-present. Approx. 300 publications. Current research interests: NMR and its applications in chemistry, biology and medicine.

Liquid Crystalline Samples: Chiral Smectic Phases

Carlo Alberto Veracini and Marco Geppi

Università degli Studi di Pisa, Pisa, Italy

1 Introduction 1
2 Molecular Alignment 1
3 Structure and Orientational Ordering: ^{2}H Methods 2
4 Structure and Orientational Ordering: ^{13}C Methods 4
5 Dynamics: ^{1}H, ^{13}C and ^{2}H Methods 5
6 Related Articles in this Volume 8
7 Related Articles in Volumes 1–8 8
8 References 8

1 INTRODUCTION

Smectic liquid crystals, in particular the chiral smectics, have dominated fundamental liquid crystal research for at least two decades while nematics still completely dominate applications. In fact, notwithstanding the great complexity of these materials as well as their mechanical fragility, they appear very promising for technological applications. Recently, the ferroelectric liquid crystals (FLC), which have been under active study since their discovery in 1975, have been complemented with antiferroelectric liquid crystals (AFLC) discovered by Chandani et al. in 1989, and with a few intermediate phases (smectic C^*_α and C^*_γ).

The mesogens giving rise to these phases are usually flexible molecules containing a chiral center; even though noticeable exceptions are present, for simplicity here we will refer to these molecules as formed by an achiral chain, a central aromatic core and a chain bearing the chiral center. In the smectic phases the molecules, which can be roughly thought of as exhibiting a rod-like shape, are arranged within layers, but, while in the smectic A (S_A) the preferred direction of the mesogen long axes (the director) is parallel to the layer normal, in the smectic C (S_C) it is tilted. In ferroelectric S_C phases (S^*_C) a spontaneous polarization is observed within each layer in a direction perpendicular to the plane formed by the tilt direction and the smectic layer normal due to the polarity of the molecules. The direction of the tilt and spontaneous polarization slowly precess as we move along the layer normal. As a result a helical structure is formed, with a pitch of the order of the wavelength of the visible light (see Figure 1a). In the antiferroelectric S_C phase (S^*_{CA}) the molecules are still tilted with respect to the smectic layer normal, but the direction of the tilt alternates, and therefore the in-plane spontaneous polarization reverses by 180°, when moving from one smectic layer to the next (see Figure 1b). The structure of the C_α and C_γ phases is less certain at the molecular level although there is a number of experimental and theoretical investigations. An hypothesis has been formulated that the smectic C_α phase is a sort of S^*_C with a much shorter helix pitch (see Figure 1c), while the ferrielectric C_γ shows two interdigitated helices as in the S^*_{CA}, but here the molecules are rotated by an angle different to 180° with respect to the helix axis when we move from one smectic layer to the next (see Figure 1d).

Over the past two years, interest in smectic liquid crystals has experienced a renaissance with active research in both the materials and their large-scale applications. Several reasons have contributed to this, in addition to the interest in AFLC and in the other S_C subphases. First of all, the mechanical fragility problem has been overcome by means of several solutions, moreover there has been the advent of FLC polymers, elastomers and polymer-reinforced FLC materials. These reasons, together with a high improvement in addressing technology, make FLCs good candidates for the next generation of Liquid Crystal Displays. However, at this moment, the molecular mechanism behind these materials, as well as their physics, and in particular the conditions responsible for the occurrence of ferroelectric and antiferroelectric phases, are still under investigation.[1] The structural behavior and, sometimes even the identification of existing subphases has not yet been performed and this is an important task which could be undertaken by spectroscopic, calorimetric and diffraction methods. This is not only fundamentally important, but it also has far-reaching consequences for applications and materials synthesis. Another important reason that has recently contributed to bring chiral smectics into focus again is that there are some very important but still unanswered fundamental questions connected with the coupling between polarity, chirality and symmetry. The chirality in smectic C phases is usually induced by using 'rod-shaped' molecules bearing a chiral center as building blocks, but recently achiral 'bow-shaped' or 'banana' molecules which form chiral smectic phases have received much attention.

For the investigation of the behavior of chiral smectic liquid crystals many spectroscopic and diffratometric techniques are used. Among them, NMR has already played and will play in the near future a major role. The structure of the mesogenic molecules, the orientational order, the structure of the aggregates, their tilt angle and magnetic alignment, as well as the structural changes at the phase transitions, are typical subjects which can be tackled with NMR. Moreover, relaxation studies allow the overall dynamics of mesogenic molecules, as well as internal and collective motions, to be investigated.

In this context, ^{13}C and ^{2}H NMR spectroscopies have almost exclusively contributed to structural and ordering studies, while ^{1}H relaxation dispersion measurements, ^{13}C and ^{2}H linewidth and relaxation studies have been employed to characterize the dynamics. Moreover, it should be mentioned that a specific structural role (e.g., in determining biasing of internal motions) has been played by ^{14}N NQR techniques.[1]

2 MOLECULAR ALIGNMENT

In the NMR of liquid crystals it is important to clarify the alignment behavior of the directors with respect to the external magnetic field. When S_C phases are obtained by lowering the temperature either from nematic or S_A phases, where the director was aligned along the external magnetic field, two types of behavior can be found: (i) the directors prefer to

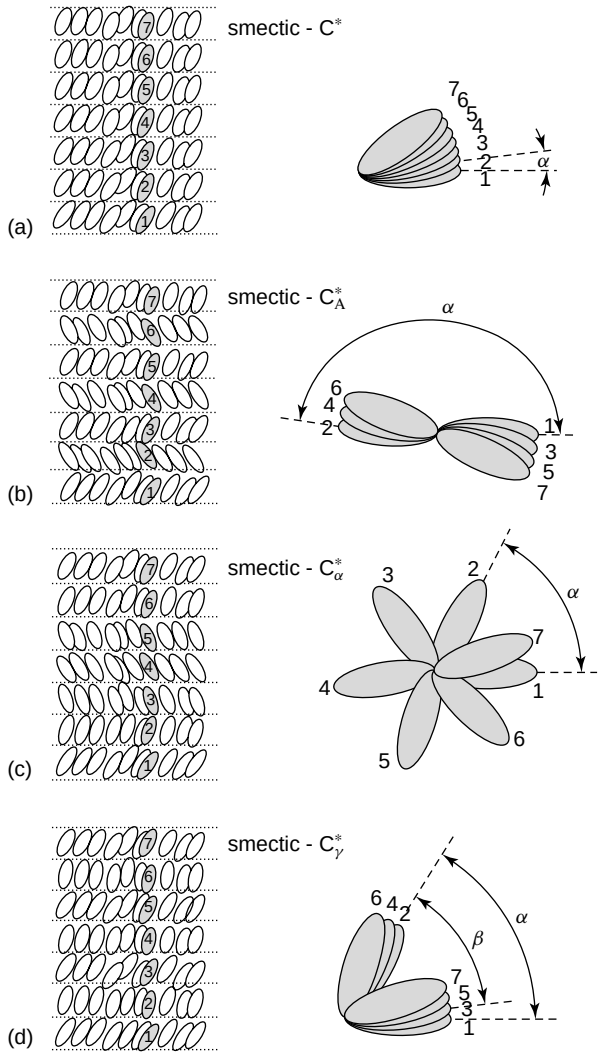

Figure 1 Scheme of different chiral smectic phases: (a) ferroelectric S_C^*, (b) anti-ferroelectric S_{CA}^*, (c) $S_{C\alpha}^*$, (d) ferrielectric $S_{C\gamma}^*$. (Reproduced by permission of American Physical Society and Professor R. Blinc from M. Skarabot, M. Cepic, B. Zeks, R. Blinc, G. Heppke, A. V. Kityk and I. Musevic, *Phys. Rev. E*, 1998, **58**, 575)

remain aligned along the magnetic field and the smectic layers tilt with respect to the field; (ii) the layers remain perpendicular to the magnetic field and the directors progressively tilt as the temperature is lowered. In the case of S_C^* the alignment is commonly governed by the chirality: in the case of high optical purity the smectic layers keep normal to the magnetic field as in the S_A phase, and the directors tilt away from the field direction within each layer and give rise to a helical structure going through the layers. However, this is not a general rule: situations where the director keeps aligned to the field, causing unwinding of the helical structures (u-S_C^*) are present and, in particular cases, a 'magnetic' transition between u-S_C^* and S_C^* can be observed within the ferroelectric range. Helix unwinding has also been found in the case of chiral smectic phases induced by chiral host molecules. When the liquid crystal is formed by racemic mixtures, the directors usually behave as in achiral smectogens, remaining aligned to the field while the smectic layers tilt. On the other hand, in the case of S_{CA}^* the directors are not aligned to the field for both optically pure samples and racemic mixtures. A particular case is that of fast spinning conditions (with a rate of the order of a kHz) about an axis not parallel to the magnetic field direction: the molecular director usually aligns along the spinning axis even for optically pure samples, but cases of partial retention of the helical structure have been observed.

3 STRUCTURE AND ORIENTATIONAL ORDERING: ^{2}H METHODS

Deuterium NMR in partially deuterated liquid crystals is an extremely powerful tool for the determination of orientational order at the molecular level, as well as for the study of the organization of liquid crystalline superstructures. In the case of FLC, AFLC and related phases, deuterium NMR has been used for the investigation of phase transitions, structural, geometrical, conformational and dynamic behavior of chiral mesogens, as well as of the helix structure and its distortion in the presence of external fields.

The deuterium nucleus has a spin $I = 1$, thus exhibiting a non-zero electric quadrupole moment (eQ). The quadrupolar Hamiltonian is the main perturbation to the Zeeman term: it does not contribute to ^{2}H spectra of isotropic phases, since it is traceless, but it dominates those of oriented phases. Here, large quadrupolar splittings $\Delta\nu_q$ can be observed depending on the local order parameters S_{ii} defined in the principal axis system (a, b, c) for the electric field gradient tensor:

$$\Delta\nu_q = \frac{3}{2} q_{aa} \left\lfloor S_{aa} + \frac{\eta}{3} (S_{bb} - S_{cc}) \right\rfloor \tag{1}$$

where the a axis is along the C–D bond, $q_{aa} = e^2 q Q/h$ is the quadrupolar coupling constant and $\eta = (V_{bb} - V_{cc})/V_{aa}$ is the asymmetry parameter, which is usually small due to the almost axial symmetry of the local electric field gradient tensor **V**. Neglecting η, equation (1) reduces to the simplified form:

$$\Delta\nu_q = \frac{3}{2} q_{aa} S_{aa} \tag{2}$$

q_{aa} assumes typical values of about 200, 185 and 170 kHz for sp, sp^2 and sp^3 carbon hybridizations, respectively, and therefore local order parameters can be obtained in a straightforward way by simple quadrupolar splitting measurements.

Sometimes, dipolar splittings due to the coupling with adjacent protons or deuterons can also be directly measured or extracted from ^{2}H NMR spectra, and they can be related to local order on the basis of the following equation:

$$\Delta\nu_d = -2K \frac{S_{\alpha\alpha}}{r^3} \tag{3}$$

where $S_{\alpha\alpha}$ is the ordering matrix element in the direction of the internuclear vector, which can be expressed in terms of S_{aa}, S_{bb} and S_{cc} depending on the molecular geometry; K is a constant depending on the nucleus coupled to the deuteron considered and r is the corresponding internuclear distance.

The expression of the local order parameters in terms of molecular order parameters is quite complex in the general case because of the molecular flexibility. This problem has been tackled either by theories which take into account how the molecular order depends on molecular conformations or

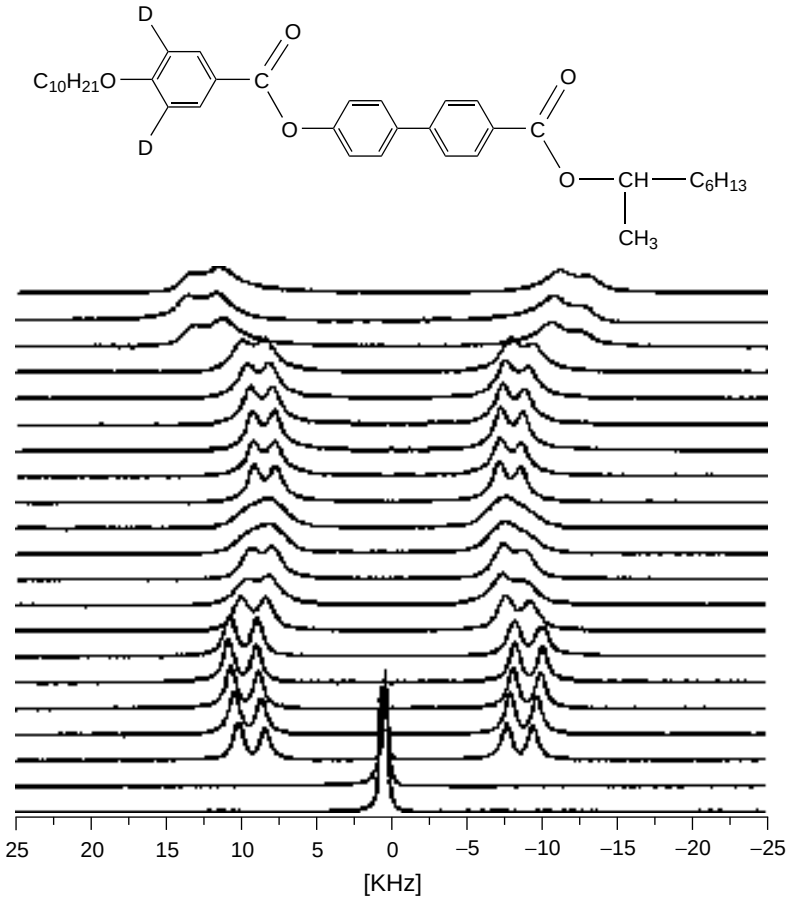

Figure 2 Variable temperature ^{2}H spectra of (S)-10B1M7-d_2 experiencing S_A, S_C^*, $S_{C\gamma}^*$, S_{CA}^* and S_J^* phases. In this example, the spectra are taken on cooling every 5 degrees starting from 403 K (bottom)

by treating the spectral data in the framework of information theories (M.E. methods). In the oversimplified, but common, assumption of rigid molecular structure, local order parameters can be written in terms of the principal order parameter S_{zz} and molecular biaxiality ($S_{xx} - S_{yy}$) through a series of spherical harmonic projections which transform the local frame into the molecular one on the basis of the molecular geometry.

Therefore, the extraction of a set of quadrupolar and dipolar couplings from ^{2}H spectra, when suitably labelled samples are available, allows the evaluation of molecular geometry and orientational order of either molecular fragments or the whole mesogenic molecule in the whole liquid crystalline range (see Figure 2).

By means of these methods structural information, such as that the core of some ferroelectric mesogens has a bent structure,[2] or that the chiral chain in AFLCs is substantially bent (as much as 43°) with respect to the molecular long axis,[3] have been found. In ferroelectric mesogens formed by two aromatic moieties joined by an ester bridge other subtle findings are that the two fragments show not only different principal local order parameters and biaxiality, but also different deuterium lineshapes within the same ^{2}H-NMR spectrum (Gaussian vs. Lorentzian). In principle, the tilt angle can be measured from the trend of the order parameter vs. temperature; however, since the measured order parameter in tilted phases is S_{zz} (the so-called 'nematic order') scaled by a factor $(3\cos^2\theta - 1)/2$, where θ is the tilt angle, this usually requires an extrapolation of S_{zz}. In favorable cases, however, a precise evaluation of the tilt angle can be performed by making measurements at two different fields, giving rise to S_C^* (low field, helix wound and molecules tilted away from the field) and u-S_C^* (high field, helix unwound, molecules aligned to the field and measured order parameter coincident with S_{zz}).

The full power of deuterium NMR can be, however, exploited in angular dependent experiments, where spectra are recorded as a function of the angle ψ between the external magnetic field and the helicoidal axis, which is parallel to the smectic layer normals.[4] In order to avoid the rearrangement of the molecules and the smectic planes with the field the sample is rotated at an angle ψ only during the short acquisition time and then quickly counterrotated to the initial position and again to $-\psi$ for the next acquisition. In this case the deuterium quadrupolar splitting is given by:

$$\Delta\nu_q = \frac{3}{4} q_{aa} S \left[3\,(\sin\psi \sin\theta \sin\phi + \cos\psi \cos\theta)^2 - 1\right] \qquad (4)$$

where S is the local order parameter relative to the director and ϕ is the director azimuth angle.

By means of this technique the soliton-like deformation of the helix and the critical magnetic field (i.e., the field causing helix unwinding) as a function of ψ can be studied. The soliton-like deformation has been found to have π and 2π symmetry for $\psi = 90°$ and $\psi \neq 90°$, respectively. The critical

magnetic field is anisotropic and it is minimum for ψ values ranging from 45 to 90°, as the tilt angle grows from 0 to 90°: reentrant S_C^*-uS_C^*-S_C^* behavior as a function of ψ has been experimentally observed.[4]

In the case of AFLC, the angular dependence of deuterium NMR spectra not only provides a microscopic verification of the alternating tilt model for S_{CA}^* phase, but it also highlights the presence of inter-layer molecular diffusion. In fact, from the point of view of angular dependent experiments, the antiferroelectric herringbone structure of the S_{CA}^* phase is similar to that of the non tilted S_A phase, as a result of the averaging of the electric field gradient tensor at the deuterium sites of two successive layers: this is produced by rapid molecular diffusion between adjacent layers followed by molecular reorientation corresponding to a 180° jump of the azimuth angle.

4 STRUCTURE AND ORIENTATIONAL ORDERING: ^{13}C METHODS

^{13}C techniques, and especially methods particular to solid state NMR, such as Magic Angle Spinning (MAS) and Cross-Polarization (CP), are useful to obtain insight into structural and orientational ordering information of chiral smectic liquid crystals. ^{13}C experiments can be carried out in static conditions or by fast spinning the sample about an axis forming an angle φ with the external magnetic field. The latter are referred to as MAS (when $\varphi = 54.7°$) or OFF-MAS experiments (when it deviates from that value). The molecular directors in tilted smectic phases can be aligned or unaligned to the magnetic field (static experiments), or to the spinning axis, depending on many factors, and a variety of behaviors have been observed, as previously discussed in Section 2.

^{13}C static spectra can experience a remarkable increase in linewidths going from isotropic to smectic phases, with a consequent loss of resolution, since the restricted mobility in the latter phases causes the anisotropic interactions affecting the spectrum to be partially reduced, but not averaged out. This allows phase transitions to be clearly identified and, possibly, the changes in the dynamic processes associated with the transitions to be unraveled.

The chemical shift in the oriented phases is strongly affected by their orientational properties, and large shifts are observed going from the isotropic towards a smectic phase. In fact, the chemical shift σ in the liquid crystalline phase can be related to the isotropic chemical shift σ_i through the following equation:

$$\sigma = \sigma_i + \frac{2}{3} S_{zz} \left[\sigma_{zz} - \frac{1}{2} \left(\sigma_{xx} + \sigma_{yy} \right) \right] + \frac{1}{3} \left(\sigma_{xx} - \sigma_{yy} \right) \left(S_{xx} - S_{yy} \right) \tag{5}$$

where the σ_{ii} are components of the chemical shift tensor and the S_{ii} are the order parameters, i.e., the principal components of the ordering matrix in an assumed rigid molecule where the z axis coincides with the long molecular axis.

This equation reduces to the simplified form of equation 6 when the biaxiality $S_{xx} - S_{yy}$ is negligible with respect to S_{zz}; $\Delta\sigma = \sigma_{zz} - 1/2 \left(\sigma_{xx} + \sigma_{yy} \right)$ is the difference between the component of the chemical shift tensor along the direction of the long molecular axis and the average component in the perpendicular plane.

$$\sigma \approx \sigma_i + \frac{2}{3} S_{zz} \Delta\sigma \tag{6}$$

Since $\Delta\sigma$ is positive for aromatic carbons and negative for aliphatic ones, a shift towards high and low frequencies is expected, respectively, in consequence of an increase of the order parameter S_{zz}, as, for instance, at the I–S_A and S_A–S_C transitions. However, when a chiral S_C phase is entered, the occurrence of the molecular tilting reduces the order parameter S_{zz} by the factor $(3\cos^2\theta - 1)/2$.

Therefore, in principle, the simple analysis of ^{13}C spectra should allow order parameters to be calculated. To this aim, two main problems need to be overcome. First, static conditions can prevent obtaining high-resolution spectra in the smectic phases, thus requiring the use of fast spinning and high-power decoupling. Even in this case, however, the large changes in chemical shifts usually make the interpretation of the ^{13}C spectrum difficult in the oriented phases on the basis of the sole spectrum of the isotropic phase, thus requiring chemical shift calculations, additional NMR experiments, such as cross-polarization, and, possibly, the preparation of suitably labeled samples. Second, in order to get S_{zz} from chemical shifts, the principal components of the chemical shift tensor have to be known (see equation 5). Since these quantities are not easily accessible, estimated values can be used, introducing, however, a large degree of uncertainty on the calculated order parameter values. Alternatively, the determination of the principal components of the chemical shift tensor can be performed for each carbon nucleus in the solid state by means of the 2D-TOSS-deTOSS experiment,[5] which gives a spinning sideband pattern for each resolved resonance in the isotropic ^{13}C spectrum.

A different approach is followed by Poon and Fung, who use the 2D-Separated Local Field (SLF) technique, which gives carbon-proton dipolar splittings ($\Delta\nu$) for each resolved resonance in the spectrum (see Figure 3).[6] The following equation can be used to determine the dipolar coupling constants D:

$$\Delta\nu = f \left[\left(3\cos^2\theta - 1 \right) D + J \right] \tag{7}$$

where f is a scaling factor characteristic of the dipolar decoupling sequence used and J is the C–H scalar coupling constant. The dipolar coupling constants so obtained can be exploited to determine the local order parameters through suitable relationships depending on the geometry and accessible conformations of the moiety which the C–H couple belongs to. This technique can also be used in combination with fast spinning at $\varphi \approx 45°$ to obtain more resolved ^{13}C spectra and remarkably reduce the proton–proton dipolar couplings. As a consequence, the experiments can be carried out with a lower decoupling power, thus reducing the temperature gradients in the sample and increasing the accuracy of the results.

The application of these techniques, also in combination with other ^{13}C experiments, has allowed some important structural aspects of chiral smectic phases to be understood. In agreement with abovementioned ^{2}H findings, in AFLCs the chiral chain is found to be bent with respect to the molecular long axis by an angle of as much as 43° not only in the

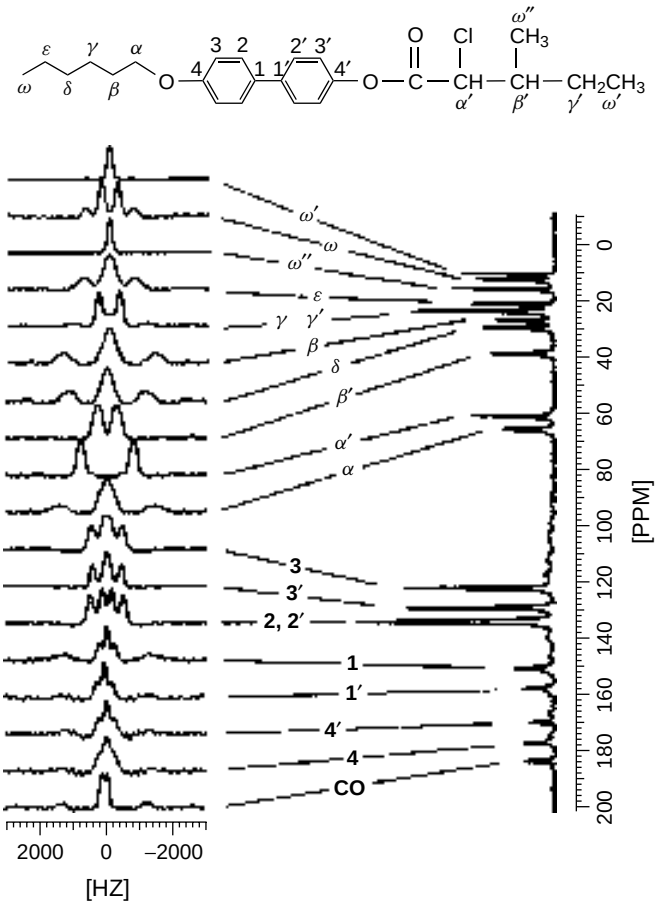

Figure 3 Application of the ^{13}C 2D-SLF technique to a ferroelectric liquid crystal. (Reproduced by permission of American Institute of Physics from C.-D. Poon and B. M. Fung, *J. Chem. Phys*., 1989, **92**, 7392)

ferro- and anti-ferroelectric phases, but also in the less ordered ones, and even in the isotropic phase.[7] Indeed, remarkable conformational changes are neither observed for optically pure mesogens throughout the liquid crystalline range, nor between optically pure mesogens and corresponding racemic mixture, thus supporting the conclusion that no new 'chiral interactions' should be invoked to explain the occurrence of chiral S_C phases, which should rather be governed by general excluded volume and/or electrostatic interactions.[8]

5 DYNAMICS: ^{1}H, ^{13}C AND ^{2}H METHODS

Dynamics in chiral smectogens by NMR is still a widely unexplored field due to the scarce experimental data so far reported in the literature and, to some extent, to the absence of theoretical models which might allow a more quantitative interpretation of these data. The papers published on this subject are mainly concerned with ^{1}H, ^{13}C or ^{2}H linewidths or spin-lattice relaxation time measurements. Each of these techniques highlights particular information, and therefore an overview on the dynamic behavior in chiral smectic phases can be obtained from their comparison.

5.1 ^{1}H

Proton spin-lattice relaxation measurements represent an important field in the investigation of the dynamics of chiral smectic phases. Some papers were published in the 80's reporting measurements at different Larmor frequencies using conventional NMR spectrometers, but a great boost in this kind of measurements took place when fast field cycling spectrometers, able to extend the Larmor frequency range down to a few Hz, became available. ^{1}H T_1 measurements covering the range 100 Hz–300 MHz are performed using fast field cycling devices and conventional NMR pulsed spectrometers for the very low frequency range (between 100 Hz and 10 MHz) and above 10 MHz, respectively.[9]

The relaxation is essentially determined by the modulation of the dipolar couplings between neighboring protons in the more rigid parts of the molecules by motions having characteristic frequencies of the order of the Larmor frequency. In the frequency range usually investigated three main kinds of dynamic processes are involved: collective motions, molecular self-diffusion (SD) and local molecular rotations. Collective motions in chiral smectics include, in principle, order director fluctuations (ODF) and Goldstone and soft modes;[1] however, the Goldstone mode has a characteristic frequency too low to be detected by this kind of measurement, and the contribution of the soft mode cannot be clearly distinguished from that of ODF, so collective motions are usually treated in terms of ODF only. On this basis, the proton spin-lattice relaxation rate $(1/T_1)$ can be expressed as a sum of terms, neglecting the contribution of possible cross terms between the different mechanisms, also considering that they usually show characteristic frequencies of different order of magnitudes:

$$\frac{1}{T_1} = \frac{1}{T_{1\mathrm{ODF}}} + \frac{1}{T_{1\mathrm{SD}}} + \frac{1}{T_{1\mathrm{Rot}}} \qquad (8)$$

As far as ODF are concerned, a frequency dependence of the type $T_1 \propto \omega$ is predicted for smectic phases by the model developed by Blinc et al.[10] The contribution of molecular SD and rotations can be expressed on the basis of a number of theoretical models; an Arrhenius dependence is usually assumed for correlation times and diffusional coefficients.

Two ranges of frequency are generally identified: at frequencies lower than 100 kHz the predominant contribution to the relaxation is represented by collective motions, while above that limit molecular rotations and SD become by far the most important relaxation mechanisms. Recently, it has been observed that the proton relaxation behavior in both ferri and anti-ferroelectric smectic C^* phases differs remarkably from that in smectic A and ferroelectric smectic C^* phases. A further dynamic process, the anti-phase azimuthal angle fluctuations, corresponding to an additional term in equation 8, can be invoked to get a good reproduction of the experimental T_1 data (see Figure 4). This process mostly contributes to the relaxation below 20 kHz, along with director fluctuations.

The main limitation of ^{1}H techniques is their difficulty in achieving site-specific information and therefore in getting insight on the dynamics of molecular fragments. This limitation can be removed, in principle, by using ^{13}C and ^{2}H techniques.

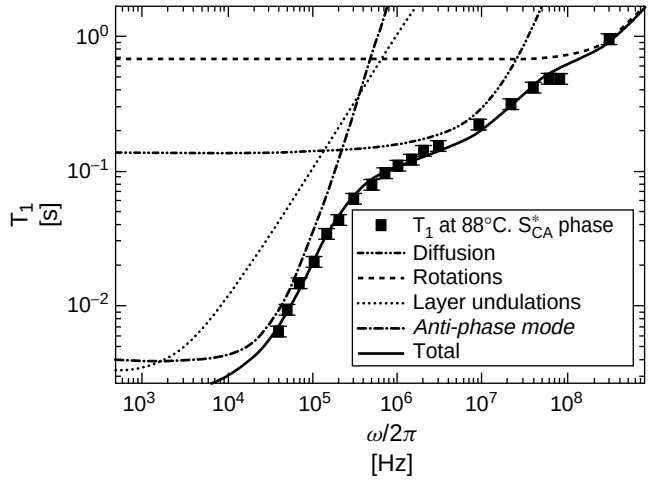

Figure 4 ^{1}H T_1 dispersion curve of an anti-ferroelectric liquid crystal, fitted by theoretical models for ODF, SD, molecular rotation and anti-phase azimuthal angle fluctuations. (Reproduced by permission of Gordon and Breach Publishers from A. Ferraz, A. C. Ribeiro and H. T. Nguyen, *Mol. Cryst. Liq. Cryst.*, 1999, **331**, 67)

5.2 ^{13}C

Some studies have been reported in which the dynamics of ferro- and/or anti-ferroelectric liquid crystals have been investigated through ^{13}C NMR solid state techniques. In fact, the high spectral resolution that can be achieved by MAS and high-power decoupling usually allows distinct peaks corresponding to the different carbon nuclei to be singled out, thus obtaining detailed dynamic information. Linewidth and relaxation time measurements can be exploited to obtain information on motions with correlation times of the same order of magnitude to the inverse of the proton decoupling and the Larmor frequency, respectively. In some cases, linewidth studies as a function of temperature highlight the presence of line broadening in the chiral smectic C phases for aromatic ^{13}C only, the linewidth of aliphatic carbon nuclei remaining substantially unchanged over the whole mesophasic range, thus revealing remarkably different internal motions between the aromatic core and both the aliphatic chains. ^{13}C T_1 measurements do not reveal any appreciable change in the MHz dynamics at the $S_A - S^*_C$ transition (see Figure 5), the only exception being represented by a change in the slope of the $\ln(T_1)$ vs 1000/T trend in the S^*_{CA} phase for the sole chiral carbon nucleus.

5.3 ^{2}H

Studies of the dynamics of liquid crystals based on the analysis of ^{2}H Zeeman (T_{1Z}) and quadrupolar (T_{1Q}) spin-lattice relaxation times have been extensively reported in the literature.[11] In fact, deuterium relaxation times, for the measurement of which the use of high-resolution solid-state devices is not necessary, are mainly determined by the intramolecular quadrupolar interaction, and therefore their interpretation is not complicated by intermolecular interactions, as

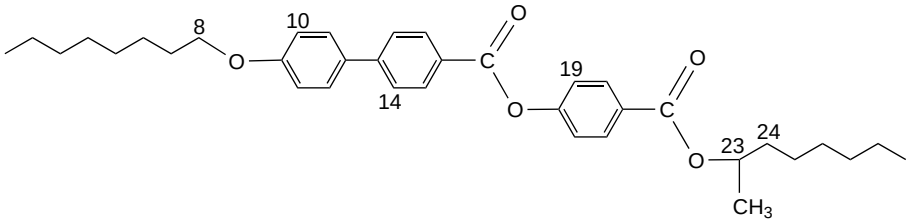

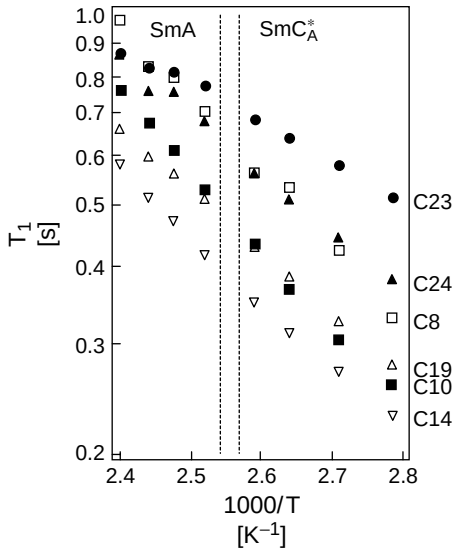

Figure 5 ^{13}C T_1 temperature dependence of some carbon nuclei from aromatic core, chiral and achiral chains of an anti-ferroelectric liquid crystal. (Reproduced by permission of the Institute of Pure and Applied Physics from K. Tokumaru, B. Jin, S. Yoshida, Y. Takanishi, K. Ishikawa, H. Takezoe, A. Fukuda, T. Nakai and S. Miyajima, *Jpn. J. Appl. Phys*., 1999, **38**, 147)

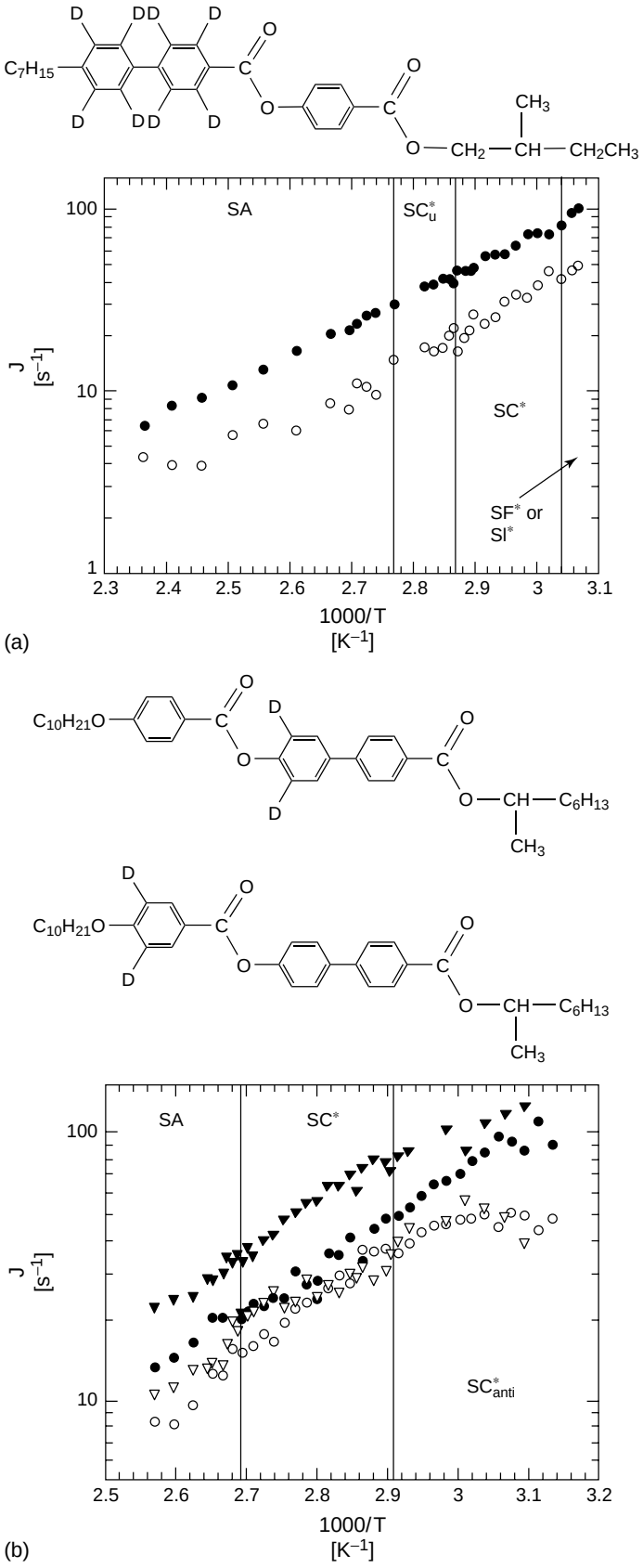

Figure 6 Logarithimic plots of ^2H spectral densities J_1 (full symbols) and J_2 (empty symbols) vs 1000/T in the different smectic phases of (a) MBHB and (b) 10B1M7 deuterated at two different aromatic core sites (triangles and circles indicate deuterons on the phenyl and biphenyl fragments, respectively). (Reproduced by permission of the American Chemical Society from D. Catalano, M. Cifelli, M. Geppi and C. A. Veracini, *J. Phys. Chem. A*, 2001, **105**, 34)

for proton relaxation. Moreover, their site-specificity allows clearly distinguished information arising from different molecular moieties to be obtained when suitably labeled samples are available. T_{1Z} and T_{1Q} are simply related to the spectral densities $J_1(\omega_0)$ and $J_2(2\omega_0)$ by means of the following equations:

$$\frac{1}{T_{1Z}} = J_1(\omega_0) + 4J_2(2\omega_0) \quad (9)$$

$$\frac{1}{T_{1Q}} = 3J_1(\omega_0) \quad (10)$$

Several models can be applied which allow these spectral densities to be expressed in terms of quantitative parameters (e.g., diffusional coefficients and activation energies) describing specific internal, overall molecular and collective motions. Unfortunately, the models available for molecular motions are based on molecular and phase symmetry assumptions which do not properly apply to chiral smectic C phases. However, even though in these phases the interpretation of ^{2}H spin-lattice relaxation times cannot be as detailed and quantitative as in nematic and smectic A phases, these measurements can contribute to unraveling the MHz dynamic behavior of FLC and AFLC. No particular changes in T_{1Z} and T_{1Q} are observed at the $S_A-S_C^*$ transition for deuterium nuclei belonging to the aromatic core, even though a change in the slope of the $\ln(J)$ trend vs 1000/T can be revealed within the anti-ferroelectric range (see Figure 6).[12] These results correspond with the ^{13}C T_1 findings previously discussed. Deuterium relaxation studies of both the chiral and achiral chains should help to clarify the extent to which internal and/or molecular motions are biased when ferroelectric and anti-ferroelectric phases are entered.

Occasionally, dynamic information can also be extracted from the analysis of variable-temperature ^{2}H spectra. For instance, a different dynamic behavior between the two aliphatic chains was observed from the occurrence of multiplets in the spectrum, ascribable to an asymmetric hindering of rotations about C–C bonds in the chiral chain. Moreover, the presence of a maximum line broadening for aromatic deuteriums in the middle of the chiral smectic C range (see Figure 2), probably highlights the same dynamic behavior revealed by the previously mentioned ^{13}C line broadening.

Summarizing, ^{1}H, ^{13}C and ^{2}H results strongly support the conclusion that no abrupt change in the fast overall dynamics in the MHz regime occurs as the smectic C* phase is entered, these motions slowing down continuously by decreasing the temperature and being more hindered within the anti-ferroelectric phase. On the other hand, particular dynamic behavior has been observed in a slower regime for both the chiral chain and the aromatic core in the chiral smectic C phases. These findings could contribute to explaining the occurrence of these phases as well as their peculiar characteristics.

6 RELATED ARTICLES IN THIS VOLUME

Chiral Discrimination Using Chiral Ordering Agents.

7 RELATED ARTICLES IN VOLUMES 1–8

Liquid Crystalline Samples: Carbon-13 NMR, Volume 4; Liquid Crystalline Samples: Deuterium NMR, Volume 4; Liquid Crystalline Samples: Relaxation Mechanisms, Volume 4; Liquid Crystalline Samples: Structure of Nonrigid Molecules, Volume 4; Liquid Crystals: General Considerations, Volume 4; Magic Angle Spinning, Volume 5; Relaxation: An Introduction, Volume 6.

8 REFERENCES

1. I. Musevic, R. Blinc, and B. Zeks, 'The Physics of Ferroelectric and Antiferroelectric Liquid Crystals', World Scientific: Singapore, 2000.
2. D. Catalano, M. Cavazza, L. Chiezzi, M. Geppi, and C. A. Veracini, *Liq. Cryst.*, 2000, **27**, 621.
3. S. Yoshida, B. Jin, Y. Takanishi, K. Tokumaru, K. Ishikawa, H. Takezoe, A. Fukuda, T. Kusumoto, T. Nakai, and S. Miyajima, *J. Phys. Soc. Jpn.*, 1999, **68**, L9.
4. B. Zalar, A. Gregorovic, M. Simsic, A. Zidansek, and R. Blinc, *Phys. Rev. Lett.*, 1998, **80**, 4458.
5. A. C. Kolbert and R. G. Griffin, *Chem. Phys. Lett.*, 1990, **166**, 87.
6. C.-D. Poon and B. M. Fung, *J. Chem. Phys.*, 1989, **91**, 7392.
7. T. Nakai, S. Miyajima, Y. Takanishi, S. Yoshida, and A. Fukuda, *J. Phys. Chem. B*, 1999, **103**, 406.
8. D. J. Photinos and E. T. Samulski, *Science*, 1995, **270**, 783.
9. H. Bender, F. Noack, M. Vilfan, and R. Blinc, *Liq. Cryst.*, 1989, **5**, 1233.
10. R. Blinc, M. Luzar, M. Vilfan, and M. Burgar, *J. Chem. Phys.*, 1975, **63**, 3445.
11. R. Y. Dong, 'Nuclear Magnetic Resonance of Liquid Crystals', Springer-Verlag: New York, 1997.
12. D. Catalano, M. Cifelli, M. Geppi, and C. A. Veracini, *J. Phys. Chem. A*, 2001, **105**, 34.

Biographical Sketches

Carlo Alberto Veracini, *b* 1942. Laurea, Pisa, Scuola Normale Superiore, 1966. Associate Professor of Molecular Spectroscopy, 1983. Full Professor of Physical Chemistry, Università di Pisa, 1986-present. Approx. 150 publications. Current interests include structure, orientational order and dynamics of mesogens and solute molecules in liquid crystals by NMR, dynamics and structure of molecules and polymers by solid state NMR.

Marco Geppi, *b* 1966. Laurea (with Professor C. A. Veracini), Pisa, 1991. Ph.D. (with Professors C. A. Veracini and F. Ciardelli), Scuola Normale Superiore, Pisa, 1997. Dipartimento di Chimica e Chimica Industriale, Università di Pisa, 1997-present. Approx. 25 publications. Current interests: structure and dynamics of liquid crystals by NMR, solid state NMR of polymeric materials.

Liquid Crystalline Samples: Deuterium NMR

Ronald Y. Dong
Brandon University, Brandon, Manitoba, Canada

1	Introduction	1
2	Orientational Ordering	2
3	Spin Relaxation and Molecular Motion	4
4	Novel NMR Experiments	6
5	Related Articles	7
6	References	8

1 INTRODUCTION

Rowell and co-workers[1,2] were first to demonstrate that deuterium is an excellent spin probe for studying liquid crystalline samples. They also used selectively deuterated compounds to simplify the proton NMR spectra. Early work in this field was devoted to measuring and interpreting spin–lattice relaxation rates[3] of protons, and to revealing orientational ordering in various mesophases[4] by means of deuterium splittings and spectral patterns. While proton NMR of liquid crystals shows broad partially resolved spectra, the deuteron NMR spectra are often characterized by well resolved quadrupolar doublets[5,6] that may contain some dipolar fine structures [Figure 1(a)]. The deuteron ($I = 1$) Zeeman levels [Figure 1(b)] are perturbed by interaction of its nuclear quadrupolar moment Q with the asymmetric EFG at the deuteron site. The static Hamiltonian $\hat{\mathcal{H}}_0$ of the system is defined by

$$\hat{\mathcal{H}}_0 = \hat{\mathcal{H}}_Z + \langle \hat{\mathcal{H}}_Q(t) \rangle \tag{1}$$

where $\hat{\mathcal{H}}_Z$ is the Zeeman Hamiltonian and $\hat{\mathcal{H}}_Q$, the quadrupolar Hamiltonian, is time dependent due to thermally driven, randomly fluctuating molecular processes. Due to a nonzero $\langle \hat{\mathcal{H}}_Q(t) \rangle$ in a partially ordered system, the two nuclear transitions are displaced at equal distances from the Larmor frequency ($\omega_0/2\pi$) as shown in Figure 1. The EFG tensor for most C–D bonds is axially symmetric, with the unique principal axis along the C–D bond direction. The quadrupolar splitting for a static C–D bond can take a maximum value of $\frac{3}{2}\chi$ or about 260 kHz, which is much less than its Larmor frequency of 46 MHz in a magnetic field of 7.1 T. For comparison, dipolar splitting between two deuterons in a methylene group is at most a few kilohertz, D–H dipolar splitting for a similar geometry is about 10 kHz, and the chemical shift is of the order of 1 kHz. It is therefore possible to neglect the chemical shift dispersion and the dipolar interaction with other nuclei and to treat the deuteron as an isolated spin-1 nucleus. The theoretical analysis of such a system is relatively simple. The quadrupolar splitting $\Delta\nu_i$ of the ith C–D bond may be approximated by[7,8]

$$\Delta\nu_i = \tfrac{3}{2}\chi S_{zz} \langle 3\cos^2\theta_i - 1 \rangle / 2 \tag{2}$$

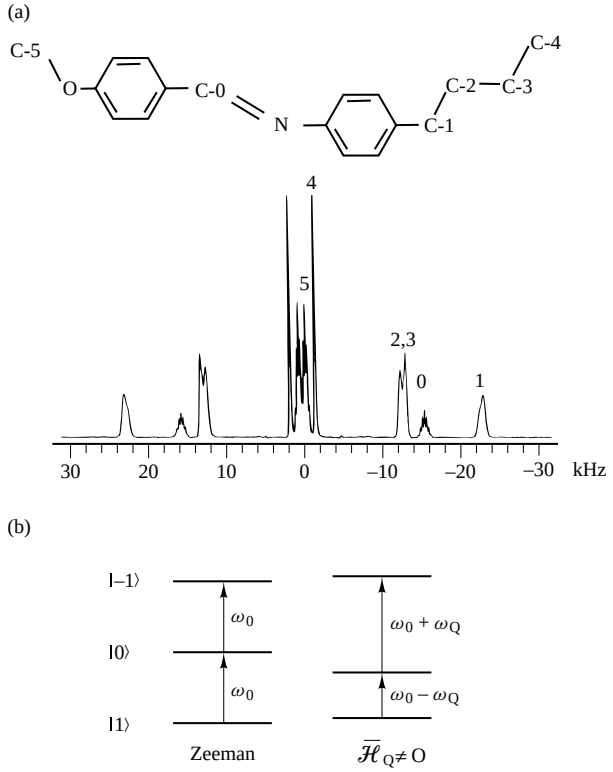

Figure 1 (a) The structure of MBBA and a typical deuterium NMR spectrum of MBBA-d_{13} in its nematic phase. (b) Energy level diagram of a deuteron spin ($\eta = 0$) in a large magnetic field. $\omega_0/2\pi$ is the Larmor frequency

where the contribution from the $S_{xx} - S_{yy}$ term is neglected, S_{zz} is the orientational order parameter of the long molecular axis with respect to the nematic director (see below), and θ_i represents the angle between the C_i–D bond and the molecular z axis. The angular brackets denote a statistical average over all allowed conformations in a flexible mesogen.

Spin relaxation has long been recognized as a useful technique for studying dynamic processes in liquid crystals.[7,8] A partial list of such processes[8] includes the order director fluctuations (ODFs), translational diffusion, order parameter fluctuations near phase transitions, molecular reorientation, and internal rotations of alkyl end chains. Deuteron is particularly suitable for getting detailed information about molecular motion in liquid crystals, since its relaxation is governed by intramolecular mechanisms, and multipulse techniques[7] may be used to determine individual spectral densities of motion from partially relaxed deuteron NMR spectra for all the resolved doublets. The quadrupolar relaxation Hamiltonian for a spin-1 system is defined by the time dependent part of $\hat{\mathcal{H}}_G(t)$ with respect to its average value $\langle \hat{\mathcal{H}}_Q(t) \rangle$:

$$\hat{\mathcal{H}}'_Q(t) = \hat{\mathcal{H}}_Q(t) - \langle \hat{\mathcal{H}}_Q(t) \rangle \tag{3}$$

The deuterium spin–lattice relaxation rates are given by[9,12]

$$\begin{aligned} \frac{1}{T_{1Z}} &= J_1(\omega_0) + 4J_2(2\omega_0) \\ \frac{1}{T_{1Q}} &= 3J_1(\omega_0) \end{aligned} \tag{4}$$

where an axially symmetric quadrupolar interaction ($\eta = 0$) is assumed. The spectral densities of motion $J_{m\mathrm{L}}$ ($m_\mathrm{L}\omega_0$) are Fourier transforms of the autocorrelation functions $G_{m_\mathrm{L}}(t)$ which involve second-rank tensor components $D^2_{m_\mathrm{L}0}(\Omega(t))$ in the relaxation Hamiltonian. The part of $\hat{\mathcal{H}}'_\mathrm{Q}(t)$ that connects spin states with $\Delta m_I = 1$ has a fluctuation spectrum described by $J_1(\omega_0)$, while the part that connects states with $\Delta m_I = 2$ is described by $J_2(2\omega_0)$. These spectral parameters and $J_0(0)$ at zero frequency (obtained in principle from one quantum spin echo or quadrupolar echo experiments) are determined without a particular choice of motional model. They must be accurately measured as a function of temperature at different Larmor frequencies, and may be used to provide critical tests of any proposed model of molecular motion. For systems with coupled deuterons, there are additional terms[13,14] in the relaxation expressions that arise from cross-correlation functions describing pairwise correlation in the motion of EFG tensor components at each deuteron. This additional information may serve as a further check of the proposed motional model.

2 ORIENTATIONAL ORDERING

One of the common features in liquid crystals is the existence of a preferred orientation of molecules along a spatial direction specified by a unit vector known as the director ***n***. Deuteron NMR spectroscopy has played a major role in establishing molecular field theories[8,15,16] for liquid crystals. These mean field theories can predict the temperature dependences of order parameters of rigid solutes and solvent molecules. The ordering of molecules in mesophases may in general be described by an orientational distribution function $f(\Omega)$ which depends on Eulerian angles $\Omega(\equiv \phi, \theta, \psi)$. The $f(\Omega)$ can be expanded in terms of Wigner rotation matrices of rank L

$$f(\Omega) = \sum_{L=0}^{\infty} \sum_{m,m'=-L}^{L} \frac{2L+1}{8\pi^2} a_{Lm'm} D^L_{m'm}(\Omega) \qquad (5)$$

where the expansion coefficients $a_{Lm'm} = \langle D^{L*}_{m'm}(\Omega)\rangle$ are the microscopic order parameters of rank L. The order parameters of rank two and four can in principle be measured, but higher rank order parameters are not as easily accessible by experiments. The potential of mean torque $V(\Omega)$ can be defined by writing $f(\Omega)$ as

$$f(\Omega) = \exp[-\beta V(\Omega)] / \int \mathrm{d}\Omega \exp[-\beta V(\Omega)] \qquad (6)$$

where $\beta = 1/k_\mathrm{B}T$. $V(\Omega)$ represents the orientational potential of a single molecule. In the Maier–Saupe theory[17,18] of nematics, $V(\Omega)$ takes on a simple form:

$$V(\cos\theta) = -\epsilon \langle P_2(\cos\theta)\rangle P_2(\cos\theta) \qquad (7)$$

where the parameter ϵ scales the strength of intermolecular interaction. The theory used a mean field approach and assumed that attractive dispersion forces among molecules are responsible for the nematic order. It was successful in predicting a first-order phase transition between a nematic and an isotropic phase, as well as the temperature dependence of the nematic order parameter $\langle P_2\rangle$ ($\equiv S_{zz}$). Using equation (2) as a first approximation, $\langle P_2\rangle$ can be calculated[1,2] from the observed quadrupolar splittings in liquid crystals. A general set of 25 rank-two order parameters[8] was defined by Saupe:

$$S^{\alpha\beta}_{ij} = \tfrac{1}{2}\langle 3 i_\alpha j_\beta - \delta_{\alpha\beta}\delta_{ij}\rangle \qquad (8)$$

where (α,β) refer to a space-fixed axis system (X,Y,Z), (i,j) refer to a molecule-fixed axis system (x,y,z), i_α denotes the projection of a unit vector ***i*** along the α axis, and the angular brackets represent an ensemble average. For uniaxial phases where ***n*** $\parallel Z$ axis, equation (8) gives the simple Saupe order matrix S_{ij} ($= \frac{1}{2}\langle 3 i_z j_z - \delta_{ij}\rangle$).

2.1 Rigid Molecules in Uniaxial Phases

For a rigid molecule (or a rigid fragment of a molecule) ordered in a uniaxial liquid crystalline phase, the partially averaged component ($\langle A_\parallel\rangle$) parallel to the director of any second rank tensor ***A*** is given by

$$\langle A_\parallel\rangle = A_0 + \tfrac{2}{3}\sum_{ij} A_{ij} S_{ij} \qquad (9)$$

where A_0 is the isotropic average of ***A***. For the EFG tensor ***q***, A_0 is zero and the splitting $\Delta\nu = \frac{3}{2}e^2Q/h\langle q_\parallel\rangle$ can be calculated using equation (9). The unknown S_{ij} elements can be determined from measuring enough independent values of $\langle q^i_\parallel\rangle$ where the superscript refers to sites in a molecule. This is usually possible for a rigid solute dissolved in a liquid crystal, where the principal axes of symmetry of the solute may be located with certainty based on its molecular symmetry. Hence deuterium NMR can provide precise measurements of S_{zz} and $S_{xx} - S_{yy}$ for a rigid molecule. Figure 2 illustrates the determination of $S_{xx} - S_{yy}$ and S_{zz} for anthracene-d_{10} in several nematogens. The solid curves are predictions based on the mean field theory of biaxial solutes where the λ parameter is a measure of the deviation in molecular symmetry of the solute from cylindrical symmetry. That the solute ordering depends on the solvent is an indication that the solute–solvent interactions cannot be dominated only by dispersion forces. For flexible mesogens, it may be possible to determine a local order matrix for a rigid fragment of the molecule provided the principal axes can be located on the fragment based on its symmetry. This is often difficult due to a lack of measurable nuclear couplings. A clear exception to this is the study of a perdeuterated fluorene group in the mesogen 2-fluorenyl-4′-tetradecyloxy benzoate-d_9 (FLOG$_4$).[20] Because of the large number (eight) of distinct deuteron sites, the location of the long molecular axis could be adjusted for the average conformer in a frame fixed to the fluorene group, and the local order parameters were unambiguously determined.

2.2 Flexible Molecules in Uniaxial Phases

Mesogenic molecules are usually composed of an aromatic core and one or more flexible alkyl chains. Due to internal

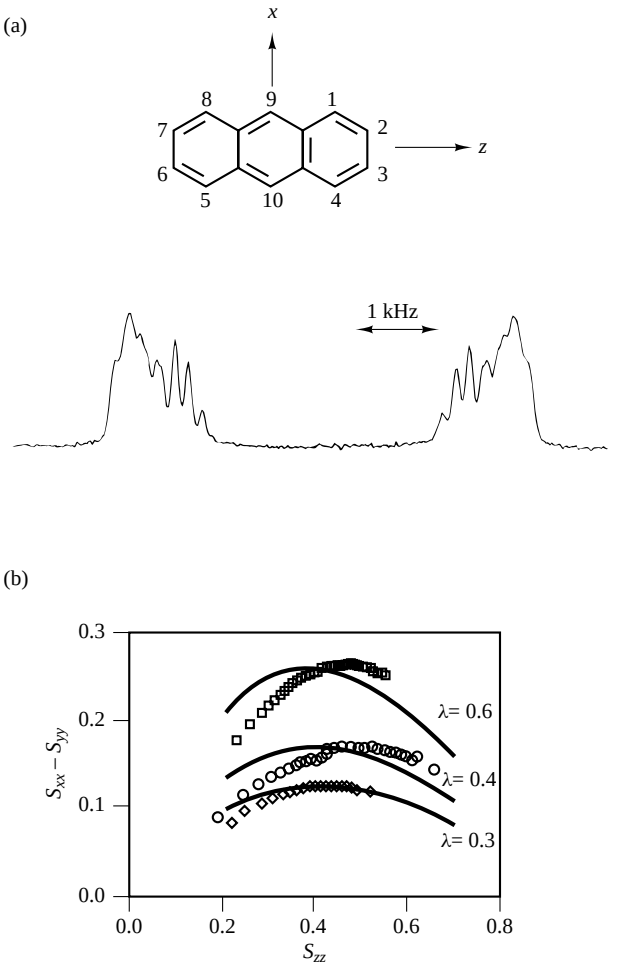

Figure 2 (a) Molecular structure of anthracene-d_{10} and the deuterium spectrum at 30.7 MHz from deuterons 1, 4, 5, 8, 9, and 10 in anthracene-d_{10} dissolved in Phase V. (b) Variation of S_{zz} with $S_{xx} - S_{yy}$ for anthracene-d_{10} dissolved in ZLI 1167 (□), E9 (○) and Phase V (◇).[19]

rotations, the chain does not always exist in an all-*trans* conformation. It is generally accepted that a single order tensor may not be enough to describe orientational ordering of different configurations. In equation (9), the average of $A_{\|}$ must also be carried out over an ensemble of molecules having all allowed configurations. The rotational isomeric state (RIS) model of Flory[21] is used to generate all chain configurations. Since a single $A_{\|}$ value would not provide quantitative information on the orientational order of the molecules, a molecular model is therefore required. Such a model using the additive potential method[15–19] was pioneered by Marcelja and later improved by Emsley and Luckhurst. The potential of mean torque which is responsible for the alignment of a conformer has its origin from the molecular field of its neighbors. It is constructed by adding up local interaction tensors of the carbon–carbon segments and the rigid aromatic core segment, which are specified by model parameters X_c and X_a, respectively. Each rigid (nth) conformer has its own order matrix $\mathbf{S}^n$ and its equilibrium probability of occurrence $P_{eq}(n)$. Equilibrium statistical mechanics is used to do the ensemble average in calculating the quadrupolar splittings $\Delta\nu_i$. The parameters X_c, X_a and E_{tg} (the energy difference between a *gauche* and a *trans* state) are varied to optimize the fits to the

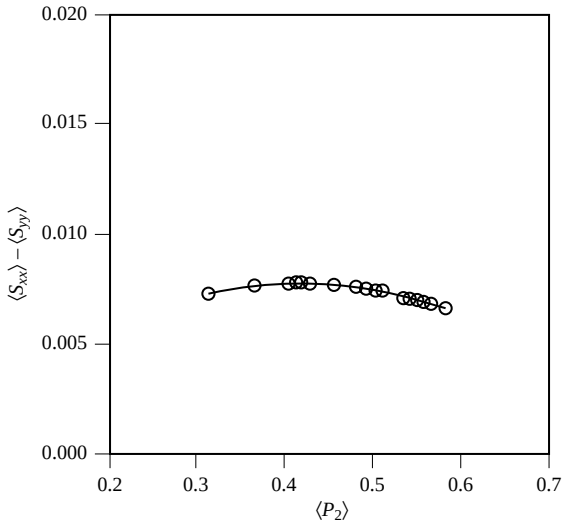

Figure 3 Plot of $\langle P_2\rangle$ versus $\langle S_{xx}\rangle - \langle S_{yy}\rangle$ for the averaged MBBA molecule.[22]

experimental splittings.[8] For example, such analysis[22] has been carried out for the splittings of MBBA (Figure 1). Knowing $S^n_{\alpha\beta}$ and $P_{eq}(n)$, it is possible to find a conformationally average order matrix $\langle\mathbf{S}\rangle$ by doing the statistical average in a common molecular frame. The principal components $\langle P_2\rangle$ and $\langle S_{xx}\rangle - \langle S_{yy}\rangle$ of the 'average' molecule can be obtained by diagonalizing the $\langle\mathbf{S}\rangle$ matrix. Figure 3 shows the plot of $\langle S_{xx}\rangle - \langle S_{yy}\rangle$ versus $\langle P_2\rangle$ of MBBA. It is interesting to note that the molecular biaxial order parameter, $\langle S_{xx}\rangle - \langle S_{yy}\rangle$, of the 'average' molecule is quite small for this flexible mesogen.

2.3 NMR in Biaxial Phases

Biaxial nematics, some smectic phases, such as S_G, and certain discotic phases[8] show phase biaxiality. Deuterium NMR may be used to detect phase biaxiality through the measurement of a nonzero motionally induced asymmetry parameter η^{LC} in the nuclear quadrupolar interaction whose EFG may have $\eta = 0$ in the solid state. Suppose that the molecule is rigid and the principal axes (X,Y,Z) of the liquid crystalline phase are chosen to coincide with the principal axes of the average EFG tensor. Letting the polar angles of the magnetic field in the (X,Y,Z) system be (θ_0, ϕ_0), the splitting is given by[8]

$$\delta\nu(\theta_0,\phi_0) = \tfrac{3}{4}\chi^{LC}\{(3\cos^2\theta_0 - 1) + \eta^{LC}\sin^2\theta_0\cos 2\phi_0\} \quad (10)$$

where χ^{LC}, a motionally averaged quadrupole coupling constant, and η^{LC} are defined by

$$\chi^{LC} = \chi\sum_m \overline{D^2_{0,m}(\theta,\psi)}D^2_{m,0}(\beta,\alpha)$$
$$\eta^{LC} = \sqrt{\tfrac{3}{2}}\frac{\chi}{\chi^{LC}}\sum_m[\overline{D^2_{2,m}(\phi,\theta,\psi)} + \overline{D^2_{-2,m}(\phi,\theta,\psi)}]D^2_{m,0}(\beta,\alpha) \quad (11)$$

where (ϕ,θ,ψ) are Euler angles that transform between a molecular frame (x,y,z) and the liquid crystalline (X,Y,Z)

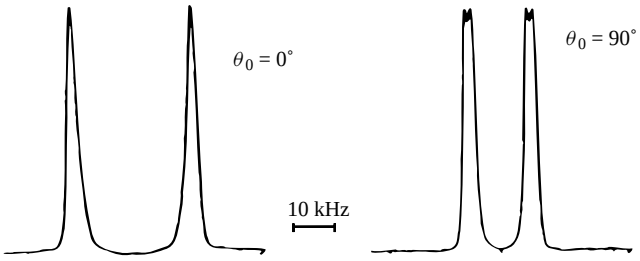

Figure 4 Experimental angular dependence of the deuterium NMR spectrum in the S_G phase of 5O.7-d_4 (aniline ring deuterated) at 31 °C.[24]

frame, and (β,α) are the polar angles of the C–D bond in the molecular frame. Phase biaxiality is reflected by $\overline{D^2_{\pm 2,m}}$ in η^{LC}, and the effect of η^{LC} on $\Delta\nu$ is maximum when the director is oriented normal to the magnetic field (i.e. $\theta_0 = 90^\circ$). It is noted that symmetry considerations involving both the nature of the molecules and of the liquid crystalline phases can considerably simplify the evaluation of the order parameters $\overline{D^2_{m',m}(\phi, \theta, \psi)}$. η^{LC} takes on a simple form if the (x,y,z) frame is chosen to be the principal frame of the order matrix. Further simplification can be made if the molecule is a cylindrical rod [$m = 0$ in equation (11)]. Then

$$\chi^{LC} = \chi S^{ZZ}_{zz}(3\cos^2\beta - 1)/2$$

$$\eta^{LC} = \sqrt{\tfrac{3}{2}}[\overline{D^2_{2,0}} + \overline{D^2_{-2,0}}]/S^{ZZ}_{zz} = (S^{XX}_{zz} - S^{YY}_{zz})/S^{ZZ}_{zz} \quad (12)$$

The $S^{XX}_{zz} - S^{YY}_{zz}$ term represents anisotropic fluctuations of the molecular z axis relative to the principal axes (X,Y,Z) of the average EFG tensor. Edge singularities (Figure 4) are predicted for the spectral pattern when $\theta_0 \neq 0$. The separation between edge singularities at $\theta_0 = 90^\circ$ is a direct measure of η^{LC}. Such a spectral pattern was first observed in an S_G phase[23] with a deuterated solute in the mesogen 6O.6. A η^{LC} value of 0.2 was obtained[24] in the S_G phase of 5O.7-d_4 (Figure 4). Phase biaxiality had been investigated in other smectic phases by Doane[25] and in discotics by Luz.[26]

3 SPIN RELAXATION AND MOLECULAR MOTION

Both nuclear spin–lattice and spin–spin relaxation rates are governed by random motion of spin-bearing molecules. Typically, a molecule remains in one state of motion for a short time (10^{-10}–10^{-12} s). After this time, it suffers a collision with one of its neighbors, which changes its state of motion. When the molecule persists in some state of motion for a time of 10^{-10} s, its motional frequency spectrum is expected to contain components ranging from zero to 10^{10} Hz, which are covered by typical NMR experiments. Several dynamic processes are known to cause deuteron spin relaxation in liquid crystals. The process known as director fluctuations is unique to liquid crystals and was first used to explain light scattering from liquid crystals. Other processes include order parameter fluctuations, molecular reorientation, and internal rotations. The latter two motions involve individual molecules as in normal liquids, while director fluctuations involve collective motions of a large number of molecules. These collective motions are influenced by macroscopic properties like elastic constants and anisotropic viscosities of the liquid crystalline medium. At best, director fluctuations can provide indirect information on the anisotropic interactions among molecules. On the contrary, molecular motion must reflect the shape of the instantaneous potential of mean torque on each molecule. Thus, it is sensitive to the nature of anisotropic interactions. Here, spin relaxation due to small cross terms between different processes will be ignored[8] for simplicity.

3.1 Solute Dynamics

To avoid dealing with internal rotations, deuterated rigid solutes dissolved in thermotropic liquid crystals were studied[7,27] by spectral density measurements. Solute reorientation and director fluctuations were used to account for the observed frequency and temperature dependences of $J_1(\omega)$ and $J_2(2\omega)$. It is now well known that director fluctuations under the small-angle approximation produce a characteristic $\omega^{-1/2}$ dependence in $J_1(\omega)$ only. Reorientation motion is often described in terms of a symmetric top reorienting in an anisotropic potential of Maier–Saupe type using a small-step rotational diffusion model.[8] This model uses a rotational diffusion tensor for the molecule which is diagonalized in a molecule-fixed frame. For weakly ordered solutes, their reorientation in a nematic solvent is often rapid to give frequency-independent spectral densities. For example, deuteron spin relaxation of p-diethynylbenzene (DEB-d_2, deuterated in the two alkynic sites) in the nematic phase of Phase V[7] clearly showed that $J_1(\omega)$ has a pronounced frequency dependence, while $J_2(2\omega)$ is essentially independent of frequency. This observation provides compelling evidence of director fluctuations in relaxing the deuterons in DEB-d_2. Smectic phases can be used to provide higher ordering of solute molecules. Similar frequency behaviors for J_1 and J_2 were obtained for DEB-d_2 in the four mesophases of 4O.8. However, J_2 showed more frequency dependence when DEB-d_2 was dissolved in 8CB.[8] A definitive explanation of the differences in these J_2 values has not yet been found. In general, analyses of experimental spectral density data would lead to rotational diffusion constants (or rotational correlation times $\tau_\parallel$, $\tau_\perp$) and a material factor A_{DF} that characterizes the strength of director fluctuations. For example, the ratio $\tau_\perp/\tau_\parallel$ is about 10 for DEB-d_2 in the nematic phase of Phase V.

3.2 Solvent Dynamics

The detection of director fluctuations in liquid crystals by means of deuteron spin relaxation in mesogens at conventional frequencies (10–50 MHz) has not met with success. This can be attributed to two factors: (1) the numerical value A_{DF} is small because most C–D bonds are oriented at an unfavorable angle to the long molecular axis; this is true for aromatic deuterons in mesogens such as 4-pentyl-4′-cyanobiphenyl (5CB), MBBA, etc., and (2) the contribution from director fluctuations to deuteron relaxation is masked by a much larger contribution due to relatively slow motions of large, sluggish molecules and fast internal motions within these molecules. To alleviate the difficulty associated with a small contribution from director fluctuations in the megahertz region, deuteron field cycling techniques have been applied[28]

to several nematogens. The techniques involve fast switching of the Zeeman field between high- and low-field levels so that detection of the NMR signal is done at a high magnetic field while the spin system is allowed to relax in a low field (in the kilohertz region). These data seem to support the findings based on the proton field cycling studies of liquid crystals that director fluctuations are slow motional processes and are effective for spin relaxation only in the kilohertz region.

To treat deuteron spin relaxation of solvent molecules in the megahertz region it is often possible to ignore the small contribution from director fluctuations. This assumption is probably necessary in modeling spectral densities of motion for various deuterated sites in flexible mesogens. In particular, correlated internal rotations in flexible chains of liquid crystals are complex to treat theoretically. Furthermore, different motional models[8] for reorientation of solvent molecules are possible. Besides the commonly used small-step rotational diffusion model, the anisotropic viscosity model of Freed and co-workers[8] is a distinct alternative. Freed used a rotational diffusion tensor that is diagonalized in the director frame to reflect the anisotropic viscosity of the liquid crystalline medium. Another motional model known as the 'third-rate' model is a simple extension of the Freed model. It has a fast rotation around the long molecular axis in addition to its motions around and toward the director. Numerous deuteron relaxation studies have been carried out in recent years to investigate molecular motion in liquid crystals. Table 1 briefly summarizes thermotropic liquid crystals in which spectral density measurements were reported.

As an example, the spectral density data of MBBA at 15.3 and 46 MHz are reproduced in Figure 5. The data are typical for thermotropic liquid crystals studied thus far. Both $J_1(\omega)$ and $J_2(2\omega)$ decrease with increasing temperature and are frequency dependent with a weaker dependence in $J_2(2\omega)$. To account for the observed site dependences of $J_1(\omega)$ and $J_2(2\omega)$, a model is required to treat internal motions in the butyl chain. A superimposed rotations model[33] was used to describe fluctuations in the orientations of the C–D bonds due to overall and internal modes of motion in the chain-deuterated nematogen 5CB. Here the internal dynamics of the pentyl chain was treated by assuming that rotations about each C–C bond are independent of each other and could be superimposed onto the rotational diffusion of the whole molecule. This motional model is, however, unrealistic and inconsistent with how quadrupolar splittings were modeled using the RIS model of Flory. The RIS model has been extended[42–44] to the time domain for liquid crystalline samples. A master equation may be used to describe transitions among all allowed configurations in the alkyl chain. The model of Nordio and co-workers[44] is inherently complex because their master equation includes configuration dependent frictional effects. The solution of the rotational diffusion problem requires a matrix representation in the full space of angular and site functions. Because of the large dimensionality of their matrix representation, the computational effort was extremely demanding. The decoupled model[42] of Dong uses three phenomenological rate constants to describe elementary jump modes: one-bond (k_1), two-bond (k_2), and three-bond (k_3) motions. The dimension of the rate matrix which is constructed in terms of these jump rate constants has the advantage of being much smaller. Both approaches,[34,42–44] however, give similar theoretical predictions for 5CB regarding site and frequency dependences of $J_1(\omega)$ and $J_2(\omega)$ as well as the observed discontinuity[33] in the spin–lattice relaxation rates at the nematic–isotropic phase transition.

The decoupled model has been successfully applied[22] to interpret the spectral densities of methylene deuterons (Figure 5) in MBBA, which are given by

$$J^{(i)}_{m_L}(m_L\omega) = \frac{3\pi^2}{2}\chi_i^2 \sum_{m_M}\sum_{n=1}^{27} c_{m_L m_M} \Big| \sum_{l=1}^{27} d^2_{m_M 0}(\beta^{(i)l}_{M,Q}) \exp[-i m_M \alpha^{(i)l}_{M,Q}] x_l^{(1)} x_l^{(n)} \Big|^2 \sum_j a^{(j)}_{m_L m_M} [(\tau^{(j)}_{m_L m_M})^{-1} + |\lambda_n|] / \{(m_L\omega)^2 + [(\tau^{(j)}_{m_L m_M})^{-1} + |\lambda_n|]^2\} \quad (13)$$

where $\beta^{(i)l}_{M,Q}$ and $\alpha^{(i)l}_{M,Q}$ are the polar angles of the C-i–D bond of the conformer l (there are 3^3 conformers in the butyl chain when the first dihedral angle at the junction of the aniline ring is allowed to sample three RISs) in a molecule-fixed frame whose z_M axis is along the ring *para* axis, λ_n and $\boldsymbol{x}^{(n)}$ are the eigenvalues and eigenvectors from diagonalizing a symmetrized rate matrix, $c_{m_L m_M}$ are the mean square of the Wigner rotation matrices, and the a, b and c coefficients are tabulated as functions of $\langle P_2 \rangle$ for a Maier–Saupe potential.[45] The correlation times $\tau^{(j)}_{m_L m_M}$ take on slightly different forms; the small-step rotational diffusion model uses

$$(\tau^{(j)}_{m_L m_M})^{-1} = [6D_\perp / b^{(j)}_{m_L m_M} + m_M^2 (D_\parallel - D_\perp)] \quad (14)$$

and the third-rate model uses

$$(\tau^{(j)}_{m_L m_M})^{-1} = h_{m_M} + [6D_\beta / b^{(j)}_{m_L m_M} + m_L^2 (D_\alpha - D_\beta)] \quad (15)$$

Table 1 Summary of Deuterium Spectral Density Measurement in Thermotropic Liquid Crystals

System	Phase	T (°C)	ν_0 (MHz)	References
1O.4 (MBBA)	N	15–40	15.3, 46	22
4O.8	N, S_A, S_B	30–79	9.2–38.4	29,30
5O.7	N, S_A, S_C, S_B	38–78	15.3, 46	31,32
5CB	N	23–35	12–46	33,34
6OCB	N	57–75.5	15.3–46	35
6OCB/8OCB	N, S_A, RN	25–78	13.8	36
1CB/5CB	N	2–28	46	37
CCH3	N	57–80	30.7	38
$FLOC_{14}$	N	130–140	38.4, 46	39
THE6	D_{h0}	68–99	46	40
8OBCAB/*n*TPCHB	N, S_A, RN	90–258	46	41

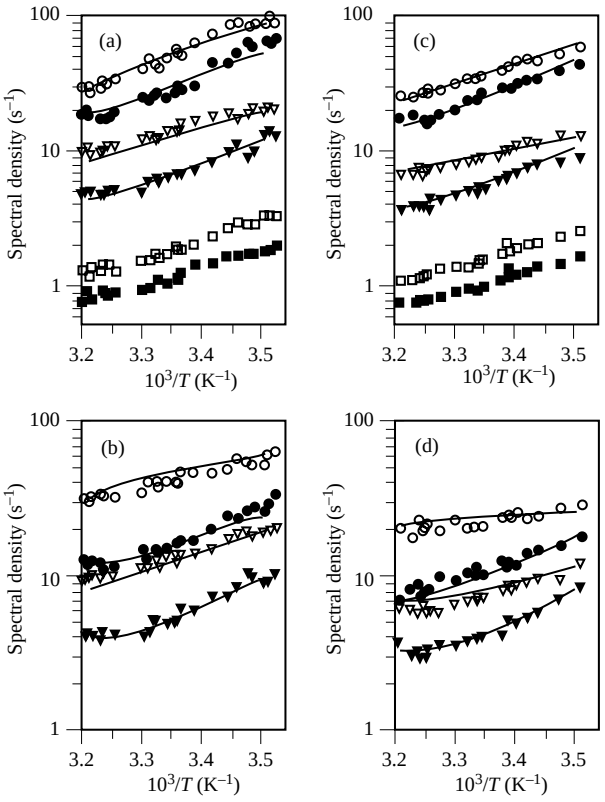

Figure 5 Plots of spectral densities versus the reciprocal temperature in the nematic phase of MBBA-d_{13}. Open symbols denote spectral densities $J_1(\omega_0)$, while solid symbols denote the corresponding $J_2(2\omega_0)$. ○ and ▽ and □ denote the C-0 and C-2 and C-4 data at (a) 15.3 MHz and (c) 46 MHz. • and ▼ denote the C-1 and C-3 data at (b) 15.3 MHz and (d) 46 MHz. Solid curves denote theoretical predictions based on the third-rate model and three jump rates for internal rotation.[22]

where $h_0 = 0$, $h_1 = D_\gamma$, and $h_2 = (3p + 1)D_\gamma$, with $p = 0$ corresponding to strong collision and $p = 1$ to small-step rotational diffusion for the γ motion. The Ds are rotational diffusion constants that are principal components of the rotational diffusion tensor of an 'average' molecule. The methine (C-0) deuteron has no internal motion, and the C-0–D bond reflects the motion of the aromatic core, giving

$$J^{(0)}_{m_L}(m_L\omega) = \frac{3\pi^2}{2}\chi_0^2 \sum_{m_M} c_{m_L m_M}[d^2_{m_M 0}(\beta_{M,Q})]^2 \times \sum_j a^{(j)}_{m_L m_M}[\tau^{(j)}_{m_L m_M}]^{-1}/[(m_L\omega)^2 + (\tau^{(j)}_{m_L m_M})^{-2}] \quad (16)$$

where $\beta_{M,Q}$ is the angle between the C–D bond and the z_M axis. Using equations (13) and (16), the fits between the calculated and experimental spectral densities are optimized by varying the rotational diffusion constants and the jump rate constants at each temperature.

Both the small-step rotational diffusion and third-rate models were examined. Both models were found to describe molecular reorientation of MBBA. The solid curves in Figure 5 are theoretical spectral densities based on equations (13) and (16) using $\tau^{(j)}_{m_L m_M}$ given by the third-rate model [equation (15)], X_a, X_c, and $\langle P_2\rangle$ given by modeling the quadrupolar splittings (E_{tg} = 2550 J mol^{-1}, $E_{g\pm g\pm}$ = 6000 J mol^{-1}). D_α and D_β are roughly the same ($\simeq 5 \times 10^7$ s^{-1} in the middle of the nematic phase), while D_γ is two orders of magnitude larger. D_α refers to the motion of the long molecular axis around the director, while D_β refers to its motion toward the director. These rotational diffusion constants decrease with decreasing temperature as expected for a thermally activated rotational process. The Nordio model has been used to derive motional parameters at different temperatures in 5CB[34] and 4-*n*-hexyloxy-4′-cyanobiphenyl (6OCB).[35] In studying the reorientation process in the smectogen 5O.7, the spectral densities of the methine and ring deuterons were measured as a function of temperature at two different Larmor frequencies in the megahertz region.[31] It was found that the large frequency dependence in $J_1(\omega)$ can only be rationalized by including director fluctuations. The third-rate model seems to produce physical rotational diffusion constants in the nematic, smectic A, and smectic C phases of 5O.7.

4 NOVEL NMR EXPERIMENTS

Some applications of newer NMR techniques to the study of liquid crystalline samples are now outlined. The proton NMR spectra of solute molecules dissolved in liquid crystals are usually complex, and iterative fitting of the NMR spectra must be used to extract dipolar couplings. Spectral simplification is possible by using partially deuterated solutes instead. When this is not practical, multiple quantum NMR spectroscopy[46] can greatly simplify spectra of complex spin systems. Multiple quantum NMR is concerned with the observation of forbidden nuclear transitions, i.e. $\Delta m_I \neq 1$. Multiple quantum coherences can only be detected indirectly. To detect all orders of multiple quantum transitions, special forms of two-dimensional NMR (2D NMR) spectroscopy are required. The high-order multiple quantum spectrum is simple due to the decrease in number of nuclear transitions with increasing order. Multiple quantum transitions of deuterons are now described.

In oriented systems, the quadrupole Hamiltonian leads to a splitting of the single quantum transitions [see Figure 1(b)]. Double quantum spectra of a deuteron (Δm_I = 2) have the advantage of eliminating quadrupolar effects. This is obvious from the deuterium energy diagram for a spin-1 system, since the quadrupolar shifts on $m_I = 1$ and $m_I = -1$ energy levels are equal. Any coherence established between these two levels will evolve at twice the Larmor frequency (as modified by chemical shift). Single- and double-quantum spectra were used[6] to study chain conformation in four members of the *n*O.7 series. It was noted that the distribution in the quadrupolar splitting is the dominant contribution to the deuteron linewidth of the single quantum spectrum. The distribution is due to a spread in the orientation of the long molecular axes in the liquid crystalline sample. Because a double quantum spectrum is not affected by quadrupolar effects, it has better spectral resolution and therefore may yield long-range dipole–dipole couplings among deuterons. Figure 6 shows a comparison of single- and double-quantum spectra of the α signal of 5O.7-αd_2 [Figure 6(a)] and the γ signal of 5O.7-$\alpha d_2 \gamma d_1$ [Figure 6(b) and (c)]. The improved resolution of the γ signal in the double quantum spectra is remarkable, and allows measurements of long-range deuterium dipolar couplings. For a two-coupled deuteron system, multiple quantum transitions can

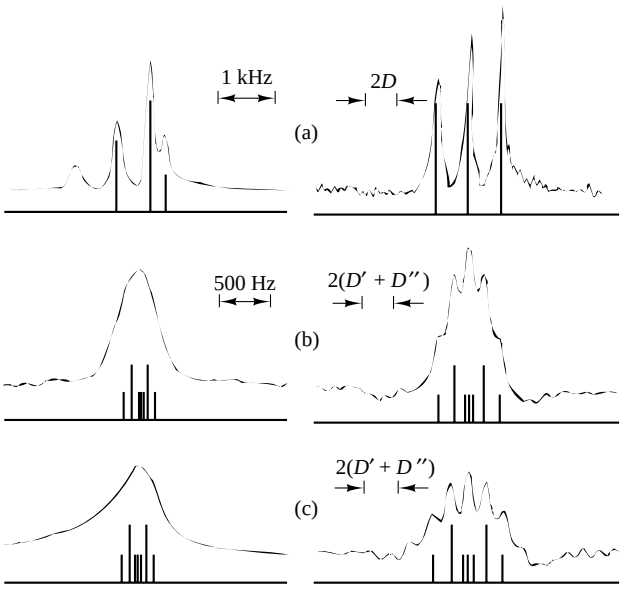

Figure 6 Single quantum (left) and double quantum (right) spectra for (a) the α signal of 5O.7-αd_2 at 57 °C, and the γ signal in 5O.7-$\alpha d_2 \gamma d_1$ at (b) 57 °C and (c) 41 °C, respectively. The stick diagrams give the corresponding theoretical spectra[6]

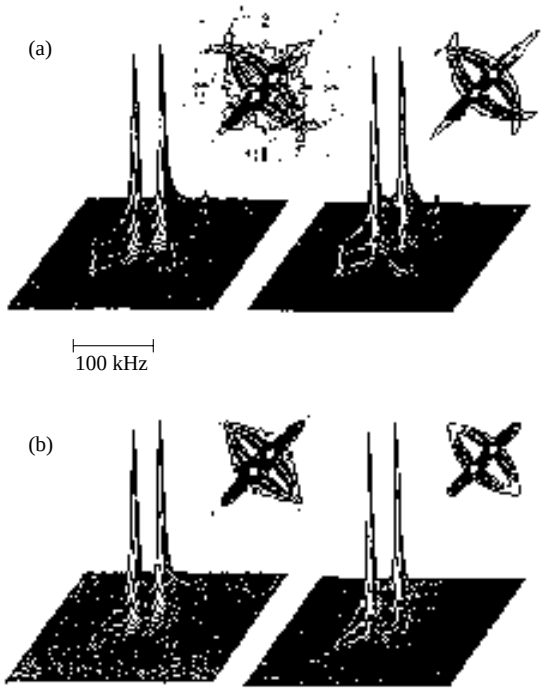

Figure 7 Experimental (left) and stimulated (right) spectra for (a) PS3 and (b) PS6 taken at 250 K with a mixing time of 100 ms. Contour plots are shown as insets[52]

reveal the correlation of relaxation mechanisms acting on two deuterium nuclei. Besides the three autocorrelation terms $J_0^{\mathrm{A}}(0)$, $J_1^{\mathrm{A}}(\omega)$, and $J_2^{\mathrm{A}}(2\omega)$, which describe the motion of the EFG tensor of either deuteron, the three cross-correlation terms $J_0^{\mathrm{C}}(0)$, $J_1^{\mathrm{C}}(\omega)$, and $J_2^{\mathrm{C}}(2\omega)$ describe correlation between the motion of the two EFG tensors. There are many relaxation studies of deuterated solutes in thermotropic liquid crystals.[13,14,27] For example, zero-, two-, and four-quantum linewidths may be used to determine the three cross-correlation terms[13,14] in acetonitrile-d_3.

2D NMR spectroscopy is now common in the study of liquid crystals. Using ^{13}C nuclei, the carbon–proton dipolar couplings can be obtained by means of the near magic angle spinning and the separated local field spectroscopy. Rapid sample spinning near the magic angle (54.7°) was incorporated to improve spectral resolution[47] so that coupling between indirectly bonded C–H pairs could be observed. A sample that has a chiral fluorinated solute dissolved in a liquid crystal was used to carry out a 2D ^{19}F spin echo[47] experiment in conjunction with the near magic angle spinning. This allows spectral analysis of small molecules to give residual dipolar coupling D_{ij} between nuclei i and j, and the isotropic spin–spin coupling J_{ij}. A deuteron 2D spin echo experiment on PAA-d_{14} allows assignment[19] of quadrupolar splittings in the NMR spectrum of perdeuterated *p*-azoxyanisole. The same technique has been used in the nematic phase of β-deuterated 5CB dispersed in polymers[48] and in model bilayer membranes[49] to determine the homogeneous linewidth of the individual lines. Another form of deuteron 2D experiment is 2D exchange spectroscopy,[50–52] which is capable of detecting slow molecular processes by monitoring the orientation of a C–D bond via its NMR frequency. A typical 2D time domain spectroscopy experiment involves four distinct periods [preparation, evolution (t_1), mixing, and detection (t_2)], leading to a time domain signal $s(t_1, t_2)$. Fourier transform of $s(t_1, t_2)$ gives $s(\omega_1, \omega_2)$, a 2D frequency spectrum. The spectrum provides information relating the frequency ω_{e} in the evolution period just before mixing and the frequency ω_{d} in the detection period just after mixing. When ω_{e} is identical to ω_{d}, this gives rise to a spectrum on the diagonal of a 2D spectrum; otherwise, off-diagonal intensity can be formed in the form of straight ridges and ellipses.[50,52] The detection of off-diagonal intensity is practical for motions that have a correlation time of the order of milliseconds or longer. As an example, deuteron 2D exchange spectroscopy in glass-forming liquid crystalline side-group polymers is described.[52] Figure 7 shows the experimental and simulated 2D spectra for poly(4-alkyloxybenzoic acid 4′-methoxyphenyl-d_4 ester)siloxane (PS*n*) with n = 3 and 6. Both PS3 and PS6 were magnetoaligned in a strong magnetic field by slow cooling from the isotropic melt into the glassy state. The glassy state of the PS6 is a frozen smectic C phase, while the glassy state of the PS3 is a frozen nematic phase. Off-diagonal intensity in the form of a partial elliptical pattern can be simulated by assuming a Gaussian distribution for the orientation distribution of the long axis of the mesogenic unit. Because the orientational order $\langle P_2 \rangle$ of PS3 is lower, the partial elliptical pattern is more pronounced for PS3 than for PS6 as seen in Figure 7. It was also found that the ring flip of 180° in PS*n* has a rather narrow angular distribution. The same technique has been used to study molecular dynamics in glass-forming discotic liquid crystals.[8]

5 RELATED ARTICLES

Amphiphilic Liquid Crystalline Samples: Nuclear Spin Relaxation; Bilayer Membranes: Deuterium and Carbon-13 NMR; Deuterium NMR in Solids; Deuteron Relaxation

Rates in Liquid Crystalline Samples: Experimental Methods; Dynamic NMR in Liquid Crystalline Solvents; Field Cycling Experiments; Liquid Crystalline Samples: Carbon-13 NMR; Liquid Crystalline Samples: Relaxation Mechanisms; Liquid Crystals: General Considerations; Lyotropic Liquid Crystalline Samples; Membranes: Deuterium NMR; Multiple Quantum Spectroscopy in Liquid Crystalline Solvents; Polymer Dispersed Liquid Crystals; Relaxation Theory: Density Matrix Formulation; Relaxation Theory for Quadrupolar Nuclei; Spinning Liquid Crystalline Samples; Two-Dimensional NMR of Molecules Oriented in Liquid Crystalline Phases.

6 REFERENCES

1. J. C. Rowell, W. D. Phillips, L. R. Melby, and M. Panar, *J. Chem. Phys.*, 1965, **43**, 3442.
2. W. D. Phillips, J. C. Rowell, and L. R. Melby, *J. Chem. Phys.*, 1964, **41**, 2551.
3. C. G. Wade, *Ann. Rev. Phys. Chem.*, 1977, **28**, 47.
4. J. W. Doane, in *Magnetic Resonance of Phase Transitions*, ed. F. J. Owens, C. P. Poole, Jr., and H. A. Farach, Academic Press, New York, 1979, Chap. 4
5. R. Y. Dong, J. Lewis, E. Tomchuk, and E. Bock, *J. Chem. Phys.*, 1978, **69**, 5314.
6. S. Hsi, H. Zimmermann, and Z. Luz, *J. Chem. Phys.*, 1978, **69**, 4126.
7. R. R. Vold, in *Nuclear Magnetic Resonance of Liquid Crystals*, ed. J. W. Emsley, Reidel, Dordrecht, 1985, Chap. 11
8. R. Y. Dong, *Nuclear Magnetic Resonance of Liquid Crystals*, Springer-Verlag, New York, 1994.
9. A. Abragam, *Principles of Nuclear Magnetism*, Oxford University Press, Oxford, 1961, Chap. 8
10. C. P. Slichter, *Principles of Magnetic Resonance*, 3rd edn., Springer-Verlag, Berlin, 1990.
11. J. P. Jacobsen, H. K. Bildsoe, and S. Schaumburg, *J. Magn. Reson.*, 1978, **23**, 153.
12. R. R. Vold and R. L. Vold, *J. Chem. Phys.*, 1977, **66**, 4018.
13. R. Poupko, R. L. Vold, and R. R. Vold, *J. Magn. Reson.*, 1979, **34**, 67.
14. D. Jaffe, R. R. Vold, and R. L. Vold, *J. Magn. Reson.*, 1982, **46**, 475.
15. G. R. Luckhurst, in *The Molecular Physics of Liquid Crystals*, ed. G. R. Luckhurst and G. W. Gray, Academic Press, London, 1979, Chap. 4
16. G. R. Luckhurst, in *Nuclear Magnetic Resonance of Liquid Crystals*, ed. J. W. Emsley, Reidel, Dordrecht, 1985, Chap. 3
17. W. Maier and A. Saupe, *Z. Naturforsch., Teil A*, 1959, **14**, 882.
18. W. Maier and A. Saupe, *Z. Naturforsch., Teil A*, 1960, **15**, 287.
19. J. W. Emsley, in *Nuclear Magnetic Resonance of Liquid Crystals*, ed. J. W. Emsley, Reidel, Dordrecht, 1985, Chap. 15
20. B. G. Wu, B. Ziemnicka, and J. W. Doane, *J. Chem. Phys.*, 1988, **88**, 1373.
21. P. J. Flory, *Statistical Mechanics of Chain Molecules*, Interscience, New York, 1969.
22. R. Y. Dong, L. Friesen, and G. M. Richards, *Mol. Phys.*, 1994, **81**, 1017.
23. T. M. Barbara and B. P. Dailey, *Mol. Cryst. Liq. Cryst.*, 1982, **87**, 239.
24. R. Y. Dong, H. Schmiedel, N. A. P. Vaz, Z. Yaniv, M. E. Neubert, and J. W. Doane, *Mol. Cryst. Liq. Cryst.*, 1993, **98**, 411.
25. J. W. Doane, in *Nuclear Magnetic Resonance of Liquid Crystals*, ed. J. W. Emsley, Reidel, Dordrecht, 1985, Chaps. 18 and 19.
26. Z. Luz, D. Goldfarb, and H. Zimmermann, in *Nuclear Magnetic Resonance of Liquid Crystals*, ed. J. W. Emsley, Reidel, Dordrecht, 1985, Chap. 14
27. R. L. Vold and R. R. Vold, *Isr. J. Chem.*, 1983, **23**, 315.
28. R. Köllner, K. H. Schweikert, F. Noack, and H. Zimmermann, *Liq. Cryst.*, 1993, **13**, 483.
29. T. M. Barbara, R. R. Vold, and R. L. Vold, *J. Chem. Phys.*, 1983, **79**, 6338.
30. T. M. Barbara, R. R. Vold, R. L. Vold, and M. E. Neubert, *J. Chem. Phys.* 1985, **82**, 1612.
31. R. Y. Dong and X. Shen, *Phys. Rev. E*, 1994, **49**, 538.
32. R. Y. Dong, *Liq. Cryst.*, 1989, **4**, 505.
33. P. A. Beckmann, J. W. Emsley, G. R. Luckhurst, and D. L. Turner, *Mol. Phys.*, 1986, **59**, 97.
34. R. Y. Dong and G. M. Richards, *J. Chem. Soc. Faraday Trans.*, 1992, **88**, 1885.
35. R. Y. Dong and G. Ravindranath, *Liq. Cryst.*, 1994, **17**, 47.
36. R. Y. Dong, G. M. Richards, J. S. Lewis, E. Tomchuk, and E. Bock, *Mol. Cryst. Liq. Cryst.*, 1987, **144**, 33.
37. G. L. Hoatson, T. Y. Tse, and R. L. Vold, *J. Magn. Reson.*, 1992, **98**, 342.
38. R. Y. Dong, J. W. Emsley, and K. Hamilton, *Liq. Cryst.*, 1989, **5**, 1019.
39. J. M. Goetz, G. L. Hoatson, and R. L. Vold, *J. Chem. Phys.*, 1992, **97**, 1306.
40. D. Goldfarb, R. Y. Dong, Z. Luz, and H. Zimmermann, *Mol. Phys.*, 1985, **54**, 1185.
41. D. Imbardelli, B. Wazynska, A. Golemme, G. Chidichimo, and R. Dabrowski, *Mol. Phys.*, 1993, **79**, 1275.
42. R. Y. Dong, *Phys. Rev. A*, 1991, **43**, 4310.
43. R. Y. Dong and G. M. Richards, *Chem. Phys. Lett.*, 1992, **200**, 541.
44. A. Ferrarini, G. J. Moro, and P. L. Nordio, *Liq. Cryst.*, 1990, **8**, 593.
45. R. R. Vold and R. L. Vold, *J. Chem. Phys.*, 1988, **88**, 1443.
46. G. P. Drobny, *Annu. Rev. Phys. Chem.*, 1985, **36**, 451.
47. J. Courtieu, J. P. Bayle, and B. M. Fung, *Prog. Nucl. Magn. Reson. Spectrosc.*, 1994, **26**, 141.
48. J. Dolinsek, O. Jarh, M. Vilfan, S. Zumer, R. Blinc, J. W. Doane, and G. Crawford, *J. Chem. Phys.*, 1991, **95**, 2154.
49. L. Müller and S. I. Chan, *J. Chem. Phys.*, 1983, **78**, 4341.
50. J. Jeener, B. H. Meier, P. Bachmann, and R. R. Ernst, *J. Chem. Phys.*, 1979, **71**, 4546.
51. C. Schmidt, B. Blümich, S. Wefing, and H. W. Spiess, *Chem. Phys. Lett.*, 1986, **130**, 84.
52. J. Leisen, C. Boeffel, R. Y. Dong, and H. W. Spiess, *Liq. Cryst.*, 1993, **14**, 215.

Acknowledgments

The financial support of the Natural Sciences and Engineering Council of Canada is gratefully acknowledged.

Biographical Sketch

Ronald Y. Dong. *b* 1942. B.A.Sc., 1966, Toronto. Ph.D. (Supervisor, Myer Bloom), 1969, University of British Columbia. Postdoctoral

work at the University of Waterloo, 1970–71, and at the National Research Council of Canada, 1971–73. Faculty in Physics, University of Winnipeg 1974–78. Faculty in Physics and Astronomy, Brandon University, 1978–present. Adjunct faculty in Physics, University of Manitoba, 1989–present. Approx. 100 publications. Research interests include solid state NMR, molecular dynamics, molecular crystals and liquid crystals.

Liquid Crystalline Samples: Diffusion

Göran Lindblom and Greger Orädd

University of Umeå, Sweden

1	Introduction	1
2	NMR Measurements of Lipid Lateral Diffusion in Oriented Bilayers	1
3	NMR Measurements of Water and Ion Diffusion in Liquid Crystals	4
4	Lipid Lateral Diffusion in Cubic Liquid Crystalline Phases	4
5	Lateral Diffusion in Other Nonlamellar Liquid Crystals	6
6	Related Articles	7
7	References	7

1 INTRODUCTION

The NMR methods involving pulsed magnetic field gradients provide one of the most attractive techniques for studies of molecular transport in lipid membranes and lyotropic liquid crystalline systems. One of the most successful applications of pulsed field gradient (PFG) NMR is found in the field of complex liquids. In particular, this has been an invaluable tool in determining the structures of cubic liquid crystalline phases.[1] Almost two decades ago, the first lateral diffusion coefficient of an amphiphile in a lamellar liquid crystalline phase was measured directly with the PFG NMR method.[2] In recent years, the range of applications of NMR diffusion techniques has been growing rapidly, due to the great improvments in the NMR equipment for diffusion and NMR microscopy.[3] We concentrate here on lyotropic liquid crystalline systems (Figure 1) containing membrane lipids or other amphiphilic molecules.

2 NMR MEASUREMENTS OF LIPID LATERAL DIFFUSION IN ORIENTED BILAYERS

The translational motion of lipids can be measured using the conventional NMR diffusion pulsed field gradient spin echo (PFG-SE) method for anisotropic liquid crystalline systems, if all static proton dipole–dipole interactions can be removed by some mechanical method. For studies of the lateral diffusion of lipids in a lamellar phase the removal of these interactions can be accomplished by a macroscopic alignment of the lamellae between, for example, glass plates.[2,4,5] In lipid bilayers, provided that the translational diffusion rapidly leads to a zero average of all the static, intermolecular dipolar interactions, the dipolar Hamiltonian $\hat{\mathcal{H}}_{\mathrm{D}}$ can be written[6,7]

$$\hat{\mathcal{H}}_{\mathrm{D}} = \sum_{i>j} \sum_{p} F_0^{(2)}(ij) D_{p0}^{(2)}(\Omega) \hat{A}_p^{(2)}(ij) \qquad (1)$$

where

$$F_0^{(2)}(ij) = 2\gamma^2 r_{ij}^3 \overline{D_{00}^{(2)}(\Omega_{ij})} \qquad (2)$$

where γ is the magnetogyric ratio, r_{ij} is the distance between the protons in an intramolecular proton pair ij, Ω_{ij} is the Eulerian angle between the proton–proton vector and the bilayer normal (the so-called 'director'), and $\overline{D_{00}^{(2)}(\Omega_{ij})}$ is a Wigner rotation matrix element.[8] The bar indicates averaging over all the fast motions. Likewise, $D_{p0}^{(2)}(\Omega)$ is a rotation matrix element, and Ω is the Eulerian angle between the bilayer director and the applied magnetic field $\boldsymbol{B}_0$. $\hat{A}_p^{(2)}(ij)$ is a component of an irreducible tensor operator of rank two operating on the nuclear spin coordinates. In a strong magnetic field only the term containing $\hat{A}_0^{(2)}(ij)$ affects the spectrum. $\hat{\mathcal{H}}_{\mathrm{D}}$ for all the protons in the hydrocarbon chain can then be written

$$\hat{\mathcal{H}}_{\mathrm{D}} = \tfrac{1}{2}(3\cos^2\theta - 1) \sum_{i>j} F_0^{(2)}(ij) \hat{A}_0^{(2)}(ij) \qquad (3)$$

From equation (3) it is obvious that if the bilayer is macroscopically aligned and oriented at the so-called magic angle $\theta = 54.7^\circ$, then $\hat{\mathcal{H}}_{\mathrm{D}} = 0$ and the static dipolar couplings are reduced. In the NMR experiment the diffusion is measured in the direction of the magnetic field gradient. For a lipid membrane or a lamellar phase the diffusion coefficient is orientation dependent and two constants D_{L} and $D_{\perp}$ describe the diffusion. D_{L} is the lateral diffusion coefficient for motion parallel with the membrane, and $D_{\perp}$ determines the diffusion perpendicular to the bilayer. The measured diffusion coefficient D for an oriented membrane system is then

$$D = D_{\mathrm{L}} \sin^2\theta + D_{\perp} \cos^2\theta \qquad (4)$$

for a lamellae oriented at the magic angle $\sin^2\theta = \frac{2}{3}$. In lipid bilayers, $D_{\perp}$ should be orders of magnitude smaller than D_{L} and the second term in equation (4) can be neglected.

Early on, this method was used to determine the lateral diffusion coefficient of a phosphatidylcholine lipid in a lamellar phase[2,4] and for potassium oleate[5] (Table 1). One of the most annoying difficulties one was faced with in the first measurements of the lateral diffusion coefficient of lipids was the contribution from water protons to the spin echo signal, which results in a diffusion coefficient for the lipids which is too large. This problem can be solved by a careful exchange of all free protons for deuterium. For example, the lateral diffusion coefficient of a typical amphiphile-like sodium octanoate (C_7COONa) was measured[2] to be equal to $2.1 \times 10^{-10}\,\mathrm{m^2\,s^{-1}}$ at 24 °C.

The lateral diffusion coefficient is also affected[9] by a change in the water content in the lamellar phase (Table 1). It was found that the lateral diffusion of dipalmitoylphosphatidylcholine (DPPC) increased by a factor of 2 for a change in the ^2H_2O content of 15 to 40 wt.%. Wu and Huang[10] have calculated the change in the lateral diffusion as a function of the water content according to the theory of Brownian motion in thin sheets. They found that the dependence of phospholipid diffusion on hydration can be attributed primarily to the change in the bulk water mobility in the multilamellar phase.

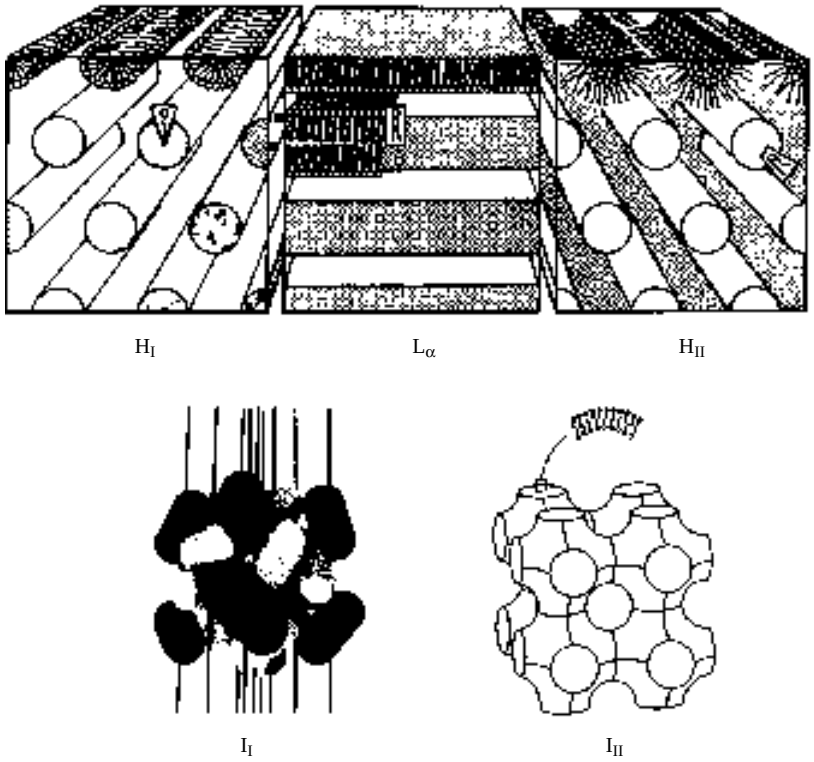

Figure 1 Structure of the most common liquid crystalline phases that membrane lipids can form: (H_I) normal hexagonal phase; (L_α) lamellar phase; and (H_{II}) reversed hexagonal phase.[98] (I_I) A scaled model of a unit cell of a cubic phase structure built up of closed micelles.[83] (I_{II}) Schematic drawing of a bicontinuous cubic phase belonging to the space group $Im3m$[1]

Recently, we reported on the effect of glycerol on the translational and rotational motions in aqueous lipid bilayers.[11] A continuous decrease in the lipid diffusion coefficient was observed upon increasing glycerol contents; thus, at room temperature $D = 12.6 \times 10^{-12}\,m^2\,s^{-1}$ for an aqueous L_α phase, while $D = 1.9 \times 10^{-12}\,m^2\,s^{-1}$ where all the water was displaced by glycerol. It was concluded that glycerol between the lipid bilayers affects the lipid diffusion due to changes in the viscosity in the interbilayer regions. This is also in accordance with the findings of Wu and Huang.[10]

As intuitively expected, the lateral diffusion coefficient depends on the hydrocarbon chain length, but the dependence is rather weak.[2,9] On the other hand, a strong dependence on the translational motion is observed for different polar headgroups of the amphiphiles.[2] Thus, lysophosphatidylcholine (lyso-PC) diffuses somewhat more slowly than the corresponding PC, although the latter has two acyl chains and the lyso compound only one.[12,13] The bulkier headgroup of the lyso-PC molecules most probably plays an important role for the lipid lateral diffusion. In studies[14,15] of the lateral diffusion of the two dominant glucolipids in the bacterium *Acholeplasma laidlawii* it was found that the translational motion of dioleoyldiglucosyldiacylglycerol (DGlcDAG) is about 10 times faster than it is in dioleoyl-PC (DOPC)[16] (Table 1). This difference in the lateral diffusion coefficients can probably be ascribed to differences in the interactions in the polar headgroup region and the packing of the lipids in the bilayer.[2,15] Addition of a monoglucolipid results[14] in a decrease in the lipid lateral diffusion, which has been suggested to be due to hydrogen bonding between the polar headgroups.[15] The theoretical models used in molecular dynamics simulations of the lateral diffusion in lipid bilayers disregard the effect on the polar headgroup, and therefore the calculated diffusion coefficients are much larger than the measured ones. A value of the diffusion coefficient which is about an order of magnitude (or even more) too large is obtained.[17–19] The reason for this discrepancy is that headgroup–headgroup interactions are essential for slowing down the diffusion process.

The effects of cholestrol on lipid membranes have been studied extensively with a number of spectroscopic methods. Cholesterol has been shown to have a condensing effect on many lipids in the lamellar phase, but it was not until recently that the ternary phase diagram of DPPC/cholesterol/water was presented.[20] As the cholesterol content in the lipid bilayer increases, two lamellar phases with different molecular ordering are formed. This unusual behavior has been explained by a theoretical model.[21] The influence of cholesterol on the lipid lateral diffusion in various lamellar liquid crystalline phases has also been investigated (Table 1) by PFG NMR.[9,16] ^{1}H NMR and bandshape simulations of phospholipid/water systems show that the addition of cholesterol to lipid bilayers in the gel phase induces a 'super-Lorentzian' ^{1}H NMR bandshape, which is a result of an enhanced lateral diffusion of the PC molecules.[22] It can be inferred from Table 1 that the cholesterol concentration has a very small effect on the phospholipid diffusion in unsaturated lipid bilayers. This is in accordance with recent molecular dynamics simulations, where it was found that cholesterol does not have any significant effect on the lateral diffusion of the chains.[18] On the other hand, cholesterol has a large influence on the molecular ordering in bilayers.[16,23–25] Thus, cholesterol increases the molecular ordering in a bilayer, but the diffusional motion

Table 1 Lateral Diffusion Coefficients D_L of Some Amphiphiles in Lamellar Phases Aligned between Glass Plates

Lipid system	Composition (wt %)	Temperature (°C)	$D_L \times 10^{11}$ ($m^2\ s^{-1}$)	Reference
Surfactants				
Octylammonium chloride	72	24	33	Lindblom and Wennerström[2]
Water	28			
Aerosol OT	71	24	1.0	Lindblom et al.[62]
Water	29	35	1.7	
Sodium octanoate	22	24	21	Lindblom and Wennerström[2]
Decanol	40			
Water	38			
Lithium perfluorooctanoate	72	25	3	Tiddy[38]
Water	28			
Biological lipids				
Monooleoylglycerol	82	22	1.1	Lindblom et al.[62]
Water	12	35	1.6	
Diglucosyldiacylglycerol (DGlcDAG)	87	45	3.9	Wieslander et al.[14]
Water	13			
Dioleoyl-PC (DOPC)	80	35	0.5	Lindblom et al.[16]
Water	20	45	0.9	
Palmitoyloleoyl-PC (POPC)	80	35	0.6	Lindblom et al.[16]
Water	20			
Dioleoyl-PC	75	35	0.5	Lindblom et al.[16]
Cholesterol	5			
Water	20			
Dioleoyl-PC	70	35	0.5	Ulmius et al.[28]
Sodium cholate	10			
Water	20			
Lysooleoyl-PC	84	26	0.2	Rilfors et al.[13]
Water	16			
Dimyristoyl-PC	75	50	1.2	Wennerström and Lindblom[7]
Water	25			
Dipalmitoyl-PC	85	52	0.6	Kuo and Wade[9]
Water	15			
Dipalmitoyl-PC	75	52	0.9	Kuo and Wade[9]
Water	25			
Dioleoyl-PC	46.2	36	0.3	Rilfors et al.[13]
Dioleoyl-PE	43.8	46	0.4	
Water	10.0	56	0.6	

is unaffected. In a study[13] of the lipid lateral diffusion of a mixture of DOPC, dioleoylphosphatidylethanolamine (DOPE), and water, both lipids were found to have about the same D_L ($5 \times 10^{-12}\ m^2\ s^{-1}$) as DOPC bilayers.[16]

The diffusional motion for powder samples of a liquid crystalline phase have also been measured.[26–28] To reduce the static dipole interactions, a combined multiple pulse homonuclear decoupling and multiple pulse gradient technique[26] has been used to determine the self-diffusion coefficient. By this method the diffusion of DPPC has been studied at 25 °C with 15 wt.% ^2H_2O in the $L_{\beta'}$ gel phase and in the lamellar phase of potassium oleate in 30 wt.% ^2H_2O. The D values obtained in this way are 1.6×10^{-14} and $1.3 \times 10^{-12}\ m^2\ s^{-1}$, respectively. Here the lateral diffusion coefficient is not obtained directly,[29] but is some kind of an average value, since the microcrystallites in the mesophase are randomly oriented. In such a measurement, the diffusion coefficient obtained is too small, compared with the local lateral diffusion. In an early study, Roberts[27] used the stimulated echo to determine the surfactant diffusion in the hexagonal and lamellar phases of potassium laurate/heavy water at 80 °C. Somewhat surprisingly he obtained a similar diffusion coefficient ($D_{lamellar} = 2.4 \times 10^{-10}\ m^2\ s^{-1}$ and $D_{hexagonal} = 2.3 \times 10^{-10}\ m^2\ s^{-1}$) for both phases, although there is a large difference in their structure.

By using pulsed field gradient double quantum spin echo decays the translational diffusion of dichloromethane dissolved in two thermotropic liquid crystals has been studied.[30] Diffusion constants of the solute were determined parallel and perpendicular to the magnetic field.

A method has been presented for simulating ^{31}P NMR spectra from a lipid vesicle dispersion. Experimental spectra are obtained by the use of a DANTE pulse sequence.[31] The

simulation was based on molecules with axially symmetric lineshapes undergoing lateral diffusion on a curved surface. By fitting a set of spectra for which the system is allowed to evolve for a variable time interval after the DANTE excitation, a lateral diffusion coefficient can be calculated from the measured correlation time. Köchy and Bayerl[32] measured ^{2}H quadrupolar transverse relaxation times obtained with the Carr–Purcell–Meiboom-Gill (CPMG) pulse sequence on spherical phospholipid bilayers on a solid support. They took advantage of the fact that the CPMG sequence can progressively filter out contributions to the T_2 relaxation arising from motions, such as lateral diffusion, which are slow on the NMR timescale. For POPC supported bilayers they got $D = 4 \times 10^{-12}\,\mathrm{m^2\ s^{-1}}$ at 30 °C, in good agreement with PFG NMR.[16] An attempt to estimate the lipid lateral diffusion in phospholipid vesicles from ^{13}C spin–spin relaxation was less successful.[33] The authors used a very simple model to describe the spin relaxation, a model which is similar to the so-called 'two-step model'.[34–36] The lateral diffusion coefficient required to fit the values of T_2 is larger by almost two orders of magnitude than the values obtained with PFG NMR.

3 NMR MEASUREMENTS OF WATER AND ION DIFFUSION IN LIQUID CRYSTALS

Most of the investigations of water diffusion in lyotropic liquid crystalline systems have been conducted on powder samples. The intermolecular exchange of protons in the water molecule is rapid on the NMR timescale, and therefore the water signal is relatively sharp even for a nonoriented sample. When the diffusion coefficient is determined for a powder sample with the NMR technique, the resulting echo has contributions from lamellae of all orientations θ, and[29]

$$S(t) = \int_{-1}^{1} \exp\left\{-\frac{2\tau}{T_2(\theta)} - \sin^2\theta\,(\gamma g\delta)^2 D(\Delta - \delta/3)\right\} \mathrm{d}\cos\theta \quad (5)$$

The first measurements of water diffusion coefficients in lamellar phases of a powder sample were performed by Blinc and co-workers.[37] However, the complications described by equation (5) were not considered in their determination of the water diffusion at different temperatures for a sample containing 70% sodium palmitate and 30% water. Assuming that the water molecules in lamellae oriented close to the magic angle make the major contribution to the spin echo, the measured diffusion coefficient should be multiplied[29] by $\frac{3}{2}$ to give $D_\mathrm{L} = 8 \times 10^{-10}\,\mathrm{m^2\ s^{-1}}$. Water diffusion coefficients have, however, also been determined for oriented lamellar phases using both protons[38] and deuterium[39] pulsed field gradient NMR. Callaghan and co-workers[39] found that the diffusion coefficients of ^2H_2O parallel and perpendicular to the bilayer surface are $D_\mathrm{L} = 1.7 \times 10^{-9}$ and $D_\perp = 5 \times 10^{-11}\,\mathrm{m^2\ s^{-1}}$. In this work they also reported the first solid echo PFG ^{2}H NMR experiment performed on a lamellar phase of potassium palmitate and water in the presence of quadrupole splittings.

In the lithium perfluorooctanoate/water system, self-diffusion coefficients are reported for water, lithium and perfluorooctanoate ions in the lamellar and viscous neat phases, as a function of temperature.[38] The difference between diffusion along the water layers and across the perfluorooctanoate bilayers was found to be small for both water and lithium ions. The lithium ion diffusion coefficient was only a factor of 3 larger than that of the perfluorooctanoate amphiphile. The lithium diffusion coefficient has also been determined in a lamellar phase composed of octanoate, water and decanol.[40] It was found that the lithium ion diffusion in this lamellar phase is independent of the composition. This is due to a constant fraction of bound ions in accordance with the ion condensation model previously used to describe the ion binding in lyotropic liquid crystals.[41,42] Recently, the PFG method was applied to estimate of the rates of ionophore-mediated transmembrane exchange of lithium ion in liposomes.[43] There was good agreement between the transmembrane exchange rate estimated from PFG and magnetization transfer ^{7}Li NMR experiments.

Water diffusion coefficients have been measured for powder samples in the two-component system of DPPC and water.[29] The diffusion coefficients were found to be 4–10 times smaller than the translational diffusion coefficient in bulk water, and essentially unaffected by changes in the phase structure.

Some recent investigations of the effect of the mesophase structure on the measured water diffusion coefficients have also been published.[44,47]

4 LIPID LATERAL DIFFUSION IN CUBIC LIQUID CRYSTALLINE PHASES

Lipid translational diffusion coefficients have been determined for a large number of different lyotropic cubic phases (Table 2). There is a great deal of interest in the structure and the properties of membrane lipids, in particular the cubic and reversed hexagonal phases, since these lipid phase structures are believed to be involved in many biologically important membrane processes such as fusion[48–50] and membrane lipid regulation.[1,15,51–53] With X-ray diffraction methods[54–57] the space group of the cubic structure can usually be obtained, but seldom is it possible to distinguish a bicontinuous structure from a structure consisting of closed micellar aggregates. The strength of the PFG NMR method is that it can discriminate between these two structures, since restricted motions in space can be easily observed.[58] The first PFG NMR study of amphiphile diffusion in a cubic phase was carried out by Charvolin and Rigny[59] for a soap system of potassium laurate which formed a cubic phase at 80 °C ($D = 2 \times 10^{-10}\,\mathrm{m^2\ s^{-1}}$). Such a large diffusion coefficient is not compatible with closed aggregates. Conclusions about whether or not a cubic phase consists of closed aggregates are based on a comparison between lipid diffusion coefficients measured by PFG NMR for neigboring phases, with which the cubic phase is in equilibrium.[2,4,60,61]

The apparent diffusion coefficients of cubic and lamellar phases can be qualitatively compared with a simple model.[2,61,62] The restricted lipid diffusion within aggregates building up the cubic lattice can be described by a local diffusion tensor, $\boldsymbol{D}$, where the component representing restricted diffusion in a certain direction is set to zero. The measured diffusion coefficient D is then an average value of the local diffusion tensor:

$$D = \tfrac{1}{3}\overline{\mathrm{Tr}\boldsymbol{D}} \quad (6)$$

where the bar denotes an average over all the sites in a unit cell of the liquid crystal. Depending on how many directions

Table 2 Lipid Diffusion Coefficients D for Some Cubic Liquid Crystalline Phases

Lipid system	Composition (wt.%)	Temperature (°C)	$D10^{11}$ (m^2 s^{-1})	Reference
Aerosol OT	72.4	24	0.36	Lindblom et al.[62]
Water	27.6	35	0.59	
Potassium octanoate	60	24	8.8	Lindblom and Wennerström[2]
Water	40			
Sodium octanoate	39.4	24	<0.1	Lindblom and Wennerström[2]
Octane	4.3			
Water	56.3			
Dodecyltrimethylammonium chloride	84.0	26	0.8	Eriksson et al.[75]
Water	16.0	47	2.0	
Monooleoylglycerol	88	43	1.5	Lindblom et al.[62]
Water	12	57	2.6	
Lysolauroyl-PC	40	29	0.006	Eriksson et al.[12]
Water	60			
Lysooleoyl-PC	79	26	0.14	Eriksson et al.[12]
Water	21			
Dioleoyl-PC	97	60	0.5	Lindblom[97]
Water	3			
Dioleoyl-PC	45	35	0.1	Ulmius et al.[28]
Sodium cholate	30			
Water	25			
Monoglucosyldiacylglycerol (MGlcDAG)	97	35	0.1	Lindblom et al.[15]
Water	3			
Dioleoyl-PC	46.2	66	0.37	Rilfors et al.[13]
Dioleoylphosphatidylethanolamine	43.8	73	0.50	
Water	10.0	83	0.64	
		90	0.78	

are effectively available for the lipid diffusion as measured by PFG NMR, three possibilities can be distinguished:

1. For a cubic phase with closed micelles, the lipid diffusion is restricted in all three directions, all the diagonal elements in the tensor are equal to zero, and D is ideally equal to zero.
2. A cubic structure of connected, long, rod-like aggregates permits lipid diffusion in one direction (along the rod) with the diffusion coefficient $D_{\|}$, and

$$D = \tfrac{1}{3}\overline{\mathrm{Tr}\boldsymbol{D}_{\mathrm{rod}}} = \tfrac{1}{3}D_{\|} \tag{7}$$

3. For a cubic phase with bilayer units, the diffusion $D_{\mathrm{L}}^{\mathrm{cub}}$ can occur in two directions, and

$$D = \tfrac{2}{3}D_{\mathrm{L}}^{\mathrm{cub}} \tag{8}$$

Thus, it can be expected that the aggregate structure in the cubic phase will appreciably influence the magnitude of the measured diffusion coefficients. In particular, PFG NMR provides a convenient method for distinguishing between bicontinuous cubic phases and those having closed aggregates. According to the above equations it should also be possible to obtain a crude estimate of the geometry of the aggregates building up the cubic phase, by comparing diffusion coefficents of lipids in the lamellar and cubic phases. Such a comparison assumes that the local environment of the molecules in the diffusing process is the same in the two phases.

For the comparison of diffusion coefficents of lipids and water in cubic phases, an attractive mathematical model based on a description of the cubic structure by periodic minimal surfaces can be used.[1,63–66] Recently, Anderson and Wennerström[66] have presented numerical results for the geometric obstruction factor of self-diffusion in different bicontinuous, cubic microstructures. The lipid diffusion was modeled as a diffusion of a particle, confined to the polar–apolar dividing surface, with a constant diffusion coefficient D_0. It was proven analytically that the effective diffusion coefficient for a particle diffusing over any minimal surface of cubic symmetry is exactly equal to $\frac{2}{3}D_0$.

4.1 Bicontinuous Cubic Phases

The most widely investigated bicontinuous cubic phases occur in the monooleoylglycerol (MO)/water system. An early X-ray diffraction and PFG NMR investigation of the lipids and water in this system suggested that the cubic phase structure was based on lamellar bilayer units.[62] The simple model described above was applied. The results of the MO system were compared with those of the aerosol OT/water system. The cubic phase of the latter system was suggested to be built up of rod-like aggregates. Using equations (7) and (8), surprisingly good predictions were made of the aggregate shape in the cubic phases.

Table 3 Water and Lipid Diffusion in Cubic Phases of Monooleoylglycerol and Water[72]

^1H_2O[a] (wt.%)	Phase	D_{cub}^{water}/D_0[b]	$D_{cub}^{lipid} \times 10^{12}(m^2s^{-1})$	p_b	n
28.0	*Ia*3*d*	0.201	14.4	0.56	4.3
30.4	*Ia*3*d*	0.237	15.1	0.49	4.2
33.4	*Ia*3*d*/*Pn*3*m*	0.276	1.53	0.41	4.1
36.6	*Pn*3*m*	0.292	15.8	0.39	4.4
39.5	*Pn*3*m*	0.300	1.69	0.38	5.0

[a] 25 °C.
[b] Measured water diffusion coefficient relative to that of pure water (see text).

The cubic phases of several monoglycerides exist over an extended water and temperature region in the phase diagrams.[67] These phases can dissolve substantial amounts of hydrophobic and amphiphilic molecules,[68–71] as well as glycerol.[11] The relationship between the water diffusion coefficient in cubic phases and the MO and water contents has been investigated. The water diffusion coefficient D_{cub}^{water} in a simple two-site model can be written[72]

$$D_{cub}^{water} = p_b D_{cub}^{lipid} + (1 - p_b)\beta D_0 \quad (9)$$

where p_b is the fraction of bound water, D_{cub}^{lipid} is the lipid diffusion coefficient in the cubic phase, β is the obstruction factor for the diffusion of unbound water in the cubic phase, and D_o is the diffusion of bulk water. The association of water obtained from the application of this simple model (Table 3) should be taken as a quantification of the extent to which the surface of the aggregates affects the dynamic properties of water. The diffusion coefficient of water[72] has a discontinuous increase at around 34% water, which harmonizes with the two-phase region between the *Ia*3*d* and *Pn*3*m* cubic structures.[73] The lipid diffusion was found to increase with increasing unsaturation of the acyl chains of the lipid, and it decreases when larger molecules such as cholesterol, gramicidin A, and lysooleoyl-PC are solubilized in the cubic phase. In a cubic liquid crystal of MO, DOPC, and water, the individual lipid diffusion coefficients can be determined simultaneously. The results obtained suggest that when probe techniques are used the choice of the probe itself may influence the measured lipid diffusion coefficient. Recently, we investigated the cubic phase of *N*,*N*-dimethyldodecylammonium oxide (DDAO) having a molar ratio of 97:3 between DDAO and gramicidin and 27 wt.% water. At 25 °C, and taking the diffusion coefficient of water as $D_{water} = 6.3 \times 10^{-11}$ m^2 s^{-1}, the measured diffusion coefficients for the methyl groups of the polar headgroup and the terminal methyl group were 7×10^{-12} m^2 s^{-1}. The latter coefficient should be compared with the coefficient for the diffusion of DDAO in a cubic phase in the absence of gramicidin; the value is 10×10^{-12} m^2 s^{-1}, i.e. gramicidin causes quite a small obstruction effect.

Several membrane lipid–water systems give rise to freeze–fracture replicas of three-dimensional regular arrays of closely packed globular elements, often called 'lipidic particles.'[74] These structural pictures have often been poorly classified, and they have been suggested to show closed lipid aggregates, such as reversed micelles. Investigations of some liquid crystalline phases, giving rise to the freeze–fractured replicas, with X-ray diffraction and PFG NMR indicate that they are: (1) cubic liquid-crystalline phases; and (2), with one exception, bicontinuous cubic phases.[13] There is a rather large accumulation of diffusion coefficients to verify the structure of bicontinuous cubic phases (Table 2).[2,12,14,15,28,53,61,75–80]

4.2 Discontinuous Cubic Phases

Usually these cubic structures are located between the micellar solution and the H_I phase in the phase diagram.[81] X-Ray diffraction showed that this structure belongs to the space group $P43n$ or $Pm3n$. For a long time it was debated whether the structure consists of closed aggregates[12,60,75,82–84] or of a network of connected rod-like micelles with enclosed spherical micelles.[55,85] This debate is now settled,[86,87] and it has been shown conclusively by PFG NMR (Table 2)[83,84,88] that this cubic structure is discontinuous. From NMR lineshapes,[83] spin relaxation,[89,90] and time-resolved quenched fluorescence[84,91] it is concluded that the structure consists of slightly elongated, closed micelles (Figure 1). Recently, a cubic phase consisting of reversed micelles was established.[92] The structure of this phase, which belongs to the space group $Fd3m$, and which is composed of DOPC and dioleoylglycerol or oleic acid and sodium oleate, was recently solved by means of low-resolution crystallography.[93] The structure consists of a complex packing of two types of quasi-spherical reversed micelles. PFG NMR has shown[94] for the cubic phase composed of DOPC and dioleoylglycerol that reversed micelles build up the structure. The diffusion coefficient of DOPC is very small, close to 10^{-13} m^2 s^{-1}, while the diffusion of water and dioleoylglycerol are much more rapid [of the order of 10^{-11} m^2 s^{-1} (Figure 2)]. It was concluded[94] that the reversed micelles contain mainly DOPC and the dioleoylglycerol merely plays the role of a solvent.

5 LATERAL DIFFUSION IN OTHER NONLAMELLAR LIQUID CRYSTALS

The translational diffusion of all three components has been measured in the ternary system DOPC/water/dodecane,[78] where dodecane induces an H_{II} phase. From a comparison between diffusion coefficients, it was concluded that dodecane resides between the water cylinders in the H_{II} phase.

Some lyotropic mesophases, called 'nematics', orient spontaneously in a strong magnetic field. Utilizing ultraviolet (UV) linear dichroism on a solubilized chromophore and PFG NMR on a nematic phase containing potassium dodecanoate, it was shown that this phase is built up of long rod-like micelles.[95,96]

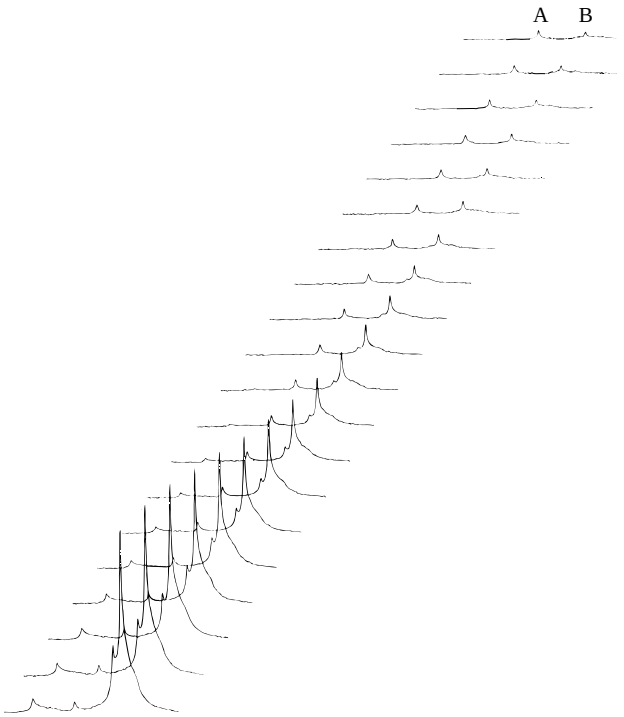

Figure 2 Stacked plot of spectra with increasing strength of the pulsed field gradient in a diffusion experiment performed on the system DOPC/1,2-dioleoylglycerol/^2H_2O (25.44/59.57/14.99) at 42 °C. The two peaks marked in the figure correspond to (A) CH_3 groups of the choline headgroup, and (B) terminal CH_3 groups of DOPC and 1,2-dioleoylglycerol. The diffusion coefficient of A is estimated to be 3×10^{-13} m^2 s^{-1}, while B shows two diffusion coefficients of 0.3×10^{-12} and 15×10^{-12} m^2 s^{-1}

The translational diffusion coefficient of the amphiphile was obtained from an aligned sample oriented at the magic angle. The surfactant diffusion along the rod was found to be $D_L = 5 \times 10^{-11}$ m^2 s^{-1} for potassium laurate and $D_L = 8 \times 10^{-11}$ m^2 s^{-1} for sodium decyl sulfate.[96] These values compare well with the lateral diffusion coefficients for the corresponding lamellar mesophases (Table 1). By means of the relationship $\langle x^2 \rangle = 2Dt$, the length can be estimated to be longer than 2000 nm.

6 RELATED ARTICLES

Amphiphilic Liquid Crystalline Samples: Nuclear Spin Relaxation; Bilayer Membranes: Deuterium and Carbon-13 NMR; Bilayer Membranes: Proton and Fluorine-19 NMR; Diffusion and Flow in Fluids; Diffusion Measurements by Magnetic Field Gradient Methods; Glycolipids; Lipid Polymorphism; Lyotropic Liquid Crystalline Samples; Membrane Lipids of Acholeplasma laidlawii; Phospholipid–Cholesterol Bilayers.

7 REFERENCES

1. G. Lindblom and L. Rilfors, *Biochim. Biophys. Acta*, 1989, **988**, 221.
2. G. Lindblom and H. Wennerström, *Biophys. Chem.*, 1977, **6**, 167.
3. P. T. Callaghan, *Principles of Nuclear Magnetic Resonance Microscopy*, Clarendon, Oxford, 1991.
4. G. Lindblom and H. Wennerström, *Magnetic Resonance of Biological Systems*, St Jovite, Quebec, 1976.
5. S. B. W. Roeder, E. E. Burnell, A.-L. Kuo, and C. G. Wade, *J. Chem. Phys.*, 1976, **64**, 1848.
6. H. Wennerström, *Chem. Phys. Lett.*, 1973, **18**, 41.
7. H. Wennerström and G. Lindblom, *Q. Rev. Biophys.*, 1977, **10**, 67.
8. D. M. Brink and G. R. Satchler, *Angular Momentum*, 3rd edn., Oxford University Press, Oxford, 1993.
9. A. L. Kuo and C. G. Wade, *Biochemistry*, 1979, **18**, 2300.
10. W.-G. Wu and C.-H. Huang, *Lipids*, 1981, **16**, 820.
11. G. Orädd, G. Wikander, G. Lindblom, and L. B.-Å. Johansson, *J. Chem. Soc., Faraday Trans. I*, 1994, **90**, 305.
12. P. O. Eriksson, G. Lindblom, and G. Arvidson, *J. Phys. Chem.*, 1987, **91**, 846.
13. L. Rilfors, P.-O. Eriksson, G. Arvidson, and G. Lindblom, *Biochemistry*, 1986, **25**, 7702.
14. Å. Wieslander, L. Rilfors, L. B.-Å. Johansson, and G. Lindblom, *Biochemistry*, 1981, **20**, 730.
15. G. Lindblom, I. Brentel, M. Sjölund, G. Wikander, and Å. Wieslander, *Biochemistry*, 1986, **25**, 7502.
16. G. Lindblom, L. B.-Å. Johansson, and G. Arvidson, *Biochemistry*, 1981, **20**, 2204.
17. P. van der Ploeg and H. J. C. Berendsen, *Mol. Physiol.*, 1983, **49**, 233.
18. O. Edholm and A. M. Nyberg, *Biophys. J.*, 1992, **63**, 1081.
19. R. M. Venable, Y. H. Zhang, B. J. Hardy, and R. W. Pastor, *Science*, 1993, **262**, 223.
20. M. R. Vist and J. H. Davis, *Biochemistry*, 1990, **29**, 451.
21. J. H. Ipsen, G. Karlström, O. G. Mouritsen, H. W. Wennerström, and M. J. Zuckermann, *Biochim. Biophys. Acta*, 1987, **905**, 162.
22. J. Ulmius, H. Wennerström, G. Lindblom, and G. Arvidson, *Biochim. Biophys. Acta*, 1975, **389**, 197.
23. G. W. Stockton and I. C. P. Smith, *Chem. Phys. Lipids*, 1976, **17**, 251.
24. E. Oldfield, M. Meadows, D. Rice, and R. Jacobs, *Biochemistry*, 1978, **17**, 2727.
25. G. Lindblom, N.-O. Persson, and G. Arvidson, *Adv. Chem. Ser.*, 1976, **152**, 121.
26. M. Silva-Crawford, B. C. Gerstein, A.-L. Kuo, and C. G. Wade, *J. Am. Chem. Soc.*, 1980, **102**, 3728.
27. R. T. Roberts, *Nature (London)*, 1973, **242**, 348.
28. J. Ulmius, G. Lindblom, H. Wennerström, L. B.-Å. Johansson, K. Fontell, O. Söderman, and G. Arvidson, *Biochemistry*, 1982, **21**, 1553.
29. G. Lindblom, H. Wennerström, and G. Arvidson, *Int. J. Quantum Chem.*, 1977, **XII** (Suppl. 2), 153.
30. J. F. Martin, L. S. Selwyn, R. R. Vold, and R. L. Vold, *J. Chem. Phys.*, 1982, **76**, 2632.
31. D. W. Larsen, J. G. Boylan, and B. R. Cole, *J. Phys. Chem.*, 1987, **91**, 5631.
32. T. Köchy and T. M. Bayerl, *Phys. Rev. E*, 1993, **47**, 2109.
33. J. F. Ellena, L. S. Lepore, and D. S. Cafiso, *J. Phys. Chem.*, 1993, **97**, 2952.
34. H. Wennerström, G. Lindblom, and B. Lindman, *Chem. Script.*, 1974, **6**, 97.
35. H. Wennerström, B. Lindman, O. Söderman, T. Drakenberg, and J. B. Rosenholm, *J. Am. Chem. Soc.*, 1979, **101**, 6860.
36. B. Halle and H. Wennerström, *J. Chem. Phys.*, 1981, **75**, 1928.

37. R. Blinc, K. Easwaran, J. Pirs, M. Volfan, and I. Zupancic, *Phys. Rev. Lett.*, 1970, **25**, 1327.
38. G. J. T. Tiddy, *J. Chem. Soc., Faraday Trans. I*, 1977, **73**, 1731.
39. P. T. Callaghan, M. A. Le Gros, and D. N. Pinder, *J. Chem. Phys.*, 1983, **79**, 6372.
40. P. O. Eriksson and G. Lindblom, *Springer Ser. Chem. Phys.*, 1980, **11**, 290.
41. H. Wennerström, B. Lindman, G. Lindblom, and G. J. T. Tiddy, *J. Chem. Soc., Faraday Trans. I*, 1979, **75**, 663.
42. G. Lindblom, L. Rilfors, J. B. Hauksson, I. Brentel, M. Sjölund, and B. Bergenståhl, *Biochemistry*, 1991, **30**, 10938.
43. A. R. Waldeck, A. J. Lennon, B. E. Chapman, and P. W. Kuchel, *J. Chem. Soc., Faraday Trans.*, 1993, **89**, 2807.
44. P. T. Callaghan and O. Söderman, *J. Phys. Chem.*, 1983, **87**, 1737.
45. L. Coppola, C. La Mesa, G. A. Ranieri, and M. Terenzi, *J. Chem. Phys.*, 1993, **98**, 5087.
46. G. Celebre, L. Coppola, and G. A. Ranieri, *J. Chem. Phys.*, 1992, **97**, 7781.
47. J. Chung and J. H. Prestegard, *J. Phys. Chem.*, 1993, **97**, 9837.
48. D. P. Siegel, *Chem. Phys. Lipids*, 1986, **42**, 279.
49. D. P. Siegel, *Biophys. J.*, 1993, **65**, 2124.
50. L. V. Chernomordik, G. B. Melikyan, and Y. A. Chizmadzhev, *Biochim. Biophys. Acta*, 1987, **906**, 309.
51. G. Lindblom, J. Hauksson, L. Rilfors, B. Bergenståhl, Å. Wieslander, and P.-O. Eriksson, *J. Biol. Chem.*, 1993, **268**, 16198.
52. L. Rilfors, Å. Wieslander, and G. Lindblom, in *Subcellular Biochemistry, Mycoplasma Cell Membranes*, eds. S. Rottem and I. Kahane, Plenum, New York, 1993.
53. L. Rilfors, J. Hauksson, and G. Lindblom, *Biochemistry*, 1994, **33**, 6110.
54. V. Luzzati, in *Biological Membranes*, ed. D. Chapman, Academic, New York, 1968.
55. P. Mariani, V. Luzzati, and H. Delacroix, *J. Mol. Biol.*, 1988, **204**, 165.
56. S. M. Gruner, P. R. Cullis, M. J. Hope, and C. P. S. Tilcock, *Ann. Rev. Biophys., Biophys. Chem.*, 1985, **14**, 211.
57. M. W. Tate, E. F. Eikenberry, D. C. Turner, E. Shyamsunder, and S. M. Gruner, *Chem. Phys. Lipids*, 1991, **57**, 147.
58. J. E. Tanner and E. O. Stejskal, *J. Chem. Phys.*, 1968, **49**, 1768.
59. J. Charvolin and P. Rigny, *J. Chem. Phys.*, 1973, **58**, 3999.
60. T. Bull and B. Lindman, *Mol. Cryst. Liquid Cryst.*, 1974, **28**, 155.
61. G. Lindblom, H. Wennerström, G. Arvidson, and B. Lindman, *Biophys. J.*, 1976, **16**, 1287.
62. G. Lindblom, K. Larsson, L. Johansson, K. Fontell, and S. Forsén, *J. Am. Chem. Soc.*, 1979, **101**, 5465.
63. L. E. Scriven, *Nature*, 1976, **263**, 123.
64. D. M. Anderson, S. M. Gruner, and S. Leibler, *Proc. Natl. Acad. Sci. USA*, 1988, **85**, 5364.
65. S. Andersson, S. T. Hyde, K. Larsson, and S. Lidin, *Chem. Rev.*, 1988, **88**, 221.
66. D. M. Anderson and H. Wennerström, *J. Phys. Chem.*, 1990, **94**, 8683.
67. E. S. Lutton, *J. Am. Oil Chem. Soc.*, 1965, **42**, 1068.
68. K. Larsson, K. Gabrielsson, and B. Lundberg, *J. Sci. Food Agric.*, 1978, **29**, 909.
69. B. Ericsson, K. Larsson, and K. Fontell, *Biochim. Biophys. Acta*, 1983, **729**, 23.
70. H. Gutman, G. Arvidson, K. Fontell, and G. Lindblom, in *Surfactants in Solutions*, eds. K. L. Mittal and B. Lindman, Plenum, New York, 1984, Vol. 1, p. 143.
71. B. Ericsson, P. O. Eriksson, J. E. Löfroth, and S. Engstrom, *ACS Symp. Ser.*, 1991, **469**, 251.
72. P. O. Eriksson and G. Lindblom, *Biophys. J.*, 1993, **64**, 129.
73. W. Longley and T. J. McIntosh, *Nature*, 1983, **303**, 612.
74. A. J. Verkleij, C. Mombers, J. Leunissen-Bijvelt, and P. H. J. T. Ververgaert, *Nature*, 1979, **279**, 162.
75. P.-O. Eriksson, A. Khan, and G. Lindblom, *J. Phys. Chem.*, 1982, **86**, 387.
76. L. Rilfors, A. Khan, I. Brentel, Å. Wieslander, and G. Lindblom, *FEBS Lett.*, 1982, **149**, 293.
77. I. Brentel, E. Selstam, and G. Lindblom, *Biochem. Biophys. Acta*, 1985, **812**, 816.
78. M. Sjölund, G. Lindblom, L. Rilfors, and G. Arvidson, *Biophys. J.*, 1987, **52**, 145.
79. J. P. Conroy, C. Hall, C. A. Leng, K. Rendall, G. J. T. Tiddy, J. Walsh, and G. Lindblom, *Prog. Colloid Polym. Sci.*, 1990, **82**, 253.
80. G. Orädd, G. Lindblom, L. B.-Å. Johansson, and G. Wikander, *J. Phys. Chem.*, 1992, **96**, 5170.
81. K. Fontell, *Adv. Colloid Interface Sci.*, 1992, **41**, 127.
82. K. Fontell, K. K. Fox, and E. Hansson, *Mol. Cryst. Liquid Cryst.*, 1985, **1**, 9.
83. P.-O. Eriksson, G. Lindblom, and G. Arvidson, *J. Phys. Chem.*, 1985, **89**, 1050.
84. G. Lindblom, L. B.-Å. Johansson, G. Wikander, P.-O. Eriksson, and G. Arvidson, *Biophys. J.*, 1992, **63**, 723.
85. A. Tardieu and V. Luzzati, *Biochim. Biophys. Acta*, 1970, **219**, 11.
86. R. Vargas, P. Mariani, A. Gulik, and V. Luzzati, *J. Mol. Biol.*, 1992, **225**, 137.
87. H. Delacroix, T. Gulik-Krzywicki, P. Mariani, and V. Luzzati, *J. Mol. Biol.*, 1993, **229**, 526.
88. P.-O. Eriksson, L. Rilfors, G. Lindblom, and G. Arvidson, *Chem. Phys. Lipids*, 1985, **37**, 357.
89. O. Söderman, H. Walderhaug, U. Henriksson, and P. Stilbs, *J. Phys. Chem.*, 1985, **89**, 3693.
90. O. Söderman and U. Henriksson, *J. Chem. Soc., Faraday Trans. I*, 1987, **83**, 1515.
91. L. B.-Å. Johansson and O. Söderman, *J. Phys. Chem.*, 1987, **91**, 5275.
92. J. M. Seddon, E. A. Bartle, and J. Mingins, *J. Phys. Condens. Matter.*, 1990, **2**, 285.
93. V. Luzzati, R. Vargas, A. Gulik, P. Mariani, J. Seddon, and E. Rivas, *Biochemistry*, 1992, **31**, 279.
94. G. Orädd, G. Lindblom, K. Fontell, and H. Ljusberg-Warren, *Biophys. J.*, 1995, **68**, 1856.
95. O. Söderman, G. Lindblom, L. B.-Å. Johansson, and K. Fontell, *Mol. Cryst. Liquid Cryst.*, 1980, **59**,
96. L. B.-Å. Johansson, O. Söderman, K. Fontell, and G. Lindblom, *J. Phys. Chem.*, 1981, **85**, 3694.
97. G. Lindblom, *Acta Chem. Scand. B*, 1981, **35**, 61.
98. L. Rilfors, G. Lindblom, Å. Wieslander, and A. Christiansson, in *Biomembranes*, eds. L. A. Manson and M. Kates, Plenum, New York, 1984, Vol. 12, p. 205.

Biographical Sketch

Göran Lindblom. *b* 1942. M.S., 1969, Ph.D., 1974, Lund, Sweden. Introduced to NMR by S. Forsén, Lund University. Professor in Physical Chemistry, University of Umeå, 1981-present. Approx. 150

publications. Research interests: structure, dynamics and function of biological membranes; physicochemical properties and structure of lyotropic liquid crystals.

Greger Orädd. *b* 1961. M.S. 1989, Ph.D., 1994, Umeå, Sweden. Introduced to NMR by G. Lindblom. Five publications. Research interests: application of NMR diffusion methods to liquid crystals.

Liquid Crystalline Samples: Relaxation Mechanisms

Pier Luigi Nordio and Alberta Ferrarini
University of Padova, Padova, Italy

1	Introduction	1
2	Experimental Observables	1
3	Dynamic Models	2
4	Related Articles	6
5	References	6

1 INTRODUCTION

In the liquid state, spin relaxation is caused by the random fluctuations of magnetic interactions resulting from Brownian rotational and translational diffusion of molecules, conformational transitions, or solvation effects. These motions act as random time-dependent perturbations, which induce transitions among the spin states and ultimately lead to Boltzmann equilibrium values of macroscopic magnetization vector components, altered by application of the excitation field in relaxation experiments. Random magnetic perturbations are characterized by the equilibrium average $\overline{\Delta}$, the mean-square value $\overline{\Delta^2}$, and the persistence or correlation time τ. It is convenient to express Δ in frequency units rather than in energy units; the strength of the interaction is therefore divided by the Planck constant $\hbar$.

In high-resolution NMR spectroscopy, a fast motional regime, characterized by the condition $(\overline{\Delta^2} - \overline{\Delta}^2)\tau^2 \ll 1$, often holds. This situation is the simplest to analyze by time-dependent perturbation theories and is generally referred to as the Redfield limit.[1] In this condition, both the longitudinal component of the macroscopic magnetization along the static field $\boldsymbol{B}_0$, and the transverse component created by the observing field $\boldsymbol{B}_1$, relax as simple exponentials, with characteristic times T_1 and T_2, respectively. The theoretical expressions predicted by the theory for T_1^{-1} and T_2^{-1} are very simple and the relaxation times come out to be of the order of $(\overline{\Delta^2} - \overline{\Delta}^2)\tau$. Thus, if the dominant relaxation mechanism is provided by modulation due to rotational diffusion of an intramolecular interaction described by an axially symmetric second-rank tensor $\boldsymbol{T}$ with principal components $T_{zz} = T_\parallel$ and $T_{xx} = T_{yy} = T_\perp$, spin relaxation times of the order of 1 s will result for $\Delta = T_\parallel - T_\perp = 10^5\,\mathrm{s}^{-1}$ (a value appropriate for the ^{13}C–H spin dipole interaction) and $\tau = 10^{-10}$ s, corresponding to the rotational correlation time of most liquids under normal conditions.

The motional processes responsible for spin relaxation in liquids are almost invariably interpreted in terms of diffusion models, so that a few comments on the underlying theoretical treatments are in order. A diffusional regime for molecular translations and rotations applies when strong impulsive interactions with the surrounding molecules interrupt the inertial motion of the particle so frequently that a random walk of infinitesimally short steps actually results. To interpret these dynamic processes, an equation of motion for the test particle can be set up, including a dissipative term in the form of a frictional force. In fact, the resulting equation is the basis of the method for describing molecular motions in fluids known as 'Brownian dynamics'.[2] (see ***Brownian Motion and Correlation Times***.)

Alternatively, a stochastic equation can be derived to interpret the time evolution of the probability distribution function specifying molecular coordinates. The treatment leading to this equation, often referred to as the 'diffusion (or Smoluchowski) equation' when inertial effects are completely quenched, is reported in specialized texts.[3] (We reserve the term 'Fokker–Planck equation' for the more general formalism which takes into account translational and angular velocity of the particle, in addition to translational and angular coordinates. According to this description, the diffusional behavior is recovered if velocities are quenched within a time shorter than the decay time for the spatial variables.) The diffusion equation is a differential equation formally similar to a time-dependent Schrödinger equation and it can solved by similar methods. In fact, after separating the time variable, the solution of the resulting second-order differential equation is reduced to the determination of eigenvalues and eigenvectors of the matrix representation of the diffusion operator on a suitable set of functions. The mathematical details are given elsewhere,[4,5] so we give here only the relevant physical factors in the diffusion equation. These are:

1. The potential function arising from forces and torques exerted on the test particle, including terms accounting for hindered internal motions.
2. Diffusion coefficients (or, more generally, diffusion tensors) which take into account frictional effects. Diffusion coefficients are determined by the molecular geometry and viscosity of the medium by the Stokes–Einstein relationships.[6,7]

The general considerations given above hold for both isotropic and anisotropic liquid phases. We will see in the following discussion how the specific nature of the liquid crystal environment may not only alter the characteristics of dynamic processes that occur in normal liquids (e.g. features of rotational and translational diffusion, or static and dynamic parameters of conformational changes), but also introduce novel relaxation mechanisms which are absent in isotropic fluids.

2 EXPERIMENTAL OBSERVABLES

NMR relaxation experiments in liquid crystals can be performed both on the molecules forming the mesophase and on solutes suitably chosen to probe the dynamic properties of the environment. Under normal experimental conditions, fast motional regimes hold, providing well-resolved spectra. Measurements on specific nuclear positions of the molecule can therefore be performed to give data which can then be processed theoretically in order to extract dynamic information. For this reason, ^{13}C (either in natural abundance or chemically enriched) and ^{2}H (introduced by specific deuteration) are the favored nuclei for use in relaxation experiments on liquid crystals. For ^{13}C and ^{2}H nuclear spins, the dominant source of spin relaxation is provided by the ^{13}C–H dipole and ^{2}H quadrupole interactions, respectively. With the very high fields used in modern spectrometers, shielding anisotropies may also have

relevant effects. In all cases, these interactions are described by second-rank Cartesian tensors.

According to the Redfield theory (see ***Relaxation Theory: Density Matrix Formulation***), the equations for ^{13}C (under proton decoupling) and ^{2}H longitudinal relaxation times are

$$1/T_1^{C} = (\tfrac{1}{12})[J_0(\omega_H - \omega_C) + 3J_1(\omega_C) + 6J_2(\omega_H + \omega_C)] \quad (1)$$

and

$$1/T_1^{D} = (\tfrac{1}{4})[J_1(\omega_D) + 4J_2(2\omega_D)] \quad (2)$$

where $J_p(\omega)$ are spectral densities, i.e. the Fourier transforms (FTs) of the correlation functions describing the time evolution of the irreducible spherical components[8] of the second-rank magnetic interactions in a laboratory reference frame. In fact, the magnetic tensor components are defined in a molecular axis system, and therefore appear to vary in time when viewed from the laboratory system, because of molecular tumbling in the liquid. The FTs are calculated at frequency values related to ^{1}H, ^{13}C, and ^{2}H resonance frequencies in the experiment. Spectral densities can be expressed in terms of the magnitude of the interactions, and of the time decay of angular functions (Wigner rotation matrix components[8]) which define the molecular orientation with respect to the laboratory fixed reference frame. The FT $j(\omega)$ of an exponential function characterized by time constant τ is

$$j(\omega) = \frac{\tau}{1 + \omega^2\tau^2} \quad (3)$$

Complete dynamic information on a system should be achieved by relaxation experiments capable of providing the various spectral densities at different frequencies. Modern experiments are actually performed at a number of working frequencies.[9,10] It is also interesting to note that equations (1) and (2) refer to standard experiments of saturation or inversion–recovery of the total longitudinal component of magnetization. In this way, individual spectral densities cannot be obtained directly from experimental data. However, they can be provided by applying appropriate sequences of radiofrequency (rf) pulses to the spin system. Equations for relaxation rates determined by various pulse experiments on a single spin $I = 1$ in ordered phases are reported in Table 3 of Vold[11] (see also ***Deuteron Relaxation Rates in Liquid Crystalline Samples: Experimental Methods***).

Experiments in liquid crystal phases are performed on samples which are macroscopically oriented by means of magnetic fields, surface effects or electric fields. In some instances, it is also possible to measure the angular dependence of the spectral densities when the axis of preferential alignment of the mesophase (the optical axis, or director) can be rotated away from the magnetic field direction. This can be easily done with uniaxial smectic-A phases. Again, explicit equations for the angular dependence of the spectral densities appropriate for this case may be found in Vold.[11]

3 DYNAMIC MODELS

In a liquid sample at thermodynamic equilibrium, the dynamic processes which cause thermal motions of the molecules are defined as random stationary. Although the system is macroscopically in equilibrium, the coordinates specifying the position and orientation of any molecule, here collectively denoted by $\boldsymbol{x}$, exhibit random walk in time. Any function of these coordinates will behave as a function $f[\boldsymbol{x}(t)]$ randomly varying in time. If a physical property of the system is related to the function $f(\boldsymbol{x})$, experimental measurements can be made to determine directly the equilibrium average:

$$\bar{f} = \int \mathrm{d}\boldsymbol{x}\ f(\boldsymbol{x})P(\boldsymbol{x}) \quad (4)$$

thus providing information on equilibrium distribution $P(\boldsymbol{x})$.

The main result of the stochastic theories is that, for random-stationary processes, knowledge of the random events occurring at the molecular level is entirely contained in a statistical property called the correlation function of $f(\boldsymbol{x})$:

$$\overline{f^*(t)f(0)} = \iint \mathrm{d}\boldsymbol{x}\,\mathrm{d}\boldsymbol{x}_0\ f^*(\boldsymbol{x})f(\boldsymbol{x}_0)P(\boldsymbol{x}, t; \boldsymbol{x}_0, 0) \quad (5)$$

where $P(\boldsymbol{x}, t; \boldsymbol{x}_0, 0)$ is the joint probability of finding the molecule in $\boldsymbol{x}_0$ at an arbitrary initial time $t_0 = 0$, and in $\boldsymbol{x}$ at the later time t. It follows from the properties of the joint probability that this function becomes equal to $P(\boldsymbol{x})\delta(\boldsymbol{x} - \boldsymbol{x}_0)$ at time zero and to the product $P(\boldsymbol{x})P(\boldsymbol{x}_0)$ at infinite time, when correlation can no longer exist. Therefore, the correlation function varies between limits $|\overline{f^2}|$ at $t = 0$ and $|\bar{f}|^2$ at $t \to \infty$. It is often convenient to define the correlation function $g(t)$ for the deviation of $f(t)$ from the equilibrium value $\bar{f}$, thus obtaining

$$g(t) = \overline{f^*(t)f(0)} - |\bar{f}|^2 \quad (6)$$

The mean square value $|\overline{f^2}|$ and average $\bar{f}$ can be calculated from the equilibrium distribution $P(\boldsymbol{x})$, but the time evolution of the joint probability function requires a mathematical model derived on the basis of a physically reasonable picture, and this is provided by solution of the diffusion equation.

The above considerations may immediately be applied to the problem of reorientational motions, which cause random fluctuations of the intramolecular anisotropic magnetic interactions, and are of particular importance for ^{13}C and ^{2}H spin relaxation in any liquid phase.

The irreducible spherical components of second-rank tensorial interactions $\boldsymbol{T}$, expressed in a laboratory frame having the Z axis parallel to the static magnetic field $\boldsymbol{B}_0$, are given by[8]

$$T_{lab}^{(2,p)} = \sum_q \mathcal{D}_{pq}^{2*}(\Omega)T_{mol}^{(2,q)} \quad (7)$$

where $T_{mol}^{(2,q)}$ are the components in a molecular frame and $\mathcal{D}_{pq}^{2}(\Omega)$ are Wigner rotation matrix elements carrying the transformation from the laboratory system (X, Y, Z) to the molecular frame (x, y, z), described by the set of Euler angles $\Omega \equiv (\alpha, \beta, \gamma)$. The time dependence of the quantities $T_{lab}^{(2,p)}$ is contained in that of the Euler angles Ω, which change randomly in time as a consequence of rotational motions. The effective perturbation induced by modulation of the $\boldsymbol{T}$

tensor components is determined by the deviation from the equilibrium value:

$$\delta T_{\text{lab}}^{(2,p)}[\Omega(t)] = \sum_q \{\mathcal{D}_{pq}^{2*}[\Omega(t)] - \overline{\mathcal{D}_{pq}^{2*}}\} T_{\text{mol}}^{(2,q)} \tag{8}$$

Of special interest, therefore, are the autocorrelation functions $g_{pq}(t)$ of the Wigner components $\mathcal{D}_{pq}^2(\Omega)$, defined as

$$g_{pq}(t) = \overline{\mathcal{D}_{pq}^{2*}(t)\mathcal{D}_{pq}^2(0)} - |\overline{\mathcal{D}_{pq}^2}|^2 \tag{9}$$

the overbar now denoting an average over the orientational degrees of freedom. The time behavior of the correlation functions $g_{pq}(t)$ is determined by the reorientational process undergone by the molecules, and the thermal averages $\overline{\mathcal{D}_{pq}^2}$ are determined by the nature of the liquid phase.

The spectral densities $J_p(\omega)$ which appear in the equations for the spin relaxation rates are

$$\begin{aligned} J_p(\omega) &= \frac{1}{2}\int_{-\infty}^{\infty} \mathrm{d}t\, \mathrm{e}^{-\mathrm{i}\omega t} \overline{\delta T_{\text{lab}}^{(2,p)*}(t)\delta T_{\text{lab}}^{(2,p)}(0)} \\ &= \sum_q |T_{\text{mol}}^{(2,q)}|^2 j_{pq}(\omega) \end{aligned} \tag{10}$$

where $j_{pq}(\omega)$ are the FTs of the correlation functions $g_{pq}(t)$.

In the case of molecules with internal degrees of freedom, the additional transformation from a fixed molecular frame to a reference system located in each molecular moiety must be considered explicitly. For a tensorial interaction located in the ith unit, equation (7) is rewritten as

$$T_{i,\text{lab}}^{(2,p)} = \sum_{q,n} \mathcal{D}_{pn}^{2*}(\Omega)\mathcal{D}_{nq}^{2*}(\Omega_i) T_i^{(2,q)} \tag{11}$$

The complex expressions resulting for correlation functions and spectral densities are given by Ferrarini et al.[12,13]

3.1 Rotational Diffusion

In isotropic media, i.e. in the case of a spherically symmetric orientational distribution, it follows from the orthogonality properties of the Wigner functions that

$$\overline{\mathcal{D}_{pq}^2} = 0, \quad \overline{|\mathcal{D}_{pq}^2|^2} = \tfrac{1}{5} \tag{12}$$

and the solution of the diffusion equation for axially symmetric molecules characterized by the principal values $D_\parallel$ and $D_\perp$ of the diffusion tensor gives

$$g_{pq}(t) = (\tfrac{1}{5}) \exp(-t/\tau_{pq}) \tag{13}$$

$$1/\tau_{pq} = 6D_\perp + (D_\parallel - D_\perp)q^2 \tag{14}$$

Since the orientational correlation time in equation (14) is independent of the index p, the spectral densities $J_p(\omega)$ all turn out to be identical.

In ordered phases, as a consequence of anisotropic interactions with the environment, the molecules are subjected to an effective orientational potential $U(\Omega)$ which, unlike the isotropic case, determines the nonuniform equilibrium distribution of orientations.

As the diffusion model is appropriate for describing the rotational dynamics of molecules in a liquid of normal density and viscosity, it is also suitable for use for liquid crystals. However, the motion in this case is better termed 'anisotropic' rotational diffusion, because of the orientational torques exerted on the molecules.

In nematics, rod-like or disk-like molecules tend to orient the symmetry axis to the director, giving rise to calamitic or discotic nematic phases, respectively. The condition of axial symmetry for the phase implies free rotations around the laboratory Z axis, and therefore $\overline{D_{pq}^2}$ must be zero for $p \neq 0$. Nematic phases are generally expected to be uniaxial, although biaxiality cannot in principle be excluded. If the molecules themselves are assumed to be uniaxial, rotations about the molecular z axis are unhindered and only terms with $q = 0$ remain. For uniaxial molecules in uniaxial phases, the only order parameter directly measured by NMR is $\overline{\mathcal{D}_{00}^2}$, which coincides with the Legendre polynomial $\overline{P}_2$.[8] The simple Maier–Saupe form

$$U(\beta)/k_{\text{B}}T = -\lambda P_2(\cos\beta) \tag{15}$$

is appropriate for this particular case, β denoting the angle between the director and the molecular symmetry axis.

The potential of the mean torque acting in nematics has two important effects on the efficiency of rotational motions as a source of spin relaxation. First, the magnitude of time-dependent perturbation is reduced with respect to the isotropic case, as the angular functions $\mathcal{D}_{pq}^2(\Omega)$ average now to non-zero values. Thermal averages $\overline{\mathcal{D}_{pq}^2}$ are called 'order parameters', because they measure the anisotropy of the orientational distribution. A second consequence of the orientational potential is to alter the features of rotational motion. Since the particles are preferentially oriented with the symmetry axis (assuming a uniaxially symmetric molecule) parallel to the director, motions can be roughly separated into fast fluctuations about the preferred orientation (with the characteristic frequencies expected to increase with the strength of the orienting field, according to the simple picture of motions in a potential well), essentially free rotations about the symmetry axis, and flippings of the long axis, which, being hindered by the orienting potential, become slower with increasing ordering. The latter motion, however, is a very important relaxation mechanism for vectorial properties, e.g. dielectric relaxation, but it is ineffective for second-rank tensorial properties. The decay of correlation functions $g_{pq}(t)$ can be calculated by solving a diffusion equation for the rotational degrees of freedom, in which the effect of the orienting potential is included.[4,5] The full solution of the diffusion equation requires expansion on the basis of the Wigner functions $\mathcal{D}_{pq}^j(\Omega)$, which are eigensolutions of the diffusional problem for the isotropic case. Correlation functions $g_{pq}(t)$ can, in most cases, be approximated by single exponentials:

$$g_{pq}(t) = C_{pq} \exp(-\alpha_{pq} t) \tag{16}$$

with the preexponential factors C_{pq} and decay rate constants α_{pq} now being dependent on the order parameters $\overline{P}_2$ and

$\overline{P_4}$, in addition to the diffusion coefficients $D_\perp$ and $D_\parallel$. Particularly simple expressions are obtained by an asymptotic solution of the diffusion problem for very highly ordered systems; these are reported in Table 2 of Chap. 18 of Nordio and Segre[4] in terms of the parameter $\delta = 1 - \overline{P_2}$, which is a measure of the deviation from perfect alignment. In the limiting case of very high ordering, the only important motion is free rotation about the molecular symmetry axis, the other motions being too rapid to produce any effective spin relaxation.

The considerations given here hold whenever uniaxial orientational order is present, such as in nematic and smectic-A phases. However, they are essentially correct also for cholesteric and smectic-C phases, because a uniaxial environment is experienced at the molecular level.

3.2 Rototranslational Couplings

In phases where both spatial and orientational order are set up, a reorientational process, which is peculiar to liquid crystal phases with spatial inhomogeneity and cannot occur in normal liquids, may result from the translational motions. We consider here the cases of smectic and cholesteric phases. In the former case, elongated molecules tend not only to orient parallel to each other, but also to organize themselves in parallel planes. In uniaxial smectic-A phases, the anisotropic potential acting on a rod-like molecule depends both on the spatial coordinate Z along the director, perpendicular to the smectic layers, and the angle β formed by the director and the molecular axis.[5,14] Because of the particular form of the potential, usually referred to as the 'McMillan potential',[15,16] the translational and rotational motions of the test molecule are coupled. Physically, a molecule traveling along the Z direction perpendicular to the smectic planes will be subjected to different orientational forces, and therefore the average value of any orientation-dependent interaction will be modulated by the translational motion. In fact, we expect that probe molecules in typical smectic systems are more oriented when surrounded by aromatic cores than when surrounded by aliphatic tails.

Modulation of intramolecular magnetic interactions by translational motion, in addition to that resulting from rotational motion, gives rise to a mechanism reminiscent of scalar relaxation of the first kind,[17] and ultimately produces similar effects. A simple interpretation of this relaxation mechanism can be given in the following way. The translational motion of the molecules is strongly anisotropic, with free diffusion within layers, and hindered diffusion across them. Translations parallel to the layers do not cause spin relaxation, because the orientational order is essentially constant. Spin relaxation results, of course, from anisotropic rotational diffusion, as in nematics. Translations perpendicular to the layers, which explore regions of a different order, are hindered by the anisotropic potential, and could be described by a diffusion equation including the McMillan potential. However, this motion can be visualized as an activated random jump process, with a correlation time given by the mean time required for the molecule to travel across layers of spacing d. The correlation time for the jump process is d^2/D_T, where D_T is the diffusion coefficient for translations perpendicular to the smectic planes. The contribution to the spin-relaxation time is proportional to

$$(\overline{P_{2\max}} - \overline{P_{2\min}})^2 (d^2/D_T) \tag{17}$$

where $\overline{P_{2\max}} - \overline{P_{2\min}}$ is the range of order parameters along Z.

In cholesteric phases too, a novel relaxation mechanism may occur, in addition to those already present in nematics, as a consequence of coupling between rotations and translations.

A simple picture of a single-domain cholesteric phase is that of a nematic in which the director moves along a helical structure, the axis of which is always perpendicular to the director itself. It follows that translation along the helical axis induces rotation of a rod-like molecule, so as to keep the long molecular axis parallel to the director. This motion gives rise to an important contribution to spin relaxation[18] by modulating the residual magnetic anisotropies left by local ordering. The correlation time for this process is the mean time required for the molecule to undergo angular displacement of the director by one radian; this time is of the order of $(p^2/4\pi^2\, D_T)$, where p is the helical pitch and D_T the diffusion coefficient for translations perpendicular to the director.

3.3 Internal Motions

The rigid rotor model is only a rough approximation for the dynamics of mesogenic molecules. Actually, molecular flexibility appears to be an important requirement for the achievement of mesomorphic states. Thus, thermotropic liquid crystals are generally made up of aromatic groups linked to flexible chains. The length and the chemical structure of the chains are important in determining their transitional properties and the nature of their mesophases. Very mobile units also characterize the lyotropics, which are water dispersions of molecules with a polar headgroup attached to long aliphatic tails. These species can be organized into structures in which regions with different characteristics can be distinguished: strong interactions of an electrostatic nature maintain the polar headgroups in hydrophilic layers separate from the hydrophobic domains of the alkyl chains. At appropriate temperatures and water concentrations, these systems may undergo transition to liquid crystal phases of different kinds, with the common feature that the chains are well aligned despite the high fluidity of the phase.

The NMR relaxation technique on specifically deuterated molecules was recognized early on as an essential tool in monitoring chain mobility, so that a large amount of experimental data is available. The timescales characterizing bond rotations depend on the specific molecule, but in most cases they range between 10^{-10} and 10^{-8} s. This means that internal motion must be an effective NMR relaxation mechanism, competing with the overall rotation of the molecule.

In the case of mesogenic molecules having a number of torsional degrees of freedom, collectively denoted by φ, the total potential undergone in the oriented phase is

$$U(\Omega, \varphi) = U^{\text{tors}}(\varphi) + U^{\text{or}}(\Omega, \varphi) \tag{18}$$

where $U^{\text{tors}}(\varphi)$ represents the torsional potential, and $U^{\text{or}}(\Omega, \varphi)$ the orientational contribution, which is now expected to depend upon the conformation assumed by the molecule.[19]

A multidimensional diffusion equation for both the orientational and the torsional degrees of freedom must be solved

in general but, under the hypothesis that internal and overall motions are decoupled, the two dynamic problems can be treated separately. Molecular reorientations are described by the diffusion model appropriate for uniaxial phases. In an analogous way, the conformational dynamics can be analyzed by solving a diffusion equation for the torsional variables. However, this procedure becomes impracticable when the number of internal degrees of freedom is greater than 3 or 4. An alternative method is based on the consideration that bond rotations are generally strongly hindered by intramolecular interactions, so that the internal potential has deep wells corresponding to a limited number of conformations. This is equivalent to assuming the so-called 'rotational isomeric state (RIS) approximation'.[20] It is therefore possible to resort to a kinetic description in terms of a master equation, for the random walk between stable conformers. This master equation can be set up phenomenologically, or be rigorously derived by asymptotic expansion of the diffusion equation in the potential minima.[21,12] The following equation is obtained for the time evolution of $P_J(t)$, the Jth conformer population:

$$\partial P_J(t)/\partial t = -\sum_{J'} W_{JJ'} P_{J'}(t) \qquad (19)$$

where $W_{JJ'}$ is the rate constant for the $J' \rightarrow J$ transition. It is calculated by generalizing to the multidimensional case the Kramers result for barrier crossing in an overdamped regime.[22] For the simple case of a single degree of freedom, as in the biphenyl molecule in which rotation about the phenyl–phenyl bond is hindered,[23] the rate constant k for a conformational jump is given by

$$k = (k_B T/2\pi\xi)\omega_m\omega_M \exp\left\{-\frac{\Delta E}{k_B T}\right\} \qquad (20)$$

where ΔE is the barrier height, ξ is the friction exerted by the viscous medium, and ω_m and ω_M are the square roots of the potential curvature along the torsional coordinate, corresponding to the starting minimum and the top of the barrier, respectively.

The structure of the master equation and the expression of the transition rate remain essentially the same in isotropic or anisotropic liquids, but the presence of the orienting potential has a twofold effect:[24]

1. A purely static effect, consisting in changes in the statistical weights of the various conformations. In calamitic nematics, the most elongated conformers can be more easily accommodated, and they are therefore stabilized at the expense of the most folded ones.
2. A dynamic effect, due to changes in the potential profile along the path of the conformational transitions, which modify the rates of such processes by altering the curvatures and activation energies.

Let us now consider mesogenic molecules formed by an elongated core and an aliphatic chain, such as those belonging to the alkylcyanobiphenyl series.[25] Conformational motions cause fast reorientations of the chain segments about the all-*trans* axis, and the whole molecule undergoes anisotropic rotational diffusion. Because of the inequivalence of the conformational sites, isomerization processes alone do not allow the chain segments to be isotropically distributed in space, and so a residual order with respect to the molecular frame is left, even in isotropic phases. The liquid crystal environment enhances the segmental order by aligning the molecular axes. If there is a timescale separation between the conformational and the overall motions, two distinct processes contributing to spin relaxation can be easily identified. Fast internal motions partially average the interaction tensors located on the various molecular segments, at rates determined by the isomerization frequencies. The partially averaged magnetic tensors are then modulated by the slow anisotropic diffusion. The same conclusions apply to the case of chains anchored to surfaces and undergoing internal and wobbling motions, and thus this can be used as a model system for studies on micelles and membranes.[13]

For illustrative purposes, we report some results obtained for a model 12-bond chain with a fixed end. Each segment of the chain can exist in one of the three states called *gauche*$_+$ (g_+), *trans*, and *gauche*$_-$ (g_-). According to the RIS approximation,[20] 531 441 different conformers are possible for this system, but only about 257 000 are physically significant, the others being rejected for steric reasons. In an isotropic liquid, the statistical weight of any conformer is never larger than 0.001. Calculations for a liquid crystalline phase of intermediate ordering show that less than 40 conformers have a global statistical weight greater than 10%. These conformers obviously include the all-*trans* configuration, the others having a single *gauche* state at chain positions not far from the free end (a *gauche* state close to the headgroup would dramatically perturb the ordered environment), and the so-called kinks, i.e. conformers with $g_\pm\ t\ g_\pm$ sequences. In all these cases an approximately cylindrical molecular shape is retained. Figure 1 shows the order parameter for the C–H (or C–D) bond and the *gauche* $\rightarrow$ *trans* isomerization rate at each chain segment of the 12-bond chain, in the isotropic and the ordered phases. The anisotropic environment significantly increases the transition rates, and dramatically changes the order parameters. Modulation of the local ordering by slow wobbling motion of the chain axis may become the most relevant mechanism for spin relaxation in the liquid crystalline phase.

3.4 Translational Diffusion and Director Fluctuations

In principle, other kinds of motion, in addition to those described so far, may operate as relaxation mechanisms in

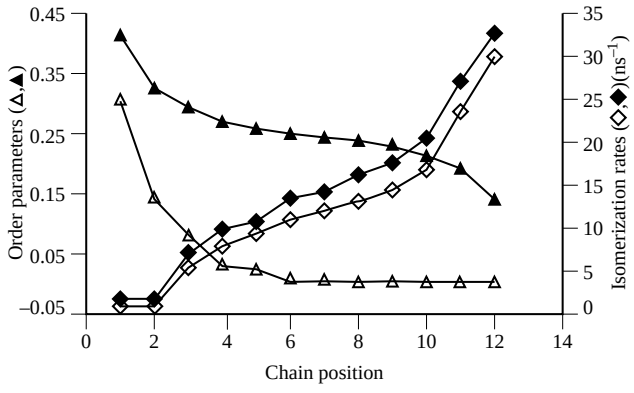

Figure 1 Order parameters and *gauche* $\rightarrow$ *trans* isomerization rates at the various segments of a substrate-supported 12-bond chain, in the isotropic (open symbols) and nematic (filled symbols) phase

liquid crystals. Since rotational diffusion and internal motion are dominant mechanisms for ^{13}C and ^{2}H spin probes at the high working frequency of standard spectrometers, they will be mentioned only briefly here.

One motional process common to all liquids is translational diffusion. This motion modulates intermolecular dipole–dipole interactions, and efficient spin relaxation results for proton nuclei, because of the abundance of hydrogen atoms in organic molecules. In the case of deuterated compounds, dipole interactions are reduced and intramolecular interactions remain, in practice, the only source of relaxation.

Another interesting process, which is specific to liquid crystal phases, results from elastic deformations of the ordered structures generated by collective thermal motions, which give rise to spontaneous alignment fluctuations. This process is responsible for the scattering of visible light, which in turn causes the turbid appearance of nematics. It also affects the spin relaxation, since it modulates the director orientation in the magnetic field. The corresponding spectral densities display characteristic frequency dependences. Director fluctuations may become the dominant relaxation mechanism at low-frequency regimes, but are relatively unimportant in high-field experiments.

4 RELATED ARTICLES

Amphiphilic Liquid Crystalline Samples: Nuclear Spin Relaxation; Bilayer Membranes: Deuterium and Carbon-13 NMR; Brownian Motion and Correlation Times; Deuteron Relaxation Rates in Liquid Crystalline Samples: Experimental Methods; Dynamic NMR in Liquid Crystalline Solvents; Liouville Equation of Motion; Liquid Crystalline Samples: Carbon-13 NMR; Liquid Crystalline Samples: Deuterium NMR; Liquid Crystalline Samples: Diffusion; Liquid Crystalline Samples: Spectral Analysis; Liquid Crystalline Samples: Structure of Nonrigid Molecules; Liquid Crystals: General Considerations; Relaxation of Coupled Spins from Rotational Diffusion; Relaxation Theory: Density Matrix Formulation.

5 REFERENCES

1. A. G. Redfield, *Adv. Magn. Reson.*, 1965, **1**, 1.
2. See, for example, R. W. Pastor, in *Molecular Description of Biological Membrane Components by Computer Aided Conformational Analysis*, ed. R. Brasseur, CRC, Boca Raton, FL, 1990.
3. N. G. van Kampen, *Stochastic Processes in Chemistry and Physics*, North-Holland, Amsterdam, 1981.
4. P. L. Nordio and U. Segre, in *The Molecular Physics of Liquid Crystals*, ed. G. R. Luckhurst and G. W. Gray, Academic, London, 1979, Chaps. 16, 18, 19.
5. G. Moro, U. Segre, and P. L. Nordio, in *Nuclear Magnetic Resonance of Liquid Crystals*, ed. J. W. Emsley, Reidel, Dordrecht, 1985, Chap. 9
6. P. Debye, *Polar Molecules*, Dover, New York, 1945.
7. J. Happel and H. Brenner, *Low Reynolds Number Hydrodynamics*, Prentice-Hall, Englewood Cliffs, NJ, 1965.
8. M. E. Rose, *Elementary Theory of Angular Momentum*, Wiley, New York, 1957.
9. W. H. Dickerson, R. R. Vold, and R. L. Vold, *J. Phys. Chem.*, 1983, **87**, 166.
10. C. R. J. Counsell, J. W. Emsley, G. R. Luckhurst, D. L. Turner, and J. Charvolin, *Mol. Phys.*, 1984, **52**, 499.
11. R. R. Vold, in *Nuclear Magnetic Resonance of Liquid Crystals*, ed. J. W. Emsley, Reidel, Dordrecht, 1985, Chap. 11
12. A. Ferrarini, G. Moro, and P. L. Nordio, *Mol. Phys.*, 1988, **63**, 225.
13. A. Ferrarini, P. L. Nordio, G. J. Moro, R. H. Crepeau, and J. H. Freed, *J. Chem. Phys.*, 1989, **91**, 5707.
14. G. Moro and P. L. Nordio, *J. Phys. Chem.*, 1985, **89**, 997.
15. W. L. McMillan, *Phys. Rev. A*, 1971, **4**, 1238; 1972, **6**, 936.
16. R. L. Humphries and G. R. Luckhurst, *Mol. Phys.*, 1978, **35**, 1201.
17. A. Abragam, *The Principles of Nuclear Magnetism*, Clarendon, Oxford, 1961.
18. Z. Luz, R. Poupko, and E. T. Samulski, *J. Chem. Phys.*, 1981, **74**, 5825.
19. A. Ferrarini, G. J. Moro, P. L. Nordio, and G. R. Luckhurst, *Mol. Phys.*, 1992, **77**, 1.
20. P. J. Flory, *Statistical Mechanics of Chain Molecules*, Interscience, New York, 1969.
21. G. Moro and P. L. Nordio, *Mol. Phys.*, 1986, **57**, 947.
22. H. Kramers, *Physica*, 1940, **7**, 284.
23. A. Ferrarini and P. L. Nordio, *J. Chem. Soc. Faraday Trans.*, 1992, **88**, 1733.
24. A. Ferrarini, A. Polimeno, and P. L. Nordio, *Liquid Cryst.*, 1993, **14**, 169.
25. A. Ferrarini, P. L. Nordio, and G. J. Moro, *Mol. Cryst. Liquid Cryst.*, 1991, **198**, 159.

Biographical Sketches

Pier Luigi Nordio. *b* 1936. Degree in Chemistry, University of Padova, 1961. Postdoctoral fellow at Stanford University, with H. M. McConnell. Associate Professor of Physical Chemistry 1968, Full Professor of Theoretical Chemistry, University of Padova, 1975–present. 100 scientific publications. Current interests include stochastic theories for molecular dynamics and conformational kinetics, interpretation of ordering in liquid crystals through molecular shape, solvation effects and photophysics of electron transfer.

Alberta Ferrarini. *b* 1957. Degree in Chemistry, 1983, Ph.D., 1989, Physical Chemistry, University of Padova, Italy. Fellowships with G. Kothe, Stuttgart University, Germany and J. H. Freed, Cornell University, USA. Presently research assistant in the Physical Chemistry Department, University of Padova. Approx. 25 publications. Current research interests: dynamics of molecules with torsional degrees of freedom, theoretical models for ordering and transitional properties in liquid crystal phases.

Liquid Crystalline Samples: Spectral Analysis

M. Longeri and G. Celebre
Università della Calabria, Cosenza, Italy

1	Introduction	1
2	Computer Programs for Spectral Analysis	2
3	Obtaining Starting Parameters for Iterations	3
4	Strategies in Spectral Analysis	4
5	Related Articles	7
6	References	7

1 INTRODUCTION

Proton (or other spin-$\frac{1}{2}$ nuclei) NMR spectra of molecules dissolved in liquid crystalline solvents differ from their isotropic analogues in a significant way. Thus, the well-known proton isotropic spectrum of ethylbenzene (composed of a triplet, a quadruplet and a broad singlet) changes into the ugly looking spectrum shown in Figure 1. Only by displaying the spectrum with a much smaller Hz/cm ratio is it possible to recognize the few thousand closely spaced, well-resolved, single transitions dispersed over a range of a few kilohertz which compose the spectrum. For molecules with a higher number of interacting spins the situation is even worse; the total intensity is dispersed over so many closely spaced, single transitions that their anisotropic spectra, except for a few highly symmetric spin systems, appear as a single unresolved band a few kilohertz in width. For this reason it is not necessary to use deuterated compounds as anisotropic solvents because the liquid crystalline phases used contain more than 20 interacting protons and contribute to the total spectrum only as the lumps and bumps which form the baseline. The lines due to the solute, which are much more intense because their total intensity is dispersed over relatively fewer transitions, can be distinguished from the baseline.[1]

These differences arise because two extra terms have to be considered in the anisotropic Hamiltonian.[1] Within the usual high field approximation the Hamiltonian is given by

$$\begin{aligned}\hat{\mathcal{H}} = {} & \frac{1}{2\pi}\sum_i \gamma_i \hat{I}_{iz}(1-\sigma_i^{\mathrm{iso}}-\bar{\sigma}_{zzi})B_z \\ & + \sum_{i<j}\{J_{ij}^{\mathrm{iso}}[\hat{I}_{iz}\hat{I}_{jz}+\tfrac{1}{2}(\hat{I}_i^+\hat{I}_j^- + \hat{I}_i^-\hat{I}_j^+)]\} \\ & + \sum_{i<j}[\bar{J}_{zzij}+2\bar{D}_{zzij}][\hat{I}_{iz}\hat{I}_{jz}-\tfrac{1}{2}(\hat{I}_i^+\hat{I}_j^- + \hat{I}_i^-\hat{I}_j^+)] \\ & + \sum_i \frac{\bar{q}_{zzi}}{4I_i(2I_i-1)}[3\hat{I}_{iz}\hat{I}_{iz}-I_i(I_i+1)] \qquad (1)\end{aligned}$$

where γ_i is the magnetogyric ratio of the ith nucleus. The fourth term is included only if $I_i \geq 1$, while the σ_i^{iso} and J_{ij}^{iso} scalars, the trace of the $\boldsymbol{\sigma}$ shielding and $\boldsymbol{J}$ indirect spin–spin coupling tensors, are the well-known spectral parameters which determine isotropic spectra; $\bar{\sigma}_{zzi}$, $\bar{J}_{zzij}$, $\bar{D}_{zzij}$ and $\bar{q}_{zzi}$ are the averaged components of the shielding, indirect coupling, direct dipolar coupling, and quadrupolar coupling tensors, respectively. The last two tensors have a null trace and so do not influence the frequencies or intensities of the peaks in isotropic spectra.

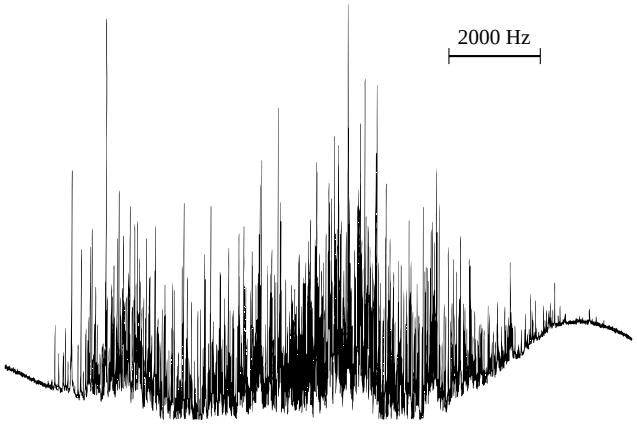

Figure 1 300 MHz (7.06 T) proton spectrum of ethylbenzene dissolved in ZLI 1132, a nematic solvent obtained from Merck

The direct dipolar couplings are related to the molecular geometries by

$$\bar{D}_{zzij} = K_{ij}\sum_{\alpha\beta} G_{ij\alpha\beta}S_{\alpha\beta}, \quad \alpha,\beta = x,y,z \qquad (2)$$

for rigid molecules, or

$$\bar{D}_{zzij} = K_{ij}\sum_n p^n \sum_{\alpha\beta} G^n_{ij\alpha\beta}S^m_{\alpha\beta} \qquad (3)$$

if internal rotational motions are present. K_{ij} depends on the magnetogyric ratio of the ith and jth nuclei, p^n is the population of conformer n, $S^m_{\alpha\beta}$ are the elements of $\mathbf{S}^n$, the Saupe orientational matrix for conformer n, $G^n_{ij\alpha\beta}$ are related to the internuclear distance r_{ij} and to its orientation with respect to a Cartesian system x, y, z fixed on the molecule.

It should be noted that the observed differences are not just due to the extra parameters present, but also, and more importantly, to the wider range of values that they can assume (from 2.5 to −5 kHz for direct couplings, and up to several kilohertz for quadrupolar couplings). If spin systems composed of only spin-$\frac{1}{2}$ nuclei are considered (for a description of how quadrupolar couplings influence anisotropic, spectra, see ***Liquid Crystalline Samples: Deuterium NMR***), the fourth term in equation (1) is zero and the spectrum shape depends mainly on the values of the dipolar couplings. Two important consequences ensue from this fact: (a) all the nuclei in the molecule have dipolar couplings larger than the experimental linewidth (4–5 Hz); and (b) no first-order features are present in the spectra of homonuclear spin systems.

Two points follow from equation (1). First, the direct spin–spin coupling $\bar{D}_{zzij}$ cannot be measured separately from $\bar{J}_{zzij}$ because only the quantity

$$\bar{T}_{zzij} = \bar{D}_{zzij} + \tfrac{1}{2}\bar{J}_{zzij} \qquad (4)$$

can be determined experimentally,[1c] and so liquid crystal NMR can be used to determine the geometry only if the pseudodipolar couplings $\bar{J}_{zzij}$ are known independently. Experimental and theoretical studies have shown that the pseudodipolar term is usually much smaller than the dipolar coupling and so, with the exception of F–F couplings, $\bar{D}_{zzij}$ can be safely equated to $\bar{T}_{zzij}$ (see ***Anisotropy of Shielding and Coupling in Liquid Crystalline Solutions***).

The second point involves magnetically equivalent nuclei (see ***Magnetic Equivalence***). The frequencies and intensities in isotropic spectra do not depend on the values of the indirect couplings between nuclei belonging to the same magnetically equivalent group, but this is not the case for anisotropic spectra. In many spectra this just means that there is one more direct coupling for each magnetically equivalent group to be taken into account in anisotropic spectral analysis, but the effects are quite dramatic for A_n (where n is the number of interacting spins) spin systems. Benzene is a very good example; all six protons have the same chemical shift and so, even though there are three different indirect couplings (J_{ortho}, J_{meta}, and J_{para}), the isotropic spectrum shows only a single transition. The spin system is correctly defined as A_6. The spectrum of benzene dissolved in an orienting medium will instead contain a maximum of 72 lines and is analyzable in terms of a chemical shift and three indirect and three direct couplings. The correct notation for the spin system is $AA'A''A'''A''''A'''''$.[1b]

2 COMPUTER PROGRAMS FOR SPECTRAL ANALYSIS

For anisotropic spectra, analytical solutions are possible only for a very limited number of simple spin systems,[1a,1b] but simulation/iteration programs are available for spectral analysis. These programs will: (a) calculate the spectrum from a trial starting set of spectral parameters using the spin Hamiltonian in equation (1); and (b) refine the parameters to fit some spectral quantities.[2]

A few methods have been proposed which use different spectral quantities in the fit, but only three of them have found application in anisotropic spectral analysis.

1. *Fully automated analysis*[3] According to this approach the full spectrum (defined by a vector containing intensity values at a fixed frequency interval) is used in the iteration procedure. No operator intervention is needed during the iteration cycles; at the end of the procedure the operator checks if the experimental spectrum has been reproduced correctly and no false minimum found (for a more detailed description of the method and computer programs, see ***Analysis of Spectra: Automatic Methods***).
2. *Swalen–Reilly method*[4] The 'experimentally' determined energy level diagram (ELD) is used in the refinement program NMRIT.[2,4b] The final parameter set, refined assuming a given assignment of calculated to experimental levels, is used to calculate the spectrum which is then compared with the experimental one. The procedure is repeated for a different assignment and the parameters giving the best fit between the calculated and experimental spectrum are assumed to be correct. The procedure can be easily automated, its main advantage deriving from the relatively low number of distinct assignments.[5] The algorithm which computes the ELD [part (a) of the program] must take into account the correct symmetry of the spin system.
3. *Castellano–Bothner-By method*[6] By far the most widely used approach,[2] this method makes use of the experimental frequencies in the parameters' refinement procedure. The method is particularly attractive because the derivatives

$$\frac{\partial F_{mn}}{\partial p_j} = \frac{\partial \Lambda_m}{\partial p_j} - \frac{\partial \Lambda_n}{\partial p_j} \tag{5}$$

where p_j is the jth spectral parameter, Λ_m is the mth eigenvalue, and F_{mn} is the calculated frequency of the transition between the mth and nth levels, can be calculated analytically. In fact,

$$\frac{\partial \Lambda_m}{\partial p_j} = \left(\mathbf{U} \frac{\partial \mathbf{H}}{\partial p_j} \mathbf{U} \right)_{mm} \tag{6}$$

where $\mathbf{U}$ is the matrix which diagonalizes the Hamiltonian matrix representation $\mathbf{H}$ in a given basis set. Care must be taken when choosing the basis set, in order to make as simple as possible the algorithm which computes the matrix $(\partial\ \mathbf{H}/\partial p_j)$.

Line identification numbers from a spectrum calculated with a trial, starting set of spectral parameters are assigned by the operator to experimental frequencies; the program will modify a selected subset of parameters to minimize the root mean square (rms) of the differences between the assigned calculated and experimental frequencies and will output the spectrum calculated with the new parameter set. The operator will compare the two spectra, recognize more lines to assign, modify or delete old assignments and choose a new subset of parameters to iterate. The cycles will be repeated until nearly all the experimental lines are assigned and a low rms obtained, having iterated the whole set of spectral parameters. The procedure is cumbersome, requiring a great deal of time and effort by the operator in the assignment step, and cannot be easily automated because only the operator can discriminate between the $N!$ different assignments (N being the number of observed transitions) on the basis of their intensities and relative positions. The probability of achieving success in the spectral analysis is low, decreases quickly as the complexity of the spin system increases, and is strictly related to the quality of the starting set, i.e. how near the starting parameter values are to the final ones.

To reduce the computational requirements [central processing unit (CPU) time and storage requirements] of part (a) of the program, much effort has been devoted to making full use of the possibilities of simplifying the Hamiltonian by using suitable basis function sets, but keeping operational the Castellano–Bothner-By iterative method. The first programs (LAOCOON[6b] and its anisotropic counterpart LAOCONOOR) took into account the so-called F_Z and X approximation factorization; magnetic equivalence factorization based on the Ferguson–Marquardt formalism[7] (composite particle formalism) was introduced in the LEQUOR program[8] in the early 1970s.

Molecular symmetry can also be used to factorize the Hamiltonian matrix if the basis function sets which are used belong to the irreducible representation of the permutation

group of the spin system.[2] This leads to an increase in the complexity of the algorithm which computes: (i) the elements of the Hamiltonian and transition probability matrices, and (ii) the analytical derivatives ($\partial \mathbf{H}/\partial_{p_i}$) in the basis set used. However, computational efficiency is greatly increased. Simulation programs which make full use of molecular symmetry exist,[9] but the iterative part has been implemented only for the C_2 permutation group (program LACX[2,10]).

The two formalisms (composite particle and symmetry factorization) have been combined in the ARCANA program,[11] which has been used to analyze such complex spin systems as those arising from the 11 protons in 4-methoxy-4′-cyanobiphenyl[12] (an AA′BB′CC′DD′E_3 spin system).

CPU times can be further reduced if more efficient ordering routines are used. The gain is quite impressive for complex spin systems, resulting in the astonishingly short time of 2 min when a Shell–Metzner ordering[13] routine was used. This compares with 102 min for the commonly used Bubble–Sort[13] for the AA′BB′CC′XX′Y_3 $\{I_A = I_B = I_C = \frac{1}{2}, I_X = I_Y = 1\}$ spin system which gives more than 10 000 transitions, and was simulated on a VAX 11/780[14] using the ARCANA program. More efficient diagonalization routines give better total performance in the simulation step, but some problems arise when they are used in the iterative step. In fact, depending on the diagonalization algorithm used, pairs of eigenvalues can change their positions arbitrarily; the line numbers change in an unpredictable way and the iteration fails. Rough prediagonalization, according to Castellano et al.,[6a] can eliminate this inconvenience if Jacobi based diagonalization routines are used.

Computer hardware is now improving at such a fast rate that the latest generation of workstations have performances in terms of mips (million instructions per second), main memory and mass storage, which are similar to, if not greater, than the largest mainframes of 10 years ago. In fact, the most important differences between programs is not now in their efficiency in simulating the spectra, or even in the iteration procedure, but rather in their ability to produce a visual representation of the spectrum on the terminal, and in the ease of assigning transitions to observed frequencies.

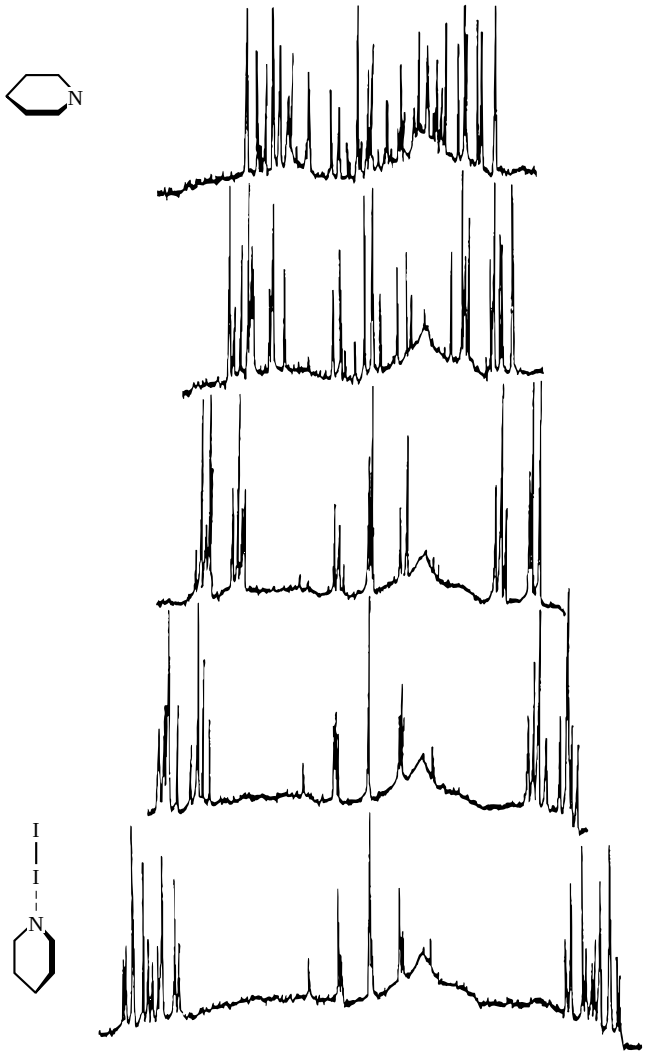

Figure 2 100 MHz (2.34 T) proton spectra of [^{14}N]pyridine in phase IV (Merck); the quantity of added I_2 increases from the top (0 mol% with respect to pyridine) to the bottom (60 mol%). The axis of highest order is perpendicular to the ring for free pyridine, parallel to the N–I–I direction for the complex. (Reproduced by permission of Royal Chemical Society from D. Catalano, C. A. Veracini, P. L. Barili, and M. Longeri, *J. Chem. Soc., Perkin Trans. II*, 1983, 171)

3 OBTAINING STARTING PARAMETERS FOR ITERATIONS

Remembering the wide range of allowed values of D_{ij}, it is easy to understand the enormous difficulties faced in analyzing anisotropic spectra. When the line density in the spectrum is low (few nuclei, strongly oriented spin systems), very approximate estimates of the D_{ij} values can quite easily give frequency/intensity patterns in the calculated spectra that can be recognized in the experimental spectra. When the spectra become crowded (the one shown in Figure 1 is a good example), a completely random trial-and-error approach is hopeless; more systematic and efficient methods have to be devised to ensure at least some probability of success in the analysis. Sometimes the spectral parameters can be guessed either from a comparison with data for similar molecules (or the same molecule in a different solvent) or from the shape of the spectrum.

The spectra of the pyridine–I_2 complex[15] shown in Figure 2 illustrate this point very well. At high concentrations of the complex, the spectrum looks fairly simple, displaying even some first-order features such as the pentuplet-like multiplet in the center of the spectrum. The two outer groups can then be thought to be due to the *ortho* and *meta* protons, the distance between the groups being related to the D_{om} coupling, while the spacing between two consecutive lines in the central multiplet is equal to $D_{op} + D_{mp}$. In addition, the chemical shifts can be guessed approximately. This behavior is due to the fact that the molecule is strongly oriented with its molecular long axis tending to lie parallel to the mesophase director. When this happens, D_{om} has a large negative value (below −1000 Hz), while both D_{op} and D_{mp} are, in absolute value, much smaller. (Note that the *ortho–meta* and *meta–para* distances are nearly the same but the direction of the interproton vector with respect to the director is very different.) For pyridine, where the N–*para*-proton axis is, on average, perpendicular to the mesophase

director, the spectrum is featureless, and no estimates of spectral parameters can be made.

A more general strategy is to prepare a solution of the fully protonated and perdeuterated isotopomers. The $S_{\alpha\beta}$ obtained from the analysis of the ^{2}H spectra (see ***Liquid Crystalline Samples: Deuterium NMR***) can be used to calculate approximate dipolar couplings from trial structures. The method works fairly well for rigid molecules, but it is not so efficient when internal rotation motions are present in the molecule (see ***Liquid Crystalline Samples: Structure of Nonrigid Molecules***). Examples of this approach are the analysis of the ^{1}H spectra of biphenyl[16] and 4-cyanobiphenyl.[17]

Alternatively, keeping an approximate molecular structure constant, it is possible to iterate over the $S_{\alpha\beta}$ values. Because the number of the variables is small (usually two or three), the approximate solution is quickly found.[18] The final parameter set is then obtained by iterating over the dipolar couplings independently.

As soon as the number of interacting spins increases, such simple considerations can no longer be applied. Monosubstituted benzenes display a behavior similar to the one already described. When the substituent does not contain protons, its spectrum looks like the one at the bottom of Figure 2, but if some interacting nucleus is present the complexity of the spectrum increases in two ways: (i) the number of the transitions increases because of the extra couplings; and (ii) groups of transitions due to these nuclei can overlap with some of the features due to the aromatic protons. This is precisely what happens for the spectrum of anisole, where the OCH_3 transitions fall in the same spectral region as the *para* proton.[19]

If these extra nuclei have different magnetogyric ratios only point (i) has to be taken into account, and first-order features due to the couplings between nuclei with different magnetogyric ratios appear in the spectrum. Such is the case for trideuteromethoxybenzene[20] (anisole-d_3) for example, where each transition of the aromatic protons is split into a septet: the septets in the outer wings are spaced by a distance approximately equal to the sum of the *ortho*-CD_3 and *meta*-CD_3 couplings, whilst the central septets are spaced by the *para*-CD_3 coupling. Being able to recognize all these structures in the spectrum, makes it possible to obtain very good values for the extra couplings and, in addition, to obtain the 'decoupled' spectrum due to the aromatic protons by selecting the central lines of each multiplet. What is left to be analyzed is just a five-spin AA′BB′C system, the spectrum of which would look like the one shown at the bottom of Figure 2. Such a spectrum can be analyzed easily. This is the case for anisole dissolved in ZLI 1115; the spectrum in I35 showed very few septet structures, and so it was not possible to determine the 'decoupled' AA′BB′C spin system.[20]

A similar approach proved to be possible for the four-proton, six-deuterium $AA'A''A'''X_3X'_3$ spin system of 1,4-bis(trideuteromethoxy)benzene.[11] The proton spectrum is composed of two complex, well-spaced groups of lines, the spacing of which is related to the coupling between the two *ortho* aromatic protons. The AA′A″A‴ spin subsystem would give the very simple spectrum shown in Figure 3, according to that obtained for symmetrically *para*-disubstituted halobenzenes. Each line would then be split into 13 subspectra corresponding to the values of m_T, the total deuteron spin quantum number, by coupling with the six deuterons: for $m_T = \pm6$, ±5, ±4, ±3, ±2, ±1, and 0, the intensities would be 1, 6, 21, 50, 90, 126, and 141, respectively. Trying to recognize all the 13 subspectra by eye is hopeless; in this case the task was easily accomplished by doing a two-dimensional homonuclear correlation experiment.

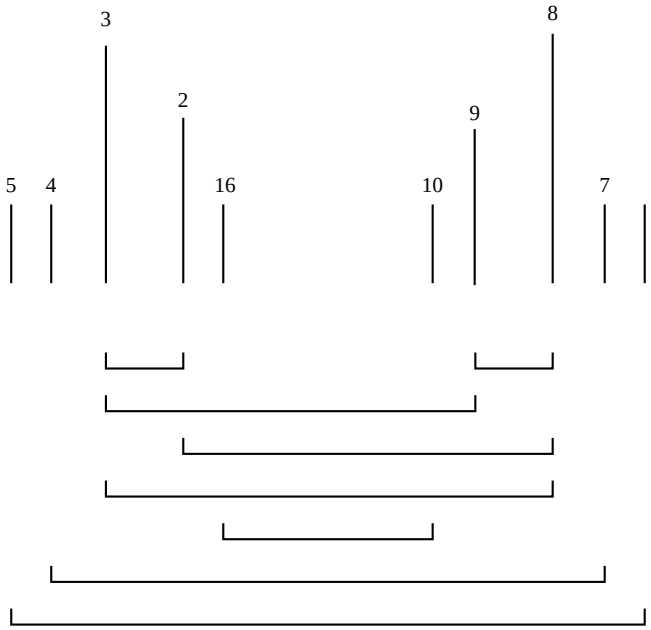

Figure 3 Sketch of the spectrum of an AA′A″A‴ system of spin-1/2 nuclei with dipolar coupling constants typical for a *para*-homodisubstituted benzene, showing how transitions are connected. (Reproduced by permission of Royal Chemical Society from J. W. Emsley, D. L. Turner, A. Giroud, and M. Longeri, *J. Chem. Soc., Faraday Trans. 2*, 1985, **81**, 603)

For an AA′A″A‴ spin system spectrum, such as the one shown in Figure 3, only two lines (the most intense ones) within the two groups share the same energy level, all the other connections being between symmetric lines belonging to the different groups. As a consequence, the off-diagonal peaks near the diagonal reveal the position of the two connected lines in each subspectrum. As shown in Figure 4, only 8 of the 13 off-diagonal peaks expected on each side of the main diagonal are visible. The lines belonging to the $m_T = 0$ subspectrum were easily spotted and then, with little effort, nearly all the subspectra (the less intense lines of the $m_T = \pm6$ subspectra are lost in the noise) were recognized.

Such elegant ways of analyzing anisotropic spectra are quite uncommon. Very often spectral analysis is an unglamorous, boring, and long task, with many unrewarding days spent in front of a terminal with little or no hope of disentangling patterns that can be recognized from the maze of lines in the experimental spectrum and few exciting moments occur when the lines begin to assume the right frequency and intensity pattern and the main features appear in the calculated spectrum.

4 STRATEGIES IN SPECTRAL ANALYSIS

Two main strategies have been developed to try to simplify the analysis of spectra: one is aimed mainly at reducing human

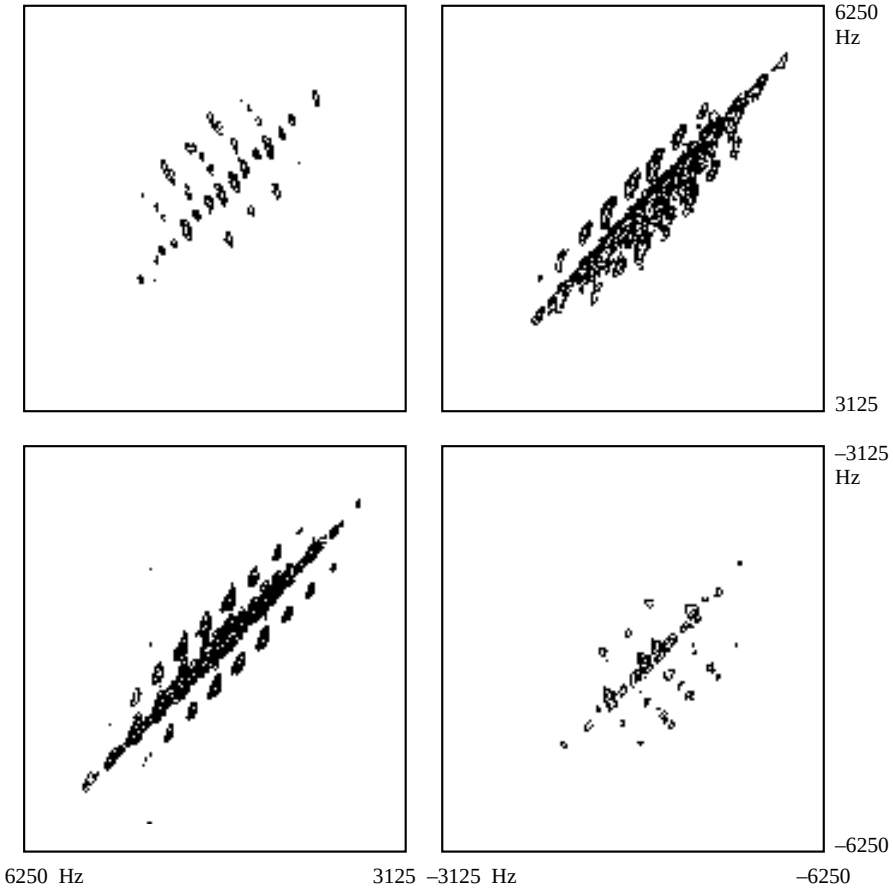

Figure 4 200 MHz (4.69 T) proton autocorrelation spectrum of 4-bis(trideuteromethoxy)benzene dissolved in the liquid crystal PCH 1132 (Merck). (Reproduced by permission of Royal Chemical Society from J. W. Emsley, D. L. Turner, A. Giroud, and M. Longeri, *J. Chem. Soc., Faraday Trans. 2*, 1985, **81**, 603)

intervention by using automated methods, and the other is aimed at simplifying spectral analysis by obtaining simpler experimental spectra.

4.1 Fully Automated Approaches

Two different approaches use the first strategy. The first approach (mentioned previously) has been used to analyze the anisotropic spectra of three allyl halides[21] and of cyclopentene,[22] an eight-spin system. The second approach makes use of the Swalen–Reilly iterative method. The use of the latter method is limited, mainly because an 'experimental' ELD is needed. Programs and/or experimental methods devoted to this task have been proposed,[2] but the complexity and peculiar characteristics of anisotropic spectra make them unsuitable candidates for analysis in this way. Pfändler and Bodenhausen[5] have proposed a two-dimensional *z* correlation spectroscopy (*z* COSY) experiment for constructing experimentally the ELD for a given spin system. Using different values of the β flip angle of the pulse sequence

$$\frac{\pi}{2} - t_1 - \beta - \tau_m - \beta - t_2 \qquad (7)$$

the authors showed that it is possible to determine the topology of two connected frequencies by observing how the intensity of the cross peak varies with β. Knowing the topology of the connections for nearly all the observed lines in the spectrum, the energy level subdiagram for an A_3B and an A_2BC spin system were constructed, even when some connections were determined incorrectly. For each different possible assignment (864 for the A_2BC, and 8 for the A_3B spin system), the spectral parameter set was refined according the Swalen–Reilly iterative method. The spectrum was calculated and the best assignment was chosen by comparing the calculated and experimental spectra.

A generalization of the method would require a library containing topologies of ELDs for spin systems of different symmetries. Improvements are needed to take into account the extensive degeneracy that can occur for larger spin systems. Such degeneracies can be due either to accidental overlaps of lines in crowded spectral regions or to the poor digital resolution of the two-dimensional spectra of liquid crystalline phases.

4.2 Spectral Simplification Based Approaches

As an alternative approach to the automated methods, experiments aimed at reducing the complexity of spectra can be planned. In this way spectral analysis will be simplified and the rate of success increased.

4.2.1 Spectral Simplification via Deuterium Decoupling

Selectively deuterated molecules give quite complex ^{1}H spectra (the anisole-d_3 spectrum in ZLI 1115 being a lucky exception), even if, at first glance, they look fairly simple. There are, in fact, a larger number of lines in such spectra, as deuterium has $I = 1$ while the larger linewidth, due to the ^{2}H quadrupolar relaxation, combined with the lower values of the D_{HD} couplings ($\gamma_H/\gamma_D \simeq 6$), causes widespread overlapping of transitions.

Spectral simplification can be obtained by performing $\{^2H\}-^1H$ decoupling experiments, and good results have been obtained with solenoid probes. Using short acquisition times (<0.2 s) when the decoupler is on, and a delay of typically 3 s to allow cooling to occur and to reduce thermal inhomogeneities, decoupled spectra from complex spin systems such the eight protons in 4-trideuteromethoxy-4′-cyanobiphenyl[12] have been recorded and successfully analyzed.

The procedure just described is the one usually followed when complex spectra are analyzed using this approach: ^{1}H spectra (with and without deuterium decoupling) of different selectively perdeuterated isotopomers are recorded under similar experimental conditions (solvent, temperature and concentration) and analyzed from the simpler to the more complex spin systems in order to obtain a good starting parameter set for the analysis of the spectrum of the fully protonated molecule. The full procedure requires much synthetic and spectral analysis work, but it is applicable whenever selective deuteration is possible and gives a very high success rate—its upper limits being an analyzable ^{1}H spectrum of the fully protonated species.

As an alternative to the high power decoupling technique, the sequence which refocuses heteronuclear coupling,

$$\left(\frac{\pi}{2}\right) - \tau_1 - (\pi) - \tau_1 - \text{Sample} \tag{8}$$

can be used:[23] τ_1 is increased at fixed intervals and the first point of each FID taken at the top of the echo is stored in a vector. The vector is Fourier transformed to give the decoupled, $\Delta\nu_i = 0$ spectrum. In fact the selective pulse sequence is such that at the top of the echo the magnetization does not depend on the heteronuclear couplings. The experiment takes a long time and has lower sensitivity than decoupling. In addition, artifacts due to pulse and phase imperfections have to be considered, but these can be significantly reduced in modern instrumentation. The spin echo experiment has the great advantage that all the heteronuclear couplings due to nuclei with different γ values are decoupled at once. If the antiecho is recorded, homonuclear couplings are refocused and the spectrum depends only on heteronuclear couplings (see ***Spin Echo Spectroscopy of Liquid Samples***).

4.2.2 Spectral Simplification via Multiple Quantum Spectroscopy

This approach is discussed elsewhere (see ***Multiple Quantum Spectroscopy in Liquid Crystalline Solvents***). Here it is sufficient to remember that for a given spin system composed of N nonequivalent spins $\frac{1}{2}$, the maximum possible number of transitions of order p is

$$Z_p = \binom{2N}{N-p} \tag{9}$$

for $1 \leq p \leq N$.[24] It is clear that even a very complex spin system will give simple spectra when p is $N - 1$ or $N - 2$ and these spectra will contain the same information that can be obtained from the single quantum ordinary spectrum with

$$Z_p = \binom{2N}{N-1} \tag{10}$$

4.2.3 Double Quantum Two-Dimensional Correlated Experiments

In a series of very elegant papers, Pines et al. applied multiple quantum (MQ) spectroscopy to a class of compounds, the n-alkanes, whose proton spectra are too complex to analyze. The molecules chosen, from n-hexane[25] to n-decane,[26] were randomly perdeuterated in such a way to have a negligible population of isotopomers with more than three protons left, but with all the possible two- and three-protonated isotopomers having a nearly uniform population distribution. This is easily done via a catalytic exchange reaction for n-alkanes, but the required population distribution may not be reached in such a direct way for other molecules having functional groups. This limits the generalization of the method to other organic compounds. A two quantum filtered experiment reduces the complexity of the spectrum leaving only AB and A_2 (16 for n-hexane) spin systems. A four-step phase cycling keeps the total number of averaged FIDs for each t_1 (96 for 24 increments in τ[25]) acceptably low, to ensure a digital resolution of nearly 30 Hz per point. The phase cycling selects even quantum coherences: the sweep width is then kept small by the isotopomer population distribution because no four or higher coherences are possible. On the other hand, it is crucial that the double quantum coherence of all the AB spin systems is present. As the D_{ij} values cover a wide range, this can be achieved only by coadding FIDs obtained with different τ values; the data acquisition time will thus be lengthened significantly. To distinguish signals belonging to different spin systems, a two-dimensional correlation experiment can be performed. The two last steps are possible using the pulse sequence

$$\left(\frac{\pi}{2}\right)_\phi - \tau - \left(\frac{\pi}{2}\right)_\phi - \frac{t_1}{2} - (\pi) - \frac{t_1}{2} - \left(\frac{\pi}{2}\right)_x - \frac{\tau_2}{2} - (\pi) - \frac{\tau_2}{2} - t_2 \tag{11}$$

All the spectra were recorded with continuous deuterium decoupling,[27] which causes considerable heating and thermal inhomogeneities, despite air-flow temperature control. All the couplings (up to 20 for n-decane) were determined with an experimental error of about 25 Hz, the low accuracy being a consequence of the low digital resolution and thermal gradients.

4.2.4 Spectral Simplification via Scaling of Dipolar Couplings

As previously stated, one of the reasons for the complexity of anisotropic spectra is the non-first-order character of the

spectra. Another way to simplify the analysis of such spectra is to scale the direct couplings by some factor, thus leaving only a few couplings (the biggest) that are greater than the spectral linewidth. In this way first-order features will appear in the spectrum if the chemical shift differences are large enough, and the number of lines in the spectrum will be reduced. In principle, all these improvements could be achieved simply by changing the experimental conditions that decrease the solute order (temperature and/or solute concentration), but this is in practice unachievable because the **S** matrix changes discontinuously at the nematic–isotropic transition temperature T_{NI}.

Courtieu et al.[28] applied the variable angle technique (using a spinning angle of 51°), developed for NMR in solids, to scale dipolar couplings, thus reducing the ABC pattern in CF_2CFBr to a first-order, easily analyzable AMX spectrum. At lower angles, non-first-order features began to appear but, because the authors were able to register the spectra at lower spinning angles, the line patterns can be easily followed and the dipolar couplings calculated at a spinning angle of 0° (***Spinning Liquid Crystalline Samples***).

Scaling of dipolar couplings can be achieved by using a suitable pulse sequence (PARDES) derived from the well-known WAHUHA and MREV sequences,[29] as described by Frydman et al.[30] The reduction in the splitting of the doublet due to CH_2Cl_2 dissolved in a nematic mesophase was followed by varying the parameters in the sequence.

5 RELATED ARTICLES

Liquid Crystals: General Considerations; Structure of Rigid Molecules Dissolved in Liquid Crystalline Solvents; Two-Dimensional NMR of Molecules Oriented in Liquid Crystalline Phases.

6 REFERENCES

1. (a) J. W. Emsley and J. C. Lindon, *NMR Spectroscopy Using Liquid Crystal Solvents*, Pergamon, Oxford, 1975; (b) P. Diehl and C. L. Khetrapal, in *NMR Basic Principles and Progress*, eds. P. Diehl, E. Fluck, and R. Kosfeld, Springer, Berlin, 1969, Vol. 1; (c) C. A. Veracini, in *NMR of Liquid Crystals*, ed. J. W. Emsley, Reidel, Dordrecht, 1985.
2. P. Diehl, H. Kellerhals, and E. Lustig, in *NMR Basic Principles and Progress*, eds. P. Diehl, E. Fluck, and R. Kosfeld, Springer, Berlin, 1972, Vol. 6.
3. (a) D. S. Stephenson and G. Binsch, *J. Magn. Reson.*, 1980, **37**, 395; (b) D. S. Stephenson and G. Binsch, *J. Magn. Reson.*, 1980, **37**, 409.
4. (a) J. D. Swalen and C. A. Reilly, *J. Chem. Phys.*, 1962, **37**, 21; (b) J. D. Swalen, in *Computer Programs for Chemistry*, ed. D. F. DeTar, Benjamin, New York, 1968, Vol. 1.
5. P. Pfändler and G. Bodenhausen, *J. Magn. Reson.*, 1991, **91**, 65.
6. (a) S. Castellano and A. A. Bothner-By, *J. Chem. Phys.*, 1964, **41**, 3863, (b) S. Castellano, in *Computer Programs for Chemistry*, ed. D. F. DeTar, Benjamin, New York, 1968, Vol. 1.
7. R. C. Ferguson and D. W. Marquardt, *J. Chem. Phys.*, 1964, **41**, 2087.
8. P. Diehl, H. P. Kellerhals, and W. Niederberger, *J. Magn. Reson.*, 1971 **4**, 352.
9. G. Hagële, M. Engelhardt, and W. Boenigk, *Simulation and automatisierte Analyse von Kernresonanzspektren*, VCH, Weinheim, 1987.
10. C. W. Haigh, *Ann. Rep. NMR Spectrosc.* 1971, **4**, 311.
11. J. W. Emsley, D. L. Turner, A. Giroud, and M. Longeri, *J. Chem. Soc. Faraday Trans. 2*, 1985, **81**, 603.
12. J. W. Emsley, G. Celebre, G. De Luca, M. Longeri, and F. Lucchesini, *Liquid Cryst.*, 1994, **16**, 1037.
13. N. Wirth, *Algorithms + Data Structures = Programs*, Prentice Hall, Englewood Cliffs, NJ, 1980.
14. E. Sicilia, Tesi di Laurea, Università della Calabria, 1988.
15. D. Catalano, C. A. Veracini, P. L. Barili, and M. Longeri, *J. Chem. Soc., Perkin Trans. II*, 1983, 171.
16. G. Celebre, G. De Luca, M. Longeri, D. Catalano, C. A. Veracini, and J. W. Emsley, *J. Chem. Soc., Faraday Trans.*, 1991, **87**, 2623.
17. J. W. Emsley, T. J. Horne, G. Celebre, G. De Luca, and M. Longeri, *J. Chem. Soc., Faraday Trans.*, 1992, **88**, 1679.
18. P. Diehl, in *NMR of Liquid Crystals*, ed. J. W. Emsley, Reidel, Dordrecht, 1985.
19. P. Diehl, H. Huber, A. C. Kunwar, and M. Reinhold, *Org. Magn. Reson.*, 1977, **9**, 374.
20. G. Celebre, G. De Luca, M. Longeri, and J. W. Emsley, *J. Phys. Chem.*, 1992, **96**, 2466.
21. D. S. Stephenson and G. Binsch, *Org. Magn. Reson.*, 1980, **14**, 226.
22. D. S. Stephenson and G. Binsch, *Mol. Phys.*, 1981, **43**, 697.
23. J. W. Emsley and D. L. Turner, *J. Chem. Soc., Faraday Trans. 2*, 1981, **77**, 1493.
24. G. Bodenhausen, *Prog. NMR Spectrosc.*, 1981, **14**, 137.
25. M. Gochin, A. Pines, M. E. Rosen, S. P. Rucker, and C. Schmidt, *Mol. Phys.*, 1990, **69**, 671.
26. M. E. Rosen, S. P. Rucker, C. Schmidt, and A. Pines, *J. Phys. Chem.*, 1993, **97**, 3858.
27. A. Pines, S. Vega, and M. Mehring, *Phys. Rev. B*, 1978, **18**, 112.
28. (a) J. Courtieu, D. W. Alderman, D. M. Grant, and J. P. Bayles, *J. Chem. Phys.*, 1982, **77**, 723; (b) J. Courtieu, D. W. Alderman, and D. M. Grant, *J. Am. Chem. Soc.*, 1983, **103**, 6783.
29. J. D. Ellett, M. G. Gibby, U. Haeberlen, L. M. Huber, M. Mehring, A. Pines, and J. S. Waugh, in *Advances in Magnetic Resonance*, ed. J. S. Waugh, Academic, San Diego, 1971, Vol. 5, p. 117.
30. L. Frydman, P. C. Rossomando, and B. Frydman, *J. Magn. Reson.*, 1991, **95**, 484.

Biographical Sketches

M. Longeri. *b* 1947. Laurea (with Professor C. A. Veracini). Pisa, 1972. Dipartimento di Chimica, Università della Calabria, 1973–present. Approx. 60 publications. Research interests: spectral and conformational analysis of molecules dissolved in liquid crystalline mesophases.

G. Celebre. *b* 1958. Laurea (with Professor M. Longeri), Calabria, 1984. Dipartimento di Chimica, Università della Calabria, 1986–present. Approx. 20 publications. Research interests: conformational analysis of molecules dissolved in liquid crystalline mesophases.

Liquid Crystalline Samples: Structure of Nonrigid Molecules

James W. Emsley

University of Southampton, Southampton, UK

1	Introduction	1
2	Averaging of Dipolar and Quadrupolar Interactions for Nuclei in Flexible Molecules in Liquid Crystalline Samples	1
3	The Maximum Entropy Method	2
4	Additive Potential Methods	3
5	Applications	5
6	Related Articles	6
7	References	7

1 INTRODUCTION

Both whole molecule and internal modes of motion are rapid enough that the dipolar couplings D_{ij} and the quadrupolar splittings $\Delta\nu_i$ which are obtained by analysis of the NMR spectrum of a sample in a liquid crystalline phase are averages over these motions. This means that, in principle, it is possible to investigate the internal motion via these averaged values, and indeed this is proving to be a valuable method for studying the flexibility of molecules in a liquid phase.

It also means that investigations of the orientational order by NMR must take the internal motion into account. NMR studies have in fact played the central role in demonstrating that molecules which form liquid crystalline phases (mesogens) are flexible, and in stimulating the development of molecular statistical theories of orientational order which allow for the internal motion. Perhaps the most important step was the realization that orientational order and internal motion are inextricably linked together.[1–3] This has the consequence that it is not possible to describe the orientational order by a single Saupe order matrix **S** (see ***Liquid Crystals: General Considerations***), but it is necessary to recognize that the elements of this matrix depend on the internal coordinates, that is they are conformationally dependent.

All mesogens discovered so far are flexible, and this should be taken into account when interpreting any measurements (not only NMR) made on them in terms of the behavior of the molecules. This is now recognized by many, although not all, in the NMR community. In the case of relaxation rates it is difficult to do this rigorously, but models of varying degrees of sophistication are used (see ***Liquid Crystalline Samples: Relaxation Mechanisms*** and ***Liquid Crystalline Samples: Deuterium NMR***). This aspect is not discussed further here.

2 AVERAGING OF DIPOLAR AND QUADRUPOLAR INTERACTIONS FOR NUCLEI IN FLEXIBLE MOLECULES IN LIQUID CRYSTALLINE SAMPLES

These are totally anisotropic interactions and so NMR experiments yield the components $T_{\mathrm{d}}^{(2,m)}$ in a frame fixed on the mesophase director, and the spherical, irreducible tensor notation is used (see ***Liquid Crystals: General Considerations***). These are related to $T_{\mathrm{d}}^{(2,m)}(\alpha, \beta, \gamma, \{\phi\})$, the values for the molecule at a fixed orientation, described by the three Euler angles α, β, and γ for the conformation described by the set of internal angles $\{\phi\}$. Thus,

$$T_{\mathrm{d}}^{(2,m)} = \int T_{\mathrm{d}}^{(2,m)}(\alpha,\ \beta, \gamma, \{\phi\}) P_{\mathrm{LC}}(\alpha, \beta, \gamma, \{\phi\}) \times \sin\beta\, \mathrm{d}\beta\, \mathrm{d}\alpha\, \mathrm{d}\gamma\, \mathrm{d}\{\phi\} \quad (1)$$

$T_{\mathrm{d}}^{(2,m)}(\alpha, \beta, \gamma, \{\phi\})$ is known for a fixed geometry of the molecule, and so the unknown quantity in equation (1) is $P_{\mathrm{LC}}(\alpha,\ \beta,\ \gamma,\ \{\phi\})$, which is the singlet, orientational distribution function for the molecules in the conformation specified by $\{\phi\}$. The object of NMR experiments on flexible molecules is to obtain this function. All properties of the ensemble of molecules which depend only on single molecules can then be calculated from $P_{\mathrm{LC}}(\alpha,\ \beta,\ \gamma,\ \{\phi\})$.

The probability, $P_{\mathrm{LC}}(\{\phi\})$, that a molecule is the conformation $\{\phi\}$ independently of its orientation relative to the director is obtained as

$$P_{\mathrm{LC}}(\{\phi\}) = \int P_{\mathrm{LC}}(\alpha, \beta, \gamma, \{\phi\})\, \mathrm{d}\alpha \sin\beta\, \mathrm{d}\beta\, \mathrm{d}\gamma \quad (2)$$

This function describes the conformational distribution of the molecules in the liquid crystalline phase. In general, this will differ from $P_{\mathrm{iso}}(\{\phi\})$, which describes the conformational distribution of the molecule, at the same temperature, in an isotropic phase of the sample.

Conformationally dependent order parameters are defined as

$$\langle D_{m,n}^{2*}(\{\phi\})\rangle = \int D_{m,n}^{2*}(\alpha, \beta, \gamma, \{\phi\}) \times P_{\mathrm{LC}}(\alpha, \beta, \gamma, \{\phi\})\, \mathrm{d}\alpha \sin\beta\, \mathrm{d}\beta\, \mathrm{d}\gamma \quad (3)$$

where $D_{m,n}^{2*}(\alpha, \beta, \gamma, \{\phi\})$ is the Wigner function describing the transformation from molecule to director fixed axes when the molecule is in conformation $\{\phi\}$.

2.1 Conformationally Dependent Saupe Order Parameters

The spherical tensor notation is particularly helpful when describing phases of different symmetries, but most NMR experiments are done either on uniaxial phases, or on biaxial phases with their director frame aligned with the applied magnetic field $\boldsymbol{B}_0$. In these cases the experiments yield just $T_{\mathrm{d}}^{(2,0)}$, and it is more convenient to use Cartesian representations of the tensors. For example, an averaged dipolar coupling, D_{ij}, is now given by

$$D_{ij} = \int P_{\mathrm{LC}}(\{\phi\}) D_{ij}(\{\phi\})\, \mathrm{d}\{\phi\} \quad (4)$$

where

$$D_{ij}(\{\phi\}) = -(\mu_0/4\pi)(h\gamma_i\gamma_j/4\pi^2 r^3_{ij\{\phi\}})S_{ij}(\{\phi\}) \quad (5)$$

and $S_{ij}(\{\phi\})$ is a conformationally dependent order parameter. Transforming $\mathbf{S}(\{\phi\})$ to give components $S_{\alpha\beta}(\{\phi\})$ in a frame fixed in a rigid subunit of the molecule gives

$$\begin{aligned} D_{ij}(\{\phi\}) = -(\mu_0/4\pi)(h\gamma_i\gamma_j/8\pi^2 r^3_{ij\{\phi\}})[&S_{zz}(\{\phi\})(3\cos^2\theta_{ijz\{\phi\}} - 1) \\ &+(S_{xx}(\{\phi\}) - S_{yy}(\{\phi\}))(\cos^2\theta_{ijx\{\phi\}} - \cos^2\theta_{ijy\{\phi\}}) \\ &+4S_{xy}(\{\phi\})\cos\theta_{ijx\{\phi\}}\cos\theta_{ijy\{\phi\}} \\ &+4S_{xz}(\{\phi\})\cos\theta_{ijx\{\phi\}}\cos\theta_{ijz\{\phi\}} \\ &+4S_{yz}(\{\phi\})\cos\theta_{ijy\{\phi\}}\cos\theta_{ijz\{\phi\}}] \end{aligned} \quad (6)$$

where $\theta_{ij\alpha\{\phi\}}$ is the angle between $\boldsymbol{r}_{ij\{\phi\}}$ and the α axis in the conformation specified by $\{\phi\}$. Similarly, the doublet splitting $\Delta\nu_i$ observed for a deuteron in a flexible molecule is given by

$$\Delta\nu_i = \tfrac{3}{2}q_{aai}[S_{aa}(\{\phi\}) + \tfrac{1}{3}\eta_i(S_{bb}(\{\phi\}) - S_{cc}(\{\phi\}))] \quad (7)$$

where *abc* are principal axes for either the quadrupolar tensor $\boldsymbol{g}_i$, or for the conformationally dependent order matrix $\mathbf{S}(\{\phi\})$.

2.2 Averaging over Single Sets of Symmetry-Related Conformations

For some molecules a reasonable approximation of the conformational distribution is that only a set of minimum energy conformations is populated [which is often referred to as the 'rotational isomeric state' (RIS) model], and that these are related by symmetry. The molecules are assumed to jump between these conformations, and this will be referred to as the 'jump model.' For example, if benzaldehyde is interconverting between two, planar conformations which are related by a mirror plane (Scheme 1), then if all other conformations are neglected:

$$S_{xx}(\mathbf{1}) = S_{xx}(\mathbf{2}), \quad S_{yy}(\mathbf{1}) = S_{yy}(\mathbf{2}), \quad S_{zz}(\mathbf{1}) = S_{zz}(\mathbf{2}) \quad (8a)$$

$$S_{xy}(\mathbf{1}) = S_{xy}(\mathbf{2}) = 0 \quad (8b)$$

$$S_{xz}(\mathbf{1}) = -S_{xz}(\mathbf{2}) \quad (8c)$$

$$S_{yz}(\mathbf{1}) = S_{yz}(\mathbf{2}) = 0 \quad (8d)$$

The observed and calculated dipolar couplings can be brought into agreement by adjusting the values of these order parameters.

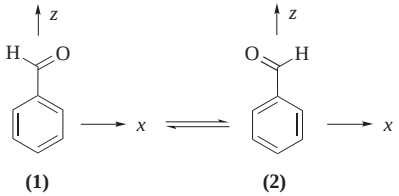

(1) (2)

Scheme 1

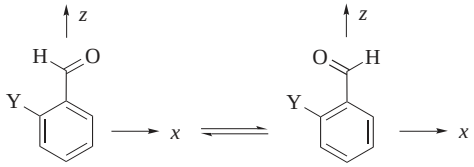

(3) (4)

Scheme 2

Equation (4) for a set of n discrete conformations becomes

$$D_{ij} = \sum_n P_{\mathrm{LC}}(n)\sum_{\alpha\beta} S_{\alpha\beta}(n)D_{ij\alpha\beta}(n) \quad (9)$$

with

$$\begin{aligned} D_{ij\alpha\beta}(n) = &-(\mu_0/4\pi)(h\gamma_i\gamma_j/8\pi^2 r^3_{ijn}) \\ &\times(3\cos\theta_{ij\alpha n}\cos\theta_{ij\beta n} - \delta_{\alpha\beta}) \end{aligned} \quad (10)$$

where $\delta_{\alpha\beta}$ is unity if $\alpha = \beta$, and zero otherwise.

2.3 Averaging over Conformations Unrelated by Symmetry

Now it is no longer possible to obtain a unique set of order matrices from the NMR (or any other!) data. The essence of the problem is illustrated by an *ortho*-substituted benzaldehyde interconverting between two planar conformations (Scheme 2). In this case,

$$\begin{aligned} D_{ij} = &\sum_{\alpha\beta} P_{\mathrm{LC}}(\mathbf{3})S_{\alpha\beta}(\mathbf{3})D_{ij\alpha\beta}(\mathbf{3}) \\ &+P_{\mathrm{LC}}(\mathbf{4})S_{\alpha\beta}(\mathbf{4})D_{ij\alpha\beta}(\mathbf{4}) \end{aligned} \quad (11)$$

and since $P_{\mathrm{LC}}(\mathbf{3}) \neq P_{\mathrm{LC}}(\mathbf{4})$, and $S_{\alpha\beta}(\mathbf{3}) \neq S_{\alpha\beta}(\mathbf{4})$ are unknown, then only the products [known as weighted order parameters $P_{\mathrm{LC}}(n)S_{\alpha\beta}(n)$] can be obtained from the data. This has not been done for *ortho*-substituted benzaldehydes, although this would be possible since there are more dipolar couplings (ten) than unknown weighted order parameters (six). An analysis of this kind has been done for the more complex case of 1-ethoxy-4-chlorobenzene.[4]

For multiple conformational states, or more generally when rotation about a bond is described by a continuous function $P_{\mathrm{LC}}(\phi)$, then the observed NMR data must be compared with values calculated from models for both $P_{\mathrm{LC}}(\phi)$ and $S_{\alpha\beta}(\phi)$, in other words, a model for $P_{\mathrm{LC}}(\beta, \gamma, \phi)$.

3 THE MAXIMUM ENTROPY METHOD

This is the least biased approach to obtaining $P_{\mathrm{LC}}(\beta, \gamma, \{\phi\})$, and was suggested initially by Zannoni,[3] and subsequently first demonstrated by application to the study of substituted biphenyls dissolved in liquid crystalline solvents by Catalano et al.[5]

Recalling that an NMR experiment on a sample in an aligned uniaxial phase (the discussion will be restricted to this

case, although the method can be extended to the more general biaxial solvent) yields values of $T_{dk}^{(2,0)}$, the spherical tensor components of a set of k dipolar or quadrupolar interactions, then application of the maximum entropy principle leads to

$$P_{\mathrm{LC}}(\beta, \gamma, \{\phi\}) = Z^{-1} \exp\left\{ -\sum_k \lambda_k T_k^{(2,0)}(\beta, \gamma, \{\phi\}) \right\} \quad (12)$$

where

$$Z^{-1} = \int P_{\mathrm{LC}}(\beta, \gamma, \{\phi\}) \sin\beta \, \mathrm{d}\beta \, \mathrm{d}\gamma \, \mathrm{d}\{\phi\} \quad (13)$$

and $T_k{}^{(2,0)}(\beta, \gamma, \{\phi\})$ is the component in a frame fixed in a rigid part of the molecule; the λ_k are adjustable parameters. For deuterium quadrupolar splittings ν_k, k will range over the number of different experimental values, and for dipolar couplings D_{ij}, λ_k must be replaced by λ_{ij}. The λ_k or λ_{ij} values are varied in order to bring calculated and observed data into agreement.

The maximum entropy method is very attractive in that no assumptions are necessary about the functional form of the rotational potentials, and it does not go beyond the information content of the data. This latter point must be recognized when interpreting the $P_{\mathrm{LC}}(\{\phi\})$ obtained by a maximum entropy analysis. Thus, the shape of $P_{\mathrm{LC}}(\{\phi\})$ depends to some extent on the degree of orientational order of the molecules in the liquid crystalline sample. This is illustrated in Figure 1, which shows the results from applying the maximum entropy method to sets of dipolar couplings simulated for the molecule 4,4′-dichlorobiphenyl (DCB), in a fixed conformation with an interring angle of 34°, and dissolved in a liquid crystal phase such that the values of S_{zz} of DCB vary from 0.2 to 0.6, in each case with $S_{xx} - S_{yy} = 0.02$. The $P_{\mathrm{LC}}(\phi)$ in each case should be a pair of delta functions at 34° and 146°, but the maximum entropy method gives continuous distributions peaked at these values but which become flatter as S_{zz} decreases. If $S_{zz} = S_{xx} - S_{yy} = 0$, then $P_{\mathrm{LC}}(\beta, \gamma, \phi)$ and $P_{\mathrm{LC}}(\phi)$ obtained from the data would both be completely flat and independent of β, γ, and ϕ. At the other extreme of complete order, $S_{zz} = 1$ and $S_{xx} - S_{yy} = 0$, the distribution $P_{\mathrm{LC}}(\phi)$ derived from the data would not be the pair of delta functions, since the maximum entropy method assumes a smooth dependence on ϕ, but a close approximation to the true distribution would be obtained.

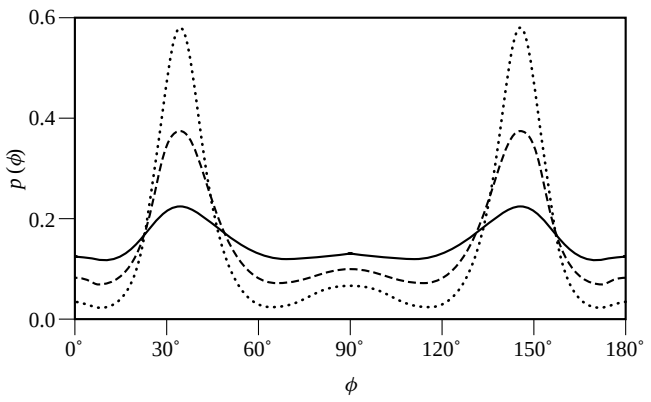

Figure 1 The probability distribution $P_{\mathrm{LC}}(\phi)$ obtained by the maximum entropy method from simulated dipolar couplings for 4,4′-dichlorobiphenyl dissolved in an uniaxial solvent. The three curves are for $S_{zz} = 0.6$ (. . . .), 0.4 (---) and 0.2 (—), in each case with $S_{xx} - S_{yy} = 0.02$

Another important point about the maximum entropy method is that it cannot yield $P_{\mathrm{iso}}(\phi)$, the probability distribution for an isotropic phase. To illuminate this point, and to set the scene for the other methods of analyzing NMR data on flexible molecules, it is useful to define a mean potential $U(\beta, \gamma, \{\phi\})$ as

$$P_{\mathrm{LC}}(\beta, \gamma, \{\phi\}) = Z^{-1} \exp[-U(\beta, \gamma, \{\phi\})/kT] \quad (14)$$

with

$$Z = \int \exp[-U(\beta, \gamma, \{\phi\})/kT] \sin\beta \, \mathrm{d}\beta \, \mathrm{d}\gamma \, \mathrm{d}\{\phi\} \quad (15)$$

The maximum entropy method derives a mean potential which is entirely anisotropic, and which vanishes in the isotropic phase, in other words a *potential of mean torque*.

4 ADDITIVE POTENTIAL METHODS

These methods differ fundamentally from the maximum entropy method in that they depend on modeling the mean potential, which means that they provide biased estimates of the distribution functions. This does have advantages, in particular that it is now possible to obtain both $P_{\mathrm{LC}}(\{\phi\})$ and $P_{\mathrm{iso}}(\{\phi\})$, and the dependence of the derived distribution functions on orientational order disappears.

The basic idea is to express $U(\beta, \gamma, \{\phi\})$ as a sum of two terms:

$$U(\beta, \gamma, \{\phi\}) = U_{\mathrm{ext}}(\beta, \gamma, \{\phi\}) + U_{\mathrm{int}}(\{\phi\}) \quad (16)$$

with $U_{\mathrm{ext}}(\beta, \gamma, \{\phi\})$ being a potential of mean torque, and $U_{\mathrm{int}}(\{\phi\})$ that part of the mean potential which depends only on $\{\phi\}$, and which does not vanish in the isotropic phase. Thus,

$$P_{\mathrm{iso}}(\{\phi\}) = Q^{-1} \exp[-U_{\mathrm{int}}(\{\phi\})/kT] \quad (17)$$

with

$$Q = \int \exp[-U_{\mathrm{int}}(\{\phi\})/kT] \, \mathrm{d}\{\phi\} \quad (18)$$

$P_{\mathrm{LC}}(\{\phi\})$ is also obtained by the additive potential methods, from equation (2), and in general will differ from $P_{\mathrm{iso}}(\{\phi\})$.

Several ways of modeling $U_{\mathrm{ext}}(\beta, \gamma, \{\phi\})$ have been proposed, and some of these are discussed in the following sections. Models for $U_{\mathrm{int}}(\{\phi\})$ may also vary, and are often specific to the molecule under consideration and the amount of experimental data available from which they may be characterized.

4.1 The Independent Fragment Model for $U_{ext}(\beta, \gamma, \{\phi\})$

This model was introduced first by Marcelja,[6] and subsequently modified by Emsley et al.;[7] it is the latter model which is discussed here. We shall refer to this as the 'AP method'. The potential of mean torque is assumed to be second rank in its orientational dependence:

$$U_{\text{ext}}(\beta, \gamma, \{\phi\}) = -\epsilon_{2,0}(\{\phi\})C_{2,0}(\beta, \gamma) - 2\ \text{Re}\,\epsilon_{2,2}(\{\phi\})C_{2,2}(\beta, \gamma) \qquad (19)$$

The $C_{2,m}(\beta, \gamma)$ are modified spherical harmonics, and the conformationally dependent interaction parameters $\epsilon_{2,m}(\{\phi\})$ are assumed to be sums of contributions $\epsilon_{2,p}(j)$ from contributions from each of j rigid subunits of the molecule:

$$\epsilon_{2,m}(\{\phi\}) = \sum_p D^2_{p,m}(\Omega_j)\epsilon_{2,\,p}(\,j) \qquad (20)$$

where Ω_j is the orientation of fragment j with respect to reference axes fixed in a rigid subunit. There will be just one contribution $\epsilon_{2,0}(j)$ from a fragment with cylindrical symmetry, and two, $\epsilon_{2,0}(j)$ and $\epsilon_{2,2}(j)$, from a fragment with lower symmetry, provided that the principal axes for $\boldsymbol{\epsilon}(j)$ are known.

For example, the $\epsilon_{2,p}(j)$ values for the rigid fragments in the mesogens 4-*n*-alkyl-4′-cyanobiphenyl (NCBs) (**5**) are as given in Table 1.

Note that, since the two rings share a common symmetry axis, then $\epsilon_{2,0}(\text{R}^1) = \epsilon_{2,0}(\text{R}^2)$.

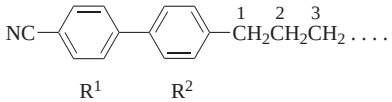

(5)

4.2 The Correlated Fragment or Chord Model

The independent fragment model does not always produce an $\epsilon(\{\phi\})$ matrix which accounts correctly for the shape of the conformer. This is illustrated in Figure 2, which shows two conformations of an alkane which give identical $\boldsymbol{\epsilon}(\{\phi\})$ matrices, but which would be expected to have different matrices because of their different shapes.

Table 1 The $\varepsilon_{2,p}(j)$ Values for the Rigid Fragments of the Mesogen (**5**)

Fragment	$\varepsilon_{z,p}\,(j)$
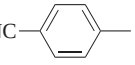	$\varepsilon_{2,0}(\text{R}^1)$, $\varepsilon_{2,2}(\text{R}^1)$
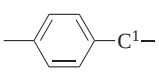	$\varepsilon_{2,0}(\text{R}^2)$, $\varepsilon_{2,2}(\text{R}^2)$
All C(i)–C(j)	$\varepsilon_{2,0}$(CC)
All C–H bonds	$\varepsilon_{2,0}$(CH)

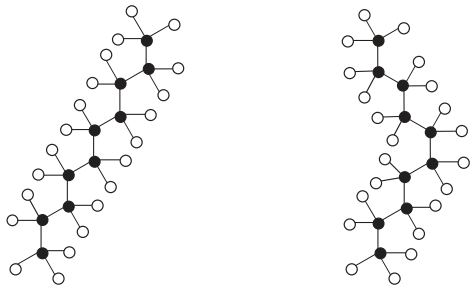

Figure 2 The conformations of decane which have different shapes, but which have identical interaction tensor elements $\epsilon_{2,\text{m}}(\{\phi\})$ when these are constructed as the sum of individual, independent C–C bond contributions. (From Photinos et al.[8])

To overcome this deficiency in the AP method, Photinos et al.[8] added terms to $U_{\text{ext}}(\beta, \gamma, \{\phi\})$ which depend on the relative orientations of different fragments. They considered fragments with cylindrical symmetry, such as C–C bonds, and proposed a potential of mean torque of the form

$$U_{\text{ext}}(\beta, \gamma, \{\phi\}) = -\sum_i w_i P_2(\cos\theta_i) - \sum_{i\neq j} w_{ij} P_{ij}(\boldsymbol{s}^i, \boldsymbol{s}^{i+j}) \qquad (21)$$

where

$$P_2(\cos\theta_i) = \tfrac{1}{2}(3\cos^2\theta_i - 1) \qquad (22)$$

and

$$P_{ij}(\boldsymbol{s}^i, \boldsymbol{s}^{i+j}) = \tfrac{1}{2}(3\cos\theta_i\cos\theta_{i+j} - \boldsymbol{s}^i \cdot \boldsymbol{s}^{i+j}) \qquad (23)$$

where θ_i is the angle between the ith C–C bond and the director, $\boldsymbol{s}^i$ and $\boldsymbol{s}^{i+j}$ are unit vectors along the ith and $(i + j)$th C–C bonds. The w_i and w_{ij} terms are the interaction strengths. For the case of an alkane, the w_i are all given the same value of w_0, and so the w_{ij} can be denoted by w_j. Note that for alkanes w_1 has a similar magnitude to w_0, and so the second terms in equation (21) should not be regarded as small corrections to the first.

Photinos et al.[8] also showed that an equivalent representation for $U_{\text{ext}}(\beta, \gamma, \{\phi\})$ is obtained by considering not bonds but chords $\boldsymbol{c}^i$ joining the midpoints of adjacent bonds, as shown in Figure 3. Note that the first and last bonds are denoted by unit vectors $\boldsymbol{t}^1$ and $\boldsymbol{t}^{N-1}$. In this chord representation, and including only nearest neighbor chord correlations (corresponding to bond correlations of next-nearest neighbors):

$$U_{\text{ext}}(\beta, \gamma, \{\phi\}) = -\Big\{ g_0 \sum_{i=1}^{N-2} P(\boldsymbol{c}^i, \boldsymbol{c}^i) + g_1 \sum_{i=1}^{N-3} P(\boldsymbol{c}^i, \boldsymbol{c}^{i+1}) + w_0^t[P(\boldsymbol{t}^1, \boldsymbol{t}^1) + P(\boldsymbol{t}^{N-1}, \boldsymbol{t}^{N-1})] + w_1^t[P(\boldsymbol{t}^1, \boldsymbol{c}^1) + P(\boldsymbol{t}^{N-1}, \boldsymbol{c}^{N-2})] \Big\} \qquad (24)$$

where $g_0 = [2\sin^2(\text{CCC}/2)]w_0$, $w_0^t = \frac{1}{2}w_0$, $w_1^t = \sin(\text{CC C}/2)\,w_1$, and $g_1 = 2\ \sin^2(\text{CCC}/2)w_1$. The terms involving g_1 and

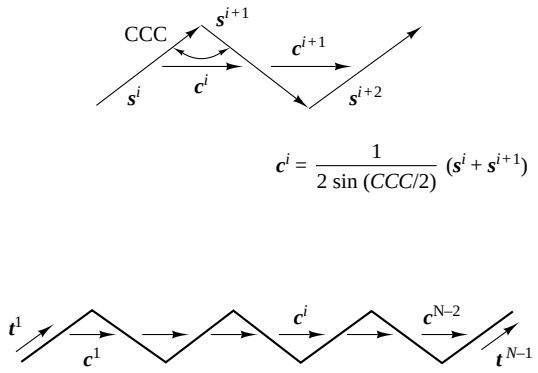

Figure 3 The unit vectors used in the chord model. (From Photinos et al.[8])

w_1^t allow for correlations between chords, and in the simplest scheme these are set to zero, w_1 is set equal to w_0, and the resulting uncoupled chord model has

$$U_{\text{ext}}(\beta, \gamma, \{\phi\}) = -\left\{ g_0 \sum_{i=1}^{N-2} P(\boldsymbol{c}^i, \boldsymbol{c}^i) + w_0^t [P(\boldsymbol{t}^1, \boldsymbol{t}^1) + P(\boldsymbol{t}^{N-1}, \boldsymbol{t}^{N-1})] \right\} \quad (25)$$

4.3 Shape Models

The mean field experienced by a molecule in a liquid crystalline phase will depend on its shape, and the chord model was introduced to improve the correlation between $U_{\text{ext}}(\beta, \gamma, \{\phi\})$ and a conformer's shape. More direct methods have been proposed for constructing shape dependent potentials of mean torque. Thus Ferrarini et al.[9] have proposed a second rank shape tensor, $T^{(2,m)}(\{\phi\})$ which is constructed as

$$T^{(2,m)}(\{\phi\}) = -\int_S \mathrm{d}S\, C^*_{2,m}(\theta, \chi) \quad (26)$$

where θ and χ are the spherical polar angles made by $\mathbf{n}_s$, the normal to the surface of the molecule at a given point. The molecular surface is constructed by placing spheres with van der Waals radii on each atom. The potential of mean torque is now

$$U_{\text{ext}}(\beta, \gamma, \{\phi\}) = -\epsilon \sum_m T^{(2,m)*}(\{\phi\}) C_{2,m}(\beta, \gamma) \quad (27)$$

where ϵ is the only adjustable parameter.

5 APPLICATIONS

Studies by NMR of flexible molecules in liquid crystalline phases are of two kinds: those of the mesogens themselves, when the motive may be to characterize the orientational order, and a conformational model is assumed, and of nonmesogenic solutes, when the main motive is to investigate the conformational distribution. Some examples are given here to illustrate both these types of investigation, but most emphasis is given to studies aimed at determining the conformational distribution.

5.1 Single Rotors

Biphenyl is an example which has been studied by both the AP and maximum entropy (ME) methods.[10] The data are the set of interproton dipolar couplings obtained by analyzing the very complex proton spectrum. The maximum entropy method gives a distribution $P_{\text{LC}}(\phi)$ peaked at 34°, whilst the AP method gives a similar shape for $P_{\text{LC}}(\phi)$ and $P_{\text{iso}}(\phi)$, with a maximum at 38°. It is important to note too that the data can be fitted to jumps between a single set of symmetry related conformations, corresponding to an interring angle of 32°. Clearly, for this molecule the data cannot discriminate between the conformational analysis methods, since all three results can be considered reasonable. Such agreement is not always found. For example, for benzyl chloride,[11] again with interproton dipolar couplings as the data, the jump model yields a structure (III) in which the C–Cl bond is at 60° to the ring plane, whilst analysis by the AP method gives the potential shown in Figure 4. The most probable structure is that with the C–Cl bond at 90° (II). Structure (I) has the C–Cl in the ring plane. Molecular orbital calculations, electron diffraction experiments, and long-range J(H, H) values all give (II) as the most probable structure, thus supporting the AP result rather than the one obtained with the jump model.

5.2 Two Rotors

The most interesting result to emerge from studies of molecules with two bond rotations is that it may be necessary to allow for cooperative rather than independent rotations. This was revealed by a maximum entropy analysis[12] of the D(H, H) values obtained for some ethoxybenzenes.[13] Continuous distributions for rotation about the ring–oxygen bond (through ψ) and about the O–CH_2 bond (through ϕ), as shown in Figure 5, were considered, the rotation about the C–CH_3 bond being approximated as three-site jumps. The probability distribution obtained for ethoxybenzene dissolved in a nematic solvent is shown in Figure 6, and this clearly shows, through the elliptical shape of the contours, that the two rotations are cooperative.

A similar coupled rotation in anisole has been revealed by an AP analysis of dipolar couplings,[14] and for this to be established it was necessary to increase the data set to include some ^{13}C–^{1}H couplings by studying anisole–$^{13}CH_3$.

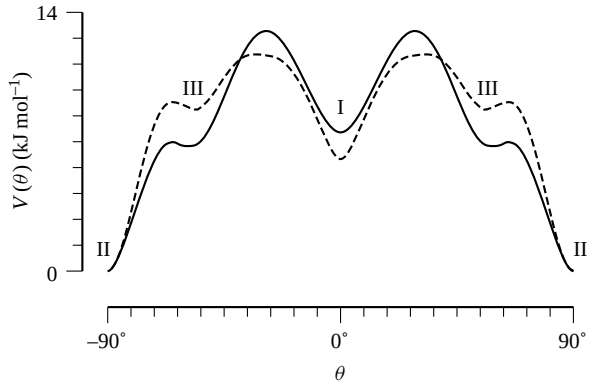

Figure 4 The potential functions determined using the AP method for benzyl chloride dissolved in the nematic solvents ZLI 1167 (—) and ZLI 1132 (---)[11]

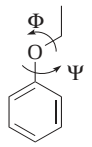

Figure 5 Ethoxybenzene

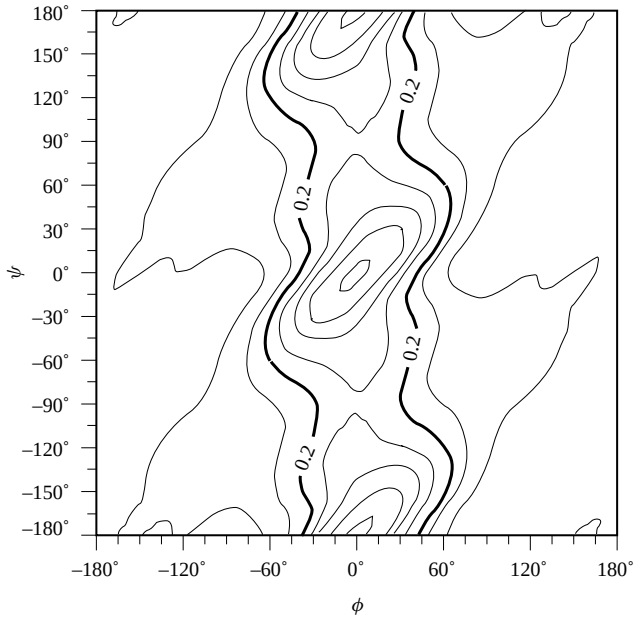

Figure 6 A contour representation of $P_{LC}(\psi, \phi)$ obtained for 4-fluoroethoxybenzene dissolved in a nematic solvent[12]

5.3 Alkanes and Alkyl Chains

As the molecules increase in size, the proton spectra become extremely complex, and it is necessary to resort to methods of spectral simplification in order to obtain interproton dipolar couplings. Thus, dipolar couplings have been obtained for a series of alkanes dissolved in nematic solvents from deuterium decoupled proton spectra obtained on 80% randomly deuterated samples (see ***Liquid Crystalline Samples: Spectral Analysis***). Dipolar couplings between ^{13}C and ^{1}H have also been obtained for mesogenic molecules by using local field spectroscopy coupled with spinning close to the magic angle (see ***Spinning Liquid Crystalline Samples*** and ***Liquid Crystalline Samples: Carbon-13 NMR***). A simpler approach is to study the deuterium spectra of deuterated samples, but with the disadvantage that the quadrupolar couplings obtained form a smaller set with which to test models for the conformational distribution (see ***Liquid Crystalline Samples: Deuterium NMR***).

When there are several bond rotations in a molecule it becomes impracticable to sample enough points for each rotation in order to be able to characterize the functional form of the potentials by NMR. The conformational distribution in such cases is usually dramatically simplified to being only the conformers at the minima in the rotational potential (the RIS model). For alkyl chains this involves the three forms shown in Figure 7. The conformations of a chain are obtained as combinations of *trans* and *gauche* forms about each C–C bond. The energy difference between *trans* and *gauche* forms

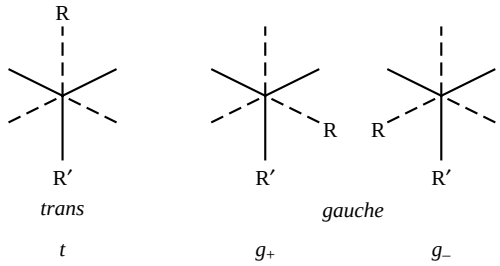

Figure 7 *Trans* and *gauche* conformations of RCH_2CH_2R' compounds

E_{tg} is the only adjustable parameter in the simplest RIS model. A term $E_{g\pm g\pm}$ is sometimes added to discriminate against conformers having $g_\pm g_\pm$ sequences.

The dipolar couplings obtained for the alkanes dissolved in a nematic solvent have been analyzed using different additive potential methods and the RIS model for the conformations.[15] The observed and calculated D_{ij} were brought into agreement by varying the parameters defining $U_{ext}(\beta, \gamma, \{\phi\})$ (which differ for each model) and E_{tg}. The quality of the fitting is similar for all the methods used, but very different values of E_{tg} were obtained. The chord model gave an E_{tg} closest to that obtained by other methods. A better fit to the data for hexane has been obtained by increasing to nine the points sampled on each C–C bond rotational potential.[16]

5.4 Mesogenic Molecules

The simplest mesogen, 4-methoxy-4′-cyanobiphenyl (1OCB) contains 11 protons and has a very complex proton spectrum, but one which has been analyzed,[17] and the data used to investigate the conformational distribution. Similar studies have been made of more complex mesogens, when dipolar couplings between protons in fragments of the molecules have been obtained by partial deuteration followed by deuterium decoupling.[18–20] Several mesogens have been studied by ^{13}C NMR using the technique of spinning close to the magic angle combined with dipolar local field spectroscopy (see ***Liquid Crystalline Samples: Carbon-13 NMR***). The RIS model has been used for the conformational distributions in these studies, and this has also been the model adopted to interpret the quadrupole splittings obtained from deuterium NMR. The objectives in most of these studies has been primarily to show that the particular models used for constructing $U_{ext}(\beta, \gamma, \{\phi\})$, together with the RIS model, are capable of fitting the data.[21–23] It is not yet clear which of the methods of constructing the potential of mean torque is the best, but there is now a clear consensus that molecular interpretations of liquid crystal properties must take into account bond rotational motion, and that, conversely, it is possible for a conformational distribution to change quite substantially on changing from an isotropic to a liquid crystalline phase.[7,22,23]

6 RELATED ARTICLES

Liquid Crystalline Samples: Spectral Analysis; Liquid Crystals: General Considerations; Structure of Rigid Molecules Dissolved in Liquid Crystalline Solvents.

7 REFERENCES

1. J. W. Emsley and G. R. Luckhurst, *Mol. Phys.*, 1980, **41**, 19.
2. E. E. Burnell and C. A. De Lange, *J. Magn. Reson.*, 1980, **39**, 461.
3. C. Zannoni, in *NMR of Liquid Crystals*, ed. J. W. Emsley, Reidel, Dordrecht, 1985.
4. J. W. Emsley, N. J. Heaton, M. K. Kimmings, and M. Longeri, *Mol. Phys.*, 1987, **61**, 433.
5. D. Catalano, L. Di Bari, C. A. Veracini, G. N. Shilstone, and C. Zannoni, *J. Chem. Phys.*, 1991, **94**, 3928.
6. S. Marcelja, *J. Chem. Phys.*, 1974, **60**, 3599.
7. J. W. Emsley, G. R. Luckhurst, and C. P. Stockley, *Proc. R. Soc. London Ser. A*, 1982, **381**, 117.
8. D. J. Photinos, E. T. Samulski, and H. Toriumi, *J. Phys. Chem.*, 1990, **94**, 4688.
9. A. Ferrarini, G. J. Moro, P. L. Nordio, and G. R. Luckhurst, *Mol. Phys.*, 1992, **77**, 1.
10. G. Celebre, G. De Luca, M. Longeri, D. Catalano, C. A. Veracini, and J. W. Emsley, *J. Chem. Soc., Faraday Trans.*, 1991, **87**, 2623.
11. G. Celebre, M. Longeri, and J. W. Emsley, *Mol. Phys.*, 1988, **64**, 715.
12. G. Celebre, M. Longeri, and J. W. Emsley, *Liq. Cryst.*, 1989, **6**, 689.
13. L. Di Bari, M. Persico, and C. A. Veracini, *J. Chem. Phys.*, 1992, **96**, 4782.
14. G. Celebre, G. De Luca, M. Longeri, and J. W. Emsley, *J. Phys. Chem.*, 1992, **96**, 2466.
15. M. E. Rosen, S. P. Rucker, C. Schmidt, and A. Pines, *J. Phys. Chem.*, 1993, **97**, 3858.
16. D. J. Photinos, E. T. Samulski, and A. F. Terzis, *J. Phys. Chem.*, 1992, **96**, 6979.
17. S. W. Sinton, D. B. Zax, J. B. Murdoch, and A. Pines, *Mol. Phys.*, 1984, **53**, 333.
18. G. Celebre, M. Longeri, E. Sicilia, and J. W. Emsley, *Liquid Cryst.*, 1990, **7**, 731.
19. J. W. Emsley, T. J. Horne, G. Celebre, M. Longeri, and H. Zimmermann, *J. Phys. Chem.*, 1992, **96**, 7929.
20. J. W. Emsley, G. Celebre, G. De Luca, M. Longeri, and F. Lucchesini, *Liquid Cryst.*, 1994, **16**, 1037.
21. D. J. Photinos, E. T. Samulski, and H. Toriumi, *J. Chem. Soc., Faraday Trans.*, 1992, **88**, 1875.
22. S. T. W. Cheung and J. W. Emsley, *Liquid Cryst.*, 1993, **13**, 265; J. W. Emsley, *Liquid Cryst.*, 1994, **16**, 671 [correction].
23. C. J. R. Counsell, J. W. Emsley, G. R. Luckhurst, and H. S. Sachdev, *Mol. Phys.*, 1988, **63**, 33.

Biographical Sketch

James W. Emsley. *b* 1934. B.Sc., 1956, Ph.D., 1960, University of Leeds (supervised by J. A. S. Smith). ICI Research Fellow, University of Liverpool, 1960–62; Research assistant and then lecturer, University of Durham, 1962–67. Since 1967 at Department of Chemistry, University of Southampton, currently as a professor. Research interests center on NMR of liquid crystalline samples. Editor of Progress in NMR Spectroscopy with Jim Feeney; about 150 scientific publications.

Liquid Crystals: General Considerations

James W. Emsley
University of Southampton, Southampton, UK

1	Introduction	1
2	Motional Averaging in Liquid Crystalline Samples	1
3	The Time-Averaged Hamiltonian $\hat{\mathcal{H}}$	2
4	Relationship Between $T_{\lambda d}^{(L,n)}$ and Components of the same Interactions in a Molecular Frame $T_{\lambda mol}^{(L,m)}$	3
5	Individual Contributions to $\hat{\mathcal{H}}$	5
6	Relaxation Rates	6
7	Proton NMR of Liquid Crystalline Samples	8
8	Carbon-13 NMR	9
9	Deuterium NMR	10
10	Related Articles	12
11	References	12

1 INTRODUCTION

The NMR spectra of liquid crystalline samples are like those of solids in that anisotropic interactions, such as dipole–dipole and nuclear electric quadrupole–electric field gradient interactions, contribute to the spectrum. The spectra are also similar to those from isotropic liquids in that relaxation rates are small, leading to narrow lines for individual resonances. These features of the spectra have ensured that NMR has become the best method for studying the structure, orientational order and dynamics of molecules in liquid crystalline phases.

The general factors which determine the form taken by the spectra of nuclei in liquid crystalline phases are discussed here. This includes a discussion of the principal contributions to the Hamiltonian, and the relationship with molecular properties of the parameters which can be obtained by analyzing the spectra. A general outline will be presented of the factors which determine relaxation rates, and this is followed by a brief discussion of the spectra observed for protons, carbon-13 and deuterium nuclei, which are the three most important nuclei for studying liquid crystalline samples.

More details of the NMR of liquid crystalline samples can be found in Emsley,[1] Dong,[2] and Emsley and Lindon,[3] and in other articles in this Encyclopedia (see Related Articles)

2 MOTIONAL AVERAGING IN LIQUID CRYSTALLINE SAMPLES

The molecules in liquid crystalline phases are moving at speeds comparable with those in isotropic liquids, with similar viscosities. This means that the spectra depend on interactions averaged over this molecular motion, and so to understand the form taken by the spectra, and to appreciate their information content, it is necessary to consider the nature of the averaging process in some detail.

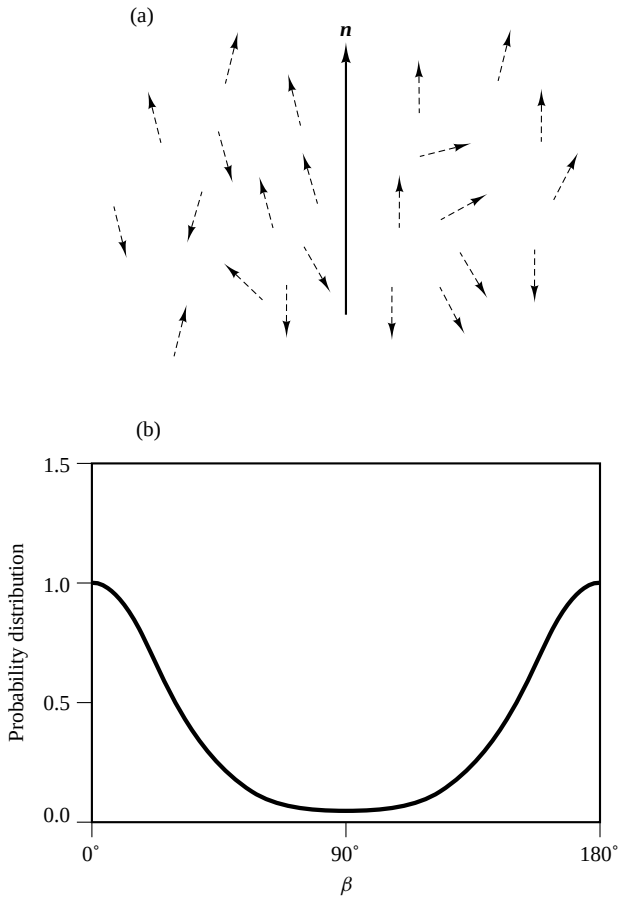

Figure 1 (a) Distribution of the symmetry axes of rigid, cylindrically symmetric molecules about the director $\boldsymbol{n}_i$. (b) The un-normalized probability $f(\beta)$ that the symmetry axis is at an angle between β and $\beta + d\beta$

2.1 The Liquid Crystal Director

Although the molecular motion is rapid, it is not random, in that at any point in the sample the molecules have a preferred orientation. The simplest phases, which are referred to as 'uniaxial,' are such that there is $D_{\infty h}$ symmetry at this point for the distribution of the molecules about a unit vector $\boldsymbol{n}_i$ known as the 'local director.' To illustrate this concept the molecules, for simplicity, but without sacrificing generality, are assumed to be rigid and cylindrical in shape and symmetry. In this case the distribution of the cylinder axes about $\boldsymbol{n}_i$ are shown in Figure 1(a), and Figure 1(b) shows the probability $f(\beta)$ that the axes are at an orientation between β and $\beta + d\beta$ with respect to $\boldsymbol{n}_i$. This singlet, orientational distribution function is symmetrical about $\beta = 90^\circ$. The direction of $\boldsymbol{n}_i$ varies continuously and randomly throughout a macroscopic sample, unless there is some external constraint acting, but $f(\beta)$ is independent of the position in the bulk sample. There is, therefore, microscopic, but not macroscopic, orientational order in an unconstrained liquid crystalline sample.

There are also liquid crystalline phases in which the symmetry about the local directors is D_{2h}, and it is now necessary to specify three unit vectors directed along axes X, Y, and Z fixed at the ith point.

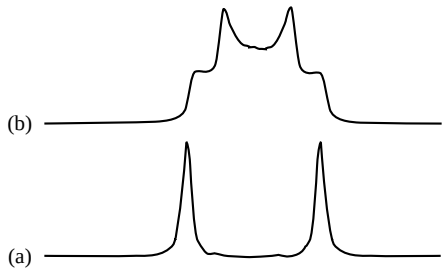

Figure 2 Deuterium spectrum observed for D_2O in a liquid crystalline sample for uniform alignment of the directors along the applied field $\boldsymbol{B}_0$ (a), and with the directors uniformly distributed at all orientations to $\boldsymbol{B}_0$ (b)

2.2 Averaging Produced by Motion Relative to the Director

When molecular motion is faster than the anisotropy ΔT in some nuclear spin interaction, then the spectrum depends on T_{XX}, T_{YY}, and T_{ZZ}, the components of the tensor in the director frame. The spectrum is also affected by the orientation of the static, applied magnetic field, $\boldsymbol{B}_0$, in the local director frames. For example, for a uniaxial phase, the deuterium spectrum produced by a group of chemically equivalent deuterons consists of a pair of lines whose separation $\Delta\nu(\theta)$ depends on the angle θ between the director and $\boldsymbol{B}_0$. Thus, for a sample in which all the directors are at a single value of θ, then

$$\Delta\nu(\theta) = \Delta\nu(0^\circ)(3\cos^2\theta - 1)/2 \tag{1}$$

where $\Delta\nu(0^\circ)$ is the splitting for $\theta = 0^\circ$. A spectrum of this kind is shown in Figure 2(a). If the directors do not adopt a single value of θ but are distributed uniformly in space, then the spectrum is a superposition of doublets, weighted according to the probability distribution for θ. This is identical in form to the spectrum observed for deuterium in polycrystalline solid samples, except for a reduction in the overall width of the spectrum (see Section 8), as shown in Figure 2(b). The spectrum observed from a liquid crystalline sample therefore changes dramatically depending on the how the directors are distributed in the magnetic field.

2.3 Alignment of Directors by a Magnetic Field

The local directors $\boldsymbol{n}_i$ of a uniaxial phase can be aligned along a common direction to create macroscopic order by applying an electric field, by confining the sample between glass plates, by spinning the sample, or by application of a magnetic field. The creation of a uniformly aligned biaxial phase requires the application of two constraints.

The alignment by a magnetic field is obviously of greatest importance for NMR experiments, although the other methods do have their uses. Magnetic field alignment occurs because the field exerts a force on the molecules, which depends upon the magnitude of χ^{mol}, the magnetic susceptibility tensor for each molecule, and on the extent of the correlations between the orientations of the molecules relative to their local director. Thus, considering a single, rigid, cylindrically symmetric molecule at a fixed orientation β_i with respect to $\boldsymbol{n}_i$ in a uniaxial phase, the contribution F_i to the magnetic energy is

$$F_i = -\tfrac{1}{4}\Delta\chi^{\text{mol}} B_0^2(3\cos^2\beta_i - 1) \tag{2}$$

F_i is a minimum for $\Delta\chi^{\text{mol}}$ positive when $\beta_i = 0^\circ$, and the molecule will want to adopt this orientation. However, collisions between molecules tend to produce an isotropic distribution of β_i, and for a normal liquid this randomizing effect is much larger than the orienting effect of $\boldsymbol{B}_0$. This means that $\bar{P}_2$, the average of the function $P_2(\cos\beta_i)$ over all the molecules, is very small ($\approx 10^{-5}$), and the samples are essentially isotropic at fields less than about 9 T. Note, however, that the effect is large enough to produce dipolar or quadrupolar splittings in higher fields when $\Delta\chi^{\text{mol}}$ is large (see ***Magnetic Field Induced Alignment of Molecules***).

A different situation prevails in a liquid crystalline phase, since now there is a net alignment of the molecules along the local directors, and the magnetic torque acting on each director becomes

$$F(\alpha_j) = -\Delta\chi^{\text{mol}}\bar{P}_2(3\cos^2\alpha_j - 1)B_0^2/6 \tag{3}$$

where α_j is the angle between the director $\boldsymbol{n}_j$ and $\boldsymbol{B}_0$. This magnetic force is now large enough relative to the thermal energy that the probability $f(\alpha)$ that a director lies between α and α + dα with respect to $\boldsymbol{B}_0$ is sharply peaked at $\alpha = 0^\circ$ when $\Delta\chi^{\text{mol}}$ is positive, and at $\alpha = 90^\circ$ when $\Delta\chi^{\text{mol}}$ is negative. This means that virtually complete alignment of the directors can be obtained for uniaxial phases in the magnets of NMR spectrometers.

The alignment is opposed by the sample's viscosity, and there may also may be a conflict with the spatial organization present in smectic, discotic, chiral, and some amphiphilic phases. In practice, alignment occurs rapidly and completely for nematic samples as soon as a sample has been placed in the magnet. Phases with spatial order behave in a more complex manner. It is usually possible, however, to obtain uniform director alignment in uniaxial smectic phases by cooling the sample from an aligned phase

3 THE TIME-AVERAGED HAMILTONIAN $\hat{\bar{\mathcal{H}}}$

3.1 The General Form

A full discussion of the form taken by the Hamiltonian has been presented by Veracini,[4] and here the discussion is restricted to presenting results and discussing their implications.

A nuclear spin Hamiltonian can be written using either Cartesian, or irreducible spherical tensors. Both will be used here, but at first the spherical tensor form is employed because it is particularly useful for showing which components are nonzero for different symmetries, either of the phase or the molecules. Thus, in this notation the general form for the Hamiltonian is

$$\hat{\bar{\mathcal{H}}} = \sum_{\lambda}\sum_{m=-L}^{+L}(-1)^m T_{\lambda}^{(L,m)}\,\hat{A}_{\lambda}^{(L,-m)} \tag{4}$$

λ denotes the different interactions contributing to $\hat{\tilde{\mathcal{H}}}$; $T_\lambda^{(L,m)}$ are the irreducible, spherical components of the tensor representing the λth interaction, and $\hat{A}_\lambda^{(L,m)}$ is the appropriate nuclear spin operator. NMR experiments are usually done with magnetic fields which are sufficiently strong that the field direction is a unique axis of quantization for the nuclear spin angular momentum (but note that this will not be the case for some quadrupolar nuclei, see ***Quadrupolar Interactions***). Confining the discussion to this high-field case means that the uniaxial symmetry about $\boldsymbol{B}_0$ restricts the terms in $\hat{\tilde{\mathcal{H}}}_\lambda$ to those involving only the components of the tensors along $\boldsymbol{B}_0$, that is those with $m = 0$, and since L is either 0 or 2, then

$$\hat{\tilde{\mathcal{H}}}_\lambda = \sum_\lambda T_\lambda^{(0,0)}\, \hat{A}_\lambda^{(0,0)} + \sum_\lambda T_\lambda^{(2,0)}\, \hat{A}_\lambda^{(2,0)} \tag{5}$$

The spherical tensor notation clearly shows that, in general, there are rotationally invariant contributions to $\hat{\tilde{\mathcal{H}}}_\lambda$ (those with $L = 0$) and anisotropic contributions (those with $L = 2$).

3.2 The Effect of Director Orientation on $\hat{\tilde{\mathcal{H}}}_\lambda$

The rotationally invariant (scalar) contributions are unaffected by director orientation, and so too are the spin operators $\hat{A}_\lambda^{(2,0)}$. The anisotropic contributions, $T_\lambda^{(2,0)}$ are related to $T_{\lambda\mathrm{d}}^{(2,0)}$, the components in a coordinate frame fixed on the director by

$$T_{\lambda\mathrm{d}}^{(2,0)} = \sum_n T_{\lambda\mathrm{d}}^{(2,n)}\, D_{0,n}^{2*}(\alpha, \beta, \gamma) \tag{6}$$

where α, β, and γ are the Euler angles (defined as in Zannoni[5]) describing the orientation of $\boldsymbol{B}_0$ in the director frame, and $D_{0,n}^{2*}(\alpha, \beta, \gamma)$ is an element of a second-rank Wigner rotation matrix. The angle α is redundant when $m = 0$, and in this case the Wigner functions can be replaced by spherical harmonics $Y_{2,n}(\beta, \gamma)$, so that

$$T_\lambda^{(2,0)} = (4\pi/5)^{1/2} \sum_n T_{\lambda\mathrm{d}}^{(2,n)}\, Y_{2,n}(\beta, \gamma) \tag{7}$$

or, in a slightly more compact form, by modified spherical harmonics $C_{2,n}(\beta, \gamma)$:

$$T_\lambda^{(2,0)} = \sum_n T_{\lambda\mathrm{d}}^{(2,n)}\, C_{2,n}(\beta, \gamma) \tag{8}$$

The angles β and γ are shown in Figure 3.

Choosing the director frame X, Y, Z to be the principal frame for $T_{\lambda\mathrm{d}}$, then n is restricted to being 0 or ± 2, and it is possible, at least in principle, to obtain both $T_{\lambda\mathrm{d}}^{(2,0)}$ $(= \sqrt{\frac{2}{3}} T_{ZZ})$, and $T_{\lambda\mathrm{d}}^{(2,2)} + T_{\lambda\mathrm{d}}^{(2,-2)}$ $(= T_{XX} - T_{YY})$.

If the liquid crystalline phase has uniaxial symmetry about the directors, then $n = 0$, and equation (7) becomes

$$T_\lambda^{(2,0)} = \tfrac{1}{2}(3\cos^2\beta - 1)\, T_{\lambda\mathrm{d}}^{(2,0)} \tag{9}$$

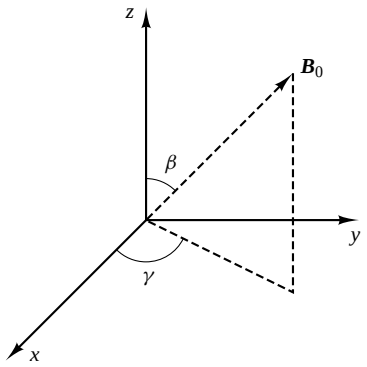

Figure 3 The orientation of $\boldsymbol{B}_0$ in the director frame XYZ

4 RELATIONSHIP BETWEEN $T_{\lambda\mathrm{d}}^{(L,n)}$ AND COMPONENTS OF THE SAME INTERACTIONS IN A MOLECULAR FRAME $T_{\lambda\mathrm{mol}}^{(L,m)}$

If the phase is biaxial it may be possible to obtain both $T_{\lambda\mathrm{d}}^{(L,0)}$ and $T_{\lambda\mathrm{d}}^{(L,\pm 2)}$, and these are related to $T_{\lambda,\mathrm{mol}}^{(L,m)}$ by

$$T_{\lambda\mathrm{d}}^{(L,m)} = \sum_{m=-2}^{2} T_{\lambda,\mathrm{mol}}^{(L,m)}\, \langle D_{m,n}^{2*} \rangle \tag{10}$$

where $\langle D_{m,n}^{2*} \rangle$ is the average over all molecules of $D_{m,n}^{2*}$ (α, β, γ), a Wigner function describing the rotation of the molecular frame into the director frame. These averages are known as *molecular order parameters*.

4.1 Molecular Order Parameters in Different Notations

A confusing aspect of the literature on the NMR of liquid crystalline samples is the alternative ways of denoting molecular order parameters. The $\langle D_{m,n}^{2*} \rangle$ is appropriate for all phase and molecular symmetries, and should be used when the phase symmetry is less than $D_{\infty h}$.

Motional constants are averages of spherical harmonics $\langle Y_{2,m}{}^* \rangle$, and are useful when there is cylindrical symmetry about the directors, and similarly in this case it is appropriate to use averages of modified spherical harmonics $\langle C_{2,m}{}^* \rangle$.

Saupe order parameters are used the most frequently, and are appropriate for uniaxial phases. They are averages of the transformation matrix elements expressed in a Cartesian molecular frame:

$$S_{\alpha\beta} = \langle (3\cos\theta_\alpha \cos\theta_\beta - \delta_{\alpha\beta})/2 \rangle \tag{11}$$

where α and β are Cartesian axes, and $\delta_{\alpha\beta}$ is 1 if $\alpha = \beta$ and zero otherwise. If a molecule is rigid and has cylindrical symmetry, then S_{zz} is the only nonzero order parameter, where z is the symmetry axis. In this case S_{zz} is often referred to as P_2.

The relationship between these order parameters is given in Table 1.

Table 1 Relationship Between Molecular Order Parameters as Averages of Wigner Functions $\langle D^2_{m,n}\rangle$, Cartesian Functions (Saupe Order Matrix $S_{\alpha\beta}$), Modified Spherical Harmonics $\langle C_{2,m}\rangle$, and Spherical Harmonics (Motional Constants C)

$S_{\alpha\beta}$	$\langle D^2_{m,n}\rangle$	$\langle C_{2,m}\rangle$	Motional constant
S_{zz}	$\langle D^2{}_{0,0}\rangle$	$\langle C_{2,0}\rangle$	$\sqrt{(1/5)}C_{3z^2-r^2}$
$S_{xx} - S_{yy}$	$\sqrt{(3/2)}[\langle D^2_{0,2}\rangle + \langle D^2_{0,-2}\rangle]$	$\sqrt{(3/2)}[\langle C_{2,2} + \langle C_{2,-2}\rangle]$	$\sqrt{(3/5)}C_{x^2-y^2}$
S_{xy}	$\mathrm{i}\sqrt{(3/8)}[\langle D^2_{0,2}\rangle - \langle D^2_{2,-2}\rangle]$	$\mathrm{i}\sqrt{(3/8)}[\langle C_{2,0}\rangle - \langle C_{2,-2}\rangle]$	$\sqrt{(3/5)}C_{xy}$
S_{xz}	$-\sqrt{(3/8)}[\langle D^2_{0,-1}\rangle + \langle D^2_{0,1}\rangle]$	$\sqrt{(3/8)}[\langle C_{2,-1}\rangle + \langle C_{2,1}\rangle]$	$\sqrt{(3/5)}C_{xz}$
S_{yz}	$\mathrm{i}\sqrt{(3/8)}[\langle D^2_{0,1}\rangle - \langle D^2_{0,-1}\rangle]$	$\mathrm{i}\sqrt{(3/8)}[\langle C_{2,1}\rangle - \langle C_{2,-1}\rangle]$	$\sqrt{(3/5)}C_{yz}$

4.2 Relationship Between Order Parameters and Molecular Orientation

The $\langle D^{2*}_{m,n}\rangle$ are related to, but are not a complete description of, the orientational order of the molecules in a liquid crystalline phase. Consider a molecule of general shape, and which may also have internal motional freedom. Fixing axes in a rigid part of the molecule, then the singlet orientational distribution function, $f(\alpha, \beta, \gamma)$, is defined as the probability that the director frame is at an orientation between α, β, γ and $\alpha + \mathrm{d}\alpha$, $\beta + \mathrm{d}\beta$, $\gamma + \mathrm{d}\gamma$. This is the generalization of the function $f(\beta)$, whose shape is shown in Figure 1, and which was introduced for the special case of a cylindrically symmetric molecule in a uniaxial phase.

The Wigner functions $D^L_{k,p}(\alpha, \beta, \gamma)$ form a complete, orthogonal set, and so $f(\alpha, \beta, \gamma)$ is conveniently expressed as

$$f(\alpha, \beta, \gamma) = \sum_{L,\text{even}}^{\infty} \sum_{k=-L}^{L} \sum_{p=-L}^{L} f_{L\,k\,p} D^L_{k,p}(\alpha, \beta, \gamma) \quad (12)$$

with the expansion coefficients $f_{L\,k\,p}$ given by:

$$f_{L\,k\,p} = [(2L+1)/8\pi^2]\langle D^{L*}_{k,p}\rangle \quad (13)$$

Thus, the second-rank order parameters which appear in equation (10) are only a small subset of the infinite set required to characterize $f(\alpha, \beta, \gamma)$. Nonetheless, they form the largest set of order parameters which are obtained easily from experimental data, and they are the principal data used to test theoretical models for $f(\alpha, \beta, \gamma)$.

4.3 Second-Rank Order Parameters and Phase and Molecular Symmetry

Most liquid crystal phases have either $D_{\infty h}$ symmetry about the directors, and are described as being uniaxial, or D_{2h} symmetry, and are biaxial phases. All symmetries are possible for the molecules in these phases. Mesogenic (a term used to describe a molecule which may form an ordered phase) molecules in liquid crystalline phases are invariably flexible to some extent, because of bond rotational motion. It is important to note the effect that this flexibility has on symmetries. Phase symmetry is unaffected by the flexibility, but for molecules the internal motion introduces additional complexity to the relationship between spectral and molecular properties. This is dealt with in detail elsewhere (see ***Liquid Crystalline Samples: Structure of Nonrigid Molecules***), but it should be noted that flexibility does not lead to any simplifications regarding molecular symmetry. In particular, it is not permissible to invoke a time-averaged structure with a higher symmetry than the individual conformations that the molecule can adopt. Unfortunately this is not always recognized. *Local order matrices*, which are for axes fixed in a rigid subunit of a molecule, are simplified by internal motion. For example, for axes fixed in the fragment 1, the local order matrix has three independent, nonzero elements S_{zz}, $S_{xx} - S_{yy}$, and S_{xz} if the A and B groups are stationary and in the xz plane. Rotation of only one of the groups A or B does not produce any simplification in S, but uncorrelated rotation of both groups through angles ϕ_1 and ϕ_2, each with potentials which have at least twofold symmetry, renders S_{xz} zero.

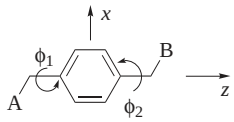

(1)

Molecular flexibility can lead to an increase in spin permutation symmetry, and hence to simpler spectra. The simplifications are similar to those produced for isotropic liquid samples, but not identically so. These aspects are discussed by Emsley and Lindon.[3]

In interpreting the spectral parameters obtained from the analysis of the spectrum it is necessary to consider four different cases. The discussion here is confined to the case of rigid molecules, and rigid fragments of flexible molecules.

4.3.1 A Biaxial Molecule in a Biaxial Phase

A biaxial molecule has a point group symmetry lower than C_3. All the terms in equation (10) are nonzero. However, choosing the reference frame on the director to be a principal frame then n is 0 or ± 2. Similarly, if the molecular frame can be chosen to be a principal frame for the interaction tensor, or for the order matrix in the case of a rigid molecule or rigid molecular fragment, then m is again restricted to 0 and ± 2.

4.3.2 A Uniaxial Molecule in a Biaxial Phase

For molecules which have C_3 symmetry or higher, m must be zero and equation (10) becomes

$$T^{(L,n)}_{\lambda\mathrm{d}} = T^{(2,0)}_{\lambda,\mathrm{mol}} \langle D^{2*}_{0,n}\rangle \quad (14)$$

A reference frame fixed on the director exists in which the only nonzero values of $\langle D^{2*}_{0,n}\rangle$ have $n = 0$ or ± 2. The location of this

principal director frame from the results of NMR experiments may, however, pose a problem.

4.3.3 A Biaxial Molecule in a Uniaxial Phase

Now n must be zero and

$$T_{\lambda d}^{(L,0)} = \sum_{m=-2}^{2} T_{\lambda,mol}^{(L,m)} \langle D_{m,0}^{2*} \rangle \tag{15}$$

Location of the principal axes of $\langle D_{m,0}^{2*} \rangle$ is possible if the molecule has two orthogonal planes of symmetry. If the molecule has one mirror plane only, then one axis is identified with the normal to the plane, and location of the other two axes requires the measurement of at least three, independent, averaged interactions, such as dipolar or quadrupolar splittings.

4.3.4 A Uniaxial Molecule in a Uniaxial Phase

Now both m and n must be zero, so that equation (10) becomes

$$T_{\lambda d}^{(L,0)} = T_{\lambda,mol}^{(2,0)} \langle D_{0,0}^{2*} \rangle \tag{16}$$

which can be simplified to

$$T_{\lambda d}^{(L,0)} = T_{\lambda,mol}^{(2,0)} \langle (3 \cos^2 \beta - 1)/2 \rangle \tag{17}$$

5 INDIVIDUAL CONTRIBUTIONS TO $\hat{\tilde{\mathcal{H}}}$

The discussion has so far been kept general, and the spherical tensor notation has been appropriate since this facilitates the identification of the effects of director orientation, and phase, and molecular symmetries. But it is more useful to use a Cartesian frame when considering individual contributions $\hat{\tilde{\mathcal{H}}}_\lambda$. Thus, the spin operators are best represented in terms of $\hat{I}_{zi}$ and the raising and lowering operators, $\hat{I}_{\pm i}$, where z is the direction of $\boldsymbol{B}_0$.

5.1 The Zeeman Interaction $\hat{\tilde{\mathcal{H}}}_Z$

$$\hat{\tilde{\mathcal{H}}}_Z = (B_0/2\pi) \sum_i \gamma_i \hat{I}_{zi} (1 - \tilde{\sigma}_{zzi}) \tag{18}$$

Note that we differ from Veracini[4] in that $\tilde{\sigma}_{zzi}$ is the component along $\boldsymbol{B}_0$ of the partially averaged (symbolized by tilde) total shielding tensor at the ith site. Thus,

$$\tilde{\sigma}_{zzi} = \sigma_i^{iso} + \sigma_{zzi}^{aniso} \tag{19}$$

The isotropic, scalar term ${\sigma_i}^{iso}$ contains contributions from the components $\sigma_{\alpha\beta}$ of the shielding tensor of a nucleus in an isolated molecule, and it is these which are most easily calculated by theoretical models, but there are also contributions from intermolecular effects, and from the magnetic shielding produced by the shape of the sample and the bulk magnetic susceptibility (see ***Anisotropy of Shielding and Coupling in Liquid Crystalline Solutions***).

The relationship between $\tilde{\sigma}_{zzi}$ and $\sigma_{\alpha\beta i}$, the components of the shielding tensor in a molecular frame for a uniaxial phase with the director aligned along $\boldsymbol{B}_0$, is

$$\begin{aligned} \tilde{\sigma}_{zzi} = \sigma_i^{iso} &+ \tfrac{2}{3} S_{aa} \{\sigma_{aai} - \tfrac{1}{2}(\sigma_{bbi} + \sigma_{cci})\} \\ &+ \tfrac{1}{3}(S_{bb} - S_{cc})(\sigma_{bbi} - \sigma_{cci}) \end{aligned} \tag{20}$$

The molecular axes a, b, and c are either principal axes for the order matrix $\mathbf{S}$, or for the shielding tensor σ.

5.2 The Indirect Spin–Spin Interaction $\hat{\tilde{\mathcal{H}}}_J$

$$\begin{aligned} \hat{\tilde{\mathcal{H}}}_J = \sum_{i<j} \{ & J_{ij}^{iso} [\hat{I}_{zi}\hat{I}_{zj} + + \tfrac{1}{2}(S_{bb} - S_{cc})(\hat{I}_{+i}\hat{I}_{-j} + \hat{I}_{-i}\hat{I}_{+j})] \\ & + J_{zzij}^{aniso} [\hat{I}_{zi}\hat{I}_{zj} - + \tfrac{1}{4}(S_{bb} - S_{cc})(\hat{I}_{+i}\hat{I}_{-j} + \hat{I}_{-i}\hat{I}_{+j})] \} \end{aligned} \tag{21}$$

The scalar coupling term J_{ij}^{iso} is, in principle, affected by the bulk medium, but in practice such effects are negligible for the lighter nuclei (see ***Anisotropy of Shielding and Coupling in Liquid Crystalline Solutions***), so that it is identical to the value observed for the isotropic phase of the sample.

The relationship between J_{zzij}^{anizo} and $J_{\alpha\beta ij}$, the components of the spin–spin coupling tensor in a molecular frame for a uniaxial phase with the director aligned along $\boldsymbol{B}_0$, is

$$\begin{aligned} J_{zzij}^{aniso} = &\tfrac{2}{3} S_{aa} \{J_{aaij} - \tfrac{1}{2}(J_{bbij} + J_{ccij})\} \\ &+ \tfrac{1}{3}(S_{bb} - S_{cc})(J_{bbij} - J_{ccij}) \end{aligned} \tag{22}$$

The molecular axes a, b, and c are either principal axes for the order matrix $\mathbf{S}$, or for the spin–spin coupling tensor $\boldsymbol{J}_{ij}$.

5.3 The Direct, Dipole–Dipole Interaction $\hat{\tilde{\mathcal{H}}}_D$

$$\hat{\tilde{\mathcal{H}}}_D = \sum_{i<j} 2\tilde{D}_{zzij} [\hat{I}_{zi}\hat{I}_{zj} - \tfrac{1}{4}(\hat{I}_{+i}\hat{I}_{-j} + \hat{I}_{-i}\hat{I}_{+j})] \tag{23}$$

This interaction is totally anisotropic. Note that the operators occur in an identical form to those involving J_{zzij}^{anizo} in equation (21), so that the two interactions are spectroscopically indistinguishable. This has important consequences when attempting to obtain the magnitudes of J_{zzij}^{anizo} (see ***Anisotropy of Shielding and Coupling in Liquid Crystalline Solutions***), or when using $\tilde{D}_{zzij}$ to investigate molecular structure (see ***Structure of Rigid Molecules Dissolved in Liquid Crystalline Solvents***).

The rapid translational and rotational motion of the molecules averages intermolecular contributions to $\tilde{D}_{zzij}$ to zero, in contrast to a solid sample where intermolecular terms lead to very broad resonances even in single crystal

samples. This means that the individual resonances in a liquid crystalline, dipolar coupled spectrum, such as from protons, have widths which range from being of the order of 1 Hz for small solute molecules, to about 100 Hz for the mesogenic molecules. For a totally rigid molecule in a uniaxial phase with the directors aligned along $\boldsymbol{B}_0$, the the value of $\tilde{D}_{zzij}$ is related to the magnitude of the internuclear vector $\boldsymbol{r}_{ij}$, and the angles $\theta_{ij\alpha}$ that this vector makes with molecular fixed axes by

$$\begin{aligned}\tilde{D}_{zzij} = & -(K_{ij}/r_{ij}^3)[S_{aa}(3\cos^2\theta_{ija}-1) \\ & +(S_{bb}-S_{cc})(\cos^2\theta_{ijb}-\cos^2\theta_{ijc}) \\ & +4S_{ab}\cos\theta_{ija}\cos\theta_{ijb}+4S_{ac}\cos\theta_{ija}\cos\theta_{ijc} \\ & +4S_{bc}\cos\theta_{ijb}\cos\theta_{ijc}]\end{aligned} \tag{24}$$

with

$$K_{ij} = (\mu_0/4\pi)h\gamma_i\gamma_j/8\pi^2 \tag{25}$$

The molecular axes a, b, and c are not special. The number of terms in equation (24) can be reduced if any of the principal axes of **S** can be identified from the symmetry of the molecule. The effects of small amplitude vibrational motion is discussed elsewhere in this Encyclopedia (see ***Structure of Rigid Molecules Dissolved in Liquid Crystalline Solvents***).

5.4 The Nuclear Electric Quadrupole–Electric Field Gradient Interaction $\hat{\tilde{\mathcal{H}}}_{\mathrm{Q}}$

The general case of a quadrupole interaction comparable with the Zeeman term is complex because the magnetic field direction is not a unique axis of quantization of the nuclear spin angular momentum (see ***Quadrupolar Interactions***). Most studies on liquid crystalline samples involve the much simpler case where the quadrupolar interaction is much smaller than the Zeeman term, and the Hamiltonian only for this situation is given here. In this case,

$$\hat{\tilde{\mathcal{H}}}_{\mathrm{Q}} = \sum_i \{\tilde{q}_{zzi}/[4I_i(2I_i-1)]\}[3\hat{I}_{zi}^2 - I_i(I_i+1)] \tag{26}$$

The term $\tilde{q}_{zzi}$ is given by:

$$\tilde{q}_{zzi} = (eQ_i\tilde{V}_{zzi})/h \tag{27}$$

where eQ_i is the nuclear electric quadrupole moment of nucleus i, and $\tilde{V}_{zzi}$ is the partially averaged component of the electric field gradient tensor measured at the nucleus, and in the direction of $\boldsymbol{B}_0$. Note that $\boldsymbol{q}$ is often used rather than χ to denote the quadrupole tensor, since this avoids confusion with the magnetic susceptibility tensor, which is also usually represented by χ.

The tensor $\boldsymbol{q}$ is purely anisotropic, which means that the values of $\tilde{q}_{zzi}$ are particularly useful for probing the orientational order in liquid crystalline samples.

The relationship between $\tilde{q}_{zzi}$ and $\tilde{q}_{\alpha\beta i}$, the components in a molecular frame, for an uniaxial phase with the directors aligned along $\boldsymbol{B}_0$, is

$$\tilde{q}_{zzi} = q_{aai}[S_{aa} + \tfrac{1}{3}\eta_i(S_{bb}-S_{cc})] \tag{28}$$

where $q_{zzi} > q_{bbi} > q_{cci}$, and

$$\eta_i = (q_{bbi}-q_{cci})/q_{aai} \tag{29}$$

6 RELAXATION RATES

Relaxation rates depend upon time–correlation functions $g_{mm,'\lambda\lambda'}(t)$, which depend on $\hat{\mathcal{H}}_\lambda(t)$ according to

$$g_{mm'\lambda\lambda'}(t) = \langle\hat{\mathcal{H}}_\lambda(\tau)\hat{\mathcal{H}}_{\lambda'}(t+\tau)\rangle - \delta_{mm'\lambda\lambda'}\hat{\tilde{\mathcal{H}}}_\lambda\hat{\tilde{\mathcal{H}}}_{\lambda'} \tag{30}$$

The angle brackets denote an average over both τ and the ensemble; $\delta_{mm'\lambda\lambda'}$ is zero unless $m = m'$ and $\lambda = \lambda'$. To understand what causes relaxation, and what can be learned from measuring relaxation rates, it is necessary to examine the contributions to $\hat{\mathcal{H}}(t)$, and to discuss what causes the time dependence. The discussion here will not be comprehensive, but will concentrate on the dominant relaxation mechanisms for nuclei in most liquid crystalline phases. Firstly, an overview is given of the sources of the time dependences, since it is the characterization of these that is the main aim of studies of relaxation rates. In later sections, the particular relaxation mechanisms which are usually dominant for protons, carbon-13, and deuterium are discussed, together with the form taken by their spectra.

6.1 Dynamic Processes Affecting Relaxation Rates in Liquid Crystalline Samples

The dynamic processes are discussed in order of their prevalence rather than their importance in determining the relaxation rate.

6.1.1 Whole Molecule Rotation and Translational Diffusion

Such motion is always present in a liquid. The molecules which form liquid crystalline phases are always strongly anisotropic in shape, so that their rotational motion is also strongly anisotropic. In addition, the dynamics are affected by the orientational and spatial order which is present. Thus, the effect of increasing orientational order alone is to decrease the spin–lattice relaxation rate R_1, and to increase the spin–spin relaxation rate R_2. A second consequence is that $R_1 \neq R_2$, even when motion is fast, in contrast with isotropic liquid samples.

Translational diffusion modulates intermolecular dipolar interactions, and may be an important relaxation mechanism for protons in all liquid crystalline phases. There can also be a coupling between translational and rotational motion in phases with spatial order (see ***Liquid Crystalline Samples: Relaxation Mechanisms***). Thus, in smectic, or similar amphiphilic and discotic phases, translation moves molecules between regions with different extents of rotational freedom, and in chiral phases the diffusion along the helical director configuration present in these phases induces a rotational motion of the molecules.

6.1.2 Internal Motion

All the molecules which have been found to form liquid crystalline phases have some internal rotational freedom. In

fact, most contain one or more alkyl chains, which are always conformationally mobile in liquid crystalline phases. The affect on relaxation rates has been demonstrated most convincingly using deuterium (see ***Liquid Crystalline Samples: Deuterium NMR***) and carbon-13 NMR.

The combination of the whole-molecule rotation and the internal rotational motion in any liquid phase presents a very complex dynamics problem, particularly when it is recognized that these two motions are probably strongly correlated in molecules as complex as mesogens. It is not surprising, therefore, that attempts to extract quantitative information from relaxation rates have used major simplifying assumptions in order to render the problems tractable. The most sophisticated models that have been used are those developed by Nordio and his colleagues, which take into account the continuous diffusive nature of both whole-molecule and internal bond rotational motions in the presence of an anisotropic, mean field ordering potential (see ***Liquid Crystalline Samples: Relaxation Mechanisms***). Dong and his colleagues have simplified the models by assuming a jump motion for the rotations about C–C bonds in alkyl chains, which is assumed to be independent of the whole molecule motion (see ***Liquid Crystalline Samples: Deuterium NMR***). Most investigators, however, have interpreted relaxation data, particularly those obtained from amphiphilic systems, by using much simpler models.

Investigations of the dynamics of molecules in liquid crystalline phases by computer simulations are just beginning to be practicable, and undoubtedly will play an important role both in testing existing theoretical models and in developing new ones.

6.1.3 Director Fluctuations

The orientation of the local directors $\boldsymbol{n}_i$ is time-dependent. This collective molecular motion would be quenched if a sufficiently large magnetic field were applied, but these fields are several orders of magnitude greater than those in use for NMR, so that fluctuations in the uniformly aligned samples still occurs (or indeed when either surface or electric field alignment is used).

Director fluctuations produce modulations in the components along $\boldsymbol{B}_0$ of all the anisotropic interactions contributing to the Hamiltonian, and so in principle will produce a contribution to relaxation rates. The only question is how large is this contribution compared with other relaxation mechanisms, and can its effect be separated from them? There does appear to be some confusion in the literature on the importance of director fluctuations as a relaxation mechanism, and an attempt is made here to clarify the position in the light of the available experimental evidence, and the current theories.

The characteristic signature for the effect produced by director fluctuations on relaxation rates is the frequency dependence of R_1. Thus, the value of R_1 for nuclei in an isotropic liquid sample, whose relaxation stems from rotational motion, is expected to depend approximately on ω_0^{-2}, where ω_0 is the Larmor frequency, when the rotational motion is slow, and becomes independent of frequency when the motion is fast. The simplest model[6] for R_1^{DF}, the contribution to relaxation from director fluctuations, predicts a dependence on $\omega_0^{-1/2}$. The frequency dependence of R_1 for all the protons in several liquid crystalline samples has been obtained by the field cycling technique (see ***Field Cycling Experiments***), and there is clearly a change from a region where the $\omega_0^{-1/2}$ dependence holds approximately, to one where R_1 varies as ω_0^{-2}. The region where director fluctuations dominate for protons is well below that used in conventional NMR spectrometers, but these experiments do not rule out a possible contribution to R_1 at higher Larmor frequencies, but of smaller magnitude than that from whole-molecule and internal motion. The conclusion from the field cycling data is that R_1^{DF} is of minor importance for relaxation rates for all nuclei in mesogenic molecules obtained above, say, 10 MHz. This is not to say, however, that R_1^{DF} can be always neglected at such frequencies, and it remains to be established just how large this term is for particular mesogens.

The experiments on proton relaxation in mesogens have the disadvantage that the proton spectrum cannot be resolved into peaks from individual protons, so that the value of R_1 obtained by experiment is an average for a set of strongly dipolar-coupled spins, and that proton relaxation may also be affected by a number of mechanisms in addition to director fluctuations, such as internal as well as whole-molecule rotational motion, and intermolecular contributions may also be important. This problem is removed by studying the relaxation rates of deuterons in dissolved, rigid solutes. Now, the relaxation is certainly dominated by modulation of the quadrupolar interaction, which is intramolecular and site specific. In addition, it is possible to obtain the spectral densities, $J_1(\omega_0)$ and $J_2(2\omega_0)$, rather than their sum R_1 (see ***Deuteron Relaxation Rates in Liquid Crystalline Samples: Experimental Methods***). This is a particular advantage since director fluctuations are predicted to contribute only to $J_1(\omega_0)$, and thus if this mechanism dominates then this spectral density should depend on $\omega_0^{-1/2}$, whilst $J_2(2\omega_0)$ will be frequency independent. This is indeed what is observed[7] for the deuterons in perdeuterated 1,4-diethynylbenzene dissolved in a nematic solvent, even though the measurements were made in the megahertz range, which is well above the range where director fluctuations are thought to produce a large contribution to the relaxation rates of nuclei in the solvent, mesogenic molecules.

This apparent paradox is resolved by theories of the magnitude of R_1^{DF}, which allow for a contribution which depends on both whole-molecule rotational motion and director motion. Thus, in a model introduced by Freed,[8]

$$R_1^{\mathrm{DF}} = A[U(\omega_c/\omega_0)\omega_0^{-1/2} - (\sqrt{8}/\pi)\tau_{\|}\omega_c^{1/2}] \qquad (31)$$

The molecules are assumed to be rigid and cylindrically symmetric, and $\tau_{\|}$ is a correlation time for rotation about an axis perpendicular to the cylinder axis. The value of A is dependent on the orientational order of the molecules and also on the viscosity and elastic constants of the bulk liquid crystal. The frequency ω_c is an upper limit to the director modes, and we shall return to a discussion of the value associated with it of λ_c, the shortest wavelength of the modes; $U(\omega_c/\omega_0)$ is a function whose form can be found in the original paper,[8] but which need not concern us now. First, note that the two terms in equation (31) are of opposite sign, and it is this which provides an explanation of the observation that director fluctuations can play a negligible role for the nuclear relaxation of nuclei in the solvent molecules, whilst dominating for nuclei in small solutes. This is because $\tau_{\|}$ is very short for small

molecules and the cross term is negligible, whilst for the mesogens themselves, this correlation time is orders of magnitude larger and hence the cross term is significant. Indeed, it is possible, in theory, for the two terms in equation (31) to cancel, or for the result to be negative! In consequence, relaxation of nuclei in molecules in liquid crystalline phases can be dominated by either director fluctuations, or molecular motions, or for director fluctuations to produce an attenuating effect on R_1.

Although Freed's theory provides an explanation of how director fluctuations can have a quite different effect on the relaxation rates of nuclei in solute and solvent molecules, it does so by extrapolating beyond the range of one of its basic assumptions, which is that director fluctuations are much slower than molecular rotations. Gertner and Lindenberg,[9] however, have shown that this difficulty is circumvented by using a generalized Langevin approach to solve the appropriate equations of motion. In this theory it is not necessary to assume that the motion of the molecules is much faster than that of the director, and they obtain essentially the same result as Freed.

One difficulty does remain. This concerns the values which are necessary for ω_c, which correspond to values of λ_c, since to fit the observed relaxation rates, these have to be of the order of a molecular length. This seems inconsistent with the continuum model used for the director modes, that is, it is assumed that the motion involves a sufficiently large number of molecules that the motion of individual molecules can be subsumed into a continuum. A short value for λ_c also implies that the order parameters obtained from NMR measurements, which are relative to $\boldsymbol{B}_0$ as a fixed direction, will be significantly smaller than values relative to an instantaneous director. If this is correct then there are important consequences for the interpretations of the orientational order parameters which are derived from dipolar or quadrupolar splittings.

6.1.4 Exchange Processes and Paramagnetic Impurities

The effect of exchange processes on spectra are discussed by Luz and Poupko (see ***Dynamic NMR in Liquid Crystalline Solvents***), and these processes can also contribute to relaxation rates.

Dipolar coupling to quadrupolar nuclei are also affected by the rate of spin–lattice relaxation of that nucleus.[10] The effect is identical to that in isotropic samples, so that fast relaxation of the quadrupolar nucleus can lead to line broadening or to complete decoupling of the dipolar interaction to a spin-$\frac{1}{2}$ nucleus, such as a proton or carbon-13 (see Section 8.1).

Paramagnetic impurities, such as oxygen, can increase relaxation rates significantly for protons, and perhaps carbon-13, and should be removed from the sample. They have a negligible effect for deuterium in most samples, partly because of the lower gyromagnetic ratio, but also because of the shorter relaxation times of this nucleus produced by the quadrupolar mechanism.

7 PROTON NMR OF LIQUID CRYSTALLINE SAMPLES

7.1 The Spectra of Mesogenic Molecules

The spectra are dominated by interproton dipolar couplings, which for most mesogens leads to very broad, unresolved spectra. An exception is provided by 4-methoxy-4′-cyanobiphenyl (1OCB), which is the simplest mesogen, and which does yield a well-resolved spectrum when in a supercooled nematic phase. This spectrum has proved impossible to analyze so far, but the better resolved spectrum (shown in Figure 4) of this mesogen dissolved in a nematic mixture (ZLI 1132) has been analyzed to yield 17 dipolar couplings.[11]

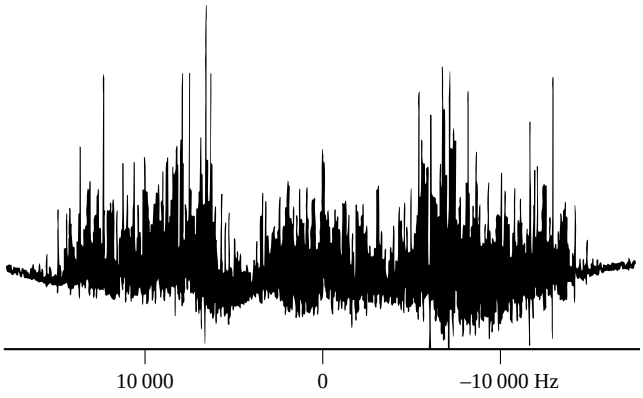

Figure 4 A 200 MHz spectrum of the protons in 4-methoxy-4′-cyanobiphenyl dissolved in the nematic phase of ZLI 1132

The analysis of such a complex spectrum is a formidable task, which was accomplished only by first analyzing the simpler, deuterium decoupled spectra from partially deuterated samples. This is a general method of simplifying complex proton spectra, which has been applied to the proton spectra of other mesogens (see ***Liquid Crystalline Samples: Spectral Analysis***).

The dipolar couplings obtained from the analysis of the proton spectrum of 1OCB were interpreted in terms of the minimum energy conformations of the molecule, the nature of the potentials governing internal bond rotations, and the orientational order. 1OCB, like all mesogens, is a flexible molecule, and an account of how to analyze such data is given elsewhere (see ***Liquid Crystalline Samples: Structure of Nonrigid Molecules***).

7.2 Proton Spectra of Solute Molecules

The proton spectra of the solute is superimposed on that of the solvent, but a separation of the two can usually be made based on the different linewidths. Thus, either convolution difference or Gaussian multiplication techniques can provide the spectrum of the solute alone. Figure 5 shows the proton spectrum of phenyl benzoate dissolved in a nematic solvent ZLI 1132, which is a mixture of three mesogenic molecules, before and after the application of Gaussian deconvolution and a baseline correction.

The maximum number of interacting protons in a molecule from which a resolved spectrum can be obtained is about 12, and this also represents the current limit on analysis. Of course, just as with mesogens, the spectra can be simplified by deuteration combined with decoupling, or multiple quantum spectroscopy, and hence more complex molecules can be studied.

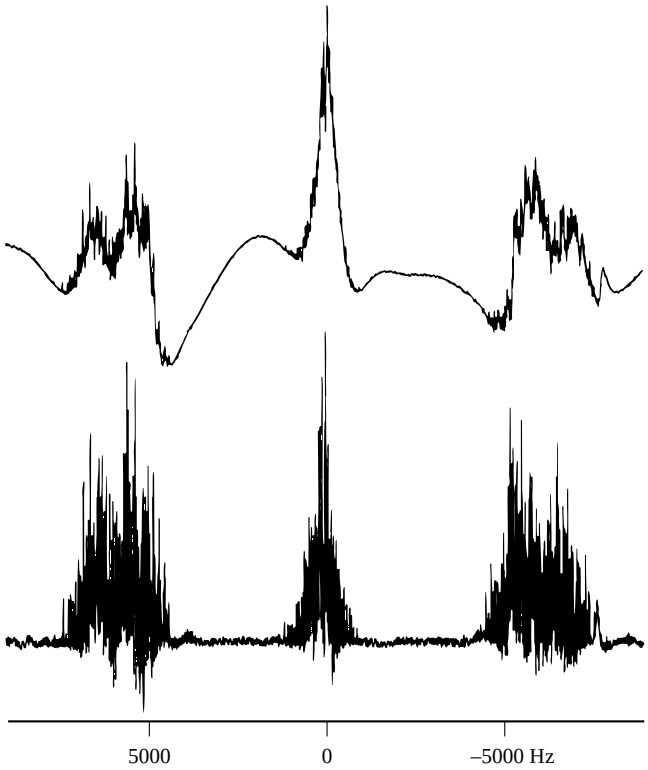

Figure 5 A 200 MHz spectra of the protons in phenyl benzoate dissolved in the nematic solvent ZLI 1132 before (top) and after (bottom) Gaussian deconvolution and baseline correction

7.3 Proton Relaxation Rates

Proton relaxation rates are similar in magnitude to those in isotropic samples of similar viscosity. As noted in Section 5.1.3, the frequency dependence of R_1 for protons in mesogens, as obtained by field cycling, have led to an understanding of the relative importance of director fluctuations as a relaxation mechanism. It is not possible, however, to obtain useful information on the dynamics of the individual molecules in liquid crystalline phases from proton relaxation, primarily because of the unresolved nature of the spectra. There would indeed be a wealth of information available from relaxation experiments on the resolved spectra that can now be easily obtained from deuterium decoupling partially deuterated samples, but no such studies have been attempted.

8 CARBON-13 NMR

8.1 Proton Decoupled Carbon-13 Spectra of Mesogenic Molecules

These are the simplest carbon-13 spectra, and have a limited information content, but they have the advantage of being very easily analyzed. The more informative local field spectra obtained with near magic angle spinning are discussed by Fung (see ***Liquid Crystalline Samples: Carbon-13 NMR***).

Decoupling the proton–carbon dipolar interactions requires more power than for isotropic samples. This can lead to a rise in temperature which is sufficient to broaden the lines, and so care must be taken in the design of the experiment. The simplest decoupling method consists in applying the proton decoupling field only when acquiring data, and in limiting this period to avoid sample heating. A delay between acquisition is introduced of about 3 s to allow the sample to cool. More efficient decoupling methods have been proposed.[12]

A case study is presented here of 4-*n*-pentyl-4′-cyanobiphenyl (5CB), which forms a nematic phase, with the aim of showing what information can be obtained from such carbon-13 spectra. Figure 6 shows proton-decoupled carbon-13 spectra of 5CB. Spectrum (a) is for the sample in the isotropic phase, and here the linewidths are limited by the probe being used (a high-power, double-tuned solenoid designed for cross-polarization studies on solid samples). Spectrum (b) is for the sample in the nematic phase, and now the lines are considerably broader, which is partly because R_2 is larger in the oriented phase, but is also probably a result of incomplete decoupling plus sample heating. Note that the presence of ^{14}N in the molecules does not lead to either resolved couplings or to line broadening.

Spectrum (b) demonstrates the basic information content of proton decoupled carbon-13 spectra. Firstly, the lines are relatively sharp, showing that the directors are aligned uniformly, in this case along $\boldsymbol{B}_0$ since the sample has a positive $\Delta\chi$. Secondly, the line positions change between the two phases. The aliphatic carbon resonances shift upfield by relatively small amounts, and come closer together, whereas the aromatic carbon resonances are all shifted downfield, and are more dispersed. Note the very large upfield shift of the nitrile carbon, which is hidden beneath the aliphatic peaks.

The shift in the line positions $\Delta\delta_i$ from isotropic to liquid crystalline phase is determined by the anisotropy in the shielding tensor $\sigma_{zzi}^{\text{aniso}}$ [see equation (19)] which, if intermolecular contributions can be neglected (see ***Anisotropy of Shielding and Coupling in Liquid Crystalline Solutions***), is related to components in a molecular frame $\sigma_{\alpha\beta i}$, and order parameters $S_{\alpha\beta}$, [see equation (20)]. The order parameters are those for axes fixed in the fragment containing nucleus i, and for a flexible molecule such as 5CB they are not order parameters for the whole molecule. To be specific, fixing axes in fragment 2, then these are principal axes for the *local* order matrix of ring 1, and

$$\Delta\delta_i = \tfrac{2}{3}S_{aa}\{\sigma_{aai} - \tfrac{1}{2}(\sigma_{bbi} + \sigma_{cci})\} + \tfrac{1}{3}(S_{bb} - S_{cc})(\sigma_{bbi} - \sigma_{cci}) \quad (32)$$

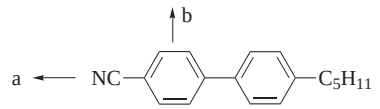

(2)

If the shielding tensor components are known, then the *local* order parameters can be obtained from the measured values of $\Delta\delta_i$. Conversely, if the local order parameters can be obtained from dipolar couplings or quadrupolar splittings, as indeed they have been[13] for 5CB, then the shielding components can be obtained. It should be noted, however, that it is

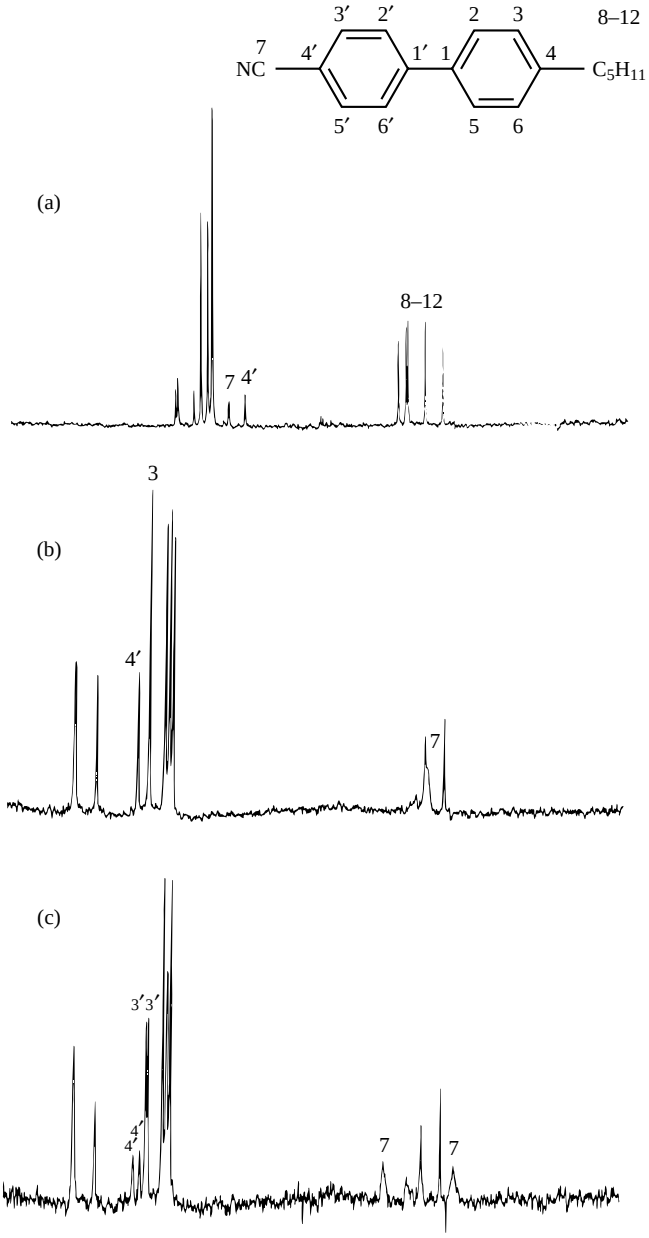

Figure 6 50 MHz proton-decoupled carbon-13 spectra of 4-*n*-pentyl-4′-cyanobiphenyl (5CB): (a) isotropic, (b) nematic, and (c) [^{15}N]5CB in the nematic phase

very difficult to measure $S_{bb} - S_{cc}$ with high precision and this, together with its small values (approximately $S_{aa}/10$), makes it impossible to separate the two terms in equation (32) experimentally. This situation occurs for most mesogenic compounds, and so it is better to approximate equation (32) as

$$\Delta\delta_i = \tfrac{2}{3} S_{aa}\{\sigma_{aai} - \tfrac{1}{2}(\sigma_{bbi} + \sigma_{cci})\} \qquad (33)$$

and to recognize that there will be a small systematic error in using this equation to obtain either S_{aa} or the molecule anisotropy $\Delta\sigma_i = \sigma_{aai} - \frac{1}{2}(\sigma_{bbi} + \sigma_{cci})$.

The values of $\Delta\delta_i$ for carbon-13 nuclei in the second ring can be used in a similar way, again to obtain S_{aa} or $\Delta\sigma_i$. The shifts for the aliphatic carbon atoms can also, in principle, be used to obtain local order parameters, or shielding tensor components. For the methyl group the rapid rotation about the C–CH_3 bond leads to

$$\Delta\delta_{CH_3} = \tfrac{2}{3} S_{CC}(\sigma_{\parallel}^{CC} - \sigma_{\perp}^{CC}) = \tfrac{2}{3} S_{CC}\Delta\sigma^{Me} \qquad (34)$$

where S_{CC} is the *local* order parameter for the C–C bond direction, and $\sigma_{\parallel}^{CC}$ and $\sigma_{\perp}^{CC}$ are components of the shielding tensors for the methyl carbon atoms parallel and perpendicular to the C–C bond direction, respectively.

The methylene carbon atoms are part of the rigid fragment 3, which has no symmetry, and therefore the location of the principal axes for the *local* order matrix is unknown. This means that the values of $\Delta\delta_i$ for methylene carbon atoms cannot be used to obtain either components of the shielding tensor elements, or the local order parameters.

(3)

Spectrum (c) in Figure 6 is of 5CB labeled with ^{15}N instead of ^{14}N, and is an example of the value of having a third, active nucleus in the molecule.[14] The carbon atoms close to the ^{15}N show doublets from ^{15}N–^{13}C dipolar plus spin–spin coupling: the splittings are $\tilde{J}_{zzij} + 2\tilde{D}_{zzij}$, and may be used[15] for this molecule to obtain local order parameters S_{aa} and $S_{bb} - S_{cc}$.

8.2 Carbon-13 Relaxation Rates

The relaxation rates R_{1i} for each resolved resonance can be obtained by the inversion–recovery experiment, and there is a clear advantage in using ^{13}C rather than ^{1}H relaxation rates to investigate the dynamics of mesogenic molecules. There have, however, been only a relatively small number of studies of ^{13}C relaxation in thermotropic liquid crystalline phases,[16–20] in part because of the difficulties in ensuring complete proton decoupling, but also because of the uncertainty in the mechanisms contributing to the values of R_{1C}. There have been more studies on amphiphilic systems,[21–23] the work prior to 1987 being summarized by Chachaty.[23]

The dominant mechanism for ^{13}C relaxation at high fields (such that director fluctuations can be ignored) is usually modulation of the ^{13}C–^{1}H dipolar interactions by whole-molecule and internal rotational motion. There may also be a contribution from modulation of the shielding anisotropy, which will increase in importance with $\boldsymbol{B}_0$.[2] Early studies by Levine et al.[21] established the importance of the bond rotational motion in alkyl chains in amphiphilic molecules, where R_{1i} decreases uniformly from carbon atoms close to the headgroup to the methyl carbon atom. A similar decrease is expected for any chain carbon atoms which are attached at one end. This, incidently, provides a method for assigning these resonances.

9 DEUTERIUM NMR

Most NMR studies on liquid crystals are of deuterium. This nucleus has advantages for studies of orientational order,

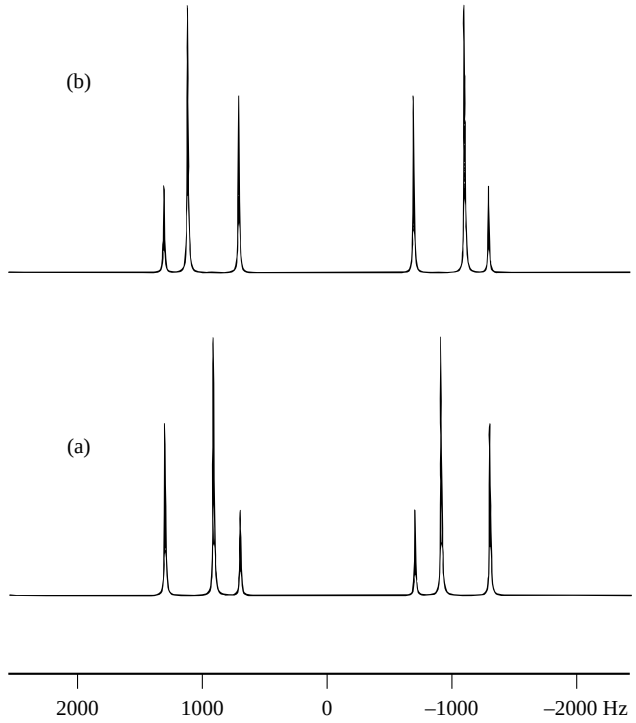

Figure 7 Simulated spectra of a pair of deuterons related by reflection symmetry (as in a CD_2 group) with $\Delta\nu/D$ (a) positive, and (b) negative

phase type, and molecular dynamics, and these outweigh the disadvantage that compounds have to be enriched with deuterium to yield observable resonances.

9.1 Deuterium Spectra

9.1.1 Deuterium Spectra of Aligned Samples

Each chemically equivalent group of deuterons gives a doublet (separation $\Delta\nu_i$) from the quadrupolar interaction, which may be split further by $^2H-^2H$ or ^2H-X dipolar couplings. The dipolar couplings are usually considerably smaller than the quadrupolar splitting $\Delta\nu_i$, so that spectra are often observed as superpositions of simple doublets. It should be noted that the splitting patterns produced by dipolar coupling D_i, between deuterons within the chemically equivalent groups can be very useful, either as sources of extra order parameters, or in giving the relative signs of $\Delta\nu_i$ and D_i. For example, Figure 7 shows the theoretical spectra for a group containing two equivalent deuterons, as in a CD_2 group, for a negative and positive value of the ratio $\Delta\nu_i/D_i$.

The spectra of CD_3 groups also depend on the sign of the ratio $\Delta\nu_i/D_i$, but now this is dependent only on the geometry of this group and not on the orientational order. The ratio is usually found[13] to lie in the range -215 ± 15.

Figure 8 shows the spectrum from the deuterons in 5CB-d_{15} in the nematic phase, and the dipolar coupling structure can be clearly seen on some of the peaks. The assignment of the lines poses a problem similar to that of $^{13}C-\{^1H\}$ spectra, but one which cannot be solved by the same methods used for isotropic samples. The only certain method of assignment of peaks of equal intensity, such as those in CD_2 groups along an

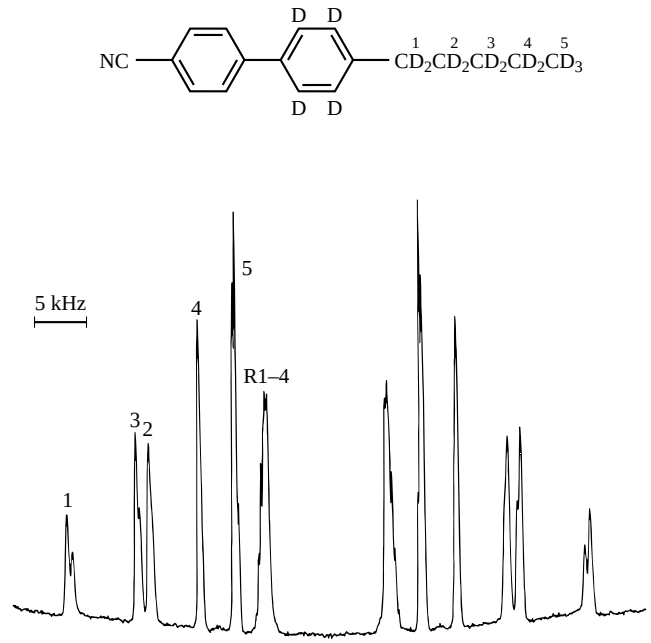

Figure 8 A 30.7 MHz spectrum of the deuterons in 5CB-d_{15} in the nematic phase. The peaks labeled 1–5 are from deuterons in the alkyl chain, 5 being the methyl group, and those labeled R1–4 are from deuterons in the alkyl substituted ring

alkyl chain, is to synthesize specifically labeled compounds. If this is not an option, the peaks from CD_2 groups in an alkyl chain can be assigned from their R_1 values, which have been found experimentally, and predicted theoretically, to decrease uniformly along the chain towards the methyl group.[24]

9.1.2 Deuterium Spectra of Unaligned Samples

A sample in which all orientations of the director with respect to $\boldsymbol{B}_0$ are equally probable gives the same lineshape as that for a polycrystalline solid sample (see Figure 2), the difference between the two cases being that the liquid crystalline powder spectrum is reduced in width. The separations of the outer edges and inner horns for a uniaxial phase are

$$\Delta\nu_{\text{outer}} = \tfrac{3}{2}q_{aa}\{S_{aa} + \eta(S_{bb} - S_{cc})\} \tag{35}$$

$$\Delta\nu_{\text{inner}} = -\tfrac{1}{2}\Delta\nu_{\text{outer}} \tag{36}$$

Here a, b, and c, are axes fixed in the rigid fragment containing the deuteron, and they are principal axes either for $\boldsymbol{q}_i$ or $\mathbf{S}^i$. Choosing them to be principal axes for $\boldsymbol{q}_i$, then they are such that $q_{aa} > q_{bb} > q_{cc}$, so that

$$\eta = (q_{bb} - q_{cc})/q_{aa} \tag{37}$$

is positive.

For deuterons in C–D bonds, a lies approximately along the bond direction, and η is usually <0.1. The effect of η on a powder spectrum is to introduce shoulders on the inner horns.

Figure 9 shows an example of the ^2H spectrum of potassium stearate-d_{35} in an unaligned sample of a lamellar

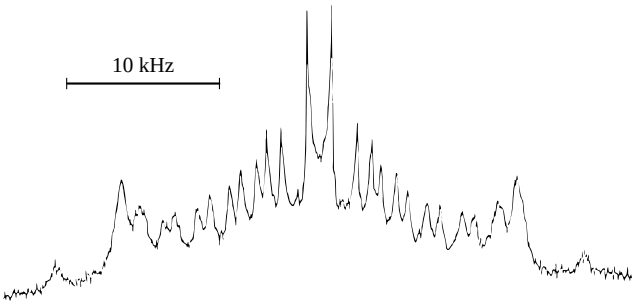

Figure 9 Deuterium spectrum of potassium stearate-d_{35} dissolved in the lamellar phase of a potassium oleate–water system[25]

phase. All 35 protons are replaced by deuterons, giving 17 overlapping powder patterns. Extracting order parameters from such a spectrum requires identifying the inner horns from each powder pattern, and this was indeed achieved for this spectrum.[25] An elegant method of deconvoluting such spectra into the separate powder patterns has been proposed by Bloom et al.,[26] and is referred to as 'de-Paking'.

Deuterium powder patterns from liquid crystalline samples are particularly useful for detecting the biaxiality of the phase. This is discussed in detail by Doane[27] for biaxial lyotropics, smectics, cholesterics (chiral nematics), and blue phases. Luz et al.[28] discuss the deuterium spectra of discotic phases, including biaxial phases.

9.2 Relaxation Rates of Deuterons

Deuterium is, without question, the nucleus of choice for studying relaxation, and hence the dynamics of molecules in liquid crystalline phases. A wealth of experimental data may be obtained, particularly for aligned samples. In this case, the spectral densities $J_1(\omega_0)$ and $J_2(2\omega_0)$ are easily obtained for each group of deuterons, giving resolved quadrupolar splittings (see ***Deuteron Relaxation Rates in Liquid Crystalline Samples: Experimental Methods***). Even more spectral densities can be obtained if the sample can be studied with different orientations Ω of the magnetic field with respect to the director. Thus,

$$J_n(n\omega_0, \Omega) = \sum_p (D^2_{p,n}(\Omega))^2 J_p(p\omega_0) \qquad (38)$$

For a uniaxial phase it is possible, in principle, to obtain $J_1(0)$, $J_1(\omega_0)$, $J_1(2\omega_0)$, $J_2(0)$, $J_2(\omega_0)$ and $J_2(2\omega_0)$ from the angular dependences of $J_1(\omega_0)$ and $J_2(2\omega_0)$.

Deuterium relaxation rates are also dominated by one mechanism, i.e. the modulation of the quadrupolar interaction. The important sources of this modulation are whole molecule rotations, and for flexible molecules, internal bond rotations. Director fluctuations are probably important only at frequencies well below those used in NMR spectrometers (see ***Liquid Crystalline Samples: Deuterium NMR***).

10 RELATED ARTICLES

Amphiphilic Liquid Crystalline Samples: Nuclear Spin Relaxation; Anisotropy of Shielding and Coupling in Liquid Crystalline Solutions; Dynamic NMR in Liquid Crystalline Solvents; Liquid Crystalline Samples: Carbon-13 NMR; Liquid Crystalline Samples: Deuterium NMR; Liquid Crystalline Samples: Diffusion; Liquid Crystalline Samples: Relaxation Mechanisms; Liquid Crystalline Samples: Spectral Analysis; Liquid Crystalline Samples: Structure of Nonrigid Molecules; Lyotropic Liquid Crystalline Samples; Polymer Dispersed Liquid Crystals; Structure of Rigid Molecules Dissolved in Liquid Crystalline Solvents; Two-Dimensional NMR of Molecules Oriented in Liquid Crystalline Phases.

11 REFERENCES

1. J. W. Emsley (ed.), *NMR of Liquid Crystals*, Reidel, Dordrecht, 1985.
2. R. Y. Dong, *Nuclear Magnetic Resonance of Liquid Crystals*, Springer, New York, 1994.
3. J. W. Emsley and J. C. Lindon, *NMR Spectroscopy Using Liquid Crystal Solvents*, Pergamon, Oxford, 1975.
4. C. A. Veracini, in *NMR of Liquid Crystals*, ed. J. W. Emsley, Reidel, Dordrecht, 1985, chap. 5
5. C. Zannoni, in *NMR of Liquid Crystals*, ed. J. W. Emsley, Reidel, Dordrecht, 1985, p. 25.
6. P. Pincus, *Solid State Commun.*, 1969, **7**, 415.
7. W. H. Dickerson, R. R. Vold, and R. L. Vold, *J. Phys. Chem.*, 1983, **87**, 166.
8. J. H. Freed, *J. Chem. Phys.*, 1977, **66**, 4183.
9. B. J. Gertner and K. Lindenberg, *J. Chem. Phys.*, 1991, **94**, 5143.
10. D. Imbardelli, G. Chidichimo, and M. Longeri, *Chem. Phys. Lett.*, 1987, **135**, 319.
11. J. W. Emsley, G. Celebre, G. De Luca, M. Longeri, and F. Lucchesini, *Liquid Cryst.*, 1994, **16**, 1037.
12. K. V. Schenker, D. Suter, and A. Pines, *J. Magn. Reson.*, 1987, **73**, 99.
13. J. W. Emsley, G. R. Luckhurst, and C. P. Stockley, *Mol. Phys.*, 1981, **44**, 565.
14. A. Hohener, L. Muller, and R. R. Ernst, *Mol. Phys.*, 1979, **38**, 909.
15. J. W. Emsley, in *NMR of Liquid Crystals*, ed. J. W. Emsley, Reidel, Dordrecht, 1985, p. 408.
16. M. Schwartz, P. E. Fagerness, C. H. Wang, and D. M. Grant, *J. Chem. Phys.*, 1974, **60**, 5066.
17. H. M. Hutton, E. Bock, E. Tomchuck, and R. Y. Dong, *J. Chem. Phys.*, 1978, **68**, 940.
18. S. Ochiai, K. Iimura, M. Takeda, M. Ohuchi, and K. Matsushita, *Mol. Cryst. Liquid Cryst.*, 1981, **78**, 227.
19. J. S. Lewis, E. Tomchuck, H. M. Hutton, and E. Bock, *J. Chem. Phys.*, 1983, **78**, 632.
20. J. S. Lewis, J. Peeling, E. Tomchuk, W. Danchura, J. Bozek, and H. M. Hutton, *Mol. Cryst. Liquid Cryst.*, 1987, **144**, 57.
21. Y. K. Levine, P. Partington, and G. C. K. Roberts, *Mol. Phys.*, 1973, **25**, 497.
22. C. Chachaty and T. Bredel, *J. Chem. Soc., Faraday Trans.*, 1992, **88**, 1893.
23. C. Chachaty, *Prog. NMR Spectrosc.*, 1987, **19**, 183.
24. J. W. Emsley, E. K. Foord, P. J. F. Gandy, D. L. Turner, and H. Zimmermann, *Liquid Cryst.*, 1994, **17**, 303.
25. N. Boden and S. A. Jones, in *NMR of Liquid Crystals*, ed. J. W. Emsley, Reidel, Dordrecht, 1985, p. 501.
26. M. Bloom, J. H. Davis, and A. L. Mackay, *Chem. Phys. Lett.*, 1981, **80**, 198.

27. J. W. Doane, in *NMR of Liquid Crystals*, ed. J. W. Emsley, Reidel, Dordrecht, 1985, pp. 413–448.
28. Z. Luz, D. Goldfarb, and H. Zimmermann, in *NMR of Liquid Crystals*, ed. J. W. Emsley, Reidel, Dordrecht, p. 343.

Biographical Sketch

James W. Emsley. *b* 1934. B.Sc., 1956, Ph.D., 1960, University of Leeds (supervised by J. A. S. Smith). ICI Research Fellow, University of Liverpool, 1960–62; Research assistant and then lecturer, University of Durham, 1962–67. Since 1967 at Department of Chemistry, University of Southampton, currently as a professor. Research interests center on NMR of liquid crystalline samples. Editor of Progress in NMR Spectroscopy with Jim Feeney; about 150 scientific publications.

Liquid Crystals: Mixed Magnetic Susceptibility Solvents

C. L. Khetrapal

Indian Institute of Science, Bangalore, India

1	Introduction	1
2	Experimental Techniques	1
3	Theoretical Interpretation	1
4	Applications	3
5	Conclusions	5
6	References	5

1 INTRODUCTION

NMR spectra of oriented molecules are extremely rich in their information content, but they become rapidly more complex as the number of interacting nuclei increases. The spectra are, in general, invariably 'strongly' coupled. This is particularly the case for spectra in thermotropic liquid crystals, unless heteronuclei are involved. On the other hand, in heteronuclear cases, it is not possible to determine the direct dipolar and the indirect spin–spin couplings individually from such spectra. Such difficulties lead to major obstacles in the routine applications of this technique to complex and heteronuclear systems. In order to enhance the scope of the technique, these problems have attracted the attention of several workers ever since the potential of the technique in the study of molecular structure and function was realized. The employment of specifically deuterated compounds with deuterium decoupling;[1,2] deuteron NMR spectroscopy in perdeuterated samples;[3] multiple quantum spectroscopy;[4] two-dimensional NMR[5] including the state correlated technique;[6] solvents with low order parameters;[7] electric[8] and magnetic[9] fields for orienting the molecules; and mixed liquid crystals of opposite diamagnetic anisotropy, are some of the steps in this direction.[10,11] This article describes the developments, progress, scope, limitations and novel applications of the NMR spectroscopy of systems oriented in mixed liquid crystals of opposite diamagnetic anisotropies ($\Delta\chi$).

2 EXPERIMENTAL TECHNIQUES

It has been observed[10,11] that the direct dipole–dipole coupling constants (D_{ij}) between two interacting nuclei i and j of the solute molecules dissolved in a mixture of two nematic liquid crystals with opposite $\Delta\chi$ values vary gradually as the relative concentrations of the two solvents are changed. When a critical point is reached, the D_{ij} values change abruptly either to twice or to half the particular value, with opposite sign, depending upon the direction of approach of the critical concentration. Beyond this point, they revert to a gradual variation. A typical plot of the proton–proton dipolar coupling [D(H,H)] in acetonitrile and the dipolar coupling between the *ortho* protons (D_{ortho}) of benzene as a function of the concentration of *N*-(*p*′-ethoxybenzylidene)-*p*-*n*-butylaniline (EBBA) ($\Delta\chi > 0$) and ZLI 1167 (Merck; an eutectic mixture of three *p*-cyano-*p*′-alkylcyclohexylcyclohexanes with propyl, pentyl and heptyl as the alkyl groups) ($\Delta\chi < 0$) is shown in Figure 1.

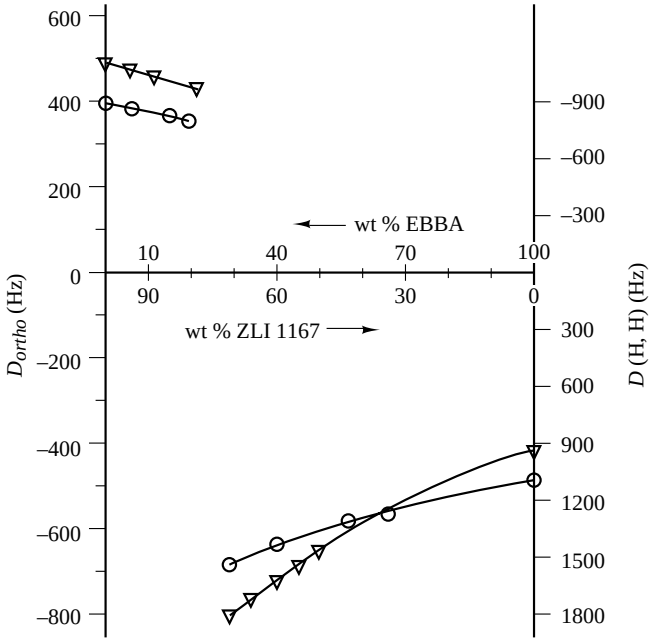

Figure 1 Dipolar couplings between methyl protons, D(H,H), in acetonitrile (○) and those between *ortho* protons (D_{ortho}) in benzene (▽) as a function of the relative concentrations of EBBA and ZLI 1167 at 270 MHz. Temperature 22°C; solute concentration 3.3 wt %

Around the critical concentration the abrupt variation in the dipolar coupling can also be obtained by changing the temperature. In fact, at the critical concentration and temperature, the observed spectrum consists of a superposition of two spectra, the dipolar couplings of one spectrum being twice those of the other, and of the opposite sign. The two spectra correspond to two different orientations of the two types of solvent. The orientation corresponding to that of the liquid crystal with $\Delta\chi > 0$ is such that the liquid crystal director is oriented parallel to the direction of the magnetic field, and in the solvent with $\Delta\chi < 0$ the director is oriented perpendicular to the magnetic field. The proton NMR spectra of acetonitrile above, below and at the critical temperature and for a given concentration are shown in Figure 2. At 21 °C two spectra are observed simultaneously.

The results can be understood in terms of the switching of the liquid crystal director by 90° at the critical point. The spectra, at temperatures and concentrations just above and just below the critical levels, result from the orientations corresponding to the solvents of positive and negative diamagnetic anisotropies. At the critical concentration and temperature where the orienting influences of both solvents are comparable, the spectra from both orientations coexist. This phenomenon has led to some new applications, which are described below.

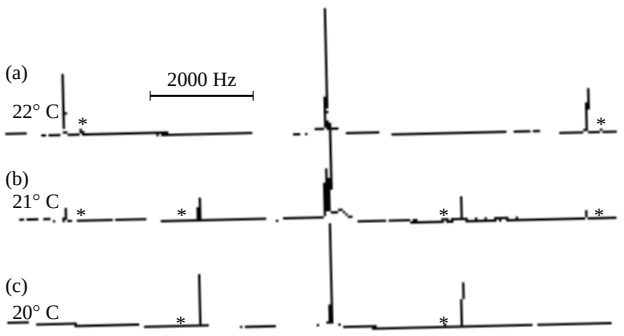

Figure 2 Proton NMR spectra of acetonitrile oriented in the nematic phase of a mixture of EBBA and ZLI 1167. Solute concentration: 3.3 wt % in 77.57% ZLI 1167 and 22.43% EBBA at different temperatures. The lines marked with an asterisk arise from traces of water in the solution. (a) 'Parallel', (b) 'coexisting', and (c) 'perpendicular' orientations

3 THEORETICAL INTERPRETATION

Mean field[12] and Landau-type theories[13–16] have been used to interpret the above-described behavior of the dipolar couplings. The theories provide good agreement for the dipolar couplings in various systems and explain the switching transition at a critical concentration and temperature and the coexistence of the two orientations.

The free energy function $F(S_\parallel, S_\perp, T)$ of the system has been expanded in terms of powers of the order parameters $S_\parallel$ and $S_\perp$:

$$F = F_0 - a(1 - X_1)S_\parallel^2 + bS_\parallel^4 - A(1 - X_2)S_\perp^2 + BS_\perp^4 + C_1\langle S_\perp^2\rangle S_\parallel^2 + C_2\langle S_\parallel^2\rangle S_\perp^2 \quad (1)$$

where X_p defines the concentration ratio of component p and is given by $X_p = \alpha_p/\alpha_{cp}$ such that α_p denotes the concentration of p and α_{cp} defines its value at the critical point. Minimization of the free energy function with respect to $S_\parallel$ or $S_\perp$ gives the following condition for the parallel- and perpendicular-orientation dominated regions, respectively:

$$S_\parallel^0 = -\left[\frac{a(1 - X_1) - C_1\langle S_\perp^2\rangle}{2b}\right]^{\frac{1}{2}} \quad (2)$$

$$S_\perp^0 = -\left[\frac{A(1 - X_2) - C_2\langle S_\parallel^2\rangle}{2B}\right]^{\frac{1}{2}} \quad (3)$$

It has been shown that the order parameter in the parallel-orientation dominated region is

$$\frac{\frac{1}{2} - 6(b/k_BT)(S_\parallel^0)^2\left[\frac{9}{28} + \left(\frac{S_\parallel^0 + \frac{1}{2}}{3}\right)^2 - \frac{3}{5}\left(S_\parallel^0 + \frac{1}{2}\right)\right]}{1 - 4(b/k_BT)(S_\parallel^0)^2\left[\frac{9}{20} + \left(S_\parallel^0 + \frac{1}{2}\right)^2 - \left(S_\parallel^0 + \frac{1}{2}\right)\right]} - \frac{1}{2} \quad (4)$$

where k_B is the Boltzmann constant and the value of $C_1 \cdot \langle S_\perp^2\rangle$ has been chosen as

$$C_1\langle S_\perp^2\rangle = C_1X_1h(1 - X_1) \quad (5)$$

where $h(1 - X_1)$ is a step function and is zero for a negative value of the argument and unity for positive values. An expression similar to equation (4) has been obtained for the perpendicular-orientation dominated regions by replacing b and $S_\parallel^0$ by B and $S_\perp^0$, respectively. The value of $C_2\langle {S_\parallel}^2\rangle$ has been chosen as in equation (5) as follows:

$$C_2S_\parallel^2 = C_2X_2h(1 - X_2) \quad (6)$$

It should be noted that, at the point of transition, the order parameter given by equation (4) and the corresponding equation for the perpendicular-orientation dominated region vanish. This implies the coexistence of the two types of orientation.

In order to compare the theoretical and the experimental findings, dipolar couplings have been used to obtain the order parameters. The order parameters were then normalized by dividing them by the largest value in each region. The coefficients to be determined are a, b, A, B, C_1, and C_2; these were estimated according to their agreement with the normalized data. The graphs obtained using these parameters derived via theoretical considerations are given in Figure 3 together with experimental data points. The agreement is very good. It shows the correct trend and switching of the order parameters near the critical concentration. It is also worth emphasizing that the parameters $(a/2b)$, (b/k_BT), $(C_1/2b)$, $(A/2B)$, (B/k_BT) and $(C_2/2B)$ were found to be almost

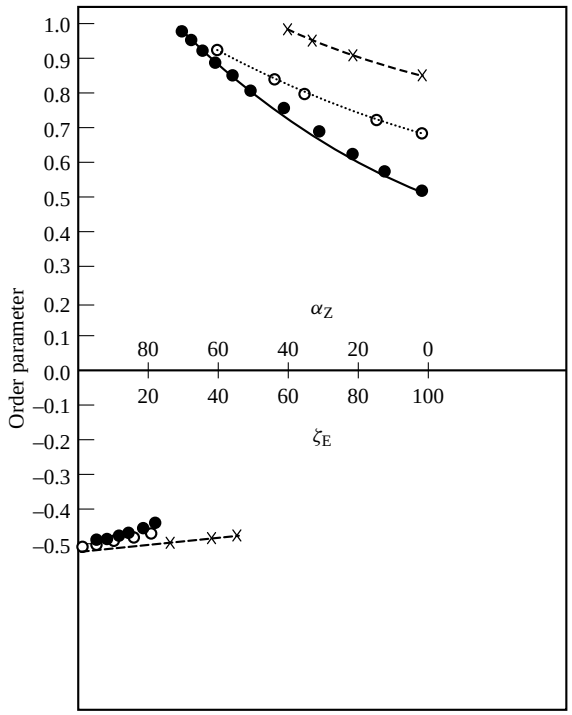

Figure 3 Calculated and experimental plots of the order parameters as a function of the relative concentrations of the liquid crystal solvents. α_E and α_Z refer to the relative concentrations of the solvents: benzene in ZLI 1167 + EBBA (•, experimental points; —, theoretical curve); acetonitrile in ZLI 1167 + EBBA (○ experimental points; ....., theoretical curve); acetonitrile in ZLI 1167 + S-1114 (×, experimental points; ----, theoretical curve)

independent of the particular solvent or the solute molecules. Similar results are shown for the switching transition observed (near the critical concentration) as a function of temperature.

Attempts have also been made to determine experimentally the exact origin of these results. The appearance of a 'powder pattern' at the critical point has been demonstrated[17] from the spectrum of 1,3,5-trichlorobenzene in a critical mixture of two nematic liquid crystals of opposite diamagnetic anisotropies. Other comments on the experimental verification of such effects have also been made.[16] In spite of these difficulties, the experiments lead to several novel applications of NMR spectroscopy of oriented molecules; these are described in the following section.

4 APPLICATIONS

The study of NMR spectra at the 'coexistence point' has led to the following novel applications:

1. separate determination of the indirect spin–spin (J_{AX}) and the direct dipolar couplings (D_{AX}) between heteronuclei;
2. determination of the chemical shift anisotropy ($\Delta\sigma$);
3. determination of the diamagnetic susceptibility anisotropy ($\Delta\chi$) of liquid crystals;
4. precise determination of spectral parameters;
5. assignments of spectral lines in the ^{13}C spectra of liquid crystals;
6. study of the dynamics of the liquid crystal director;
7. study of the orientation and distortions in tetrahedral and spherical molecules.

4.1 Determination of Indirect Couplings Between Heteronuclei (J_{AX})

When A and X are heteronuclei, NMR spectra of oriented molecules provide the sum (J_{AX} + $2D_{AX}$) instead of the individual coupling constants. Therefore, to obtain correct values of D_{AX}, the values of J_{AX} must be known. As J_{AX} may be solvent and temperature dependent, especially when heavier nuclei are involved, it is worth obtaining values in the nematic phase itself without changing the experimental conditions. These values may be obtained from the spectra at the 'coexistence point'. The parameters (J_{AX} + $2D_{AX}$) and (J_{AX} − D_{AX}) can thus be obtained, where D_{AX} is the dipolar coupling for the orientation corresponding to that for the parallel orientation. The values of J_{AX} and D_{AX} can then be determined.

The first demonstration of this particular application was for acetonitrile. The values of the various heteronuclear indirect spin–spin couplings thus obtained were found to agree well with those reported from studies in the isotropic media.[11]

No values for the indirect selenium–proton couplings in phenylselenyl halides (chloride and bromide) have been reported. The proton spectra of the isotropic media contain ^{77}Se satellites. These small satellite lines are masked by the huge proton lines arising from species having a much greater abundance of the nonmagnetic selenium isotopes, and thus the selenium–proton couplings cannot be easily determined. However, the values have been determined from the spectra of the phenylselenyl halides in a mixture of ZLI 1167 and Merck Phase IV at the 'coexistence point'.[18,19] In addition to determining the vibrationally corrected r_α structure, the chemical shift anisotropy, and the sign and magnitude of the indirect P–H coupling in methyldichlorophosphine, the authors interpreted the abnormal orientation of the molecule in terms of the formation of a solvent–solute complex.[20] Typical spectra are shown in Figure 4.

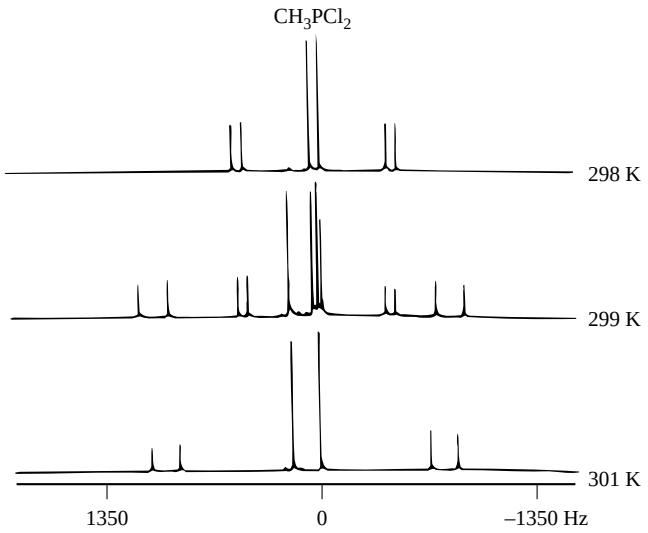

Figure 4 Proton NMR spectra of a 7 wt% solution of CH_3PCl_2 oriented in 1:1 wt % solution of S-1114 and ZLI 1167 at 270 MHz

4.2 Determination of Chemical Shift Anisotropy $\Delta\sigma$

Various methods are available for determining $\Delta\sigma$ from NMR spectra of oriented molecules. Most of these methods suffer from drawbacks arising from changes in the experimental conditions, such as temperature and concentration, and the use of external or internal references. All these factors lead to uncertainties in the values of $\Delta\sigma$ determined. An interesting comparison has been made of the values of the chemical shift anisotropies determined using the various methods.[21] It is observed that the uncertainties, particularly those in the proton chemical shift anisotropies, may sometimes be larger than the magnitudes of $\Delta\sigma$. However, when the spectra recorded at the 'coexistence point' are used, $\Delta\sigma$ can be obtained without changing the experimental conditions and also in the absence of a reference compound. This approach provides very consistent results for $\Delta\sigma$ in various solvents, virtually independent of the solvent effects.

The chemical shift in the nematic phase (σ_a) for a molecule with a three-fold or higher axis of symmetry is given by

$$\sigma_a = \sigma_i + \tfrac{2}{3}\Delta\sigma \cdot S_{C_3} \tag{7}$$

where σ_i is the isotropic chemical shift and S_{C_3} is the order parameter of the C_3 axis of symmetry.

The use of the condition in which the order parameters for the coexistence of the two orientations are related by $(S_{C_3})_\parallel = -2(S_{C_3})_\perp$, leads to

$$\Delta\delta = \frac{(\sigma_a)_\parallel - (\sigma_a)_\perp}{(S_{C_3})_\parallel} \tag{8}$$

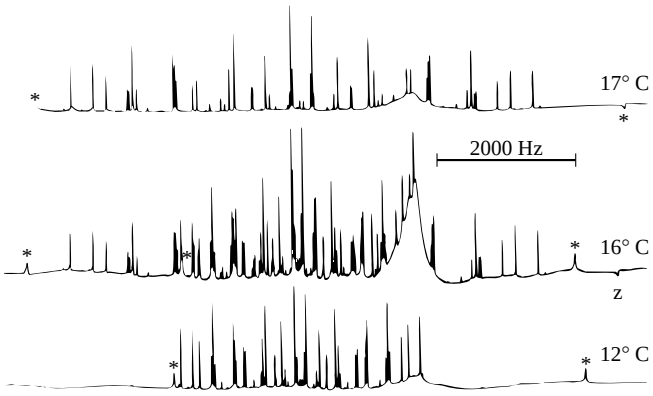

Figure 5 Proton NMR spectra of 3 wt % benzene oriented in a 0.3:1.0 (by weight) mixture of EBBA + ZLI 1167 at 270 MHz. The lines marked with an asterisk arise from traces of water in the solution

where $(\sigma_a)_\parallel$ and $(\sigma_a)_\perp$ are the chemical shifts for the conditions $\Delta\chi > 0$ and $\Delta\chi < 0$, respectively.

The first such measurement of $\Delta\sigma$ (for acetonitrile protons) gave a value of -2.01 ± 0.01 ppm.[11] Subsequently, the method has been used to measure $\Delta\sigma$ for acetonitrile in a large number of mixtures, and has given very consistent results.[21] This method of determining $\Delta\sigma$ has been named the 'NEMIX method'.[21] Measurements of the proton chemical shift anisotropies of systems such as benzene and 1,3,5-trichloro-, bromo-, and nitrobenzenes using this technique have also been reported.[22] Typical spectra for benzene are shown in Figure 5. For benzene, a value of -1.49 ± 0.01 ppm was obtained, which is smaller than the values obtained using other techniques. This might be due to different local effects of the various methods and to additional unknown factors influencing the various techniques. Using this technique, the ^{13}C chemical shift anisotropy for the methyl carbon in acetonitrile was found to be 16.6 ± 0.4 ppm. The corresponding values for 1,3,5-tribromobenzene are -260 and -275 ppm for the carbon atoms attached to proton and bromine, respectively.

It should be emphasized that different local effects may play an important role even in this method. This has been clearly demonstrated by measuring the proton chemical shift anisotropy of tetramethylsilane (TMS) using spectra recorded at the 'coexistence point' in EBBA + ZLI 1167. It was found that the TMS spectra corresponding to the parallel and perpendicular orientations do not have signals at the same frequency, but are chemically shifted by 0.421 ppm.[23,24] This results in an absurd value of $\Delta\sigma$. An NMR study of methanol recorded at the 'coexistence point' provided a value of -104.3 ppm for the chemical shift anisotropy of the methyl protons.[23] This value of $\Delta\sigma$ is abnormally large and unrealistic. Such behavior can be understood in terms of a multiple site theory analogous to that reported for dipolar and quadrupolar couplings, and solvent effects.

4.3 Determination of Diamagnetic Susceptibility Anisotropy ($\Delta\chi$)

At the critical point, the macroscopic diamagnetic anisotropy of the system vanishes. This implies that

$$p(\Delta\chi)_\parallel + (1-p)(\Delta\chi)_\perp = 0 \tag{9}$$

where p is the mole fraction of the solvent with $\Delta\chi > 0$. Both $(\Delta\chi)_\parallel$ and $(\Delta\chi)_\perp$, which are the diamagnetic anisotropies of components with $\Delta\chi > 0$ and $\Delta\chi < 0$, respectively, are dependent on the degree of order of the liquid crystal (S_{LC}) as $\Delta\chi = S_{LC}\Delta\chi_a$, where $\Delta\chi_a$ is the molar susceptibility anisotropy.

The relative diamagnetic anisotropies of the solvents can be derived using a solute molecule as a probe. This method has been used to obtain relative $\Delta\chi$ values with acetonitrile as the probe molecule.[25] Knowledge of the diamagnetic anisotropy of one component gives the value of the other. A value of $\Delta\chi$ at 295 K for ZLI 1167 has thus been obtained as $-4.5 \pm 0.2 \times 10^{-8}$ cgs cm^{-3}. This value has been used to determine $\Delta\chi$ for a number of other liquid crystals with $\Delta\chi > 0$.

4.4 Precise Determination of Spectral Parameters

In a spin system with a relatively small number of independent transitions, the spectral parameters determined may contain large uncertainties. Such a situation has been encountered[26] in 2,6-dichlorophenol, the proton spectrum for which is of the AB_2 type (due to rapid exchange of OH protons in a mixture of EBBA and ZLI 1167). Each spectrum contains nine lines with fairly large linewidths ($\simeq$20 Hz). When all the spectral parameters [(i.e. $\nu_A - \nu_B$, D_{AB}, D_{BB}, and J_{AB} (J_{BB} does not influence the spectrum)] were derived from each spectrum separately, the values determined, particularly those for J_{AB}, were not in agreement with each other or with the literature values for similar systems. However, when the two spectra recorded at the 'coexistence point' were investigated and the fact that the dipolar couplings in the two are not independent (related by a factor of -2) was taken into consideration, it was found that all the parameters could be obtained with reasonable accuracy. J_{AB} determined from the individual spectra were -7.3 and $+10.1$ Hz, but using the 'coexisting phase' spectrum a value of 8.3 Hz was obtained. A separate determination of the value in the isotropic phase also yielded a value of 8.3 Hz for J_{AB}.

4.5 Assignment of ^{13}C Spectral Lines in the ^{13}C Spectra of Liquid Crystals

Assignments of the resonances in the ^{13}C NMR spectra of isotropic systems can be made from off-resonance decoupled spectra and two-dimensional $^{13}C/^{1}H$ heteronuclear COSY experiments. However, it is not so easy to make these assignments of ^{13}C spectra in the nematic phase. The mixture of liquid crystals of opposite diamagnetic anisotropies provides a convenient technique for such a purpose, as described below.

The chemical shift in the nematic phase for a nucleus i in the parallel and perpendicular orientations [$(\sigma_a)_\parallel$ and $(\sigma_a)_\perp$ respectively], the isotropic chemical shift α_i, the order parameter S, and the chemical shift anisotropy $\Delta\sigma$, are related as follows:

$$(\sigma_a)_\parallel = \sigma_i + \tfrac{2}{3}\Delta\sigma \cdot S \tag{10}$$

$$(\sigma_a)_\perp = \sigma_i - \tfrac{1}{3}\Delta\sigma \cdot S \tag{11}$$

The equations imply that the order parameter in the perpendicular orientation is $-\frac{1}{2}S$ at the critical concentration

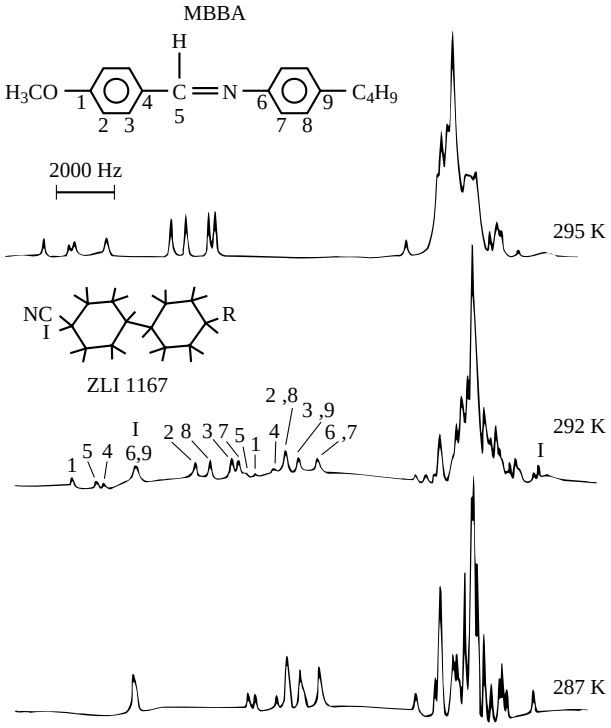

Figure 6 Proton decoupled ^{13}C NMR spectra of a 0.3:1.0 wt % mixture of MBBA and ZLI 1167 at 75.47 MHz. In the assignments of the peaks the primes denote the perpendicular orientation; unprimed numbers denote the parallel orientation

where both orientations coexist. The equations also suggest that the separation between the line for the isotropic phase and the line for the parallel orientation is twice, and with opposite sign, compared with that between the isotropic phase and the perpendicular orientation. Thus the line pairs in the parallel and perpendicular orientations for the same nucleus can be assigned using the line positions in the spectra of isotropic media. This leads to unambiguous assignment of spectral lines in ^{13}C spectra. The technique has been applied[27] to liquid crystals such as *N*-(*p′*-methoxybenzylidene)-*p*-*n*-butylaniline (MBBA) and *trans*-4-pentyl-4-(4-cyanophenyl)cyclohexane (S-1114). Typical spectra for MBBA + ZLI 1167 are shown in Figure 6, and the chemical shift anisotropies of the individual carbon atoms were finally obtained.

4.6 Study of the Dynamics of the Liquid Crystal Director

Experiments have been carried out to study the dynamics of the liquid crystal director in 'near magic angle spinning' experiments on liquid crystal mixtures with near-zero macroscopic diamagnetic anisotropy.[28] The ^2H quadrupole splitting of deuterochloroform dissolved in liquid crystals has been monitored. In systems with weakly positive diamagnetic susceptibility anisotropy, the director has been observed to switch from an orientation parallel to the spinning axis at low rotational speeds to one perpendicular to the spinning axis at high rotational speeds. This occurs when the angle θ which the axis of rotation makes with the magnetic field is smaller than the magic angle θ_m. For systems with small negative $\Delta\chi$, a similar director behavior has been observed for $\theta > \theta_m$.

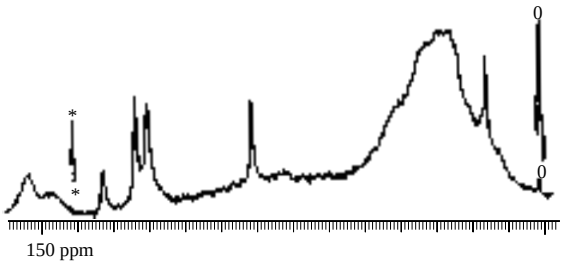

Figure 7 ^{13}C NMR spectra of 0.2 wt % of fullerene (C_{60}) containing 4.2 wt % of TMS in a 1:1 mixture of S-1114 and ZLI 1167 at 332.4 K. The coexistence of the two spectra is evident in the case of tetramethylsilane (○). The C_{60} line is marked by asterisks

4.7 Orientation and Distortions of Tetrahedral and Spherical Molecules

Studies of this type have attracted the attention of several workers[24,29–32] ever since the observation in 1966 of the splittings in the proton NMR spectra of oriented tetramethylsilane.[33] The splittings have been attributed to the small anisotropic pressures of the anisotropic media, which result in minor distortions of the molecules from perfect symmetry. A distortion of about 0.1° in the H–C–H or H–C–Si bond angles from the tetrahedral value in tetramethylsilane has thus been estimated. Subsequently, several theoretical and experimental reports have emerged in which attempts have been made to understand the behavior. Mixed liquid crystals containing opposite diamagnetic anisotropies have also been used in trying to understand such effects. In fact, the critical mixture proposed and used by Jokisaari et al. is the one in which the splittings in the proton spectrum of methane are minimal.[29] An experiment set up to study the extent of the distortion, (if any) in fullerene (C_{60}) has been reported; mixtures of liquid crystals of opposite diamagnetic anisotropies were used. The experiments were performed in a solution of fullerene in the critical mixture of S-1114 and ZLI 1167 containing small quantities of TMS (Figure 7). At the critical point where the ^{13}C spectrum of tetramethylsilane shows two lines due to two different orientations, fullerene shows a single line. The results indicate that fullerene remains undistorted in the liquid crystalline media and its perfect spherical symmetry is retained.

It should be noted that information on a system like fullerene cannot be easily obtained in any other way, as fullerene shows no $^{13}C–^{13}C$ dipolar splittings under normal conditions due to the low natural abundance of ^{13}C and the poor solubility in liquid crystalline media.

5 CONCLUSIONS

The above discussion demonstrates that the NMR spectra of systems oriented in mixtures of liquid crystals of opposite diamagnetic anisotropies exhibit interesting features that lead to novel applications of NMR.

6 REFERENCES

1. R. C. Hewitt, S. Meiboom, and L. C. Snyder, *J. Chem. Phys.*, 1973, **58**, 5089.

2. L. C. Snyder and S. Meiboom, *J. Chem. Phys.*, 1973, **58**, 5096.
3. J. W. Emsley and D. L. Turner, *J. Chem. Soc., Faraday Trans. 2*, 1981, **77**, 1493.
4. A. Pines, D. Wemmer, J. Tang, and S. Sinton, *Bull. Am. Phys. Soc. 2*, 1978, **23**, 21.
5. J. W. Emsley and D. L. Turner, *Chem. Phys. Lett.*, 1981, **82**, 447.
6. K. Akaska, A. Naito, and M. Imanari, *XI ISMAR, Vancouver, Canada, 1992*.
7. C. L. Khetrapal, A. C. Kunwar, and A. V. Patankar, *Org. Magn. Reson.*, 1974, **6**, 556.
8. P. Diehl, C. L. Khetrapal, H. P. Kellerhals, U. Lienhard, and W. Niederberger, *J. Magn. Reson.*, 1969, **1**, 527.
9. P. C. M. van Zijl, C. MaClean, and A. A. Bothner-By, *J. Chem. Phys.*, 1985, **83**, 4410.
10. C. L. Khetrapal and A. C. Kunwar, *Mol. Cryst. Liquid Cryst.*, 1981, **72**, 13.
11. C. L. Khetrapal and A. C. Kunwar, *Chem. Phys. Lett.*, 1981, **82**, 170.
12. G. F. Kventsel, J. Katriel, and T. J. Sluckin, *Mol. Cryst. Liquid Cryst. Lett.*, 1987, **4**, 145.
13. K. P. Sinha, R. Subburam, and C. L. Khetrapal, *Chem. Phys. Lett.*, 1983, **96**, 472.
14. K. P. Sinha, R. Subburam, and C. L. Khetrapal, *Mol. Cryst. Liquid Cryst.*, 1983, **94**, 375.
15. K. P. Sinha, R. Subburam, A. C. Kunwar, and C. L. Khetrapal, *Mol. Cryst. Liquid Cryst.*, 1983, **101**, 283.
16. G. F. Kventsel and T. J. Sluckin, *Phys. Rev. A*, 1987, **36**, 4486.
17. J. Jokisaari and Y. Hiltunen, *Chem. Phys. Lett.*, 1985, **115**, 441.
18. N. Suryaprakash, A. C. Kunwar, and C. L. Khetrapal, *J. Magn. Reson.*, 1983, **54**, 502.
19. N. Suryaprakash, A. C. Kunwar, and C. L. Khetrapal, *J. Organomet. Chem.*, 1983, **252**, 301.
20. C. L. Khetrapal, S. Raghothama, and N. Suryaprakash, *J. Magn. Reson.*, 1987, **71**, 140.
21. P. Diehl, J. Jokisaari, and F. Moia, *J. Magn. Reson.*, 1982, **49**, 498.
22. C. L. Khetrapal, A. C. Kunwar, and M. R. Lakshminarayana, *Liquid Cryst. Ordered Fluids*, 1984, **4**, 1033.
23. C. L. Khetrapal, A. C. Kunwar, and M. R. Lakshminarayana, *Mol. Cryst. Liquid Cryst.*, 1984, **111**, 189.
24. E. E. Burnell and C. A. deLange, *Chem. Phys. Lett.*, 1987, **136**, 87.
25. P. Diehl and J. Jokisaari, *Chem. Phys. Lett.*, 1982, **87**, 494.
26. C. L. Khetrapal and A. C. Kunwar, *Isr. J. Chem.*, 1983, **23**, 299.
27. B. S. Arunkumar, N. Suryaprakash, K. V. Ramanathan, and C. L. Khetrapal, *J. Magn. Reson.*, 1988, **76**, 256.
28. B. S. Arunkumar, N. Suryaprakash, K. V. Ramanathan, and C. L. Khetrapal, *Chem. Phys. Lett.*, 1987, **136**, 227.
29. O. Muenster, J. Jokisaari, and P. Diehl, *Mol. Cryst. Liquid Cryst.*, 1991, **206**, 179.
30. J. P. Bayle, J. Courtieu, and J. Jullien, *J. Chim. Phys., Chim. Biol.*, 1988, **85**, 147.
31. C. L. Khetrapal and N. Suryaprakash, *Liquid Cryst.*, 1993, **14**, 1479.
32. C. N. R. Rao, T. Pradeep, R. Seshadri, R. Nagarajan, V. Narasimha Murthy, G. N. Subbanna, F. D'Souza, V. Krishnan, G. A. Nagana Gowda, N. Suryaprakash, C. L. Khetrapal, and S. V. Bhat, *Ind. J. Chem.*, 1991, **31A/B**, F5.
33. L. C. Snyder and S. Meiboom, *J. Chem. Phys.*, 1966, **44**, 4057.

Biographical Sketch

Chunni L. Khetrapal. *b* 1937. M.Sc., 1959, Allahabad, Ph.D., 1965, Bombay. Introduced to NMR by S. S. Dharmatti. Worked at Tata Institute of Fundamental Research, Bombay, 1959–73 in various positions, the last one being reader; Raman Research Institute, Bangalore, 1973–84, as associate professor and Indian Institute of Science, Bangalore, 1984–present, as Professor and Head, Sophisticated Instruments Facility. Nearly 200 publications and several reviews, books and monographs. Research interests include NMR of oriented systems with emphasis on molecular structure and function, developments of novel techniques, and applications of NMR imaging and in vivo spectroscopy to problems of agricultural interest.

Local Field Experiments in Liquid Crystals

Stefano Caldarelli

CRRMN Université d'Aix Marseille III, Marseille, France

1 Introduction 1
2 Definitions 1
3 Methods to Measure Dipolar Couplings 2
4 Methods for Quadrupolar Couplings (DECOR) 5
5 Related Articles in Volumes 1–8 7
6 References 7

1 INTRODUCTION

The analysis of NMR spectra of aligned liquid crystalline samples provides insight into the structure and dynamics of the molecular constituents or of dissolved molecular probes. However, the NMR spectra of ordinary liquid crystal samples are often too complicated to analyze. This is because the presence of proton-proton dipolar couplings renders the system strongly coupled. Substitution of the protons by deuterons might simplify the analysis, although the assignment of the signals remains uncertain. Separated local field methods for liquid crystals provide a tool to measure and/or assign in a straightforward manner interactions such as heteronuclear dipolar couplings or quadrupolar couplings in deuterium labeled compounds.

1.1 Relevance of the Separate Local Field Approach for Liquid Crystals

The dipolar coupling between protons is a long-range interaction, which is still active over several Angstroms. Any organic molecule is thus a system of mutually coupled spins, the size of which can become rather large already for small molecular weights. The spectral complexity increases accordingly, the number of lines for a system of N coupled spin 1/2 being

$$n_l = \left(\frac{2N}{N-1}\right)$$

For example, a system of 6 coupled spin-1/2 nuclei leads to 763 transitions. Molecular symmetry may reduce this number, but even so the problem of solving the proton spectrum becomes untractable for $N \sim 10$, where $n_l > 10\,000$. Conversely, the spectrum of diluted spins, such as ^{13}C, can be well resolved as, under ^{1}H decoupling, it is dominated by its chemical shift, the next NMR active neighbors being far in space. The separation of the local fields is a multidimensional NMR method in which the chemical shift of a diluted nucleus can be used to spread out other interactions using a two-dimensional scheme. Heteronuclear interactions can be measured and/or assigned in the second dimension in a more straightforward fashion. The ability to assign a coupling to a determined internuclear vector is not a trivial matter in liquid crystalline samples. In these materials, the size of the interaction depends on the molecular structure and orientation. In the absence of direct knowledge on the coupling partners, the assignment is carried out on the basis of the expected length and/or orientation of internuclear vectors. This approach yielded often reasonable results. However, labeling of the coupling partners by their chemical shift constitutes a sounder approach that may help for uncertain cases. Since the assignment obtained this way is model-free, the information obtained can be used to determine fine aspects of the molecular dynamics.

2 DEFINITIONS

2.1 Liquid Crystal Hamiltonians

The interactions measured by NMR in liquid crystals are average quantities, due to the presence of molecular motion:

$$\langle A \rangle = \int A(\Omega) f(\Omega) d\Omega \tag{1}$$

where the integral runs over the orientational coordinates and $f(\Omega)$ is the associated probability distribution function.

Due to motional averaging the NMR spectrum of magnetically or mechanically aligned samples, although still anisotropic in nature, does not show a powder-like line shape, but it is rather constituted of narrow lines.

In the case of molecules with some degree of internal flexibility, the average must be extended over internal (ϕ) and external orientational coordinates (Ω):

$$\langle A \rangle = \int A(\Omega, \phi) f(\Omega, \phi) d\Omega d\phi \tag{2}$$

These average quantities can be interpreted in terms of molecular dynamics, or as constraints in modeling an overall anisotropic potential, $U(\Omega, \phi)$, such as $f(\Omega, \phi) \propto e^{-U(\Omega,\phi)/kT}$ (see **Liquid Crystalline Samples: Structure of Nonrigid Molecules,** Volume 4).

The relevant NMR interactions for organic molecules (or for the organic part of an organometallic moiety) are the chemical shift, indirect scalar coupling and the magnetic dipolar coupling. Deuterium labeling is often used to simplify the spectra. In this case, the dominant interaction becomes the nuclear electric quadrupolar coupling. Chemical shift and quadrupolar couplings are often used to investigate the local order, especially as a function of the temperature in a phase diagram, capitalizing on the orientational dependence of these interactions (see **Liquid Crystalline Samples: Carbon-13 NMR,** Volume 4 and **Liquid Crystalline Samples: Deuterium NMR,** Volume 4). The dipolar coupling may play a similar role, with the additional important property of being an extremely sensitive probe of the internal dynamics, due to its dependence on the internuclear distance. In this respect, dipolar couplings between nuclei far apart are particularly useful, as their distance is more likely to vary between molecular conformations.

2.2 The Separate Local Field (SLF) Principle

The local field separation is a heteronuclear correlation two-dimensional experiment, first introduced by Waugh and coworkers.[1,2] As mentioned earlier, the resolution of the chemical shift dimension of a diluted nucleus is exploited to spread out (and measure) anisotropic interactions. A successful implementation of this scheme can be achieved only if the local fields relative to each probe nucleus are magnetically isolated from each other. That is to say, the corresponding 1D spectrum has to be the sum of distinct contributions, rather than the complicated one arising from a strongly coupled system. In practical terms, a prerequisite is the removal of long-range contacts, which in liquid crystals are provided by proton-proton dipolar couplings. The latter need to be effectively and selectively suppressed in order to implement any SLF scheme. This can be achieved either by employing dedicated pulse sequences (see **CRAMPS,** Volume 3), or chemically, by deuterium substitution. Each one of the mentioned options gives rise to a family of local field experiments, one to measure and assign short-range and long-range heteronuclear dipolar couplings, and the other to assign quadrupolar couplings.

3 METHODS TO MEASURE DIPOLAR COUPLINGS

3.1 Basic Pulse Sequences

The local fields concerned in this case are heteronuclear dipolar couplings (e.g., C–H or P–H). The measured quantity is actually a combination of a dipolar and a scalar interaction, as they share the same operator dependence. In the case of an isolated pair, the splitting of the transitions due to the heteronuclear coupling is shown in equation (3) (see **Liquid Crystalline Samples: Carbon-13 NMR,** Volume 4),

$$A = (2D + J) * f_S \tag{3}$$

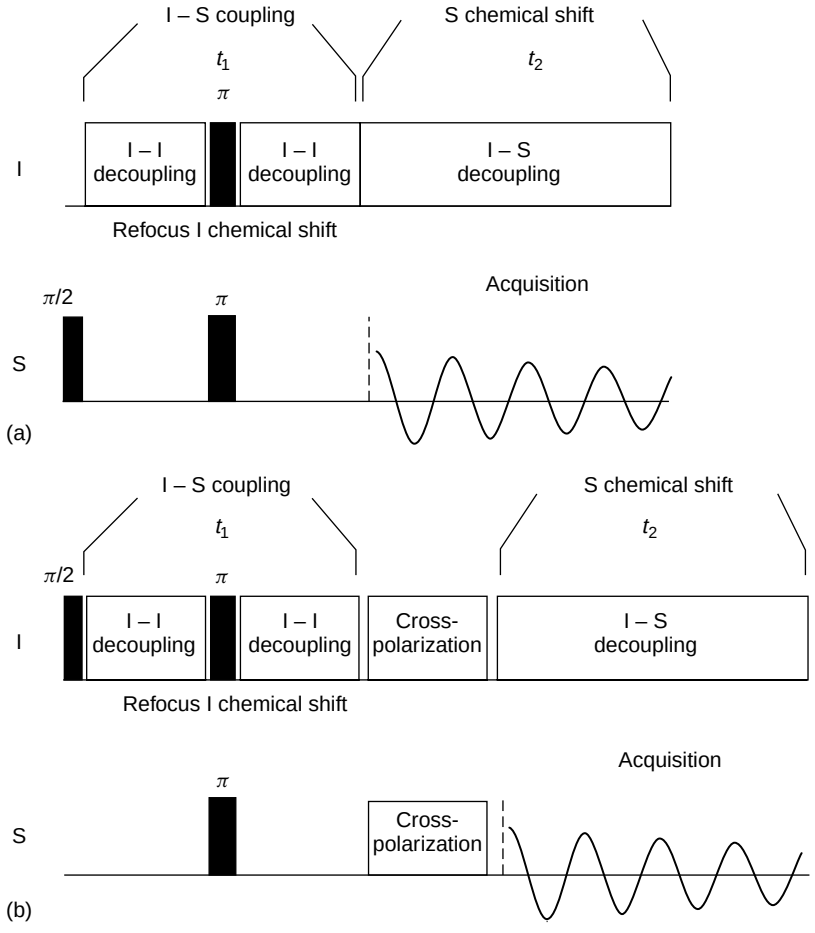

Figure 1 Pulse sequence schemes for "dipolar" separate local field experiments. (a) SLF pulse sequence. After excitation of S coherence with a $\pi/2$ pulse, evolution is allowed to occur under the pure I–S heteronuclear interaction (t_1). Other interactions are removed either by a simultaneous pair of π pulses on I and S (chemical shift) or by a dedicated irradiation scheme for selective I–I decoupling (see text). Typically, a multiple-pulse sequence is used for this purpose. This latter is encased by two extra pulses to tilt the relevant density matrix into suitable directions to achieve maximum efficiency when integrated with the other elements of the sequence. High-power I–S decoupling assures that the S chemical shift is the only active interaction during acquisition (t_2). (b) PELF (PDLF) pulse sequence. I nucleus coherence is first excited by a $\pi/2$ pulse, then allowed to evolve (t_1) under I–S coupling in analogy to the previous scheme; this same coherence is then cross-polarized onto nucleus S, which is observed during acquisition under high-power I–S decoupling. Some published sequences may include other optional elements, such as a presaturation pulse train on S or z-filters to facilitate pure-phase 2D spectroscopy. Adapted from Ref.[8], reproduced by permission of the American Chemical Society

where f_S is the scaling factor associated with the use of a multiple-pulse sequence to remove the homonuclear couplings. The largest known theoretical value for f_S is about 0.575.[3,4]

In the case of a diluted nucleus S, such as a carbon or a phosphorous atom, surrounded by many abundant (proton) I nuclei, two different ways to measure I–S coupling have been proposed (Figure 1).

In the first scheme (Figure 1(a)), the heteronuclear dipolar Hamiltonian is allowed to act on carbon coherence (created by a pulse). The relevant operators carrying the information about the heteronuclear coupling will be of the form shown in equation (4).

$$S_x \prod_k \cos(A_k t) + \sum_k 2S_y I_z \sin(A_k t) \tag{4}$$

In the second half of the sequence, only the first term is observed, under proton decoupling. In the example of an organic molecule, the presence of N protons thus split the carbon spectrum into a complex multiplet with 2^N lines. An example of application to the liquid crystal 5CB (4-*n*-pentyl-4′-cyanobiphenyl) is shown in Figure 2(a).[5]

This approach was the first to be introduced, following the original idea of local field separation as proposed by Waugh.[6,7] In the case of liquid crystal applications, this pulse sequence has been going under the simple acronym of SLF (Separate Local Field) experiment. Each trace of the 2D diagram is a combination spectrum arising from sums and differences of several heteronuclear couplings. A simultaneous fitting of all lines has to be performed in order to extract the values of the interactions. This part of the analysis may prove difficult, as it requires the resolution of all lines, especially the many ones in the center of the spectrum.

Another possible implementation of the local field separation consists in allowing the heteronuclear couplings to act upon proton coherence (Figure 1(b)).[8] In this case, the operators carrying the information on the heteronuclear coupling are in the form shown in equation (5),

$$\sum_k I_x \cos(A_k t) + \sum_k 2I_y S_z \sin(A_k t) \tag{5}$$

as it is unlikely for any proton k to have more than one coupling partner of the diluted species. The first term in equation (5) is transferred via cross-polarization into observable S_x terms. The spectrum is thus a sum of doublets, with a total of $2N$ lines. This second approach has several advantages. Firstly, the reduced number of lines ($2N$ vs 2^N) translates into a better S/N. Moreover, it is easier to measure dipolar coupling, as each doublet in the traces splits according to equation (1) (see Figure 2(b)). The lack of resolution on part of the spectrum does not affect the measurement of the other couplings. For example, in the case of C–H pairs, the measurement of the largest splitting, corresponding to directly bond partners, yields information equivalent to deuterium NMR of labeled compounds, but without chemistry required.[9] This second implementation was originally dubbed proton-detected local field (PDLF) then changed to proton-encoded local field (PELF) to avoid confusion since the actual detection in practical cases occurs on the diluted nucleus.[5,10,11]

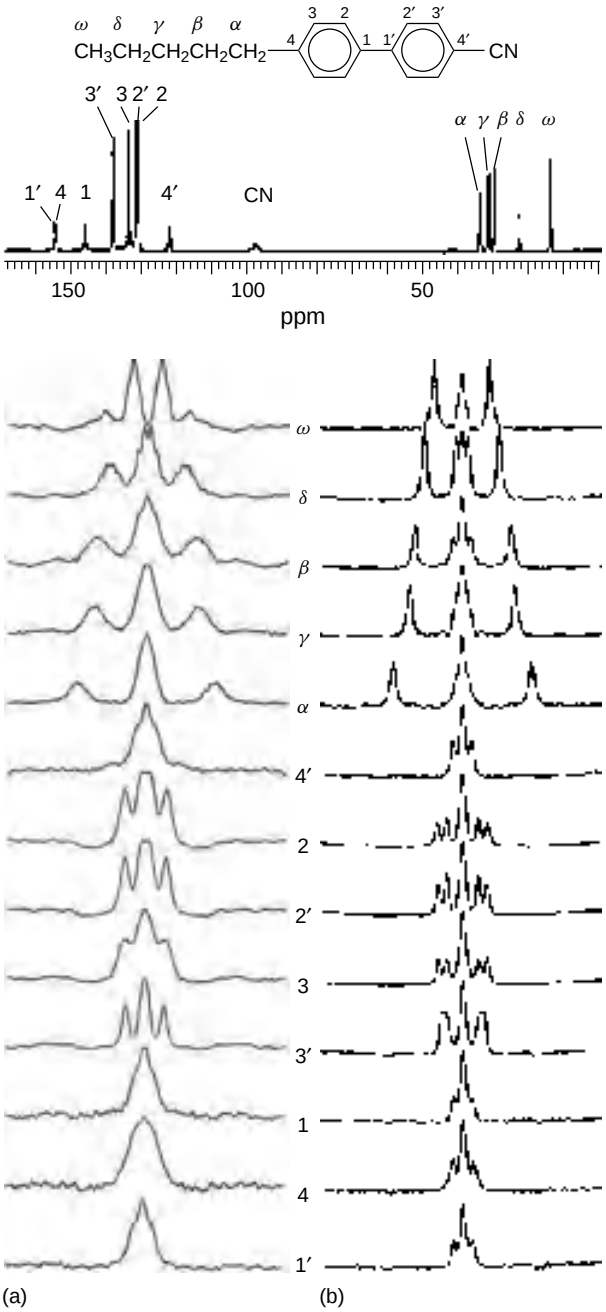

Figure 2 A comparison of the SLF and PELF methods for the nematic liquid crystal 5CB (4-*n*-pentyl-4′-cyanobiphenyl), the structure and ^{13}C NMR spectrum of which are reported on top. The left column shows traces of the 2D SLF experiment [Figure 1(a)] extracted at a chemical shift for a given carbon site. The right column (b) shows the equivalent for the PELF experiment [Figure 1(b)]. Note the different structure of the traces. SLF spectra are complex multiplets, while PELF spectra are the sum of doublets. Smaller long-range couplings produce the unresolved doublets in the center of PELF spectra. In both cases I–I decoupling was achieved by BLEW-48. Reproduced from Ref.[5] by permission of Academic Press

3.2 Off Magic-Angle (OMAS) or Variable-Angle (VAS) Spinning Experiments

Spinning of nematic liquid crystalline samples in the presence of a magnetic field introduces an additional torque

to the nematic director due to the action of viscous forces. This effect competes with magnetic alignment due to the anisotropy of the magnetic susceptibility (see **Spinning Liquid Crystalline Samples,** Volume 7) and tends to orient the directors along the axis of rotation. The 'viscosity' alignment mechanism dominates when the spinning rate is in excess of a threshold value. This kind of alignment is possible only for a given range of subtended angles between the rotor axis and the magnetic field, below or above the magic angle, depending on whether the anisotropy of the magnetic susceptibility is positive or negative, respectively. Considering that anisotropic NMR interactions depend on their orientation with respect to the magnetic field, spinning of the sample can be used to scale down the size of the heteronuclear coupling. In the case of a nematic liquid crystal, the dipolar coupling becomes as shown in equation (6),

$$D' = D\frac{(3\cos^2\beta - 1)}{2} \tag{6}$$

where β is the angle subtended between the rotor axis and the magnetic field (see **Spinning Liquid Crystalline Samples,** Volume 7). The possibility of reducing the anisotropic interactions by this effect, particularly the proton-proton dipolar couplings, has been used to facilitate the suppression of the proton homonuclear couplings. PELF or SLF experiments can be performed under OMAS, and in some cases increased resolution has been observed.[7] However, one should bear in mind that heteronuclear couplings are scaled down according to equation (6). An optimal OMAS (β) angle should be chosen in order to balance these two counteracting effects, especially if one is interested in measuring small long-range couplings. Local field experiments performed off magic-angle are often referred to as variable angle spinning (VAS) methods, since they can be performed, in principle, at different angles.

3.3 Accuracy and Precision of the Measurements

Many effects contribute to the experimental error on the measured couplings (variation of the local order, sample inhomogeneity, etc.). A pervasive source of error, typical of local field experiments, is the difficulty to accurately assess the scaling factor f_S in equation (3). The latter is theoretically known, but often depends on experimental details such as the ratio of the dipolar coupling to the RF field. Moreover, the scaling factor may not be homogeneous throughout the spectrum, as it may depend on the offset.[12,13] In the case of the SLF experiment (Figures 1 and 2(a)), either performed in a static or VAS scheme, all sources of error are mirrored by the goodness of the fit of the spectrum. In fact, the spectrum in this case is the product of combinations of many dipolar couplings involving different partners, and so the individual uncertainties propagate and combine into the line positions. Accuracy and precision of the measurements are directly related here. Conversely, precision for PELF schemes can be as high as the digital resolution of the spectrum, as the coupling is measured from the frequency difference of the lines of a doublet. This precision is expected to largely exceed the reasonable value of the accuracy. In the case when the RF coil in the VAS probe is oriented along the sample holder, the accuracy of the measurement can be evaluated by performing a series of VAS PELF spinning at different angles. By varying the rotor angle, the dipolar couplings will change according to equation (6), but the effective RF field will scale linearly. The consequent modulation of the ratio between the homonuclear proton-proton coupling and the irradiating field will affect the experimental scaling factor in a way that would mimic the variation in the effective RF field caused by the offset in a different part of the spectrum. The accuracy of the experiment can be thus inferred by a linear regression of the splitting $\Delta\nu$ measured along a series of VAS experiments to a combination of equations (5) and (6). Experimental errors measured this way showed a consistent value (about 5% in the case of MREV8) between SLF and PELF experiments.[10]

3.4 Efficiency of Homonuclear Decoupling Sequences

A crucial step toward achieving the best resolution in SLF experiments is to optimize the performance of the

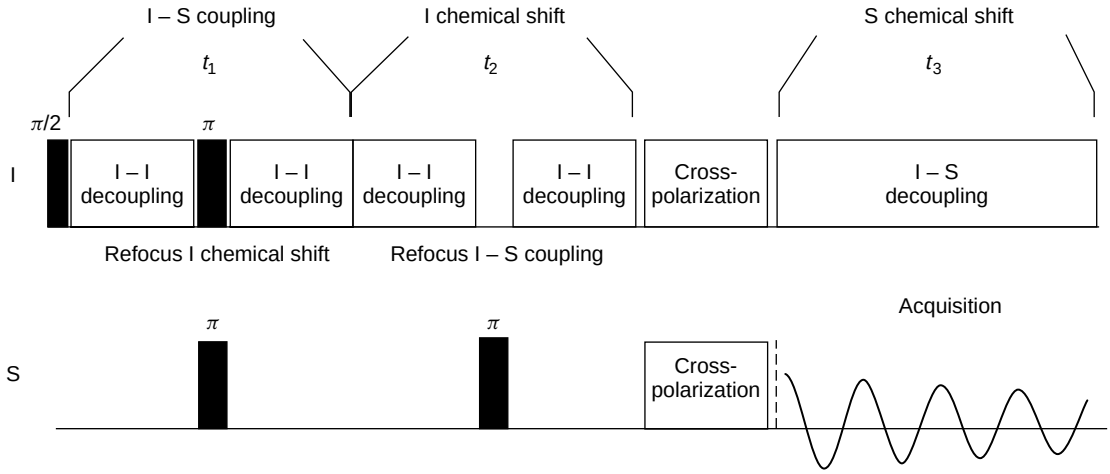

Figure 3 3D extension of the PELF (PDLF) scheme of Figure 1(a). An extra dimension, corresponding to pure I chemical shift evolution, is achieved by combining I–I decoupling and a π pulse on S, which refocuses the heteronuclear I–S couplings. In the literature, two versions of this scheme have been implemented: one in which evolution times t_1 and t_2 were incremented synchronously and the full 3D experiment. Adapted from Ref.[11] by permission of the American Chemical Society

proton homonuclear decoupling.[9,12,13] Historically, MREV8 or BLEW48 were used, but more recent and better-performing sequences can be easily integrated into the method.[9,14–16] Liquid crystal samples present the additional constraint that long, high-power pulse trains may induce thermal gradients, which could perturb the local order of the sample. This can be a serious nuisance in the case of liquid crystalline phases that are stable only over a narrow range of temperatures. Fortunately, the size of the proton-proton coupling to be removed is scaled down by the molecular motion, so that it is often not necessary to employ more than moderate power levels for homonuclear decoupling. If possible, a sequence providing a large and homogeneous (as a function of the offset) scaling factor should be chosen.

3.5 3D Methods for Long-range Couplings

Long-range dipolar couplings are particularly useful as constraints in the study of the dynamics of flexible molecules, as they are extremely sensitive to conformational modifications. It is apparent from Figure 2(b) that the PELF method can provide a reliable measurement for long-range couplings, associated to the many resolved doublets toward the center of the traces. However, these interactions cannot be fully assigned, as the carbon chemical shift only provides a label for one of the partners of the coupling. A possible ploy to avoid recourse to geometrical models is the 'natural' development to a three-dimensional extension of the PELF method, adding as a third dimension the proton chemical shift (Figure 5), which makes the assignment complete.[17,18] Although in principle being the perfect method, the performance of the 3D version of the PELF relies upon a good resolution of the proton spectrum. It is thus relatively easy to distinguish couplings between a given carbon and well-resolved protons, for instance belonging to an aromatic or aliphatic part of the molecule. Another good candidate, as shown in Figure 4, is the tail of an aliphatic chain, as the methyl proton resonance is usually well isolated. Couplings between partners of up to 4 bonds away can be measured in the case of the liquid crystal 5CB (Figure 3). On the other hand, assignment of couplings inside an aliphatic chain may prove more difficult.

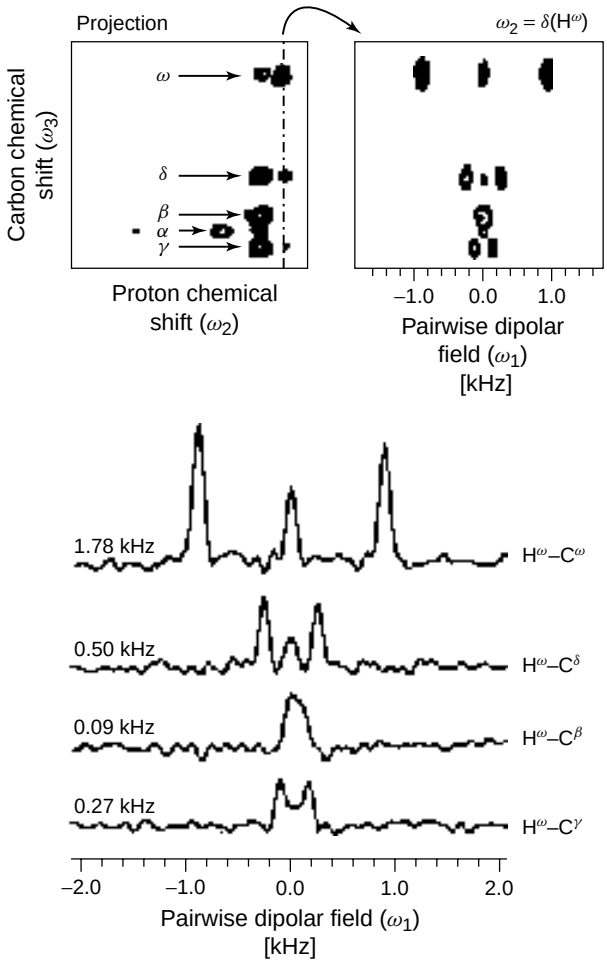

Figure 4 3D PELF spectrum of the aliphatic region of the liquid crystal 5CB. The ω_2/ω_3 plane projection yields an heteronuclear correlation spectrum (upper left). In the proton dimension, the α and ω sites are well resolved, while all other signals overlap. The methyl protons show dipolar contacts with several carbon atoms, the details of which are unveiled in the corresponding ω_2 plane (upper right), in which the size of the H_ω–C^X ($X = \alpha, \ldots, \omega$) interaction is proportional to the splitting (equation (1)). The corresponding traces are shown in the lower part of the figure. The small H^ω–C^β coupling, corresponding to a partially unresolved splitting, was evaluated by fitting of the line shape. Reproduced from Ref.[11] by permission of the American Chemical Society

4 METHODS FOR QUADRUPOLAR COUPLINGS (DECOR)

Spectral simplification in organic liquid crystals can be achieved by isotopic substitution of protons with deuterium (see **Liquid Crystalline Samples: Deuterium NMR,** Volume 4). The spectrum of a spin-1 nucleus is dominated by the quadrupolar interaction, and the dipolar couplings between hydrogens are scaled down by a factor of about 36 (by γ_H^2/γ_D^2) upon isotopic substitution. Consequently the spectrum is constituted of quadrupolar doublets, split by twice the quadrupolar frequency ω_Q, with residual dipolar couplings acting as a fine, often unresolved structure. The deuterium spectrum is usually well resolved for molecules of moderate size. However, similar to the case of dipolar spectra, the assignment of uniformly labeled compounds is obtained on the basis of geometric arguments. In the case of molecules with some degree of internal flexibility, such an assumption implies prior knowledge of the average molecular shape in solution and its correlation with the orientation. An independent way of assigning a deuterium site to a specific C–D bond is to use the ^{13}C chemical shift as a label, analogously to the PELF idea for heteronuclear dipolar couplings. Deuterium-carbon correlation can be achieved using a pulse scheme analogous to PELF (Figure 5), but simplified because of the absence of a strongly coupled network of deuterium nuclei.[19,20]

This method has been dubbed DECOR (DEuterium CORrelation spectroscopy). The (optional) 180 degree pulse on deuterium during t_1 (Figure 5) is sufficient in this case to remove the (reduced) C–D dipolar coupling. The latter may otherwise be revealed (and measured) as a splitting or line broadening (see Figure 4) in the DECOR spectra.

Besides providing a way for assigning deuterium spectra, this technique can be helpful in measuring quadrupolar couplings that are not resolved in the one-dimensional spectrum.

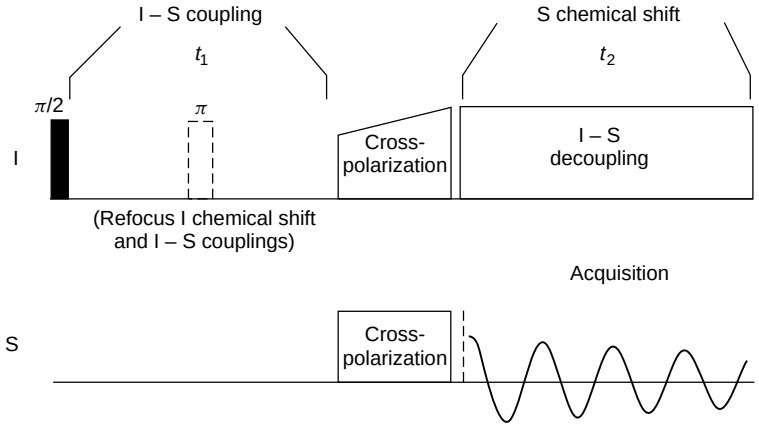

Figure 5 Pulse sequence for the separate local field experiments involving quadrupolar nuclei. In liquid crystals this concerns assignment of quadrupolar couplings in deuterated samples, and for this reason it was dubbed DECOR (DEuterium CORrelation spectroscopy). The first dimension (t_1) is simply the deuterium (I) evolution, with an optional π pulse to refocus I–S (i.e., deuterium–carbon) couplings and I chemical shift to obtain a purely quadrupolar dimension. Acquisition takes place on the S spins under I–S decoupling, after cross polarization. The latter requires special care to insure a match condition sufficiently broad to cover all C–D pairs. In the example in Figure 6, only one of the two lines of the quadrupolar doublet was used for the transfer (single-quantum cross-polarization). Even with this restriction, variable-amplitude spin-lock was still required to further broaden the match condition. Adapted from Ref.[19] by permission of the American Chemical Society

4.1 Deuterium to Carbon Cross-polarization

A delicate part in the DECOR pulse sequence is the cross-polarization step due to the large span of the deuterium spectrum, which defies the ability of a RF field to spin-lock the magnetization ($\omega_{RF} \ll \omega_Q$). Efficient cross-polarization with weak RF fields can be recovered by focussing on half of the symmetrical spectrum typical of the spin-1 deuterium. That is to say, only one of the two single-quantum transitions (i.e., one of the two lines of the doublet) is used to cross-polarize to the carbons, without loss of information. In fact, the main cause of spectral dispersion for a typical liquid crystal sample is the dispersion of the average quadrupolar couplings, essentially due to differences in mobility or average orientation of the molecular segments. The spectrum can be seen as two almost symmetrical groups of lines, in most cases well separated. In fact, single-quantum transitions are further shifted by the chemical shift and split by the dipolar coupling, which are usually much weaker interactions than the quadrupolar coupling ($\omega_{CS}, \omega_D \ll \omega_Q$). One can thus focus on half of the spectrum without losing any site resonance. The match condition for cross-polarization modifies accordingly: $\omega_S = \sqrt{2}\omega_I$.[19,20] The spectral breadth of the ensemble of the SQ-transitions can still be too large to be effectively spin-locked ($|\omega_Q^{max} - \omega_Q^{min}| > \omega_{RF}$), depending on the experimental conditions.[21] In the original experiment, a variable-amplitude cross-polarization scheme was necessary to broaden the match condition enough to achieve a homogeneous transfer over the entire spectrum.[22]

As a consequence of the use of only one SQ transition, in the DECOR 2D diagrams (see Figure 4) only half of the 1D deuterium spectrum correlates with the ^{13}C spectrum. This is sufficient to assign the deuterium spectrum, due to its mirror symmetry (neglecting to first order the effect of chemical shift).

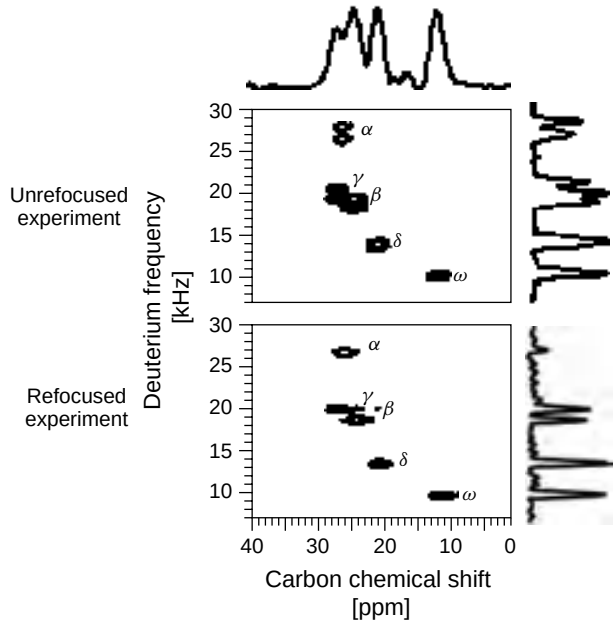

Figure 6 DECOR spectrum of the aliphatic region of a fully deuterated sample of 5CB, using the pulse sequence in Figure 5. The deuterium frequency dimension shows only half of the characteristic quadrupolar doublets because of the selective single-quantum deuterium to carbon cross-polarization scheme used (see text). The effects of the 180 degree pulse on deuterium at $t_1/2$ are demonstrated by the further splitting of some of the peaks in the upper spectrum as compared to the lower one. The effect, as the C–D dipolar coupling, scales with the quadrupolar frequency, since the two interactions are co-linear. Reproduced from Ref.[20] by permission of the American Chemical Society

4.2 Exploiting Long-range Correlations to Resolve Assignment Ambiguities

In some cases, the dipolar coupling between a directly bonded C–D pair and a pair of second neighbors may assume similar values, because of particular orientation effects. For instance, the C–D coupling of directly bonded pairs in the aromatic ring of perdeuterated 5CB is severely reduced as the bond aligns close to the magic angle with respect to the magnetic field. As a consequence, its size becomes comparable

with that of the coupling relative to next neighbors. A same quadrupolar signal in the deuterium dimension can thus correlate to two carbon signals in a DECOR experiment. This kind of ambiguity in the assignment can be lifted by using longer mixing times in the CP transfer, by which the search for correlations is pushed further to smaller couplings, and thus farther neighbors.

5 RELATED ARTICLES IN VOLUMES 1–8

CRAMPS, Volume 3; Liquid Crystalline Samples: Carbon-13 NMR, Volume 4; Liquid Crystalline Samples: Deuterium NMR, Volume 4; Liquid Crystalline Samples: Spectral Analysis, Volume 4; Liquid Crystalline Samples: Structure of Nonrigid Molecules, Volume 4; Liquid Crystals: General Considerations, Volume 4; Spinning Liquid Crystalline Samples, Volume 7

6 REFERENCES

1. R. K. Hester, J. L. Ackermann, B. L. Neff, and J. S. Waugh, *Phys. Rev. Lett.*, 1976, **36**, 1081.
2. S. J. Opella and J. S. Waugh, *J. Chem. Phys.*, 1977, **66**, 4919.
3. M. Lee and W. I. Goldburg, *Phys. Rev.*, 1965, **A140**, 1261.
4. A. Bielecki, A. C. Kolbert, and M. H. Levitt, *Chem. Phys. Lett.*, 1989, **155**, 341.
5. B. M. Fung, K. Ermolaev, and Y. Yu, *J. Magn. Reson.*, 1999, **138**, 28.
6. B. M. Fung and J. Afzal, *J. Am. Chem. Soc.*, 1986, **108**, 1107.
7. B. M. Fung and J. Afzal, *J. Chem. Phys.*, 1986, **85**, 4808.
8. K. Schmidt-Rohr, D. Nanz, L. Emsley, and A. Pines, *J. Phys. Chem.*, 1994, **98**, 6668.
9. C. Canlet and B. M. Fung, *J. Phys. Chem.*, 2000, **B104**, 6181.
10. M. Hong, K. Schmidt-Rohr, and A. Pines, *J. Am. Chem. Soc.*, 1995, **117**, 3310.
11. S. Caldarelli, M. Hong, L. Emsley, and A. Pines, *J. Phys. Chem.*, 1996, **100**, 18 696.
12. B. M. Fung, *J. Magn. Reson.*, 1986, **66**, 525.
13. B. M. Fung, *J. Magn. Reson.*, 1987, **72**, 353.
14. P. Mansfield, *J. Phys. Chem.*, 1971, **4**, 1444.
15. W. K. Rhim, D. D. Elleman, and R. W. Vaughn, *J. Chem. Phys.*, 1972, **59**, 3740.
16. D. P. Burum, N. Linder, and R. R. Ernst, *J. Magn. Reson.*, 1981, **44**, 173.
17. M. Hong, S. Caldarelli, and A. Pines, *J. Phys. Chem.*, 1996, **100**, 14 815.
18. S. Caldarelli, A. Lesage, and L. Emsley, *J. Am. Chem. Soc.*, 1996, **118**, 12 224.
19. C. Auger, A. Lesage, S. Caldarelli, P. Hodgkinson, and L. Emsley, *J. Am. Chem. Soc.*, 1997, **119**, 12 000.
20. C. Auger, A. Lesage, S. Caldarelli, P. Hodgkinson, and L. Emsley, *J. Phys. Chem.*, 1998, **102**, 3718.
21. P. J. Hodgkinson, C. Auger, and L. Emsley, *J. Chem. Phys.*, 1998, **109**, 1873.
22. G. Metz, X. Wu, and S. O. Smith, *J. Magn. Reson.*, 1994, **A110**, 219.

Biographical Sketch

Stefano Caldarelli, *b* 1962 in Spoleto, Italy. Ph.D., 1992 Pisa, Italy. Approx. 30 papers. After a beginning as an organometallic chemist, he quickly found his way into NMR of liquid crystals. An initial stay in the Pines' group in Berkeley expanded his research interests to cover all aspects of NMR for materials sciences: gas, liquids, interfaces, surfaces and solids. His scientific peregrination led him from Pisa, Italy, through Berkeley, USA, Lausanne, Switzerland and Lyon, France to the temporary permanent settlement as a chemistry professor in Marseille, France.

Lyotropic Liquid Crystalline Samples

Alan S. Tracey

Simon Fraser University, Burnaby, BC, Canada

1	Surfactant Structures	1
2	Nuclear Magnetic Resonance	3
3	The Microstructure of Lyotropic Mesophases	5
4	Summary	8
5	Related Articles	8
6	References	8

1 SURFACTANT STRUCTURES

1.1 Introduction

Amphiphilic liquid crystalline materials are most familiar as soaps or detergents in water. They are, perhaps, much less familiar as one of the fundamental building blocks of living materials.[1] It is, however, the ability of lipids spontaneously to generate the lipid bilayer membranes of cells that makes possible the functioning of life as we know it (see also ***Bilayer Membranes: Deuterium and Carbon-13 NMR*** and ***Bilayer Membranes: Proton and Fluorine-19 NMR***).

Chemical compounds capable of forming liquid crystals are known as *mesogens*. Liquid crystals formed by heating a single compound are known as *thermotropic liquid crystals*, while those formed by solvation, i.e. dissolution of a solute in a solvent, are called *lyotropic liquid crystals*. The name 'liquid crystal' arises because, although the materials are fluids, they also have anisotropic properties, such as birefringence, that are usually associated with crystals. There are two main types of lyotropic liquid crystals. The first type arises from the action of an organic solvent on a polymer (see ***Polymer Dispersed Liquid Crystals***). The second type of lyotropic liquid crystal is formed by the action of a solvent, usually water, on an amphiphile, and this type is the topic of this article (see also ***Micellar Solutions and Microemulsions***). An amphiphilic substance has a dual nature—usually a headgroup which is hydrophilic (has an affinity for water), and a hydrocarbon chain which is hydrophobic (lacks an affinity for water). These properties lead to the formation of structured arrays of amphiphile aggregates, where the headgroups provide an interface between the water and the hydrocarbon chains and help keep the aggregates in solution.[2,3] Examples of amphiphiles are detergents, flocculants, dispersants, and lipids.

Somewhat surprisingly, despite the apparently simple nature of the amphiphiles themselves, they form a rather complicated set of macroscopic structures.[4,5] These structures are based principally on three motifs: spherical or semispherical arrays of limited size; cylindrically shaped arrays of finite cross section but of indefinite length; and planar arrays of indefinite extent in two dimensions but of limited thickness.

1.2 The Structural Motifs

There is a progression in structure associated with changes in the concentration of the amphiphile in water. In very dilute solution the amphiphiles exist essentially as individual ionic species that interact only transiently with each other. At a certain concentration, known as the critical micelle concentration, the amphiphiles aggregate into stable semispherical entities and give rise to the isotropic micellar solution. With a continued increase in amphiphile concentration a phase transition occurs, generally to the cylindrical or middle soap structure. The individual aggregates of this mesophase tend to, though do not necessarily,[5] arrange themselves into a hexagonally-packed array and this is often referred to as the *hexagonal or H_1 phase*. Occasionally a cubic-packed arrangement occurs, and this is known as the *rectangular phase*. Further increases in amphiphile concentration will cause an additional phase transition and the *neat or lamellar (L_α) mesophase* is formed. This structure generally persists into the truly crystalline state.

On occasion, before a phase transition to the cylindrical or lamellar structure occurs, the micelles pack together in a cubic-close-packed array to form a second type of isotropic phase. These tend to be highly viscous materials and are referred to as the *viscous isotropic (I_1) phase*. Two forms exist and correspond to body-centered-cubic or face-centered-cubic arrays. Often, aggregates of intermediate structure are formed. For instance, ribbon-like structures can be generated as an intermediate stage in the progression from cylindrical to lamellar arrays. Instead of a circular cross section as in the cylindrical phase, a cross section of the *ribbon (R_1) phase* reveals an ellipsoidal structure. Aggregate structures corresponding to the isotropic micellar mesophase and the three anisotropic mesophases are depicted in Figure 1.

Of particular interest, from the NMR point of view, are the intermediate structures formed from micelles. Incorporation of additional amphiphile into a micellar solution can cause a phase change to a structure in which the micelles become elongated to form cylindrically shaped micelles. These micelles are closely related to the cylindrical aggregates of the hexagonal mesophase but are of limited length. This intermediate structure is not necessarily adopted; instead, a phase transition may occur to disk-like aggregates that have a close resemblance to the components of the lamellar mesophase. These entities are thermodynamically well defined and undergo phase transitions to and from other aggregate structures and form optically uniaxial mesophases. In binary systems of amphiphile in water these two intermediate structures are not well known. However, they, are much more readily formed if an electrolyte or a long-chain aliphatic alcohol is added to the medium. In addition, it is often possible to induce phase transitions between these disk and cylindrical structures by changing the electrolyte concentration or decanol or water content. Occasionally, an intermediate structure is formed that is optically biaxial.[6] Unlike the systems described previously, this latter mesophase has two unique axes and alignment occurs about both directors simultaneously. The structure of the biaxial phase is not known, but may well be a truncated form of the ribbon phase.

Additional structures are formed if the water of the mesophase is replaced by an organic solvent. In this event, the inverse phases are formed in which the organic region of the detergent solution is continuous and the residual water, ions,

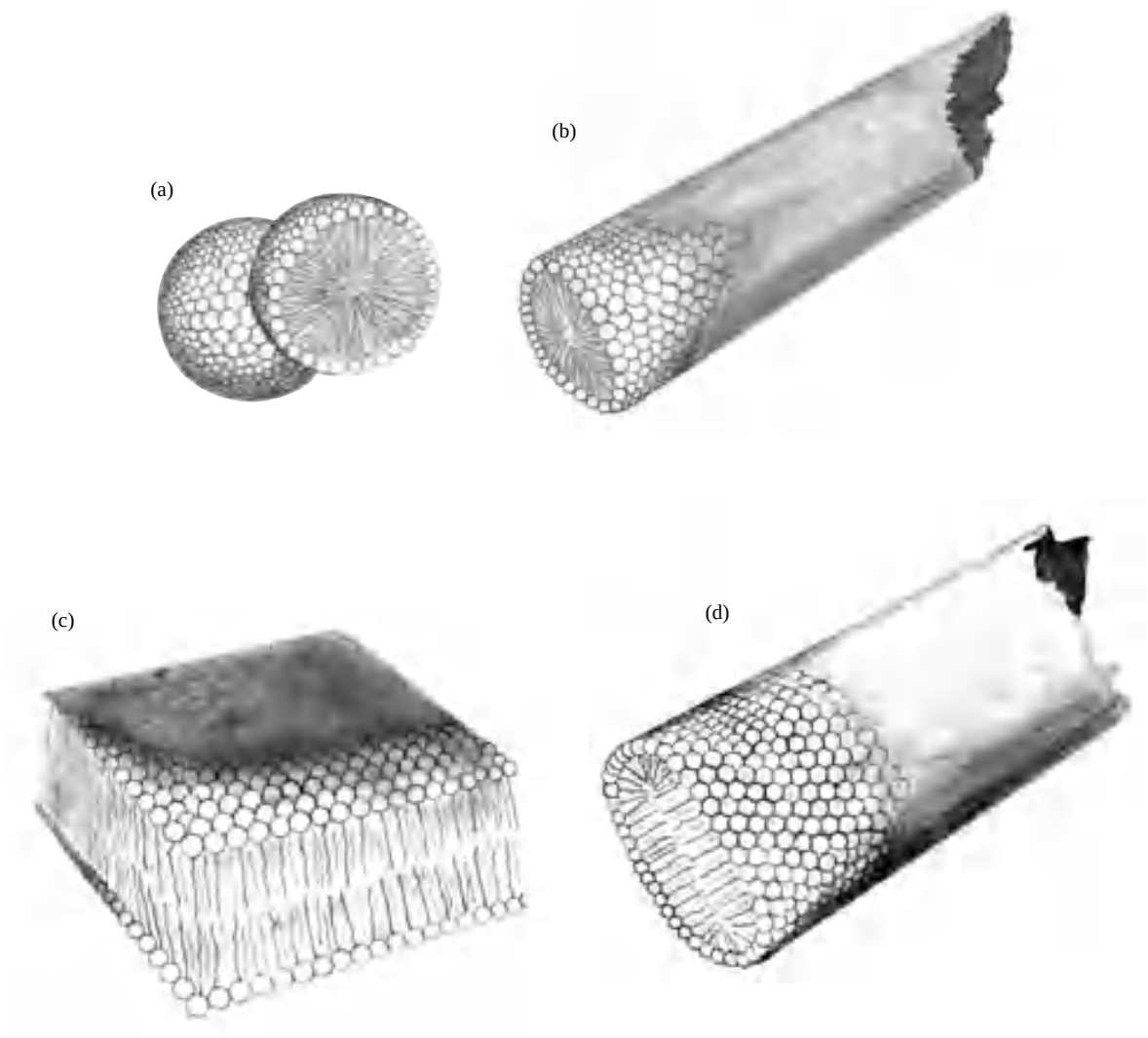

Figure 1 Diagrammatic illustration of the four major structures formed by surfactant materials. Not all structures are formed for all amphiphiles. (a) The spheroidal entities that give rise to the isotropic micellar phase. (b) The cylindrical shaped aggregates of indefinite length that generate the hexagonal and cubic-close-packed mesophases. (c) The planar aggregate of indefinite extent in two dimensions that forms the lamellar mesophase. (d) The structure intermediate between the cylindrical and planar aggregates, which forms the ribbon phase

and amphiphile headgroups aggregate into discrete regions. This situation gives rise to the inverse micellar, cylindrical, and other phases.[7–9] These materials, although of great interest, are not the topic of this article.

On consideration of the cylindrical structure of the elongated micelle, it is evident that a unique axis can be defined which runs lengthwise through the cylinder. Correspondingly, a unique axis can be defined that is perpendicular to the plane of the disk-like micelle. These axes are known as *directors*. Cooperative long-range interactions occur between micelles that cause the individual director axes to align with one another to form, in effect, microcrystalline regions. Within these regions, on average, all micelles have their directors aligned parallel to each other and the directors behave cooperatively.

Because fully extended hydrocarbon chains are long compared to their cross-sectional area, the diamagnetism associated with the molecular structure is anisotropic. The diamagnetic anisotropy is negative. This means that if hydrocarbon chains are fully or partially extended and subjected to a magnetic field, there is a tendency to align in the field with their long axis perpendicular to the applied field. This tendency is enhanced when many alkyl chains can act together, as in the cylindrical or disk micelles. This effect is further enhanced because of the cooperative behavior between micelles. The net result is that when these types of amphiphilic solution are placed in a magnetic field, as in an NMR spectrometer, all micelles align with their directors parallel to each other. The result is a liquid that, in many respects, behaves as a single crystalline entity. These are called *nematic lyotropic liquid crystals*. The disk-like micelles align with the director axis perpendicular to the applied field to accommodate the diamagnetic anisotropy of the hydrocarbon chains. The cylindrical micelles align with their directors parallel to the applied field. It is, therefore, relatively easy to distinguish between these two mesophases with an NMR experiment. The two phases are designated as *nematic lamellar (N_L) phase* and *nematic cylindrical (N_C) phase* because of the close correspondence in structures between these and the lamellar and cylindrical phases. When in a magnetic field, the biaxial mesophase will

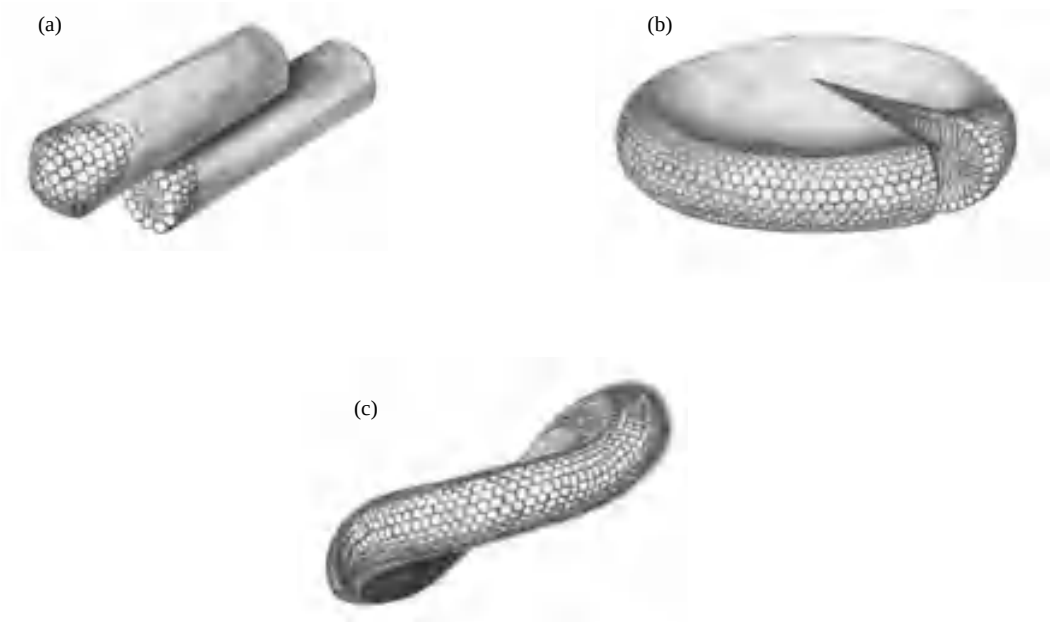

Figure 2 Diagrammatic illustration of the most commonly encountered mesophases that spontaneously align in an applied magnetic field. (a) The nematic cylindrical phase. (b) The nematic disk phase. (c) The cholesteric mesophase derived from a disk-like nematic phase

undergo simultaneous forces for alignment along both directors. This mesophase is designated the *nematic biaxial (N_{BX}) phase*. Neither the parent structures, the lamellar phase, the cylindrical phase, nor the ribbon phase orients in an applied field, because of their high viscosity.

If the amphiphile of the nematic mesophase contains a chiral center, or if a chiral additive is added to the mesophase, asymmetric interactions occur within the micellar structure. The result of these interactions is the generation of a chiral micelle. Because of the nematic character of the solution, the micelles still align in a magnetic field. However, the additional asymmetric long range interaction between the chiral micelles introduces a helical twist into the mesophase structure. These special nematic mesophases are known as *cholesteric lyotropic liquid crystals* and are denoted by Ch_C or Ch_L, to designate their origin from cylinder-like or lamellar-like precursors, respectively. Figure 2 depicts the structural units of the two common types of nematic mesophase and also a cholesteric modification derived from a nematic disk phase. The close structural correspondence between these aggregates and those shown in Figure 1 is exemplified by the drawings in Figure 2.

1.3 The Building Blocks

On the molecular scale there are only small differences between the aggregate structures of the various amphiphilic materials. These differences arise from the motional restrictions imposed by surface curvature and from the packing of the hydrocarbon chains within the various structures. The motional properties of the various components of the individual aggregates are addressed in other chapters of this Encyclopedia (see ***Amphiphilic Liquid Crystalline Samples: Nuclear Spin Relaxation*** and ***Liquid Crystalline Samples: Diffusion***). The influence of charge, electrolyte, and changes in counterions will be discussed briefly here, as will the effects of combining amphiphiles of different headgroup or charge state.

On a microscale, these amphiphilic materials all contain three distinct regions: the aqueous region, the interface region, and the organic region. The aqueous region contains the water, the counterions to the charged amphiphiles, and any added electrolyte. This region serves to mediate the reactions occurring between the aggregates. The headgroups of the amphiphiles, in combination with the bound counterions and associated water, form the interface region. The headgroups of added amphiphiles, such as the hydroxyl group of decanol, will also be located in the interface and the interface separates the aqueous region from the organic region of the system.

The alkyl group of the amphiphile is located in the interior of the aggregates. Hydrophobic additives are also located in this region. This and the other two regions of the lyotropic system are all readily studied by means of NMR techniques.

2 NUCLEAR MAGNETIC RESONANCE

NMR has provided an excellent tool for the study of lyotropic liquid crystals.[4,10–12] The usefulness of this tool lies mainly in its ability to observe directly the individual components of the mesophase. On the other hand, the liquid crystalline behavior of the mesophase itself strongly enhances the power of NMR spectroscopy. Because the motions of the amphiphilic aggregates are anisotropic there is incomplete motional averaging of various interactions, and this leads to NMR observables that give details about the properties of the amphiphilic material.

The two interactions most utilized for the study of anisotropic systems are the dipolar coupling and quadrupole splitting. Of these two, the dipolar coupling has been utilized mostly for studying the structure of solutes (see ***Structure of Rigid Molecules Dissolved in Liquid Crystalline Solvents***), while the quadrupolar interaction has allowed many of the details of the structure of lyotropic mesophases to be determined.

2.1 Quadrupolar Interactions

2.1.1 Quadrupole Splittings

In the generally observed case when a nucleus of spin $I > \frac{1}{2}$ is subjected to an anisotropic environment, the NMR spectrum is split into $2I$ equally spaced transitions with an interaction energy B given by

$$B = \frac{eQ \cdot V_{zz}}{h4I(2I-1)}[3S_{zz} + \eta(S_{xx} - S_{yy})] \qquad (1)$$

where eQ is the nuclear quadrupole moment, eQV_{zz}/h is the quadrupole coupling constant, η represents the asymmetry in the electric field gradient tensor $\boldsymbol{V}$, and h is Planck's constant. The S_{ii} terms represent the alignment of the nuclear fixed coordinate system in the magnetic field of the NMR spectrometer. The observed spacing in the NMR spectrum, $\Delta\nu$, is equal to $2B$.

The coordinates of the electric field gradient tensor are chosen so that $|V_{zz}| \geq |V_{yy}| \geq |V_{zz}|$, since $V_{xx} + V_{yy} + V_{zz} = 0$. The asymmetry parameter $\eta = (V_{xx} - V_{yy})/V_{zz}$ takes the values $0 \leq \eta \leq 1$; $\eta = 0$ corresponds to the special case of axial symmetry, while the condition that $V_{xx} + V_{yy} + V_{zz} = 0$ means that if the nucleus is located at a position of cubic or higher symmetry the quadrupole splitting vanishes. As a consequence of this, the observation of quadrupole splittings from ions such as Na^+, Li^+, Cl^-, or other similar species means that distortions from high symmetry occur.

2.1.2 Quadrupolar Induced Relaxation

Relaxation of quadrupolar nuclei is, even for nominally spherical ions such as Na^+, K^+, Cl^-, or Br^-, dominated by the interaction between the nuclear quadrupole moment and the fluctuating electric field gradients at the nucleus (see ***Amphiphilic Liquid Crystalline Samples: Nuclear Spin Relaxation***). The relaxation rate $(1/T_1)$ is given by

$$\frac{1}{T_1} = \frac{3}{40}\frac{2I+3}{I^2(2I-1)}\left(\frac{eQV_{zz}}{\hbar}\right)^2 \tau_c \qquad (2)$$

where the asymmetry in the electric field gradients is ignored. τ_c is the correlation time for the fluctuation in the orientation of electric field gradient in the magnetic field. This expression is valid in the case when fluctuations are much faster than the nuclear precession frequency, i.e. when $\omega_0\tau_c \ll 1$.

Ion binding in amphiphilic materials has generally been studied by relaxation techniques in order to obtain information concerning the motional properties of the ions in the interface. In anisotropic systems, such as nematic lyotropic liquid crystals, the quadrupolar nucleus gives rise to a quadrupole splitting in the NMR spectrum, the origin of which is the same as that leading to quadrupolar relaxation.

2.1.3 Quadrupolar Splittings from Pseudospherical Ions

The observation of quadrupolar splittings from alkali metal or halide ions shows that these materials have nonspherical components in their structures that have lower than tetrahedral symmetry. For the most commonly observed case, the quadrupole splitting is small compared with the Zeeman splitting. Consequently, it is 'first order' and is given by equation (1). However, it is generally assumed that the distortions of the solvated ions which give rise to the quadrupole splitting are symmetric so that the electric field gradient tensor has rotational symmetry. Under these circumstances, the splitting $\Delta\nu$ is given by

$$\Delta\nu = \frac{3eQV_{zz}}{h2I(2I-1)}S \qquad (3)$$

which can be written in terms of a quadrupole coupling constant Q equal to eQV_{zz}/h, so that

$$\Delta\nu = \frac{3}{2I(I-1)}QS \qquad (4)$$

The quadrupole coupling constant Q and the order parameter S cannot be separated unambiguously for ions such as those of interest here. This separation, however, can be accomplished in complex systems where dipolar couplings are present. Figure 3 shows a typical NMR spectrum obtained from a quadrupole split resonance, in this case of the Cs^+ ion. The spectrum is characterized by $2I$ transitions of repeated spacing $\Delta\nu$.

Ions such as the halides, alkali metals, or other monatomic species are highly symmetric species surrounded by a solvent shell. The distortions that lead to the observation of quadrupole splittings occur primarily by two mechanisms. Specific binding of the ion to sites within the amphiphilic system can occur. Under these circumstances the binding gives rise to electric field gradients about the nucleus which result in the quadrupole splitting.[13] A second means of distorting the solvation shell is for it to undergo anisotropic nonbonding interactions with its environment. Since the interaction forces are fixed in direction, the nucleus together with its hydration shell (although tumbling freely) is still affected by these forces, which distort the solvent shell. The direction of distortion is constant and the result gives rise to the splitting.[14] Both these mechanisms are possible for most amphiphilic systems. Furthermore, more than one specific binding site could well occur. The product,

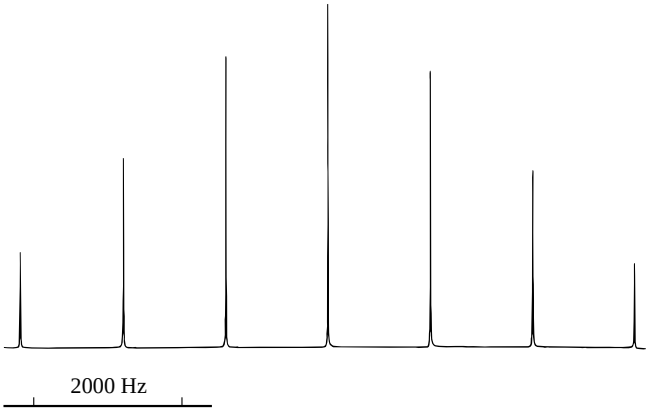

Figure 3 A ^{133}Cs NMR spectrum (52.4 MHz) of the Cs^+ ion in a nematic mesophase prepared from cesium decyl sulfate, decanol, and water. The observation of quadrupole splittings from this ion is consistent with it undergoing strong binding interactions in the interface region of the nematic (N_L) mesophase

QS, in equation (4) can be expected to be reasonably constant for any particular binding site, but different from one site to the other. If chemical exchange is fast compared with the difference of these terms for all sites involved, an averaged quadrupole splitting will be observed as described by

$$\Delta\nu = \sum_i X_i \Delta\nu_i \tag{5}$$

where X_i is the mole fraction of ions in site i, and $\Delta\nu_i$ is the corresponding quadrupole splitting. As it is possible that $\Delta\nu_i$ for any particular site i can be opposite in sign from $\Delta\nu_j$ for a second site j, then the observed splitting can be zero. A consequence of this is that quadrupole splittings might not be observed in some anisotropic systems, even though the nuclear relaxation is clearly quadrupole dominated.

3 THE MICROSTRUCTURE OF LYOTROPIC MESOPHASES

As mentioned previously, lyotropic mesophases contain three regions, each of which has distinct chemical properties. The three regions are the interstitial aqueous region, the interface region, and the organic region. All regions have been studied by NMR techniques.

3.1 The Interstitial Region

The interstitial region of a lyotropic mesophase consists mostly of water with some counterions. Additives, such as electrolyte or water soluble organic materials, will be dispersed throughout this region.

The interstitial region appears to be nearly isotropic in character. Dipolar couplings between organic co-ions (ions with the same charge as the amphiphile, for instance acetate in a sodium decyl sulfate mesophase) and other hydrophilic additives such as methanol, are quite small. Similarly, quadrupole splittings from inorganic co-ions are much smaller than when they are in solution as counterions. There must be some anisotropic character of the water region, but in general the effects are small. This anisotropy will be minimal for the mesophases of high water content, such as the nematic and cholesteric materials, but will be substantial for some of the low water content lamellar phases. Recent molecular dynamics simulations agree with this picture of the interstitial region, suggesting that the bulk properties of water are quickly attained as the water diffuses from the interface region of a membrane.[15] This view has also been supported by self-diffusion measurements in liquid crystalline materials.[16]

3.2 The Interface Region

The interface region is characterized by three components. These are the headgroup of the amphiphile, the counterions that balance the charge, and the associated water. This region is frequently referred to as the *Stern layer*.

3.2.1 The Headgroup

A number of headgroups have been studied by NMR spectroscopy, the most informative one probably being the headgroup in the potassium *N*-dodecanoyl-L-alaninate amphiphile. Other headgroups that have been studied include pyridinium and trimethylammonium. The studies show that, as a general rule, the overall orientational order of the headgroup is comparable to that of the adjacent methylene segments of the attached hydrocarbon chain.

The headgroup of potassium *N*-dodecanoyl-L-alaninate contains a chiral center, and therefore this amphiphile gives rise to a cholesteric mesophase. Studies of this amphiphile have revealed a direct link between rotational isomerization within the headgroup of the amphiphile and the overall headgroup alignment. Furthermore, a linear correlation between the alignment of the headgroup and the twist (inverse pitch) of the helical axis of the phase was observed for this system. It was also found that the quadrupole splitting from the counterions in the mesophase was directly proportional to the alignment of the headgroup.[17] These observations established that there is a direct connection between the molecular behavior (rotational isomerization) of the amphiphile and the macroscopic generation of a helical axis, and clearly showed that structural modifications within the Stern layer have a direct influence on the properties of the mesophase itself.

Often, a long-chain alcohol is added to an amphiphilic solution in order to modify the Stern layer and to cause phase changes. An alcohol frequently used is 1-decanol. Addition of decanol serves to promote the formation and to extend the range of the nematic mesophase. The role of decanol is not well understood, but the hydroxyl group seems to act as a spacer between headgroups; it allows headgroups to be spaced farther apart while simultaneously promoting a hydrogen-bonded water network throughout the interface. Decanol can often be replaced by other long-chain alcohols, decylamine or even amphiphiles carrying a charge of sign opposite to that of the primary amphiphile. Decanol is often the component of choice simply because it is innocuous, easy to work with, and readily purified.

3.2.2 Ion Binding

A procedure commonly employed in order to modify the interface region is to change the counterions. Such a modification is frequently sufficient to cause large changes in the mesophase structure, often resulting in phase transitions, for example from cylindrical to lamellar or lamellar to nematic.[18–20] These changes are clearly associated with the interactions specific to the type of counterion employed.

The NMR methods commonly employed to study counterion interactions are relaxation (see ***Amphiphilic Liquid Crystalline Samples: Nuclear Spin Relaxation***) and self-diffusion studies (see ***Liquid Crystalline Samples: Diffusion***), and observation of the nuclear quadrupole splittings. The most commonly studied ions are the alkali metal and halide ions, although the interactions of transition metal complexes are attracting increasing attention.[21] The relaxation time and self-diffusion studies have shown that the counterions undergo fast translational motion within the interface and exchange rapidly between the free and bound states. The details of the interface structure have emerged from utilization of the

quadrupole splitting of counterions. Probably the most salient result of the NMR studies was the finding that the number of headgroups involved in binding counterions was counterion specific.[22] For instance, in a nematic dodecanoate mesophase, the lithium cation was held by two amphiphiles, the sodium ion by three, and the larger alkali metal ions by four amphiphiles. Halide ions showed a similar behavior in their binding to alkyltrimethylammonium amphiphiles. This chemistry, to a large extent, will account for the influence that the counterion has on the phase behavior of lyotropic mesophases.

3.3 The Organic Region

Studies of the aliphatic region of surfactant aggregates have concentrated on the ^{13}C relaxation times of the carbon signals for isotropic materials, ESR studies of nitroxide-labeled amphiphiles, and deuterium studies of deuterium-labeled amphiphiles for the anisotropic phases. The power of the ^{13}C relaxation studies and the deuterium NMR studies lies in their ability to extract an order parameter for the individual positions along the aliphatic chain.

3.3.1 The Deuterium Order Parameter

NMR spectra from deuterium nuclei in anisotropic systems are dominated by the deuterium quadrupole splitting [equation (1)] which for a spin-1 nucleus is given by equation (6) (see also ***Liquid Crystalline Samples: Deuterium NMR***):

$$\Delta\nu = \frac{eQV_{zz}}{2h}[3S_{zz} + \eta(S_{xx} - S_{yy})] \qquad (6)$$

The deuterium quadrupole coupling constant eQV_{zz}/h is often referred to as Q_D, the D specifying deuterium. Q_D is close to 170 kHz for the C–D bonds of methylene groups. Although η can be significant for quadrupolar nuclei other than deuterium, it is generally small for deuterium, and for most applications can be neglected. The various S_{ii} terms in equation (6) are order parameters describing the alignment of the electric field gradients, about the deuterium nucleus, in the magnetic field of the NMR spectrometer. For deuterium attached to carbon, the major axis of the electric field gradient, V_{zz} deviates only slightly from the C–D bond and, consequently, S_{zz} is equal to S_{CD}. With η being negligible, equation (6) can be rewritten as:

$$\Delta\nu = \tfrac{3}{2}Q_D S_{CD} \qquad (7)$$

The parameter S_{CD} is an average value given by:

$$S_{CD} = \tfrac{1}{2}\langle 3\cos^2\theta - 1\rangle \qquad (8)$$

where θ is the instantaneous angle between the magnetic induction $\boldsymbol{B}_0$ and the bond axis vector. An interesting property of the order parameter is that terms for motional averaging which result from the occurrence of fixed angles, for instance a precession about an axis a at the angle γ, can be readily extracted:

$$S_{CD} = \tfrac{1}{2}(3\cos^2\gamma - 1)S^{o} \qquad (9)$$

S° provides a measure of the alignment of the C–D bond resolved along the axis a. This process can be repeated for all such rigid body motions until an order parameter is obtained which reflects the alignment that would be observed if the C–D bond were directed preferentially along the magnetic field of the NMR spectrometer. The effects of a motion such as translation about the axis of a cylinder are thus readily accounted for.

3.3.2 The Order Profile

Investigation of the properties of hydrocarbon chains in liquid crystalline systems has depended to a large extent on the behavior of the observed order parameter as a function of position along the hydrocarbon chain. Early work in this area focused on the study of spin-labeled fatty acids and their derivatives.[23] It was found that the alignment of the spin label decreased in an exponential fashion with its position along the hydrocarbon chain, counting from the headgroup to the terminal position of the chain. It was soon found that the spin label was a poor reporter of the motion of *n*-alkyl hydrocarbon chains.[24] Deuterium quadrupole splittings from deuterated hydrocarbon chains showed not an exponential decrease in splitting with position, but rather a region of splittings of relatively constant magnitude extending over a high proportion of the chain length followed by a gradual decrease in quadrupole splittings. Figure 4 shows some

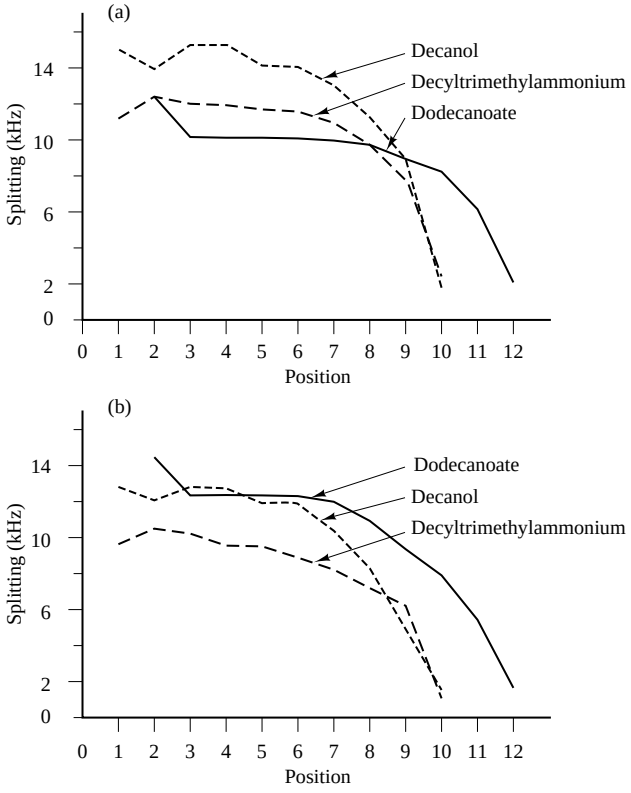

Figure 4 Deuterium quadrupole coupling splittings plotted as a function of methylene position for three different amphiphiles of a mixed detergent nematic (N_L) phase prepared from potassium dodecanoate, decyltrimethylammonium bromide, decanol and sodium bromide. (a) 90 mol% dodecanoate in total detergent; (b) 35 mol% dodecanoate in total detergent. For details see Lee et al.[28]

excellent examples of this behavior. Several points are made obvious by this figure. The first point is that the plateau region is not necessarily particularly flat. Secondly, the behavior of quadrupole splittings with position along the chain is highly headgroup specific, so much so that it almost serves as a signature. A third point which can be made from Figure 4 is that the magnitude of the splitting which defines the plateau region is also headgroup specific. These characteristics of the hydrocarbon chain quadrupole splitting profile make it clear why spin labels are such poor probes of chain motions. As is obvious from Figure 4, changing the headgroup is sufficient to cause changes in the quadrupole splitting of 40% or more. Clearly, these effects are a result of the different interface interactions associated with those headgroups. Changes in the length of the hydrocarbon chains has a minimal effect on the quadrupole splittings throughout the regions that are comparable.[25] Recent studies of a sodium octanoate phase showed an essentially identical behavior.[26] The quadrupole splittings give the order parameter directly from equation (7) and the known value of Q_D. The quadrupole splitting (or alternatively S_{CD}) when plotted as a function of the methylene group position is generally referred to as an 'order profile'. As mentioned above, this profile is highly headgroup specific and it can be nearly flat or can show large deviations from flatness.

There are various aspects of the order profile which provide information concerning the dynamic properties of the hydrocarbon chain (see ***Liquid Crystalline Samples: Structure of Nonrigid Molecules***). The magnitude of the order parameter itself is in some regards highly misleading, since contributions to S from rigid body motions may not be properly accounted for, as is clear from the study of relaxation times. Indeed, rigid body motions may well be, and probably are, different from one component of a bilayer to another. To circumvent this problem, ratios of quadrupole splittings, usually with the terminal methyl group being used as the reference, can be obtained.

In the event that a hydrocarbon chain is rigid and rotating freely about the long axis, the ratio of deuterium splittings of the methylene groups to methyl groups would be about 3.0, assuming only small distortions from tetrahedral geometry. With an increase in mobility of the terminal position with respect to the initial positions, the ratio of splittings becomes larger than 3.0 and, depending on internal motions, the plateau will no longer be flat. The closer the ratio of the plateau splitting to the methyl group splitting is to 3.0, the more the molecule behaves as a rigid entity. The number of carbon atoms over which the plateau extends is a further measure of this, as is the flatness of the plateau region. Figure 5 demonstrates the simultaneous changes of these three parameters as various amphiphiles are incorporated into a progressively less restrictive bilayer (bottom to top traces). Figures 4(a) and 4(b) show the quadrupole splittings corresponding to the 90 and 35 mol% potassium dodecanoate, respectively, in Figure 5. It is clear that the hydrocarbon group of the amphiphile with the larger quadrupole splittings (decanol) behaves least like a rigid rapidly rotating chain. Even though it is apparently the most highly aligned of the mesophase components, internal *cis*/*trans* isomerization about the C–C bonds is not as restricted as for the other two amphiphiles. The motions that cause the deviations of the plateau from flatness have their origins in the specificity of anchoring of the polar headgroup in the interface. These

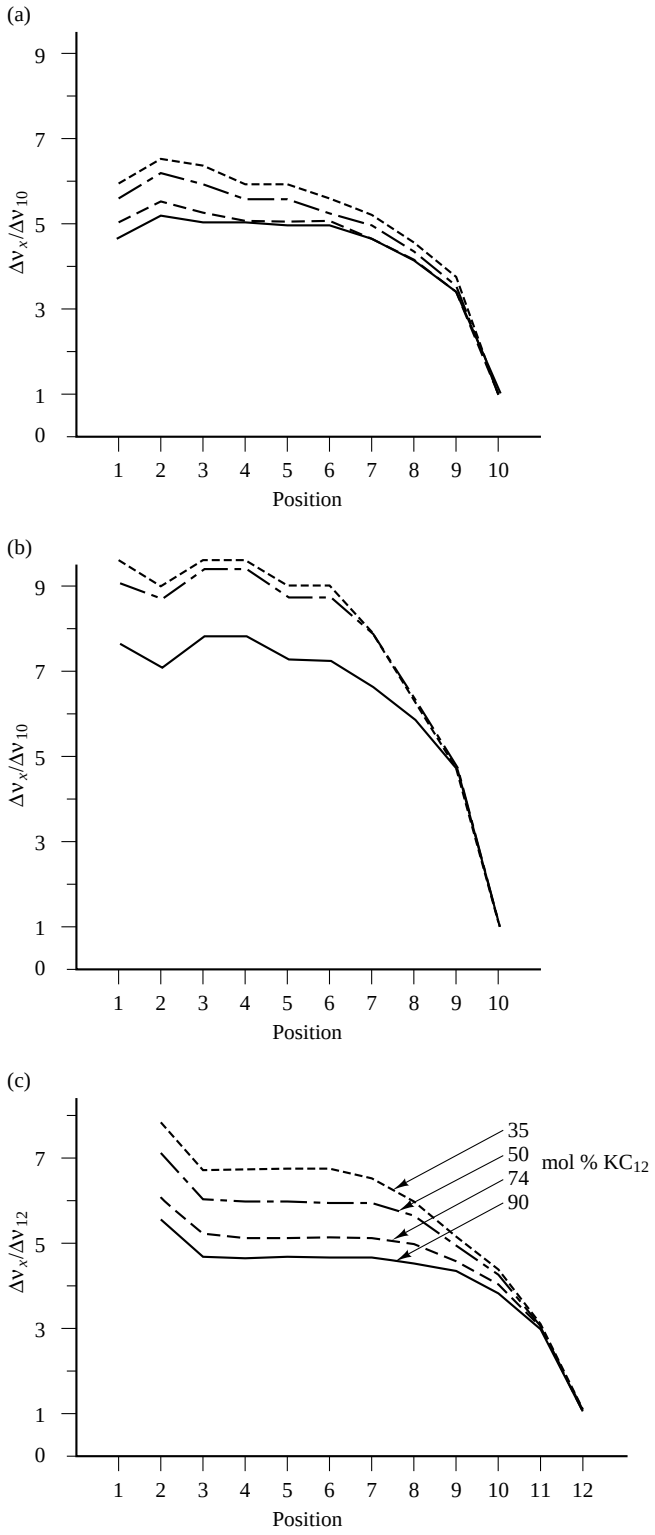

Figure 5 Quadrupole splitting profiles for the three components of a mixed amphiphilic nematic mesophase showing the effects of changes in composition. The mole per cent KC_{12} refers to the molar proportion of potassium dodecanoate in the total of potassium dodecanoate plus decyltrimethylammonium bromide. The mesophase system corresponds to that in Figure 4. (a) Decyltrimethylammonium; (b) decanol; (c) dodecanoate

motions are presumably the fast motions which are observed from relaxation time measurements and which occur on a timescale of the order of 10^{-12} s.[27] The selectively restricted motional properties of the individual amphiphiles no doubt contribute strongly to the structure-building properties associated with different headgroups.

4 SUMMARY

The aggregate structures commonly associated with lyotropic liquid crystalline materials have been briefly discussed and the correspondence in structure between the nematic and non-nematic materials described. NMR spectroscopy has provided much of the information concerning the details of the various regions of these materials. The aqueous region of the mesophases is largely isotropic in character, but it can be used to attenuate and regulate the interactions between the amphiphilic aggregates through changes in water content or incorporation of electrolytes. It is the interface region that dominates the structural characteristics of the mesophase. The two main components of the interface, the counterions to the amphiphile headgroups and the headgroups themselves, strongly influence the properties of the interface and mesophase structure. In addition, the individual headgroups play a dominant role in the alignment and motional properties of the attached hydrocarbon chain. As a consequence, there is a marked heterogeneity in the behavior of the individual hydrocarbon chains when several amphiphiles are incorporated into a mixed mesophase.

5 RELATED ARTICLES

Amphiphilic Liquid Crystalline Samples: Nuclear Spin Relaxation; Bilayer Membranes: Deuterium and Carbon-13 NMR; Liquid Crystalline Samples: Deuterium NMR; Liquid Crystalline Samples: Diffusion; Liquid Crystals: General Considerations; Micellar Solutions and Microemulsions; Polymer Dispersed Liquid Crystals.

6 REFERENCES

1. G. H. Brown and J. J. Wolken, *Liquid Crystals and Biological Structures*, Academic, New York, 1979.
2. D. Fennell Evans and B. W. Ninham, *J. Phys. Chem.*, 1986, **90**, 226.
3. D. Fennell Evans and D. D. Miller, in *Organized Solutions: Surfactants in Science and Technology*, ed. S. E. Friberg and B. Lindman, M. Dekker, New York, 1992, pp. 33–45.
4. R. Bartolino, M. Meuti, G. Chidichimo, and G. A. Ranieri, in *Proceedings of the International School of Physics "Enrico Fermi"*, ed. V. Degiorgio and M. Corti, North-Holland, Amsterdam, 1985, pp. 524–546.
5. M. E. Cates and S. J. Candau, *J. Phys. C: Condens. Matter*, 1990, **2**, 6869.
6. A. Saupe, P. Boonbrahm, and L. J. Yu, *J. Chim. Phys.*, 1983, **80**, 7.
7. A. Ceglie, G. Colafemmina, and M. Della Monica, *Langmuir*, 1993, **9**, 1449.
8. K. Kon-no, in *Surface and Colloid Science*, ed. E. Matijevic, Plenum, New York, 1993, Vol. 15, p. 125.
9. M. P. Pileni (ed.), *Structure and Reactivity in Reverse Micelles*, Elsevier, Amsterdam, 1989.
10. M. Iida and A. S. Tracey, in *Structure and Dynamics of Solutions*, ed. H. Ohtaki and H. Yamatera, Elsevier, Amsterdam, 1992, pp. 176–189.
11. S. Forsén, T. Drakenberg, and H. Wennerstrom, *Quart. Rev. Biophys.*, 1987, **19**, 83.
12. S. E. Friberg and B. Lindman (eds), *Organized Solutions: Surfactants in Science and Technology*, M. Dekker, New York, 1992.
13. H. Wennerstrom, G. Lindblom, and B. Lindman, *Chem. Script.*, 1974, **6**, 97.
14. D. Bailey, A. D. Buckingham, F. Fujiwara, and L. W. Reeves, *J. Magn. Reson.*, 1975, **18**, 344.
15. S.-J. Marrink, M. Berkowitz, and H. J. C. Berendsen, *Langmuir*, 1993, **9**, 3122.
16. J. Chung and J. H. Prestegard, *J. Phys. Chem.*, 1993, **97**, 9837.
17. A. S. Tracey and X. Zhang, *J. Phys. Chem.*, 1992, **96**, 3889.
18. S. Mishra, B. K. Mishra, S. D. Samant, J. Narayanan, and C. Manohar, *Langmuir*, 1993, **9**, 2804.
19. J. Zhao and B. M. Fung, *Langmuir*, 1993, **9**, 1228.
20. K. Radley, L. W. Reeves, and A. S. Tracey, *J. Phys. Chem.*, 1976, **80**, 174.
21. M. Iida, Y. Miyagawa, S. Kohri, and Y. Ikemoto, *Bull. Chem. Soc. Jpn.*, 1993, **66**, 2840.
22. A. S. Tracey and T. L. Boivin, *J. Phys. Chem.*, 1984, **88**, 1017.
23. J. Seelig, H. Limacher, and P. Bader, *J. Am. Chem. Soc.*, 1972, **94**, 6364.
24. J. Charvolin, P. Manneville, and B. Deloche, *Chem. Phys. Lett.*, 1973, **23**, 345.
25. B. J. Forrest, F. Y. Fujiwara, and L. W. Reeves, *J. Phys. Chem.*, 1980, **84**, 662.
26. Y. Sasanuma, M. Nakamura, and A. Abe, *J. Phys. Chem.*, 1993, **97**, 5155.
27. N. Mahieu, P. Tekely, J.-C. Boubel, J. M. Cases, and D. Canet, *J. Phys. Chem.*, 1993, **97**, 9513.
28. Y. Lee, L. W. Reeves, and A. S. Tracey, *Can. J. Chem.*, 1980, **58**, 110.

Biographical Sketch

Alan S. Tracey. *b* 1943. B.Sc., 1967, University of British Columbia; Ph.D., 1971, Chemistry, Simon Fraser University, Canada. Approx. 100 publications. Current research interests: NMR studies of the aqueous chemistry of vanadium and molybdenum oxoanions, applications in biochemistry; NMR in protein/peptide interactions–structures of bound enzyme inhibitors; NMR studies of ion interactions in lyotropic liquid crystalline systems.

Micellar Solutions and Microemulsions

Olle Söderman and Ulf Olsson
University of Lund, Lund, Sweden

1	Introduction	1
2	Self-Diffusion Studies	1
3	Relaxation Studies	5
4	Related Articles	11
5	References	11

1 INTRODUCTION

Surfactants are molecules with two distinctively different parts, one of which is hydrophilic and one which is hydrophobic. This feature of surfactants determines their properties in aqueous or oleic solutions. At low enough concentrations they form molecularly dispersed solutions. As the concentration is increased, they self-assemble into aggregates at a rather well-defined concentration, which is termed the *critical micellar concentration* (cmc) on account of the fact that the aggregates formed are termed *micelles*. As the concentration of surfactant is further increased, the aggregates crystallize into liquid crystalline phases with long-range order, the structures of which may vary rather substantially. The addition of a third component, giving rise to a water–oil–surfactant (where 'oil' is taken to be a generic term for an oleic component) system, results in an amazingly rich phase behavior, involving both liquid crystalline phases and liquid solution phases.

The present contribution will be concerned with the characterization by means of NMR techniques of two particular types of liquid solution of surfactant, the first being micellar solutions and the second being microemulsions. Having said this, we run into a problem of definition. How do we decide whether a particular solution belongs to one of these classes or perhaps to yet another class of solutions? Commonly, microemulsions are defined as thermodynamically stable solutions containing a surfactant (where 'surfactant' is a generic term for a single surfactant or mixtures of different amphiphilic molecules), water and oil. We shall adhere to this definition. Consequently, a micellar solution is one containing a surfactant and water (possibly with added salt) or oil, while the addition of oil or water to a micellar solution turns it into a microemulsion. Possible ambiguities of these definitions will be pointed out as we go along. [The name 'microemulsion' is somewhat unfortunate as it implies that the structure in the solution is one of discrete droplets of either water in oil (W/O) or oil in water (O/W). This is only partly true, as a rich variety of structures can indeed be found in addition to these two droplet structures. The literature is abundant with contributions which ignore this fact and only treat the two droplet structures.]

Studies of surfactant solution systems have had a central place in physical chemistry ever since the pioneering work of McBain at the beginning of this century,[1–4] not least due to the fact that these systems have important roles in a variety of applied processes. Questions asked pertain to the structure of the aggregates formed as well as the properties on a molecular level of the molecules comprising the systems.

It is fair to state that NMR has played a central role as a tool in tackling these questions, and much of our current understanding of surfactant solutions derives from NMR studies where two NMR methods have been especially important. The first of these is NMR relaxation studies, which have evolved to become an indispensable tool in studies of liquid surfactant solutions. The second one is measurements of self-diffusion coefficients by means of pulsed field gradients (PFG), an experiment which yields direct and easily interpretable information regarding many different aspects of surfactant solutions. In fact, our present understanding of the structure in microemulsions is to a large extent derived from PFG work in combination with various scattering approaches.

In the present article we discuss the two NMR approaches and describe applications which we consider to be those where NMR has contributed significantly to our present understanding of liquid solution phases of surfactants.

2 SELF-DIFFUSION STUDIES

Measurements of self-diffusion coefficients by means of PFG techniques have evolved to become one of the most important tools in the characterization of liquid surfactant systems. There are essentially two reasons for this, one of which has to do with the measuring technique itself. Thus the PFG approach offers a convenient method of determining self-diffusion coefficients. The technique is outlined in another article in this Encyclopedia (see ***Diffusion Measurements by Magnetic Field Gradient Methods***) and has also been described in a number of review articles.[5,6] Thus we shall not dwell on the technical aspects here. Suffice is to say that the technique requires no isotopic labeling (thus avoiding possible disturbances due to addition of probes); furthermore, it gives component resolved diffusion coefficients with great precision in a minimum of measuring time.

The second reason for its success rests on the fact that the method monitors transport over macroscopic distances (typically of the order of micrometers), and therefore the determined diffusion coefficients reflect aggregate sizes and obstruction effects, yielding information which is easily interpretable in terms of the microstructure of surfactant solutions. The fact that the information is obtained without the need to invoke complicated models, as is the case in the NMR relaxation approach, is particularly important. In this context it should be stressed that the PFG approach measures the self-diffusion rather than the collective diffusion coefficient.

The foundation for the use of NMR to monitor diffusion was laid in 1950 in the seminal paper by Hahn.[7] Another milestone occurred in the mid-1960s when Stejskal and Tanner demonstrated,[8] following a suggestion by Douglass and coworkers,[9] the use of pulsed gradients. Finally, towards the end of the 1960s the method became component resolved when the FT approach was introduced.[10]

In its simplest version, the method consists of two equal and rectangular gradient pulses of magnitude g and length δ, sandwiched on either side of the 180° rf pulse in a simple Hahn

echo experiment. For molecules undergoing free (Gaussian) diffusion characterized by a diffusion coefficient of magnitude D, the echo attenuation due to diffusion is given by[8,11]

$$I(\Delta, \delta, g) = I_0 \exp\left[-\gamma^2 g^2 \delta^2 \left(\Delta - \frac{\delta}{3}\right) D\right] \qquad (1)$$

where Δ represents the distance between the two gradient pulses, γ is the magnetogyric ratio of the monitored spin, and I_0 denotes the echo intensity in the absence of any field gradient. By varying either g, δ, or Δ (while at the same time keeping the distance between the two rf pulses constant), D can be determined by fitting equation (1) to the observed intensities.

In the following we use some illustrative examples to show how the PFG approach can be used to obtain information on surfactant solutions.

2.1 Micellar Solutions

2.1.1 The Micellization Process

The PFG method provides a unique way of investigating the process of micellization. The approach is based on the fact that the observed surfactant self-diffusion rates constitute a population weighted average between micellized and monomeric surfactant. This follows since the surfactant lifetime in the micelle is short on the relevant NMR timescale (which is essentially Δ in equation (1), and thus typically around 100 ms). Thus the observed surfactant diffusion coefficient is given by

$$D_{\text{obs}} = p_{\text{mic}} D_{\text{mic}} + (1 - p_{\text{mic}}) D_{\text{free}} \qquad (2)$$

where D_{mic} and D_{free} represent the diffusion coefficients of micellized and free surfactant, respectively, and p_{mic} is the fraction of micellized surfactant. Equation (2) can be rearranged to

$$p_{\text{mic}} = \frac{D_{\text{free}} - D_{\text{obs}}}{D_{\text{free}} - D_{\text{mic}}} \qquad (3)$$

Clearly, one can obtain the degree of micellization as a function of total surfactant concentration from the concentration dependence of D_{obs}, provided that D_{free} and D_{mic} are known. D_{free} can be obtained from measurements below cmc, while D_{mic} can be obtained from the diffusion coefficient of a hydrophobic probe which is solubilized into the micelles and for which p_{mic} is unity. A suitable probe is hexamethyldisilane (HMDS) which, if it is added in small amounts (on average one probe per micelle is a recommended concentration), seems only negligibly to disturb the micelles (although for some systems it should be used with some care[12]). Once D_{free} and D_{mic} are known, p_{mic} is obtained without the need to invoke any model for the micellization process. For ionic surfactants the same approach can also be used to obtain the degree of counterion association with the micelles, provided that the counterions contain nuclei suitable for PFG work, which is the case for surfactants with organic counterions.

The result of the approach outlined above is shown in Figure 1, in which a textbook example of the micellization process is presented. Data are obtained for a system with an organic counterion.[13] It is difficult to conceive of any other method that would give the same richness of detail concerning the micellization process. Data such as those presented in Figure 1 have been instrumental in testing various models for describing the micellization process. For instance, approaches based on the Poisson–Boltzmann equation have been very successful in rationalizing the process of micellization for ionic surfactants.[14,15]

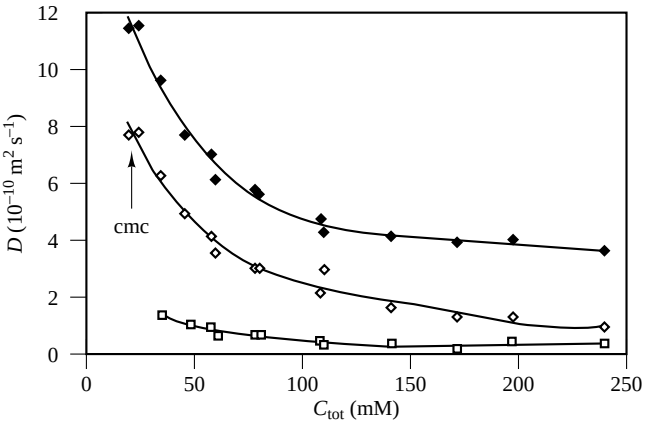

Figure 1 Self-diffusion data for the surfactant ion ($C_{10}H_{21}ND_3^+$) (◊) and counterion ($CHCl_2COO^-$) (♦) of a cationic surfactant with an organic counterion. Also given are the diffusion coefficients of the micelles (□), as measured by solubilizing a small amount of HMDS into the micelles. By applying the two-site model given by equation (3) one can estimate both the fraction of micellized surfactant and the degree of counterion binding to the micelles from the diffusion coefficients. For instance, at 140 mM total concentration of surfactant p_{mic} = 0.8, while the degree of counterion binding (defined as the ratio of the concentration of micelle associated counterions to the concentration of micellized surfactant cations) is 0.8. (Data from Jansson and Stilbs.[13])

2.1.2 Micellar Size and Structure

Questions pertaining to micellar size and structure may be tackled in two ways by means of PFG studies. The first concerns the measurement of self-diffusion of water (or other small molecules) in the system. Any aggregate present obstructs the diffusion of the water and, as the degree of obstruction depends on the volume fraction of the particles present as well as their geometry, information concerning the latter may be obtained. The mathematical description of such obstruction effects was worked out by Jönsson et al.,[16] who presented results for spheres, prolates, and oblates of different sizes and solution volume fractions.

The other approach to investigating micellar structure is based on Einstein's law, in which the (micellar) diffusion coefficient is related to the frictional factor f through

$$D = \frac{k_{\text{B}} T}{f} \qquad (4)$$

where k_{B} is the Boltzmann constant, and T is the absolute temperature.

The friction coefficient depends on the geometry and size of the diffusing particle as well as on the solvent viscosity η. Expressions relating f to the dimensions exist for several

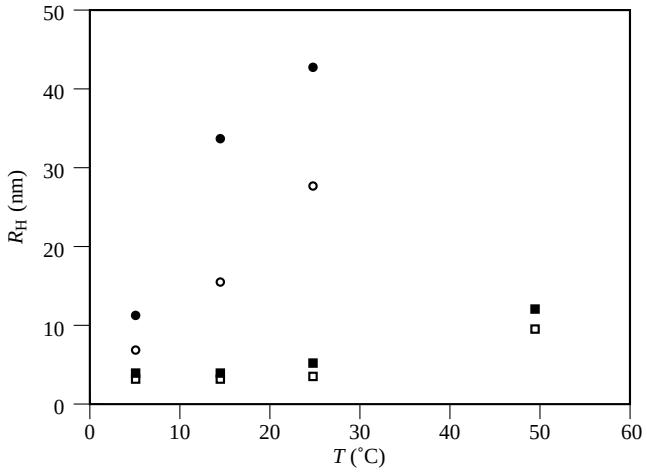

Figure 2 Micelle hydrodynamic radii for two concentrations of $C_{12}H_{25}(OCH_2CH_2)_5OH$ [(●) 2.73 wt%, (○) 0.92 wt% surfactant] and $C_{12}H_{25}(OCH_2CH_2)_8OH$ [(■) 3.06 wt%, (□) 1.02 wt%]. (Data from Nilsson et al.[18,19])

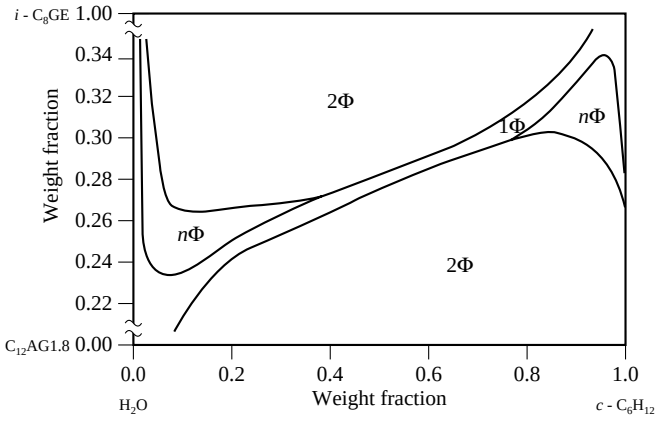

Figure 3 Phase diagram of an alkylpolyglucoside/cosurfactant/water/cyclohexane system at 25 °C with a total surfactant + cosurfactant concentration of 4 wt%. The number of phases present in the various regions of the phase diagram is indicated (for example, the one-phase microemulsion is denoted by 1Φ). (Reproduced with permission from Fukuda et al.[24])

different geometries, the simplest being that for a sphere of hydrodynamic radius R_H, which is:

$$f = 6\pi\eta R_H \tag{5}$$

For cases where the geometry is not known, one often uses equation (5) and computes a hydrodynamic radius, on the assumption that the diffusing species is a sphere. An example of this approach is shown in Figure 2, which gives the hydrodynamic radii for micelles formed by nonionic surfactants of the oligo(ethylene oxide) type as a function of temperature. Questions pertaining to the aggregate growth as a function of temperature and concentration in these systems have been the subject of rather lively discussion over the years.[17] Clearly, data such as those presented in Figure 2 are important in this context.[18–20]

Although the method outlined above is certainly useful, one should be aware of the limitations inherent in the approach. First, equations (4) and (5) assume infinite dilution. As micelles are self-assembled units, one must be aware of the fact that dilution may change their properties. At higher concentrations particle–particle obstruction effects become important, and these must be taken into account.[21,22]

2.2 Microemulsions

Microemulsions are defined as thermodynamically stable systems containing an oleic solvent (in most basic research a simple hydrocarbon is used), a hydrophilic solvent (most often water or brine), and a surfactant (which can be a combination of several amphiphilic molecules). For weakly amphiphilic molecules the system is molecularly dispersed; this will not be discussed here.

Of particular interest are systems in which small amounts of surfactant may bring equal volumes of oil and water into solution. This can be achieved with less than 1% surfactant, and such systems are usually termed 'balanced'.[23] In many of these systems one may vary the oil to water volume ratio extensively without ever leaving the one-phase microemulsion region. This is achieved by varying some parameter. Such a parameter is constituted by the temperature in the case of nonionic surfactants of the C_xE_y type, the salinity of the water for ionic surfactants, and the cosurfactant/surfactant ratio in a mixed surfactant system. An example of such behavior is shown in Figure 3, where a recently compiled phase diagram for an alkylpolyglucoside surfactant is displayed. In this case it is the proportion of the cosurfactant (which is a branched alkyl glycerol monoether) in the surfactant mixture which was varied.[24]

It is a considerable challenge to model such a system, and a prerequisite for such an endeavor is the availability of structural information. It is perhaps in this context that the PFG approach has achieved its most spectacular successes, not least due to the fact that very few other methods can yield such information for microemulsions. How then do we infer structural information from self-diffusion coefficients which are dynamic quantities? The basis of the approach is the fact that the mean distance traveled by the molecules is of the order of $\sqrt{\Delta D}$, which quantity is of the order of micrometers for low molecular weight liquids. Thus any obstruction effects or confinement to droplets of colloidal dimensions affects the diffusion coefficient.

Broadly speaking, one can differentiate between a microstructure of closed particles, whether they are normal (enclosing the oil component) or reversed (enclosing the water), and a microstructure which is bicontinuous. The latter term is often used without being properly defined. We shall take it to imply that a large fraction of both the oil and water molecules exists in domains which span macroscopic distances in three dimensions.

For the case of discrete particles, the continuous phase displays a diffusion behavior similar to that of the neat liquid. There will be solvation effects, i.e. some of the continuous solvent may be associated with the surfactant and, as a consequence, will have an altered diffusional behavior. However, for low surfactant concentration this effect is negligible. Thus any reduction in the reduced diffusion coefficient for the continuous solvent (in PFG studies of microemulsions one preferably reports the reduced diffusion

coefficient, defined as D/D_0, where D_0 is the bulk diffusion coefficient of the neat liquid at the same temperature) can be attributed to particle obstruction effects (see above). If both the dispersed phase and the surfactant have negligible solubility in the continuous phase, their diffusion is given by the particle diffusion, and so both have the same diffusion coefficient, the value of which can be used to estimate the size of the diffusion particle from equation (4), while the concentration dependence of the diffusion coefficient can be used to infer information about the interaggregate interactions.[22]

Turning to the bicontinuous case we note first that both the water and the oil component diffuse rapidly. Careful PFG work using mixtures of oil has revealed that the diffusion process of the oil component is very similar to the diffusion in neat oil.[25,26] The same holds for the water component.[27] This is an important observation, which implies that any reduction in the reduced diffusion coefficient can be attributed to the obstruction effects due to the presence of the surfactant film. Effects such as exchange between droplets and fusion–fission processes cannot explain the rapid oil and water diffusion. Any structural model of microemulsions must not be at variance with this statement. It should be emphasized that, at present, the PFG method is the only way in which bicontinuity may be proved or disproved. Two-dimensional images cannot prove bicontinuity, since it cannot exist in two dimensions.[28]

Let us now investigate whether the diffusion data for the system in Figure 3 is in line with this reasoning. Figure 4 shows the reduced diffusion coefficients for the water and oil components in the system shown in Figure 3 as a function of the volume fraction of hydrocarbon in the solvent mixture (Φ_{oil}). The data in Figure 4 are typical for microemulsions where the oil content can be varied continuously from no oil to pure oil. Thus the water and oil component diffusion changes continuously from rapid to slow as the fraction of each component is decreased, and the plots of the reduced diffusion coefficients versus the volume fraction of oil in the solvent mixture show a rather characteristic 'sigmoidal' curve for both components. At equal volume fractions of oil and water the curves intersect, and the value of both reduced diffusion coefficients is around 0.6 at the point of intersection. In line with the discussion above, this points to discrete particles at low and high values of Φ_{oil} and a bicontinuous structure in between. Based on the information inherent in PFG data such as those presented in Figure 4, how should we picture the bicontinuous microemulsions?

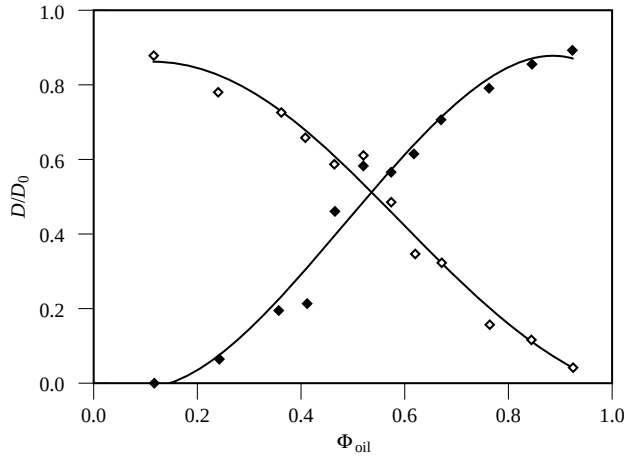

Figure 4 The relative self-diffusion coefficients of water (◊) and hydrocarbon (♦) as a function of the volume fraction, Φ_{oil} of hydrocarbon in the solvent mixture, for microemulsions formed in the alkylpolyglucoside/cosurfactant/water/cyclohexane system, the phase diagram of which is shown in Figure 3. (Data from Fukuda et al.[24])

A most fruitful way of looking at these phases is due to Scriven[29] who proposed the idea that the structure could be described as a melted liquid crystalline cubic phase, for which the structure is known on account of the scattering studies that can be performed on these systems [cubic phases come in two varieties (discrete and bicontinuous); Scriven had the latter class in mind]. These are formed by two interwoven subvolumes of the same material (polar or nonpolar), which are separated by a film of the opposite material. This dividing film is described as a 'minimal surface', having zero mean curvature.

Now, allow this structure to melt, so that the long range order is lost, but locally the structure is retained. When the material on both sides is equal, L_3 phases or bicontinuous micellar solutions (see below) are formed, and the dividing film is a bilayer, while for the case where the two subvolumes are not equal, microemulsions are formed. For this case the dividing film is a monolayer, with a curvature towards the oil or water depending on the volume fraction of the two components.

In an important contribution, Anderson and Wennerström[30] have computed the obstruction effect for components in the subvolumes and for components diffusing along the dividing surface. Indeed, these workers found that the reduced diffusion coefficient for a bicontinuous microemulsion with roughly equal oil and water volume fractions is around 0.6, giving further credence to Scriven's suggestion.

Finally, we note that, when measurements are possible, the value of the surfactant self-diffusion coefficient often displays a maximum with respect to changes in the solvent composition at equal oil and water volume fractions. This observation is more difficult to interpret in terms of a particular microstructure, owing to the difficulties of finding a suitable reference value for the lateral diffusion coefficient for the surfactant along the surfactant film, but it does indicate that the surfactant is diffusing over surfaces that extend over several micrometers with only minor disturbances for diffusions. Consider, for example, the case of a sodium dodecyl sulfate (SDS) microemulsion,[31] where D for the surfactant was found to be $1.5 \times 10^{-10}\,m^2\ s^{-1}$ at 27 °C, a value which is in good agreement with the values found for lateral diffusion of SDS over a micellar surface of spherical[32] ($D = 1.0 \times 10^{-10}\,m^2\ s^{-1}$ at 30 °C) and cylindrical[33] ($D = 1.69 \times 10^{-10}\,m^2\ s^{-1}$ at 30 °C) geometry, where the diffusion is indeed unhindered.

2.3 L_3-Phases and Bicontinuous Micellar Solutions

The properties of L_3 phases and bicontinuous micellar solutions have been discussed extensively, and they constitute an illustrative example of the power of the PFG method in unravelling solution structure. Both types of solution have a connected structure, and again a fruitful starting point is the (known) structure of the cubic phases. If a cubic phase is diluted with the material of the subvolumes, an L_3 phase

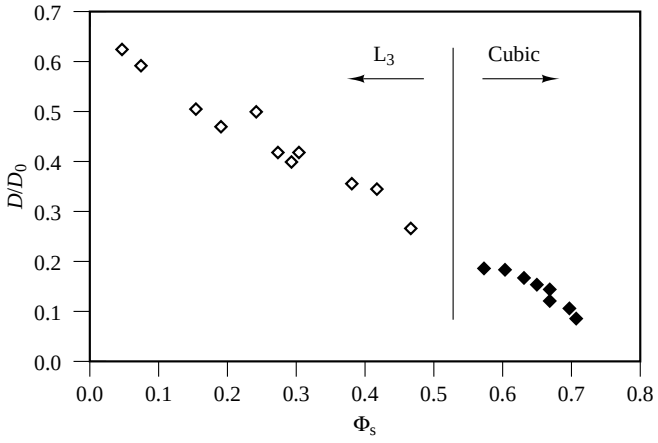

Figure 5 Variation in the reduced water diffusion coefficient with the volume fraction of surfactant in the L_3 (◊) and cubic (♦) phases formed in the AOT/water/NaCl system. (Data from Balinov et al.[34])

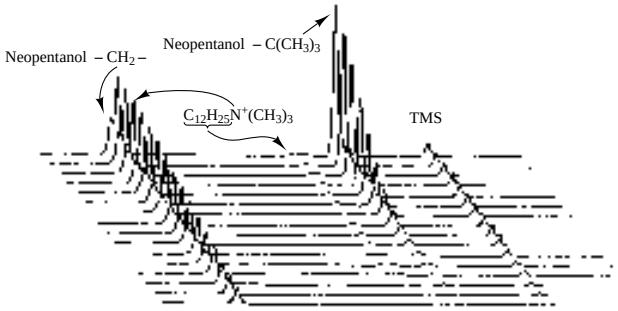

Figure 6 A ^{1}H NMR FT PFG experiment at 100 MHz on the solubilization of neopentanol into dodecyltrimethylammonium chloride micelles (solvent D_2O). The degree of solubilization is obtained directly from the evaluated D values for neopentanol in the micellar solution and in an aqueous solution [see equation (3)]. The value for the micellar diffusion coefficient, which is obtained from a small amount of solubilized tetramethylsilane (TMS), is also needed. The gradient current was varied linearly between successive spectra, which were obtained at fixed intergradient (Δ) and rf pulse (τ) intervals

(sometimes known as L* or 'sponge' phase) is formed, while dilution with the material of the dividing film gives rise to a bicontinuous micellar solution. Let us consider the L_3 phase formed in the sodium bis(2-ethylhexyl)sulfosuccinate (AOT)/brine system. In this system, the L_3 phase is in equilibrium with a bicontinuous cubic phase via a two-phase region.[34] Figure 5 gives the reduced diffusion coefficients for the water as a function of the surfactant volume fraction Φ_s in both the L_3 and the cubic phase.

There are two noteworthy features of the data shown in Figure 5. First, there is a continuous change in D/D_0 with Φ_s over the two-phase area between the L_3 and cubic phases. Secondly, at high dilution, a limiting value of D/D_0 of around 0.65 is obtained. The first observation indicates that the microstructures in the two phases are similar, since the translational diffusion of water reflects the microstructure of the solution. The second point can be used to infer information about the microstructure in a slightly more rigorous way. Consider a structure of discrete particles. According to the obstruction factors derived by Jönsson et al.,[16] the only geometry that would give rise to a reduction in D/D_0 from 1 to 0.65 would be large disks with an axial ratio in excess of 100:1. This is not in agreement with the surfactant diffusion, which, for the case of disks, implies an axial ratio of 12:1. Thus we are forced to think of alternative microstructures. Following the suggestion inherent in the first feature of the data in Figure 5, i.e. that the microstructures are similar in the L_3 and cubic phases, let us consider the case of a bilayer continuous structure. As noted above, this case has been treated by Anderson and Wennerström,[30] who obtained a value of 0.65 for the reduced diffusion coefficient for the solvent diffusion at low volume fraction of bilayer (in fact, for an infinitely thin multiply connected bilayer, the limiting value is $\frac{2}{3}$, on account of the dimensionality of the bilayer). Moreover, by analyzing the dependence of D/D_0 on Φ_s, information can be obtained regarding the coordination number of the obstructing surface.[35]

The analysis of the bicontinuous micellar solution structure as based on PFG data follows the same approach as the one described above. Readers interested in this particular micellar solution are referred to the paper by Monduzzi et al.[36]

2.4 Solubilization

As a final illustration of the power of the PFG approach, we consider the topic of solubilization. By 'solubilization' we mean the incorporation of molecules which are not water soluble into the micellar subvolume of a micellar solution. An important question pertaining to the phenomenon of solubilization concerns the degree of partitioning between the micelles and the water. This question is related to that pertaining to the micellization process (see above), and the same approach used to study that process can be used to investigate solubilization. Thus the degree of solubilization p can be determined by measuring the diffusion coefficient of the solubilizate in the absence and presence of micelles, and determining the diffusion coefficient for the micelle (using the approach outlined above) by using equation (3). From the volume or weight fraction of the micellar subvolume and the value of p, one can then determine the desired partition coefficient. A typical PFG solubilization experiment is shown in Figure 6.[37]

There are several advantages of the PFG approach as compared with other techniques for studying solubilization. The experiment is simple as well as selective. The latter point is particularly important, as one can determine the solubilization of several different solubilizates simultaneously, and each individual value of p can be determined. The presence of impurities is normally not a problem. The quantity p is well defined and easily interpreted. Finally, by measuring the surfactant diffusion one can independently check whether the micelles as such are altered by the presence of solubilizates. Clearly, the whole topic of solubilization becomes somewhat less meaningful if one does not have control over the state of the micelles.

3 RELAXATION STUDIES

NMR relaxation has proven to be a useful experimental technique for studying surfactant aggregation in liquid solutions

and liquid crystals.[20,38–40] The experiment yields information on the local dynamics and conformational state of the surfactant hydrocarbon chain and has demonstrated the liquid-like interior of surfactant micelles. However, the main purpose of NMR relaxation studies of isotropic micellar solutions and microemulsions has been to study properties such as the aggregate size.

The reorientation dynamics of aggregated surfactant molecules, which are discussed in more detail below, are characterized by the fact that they locally have a preferred orientation, forming essentially a monomolecular film of oriented molecules. Locally, surfactant molecules undergo rapid internal motions, such as *trans–gauche* isomerizations in the hydrocarbon chain. These motions are, due to the preferred orientation, slightly anisotropic. The situation can be pictured as the polar headgroups being anchored at the polar–apolar interface, leaving room for dangling motions of the hydrocarbon chains, with certain restrictions on the number of conformations due to packing constraints in the film. In isotropic solutions the residual interaction or anisotropy is further averaged by the thermal tumbling of the aggregates in combination with the diffusion of surfactant molecules within the curved surfactant film.

NMR spectra from surfactants in micellar solutions and microemulsions are generally in the motional narrowing regime, and the spin dynamics are characterized by well-defined relaxation times. Exceptions can be found in solutions of very long ($>10^2$ nm) wormlike cylindrical micelles where the large size in connection with steric overlap gives rise to a very slow (about 10^{-4} s) aggregate reorientation.[41,42] On the other hand, the dynamics are typically outside the extreme narrowing regime, and one often observes $R_2 \gg R_1$, where R_1 and R_2 are the longitudinal and transverse relaxation rates, respectively. Micellar aggregates reorient on a timescale of 10^{-9} s or slower. Thus, at conventional magnetic field strengths, the essential information on the surfactant aggregates is stored in the transverse relaxation rate R_2.

A hydrocarbon, typically an alkyl chain of 12–16 carbon atoms, constitutes the major part of surfactant molecules, offering ^{1}H and ^{13}C nuclei for NMR studies. Being spin-$\frac{1}{2}$ nuclei, the relaxation is mainly due to dipole–dipole interactions (although chemical shift anisotropy and scalar interaction can sometimes be important in the case of ^{13}C). The easy access and the relatively high sensitivity (which was particularly important in early CW NMR studies) has made ^{1}H NMR (in particular bandwidth measurements) studies particularly popular. Micellar growth can easily be studied qualitatively by monitoring the bandwidth of aliphatic ($-CH_2-$) protons in the spectrum. Quantitative analysis is, however, complicated by the coupling of the various protons having locally different motional characteristics along the alkyl chain. In an alkyl chain of, say, 16 carbon atoms, the protons constitute a coupled spin system of approximately 2^{16} spin states, which can have a broad spectrum of transition rates, resulting in significant deviations from a Lorentzian bandshape of the CH_2 resonance.[41,43] This complexity can, however, be turned into an advantage in that it allows for a continuum description of the transition rate spectrum. The ^{1}H bandshape problem was analyzed by Wennerström et al.[41,43] within the two-step formalism (see below), and quantitative ^{1}H bandshape analyses have been performed in systems of large, slowly reorienting micelles.[41,42] In contrast to the non-Lorentzian band shape, one often observes an exponential longitudinal relaxation due to rapid internal equilibration of the spin system (spin diffusion), and the frequency dependence of R_1 has been measured by using field cycling techniques.[44,45]

In an alkyl chain, the ^{13}C nuclei are relaxed by the fluctuating dipole–dipole coupling to the directly bound protons. The various carbon atoms along the chain are normally resolved. Usually, one applies broadband proton decoupling, resulting in exponential longitudinal relaxation of the individual ^{13}C magnetizations, and it is possible to determine R_1 and the nuclear Overhauser enhancement of the different methylene segments. On the other hand, it is difficult to measure R_2 on ^{13}C. Therefore, ^{13}C is mainly useful for studying local chain dynamics and segmental order, since the aggregate dynamics occur on timescales which are normally long relative to the inverse ^{13}C resonance frequency.

Certain surfactants carry phosphate or ammonium polar headgroups, offering ^{31}P and ^{14}N nuclei, respectively, for relaxation studies. The phosphate ^{31}P ($I = \frac{1}{2}$) has a relatively large chemical shift anisotropy which is strongly dependent on the pH (degree of protonation), complicating the analysis of relaxation data. ^{14}N is a $I = 1$ nucleus and its relaxation is dominated by the strong quadrupolar interaction. Except for the case of quaternary ammonium groups, the magnitude and asymmetry of the quadrupolar coupling is also pH dependent, and special care has to be taken.

The most suitable nucleus for relaxation studies of surfactant systems is ^{2}H, which can be incorporated synthetically into the hydrocarbon chain of the surfactant molecule. Normally, one selectively labels a single methylene segment, typically one adjacent to the polar headgroup, in order to avoid resonance overlap in the spectrum. ^{2}H is a $I = 1$ nucleus, and the dominating interaction governing the relaxation is the strong quadrupolar interaction. For aliphatic ($C-^2H$) deuterons, the analysis is further simplified by the fact that the electric field gradient tensor has essentially cylindrical symmetry around the $C-^2H$ bond direction, resulting in a vanishing asymmetry parameter. The ease with which both R_1 and R_2 can be accurately measured, the relatively simple interaction Hamiltonian, and the sufficiently high sensitivity allowing measurements to be made at low resonance frequencies (down to 2 MHz using variable field electromagnets), give ^{2}H NMR relaxation a particularly important role among the different experimental tools available for studying surfactant systems.

The utility of the NMR technique as an experimental tool in surfactant science can be made apparent by comparing the strengths and weaknesses of the NMR relaxation technique with those of other experimental techniques. In comparison with other experimental methods used in studying, for example, micellar size, the NMR relaxation technique has two major advantages, both of which are associated with the fact that it is reorientational motions which are measured. One is that the relaxation, i.e. R_2, is sensitive to small variations in micellar size. Consider, for example, a sphere for which the rotational correlation time is proportional to the cube of the radius. This can be compared with the translational self-diffusion coefficient which varies linearly with the radius. The second, and perhaps most important advantage is the fact that the rotational diffusion of particles in solution is essentially independent of interparticle interactions (electrostatic and hydrodynamic). This is in contrast to most

other techniques (such as viscosity, collective and self-diffusion, scattered light intensity, etc.) available for studying surfactant systems or colloidal systems in general. In this latter respect, NMR relaxation experiments are comparable with form factor determinations with small angle X-ray or neutron scattering experiments. A weakness of the NMR relaxation approach to aggregate size determinations, compared with form factor determinations, would be the difficulties of absolute calibration, since the transformation from information on dynamics to information on structure must be performed by means of a motional model.

3.1 Timescale Separation: The Two-Step Model

In this section we discuss a motional model[46–48] of aggregated surfactant molecules, which involves a timescale separation of fast local and slow global motions. This model has been applied extensively to, and shown to rationalize, NMR relaxation data from aggregated surfactant systems. We discuss the model in connection with ^{2}H relaxation experiments, since the most extensive experimental studies have been performed on ^{2}H-labeled surfactants. We begin by recalling that the longitudinal (R_1) and transverse (R_2) relaxation rates of an $I = 1$ nucleus, due to the quadrupolar interaction in an isotropic solution, are given by[49]

$$R_1 = \frac{3\pi^2}{40}\chi^2[2j(\omega_0) + 8j(2\omega_0)] \tag{6a}$$

$$R_2 = \frac{3\pi^2}{40}\chi^2[3j(0) + 5j(\omega_0) + 2j(2\omega_0)] \tag{6b}$$

where χ is the quadrupolar coupling constant, and $j(\omega_0)$ is the reduced spectral density function evaluated at the Larmor frequency ω_0.

Based on existing knowledge of surfactant aggregate structures, Wennerström and co-workers[46–48] suggested that the reorientational motion of surfactant molecules can be divided into: (i) fast local motions (equilibration of internal modes), which are slightly anisotropic due to the preferred orientation of the surfactant molecules; and (ii) slow isotropic motions, associated with the aggregate tumbling and the lateral diffusion of surfactant molecules within the aggregates. If these two motions occur on significantly different timescales, the fast motions generate a well-defined residual anisotropy to be averaged by the slow motions, and the spectral density can be written as a weighted sum of the fast and the slow components

$$j(\omega_0) = (1 - S^2)j_f(\omega_0) + S^2 j_s(\omega_0) \tag{7}$$

where $j_f(\omega_0)$ and $j_s(\omega_0)$ are the reduced spectral density functions describing the fast and slow motions, respectively. The parameter S is often referred to as an 'order parameter' and is given by the average

$$S = \tfrac{1}{2}\langle 3\cos\theta_{MD} - 1\rangle_f \tag{8}$$

where θ_{MD} is the angle between the axis of the maximum component of the electric field gradient tensor and the director axis.

The situation for the case of a ^{2}H-labeled methylene segment of a surfactant molecule residing in a micelle is illustrated in Figure 7. The director axis Z_D corresponds to the micellar surface normal. The field gradient tensor is cylindrically symmetric around the C–D bond axis, with the maximum component in the bond axis direction Z_M.

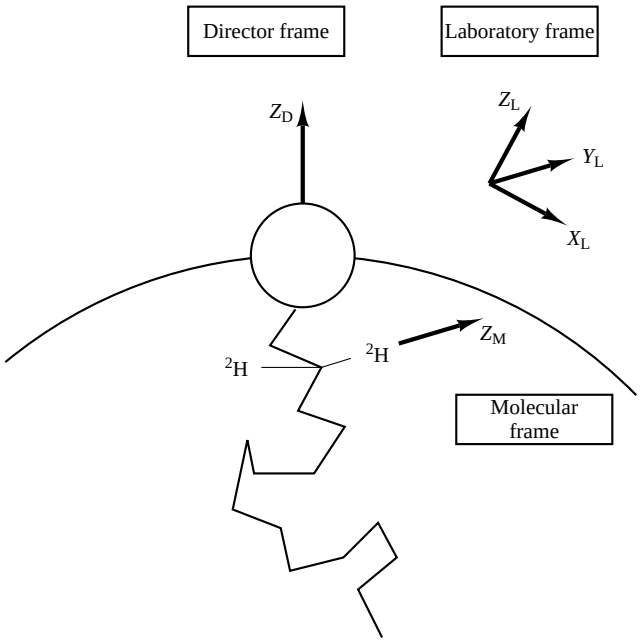

Figure 7 Schematic illustration of the various coordinate frames considered within the two-step model, for the case of a specifically ^{2}H-labeled methylene segment in the surfactant hydrocarbon chain. The laboratory frame (L) is set by the direction of the external magnetic field, where Z_L is the field direction. In this frame the nuclear quadrupolar moment tensor is diagonal. The director frame (D) is associated with the micellar aggregate, where Z_D specifies the micellar surface normal. It is assumed that the fast local dynamics occur with an essentially cylindrical symmetry around Z_D. The molecular frame (M) corresponds to the principal axis of the electric field gradient tensor. For the case of a methylene segment, Z_M specifies the maximum component of the field gradient tensor, which is also cylindrically symmetric around Z_M

In equation (7) it is also assumed that the fast motions have an effective three-fold or higher symmetry around the director. For most situations, however, one may expect an effectively cylindrical symmetry. For lower than three-fold symmetry, equation (7) must be extended to include a second-order parameter, describing the residual order in the plane perpendicular to the director. A similar extension is also necessary when the electric field gradient has a nonvanishing asymmetry parameter (for an extensive discussion, see Halle and Wennerström[48]).

3.2 Frequency Dependent Relaxation Studies of Small Spherical Micelles

The fast motions, described by the spectral density function $j_f(\omega_0)$, are expected to occur on a similar timescale ($\tau_f \approx 10^{-11}$ s) as in the corresponding liquid alkane. Thus this motion is in extreme narrowing ($\tau_f \ll 1/\omega_0$) in the accessible frequency range, and we may assume that $j_f(2\omega_0) \approx j_f(\omega_0) \approx j_f(0) = 2\tau_f$, where τ_f should be considered as an effective correlation time, representing the integral over a nonexponential correlation function.

The slow motion is a combination of micelle tumbling and the lateral diffusion of surfactant molecules within the surfactant film. For spherical aggregates, this motion is described by a Lorentzian spectral density function:

$$j_s(\omega_0) = \frac{2\tau_s}{1 + (\omega_0\tau_s)^2} \tag{9}$$

where τ_s is the correlation time. The tumbling and the lateral diffusion are expected to be statistically independent, in which case the correlation function can be factorized:

$$G_s = G_t G_d = e^{-t/\tau_t}\, e^{-t/\tau_d} = e^{-t/\tau_s} \tag{10}$$

where subscripts t and d refer to tumbling and lateral diffusion, respectively, and the slow correlation time can be written as

$$\frac{1}{\tau_s} = \frac{1}{\tau_t} + \frac{1}{\tau_d} \tag{11}$$

The correlation time associated with the tumbling of a sphere of radius R is given by

$$\tau_t = \frac{4\pi\eta R^3}{3k_B T} \tag{12}$$

where η represents the solvent viscosity, and $k_B T$ is the thermal energy. The effect of lateral diffusion can be described in terms of diffusion on the surface of a sphere of radius R. In this case, the correlation time can be written as

$$\tau_d = \frac{R^2}{6D_{lat}} \tag{13}$$

where D_{lat} is the lateral diffusion coefficient.

With the assumptions of (i) extreme narrowing conditions for the fast motions and (ii) a Lorentzian spectral density function of the slow motion, the expressions for the relaxation rates become, with equation (7)

$$R_1 = \frac{3\pi^2}{40}\chi^2 \left\{ (1 - S^2)20\tau_f + S^2 \times \left[\frac{4\tau_s}{1 + (\omega_0\tau_s)^2} + \frac{16\tau_s}{1 + (2\omega_0\tau_s)^2} \right] \right\} \tag{14a}$$

$$R_2 = \frac{3\pi^2}{40}\chi^2 \left\{ (1 - S^2)20\tau_f + S^2 \times \left[6\tau_s + \frac{10\tau_s}{1 + (\omega_0\tau_s)^2} + \frac{4\tau_s}{1 + (2\omega_0\tau_s)^2} \right] \right\} \tag{14b}$$

Equations (14a) and (14b) have been applied in a large number of ^{2}H NMR relaxation studies of micellar systems. It turns out that frequency dependent relaxation studies are particularly useful for studying small spherical micelles, which typically have a radius of about 2 nm. Using the water viscosity and equation (12) we obtain $\tau_t \approx 7$ ns at room temperature (25 °C). Including the effect of lateral diffusion, a typical value of the slow correlation time is $\tau_s \approx 5$ ns. Thus, the relaxation dispersion from the slow motion occurs around $\nu_0 \approx (2\pi\tau_s)^{-1} \approx 30$ MHz, which is well within the accessible Larmor frequency range for ^{2}H.

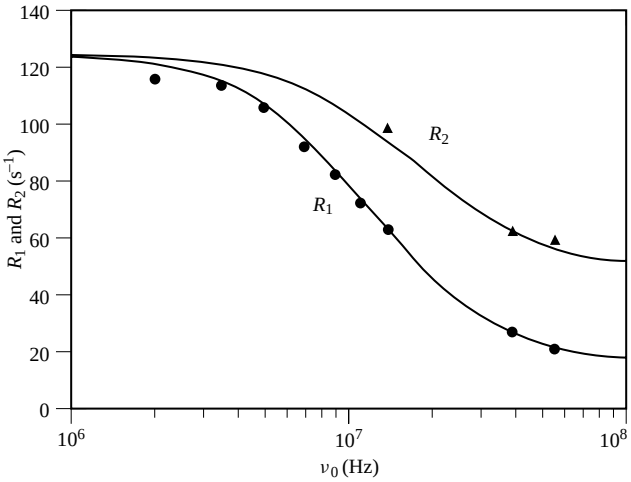

Figure 8 The variation in R_1 and R_2 with the Larmor frequency for ^{2}H nuclei bound to the α-methylene segment of the surfactant hexadecyltrimethylammonium chloride. The sample was an aqueous micellar solution containing 13 wt% of the surfactant. Experiments were performed at 27 °C. (Data from Söderman et al.[51])

To investigate the applicability of the motional model, Söderman and co-workers[50,51] studied aqueous micellar systems of alkyltrimethylammonium chloride surfactants of two different alkyl chain lengths: dodecyl and hexadecyl chains. The alkyl chains were ^{2}H labeled in the α-methylene segment, adjacent to the ammonium polar headgroup, and the relaxation rates R_1 and R_2 were measured in the Larmor frequency range 2–55 MHz, in order to cover the dispersion of the slow motion. The lower frequencies were obtained by using a variable field electromagnet. The results[51] obtained for the hexadecyltrimethylammonium chloride micelles (concentration 13 wt%) are shown in Figure 8. The solid lines are best fits of equations (14a) and (14b) to the whole data set, using τ_f, τ_s, and S as adjustable parameters. As can be seen from Figure 8, the data are well described by a Lorentzian spectral density function superimposed on a constant offset in the investigated frequency range, thus supporting the assumption of timescale separation. The fit yielded $\tau_f = 42 \pm 1$ ps, $\tau_s = 7.6 \pm 0.4$ ns, and $S = 0.186 \pm 0.003$, where the uncertainties correspond to an approximately 80% confidence interval taking only random errors into account, and a value of $\chi = 167$ kHz was used for the quadrupolar coupling constant.

The slow correlation time was interpreted in terms of equations (11)–(13), which contain two unknown parameters, R and D_{lat}. However, D_{lat} can be measured in phases of extended surfactant films, such as bicontinuous cubic phases, and R is expected to be close to the overall length of the surfactant molecule. Using $D_{lat} \approx 1 \times 10^{-11}$ m^2 s^{-1}, as measured in a bicontinuous cubic phase of the similar surfactant hexadecylammonium fluoride, and the radius $R = 2.37$ nm, a slow correlation time of approximately 10 ns was calculated from equations (11)–(13), which is in reasonable agreement with the experimentally determined value.

The applicability of the two-step model receives further support when comparing the S value obtained from the fit to the relaxation dispersion with that measured from quadrupolar

splittings in liquid crystalline phases formed at higher surfactant concentrations. In the liquid crystalline phases, extended surfactant aggregates are 'locked' in a crystalline array. Two very common structures are the lamellar phase, where surfactant bilayers are stacked with one-dimensional order, and the hexagonal phase, where cylindrical aggregates are packed on a two-dimensional hexagonal lattice. In these phases one has effectively frozen the slow motion, and the nuclei experience a static quadrupolar Hamiltonian $\langle\hat{\mathcal{H}}_Q\rangle_f$ in addition to the Zeeman term, where the average is taken over the fast local motions. This results in a quadrupolar splitting of magnitude[46]

$$\Delta_{lam} = \tfrac{3}{4}\chi|S| \tag{15}$$

in the lamellar phase with planar films. In the hexagonal phase, the rapid surfactant diffusion around the cylinder axis results in an additional averaging of the interaction by a factor of 2 and the splitting is given by

$$\Delta_{hex} = \tfrac{3}{8}\chi|S| \tag{16}$$

One may expect that the local motions, and hence the S value, should be similar in the liquid crystalline surfactant aggregates and the micelles in the dilute solution phase. This is in fact found to be the case. As mentioned above, the S value obtained from the fit to the relaxation dispersion (Figure 8) was found to be $S = 0.186$. A very similar value (0.192) was measured in the hexagonal phase at higher concentrations.[51]

3.3 Larger Aggregates: Use of the Zero Frequency Spectral Density

The small spherical micelles ($R \approx 2$ nm) can be seen as a limiting case, and in general surfactant aggregates have much larger extensions. When the size of the aggregates increases, τ_s increases as well, and the relevant relaxation dispersion moves out of the accessible frequency window. In some extreme cases, for example with long, entangled wormlike micelles, the dynamics may even move out of motional narrowing, showing slow motion effects in the NMR spectrum.[42] However, for most micellar and microemulsion systems, the motional narrowing condition applies. In these cases, valuable information may be obtained by measuring R_1 and R_2 for ^{2}H-labeled surfactants at a single Larmor frequency. For larger aggregates, the relevant information on the aggregate size is contained in the zero frequency spectral density only. Assuming that the fast motions are in extreme narrowing, in which case they contribute to a constant offset of both R_1 and R_2, it is useful to consider the difference $\Delta R = R_2 - R_1$ which then depends only on the slow motions. For the case of very slow motions, we also have $j_s(0) \gg j_s(\omega_0) \approx j_s(2\omega_0)$, and ΔR can be approximated by

$$\Delta R = \frac{9\pi^2}{40}(\chi S)^2 j_s(0) \tag{17}$$

This expression has been used to study variations in the shape of surfactant aggregates in different microemulsion systems.[52,53] Here, the micellar aggregates are swollen by the addition of a third component (normal micelles in aqueous solution are swollen by oil; reverse micelles in oil are swollen by water), where spherical aggregates can have radii of the order of 10 nm. Quantitative applications of equation (17) require reliable determinations of S from adjacent liquid crystalline phases. Furthermore, they require assumptions concerning the aggregate shape, and a knowledge of D_{lat}, to determine, for example, an aggregate radius of spherical aggregates. So, obviously, there are some uncertainties involved concerning the 'absolute calibration' of the method.

The situation can, however, be optimized by noting that the aggregates are formed under the constraint of a constant average interfacial area/enclosed volume ratio, set by the surfactant/internal component concentration ratio. With this constraint, the minimum aggregate size corresponds to a spherical shape. Due to the entropy of mixing, spherical aggregates, representing the minimum aggregate size, will always be stable at high dilutions, where the experiment can be calibrated. In many cases, D_{lat} is also known quite accurately from the various bicontinuous phases of the different systems.

Deviations from spherical shape can be modeled as a growth into prolate or oblate shapes. The interfacial area/enclosed volume constraint implies a constraint on the possible values of the two semiaxes describing the particle size. Halle[54] has calculated the correlation functions for the combined particle tumbling and surface diffusion of prolate and oblate particles. His results have been applied to, for example, microemulsion systems,[52,53] focusing on the ratio $j_{s,pr}(0)/j_{s,sph}(0)$, where the subscripts pr and sph refer to prolate and spherical particles, respectively. For a given interfacial area/enclosed volume ratio, which specifies the radius R of the sphere, $j_{s,pr}(0)/j_{s,sph}(0)$ is a function of the prolate axial ratio D_{lat}, and R. Knowing D_{lat} and R from other experiments it is possible to determine the aggregate axial ratio from the relaxation experiment.

As mentioned above, the strength of the NMR relaxation technique in comparison to other (e.g. scattering) techniques for studying micelles and microemulsions is related to the fact that rotational dynamics are monitored. This has the advantages that (i) the dynamics are sensitive to small size variations, and (ii) the dynamics are essentially independent of interactions. In an extensive study of a three-component microemulsion system composed of the nonionic surfactant pentaethyleneoxide dodecyl ether, water, and decane, oil swollen micelles dispersed in water were investigated over a large concentration range.[52]

With a nonionic surfactant, spherical aggregates are formed at lower temperatures, while the aggregates grow in size with increasing temperature.[17] Figure 9 shows the variation of ΔR with temperature for two compositions, $\Phi = 0.12$ and 0.23, in the microemulsion phase.[52] Here, $\Phi = \Phi_s + \Phi_O$ is the total volume fraction of surfactant (Φ_s) and oil (Φ_O), and the ratio $\Phi_s/\Phi_O = 0.815$ was kept constant.

The value of ΔR decreases when the temperature is decreased in the microemulsion phase and levels off at lower temperatures at a minimum value ΔR_{min}, when the aggregates have reached the limiting spherical shape, corresponding to the minimum size. Note that the minimum ΔR value is the same for the two concentrations, as is expected because the radius, dictated by Φ_s/Φ_O, should be the same. By considering

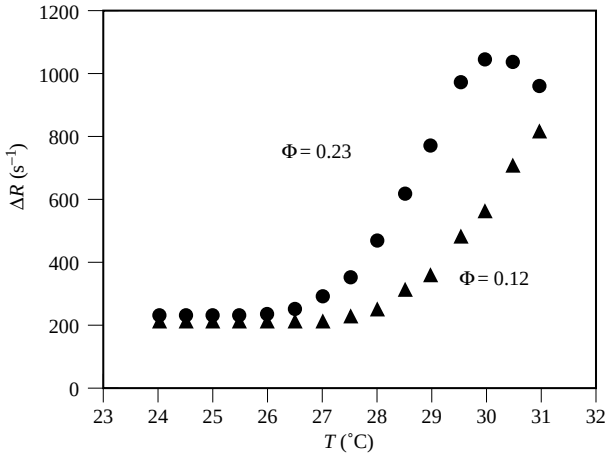

Figure 9 Variation in ^{2}H $\Delta R = R_2 - R_1$ with temperature of the ^{2}H-labeled nonionic surfactant pentaethyleneoxide dodecyl ether $[CH_3(CH_2)_{10}C^2H_2(OCH_2CH_2)_5OH]$ in a ternary system with water and decane. The ratio Φ_s/Φ_O is 0.815, where Φ_s and Φ_O are the surfactant and oil volume fractions, respectively. The concentrations are $\Phi=\Phi_s + \Phi_O$ = 0.12 and 0.23, respectively. (Data from Leaver et al.[52])

the reduced ΔR value, $\Delta R/\Delta R_{min} = j_{s,pr}(0)/j_{s,sph}(0)$, it was possible to calculate the increase in the axial ratio of the aggregates with increasing temperature, assuming a growth into prolate aggregates. The variation in the axial ratio obtained is shown in Figure 10.

Very large micelles may also form in binary surfactant systems. These are long wormlike micelles which become entangled at higher concentrations, giving rise to rheological properties similar to those in polymer solutions. Such systems have been examined by means of ^{1}H bandshape analysis.[41,42] The protons of the surfactant hydrocarbon chain form a very large dipolar coupled spin system, with essentially a continuum distribution of transverse relaxation rates. The distribution of relaxation rates is related to the distribution of order parameters,[43] which can be obtained from analyzing the bandshape in the liquid crystalline (lamellar or hexagonal) phases, where the bandshape is associated with a continuum distribution of residual dipolar splittings.[55]

Slow motions have also been studied by measuring the differential line broadening (DLB) of proton J coupled ^{13}C nuclei.[56] Here the difference in bandwidth of the different resonances in a ^{13}C multiplet can be attributed to the interplay between the dipole–dipole and chemical shift anisotropy relaxation mechanisms, and by analyzing the difference, information on the slow motion may be obtained.

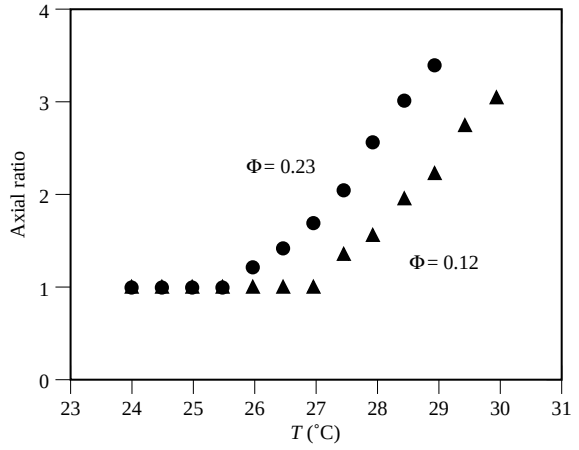

Figure 10 Variation in the micellar axial ratio with temperature, assuming a monodisperse prolate growth, as deduced from the relaxation data in Figure 9 by using the correlation function due to Halle,[54] for the combined motion of aggregate tumbling and surface diffusion

3.4 Relaxation Measurements on Water and Counterion Nuclei

Relaxation measurements on water and counterion nuclei may also give information about the surfactant aggregate size and shape. Such measurements may be particularly useful in reverse micellar systems, where water and surfactant counterions are contained in small water pools covered by a surfactant monolayer. In a ^{23}Na ($I = \frac{3}{2}$) spin relaxation study of a reverse micellar system, the presence of slow motions was found to result in a biexponential free induction decay (FID).[57] Using the two transverse relaxation rates and an effective longitudinal relaxation rate, it was possible to determine all three spectral density values: $j(0)$, $j(\omega_0)$, and $j(2\omega_0)$. From the fit of the imaginary part of the FID it was also possible to determine the second-order quadrupolar dynamic shift, allowing for an additional test of the motional model invoked in the interpretation of the data.

An interesting application of water nuclei relaxation in microemulsions concerns the so-called 'nuclear spin quenching' studied by Carlström and Halle.[58] Here, the effect of chemical exchange of water protons, mediated by the presence of prototropic ions, H_3O^+ and OH^-, on the ^{17}O bandshape in a reverse micellar system was investigated. By careful analysis of the ^{17}O bandshape, information on the water exchange kinetics between droplets as well as the droplet size was obtained.

3.5 Surfactant Hydrocarbon Chain Conformations in Micelles

The early findings of narrow ^{1}H bands from the surfactant hydrocarbon chains in small spherical micelles revealed that the micellar interior is in a liquid-like state. Magnetic field dependent ^{13}C R_1 relaxation experiments confirmed those ideas, and a segmental order parameter profile, similar to that obtained from ^{2}H quadrupolar splittings in lipid bilayer systems, was obtained within the two-step formalism.[59] By studying the dynamics of a symmetric probe molecule solubilized in micelles, it was concluded that the micellar interior was characterized by an effective viscosity similar to that of the neat hydrocarbon.[60]

Chachaty and co-workers[40,61] have studied the enhanced relaxation rate due to the presence of paramagnetic counterions. The multivalent paramagnetic counterion is expected to be selectively adsorbed onto the charged micellar surface. Thus, by analyzing the effect on the ^{13}C relaxation along the chain, the distribution in the distance from the micellar surface could be estimated for the various methylene segments.

A conceptually similar study was reported recently by Palmas et al.[62] Here, cross relaxation effects between ^{13}C and nondirectly bonded protons were examined by two-dimensional heteronuclear Overhauser effect spectroscopy (HOESY). This study revealed the significance of intermolecular $^{1}H-^{13}C$ dipolar interactions. Correlations between carbon atoms and protons belonging to different segments were observed in the lower part of the hydrocarbon chains, while they were found to be absent in the vicinity of the polar headgroup, where the chain configuration is more rigid.

4 RELATED ARTICLES

Amphiphilic Liquid Crystalline Samples: Nuclear Spin Relaxation; Bilayer Membranes: Deuterium and Carbon-13 NMR; Brownian Motion and Correlation Times; Colloidal Systems; Diffusion Measurements by Magnetic Field Gradient Methods; Liquid Crystalline Samples: Diffusion; Liquid Crystalline Samples: Structure of Nonrigid Molecules.

5 REFERENCES

1. J. W. McBain and M. Taylor, *Ber.*, 1910, **43**, 321.
2. J. W. McBain, E. C. V. Cornish, and R. C. Bowden, *J. Chem. Soc.*, 1912, **101**, 2042.
3. J. W. McBain, *Trans. Faraday Soc.*, 1913, **9**, 99.
4. J. W. McBain and C. S. Salmon, *J. Am. Chem. Soc.*, 1920, **42**, 426.
5. P. T. Callaghan, C. M. Trotter, and K. W. Jolley, *J. Magn. Reson.*, 1980, **37**, 247.
6. P. Stilbs, *Prog. Nucl. Magn. Reson. Spectrosc.*, 1987, **19**, 1.
7. E. L. Hahn, *Phys. Rev.*, 1950, **80**, 580.
8. E. O. Stejskal and J. E. Tanner, *J. Chem. Phys.*, 1965, **42**, 288.
9. D. W. McCall, D. C. Douglass, and E. W. Anderson, *Ber. Bunsenges. Phys. Chem.*, 1963, **67**, 336.
10. R. L. Vold, J. S. Waugh, M. P. Klein, and D. E. Phelps *J. Chem. Phys.*, 1968, **48**, 3831.
11. J. E. Tanner, Thesis, University of Wisconsin, Madison, WI, USA, 1966.
12. G. Oraedd, G. Lindblom, L. B. A. Johansson, and G. Wikander, *J. Phys. Chem.*, 1992, **96**, 5170.
13. M. Jansson and P. Stilbs *J. Phys. Chem.*, 1985, **89**, 4868.
14. G. Gunnarsson, B. Jönsson, and H. Wennerström, *J. Phys. Chem.*, 1980, **84**, 3114.
15. H. Hagslätt, O. Söderman, B. Jönsson, and L. Johansson, *J. Phys. Chem.*, 1991, **95**, 1703.
16. B. Jönsson, H. Wennerström, P. Nilsson, and P. Linse, *Colloid Polymer Sci.*, 1986, **264**, 77.
17. B. Lindman and H. Wennerström, *J. Phys. Chem.*, 1991, **95**, 6053.
18. P. G. Nilsson, H. Wennerström, and B. Lindman, *J. Phys. Chem.*, 1983, **87**, 1377.
19. P. G. Nilsson, H. Wennerström, and B. Lindman, *Chem. Script.*, 1985, **25**, 67.
20. B. Lindman, O. Söderman, and P. Stilbs, in *Surfactants in Solutions*, ed. K. L. Mittal, Plenum, New York, 1989, Vol. 7.
21. O. Söderman, E. Hansson, and M. Monduzzi, *J. Colloid Interface Sci.*, 1991, **141**, 512.
22. U. Olsson and P. Schurtenberger, *Langmuir*, 1993, **9**, 3389.
23. K. Shinoda and B. Lindman, *Langmuir*, 1987, **3**, 135.
24. K. Fukuda, O. Söderman, B. Lindman, and K. Shinoda, *Langmuir*, 1993, **9**, 2921.
25. U. Olsson, K. Nagai, and H. Wennerström, *J. Phys. Chem.*, 1988, **92**, 6675.
26. U. Olsson, M. Jonströmer, K. Nagai, O. Söderman, H. Wennerström, and G. Klose, *Prog. Colloid Polym. Sci.*, 1988, **76**, 75.
27. M. Jonströmer, W. O. Parker, and U. Olsson, *Langmuir*, 1995, **11**, 61.
28. B. Lindman, K. Shinoda, U. Olsson, D. Anderson, G. Karlström, and H. Wennerström, *Colloid Surfaces*, 1989, **38**, 205.
29. L. E. Scriven, *Nature*, 1976, **263**, 123.
30. D. M. Anderson and H. Wennerström, *J. Phys. Chem.*, 1990, **94**, 8683.
31. M. T. Clarkson, D. Beaglehole, and P. T. Callaghan, *Phys. Rev. Lett.*, 1985, **54**, 1722.
32. O. Söderman, G. Carlström, U. Olsson, and T. C. Wong, *J. Chem. Soc., Faraday Trans. 1*, 1988, **84**, 4475.
33. P.-O. Quist, B. Halle, and I. Furo, *J. Chem. Phys.*, 1991, **95**, 6945.
34. B. Balinov, U. Olsson, and O. Söderman, *J. Phys. Chem.*, 1991, **95**, 5931.
35. U. Olsson, B. Balinov, and O. Söderman, in *The Structure and Conformation of Amphiphilic Membranes* (*Springer Proceedings in Physics, Vol. 66*), ed. R. Lipowsky and K. Kremer, Springer, Berlin, 1992.
36. M. Monduzzi, U. Olsson, and O. Söderman, *Langmuir*, 1993, **9**, 2914.
37. P. Stilbs, in *Solubilization* (*Surfactant Science Series*), ed. D. Christian and J. F. Scamehorn, M. Dekker, New York, 1994.
38. B. Lindman, O. Söderman, and H. Wennerström, in *Surfactant Solutions. New Methods of Investigation*, ed. R. Zana, M. Dekker, New York, 1987, p. 295.
39. B. Lindman, O. Söderman, and H. Wennerström, *Ann. Chim. (Rome)*, 1987, **77**, 1.
40. C. Chachaty, *Prog. Nucl. Magn. Reson. Spectrosc.*, 1987, **19**, 183.
41. J. Ulmius and H. Wennerström, *J. Magn. Reson.*, 1977, **28**, 309.
42. U. Olsson, O. Söderman, and P. Guéring, *J. Phys. Chem.*, 1986, **90**, 5223.
43. H. Wennerström and J. Ulmius, *J. Magn. Reson.*, 1976, **23**, 431.
44. F. Noack, *Prog. Nucl. Magn. Reson. Spectrosc.*, 1986, **18**, 171.
45. W. Kühner, E. Rommel, F. Noack, and P. Meier, *Z. Naturforsch., Teil A*, 1987, **42**, 127.
46. H. Wennerström, G. Lindblom, and B. Lindman, *Chem. Script.*, 1974, **6**, 97.
47. H. Wennerström, B. Lindman, O. Söderman, T. Drakenberg, and J. B. Rosenholm, *J. Am. Chem. Soc.*, 1979, **101**, 6860.
48. B. Halle and H. Wennerström, *J. Chem. Phys.*, 1981, **75**, 1928.
49. A. Abragam, *The Principles of Nuclear Magnetism*, Clarendon, Oxford, 1961.
50. O. Söderman, H. Walderhaug, U. Henriksson, and P. Stilbs, *J. Phys. Chem.*, 1985, **89**, 3693.
51. O. Söderman, U. Henriksson, and U. Olsson, *J. Phys. Chem.*, 1987, **91**, 116.
52. M. S. Leaver, U. Olsson, H. Wennerström, and R. Strey, *J. Phys. II*, 1994, **4**, 515.
53. R. Skurtveit and U. Olsson, *J. Phys. Chem.*, 1992, **96**, 8640.
54. B. Halle, *J. Chem. Phys.*, 1991, **94**, 3150.
55. H. Wennerström, *Chem. Phys. Lett.*, 1973, **18**, 41.
56. L. Hwang, P. Wang, and T. C. Wong, *J. Phys. Chem.*, 1988, **92**, 4753.

57. P. H. Kenez, G. Carlström, I. Furo, and B. Halle, *J. Phys. Chem.*, 1992, **96**, 9524.
58. G. Carlström and B. Halle, *Mol. Phys.*, 1988, **64**, 659.
59. H. Walderhaug, O. Söderman, and P. Stilbs, *J. Phys. Chem.*, 1984, **88**, 1655.
60. P. Stilbs, H. Walderhaug, and B. Lindman, *J. Phys. Chem.*, 1983, **87**, 4762.
61. Y. Chevalier and C. Chachaty, *J. Phys. Chem.*, 1985, **89**, 875.
62. P. Palmas, P. Tekely, P. Mutzenhardt, and D. Canet, *J. Chem. Phys.*, 1993, **99**, 4775.

Biographical Sketches

Olle Söderman. *b* 1951. B.Sc., 1976, Ph.D. (supervisor Göran Lindblom), 1981, Lund Institute of Technology. Introduced to NMR by S. Forsén and G. Lindblom. Visiting graduate student at University of British Columbia (with Myer Bloom). Joined Faculty of Physical Chemistry, University of Lund, 1981. Currently, lecturer, University of Lund. Approx. 80 publications. Current research interests: pulsed field gradient NMR applied to colloidal systems.

Ulf Olsson. *b* 1957. B.Sc., 1981, Ph.D. (supervisor Olle Söderman), 1988, Lund University. Postdoctoral research, Centre de Recherche Paul Pascal, Pessac France, 1989. Faculty of Physical Chemistry, Lund University, 1989. Approx. 40 publications. Current research interests: structure and phase equilibria of surfactant/water/oil systems.

Multiple Quantum Spectroscopy in Liquid Crystalline Solvents

Leslie D. Field
Sydney University, NSW, Australia

1	Introduction	1
2	Multiple Quantum NMR of Samples Dissolved in Liquid Crystalline Solvents	1
3	Excitation of Multiple Quantum Coherences	2
4	Detection of Multiple Quantum Coherences	3
5	Methods of Spectral Analysis and Spectral Simulation	5
6	Applications of MQ NMR to Samples Dissolved in Liquid Crystalline Solvents	5
7	Related Articles	8
8	References	8

1 INTRODUCTION

Liquid crystals can be loosely defined as materials with properties intermediate between those of solids and liquids (mesophases). Liquid crystals typically flow like viscous liquids but the phase exhibits some degree of molecular packing or structure whereby individual molecules tend to align, making the mesophase anisotropic.

1.1 NMR in Liquid Crystalline Solvents

Most molecules that form a nematic mesophase are able to dissolve a small amount of solute compound without destroying the mesophase. Since the first reports of using liquid crystals as solvents for NMR spectroscopy, high resolution NMR in liquid crystalline solution has developed into an important area.[1] The amount of solute that can be dissolved in a nematic mesophase depends on the mesophase and the solute, but solute concentrations of 5 wt % are common and concentrations of 10–15 wt % are sometimes achievable without disrupting the liquid crystalline properties of the solvent.

The motion of solute molecules dissolved in a nematic mesophase is restricted by the arrangement of the mesophase molecules. The anisotropy of the arrangement of the solvent molecules induces anisotropy in the movement of the solute molecules via dispersion forces. A solute dissolved in an oriented mesophase is forced to undergo nonrandom (anisotropic) motion because of its interactions with the aligned solvent. If the nematic mesophase is aligned in a magnetic field then alignment of the mesophase is reflected in the anisotropy of the motion of the solute molecules.

The rapid motion of molecules in an oriented mesophase results in the averaging of the intermolecular dipolar interactions to zero. However, the intramolecular dipolar interactions have a nonzero average.

Qualitatively the NMR spectra of solutes oriented in mesophases are more complex than the spectra obtained in isotropic solvents, for two reasons (see ***Liquid Crystalline Samples: Spectral Analysis***):

1. The nonzero averaging of dipolar couplings results in many more coupling constants (splittings) being expressed in the spectrum. A dipolar coupling constant appears for every pair of interacting nuclei.
2. The magnitude of the dipolar coupling constants (D_{ij}), between a pair of interacting nuclei is generally large (up to a few kilohertz) compared with the indirect coupling constants (typically a few hertz). This results in virtually all spectra of solutes dissolved in an oriented mesophase being highly second order and adds to the spectral complexity.

2 MULTIPLE QUANTUM NMR OF SAMPLES DISSOLVED IN LIQUID CRYSTALLINE SOLVENTS

The signals observed in a conventional NMR spectrum (single rf pulse followed by signal acquisition and FT of the resulting FID) are governed by selection rules which dictate that transitions can only be induced between energy levels differing in total spin quantum number by $\Delta M = \pm 1$ (single quantum transitions). Multiple quantum NMR (MQ NMR)[2] is concerned with the observation of nuclear transitions where $\Delta M \neq \pm 1$.

The number of transitions in the single quantum NMR spectrum of a solute dissolved in an anisotropic solvent increases rapidly with the number of coupled spins. A molecule with a single proton would have a ^{1}H spectrum with only one transition. A system containing two protons would have four possible transitions, and a spin system composed of three nonequivalent protons has 15 transitions.

The number of transitions for an unsymmetrical spin system (disregarding symmetry considerations) can be calculated as[3]

$$\text{No. single quantum transitions} = (2N)!/[(N-1)!(N+1)!] \quad (1)$$

This is an exponential function where the number of transitions increases dramatically as the number of interacting spins increases (Figure 1). In an 8-spin system there would be 1.14×10^3 transitions in the single quantum spectrum; in a 10-spin system there would be 1.67×10^5 transitions.

If there is symmetry present in the spin system (i.e. chemically or magnetically equivalent nuclei) the number of transitions is reduced. For the symmetrical six proton spin system of benzene there are 72 transitions, compared with 792 transitions in a six proton system with no symmetry.

Given a reasonable linewidth for each transition, substantial overlap occurs in the single quantum spectrum of a large spin system, and the spectrum rapidly degenerates to an unresolved broad lump. In higher spin systems, it becomes impossible to resolve or assign individual transitions for an iterative computer analysis. MQ NMR can considerably reduce the complexity of the spectrum of a solute dissolved in a liquid crystalline solvent, and the main benefit of MQ NMR lies in the fact that there are fewer transitions in the very high MQ spectra.

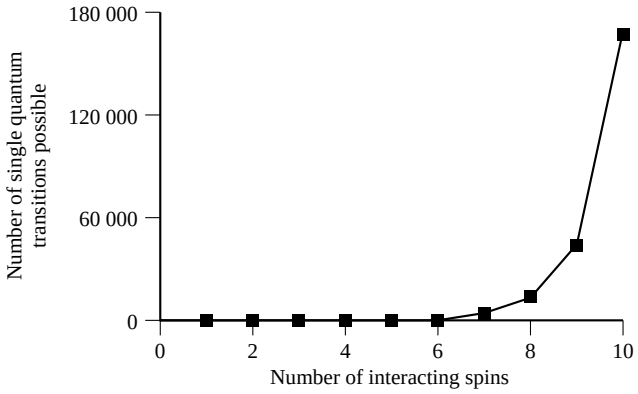

Figure 1 The number of single quantum transitions as a function of the number of interacting nuclei ($I = \frac{1}{2}$)

The number of M quantum transitions in a system of N nuclei ($I = 1/2$), neglecting symmetry, is given by

$$\text{No. of } M \text{ quantum transitions} = (2N)!/[(N - M)!(N + M)!] \quad (2)$$

Representative values are summarized in Table 1.

In the N quantum spectrum of an N-spin system, there will always be only one transition. The $(N - 1)$ quantum spectrum of an N-spin system will contain only $2N$ transitions. For large N, the $N - 1$ and $N - 2$ quantum spectra will contain only a few transitions and will be much less complex and more easily analyzed than the single quantum spectrum.

3 EXCITATION OF MULTIPLE QUANTUM COHERENCES

Coherence between states separated by $\Delta M \neq 1$ cannot be observed directly, but is usually detected indirectly by its modulation of single quantum coherence in a two-dimensional NMR experiment. A two-dimensional NMR experiment[4] for exciting and detecting MQ spectra can be divided schematically into five time frames, as shown in Table 2.

Providing that MQ coherences (MQCs) can be produced by a suitable preparation sequence, and mixed to observable single quantum coherence with an appropriate 'mixing' sequence, the MQ frequencies of a spin system can be obtained by systematically varying the duration of the 'evolution' period (t_1) followed by Fourier transformation over t_1. Compared with samples in isotropic solution, MQCs can be excited relatively easily in samples dissolved in liquid crystalline solution. The large dipolar coupling constants expressed ensure that coherences evolve rapidly and MQC can be excited efficiently before the effects of relaxation complicate coherence development in the spin system.

3.1 Nonselective Excitation

The most common (and simplest) method for preparing MQC is by use of two $\pi/2$ pulses separated by a fixed delay. The simplest mixing sequence is a single $\pi/2$ pulse and this means that a three-pulse sequence (Figure 2) can be used to record multiple quantum spectra.

The sequence of two hard pulses in the preparation part in Figure 2 nonselectively generates coherence of all orders possible in the spin system. Coherences are not excited uniformly and the efficiency with which MQC is excited depends specifically on the couplings and chemical shifts of the nuclei in the spin system and the choice of the interval d_1. Broad band excitation techniques have been proposed[5] where the value of d_1 in the preparation sequence is varied either in a pseudorandom or systematic fashion to achieve a more uniform excitation in the multiple quantum domain. Weitekamp et al.[6] have devised an experimental search procedure for optimizing the delays in the preparation period of the MQ excitation sequence.

Table 1 The Number of Transitions in the M Quantum Spectra as a Function of the Number of Interacting Nuclei ($I = \frac{1}{2}$)

	Number of spins ($I = \frac{1}{2}$)						
ΔM	2	4	6	8	10	15	20
1	4	56	792	11440	1.68×10^5	1.45×10^8	1.31×10^{11}
2	1	28	495	8008	1.26×10^5	1.19×10^8	1.13×10^{11}
4		1	220	1820	38760	5.46×10^7	6.28×10^{10}
6			1	120	4845	1.43×10^7	2.32×10^{10}
8				1	190	2.04×10^6	5.58×10^9
10					1	1.42×10^5	8.48×10^8
15						1	6.58×10^5
20							1

Table 2 The Five Time Frames in the Two-dimensional MQ NMR Experiment[a]

Relaxation	Preparation	Evolution	Mixing	Detection
Spin system relaxes between experiments	Generate MQC in the coupled spin system	MQC evolves with time (t_1)	Mixes MQC to observable SQC	Detect SQC as a FID (t_2)

[a]MQC, multiple quantum coherence; SQC, single quantum coherence.

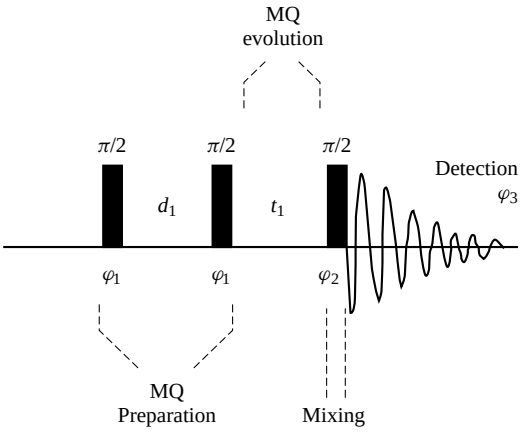

Figure 2 Three-pulse sequence for the observation of MQ spectra

3.2 Selective Excitation

Nonselective excitation of MQC excites all possible coherences, but leaves most of the spectral intensity in the single quantum and low multiple quantum spectra because these spectra have the most transitions.[3b] As a result, the simpler high-order coherences are comparatively weak. An alternative approach to the excitation of MQC is selectively to excite only a few orders of coherence and more effectively channel or focus the available signal into one order (or a few selected orders).

Order selective excitation has been achieved by the use of phase-cycled sequences of rf pulses[7] and composite pulse trains.[8] Pines et al.[7,9] have established that an nk quantum selective excitation sequence ($k = 0, \pm1, \pm2, \cdots$) can be constructed by repeating an appropriate sequence with a phase increment $2\pi/n$ between repetitions:

$$\varphi = 0 \quad \varphi = 2\pi/n \; \varphi = 4\pi/n \quad \varphi = 2(n-1)\pi/n$$
$$[p_1 \ldots p_q]\,[p_1 \ldots p_q]\,[p_1 \ldots p_q] \ldots [p_1 \ldots p_q]$$

The pulse sequences $[p_1 \cdots p_q]$ employed in each section of the sequence can be nonselective; however, only certain sequences are effective in efficiently generating the desired orders of MQC. Sequences involving several thousand cycled pulses have been explored.[7,9] An upper limit on the length of the excitation sequence is set by relaxation processes in the spin system. Effective phase-cycled excitation sequences must generate MQC efficiently and compensate for the effects of imperfect rf hardware and pulses.

4 DETECTION OF MULTIPLE QUANTUM COHERENCES

The frequencies of MQCs are obtained indirectly using two-dimensional NMR sequences whereby the multiple quantum frequencies modulate the observable single quantum spectrum. The two-dimensional spectrum contains multiple quantum frequencies in F_1 and single quantum frequencies in F_2. The frequencies of the multiple quantum spectrum are most conveniently obtained as F_1 projections from the two-dimensional spectrum.

It is not necessary to acquire an entire two-dimensional data set to obtain the multiple quantum frequencies. MQ spectra can be obtained by acquiring a single point in t_2 (at $t_2 = 0$ or some other value) and then transforming the resulting one-dimensional sequence of points as a function of t_1. In theory, the FT of the $t_2 = 0$ row of a two-dimensional data set is identical to the F_1 projection of the entire two-dimensional data set.[10]

If the MQ preparation sequence does not perfectly select coherences from an individual MQ order, then the MQ spectrum detected will be a complex superposition of subspectra from the various MQCs excited. There are several methods available to filter or separate the MQ spectra of various orders.

4.1 Order Selective Detection

4.1.1 Dependence on Resonance Offset

n Quantum coherence evolves n-fold more rapidly during the t_1 evolution period of the MQ experiment than does single quantum coherence. If the single quantum spectrum is centered at a frequency approximately $\Delta\omega$ from the rf transmitter, transitions in the n quantum spectrum are centered at a frequency $n\Delta\omega$. With nonselective excitation, multiple quantum spectra are separated by $\Delta\omega$ and by judicious selection of the transmitter offset, the spectra of various multiple quantum orders can be cleanly separated (Figure 3) in the frequency domain.

The main disadvantages of using transmitter offsets to separate various orders of MQC are: (i) offset frequencies of 10–30 kHz are often required to obtain clean separation of the coherence orders and the large offset results in nonuniform rf distribution and homogeneity across the spectrum: and (ii) for a nonselective experiment where all orders of coherence (up to $\pm N$ orders in an N-spin system) are detected, the total sweep width required in F_1 is prohibitively large. The F_1 sweep width is approximately $N*SW$, where SW is the approximate spectral width of any of the orders of coherence in the spin system; SW may be 100–300 kHz and necessarily gives rise to poor digital resolution.

4.1.2 Time Proportional Phase Incrementation

Time proportional phase incrementation (TPPI) enables the separation of spectra of various coherence orders. If the phase of the excitation radiation is incremented by $\Delta\phi = \Delta\omega{\cdot}\Delta t_1$ each time that t_1 is incremented by Δt_1, the n quantum spectrum is centered at a frequency $n\Delta\omega$ from the transmitter in the two-dimensional MQ NMR spectrum. MQ orders are separated in frequency by $\Delta\omega$ in the same fashion as if an offset had been employed.

4.1.3 Order Selective MQ Filtration Using Phase Cycling

Order selective detection of the spectrum of a desired order n is achieved by coadding $4n$ FIDs at each value of τ_1 with the phase of the preparation rf radiation (φ_1 in Figure 2) incremented from $2\pi/4n$ to 2π in steps of $2\pi/4n$ with the receiver phase (φ_3 in Figure 2) incremented by $\pi/2$ at each step.[11] Two-dimensional Fourier transformation over τ_1 and τ_2 affords a two-dimensional spectrum which has the MQ

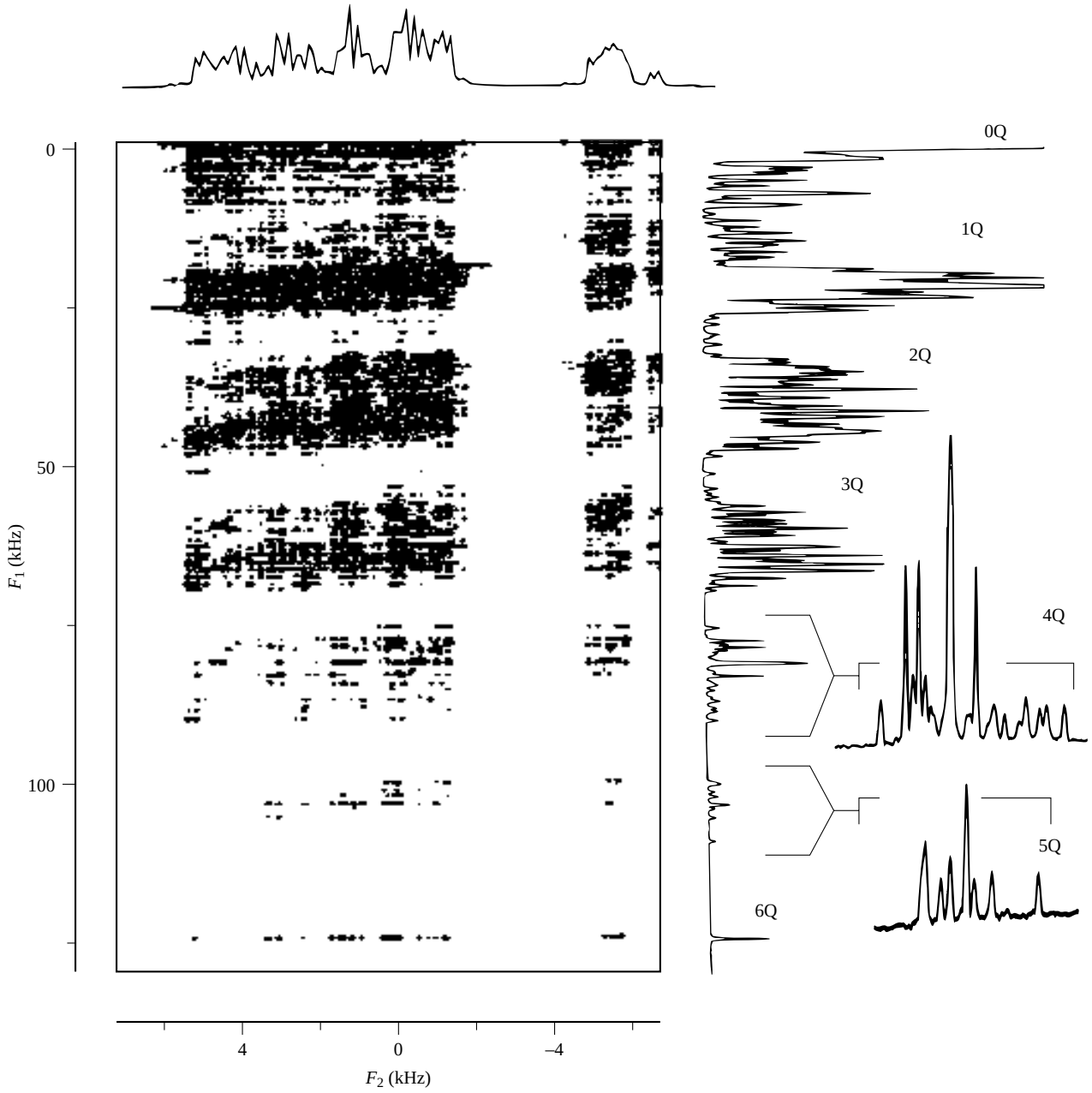

Figure 3 The separation of MQ spectra by employing a transmitter offset: ^{1}H spectrum of 2-methylthiophene aligned in a liquid crystalline solvent. The spectrum was acquired with the pulse sequence shown in Figure 2 with the transmitter offset approximately 20.7 kHz from the center of spectrum. The full spectrum is symmetrical about $F_1 = 0$ and only half of the spectrum is shown. Frequencies in the MQ spectrum are obtained from an F_1 projection of the two-dimensional data set

frequencies of the desired order of MQC in F_1 and the MQ filtered single quantum spectrum in F_2.

4.1.4 Coherence Echo Filtration

Order selective detection of the spectrum of a desired order n has been achieved by exploiting the phase properties of MQC transfer echoes. An additional (fixed) period d_e is inserted in the MQ pulse sequence, prior to the mixing pulse of the MQ pulse sequence (Figure 4). The delay d_e results in the MQCs evolving beyond the normal τ_1 period and coherence transfer echoes of the n quantum coherences maximize in the detection period at nd_e.[12] Different coherence orders give rise to echoes which maximize at different times in the detection period. The spectra derived from individual orders of coherence can be obtained by selecting a detection window to coincide with the maximum signal of the desired order of coherence.

4.1.5 Use of Magnetic Field Gradients

Order selective detection of the spectrum of a desired order n has been achieved by using field gradients.[13] A field gradient pulse of amplitude g is applied at the end of the MQ evolution

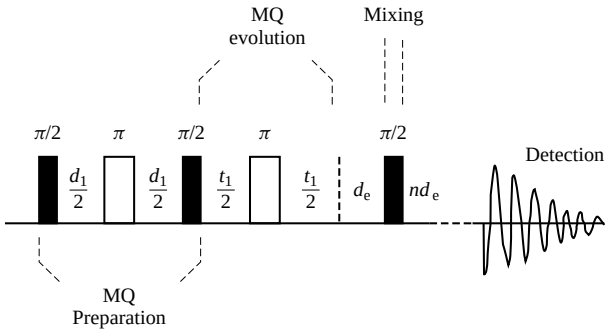

Figure 4 Pulse sequence for selectively observing MQC transfer echoes

period, prior to the mixing section of the MQ pulse sequence (Figure 5). A refocusing gradient of amplitude *ng* immediately after the mixing sequence selects only signals from the *n*-quantum spectrum.[12a,14]

4.1.6 Phase Sensitive MQ Spectra

A disadvantage of most simple mixing sequences which convert MQCs to detectable single quantum coherence is that the detectable single quantum spectrum has both absorption and dispersion components. As spin systems become larger, the single quantum spectrum degenerates to a mass of overlapping resonances, and any mixing sequence which results in signals of differing phase causes signal cancellation. In larger, more complex spin systems, the single quantum spectrum becomes weaker and inherently more difficult (or impossible) to detect. Pines et al.[15] have developed a general class of MQ experiments where the MQ preparation sequence is matched with a mixing sequence (a time reversal sequence) to give a single quantum spectrum which is in-phase. There are a number of matched preparation/mixing sequences and these have been used to observe high-order MQ spectra, including those in solids.

Another consequence of simple MQ sequences is that the MQ spectra obtained are obtained as spectra that cannot be phased. Most MQ spectra which have been recorded from samples dissolved in liquid crystalline solution have been transformed as magnitude spectra. Using appropriately matched preparation and mixing sequences, pure absorption spectra

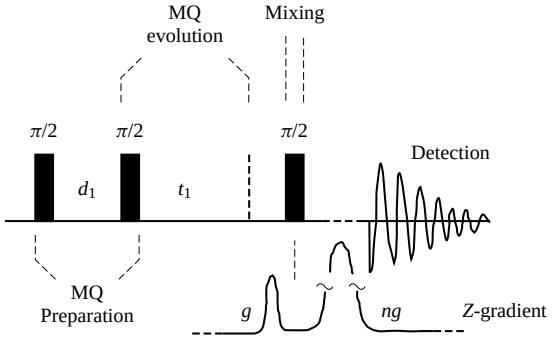

Figure 5 Pulse sequence for selectively observing MQC using field gradient filtration

have been recorded,[2b,16] and these show improved sensitivity and resolution compared with corresponding magnitude spectra.

5 METHODS OF SPECTRAL ANALYSIS AND SPECTRAL SIMULATION

The energy levels of an *n*-spin system can be calculated if the dipolar coupling constants D_{ij}, scalar coupling constants J_{ij}, chemical shifts ν_i, and quadrupolar coupling constants q_{ij} are known. The energy levels are grouped into manifolds according to their Zeeman quantum number (M) and irreducible symmetry representations. m Quantum transitions occur between energy levels of the same symmetry where $\triangle M = m$. The frequencies of MQ transitions are not difficult to calculate and the frequencies in experimental MQ spectra have been fitted iteratively to calculated frequencies using modifications of LAOCOON type[17] computer algorithms. The calculation of the correct intensities of MQ transitions is more demanding since the transition intensities are a complex function of the specific pulse sequence used to generate the spectrum. Transition intensities in MQ spectra derived from a simple three-pulse sequence (Figure 2) have been estimated using a statistical approach whereby all symmetry-allowed transitions are assumed to be equally excited. Averaging over a range of d_1 values, the integrated intensity per order decreases as $\triangle M$ increases, but the average intensity per transition increases as $\triangle M$ increases.[3b] The estimation of transition intensities in MQ spectra has been extended to excitation sequences involving order selective composite pulse excitation, and the calculations provide a reliable means for theoretically optimizing the efficiency of the excitation sequence.[18]

6 APPLICATIONS OF MQ NMR TO SAMPLES DISSOLVED IN LIQUID CRYSTALLINE SOLVENTS

6.1 Structural Studies

In the spectra of compounds dissolved in liquid crystalline solution, dipolar interactions between nuclei are not averaged to zero and the spectra can, in principle, be analyzed to obtain values for the dipolar coupling constant D_{ij} between each pair of nuclei (i and j) in the solute spin system. Since the D_{ij} are inversely proportional to the cube of the internuclear distances r_{ij} [equation (3)], the relative positions of the nuclei in the spin system can be determined and the shape of the molecule as well as its average orientation in the magnetic field can be deduced, providing enough independent D_{ij} values can be measured. For a system of coupled $I = 1/2$ nuclei, the transition frequencies in the MQ spectra are determined by the dipolar coupling constants, the scalar coupling constants, and the chemical shifts of the nuclei. In theory, the spectra of order $n - 1$ and $n - 2$ contain sufficient transitions to measure all the dipolar coupling constants and chemical shifts in an *n*-spin system:

$$D_{ij} = -(h\gamma_H^2/4\pi^2)S_{ij}/r_{ij}^3 \qquad (3)$$

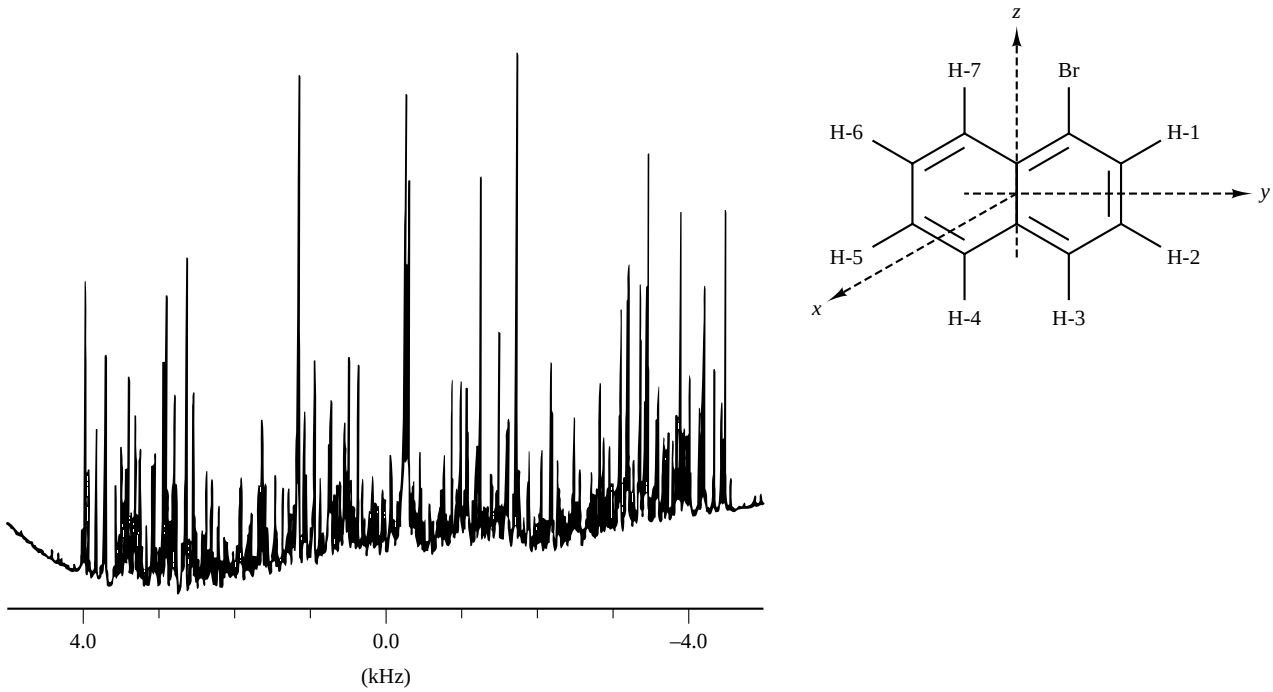

Figure 6 Single quantum proton spectra of 1-bromonaphthalene aligned in liquid crystalline solution. Reproduced by permission of Academic Press from Reference [20a]

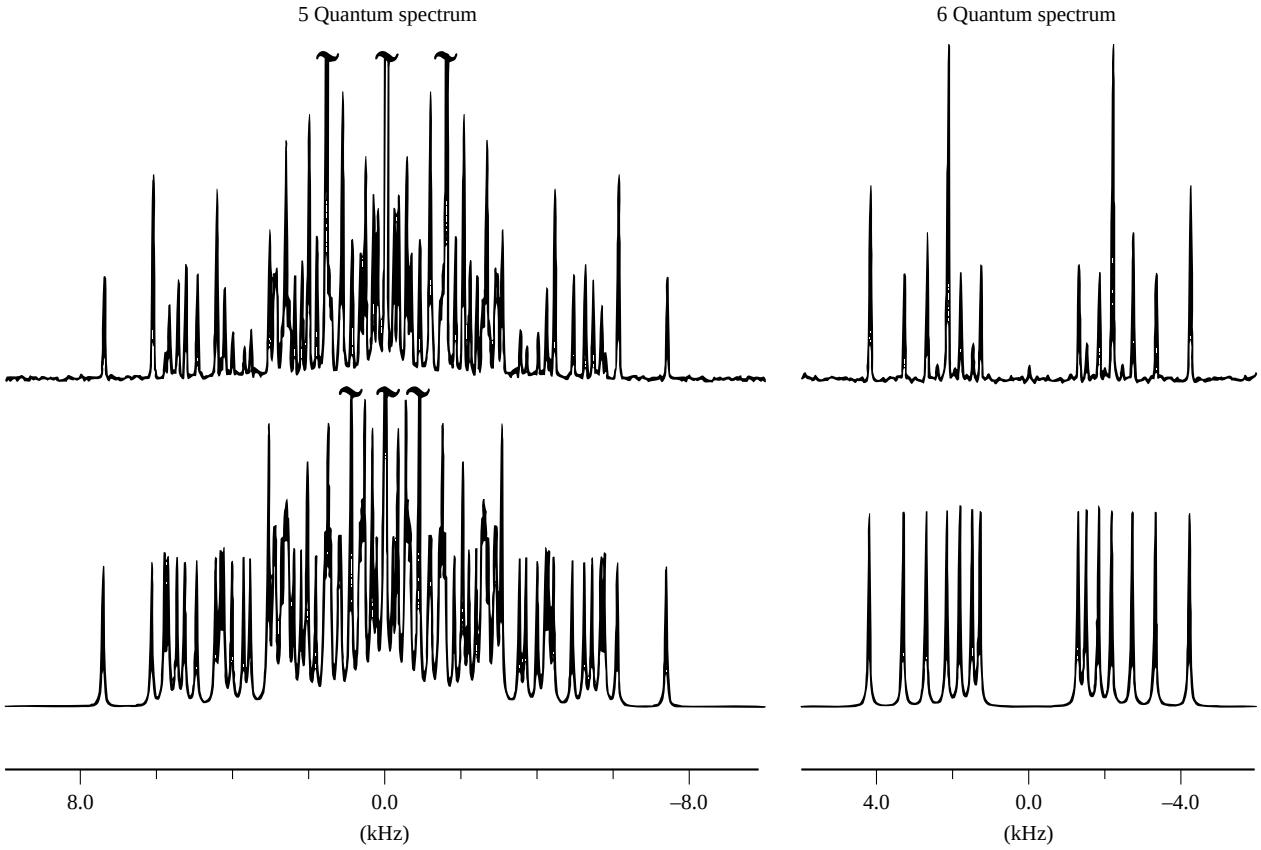

Figure 7 Experimental (upper) and simulated (lower) multiple quantum spectra of 1-bromonaphthalene aligned in liquid crystalline solution. Experimental spectra were acquired with chemical shift refocusing in F_1 and spectra were symmetrized about $F_1 = 0$. Simulations assume all transitions have the same intensity. Reproduced by permission of Academic Press from Reference [20a]

where γ_H is the proton magnetogyric ratio, r_{ij} is the internuclear distance between protons i and j, and S_{ij} is the order of the internuclear vector between i and j.[19] There have been only a few studies in which the geometry of a spin system has been established using MQ NMR.

6.1.1 Structure of Rigid Molecules: Structure of 1-Bromonaphthalene

1-Bromonaphthalene has a proton spin system containing seven nonequivalent spins. In liquid crystalline solution the ^{1}H NMR spectrum contains more than 3000 transitions (Figure 6).[20] The five and six quantum spectra have been recorded and solved simultaneously (Figure 7) to give values for the 21 independent dipolar coupling constants, and from the D_{ij} values the geometry of the planar seven spin system was determined.[20]

6.1.2 Chain Mobility in n-Hexane-d_6

MQ NMR has been employed to study chain mobility in alkanes dissolved in liquid crystalline solution. Drobny[2b] has reported the MQ spectra of *n*-hexane-d_6 (deuterated in the terminal methyl groups) dissolved in a nematic solvent. MQ spectra were recorded and the high quantum spectra (six and seven quantum) analyzed to give dipolar couplings. The six quantum proton spectrum contains 36 transitions and the seven quantum spectrum contains four transitions, as expected for an eight proton spin system with C_{2h} symmetry. The best fit of theoretically generated MQ NMR spectra to the experimental spectra was obtained with a model where only the minimum energy conformations of the alkane chain were appreciably populated.

6.1.3 Structure of 4-Cyano-4′-n-pentylbiphenyl

4-Cyano-4′-*n*-pentylbiphenyl is a nematic liquid crystal at room temperature. The five, six, and seven quantum MQ NMR spectra of the eight proton spin system of a partially deuterated compound (with the pentyl side chain completely deuterated) have been analyzed to give the interproton dipolar couplings in the biphenyl core of the molecule.[21] The best match between the experimental and simulated MQ NMR spectra were obtained when the biphenyl system was not planar, but when there was an angle of about 32° between the linked phenyl groups.

6.2 Counting Spins in Clusters

In MQ NMR, individual spins become correlated with each other over time through their dipolar couplings. The rate at which MQCs develop is a complex function of the coupling constants present in the spin system. In solids, where the distribution of dipole coupled spins is effectively infinite, the correlations between spins develop in a monotonic fashion. As time progresses, more spins can absorb more quanta and high order MQC can be generated.[22] In systems where there are effectively isolated clusters of spins (e.g. liquid crystals, molecules dissolved in liquid crystalline phases, and polycrystalline solids) the time development of MQC is interrupted and the system can only support MQC up to the size of coupled spin clusters. In the 21-spin system of the liquid crystal 4-cyano-4′-heptylbiphenyl, the effective spin system size increases to a maximum of 21 spins as the preparation time for MQC increases (Figure 8).

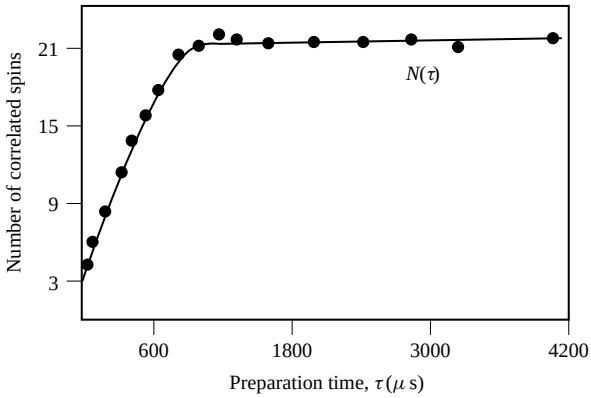

Figure 8 The effective system size $N(\tau)$ as a function of the preparation time τ for the liquid crystal 4-cyano-4′-heptylbiphenyl. After an induction period of approximately 1000 μs, $N(\tau)$ levels off to a value of 21, reflecting the number of spins in the isolated molecular cluster. Reprinted by permission of the American Chemical Society from Baum and Pines[22]

The rate of MQC development in a mixture of liquid crystalline materials has also been used to identify and observe distinct subsections of molecules comprising the liquid crystals. Separate MQ signals were observed for effectively isolated spin pairs (phenyl rings) and weakly coupled multispin clusters (alkyl tails)[23] in a mixture of 4-cyanophenyl 4′-butylbenzoate and 4-cyanophenyl 4′-heptylbenzoate.

6.3 Measurements of Diffusion

MQC has been used to extend the normal NMR spin echo measurement of diffusion. In typical spin echo experiments, molecules are labeled by their position in a magnetic field gradient after an initial rf pulse and diffusion is measured by monitoring the amplitude of the spin echo following a second pulse. MQ NMR spectroscopy exploits the fact that *n* quantum coherence dephases *n*-times more quickly than does single quantum coherence, so higher quantum coherences are significantly more sensitive to diffusion.

Martin et al.[24] measured the diffusion of dichloromethane (CH_2Cl_2) in various liquid crystal solvents by following the decay of the double quantum coherence. In measurements of the diffusion of benzene in a nematic liquid crystal, Zax and Pines[25] used a pulse sequence [Figure 9(a)] to excite MQC nonselectively and then selectively monitored the decay of the coherence echo of the $n = 1$ to $n = 6$ orders of coherence following field gradient pulses. The amplitude of echo decay for all orders of coherence was fitted to a modified Stejskal–Tanner equation[26] (Figure 9), thus verifying that the rate of echo decay is proportional to n^2.

6.4 Molecular Motion and Relaxation

The spectral densities of molecule motion $J_q(\omega)$ are usually estimated by simultaneously analyzing a combination of

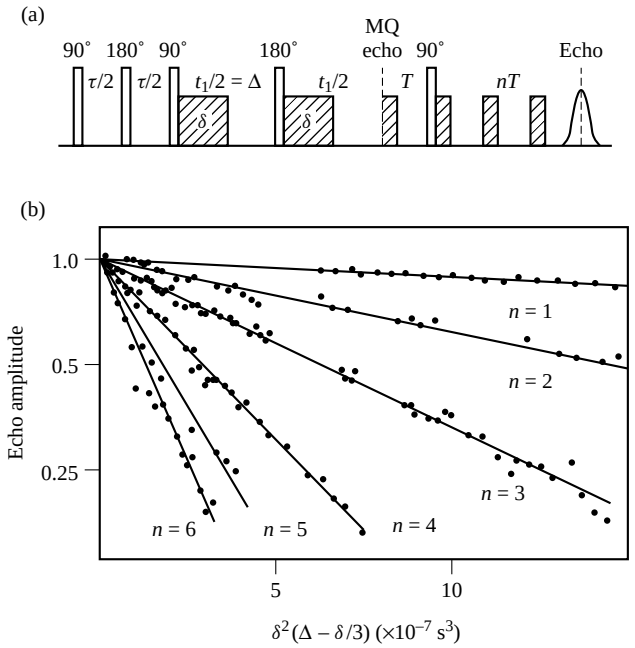

Figure 9 (a) Pulse sequence for an NMR pulsed field gradient experiment. (b) Normalized echo amplitudes plotted against the gradient pulse timing parameter $[\delta^2(\Delta - \delta/3)]$ of the Stejskal–Tanner equation.[26] (Reproduced by permission from D. Zax and A. Pines, *J. Chem. Phys.*, 1983, **78**, 6333)

relaxation measurements. Spectral densities may be measured from the decay of MQC and, particularly in $I = 1$ systems where the relaxation mechanism is dominated by the nuclear quadrupole, the relaxation of zero, double, triple and higher order coherences have been used to determine the spectral densities of motion for small deuterated organic molecules ($CDCl_3$,[27] $D{-}C{\equiv}C{-}C{\equiv}N$,[27b] CD_2Cl_2,[28] and $CD_3{-}C{\equiv}N$,[29]) dissolved in liquid crystalline solution. The relaxation of the two and three quantum resonances of ^{23}Na ($I = \frac{3}{2}$) and the four and five quantum resonances of ^{17}O ($I = \frac{5}{2}$) have been measured in lyotropic liquid crystals.[30]

6.5 Heteronuclear MQC

Heteronuclear MQC (HMQC) (coherence involving spins of different type, e.g. $^1H/^2H$ or $^1H/^{15}N$) have been used to study molecules in liquid crystal solution. Minoretti et al.[31] have demonstrated that there is a significant sensitivity advantage when the MQCs of a relatively insensitive nucleus (e.g. ^2H) can be detected indirectly by observing ^1H nuclei coupled to the heteronuclear spin system.

7 RELATED ARTICLES

Amphiphilic Liquid Crystalline Samples: Nuclear Spin Relaxation; Liquid Crystalline Samples: Deuterium NMR; Liquid Crystalline Samples: Diffusion; Liquid Crystalline Samples: Relaxation Mechanisms; Liquid Crystalline Samples: Spectral Analysis; Liquid Crystalline Samples: Structure of Nonrigid Molecules; Liquid Crystals: General Considerations; Lyotropic Liquid Crystalline Samples; Multidimensional Spectroscopy: Concepts; Multiple Quantum NMR in Solids; Multiple Quantum Spectroscopy of Liquid Samples; Structure of Rigid Molecules Dissolved in Liquid Crystalline Solvents; Two-Dimensional NMR of Molecules Oriented in Liquid Crystalline Phases.

8 REFERENCES

1. For leading references on NMR in liquid crystalline solvents see: (a) J. W. Emsley and J. C. Lindon, *NMR Spectroscopy Using Liquid Crystal Solvents*, Pergamon, Oxford, 1975; (b) J. W. Emsley (ed.), *Nuclear Magnetic Resonance of Liquid Crystals*, Riedel, Dordrecht, 1985.
2. For leading references on multiple quantum NMR spectroscopy, including studies of molecules in ordered phases see: (a) M. Munowitz and A. Pines, *Adv. Chem. Phys.*, 1987, **66**, 1; (b) G. P. Drobny, *Ann. Rev. Phys. Chem.*, 1985, **36**, 451; (c) D. Weitekamp, *Adv. Magn. Reson.*, 1983, **11**, 111; (d) G. Bodenhausen, *Progr. NMR Spectrosc.*, 1981, **14**, 137.
3. (a) S. Sinton, *Ph.D. Thesis*, University of California, Berkeley, 1982; (b) J. B. Murdoch, W. S. Warren, D. Weitekamp, and A. Pines. *J. Magn. Reson.*, 1984, **60**, 205; (c) A. Wokaun and R. R. Ernst, *Mol. Phys.*, 1978, **36**, 317; (d) R. A. Hoffman, *Adv. Magn. Reson.*, 1970, **4**, 87.
4. For general references to two-dimensional NMR spectroscopy see, for example: (a) A. E. Derome, *Modern NMR Techniques for Chemistry Research*, Pergamon, Oxford, 1989; (b) R. R. Ernst, G. Bodenhausen, and A. Wokaun, *Principles of Nuclear Magnetic Resonance in One and Two Dimensions*, Clarendon, Oxford, 1987.
5. (a) G. Drobny, A. Pines, S. Sinton, D. P. Weitekamp, and D. Wemmer, *Faraday Div. Chem. Symp.*, 1979, **13**, 49; (b) L. Braunschweiler, G. Bodenhausen, and R. R. Ernst, *Mol. Phys.*, 1983, **48**, 535; (c) O. W. Sorenson, M. Levitt, and R. R. Ernst, *J. Magn. Reson.*, 1983, **55**, 104.
6. D. P. Weitekamp, J. R. Garbow, and A. Pines, *J. Magn. Reson.*, 1982, **46**, 529.
7. (a) W. S. Warren and A. Pines, *J. Chem. Phys.*, 1981, **74**, 2808; (b) W. S. Warren, S. Sinton, D. P. Weitekamp, and A. Pines, *Phys. Rev. Lett.*, 1979, **43**, 1791; (c) W. S. Warren, D. P. Weitekamp, and A. Pines, *J. Magn. Reson.*, 1980, **40**, 581; (d) W. S. Warren, D. P. Weitekamp, and A. Pines, *J. Chem. Phys.*, 1980, **73**, 2084; (e) W. S. Warren and A. Pines, *Chem. Phys. Lett.*, 1982, **88**, 441.
8. T. M. Barbara, R. Tycho, and D. P. Weitekamp, *J. Magn. Reson.*, 1985, **62**, 54.
9. G. Drobny, A. Pines, S. Sinton, W. S. Warren, and D. P. Weitekamp, *Phil. Trans. R. Soc. London, Ser. A*, 1981, **299**, 585.
10. K. Nagayama, P. Bachmann, K. Wurthrich, and R. R. Ernst, *J. Magn. Reson.*, 1978, **31**, 133.
11. Order Selective detection: (a) A. Wokaun and R. R. Ernst, *Chem. Phys. Lett.*, 1977, **52**, 407; (b) G. Drobny, *Chem. Phys. Lett.*, 1984, **109**, 132.
12. Coherence transfer echoes: (a) A. Bax, P. G. DeJong, A. F. Mehlkopf, and J. Schmidt, *Chem. Phys. Lett.*, 1980, **69**, 567; (b) Y. S. Yen and D. P. Weitekamp, *J. Magn. Reson.*, 1982, **47**, 476; (c) D. P. Weitekamp, J. R. Garbow, and A. Pines, *J. Chem. Phys.*, 1982, **77**, 2870.
13. G. K. Pierens, T. A. Carpenter, L. D. Colebrook, L. D. Field, and L. D. Hall, *J. Magn. Reson.*, 1992, **99**, 398.
14. (a) R. L. Vold, J. S. Waugh, M. P. Klein, and D. E. Phelps, *J. Chem. Phys.*, 1968, **48**, 3831; (b) J. F. Martin, L. S. Selwyn, R. R. Vold, and R. L. Vold, *J. Chem. Phys.*, 1982, **76**, 2632; (c)

D. Zax and A. Pines, *J. Chem. Phys.*, 1983, **78**, 6333; (d) A. A. Maudsley, A. Wokaun, and R. R. Ernst, *Chem. Phys. Lett.*, 1978, **55**, 9.

15. Time reversal sequences: (a) W. S. Warren, S. Sinton, D. P. Weitekamp, and A. Pines, *Phys. Rev. Lett.*, 1979, **43**, 1791; (b) W. S. Warren, D. P. Weitekamp, and A. Pines, *J. Magn. Reson.*, 1980, **40**, 581; (c) W. S. Warren, D. P. Weitekamp, and A. Pines, *J. Chem. Phys.*, 1980, **73**, 2084.
16. G. Drobny and J. Listerud, *Mol. Phys.*, 1986, **58**, 1021.
17. (a) S. Castellano and A. A. Bothner-By, *J. Chem. Phys.*, 1964, **41**, 3863; (b) J. A. Ferretti, R. K. Harris, and R. B. Johannesen, *J. Magn. Reson.*, 1970, **84**, 3.
18. W. S. Warren, J. B. Murdoch, and A. Pines, *J. Magn. Reson.*, 1984, **60**, 236.
19. P. Diehl and C. L. Khetrapal, in *NMR, Basic Principles and Progress*, ed. P. Diehl, E. Fluck, and R. Kosfeld, Springer, Berlin, 1969, Vol. 1.
20. (a) L. D. Field, G. K. Pierens, K. J. Cross, and M. L. Terry, *J. Magn. Reson.*, 1992, **97**, 451; (b) L. D. Field and M. L. Terry, *J. Magn. Reson.*, 1986, **69**, 176.
21. (a) S. W. Sinton, D. Zax, J. B. Murdoch, and A. Pines, *Mol. Phys.*, 1984, **53**, 333; (b) S. W. Sinton and A. Pines, *Chem. Phys. Lett.*, 1980, **76**, 263.
22. J. Baum and A. Pines, *J. Am. Chem. Soc.*, 1986, **108**, 7447.
23. W. V. Gerasimowicz, A. N. Garroway, and J. B. Miller, *J. Am. Chem. Soc.*, 1990, **112**, 3726.
24. J. F. Martin, L. S. Selwyn, R. R. Vold, and R. L. Vold, *J. Chem. Phys.*, 1982, **76**, 2632.
25. D. Zax and A. Pines, *J. Chem. Phys.*, 1983, **78**, 6333.
26. E. O. Stejskal and J. E. Tanner, *J. Chem. Phys.*, 1965, **42**, 288.
27. (a) R. R. Vold and R. L. Vold, *J. Chem. Phys.*, 1977, **66**, 4018; (b) R. R. Vold, R. L. Vold, and N. Szerverenyi, *J. Phys. Chem*, 1981, **85**, 1934.
28. (a) R. Poupko, R. R. Vold, and R. L. Vold, *J. Magn. Reson.*, 1979, **34**, 67; (b) G. Bodenhausen, R. R. Vold, and R. L. Vold, *J. Magn. Reson.*, 1980, **37**, 93; (c) R. R. Vold, R. L. Vold, R. Poupko, and G. Bodenhausen, *J. Magn. Reson.*, 1980, **38**, 141.
29. (a) D. Jaffe, R. R. Vold, and R. L. Vold, *J. Magn. Reson.*, 1982, **46**, 475; (b) D. Jaffe, R. R. Vold, and R. L. Vold, *J. Magn. Reson.*, 1982, **46**, 496; (c) D. Jaffe, R. R. Vold, and R. L. Vold, *J. Chem. Phys.*, 1983, **78**, 4852.
30. I. Furo and B. Halle, *Mol. Phys.*, 1992, **76**, 1169.
31. A. Minoretti, W. P. Aue, M. Reinhold, and R. R. Ernst, *J. Magn. Reson.*, 1980, **40**, 175.

Biographical Sketch

Leslie D. Field. *b* 1953. B.Sc., 1975, Ph.D., 1979, Sydney. Faculty in Chemistry, Sydney University, 1982–present. Approx. 100 publications. Research interests: organometallic chemistry (C–H bond activation, catalytic activation of hydrocarbons, organometallic polymers, the mechanism of organometallic reactions); organic, organometallic, and inorganic synthesis; chemical applications of multinuclear MR spectroscopy, multiple quantum NMR spectroscopy, and NMR spectroscopy of molecules aligned in ordered solvents.

Polymer Dispersed Liquid Crystals

J. William Doane and Gregory P. Crawford
Kent State University, Kent, OH, USA

1	Introduction	1
2	Confining Materials	1
3	Deuterium NMR of Confined Liquid Crystals	2
4	Probing Nematic Director Configurations	3
5	Detection of Surface Ordering	4
6	Summary	5
7	Related Article	5
8	References	5

1 INTRODUCTION

Nuclear magnetic resonance studies of liquid crystals confined to submicrometer cavities of polymer dispersed liquid crystals (PDLC) pose problems of both basic and applied interest. The high surface-to-volume ratio imposed by the cavities and the high density of cavities present in the confining matrices allow for NMR studies of unusual surface phenomena not possible before the development of this powerful experimental technique. Unique measurements of surface molecular anchoring energies and angles, effects of surface confinement on molecular orientational ordering, and surface layer transitions predicted by theory are shown to be accessible by this method. Nematic director configurations and pretransitional ordering at cavity surfaces are the subject of this article.

Golemme and co-workers[1] pioneered NMR studies of confined liquid crystals in PDLCs. Using composites of polymer and spherical liquid crystal droplets composed of low molecular weight liquid crystal (selectively deuterated) of uniform size ranging from 2.0 to 0.02 μm in diameter, they were able to use deuterium NMR to study the molecular orientational order parameter of the confined liquid crystal. The results revealed that, for sufficiently small droplets, the isotropic fluid phase is replaced by a paranematic phase where a small but finite amount of order persists and that the nematic–isotropic transition is replaced by the continuous evolution of orientational order. Golemme and co-workers[2] also presented an elegant study of the nematic director fields that are stable in spherical cavities below the nematic–isotropic transition. This work prompted researchers[3] to study the molecular dynamics of liquid crystal molecules under spherical confinement and to develop further the theory of ordering within spherical geometries.

The successful work on liquid crystal droplets led to subsequent studies of confined liquid crystals in other cavity shapes and sizes. The study of nematic liquid crystal director fields was extended[4] to submicrometer cylindrical cavities of diameter 0.6 and 0.4 μm, demonstrating the effectiveness of this technique in confirming nematic director configurations in high detail to the point of even identifying singular defect structures and their densities. Confining liquid crystals to cylindrical rather than spherical cavities has two distinct advantages: the internal cavity surfaces are easily modified by chemical treatments that alter the molecular anchoring energies and angles at the cavity wall, and the cylindrical symmetry simplifies the analysis of the deuterium NMR spectra. Deuterium NMR has proven to be the most effective experimental tool in probing the ordering effects of confined liquid crystals, and has furthered the understanding of these systems to the point of being useful in optimizing the performance of electrooptic displays that rely on confinement.[5]

2 CONFINING MATERIALS

There are two ways in which liquid crystals have been prepared for NMR experiments. The phase separation technique is used to form spherical liquid crystal droplets surrounded by a polymer where diameters can be controlled down to 0.02 μm in diameter.[5] The most common liquid crystal used for deuterium NMR experiments on confined liquid crystals is 4′-pentyl-4-cyanobiphenyl (5CB), either deuterated in the α- or β-position of the hydrocarbon chain. The liquid crystal is usually soluble in the polymer or prepolymer, and after polymerization occurs, the liquid crystal phase separates out to form nearly spherical droplets. The size of the droplets can be adjusted by varying the relative amounts of the liquid crystal to the polymer or by varying the cure temperature; for instance, less liquid crystal in the solution leads to more rapid polymerization, which reduces the droplet size. Scanning electron microscope (SEM) photographs of the spherical cavities found in the polymer matrix are presented in Figure 1(a).

The other technique used to confine liquid crystals is to permeate a prefabricated porous matrix with a deuterated liquid crystal. These matrices are commercially available with either well-defined or random-type cavities. The pores of Nuclepore membranes, presented in Figure 1(b), and those of Anopore membranes, presented in Figure 1(c), are well-defined cylindrical channels. Nuclepore membranes are fabricated from 10 μm polycarbonate sheets in a variety of pore sizes, ranging between 12 and 0.015 μm, with a 12% porosity. An important property inherent to Nuclepore membranes is the presence of corrugations on the inner cavity walls, which prove useful for uniform homogeneous alignment. Anopore membranes are alumina-based membranes available only in 0.2 μm pore sizes, but with a porosity of nearly 40%, a thickness of 60 μm, and an extremely narrow pore size distribution. Anopore membranes have advantages compared with Nuclepore membranes because they are easier to handle when preparing an NMR sample, and their larger porosity gives rise to a better signal-to-noise ratio. However, they are only manufactured in the 0.2 mm pore size, whereas Nuclepore membranes are available in a large variety of pore sizes. For a sufficient signal-to-noise ratio, approximately forty 5 mm $\times$ 25 mm sheets of permeated Anopore membranes or nearly two hundred 5 mm $\times$ 25 mm sheets of permeated Nuclepore membranes stacked uniformly and secured in a 5 mm NMR sample tube are required. Both Nuclepore and Anopore membranes can be filled with most liquid crystals. The material dodecylcyanobiphenyl (12CB) deuterated in the α position was also used in these matrices to study the effect of confinement

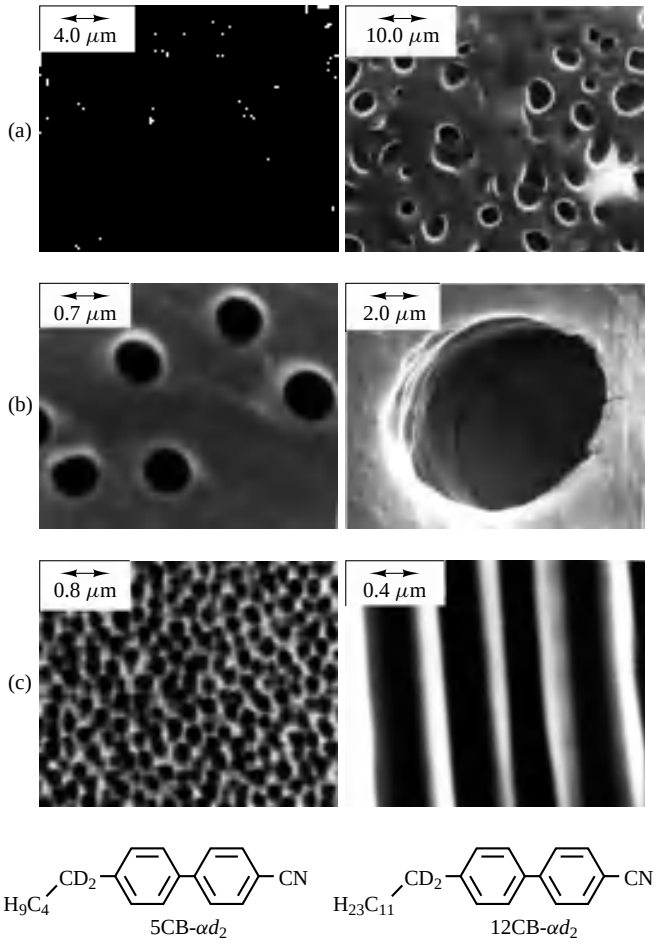

Figure 1 Scanning electron microscope photographs of various types of matrices used to confine liquid crystals. (a) The polymer matrices of PDLC materials with spherical inclusions are shown for two different droplet sizes formed by polymerization-induced phase separation techniques. (b) Nuclepore membranes with cylindrical inclusions are shown for two different pore sizes; the close-up photograph of the inner polymer surface of the pore reveals corrugations. (c) Anopore membranes are alumina-based matrices that consist of 0.2 mm cylindrical pores; the cross-sectional photograph reveals the cylindrical nature of the pore and its narrow pore size distribution. The structures of two of the deuterated liquid crystalline compounds commonly used in confinement studies are shown at the bottom

on the smectic A–isotropic transition temperature. There are comprehensive reviews of the properties of these membranes,[6] as well as of those matrices that exhibit a random-type confinement.[7]

3 DEUTERIUM NMR OF CONFINED LIQUID CRYSTALS

The molecular orientational order in confined liquid crystals strongly influences the deuterium NMR lineshape. Because of the positional dependence of the molecular orientation and orientational order parameter in confined liquid crystals, molecular self-diffusion can induce additional motional averaging. Considering typical values for the translational diffusion constant for nematic liquid crystals $D \approx 10^{-11}\,\mathrm{m^2\,s^{-1}}$, and for a cavity diameter on the order of $1\,\mu$m, the influence of self-diffusion is significant for splittings below 1 kHz, while spectra with splittings in the 100 kHz range will not be affected by diffusion. Neglecting averaging effects caused by translational motions and in a frame determined by the external magnetic field $\boldsymbol{B}$, the quadrupole splitting for a nucleus with spin $I = 1$ at the position $\boldsymbol{r}$ can be expressed by the following relationship:[8]

$$\delta\nu = \frac{1}{2}\frac{S(r)}{S_\mathrm{B}}\delta\nu_\mathrm{B}\{[3\cos^2\theta_n(\boldsymbol{r}) - 1] + \eta(\boldsymbol{r})\sin^2\theta_n(\boldsymbol{r})\cos[2\psi_n(\boldsymbol{r})]\} \quad (1)$$

where $\theta_n(\boldsymbol{r})$ and $\psi_n(\boldsymbol{r})$ express the orientation of $\boldsymbol{B}$ in the principal axis frame of the local electric field gradient (EFG) tensor averaged over fast orientational fluctuations, S_B and $\delta\nu_\mathrm{B}$ are the orientational order parameter and the quadrupole splitting frequency of the bulk liquid crystal material, respectively, and $S(\boldsymbol{r})$ is the local order parameter at position $\boldsymbol{r}$ inside the cavity. The bulk quadrupole splitting frequency $\delta\nu_\mathrm{B}$ is directly proportional to the degree of orientational order of the C–D bond direction with respect to $\boldsymbol{B}$.[8] The asymmetry parameter $\eta(\boldsymbol{r})$ is zero for uniaxial liquid crystals, but can be nonzero for confined liquid crystals because the averaging motions (orientational fluctuations) lose their symmetry under confinement. The effect is predicted to be small;[9] therefore, $\eta(\boldsymbol{r})$ is typically neglected.

The analysis of spectra recorded for nematic liquid crystals confined to cavities of diameters ranging between 0.1 and $1.0\,\mu$m is simplified for the following three reasons. The characteristic diffusion length is approximately $d \approx (D/\delta\nu)^{1/2} \approx 0.02\,\mu$m for $D \approx 10^{-11}\,\mathrm{m^2\,s^{-1}}$ and $\delta\nu \approx 50$ kHz, which is substantially less than the cavity diameters; therefore, the deuterium NMR spectra are indicative of the director distribution. The aligning effect of $\boldsymbol{B}$ on the nematic directors is negligible because the magnetic coherence length $\xi_\mathrm{m} \approx (\mu_0 K/\Delta\chi)^{1/2}/\boldsymbol{B} \approx 1.7\,\mu$m is substantially larger than the cavity diameters for typical values of the bulk elastic constant K and diamagnetic susceptibility $\Delta\chi$ for the 5CB compound when a 4.7 T magnetic field is employed. The order parameter can also be taken as constant throughout the cavity volume: $S(\boldsymbol{r})$ = constant = S_B in the nematic phase for these cavity sizes.[4] The deuterium NMR spectral distributions are calculated from the free induction decay (FID), which is a function describing the attenuation of nuclear magnetization in the time domain. The FID is described in terms of the resonance frequency expressed by equation (1) given by the following relationship:[10]

$$G(t) = \left\langle \exp\left\{\mathrm{i}\int_0^t \pi\delta\nu[r(t')]\,\mathrm{d}t'\right\}\right\rangle = \sum_j \exp[\mathrm{i}\pi\delta\nu(r_j)t]\,P(r_j) \quad (2)$$

where the time interval $(0, t)$ is divided into equal parts, $\langle\ \rangle$ represents the ensemble average, and P is the time-independent probability that there is a molecule with frequency $\delta\nu$ at position r_j. The frequency spectrum is obtained by the Fourier transformation of equation (2) given by the expression

$$I(\delta\nu) = \int_{-\infty}^{\infty} G(t)\exp(-\mathrm{i}\pi\delta\nu t)\,\mathrm{d}t \quad (3)$$

Line broadening is included by convoluting $I(\delta\nu)$ with the Gaussian distribution function. Motional averaging can be included in this formalism, if necessary, by incorporating an instantaneous value of the quadrupole splitting frequency and time-dependent probability in equation (2).

In the isotropic phase, confined liquid crystals in submicrometer cavities exhibit a small but measurable quadrupole splitting frequency due to the induced order at the cavity wall. In this case, the characteristic diffusion length $d \approx (D/\delta\nu)^{1/2} \approx 0.3\,\mu$m now becomes comparable to the cavity radii, resulting in spectra that are motionally averaged. Furthermore, the orientational order parameter depends on position $\boldsymbol{r}$. Assuming $S(r) = S_0 \exp[-(R - r)/\xi]$ for a liquid crystal confined to a cylindrical cavity of radius R, where R is comparable to the characteristic diffusion length, the time-averaged quadrupole splitting frequency can be expressed as

$$\langle\delta\nu\rangle = \frac{\delta\nu_{\mathrm{B}}}{S_{\mathrm{B}}}\langle S\rangle = \frac{\int_0^R S(r)r\,\mathrm{d}r}{\int_0^R r\,\mathrm{d}r} = \frac{2\delta\nu_{\mathrm{B}}S_0\xi}{S_{\mathrm{B}}R} \qquad (4)$$

where S_0 is the orientational order parameter of the molecules at the surface and ξ is the penetration length of nematic-like order, which propagates away from the cavity wall. Far from the cavity wall of the confining cylinder, $S(r)$ is zero, and the quadrupole interactions are completely averaged. Equation (4) demonstrates the usefulness of deuterium NMR as a tool for probing surface-induced phenomena.

4 PROBING NEMATIC DIRECTOR CONFIGURATIONS

Deuterium NMR is useful for identifying nematic director fields inside confined geometries. One example is presented in Figure 2 for the liquid crystal material 5CB-βd_2 confined to the 0.4 and 0.5 μm cavities of Nuclepore membranes. Before the liquid crystal was filled into the pores of Nuclepore membranes, however, the pores were rinsed with a lecithin solution to promote perpendicular aligning conditions of the liquid crystal molecules at the cavity wall. One advantage of cylindrical pores in Nuclepore and Anopore membranes is that they can be placed in different orientations within the magnetic field to double-check nematic director distributions and remove ambiguity in the deuterium NMR measurement. Two orientations were studied: $\theta_{\mathrm{B}} = 0^\circ$ and 90°, corresponding to the cylinder axis being parallel and perpendicular to the magnetic field, respectively. For the 0.4 μm sample, the $\theta_{\mathrm{B}} = 0^\circ$ orientation resulted in a splitting that is $\frac{1}{2}\delta\nu_{\mathrm{B}}$, and the $\theta_{\mathrm{B}} = 90^\circ$ orientation resulted in a splitting that is identical to $\delta\nu_{\mathrm{B}}$, with a slight broadening inside the peaks. For the 0.5 μm sample, the $\theta_{\mathrm{B}} = 0^\circ$ orientation has a splitting of $\frac{1}{2}\delta\nu_{\mathrm{B}}$, with a significant contribution in the center of the spectrum, and the $\theta_{\mathrm{B}} = 90^\circ$ orientation appears to be a cylindrical powder pattern. The change in the spectral patterns as the pore size is changed indicates that a nematic director field configuration transition[11] has taken place.

To help in analyzing the spectral patterns in Figure 2, Frank elastic theory was employed to predict the stable director field,

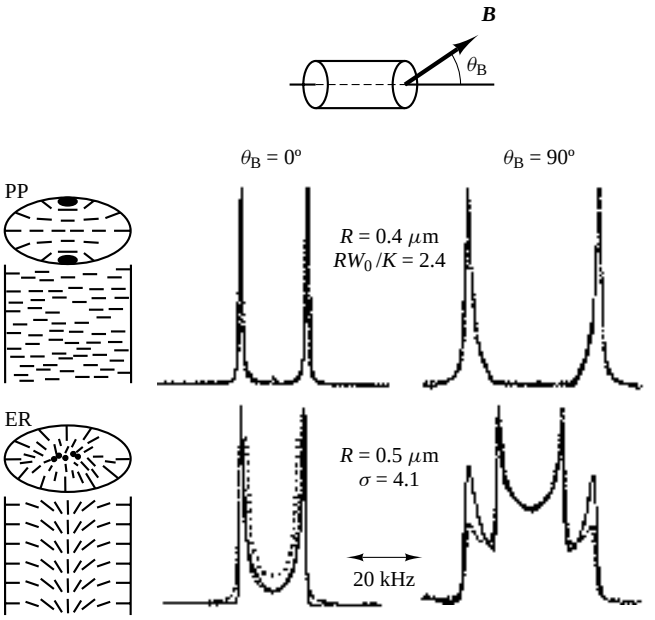

Figure 2 Experimental deuterium NMR spectra (solid line) of 5CB-βd_2 in the cylindrical pores of Nuclepore cavities fitted to theoretical spectra (dotted line) simulated from director distributions derived from elastic theory. Parallel ($\theta_{\mathrm{B}} = 0^\circ$) and perpendicular ($\theta_{\mathrm{B}} = 90^\circ$) orientations of the cylinder axis in the magnetic field are recorded for two samples with different pore sizes. The director field distributions that are consistent with the spectra are the planar-polar (PP) and the escaped-radial (ER) configurations

which is expressed as

$$F = \frac{1}{2}\int_{\mathrm{vol}} \{K_{11}(\nabla\cdot\boldsymbol{n})^2 + K_{22}(\boldsymbol{n}\cdot\nabla\times\boldsymbol{n})^2 + K_{33}(\boldsymbol{n}\times\nabla\times\boldsymbol{n})^2 - K_{24}\nabla(\boldsymbol{n}\times\nabla\times\boldsymbol{n} + \boldsymbol{n}\nabla\cdot\boldsymbol{n})\}\,\mathrm{d}V + \frac{1}{2}\int_{\mathrm{surf}} W_0\sin^2\phi\,\mathrm{d}S \qquad (5)$$

where $\boldsymbol{n}$ represents the nematic director, K_{11}, K_{22}, and K_{33} are the splay, twist, and bend phenomenological elastic constants, and K_{24} is the saddle–splay surface elastic constant; ϕ is the molecular anchoring angle of the liquid crystal molecules with respect to the cavity wall normal, and W_0 is its associated interaction energy (surface anchoring energy). Using this phenomenological expression, stable nematic director fields were derived, and are presented in Figure 2, along with their corresponding spectral patterns (dotted line), which are overlaid on the experimental spectra (solid line). The fitting parameter for the planar-polar (PP) director field stable in the $R = 0.4\,\mu$m cavities is RW_0/K; therefore, the surface anchoring strength was determined to be $W_0 = 3 \times 10^{-5}$ J m^{-2} for $K_{11} = K_{22} = K_{33} = K = 5 \times 10^{-12}$ J m^{-1}. The fitting parameter for the escaped-radial (ER) director field stable in $R = 0.5\,\mu$m cavities is $\sigma = RW_0/K + K_{24}/K - 1$, which allows the determination of $K_{24}/K \approx 1$ using the value of RW_0/K determined from the PP configuration. Using this value of W_0/K is justified, since the surfaces are identical. Measuring K_{24} was a great feat[12] in liquid crystal physics, because its magnitude eluded measurement for many years. There have been other studies in Nuclepore cavities for different

boundary conditions[13] and liquid crystal materials,[14] which have furthered the understanding of interfacial phenomena of liquid crystals and finite-size effects.

5 DETECTION OF SURFACE ORDERING

Deuterium NMR is a very powerful tool for studying surface-induced orientational ordering of liquid crystals in the isotropic phase. It can be used to determine the orientational order parameter at the surface and how far inside the cavity the order penetrates. For a truly isotropic phase, the quadrupole interactions average out and there is no quadrupole splitting—hence no orientational order. When the liquid crystal compound 5CB-βd_2 is confined to a small cavity, such as a Nuclepore cavity of radius 0.1 μm, a small but finite quadrupole splitting exists, indicative of surface-induced orientational order[15] (see Figure 3). As the cylinder size decreases, the quadrupole splitting frequency increases in the isotropic phase because of the increased surface-to-volume ratio. The simple order parameter profile $S(r) = S_0 \exp[-(R - r)/\xi]$ does not describe the complete temperature dependence of the quadrupole splitting frequency. In fact, when the system is deep in the isotropic phase, a quadrupole splitting frequency still persists that is not predicted by theory. Such behavior is expected, however, when the dominant ordering interactions are local in nature. Better agreement between theory and experiment can be obtained by assuming a constant order within the first layer (= S_0) with a thickness equal to the molecular length followed by the exponential decay of the order parameter profile as shown in Figure 3. This model enables good fits between experiment (solid line) and theory (dashed line) in Figure 3, and describes the strong quadrupole splitting frequency observed deep in the isotropic phase.[15]

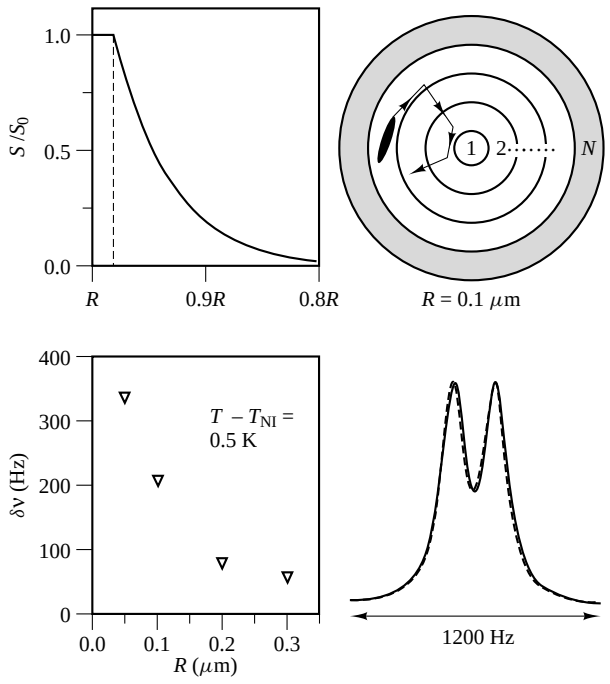

Figure 3 Experimental deuterium NMR spectrum (solid line) of 5CB-βd_2 in Nuclepore cavities above the nematic–isotropic transition temperature fitted to theoretical prediction (dotted line) is shown, lower right. The quadrupole splitting frequency $\delta\nu$ as a function of pore size recorded just above the nematic–isotropic transition temperature ($T - T_{NI}$ = 0.5 K) is shown (lower left). The model that describes the data includes a variation in the orientational order parameter S (upper left) and an inhibited diffusion constant at the cavity surface (upper right)

Additional evidence of different behavior in the first molecular layer comes from the positional dependence of the self-diffusion constant, which can be determined by simultaneously fitting the spectra of different pore sizes. As shown in Figure 3, the shaded region at the surface of the cylinder represents a different self-diffusion constant, which is used to explain the broadening in the lineshapes as the pore size is decreased. This enables the measurement of the molecular exchange rate between the surface layer, which is found to be on the order of $10^3\ s^{-1}$. Similar experiments were performed using Anopore membranes[16] as the confining matrix.

Recently, deuterium NMR was used to show that the surface order parameter at the cavity wall of Anopore membranes could be controlled systematically. By treating the membranes with an aliphatic acid surfactant $C_nH_{2n+1}COOH$, the ordering of the 5CB-αd_2 liquid crystal molecules at the cavity wall was found to depend strongly on the length (carbon number n) of the aliphatic surfactant that attaches itself to the alumina Anopore surfaces. For n = 7, 9, and 15, perpendicular anchoring of the liquid crystal molecules was found to exist at the cavity walls, while for shorter chain lengths n = 5 and 6, parallel anchoring of the liquid crystal molecules at the surface was preferred.[17] In addition, the orientational order parameter at the cavity wall in the isotropic phase was found to increase with n for homeotropic anchoring conditions, while the reverse trend was observed for parallel anchoring. This was attributed to the interaction of the long alkyl chains of the aliphatic acid surfactant and the liquid crystal molecules being predominately sterical, resulting in perpendicular anchoring, while for shorter aliphatic chain lengths, strong interactions between the core of the liquid crystal molecules and the alumina Anopore surfaces enforced parallel anchoring conditions.

The temperature dependence of the quadrupole splitting in these systems was monitored, and the surface-induced orientational order parameter at cavity wall above the nematic–isotropic transition temperature (T_{NI}) was derived using a phenomenological free energy density in terms of the orientational order parameter. The data (derived from quadrupole splitting) and corresponding theoretical fits (solid line) are presented in Figure 4. For n = 15, the order parameter approaches S_0 = 0.1 near T_{NI}, which is still less than the bulk nematic order parameter at the transition, which is about 0.3. However, the n = 5 sample that promotes parallel anchoring conditions shows a noncritical behavior in S_0, which is found to be negative. A negative S_0 implies that the liquid crystal molecules are anchored with their long axis parallel to the surface by random orientation; therefore, the director is perpendicular to the surface, resulting in a negative S_0.[17] Deuterium NMR cannot directly distinguish whether S_0 is positive or negative, but the model can decipher its sign based on the temperature dependence of S_0, i.e., the temperature dependence of $\langle\delta\nu\rangle$.

Deuterium NMR can be used to study a very interesting surface parameter that characterizes the wetting regime of the confined liquid crystal system. The adsorption parameter is defined as $\Gamma = \int_0^\infty [S(z) - S_B]dz$, where z is the distance

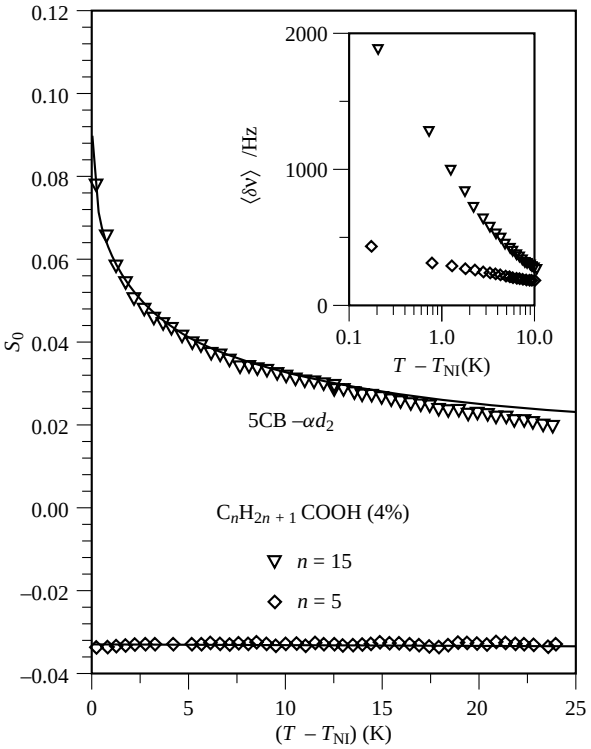

Figure 4 The orientational order parameter S_0 at the cavity surface of 5CB-αd_2 confined to the cylindrical channels of Anopore membranes derived from the measured quadrupole splitting frequency $\langle \delta\nu \rangle$ (inset). The channels of the Anopore membranes were modified with an aliphatic acid surfactant ($C_nH_{2n+1}COOH$) to introduce different interactions between the 5CB-αd_2 molecules and the surface. This is apparent from the dramatic temperature behavior of $\langle \delta\nu \rangle$ and S_0

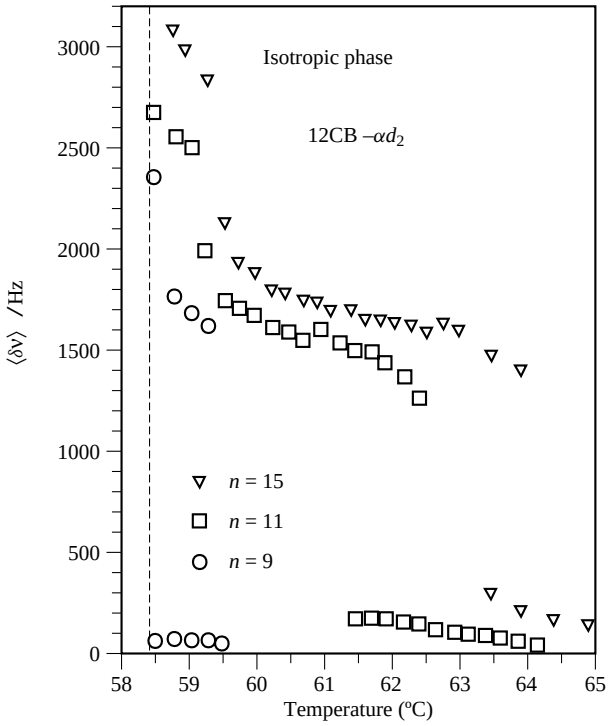

Figure 5 The average quadrupole splitting frequency $\langle \delta\nu \rangle$ as a function of temperature for the liquid crystal compound 12CB-αd_2 confined to the treated channels ($C_nH_{2n+1}COOH$) of Anopore membranes. Two discontinuities in $\langle \delta\nu \rangle$ are observed for all samples before the bulk smectic A–isotropic transition temperature (vertical dotted line), which is consistent with the formation of smectic layers

from the cavity wall. Γ diverges for complete wetting, and remains finite for partial wetting at the nematic–isotropic transition temperature. This adsorption parameter is easily related to the averaged quadrupole splitting frequency[17] by $\Gamma = RS_B\langle \delta\nu \rangle / 2\delta\nu_B$. According to theory,[17] Γ exhibits a logarithmic divergence at the nematic–isotropic transition temperature for complete wetting; therefore, graphing $\langle \delta\nu \rangle$ on a semilogarithmic plot as shown in the inset in Figure 4 helps characterize the orientational wetting behavior. It appears that Γ exhibits weak divergence corresponding to complete wetting for the n = 15 surface; however, Γ definitely remains finite for the n = 5 surface. This provides an ideal way to characterize pretransitional orientational wetting behavior.

The power of deuterium NMR as a surface-sensitive technique is obvious from Figure 5. The average quadrupole splitting frequency in the isotropic phase of the liquid crystal compound 12CB-αd_2 confined to Anopore membranes was monitored on approaching the smectic A–isotropic transition for different lengths (carbon number n) of the aliphatic acid surfactant surface treatment attached to the cavity wall. It is clear that there are two discontinuities in $\langle \delta\nu \rangle$ as the bulk transition is approached from above. These are attributed to pretransitional smectic layering. Additionally, as the chain length n of the aliphatic surfactant decreases, the smectic layering transitions are shifted towards the bulk smectic A–isotropic transition temperature, and $\langle \delta\nu \rangle$ also decreases. The phenomenological theory behind these smectic layering transitions is currently being pursued.

6 SUMMARY

The scope of NMR for studying confined liquid crystals appears boundless. Its sensitivity to nematic director distributions of confined liquid crystals in various geometries, and to the surface-induced orientational order parameter has furthered the understanding of elasticity and pretransitional ordering. Studies of the dynamics of liquid crystals under confinement[18] and liquid crystals constrained to random porous glass[19] have also been very intriguing, and are attracting considerable interest. To date, the deuterium NMR technique has made the biggest impact on the fundamental understanding of confined liquid crystals, particularly in the field of PDLCs, and its role in the future looks very promising.

7 RELATED ARTICLES

Liquid Crystals: General Considerations.

8 REFERENCES

1. A. Golemme, S. Zumer, D. W. Allender, and J. W. Doane, *Phys. Rev. Lett.*, 1988, **61**, 2937.
2. A. Golemme, S. Zumer, J. W. Doane, and M. E. Neubert, *Phys. Rev. A*, 1988, **37**, 559.

3. M. Vilfan, R. Rutar, S. Zumer, G. Lahajnar, R. Blinc, J. W. Doane, and A. Golemme, *J. Chem. Phys.*, 1988, **89**, 579; J. Dolinsek, O. Jarh, M. Vilfan, S. Zumer, R. Blinc, J. W. Doane, and G. P. Crawford, *J. Chem. Phys.*, 1991, **95**, 2154.
4. G. P. Crawford, M. Vilfan, J. W. Doane, and I. Vilfan, *Phys. Rev. A*, 1991, **43**, 835.
5. J. W. Doane, *MRS Bull.*, 1991, **XVII**, 22.
6. G. P. Crawford, L. M. Steele, R. J. Ondris-Crawford, G. S. Iannacchione, C. J. Yeager, J. W. Doane, and D. Finotello, *J. Chem. Phys.*, 1992, **96**, 7788.
7. P. Levitz, G. Ehret, S. K. Sinha, and J. M. Drake, *J. Chem. Phys.*, 1991, **95**, 6151.
8. J. W. Doane, *Magnetic Resonance of Phase Transitions*, eds. F. J. Owens, C. P. Poole, Jr., and H. A. Farach, Academic Press, New York, 1979.
9. N. Schopohl and T. J. Sluckin, *Phys. Rev. Lett.*, 1987, **59**, 2582.
10. A. Abragam, *The Principles of Nuclear Magnetism*, Oxford University Press, London, 1961.
11. D. W. Allender, G. P. Crawford, and J. W. Doane, *Phys. Rev. Lett.*, 1991, **67**, 1442.
12. G. P. Crawford, D. W. Allender, and J. W. Doane, *Phys. Rev. A*, 1992, **45**, 8693.
13. R. J. Ondris-Crawford, G. P. Crawford, S. Zumer, and J. W. Doane, *Phys. Rev. Lett*, 1993, **70**, 194.
14. R. J. Ondris-Crawford, G. P. Crawford, J. W. Doane, S. Zumer, M. Vilfan, and I. Vilfan, *Phys. Rev. E*, 1993, **48**, 1998.
15. G. P. Crawford, D. K. Yang, S. Zumer, D. Finotello, and J. W. Doane, *Phys. Rev. Lett.*, 1991, **66**, 723.
16. G. P. Crawford, R. Stannarius, and J. W. Doane, *Phys. Rev. A*, 1991, **44**, 2558.
17. G. P. Crawford, R. J. Ondris-Crawford, S. Zumer, and J. W. Doane, *Phys. Rev. Lett.*, 1993, **70**, 1838.
18. N. Vrbancic, M. Vilfan, R. Blinc, J. Dolinsek, G. P. Crawford, and J. W. Doane, *J. Chem. Phys.*, 1993, **98**, 3540.
19. G. S. Iannacchione, G. P. Crawford, S. Zumer, J. W. Doane, and D. Finotello, *Phys. Rev. Lett.*, 1993, **71**, 2595.

Biographical Sketches

J. William Doane. *b* 1935. Ph.D., 1965, University of Missouri, USA. Currently Director of the Liquid Crystal Institute, the National Science Foundation Science and Technology Center for Advanced Liquid Crystalline Optical Materials (ALCOM), a consortium of Kent, Case Western Reserve, and Akron Universities, 1983–present Professor of Physics at Kent State University, 1991–present. Fellow of the American Physical Society. 180 publications.

Gregory P. Crawford. *b* 1965. B.S., 1987, Ph.D., 1991, Kent State University, USA. Introduced to NMR by Professor J. William Doane at the Liquid Crystal Institute. Postdoctoral fellow at the Liquid Crystal Institute, 1991–1993. National Research Council postdoctoral fellow at the Naval Research Laboratory, 1993–95. Currently a member of the research staff at Xerox PARC (1995–present). Approx. 40 publications. Research specialty: applications of NMR to confined liquid crystals and polymer dispersion systems, ferroelectric and electroclinic materials, spatial light modulators, flat panel displays, and physics education.

Spinning Liquid Crystalline Samples

Jacques Courtieu

University of Paris-Sud, Orsay, France

1	Introduction	1
2	NMR Implications of Tilting the Director from B_0	2
3	The Slow Sample Rotation Technique	2
4	Spinning at Various Angles	4
5	Application of VAS to the NMR of Dissolved Molecules	5
6	Perspectives	7
7	Related Articles	7
8	References	7

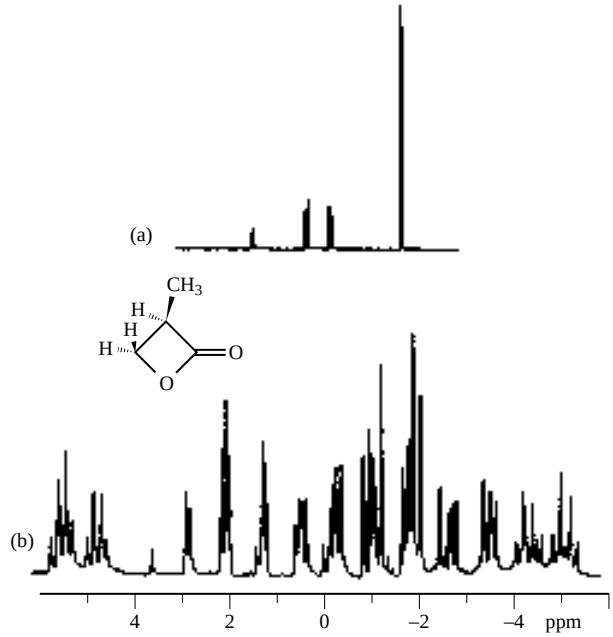

Figure 1 ^{1}H NMR spectra of β-butyrolactone at 250 MHz and 20 °C: (a) Spectrum of an isotropic solution in $CDCl_3$: (b) Spectrum of an anisotropic solution in the liquid crystal solvent ZLI 1167. Many overlapping peaks are not resolved in this experimental spectrum

1 INTRODUCTION

The analytical power of the use of nematic liquid crystals as solvents in high-resolution NMR, due primarily to the pioneering work of Saupe and Englert,[1–3] has excited a part of the NMR community since 1963. The basic phenomenon is that molecules dissolved in these ordered media are partially oriented in such a way that, while the intermolecular interactions are still averaged to zero through rapid molecular motions, all the intramolecular anisotropic interactions are no longer averaged to zero. This effect gives chemists a very powerful tool to measure, among others, shielding anisotropies, internuclear dipole–dipole interactions, quadrupolar interactions, and the anisotropic parts of the scalar coupling constants. Special emphasis must be given to the dipole–dipole interaction, because its classical relationship to molecular geometry through the well-known equation

$$D_{ij} = -\frac{h\gamma_i\gamma_j}{8\pi^2}\left\langle \frac{3\cos^2\theta - 1}{r_{ij}^3} \right\rangle \qquad (1)$$

provides a very precise method of investigating the geometry of the dissolved molecules. In this equation, h is Planck's constant, D_{ij} is the dipolar coupling constant between nuclei i and j, γ_i and γ_j are their magnetogyric ratios, r_{ij} is the magnitude of the internuclear vector $\boldsymbol{r}_{ij}$, θ is the angle between $\boldsymbol{r}_{ij}$ and the magnetic field, and the angle brackets indicate the time average. Several reviews have been written on the subject,[4–9] and readers who are not familiar with this kind of nonclassical NMR should refer to these. In spite of this great advantage, NMR studies using liquid crystal solvents have declined somewhat since the late 1970s, the reasons for which can be understood by considering the following.

Although the spectra of molecules dissolved in ordered media are much more informative than those in isotropic solvents, they are also considerably more complicated for two reasons. First, many of the residual dipolar couplings are generally much larger than the resonance frequency differences, often having values of 2 or 3 kHz. Consequently, the classical first-order approximation, which can be used when the couplings are small compared with the $\Delta\nu_i$, is no longer valid, even at high fields. Second, the appearance of the partially averaged dipolar couplings lifts the degeneracies among spin systems containing chemically or magnetically equivalent nuclei. Thus, for molecules dissolved in a nematic medium, one generally obtains second-order spectra that are difficult and sometimes even impossible to analyze by calculations using the spin Hamiltonian.

The complexity of this kind of nonclassical NMR is well illustrated by the spectra of β-butyrolactone shown in Figure 1. The isotropic spectrum shows a simple $AMKX_3$ pattern, which can be easily recognized. On the other hand, the anisotropic spectrum is very complicated, and has hundreds of transitions, many of which overlap in the experimental spectrum. Such a spectrum could be analyzed, and consequently the geometric parameters derived. However, the analysis would require a good computer, some skill, and weeks of effort. The reader should be aware of the fact that if the molecule under investigation does not possess any element of symmetry and the number of spins is larger than six, its spectrum would often become impossible to calculate. Our drawers are full of spectra that we have never been able to calculate, and the situation is probably the same in many specialized laboratories around the world. Finally, perhaps the most important point is the fact that we have not found in the scientific literature a geometrical analysis of a chiral molecule through this otherwise very precise method, which allows internuclear distances to be evaluated with a precision within the amplitude of bond vibrations.

The limitations mentioned above have become a challenge, and many investigators in this field have tried to overcome them. Their basic idea is as follows: if it is possible to reduce the magnitude of the dipolar couplings to make them smaller than the frequency shift differences, or even comparable in magnitude to the isotropic part of the scalar couplings, it would be possible to convert the very strong second-order pattern

commonly shown in the spectra into a first-order spectrum analyzable by any NMR spectroscopist. It has been known from the very beginning of the NMR study of liquid crystals that this can be achieved when the director is tilted at an angle β from the magnetic field. Section 2 is devoted to showing this effect. Then it will be shown that, in some circumstances, it is possible to tilt the director from the magnetic field through sample rotation.

The first experiments on the rotation of a nematic liquid crystal around an axis perpendicular to the magnetic field were performed by the physicists Tsvetkov[10] and Lippmann.[11] Then, Snyder[12] in 1965 and Diehl and Khetrapal[13] in 1967 applied this old idea to the NMR study of liquid crystals. The details of the effects of this technique, which we shall refer to as the slow sample rotation experiment, were first studied by Leslie, Luckhurst, and Smith for EPR[14] and by Emsley, Lindon, Luckhurst, and Shaw for applications in NMR.[15] This experiment will provide us with a starting point, which will be the content of Section 3. The reason to begin our discussion with tilting the axis of rotation by 90° is not only because of the historical chronology but also because it contains all of the main ingredients to introduce the variable angle spinning technique. Unfortunately, there are two serious limitations to this approach: first, it is theoretically impossible to reduce the anisotropic interactions by more than a factor of four; second, the reduction is accompanied by an increase in linewidth, which further limits the useful reduction factor to barely one-half.

In Section 4, we shall derive the behavior of the director of a nematic when it is spun around an axis tilted at an angle β from the magnetic field, which constitutes the basis of variable angle sample spinning (VAS). The first idea of spinning nematics neither parallel nor perpendicular to the magnetic field but in between as a means to reorient the director was due to Hornreich[16] in 1977, and the technique was first applied in EPR by Yo, Poupko, and Hornreich[17] in 1978. The NMR applications were worked out by ourselves[18] in 1981, and independently by Lippmaa et al. at Tallinn[19] in 1982. Then, a detailed theoretical analysis[20] and a review[21] were given shortly after the initial experimental demonstrations of VAS.

Section 5 will be devoted to the principal applications of the technique to the NMR of molecules dissolved in nematics. Applications to the NMR of liquid crystals themselves are described in ***Liquid Crystalline Samples: Carbon-13 NMR***.

In the concluding Section 6, we shall try to evaluate the prospects of the VAS method for the near future, which may help the further development of one of the most fascinating aspects of NMR in chemistry, namely the structural and dynamic analysis of molecules in an anisotropic environment.

2 NMR IMPLICATIONS OF TILTING THE DIRECTOR FROM B_0

The arguments presented here are based on the assumption that the nematic sample is placed in a magnetic field of 1 T or more, so that nuclear magnetic moments are quantized along this field and that nematic director dynamics are dominated by magnetic field interactions and the mechanical motion of the sample. It will also be assumed that the rotational motions of individual molecules are fast on the NMR timescale, so that interactions can be expressed as averages.

Molecules dissolved in liquid crystals tumble rapidly but with unequal orientational probabilities, so that anisotropic intramolecular interactions are averaged to nonzero values. Only the averages of these second-rank tensorial properties in the direction of spin quantization are measurable. Quantization is along the externally applied magnetic field, which is arbitrarily defined as the laboratory z axis. We have

$$\bar{T}_{zz} = \tfrac{1}{3}(T_{11} + T_{22} + T_{33}) + \frac{2}{3}\sum_{\alpha,\beta} \tfrac{1}{2}\langle 3\cos\theta_\alpha^z \cos\theta_\beta^z - \delta_{\alpha\beta}\rangle T_{\alpha\beta} \qquad (2)$$

where T_{zz}, the z component of a tensorial property T, corresponds to our measure along the magnetic field. $\frac{1}{3}(T_{11} + T_{22} + T_{33})$ is the isotropic average of the interaction, often referred to as T^{iso}. The sum, which depends on the orientation through the angles

$$\theta_\alpha^z$$

between the molecular axes $(\alpha,\beta) \equiv (1,2,3)$ and the magnetic field, is the anisotropic part of the interaction ΔT.

In uniaxial liquid crystals such as nematics it has been shown[12] that the anisotropic part is sensitive to the angle β between the axis of orientation, the director, and the magnetic field through the simple equation

$$\bar{T}_{zz} = T^{\text{iso}} + \tfrac{1}{2}(3\cos^2\beta - 1)\Delta T \qquad (3)$$

which indicates that the average property measured along the z magnetic field is made up of two terms. The first term is the invariant under the rotation of T, and the second term is the anisotropic contribution scaled by the factor $\frac{1}{2}(3\cos^2\beta - 1)$. In other words, this equation means that if it is possible to orient the director of a uniaxial liquid crystal at an angle β to the magnetic field then the anisotropic part of the interaction will be reduced by a factor $\frac{1}{2}(3\cos^2\beta - 1)$, which lies between 1 and -0.5 for $0 > \beta > \frac{1}{2}\pi$. This is true for the shielding anisotropy, the anisotropy of the scalar coupling, and for the dipolar and quadrupolar couplings that are purely anisotropic interactions.

Of course, the difficulty is that the angle β must be the same all over the sample. If this is not the case then the spectrum will not be high-resolution but a powder pattern. In other words, a homogeneous orientation is needed. This can be obtained by spinning the sample.

Having established the NMR consequences when the director is tilted from the magnetic field, we must now describe how it is possible to move the director from its equilibrium position.

3 THE SLOW SAMPLE ROTATION TECHNIQUE

3.1 Magnetic Torque Against Viscous Torque

When subjected to an external magnetic field $\boldsymbol{B}_0$ of sufficient magnitude (usually about 0.5 T or higher), the local order directors of a nematic liquid crystal have a uniform alignment, producing a single well-defined bulk nematic director $\boldsymbol{n}$. This is due to the interaction between the external field and the anisotropy of the diamagnetic susceptibility, which is defined as

$$\Delta\chi = \chi_{\parallel} - \chi_{\perp} \qquad (4)$$

where $\chi_{\parallel}$ and $\chi_{\perp}$ are the susceptibilities parallel and perpendicular to $\boldsymbol{n}$, respectively. Although $\Delta\chi$ is relatively small, the collective effect in the bulk sample is sufficient to overcome thermal disordering motions. Quantitatively, this can be expressed as a change in the potential energy P of the system:[22]

$$P = -\tfrac{1}{3}\Delta\chi B_0^2 \tfrac{1}{2}(3\cos^2\beta - 1) \tag{5}$$

where β is the angle between the director and the magnetic field. For many nematics, $\Delta\chi$ is positive, so the potential energy is minimum for $\beta = 0^\circ$, and the equilibrium alignment of $\boldsymbol{n}$ will be along $\boldsymbol{B}_0$. For a few liquid crystals, most of which have no aromatic rings, $\Delta\chi$ is negative and P is minimum for $\beta = 90^\circ$; therefore, $\boldsymbol{n}$ will tend to be perpendicular to $\boldsymbol{B}_0$. Since nematics are moderately viscous fluids, the alignment of $\boldsymbol{n}$ is not instantaneous, but requires some time to reach equilibrium. This is governed by the competition between the viscous torque and the magnetic torque.

The potential energy gives rise to a magnetic torque τ_m on the liquid crystal director whose magnitude per unit volume is

$$\tau_m = \Delta\chi B_0^2 \cos\beta \sin\beta \tag{6}$$

According to Leslie,[23,24] the viscous torque τ_v can be written as

$$\tau_v = \gamma_1 \dot{\beta} \tag{7}$$

where γ_1 is the Leslie rotational twist coefficient and $\dot{\beta}$ is the time rate of change of β.

The return of $\boldsymbol{n}$ to its equilibrium condition is related to a characteristic motional frequency expressed as ω_c, which is a function of these competing torques. Equating τ_v and τ_m in equations (6) and (7), an expression for ω_c can be obtained:

$$\gamma_1\dot{\beta} = \Delta\chi B_0^2 \cos\beta \sin\beta \tag{8}$$

$$\dot{\beta} = \omega_c \cos\beta \sin\beta \tag{9}$$

with

$$\omega_c = \frac{\Delta\chi B_0^2}{\gamma_1} \tag{10}$$

For typical nematic liquid crystals, $\omega_c/{B_0}^2$ is of the order of 4.8 Hz T^{-2}, which means that ω_c is approximately 30 Hz at 2.35 T (100 MHz proton NMR), 200 Hz at 5.87 T (250 MHz), and 1.1 kHz at 14.10 T (600 MHz).

3.2 Slow Spinning Perpendicular to the Magnetic Field

The behavior of a nematic mesophase of $\Delta\chi > 0$ being spun around an axis perpendicular to the director was first studied by Lippmann,[11] but it was the EPR and NMR spectra of probes dissolved in nematic phases that provided a detailed description of the director behavior.[14,15,25–29]

The quantitative relation can be easily derived from the equality of the two torques expressed in Equation (8). According to this, at equilibrium, the director adopts an angle β relative to $\boldsymbol{B}_0$ given by

$$\sin 2\beta = \frac{2\gamma_1\omega_r}{\Delta\chi B_0^2} \tag{11}$$

where $\omega_r = \dot{\beta}$ is the angular velocity of the spun sample. From equation (11), it can be seen that the maximum theoretical value for β is 45°, which is achieved when ω_r reaches a critical angular velocity that is half of the characteristic motional frequency defined in equation (10):

$$\omega_r^{\text{critical}} = \frac{\Delta\chi B_0^2}{2\gamma_1} = \tfrac{1}{2}\omega_c \tag{12}$$

For $\omega_r < \frac{1}{2}\omega_c$, the director will reach an equilibrium angle

$$\beta = \tfrac{1}{2}\sin^{-1}\left(\frac{2\omega_r}{\omega_c}\right) \tag{13}$$

When $\omega_r > \frac{1}{2}\omega_c$, it can be shown that the director rotates about the spinning axis.

3.3 Experiments and Limitations

The 94.1 MHz fluorine spectra of CF_3COOH dissolved in Phase V, obtained at various rotation speeds by Emsley and Lindon,[6] provide a nice way to show the power and the limitations of the slow spinning technique, Figure 2. In this A_3 spin system, the line positions are determined by the F–F dipolar coupling and the electronic shielding $\sigma_F^{iso} + \Delta\sigma_F$. Compared with the static spectrum (a), the reduction of the dipolar interaction in spectrum (b) is clear, together with a shift of the central line due to the reduction of the shielding anisotropy. Unfortunately, it must also be noted that this spectrum is no longer a simple 1–2–1 triplet, and the outer lines are broadened. This effect is more pronounced in spectrum (c), where $\omega_r = \frac{1}{2}\omega_c$. Spectra (c) and (d) show clear

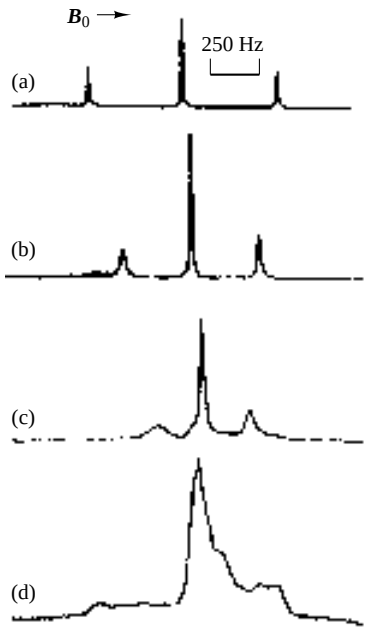

Figure 2 ^{19}F NMR spectra of CF_3COOH dissolved in the nematic liquid crystal Merck Phase V at 94.1 MHz, with ω_r(critical) = 11.8 Hz. The sample was rotated about an axis perpendicular to the magnetic field, and values of the rotation rate ω were (a) 0.0 Hz,; (b) 9.3 Hz; (c) 11.8 Hz; (d) 14.4 Hz

evidence of being weighted sums of spectra with values of β lying in a wide range between 0° and 90°. The distribution of the values of β was first analyzed in the ESR spectra of spin probes dissolved in rotating nematic phases by Carr et al.[25] They showed that the results are consistent with an elliptical distribution of the angle β.

Although slow sample rotation is limited to small tilting angles of the director, where the value of the reduction factor $\frac{1}{2}(3\cos^2\beta - 1)$ is not very different from unity, this technique has been used by Emsley and Lindon[27,28] to separate the anisotropic from the isotropic interactions, such as J^{iso} from D, or σ^{iso} from $\Delta\sigma$. However, the original goal, which is to reduce the dipolar interaction to such an extent that a first-order spectrum can be obtained, cannot be reached by this method. On the other hand, the beauty of the VAS technique, which we are going to describe in the next section, is to actually narrow the lines as the tilt angle between the magnetic field and the director increases. Because the slow sample rotation technique was discovered first, and all the necessary theoretical backgrounds have been discussed, the equations developed in this section will be found useful below.

4 SPINNING AT VARIOUS ANGLES

The work on slow spinning samples was done very early—most probably because many of the experiments were performed on conventional spectrometers with electromagnets, in which the probes are designed to spin the samples about an axis perpendicular to $\boldsymbol{B}_0$. There is another well-known situation in these electromagnets, namely the case of nematics with negative $\Delta\chi$. These orient spontaneously with the director perpendicular to the magnetic field. In this case, it is commonly said that rotation does not affect the orientation of a nematic; but this is not true. If the sample is kept static in the field, the directors distribute in a plane perpendicular to $\boldsymbol{B}_0$. When the sample is rotated, the directors reorient about the unique rotation axis, which remains perpendicular to $\boldsymbol{B}_0$. This, of course, would not change the NMR measurement, but the interesting point is that the difference of the director behavior between the two cases indicates the roles of $\boldsymbol{B}_0$, $\Delta\chi$, and the rotation axis in this problem.

In the following discussion, the derivation of Hornreich[16] together with that of Courtieu et al.[20] are followed.

4.1 Average Potential Theory

If the liquid crystal were spun around an axis tilted from $\boldsymbol{B}_0$ by an angle β at an angular velocity larger than ω_c, the director would not have time to orient parallel to the field, but would orient in such a way that the average of the potential energy over one cycle of the rotation is minimum. This average potential energy P is obtained from Equation (5) by averaging $\cos^2\beta$ over one cycle of the rotation. To calculate the average of $\cos^2\beta$, consider a reference frame fixed relative to the bulk of the liquid crystal, with the polar axis along the spinning axis as shown in Figure 3. Here we denote the principal axis of the bulk liquid crystal as $\boldsymbol{R}$, which will be defined as the spinning axis later.

Assume that the director is stationary relative to the bulk liquid and is described by a polar angle δ and an azimuthal angle ϕ. Since the angle between the spinning axis and the magnetic field is η, in this frame the magnetic field has a constant polar angle η and a constantly changing azimuthal angle $\phi_m = \omega_r t$. The cosine of the angle β between the director and the magnetic field is

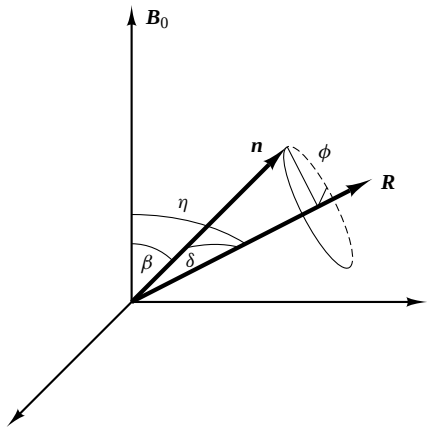

Figure 3 Definition of the axes and angles used in the text: $\boldsymbol{B}_0$, $\boldsymbol{n}$, and $\boldsymbol{R}$ are the magnetic field, the director, and the spinning axis, respectively; β is the angle between $\boldsymbol{B}_0$ and $\boldsymbol{n}$, η is that between $\boldsymbol{B}_0$ and $\boldsymbol{R}$, and δ is that between $\boldsymbol{n}$ and $\boldsymbol{R}$

$$\cos\beta = \cos\eta\cos\delta + \sin\eta\sin\delta\cos(\phi_m - \phi) \tag{14}$$

The average of $\cos^2\beta$ over one cycle of the rotation is

$$\cos^2\beta = \cos^2\eta\cos^2\delta + \tfrac{1}{2}\sin^2\eta\sin^2\delta \tag{15}$$

Inserting this into Equation (5) and simplifying the result, the average potential energy is obtained:

$$\begin{aligned}\bar{P} &= -\tfrac{1}{3}\Delta\chi B_0^2[\tfrac{1}{2}(3\cos^2\eta - 1)][\tfrac{1}{2}(3\cos^2\delta - 1)] \\ &= \tfrac{1}{3}\Delta\chi B_0^2 f(\eta,\delta)\end{aligned} \tag{16}$$

The angular part of the function $f(\eta,\delta)$ is plotted in Figure 4 for different values of η. Defining the magic angle as $\theta_m = \arccos(\frac{1}{3})^{1/2} = 54°\ 44'$, it can be analyzed in the following way for $0° \le \eta \le 90°$.

1. For nematics with $\Delta\chi > 0$, (a) when $\eta < \theta_m$, the potential energy is minimum at $\delta = 0°$, and the director tends to align along the rotation axis; (b) when $\eta = \theta_m$, the potential energy is independent of δ, which means that the director has no preferred orientation; (c) when $\eta > \theta_m$, the potential energy is minimum at $\delta = 90°$, and the director is distributed in a plane perpendicular to the rotation axis.
2. For nematics with $\Delta\chi < 0$, the situation of the minimum potential changes so that, (a) when $\eta < \theta_m$, the director is distributed in a plane perpendicular to the rotation axis; (b) when $\eta = \theta_m$, the director does not show a preferred orientation; (c) when $\eta > \theta_m$, the director aligns along the rotation axis.

The average potential treatment presented above is semi-quantitative, and holds only for high spinning speed. However, it does give a simple understanding of the phenomenon. A complete mechanistic analysis been given by Hornreich[16] and by Courtieu et al.[20] It leads to the conclusion that the theoretical situation described in Sections 2 and 3 can be achieved through sample spinning at an angular frequency five or more

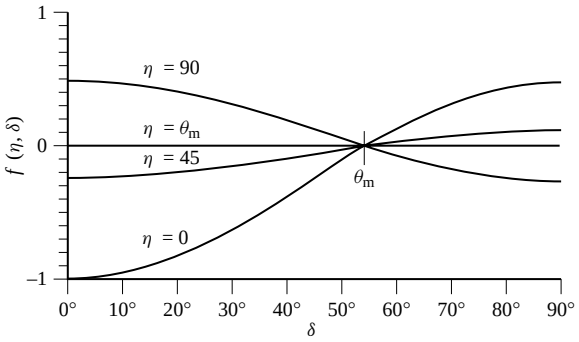

Figure 4 Plot of the function $f(\eta,\delta) = -\frac{1}{4}(3\cos^2\eta - 1)(3\cos^2\delta - 1)$

time the critical spinning rate. In this situation, the angle β reaches a steady-state position where the director is homogeneously aligned on the rotation axis, $\beta \approx \eta$, as long as we are inside the region of stability. The latter depends only on the sign of the diamagnetic susceptibility anisotropy. The next section will be devoted to the experimental confirmation of the above derivation using NMR.

5 APPLICATION OF VAS TO THE NMR OF DISSOLVED MOLECULES

In this section, we shall show some examples of the application of VAS to study the NMR of small molecules dissolved in nematic solvents. The basis of these applications is the ability of VAS to reduce various anisotropic interactions by a factor of $\frac{1}{2}(3\cos^2\beta - 1)$, as expressed by Equation (3). Actually, the tremendous advantage of the VAS technique in reducing H–H dipolar couplings has found another important application in the simplification of the ^{1}H and ^{13}C spectra of liquid crystals (see ***Liquid Crystalline Samples: Carbon-13 NMR***).

5.1 Practical Considerations for VAS

We have seen in Section 4 that in VAS, the orientation of the nematic director is dependent on the spinning angle η, the spinning rate, and the magnetic anisotropy $\Delta\chi$. When the spinning rate is fast, for a liquid crystal with $\Delta\chi > 0$, the director orients along the spinning axis for $0^\circ < \eta < \theta_m = 54^\circ\,44'$, lies around a cone about the spinning axis for η near the magic angle, and is distributed perpendicular to the spinning axis for $\theta_m < \eta < 90^\circ$. The situation is opposite for a liquid crystal with $\Delta\chi < 0$. However, when the spinning angle is near θ_m, the situation is more complicated. For example, for a nematic liquid crystal with $\Delta\chi < 0$, the director orients perpendicular to the spinning axis when η is between 0° and 52°, but lies around a cone in the vicinity of the magic angle, and spinning sidebands become a prominent feature of the spectra.[29] The patterns and intensities of the sidebands depend upon the dipolar interactions and frequency shifts of the system as well as the spinning rate and spinning angle. A study of these effects was made by studying the ^{19}F spectra of CF_2ClCCl_3 in two liquid crystal solvents (Merck ZLI 2334, $\Delta\chi > 0$; ZLI 1167, $\Delta\chi < 0$). The details of the theoretical analysis will not be repeated here; it is sufficient to say that the results agree quite well with the experimental data.

The spinning sidebands are, of course, not desirable in most applications of the VAS method. Fortunately, they can be avoided and even totally eliminated by setting the spinning rate fast enough and the angle η far away enough from the magic angle. In the experiments described in the rest of this section, the conditions were such that the fast spinning limit is reached. However, other complications would appear at very high spinning rates, where inertial forces become important.[21]

5.2 Reduction of Dipolar Interactions

The original goal of the VAS technique was to reduce the dipolar interaction and change second-order spectra into first-order ones. This goal was successfully reached,[20] and the result is illustrated in Figure 5, which shows the change in the ^{19}F spectra of $CF_2{=}CFBr$ dissolved in a nematic solvent. When the sample is stationary or spun at $\eta = 0^\circ$, the spectrum is of the ABC type, because the D_{ij} values are of the same order of magnitude as the frequency shifts. Tilting the spinning axis reduces D_{ij} more than the frequency shift differences, and the second-order spectrum gradually changes into a first-order one when η increases. At $\eta = 51^\circ$, the ABC pattern is converted

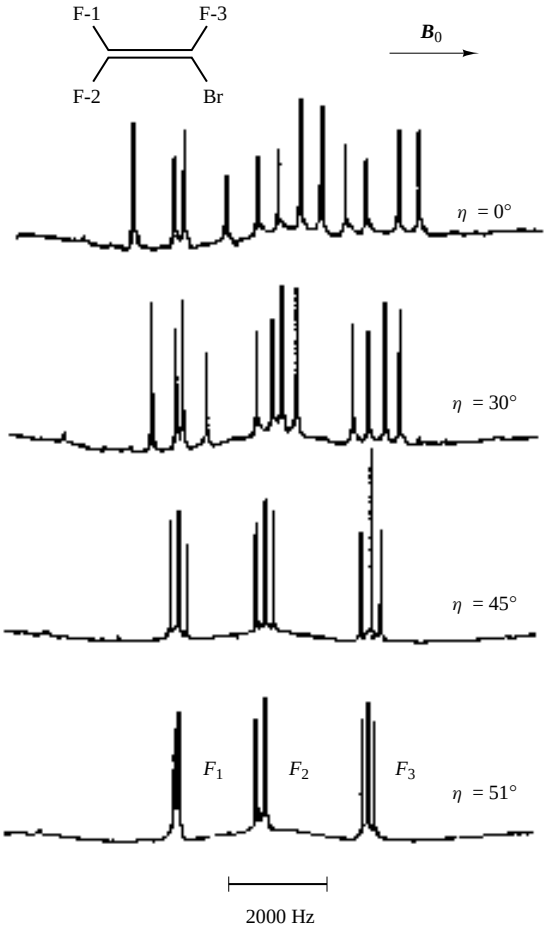

Figure 5 ^{19}F NMR spectra of $CF_2{=}CFBr$ dissolved in the nematic liquid crystal *p*-*n*-pentylphenyl 2-chloro-4-(*p*-*n*-pentylbenzoyloxy)benzoate at 75.25 MHz and 31 °C. The spinning rate was 75 Hz, and values of the spinning angle η are indicated in the spectra

into an AMX pattern, from which the values of the couplings can be obtained directly. An analysis of the spectra yields the relative signs of D_{ij} and J_{ij}. In the limit of $\eta = \theta_m$, only the isotropic scalar couplings remain, and the centers of the multiplets give the isotropic shielding in the liquid crystal solvent.

A reduction of the dipolar coupling constants, of course, also simplifies the ^{1}H spectrum of solute molecules in liquid crystal solvents. For example, the ^{1}H spectrum of norbornadiene, an eight-spin system, is quite complicated and difficult to analyze, but it becomes essentially first-order when the system is spun at $\eta = 45.2^\circ$.[30] Some peaks in the VAS spectrum overlap with each other because the order parameters are quite small, but the three largest coupling constants can be immediately obtained from the spectrum with VAS. From these data, very good initial estimates of the order parameters were made to aid the analysis of the complicated spectrum for $\eta = 0^\circ$. A simplification of the spectra of thiophene dissolved in two nematic solvents, one with $\Delta\chi > 0$, and the other with $\Delta\chi < 0$, was also observed.[31] The proton dipolar coupling constants of these systems were measured, and it was confirmed that in both cases, the coupling constants are scaled by the angular factor predicted by the theory discussed in the previous section.

In a VAS experiment, it is essential to determine the angle η between the spinning axis and the magnetic field accurately. The determination can be made by the use of an optical pointer.[32] Another way of determining η is to take advantage of the reduction in the dipolar coupling constant by comparing the dipolar splittings of a solute molecule with and without sample spinning. If the director of the liquid crystalline solvent aligns along the spinning axis, the ratio between the dipolar splittings in the two cases is $\frac{1}{2}(3\cos^2\eta - 1)$; if it aligns perpendicularly to the spinning axis, the factor is $-\frac{1}{4}(3\cos^2\eta - 1)$. The ^{1}H signal of CH_2Cl_2,[33] the ^{19}F signal of CF_2ClCCl_3,[34] and the ^{13}C signals of CH_2I_2[20] and $CHCl_3$[35] have been used for this purpose.

5.3 Shielding Anisotropy

The use of liquid crystals as solvents to determine the shielding anisotropy of solute molecules is a well-known method[36] (see ***Anisotropy of Shielding and Coupling in Liquid Crystalline Solutions***). The principle of the technique is to follow the resonance frequencies of the solute as its molecular orientation changes. This change can be induced by several methods, including changes of phase, solute concentration, or temperature. However, each has its own disadvantage, leading to various uncertainties in the results.[36] On the other hand, the VAS method does not require any internal change in the system itself, and may avoid some of these problems.

Väänänen et al. have demonstrated the use of the VAS technique to determine the shielding anisotropy in CH_3I.[32] To do this, it should be recalled that Equation (3) is applicable to both the dipolar coupling constant and the shielding anisotropy. By taking the ratio of these two kinds of interactions, the factor $\frac{1}{2}(3\cos^2\beta - 1)$ can be eliminated to give

$$\sigma^{\exp} = \sigma^{\mathrm{iso}} + \tfrac{2}{3}\Delta\sigma_H S_{zz}\frac{D^{\eta}_{HH}}{D^{0}_{HH}} \tag{17}$$

where $\sigma^{\exp}$ is the experimental electronic shielding. Then, the shielding anisotropy $\Delta\sigma_H$ was obtained from the slope of the plot of $\sigma^{\exp}$ versus the observed dipolar coupling constant D^{η}_{HH} as the angle was varied gradually. Using this approach, it was found that $\Delta\sigma_H$ was dependent on the liquid crystal solvent, which could be caused by the anisotropy of the local effects on $\sigma^{\exp}$ and different deformational effects of the liquid crystal solvents on the methyl groups of methyl iodide and the reference molecule, tetramethylsilane. This observation confirms similar results reported earlier that both the ^{1}H and the ^{13}C shielding anisotropies of CH_3CN are dependent on the liquid crystal solvent, and that they are linearly related to each other.[37]

5.4 Quadrupolar Interactions

When VAS is used to cause the nematic director to align along an axis forming an angle β with respect to $\boldsymbol{B}_0$, the quadrupolar interaction is also scaled by a factor of $\frac{1}{2}(3\cos^2\beta - 1)$. This causes the NMR peaks of quadrupolar nuclei to be much sharper and the splittings to be less. Taking advantage of this effect and following the example of an earlier study by proton NMR,[38] Kumar et al.[39,40] used deuterochloroform as a probe to investigate the effect of very small $\Delta\chi$, which was reached by mixing liquid crystals with positive and negative values of $\Delta\chi$ in proper ratios, on the orientation of the nematic directors in VAS experiments. To do this, they measured the deuterium NMR spectra of $CDCl_3$ in several mixtures of liquid crystals with different values of $\Delta\chi$. Their results show that, for a liquid crystal with a positive $\Delta\chi$ spinning along an axis with $\beta < 54^\circ\,44'$, the director orients parallel to the spinning axis above a critical spinning rate, as discussed in the previous section. However, for a system with nearly zero but positive $\Delta\chi$, the nematic director orients along the spinning axis at low spinning speeds, but orients perpendicularly to the spinning axis at high speeds, for $\beta < \theta_m = 54^\circ\,44'$. For a system with a very small but negative value of $\Delta\chi$, the behavior is similar for $\eta > 54^\circ\,44'$, but no change in the director orientation with spinning speed was observed for $\beta < 54^\circ\,44'$, but some spinning sidebands were observed indicating director reorientation.

A rather different application of VAS to deuterium NMR is the study of side-chain nematic liquid crystal polymers.[41,42] Because these polymers have very high rotational viscosities, ω_c is of the order of 0.001–0.1 Hz at $B_0 = 7.1$ T [see Equation (10)], so that very slow spinning was used to study the systems. However, it takes these liquid crystal polymers a very long time to reach equilibrium because of their high viscosities. Therefore, the initial stage of the time dependence of the deuterium NMR spectra were investigated, using synchronized data acquisition with the sample rotation. The kinetic results were used to measure the rotation viscosities[41] and study the convection director structures.[42]

5.5 Two-Dimensional NMR with VAS

Two-dimensional NMR of solute molecules in liquid crystal solvents has not enjoyed the success of that for isotropic solutions. This is mainly because the large dipolar interactions make the spectra second order, so that correlation relations, which are the essential features in 2D NMR, are usually not very informative. This problem can be overcome partly by symmetry filtering,[43–45] but the scope is still rather limited.

On the other hand, because the VAS method can simplify a second-order spectrum into a first-order one, it has a potential application in the 2D NMR of liquid crystal solutions.

As an example of this application, the ^{19}F spin echo spectra of the chiral molecule $CF_3CFBrCF_2Br$ dissolved in a liquid crystal with a negative $\Delta\chi$ (Merck ZLI 2806) was studied.[21] The normal 1D spectrum is a complicated ABC_3X type and very difficult to analyze, and the 2D spin echo spectrum is practically impossible to interpret. However, the spectrum turned into an ABM_3X type when the sample was spun at η = 63.9° or 58.4°.[46] The 2D spin echo spectra can be regarded as first-order J-resolved spectra, where the residual dipolar couplings appear in the ω_1 dimension, and the resonance frequencies in the ω_2 dimension. The analysis of the spectra in the ω_1 dimension then yielded the values of D_{ij} for this chiral molecule.

6 PERSPECTIVES

The most important characteristic of liquid crystals is the presence of orientational ordering without long-range positional ordering. Various kinds of anisotropic interactions, including dipolar couplings, quadrupolar couplings, and electronic shielding, can be used to study the orientational ordering and dynamics of liquid crystals, as well as the structures and motions of solute molecules. However, these interactions are often so large that the NMR spectra are either too broad or too complicated to be tractable. When liquid crystals are spun at high speeds along the magic angle, the NMR linewidths can be greatly reduced, just like those for solids, but information on anisotropic interactions is lost. On the other hands, the use of VAS can reduce the anisotropic interactions to yield simplified spectra, and in the mean time preserve the valuable anisotropic interactions, which are scaled by a proper factor. Solute spectra are greatly simplified, and the linewidths of bulk liquid crystals are reduced, bringing important advantages for the spectral analysis. So far, the potential of using VAS for the structural determination of complex solute molecules has not been fully realized, but investigations of the order parameters of various types of liquid crystals have been very successful.

It must be pointed out again that the reduction of the anisotropic interactions in liquid crystals by VAS is not a time-averaging effect as in MAS experiments for solids, but an effect of the alignment of the director. Therefore, a fundamental requirement for VAS experiments to be effective is the presence of macroscopic ordering of the liquid crystal director along the magnetic field in a static situation. This situation is fulfilled for nematic liquid crystals at $B_0 > 0.5\,T$, and for smectics that can be aligned through cooling from the nematic phase. However, for cholesterics and chiral smectics that have short pitches, and for smectics that have no or very short nematic ranges, powder patterns are often obtained, and the VAS technique is not very useful. In these cases, deuterium NMR without sample spinning is most advantageous. (See ***Liquid Crystalline Samples: Deuterium NMR***).

7 RELATED ARTICLES

Liquid Crystalline Samples: Carbon-13 NMR; Liquid Crystals: General Considerations; Structure of Rigid Molecules Dissolved in Liquid Crystalline Solvents.

8 REFERENCES

1. A. Saupe and G. Englert, *Phys. Rev. Lett.*, 1963, **11**, 462.
2. G. Englert and A. Saupe, *Z. Naturforsch. A*, 1964, **19**, 172.
3. A. Saupe, *Angew. Chem., Int. Ed. Engl.*, 1968, **7**, 107.
4. A. D. Buckingham and K. A. Mc Lauchlan, in *Progress in Nuclear Magnetic Resonance Spectroscopy*, eds. J. W. Emsley, J. Feeney, and L. H. Sutcliffe, Pergamon Press, Oxford, 1967, Vol. 2, p. 63.
5. P. Diehl and C. L. Khetrapal, in *NMR Basic Principles and Progress*, eds. P. Diehl, E. Fluck, and R. Kosfeld, Springer-Verlag, Berlin, 1969, Vol. 1, p. 1.
6. J. W. Emsley and J. C. Lindon, *NMR Spectroscopy Using Liquid Crystal Solvents*, Pergamon Press, Oxford, 1975.
7. C. L. Khetrapal and A. C. Kunvar, in *Advances in Magnetic Resonance*, ed. J. S. Waugh, Academic Press, New York, 1977, Vol. 9, p. 302.
8. C. Zannoni, in *Nuclear Magnetic Resonance of Liquid Crystals*, ed. J. W. Emsley, Reidel, Dordrecht, 1985, p. 1.
9. P. Diehl, in *Nuclear Magnetic Resonance of Liquid Crystals*, ed. J. W. Emsley, Reidel, Dordrecht, 1985, p. 147.
10. V. Tsevtkow, *Zh. Eksp. Theor. Fiz.*, 1935, **9**, 603.
11. H. Lippmann, *Ann. Phys. (Leipzig)*, 1958, **1**, 157.
12. L. C. Snyder, *J. Chem. Phys.*, 1965, **43**, 4041.
13. P. Diehl and C. L. Khetrapal, *Mol. Phys.*, 1967, **14**, 283.
14. F. M. Leslie, G. R. Luckhurst, and H. J. Smith, *Chem. Phys. Lett.*, 1972, **13**, 368.
15. J. W. Emsley, J. C. Lindon, G. R. Luckhurst, and D. Shaw, *Chem. Phys. Lett.*, 1973, **19**, 345.
16. R. M. Hornreich, *Phys. Rev. A*, 1977, **15**, 1767.
17. C. H. Yo, R. Poupko, and R. M. Hornreich, *Chem. Phys. Lett.*, 1978, **54**, 142.
18. J. Courtieu, D. W. Alderman, and D. M. Grant, *J. Am. Chem. Soc.*, 1981, **103**, 6783.
19. R. Teeaar, M. Alla, and E. Lippmaa, *Org. Magn. Reson.*, 1982, **19**, 134.
20. J. Courtieu, D. W. Alderman, D. M. Grant, and J. P. Bayle, *J. Chem. Phys.*, 1982, **77**, 723.
21. J. Courtieu, J. P. Bayle, and B. M. Fung, in *Progress in Nuclear Magnetic Resonance Spectroscopy*, eds. J. W. Emsley, J. Feeney, and L. H. Sutcliffe, Pergamon Press, Oxford, 1994, Vol. 26, p. 141.
22. P. G. de Gennes, *The Physics of Liquid Crystals*, Clarendon Press, Oxford, 1976.
23. F. M. Leslie, *Q. J. Mech. Appl. Math.*, 1966, **19**, 357.
24. F. M. Leslie, *Arch. Rat. Mech. Anal.*, 1968, **28**, 265.
25. S. G. Carr, G. R. Luckhurst, R. Poupko, and H. J. Smith, *Chem. Phys.*, 1975, **7**, 278.
26. S. D. Goren, S. B. Stephen, and R. Potashnik, *Chem. Phys. Lett.*, 1974, **28**, 400.
27. J. W. Emsley and J. C. Lindon, *Chem. Phys. Lett.*, 1974, **26**, 361.
28. J. W. Emsley and J. C. Lindon, *Mol. Phys.*, 1974, **28**, 1253.
29. J. P. Bayle, A. Khandar, P. Gonord, and J. Courtieu, *J. Chim. Phys.*, 1986, **83**, 177.
30. W. A. Heeschen, D. W. Alderman, and D. M. Grant, *J. Phys. Chem.*, 1988, **92**, 6504.
31. T. Väänänen, J. Jokisaari, and M. Seläntaus, *Chem. Phys. Lett.*, 1986, **129**, 399.
32. T. Väänänen, J. Jokisaari, and M. Seläntaus, *J. Magn. Reson.*, 1987, **72**, 414.
33. B. M. Fung and J. Afzal, *J. Am. Chem. Soc.*, 1986, **108**, 1107.
34. W. Richter, D. Reimer, B. M. Fung., R. J. Twieg, and K. Betterton, *Liq. Cryst.*, 1990, **8**, 687.

35. C. L. Khetrapal, B. S. A. Kumar, K. V. Ramanathan, and N. Suryaprakash, *J. Magn. Reson.*, 1987, **73**, 516.
36. J. Lounila and J. Jokisaari, in *Progress in Nuclear Magnetic Resonance Spectroscopy*, eds. J. W. Emsley, J. Feeney, and L. H. Sutcliffe, Pergamon Press, Oxford, 1982, Vol. 15, p. 249.
37. P. Diehl, J. Jokisaari, and F. Moia, *J. Magn. Reson.*, 1982, **49**, 498.
38. J. P. Bayle, A. Khandar, and J. Courtieu, *Liq. Cryst.*, 1986, **1**, 189.
39. B. S. A. Kumar, N. Suryaprakash, K. V. Ramanathan, and C. L. Khetrapal, *Chem. Phys. Lett.*, 1987, **136**, 227.
40. B. S. A. Kumar, K. V. Ramanathan, and C. L. Khetrapal, *Chem. Phys. Lett.*, 1988, **149**, 306.
41. D. Van der Putten, N. Schwenk, and H. W. Spiess, *Liq. Cryst.*, 1992, **12**, 735.
42. N. Schwenk, C. Boeffel, and H. W. Spiess, *Liq. Cryst.*, 1989, **4**, 341.
43. D. L. Turner, *J. Magn. Reson.*, 1982, **46**, 213.
44. A. G. Avent, J. W. Emsley, and D. L. Turner, *J. Magn. Reson.*, 1983, **52**, 57.
45. K. Rukmani and A. Kumar, *Chem. Phys. Lett.*, 1987, **133**, 485.
46. Nguyen Thoi Lai, J. P. Bayle, J. H. Ouvrard, and J. Courtieu, *Liquid Crystals*, 1988, **3**, 745.

Biographical Sketch

Jacques Courtieu. *b* 1944. Ph.D., 1974, University of Paris. Introduced to NMR by David M. Grant, U. of Utah, 1975–76. Faculty in Chemistry at the University of Orsay, 1969–present. Approx. 100 publications. Research interests: theory, practice and applications of liquid crystal NMR: dipolar couplings and molecular topology, relaxation in coupled systems, coherent averaging in spin space and in physical space, chiral recognition in cholesterics.

Structure of Rigid Molecules Dissolved in Liquid Crystalline Solvents

Peter Diehl

University of Basel, Basel, Switzerland

1	Introduction	1
2	Liquid Crystals as Solvents	1
3	Degree of Order of the Solute	1
4	Direct Dipolar Coupling and Molecular Geometry	3
5	Spectra of Oriented Spin Systems	3
6	Determination of Structure from Dipolar Coupling	7
7	Possible Accuracy of Structure Determination	7
8	Molecules Studied	7
9	Factors Limiting the Accuracy of Structure Determination	8
10	Combination of NMR Structural Information with Data from Other Spectroscopies	10
11	Conclusions	11
12	Related Articles	11
13	References	11

1 INTRODUCTION

As a result of Brownian motion in liquids, not only are the direction-dependent properties of chemical shift and indirect dipole–dipole coupling lost, and only one-third of the traces of the respective tensors observed, but also the direct dipole–dipole coupling as well as the quadrupolar coupling are averaged to zero, so that these interactions can only contribute to relaxation. In particular, the loss of direct dipolar coupling is very serious, because it has a quite simple geometrical meaning in that it depends upon the inverse cube of the internuclear distance, the degree of orientation of the internuclear axis with respect to the applied magnetic field, and the product of the gyromagnetic ratios of the interacting nuclei. In solids that are 'fully oriented', the direct coupling was, of course, observed in the 1950s; however the large number of interacting spins led to very complex spectra, with broad features, resulting in low accuracy of information on internuclear distances.

NMR spectroscopists have always been aware of this missing information in liquid samples, and have repeatedly tried to produce partially oriented systems by various means. But only in 1963, when Saupe and Englert[1] used liquid crystals as solvents, were the first highly resolved spectra showing direct dipolar coupling observed. The main idea of this approach was that in liquid crystal solvents the solute molecules still rotate and diffuse as in normal liquids, but, owing to their interaction with the anisotropic solvent, they are partially oriented. The diffusion and rotation are responsible for the averaging out of intermolecular direct dipolar coupling, i.e., we observe the 'isolated' spin system of one solute molecule, and the liquid crystal, which in the magnetic field is uniaxially oriented, keeps the solute molecular axes partially parallel (i.e., oriented), causing the average dipolar coupling to deviate from zero. Since the motion of the solute molecules does not deviate appreciably from that of normal liquids, the relaxation times of partially oriented molecules are similar to those of the liquid. Therefore linewidths of the order of 1 Hz can be obtained, and dipolar couplings (i.e., molecular structure) can be measured with considerable accuracy.[2–11]

This method of structure determination is relatively fast compared with other approaches such as microwave spectroscopy, which usually needs spectra of several isotopically substituted species, and furthermore only allows one to study dipolar molecules, or electron diffraction, which determines the position of light nuclei such as protons with low accuracy and furthermore has difficulties in discriminating between similar interatomic distances. NMR of oriented molecules, on the other hand, has the limitation that coupling to quadrupolar nuclei except ^{2}D is rarely observed, because it is fully or partially averaged out by quadrupolar relaxation.

2 LIQUID CRYSTALS AS SOLVENTS

The liquid crystals used as orienting solvents consist of nonspherical, either rod- or disk-shaped, molecules that below a certain transition temperature are partially oriented owing to attractive dispersive—as well as repulsive—interactions. In spite of their orientation, they have liquid-like properties such as diffusion and flow.

Of the three main types of liquid crystals—nematic, smectic, and cholesteric—it is mainly the nematic phases, which have long-range order in the molecular axes but not in the centers of gravity, and the smectic phases, which have order in both, that are used in practice (see Figure 1). They may be pure compounds (thermotropics) or mixtures of various compounds (lyotropics). The latter contain molecules with hydrophobic paraffin chains and hydrophilic headgroups as well as water.

The most important compounds are the thermotropic azo-, azoxy-, and azine-type molecules, biphenyls, phenylcyclohexanes or bicyclohexanes, and lyotropic mixtures of alkyl sulfates, alcohols, sodium phosphate, and water.

Liquid crystal solvents are uniaxially oriented by the applied magnetic field (>0.1 T) or by electric fields. The reason is the diamagnetic or dielectric anisotropy of the molecular aggregates. The axis of largest diamagnetic susceptibility is oriented perpendicularly to the magnetic field.

Molecular solutes in the liquid crystal solvent are also oriented. The degree of order is usually smaller than 0.1, and depends upon the concentration of the solute and the temperature (roughly 1% change K^{-1}). Obviously, in order to obtain small linewidths of the spectra, concentration and temperature gradients must be avoided.

Because many liquid crystals contain aromatic rings with large diamagnetic susceptibilities perpendicular to the ring plane, usually the optic axis of the liquid crystal is oriented along the magnetic field; exceptions are cyclohexane ring-containing compounds.

The orientation of smectic liquid crystals is quite slow, and consequently stable, so that probes at arbitrary angles between the optical axis and the magnetic field may be studied. In contrast the orientation of nematic liquid crystals is fast.

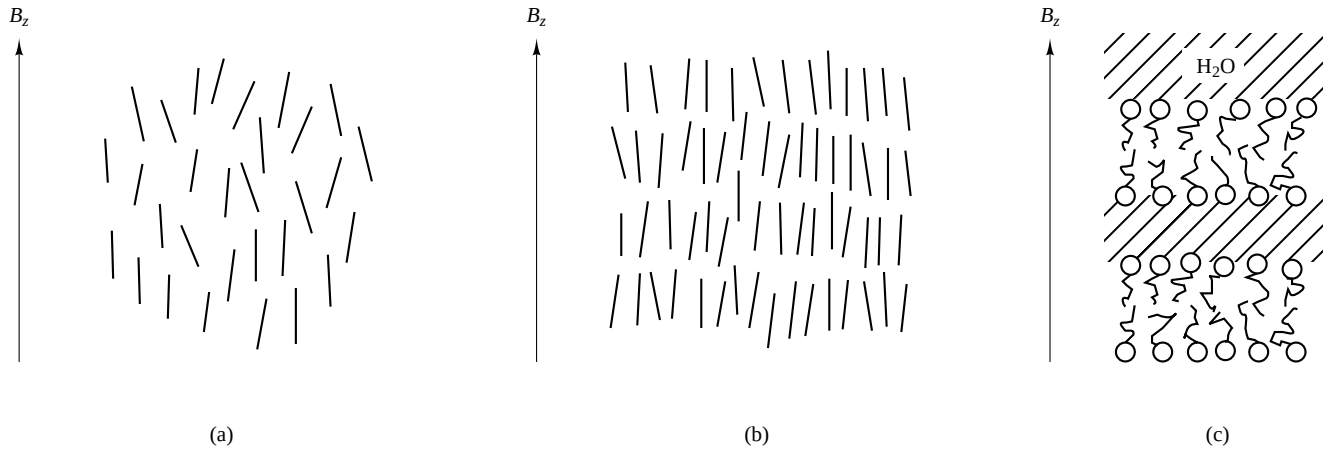

Figure 1 Schematic representation of liquid crystal phases in a magnetic field: (a) thermotropic nematic; (b) thermotropic smectic; (c) lamellar lyotropic with water layers, ionic hydrophilic head groups, and hydrophobic tail paraffin chains

3 DEGREE OF ORDER OF THE SOLUTE

Molecules dissolved in liquid crystals are oriented because of their interaction with the anisotropic solvent. The degree of order may be described by the order tensor $\boldsymbol{S}$:[12]

$$S_{pq} = \tfrac{1}{2}\langle 3\cos\Theta_{pz}\cos\Theta_{qz} - \delta_{pq}\rangle \tag{1}$$

where Θ_{pz} is the angle between the liquid crystal optical axis and the p axis in a molecule-fixed coordinate system. δ_{pq} is the Kronecker delta, and the z axis is parallel to the optical axis.

$\boldsymbol{S}$ is a traceless symmetric tensor with five independent elements. Solute symmetry reduces the number of elements required for a description of order. A plane of symmetry (x,y) is fully characterized by the elements S_{xx}, S_{yy} and S_{xy}. If there is also a C_2 axis (y) then S_{xx} and S_{yy} define the order. An n-fold axis of symmetry (y) reduces the necessary $\boldsymbol{S}$ components to S_{yy}, which is equal to $-2S_{xx} = -2S_{zz}$. For S values reported in the literature, it is usually assumed that the liquid crystal optical axis is parallel to the applied field. If the axis is at an angle of β with respect to the field then the measured S also contains a factor of $\frac{1}{2}(3\cos^2\beta - 1)$.

The degree of order of any axis ij in a molecule without symmetry can be derived from the $\boldsymbol{S}$ components in the molecular axis system (x, y, z):

$$\begin{aligned} S_{ij} &= \sum_{p.q}\cos\Theta_{ijp}\cos\Theta_{ijq}S_{pq} \\ &= \tfrac{1}{2}S_{zz}(3\cos^2\Theta_{ijz} - 1) + \tfrac{1}{2}(S_{xx} - S_{yy})(\cos^2\Theta_{ijx} - \cos^2\Theta_{ijy}) \\ &\quad + 2S_{xy}\cos\Theta_{ijx}\cos\Theta_{ijy} + 2S_{xz}\cos\Theta_{ijx}\cos\Theta_{ijz} \\ &\quad + 2S_{yz}\cos\Theta_{ijy}\cos\Theta_{ijz} \end{aligned} \tag{2}$$

In analogy with the fact that two nuclei whose internuclear axis makes an angle of 54° 44′ (the magic angle) with the applied magnetic field have zero direct dipolar coupling, there exists in every molecule a continuum of directions that have a degree of order of zero; i.e., nuclei whose connecting axis lies on this continuum have no dipolar interaction. The continuum consists of a double cone that, for molecules with two planes of symmetry, cuts the planes at directions $x/y = \pm(-S_{yy}/S_{xx})^{1/2}$. Consequently, if the two degrees of order of the plane have different signs then there is a direction in the plane in which two nuclei will not interact. On neighboring axes, the interaction is small, i.e., the structure information is of poor quality because of the relative uncertainties of the necessary corrections for vibrations and for deformation. (See Sections 9.2.1 and 9.2.2.)

In principle, a priori, there is no information available on the magnitude of molecular S values nor on the interdependence between molecular structure and order parameters. There is, however, a possibility to gain some insight if the assumptions of the deformation theory[13] (see Section 9.2.2) are used.

For a planar molecule (x, y), the segment n (bond or larger structure) makes the following contributions to the molecular interaction tensor $\boldsymbol{A}$, which determines the orientation:

$$\left.\begin{aligned} A^n_{xx} &= \Delta A_n[\tfrac{2}{3} - (1 - \tfrac{1}{3}\eta_n)\sin^2\Theta_n] \\ A^n_{yy} &= \Delta A_n[\tfrac{2}{3} - (1 - \tfrac{1}{3}\eta_n)\cos^2\Theta_n] \\ A^n_{zz} &= -\tfrac{1}{3}\Delta A_n(1 + \eta_n) \\ A^n_{xy} &= \tfrac{1}{2}\Delta A_n(1 - \tfrac{1}{3}\eta_n)\sin 2\Theta_n \\ A^n_{xz} &= A^n_{yz} = 0 \end{aligned}\right\} \tag{3}$$

Here the z axis is perpendicular to the plane and Θ_n is the angle between the bond axis and the molecular x axis. The degrees of order may be obtained by integration as described in Section 9.2.2.

As an example, in benzene, the relation between the ordering matrix

$$S_{\alpha\beta} = S\begin{bmatrix} -\frac{1}{2} & 0 & 0 \\ 0 & -\frac{1}{2} & 0 \\ 0 & 0 & 1 \end{bmatrix} \tag{4}$$

and the interaction parameters is

$$\begin{aligned} A_{xx} &= A_{yy} = -\tfrac{1}{2}A_{zz} = \Delta A_{\mathrm{CC}}(1 + \eta_{\mathrm{CC}}) + \Delta A_{\mathrm{CH}}(1 + \eta_{\mathrm{CH}}) \\ &= -\tfrac{2}{9}ck_{\mathrm{B}}T = U_{\mathrm{ext}} \end{aligned} \tag{5}$$

with

$$S_{zz} = \frac{3}{4c}\left[\mathrm{e}^c\left(\int_0^1 \mathrm{e}^{cx^2}\,\mathrm{d}x\right)^{-1} - 1\right] - \frac{1}{2} \tag{6}$$

Here ΔA is the anisotropy and η_A the asymmetry of the interaction tensor $\boldsymbol{A}$, and U_{ext} is the orienting potential energy; k_B is Boltzmann's constant. For benzene, the ηs are small or zero, but the ΔAs vary considerably with the liquid crystal solvent. ΔA_{CC} is in the range $(12-18) \times 10^{-22}$ J and ΔA_{CH} varies between -4×10^{-22} and $+7 \times 10^{-22}$ J. The change of sign indicates a change of the preferred orientation of the bond parallel (+) or perpendicular to the liquid crystal axis.

For the addition of ΔAs, bonds may be shifted to any position, as long as they retain their orientation. 1,2- and 1,3-disubstituted benzenes with equal substituents should have the same degrees of order (with exchanged C_2 axes). This is only approximately fulfilled, indicating the limitations of the approach.

4 DIRECT DIPOLAR COUPLING AND MOLECULAR GEOMETRY

The direct dipolar coupling is defined as follows:

$$D_{ij} = -K_{ij} S_{ij} / r_{ij}^3 \tag{7}$$

where

$$K_{ij} = -\mu_0 \hbar \gamma_i \gamma_j / 8\pi^2 \tag{8}$$

depends upon the gyromagnetic ratios of the nuclei i and j.

K_{ij} may be split into the individual nuclear contributions $K_{ij} = k_i k_j$. For $S_{ij} = 1$ and $r_{ij} = 0.1$ nm, the ks as well as the K_{ij} are summarized in Table 1.

For partially oriented solutes, the degree of order is normally of the order of 0.1, and internuclear distances are larger than 100 pm, so that the direct couplings will not usually exceed 3 kHz.

As equation (7) demonstrates, each direct coupling contains two unknown parameters, r_{ij} and S_{ij}, which cannot be determined separately. Also, in systems of several nuclei for which a network of direct couplings has been measured, it is only possible to determine distance ratios but not absolute distances unless a reference absolute distance determined by a different spectroscopy has been introduced. The reference length will then determine all the absolute distances as well as the S values.

For simple spin systems, the relations between the molecular geometry and the direct couplings can be represented analytically. An almost trivial case is benzene, for which the distance ratios r_o/r_p and r_m/r_p in the proton hexagon of $\frac{1}{2}$ and $\frac{1}{2}\sqrt{3}$ lead to ratios of direct couplings $D_o/D_p = 2^3$ and $D_m/D_p = (2/\sqrt{3})^3$. Real structural information can only be derived if the couplings from the protons to a carbon (^{13}C) are also observed. One structural parameter, r_{CH}/r_{HH}^0, fully determines the problem.

For a methyl group, the following equation is valid:

$$\frac{D_{CH}}{D_{HH}} = \frac{\gamma_C}{\gamma_H} \left(\frac{r_{HH}}{r_{CH}}\right)^3 \left[\left(\frac{r_{HH}}{r_{CH}}\right)^2 - 2\right] \tag{9}$$

which determines the distance ratio from the measured direct coupling ratio. The angle β between the C_3 axis and the CH bond is obtained from

$$\sin\beta = 3^{-1/2} r_{HH}/r_{CH} \tag{10}$$

The relation for a rectangular system of four nuclei,[14]

$$\frac{D_{12}}{D_{23}} \left(\frac{r_{12}}{r_{23}}\right)^5 - \frac{D_{13}}{D_{23}} \left[1 + \left(\frac{r_{12}}{r_{23}}\right)^2\right]^{5/2} + 1 = 0 \tag{11}$$

shows that, with an increasing number of nuclei, the help of computers for a solution of the equation is necessary. On the other hand, such relations are of interest, because they allow the discussion of the uniqueness of solutions as well as the possible accuracy of the geometrical information obtained. So, for instance, the shape of the rectangle has two solutions for $|D_{12}| > |D_{13}| < |D_{23}|$, and only one solution for $|D_{12}| < |D_{13}| < |D_{23}|$. The situation is particularly difficult if, by coincidence, the relation $D_{13}/D_{23} = |D_{12}/D_{23}|[(D_{12}/D_{23})^{2/3} + 1]^{-3/2}$ is fulfilled, because then, depending upon small errors in the Ds, there exist two very similar, one, or no solutions.

In general, therefore, it is recommended to record several spectra in different solvents, which preferably have different ratios of S values. The latter condition reduces the errors in a combined fit.

The number of different D couplings in a system of n nuclei without symmetry is equal to $\frac{1}{2}n(n-1)$. These couplings must define the five S values as well as the $3(n-2)$ coordinates of the spin system (six coordinates define an absolute distance as a basis). In order to have a fully determined system, the following relation must be fulfilled:

$$\tfrac{1}{2}n(n-1) - 5 - 3(n-2) \geq 0, \quad \text{i.e.,} \quad n \geq 7 \tag{12}$$

By similar arguments, it can be shown that in planar molecules without symmetry, $n \geq 5$, and with C_2 symmetry, the condition is $n \geq 4$. There are two ways out of the difficulty if a system is underdetermined. Either several spectra are combined, which is only recommended if the solvent effects on the structure (deformation—see Section 9.2.2) are corrected, or the number of couplings is increased by also considering ^{13}C information, i.e., satellite spectra of protons or ^{13}C spectra.[15] In the latter case, the information content of subsystems corresponding to ^{13}C in a particular position must be analyzed separately; some may be overdetermined or just determined, while simultaneously others can be underdetermined.

Table 1 Relative Size of Direct Dipolar Couplings K_{ij} for $S_{ij} = 1$ and $r_{ij} = 0.1$ nm and Nuclear Contribution Factors k_i ($K_{ij} = k_i k_j$)

Nucleus	k_i (kHz$^{1/2}$ pm$^{3/2}$)	Nuclear pair	K_{ij} (MHz pm^3)
^{1}H	346.506	^{1}H ^{1}H	120 067
^{2}D	53.190	^{1}H ^{2}D	18 431
^{13}C	87.123	^{2}D ^{2}D	2 829
^{14}N	25.034	^{1}H ^{13}C	30 188
^{15}N	−35.118	^{1}H ^{15}N	−12 169
^{19}F	325.989	^{1}H ^{35}P	48 606
^{31}P	140.276	^{1}H ^{57}Fe	3 895
^{57}Fe	11.24	^{1}H ^{107}Ag	4 855
^{107}Ag	14.01	^{13}C ^{13}C	7 590

5 SPECTRA OF ORIENTED SPIN SYSTEMS

5.1 Experimental Details

Preparation of samples is relatively simple. Approximately 10 mol% of the solute is brought into the liquid crystal solvent, which has been heated in the NMR sample tube to the isotropic range. Care is taken to mix thoroughly the components in order to avoid concentration gradients, which, via the concentration dependence of the S value, would produce considerable line broadening in the wings of the spectral range. Temperature gradients can be reduced by using double walled sample tubes with, for example, D_2O, in the interwall space. This liquid, which can also be used as a locking substance provides faster convection than the viscous liquid crystal in the inner tube.

Smectic samples must be cooled from the isotropic state in the magnetic field in order to produce homogeneous orientation, whereas nematic samples orient easily and rapidly after being brought into the field. Nematic samples can be rotated in the field of superconducting magnets in order to average out field gradients. The spectral width is usually several kilohertz, and a good signal-to-noise ratio for ^{1}H is reached with $1-10^2$ FIDs. If ^{13}C satellites at natural abundance are studied, 10^2-10^4 FIDs are required. For ^{13}C spectra at natural abundance, the relative receptivity of the nucleus (2×10^{-4}) with respect to the protons considerably increases the measuring time.

5.2 Theory

NMR spectra of molecules partially oriented in liquid crystal solvents are, for nuclei with $I = \frac{1}{2}$, characterized by the following Hamiltonian (in frequency units):

$$\hat{\mathcal{H}} = -(2\pi)^{-1} \sum_i \gamma_i \hat{\boldsymbol{I}}_i \cdot (\boldsymbol{1} - \boldsymbol{\sigma}_i) \cdot \boldsymbol{B} + \sum_{i<j} \hat{\boldsymbol{I}}_i \cdot \boldsymbol{T}_{ij} \cdot \hat{\boldsymbol{I}}_j \tag{13}$$

where $\boldsymbol{B}$ is the applied magnetic field in the z direction, γ_i is the gyromagnetic ratio of nucleus i, and the general coupling tensor $\boldsymbol{T}_{ij} = \boldsymbol{J}_{ij} + 2\boldsymbol{D}_{ij}$. Neglecting terms that do not commute with the total spin components in the z direction, we obtain

$$\begin{aligned}\hat{\mathcal{H}} = &-(2\pi)^{-1} \sum_i \gamma_i \hat{I}_{iz}(1 - \sigma_{izz}) B_z \\ &+ \sum_{i<j} [T_{ijzz} \hat{I}_{iz} \hat{I}_{jz} + \tfrac{1}{4}(T_{ijxx} + T_{ijyy})(\hat{I}_{i+}\hat{I}_{j-} + \hat{I}_{i-}\hat{I}_{j+}) \\ &+ \tfrac{i}{4}(T_{ijxy} + T_{ijyx})(\hat{I}_{i+}\hat{I}_{j-} - \hat{I}_{i-}\hat{I}_{j+})]\end{aligned} \tag{14}$$

where $\hat{I}_+$ and $\hat{I}_-$ are the raising and lowering operators, respectively.

Averaged over the anisotropic tumbling motion, we find in a laboratory-fixed coordinate system (x',y',z'),

$$\langle T_{x'x'} \rangle = \langle T_{y'y'} \rangle = \tfrac{3}{2} T^{\text{iso}} - \tfrac{1}{2} \langle T_{z'z'} \rangle \tag{15}$$

where

$$T^{\text{iso}} = \tfrac{1}{3}(T_{x'x'} + T_{y'y'} + T_{z'z'}) \tag{16}$$

$$\langle T_{z'z'} \rangle = T^{\text{iso}} + T'^{\text{aniso}} \tag{17}$$

with

$$T'^{\text{aniso}} = \frac{2}{3} \sum_{\alpha,\beta} S_{\alpha\beta} T_{\alpha\beta} \tag{18}$$

$$S_{\alpha\beta} = \tfrac{1}{2} \langle 3 \cos \Theta_{\alpha z'} \cos \Theta_{\beta z'} - \delta_{\alpha\beta} \rangle \tag{19}$$

Transformed to a molecule-fixed system (x,y,z), we have

$$\langle T_{ab} \rangle = \left(T^{\text{iso}} - \tfrac{1}{2} T'^{\text{aniso}}\right) \delta_{ab} + \tfrac{3}{2} T'^{\text{aniso}} \cos \Theta_{z'a} \cos \Theta_{z'b} \tag{20}$$

$$T^{\text{aniso}} = \tfrac{1}{2}(3 \cos^2 \alpha - 1) T'^{\text{aniso}} \tag{21}$$

where α is the angle between the optical axis of the liquid crystal and the magnetic field.

Finally, the effective Hamiltonian is

$$\begin{aligned}\hat{\mathcal{H}} = &-(2\pi)^{-1} \sum_i \gamma_i \hat{I}_{iz}(1 - \sigma_i^{\text{iso}} - \sigma_i^{\text{aniso}}) B_z \\ &+ \sum_{i<j} \{T_{ij}^{\text{iso}} [\hat{I}_{iz}\hat{I}_{jz} + \tfrac{1}{2}(\hat{I}_{i+}\hat{I}_{j-} + \hat{I}_{i-}\hat{I}_{j+}) \\ &+ T_{ij}^{\text{aniso}} [\hat{I}_{iz}\hat{I}_{jz} - \tfrac{1}{4}(\hat{I}_{i+}\hat{I}_{j-} + \hat{I}_{i-}\hat{I}_{j+})]\}\end{aligned} \tag{22}$$

T'^{aniso} of equation (18) can be expanded in terms of a molecule-fixed system (x, y, z) as

$$\begin{aligned}T'^{\text{aniso}} = &\tfrac{2}{3} S_{zz} \left[T_{zz} - \tfrac{1}{2}(T_{xx} + T_{yy})\right] + \tfrac{1}{3}(S_{xx} - S_{yy})(T_{xx} - T_{yy}) \\ &+ \tfrac{2}{3} S_{xy}(T_{xy} + T_{yx}) + \tfrac{2}{3} S_{xz}(T_{xz} + T_{zx}) \\ &+ \tfrac{2}{3} S_{yz}(T_{yz} + T_{zy})\end{aligned} \tag{23}$$

In the Hamiltonian, $T_{ij}^{\text{iso}} = J_{ij}^{\text{iso}} = J_{ij}$ is the indirect spin–spin coupling constant and $T_{ij}^{\text{aniso}} = J_{ij}^{\text{aniso}} + 2D_{ij}$, where J_{ij}^{aniso} is the pseudodipolar coupling, which cannot easily be separated from the direct coupling (see Section 9.1.2).

$D_{ij} = -(\mu_0 \hbar \gamma_i \gamma_i / 8\pi^2 r_{ij}^3) S_{ij}$ contains the structural information.

In an experiment, the measured T_{ij}^{aniso} is usually called $2D_{ij}$, so that the parameter D_{ij} contains a contribution of $\frac{1}{2} J_{ij}^{\text{aniso}}$.

In conclusion, it may be stated that the Hamiltonian of an oriented spin system can be derived from that of the isotropic system simply by adding the anisotropic shift component to the shift part, and substituting $J_{ij} + 2D_{ij}$ for J_{ij} in the diagonal contributions to the Hamiltonian and $J_{ij} - D_{iij}$ for J_{ij} in the off-diagonal contributions.

5.3 Nomenclature and Characterization of Spectra

Although the spectra of oriented molecules can be calculated by a relatively minor modification of the Hamiltonian of the nonoriented spin system, there are no simple transformations with, for example, effective Larmor frequencies or effective coupling constants (as in subspectra) that transform the spectrum of an oriented system into that of a nonoriented system; consequently, there are some clear differences. First of all, the notion of magnetic equivalence must be redefined, and the term ‘full equivalence’, which means the same coupling between nuclei of same chemical shift, must be introduced,

because, in oriented systems, the spectra of magnetically equivalent nuclei such as the protons of benzene (which, when nonoriented, displays one transition) depend upon all the direct as well as the indirect coupling constants. Only in a fully equivalent group such as CH_3 is the spectrum of the oriented molecule independent of J(H,H). However, it still displays information on the Ds: spectra of n fully equivalent nuclei of spin-$\frac{1}{2}$ consist of n-line multiplets with spacing $3D$. Magnetic equivalence does not exist for $I \geq 1$.

Also, the term 'weak coupling', which in normal NMR is usually (but wrongly!) defined as $J_{AX} \ll \delta_{AX}$ and which should actually be defined as $J^2/\delta_{AX} \ll$ (measurable difference in line position), loses its meaning in oriented NMR. The exception is when, in a system of, for example, three spins ABC, there is one direct coupling D_{AB} that exceeds all the δs, Js, and other Ds. In this case, in analogy with an ABX spectrum, the C nucleus is isolated and acts as a weakly coupled X nucleus; i.e., we observe AB doublets with splitting of $3D_{AB}$ with effective Larmor frequencies, i.e., centers of gravity, at

$$\tfrac{1}{2}(\nu_A + \nu_B) \pm \tfrac{1}{2}[\tfrac{1}{2}(J_{AC} + J_{BC}) + (D_{AC} + D_{BC})] \quad (24)$$

The appearance of a spectrum of two oriented nuclei AB is similar to that of the nonoriented system only if either J or δ and J are large with respect to D. In all other cases, i.e., $J = \delta = D$, $\delta = D > J$, $J = D < \delta$, $\delta = J < D$, and $J = D > \delta$, the intensity pattern is reversed, i.e., the inner lines are weaker.

Finally, a peculiarity of the spectra of oriented systems of three nuclei AA′A″ in which the Ds dominate may be mentioned. These spectra have a continuum of solutions, because only $D_{AA'} + D_{AA''} + D_{A'A''}$ as well as $D_{AA'}\,D_{AA''} + D_{AA'}\,D_{A'A''} + D_{AA''}D_{A'A''}$ can be determined, even if the line intensity is also considered.

5.4 Spectral Analysis

Spectra of oriented molecules are usually analyzed with the help of computers. Various programs such as LEQUOR,[16] which has been derived from LAOCOON simply by modification of the Hamiltonian (see Section 5.3), are available. The analysis is often quite complex, because, even if an appropriate molecular geometry can be guessed, the degrees of order cannot be predicted. In the fitting process illustrated in Figure 2, the indirect couplings J as fixed parameters as well as starting values of isotropic chemical shifts are taken from spectra of the nonoriented molecules, and Ds as well as δs are then iterated. As an example of a spectral analysis, we cite the proton spectrum of benzene shown in Figure 3. It is, of course, not representative of a typical structure determination, because the protons must form a hexagon. However, it will be interesting for a discussion of effects that must be corrected, such as vibration and deformation (see Section 9). The analysis of the spectrum is relatively trivial, because the degree of order is the only principal unknown, and the assignment of transitions is possible by inspection of a series of calculated spectra with assumed perfect hexagonal structure and with variable S value. Such inspection methods still work for two different degrees of order and with a two-dimensional display of the calculated spectra. For more than two unknown S values, however, the method fails.

Coming back to the benzene case, we should mention that the measured direct coupling constants do not quite agree with the hexagonal values, and depend quite strongly upon the liquid crystal solvent. The observed ranges in smectic, nematic lyotropic, mixed cholesteric, and nematic thermotropic solvents are for r_p/r_o (which should be 2.000) from 1.989 to 2.004 and for r_m/r_o (which should be 1.732) from 1.725 to 1.735.

In order to simplify the analysis procedure, two different approaches have been developed. In the first, an approximate guessed molecular structure is kept fixed during the iterative analysis of the spectrum, and only the S values are varied. The great advantage of such a scheme is the reduction of the number of unknowns for n nuclei of the order of n^2 to less than five, depending upon the symmetry, i.e., a very low number of assigned transitions allows a more rapid approach to an approximate solution. Of course, a normal analysis with a maximum of assigned transitions has to be performed at the end of this procedure, because the assumed geometry is not quite correct. However, the assignment of lines is then quite easy.

In the second simplifying approach, programs were developed that analyze the spectra automatically, i.e., no line assignment is necessary. The programs were based on the observation that in a fit that minimizes the average square deviation of line positions, there are local minima of this function that stop the fitting process whenever a transition of the measured spectrum coincides accidentally with one of the calculated spectrum. Therefore, in order to fit a spectrum, its properties should be 'smeared out', and only the rough features should be considered—as is actually done in analysis 'by hand'. For this purpose, either the lines may be artificially broadened to begin with and subsequently sharpened again during the fitting process, or the whole spectral information may be transformed into values, each of which characterizes a property of the spectrum but is independent of the others (integral transformations). Then the fit consists of a comparison of experimental with theoretical transforms. Again, a 'smeared out' appearance of the information is obtained—this time by using first a limited number of transforms (e.g., the lowest frequency Fourier transforms) and subsequently increasing the number during the fit as, for example, in the program STREAK.[17] Automatic analysis programs have successfully been used in practice.

5.5 Simplification of Spectra

5.5.1 Decoupling

The number of intense transitions for spectra of n spins $\frac{1}{2}$ increases as $n2^{n-1}$; i.e., a system of eight spins with approximately 1000 transitions is already quite tedious to analyze. For larger systems, one way out of trouble is a partial deuteration of the molecule, which, owing to the spin 1 of the deuterons, at first makes the proton spectrum more complex, although all the couplings to deuterons are reduced by a factor of 6.514 with respect to the proton case. The spectrum can then be simplified considerably by decoupling the deuterons[18] from the protons by irradiation at the center of gravity of the deuteron quadrupolar-split doublets, inducing double quantum transitions between the two deuteron levels with spins +1 and −1.

5.5.2 Two-Dimensional Spectroscopy

An alternative approach[19] is provided by random deuteration and subsequent use of quantum filtered and

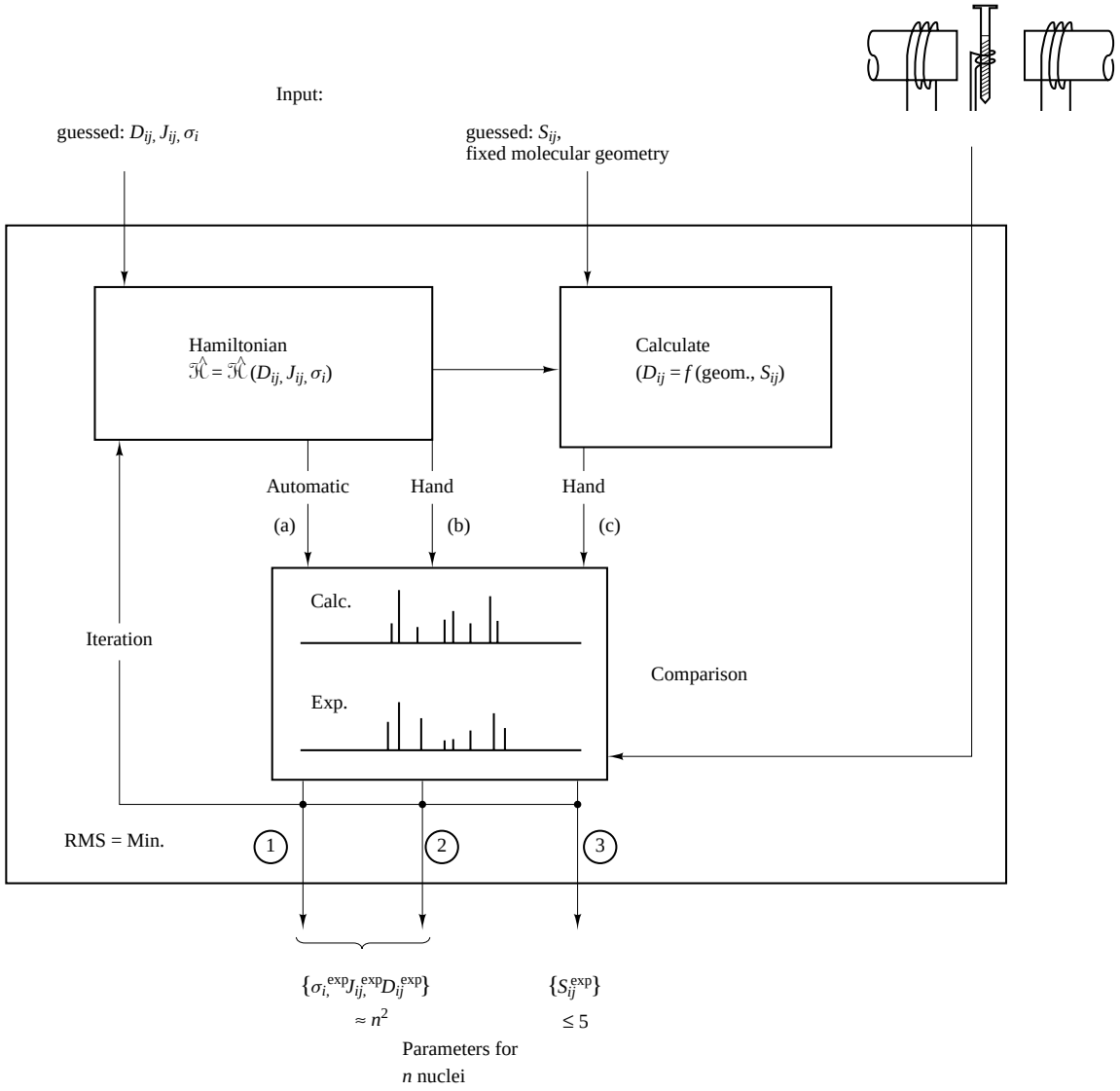

Figure 2 Schematic representation of spectral analysis: (a) automatic, comparison of experimental with theoretical data via integral transformations of spectrum (see Section 5.4); (b) normal 'hand' analysis with line assignment and iteration of σ_i, J_{ij}, and D_{ij}; (c) 'hand' analysis, with line assignment and assumed approximate molecular geometry, iteration of σ_i, J_{ij}, and S_{ij}

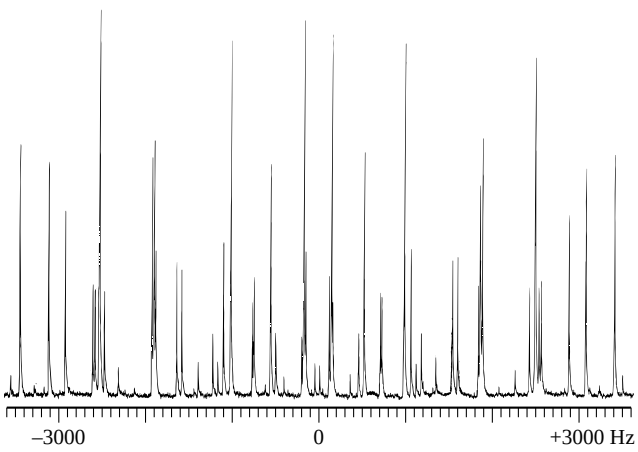

Figure 3 Proton spectrum of benzene, 6 mol% partially oriented in the nematic liquid crystal solvent ZLI 1132 (see Table 4) at 303 K

two-dimensional correlated spectroscopy, which leads to the separation of spectra of isotopically different molecules, each, of course, with a reduced number of protons.

5.5.3 Sample Rotation

Samples can be rotated[20] near the magic angle orientation with spinning speeds of a few kilohertz, and the direct couplings are thus reduced so that two-dimensional techniques, which normally fail in the strongly coupled spin systems of oriented molecules, become possible and assist the analysis.

5.5.4 Satellite Enhancement

X-nucleus satellite spectra of protons are very useful for a determination of structure information on, for example, ^{13}C and ^{15}N. Although they are usually quite weak because of the low abundance of the X nucleus, they are still easier to detect

Table 2 Gain Factor in the Signal-to-Noise Ratio if Direct Coupling D_{HX} is Not Observed in the X Spectrum but as a Satellite in the H Spectrum

Nucleus	Gain factor	Nucleus	Gain factor
H	1	^{77}Se	144
^{13}C	63	^{107}Ag	15 106
^{15}N	961	^{113}Cd	91
^{29}Si	128	^{117}Sn	22
^{31}P	15	^{199}Hg	176
^{57}Fe	29 590	^{195}Pt	101

than the X spectra. As an example, the gain in signal-to-noise ratio which is obtained if the C–H direct coupling is observed as a satellite in the proton spectrum and not as a splitting in the ^{13}C spectrum is 63. The corresponding gain for ^{15}N is 961. Further values are shown in Table 2.

In order to separate the weak satellite spectra from the much stronger pure proton spectrum, special difference methods may be applied. Thus, for instance, the ^{1}H spectrum minus a ^{1}H{^{13}C} spectrum gives simply the satellite spectrum with positive amplitude as well as the ^{1}H spectrum with total intensity equal to the ^{13}C satellite spectrum with negative amplitude.

5.5.5 *Multiple Quantum Transitions*

In normal NMR, we always observe one quantum transitions, i.e., the energy or frequency of the transitions is obtained as the difference of two eigenvalues of two Hamiltonian submatrices corresponding to total spins m and $m - 1$. For systems of more than two spins without symmetry, these matrices may have dimensions of 3×3 or larger, so that usually the transitions are not given by analytical expressions in the NMR parameters. In systems with symmetry, the breakdown of the Hamiltonian matrix into submatrices corresponding to symmetry species is responsible for transitions that can be expressed analytically.

A method that provides simplification of the information is the induction of multiple quantum transitions.[21] Thus, for instance, in a system of n spins $\frac{1}{2}$, the transition from total spin $+\frac{1}{2}n$ to $-\frac{1}{2}n$, i.e., the n quantum transition, is observed as the average Larmor frequency of the n nuclei, because in both eigenvalues all the couplings contribute equally and therefore disappear in the difference.

In the benzene six-spin system, for example, the six quantum transition is located at ν_H (benzene), but the five quantum transitions are also still simple sums of J and D couplings, because in the Hamiltonian subsystems corresponding to the symmetry species A_1, these transitions connect 1×1 submatrices. Some of the four quantum transitions (species A_1, B_1, E_1, E_2) again appear at ν_H (benzene), but some others (species A_1) are nonanalytical. The main simplification, however, lies in the drastic reduction in the number of transitions and in the easy identification of their origin, which, with the help of a computer, allows faster analysis. On the other hand, the method has not found routine application, because the measuring time for a reasonable signal-to-noise ratio is large.

5.5.6 *Very High Fields*

Except for an increased signal-to-noise ratio, very high fields do not contribute to the simplification of spectra of oriented molecules, because, even for 750 MHz proton spectra, the weak coupling condition limits D values to less than 100 Hz if deviations from the weak coupling behavior are not to exceed 1 Hz.

On the other hand, high magnetic fields are able to orient molecules whose anisotropy of diamagnetic susceptibility is large enough, so that dipolar splittings may be observed in 'isotropic' liquids. This effect is, however, small, because the degrees of orientation that may be reached are 10^{-6}–10^{-5} for diamagnetic and 10^{-5}–10^{-4} for paramagnetic molecules, whereas in liquid crystals we easily reach 10^{-2}–10^{-1}. Orientation by magnetic field for determining accurate structures is therefore out of the question.

6 DETERMINATION OF STRUCTURE FROM DIPOLAR COUPLING

For the determination of molecular structure from measured direct couplings, computer programs such as SHAPE[22] may be used, which, starting from a guessed molecular geometry, defined symmetries, and an assumed basis, calculates a set of theoretical direct couplings that is iteratively compared with the measured values weighted according to their variance until a minimum square deviation is found. As a result of the fit, the relative internuclear distances, absolute angles, and S values, as well as errors (variances and covariances), are obtained. For the calculation of error propagation, the mean-square error of the spectral fit is fed into the program. If this error is smaller than the average line position error (i.e., the problem is just determined or slightly overdetermined) then the latter is used as input. Actually, it is generally meaningful to use an increased error (e.g., 1–2 Hz) that takes into account the imprecision of the theoretical assumptions made in the corrections (see Section 9.2).

7 POSSIBLE ACCURACY OF STRUCTURE DETERMINATION

Most observed direct couplings are in the range of 10^2–10^3 Hz. It is usually possible to obtain linewidths of the order of 1 Hz, so that 10^{-1} Hz can definitely be determined (sometimes even 10^{-2} Hz), so that the relative accuracy of couplings is usually 10^{-4}. Since the internuclear distances are proportional to $D^{-1/3}$, the relative accuracy of the distances is also further increased to 3×10^{-5}. Consequently, distances should, in principle, be measurable with an accuracy of at least 10^{-2} pm. Unfortunately, this accuracy is not meaningful, because several approximations are made in the necessary corrections to the measured direct couplings. These are neglect of pseudodipolar coupling contributions to the measured Ds, limited accuracy in the vibration corrections, and assumptions made in the deformation corrections (see Section 9.2.2).

Taking these facts into account, it is possible to state that an accuracy of distance determination by NMR of oriented molecules exceeding 0.1 pm in bond lengths and 0.1° in bond angles is definitely unrealistic, However 1 pm may be measured reliably.

8 MOLECULES STUDIED

Between 1968 and 1983, the structures of over 500 molecules were determined by NMR in liquid crystal solvents. The initial intensity of research, with approximatively 30 structures per year, has more recently been reduced to approximately 10 structures per year. On the other hand, the interest in high-resolution NMR in liquid crystals in general has steadily increased from 40–50 papers per year in the 1970s to 80–100 papers per year in the 1980s and early 1990s.

The reasons for the reduction in structure studies are obviously that practically all the interesting small molecules with six or less spins have already been considered, and the expansion to larger spin systems is still slow. For the first studied 500 molecules, the relative contributions of systems with 4, 5, 6, 7, and 8 or more spins were 30, 20, 30, 10, and 10%. These ratios have not changed appreciably since then. Still ^{1}H with and without satellites and ^{13}C are the most studied nuclei, with additional interest in ^{2}H, ^{19}F, and ^{31}P, and occasional interest in ^{11}B, ^{14}N, ^{15}N, ^{17}O, ^{111}Cd, ^{113}Cd, ^{119}Sn, and ^{199}Hg. The spectra of relatively few molecules (less than 20) have so far been 'properly' analyzed in the sense that vibrational as well as deformational corrections have been performed. Structural data obtained by NMR of oriented molecules have been collected in books and reviews.[23,24]

9 FACTORS LIMITING THE ACCURACY OF STRUCTURE DETERMINATION

9.1 Principal Limits or Factors That at Present Practically Cannot Be Corrected

9.1.1 Signal-to-Noise Ratio

One of the limiting factors to the accuracy of structure determination is the signal-to-noise ratio (S/N) of the spectra, because the errors in line position (Δ) depend upon the point resolution ν_p, the linewidth ν_L and S/N as follows:

$$\Delta = \left(\frac{\nu_L^2}{\mathrm{S/N}} + \frac{\nu_p^2}{12} \right)^{1/2} \tag{25}$$

The S/N can be increased by a factor of n if the measurement time is increased by n^2.

In ^{13}C satellites of proton spectra, Δ is usually 10 times larger than in the strong proton transitions. Consequently, the accuracy of the D_{HH}s exceeds that of the D_{CH}s.

9.1.2 Anisotropy of Indirect Coupling Constants (Pseudodipolar Coupling)

As pointed out in Section 7, the measured direct coupling constants contain contributions from the pseudodipolar coupling, i.e., the anisotropy of the indirect coupling; for example, for a planar molecule with C_2 symmetry,

$$\begin{aligned} D_{ji}^{\mathrm{exp}} &= D_{ji} + \tfrac{1}{2} J_{ij}^{\mathrm{aniso}} \\ &= \tfrac{1}{2}(3\cos^2\alpha - 1)\left\{ S_{33}\left[-\frac{K}{r_{ij}^3}\tfrac{1}{2}(\cos^2\Theta_3 - 1) + \tfrac{1}{3}\Delta J \right] \right. \\ &\quad + (S_{11} - S_{22}) \\ &\quad \left. \times \left[-\frac{K}{r_{ij}^3}\tfrac{1}{2}(\cos^2\Theta_1 - \cos^2\Theta_2) + \tfrac{1}{6}(J_{11} - J_{22}) \right] \right\} \end{aligned} \tag{26}$$

with

$$\Delta J = J_{33} - \tfrac{1}{2}(J_{11} + J_{22}), \quad K = \mu_0 \hbar \gamma_i \gamma_j / 8\pi^2 \tag{27}$$

If $J_{ij}^{\mathrm{iso}} = \frac{1}{3}(J_{11} + J_{22} + J_{33})$ is small then usually the individual components $J_{\mu\mu}$ will also be small, i.e., the contribution of J^{aniso} may be neglected. This is certainly the case for couplings between two protons, for which $J_{ij}^{\mathrm{aniso}}/D_{ij}$ has been found to be of the order of 10^{-4}. Also, for one-bond C–H couplings, $J_{ij}^{\mathrm{aniso}}/D_{ij}$ has been determined experimentally as well as theoretically to be smaller than 10^{-3}. For other nuclear pairs, such as C–F, F–F, C–C, and C–N, the values are between 10^{-2} and 10^{-1}. Unfortunately J anisotropies are very difficult to determine—at any rate, vibrational as well as deformational corrections have to be performed in order to obtain meaningful results. Furthermore, the determinacy problem arises.[25]

If a molecular structure is defined by G and the order by O parameters then the number of measured couplings C must exceed the sum $G + O$. If we also count the J^{aniso} contributions, of which we have CO, then the condition

$$C \rangle G + O + CO \tag{28}$$

is only fulfilled if several spectra (n) are recorded:

$$nC \rangle G + nO + CO \tag{29}$$

i.e.,

$$n(C - O) \rangle G + CO \tag{30}$$

which is possible for large n if $C > O$.

The situation is even worse if the necessary deformational corrections are also considered. They introduce, instead of the O order parameters, a number of unknowns equal to twice the number of different bond types of the studied molecule, a figure that is always larger than O.

In conclusion, the neglect of J^{aniso} limits the obtainable accuracy in structure determination. As long as only H–H and C–H dipolar couplings are considered, the relative error is of the order of 3×10^{-4}, i.e., the contribution is of similar magnitude to that of the imprecise vibrational correction (see Section 9.2.1).

9.2 Factors That Can Be Corrected

9.2.1 Molecular Vibration

Apparent geometries of rigid solute molecules calculated from NMR spectra in nematic solvents must be corrected for effects due to their vibrational motions. These motions affect the direct couplings not only via the time dependence of the internuclear distance r_{ij} but also that of the degree of order of the ij axis. (The molecular degree of order is assumed to be constant during the vibrational period.) If we consider the substantial mean amplitudes of vibration of, for example, a C–H bond (7.8 pm) or of a nonbonded pair H–C–H (13.5 pm), it is obvious that different structure determination methods will, if uncorrected, provide different results for the average of

r_{ij}: $\langle r_{ij}\rangle$ from electron diffraction, $\langle r_{ij}^{-2}\rangle^{-1/2}$ from microwave spectroscopy, and $\langle r_{ij}^{-3}\rangle^{-1/3}$ from NMR.

An expansion for small amplitudes of vibration provides the relation

$$D_{ij}^{\text{exp}} = D_{ij}^{\text{e}} + D_{ij}^{\text{a}} + D_{ij}^{\text{h}} \tag{31}$$

where D_{ij}^{e} corresponds to the hypothetical molecular equilibrium structure that minimizes the electronic potential within the Born–Oppenheimer approximation. D^{a} is the anharmonic term, which for a pair of nuclei at distance R on the z axis is given by $D^{\text{a}} = -3\langle\Delta z\rangle\, D^{\text{e}}/R$, where $\langle\Delta z\rangle$ is the average z-vibration amplitude. D^{h} is the harmonic term, which is given by $D^{\text{h}} = 6(C^{\parallel} - C^{\perp})D^{\text{e}}/R^2$, where $C^{\parallel}$ and $C^{\perp}$ are the diagonal terms of the covariance matrix of vibrations.

For the vibrational corrections of NMR data, the force field of the molecule under study must be known. Computer programs are available (e.g., VIBR[26]) that from a force field and the corresponding assumed molecular geometry derive normal coordinates, vibrational frequencies (as a test), covariance matrices of quadratic displacements, and, finally, D_{ij}^{h}. The corrected coupling $D_{ij} - D_{ij}^{\text{h}} = D_{ij}^{\text{e}} + D_{ij}^{\text{a}}$ corresponds to a so-called additive r_α structure, i.e., to the average projection of the bond length onto a line joining the equilibrium positions.

Owing to their R^{-2} dependence, the harmonic vibrational corrections are particularly large for directly bonded nuclei such as C–H, for which the correction, for example, in benzene, is of the order of 8%, leading to an error in the bond length of close to 3% if it is not taken into account (see Table 3).

Relative corrections can also become particularly large for planar molecules of which two perpendicular axes in the plane have oppositely signed degrees of order. From Table 3, it can be concluded that if the required relative structural precision is of the order of 0.5% then, for not too small degrees of order and pure proton structure, harmonic corrections are not required.

The accuracy of harmonic vibrational corrections depends upon the force field, and is also affected by the approximation of r_{e} by r_α in the derivation of the corrections. However, the errors introduced are generally smaller than 4% (C–H bond) of the correction, corresponding to distance errors of 0.1 pm.

Anharmonic corrections may be computed by the program AVIBR[27] if the cubic force constants are available. Even if they are not, approximate corrections can still be calculated. A considerable part of the anharmonicity is artificial in that it originates from the use of rectilinear coordinates for a curvilinear pure harmonic motion. Obviously, this part can be derived from the harmonic force constants. The intrinsic anharmonicity stems principally from the potential functions associated with bond stretching. Using the Morse potential $V(\Delta r) = D[1 - \exp(-a\ \Delta r)^2]$ and expanding in terms of the bond stretch coordinate, it is possible to derive the cubic force constant in terms of the quadratic one as $f_{\text{cubic}} = -3af_{\text{quad}}$, where a turns out to be $0.02\,\text{pm}^{-1}$, even for very different bonds.

Table 3 Harmonic Vibrational corrections for Benzene, $D_{\text{corr}} = D_{\text{exp}}(1 + \alpha)$

Coupling	100 α
D_{HH}^{o}	+1.418
D_{HH}^{m}	+0.719
D_{HH}^{p}	+0.446
D_{CH}	+8.054
D_{CH}^{o}	+1.845
D_{CH}^{m}	+0.677
D_{CH}^{p}	+0.384

9.2.2 Molecular Deformation

The energy of molecules dissolved in liquid crystals contains contributions from their orientation and also from their vibration (quadratic in the normal coordinates). Because the vibrating molecule is subject to external forces, there must be a further contribution that is linear in the normal coordinates Q_k ($U_k Q_k$, where $U_k = \partial U_{\text{ext}}/\partial Q_k|_{\text{e}}$). This linear term, if added to the quadratic one ($\omega_k^2 Q_k^2$), shifts the energy minimum, i.e., the nuclei vibrate around a position displaced by U_k/ω_k^2. In other words, the molecules are deformed, the deformation depending upon the orientation of the molecule with respect to the liquid crystal director. Various names have been used for this phenomenon—for example, vibrational–rotational interaction or correlated deformation. The fact that to a certain orientation of a molecule there corresponds a deformation can also be reinterpreted as follows: orientation of a molecule requires that certain torques be applied to the bonds, and these torques will of course deform the molecular structure.

Correlated deformation[28] leads to additional terms in direct couplings D^{d}:

$$D^{\text{d}} = -K\sum_k \frac{1}{\omega_k^2}\left[\frac{3}{10}\sum_{\alpha\beta}\frac{\partial\Phi_{\alpha\beta}^{ij}}{\partial Q_k}\frac{\partial A_{\alpha\beta}}{\partial Q_k} + \frac{2}{7}\sum_{\alpha\beta\mu}\left(3\frac{\partial\Phi_{\alpha\mu}^{ij}}{\partial Q_k}\frac{\partial A_{\beta\mu}}{\partial Q_k} - \frac{\partial\Phi_{\mu\mu}^{ij}}{\partial Q_k}\frac{\partial A_{\alpha\beta}}{\partial Q_k}\right)S_{\alpha\beta}\right] \tag{32}$$

where

$$\Phi_{\alpha\beta}^{ij} = \langle\cos\Theta_{ij\alpha}\cos\Theta_{ij\beta}/r_{ij}^3\rangle \tag{33}$$

$\Theta_{ij\alpha}$ is the angle between internuclear vector $\boldsymbol{r}_{ij}$ and the α axis of the reference system, and $A_{\alpha\beta}$ are the elements of the interaction tensor, where

$$U_{\text{ext}} = -\frac{1}{2}\sum_{\alpha\beta}A_{\alpha\beta}(3\cos\Theta_\alpha\cos\Theta_\beta - \delta_{\alpha\beta}) \tag{34}$$

with Θ_α the angle between the α axis of the reference system and the liquid crystal director. As pointed out above, the interaction tensor must also define the order tensor of the molecule:

$$S_{\alpha\beta} = \frac{1}{Z_{\text{c}}}\int(3\cos\Theta_\alpha\cos\Theta_\beta - \delta_{\alpha\beta})\exp\left(-\frac{U_{\text{ext}}}{k_{\text{B}}T}\right)\mathrm{d}\Omega \tag{35}$$

$$Z_{\text{c}} = \int\exp\left(-\frac{U_{\text{ext}}}{k_{\text{B}}T}\right)\mathrm{d}\Omega \tag{36}$$

where Ω is the orientation of the molecular axis with respect to the laboratory-fixed frame.

It is interesting to note that even for $S_{\alpha\beta} = 0$ there is a remaining contribution to D^{d}. This explains the well known

fact that tetrahedral molecules dissolved in liquid crystals also display direct couplings. Obviously, this contribution increases drastically the relative importance of deformational corrections for molecules with small degrees of order. Furthermore, it should be mentioned that actual distortions of molecules (e.g., a change in bond angle between parallel and perpendicular orientations of the molecule with respect to the liquid crystal director) are amplified considerably by the correlated deformation process, and may lead, if uncorrected, to apparent distortions of the order of 10 times the actual distortion.

In order to determine solvent-independent molecular structures, the measured couplings must definitely be corrected for deformation. Since nothing is known initially about the interaction tensor, the elements $A_{\mu\nu}$ must be treated as unknown. The simplest approach is the assumption that the tensor $\boldsymbol{A}$ is a sum of individual bond interactions and that bond stretching may be neglected with respect to bond bending. In the iterative determination of molecular structure, not only the nuclear positions but also bond interaction tensors, i.e., their anisotropies $\Delta A = A_{zz} - \frac{1}{2}(A_{xx} + A_{yy})$ and asymmetries $\eta = (A_{yy} - A_{xx})/A_{zz}$, are iterated. As shown above, the As simultaneously determine the degrees of order (see also Section 3). In such a fit, the number of unknowns increases, but data obtained in various solvents may be fitted in one run.

The corresponding program MASTER[29] (see Figure 4) needs an input of the force field with the corresponding molecular structure and a definition of bonds; it then calculates in a modified subprogram of the type VIBR (see Section 9.2.1) the normal coordinates, the vibrational frequencies, and the basis for the harmonic contributions to the direct couplings and for the derivatives of direct coupling tensors and interaction tensors with respect to the normal coordinates. These data are fed into a modified version of SHAPE (see Section 6), together with the definition of the iteration parameters, experimental direct couplings, symmetries, gyrometric ratios, guessed starting structure, and guessed starting interaction tensors. SHAPE then calculates order parameters (S) from interaction parameters (ΔA, η_A) by numerical integration, the equilibrium Ds (D^{e}); harmonic corrections (D^{h}) and deformation corrections (D^{d}). By subsequent iteration of ΔA, η_A, and molecular structure, a minimum RMS error is obtained, and the output of the program lists molecular structure, interaction parameters, and δ values, with corresponding errors.

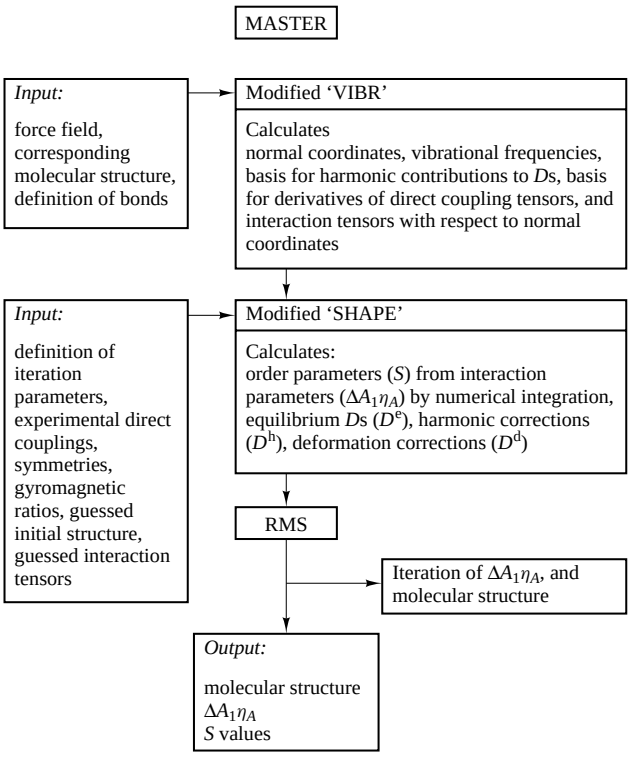

Figure 4 Schematic representation of molecular structure determination with corrections for harmonic vibrations and for deformation (program MASTER)

As an example of deformational corrections we compare in Table 4 the relative deviations of distance ratio in benzene $\Delta(r_\mu/r_v)$ derived from the measured direct couplings, with the data corrected for vibration only and for vibration as well as deformation from the theoretical hexagonal values.

The table shows that the effects of vibrational and deformational corrections on the resulting structure can be of similar magnitude; however, their signs may be opposite, so that the uncorrected structure can be closer to the real structure than the one corrected for harmonic vibration. A typical example is the solvent EBBA, in which the deviation from a hexagon is increased by the harmonic vibrational correction, but is reduced to zero by the deformational correction. Table 4 also demonstrates that, because the sign of the deformational correction can be positive or negative, depending upon the liquid crystal, it is possible to minimize the deformation—in particular, the C–H bending contribution—by using a mixture of solvents. There is, however, no ideal solvent in general, because different bond interactions may contribute to the distortion even if the C–H contribution disappears. The program MASTER, and the underlying theory, have been very successful. They explain the direct couplings in tetrahedral molecules, the deviation from the apparent benzene structure from the hexagonal one after harmonic vibrational corrections, the methyl angle variation with solvent in molecules of the type CH_3X with an apparent distortion of 2° and an actual one of 0.2°, and the apparent variation of the distance ratio r_{CH}/r_{CN} by 50% in HCN for small S values, as well as disagreements between NMR and different methods of structure determination (e.g., in the deformation of benzene by substituents).

10 COMBINATION OF NMR STRUCTURAL INFORMATION WITH DATA FROM OTHER SPECTROSCOPIES

Because of their large coupling constants, the positions of protons can be determined with high accuracy. Positions of carbon or nitrogen are obtainable with less accuracy. Nuclei such as oxygen, sulfur, or chlorine with spin $I \geq 1$ cannot be located, because, owing to their quadrupolar relaxation, they are effectively decoupled from the other nuclei. Deuterium and quadrupolar nuclei in highly symmetrical structural environments are exceptions. Their dipolar (as well as quadrupolar) interactions can be measured.

The lack of information has induced several authors right from the beginning of work on NMR of oriented molecules

Table 4 Relative Deviations $\Delta(r_\mu/r_\nu) = [(r_\mu/r_\nu) - (r_\mu/r_\nu)_{\text{hex}}]/(r_\mu/r_\nu)_{\text{hex}}$ from Theoretical Hexagonal Distance Ratios for Protons $r_p/r_o = 2.0000$ and $r_p/r_m = 2/\sqrt{3} = 1.1547$ in Benzene (accuracy $> \pm 0.7$); A Deviation of 10^{-4} Corresponds to 0.025 pm in r_o, or 0.043 pm in r_m, or 0.05 pm in r_p

Liquid crystal solvent[a]	Measured	Vibration	Corrected for Vibration and Deformation
1132	−41.1/−13.4	−9.6/−4.5	0/0
EBBA	+19.7/+7.4	+51.4/+16.4	0/0
1132 (55%) + EBBA (45%)	−30/−9.5	+1.8/0	0/0

[a]1132 = mixture of three *trans*-4-*n*-alkyl(4-cyanophenyl)cyclohexanes and *trans*-4-*n*-pentyl(4′-cyanobiphenyl-4-yl)cyclohexane; EBBA = *n*-(*p*-ethoxybenzylidene)-*p*-*n*-butylaniline.

to combine information from different spectroscopies with NMR.[30,31] Other spectroscopies, each of which has its own limitations, can profit from this. For example, electron diffraction and microwave spectroscopy provide absolute internuclear distances with reliable heavy atom positions, whereas NMR gives relative distances with high accuracy for the location of the light nucleus, namely the proton. In combined fits, relative weights proportional to the inverse square of their uncertainties are given to the parameters. Of course, harmonic vibrational corrections must be performed for all the spectroscopies, and, in particular, deformational corrections are essential for NMR in order to remove solvent effects. Furthermore, in NMR, couplings to heavy nuclei should be excluded, because of their pseudodipolar coupling component. Finally, variances as well as covariances should be considered.

11 CONCLUSIONS

NMR of oriented molecules is a simple and fast method for obtaining information on molecular structure in the form of highly accurate direct coupling constants. It can be used for groups of up to 10 magnetic nuclei (with spin-$\frac{1}{2}$) in small molecules or in larger molecules in which the remaining nuclei are decoupled. The method provides accurate proton positions, which are difficult to obtain by other spectroscopies. It can definitely compete with microwave spectroscopy and electron diffraction and, for small molecules, with X-ray diffraction.

The main disadvantage of the method lies in the fact that it studies molecules that are not free but are dissolved in liquid crystals, which deform the molecular structure by anisotropic interaction and make it solvent-dependent. However, the solvent dependence can now be removed by calculation of deformational corrections. In these calculations, approximations have to be made in order to reduce the number of unknowns:

1. deformations are taken to consist of bond bending exclusively, and stretching is neglected;
2. the interaction is assumed to be described as a sum of bond contributions.

These simplifications, together with the neglect of pseudodipolar coupling, lead to a reduction of structural accuracy, which, on the basis of measurement errors, could easily have reached 0.01 pm, to approximately 0.1 pm in bond lengths and 0.1° in angles.

12 RELATED ARTICLES

Anisotropy of Shielding and Coupling in Liquid Crystalline Solutions; Liquid Crystalline Samples: Structure of Nonrigid Molecules; Two-Dimensional NMR of Molecules Oriented in Liquid Crystalline Phases.

13 REFERENCES

1. A. Saupe and G. Englert, *Phys. Rev. Lett.*, 1963, **11**, 462.
2. P. Diehl and C. L. Khetrapal, in *NMR Basic Principles and Progress*, eds. P. Diehl, E. Fluck, and R. Kosfeld, Springer-Verlag, Berlin, 1969, Vol.1, p. 3.
3. J. Bulthuis, C. W. Hilbers, and C. MacLean, *MTP Int. Rev., Sci., Phys., Chem. Ser. 1*, 1972, **4**, 401.
4. L. C. Snyder and S. Meiboom, In *Critical Evaluation of Chemical and Physical Structural Information*, eds. D. R. Lide and M. A. Paul, National Academy of Sciences, Washington, DC, 1974, p. 143.
5. J. W. Emsley, J. C. Lindon, *NMR Spectroscopy Using Liquid Crystal Solvents*, Pergamon Press, Oxford, 1975.
6. C. L. Khetrapal, A. C. Kunwar, A. S. Tracey, and P. Diehl, in *NMR Basic Principles and Progress*, eds. P. Diehl, E. Fluck, and R. Kosfeld, Springer-Verlag, Berlin, 1975, Vol.9, p. 3.
7. L. Lunazzi, In *Determination of Organic Structures by Physical Methods*, eds. F. C. Nachod, J. J. Zuckermann, and E. W. Randall, Academic Press, New York, 1976, Vol.6, p. 235.
8. P. Diehl, in *Nuclear Magnetic Resonance of Liquid Crystals*, ed. J. W. Emsley, Reidel, Dordrecht, 1985, p. 147.
9. P. Diehl and J. Jokisaari, in *NMR in Stereochemical Analysis*, eds. Y. Takeuchi and A. M. Marchand, VCH, Dearfield Beach, FL, 1986, p. 4.
10. P. Diehl, in *Accurate Molecular Structures*, eds. A. Domenicano and I. Hargittai, Oxford University Press, Oxford, 1992, p. 299.
11. C. L. Khetrapal and K. V. Ramanathan, in *Specialist Periodical Reports on NMR*, ed. R. J. Abraham, The Royal Society of Chemistry, London, 1992, and earlier reports since 1972 cited therein.
12. A. Saupe, *Z. Naturforsch. A*, 1964, **19**, 161.
13. J. Lounila and P. Diehl, *Mol. Phys.*, 1984, **52**, 827.
14. P. Diehl, C. L. Khetrapal, and U. Lienhard, *Can. J. Chem.*, 1968, **46**, 2645
15. E. E. Burnell, P. Diehl, and W. Niederberger, *Can. J. Chem.*, 1974, **52**, 151.
16. P. Diehl, H. P. Kellerhals, and W. Niederberger, *J. Magn. Reson.*, 1971, **4**, 352.
17. P. Diehl, S. Sykora, and J. Vogt, *J. Magn. Reson.* 1975, **19**, 67.

18. S. Meiboom, R. C. Hewitt, and L. C. Snyder, *Pure Appl. Chem.*, 1972, **32**, 251.
19. M. Gochin, A. Pines, M. E. Rosen, S. P. Rucker, and C. Schmidt, *Mol. Phys.*, 1990, **69**, 671.
20. J. Courtieu, P. W. Aldermann, and D. M. Grant, *J. Am. Chem. Soc.*, 1981, **103**, 6783.
21. A. G. Avent *J. Magn. Reson.*, 1983, **53**, 513.
22. P. Diehl, P. M. Henrichs, and W. Niederberger, *Mol. Phys.*, 1971, **20**, 139.
23. C. Schumann, in *Handbook of Liquid Crystals*, ed. H. Kelker and R. Hatz, Verlag Chemie, Weinheim, 1980, p. 426.
24. C. L. Khetrapal and A. C. Kunwar, in *Advances in Magnetic Resonance*, ed. J. S. Waugh, Academic Press, New York, 1977, Vol.9, p. 301.
25. J. Lounila and J. Jokisaari, in *Progress in NMR Spectroscopy*, eds. J. W. Emsley, J. Feeney, and L. H. Sutcliffe, Pergamon Press, Oxford, 1982, Vol.15, Part 3, p. 249.
26. S. Sykora, J. Vogt, H. Bösiger, and P. Diehl, *J. Magn. Reson.*, 1979, **36**, 53.
27. J. Lounila, R. Wasser, and P. Diehl, *Mol. Phys.*, 1987, **62**, 19.
28. J. Lounila and P. Diehl, *J. Magn. Reson.*, 1984, **56**, 254.
29. R. Wasser, M. Kellerhals, and P. Diehl, *Magn. Reson. Chem.*, 1989, **27**, 335.
30. G. Englert and A. Saupe, *Mol. Cryst. Liq. Cryst.*, 1969, **8**, 233.
31. D. W. H. Rankin, in *Stereochemical Applications of Gas-Phase-Electrondiffraction*, eds. I. Hargittai and M. Hargittai, VCH, New York 1988, Part A, p. 451.

Biographical Sketch

Peter Diehl. *b* 1931. Ph.D., 1958, physics, University of Basel, Switzerland. Postdoctoral work at Oxford (with Rex Richards), Teddington (with John Pople) and Ottawa (with Harold Bernstein). Research Professor, University of Basel, 1964–present. Approximately 200 publications, including 3 books. Research specialties: ^{17}O spectroscopy, spectral analysis, ^{2}D spectroscopy, oriented molecules in liquid crystals, noble gas NMR.

Two-Dimensional NMR of Molecules Oriented in Liquid Crystalline Phases

Anil Kumar

Indian Institute of Science, Bangalore, India

1	Introduction	1
2	Two-Dimensional Spin Echo Resolved Spectroscopy	1
3	Two-Dimensional Correlation Spectroscopy	2
4	Experiments Utilizing Longitudinal Spin Order	7
5	Other Studies	8
6	Related Articles	9
7	References	9

1 INTRODUCTION

The direct dipole–dipole interaction between nuclear spins plays a dominant role in magnetic resonance. Several kilohertz in magnitude, it causes severe line broadening of NMR lines in solids owing to the presence of a large number of coupled spins. Anisotropic reorientation coupled with translational diffusion of molecules embedded in ordered matrices, such as a liquid crystalline medium, yields extremely interesting NMR spectra.[1] In such cases, the intermolecular dipolar interactions are averaged to zero, and the intramolecular interactions, scaled by the order parameter, are reduced to a few hundreds of hertz. As a result, only a finite number of spins are dipolar-coupled, yielding a large number of sharp and often well-resolved spectral lines. These dipolar-coupled spectra are extremely useful, and contain detailed information on the conformation, symmetry and anisotropy of reorientation of the molecules. However, since the dipolar couplings are often large compared with the chemical shifts, the spectra exhibit strong coupling features, making the analysis of such spectra nontrivial.[2–5] Only in some simple spin systems is the Hamiltonian analytically diagonalizable, allowing straightforward interpretation of the spectra. In most cases, one has to perform a numerical analysis using iterative computer programs such as LAOCOON[6] and its various modifications.[4,7,8] The input to these programs comprises the line frequencies, intensities, and initial parameters of the Hamiltonian. Trapping of the algorithm into local minima is a frequently encountered problem, and any additional information about the spectrum, the spin system, and the molecular reorientations is extremely useful.

Two-dimensional (2D) NMR spectroscopy has played a significant role in simplifying spectra and in often providing the key information. The various 2D NMR studies of oriented molecules discussed in this article are classified into the following categories:

1. resolved spectroscopy;
2. experiments utilizing transverse spin orders using single and multiple quantum coherences;
3. experiments utilizing longitudinal spin orders such as NOESY and Z-COSY.

The emphasis in this article is on proton spectra of small molecules oriented in liquid crystal matrices. Reference may be made to a review on this subject,[9] and periodic reviews of NMR of oriented molecules.[10]

2 TWO-DIMENSIONAL SPIN ECHO RESOLVED SPECTROSCOPY

The spin echo 2D resolved experiment utilizes a pulse sequence (90°, $\frac{1}{2}t_1$, 180°, $\frac{1}{2}t_1$, t_2). The 180° pulse reverses the sign of all terms linear in spin operators over which the 180° pulse acts, and leaves all bilinear terms invariant. For homonuclear (spin-$\frac{1}{2}$) spins, the various terms contributing to the spectra of oriented molecules are

$$\hat{\mathcal{H}} = \hat{\mathcal{H}}_{\mathrm{Z}} + \hat{\mathcal{H}}_{\mathrm{J}} + \hat{\mathcal{H}}_{\mathrm{D}} \tag{1}$$

where $\hat{\mathcal{H}}_{\mathrm{Z}}$ involves chemical shift terms linear in spin operators, and $\hat{\mathcal{H}}_{\mathrm{J}}$ and $\hat{\mathcal{H}}_{\mathrm{D}}$ are the indirect spin–spin and direct dipole–dipole couplings, respectively, which are both bilinear in spin operators. The 180° pulse reverses the sign of $\hat{\mathcal{H}}_{\mathrm{Z}}$ and leaves $\hat{\mathcal{H}}_{\mathrm{J}}$ and $\hat{\mathcal{H}}_{\mathrm{D}}$ invariant. If all the terms commute, as happens only in weakly coupled isotropic cases where $\hat{\mathcal{H}}_{\mathrm{D}}$ is absent and $\hat{\mathcal{H}}_{\mathrm{Z}} \gg \hat{\mathcal{H}}_{\mathrm{J}}$, then $\hat{\mathcal{H}}_{\mathrm{Z}}$ refocuses, and the effective Hamiltonian is simply $\hat{\mathcal{H}}_{\mathrm{J}}$. In such cases, the 2D spin echo spectrum consists of a simple separation of chemical shifts and couplings, with the multiplets of each chemical site appearing along a 45° line from the $\omega_1 = 0$ axis[11,12] (see ***Two-Dimensional J-Resolved Spectroscopy***). When the various terms in equation (1) do not commute, the 180° pulse causes coherence transfer between various transitions, and calculations performed for strongly coupled spins show that the line intensities and frequencies along the ω_1 direction are modified and that there are additional lines in the 2D spectra.[13,14]

The first application of this experiment in oriented systems was on an AB spin system formed by the protons of 1-thio-3-selenole-2-thione oriented in MBBA.[15] The 1D spectrum of the two spins consists of four lines symmetrically displaced from the average chemical shift. The difference between the outer and inner lines is the sum $|J_{\mathrm{AB}} + 2D_{\mathrm{AB}}|$. To assign the lines, one needs additional information, which can be provided by conventional double resonance experiments or by the above 2D resolved experiment. The 2D resolved experiment has eight lines, two of which appear with negative intensity (Figure 1). There are four lines of equal intensity along the ω_1 dimension, uniquely identifying the parameter $|J_{\mathrm{AB}} + 2D_{\mathrm{AB}}|$.[15]

Another 2D spin echo study has been carried out on the AB_2 spin system of 1-bromo-2,6-dinitrobenzene oriented in the room temperature nematic, Merck Phase V.[16] Significant rf inhomogeneity gave rise to artifacts in the spectra, which were simulated as errors in the refocusing 180° pulse. Errors in the 180° pulse cause additional coherence transfer pathways of the type obtained in spin echo correlated spectroscopy (SECSY),[17] and such spectra thus have features of resolved spectroscopy and SECSY, both affected by strong couplings.

Accurate values for homonuclear dipolar couplings have been extracted from 1D spin echo spectroscopy of oriented

Figure 1 Phase-sensitive spin echo 2D resolved spectrum of two strongly coupled protons of 1-thio-3-selenole-2-thione oriented in MBBA [obtained using the pulse sequence (90°, $\frac{1}{2}t_1$, 180°, $\frac{1}{2}t_1$, t_2)], recorded at 270 MHz. While the 1D spectrum consists of four lines, the 2D spectrum has eight, two of which appear with negative intensity. (Reproduced by permission of Academic Press from Khetrapal et al.[15])

molecules containing AA′BB′-type spin systems, formed by the protons in *para*-substituted pyridines, which are coupled to an increasingly complex group of heteronuclei and to fluorines in tetrafluorinated benzenes.[18] All the echo spectra were analyzed with a modified LAOCOON-type computer program.[16,19] The echo spectra differed from the normal spectra principally in the presence of extra lines, which were interpreted as being due to $\boldsymbol{B}_1$ inhomogeneity and analyzed iteratively assuming a refocusing pulse of angle 160° ± 10°.[18]

3 TWO-DIMENSIONAL CORRELATION SPECTROSCOPY

3.1 Single Quantum Correlation (COSY)

Two-dimensional COSY utilizes a pulse sequence (90°, t_1, 90°, t_2), and gives cross peaks between transitions that are coupled to each other in a coupled network. The first application of COSY for the spectra of oriented molecules was to the AA′BB′ spin system formed by the protons of benzoselenodiazole oriented in the liquid crystal EBBA.[20] The COSY spectrum separated the symmetric and antisymmetric transitions by the absence of cross peaks between them. This separation further facilitated complete identification and analysis of the antisymmetric part of the spectrum, virtually by inspection. A more detailed analysis of the intensities of the cross peaks, by changing the flip angle of the coherence transfer pulse (the second pulse of COSY), further facilitated identification of connected transitions and the assignment of resonances.[20]

The absence of cross peaks between symmetric and antisymmetric domains in COSY has been exploited further for systems with higher symmetry. The proton spectra of oriented acetone and oriented benzene have been studied.[21] Acetone has two rotating methyl groups, each having C_{3v} symmetry, yielding a spin system of the type A_3A_3'. The eigenstates of the Hamiltonian can be grouped into four irreducible representations, namely, A_g, A_u, G_1, and G_{2g}, with analytical expressions available for the energies. The 2D technique separated the spectrum into four parts, with cross peaks within each group and no cross peaks between the groups. This yielded a complete symmetry filtering of all the transitions, with straightforward identification of each group and the values of the dipolar couplings. Benzene has D_{6h} symmetry, and the spin states are divided into six irreducible representations (A_1, A_2, B_1, B_2, E_1, and E_2). The A_2 representation has only one spin state and no transition. The remaining five representations are filtered by COSY (Figure 2) in a straightforward manner, and separate iteration of each of the domains using a modified LACOONOR program yielded all the parameters in an efficient manner.[21]

Flip-angle-dependent COSY (COSY-30; 90°, t_1, 30°, t_2) experiments have also been performed on the protons of *p*-dimethoxy[$^2H_6$]benzene oriented in the liquid crystal PCH 1132, yielding information on the directly connected transitions.[8] This system of four ring protons coupled to six methyl deuteriums forms one of the largest spin systems giving a well-resolved spectrum. The $^1H-^2H$ dipolar couplings were focused by a spin echo experiment yielding a 10-line spectrum typical of an AA′A″A‴ spin system. The connectivity information allowed a complete analysis of this spectrum, and yielded the various spectral parameters.[8] The 2D COSY spectrum of ethyl iodide oriented in a nematic phase has also been reported.[22]

3.2 Multiple Quantum Correlation

In the previous section, the use of experiments that correlate single quantum coherences with each other were described. In this section, the use of the correlation of multiple quantum coherences to single quantum coherences by 2D spectroscopy (MQ spectroscopy) and simplification of COSY spectra by multiple quantum filtering is discussed.

3.2.1 MQ Spectroscopy

Two-dimensional multiple quantum spectra are obtained by the use of the pulse sequence (90°, τ, 90°, t_1, 90°, t_2), where the (90°, τ, 90°) pulse sandwich excites all orders. These multiple quantum coherences cannot be detected directly, and therefore are monitored indirectly by the use of 2D NMR. These coherences, allowed to evolve during the period t_1, are frequency-labeled, and at the end of t_1, a 90° pulse is used to transform them into single quantum (SQ) coherences, which are detected during the period t_2. Thus, the 2D spectrum contains MQ frequencies in the ω_1 dimension correlated with various SQ frequencies in the ω_2 dimension.[12,23,24] There is no net transfer of magnetization from one order to another, but only a differential transfer; therefore, many correlations appear with negative intensity. The projection of the absolute mode of the 2D spectrum on the ω_1 axis yields a 1D MQ spectrum, which can also be obtained by single point detection of the signal in t_2.[22,25–40] While most of the applications have been demonstrated using such one-dimensional spectra, 2D spectra have also been recorded (see ***Multiple Quantum Spectroscopy of Liquid Samples***). Figure 3 shows the 2D MQ spectrum of oriented benzene.[22,39] The spectrum becomes progressively simpler as one goes to higher multiple quantum orders, there being seven four-quantum frequencies, two five-quantum frequencies, and one six-quantum frequency present in the six-proton system of oriented benzene.

The various multiple quantum orders in Figure 3 have been separated by offsetting the carrier from the middle of the single quantum spectrum. If $\Delta\omega$ is the offset parameter then various orders are separated out by $n\ \Delta\omega$. The magnetic field inhomogeneity contribution to the linewidth increases

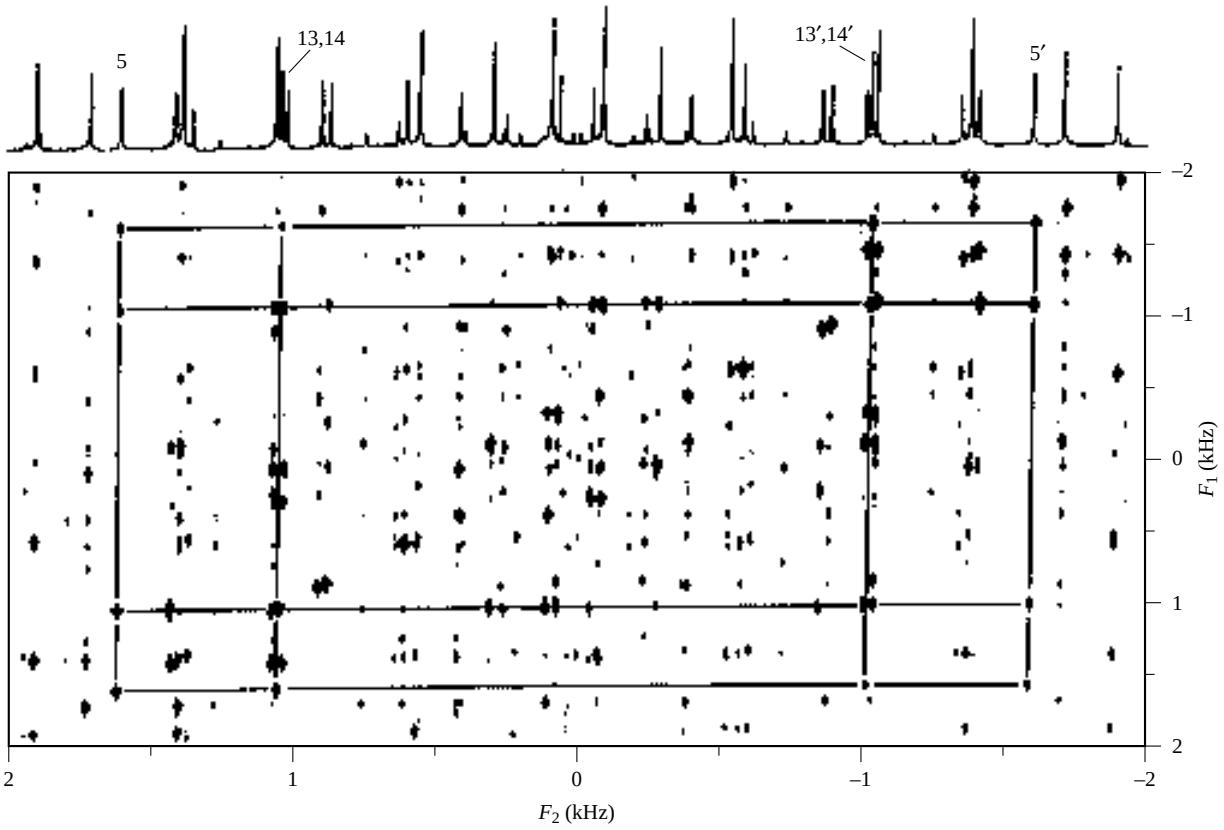

Figure 2 COSY spectrum of benzene oriented in ZLI-1167, recorded at 270 MHz. The connectivity in the B_1 symmetry domain containing lines 5, 13, 14, 14′, 13′, and 5′ is marked in the spectrum. (Reproduced by permission of Elsevier Science Publishers BV from Rukmani and Kumar[21])

proportionally for various MQ orders. In order to focus the field inhomogeneity, a 180° pulse has been introduced in the middle of the period t_1, which also focuses the offset dependence of various MQ orders. The various MQ orders in such cases are separated out by the use of time proportional phase incrementation (TPPI),[25] in which the phases of all the pulses in the excitation sequence are incremented in sequential t_1 experiments as $\phi = \Delta\omega\ t_1$. This results in a separation of various MQ orders by an effective offset parameter of $n\ \Delta\omega$. The 180° pulse in the middle of the period t_1 leaves all homonuclear couplings invariant, and, if there are no chemical shifts, yields an undistorted MQ spectrum, for example, in benzene.[25,26,32] However, if there are chemical shifts present along with dipolar and/or J couplings and the spectra are strongly coupled then the 180° pulse causes coherence transfer within each order, giving rise to new transitions and changed frequencies.[13,41,42]

Using the above pulse sequences, the 1D MQ spectrum has been obtained for the partially deuterated nematic liquid crystal 4-cyano-4′-(*n*-pentyl-d_{11})biphenyl (5CB-d_{11}), which has eight ring protons coupled to each other and yields a rather broad deuterium-decoupled single-quantum spectrum, but well-resolved five-, six-, and seven-quantum spectra (Figure 4).[33] Detailed analyses of these spectra have been carried out to obtain the dipolar couplings between various protons. The two biphenyl rings were either considered equivalent (D_4 symmetry) or inequivalent (D_2 symmetry). While an unequivocal fit was not obtained for either model, the D_4 symmetry resulted in the most physically reasonable molecular parameters. However, several splittings could not be explained by either of these models or by the effect of strong couplings, and it was suggested that rf inhomogeneity might provide an explanation for the extra splittings not predicted by the D_4 symmetry.[33]

3.2.2 Selectivity of Excitation and Detection

Attempts have been made to excite/retain only a few selected orders instead of all orders of MQ, thereby increasing the intensity of the particular order and the resolution of the detected order. Retaining a particular order is rather straightforward by phase cycling the detection pulse (the third 90° pulse) and the receiver or the excitation sequence and the receiver, in a concerted manner.[12] An example is shown in Figure 5.[34] The selection of a particular MQ order can also be achieved by using the technique of coherence transfer echo filtering (CTEF). A field gradient pulse of length τ in the MQ evolution period followed by a field gradient pulse of length $n\tau$ during the detection period refocuses only the nth order. This has been demonstrated on hexachloroethane oriented in EBBA.[43]

A large amount of effort has been made by Pines and coworkers in attempting to excite selectively all the transitions of a particular order using dipolar refocusing.[26,29,38–40] The introduction of a 180° pulse in the middle of the excitation sequence, along with appropriate phases of the two 90° pulses, yields an even- or odd-order excitation sequence for weakly coupled spins.[12] However, for dipolar-coupled spins,

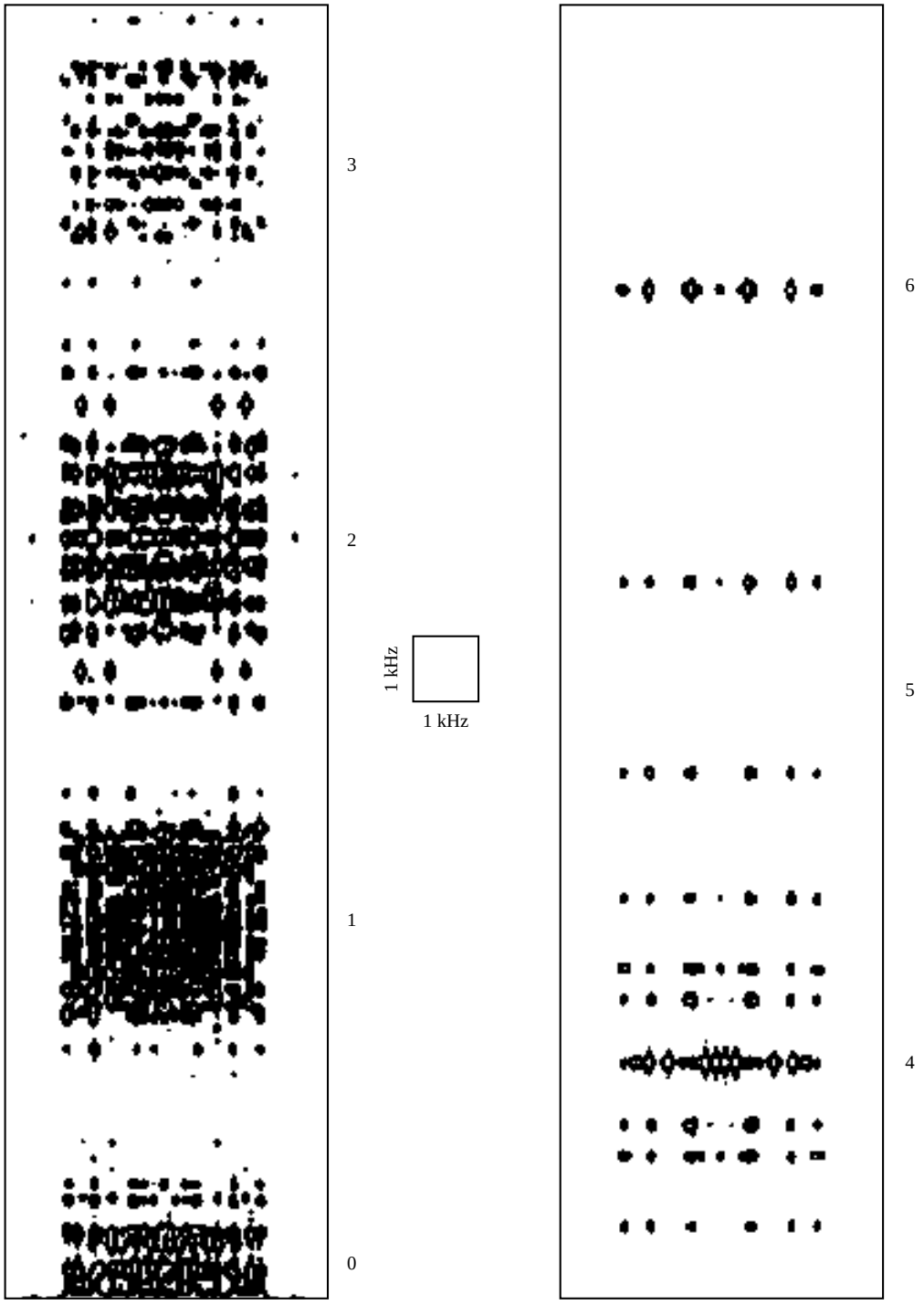

Figure 3 Two-dimensional multiple quantum spectrum of oriented benzene obtained using the pulse sequence (90°, τ, 90°, t_1, 90°, t_2), recorded at 200 MHz with a spectral offset of 6 kHz. (Reproduced by permission of Elsevier Science Publishers BV from Drobny[22])

it is possible to reverse the sign of the effective dipolar Hamiltonian by using multiple pulses, allowing one to design pulse sequences for exciting a particular order. The basic building block of the pulse sequence is shown in Figure 6. This block replaces the nonselective excitation sequence $90^\circ - \tau - 90^\circ$. Each sub-block consists of three parts. The first has a sequence of 90° pulses with interval τ, yielding a first-order average Hamiltonian $\hat{\mathcal{H}}_p$, and is applied for a time T. The second part consists of a delay $\Delta\tau_p$, and the third consists of a sequence of 90° pulses with delays of τ and 2τ, having an average Hamiltonian $-\hat{\mathcal{H}}_p'$ applied for a time T' such that $\hat{\mathcal{H}}_p T = \hat{\mathcal{H}}_p' T'$. Together, these yield the first sub-block, having an average Hamiltonian $\hat{\mathcal{H}}_0$, where the subscript refers to the phase of this sub-block. These sub-blocks are repeated n times, where n is the order to be selected, and the phase is

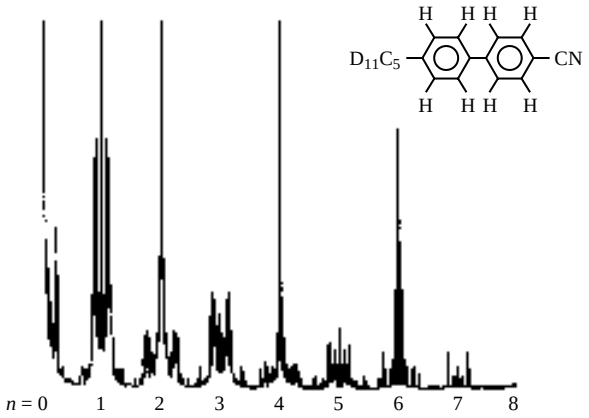

Figure 4 Multiple quantum proton spectrum of 5CB-d_{11} obtained using the pulse sequence (90°, τ, 90°, $\frac{1}{2}t_1$, 180°, $\frac{1}{2}t_1$, 90°, τ), at 182 MHz. The various multiple quantum orders are separated by TPPI, and the spectrum is the sum of magnitude mode spectra recorded for several values of τ ranging from 0.4 to 1.4 ms. (Reproduced by permission of Elsevier Science Publishers BV from Sinton and Pines[27])

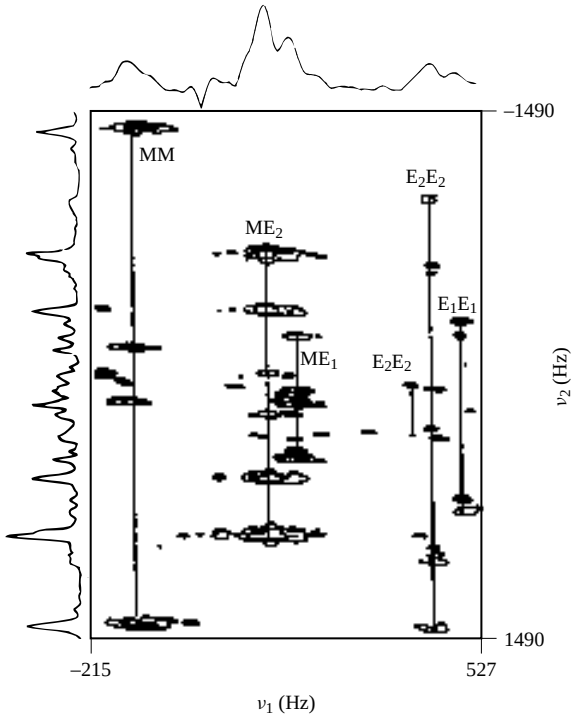

Figure 5 Double quantum versus single quantum correlation proton spectrum of 81% randomly deuterated *n*-hexane recorded by the sequence (90°$_\phi$, $\frac{1}{2}\tau_1$, 180°$_\phi$, $\frac{1}{2}\tau_1$, 90°$_\phi$, t_1, 90°$_\alpha$, $\frac{1}{2}\tau_2$, 180°$_\alpha$, $\frac{1}{2}\tau_2$, t_2), recorded at 360 MHz, under deuterium decoupling. The phase ϕ was incremented by 90° while the receiver phase was incremented by 180°. This retains double quantum coherences. Six vertical lines have been drawn at ν_1 frequencies corresponding to double quantum frequencies $2\nu_M$, $\nu_M+\nu_E$, $\nu_M+\nu_E$, $2\nu_E$, $2\nu_E$, and $\nu_E+\nu_E$. (Reproduced by permission of the American Chemical Society from Gochin et al.[34])

incremented each time for the entire subcycle by $\phi = 2\pi/n$. For better selectivity, the whole sequence may be repeated N times, where N may be 4 or 5. The results of such selective excitation are shown in Figure 7. More details about such

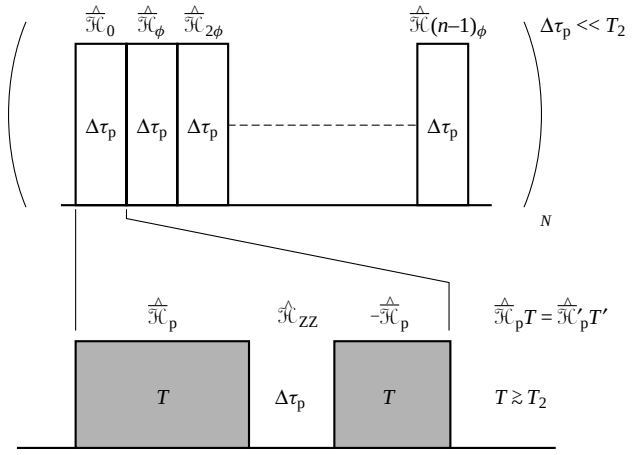

Figure 6 Pulse scheme for selective excitation of the *n*-quantum spectrum of dipolar-coupled spins. The order n is selected by incrementing ϕ in steps of $2\pi/n$. (Reproduced by permission of the American Physical Society from Warren et al.[26])

excitations are given by Warren et al.[26,29] and Drobny et al.[40] The highest order spectrum of N coupled spins $\frac{1}{2}$ is always a single line, whose position is determined by the sum of the chemical shifts of the coupled spins and is independent of spin−spin and dipolar couplings. Pines and co-workers have demonstrated that the $(N-1)$th- and $(N-2)$th-order spectra contain enough information to allow a spectral fit by iteration on the dipolar couplings, if there are no chemical shift differences, and, in general, it is possible to derive all the information from high-order MQ spectra that have a finite number of lines to be iterated upon.[25,28,30,35–40]

Most of the spectra using the above experimental procedures have been recorded using 2D pulse sequences, but recorded in a 1D manner using a single point detection in t_2. We shall restrict further discussion to 2D spectra.

3.2.3 Simplification of Spectra by Specific and Random Deuteration

As the number of dipolar-coupled spins increases beyond six or seven, the spectra become too complex for analysis by conventional procedures. Specific deuteration, coupled with deuterium decoupling—a straightforward technique for reducing the number of coupled protons—has been used in several cases. The main studies have been carried out on *n*-hexane-d_6, deuterated at methyl positions, and on 4-cyano-4′-(*n*-pentyl-d_{11})biphenyl (5CB-d_{11}), in which all the aliphatic protons have been deuterated, reducing both to systems of eight coupled protons.[27,33,35,39] The six- and seven-quantum 2D MQ spectra of *n*-hexane-d_6 (Figure 8) have been used to obtain the various dipolar couplings and their signs to estimate the dynamic molecular structure in the form of conformational probabilities.[35,39]

Another method of reducing the size of the spin system, but retaining information on dipolar couplings between all the protons of a molecule, is the technique of random deuteration combined with multiple quantum 2D spectroscopy or multiple quantum filtered COSY.[24,36,44,45] For example, an 81% random deuteration of *n*-hexane, which has 14 protons, yields approximately 6%, 18%, 25%, 25%, 14%, 5%, 3%, 2%,

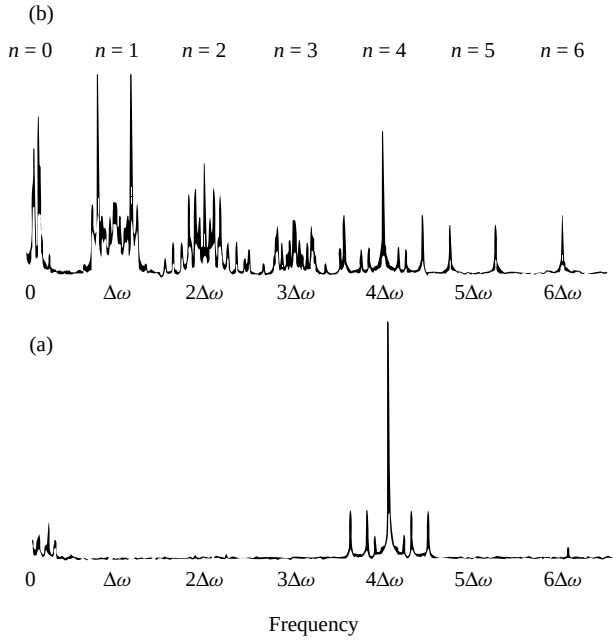

Figure 7 Four-quantum selective (a) and nonselective (b) MQ spectra of oriented benzene. (Reproduced by permission of the American Institute of Physics from Warren et al.[29])

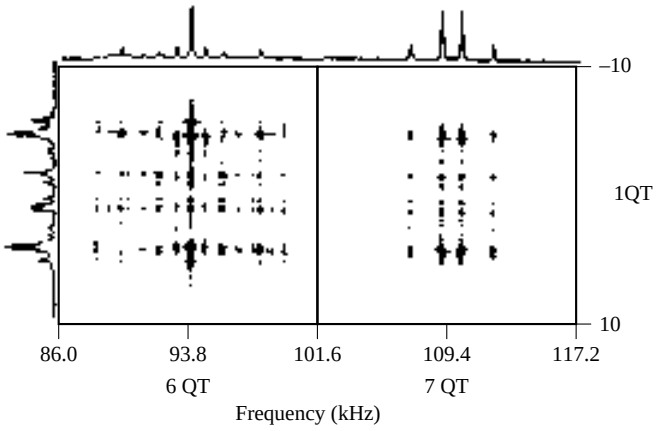

Figure 8 Absolute value six- and seven-quantum versus single-quantum correlation 2D spectrum of *n*-hexane-d_6 deuterated at methyl positions obtained by using the same pulse sequence as in Figure 5. The various orders were separated by TPPI using $\Delta\phi = 22.5°$. (Reproduced by permission of Elsevier Science Publishers BV from Gochin et al.35)

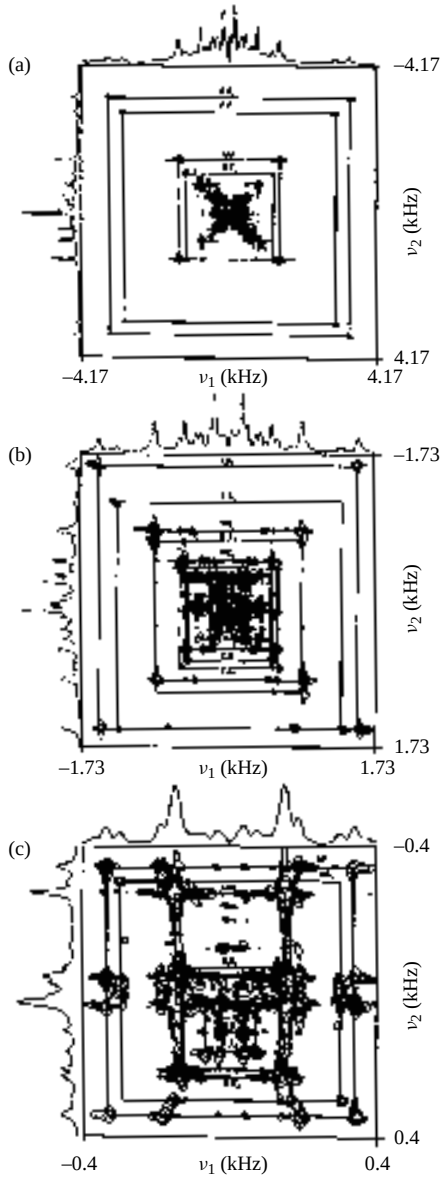

Figure 9 Double quantum filtered COSY (DQFC) spectrum of 81% randomly deuterated *n*-hexane-$d_{0.81}$ obtained using the pulse sequence ($90°_{\phi}$, $\frac{1}{2}t_1$, $180°_{\phi}$, $\frac{1}{2}t_1$, $90°_{\phi}$, $\frac{1}{2}\tau_1$, $180°_{x}$, $\frac{1}{2}\tau_1$, $90°_{x}$, $\frac{1}{2}\tau_2$, $180°$, $\frac{1}{2}\tau_2$, t_2), with phase cycling to retain double quantum coherence during the period τ_1. (a), (b), and (c) show successively expanded regions of the spectrum. The various two-spin systems are identified with square patterns. (Reproduced by permission of Taylor and Francis Ltd. from Gochin et al.[44])

and 1% molecules having 0, 1, 2, 3, 4, 5, 6, 7, and 8 protons, respectively.[36] Of these, only the one-, two-, and three-proton cases give significant intensity. The one-proton spectra can be easily filtered out using double quantum spectroscopy/filtering. The three- and high-spin spectra are quite low in intensity owing to the large number of lines and large number of possible spin systems. The double quantum filtered COSY (DQFC) spectrum thus contains prominently only the spectra of two coupled spins, and yields square patterns for each of the spin systems.[34,36] Numbering the carbons as M, E_1, E_2, E_2', E_1', and M′ in *n*-hexane, the various two-spin systems will be of the A_2 type for the protons in MM, E_1E_1, E_2E_2, E_2E_2'(*cis*), E_2E_2'(*trans*), E_1E_1'(*cis*), E_1E_1'(*trans*), and MM′ positions, and of AB type for ME_1, ME_2, ME_1', E_1E_2(*cis*), E_1E_2(*trans*), E_1E_2'(*cis*), and E_1E_2'(*trans*) positions. All such spin systems have been readily identified in the DQFC spectrum of 81% deuterated *n*-hexane recorded under deuterium decoupling (Figure 9), and several in the double-quantum 2D spectrum (Figure 5).[34,36] This yields all the dipolar couplings in *n*-hexane. Detailed analysis of the measured dipolar couplings has been carried out in terms of conformation and orientations of *n*-hexane in the liquid crystal solvent.

Recently, this idea has been extended to a series of *n*-alkanes, from hexane to decane (random deuteration level

of 80–90%), oriented in a nematic liquid crystal.[44] The DQFC spectrum in each case yields a large number of square patterns, each of which belongs to a two-spin system, yielding the totality of dipolar couplings between pairwise protons in the above molecules. The interpretation of the measured dipolar couplings is complicated, since they are averaged over molecular conformations and orientations sampled by the molecules. Nevertheless, they provide constraints on the time-averaged conformations and orientations of the molecules, which in turn allow an examination of various possible models for the solute–liquid crystal interactions.[44]

DQFC spectroscopy has also been utilized for a study of 78.7% randomly deuterated benzene oriented in a nematic phase.[36] Subspectra of three diprotonated and three triprotonated species could be identified in the spectrum. The subspectra were compared with the simulated spectra for various assignments, and the spectral parameters were obtained. A five-quantum versus single-quantum correlation 2D spectrum was also recorded for 34% randomly deuterated benzene. The five-quantum spectrum can be obtained either from fully protonated species or singly deuterated species. The singly deuterated species has only one five-quantum transition, while the fully protonated species has two five-quantum transitions, the correlation of which with various single quantum transitions yields various spectral parameters.[36]

3.2.4 Application to Chemically Exchanging Systems

Multiple quantum 2D spectroscopy has also been applied to chemically rearranging systems of oriented *s*-trioxane, which undergoes ring inversion, and oriented cyclooctatetracene, which undergoes a bond shift rearrangement.[46] Two-dimensional MQ–SQ correlation spectra were recorded at various temperatures, from which projected MQ spectra were obtained. The high-order (four and six) MQ spectra are much simpler than the single-quantum spectra, and exhibit characteristic exchange broadening and narrowing effects very similar to the single-quantum spectra. It is much easier to compare the high-order MQ spectra with the simulated spectra, calculated using exact as well as approximate expressions for the dynamic lineshapes, which then yield information on the rates of the dynamic processes. The uses, advantages, and limitations of the technique have been discussed in detail.[46]

4 EXPERIMENTS UTILIZING LONGITUDINAL SPIN ORDER

4.1 Effect of Strong Coupling in NOESY

It is known that each cross-section of the NOESY experiment using the (90°, t_1, 90°, τ_m, 90°, t_2) sequence is equivalent to a 1D difference NOE experiment in which the spin corresponding to the diagonal peak is selectively inverted at $\tau_m = 0$. It has been shown recently that this equivalence breaks down for strongly coupled spins, resulting in cross peaks in NOESY experiments, even without relaxation.[47,48] Explicit theoretical calculations have been carried out for an AB spin system, and the results are given in Figure 10.

Calculations have also been carried out for an ABX spin system, showing the existence of cross peaks between

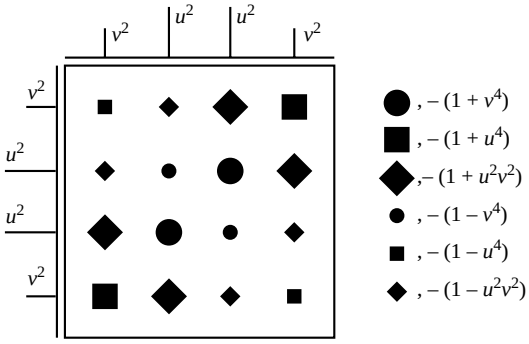

Figure 10 Schematic spectrum of an AB spin system calculated for the NOESY experiment (90°, t_1, 90°, τ_m, 90°, t_2), with phase cycling to retain longitudinal magnetization during the short period τ_m. The intensities of the 2D peaks are obtained by multiplying the symbols with the 1D intensities indicated on the ω_1 and ω_2 axes. For example, the intensity of the bottom left diagonal peak is given by $-v^4(1 + u^4)$, where $u = \cos\theta + \sin\theta$, $v = \cos\theta - \sin\theta$, and $\tan 2\theta = J_{AB}/(\nu_A - \nu_B)$. All cross peaks disappear for weakly coupled spins ($\theta = 0$, $u = v = 1$). (Reproduced by permission of the *Bulletin of Magnetic Resonance* from Christy Rani Grace and Kumar[48])

all X and AB transitions, even when X is only weakly coupled to AB.[48] The existence of such cross peaks has been experimentally demonstrated in oriented acetone (Figure 11), where a quantitative fit to the experimental cross sections, after removal of zero quantum interference, has been demonstrated by detailed calculations.[47] These cross peaks arise owing to the combined effect of strong coupling and the nonlinearity of the rf pulses. In order to examine whether the cross peaks are due to nonlinearity of the second or the third pulse in the NOESY experiment, calculations for the ABX spin system have been carried out for a small-angle second or third pulse. In an ABX spin system, there are two X transitions between pure states. In the experiments with the second pulse being of small angle and the third being 90°, there are no cross peaks from these X transitions to the AB transitions. Similarly, in the experiment in which the second pulse is 90° and the third is of small angle, there are no cross peaks from AB transitions to these X transitions. These observations indicate that the nonlinearity of a pulse is restricted to transitions within a spin or within groups of strongly coupled spins.[48]

4.2 Construction of Energy Level Diagrams

4.2.1 Using NOESY-α,β

In the linear regime, the NOESY-α,β experiment corresponds to the sequence (90°, t_1, α, τ_m, β, t_2), where α is a small-angle pulse and only longitudinal magnetization is retained during the period τ_m. It has been shown recently that, irrespective of the strength of coupling, each cross section of this experiment is equivalent to a 1D difference experiment in which the peak corresponding to the diagonal is selectively inverted at $\tau_m = 0$ and the state of spin system is monitored by the β pulse. If β is also a small-angle pulse then the state of the spin system is measured faithfully. In a coupled spin system, selective inversion of a transition gives rise to a direct population effect on all the transitions that share energy levels with the inverted transition. The transitions that increase or

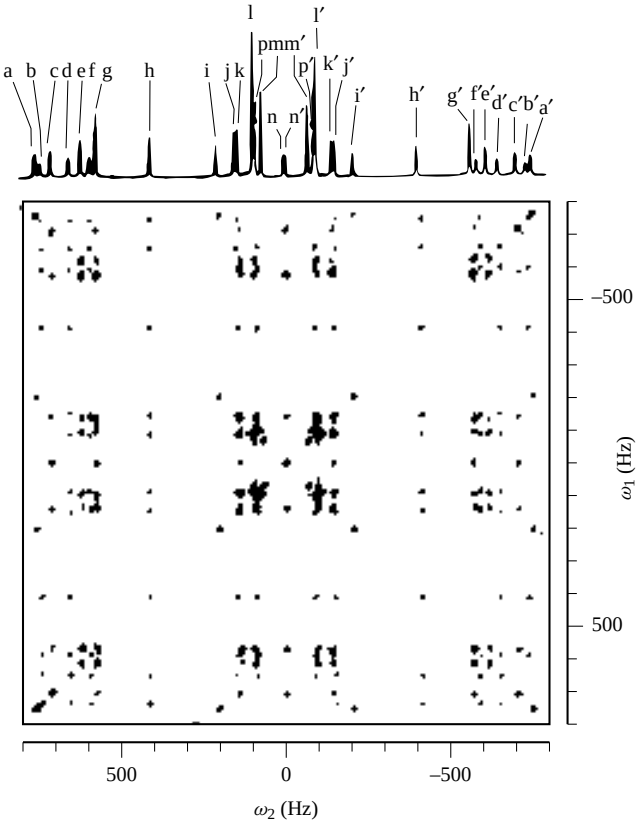

Figure 11 Phase-sensitive NOESY spectrum of oriented acetone obtained using the pulse sequence (90°, t_1, 90°, τ_m, 90°, t_2), with phase cycling to retain longitudinal magnetization during the short period τ_m (= 20 μs). Filled contours represent negative intensity. The various cross peaks here arise mainly owing to the strong coupling effect. (Reproduced by permission of Academic Press from Christy Rani Grace and Kumar[47])

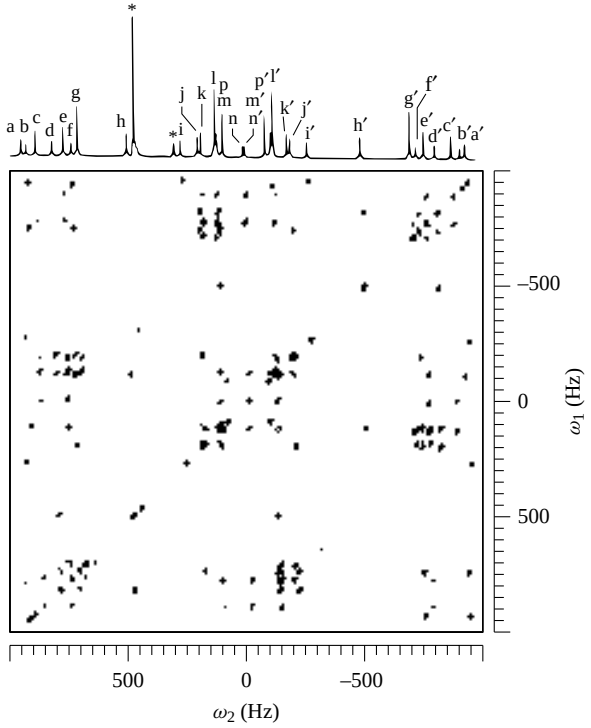

Figure 12 Phase-sensitive small-flip-angle NOESY (NOESY-α,β) spectrum of oriented acetone for α=β = 14° and τ_m = 20 μs, using the sequence (90°, t_1, α, τ_m, β, t_2) while retaining only the longitudinal magnetization during the short interval τ_m. Each diagonal peak has cross peaks only to directly connected transitions within the irreducible representation. Filled contours represent negative intensity. (Reproduced by permission of Academic Press from Christy Rani Grace and Kumar[49])

decrease in intensity are called progressively or regressively connected to the inverted transition, respectively. Use has been made of this information, without bringing in relaxation (for small values of τ_m), to construct energy level diagrams of oriented molecules.[49] This experiment is similar to a Z-COSY experiment,[50] as well as to a large number of difference 1D experiments in which one peak is selectively inverted at a time.

Figure 12 shows the 2D spectrum of oriented acetone recorded using NOESY-α,β for τ_m = 10 μs and α = β = 14°. As in COSY-β, the cross peaks here are also only between directly connected transitions within each irreducible representation, with the advantage that the 2D spectrum has pure absorptive lines.[49] From various cross sections of such spectra, a connectivity matrix is built up by entering (+1), (−1), and 0 for progressively, regressively, and unconnected transitions, respectively. This connectivity matrix is supposed to be symmetric, and its systematic analysis leads to a complete identification of the connected network of transitions, and in turn the complete energy level of a given symmetry.[49] The well-known problems of zero quantum coherences, which are not cancelled by NOESY phase cycling, also interfere in this experiment, and therefore have to be removed by known procedures.[12] The connectivity information has also been utilized for the analysis of the spectrum of *cis*,*cis*-mucanonitrile oriented in ZL1-1167, a four-spin system having C_{2h} symmetry.[51]

4.2.2 Using Z-COSY

Similar experiments (Z-COSY: 90°, t_1, α, τ_m, α) have also been performed on oriented methanol (an A_3B type of spin system) and oriented 1,3-dichlorobenzene (A_2BC). By systematically reducing the flip angle α, the direct progressive and regressive connectivities were identified. Patterns of connectivity were identified with the help of such spectra, which were then utilized for the construction of energy level diagrams. This information was in turn utilized for iteratively obtaining the complete Hamiltonian and its parameters.[50]

5 OTHER STUDIES

There has been an interesting application of near-magic-angle sample spinning combined with 2D NMR (COSY and 2D *J*-resolved experiments) of substituted benzenes dissolved in lyotropic liquid crystals. The normal spectra of these molecules were too complex to be analyzed. The near-magic-angle spinning simplified the spectrum considerably, and, in addition, the 2D *J*-resolved spectrum showed well-resolved multiplet patterns for various protons, while COSY helped in identifying the peaks of these protons.[52]

Another interesting study has been a 2D correlation of the liquid crystal spectrum with the isotropic spectrum by the use of a temperature jump during the mixing period. This allows a straightforward separation of the liquid crystal spectrum into various chemical sites.[53] There are several detailed and informative 2D NMR studies of both the spin echo and the correlated type of $I \geq 1$ spins in oriented systems, as well as many 2D NMR studies of liquid crystal molecules with and without magic angle sample spinning. Further, there have been several studies of zero field NMR of molecules oriented in liquid crystal matrices. These studies are discussed in other articles in this Encyclopedia.

6 RELATED ARTICLES

Analysis of High-Resolution Solution State Spectra; Analysis of Spectra: Automatic Methods; COSY Spectra: Quantitative Analysis; COSY Two-Dimensional Experiments; Deuterium NMR in Solids; INADEQUATE Experiment; Liquid Crystalline Samples: Carbon-13 NMR; Liquid Crystalline Samples: Deuterium NMR; Liquid Crystalline Samples: Diffusion; Liquid Crystalline Samples: Relaxation Mechanisms; Liquid Crystalline Samples: Spectral Analysis; Liquid Crystalline Samples: Structure of Nonrigid Molecules; Multidimensional Spectroscopy: Concepts; Multiple Quantum NMR in Solids; NOESY; Spin Echo Spectroscopy of Liquid Samples; Spinning Liquid Crystalline Samples; Two-Dimensional J-Resolved Spectroscopy; Zero Field NMR.

7 REFERENCES

1. A. Saupe and G. Englert, *Phys. Rev. Lett.*, 1963, **11**, 462.
2. A. D. Buckingham and K. A. McLauchlan, in *Progress in Nuclear Magnetic Resonance Spectroscopy*, ed. J. W. Emsley, J. Feeney, and L. H. Sutcliffe, Pergamon Press, Oxford, 1967, Vol. 2, p. 63.
3. P. Diehl and C. L. Khetrapal in *NMR Basic Principles and Progress*, ed. P. Diehl, E. Fluck, and R. Kosfeld, Springer-Verlag, Berlin, 1969, Vol. 1, p. 1.
4. P. Diehl, C. L. Khetrapal, and H. P. Kellerhals, *Mol. Phys.*, 1968, **15**, 333.
5. J. W. Emsley and J. C. Lindon, *NMR Spectroscopy Using Liquid Crystal Solvents*, Pergamon Press, Oxford, 1975.
6. S. Castellano and A. A. Bothner-By, *J. Chem. Phys.*, 1964, **41**, 3863.
7. P. Diehl, H. P. Kellerhals, and W. Niederberger, *J. Magn. Reson.*, 1971, **4**, 352.
8. J. W. Emsley, D. L. Turner, A. M. Giroud, and M. Longeri, *J. Chem. Soc., Faraday Trans. 2*, 1985, **81**, 603.
9. A. Kumar, *Current Sci.*, 1988, **57**, 109.
10. C. L. Khetrapal and K. V. Ramanathan, in *Specialist Periodical Reports on NMR*, ed. G. A. Webb, The Royal Society of Chemistry, London, 1994, Vol. 23, p. 439 and references therein.
11. W. P. Aue, J. Karhan, and R. R. Ernst, *J. Chem. Phys.*, 1976, **64**, 4226.
12. R. R. Ernst, G. Bodenhausen, and A. Wokaun, *Principles of Nuclear Magnetic Resonance in One and Two Dimensions*, Clarendon Press, Oxford, 1987.
13. A. Kumar, *J. Magn. Reson.*, 1978, **30**, 227 (erratum, 1980, **40**, 413).
14. A. Kumar and C. L. Khetrapal, *J. Magn. Reson.*, 1978, **30**, 137.
15. C. L. Khetrapal, A. Kumar, A. C. Kunwar, P. C. Mathias, and K. V. Ramanathan, *J. Magn. Reson.*, 1980, **37**, 349.
16. D. L. Turner, *J. Magn. Reson.*, 1982, **46**, 213.
17. K. Nagayama, A. Kumar, K. Wüthrich, and R. R. Ernst, *J. Magn. Reson.*, 1980, **40**, 321.
18. A. G. Avent, J. W. Emsley, and D. L. Turner, *J. Magn. Reson.*, 1983, **52**, 57.
19. J. W. Emsley and D. L. Turner, *J. Chem. Soc., Faraday Trans. 2*, 1981, **77**, 1493.
20. M. Albert Thomas, K. V. Ramanathan, and A. Kumar, *J. Magn. Reson.*, 1983, **55**, 386.
21. K. Rukmani and A. Kumar, *Chem. Phys. Lett.*, 1987, **133**, 485.
22. G. Drobny, *Chem. Phys. Lett.*, 1984, **109**, 132.
23. W. P. Aue, E. Bartholdi, and R. R. Ernst, *J. Chem. Phys.*, 1976, **64**, 2229.
24. A. Wokaun and R. R. Ernst, *Chem. Phys. Lett.*, 1977, **52**, 407.
25. G. Drobny, A. Pines, S. Sinton, D. P. Weitekamp, and D. Wemmer, *Faraday Symp. Chem. Soc.*, 1978, **13**, 49.
26. W. S. Warren, S. Sinton, D. P. Weitekamp, and A. Pines, *Phys. Rev. Lett.*, 1979, **43**, 1791.
27. S. Sinton and A. Pines, *Chem. Phys. Lett.*, 1980, **76**, 263.
28. J. Tang and A. Pines, *J. Chem. Phys.*, 1980, **72**, 3290; 1980, **73**, 2512.
29. W. S. Warren, D. P. Weitekamp, and A. Pines, *J. Chem. Phys.*, 1980, **73**, 2084.
30. W. S. Warren and A. Pines, *J. Chem. Phys.*, 1981, **74**, 2808; *J. Am. Chem. Soc.*, 1981, **103**, 1613.
31. D. P. Weitekamp, J. R. Garbow, and A. Pines, *J. Magn. Reson.*, 1982, **46**, 529; *J. Chem. Phys.*, 1982, **77**, 2870.
32. J. B. Murdoch, W. S. Warren, D. P. Weitekamp, and A. Pines, *J. Magn. Reson.*, 1984, **60**, 205.
33. S. W. Sinton, D. B. Zax, J. B. Murdoch, and A. Pines, *Mol. Phys.*, 1984, **53**, 333.
34. M. Gochin, K. V. Schenker, H. Zimmermann, and A. Pines, *J. Am. Chem. Soc.*, 1986, **108**, 6813.
35. M. Gochin, H. Zimmermann, and A. Pines, *Chem. Phys. Lett.*, 1987, **137**, 51.
36. M. Gochin, D. Hugi-Cleary, H. Zimmermann, and A. Pines, *Mol. Phys.*, 1987, **60**, 205.
37. M. Munowitz and A. Pines, *Science (Washington, DC)*, 1986, **233**, 525.
38. W. S. Warren, J. B. Murdoch, and A. Pines, *J. Magn. Reson.*, 1984, **60**, 236.
39. G. P. Drobny, *Annu. Rev. Phys. Chem.*, 1985, **36**, 451.
40. G. P. Drobny, A. Pines, S. W. Sinton, W. S. Warren, and D. P. Weitekamp, *Phil. Trans. R. Soc. Lond., Ser. A*, 1981, **299**, 585.
41. M. Albert Thomas and A. Kumar, *J. Magn. Reson.*, 1982, **47**, 535.
42. M. Albert Thomas and A. Kumar, *J. Magn. Reson.*, 1984, **56**, 479.
43. H. Fujiwara, N. Shimizu, T. Takagi, Y. Sasaki, and K. Takahashi *J. Magn. Reson.*, 1985, **64**, 325.
44. M. Gochin, A. Pines, M. E. Rosen, S. P. Rucker, and C. Schmidt, *Mol. Phys.*, 1990, **69**, 671.
45. M. E. Rosen, S. P. Rucker, C. Schmidt, and A. Pines, *J. Phys. Chem.*, 1993, **97**, 3858.
46. D. Gamliel, A. Maliniak, Z. Luz, R. Poupko, and A. J. Vega, *J. Chem. Phys.*, 1990, **93**, 5379.
47. R. Christy Rani Grace and A. Kumar, *J. Magn. Reson.*, 1992, **97**, 184.
48. R. Christy Rani Grace and A. Kumar, *Bull. Magn. Reson.*, 1992, **14**, 42.

49. R. Christy Rani Grace and A. Kumar, *J. Magn. Reson.*, 1992, **99**, 81.
50. P. Pfländler and G. Bodenhausen, *J. Magn. Reson.*, 1991, **91**, 65.
51. R. Christy Rani Grace, N. Suryaprakash, A. Kumar and C. L. Khetrapal, *J. Magn. Reson., Ser. A*, 1994, **106**, 79.
52. H. Fujiwara, in *Proceedings of 11th Conference of the International Society of Magnetic Resonance, Vancouver, 1992*, Abstract 0–69, p. 114; in *Proceedings of 32nd Annual NMR Symposium, Japan, 1993*, L35 p. 141.
53. K. Akasaka, A. Naito, and M. Kimura, in *Proceedings of 11th Symposium of the International Society of Magnetic Resonance, Vancouver, 1992*, Abstract 0–36, p. 81; A. Naito, M. Imanari, and K. Akasaka, *J. Magn. Reson.*, 1991, **92**, 85; K. Akasaka, A. Naito, and M. Imanari, *J. Am. Chem. Soc.*, 1991, **113**, 4688.

Biographical Sketch

Anil Kumar. *b* 1941. M.Sc., 1961, Agra, Ph.D., 1969, Indian Institute of Technology, Kanpur (supervisor, B. D. N. Rao). Postdoctoral research at Georgia Tech., Atlanta, GA (Sidney Gordon) 1969–70, University of North Carolina, Chapel Hill, NC (Charles Johnson) 1970–72, and E.T.H. Zürich, Switzerland (Richard Ernst) 1973–76. Faculty of Physics, Indian Institute of Science, Bangalore, 1977–present. Sabbatical leave at E.T.H. Zürich with Kurt Wüthrich, 1979–80. Approx 100 publications. Research interests: methodology of NMR, two-dimensional techniques, relaxation studies, applications to structure determination of biomolecules and characterization of molecular motions.

Chemical Exchange on Solid Metal Surfaces

Frank Engelke
Ames Laboratory, Ames, IA, USA

1	Introduction	1
2	Theory of Magnetization Exchange	1
3	Advanced NMR Techniques to Monitor Exchange	2
4	Chemical Exchange of Adsorbed Species on Metal Surfaces: Examples	3
5	Related Articles	4
6	References	4

1 INTRODUCTION

Chemical exchange, i.e. the transfer of atoms, molecules or molecular groups between two or more different environments or regions, is a phenomenon encountered frequently in studies by NMR of a wide variety of chemical, physical and biological systems. Different environments are usually revealed in NMR experiments through distinct resonance frequencies, spin–spin coupling constants, or relaxation times characteristic of the regions between which chemical exchange takes place. The types of atomic or molecular motion most often investigated on metal surfaces include surface diffusion, adsorption and desorption, exchange between different surface sites or different types of adsorbed species, molecular reorientation, and reorientation of molecular groups.

Because NMR requires at least ca. 10^{18} spins at the surface to be able to detect a signal, single crystal surfaces cannot be studied (10^{15} spins). However, introducing the metal in the form of small particles with diameters in the order of nanometers into porous materials, provides a sufficiently high number of surface sites for adsorption to be studied by NMR. These support materials are mostly oxide compounds like silica, alumina, titania, or zeolites with high internal surfaces of several hundred square meters. At the same time, highly dispersed supported metals, e.g. group VIII elements like ruthenium, rhodium, palladium, osmium, iridium, and platinum, are very often of interest in basic and applied research in catalysis (see also ***Supported Metal Catalysts***, and ***Adsorbed Species: Spectroscopy and Dynamics***).

Several NMR techniques are available to study exchange phenomena of adsorbed species. Spin–lattice relaxation[1] measurements are useful if chemical exchange dominates as a source for relaxation, or can be separated from other relaxation mechanisms, e.g. relaxation via the conduction electrons of the metal, called Korringa relaxation (see ***Electron–Nuclear Hyperfine Interactions***). To be investigated by relaxation measurements, the characteristic time constants of exchange τ_{ex} have to be in the order of 10^{-9} s for spin–lattice relaxation in the laboratory frame to 10^{-5} s for spin–lattice relaxation in the rotating frame.[1] For a review of the relaxation method used to study the dynamics on surfaces we refer the reader to the literature.[2–4] The analysis of lineshapes or resonance shifts obtained by conventional NMR techniques are sensitive in the dynamic range of $10^{-6} \leq \tau_{ex} \leq 10^{-3}$ s. Spin labeling methods extend this range up to more than 10^{-1} s. Two-dimensional NMR techniques, applicable in approximately the same slow dynamic range, are most effective if the exchanging species exhibit separate NMR peaks or if well-defined lineshapes due to anisotropic interactions can be observed.[5]

In the present article the theoretical basis necessary to understand the evolution of nuclear spin magnetization influenced by chemical exchange is outlined briefly. The reader is introduced to spin-labeling and two-dimensional (2D) NMR techniques, which are frequently used to monitor exchange. Finally, experimental examples regarding chemical exchange on metal surfaces are discussed.

2 THEORY OF MAGNETIZATION EXCHANGE

In the following it is assumed that the spatial motion of molecules or atoms can be described classically. If all spin interactions are secular with respect to the Zeeman interaction, i.e., the corresponding interaction Hamiltonians commute with the Zeeman Hamiltonian, then each spin can be considered as being subjected to a local field arising from the environment, superimposed on the external static field. Chemical exchange has the effect of causing random fluctuations of the local field. For example, a nuclear spin situated in a molecule or atom, which jumps randomly between two regions on a surface, such that each region gives rise to a different isotropic resonance shift, experiences a random modulation of its resonance frequency. The influence of such frequency fluctuations upon the NMR lineshape was first treated by Hahn, Maxwell, Gutowsky, McCall, and Slichter.[6]

If the spin Hamiltonian contains nonsecular terms, arising, for example, from J couplings observed commonly in liquids, a quantum-mechanical treatment (spin density matrix formalism) is required.[7] Splittings due to J couplings are often difficult to detect in NMR studies of adsorbates on metal surfaces because of insufficient spectral resolution, caused by the heterogeneity of the system, leading to distributions of isotropic chemical or Knight shifts, and/or the presence of 'solid-like' spin interactions much stronger than J coupling, like chemical shift anisotropy (see ***Internal Spin Interactions and Rotations in Solids***) and paramagnetic shifts.

We confine ourselves here exclusively to the case of secular spin interactions, leading to a classical probabilistic model for the magnetization exchange originating from chemical exchange processes. The probabilistic model is commonly represented by a stationary Markov process,[8,9] allowing the derivation of equations of motion for the nuclear spin magnetization in the form of generalized Bloch equations.[9–11] The evolution of longitudinal and transversal magnetization components for all regions, between which exchange takes place, are given as a system of coupled differential equations with rate coefficients describing the magnetization exchange process. Solving these equations is a standard problem of analysis and matrix algebra (see Ernst et al.[11] and Jeener et al.[13]) and enables explicit calculation of NMR lineshapes.

Figure 1 illustrates the principal effects on the NMR lineshapes originating from magnetization exchange between two regions or sites. Regions A and B, populated by N_A and N_B spins, respectively, are characterized by distinct resonance

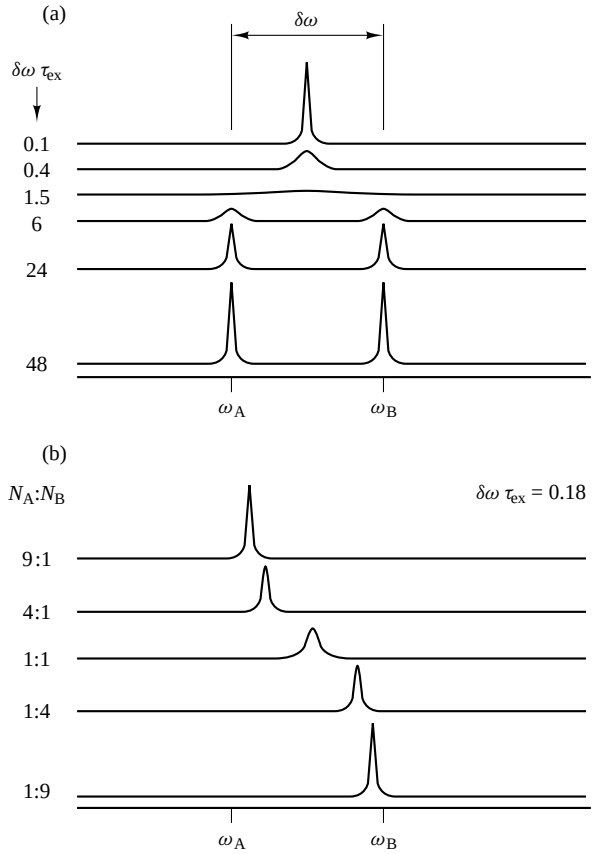

Figure 1 (a) NMR lineshape versus $\delta\omega\tau_{ex}$ for symmetric two-site exchange ($N_A = N_B$). (b) Variation of the resonance frequency in the fast exchange limit as a function of N_A:N_B

frequencies ω_A and ω_B, $\delta\omega = \omega_B - \omega_A$. This difference of resonance freqencies may be caused by different isotropic chemical or Knight shifts. In the slow exchange limit, $\delta\omega\tau_{ex} \gg 1$, where τ_{ex} is a characteristic time constant for the exchange process, two separate lines appear in the NMR spectrum [Figure 1(a)], which become broadened with decreasing $\delta\omega\tau_{ex}$, and coalesce to a single broad line at $\delta\omega\tau_{ex} \approx 1$. With $\delta\omega\tau_{ex}$ decreasing further, only one single 'exchange-averaged' narrow line is observed (fast exchange limit, $\delta\omega\tau_{ex} \ll 1$). The spectra in Figure 1(b) were calculated for the fast exchange limit varying the ratio N_A:N_B of spin numbers in regions A and B, leading to a variation in the resonance frequency of the exchange averaged resonance line as well as to a broadening for values of N_A:N_B near unity. The dependence of the resonance shift δ on N_A and N_B can be expressed for the fast exchange limit as the weighted average:

$$\delta = \frac{N_A}{N_A + N_B} + \delta_A \frac{N_B}{N_A + N_B}\delta_B \qquad (1)$$

of the individual resonance shifts δ_A and δ_B. The mathematical formalism to calculate the above lineshapes is still applicable if anisotropic interactions, to be described by interaction tensors, e.g. chemical shift anisotropy, are present. However, because of the random spatial orientations of the principal tensor axes in a powder sample, the resulting orientation dependence of the resonance frequencies has to be taken into account to obtain the lineshape.[10]

3 ADVANCED NMR TECHNIQUES TO MONITOR EXCHANGE

As shown above, no significant changes of the one-dimensional NMR lineshapes or frequencies occur in the slow exchange limit. More advanced NMR techniques are available to detect such slow exchange processes.

3.1 Spin Labeling by Selective Excitation

The idea of spin labeling is based on the fact that the actual chemical exchange process, being in thermal equilibrium, causes an exchange of spin magnetization.[12] The latter is initially prepared by irradiation of rf pulses to be in nonequilibrium. The irradiation of an rf pulse, or a sequence of rf pulses affects only spins resonating within the spectral excitation window defined by the Fourier transform of the pulse sequence [Figure 2(a) and (b)]. Although this Fourier picture is only an approximation when selective saturation or inversion is considered,[12] it is a useful qualitative description. Denoting the length of a single rf pulse or the total duration of a pulse sequence by τ_p, the excitation width in the frequency domain is proportional to $1/\tau_p$, with the rf carrier frequency in the center of the excitation window. The irradiation of either a long pulse of low rf power or a sequence of strong, but very short pulses, as indicated in Figure 2(a), allows selective excitation of spins. The pulse sequence can be adjusted to act in total like a 90° pulse (selective saturation) or a 180° pulse [selective inversion, illustrated in Figure 2(c)]. Therefore, spins within the spectral window can be labeled, for example, by inversion of their magnetization, while spins which resonate outside the window remain unaffected. If a pulse sequence is used, excitation sidebands also occur [Figure 2(b)]. During a subsequent time interval τ_m [Figure 2(a)] the spin system is allowed to undergo free time evolution. The NMR signal is detected finally by a short (nonselective) 90° pulse. Selective excitation (saturation or inversion) of a narrow frequency band within a broad NMR line, for example, caused by chemical shift anisotropy, is called 'spectral hole-burning'. If chemical exchange is present, the labeled spins may change their resonance frequencies resulting in a redistribution of spin

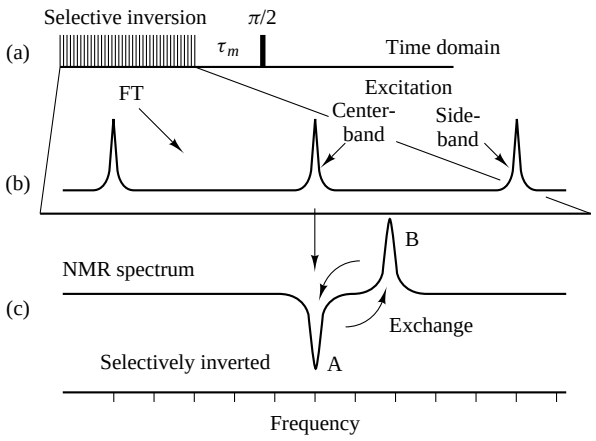

Figure 2 Spin labeling by selective excitation: (a) pulse sequence, (b) Fourier transformation of the train of equidistant pulses, and (c) NMR spectrum showing a selectively inverted line

magnetization toward spectral regions outside of the selected window. The recovery of the spectral hole, or of the intensity of an inverted single resonance line, can be measured as a function of the recovery time τ_m to reveal the kinetics of a chemical exchange process.

Magnetization recovery is also caused by spin–lattice relaxation of the spin magnetization. Only exchange processes with a characteristic time τ_{ex} shorter than the spin–lattice relaxation time T_1 can be observed. Spin-labeling becomes ineffective if the chemical exchange process is faster than the spin-labeling process itself (characteristic time constant τ_p). Thus accessible by spin-labeling techniques are exchange processes within a timescale $\tau_p < \tau_{ex} < T_1$.

3.2 Two-Dimensional Exchange NMR

Two-dimensional exchange NMR techniques[13] are based on the idea of measuring the frequency of spin magnetization components at two different times during the NMR experiment. After the initial preparation period, which consists of a waiting period to allow equilibration of the longitudinal magnetization and irradiating the first $\pi/2$ pulse, transversal magnetizations are present, oscillating with frequencies ω_A and ω_B during the time t_1 [evolution period, Figure 3(a)] corresponding to spins located in regions A and B. A second $\pi/2$ pulse converts the magnetization present at time t_1 into longitudinal magnetization. During the mixing time τ_m (usually much longer than the time t_1) slow chemical exchange leads to a random modulation of the precession frequencies of the two magnetization components M_{zA} and M_{zB}. Spins which were resonating at ω_A at the end of the period t_1 may resonate at either ω_A or ω_B at the end of the mixing period τ_m (and vice versa). The NMR signal is detected after the final $\pi/2$ pulse during the time period t_2. Repeating the experiment by incrementing the time t_1 in small steps, yields a two-dimensional time-domain interferogram which after 2D Fourier transformation[11] with respect to t_1 and t_2 gives the 2D NMR spectrum $S(\omega_1,\omega_2)$. If exchange occurs between A and B, cross peaks are observed, labeled A → B and B → A in Figure 3(b), in addition to main peaks A and B located along the principal diagonal.[14]

4 CHEMICAL EXCHANGE OF ADSORBED SPECIES ON METAL SURFACES: EXAMPLES

Chemical exchange phenomena at or near metal surfaces observed by NMR encompass a wide dynamical range extending from the fast exchange limit ($\tau_{ex} < 10^{-5}$ s) to extremely slow processes ($\tau_{ex} > 1$ s). The details of the chemical exchange processes might be quite different, originating, for example, from adsorption or desorption, exchange between different surface sites, exchange between different populations of adsorbed species or surface diffusion.[15]

4.1 Exchange Dynamics of CO Adsorbed on Metals

Carbon-13 spin labeling techniques have been applied by Duncan, et al.[16] to elucidate in detail surface diffusion of CO and slow exchange between different carbonyl species adsorbed on rhodium. Molitor and Apple[17] performed ^{13}C NMR powder lineshape calculations for reorientating dicarbonyl groups bonded to rhodium. Surface diffusion of CO chemisorbed on palladium has been investigated by means of ^{13}C relaxation measurements and lineshape analysis.[18]

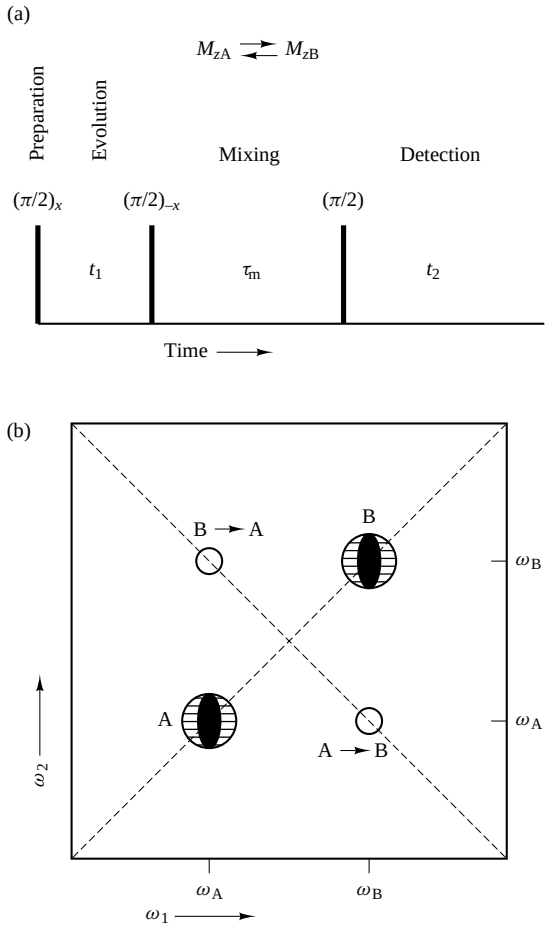

Figure 3 (a) Basic 2D NMR pulse sequence to monitor exchange. (b) Schematic representation of a 2D NMR spectrum for exchange between two sites A and B

4.2 Fast Exchange of Hydrogen on Metal Surfaces

Proton NMR peaks of hydrogen interacting with metal surfaces are commonly shifted to lower frequency (i.e. upfield) due to the Knight shift interaction and reveal relatively small linewidths, especially at elevated external H_2 pressures and temperatures above room temperature, indicating high intrinsic mobility. Variations of the resonance frequency of ^1H NMR peaks, attributed to hydrogen on the metal surface, versus pressure (i.e. changing the number of hydrogen atoms or molecules on the surface) may be caused by at least two different mechanisms: (i) fast exchange between surface environments with different Knight shifts [as illustrated in Figure 1(b)]; and (ii) by a variation of the Knight shift interaction itself, because the latter may be a function of the surface coverage. As pointed out above, fast exchange between two regions leads to an averaged NMR line representing hydrogen in both regions. Variation of the resonance shift

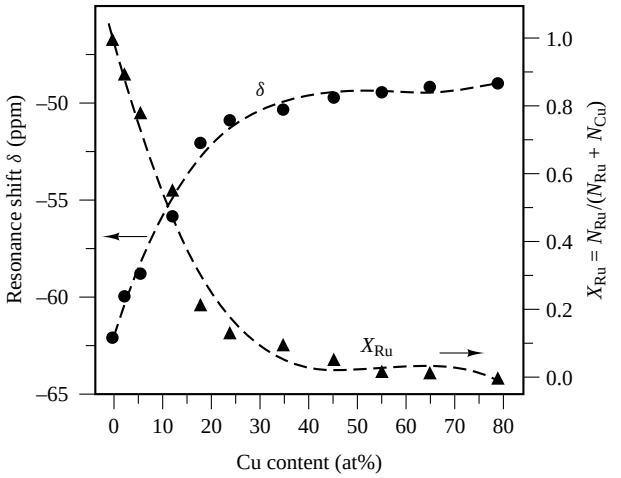

Figure 4 ^{1}NMR resonance shift δ for hydrogen adsorbed on ruthenium–copper bimetallic particles and fraction X_{Ru} of surface ruthenium as a function of the copper content

with pressure, or coverage, has been observed quite frequently by ^{1}H NMR[19] or ^{2}H NMR[20] for hydrogen adsorbed on various metals like platinum, rhodium, and ruthenium (see also refs. [18–20] and 23–24 given in Wu et al.[19]). The resonance shift variation of hydrogen due to fast exchange between different surfaced regions has been used to monitor the surface composition of bimetallic particles.[21] In this case hydrogen atoms are rapidly exchanging between sites on the bimetallic particle surface, composed of sites with different Knight shifts for adsorbed hydrogen. As shown in Figure 4, on particles consisting of pure ruthenium, hydrogen resonates at −62 ppm [to low frequency relative to tetramethylsilane (TMS)]. Increasing the total copper content of the sample leads to a systematic decrease of the ^{1}H resonance shift δ, approaching asymptotically the value of −49 ppm for a copper content near 80 at%. This shift value is regarded as the resonance shift for hydrogen adsorbed on copper sites of ruthenium–copper bimetallic particles. Applying equation (1) inserting $\delta_{Cu} = -49$ ppm and $\delta_{Ru} = -62$ ppm, the fraction $X_{Ru} = N_{Ru}/(N_{Ru} + N_{Cu})$ of ruthenium atoms exposed at the particle surface can be determined (see Figure 4). Therefore, in this example the ^{1}H NMR resonance shift provides a sensitive measure for the composition of the surface.

4.3 Slow Exchange Between Different Hydrogen Populations on the Metal Surface

Figure 5(a) shows an in situ ^{1}H NMR spectrum of silica supported ruthenium, obtained at T = 400 K and at an external H_2 pressure of 300 Torr.[22] Two distinct resonance lines (denoted as α and β) are observed, originating from two different hydrogen species, characterized by different heats of adsorption. The 2D exchange NMR spectrum [Figure 5(b)] was obtained by the pulse sequence illustrated in Figure 3(a). The cross peaks reveal a slow exchange process within the timescale of the experiment, given by the mixing time τ_{mix} = 2 ms, occurring between α and β hydrogen, but there is no exchange within this timescale between the α or β species and the hydrogen residing on the silica support. Spin

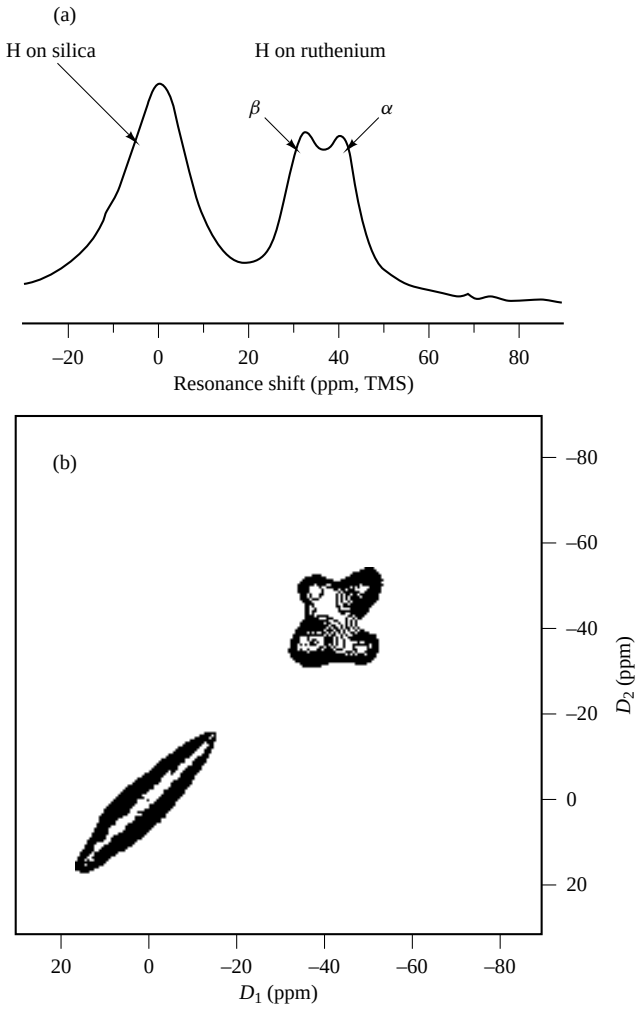

Figure 5 (a) Conventional ^{1}H NMR spectrum of silica supported ruthenium. (b) 2D exchange NMR spectrum at T = 400 K and external H_2 pressure p = 300 Torr

labeling of one of the two spin species, α or β, by selective excitation (Figure 2) allows the determination of the average time constant, τ_{ex} = 700 μs, for the magnetization exchange between α and β hydrogen.

5 RELATED ARTICLES

Adsorbed Species: Spectroscopy and Dynamics; Brønsted Acidity of Solids; Diffusion in Porous Media; Electron–Nuclear Hyperfine Interactions; Internal Spin Interactions and Rotations in Solids; Microporous Materials and Xenon-129 NMR; Silica Surfaces: Characterization; Spin Diffusion in Solids; Supported Metal Catalysts

6 REFERENCES

1. C. P. Slichter, *Principles of Magnetic Resonance*, 3rd edn., Springer, Berlin 1990, Chaps. 4–6.
2. H. Pfeifer, in *NMR Basic Principles and Progress*, eds. P. Diehl, E. Fluck, and R. Kosfeld, Springer, Berlin, 1972, Vol. 7, p. 53.

3. H. Winkler and D. Michel, *Adv. Colloid Interface Sci.*, 1985, **23**, 149.
4. C. P. Slichter, *Ann. Rev. Phys. Chem.*, 1986, **37**, 25.
5. H.-W. Spiess, *Chem. Rev.*, 1991, **91**, 1321.
6. E. L. Hahn and D. E. Maxwell, *Phys. Rev.*, 1952, **88**, 1070; H. S. Gutowsky, D. W. McCall, and C. P. Slichter, *J. Chem. Phys.*, 1953, **21**, 279.
7. J. I. Kaplan and G. Fraenkel, *NMR of Chemically Exchanging Systems*, Academic, New York, 1980.
8. A. Abragam, *The Principles of Nuclear Magnetism*, Clarendon, Oxford, 1961, Chap. X.
9. C. S. Johnson, Jr., in *Advances in Magnetic Resonance*, ed. J. S. Waugh, Academic, New York, 1965, Vol. 1, p. 33.
10. M. Mehring, *Principles of High Resolution NMR in Solids*, 2nd edn., Springer, Berlin, 1983, Chap. 28.
11. R. R. Ernst, G. Bodenhausen, and A. Wokaun, *Principles of Nuclear Magnetic Resonance in One and Two Dimensions*, Clarendon, Oxford, 1987, Chaps. 2.4, 4.6, 6.4 and 9.
12. G. A. Morris and R. Freeman, *J. Magn. Reson.*, 1978, **29**, 433; R. Freeman, *Chem. Rev.*, 1991, **91**, 1397.
13. J. Jeener, B. H. Meier, P. Bachmann, and R. R. Ernst, *J. Chem. Phys.*, 1979, **71**, 4546.
14. If direct dipolar spin–spin couplings are present, spin diffusion (a process to be distinguished from chemical exchange) may also lead to cross peaks (see Jeener et al.[13] and ***Spin Diffusion in Solids***).
15. Spin labeling is well suited to monitor surface diffusion. However, the theoretical treatment of surface diffusion is based on the diffusion equation, and not on Bloch-type equations to describe exchange as discrete jumps between distinct environments.
16. T. M. Duncan, A. M. Thayer, and T. W. Root, *Phys. Rev. Lett.*, 1989, **63**, 62. See also: T. M. Cuncan, *Colloids Surfaces*, 1990, **45**, 11, and references therein.
17. P. Molitor and T. Apple, *J. Phys. Chem.*, 1989, **93**, 7055.
18. S. E. Shore, J.-P. Ansermet, C. P. Slichter, and J. H. Sinfelt, *Phys. Rev. Lett.*, 1987, **58**, 953.
19. X. Wu, B. C. Gerstein, and T. S. King, *J. Catal.*, 1989, **118**, 238.
20. T. Chang, C. P. Cheng, and C. Yeh, *J. Phys. Chem.*, 1991, **95**, 5239.
21. X. Wu, B. C. Gerstein, and T. S. King, *J. Catal.*, 1990, **121**, 271.
22. F. Engelke, S. Bhatia, T. S. King, and M. Pruski, *Phys. Rev. B*, 1994, **49**, 2730; F. Engelke, R. Vincent, T. S. King, and M. Pruski, *J. Chem. Phys.*, 1994, **101**, 7262.

Biographical Sketch

Frank Engelke. *b* 1955. M.Sc. (physics), Ph.D. (supervisor Dieter Michel) 1985, habilitation, University of Leipzig, Germany. Postdoctoral work at Saarbruecken University, Germany (with Jörn Petersson), and since 1992–1994 at Ames Laboratory, USA (with Bernie Gerstein, Marek Pruski and Terry King). Since 1994 affiliated with Bruker Analytische Messtechnik. Approx. 20 publications. Current research specialties: solid state NMR in rotating solids, solid state NMR applications on metal surfaces, NMR probe development.

Micellar Solutions and Microemulsions

Olle Söderman and Ulf Olsson
University of Lund, Lund, Sweden

1	Introduction	1
2	Self-Diffusion Studies	1
3	Relaxation Studies	5
4	Related Articles	11
5	References	11

1 INTRODUCTION

Surfactants are molecules with two distinctively different parts, one of which is hydrophilic and one which is hydrophobic. This feature of surfactants determines their properties in aqueous or oleic solutions. At low enough concentrations they form molecularly dispersed solutions. As the concentration is increased, they self-assemble into aggregates at a rather well-defined concentration, which is termed the *critical micellar concentration* (cmc) on account of the fact that the aggregates formed are termed *micelles*. As the concentration of surfactant is further increased, the aggregates crystallize into liquid crystalline phases with long-range order, the structures of which may vary rather substantially. The addition of a third component, giving rise to a water–oil–surfactant (where 'oil' is taken to be a generic term for an oleic component) system, results in an amazingly rich phase behavior, involving both liquid crystalline phases and liquid solution phases.

The present contribution will be concerned with the characterization by means of NMR techniques of two particular types of liquid solution of surfactant, the first being micellar solutions and the second being microemulsions. Having said this, we run into a problem of definition. How do we decide whether a particular solution belongs to one of these classes or perhaps to yet another class of solutions? Commonly, microemulsions are defined as thermodynamically stable solutions containing a surfactant (where 'surfactant' is a generic term for a single surfactant or mixtures of different amphiphilic molecules), water and oil. We shall adhere to this definition. Consequently, a micellar solution is one containing a surfactant and water (possibly with added salt) or oil, while the addition of oil or water to a micellar solution turns it into a microemulsion. Possible ambiguities of these definitions will be pointed out as we go along. [The name 'microemulsion' is somewhat unfortunate as it implies that the structure in the solution is one of discrete droplets of either water in oil (W/O) or oil in water (O/W). This is only partly true, as a rich variety of structures can indeed be found in addition to these two droplet structures. The literature is abundant with contributions which ignore this fact and only treat the two droplet structures.]

Studies of surfactant solution systems have had a central place in physical chemistry ever since the pioneering work of McBain at the beginning of this century,[1–4] not least due to the fact that these systems have important roles in a variety of applied processes. Questions asked pertain to the structure of the aggregates formed as well as the properties on a molecular level of the molecules comprising the systems.

It is fair to state that NMR has played a central role as a tool in tackling these questions, and much of our current understanding of surfactant solutions derives from NMR studies where two NMR methods have been especially important. The first of these is NMR relaxation studies, which have evolved to become an indispensable tool in studies of liquid surfactant solutions. The second one is measurements of self-diffusion coefficients by means of pulsed field gradients (PFG), an experiment which yields direct and easily interpretable information regarding many different aspects of surfactant solutions. In fact, our present understanding of the structure in microemulsions is to a large extent derived from PFG work in combination with various scattering approaches.

In the present article we discuss the two NMR approaches and describe applications which we consider to be those where NMR has contributed significantly to our present understanding of liquid solution phases of surfactants.

2 SELF-DIFFUSION STUDIES

Measurements of self-diffusion coefficients by means of PFG techniques have evolved to become one of the most important tools in the characterization of liquid surfactant systems. There are essentially two reasons for this, one of which has to do with the measuring technique itself. Thus the PFG approach offers a convenient method of determining self-diffusion coefficients. The technique is outlined in another article in this Encyclopedia (see ***Diffusion Measurements by Magnetic Field Gradient Methods***) and has also been described in a number of review articles.[5,6] Thus we shall not dwell on the technical aspects here. Suffice is to say that the technique requires no isotopic labeling (thus avoiding possible disturbances due to addition of probes); furthermore, it gives component resolved diffusion coefficients with great precision in a minimum of measuring time.

The second reason for its success rests on the fact that the method monitors transport over macroscopic distances (typically of the order of micrometers), and therefore the determined diffusion coefficients reflect aggregate sizes and obstruction effects, yielding information which is easily interpretable in terms of the microstructure of surfactant solutions. The fact that the information is obtained without the need to invoke complicated models, as is the case in the NMR relaxation approach, is particularly important. In this context it should be stressed that the PFG approach measures the self-diffusion rather than the collective diffusion coefficient.

The foundation for the use of NMR to monitor diffusion was laid in 1950 in the seminal paper by Hahn.[7] Another milestone occurred in the mid-1960s when Stejskal and Tanner demonstrated,[8] following a suggestion by Douglass and coworkers,[9] the use of pulsed gradients. Finally, towards the end of the 1960s the method became component resolved when the FT approach was introduced.[10]

In its simplest version, the method consists of two equal and rectangular gradient pulses of magnitude g and length δ, sandwiched on either side of the 180° rf pulse in a simple Hahn

echo experiment. For molecules undergoing free (Gaussian) diffusion characterized by a diffusion coefficient of magnitude D, the echo attenuation due to diffusion is given by[8,11]

$$I(\Delta, \delta, g) = I_0 \exp\left[-\gamma^2 g^2 \delta^2 \left(\Delta - \frac{\delta}{3}\right) D\right] \qquad (1)$$

where Δ represents the distance between the two gradient pulses, γ is the magnetogyric ratio of the monitored spin, and I_0 denotes the echo intensity in the absence of any field gradient. By varying either g, δ, or Δ (while at the same time keeping the distance between the two rf pulses constant), D can be determined by fitting equation (1) to the observed intensities.

In the following we use some illustrative examples to show how the PFG approach can be used to obtain information on surfactant solutions.

2.1 Micellar Solutions

2.1.1 The Micellization Process

The PFG method provides a unique way of investigating the process of micellization. The approach is based on the fact that the observed surfactant self-diffusion rates constitute a population weighted average between micellized and monomeric surfactant. This follows since the surfactant lifetime in the micelle is short on the relevant NMR timescale (which is essentially Δ in equation (1), and thus typically around 100 ms). Thus the observed surfactant diffusion coefficient is given by

$$D_{\text{obs}} = p_{\text{mic}} D_{\text{mic}} + (1 - p_{\text{mic}}) D_{\text{free}} \qquad (2)$$

where D_{mic} and D_{free} represent the diffusion coefficients of micellized and free surfactant, respectively, and p_{mic} is the fraction of micellized surfactant. Equation (2) can be rearranged to

$$p_{\text{mic}} = \frac{D_{\text{free}} - D_{\text{obs}}}{D_{\text{free}} - D_{\text{mic}}} \qquad (3)$$

Clearly, one can obtain the degree of micellization as a function of total surfactant concentration from the concentration dependence of D_{obs}, provided that D_{free} and D_{mic} are known. D_{free} can be obtained from measurements below cmc, while D_{mic} can be obtained from the diffusion coefficient of a hydrophobic probe which is solubilized into the micelles and for which p_{mic} is unity. A suitable probe is hexamethyldisilane (HMDS) which, if it is added in small amounts (on average one probe per micelle is a recommended concentration), seems only negligibly to disturb the micelles (although for some systems it should be used with some care[12]). Once D_{free} and D_{mic} are known, p_{mic} is obtained without the need to invoke any model for the micellization process. For ionic surfactants the same approach can also be used to obtain the degree of counterion association with the micelles, provided that the counterions contain nuclei suitable for PFG work, which is the case for surfactants with organic counterions.

The result of the approach outlined above is shown in Figure 1, in which a textbook example of the micellization process is presented. Data are obtained for a system with an organic counterion.[13] It is difficult to conceive of any other method that would give the same richness of detail concerning the micellization process. Data such as those presented in Figure 1 have been instrumental in testing various models for describing the micellization process. For instance, approaches based on the Poisson–Boltzmann equation have been very successful in rationalizing the process of micellization for ionic surfactants.[14,15]

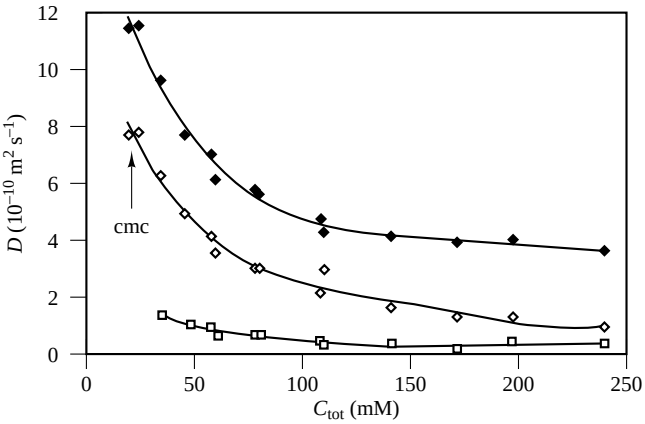

Figure 1 Self-diffusion data for the surfactant ion ($C_{10}H_{21}ND_3^+$) (◊) and counterion ($CHCl_2COO^-$) (♦) of a cationic surfactant with an organic counterion. Also given are the diffusion coefficients of the micelles (□), as measured by solubilizing a small amount of HMDS into the micelles. By applying the two-site model given by equation (3) one can estimate both the fraction of micellized surfactant and the degree of counterion binding to the micelles from the diffusion coefficients. For instance, at 140 mM total concentration of surfactant p_{mic} = 0.8, while the degree of counterion binding (defined as the ratio of the concentration of micelle associated counterions to the concentration of micellized surfactant cations) is 0.8. (Data from Jansson and Stilbs.[13])

2.1.2 Micellar Size and Structure

Questions pertaining to micellar size and structure may be tackled in two ways by means of PFG studies. The first concerns the measurement of self-diffusion of water (or other small molecules) in the system. Any aggregate present obstructs the diffusion of the water and, as the degree of obstruction depends on the volume fraction of the particles present as well as their geometry, information concerning the latter may be obtained. The mathematical description of such obstruction effects was worked out by Jönsson et al.,[16] who presented results for spheres, prolates, and oblates of different sizes and solution volume fractions.

The other approach to investigating micellar structure is based on Einstein's law, in which the (micellar) diffusion coefficient is related to the frictional factor f through

$$D = \frac{k_{\text{B}} T}{f} \qquad (4)$$

where k_{B} is the Boltzmann constant, and T is the absolute temperature.

The friction coefficient depends on the geometry and size of the diffusing particle as well as on the solvent viscosity η. Expressions relating f to the dimensions exist for several

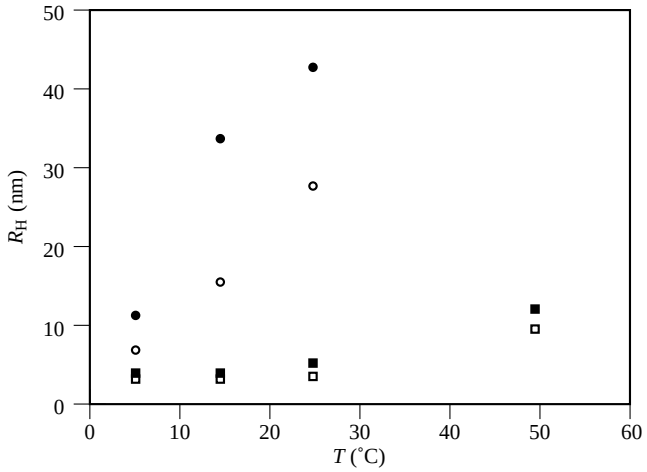

Figure 2 Micelle hydrodynamic radii for two concentrations of $C_{12}H_{25}(OCH_2CH_2)_5OH$ [(●) 2.73 wt%, (○) 0.92 wt% surfactant] and $C_{12}H_{25}(OCH_2CH_2)_8OH$ [(■) 3.06 wt%, (□) 1.02 wt%]. (Data from Nilsson et al.[18,19])

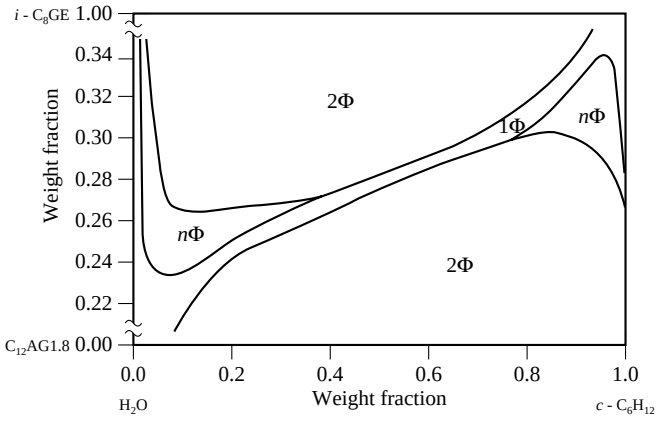

Figure 3 Phase diagram of an alkylpolyglucoside/cosurfactant/water/cyclohexane system at 25 °C with a total surfactant + cosurfactant concentration of 4 wt%. The number of phases present in the various regions of the phase diagram is indicated (for example, the one-phase microemulsion is denoted by 1Φ). (Reproduced with permission from Fukuda et al.[24])

different geometries, the simplest being that for a sphere of hydrodynamic radius R_H, which is:

$$f = 6\pi\eta R_H \tag{5}$$

For cases where the geometry is not known, one often uses equation (5) and computes a hydrodynamic radius, on the assumption that the diffusing species is a sphere. An example of this approach is shown in Figure 2, which gives the hydrodynamic radii for micelles formed by nonionic surfactants of the oligo(ethylene oxide) type as a function of temperature. Questions pertaining to the aggregate growth as a function of temperature and concentration in these systems have been the subject of rather lively discussion over the years.[17] Clearly, data such as those presented in Figure 2 are important in this context.[18–20]

Although the method outlined above is certainly useful, one should be aware of the limitations inherent in the approach. First, equations (4) and (5) assume infinite dilution. As micelles are self-assembled units, one must be aware of the fact that dilution may change their properties. At higher concentrations particle–particle obstruction effects become important, and these must be taken into account.[21,22]

2.2 Microemulsions

Microemulsions are defined as thermodynamically stable systems containing an oleic solvent (in most basic research a simple hydrocarbon is used), a hydrophilic solvent (most often water or brine), and a surfactant (which can be a combination of several amphiphilic molecules). For weakly amphiphilic molecules the system is molecularly dispersed; this will not be discussed here.

Of particular interest are systems in which small amounts of surfactant may bring equal volumes of oil and water into solution. This can be achieved with less than 1% surfactant, and such systems are usually termed 'balanced'.[23] In many of these systems one may vary the oil to water volume ratio extensively without ever leaving the one-phase microemulsion region. This is achieved by varying some parameter. Such a parameter is constituted by the temperature in the case of nonionic surfactants of the C_xE_y type, the salinity of the water for ionic surfactants, and the cosurfactant/surfactant ratio in a mixed surfactant system. An example of such behavior is shown in Figure 3, where a recently compiled phase diagram for an alkylpolyglucoside surfactant is displayed. In this case it is the proportion of the cosurfactant (which is a branched alkyl glycerol monoether) in the surfactant mixture which was varied.[24]

It is a considerable challenge to model such a system, and a prerequisite for such an endeavor is the availability of structural information. It is perhaps in this context that the PFG approach has achieved its most spectacular successes, not least due to the fact that very few other methods can yield such information for microemulsions. How then do we infer structural information from self-diffusion coefficients which are dynamic quantities? The basis of the approach is the fact that the mean distance traveled by the molecules is of the order of $\sqrt{\Delta D}$, which quantity is of the order of micrometers for low molecular weight liquids. Thus any obstruction effects or confinement to droplets of colloidal dimensions affects the diffusion coefficient.

Broadly speaking, one can differentiate between a microstructure of closed particles, whether they are normal (enclosing the oil component) or reversed (enclosing the water), and a microstructure which is bicontinuous. The latter term is often used without being properly defined. We shall take it to imply that a large fraction of both the oil and water molecules exists in domains which span macroscopic distances in three dimensions.

For the case of discrete particles, the continuous phase displays a diffusion behavior similar to that of the neat liquid. There will be solvation effects, i.e. some of the continuous solvent may be associated with the surfactant and, as a consequence, will have an altered diffusional behavior. However, for low surfactant concentration this effect is negligible. Thus any reduction in the reduced diffusion coefficient for the continuous solvent (in PFG studies of microemulsions one preferably reports the reduced diffusion

coefficient, defined as D/D_0, where D_0 is the bulk diffusion coefficient of the neat liquid at the same temperature) can be attributed to particle obstruction effects (see above). If both the dispersed phase and the surfactant have negligible solubility in the continuous phase, their diffusion is given by the particle diffusion, and so both have the same diffusion coefficient, the value of which can be used to estimate the size of the diffusion particle from equation (4), while the concentration dependence of the diffusion coefficient can be used to infer information about the interaggregate interactions.[22]

Turning to the bicontinuous case we note first that both the water and the oil component diffuse rapidly. Careful PFG work using mixtures of oil has revealed that the diffusion process of the oil component is very similar to the diffusion in neat oil.[25,26] The same holds for the water component.[27] This is an important observation, which implies that any reduction in the reduced diffusion coefficient can be attributed to the obstruction effects due to the presence of the surfactant film. Effects such as exchange between droplets and fusion–fission processes cannot explain the rapid oil and water diffusion. Any structural model of microemulsions must not be at variance with this statement. It should be emphasized that, at present, the PFG method is the only way in which bicontinuity may be proved or disproved. Two-dimensional images cannot prove bicontinuity, since it cannot exist in two dimensions.[28]

Let us now investigate whether the diffusion data for the system in Figure 3 is in line with this reasoning. Figure 4 shows the reduced diffusion coefficients for the water and oil components in the system shown in Figure 3 as a function of the volume fraction of hydrocarbon in the solvent mixture (Φ_{oil}). The data in Figure 4 are typical for microemulsions where the oil content can be varied continuously from no oil to pure oil. Thus the water and oil component diffusion changes continuously from rapid to slow as the fraction of each component is decreased, and the plots of the reduced diffusion coefficients versus the volume fraction of oil in the solvent mixture show a rather characteristic 'sigmoidal' curve for both components. At equal volume fractions of oil and water the curves intersect, and the value of both reduced diffusion coefficients is around 0.6 at the point of intersection. In line with the discussion above, this points to discrete particles at low and high values of Φ_{oil} and a bicontinuous structure in between. Based on the information inherent in PFG data such as those presented in Figure 4, how should we picture the bicontinuous microemulsions?

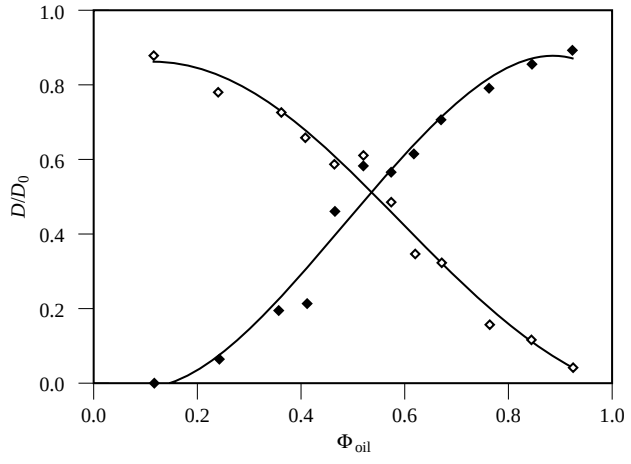

Figure 4 The relative self-diffusion coefficients of water (◊) and hydrocarbon (♦) as a function of the volume fraction, Φ_{oil} of hydrocarbon in the solvent mixture, for microemulsions formed in the alkylpolyglucoside/cosurfactant/water/cyclohexane system, the phase diagram of which is shown in Figure 3. (Data from Fukuda et al.[24])

A most fruitful way of looking at these phases is due to Scriven[29] who proposed the idea that the structure could be described as a melted liquid crystalline cubic phase, for which the structure is known on account of the scattering studies that can be performed on these systems [cubic phases come in two varieties (discrete and bicontinuous); Scriven had the latter class in mind]. These are formed by two interwoven subvolumes of the same material (polar or nonpolar), which are separated by a film of the opposite material. This dividing film is described as a 'minimal surface', having zero mean curvature.

Now, allow this structure to melt, so that the long range order is lost, but locally the structure is retained. When the material on both sides is equal, L_3 phases or bicontinuous micellar solutions (see below) are formed, and the dividing film is a bilayer, while for the case where the two subvolumes are not equal, microemulsions are formed. For this case the dividing film is a monolayer, with a curvature towards the oil or water depending on the volume fraction of the two components.

In an important contribution, Anderson and Wennerström[30] have computed the obstruction effect for components in the subvolumes and for components diffusing along the dividing surface. Indeed, these workers found that the reduced diffusion coefficient for a bicontinuous microemulsion with roughly equal oil and water volume fractions is around 0.6, giving further credence to Scriven's suggestion.

Finally, we note that, when measurements are possible, the value of the surfactant self-diffusion coefficient often displays a maximum with respect to changes in the solvent composition at equal oil and water volume fractions. This observation is more difficult to interpret in terms of a particular microstructure, owing to the difficulties of finding a suitable reference value for the lateral diffusion coefficient for the surfactant along the surfactant film, but it does indicate that the surfactant is diffusing over surfaces that extend over several micrometers with only minor disturbances for diffusions. Consider, for example, the case of a sodium dodecyl sulfate (SDS) microemulsion,[31] where D for the surfactant was found to be $1.5 \times 10^{-10}\,m^2\ s^{-1}$ at 27 °C, a value which is in good agreement with the values found for lateral diffusion of SDS over a micellar surface of spherical[32] ($D = 1.0 \times 10^{-10}\,m^2\ s^{-1}$ at 30 °C) and cylindrical[33] ($D = 1.69 \times 10^{-10}\,m^2\ s^{-1}$ at 30 °C) geometry, where the diffusion is indeed unhindered.

2.3 L_3-Phases and Bicontinuous Micellar Solutions

The properties of L_3 phases and bicontinuous micellar solutions have been discussed extensively, and they constitute an illustrative example of the power of the PFG method in unravelling solution structure. Both types of solution have a connected structure, and again a fruitful starting point is the (known) structure of the cubic phases. If a cubic phase is diluted with the material of the subvolumes, an L_3 phase

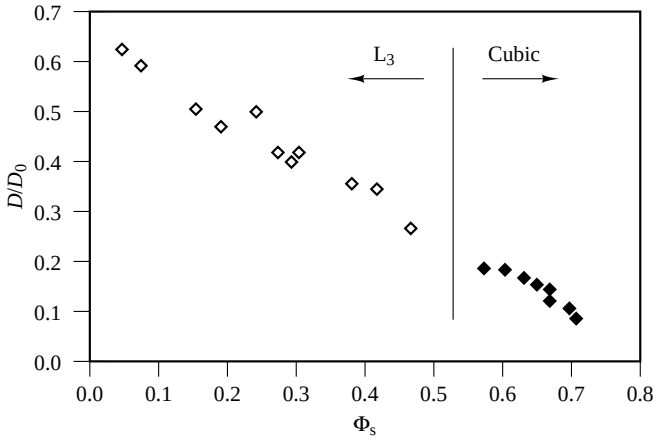

Figure 5 Variation in the reduced water diffusion coefficient with the volume fraction of surfactant in the L_3 (◊) and cubic (♦) phases formed in the AOT/water/NaCl system. (Data from Balinov et al.[34])

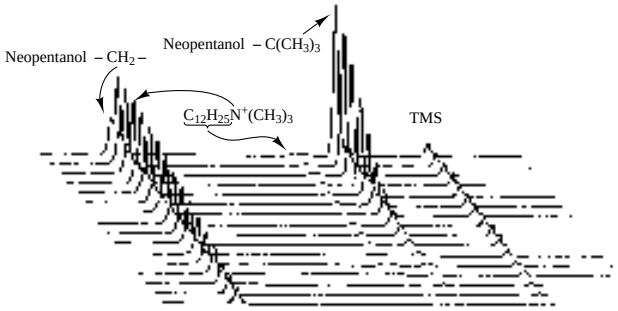

Figure 6 A ^{1}H NMR FT PFG experiment at 100 MHz on the solubilization of neopentanol into dodecyltrimethylammonium chloride micelles (solvent D_2O). The degree of solubilization is obtained directly from the evaluated D values for neopentanol in the micellar solution and in an aqueous solution [see equation (3)]. The value for the micellar diffusion coefficient, which is obtained from a small amount of solubilized tetramethylsilane (TMS), is also needed. The gradient current was varied linearly between successive spectra, which were obtained at fixed intergradient (Δ) and rf pulse (τ) intervals

(sometimes known as L* or 'sponge' phase) is formed, while dilution with the material of the dividing film gives rise to a bicontinuous micellar solution. Let us consider the L_3 phase formed in the sodium bis(2-ethylhexyl)sulfosuccinate (AOT)/brine system. In this system, the L_3 phase is in equilibrium with a bicontinuous cubic phase via a two-phase region.[34] Figure 5 gives the reduced diffusion coefficients for the water as a function of the surfactant volume fraction Φ_s in both the L_3 and the cubic phase.

There are two noteworthy features of the data shown in Figure 5. First, there is a continuous change in D/D_0 with Φ_s over the two-phase area between the L_3 and cubic phases. Secondly, at high dilution, a limiting value of D/D_0 of around 0.65 is obtained. The first observation indicates that the microstructures in the two phases are similar, since the translational diffusion of water reflects the microstructure of the solution. The second point can be used to infer information about the microstructure in a slightly more rigorous way. Consider a structure of discrete particles. According to the obstruction factors derived by Jönsson et al.,[16] the only geometry that would give rise to a reduction in D/D_0 from 1 to 0.65 would be large disks with an axial ratio in excess of 100:1. This is not in agreement with the surfactant diffusion, which, for the case of disks, implies an axial ratio of 12:1. Thus we are forced to think of alternative microstructures. Following the suggestion inherent in the first feature of the data in Figure 5, i.e. that the microstructures are similar in the L_3 and cubic phases, let us consider the case of a bilayer continuous structure. As noted above, this case has been treated by Anderson and Wennerström,[30] who obtained a value of 0.65 for the reduced diffusion coefficient for the solvent diffusion at low volume fraction of bilayer (in fact, for an infinitely thin multiply connected bilayer, the limiting value is $\frac{2}{3}$, on account of the dimensionality of the bilayer). Moreover, by analyzing the dependence of D/D_0 on Φ_s, information can be obtained regarding the coordination number of the obstructing surface.[35]

The analysis of the bicontinuous micellar solution structure as based on PFG data follows the same approach as the one described above. Readers interested in this particular micellar solution are referred to the paper by Monduzzi et al.[36]

2.4 Solubilization

As a final illustration of the power of the PFG approach, we consider the topic of solubilization. By 'solubilization' we mean the incorporation of molecules which are not water soluble into the micellar subvolume of a micellar solution. An important question pertaining to the phenomenon of solubilization concerns the degree of partitioning between the micelles and the water. This question is related to that pertaining to the micellization process (see above), and the same approach used to study that process can be used to investigate solubilization. Thus the degree of solubilization p can be determined by measuring the diffusion coefficient of the solubilizate in the absence and presence of micelles, and determining the diffusion coefficient for the micelle (using the approach outlined above) by using equation (3). From the volume or weight fraction of the micellar subvolume and the value of p, one can then determine the desired partition coefficient. A typical PFG solubilization experiment is shown in Figure 6.[37]

There are several advantages of the PFG approach as compared with other techniques for studying solubilization. The experiment is simple as well as selective. The latter point is particularly important, as one can determine the solubilization of several different solubilizates simultaneously, and each individual value of p can be determined. The presence of impurities is normally not a problem. The quantity p is well defined and easily interpreted. Finally, by measuring the surfactant diffusion one can independently check whether the micelles as such are altered by the presence of solubilizates. Clearly, the whole topic of solubilization becomes somewhat less meaningful if one does not have control over the state of the micelles.

3 RELAXATION STUDIES

NMR relaxation has proven to be a useful experimental technique for studying surfactant aggregation in liquid solutions

and liquid crystals.[20,38–40] The experiment yields information on the local dynamics and conformational state of the surfactant hydrocarbon chain and has demonstrated the liquid-like interior of surfactant micelles. However, the main purpose of NMR relaxation studies of isotropic micellar solutions and microemulsions has been to study properties such as the aggregate size.

The reorientation dynamics of aggregated surfactant molecules, which are discussed in more detail below, are characterized by the fact that they locally have a preferred orientation, forming essentially a monomolecular film of oriented molecules. Locally, surfactant molecules undergo rapid internal motions, such as *trans–gauche* isomerizations in the hydrocarbon chain. These motions are, due to the preferred orientation, slightly anisotropic. The situation can be pictured as the polar headgroups being anchored at the polar–apolar interface, leaving room for dangling motions of the hydrocarbon chains, with certain restrictions on the number of conformations due to packing constraints in the film. In isotropic solutions the residual interaction or anisotropy is further averaged by the thermal tumbling of the aggregates in combination with the diffusion of surfactant molecules within the curved surfactant film.

NMR spectra from surfactants in micellar solutions and microemulsions are generally in the motional narrowing regime, and the spin dynamics are characterized by well-defined relaxation times. Exceptions can be found in solutions of very long ($>10^2$ nm) wormlike cylindrical micelles where the large size in connection with steric overlap gives rise to a very slow (about 10^{-4} s) aggregate reorientation.[41,42] On the other hand, the dynamics are typically outside the extreme narrowing regime, and one often observes $R_2 \gg R_1$, where R_1 and R_2 are the longitudinal and transverse relaxation rates, respectively. Micellar aggregates reorient on a timescale of 10^{-9} s or slower. Thus, at conventional magnetic field strengths, the essential information on the surfactant aggregates is stored in the transverse relaxation rate R_2.

A hydrocarbon, typically an alkyl chain of 12–16 carbon atoms, constitutes the major part of surfactant molecules, offering ^{1}H and ^{13}C nuclei for NMR studies. Being spin-$\frac{1}{2}$ nuclei, the relaxation is mainly due to dipole–dipole interactions (although chemical shift anisotropy and scalar interaction can sometimes be important in the case of ^{13}C). The easy access and the relatively high sensitivity (which was particularly important in early CW NMR studies) has made ^{1}H NMR (in particular bandwidth measurements) studies particularly popular. Micellar growth can easily be studied qualitatively by monitoring the bandwidth of aliphatic ($-CH_2-$) protons in the spectrum. Quantitative analysis is, however, complicated by the coupling of the various protons having locally different motional characteristics along the alkyl chain. In an alkyl chain of, say, 16 carbon atoms, the protons constitute a coupled spin system of approximately 2^{16} spin states, which can have a broad spectrum of transition rates, resulting in significant deviations from a Lorentzian bandshape of the CH_2 resonance.[41,43] This complexity can, however, be turned into an advantage in that it allows for a continuum description of the transition rate spectrum. The ^{1}H bandshape problem was analyzed by Wennerström et al.[41,43] within the two-step formalism (see below), and quantitative ^{1}H bandshape analyses have been performed in systems of large, slowly reorienting micelles.[41,42] In contrast to the non-Lorentzian band shape, one often observes an exponential longitudinal relaxation due to rapid internal equilibration of the spin system (spin diffusion), and the frequency dependence of R_1 has been measured by using field cycling techniques.[44,45]

In an alkyl chain, the ^{13}C nuclei are relaxed by the fluctuating dipole–dipole coupling to the directly bound protons. The various carbon atoms along the chain are normally resolved. Usually, one applies broadband proton decoupling, resulting in exponential longitudinal relaxation of the individual ^{13}C magnetizations, and it is possible to determine R_1 and the nuclear Overhauser enhancement of the different methylene segments. On the other hand, it is difficult to measure R_2 on ^{13}C. Therefore, ^{13}C is mainly useful for studying local chain dynamics and segmental order, since the aggregate dynamics occur on timescales which are normally long relative to the inverse ^{13}C resonance frequency.

Certain surfactants carry phosphate or ammonium polar headgroups, offering ^{31}P and ^{14}N nuclei, respectively, for relaxation studies. The phosphate ^{31}P ($I = \frac{1}{2}$) has a relatively large chemical shift anisotropy which is strongly dependent on the pH (degree of protonation), complicating the analysis of relaxation data. ^{14}N is a $I = 1$ nucleus and its relaxation is dominated by the strong quadrupolar interaction. Except for the case of quaternary ammonium groups, the magnitude and asymmetry of the quadrupolar coupling is also pH dependent, and special care has to be taken.

The most suitable nucleus for relaxation studies of surfactant systems is ^{2}H, which can be incorporated synthetically into the hydrocarbon chain of the surfactant molecule. Normally, one selectively labels a single methylene segment, typically one adjacent to the polar headgroup, in order to avoid resonance overlap in the spectrum. ^{2}H is a $I = 1$ nucleus, and the dominating interaction governing the relaxation is the strong quadrupolar interaction. For aliphatic ($C-^2H$) deuterons, the analysis is further simplified by the fact that the electric field gradient tensor has essentially cylindrical symmetry around the $C-^2H$ bond direction, resulting in a vanishing asymmetry parameter. The ease with which both R_1 and R_2 can be accurately measured, the relatively simple interaction Hamiltonian, and the sufficiently high sensitivity allowing measurements to be made at low resonance frequencies (down to 2 MHz using variable field electromagnets), give ^{2}H NMR relaxation a particularly important role among the different experimental tools available for studying surfactant systems.

The utility of the NMR technique as an experimental tool in surfactant science can be made apparent by comparing the strengths and weaknesses of the NMR relaxation technique with those of other experimental techniques. In comparison with other experimental methods used in studying, for example, micellar size, the NMR relaxation technique has two major advantages, both of which are associated with the fact that it is reorientational motions which are measured. One is that the relaxation, i.e. R_2, is sensitive to small variations in micellar size. Consider, for example, a sphere for which the rotational correlation time is proportional to the cube of the radius. This can be compared with the translational self-diffusion coefficient which varies linearly with the radius. The second, and perhaps most important advantage is the fact that the rotational diffusion of particles in solution is essentially independent of interparticle interactions (electrostatic and hydrodynamic). This is in contrast to most

other techniques (such as viscosity, collective and self-diffusion, scattered light intensity, etc.) available for studying surfactant systems or colloidal systems in general. In this latter respect, NMR relaxation experiments are comparable with form factor determinations with small angle X-ray or neutron scattering experiments. A weakness of the NMR relaxation approach to aggregate size determinations, compared with form factor determinations, would be the difficulties of absolute calibration, since the transformation from information on dynamics to information on structure must be performed by means of a motional model.

3.1 Timescale Separation: The Two-Step Model

In this section we discuss a motional model[46–48] of aggregated surfactant molecules, which involves a timescale separation of fast local and slow global motions. This model has been applied extensively to, and shown to rationalize, NMR relaxation data from aggregated surfactant systems. We discuss the model in connection with ^{2}H relaxation experiments, since the most extensive experimental studies have been performed on ^{2}H-labeled surfactants. We begin by recalling that the longitudinal (R_1) and transverse (R_2) relaxation rates of an $I = 1$ nucleus, due to the quadrupolar interaction in an isotropic solution, are given by[49]

$$R_1 = \frac{3\pi^2}{40}\chi^2[2j(\omega_0) + 8j(2\omega_0)] \tag{6a}$$

$$R_2 = \frac{3\pi^2}{40}\chi^2[3j(0) + 5j(\omega_0) + 2j(2\omega_0)] \tag{6b}$$

where χ is the quadrupolar coupling constant, and $j(\omega_0)$ is the reduced spectral density function evaluated at the Larmor frequency ω_0.

Based on existing knowledge of surfactant aggregate structures, Wennerström and co-workers[46–48] suggested that the reorientational motion of surfactant molecules can be divided into: (i) fast local motions (equilibration of internal modes), which are slightly anisotropic due to the preferred orientation of the surfactant molecules; and (ii) slow isotropic motions, associated with the aggregate tumbling and the lateral diffusion of surfactant molecules within the aggregates. If these two motions occur on significantly different timescales, the fast motions generate a well-defined residual anisotropy to be averaged by the slow motions, and the spectral density can be written as a weighted sum of the fast and the slow components

$$j(\omega_0) = (1 - S^2)j_f(\omega_0) + S^2 j_s(\omega_0) \tag{7}$$

where $j_f(\omega_0)$ and $j_s(\omega_0)$ are the reduced spectral density functions describing the fast and slow motions, respectively. The parameter S is often referred to as an 'order parameter' and is given by the average

$$S = \tfrac{1}{2}\langle 3\cos\theta_{MD} - 1\rangle_f \tag{8}$$

where θ_{MD} is the angle between the axis of the maximum component of the electric field gradient tensor and the director axis.

The situation for the case of a ^{2}H-labeled methylene segment of a surfactant molecule residing in a micelle is illustrated in Figure 7. The director axis Z_D corresponds to the micellar surface normal. The field gradient tensor is cylindrically symmetric around the C–D bond axis, with the maximum component in the bond axis direction Z_M.

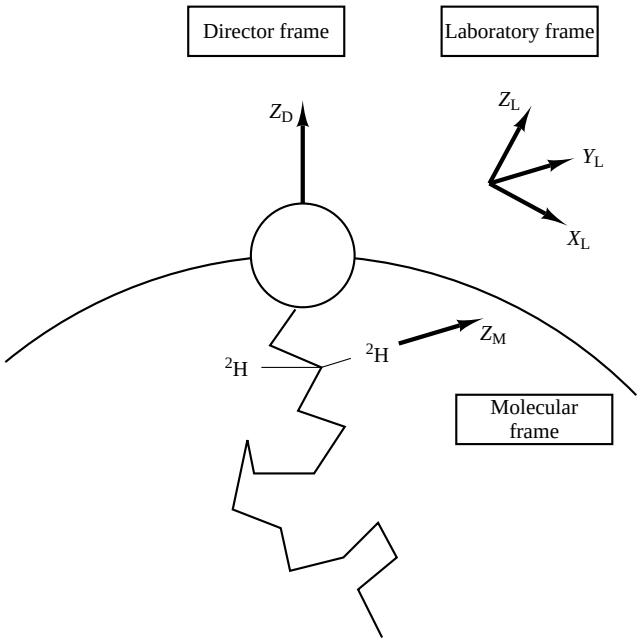

Figure 7 Schematic illustration of the various coordinate frames considered within the two-step model, for the case of a specifically ^{2}H-labeled methylene segment in the surfactant hydrocarbon chain. The laboratory frame (L) is set by the direction of the external magnetic field, where Z_L is the field direction. In this frame the nuclear quadrupolar moment tensor is diagonal. The director frame (D) is associated with the micellar aggregate, where Z_D specifies the micellar surface normal. It is assumed that the fast local dynamics occur with an essentially cylindrical symmetry around Z_D. The molecular frame (M) corresponds to the principal axis of the electric field gradient tensor. For the case of a methylene segment, Z_M specifies the maximum component of the field gradient tensor, which is also cylindrically symmetric around Z_M

In equation (7) it is also assumed that the fast motions have an effective three-fold or higher symmetry around the director. For most situations, however, one may expect an effectively cylindrical symmetry. For lower than three-fold symmetry, equation (7) must be extended to include a second-order parameter, describing the residual order in the plane perpendicular to the director. A similar extension is also necessary when the electric field gradient has a nonvanishing asymmetry parameter (for an extensive discussion, see Halle and Wennerström[48]).

3.2 Frequency Dependent Relaxation Studies of Small Spherical Micelles

The fast motions, described by the spectral density function $j_f(\omega_0)$, are expected to occur on a similar timescale ($\tau_f \approx 10^{-11}$ s) as in the corresponding liquid alkane. Thus this motion is in extreme narrowing ($\tau_f \ll 1/\omega_0$) in the accessible frequency range, and we may assume that $j_f(2\omega_0) \approx j_f(\omega_0) \approx j_f(0) = 2\tau_f$, where τ_f should be considered as an effective correlation time, representing the integral over a nonexponential correlation function.

The slow motion is a combination of micelle tumbling and the lateral diffusion of surfactant molecules within the surfactant film. For spherical aggregates, this motion is described by a Lorentzian spectral density function:

$$j_s(\omega_0) = \frac{2\tau_s}{1 + (\omega_0\tau_s)^2} \tag{9}$$

where τ_s is the correlation time. The tumbling and the lateral diffusion are expected to be statistically independent, in which case the correlation function can be factorized:

$$G_s = G_t G_d = e^{-t/\tau_t}\, e^{-t/\tau_d} = e^{-t/\tau_s} \tag{10}$$

where subscripts t and d refer to tumbling and lateral diffusion, respectively, and the slow correlation time can be written as

$$\frac{1}{\tau_s} = \frac{1}{\tau_t} + \frac{1}{\tau_d} \tag{11}$$

The correlation time associated with the tumbling of a sphere of radius R is given by

$$\tau_t = \frac{4\pi\eta R^3}{3k_B T} \tag{12}$$

where η represents the solvent viscosity, and $k_B T$ is the thermal energy. The effect of lateral diffusion can be described in terms of diffusion on the surface of a sphere of radius R. In this case, the correlation time can be written as

$$\tau_d = \frac{R^2}{6D_{lat}} \tag{13}$$

where D_{lat} is the lateral diffusion coefficient.

With the assumptions of (i) extreme narrowing conditions for the fast motions and (ii) a Lorentzian spectral density function of the slow motion, the expressions for the relaxation rates become, with equation (7)

$$R_1 = \frac{3\pi^2}{40}\chi^2 \left\{ (1 - S^2)20\tau_f + S^2 \times \left[\frac{4\tau_s}{1 + (\omega_0\tau_s)^2} + \frac{16\tau_s}{1 + (2\omega_0\tau_s)^2} \right] \right\} \tag{14a}$$

$$R_2 = \frac{3\pi^2}{40}\chi^2 \left\{ (1 - S^2)20\tau_f + S^2 \times \left[6\tau_s + \frac{10\tau_s}{1 + (\omega_0\tau_s)^2} + \frac{4\tau_s}{1 + (2\omega_0\tau_s)^2} \right] \right\} \tag{14b}$$

Equations (14a) and (14b) have been applied in a large number of ^{2}H NMR relaxation studies of micellar systems. It turns out that frequency dependent relaxation studies are particularly useful for studying small spherical micelles, which typically have a radius of about 2 nm. Using the water viscosity and equation (12) we obtain $\tau_t \approx 7$ ns at room temperature (25 °C). Including the effect of lateral diffusion, a typical value of the slow correlation time is $\tau_s \approx 5$ ns. Thus, the relaxation dispersion from the slow motion occurs around $\nu_0 \approx (2\pi\tau_s)^{-1} \approx 30$ MHz, which is well within the accessible Larmor frequency range for ^{2}H.

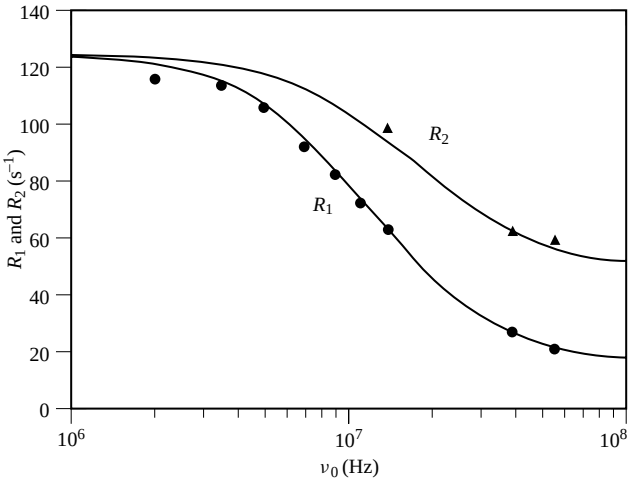

Figure 8 The variation in R_1 and R_2 with the Larmor frequency for ^{2}H nuclei bound to the α-methylene segment of the surfactant hexadecyltrimethylammonium chloride. The sample was an aqueous micellar solution containing 13 wt% of the surfactant. Experiments were performed at 27 °C. (Data from Söderman et al.[51])

To investigate the applicability of the motional model, Söderman and co-workers[50,51] studied aqueous micellar systems of alkyltrimethylammonium chloride surfactants of two different alkyl chain lengths: dodecyl and hexadecyl chains. The alkyl chains were ^{2}H labeled in the α-methylene segment, adjacent to the ammonium polar headgroup, and the relaxation rates R_1 and R_2 were measured in the Larmor frequency range 2–55 MHz, in order to cover the dispersion of the slow motion. The lower frequencies were obtained by using a variable field electromagnet. The results[51] obtained for the hexadecyltrimethylammonium chloride micelles (concentration 13 wt%) are shown in Figure 8. The solid lines are best fits of equations (14a) and (14b) to the whole data set, using τ_f, τ_s, and S as adjustable parameters. As can be seen from Figure 8, the data are well described by a Lorentzian spectral density function superimposed on a constant offset in the investigated frequency range, thus supporting the assumption of timescale separation. The fit yielded $\tau_f = 42 \pm 1$ ps, $\tau_s = 7.6 \pm 0.4$ ns, and $S = 0.186 \pm 0.003$, where the uncertainties correspond to an approximately 80% confidence interval taking only random errors into account, and a value of $\chi = 167$ kHz was used for the quadrupolar coupling constant.

The slow correlation time was interpreted in terms of equations (11)–(13), which contain two unknown parameters, R and D_{lat}. However, D_{lat} can be measured in phases of extended surfactant films, such as bicontinuous cubic phases, and R is expected to be close to the overall length of the surfactant molecule. Using $D_{lat} \approx 1 \times 10^{-11}$ m^2 s^{-1}, as measured in a bicontinuous cubic phase of the similar surfactant hexadecylammonium fluoride, and the radius $R = 2.37$ nm, a slow correlation time of approximately 10 ns was calculated from equations (11)–(13), which is in reasonable agreement with the experimentally determined value.

The applicability of the two-step model receives further support when comparing the S value obtained from the fit to the relaxation dispersion with that measured from quadrupolar

splittings in liquid crystalline phases formed at higher surfactant concentrations. In the liquid crystalline phases, extended surfactant aggregates are 'locked' in a crystalline array. Two very common structures are the lamellar phase, where surfactant bilayers are stacked with one-dimensional order, and the hexagonal phase, where cylindrical aggregates are packed on a two-dimensional hexagonal lattice. In these phases one has effectively frozen the slow motion, and the nuclei experience a static quadrupolar Hamiltonian $\langle\hat{\mathcal{H}}_Q\rangle_f$ in addition to the Zeeman term, where the average is taken over the fast local motions. This results in a quadrupolar splitting of magnitude[46]

$$\Delta_{lam} = \tfrac{3}{4}\chi|S| \tag{15}$$

in the lamellar phase with planar films. In the hexagonal phase, the rapid surfactant diffusion around the cylinder axis results in an additional averaging of the interaction by a factor of 2 and the splitting is given by

$$\Delta_{hex} = \tfrac{3}{8}\chi|S| \tag{16}$$

One may expect that the local motions, and hence the S value, should be similar in the liquid crystalline surfactant aggregates and the micelles in the dilute solution phase. This is in fact found to be the case. As mentioned above, the S value obtained from the fit to the relaxation dispersion (Figure 8) was found to be $S = 0.186$. A very similar value (0.192) was measured in the hexagonal phase at higher concentrations.[51]

3.3 Larger Aggregates: Use of the Zero Frequency Spectral Density

The small spherical micelles ($R \approx 2$ nm) can be seen as a limiting case, and in general surfactant aggregates have much larger extensions. When the size of the aggregates increases, τ_s increases as well, and the relevant relaxation dispersion moves out of the accessible frequency window. In some extreme cases, for example with long, entangled wormlike micelles, the dynamics may even move out of motional narrowing, showing slow motion effects in the NMR spectrum.[42] However, for most micellar and microemulsion systems, the motional narrowing condition applies. In these cases, valuable information may be obtained by measuring R_1 and R_2 for ^{2}H-labeled surfactants at a single Larmor frequency. For larger aggregates, the relevant information on the aggregate size is contained in the zero frequency spectral density only. Assuming that the fast motions are in extreme narrowing, in which case they contribute to a constant offset of both R_1 and R_2, it is useful to consider the difference $\Delta R = R_2 - R_1$ which then depends only on the slow motions. For the case of very slow motions, we also have $j_s(0) \gg j_s(\omega_0) \approx j_s(2\omega_0)$, and ΔR can be approximated by

$$\Delta R = \frac{9\pi^2}{40}(\chi S)^2 j_s(0) \tag{17}$$

This expression has been used to study variations in the shape of surfactant aggregates in different microemulsion systems.[52,53] Here, the micellar aggregates are swollen by the addition of a third component (normal micelles in aqueous solution are swollen by oil; reverse micelles in oil are swollen by water), where spherical aggregates can have radii of the order of 10 nm. Quantitative applications of equation (17) require reliable determinations of S from adjacent liquid crystalline phases. Furthermore, they require assumptions concerning the aggregate shape, and a knowledge of D_{lat}, to determine, for example, an aggregate radius of spherical aggregates. So, obviously, there are some uncertainties involved concerning the 'absolute calibration' of the method.

The situation can, however, be optimized by noting that the aggregates are formed under the constraint of a constant average interfacial area/enclosed volume ratio, set by the surfactant/internal component concentration ratio. With this constraint, the minimum aggregate size corresponds to a spherical shape. Due to the entropy of mixing, spherical aggregates, representing the minimum aggregate size, will always be stable at high dilutions, where the experiment can be calibrated. In many cases, D_{lat} is also known quite accurately from the various bicontinuous phases of the different systems.

Deviations from spherical shape can be modeled as a growth into prolate or oblate shapes. The interfacial area/enclosed volume constraint implies a constraint on the possible values of the two semiaxes describing the particle size. Halle[54] has calculated the correlation functions for the combined particle tumbling and surface diffusion of prolate and oblate particles. His results have been applied to, for example, microemulsion systems,[52,53] focusing on the ratio $j_{s,pr}(0)/j_{s,sph}(0)$, where the subscripts pr and sph refer to prolate and spherical particles, respectively. For a given interfacial area/enclosed volume ratio, which specifies the radius R of the sphere, $j_{s,pr}(0)/j_{s,sph}(0)$ is a function of the prolate axial ratio D_{lat}, and R. Knowing D_{lat} and R from other experiments it is possible to determine the aggregate axial ratio from the relaxation experiment.

As mentioned above, the strength of the NMR relaxation technique in comparison to other (e.g. scattering) techniques for studying micelles and microemulsions is related to the fact that rotational dynamics are monitored. This has the advantages that (i) the dynamics are sensitive to small size variations, and (ii) the dynamics are essentially independent of interactions. In an extensive study of a three-component microemulsion system composed of the nonionic surfactant pentaethyleneoxide dodecyl ether, water, and decane, oil swollen micelles dispersed in water were investigated over a large concentration range.[52]

With a nonionic surfactant, spherical aggregates are formed at lower temperatures, while the aggregates grow in size with increasing temperature.[17] Figure 9 shows the variation of ΔR with temperature for two compositions, $\Phi = 0.12$ and 0.23, in the microemulsion phase.[52] Here, $\Phi = \Phi_s + \Phi_O$ is the total volume fraction of surfactant (Φ_s) and oil (Φ_O), and the ratio $\Phi_s/\Phi_O = 0.815$ was kept constant.

The value of ΔR decreases when the temperature is decreased in the microemulsion phase and levels off at lower temperatures at a minimum value ΔR_{min}, when the aggregates have reached the limiting spherical shape, corresponding to the minimum size. Note that the minimum ΔR value is the same for the two concentrations, as is expected because the radius, dictated by Φ_s/Φ_O, should be the same. By considering

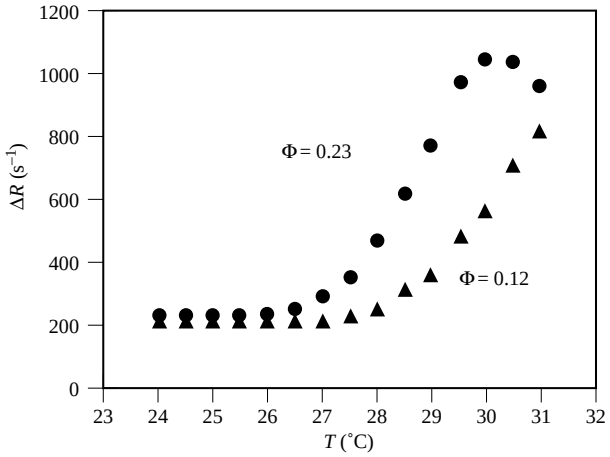

Figure 9 Variation in ^{2}H $\Delta R = R_2 - R_1$ with temperature of the ^{2}H-labeled nonionic surfactant pentaethyleneoxide dodecyl ether $[CH_3(CH_2)_{10}C^2H_2(OCH_2CH_2)_5OH]$ in a ternary system with water and decane. The ratio Φ_s/Φ_O is 0.815, where Φ_s and Φ_O are the surfactant and oil volume fractions, respectively. The concentrations are $\Phi=\Phi_s + \Phi_O$ = 0.12 and 0.23, respectively. (Data from Leaver et al.[52])

the reduced ΔR value, $\Delta R/\Delta R_{min} = j_{s,pr}(0)/j_{s,sph}(0)$, it was possible to calculate the increase in the axial ratio of the aggregates with increasing temperature, assuming a growth into prolate aggregates. The variation in the axial ratio obtained is shown in Figure 10.

Very large micelles may also form in binary surfactant systems. These are long wormlike micelles which become entangled at higher concentrations, giving rise to rheological properties similar to those in polymer solutions. Such systems have been examined by means of ^{1}H bandshape analysis.[41,42] The protons of the surfactant hydrocarbon chain form a very large dipolar coupled spin system, with essentially a continuum distribution of transverse relaxation rates. The distribution of relaxation rates is related to the distribution of order parameters,[43] which can be obtained from analyzing the bandshape in the liquid crystalline (lamellar or hexagonal) phases, where the bandshape is associated with a continuum distribution of residual dipolar splittings.[55]

Slow motions have also been studied by measuring the differential line broadening (DLB) of proton J coupled ^{13}C nuclei.[56] Here the difference in bandwidth of the different resonances in a ^{13}C multiplet can be attributed to the interplay between the dipole–dipole and chemical shift anisotropy relaxation mechanisms, and by analyzing the difference, information on the slow motion may be obtained.

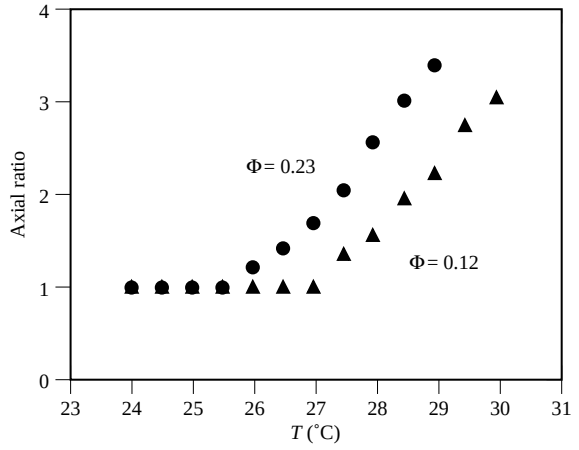

Figure 10 Variation in the micellar axial ratio with temperature, assuming a monodisperse prolate growth, as deduced from the relaxation data in Figure 9 by using the correlation function due to Halle,[54] for the combined motion of aggregate tumbling and surface diffusion

3.4 Relaxation Measurements on Water and Counterion Nuclei

Relaxation measurements on water and counterion nuclei may also give information about the surfactant aggregate size and shape. Such measurements may be particularly useful in reverse micellar systems, where water and surfactant counterions are contained in small water pools covered by a surfactant monolayer. In a ^{23}Na ($I = \frac{3}{2}$) spin relaxation study of a reverse micellar system, the presence of slow motions was found to result in a biexponential free induction decay (FID).[57] Using the two transverse relaxation rates and an effective longitudinal relaxation rate, it was possible to determine all three spectral density values: $j(0)$, $j(\omega_0)$, and $j(2\omega_0)$. From the fit of the imaginary part of the FID it was also possible to determine the second-order quadrupolar dynamic shift, allowing for an additional test of the motional model invoked in the interpretation of the data.

An interesting application of water nuclei relaxation in microemulsions concerns the so-called 'nuclear spin quenching' studied by Carlström and Halle.[58] Here, the effect of chemical exchange of water protons, mediated by the presence of prototropic ions, H_3O^+ and OH^-, on the ^{17}O bandshape in a reverse micellar system was investigated. By careful analysis of the ^{17}O bandshape, information on the water exchange kinetics between droplets as well as the droplet size was obtained.

3.5 Surfactant Hydrocarbon Chain Conformations in Micelles

The early findings of narrow ^{1}H bands from the surfactant hydrocarbon chains in small spherical micelles revealed that the micellar interior is in a liquid-like state. Magnetic field dependent ^{13}C R_1 relaxation experiments confirmed those ideas, and a segmental order parameter profile, similar to that obtained from ^{2}H quadrupolar splittings in lipid bilayer systems, was obtained within the two-step formalism.[59] By studying the dynamics of a symmetric probe molecule solubilized in micelles, it was concluded that the micellar interior was characterized by an effective viscosity similar to that of the neat hydrocarbon.[60]

Chachaty and co-workers[40,61] have studied the enhanced relaxation rate due to the presence of paramagnetic counterions. The multivalent paramagnetic counterion is expected to be selectively adsorbed onto the charged micellar surface. Thus, by analyzing the effect on the ^{13}C relaxation along the chain, the distribution in the distance from the micellar surface could be estimated for the various methylene segments.

A conceptually similar study was reported recently by Palmas et al.[62] Here, cross relaxation effects between ^{13}C and nondirectly bonded protons were examined by two-dimensional heteronuclear Overhauser effect spectroscopy (HOESY). This study revealed the significance of intermolecular $^{1}H-^{13}C$ dipolar interactions. Correlations between carbon atoms and protons belonging to different segments were observed in the lower part of the hydrocarbon chains, while they were found to be absent in the vicinity of the polar headgroup, where the chain configuration is more rigid.

4 RELATED ARTICLES

Amphiphilic Liquid Crystalline Samples: Nuclear Spin Relaxation; Bilayer Membranes: Deuterium and Carbon-13 NMR; Brownian Motion and Correlation Times; Colloidal Systems; Diffusion Measurements by Magnetic Field Gradient Methods; Liquid Crystalline Samples: Diffusion; Liquid Crystalline Samples: Structure of Nonrigid Molecules.

5 REFERENCES

1. J. W. McBain and M. Taylor, *Ber.*, 1910, **43**, 321.
2. J. W. McBain, E. C. V. Cornish, and R. C. Bowden, *J. Chem. Soc.*, 1912, **101**, 2042.
3. J. W. McBain, *Trans. Faraday Soc.*, 1913, **9**, 99.
4. J. W. McBain and C. S. Salmon, *J. Am. Chem. Soc.*, 1920, **42**, 426.
5. P. T. Callaghan, C. M. Trotter, and K. W. Jolley, *J. Magn. Reson.*, 1980, **37**, 247.
6. P. Stilbs, *Prog. Nucl. Magn. Reson. Spectrosc.*, 1987, **19**, 1.
7. E. L. Hahn, *Phys. Rev.*, 1950, **80**, 580.
8. E. O. Stejskal and J. E. Tanner, *J. Chem. Phys.*, 1965, **42**, 288.
9. D. W. McCall, D. C. Douglass, and E. W. Anderson, *Ber. Bunsenges. Phys. Chem.*, 1963, **67**, 336.
10. R. L. Vold, J. S. Waugh, M. P. Klein, and D. E. Phelps *J. Chem. Phys.*, 1968, **48**, 3831.
11. J. E. Tanner, Thesis, University of Wisconsin, Madison, WI, USA, 1966.
12. G. Oraedd, G. Lindblom, L. B. A. Johansson, and G. Wikander, *J. Phys. Chem.*, 1992, **96**, 5170.
13. M. Jansson and P. Stilbs *J. Phys. Chem.*, 1985, **89**, 4868.
14. G. Gunnarsson, B. Jönsson, and H. Wennerström, *J. Phys. Chem.*, 1980, **84**, 3114.
15. H. Hagslätt, O. Söderman, B. Jönsson, and L. Johansson, *J. Phys. Chem.*, 1991, **95**, 1703.
16. B. Jönsson, H. Wennerström, P. Nilsson, and P. Linse, *Colloid Polymer Sci.*, 1986, **264**, 77.
17. B. Lindman and H. Wennerström, *J. Phys. Chem.*, 1991, **95**, 6053.
18. P. G. Nilsson, H. Wennerström, and B. Lindman, *J. Phys. Chem.*, 1983, **87**, 1377.
19. P. G. Nilsson, H. Wennerström, and B. Lindman, *Chem. Script.*, 1985, **25**, 67.
20. B. Lindman, O. Söderman, and P. Stilbs, in *Surfactants in Solutions*, ed. K. L. Mittal, Plenum, New York, 1989, Vol. 7.
21. O. Söderman, E. Hansson, and M. Monduzzi, *J. Colloid Interface Sci.*, 1991, **141**, 512.
22. U. Olsson and P. Schurtenberger, *Langmuir*, 1993, **9**, 3389.
23. K. Shinoda and B. Lindman, *Langmuir*, 1987, **3**, 135.
24. K. Fukuda, O. Söderman, B. Lindman, and K. Shinoda, *Langmuir*, 1993, **9**, 2921.
25. U. Olsson, K. Nagai, and H. Wennerström, *J. Phys. Chem.*, 1988, **92**, 6675.
26. U. Olsson, M. Jonströmer, K. Nagai, O. Söderman, H. Wennerström, and G. Klose, *Prog. Colloid Polym. Sci.*, 1988, **76**, 75.
27. M. Jonströmer, W. O. Parker, and U. Olsson, *Langmuir*, 1995, **11**, 61.
28. B. Lindman, K. Shinoda, U. Olsson, D. Anderson, G. Karlström, and H. Wennerström, *Colloid Surfaces*, 1989, **38**, 205.
29. L. E. Scriven, *Nature*, 1976, **263**, 123.
30. D. M. Anderson and H. Wennerström, *J. Phys. Chem.*, 1990, **94**, 8683.
31. M. T. Clarkson, D. Beaglehole, and P. T. Callaghan, *Phys. Rev. Lett.*, 1985, **54**, 1722.
32. O. Söderman, G. Carlström, U. Olsson, and T. C. Wong, *J. Chem. Soc., Faraday Trans. 1*, 1988, **84**, 4475.
33. P.-O. Quist, B. Halle, and I. Furo, *J. Chem. Phys.*, 1991, **95**, 6945.
34. B. Balinov, U. Olsson, and O. Söderman, *J. Phys. Chem.*, 1991, **95**, 5931.
35. U. Olsson, B. Balinov, and O. Söderman, in *The Structure and Conformation of Amphiphilic Membranes* (*Springer Proceedings in Physics, Vol. 66*), ed. R. Lipowsky and K. Kremer, Springer, Berlin, 1992.
36. M. Monduzzi, U. Olsson, and O. Söderman, *Langmuir*, 1993, **9**, 2914.
37. P. Stilbs, in *Solubilization* (*Surfactant Science Series*), ed. D. Christian and J. F. Scamehorn, M. Dekker, New York, 1994.
38. B. Lindman, O. Söderman, and H. Wennerström, in *Surfactant Solutions. New Methods of Investigation*, ed. R. Zana, M. Dekker, New York, 1987, p. 295.
39. B. Lindman, O. Söderman, and H. Wennerström, *Ann. Chim. (Rome)*, 1987, **77**, 1.
40. C. Chachaty, *Prog. Nucl. Magn. Reson. Spectrosc.*, 1987, **19**, 183.
41. J. Ulmius and H. Wennerström, *J. Magn. Reson.*, 1977, **28**, 309.
42. U. Olsson, O. Söderman, and P. Guéring, *J. Phys. Chem.*, 1986, **90**, 5223.
43. H. Wennerström and J. Ulmius, *J. Magn. Reson.*, 1976, **23**, 431.
44. F. Noack, *Prog. Nucl. Magn. Reson. Spectrosc.*, 1986, **18**, 171.
45. W. Kühner, E. Rommel, F. Noack, and P. Meier, *Z. Naturforsch., Teil A*, 1987, **42**, 127.
46. H. Wennerström, G. Lindblom, and B. Lindman, *Chem. Script.*, 1974, **6**, 97.
47. H. Wennerström, B. Lindman, O. Söderman, T. Drakenberg, and J. B. Rosenholm, *J. Am. Chem. Soc.*, 1979, **101**, 6860.
48. B. Halle and H. Wennerström, *J. Chem. Phys.*, 1981, **75**, 1928.
49. A. Abragam, *The Principles of Nuclear Magnetism*, Clarendon, Oxford, 1961.
50. O. Söderman, H. Walderhaug, U. Henriksson, and P. Stilbs, *J. Phys. Chem.*, 1985, **89**, 3693.
51. O. Söderman, U. Henriksson, and U. Olsson, *J. Phys. Chem.*, 1987, **91**, 116.
52. M. S. Leaver, U. Olsson, H. Wennerström, and R. Strey, *J. Phys. II*, 1994, **4**, 515.
53. R. Skurtveit and U. Olsson, *J. Phys. Chem.*, 1992, **96**, 8640.
54. B. Halle, *J. Chem. Phys.*, 1991, **94**, 3150.
55. H. Wennerström, *Chem. Phys. Lett.*, 1973, **18**, 41.
56. L. Hwang, P. Wang, and T. C. Wong, *J. Phys. Chem.*, 1988, **92**, 4753.

57. P. H. Kenez, G. Carlström, I. Furo, and B. Halle, *J. Phys. Chem.*, 1992, **96**, 9524.
58. G. Carlström and B. Halle, *Mol. Phys.*, 1988, **64**, 659.
59. H. Walderhaug, O. Söderman, and P. Stilbs, *J. Phys. Chem.*, 1984, **88**, 1655.
60. P. Stilbs, H. Walderhaug, and B. Lindman, *J. Phys. Chem.*, 1983, **87**, 4762.
61. Y. Chevalier and C. Chachaty, *J. Phys. Chem.*, 1985, **89**, 875.
62. P. Palmas, P. Tekely, P. Mutzenhardt, and D. Canet, *J. Chem. Phys.*, 1993, **99**, 4775.

Biographical Sketches

Olle Söderman. *b* 1951. B.Sc., 1976, Ph.D. (supervisor Göran Lindblom), 1981, Lund Institute of Technology. Introduced to NMR by S. Forsén and G. Lindblom. Visiting graduate student at University of British Columbia (with Myer Bloom). Joined Faculty of Physical Chemistry, University of Lund, 1981. Currently, lecturer, University of Lund. Approx. 80 publications. Current research interests: pulsed field gradient NMR applied to colloidal systems.

Ulf Olsson. *b* 1957. B.Sc., 1981, Ph.D. (supervisor Olle Söderman), 1988, Lund University. Postdoctoral research, Centre de Recherche Paul Pascal, Pessac France, 1989. Faculty of Physical Chemistry, Lund University, 1989. Approx. 40 publications. Current research interests: structure and phase equilibria of surfactant/water/oil systems.

Conducting Polymers

Takehiko Terao
Kyoto University, Japan
and

Kiyoshi Kume
Tokyo Metropolitan University, Japan

1	Introduction	1
2	Undoped Polyacetylene	1
3	Doped Polyacetylene	2
4	References	4

1 INTRODUCTION

Conducting polymers have attracted a great deal of interest because of their peculiar electrical behavior. The characterization of these materials is, of course, very important, in order to provide a background for understanding their complex nature. Many of the most important results regarding the characterization of conducting polymers have been obtained using solid state NMR, which is potentially one of the most useful techniques for determining the static and dynamic properties of conducting polymers.

This article discusses solid state NMR studies of polyacetylene; this has been the most investigated of the various conducting polymers, because it is the simplest prototype and shows most of the characteristic features of such polymers. Supplementary information on this subject can be obtained from two review articles: the review by Clark and Scott[1] is concerned with the NMR of polyacetylene, and the one by Kahol et al.[2] reviews the magnetic properties of polyacetylene (mainly) and other conjugated polymers (briefly).

2 UNDOPED POLYACETYLENE

Polyacetylene is typically synthesized as the *cis* isomer (**1**) in the form of crystalline films, and can be converted to the thermodynamically more stable *trans* isomer (**2**) by heating. The ^{13}C CP MAS peaks of the *cis* and *trans* isomers appear at 127.7 and 137.3 ppm, respectively,[3] unequivocally confirming the structural configuration of each isomer. The principal values of the *cis* and *trans* ^{13}C chemical shift tensors were determined to be (218, 138, 22) and (219, 144, 47), respectively.[3] The chemical shift tensor orientations were also obtained for *trans*-$(CH)_x$ with respect to the single and double carbon–carbon bonds[4,5] and for *cis*- and *trans*-$(CH)_x$ with respect to the C–H bond.[6] These chemical shift parameters (see also Kahol et al.)[2] reflect the local electronic structures and serve as a reference for the purpose of comparison with those of doped $(CH)_x$ and other polyacetylenes with different structures.

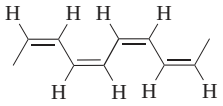

(1)

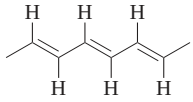

(2)

A weaker line was found at about 47 ppm with an area intensity of 3.4% of that of the whole ^{13}C CP MAS spectrum in 30% ^{13}C-enriched *trans*-$(CH)_x$.[3] This line was assigned to sp^3 hybridized carbon atoms existing as defects in the polymer chain, which may originate from the Ziegler–Natta catalyst. These defects may interrupt the conjugated system and decrease the electrical conductivity. A similar line was also observed in the DNP-enhanced ^{13}C NMR spectrum (see ***Dynamic Nuclear Polarization and High-Resolution NMR of Solids***).[7]

The *cis–trans* thermal isomerization process has been studied by ^{13}C CP MAS NMR.[3] The *trans* peaks in partially isomerized $(CH)_x$ show shielding shifts and broader linewidths with respect to the pure *trans* peak. The shifts indicate that the structure of partially isomerized $(CH)_x$ differs from that of pure *trans*-$(CH)_x$, and the broad linewidths demonstrate that the structure is disordered. On the other hand, the *cis* peaks in partially isomerized $(CH)_x$ show neither shifts nor line broadening compared with the spectrum of pristine *cis*-$(CH)_x$, indicating no changes in the structure of the *cis* parts. These results suggest that the isomerization proceeds inhomogeneously, probably from the surface of fibrils, with the core remaining in the regular *cis* structure.

The disordered nature of polyacetylene films prevents reliable structural determination by diffraction methods. Although conventional wideline NMR spectra of undoped and doped polyacetylene have been observed in order to obtain structural information, no two sets of data agree.[1] Reliable second and fourth moments can be obtained using the magic echo technique, thus confining the structural possibilities to a few of many proposed structures.[2]

The carbon–carbon bond lengths in both *cis*- and *trans*-$(CH)_x$ were obtained with the use of nutation NMR spectroscopy.[8] By this approach, ^{13}C Pake doublets were observed in polyacetylene polymerized from a mixture of 4% doubly ^{13}C-enriched acetylene in doubly ^{13}C-depleted acetylene. The proton-decoupled ^{13}C nutation spectrum of a *cis* sample and the corresponding simulated spectrum are shown in Figure 1(a). The observed spectrum was well simulated by assuming the existence of only one carbon–carbon bond distance of 0.137 nm, which corresponds to a double bond length. This result strongly suggests that the Ziegler–Natta reaction leaves the original carbon pair doubly bonded in the resulting polymer. Unlike the spectrum of *cis*-$(CH)_x$, the spectrum of the corresponding *trans* isomer shows two overlapping Pake doublets [Figure 1(b)]. The simulation is a composite of two Pake patterns of equal intensity corresponding to bond lengths of 0.144 and 0.136 nm, which may be assigned to the single and double bonds, respectively, in *trans*-$(CH)_x$.

These carbon–carbon bond lengths were found to be independent of temperature in the range 4.2–300 K. Almost the same bond lengths and a C–C=C bond angle of 120.7 ± 1.5° were obtained for *trans*-$(CH)_x$ using ^{13}C two-dimensional NMR in combination with DNP.[5]

An interesting problem in *trans*-$(CH)_x$ is the existence and diffusive motion of neutral (spin) solitons. As shown in

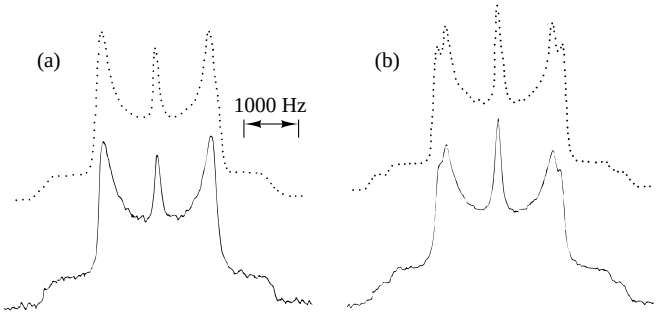

Figure 1 Experimental (—) and simulated (. . .) ^{13}C nutation NMR spectra observed at 77 K: (a) *cis*-$(CH)_x$ and (b) *trans*-$(CH)_x$. The samples were weakly enriched in ^{13}C pairs. (Reproduced by permission of The American Physical Society from C. S. Yannoni and T. C. Clarke, *Phys. Rev. Lett.*, 1983, **51**, 1991)

Figure 2, two kinds of domain can coexist, where the positions of the single and double bonds are exchanged. Between the two domains a defect occurs as a domain wall, where an electron is unpaired. Actually, the unpaired electron extends over several carbon atoms, and is considered to move along the chain. Thus, the defect is a kind of kink soliton.[9] This is called a spin soliton or a neutral soliton, because it carries a spin but not a charge. The concentration of such a defect is known to be about 1/3000 carbon atoms. The spin density distribution over the several carbon atoms, which is associated with the solitons, has been determined using ENDOR (see ***Electron–Nuclear Multiple Resonance Spectroscopy***).[10–12]

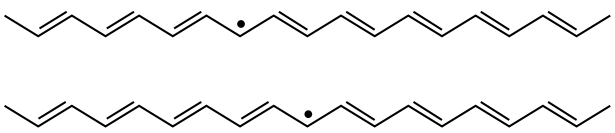

Figure 2 Diffusive motion of a neutral (spin) soliton along the chain of *trans*-polyacetylene

The experimental evidence for the diffusive motion of neutral solitons was proposed by a ^{1}H NMR $T_1{}^{-1}$ frequency dependence experiment. The $T_1{}^{-1}$ was found to vary proportionally with $\omega^{-1/2}$ between 10 and 340 MHz.[13] This shows that the solitons make a one-dimensional diffusive motion. The obtained diffusion rate D is about 6×10^{13} rad s^{-1} at room temperature. A similar frequency dependence experiment was also done using the ESR method and a somewhat smaller value of D was obtained.[14] The ESR method is considered to be important because the nuclear spin diffusion process, which gives the same frequency dependence as the one-dimensional diffusive motion, is ineffective for the ESR. The diffusive motion of neutral solitons is also supported by the results of a DNP experiment.[13]

The temperature dependence of D determined experimentally has been a controversial subject. When the ^{1}H NMR $T_1{}^{-1}$ data were directly analyzed, D was found to decrease with increasing temperature.[15] This means that the soliton motion is interrupted by phonons. On the other hand, when the effect of trapping was assumed, the conclusion was reversed; D was found to increase with T^2. This means that the solitons are assisted by phonons. Although the latter appears to be consistent with the ESR motional narrowing experiment,[16] the trapping effect should also be taken into account in interpreting the results of this experiment. From the DNP experiment a temperature dependence of $D \propto T^{\frac{1}{2}}$ was obtained.[17] The D from μSR is almost independent of temperature.[18] Extensive theoretical discussions have been carried out on the temperature variation of D.[19] The D obtained from the ^{13}C NMR $T_1{}^{-1}$ was found to be almost independent of frequency. This was explained by a model of confined soliton motion and a nuclear spin diffusion process.[20]

3 DOPED POLYACETYLENE

When polyacetylene films are heavily doped with donor or acceptor ions they become metallic. This metallic nature has been demonstrated by Pauli paramagnetism, thermoelectric power, and optical absorption experiments. The maximum reported electrical conductivity reaches ca. 1×10^5 S cm^{-1}, which is rather close to that of copper. Carbon-13 solid state NMR has played an important role in obtaining information on the electronic states of doped polyacetylene.

Initially a deshielding shift was observed with line broadening in AsF_6-doped $(CH)_x$, and there was a controversy as to whether it was a Knight shift or a chemical shift.[1] In order to provide a final answer to this question, ^{13}C spectra of acceptor-doped $(CH)_x$ and donor-doped $(CH)_x$ were measured.[21] Figure 3(a) and (b) show the spectra of 7.6 mol% AsF_6-doped *trans*-$(CH)_x$ and 9 mol% K-doped *trans*-$(CH)_x$, respectively,

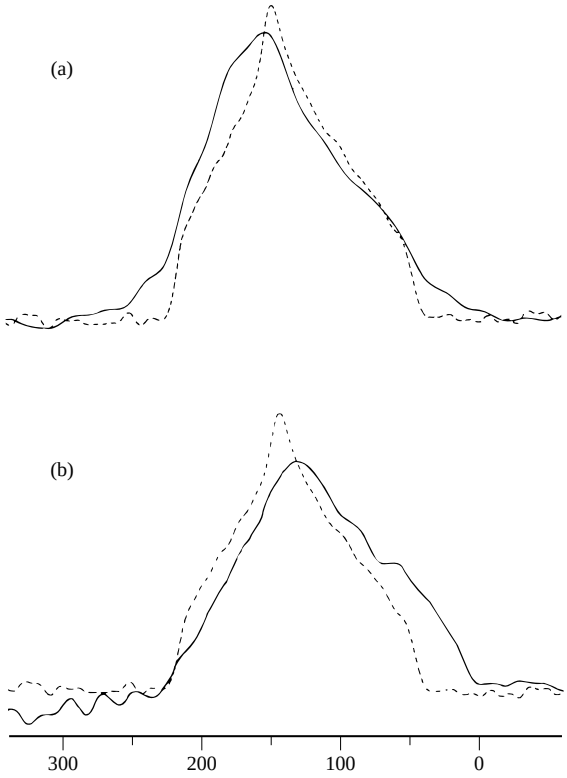

Figure 3 Carbon-13 chemical shift powder patterns of: (a) *trans*-$[CH(AsF_6)_{0.076}]_x$, (b) *trans*-$(CHK_{0.09})_x$. (. . .) *trans*-$(CH)_x$. (Reproduced by permission of Elsevier Science Ltd from T. Terao, S. Maeda, T. Yamabe, K. Akagi, and H. Shirakawa, *Solid State Commun.*, 1984, **49**, 829)

which were obtained without sample spinning. The spectrum of *trans*-$[CH(AsF_6)_{0.076}]_x$ clearly shows a deshielding shift with a broader width with respect to that of undoped *trans*-$(CH)_x$; the observed deshielding shift of the center of gravity of the spectrum is 9 ppm. On the other hand, the spectrum of *trans*-$(CHK_{0.09})_x$ exhibits a shielding shift of 12 ppm. It is known that a ^{13}C line shows a deshielding or shielding shift of 160 ppm according to whether the π-electron density decreases or increases, respectively, by one electron per carbon. From this fact we can expect a deshielding shift of 12 ppm in *trans*-$[CH(AsF_6)_{0.076}]_x$ and a shielding shift of 14 ppm in *trans*-$(CHK_{0.09})_x$ from the resonance of undoped *trans*-$(CH)_x$. On the other hand, the Knight shift was estimated to be 2 ppm. Both the direction and the magnitude of the observed shifts agree with the estimation of the chemical shifts, within an experimental error of 3 ppm, distinctly indicating that the observed shifts are chemical in origin. The contribution of the Knight shift is concluded to be smaller than 3 ppm, which is in agreement with the theoretical estimation.

Figure 4 shows the CP MAS spectrum of *trans*-$(CHBr_{0.103})_x$.[21] The main peak composed of a broad peak and a rather sharp line superimposed on it is ascribed to the alkenic carbon atoms. The broad signal is shifted in the deshielding direction from the peak position of 137.3 ppm for undoped $(CH)_x$, which is considered to be a chemical shift due to the removal of π electrons from sp^2 hybridized carbon atoms, as discussed above. The shift is smaller than the value (30–40 ppm) expected in the case when all bromine atoms of 10.3 mol% contribute to the removal of π electrons. This leads to the conclusion that only some bromine atoms contribute to charge transfer, the remaining bromine atoms adding to double bonds or substituting hydrogen atoms. The broad linewidth can be rationalized by considering that the charges on a polyacetylene chain are not homogeneously distributed, but may be positive or negative and of various magnitudes. Some theoretical studies based on the charged soliton model[9] support this consideration, giving the observed linewidth.[22–24] The chemical shift of the sharp peak is 137.3 ppm, in agreement with that of undoped *trans*-$(CH)_x$. The result shows the existence of undoped regions in a fibril; the amount of the undoped regions can be estimated to be about 50% from the relative intensity of the sharp line. A swelling near the bottom of the sharp part of the sp^2 signal on the high frequency side is due to bromine-substituted carbon atoms and/or sp^3-adjacent carbons.

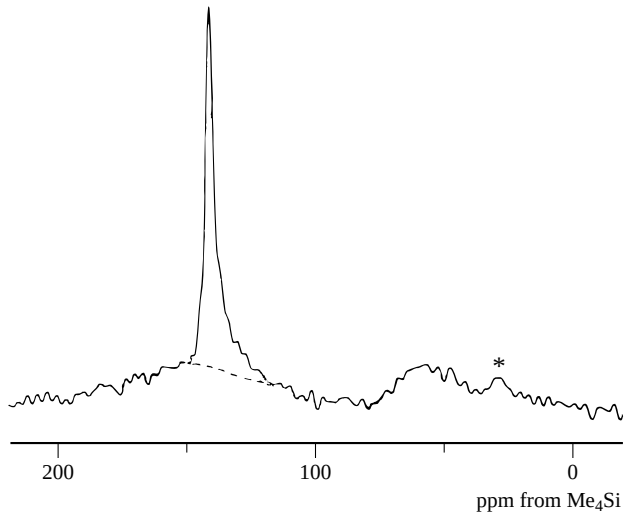

Figure 4 Carbon-13 CP MAS spectrum of *trans*-$(CHBr_{0.103})_x$. The peak marked with an asterisk is a spinning sideband. (Reproduced by permission of Elsevier Science Ltd from T. Terao, S. Maeda, T. Yamabe, K. Akagi, and H. Shirakawa, *Solid State Commun.*, 1984, **49**, 829)

A weaker peak can be seen at about 60 ppm, which is in the region of chemical shifts for sp^3 hybridized carbon atoms. The intensity ratio of 20% to the whole spectrum, however, cannot be explained even if all bromine atoms of 10.3 mol% are added to double bonds (it implies that the sample is an insulator). A considerable number of sp^3 carbon atoms are supposed to result from cross-linking induced by addition of bromine atoms.[21] Cross-linking, as well as bromine addition, ought to disturb the conjugated system seriously and result in the low conductivity of bromine-doped $(CH)_x$. Iodine-doped $(CH)_x$ also exhibits a peak around 50 ppm.[21,25]

The NMR of dopants is also important when investigating their electronic states. It was found that the resonance frequencies of ^7Li and ^{23}Na doped in $(CH)_x$ are very close to the purely ionic values, irrespective of the dopant concentration.[26] This shows that these alkali metals in polyacetylene are completely ionized. On the other hand, the ^{133}Cs resonance in cesium-doped $(CH)_x$ shows a peak at -200 ppm from the reference (aqueous solution of $CsNO_3$) at all concentrations and another peak at 12 100 ppm at room temperature for a concentration of 16 mol%.[26] Two-dimensional nutation NMR (see ***Nutation Spectroscopy of Quadrupolar Nuclei***) of the central transition of the ^{23}Na resonance in sodium-doped $(CH)_x$ was observed.[25] The spectrum consists of a broad line and a narrow line in the chemical shift dimension through doping levels from 2.8 to 28.8 mol%. This result shows the presence of at least two different crystal phases in sodium-doped $(CH)_x$.

The temperature dependence of the electrical conductivity for doped polyacetylene is largely semiconductive, except for a small region near room temperature; this is considered to be due to the fibrillar structure of polyacetylene. The conductivity inside the fibrils would be metallic. The NMR method should be a powerful tool to pick up the inside metallic conductivity. The frequency dependence experiment of the ^1H NMR ${T_1}^{-1}$ was extended to doped polyacetylene. A $\omega^{-1/2}$ law was also observed on a heavily AsF_6-doped sample.[13] By applying the expression for one-dimensional diffusive motion, a conductivity of 5×10^4 S cm^{-1} at room temperature was obtained.

However, the temperature dependence experiment has not been very successful at detecting the metallic behavior. Even in the most recent experiment, heavily FSO_3^--, ClO_4^--, I_3^--, and K^+-doped samples showed curious temperature dependences of ${T_1}^{-1}$, which are quite different from metallic samples.[27] The heavily AsF_6^--doped sample also showed a similar behavior, which cannot be simply attributed to the metallic origin.[28] The curious experimental results were recently interpreted as being due to some restricted motion of residual spins.[27]

The only exception was a Br_3-doped sample. The metallic T_1T = Constant law was observed nearly 10 years ago.[15,28] Recently, an aging effect was discovered on the Br_3-doped samples.[27] For samples just after doping, the ${T_1}^{-1}$ showed a similar curious behavior to the other dopants. However, this changed gradually. After 6 weeks the behavior of T_1T = Constant appeared, and after 6 months this changed to a

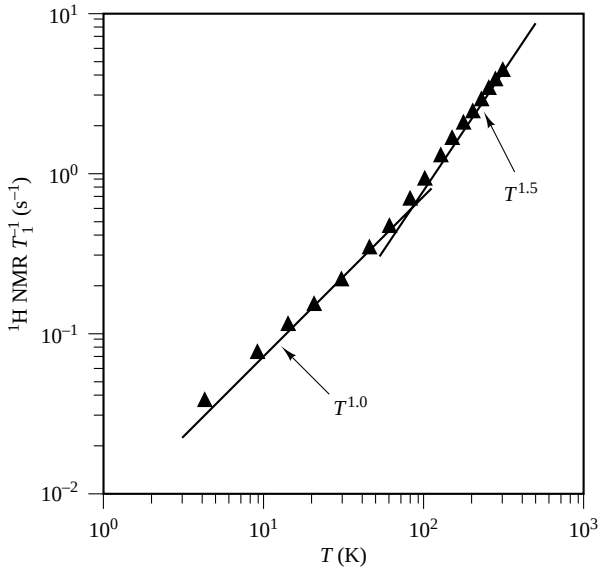

Figure 5 Temperature dependence of ^{1}H NMR ${T_1}^{-1}$ in $[CH(Br_3^-)_{0.15}]_x$ at 50.5 MHz

bent curve as shown in Figure 5. To confirm the origin of this behavior new samples were prepared where bromine atoms were substituted or added to polyacetylene chains. Their ${T_1}^{-1}$ showed the same behavior as in Figure 5. The frequency dependence obeyed a $\omega^{-1/2}$ law as shown in Figure 6. This result shows that the aging is due to the substitutional or additional effect of bromine. The reason why the metallic behavior was observed only for Br_3 as dopant is that the ${T_1}^{-1}$ due to the residual spins was reduced by bromine substitution or addition, and that the metallic ${T_1}^{-1}$ was instead enhanced by the reduction of conductivity. The bent curve in Figure 5 is reasonably accounted for by the one-dimensional metallic diffusive motion. The $T^{1.5}$ asymptotic line at high temperatures corresponds to T-linear resistivity due to phonon scattering. With the observed Pauli susceptibility $\chi_p \simeq 3.0 \times 10^{-6}$ emu mol^{-1} C, the conductivity at room temperature was calculated to be 2.5×10^3 S cm^{-1}.

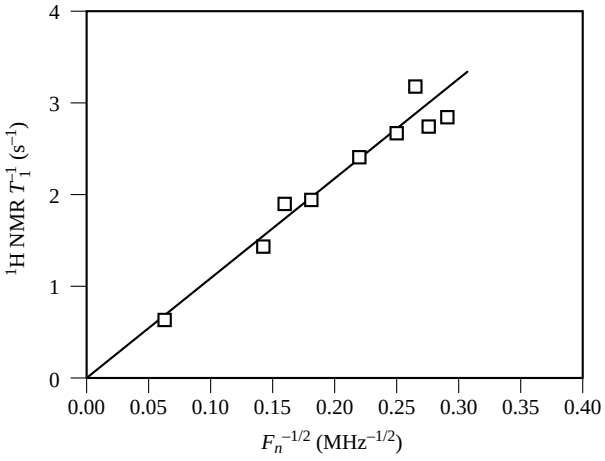

Figure 6 Frequency dependence of ^{1}H NMR ${T_1}^{-1}$ in $[CH_{0.91}Br_{0.11}(Br_3^-)_{0.041}]_x$ at 200 K

4 REFERENCES

1. T. C. Clarke, and J. C. Scott, in *Handbook of Conducting Polymers*, ed. T. A. Skotheim, Marcel Dekker, New York, 1986, Vol. 2, p. 1127
2. P. K. Kahol, G. C. Clark, and M. Mehring, in *Conjugated Conducting Polymers (Springer Series in Solid-State Science)*, ed. H. Kiess, Springer, Berlin, 1992, Vol. 102, p. 217.
3. T. Terao, S. Maeda, T. Yamabe, K. Akagi, and H. Shirakawa, *Chem. Phys. Lett.*, 1984, **103**, 347.
4. A. Manenschijn, M. J. Duijvestijn, J. Smidt, R. A. Wind, C. S. Yannoni, and T. C. Clarke, *Chem. Phys. Lett.*, 1984, **112**, 99.
5. M. J. Duijvestijn, A. Manenschijn, J. Smidt, and R. A. Wind, *J. Magn. Reson.*, 1985, **64**, 461.
6. T. Nakai, T. Terao, and H. Shirakawa, *Chem. Phys. Lett.*, 1988, **145**, 90.
7. R. A. Wind, M. J. Duijvestijn, and J. Vriend, *Solid State Commun.*, 1985, **56**, 713.
8. C. S. Yannoni and T. C. Clarke, *Phys. Rev. Lett.*, 1983, **51**, 1191.
9. W. P. Su, J. R. Schrieffer, and A. J. Heeger, *Phys. Rev. B*, 1980, **22**, 2099.
10. S. Kuroda and H. Shirakawa, *J. Phys. Soc. Jpn.*, 1992, **61**, 2930.
11. H. Thomann, L. R. Dalton, M. Grabowski, and T. C. Clarke, *Phys. Rev. B*, 1985, **31**, 3141.
12. M. Mehirng, A. Grupp, P. Hofer, and H. Kass, *Synth. Metals*, 1989, **28**, D399.
13. M. Nechtschein, F. Devreux, R. L. Greene, T. C. Clarke, and G. B. Street, *Phys. Rev. Lett.*, 1980, **44**, 356.
14. K. Kume and K. Mizoguchi, *Prog. Theor. Phys. Suppl.*, 1993, **113**, 91; K. Mizoguchi, S. Masubuchi, K. Kume, K. Akagi, and H. Shirakawa, *Phys. Rev. B*, 1995, **51**, 8664.
15. K. Kume, K. Mizuno, K. Mizoguchi, K. Nomura, J. Tanaka, M. Tanaka, and H. Fujimoto, *Mol. Cryst. Liq. Cryst.*, 1982, **83**, 99.
16. B. R. Weingerger, E. Ehrenfreund, A. Pron, A. J. Heeger, and A.G. MacDiarmid, *J. Chem. Phys.*, 1980, **72**, 4749.
17. W. G. Clarke, K. Glover, G. Mozurkewich, S. Etemad, and M. Maxfield, *Mol. Cryst. Liq. Cryst.*, 1985, **117**, 447.
18. K. Ishida, K. Nagamine, T. Matsuzaki, Y. Kuno, T. Yamazaki, E. Torikai, H. Shirakawa, and J. H. Brewer, *Phys. Rev. Lett.*, 1985, **55**, 2009.
19. Y. Wada, *Prog. Theor. Phys. Suppl.*, 1993, **113**, 1.
20. P. K. Kahol, M. Mehring, and X. Wu, *J. de Physique*, 1985, **46**, 1683.
21. T. Terao, S. Maeda, T. Yamabe, K. Akagi, and H. Shirakawa, *Solid State Commun.*, 1984, **49**, 829.
22. M. Sasai and H. Fukutome, *Solid State Commun.*, 1984, **51**, 609.
23. L. M. Tolbert and M. E. Ogle, *Mol. Cryst. Liq. Cryst.*, 1990, **189**, 279.
24. A. U. Kon and I. A. Misurkin, *J. Struct. Chem.*, 1989, **30**, 480.
25. A. Vainrub, I. Heinmaa, E. Lippmaa, and G. I. Kozub, *Synth. Metals*, 1993, **55**, 660.
26. P. Bernier, K. Zniber, F. Rachdi, H. Bleier, and C. Fite, in *Springer Series in Solid State Science*, ed. H. Kuzmany, M. Mehring, and S. Roth, Springer, Berlin, 1989, Vol. 91, p. 193.
27. F. Shimizu, K. Mizoguchi, S. Masubuchi, and K. Kume, *Synth. Metals*, 1995, **69**, 43.
28. K. Kume, K. Mizuno, K. Mizoguchi, K. Nomura, H. Takayama, S. Ishihara, J. Tanaka, M. Tanaka, H. Fujimoto, and H. Shirakawa, *J. de Physique*, 1983, **44**, C3-353.

Biographical Sketches

Takehiko Terao. *b* 1941. B.S., 1966, Ph.D., 1973, Physics, Kyoto University, Japan, where he was introduced to NMR by Tsuneo Hashi. Faculty of Science, Kyoto Sangyo University, 1971–75. Department of Chemistry, Faculty of Science, Kyoto University, 1975–present. Research specialty: solid state NMR and its applications in the chemistry of materials.

Kiyoshi Kume. *b* 1933. B.S., 1955, Ph.D., 1960, Physics, University of Tokyo. The Institute for Solid State Physics, University of Tokyo, 1960–65. Department of Physics, Faculty of Science, Tokyo Metropolitan University, 1965–present. Research specialty: NMR and ESR studies in solid state physics.

Coupled Spin Relaxation in Polymers

Michael M. Fuson
Denison University, Granville, OH, USA

1	Introduction	1
2	Spin–Lattice Relaxation of $^{13}CH_2$	1
3	Obtaining Motional Information from Coupled Spin Relaxation Data	2
4	Experimental Methods for Polymer Studies	3
5	Results from Polymer Studies	4
6	Related Articles	6
7	References	6

1 INTRODUCTION

Coupled spin relaxation is the generally accepted term for the spin–lattice relaxation of a scalar-coupled spin system such as a ^{13}C-containing methylene group, $^{13}CH_2$. It is a powerful method to probe motional dynamics in solution, particularly in molecules with internal motions such as polymers.

Nuclear spin relaxation was recognized as a powerful probe of motional dynamics since the observation of unexpectedly sharp resonance lines in liquids in the early days of magnetic resonance spectroscopy in the 1940s. These phenomena were explained almost immediately in terms of the effect of thermal motion by Bloembergen, Purcell, and Pound.[1] This sensitivity to motion has its basis in the fact that the energy of a spin state in a static magnetic field usually depends on an orientation, whether it is the orientation of a chemical shift tensor or a dipole–dipole interaction between two spins or a quadrupole coupling tensor. Orientational fluctuations, that is 'motional dynamics', cause fluctuations in the spin energy levels that can couple to each other or the surrounding lattice to produce the various phenomena of spin relaxation. Measurement of spin relaxation times in order to obtain information about dynamics has been widely exploited (see ***Carbon-13 Relaxation Measurements: Organic Chemistry Applications***, etc.).

In the 1960s Woessner, amongst others, recognized the potential of using a series of relaxation interactions that are rigidly oriented relative to each other to obtain information about the anisotropy, or relative rates in different directions, of motion (see ***Brownian Motion and Correlation Times***). The requirement of a series of independent spin systems all oriented rigidly relative to each other in a molecule is a stringent one however, and the method did not receive wide application.

In the 1970s several groups showed that a more productive approach was to use the multiplicity of interactions amongst a *single* spin system of three or more scalar-coupled spins to generate sufficient information to determine the full diffusion tensor of a small molecule[2,3] (see ***Relaxation Processes in Coupled-Spin Systems***). In addition, coupled spin relaxation has the advantage that a three spin system such as $^{13}CH_2$ can be incorporated in a flexible chain and thus provides a powerful probe of internal motion. Application of these techniques to internal dynamics in small molecules has recently been reviewed.[4]

The basis for the method can be summarized briefly. The relaxation of dipolar coupled spins is generally described in terms of autocorrelation spectral densities which are the Fourier transforms of correlation functions relating the orientation of an internuclear dipole to itself at a later time. For multiple coupled spins, for example $^{13}CH_2$, a complete description of the relaxation also includes cross-correlation terms between *pairs* of dipolar vectors. The traditional approach has been to regard these as unimportant and, using our example, to decouple the ^{1}H spins to enhance the ^{13}C sensitivity. Invariably, the proton-decoupled methylene ^{13}C spin will relax with an 'effective' single exponential recovery law as the multiple exponential relaxation behavior of the coupled spins is obscured with the collapse of the proton-induced multiplet under decoupling.

Study of the fully coupled multiplets provides significant additional information. For a methylene group, four independent spectral densities are required to describe the relaxation, even in the extreme narrowing limit. These can be used to calculate four correlation times describing reorientation of the x, y, and z axes of a molecule fixed reference frame.

This article describes the application of coupled spin relaxation to the reorientational dynamics of polymer chains in solution. These dynamics have been of considerable interest in recent years. Technologically important properties such as elasticity, phase transition temperatures, and solution and melt viscosities are thought to be correlated with molecular motion.[5] Thus, understanding the relationship between chain structure and chain motion is an important factor in predicting polymer properties.

Spin–lattice relaxation has been widely used to investigate such systems and, typically, in these studies the ^{1}H or ^{13}C T_1 values of the polymer are studied as a function of temperature and/or field strength. The results are then fitted to expressions derived from the theoretical models. Discrimination between models has been difficult, however. While experiments such as those described are very sensitive to the motional *timescales*, they lack descriptive details of the *geometry* of motion. This latter information is often needed to discriminate one model from another and can be provided by coupled spin relaxation methods.

In addition, computer simulations of the dynamics of simple polymers are now practical. Recent simulations of chain dynamics have included studies of polyethylene (PE), polyisoprene, and poly(ethylene oxide) (PEO).[6] The Cartesian correlation times (described below) calculated from coupled spin relaxation measurements can be obtained directly from such simulated dynamics trajectories.

Coupled spin relaxation methods have now been applied to a series of linear polymers, most notably polyoxides. In the following, the theory and methods used in these studies are described and recent results are then summarized. The results show quite strikingly the dependence of dynamic properties on chain structure.

2 SPIN–LATTICE RELAXATION OF $^{13}CH_2$

As noted above, the $^{13}CH_2$ spin system makes an excellent probe of chain dynamics. The relative positions of the nuclei

in the methylene group are independent of the orientation or rotational state of the chain. Spin relaxation of the group then depends on its overall reorientation, not the motion of the three nuclei relative to each other. Dipole–dipole interactions among the ^{13}C and ^{1}H spins are sufficiently strong that they are the dominant relaxation mechanisms under most circumstances. These characteristics make the spin relaxation behavior itself relatively simple to interpret. In addition, there are experimental advantages to this spin system. The coupled spin relaxation can be characterized entirely from observing the ^{1}H coupled ^{13}C multiplet and individual ^{13}C signals are often easily resolved, even in complex samples. The ability to excite ^{13}C and ^{1}H spins separately makes it possible to dispense with most selective excitation experiments.

Relaxation in scalar-coupled spin systems has been described using Bloch–Redfield theory and then recasting the density matrix in terms of 'magnetization modes'. A full description is given elsewhere and will not be repeated here except to summarize pertinent details (see ***Relaxation Processes in Coupled-Spin Systems*** and ***Relaxation Mechanisms: Magnetization Modes***).

An energy level diagram for the AX_2 spin system (of which $^{13}CH_2$ is an example) is given in Figure 1. Application of Bloch–Redfield theory to the AX_2 spin system in the eigenstate representation yields an expression for the time evolution of the populations of the various states, N_κ,

$$\frac{\mathrm{d}\boldsymbol{N}}{\mathrm{d}t} = \mathbf{W}[\boldsymbol{N} - \boldsymbol{N}(\infty)] \tag{1}$$

where the elements of $\boldsymbol{N}$ are the diagonal members of the spin density matrix: $N_\kappa = \sigma_{\kappa\kappa} = \langle\kappa|\hat{\sigma}|\kappa\rangle$. The elements of the matrix $\mathbf{W}$ are a subset of the full Redfield matrix, $W_{\kappa\lambda} = R_{\kappa\kappa\lambda\lambda}$, and may be considered as simple transition probabilities.

For convenience magnetization modes, ν, corresponding to a maximum number of observables are constructed by taking linear combinations of the diagonal density matrix elements. Thus

$$\nu_\kappa = \sum_\lambda T_{\kappa\lambda} N_\lambda \quad \text{or} \quad \boldsymbol{\nu} = \mathbf{T}\boldsymbol{N} \tag{2}$$

where $T_{\kappa\lambda}$ are the elements of the transformation matrix. If $\mathbf{\Gamma} = \mathbf{TWT}^{-1}$, then

$$\frac{\mathrm{d}\boldsymbol{\nu}}{\mathrm{d}t} = \mathbf{\Gamma}[\boldsymbol{\nu} - \boldsymbol{\nu}(\infty)] \tag{3}$$

As line intensities depend on the difference between diagonal density matrix elements, the magnetization modes can also be expressed as combinations of line intensities. The members of a convenient set of modes for the AX_2 spin system which are observable in isotropic solution are:

$$\left.\begin{aligned}
{}^{\mathrm{a}}\nu_{\mathrm{A}} &= \tfrac{1}{k_{\mathrm{A}}}(L_1 + L_2 + L_3) \\
{}^{\mathrm{a}}\nu_{\mathrm{X}} &= \tfrac{1}{k_{\mathrm{X}}}(L_4 + L_5) \\
{}^{\mathrm{a}}\nu_{+-+} &= \tfrac{1}{k_{\mathrm{A}}}(L_1 - L_2 + L_3) \\
{}^{\mathrm{a}}\nu_{\pm\mp} &= \tfrac{1}{k_{\mathrm{X}}}(L'_4 - L''_4 - L'_5 + L''_5) \\
&= \tfrac{1}{k_{\mathrm{A}}}(L_1 - 2L'_2 + L_3) \\
{}^{\mathrm{s}}\nu_{+0-} &= \tfrac{1}{k_{\mathrm{A}}}(L_1 - L_3) = \tfrac{1}{k_{\mathrm{X}}}(L_4 - L_5)
\end{aligned}\right\} \tag{4}$$

where line labels are given in Figure 1 and k_{A} and k_{X} are scaling factors. The quantities ${}^{\mathrm{a}}\nu_{\mathrm{A}}$, ${}^{\mathrm{a}}\nu_{+-+}$, and ${}^{\mathrm{s}}\nu_{+0-}$ are all directly observable from the A spectrum (^{13}C in a $^{13}CH_2$ study). The quantity ${}^{\mathrm{a}}\nu_{\mathrm{A}}$ is proportional to the the sum of the intensities of all the lines in the A multiplet. The quantity ${}^{\mathrm{a}}\nu_{+-+}$ is proportional to the difference between the intensities of the outer and inner lines of the multiplet, while ${}^{\mathrm{s}}\nu_{+0-}$ is related to the difference between the two outer lines of the multiplet. The quantity ${}^{\mathrm{a}}\nu_{\mathrm{X}}$ is simply the total X (^{1}H) magnetization. Application of a 90° X pulse simultaneous with an observe pulse on the A spins exchanges triplet intensities in the A manifold and allows, by difference, evaluation of ${}^{\mathrm{a}}\nu_{\pm\pm}$.

The elements of the relaxation matrix, $\mathbf{\Gamma}$, are made up of linear combinations of spectral densities arising from the interactions important in the system under study. These might include dipole–dipole, chemical shift anisotropy, spin rotation, and random field interactions among others. The relaxation matrix for the AX_2 spin system including only contributions from dipole–dipole and random field interactions and corresponding to the set of magnetization modes used here is given in full elsewhere.[4]

In the limit of extreme narrowing, the dipolar relaxation of an AX_2 or $^{13}CH_2$ spin system is completely described by four frequency-independent spectral densities. Two of these are autocorrelation terms related to the CH or HH′ internuclear vectors (J_{CH} and J_{HH}). The others are cross-correlation terms relating one CH vector to the other (J_{HCH}) or to the HH′ vector (J_{CHH}). A complete set of random field spectral densities would include an autocorrelation term at the carbon (j_{C}), an autocorrelation term at each hydrogen (j_{H}), and a cross-correlation term between the two hydrogens (j_{HH}).

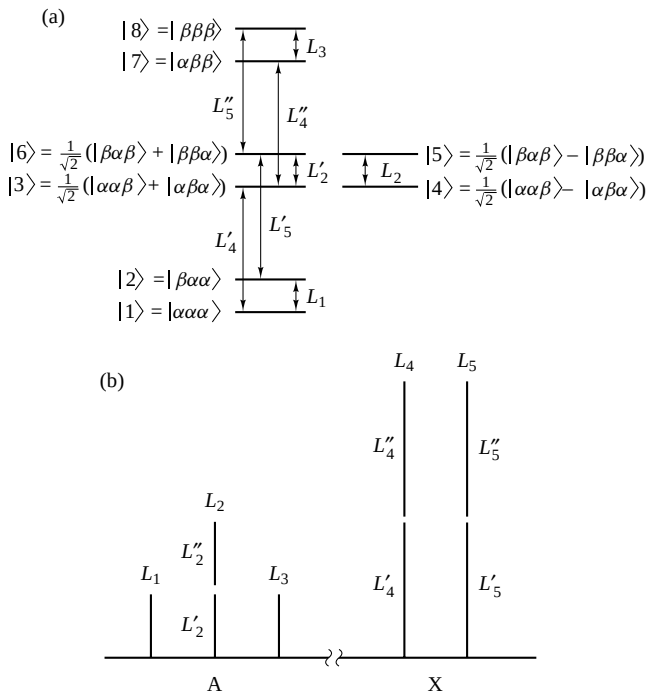

Figure 1 (a) The energy level diagram and eigenstates of the static Hamiltonian, $\hat{\mathcal{H}}_0$, for an AX_2 spin system. The first label gives the state of the A spin and subsequent labels the states of the two X spins. Allowed single quantum transitions are labeled. (b) A schematic diagram of the AX_2 spectrum in isotropic solution

3 OBTAINING MOTIONAL INFORMATION FROM COUPLED SPIN RELAXATION DATA

As noted above, the spectral densities are the Fourier transforms of correlation functions relating the orientation of an internuclear dipole to a second dipole at a later time. In the simplest case, these correlation functions decay as simple exponentials which can be characterized by a correlation time, τ_c. The value of the spectral density then depends on the magnitude of τ_c and the frequency at which it is sampled. When the dynamics are more complex, the correlation function can be a complex sum of exponentials with various time constants. The resulting spectral densities do not reflect the values of these time constants in any simple way.

Two general approaches to this problem have been established. One is to sample a spectral density function at a range of frequencies, perhaps by performing conventional T_1 experiments at several field strengths. This is often effective in enabling the investigator to estimate the timescales involved in a dynamic process, but is less effective in establishing the associated geometrical factors. The other approach, embodied in the coupled spin relaxation experiment, is to sample a wider variety of spectral density functions. The ratios of the different spectral densities at a given frequency are often a sensitive function of the geometry of the motion.

It remains to establish the relationship between the measured spectral densities and appropriate motional parameters. Again, two approaches have been used. The first, dating to the very first use of spin relaxation to elucidate dynamic parameters, is to assume a particular motional model and then calculate the associated correlation function and, by taking the Fourier transform, spectral density function. The assumption of diffusive isotropic motion, which leads to an exponential correlation function and a Lorentzian spectral density function, is the classic example of this approach, but it has also been applied to much more complex models.

A second approach that has been used recently is to take the four spectral densities measured in the coupled spin relaxation experiment (J_{CH}, J_{HH}, J_{HCH}, and J_{CHH}) and to reexpress them in terms of four autocorrelated Cartesian spectral densities, which are in turn simply related to four correlation times (τ_{xx}, τ_{yy}, τ_{zz}, and τ_{xy}).[7] These transformations are model-independent and are extremely useful in several ways. First, the difficulty of interpreting cross-correlation functions is removed. Second, the results are presented in a molecule fixed Cartesian axis system commonly used in dynamics simulations (see Figure 2) and are readily interpretable. The correlation times describe the reorientation of geometrical constructs having the shape of d orbitals. Thus τ_{xx} represents the motion of a d_0 construct fixed on the x axis or the bisector of the HCH angle. Lastly, it should be emphasized that in the transformation to this basis no biases or assumptions about the dynamical behavior of the molecule are introduced, as are encountered in using diffusional models.

As will be discussed below, in spin relaxation studies of unlabeled polymers it is difficult to determine J_{HH} reliably. Under these circumstances some assumption must be made in order accomplish the transformation. A reasonable assumption is to set τ_{xx} and τ_{yy} equal to each other and defining a $\tau_\perp$ term. The quantities τ_{xx} and τ_{yy} have been shown to be very similar in value in simulations of flexible chains.

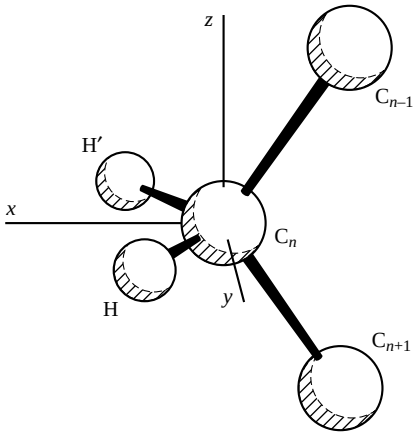

Figure 2 Orientation of the Cartesian axis system in the frame of reference of the methylene group

Reduced spectral densities are defined as

$$\hat{J}_{ijkl} = \frac{20}{9K_{ijkl}} J_{ijkl}(\omega = 0) \tag{5}$$

where $K_{ijkl} = \gamma_i\gamma_j\gamma_k\gamma_l h^2/r_{ij}^3 r_{kl}^3$ and i, j, k, and l represent the spins involved. If the reduced autocorrelation spectral densities $\hat{J}_{xx}$ and $\hat{J}_{yy}$ are set equal to each other than it can be shown:

$$\left.\begin{aligned} \tau_\perp = \tau_{xx} = \tau_{yy} &= \tfrac{3}{4(\alpha^4-\beta^4)}(\hat{J}_{AX} + \hat{J}_{XAX} - 4\beta^2\hat{J}_{AXX}) \\ \tau_\parallel = \tau_{zz} &= \tfrac{3}{2\alpha^2}(\hat{J}_{AX} + \hat{J}_{XAX} - (2-4\beta^2)\hat{J}_{AXX}) \\ \tau_{xy} &= \tfrac{1}{4\alpha^2\beta^2}(\hat{J}_{AX} - \hat{J}_{XAX}) \end{aligned}\right\} \tag{6}$$

where $\alpha = \cos(\theta/2)$, $\beta = \sin(\theta/2)$, and θ = HCH angle.

4 EXPERIMENTAL METHODS FOR POLYMER STUDIES

Spectroscopic samples are typically 1% w/v polymer in good solvents. Samples are degassed either by flushing the solvent with dry nitrogen and then assembling and sealing the sample under nitrogen, or by subjecting the sample to five freeze–pump–thaw cycles and then sealing under vacuum.

Spin relaxation measurements use variations on the inversion recovery pulse sequence. Four different initial perturbations of the coupled $^{13}CH_2$ spin system are used: (1) a ^{13}C 180° pulse inverting the ^{13}C triplet; (2) a ^1H 180° pulse inverting the proton doublet; (3) a low power ^1H pulse inverting only the low-frequency line of the ^1H doublet; and (4) a J pulse preparation on the ^1H magnetization (resembling a spin echo) resulting in the inversion of the outer lines of the ^{13}C triplet. In each case the initial perturbation of the spin system is followed by a variable delay period and a ^{13}C sampling pulse as in a normal inversion recovery experiment. For each experiment 17 or 18 different delay times are used. The delay times are ordered randomly to reduce systematic errors. Recycle delays are adjusted to be at least 10-times the nominal T_1 value of the sample.

FIDs are subjected to appropriate exponential multiplication before Fourier transformation. Line amplitudes are then obtained, typically after applying a linear baseline correction over a 500 Hz region centered on the appropriate ^{13}C multiplet. Relaxation parameters are obtained from a multiparameter least squares curve fitting routine using an implementation of the Levenberg–Marquardt algorithm. Theoretical values of the intensities of the modes are calculated first using the normalized, symmetric set of modes described by Werbelow and Grant[8] and then taking appropriate linear combinations to generate the modes described here. Parameters for the fit include not only dipolar and random field spectral densities, but also several experimental parameters.[9] To account for any systematic instrumental imperfections or differences in widths of inner and outer lines of the multiplet, the line amplitudes for each data set are scaled by two parameters β and δ such that the ^{13}C multiplet has the expected 1:2:1 intensity ratio when fully relaxed. The term L_3 (see Figure 1) is multiplied by δ to equalize the outer line intensities and then both outer lines are multiplied by β to equalize the intensities of the sum of the outer lines and the inner line of the multiplet. A third parameter associated with each data set is a normalization constant such that $^{a}\nu_c(\infty)$ is scaled to unity. Additional parameters are pulse efficiencies and differential pulse efficiencies.

Spectral densities included in the fit include four frequency independent spectral densities describing the dipolar relaxation of a methylene group ($^{13}CH_2$) in the limit of extreme narrowing (J_{CH}, J_{HH}, J_{HCH}, and J_{CHH}). Random field spectral densities are also included to account for other relaxation mechanisms operating in the sample, primarily remote dipolar interactions. For the methylene spin system, a complete set of random field spectral densities would include an autocorrelation term at the carbon (j_C), an autocorrelation term at each hydrogen (j_H), and a cross correlation term between the two hydrogens ($j_{HH'}$). At high fields or in a more anisotropic electronic environment caused by insertion of an oxygen into the polymer chain, cross correlation between chemical shift anisotropy (CSA) and dipolar relaxation mechanisms is possible. Where appropriate, this requires inclusion of four more spectral densities in the fit: $J_{CH,C}$, the cross term between the CH dipolar interaction and the carbon CSA; $J_{CH,H}$, the cross term between the CH dipolar interaction and the proton CSA; $K_{CH,H'}$, the cross term between the CH dipolar interaction and the CSA on the other proton (H′); and finally $J_{HH,H}$, the cross term between the HH dipolar interaction and the proton CSA.[10]

Rigorous characterization of dipolar interactions as random fields requires that both the rotational and translational motion of the interacting spins be independent. This independence of motion is not satisfied for protons bonded to carbons adjacent to the methylene group of interest. A study of isotopomers of 5-^{13}C nonane has shown that inclusion of random field terms in the relaxation matrix is not enough to allow accurate measurement of all four dipolar spectral densities in the presence of protons on neighboring carbons.[9] However, that study showed that as long as the random field term j_C is held equal to zero in the fitting procedure, then J_{CH}, J_{HCH}, and J_{CHH} may be reliably evaluated; J_{HH} remains strongly correlated to j_H. The results reported here follow this practice.

5 RESULTS FROM POLYMER STUDIES

These methods have been applied to a series of homologous polyethers with increasing numbers of methylenes between the oxygens: poly(oxymethylene) (POM),[11] poly(ethylene oxide) (PEO),[12] and poly(tetramethylene oxide) (PTMO),[12] and to poly(*cis*-1,4-butadiene) (CBD).[13] In the absence of data on polyethylene, CBD serves as a model for the dynamics of the infinite polymethylene chain. Recent simulations of polyethylene and polyisoprene suggest the dynamics are quite similar despite the structural differences and justify this analogy.[6] Data from the smaller hydrocarbon [11-^{13}C]heneicosane are also included for comparison.[14] These polymers exhibit a wide range of equilibrium conformations with POM most stable in a helical conformation and CBD in an extended, all-*trans* conformation. PEO and PTMO are more flexible and intermediate in conformational preferences. As such they provide an interesting opportunity to probe the impact of chain conformation on dynamics with only minimal variations in structure.

Each of the polymers studied has a single type of methylene group, except for PTMO which has two distinct types of methylene groups with the carbons adjacent to the oxygen (C-α) absorbing at 67.4 ppm and the central carbons (C-β) absorbing at 25.3 ppm. Only POM and heneicosane were isotopically labeled to provide truly isolated $^{13}CH_2$ spin systems.

Three 'magnetization nodes' of each $^{13}CH_2$ spin system can be obtained while observing only the ^{1}H coupled ^{13}C spectrum of a given polymer: $^{a}\nu_C$, the total ^{13}C magnetization; $^{a}\nu_{+-+}$, the difference between the inner and outer line intensities of the ^{13}C triplet; and $^{s}\nu_{+0-}$, the difference between the intensities of the outer two lines of the ^{13}C triplet. Figure 3 shows typical relaxation curves for C-α of PTMO.

The three dipolar spectral densities which have been reliably evaluated in all cases can be reexpressed in terms of three second rank autocorrelation times ($\tau_\perp = \tau_{xx} = \tau_{yy}$, τ_{zz}, and τ_{xy}). The transformation to Cartesian correlation times requires that the geometry of the spin system be known. In most cases these geometries must be inferred from small molecule analogs. As hydrogens are not located accurately in most X-ray diffraction studies, it is generally necessary to rely on other structural techniques such as electron or neutron diffraction. For methylenes in hydrocarbon chains, electron diffraction studies of small alkanes provide the HCH angle of 108.5° and a CH distance of 1.12 Å. For protons bonded to carbons adjacent to oxygen, the value of 1.11 Å for the CH distance given by the electron diffraction study of the small molecule analog 1,2-dimethoxyethane has been adopted. The HCH angle was not determined in that study. The Cartesian correlation times calculated using these parameters are given in Table 1. Uncertainties reported are standard errors in the last significant figure of the associated value.

The timescales of tens of picoseconds reported in Table 1 are consistent with those generally found for local segmental motion of polymers in dilute solution. Because of differences in temperature and viscosity among the samples, comparing the absolute values of the correlation times is not as interesting as comparing ratios of correlation times which gives insight into the anisotropy of motion. Table 2 gives these ratios.

If we examine the anisotropies of motion of the most conformationally distinct polymers, POM and CBD, we see

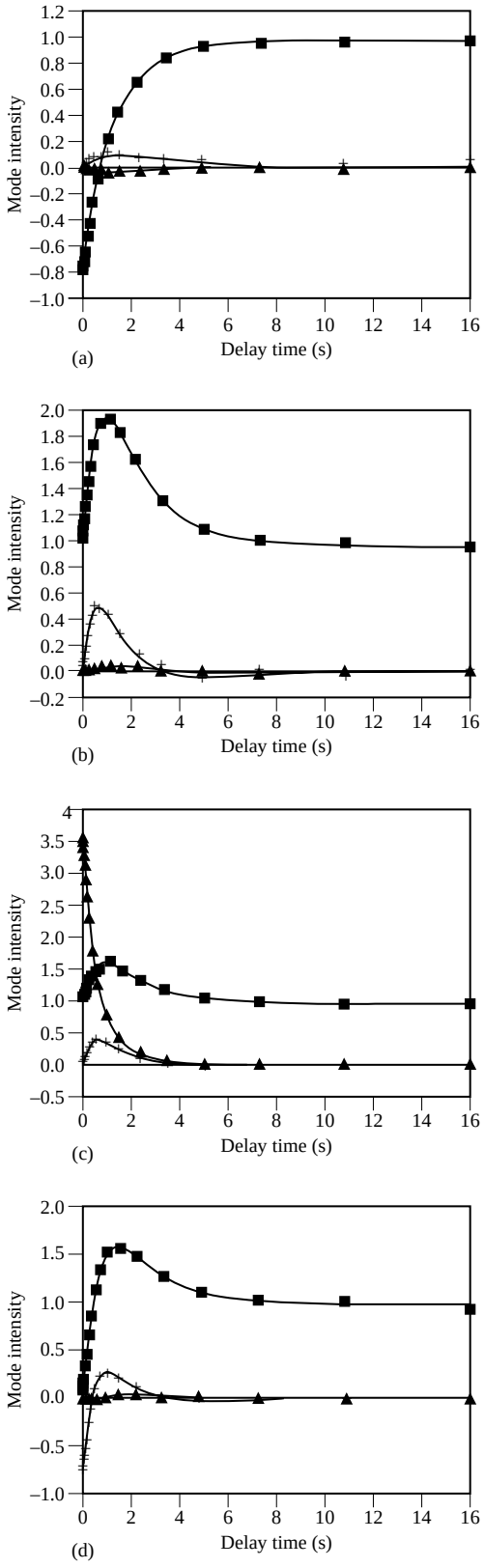

Figure 3 Magnetization mode intensities for C-α of PTMO. Intensity units are defined by setting $^{a}\nu_{C}$ (∞) to unity. Experimental values for $^{a}\nu_{C}$, ■; experimental values for $^{a}\nu_{+-+}$, +; experimental values for $^{s}\nu_{+0-}$, ▲. Solid lines are calculated from fitted parameters. (a) After ^{13}C inversion. (b) After ^{1}H inversion. (c) After selective inversion of one line of the ^{1}H doublet. (d) After J pulse preparation of the ^{1}H spins, resulting in ^{1}H inversion and inversion of the outer lines of the ^{13}C multiplet

Table 1 Cartesian Correlation Times of Polymers in Solution

	$\tau_{\perp}$ (ps)	τ_{zz} (ps)	τ_{xy} (ps)
POM (phenol-d_6, 86 °C)	21(1)	36(6)	12.1(8)
PEO (D_2O, 25 °C)	42(9)	115(11)	44(3)
PTMO(C-α) (toluene-d_8, 28 °C)	21(2)	64(3)	10.4(6)
PTMO(C-β) (toluene-d_8, 28 °C)	15(2)	45(2)	15.2(6)
CBD (CD_2Cl_2, 20 °C)	23(2)	55(6)	11(1)
C11-heneicosane (diglyme-d_{14}, 40 °C)	21(1)	48(3)	9(1)

Table 2 Motional Anisotropies of Polymers in Solution

	$\tau_{zz}/\tau_{\perp}$	τ_{zz}/τ_{xy}	$\tau_{\perp}/\tau_{xy}$
POM	1.6	2.6	1.6
PEO	2.7	2.6	1.0
PTMO(C-α)	3.0	6.2	2.0
PTMO(C-β)	3.0	3.0	1.0
poly(*cis*-1,4-butadiene)	2.4	5.0	2.1
C11-heneicosane	2.3	5.1	2.2

that they are quite different. POM has reduced anisotropies of motion compared with CBD methylenes, which in turn have anisotropies of motion which are very similar to those of the central methylene of the smaller hydrocarbon heneicosane. These differences have been interpreted in terms of the relative importance of transitions between rotational isomeric states and librational motion within a given potential energy well in the spin relaxation of these polymers. The lowest energy conformation of POM in solution is predicted to be helical, with no readily available rotational transitions that do not involve major chain translocation. In such a situation it is reasonable to expect librational motion to be an important relaxation mechanism. In CBD the extended chain structure make possible 'crankshaft'-type correlated motions of a few bonds. Supporting the interpretation that these might be important are simulations of hydrocarbon chains which show contributions from both correlated and uncorrelated chain motions. The correlated motions in these simulations have a similar ratio of $\tau_{zz}/\tau_{\perp}$ to that observed for CBD and heneicosane.[15]

New patterns emerge when examining the anisotropies of motion for PEO and PTMO. Overall the pattern for C-α of PTMO is much like those seen previously in hydrocarbons, although with slightly greater anisotropies. PEO and the C-β position of PTMO have very similar anisotropies of a reduced magnitude and a much different pattern from any observed previously. The ratios $\tau_{zz}/\tau_{\perp}$ and τ_{zz}/τ_{xy} are nearly identical and the ratio $\tau_{\perp}/\tau_{xy}$ is essentially unity. The relative anisotropies of C-α and C-β of PTMO are the opposite of what might be naively expected. Based on the similarity of the energetics of conformations involving C-α and its adjacent atoms to those in PEO, and of conformations involving C-β to those in PE, one might expect the opposite result.

Do the differences in dynamics in PEO and PTMO originate at the librational level or in transitions between rotational isomeric states? It is difficult to imagine that the differences in

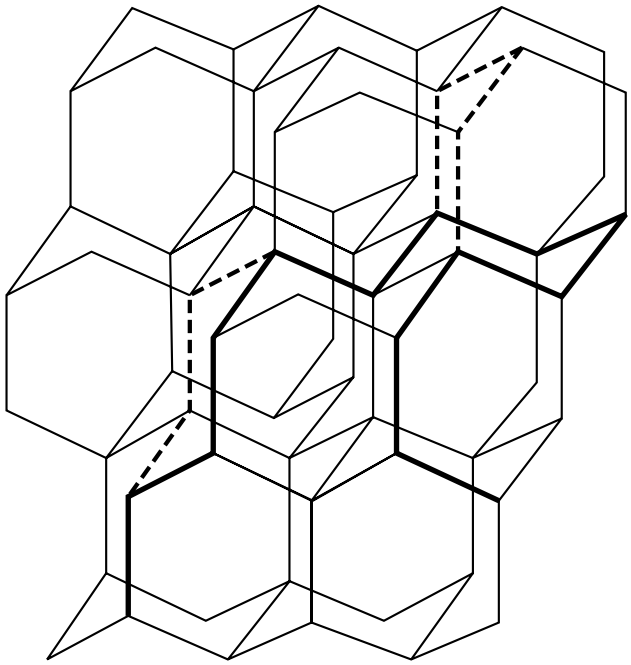

Figure 4 Examples of chain motion on a tetrahedral lattice. An example of three bond motion is at the bottom and of four bond motion is at the top

librational motion between C-α and C-β, adjacent carbons in the PTMO chain, are large enough to give rise to the measured difference in anisotropies. A plausible model does exist for differences in rotational transitions.

Geny and Monnerie have simulated the motion of the various linear polyoxides as motions involving three or four bonds on a tetrahedral lattice.[16] Examples of such motions are shown in Figure 4. The three bond motions are essentially the 'crankshaft'-type motions referred to above. Four bond motions involve the pivoting of a segment back and forth, without the option of continuing around the chain axis. Three bond motions occur in all their simulations of the polyoxides although with markedly less 'efficiency' in POM due to the stability of its helical form. Four bond motions such as shown are forbidden in PE due to the 'pentane effect' (which rules out g^+g^- sequences because of steric interactions of the hydrogens on carbon i and i + 4 along the chain). In the polyoxides these motions are allowed as long as at least one oxygen atom is at the 'foot' of the pivoting segment. Geny and Monnerie found these motions even more common than three bond motions in PEO, significant in PTMO, and again rarely observed in POM.

Of course, full recognition must be given to the limitations of the model of the polymer chain as moving on a tetrahedral lattice. In this model all motions must be cooperative, in the sense that any configurational transition is accompanied by compensatory transitions elsewhere in order not to force large motions of the chain. In contrast, Brownian dynamics simulations of the PE chain showed that at least two-thirds of the configurational transitions in PE were 'isolated' rotations about bonds along the chain accompanied by orientational relaxation of neighboring segments. Simulations of polyisoprene suggest that three bond motions are largely absent in polyisoprene. Furthermore, analysis of the motion in isolated configurational transitions and in 'three bond motions' in PE finds them to be nearly identical, leading into question the importance of cooperative motions in analyzing polymer dynamics.

Even so, the reduced anisotropy of PEO relative to the hydrocarbons may be due to the combination of three- and four-bond motions available to the former. In particular, the ratio $\tau_\perp/\tau_{xy}$ becomes unity only when there is efficient averaging with respect to the z axis of the coordinate system we have defined. Remembering that the z axis is perpendicular to the HCH plane or parallel to the vector between adjacent atoms on either side of the methylene along the polymer chain, efficient averaging around this axis occurs whenever the methylene is located at the 'point' of the four bond section which is pivoting.

The results for PTMO may then be explained by noting that only C-β can be at the 'point' of the pivoting section when there is an oxygen at the 'foot', making the four bond motion possible. The motion of a methylene at the 'side' of the four bond segment is similar to that caused by a three bond motion and thus although PTMO as a whole appears to undergo three and four bond motions, C-α can only experience 'three bond like' motion and thus is very similar in anisotropy to hydrocarbons studied previously. Thus while four bond motions may be minor components of the overall dynamics, by introducing a distinctly different reorientational motion they may have an apparently disproportionate impact on the measured anisotropy. A more complete analysis of the importance of these motions must await more realistic simulations of the polyoxide chains. A molecular dynamics simulation of PEO in water has been published recently, but it was on a fairly short chain (13 units) and the question of cooperative transitions was not addressed.

6 RELATED ARTICLES

Brownian Motion and Correlation Times; Carbon-13 Relaxation Measurements: Organic Chemistry Applications; Protein Dynamics from NMR Relaxation; Relaxation Mechanisms: Magnetization Modes; Relaxation Processes in Coupled-Spin Systems; Relaxation Processes: Cross Correlation and Interference Terms; Relaxation Theory: Density Matrix Formulation

7 REFERENCES

1. N. Bloembergen, E. M. Purcell, and R. V. Pound, *Phys. Rev.*, 1948, **73**, 679.
2. L. G. Werbelow and D. M. Grant, *Adv. Magn. Reson.*, 1977, **9**, 189.
3. R. L. Vold and R. R. Vold, *Prog. Nucl. Magn. Reson. Spectrosc.*, 1978, **12**, 79.
4. D. M. Grant, C. L. Mayne, F. Liu, and T.-X. Xiang, *Chem. Rev.*, 1991, **91**, 1591.
5. L. Monnerie, *Makromol. Chem., Macromol. Symp.*, 1991, **48–49**, 125.
6. M. D. Ediger and D. B. Adolf, *Adv. Polym. Sci.*, 1994, **116**, 73.
7. M. M. Fuson, M. S. Brown, D. M. Grant, and G. T. Evans, *J. Am. Chem. Soc.*, 1985, **107**, 6695.
8. L. G. Werbelow and D. M. Grant, *J. Chem. Phys.*, 1976, **63**, 544.
9. M. M. Fuson and A. M. Belu, *J. Magn. Reson., Ser. A*, 1994, **107**, 1.

10. Z. Zheng, C. L. Mayne, and D. M. Grant, *J. Magn. Reson., Ser. A,* 1993, **103**, 268.
11. M. M. Fuson and D. M. Grant, *Macromolecules*, 1991, **24**, 2594.
12. M. M. Fuson and J. B. Miller, *Macromolecules*, 1993, **26**, 3218.
13. M. M. Fuson and D. M. Grant, *Macromolecules*, 1988, **21**, 944.
14. M. S. Brown, D. M. Grant, W. J. Horton, C. L. Mayne, and G. T. Evans, *J. Am. Chem. Soc.*, 1985, **107**, 6698.
15. T. A. Weber and E. Helfand, *J. Chem. Phys.*, 1983, **78**, 2881.
16. F. Geny and L. Monnerie, *J. Polym. Sci., Polym. Phys. Ed.*, 1979, **17**, 131, 147, 173.

Biographical Sketch

Michael M. Fuson. *b* 1954. B.A., 1976, Haverford, Ph.D., 1982, Yale (supervisor J. H. Prestegard). Postdoctoral studies at the University of Utah (with D. M. Grant). Faculty in Chemistry at Wabash College (1984–89) and Denison University (1989–present). Approx. 10 publications. Research interests: coupled spin relaxation and molecular motion in macromolecules.

Polymer Blends: Miscibility Studies

Wiebren S. Veeman

Gerhard-Mercator-Universität Duisburg, Germany

1	Introduction	1
2	Polymer Blends	1
3	The Dipolar Interaction	1
4	Short-Range Techniques	1
5	Long-Range Techniques	5
6	Other NMR Methods	7
7	Related Articles	8
8	References	8

1 INTRODUCTION

Most industrially important organic polymer materials are multicomponent systems, like polymer blends (mixture of two polymers) and polymer composites (consisting of a polymer and a filler, usually inorganic, such as silica or talcum). The macroscopic properties of such materials are determined not only by the molecular properties of the polymers, but also by the miscibility, morphology, and structure of the interfaces between the various components. By choosing the right components and controlling the adhesion between them in the interfaces, materials with optimal macroscopic properties can be prepared. Solid state NMR is well suited for studying the microscopic structure of heterogeneous polymer materials, although its inherent low sensitivity is often a limitation, particularly for the study of the interfacial region between the components when they form large domains.

In this article, we shall discuss various solid state NMR techniques that can be used to study the miscibility of and domain sizes in polymer blends.

2 POLYMER BLENDS

In many practical instances, the critical property that is used to classify a polymer blend as miscible or not miscible is the glass transition temperature T_g. A blend with one T_g, in between those of the pure components, is usually classified as miscible and described as a mixed, single-phase material. For a material with a single T_g, it is still possible that domains of the separate components exist. If they do, it is believed that their dimensions are at most 10–20 nm.[1]

Solid state NMR is very well suited for investigating the heterogeneity of polymer blends at the scale below 10–20 nm. As with many other applications of NMR, the enormous freedom and flexibility of the NMR experiment has resulted in many different approaches, each employing specific solid state NMR experiments.

3 THE DIPOLAR INTERACTION

All NMR studies of polymer–polymer miscibility have in common that some NMR parameter of one component that is sensitive to the near presence of another component is measured. Although it does happen that the chemical shift of a nuclear spin in component A is affected by the presence of units of component B, most studies rely in some way on the magnetic interaction between neighboring spin dipoles, that is, the dipolar interaction.

For two spins with angular momentum operators $\hat{\boldsymbol{I}}_1$ and $\hat{\boldsymbol{I}}_2$ and internuclear vector $\boldsymbol{r}_{12}$, the dipolar interaction can be written in the form[2]

$$\hat{\mathcal{H}}_D = \frac{\gamma^2\hbar^2}{r_{12}^3}\left[\hat{\boldsymbol{I}}_1 \cdot \hat{\boldsymbol{I}}_2 - 3\frac{(\hat{\boldsymbol{I}}_1 \cdot \boldsymbol{r}_{12})(\hat{\boldsymbol{I}}_2 \cdot \boldsymbol{r}_{12})}{r_{12}^2}\right] \tag{1}$$

or as

$$\hat{\mathcal{H}}_D = \frac{\gamma^2\hbar^2}{r_{12}^3}(\hat{A} + \hat{B} + \hat{C} + \hat{D} + \hat{E} + \hat{F}) \tag{2}$$

where

$$\left.\begin{aligned}
\hat{A} &= \hat{I}_{1z}\hat{I}_{2z}(1 - 3\cos^2\theta) \\
\hat{B} &= -\tfrac{1}{4}(\hat{I}_1^+\hat{I}_2^- + \hat{I}_1^-\hat{I}_2^+)(1 - 3\cos^2\theta) \\
\hat{C} &= -\tfrac{3}{2}(\hat{I}_1^+\hat{I}_{2z} + \hat{I}_{1z}\hat{I}_2^+)\sin\theta\cos\theta\,\mathrm{e}^{-\mathrm{i}\phi} \\
\hat{D} &= -\tfrac{3}{2}(\hat{I}_1^-\hat{I}_{2z} + \hat{I}_{1z}\hat{I}_2^-)\sin\theta\cos\theta\,\mathrm{e}^{\mathrm{i}\phi} \\
\hat{E} &= -\tfrac{3}{4}\hat{I}_1^+\hat{I}_2^+\sin^2\theta\,\mathrm{e}^{-2\mathrm{i}\phi} \\
\hat{F} &= -\tfrac{3}{4}\hat{I}_1^-\hat{I}_2^-\sin^2\theta\,\mathrm{e}^{2\mathrm{i}\phi}
\end{aligned}\right\} \tag{3}$$

and the angles θ and ϕ define the internuclear vector in an axis system where the external magnetic field is along the z axis. As a result of this dipolar interaction, in general a spin feels a local field due to the presence of other spins. Because the nuclear magnetic moments are small and the magnitude of this local field decreases sharply (r^{-3}) with the internuclear distance, the presence of a nucleus can be felt over short distances, ranging from a few tenths of nanometer to the order of 10 nm, depending on the technique in question. The NMR methods that we shall discuss are therefore excellently suited for studying the miscibility of polymer blends at a scale below 10 nm.

The various NMR techniques can be distinguished in different ways. Here we divide them into really short-range techniques (up to about 0.6 nm) and techniques that are suitable for studying the miscibility of polymers over distances from 0.6 nm to the order of 10 nm.

4 SHORT-RANGE TECHNIQUES

At least five techniques that have been reported for the study of the miscibility of polymer blends fall into the short-range category. They are based on the use of the chemical shift as a local probe, or employ one of the following (solid state) NMR techniques: cross polarization,[3] the nuclear Overhauser effect (see ***Nuclear Overhauser Effect***), two-dimensional heteronuclear correlation NMR (see ***Heteronuclear Shift Correlation Spectroscopy***), or rotor-driven ^{13}C spin diffusion (see ***Rotating Solids***).

4.1 Short-Range Techniques Based on Carbon-13 Chemical Shifts

The chemical shift of a nucleus is sensitive to the local electron density. When an interaction occurs between the different components in a polymer blend, this may affect the electron density locally near an NMR nucleus and change the chemical shift. Since the spectral resolution in a solid state NMR spectrum is rather low, to observe such a change of chemical shift two conditions have to be fulfilled. First, the interaction between the components of the blend has to be relatively strong. Direct detection of intermolecular interaction in polymer blends has been reported only for cases where hydrogen bonding or charge transfer between the components occurs. The second condition is that the spectrum shows a resolution high enough to detect such changes in chemical shift. In general, such a high resolution has been obtained only with carbon-13 NMR, where the line broadening due to dipolar couplings with protons has been removed by dipolar decoupling (DD) and the line broadening due to chemical shift anisotropy by magic angle spinning (MAS).[4] Although changes of chemical shift in a solid state proton spectrum, obtained under high-resolution conditions with multiple pulse decoupling and MAS [CRAMPS (see ***CRAMPS***)] have been reported for a complex between a polymer and a monomer,[5] as far as we know, no such studies have been reported for polymer blends.

4.2 Intermolecular Cross Polarization (CP)

In most CP experiments, magnetization is transferred from abundant proton spins I to rare carbon-13 spins S to enhance the carbon-13 signal. This results in relatively strong and highly resolved carbon-13 spectra. However, since the CP transfer is mediated by the short-range dipolar interactions, CP can also be used to detect whether I and S spins are physically near each other.

Many studies of polymer miscibility make use of this fact. Let us assume that in a binary blend one of the components, A, has only spins I and both components A and B have spins S. Further, we assume that in the S-spin spectrum, obtained with the highest possible resolution, at least one S-spin NMR line of component B at frequency ν_B does not overlap with any of the S-spin NMR lines of component A. When in such a situation a CP transfer of magnetization from I spins in component A to S spins in A and B results in intensity at frequency ν_B, then this proves that the S spins responsible for the intensity at ν_B are only a few tenths of a nanometer separated from an I spin. Situations are also found where only component B has S spins.

The distinction between the different studies that have been reported with this technique lies in the choice of nuclear spins I and S. A popular approach is to perdeuterate one of the components in the blend, say B.[6] Both components contain carbon-13 spins, and $^1H-^{13}C$ CP from protons in A to carbons in B can establish whether or not the two components are mixed on a molecular scale. Direct cross polarization between protons and deuterons can also be employed.[7] A disadvantage of this technique is that the miscibility between two polymers may be affected when one of the components has to be deuterated. In fact, it has been reported that even polymer isotope mixtures are not simple mixtures.

The blend poly(vinylidene fluoride)/poly(methyl methacrylate) (PVDF/PMMA) has been investigated in great detail with $^{19}F-^{13}C$ cross polarization and $^{19}F-^1H-^{13}C$ double cross polarization.[8] Figure 1 shows the ^{13}C spectrum of the PVDF/PMMA 40/60 blend, obtained from $^{19}F-^{13}C$ cross polarization with proton decoupling and magic angle spinning. The small lines of PMMA in this spectrum show the presence of PMMA units near fluorines of PVDF.

An important aspect of the CP technique for the study of blends is to obtain distance information from such experiments. For a perfectly tuned CP process between N_I abundant I spins (spin quantum number I) and N_S dilute S spins (spin quantum number S) the signal intensity of the S

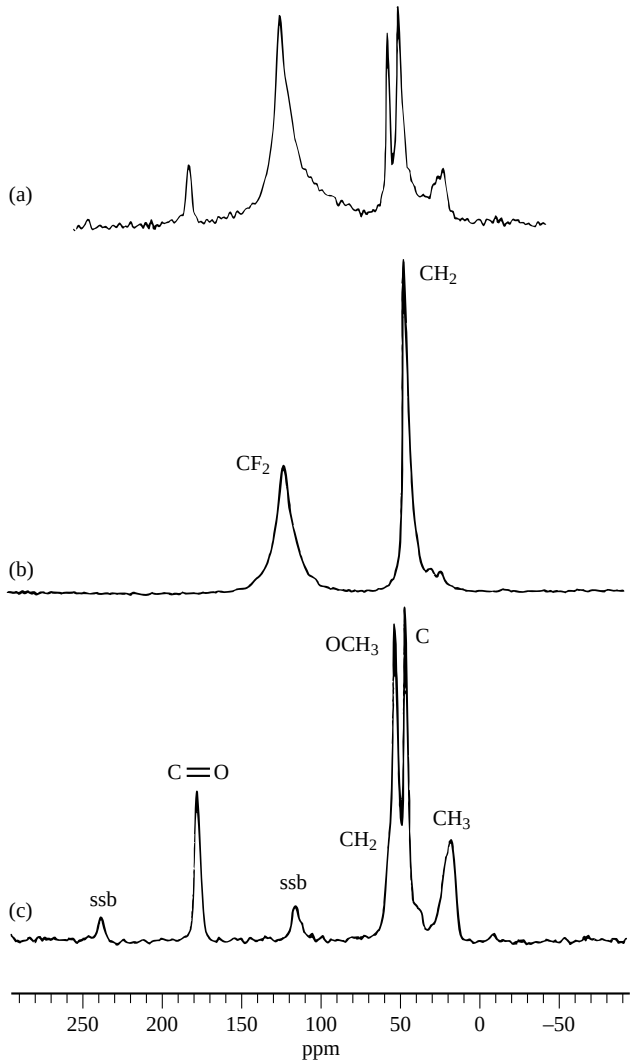

Figure 1 (a) Carbon-13 spectrum of a PMMA/PVDF 60/40 blend, obtained with $^{19}F \rightarrow {}^{13}C$ intermolecular cross polarization (fluorine spins in PVDF; carbon-13 spins in both PVDF and PMMA), proton decoupling and magic angle spinning. (b, c) Carbon-13 CP MAS NMR spectra of the PVDF (b) and PMMA (c) components, obtained with $^1H \rightarrow {}^{13}C$ cross polarization. By comparing the blend spectrum with the spectra of the individual blend components, it is clear that a substantial fraction of the PMMA C=O, OCH_3 and CH_3 groups are within a few tenths of a nanometer away from a PVDF fluorine. The quaternary carbon of PMMA (indicated by C in (c)) is not detected in the blend, since the fluorine–quaternary carbon distance is too large

spins, $I_S(t)$, as a function of the $I \rightarrow S$ CP transfer time t can be expressed as[9]

$$I_S(t) = \frac{I_S(\infty)}{a_+ - a_-}\left[\exp\left(\frac{-a_- t}{T_{IS}}\right) - \exp\left(\frac{-a_+ t}{T_{IS}}\right)\right] \quad (4)$$

where

$$\left.\begin{aligned} a_\pm &= a_0\left(1 \pm \sqrt{1 - b/a_0^2}\right) \\ a_0 &= \frac{1}{2}\left(1 + \varepsilon + \frac{T_{IS}}{T_{1\rho}^I} + \frac{T_{IS}}{T_{1\rho}^S}\right) \\ b &= \frac{T_{IS}}{T_{1\rho}^I}\left(1 + \frac{T_{IS}}{T_{1\rho}^S}\right) + \varepsilon\frac{T_{IS}}{T_{1\rho}^S} \\ \varepsilon &= \frac{N_S S(S+1)}{N_I I(I+1)} \end{aligned}\right\} \quad (5)$$

T_{IS} is the CP transfer time and $T_{1\rho}$ the spin–lattice relaxation time in the rotating frame for the I or S spins. $I_S(\infty)$ is the maximum S-spin magnetization available through CP in the absence of relaxation processes. Demco et al.[10] have approximated the CP rate T_{IS}^{-1} as

$$T_{IS}^{-1} = \tfrac{1}{2} M_{2,SI} J_X \quad (6)$$

where

$$M_{2,SI} = \frac{\langle \Delta\omega^2 \rangle}{4\pi^2} \quad (7)$$

is the van Vleck second moment of the S-spin resonance line determined by the dipolar coupling of the S spins with I spins, and J_X is the cross polarization spectral density function of the I spins. The second moment expresses the static dipolar interaction between S and I spins, while the spectral density function is determined by fluctuations in the I-spin system due to spin flip–flop transitions induced by the B term of equation (2). The spectral density function can be approximated by assuming a Gaussian shape for the correlation function,[10] leading to the following expression for J_X:

$$J_X = \tfrac{1}{2}\sqrt{\pi}\,\tau_c \quad (8)$$

where τ_c is the correlation time, which is of the order of the I-spin T_2 and can be estimated from the I-spin linewidth. The second moment can be described, according to Slichter,[2] as

$$\langle \Delta\omega^2 \rangle = \tfrac{1}{3}\gamma_I^2\gamma_S^2\hbar^2\left(\frac{\mu_0}{4\pi}\right)^2 I(I+1)\sum_{I,S}(1 - 3\cos^2\theta_{IS})^2 r_{IS}^{-6} \quad (9)$$

in which r_{IS} is the distance between I and S spins and θ_{IS} the angle between the internuclear vector and the external field direction. For a given S spin, the second moment contains contributions from all I spins that are dipolar-coupled to this S spin. Because of the r^{-6} dependence of the second moment, the summation in equation (9) can be limited to nearest neighbors. For a polycrystalline solid with the powder average of $1 - 3\cos^2\theta_{IS}$,

$$\langle \Delta\omega^2 \rangle = \tfrac{4}{15}\gamma_I^2\gamma_S^2\hbar^2\left(\frac{\mu_0}{4\pi}\right)^2 I(I+1)\sum_{I,S} r_{IS}^{-6} \quad (10)$$

From a CP experiment where the S-spin signal intensity is measured as a function of the contact time t, T_{IS} can be determined from the fit of equation (4) to the experimental data. For an accurate determination of T_{IS}, the carbon-13 and proton $T_{1\rho}$ have to be measured in separate experiments. Once the CP time T_{IS} and the correlation time τ_c are known, the term

$$\sum_{I,S} r_{IS}^{-6} \quad (11)$$

can be calculated using equations (6), (8), and (10). In particular, for the situation of a polymer blend where we cross polarize from I spins in one component to S spins in the other, we can expect that one I–S distance is shorter than all others. Owing to the r^{-6} dependence, it then seems reasonable to approximate the sum in equation (11) by

$$\sum_{I,S} r_{IS}^{-6} \approx \langle r \rangle_{IS}^{-6} \quad (12)$$

where $\langle r \rangle_{IS}$ is the average nearest I–S distance.

By combining equations (6), (8), (10), and (12), and taking $I = \frac{1}{2}$, we find for protons and carbon-13 spins,

$$\begin{aligned} \langle r \rangle_{IS} &= \left[\tfrac{1}{80}\pi^{-3/2}\gamma_I^2\gamma_S^2\hbar^2\left(\frac{\mu_0}{4\pi}\right)^2 \tau_c T_{IS}\right]^{1/6} \\ &= (7.8 \times 10^{-53}\tau_c T_{IS})^{1/6} \end{aligned} \quad (13)$$

For the PVDF/PMMA[8] blend, a PVDF fluorine–PMMA carbon average distance of about 0.3 nm has been found, independent of composition.

In practical situations, the range of T_{IS} values that can be measured is limited by the length of the proton and carbon-13 $T_{1\rho}$ values. We can therefore estimate the longest $\langle r \rangle_{IS}$ that one can hope to find from a CP experiment. When we assume that in most cases T_{IS} values longer than about 30 ms cannot be determined, we find for the ^1H–^{13}C distance in a rigid proton system with τ_c = 1 ms a value of

$$\langle r \rangle_{max} \approx 0.36\,\text{nm} \quad (14)$$

4.3 Nuclear Overhauser Effect

Two-dimensional nuclear Overhauser effect spectroscopy (2D NOESY) is an important technique for structural and conformational analysis of biomacromolecules in solution. The nuclear Overhauser effect (NOE) also plays an important role in a number of blend NMR studies. An early example is the work of Douglass and McBrierty,[11] who exploited the transient NOE in blends of PVDF and PMMA and of PVDF and poly-(ethyl methacrylate) (PEMA). Here, because of the effects of spin diffusion, these experiments should be classified as belonging to the long-range category. White and Mirau[12] used the NOE technique in a one-dimensional fashion to study the miscibility of deuterated polystyrene (PS) and poly(vinyl methyl ether) (PVME) in the solid phase. They were able to show that the motion of the methyl group protons in PVME modulates the dipolar local field at the PS phenyl ring carbons in blends cast from toluene, in contrast to blends cast from chloroform.

4.4 Two-Dimensional $^{13}C-^{1}H$ Correlation NMR

In order to correlate in a two-dimensional fashion a high-resolution carbon-13 spectrum with a high-resolution proton spectrum for solids, three conditions have to be fulfilled:

1. during the evolution period, the proton–proton and proton–carbon dipolar couplings and the proton chemical shift anisotropy have to be eliminated;
2. during the mixing period, coherence has to be transferred from the proton spins to the carbons; and
3. during the detection period, a high-resolution carbon-13 spectrum has to be acquired.

Figure 2 shows a two-dimensional $^{13}C-^{1}H$ correlated spectrum of poly(vinylphenol) and poly(methyl acrylate).[13] During the evolution time, homo- and heteronuclear dipolar couplings are eliminated by appropriate multiple pulse sequences. The carbon-13 spectrum is obtained under proton-decoupling conditions, while MAS eliminates all line boadenings due to proton and carbon chemical shift anisotropies. Since the distance-determining step is basically a one-step process mediated by the dipolar coupling between protons and carbons, this technique should be listed under the techniques that can provide information about short-range effects. From the spectrum in Figure 2, a direct interaction between the hydroxyl hydrogen of poly(vinylphenol) and the carbonyl carbon of poly(methyl acrylate) can be deduced.

4.5 Rotational Resonance

Although rotational resonance or rotor-driven ^{13}C spin diffusion is an example of the spin diffusion methods discussed in the next section, it is mentioned here since the distance between molecules that can be bridged by this technique falls in the range covered in this section. Owing to the presence of the B term in the dipolar interaction, two spins I_1 and I_2 can undergo flip–flop transitions. When the two spins I_1 and I_2 are both carbon-13 spins under ^{1}H-decoupling conditions, the probability of such transitions is negligible, unless the coupling B term is at least of the same order of magnitude as $\Delta\delta$, the difference in chemical shift (in energy units) of the two spins. Without ^{1}H decoupling, the proton–carbon dipolar interactions can help to bridge this energy difference $\Delta\delta$. Even in the last case, spin diffusion between ^{13}C spins at natural abundance is relatively slow and not so attractive for the study of the miscibility of polymer blends. For carbon-enriched systems, the average dipolar interaction is drastically increased, and carbon–carbon spin diffusion times are reduced by two orders of magnitude. Spin exchange between two carbons of two components in a blend can then be used to obtain information about specific nearest-neighbor interactions. We shall not discuss this technique here, since a good overview has been given by Linder et al.[14] We do discuss another technique for enhancing the carbon–carbon flip–flop rate,

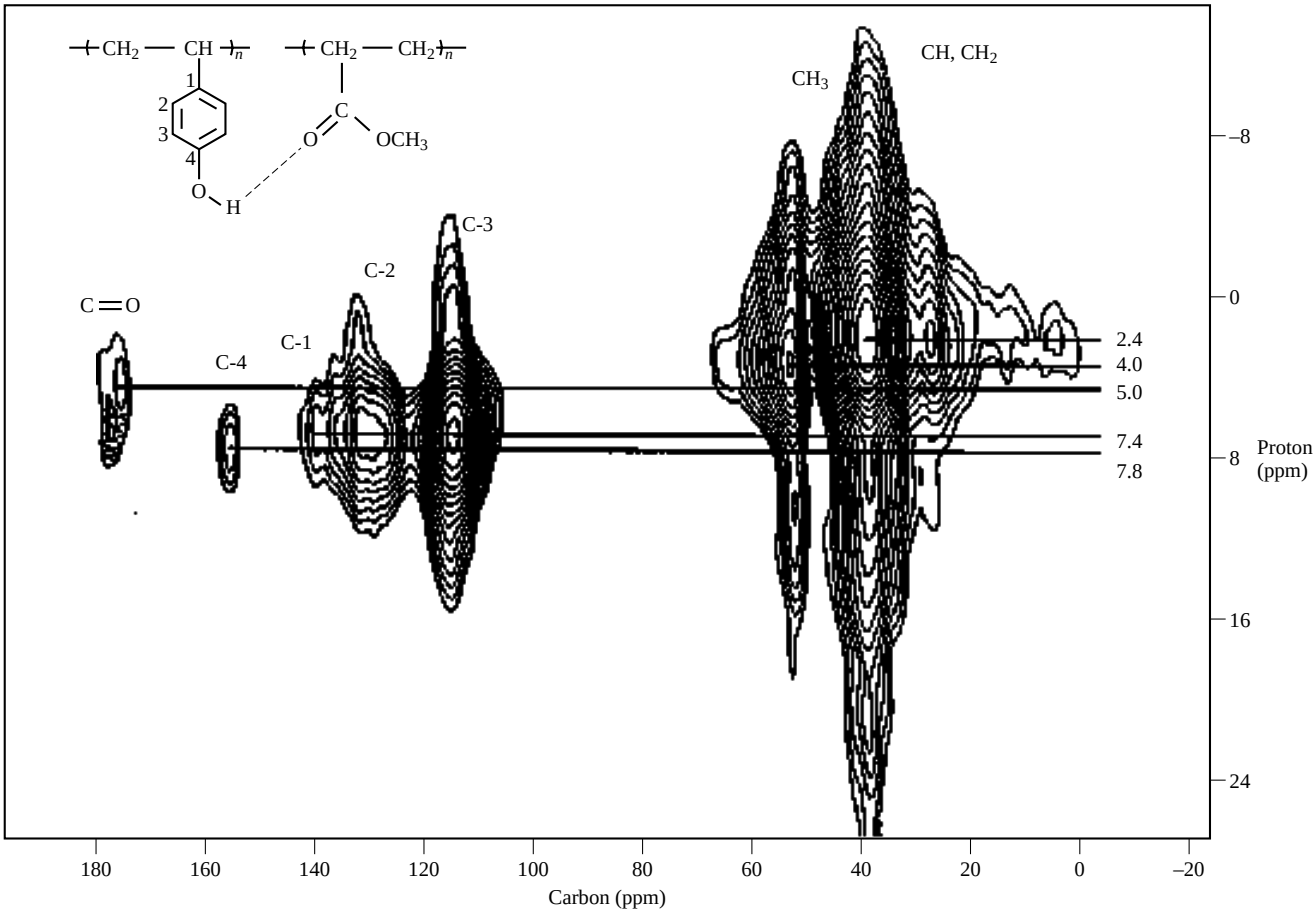

Figure 2 Two-dimensional $^{1}H-^{13}C$ correlation spectrum of a 1:1 molar blend of poly(vinylphenol) and poly(methyl acrylate). The carbonyl resonance at 176 ppm is correlated with the hydroxyl proton at 5.0 ppm, as indicated. Surprisingly, the C-4 carbon does not seem to correlate with the C-3 proton. (Reprinted, with permission, from White and Mirau[13])

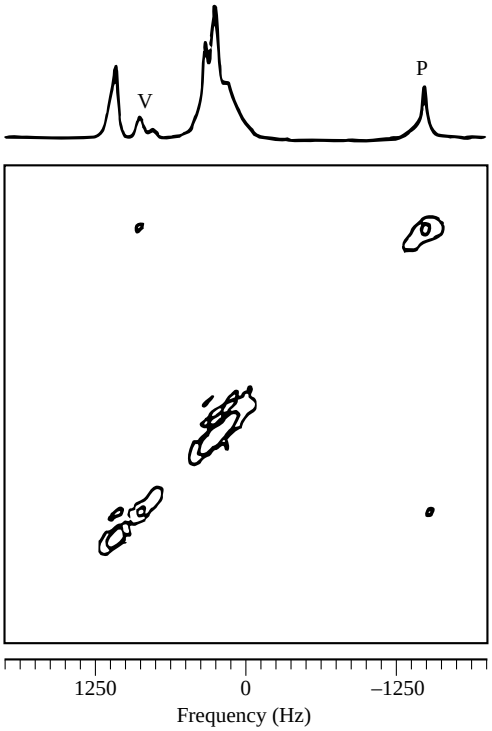

Figure 3 Two-dimensional rotor-driven ^{13}C spin diffusion spectra of annealed 50/50 blends of a random copolyester Vectra-A, containing 73%*p*-hydroxybenzoic acid and 27% hydroxynaphthoic acid, and poly(ethylene terephthalate) (PET). The one-dimensional ^{13}C MAS spectrum is shown at the top, with aliphatic PET resonances and quaternary Vectra-A carbons marked P and V, respectively. The small cross peaks between the P and V diagonal lines indicate intimate mixing. (Reprinted, with permission, from Tang et al.[15])

namely, rotor-driven spin diffusion or rotational resonance (see ***Rotating Solids***). This experiment can be employed to study the miscibility in blends by using a standard two-dimensional exchange experiment.[15] When the magic angle spinning frequency is tuned to the frequency difference of two carbons C_A and C_B, where C_A is in component A and C_B in component B, then the occurrence of cross peaks between the diagonal lines of C_A and C_B implies miscibility on a molecular scale between polymer A and polymer B. So far, only carbon-13 enriched samples have been used, and an example is given in Figure 3.[15]

5 LONG-RANGE TECHNIQUES

5.1 Spin Diffusion

All long-range techniques rely in some way on the process of spin diffusion. Spin diffusion is, like rotational resonance, a consequence of the B term in the dipolar interaction, equation (2). For a large network of dipolar-coupled spins, the effect of successive energy-conserving spin flip–flops can be described as a diffusion process where a local disturbance of the spin system (a nonequilibrium value of the spin magnetization) is dissipated to sites spatially removed from the original disturbance.

A radial spin diffusion process with an isotropic diffusion constant D can be described by the diffusion equation[16]

$$\frac{\partial m(r,t)}{\partial t} = D\frac{\partial^2 m(r,t)}{\partial r^2} \tag{15}$$

where $m(r,t)$ is the magnetization at time t at position r. For spherical diffusion from a point source at $r = 0$, the solution of equation (15) is[16]

$$m(r,t) = \frac{m_0}{8(\pi Dt)^{3/2}} \exp\left(-\frac{r^2}{4Dt}\right) \tag{16}$$

where m_0 is the total magnetization. The fraction of the magnetization in the volume $4\pi r^2\,\mathrm{d}r$ between two spheres with radii r and $r + \mathrm{d}r$, respectively, at time t is

$$4\pi r^2\,\mathrm{d}r\frac{m(r,t)}{m_0} \tag{17}$$

The mean-square distance $\langle r^2\rangle$ that this magnetization has moved from the point source in a time t is given by

$$\langle r^2\rangle = \int_0^\infty 4\pi r^4 \frac{m(r,t)}{m_0}\,\mathrm{d}r = 6Dt \tag{18}$$

To simplify the problem, we assume that after a disturbance at some point, spin diffusion during a time period t can equalize the magnetization in a spherical domain of radius $\sqrt{6Dt}$. Some workers have assumed a lamellar morphology for polymer blends, and spin diffusion must then be described as a one-dimensional process. Since the root-mean-square distance traveled for such a linear process differs by only a small factor from the three-dimensional case, we shall not worry here about the best model, and shall simply assume that the three-dimensional model describes spin diffusion in polymer blends. For a recent and more extensive discussion of spin diffusion in heterogeneous solids, see Clauss et al.[17]

As equation (18) shows, the process of spin diffusion can provide information about domain sizes in polymer blends. Although spin diffusion may occur in every spin system, it will be clear that the diffusion rate can be relatively high only for dense systems with like spins. For carbon-13 spins, for example, the average dipolar interaction is relatively small because of the large average internuclear distances associated with a natural abundance of 1.1%. For such spins, the spin diffusion is almost negligible, especially because in general the dipolar interaction is much smaller than the chemical shift differences. Although one can think of several experiments that eliminate this chemical shift difference, thereby increasing the spin diffusion rate by more than one order of magnitude (e.g., spin locking,[18] and rotational resonance, see Section 4.5), we shall not consider them here. We limit ourselves in the discussion in this section to spin diffusion among proton spins.

We can distinguish

1. direct spin diffusion experiments where the rate of diffusion during a certain time is measured; and
2. indirect experiments where some other parameter is measured whose magnitude is determined by spin diffusion.

A direct experiment always consists of two parts. In the first, the spins are prepared in such a way that different domains have different magnetizations. In the second, spin diffusion restores equilibrium, and the rate of this relaxation process is measured and related to an equation like equation (18). We shall first discuss the direct experiments and the different ways in which the magnetization gradient can be generated and how spin diffusion is manifested.

5.2 Direct Spin Diffusion Experiments

For a direct proton spin diffusion experiment on a binary polymer blend A/B, proton spins in A have to differ in some respect from spins in B, for example, because of a different chemical shift, or because of a difference in relaxation behavior. In the case of a different chemical shift, two possible ways are open: a two-dimensional experiment or selective excitation. An early example of the study of the miscibility in polymer blends is the two-dimensional proton experiment by Caravatti et al.[19] In this Jeener exchange experiment[20] on PS/PVME blends, the aromatic protons of PS and the aliphatic protons in PVME are distinguished in the evolution and detection period by eliminating the line broadening due to dipolar interactions and chemical shift anisotropy in a CRAMPS experiment, while during the mixing period, spin diffusion takes care of the exchange of magnetization between PS and PVME protons. The occurrence of such spin diffusion, and the proof that the two components are mixed on a molecular scale, is shown by the presence of cross peaks in the two-dimensional spectrum, reproduced in Figure 4. The same authors[21] showed for the same blend that the spectral resolution also allowed selective excitation experiments, from which it could be confirmed that the PS/PVME blend can be described as a three-phase system.

In these experiments, magnetization differences are generated among the proton spins, and also the proton spins are detected. An obvious extension of this experiment is to monitor the progression of proton spin diffusion via cross polarization to the carbon spins. The much higher resolution in the carbon-13 spectrum can be exploited to improve the selectivity.[17,22,23]

A much-used technique to study proton spin diffusion is based on differences in mobility of the two components forming a binary blend. In the original approach of Goldman and Shen,[24] a magnetization gradient can be achieved based on the different dipolar strengths of the two components due to molecular motions. Since the dipolar interaction is orientation-dependent, a relatively fast molecular motion may partly or completely average out the dipolar interaction. This means that, for a blend where the two components exhibit significantly different molecular mobilities, the transverse magnetization of one component decays much faster than that of the other. A magnetization gradient is then created, which spin diffusion tries to eliminate. This has been recently used by Spiess and co-workers[23] in a two-dimensional experiment (WISE, wide line separation). In the two-dimensional spectrum, the wide line proton spectrum appears along one axis, with the high-resolution spectrum of the carbon-13 spins coupled to the protons in the other dimension. When two components in a heterogeneous polymer system have different proton linewidths, or different proton T_2 values, this creates a magnetization gradient in the evolution time. By inserting a variable mixing time between the evolution and detection period, proton spin diffusion can be detected via the high-resolution carbon spectrum, and domain sizes can be determined.

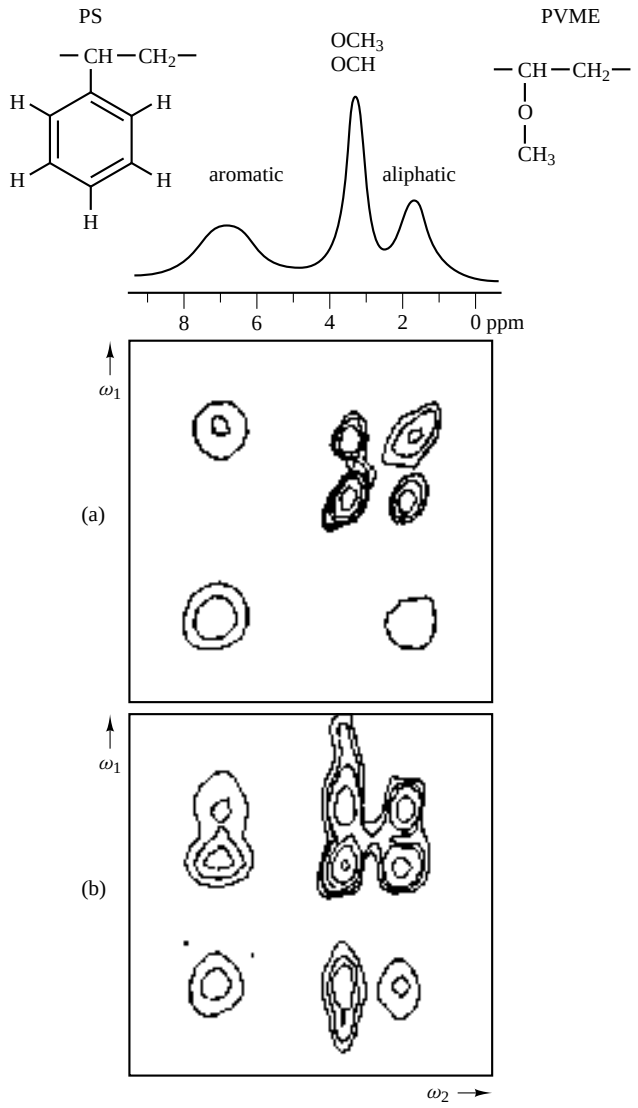

Figure 4 Two-dimensional proton spin diffusion spectra of blends of polystyrene (PS) and poly(vinyl methyl ether) (PVME): (a) cast from chloroform; (b) cast from toluene. Strong cross peaks between aromatic PS protons and OCH and OCH_3 PVME protons appear in spectrum (b). (Reprinted, with permission, from Caravatti et al.[19])

Of course, the decay of the transverse magnetization described by a T_2 relaxation time is just one of the relaxation processes, and differences between other relaxation parameters can also be exploited to generate magnetization gradients.

5.3 Effects of Indirect Spin Diffusion

The most common technique for the study of miscibility in polymer blends uses the fact that when the two separate components have different proton relaxation times (mostly T_1 and $T_{1\rho}$ are used), spin diffusion between protons in the blend may or may not equalize the two values, depending on the size of the domains. The procedure is simple:

measure the appropriate relaxation time and compare it with the component values. There are two limiting possibilities: the blend relaxation process can be described by a single exponential or by two exponentials. In the first case, one can assume that the domains are small enough for spin diffusion to average the values from the two components; in the latter case, the domains are too large for spin diffusion to equalize the individual relaxation times. When the relaxation times of component A and B are T_A and T_B, the blend relaxation time T_k averaged by spin diffusion can then be written as

$$T_k^{-1} = p_A T_{kA}^{-1} + p_B T_{kB}^{-1} \tag{19}$$

where p_A and p_B represent the relative proton signal intensities for components A and B, and T_k is T_1 or $T_{1\rho}$.

From our equation (18), we can immediately estimate the limiting size L_D of the domains by realizing that spin diffusion can proceed during a time of the order of the appropriate relaxation time T_k:

$$L_D = \sqrt{\langle r^2 \rangle} = \sqrt{6DT_k} \tag{20}$$

The diffusion coefficient D depends on the density of the proton spins and the proton linewidth. It is generally assumed that D scales as the one-third power of the proton density.[25] In many systems, D is of the order of 10^{-15}–$10^{-16}\,m^2\,s^{-1}$; for polyethylene, for instance, $D = 6.2 \times 10^{-16}\,m^2\,s^{-1}$.[25] When we take for D an average value of $5 \times 10^{-16}\,m^2\,s^{-1}$, for the proton $T_{1\rho} = 10\,ms$, and for the proton $T_1 = 1\,s$, we find for L_D in the case of $T_{1\rho}$ experiments (remember that for spin diffusion in the rotating frame, D is scaled by a factor of one-half),

$$L_D(T_{1\rho}) \approx 4\,nm \tag{21}$$

and for T_1 experiments,

$$L_D(T_1) \approx 50\,nm \tag{22}$$

With these values, one can make a quick estimate of domain sizes in a blend by measuring proton T_1 and $T_{1\rho}$ values. Assuming that the component relaxation times are sufficiently different, one has the following possibilities:

1. the blend has one proton T_1 and one proton $T_{1\rho}$, implying that domains, when present, are smaller than 4 nm and that there is molecular mixing;
2. the blend has one proton $T_{1\rho}$ and two T_1's, implying that average domain sizes are between 4 and 50 nm;
3. the blend has two values for each type of spin–lattice relaxation time T_1 and $T_{1\rho}$, implying that the average domain size is larger than 50 nm.

So far, we have discussed only proton spin–lattice relaxation, but further information about miscibility can also be obtained from carbon-13 relaxation parameters. However, because, in general, carbon-13 spin diffusion, as discussed above, is a very slow process, the information from such experiments is not usually as clear as that from proton measurements. Therefore, we shall not discuss such experiments here.

A significant improvement of the proton spin–lattice relaxation experiment for determination of miscibility can be obtained when the actual detection of the proton signal is made indirectly via the carbon-13 spins.[26] For that purpose, at the end of the spin–lattice relaxation measurement, one transfers proton magnetization to the carbon spins via cross polarization. When one component of the blend has at least one carbon-13 NMR line that does not overlap with the carbon lines of the other component, the proton relaxation of that component can then be measured separately. In that way, there is no need to decompose proton spin–lattice relaxation curves in order to see whether there is one relaxation time or two.

5.4 Dynamic Nuclear Polarization (DNP)

So far, we have discussed NMR techniques that are suitable for investigating miscible blends, or, in other words, blends where the total interface area between the components is very large. For immiscible blends, all the techniques we have discussed so far do not work, because the interface area is too small and the number of spins in these interface areas is not large enough to be detected. NMR is basically a bulk technique. With DNP, it is possible to enhance the signal from nuclei in interfaces between polymer components, one of which has unpaired electrons. In this way, two advantages are obtained: first, since the DNP mechanism again relies on the dipolar interaction—this time between electron spins and nuclear spins—the nuclear spins that are influenced by the DNP process have to be close to the interface; secondly, the detection limit of such spins is appreciably lowered. This technique has been applied to polyacetylene/polyethylene[27] and to polystyrene/polycarbonate blends.[28] For a discussion of the DNP effect and the application to blends, we refer to these publications. Here it suffices to say that the experiment is rather involved, while, in addition to the normal solid state carbon-13 NMR experiment with magic angle spinning, one also has to saturate the electron spin resonance (ESR) line of the unpaired electrons. The success of the DNP method is further crucially determined by the ESR linewidth and other parameters. For the cases where it works, it is a unique method, since one can observe spins in areas that are not usually accessible to NMR observation but are of great interest in polymer research.

The DNP process can be used for direct electron–carbon-13 transfer or for electron–proton transfer, followed by proton spin diffusion and proton–carbon-13 transfer via CP. The problem with the first process seems to be that carbons with strong enough coupling with the electrons to show DNP enhancements also have, because of this interaction, broadened NMR lines.[28]

6 OTHER NMR METHODS

In the proceeding two sections, we have discussed the main methods for studying miscibility of polymer blends by solid state NMR. However, other techniques are certainly worth mentioning. VanderHart et al.[29] have shown that in a mixture where one component is deuterated and the mixing is not intimate the dilute protons in the 98–99% deuterated component show a MAS spectrum with a centerband and spinning sidebands on top of the broad proton spectrum from the protonated component. In the case of intimate mixing, when the environment of the deuterated units contains

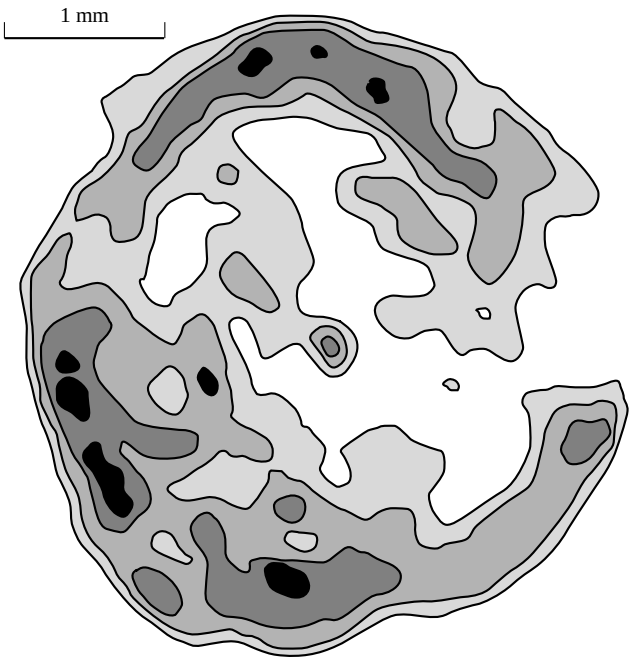

Figure 5 Proton NMR image of a blend of polybutadiene (PB) and polystyrene (PS) obtained with magic angle spinning imaging. The rigid PS escapes detection; the density of PB is indicated[34]

protons from the protonated component, there is a significant weakening of or complete disappearance of the spinning sideband pattern.

Xenon-129 NMR has also been used to study polymer blends.[30,31] It is well known that the chemical shift of Xe is very sensitive to its environment, and when the Xe atoms reside in the free volume of an immiscible polymer blend, it may show more than one line at temperatures low enough that no rapid exchange takes place between the different adsorption sites.[32]

A final technique to be mentioned is that of NMR imaging. The problem with this technique is the low inherent sensitivity of NMR and consequently the poor spatial resolution. Therefore, NMR imaging cannot give information about molecular mixing in polymer blends. However, the combination of imaging with further discrimination with the help of NMR parameters like relaxation times or chemical shift makes it an attractive alternative to microscopy for studying noncompatible blends. Some images of heterogeneous materials have been published.[33,34] Figure 5 shows the image of a polybutadiene/polystyrene blend obtained with magic angle spinning imaging.[34]

7 RELATED ARTICLES

Diffusion in Solids; Polymer Dynamics and Order from Multidimensional Solid State NMR; Spin Diffusion in Solids.

8 REFERENCES

1. O. Olabisi, L. M. Robeson, and M. T. Shaw, *Polymer–Polymer Miscibility*, Academic Press, New York, 1979.
2. C. P. Slichter, *Principles of Magnetic Resonance*, 3rd edn., Springer-Verlag, Berlin, 1990.
3. A. Pines, M. G. Gibby, and J. S. Waugh, *J. Chem. Phys.*, 1973, **59**, 569.
4. E. R. Andrew, in *Progress in Nuclear Magnetic Resonance Spectroscopy*, eds. J. W. Emsley, J. Feeney, and L. H. Sutcliffe, Pergamon Press, Oxford, 1971, Vol. 8, p. 1.
5. L. A. Belfiori, T. J. Lutz, C. Cheng, and C. E. Bronnimann, *J. Polym. Sci., Part B: Polym. Phys.*, 1990, **28**, 1261.
6. G. C. Gobbi, R. Silvestri, T. P. Russell, J. R. Lyerla, and W. W. Fleming, *J. Polym. Sci, Part C: Polym. Lett.*, 1987, **25**, 61.
7. N. Zumbulyadis, C. J. T. Landry, and T. E. Long, *Macromolecules*, 1993, **26**, 2647.
8. C. H. Klein Douwel, W. E. J. R. Maas, W. S. Veeman, G. H. Werumeus Buning, and J. M. J. Vankan, *Macromolecules*, 1990, **23**, 406; W. E. J. R. Maas, W. A. C. van der Heijden, W. S. Veeman, J. M. J. Vankan, and G. H. Werumeus Buning, *J. Chem. Phys.*, 1991, **95**, 4698; A. P. A. Eijkelenboom, W. E. J. R. Maas, W. S. Veeman, G. H. Werumeus Buning, and J. M. J. Vankan, *Macromolecules*, 1992, **25**, 18.
9. M. Mehring, in *NMR, Basic Principles and Progress*, eds. P. Diehl, E. Fluck, and R. Kosfeld, Springer-Verlag, New York, 1983, Vol. 12, 2nd edn.
10. D. E. Demco, J. Tegenfeldt, and J. S. Waugh, *Phys. Rev. B*, 1975, **11**, 4133.
11. D. C. Douglass and V. J. McBrierty, *Macromolecules*, 1978, **11**, 766.
12. J. L. White and P. A. Mirau, *Macromolecules*, 1993, **26**, 3049.
13. J. L. White and P. A. Mirau, *Macromolecules*, 1994, **27**, 1648.
14. M. Linder, P. M. Henrichs, J. M. Hewitt, and D. J. Massa, *J. Chem. Phys.* 1985, **82**, 1585.
15. P. Tang, J. A. Reimer, and M. M. Denn, *Macromolecules*, 1993, **26**, 4269.
16. J. Crank, *Mathematics of Diffusion*, Clarendon Press, Oxford, 1956.
17. J. Clauss, K. Schmidt-Rohr, and H. W. Spiess, *Acta Polym.*, 1993, **44**, 1.
18. R. R. Ernst, G. Bodenhausen, and A. Wokaun, *Principles of Nuclear Magnetic Resonance in One and Two Dimensions*, Clarendon Press, Oxford, 1987.
19. P. Caravatti, P. Neuenschwandler, and R. R. Ernst, *Macromolecules*, 1986, **19**, 1895.
20. J. Jeener, B. H. Meier, P. Bachmann, and R. R. Ernst, *J. Chem. Phys.*, 1979, **71**, 462.
21. P. Caravatti, P. Neuenschwandler, and R. R. Ernst, *Macromolecules*, 1986, **19**, 1889.
22. P. M. Henrichs, J. Tribone, D. J. Massa, and J. M. Hewitt, *Macromolecules* 1988, **21**, 1282.
23. K. Schmidt-Rohr, J. Claus, and H. W. Spiess, *Macromolecules*, 1992, **25**, 3273.
24. M. Goldman and L. Shen, *Phys. Rev.*, 1966, **144**, 321.
25. J. R. Havens and D. L. VanderHart, *Macromolecules*, 1985, **18**, 1663.
26. E. O. Stejskal, J. Schaefer, M. D. Sefcik, and R. A. McKay, *Macromolecules*, 1981, **14**, 275.
27. G. G. Maresch, R. D. Kendrick, C. S. Yannoni, and M. E. Galvin, *Macromolecules*, 1988, **21**, 3525.
28. M. Afeworki, R. A. McKay, and J. Schaefer, *Macromolecules*, 1992, **25**, 4084.
29. D. L. VanderHart, W. F. Manders, R. S. Stein, and W. Herman, *Macromolecules*, 1987, **20**, 1726.

30. J. H. Walton, J. B. Miller, and C. M. Roland, *J. Polym. Sci., Part B: Polym. Phys.*, 1992, **30**, 527.
31. J. H. Walton, J. B. Miller, C. M. Roland, and J. B. Nagode, *Macromolecules*, 1993, **26**, 4052.
32. M. Mansfeld and W. S. Veeman, *Chem. Phys. Lett.*, 1993, **213**, 153.
33. S. N. Sarkar and R. A. Komoroski, *Macromolecules*, 1992, **25**, 1420.
34. D. G. Cory, J. C. de Boer, and W. S. Veeman, *Macromolecules*, 1989, **22**, 1618.

Biographical Sketch

Wiebren Sjoerd Veeman. *b* 1942. Engineering degree in Technical Physics, 1967, Technical University of Delft; Ph.D., 1972, University of Leiden. Postdoctoral Fellow IBM Research San José, 1973–74. Wetenschappelijk medewerker, University of Nijmegen 1974–86. Professor of Physical Chemistry, University of Nijmegen, 1986–91. Professor of Physical Chemistry, University of Duisburg, 1991–present. Research interests: spectroscopy and its applications to materials.

Polymer Conformations in Glassy Solutions as Studied by Off-resonance Radiation

Jacques-François Jacquinot and Maurice Goldman

CEA Saclay, Gif-sur-Yvette Cedex, France

1 Introduction 1
2 Basics of Relaxation by Fixed Paramagnetic Centers 2
3 The Model Structure of Linear Polymers 4
4 Experimental Methods – Validation on a 3-D System 4
5 Results for Polymer Solutions 5
6 The Problem of Spin Diffusion 7
7 Conclusion and Perspectives 8
8 References 9

1 INTRODUCTION

The statistical structure of linear polymers in dilute or semi-dilute solution, whose main characteristic is its fractal dimension, has been the subject of extensive studies in modern times, on both theoretical and experimental levels. The interest it raised in physics is because, as a branch of theoretical statistical physics, it is amenable to extremely clean and elaborate treatments making use of sophisticated mathematical techniques.[1–3] It also offered an ample field for experimentation. One of the most sensitive and most extensively used tools for these polymer studies is small angle neutron scattering (SANS), which yields the Fourier transform of the average space correlation of pairs of nuclei. This kind of approach corresponds to an exploration of the reciprocal or k space of the polymers.

NMR has been largely absent so far from this class of problems; there are a few exceptions. The numerous NMR studies of polymers (for example, see the articles on polymers in the *Encyclopedia of NMR*) are centered on different properties of these systems. The first exception is the use of dynamic polarization in partly protoned and partly deuterated polymers in solid glassy solutions, in connection with SANS, whose unique quality is that it enables one to change continuously the neutron scattering *amplitude* by the polarized nuclei, an enormous advantage for disentangling the various contributions to the neutron scattered intensity.[4,5] The second exception is mentioned later.

The approach described is to study the influence of the average polymer structure on the characteristics of spin-lattice relaxation.[6,7] More precisely, we study nuclear relaxation without spin diffusion, under the influence of paramagnetic centers, in polymers in solution in a solid glass. The advantage of this is that, since the various spins relax independently of one another, we can see the sum of the individual magnetization evolutions, which is an additive phenomenon. Therefore, the bulk evolution under relaxation of the NMR signal reflects the statistical structural distribution of the polymers. This statistical sensitivity to the environment is well known in ordinary 3D solids, as is discussed later.

Several conditions are required for this study of polymers.

1. The polymers must be static, that is embedded in a solid, which must be a glass, so as not to strain their structure with respect to that in liquid solution. This constraint does not exist in standard SANS, because the high energy of the neutrons (by comparison with the kinetic energy of the atoms or molecules), the polymer motions in a liquid are completely unnoticed by them: for neutrons, a liquid is as 'static' as a solid.
2. Only the nuclei of the polymer must have a large nuclear moment, and not those of the solvent, to investigate the structure of the polymer itself, without contributing to relaxation from the solvent nuclei. The obvious choice is that of protonated polymers in a deuterated solvent. The latter must be a good solvent down to the glassy transition, so as to preserve the structure of the polymers and to avoid their segregation.
3. The only sufficiently tractable case is that when the paramagnetic centers are located on the polymer itself, and not in the solvent. For usual protonated polymers, the choice is most often limited to nitroso radicals. Furthermore, these radicals must be easily grafted to the polymers.
4. The electronic relaxation time, which in practice is the correlation time for the nuclear relaxation, must have an adequate value which imposes that the sample temperature be in the liquid nitrogen range.
5. In order for the time required for nuclear relaxation to remain within a reasonable range, it is necessary for the concentration of paramagnetic centers relative to the relaxing nuclei not to be too small. In the case when only one center is grafted on each polymer, this imposes in practice a maximum size for the polymers.

An experiment of diffusion-free nuclear relaxation by impurities on fractal systems has already been done. (This is the second exception to non-NMR studies to polymer-like fractal structure.) It was performed on ^{29}Si by Devreux et al. in silica aerogels.[8] These have a network structure characterized by a fractal dimension D slightly in excess of two. Using an angular average for the individual relaxation rates, the authors showed that the initial variation of the nuclear polarization was proportional to $t^{D/6}$. This was tentatively extended to an exponential law of the form

$$\langle p(t) - p_{eq} \rangle \propto \exp\left[-\left(\frac{t}{\tau_1} \right)^{D/6} \right] \tag{1}$$

Experimentally, spin diffusion was quenched by averaging the dipole-dipole interactions between ^{29}Si nuclei to zero by

sample spinning at the magic angle $\theta = \text{acos}(1/\sqrt{3})$, and the results correlated well with theory.

In this article, diffusion-free relaxation is investigated in the absence of irradiation, or under off-resonance nuclear irradiation as a function of the angle between the effective field in the rotating frame and the steady field. The measurements concern both the rate of evolution of the bulk nuclear magnetization along the effective field and its steady-state limit. Two types of systems were studied: the paramagnetic centers are grafted at random positions on the polymer; or only one center is grafted on each polymer in a well defined position, usually at one end. For the results to be interpretable, the polymers are monodispersed.

The article is organized in the following sections:

1. A review of the basic facts of nuclear relaxation by dipolar coupling with paramagnetic centers.
2. Description of the experimental procedure and its validation in a 3D solid.
3. Statistical properties of linear polymers in dilute or semi-dilute solution, as results from theory backed by neutron scattering experiments.
4. Description of the investigation of several systems and comparison with theory.
5. Discussion of the problem of spin 'diffusion'.
6. Conclusion and perspectives.

2 BASICS OF RELAXATION BY FIXED PARAMAGNETIC CENTERS

This section is essentially a short summary of well-known facts of NMR.

It has been known since 1949[9] that in insulating solids, the relaxation of nuclear spins 1/2 proceeds from the combination of two processes: direct relaxation by paramagnetic centers, usually present at low concentration, combined with homogenization of the polarization throughout the sample via dipolar-induced flip-flops among the nuclear spins, described by a diffusion equation, leading to an exponential decay of the bulk polarization. The situation is changed when the flip-flops are quenched by a decrease of the effective dipolar interactions, for instance through a strong off-resonance rf irradiation so as to orient the effective field in the rotating frame at the magic angle from the external field.[10–12] Then, one observes the independent direct relaxation of the individual spins. Even when the dipolar interactions are not completely averaged to zero, it is generally possible to observe the diffusion-free relaxation at the beginning of the nuclear magnetization evolution. These are the conditions used in the present study.

2.1 Nuclear Spins Subjected to Strong rf Irradiation

A system of nuclear spins I in a steady magnetic field is subjected to a strong rf field B_1 rotating at a frequency ω at a value $\Delta = \omega_0 - \omega$ from the Larmor frequency. In a frame rotating at frequency ω, the spins are subjected to a steady magnetic field B_{eff} of components $-\Delta/\gamma$ and B_1 along the axes Oz and Ox respectively, that is oriented along an axis OZ tilted by the angle $\theta = \text{atan}\,(B_1/(-\Delta/\gamma))$ Oz (see Figure 1). The effective Hamiltonian has the form

$$\mathcal{H}_{\text{eff}} = \Delta I_z + \omega_1 I_x + \mathcal{H}'_{Dz} = \Omega I_Z + \mathcal{H}'_{Dz} \tag{2}$$

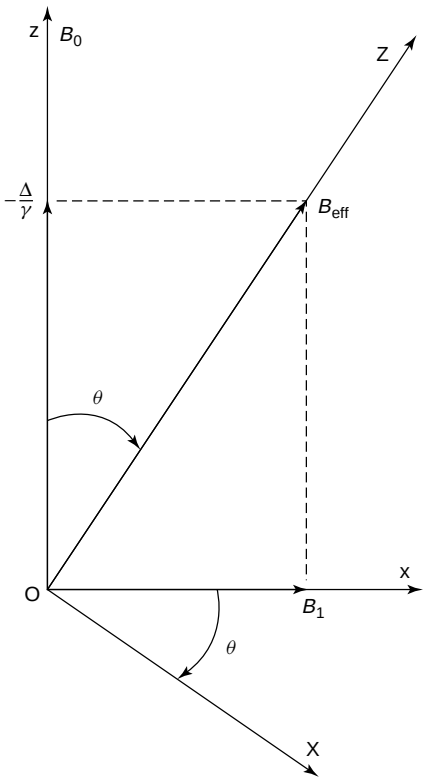

Figure 1 Effective field in the rotating frame under off-resonance irradiation

where, in the last term on the right-hand side, we express the effective Zeeman interaction with respect to the orientation OZ of the effective field (see Figure 1), and $\mathcal{H}'_{Dz}$ is the secular dipolar interaction in the rotating frame, commuting with the operator I_z.

If as we assume, the effective Zeeman interaction is much larger than the dipolar one, the latter has to be truncated so as to retain only its part which commutes with the effective Zeeman interaction, that is with the spin operator I_Z. This is done by rewriting the dipolar Hamiltonian in the system of axes OXYZ and rejecting all terms which differ from $\mathcal{H}'_{Dz}$, of the same form as $\mathcal{H}'_{Dz}$ but expressed in the new system of axes. The corresponding coefficient is equal to $1/2(3\cos^2\theta - 1)$, a standard result recalled in Tabti et al. and discussed at length in Blumberg, Tse and Hartmann, and Lin and Hartmann.[7,9–11] It is easily recovered by an elementary calculation The new effective dipolar interaction is then

$$\mathcal{H}''_{Dz} = \frac{1}{2}(3\cos^2\theta - 1)\mathcal{H}'_{Dz} \tag{3}$$

The magnitude $1/2|3\cos^2\theta - 1|$ can be modified at will within limits by adjusting the angle θ. If we use a second rotating frame, of frequency Ω around OZ, the evolution of the spin system is governed by the effective dipolar interaction $\mathcal{H}''_{Dz}$.

2.2 Local Nuclear Relaxation by a Paramagnetic Center

We consider a paramagnetic spin S at the origin and a nuclear spin I with polar coordinates (r, α, β) Under rf irradiation, the orientation of the spin I is locked along the

direction OZ of its effective field in the rotating frame. Its relaxation through its dipolar coupling with the spin S is calculated through a combination of the methods of Abragam and Tomita.[13,14] The spin S components fluctuate randomly under the effect of its own spin-lattice relaxation, with a longitudinal time T_{1e}. We assume that $\omega_e T_{1e} \gg 1$, where ω_e is the electronic Larmor frequency, so that the only effective S spin component contributing to the nuclear relaxation is S_z, and the correlation time of the random $I - S$ coupling is $\tau_c = T_{1e}$. The relaxing Hamiltonian is of the form

$$\mathcal{H}_{IS}(t) = AS_z(t)I_z + \{BS_z(t)[I_x + iI_y] + h.c.\} \tag{4}$$

with

$$A = \frac{\gamma_I \gamma_S \hbar}{r^6}(1 - 3\cos^2\alpha),$$
$$B = -\frac{3}{2}\frac{\gamma_I \gamma_S \hbar}{r^6}\sin\alpha\cos\alpha\exp(-i\beta) \tag{5}$$

In the hypothesis, often realistic, that $\Omega\tau_c \ll 1$, the relaxation evolution of the component I_Z is a weighted average of those of I_z and I_x. It corresponds to the equation

$$\frac{d}{dt}\langle I_Z\rangle = -\frac{1}{T_1}[\langle I_Z\rangle - \langle I_Z\rangle_{st}] \tag{6}$$

where a standard relaxation calculation yields

$$\frac{1}{T_1} = \frac{S(S+1)}{3}[A^2\sin^2\theta\, J(0) + 2|B|^2(1+\cos^2\theta)J(\omega)] \tag{7}$$

The spectral densities are of the usual form

$$J(\omega) = \frac{\tau_c}{1+\omega^2\tau_c^2} \tag{8}$$

The relaxation rate, equation (7), can be written under the general form

$$\frac{1}{T_1}(\alpha, r) = \frac{C(\alpha)}{r^6} \tag{9}$$

where $C(\alpha)$, which depends on the angle α between the direction of the vector SI and the external field through the square of its sine or cosine, also depends on the angle θ between effective and external fields.

Equation (7) agrees with the relaxation rates derived for the z and x components

$$\frac{1}{T_{1z}} = \frac{1}{T_1}(\theta = 0); \quad \frac{1}{T_{1x}} = \frac{1}{T_1}(\theta = 90^\circ) \tag{10}$$

As for the steady-state value towards which $\langle I_Z\rangle$ evolves, it corresponds to a compromise between the tendency of $\langle I_z\rangle$ to evolve towards the thermal equilibrium value I_0 and that of $\langle I_x\rangle$ to evolve towards 0. The result is

$$\langle I_Z\rangle_{st} = I_0\frac{\cos\theta}{\cos^2\theta + (T_{1z}/T_{1x})\sin^2\theta} \tag{11}$$

All these results can be cleanly derived, and they can be extended to the case when the condition $\Omega\tau_c \ll 1$ is not fulfilled: one must simply replace $J(0)$ with $J(\Omega)$ in equation (7).[15]

2.3 The Steady-State Polarization in a Bulk Sample

The steady-state polarization for a single spin I given in equation (11) depends on the polar angle α through the dependence of T_{1z} and T_{1x} on this angle. In a bulk sample, flip-flop processes, when given enough time to take place, homogenize these steady-state values. The final result is a bulk steady-state polarization of the form

$$\frac{\langle I_Z\rangle_{st}}{I_0} = \frac{\cos\theta}{\cos^2\theta + f(\tau_c)\sin^2\theta}, \tag{12}$$

where the factor $f(\tau_c)$ is equal to a ratio of average relaxation rates

$$f(\tau_c) = \overline{\left(\frac{1}{T_{1x}}\right)}\Big/\overline{\left(\frac{1}{T_{1z}}\right)} \tag{13}$$

Its formal expression is

$$f(\tau_c) = \frac{1}{2} + \frac{2}{3}\omega^2\tau_c^2 \tag{14}$$

The importance of equations (12) and (14) is that by merely measuring the steady-state NMR signal as a function of the angle θ between effective and external field, one obtains an accurate determination of the correlation time τ_c, that is the spin-lattice relaxation time of the paramagnetic centers, irrespective of whether the EPR linewidth is homogeneous or inhomogeneously broadened. This very general result, independent of the structure of the system, may be considered a by-product of some value of the present study.

2.4 Diffusion-Free Relaxation in a Bulk Sample

We give here but an outline of the way of handling the problem of determining the shape of the relaxation evolution of the bulk polarization towards its steady-state value.

The problem is essentially of statistical nature. The magnetization of each individual nuclear spin evolves according to the equation

$$\langle I_Z^i\rangle(t) = \langle I_Z^i\rangle_{st} + (\langle I_Z^i\rangle(0) - \langle I_Z^i\rangle_{st})\exp\left(\frac{-t}{T_1^i}\right) \tag{15}$$

One must sum over all spins, or else consider a 'typical' spin and calculate its average evolution through the probability distribution of relaxation times and steady-state limits

$$\langle I_Z\rangle(t) = \overline{\langle I_Z\rangle_{st}} + \langle I_Z\rangle(0)\overline{\exp\left(\frac{-t}{T_1}\right)} - \overline{\langle I_Z\rangle_{st}\exp\left(\frac{-t}{T_1}\right)} \tag{16}$$

Where the overbar means a bulk statistical average, whereas the brackets correspond as usual to quantum-mechanical expectation values.

As a general rule, all initial magnetizations are equal, which is why the second average on the right-hand side of equation (16) is only on the time-dependent term. This average is relatively easy to calculate. This is not the case for the last joint average, because both the individual $\langle I_Z^i\rangle_{st}$ and T_1^i produced by a single paramagnetic center depend on the polar angle α. This is not too severe when the paramagnetic centers are distributed at random, because most spins will be relaxed by several centers, and the local $\langle I_Z^i\rangle_{st}$ will not differ much from the average. The problem might arise in the case of dilute polymers with only one center grafted on each, that is when

all nuclear spins are relaxed only by one center. However, in all cases studied so far, one always had $\omega\tau_c \gg 1$, so that except in a very small domain of angles α around the magic value, one has $T_{1z}^i/T_{1x}^i \gg 1$ and $\langle I_Z^i\rangle_{st}$ is small compared with $\langle I_Z\rangle(0)$, so that its exact value is of little importance over most of the evolution.

The methods used for calculating the average $\overline{\exp(-t/T_1^i)}$ will not be detailed here, and we will only give and briefly comment on the results for the various cases under study.

3 THE MODEL STRUCTURE OF LINEAR POLYMERS

Although the experimental study was made with finite and relatively short polymers, we describe them by the same model as that derived theoretically in the limit of very long polymers.[1–3]

Linear polymers in dilute solution, that is at a concentration c smaller than the overlap concentration c^*, to be defined later, are independent of each other. Being flexible, they can be present under a variety of configurations. One can define a mean statistical structure by performing an average of all possible configurations. This structure is of spherical symmetry and is characterized by a fractal dimension D. What is meant by this is that around any point of the polymer the number of monomers (or the number of nuclei) present in a sphere of radius r is of the form

$$n_n(r) = \lambda r^D \tag{17}$$

from which we can define an average nuclear density $\rho(r)$ through

$$\frac{d}{dr} n_n(r) = D\lambda r^{D-1} = 4\pi r^2 \rho(r) \tag{18}$$

that is

$$\rho(r) = \frac{1}{4\pi} D\lambda r^{D-3} \tag{19}$$

For linear polymers in solution in a good solvent, this dimension is equal to $D = 1.7$.

We define an effective radius R as that of a sphere that contains all the nuclei N_n of the polymer

$$R = \left(\frac{N_n}{\lambda}\right)^{1/D} \tag{20}$$

and we assume that the density $\rho(r)$ is of the form shown in equation (19) up to $r = R$ and vanishes at larger values. This is obviously an oversimplification, but it will turn out to be convenient.

Among other kinds of radii used in the study of polymers there is the so-called gyration radius R_G defined through

$$R_G^2 = \frac{1}{2(N+1)^2} \sum_{i,j} (\mathbf{r}_i - \mathbf{r}_j)^2 \tag{21}$$

where N is the number of monomers and $\mathbf{r}_i - \mathbf{r}_i$ is the vector joining the monomers i and j. Its value is experimentally derived by small angle neutron scattering.

Another radius, called R_F, equal to the r.m.s. end-to-end distance of the polymer, is theoretically related to R_G through $R_F = 2.51\, R_G$. The vector R of equation (20) is likely to be of an order of magnitude that is similar to these radii.

Among several different definitions of the polymer overlap concentration c^*, the simplest one in the present case is

$$4\pi R^3 c^* = 1 \tag{22}$$

The polymers are said to be in semi-dilute solution when their concentration c is somewhat larger than the concentration c^*, so that they partly overlap. In this case, all points of the polymer are still statistically equivalent: in a sphere of radius ξ around a 'typical' point, the fractal dimension has the same value $D = 1.7$ as in dilute solution, and beyond this distance, the dimension is the same as that of the host medium, that is $D = d = 3$.

The knowledge of the fractal dimension is sufficient to determine the shape of the signal evolution at short time, when only those nuclei close to a paramagnetic center are substantially relaxed. The centers are at low concentration, so that these nuclei are only relaxed by one impurity. The centers being grafted on the polymers, the density of nuclei around them corresponds to the same fractal dimension as the polymers. Starting from zero initial saturation, the evolution of the nuclei at a polar angle α with respect to the center is approximately of the form

$$\langle I_Z\rangle(\alpha; t) \propto \langle I_Z\rangle_{st} \int_{r=b_0}^{\infty} \left[1 - \exp\left(\frac{-C(\alpha)t}{r^6}\right)\right] d(r^D) \tag{23}$$

where b_0 is the barrier within which the nuclei, of frequency shifted by the average electronic dipolar field, are not observed. For $ct/b_0^6 \gg 1$, and by using the notation

$$x = \frac{C(\alpha)t}{r^6} \tag{24}$$

we obtain a result of the form

$$\langle I_Z\rangle(\alpha; t) = \langle I_Z\rangle_{st}(1 - \zeta t^{D/6}) \tag{25}$$

This form remains true when integrating over the angle α. As for the complete form of the evolution, it requires a more elaborate calculation, and it depends on the distribution of the relaxing centers around the nuclei.

4 EXPERIMENTAL METHODS – VALIDATION ON A 3-D SYSTEM

4.1 Experimental Procedure

Within an electromagnet producing a horizontal field, the sample is cooled in a cryostat by flowing cooled nitrogen gas around it. A resistor is used to adjust the gas temperature to within 0.5 K between liquid nitrogen and room temperatures. The sample temperature was as a rule around 100 K. The pulsed spectrometer operates at a frequency around 100 MHz. The field B_1 is of the order of 1 mT, rotating component, that is much larger than the local field of the compounds used, about 0.2 to 0.3 mT. The rf field can be applied up to 9 s without problems.

The measuring sequence goes as follows: the thermal equilibrium magnetization is spin-locked along the direction OZ of the effective field; after an evolution time t, the

magnetization is as a rule realigned with the steady field and then subjected to a $\pi/2$ pulse, and the FID amplitude is measured. The manipulations of the magnetization directions are performed by appropriate pulses and evolution periods.

4.2 Validation on a 3-D Solid: Protonated *O*-Terphenyl

The sample was protonated *o*-terphenyl (OTP) doped with the radical 4-hydroxyl TEMPO (tetramethyl-2,2,6,6 piperidinol-4 oxyle-1) at a concentration of $4.3 \times 10^{19}\,\mathrm{cm}^{-3}$. It was degassed and cooled at 143 K. The centers were then randomly distributed. The relaxation time without rf irradiation was 0.78 s.

For randomly distributed relaxing centers, the theoretical evolution of the nuclear magnetization is an exponential function of $\sqrt{t}$, in accordance with the initial law (see equation (25)).[6,7,10–12,16]

$$\langle I_Z\rangle(t) - \langle I_Z\rangle_{st} = (\langle I_Z\rangle(0) - \langle I_Z\rangle_{st}) \exp\left[-\left(\frac{t}{\tau_1}\right)^{1/2}\right] \quad (26)$$

This law is deduced from a statistical analysis of the paramagnetic center random distribution, and from the fact that, when 'seeing' several paramagnetic centers, the relaxation rate of a given nucleus is the sum of those due to the individual centers.

The expressions for the relaxation rates and steady-state magnetizations as a function of the angle θ between external and effective fields are given in Tabti and Tabti et al. with only two adjustable parameters: the correlation time $\tau_c = T_{1e}$ and the concentration of the relaxing centers. The variation of the steady-state reduced magnetization as a function of the angle θ is shown in Figure 2, together with a best-fit theoretical curve corresponding to

$$\tau_c = 6.5 \pm 0.2 \times 10^{-8}\,\mathrm{s}. \quad (27)$$

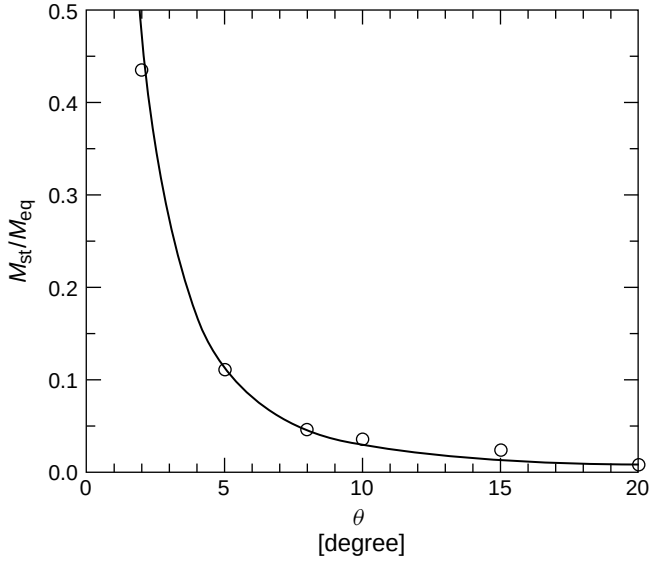

Figure 2 Reduced steady-state magnetization as a function of the angle θ between external and effective field in protonated OTP, together with a best-fit theoretical curve with $\tau_c = 6.5 \pm 0.2 \times 10^{-8}$ s

As for the time-decaying part, it consists of three parts: an initial plateau due to the non-observation of the nuclei close to the centers, an exponential function of $\sqrt{t}$ of the form shown in equation (26), and a final exponential decay as a function of t, when spin diffusion becomes faster than direct relaxation. For the part evolving according to equation (26), the variation of $\tau_{1/2}$ as a function of the angle θ is shown in Figure 3 together with a best-fit curve.

Using the preceding value of τ_c, it yields the concentration of paramagnetic centers

$$N_p = 6.4 \pm 0.1 \times 10^{19}\,\mathrm{cm}^{-3} \quad (28)$$

The fact that this concentration is larger than the nominal one is attributed to the evaporation of some OTP during the degassing process.

These results constitute a validation of the experimental procedure, and provide in addition two pieces of information: the electronic relaxation time and the concentration of the centers.

5 RESULTS FOR POLYMER SOLUTIONS

5.1 Polymers with Randomly Distributed Paramagnetic Centers

The only system studied consisted of poly 2-vinyl pyridine (P_2VP) of average molecular mass $2 \times 10^5\,\mathrm{g\,mole}^{-1}$ on which paramagnetic vanadyl sulphate $VOSO_4$ was grafted at random. It was in semi-dilute solution ($c = 0.05\,\mathrm{g\,cm}^{-3}$) in deuterated glycerol. This system, studied only for illustration purposes, did not use rf irradiation, and it concerns only the longitudinal relaxation.

For polymers of fractal dimension D with random relaxing centers grafted on them, a statistical calculation analogous to that use for 3-D solids yields an evolution law of the magnetization of the form

$$\langle I_Z\rangle(t) - \langle I_Z\rangle_{st} = (\langle I_Z\rangle(0) - \langle I_Z\rangle_{st}) \exp\left[-\left(\frac{t}{\tau_1}\right)^{D/6}\right] \quad (29)$$

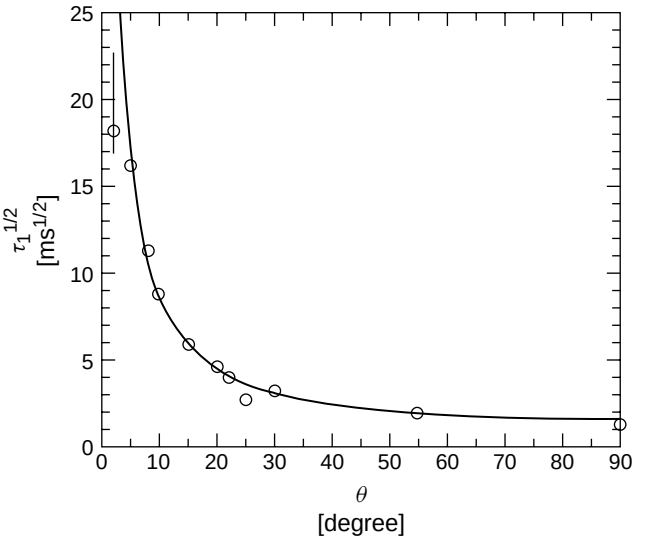

Figure 3 Variation of $\tau_1^{1/2}$ as a function of the angle θ in protonated OTP, together with a best-fit curve with $N_p = 6.4 \pm 0.1 \times 10^{19}\,\mathrm{cm}^{-3}$

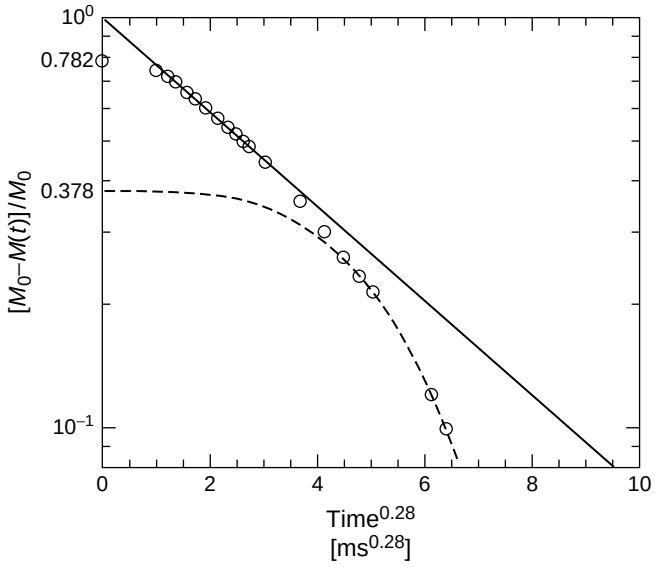

Figure 4 Longitudinal relaxation curve for a semi-dilute solution of P_2VP. The initial decay, an exponential function of $t^{D/6} = t^{0.28}$ (solid line), is followed by an exponential function of time (dashed curve)

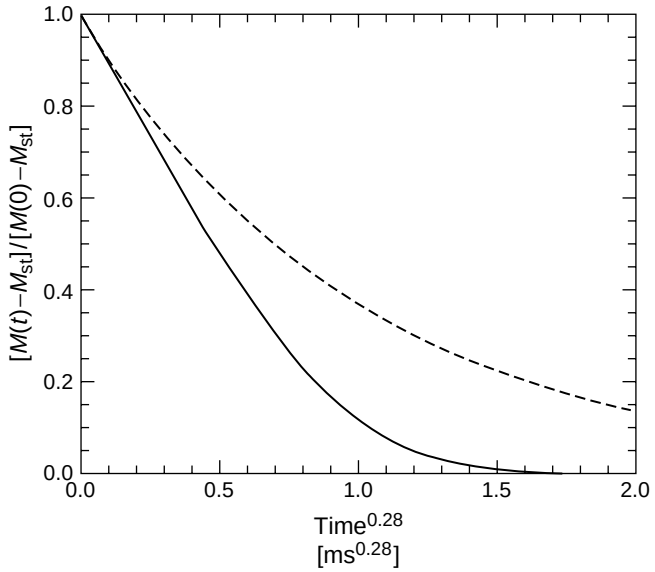

Figure 5 Theoretical variation of the reduced magnetization as a function of $t^{0.28}$ in a dilute solution of polymers with one relaxation center at one end (solid curve). For comparison, the dashed curve is an exponential with the same initial slope

The experimental magnetization evolution, shown in Figure 4, does indeed display such an initial behavior, followed at longer times by an exponential variation, when spin diffusion takes over.

5.2 Polymers with One Paramagnetic Center at One End

The situation for relaxation is markedly different from the preceding one. Indeed, for dilute solution, the relaxation of the nuclei of a polymer is essentially produced by only one center, the one located on the polymer. What the statistical calculation predicts is that over a substantial range, the evolution of the magnetization is a *linear* function of $t^{D/6}$

$$\langle I_Z\rangle(t) - \langle I_Z\rangle_{st} = (\langle I_Z\rangle(0) - \langle I_Z\rangle_{st})\left(1 - \left(\frac{t}{\tau_1}\right)^{D/6}\right) \quad (30)$$

The theoretical curve for the model used is shown in Figure 5, together with an exponential of equal initial slope for comparison. The expected variation for the polymer is indeed linear from initial value 1 down to about 0.4–0.3. We come now to the experimental investigation.

The polymer used is polystyrene of molecular mass of about 8000 (i.e., corresponding to 80 monomers) at the end of which was grafted the radical tetramethyl-2,2,5,5 carboxy-3 pyrrolinyl oxyle-1 (commercial name 3-carboxy PROXYL), diluted in deuterated OTP and then cooled to 120 K The overlap concentration c^* is estimated to about $0.25\,\mathrm{g\,cm^{-3}}$. Experiments were performed on dilute and semi-dilute solutions.

From a study of the steady-state reduced polarization as a function of the angle θ, shown in Figure 6, the best-fit value for the correlation time is

$$\tau_c = 2.6 \pm 0.4 \times 10^{-8}\,\mathrm{s}. \quad (31)$$

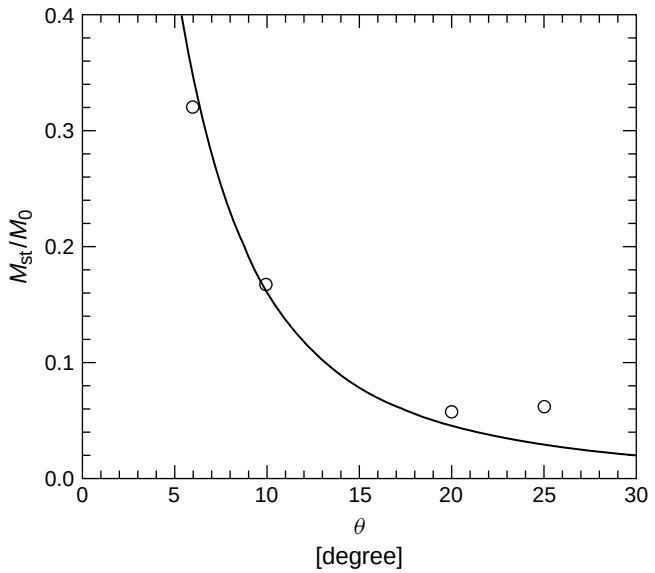

Figure 6 Dilute solution of polystyrene with one relaxing center at one end. Reduced steady-state magnetization as a function of the angle θ, together with a best-fit theoretical curve with $\tau_c = 2.5 \pm 0.4 \times 10^{-8}\,\mathrm{s}$

5.2.1 Dilute Solution

The polystyrene concentration was $0.05\,\mathrm{g\,cm^{-3}}$. A typical evolution curve, for the magic angle $\theta = \mathrm{acos}(1/\sqrt{3})$, is shown in Figure 7.

One observes indeed a linear variation, but down to about 0.1, that is beyond theoretical expectation. This may be due to the crude structure model used: a sudden drop of the nuclear concentration beyond R, or to the interaction with the other polymers. In the absence of any firm theoretical model for the concentration variation of the nuclear density at the largest

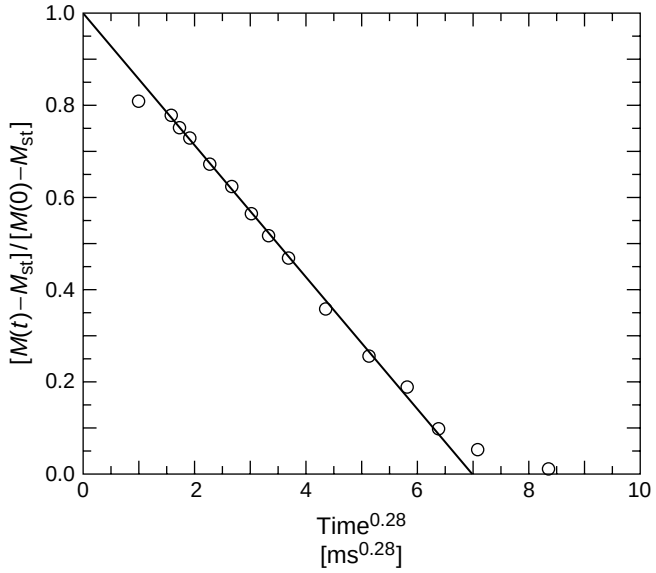

Figure 7 Dilute solution of polystyrene with one relaxing center at one end. Relaxation along an effective field at the magic angle from the external field. Linear reduced magnetization as a function of $t^{0.28}$

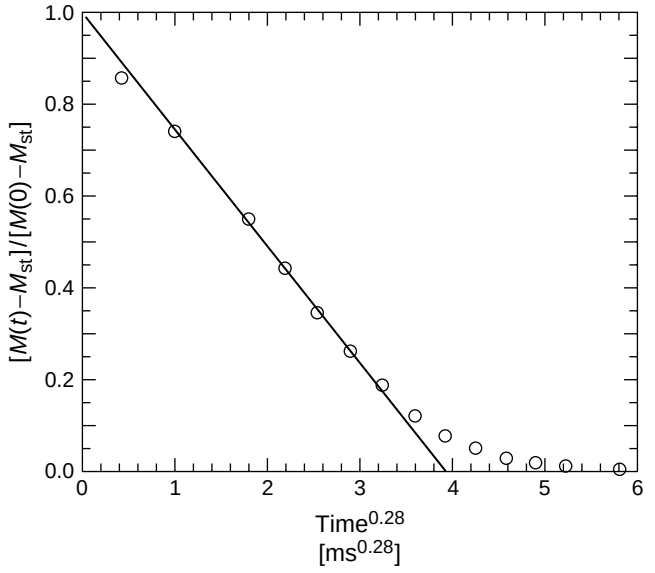

Figure 8 Semi-dilute solution of polystyrene with one relaxing center at one end, under irradiation at resonance. Linear reduced magnetization as a function of $t^{0.28}$

distances, we did not investigate this matter further. Knowing τ_c from the steady-state variation, it is possible to determine the radius R from the evolution with angle θ of the value of τ_1 in equation (30). The best fit value is:

$$R = 3.1 \pm 0.15\,\text{nm}, \tag{32}$$

to be compared with the neutron-scattering-measured value $R_G = 2.1\,\text{nm}$ and the corresponding $R_F = 5.2\,\text{nm}$ All three radii are indeed of the same order of magnitude.

5.2.2 Semi-dilute Solution

The same polystyrene polymers were used at a concentration of $0.30\,\text{g cm}^{-3}$, slightly above the overlap concentration $c^* = 0.25\,\text{g cm}^{-3}$. The experimental relaxation evolution is shown in Figures 8 and 9 for $\theta = 90°$. In Figure 8, the signal is plotted as a function of $t^{D/6}$ and it exhibits the same linear variation as for the dilute solution. In Figure 9, the signal is plotted as a function of $t^{1/2}$ on a logarithmic scale, showing that in the end the signal varies as an exponential function of $\sqrt{t}$. All these features agree qualitatively with the model of semi-dilute solutions of polymers: a region of fractal dimension 1.7 with at most one impurity, surrounded by a homogeneous medium with randomly distributed paramagnetic centers.

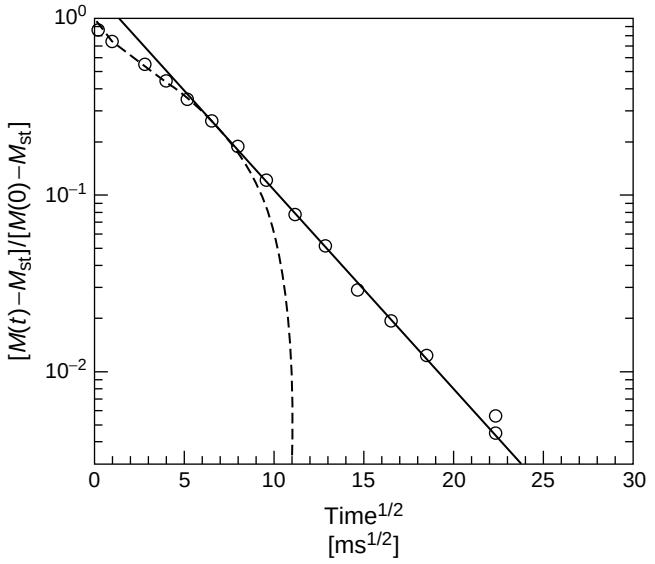

Figure 9 Same as Figure 8, but with different scales: Logarithm of the reduced magnetization as a function of $t^{1/2}$ (solid line), and its variation as a function of $t^{0.28}$ (dashed curve)

6 THE PROBLEM OF SPIN DIFFUSION

This topic, which is not directly connected with the NMR investigation of the polymer structure, will be given a schematic discussion only.

When the angle between the effective and external fields is different from the magic angle, i.e., when the effective secular dipolar interactions do not vanish, the end of evolution of the signal is an exponential function of time. This is brought about by the homogenization of the polarization through flip-flop processes under the influence of the secular dipole-dipole interactions. In usual 3-D solids, this nuclear polarization transfer through space is tentatively described by a diffusion equation, and referred to as spin diffusion. All experimental results on nuclear relaxation by paramagnetic centers in non-conducting solids are in good agreement with this description.

Besides more or less complicated and approximate theoretical treatments of this problem, a particularly enlightening picture of spin-diffusion-induced exponential evolution is that of Blumberg. We summarize it for the so-called diffusion-limited case, in a spherical system of radius R with a relaxing center at the origin, and neglect the angular dependence of the

coefficient C, in equation (9), as well as that of the diffusion coefficient D. The time necessary for direct relaxation to reach the distance r is of the order of $t_r = r^6/C$, whereas the corresponding time for diffusion is of the order of $t_d = r^2/D$. Both times are equal at a distance

$$b \approx \left(\frac{C}{D}\right)^{1/4} \tag{33}$$

Up to this distance, relaxation acts independently on the nuclei, and beyond it diffusion homogenizes the polarization. The relaxation of this part is exponential, with a relaxation rate equal to the average of the individual rates. If ρ is the nuclear density, we obtain

$$\frac{1}{T_1} \approx \frac{C\int_b^R \rho r^{-4}\,dr}{\int_b^R \rho r^2\,dr} \tag{34}$$

which, for a 3-D solid where the density is constant and for $b \ll R$, yields

$$\frac{1}{T_1} \approx \frac{C}{R^3 b^3} \tag{35}$$

a result equal, within a numerical factor of order unity, to that predicted by more sophisticated methods, and in agreement with experiment for randomly distributed centers at low concentration, with R equal to the average distance between centers. We can compare it with the time τ necessary for diffusion to travel the distance R

$$\tau \approx \frac{R^2}{D} \tag{36}$$

We obtain from equations (33) and (35)

$$\frac{\tau}{T_1} \approx \frac{(C/D)R^2}{R^3 b^3} \approx \frac{b}{R} \ll 1 \tag{37}$$

which validates the coherence of the model.

This approach is not adapted to dilute polymers of fractal dimension $D = 1.7$, for two reasons. First, and contrary to direct relaxation, it is hardly justified to use an 'average' polymer, since the dipolar-induced transport of polarization is likely to depend critically on the spatial structure of each polymer. In particular, linear polymers make loops, and there is at present no clean theory of the relative importance of polarization transport along the polymer and through monomers well separated in the linear polymer but accidentally close in space. It is even not known whether this transport can be described by a diffusion equation, nor if the average square distance over which polarization is transported is proportional to time. The second reason why the Blumberg approach fails is that it would yield unphysical predictions even if we could use an average polymer structure and a diffusion equation. We see this briefly. Let us assume that in a polymer both equations (33) and (34) are valid. With a density $\rho \propto r^{D-3}$, we obtain for $b \ll R$, and after a little algebra

$$\frac{1}{T_1} \approx \frac{C}{R^D b^{6-D}} \text{ and } \frac{\tau}{T_1} \approx \left(\frac{b}{R}\right)^{D-2} \tag{38}$$

For $D < 2$, the last ratio is larger than unity! This is in contradiction with the hypotheses of the model. The conclusion is that for a system of low dimensionality, diffusion can take over direct relaxation only at distance substantially larger than b as given by equation (33). This conclusion is confirmed by the experimental results on dilute and semi-dilute solutions of polystyrene. As an example, for an angle $\theta = 25°$ between effective and external fields in a dilute solution of polystyrene, the exponential part of the signal corresponds approximately to 30 per cent of the total signal. The distance r_1 beyond which the polarization is homogenized by diffusion corresponds to $(r_1/R)^D \simeq 0.7$ that is $(r_1/R \simeq 0.8)$. We use this value in equation (34), with the integrations between r_1 and R for calculating T_1. As for the diffusion time, it has to be taken from r_1 to $R : \tau \approx (R - r_1)^2/D$. We obtain finally, with the help of equation (33)

$$\frac{\tau}{T_1} \approx 0.03\left(\frac{b}{R}\right)^4 \ll 1, \tag{39}$$

which lifts the inconsistency.

It would be pointless to extend the discussion further, both because of the doubtful validity of a spin diffusion equation for a collection of polymers and because it is at distances close to R that the model for the variation of the nuclear density with distance should cease to be strictly valid.

7 CONCLUSION AND PERSPECTIVES

The study of direct spin-lattice relaxation of polymers by fixed paramagnetic centers grafted on the polymers turns out to be indeed a useful complement to their investigation by small angle neutron scattering, in particular for confirming their fractal structure. At the present experimental stage, it cannot be claimed that NMR by itself can actually determine the fractal dimension with great accuracy, but it confirms the findings of SANS from a very different type of approach.

However, NMR has potential capabilities that might go beyond those of SANS. An example provided by the experiments on dilute solutions of polystyrene is the shape of the relaxation decay, distinctly different in its last part from theoretical expectation, which hints at the possibility of refining the form of nuclear density near the edge of the polymer. We list a number of openings for which NMR could equally well provide information essentially unavailable by other means:

- placing the paramagnetic centers in the solvent rather than on the polymers, which could provide information on the space excluded by the presence of the polymers and its shape.
- use of a polycrystalline host in order to reveal whether this has an influence on the polymer shape. This possibility is forbidden to SANS, since the grain boundaries would cause a neutron scattering far larger than that due to the polymers.
- use of partly deuterated polymers, so as to have access to the position of given parts of the polymer relative to the end where the relaxing center is grafted.
- consider other polymer configurations. A general but still preliminary study has in fact been made on the relaxation characteristics of polymers close to a surface where paramagnetic centers are located, either grafted to the surface

or adsorbed by the surface, as a function of the surface density of the polymers with respect to their length.[16] This study also envisioned the interest of using partly deuterated polymers.

8 REFERENCES

1. P. Flory, 'Statistical Mechanics of Chain Molecules', reprinted edn., Hanser Publishers: Munich, 1989.
2. P. G. de Gennes, 'Scaling Concepts in Polymer Physics', Cornell University Press: Ithaca and London, 1979.
3. J. des Cloizeaux and G. Jannink, 'Polymers in Solution: Their Modelling and Structure', Clarendon Press: Oxford, 1990.
4. M. G. D. Van der Grinten, H. Glättli, C. Fermon, M. Eisenkremer, and M. Pinot, *Nucl. Instrum. Methods Phys. Res.*, 1995, **A356**, 422–431.
5. H. B. Stuhrmann, *Physica*, 1999, **B267–268**, 92.
6. T. Tabti, *Thèse de Doctorat*, Université de Paris XI, 1995, No. 3699.
7. T. Tabti, M. Goldman, J.-F. Jacquinot, C. Fermon, and G. Le Goff, *J. Chem. Phys.*, 1997, **107**, 9239.
8. F. Devreux, J.-P. Boilot, F. Chaput, and B. Sapoval, *Phys. Rev. Lett.*, 1990, **65**, 614.
9. N. Bloembergen, *Physica*, 1949, **15**, 386.
10. W. E. Blumberg, *Phys. Rev.*, 1960, **119**, 79.
11. D. Tse and S. R. Hartmann, *Phys. Rev. Lett.*, 1968, **21**, 511.
12. N. A. Lin and S. R. Hartmann, *Phys. Rev.*, 1973, **B8**, 4079.
13. A. Abragam, 'The Principles of Nuclear Magnetism', Oxford University Press: Oxford, 1961.
14. K. Tomita, *Prog. Theor. Phys.*, 1958, **19**, 541.
15. M. Goldman, *J. Magn. Reson.*, 2001, **149**, 160–187.
16. T. Tabti, J. Chikina, J.-F. Jacquinot, and M. Daoud, *Phys. Rev. E*, 1999, **60**, 645.

Biographical Sketches

Jacques-François Jacquinot, *b* 1946. Studied at Ecole Normale Supérieure de Saint Cloud. Senior Physicist at Commissariat à l'Energie Atomique (CEA) 1974–present. Research specialties: spin temperature, nuclear magnetic ordering, relaxation in solids, solid state NMR, spin dynamics in rotating samples.

Maurice Goldman, *b* 1933. Diplôme d'Ingénieur Chimiste ESPCI, 1955; Doctorat d'Etat, 1967, University of Paris. Physicist, Commissariat à l'Energie Atomique (CEA), 1955–69 and 1984–89. Vice-Director, Collège de France, 1969–83. Research Director, CEA, 1989–93. Scientific Advisor, CEA, 1993–present. Vice-President, President, Past-President of ISMAR, 1992–present. Approx.130 publications, including three books. Research specialties: spin temperature and thermodynamics, dynamic nuclear polarization, nuclear magnetic ordering, relaxation in liquids and solids, and quantum theory of high-resolution NMR.

Polymer Dynamics and Order from Multidimensional Solid State NMR

Hans Wolfgang Spiess

Max-Planck-Institut für Polymerforschung, Mainz, Germany

1	Introduction	1
2	Solid State NMR	1
3	Applications	4
4	Conclusions	13
5	Related Articles	14
6	References	14

1 INTRODUCTION

One of the key goals of materials science is the establishment of structure–property relationships in order to improve known and design new materials. This holds in particular for synthetic polymers, whose properties depend on both the molecular structure and the organization of the macromolecules in the solid state: their phase structure, morphology, molecular order and molecular dynamics.[1,2] Macroscopic as well as microscopic parameters are influenced by processing that follows the chemical synthesis. This calls for powerful analytical tools that can probe these aspects in the material as it is used, predominantly in the solid state. The structural aspects are studied mostly by scattering techniques or by microscopy. Information about dynamic aspects are deduced mainly from scattering or relaxation experiments.[3] Among these, nuclear magnetic resonance[4,5] is well established in structural characterization of liquids or compounds in solution; however, this is much less the case for solids.[6,7] Moreover, NMR offers numerous ways to study dynamic aspects over a large range of characteristic rates. The main advantage of NMR is its unprecedented selectivity. Thus, it is desirable to exploit this technique for studying the structure and dynamics of solid polymers.[7,8] However, owing to the presence of angular-dependent anisotropic interactions, the spectral resolution of solid state NMR spectra is orders of magnitude lower than that of high-resolution NMR in liquids. Important improvements were achieved in the 1970s by combining high-speed mechanical rotation of the sample with ingenious manipulations of the nuclear spins, such as multiple pulse irradiation, high-power decoupling and cross polarization.[9] Moreover, two- and higher-dimensional NMR techniques have been introduced that offer fundamental advantages.[10] First, as in liquids, the introduction of a new frequency dimension provides a means to increase the spectral resolution. Even more importantly, multidimensional spectroscopy also provides routes to new information, unavailable from 1D spectra even in the limit of high resolution. Experiments can be designed that correlate different spin interactions providing different structural information, or relate various states taken up by the molecular unit during different time periods by exchange, and in this way they can probe dynamic processes in real time.

Progress in multidimensional solid state NMR has been hampered by experimental and conceptual difficulties, which have now been overcome.[11–14] This article briefly outlines some of the main concepts and illustrates the information available from multidimensional solid state NMR spectra about polymer structure and dynamics through selected experimental examples, mainly from the author's laboratory.

Polymer dynamics is of central interest in our studies. Of the great variety of molecular motions possible in polymers (e.g., translations, rotations, and vibrations), rotations have the most pronounced effects on NMR lineshapes and relaxation parameters. Thus, multidimensional NMR provides, in particular, unique information about rotational motions. Their timescales are followed in real time over many orders of magnitude, covering in particular the regime of slow motions, which govern the mechanical properties of polymers. Moreover, the higher-order correlation functions provided by multidimensional NMR yield previously inaccessible model-independent information about the geometry of rotational motions, the orientational memory of molecular units involved in complex dynamics, and the nature of nonexponential relaxation in disordered systems. This information collected for a variety of polymers should eventually lead to a better understanding of their mechanical and rheological behavior, which is of interest not only for conventional but also for new advanced polymeric materials.

Two other aspects are particularly important for establishing structure–property relationships for polymer materials, namely, chain alignment in partially ordered systems and domain sizes in heterogeneous polymer materials. The orientation of macromolecular units is used to improve the properties of polymers for such different applications as high-tensile-strength fibres and nonlinear optical materials for information technology. Advanced polymer materials almost inevitably consist of more than one component, which often leads to phase separation. Careful design of the molar ratios as well as the size, composition, and morphology of the different phases offers a means to control the mechanical, electrical, and optical properties. Small domains that extend over only a few nanometers, as well as interfacial regions between the different phases, are particularly difficult to characterize. Major advances have been achieved in these areas by introducing the concepts of multidimensional spectroscopy. The new solid state NMR techniques nicely supplement well-established scattering and microscopic methods, as demonstrated by various experimental examples and by explicit comparison.

2 SOLID STATE NMR

The various aspects of solid state NMR are treated in detail in other articles in this Encyclopedia. Therefore, only a brief outline of the techniques used in the applications described below are given here. A full treatment is also available in our extended monograph on solid state NMR and polymers.[14]

2.1 One-Dimensional NMR

Solid state NMR exploits anisotropic, angular-dependent interactions of nuclear spins with their surroundings,[4,5] in particular magnetic dipole–dipole coupling of nuclei among themselves. This leads to broad NMR lines covering approximately 50 kHz for ^{1}H–^{1}H homonuclear coupling and approximately 25 kHz for ^{1}H–^{13}C heteronuclear coupling. The anisotropy of the chemical shift results in powder patterns covering approximately 15 kHz at a field strength of 7 T. In addition to these magnetic interactions, nuclei with spin $I > \frac{1}{2}$ can also have electric quadrupole moments and are subject to quadrupole coupling to the electric field gradient at the nuclear site. For ^{2}H ($I = 1$) in C–^{2}H bonds, it leads to spectral splittings of about 250 kHz. Since C–H bonds are common in polymers, ^{2}H labeling is particularly useful.

If one of the above mentioned couplings dominates, either because of its strength or because the others have been suppressed by decoupling, the angular dependence of the NMR frequency in high magnetic fields is alike for all couplings, and is given by

$$\omega = \omega_{\mathrm{L}} + \tfrac{1}{2}\Delta(3\cos^2\theta - 1 - \eta\sin^2\theta\cos 2\phi) \qquad (1)$$

Here ω_{L} is the Larmor frequency, Δ describes the strength of the anisotropic coupling (i.e., the anisotropic chemical shift or ^{13}C–^{1}H dipole–dipole coupling for ^{13}C or the quadrupole coupling for ^{2}H), and η is the asymmetry parameter describing the deviation of the anisotropic coupling from axial symmetry ($0 \leq \eta \leq 1$). The angles θ and ϕ are the polar angles of the magnetic field $\boldsymbol{B}_0$ in the principal axis system of the coupling tensor. This in turn is often simply related to the molecular geometry, with the unique axis lying along a bond direction (e.g., for dipole–dipole coupling along the ^{13}C–^{1}H bond, and for quadrupole coupling along the C–^{2}H bond), or perpendicular to an sp^2 plane as for ^{13}C chemical shift tensors in aromatic rings, etc. Depending on the total spin involved, signals described by equation (1) and their mirror images with respect to ω_{L} may be superimposed, and in powder samples spectra for all orientations are added to yield the powder lineshape (e.g., the Pake pattern for ^{2}H with spin $I = 1$).

These anisotropic interactions can be removed under rapid magic angle spinning (MAS), yielding liquid-like spectra if the spinning frequency ω_{R} is significantly larger than the width of the anisotropic powder pattern ($\omega_{\mathrm{R}} \gg \Delta$). In the slow-spinning regime, $\omega_{\mathrm{R}} < \Delta$, the centerband at the isotropic chemical shift is flanked by sidebands at multiples of ω_{R}, thus retaining information about the anisotropic coupling.

A few examples of 1D NMR spectra are collected in Figure 1, displaying single ^{13}C lines at the isotropic chemical shifts [Figure 1(a)], a chemical shift powder pattern for ^{13}C in a carboxyl group and its relation to the molecular geometry [Figure 1(b)], a ^{13}C MAS sideband pattern [Figure 1(c)], and ^{2}H NMR lineshapes for an isotropic powder [Pake pattern, Figure 1(d)], a uniaxially drawn fiber [Figure 1(e)], and a phenyl ring with motional averaging due to flipping about the axis shown [Figure 1(f)].

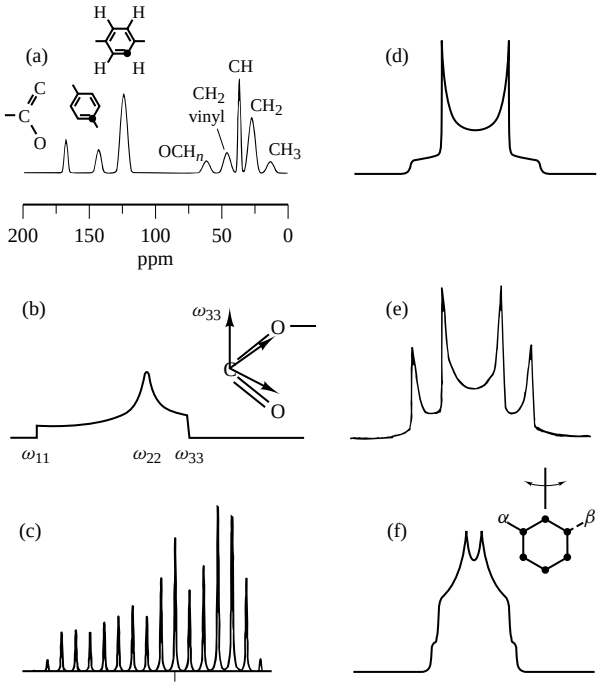

Figure 1 Examples of solid state NMR spectra: (a) ^{13}C CP MAS spectrum displaying isotropic chemical shifts of different functional groups; (b) ^{13}C powder pattern for carboxyl group, governed by chemical shift anisotropy and relationship of the principal axes system of the shielding tensor to the molecular framework; (c) ^{13}C sidebands due to anisotropic chemical shift and slow MAS; (d) ^{2}H NMR lineshape for rigid isotropic powder (Pake pattern); (e) ^{2}H NMR lineshape for a uniaxial fiber; (f) ^{2}H NMR lineshape for flipping phenyl rings

2.2 Two-Dimensional NMR

A 2D NMR spectrum is generated by recording a two-dimensional data set following pulsed irradiation as a function of two time variables, as shown schematically in Figure 2(a), and subsequent double Fourier transformation. The development of the nuclear spin system in the evolution period with incremented time t_1 at the beginning of the pulse sequence provides the basis for the first frequency dimension ω_1. The NMR signal is detected in the detection period with time t_2 at the end of the pulse sequence, providing the basis for the second frequency dimension ω_2. In the exchange experiments described here, a variable mixing period of duration t_{m}, during which dynamic processes can take place, is inserted between evolution and detection. In this way, slow molecular dynamics are probed in real time. The concept of 2D spectroscopy is readily extended to three and higher dimensions by inserting additional evolution and mixing times.

The most important aspects of 2D NMR are exemplified in Figure 2(b)–(d). First, 2D NMR is often used to increase the spectral resolution of solid state NMR spectra by separating different interactions. As an example, consider 1D sideband patterns. These are often hampered by a severe loss of spectral resolution due to overlapping sidebands of ^{13}C with different isotropic chemical shifts. This loss of resolution is circumvented at the expense of a new frequency dimension, as demonstrated in Figure 2(b), where the sideband patterns for the different sites experiencing different isotropic chemical shifts are separated from each other.

Other 2D NMR techniques aim at obtaining new information by correlating different interactions. As a specific example, Figure 2(c) displays a 2D NMR spectrum correlating a ^{13}C chemical shift with a ^{13}C–^{1}H dipolar powder

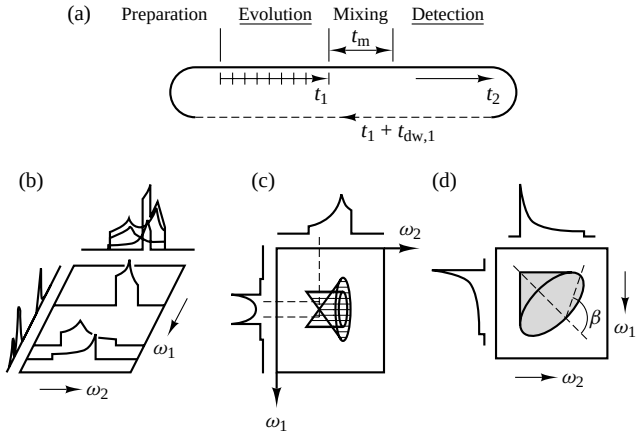

Figure 2 Principles of 2D NMR spectroscopy: (a) basic pulse sequence; (b) separation of isotropic and anisotropic chemical shifts; (c) correlation of anisotropic chemical shift and dipolar interaction; (d) 2D exchange spectrum reflecting the reorientation about the angle β through an elliptical exchange ridge

pattern. Since the dipole–dipole coupling is well understood in terms of bond lengths and angles, such spectra provide valuable information about the orientation of the principal axes of the chemical shift tensor in relation to structural units such as CH_2– groups etc.

As far as applications to polymers are concerned, 2D exchange NMR has proved to be particularly valuable. First of all, by varying the mixing time t_m, slow dynamic processes in the range of milliseconds to seconds can be followed in real time. Moreover, 2D exchange NMR spectra yield unique and model-independent information about the geometry of rotational motions. In fact, for axially symmetric tensors, ubiquitous in ^{2}H NMR of polymers, the 2D exchange spectrum yields elliptical ridge patterns from which the angle about which the molecules have rotated can be read off with a ruler [Figure 2(d)].

2.3 Multidimensional NMR

The concepts of 2D NMR are readily extended to higher dimensions. By combining the different schemes of 2D NMR, a large variety of three-dimensional experiments can be designed, as discussed, for example, for liquid state NMR by Griesinger et al.[15] In liquid state NMR, 3D techniques are mainly used to increase the spectral resolution. Although this is also an important aspect in solid state NMR (see below), 3D exchange NMR as shown schematically in Figure 3 offers fundamentally new information about higher-order correlation functions of complex motions in the solid state. Since the orientation of a given molecule is probed three times, different pathways taken by the molecule from the beginning to the end lead to different exchange signals. Thus, different motional mechanisms may be distinguished. Such information is inaccessible from 2D NMR, where the orientation of the molecule is measured only twice, and therefore no information is available about the trajectory a molecule follows when rotating from one orientation to another. Specific examples of applying three- and higher-dimensional NMR techniques to polymers are discussed below.

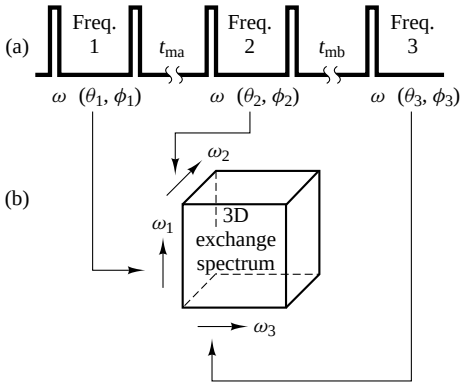

Figure 3 Principle of 3D exchange NMR: (a) pulse sequence; (b) corresponding spectral cube

2.4 Spin Diffusion

Solid state NMR can also provide information about intermolecular distances and domain sizes in heterogeneous polymers by means of spin diffusion, i.e., the diffusion of nuclear magnetization through the sample without transport of material. It is mediated by dipolar couplings, and therefore is most efficient among protons.[4] Figure 4 demonstrates schematically the connection between the spatial distribution of proton magnetization within the sample and the solid state NMR spectra for a two-phase system with spatially constant proton density. In equilibrium, the proton polarization is spatially constant, and the relative signal intensities in an NMR spectrum reflect the integral chemical composition of the sample. Differences in the chemical structure or in local molecular mobility can be used to select the proton magnetization in one component (A) and suppress it in the other (B) [Figure 4(a)]. The subsequent redistribution of magnetization by ^{1}H spin diffusion is monitored by NMR spectroscopy [Figure 4(b)]. For short times, the mean-square distance $\langle x^2 \rangle$ that the magnetization moves within time t is given by $\langle x^2 \rangle = aDt$, where D is the spin diffusion constant of the system under study. The factor a depends on the geometry of the packing (e.g., lamellar, cylindrical, or spherical). The spin diffusion constant D is related to the strength of the dipolar coupling as reflected in the width of the ^{1}H NMR

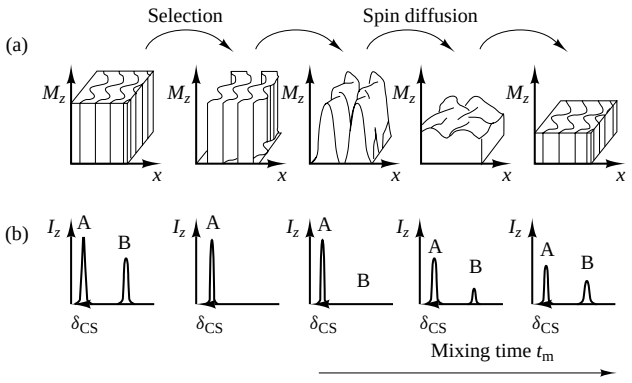

Figure 4 Schematic representation of ^{1}H spin diffusion in a two-phase system (A,B) with spatially constant proton density: (a) spatial distribution of ^{1}H magnetization; (b) NMR spectra for different mixing times t_m

spectrum, and has been calibrated for polymers of different molecular mobility by comparing spin diffusion data with direct measurements of domain sizes by X-ray scattering and electron microscopy.[16,17]

3 APPLICATIONS

3.1 Conformational Structure

The packing behavior of polymers depends strongly on their chain microstructure.[18] In particular, it is well known that only stereoregular macromolecules can crystallize. A schematic representation of the carbon backbone of an amorphous polymer is depicted in Figure 5(a). In order to specify the conformation of such a segment, one must know the bond length l, the valence angle Θ and the rotational angles Φ_i. The rotational potential $E(\Phi_i)$ around the central C–C bond in n-butane is plotted in Figure 5(b). The minima for the *gauche* conformers are higher than that of the *trans* by about 3.5 kJ mol^{-1}. Since this energy difference is comparable to the thermal energy at ambient temperatures, a large number of conformations is normally present in an amorphous polymer. Therefore, experimental techniques are needed that can check the conformational statistics.

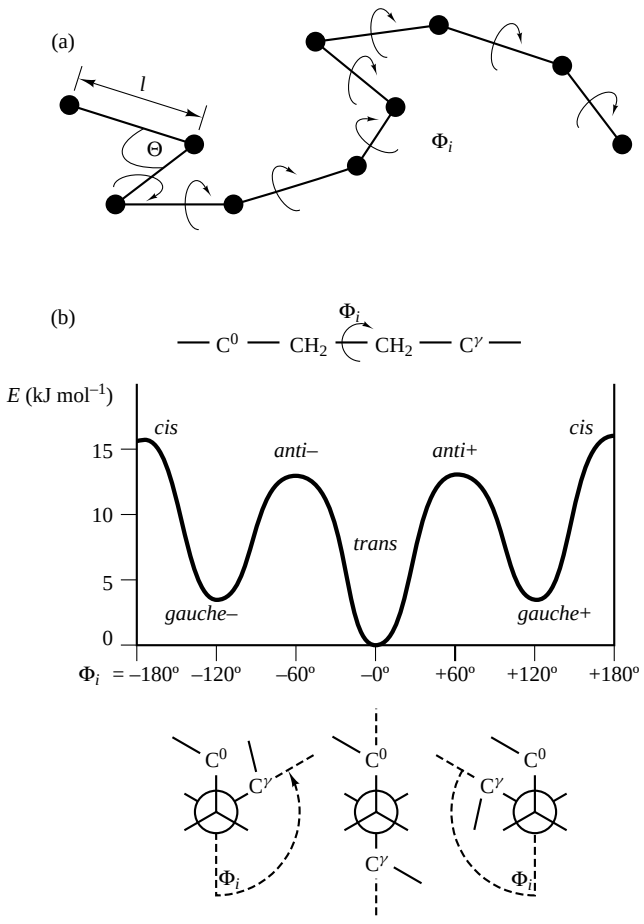

Figure 5 (a) Schematic representation of a carbon-backbone polymer chain in the amorphous state. (b) The potential energy E for rotation about the central carbon of a butane unit in a polymer chain together with Newman projections illustrating the different interactions between the atom C^0 and its γ-*gauche* substituent $C\gamma$ for the conformations *gauche*− ($g-$), *trans* (t) and *gauche*+ ($g+$)

NMR of polymers in solution is well established for determining the chain microstructure.[6,19] Glassy solid state amorphous polymers typically display broad ^{13}C *c*ross *p*olarization *m*agic *a*ngle *s*pinning (CP MAS) NMR lines due to an inhomogenous superposition of contributions from different conformations. These conformational effects on ^{13}C chemical shift have traditionally been attributed to the shielding of a reference carbon C^0 by the γ-substituent C^γ [see Figure 5(b)] in a semiempirical fashion ('the γ-*gauche* effect').[6,8,19] It has been shown that these shifts can be calculated quantitatively on the ab initio level[20] by exploiting the high computing power of modern workstations and advanced schemes for calculating NMR chemical shifts, such as *i*ndividual *g*auge for *l*ocalized *o*rbitals (IGLO).[21] Thus, it is hoped that eventually the spread in chemical ^{13}C shifts in amorphous polymers can be analyzed to provide structural information, in particular because profound correlations of the chemical shift with specific geometrical aspects such as C–C bond lengths and dihedral angles emerge.

As a specific example, Figure 6(a) displays the ^{13}C CP MAS spectrum of atactic polypropylene (aPP), with the assignment of the two partially resolved peaks and the shoulder corresponding to specific conformations of a tetrameric unit depicted in Figure 6(b). The assignment is readily made by comparison with the chemically shifted peak positions of the solid state ^{13}C NMR spectra of crystalline isotactic[22] and syndiotactic polypropylene.[23] In the glassy state, the peaks are broadened owing to differences in the geometry[20] and to the fact that numerous configurations contribute to the three main conformations, as discussed in detail elsewhere.[24]

3.2 Molecular Order

Structural characterization of polymers often requires the determination of the alignment of macromolecular chains.[25] Orientation in polymers is often induced by the production process, and has strong effects on product properties. Through the angular-dependent NMR interactions, orientation is amenable to NMR experiments. As opposed to most classical techniques, the order of both crystalline and amorphous components can be studied. For ^{2}H- or ^{13}C-enriched samples, one-dimensional experiments are sufficient to obtain orientation distributions in terms of a single angle.[26] In order to reconstruct two-dimensional orientation distributions, or to resolve overlapping patterns in natural abundance ^{13}C spectra, multidimensional spectra are required. Two examples are discussed here. Both involve 3D spectra of ^{13}C in natural abundance.

3.2.1 Chain Alignment in Drawn Poly(ethylene terephthalate)

In the case of a biaxially drawn film of poly(ethylene terephthalate) (PET) from an industrial process line, the orientational distribution was mapped out in the 3D exchange NMR spectrum by flipping the sample between different orientations with respect to the magnetic field (*d*irection *e*xchange with *c*orrelation for *o*rientation *d*istribution *e*valuation and *r*econstruction, DECODER).[27] The NMR signals of the different structural units of PET are completely resolved in the

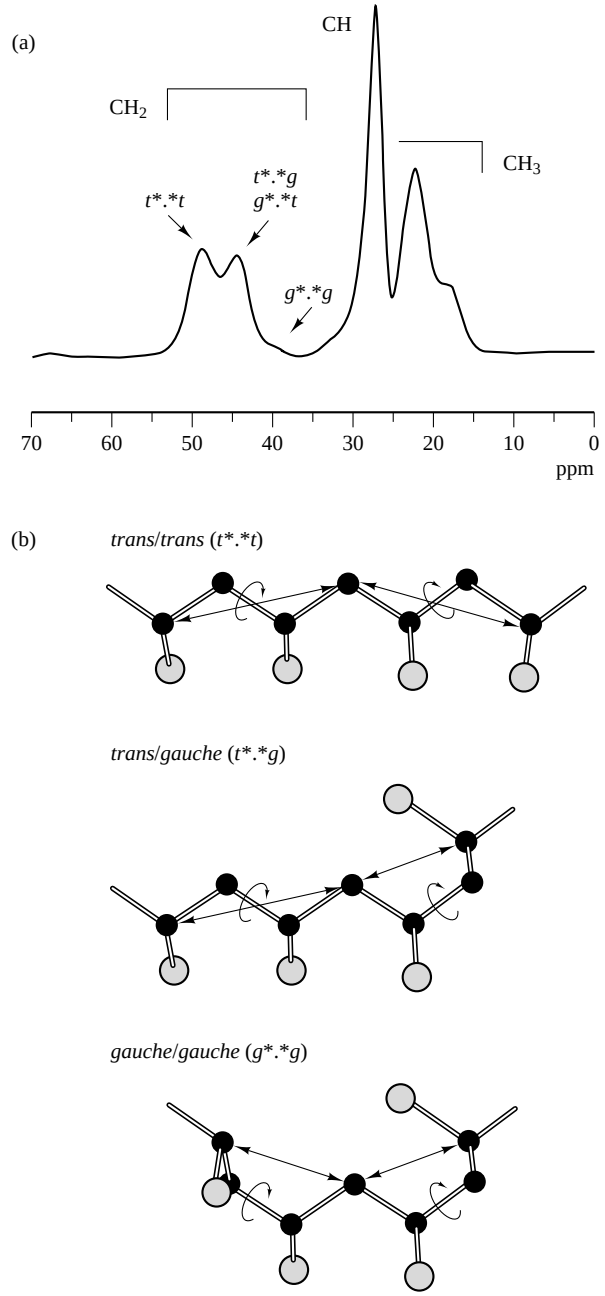

Figure 6 (a) ^{13}C CP MAS NMR spectrum of an amorphous polypropylene at T = 252 K (T_g − 6 K).[24] Note that the observed splitting is due to conformational effects. (b) Schematic representation of the conformations of a tetrameric unit in polypropylene relevant for the γ-*gauche* effect of the methylene group C^0H_2. One particular configuration, the mrr tetrad, is selected, here. The abbreviation *t**.**g* stands for a conformational unit around a carbon center denoted by '.' with undefined conformations of the neighboring bonds and *t* and *g* conformations of the next-neighboring bonds

3D cube, and their orientation distributions thus separately determined.[28] As depicted in Figure 7(b), the chain axes are confined to the film plane (full-width at half-maximum, fwhm, of 15°), while the in-plane distribution is much broader (fwhm ≈90°). The planes containing the phenylene rings and the carboxyl group are oriented preferentially parallel to the plane of the film (fwhm = 55°).

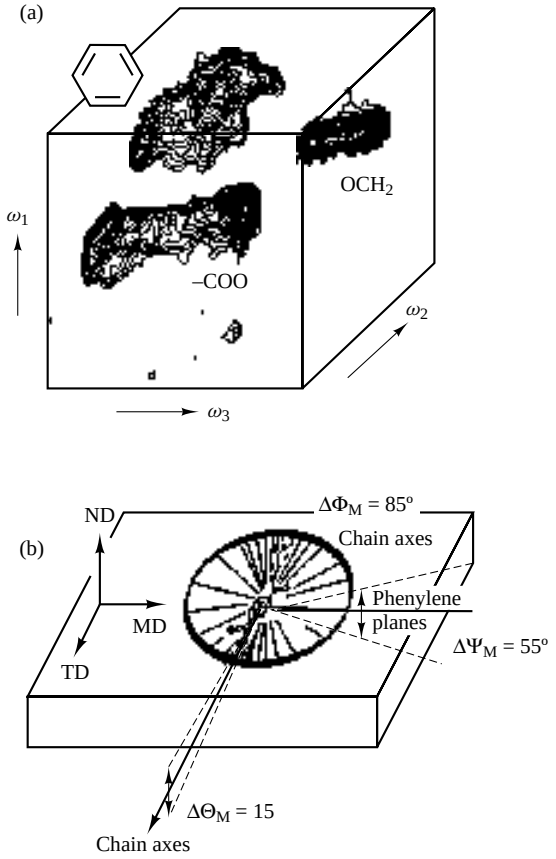

Figure 7 (a) ^{13}C 3D DECODER NMR spectrum of an industrial biaxially drawn film of poly(ethylene terephthalate), (PET).[28] (b) Schematic representation of orientation distribution derived from it

3.2.2 Molecular Order in Liquid Crystalline Polymers

New polymeric materials often contain mesogenic groups that are able to form liquid crystalline phases.[29,30] The interest in such liquid crystalline polymers (LCPs) comes from the fact that in the liquid crystalline phase, they can be macroscopically oriented not only by electric or magnetic fields but also by mechanical forces. The order thus generated in the mesophase can subsequently be retained in the solid material. This offers interesting applications, ranging from high-tensile-strength fibers to nonlinear optics and optoelectronics. In order to relate the material properties of LCPs to molecular structure, the degree of alignment as well as the mobility of the different structural units must be determined. This calls for highly selective analytical tools like NMR. In fact, pulsed ^2H NMR of selectively deuterated systems[31,32] as well as multidimensional NMR[33] have provided already a wealth of information about the structure and dynamics of these systems.

As a specific example, let us consider a side group LCP as depicted in Figure 8(a). The development of such materials has been stimulated by the concept that the mesogens with their tendency to form ordered structures can be decoupled from the polymer chain with its tendency to form a random coil by inserting a flexible spacer. By advanced 3D MAS NMR of ^{13}C in natural abundance, involving rotor-synchronized detection of molecular order with sideband separation,[34] the alignment of all structural units can be studied simultaneously. Figure 8(b) displays a 3D MAS spectrum of the frozen smectic

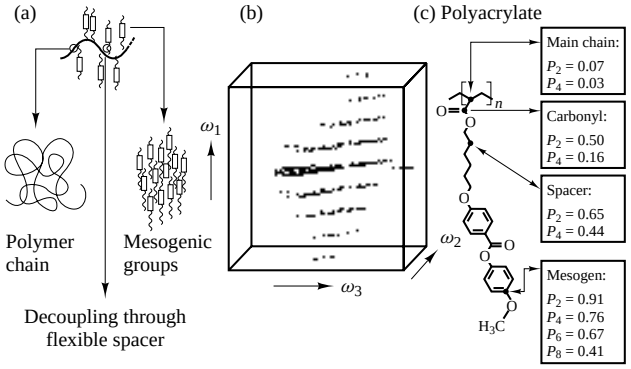

Figure 8 Molecular order in calamitic liquid crystalline side group polymers: (a) spacer model; (b) 3D CP MAS NMR spectrum of ^{13}C in natural abundance; (c) order parameters of different functional groups derived from it. For details see Titman et al.[34]

LCP aligned in the liquid crystalline phase in the magnetic field. Each dot in the spectrum corresponds to a single spinning sideband of a single resolvable carbon in the repeat unit, from which the degree of alignment of the corresponding unit can be retrieved. The results of the analysis in terms of order parameters $\langle P_2\rangle$, ... ,$\langle P_8\rangle$ are displayed in Figure 8(c). This not only reveals a pronounced order gradient from the aligned mesogen to the disordered chain, it also shows that the acrylic carbonyl group exhibits much higher order than the hydrocarbon units of the main chain. Because of its selectivity, high-resolution solid state NMR is able to reveal that the carbon–carbon bond that links the acrylic carbonyl to the main chain plays a crucial role in the decoupling of the ordered side groups from the disordered polymer chain. This information is needed to understand the differences in chain order for different backbones,[31] and the rheological behavior[35] as well as the ordering behavior of mechanically deformed LC elastomers.[36]

3.3 Molecular Dynamics

The molecular dynamics of polymer chains depend first of all on their phase structure. Most synthetic polymers are amorphous, forming a coiled shape as indicated in Figure 9(a). Stereoregular polymers can crystallize. However, owing to the enormous loss of conformational degrees of freedom, crystallization is incomplete and leads to semicrystalline materials that typically form lamellar structures, as depicted in Figure 9(b). Different aspects of the molecular dynamics are important in amorphous and semicrystalline systems, and the application of multidimensional solid state NMR has recently provided detailed information about chain dynamics for both cases.[14]

3.3.1 Rotational Motions in Crystalline Regions

Two-dimensional exchange NMR provides detailed information about the geometry of rotational motions. This was demonstrated, among other ways, by ^2H 2D exchange NMR of poly(vinylidene fluoride) (PVF_2).[37] This polymer is of particular interest because of its electrical properties.[38] The 2D spectrum for the crystalline α phase at 370 K, shown in

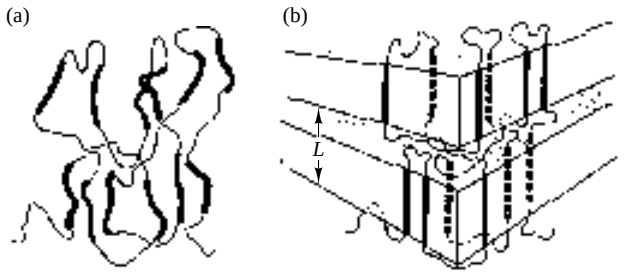

Figure 9 Schematic representation of (a) amorphous and (b) semicrystalline polymers

Figure 10(a), in addition to a well-defined powder spectrum (Pake pattern) along the diagonal, displays well-developed elliptical exchange ridges. The latter indicates jump motions of the PVF_2 chains through the crystal lattice, which interchange C–^{2}H bond directions differing by 113°, in agreement with the refined crystal structure. Altogether, 16 conformational defects had previously been proposed to be responsible for the chain dynamics in this polymer. Together with knowledge of the change in dipole moment generated by the motion, a specific conformational change $tg\bar{t}\bar{g} \leftrightarrow \bar{g}tgt$ of a chain defect

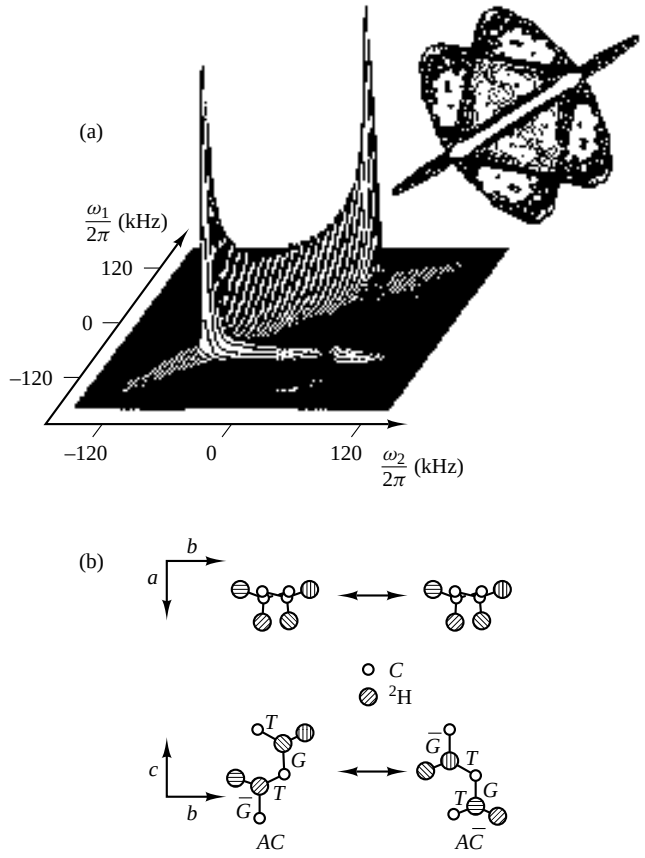

Figure 10 Chain motion in the crystalline α phase of poly(vinylidene fluoride), (PVF_2).[37] (a) Experimental ^2H 2D exchange NMR spectrum at T = 370 K, mixing time t_m = 200 ms. (b) Geometry of the conformational jumps, T and G refer to *trans* and *gauche* conformations of the respective bonds, while A and C describe the direction of the dipole moment with respect to the a and c crystal axes

[Figure 10(b)] was identified as being responsible for the mechanical and dielectric relaxation in the crystalline regions of this polymer.[37]

In other semicrystalline polymers like polypropylene, poly(oxymethylene), and poly(ethylene oxide), slow chain motions in the crystalline regions have been detected, and 2D exchange NMR of ^{2}H and ^{13}C has identified these motions as being due to helical jumps.[12–14,39]

3.3.2 Chain Diffusion between Crystalline and Amorphous Regions

Not only can two-dimensional exchange NMR detect molecular dynamics via the resulting rotations of individual groups of the monomer unit, but it is also able to detect chain diffusion from crystalline to amorphous regions in semicrystalline polymers.[40] Although occasionally postulated,[41] this process has not been accepted as a general concept, most likely because of lack of experimental evidence.

Our 2D experiment makes use of the fact that, under MAS, the all-*trans* conformation in the crystalline regions of polyethylene (PE) has an isotropic chemical shift that differs by approximately 2 ppm from that of the *gauche*-containing conformers in the amorphous regions. In the sketch of polyethylene (PE) chains in a crystallite near the interface with an amorphous region shown in Figure 11(a), carbons 1 and 2 would contribute to the "amorphous" signal [marked *a* in Figure 11(b)] and the carbons 9 and 10 would contribute to the "crystalline signal" (marked *c*). The exchange intensity between the ^{13}C signals for CH_2 groups in the crystalline and amorphous regions is clearly visible in Figure 11(b). This directly proves chain diffusion taking CH_2 groups from the crystalline into the amorphous regions and vice versa. This translational diffusion in the solid state results from the well-known α process, assigned to 180° jumps of the chain stems in the crystallites,[41] accompanied by a translation by one CH_2 unit. The quantitative analysis of our 2D NMR and relaxation data yields jump rates in complete agreement with previously reported values (activation energy E_a = 105 kJ mol^{-1}). It shows that the root-mean-square displacement of individual CH_2 groups amounts to more than 100 nm within 100 s near 360 K, corresponding to a translational diffusion constant of 10^{-14} cm^2 s^{-1}. In commercial materials, chain diffusion, as detected here, is suppressed by branching, since it leads to deterioration of the long-term mechanical properties owing to creep.

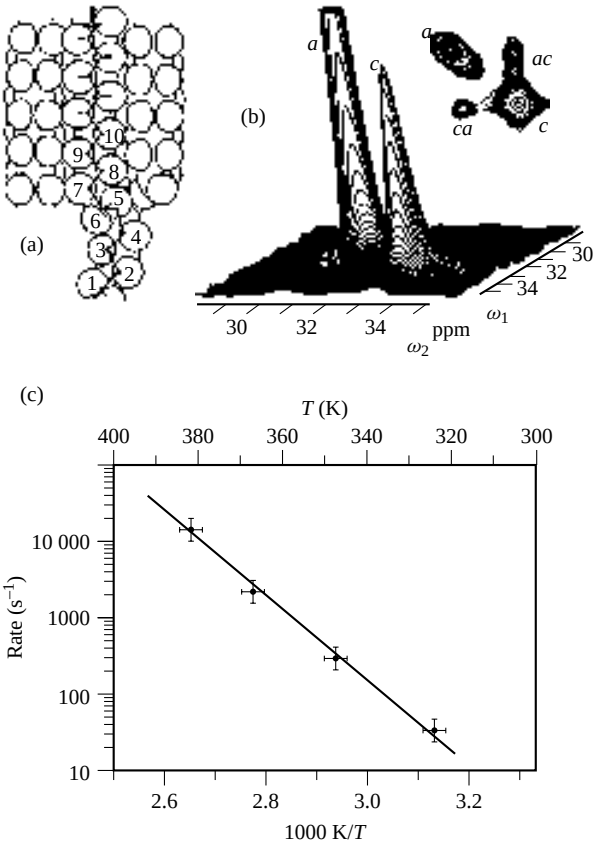

Figure 11 Chain diffusion in solid polyethylene, (PE).[40] (a) Sketch of PE chains in a crystallite, near the interface with an amorphous region. (b) ^{13}C 2D MAS NMR spectrum at T = 363 K; signal of the crystalline regions suppressed through single pulse irradiation. (c) Arrhenius plot of jump rates for the primary step of chain diffusion in PE

3.3.3 Chain Motions of Amorphous Polymers at the Glass Transition

As an amorphous polymer is heated above its glass transition temperature T_g, its mechanical properties change significantly within a temperature range of typically 20–30 K where the material transforms from a glassy solid to a highly viscous melt.[1–3,42] (An excellent overview of dynamic phenomena at the glass transition is given in special issues of the *Journal of Non-Crystalline Solids*.[43]) However, the dynamic processes on a molecular level, responsible for these changes in the macroscopic behavior, are not sufficiently well characterized. Multidimensional exchange NMR has now provided information about the chain dynamics at the glass transition in unprecedented detail.[14]

Conformational (*trans*–*gauche*) transitions are usually considered as an important aspect of polymer chain dynamics in the melt and in solution.[44] Slow conformational transitions at temperatures slightly above T_g have indeed been observed in various polymers.[24,45] This is demonstrated for aPP in Figure 12. The ^{13}C 2D exchange NMR spectrum was recorded under rapid MAS, such that isotropic lines were obtained. The conformational exchange clearly manifests itself by pronounced cross peaks between the lines corresponding to the *t**.**t* and the *t**.**g* conformers discussed earlier (see Figures 5 and 6).

However, as pointed out, for example, by Helfand et al.,[46] such motions need not be strictly local processes described by kink[47] or three-bond motions on a diamond lattice,[48] involving rotations by well-defined angles about spatially fixed C–C axes. Conformational transitions may also arise from relaxation processes involving longer chain units, leading to translational and angular displacements of different amplitudes of the corresponding monomer units. Indeed, ^{2}H 2D exchange NMR of aPP of the chain dynamics does not show any sign of preferred rotational angles.[49] As demonstrated in Figure 12(b), the ^{2}H spectra could be fitted adequately on the basis of an isotropic rotational diffusion model involving small angular steps.

The correlation times of the conformational dynamics agree remarkably well with those of the rotational motions. This is

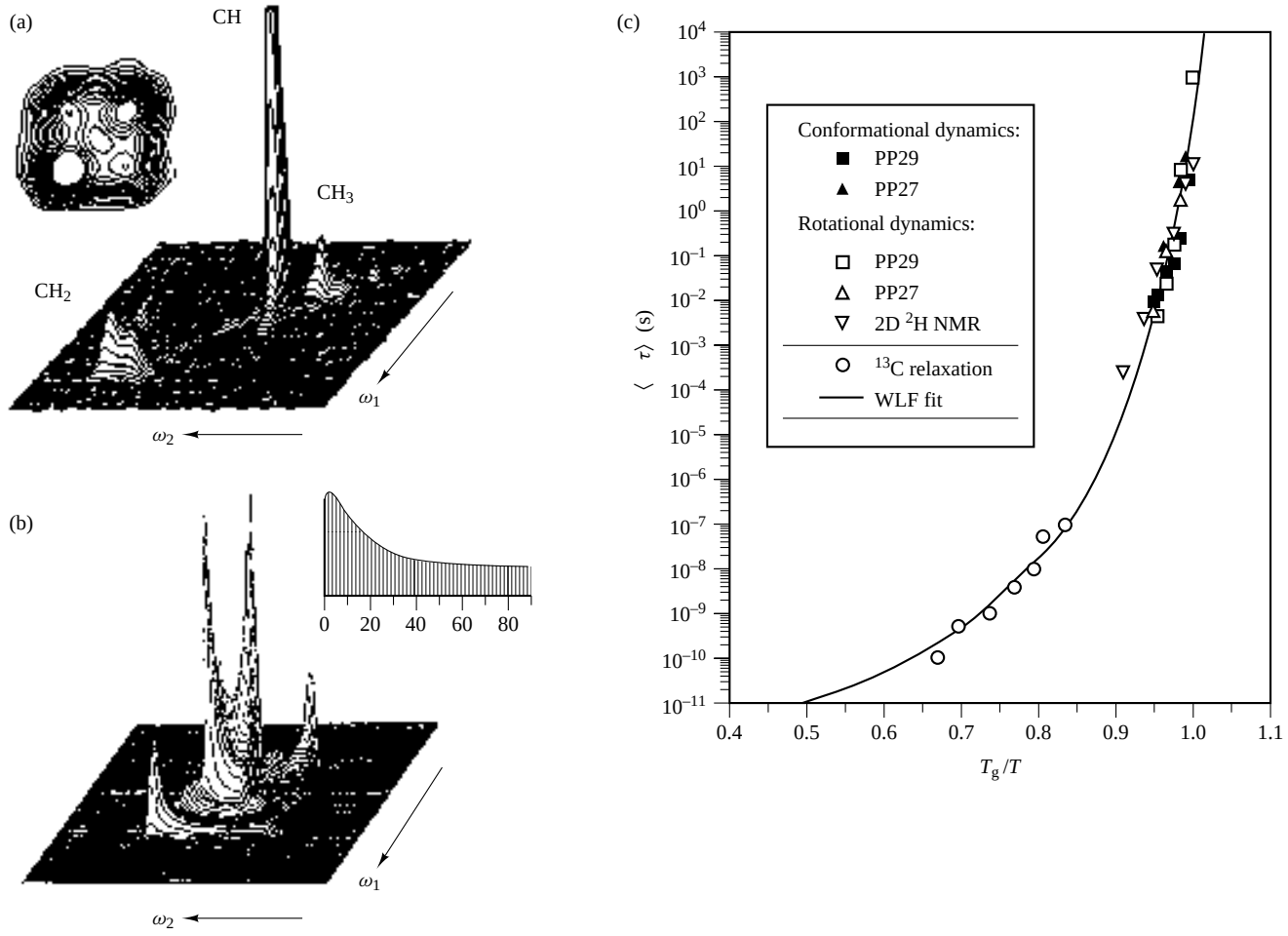

Figure 12 Chain motion of atactic polypropylene, (aPP), at the glass transition. (a) ^{13}C 2D CP MAS spectrum at T = 250 K (T_g + 12 K) and mixing time t_m = 500 ms. The cross peaks indicate conformational transitions.[45] (b) ^{2}H 2D exchange NMR spectrum at T = 270 K (T_g + 17 K) and mixing time t_m = 50 ms. The broad exchange features indicate rotational motions, which can be fitted by small-angle step rotational diffusion;[49] see also the reorientational angle distribution obtained from a quantitative fit of the spectrum. (c) Mean correlation times for the various aspects of the chain dynamics in different polypropylene samples plotted versus reduced temperature from ^{13}C and ^{2}H NMR; for details see Zemke et al.,[24] Schaefer et al.,[49] and Dekmezian et al.[50]

demonstrated in Figure 12(c), where mean correlation times determined by various techniques on different amorphous PP samples are shown.[24] Also included are values determined earlier through ^{13}C spin–lattice relaxation times by Mandelkern and co-workers[50] at elevated temperatures. All these correlation times can be fitted by the Williams–Landel–Ferry (WLF) equation[42] describing mechanical relaxation over more than 12 orders of magnitude. Thus, as noted before,[45,48,51] the timescales of the chain dynamics as probed for individual CH_2 units by 2D NMR are in excellent agreement with those of the collective processes responsible for the strong temperature dependence of the α process at the glass transition.[3,42,43]

3.3.4 Geometry of Chain Motion in Amorphous Polymers

As noted in the preceding section, conformational transitions in a vitrifying melt need not be strictly local processes involving rotations by well-defined angles in a potential that is static with respect to an external reference frame. If conformational transitions do indeed arise from relaxation processes of larger chain units[46] involving translational and angular displacements of different amplitude along such a unit then the rotational potential around a given C–C bond, which with respect to an internal frame would still look like that plotted in Figure 5(b), can be displaced by large angles after a conformational transition has occurred around that bond. Such displacements are difficult to prove experimentally. In fact, we are unaware of techniques or attempts in other groups that tackle this question. Yet it is of profound importance in order to understand the coupling of molecular dynamics and macroscopic properties such as viscosity or dynamic mechanical relaxation. Indeed, there are several ways in which such angular displacements manifest themselves in multidimensional NMR experiments.[14] A particularly direct way of proving their existence is provided by 3D exchange NMR. There the orientation of a selected group is measured at three distinct points in time through their frequencies ω_1, ω_2, ω_3, displaced by two mixing times t_{ma} and t_{mb} [Figure 3(a)]. If the conformational transitions occurred in a potential that was static on average, at least on the timescale of several jumps,

the groups under study should exhibit long-term orientational memory,[14] which should manifest itself by jumps back to the starting orientation. These can directly be probed by 3D exchange NMR, where return jumps lead to ridges with $\omega_1 = \omega_3$.

Poly(vinyl acetate) (PVAc) provides a means to check such long-term orientational memory by 3D exchange NMR. This is due to the fact that, even in the ^{13}C NMR spectrum of a nonrotating sample, the powder pattern of the carbonyl carbon is completely separated from the signals of the aliphatic carbons. Thus it was possible to record a complete 3D exchange spectrum for that position.[14] In Figure 13, it is compared with a 3D exchange NMR spectrum of poly(ethylene oxide), (PEO), a highly disordered semicrystalline polymer.[52] In both cases, the mixing times t_{ma} and t_{mb} were set equal. The ridge in the diagonal plane $\omega_1 = \omega_3$ due to return jumps indicating long-term orientational memory is a prominent feature of the PEO spectrum [Figure 13(b)], but is absent from the PVAc spectrum [Figure 13(a)]. Thus, the disordered 7_2 helix of PEO has a finite probability to return to the start position even after numerous helical jumps,[14] whereas the repeat unit of PVAc apparently loses its orientational memory at each large-angle jump. This proves that in a semicrystalline polymer the chain moves in a potential that, on average, is static, whereas no such average static potential can be associated with the chain motion of an amorphous polymer above T_g. This also means that a tight coupling of molecular and cooperative dynamics must exist in amorphous polymers.

3.3.5 *Nature of Nonexponential Relaxation above T_g*

The time dependence of relaxation processes in amorphous polymers above T_g cannot be described by single exponentials. This is inferred from nonexponential correlation functions measured by conventional relaxation techniques,[42,43] and also shows up in 2D exchange NMR.[14,49,51] This is illustrated in Figure 14 for poly(vinyl acetate), where again the carboxyl carbon only is considered.[53] From the ratio of diagonal and off-diagonal intensity of 2D exchange spectra as a function of t_m, the correlation function $\langle\omega(0)\,\omega(t_m)\rangle$ is obtained and is plotted in Figure 14(a). The nonexponential decay is consistent with a stretched exponential Kohlrausch–Williams–Watts function

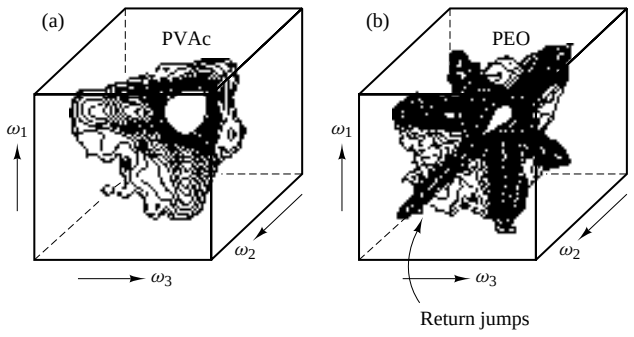

Figure 13 ^{13}C 3D exchange CP NMR spectra without MAS, comparing the chain motion in an amorphous and in a crystalline polymer: (a) poly(vinyl acetate), (PVAc), at T = 311 K (T_g + 10 K) and mixing times $t_{ma} = t_{mb}$ = 500 ms; only the carbonyl region of the spectrum is shown; (b) poly(ethylene oxide), (PEO), at T = 225 K and $t_{ma} = t_{mb}$ = 1 s; frequency scales in (a) and (b) are different for better comparison[14]

exp $[-(t/\tau_0)^{\beta}]$[54,55] with a mean correlation time τ_0 = 20 ms and β = 0.3, which translates into an asymmetric distribution of correlation times with a width of approximately three decades, as plotted in Figure 14(b).

The nature of such observations has been a matter of dispute for a long time. Two conflicting views offer explanations in terms of (i) a spatially heterogeneous distribution of correlation times (parallel processes, nonergodic) or (ii) an intrinsically nonexponential loss of correlation in a homogeneous system (a serial process, ergodic). Experimental techniques that are able to distinguish these views on a timescale relevant for the glass process, i.e., a second or so, were lacking. This distinction can be achieved by multidimensional exchange NMR, where the orientation of the same molecule can be measured by three or more subsequent points in time. In the reduced 4D exchange experiment [Figure 14(c)], we keep the first two evolution times t_1 and t_2 constant and equal. Units for which $\omega(\theta_1) = \omega(\theta_2)$, i.e., that have the same orientation before and after t_{ma}, generate a stimulated echo. The magnetization generated by the 'slow molecules' is then stored by a 90° pulse, and a 2D exchange spectrum of that selected subensemble of slow molecular units is recorded at later times, after t_{mb}, constituting a reduced 4D exchange spectrum.

In Figure 14(d)–(f), two reduced 4D exchange spectra are compared with a reference 2D NMR spectrum. The mixing times t_{ma} and t_{mc} were kept equal and comparable to τ_0. Whereas the 2D spectrum for that mixing time [Figure 14(d)] is a superposition of a diagonal ridge and broad exchange features, the reduced 4D spectrum for $t_{mb} = t_{ma} = t_{mc}$ exhibits the diagonal ridge only [Figure 14(e)]. This proves directly that the system is heterogeneous (nonergodic) on the timescale of the mean correlation time τ_0, since the spectrum of the selected subensemble is entirely different from that of the total ensemble. However, on lengthening t_{mb} by two orders of magnitude (point V in Figure 14(b)), considerable off-diagonal intensity is observed [Figure 14(e)]. This means that a significant number of units that were slow initially ($\tau \gg \tau_0$) have changed their correlation time to $\tau < \tau_0$. Thus, in the vitrifying melt, fluctuations are detected that change the reorientational dynamics of chain units. Markedly, these fluctuations causing the system to become homogeneous (ergodic) occur on timescales within the "long-time tail" of the distribution of correlation times. These experiments clearly show that, during the glass transition, the molecular units undergo non-Markovian motion with time-dependent correlation times, though not on the timescale of the mean correlation time but rather in a process limiting the longest correlation time.

3.3.6 *Local Motions in the Glassy State and Their Relation to Mechanical Properties*

The favorable mechanical properties of glassy polymers stem from relaxation processes that are possible even in the solid state.[2,3,42] However, little is known about the geometry of molecular dynamics responsible for such processes. Mechanical measurements[56,57] and ^2H 1D NMR[58] have previously established a connection between the low-temperature γ relaxation and phenylene ring motions in polycarbonate (PC), a polymer with especially favorable mechanical properties. The ring motion was identified as a flip by 180° [Figure 1(f)]. This was subsequently verified by ^{13}C NMR.[59,60] However,

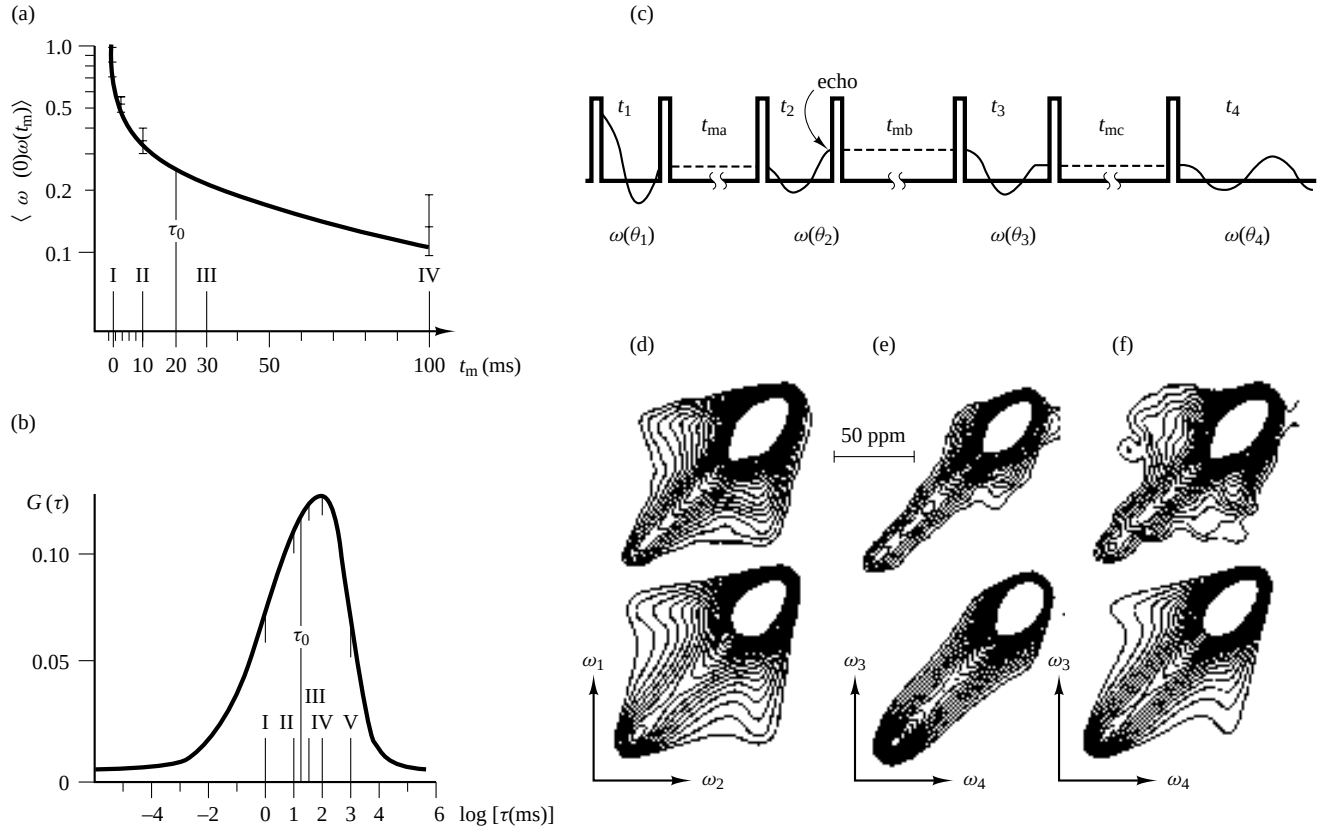

Figure 14 Nature of nonexponential loss of correlation above the glass transition.[53] (a) Nonexponential decay of correlation function with experimental points for poly(vinyl acetate), (PVAc). (b) Distribution of correlation times $G(\tau)$ derived from it. (c) Pulse sequence for reduced 4D exchange NMR. (d) Experimental and simulated ^{13}C 2D exchange NMR spectrum at T = 320 K (T_g + 20 K) and mixing time t_m = 10 ms. (e) Experimental and simulated ^{13}C reduced 4D exchange NMR spectrum at the same temperature and mixing times $t_{ma} = t_{mb} = t_{mc}$ = 10 ms. (f) Similar to (e), but with t_{mb} = 1 s and $t_{ma} = t_{mc}$ = 10 ms

the NMR lineshapes are unable to provide information about the detailed geometry of the phenylene motion at low temperatures, where it occurs on a timescale of hundreds of milliseconds, which can be probed directly by mechanical relaxation experiments. Again, such slow molecular dynamics can be detected by 2D exchange NMR, as demonstrated in Figure 15. The ^{2}H 2D exchange NMR spectrum of a sample selectively deuterated at the phenylene rings, PC-d_4, exhibits somewhat broadened elliptical ridges [Figure 15(a)],[61] which confirm the geometry of the phenylene motion as rotations around the *para* axis as indicated. However, the flip typically does not involve a rotation by exactly 180°, but by angles that can differ substantially from this mean value [Figure 15(b)]. This means that, after a rotation, the phenylene group finds itself in a slightly different environment, which readily explains the connection between this molecular dynamic process and the mechanical relaxation. Indeed, when the 2D spectrum is recorded under tensile stress, such that the sample is stretched up to the nonlinear region, yet below the yield point, the angular uncertainty in the flip angle increases further[61] [Figure 15(b)]. This is consistent with the reported increase in the strength of the mechanical relaxation under such conditions.[62] The timescale of the phenylene flips is not uniform but displays a broad distribution of correlation times[63] reflecting different activation energies in different regions of the sample.

3.3.7 Geometry of Side Group Motion in the Glassy State

The β relaxation observed in poly(methyl methacrylate), (PMMA), by means of both dielectric and dynamic–mechanical relaxation,[3] is often considered as the archetype of a localized (β) relaxation in polymers. Since this relaxation is very prominent in dielectric relaxation, it has traditionally been attributed to the carboxyl side group with its large dipole moment [Figure 16(a)]. However, quantitative analysis of relaxation strengths in both techniques is virtually impossible. Thus, neither was the geometry of the side group motion known, nor whether all or only a fraction of the groups are participating in the motion in the glassy state. A study involving both ^{13}C and ^{2}H multidimensional exchange NMR gave answers to these questions.[64] In fact, the geometry of the side group motion turned out to be more complex than originally anticipated. It involves ill-defined flips by 180° ± 20° about the C–C bond linking the carboxyl side group to the polymer backbone. This flip motion is coupled to a "rocking" motion about the local chain axis [Figure 16(a)], with a 20° root-mean-square amplitude. This motion can be detected in both ^{13}C and ^{2}H NMR, whereas the flip shows up only in the ^{13}C spectra. In the latter, the two coupled motional processes manifest themselves in the unstructured exchange intensity covering most of the 2D plane [Figure 16(b)], whereas the angular more restricted "rocking" motion leads to the exchange intensity in the ^{2}H spectrum being restricted to the vicinity of the diagonal[64] [Figure 16(c)].

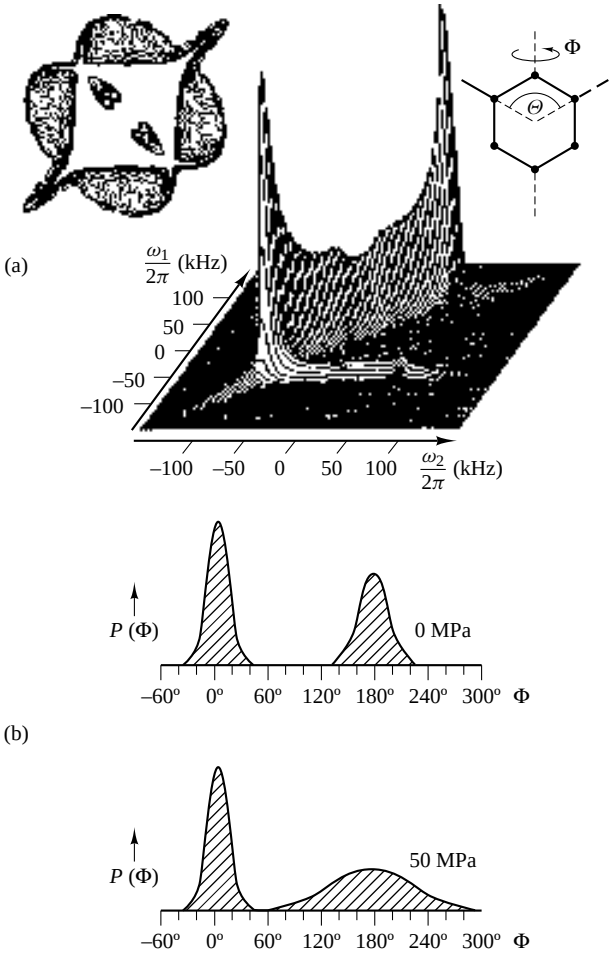

Figure 15 Phenylene motion and mechanical behavior in bisphenol-A-polycarbonate, (PC)[61]. (a) ^{2}H 2D exchange NMR spectrum of phenylene deuterated sample at T = 223 K, mixing time t_m = 500 ms. The elliptical figures (see inset) correspond to $\Phi = 180^\circ \pm 25^\circ$ phenylene flips with reorientational angle distributions shown in (b). (c) After application of 50 MPa stress, a significant broader distribution of flip angles around the same mean 180° is observed

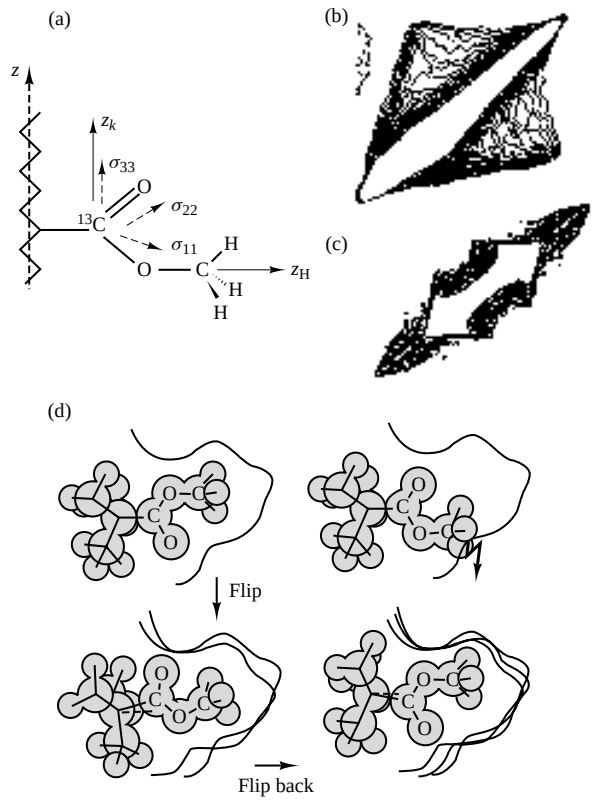

Figure 16 Side group motion in poly(methyl methacrylate), (PMMA).[64] (a) Sketch of the PMMA geometry and the principal axes for ^{13}C (carboxyl group) and ^{2}H (*O*-methyl group) NMR. (b) ^{13}C 2D exchange NMR spectrum at T = 333 K and mixing time t_m = 50 ms. (c) ^{2}H 2D exchange NMR spectrum at T = 355 K and mixing time t_m = 500 ms. (d) Sketch of the dynamics of an asymmetric side group in its correspondingly asymmetric environment, indicating that in order to fit the asymmetric side group into the volume that it had occupied before the flip, a twist around the local chain axis ("rocking" motion) is required

These findings are ascribed to the fact that the asymmetric side group, after the flip, does not fit into its original environment as depicted in Figure 16(d). Remarkably, the side group exhibits long-term orientational memory. As checked by ^{13}C 3D exchange NMR, despite the featureless exchange intensity in the 2D spectrum, the reorientation of each segment involves only two, relatively well-defined, potential energy minima. Thus, after two subsequent flips, the carboxyl group is back to almost the initial orientation [Figure 16(d)]. It is also important to realize that in the glassy state of PMMA, only about 50% of the side groups can undergo this motion. Since the side group flip requires the "rocking" motion around a locally extended chain axis, this was related to the fraction of syndiotactic triads in this polymer, which indeed favor extended conformations.[64]

This example demonstrates how complex a seemingly simple side group motion in a glassy polymer can be. The complex geometry of the side group dynamics stems from its asymmetry, since the packing apparently does provide enough free volume for a methyl group, in which it could fit after a flip. Obviously, this finding should be of interest not only for the understanding of the relation between molecular dynamics and the mechanical properties of amorphous polymers, but also in biophysics, where motions of asymmetric side groups are common dynamic processes, e.g., in proteins.[65]

3.4 Heterogeneous Polymers

In heterogeneous polymers, i.e., polymer blends or block copolymers,[1,2] domain sizes, or structures on the scale from a few to some tens of nanometers, can be be investigated by NMR spin diffusion experiments. Thus, NMR is particularly suited for characterizing small domains, nanoheterogeneities, or concentration fluctuations on lengthscales of a few nanometers, where other methods often fail owing to limitations in resolution or contrast. Thus, spin diffusion measurements are well established in solid state NMR of polymers.[8] Moreover, several advanced approaches exploiting ^{1}H spin diffusion with highly selective ^{13}C detection have been introduced.[14]

3.4.1 Wideline Separation Experiments on Polymer Blends

Spin diffusion experiments require that the different components contained in the sample be distinguished in their

NMR parameters. This is particularly straightforward if the components differ in their mobility. In fact, a long-standing method for a qualitative characterization of molecular mobility is ^{1}H wideline NMR spectroscopy.[8] There, rapid large-amplitude motions are detected through the reduction of dipolar linewidths. However, 1D proton lineshapes leave many questions open, since they typically represent superpositions of broad and narrow lines, and their relation to different structural units is often not obvious. In a straightforward combination of ^{1}H wideline NMR, cross polarization and ^{13}C MAS spectroscopy in a 2D experiment,[66] it is possible to separate the dipolar patterns for the different structural units (*wi*deline *se*paration, WISE).

The power of this technique is demonstrated in Figure 17, where data on a 50:50 wt% blend of polystyrene, (PS), and poly(vinyl methyl ether), (PVME), cast from toluene, are presented. This blend appears homogeneous by most classical techniques. The ^{1}H wideline spectrum [Figure 17(a)] consists of a rather featureless superposition of components with different dipolar linewidths, which are nicely separated in the second frequency dimension [Figure 17(b)] and related to their ^{13}C chemical shifts. Substantial motional heterogeneities, PVME being more mobile than PS, are detected despite the fact that the spectrum is recorded about 60 K above the caloric glass transition of the blend. By introducing a mixing time[66] to allow for spin diffusion, the ^{1}H lineshapes equilibrate after only 5 ms [Figure 17(c)]. From this, the domain sizes for the regions of different mobility were estimated to be 3.5 ± 1.5 nm. Thus, these advanced NMR techniques reveal substantial motional differences in different regions of this blend, which rather than homogeneous should better be described as nanoheterogeneous.

3.4.2 Domain Sizes from Spin Diffusion Experiments

Another advanced approach towards quantitative use of spin diffusion experiments exploits ^{1}H spin diffusion after high-resolution ^{1}H solid state NMR by *c*ombined *r*otation *a*nd *m*ultiple-*p*ulse *s*pectroscopy (CRAMPS), with high-resolution ^{13}C MAS detection.[14,16] In a particularly clear-cut case, this technique has been applied to a series of symmetric diblock copolymers of PS and PMMA.[16] In Figure 18(a), the increase

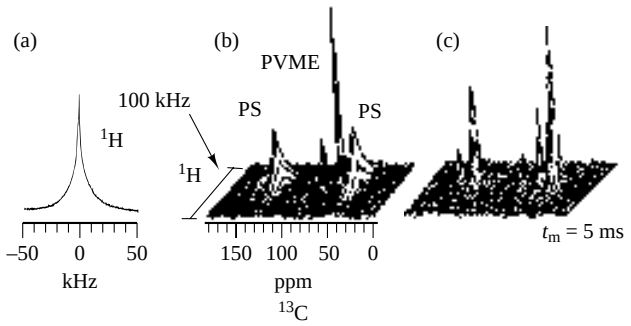

Figure 17 2D WISE NMR separating ^{1}H wideline spectra for different structural units according to their ^{13}C chemical shifts. (a) Conventional ^{1}H wideline spectrum of a blend of polystyrene, (PS), and poly(vinyl methyl ether), (PVME). (b) 2D ^{1}H ^{13}C WISE NMR spectrum at T = 320 K, note the different ^{1}H linewidths for PS and PVME. (c) Similar to (b), but with spin diffusion over a time t_m = 5 ms; note that now all lines have equal ^{1}H linewidths

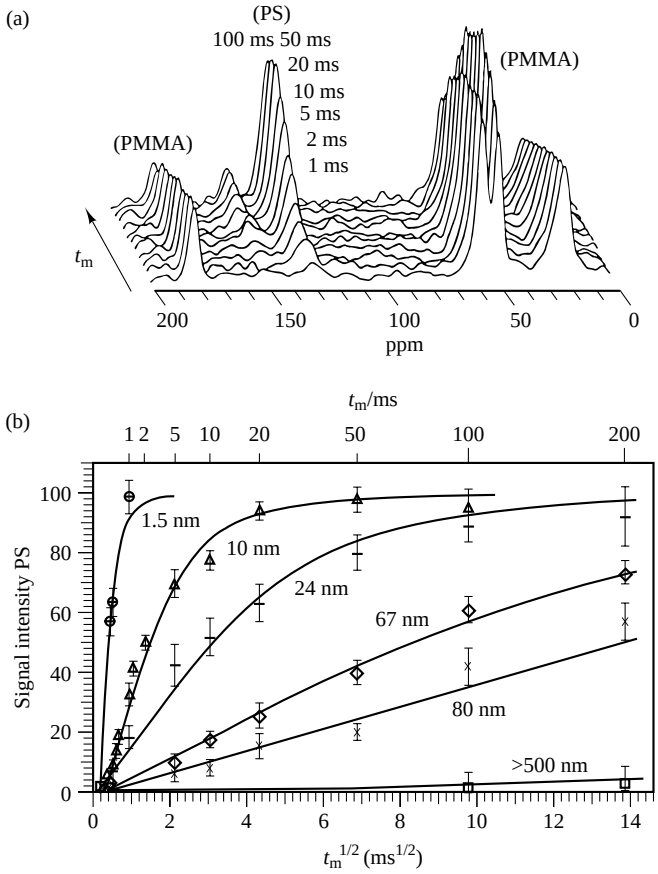

Figure 18 Spin diffusion as a tool for determining domain sizes in heterogeneous polymers.[16] (a) ^{13}C MAS spectra of the symmetric diblock copolymer PS-*b*-PMMA as a function of the diffusion time t_m after selection of proton magnetization of the methoxy group in PMMA. (b) Signal intensity of the phenyl carbons in PS as a function of t_m for different molecular weights. The numbers indicate the domain sizes obtained from the respective fits

in the carbon signal of the phenyl ring in the PS block after selection of the PMMA block is plotted against the spin diffusion time t_m for various block lengths. The equal lengths of both blocks in the symmetric copolymer ensures a lamellar structure, which makes quantitative analysis of the data easy. PMMA and PS are known to be immiscible. The spin diffusion data yield domain sizes that are consistent with the scaling law $M_n^{0.66}$, where M_n denotes the molar mass of the block, as predicted theoretically.[2] For comparison, a statistical copolymer, in which no phase separation is possible, and a blend of both homopolymers were included in the data set. The close agreement between experimental intensities and the time dependence calculated from the diffusion equation is apparent in Figure 18(b), and demonstrates that domain sizes between 0.5 and 100 nm can be determined quantitatively.

3.4.3 Packing and Mobility in Rigid Rod Systems

Advanced solid state NMR has also been applied to study the structure and dynamics of advanced polymer materials.[33] As a specific example, consider rigid rod systems consisting of *para*-substituted aromatics as stiff macromolecules, such as polyesters, polyamides and polyimides. These have attracted

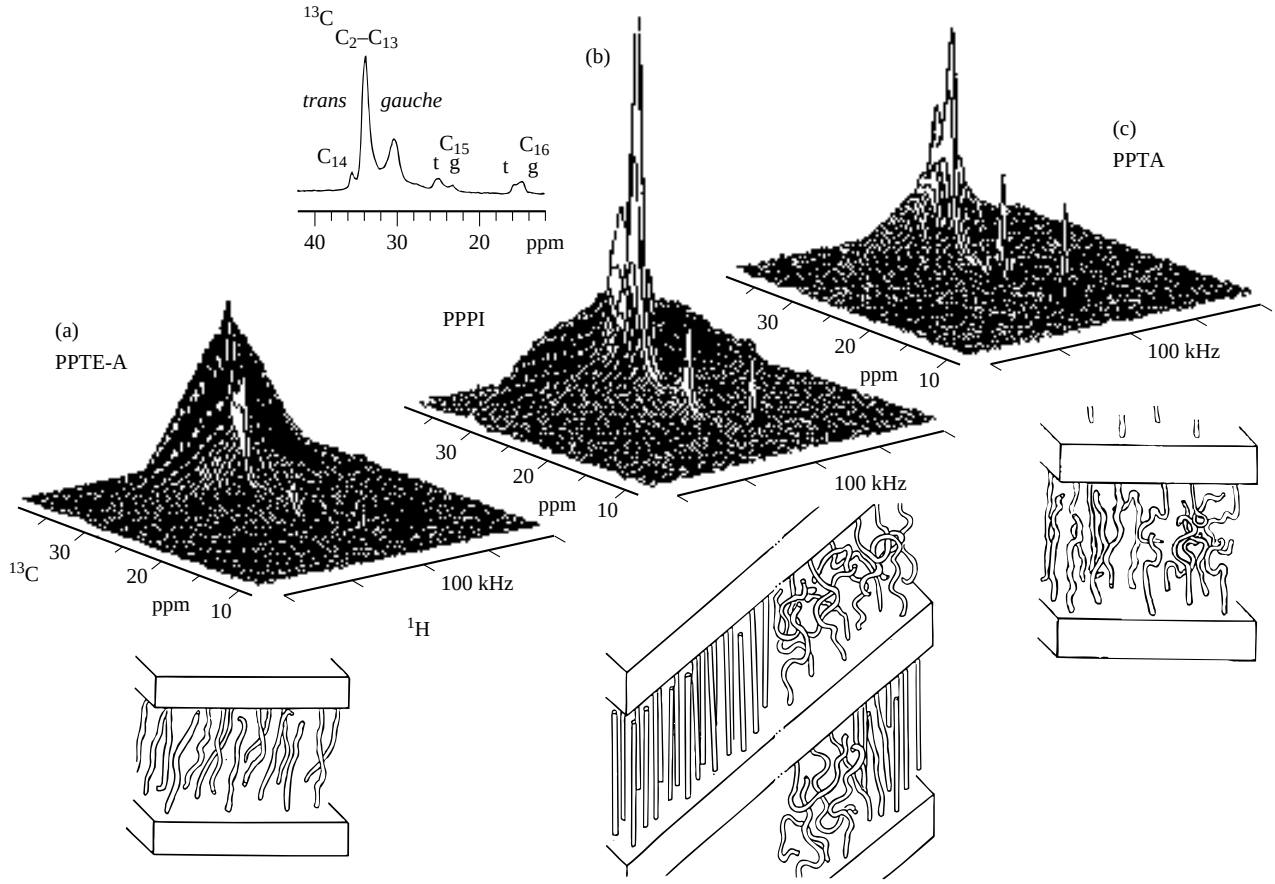

Figure 19 2D WISE NMR spectra of aliphatic side chains of various rigid rod macromolecules and structural models derived from them and spin diffusion measurements:[69] (a) polyester, A-form, PPTE-A; (b) polyimide PPPI; (c) polyamide, PPTA

considerable interest because of their unusual mechanical properties.[67] When processed from a nematic mesophase, the parallel packing of the stiff macromolecules results in high-modulus fibers. In order to increase the processability of such materials, flexible side chains are attached. However, owing to the inherent incompatibility of stiff backbone and flexible side chains, layer structures are formed where these different building elements are separated[68] (see Figure 19). Depending on the packing requirements of the stiff macromolecules, highly crystalline [form B, Figure 19(b)] or disordered amorphous [form A, Figure 19(a) and (c)] structures are formed. This imposes packing restrictions on the side chains, favoring crystallization or preventing it. Whereas X-ray scattering has been invaluable in establishing the basic features of the packing, it is difficult to provide clear-cut information about the details of the molecular organization in such complex systems.

Here, advanced 2D solid state NMR methods offer interesting alternatives. Figure 19 displays the results of 2D WISE NMR and spin diffusion experiments[69] on the side chains of a polyester (PPTE-A), a polyimide (PPPI), and a polyamide (PPTA). A high-resolution ^{13}C CP MAS spectrum of the polyimide is also displayed as an insert. The ^{1}H wideline spectra reflect the molecular dynamics of the different methylene groups. They are superpositions of broad and narrow components, even at the chain end (C_{16}). The different side-chain packings of the three systems—almost homogeneous with rather extended chain in the polyester PPTE-A, separated crystalline regions with all-*trans* chains and amorphous regions with disordered chains in the polyimide PPPI, and separated regions with extended and disordered chains in the polyamide PPTA—are nicely reflected in the different WISE NMR spectra.[69]

The delicate balance between the organization of the incompatible rigid main chains and flexible side chains in their respective layers thus leads to a considerable variety in the packing. Advanced NMR techniques yield specific information supplementing computer-aided X-ray studies, because NMR is sensitive to conformation, mobility, and spatial proximity of different structural elements.

4 CONCLUSIONS

High-resolution NMR in liquids is an indispensable analytical tool for structural characterization in chemistry, including the stereochemistry of polymers. Particularly in biochemical applications, the necessary spectral resolution can only be achieved, however, by two- and higher-dimensional spectroscopy. An analogous situation is encountered in solid polymers. Unless isotopic labeling is employed, the different anisotropic spin interactions can be separated only via multidimensional techniques. Besides providing highly selective structural information, advanced solid state NMR

offers unique possibilities for characterizing slow molecular dynamics and relating it to macroscopic material behavior.

5 RELATED ARTICLES

Brownian Motion and Correlation Times; Chemical Shift Tensors; CRAMPS; Cross Polarization in Solids; Deuterium NMR in Solids; Diffusion in Solids; Dipolar and Indirect Coupling Tensors in Solids; Dynamic Angle Spinning; HETCOR in Organic Solids; Internal Spin Interactions and Rotations in Solids; Line Narrowing Methods in Solids; Liquid Crystalline Samples: Deuterium NMR; Liquid Crystals: General Considerations; Magic Angle Spinning; Multidimensional Spectroscopy: Concepts; Polymer Blends: Miscibility Studies; Polymer MRI; Polymer Physics; Polymers: Regio-Irregular Structure; Polymers: Relaxation and Dynamics of Synthetic Polymers in Solution; Protein Dynamics from Solid State NMR; Quadrupolar Nuclei in Solids; Rotating Solids; Shielding Calculations: IGLO Method; Sideband Analysis in Magic Angle Spinning NMR of Solids; Slow and Ultraslow Motions in Biology; Sodium-23 Magnetic Resonance of Human Subjects; Two-Dimensional Methods of Monitoring Exchange; Two-Dimensional Powder Correlation Methods; Ultraslow Motions in Solids.

6 REFERENCES

1. P. J. Flory, *Principles of Polymer Chemistry*, Cornell University Press, Ithaca, NY, 1953.
2. J. I. Kroschwith (ed.), *Concise Encyclopedia of Polymer Science and Technology*, Wiley, New York, 1990.
3. N. G. McCrum, B. E. Read, and G. Williams, *Anelastic and Dielectric Effects in Polymeric Solids*, J. Wiley, New York, 1967.
4. A. Abragam, *The Principles of Nuclear Magnetism*, Oxford University Press, London, 1961.
5. C. P. Slichter, *Principles of Magnetic Resonance*, Springer-Verlag, Berlin, 1980.
6. F. A. Bovey, *Chain Structure and Conformation of Macromolecules*, Academic Press, New York, 1982.
7. R. A. Komoroski (ed.), *High Resolution NMR of Synthetic Polymers in Bulk*, VCH, Deerfield Beach, FL, 1986.
8. V. J. McBrierty, and K. J. Packer, *Nuclear Magnetic Resonance of Solid Polymers*, Cambridge University Press, Cambridge, 1993.
9. M. Mehring, *High Resolution NMR in Solids*, Springer-Verlag, Berlin, 1983.
10. R. R. Ernst, G. Bodenhausen, and A. Wokaun, *Principles of Nuclear Magnetic Resonance in One and Two Dimensions*, Oxford University Press, Oxford, 1987.
11. B. Blümich and H. W. Spiess, *Angew. Chem., Int. Ed. Engl.*, 1988, **27**, 1655.
12. A. Hagemeyer, K. Schmidt-Rohr, and H. W. Spiess, *Adv. Magn. Reson.*, 1989, **13**, 85.
13. H. W. Spiess, *Chem. Rev.*, 1991, **91**, 1321.
14. K. Schmidt-Rohr and H. W. Spiess, *Multidimensional Solid-State NMR and Polymers*, Academic Press, London, 1994.
15. C. Griesinger, O. W. Sørensen, and R. R. Ernst, *J. Magn. Reson.*, 1989, **84**, 14.
16. J. Clauss, K. Schmidt-Rohr, and H. W. Spiess, *Acta Polym.*, 1993, **44**, 1.
17. S. Spiegel, K. Schmidt-Rohr, C. Boeffel, and H. W. Spiess, *Polymer*, 1993, **34**, 4566.
18. P. J. Flory, *Statistical Mechanics of Chain Molecules*, Wiley-Interscience, New York, 1969.
19. A. E. Tonelli, *NMR Spectroscopy and Polymer Microstructure: The Conformational Connection*, VCH, New York, 1989.
20. R. Born, H. W. Spiess, W. Kutzelnigg, U. Fleischer, and M. Schindler, *Macromolecules*, 1994, **27**, 1500.
21. W. Kutzelnigg, U. Fleischer, and M. Schindler, in *NMR, Basic Principles and Progress*, ed. P. Diehl, E. Fluck, H. Günther, R. Kosfeld, and J. Seelig, Springer-Verlag, New York, 1991, Vol. 23, p. 165.
22. A. Bunn, M. E.A. Cudby, R. K. Harris, K. J. Packer, and B. J. Say, *Polymer*, 1982, **23**, 694.
23. A. Bunn, M. E.A. Cudby, R. K. Harris, K. J. Packer, and B. J. Say, *J. Chem. Soc., Chem. Commun.*, 1981, 15.
24. K. Zemke, K. Schmidt-Rohr, and H. W. Spiess, *Acta Polym.*, 1994, **45**, 148.
25. I. M. Ward (ed.), *Structure and Properties of Oriented Polymers*, Applied Science, London, 1975.
26. H. W. Spiess, in *Developments in Oriented Polymers*, ed. I. M. Ward, Applied Science, London, 1987, Vol. 1, p. 44.
27. K. Schmidt-Rohr, M. Hehn, D. Schaefer, and H. W. Spiess, *J. Chem. Phys.*, 1992, **97**, 2247.
28. B. F. Chmelka, K. Schmidt-Rohr, and H. W. Spiess, *Macromolecules*, 1993, **26**, 2282.
29. A. Ciferri (ed.), *Liquid Crystallinity in Polymers: Principles and Fundamental Properties*, VCH, Weinheim, 1991.
30. C. B. McArdle (ed.), *Liquid-Crystalline Side Group Polymers*, Blackie, Glasgow, 1988.
31. C. Boeffel and H. W. Spiess, in *Liquid-Crystalline Side Group Polymers*, ed. C. B. McArdle, Blackie, Glasgow, 1988, p. 224.
32. K. Müller, P. Meier, and G. Kothe, in *Progress in NMR Spectroscopy*, eds. J. Emsley, J. Feeney, and L. Suttcliffe, Pergamon Press, Oxford, 1985, Vol. 17, p. 211.
33. H. W. Spiess, *Ber. Bunsenges. Phys. Chem.*, 1993, **97**, 1294.
34. J. J. Titman, S. Féaux de Lacroix, and H. W. Spiess, *J. Chem. Phys.*, 1993, **98**, 3816.
35. R. M. Kannan, J. A. Kornfield, N. Schwenk, and C. Boeffel, *Macromolecules*, 1993, **26**, 2050.
36. W. Gleim and H. Finkelmann, in *Liquid Crystalline Side Group Polymers*, ed. C. B. McArdle, Blackie, Glasgow, p. 287.
37. J. Hirschinger, D. Schaefer, H. W. Spiess, and A. J. Lovinger, *Macromolecules*, 1991, **24**, 2428.
38. A. J. Lovinger, in *Developments in Crystalline Polymers*, ed. C. D. Bassett, Applied Science, London, 1981, Vol. 1, p. 195.
39. A. P. M. Kentgens, A. F. de Jong, E. de Boer, and W. S. Veeman, *Macromolecules*, 1985, **18**, 1045.
40. K. Schmidt-Rohr and H. W. Spiess, *Macromolecules*, 1991, **24**, 5288.
41. M. Mansfield and R. H. Boyd, *J. Polym. Sci., Polym. Phys. Ed.*, 1978, **16**, 1227.
42. J. D. Ferry, *Viscoelastic Properties of Polymers*, 3rd edn., Wiley, New York, 1980.
43. *J. Non-Crystal. Solids*, 1991, **131–133**; *J. Non-Crystal. Solids*, 1994, **172–174**.
44. L. Monnerie, *Makromol. Chem., Makromol. Symp.*, 1991, **48/49**, 125.
45. K. Zemke, B. F. Chmelka, K. Schmidt-Rohr, and H. W. Spiess, *Macromolecules*, 1991, **24**, 6874.
46. E. Helfand, Z. R. Wassermann, T. A. Weber, J. Skolnick, and J. H. Runnels, *J. Chem. Phys.*, 1981, **75**, 4441.

47. W. Pechold and S. Blasenbrey, *Kolloid Z.*, 1967, **216/217**, 235.
48. F. Gény and L. Monnerie, *J. Polym. Sci., Polym. Phys. Ed.*, 1979, **17**, 131, 147.
49. D. Schaefer, H. W. Spiess, U. W. Suter, and W. W. Fleming, *Macromolecules*, 1990, **23**, 3431.
50. A. Dekmezian, D. E. Axelson, J. J. Dechter, B. Bohra, and L. Mandelkern, *J. Polym. Sci., Polym. Phys. Ed.*, 1985, **23**, 367.
51. U. Pschorn, E. Rössler, H. Sillescu, S. Kaufmann, D. Schaefer, and H. W. Spiess, *Macromolecules*, 1991, **24**, 398.
52. Y. Tagahashi and H. Tadoroko, *Macromolecules*, 1973, **6**, 672.
53. K. Schmidt-Rohr and H. W. Spiess, *Phys. Rev. Lett.*, 1991, **66**, 3020.
54. R. Kohlrausch, *Pogg. Ann. Phys.*, 1854, **4**(17), 56.
55. G. Williams and D. C. Watts, *Trans. Faraday Soc.*, 1970, **66**, 80.
56. A. F. Yee and S. A. Smith, *Macromolecules*, 1981, **14**, 54.
57. E. W. Fischer, G. P. Hellmann, H. W. Spiess, F. J. Hörth, U. Ecarius, and M. Wehrle, *Macromol. Chem. Suppl.*, 1985, **12**, 189.
58. H. W. Spiess, *Colloid. Polym. Sci.*, 1983, **261**, 193.
59. P. T. Inglefield, R. M. Amici, J. F. O'Gara, C.-C. Hung, and A. A. Jones, *Macromolecules*, 1983, **16**, 1552.
60. J. Schaefer, E. O. Stejskal, R. A. McKay, and W. T. Dixon, *Macromolecules*, 1984, **17**, 1479.
61. M. T. Hansen, B. Blümich., C. Boeffel, H. W. Spiess, L. Morbitzer, and A. Zembrod, *Macromolecules*, 1992, **25**, 5542.
62. M. H. Litt and S. J. Torp, *Appl. Phys.*, 1973, **44**, 4282.
63. M. Wehrle, G. P. Hellmann, and H. W. Spiess, *Colloid. Polym. Sci.*, 1987, **265**, 815.
64. K. Schmidt-Rohr, A. S. Kulik, H. W. Beckham, A. Ohlemacher, U. Pawelzik, C. Boeffel, and H. W. Spiess, *Macromolecules*, 1994, **27**, 4733.
65. E. Clementi and S. Chin (eds), *Structure and Dynamics of Nucleic Acids, Proteins, and Membranes*, Plenum, New York, 1986.
66. K. Schmidt-Rohr, J. Clauss, and H. W. Spiess, *Macromolecules*, 1992, **25**, 3273.
67. W. J. Jackson, Jr., *Br. Polym. J.*, 1980, **12**, 147.
68. M. Ballauff, *Angew. Chem.*, 1989, **101**, 261.
69. J. Clauss, K. Schmidt-Rohr, A. Adam, C. Boeffel, and H. W. Spiess, *Macromolecules*, 1992, **25**, 5208.

Biographical Sketch

Hans Wolfgang Spiess. *b* 1942. Ph. D. 1968, Physical Chemistry, University of Frankfurt, Germany. Research associate, Florida State University, 1968–70; Max-Planck-Institute, Heidelberg with K. H. Hausser, 1970–75; University of Mainz, 1975–78. Professor at University of Mainz, 1978–80, University of Münster, 1981–82, University of Bayreuth, 1983–84. Director, Max-Planck-Institut for Polymer Research, Mainz since 1984. Approx. 250 publications. Current research interests: solid state NMR and its applications in polymer science.

Polymer Physics

Ian M. Ward and Philip G. Klein
Leeds University, Leeds, UK

1	Introduction	1
2	Molecular Orientation	1
3	Analysis of Composite NMR Spectra: Determination of Rigid/Mobile Fraction and Crystallinity	5
4	Relaxation Parameters and Polymer Dynamics	7
5	Polymer Networks and Chain Entanglements	10
6	Related Articles	13
7	References	13

1 INTRODUCTION

The study of polymer structure, morphology, orientation, order, and chain dynamics by NMR is an extremely active area. In this article, the application of NMR techniques to selected aspects of polymer physics will be addressed, and these have been chosen in order to show how NMR can provide complementary and additional information to that obtained by other spectroscopic techniques and by mechanical measurements. The first part of the article provides a detailed description of how orientation in particular as well as crystallinity in solid polymers can be quantified using proton second-moment and lineshape analysis. This then leads into an explanation of how relaxation time measurements can give an insight into the nature of polymer relaxations and transitions, and finally we discuss the application of NMR to the study of polymer networks in the melt. A more detailed introduction to each of these areas will be found at the beginning of the relevant section.

2 MOLECULAR ORIENTATION

In many commercial applications of polymers, molecular orientation is introduced as a means of enhancing properties. This is the case for fibers and films, where the production of a highly ordered aligned structure can be used to give increased stiffness and strength, as well as improvements in chemical resistance and thermal stability. Orientation is also a valuable tool for the polymer physicist, because it can often enable more precise relationships to be established between structure and properties and to gain a more precise understanding of molecular relaxation processes. This is essentially a result of the greater complexity of structure and properties observed in an oriented polymer and the correspondingly greater discrimination that can be achieved, the increase in precise information gained usually leading to greater understanding.

NMR studies of oriented polymers are most valuable when they are combined with other structural techniques such as X-ray diffraction, infrared and Raman spectroscopy and with measurements of physical properties, especially mechanical and dielectric relaxation. The starting point for a quantitative understanding at a molecular level for all these techniques is to consider that the bulk polymer is an aggregate of anisotropic structural units.

At the simplest level, consider a pair of identical nuclei of spin-$\frac{1}{2}$ (i.e. protons). The dipole–dipole interaction will give rise to a doublet signal with linewidth splitting

$$\Delta B = \frac{\mu_0}{4\pi}\frac{3\gamma\hbar}{r^3}(3\cos^2\beta - 1) \tag{1}$$

where β is the angle between the line joining the protons and the field $\boldsymbol{B}_0$. In some oriented polymers where the predominant dipolar interactions arise from a proton pair, e.g. CH_2 in polyethylene $(CH_2)_n$ and poly(vinylidene fluoride) $(CH_2CF_2)_n$ or the proton pairs on each side of a phenyl ring in liquid crystalline copolyesters, such simple doublet structures can be observed with some broadening due to other internuclear dipolar interactions, and the doublet splitting will be dependent on the direction of $\boldsymbol{B}_0$ according to the function $3\cos^2\beta - 1$.

For a more quantitative discussion, it is usual to use the Van Vleck[1] equations, which relate the even moments of the lineshape to all the intermolecular distances in the polymer. For an absorption line described by $f(B)$, the nth moment is defined by

$$\begin{aligned}\langle \Delta B^n \rangle &= \langle (B - B^*)^n \rangle \\ &= \frac{\int_{-\infty}^{\infty} f(B)(B - B^*)^n \,\mathrm{d}(B - B^*)}{\int_{-\infty}^{\infty} f(B)\,\mathrm{d}(B - B^*)}\end{aligned} \tag{2}$$

where B^* is the applied field at the center of resonance.

The Van Vleck second-moment equation is

$$\langle \Delta B^2 \rangle = \left(\frac{\mu_0}{4\pi}\right)^2 \frac{G}{N}\sum_{j,k} r_{jk}^{-6}(3\cos^2\beta_{jk} - 1)^2 \tag{3}$$

where $G = \frac{3}{2}I(I+1)\gamma^2$, I is the nuclear spin number (= $\frac{1}{2}$ for protons), N the number of nuclei over which the sum is taken, r_{jk} the length of the vector joining nuclei j and k, and β_{jk} the angle between the vector r_{jk} and the direction of the steady magnetic field $\boldsymbol{B}_0$. Equation (3) ignores any interactions with nonresonant nuclei, and can be seen to be a direct generalization of equation (1).

It is not difficult to envisage how equations (1) and (3) can describe the changes in the NMR signal for an isolated proton pair or for a single crystal of a solid as the direction of $\boldsymbol{B}_0$ is varied. In practice, polymers are usually not fully aligned, but there is a distribution of molecular orientations, depending critically on the fabrication processing. To develop a quantitative treatment, it is assumed that the polymer can be regarded as an aggregate of anisotropic units of structure, each of which possesses the properties of the fully oriented polymer. In one of the first applications of this approach, for polyethylene, it was assumed that the structural units were an infinite crystal lattice. Because the NMR second moment depends primarily on nearest-neighbor interactions [the r_{ij}^{-6} term in equation (3)], it is only necessary to calculate interactions accurately within a range of about 0.5 nm. This means that quantitative studies of NMR anisotropy can be extended successfully to liquid crystalline polymers and even amorphous polymers.

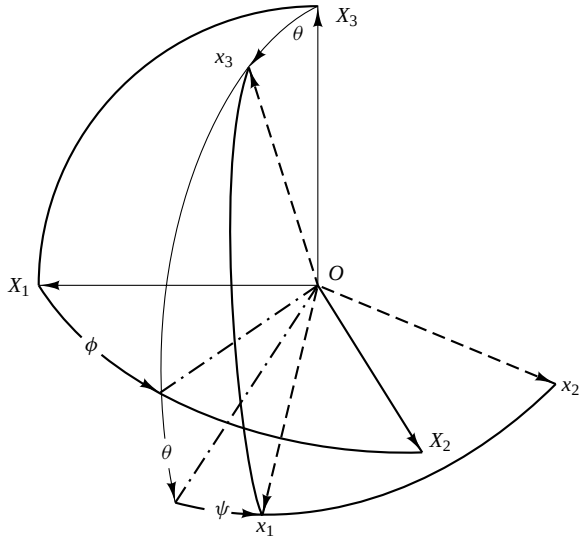

Figure 1 Definition of Euler angles. Reproduced by permission from D. A. Jarvis, I. J. Hutchinson, D. I. Bower, and I. M. Ward, *Polymer*, 1980, **21**, 41. © (1981) Butterworth–Heinemann

2.1 Definition of Orientation and Orientation Distribution Functions

The bulk polymer is usually in the form of a film or fiber, with overall orthorhombic or hexagonal symmetry, respectively. A system of rectangular coordinate axes $OX_1X_2X_3$ can be chosen fixed in the polymer sample, conventionally with the initial draw direction in the film or the fiber axis as X_3, and X_2 as the normal to the film plane (Figure 1). A second set of axes $Ox_1x_2x_3$ is chosen in the structural unit, which is also implicitly assumed to have at least orthorhombic symmetry. (This is not always true at a molecular level, which leads to a further degree of complication.) The orientation of the structural unit with respect to the bulk polymer is defined by the three Euler angles as shown in Figure 1, which represent the three successive rotations through angles ψ, ϕ and θ that would bring the $Ox_1x_2x_3$ axes into exact coincidence with the $OX_1X_2X_3$ axes.

For an aggregate of units, the distribution of orientations is then described by a function $N(\theta, \phi, \psi)$, where $N((\theta, \phi, \psi)$ $\sin\theta\ \mathrm{d}\theta\ \mathrm{d}\phi\ \mathrm{d}\psi$ is the fraction of units whose axes lie in the solid angle $\sin\theta\ \mathrm{d}\theta\ \mathrm{d}\phi\ \mathrm{d}\psi$. It is usual to express this function in a series of generalized spherical harmonic functions

$$N(\theta, \phi, \psi) = \sum_{l=0}^{\infty} \sum_{m=-1}^{+1} \sum_{n=-1}^{+1} P_{lmn} Z_{lmn}(\cos\theta) \mathrm{e}^{-\mathrm{i}m\phi} \mathrm{e}^{-\mathrm{i}n\psi} \quad (4)$$

where the Z_{lmn} are generalizations of the Legendre function, and a non-normalized form of Z_{lmn} is chosen that makes $P_{000} = 1$ and P_{100} equal to the average over the distribution of the lth-order Legendre polynomial in $\cos\theta$.

Although we now have the basis for a general theory, it is instructive (and often adequate in practice) to consider an aggregate of units with fiber symmetry (i.e. defined by the orientation of the Ox_3 axis) where the aggregate also has fiber symmetry (so that the molecule orientation is defined only by the orientation of the Ox_3 axes with respect of the OX_3 axis of the bulk sample). The distribution function equation (4) then reduces to

$$N(\theta) = \sum_{l=0}^{\infty} (l + \tfrac{1}{2}) \langle P_l(\cos\theta) \rangle P_l(\cos\theta) \quad (5)$$

where $\langle P_l(\cos\theta) \rangle = \int_0^{\pi} N(\theta) P_l(\cos\theta) \sin\theta \mathrm{d}\theta$ and the orientation distribution is described by two principal averages

$$P_{200} = \langle P_2(\cos\theta) \rangle = \tfrac{1}{2} \langle 3\cos^2\theta - 1 \rangle \quad (6)$$

$$P_{400} = \langle P_4(\cos\theta) \rangle = \tfrac{1}{8} \langle 3 - 30\cos^2\theta + 35\cos^4\theta \rangle \quad (7)$$

P_{200} is the well-known Hermans orientation function,[2] which is proportional to the birefringence in an optically anisotropic polymer.

It is now necessary to develop the relationship between the anisotropy of the NMR signal as determined say from the second moment, equation (3), and therefore related to a function of the angle β, which defines the angle between the internuclear vectors and the steady magnetic field, and the orientation distribution function for the units of structure, which is defined by the spherical harmonic average functions.[3] The second-moment anisotropy, equation (3), is written as

$$\langle \Delta B^2 \rangle = \left(\frac{\mu_0}{4\pi}\right)^2 \frac{4G}{N} \sum_{j,k} r_{jk}^{-6} P_2^2(\cos\beta_{jk}) \quad (8)$$

First, the orientation of given internuclear vector is defined by polar and azimuthal angles (Ξ, η) as shown in Figure 2(a). Because the structural units are transversely isotropic, the second moment will involve functions of Ξ only, the functions of η being replaced by their average values.

Similarly, although the orientation of each structural unit must be defined by polar and azimuthal angles θ and ϕ as shown in Figure 2(b), because the bulk sample is also transversely isotropic, the observed second moment will depend only on P_{200} and P_{400}, the functions involving ϕ taking fixed average values.

Finally, the magnitude of $\langle \Delta B^2 \rangle$ depends on the direction of $\boldsymbol{B}_0$ with respect to the sample axes, which is defined by polar and azimuthal angles Δ and Δ_ϕ, as shown in Figure 2(b). Again, because we assumed uniaxial symmetry for both the sample and the structural units, $\langle \Delta B^2 \rangle$ will depend only on Δ, because there is no preferred orientation in the plane normal to OX_3.

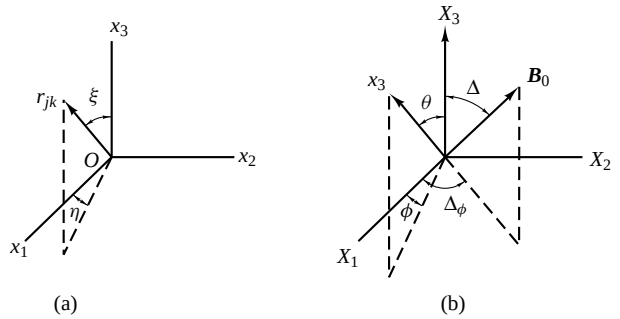

Figure 2 Polar and azimuthal angles used for relating second-moment anisotropy to the orientation distribution function

The assumptions of uniaxiality for sample and structural units enables us to use the Legendre addition theorem to write

$$\langle P_2^2(\cos\beta_{jk})\rangle_{\eta_{jk},\phi} = \sum_l a_l P_l(\cos\theta) P_l(\cos\xi_{jk}) P_l(\cos\Delta) \quad (9)$$

(where the subscripts on the angular brackets $\langle\ \rangle$ indicate the angles over which the average is taken) and the second moment $\langle\Delta B^2\rangle$ as

$$\langle\Delta B^2\rangle = \left(\frac{\mu_0}{4\pi}\right)^2 4G \sum_{l=0,2,4} a_l S_l P_l(\cos\Delta)\langle P_l(\cos\theta)\rangle \quad (10)$$

where

$$S_l = \frac{1}{N}\sum_{j>k}^{N} P_l\cos(\xi_{jk}) r_{jk}^{-6} \quad (11)$$

and $a_0 = \frac{1}{5}$, $a_2 = \frac{2}{7}$, $a_4 = \frac{18}{35}$. The second-moment anisotropy can therefore be seen to depend on the direction of $\boldsymbol{B}_0$ through the term P_l (cos Δ), the orientation distribution averages P_{200} and P_{400}, and the quantities S_l, which we call the lattice sums and which can be calculated from knowledge of the spatial coordinates of the magnetic nuclei.

2.2 NMR Anisotropy When There are Molecular Motions

In this section, we shall consider the situation where the NMR signal is narrowed owing to molecular motion but the molecular orientation is essentially retained. We shall confine the discussion to molecular rotation about a single axis, and not discuss the situation that occurs in the melt or even in the solid at temperatures close to the melting point, where rotations about several axes occur together with diffusion of the molecules.

Where molecular motion occurs, the dipolar interaction terms must be time-averaged, so that, for example, the second moment is now

$$\langle\Delta B^2\rangle_{\text{motion}} = \left(\frac{\mu_0}{4\pi}\right)^2 \frac{G}{N}\left\langle\frac{3\cos^2\beta_{jk^{-1}}}{r_{jk}^3}\right\rangle_{\text{motion}} \quad (12)$$

The evaluation of equation (12) for all dipolar interaction terms in a polymer in general involves somewhat laborious calculations. As an illustration, we can consider the case of the proton pair interaction only in a polyethylene fiber with full orientation and rotation of the chain around its axis at a frequency greater than the linewidth in hertz. The length of the intermolecular vector $\boldsymbol{r}$ is unchanged by the motion, and the contribution to the second moment from the proton pair interaction is

$$\begin{aligned}\langle\Delta B^2\rangle_{\text{motion}} &= \left(\frac{\mu_0}{4\pi}\right)^2 \frac{G}{N}\frac{\langle 3\cos^2\beta - 1\rangle^2}{r^6} \\ &= \left(\frac{\mu_0}{4\pi}\right)^2 \tfrac{5}{16}\langle\Delta B^2\rangle_{\text{iso}}(3\cos^2\Delta - 1)^2 \quad (13)\end{aligned}$$

where $\langle\Delta B^2\rangle_{\text{iso}}$ is the rigid lattice isotropic second moment and Δ is the angle between the fiber axis and $\boldsymbol{B}_0$. In terms of the more sophisticated development using spherical harmonic analysis,[4] the equation equivalent to equation (10) is

$$\langle\Delta B^2\rangle = \left(\frac{\mu_0}{4\pi}\right)^2 \frac{4G}{N} S \sum_l a_l P_l(\cos\Delta)\langle P_l(\cos\theta)\rangle \quad (14)$$

where S is a lattice sum defined by

$$S = \sum_{j>k} r_{jk}^{-6} P_2^2(\cos\xi_{jk}) \quad (15)$$

and may also be written as

$$S = \sum_{j>k} r_{jk}^{-6} \sum_l a_l P_l(\cos\xi_{jk}) \quad (16)$$

2.3 Theoretical Predictions of Orientation Distribution Functions from Models for Molecular Alignment

Theoretical predictions of molecular orientation stem principally from two different but related mathematical models. These models seek to relate the molecular alignment to the macroscopic deformation, i.e., the degree of permanent strain, usually defined in terms of the principal extension ratios λ_1, λ_2, λ_3 related to a set of rectangular coordinate axes 1, 2, 3, where λ_1 is the ratio of the length of a line in the 1 direction in the deformed polymer to its length in the undeformed polymer, and similarly for λ_2 and λ_3.

The first model, originally proposed by Kratky[5] for crystalline orientation in a semicrystalline polymer, assumes that the polymer consists of an aggregate of transversely isotropic units whose symmetry axes rotate on deformation in the same manner as joining pairs of points in the bulk material, which is assumed to deform at constant volume. For uniaxial deformation $\lambda_1 = \lambda$ and $\lambda_2 = \lambda_3 = \lambda^{-1/2}$, and it can be shown that

$$P_{200} = \frac{1}{2}\left[\frac{2\lambda^3+1}{\lambda^3-1} - \frac{3\lambda^{1/2}\cos^{-1}\lambda^{-3/2}}{(\lambda^3-1)^{3/2}}\right] \quad (17)$$

$$\begin{aligned}P_{400} = {} & \frac{1}{8}\frac{35\lambda^6}{(\lambda^3-1)^2}\left[1 + \frac{1}{2\lambda^3} - \frac{3\cos^{-1}\lambda^{-3/2}}{2(\lambda^3-1)}\right] \\ & - \left[\frac{30\lambda^3}{\lambda^3-1}\left(1 - \frac{\cos^{-1}\lambda^{-3/2}}{\lambda^3-1}\right) + 3\right] \quad (18)\end{aligned}$$

Similarly, it is possible to calculate P_{200}, P_{220}, etc. for a biaxially oriented aggregate.

This deformation scheme ignores the fact that, on deformation, the line joining two points in the bulk polymer will in general change its length as well as rotate. It has therefore been called the 'pseudoaffine' deformation scheme to distinguish it from the 'affine' deformation scheme, which was devised by Kuhn and Grün[6] for the deformation of a rubber-like network where the vectors joining the junction points of the network both rotate and change their length, and the chain segments between the junction points adopt the most probable distribution of molecular orientations consistent with maximizing the entropy for the new length between these junction points

in the deformed state. For this deformation scheme, the true network of chains can be modeled by an idealized network of chains consisting of rotatable rigid segments called random links, each chain containing an identical number N' of such links. Using the Treloar expression for the inverse Langevin function,[7] it can be shown that

$$P_{200} = \frac{1}{5N'}\left(\lambda^2 - \frac{1}{\lambda}\right) + \frac{1}{25N'^2}\left(\lambda^4 + \frac{\lambda}{3} - \frac{4}{3\lambda^2}\right) + \frac{1}{35N'^3}\left(\lambda^6 + \frac{3\lambda^2}{5} - \frac{8}{5\lambda^2}\right) \quad (19)$$

for uniaxial deformation to an extension ratio λ. Further expressions have been given for P_{200}, P_{220}, etc. in the case of a biaxially oriented rubber network, and

$$P_{400} = \frac{3}{175N'^2}\left(\lambda^4 - 2\lambda + \frac{1}{\lambda^2}\right) + \frac{216}{13\,475N'^3}\left(\lambda^6 - \frac{4\lambda^3}{5} - \frac{7}{5} + \frac{6}{5\lambda^3}\right) \quad (20)$$

Equations (17)–(20) are shown schematically in Figure 3.

2.4 Experimental Studies of NMR Anisotropy

Quantitative studies of molecular orientation using NMR anisotropy have been largely concerned with second-moment measurements using the theoretical developments leading to equations (10) and (14), which provide information regarding P_{2mn} and P_{4mn}, most usually P_{200} and P_{400} for samples possessing uniaxial symmetry. Fourth-moment measurements have also been used to obtain values for higher-order orientation functions such as P_{600} and P_{800}.

One of the earliest applications of the theory outlined above was to cold-drawn low-density polyethylene,[3] where the development of NMR anisotropy was determined from quantitative measurements of the second and fourth moments as functions of the direction of $\boldsymbol{B}_0$. A further complication in the analysis arises from the fact that we are dealing with a semicrystalline polymer, i.e., there are crystalline and amorphous regions with different degrees of molecular orientation. It was found adequate to assume that the NMR anisotropy arose entirely from the crystalline regions and that the amorphous regions made a constant contribution in proportion to their concentration. With this assumption, the NMR anisotropy was shown to be consistent with the pseudoaffine deformation scheme [equations (17) and (18) for P_{200} and P_{400}, respectively] (Figure 4). A result of particular practical value was that the values of P_{200} and P_{400} could be used to give a very successful prediction of the mechanical anisotropy, for example, the change in Young's modulus as a function of draw ratio.

A second polymer that has been studied in some detail is poly(ethylene terephthalate), (PET).[8] There are several major differences with the previous case of PE. First, PET appears to conform on deformation to the rubber network model so that P_{200} and P_{400} are now given by equations (19) and (20). Secondly, an important distinction at a structural level is between *trans* and *gauche* conformations of the glycol residue, and although the crystalline regions are solely *trans*, the amorphous regions can be both *gauche* and *trans* (the so-called 'amorphous *trans*' material).

It has been shown that the NMR anisotropy relates primarily to the all-*trans* material, irrespective of whether this is in the crystalline or amorphous regions. For a quantitative analysis of the NMR anisotropy, the *gauche*/*trans* ratio must also be determined (e.g., by infrared spectroscopy). The situation is analogous to that for low-density polyethylene, where the fractional crystallinity was required.

Similar studies to the above have been undertaken for many crystalline polymers, including the situation where

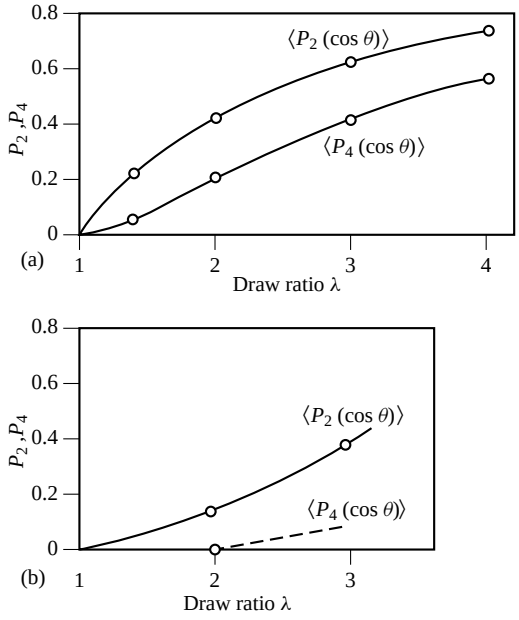

Figure 3 P_{200} and P_{400} as functions of draw ratio λ for (a) the pseudoaffine deformation scheme (uniaxially oriented sample) and (b) the rubber network affine deformation scheme (N' = 6, uniaxially oriented sample). Reprinted by permission from I. M. Ward, *J. Polym. Sci., Polym. Symp.*, 1977, **58**, 1. © (1977) John Wiley & Sons, Inc.

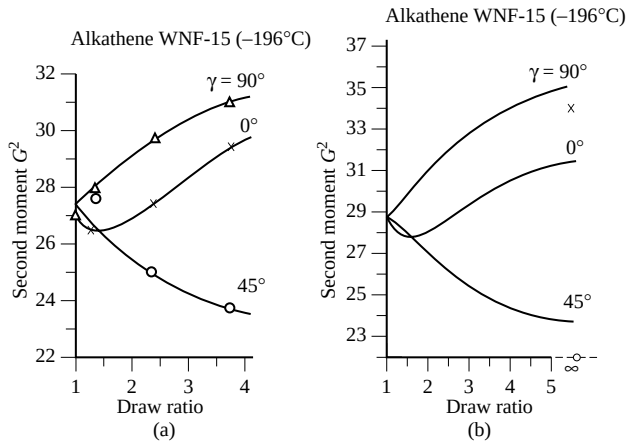

Figure 4 The second moment plotted against draw ratio: (a) the observed variation; (b) theoretical variation on pseudoaffine deformation scheme. Reprinted by permission from V. J. McBrierty and I. M. Ward, *Br. J. Appl. Phys. (J. Phys. D)*, 1968, **1**, 1529. © (1968) IOP Publishing Ltd.

molecular motions occur. Particularly notable early investigations were those of Slichter[9] on polytetrafluoroethylene, Olf and Peterlin[10] on poly(oxymethylene) and polyethylene, and Folkes and Ward[4] on polyethylene.

Second-moment anisotropy studies have also been analyzed quantitatively for noncrystalline polymers [e.g., poly(methyl methacrylate)] poorly crystalline polymers [e.g., poly(vinyl chloride)], and liquid crystalline polymers (e.g., linear thermotropic copolyesters of hydroxybenzoic acid and hydroxynaphthoic acid). In these polymers, the lattice sums can be estimated by assuming that the magnetic anisotropy arises entirely from the intramolecular interactions, and that the intermolecular interactions are isotropic. The lattice sums for the intramolecular interactions are then calculated exactly for the molecular chains on the basis of a configurational model for the chain, and the intermolecular interactions give a small additional term in the isotropic S_0 lattice sum that can be found from a least-squares fit to the data. In the case of liquid crystalline copolyesters, the existence of random chain substitution is taken into account by Monte Carlo statistics.

2.5 Chemical Shift Anisotropy

In oriented polymers, there is also an effect that can be observed relating to the fact that the chemical shift depends on the direction between the steady magnetic field $\boldsymbol{B}_0$ and the orientation of the local environment of the resonant nucleus. This is called chemical shift anisotropy. Consider the situation where the chemical shift can be represented by an axially symmetric chemical shift tensor. The position of the resonance line is then given by

$$\sigma(\beta) = \sigma_{\parallel} \cos^2 \beta + \sigma_{\perp} \sin^2 \beta \tag{21}$$

where $\sigma_{\parallel}$ and $\sigma_{\perp}$ are the chemical shifts when the unique axis of the tensor is parallel or perpendicular to $\boldsymbol{B}_0$, respectively, and β is the angle between the unique axis and $\boldsymbol{B}_0$. In practice, this simple situation is complicated for two major reasons. First, there is a distribution of molecular orientations, so that the total NMR signal will have a lineshape that relates to the distribution with the chemical shift anisotropy for each proton given by equation (21) with the appropriate value of β. Second, this lineshape must also be convoluted with a broadening function to account for relaxation broadening or dipolar interactions. It has been shown to be adequate to approximate these broadening effects by a simple Gaussian function[11] (analogous to that procedure for the Pake doublet broadening).

A quantitative treatment of chemical shift anisotropy relates the orientation distribution parameters P_{lmn} to the first-moment anisotropy, i.e., the shift in the center of gravity of the absorption as a function of the direction of $\boldsymbol{B}_0$, which is most generally defined by the polar and azimuthal angles Δ and ϕ_{Δ} that this makes with the 3 axis of the sample. Most studies of chemical shift anisotropy have been confined to samples with uniaxial (fiber) symmetry. For this situation, it can be shown that the first-moment anisotropy $\Delta\sigma_1$ is given by

$$\Delta\sigma_1 = \Delta\sigma\, P_2(\cos\theta)(\tfrac{2}{3} - \sin^2 \Delta) \tag{22}$$

where $\Delta\sigma = \sigma_{\parallel} - \sigma_{\perp}$, $\langle P_2(\cos\theta)\rangle$ is the molecular orientation function average, and Δ is the angle between $\boldsymbol{B}_0$ and the symmetry axis of the sample (the fiber axis or draw direction). A further complication required to obtain quantitative information is the need to take into account the different chemical shift anisotropies for the crystalline and amorphous regions in a semicrystalline polymer. The first-moment anisotropy is divided into two components, so that

$$\Delta\sigma_1 = f_c \Delta\sigma_{1c} + (1 - f_c)\Delta\sigma_{1a} \tag{23}$$

where f_c is the crystalline fraction, and $\Delta\sigma_{1c}$ and $\Delta\sigma_{1a}$ refer to crystalline and amorphous regions respectively.

Experimental studies of chemical shift anisotropy have now been reported for several polymers. Particularly notable are the pioneering research of Garroway[12] and co-workers and Brandolini et al.[11] on poly(tetrafluoroethylene), van der Hart and co-workers[13] on polyethylene, and more recently Monnerie et al.[14] on liquid crystalline copolyesters.

3 ANALYSIS OF COMPOSITE NMR SPECTRA: DETERMINATION OF RIGID/MOBILE FRACTION AND CRYSTALLINITY

3.1 Broadline Line Shape and Measurements of the Free Induction Decay

Wilson and Pake[15] showed that the broadline (continuous wave) spectra for proton resonance in polyethylene and for fluorine resonance in poly(tetrafluorethylene) were composite in form, consisting of a broad and a narrow component. These two components were attributed to the crystalline region (broad 'rigid' component) and the amorphous regions (narrow 'mobile' component), respectively. These preliminary results have been extended in several respects.

(i) *Recognition that a two-component analysis may be inadequate*.[16] Although it can be concluded with some certainty that the rigid broad component has usually been shown to relate predominantly to the crystalline phase, the mobile component is often heterogeneous. Sometimes, as has been observed for oriented fibers, two 'narrow' components can be identified, and only in exceptional cases is the narrow component truly liquid-like with a Lorentzian lineshape.

(ii) *Attempts to produce quantitative lineshapes for the several components, especially the rigid crystalline phase*. In polyethylene and poly(vinylidene fluoride), the structure shows that the predominant intramolecular dipolar interaction arises from the pairs of protons attached to a carbon atom. It has been found very satisfactory[17,18] to model the lineshape for the crystalline component as a Gaussian doublet [Figure 5], defined as

$$Y(\Delta B) = a_1 \left\{ \exp\left[-\frac{(\Delta B - a_2)^2}{2a_3^2} \right] + \exp\left[-\frac{(\Delta B + a_2)^2}{2a_3^2} \right] \right\} \tag{24}$$

This describes the superposition of two identical Gaussian lineshapes whose individual second moments about their

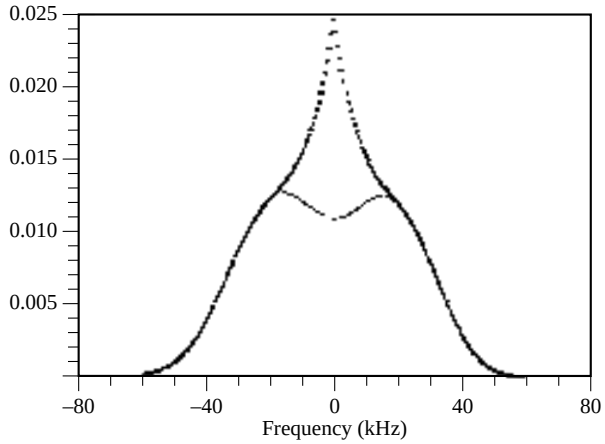

Figure 5 Proton NMR spectrum of polyethylene, obtained by Fourier transformation of FID following a solid echo pulse sequence. The solid line is the fit to equation (24), giving a crystallinity of 84%

centers are a_3^2, separated by a field interval $2a_2$. The variable $\Delta B = B - B_0$, where B_0 is the magnetic field at the center of the doublet. The area under the curve can be shown to be $(8\pi)^{1/2}a_1a_3$, and the second and fourth moments are

$$\langle \Delta B^2 \rangle = a_2^2 + a_3^2 \tag{25}$$

$$\langle \Delta B^4 \rangle = a_2^2 + 3a_3^4 + 6a_2^2a_3^2 \tag{26}$$

A recommended procedure when the spectrum is composite in nature is to fit the outer part of the experimental spectrum with a_1, a_2, and a_3 as adjustable parameters, using a least-squares procedure with parabolic extrapolation,[17] minimizing the sum

$$\chi^2 = \sum_i \frac{[A_i - Y(\Delta B_i)]^2}{\sigma_i^2} \tag{27}$$

where A_i is the experimental value of the absorption at the *ith* point and $Y(\Delta B_i)$ the corresponding value of the Gaussian doublet. χ^2 can be considered as a function of a_1, a_2, and a_3 represented by a three-dimensional hypersurface, which must be searched for the correct global minimum. This is ensured by choosing initial values for a_2 and a_3 by calculating the value of a_2 appropriate to the proton pair in the CH_2 group and then deriving a_3 from the theoretical second moment using $\langle \Delta B^2 \rangle = a_2^2 + a_3^2$. With these two parameters chosen, the choice of an initial value for a_1 could easily be made. For isotropic samples, Pranadi and Manuel[17] showed that confirmation of the satisfactory nature of this fitting procedure can be obtained by comparing the ratio of the squares of the second moment to the fourth moment for the Gaussian doublets fitted to the theoretical value for an isotropic fully crystalline sample. For oriented samples, Clements et al.[18] carried out the fitting procedures for different directions of $\boldsymbol{B}_0$ with respect to the sample symmetry axis (fiber symmetry), and showed that these led to very similar crystallinity values, and also that the values of $\langle P_2(\cos\Delta)\rangle$ and $\langle P_4(\cos\Delta)\rangle$ obtained in this way agreed well with these obtained from X-ray diffraction measurements.

Bergmann and Nawotki,[19] and subsequently Kitamaru et al.,[20] have proposed that the spectra of isotropic semicrystalline polymers consist of three superimposed lines of different widths, although the narrow and intermediate lines are not separately resolved in the broadline spectrum. Both sets of workers obtained the lineshape for the broad crystalline component from the measured spectrum of a very highly crystalline linear polyethylene at a low temperature, correcting this for increases in lattice spacing at higher temperatures. The lineshape for the intermediate component was obtained from the spectrum calculated by Gutowsky and Pake[21] for an isotropic assembly of proton pairs undergoing hindered rotation about the line joining them, and broadened by convolution with a Gaussian function. The narrow component was assumed to have a Lorentzian shape. Bergmann and his co-workers applied these procedures to many semicrystalline polymers, including poly(oxymethylene), poly(ethylene oxide), poly(vinylidene fluoride), Nylon 6 and polypropylene. Kitamaru and his colleagues concentrated their efforts on polyethylene, exploring the effects of molecular weight on both melt-crystallized and solution-crystallized materials. Kitamaru and Horii[22] also reported measurements on oriented fibers where a three-component structure could be clearly identified (Figure 6). Similar results were reported by Smith et al.[23] for highly drawn polyethylene fibers, and an attempt was made

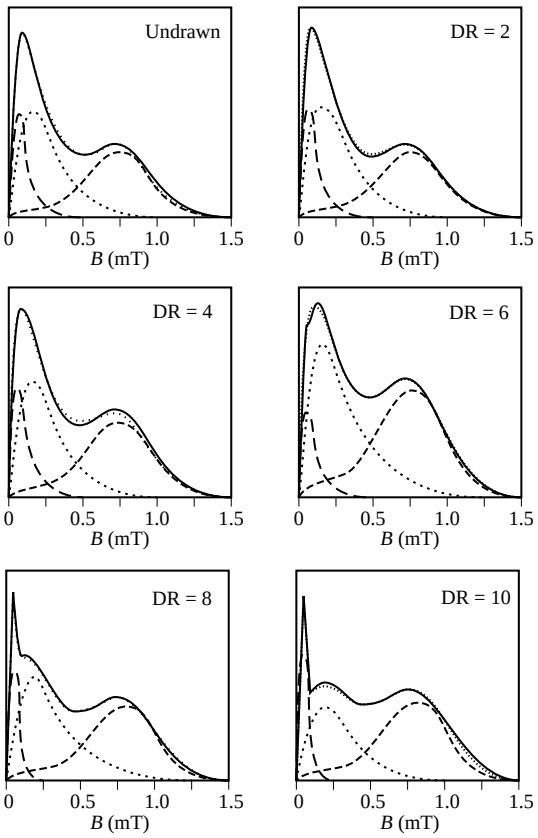

Figure 6 Three-component analysis at room temperature for fibers drawn to different degrees. The draw ratio (DR) is indicated. Dashed, dotted, and broken lines indicate narrow, medium, and broad components, respectively. Thick dotted and solid lines indicate the composite curve for the three components and the experimental spectrum, respectively. R. Kitamaru and F. Horii, *Adv. Polym. Sci.*, 1978, **26**, 137. © (1978) Springer-Verlag

to determine the orientation functions $\langle P_2(\cos\Delta)\rangle$ and $\langle P_4(\cos\Delta)\rangle$ for the intermediate component from the anisotropy of the second moment of this component on the assumption that this arises from oriented chains undergoing rotation about the chain axis.

A major disadvantage of the broadline CW technique (apart from the availability of suitable equipment) is the inevitable distortion of the linewidth due to the field modulation method of detection. Although correction procedures can be applied, these are least satisfactory for the narrowest components. There are therefore considerable incentives to use the latest NMR facilities and obtain the lineshape in the frequency domain, i.e., to measure the free induction decay (FID). In fact, attempts to interpret the FID for semicrystalline polymers appear to be more empirical and less quantitative than the CW studies described in detail above. Bergmann[24] has suggested decomposition of the FID into components: the crystalline component as a Gaussian multiplied by a sinc function (the 'Abragam function' proposed for the FID of CaF_2), and a Gaussian distribution of Kubo–Tomita functions to represent the remaining mobile regions (i.e., including at least two components analyzed from CW studies). Although useful empirical information has been obtained from this and similar procedures, it can only be concluded that this area is still unresolved.

3.2 High-Resolution Spectra

High-resolution ^{13}C measurements have also been shown to provide detailed information on the phase studies of semicrystalline polymers. Kitamaru and his colleagues[25] showed that for uniaxially oriented polyethylene films, two sharp lines were observed, which could be assigned to the crystalline and noncrystalline regions, respectively. The noncrystalline line was further resolved on the basis of spin–spin relaxation into two components—attributed to a true amorphous component and a crystalline–amorphous interface, respectively. The presence of three components was confirmed by lineshape analysis (Figure 7). Finally, it was concluded from selective relaxation experiments that the crystalline line is composed of three components with different spin–lattice relaxation times.

3.3 Longitudinal Relaxation T_1

The inversion–recovery method for measuring T_1 where the FID following a $180_y^\circ - \tau - 90_x^\circ$ pulse sequence is recorded can also be used to separate the components in a composite spectrum, and hence assist the decomposition procedures. Direct measurements of T_1 for protons do not generally show other than a single exponential decay owing to very efficient spin diffusion between protons.

3.4 Relaxation in the Rotating Frame; $T_{1\rho}$

Measurements of $T_{1\rho}$ have been used successfully to identify different phases and to provide new understanding of the role of spin diffusion as well as relating this to the dimensions of sample morphology (e.g. lamellar thicknesses). Packer and his colleagues[26] have made notable contributions to this subject.

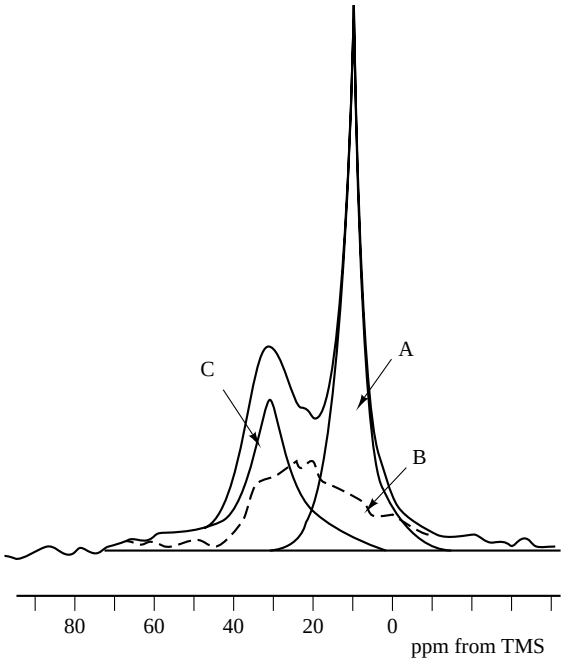

Figure 7 Component analysis of ^{13}C spectrum of polyethylene, showing, crystalline (A), interfacial (B), and amorphous (C) components. Reprinted by permission from M. Nakagawa, F. Horii, and R. Kitamaru, *Polymer*, 1990, **31**, 323. © (1990) Butterworth–Heinemann

4 RELAXATION PARAMETERS AND POLYMER DYNAMICS

One of the main areas of interest in the application of NMR to the study of solid polymers is in the relationship between the temperature dependence of the NMR relaxation times and the locations and activation energies of transitions observed by dynamic mechanical and dielectric relaxation studies. The advantage of NMR in this respect is that is that it can help identify the precise molecular origin of polymer transitions. This is particularly true for isotopically labeled structures, and in the case of high-resolution ^{13}C studies, where as a result of the chemical shift, and the absence of spin diffusion effects, the relaxation times of chemically distinct carbons can be measured.

4.1 Relaxation Theory

Let us take as a starting point the expression for T_1 derived by Bloembergen, Purcell and Pound,[27] as modified by Kubo and Tomita,[28] written here for homonuclear dipolar interactions between protons:

$$\frac{1}{T_1} = \frac{3}{20}\left(\frac{\mu_0}{4\pi}\right)^2 \gamma^4 \hbar^2 \sum_j r_j^{-6}[J(\omega_0) + 4J(2\omega_0)] \quad (28)$$

where $J(\omega)$ is the spectral density, which is obtained by considering a single exponential autocorrelation function, followed by a Fourier transformation, as follows:

$$G(t) = \exp\left(-\frac{t}{\tau_c}\right) \quad (29)$$

$$J(\omega) = \int_{-\infty}^{\infty} G(t) \exp(-\mathrm{i}\omega t)\, \mathrm{d}t \tag{30}$$

This leads to an expression containing a single correlation time τ_c:

$$\frac{1}{T_1} = \frac{3}{10}\left(\frac{\mu_0}{4\pi}\right)^2 \gamma^4 \hbar^2 \sum_j r_j^{-6} \left(\frac{\tau_c}{1+\omega_0^2\tau_c^2} + \frac{4\tau_c}{1+4\omega_0^2\tau_c^2}\right) \tag{31}$$

It will be more convenient to write this in a form containing the isotropic second moment M_2, written here in frequency units, such that

$$\frac{1}{T_1} = \frac{2M_2}{3}\left(\frac{\tau_c}{1+\omega_0^2\tau_c^2} + \frac{4\tau_c}{1+4\omega_0^2\tau_c^2}\right) \tag{32}$$

The shortcomings of considering a single correlation time will be addressed in due course. For now, however, this assumption is more useful for illustrating the general features of relaxation behavior than considering the additional complexities introduced by a distribution of correlation times, at this stage. As illustrated in Figure 8, equation (32) predicts T_1 to pass through a minimum, and this occurs when $\omega_0\tau_c$ is approximately 0.62.

On the long-τ_c side of the minimum, T_1 decreases with decreasing τ_c (or increasing temperature), and this will generally be the case for a solid polymer. The observation of a minimum in the T_1 plot is then taken as a good indication of the onset of a mechanical transition, which would be observable by a drop in the dynamic storage modulus, or by a peak in the loss modulus or damping factor in, say, a dynamic mechanical experiment. However, the frequency of the NMR T_1 measurement will be in the region of hundreds of megahertz, and this presents at least two problems. First, the nature of the polymer chain motion at such high frequencies may well be different from the motion at the lower frequencies (Hz–kHz) encountered in dynamic mechanical and dielectric analysis. Second, depending on the activation energy of the process, to observe the transition at megahertz frequencies may require prohibitively high temperature. As a result, it is usually more rewarding to study the temperature dependence of $T_{1\rho}$. The relaxation rate as a function of τ_c is obtained in a similar manner to before, and the expression, again for a single τ_c, is given by

$$\frac{1}{T_{1\rho}} = \frac{M_2}{3}\left(\frac{3\tau_c}{1+4\Omega_1^2\tau_c^2} + \frac{5\tau_c}{1+\omega_0^2\tau_c^2} + \frac{2\tau_c}{1+4\omega_0^2\tau_c^2}\right) \tag{33}$$

Ω_1 is now the strength of the B_1 spin locking field in the on-resonance rotating frame. This frequency is usually at least three orders of magnitude less than the Larmor frequency ω_0 applicable to T_1 relaxation. The dependence of $T_{1\rho}$ on τ_c is similar to that of T_1 (Figure 8), but the consequence of the lower-frequency measurement is that the minimum appears at much higher correlation times, and therefore at lower, more accessible, temperatures. For completeness, the dependence of T_2 is also shown, and the relevant expression is given by

$$\frac{1}{T_2} = \frac{M_2}{3}\left(3\tau_c + \frac{5\tau_c}{1+\omega_0^2\tau_c^2} + \frac{2\tau_c}{1+4\omega_0^2\tau_c^2}\right) \tag{34}$$

The dominant contributions to T_2 in solids arise from the frequency-independent term, and so the temperature at which a transition is indicated, by an increase in T_2, is not usually affected by the NMR frequency,[29] at least at frequencies corresponding to the linewidth, in hertz. Analogous expressions to those above can be obtained for heteronuclear interactions,[30] pertaining to, for example, ^{13}C relaxation.

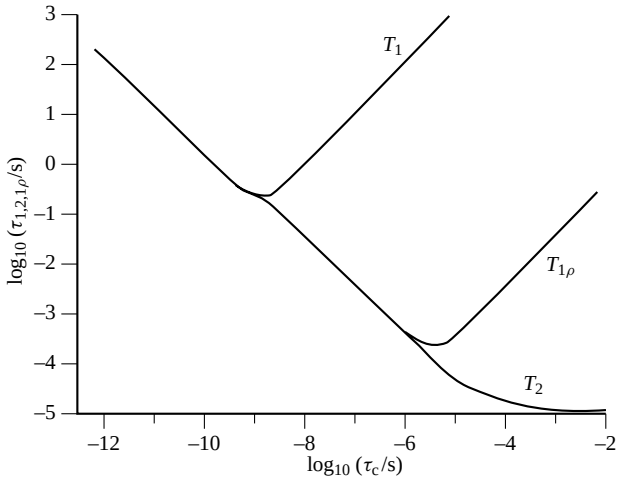

Figure 8 Dependence of T_1, T_2, and $T_{1\rho}$ on correlation time τ_c for frequencies $\omega_0/2\pi$ = 100 MHz and $\Omega_1/2\pi$ = 40 kHz. Reprinted by permission from R. K. Harris, Nuclear Magnetic Resonance Spectroscopy, Revised reprint, Longman. © (1986) Robin K. Harris

4.2 Calculation of the Activation Energy

The frequency dependence of the glass transition in polymers is usually best described by the Williams–Landel–Ferry equation (WLF), or its close equivalent, the Vogel–Fulcher–Tammann (VFT) equation:

$$\tau_c = \tau_0 \exp\left(\frac{B}{T - T_0}\right) \tag{35}$$

where B is related to the activation energy and T_0 is a reference temperature equal to $T_g - C_2$, where C_2 is the WLF constant. On the other hand, minor local relaxations and transitions often conform to the Arrhenius equation, such that

$$\tau_c = \tau_0 \exp\left(\frac{E}{RT}\right) \tag{36}$$

where E is the activation energy. An inspection of the plots in Figure 8 shows that, beyond a certain displacement either side of the T_1 or $T_{1\rho}$ minimum, the plot of ln T_1 or ln $T_{1\rho}$ versus ln τ_c is linear. A combination of this observation with equation (36) suggests that a plot of ln T_1 or ln $T_{1\rho}$ versus T^{-1} should yield a straight line of slope $+E/R$ or $-E/R$, corresponding to the long τ_c or short τ_c sides of the minimum, respectively. Of course, for T_g behavior, the relevant abscissa would be $(T - T_0)^{-1}$. Now, it is usually the case that activation energies

Table 1 Correlation Time (τ_c) Relationships, and the Range of τ_c Appropriate to Each Measurement (Adapted from V. J. McBrierty and D. C. Douglass, *J. Polym. Sci., Macromol. Rev.* 1981, **16**, 295. © (1981) John Wiley & Sons, Inc. Reprinted with permission)

NMR feature	Expression for τ_c (s)	Range of τ_c (s)
T_1 minimum	$(\sqrt{\omega}\omega_0)^{-1}$	4×10^{-8}–4×10^{-10}
$T_{1\rho}$ minimum	$(\gamma B_1)^{-1}$	2×10^{-5}–3×10^{-7}
T_2 transition	T_{2LT}[a]	2×10^{-5}–2×10^{-6}
Linewidth transition	$(\gamma \delta H_{LT})^{-1}$[b]	2×10^{-5}–2×10^{-6}

[a] $T_{2LT}^{-2} = T_{2lt}^{-2} - T_{2ht}^{-2}$, where T_{2lt} and T_{2ht} are the values of T_2 on the low- and high-temperature sides of the transition.
[b] δH_{LT} is the linewidth between points of inflection.

calculated by this method are much smaller, typically by an order of magnitude, than those calculated from dielectric or dynamic mechanical data. The source of this discrepancy lies in the distribution of correlation times, which will be addressed shortly. However, a means of avoiding this difficulty has been discussed by McBrierty and Douglass.[31] They point out that the positions of the minima in T_1 and $T_{1\rho}$ plots, or points of inflection in the case of T_2 and linewidth changes, are unaffected by the correlation time distribution. A value for τ_c associated with each of these features can be determined using Table 1, and the activation energy again calculated by applying equation (36).

Another similar method is to use the temperatures of T_1 and $T_{1\rho}$ minima obtained at a number of different B_0 and B_1 field strengths. However, it is difficult in practice to use more than a couple of different B_0 fields, and the experimental range of B_1 field strengths that can be used in a $T_{1\rho}$ experiment is limited, since the amplitude of B_1 must be larger than the frequency spread in the spectrum of the spin system.[32] The upper limit will be dictated by probe stability, so these considerations would typically restrict the B_1 field strength to the range 20–80 kHz, which is rather a small range for the purposes of activation energy calculations.

4.3 The Distribution of Correlation Times

As mentioned earlier, the assumption of a single correlation time leads to much smaller activation energies than those calculated from other methods. Connor[33] has discussed an approach whereby the expression for T_1, equation (32), can be modified to embrace a continuous distribution of correlation times, described by a normalized density function $H(\tau)$, to give

$$\frac{1}{T_1} = \frac{2M_2}{3}\left[\int_0^\infty \frac{\tau_c H(\tau_c)\,d\tau_c}{1+\omega_0^2\tau_c^2} + 4\int_0^\infty \frac{\tau_c H(\tau_c)\,d\tau_c}{1+4\omega_0^2\tau_c^2}\right] \quad (37)$$

Schaefer[34] has analyzed solution and solid state ^{13}C NMR relaxation times and has devised a log χ^2 distribution function to fit the experimental data, with reasonable success. Several other empirical distribution functions have been suggested, mainly to fit dielectric relaxation data, which can then be extended to NMR. The procedure involves introducing a distribution function $H(\tau_D)$, where τ_D is the correlation time appropriate to dielectric loss, and is related to the NMR correlation time via $\tau_D \approx 3\tau_c$. If τ_0 is the center of the distribution on a logarithmic timescale then we define another parameter s such that

$$s = \ln\left(\frac{\tau_D}{\tau_0}\right) \quad (38)$$

$H(\tau_D)$ is now replaced by another function $F(s)$, where

$$\tau_D H(\tau_D) = F(s) \quad (39)$$

Several forms of the function $F(s)$, such as Gaussian, Fuoss–Kirkwood and Cole–Cole have been suggested,[33] and used to fit dielectric relaxation data with varying degrees of success. The same functions can then be employed to fit the T_1 data, by substitution into equation (37) and subsequent integration. However, the extension of this approach to the expressions for $T_{1\rho}$ and T_2 is more complex, and so these distribution functions will not be considered further here. The exception to this is the Cole–Davidson function,[33] which is potentially more useful, since it accommodates the possibility of an asymmetric distribution, and is more amenable to extension to $T_{1\rho}$ data. This function is given by

$$F(s) = \begin{cases} \dfrac{\sin \delta\pi}{\pi}(1 - e^{-s})^{-\delta} & (\tau_c < \tau_0) \\ 0 & (\tau_c > \tau_0) \end{cases} \quad (40)$$

where δ is an adjustable parameter quantifying the width of the distribution. This leads to the following expression for T_1:

$$\frac{1}{T_1} = \frac{2M_2\delta}{3}\left[\frac{\tau_c}{(1+\omega_0^2\tau_c^2)^{\delta/2}(1+\delta^2\omega_0^2\tau_c^2)^{1/2}} + \frac{4\tau_c}{(1+4\omega_0^2\tau_c^2)^{\delta/2}(1+4\delta^2\omega_0^2\tau_c^2)^{1/2}}\right] \quad (41)$$

Extension of this to the expression for $T_{1\rho}$ is obvious. Calculation of the activation energies can be done in the same manner as before, by taking the slope of the ln T_1 or ln $T_{1\rho}$ versus T^{-1} plot in the linear region. Now, however, the slope of the low-temperature side of the plot depends on the width parameter δ, having the value $+\delta E/R$, but the consequence of the asymmetry is that the high-temperature slope is unaffected, and is $-E/R$, as for the single-τ_c case.

More recently, a different and potentially more useful approach has appeared. This is the use of Williams–Watts stretched exponential correlation function,[35] again borrowed from dielectric relaxation studies, which has the form

$$G(t) = \exp\left[\left(\frac{-t}{\tau_c}\right)^\beta\right] \quad (42)$$

The stretched exponential representation is finding increasing use in studies by a number of experimental techniques of a whole range of glass-forming systems, including solid polymers, and the value of β obtained from the fit is used to classify materials in terms of 'strong' and 'weak' glasses. Garroway et al.[36] have used this formulation to interpret changes in the lineshape of ^{13}C in phenylene with temperature

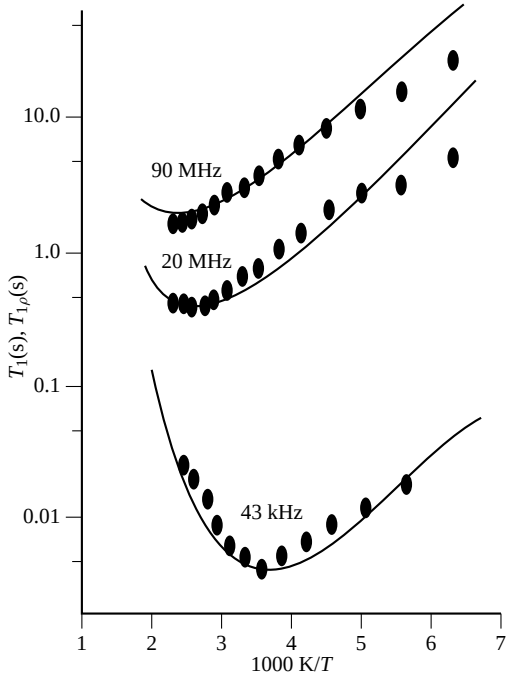

Figure 9 Proton T_1 and $T_{1\rho}$ versus inverse temperature for chloral polycarbonate. The solid lines are fits to the stretched exponential correlation function. Reprinted with permission from A. A. Jones, J. F. O'Gara, P. T. Inglefield, J. T. Bendler, A. F. Yee, and K. L. Ngai, *Macromolecules*, 1983, **16**, 658. © (1983) American Chemical Society

in epoxy resins, using a value for β of 0.3. Roy et al.[37] also found this value of β in their study of phenylene ring flips in poly(butylene terephthalate) using deuterium NMR. Jones and co-workers[38] have used the stretched exponential to interpret the temperature dependence of the proton T_1 and $T_{1\rho}$ in polycarbonate, through the sub-T_g transition. The procedure is to obtain the spectral density $J(\omega)$ by a Fourier transformation of equation (42) [compare with equation (29)] and substitute it into the appropriate expressions for T_1 and $T_{1\rho}$, equations (32) and (33). Two B_0 field strengths were used (90 and 20 MHz), and the B_1 field strength was 43 kHz. As shown in Figure 9, the fit to any one set of data is adequate rather than spectacular, but what is impressive is that the same value of β (0.2) was used to fit the data at all three frequencies. More recently, Colmenero et al.[39] used this procedure to fit ^{13}C T_1 and $T_{1\rho}$ relaxation times with temperature, in a study of the glass transition in poly(vinyl methyl ether). The NMR data were complemented with dielectric, dynamic mechanical, and neutron scattering studies, and a universal value of β = 0.44 was found. It would appear, then, that the stretched exponential representation of the correlation time distribution in polymers will prove to be the method of choice in future.

5 POLYMER NETWORKS AND CHAIN ENTANGLEMENTS

Above the glass transition temperature, or above the melting temperature in the case of semicrystalline materials, polymers whose chains are below the molecular weight necessary for entanglement formation (M_e) are best described as viscous liquids. Above M_e, polymers display a temporary rubber–elastic behavior as a direct consequence of the formation of an entanglement network. If permanent chemical cross-links are also incorporated into the structure, polymers in this temperature regime become true rubbers, with the elastic behavior characterized by contributions from the permanent cross-links, and the chain entanglements trapped between them. The rheological and mechanical properties of polymers in this state have been extensively studied,[40] and the theoretical description of the chain dynamics contributing to the permanent and temporary rubber–elastic behavior is now quite well advanced.[41] NMR studies of the dynamics have also been carried out, although perhaps less extensively, and recently a theoretical understanding has begun to emerge.

5.1 Experimental Considerations

The most common experiment for studying the dynamics of polymer melts by NMR is the observation of the proton transverse relaxation behavior. The shape and the rate of decay of the transverse magnetization are dictated by the residual dipolar interactions between protons that are not averaged to zero by molecular motion. The transverse relaxation can, in principle, be described by the FID following a 90° pulse. However, the inevitable $\boldsymbol{B}_0$ field inhomogeneity causes different protons to have slightly different Larmor frequencies, and this contributes to a dephasing of spins in the x–y plane that shortens the FID significantly for liquid-like signals. A commonly used technique to overcome this problem is the Carr–Purcell–Meiboom–Gill[42] (CPMG) echo train: 90°–(τ–180°–τ–echo–)$_n$. This is illustrated in Figure 10. After the initial 90° pulse, the magnetization is allowed to decay for a time τ (which is long compared with the pulse width), and then subjected to a 180° pulse. The result is that the magnetization is then refocused, forming an 'echo' at a time τ later. The magnitude of successive echoes then forms the true FID. A preferred refinement to this is the Levitt–Freeman[43] modification, which is the sequence $90_x{}^\circ$–τ–($90_x{}^\circ$–$180_y{}^\circ$–$90_x{}^\circ$–2τ)$_n$. This is a self-compensating pulse sequence that corrects for any slight error in the pulse widths by ensuring that every second echo is correct, providing that diffusional processes are not significant.

5.2 Interpretation of the FID from Polymer Melts

5.2.1 Phenomenological Features

For low molecular weight polymers, the FID tends to be a single exponential, characterized by a time constant T_2, the spin–spin relaxation time. The magnitude of T_2

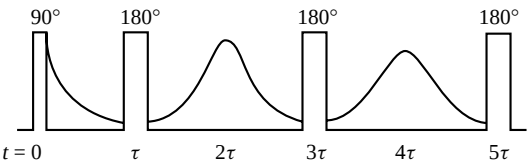

Figure 10 The CPMG pulse sequence for measuring the transverse relaxation function

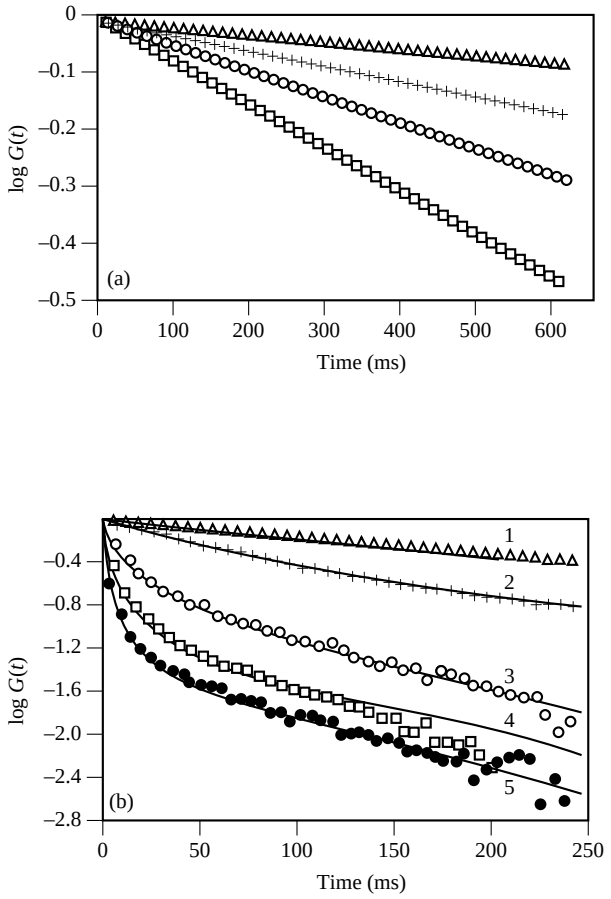

Figure 11 Transverse relaxation functions for monodisperse polyethylenes. (a) Molecular weights below the entanglement point: Δ, 342; +, 525; ○, 900; □, 1700 g mol^{-1}. (b) Showing the transition from unentangled to entangled chains: Δ, 5700; +, 11 400; ○, 30 600; □, 55 700; •, 107 000 g mol^{-1}. The lines through the data are fits to the Brereton model. M. Ward, N. Boden, and P. Wright, *Macromolecules*, 1991, **24**, 2068. © (1991) American Chemical Society

decreases as the molecular weight increases, until M_e is reached, and the decay is no longer simply exponential. This effect is illustrated in Figure 11 for samples of monodisperse polyethylene. Cross-linked polymer networks show the same general features as highly entangled systems, and a phenomenological interpretation of the FID was provided by Charlesby and co-workers in a number of papers.[44,45] They described the FID for irradiated (and therefore cross-linked) poly(dimethylsiloxane) (PDMS) in terms of two exponential components, characterized by two time constants T_{2S} and T_{2L}, referring to the short and long relaxation times, respectively, such that

$$\frac{I(t)}{I(0)} = f \exp\left(-\frac{t}{T_{2S}}\right) + (1-f)\exp\left(-\frac{t}{T_{2L}}\right) \quad (43)$$

It is found that f corresponds well to the gel fraction obtained by extraction techniques, with T_{2S} being directly proportional to the number average molecular weight between cross-links,[45] M_c, and T_{2L} related to the M_n of the chains forming the sol fraction. This approach can also be extended to entanglement networks, where now T_{2S} is related to the entanglement density manifested at a particular temperature. On the timescale of the NMR experiment, then, this suggests that some entanglements will appear to be static. Charlesby has shown that this is similar and indeed related to the observation of the plateau modulus in dynamic shear experiments.[46]

5.2.2 *Theories Based on Scale-Invariant Models*

5.2.2.1 The Cohen-Addad NMR Submolecule. Although extremely useful for the characterization of polymer networks, the preceding analysis has little theoretical basis. In this respect, a more satisfactory description is given by the work of Cohen-Addad,[47] who developed a scale-invariant model of the polymer chain by application of the submolecule concept. This is based on the idea that the whole relaxation time spectrum of polymer chains in the melt must consist of two well-separated dispersions Ω_1 and Ω_2. The Ω_1 spectrum is associated with high-frequency relaxation processes of short segments within a submolecule, which comprises a number N_a of monomer units, typically about 10, each of step length a. Each bond is considered to carry a proton pair, of separation b, and interactions between proton pairs are neglected. The set Ω_2 of long relaxation times characterizes the long-range configurational changes, involving several submolecules and motions beyond entanglements. Under these conditions, the transverse relaxation function $G(t)$ is given by

$$G(t) = \exp\left(-\frac{t}{T_2}\right)\left\{\frac{1+3\theta^2+[(1+3\theta^2)^2+4\theta^6]^{1/2}}{2[(1+3\theta^2)^2+4\theta^6]}\right\}^{1/2} \quad (44)$$

where $\theta = \frac{1}{3}t(M_2^M)^{1/2}$, M_2^M being the second moment associated with the residual spin coupling interactions induced by entanglements, and is given by

$$M_2^M = \frac{0.6M_2^G}{N_a^2} = \frac{0.27\gamma^4\hbar^2}{N_a^2 b^6} \quad (45)$$

where, in turn, M_2^G is the rigid-lattice second moment. At long times, $G(t)$ varies as $\theta^{-3/2}$, not the exponential function of simple T_2 behavior. Equation (45) was fitted to experimental data on highly entangled PDMS chains in high concentration in chloroform solution,[47] and from the fit a molecular weight between chain entanglements of 8224 g mol^{-1} was obtained, comparing well to the value of 8100 g mol^{-1} determined from viscoelastic measurements.

5.2.2.2 The Hierarchical Brereton Model. More recently, Brereton[48–51] has produced an exact expression for the transverse relaxation function, using a similar scale-invariant model to Cohen-Addad. Considering dipolar interactions within a proton pair separated by a distance d leads to the following expression for $G(t)$:

$$G(t) = \left\langle \cos\left\{\delta\int_0^t [3\cos^2\alpha(t') - 1]\,dt'\right\}\right\rangle \quad (46)$$

where $\alpha(t')$ is the angle the internuclear vector $\boldsymbol{d}$ makes with the static magnetic field $\boldsymbol{B}_0$, and δ is given by

$$\delta = \frac{3\gamma^2\hbar}{4d^3} \quad (47)$$

We now again consider a submolecule, of length b, comprising N_a repeat units, making an angle θ with respect to $\boldsymbol{B}_0$, leading to

$$G(t) = \left\langle \cos\left[\frac{3\Delta}{b^2}\int_0^t (2z^2 - x^2 - y^2)\,\mathrm{d}t'\right]\right\rangle \tag{48}$$

where Δ is a rescaled dipolar interaction, given by

$$\Delta = \frac{3}{2}\frac{\gamma^2\hbar}{N_a d^3} \tag{49}$$

If N_a is large then x, y and z are independent and can be described by the following Gaussian random time process:

$$g(\Delta, t) = \left\langle \exp\left(\frac{3\Delta \mathrm{i}}{2b^2}\int_0^t x^2(t')\,\mathrm{d}t'\right)\right\rangle \tag{50}$$

and then

$$G(t) = \mathrm{Re}[g(2\Delta, t)g(-\Delta, t)g(-\Delta, t)] \tag{51}$$

Equation (51) can be solved to give a functional form of $G(t)$ for different levels of dynamics. For molecular weights less than M_e, we consider fast dynamics appropriate for a Rouse chain[48] consisting of N submolecules. $G(t)$ is then predicted to be a single exponential:

$$G(t) = \exp\left(-\frac{6\Delta^2\tau\ \ln\ N}{\pi}t\right) \tag{52}$$

where τ is the fastest relaxation time for the smallest length, corresponding to one submolecule. Experimentally, of course, we associate the spin–spin relaxation time with the single exponential, such that $G(t) = \exp(-t/T_2)$. Equating this to equation (52) leads to the relationship

$$\frac{1}{T_2} = \frac{6\Delta^2\tau}{\pi}[\ln\ M_n - \ln(mN_a)] \tag{53}$$

where M_n is the molecular weight of the chain, and m the molecular weight of a repeat unit. It is apparent from equation (53) that a plot of the relaxation rate $1/T_2$ versus $\ln M_n$ should be linear, allowing the parameters N_a, Δ, and τ to be determined from the slope, intercept, and equation (49). For the polyethylene data[49] shown in Figure 12 this plot is indeed linear up to M_e, and it is found that N_a, the number of monomer units in a submolecule (in this case, the Rouse unit), is 9.0, and the fastest Rouse relaxation time is 1.49×10^{-8} s.

Similar studies have also been undertaken on polyethylene oxide, a much more highly coiled and flexible chain, and here it is found that N_a is correspondingly smaller, at only 1.5 repeats. The onset of entanglement formation is indicated in Figure 12 for polyethylene by the departure from the linearity expressed by equation (53). At this point, the FID is no longer a single exponential, and the characterization of the decay by T_2 has no real meaning. However, for the purposes of indicating this departure from fast dynamics, T_2* has been plotted, which is simply the time taken for the magnetization to decay to e^{-1} of its original value. With the onset of entanglement formation,

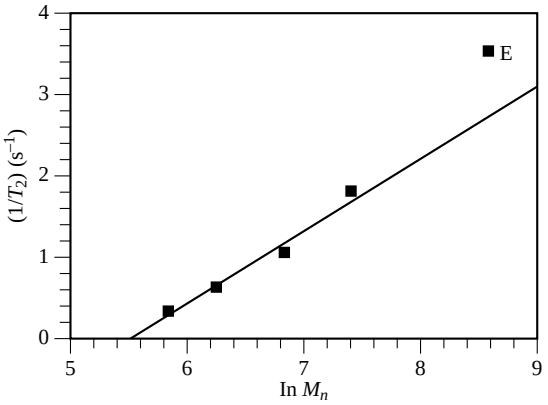

Figure 12 T_2^{-1} versus $\ln M_n$ for monodisperse polyethylenes. The solid line is the fit to the Rouse chain model, equation (53). The point marked E represents the onset of entanglements. Reprinted with permission from M. G. Brereton, I. M. Ward, N. Boden, and P. Wright, *Macromolecules*, 1991, **24**, 2068. © (1991) American Chemical Society

we encounter the next level in the hierarchical model,[49] shown in Figure 13.

We now have a number N_b of our submolecules spanning entanglement points, defining a vector $\boldsymbol{R}$. In the model, the Rouse dynamics is retained for each of the $\boldsymbol{b}$ bonds, and R is considered to be a reptating chain with a single relaxation time T_R, related to the bond correlation function:

$$\frac{\langle R_i(t)R_i(0)\rangle}{\langle R^2\rangle} = \exp\left(-\frac{t}{T_R}\right) \tag{54}$$

The full expression for $G(t)$ is obtained by numerical evaluation of the following product formula:

$$g(\Delta, t) = \prod_\alpha [1 - 3\mathrm{i}t\Delta_\alpha(t)]^{-1/2} \tag{55}$$

where α is an integer variable and $\Delta_\alpha(t)$ is related to the bond correlation functions. As can be seen from Figure 11(b),

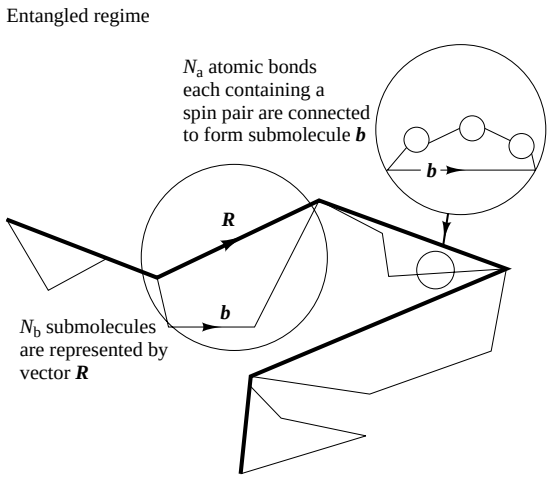

Figure 13 Illustration of the Brereton model, showing two structural levels: the atomic bonds forming one $\boldsymbol{b}$ vector, and the $\boldsymbol{b}$ vectors constituting the larger $\boldsymbol{R}$ vectors

the model provides good fits to the polyethylene data above the entanglement point.[49] From these fits, the average number of ***b*** bonds in the R chain is 25. Combining this with the number of monomer units in the ***b*** bond leads to a value of 6300 g mol^{-1} for M_e, which compares well to results from viscoelastic studies of polyethylene at the same temperature (149 °C), and with the departure from linearity of the FIDs. Furthermore, the plot of ln T_R versus ln M_n is linear, and of slope 3.5, in other words $T_R \propto M_n^{3.5}$, which is consistent with viscoelastic relaxation data on polymer melts in the entangled regime. A detail of the fitting procedure for the entangled polymers is that a small fraction of free chain ends needs to be invoked to accommodate the exponential tail of the FID at long times. In general, the fraction of free ends obtained from the fit is consistent with that expected from the molecular weight of the chain and the entanglement density.

5.2.3 The Effect of Deformation

Brereton[51] has developed the model to incorporate the effect of permanent chemical cross-links and the effect of deformation. Here, the cross-links are permitted a certain fluctuation volume, which is considered to be strain-dependent, the fluctuations increasing in the direction of strain. Other notable contributions to the study of network deformation by NMR have been made by Sotta and Deloche.[52,53] They have studied the deuterium NMR of deuterated PDMS networks,[52] and of deuterated linear 'probe' polymer chains within networks.[53] In both cases, they have observed a line splitting of the order of 100 Hz, which increases with deformation, and is attributed to the residual quadrupolar interactions induced by uniaxial orientational order in the network. Recently, however, Brereton[51] has reinterpreted these data, and attributed the line splitting to the cross-link fluctuations.

6 RELATED ARTICLES

Polymer Blends: Miscibility Studies; Polymer Dynamics and Order from Multidimensional Solid State NMR; Polymers: Relaxation and Dynamics of Synthetic Polymers in Solution.

7 REFERENCES

1. J. H. Van Vleck, *Phys. Rev.*, 1948, **74**, 1168.
2. P. H. Hermans, *Contribution to the Physics of Cellulose Fibres* Elsevier, Amsterdam, 1946, p. 195.
3. V. J. McBrierty and I. M. Ward, *Br. J. Appl. Phys. (J. Phys. D)*, 1968, **1**, 1529.
4. M. J. Folkes and I. M. Ward, *J. Mater. Sci.*, 1971, **6**, 582.
5. O. Kratky, *Kolloid-Z.*, 1933, **64**, 213.
6. W. Kuhn and F. Grün, *Kolloid-Z.*, 1942, **101**, 248.
7. L. R. G. Treloar, *Trans. Faraday Soc.*, 1954, **50**, 881.
8. A. Cunningham, A. J. Manuel, and I. M. Ward, *Polymer*, 1976, **17**, 125.
9. W. P. Slichter, *J. Polym. Sci.*, 1957, **24**, 173.
10. H. G. Olf and A. Peterlin, *J. Polym. Sci.*, 1970, **A2**, **8**, 791.
11. A. J. Brandolini, T. M. Apple, C. Dybowski, and R. G. Pembleton, *Polymer*, 1982, **23**, 39.
12. A. N. Garroway, D. C. Stalker, and P. Mansfield, *Polymer*, 1975, **16**, 161.
13. D. L. van der Hart and F. Khoury, *Polymer*, 1984, **25**, 1589.
14. A. Gerard, F. Laupetre, and L. Monnerie, *Macromolecules*, 1993, **26**, 3313.
15. C. W. Wilson and G. E. Pake, *J. Polym. Sci.*, 1953, **10**, 503.
16. D. Hyndman and G. F. Origlio, *J. Polym. Sci.*, 1959, **39**, 556.
17. H. Pranadi and A. J. Manuel, *Polymer*, 1980, **21**, 303.
18. J. Clements, G. R. Davies, and I. M. Ward, *Polymer*, 1985, **26**, 208.
19. K. Bergmann and K. Nawotki, *Kolloid-Z. u. Z. Polymere*, 1967, **219**, 132.
20. R. Kitamaru, F. Horii, and S. H. Hyai, *J. Polym. Sci., Polym. Phys. Ed.*, 1977, **15**, 821.
21. H. S. Gutowsky and G. E. Pake, *J. Chem. Phys.*, 1950, **18**, 16.
22. R. Kitamaru and F. Horii, *Adv. Polym. Sci.*, 1978, **26**, 137.
23. J. B. Smith, A. J. Manuel, and I. M. Ward, *Polymer*, 1975, **16**, 57.
24. K. Bergmann, *Kolloid-Z. u. Z. Polymere*, 1973, **251**, 1962.
25. M. Nakagawa, F. Horii, and R. Kitamaru, *Polymer*, 1990, **31**, 323.
26. K. J. Packer, I. J. F. Poplett, and M. J. Taylor, *J. Chem. Soc., Faraday Trans.*, 1988, **84**, 3851.
27. N. Bloembergen, E. M. Purcell, and R. V. Pound, *Phys. Rev.*, 1948, **73**, 679.
28. R. Kubo and K. Tomita, *J. Phys. Soc. Jpn.*, 1954, **9**, 888.
29. M. Andreis and J. L. Koenig, *Advances in Polymer Science 89*, Springer-Verlag, Berlin, 1989, p. 82.
30. R. K. Harris, *Nuclear Magnetic Resonance Spectroscopy*, Revised reprint, Longman, Harlow, UK, 1986, p. 100.
31. V. J. McBrierty and D. C. Douglass, *J. Polym. Sci., Macromol. Rev.*, 1981, **16**, 295.
32. V. J. McBrierty and K. J. Packer, *Nuclear Magnetic Resonance in Solid Polymers*, Cambridge University Press, Cambridge, 1993, p. 97.
33. T. M. Connor, *Trans. Faraday Soc.*, 1964, **60**, 1574.
34. J. Schaefer, *Macromolecules*, 1973, **6**, 882.
35. G. Williams and D. C. Watts, *Trans. Faraday Soc.*, 1970, **66**, 80.
36. A. N. Garroway, W. M. Ritchey, and W. B. Moniz, *Macromolecules*, 1982, **15**, 1051.
37. A. K. Roy, A. A. Jones, and P. T. Inglefield, *Polym. Prepr., Am. Chem. Soc. Div. Polym. Chem.*, 1986, **27**, 451.
38. A. A. Jones, J. F. O'Gara, P. T. Inglefield, J. T. Bendler, A. F. Yee, and K. L. Ngai, *Macromolecules*, 1983, **16**, 658.
39. J. Colmenero, A. Alegria, J. M. Alberdi, F. Alvarez, and B. Frick, *Phys. Rev. B*, 1991, **44**, 7321.
40. J. D. Ferry, *Viscoelastic Properties of Polymers*, 3rd edn., Wiley, New York, 1980.
41. S. F. Edwards and T. Vilgis, *Polymer*, 1986, **27**, 483.
42. H. Y. Carr and E. M. Purcell, *Phys. Rev.*, 1954, **94**, 630.
43. M. H. Levitt and R. J. Freeman, *J. Magn. Reson.*, 1981, **43**, 65.
44. R. Folland and A. Charlesby, *Int. J. Radiat. Phys. Chem.*, 1976, **8**, 555.
45. A. Charlesby, R. Folland, and J. H. Steven, *Proc. R. Soc. Lond., Ser. A*, 1977, **355**, 189.
46. A. Charlesby and E. M. Jaroszkiewicz, *Eur. Polym. J.*, 1985, **21**, 55.
47. J. P. Cohen-Addad and R. Dupeyre, *Polymer*, 1983, **24**, 400.
48. M. G. Brereton, *Macromolecules*, 1989, **22**, 3667.
49. M. G. Brereton, I. M. Ward, N. Boden, and P. Wright, *Macromolecules* 1991, **24**, 2068.

50. M. G. Brereton, *Macromolecules*, 1990, **23**, 1119.
51. M. G. Brereton, *Prog. Colloid Polym. Sci.*, 1992, **90**, 90.
52. P. Sotta and B. Deloche, *Macromolecules*, 1990, **23**, 1999.
53. P. Sotta, B. Deloche, J. Herz, A. Lapp, D. Durand, and J. C. Rabadeux, *Macromolecules*, 1987, **20**, 2769.

Biographical Sketches

Ian M. Ward. *b* 1928. B.A. (Physics) 1951, D. Phil. 1954, University of Oxford, UK. Technical officer, section head and research associate, ICI Fibres, 1954–66. Senior Lecturer in Physics of Materials, University of Bristol, 1966–70. Professor of Physics, University of Leeds, 1970–present, Head of Department 1975–78, 1987–89. Director, IRC in Polymer Science and Technology, Universities of Leeds, Bradford and Durham, 1989–1994. FRS, 1983. Approx. 400 publications on infrared and NMR spectroscopy, mechanical properties of polymers.

Philip G. Klein. *b* 1957. B.Sc.(Hons.), 1978, M.Sc., 1979, Ph.D., 1982, University of Lancaster, UK. Postdoctoral work in NMR at Case Western Reserve University, Cleveland, Ohio, 1983, with W. M. Ritchey. Research fellow (1984–86) and lecturer (1986–present), Department of Physics, University of Leeds, UK; currently on secondment to IRC in Polymer Science and Technology. Research interests: NMR of solid polymers, and polymer gels and networks.

Polymer Reactions

H. N. Cheng

Hercules Incorporated Research Center, Wilmington, DE, USA

1	Introduction	1
2	Oxidation Reactions	1
3	Chlorination and Bromination	1
4	Irradiation	2
5	Formation of Functionalized Polymers	4
6	Cross-Linking Reactions	4
7	Heat Degradation and Pyrolysis	5
8	Curing Reactions	6
9	Ester and Amide Interchange Reactions	6
10	Related Articles	6
11	References	6

1 INTRODUCTION

Synthetic polymers undergo organic and inorganic reactions just like their low molecular weight counterparts. Many of these reactions are commercially important, leading to modified polymers with improved properties. Included in this category are chlorination and bromination reactions, irradiated polymers, functionalization, and cross-linking reactions. Many thermosetting polymers need to be cured during or after polymerization. Some high-performance materials (e.g., ceramics and carbon fibers) are formed by heating the precursor polymers in controlled atmospheres at high temperatures. Not all polymer reactions are desirable; for example, oxidative and degradative processes tend to degrade the polymer properties, and should be controlled.

In many of these processes, NMR has been used as a characterization technique. If the polymers involved are soluble, studies using liquid state NMR are usually preferred. In many reactions (e.g., cross-linking, curing, and pyrolysis), the resulting polymers are insoluble or partially soluble. In these cases, solid state CP MAS techniques can be used to give chemical information. In many cases, nuclear relaxation times alone (especially T_2) can provide very useful information.

Because of the scope of the published literature, this article will selectively review the major types of polymer reactions as studied by NMR. Space limitations necessitate the exclusion of polymer/polymer transformations, metal chelation, graft copolymerization, polymer blending, biodegradable processes, and reactions involving cellulose.

2 OXIDATION REACTIONS

The oxidative degradation of polymers is of major industrial importance. Almost all commercial polymers undergo oxidation with time, and have to be stabilized with antioxidants and antiozonants. Sometimes, oxidation is carried out deliberately in order to provide a more polar polymer surface. The major oxidation pathways (Scheme 1) are fairly well understood.[1]

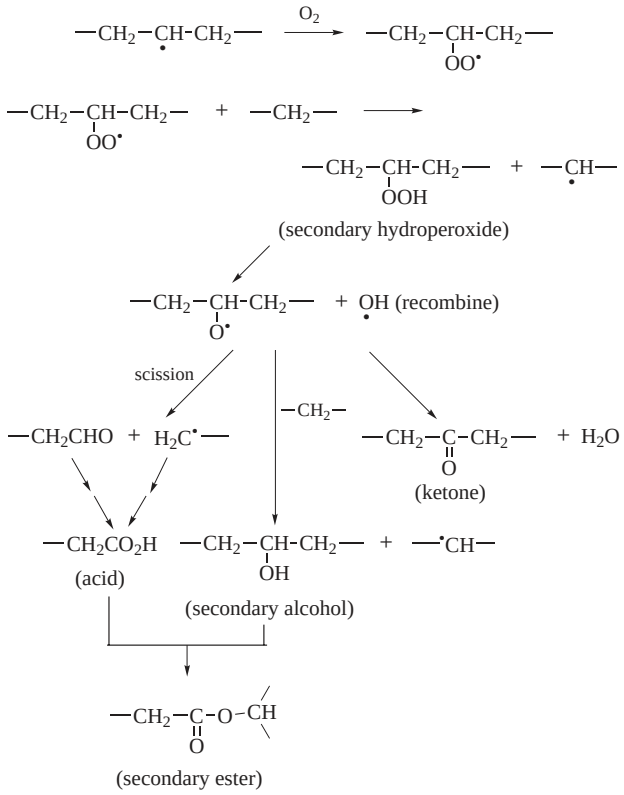

Scheme 1

Scheme 1 is valid for saturated polymers like polyethylene and polypropylene. Many of the mechanistic studies have been carried out using IR (see, e.g., Adams[2]). Liquid state ^{13}C NMR has been shown[3,4] to give detailed information on polyethylene oxidation. The ^{13}C NMR spectra of low-density polyethylene (LDPE) and oxidized LDPE[3] are given in Figure 1. The oxidized sample gives many resonances, from which hydroperoxide, alcohol, ketone, acid, peracid, ester, and γ-lactone can be clearly identified.

When the oxidation process is carried out over time, the distribution of these various oxidation products changes. A plot of concentration versus time is shown in Figure 2.[3] As expected, the hydroperoxide forms in the early phase of oxidation. At the oxidation temperature employed (140 °C), hydroperoxide is unstable and degrades in time to the other oxidation products. At very high levels of oxidation, acids and ketones are the major products.

A similar NMR study of the oxidation of natural rubber has been carried out by Golub et al.[5] The main difference with polyethylene is the ready formation of hydroperoxide and peroxide (owing to the reactivity of the allylic hydrogen) and the occurrence of epoxide. Studies have also been conducted on the photooxidation[6a,6b] and thermal oxidation[6c] of polybutadiene using NMR and other analytical techniques, and on other oxidized polymeric systems.[7]

3 CHLORINATION AND BROMINATION

The chlorination reaction is often carried out on hydrocarbon polymers and poly(vinyl chloride). The NMR spectra are

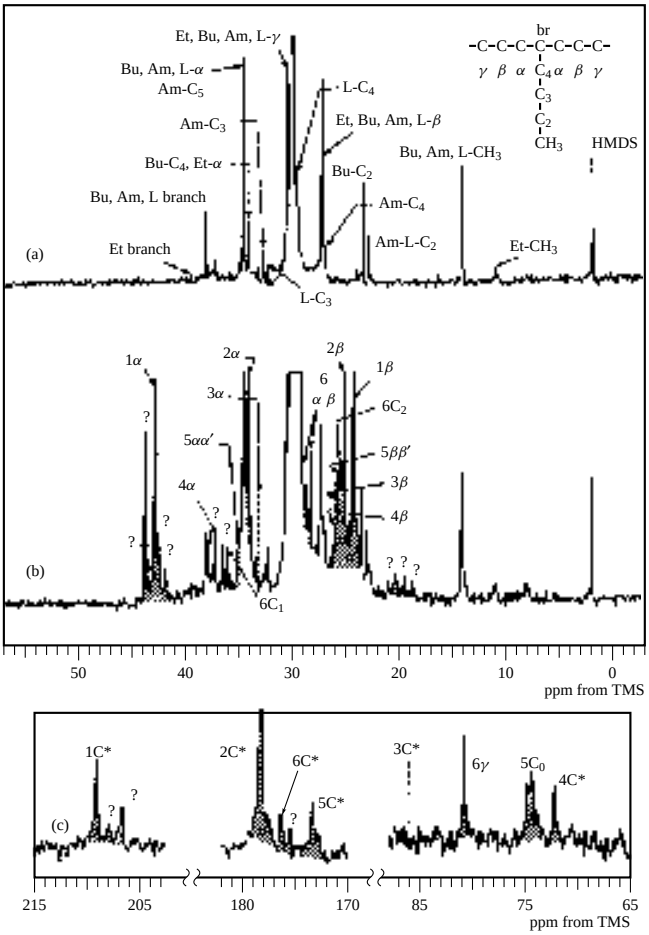

Figure 1 ^{13}C NMR spectra (at 25 MHz) of LDPE before oxidation (a), and after oxidation (b), (c). The oxidation products are identified by numbers as follows: 1, ketone; 2, acid; 3, secondary hydroperoxide; 4, secondary alcohol; 5, ester of acid and secondary alcohol; 6 = γ-lactone.[3] The designations α, β, γ refer to the carbons located at α, β, γ away from the functionality, and C* is the carbon bonded to oxygen. In 5 and 6, the carbons attached to O through σ bonds are $5C_0$ and 6γ, respectively. (Reproduced by permission of the American Chemical Society)

typically very complex, frequently with multiple resonances and broad, nondescript spectral features. For example, the ^{13}C NMR spectra[8] of chlorinated polyethylene and chlorinated polyisoprene are given in Figure 3.

The chemical structure of chlorinated polyethylene has been much studied using NMR.[9–13] The chlorination reaction occurs in a stepwise fashion, starting with $-CH_2-$ (designated 0), and generating $-CHCl-$ (designated 1) and $-CCl_2-$ (designated 2). Some reactions are shown in Scheme 2. The ^{13}C spectral assignments (primarily from Hösselbarth et al.[13]) are given in Figure 3(a).

The chlorination of polyisoprene is inherently a more complex reaction, but it gives a deceptively simple spectrum.[8,14,15] Eskina et al.[15] recently carried out a detailed NMR study of this reaction. They identified the main reaction pathways, pointing out the presence of linear reaction products and five-membered ring structures. Their results have been incorporated in Scheme 3. In view of their work, the ^{13}C NMR spectrum [shown in Figure 3(b)] can be interpreted[8] on the basis of

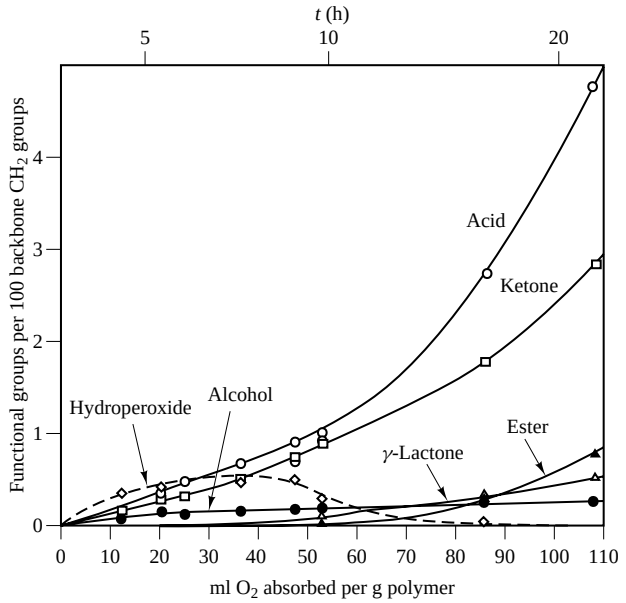

Figure 2 Distribution of oxidation products of polyethylene as a function of the extent of oxidation (lower scale: O_2 absorbed; upper scale: time of reaction).[3] (Reproduced by permission of the American Chemical Society)

two main structures. The linear product (**1**) has been assigned previously by Eskina et al.[15] The five-membered cyclic product (**2**) was assigned[8] on the basis of empirical additive shift rules.[16,17]

Other NMR studies have been reported for chlorinated polypropylene,[18,19] chlorinated ethylene/propylene copolymer,[20] chlorinated polybutadiene,[21] and chlorinated poly(vinyl chloride).[13,22–24] Keller and co-workers[10,13,18,19] have made the most detailed studies of chlorinated polymers using ^{13}C NMR. For example, a series of spectra of chlorinated polypropylene[18] showing an increasing level of chlorination is given in Figure 4. Using a large number of model compounds, Keller et al.[18] devised general shift rules and made rather detailed assignments.

Bromination has been used to functionalize polymers and to improve their flame-retardant properties. For example, hydrobromination[25] has been performed on natural rubber, and has been studied using ^{13}C NMR. Polystyrene has been brominated to give a flame-retardant polymer. Under the reaction conditions, bromination occurs on the benzene ring, and has been studied by NMR.[26–28] Other NMR studies include those of brominated poly(arylene ether sulfone),[29] a brominated copolymer of styrene and 2,6-dimethyl-1,4-phenylene oxide,[30] and brominated diacetylene.[31]

4 IRRADIATION

Irradiation with electrons or γ-rays is often used to improve the rheological behavior of polyolefins. In general, two reactions compete: cross-linking and chain scission. In polyethylene, cross-linking is the dominant reaction; in polypropylene, both reactions occur.

NMR studies of the irradiated polymers are difficult because the concentrations of the chemical species formed as a result

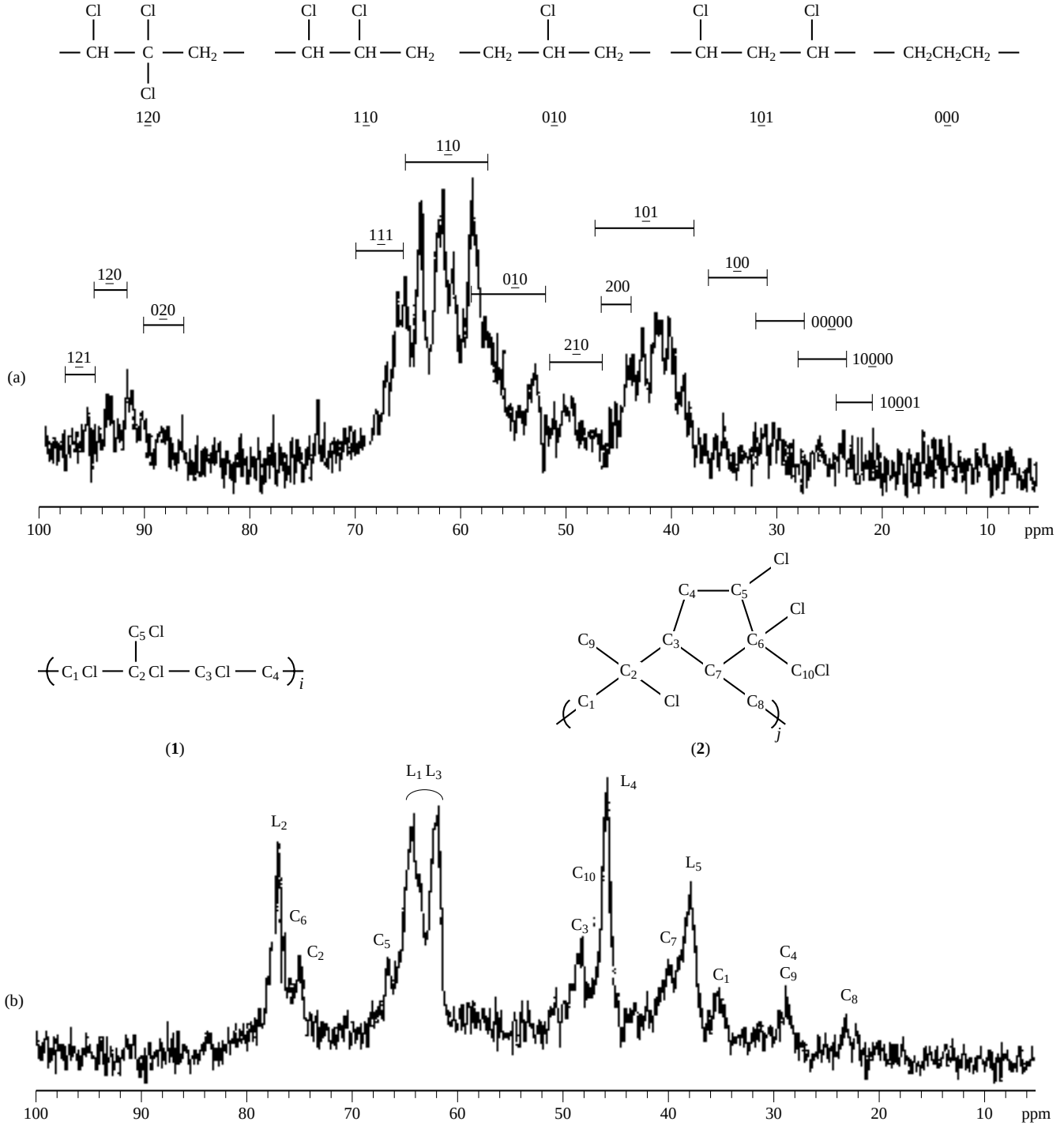

Figure 3 ^{13}C NMR spectra at 90 MHz of (a) chlorinated polyethylene (0, CH_2; 1, CHCl; 2, CCl_2; groups being assigned are underlined) and (b) chlorinated polyisoprene. The spectrum can be assigned to two main structures: a linear product L_i (**1**), where i = 1, ... 5, and a cyclic product C_i (**2**), where j = 1, ... ,10 (hydrogens are omitted for simplicity)

of irradiation are usually very low. One approach, successfully used by a number of workers,[32–34] is to monitor the T_2 values on bulk polymers. With irradiation, a short relaxation time component is formed owing to decreased mobility. As expected, the amount of this short T_2 component increases with increasing irradiation. Charlesby and co-workers[32,33] have carried out extensive studies of irradiated polyethylene, polyisoprene, poly(dimethylsiloxane), poly(ethylene oxide), polyisobutylene, and polyacrylamide. An example of irradiated aqueous polyacrylamide[33] is shown in Figure 5.

Direct observation of the chemical structure of irradiated polymers can be achieved using liquid state NMR in some cases. Through the use of high radiation doses, and sometimes with model compounds, it is possible to identify the major structures. This is the case with polyethylene.[35–39] Structures identified include internal olefins, saturated end groups, vinyl

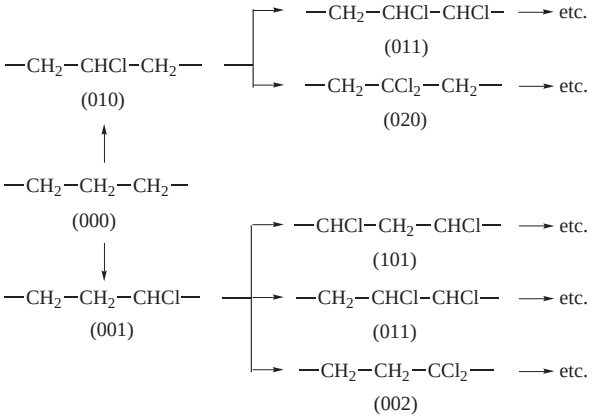

Scheme 2

end groups, short branches, H-shaped cross-links, and Y-shaped branches.

Several studies have been carried out on irradiated polypropylene.[40–42] The following observations have been made.

1. The tacticity of isotactic polypropylene decreases after irradiation.[40,41]
2. Vinyl and saturated chain ends are formed through chain scission.[41,42]
3. There is an increase in the number of head-to-head and tail-to-tail structures.[42]
4. Although cross-linked structures are expected in this system, NMR evidence for them has been suggestive rather than definitive.[42]

5 FORMATION OF FUNCTIONALIZED POLYMERS

Polymers are often reacted in order to place a special functional group or functional groups on the polymer chain. NMR has been used routinely to monitor the extent of the functionalization.

As an example, Rengarajan et al.[43] studied polypropylene that had been adducted with maleic anhydride using peroxide. The maleic functionality was detected at 175 ppm via solid state ^{13}C NMR, but was not seen by liquid state NMR. Structure (**3**) previously proposed from FTIR data,[44] was confirmed.

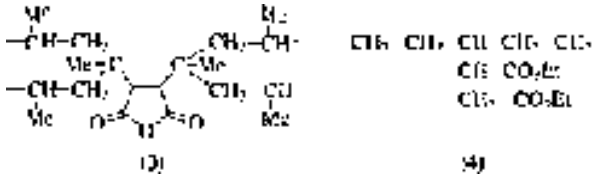

Aglietto et al.[45] studied high-density polyethylene (HDPE) adducted with diethyl maleate. The maleate signals were observed directly as multiple resonances at 172–179 ppm through liquid state ^{13}C NMR. A number of model compounds were used for spectral assignments. The authors concluded that structure (**4**) was found in the functionalized polymer.

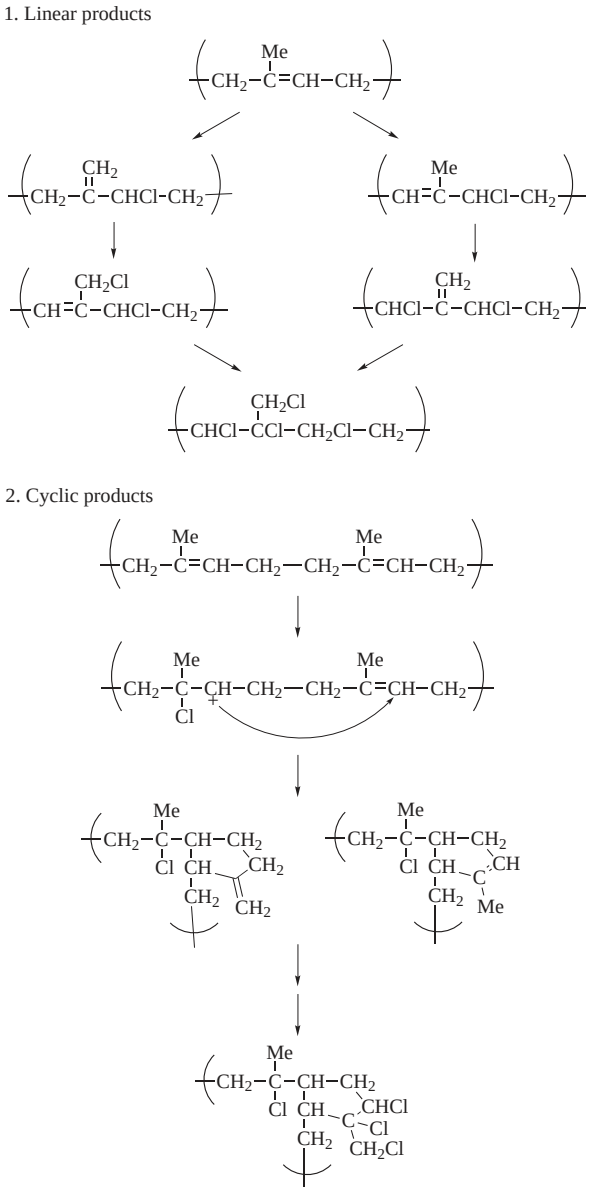

Scheme 3

In a related study, Aglietto et al.[46] introduced isolated CH_2COOEt units onto polyethylene using ethyl diazoacetate, and characterized the polymer structure using ^{13}C NMR.

Another reaction attracting attention is the dichlorocarbene adduction of 1,4-polybutadiene.[47–50] Other recent examples of functional polymers include those arising from the nucleophilic substitution reaction of poly(vinyl chloride) with sodium benzenethiolate and related compounds,[51,52] from the adduction of styrene onto the backbone of poly(methylsiloxane),[53] from the reaction of ethanolamine with poly(methyl acrylate),[54] and from the reaction of formaldehyde with polyamide.[55]

6 CROSS-LINKING REACTIONS

Cross-linking by irradiation has been discussed in Section 4. Chemical means of cross-linking are exemplified by cross-

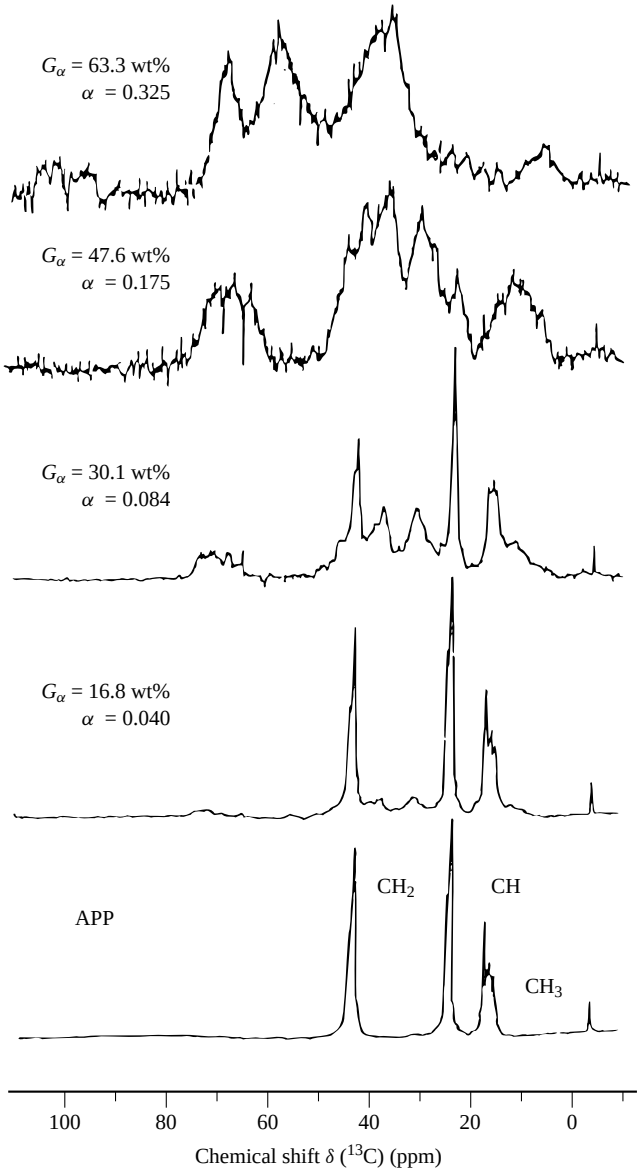

Figure 4 ^{13}C NMR spectra at 22.6 MHz of chlorinated polypropylene with different chlorine content G_α and degree of chlorination α.[18] (Reproduced by permission of *Acta Polymerica*)

linked poly[(chloromethyl)styrene], studied by liquid state ^{13}C NMR.[56] Another important reaction pertains to elastomers, where cross-linking by sulfur and peroxide is commonly practiced. Solid state ^{13}C NMR has been used extensively,[57] primarily by Koenig et al. Sulfur vulcanization can also be followed by T_2 measurements.[58] Continuous wave ^1H NMR has been carried out[59] on swollen polymers to determine the extent of cross-linking in vulcanized polymer blends.

7 HEAT DEGRADATION AND PYROLYSIS

Upon heating in a controlled atmosphere, polymers undergo thermal reaction and (at higher temperatures) pyrolysis. Both liquid and solid state NMR can be used to study these reactions. For example, polyisoprene[60] and polybutadiene[60,61]

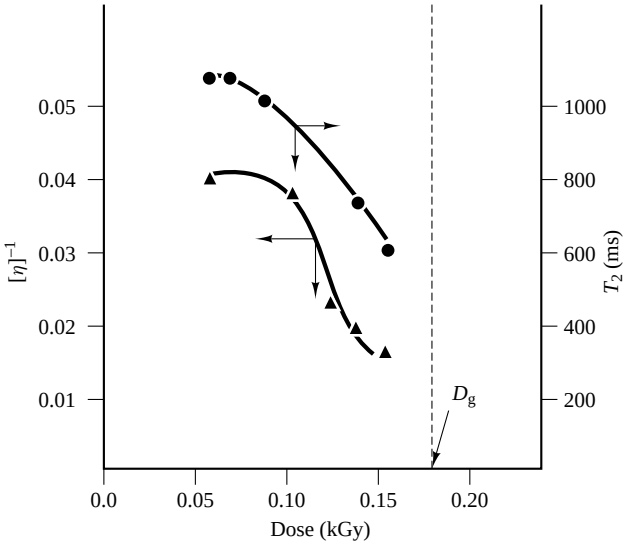

Figure 5 T_2 and intrinsic viscosity $[\eta]$ of aqueous polyacrylamide (20% solution) as a function of irradiation dose. T_2 was measured on the ^1H signal at 90 MHz. D_g is the dosage when the polymer gels.[33] (Reproduced by permission of Elsevier)

will undergo cyclization reactions to form fused ring structures [see equation (1)], and will also depolymerize. NMR has been used to follow the degradation of poly(vinyl chloride) to form polyenes,[62] polyacrylonitrile to form a ladder polymer,[63–65] and polyacrylamide and acrylamide copolymers to form cyclic imides;[66,67] see equations (2), (3), and (4), respectively.

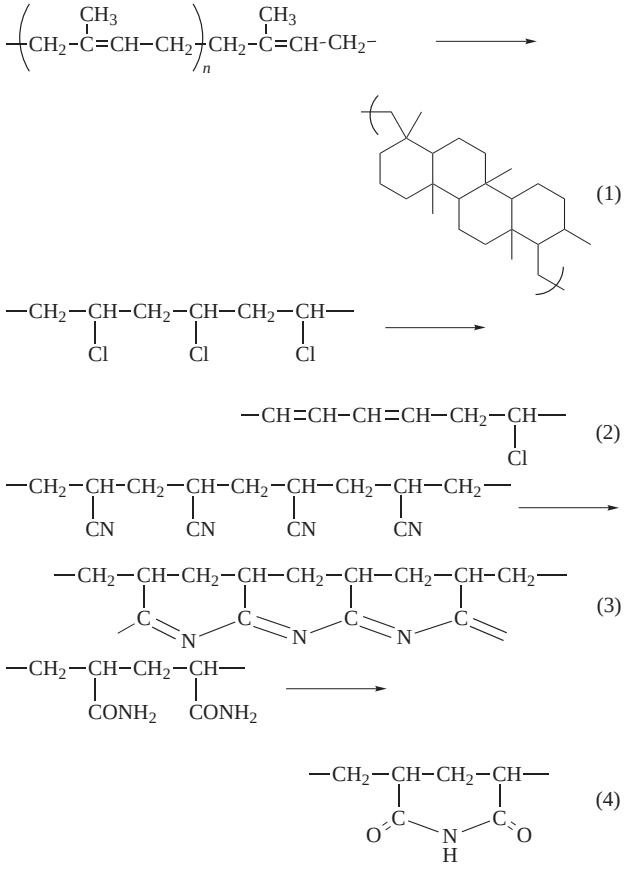

In the above examples, the reactions are not as clean as depicted, and many reaction pathways are involved, with different products identified.

Recent degradation studies include thermal degradation of polychloroprene,[68] polyurethanes,[69] vinyl alcohol copolymers,[70] and thermal decomposition and branching reactions of aromatic esters.[71]

In view of current interest in ceramics, a number of papers have appeared describing the use of NMR to study polymeric precursors and the pyrolytic processes leading to the formation of ceramics. For example, the pyrolyses of polysilazane (precursor to silicon nitride),[72,73] and of polycarbosilane and polysilane (precursor to silicon carbide)[72] have been studied using solid state NMR techniques.

8 CURING REACTIONS

For thermosetting polymers, the curing reactions are a key step to achieve their end-use properties. In the early stages of curing when the reaction mixture is a liquid, the reaction can often be studied by liquid state NMR. Beyond the gel point, solid state NMR techniques have to be used.

A fair number of publications have appeared on thermosetting polymer systems. Some examples include phenol/formaldehyde resins,[74–77] furfuryl alcohol resins,[79] cyanate polymers,[80] urea–formaldehyde resins,[78] acetylene-terminated polyimides,[82] and polymers containing maleimide.[83,84]

9 ESTER AND AMIDE INTERCHANGE REACTIONS

Blends of condensation polymers may undergo interchange reactions that may promote polyblend phase homogeneity.[85,86] An example of polyamide/polyamide interchange is that with poly(*m*-xylene adipamide) and Nylon-6.[87] Examples of polyester/polyester interchange include those of polyarylate/poly(butylene terephthalate),[88] polycarbonate/poly (butylene terephthalate),[89] and polycarbonate/poly(ethylene terephthalate).[90]

10 RELATED ARTICLES

Polymer Dynamics and Order from Multidimensional Solid State NMR; Polymerization and Statistical Models; Polymers: Relaxation and Dynamics of Synthetic Polymers in Solution.

11 REFERENCES

1. (a) W. L. Hawkins (ed), *Polymer Stabilization*, Wiley-Interscience, New York, 1970. (b) D. L. Allara and W. L. Hawkins (eds), *Stabilization and Degradation of Polymers*, *Advances in Chemistry Series, Vol. 169*, American Chemical Society, Washington, DC, 1978.
2. J. H. Adams, *J. Polym. Sci., Part A-1*, 1970, **8**, 1077, 1279.
3. H. N. Cheng, F. C. Schilling, and F. A. Bovey, *Macromolecules*, 1976, **9**, 363.
4. L. W. Jelinski, J. J. Dumais, J. P. Luongo, and A. L. Cholli, *Macromolecules*, 1984, **17**, 1650.
5. M. A. Golub, M. S. Hsu, and L. A. Wilson, *Rubber Chem. Technol.*, 1975, **48**, 953.
6. (a) M. A. De Paoli, *Eur. Polym. J.*, 1983, **19**, 761. (b) C. Adam, J. Lacoste, and G. Dauphin, *Polym. Commun.*, 1991, **32**, 317, and references therein. (c) C. Tang, *ACS Polym. Mater. Sci. Eng.*, 1987, **57**, 598.
7. (a) K. R. Carduner, D. R. Bauer, J. L. Gerlock, and D. F. Mielewski, *Polym. Degrad. Stab.*, 1992, **35**, 219. (b) J. Sohma, M. Tabata, F. Ebisawa, and M. Hatano, *Polym. Degrad. Stab.*, 1987, **17**, 5.
8. H. N. Cheng, unpublished work.
9. B.-M. Quenum, P. Berticat, and Q.-T. Pham, *Eur. Polym. J.*, 1971, **7**, 1527.
10. F. Keller, M. Michajlov, and S. Stoeva, *Acta Polym.*, 1979, **30**, 694.
11. W. Busch, F. Kloos, and J. Brandrup, *Angew. Makromol. Chem.*, 1982, **105**, 187.
12. B. Bikson, J. Jagur-Grodzinski, and D. Vofsi, *Polymer*, 1982, **23**, 1163.
13. B. Hösselbarth, F. Keller, and M. Findeisen, *Acta Polym.*, 1989, **40**, 371.
14. S. Makani, M. Brigodiot, E. Marechal, F. Dawans, and J.-P. Durand, *J. Appl. Polym. Sci.*, 1984, **29**, 4081.
15. M. V. Eskina, A. S. Khachaturov, L. B. Krentsel, and A. D. Limanovitch, *Eur. Polym. J.*, 1990, **26**, 181.
16. E. Pretsch, J. Seibl, W. Simon, and J. T. Clerc, *Tables of Spectral Data for Structure Determination of Organic Compounds*, Springer-Verlag, Berlin, 1983.
17. (a) H. N. Cheng and M. A. Bennett, *Anal. Chim. Acta*, 1991, **242**, 43. (b) H. N. Cheng and L. J. Kasehagen, *Anal. Chim. Acta*, 1994, **285**, 223.
18. P. Pinther, F. Keller, and M. Hartmann, *Acta Polym.*, 1980, **31**, 299.
19. F. Keller, P. Pinther, M. Hartmann, *Acta Polym.*, 1980, **31**, 439.
20. K. Liao and S. Zhong, *Zhongshan Daxue Xuebao, Ziran Kexueban*, 1991, **30**, 66.
21. H. Kawaguchi, Y. Sumida, J. Muggee, and O. Vogl, *Polymer*, 1982, **23**, 1805.
22. R. Lukas, M. Kolinsky, and D. Doskocilova, *J. Polym. Sci., Polym. Chem. Ed.*, 1979, **17**, 2691.
23. R. Lukas, J. Svetly, and M. Kolinsky, *J. Polym. Sci., Polym. Chem. Ed.*, 1981, **19**, 295, and references therein.
24. R. A. Komoroski, R. G. Parker, and M. H. Lehr, *Macromolecules*, 1982, **15**, 844.
25. J. H. Bradbury, J. A. Elix, and M. C. S. Perera, *Polymer*, 1987, **28**, 1098.
26. M. J. Farrall and J. M. J. Frechet, *Macromolecules*, 1979, **12**, 426.
27. I. C. McNeill and M. Coskun, *Polym. Degrad. Stab.*, 1989, **23**, 175.
28. M. Camps, J. P. Montheard, F. Benrokia, J. M. Camps, and Q.-T. Pham, *Eur. Polym. J.*, 1990, **26**, 53.
29. I. Esser, I. W. Parsons, *Polym. Commun.*, 1991, **32**, 538.
30. E. A. Williams, E. M. Skelly Frame, P. E. Donahue, N. A. Marotta, and R. P. Kambour, *Appl. Spectrosc.*, 1990, **44**, 1107.
31. H. Eckert, J. P. Yesinowski, D. J. Sandman, C. S. Velazquez, *J. Am. Chem. Soc.*, 1987, **109**, 761.
32. (a) A. Charlesby, R. Folland and J. H. Stevens, *Proc. R. Soc. London, Ser. A*, 1977, **355**, 189, and references therein. (b) A. Charlesby and R. Folland, *Radiat. Phys. Chem.*, 1980, **15**, 393. (c) A. Charlesby, *J. Radioanal. Nucl. Chem.*, 1986, **101**, 401, and references therein.

33. J. Rosiak, K. Burczak, W. Pekala, N. Pislewski, S. Idziak, and A. Charlesby, *Radiat. Phys. Chem.*, 1988, **32**, 793.
34. For example, O. Giraud, A. Guillermo, and J. P. Cohen-Addad, *Makromol. Chem., Makromol. Symp.*, 1989, **30**, 69.
35. F. A. Bovey, F. C. Schilling, H. N. Cheng, in *Stabilization and Degradation of Polymers*, eds. D. L. Allara and W. L. Hawkins, *Advances in Chemistry Series, Vol. 169*, American Chemical Society, Washington, DC, 1978, p. 133.
36. J. C. Randall, F. J. Zoepfl, and J. Silverman, *Radiat. Phys. Chem.*, 1983, **22**, 183.
37. J. C. Randall, F. J. Zoepfl, and J. Silverman, in *NMR and Macromolecules*, ed. J. C. Randall, *ACS Symposium Series, Vol. 247*, American Chemical Society, Washington, DC, 1984, p. 245.
38. Q. Zhu, F. Horii, R. Kitamaru, H. Yamaoka, *J. Polym. Sci., Polym. Chem. Ed.*, 1990, **28**, 2741.
39. F. Horii, Q. Zhu, R. Kitamaru, H. Yamaoka, *Macromolecules*, 1990, **23**, 977.
40. W. K. Busfield, J. V. Hanna, J. H. O'Donnell, and A. K. Whittaker, *Br. Polym. J.*, 1987, **19**, 223.
41. W. K. Busfield and J. V. Hanna, *Polym. J.*, 1991, **23**, 1253.
42. H. N. Cheng, unpublished work.
43. R. Rengarajan, V. R. Parameswaran, S. G. Lee, M. Vicic, and P. L. Rinaldi, *Polymer*, 1990, **31**, 1703.
44. Y. Minoura, M. Ueda, S. Mizunuma, and M. Oba, *J. Appl. Polym. Sci.*, 1969, **13**, 1625.
45. M. Aglietto, R. Bertani, G. Ruggeri, and A. L. Segre, *Macromolecules*, 1990, **23**, 1928.
46. M. Aglietto, R. Bertani, G. Ruggeri, M. Fiordiponti, and A. L. Segre, *Macromolecules*, 1989, **22**, 1492.
47. C. J. Carman, R. A. Komoroski, and S. E. Horne, in *NMR and Macromolecules*, ed. J. C. Randall, *ACS Symposium Series, Vol. 247*, American Chemical Society, Washington, DC, 1984, p. 167.
48. S. Siddiqui, R. E. Cais, *Macromolecules*, 1986, **19**, 595, 998.
49. R. E. Cais, and S. Siddiqui, *Macromolecules*, 1987, **20**, 1004.
50. R. E. Cais, P. A. Mirau, and S. Siddiqui, *Br. Polym. J.*, 1987, **19**, 189.
51. S. Marian and G. Levin, *J. Appl. Polym. Sci.*, 1981, **26**, 3295.
52. J. Millan, G. Martinez, C. Mijangos, A. Mendez, J. M. Gomez-Elvira, and M. Gomez-Daza, *Makromol. Chem., Macromol. Symp.*, 1988, **20/21**, 49.
53. Y. Kuwae and N. Kushibiki, *J. Polym. Sci., Polym. Chem. Ed.*, 1989, **27**, 3969.
54. Y. L. Yu and G. R. Brown, *Macromolecules*, 1992, **25**, 6658.
55. H. Ketels, R. Schellekens, J. Beulen, and G. Van der Velden, *Polym. Commun.*, 1988, **29**, 189.
56. S. Mohanraj and W. T. Ford, *Macromolecules*, 1985, **18**, 351.
57. (a) D. J. Patterson, J. L. Koenig, and J. R. Shelton, *Rubber Chem. Technol.*, 1983, **56**, 971. (b) R. A. Komoroski, J. P. Shockcor, E. C. Gregg, and J. L. Savoca, *Rubber Chem. Technol.*, 1986, **59**, 328. (c) A. M. Zaper and J. L. Koenig, *Rubber Chem. Technol.*, 1987, **60**, 252 and 278. (d) M. Andreis, J. Liu, and J. L. Koenig, *J. Polym. Sci., Polym. Phys. Ed.*, 1989, **27**, 1389. (e) A. M. Zaper and J. L. Koenig, *Makromol. Chem.*, 1988, **189**, 1239. (f) R. S. Clough and J. L. Koenig, *Rubber Chem. Technol.*, 1989, **62**, 908. (g) M. R. Krejsa and J. L. Koenig, *Rubber Chem. Technol.*, 1991, **64**, 40. (h) S. R. Smith and J. L. Koenig, *Rubber Chem. Technol.*, 1992, **65**, 176.
58. M. R. Krejsa and J. L. Koenig, *Rubber Chem. Technol.*, 1992, **65**, 427, 956, and references therein.
59. M. J. R. Loadman and A. J. Tinker, *Rubber Chem. Technol.*, 1989, **62**, 234, and references therein.
60. M. A. Golub and R. J. Gargiulo, *J. Polym. Sci., Part B*, 1972, **10**, 41.
61. B. Schneider, D. Doskocilova, J. Stokr, and M. Svoboda, *Polymer*, 1993, **34**, 432.
62. H. N. Cheng and F. A. Bovey, unpublished work.
63. W. T. K. Stevenson, A. Garton, J. A. Ripmeester, D. M. Wiles, *Polym. Degrad. Stab.*, 1986, **15**, 125.
64. T. Usami, T. Itoh, H. Ohtani, and S. Tsuge, *Macromolecules*, 1990, **23**, 2460.
65. K. Frigge, A. Büchteman, and H.-P. Fink, *Acta Polym.*, 1991, **42**, 322.
66. K. Y. Park, E. R. Santee, and H. J. Harwood, *Polym. Prepr., Am. Chem. Soc. Div. Polym. Chem.*, 1986, **27**(2), 81.
67. W. M. Leung, D. E. Axelson, and J. D. Van Dyke, *J. Polym. Sci., Polym. Chem. Ed.*, 1987, **25**, 1825.
68. Y. Miyata and M. Atsumi, *J. Polym. Sci., Polym. Chem. Ed.*, 1988, **26**, 2561.
69. D. W. Duff and G. E. Maciel, *Macromolecules*, 1991, **24**, 651.
70. X. Zhang, K. Takegoshi, and K. Hikichi, *Polymer*, 1992, **33**, 718.
71. S. J. Ting and J. H. Noggle, *J. Polym. Sci., Polym. Chem. Ed.*, 1989, **27**, 2325.
72. F. Babonneau, J. Livage and R. M. Laine, *Polym. Prepr., Am. Chem. Soc. Div. Polym. Chem.*, 1991, **32**(3), 579.
73. N. Brodie, J. P. Majoral, and J. P. Disson, *Inorg. Chem.*, 1993, **32**, 4646.
74. D. D. Werstler, *Polymer*, 1986, **27**, 750.
75. E. A. Mertzel, D. R. Perchak, W. M. Ritchey, and J. L. Koenig, *Ind. Eng. Chem. Res.*, 1988, **27**, 586.
76. (a) M. G. Kim, L. W. Amos, and E. E. Barnes, *Ind. Eng. Chem. Res.*, 1990, **29**, 2032. (b) S. So and A. Rudin, *J. Appl. Polym. Sci.*, 1990, **41**, 205.
77. A. Fischer, K. Schlothauer, A. Pfitzmann, and J. Spavacek, *Polymer*, 1992, **33**, 1370.
78. I. S. Chuang and G. E. Maciel, *Macromolecules*, 1992, **25**, 3204; I. S. Chuang and G. E. Maciel, *Polymer*, 1994, **35**, 1602, 1621.
79. I. S. Chuang, G. E. Maciel, and G. E. Myers, *Macromolecules*, 1984, **17**, 1087.
80. C. A. Fyfe, J. Niu, S. J. Rettig, N. E. Burlinson, C. M. Reidsema, D. W. Wang, and M. Poliks, *Macromolecules*, 1992, **25**, 6289.
81. M. F. Grenier-Loustalot and P. Grenier, *High Perform. Polym.*, 1991, **3**, 113.
82. S. A. Swanson, W. W. Fleming, and D. C. Hofer, *Macromolecules*, 1992, **25**, 582.
83. G. D. Lyle, J. S. Senger, D. H. Chen, S. Kilic, S. D. Wu, D. K. Mohanty, and J. E. McGrath, *Polymer*, 1989, **30**, 978.
84. C. G. Fry and A. C. Lind, *New Polym. Mater.*, 1990, **2**, 235.
85. R. Yamadera and M. Murano, *J. Polym. Sci., Part A-1*, 1967, **5**, 2259.
86. J. Devaux, P. Godard, and J. P. Mercier, *J. Polym. Sci., Polym. Phys. Ed.*, 1982, **20**, 1875, 1881, and references therein.
87. Y. Takeda and D. R. Paul, *Polymer*, 1991, **32**, 2771.
88. E. Espinosa, M. J. Fernandez-Berridi, I. Maiza, and M. Valero, *Polymer*, 1993, **34**, 382.
89. G. Van der Velden, G. Kolfschoten-Smitsmans, and A. Veermans, *Polym. Commun.*, 1987, **28**, 169.
90. W. G. Zheng, Z. H. Wan, Z. N. Qi, and F. S. Wang, *Polymer*, 1993, **34**, 4982.

Biographical Sketch

H. N. Cheng. *b* 1947. B.S., 1969, University of California Los Angeles, USA; Ph.D., 1974 University of Illinois, physical chemistry (supervisor, H. S. Gutowsky). Postdoctoral work at Bell Laboratories, Murray Hill, NJ with Frank A. Bovey. Senior research chemist at GAF Corporation, 1976–79. Research staff, Hercules Research Center, 1979–83; Research supervisor, spectroscopy/microscopy/surface analysis, 1983–90; Research fellow, 1990, Research associate, new business R&D, 1991–present. Approx. 85 publications. Current research interests: NMR of polymers, statistical models and computer modeling of polymerization, polymer reactions, and automated methods for ^{13}C spectral interpretation and shift prediction.

Polymerization and Statistical Models

H. N. Cheng

Hercules Incorporated, Research Center, Wilmington, DE, USA

1	Introduction	1
2	One State Models	1
3	Two State Models	5
4	MultiState Models	6
5	Perturbed Models	7
6	Analytical Methodologies	7
7	Related Articles	7
8	References	7

1 INTRODUCTION

Synthetic polymers can be made from monomers through either addition or condensation polymerization.[1] Condensation (or step-growth) polymers are made from monomers through condensation or related reactions, frequently involving the loss of a small molecule. An example is the production of Nylon-6,6, which is a polyamide:

$$\begin{aligned} &NH_2\text{–}(CH_2)_6\text{–}NH_2 + HOCO\text{–}(CH_2)_4\text{–}COOH \\ &\quad \rightarrow \text{–}(CO\text{–}(CH_2)_4\text{–}CONH\text{–}(CH_2)_6\text{–}NH)_n\text{–} \end{aligned} \tag{1}$$

Other condensation polymers include polyesters, polyurethanes, polysiloxanes, polysulfides, cellulosic derivatives, and phenol–formaldehyde, urea–formaldehyde and melamine–formaldehyde resins.

Addition (or chain-growth) polymers are those made from monomers without the loss of small molecules, the most common being vinyl and vinylidene polymers, i.e.,

$$CH_2{=}\ CXY \rightarrow \text{–}(CH_2\text{–}CXY)_n\text{–} \tag{2}$$

where X and Y can be any substituents, e.g., hydrogen and halogen, alkyl and aryl, carboxyl and carbonyl, alcohol and ether. Polymerization may be accomplished through a reaction mechanism involving free radical, cationic, anionic, or metal complexes. Other common addition polymers are made from dienes, acetylenes, and aldehydes. A related category comprises polymers made from ring-opening polymerization, e.g., the polyethers:

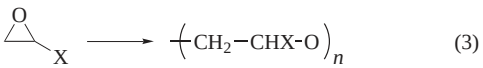

(3)

In polymer studies, NMR has been extensively used to identify major or minor components in polymers, to determine polymer stereochemistry (tacticity), copolymer sequence structures, and substitution patterns in cellulosic derivatives, to identify and quantify chain branching, defect structures, and chain ends, and to study polymerization reaction mechanisms. The literature is rather voluminous, and has been reviewed previously.[2–4]

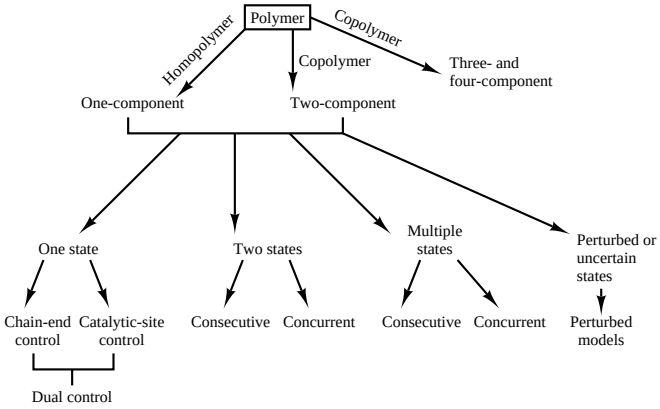

Figure 1 Statistical models of polymerization

In NMR studies of polymer microstructure and polymerization mechanisms, statistical probability models have been found to be a convenient theoretical framework for analysis. Over the years, many statistical models have been devised, and are now used routinely. Associated with these models are a number of analytical methodologies that have been developed to treat NMR data. For convenience, these models are shown schematically in Figure 1.

2 ONE STATE MODELS

In most applications of NMR to polymers, the one-component statistical model is used. The polymer is assumed to form homogeneously via one reaction mechanism that can be described by one statistical model. Two types of structural features are commonly observed: stereochemistry (tacticity) of homopolymers and sequence placements of copolymers. A third type (regioirregular structures) can also occur, but is less frequently studied.

2.1 Copolymer Sequence

The simplest model is based on Bernoullian (B) statistics, where the addition of a monomer to a growing polymer chain does not depend on the identity of the monomer on the chain, but only on the instantaneous concentrations of the comonomers present. Thus, for a copolymer derived from comonomers M_1 and M_2, the propagation equations are

$$(-) * + M_1 \xrightarrow{k_1} y(-)M_1* \tag{4}$$

$$(-) * + M_2 \xrightarrow{k_2} (-)M_2* \tag{5}$$

where $(-)$ represents the polymer chain, * represents a free radical, a cation, an anion, or a metal in a catalytic complex, and k_1 and k_2 are the rate constants of the comonomer addition reaction. The reactivity ratio r can be defined as

k_1/k_2. The conditional probabilities for M_1 and M_2 (P_1 and P_2, respectively) are

$$P_1 = \frac{rx}{1+rx}, \quad P_2 = \frac{1}{1+rx} \tag{6}$$

where $x = (M_1)/(M_2)$, with (M_1) and (M_2) the feed concentrations of M_1 and M_2.

A slightly more complex model occurs when the addition depends not only on x but also on the reactivity of the last unit on the growing polymer chain. This is the first-order Markovian (**M1**), or terminal, statistical model:

$$(-)M_1* + M_1 \xrightarrow{k_{11}} (-)M_1M_1* \tag{7}$$

$$(-)M_1* + M_2 \xrightarrow{k_{12}} (-)M_1M_2* \tag{8}$$

$$(-)M_2* + M_1 \xrightarrow{k_{21}} (-)M_2M_1* \tag{9}$$

$$(-)M_2* + M_2 \xrightarrow{k_{22}} (-)M_2M_2* \tag{10}$$

The conditional probabilities are

$$P_{12} = \frac{1}{1+r_1x}, \quad P_{21} = \frac{1}{1+r_2/x} \tag{11}$$

where P_{ij} is the probability of comonomer j adding to a propagating chain terminating in monomer residue i, and the reactivity ratios $r_1 = k_{11}/k_{12}$ and $r_2 = k_{22}/k_{21}$. Reaction probability expressions for the various n-ad sequences can be derived for the Bernoullian and first-order Markovian models.[3–5] These are given in Table 1.

In the second-order Markovian (**M2**), or penultimate, statistical model, the probability of monomer addition depends on the identity of the last *two* units of the propagating chain. Four conditional probabilities are needed: $\alpha = P_{111}$, $\beta = P_{121}$, $\gamma = P_{211}$, and $\delta = P_{221}$, where P_{ijk} is the probability of comonomer k adding to a propagating chain terminating in residues i and j. For completeness, the reaction probability expressions[3–5] for this model are also given in Table 1.

For example, the two-dimensional $^{13}C/^1H$ shift-correlated plot[6] for a copolymer of ethylene (E) and vinyl chloride (V) is given in Figure 2. The spectral assignments are given in Table 2, where the nomenclature shown for (**1**)–(**4**) is used.[7]

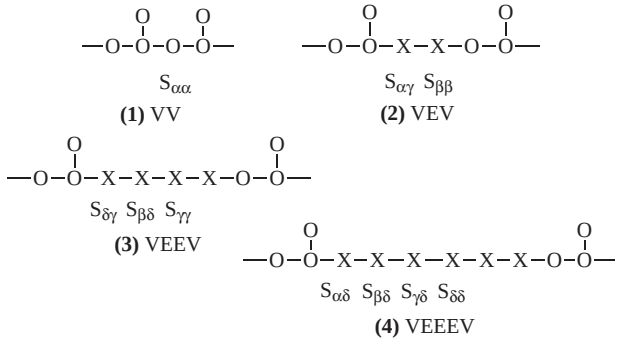

The comonomer sequence distribution can be derived from the spectral intensities of either the ^1H or the ^{13}C NMR spectrum.[6,8–10] The sample shown in Figure 2 has the

Table 1 Reaction Probability Expressions in the Bernoullian (B), First-Order Markovian (M1), Second-Order Markovian (M2), and Enantiomorphic-Site (E) Models

Sequence	Tacticity[a]	**B**	**M1**	**M2**[b]	**E**[c]
A	m	P_a	P_{ba}	$(\overline{\alpha} + \gamma)\,\delta$	$1 - 2t$
B	r	P_b	P_{ab}	$(\overline{\beta} + \delta)\,\overline{\alpha}$	$2t$
AA	mm	P_a^2	$P_{ba}P_{aa}$	$\gamma\delta$	$1 - 3t$
AB	mr	$2P_aP_b$	$2P_{ba}P_{ab}$	$2\overline{\alpha}\delta$	$2t$
BB	rr	P_b^2	$P_{ab}P_{bb}$	$\overline{\alpha}\overline{\beta}$	t
AAA	mmm	P_a^3	$P_{ba}P_{aa}^2$	$\alpha\gamma\delta$	$1 - 4t + 2t$
AAB	mmr	$2P_a^2P_b$	$2P_{ba}P_{aa}P_{ab}$	$2\overline{\alpha}\gamma\delta$	$2t - 4t^2$
BAB	rmr	$P_aP_b^2$	$P_{ab}^2P_{ba}$	$\overline{\alpha\gamma}\delta$	$2t^2$
ABA	mrm	$P_a^2P_b$	$P_{ab}P_{ba}^2$	$\overline{\alpha}\beta\delta$	$2t^2$
BBA	rrm	$2P_aP_b^2$	$2P_{ab}P_{bb}P_{ba}$	$2\overline{\alpha}\overline{\beta}\delta$	$2t - 9t^2$
BBB	rrr	P_b^3	$P_{ab}P_{bb}^2$	$\overline{\alpha}\overline{\beta\delta}$	$2t^2$
AAAA	mmmm	P_a^4	$P_{ba}P_{aa}^3$	$\alpha^2\gamma\delta$	$1 - 5t + 5t^2$
AAAB	mmmr	$2P_a^3P_b$	$2P_{ba}P_{aa}^2P_{ab}$	$2\alpha\overline{\alpha}\gamma\delta$	$2t - 6t^2$
BAAB	rmmr	$P_a^2P_b^2$	$P_{ab}^2P_{ba}P_{aa}$	$\overline{\alpha}^2\gamma\delta$	t^2
AABB	mmrr	$2P_a^2P_b^2$	$2P_{ba}P_{aa}P_{ab}P_{bb}$	$2\overline{\alpha}\overline{\beta}\gamma\delta$	$2t - 6t^2$
AABA	mmrm	$2P_a^3P_b$	$2P_{ba}^2P_{aa}P_{ab}$	$2\overline{\alpha}\beta\gamma\delta$	$2t^2$
BABB	rmrr	$2P_aP_b^3$	$2P_{ab}^2P_{ba}P_{bb}$	$2\overline{\alpha}\overline{\beta}\gamma\delta$	$2t^2$
BABA	rmrm	$2P_a^2P_b^2$	$2P_{ab}^2P_{ba}^2$	$2\overline{\alpha}\beta\overline{\gamma}\delta$	$2t^2$
ABBA	mrrm	$P_a^2P_b^2$	$P_{ba}^2P_{ab}P_{bb}$	$\overline{\alpha}\overline{\beta}\delta^2$	$t - 3t^2$
BBBA	rrrm	$2P_aP_b^3$	$2P_{ab}P_{bb}^2P_{ba}$	$2\overline{\alpha}\overline{\beta}\delta\overline{\delta}$	$2t^2$
BBBB	rrrr	P_b^4	$P_{ab}P_{bb}^3$	$\overline{\alpha}\overline{\beta}\overline{\delta}^2$	t^2
Sum		$(P_a + P_b)$	$(P_{ba} + P_{ab})$	$(\overline{\alpha}\overline{\beta} + 2\overline{\alpha}\delta + \gamma\delta)$	1.0

[a]For tacticity, the substitution (A → m, and B → r) should be made in the expressions for the **B**, **M1** and **M2** models.
[b]$\alpha = P_{aaa}$, β ;= P_{aba}, $\gamma = P_{baa}$, $\delta = P_{bba}$.
[c]$t = P_1(1 - P_1)$.

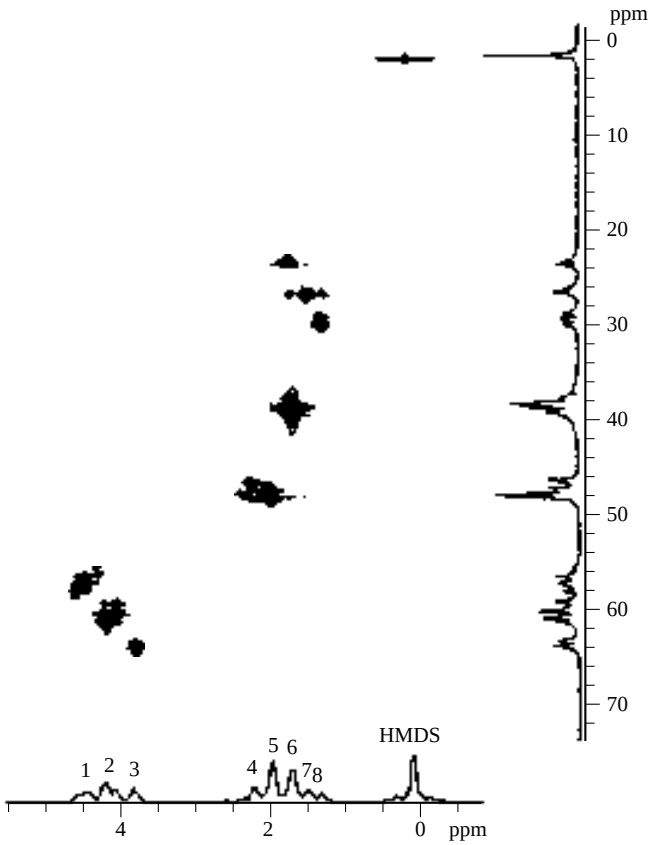

Figure 2 Two-dimensional $^{13}C-^{1}H$ shift-correlation plot for ethylene–vinyl chloride copolymer, obtained at 300 MHz (^{1}H) and 75 MHz (^{13}C).[6] The shift reference is hexamethyldisiloxane (HMDS). The numbering conforms to Table 2. Reproduced by permission of the American Chemical Society

composition E : V = 0.43 : 0.57. It turns out that this copolymer conforms well to a first-order Markovian model. The observed and calculated ^{1}H intensities are given in Table 2. The product $r_1 r_2$ of the reactivity ratios is 1.4.

An example of a condensation polymer can be given for the copolymer of dimethylsiloxane (M) and diphenylsiloxane (P). The ^{29}Si spectra of two copolymers prepared through ring-opening polymerization of methyl tetramer and phenyl

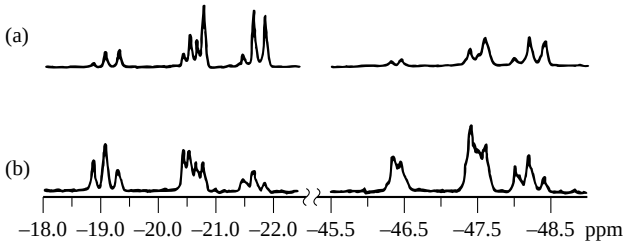

Figure 3 ^{29}Si NMR spectra of poly(dimethylsiloxane-co-diphenylsiloxane), obtained at 79.5 MHz: (a) sample 3; (b) sample 1.[11] Reproduced by permission of the American Chemical Society

tetramer are given[11] in Figure 3. The high-frequency (downfield) resonances (at approx. −20 ppm) are due to ($SiMe_2O$), and the low-frequency resonances (at approx. −47 ppm) are due to ($SiPh_2O$). In both regions, the ^{29}Si resonances are sensitive to pentads[12–14] (Table 3). The polymerization reaction in this case is random; the spectral intensities conform to the Bernoullian model. The calculated versus the observed intensities are also shown in Table 3.

Thus far, only copolymers containing two comonomers have been considered. In three-component copolymerization, three comonomers are polymerized, and the first-order Markovian model has been derived[7,15] and used for the analysis of the ^{13}C NMR data of ethylene/propylene rubber[7] and ethylene/vinyl alcohol copolymers.[15]

Occasionally, four-component copolymerization is needed. The first-order Markovian model for this copolymerization is more complex,[16] and has been formulated in a convenient form for NMR applications.[17a] The model has been successfully applied to ^{13}C NMR data on styrene/butadiene rubber.[17b] More recently, the same model has been modified to be used in a general way for the treatment of the NMR data of regio-irregular polymers.[18]

Three other statistical models should be mentioned: the Markovian model with reversible propagation, the complex participation model, and the bootstrap model. These models are useful in specific cases. For example, some monomers have low ceiling temperatures such that propagation and depropagation can occur during polymerization. Polymerizations involving methyl methacrylate, α-methylstyrene, and sulfur dioxide may exhibit this effect. In such cases, the Markovian model

Table 2 First-Order Markovian Expressions for ^{1}H Spectral Intensities of Ethylene (E)/Vinyl Alcohol (V) Copolymer

				Indensity	
Line	Assignment	Sequence	Probability expression	Observed	Calculated
1	$T_{\beta\beta}$	VVV	$kP_{EV}(1-P_{VE})^2$	0.106	0.106
2a	$T_{\beta\delta}$(r)	VVE	$2kP_{EV}P_{VE}(1-P_{VE})(1-P_m)$	0.091	0.100
2b	$T_{\beta\delta}$(m)	VVE	$2kP_{EV}P_{VE}(1-P_{VE})P_m$	0.037	0.037
3	$T_{\delta\delta}$	EVE	$kP_{EV}P_{VE}^2$	0.053	0.044
4	$S_{\alpha\alpha}$(m)	VV	$2kP_{EV}(1-P_{VE})P_m$	0.041	0.047
5	$S_{\alpha\alpha}$(r)	VV	$2kP_{EV}(1-P_{VE})(1-P_m)$	0.130	0.127
6	$S_{\beta\beta}$, $S_{\alpha\gamma}$, $S_{\alpha\delta}$	VE	$2k(2P_{EV}P_{VE}+P_{EV}^2P_{VE})$	0.283	0.283
7	$S_{\beta\delta}$	VE	$4kP_{EV}P_{VE}(1-P_{EV})$	0.120	0.106
8	$S_{\gamma\gamma}$, $S_{\gamma\delta}$, $S_{\delta\delta}$	EE	$2k[P_{VE}(1-P_{EV})+P_{VE}(1-P_{EV})^2]$	0.136	0.149
Sum			$k(3P_{EV}+4P_{VE})$		P_{EV} = 0.525 P_{VE} = 0.392

Table 3 ^{29}Si Shift, Sequence, and Intensities for Two Samples of Poly(dimethylsiloxane-co-diphenylsiloxane)

		Sample 1		Sample 3	
Shift	Sequence	I (obsd)	I (calc)	I (obsd)	I (calc)
−18.78	PPMPP	8	9	1	1
−19.00	PPMPM	16	15	5	5
−19.21	MPMPM	8	6	6	5
−20.34	PPMMP	14	15	9	5
−20.45	MPMMP	14	12	11	10
−20.58	PPMMM	11	12	9	10
−20.71	MPMMM	11	10	21	20
−21.43	PMMMP	6	6	5	5
−21.63	PMMMM	8	10	16	20
−21.85	MMMMM	3	4	19	19
−46.30	PPPPP	25	9	0	1
−46.39	PPPPM		15	3	5
−46.55	MPPPM		6	5	5
−47.12	PPPMP	51	15	11	5
−47.33	MPPMP		12		10
−47.46	PPPMM		12	7	10
−47.54	MPPMM		10	21	20
−47.86	PMPMP	8	6	7	5
−48.13	PMPMM	12	10	23	20
−48.33	MMPMM	4	4	21	19

must be modified to account for depropagation.[19] The treatment has been generalized to equilibrium copolymerizations.[20]

In some copolymerizations, two comonomers may form a complex. Upon copolymerization, the two comonomers would then have a greater tendency to alternate. The complex participation model takes this complexation into account.[21,22] This model is useful, for example, for copolymers involving maleic anhydride, which has a tendency to complex with many comonomers.

In the bootstrap model,[23a] the comonomer concentration at the polymerization center is different from that in the bulk. It has been suggested for styrene/methyl methacrylate copolymerization that the comonomer concentration ratio at the polymerization center is related to the bulk concentration ratio through an equilibrium constant K, which then describes the bootstrap effect. The bootstrap model has now found additional experimental verification.[23b]

2.2 Homopolymer Tacticity

In vinyl homopolymers, the configuration of the substituents X gives rise to tacticity [structures (**5**)–(**7**)]:

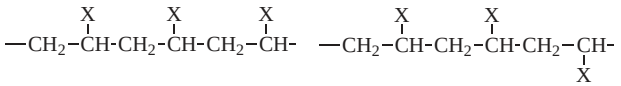

(5) Isotactic (111 or mm)

(6) Heterotactic ($11\bar{1}$ or mr)

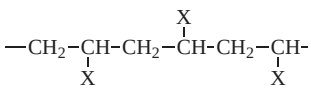

(7) Syndiotactic ($\bar{1}1\bar{1}$ or rr)

Two terminologies can be used for tacticity. In absolute configuration terms, the heterotactic sequence above can be represented as ($11\bar{1}$), where 1 represents the *up* configuration, and $\bar{1}$ denotes the *down* configuration. Alternatively, one can consider the relative configuration of pairwise adjacent substituents; the heterotactic sequence is then (mr). Statistical models can be carried out using either terminology. In the absolute configuration (Price formalism),[24] one considers the polymer as a copolymer of two 'comonomers' (1) and ($\bar{1}$). In the relative configuration scheme (Bovey formalism),[3] the polymer is regarded as a copolymer of two 'comonomers' (m) and (r).

Note that in NMR measurements, only the relative configuration is actually observed; thus, the Bovey formalism is more commonly used. The Price configuration is useful in Ziegler–Natta polymerization, where most catalysts are stereospecific. The statistical models (Bernoullian and Markovian) hold for both formalisms, although they take on different meanings.[5] In the Bovey formalism (**8**), the first-order Markovian model means that the tacticity of the incoming monomer j depends on the previous tacticity (between units i and $i-1$ on the propagating chain). In the Price formalism (**9**), this means that the configuration of unit j depends on the configurations of *two* previous units (i and $i-1$). This represents the second-order Markovian model (in the Price formalism).

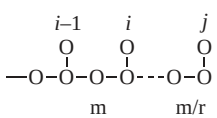

(8) Bovey (1st-order Markov)

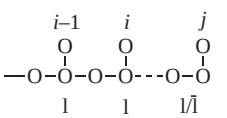

(9) Price (2nd-order Markov)

The reaction probability in both formalisms can be derived just as in the case of the copolymers. In the conventional first-order Markovian model (i.e., the Bovey formalism), the first-order Markovian probabilities are P_{mr} and P_{rm}. In the

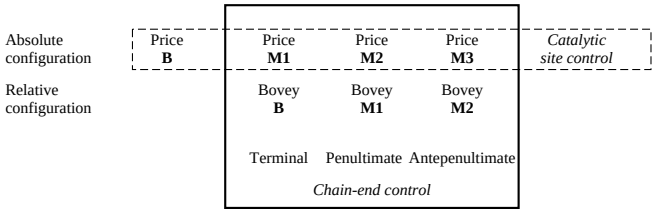

Figure 4 Relationships between the Bernoullian (**B**), first-order Markov (**M1**), and second-order Markov (**M2**) models in the Bovey and the Price formalisms

Price formalism, four second-order Markovian probabilities are needed: $\alpha = P_{111}$, $\beta = P_{1\bar{1}1}$, $\gamma = P_{\bar{1}11}$, and $\delta = P_{\bar{1}\bar{1}1}$. For convenience, $\overline{\alpha} = 1 - \alpha$, $\overline{\beta} = 1 - \beta$, etc. The tacticity expressions are

$$\text{Bovey} \quad (\text{m}) = kP_{\text{rm}} \tag{12}$$

$$(\text{r}) = kP_{\text{mr}} \tag{13}$$

$$\text{Price} \quad (\text{m}) = (11) + (\bar{1}\bar{1}) = k'(\gamma\delta + \bar{\alpha}\bar{\beta}) \tag{14}$$

$$(\text{r}) = (1\bar{1}) + (\bar{1}1) = k'(2\bar{\alpha}\delta) \tag{15}$$

where $k = (P_{\text{mr}} + P_{\text{rm}})^{-1}$ and $k' = (\overline{\alpha}\overline{\beta} + 2\overline{\alpha}\delta + \gamma\delta)^{-1}$.

An analogous situation occurs in Bovey's Bernoullian model, which corresponds to the first-order Markovian model in the Price formalism. The relationship between the two formalisms has been reviewed,[5] and is summarized in Figure 4.

The special case of the Price Bernoullian model needs to be considered; this model has no equivalence in the Bovey formalism. The catalytic site will have a reaction probability P_1 for the 1-configuration and $P_{\bar{1}}$ (or $1 - P_1$) for the $\bar{1}$-configuration. The various n-ad sequences are as follows:

$$(\text{m}) = (11) + (\overline{1\bar{1}}) = P_1^2 + (1 - P_1)^2 \tag{16}$$

$$(\text{r}) = (1\bar{1}) + (\bar{1}1) = 2P_1(1 - P_1) \tag{17}$$

$$(\text{mm}) = (111) + (\overline{1\bar{1}1}) = P_1^3 + (1 - P_1)^3 \tag{18}$$

$$(\text{mr}) = (1\overline{1\bar{1}}) + (\overline{1\bar{1}1}) + (\bar{1}11) + (11\bar{1})$$

$$= 2P_1(1 - P_1)^2 + 2P_1^2(1 - P_1) \tag{19}$$

$$(\text{rr}) = (1\bar{1}1) + (\bar{1}1\bar{1}) = P_1(1 - P_1)^2 + P_1^2(1 - P_1) \tag{20}$$

The Price Bernoullian model is also known as the symmetrical enantiomorphic-site (**E**) model,[25–28] and is found to be suitable for stereospecific Ziegler–Natta polymers, where the polymerization is determined by catalytic sites only.

In general, the Bovey formalism is used for polymerizations which are controlled by the propagating chain ends; this is the most frequently encountered case. For polymerizations catalyzed by metal complexes (e.g., Ziegler–Natta catalysts), the catalytic site may dominate the reaction probability, and the Price formalism may be appropriate. The various mechanisms of stereochemical control and the suitable models can be summarized as follows:[5,29]

1. pure chain-end control: Bovey **B**, **M1** and **M2** models;
2. pure catalyst-site control: **E** model (Price **B** model);
3. both catalyst-site and chain-end control: Price **M1** and **M2** models.

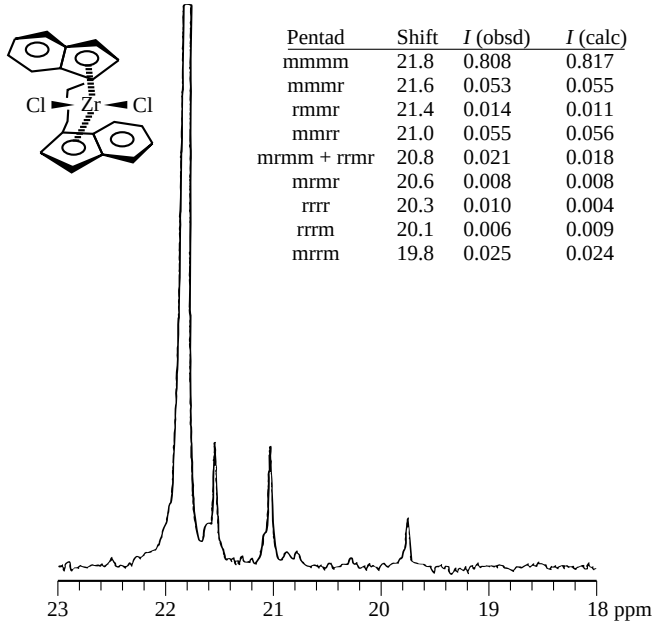

Pentad	Shift	*I* (obsd)	*I* (calc)
mmmm	21.8	0.808	0.817
mmmr	21.6	0.053	0.055
rmmr	21.4	0.014	0.011
mmrr	21.0	0.055	0.056
mrmm + rrmr	20.8	0.021	0.018
mrmr	20.6	0.008	0.008
rrrr	20.3	0.010	0.004
rrrm	20.1	0.006	0.009
mrrm	19.8	0.025	0.024

Figure 5 ^{13}C NMR spectrum of the methyl region (obtained at 90 MHz) for a sample of polypropylene made with Et $(\text{Ind})_2\text{ZrCl}_2$ (shown on the left) at 50°C

As an example, the ^{13}C NMR spectrum of the methyl substituent of polypropylene, prepared with a Zr metallocene/methyl aluminoxane,[30] is shown in Figure 5. The assignments[31] are shown with the spectrum. The resonances are sensitive to the pentad level. For this sample,[30] the tacticity agrees with the **E** model with $P_1 = 0.92$.

2.3 Regioirregular Structures

In some polymers, head-to-head (**11**) and tail-to-tail (**12**) structures are found together with the normal, head-to-tail structure (**10**):

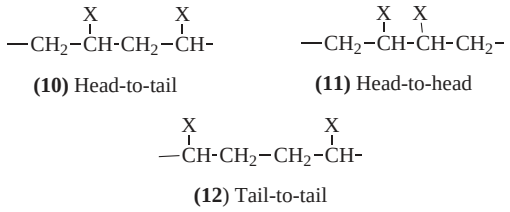

For a more detailed discussion of these regioirregular structures, see ***Polymers: Regio-Irregular Structure***. The statistical models used for regioirregular structures have been reviewed in a recent article.[18]

3 TWO STATE MODELS

For convenience, one can distinguish two types of two state models.[32] In *concurrent two state models*, two separate polymer components are present, which may be a result of deliberate polymer blending, programmed comonomer feed concentrations, or phase separation. Another possibility is

when two separate polymerization centers (or catalytic sites) are present, each center making its own polymer according to its propagation statistics. This is sometimes the case with some emulsion and Ziegler–Natta polymerizations.

In *consecutive two state models*, two polymerization centers are present, but they switch back and forth even as polymerization proceeds. As a result, one gets a block copolymer consisting of blocks that conform to different statistical models. Another case where this model holds is when sudden fluctuations in the reaction conditions occur during polymerization (e.g., changes in temperature, pressure, or comonomer concentrations). The polymer made during the change may also conform to the consecutive model.

The classic work on two state models is that of Coleman and Fox.[33] Their theory assumes two Bernoullian states (i.e., two state **B**/**B**), and includes both consecutive and concurrent cases. Its application to NMR data has been described by Frisch et al.,[34] especially in relation to the anionic polymerization of methyl methacrylate. An alternative two state model for anionic polymerization has been proposed by Khan and Hogan-Esch.[35] A generalized treatment of two state consecutive models has been devised[32] using a structural approach. The general model can be used for consecutive two state **B**/**B**, **B**/**E**, and **E**/**E** cases. These models have been tested on anionic PMMA data and also on the tacticity data of polypropylene produced by nonsymmetric *ansa*-titanocene catalysts.[32]

Concurrent two state models have been used for Ziegler–Natta polymers. Zambelli et al.[36] and Chujo et al.[37] first used the concurrent **E**/**B** model for the treatment of polypropylene tacticity, and the concurrent **B**/**B** model has been applied to olefin copolymers by Ross[38] and others.[39–41] The mode of application of these concurrent two state models to the analysis of NMR data is similar to that of concurrent multistate models (see Section 4).

As a result of intensive research activities on homogeneous Group IV metallocene catalysts, a number of new two state models have been proposed. To rationalize the NMR data of syndiotactic polypropylene made with metallocene catalysts, Ewen et al.[42] proposed a two state model based on dual catalytic-site and chain-end control. Cheng and Kasehagen[43a] have devised a two state model, attempting to explain the NMR tacticity data of polypropylene in general. Serveral other models have also been proposed.[43b–d]

4 MULTISTATE MODELS

In many polymers of commercial interest, more than one or two components may be present. For example, heterogeneous Ziegler–Natta catalysts are known to contain at least three active sites.[44,45] The NMR data for a polymer made with such a catalyst would have contributions from all the multiple components. A general methodology for the treatment of the NMR data of these polymers has been devised.[41] Whereas the methodology can be used on the NMR data of the polymer as is, it has been found that best results are obtained when the NMR data of a *series* of polymer samples are available; for example, in the following cases.

1. The polymer is fractionated by a suitable means.[41,46–51]
2. During polymerization, the polymerization reaction mixture is sampled at various conversions.
3. For copolymers, different copolymer compositions are made under similar reaction conditions, but with different feed comonomer concentrations.[52]
4. A related series of polymers is obtained, prepared with essentially the same reaction conditions except that one experimental variable has been systematically varied.[53] That experimental variable should change the proportions of the components making up the polymer, but does not significantly change the polymer microstructure (e.g., stereospecificity, regiospecificity, and reactivity ratios).

In all four cases, the NMR data for the series of polymer samples or fractions are obtained and analyzed in a systematic manner. The methodology has been applied to copolymer sequence analysis of ethylene/propylene copolymer,[41,46,47,52,53] propylene/1-butene copolymer,[41] ethylene/1-butene copolymer,[48,54] ethylene/1-hexene copolymer,[52,55] and ethylene oxide/epichlorohydrin copolymer,[50] and to the tacticity determination of polypropylene,[41,49,53] poly(1-butene),[41,46] and polyepichlorohydrin.[51]

Table 4 Observed ^{13}C Methyl Pentad Intensities[a] and Molecular Weight Data[a] for Polypropylene Made with a Heterogeneous Catalyst and Its Fractions; Values in Parentheses are Calculated[49] from the Four-Component E/E/E/B Model

				Pentad Intensities								
Fraction[b]	Weight %	M_n ($\times 10^4$)	M_w ($\times 10^4$)	mmmm	mmmr	rmmr	mmrr	xmrx	mrmr	rrrr	rrrm	mrrm
Whole	100	0.83	4.59	—	—	—	—	—	—	—	—	—
Polymer		(0.82)	(4.20)									
C5 sol.	43.9	0.46	2.28	23.4	12.5	2.9	15.1	12.4	3.6	12.1	11.1	6.7
		(0.50)	(2.37)	(25.0)	(12.2)	(2.7)	(13.6)	(13.6)	(5.4)	(11.2)	(9.6)	(6.8)
C5 insol.	16.5	0.99	3.02	59.4	10.0	0.6	10.0	3.2	0.7	3.1	2.3	4.7
C6 sol.		(1.02)	(3.06)	(59.4)	(9.1)	(1.3)	(9.4)	(6.0)	(2.6)	(3.6)	(3.8)	(4.7)
C6 insol.	10.9	1.21	3.11	77.5	7.3	0.5	6.9	3.1	0.1	0.9	0.8	2.9
C7 sol.		(1.38)	(3.17)	(77.6)	(6.2)	(0.6)	(6.3)	(2.5)	(1.2)	(1.1)	(1.4)	(3.1)
C7 insol.	7.2	1.82	4.91	85.5	4.9	0.3	4.7	1.1	0.2	0.7	0.6	2.0
T sol.		(1.64)	(4.95)	(84.2)	(4.5)	(0.3)	(4.6)	(1.5)	(0.7)	(0.9)	(0.9)	(2.3)
T insol.	21.5	3.50	8.75	93.5	2.7	0	2.3	0.3	0.1	0	0.1	1.0
		(3.76)	(8.84)	(93.8)	(2.4)	(0)	(2.4)	(0.1)	(0)	(0)	(0)	(1.2)

[a]Observed data taken from T. Tsutsui, N. Ishimaru, A. Mizuno, A. Toyota, and N. Kashiwa, *Polymer*, 1989, **30**, 1351.
[b]C5 = pentane, C6 = hexane, C7 = heptane, T = toluene.

An example is given for the NMR data of polypropylene made with a heterogeneous Ziegler–Natta catalyst.[49] The polymer has been fractionated and the NMR pentad intensities for the methyl resonances obtained (Table 4).

The data have been treated using the computerized analytical approach.[49] First, the pentad data for each fraction are analyzed using the one state and two state models. If there is strong evidence that the polymer contains multiple components then the pentad data from pairwise fractions are taken and simultaneously analyzed using the two state and the three state models. The results are compiled and checked for trends. Additional information (e.g., M_n and M_w) is included in the analysis. If the precision in the data is good, a decision can often be made as to the minimum number of states that the data need in order to obtain satisfactory goodness-of-fit. Finally, a global data fit can be carried out including the data of all the fractions. The result of this analysis for the polymer example is shown in Table 4. The polymer consists of at least four distinct components; three of them conform to the **E** model and one to the **B** model. Thus, the catalyst contains at least four active sites. Through further calculation,[49] it can be shown that the sites contribute 24.8%, 20.0%, 39.9%, and 15.3%, respectively, to polymer yield.

5 PERTURBED MODELS

As with molecular weights, most polymers do not have a single uniform composition; instead, a distribution of composition is obtained. This compositional heterogeneity can come about through many means,[56,57] for example,

1. copolymer sequence
   (a) statistical,
   (b) conversion,
   (c) multistate,
   (d) process;
2. homopolymer tacticity
   (a) statistical,
   (b) chain end,
   (c) multistate,
   (d) process.

Statistical heterogeneity occurs as a result of different statistical combinations of the comonomers in a given polymer chain. Conversion heterogeneity is found in copolymers when two comonomers have different reactivities; thus, at low conversions, the polymer chains produced are enriched in the more reactive comonomers, and at high conversions, the polymer contains the comonomers that are left over. Multistate heterogeneity has been described in the previous section. Process heterogeneity is a result of fluctuations in the polymerization processes. These various heterogeneities separately or together have an effect on the copolymer sequence or tacticity. Perturbed Markovian[58] and enantiomorphic-site[59] models have been developed. Similar equations for the Bernoullian model were derived earlier by Ross.[38] Using the perturbed model, one can analyze[58] or simulate[56,57] the NMR data and the compositional distribution curves.

The perturbation model is particularly useful[60] when the polymer molecular weights are low, or when there are large fluctuations in the reaction conditions during polymerization. Another pertinent situation occurs in copolymerization when the reactivity of the comonomers involves uncertainty (e.g., with the active catalytic site exhibiting a distribution of selectivities). The resulting reaction probability would then have a range of values: $P_{ij} = \langle P_{ij} \rangle \pm \epsilon$, where P_{ij} and $\langle P_{ij} \rangle$ are the actual and average reaction probabilities, respectively, and ϵ is a measure of the distribution. A similar situation may arise if the tacticity control of the active site is partial or imprecise.

6 ANALYTICAL METHODOLOGIES

In order to apply these various models to actual data, appropriate analytical methodologies are needed. In the *analytical* (model-fitting) approach,[14,15,41,49,52,53,61,62] the observed NMR spectrum is interpreted and the spectral intensities fitted to a reaction probability model:

$$\text{observed data} \longrightarrow \text{spectral interpretation} \longrightarrow \text{fitting algorithm} \longrightarrow \text{probability model} \qquad (21)$$

This approach has been used for the analyses of the data in the preceding sections. The analyses can be facilitated with the use of computers.

In the *synthetic* (or computer simulation) approach,[29,56,57,61,63,64] one starts with the statistical model and carries out 'model calculations' to derive the predicted NMR information:

$$\text{probability model} \longrightarrow \text{model calculations} \longrightarrow \text{bookkeeping procedures} \longrightarrow \text{predicted results} \qquad (22)$$

The 'model calculations' may involve theoretical derivations of reaction probabilities, or Monte Carlo simulation of polymerization to generate an ensemble of polymer chains. In the latter case, one then needs to count the polymer chains and sort them according to the information needed. In this way, polymer sequence, composition distribution, molecular weights, and even simulated NMR spectra can be obtained.

The relative merits of these two approaches have been discussed in the literature.[61] In general, they are complementary; the use of both can provide a rather detailed understanding of the polymer in question.

7 RELATED ARTICLES

Polymer Reactions; Polymers: Regio-Irregular Structure; Polymers: Relaxation and Dynamics of Synthetic Polymers in Solution.

8 REFERENCES

1. (a) G. Odian, *Principles of Polymerization*, 2nd edn., Wiley, New York, 1981. (b) R. W. Lenz, *Organic Chemistry of Synthetic High Polymers*, Wiley-Interscience, New York, 1967.
2. (a) F. A. Bovey, in *Comprehensive Polymer Science*, eds. G. Allen and J. C. Bevington, Pergamon, Oxford, 1989, Vol. 1, p. 377. (b) A. E. Tonelli, *NMR Spectroscopy and Polymer Microstructure*, VCH Publishers, New York, 1989. (c) F. Heatley, *Nucl. Magn. Reson.*, 1989, **18**, 259. (d) H. N. Cheng, in *Modern Methods of Polymer Analysis*, eds. H. G. Barth and J. W. Mays, Wiley, New York, 1991, Chap. 11
3. F. A. Bovey, *High Resolution NMR of Macromolecules*, Academic Press, New York, 1972.

4. J. L. Koenig, *Chemical Microstructure of Polymer Chains*, Wiley, New York, 1980.
5. H. N. Cheng, *J. Appl. Polym. Sci.*, 1988, **36**, 229.
6. H. N. Cheng and G. H. Lee, *Macromolecules*, 1988, **21**, 3164.
7. C. J. Carman, R. A. Harrington, and C. E. Wilkes, *Macromolecules*, 1977, **10**, 536.
8. J. Schaefer, *J. Chem. Phys.*, 1966, **70**, 1975.
9. A. E. Tonelli and F. C. Schilling, *Macromolecules*, 1981, **14**, 74.
10. F. C. Schilling, A. E. Tonelli, and M. Valenciano, *Macromolecules*, 1985, **18**, 356.
11. G. N. Babu, S. S. Christopher, and R. A. Newmark, *Macromolecules*, 1987, **20**, 2654.
12. H. Jancke, G. Engelhardt, H. Kriegsmann, and F. Keller, *Plaste u. Kautsch.*, 1979, **26**, 612.
13. G. Englehardt and H. Jancke, *Polym. Bull.*, 1981, **5**, 577.
14. P. J. A. Brandt, R. Subramanian, P. M. Sormani, T. C. Ward, and J. E. McGrath, *Polym. Prepr., Am. Chem. Soc. Div. Polym. Chem.*, 1985, **26**(2), 213.
15. T. Moritani and H. Iwasaki, *Macromolecules*, 1978, **11**, 1251.
16. C. Wallings and E. R. Briggs, *J. Am. Chem. Soc.*, 1945, **67**, 1774.
17. (a) M. T. Roland and H. N. Cheng, *Macromolecules*, 1991, **24**, 2015. (b) H. N. Cheng and M. T. Roland, *Polym. Prep., Am. Chem. Soc. Div. Polym. Chem.* 1991, **32**(1), 549.
18. H. N. Cheng, *Makromol. Chem., Theory Simul.*, 1994, **3**, 979.
19. (a) B. K. Kang, K. F. O'Driscoll, and J. A. Howell, *J. Polym. Sci., Part A-1*, 1972, **10**, 2349. (b) M. Izu, K. F. O'Driscoll, R. J. Hill, M. J. Quinn, and H. J. Harwood, *Macromolecules*, 1972, **5**, 90, and references therein. (c) R. E. Cais, D. J. T. Hill, and J. H. O'Donnell, *J. Macromol. Sci., Chem., A*, 1982, **17**, 1437.
20. (a) M. Szwarc and C. L. Perrin, *Macromolecules*, 1985, **18**, 528. (b) G. Cai and D. Yan, *J. Macromol. Sci., Chem., A*, 1987, **24**, 869.
21. J. A. Seiner and M. Litt, *Macromolecules*, 1971, **4**, 308.
22. D. J. T. Hill, J. H. O'Donnell, P. W. O'Sullivan, *Prog. Polym. Sci.*, 1982, **8**, 215, and references therein.
23. (a) H. J. Harwood, *Makromol. Chem., Makromol. Symp.*, 1987, **10/11**, 331. (b) H. J. Harwood, private communication.
24. F. P. Price, in *Markov Chains and Monte Carlo Calculations in Polymer Science*, ed. G. G. Lowry, Marcel Dekker, New York, 1970, Chap. 7
25. R. A. Sheldon, T. Fueno, T. Tsunetsuga, and J. Furukawa, *J. Polym. Sci., Part B*, 1965, **3**, 23.
26. J. Furukawa, *Polym. Prepr., Am. Chem. Soc. Div. Polym. Chem.*, 1967, **8**(1), 39.
27. Y. Doi, *Makromol. Chem., Rapid Commun.*, 1982, **3**, 635.
28. A. Zambelli, P. Locatelli, M. C. Sacchi, and I. Tritto, *Macromolecules*, 1982, **15**, 831.
29. H. N. Cheng, in *Transition Metal Catalyzed Polymerizations*, ed. R. P. Quirk, Cambridge University Press, Cambridge, 1988, p. 599.
30. (a) J. A. Ewen, L. Haspelagh, M. J. Elder, J. L. Atwood, H. Zhang, and H. N. Cheng, in *Transition Metals and Organometallics as Catalysts for Olefin Polymerization*, eds. W. Kaminsky and H. Sinn, Springer-Verlag, Berlin, 1988, p. 281. (b) H. N. Cheng and J. A. Ewen, unpublished work.
31. A. Zambelli, P. Locatelli, G. Bajo, and F. A. Bovey, *Macromolecules*, 1975, **8**, 687, and references therein.
32. H. N. Cheng, G. N. Babu, R. A. Newmark, J. C. W. Chien, *Macromolecules*, 1992, **25**, 6980.
33. B. D. Coleman, T. G. Fox, *J. Chem. Phys.*, 1963, **38**, 1065.
34. H. L. Frisch, C. L. Mallows, F. Heatley, F. A. Bovey, *Macromolecules*, 1968, **1**, 533.
35. I. M. Khan and T. E. Hogen-Esch, in *Recent Advances in Anionic Polymerization*, eds. T. E. Hogen-Esch and J. Smid, Elsevier, New York, 1987, p. 261.
36. A. Zambelli, P. Locatelli, A. Provasoli, and D. R. Ferro, *Macromolecules*, 1980, **13**, 267.
37. S.-N. Zhu, X.-Z. Yang, and R. Chujo, *Polym. J. (Tokyo)*, 1983, **15**, 859, and references therein.
38. J. F. Ross, in *Transition Metal Catalyzed Polymerizations, Alkenes and Dienes*, ed. R. P. Quirk, Harwood Academic, New York, 1983, p. 799.
39. C. Cozewith, *Macromolecules*, 1987, **20**, 1237.
40. S. Floyd, *J. Appl. Polym. Sci.*, 1987, **34**, 2559.
41. H. N. Cheng, *J. Appl. Polym. Sci.*, 1988, **35**, 1639.
42. J. A. Ewen, M. J. Elder, R. L. Jones, S. Curtis, H. N. Cheng, in *Catalytic Olefin Polymerization*, eds. T. Keii and K. Soga, Kodansha, Tokyo, 1990, p. 439.
43. (a) H. N. Cheng and L. J. Kasehagen, manuscript in preparation. (b) T. Asanuma, Y. Nishimori, M. Ito, and T. Shiomura, *Makromol. Chem., Rapid Commun.*, 1993, **14**, 315. (c) M. Farina and A. Terragni, *Makromol. Chem., Rapid Commun.*, 1993, **14**, 791. (d) M. Farina, G. DiSilvestro, and P. Sozzani, *Macromolecules*, 1993, **26**, 946.
44. Y. V. Kissen, *Isospecific Polymerization of Olefins*, Springer-Verlag, New York, 1985.
45. (a) J. C. W. Chien, in *Transition Metal Catalyzed Polymerizations*, ed. R. P. Quirk, Cambridge University Press, Cambridge, 1988, p. 55. (b) J. Mejzlik, M. Lesna, and J. Kratochvila, *Adv. Polym. Sci.*, 1987, **81**, 84. (c) J. J. A. Dusseault and C. C. Hsu, *J. Appl. Polym. Sci.*, 1993, **50**, 431.
46. H. N. Cheng, in *Computer Applications in Applied Polymer Science II*, ed. T. Provder, *ACS Symposium Series, Vol. 404*, American Chemical Society, Washington, DC, 1989, p. 174.
47. H. N. Cheng and M. Kakugo, *Macromolecules*, 1991, **24**, 1724.
48. H. N. Cheng, *Polym. Bull.*, 1990, **23**, 589.
49. H. N. Cheng, *Makromol. Chem., Theor. Simul.*, 1992, **1**, 415.
50. H. N. Cheng, in *Catalysis in Polymer Synthesis*, eds. E. J. Vandenberg and J. C. Salamone, *ACS Symposium Series, Vol. 496*, American Chemical Society, Washington, DC, 1992, p. 157.
51. H. N. Cheng, *Polym. Prepr., Am. Chem. Soc. Div. Polym. Chem.*, 1991, **32**(1), 549.
52. H. N. Cheng, in *New Advances in Polyolefins*, ed. T. C. Chung, Plenum Press, New York, 1993, p. 159.
53. H. N. Cheng, *Makromol. Chem., Theor. Simul.*, 1993, **2**, 901.
54. H. N. Cheng, *Macromolecules*, 1991, **24**, 4813.
55. H. N. Cheng, *Polym. Bull.*, 1991, **26**, 325.
56. H. N. Cheng, S. B. Tam, and L. J. Kasehagen, *Macromolecules*, 1992, **25**, 3779.
57. H. N. Cheng and L. J. Kasehagen, *Macromolecules*, 1993, **26**, 4774.
58. H. N. Cheng, *Macromolecules*, 1992, **25**, 2351.
59. H. N. Cheng, *Makromol. Chem., Theor. Simul.*, 1993, **2**, 561.
60. H. N. Cheng, *J. Appl. Polym. Sci., Appl. Polym. Symp.*, 1992, **51**, 21.
61. H. N. Cheng, *J. Appl. Polym. Sci., Appl. Polym. Symp.*, 1989, **43**, 129, and references therein.
62. H. N. Cheng, *J. Chem. Inf. Comput. Sci.*, 1987, **27**, 8.
63. H. N. Cheng and M. A. Bennett, *Anal. Chem.*, 1984, **56**, 2320.
64. H. N. Cheng and M. A. Bennett, *Makromol. Chem.*, 1987, **188**, 2665.

Biographical Sketch

H. N. Cheng. *b* 1947. B.S., 1969, University of California, Los Angeles, USA; Ph.D., 1974 University of Illinois, Physical Chemistry (supervisor, H. S. Gutowsky). Postdoctoral work at Bell Laboratories, Murray Hill, NJ with Frank A. Bovey. Senior research chemist at GAF Corporation, 1976–79. Research staff, Hercules Research Center, 1979–83; Research supervisor, spectroscopy/microscopy/surface analysis, 1983–90; Research fellow, 1990, Research associate, new business R&D, 1991–present. Approx. 85 publications. Current research interests: NMR of polymers, statistical models and computer modeling of polymerization, polymer reactions, and automated methods for ^{13}C spectral interpretation and shift prediction.

Polymers: Regio-Irregular Structure

Tetsuo Asakura
Tokyo University of Agriculture and Technology, Koganei, Tokyo, Japan

1	Introduction	1
2	^{13}C NMR Spectrum of Regio-Irregular Polypropylene	1
3	2D INADEQUATE Spectrum of Regio-Irregular Polypropylene	2
4	^{13}C NMR Assignment of Regio-Irregular Polypropylene	5
5	Other Regio-Irregular Polymers	5
6	References	6

1 INTRODUCTION

'Regio-irregular structure' generally refers to the structure of regio-irregular polymers prepared with unsymmetrically substituted vinyl monomers ($CHR{=}CH_2$). The orientational mode adopted by such an asymmetric monomer on entering the growing chain leads normally to a regular chemical arrangement of the monomer units, i.e., head-to-tail (H-T) (**1**), in addition polymerization reactions.

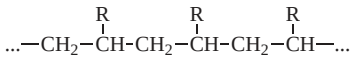

(1)

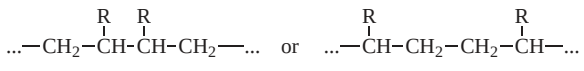

(2)

In contrast, the alternative head-to-head (H-H) and the accompanying tail-to-tail (T-T) structures (**2**) are not favored, although some of these sequences may be found in some polymers. In a few cases the proportion of (H-H) and (T-T) structures can be relatively high; it can reach 30–40% in polypropylene (PP),[1] poly(1-butene)[2] and poly(vinyl fluoride), but about 5% is a more usual level.[3,4]

The presence of such arrangements must be taken into account while interpreting the ^{13}C or ^{19}F NMR spectra of these polymers, because this probe is very sensitive both to chemical and steric structure, and, from a detailed knowledge of the structure, information can be drawn on the polymerization mechanism.[4]

As the proportion of the regio-irregular structure in the sample increases, peak assignment becomes very complex because of the coexistence of several kinds of sequence containing inverted units and also the fine splitting of each peak due to stereoregularity. Several NMR techniques including sample preparation have been used for peak assignment: 2D INADEQUATE,[1,2] INEPT and DEPT,[1,2,5] ^{13}C-γ shielding calculations with a rotational isomeric state (ris) model,[5,6] empirical chemical shift rules,[7] and the preparation of several ^{13}C-enriched model compounds for irregularly arranged sequences in the polymers.[8] Since the ^{13}C NMR assignment of regio-irregular PP has been reported most frequently, the assignment will be described here in detail. Then the NMR analysis of other regio-irregular polymers will be reviewed.

2 ^{13}C NMR SPECTRUM OF REGIO-IRREGULAR POLYPROPYLENE

Figure 1 shows the ^{13}C NMR spectrum of regio-irregular PP containing up to 40 mol% of inverted propylene units along with the stick spectra calculated according to the Lindeman–Adams empirical rules.[9,10] Here, the letters S, T and P are used when we refer to secondary (CH_2), tertiary (CH), and primary (CH_3) carbons, respectively. Two Greek subscripts are used, referring to the distances of the nearest methyl groups from the carbon in question. Four Greek subscripts are used when referring to the distances of the two nearest methyl substituents on each side of the given carbon.[11–13] The sample giving rise to Figure 1 is atactic, judging from the peak patterns of the carbons, $P_{\beta\beta}$ and $S_{\gamma\alpha\alpha\gamma}$.[14] For the empirical chemical shift calculation, the presence of five kinds of sequence containing H-H and/or T-T units in the sample is assumed as follows:

1. the sequence (**3**) where an isolated H-H unit is involved,

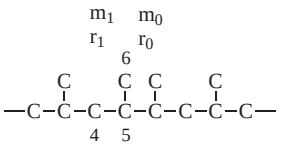

(3)

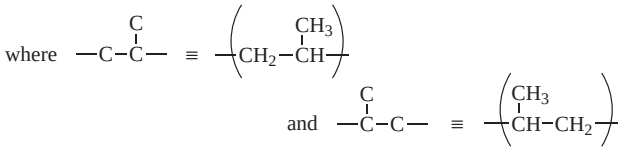

2. the sequence (**4**) where an isolated T-T unit is involved,

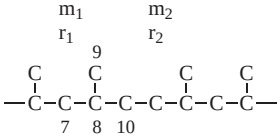

(4)

3. the sequence 1-r (**5**), where a single inverted unit in the successive H-T units is involved,

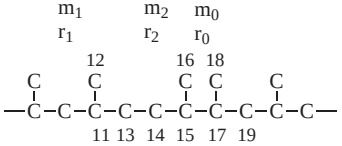

(5)

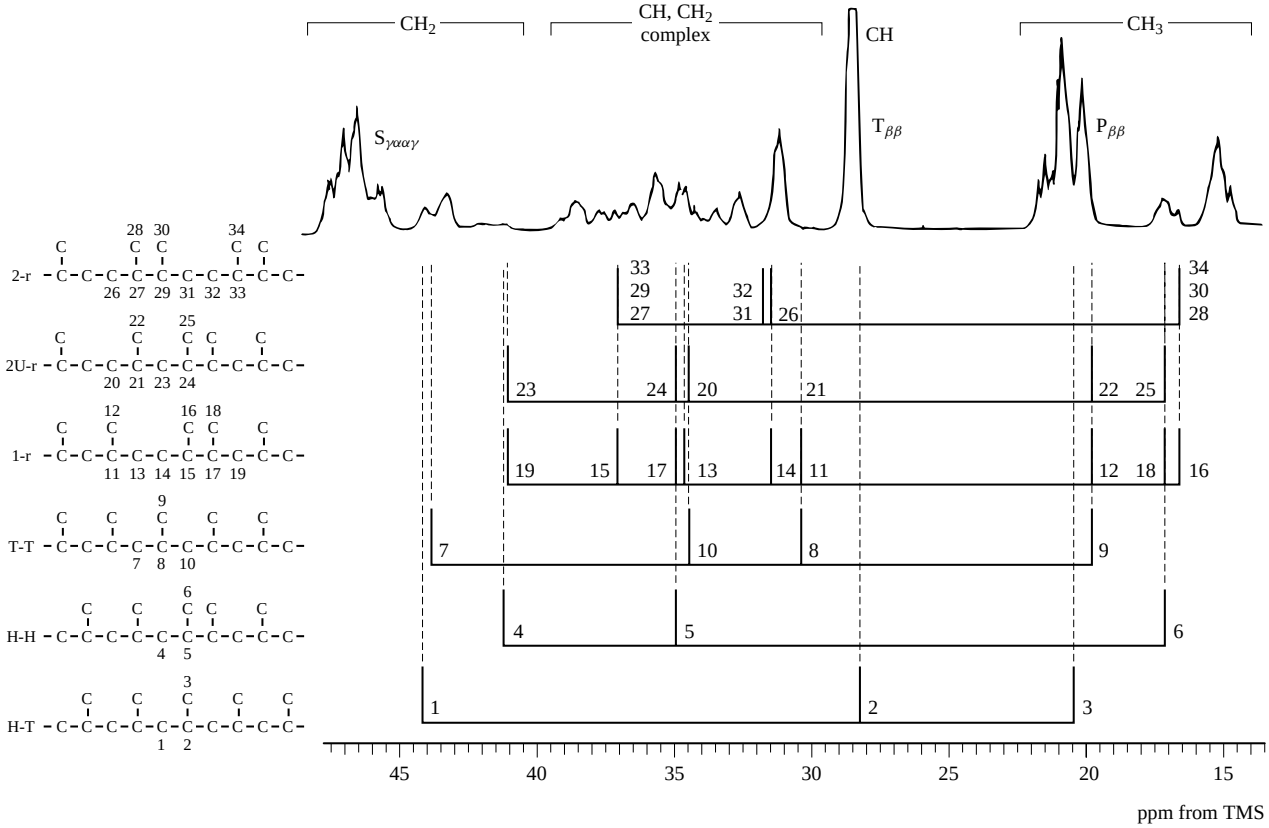

Figure 1 100 MHz ^{13}C NMR spectrum of regio-irregular polypropylene containing many inverted propylene units [sample concentration 12% (w/v), 15 254 pulses]. The stick spectra were calculated using the Lindeman–Adams chemical shift empirical rules by assuming the presence of several kinds of sequence in the chain

4. the sequence 2U-r (**6**), where two successive inverted units in the H-T units are involved,

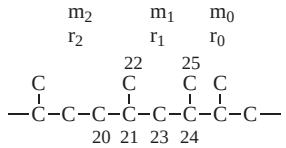

(6)

5. the sequence 2-r (**7**), where an inversion occurs, followed by a second inversion,

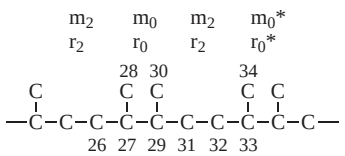

(7)

It is possible to speculate on the presence of several kinds of sequences from a comparison of the calculated and observed chemical shifts, although the agreement is extremely poor in the methylene carbon region. Consequently, it is difficult to assign these peaks to the individual carbons of the sequences assumed.

The ^{13}C NMR spectral assignment is not easy because of overlapping of the peaks, especially in the region from 30 to 40 ppm. One of the reasons for the complexity of this spectral region is overlapping of the CH and CH_2 peaks. Therefore, assignment of these peaks to the CH and CH_2 carbons is performed using the INEPT technique,[15] as shown in Figure 2.

The INEPT ($\Delta = 2/4J^*$) observation gives only the CH spectrum (b). Then, only the CH_2 spectrum (c) is obtained from the difference between the ^1H-decoupled (a) and INEPT ($\Delta = 2/4J^*$) (b) spectra. Here the peak of the CH carbon in the successive H-T units, $T_{\beta\beta}$, was used as a reference. From these spectra, it is observed that all peaks between 36.5 and 39 ppm are clearly assigned to CH carbons, and the peaks at 32.6 and 33.4 ppm to the CH_2 carbons. The CH and CH_2 peaks overlap in the spectral region 34–36.5 ppm, and are identified for each carbon by the INEPT technique. In addition, small CH_2 peaks overlapping with the CH peak at 31 ppm are detected in the difference spectrum. Thus, all of the peaks are classified into the CH, CH_2, and CH_3 carbons.

3 2D INADEQUATE SPECTRUM OF REGIO-IRREGULAR POLYPROPYLENE

A 2D INADEQUATE experiment, which makes it possible to assign carbons to specified sequences through the ^{13}C–^{13}C connectivities, is then performed.[16]

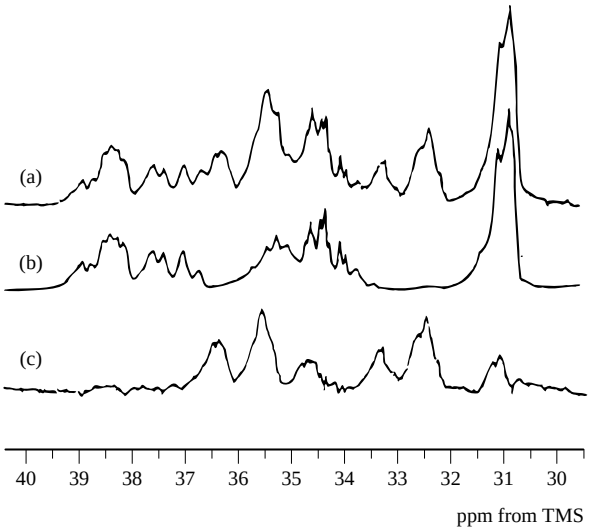

Figure 2 100 MHz ^{13}C NMR spectra of regio-irregular polypropylene (the spectral region 29.9–40 ppm is expanded): (a) ^{1}H completely decoupled; (b) INEPT ($\Delta = 2/4J^*$, 17 497 pulses) CH only; (c) difference, (a) − (b), CH_2-only. The CH peak $T_{\beta\beta}$ carbon in head-to-tail units was used as a reference to obtain the difference spectrum (c)

Figure 3 shows the 2D INADEQUATE spectrum of regio-irregular PP. The $^{13}C-^{13}C$ connectivities of the carbons in the isolated H-H and T-T units are shown as solid and broken lines, respectively. Assignment of the peaks attributable to the carbons in these units is relatively easy. The assignments due to stereoregularity are also possible at the diad level. In the

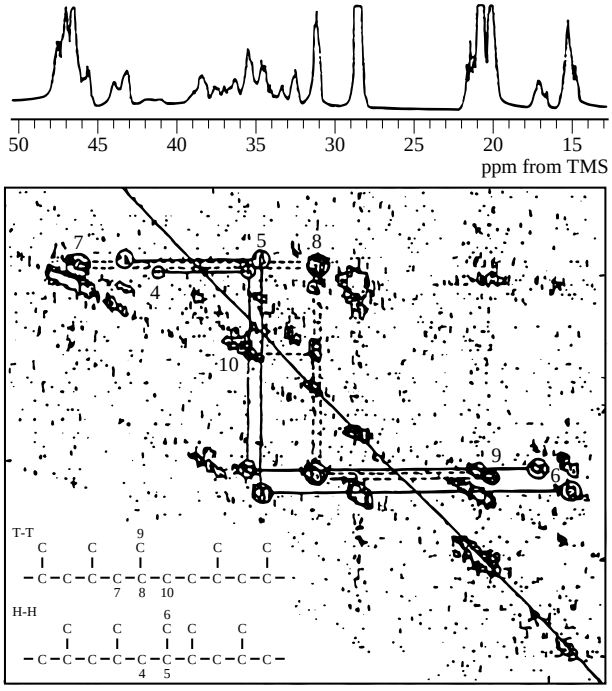

Figure 3 100 MHz 2D INADEQUATE ^{13}C NMR spectrum of regio-irregular polypropylene. The $^{13}C-^{13}C$ connectivities of the carbons in the isolated head-to-head and tail-to-tail units are shown as solid and broken lines, respectively

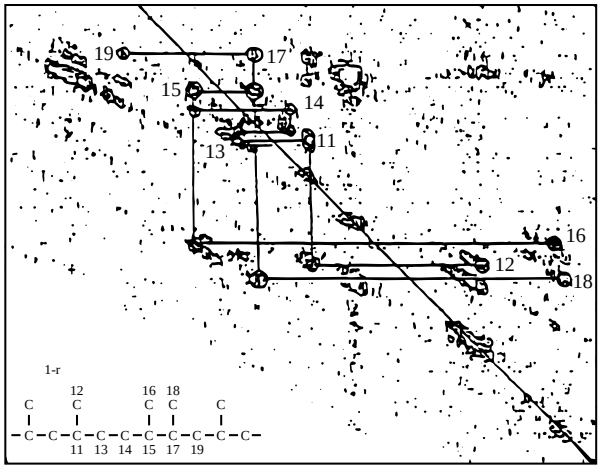

Figure 4 100 MHz 2D INADEQUATE ^{13}C NMR spectrum of regio-irregular polypropylene. The $^{13}C-^{13}C$ connectivity of the carbons in the sequence 1-r, where there is a single inverted unit in the successive head-to-tail units, is shown as a solid line

region 14–18 ppm, the lower-frequency (higher field) peak at 14.7–15.1 ppm has already been assigned to be the carbon r_0-$P_{\alpha\beta}$, and the higher-frequency peak at 16.6–17.2 ppm is assigned to $m_0-P_{\alpha\beta}$ in the H-H unit of PP. Therefore, in the CH spectrum of Figure 2(b), the spectral region 34.2–35.6 ppm is assigned to the carbon $T_{\alpha\beta}(5)$ in the H-H units from the $^{13}C-^{13}C$ connectivities (solid lines). The number in parentheses refers to the carbon in the structure in Figure 1. The peaks between 34.2 and 34.8 ppm are assigned to the r_0-$T_{\alpha\beta}$ carbons, and the peaks between 35.4 and 35.6 ppm to the $m_0-T_{\alpha\beta}$ carbon. Similarly, in the region 40–45 ppm, the peaks at 40.9–42.3 ppm are assigned to $m_0-S_{\beta\alpha\alpha\gamma}$, and the higher-frequency peaks at 43.3–44.1 ppm to $r_0-S_{\beta\alpha\alpha\gamma}$. Further splittings of these peaks are due to both the stereoregularity and the presence of other carbons in the sequences, except for the isolated H-H and T-T units. The assignments of the peaks of the carbons in the T-T unit are also performed by the 2D INADEQUATE method.

Table 1 ^{13}C NMR Chemical Shifts of the Carbon $S_{\gamma\alpha\beta\gamma}$ [see (**8**)] in the Sequence 1-r Calculated at the Pentad Level on the Basis of the ^{13}C NMR γ-Effect and Ris Model, (a) and with the Empirical Additivity Rules Proposed by Cheng and Bennett (b)

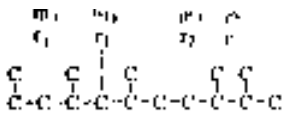

Sequence	(a)[a]	(b)
[illegible]	0.08	0.00
[illegible]	−0.09	0.05
[illegible]	0.96	1.07
[illegible]	0.92	1.8
[illegible]	0.75	1.04
[illegible]	0.68	0.92
[illegible]	0.73	0.86
[illegible]	0.97	0.16

[a] In ppm downfield from the m_0m_0 resonance (assumed to be the origin).

The appearance of the peak at 32.6 ppm, assigned to the $S_{\delta\beta\alpha\beta}(14)$ carbon, indicates the presence of the sequence 1-r (see Figure 1). This is supported by the $^{13}C-^{13}C$ connectivities of the 2D INADEQUATE spectrum (solid line in Figure 4).

Grassi et al.[17] have reported the ^{13}C NMR spectrum of *isotactic* regio-irregular PP containing exclusively the sequence 1-r in successive H-T units. Their data constitute a reference for the chemical shifts of the isotactic peaks of the sequence 1-r. By comparison, the absence of the $m_0-S_{\delta\beta\alpha\beta}$ peak in this spectrum is clearly indicated because there are no peaks around 30.4 ppm. Thus, there is a $^{13}C-^{13}C$ connectivity between $r_0-P_{\alpha\beta}$ and $r_0-S_{\beta\alpha\alpha\gamma}$ but no connectivity between the $m_0-P_{\alpha\beta}$ and $r_0-S_{\beta\alpha\alpha\gamma}$ peaks.

Nine kinds of carbons, 11–19 in the sequence 1-r, can be assigned through $^{13}C-^{13}C$ connectivities (Figure 4). The peaks of three kinds of CH carbons, namely, $T_{\delta\beta\gamma\delta}(11)$, $T_{\delta\gamma\alpha\gamma}(15)$, and $T_{\delta\alpha\beta\delta}(17)$, were observed. The peak position of the $T_{\delta\beta\gamma\delta}$ carbon in the sequence 1-r coincides with that of the $T_{\delta\beta\gamma\delta}$ carbon in the isolated T-T unit. In addition, the peak of the $r_0-T_{\delta\alpha\beta\delta}$ carbon, which was separated from the CH_2 peaks by the INEPT technique (Figure 2), appears at 34.5 ppm, the same region as the peak of the carbon $r_0-T_{\alpha\beta}$ in the H-H unit.

There are also three kinds of CH_2 carbons, namely, $S_{\gamma\alpha\beta\gamma}(13)$, $S_{\delta\beta\alpha\beta}(14)$, and $S_{\beta\alpha\alpha\gamma}(19)$, in the sequence 1-r. The peak at 32.6 ppm is assigned to the $r_0-S_{\delta\beta\alpha\beta}$ carbon as mentioned above. In the resonance region, 34–36.7 ppm, three CH_2 peaks are observed (Figure 2). The lowest-frequency peak has already been assigned to the $m_1-S_{\gamma\alpha\beta\delta}$ carbon, and the center peak to the $r_1-S_{\gamma\alpha\beta\delta}$ carbon. The ^{13}C NMR chemical shifts of the $S_{\gamma\alpha\beta\gamma}$ carbon in the sequence 1-r are calculated on the basis of the γ-shielding effect and the ris model.[5,6,18] The chemical shifts of the same carbon are also calculated with the empirical rules reported by Cheng and Bennett.[7] The results are listed in Table 1. Both calculated results indicate that the peak of the $r_1-S_{\gamma\alpha\beta\gamma}$ carbon should appear at higher frequency by approx. 0.6–1 ppm from the peak of the $m_1-S_{\gamma\alpha\beta\gamma}$ carbon, where m_1 and r_1 imply the stereoregularity indicated by the arrow in Table 1. Thus, the CH_2 peak at 36.5 ppm is assigned to the $r_1-S_{\gamma\alpha\beta\gamma}(13)$ carbon in the sequence 1-r. The peak at 35.5 ppm, which was already assigned to the $r_1-S_{\gamma\alpha\beta\delta}$ carbon in the isolated T-T unit might contain the $m_1-S_{\gamma\alpha\beta\gamma}$ carbon in the sequence 1-r. The peak of the $r_0-S_{\beta\alpha\alpha\gamma}(19)$ carbon is observed at 43–44 ppm, where the peak of the $r_0-S_{\gamma\alpha\alpha\beta}$ carbon in the H-H unit also appears. The peaks of the CH_3

Table 2 ^{13}C NMR Chemical Shift Assignments of Regio-Irregular Polypropylene

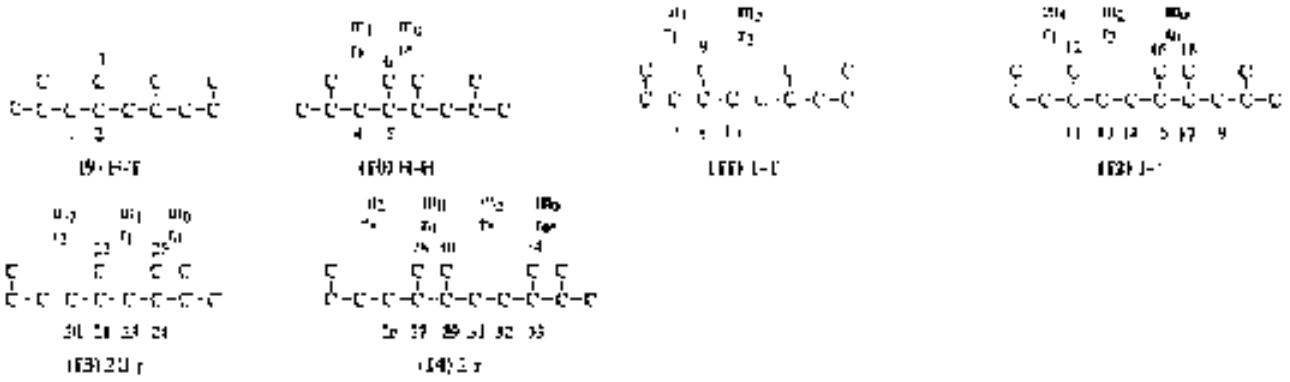

Chemical shift (ppm, from TMS)	H-T (9)	H-H (10)	T-T (11)	1-r (12)	2D-r (13)	3-r (14)
45.7–47.7	$S_{\alpha\alpha\gamma\gamma}(19)$					
43.3–44.1		$r_0S_{\alpha\alpha\gamma\gamma}$ (19)		$r_0S_{\alpha\alpha\gamma\gamma}(19)$	$S_{\alpha\alpha\gamma\gamma}(27)$	
40.6–42.9		m_0-$S_{\alpha\alpha\gamma\gamma}$(19)				
36.8–39.1				r_0-$T_{\delta\gamma\alpha\gamma}$(15)		$T_{\delta\alpha\beta\delta}$(27) and (29); $T_{\delta\gamma\alpha\gamma}$(31)
36.5				$r_1S_{\gamma\alpha\beta\gamma}$(13)		
35.4–35.6		m_0-$T_{\alpha\beta}$(5)	r_1-$S_{\gamma\alpha\beta\delta}$(10)	m_1-$S_{\gamma\alpha\beta\gamma}$(13)	r_1-$S_{\gamma\alpha\beta\delta}$(20) m_0-$T_{\alpha\beta}$(24)	
34.2–34.8		r_0-$T_{\alpha\beta}$(5)	m_1-$S_{\gamma\alpha\beta\delta}$(10)	r_0-$T_{\delta\beta\gamma\delta}$(17)	m_1-$S_{\gamma\alpha\beta\delta}$(20) r_0-$T_{\delta\beta\gamma\delta}$(24)	
33.4						r_0-$S_{\delta\beta\alpha\beta}$(31)
32.6				$r_0S_{\delta\beta\alpha\beta}$(14)		$r_0S_{\delta\beta\alpha\beta}$(26)
31.1–31.3			$T_{\beta\alpha\alpha\gamma}$(18)	$T_{\beta\alpha\alpha\gamma}$(18)	$T_{\beta\alpha\alpha\gamma}$(21)	r_0-$S_{\gamma\alpha\alpha\beta}$(32)?
28.3–28.4	$T_{\alpha\beta}$(3)					
20.1–20.7	$P_{\alpha\beta}$(3)					
20.1–20.5			m_0-$P_{\alpha\beta}$(9) r_0-$P_{\alpha\beta}$(9)	m_0-$P_{\alpha\beta}$(12) r_0-$P_{\alpha\beta}$(13)	m_0-$P_{\alpha\beta}$(22) r_0-$P_{\alpha\beta}$(22)	
16.6–17.1		m_0-$P_{\alpha\beta}$(6)			m_0-$P_{\alpha\beta}$(23)	m_0-$P_{\alpha\beta}$(34)
14.7–15.1		r_0-$P_{\alpha\beta}$(6)		r_0-$P_{\alpha\beta}$(16, r_0-$P_{\alpha\beta}$(18)	r_0-$P_{\alpha\beta}$(23)	r_0-$P_{\alpha\beta}$(28) and (30)

[a] Tentative assignment.

carbons, $r_0-P_{\delta\gamma\alpha\gamma}(16)$ and $r_0-P_{\delta\alpha\beta\delta}(18)$ in the sequence 1-r coincide with the peak of the $r_0-P_{\alpha\beta}$ carbon in the isolated H-H unit. There remain other $^{13}C-^{13}C$ connectivities, and it is therefore necessary to consider the presence of other sequences in this regio-irregular PP.

Most of the peaks of the carbons in the sequence 2U-r occur where two successive inverted H-T units overlap with those in the isolated H-H and T-T units (Figure 1). However, the presence of the $^{13}C-^{13}C$ connectivities among carbons-21, -23 and -24 in the 2D INADEQUATE spectrum indicates strongly the presence of the sequence 2U-r. This is a merit of the 2D INADEQUATE method, because it is difficult to detect a 2U-r sequence in the usual one-dimensional NMR spectrum.

The presence of the sequence 2-r where an inversion occurs, followed by a second inversion, is also considered for the following reasons.

1. The CH_2 peak at 33.4 ppm (Figure 2c) remains unassigned. If there is a sequence 2-r then the appearance of the peaks of carbons-31 and -32 is predicted to be at a slightly higher frequency than the peak of the $r_0-S_{\alpha\beta\alpha\beta}$ carbon (32.6 ppm) in the sequence 1-r (Figure 1).
2. The CH_2 peak at 31.2 ppm (Figure 2c) remains unassigned.
3. The peak intensity of the $T_{\alpha\gamma}$ carbon (36.8–39.1 ppm) in the sequence 1-r is too strong (Figure 2b). The discrepancy is reasonably interpreted with the appearance of the $T_{\alpha\gamma}(27)$, (29), and (33) peaks by assuming the presence of the sequence 2-r.
4. The presence of the sequence 2-r, as well as the other sequences, is confirmed in a regio-irregular poly(1-butene) sample containing many inverted butene units. The catalytic system of polymerization is similar to that used in the case of the regio-irregular PP considered here.

4 ^{13}C NMR ASSIGNMENT OF REGIO-IRREGULAR POLYPROPYLENE

The chemical shifts and final assignments are summarized in Table 2. It should be emphasized here that detailed assignment of the carbon resonances of regio-irregular PP is performed using the 2D INADEQUATE technique, the INEPT technique, and ^{13}C chemical shift calculations. An analytical approach on the basis of the assigned peaks of regio-irregular PP has been developed using the reaction probability model by Cheng.[4]

5 OTHER REGIO-IRREGULAR POLYMERS

A similar approach has also been applied to the ^{13}C NMR assignment of regio-irregular poly(1-butene), PB.[2] Only the spectrum and the final assignments are shown in Figure 5, where the side-chain secondary and primary carbons are designated by s-S and P, respectively, and the main-chain secondary and tertiary carbons by m-S and T, respectively. The sequences containing H-H and/or T-T units in the regio-irregular PB sample are the same as those in the regio-irregular PP sample.

Poly(vinylidene fluoride) (PVF_2), $-(CF_2-CF_2)-$, as normally obtained by free radical polymerization, is not completely regio-regular, resulting in the creation of between 3.5 and 6% defects or regio-irregularities.[19] Figure 6 presents the completely decoupled ^{13}C NMR spectrum of PVF_2 obtained using the triple resonance technique to delete the usual multi-triplet pattern of ^{19}F-coupled ^{13}C resonances.

The ^{13}C chemical shift calculations have been performed on the basis of the β- and γ-shielding effects and the ris model for the sequence containing inverted monomer units as shown in Figure 6. The agreement between the calculated

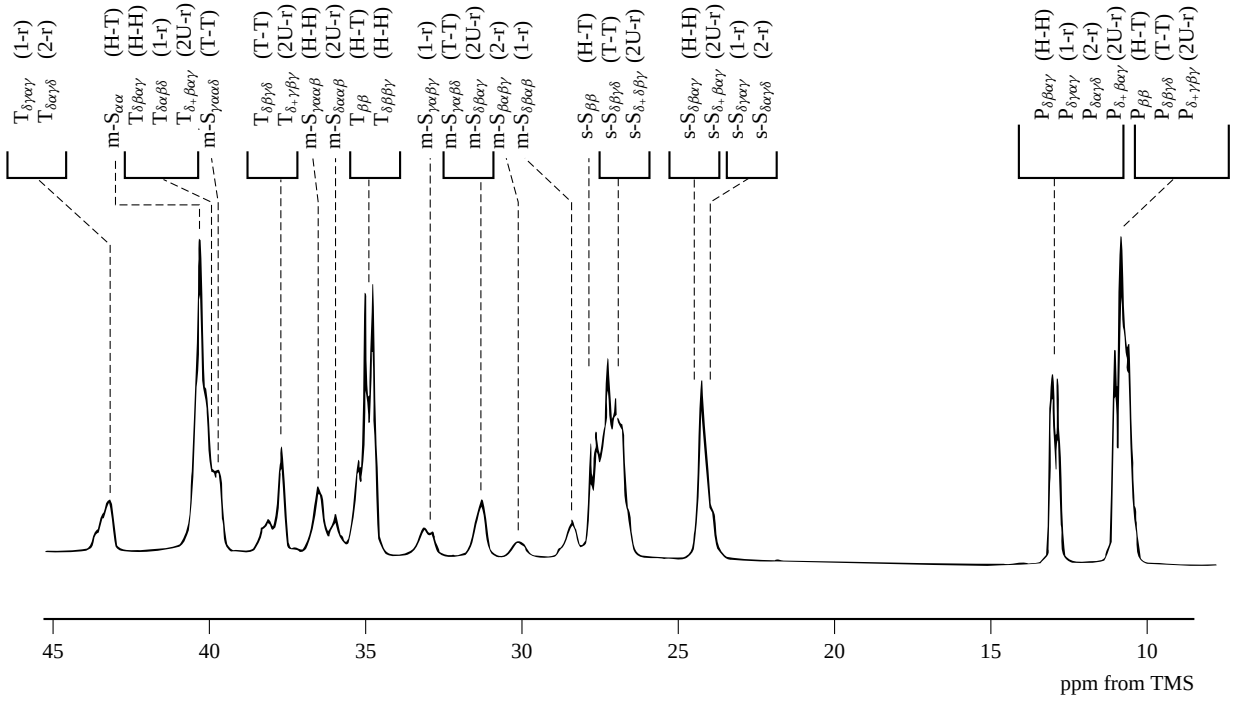

Figure 5 67.8 MHz ^{13}C NMR spectrum of regio-irregular poly(1-butene), together with the assignments

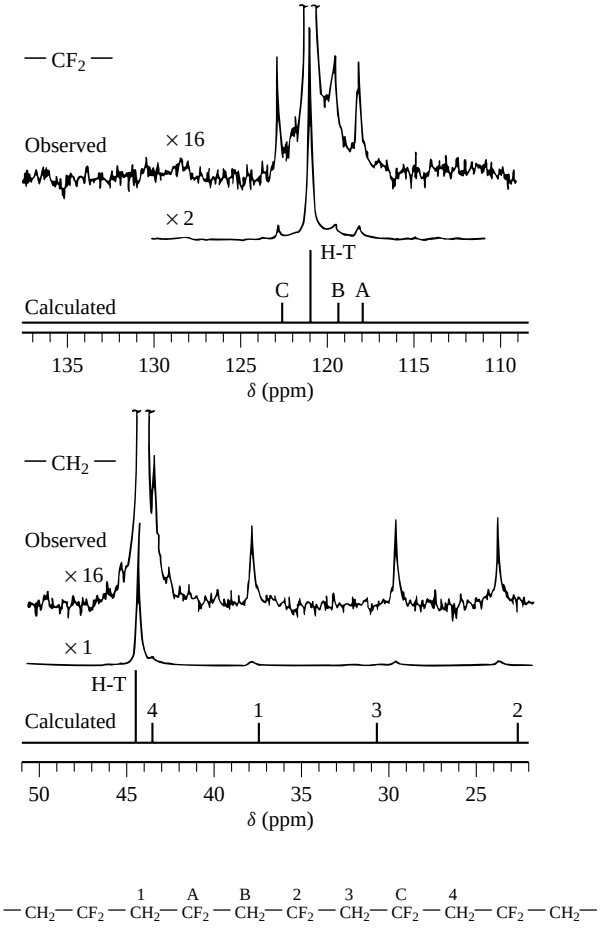

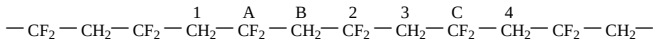

Figure 6 22.5 MHz ^{13}C NMR spectra of poly(vinylidene fluoride). The stick spectra are calculated on the basis of the β- and γ-shielding effects and the ris model for the sequence containing inverted monomer units

(stick spectra) and observed chemical shifts is good, and the assignment is easily performed.[20] The ^{19}F NMR spectrum has also been observed, and the assignment is reported on the basis of similar chemical shift calculations.[21]

Regio-sequence defects in propylene oxide have been analyzed in detail by Tonelli and co-workers[22] using ^{13}C NMR.

6 REFERENCES

1. T. Asakura, N. Nakayama, M. Demura, and A. Asano, *Macromolecules*, 1992, **25**, 4876.
2. T. Asakura and N. Nakayama, *Polymer*, 1992, **33**, 650.
3. T. Asakura, I. Ando, A. Nishioka, Y. Doi, and T. Keii, *Makromol. Chem.* 1977, **178**, 791.
4. H. N. Cheng, *Polym. Bull.*, 1985, **14**, 347.
5. T. Asakura, Y. Nishiyama, and Y. Doi, *Macromolecules*, 1987, **20**, 616.
6. T. Asakura, I. Ando, and A. Nishioka, *Makromol. Chem.*, 1976, **177**, 1493.
7. H. N. Cheng and M. A. Bennett, *Makromol. Chem.*, 1987, **188**, 135.
8. A. Zambelli, and G. Gatti, *Macromolecules*, 1978, **11**, 485.
9. D. M. Grant and E. G. Paul, *J. Am. Chem. Soc.*, 1964, **86**, 2984.
10. L. P. Lindeman and J. Q. Adams, *Anal. Chem.*, 1971, **43**, 1245.
11. C. J. Carman, R. A. Harrington, and C. E. Wilkes, *Macromolecules*, 1977, **10**, 536.
12. Y. Doi, *Macromolecules*, 1979, **12**, 248.
13. W. V. Smith, *J. Polym. Sci., Polym. Phys. Ed.*, 1980, **18**, 1573.
14. F. A. Bovey and L. W. Jelinski, *Chain Structure and Conformation of Macromolecules*, Academic Press, New York, 1982.
15. D. P. Burum, and R. R. Ernst, *J. Magn. Reson.*, 1980, **39**, 163.
16. A. Bax, R. Freeman, and T. Frenkiel, *J. Am. Chem. Soc.*, 1981, **103**, 2102.
17. A. Grassi, A. Zambelli, L. Resconi, E. Albizzati, and R. Mazzocchi, *Macromolecules*, 1988, **21**, 617.
18. W. Ritter, M. Möller, and H.-J. Cantow, *Polym. Bull.*, 1980, **2**, 533.
19. V. M. Görlitz, R. Minke, W. Trautvetter, and G. Weisgerber, *Angew. Makromol. Chem.*, 1973, **29/30**, 137.
20. A. E. Tonelli, F. C. Schilling, and R. E. Cais, *Macromolecules*, 1981, **14**, 560.
21. A. E. Tonelli, F. C. Schilling, and R. E. Cais, *Macromolecules*, 1982, **15**, 849.
22. A. E. Tonelli, *NMR Spectroscopy and Polymer Microstructure*, VCH Publishers, Weinheim, 1989.

Biographical Sketch

Tetsuo Asakura. *b* 1949. B.S., 1972, Tokyo Science University, Japan; Ph.D., 1977, Tokyo Institute of Technology. Introduced to NMR by A. Nishioka. Faculty of Polymer Science, Tokyo Institute of Technology, 1973–present. Approx. 130 publications. Research interests include structural analyses of polymers such as polyolefins and proteins, including silk, with solution and solid state NMR.

Polymers: Relaxation and Dynamics of Synthetic Polymers in Solution

Frank Heatley

University of Manchester, Manchester, UK

1	Introduction	1
2	Basic Aspects of Relaxation Studies of Polymers	1
3	General Features of Polymer Relaxation	2
4	Quantitative Analysis of Relaxation Times	3
5	Related Articles	6
6	References	6

1 INTRODUCTION

This article is concerned with the application of high-resolution NMR relaxation techniques in studying the mechanisms and rates of motions of synthetic polymers in dilute solutions. Such measurements provide data on the physical state of dissolved polymers, on polymer–solvent interactions, and on the intramolecular factors which control chain dynamics.

Perhaps the first qualitative observation on this subject was made by Bovey et al.[1] in their pioneering work on the use of high-resolution NMR to determine the structure of polymers, where they found that high-resolution spectra were obtained from solutions of polymers of such high molecular weight that the rate of overall tumbling of the molecule as a whole would be far too slow to average dipole–dipole coupling. Their conclusion, that magnetic relaxation was in fact largely controlled by rapid small-scale segmental motions, has formed the basis of subsequent approaches to the interpretation of relaxation measurements of random coil polymers in dilute solution. Exceptions to this general principle are found in three situations: (i) when the polymer is capable of adopting a regular relatively rigid conformation, e.g. the helical conformation of synthetic polypeptides; (ii) when the polymer may associate into a colloidal structure, e.g. the micellar structure adopted by block copolymers in selective solvents; and (iii) solutions which are sufficiently concentrated that chain entanglements hinder the complete averaging of dipole–dipole coupling. This article first surveys the general features of relaxation of single chains in solution, then describes the theoretical approaches which have been developed to interpret relaxation times quantitatively in terms of chain motions. These topics have been covered in considerable detail previously in numerous books and reviews.[2–7] A useful annual survey appears in the Nuclear Magnetic Resonance volume of the Specialist Periodical Reports published by the Royal Society of Chemistry, London, UK.

2 BASIC ASPECTS OF RELAXATION STUDIES OF POLYMERS

The vast majority of studies of the type under discussion here have used either ^{1}H or natural abundance ^{13}C NMR. In polymers, the relaxation of protons and protonated saturated ^{13}C nuclei is determined essentially by intramolecular dipole–dipole (DD) interactions with neighboring ^{1}H nuclei. The spin–rotation (SR) mechanism and relaxation by dissolved oxygen are usually insignificant, though the chemical shift anisotropy (CSA) mechanism is important for unsaturated ^{13}C nuclei at magnetic fields above ca. 5 T. Carbon-13 NMR has two advantages which outweigh its greatly reduced sensitivity compared to ^{1}H NMR. First, the resolution of small structural differences in ^{13}C spectra is better so that the motions of different chain fragments can be studied more closely. Second, relaxation of a protonated ^{13}C nucleus is determined almost entirely by DD interaction with the attached proton(s). Since the C–H bond length may be estimated with reasonable accuracy, the precise determination of correlation times is thereby facilitated. In contrast, ^{1}H NMR spectra are frequently poorly resolved, while ^{1}H relaxation is controlled by DD interactions with numerous geminal, vicinal, or more distant neighbors whose separations depend on perhaps poorly characterized chain configuration and conformation.

The ultimate objective of dynamic studies is to determine the correlation function, $G(\tau)$, for some time-dependent function which depends on the relaxation mechanism (see ***Brownian Motion and Correlation Times***). For DD relaxation, the functions are second-order harmonic functions of the Euler angles describing the orientation of internuclear vectors. NMR relaxation times depend on $G(\tau)$ indirectly through the spectral density function, $J(\omega)$, which is related to $G(\tau)$ via

$$J(\omega) = \int_{-\infty}^{+\infty} G(\tau) \exp(\mathrm{i}\omega\tau)\, \mathrm{d}\tau \qquad (1)$$

In a given magnetic field, relaxation times depend on values of $J(\omega)$ at a limited number of frequencies. For relaxation of the ^{13}C nucleus in a $^{13}CH_n$ group by DD interaction with the attached protons under ^{1}H-decoupled conditions, $G(\tau)$ is the autocorrelation function for the C–H bond, and T_{1C}, T_{2C}, and the ^{13}C-{^{1}H} nuclear Overhauser enhancement factor, η, are given by

$$\frac{1}{T_{1C}} = Q[J(\omega_H - \omega_C) + 3J(\omega_C) + 6J(\omega_H + \omega_C)] \qquad (2)$$

$$\frac{1}{T_{2C}} = \frac{Q}{2}[4J(0) + J(\omega_H - \omega_C) + 3J(\omega_C) + 6J(\omega_H) + 6J(\omega_H + \omega_C)] \qquad (3)$$

$$\eta = \left(\frac{\gamma_H}{\gamma_C}\right)\left[\frac{6J(\omega_H + \omega_C) - J(\omega_H - \omega_C)}{J(\omega_H - \omega_C) + 3J(\omega_C) + 6J(\omega_H + \omega_C)}\right] \qquad (4)$$

where

$$Q = \frac{1}{20}\left(\frac{\mu_0}{4\pi}\right)^2 \frac{n\gamma_H^2\gamma_C^2h^2}{4\pi^2 r_{CH}^6} \qquad (5)$$

r_{CH} is the C–H bond length and other symbols have their standard meanings. [Note that in these equations, the functions

$J(\omega)$ are defined in terms of a normalized correlation function, i.e., $G(0) = 1$.]

For ^{1}H relaxation, except for a few very simple chains, there are usually several resolvable groups of protons. Longitudinal relaxation is governed by the set of coupled equations

$$\frac{dM_{zi}}{dt} = -\rho_i(M_{zi} - M_{zi}^0) - \sum_{j\neq i}\sigma_{ij}(M_{zj} - M_{zj}^0) \quad (6)$$

where M_{zi} is the longitudinal magnetization of spin i, the superscript 0 denotes equilibrium values, and the relaxation coefficients are given by

$$\rho_i = \sum_{j\neq i} C_{ij}[J(\omega_i - \omega_j) + 3J(\omega_i) + 6J(\omega_i + \omega_j)] \quad (7)$$

$$\sigma_{ij} = C_{ij}[6J(\omega_i + \omega_j) - J(\omega_i - \omega_j)] \quad (8)$$

$$C_{ij} = \frac{1}{20}\left(\frac{\mu_0}{4\pi}\right)^2 \frac{\gamma_H^4 h^2}{4\pi^2 r_{ij}^6} \quad (9)$$

(See ***Relaxation Processes in Coupled-Spin Systems***). For nonselective pulses under extreme narrowing $[(\omega_i + \omega_j)^2\tau_c^2 \ll 1]$, each spin relaxes at a characteristic rate with a time constant given approximately by

$$\frac{1}{T_{1i}} = \rho_i + \sum_{j\neq i}\sigma_{ij} \quad (10)$$

However for slow motion $[(\omega_i + \omega_j)^2\tau_c^2 \gg 1]$, rapid cross relaxation (spin diffusion) arising from the $J(\omega_i - \omega_j)$ terms maintains a uniform spin temperature, and all spins relax at the same population-weighted average rate. The cross-relaxation rate σ_{ij} gives access to the spectral density at very low frequencies of the order of differences in ^{1}H resonance frequencies, and can be measured using selective perturbation methods.[4] It also gives rise to ^{1}H–^{1}H NOEs, much used in the study of the structure of biological macromolecules but only rarely applied to synthetic polymers. Recently NOEs have been used to study the conformation of polyesters[8] and the miscibility of poly(methyl acrylate) and poly(vinyl acetate) in solution.[9]

Because NMR relaxation depends on the motion of a single bond or short range internuclear vector, relaxation measurements are in principle capable of giving detailed insight into the nature of the polymer motions at the functional group level.

For isotropic rotation, $G(\tau)$ is exponential:

$$G(\tau) = \exp(-|\tau|/\tau_c) \quad (11)$$

and $J(\omega)$ becomes

$$J(\omega) = \frac{2\tau_c}{1 + \omega^2\tau_c^2} \quad (12)$$

where τ_c is the correlation time. However in a complex dynamic system such as a random coil in solution, it is not to be expected, nor do experimental data show, that $G(\tau)$ is such a simple function. In order to gain insight into the form of $G(\tau)$, and hence the motional mechanism, it is necessary to measure several relaxation parameters at different resonance frequencies. For ^{13}C measurements, the relaxation data set normally comprises T_1 and ^{13}C-{^{1}H} NOE measurements, though ^{13}C T_2 data are also accessible. For ^{1}H, the data set normally includes T_1 and T_2. In analyzing relaxation data in terms of a dynamic model, it is a great advantage to have T_2 data available, since T_2 depends on the spectral density at zero frequency whereas T_1 and ^{13}C-{^{1}H} NOEs depend on the spectral density only at frequencies on the order of the resonance frequencies. In ^{1}H NMR, data which effectively replicate T_2 by sampling the spectral density at very low frequencies on the order of differences in ^{1}H resonance frequencies can be obtained[4] by measuring T_1 of one type of proton while another is kept saturated by a decoupling frequency, or by monitoring the transient NOE following selective inversion of one group of ^{1}H nuclei. Measurements of $T_{1\rho}$, which also monitor the spectral density at kHz frequencies, have found limited application to polymers in solution.[10]

3 GENERAL FEATURES OF POLYMER RELAXATION

3.1 Effect of Chain Length

Early work[2,5] showed that for random coils in solution, relaxation times as a function of chain length attained an asymptotic value at a fairly low critical chain length on the order of 100 units, corresponding to a molar mass on the order of 10^4. This behavior was attributed to control of relaxation above the critical length by local segmental motions independent of chain length. Below the critical length, overall molecular tumbling is sufficiently rapid to contribute to a shortening of the effective correlation time. The few exceptions to this general principle are observed for polymers which adopt a well-defined persistent conformation, such as the polypeptide α-helix. For example, measurements on poly(γ-benzyl-L-glutamate) in helix-supporting solvents show that relaxation is determined to a considerable extent by slow end-over-end and axial rotational diffusion.[11]

3.2 Effect of Concentration

For random coil polymers, numerous studies[2,5] have found that relaxation times are generally insensitive to concentration up to quite high values on the order of 5–10 wt.% depending on the chain chemical structure and molar mass, even though the bulk viscosity may change by several orders of magnitude. This behavior is further evidence for the control of relaxation by local segmental motions, whose rates are determined by a 'microviscosity' of the chain and its immediate solvent environment. At higher concentrations, the relaxation times show the effects of increasing motional hindrance, the changes in T_2 appearing at a somewhat lower concentration than those in T_1 because of the greater sensitivity of T_2 to slow long-range motions. For polystyrene in $CDCl_3$,[12] the concentration at which T_1 and T_2 become concentration-dependent depends on molar mass, and correlates with the concentration at which the chains begin to overlap.

At high concentrations, chain motion becomes restricted by physical entanglements of such severity that DD coupling is no longer averaged to zero, and strong line broadening is encountered. The spectrum exhibits a 'pseudosolid' character which may be detected in several ways, for example from the characteristic shape of the FID,[13] or from the line-narrowing effect of sample rotation.[14]

3.3 Effect of Solvent

The chemical structure of the solvent affects the polymer motions in two ways,[2,5] first dynamically through its effect on the environment 'microviscosity', and second thermodynamically through its effect on the chain conformation. In thermodynamically good solvents of comparable chemical structure, there is a reasonable consistent relationship between relaxation times and bulk solvent viscosity, as has been shown by studies of ^{13}C relaxation in poly(oxyethylene)[15] and poly(isoprene)[16] solutions in solvents covering a wide range of viscosities. The effect of solvent viscosity on the rate of segmental motions has usually been approached through Kramers' theory[17] for the rate of passage over an energy barrier E_a between two potential wells in a frictional medium. In the high-friction limit, the rate constant is given by

$$k = \frac{(\gamma_a \gamma_b)^{1/2}}{2\pi\zeta} \exp(-E_a/RT) \tag{13}$$

where γ_a and γ_b are the curvature coefficients of the potential energy at the minimum and maximum and ζ is the medium friction coefficient. Assuming that the correlation time for segmental motion, τ_c, is inversely proportional to k, the dependence of τ_c on the solvent viscosity η can then be written as

$$\tau_c = A\eta \exp(E_a/RT) \tag{14}$$

where A is a constant for a particular polymer. A plot of log τ_c against log η should be linear with a slope of unity. For poly(isoprene),[16] such a graph is linear, but the slope is only 0.41. A similar plot of data of poly(oxyethylene)[15b] made by the writer gives a slope of 0.66. Thus it appears that equation (14) is better written as

$$\tau_c = A\eta^{\alpha} \exp(E_a/RT) \tag{15}$$

where α is an empirical exponent less than unity. Equation (15) has been rationalized[16] in terms of the modification of Kramers's theory by Grote and Hynes[18] in which the frequency dependence of the friction constant is taken into account. From equation (15), the Arrhenius activation energy for τ_c is equal to $E_a + \alpha E_\eta$ where E_η is the activation energy for the viscosity.

3.4 Effect of Chain Structure

In order to evaluate the effect of chemical structure on chain mobility, it is necessary to use a standard basis for the comparison. The most reliable basis is the value of nT_{1C} for protonated backbone ^{13}C nuclei measured at the same resonance frequency, concentration, and temperature in good solvents of similar viscosity. Unfortunately, such consistency in conditions is not a common feature of reported studies; however, a representative selection of values of nT_{1C} for common chain structures is given in Table 1, together with apparent correlation times obtained using equations (2) and (12).

In general, it is found that correlation times for random coil chains at ambient temperature or above lie in the vicinity of the T_1 minimum or shorter, as indicated by the facts that substantial ^{13}C-{^1H} NOEs are observed and that T_1 increases with increasing temperature. The two exceptions in Table 1 are poly(4-vinyl-*N*-octylpyridinium bromide) and poly(but-1-ene sulfone). The most mobile chains are those containing a heteroatom [e.g. poly(oxyethylene)] or double bonds [e.g. poly(butadiene)], consistent with the lower barriers to rotation about CH_2-O and allylic bonds (ca. 4 kJ mol^{-1}) compared with CH_2-CH_2 bonds (ca. 16 kJ mol^{-1}). As expected, the presence of substituents decreases chain mobility, the effect increasing with the size of the substituent. However, it is perhaps surprising that two geminal substituents are not significantly more effective in hindering motion than is a single substituent [cf. poly(propylene) with poly(isobutene) or polystyrene with poly(methyl methacrylate)]. The explanation, supported by conformational calculations,[19] appears to be that the introduction of a second group into the monosubstituted chains engenders such severe steric interactions that the energies of all conformations, including transition states, are raised, so leaving the barrier unaffected.

Two comparisons of pairs of polymers with similar structures but quite different relaxation times exemplify the insight into polymer conformation provided by relaxation measurements. The lower mobility of poly(oxymethylene) (POM) compared with poly(oxyethylene) (POE) has been explained[20] by the fact that POE has several well-populated conformations, whereas POM is substantially restricted to a single conformation, thus inhibiting segmental motions. The large difference in correlation time between the isomeric pair poly(but-1-ene sulfone) and poly(but-2-ene sulfone) has also been explained[21] in conformational energy terms, the former predominantly occupying a *gauche* conformation with strong ordering between adjacent SO_2 dipoles and the latter predominantly occupying a *trans* conformation with independent SO_2 groups.

4 QUANTITATIVE ANALYSIS OF RELAXATION TIMES

4.1 Cross Correlation

In quantitative interpretations of relaxation in polymers, the simple Bloembergen, Purcell, and Pound approach[22] has normally been used, rather than the formally correct density matrix theory[23] (see also ***Relaxation Processes: Cross Correlation and Interference Terms*** and ***Coupled Spin Relaxation in Polymers***). An early example of a relaxation phenomenon for which the sophisticated theory is required is the observation of nonexponential T_1 relaxation of the CH_3 protons in poly(2,6-dimethyl-1,4-phenylene oxide)[24] which arises from a cross-correlation effect associated with very rapid internal CH_3 rotation. Recently advances in both theory and experimental techniques have been applied to the study of

Table 1 Representative ^{13}C Relaxation Times and Apparent Isotropic Correlation Times for Backbone Carbons[a]

Polymer	Solvent	Temp. (°C)	Conc. (wt. %)	nT_{1C} (s)	τ_c(app.) (ns)
Ethylene	ODCB[b]	100	25	2.70	0.018
	ODCB	30[c]	25	1.24	0.04
Propylene	ODCB	100	25	1.13	0.044
	ODCB	30[d]	25	0.39	0.13
But-1-ene	CCl_3CHCl_2	100	10	0.34[e]	0.14
Isobutene	CCl_4	45	5	0.37	0.13
Styrene	Toluene-d_8	30	15	0.10	0.49
4-Vinyl-*N*-octylpyrinidium bromide	CD_3OD	27	25	0.069	42
Methyl methacrylate					
isotactic	$CDCl_3$	38	10	0.13	0.39
syndiotactic	$CDCl_3$	38	10	0.08	0.62
L-Lysine	D_2O (pD = 7)	30		0.12	0.42
cis-Butadiene	$CDCl_3$	54	20	3.00	0.016
trans-Butadiene	$CDCl_3$	54	20	2.38	0.021
Oxymethylene	HFIP[f]	30	3	0.60	0.082
Oxyethylene	C_6D_6	30	5	2.80	0.018
But-1-ene sulfone	$CDCl_3$	40	25	0.090	23
But-2-ene sulfone	$CDCl_3$	30	11	0.112	0.47
2,6-Dimethyl-1,4-phenylene oxide	$CDCl_3$	30	10	0.093	0.57
Bisphenol A polycarbonate	$CDCl_3$	40	10	0.092	0.051

[a]All measurements at 25.14 MHz except as noted. Full source data can be found in Heatley.[5]
[b]*o*-Dichlorobenzene.
[c]Extrapolated from high-temperature data using E_a = 10.5 kJ mol^{-1}.
[d]Extrapolated from high-temperature data using E_a = 14.3 kJ mol^{-1}.
[e]22.6 MHz.
[f]Hexafluoro-2-propanol.

^{13}C relaxation under ^1H coupled conditions in poly(ethers).[25] These experiments involve studying relaxation following a variety of selective and nonselective excitations of ^1H and ^{13}C transitions, and permit the determination of spectral densities for both auto- and cross-correlation functions of C−H and H−H interaction vectors, thus giving a detailed insight into the nature of chain dynamics. It is anticipated that this approach will repay further attention.

4.2 Correlation Functions for Segmental Motions

Initial investigations rapidly revealed that relaxation data for polymers could not be interpreted quantitatively using the isotropic rotation model. Even a simple measurement of the value of T_1 at its minimum at a single frequency was sufficient to show this deficiency, which is not unexpected in view of the multitude of conformational transitions available to a macromolecule. The first attempt[26] to rationalize data on ^{13}C T_1 and NOE values represented the segmental motions by an empirical log χ^2 distribution of exponential correlation functions, emulating the methodology which had been used for some time in dielectric and viscoelastic relaxation studies. However, while successful in allowing an interpretation of all the experimental data by a single form for the correlation function, this approach gives little insight into the nature of the segmental motions in terms of specific conformational processes.

The first general analytical expression for the NMR segmental correlation function at a molecular level was developed by Valeur et al.[27] using a model based on concerted motions on a diamond lattice. Only three- or four-bond segmental motions were considered, such that the remainder of the chain was unaffected. Although the model possessed realistic elements in that the discrete jumps through realistic angles were allowed, no account was taken of possible differences in conformational probabilities, and the solution of the discrete differential equations for the bond orientational time-dependence was obtained using a continuum equation. This model, denoted the VJGM model, considered coupled motions for an infinite chain and resulted in a correlation function

$$G(\tau) = \exp(-|\tau|/\theta)\exp(|\tau|/\rho)\,\mathrm{erfc}(|\tau|/\rho)^{1/2} \qquad (16)$$

where θ and ρ are correlation times characterizing the three- and four-bond motions and erfc represents the error function complement. The corresponding spectral density is

$$J(\omega) = \frac{2\theta\rho(\theta-\rho)}{(\theta-\rho)^2+(\omega\theta\rho)^2}\left\{\left(\frac{\theta}{2\rho}\right)^{1/2}\left[\frac{(1+\omega^2\theta^2)^{1/2}+1}{1+\omega^2\theta^2}\right]^{1/2} + \left(\frac{\theta}{2\rho}\right)^{1/2}\left(\frac{\omega\theta\rho}{\theta-\rho}\right)\left[\frac{(1+\omega^2\theta^2)^{1/2}-1}{1+\omega^2\theta^2}\right]^{1/2}-1\right\} \qquad (17)$$

It was later recognized that although this equation resulted from a specific molecular model of conformational transitions, it represented a more general description. The terms in ρ represent cooperative processes leading to diffusion of orientation along the chain, while the term in θ also represents reorientations not necessarily linked to transitions of neighboring bonds.

The VJGM model was subsequently modified by two groups. First, Jones and Stockmayer[28] suggested that the three-bond motions be restricted to a finite segment of $2m-1$ bonds on the basis that in a real chain conformational correlation

would not be strictly obeyed (the JS model). The correlation function was obtained as a discrete sum of exponentials

$$G(\tau) = \sum_{k=1}^{s} B_k \exp(-|\tau|/\tau_k) \tag{18}$$

with a corresponding spectral density

$$J(\omega) = \sum_{k=1}^{s} \frac{2B_k\tau_k}{1+\omega^2\tau_k^2} \tag{19}$$

where $s = (m + 1)/2$ and the coefficients B_k and τ_k (tabulated in Jones and Stockmayer[28]) depend on m.

Further modifications to the VJGM model were made by Yaris and co-workers.[29] They generalized the VJGM master differential equation with the explicit inclusion of a diffusion term and, recognizing that the solution of the diffusion equation is an integral of the wavevector of a plane wave, imposed both lower and upper limits on the allowed wavelengths, i.e. on the minimum and maximum size of the mobile segment.

The VJGM and JS models have been used successfully to interpret a wide range of experimental measurements of ^{1}H and ^{13}C relaxation parameters in a number of polymers of different backbone structure; the results have been summarized by the author.[4] Figure 1 shows the simulation of ^{1}H T_1 and T_2 data for syndiotactic poly(methyl methacrylate) using the VJGM model. In general, it is found that in the VJGM model, the ratio ρ/θ lies in the range 0.1–1 and is independent of temperature. Cooperative processes dominate the chain motions. In the JS model, it is found that the values of the coupling length $2m + 1$ typically lie in the range 5–13.

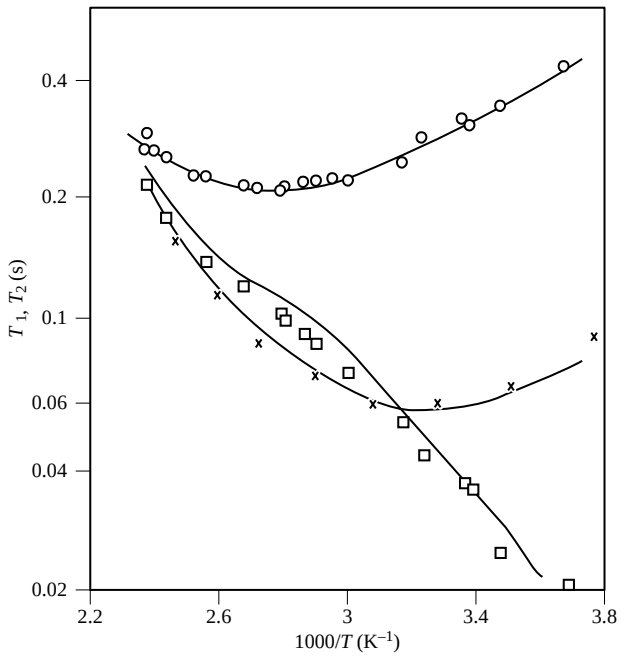

Figure 1 Variation of the backbone CH_2 ^{1}H relaxation times with temperature for a 1% solution of syndiotactic poly(methyl methacrylate) in toluene-d_8: ○ T_1 at 300 MHz; □ T_2 at 300 MHz; × T_1 at 80 MHz. The lines are simulations using the VJGM model, equation [13], with ρ/θ = 0.7. (Reproduced by permission of Pergamon Press from Heatley[5])

In recent years, increases in computing power have allowed more realistic investigations of polymer dynamics using two approaches, first molecular dynamics simulations,[30] and second time-dependent rotational isomeric state (RIS) statistical theory.[31] The dynamics simulation technique generally involves numerical solution of the Langevin equation of motion of a chain of atoms moving in a viscous medium subject to forces from bond rotations, bond stretching, and bond angle bending, as well as a random Brownian force. A significant result is that rotations about one bond only are not as hindered as might be expected by the fact that such a motion necessarily requires the long polymer 'tails' to move through the medium. Evidently the movement of the tails is initially accommodated by elastic distortion of neighboring bond torsion angles. The simulations also show that the correlation function depends on the orientation of the vector relative to the chain backbone,[30a] indicating that the correlation function for ^{1}H relaxation may be different to that for ^{13}C relaxation. In heterogeneous chains, e.g. polyisoprene,[30c] C–H bonds in different groups are found to have different correlation functions, consistent with the experimental observation of different values of nT_{1C}. It has been shown[30a,32] that numerically simulated correlation functions are well represented by the following analytic expression (the HWH model)

$$G(\tau) = \exp(-|\tau|/\tau_0)\exp(-|\tau|/\tau_1)\, I_0(|\tau|/\tau_1) \tag{20}$$

where I_0 is the Bessel function, and τ_0 and τ_1 are correlation times representing single-bond and cooperative transitions, respectively. The spectral density is

$$J(\omega) = 2(\alpha^2+\beta^2)^{-1/4}\cos\left[\frac{1}{2}\arctan\left(\frac{\beta}{\alpha}\right)\right] \tag{21}$$

where $\alpha = \tau_0^{-2} + 2(\tau_0\tau_1)^{-1} - \omega^2$ and $\beta = 2\omega(\tau_0^{-1} + \tau_1^{-1})$.

Although the various expressions for the correlation function given above differ markedly in mathematical form, it has been found in practice that with suitable choice of parameters they coincide closely in shape,[4] and experimental results can often be satisfactorily simulated by different models.[33]

The RIS theory expresses both conformational and transition probabilities by matrices whose order is determined by the degree of conformational and dynamic interdependence of the chain bonds. The general solution leads[34] to a correlation function expressed as a discrete distribution of exponential functions. The method is capable of embodying the characteristic properties of a particular chain, and calculations have been carried out for several chains whose conformations are well-understood, including polyethylene[35] and poly(oxyethylene).[36] For polyethylene,[35] it was found that the results from RIS calculations could be well-represented by the JS or HWH functions. For poly(oxyethylene),[36] the RIS theory was combined with Kramers's theory[17] of the medium effect on transition rates [equation (11)] to calculate a priori the effect of solvent viscosity on ^{13}C correlation times: the results were in good agreement with experiment.

4.3 Other Polymer Motions

4.3.1 Librations

In polymers known to have a relatively persistent conformation, such as the fixed conformation of biological

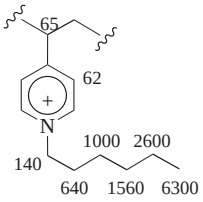

Figure 2 Values of nT_{1C} for ^{13}C nuclei in poly(*N*-hexyl-4-pyridinium bromide) at 25.14 MHz in CD_3OD at 26 °C. (Data from Radiotis et al.[39])

macromolecules, or the helical structure of regular polypeptides in some solvents, it has been found[37] that in order to understand relaxation parameters quantitatively, it is necessary to include a high-frequency limited-amplitude libration arising from vibrations and torsional oscillations. This motion has also been found necessary to understand relaxation in molten synthetic polymers,[38] and it is also manifest in dynamics simulations.[30c] The motion is much more rapid than segmental motions, and falls into the extreme narrowing regime. It is usually modeled[38] by the 'diffusion-in-a-cone' model in which the internuclear vector diffuses freely within a cone of semi-angle ϕ, while the axis of the cone undergoes reorientation according to the dynamics of the backbone. The appropriate correlation function is

$$G(\tau) = A\exp(-|\tau|/\tau_v) + (1 - A)G_b(\tau) \qquad (22)$$

where τ_v is the libration correlation time and $G_b(\tau)$ is the segmental correlation function given by one of the expressions above. The quantity A expresses the loss of correlation by the libration and is related to ϕ by

$$A = 1 - \left[\frac{\cos\phi - \cos^3\phi}{2(1 - \cos\phi)}\right]^2 \qquad (23)$$

Recent work, for example a study of multiple-frequency ^{13}C relaxation data for poly(vinyl chloride) in solution,[39] has shown that the combination of equations (20) and (23) generally gives the best fit to experimental data. Typically, $\phi \approx 30^\circ$ and $\tau_v \approx 10^{-12}$ s.

4.4 Side-Chain Motions

Generally, nuclei in side chains have shorter average correlation times than backbone nuclei because internal rotation of the side group is commensurate with or faster than segmental motions.[2–5] As an example, Figure 2 illustrates the positional dependence of ^{13}C T_1 values in poly(*N*-hexyl-4-pyridinium bromide) in CD_3OD.[40] Quantitatively, multiple internal rotations have been modeled by stochastic, independent, rotational diffusion about successive bonds,[41] though for aromatic rings a model of restricted rotation has proved more appropriate.[42]

5 RELATED ARTICLES

Brownian Motion and Correlation Times; Coupled Spin Relaxation in Polymers; Micellar Solutions and Microemulsions; Molecular Motions: T_1 Frequency Dispersion in Biological Systems; Nuclear Overhauser Effect; Protein Dynamics from NMR Relaxation; Relaxation: An Introduction; Relaxation Processes in Coupled-Spin Systems; Relaxation Processes: Cross Correlation and Interference Terms.

6 REFERENCES

1. F. A. Bovey, G. V. D. Tiers, and G. Filipovich, *J. Polym. Sci.*, 1959, **28**, 73.
2. F. Heatley, *Prog. NMR Spectrosc.*, 1979, **13**, 47.
3. F. A. Bovey and L. W. Jelinski, *J. Phys. Chem.*, 1985, **89**, 571.
4. F. Heatley, *Annu. Rep. NMR Spectrosc.*, 1986, **17**, 179.
5. F. Heatley, in *Comprehensive Polymer Science*, eds. C. Booth and C. Price, Pergamon Press, Oxford, UK, 1989, Vol. 1, Chap. 18
6. J. L. Koenig, *Spectroscopy of Polymers*, American Chemical Society, Washington, DC, 1992, Chap. 10
7. O. W. Howarth, in *NMR Spectroscopy of Polymers*, ed. R. N. Ibbett, Chapman & Hall, London, 1993, Chap. 4
8. S. Spera, R. Po', and L. Abis, *Polymer*, 1993, **34**, 3380.
9. K. Takegoshi, Y. Ohya, and K. Hikichi, *Polym. J.*, 1993, **25**, 59.
10. A. A. Jones and F. P. Shea, *J. Polym. Sci., Polym. Phys. Ed.*, 1982, **20**, 681.
11. A. Allerhand and E. Oldfield, *Biochemistry*, 1973, **12**, 3428; P. M. Budd, F. Heatley, T. J. Holton, and C. Price, *J. Chem. Soc., Faraday Trans. 1*, 1981, **77**, 759.
12. P. Stilbs and M. E. Moseley, *Polymer*, 1981, **22**, 321.
13. J. P. Cohen-Addad and R. Dupeyre, *Polymer*, 1983, **24**, 400.
14. J. P. Cohen-Addad and J. P. Faure, *J. Chem. Phys.*, 1974, **61**, 1571; J. P. Cohen-Addad and C. Roby, *J. Chem. Phys.*, 1975, **63**, 3095.
15. (a) K. J. Liu and J. E. Anderson, *Macromolecules*, 1970, **3**, 163; (b) M.-C. Lang, F. Lauprêtre, C. Noêl, and L. Monnerie, *J. Chem. Soc., Faraday Trans. 1*, 1979, **75**, 349.
16. S. Glowinkowski, D. J. Gisser, and M. D. Ediger, *Macromolecules*, 1990, **23**, 3520.
17. H. A. Kramers, *Physica*, 1940, **7**, 284.
18. R. F. Grote and J. T. Hynes, *J. Chem. Phys.*, 1980, **73**, 2715.
19. R. H. Boyd and S. M. Breitling, *Macromolecules*, 1972, **5**, 1; P. R. Sundararajan and P. J. Flory, *J. Am. Chem. Soc.*, 1974, **96**, 5025.
20. F. Gény and L. Monnerie, *J. Polym. Sci., Polym. Phys. Ed.*, 1979, **17**, 131, 147.
21. A. H. Fawcett, S. H. Fee, and L. Waring, *Polymer*, 1983, **24**, 1571.
22. N. Bloembergen, E. M. Purcell, and R. V. Pound, *Phys. Rev.*, 1948, **73**, 679.
23. A. G. Redfield, *Adv. Magn. Reson.*, 1965, **1**, 1.
24. R. P. Lubianez and A. A. Jones, *J. Magn. Reson.*, 1980, **38**, 331.
25. M. M. Fuson, D. J. Anderson, F. Liu, and D. M. Grant, *Macromolecules*, 1991, **24**, 2594; M. M. Fuson and J. B. Miller, *ibid.*, 1993, **26**, 3218.
26. J. Schaefer, *Macromolecules*, 1973, **6**, 882.
27. B. Valeur, J. P. Jarry, F. Gény, and L. Monnerie, *J. Polym. Sci., Polym. Phys. Ed.*, 1975, **13**, 667, 2251; B. Valeur, L. Monnerie, and J. P. Jarry, *ibid.*, 1975, **13**, 675.
28. A. A. Jones and W. H. Stockmayer, *J. Polym. Sci., Polym. Phys. Ed.*, 1977, **15**, 847.
29. J. T. Bendler and R. Yaris, *Macromolecules*, 1978, **11**, 650 (correction: F. Heatley and J. T. Bendler, *Polymer*, 1979, **20**,

1578); J. Skolnick and R. Yaris, *Macromolecules*, 1982, **15**, 1041 (correction: *ibid.*, 1983, **16**, 491).

30. (a) T. A. Weber and E. Helfand, *J. Phys. Chem.*, 1983, **87**, 2881; (b) I. Zúñiga, I. Bahar, R. Dodge, and W. L. Mattice, *J. Chem. Phys.*, 1991, **95**, 5348; (c) D. B. Adolf and M. D. Ediger, *Macromolecules*, 1991, **24**, 5834.
31. (a) R. L. Jernigan, in *Dielectric Properties of Polymers*, ed. F. E. Karasz, Plenum Press, New York, 1972, p. 99; (b) I. Bahar and B. Erman, *Macromolecules*, 1987, **20**, 1368.
32. C. K. Hall and E. Helfand, *J. Chem. Phys.*, 1982, **77**, 3275.
33. D. J. Gisser, S. Glowinkowski, and M. D. Ediger, *Macromolecules*, 1991, **24**, 4270.
34. I. Bahar, B. Erman, and L. Monnerie, *Polym. Commun.*, 1988, **29**, 349.
35. I. Bahar, B. Erman, and L. Monnerie, *Macromolecules*, 1989, **22**, 431.
36. I. Bahar, B. Erman, and L. Monnerie, *Macromolecules*, 1989, **22**, 2396.
37. O. W. Howarth, *J. Chem. Soc., Faraday Trans. 2*, 1979, **75**, 863.
38. R. Dejean de la Batie, F. Lauprêtre, and L. Monnerie, *Macromolecules*, 1988, **21**, 2045.
39. T. Radiotis, G. R. Brown, and P. Dais, *Macromolecules*, 1993, **26**, 1445.
40. T. Yasukawa, D. Ghesquiere, and C. Chachaty, *Chem. Phys. Lett.*, 1977, **45**, 279.
41. R. E. London and J. Avitabile, *J. Chem. Phys.*, 1976, **65**, 2443.
42. A. Spyros and P. Dais, *Macromolecules*, 1992, **25**, 1062.

Biographical Sketch

Frank Heatley. *b* 1943. B.Sc., 1964, Ph.D., 1967, chemistry, University of Manchester, UK. Postdoctoral Fellowship at Bell Telephone Laboratories, NJ (with Frank A. Bovey), 1967–69. Lecturer and senior lecturer in Chemistry, University of Manchester, 1970–present. Approx. 110 publications. Current interests include relaxation studies of block copolymer colloids and the application of high-resolution solid state NMR to polymers.

Polymers Under Mechanical Tension

Wiebren S. Veeman

Gerhard-Mercator-Universität, Duisburg, Germany

&

Angelika Schmidt

DSM Research, Geleen, The Netherlands

1 Introduction 1
2 A Simple Introduction to the Deformation Theory of Solid Polymers and Consequences for NMR 1
3 Spectroscopical Studies of Deformed Polymer Materials 2
4 NMR Imaging of Polymers Under Tension 9
5 Conclusions 10
6 Related Articles in Volumes 1–8 10
7 References 10

1 INTRODUCTION

For many engineering applications of polymeric materials it is important to know how the material behaves under elastic or plastic deformation. Since the mechanical properties of such a material are a consequence of the chemical composition and the physical microstructure of the material, it should be possible in principle to predict the mechanical properties from the microscopic structure. However, especially for heterogeneous polymeric materials (copolymers, polymer blends and polymer composites) a complete prediction of the behavior under mechanical stress, starting from the microscopic structure, is still too difficult. Therefore experimental techniques are necessary, which allow the detection of changes in the microstructure when the material is mechanically deformed.

In a polymeric material under stress the polymer chains can react to the stress by changing their orientation, their conformation, their mobility or even by breaking. Although many techniques exist which can probe microscopic changes in a polymer material, the advantage of NMR to study materials under stress is that NMR is able to detect the effect of stress on the structure of a material on a molecular level. On the other hand, the combination of the NMR technique, where usually the sample is located in a strong magnetic field, and the devices to mechanically deform materials, in general do not form great combinations. Therefore a great number of NMR publications deal with the study of polymeric materials, which have *prior* to the NMR experiment undergone some kind of deformation by a mechanical force. The NMR is performed on samples in the relaxed state, which may be quite different from the state of the material under tension.

Also to keep the size of this paper within certain limits, we only review here those NMR experiments on solid or gel-like materials where the material is under mechanical tension *during the NMR experiment*. We therefore also exclude the many NMR experiments on polymer melts or polymer solutions. In other words, we limit ourselves to NMR experiments where the probe head contains a device to keep the sample under stress.

This restriction implies that in most of these experiments the information has to come from a wide-line NMR spectrum, usually either from a wide-line proton spectrum or from a deuterium spectrum. Exceptions are investigations on elastomers, where the high polymer chain mobility provides high-resolution spectra for spectroscopic studies or allows standard imaging NMR techniques, and experiments where the sample under stress is contained in a magic angle rotor so that high-resolution ^{13}C CPMAS techniques can be used. For this reason most experiments which we will summarize, are experiments on elastomers.

After a short introduction to the macroscopic theory of polymer deformation, the paper is divided in two sections: NMR spectroscopy and NMR imaging. The spectroscopical section is subdivided with respect to the nucleus investigated: proton, deuterium or carbon-13.

2 A SIMPLE INTRODUCTION TO THE DEFORMATION THEORY OF SOLID POLYMERS AND CONSEQUENCES FOR NMR

In this section we want to give a short introduction to the main notions of deformation theory and summarize those macroscopic aspects that are important to understand the results discussed here. For an introduction to the mechanical properties of solid polymers, see for instance the textbook by Ward and Hadley.[1]

For an ideally elastic rectangular or cylindrical solid rod with a cross-section area A and length ℓ, subjected to a force F in the length direction of the rod, the strain ε is proportional to the stress σ:

$$\sigma = \mathrm{E}\varepsilon \quad \text{(Hooke's law)} \tag{1}$$

Here $\sigma = \mathrm{F/A}$, $\varepsilon = \Delta\ell/\ell$ and E is the elasticity modulus (or Young's modulus).

Although for small strains many polymeric materials behave elastically, in general E is dependent on ε. Typical stress-strain curves for different types of polymers are shown in Figure 1. Also for most polymers E shows a characteristic temperature dependence, see e.g., Figure 2 for an amorphous polymer. At temperatures $T < T_\mathrm{g}$ (T_g is the glass-transition temperature) the material of Figure 2 is in a glassy rigid state with elastic behavior. Above T_g to a first approximation the material behaves rubbery and at temperatures above T_m (T_m = melting temperature) viscous flow is observed. A more detailed view at the temperature regime $T_\mathrm{g} < T < T_\mathrm{m}$ reveals that the material does not show ideally elastic behavior but also has viscous properties. The polymer is in a visco-elastic state, which is in between the ideal Hookian behavior (stress proportional to strain) and the ideal Newtonian flow of a liquid (shear stress proportional to the shear rate). For visco-elastic polymers the stress and strain curves are time dependent, which

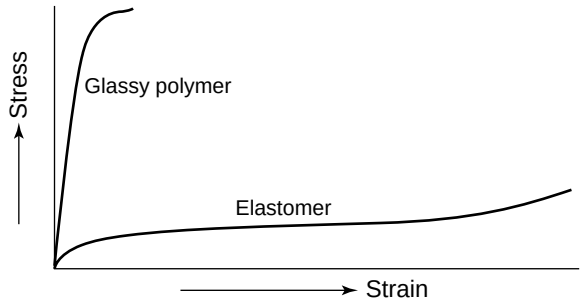

Figure 1 Schematic stress-strain curves for glassy and rubbery polymers (elastomers). For small strain values the slope of the curves represent the elastic modulus E

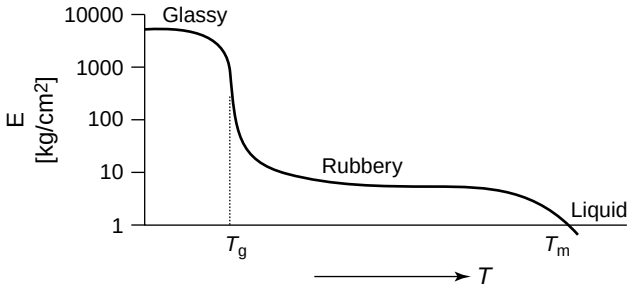

Figure 2 The temperature dependence of the elastic modulus E for a typical non-cross-linked polymer. Below T_g the polymer is glassy with a high E (see also Figure 1), between T_g and T_m the polymer shows visco-elastic behavior and above T_m the polymer is viscous

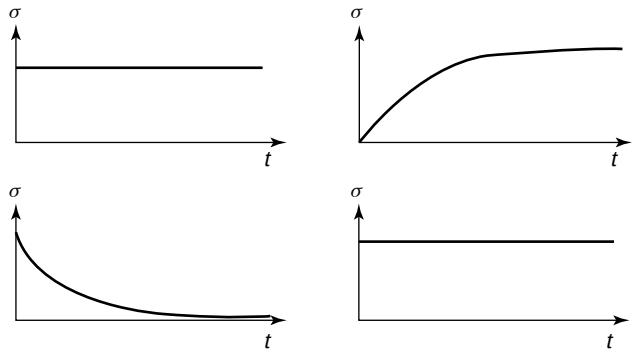

Figure 3 A schematic representation of visco-elastic behavior: (a) at a sudden increase of the stress at $t = 0$ to a constant value, the elongation ε follows with a time lag (creep). An ideally elastic solid would show an immediate constant elongation. (b) After a stepwise increase of the elongation ε, the stress decreases in time (relaxation). An ideally elastic solid would show a constant stress value

results in creep and relaxation phenomena, as schematically shown in Figure 3.

The complex response of a polymer to mechanical stress will result in changes of some NMR parameter. A complete description of the effect of stress or strain on NMR parameters is a formidable theoretical problem. To realize the difficulty of this problem let us consider the following example. We will see later that for spectroscopic studies, as well as in NMR imaging experiments, the NMR parameter that is often used to monitor the strain or stress in a material, is the proton T_2. The proton T_2 in a not completely rigid material depends on anisotropic molecular motions, for instance in a cross-linked polymer the hindered rotations and translations of those segments of the polymer chain between the cross-linked joints.

By applying stress to a heterogeneous polymeric material a spatially dependent deformation with tensorial character develops. To predict the effect of this deformation on the proton T_2, it would be necessary to calculate how the local anisotropic molecular motions are affected by the anisotropic deformation and then how the changed molecular motions influence the proton dipolar interactions. The result of the interplay between all these tensorial interactions is finally monitored by the *scalar* parameter T_2. It will be clear that in practice a theoretical description has to be simplified.

The intermediate visco-elastic state between the low temperature glass state and the high temperature molten state is a rubbery phase. In this state a small stress causes a very large extension. When a material in the rubbery state is extended, the restoring force is mainly due to the change in entropy and not, like for steel, due to a change in the internal energy. It can be shown from thermodynamic arguments that for an incompressible cross-linked rubber material at constant temperature the tensile stress σ is given by:[1]

$$\sigma = \frac{\rho \mathrm{RT}}{\mathrm{M}} \left(\lambda - \frac{1}{\lambda^2} \right) \tag{2}$$

where $\lambda = \ell + \Delta\ell/\ell = 1 + \varepsilon$, M is the mean molecular mass between cross-links and ρ the density of the polymer. Equation (2) reduces to equation (1) for small strains for which $\lambda \approx 1$.

For an incompressible solid a small elongation by $\Delta\ell$ reduces the cross-section area from A to A/λ. When the stress is referred to the original cross-section area A in the absence of stress ('engineering' or 'nominal' stress), equation 2 changes to:

$$\sigma' = \frac{\rho \mathrm{RT}}{\mathrm{M}} \left(\lambda^2 - \frac{1}{\lambda} \right) \tag{3}$$

For polymers in the rubbery phase usually the chains are very mobile. This can be easily experimentally observed when the chains contain proton or deuteron spins. At a temperature below T_g the proton NMR spectrum will be very broad due to the dipolar interactions between the spins. In the case of deuterium spins the spectrum will show the well-known Pake-doublet line shape of deuterium in a non-ordered rigid solid. For temperatures above T_g the chain mobility can be so high, that the dipolar or quadrupolar interaction is averaged to a very small value, resulting in spectra with a single narrow line.

3 SPECTROSCOPICAL STUDIES OF DEFORMED POLYMER MATERIALS

3.1 The Effect of Mechanical Tension Studied by Proton NMR

In the proton NMR studies of deformation in polymeric materials the attention is focussed on the transverse magnetization decay, as measured by the free induction decay (FID) or by a spin-echo experiment. It is assumed that the proton

transverse relaxation is fully governed by the proton dipole-dipole interactions, possibly reduced by the rotational motions of the chain segments.

Different general theories exist that describe the transverse relaxation in the presence of molecular motions. The usefulness of these theories can be classified with the help of a motional correlation time τ_c, which is here very loosely defined as the characteristic time lap during which the rotational or translational coordinates of a molecular segment have changed so much by random molecular motions that there is no resemblance to the coordinates of the initial state anymore. This motional correlation time varies strongly when we go from a rigid solid, where $\Delta\omega_{rl}\tau_c \gg 1$ ($\tau_c \gg 10^{-5}$ s, $\Delta\omega_{rl}$ is the rigid-lattice proton line width), to a liquid of small molecules, where $\omega_0\tau_c \ll 1$ ($\tau_c \ll 10^{-9}$ s, ω_0 is the resonance frequency).

The Bloch-Wangness-Redfield theory[2] is valid in the range between complete motional averaging ($\omega_{rl}\tau_c \ll 1$) and beyond extreme motional averaging ($\omega_0\tau_c \ll 1$). In this range the transverse magnetization decays exponentially with a characteristic time T_2:

$$M(t) = M(0)\exp\left[-\frac{t}{T_2}\right] \tag{4}$$

representing a Lorentzian line shape in the frequency domain.

For incomplete motional averaging, when the condition $\omega_{rl}\tau_c \ll 1$ is not fulfilled, the Anderson-Weiss[3] and the Kubo-Tomita[4] theories can be applied. Although these two theories have a different theoretical basis, they both lead to the same expression for the transverse relaxation function:

$$M(t) = M(0)\exp\left[-(\Delta\omega_{rl})^2\int_0^t (t-\tau)\,g(\tau)\,d\tau\right] \tag{5}$$

where $g(\tau)$ is a normalized correlation function, $g(0) = 1$.

When an exponential correlation function is assumed:

$$g(\tau) = \exp\left[-\frac{\tau}{\tau_c}\right] \tag{6}$$

Equation 5 reduces to:

$$M(t) = M(0)\exp\left[-(\Delta\omega_{rl})^2\tau_c^2\left\{\exp\left[-\frac{t}{\tau_c}\right] + \frac{t}{\tau_c} - 1\right\}\right] \tag{7}$$

In the case where the correlation time $\tau_c \gg t$, t being the length of the FID (no motions), we find the rigid lattice limit by expanding $\exp[-t/\tau_c]$ in a power series:

$$M(t) = M(0)\exp\left[-\frac{1}{2}(\Delta\omega_{rl})^2 t^2\right] \tag{8}$$

This Gaussian decay function represents a Gaussian solid state NMR line.

In the motional averaging limit $\Delta\omega_{rl}\,\tau_c \ll 1$ the integral in equation (5) can be written as:[5]

$$\int_0^t (t-\tau)g(\tau)\,d\tau \approx t\int_0^\infty g(\tau)\,d\tau = \tau_c\, t \tag{9}$$

which yields a Lorentzian line shape:

$$M(t) = M(0)\exp\left[-(\Delta\omega_{rl})^2\tau_c t\right] \tag{10}$$

with the reduced line width

$$\frac{1}{T_2} = (\Delta\omega_{rl}\tau_c)\Delta\omega_{rl} \tag{11}$$

Most polymer materials behave like a network in which the chains are cross-linked, either by covalent bonds, as in vulcanised rubber, or by physical cross-links like entanglements or crystalline domains. With respect to the general relaxation theories summarized above, such network polymers constitute a special class of materials, since they can reflect both solid-like and liquid-like behavior at the same time. For a cross-linked polymer below T_g the FID is that of a strongly dipolar coupled rigid proton spin system (equation 8). Above T_g those parts of the chains relatively far from the junctions can execute fast, almost isotropic motions (liquid-like behavior), while the motion of those parts of the chains near cross-links is severely hindered (solid-like behavior). In addition some chains may exist (dangling ends) which are joined to the network by one end only and it can be expected that these chains are even more free to move than the segments between cross-links.

The transverse magnetization decay function $M(t)$ of such a network reflects the mobility of all parts of those chains and therefore it can be expected that the general relaxation theories discussed above are not able to accurately describe the transverse magnetization decay. Indeed, several special transverse relaxation functions have been used for polymers.

In the work of Simon et al.[6] a Bloch type exponential relaxation decay (equation 4) was assumed for the dangling ends and an Anderson-Weiss/Kubo-Tomita type decay (equation 7) for the chains between two cross-links.

A completely different approach was taken by Sotta et al.[7] who realized that for a polymer network transverse relaxation is not only caused by irreversible ('homogeneous broadening') processes due to chain mobility, as we discussed above, but that due to the constraints by the chain junctions the local dipolar interactions are not averaged to zero. This causes a spread in resonance frequencies ('inhomogeneous broadening'). High enough above T_g these authors assume that the decay induced by the chain motions is so much slower than the decay due to the residual local dipolar field that only the heterogeneous contribution has to be considered. From a statistical analysis they found for polymer chains consisting of N segments, each segment carrying one isolated proton pair with dipolar coupling strength Δ:

$$M(t) = \mathrm{Re}\left[\frac{M_0}{\left(1+\frac{1}{3}ikN^{-1}\Delta t\right)\sqrt{1-\frac{2}{3}ikN^{-1}\Delta t}}\right] \tag{12}$$

where k is a geometrical factor.[8]

After summarizing some different expressions for the decay of transverse magnetization we review the results of typical proton NMR experiments on polymers under tension.

Nishi and Chikaraishi[9] investigated the transverse magnetization decay of cross-linked natural and synthetic rubber samples as a function of cross-link density for various elongations. By fitting their results with equations (4) and (11) they found that T_2 depends on the elongation factor λ mainly via the dependence of the correlation time τ_c on λ, the dependence

of the rigid-lattice line width on stretching was small. The λ-dependence of T_2 could be fitted with an empirical relation of the form:

$$T_2(c, \lambda - 1) = T_{2,0}(c)\ \exp[-kc(\lambda - 1)] \tag{13}$$

where c is the crosslink density, $T_{2,0}$ the T_2 in the absence of deformation and k a constant (1.1×10^3 cc/mol). This shows that mechanical tension on a polymeric material can influence the chain mobility. Here τ_c increased with tension, probably due to the fact that the stretching of the rubber induced crystallization, as is apparent from the fact that at $\lambda > 5$ a second component in the FID appears with a much shorter T_2. In one of the next subsections we will consider this strain-induced crystallization in more detail.

Fukumori et al.[10] studied a styrene-butadiene-styrene (SBS) blockpolymer. Here the rigid styrene blocks act as physical crosslinks or 'hard' segments in the rubbery polybutadiene matrix. Also here a dependence of T_2 on λ as shown in equation (13) was found.

Another approach to the dependence of the transverse magnetization decay on stretching was followed by Cohen-Addad and Huchot.[11] They found for vulcanized polybutadiene of different chain lengths and cross-link density c that the initial slope s of the proton magnetization decay at time $t = 0$ is given by:

$$s = s_0 + \left(\lambda^2 - \frac{1}{\lambda}\right) \left|3\cos^2(\theta) - 1\right| \kappa(c) \tag{14}$$

where $\kappa(c)$ is a function of the cross-link density c and s_0 the slope observed in the absence of any deformation. The angle θ is the angle between the stretching direction and the magnetic field. Figure 4 shows how well the experimental results on vulcanised polybutadiene fit equation (14). Equation (14) shows the same dependence on the stretching variable λ as the stress referenced to the original cross-section area, equation (3).

Equations (13) and (14), however, are not completely identical, which becomes clear when the initial slope of the free induction decay in the motional averaging limit is related to T_2 according to equation (4):

$$s = -\frac{M_0}{T_2} \tag{15}$$

With equation (15) we can rewrite equation (13) in a form which can be directly compared to equation (14):

$$s = s_0 \exp[kc(\lambda - 1)] \tag{16}$$

Although equations (14) and (16) are not identical, for certain values of k, c and $\kappa(c)$ and a limited range of λ-values their λ-dependences are similar.

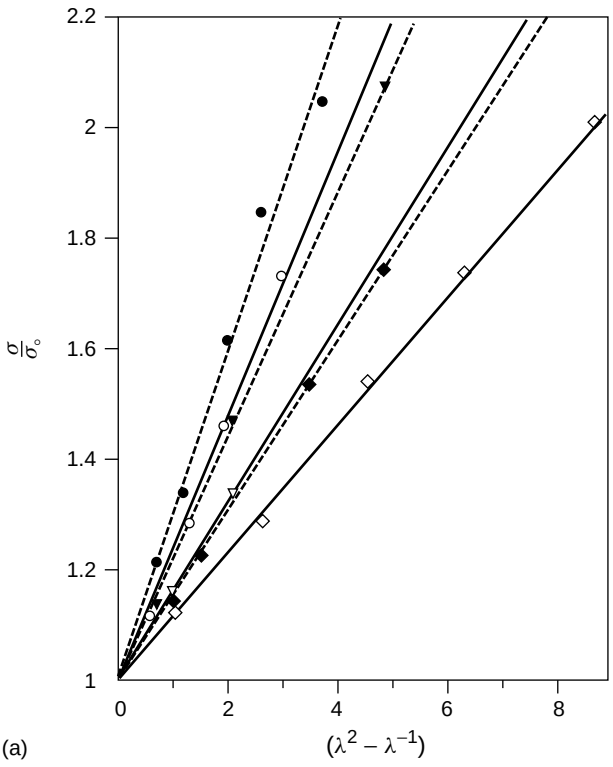

Figure 4 (a) The stress ratio σ/σ_0 of vulcanised polybutadiene as a function of the stretching parameter $\lambda^2 - 1/\lambda$ for vulcanized polybutadiene for different molecular weights and/or sulfur concentration c: open and filled circles $\overline{M}_n = 2.5 \times 10^5$, $c = 1\%$; open and filled triangles $\overline{M}_n = 3.6 \times 10^5$, $c = 0.5\%$; open and filled diamonds $\overline{M}_n = 2.5 \times 10^5$, $c = 0.5\%$. Open symbols correspond to $\theta = \pi/2$, while for closed symbols $\theta = 0$, where θ is the angle between the stretching direction and the magnetic field. (Reproduced with permission from Cohen-Addad and Huchot[11])

Cohen-Addad and Huchot[11] conclude further from their experiments on several vulcanised systems that the elasticity modulus E is proportional to the factor $\kappa(c)$ from equation (14). Therefore the slope of the curves in Figure 4a is proportional to E.

3.2 Deuterium NMR

^{2}H is by far the most popular NMR nucleus to study the effect of deformation on the molecular orientation and motions in polymer systems. The reason is that the characteristic quadrupole broadened deuterium NMR spectrum for randomly oriented rigid polymer chains ('Pake doublet') can be strongly and characteristically affected by molecular orientation and/or molecular motions, effects which can both be induced by mechanical deformation. In addition, the simulation of a motionally averaged spectrum or the spectrum of partly oriented samples is relatively easy, so that order parameters and/or motional parameters can be determined from the experimental spectra.

3.2.1 The Effect of Deformation on Molecular Motion

The first example of the effect of in-situ stress on NMR parameters was published by Hansen et al.[12] who investigated

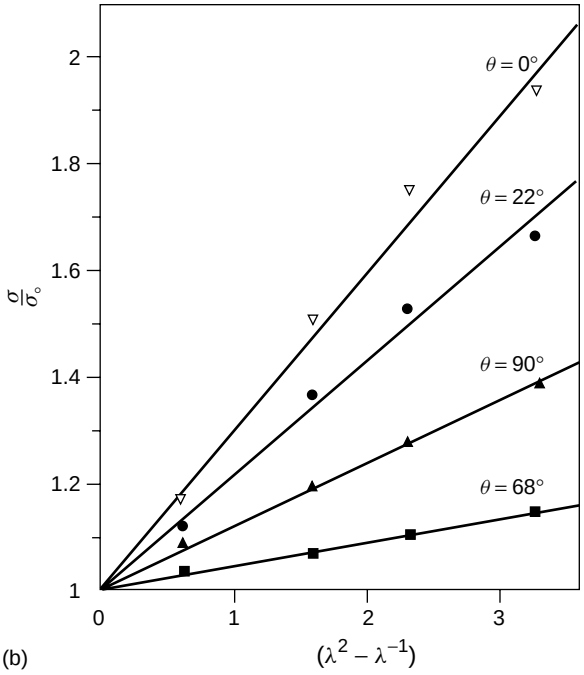

Figure 4 (b) The stress ratio σ/σ_0 of vulcanised polybutadiene as a function of the stretching parameter $\lambda^2 - 1/\lambda$ for vulcanized polybutadiene for different angles between the stretching direction and the magnetic field. The molecular weight $\overline{M}_n = 2.5 \times 10^5$. (Reproduced with permission from Cohen-Addad and Huchot[11])

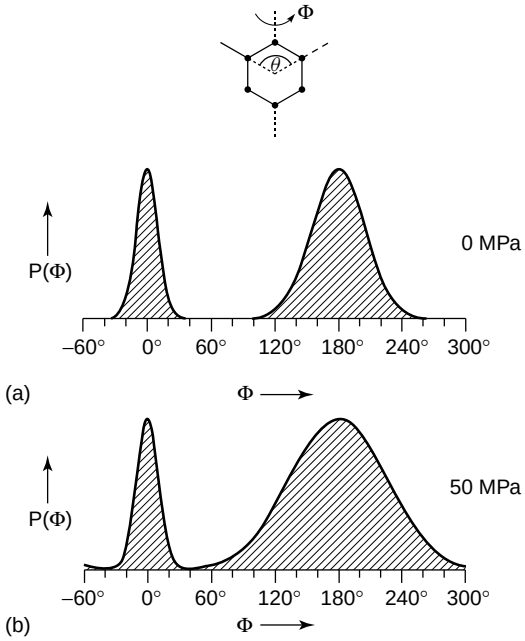

Figure 5 Distribution of the flip angles of the phenylene ring in polycarbonate for the unstretched and the stretched sample. (Reproduced with permission from Hansen et al.[12])

phenylene ring flips in polycarbonate as a function of the applied stress. A pneumatically driven stretching apparatus,[13] good for forces up to 1500 N, could be triggered by the spectrometer software to synchronize rf pulsing and the application of stress. The effect of the applied stress was monitored by ^{2}H two-dimensional exchange spectroscopy[14] and echo experiments. In polycarbonate the phenyl rings can make 180° flips. By simulation of the experimental 2D-exchange spectra it was found that prior to a flip the ring executes small angle rotations and also that the ring flip angle is not always exactly 180°. The main results of Hansen et al. are reproduced in Figure 5. This figure shows the remarkable result that the width of the distribution of the phenylene ring small angle rotations before a flip is independent of the applied stress, while the width of the distribution of the flip angles itself, with a mean value of 180°, increases with stress. Apparently, the application of stress loosens the angular restriction for the ring flip, allowing larger deviations from 180° than in the absence of an applied stress. At the same time echo experiments have shown that the distribution of correlation times of this motion is not affected by the stress. Here stretching does not increase the motional correlation time, as in one of the examples of section IIIa, but stretching does enhance deviations from the average flip angle 180°.

Schaefer et al.[15] also conclude that stress enhances the phenylene ring flip motion in poly(*p*-phenyleneterephthalamide) fibers. These authors lead a suspended bundle of fibers through a 5 mm saddle-coil in the probe head. The bundle can be loaded with 31 steel (!) plates to a total weight of 300 kg, which causes an elongation of ca. 1% at 55% of the breaking stress.

Another example of the use of deuterium NMR to investigate the chain mobility in polymers under stress was reported by Loo et al.[16] Here polyamide-6 rods were deuterated by immersing the rods in D_2O for several weeks. By H-D exchange between D_2O and nylon-6 it is assumed that only the polyamide N-H groups in the amorphous domains were deuterated. The experiments show that at 70 °C, which is near T_g, the mobility of the chains in the amorphous regions is increased by stretching. At room temperature such an effect is not observed.

3.2.2 The Effect of Deformation on Orientation

Two approaches have been followed to study the effect of mechanical deformation on the polymer chain orientation, the deuterium atoms are part of small solvent molecules which are absorbed by the polymer system (swelling) or the polymer chains itself are (partly) deuterated. In the first case, in general the solvent molecules are highly mobile and the quadrupolar spectrum does not show a splitting, but is broadened by T_2 effects as described in section IIIa. When the polymer material is stretched, the rotational diffusion of these molecules becomes non-isotropic and this results in a quadrupolar splitting $\Delta\nu$.[17]

$$\Delta\nu = \frac{3e^2qQ}{2h}\left(\langle P_2(\cos\theta)\rangle + \frac{1}{2}\eta\langle\sin^2\theta\cos 2\phi\rangle\right) P_2(\cos\Omega) \quad (17)$$

where:

$\frac{e^2qQ}{h}$ = quadrupolar coupling constant
η = quadrupolar asymmetry parameter, usually $\eta \approx 0$
θ, ϕ = the polar angles between the C–D bond and the stretching direction

Ω = angle between the stretching direction and the magnetic field and,
$\langle\rangle$ = averaging over all angles.

Equation 17 shows that the resulting quadrupole splitting is proportional to the average order parameter S if $\eta = 0$:

$$S = \langle P_2(\cos\theta)\rangle = \tfrac{1}{2}\langle(3\cos^2\theta - 1)\rangle \tag{18}$$

Theoretically[18] it has been shown that for ideally elastic polymer networks S is proportional to $E(\lambda^2 - 1/\lambda)$, where E is the modulus. Many authors[19,20] indeed confirmed experimentally that the residual quadrupolar splitting $\Delta\nu$, induced by uniaxial stretching of an elastic polymer network depends on the stretching constant λ as:

$$\Delta\nu \propto \left(\lambda^2 - \frac{1}{\lambda}\right) \tag{19}$$

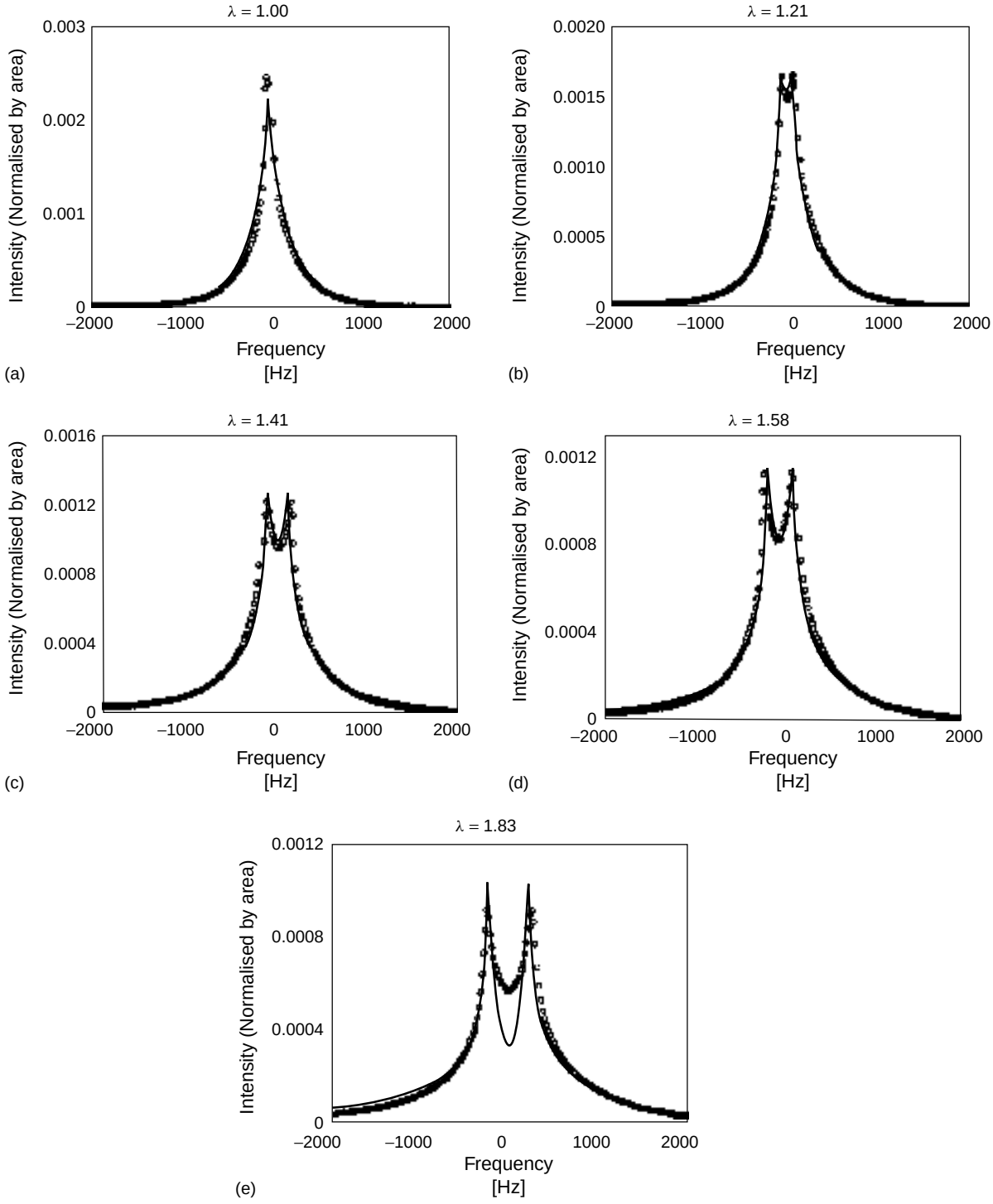

Figure 6 The deuterium spectra of cross-linked polybutadiene as a function of the elongation factor λ. (Reproduced with permission from Ries et al.[20])

where the stretching variable is the same as in equation (3) (see Figure 6).

When a network is deformed, the spatial positions of the network junctions are changed and one might expect that the anisotropy caused by these displacements is the cause of the induced quadrupole splitting. However, Brereton[21] theoretically studied ideal networks in which the chains between junctions are free to move and do not interact with each other. He found that the displacement of the chain junctions in the network by the mechanical deformation was not sufficient to obtain a quadrupolar splitting. A splitting of the line shape of deuterons in the chains of the network is induced by an uniaxial deformation only when interactions between the chain segments in the network are introduced. This result was confirmed by Warner et al.[22]

When the deformation of a polymer network is probed by an absorbed solvent molecule, an important question here is in how far the solvent molecule and the network have the same degree of orientation. This problem was tackled by Jacobi et al.[23] who showed for cross-linked deuterated polybutadiene, swollen to different degrees by free deuterated butadiene oligomers, that for low degrees of swelling the orientation of the solvent molecules and of the network as a function of uniaxial strain are the same. For larger fractions of solvent molecules, however, the orientation of the oligomers is considerably lower than that of the network. Two explanations have been offered for the experimental observation that solvent molecules with the *same* chemical composition as the network molecules follow the orientation of the deformed network. The first explanation assumes an interaction like between the molecules in a nematic liquid crystal, the second suggests that competition for space causes an orientational coupling due to entropic interactions.[24,25] Experiments by McLoughlin et al.[19] seem to confirm the latter explanation.

An example of the use of small deuterated molecules in deformed samples forms the work by Loo et al.[26] Here polyamide-6 is investigated by letting phenol-d5 from the solvent CCl_4 diffuse into the amorphous domains of the polymer. Since it is known that phenol plasticizes polyamide-6 it is the combination of polyamide-6 with phenol (the investigated polyamide contained 40% wt phenol) that is been investigated, not the polymer itself. The deuterium quadrupole spectrum of phenol-d5 was recorded as a function of an elongation up to twice the original length, see Figure 7. By deconvoluting the spectra reproduced in Figure 7 with two Lorentzians, the authors found that the quadrupole splitting, as defined by equation (18), of the phenol deuterons in the amorphous domains of polyamide-6 approximately increased linearly with the strain, while the line widths showed an S-shaped relation with strain. This difference in behavior of the quadrupole splitting and the deuterium line width as a function of strain can be due to the difference in the local property that is probed by the quadrupole interaction. For the quadrupole splitting the average orientation of the probe molecule is important, for the line width the motional correlation time is decisive.

The near proportionality between the quadrupole splitting $\Delta\nu$ and the strain in this work clearly deviates from the quadratic dependence shown in other elastomer networks (equation 19), although the crystalline domains in the polyamide-6 material can be considered as the physical junctions in a network of plasticized amorphous chains.

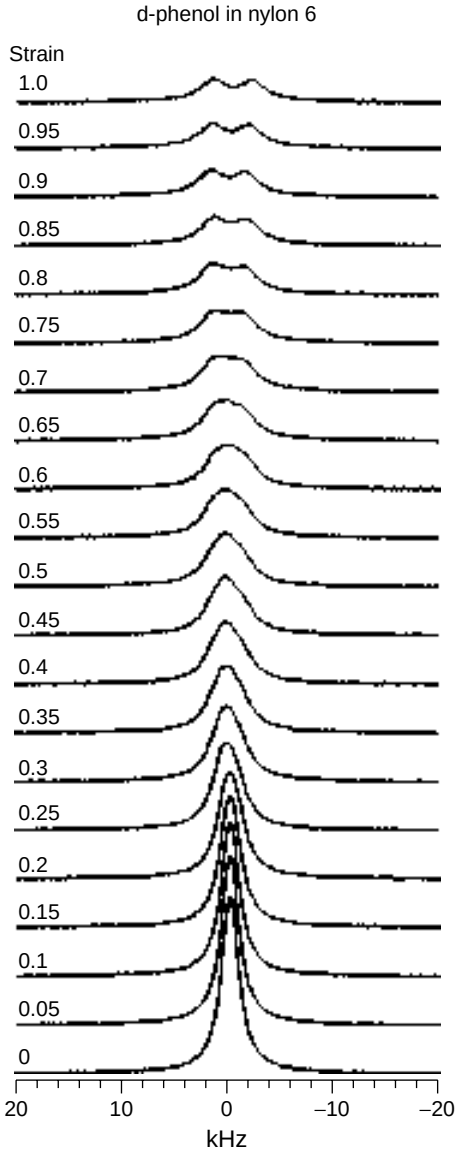

Figure 7 The deuterium spectra of phenol-d5 in polyamide-6 rods undergoing an elongation with a rate of 0.25 mm/min. (Reproduced with permission from Loo et al.[26])

In the investigations discussed above, the polymer networks were considered to be homogeneous in the way that all chains were cross-linked on both ends. In more recent work the magnetization decays are decomposed into two fractions. One fraction results from chains that are cross-linked at both ends, intercrosslinked chains, the other fraction from dangling ends. It was assumed that the dangling ends (and possibly some free chains) can reorient isotropically and their magnetization decay is represented by an exponential decay with relaxation time T_2. The decay of the intercrosslinked chains is represented by a relation like shown in equation (7).

Using such a decomposition, Menge et al.[27] related for partly deuterated polybutadiene the polymer segment order parameter S with the stretching parameter, for both the intercrosslinked and the dangling chains. Figure 8 shows a linear relation between the stretching parameter and S, but with different slopes for the intercrosslinked and the dangling chains.

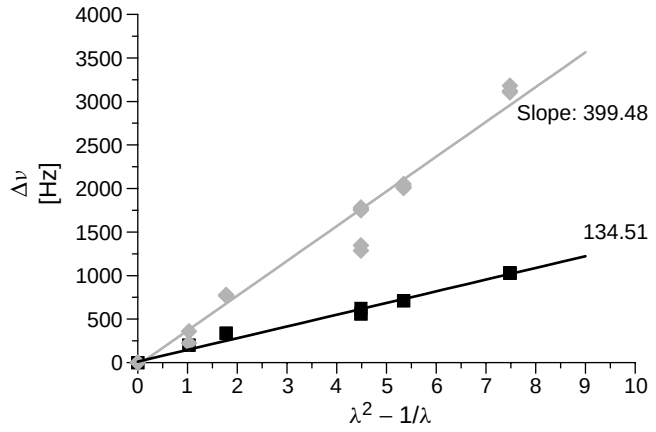

Figure 8 Dependence of the deuterium splitting $\Delta\nu$ as a function of the stretching parameter $\lambda^2 - 1/\lambda$ for two components with different T_2 in polybutadiene networks; ♦ represent the chains cross-linked at both ends with short T_2, ■ stands for pendant chains with a long T_2. (Reproduced with permission from Menge et al.[27])

Also it was found that the line width of the intercrosslinked chains increased strongly with stretching (meaning an increase of the correlation time τ_c, see equation (7)), in contrast to the line width of the dangling ends, which remained constant.

Thus far we discussed experiments where the stress during the NMR experiment was considered to be constant. NMR, however, is also able to follow the time-dependent mechanical relaxation behavior after a stress step. In experiments by Dardin et al.[28] on elastomers networks in which the cross-linking was performed by hydrogen bonds between units randomly attached to partly deuterated polybutadiene chains, the stress relaxation could be followed in time by the slow decrease of the quadrupole splittings. Figure 9 shows the decrease of the deuterium quadrupole splitting of such a network as a function of time.[28] The quadrupole splitting disappears with time, evidently due to a gradual breakdown of the hydrogen bonded junctions.

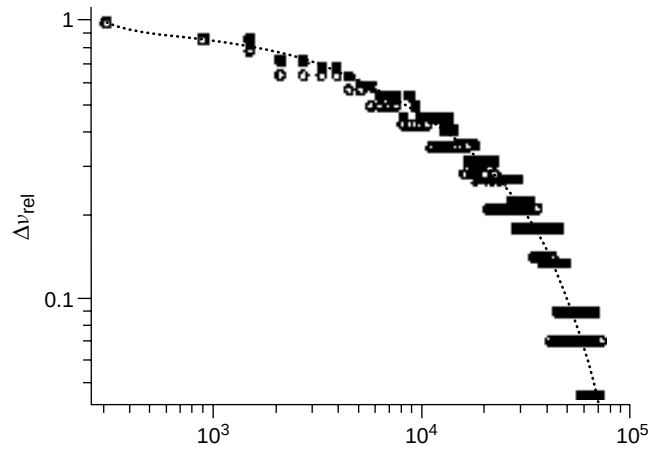

Figure 9 Decrease of the relative deuterium quadrupole splittings $\Delta\nu$ as a function of time in a polybutadiene network where the cross-links are formed by hydrogen bonds between units randomly placed along the polybutadiene chains, for two different initial elongations $\lambda = 2.2$ (■) and $\lambda = 3.1$ (○). (Reproduced with permission from Dardin et al.[28])

3.3 ^{13}C NMR

At first sight ^{13}C NMR seems not the best nucleus for NMR experiments on polymers under tension. Because of experimental reasons most combinations of mechanical deformation and NMR rely on the dependence of some anisotropic spin interaction on deformation. Anisotropic spin interactions are sensitive to both molecular rotations and orientation and therefore provide evidence of the effect of sample deformation on molecular mobility and orientation. As discussed above, for proton spins the proton-proton dipolar interaction and for deuterium the quadrupole interaction is used. For ^{13}C NMR in principle the ^{13}C chemical shift anisotropy or the proton-carbon dipolar interactions are available and could be employed in the same way as for instance for protons. At this point we have not discussed an example where the isotropic chemical shift is used, although the isotropic chemical shift is a parameter which depends on the local structure, much more so than the dipolar interactions or the quadrupole interaction. A disadvantage of the isotropic chemical shift is that its value is hardly affected by molecular motions or orientations.

The problem with using isotropic chemical shifts is that the line broadening effects of the anisotropic interactions, like the dipolar interactions or the chemical shift anisotropy, have to be eliminated. In other words, solid state high resolution techniques like magic angle spinning have to be used.

The combination of a stretching device and a magic angle rotor is not an easy combination. However, it has been shown by Schmidt et al.[29] that it is possible to bring prestretched samples *under stress* into a standard magic angle rotor (see Figure 10). Standard CP-MAS[30] experiments can then be performed as a function of the stress. The advantage of this method is that, without the need for preparing selectively deuterated samples, the high resolution CP-MAS spectrum under stress provides information about the effect of mechanical deformation on each chemical group in the material that causes a distinguishable ^{13}C NMR line.

Schmidt et al.[29] investigated materials composed of semi-crystalline block copolymers of poly(butylene terephthalate) (PBT) and poly(tetramethylene oxide) (PTMO). In this thermoplastic copolymer material the PBT segments form hard, crystalline blocks in a soft amorphous matrix of PTMO and PBT. The experiments have shown that the amorphous matrix is phase-separated into a very mobile PTMO-rich phase and a PBT/PTMO mixed phase with restricted mobility. It is clear that these block copolymers can again be considered as a network where the PBT crystalline domains form the physical cross-links. This material is a typical example of modern polymeric materials, in which two components are combined to form a cross-linked elastomer which can be melted.

Figure 11 displays the effect of increased strain on part of the ^{13}C CP-MAS spectrum of the PBT/PTMO copolymer. The spectra of the sample, which is transferred to the rotor in the way depicted in Figure 10 ('in-situ stretched') and of the samples brought into the rotor after the samples were allowed to relax after stretching ('stretched') can be compared. Upon stretching a new resonance for the PTMO OCH_2 carbons shows up at 72.5 ppm, shifted by ca. 1.3–1.4 ppm down field relative to the corresponding peak of the unstretched material, and with an intensity proportional to the strain. This peak is assigned to crystalline PTMO, which is induced by the stretching. It is found that the strain-induced crystallization depends on the temperature and on the PTMO block length.

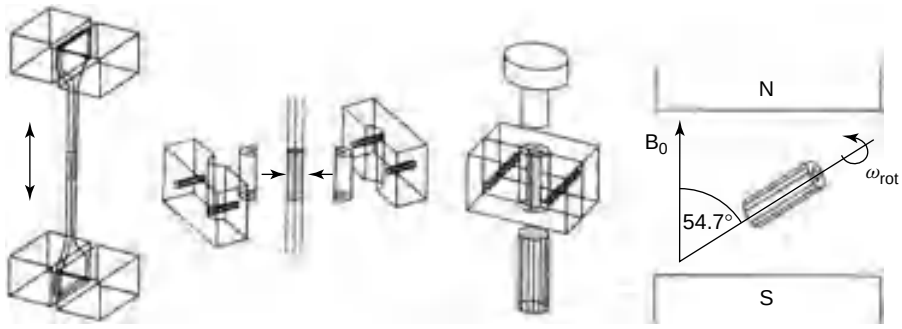

Figure 10 A schematic representation how a sample under stress is transferred from the stretching machine into a standard 7 mm magic angle rotor. (Schmidt et al.[29])

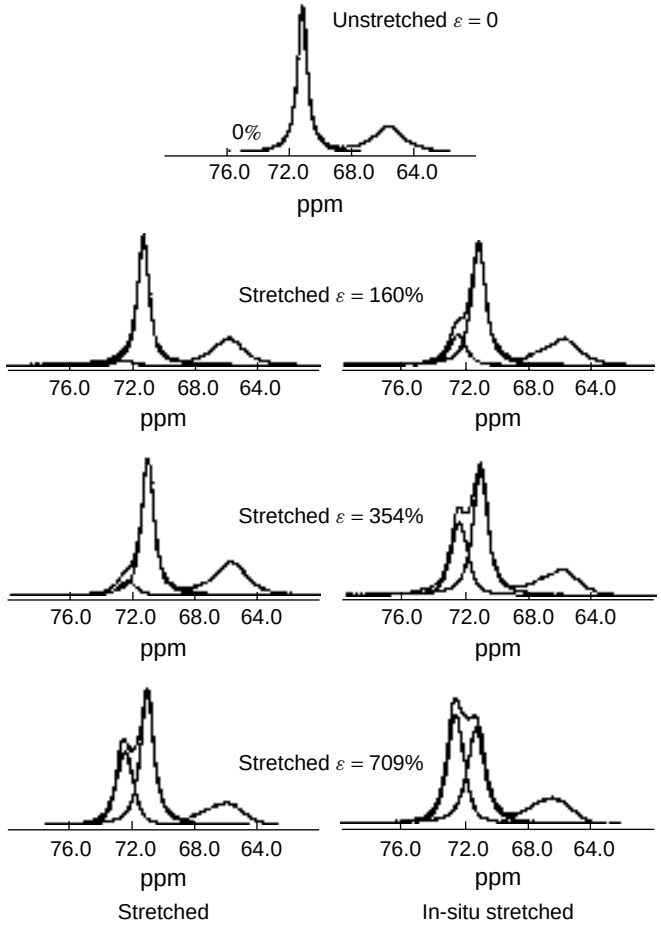

Figure 11 ^{13}C CP-MAS spectra of PBT/PTMO copolymers as a function of the elongation factor ε. The 'stretched' spectra result from samples stretched before the measurement and then relaxed, the 'in-situ stretched' spectra are from samples under stress in the rotor. (Schmidt et al.[29])

4 NMR IMAGING OF POLYMERS UNDER TENSION

NMR imaging finds most of its applications in medical diagnostics but can also be used for materials science.[31,32] The spatial resolution of an NMR imaging experiment is dependent on the width of the resonance line,[33] the smaller the line width, the higher the obtainable resolution. Therefore NMR imaging is particularly useful for elastomers, where the molecular motions are so fast that the rigid solid state line width for protons or deuterons is reduced to values comparable to those of solution NMR. Nevertheless the spatial resolution usually is not better than ca. 100 μm.

Although with respect to spatial resolution NMR imaging is unattractive when compared to other modern microscopical techniques, like e.g., atomic force microscopy, NMR imaging also has some definite advantages:

(a) the large number of parameters which can be used to obtain image contrast and
(b) the fact that NMR imaging can be used to image the inside of materials in a non-invasive way.

As remarked above, in the imaging of elastomers it is very helpful that the high molecular mobility at temperatures above T_g strongly reduces the proton line width. On the other hand, by using contrast filters based on residual dipolar interactions, the experiments can be modified in such a way that those parts of the sample with residual dipolar interactions are represented in the image. Among the various contrast parameters for such experiments the proton transverse relaxation time T_2 is particularly important, while it can easily be used to discriminate between more rigid-like and more liquid-like domains, since the value depends on the motional correlation time τ_c, as discussed in section 3.1. Another contrast technique, which also depends on the polymer chain mobility and residual dipolar interactions, is multi-quantum filtering. In chains of elastomers not undergoing fast isotropic motions, the dipolar interactions, especially within CH_2 and CH_3 groups, are not completely averaged out and therefore single and double quantum coherences can be generated. The contrast parameter to be used of course has to be dependent on stress, but both T_2 and multi-quantum filtering fulfil this condition.

A beautiful example of NMR imaging of materials is the imaging of the distribution of strain in a polymer material. NMR imaging in this sense is comparable to certain optical techniques (polariscope, Moiré method), which are used to image strain in optically transparent materials,[34] except that, obviously, for NMR the material does not need to be optically transparent. An example of the imaging of strain is reproduced in Figure 12, where a double-quantum-filtered proton image of a stressed rubber band with a cut is presented.[35]

A different possibility is the imaging of the temperature profile of a polymer material, which arises when the material

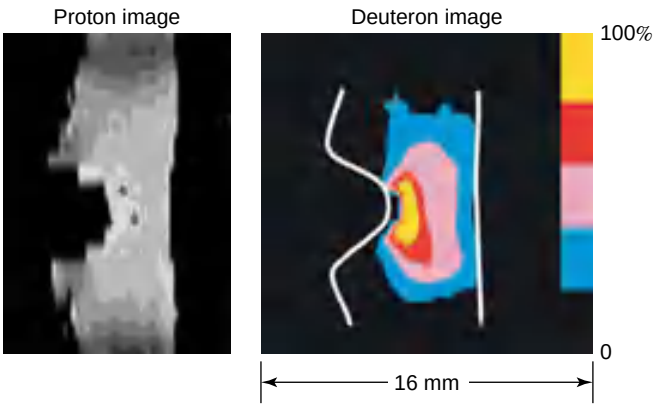

Figure 12 ^{1}H-NMR image of a rubber band with cut under stress. (Reproduced with permission from Demco et al.[35])

is subjected to a dynamic deformation. When the T_2 value is temperature dependent, the T_2 profile of the material represents the spatial changes of the value of the loss module,[36] since the loss module determines the amount of heat generated by a dynamic deformation. Another important development by Blümich et al. is a mobile surface NMR sensor ('NMR mouse'), which can be used to determine the stress behavior of arbitrarily large objects.[37]

5 CONCLUSIONS

Although certainly not all examples of the use of NMR for the study of polymeric materials under tension have been summarized in this review, the examples that were discussed are typical enough to show the possibilities and impossibilities of NMR for such investigations. It is clear that the combination of stretching (or compression) devices with NMR spectrometers severely limits the type of NMR experiments that can be explored. Nevertheless, enough possibilities remain to study polymers under stress with NMR, as shown for instance by the study of polymer networks. The combination of statistical theoretical techniques and experimental deuterium or wide-line proton NMR has lead to a high degree of understanding of the behavior of such systems under stress.

Another field, which has not been reviewed here, but certainly deserves to be considered as a powerful demonstration of the possibilities of NMR, is the study of the viscous behavior of polymer melts under the action of shear.

6 RELATED ARTICLES IN VOLUMES 1–8

Brownian Motion & Correlation Times, Volume 2; Deuterium NMR in Solids, Volume 3; Imaging: A Historical Overview, Volume 4; Imaging Techniques for Solids and Quasi-solids, Volume 4; Magic Angle Spinning, Volume 5; Polymer MRI, Volume 6; Polymer Physics, Volume 6; Relaxation: An Introduction, Volume 6.

7 REFERENCES

1. I. M. Ward and D. W. Hadley, 'An Introduction to the Mechanical Properties of Solid Polymers', Wiley, 1997.
2. R. K. Wangness and F. Bloch, *Phys. Rev.*, 1953, **89**, 728; F. Bloch, *Phys. Rev.*, 1956, **102**, 104; A. G. Redfield, *IBM J. Res. Dev.*, 1957, **1**, 19.
3. P. W. Anderson and P. R. Weiss, *Rev. Mod. Phys.*, 1953, **25**, 269.
4. R. Kubo and K. Tomita, *J. Phys. Soc. Jpn.*, 1954, **9**, 888.
5. R. Kimmich, 'NMR-Tomography, Diffusometry and Relaxometry', Springer, 1997.
6. G. Simon, K. Baumann, and W. Gronski, *Macromolecules*, 1992, **25**, 3624.
7. P. Sotta, C. Füber, D. E. Demco, B. Blümich, and H. W. Spiess, *Macromolecules*, 1996, **29**, 6222.
8. P. Sotta and B. Deloche, *Macromolecules*, 1990, **23**, 1999.
9. T. Nishi and T. Chikaraishi, *J. Macromol. Sci.-Phys.*, 1981, **B19**, 445.
10. K. Fukumori, T. Kuraughi, and O. Kamigaito, *J. Appl. Pol. Sc.*, 1989, **38**, 1313.
11. J. P. Cohen-Addad and P. Huchot, *Macromolecules*, 1991, **24**, 6591.
12. M. T. Hansen, B. Blümich, C. Boeffel, and H. W. Spiess, *Macromolecules*, 1992, **25**, 5542.
13. M. T. Hansen, Ph.D. Thesis, University of Mainz, 1991.
14. K. Schmidt-Rohr and H. W. Spiess, 'Multidimensional Solid-State NMR and Polymers', Academic Press, 1994.
15. D. J. Schaefer, R. J. Schadt, K. H. Gardner, V. Gabara, S. R. Allen, and A. D. English, *Macromolecules*, 1995, **28**, 1152.
16. L. S. Loo, R. E. Cohen, and K. K. Gleason, *Science*, 2000, **288**, 116.
17. B. Deloche and E. T. Samulski, *Macromolecules*, 1981, **14**, 575; W. Gronski, R. Stadler, and M. M. Jacobi, *Macromolecules*, 1984, **17**, 741; H. E. Gottlieb and Z. Luz, *Macromolecules*, 1984, **17**, 1959; J. L. Hutchison, N. S. Murphy, and E. T. Samulski, *Macromolecules*, 1996, **29**, 5551.
18. W. Kuhn and F. Grun, *Kolloid Zeitschr.*, 1942, **101**, 248.
19. K. McLoughlin, J. K. Waldbieser, C. Cohen, and T. M. Duncan, *Macromolecules*, 1997, **30**, 1044.
20. M. E. Ries, M. G. Brereton, P. G. Klein, I. M. Ward, P. Ekanayaka, H. Menge, and H. Schneider, *Macromolecules*, 1999, **32**, 4961.
21. M. G. Brereton, *Macromolecules*, 1993, **26**, 1152.
22. M. Warner, P. T. Callaghan, and E. T. Samulski, *Macromolecules*, 1997, **30**, 4733.
23. M. M. Jacobi, V. Abetz, R. Stadler, and W. Gronski, *Polymer*, 1996, **37**, 1669.
24. C. Ylitalo, J. Zawada, G. Fuller, V. Abetz, and R. Stadler, *Polymer*, 1992, **33**, 2949.
25. M. G. Brereton and M. E. Ries, *Macromolecules*, 1996, **29**, 2644.
26. L. S. Loo, R. E. Cohen, and K. K. Gleason, *Macromolecules*, 1999, **32**, 4359.
27. H. Menge, S. Hotopf, and H. Schneider, *Polymer*, 2000, **41**, 4189.
28. A. Dardin, H. W. Spiess, R. Stadler, and E. Samulski, *Polymer gels and Networks*, 1997, **5**, 37.
29. A. Schmidt, W. S. Veeman, V. M. Litvinov, and W. Gabriëlse, *Macromolecules*, 1998, **31**, 1652.
30. F. Engelke, in 'Encyclopedia of NMR', eds D. M. Grant and R. K. Harris, Wiley: Chichester, 1996, Vol. 3, p. 1529; D. Burum, in 'Encyclopedia of NMR', eds D. M. Grant and R. K. Harris, Wiley: Chichester, 1996, Vol. 3, p. 1535.
31. B. Blümich and W. Kuhn, eds, 'Magnetic Resonance Microscopy', VCH: Weinheim, 1992.
32. P. Blümler, B. Blümich, R. Botto, and E. Fukushima, eds, 'Spatially Resolved Magnetic Resonance', Wiley-VCH: Weinheim, 1998.
33. W. S. Veeman, in 'Magnetic Resonance Microscopy', eds B. Blümich and W. Kuhn, VCH: Weinheim, 1992, p. 29.
34. S. P. Timoshenko and J. N. Goodier, 'Theory of Elasticity', 3rd edn., McGraw-Hill, 1970.

35. D. E. Demco and B. Blümich, 'Current Opinion in Solid State and Materials Science', in press.
36. D. Hauck, P. Blümler, and B. Blümich, *Macromol. Chem. Phys.*, 1997, **198**, 2729.
37. G. Eidmann, R. Savelsberg, P. Blümler, and B. Blümich, *J. Magn. Reson.*, 1996, **A122**, 104.

Biographical Sketches

Wiebren S. Veeman, *b* 1942. M.S., 1967, Technical Physics, University of Delft (supervisor J. Smidt), Ph.D. 1972, University of Leiden (supervisor J. H. van der Waals). Postdoctoral fellow, IBM Research, San Jose, Ca., 1973–74. Wetenschappelijk medewerker, University of Nijmegen, 1974–86. Professor in Physical Chemistry, University of Nijmegen, 1986–91, Lehrstuhl für Physikalische Chemie, Gerard-Mercator-Universität, Duisburg, 1991–present. About 150 publications, research interests: the application of NMR to materials and biosystems.

Angelika Schmidt, *b* 1970. Chemistry Diplom Gerhard-Mercator-Universität Duisburg 1994, Ph.D. Gerhard-Mercator-Universität Duisburg (supervisor W. S. Veeman) 1998, Research Associate DSM Research 1999–present; expert in the Competence Center Material Properties, research interests: permeability and elasticity of polymer.

Polysaccharide Solid State NMR

Hazime Saitô

Himeji Institute of Technology, Kamigori, Hyogo, Japan

1	Introduction	1
2	Conformation-Dependent ^{13}C Chemical Shifts	1
3	Secondary Structure of Gel-Forming Polysaccharides	1
4	Dynamic Aspects of Polysaccharide Gels	4
5	Concluding Remarks	5
6	Related Article	5
7	References	5

1 INTRODUCTION

A variety of polysaccharides are known to play essential roles as the structural components in the cell walls of plant and microorganisms, in insect cuticles, as storage polysaccharides, as matrix components in animal fluids and connective tissues, and as molecular signals for biological recognition. These functions are strongly related to their respective secondary structures, taking in the solid, gel, or solution states. Nevertheless, it is not easy to reveal the secondary structures of these polysaccharides either in the solid or in solution, as compared with those of globular proteins or nucleic acids which have been extensively studied by X-ray diffraction or multidimensional NMR spectroscopy. This is mainly because the crystallization of polysaccharides for an X-ray diffraction study is extremely difficult and the number of interresidual nuclear Overhauser enhancements in solution NMR is not sufficient for the purpose of model building. Moreover, it should be emphasized that the secondary structures of polysaccharides are generally very heterogeneous, especially in the gel state in which several different kinds of domain are simultaneously present.

Conformational elucidation by solid state NMR spectroscopy as a means for in situ structural analysis is especially important for a number of polysaccharides, because they are in many instances not soluble in mild solvent systems (such as aqueous solution) and other spectroscopic means for this purpose are virtually unavailable. It should be anticipated that solubilization in either alkaline or DMSO solution can usually be associated with a conformational change. In addition, too much reliance should not be laid on a secondary structure as deduced by fiber X-ray diffraction studies, because any physical treatment to improve the crystallinity (such as thermal treatment) may cause a conformational change. There remains an ambiguity about secondary structure owing to the limited number of diffraction data available. In this respect solid state NMR is invaluable as a complement to fiber X-ray diffraction as well as a means to gain insight into the dynamic aspects of polysaccharides, especially in relation to a study of gel networks.

2 CONFORMATION-DEPENDENT ^{13}C CHEMICAL SHIFTS

We have previously shown that the ^{13}C chemical shifts of a variety of molecular systems, including polypeptides and proteins, carbohydrates and polysaccharides, ionophores, etc., vary by as much as 8 ppm depending on their conformations.[1,2] In principle, such a conformation-dependent change in polysaccharides is observable either in the solid state or in solution when rapid conformational isomerism about the glycosidic linkages is frozen. However, there are a limited number of examples which exhibit the existence of conformation-dependent ^{13}C chemical shifts: ^{13}C chemical shifts recorded in solution are generally identical, within experimental error, to those observed in the solid state, as in higher molecular weight (1 → 3)-β-D-glucans and α-cycloamylose. The situation arose when rapid rotational motion about the glycosidic linkages was frozen (even in solution) due to the formation of cross-links or to the presence of cyclic structures for the (1 → 3)-β-D-glucans and α-cycloamylose, respectively.

The existence of conformation-dependent ^{13}C chemical shifts, however, is more clearly visualized by an examination of the ^{13}C chemical shifts of solid polysaccharides which have a variety of polymorphs. It is also useful to examine the ^{13}C NMR spectra of crystalline cycloamyloses enclosing a variety of guest molecules, because detailed conformational data for such complexes are available from single crystal X-ray diffraction studies. We previously demonstrated that the C-1 and C-4 ^{13}C chemical shifts of crystalline cycloamyloses enclosing various types of guest molecules could be well related to a set of torsion angles about the glycosidic linkages (ϕ, ψ).[3] Later, similar but slightly different relationships[4,5] were proposed. Therefore, conformational elucidation by means of solid state NMR is feasible on the basis of the concept of conformation-dependent ^{13}C chemical shifts.[1,2]

3 SECONDARY STRUCTURE OF GEL-FORMING POLYSACCHARIDES

It is well recognized that cross-links of polysaccharide gels are formed via several degrees of molecular association of the ordered polysaccharide chains. It is thus important to obtain the detailed in situ secondary structure of various polymorphs of polysaccharides by solid state NMR as reference data useful for conformational studies of gel samples.

3.1 (1 → 3)-β-D-Glucans

As an illustrative example, we first demonstrate comparative ^{13}C NMR studies on linear and branched (1 → 3)-β-D-glucans isolated from bacteria and reserve polysaccharide, and fungi (edible mushrooms), respectively.[6,7] Curdlan [(**1**), Figure 1], a bacterial linear (1 → 3)-β-D-glucan from *Alcaligenes faecalis* (Wako Pure Chemicals, Osaka, Japan) is able to form a firm elastic gel when its aqueous suspension is heated at a temperature above 54 °C. On the other hand, several branched glucans such as lentinan (Ajinomoto Co. Japan), schizophyllan (Taito, Japan), etc. (**2**) from various types of mushrooms are able to form gels of a rather brittle type at higher

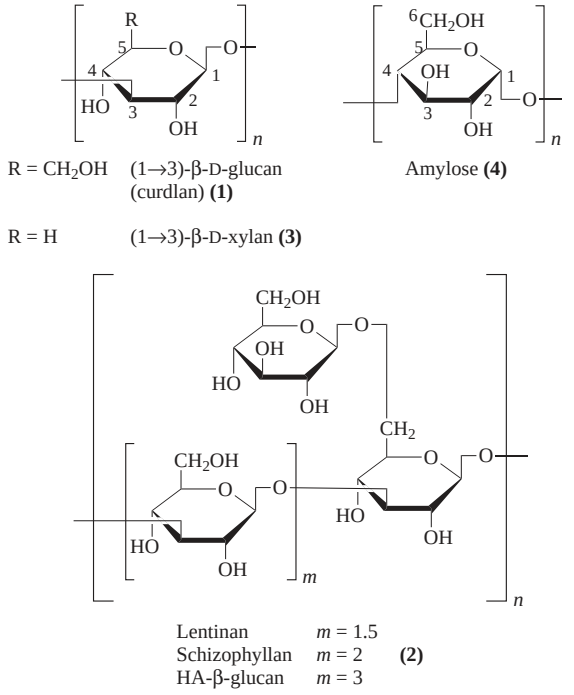

Figure 1 Primary structures of a variety of polysaccharides

concentrations (>10%). Such a difference in macroscopic texture of these gel samples is closely related to a different architecture of the network structure between the two types of gels, as will be discussed later in more detail. In fact, rather sharp ^{13}C NMR signals (about 40% of the total NMR spectrum) are visible from curdlan gel using conventional liquid state NMR with broadband decoupling.[8] The C-1 and C-3 ^{13}C chemical shifts from the elastic gel were displaced to high frequency by 2.8 and 3.2 ppm, respectively, as compared with those of a lower molecular weight glucan with a random coil conformation. As pointed out in the previous section, such a conformation-dependent ^{13}C chemical shift of (1 → 3)-β-D-glucans arises from the fact that the rotational motions of the polysaccharide backbone about the glycosidic linkages are frozen due to the formation of an ordered helical conformation. The polysaccharide chain in this case must be a *single* helical species in spite of the existence of a triple helical model, based on fiber X-ray diffraction studies,[9,10] because the molecular chain is found to be rather flexible, as demonstrated by relaxation parameters such as the spin–lattice relaxation times and the NOE.[6] In contrast, all of the ^{13}C NMR signals of the branched glucans were found to be completely suppressed in the gel state as recorded on a traditional solution state NMR spectrometer.[11] This finding implies that the molecular conformations of these two types of polysaccharides are different from each other. It is essential for this reason to examine the solid state ^{13}C NMR spectra of various types of polymorphs in (1 → 3)-β-D-glucans for use as reference data.

Figure 2 illustrates the ^{13}C NMR spectrum of a hydrated sample of curdlan (b) obtained by placing it in a desiccator at 96% relative humidity for 8 h compared with that of the anhydrous powder as received from the manufacturer (a)[12] and annealed curdlan[13] prepared by heating an aqueous suspension at 150 °C followed by slow cooling (c). It is noteworthy

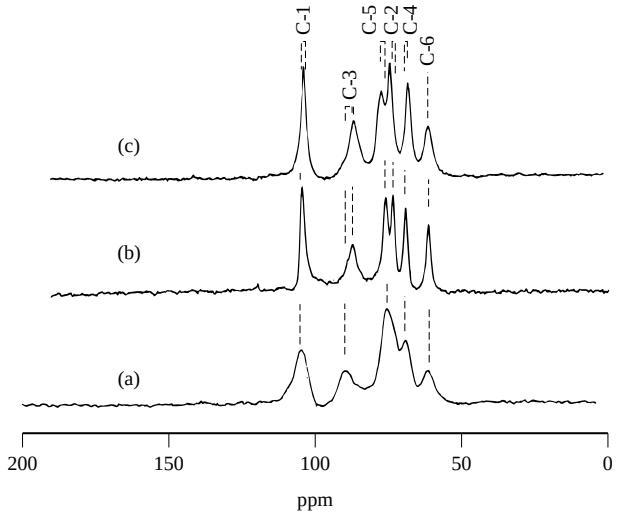

Figure 2 ^{13}C CP MAS NMR spectra of curdlan in the solid state: (a) anhydrous; (b) hydrated; and (c) annealed[12]

that the ^{13}C NMR linewidths of the hydrated sample are considerably narrowed in comparison to those of the anhydrous sample and are comparable to those of the annealed curdlan [Figure 2(c)]. The C-3 ^{13}C chemical shift of curdlan hydrate is displaced to low frequency by 2.5 ppm with respect to that of the anhydrous state. Distinction between the hydrated and annealed curdlan is straightforward by means of the C-5 chemical shifts (75.8 ppm and 77.5 ppm for the former and latter, respectively) and the peak separation between the C-5 and C-2 signals (2.0 and 3.2 ppm, respectively). Lyophilized curdlan from DMSO solution gave rise to narrower spectra but the peak positions were exactly the same as those for the anhydrous sample.[14] Annealed curdlan may be related straightforwardly to the triple-helix form on the basis of its powder X-ray diffraction by reference to previous fiber diffraction data.[9,10]

Hydrated curdlan gave rise to ^{13}C NMR signals which were identical to those observed in the gel state. Hence, this form was ascribed to the flexible single helix already mentioned. Consistent with this view, a recent fiber X-ray diffraction[15] study showed the presence of a 6/1 single helix conformation for the curdlan gel prepared by heating an aqueous suspension at 70 °C for 10 min, although Fulton and Atkins previously ascribed a similar diffraction pattern to a 7/1 triple helix conformation.[16] It is surprising that the C-1 and C-3 chemical shifts of the single helical curdlan hydrate are very similar to those of the triple helical annealed curdlan, although distinction between the two forms is possible from the C-2 and C-5 peaks. This is because the two pairs of the torsion angles about the glycosidic linkages (ϕ, ψ) are very similar, as revealed by X-ray diffraction studies.[10,15] The anhydrous form, on the other hand, is ascribed to a single-chain form whose torsion angles vary to some extent from those of the single helix form owing to loss of hydrated water molecules (which are essential for stability in the single helix conformation). In a similar manner, DMSO molecules in the single-chain form are complexed with the polysaccharide chains (ca. 0.5 DMSO molecules per residue)[14] and may play an important role for the conformational stabilization, although they are readily replaced by water molecules on hydration

to yield the single helix form.[12,14] This situation is very similar to the case of DMSO molecules complexed with V-amylose, which are very easily replaced by water molecules by hydration, leading to the conversion to the B- form, as will be described later.

Linear (1 → 3)-β-D-glucans of low molecular weight oligomers such as laminariheptaose and acid-degraded curdlan with a degree of polymerisation (*DP*) of 14 can adopt neither the single helix nor triple helix form, as judged from the characteristic ^{13}C signals.[12,13,17] Interestingly, glucans of either short-chain (*DP* < 14) or longer-chain species are incapable of forming triple helices by lyophilization from aqueous solution. Laminaran from *Laminaria* species (*DP* 39) turned out to be able to exist in the triple helix form by lyophilization from aqueous solution, although this polysaccharide adopts a random coil form in aqueous solution.[13] In contrast, triple helix conformations were achieved when high molecular weight branched (1 → 3)-β-D-glucans such as schizophyllan or HA-β-glucan were lyophilized from their aqueous solution, although the single-chain form was available from an aqueous solution of lentinan.[17] It is now clear that the obvious preponderance of the single helix conformation for the linear (1 → 3)-β-D-glucans of high molecular weight arises mainly from insufficient hydration. Once this molecule is completely dissolved in an aqueous solution at a temperature above 150 °C, it is able to refold to yield the triple helical conformation when cooled slowly to ambient temperature.[13] It is thus expected that such a conversion is inefficient when heated samples are cooled rapidly (at most 50%).[13] It is noteworthy that conversion of the single helix to the triple helix by annealing at 150 °C is accompanied by fragmentation of the polymer chain due to thermal degradation from an initial *DP* of 3930 to a final *DP* of 110.[18] Such an annealing is not necessary in the case of the branched glucans, because these molecules are well hydrated in aqueous media at ambient temperature. It appears that rather weak intermolecular association of the branched glucan (as compared with that of the linear glucan) arises from the presence of a pendant glucose moiety (Figure 1) for every two or three glucose residues. This is the reason why the branched (1 → 3)-β-D-glucans and laminaran have a preponderance of the triple helix over the single helix conformations.

In general, several types of polysaccharides including (1 → 3)-β-D-glucans can acquire the double or triple stranded form as the most energetically stable, as expected from a molecular mechanics calculation.[19] Nevertheless, any given polysaccharide sample does not always take the energetically most stable conformation, because of different sample histories. Distinction between the single and multiple helical chains, however, is not always straightforward to obtain by X-ray diffraction, because distinguishing multiple stranded coaxial helices and nested single helices is one of the most difficult problems encountered in interpreting fiber diffraction data.[20] It should be emphasized that this problem is readily solved by examination of the conversion diagram of these polysaccharides after a series of physical treatments, as summarized in Figure 3. The present approach can be further extended to any types of polysaccharide. In fact, a very similar conversion diagram was recently obtained for (1 → 3)-β-D-xylan (**3**), which is also found to acquire the three above-mentioned types of conformation, as may be expected from its structural similarity with (1 → 3)-β-D-glucans.[21] The

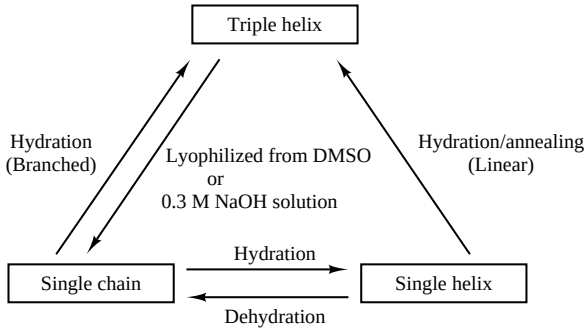

Figure 3 Conversion diagram for (1 → 3)-β-D-glucans by various physical treatments (based on Saitô et al.[12,13])

triple helical conformation was initially proposed for (1 → 3)-β-D-xylan[22] and then adopted for (1 → 3)-β-D-glucan, because the C-6 hydroxymethyl group of the latter is located outside the helical chains. It turned out that the triple helix conformation of the former is more stable than that of the latter because of the greater hydrophobic character in the polymer chain and it cannot be readily converted to the single chain form even if dissolved in DMSO. This type of conversion was made possible by dissolution of the sample in aqueous zinc chloride solution in place of the more common DMSO solution.[21]

3.2 Amylose and Starch

Amylose (**4**) has a common feature with (1 → 3)-β-D-glucans as viewed from the presence of the single helical conformation, which is stabilized by DMSO molecules, and also from its gel-forming ability. Amylose and starch are known to have the following four kinds of polymorphs: V-, A-, B-, and C-forms.[23,24] The V form exists as a complex with a variety of small organic molecules and has a left-handed single helical conformation. The A- and B-forms are found in cereal and tuber starches, respectively, and can be distinguished by the splittings of the C-1 peaks as triplet and doublet peaks, respectively.[25–27] In contrast, V-amylose gives rise to single lines.[28] The C-4 peak of V-amylose is particularly displaced to high frequency by ca. 4–5 ppm from that of the B form. These amylose polymorphs can also be mutually interconverted by a series of physical treatments in a similar manner to (1 → 3)-β-D-glucan, as demonstrated for amylose of low molecular weight (*DP* 17, Figure 4).[29] Obviously, anhydrous amylose lyophilized from a DMSO solution [Figure 4(b)] gave rise to a spectral pattern of the V form. The anhydrous powder as received, however, has an amorphous structure distorted from the B form, as judged from the broad envelope of the ^{13}C NMR signal in the C-1 region and the absence of the C-4 peak at 81 ppm [Figure 4(a)]. Furthermore, hydration of the anhydrous powder or V-amylose resulted in conversion to the B-amylose as judged from the ^{13}C NMR spectra [Figure 4(c)]. It is interesting that such conversion occurs efficiently for amylose of either low (*DP* 17) or high (*DP* 1000) molecular weight but was incomplete for amylose of intermediate molecular weight (*DP* 100).[29]

The secondary structure of the B form was initially considered to be the single helical conformation,[30] since the conversion of the V- to the B-form amylose takes place on humidification.[31] Later, however, the structure was refined as

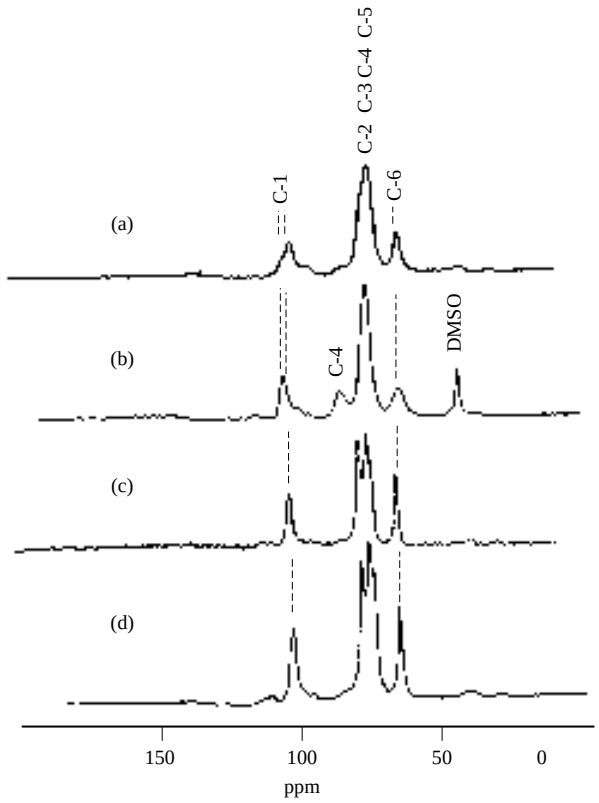

Figure 4 ^{13}C CP MAS NMR spectra of low molecular weight amylose (*DP* 17): (a) anhydrous powder; (b) anhydrous lyophilized sample from DMSO solution; (c) hydrated amylose power; and (d) hydrated iodine complex[29]

a right-handed double helix in an antiparallel fashion.[32] The handedness of the double helix form, however, was recently revised as a left-handed double helix.[33] Nevertheless, it is hardly likely that simple humidification of amylose by placing it in a desiccator at a relative humidity of 96% causes such a drastic conformational change. In this connection, it is crucially important to clarify whether the secondary structure of B-amylose is a left-handed single helix as suggested from solid state NMR or a left-handed double helix as suggested from fiber X-ray diffraction study.

It was expected that ^{2}H NMR spectra of ^2H_2O or DMSO-d_6 complexed to amylose by forming the B- or V-form would be split into a doublet pattern, with the separation of peaks being about 100–200 kHz and 40 kHz (with C_3 rotation of the methyl group), respectively, if they are tightly bound to the polymer chains (static). It emerged, however, that only a singlet was visible as a result of rapid isotropic averaging of the quadrupole interaction in the solid state, with correlation times on the order of 10^{-6} s. The correlation times of isotropic tumbling of ^2H_2O and DMSO-d_6 as estimated from ^{2}H spin–lattice relaxation times are found to be in the vicinity of the T_1 minimum and on the high-temperature side of the T_1 minimum, respectively.[29]

4 DYNAMIC ASPECTS OF POLYSACCHARIDE GELS

Network structures of gel samples should be highly heterogeneous from the conformational and dynamic point of view. Any single NMR measurement, however, does not give rise to such information, because the correlation times of the molecular motions may be broadly distributed from the liquid- to solid-like domains. We have already demonstrated that ^{13}C NMR signals from the liquid-like domains are easily visible with a conventional solution state spectrometer but those of the solid-like domains are not.[5,6] It is therefore necessary to record NMR signals from these solid-like domains in order to gain some insight into the gel structure and dynamics. It is accordingly a major advantage of the NMR approach that it is able to select a particular domain from a variety of motionally different domains.

We have recorded ^{13}C NMR spectra of curdlan gels (Figure 5) by various methods including broadband decoupling for the liquid-like domain as discussed above (b), high-power dipolar decoupling with magic angle spinning (MAS) for intermediate domains between the liquid- and solid-like domains (c), and cross-polarization magic angle spinning (CP MAS) for the solid-like domains (d), and have compared these with the ^{13}C NMR spectrum of hydrated curdlan (a).[34] Such comparison indicated that the single helix form is dominant for all of the motionally different domains of an elastic curdlan gel, although a low intensity peak arising from the contribution from the triple helix is visible in the solid-like domains as shown by the arrowed peak in the CP MAS NMR spectrum. It is worthwhile to relate here the present view of the gel structure with the data for gel strength as a function of heating temperature:[35] the gel strength is almost the same at temperatures between 60–80 °C (low-set gel) and thereafter increases with heating temperature together with the development of turbidity and shrinkage of the gel (high-set gel). The first step of gelation thus corresponds to the formation of pseudo cross-links by hydrophobic association of

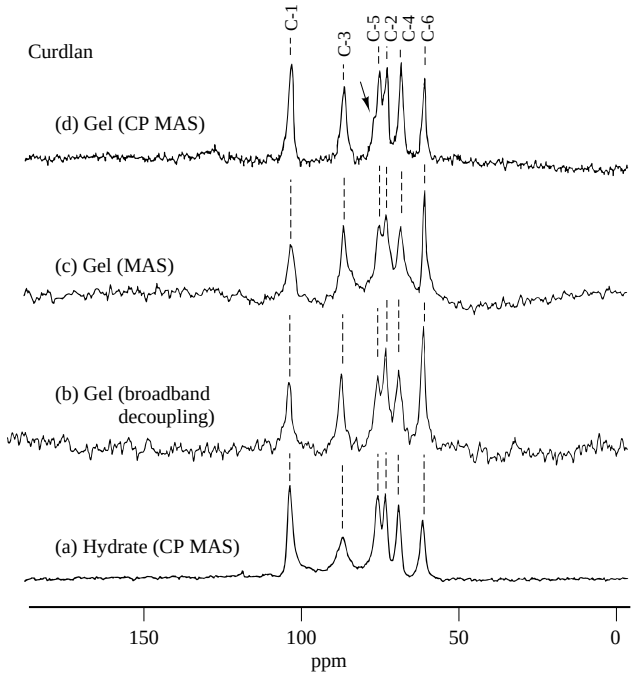

Figure 5 ^{13}C NMR spectra of curdlan gel (b–d) and curdlan hydrate (a) recorded by various types of NMR measurements: (a) and (d) by CP MAS; (b) by broadband decoupling; and (c) by MAS experiments[34]

the single helical chain. The increased gel strength in the high-set gel is well explained in terms of an increased proportion of the triple helical conformation.[5,6]

On the other hand, we found that ^{13}C NMR spectra of branched glucans such as lentinan, schizophyllan, and HA-β-glucan exhibited characteristic peaks of the triple helix conformation.[34] As pointed out, such a preponderance of the triple helix forms resulted in the complete absence of the peaks from the liquid-like domains.[5,6] In this connection, Yanaki and co-workers[36] showed that the triple helical chain of (1 → 3)-β-D-glucans is stiffer than that of native collagen, as manifested from the measurements of persistent chain length for schizophyllan (2000 ± 300 Å). This means that the resulting slow tumbling motion of the stiff rod-like triple helices is not sufficient to average out the dipolar or chemical shift anisotropy interactions in the gel state. Thus, it follows that the major gelation mechanism for the branched (1 → 3)-β-D-glucans proceeds from partial association of the triple helical chains. It appears that the absence of the flexible molecular chain is consistent with the property of a brittle gel. Here we point out that the linear and branched (1 → 3)-β-D-glucans so far discussed are involved in a variety of host-defence biological responses such as antitumor activity, activation of the coagulation system of horseshoe crab amebocyte lysate (LAL), etc. It is interesting that such biological response is initiated by recognition of the molecular chains of the single helical conformations.[18,37,38]

Gidley[39] showed that amylose gel exhibits two kinds of ^{13}C NMR signals: B type signals from motionally restricted regions as recorded by the CP MAS technique and signals identical to those found in aqueous solution. Obviously the latter signals can be ascribed to the presence of a mobile region (liquid-like domain) in the network whose conformation is random coil. The former peaks are naturally ascribed to the solid-like domain with cross-links, either consisting of double helical junction zones,[39] or aggregated regions of the single helical chains[29] as discussed in the previous section. To date, two different views have been presented for the gelation mechanism of amylose: Miles et al.[40] have suggested that gels are formed upon cooling molecularly entangled solutions as a result of phase separation of the polymer-rich phase, whereas Wu and Sarko[33] proposed that gelation occurs through cross-linking by double helical junction zones. Recently, we measured the ^{13}C spin−lattice relaxation times of the liquid- and solid-like domains of starch gel by means of dipolar decoupled single pulse MAS and CP MAS, respectively.[41] It turned out that the T_1 of the C-6 carbon is 0.16 s and 2.1 s for the former and latter, respectively. It appears that such a long T_1 for the latter as compared with that of other types of swollen gels (<0.5 s) arises mainly from motionally restricted crystalline portions consisting of aggregated molecular species such as single helical chains. In any case, it is crucially important to distinguish single helical chains from double helical chains by means of solid state NMR spectroscopy.

5 CONCLUDING REMARKS

It has been demonstrated that the solid state NMR approach is a very powerful means of clarifying conformational features of a variety of polysaccharides in an empirical manner based on the concept of the conformation-dependent displacements of ^{13}C chemical shifts. Careful examination of an NMR-based conversion diagram by a series of physical treatments has proved to be a very useful means for the distinction of single-chain/multiple helices. The application of a modern methodology is urgently required to determine the secondary structure in a nonempirical manner, such as rotational echo double resonance or rotational resonance as currently being applied to a variety of peptides or proteins in the solid state.

6 RELATED ARTICLES

Solid Biopolymers.

7 REFERENCES

1. H. Saitô, *Magn. Reson. Chem.*, 1986, **24**, 835.
2. H. Saitô and I. Ando, *Annu. Rep. NMR Spectrosc.*, 1989, **21**, 209.
3. H. Saitô, G. Izumi, T. Mamizuka, S. Suzuki, and R. Tabeta, *J. Chem. Soc., Chem. Commun.*, 1982, 1386.
4. J. A. Ripmeester, *J. Inclusion Phenom.*, 1985, **4**, 179.
5. R. G. Veregin, C. A. Fyfe, R. H. Marchessault, and M. G. Taylor, *Carbohydr. Res.*, 1987, **160**, 41.
6. H. Saitô, *ACS Symp. Ser.*, 1981, **150**, 125.
7. H. Saitô, *ACS Symp. Ser.*, 1992, **489**, 296.
8. H. Saitô, T. Ohki, and T. Sasaki, *Biochemistry*, 1977, **16**, 908.
9. R. H. Marchessault, Y. Deslandes, K. Ogawa, and P. R. Sundarajan, *Can. J. Chem.*, 1977, **55**, 300.
10. C. T. Chuah, A. Sarko, Y. Deslandes, and R. H. Marchessault, *Macromolecules*, 1983, **16**, 1375.
11. H. Saitô, T. Ohki, and T. Sasaki, *Carbohydr. Res.*, 1979, **74**, 227.
12. H. Saitô, M. Yokoi, and Y. Yoshioka, *Macromolecules*, 1989, **22**, 3892.
13. H. Saitô, R. Tabeta, M. Yokoi, and T. Erata, *Bull. Chem. Soc. Jpn.*, 1987, **60**, 4259.
14. H. Saitô and M. Yokoi, *Bull. Chem. Soc. Jpn.*, 1989, **62**, 392.
15. K. Okuyama, A. Otsubo, Y. Fukuzawa, M. Ozawa, T. Harada, and N. Kasai, *J. Carbohyr. Chem.*, 1991, **10**, 645.
16. W. S. Fulton and E. D. T. Atkins, *ACS Symp. Ser.*, 1980, **141**, 385.
17. H. Saitô, R. Tabeta, T. Sasaki, and Y. Yoshioka, *Bull. Chem. Soc. Jpn.*, 1986, **59**, 2093.
18. Y. Yoshioka, N. Uehara, and H. Saitô, *Chem. Pharm. Bull.*, 1992, **40**, 1221.
19. T. L. Bluhm and A. Sarko, *Can. J. Chem.*, 1977, **55**, 293.
20. T. A. Foord and E. D. T. Atkins, *Biopolymers*, 1987, **28**, 1345.
21. H. Saitô, J. Yamada, Y. Yoshioka, Y. Shibata and T. Erata, *Biopolymers*, 1991, **31**, 933.
22. E. D. T. Atkins, K. D. Parker, and R. D. Preston, *Proc. R. Soc. London, Ser. B.*, 1969, **173**, 209.
23. A. Sarko and P. Zugenmaier, *ACS Symp. Ser.*, 1980, **141**, 459.
24. D. French, *Starch: Chemistry and Technology*, ed. R. L. Whistler and E. D. Pascal, 2nd edn., Academic Press, New York, 1984, p. 183.
25. R. P. Veregin, C. A. Fyfe, R. H. Marchessault, and M. G. Taylor, *Macromolecules*, 1986, **19**, 1030.
26. M. J. Gidley and S. M. Bociek, *J. Am. Chem. Soc.*, 1985, **107**, 7040.
27. F. Horii, H. Yamamoto, A. Hirai, and R. Kitamaru, *Carbohydr. Res.*, 1987, **160**, 29.

28. H. Saitô and R. Tabeta, *Chem. Lett.*, 1981, 713.
29. H. Saitô, J. Yamada, T. Yukumoto, H. Yajima, and R. Endo, *Bull. Chem. Soc. Jpn.*, 1991, **64**, 3528.
30. J. B. Blackwell, A. Sarko, and R. H. Marchessault, *J. Mol. Biol.*, 1969, **42**, 379.
31. F. R. Senti and L. P. Witnauer, *J. Am. Chem. Soc.*, 1948, **70**, 1438.
32. H. C. H. Wu and A. Sarko, *Carbohydr. Res.*, 1978, **61**, 7.
33. A. Imberty and S. Perez, *Biopolymers*, 1988, **27**, 1205.
34. H. Saitô, Y. Yoshioka, M. Yokoi, and J. Yamada, *Biopolymers*, 1990, **29**, 1689.
35. T. Harada, *ACS Symp. Ser.*, 1977, **45**, 265.
36. T. Yanaki, T. Norisue, and H. Fujita, *Macromolecules*, 1980, **13**, 1462.
37. H. Saitô, Y. Yoshioka, N. Uehara, J. Aketagawa, S. Tanaka, and Y. Shibata, *Carbohydr. Res.*, 1991, **217**, 181.
38. J. Aketagawa, S. Tanaka, H. Tamura, Y. Shibata, and H. Saito, *J. Biochem (Tokyo)*, 1993, **113**, 683.
39. M. J. Gidley, *Macromolecules*, 1989, **22**, 351.
40. M. J. Miles, V. J. Morris, and S. G. Ring, *Carbohydr. Res.*, 1985, **135**, 257.
41. H. Saitô, H. Shimizu, T. Sakagami, A. Tuzi, and A. Naito, in *Magnetic Resonance in Food Science*, ed. P. S. Bolton, I. Delgadillo, A. M. Gil, and G. A. Webb, Royal Society of Chemistry, London, 1995, p. 257.

Biographical Sketch

Hazime Saitô. *b* 1937. B.S., 1961, Ph.D., 1968 (supervisor Teijiro Yonezawa), applied chemistry, Kyoto University, Japan. Postdoctoral work at The National Research Council, Canada (with Ian C. P. Smith). Research chemist, Toray Industries, 1963–75, section head, Biophysics Division, National Cancer Center Research Institute, Tokyo, 1975–90, Professor, Himeji Institute of Technology, 1990–present. Approx. 200 publications. Current research specialty: solid state NMR and its application to biophysical chemistry/structural biology.

Polysaccharides and Complex Oligosaccharides

C. Allen Bush

University of Maryland, Baltimore County, Baltimore, MD, USA

1	Introduction	1
2	Covalent Structure Determination	1
3	Conformation and Dynamics	3
4	Related Articles	5
5	References	5

1 INTRODUCTION

Complex oligosaccharides and polysaccharides are composed of a wide variety of different monosaccharides in different linkages. They are not involved as energy sources in metabolism but should be considered rather as 'informational macromolecules' encoding information which is generally important in intercellular communication. The information which they store is decoded by interaction with specific binding proteins known as lectins.[1] The cell surface oligosaccharides of membrane glycoproteins and glycolipids have been implicated in such important biological functions as inflammation[2] and cellular differentiation.[3] The cell surface polysaccharides of bacteria, including lipopolysaccharides, capsular polysaccharides, and other cell wall polysaccharides are implicated in bacterial adhesion and coaggregation.[4,5] Two different aspects of the structure are important to an understanding of the biology of these interactions. First, one must determine the covalent chemical structure of complex oligosaccharides and polysaccharides including the absolute configuration of the constituent monosaccharides. Secondly, one must also determine their three-dimensional folding and their conformation. If they do not adopt a single conformation but rather exist in multiple conformations which exchange, then one must also determine the dynamics of the conformational exchange. This knowledge will make a major contribution to our understanding the interactions of complex oligosaccharides with lectins. High-resolution NMR spectroscopy has been important in all three facets of the structure of complex oligosaccharides and polysaccharides.

2 COVALENT STRUCTURE DETERMINATION

Determination of the covalent structure of a complex oligosaccharide or polysaccharide is not so simple as determination of a peptide sequence or of a nucleotide sequence. With the possibility of two sugar ring forms (furanoside or pyranoside) and of two anomeric forms (α and β) as well as multiple linkage positions, much more detailed information is required for a description of the structure of a complex oligosaccharide which often includes branching. At present there is no single established method for structure determination and many different methods involving enzymatic digestion, chemical degradation, and methylation analysis are used for various problems. The catalog of available *endo*- and *exo*-glycosidases is inadequate and the outcome of chemical reactions involving sugars is notoriously unpredictable. These facts contribute to the attractiveness of instrumental methods such as mass spectrometry and NMR spectroscopy which require minimal chemistry.

2.1 Proton NMR Spectroscopy

The first major contribution of high-resolution ^{1}H NMR spectroscopy to this problem was the structural reporter group method which became useful with the introduction of high-field superconducting spectrometers operating at 360 MHz. An oligosaccharide or polysaccharide in the quantity range of 100 nmol to 1 μmol is dissolved in D_2O and a ^{1}H spectrum is recorded with chemical shifts referred to DSS.[6,7] In this method, which was first used in glycopeptides and was later extended to glycolipids in DMSO solution, certain well-resolved resonances can often be recognized in one-dimensional spectra. For example the anomeric region at ca. 4.4–5.4 ppm usually contains resonances of anomeric protons most of which are isolated (see ***Carbohydrates and Glycoconjugates***). Accurately measured values of the chemical shift can be combined with the multiplet splitting to characterize the oligosaccharide or polysaccharide. Other structural reporter resonances which contribute to the fingerprint include methyl doublets near 1.3–1.5 ppm typical of 6-deoxyhexoses and methyl singlets around 2.0 ppm characteristic of *N*- or *O*-acetyl methyl groups. Methylene resonances of 3-deoxy sugars can be found between 1.8 and 2.3 ppm. But many overlapping resonances of the methine protons between 3.5 and 4.0 ppm are unresolved and contribute minimal information. The chemical shifts and multiplet structures of the isolated structural reporter resonances can be used to characterize the oligosaccharide or polysaccharide, since no two distinct structures have ever been found to have the same NMR spectrum.

Although the structural reporter method has been used primarily for *N*-linked glycopeptides and glycolipids, it can be used on any oligosaccharide or polysaccharide for which a reference library of closely related structures is available (see ***Carbohydrates and Glycoconjugates***). The method has also been used extensively for the oligosaccharide alditols isolated from the alkaline borohydride degradation of mucin glycoproteins.[8–10] In polysaccharides with a repeating subunit, only the structural reporter resonances of the repeat unit are observed and the spectrum resembles that of an oligosaccharide without a reducing terminal. The method works well in any system of closely related bacterial polysaccharides.[11] Although the structural reporter method has been generally associated with ^{1}H NMR spectroscopy, a very similar approach has been used in the ^{13}C NMR of bacterial polysaccharides as will be described below. The structural reporter method for ^{1}H spectra is fast (~30 min) requiring less spectrometer time than other NMR methods and is comparatively sensitive yielding at least some information on samples as small as 20–100 nmol.

A complete assignment of all the proton signals is more difficult, but it provides much more information

on the structure of a polysaccharide for which there are no available spectra for closely similar compounds. A complete assignment of the ^{1}H spectrum can in principle be established by spin correlation since each sugar ring forms a chain of scalar coupled spins. While correlation by scalar coupling was originally done by spin decoupling, usually by difference methods, two-dimensional methods such as COSY are generally preferred for modern instrumentation. The experiment is usually performed in a phase-sensitive mode with a double quantum filter.[11,12] Spin correlation is started at the anomeric proton resonance or at some other structural reporter resonance such as a methyl doublet of a 6-deoxyhexose. Correlation through the entire spin system by COSY can be augmented by 2D HOHAHA or TOCSY which is especially valuable for resonances which are close in chemical shift, giving rise to COSY cross peaks close to the diagonal.[13] From these 2D COSY and TOCSY spectra, one can extract the homonuclear coupling constants which are very useful in assigning the stereochemistry of the sugar pyranoside residue. Two vicinally coupled protons which are axial make a dihedral angle of 180° implying a large coupling constant which is observed in practice to range from 7–11 Hz, whereas any coupling involving equatorial protons exhibits a small *gauche* coupling constant ranging in practice from 0.5–3 Hz (see ***Vicinal Coupling Constants and Conformation of Biomolecules***). Hence these data reveal whether substituents are axial or equatorial, providing the anomeric configuration of the glycosidic linkage as well as the identity of the sugar residue. The identities of the monosaccharides are then to be confirmed by carbohydrate analysis by a method such as HPLC.

Two common difficulties arise which may prevent the above scheme from providing a successful assignment of the ^{1}H spectrum. The first problem is strong coupling which is all too common in the crowded 3.4–4.4 ppm region of the carbohydrate spectrum. It arises when the chemical shifts of two resonances which are coupled are separated by an amount which is not large compared with the coupling constant. Homonuclear two-dimensional TOCSY or HOHAHA spectroscopy can be used to obtain cross peaks which are well removed from the diagonal in many cases. But if the difference in chemical shift is less than twice the coupling constant, the multiplet shape cannot be extracted interfering with the assignment of stereochemistry by homonuclear coupling, ^3J(H,H). In this case, heteronuclear NMR methods involving ^{13}C resolution are required, as will be discussed below. A second problem in spin correlation about the ring arises for very small values of ^3J(H,H) associated with some *gauche* protons.

NOESY correlations can often be used to correlate such *gauche* protons since they are close in space. A hybrid homonuclear method combining TOCSY with ROESY or NOESY may be useful in such cases and long-range heteronuclear coupling correlation can also be useful as will be described below (see ***Carbohydrates and Glycoconjugates***).

Although the scheme outlined above for spin correlation can be used to assign all proton resonances in a ring and to identify the sugar residues and their anomeric configuration, it does not provide the sequence of residues or their linkage and branching. For this purpose, homonuclear spin correlation is not informative and correlation through space by NOESY can be employed. The anomeric proton of one residue is often close to the aglycone proton directly across the glycosidic linkage, giving rise to NOESY cross peaks which identify the linkage.[13,14] Unfortunately this proximity depends on the conformation of the glycosidic linkage and many exceptions are observed in which a large NOE is seen between the anomeric proton resonance and that of the proton adjacent to the linkage position. This situation arises most often when the adjacent proton is equatorial.[11,13] Although the NOESY data can be useful for the assignment of oligosaccharide sequences, the information on the linkage position is not definitive unless the conformation is known, which is usually not the case for a completely new polysaccharide of unknown structure. Thus the linkage position must be confirmed by some other type of data, such as methylation analysis or long-range heteronuclear correlation to be described below.

Observation of NOESY in oligosaccharides and polysaccharides is complicated by difficulties arising from a dependence on the rotational correlation time. NOE is positive for small molecules and negative for larger ones such as proteins and DNA duplexes.[15] (See ***Nuclear Overhauser Effect***.) For intermediate sized molecules having a rotational correlation time τ_c approximately equal to the reciprocal of the spectrometer frequency ω, the NOE disappears altogether. This is approximately the case for a tetrasaccharide at 500 MHz. One solution to this problem is to change the viscosity of the solution, and thus the τ_c, by changing the sample probe temperature[16] or the viscosity of the solvent by the addition of a viscous cosolvent such as DMSO.[17,18] If it is not desirable to alter the solvent conditions, one can resort to NOE in the rotating frame for which NOEs are positive for all rotational correlation times (see ***ROESY*** and ***Carbohydrates and Glycoconjugates***.) One difficulty with this experiment, which is known as ROESY, is that one must be careful to account for magnetization transfer by the HOHAHA mechanism which leads to cross peaks of the opposite sign and which may cancel ROESY peaks.

The observation of a NOE in polysaccharides is usually straightforward since it is commonly large and negative. Wide variations in flexibility are observed among polysaccharides depending strongly on the linkages. Thus wide variations of linewidth are observed, but generally the NOE is negative.[11] The dynamics of the internal motion in polysaccharides is a complex topic which will be addressed below.

2.2 Carbon-13 NMR Spectroscopy

The ^{13}C spectra of carbohydrates generally show much better chemical shift dispersion than do the ^{1}H spectra. In D_2O solution referenced to DSS, the anomeric signals are dispersed between 95 and 110 ppm and methyl carbon resonances are observed at 15–25 ppm. Since the signals corresponding to the methine carbon atoms of the sugar ring are spread over a much wider spectral region (between 55 and 85 ppm) than are the corresponding signals in the ^{1}H spectrum, there is only a moderate amount of overlap of the signals even at the low fields typical of iron core magnet NMR spectrometers (20–25 MHz carbon ^{13}C frequency). With the introduction of Fourier transform ^{13}C spectroscopy in the 1970s, the spectra of many carbohydrates were recorded, revealing both the promise and some of the difficulties with this type of spectroscopy. A major problem arises from the low sensitivity associated with the direct observation of ^{13}C in natural abundance, especially

with low magnetic field strength spectrometers. Although the requirement for sample sizes of 20–50 μmol severely limited applications to oligosaccharides from eukaryotic glycopeptides and glycolipids, bacterial polysaccharides are often available in such quantities and spectra were reported for a number of bacterial polysaccharides such as the *O*-antigen chains of lipopolysaccharides (LPS), capsular polysaccharides, and other bacterial cell wall polysaccharides.[19–21] A second problem with these early studies of ^{13}C NMR spectra of carbohydrates was the lack of a simple method for the rigorous assignment of ^{13}C signals analogous to the ^3J(H,H) correlation method described above for the assignment of ^{1}H spectra. In the absence of a correlation method, the only data upon which to base resonance assignments were ^{13}C chemical shifts and extensive sets of rules for 'glycosylation shifts' were developed.[22,23] Recently more sophisticated computer-based schemes for this type of correlation have been developed for complex oligosaccharides.[24–26] Although the large chemical shift dispersion of ^{13}C spectra leads to well-resolved spectra, the large effects complicate any rational scheme for assignment based on regular differences in chemical shifts. This situation has led to many revisions of the spectral assignments of the ^{13}C spectra of complex carbohydrates as more rigorous correlation-based methods for assignment were introduced. These methods include specific ^{13}C incorporation by chemical synthesis,[27] DEPT methods which count the protons bonded to a particular carbon atom,[28] or comparison of chemical shifts in D_2O and H_2O solution (DIS).[29] In spite of the difficulties in obtaining reliable ^{13}C resonance assignments in these early ^{13}C studies, the data proved to be immensely useful in studies of bacterial polysaccharide structure.[19,20]

Major advances in ^{13}C NMR spectroscopy of polysaccharides have resulted from the more common use of correlation methods which follow chemical bonds. Rigorous assignment of the ^{13}C spectrum can be derived from the ^{1}H assignment by one-bond C–H coupling correlation. While such a correlation is not very practical for ^{13}C detection in macromolecules, the recent introduction of inverse detection or ^{1}H-detected ^{13}C spectroscopy has greatly increased the utility of this approach. Not only is the sensitivity of ^{1}H-detected ^{13}C spectra greatly improved, but it also gives the ^{1}H spectrum the higher resolution of the detected dimension where it is most needed. In a convenient implementation called HMQC[30] the rather crowded ^{1}H spectrum is resolved in the F_1 dimension by the excellent dispersion of the ^{13}C dimension. This spreads out the resonances that would otherwise overlap in the ^{1}H spectrum and also provides a scheme for the assignment of the ^{13}C resonances once a rigorous assignment of the ^{1}H spectrum is derived from homonuclear spin correlation as described above.[31] Another advantage of HMQC arises in the case of strongly coupled ^{1}H resonances, which are often resolved by the difference in ^{13}C chemical shift. The large value of ^1J(C,H) (~140 Hz) removes the strong coupling for natural abundance samples in which there is only one ^{13}C atom in the average sugar ring.[11] In the absence of strong coupling, the correct homonuclear multiplet shape can be deduced as required for the assignment of the stereochemistry of the pyranoside ring and identification of the sugar. With hybrid methods such as coupled HMQC–COSY, one can assign the correct multiplet shape and chemical shift even in cases for which the ^{1}H resonances exactly overlap.[32] The combination of ^{1}H homonuclear correlation and ^{1}H-detected ^{13}C correlation enables a complete assignment of both spectra for complex carbohydrates which are available in quantities of about 1 μmol. This is reasonable for bacterial polysaccharides, but may not be suitable for glycopeptides or glycolipids from eukaryotes which are often not available in such large quantities.

Another important extension of these heteronuclear methods is long-range correlation of ^{1}H with ^{13}C over two and three bonds by the method popularly known as HMBC.[33] The pulse sequence is similar to that used for HMQC but it involves longer delays to allow antiphase magnetization to develop over the smaller coupling. In this experiment, there is a reduction in sensitivity due to the long delays (30–50 ms) which are required and if T_2 is not much longer than the delays, substantial signal is lost. Particularly for polysaccharide samples with wide lines, this experiment is less sensitive than HMQC and can require as much as 10 μmol of sample depending on the linewidth. HMBC spectra provide valuable confirmation of ^{1}H and ^{13}C resonance assignments through correlation within the sugar ring, and also complete assignments for cases in which vicinal homonuclear coupling constants are too small to provide correlation.[11] But the main function of HMBC spectra is correlation across the glycosidic linkage.[31] This allows assignment of the glycosidic linkage in a rigorous way which follows the chemical bonds. This method has found a number of recent applications for determining glycosidic linkages in bacterial polysaccharides.[11] In favorable cases, this information can take the place of data from methylation analysis and a complete structure of a polysaccharide can be determined essentially by NMR methods with very little ancillary data.

3 CONFORMATION AND DYNAMICS

The question of the three-dimensional conformation of complex oligosaccharides and polysaccharides is distinct from the primary or covalent structure. A truly detailed understanding of the conformation and dynamics requires contributions from a number of techniques, but at the present time data from NMR spectroscopy have made the most significant contributions to the solution of this problem. Computer molecular modeling is generally essential to the satisfactory interpretation of the experimental NMR data.[34] It seems likely that contributions from other experimental biophysical methods such as X-ray crystallography and fluorescence spectroscopy can be expected to increase as the importance of oligosaccharide–lectin interactions becomes more apparent.[35]

An early contribution of NMR data to oligosaccharide conformation was the homonuclear ^3J(H,H) values which are especially useful for determining the puckering of the pyranoside rings of sugars. Since the six-membered pyranoside rings generally assume defined chairs, their ^3J(H,H) values are either large (7–11 Hz) for coupling between axial protons or small (0–3 Hz) for coupling involving equatorial protons, as is described above in connection with the assignment of ring stereochemistry. For furanosides, the pucker is much more complicated, with the five-membered rings adopting envelope conformations in rapid exchange. Measurements of ^3J(H,H) for furanosides have been useful in determining the relative contributions from the various envelope conformations which are important in DNA and RNA conformation.[36]

(See ***Vicinal Coupling Constants and Conformation of Biomolecules***.) A combination of empirical and ab initio calculations has been used to model the furanoside rings and to fit the ^3J(H,H) data to the model.

For oligosaccharides composed of relatively rigid pyranoside rings, the glycosidic dihedral angles describe the conformation and dynamics of the polysaccharide.[37] Homonuclear coupling data are uninformative regarding the relative conformation of the rings with respect to each other and much more information on oligosaccharide and polysaccharide conformation has been derived from ^{1}H NOE data which report on distances through space.[15] (See ***Nuclear Overhauser Effect***.) The strategy is similar to that used in the determination of protein structure in solution by NMR methods which relies heavily on computer modeling methods for an interpretation of the NMR data (See ***Structures of Larger Proteins, Protein-Ligand, and Protein-DNA Complexes by Multi-Dimensional Heteronuclear NMR***). The earliest studies of oligosaccharide conformation were performed on chemically synthesized models of blood group oligosaccharides in which steady-state NOEs were interpreted qualitatively.[38] Models were built with a simple empirical energy function and the NOE data were interpreted qualitatively to confirm these models. This method has also been used in bacterial polysaccharides.[39,40]

A more quantitative method for incorporating the NOE data into molecular modeling schemes follows methods often used in the interpretation of NMR data of proteins in which experimental distance constraints are derived from the NOE data. The distance constraints, which are most commonly derived from the 'isolated spin pair approximation', are treated as pseudo energy terms in the modeling to force a conformation which is consistent with the experimental NOE data (see ***Structures of Larger Proteins, Protein-Ligand, and Protein-DNA Complexes by Multi-Dimensional Heteronuclear NMR***). Choe et al.[41] have used NOE constraints to study the core oligosaccharide of the glycosamino glycans and Scarsdale et al.[42] have described an application to gangliosides. Homans and Forster[43] have also outlined a detailed method for restrained molecular dynamics for oligosaccharides.

A slightly different approach to the quantitative evaluation of NOE data for modeling of oligosaccharides is spin matrix analysis. In this method a molecular model is built and interactions among all the ^{1}H spins are treated to include three spin effects and spin diffusion (see ***Protein Structures: Relaxation Matrix Refinement***). The model is then adjusted to determine whether any conformation can be found for which all the simulated NOE data agree with experiment. This method was first introduced by Brisson and Carver[44] for steady-state NOE in glycopeptides. The matrix method for oligosaccharides was later extended to transient two-dimensional NOESY data which are technically more convenient.[45] The spin matrix method has been adapted to include quantitative interpretation of rotating frame or ROESY data.[46]

An inherent problem with both methods outlined above for the quantitative interpretation of NOE data for oligosaccharides is that they ignore internal motion. The matrix method begins with the assumption of a simple isotropically rotating rigid model and the restrained molecular modeling methods are generally assumed to converge to a single conformation. Careful analysis of the results of either method can be used to test for consistency of a single rigid model with the experimental data, but it is difficult to incorporate internal motion into a quantitative NOESY calculation. The question of the flexibility of complex oligosaccharides is important and remains somewhat controversial.[47,48] Certainly, the relatively narrow lines observed in NMR spectra of polysaccharides (2–15 Hz) having molecular weights as high as 100 kDa suggest that there must be some type of flexibility. One possible interpretation is that certain types of oligosaccharides, such as the blood group epitopes, do assume relatively rigid conformations, while other sugar linkages are flexible, providing structural 'hinges'.[34,48]

One approach to the interpretation of NOE in the presence of internal motion is to assume that the molecular modeling results are correct, assign statistical weights to the minimum energy conformations, and then calculate average NOE. Under the assumption that the rate of conformational exchange is fast compared with T_1 but slow compared with the overall τ_c of the oligosaccharide, one may average the values of the spin matrix elements and then solve the problem.[45,48] Unfortunately it is not known whether this assumption about the kinetics of conformational exchange is correct.

The uncertainty about the details of the conformational dynamics of polysaccharides suggests that additional types of experimental information are needed. The interpretation of NOESY data for a system with internal motion can be quite complex since motion can modulate not only the orientation of ^{1}H–^{1}H vectors but also the distances between protons. It has been recognized for many years that heteronuclear coupling ^3J(C,H) values could be used to correlate with dihedral angles (see ***Vicinal Coupling Constants and Conformation of Biomolecules***). Interpretation of coupling data such as ^3J(C,H) in an oligosaccharide with internal motion is much simpler than NOE since the motion is almost certainly fast compared with the timescale of the interaction (ms). But it has proven to be technically very difficult to measure these coupling constants for macromolecules with ^{13}C in natural abundance. Data were first reported from 1D ^{13}C spectra and ^{1}H spectra of oligosaccharides synthesized with specific ^{13}C enrichment.[27] More recently, long-range heteronuclear coupling constants have been measured in natural abundance by ^{13}C-detected ^{1}H spin echo methods.[49] But the low sensitivity of ^{13}C-detected methods presents a serious limitation and this method requires a resolved ^{1}H spectrum which is a rarity in complex carbohydrates. The improved sensitivity of ^{1}H detection, which has been described above for long-range ^{13}C–^{1}H correlation, provides a method for encoding values of ^3J(C,H).[50] Several one-dimensional versions of ^{1}H-detected ^3J(C,H) have been demonstrated in disaccharides and trisaccharides by Poppe and van Halbeek.[51] In spite of the improved sensitivity, cancellation of the antiphase components of heteronuclear doublets hampers accurate measurements for macromolecules. When the linewidths are comparable to the values of the coupling constants (1–8 Hz), the latter cannot be accurately measured due to antiphase cancellation. In the ECOSY method of Montelione et al.,[52] large one-bond coupling to resolve the long-range coupling removes the problem of overlap making it possible to measure accurately coupling constants much smaller than the linewidth.[53] (See ***Coupling Constants Determined by ECOSY***.) This approach has been used in carbohydrates in natural abundance with ^{13}C selective filters,[54] and in polysaccharides with uniform ^{13}C enrichment.[55]

The question of internal motion in complex polysaccharides can also be addressed by spin relaxation methods in which $J(\omega)$, the spectral density, is sampled at a number of different frequencies to measure the different types of motion which contribute to nuclear relaxation. Measurements of different relaxation rates, T_1, T_2, $T_{1\rho}$, and NOE of ^{15}N or ^{13}C can be combined in order to provide this information.

4 RELATED ARTICLES

Carbohydrates and Glycoconjugates; Coupling Constants Determined by ECOSY; Glycolipids; NOESY; Nuclear Overhauser Effect; Polysaccharide Solid State NMR; ROESY; Structures of Larger Proteins, Protein-Ligand, and Protein-DNA Complexes by Multi-Dimensional Heteronuclear NMR; Vicinal Coupling Constants and Conformation of Biomolecules.

5 REFERENCES

1. K. Drickamer, *J. Biol. Chem.*, 1988, **263**, 9557.
2. A. Varki, *Curr. Opin. Cell Biol.*, 1992, **4**, 257.
3. T. Feizi, *Curr. Opin. Struct. Biol.*, 1991, **1**, 766.
4. I. Ofek and R. J. Doyle, *Bacterial Adhesion to Cells and Tissues*, Chapman & Hall, New York, 1993.
5. P. E. Kolenbrander, N. Ganeshkumar, F. J. Cassels, and C. V. Hughes, *FASEB J.*, 1993, **7**, 406.
6. J. F. G. Vliegenthart, H. van Halbeek, and L. Dorland, *Pure Appl. Chem.*, 1981, **53**, 45.
7. J. F. G. Vliegenthart, L. Dorland, and H. van Halbeek, *Adv. Carbohydr. Chem. Biochem.*, 1983, **41**, 209.
8. A. Klein, C. Carnoy, G. Lambin, P. Roussel, J. A. van Kuik, P. de Waard, and J. F. G. Vliegenthart, *Eur. J. Biochem.*, 1991, **198**, 151.
9. J. A. van Kuik, P. de Waard, J. F. G. Vliegenthart, A. Klein, C. Carnoy, G. Lambin, and P. Roussel, *Eur. J. Biochem.*, 1991, **198**, 169.
10. G. Strecker, J. M. Wieruszeski, O. Cuvillier, J. C. Michalski, and J. Montreuil, *Biochimie*, 1992, **74**, 39.
11. C. Abeygunawardana and C. A. Bush, *Adv. Biophys. Chem.*, 1993, **3**, 199.
12. J. Dabrowski, *Methods Enzymol.*, 1989, **179**, 122.
13. C. A. Bush, *Bull. Magn. Reson.*, 1988, **10**, 73.
14. T. A. W. Koerner, Jr., J. H. Prestegard, P. C. Demou, and R. K. Yu, *Biochemistry*, 1983, **22**, 2687.
15. D. Neuhaus and M. Williamson, *The Nuclear Overhauser Effect in Structural and Conformational Analysis*, VCH Publishers, New Yorka, 1989.
16. B. N. N. Rao, V. K. Dua, and C. A. Bush, *Biopolymers*, 1985, **24**, 2207.
17. H. Kovacs, S. Bagley, and J. Kowalewski, *J. Magn. Reson.*, 1989, **85**, 530.
18. P. Cagas and C. A. Bush, *Biopolymers*, 1992, **32**, 277.
19. P. A. J. Gorin, *Adv. Carbohydr. Chem. Biochem.*, 1981, **38**, 113.
20. H. J. Jennings, *Adv. Carbohydr. Chem. Biochem.*, 1983, **41**, 155.
21. P. K. Agrawal, *Phytochemistry*, 1992, **31**, 3307.
22. A. Allerhand and E. Berman, *J. Am. Chem. Soc.*, 1984, **106**, 2400.
23. A. Allerhand and E. Berman, *J. Am. Chem. Soc.*, 1984, **106**, 2412.
24. P. E. Jansson, L. Kenne, and G. Widmalm, *J. Chem. Inf. Comput. Sci.*, 1991, **31**, 508.
25. P. E. Jansson, L. Kenne, and G. Widmalm, *Anal. Biochem.*, 1991, **199**, 11.
26. G. M. Lipkind, A. S. Shashkov, N. E. Nifantev, and N. K. Kochetkov, *Carbohydr. Res.*, 1992, **237**, 11.
27. R. Barker and A. S. Serianni, *Acc. Chem. Res.*, 1986, **19**, 307.
28. D. M. Doddrell, D. T. Pegg, and M. R. Bendall, *J. Magn. Reson.*, 1982, **48**, 323.
29. P. E. Pfeffer, K. M. Valentine, and F. W. Parrish, *J. Am. Chem. Soc.*, 1979, **101**, 1265.
30. A. Bax, R. H. Griffey, and B. L. Hawkins, *J. Magn. Reson.*, 1983, **55**, 301.
31. R. A. Byrd, W. Egan, M. F. Summers, and A. Bax, *Carbohydr. Res.*, 1987, **166**, 47.
32. C. Abeygunawardana, C. A. Bush, and J. O. Cisar, *Biochemistry*, 1991, **30**, 8568.
33. A. Bax and M. F. Summers, *J. Am. Chem. Soc.*, 1986, **108**, 2093.
34. C. A. Bush, *Curr. Opin. Struct. Biol.*, 1992, **2**, 655.
35. K. G. Rice, P. Wu, L. Brand, and Y. C. Lee, *Curr. Opin. Struct. Biol.*, 1993, **3**, 669.
36. J. Raap, J. H. Van Boom, H. C. Van Lieshout, and C. A. G. Haasnoot, *J. Am. Chem. Soc.*, 1988, **110**, 2736.
37. J. W. Brady, *Adv. Biophys. Chem.*, 1990, **1**, 155.
38. T. H. Thogersen, R. U. Lemieux, K. Bock, and B. Meyer, *Can. J. Chem.*, 1982, **60**, 44.
39. T. Peters, J.-R. Brisson, and D. R. Bundle, *Can. J. Chem.*, 1990, **68**, 979.
40. K. Bock, H. Lönn, and T. Peters, *Carbohydr. Res.*, 1990, **198**, 375.
41. B.-Y. Choe, G. C. Ekborg, L. Rodén, S. C. Harvey, and N. R. Krishna, *J. Am. Chem. Soc.*, 1991, **113**, 3743.
42. J. N. Scarsdale, P. Ram, J. H. Prestegard, and R. K. Yu, *J. Comput. Chem.*, 1988, **9**, 133.
43. S. W. Homans and M. Forster, *Glycobiology*, 1992, **2**, 143.
44. J. R. Brisson and J. P. Carver, *Biochemistry*, 1983, **22**, 1362.
45. C. A. Bush, *Methods Enzymol.*, 1994, **240**, 446.
46. R. Bazzo, C. J. Edge, M. R. Wormald, T. W. Rademacher, and R. A. Dweck, *Chem. Phys. Lett.*, 1990, **174**, 313.
47. J. P. Carver, *Curr. Opin. Struct. Biol.*, 1991, **1**, 716.
48. C. A. Bush and P. Cagas, *Adv. Biophys. Chem.*, 1992, **2**, 149.
49. C. Morat, F. R. Taravel, and M. R. Vignon, *Magn. Reson. Chem.*, 1988, **26**, 264.
50. T. J. Norwood, J. Boyd, N. Soffe, and I. D. Campbell, *J. Am. Chem. Soc.*, 1990, **112**, 9638.
51. L. Poppe and H. van Halbeek, *J. Magn. Reson.*, 1991, **93**, 214.
52. G. T. Montelione, M. E. Winkler, P. Rauenbuehler, and G. Wagner, *J. Magn. Reson.*, 1989, **82**, 198.
53. C. Biamonte, C. B. Rios, B. A. Lyons, and G. T. Montelione, *Adv. Biophys. Chem.*, 1994, **4**, in press.
54. L. Poppe, W. S. York, and H. van Halbeek, *J. Biomol. NMR*, 1993, **3**, 81.
55. R. Gitti, G. Lond, and C. A. Bush, *Biopolymers*, 1994, **34**, 1327.

Acknowledgments

Research supported by NIH Grant GM 31449.

Biographical Sketch

C. Allen Bush. *b* 1938. B.A., 1961, Cornell University, Ph.D., 1965, University of California, Berkeley. Faculty, Illinois Institute of Technology, 1968–89. Currently Professor of Biochemistry, University of Maryland, Baltimore County. Approx. 100 publications. Research interests: structural chemistry of complex carbohydrates by NMR, computer modeling, circular dichroism and HPLC.

Solid Biopolymers

Isao Ando and Shigeki Kuroki

Tokyo Institute of Technology, Japan

1	Introduction	1
2	Solid State ^{13}C NMR of Polypeptides and Proteins	1
3	Solid State NMR Studies of ^{15}N in Synthetic Polypeptides	6
4	Solid State ^{17}O NMR of Synthetic Polypeptides	7
5	Related Articles	9
6	References	9

1 INTRODUCTION

The structural investigation of peptides, polypeptides, proteins, and other biopolymers in the solid state is being pursued increasingly by means of high-resolution solid state NMR.[1–8] Most of the biopolymers considered here consist of repeating sequences of peptide bonds with 20 different types of substituent at the α carbon. The secondary structures of these biopolymers are classified as α-helix, β-sheet, ω-helix, and so on, by means of a set of dihedral angles (ϕ, ψ).

In the solution state, the NMR chemical shifts of biopolymers with internal rotations are often the averaged values for all internal rotations because of rapid interconversion by rotation about peptide bonds. In the solid state, however, chemical shifts are often characteristic of specific conformations because of highly restricted rotation about the peptide bonds. The NMR chemical shift is affected by a change in the electronic state arising from the conformational change.[9] NMR chemical shifts in the solid state, therefore, provide useful information about the electronic state and conformation of a biopolymer with a fixed structure.[10]

The present article concentrates on the use of solid state ^{13}C, ^{15}N, and ^{17}O NMR studies in the structural investigation of biopolymers such as polypeptides, proteins, and similar compounds.

2 SOLID STATE ^{13}C NMR OF POLYPEPTIDES AND PROTEINS

2.1 Synthetic Polypeptides

Synthetic polypeptides consist of repeating sequences of certain amino acids and their structures are not as complicated as those of proteins. For this reason, synthetic polypeptides are sometimes used as model compounds for proteins. Their conformations are classified as α-helix, β-sheet, ω-helix, and so on. High-resolution solid state ^{13}C NMR spectroscopy has proved to be a very powerful tool for determining the structure of polypeptides in the crystalline state.[1,5–8] It has been demonstrated that the ^{13}C chemical shifts are related to particular conformations. Carbon-13 CP MAS NMR spectra of solid poly(L-alanine) ([Ala]$_n$) show the C-α, C-β, and C=O carbon signals to be well resolved between the α-helix and β-sheet forms.[11] The ^{13}C chemical shifts are plotted against the number-average degree of polymerization in Figure 1. Clearly, ^{13}C chemical shifts of [Ala]$_n$ ($n > 16$) are unchanged for the peptides of various molecular weights within experimental error, and thus can serve to characterize the α-helix form. The chemical shifts of the C-α and carbonyl carbons of the α-helix are displaced significantly to high frequency (downfield) by 4.2 and 4.6 ppm, respectively relative to those of the β-sheet form, while the chemical shift of the C-β carbon of the α-helix is displaced to low frequency by about 5 ppm with respect to that of the β-sheet (−5.0 ppm). For this reason, the value of the ^{13}C chemical shift can be used to describe the local conformation.[12] In addition, the ^{13}C chemical shifts of randomly coiled poly(L-alanine) in trifluoroacetic acid solution have values between those of the α-helix and β-sheet forms.

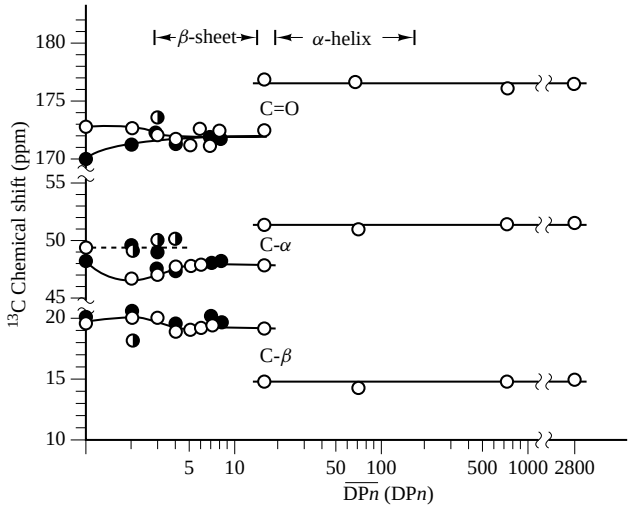

Figure 1 Plots of the ^{13}C chemical shifts of oligo-L-Ala and poly-L-Ala against the number-average degree of polymerization ($\overline{DP_n}$)

The existence of such characteristic displacements of ^{13}C chemical shifts is not limited to the Ala residue. In Table 1 are summarized the ^{13}C chemical shift values of various amino acid residues in the α-helix and β-sheet forms.[5,6] Here it is seen that the C-α and C=O peaks of the α-helix form are all displaced to high frequency with respect to those of the β-sheet form, which is consistent with the data of poly(L-alanine). The absolute ^{13}C chemical shifts of the C-α and C-β carbons are affected by the chemical structure of the individual amino acid residues and can be used effectively for conformational studies of particular amino acid residues in polypeptides and proteins. On the other hand, the C=O chemical shifts do not seem to be affected by residue structure and can be used for diagnosing the main chain conformation.

Poly(β-benzyl L-aspartate) (PBLA) in the solid state adopts various conformations such as a right-handed $\alpha(\alpha_R)$-helix, a left-handed $\alpha(\alpha_L)$-helix, a left-handed $\omega(\omega_L)$-helix, and a β-sheet form depending upon the temperature. The measured values for the ^{13}C chemical shifts depend significantly on the conformations of the peptide as shown in Table 2.[13] Variable temperature ^{13}C CP MAS NMR spectra of PBLA are shown in Figure 2.[14] The temperatures of the conformational changes of PBLA are indicated in the Figure. From this, it is clear that

Table 1 Carbon-13 Chemical Shift Characteristics of the α-helix and β-Sheet Forms (±0.5 ppm; from TMS)

	C-α			C-β			C=O		
Polypeptides[a]	α-Helix	β-Sheet	Δ[b]	α-Helix	β-Sheet	Δ[b]	α-Helix	β-Sheet	Δ[b]
$(Ala)_n$	52.4	48.2	4.2	14.9	19.9	−5.0	176.4	171.8	4.6
	52.3	48.7	3.6	14.8	20.0	−5.2	176.2	171.6	4.6
	52.8	49.3	3.5	15.5	20.3	−4.8	176.8	172.2	4.6
$(Leu)_n$	55.7	50.5	5.2	39.5	43.3	−3.8	175.7	170.5	5.2
	55.8	51.2	4.6	43.7[c]	39.6[c]	(4.1)	175.8	171.3	4.5
$[(Glu(OBzl)]_n$	56.4	51.2	5.2	25.6	29.0	−3.4	175.6	171.0	4.6
	56.8	51.1	5.7	25.9	29.7	−3.8	175.4	172.2	3.2
$[(Asp(OBzl)]_n$	53.4	49.2	4.2	33.8	38.1	−4.3	174.9	169.8	5.1
	53.6[d]			34.2[d]			174.9[d]		
$(Val)_n$	65.5	58.4	7.1	28.7	32.4	−3.7	174.9	171.8	3.1
		58.2			32.4			171.5	
$(Ile)_n$	63.9	57.8	6.1	34.8	39.4	−4.6	174.9	172.7	2.2
		57.1			33.1			171.0	
$(Lys)_n$[e]	57.4			29.9			176.5		
$[(Lys(Z))]_n$	57.6	51.4	6.2	29.3	28.5	−0.8	175.7	170.4	5.3
$(Arg)_n$[e]	57.1			28.9			176.8		
$(Phe)_n$	61.3	53.2	8.1	35.0	39.3	−4.3	175.2	169.0	6.2
$(Met)_n$	57.2	52.2	5.0	30.2	34.8	−4.6	175.1	170.6	4.5
$(Gly)_n$		43.2						168.4	
		44.3						169.2	
			5.1 ± 1.0[f]			−4.1 ± 0.7	175.8 ± 0.8	170.9 ± 1.2	4.9 ± 1.1

[a]Ala = alanine, Leu = leucine, Glu = glutamic acid, Asp = aspartic acid, Val = valine, Ile = isoleucine, Lys = lysine, Arg = arginine, Phe = phenylalanine, Met = methionine, Gly = glycine.
[b]Difference of the ^{13}C chemical shifts of the α-helix relative to those of the β-sheet form.
[c]Mistyping or erroneous assignment.
[d]Erroneously assigned to the left-handed α-helix.
[e]Data taken in neutral aqueous solution.
[f]Average values.

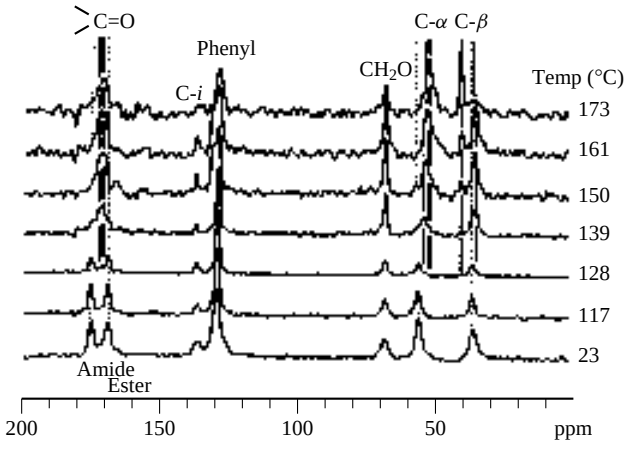

Figure 2 Variable temperature ^{13}C CP MAS TOSS NMR spectrum of poly(β-benzyl L-aspartate) in the solid state at various temperatures: *dashed line*, α_R-helix form; *light solid line*, ω_L-helix form; *bold solid line*; β-sheet form

the conformational changes α_R-helix → ω_L-helix → β-sheet occur with increasing temperature.

The conformations of polypeptides such as poly(L-alanine), polyglycine, and so on in the solid state are in many instances quite fixed. However, additional types of conformation can be formed when a small amount of guest glycine[15] or L-Ala[16] residues are incorporated into the host polypeptides. For example, solid state ^{13}C CP MAS NMR spectra of PBLA containing [3-^{13}C]L-Ala residues have been measured. The Ala C-β carbon shows significant displacements of the ^{13}C chemical shift depending on the conformational change.

Using the reference data, the helical sense of the ω-helix of poly(L-phenylalanine) has been shown to be right-handed, and this could not have been determined absolutely by X-ray diffraction. Furthermore, the side-chain conformation-dependent ^{13}C chemical shifts of this polymer and the L-phenylalanine residue in oligopeptides have been determined.[17]

The principal values of the ^{13}C chemical shift tensors (σ_{11}, σ_{22}, and σ_{33}) determined from the ^{13}C powder pattern spectrum are valuable as parameters for obtaining structural information which can be related to the electronic state more directly than the isotropically averaged value [$\sigma_{iso} = (\sigma_{11} + \sigma_{22} + \sigma_{33})/3$].[10] Nevertheless, very few data are available for the ^{13}C chemical shift tensor for carbon atoms in peptides. There have been a few studies of conformation using ^{13}C chemical shift tensors of polypeptides in the solid state. Solid state ^{13}C CP MAS NMR spectra of a variety of polypeptides containing [1-^{13}C]glycine residues as a minor component (<8%) have also been recorded. This was to obtain the ^{13}C isotropic average chemical shifts, and the principal values of the chemical shift tensors of the glycine (Gly) carbonyl carbon in β-sheet, α-helix, ω-helix, and 3_1-helix forms.[15] The last two conformations were obtained only when Gly residues were incorporated into the homopolypeptides. It was found that the magnitudes of displacements of chemical shifts upon conformational changes are larger for σ_{22} and σ_{33} than the

Table 2 Carbon-13 Chemical Shifts of Various Conformations of Poly(β-benzyl L-aspartate) in the Solid State (ppm from TMS; $\pm$0.5 ppm)

Sample	Conformation	C-α	C-β	C=O(amide)	C=O(ester)	Phenyl	CH_2O
Polymer	α_R-helix	53.4	33.8	174.9	167.0	129.8	65.7
	α_L-helix	50.9	33.8	171.1	169.0	129.2	66.1
	ω-helix	50.5	32.9	171.3	167.8	129.0	65.3
	β-sheet	49.2	38.2; 35.1	169.6	169.5	129.2	65.9
Oligomers							
DP_n5[a]	β-sheet	49.1	38.0	169.8	168.2	129.0	65.5
DP_n10	β-sheet	49.5	36.8	169.6	168.0	128.4	65.9

[a]DP = degree of polymerization.

isotropic chemical shift values, while σ_{11} is almost unaffected by any conformational change.

A solid state ^{13}C NMR study of some polypeptides containing [2-^{13}C]glycine residues has been carried out in order to clarify a conformational effect on the ^{13}C chemical shift tensors. It was found that the isotropic chemical shifts and principal values of the chemical shift tensor of Gly C-α incorporated in some homopolypeptides are displaced.

Hydrogen bonding plays an important role in the adoption of any specific conformation in peptides and polypeptides in the solid state. The effect of hydrogen bonding on the solid state ^{13}C chemical shifts of carbonyl carbons in peptides has been examined. Carbon-13 chemical shifts were determined for a series of oligopeptides containing glycine (Gly), L-Ala, L-valine, and L-leucine residues, for which the crystal structures were already available from X-ray diffraction studies. It was found that the ^{13}C chemical shifts of the carbonyl carbons in the $-C{=}O\cdots H-N-$type of hydrogen bond move linearly to high frequency with a decrease in the hydrogen bond length (R_{N-O}) as $\delta = a\ R_{N-O} + b$ (ppm). For the Gly, L-Ala, L-valine, and L-leucine residues, a and b are -12.4 and 206, -21.7 and 237.5, -14.2 and 215.4 and -10.0 and 202.2 ppm, respectively.[18,19] Using these relations, the hydrogen-bond length can be determined from the observed ^{13}C chemical shift values for the carbonyl carbons. These experimental results were explained by using ^{13}C chemical shift calculations based on the finite perturbation theory (FPT) intermediate neglect of differential overlap (INDO) method.

The conformational structures of poly(α-L-glutamic acid) [poly(Glu)], poly(α-L-aspartic acid) [poly(Asp)] and irregular poly(α,β-D,L-Asp) in the solid state have been studied by means of ^{13}C CP MAS NMR in conjunction with results from X-ray diffraction and infrared spectroscopy studies.[20] From these, it has been shown that poly(Glu) and poly(Asp) in the free acid form exhibit both α-helical and β-sheet forms, whereas the random coil form predominates in their sodium salts. Both the free acid and sodium salt of poly(α,β-Asp) exist predominantly in the random coil form. It turns out that the sodium salts are especially suitable for determining the NMR characteristics of the random coil conformation in the solid state.

2.2 Proteins

2.2.1 Fibrous Proteins

Since fibrous proteins generally have periodic amino acid sequence and higher order structures, the clarification of their fine structure in the solid state becomes very important not only when discussing the physical and chemical properties, but also when obtaining information about the molecular design of synthetic polypeptides. Indeed, a comparison of some fibrous proteins and their model synthetic polypeptides has been carried out. The conformation-dependent ^{13}C chemical shifts are useful for the determination of the conformational features of fibrous proteins.

Silk fibroin is one of the fibrous proteins having a simple amino acid composition, and isotopic enrichment can be performed easily. More detailed analyses of static or dynamic structures have been made by solid state NMR.[1,21,22] The amino acid composition of silk varies with the species of silkworm. In reflecting the higher Ala content of *Phylosamia cynthia ricini* fibroin it has been shown that the ^{13}C chemical shifts of the Ala residues of a dried sample, taken from the silk gland of *P.c. ricini*, are identical to those of the α-helical $[Ala]_n$. In contrast, the cocoon of *P.c. ricini* was found to have an antiparallel β-sheet form, as determined from the ^{13}C chemical shifts of the Ala and serine (Ser) residues. On the other hand, the ^{13}C peaks of the Ala and Gly residues of the silk II form of *Bombyx mori* silk fibroin are in good agreement with those of $[Ala\text{-}Gly]_n$ II as well as $[Gly]_n$ II and $[Ala]_n$ in the β-sheet form. The ^{13}C chemical shifts of samples taking the silk I form are significantly displaced from those of the silk II form. Models for the silk I structure of *B. mori* silk fibroin have been proposed on the basis of ^{13}C NMR data, X-ray diffraction data, and conformational energy calculations.

Collagen is composed of a triple-stranded helix. The individual triple chains are composed of the repeating pattern, $[Gly\text{-}X\text{-}Y]_n$, where X and Y are frequently occupied by proline (Pro) and hydroxyproline residues, respectively. Torchia and co-workers[23,24] have reported substantial work on the molecular dynamics of collagens by means of multinuclear solid state MR, using isotopically labeled samples which were obtained by cultivation techniques. Saito et al.[25] have found that most of the ^{13}C signals of collagen fibrils from bovine tendon and skin are in good agreement with those of $[Pro\text{-}Gly\text{-}Pro]_n$, although some peaks characteristic of the collagen are slightly displaced from those of the model polypeptides. All of the peaks of collagen fibrils have been assigned on the basis of computer simulation by utilizing amino acid composition and chemical shift data from the solid state and solution.

Carbon-13 CP MAS NMR spectra of tropomyosin, one of the muscle proteins, were measured in the solid state, in order to elucidate the higher order structure of the protein via the observation of the ^{13}C chemical shifts of the amino acid residues and their mobility. The higher order structure of tropomyosin is a right-handed α-helix coiled-coil structure,

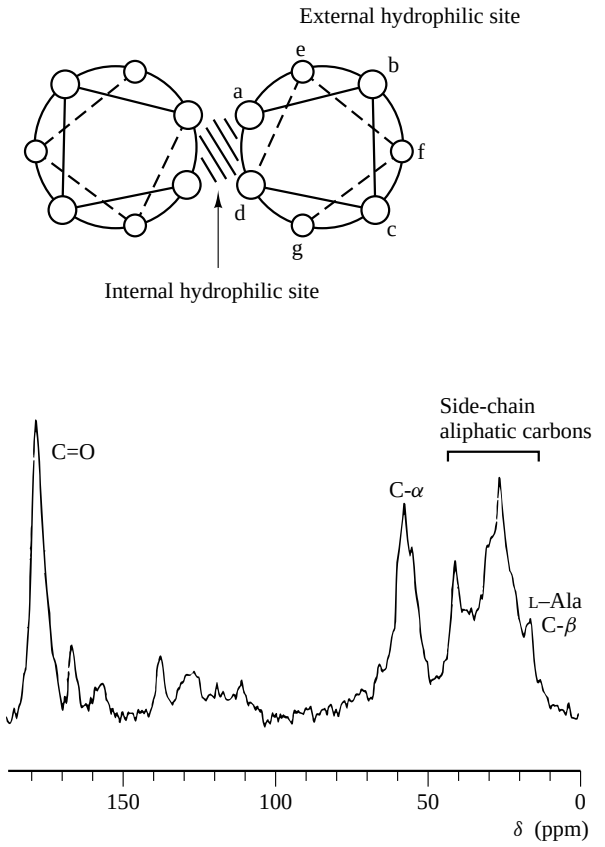

Figure 3 A schematic picture of the cross-section of the coiled-coil structure in tropomyosin (top), and the typical ^{13}C CP MAS NMR spectrum of tropomyosin at room temperature (bottom)

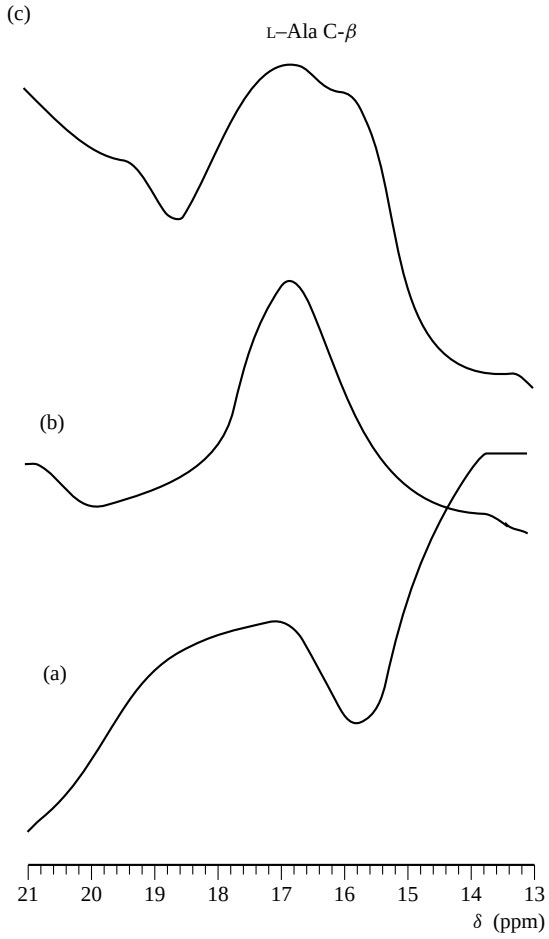

Figure 4 The expanded ^{13}C NMR spectra of the Ala C-β carbon atoms of tropomyosin, measured using the inversion–recovery method at room temperature. Recovery time, t: (a) 10 ms; (b) 500 ms; (c) 3500 ms

which contains two different sites. These are characterized by an internal hydrophobic site and an external hydrophilic site (Figure 3). A typical ^{13}C CP MAS NMR spectrum for tropomyosin in the solid state is shown in Figure 3.[26] Since the Ala residue is one of the major components, the ^{13}C signal which appears at 15–17 ppm can be assigned readily to the Ala C-β carbons, and it is seen that this signal consists of two peaks. Figure 4 shows the expanded Ala C-β signal, measured using the inversion–recovery method. These peaks indicated that there are at least two kinds of Ala C-β carbons. Furthermore, the carbon atoms contributing to the peak at 15.8 ppm have a larger value of T_1 than those at 16.7 ppm. This indicates that the former carbons are more mobile than the latter carbons, because the Ala C-β carbons in tropomyosin have correlation times with values appearing in an extremely narrow region at room temperature. The distance between the two α-helical axes in the coiled-coil structure is shorter than in coiled-coil helices which are packed in parallel in native muscle, as shown from X-ray studies. Therefore, it can be argued that the mobility of the Ala C-β carbon atoms in the internal site is expected to be more restricted than that in the external site. The two peaks at 15.8 and 16.7 ppm therefore are assigned to the Ala C-β carbons in the external and internal sites of the coiled-coil structure, respectively.

Native wool fiber consists of intermediate filaments composed of low-sulfur-containing proteins which are embedded in a nonfilamentous matrix. The nonfilamentous matrix usually consists of two classes of proteins; one is a high-sulfur-containing protein and the other is a protein containing Gly and tyrosine (Tyr) residues. Wool keratin can be divided into three main fractions after reducing the disulfide bonds and protection of the resulting thiol groups with iodoacetic acid to form *S*-carboxymethylkerateine (SCMK). The solid state ^{13}C CP MAS TOSS NMR spectra of wool and four kinds of SCMKs extracted from low-sulfur fractions (SCMKA), helix-rich fragments (SCMKA-hf), high-sulfur fractions (SCMKB), and high-Gly-Tyr fractions (HGT) are shown in Figure 5.[27,28] For characterization of the main-chain conformation of polypeptides and proteins in the solid state, it is very useful to use the ^{13}C chemical shift value of the main-chain carbonyl carbon, because it is strongly influenced by the conformation of the main chain but not by the type of amino acids and/or a specific amino acid sequence. Hence, it can be argued that the lineshape of the ^{13}C signals in the carbonyl region for proteins reflects the main-chain conformation.

The carbonyl ^{13}C signal can be resolved into four peaks by computer fitting. The relative intensity of the high-frequency peak at about 176 ppm corresponds to the proportion of the α-helix component, because this peak comes from the main-chain carbonyl carbons in the α-helix form. The proportion of

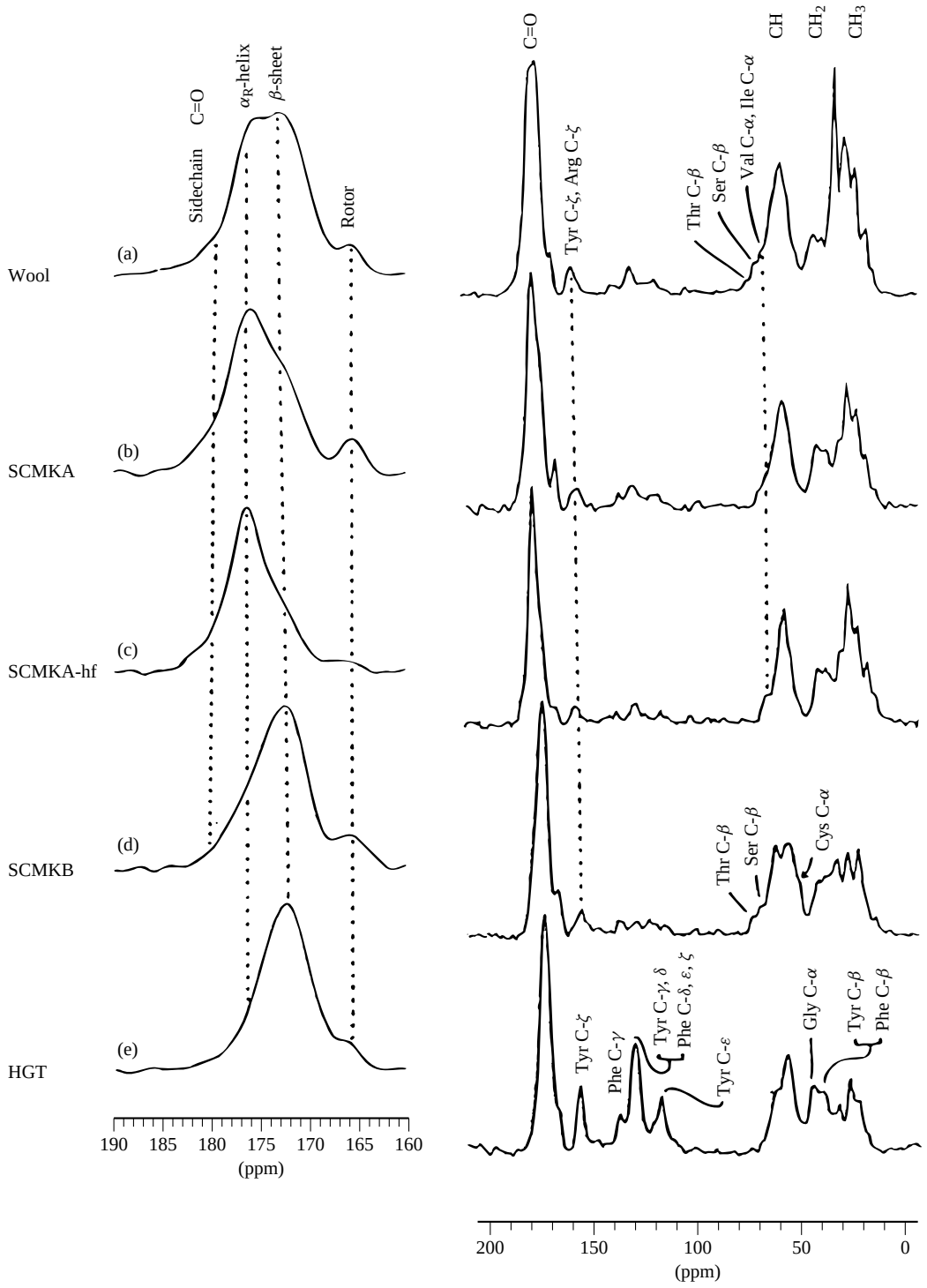

Figure 5 ^{13}C CP MAS TOSS NMR spectra of (a) wool, (b) SCMKA, (c) SCMKA-hf, (d) SCMKB, and (e) HGT, and their expanded spectra of the carbonyl carbon region. Arg = arginine, Thr = threonine, Val = valine, Ile = isoleucine, Cys = cysteine, Phe = phenylalanine

the α-helix component increases in the order: wool, SCMKA, SCMKA-hf. On the other hand, the low-frequency peak at 172 ppm is characteristic of the main-chain carbonyl carbons in the β-sheet form. On the basis of the above assignment, it can be said that the β-sheet form is predominant in SCMKB and HGT. These findings are also confirmed from the peaks in other carbon regions. Furthermore, it is suggested that the coiled-coil structure exists in wool, SCMKA, and SCMKA-hf, because the ^{13}C chemical shift values of the Ala C-β carbons in these samples coincide, within experimental error, with that of the Ala residue located in the internal site of the coiled-coil structure in tropomyosin.

This conformational analysis, using conformation-dependent ^{13}C chemical shifts, has been applied to investigate the conformational transition of SCMKA induced by stretching, heating, or steam-treating. The β-sheet form appears and the proportion

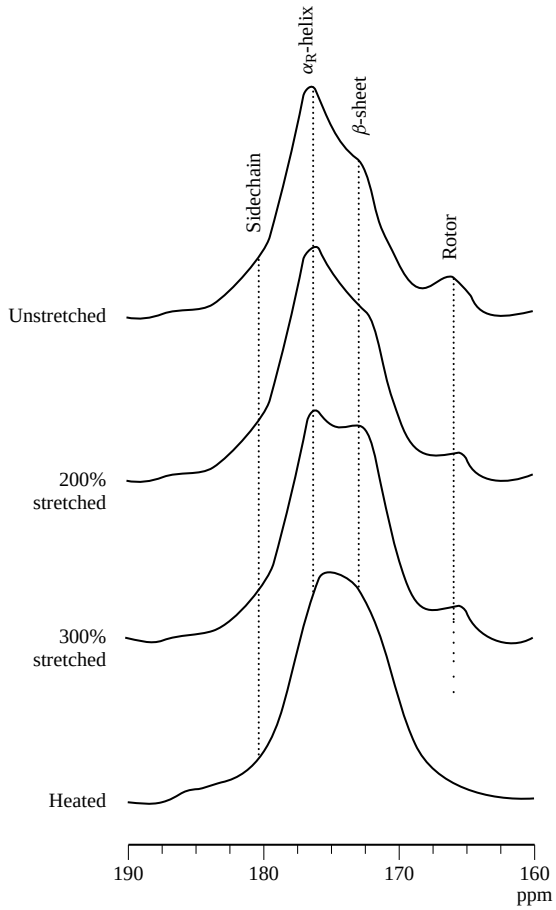

Figure 6 Expanded ^{13}C CP MAS TOSS NMR spectra for the carbonyl carbon region in SCMKA films cast from aqueous solution

of the α-helix form decreases upon stretching and steam-treating as shown in Figure 6.[28] For the SCMKA heated at 200 °C for 3 h in vacuo, the ^{13}C CP MAS spectrum shows that each peak is broader than those of other treated specimens. This indicates the existence of various conformations and/or different microenvironments in the heated SCMKA. Thus, it can be said that the random coil form appears by heating. From X-ray diffraction measurements, the α-helix form completely vanishes in SCMKA heated under the same conditions. However, Figure 6 shows that the α-helix form remains to an appreciable extent in the heated sample, although the random coil form also appears. The difference between the results from X-ray diffraction and NMR spectroscopy studies suggests that only the packing of the ordered structure (the α-helix form) in SCMKA is disrupted by heating, but that the secondary structure is retained. On the other hand, in the case of the structural transition for the same protein, the change of the lineshape for the α-methine carbons can be attributed mainly to the conformational change.

The dynamics and structure of mouse keratin intermediate filaments has been investigated by solid state ^{13}C and ^{2}H NMR spectroscopy, using isotopically labeled samples.[29]

2.2.2 Membrane Proteins

The structural and dynamic analysis of membrane proteins is readily achieved by solid state ^{13}C NMR. The reasons are as follows: firstly, biological membranes greatly restrict the motion of embedded proteins and consequently are difficult to study by solution NMR methods; secondly, only a few membrane proteins have been crystallized and studied by X-ray diffraction methods; thirdly, if the membrane protein is uniaxially oriented in the lipid, there is the advantage of being able to determine the structure at the atomic level by NMR as well as X-ray crystallography. Further, since phospholipids coexist in many cases in membranes, the NMR method is still suitable because of its ability to observe selectively by means of isotopic labeling, multinuclear MR, and utilizing the differences of relaxation times. Thus phospholipids, for example, are readily and selectively studied by solid state NMR methods using specifically ^{31}P NMR.[30]

The ^{13}C CP MAS spectra of ^{13}C-labeled gramicidin A (GA) were measured to determine directly the structure of this peptide in a lipid membrane.[31] The seven GA analogs, each labeled at a single carbonyl group of each of some amino acid residues, were synthesized by the solid phase method. These ^{13}C-labeled GAs were incorporated into aligned multilayers of dimyristoylphosphatidylcholine or diether lipid bearing 14- or 16-carbon chains, at a 1:15 peptide:lipid molar ratio. Carbon-13 CP NMR spectra were obtained at several temperatures and over a range of sample orientations with respect to the spectrometer magnetic field. The observed chemical shielding anisotropies indicate that all of the labeled carbonyl bonds are oriented almost parallel to the molecular long axis and perpendicular to the lipid bilayer plane. These orientations are consistent with GA forming a β6.3 single-strand helix that is oriented parallel to the methylene chains of the lipid molecules. Comparison of the linewidths from labeled residues that are in the innermost turn of the helix, and in the turn nearest the lipid bilayer surface suggests that although the peptide behaves largely as a right-handed barrel, segments of the peptide close to the membrane surface possess greater motional freedom.

Bacteriorhodopsin and rhodopsin are integral membrane proteins that contain the vitamin A aldehyde, retinal, as a photoreactive chromophore. Many solid state NMR studies on the structure and environment of the retinal chromophore in these proteins have been reported, using mainly specifically ^{13}C-labeled retinals.[2,32,33] It may reasonably be said that the structure of retinal in bacteriorhodopsin and rhodopsin has been determined by solid state NMR. Hence, solid state NMR is an extremely important experimental procedure in investigating the mechanism of sight. Most recently, the spectrum of ^{13}C-labeled bacteriorhodopsin in purple membranes was recorded. On the basis of the ^{13}C CP MAS NMR experiments, a discussion has been presented of the change of the manner of mutual orientation between α-helices as induced by hydration/dehydration.

Also, soluble proteins such as enzymes, conjugated proteins such as glycoproteins, and proteins which are in more complex systems have been investigated by solid state NMR.[34–36]

3 SOLID STATE NMR STUDIES OF ^{15}N IN SYNTHETIC POLYPEPTIDES

It has been demonstrated that the isotropic ^{15}N chemical shifts of systems such as poly(Gly) (PG), poly(L-Ala), poly(L-leucine), poly(L-isoleucine) poly(L-valine), poly

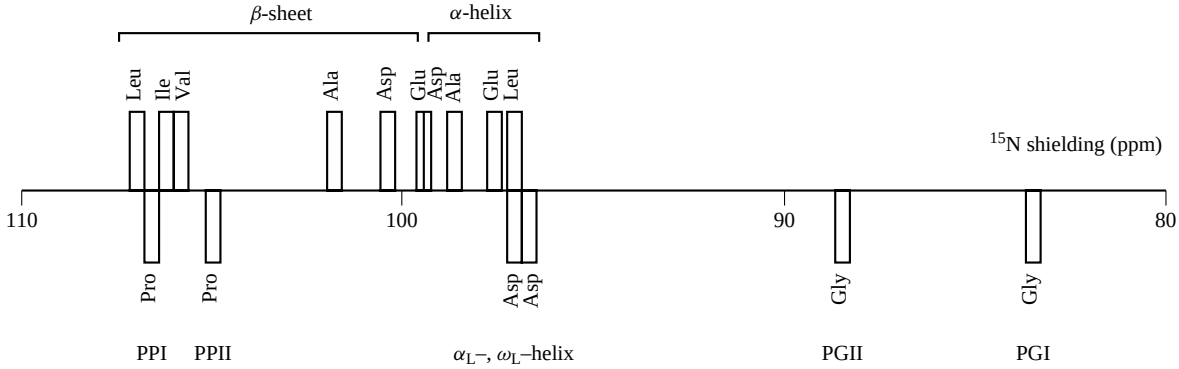

Figure 7 Diagram of the observed isotropic ^{15}N shielding of some homopolypeptides $[X]_n$ with various conformations (α-helix, β-sheet, α_L-helix, ω_L-helix, PG I, PG II, PP I, and PP II forms). Leu = leucine, Ile = isoleucine, Val = valine, Glu = glutamic acid

(L-phenylalanine), poly(γ-methyl L-glutamate), poly(β-benzyl L-aspartate) and poly(L-Pro) (PP) in the peptide backbone of polypeptides in the solid state exhibit a significant conformation-dependent change. Both experimental observation and theoretical calculation confirm this.[37–39] The σ_{iso} for the α-helix form (97.0−99.2 ppm) appears to low frequency by about 1.2−10.0 ppm with respect to that for the β-sheet form (99.5−107.0 ppm) of polypeptides, which obviously depends on the structure of the individual amino acid residue, as shown in Figure 7 (relative to $^{15}NH_4NO_3$). Some ^{15}N chemical shift differences are rather small, but are meaningful in the context of polypeptides. The variations of the σ_{iso} for various kinds of polypeptides are about 2.5 ppm in the α-helix form and about 7.5 ppm in the β-sheet form. In addition, the σ_{iso} of the β-sheet form of the L-leucine, L-valine, and L-isoleucine residues, which possess alkyl side chains, appear to high frequency with respect to that of the L-Ala residue. In contrast, the σ_{iso} value for the β-sheet form of the L-Asp(OBzl), L-Glu(OBzl), and L-Glu(OMe) residues (where Glu = glutamic acid), which possess a side-chain ester, is to low frequency with respect to that of the L-Ala residue. These results indicate that the ^{15}N chemical shift difference between the α-helix and β-sheet forms depends on the side-chain structure of individual amino acid residues.

Further, σ_{iso} gives information about the helix sense (α_R-helix or α_L-helix) of poly(β-benzyl L-aspartate) (ω-helix: 99.2 ppm; α_L-helix: 97.0 ppm).[40] In addition, the ^{15}N chemical shift value of PBLA with low molecular weight (β-sheet form) is identical with that of PBLA with high molecular weight (β-sheet form), indicating that the ^{15}N chemical shift of solid polypeptides is independent of the chain length, if no conformational changes occur. Accordingly, the ^{15}N chemical shift depends mainly on the conformation and side-chain structure of individual amino acid residues. In order to support this view theoretical calculations of ^{15}N chemical shifts are required, using the electronic states derived by quantum chemical methods. The relative ^{15}N NMR chemical shift of a dipeptide fragment forming hydrogen bonds with two formamide molecules has been calculated using the FPT INDO theory.[37]

The relation between the isotropic ^{15}N chemical shift or chemical shift tensor and the structures of various kinds of synthetic copolypeptides in the solid state have been studied.[38–40] It was found that the ^{15}N chemical shifts indicate strong neighboring sequence effects.

An analytical method for the determination of dihedral angles of the GA backbone from solid state ^{15}N NMR spectroscopic data has been demonstrated.[31,41] Advantage is taken of the ^{15}N−^{1}H and ^{15}N−^{13}C dipolar interactions as well as the ^{15}N chemical shift interaction in the oriented samples. The dihedral angles for the L-Ala$_3$ site are determined by obtaining the NMR data for both the Gly$_2$-L-Ala$_3$ and L-Ala$_3$-D-leucine$_4$ peptide linkages. Two possible sets of torsion angles for the L-Ala$_3$ site are obtained (ϕ,ψ = − 129°, 153° and − 129°, 122°), both of which are consistent with a right-handed α-helix. In addition, the dynamics of the backbone of GA in dimyristoylphosphatidylcholine bilayers have been investigated using solid state ^{15}N NMR.[41] Nitrogen-15 CP NMR spectra of single-site ^{15}N-labeled GA at 8 °C were analyzed to yield a spatial model for local backbone motion. This model includes the axis of motion, the mean orientation, and the maximum amplitude of displacement for individual peptide planes. Specific sites in the first turn of the amino terminus were investigated, with emphasis on the L-Ala$_3$ and D-leucine$_4$ linkages, for which the orientation of the ^{15}N chemical shift tensor with respect to the molecular frame has been determined.

4 SOLID STATE ^{17}O NMR OF SYNTHETIC POLYPEPTIDES

The oxygen atom is an important atom in the hydrogen bonding structure in peptides and polypeptides. Nevertheless, a solid state ^{17}O NMR study of peptides and polypeptides has never been carried out, to our knowledge. This is due to the very low sensitivity of solid state ^{17}O NMR measurements which arises for two reasons. One is that the ^{17}O nucleus is in very low natural abundance, 0.037%. The other is that the ^{17}O nuclear spin quantum number (I) is $\frac{5}{2}$, which is a quadrupolar nucleus, and so the ^{17}O signal is broadened by nuclear quadrupolar effects in the solid. On the other hand, solution state ^{17}O NMR spectroscopy has been employed successfully to elucidate a number of structural problems in organic chemistry,[42] because the ^{17}O signal becomes very sharp due to the removal of quadrupolar interaction by isotropic fast reorientation in solution. For example, as the oxygen atom is directly associated with the formation of hydrogen bonds, hydrogen bonding for the carbonyl group

in various compounds often results in large low-frequency shifts of the carbonyl ^{17}O NMR signal.[43] From these results, solution state ^{17}O NMR has been established as a means of investigating structural characterizations.

Clearly therefore, solid state ^{17}O NMR does offer a unique opportunity for understanding the hydrogen-bonding structure in solid peptides and polypeptides. Kuroki et al.[44] have observed high-resolution ^{17}O NMR spectra of systems with a wide range of hydrogen bond length, of PG I, PG II, glycylglycine (GlyGly) and glycylglycine nitrate (GlyGly·HNO_3) in the solid state, in order to obtain three kinds of NMR parameters: chemical shift, the quadrupolar coupling constant (e^2qQ/h) and the asymmetric parameter (η_Q), and to understand the relationship between the hydrogen bonding structure and these NMR parameters.

Static ^{17}O CP NMR spectra of GlyGly were observed at 36.6, 54.2, and 67.8 MHz. The spectra at 36.6 and 54.2 MHz consist of two major split signals, but that at 67.8 MHz becomes one major signal. Such splitting comes from the quadrupolar interaction. By computer simulation, the quadrupolar coupling constant e^2qQ/h was determined to be 8.55 MHz. This value is much larger than that for the amide ^{14}N nitrogen nucleus (1.11 MHz). It is seen that the NMR spectra depend strongly on the measurement frequency because the quadrupolar effect depends on the measurement frequency, and the broadening of the ^{17}O NMR signal is further increased by the quadrupolar effect as the measurement frequency is decreased. Thus, it is clear that high-frequency measurements are needed for quadrupolar nuclei such as ^{17}O.

Figure 8 shows 67.8 MHz static ^{17}O CP NMR spectra of PG I, PG II, GlyGly, and GlyGly·HNO_3 (points), compared with the computer simulations (continuous lines). The ^{17}O NMR parameters of PG I, PG II, GlyGly, and GlyGly·HNO_3 obtained by computer simulations are shown in Table 3. From these results, the δ_{11}, δ_{22}, and δ_{33} values of the samples were found to change from 546 to 574 ppm, 382 to 425 ppm, and − 132 to − 101 ppm, respectively. The magnitude of the chemical shift change is much larger than that of the carbonyl

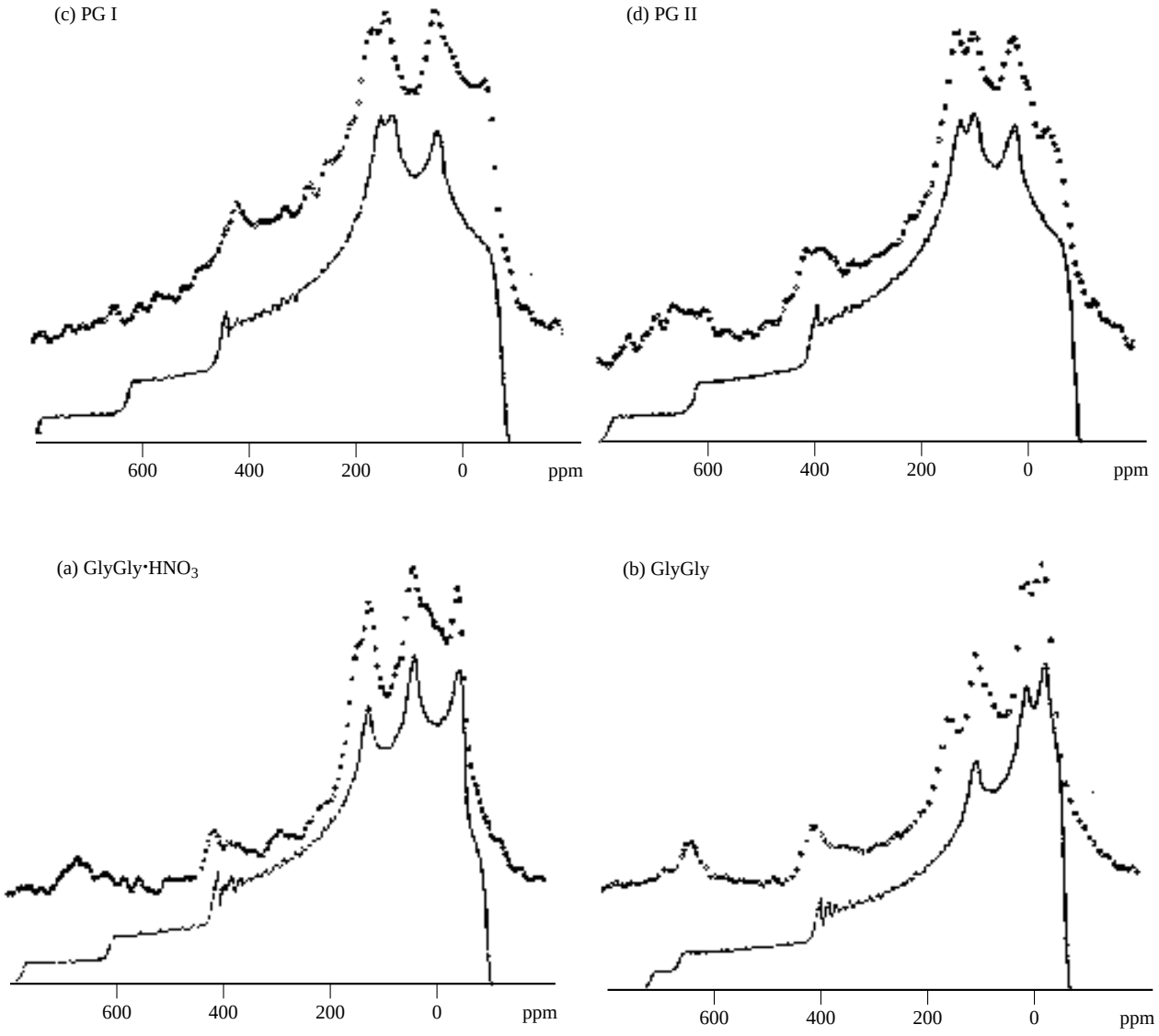

Figure 8 ^{17}O 67.8 MHz CP static NMR spectra of GlyGly·HNO_3 (a), GlyGly (b), PG I (c), and PG II (d), together with theoretically simulated spectra

Table 3 Determined ^{17}O NMR Parameters of Solid Peptides and Polypeptides Containing a Gly Residue

Sample	e^2qQ/h (MHz)	η_Q	Chemical shift tensor (ppm)						Angle Δ[a] (deg)		
			δ_{11}	δ_{22}	δ_{33}	δ_{iso}	$\Delta\delta$[b]	η[c]	α	β	γ
Polypeptides											
PG II	8.30	0.29	562	410	−108	288	396	0.38	92	89	−81
PG I	8.55	0.26	574	425	−101	299	400	0.37	100	91	−79
Oligopeptides											
GlyGly	8.55	0.45	546	382	−132	265	397	0.41	94	90	−87
GlyGly·HNO_3	8.75	0.47	559	408	−127	280	407	0.37	94	89	−81

[a]Angle Δ indicates the Euler angles between the principal axes of the quadrupolar tensor and the chemical shift tensor.
[b]$\Delta\delta = \delta_{iso} - \delta_{33}$.
[c]$\eta = (\delta_{11} - \delta_{22})/\Delta\delta$.

^{13}C and amide ^{15}N chemical shift. Every $\Delta\delta$ defined by $\Delta\delta = \delta_{33} - \delta_{iso}$, is about 400 ppm, which is much larger than that of the carbonyl ^{13}C and amide ^{15}N chemical shifts by about 170, 100 ppm, respectively. Every η value, defined by $\eta = (\delta_{22} - \delta_{11})/\Delta\delta$, is roughly 0.4. These values are common to the carbonyl oxygen in peptides. Although the chemical shift tensor is axially symmetric ($\delta_{11} = \delta_{22}$) for the case of the carbonyl oxygen of L-Ala as reported by Fiat and co-workers,[45,46] the chemical shift tensor of the carbonyl oxygen in the peptides considered here is not axially symmetric.

The e^2qQ/h values change from 8.30 to 8.75 MHz. These values are larger than the e^2qQ/h value of χ for L-leucine, which is 8.0 MHz at 190 K.[46] The η_Q values of polypeptides such as PG I and II are 0.26 and 0.29, and the η_Q values of oligopeptides such as GlyGly and GlyGly·HNO_3 are 0.45 and 0.47, respectively. The difference may come from a difference in molecular packing between them. Further, it is found that the principal axis of the quadrupolar tensor and the principal axis of the ^{17}O chemical shielding tensor for the carbonyl oxygen of the peptides and polypeptides are not coincident with each other. From these experimental results it can be said that each of the above NMR parameters is strongly influenced by the electronic structure of molecules.

So far, there has been little study aimed at determining the direction of the principal axes of the electric field gradient tensor and the chemical shielding of carbonyl oxygen of peptides and polypeptides from NMR experiments. The direction of the principal axes of the chemical shielding of the carbonyl oxygen of peptides and polypeptides has been calculated using FPT-MNDO-PM3 methods. It was found that the σ_{22} component lies approximately along the C=O bond, the σ_{11} component is aligned in the direction perpendicular to the C=O bond on the peptide plane, and σ_{33} which is the most shielded component is aligned in the direction perpendicular to the peptide plane. In the case of the electric field gradient tensor of the carbonyl oxygen, it was shown that the V_{22} component lies approximately along the C=O bond, the V_{33} component is aligned in the direction perpendicular to the C=O bond on the peptide plane, and the V_{11} component is aligned in the direction perpendicular to the peptide plane. These results show that the largest component V_{33} of the electric field gradient lies along the molecular chain direction. The relationship between the electric field gradient tensor and the chemical shielding obtained by this calculation agree with the experimental results.

The plot of the observed e^2qQ/h values vs. the hydrogen bond length shows that the e^2qQ/h values decrease linearly with a decrease in the hydrogen-bond length (R_{N-O}) (in Å) as expressed by e^2qQ/h (MHz) = 5.15 + 1.16R_{N-O}. This shows that the decrease of the hydrogen-bond length leads to a decrease in electric gradient (q). The value of q is very sensitive to the hydrogen-bond-length change. From this relationship it is apparent that the hydrogen-bond length can be determined by the observation of the e^2qQ/h value. The plot of the observed isotropic ^{17}O chemical shift values (δ_{iso}) against the hydrogen-bond length (R_{N-O}) shows that the δ_{iso} values in both peptides and polypeptides move upfield with a decrease in the hydrogen-bond length (R_{N-O}). The plot of the observed principal values of ^{17}O chemical shifts against the hydrogen-bond length (R_{N-O}) also shows every principal value in both the peptides and polypeptides and moves to low frequency with a decrease in the hydrogen-bond length (R_{N-O}).

From these experimental findings, it is clear that ^{17}O NMR spectroscopy will become a powerful tool for elucidating the hydrogen-bonding structure in solid peptides and polypeptides.

5 RELATED ARTICLES

Chemical Shift Tensors; Chemical Shifts in Biochemical Systems; Membrane Proteins; Oxygen-17 NMR; Protein Dynamics from Solid State NMR; Quadrupolar Nuclei in Solids.

6 REFERENCES

1. H. Saito, T. Tabeta, A. Shoji, I. Ando, and T. Asakura, in *Magnetic Resonance in Biology and Medicine*, eds. G. Govil, C. L. Kheterapal, and A. Saran, Tata McGraw-Hill, New Delhi, 1985, p. 195
2. S. O. Smith and R. G. Griffin, *Annu. Rev. Phys. Chem.*, 1988, **39**, 511.
3. G. A. Hartfield and G. E. Maciel, *Methods Protein Anal.*, **1988**, 214.
4. S. J. Opella and P. L. Stewart, *Methods Enzymol.*, 1989, **176**, 242; S. J. Opella, *Biol. Magn. Reson.*, 1990, **9**, 177.
5. H. Saito and I. Ando, *Annu. Rep. NMR Spectrosc.*, 1989, **21**, 210.
6. I. Ando, T. Yamanobe, and T. Asakura, *Prog. NMR Spectrosc.*, 1990, **22**, 349.
7. A. Shoji, S. Ando, S. Kuroki, I. Ando, and G. A. Webb, *Annu. Rep. NMR Spectrosc.*, 1993, **26**, 55.

8. H. Kurosu, S. Ando, H. Yoshimizu, and I. Ando, *Annu. Rep. NMR Spectrosc.*, 1994, **28**, 189.
9. I. Ando and G. A. Webb, *Theory of NMR Parameters*, Academic Press, London, 1983.
10. I. Ando, T. Yamanobe, H. Kurosu, and G. A. Webb, *Annu. Rep. NMR Spectrosc.*, 1989, **22**, 205.
11. H. Saito, R. Tabeta, A. Shoji, T. Ozaki, and I. Ando, *Macromolecules*, 1983, **16**, 1050.
12. I. Ando, H. Saito, R. Tabeta, A. Shoji, and T. Ozaki, *Macromolecules*, 1984, **17**, 457.
13. H. Saito, R. Tabeta, I. Ando, T. Ozaki, and A. Shoji, *Chem. Lett.*, 1983, 1437.
14. T. Akieda, H. Mimura, S. Kuroki, H. Kurosu, and I. Ando, *Macromolecules*, 1992, **25**, 5794.
15. S. Ando, T. Yamanobe, I. Ando, A. Shoji, T. Ozaki, R. Tabeta, and H. Saito, *J. Am. Chem. Soc.*, 1985, **107**, 7648.
16. S. Tuzi, T. Komoto, I. Ando, H. Saito, A. Shoji, and T. Ozaki, *Biopolymers*, 1987, **26**, 1983.
17. H. Miyamoto, T. Komoto, H. Kurosu, I. Ando, T. Ozaki, and A. Shoji, *J. Mol. Struct.*, 1990, **220**, 251.
18. S. Ando, I. Ando, A. Shoji, and T. Ozaki, *J. Am. Chem. Soc.*, 1988, **110**, 3380.
19. N. Asakawa, S. Kuroki, H. Kurosu, I. Ando, A. Shoji, and T. Ozaki, *J. Am. Chem. Soc.*, 1992, **114**, 326.
20. H. Piocova, V. Sasudek, P. Schmidt, D. Hlavata, J. Plestill, and F. Lauprette, *Polymer*, 1987, **28**, 1991.
21. H. Saito, R. Tabeta, T. Asakura, Y. Iwanaga, A. Shoji, T. Ozaki, and I. Ando, *Macromolecules*, 1984, **17**, 1405.
22. T. Asakura, M. Demura, Y. Watanabe, and K. Sata, *J. Polym. Sci., Polym. Phys. Ed.*, 1992, **30**, 693.
23. D. A. Torchia and D. L. VanderHart, *J. Mol. Biol.*, 1976, **104**, 315.
24. Y. Hiyama and D. A. Torchia, *Basic Life Sci.*, 1990, **56**, 273.
25. H. Saito, R. Tabeta, A. Shoji, T. Ozaki, I. Ando, and T. Miyata, *Biopolymers*, 1984, **23**, 2279.
26. S. Tuzi, S. Sakamaki, and I. Ando, *J. Mol. Struct.*, 1990, **221**, 289.
27. H. Yoshimizu and I. Ando, *Macromolecules*, 1990, **23**, 2908.
28. H. Yoshimizu, H. Mimura, and I. Ando, *Macromolecules*, 1991, **24**, 862.
29. J. W. Mack, D. A. Torchia, and M. Steinert, *Biochemistry*, 1988, **27**, 5418.
30. H. Tournois, J. L. Bijvelt, C. W. M. Haest, J. Ier, and B. Kruiff, *Biochemistry*, 1987, **26**, 6613.
31. L. K. Nicholson, F. Moll, T. E. Mixon, P. V. LoGrasse, J. C. Lay, and T. A. Cross, *Biochemistry*, 1987, **26**, 6621.
32. G. S. Harbison, J. Herzfeld, and R. G. Griffin, *Biochemistry*, 1983, **22**, 1.
33. S. O. Smith, H. J. M. De Groot, R. Gebhard, J. M. L. Courtin, J. Lugtenburg, J. Herzfeld, and R. G. Griffin, *Biochemistry*, 1989, **28**, 8897.
34. R. A. Santos, E. S. Gruff, S. A. Koch, and G. S. Harbison, *J. Am. Chem. Soc.*, 1991, **113**, 469.
35. J. R. Garbow, H. Fujiwara, C. R. Sharp, and E. W. Logusch, *Biochemistry*, 1991, **30**, 7057.
36. J. Schaefer, K. J. Kramer, J. R. Garbow, G. S. Jacob, E. O. Stejskal, T. L. Hopkins, and R. D. Speirs, *Science*, 1987, **235**, 1200.
37. A. Shoji, T. Ozaki, T. Fujito, K. Deguchi, and I. Ando, *Macromolecules*, 1987, **20**, 2441.
38. A. Shoji, T. Ozaki, T. Fujito, K. Deguchi, S. Ando, and I. Ando, *Macromolecules*, 1989, **22**, 2860.
39. A. Shoji, T. Ozaki, T. Fujito, K. Deguchi, S. Ando, and I. Ando, *J. Am. Chem. Soc.*, 1990, **112**, 4693.
40. A. Shoji, T. Ozaki, T. Fujito, K. Deguchi, and I. Ando, in preparation.
41. L. K. Nicholson and T. A. Cross, *Biochemistry*, 1991, **28**, 607.
42. ed. D. W. Boykin, *^{17}O NMR Spectroscopy in Organic Chemistry*, CRC Press, Boca Raton, FL, 1991.
43. D. W. Boykin and A. L. Baumstark, *New J. Chem.*, 1992, **16**, 357.
44. S. Kuroki, A. Takahashi, I. Ando, A. Shoji, and T. Ozaki, *J. Mol. Struct.*, 1994, **323**, 197.
45. R. Goc, E. Ponnusomy, J. Tritt-Goc, and D. Fiat, *Int. J. Pept. Protein Res.*, 1988, **31**, 130.
46. R. Goc, J. Tritt-Goc, and D. Fiat, *Bull. Magn. Reson.*, 1989, **11**, 238.

Biographical Sketches

Isao Ando. *b* 1941. Ph.D., 1972 (supervisor Atsuo Nishioka), polymer chemistry, Tokyo Institute of Technology, Japan. Postdoctoral work at University of Illinois, Urbana (with Herb Gutowsky). Successively research associate, associate professor, and professor, Tokyo Institute of Technology. Approx. 250 publications. Research specialties: structures and electronic states of solid polymers and biopolymers, solid state NMR, and nuclear shielding calculation.

Shigeki Kuroki. *b* 1965. Ph.D., 1994 (supervisor Isao Ando), polymer chemistry; postdoctoral fellowship, 1994–present, Tokyo Institute of Technology. Approx. 15 publications. Research specialties: structures of solid biopolymers, and solid state NMR.

Solid Polymers: Shielding and Electronic States

Takeshi Yamanobe
Gunma University, Kiryu, Gunma, Japan
and
Hiromichi Kurosu
Tokyo Institute of Technology, Ookayama, Meguro-ku, Tokyo, Japan

1 Introduction 1
2 Theoretical Aspects of Electronic State and Nuclear Shielding in Solid Polymers 1
3 Interpretation of Nuclear Shielding by the TB Method 2
4 Related Articles 6
5 References 6

1 INTRODUCTION

Nuclear shielding data offer microscopic information about the stereochemical and crystal structures of polymers, which in turn are important factors in understanding physical properties. Details of electronic structure can also be deduced from nuclear shielding data, and this is also important in controlling physical properties.[1] In order to obtain information about the electronic structure of polymers from nuclear shielding data, it is necessary to use a theoretical approach in addition to an experimental one.

In general, there are two possibilities for obtaining such information by theoretical methods. One is to use a fragment of polymer such as a dimer, trimer, etc. for theoretical calculations. Such an approach is useful, because the nuclear shielding is sometimes governed by the local electronic structure. However, there is doubt whether the electronic structure obtained from the model compound appropriately reproduces that of the polymer chain. Another approach is to employ directly an infinite polymer chain with a periodic structure. This leads to the application of the tight-binding (TB) molecular orbital approximation, which was developed in the field of solid state physics.[2] Its advantages are that it treats the polymer directly and that relatively long range intrachain interactions such as hydrogen bonding in the α-helix form of polypeptides can be easily taken into account.

In using the model compound approach, the electronic structure of large chains can be visualized by drawing the orbital energies associated with chains of increasing length. On the other hand, for an infinite polymer chain, the energy levels are built up as a continuous band structure. As the rotation about the bond is strongly restricted in solid polymers, the periodicity of the polymer chain is retained. From the point of view of calculating nuclear shielding, use of the TB model for calculations of the electronic structures of polymers has been successful. Here we describe the basic ideas for deducing the electronic structure and nuclear shielding of solid polymers by the TB approximation.

2 THEORETICAL ASPECTS OF ELECTRONIC STATE AND NUCLEAR SHIELDING IN SOLID POLYMERS

Polymers can be characterized by a possible periodicity in their conformational structure and a large number of electrons. In this system, the potential energy that an electron experiences is periodic. Periodic systems have the advantage of translational symmetry when compared with aperiodic systems. It is possible to exploit this symmetry in order to reduce to reasonable proportions the formidable task of computing the electronic states of an extended system. The TB molecular orbital model is employed to describe the electronic structure of linear periodic polymers within the framework of a 'linear combination of atomic orbitals' approximation for electronic eigenfunctions. By means of Bloch's theory,[3] the eigenfunction $\Phi_n(k)$ for an electron at position r, belonging to the nth crystal orbital is given by

$$\Phi_n(k) = N^{-1/2} \sum_{j=-(N-1)/2}^{(N-1)/2} \sum_{\nu=1}^{s} \mathrm{e}^{\mathrm{i}jkb} C_{\nu n}(k) \phi_\nu(r - jb) \tag{1}$$

where k is the wavenumber, ν is an orbital index for the jth cell, s is the total number of atomic orbitals in a given cell, N is the total number of cells considered, and b is the unit vector of translational symmetry. In equation (1) $\phi_\nu(r - jb)$ represents the νth atomic orbital in the jth cell and $C_{\nu n}(k)$ its expansion coefficient in the linear combination of atomic orbitals. The limits of k, within a given Brillouin zone, are $-\frac{1}{2}\pi$ and $\frac{1}{2}\pi$. Using equation (1), the total energy E of the polymer can be expressed as

$$E(k) = \sum_{n}^{\mathrm{occ}} \langle \Psi_n(k) | \hat{\mathcal{H}} | \Psi_n(k) \rangle \tag{2}$$

where $\Psi_n(k)$ is the Slater determinant composed of the $\Phi_n(k)$. $\hat{\mathcal{H}}$ is the Hamiltonian, consisting of terms representing the kinetic energy, the potential energy of the electronic field of the polymer, and the electron repulsion energy. The advantage of equation (1) is that calculation of the electronic structure of an infinite polymer can be reduced to the calculation for a unit cell (monomer unit) interacting with all other unit cells, using the periodicity of the polymer.

In general, calculations on small molecules using ab initio MO methods can provide very satisfactory estimates of nuclear shielding.[1] For larger monomeric species, semiempirical molecular orbital calculations such as CNDO/2 and INDO/S are still the workhorses. The diagonal and off-diagonal elements of the Fock matrix, $F_{\mu\mu}$ and $F_{\mu\mu'}$, respectively, based on CNDO/2, are expressed as follows:

$$\begin{aligned} F_{\mu\mu}(k) = {} & -\tfrac{1}{2}(I_\mu + A_\mu) + \tfrac{1}{2}(1 - P_{\mu\mu})\gamma_{\mathrm{AA}}^{00} \\ & + \sum_{\mathrm{B}} \sum_{j=-M}^{M} (P_{\mathrm{B}} - Z_{\mathrm{B}})\gamma_{\mathrm{AB}}^{0j} \\ & + 2K_\pi \beta_{\mathrm{A}} \sum_{j=1}^{M} S_{\mu\mu}^{0j} \cos kj - \sum_{j=1}^{M} \gamma_{\mathrm{AA}}^{0j} P_{\mu\mu}^{-jR} \cos kj \end{aligned} \tag{3}$$

$$\begin{aligned} F_{\mu\mu'}(k) = {} & \tfrac{1}{2} K_\pi (\beta_{\mathrm{A}} + \beta_{\mathrm{B}}) \sum_{j=-M}^{M} S_{\mu\mu'}^{0j} \mathrm{e}^{\mathrm{i}kj} \\ & - \tfrac{1}{2} \sum_{j=-M}^{M} P_{\mu'\mu}^{-jR} \gamma_{\mathrm{AB}}^{0j} \mathrm{e}^{\mathrm{i}kj} \end{aligned} \tag{4}$$

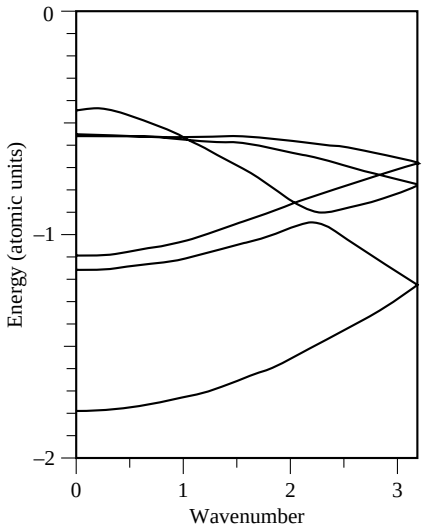

Figure 1 Electronic band structure of polyethylene with *trans* zigzag conformation calculated using CNDO/2 TB MO

where I_μ and A_μ are the ionization potential energy and electron affinity, respectively, γ_{AB} represents the Coulomb repulsion integral between the atomic orbital μ on atom A in the original cell and the atomic orbital μ' on atom B in the jth cell. $S^{0j}_{\mu\mu'}(k)$ is the overlap integral between the μth atomic orbital in the original cell and the μ'th atomic orbital in the jth cell. $P_{\mu\mu'}$ is the bond order matrix, P_B is the electron density on atom B, $P^{-jR}_{\mu'\mu}$ is the bond order matrix between the μth atomic orbital in the original cell and the μ'th atomic orbital in the $\pm j$th cell, and Z_B is the core charge of atom B. K_π is a correction factor for the $\pi-\pi$ electron interaction.[4,5]

By solving the Fock matrix defined by equations (3) and (4), the expansion coefficients in equation (1) can be obtained. These expansion coefficients and energies are dependent on k, which leads to a band structure for the polymer chain. Figure 1 shows the calculated band structure of polyethylene with a *trans* zig–zag conformation. As only six valence electrons in a monomer unit cell are included in the calculation, the corresponding six valence bands can be seen in Figure 1. Calculation with model compounds gives discrete energy levels. In a series of homogeneous molecules, the number of energy levels increases with the molecular size, and correspondingly the separation between these energy levels decreases. For an infinite polymer chain, the energy level is a continuous band structure, as shown in Figure 1. The electronic structure of solid polymers is characterized by this band structure, with a dependence of the energy level on k.

The nuclear shielding for the various nuclei in a given macromolecule can be calculated from the electronic band structure obtained, $C_{\nu n}(k)$, and $E_n(k)$. In general, the nuclear shielding can be written as[1]

$$\sigma = \sigma^{d} + \sigma^{p} + \sigma' \tag{5}$$

where σ^d and σ^p are diamagnetic and paramagnetic contributions, respectively, and σ' is the contribution from neighboring atoms. For a carbon atom, σ' is much less than 1 ppm, and can be considered negligible. Thus, σ can be estimated as the sum of σ^d and σ^p. Based on the TB MO, σ^d and σ^p are obtained by the sum-over-states method as follows:[5–7]

$$\sigma^{d}_{A}(k) = \frac{\mu_0 e^2}{6\pi m_e^2} \sum_{\nu}^{A} \sum_{\nu'}^{A} P_{\nu\nu'}(k) \langle \phi_\nu(r) | r^{-1} | \phi_{\nu'}(r) \rangle \tag{6}$$

$$\begin{aligned}\sigma^{p}_{A,\alpha\beta}(k) = -\frac{\mu_0 h^2 e^2}{4\pi m_e^2} \sum_{m}^{occ} \sum_{n}^{unocc} \sum_{j}^{A} \langle r^{-3} \rangle_{2p} ({}^1E^n_m - {}^1E_0)^{-1} \\ \times \sum_{j}^{B} \sum_{l}^{B} [X(k,j,m,n,\beta,\gamma) X(l,m,n,\gamma,\alpha) \\ - Y(j,m,n,\beta,\gamma) Y(l,n,m,\gamma,\alpha) \\ + X(j,m,n,\gamma,\alpha) X(l,n,m,\beta,\gamma) \\ - Y(j,m,n,\gamma,\alpha) Y(l,n,m,\beta,\gamma)]\end{aligned} \tag{7}$$

Here e is the charge and m_e the mass of the electron, μ_0 is the permeability of free space,

$$P_{\nu\nu'}(k) = \sum_{m}^{occ} C^*_{\nu m}(k) C_{\nu' m}(k) \tag{8}$$

where m refers to the number of occupied crystal orbitals and n to those that are unoccupied, E_0 is the electronic energy of the ground state, and E^n_m is the energy of the state created by promoting an electron from orbital m to orbital n. j and l are atomic orbitals on centers A and B, respectively, and

$$X(j,m,n,\beta,\gamma) = C^{R\beta}_{jm} C^{I\gamma}_{jn} + C^{R\beta}_{jn} C^{I\gamma}_{jm} - C^{R\gamma}_{jn} C^{I\beta}_{jm} - C^{R\gamma}_{jm} C^{I\beta}_{jn} \tag{9}$$

$$Y(j,m,n,\beta,\gamma) = C^{R\beta}_{jm} C^{R\gamma}_{jn} + C^{R\gamma}_{jn} C^{R\beta}_{jm} - C^{I\beta}_{jn} C^{I\gamma}_{jm} - C^{I\gamma}_{jm} C^{I\beta}_{jn} \tag{10}$$

where α, β, and γ refer to the x, y, and z components of the shielding tensor in cyclic order, and R and I indicate the real and imaginary parts of the coefficients $C_{\nu n}(k)$. As shown by equations (6) and (7), the nuclear shielding is calculated as a function of k. In order to be able to compare the calculated and experimental values of the nuclear shielding, it is necessary to average the calculated data over k, within the first Brillouin zone, as given by

$$\sigma = \int_{-\pi/b}^{\pi/b} \sigma(k) D(k)\, dk \tag{11}$$

where $D(k)$ is the density of states, namely, the number of states per unit amount of energy. Thus, the nuclear shielding can be obtained through the electronic band structure of polymers—especially solid polymers.

The quantities calculated using equations (6) and (7) are nuclear shieldings σ, and so the negative sign means deshielding. On the other hand, a negative sign for the observed chemical shift δ means an increase in shielding. Hereinafter, calculated and observed shieldings are expressed as shielding and chemical shift, respectively. The absolute value of the calculated shielding should be compared directly with the observed chemical shift.

3 INTERPRETATION OF NUCLEAR SHIELDING BY THE TB METHOD

The shielding of ^{13}C reflects the magnetic environment of the atom considered, and this depends on the conformation, configuration, and crystal structure of polymers. In order to understand ^{13}C shielding, examples illustrating the applications of TB MO methods to some polymers will be described.

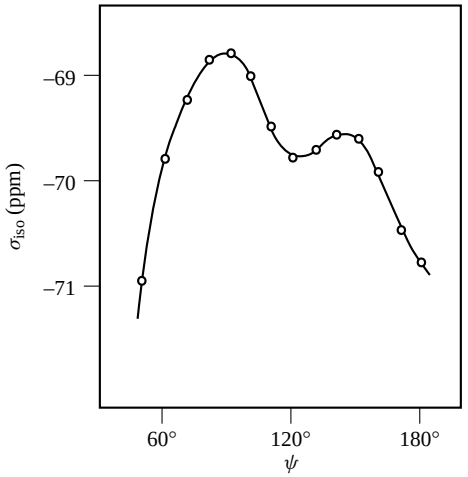

Figure 2 Dependence of the calculated ^{13}C NMR shielding of polyoxymethylene on dihedral angle ψ

3.1 Conformation

It is known from an X-ray diffraction study that a polyoxymethylene chain in the crystalline region takes an all-*gauche* conformation with a 9/5 helix.[8] However, in the noncrystalline region, the structure has not yet been determined exactly, because of the complicated conformation of the chain. It has been reported that the observed ^{13}C chemical shifts of polyoxymethylene in crystalline and noncrystalline regions appear at 88.5 and 89.5 ppm, respectively.[9] Figure 2 shows the dependence of the calculated isotropic ^{13}C shielding on the dihedral angles ψ within the framework of CNDO/2 TB MO.

The isotropic shielding of ^{13}C increases as ψ is increased from 50° to 90°, and the shielding decreases through a minimum value as ψ is increased from 90° to 180°. The values of 60° and 180° for ψ correspond to the all-*gauche* and all-*trans* conformations, respectively. The calculated isotropic ^{13}C shielding of the all-*gauche* conformation appears at lower frequency by about 1 ppm than that of the all-*trans* conformation. Dividing the difference of ^{13}C shielding between all-*gauche* and all-*trans* conformations, for the diamagnetic term, the difference between the all-*gauche* and all-*trans* conformations is 0.1 ppm, and for the paramagnetic term the corresponding difference is 0.9 ppm. The contribution to the relative ^{13}C shielding is due mainly to a change in the paramagnetic term. The diamagnetic term is determined only by the ground state, whereas the paramagnetic term involves interactions between the ground and excited states, as seen from equations (6) and (7). Thus, the observed chemical shift difference between the crystalline and noncrystalline regions comes from a variable interaction due to a conformational change. Therefore, it can be argued that the calculated value confirms well the experimental finding that the ^{13}C shielding for the crystalline region is greater by about 1 ppm than that for the noncrystalline region.

Calculated values of $\Delta\sigma$ ($= \sigma_{yy} - \sigma_{zz}$; spectrum breadth) for the all-*gauche* and all-*trans* conformations are 37.7 and 1.8 ppm, respectively. $\Delta\sigma$ for the all-*gauche* conformation is much larger than that for the all-*trans* conformation. On the other hand, the experimental values of $\Delta\delta$ for the crystalline and noncrystalline regions are about 35 ppm and 7–10 ppm, respectively.[9] The calculated and experimental values agree relatively well with each other. The fact that the calculated value of $\Delta\sigma$ for the all-*trans* conformation is rather small suggests that the electronic environment around the carbon nucleus considered here is relatively symmetric. The small observed value for $\Delta\delta$ may be due mainly to the high symmetry of the electronic environment in addition to the averaging of ^{13}C shielding anisotropy with molecular motion. Further, we are concerned with the behavior of δ_{22}, whose value is obtained from the apex of the tent-like powder pattern. In the experimental data, δ_{22} for the crystalline region appears at about 5 ppm to low frequency when compared with that for the noncrystalline region. However, the calculated value of σ_{xx} for the all-*gauche* conformation appears at lower frequency by about 2.5 ppm when compared with that for the all-*trans* conformation. Thus, the calculation explains the experimental observation reasonably, despite the rough assumption of an all-*trans* conformation for the noncrystalline region.

There has also been some interest in polypeptides. It has been demonstrated that the ^{13}C chemical shifts of C-α, C-β, and the carbonyl carbons are displaced by up to 7 ppm, depending on the particular conformations such as α-helix and β-sheet. Such conformation-dependent chemical shifts of ^{13}C can be understood through changes of the electronic band structure varying with the dihedral angles (ϕ and ψ) of the skeletal bond.

Table 1 shows the calculated and observed ^{13}C shieldings of a polyglycine chain with forms I and II.[7] The observed carbonyl ^{13}C signal for form I is shielded by about 4 ppm compared with that for form II. The calculated ^{13}C shielding for form I is larger by about 11 ppm than that for form II, which matches the experimental finding. There is no significant difference between the methylene ^{13}C chemical shifts for forms I and II within experimental error. At this stage, it cannot be determined whether the methylene shielding for form I or that for II is the larger. The calculated shielding of ^{13}C for form I is smaller by about 3 ppm than that for form II, so the calculation predicts the existence of a shielding difference (about 3 ppm) between forms I and II. It appears that the calculated shieldings are somewhat exaggerated compared

Table 1 Observed and Calculated ^{13}C Chemical Shifts and Shieldings of an Isolated Polyglycine Chain

	δ_{obs} (ppm)[a]		δ_{calc} (ppm)[b]	
	Form I	Form II	Form I	Form II
CH_2	43.5	43.5	−127.2	−124.4
C=O	168.4	172.3	−236.7	−248.1

[a]From TMS. The positive sign means deshielding.
[b]The negative sign means deshielding.

with the observed values. Nevertheless, the observed trend that the ^{13}C chemical shift difference for the methylene carbon is very small when compared with that for carbonyl carbon is reproduced qualitatively by the calculation.

3.2 Configuration

Polyacetylene (PA) is the simplest conjugated polyene, and has two configurations (*cis* and *trans*). It has been reported that shielding of ^{13}C in *cis*-PA appears at lower frequency by about 10 ppm than that of *trans*-PA.[10] Calculations of ^{13}C shielding in PAs have been carried out based on the use of CNDO/2 TB MO and INDO/S TB MO. The differences in the isotropic shielding of ^{13}C between *cis*- and *trans*-PAs, calculated using CNDO/2 and the INDO/S TB MO, are about 2.0 and 3.5 ppm, respectively,[11] i.e., the results differ by a factor of about 2. As the observed difference is about 10 ppm, both types of calculation somewhat underestimate the real values in this case.

Figure 3 shows the observed[12] and calculated components of the ^{13}C shielding tensors of *cis*- and *trans*-PA. As can be seen, the absolute values of σ_{zz} and σ_{xx} calculated using INDO/S TB MO are smaller by about 40 ppm than those obtained using CNDO/2 TB MO. The value of σ_{yy} calculated using INDO/S TB MO is larger by about 10 ppm than that obtained using CNDO/2 TB MO. Consequently, the separation between the values of σ_{xx} and σ_{yy} calculated using INDO/S TB MO is much larger than that obtained using CNDO/2 TB MO. Furthermore, it has been shown that in going from the calculation using CNDO/2 to that using INDO/S, the values of σ_{zz} and σ_{xx} are changed considerably. The most remarkable difference is the estimation of the $\pi-\pi$ overlap integral. Values of σ_{zz} and σ_{xx} are affected by the distribution of π electrons.

The electronic band structure of a PA consists of five valence bands within the framework of the semiempirical method. The highest occupied band has π symmetry. Comparing the electronic band structures calculated using CNDO/2 TB MO with that using INDO/S TB MO, the energies of the three high-energy bands increase, in particular that of the highest occupied band. As can seen from Equation (5), σ^{p} contains a term proportional to the inverse of the excitation energy. The increase in the energies of the three high-energy bands is one of the factors leading to the deshielding of σ_{zz} and σ_{xx}, which implies a lower excitation energy. In fact, the band gaps (the energy difference between the highest occupied and the lowest unoccupied band) for *trans*-PA calculated using CNDO/2 and INDO/S TB MO are about 8.0 and 4.2 eV, respectively. The observed band gap for *trans*-PA is about 1.9 eV. Thus, the contribution of these high-energy bands to σ_{xx} and σ_{zz} is remarkably improved in going from CNDO/2 to INDO/S TB MO.

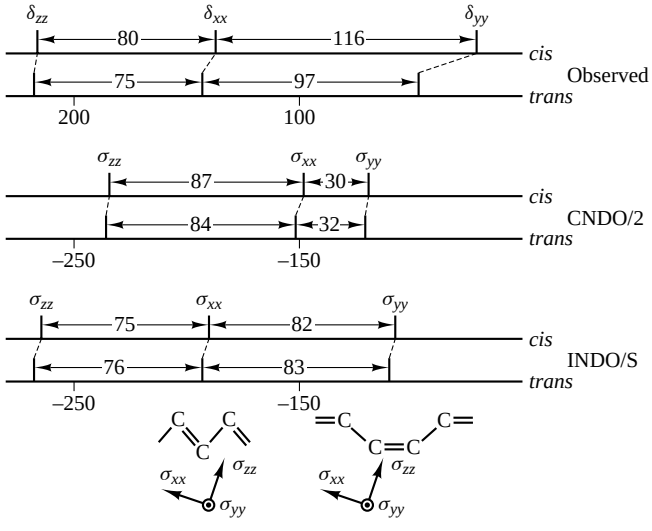

Figure 3 Observed and calculated components of ^{13}C NMR shielding tensors of *cis*- and *trans*-PAs. The directions of the principal axes are indicated at the bottom

It is clear from Figure 3 that the reason why the calculated difference in isotropic shielding of ^{13}C between *cis*- and *trans*-PAs is underestimated is that the difference in σ_{yy} cannot be reasonably reproduced. In order to reproduce more reasonably the observed difference in σ_{yy} between *cis*- and *trans*-PAs, it may be necessary to use MOs that can properly describe band structures that have σ symmetry.

Polypyrrole is one of a series of heterocyclic polymers that has attracted much attention because of its characteristic electric and electronic properties. Fundamental structural formulas have been proposed for undoped and doped polypyrroles, where the aromatic form corresponds to the undoped state and the quinoid form to the doped state. From analysis of high-resolution solid state ^{15}N NMR, it is known that the ^{15}N chemical shift for the quinoid form appears to high frequency from that for the aromatic form. In order to obtain information about ^{15}N chemical shifts and electronic band structures of an infinite polypyrrole chain with aromatic or quinoid forms, calculations were carried out using INDO/S TB MO.[13]

As listed in Table 2, the calculated shielding of ^{15}N for the quinoid form appears to high frequency compared with that for the aromatic form. The calculated results agree with observed ones, suggesting that the electronic band structure has been properly estimated. From the calculated electronic band structure, the band gaps for the aromatic and quinoid forms are 5.1 and 2.9 eV, respectively. This result implies that the electrical conductivity of the quinoid form is larger than that of the aromatic form. Therefore, it can be expected that if the amount of the quinoid form is increased, polypyrrole with a higher electric conductivity can be obtained.

3.3 Crystal Structure

The crystal structure in the solid state, which describes how molecules condense, is an important factor when discussing physical properties. The effect of crystal structure on the nuclear shielding can, in principle, be separated from the effect of conformation and configuration to within the limitations of a quantum chemical model.

Experimentally, it is reported that the ^{13}C chemical shifts of the CH_2 carbon for *n*-paraffins, cyclic paraffins,

Table 2 Calculated ^{15}N Shieldings and Band Gaps for Aromatic and Quinoid Polypyrrole Models Using INDO/S TB MO

Structure	Calculated shielding σ_{iso} (ppm)	Band gap (eV)
Aromatic	−223.50	5.12
Quinoid	−232.51	2.86

and polyethylene with *trans* zigzag conformations in the orthorhombic and triclinic forms are about 33 and 34 ppm, respectively.[14,15] As the conformation is the same in each case, the difference of about 1 ppm may be due to a local change in intermolecular interactions resulting from the change of the orthorhombic to the triclinic form. Paraffins can be considered as models for the crystallographic form of the polyethylene. The results of X-ray diffraction studies suggest that the *trans* zigzag plane of any specified chain in the orthorhombic and triclinic forms is, respectively, perpendicular and parallel to that of the neighboring chains. The chemical shift of ^{13}C in polyethylene with a monoclinic form appears at higher frequency by 1.4 ppm compared with that of polyethylene with a orthorhombic form. The orientation of the *trans* zigzag plane in the monoclinic form is very close to that in the triclinic form.[16] Thus, the solid state ^{13}C NMR chemical shift depends on the orientation of the C–C–C plane in the *trans* zigzag chains.

Since the chains lie periodically in space in the solid state, calculations of chemical shifts should be employed that take account of the three-dimensional structure, including interactions between chains. In order to take into account the interchain interaction, a 'seven-polyethylene-chains model' has been used to compute the ^{13}C shielding.[17] Figure 4 shows models for polyethylenes with an orthorhombic form and a monoclinic form. The setting angle ψ for orthorhombic polyethylene is not clearly determined. Figure 5 shows the ψ dependence of the difference in shielding of ^{13}C between orthorhombic and monoclinic polyethylenes ($\sigma_{orth} - \sigma_{mono}$) calculated using INDO/S TB MO. As can be seen, the calculated difference in shielding of ^{13}C between these forms is positive in the case of $\psi = 25^\circ - 42^\circ$, and negative in the case of $\psi = 20^\circ - 25^\circ$ and $\psi = 42^\circ - 55^\circ$. The largest difference occurs at $\psi = 35^\circ$. From these results, the angle of $\psi = 25^\circ - 42^\circ$ is good for the setting angle of orthorhombic polyethylene, and can reasonably reproduce the observed data. This result shows that the difference in chemical shift between the orthorhombic and monoclinic forms is caused by the difference in interchain interaction through the electronic band structure.

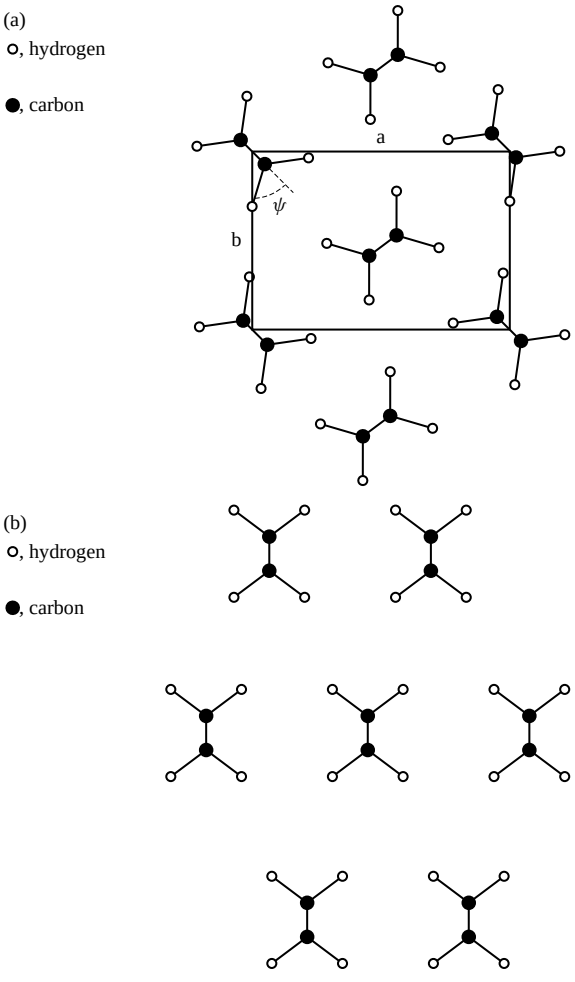

Figure 4 The 'seven-polyethylene-chains' model: (a) orthorhombic form; (b) monoclinic form

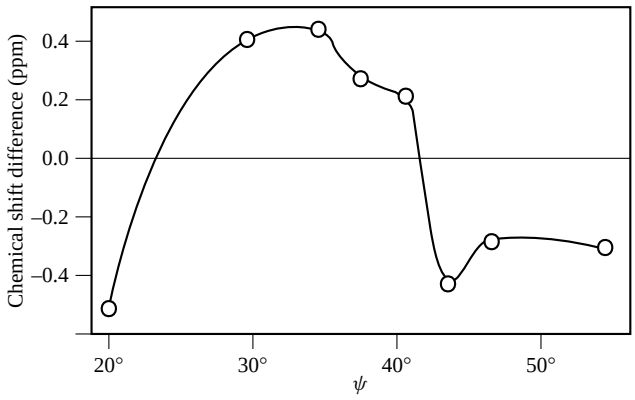

Figure 5 The ^{13}C NMR chemical shift difference between the orthorhombic and monoclinic polyethylene chains calculated using the seven-chains model, as functions of the setting angle ψ

The effect of crystal structure on the nuclear shielding of *cis*- and *trans*-PA is also relevant. A specified polymer chain is surrounded locally by six neighboring chains in the crystal, and these six chains can be separated into three groups. Each chain group consists of two chains, which are equivalent with respect to the central chain. In order to take interchain interaction into account, the 'seven-chains model' has been used to compute the ^{13}C shielding as shown in Figure 6.[18]

The calculated values depend on the chain arrangement. The total energies of *cis*- and *trans*-PAs show minima at $\Delta b = -10$ pm, where Δb is the deviation of b from the value determined by X-ray diffraction. A small decrease from the original crystal lattice values determined by X-ray methods leads to energetically stable results in the calculations for both PAs. This arises from the fact that CNDO/2 slightly underestimates the interaction distances, as is already known.[19] However, an extreme decrease in the interchain distance leads to a large instability. Therefore, when comparing *cis*- and *trans*-PAs, it might be appropriate to consider the arrangement with a somewhat shorter distance. With respect to the band gap, the smaller the value of b, the smaller the band gap becomes. The decreases in the lattice parameters in the calculation correspond to the PA system under high pressure, where a shrinkage of the interchain distance occurs. It is therefore suggested that the electric conductivity of PA samples will increase with an increase in pressure. Comparing the isomers, the band gap value of *trans*-PA is smaller than that of *cis*-PA. This explains the experimental observation that *trans*-PA has a higher conductivity than *cis*-PA. The calculated values

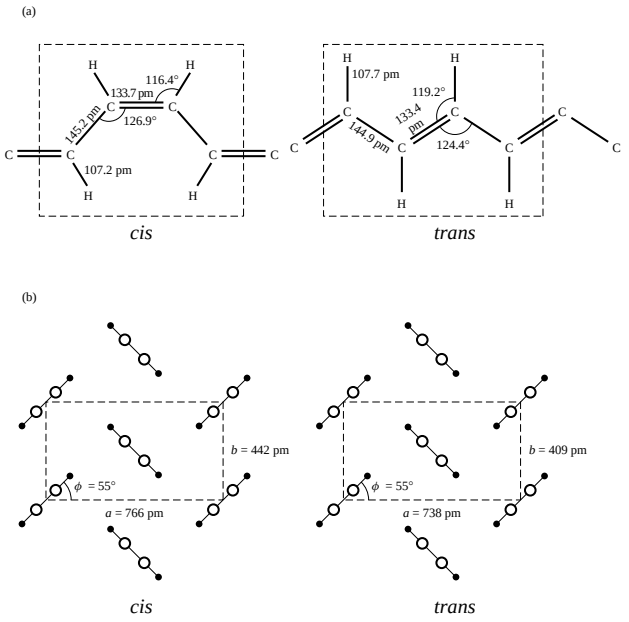

Figure 6 Geometrical parameters of *cis*- and *trans*-PA: (a) valence geometries; (b) lattice parameters

are very large for the arrangement given by the original lattice parameters. The arrangement with a small value of b is near to the real form in the crystal. It has been shown experimentally that the lattice parameters a and b for *cis*-PA are larger than those for *trans*-PA (Figure 6); that is, the interchain distance of *cis*-PA is longer than that of *trans*-PA. This may be due to the different shapes of the PA chains. In the comb-like *cis*-PA chains, some of the hydrogen and carbon atoms tend to be very close in interatomic distance, and so they become repulsive (in fact, the nearest-neighbor C−H distance between the chains in *cis*-PA is shorter than that in *trans*-PA in the case using the original geometries). Therefore, the *cis*-PA crystal becomes more stable at the arrangement with the larger lattice parameters than does the *trans*-PA crystal, and these long interchain distances lead to a large band gap and so to a low conductivity for *cis*-PA.

Figure 7 shows the calculated dependence of the shielding of ^{13}C for *cis*- and *trans*-PA on Δb. In the arrangement with

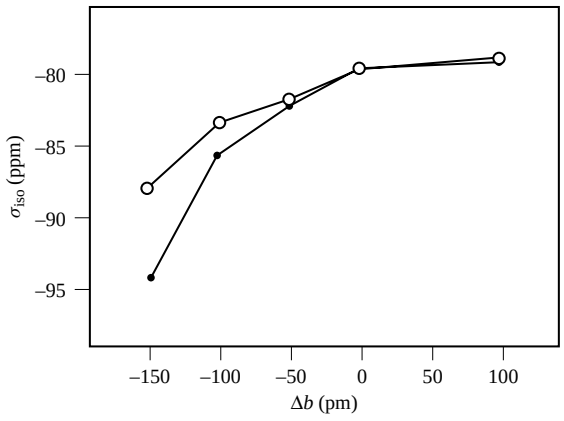

Figure 7 Dependence on b of the calculated isotropic ^{13}C shielding of PA chains in the seven-chains model: ○, *cis*; ●, *trans*

the original lattice parameters, the calculated values of σ_{iso} do not reproduce the observed large difference between the two isomers. However, in the arrangement with short interchain distances, the calculations agree well with the experiments. With regard to the chemical shift tensors, not only σ_{33} but also the components σ_{11} and σ_{22} decrease as the interchain distance is decreased. The most variable component for a change of the interchain distance is σ_{22}, whose direction is along that of the molecular chain. The effect of the interchain interactions might appear strongly in this direction. At $\Delta b = -100$ pm, the difference in σ_{22} between the isomers agrees quantitatively with the experimental data. From these results, the effect of crystal structure on nuclear shielding can be explained via the electronic structure in addition to the effect of the chain configuration.

4 RELATED ARTICLES

Chemical Shift Tensors; Conducting Polymers; Shielding Calculations: IGLO Method; Shielding Calculations: Perturbation Methods; Shielding: Overview of Theoretical Methods; Shielding in Small Molecules; Shielding Tensor Calculations; Shielding Theory: GIAO Method.

5 REFERENCES

1. I. Ando and G. A. Webb, *Theory of NMR Parameters*, Academic Press, London, 1983.
2. A. Imamura, *J. Chem. Phys.*, 1970, **52**, 3168.
3. F. Bloch, *Z. Phys.*, 1928, **52**, 555.
4. M. Kondo, I. Ando, R. Chujo, and A. Nishioka, *J. Magn. Reson.*, 1976, **24**, 315.
5. T. Yamanobe and I. Ando, *J. Chem. Phys.*, 1985, **83**, 3154.
6. T. Yamanobe, R. Chujo, and I. Ando, *Mol. Phys.*, 1983, **50**, 1231.
7. T. Yamanobe, I. Ando, H. Saito, R. Tabeta, A. Shoji, and T. Ozaki, *Bull. Chem. Soc. Jpn.*, 1985, **58**, 23.
8. H. Tadokoro, M. Kobayashi, Y. Kawaguchi, A. Kobayashi, and S. Murashashi, *J. Chem. Phys.*, 1963, **38**, 703.
9. H. Kurosu, T. Yamanobe, T. Komoto, and I. Ando, *Chem. Phys.*, 1987, **116**, 391.
10. M. M. Maricq, J. S. Waugh, A. G. MacDiarmid, H. Shirakawa, and A. T. Heeger, *J. Am. Chem. Soc.*, 1978, **100**, 7729.
11. T. Yamanobe, I. Ando, and G. A. Webb., *J. Mol. Struct.*, 1987, **151**, 191.
12. T. Terao, S. Maeda, T. Yamabe, K. Akagi, and H. Shirakawa, *Chem. Phys. Lett.*, 1984, **103**, 347.
13. M. Kiuchi, H. Kurosu, and I. Ando, *J. Mol. Struct.*, 1992, **29**, 193.
14. T. Yamanobe, T. Sorita, T. Komoto, I. Ando, and H. Sato, *J. Mol. Struct.*, 1985, **131**, 267.
15. D. L. VanderHart, *J. Magn. Reson.*, 1981, **44**, 117.
16. D. L. VanderHart and F. Khoury, *Polymer*, 1984, **25**, 1589.
17. H. Kurosu, I. Ando, and T. Yamanobe, *J. Mol. Struct.*, 1989, **201**, 239.
18. T. Ishii, H. Kurosu, T. Yamanobe, and I. Ando, *J. Chem. Phys.*, 1988, **89**, 7315.
19. K. Morokuma, *Chem. Phys. Lett.*, 1971, **19**, 129.

Biographical Sketches

Takeshi Yamanobe. *b* 1958. B.E., 1981, Ph.D., 1986, Tokyo Institute of Technology. Introduced to NMR by I. Ando. Dept. Industrial Chemistry, Tokyo Institute of Polytechnic, 1987–1993. Currently associate professor of Materials Engineering, Gunma University, Japan, 1993–present. Approx. 30 publications. Research interests include the electronic structure and NMR chemical shift of polymers, and structure and dynamics of polymeric materials by solid state NMR.

Hiromichi Kurosu. *b* 1962. Ph.D., 1990, Tokyo Institute of Technology (supervisor Isao Ando). Postdoctoral work at the University of Surrey (with Graham A. Webb). Assistant professor, Department of Polymer Chemistry, Tokyo Institute of Technology, 1989–present. Approx. 40 publications. Research specialties: solid state NMR and NMR shielding calculations, and structures and electronic states of solid polymers.

Structural and Dynamic Characterization of Soft Polymers by Solid State NMR and Field Gradient NMR

Isao Ando, Masatoshi Kobayashi, Chenhua Zhao, Yige Yin, and Shigeki Kuroki

International Research Center of Macromolecular Science, Tokyo Institute of Technology, Tokyo, Japan

1 Introduction 1
2 Microscopic Structure and Dynamics of Polymer Gels 1
3 References 18

1 INTRODUCTION

Most recently, the term '*soft* materials' is frequently used in the field of materials science. *Soft* polymers considered here are classified into soft materials, and contain polymer gels, polymer liquid crystals, vulcanized elastomers, etc., in which molecular motion is much higher compared with solid polymers. Most recently *soft* polymers have attracted attention as useful materials as detailed below.

Polymer gels consist of two components of network polymer chains and solvent. Further, a third component such as a low molecular-weight compound or polymer is often contained in the gels. Polymer gels have attracted considerable attention from the point-of-view of various physical and chemical properties.[1] For example, hydroelectrolyte gels show a dramatic change in volume in response to change in solvent composition, pH, ionic strength and temperature. They contract upon application of an electric field. Further, water-swollen polymer gels can convert chemical energy into mechanical energy. These properties lead to the vitality of polymer research and development of a diversity of interests in polymer gel systems. In order to develop new polymer materials, polymer gel design has been performed on the basis of advanced polymer science and technology. The properties of polymer gels are closely related to their structures and dynamics. From such situations, the establishment of methods for elucidating the structures and dynamics is important for making reliable polymer gel design and developing new advanced polymer gels. In polymer gels, although the mobility of network polymer chains is much higher than solids, it is much lower than solvent and the low-molecular weight molecules. Thus, by taking into account such a difference in molecular motion between the mobile and immobile regions, solid-state high-resolution NMR proves to be a useful tool to characterize such systems.

On the other hand, liquid crystalline polymers have both positional and orientational orders in the liquid crystalline phase.[2] The amount of order in a liquid crystal is quite small compared with a crystal. The polymer chain is rapidly rotating around the long axis and diffusing along and perpendicular to the long axis. Such anisotropic structures induce various characteristic properties to be used as materials.

From such a background, the structure and dynamics of polymer gels, liquid crystalline polymers and vulcanized elastomers by solid-state NMR, and the diffusion process of polymer gels by pulse-field-gradient spin-echo (PFGSE) NMR have been widely used in order to make reliable polymer gel and liquid crystalline polymer designs and to develop new advanced polymer gels and liquid crystalline polymers.[3–5] Details of this work will be described.

2 MICROSCOPIC STRUCTURE AND DYNAMICS OF POLYMER GELS

Polymer gels consist of mobile and immobile regions. For this, conventional solution NMR gives useful information about mobile regions, but sometimes not on the more rigid regions. To obtain structural information on relatively rigid regions, solid-state NMR is required. Then, in order to elucidate structure and dynamics of the immobile and mobile regions in polymer gels, we must use some appropriate NMR methods or must design special methods. In this section, some studies of microscopic structure of polymer gels by ^{1}H pulse NMR (including use of gradient-field) and high-resolution solid-state ^{13}C NMR will be introduced.

2.1 Approach by ^{1}H Pulse NMR Method

In the pulse NMR experiment, high power radio-frequency (rf) pulses are applied and the free induction decay (FID) of the T_2 component is detected as a time-dependent function that becomes a measure of the mobility.[53] The Fourier transform converts the FID into the corresponding frequency spectrum, in which the chemical shift gives information about chemical structures. On the other hand, the FID contains information about molecular dynamics, and so the experiment with some rf pulses gives T_1, T_2 and the diffusion coefficient (D).[6] T_1 and T_2 are closely related with the correlation-time for molecular motion by BPP (Bloembergen–Purcell–Pound) theory when they are governed by dipolar interactions, and D as obtained by pulse NMR under a field gradient provides information about the translational motion.[7] Therefore, pulse NMR is useful method for the elucidation of molecular dynamics in polymer systems.

2.1.1 Volume Transition of a Poly(N-Isopropylacrylamide) Gel

It is known that the volume of a poly(*N*-isopropylacrylamide) (PNIPAM) gel with water as solvent experiences a transition with temperature at about 33 °.[8] In order to elucidate molecular motion of water in the gel through the transition temperature (T_{vt}) by temperature variation, the ^{1}H T_2 has been measured as a function of temperature.[9]

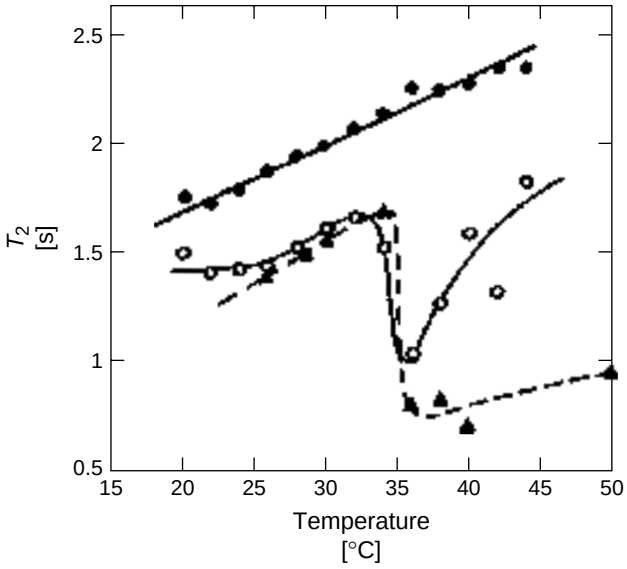

Figure 1 Plots of the ^{1}H T_2 values of H_2O in neat water (●) and in the PNIPAM gel (○) against temperature at atmospheric pressure

Figure 1 shows plots of the ^{1}H T_2 values of H_2O in neat water (●) and water in the PNIPAM gel (○), as a function of temperature at atmospheric pressure. The T_2 value of neat water increases as the temperature is linearly increased. This shows that the mobility of water is monotonically increased with increase in temperature in the measurement temperature range. The T_2 of HDO in the PNIPAM gel increases as the temperature increases up to 33 °C. At T_{vt} (33 °C), the T_2 value is transitionally decreased. As the temperature is further increased, the T_2 value is transitionally decreased. Such behavior is similar to that of water in aqueous PNIPAM solution as reported previously.[10] During the NMR measurements, the gel shrinks with an increase in temperature and exuded water is physically removed. The degree of swelling Q, which is defined by the ratio of the mass of swollen gel to the mass of dried gel and shows a measure of the size of the network. This implies that the mobility of water in the gel increases with an increase in temperature up to 33 °C in spite of much smaller change of the Q value, but decreases transitionally at 33 °C due to a large decrease in the Q value and increases again with a further increase in temperature during which the Q value does not change. Such a behavior can be understood by assuming that intermolecular interaction between the network polymer chains above the transition temperature occurs and so the mobility of water molecules is more restricted by the polymer networks than that below the transition temperature.

2.1.2 Gelation of Poly(N-isopropylacrylamide) Aqueous Solution

PNIPAM in water undergoes a phase transition from sol to gel at around 32 °C[11] ^{1}H pulse NMR experiments provide useful information about molecular motion of the polymer and solvent in the solution and gel state. The abrupt change in molecular motion for solvent in the gel is caused by the formation of the gel structure at the phase transition temperature and therefore, the change of relaxation times sensitively reflects the change of states.

The ^{1}H T_2 values for water in 1, 2.5, 5 and 10% w/v PNIPAM/water solutions and for neat water against temperature were measured as a function of temperature.[10] The ^{1}H T_2 value increases as the temperature is increased up to 30 °C, where an increase in T_2 means an increase in molecular motion according to BPP theory.[7] The ^{1}H T_2 value of neat water increases linearly with temperature up to 50 °C. At the gelation temperature (about 32 °C), the ^{1}H T_2 value in all of the polymer solutions transitionally decreases. As temperature is further increased, the T_2 value increases again. The mobility of water increases with increasing temperature up to 30 °C, then decreases transitionally at about 32 °C due to the gelation of the system and increases again with a further increase of temperature. This trend is very different from that of neat water. Furthermore, it is seen that the increase in the polymer concentration leads to a decrease in ^{1}H T_2 for water. The molecular motion of water is restricted by an increase in intermolecular interactions between the polymer chains and water. As the polymer concentration increases up to 5% at the gelation temperature, the magnitude of the decrease for ^{1}H T_2 value is larger. As the concentration increases further up to 10% w/v, the magnitude of the change in T_2 value for the transition becomes smaller.

The ^{1}H T_1 value of water molecules in 5% w/v PNIPAM/water solution was measured as a function of temperature. The ^{1}H T_1 value slowly increases as does the ^{1}H T_2 mentioned above as the temperature is increased. At the gelation temperature, the T_1 value transitionally decreases. As the temperature is further increased, the ^{1}H T_1 value slowly increases. This behavior is very similar to that for T_2. As seen from the observed ^{1}H T_1 and T_2 behaviors, the water molecules are in the fast motion region ($\omega\tau_c \ll 1$, where ω is the resonance frequency). At 1, 2.5 and 10% w/v solutions, similar results were obtained. Therefore, the ^{1}H T_1 and T_2 values for water in the PNIPAM/water system are very sensitive to the phase transition and provide dynamic information.

In PNIPAM/deuterated water solution, the ^{1}H T_2 signal is composed mainly of two components, a long T_2 component corresponding to the side chains and extremely short T_2 component corresponding to the main chain. The T_2 value for the main chain and side chains of PNIPAM in 10% w/v PNIPAM/deuterated water solution were determined as a function of temperature. For the main chain, at temperatures from 10 to 30 °C, the T_2 value is almost constant, but at the gelation temperature (32 °C) it decreases transitionally, and at temperatures of 40–50 °C it returns to being constant. This indicates that at the gelation temperature, the molecular motion of the main chain is greatly restricted. On the other hand, for the side chains, at temperatures from 10 to 30 °C the T_2 value remains almost constant, increases transitionally at the gelation temperature, and at temperatures from 40 to 50 °C it becomes a constant again. This is evidence that the molecular motion of the side chains increases transitionally at the gelation temperature.

By evaporating water slowly from PNIPAM aqueous solution, a PNIPAM gel is obtained. The ^{1}H T_2 behavior of water for this gel is very similar to that for PNIPAM aqueous solution. This shows that temperature changes of structure and dynamics for both of these systems up to 32 °C are very similar to each other.[10] Further insight into structural and dynamic changes by changing temperature has been studied by high-resolution solid-state ^{13}C NMR technique.

2.1.3 *Structure and Dynamics of Poly(vinyl alcohol) Gel*

Amorphous-poly(vinyl alcohol) (PVA) gel prepared by repeating freeze-thaw cycles from its aqueous solution is one of the physical gels.[12] A ^{1}H spin echo signal of PVA gel measured is composed of three components such as a long T_2 component corresponding to the mobile region (C), a short T_2 component corresponding to the immobile region (A) and an intermediate T_2 component corresponding to the interfacial region (B), which exists between the mobile and immobile regions.[13] It can be said that the mobile region (C) comes from the non-crosslinked region, the immobile region (A) comes from the crosslinked region and the interfacial region (B) comes from the vicinity of the crosslinked region in the gel. With an increase in the polymer concentration, ^{1}H T_2 of three regions are slowly decreased. This means that the molecular motion is restrained, as the polymer concentration is increased. The fractions of the corresponding three regions were determined as a function of polymer concentration. The fractions of the mobile and immobile regions are largely decreased and increased with an increase in the polymer concentration, respectively. The fraction of the intermediate region over a wide range of polymer concentrations is very small.

2.1.4 *Gelation of Poly(vinyl alcohol)/Water System Under High Pressure*

As mentioned above, PVA aqueous solution forms a gel by undergoing freeze-thaw cycles. The gelation is induced by network formation, and at the initial step of the gelation phase separation occurs by forming polymer-aggregation region and polymer-unaggregation regions. It has been suggested that the cause of the gel formation in PVA aqueous solution is due to the formation of intermolecular hydrogen bonds.[14,15]

The use of variable pressure is very effective in overcoming the limited interpretability of the results obtained at atmospheric pressure. Additionally, a change in pressure is expected to provide another dimension in the investigation of aqueous PVA solution and gel because volume changes by the application of pressure lead to reduction of intermolecular distance and to a major effect on molecular motion in the system compared with experiments conducted at atmospheric pressure. As viewed from high pressure NMR experiments, it can provide more useful information about intramolecular dynamics, structures of liquids, molecular conformations and intermolecular interactions through the observation of some NMR parameters such as chemical shift, T_1, T_2 and dipolar splitting.[13,16] From such a situation, it can be expected that more detailed information about the dynamical behavior of PVA/water system is obtained by the application of pressure. Therefore, the dynamical behavior of PVA aqueous solution and gel through the observation of ^{1}H T_2 values is elucidated as a function of pressure from 1 to 500 kg cm^{-2} by using high pressure ^{1}H pulse NMR.[17]

The degree of polymerization of amorphous PVA used in this experiment was 300. PVA was dissolved in D_2O at 90 °C to observe the ^{1}H signal from the polymer. To remove the ^{1}H signal from HDO, which came from chemical exchange between hydroxyl proton and deuteron in PVA and D_2O, the following procedure was performed. By adding PVA/D_2O solution into excess acetonitrile, PVA substituted hydroxyl proton by deuterium (*d*-PVA) was precipitated. The precipitated *d*-PVA was dried by a vacuum pump. The obtained *d*-PVA was dissolved in D_2O again. This procedure was repeated three times. Deuterated PVA samples were dissolved in D_2O at 90 °C. The concentration was 10% (w/w). The solution was cooled to 25 °C and kept for 10 days (sample I). PVA chains in aqueous solution aggregate slightly by such a cooling process. For this, the ^{1}H T_2 value for the PVA solution was measured as a function of the elapsed time during the cooling process. It is obvious that the change of the ^{1}H T_2 with the elapsed time is much smaller compared with that under pressure. PVA gel was prepared from PVA/D_2O solution by repeating freeze-thaw cycles 3 times (frozen and kept at −15 °C for 3 hours, and melted and kept at 25 °C for 2 hours) (sample II).

Pulse ^{1}H NMR measurements were carried out at 20 MHz. ^{1}H T_2 was determined by the CPMG (Carr–Purcell–Meiboom–Gill) method to obtain information about the molecular motion of PVA chain in the solution state, and was determined by the solid echo pulse sequence to obtain information about the molecular motion of the immobile component in the gel state. The T_2 decay for the PVA solution was analyzed as a sum of Lorentzian-type decays and for the PVA gel was analyzed as sum of Gaussian-type decays using the nonlinear least-squares method.

In high pressure experiments, the sample cell was made from a Pyrex glass capillary tube with an outside diameter of 5.0 mm and an inside diameter of 2.6 mm. The cracks on the surface of the outside and inside of the capillary tube were etched by aqueous HF solution. The capillary was glued to a nonmagnetic stainless steel tube using epoxy resin. The pressure can be changed from 1 to 500 kg cm^{-2} with no failure of the system.

From the ^{1}H CPMG experiments on PVA aqueous solution at room temperature, the T_2 signal is mainly composed of two components. The PVA chains in aqueous solution aggregate partly by the cooling process when the solution is prepared. From such a situation, the long T_2 component comes from the mobile region, which is assigned to non-aggregated PVA chains. The short T_2 component comes from the immobile region, which is assigned to aggregated PVA chains in the solution state. The ^{1}H FID signals of PVA/D_2O solution are shown as a function of pressure in Figure 2. The ^{1}H FID signals of PVA chains at pressures from 1 to 100 kg cm^{-2} slowly decay, and at pressures over 200 kg cm^{-2} the variation of decay increases. The ^{1}H T_2 values for PVA/D_2O solution were determined as a function of temperature. The ^{1}H T_2 value for the immobile region is almost a constant to be about 25 ms at pressures from 1 to 500 kg cm^{-2}. On the other hand, the ^{1}H T_2 value for the mobile region is changed by pressure. The ^{1}H T_2 value is lowered from ca. 650 to 600 ms in the pressure range from 1 to 100 kg cm^{-2}, and again decreases from ca. 600 to ca. 100 ms in the pressure range from 100 to 200 kg cm^{-2}. At pressures over 200 kg cm^{-2}, the ^{1}H T_2 values for the long T_2 component are constant at about 100 ms. These experimental results indicate that the molecular motion of PVA chains in the aggregated region is not changed by varying pressure up to 500 kg cm^{-2}, but the molecular motion in the non-aggregated region is affected by pressure in the pressure range over 200 kg cm^{-2}. The ^{1}H T_2 value for mobile component is about 320 ms and the ^{1}H T_2 value for mobile component at 1 kg cm^{-2} decreases by applying pressure. The long T_2 component disappears in the pressure range over 200 kg cm^{-2}

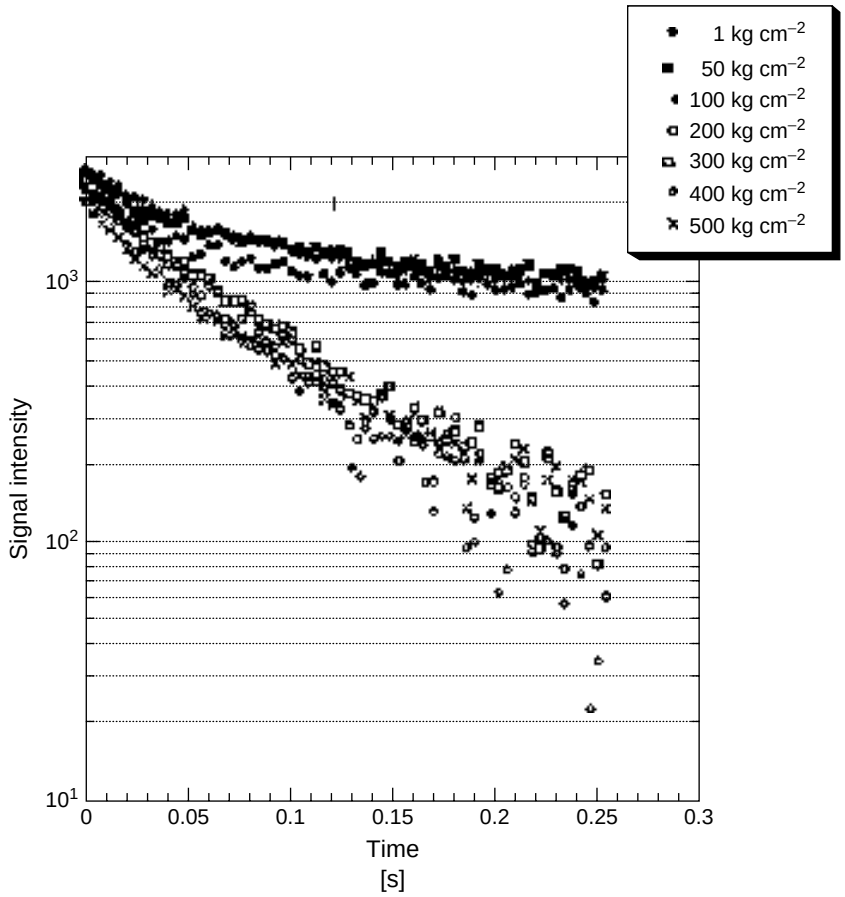

Figure 2 Pressure dependence of ^{1}H T_2 signal of PVA/D_2O solution obtained by the CPMG method

and the fraction of the short T_2 component increases up to 200 kg cm^{-2}. In the pressure range over 200 kg cm^{-2}, the short T_2 component occupies the whole fraction. From these results, it can be said that the molecular motion of PVA chains in non-aggregated region is restricted by applying pressure up to 500 kg cm^{-2}, and the process of gelation is induced. Finally, it can be said that high-pressure ^{1}H pulse NMR gives useful information about the dynamics of PVA chains in aqueous solution state and in gel state.

2.1.5 Structure and Dynamics of (Ethylene-Vinyl Alcohol) Copolymer Gels

Ethylene-vinyl alcohol (EVOH) copolymer gel can be prepared by repeating freeze-thaw cycles from its aqueous solution similarly to the preparation of the PVA gel. The ^{1}H T_2 signal of EVOH gel with a relatively high ethylene content of 32% as obtained by ^{1}H solid echo method was observed.[18] The ^{1}H T_2 value is determined from the slope of the plot of ln M against t^2, where M is the amplitude of the spin echo signal and the T_2 signal is assumed to be a Gaussian decay in the spectral analysis. According to the BPP theory for NMR relaxation, T_2 decreases continuously as the correlation time τ_c in molecular motion is increased.[7] This means that shorter T_2 corresponds to slower molecular motion. Thus, T_2 can give dynamic information about the gels through the BPP theory. The ^{1}H T_2 curve is composed of three kinds of the components; the short T_2 component corresponding to the immobile region (A), the intermediate T_2 component corresponding to the interfacial region (B), which exists between the mobile and immobile regions, and the long T_2 component corresponding to the mobile region (C). By aid of the computer-fitting, the ^{1}H T_2 value was obtained from the T_2 signal with experimental error of $\pm$5%. The result is the same as that of PVA gel.[13] It can be said that the short T_2 component corresponding to the immobile region comes from the crosslinked region in the EVOH gels, the long T_2 component corresponding to the mobile region comes from the non-crosslinked region, the intermediate T_2 component with the intermediate mobility comes from the vicinity of the crosslinked region.

The ^{1}H T_2 values determined for the individual regions were plotted against the ethylene content. It is found that the ^{1}H T_2 values for the immobile, mobile and intermediate regions are gradually decreased with an increase in ethylene content. The increase of the ethylene content in EVOH samples in the gel state leads to reduction in molecular motion for the individual regions.

The fraction of each of the immobile, mobile and intermediate regions with different molecular motion were determined as a function of ethylene content. In the range of ethylene content less than 55%, the fractions of three kinds of regions with different mobilities are almost independent of ethylene content. In the ethylene content range greater than 55%, the fractions of the mobile region are rapidly decreased with an increase in ethylene content. On the other hand, the fractions

of the intermediate and immobile regions are largely increased with an increase in ethylene content. Their fractions are similar in value. This means that the fraction of the crosslinked region as formed by an addition of hydrophobic interaction between the ethylene parts to hydrogen bonds between the vinyl alcohol units is increased with an increase in ethylene content. From such a situation, the molecular motion for all of the three regions are more restrained with an increase in ethylene content.

2.1.6 Structure and Dynamics of Swollen Polymer Networks

The structural and dynamic characterization of swollen polymer networks has been one of the important research programs in polymer science. Samulski, et al. have elucidated the effect of orientation on residual quadrupolar splitting of deuterated solvents in swollen strained polyisoprene by ^{2}H NMR.[57] The quadrupolar splitting depends linearly on $\lambda^2-\lambda^{-1}$ over a large range of the extension ratios (λ) and the degree of swellings. A phenomenological description based on a lattice model of the deformed, swollen network, which induces short-range nematic-like interactions successfully accounts for the observations. Also, the structural characterization of the other swollen networked polymers have been studied by ^{2}H NMR.[58–60]

2.2 Approach by High-Resolution Solid-State ^{13}C NMR

It is well known that ^{13}C CP/MAS (cross polarization/magic angle spinning) NMR method obtains high-resolution solid-state NMR spectra of solid polymers and enhances the peak intensity of carbons in the immobile region.[3,19–21] The CP efficiency is relatively high for carbons in rigid solid polymers. Polymer gels and polymers in the liquid crystalline state are relatively mobile. For this reason, care must be exercised to obtain ^{13}C CP/MAS NMR spectra because the ^{13}C signals of carbons in the mobile region may not appear due to the large reduction of the CP efficiency. It is often convenient to use MAS with strong ^{1}H decoupling, which leads to NOE (Nuclear Overhauser Effect), and without CP for obtaining the ^{13}C signals of carbons in the mobile state, for example, the PST (pulse saturation transfer)/MAS is often used, in which ^{1}H decoupling is carried out by using a number of pulses.[22] MAS removes effectively weak dipolar coupling of carbons in the mobile state. In the case of polymer gels there exist mobile and immobile regions. For this, ^{13}C CP/MAS and PST/MAS methods are often used to get useful information about both regions. This leads to reasonable structural characterization of polymer gels.

If a conventional NMR rotor is used under high speed rotation (about 4 kHz), polymer gels and polymer liquid crystals come out of a conventionally sealed NMR rotor due to high speed rotation. From such a situation, it is convenient to use an NMR rotor sealed with an O-ring rubber, the use of which prevents loss of samples.[14]

2.2.1 Structural Characterization of Poly(Vinyl Alcohol) Gel

As mentioned above, amorphous-PVA gel is prepared by repeating freeze-thaw cycles from its aqueous solution. At the beginning of the gelation of the PVA aqueous solution, phase separation into polymer-rich and polymer-poor regions occurs with a decrease in temperature. It is suggested that the gel formation is due to the formation of intermolecular hydrogen bonds.[14] The structure and the amount of hydrogen bonds may play an important role for properties of PVA gel, and high-resolution solid-state ^{13}C NMR gives useful information about them.[14,15] Figure 3 shows ^{13}C NMR spectra for PVA in the solution (a), gel (b–d) and solid (e) states as measured by solution and solid-state NMR. In conventional solution ^{13}C NMR spectrum for PVA gel shown in Figure 3(b), the ^{13}C signal for the CH carbon splits into three peaks assigned to mm, mr and rr triads. The signals for the CH and CH_2 carbons become broader as compared with those for PVA solution (Figure 3(a)). This is caused by the increase in dipole–dipole interactions due to a decrease in molecular motion. The ^{13}C PST/MAS NMR spectrum of the PVA gel shown in Figure 3(c) is similar to the solution NMR spectrum of Figure 3(b). However, the resolution of spectrum (c) is better than that of spectrum (b), because of a MAS and a high-power proton decoupling. NOE enhancement is used to obtain more intense ^{13}C signal using PST method.[22] The PST method effectively enhances peak intensity for the mobile regions in samples as compared with CP and vice versa. This means that the mobile region in the PVA gel is observed in both spectra (b) and (c). The ^{13}C signal for the CH carbon of the solid PVA has three-split broad peaks in the ^{13}C CP/MAS NMR spectrum

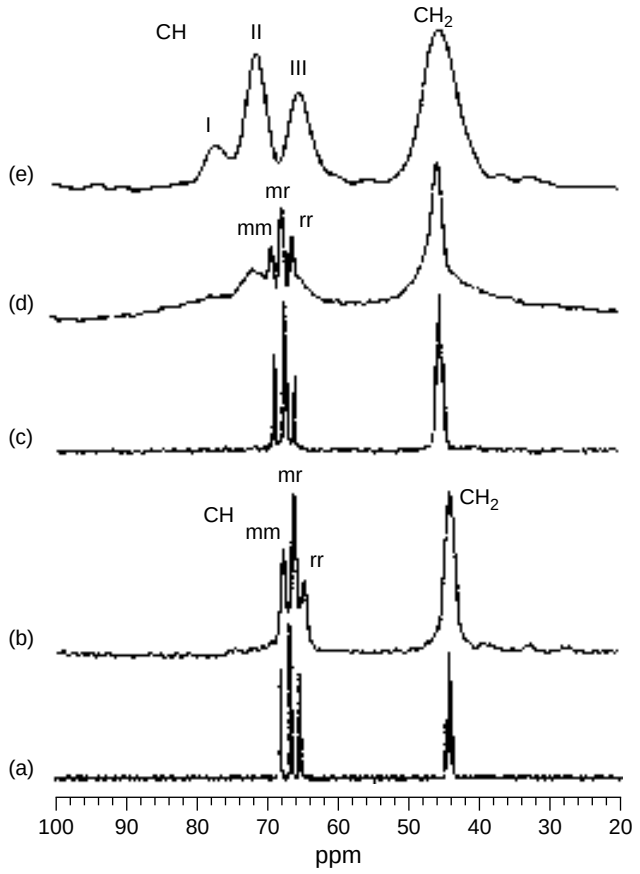

Figure 3 ^{13}C NMR spectra for the PVA in the solution, gel and solid states as measured by solution and solid-state NMR methods. For solution NMR method: PVA/D_2O solution (a) and PVA gel (b); for solid-state NMR method: PVA gel by PST/MAS (c) and CP/MAS (d), and solid PVA by CP/MAS (e)

as shown in Figure 3(e). Such a splitting is explained by the number of intramolecular hydrogen bonds formed among neighboring hydroxyl groups. Assuming that the ^{13}C chemical shift value for the CH carbon shifts to downfield by 6 ppm per one intermolecular or intramolecular hydrogen bond, the most deshielded peak (peak I) can be assigned to the CH carbon with two hydrogen bonds, the central peak (peak II) to the CH carbon with one hydrogen bond and the most shielded peak (peak III) to the CH carbon with no hydrogen bonds, respectively.[23] In the ^{13}C CP/MAS spectrum for the PVA gel as shown in Figure 3(d), the CH signal is composed of the three splitting peaks corresponding to the triad tacticity and the broad peaks as found in the solid PVA. This means that in this case both of the immobile and mobile regions of the PVA gel are observed by CP/MAS.

Figure 4 shows ^{13}C CP/MAS NMR spectra of the PVA gels with different polymer concentrations.[14] The polymer concentrations of samples (a), (b), (c) and (d) are 9.1, 11.8, 13.8 and 35.0% (w/w), respectively. The intensities of the three-split peaks due to stereochemical configurations decrease and those of peaks I, II and III increase with a decrease in water fraction in the gel. The three peaks due to stereochemical configurations completely disappear in sample (d). The schematic crosslinked structure of PVA gel formed by intermolecular and intramolecular hydrogen bonds can be inferred from these spectra. The increase in the fraction of the immobile region and the formation of hydrogen bonds are promoted by the increase in the polymer concentration of the gel.

In order to clarify the dynamics of PVA gel, ^{13}C T_1 measurements were carried out.[12] The ^{13}C T_1 values for the mobile region in a PVA gel were determined by the inversion-recovery method combined with the PST/MAS technique and the immobile region was also determined using CP/MAS combined with Torchia's pulse sequence.[54] The T_1 values for the triads are

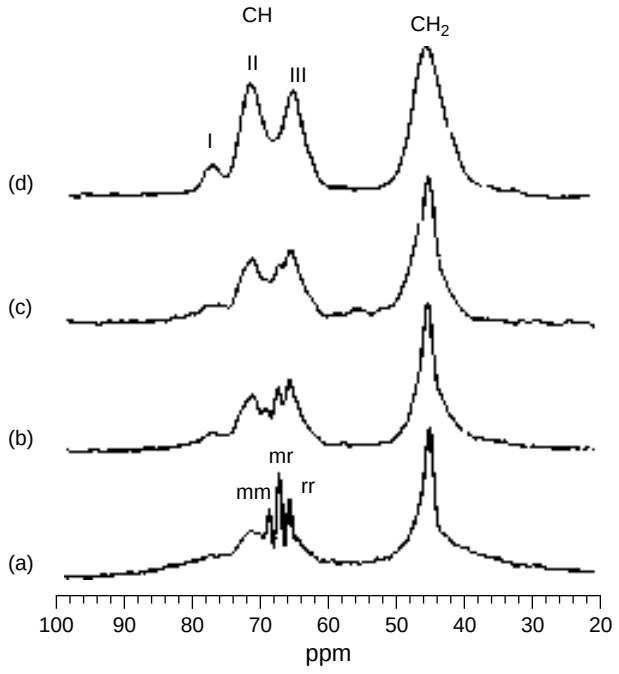

Figure 4 ^{13}C CP/MAS NMR spectra for PVA gels with different polymer concentrations. The polymer concentrations are (a) 9.1, (b) 11.8, (c) 13.8 and (d) 35.0% (w/w), respectively

smaller than those for peaks II and III. The immobile region corresponds to the CH carbons in the crosslinked regions formed by intermolecular and intramolecular hydrogen bonds in the gel, and the mobile ones to the regions away from the crosslinked regions that undergo fast molecular motion in the gel. The mobility of the network polymer in the PVA gel is restrained by hydrogen bonds and especially that of the crosslinked region is very low.

2.2.2 *Gelation Mechanism of Poly(Vinyl Alcohol) in Aqueous Solution*

PVA in aqueous solution forms a gel by undergoing freeze-thaw cycles. We have studied the structure and dynamics of PVA gels that were prepared using PVA samples with different microtacticity at some polymer concentrations under atmospheric pressure and high pressure by high-resolution solid-state ^{13}C NMR and ^{1}H pulse NMR.[14,15,17] From these studies, we have demonstrated that the crosslinked region is formed by the formation of intermolecular hydrogen bonds. From such a situation, in this work we aim to measure high-resolution solid-state ^{13}C NMR spectra during the freeze-thaw cycles, and to elucidate the mechanism of gelation process for PVA in aqueous solution.

The degree of polymerization and the degree of saponification of amorphous PVA were 1700 and 99.9%, respectively. The PVA sample was dissolved into water at 120 °C using an autoclave. The polymer concentration was 10% (g dl^{-1}). The obtained PVA aqueous solution was cooled to room temperature and was contained in a cylindrical rotor with a rubber O-ring to prevent loss of water during the NMR measurements. Prior to NMR measurement, it was kept at room temperature for one month to reach a stable state.

^{13}C CP/MAS NMR spectra of PVA/water system during the freeze-thaw cycles are shown in Figure 5.[24] There are no signals in the ^{13}C CP/MAS NMR spectrum of aqueous PVA solution at 40 °C, because in the solution state the PVA chains are undergoing much faster molecular motion compared with a frequency of ^{1}H decoupling to be ca. 60 kHz used in this experiment, and so the CP efficiency is quite reduced. In the ^{13}C CP/MAS NMR spectrum of the PVA/water system in the freezing state at −30 °C, three peaks I, II and III for the CH signal, which come from the formation of hydrogen bonds as reported previously appear clearly.[14] Peak I was assigned to carbons with two intermolecular or intramolecular hydrogen bonds, peak II to those with one intermolecular or intramolecular hydrogen bond, and peak III with no hydrogen bond. From this spectrum, it can be seen that some hydroxyl groups form hydrogen bonds at −30 °C as in the PVA gel. If the temperature is increased from −30 to 40 °C again, peak II at 71 ppm becomes broad and the three splitting peaks due to the triad configurations (mm, mr and rr) appear. This result shows that the molecular motion of PVA chains is decreased compared with that in the original solution state due to the formation of hydrogen bonds, and so the CP efficiency was enhanced. This means that the freeze-thaw process induces gel formation. In ^{13}C CP/MAS NMR spectrum of the PVA/water system in the 2nd frozen state, the three CH peaks are observed as clearly as the case in the 1st frozen state. The ^{13}C CP/MAS NMR spectra in the 3rd and 4th frozen states are almost identical. On the other hand, in the ^{13}C CP/MAS NMR spectrum of the PVA/water system in the thawing state

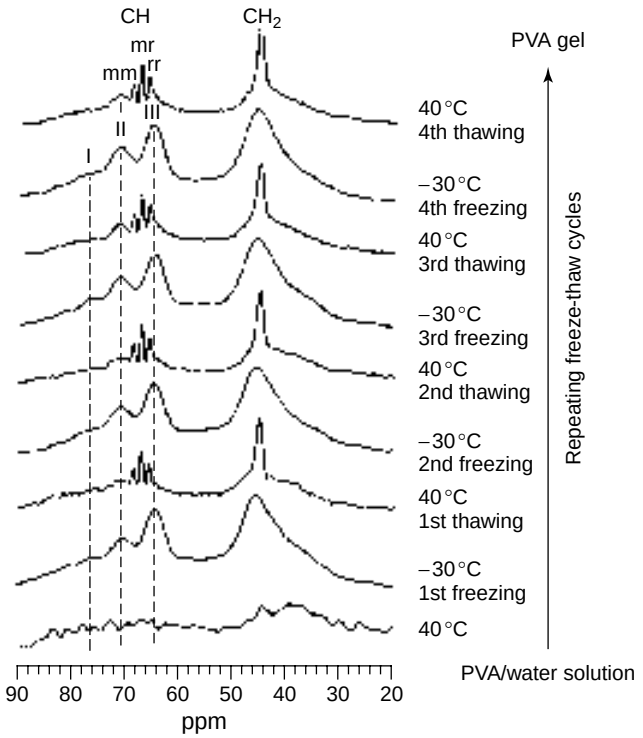

Figure 5 ^{13}C CP/MAS NMR spectra for PVA/water system under the freeze-thaw cycles

at 40 °C, the intensity of peak II is gradually increased with an increase in the number of freeze-thaw cycles. In the 4th thawing state, peak II clearly appeared. This shows that the amount of hydrogen bonds in the course of the formation of the PVA gel is increased by repeating the freeze-thaw cycles. These experimental results mean that the repeating of freeze-thaw cycles induces the gelation of the PVA/water system.

From these experiments, the mechanism of gelation for the PVA/water system was proposed as follows: in the solution state, there are no strong intermolecular hydrogen bonds and so the corresponding CH peak cannot be obtained using ^{13}C CP/MAS NMR method. In the frozen state, water is frozen and the PVA chains aggregate to form the polymer-rich domain. In the polymer-rich region, strong intermolecular hydrogen bonds may be formed and the corresponding CH peaks are clearly observed by ^{13}C CP/MAS NMR. By repeating the freeze-thaw cycles, the fraction of the polymer-rich regions is increased, and then the crosslinked region is formed, which consists of strong hydrogen bonds. Therefore, it can be said that the process of repeating the freeze-thaw cycles induce intermolecular hydrogen bonds and so is essential for the gelation of the PVA/water system.

2.2.3 *Structure and Dynamics of Poly(γ-Methyl L-Glutamate) Gel*

The properties of the polymer gels swollen in organic solvents are different from those of hydro-swollen gels. Crosslinked poly(γ-methyl L-glutamate) (PMLG) is prepared by the ester-amide exchange reaction using diaminododecane as a cross-linker and is swollen in trifluoroacetic acid (TFA) and $CHCl_3$. The PMLG gel was studied by using high-resolution solid-state ^{13}C NMR spectroscopy.[55] A typical ^{13}C PST/MAS NMR spectrum of PMLG gel swollen in $CHCl_3$ is shown in Figure 6. The amide and ester carbonyl carbons of PMLG appear at 176.2 and 173.5 ppm, respectively. The Cα, OCH_3, Cγ and Cβ carbons appear at 57.6, 52.3, 31.3, and 26.1 ppm, respectively. The peak intensities of the side chain carbons is more intense than that of the main chain carbons.

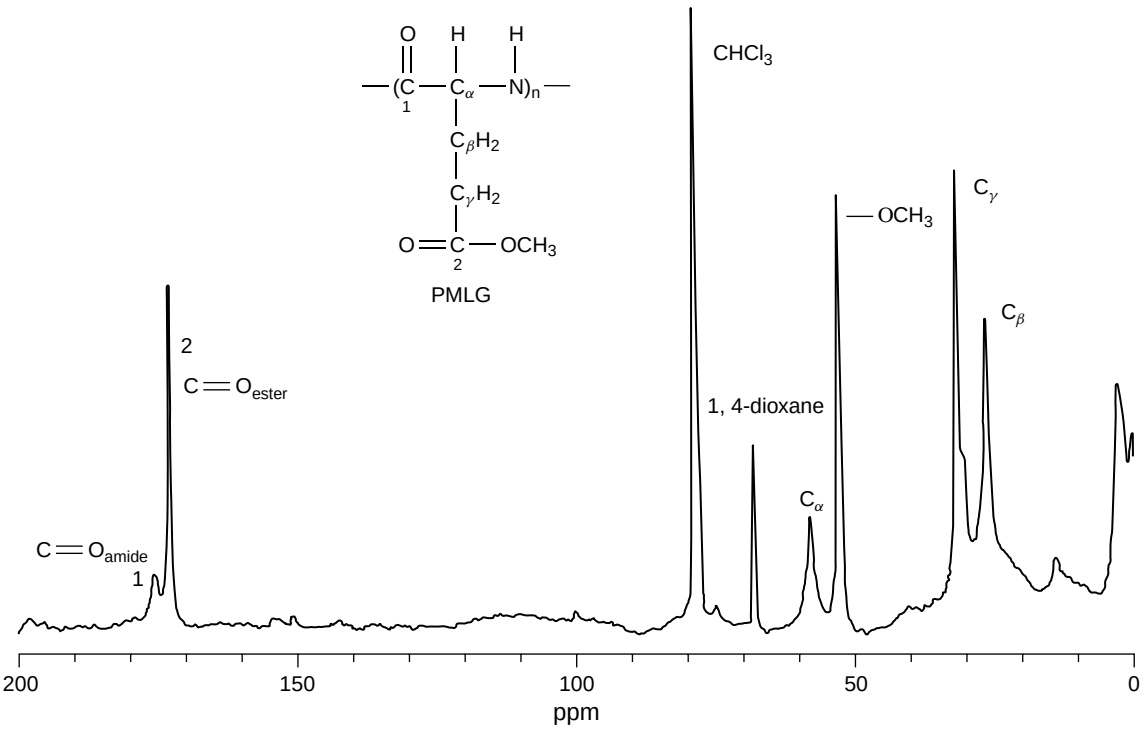

Figure 6 ^{13}C PST/MAS NMR spectrum of PMLG gel swollen in $CHCl_3$

This means that the side chains are undergoing faster molecular motion compared with the main chain.

The ^{13}C chemical shifts of the individual carbons of PMLG gel are changed as a function of the TFA content (f_{TFA}) in a mixture of $CHCl_3$ and TFA. In the PMLG gel with $CHCl_3$, the ^{13}C chemical shift values of the main chain amide C=O and Cα carbons are 176.2 and 57.6 ppm, respectively. The PMLG chain part of the crosslinked network takes the α-helix conformation as determined by reference data[25] of solid polypeptides at about 176 and 57 ppm. The amide C=O and Cα ^{13}C chemical shifts change transitionally from 176.5 and 57.6 ppm to 174.0 and 54.4 ppm, respectively, and so move upfield with an increase in TFA content. Such a transitional upfield shift shows that the main chain conformation of the PMLG network changes from the α-helix to the random coil form. The midpoint of the transition is at about $f_{TFA} = 0.15$. On the other hand, it is shown that in the side chain carbons the ester C=O carbon moves downfield at the transition point, but the chemical shifts of the other carbons do not change clearly. The chemical shift of the main chain arises from the conformational change due to the formation of intramolecular hydrogen bond between the C=O and N–H in the main chain. The main chain chemical shift is considered to be very sensitive to the helix-coil transition. The large shift difference of the ester carbonyl carbons is due to the interaction with TFA. The ^{13}C chemical shifts of the other side chain carbons also show small changes at $f_{TFA} = 0.15$.

The degree of swelling for the PMLG gel is a function of f_{TFA}. The degree of swelling is transitionally decreased at 0–0.05 f_{TFA}, is constant at 0.05–0.2 f_{TFA} and is gradually increased at $f_{TFA} > 0.2$. In the range 0.05–0.2, the fraction of the random coil form is increased gradually with an increase in f_{TFA} and the degree of swelling is constant. The TFA content dependence of the ^{13}C T_1 of amide C=O and ester C=O carbons was observed at 20 and 40 °C. As the temperature decreases from 40 to 20 °C, the ^{13}C T_1 for the amide C=O carbon increases and that of the ester C=O carbon decreases. The molecular motion of the amide C=O carbon is in the slow motion region ($\omega\tau_c \gg 1$, where ω is the resonance frequency) and that of the ester C=O carbon is in the fast motion region ($\omega\tau_c \ll 1$) according to the BPP theory. The decrease in ^{13}C T_1 of the ester C=O carbon in f_{TFA} from 0 to 0.05 shows that the decrease in molecular motion of side chain caused by a rapid shrinkage of the gel. In the range $f_{TFA} = 0.05–0.20$, ^{13}C T_1 of the amide C=O carbon decreases with an increase in TFA content. This means that the molecular motion of main chains is increased in going from the α-helix to the random coil in the constant degree of swelling. On the other hand, the molecular motion of the side chains is not so affected by the helix-coil transition.

2.2.4 Structural and Dynamic Characterization of EVOH Gels

In the CP method, enhancement of the ^{13}C magnetization is effective for the relatively immobile solid-like region, but is greatly reduced for the mobile region in gels. For this, it is expected that ^{13}C CP/MAS NMR gives us dynamic information about gels in an addition to structural information. ^{13}C CP/MAS NMR spectra of EVOH gel samples were measured over a wide range of ethylene contents from 5 to 74% at room temperature.[18] Only the intense background signal in the ^{13}C CP/MAS spectra of EVOH gels with low ethylene contents from 5 to 48% appears. This results from the following reasons. At the measurement temperature, the gels are very soft, so the mobility of EVOH network chains becomes high. This leads to a large reduction of the CP efficiency. Thus, the background signal that comes from the polymer materials used in an NMR probe appears intensely in the spectrum. This was recognized from the CP/MAS experiment using an NMR rotor containing no sample. The ^{13}C CP/MAS spectra of EVOH samples with high ethylene content of 55 and 74% were obtained with a reasonable signal-to-noise ratio. It is found that the spectral patterns for the CH carbon of the V units and for the CH_2 carbon of the E and V units are greatly changed by varying the ethylene content. In order to obtain the sufficient CP efficiency for the immobile component of EVOH gels with low ethylene content, ^{13}C CP/MAS NMR spectra of EVOH gel with the ethylene content of 5% were measured with repetition time of 5 s by changing of the contact time in the range from 100 to 2000 μs. At long contact time the noncrystalline region that is undergoing slow molecular motion can be often observed.

The ^{13}C PST/MAS NMR spectrum of EVOH gel with ethylene content of 5% was shown in Figure 7(b). This spectrum is similar to solution-state ^{13}C NMR spectrum of EVOH, like the case of PVA gel.[14,15] In the spectrum, the mm, mr and rr triad peaks for the CH carbon (in the 65–69 ppm region), and the m and r diad peaks for the CH_2 carbon (in the 45–48 ppm region) of V units in EVOH appear clearly. It can be said that the V units in the highly mobile region are observed by the PST/MAS NMR. On the other hand, ^{13}C CP/MAS NMR spectrum of its gel was measured under different conditions of the contact time of 1000 μs, the repetition time of 3 s and the accumulation number of 150 000 from the measurement condition used for the observed ^{13}C CP/MAS NMR spectra (see Figure 7(a)). In this spectrum, peaks I, II and III for the CH carbon of V units, which come from the immobile region, and the mr peak of the triad peaks (as appeared in the 65–69 ppm region) for the CH carbon, which comes from the mobile region appears clearly as shown in Figure 7(a). On the other hand, EVOH gel samples with higher ethylene-content become very hard, and thus ^{13}C CP/MAS NMR spectra of EVOH gels with the ethylene contents of 55 and 74% appear more clearly with a reasonable signal-to-noise ratio even at room temperature because the gels are solid-like, so their molecular motion is greatly restrained. This does not conflict with the pulse ^{1}H NMR results, in which the ^{1}H T_2 value of EVOH gels is decreased with ethylene content and the fractions of the mobile and intermediate regions (corresponding to the crosslinked and non-crosslinked regions, respectively) in EVOH gels with ethylene content larger than 55% are increased.

Next, we are concerned with temperature-variable ^{13}C CP/MAS NMR spectra of EVOH gels to obtain further dynamic information on the gels. ^{13}C CP/MAS NMR spectra of EVOH gels with ethylene content of 32% at 0 and 23 °C are shown in Figure 8. The ^{13}C CP/MAS NMR spectrum at 23 °C has very low signal-to-noise ratio and thus the intense background signal appears as a whole as shown in Figure 8(a). This means that the CP efficiency of the gels becomes insufficient by undergoing fast molecular motion at 23 °C, where these gel samples are very soft and thus mobility is high. As temperature is decreased, the individual peaks

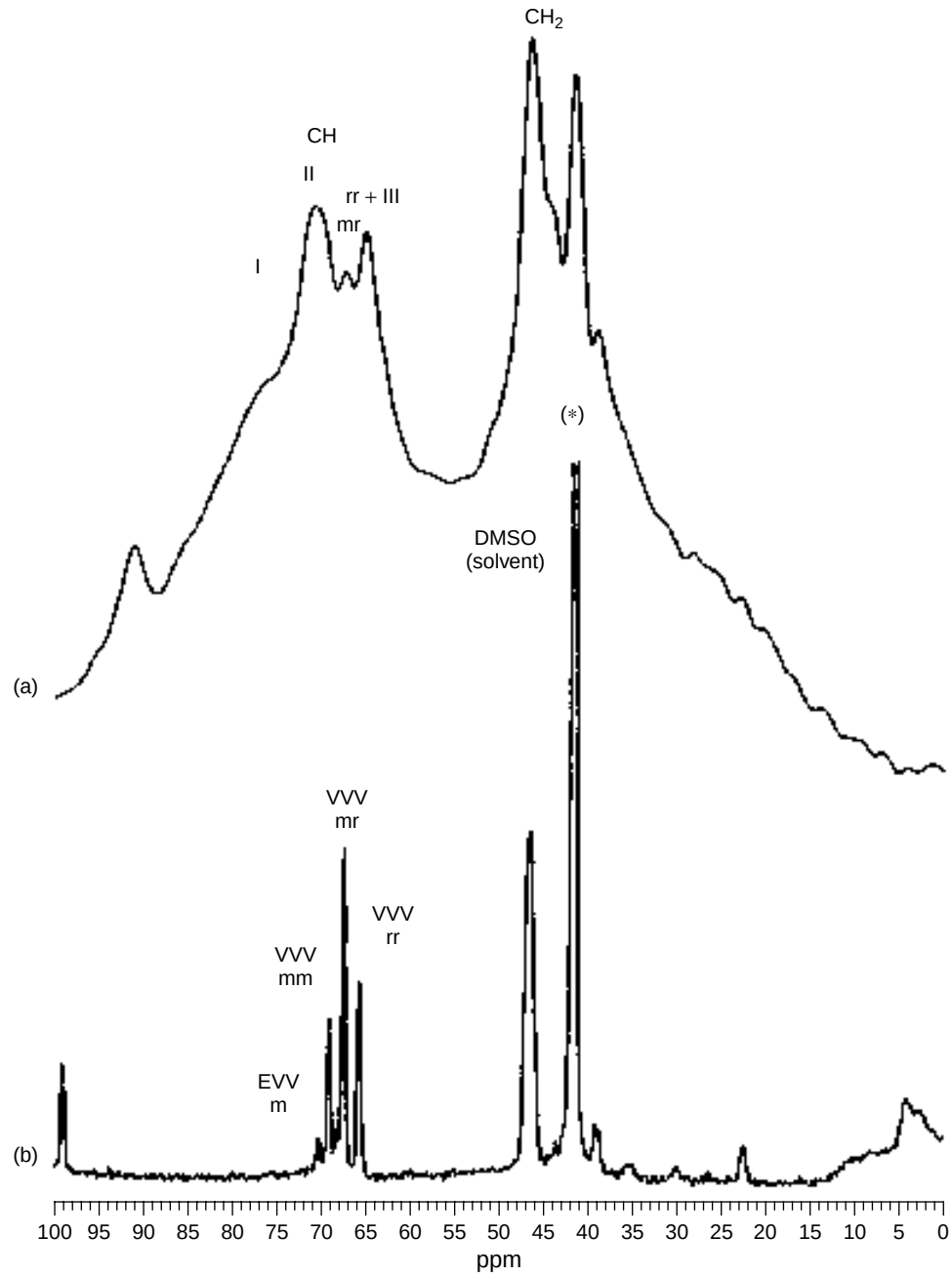

Figure 7 67.8 MHz ^{13}C NMR spectra of EVOH gel with ethylene content of 5% at room temperature. (a) CP/MAS NMR spectrum and (b) PST/MAS NMR spectrum

in the spectrum (a) at 0 °C appear more clearly compared with the spectrum (b) at 23 °C. This is due to an increase in the CP efficiency by reduction of molecular motion at low temperature. The three peaks I, II and III for the CH carbon of the V units appear like the ^{13}C CP/MAS NMR spectra of solid EVOH samples.[29] Further, the EVOH copolymer gel prepared by using a mixture of DMSO and water as solvent is relatively harder compared with one prepared by using DMSO as solvent. This is because the intermolecular affinity between EVOH and mixture solvent of DMSO and water becomes much lower compared with that between EVOH and DMSO solvent, and then the hydrophobic and/or hydrophilic interactions between polymer chains are enhanced. Thus, the EVOH copolymer with the ethylene content of 32% as prepared by using a mixture of DMSO and water as solvent becomes relatively solid-like. This leads to the ^{13}C CP/MAS NMR spectrum of the EVOH gel being well resolved with a reasonable signal-to-noise ratio, similar to solid EVOH.[26–29] All peaks in these spectra can be assigned in the same way as already assigned in PVA gel[14] and solid EVOH[29] as below.[14,29]

Next, we are concerned with the spectral analysis. The spectral assignment was made according to the previous assignments on solid EVOH samples.[29] First, the assignment of the ^{13}C peaks of the CH carbon was made. The assignment of three peaks I, II and III of the CH carbon in EVOH gel with low ethylene content, which appeared at about 77, 71 and

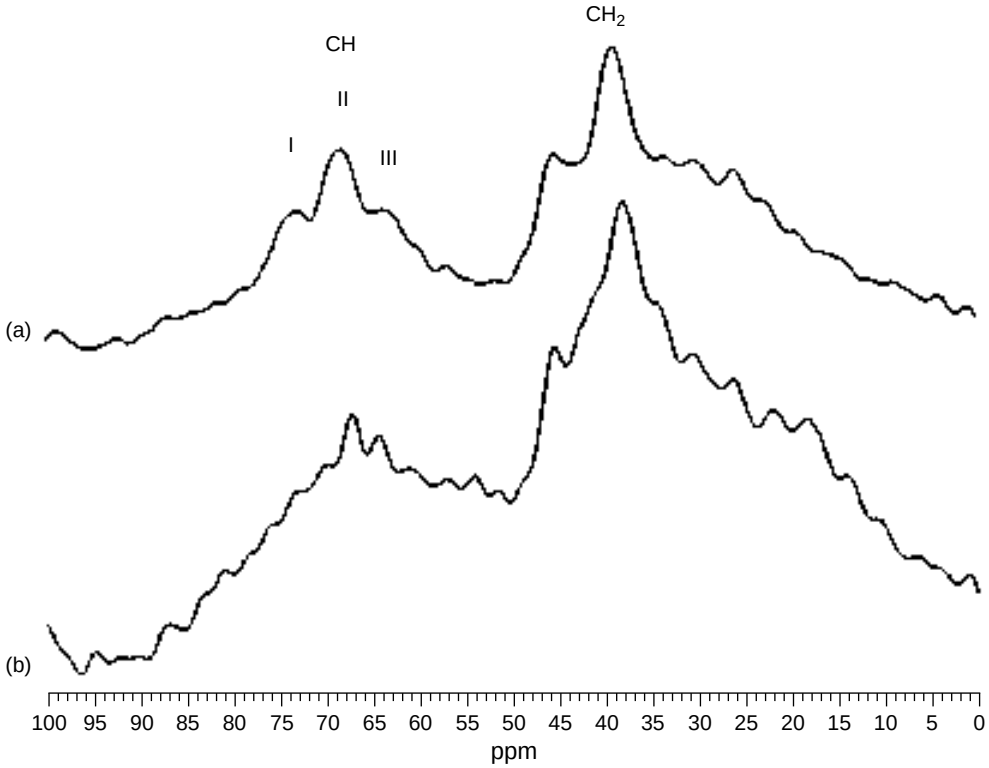

Figure 8 67.8 MHz ^{13}C CP/MAS NMR spectra of EVOH gel with ethylene content of 32% at 0 °C (a) and 23 °C (b)

65 ppm, respectively, can be made according to the assignment of the CH peaks in PVA gel.[14] Peak I comes from the formation of two intramolecular or intermolecular hydrogen-bonds, peak II from the formation of one intramolecular or intermolecular hydrogen-bond, and peak III from no hydrogen bond. On the other hand, in EVOH gel samples with high ethylene content, the ^{13}C chemical shift positions of peaks I and II are different from those in EVOH gel samples with low ethylene content. This is due to appearance of new configurational arrangements by the large amount of the ethylene units in the copolymers. From such a situation, according to the previous assignment we assign peak I to CH carbon of the V unit in EVE sequence as the major contribution in addition to two intramolecular or intermolecular hydrogen-bonded CH carbon of the V units as the minor contribution, and peak II from one intramolecular or intermolecular hydrogen bonded CH carbon of the central V unit in VVV sequences as the minor contribution.[29] Further, by analyzing the partially-relaxed spectra of EVOH gel (with the ethylene content of 5%) by using the Torchia method, it was found that each of three CH peaks I, II and III in EVOH gel remains even at longer delay time (=15 000 ms). This arises from the fact that peaks I, II and III in EVOH gel are frozen in molecular motion on the NMR timescale, because these three peaks comes from the crosslinking region in the gel. From the present results and the previous results in the sample of low ethylene content, it is concluded that the formation of hydrogen bonds between vinyl alcohol parts of EVOH contributes to gel formation.[16,17]

Further, we are concerned with the peak assignment of the CH_2 carbon in EVOH gel with high ethylene content. The CH_2 peaks at 30 and 33 ppm come from the asterisked central CH_2 carbons in both of the $–CH_2–CH_2–CH_2*–CH_2–CH_2–$ unit and $–CH_2–CH_2–CH_2*–CH_2–CH_2–$ unit with and without fast exchange between the *trans* and *gauche* conformations, respectively. The CH_2 peak at 30 ppm decays more rapidly than the CH_2 peak at 33 ppm. This arises from the fact that the CH_2 carbons of the ethylene units with the *trans* zigzag conformation in the crystalline region, which appear at 33 ppm, are frozen on the NMR timescale. On the other hand, the CH_2 carbons in the non-crystalline region, which appear at 30 ppm, are undergoing fast exchange between the *trans* and *gauche* conformations at room temperature.[30,31] In this case, in EVOH samples with high ethylene content, the gel may be formed in the crystalline region by hydrophobic interactions between the ethylene units of EVOH.

2.2.5 *Structural Characterization of Poly(Methacrylic Acid) Gel*

The structural and dynamic characterization of poly(methacrylic acid) gel with water as a function of degree of crosslinking was carried out through the observation of high-resolution solid-state ^{13}C NMR spectra by using ^{13}C PST/MAS NMR.[41] ^{13}C PST/MAS NMR spectra of PMAA gels with $Q = 3.4, 21.7$ and 105.8 are shown in Figure 9.[56] It is seen that high-resolution spectra are obtained. This indicates that the efficiency of MAS to obtain high resolution spectrum is very high for polymer gel systems. The peaks of the PMAA gel can be assigned to the C=O, CH_2, quaternary C, and CH_3 carbons from downfield. Each of the C=O and CH_3 carbon signals is split into three peaks due to the triad configurations of PMAA. These peaks are designated by the C=O (rr:182.5 ppm), C=O (mr:181.5 ppm), C=O (mm:180.8 ppm), CH_3 (mm:22.3 ppm), CH_3 (mr:19.8 ppm)

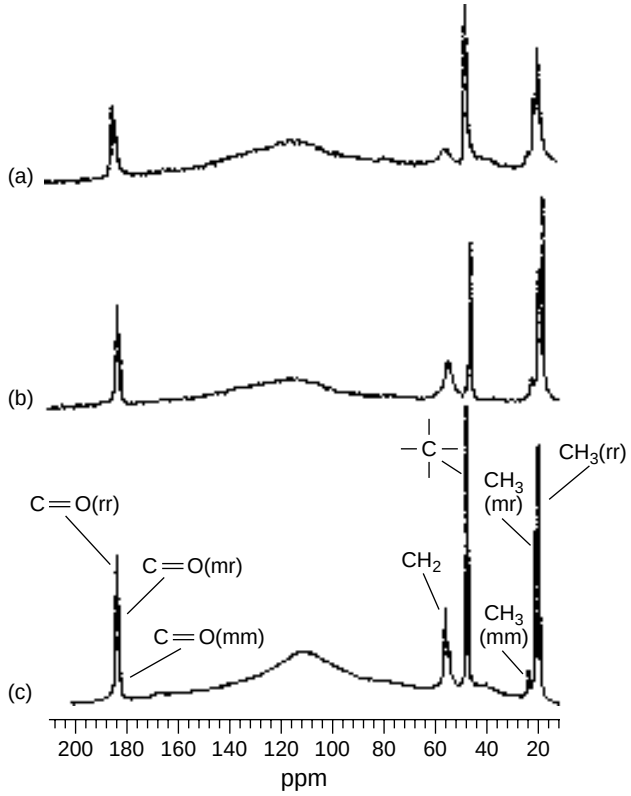

Figure 9 ^{13}C PST/MAS spectra of PMAA gels with $Q = 105.8$ (a), 21.7 (b) and 3.4 (c) at 300 K

and CH_3 (mm:18.2 ppm). The peak intensity ratio of these triad signals corresponds to the triad fraction. From the CH_3 signals, the triad fraction is evaluated as rr : mr : mm = 67.4 : 27.1 : 5.5%. The ^{13}C chemical shift values for the PMAA gels are independent of Q. This means that there is no specific effect on the ^{13}C chemical shift by changing Q.

From the ^{13}C T_1 measurements, it was found that molecular motion of the side chain carbons is in the extremely narrowing region in the BPP theory and that of the main chain carbons is in the slow motion region, and an increase in the degree of crosslinking in the PMAA gel leads to restraint in the segmental motion of the network polymer.

2.2.6 Structural and Dynamic Characterization of Poly(L-Glutamates) with N-Alkyl Side Chains in the Thermotropic Liquid Crystalline State

It is known that in a series of α-helical poly(L-glutamates) with n-alkyl side chains of various lengths, n-alkyl side chains longer than $n = 10$ form a crystalline phase composed of paraffin-like crystallites together with an α-helical main chain packing into a characteristic layer structure. The polymers form thermotropic liquid crystals by the melting of the side chain crystallites. The structural and dynamic behavior of the polymers over a wide range of temperatures in going from the solid state to the thermotropic liquid crystalline state has been elucidated by variable temperature ^{13}C CP/MAS NMR.[33,34] It has been demonstrated that the ^{13}C chemical shifts of the main chain amide carbonyl and Cα carbons in polypeptides are conformation-dependent and thus the main chain conformation can be determined by the ^{13}C chemical shift position of the main chain carbons.[25] Also, like polypeptides the conformation of long n-alkyl side chains can be determined by the ^{13}C chemical shift position.[46]

In Figure 10 the ^{13}C CP/MAS NMR spectra of poly(γ-n-octadecyl L-glutamate) (POLG) with long n-alkyl[$-(CH_2)_{17}CH_3$] side chains are shown over a wide range of temperatures from −40 to 230 °C. Assignments for peaks are straightforward as indicated in the spectra. The ^{13}C chemical shift values of the amide carbonyl and Cα carbons are 176.2 and 57.4 ppm, respectively. These values are characteristic of the right-handed α-helix conformation of the main chain of POLG. On the other hand, the assignment for peaks of n-alkyl side chains of POLG is performed by the using reference data on n-alkanes. At temperatures from −40 to 40 °C, the ^{13}C chemical shift values of the inner CH_2 carbons of the side chains are 33 ppm. This means that the inner CH_2 carbons of the side chains take an all-*trans* zigzag conformation in the orthorhombic form. At temperatures above 50 °C, the ^{13}C chemical shift value moves transitionally upfield by ca. 3 ppm. This means that n-alkyl side chains melt like liquid n-alkanes and then the fast exchange between the *trans* and *gauche* conformations occurs. Such an upfield shift occurs according to equation (1)

$$\delta_{obs} = \delta_o - 2\gamma f_g \quad (1)$$

where δ_{obs} and δ_o are the observed ^{13}C chemical shift and the ^{13}C chemical shift for the *trans* conformation, f_g is the fraction of the *gauche* conformation, and γ is attributed to the chemical shift difference (ca. 5.3 ppm) between the *trans* and *gauche* conformations.[30] At temperatures above 50 °C, this polymer forms a thermotropic liquid crystalline state.

In Figure 10 it is shown that the broadening phenomenon for peaks of the main chain carbons can be explained on the basis of the consideration that when the orientation rate of the main chain in the liquid crystalline state is close to a frequency corresponding to the amplitude of the proton decoupling field (about 60 kHz for this experiment), the efficiency of the proton decoupling is considerably reduced and the line width becomes the maximum. Thus, it can be said that the main chain is undergoing reorientation at a frequency of ca. 60 kHz in the temperature range from 50 to 90 °C.

In poly(L-glutamate) with long oleyl [$-(CH_2)_8CH{=}CH(CH_2)_7CH_3$] side chains which contain a double bond (POLLG), the melting of the side chain crystallites is at a much lower temperature than that of POLG. This polymer forms thermotropic liquid crystals from lower temperature.[45] The spectral behavior is very similar to POLG.[34]

2.3 Approach by Pulse Field-Gradient Spin-Echo ^{1}H NMR

2.3.1 Pulse Field-Gradient Spin-Echo ^{1}H NMR Measurements

In order to determine the diffusion coefficient of solvent and probe molecules in a gel, pulse field-gradient spin-echo (PFGSE) NMR is used. This method is very powerful.[5,35,36] However, if one wants to determine relatively small diffusion coefficients with high accuracy, a strong strength of the field gradient must be used. We have designed two kinds of PFGSE NMR probe systems of generating the strength of the field

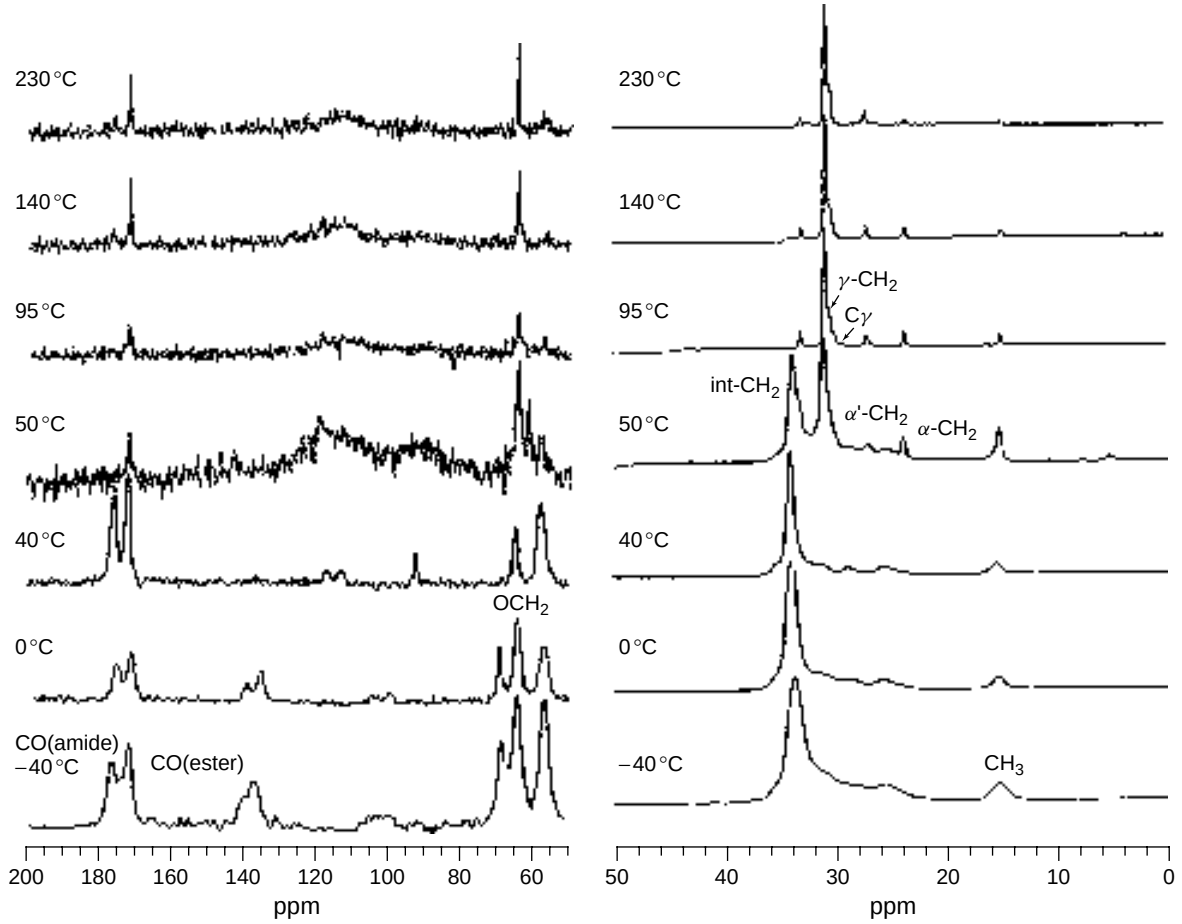

Figure 10 ^{13}C CP/MAS NMR spectra of poly(γ-octadecyl L-glutamate) over a wide range of temperatures

gradient pulse of $7.8\,\mathrm{T\,m^{-1}}$ and $22.8\,\mathrm{T\,m^{-1}}$.[3] This leads to a determination of the diffusion coefficient on the order of $10^{-14}\,\mathrm{m^2\,s^{-1}}$. As the PFGSE pulse sequence, two field gradient pulses are added to the ($\pi/2$ pulse $-\tau-\pi$ pulse) sequence, in which the first field gradient pulse is added at the mid position between the $\pi/2$ and π pulses (that is, at the position of τ^* after the $\pi/2$ pulse), and the second at the position of τ^* after the π pulse.[37]

The relationship between the echo signal intensity and pulse field gradient parameters is given by equation (2)

$$\mathrm{A}(\delta)/\mathrm{A}(0) = \exp[-\gamma^2 G^2 D\delta^2(D-\delta/3)] \qquad (2)$$

where A(δ) and A(0) are echo signal intensities at $t = 2\tau$ with and without the magnetic field gradient pulse, respectively, whose length is δ. τ is the pulse interval, γ the gyromagnetic ratio of the proton ($\gamma = 2.675 \times 10^8$ rad $T^{-1}\,\mathrm{s^{-1}}$), G the field gradient strength, D the self-diffusion coefficient, and Δ the gradient pulse interval. The echo signal intensity was measured as a function of δ. The plot of ln[A(δ)/A(0)] against $\gamma^2G^2\delta^2$ $(\Delta-\delta/3)$ gives a straight line with a slope of $-D$. Therefore, D can be determined from the slope. The τ, Δ and δ values employed in these experiments were 10, 10 and 0.001–0.12 ms, respectively. The D value of $2.5 \times 10^{-9}\,\mathrm{m^2\,s^{-1}}$ for water at 303 K was used as the calibration of the field gradient strength.[3] The experimental error for the D value is estimated to be less than ca. 5%.

2.3.2 *Diffusional Behavior of Synthetic Polymer Gels*

2.3.2.1 *Diffusional Behavior of Water in Poly(methacrylic acid) Gels*

In order to investigate changes in the translational motion of water contained in the poly(methacrylic acid) (PMAA) gel by a change in the degree of crosslinking, the diffusion coefficient of water molecules ($D_{\mathrm{H_2O}}$) in PMAA gels with the degree of swelling $Q = 3.4$–105.8 was determined by PFGSE ^{1}H NMR method at 300 K.[38] As seen from this table, $D_{\mathrm{H_2O}}$ increases as Q is increased. This means that an increase in Q leads to an increase in mobility of water molecules. If the $D_{\mathrm{H_2O}}$ increases are plotted against $Q^{1/3}$, it is seen from Figure 11 that $D_{\mathrm{H_2O}}$ increases linearly from 1.37×10^{-9} to $2.19 \times 10^{-9}\,\mathrm{m^2\,s^{-1}}$ with increasing $Q^{1/3}$.[39] This shows that the translational molecular motion of water molecules in the PMAA gel increases with an increase in the degree of swelling. The $D_{\mathrm{H_2O}}$ value of neat water at 300 K is $2.5 \times 10^{-9}\,\mathrm{m^2\,s^{-1}}$. Therefore, it can be said that the translational molecular motion of water molecules in the gel is more restrained compared with that of neat water by the intermolecular interactions with the polymer network.

We are concerned with the reason why there exists a linear relationship between the $D_{\mathrm{H_2O}}$ and $Q^{1/3}$. The volume for the gel that contains network polymer and water may be associated with $Q^{1/3}$. Assuming that the volume for the gel is a cube with the length of an edge being r, the degree of swelling for the

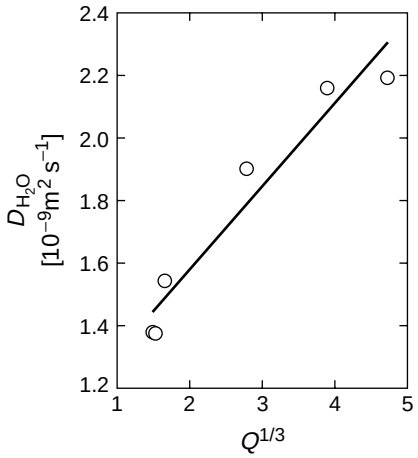

Figure 11 Plots of diffusion coefficient of water (D_{H_2O}) in PMAA gel against $Q^{1/3}$ at 300 K

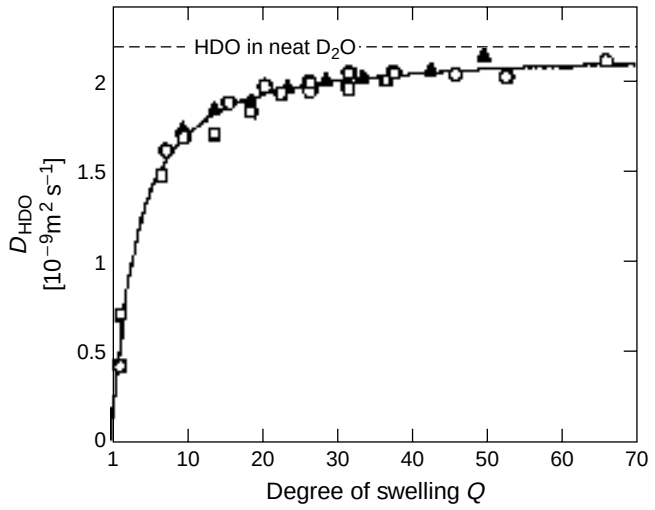

Figure 12 Dependence of the diffusion coefficient of water molecules (D_{HDO}) on the degree of swelling (Q) in a PDMAA gel containing PEG with $M_w = 4250$ (□), 10 890 (▲) and 20 000 (○) at 303 K

gel is rearranged as equation (3)

$$Q = M_{swollen}/M_{dry} = (\rho_{swollen} \cdot V_{swollen})/M_{dry} = (\rho_{swollen}/M_{dry})r^3 \quad (3)$$

where $\rho_{swollen}$ is the density of swollen polymer gel and $V_{swollen}$ the volume of swollen polymer gel. M_{dry} is a constant. By rearranging equation (3), we obtain equation (4)

$$r = (M_{dry}/\rho_{swollen})^{1/3} Q^{1/3} \quad (4)$$

If Q is changed as a function of the degree of crosslinking of the gel, $\rho_{swollen}$ does not change greatly (at 300 K $\rho_{swollen} = 1.001\,g\,cm^{-3}$ at $Q = 3.4$ and $\rho_{swollen} = 0.997 \times 10^3\,Kg\,m^{-3}$ at $Q = 106$). Therefore, it can be said that the length of an edge of the volume of the gel (r) is proportional to $Q^{1/3}$. This means that r of the volume containing a constant amount of network polymer increases with an increase in $Q^{1/3}$ and so the size of the polymer network in the gel expands the intermolecular distance between water molecules increases. For this, the molecular motion of molecules increases with an increase in $Q^{1/3}$. From the linear relationship between the D_{H_2O} and $Q^{1/3}$, it can be said that the molecular motion of water depends on intermolecular distance.

2.3.2.2 *Diffusional of Water and Poly(Ethylene Glycol) in Poly(Dimethylacrylamide) Gels*

The diffusion coefficients of HDO(D_{HDO}) and poly(ethylene glycol) (PEG) contained in poly(dimethylacrylamide) (PDMAA) gel were determined by the PFGSE ^{1}H NMR method as described above at 303 K varying Q and molecular weight (M_w) of PEG.[40] The D_{HDO} values obtained were plotted against Q as shown in Figure 12. As seen from this figure, D_{HDO} increases as Q is increased, and is almost independent of M_w of PEG contained in the gel. The change of D_{HDO} in the small Q region is much larger than that in the large Q region. The D_{HDO} value in the large Q region asymptotically approaches that for HDO in neat D_2O ($2.22 \times 10^{-9}\,m^2\,s^{-1}$). Therefore, it can be said that the intermolecular interaction between water and polymer network, of which the strength depends on the size of a network, restrains translational motion of the water. There is almost no effect on the molecular motion of HDO by the change of M_w of PEG, indicating that the diffusion of HDO is independent of M_w of PEG.

We can understand these results by using the modified free volume theory proposed by Fujita.[41] The diffusion coefficient is related to the friction ζ by the equation $D = kT/\zeta$, where k is the Boltzmann constant and T the absolute temperature. The dependence of ζ on solvent concentration is expressed as an exponential function of the fractional free volume f. Thus, we have equation (5)

$$D_{HDO} = D^0_{HDO} \exp[Q^{-1}/(Q^{-1} f_{solv} - f^2_{solv}/\beta)] \quad (5)$$

The dynamic behavior of a probe polymer in a gel can be analyzed by the ratio of the screening length of polymer network to the dimensional size of PEG. It is shown that the diffusion of a particle in semi-dilute polymer solution and in a polymer gel is obeyed by the relation shown in equation (6)

$$D/D^0 = \exp(-\kappa R) \quad (6)$$

where D^0 is the diffusion coefficient of an isolated particle, R the radius of a particle and κ^{-1} the dynamical screening length of the polymer chain. When $D/D^0 = \kappa^{-1}$, κ^{-1} is equivalent to R. This relation has also been employed for elucidating the self-diffusion of random-coil polymers in solution and gel, in which the values of κ^{-1} are large enough for probe polymers to have the same motion as for a hard sphere. In these cases, the interchain hydrodynamic interactions more significantly contribute to the diffusion process compared with the topological constraints. For this, the hydrodynamic radius of a probe polymer can be replaced by R. When the topological constrains cannot be neglected compared with the interchain hydrodynamic interactions, Ds becomes larger than the value expected from equation (6). When the diffusion coefficient of an isolated PEG (D^0_{PEG}) is determined from the diffusion coefficient of PEG in aqueous dilute solution (D^{soln}_{PEG}), it is necessary to take into account the change of local friction of polymer, which is estimated by the change for the

diffusion coefficient of the solvent. Then, D^0_{PEG} is given by equation (7)

$$D^0_{PEG} = D^{soln}_{PEG}/(D^{neat}_{HDO}/D_{HDO}) \quad (7)$$

where D^{neat}_{HDO} is the diffusion coefficient of HDO in D_2O. In this work, the diffusion of water and PEG in a PDMAA gel has been analyzed by the above mentioned equations (6) and (7).

2.3.2.3 *Diffusion Coefficient of HDO in a PDMAA Gel*

We can more clearly understand the dynamic behavior of water in the gel system using equation (5) obtained from modified free volume theory.[31,41] The solid curve obtained from a least-squares fitting to the experimental data using equation (5) is shown in Figure 12. The theoretical curve agrees well with the experimental data. From this result, the diffusion coefficient for HDO in infinite swollen gel ($Q \rightarrow \infty$) is obtained to be $D^0_{PEG} = 2.16 \times 10^{-9}\,m^2\,s^{-1}$, which is lower than HDO in neat D_2O ($2.22 \times 10^{-9}\,m^2\,s^{-1}$). This means that the diffusion coefficient for HDO in neat D_2O is different from the Q-extrapolated value to infinity given by the modified free volume theory for the diffusion concentration dependence. The diffusion coefficient for an isolated HDO molecule in bulk PDMAA ($Q \rightarrow 1$) obtained from Figure 12 was $2.5 \times 10^{-11}\,m^2\,s^{-1}$. It is seen that the translational motion of isolated water in bulk polymer is more strongly restrained compared to that in the gel. Further, it can be said that the rapid decrease of D_{HDO} in the small Q region can be explained by the decrease in free volume.

2.3.2.4 *Diffusion Coefficient of PEG in a PDMAA Gel*

In order to investigate the translational motion of PEG contained in PDMAA gel as a probe polymer, the diffusion coefficient of PEG (D_{PEG}) was determined by PGSE ^1H NMR at 303 K varying Q and M_w of PEG contained in the gel. It was found that D_{PEG} increases as Q is increased and also depends on M_w of PEG. The D_{PEG} value in the gel is smaller than that at 1% wt aqueous PEG solution (D^{soln}_{PEG}) at 303 K. Therefore, it can be said that the translational motion of PEG in the gel is more restrained by large intermolecular interaction with polymer network as compared with PEG in aqueous solution and that PEG with higher M_w is more strongly restrained.

Next, we are concerned with the relationship between the degree of restraint in molecular motion of PEG in the gel and the ratio of the screening length of polymer network to the size of PEG.[40] The dynamic behavior of PEG in the gel can be analyzed by using equation (6). The relationship between the dynamic screening length (κ^{-1}) and the concentration of network polymer (c) or the degree of swelling (Q) is expressed by equation (8)

$$\kappa^{-1} = c^u = Q^{-u} \quad (8)$$

where u may be a constant in the range from -0.5 to -1.0, but depends largely on the polymer species. Substitution of equations (6) and (7) into equation (8) gives equation (9)

$$D_{PEG}\,D^{neat}_{HDO}/D^{soln}_{PEG}\,D_{HDO} = \exp(-Q^u R). \quad (9)$$

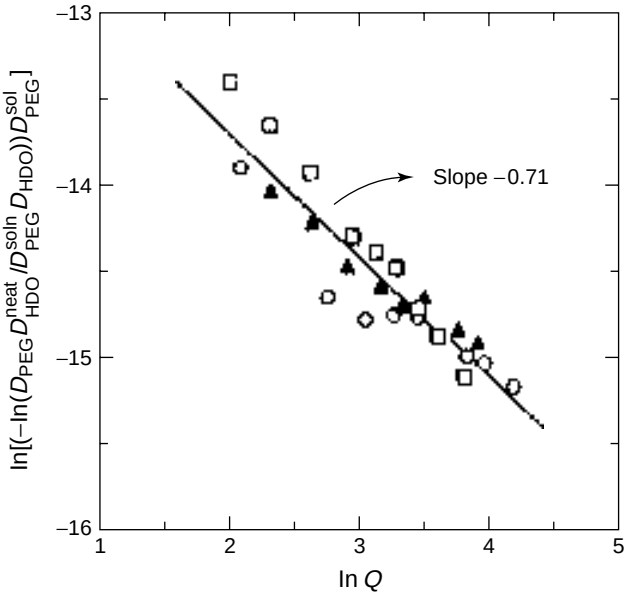

Figure 13 Plots of $\ln(-\ln(D_{PEG}D^{neat}_{HDO}/D^{soln}_{PEG}D_{HDO}))$ against $\ln Q$ at 303 K. M_ws of PEGs used are 4250 (□), 10 890 (▲) and 20 000 (○)

It is convenient to rewrite it in the form shown in equation (10)

$$\ln\left(-\ln\frac{D_{PEG}D^{neat}_{HDO}}{D^{soln}_{PEG}D_{HDO}}\right) = u\ln Q + \ln R. \quad (10)$$

In Figure 13, the $\ln[(-\ln(D_{PEG}D^{neat}_{HDO}/D^{soln}_{PEG}D_{HDO}))D^{soln}_{PEG}]$ value calculated using the experimental data is plotted against $\ln Q$. A straight line with a slope of – 0.71 is obtained and so $u = -0.71$. Therefore, we have $\kappa^{-1} \sim Q^{0.71} = c^{-0.71}$. Depending on the nature of network and solvent, there are a variety of theoretical calculations for the concentration dependence of the dynamical screening length. de Gennes proposed that for flexible polymer chains in a gel with good solvent the relationship $\kappa^{-1} \sim c^{-0.71}$ is obtained.[54] This prediction is in agreement with the above experimental results.

2.3.2.5 *Diffusion Behavior and Intermolecular Hydrogen-Bond Between Probe Polymer and Network Polymer in (N,N-Dimethylacrylamide–Acrylic Acid) Copolymer Gels*

Molecular dynamics of a probe polymer is strongly affected in polymer gel systems with various kinds of intermolecular interactions between the probe polymer and the network polymer, such as hydrogen-bonding interactions, hydrophobic interactions, Coulomb interactions, etc. For example, by adding aqueous PEG solution to aqueous poly(acrylic acid) (PAA) solution the complex between PEG and PAA is formed by the formation of hydrogen bonds between the oxygen atoms of PEG and the carboxyl groups of PAA. Also, in PMAA hydrogel the complex between PEG and PMAA is formed by the same interaction. The justification for the formation of such complexes has been carried out by macroscopic methods such as viscosity measurements for solutions and mass measurements for gels. Nevertheless, in order to clarify more clearly such intermolecular interactions between probe polymer and network polymer in the gel systems, systematic studies by microscopic methods such as NMR spectroscopy are needed.[43]

2.3.2.6 *Diffusion Coefficient of HDO in (DMAA-AA) Copolymer Gels*

The diffusion coefficients of HDO (D_{HDO}) contained in PDMAA gels, PAA gels and (DMAA-AA) copolymer gels with PEG were determined by PGSE ^{1}H NMR at 303 K varying Q and f_{AA}.[44] The D_{HDO} values obtained were plotted against Q. From this plot, it was found that the D_{HDO} increases as Q is increased. The molecular motion of HDO is not affected by a change of f_{AA} in the region of $f_{AA} < 0.9$. This means that the translational motion of the HDO molecule increases as the size of the network becomes larger. The dynamic behavior of solvent in a gel can be analyzed by the modified free volume theory. As described above D_{HDO} in a PDMAA gel can be expressed by equation (9). From a least-squares fit to the experimental data for PDMAA gels using equation (9), we can determine D^0_{HDO}, f_{solv} and β to be $2.16 \times 10^{-9}\,m^2\,s^{-1}$, 0.178 and 0.079, respectively. The calculation by using equation (6) and parameters obtained for PDMAA gels, agrees well with the experimental data obtained for (DMAA-AA) copolymer gels with f_{AA} value less than 0.9. This indicates that the diffusion of HDO is independent of the concentration of carboxylic acid group in this region. D_{HDO}s in PAA gels are larger than those in (DMAA-AA) copolymer gels. This may be because the concentration of H^+ ions dissociated from carboxylic acid groups in PAA gels, which diffuse faster than HDO, is higher than that in (DMAA-AA) copolymer gel.

2.3.2.7 *Diffusion Coefficient of PEG in (DMAA-AA) Copolymer Gels*

In order to investigate the translational motion of PEG contained in PDMAA gels and PAA gels as probe polymer, the diffusion coefficient of PEG (D_{PEG}) was determined by PGSE ^{1}H NMR at 303 K varying Q of the gel.[44] The D_{PEG} value in PDMAA gel is smaller than that in aqueous 1% wt PEG solution (dashed line), and increases as Q is increased. From the plot of $\ln(-\ln(D/D_0))$ against $\ln Q$, it was shown that this behavior is followed by $D/D_0 = \exp(-Q^{\alpha}R)$, and is similar to that mentioned above. Therefore, it can be said that the translational motion of PEG in PDMAA gel is restrained by hydrodynamic interaction with polymer network. This means that polymer network is working as only a spatial obstruction for the displacement of PEG. The D_{PEG} value in PAA gels is much smaller than that in PDMAA gel. This suggests that the loose complex of PEG and PAA network is formed by intermolecular hydrogen-bond interactions between the oxygen atoms of PEG and the carboxyl groups of PAA.[49] By addition of a small amount of HCl into the solution for the gel to be 0.15 mM in concentration, the gel shrinks and D_{PEG} is decreased. The complexation arises from intermolecular hydrogen-bond interaction between oxygen atoms of PEG and the carboxylic groups of AA units in the undissociated state as shown below. Therefore, it can be said that the addition of HCl leads to an increase in the amount of undissociated carboxylic groups and so enhances the formation of the complex and induces the shrinkage of the gel. This leads to slow diffusion of PEG. The addition of amine decreases the amount of dissociated carboxylic group and so inhibits the formation of the complex. This leads to fast diffusion of PEG and the swelling of the gel.

2.4 Diffusion Behavior of Polypeptide Gels

NMR methods involving pulsed magnetic field gradients provide one of the most attractive techniques for studies of molecular dynamics in polypeptide solution and gel systems. In particular, PFGSE NMR has been an invaluable tool in determining the anisotropic structures of polypeptide lyotropic liquid crystalline phase. Almost two decades ago, the first lateral diffusion coefficient of an amphiphile in a lamellar liquid crystalline phase was measured directly using PFGSE NMR. In recent years, the range of applications of NMR diffusion techniques has been growing rapidly, due to the great improvements in the NMR equipment for the diffusion microscopy. The diffusion behavior of solvent molecule in polypeptide gel system with α-helix-random coil transition, and on the diffusion behavior of solvent and probe n-alkanes molecules in polypeptide gel system with highly-oriented structures is introduced.

2.4.1 *Diffusion Behavior of Solvents in Unoriented Polypeptide Gels*

In high-resolution solid-state ^{13}C NMR experiments on cross-linked poly(γ-methyl L-glutamate) (PMLG) gel, we have found that the conformation of cross-linked PMLG with a mixture of chloroform ($CHCl_3$) and trifluoroacetic acid (TFA) largely depends on the solvent composition. The increase of volume fraction of TFA (f_{TFA}) in a mixture of $CHCl_3$ and TFA induces the α-helix-random coil transition of the main chain of cross-linked PMLG. $CHCl_3$ and TFA are sometimes so-called 'helix' and 'coil' solvents, respectively. It is important for gel science in polypeptide gel systems to elucidate how the translational motion of these solvents is affected when the main-chain of PMLG changes from the α-helix form to the random coil form. In such systems, the diffusion of solvent molecules contained in the polypeptide gel system strongly depends on the dynamics of polypeptide chains. As demonstrated above, PFGSE NMR gives useful information about the diffusion process of polymer gel system. From such a background, the dynamics of solvents in cross-linked PMLG gel with a mixture of $CHCl_3$ and TFA on going from the α-helix form to the random coil form through the diffusion coefficients were determined by PFGSE ^{1}H NMR.[45]

2.4.2 *Diffusion Behavior of Solvent and Probe-Molecules in Highly-Oriented Polypeptide Gels*

As is well known, poly(γ-benzyl L-glutamate) (PBLG) forms the lyotropic liquid crystalline state in good solvents such as dichloromethane, dioxane, chloroform, etc. and when the PBLG liquid crystalline solution is placed in a strong magnetic field, the main chain can be oriented in the direction of the magnetic field. The molecular motion of solvent and PBLG in the liquid crystalline solution is considerably influenced by intermolecular interactions. By reacting highly-oriented PBLG chains with a cross-linker in a strong magnetic field, cross-linked PBLG gel with the highly-oriented α-helical chains is assumed to be formed.[46] We are interested in the problem of the diffusion process of solvent and n-alkanes with relatively extended conformation in the gel with anisotropic structure. The interest lies in the fact that n-alkanes are basic

molecules for understanding structure and dynamics of linear polymer chains.

According to the work on the orientation of *n*-alkanes in PBLG liquid crystalline solution by ^{1}H NMR, in which PBLG chains are highly oriented, *n*-alkanes being guest molecules are highly oriented to the magnetic field of an NMR magnet with the relatively extended conformation along the α-helical PBLG chains.[47] Also, as elucidated by NMR *n*-alkanes in the rotator phase take an extended conformation, which are rotating rapidly around the long axis. Thus, the diffusion coefficients for the directions parallel and perpendicular to the long axis differ.[36,37]

With this as a background, cross-linked PBLG gels with highly-oriented α-helical chains are prepared. The diffusion coefficient of the solvent and *n*-alkanes in the gel for the directions parallel and perpendicular to the α-helical PBLG axis by using the PFGSE ^{1}H NMR method with strong field-gradient strength has been studied. In the liquid crystalline and gel states, the orientation of the PBLG chains can be determined by using high-resolution solid-state ^{13}C NMR.

2.4.3 Diffusional Process of Water in Starch Gels

The diffusional phenomena of compartmentalized water such as water in biological cells reflect the size and shape of the microstructure of the compartments and permeability of the barriers. The diffusion coefficients of water in corn starch gels, various wheat starch pastes and potato starch gels were measured.[48–50] The diffusion coefficient (D_0) of water, the permeability of the barriers and the size of microstructure in potato starch gels have been determined by using the equation of restricted diffusional motion. The D_0 value is gradually decreased with an increase in the starch concentration and approaches a constant value of about $1.0 \times 10^{-9}\,\mathrm{m^2\,s^{-1}}$. If the diffusion comes from restricted diffusion by a structural barrier (a), the interbarrier diffusion coefficient may be equal to the diffusion coefficient of pure water. These results show that the diffusion coefficient is affected by obstruction and hydration effects by polymers that are dispersed in the water compartments. The compartmentalized water experiences higher viscosity and/or a longer lifetime in the hydration sphere of starch chains. The permeability is gradually decreased with an increase in the starch concentration and is reached a constant value at more than 30% concentration. This shows that the polymer network of barriers is more dense in the gels at higher concentration. This does not conflict with general experimental results that the higher is the starch concentration, the stiffer is corresponding gel. The value of the distance between the neighboring barriers is independent of the starch concentration for fresh gels. The increase in polymer concentration causes an increase in the density of barriers until the latter reaches its limiting value. The density of barriers reaches the limit value (at a concentration between 33.3 and 37.9%), further increase in the concentration causes a decrease in the a value. From these experimental results, the fresh starch gel structure may be pictured that some of the polymers aggregate to make the starch network of the gel and the remaining polymers, and/or parts of polymer chain, are free from the starch network and function as a solute in water compartmentalized by the network.

2.5 Diffusion in Poly(γ-*n*-octadecyl L-glutamate) and Poly(γ-oleyl L-glutamate) (POLLG) in the Thermotropic Liquid Crystalline State

In order to elucidate more deeply dynamics of the polypeptides in the thermotropic liquid crystalline state, it is important to have some knowledge of the magnitude of the diffusion coefficient and the anisotropy of the diffusion for the directions parallel and perpendicular to the α-helical chain axis. For measurements of the diffusion coefficients, it has been demonstrated that PFGSE ^{1}H NMR can provide useful information to elucidate the diffusion process of solvents for polypeptides in the liquid crystalline state, in addition to polymer gel systems and *n*-alkanes in the rotator phase like the liquid crystalline state.[51]

To this end, the isotropic and anisotropic diffusion coefficients of the POLG chain in an highly-oriented sample prepared in the magnetic field produced by 500 MHz NMR equipment and the isotropic diffusion coefficients of the POLLG chain in the thermotropic liquid crystalline state were measured over a wide range of temperatures.[52] Further, T_2 of the side chain protons of POLG and POLLG were measured over a wide range of temperatures, and then the dynamics of the side chains were elucidated.

The highly-oriented POLG sample was prepared by the following procedure:

1. POLG was dissolved in 1,2-dichloroethane in an NMR glass tube to form the lyotropic liquid crystalline state.
2. the sample was placed in an NMR glass tube with a diameter of 5 mm and thence into the magnetic field of a 500 MHz NMR magnet for 60 hours until the POLG chains were aligned parallel to the magnetic field. The direction of the magnetic field was along the long axis of the NMR tube. After the full orientation of the polypeptide chains, solvent was vaporized from the NMR tube and then the highly-oriented film was obtained on the wall of the NMR tube. The complete orientation of the POLG chains in the film was confirmed by cross-polarized microscopy.

2.5.1 Diffusional Behavior and Dynamics of POLG and POLLG

In the spin-echo ^{1}H NMR spectra of POLG in the liquid crystalline state at 80 °C, an asymmetric relatively sharp signal appears, which has a chemical shift position (0.9 ppm) at the peak. This peak can be straightforwardly assigned to the methyl protons in the side chains. The upper shoulder peaks may be assigned to the methylene protons in the side chains. The peaks that come from the main chain protons such as α-CH proton and amide proton do not appear within the measurement temperature range. This is due to dipolar-broadened signal because of anisotropic molecular motion slow compared to the dipolar frequency, $\omega_0/2\gamma$. However, the spin-echo ^{1}H NMR spectra of POLLG are similar to those of POLG. Thus, the peak assignment can be made by comparison.

The plots of $\ln[\mathrm{A}(\delta)/\mathrm{A}(0)]$ against $\gamma^2G^2\delta^2\,(\Delta - \delta/3)$ for the above-mentioned peak (at ca. 0.9 ppm) in the PFGSE ^{1}H NMR spectra of POLG and POLLG, become straight lines (not shown here). This shows that the diffusion of POLG and POLLG consists of a single component during the observation time. Hence, the diffusion coefficients for POLG and POLLG

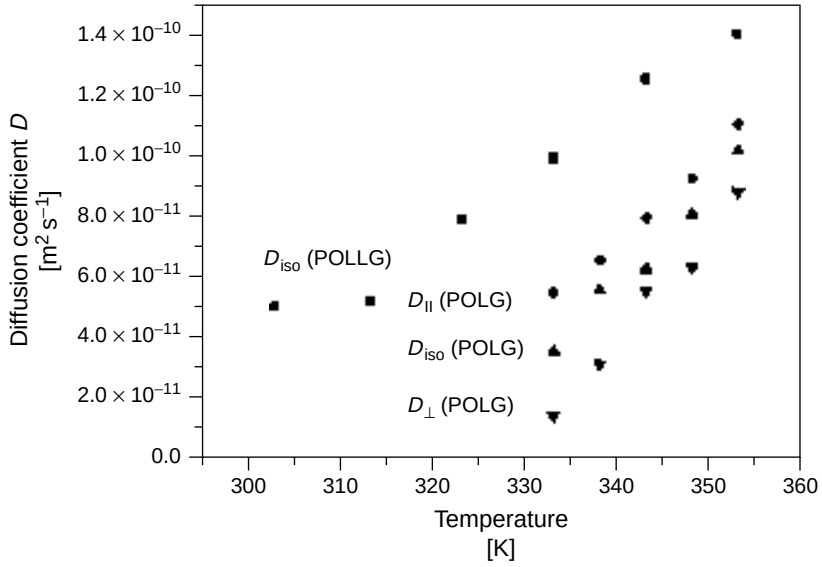

Figure 14 Temperature dependence of the diffusion coefficients of POLG chains in the direction parallel and perpendicular to the α-helical axis magnetic field and the isotropic diffusion coefficients (D_{iso} ($= D_{\parallel} + 2D_{\perp})/3$), and the isotropic diffusion coefficients of POLLG within the temperature range from 30 to 80 °C

considered here were determined from the slope of the straight line as seen from equation (1).[52]

The diffusion coefficients of the rod-like polypeptide chains for the directions parallel ($D_{\parallel}$) and perpendicular ($D_{\perp}$) to the α-helical chain axis were determined, and the isotropic diffusion coefficient (D_{iso}) was estimated by an average of the determined $D_{\parallel}$ and $D_{\perp}$ values as $(D_{\parallel} + 2D_{\perp})/3$ (Figure 14). As the temperature is increased from 60 to 80 °C, the $D_{\parallel}$ values of POLG in the liquid crystal state increase monotonically from 5.48×10^{-11} to $1.11 \times 10^{-10}\,m^2\,s^{-1}$ and, the $D_{\perp}$ values increase monotonically from 1.41×10^{-11} to $8.87 \times 10^{-11}\,m^2\,s^{-1}$. The determined $D_{\parallel}$ and $D_{\perp}$ values at 60 °C are 5.48×10^{-11} and $1.41 \times 10^{-11}\,m^2\,s^{-1}$, respectively, and those at 80 °C are 1.11×10^{-10} and $8.87 \times 10^{-11}\,m^2\,s^{-1}$, respectively. The diffusion of POLG in the thermotropic liquid crystalline state is anisotropic. The diffusion of the polypeptide along the long α-helical chain axis at 60 °C is roughly four times faster than that perpendicular to the long α-helical chain axis. At 80 °C, their diffusion coefficients are close to each other. As reported previously, the determined $D_{\parallel}$ and $D_{\perp}$ values of *n*-alkane, *n*-$C_{24}H_{50}$, in the rotator phase like the liquid crystalline state, which takes the all-*trans* zigzag conformation, are 1.64×10^{-10} and $2.70 \times 10^{-10}\,m^2\,s^{-1}$, respectively. The diffusion of the *n*-alkane in the rotator phase along the long chain axis is slower by roughly two times than that perpendicular to the long chain axis. This is opposite to the results of POLG. From the number of amino acid residues of POLG (ca. 780) considered here, the α-helical chain length is roughly estimated to be ca. 117 nm by using the pitch of an α-helix chain per one amino acid residue to be 0.15 nm. However, the chain length of *n*-$C_{24}H_{50}$ with the all-*trans* zigzag conformation is roughly estimated to be ca. 1.8 nm. From these simple estimations, it is seen that the corresponding rod-like POLG is much longer than *n*-$C_{24}H_{50}$. This leads to the experimental finding that the diffusion of the POLG along the long α-helical chain axis is much faster than that perpendicular to the long α-helical chain axis.

As for POLLG, only the isotropic diffusion coefficients were determined for an interval of 10 °C in the temperature range from 30 to 80 °C (Figure 14). The diffusion coefficients of POLLG in the liquid crystalline state were determined as a function of temperature similarly to POLG. It is shown that with an increase in temperature from 30 to 80 °C, the D value increases gradually from 4.9×10^{-11} to $1.4 \times 10^{-10}\,m^2\,s^{-1}$. Let us compare these D_{iso} values with those of POLG calculated from the determined $D_{\parallel}$ and $D_{\perp}$ values. As the temperature is increased from 60 to 80 °C, the D_{iso} values of POLG increase gradually from 3.53×10^{-11} to $1.02 \times 10^{-10}\,m^2\,s^{-1}$ and those of POLLG increase from 4.9×10^{-11} to $1.40 \times 10^{-10}\,m^2\,s^{-1}$. At 60 °C, POLLG in the thermotropic liquid crystalline state diffuses faster by ca. 2.8 times than POLG irrespective of the same α-helical chain length and at 80 °C their diffusion rates are close to each other. At 60 °C such a large difference in D_{iso} between POLG and POLLG may come from large differences in their side-chain conformation and molecular motion (as seen from the T_2 experiments below). The melting temperature of side chain crystallites in POLG is ca. 60 °C and that of POLLG is below −40 °C as DSC measurements as reported previously.[34] This means that at 60 °C the side chains of POLLG are undergoing much faster *trans-gauche* exchange around the C–C bond compared with those of POLG, and the expansion of the side chains from the main chain in the former is much smaller than that of the latter. At a higher temperature (80 °C) their mobilities are close to each other. This leads to the difference in D_{iso} between POLG and POLLG.

In order to understand the diffusion process of the polypeptide in the thermotropic liquid crystalline state more thoroughly, the activation energy $E^{\ddagger}$ for diffusion process can be determined. $E^{\ddagger}$ can be obtained from the plots of $\ln D$ against $1/T$ within the temperature range from 60 to 80 °C. As for POLG, the measured values of $E^{\ddagger}$ are 33.4, 77.4 and 49.8 kJ mol^{-1} for $D_{\parallel}$, $D_{\perp}$, and D_{iso}, respectively. However, the activation energy for D_{iso} of POLLG is determined to be 20.6 kJ mol^{-1}. From these experimental results, it can be said

that the activation energy for the diffusion process for POLLG in the thermotropic liquid crystalline state is much lower than that of POLG. In the case of POLG, the activation energy for the diffusion along the α-helical chain axis is much lower than that in the direction perpendicular to the α-helical chain axis.

3 REFERENCES

1. (a) Y. Osada and K. Kajiwara, 'Polymer Gels Handbook', Academic Press: New York, 2000; (b) D. DeRossi, K. Kajiwara, Y. Osada, and A. Yamauchi, 'Polymer Gels – Fundamentals and Biomedical Applications', Plenum Press: New York, 1991; (c) Y. Osada, *Adv. Polym. Sci.*, 1987, **82**, 1.
2. (a) P. J. Collings and M. Hird, 'Introduction to Liquid Crystals', Taylor and Francis: London, 1998; (b) V. P. Shibaeb and Lui Lan, 'Liquid Crystalline and Mesomorphic Polymers', Springer-Verlag: Berlin, 1993.
3. (a) I. Ando and T. Asakura, 'Solid State NMR of Polymers', Elsevier Science: Amsterdam, 1998; (b) I. Ando, M. Kobayashi, M. Kanekiyo, S. Kuroki, S. Ando, S. Matsukawa, H. Kurosu, H. Yasunaga, and S. Amiya, 'Experimental Methods in Polymer Science', John Wiley: New York, 1999, Chapter 4, pp 261–483.
4. M. Mori and J. L. Koenig, *Annu. Rept. NMR Spectrosc.*, 1997, **34**, 231.
5. (a) S. Matsukawa, H. Yasunaga, C. Zhao, S. Kuroki, H. Kurosu, and I. Ando, *Prog. Polymer Sci.*, 1999, **24**, 995; (b) I. Ando, H. Kurosu, S. Matsukawa, A. Yamazaki, Y. Hotta, and N. Tanaka, 'The Wiley Polymer Networks Review Series', Vol. 1, eds K. te Nijenhuis and W. J. Mijs, Wiley: New York, 1998, pp 331–346.
6. P. T. Callaghan, 'Principles of Nuclear Magnetic Resonance Microscopy', Claredon Press: Oxford, 1991.
7. N. Bleombergen, E. M. Purcell, and R. V. Pound, *Phys. Rev.*, 1948, **73**, 679.
8. T. Tanaka, *Phys. Rev. Lett.*, 1978, **244**, 110.
9. N. Tanaka, S. Matsukawa, H. Kurosu, and I. Ando, *Polymer*, 1998, **39**, 4703.
10. H. Ohta, I. Ando, S. Fujishige, and K. Kubota, *J. Polymer Sci.*, 1991, **B29**, 963.
11. M. Heskins and J. E. Guillet, *Macromol. Sci. Chem.*, 1986, **A2**, 1441.
12. A. Takahashi and S. Hiramitsu, *Polymer J.*, 1974, **6**, 103.
13. M. Kanekiyo, M. Kobayashi, I. Ando, H. Kurosu, T. Ishii, and S. Amiya, *J. Mol. Struct.*, 1998, **447**, 49.
14. M. Kobayashi, I. Ando, T. Ishii, and S. Amiya, *Macromolecules*, 1995, **28**, 6677.
15. M. Kobayashi, I. Ando, T. Ishii, and S. Amiya, *J. Mol. Struct.*, 1998, **440**, 155.
16. J. Jonas and A. Jonas, *Annu. Rev. Biophys. Biomol. Struct.*, 1994, **23**, 287.
17. M. Kobayashi, M. Kanekiyo, and I. Ando, *Polymer Gels Networks*, 1998, **6**, 347.
18. M. Kanekiyo, M. Kobayashi, I. Ando, H. Kurosu, and S. Amiya, *Macromolecules*, 2000, **33**, 7971.
19. J. Schaefer and E. O. Stejskal, *J. Am. Chem. Soc.*, 1976, **98**, 1031.
20. J. Schaefer and E. O. Stejskal, *Macromolecules*, 1977, **10**, 384.
21. B. C. Gerstein and C. R. Dybowski, 'Transient Techniques in NMR of Solids', Academic Press: New York, 1985.
22. T. Fujito, K. Deguchi, M. Ouchi, M. Imanari, and M. J. Albright, 'The Twentieth Meeting in NMR', Tokyo, 1981, p 68.
23. T. Terao, S. Maeda, and A. Saika, *Macromolecules*, 1983, **16**, 1535.
24. M. Kobayashi, M. Kanekiyo, I. Ando, and S. Amiya, *Polymer Gels Networks*, 1998, **6**, 425.
25. H. Saito and I. Ando, *Annu. Rept. NMR Spectrosc.*, 1989, **21**, 210.
26. H. Ketels, J. Buelen, and G. Velden, *Macromolecules*, 1988, **21**, 2032.
27. H. Ketels, J. de. Haan, A. Aerdts, and G. Velden, *Polymer*, 1990, **31**, 1419.
28. D. L. VandeHart, S. Simmons, and J. W. Gilman, *Polymer*, 1995, **36**, 4223.
29. M. Kanekiyo, M. Kobayashi, I. Ando, H. Kurosu, and S. Amiya, *Polymer*, 2000, **41**, 2391.
30. (a) A. E. Tonelli, *Accts. Chem. Res.*, 1981, **14**, 233; (b) A. E. Tonelli, *Annu. Rept. NMR Spectrosc.*, 1997, **34**, 185.
31. W. L. Earl and D. L. VanderHart, *Macromolecules*, 1979, **12**, 769.
32. H. Yasunaga and I. Ando, *J. Mol. Struct.*, 1993, **301**, 129.
33. T. Yamanobe, M. Tsukahara, T. Komoto, J. Watanabe, I. Ando, I. Uematsu, K. Deguchi, T. Fujito, and M. Imanari, *Macromolecules*, 1998, **21**, 48.
34. B. Mohanty, T. Komoto, J. Watanabe, I. Ando, and T. Shiibashi, *Macromolecules*, 1989, **22**, 4451.
35. W. S. Price, *Annu. Rept. NMR Spectrosc.*, 1996, **32**, 51.
36. A. K. Whittaker, *Annu. Rept. NMR Spectrosc.*, 1997, **34**, 105.
37. J. E. Tanner and E. O. Stejskal, *J. Chem. Phys.*, 1968, **49**, 1768.
38. H. Yasunaga and I. Ando, *Polymer Gels Networks*, 1993, **1**, 267.
39. H. Yasunaga and I. Ando, *Polymer Gels Networks*, 1993, **1**, 81.
40. S. Matsukawa and I. Ando, *Macromolecules*, 1996, **29**, 7136.
41. H. Fujita, *Advance Polymer Sci.*, 1961, **3**, 1.
42. P. G. de Gennes, *Macromolecules*, 1976, **9**, 594.
43. S. Matsukawa and I. Ando, *Macromolecules*, 1997, **30**, 8310.
44. S. Matsukawa and I. Ando, *Macromolecules*, 1999, **31**, 1865.
45. C. Zhao, S. Matsukawa, H. Kurosu, and I. Ando, *Macromolecules*, 1998, **31**, 3139.
46. C. Zhao, H. Zhang, T. Yamanobe, S. Kuroki, and I. Ando, *Macromolecules*, 1999, **32**, 3389.
47. C. Zhao, S. Kuroki, and I. Ando, *Macromolecules*, 2000, **33**, 4486.
48. W. von Basler and H. Lechert, *Staeke*, 1974, **2**, 39.
49. P. T. Callaghan, K. W. Levievre, and R. K. B. King, *J. Coll. Interface Sci.*, 1983, **92**, 332.
50. A. Ohtsuka and T. Watanabe, *Carbohydr. Polymers*, 1996, **30**, 135.
51. H. Yamakawa, S. Matsukawa, H. Kurosu, S. Kuroki, and I. Ando, *J. Chem. Phys.*, 1999, **111**, 7110.
52. Y. Yige, C. Zhao, S. Kuroki, and I. Ando, *J. Chem. Phys.*, 2000, **113**, 9606.
53. T. C. Farra and E. D. Becker, 'Pulse and Fourier Transform NMR', Academic Press: New York, 1971.
54. D. A. Torchia, *J. Magn. Reson.*, 1978, **30**, 613.
55. C. Zhao, S. Matsukawa, M. Kobayashi, and I. Ando, *J. Mol. Struct.*, 1998, **442**, 235.
56. H. Ohta, I. Ando, S. Fujishige, and K. Kubota, *J. Mol. Struct.*, 1991, **245**, 391.
57. B. Beloche and E. T. Samulski, *Macromolecules*, 1981, **14**, 575.
58. W. Gronski, R. Stadler, and M. M. Jacobi, *Macromolecules*, 1984, **17**, 741.
59. H. E. Gottlieb and Z. Luz, *Macromolecules*, 1984, **17**, 1959.
60. M. I. Lifshits, *Polymer*, 1987, **28**, 454.
61. W. Gronski, F. Foster, W. Pyckhout-Hintzen, and T. Springer, *Macromol. Chem., Macromol. Symp.*, 1990, **40**, 121.
62. D. Yang, F. Li, and Z. Qiu, *J. Macromol. Sci., Chem.*, 1990, **A27**, 149.

Incommensurate Systems

Robert Blinc
J. Stefan Institute, University of Ljubljana, Ljubljana, Slovenia

and

David C. Ailion
Department of Physics, University of Utah, Salt Lake City, UT, USA

1	Introduction	1
2	Single-q (1-q) Modulated Plane Wave Limit	1
3	Multiple-q Modulated Incommensurate Systems	9
4	Related Articles	12
5	References	12

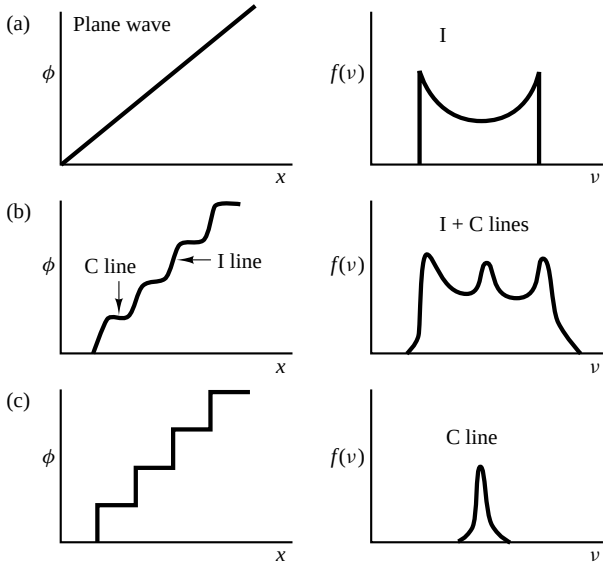

Figure 1 NMR lineshapes in I systems: (a) plane wave limit, (b) multisoliton lattice, (c) sequence of commensurate phases. (Reproduced by permission of Elsevier from R. Blinc[2])

1 INTRODUCTION

In incommensurate (I) systems[1] the periodicity $\boldsymbol{q}_\mathrm{I}$ of at least one of the modulation waves cannot be expressed as a rational fraction of the periodicity $\boldsymbol{q}_\mathrm{L}$ of the underlying lattice:

$$\frac{q_\mathrm{I}}{q_\mathrm{L}} \neq \frac{M}{N}, \qquad M, N = 1, 2, 3, \ldots \tag{1}$$

As a result, translational periodicity is lost in at least one dimension in spite of the existence of perfect long range order. In the general case, incommensurately modulated phases can be formed when several spatially periodic modulations with wave vectors $\boldsymbol{q}_i$ are incommensurate with the characteristic wave vectors of the underlying lattice. The modulation waves can be either of the plane wave (sinusoidal) type or soliton-like, consisting of nearly commensurate regions where the phase of the order parameter is practically constant and other regions (phase solitons) where it changes rapidly (Figure 1). Translational lattice periodicity is generally restored at lower temperatures by a 'lock-in' phase transition where the lattice modulation changes from incommensurate to commensurate.

The usefulness[1,2] of NMR and NQR for the study of incommensurate systems is based on the fact that the resonance frequency varies in space in a way that reflects the spatial variation of the incommensurate modulation. In commensurate systems the number of magnetic resonance lines equals the (usually very small) number of physically nonequivalent nuclei per unit cell. In incommensurate systems, where the translational lattice periodicity is lost, there is in essence an infinite number of nonequivalent nuclei contributing to the magnetic resonance spectrum. Except in the narrow soliton limit, the incommensurate spectrum should be characterized by a quasicontinuous distribution of NMR frequencies instead of sharp lines as in commensurate crystals.

The nature of this distribution depends critically on the spatial variation of the phase of the incommensurate modulation, $\Phi = \Phi(x)$. A plane wave modulation thus produces a lineshape that differs strongly from the one expected for a multisoliton lattice. As the width of the phase solitons decreases and the soliton–soliton spacing increases, more and more nuclei will find themselves in locally commensurate domains, so that new lines will appear at positions corresponding to the ones in the commensurate phase. These lines become stronger as the soliton density decreases, thereby allowing for a quantitative determination of the variation of the soliton density with temperature.

NMR and NQR are thus among the most sensitive means for studying the local nature of the incommensurate modulation.

2 SINGLE-q (1-q) MODULATED PLANE WAVE LIMIT

2.1 Lineshapes in the Plane Wave Limit

In the 1-$\boldsymbol{q}$ plane wave modulation limit the phase of the modulation wave is a linear function of the spatial coordinate x, and the incommensurate distortion is characterized by a single Fourier component $\boldsymbol{q}_\mathrm{I}$:

$$u = A\cos\Phi(x) = A\cos(q_\mathrm{I}x + \Phi_0), \qquad \Phi_0 = \text{const.} \tag{2}$$

In the local approximation the resonance frequency ν_i of a given nucleus depends only on the incommensurate displacement u_i of the resonating nucleus and the displacement of atoms moving in phase with it:

$$\nu_i = \nu[u_i(x_i)] \tag{3}$$

This relation can be expanded in powers of the displacements:

$$\nu_i = \nu_0 + a_1u_i(x) + \tfrac{1}{2}a_2u_i^2(x) + \ldots \tag{4a}$$

yielding

$$\nu_i = \nu_0 + \nu_1\cos\Phi(x) + \tfrac{1}{2}\nu_2\cos^2\Phi(x) + \ldots \tag{4b}$$

where cos $\Phi(x)$ nearly continuously takes on all values between +1 and −1, and where $\nu_1 \propto A \propto (T_I - T)^{\beta}$ and $\nu_2 \propto A^2 \propto (T_I - T)^{2\beta}$. Here the phase $\Phi(x)$ and the amplitude A of the modulation wave constitute the two-component order parameter of the 1-***q*** normal–incommensurate phase transition.

The intensity of the resonance line in a frequency interval between ν and $\nu + d\nu$ is proportional to the number of nuclei resonating in this interval. Knowing the function $\nu_i = \nu[u_i(x)]$, one can calculate the frequency distribution $f(\nu)$ in I systems from

$$f(\nu)\,d\nu = C\,dx \tag{5}$$

or

$$f(\nu) = \frac{C}{\left|\frac{d\nu}{d\Phi}\,\frac{d\Phi}{dx}\right|} \tag{6}$$

In the plane wave limit $d\Phi/dx$ = const and $f(\nu)$ is determined simply by $d\nu/d\Phi$. In the multisoliton limit, however, $d\Phi/dx$ is a function of x (and thus of frequency) and thereby influences the lineshape. Typically, $d\nu/d\Phi$ is obtained from relationships like equation (4a).

2.1.1 The Linear and the Quadratic Cases

In the *linear case*, where $\nu(x) = \nu_0 + \nu_1 \cos \Phi(x)$, the frequency distribution is

$$f(\nu) = \frac{\text{const.}}{\sqrt{1 - (\nu - \nu_0)^2 \nu_1^2}} \tag{7a}$$

and is shown in Figure 1(a). Here the splitting $\Delta\nu$ between the two edge singularities at

$$\nu_{\pm} = \nu - \nu_0 = \pm\nu_1 \tag{7b}$$

increases with the critical exponent β, since

$$\Delta\nu = 2\nu_1 \propto (T_I - T)^{\beta} \tag{7c}$$

This lineshape has been observed[1] for the ^{87}Rb $\frac{1}{2} \rightarrow -\frac{1}{2}$ transition in Rb_2ZnCl_4 (Figure 2).

In the *quadratic case*, where $\nu(x) = \nu_0 + \frac{1}{2}\nu_2 \cos^2\Phi(x)$, the frequency distribution is

$$f(\nu) = \frac{\text{const.}}{\sqrt{(\nu - \nu_0)\left[\frac{1}{2}\nu_2 - (\nu - \nu_0)\right]}} \tag{8a}$$

The edge singularities occur now at

$$\nu_{(a)} = \nu_0 \tag{8b}$$

and

$$\nu_{(b)} = \nu_0 + \frac{\nu_2}{2} \tag{8c}$$

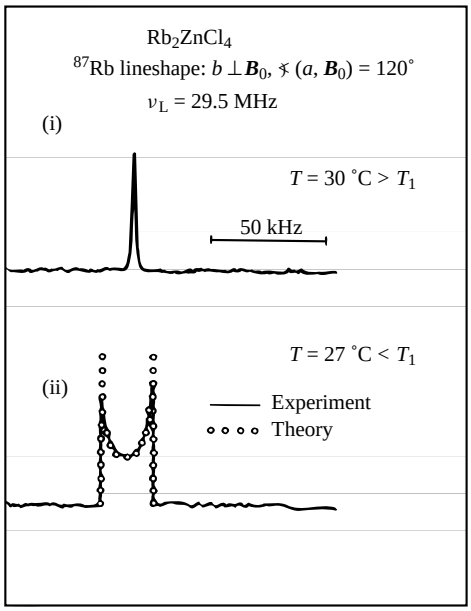

Figure 2 NMR lineshape of the ^{87}Rb $\frac{1}{2} \rightarrow -\frac{1}{2}$ transition in the (i) paraelectric and (ii) incommensurate phases of Rb_2ZnCl_4. (Reproduced by permission of the International Society of Magnetic Resonance from R. Blinc, *Bull. Magn. Reson.*, 1984, **6**, 38)

The position of the singularity at $\nu_{(a)}$ will not depend critically on temperature, but the position of the singularity $\nu_{(b)}$ will shift proportionally to the square of the order parameter so that

$$\Delta\nu = [\nu_{(b)} - \nu_{(a)}] \propto (T_I - T)^{2\beta} \tag{8d}$$

The quadratic case will be important for systems in which the linear term in equation (5) is forbidden by symmetry. If both linear and quadratic terms have to be taken into account, the frequency distribution will exhibit three singularities ν_+, ν_-, and $\nu_{(c)}$ if $|\nu_2| \geq |\nu_1|$. These singularities will occur at

$$\nu_{\pm} = \nu_0 \pm \nu_1 + \frac{\nu_2}{2} \tag{9a}$$

and at

$$\nu_{(c)} = \nu_0 - \frac{\nu_1^2}{2\nu_2} \tag{9b}$$

2.1.2 Nonlocal Effects

In the general case the dependence of the resonance frequency on the lattice displacements is nonlocal[2] (i.e., the resonance frequency of the ith nucleus depends not only on its displacement but also on the displacement of other nuclei), as given by

$$\nu_i = \nu[u_i(x_i), u_j(x_j), \ldots], \qquad i \neq j \tag{10}$$

This dependence can reflect the nonlocal nature of such quantities as the electric field gradient (EFG) tensor or the chemical shift tensor, which, in addition to the external magnetic field, determine the NMR resonance frequency.

Only when the dominant contribution to the NMR resonance frequency comes from a region whose dimensions are small compared with the wavelength of the incommensurate modulation wave can the relationship between ν_i and u_i be treated as local, so that equation (3) becomes strictly valid.[2]

In the nonlocal case equation (10) yields the spatial dependence of the NMR frequency[2]

$$\nu(x) = \nu_0 + \nu_1 \cos[\Phi(x) - \Phi_1] + \tfrac{1}{2}\{\nu_{2'} + \nu_{2''} \cos 2[\Phi(x) - \Phi_2]\} + \dots \quad (11a)$$

or, after introducing $\psi = \Phi - \Phi_2$ and $\tilde{\Phi} = \Phi_2 - \Phi_1$,

$$\nu(x) = \nu_0 + \nu_1 \cos[\psi(x) + \tilde{\Phi}] + \nu'_2 + \nu_2 \cos^2 \psi(x) + \dots \quad (11b)$$

where $\nu_2 = \nu_{2''}$ and $\nu'_2 = \frac{1}{2}(\nu_{2'} - \nu_2)$. Equation (11b) is similar to the local expression, equation (4b), except for the fact that there is now a phase shift $\tilde{\Phi} \neq 0$ between the linear and the quadratic terms and there is a uniform frequency shift $\nu'_2 \neq 0$.

In the *linear* approximation ($\nu_1 \neq 0$, $\nu_2 = \nu'_2 = 0$) there is no difference between the local and the nonlocal cases. In the *quadratic* approximation ($\nu_1 = 0$, $\nu_2 \neq 0$, $\nu'_2 \neq 0$) the frequency distribution is different from the one obtained in the local case. It is given by

$$f(\nu) = \frac{\text{const.}}{\sqrt{(\nu - \nu'_2 - \nu_0)(\nu_2 + \nu'_2 + \nu_0 - \nu)}} \quad (12a)$$

The edge singularities occur at

$$\nu - \nu_0 = \nu'_2 \quad (12b)$$

and

$$\nu - \nu_0 = \nu_2 + \nu'_2 \quad (12c)$$

The positions of both singularities now vary with temperature as $(T_I - T)^{2\beta}$. The lineshapes and splittings for the local and nonlocal cases are illustrated in Figure 3 for both the linear and the quadratic approximations. If both linear and quadratic terms are present, the shape of the spectrum in the nonlocal case will depend strongly on the ratio between the magnitudes of ν_1 and ν'_2 and on the relative phase shift $\tilde{\Phi}$ between them. At lower temperatures, if $\tilde{\Phi}$ does not equal 0° or 90°, there will be *four* edge singularities and not *three*,[2] as in the local case.

2.1.3 *Effects of Thermal Fluctuations*

Let us now take into account thermal fluctuations[3] of the phase,

$$\Phi(x, t) = \Phi(x) + \delta\Phi(x, t) \quad (13a)$$

and the amplitude,

$$A(x, t) = A_0 + \delta A(x, t) \quad (13b)$$

of the modulation wave. The NMR frequency of a given nucleus is now both time-dependent and space-dependent [i.e. $\Omega = \Omega(x,t)$]. Let us, for the sake of simplicity, assume that the NMR frequency $\Omega(x,t)$ of a nucleus at site x is related linearly to the nuclear displacement $u(x,t)$ at this site. Then[3]

$$\Omega(x, t) = \Omega_0 + a u(x, t) \quad (14)$$

and

$$u(x, t) = A(x, t) \cos(q_I x) + \delta\Phi(x, t) \sin(q_I x) \quad (15)$$

The adiabatic NMR lineshape is given by

$$I(\omega) = \int G(t) \exp(\mathrm{i}\omega t)\, \mathrm{d}t \quad (16a)$$

where

$$G(t) = \exp(-\mathrm{i}\Omega_0 t) \left\langle\!\!\left\langle \exp\left\{ -\mathrm{i} \int_0^t [\Omega(x, t') - \Omega_0]\, \mathrm{d}t' \right\} \right\rangle\!\!\right\rangle_x \quad (16b)$$

The inner brackets stand for an ensemble average and $\langle\rangle_x$ represents an average over the static inhomogeneous distribution of resonance frequencies discussed in the preceding section. Inserting equations (14) and (15) into equation (16b), we find the autocorrelation function $G(t)$ in the form

$$G(t) = \exp(-\mathrm{i}\Omega_0 t) \langle\!\langle G_1(t) G_2(t) \rangle\!\rangle_x \quad (17)$$

Here $G_1(t)$ represents the static inhomogeneous frequency distribution limited by two edge singularities and $G_2(t)$ describes the effects of the amplitudon and phason thermal fluctuations of the modulation wave. Since the product of two functions in the time domain is equivalent to the convolution of their Fourier transforms in the frequency domain, the Fourier transform of $G(t)$ represents a convolution of the dynamic and static lineshapes.[3] $I(\omega)$ is now given by

$$I(\omega) = \int_{-1}^{+1} \frac{\mathrm{d}x}{\sqrt{1 - x^2}} \int_0^\infty \mathrm{d}t\, \exp[\mathrm{i}(\omega - \Omega_0 - \Omega_1 x)t] \times \exp\{-[\omega_{\mathrm{loc}1} t x^2 + (\omega_{\mathrm{loc}2} t)^{3/2}(1 - x^2)]\} \quad (18)$$

where $x = \cos(\boldsymbol{q}_I x)$, $\Omega_1 = aA_0$ and $\omega_{\mathrm{loc}1}$ and $\omega_{\mathrm{loc}2}$ are parameters[3] that measure the relative sizes of amplitudon and phason fluctuations compared with the static order parameter. The fluctuation correction, determined by the Fourier transform of $G_2(t)$, determines the form of the incommensurate NMR spectrum close to the paraelectric–incommensurate transition T_I. This feature is illustrated in Figure 4.

2.1.4 *Sliding of the Modulation Wave*

In $NbSe_3$ and other charge density wave (CDW) systems the CDW has been depinned[4] by an applied electric field which was larger than a critical value. In such a case the NMR resonance frequencies are again both time- and space-dependent [$\Omega = \Omega(x, t)$]. The NMR lineshape is again given by equations (16a) and (16b). For the case of a *uniform sliding*

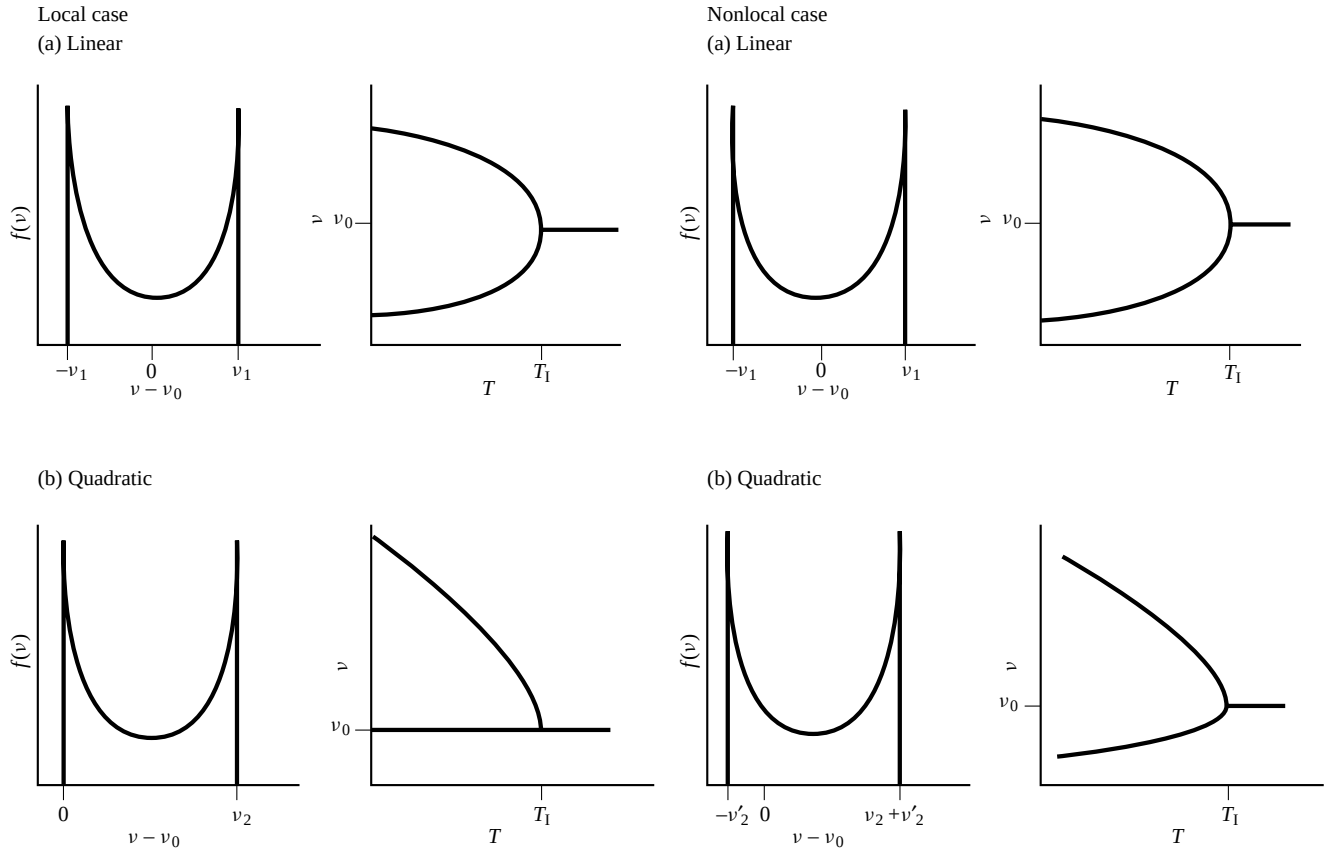

Figure 3 NMR lineshapes and T-dependence of splitting between edge singularities in the 'local' and 'nonlocal' cases: (a) linear, (b) quadratic, approximation. (Reproduced by permission of Elsevier from R. Blinc, P. Prelovšek, V. Rutar, J. Seliger, and S. Žumer, in 'Incommensurate Phases in Dielectrics', eds. R. Blinc and A. P. Levanyuk, 1986, Vols. I and II)

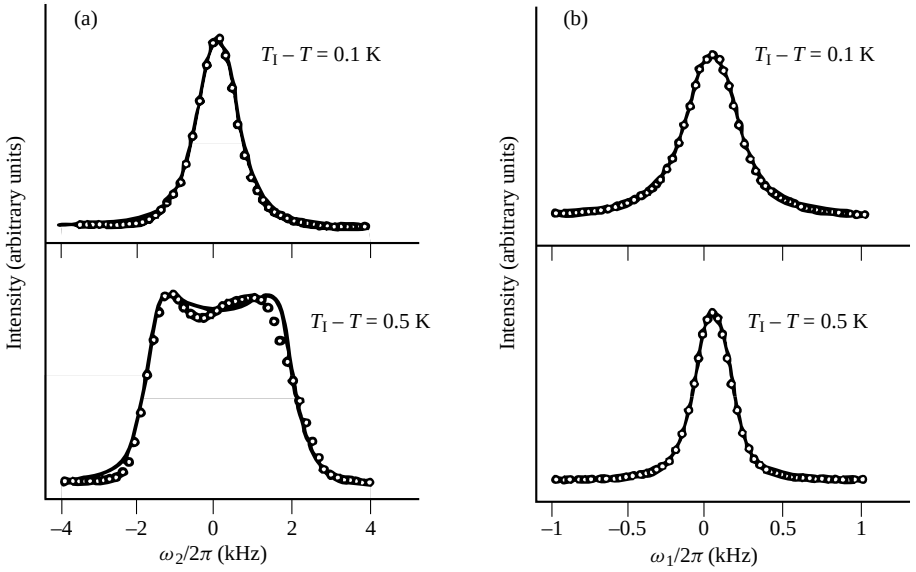

Figure 4 (a) Inhomogeneous and (b) homogeneous ^{87}Rb $\frac{1}{2} \rightarrow -\frac{1}{2}$ lineshapes obtained by two-dimensional NMR in Rb_2ZnCl_4 close to T_I. (Reproduced by permission of The American Physical Society from A. M. Fajdiga et al.[3])

of the 'plane wave' like modulation wave with a velocity v and a wave vector $\boldsymbol{q}_1$ we have

$$u(x,t) = A\cos[q_I(x+vt)+\Phi_0] = A\cos(q_I x+\omega_v t+\Phi_0) \quad (19a)$$

Uniform sliding of the modulation wave thus corresponds to a harmonic oscillation of a given nucleus with a frequency

$$\omega_v = q_I v \quad (19b)$$

For

$$\Omega(x,t) = \Omega_0 + au(x,t) = \Omega_0 + \Omega_1\cos(q_I x+\omega_v t+\Phi_0) \quad (20)$$

we get[5]

$$G(T) = J_0\left[\frac{2}{w}\sin(\pi T)\right] \quad (21)$$

where J_0 is the cylindrical Bessel function of order zero, $T = (w/2\pi)\Omega_1 t$, and $w = \omega_v/\Omega_1$. In contrast to the case of a stochastic thermal motion, here $G(T)$ is periodic due to the uniform sliding of the modulation wave. This is an example of 'coherent' averaging, similar to the uniform magic angle spinning of a sample in the magnet.

The lineshape can be expressed[5] as the Fourier transform of $G(T)$,

$$I(\omega) = \sum_{n=-\infty}^{+\infty} J_n^2\left(\frac{1}{w}\right)\delta\left(\frac{\omega-\Omega_0}{\Omega_1}-nw\right) \quad (22)$$

It consists of a series of delta functions weighted by the square of the Bessel function of order n. In the general case a three-component lineshape is expected with peaks around $\omega = 0$ and $\omega = \pm\,\Omega_1$. The relative intensities of these lines and the positions of the center peaks vary strongly with w (Figure 5). For small sliding velocities the characteristic static incommensurate lineshape is preserved, but for large sliding velocities the incommensurate effects are motionally averaged out and a single sharp 'paraelectric' line at Ω_0 is obtained.

2.2 Lineshapes in the Multisoliton Lattice Limit

Consider, for the sake of simplicity, the static local case where the spatial variation of the NMR frequency $\nu(x)$ reflects the spatial variation of the frozen-out modulation wave $u(x)$. Here we have $\nu(x) = \nu[u(x)]$.

For a space-varying frequency $\nu(x)$ the spectral distribution at ν' is given by

$$f(\nu') = \int \delta[\nu'-\nu(x)]\,\mathrm{d}x \quad (23a)$$

yielding

$$f(\nu) = \frac{\text{const.}}{\left|\frac{\mathrm{d}\nu}{\mathrm{d}u}\right|\left|\frac{\mathrm{d}u}{\mathrm{d}\Phi}\right|\left|\frac{\mathrm{d}\Phi}{\mathrm{d}x}\right|} \quad (23b)$$

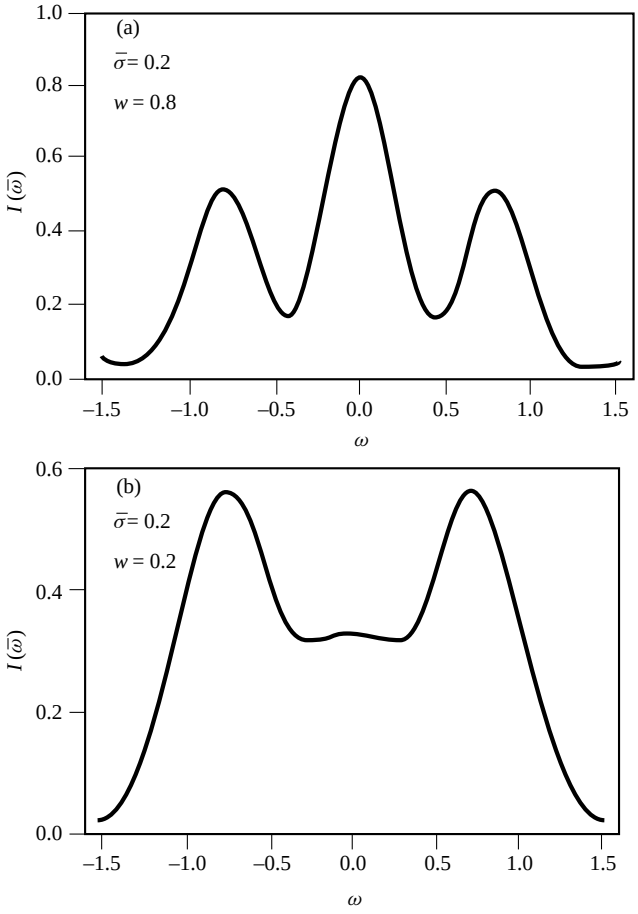

Figure 5 Dependence of the incommensurate NMR lineshape $I(\omega)$ on the sliding velocity[5] in the plane wave limit: (a) w = 0.8, (b) w = 0.2. The spectra have been convoluted with a Gaussian representing the width of the individual lines. (Reproduced by permission of Gordon and Breach Science Publishers from R. Blinc, *Phase Transitions*, 1988, **11**, 255)

The lineshape will be peaked whenever

$$\text{(i) } \mathrm{d}\nu/\mathrm{d}u \to 0 \quad (23c)$$

$$\text{(ii) } \mathrm{d}u/\mathrm{d}\Phi \to 0 \quad (23d)$$

or

$$\text{(iii) } \mathrm{d}\Phi/\mathrm{d}x \to 0 \quad (23e)$$

Whereas points (i) and (ii) give rise to singularities in the spectrum in the plane wave limit, it is point (iii), $\mathrm{d}\Phi/\mathrm{d}x \to 0$, that is unique to the multisoliton lattice limit, and which allows for a determination of the soliton density. Here the spatial variation of the phase $\Phi(x)$ of the modulation wave is determined from the nonlinear sine–Gordon equation

$$\frac{\mathrm{d}^2\Phi}{\mathrm{d}x^2} = -\frac{n}{2}\frac{\gamma}{\kappa}A_0^{n-2}\sin(n\Phi) \quad (24)$$

Here n represents the lowest power of the 'lock-in' term[1,2,6] describing the effect of the discrete crystal lattice; γ is a

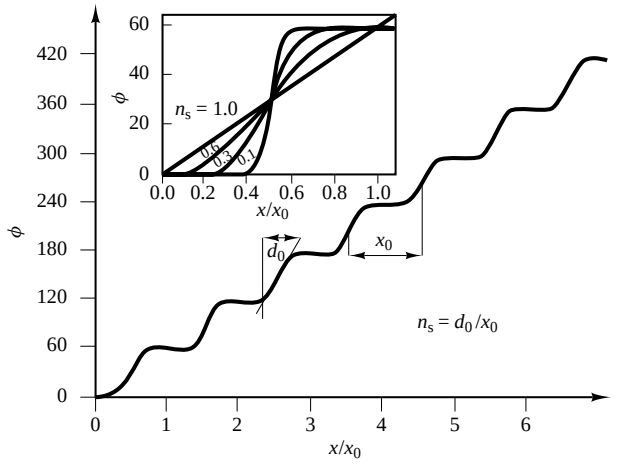

Figure 6 Spatial variation of the phase of the modulation wave for different soliton densities $n_s = d_0/x_0$. Here d_0 is the soliton width and x_0 the intersoliton spacing. (Reproduced by permission of Elsevier from R. Blinc, P. Prelovšek, V. Rutar, J. Seliger, and S. Žumer, in 'Incommensurate Phases in Dielectrics', eds. R. Blinc and A. P. Levanyuk, 1986, Vols. I and II)

coefficient describing the strength of the lock-in term, and κ is an elastic constant.

It should be noted that $n = 10$ for $[N(CH_3)_4]_2ZnCl_4$, $n = 6$ for Rb_2ZnCl_4, $n = 4$ for $(NH_4)_2BeF_4$, and $n = 2$ for chiral smectic liquid crystals in an external magnetic field.[2]

Close to T_I, where $A_0 \propto (T_I - T)^\beta \rightarrow 0$, $\Phi(x)$ is nearly linear in x and we are in the 'plane wave' modulation limit. At lower temperatures, where A_0 is larger, Φ becomes nonlinear in x and the multisoliton lattice limit is approached. Nearly commensurate regions where $\Phi(x) \approx$ const. are separated by soliton-like 'discommensurations' where the phase changes rapidly (Figure 6). The soliton density[1]

$$n_s = \frac{d_0}{x_0} \tag{25}$$

is the ratio of the soliton width d_0 to the intersoliton spacing x_0 and corresponds to the volume fraction of the crystal occupied by the phase soliton domain walls (i.e. the 'discommensurations'). The soliton density is unity in the plane wave limit just below T_I and zero at the 'lock-in' transition to the commensurate phase at T, where $x_0 \rightarrow \infty$.

By a straightforward integration of equation (24) we can obtain $d\Phi/dx$ so that $f(v)$ becomes:

$$f(v) = \frac{\text{const.}}{\left|\frac{dv}{du}\right| \left|\frac{du}{d\Phi}\right| \sqrt{\Delta^2 + \cos^2\left\{\frac{1}{2}n[\Phi(x) - \Phi_0]\right\}}} \tag{26a}$$

where Φ_0 is an initial phase that depends on the position of the nucleus in the paraelectric unit cell. The integration constant Δ^2 is related to the soliton density n_s via[2]

$$n_s = \frac{\pi/2}{K(k)} \tag{26b}$$

where

$$k = \frac{1}{\sqrt{1 + \Delta^2}} \tag{26c}$$

and $K(k)$ is the complete elliptic integral of the first kind

$$K(k) = \int_0^{\pi/2} \frac{d\Phi}{\sqrt{1 - k^2 \sin^2 \Phi}} \tag{26d}$$

Δ^2 is obtained experimentally by fitting the observed lineshape to equation (26a).

It should be noted[2] that for $T \rightarrow T_I$, $A_0 \rightarrow 0$, $k^2 \rightarrow 0$, $\Delta^2 \rightarrow \infty$, and $K(k) \rightarrow \pi/2$ so that $n_s \rightarrow 1$. For $T \rightarrow T_c$, however, $k^2 \rightarrow 1$, $K(k) \rightarrow \infty$, and $n_s \rightarrow 0$.

Equation (26a) yields the same lineshape as that obtained in the plane wave limit if $\Delta^2 \gg 1$, but up to n new lines are found[2] in the multisoliton limit (where $\Delta^2 \ll 1$). The new lines are in addition to the singularities formed in the plane wave limit and appear for $\Delta^2 \ll 1$ when $\cos^2\{\frac{1}{2}\, n[\Phi(x) - \Phi_0]\} = 0$, i.e. when

$$\Phi = (2m + 1)\pi/n + \Phi_0, \qquad m = 0, 1, 2, \ldots n - 1 \tag{27}$$

At special values of Φ_0 the number of new 'commensurate' lines will be smaller than n. The gradual appearance of these lines[7] is illustrated in Figure 7 and the corresponding temperature dependence of n_s is shown in Figure 8.

2.3 Long Period Commensurate Phases

In incommensurate phases the periodicity $\boldsymbol{q}_I$ of the order parameter and the periodicity of the basic lattice cannot be

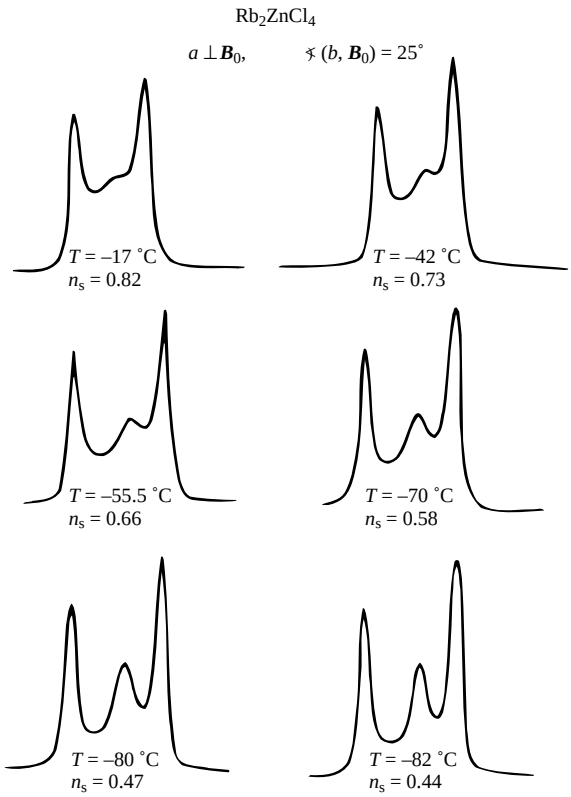

Figure 7 $^{87}Rb\ \frac{1}{2} \rightarrow -\frac{1}{2}$ NMR lineshapes for different soliton densities n_s. (Reproduced by permission of the International Society of Magnetic Resonance from R. Blinc, *Bull. Magn. Reson.*, 1984, **6**, 38)

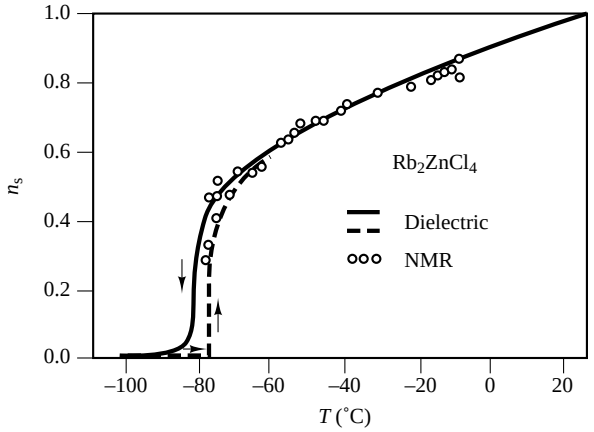

Figure 8 T-dependence of soliton density n_s in Rb_2ZnCl_4. (Reproduced by permission of the International Society of Magnetic Resonance from R. Blinc, *Bull. Magn. Reson.*, 1984, **6**, 38)

expressed as a ratio of two integers, resulting in a loss of translational periodicity. Long period commensurate (C) phases exist[2] where $\boldsymbol{q}_I$ varies in steps and 'locks in' at an infinity of rational multiples of the periodicity of the basic lattice. The $T-\boldsymbol{q}_I$ phase diagram of such a system consists of an infinity of C phases which may or may not be separated by I phases in which $\boldsymbol{q}_I$ varies continuously with T. The first of these two cases is known as the incomplete and the second as the complete devil's staircase.[6,8] Such phases have been observed in betaine calcium chloride dihydrate,[9,10] thiourea, $[N(CH_3)_4]_2ZnCl_4$ and other systems.

In the C region the phase becomes a constant, $\Phi(x) = K$, which is equivalent to a renormalization of the initial phase, $\Phi_0 \rightarrow \tilde{\Phi}_0$. If the commensurate wave vector $\boldsymbol{q}_c^x$ in the presence of a devil's staircase is expressed as

$$\boldsymbol{q}_c^x = \boldsymbol{b}^x \frac{M}{N} \tag{28a}$$

where $\boldsymbol{b}^x$ is a reciprocal lattice vector of the high-temperature phase and M and N are integers, the NMR frequency can be expressed[10] in the linear case as

$$\nu^{(M,N)} = \nu_0 + \nu_1 \cos\left(2\pi \frac{M}{N} + \tilde{\Phi}_0\right), \quad M = 0, 1, \ldots, N-1 \tag{28b}$$

Equation (28b) yields the NMR frequencies in a commensurate unit cell which is N times larger than the high-temperature unit cell. The frequency distribution $f(\nu)$ is now obtained[10] as

$$f(\nu) = \frac{1}{N} \sum_{M=0}^{N-1} \delta\left[\nu - \nu_0 - \nu_1 \cos\left(2\pi \frac{M}{N} + \tilde{\Phi}_0\right)\right] \tag{28c}$$

which yields N commensurate lines with a splitting $\Delta\nu \approx 2\nu_1/N - 1$. For $N \rightarrow \infty$ the incommensurate lineshape is recovered. However, because of the natural width of the individual NMR lines, it is hard to discriminate between I phases and long period C phases for $N > 20$.

2.4 T_1 Effects

Spin–lattice relaxation is often due to phonon scattering processes which are accompanied by spin flips. The probability of such processes increases with increasing phonon occupation number and increasing relative displacement of the lattice nuclei leading to fluctuations in the EFG, the chemical shift, or the magnetic dipolar coupling tensors. In translationally periodic crystals undergoing structural phase transitions, the main contribution to spin–lattice relaxation is usually made by the lowest frequency soft optic modes. The contribution of long wavelength acoustic modes is usually negligible, since the relative displacements of the nearest neighbors are too small.

The situation is quite different in I systems. The excitation spectrum consists here in the simplest case of two modes: an optic-like amplitudon branch, $A = A_0 + \delta A(t)$, corresponding to oscillations of the amplitude of the modulation wave, and an acoustic-like phason branch, $\Phi = \Phi_0 + \delta\Phi(t)$, representing the sliding of the I modulation wave. The phason with wave vector $\boldsymbol{q}_I$ corresponds to the Goldstone mode, which recovers the broken translational periodicity of the I phase. It is gapless in the continuum limit, since the free energy of the I phase does not depend on the phase of the modulation wave. In contrast to acoustic phonons, the phason has zero frequency at a nonzero wave vector $\boldsymbol{q}_I$. The number of thermally excited phasons is of the order of the number of acoustic phonons, but the relative nuclear displacements are not small since $\boldsymbol{q}_I \neq 0$. This leads to an extremely efficient spin–lattice relaxation mechanism for quadrupolar nuclei. The rather short value of the phason-induced T_1 is thus one of the prominent signs of the presence of an I phase.

2.4.1 Amplitudons and Phasons: One Phonon Processes

In the presence of pinning effects the phason dispersion relation is

$$\omega_\Phi^2 = \Delta_\Phi^2 + \kappa(q - q_I)^2, \qquad T < T_I \tag{29a}$$

where Δ_Φ is the phason gap which vanishes in the absence of pinning in the continuum limit. The amplitudon dispersion relation, however, is

$$\omega_A^2 = \Delta_A^2 + \kappa(q - q_I)^2, \qquad T < T_I \tag{29b}$$

where

$$\Delta_A^2 = 2a(T_I - T), \qquad T < T_I \tag{29c}$$

One-phonon processes will dominate the relaxation rate if the above order parameter fluctuation modes are overdamped. In the simplest 'linear' case we find within the 'local' model that T_1^{-1} varies over the I frequency distribution $f(\nu)$ as

$$\frac{1}{T_1} = \frac{1}{T_{1A}} X^2 + \frac{1}{T_{1\Phi}}(1 - X^2) \tag{30a}$$

where

$$X = \frac{\nu - \nu_0}{\nu_1} \tag{30b}$$

and T_{1A} and $T_{1\Phi}$ are the spin–lattice relaxation times for amplitudons and phasons, respectively. The two 'edge' singularities, where $X = \pm 1$, will thus be relaxed by amplitudons whereas the central part of $f(\nu)$, where $X = 0$, will be relaxed by phasons.[11] Here one finds[11]

$$T_{1\Phi}^{-1} = C\frac{\pi}{2\sqrt{2}}\kappa^{-3/2}\sqrt{\frac{\Gamma_\Phi}{\Omega_0}} \tag{31a}$$

if

$$\Gamma_\Phi \gg \Omega_0 \gg \Delta_\Phi \tag{31b}$$

i.e. if the phason gap is smaller than the Larmor frequency Ω_0. Γ_Φ is the phason damping constant ($\Gamma_\Phi \approx 10^{11} - 10^{12}$ Hz) and C is a constant proportional both to the square of the fluctuating quadrupole coupling tensor components and to kT.

If, however, the phason gap Δ_Φ is larger than the Larmor frequency Ω_0, $T_{1\Phi}$ depends on the phason gap Δ_Φ:

$$T_{1\Phi}^{-1} = C\frac{\pi}{4}\kappa^{-3/2}\frac{\Gamma_\Phi}{\Delta_\Phi} \tag{32a}$$

if

$$\Delta_\Phi \gg \Omega_0 \tag{32b}$$

The amplitudon-induced spin–lattice relaxation rate is similarly obtained as

$$T_{1A}^{-1} = C\frac{\pi}{4}\kappa^{-3/2}\frac{\Gamma_A}{\Delta_A} \tag{33a}$$

Since $\Gamma_A \approx \Gamma_\Phi = \Gamma$ and $\Omega_0 \ll \Gamma \ll \Delta_A$, one gets

$$\frac{T_{1\Phi}}{T_{1A}} = \frac{\Delta_\Phi}{\Delta_A}, \quad \Delta_\Phi \gg \Omega_0 \tag{33b}$$

and

$$\frac{T_{1\Phi}}{T_{1A}} = \frac{\sqrt{\Omega_0\Gamma}}{\Delta_A}, \quad \Delta_\Phi \leq \Omega_0 \tag{33c}$$

A measurement of $T_{1\Phi}$ and T_{1A} in the I phase thus permits a determination of Δ_Φ in terms of Δ_A, which can be easily determined by Raman or neutron scattering.[2] Such a measurement is performed by selective frequency irradiation of the various parts of $f(\nu)$ and a determination of the variation of the effective $T_1{}^{-1}$ over the incommensurate lineshape (Figure 9).

The above theoretical predictions have been verified by numerous experiments[1,2] (Figure 10). It should be noted that only in biphenyl[12] and in bis(4-chlorophenyl) sulfone[13] was the phason gap found to be smaller than Ω_0. In all other I systems investigated so far $\Delta_\Phi > \Omega_0$, since the modulation wave is pinned by defects or discrete lattice effects.

2.4.2 Amplitudons and Phasons: Raman Processes

For two-phonon Raman processes the spin–lattice relaxation rates are proportional[11] to $(kT)^2$, in contrast to the direct

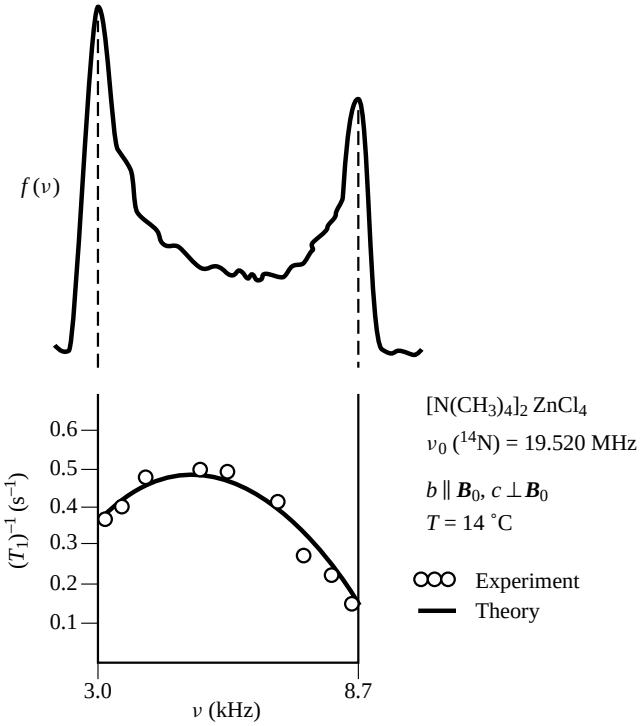

Figure 9 Variation of the effective ^{14}N spin–lattice relaxation rate over the incommensurate ^{14}N NMR lineshape in $[N(CH_3)_4]_2ZnCl_4$. (Reproduced by permission of Elsevier from R. Blinc, P. Prelovšek, V. Rutar, J. Seliger, and S. Žumer, in 'Incommensurate Phases in Dielectrics', eds. R. Blinc and A. P. Levanyuk, 1986, Vols. I and II)

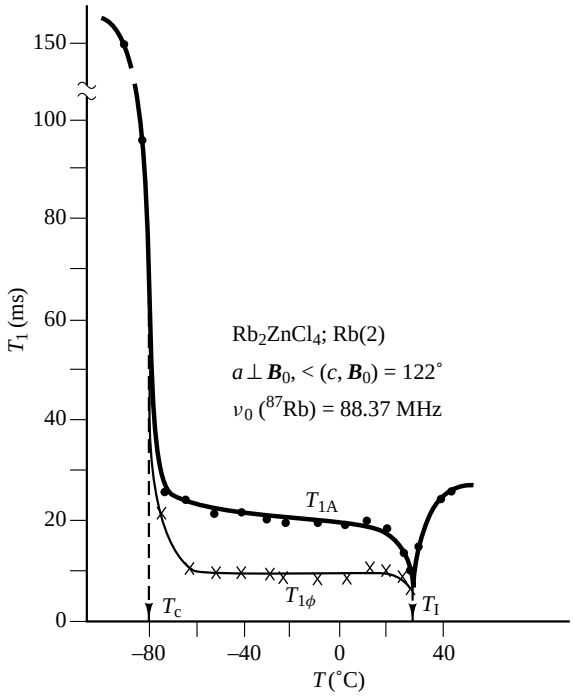

Figure 10 Temperature dependence of the ^{87}Rb $\frac{1}{2} \rightarrow -\frac{1}{2}$ spin–lattice relaxation time in the P, I, and C phases of Rb_2ZnCl_4. (Reproduced by permission of Elsevier from R. Blinc, P. Prelovšek, V. Rutar, J. Seliger, and S. Žumer, in 'Incommensurate Phases in Dielectrics', eds. R. Blinc and A. P. Levanyuk, 1986, Vols. I and II)

case where they are proportional to kT. The frequency variation of T_1 over the inhomogeneous frequency distribution is here slightly more complicated. For the 'linear' case one finds[14] that

$$\frac{1}{T_1} = \frac{1}{T_{1\mathrm{AA}}}X^4 + \frac{1}{T_{1\Phi\Phi}}(1-X^2)^2 + \left(\frac{1}{T_{1\mathrm{A}\Phi}} + \frac{1}{T_{1\Phi\mathrm{A}}}\right)X^2(1-X^2) \qquad (34)$$

where $T_{1\mathrm{AA}}^{-1}$ and $T_{1\Phi\Phi}^{-1}$ are spin–lattice relaxation rates for processes involving two amplitudons and two phasons, respectively, and $T_{1\mathrm{A}\Phi}^{-1} = T_{1\Phi\mathrm{A}}^{-1}$ are for Raman processes involving one amplitudon and one phason. By selective irradiation we can measure $T_{1\mathrm{AA}}$ at $X = 1$ and $T_{1\Phi\Phi}$ at $X = 0$. Using this technique the phason gap in $TlBr_4$ has been determined.[14] Furthermore, the $(kT)^2$ dependence predicted for Raman relaxation was confirmed experimentally[14] in this system.

2.4.3 T_1 in the Multisoliton Lattice Limit

The periodicity of the multisoliton lattice results in a splitting of the phason mode[1,2,6] [equation (29a)] into two branches separated by an energy gap: an 'acoustic-like' branch for $|k_z| < \pi/x_0$ and an 'optic-like' branch for $|k_z| > \pi/x_0$ (Figure 11). The 'acoustic' branch corresponds to phase oscillations of the multisoliton lattice, whereas the 'optic-like' branch corresponds to phase oscillations in the commensurate regions. On approaching the 'lock-in' transition the 'acoustic-like' branch vanishes (Figure 11) resulting in a critical decrease[13] of the 'acoustic phason'-induced spin–lattice relaxation rate

$$\left(\frac{1}{T_1}\right)_{\mathrm{ac},\Phi} = C[(\pi\Gamma_\Phi\Lambda_\perp^2)/(2\Delta_\Phi^4)]x_0^{-1} \qquad (35a)$$

where

$$x_0 = \ln(1 - T_\mathrm{c}/T) \qquad (35b)$$

and $\Lambda_\perp$ is the maximum value of the corresponding wave vector components. This effect has indeed been observed[13] in Rb_2ZnCl_4 close to the 'lock-in' transition T_c (Figure 12).

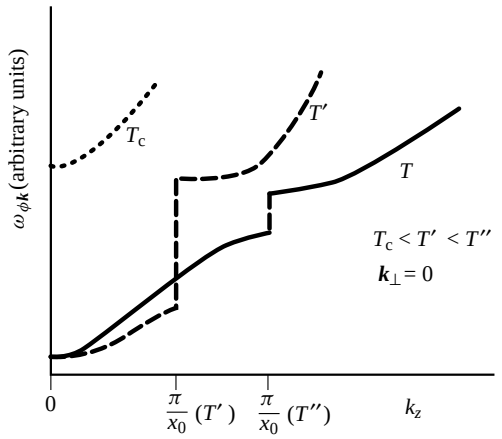

Figure 11 Temperature dependence of the phason dispersion relation in a multisoliton lattice showing the splitting into 'acoustic-like' and 'optic-like' branches. The acoustic-like branch vanishes on approaching the lock-in transition T_c. (Reproduced by permission of The American Physical Society from R. Blinc et al.[13])

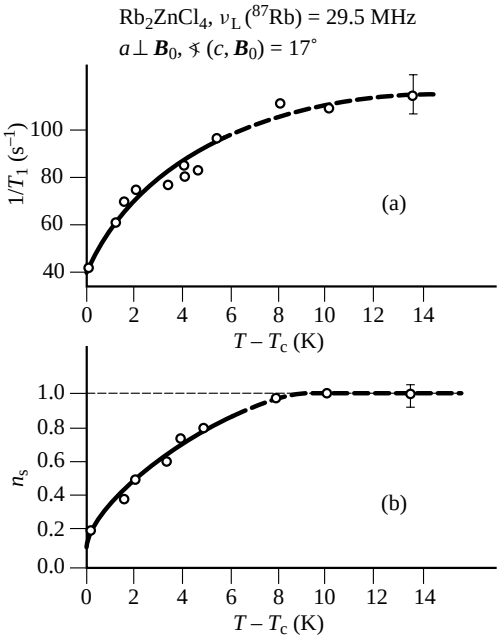

Figure 12 (a) Temperature dependence of the 'acoustic-like' phason-induced ^{87}Rb spin–lattice relaxation rate $T - 1/1$, and (b) temperature dependence of the soliton density n_s in Rb_2ZnCl_4 as $T \rightarrow T_\mathrm{c}$. (Reproduced by permission of The American Physical Society from R. Blinc et al.[13])

3 MULTIPLE-*q* MODULATED INCOMMENSURATE SYSTEMS

Consider now the NMR properties of I systems with a $2n$-component order parameter,

$$Q_{i\pm} = A_i \exp(\pm \mathrm{i}\Phi_i), \qquad i = 1, 2, \ldots n \qquad (36a)$$

corresponding to an n-dimensional modulation wave

$$u = \sum_{p=1}^{n} A_p \cos[\Phi_p(\boldsymbol{r}) + \Phi_{p0}] \qquad (36b)$$

For the sake of simplicity let us first assume that the relation between the NMR frequency and the incommensurate displacements is purely local and linear, so that

$$\nu(\Phi_1, \ldots, \Phi_n) = \nu_0 + \sum_{i=1}^{n} \nu_i \cos\Phi_i \qquad (37a)$$

Here ν_i is proportional to the amplitude A_i of the ith component of the modulation wave. In the plane wave limit

we have

$$\Phi_i = \boldsymbol{q}_i \cdot \boldsymbol{r}_i + \Phi_{pi0} \tag{37b}$$

where the modulation vectors $\boldsymbol{q}_i$ are incommensurate to the basic crystal lattice. The phases Φ_i take on any value in the interval $(-\infty, +\infty)$ with equal probability. The frequency distribution is now obtained[15] as

$$f(\nu) = \int \cdots \int \mathrm{d}\Phi_1\, \mathrm{d}\Phi_2 \cdots \mathrm{d}\Phi_n \delta \times [\nu - \nu(\Phi_1, \ldots, \Phi_n)] \tag{38a}$$

When the modulation waves are independent, $f(\nu)$ is given by a multiple convolution,

$$f(\nu) = \int_{-\infty}^{+\infty} f_1(\nu_1') f_2(\nu_2') \cdots f_{n-1}(\nu_{n-1}') \times f_n\left(\nu - \sum_{j=1}^{n-1} \nu_j'\right) \mathrm{d}\nu_1'\, \mathrm{d}\nu_2' \cdots \mathrm{d}\nu_{n-1}' \tag{38b}$$

of frequency distributions $f_i(\nu)$ for purely one-dimensional modulations.[16]

The modulation waves are independent if the number of modulation waves is smaller than the dimension of space spanned by the corresponding wave vectors and if the initial phases Φ_{i0} are not correlated.[15] In quartz,[2] for instance, the three modulation waves are coplanar ($|\boldsymbol{q}_1| = |\boldsymbol{q}_2| = |\boldsymbol{q}_3|$ and $\boldsymbol{q}_1 + \boldsymbol{q}_2 + \boldsymbol{q}_3 = 0$) and therefore correlated so that the 3-$\boldsymbol{q}$ case is in fact reduced to a 2-$\boldsymbol{q}$ case.

The NMR lineshapes $f(\nu)$ for multiple-$\boldsymbol{q}$ modulations are illustrated in Figure 13 for the linear case in both the plane wave and the multisoliton lattice limits ($n_s = 0.6$).

3.1 Lineshapes in 2-q Modulated Systems

Let us now consider a case where the angle between the two modulation vectors $\boldsymbol{q}_1$ and $\boldsymbol{q}_2$ equals $\gamma \neq 0$. Here

$$u = A_1 \cos \Phi_1 + A_2 \cos \Phi_2 \tag{39a}$$

where $\Phi_1 = \boldsymbol{q}_1 x$ and $\Phi_2 = \boldsymbol{q}_2 x \cos\gamma + \boldsymbol{q}_{2y} \sin\gamma + \Phi_0$. The lineshape $f(\nu)$ is given by

$$f(\nu) = \int_{-\infty}^{+\infty} f_1(\nu') f_2(\nu - \nu')\, \mathrm{d}\nu' \tag{39b}$$

For $A_1 = A_2$ and $\nu_1 = \nu_2$ the lineshape reduces to a central logarithmic singularity

$$f(\nu) = -\ln[(\nu - \nu_0)/\nu_1]/\nu_1 \tag{39c}$$

for $\nu - \nu_o \to 0$ (Figure 13). $f(\nu)$ does not depend on γ or on the ratio $|\boldsymbol{q}_1|/|\boldsymbol{q}_2|$ since the two modulation waves are independent. If $\gamma = 0$, so that $\boldsymbol{q}_1$ is parallel to $\boldsymbol{q}_2$, this is still true as long as $|\boldsymbol{q}_1|$ is incommensurate to $|\boldsymbol{q}_2|$. If however the ratio $|\boldsymbol{q}_1|/|\boldsymbol{q}_2|$ is commensurate, the two waves are correlated and the lineshape is the same as in the 1-$\boldsymbol{q}$ case. Barium sodium niobate, biphenyl, and $BaMnF_4$ represent examples of 2-$\boldsymbol{q}$ modulated systems.[2]

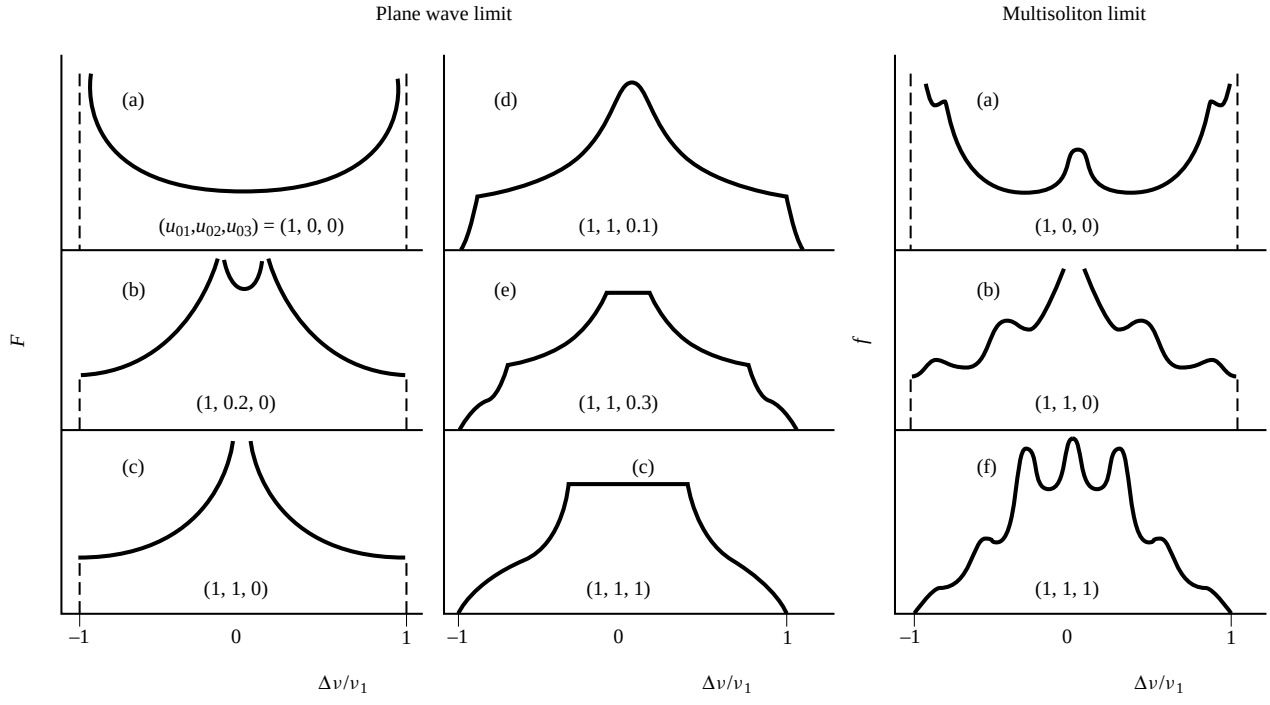

Figure 13 Frequency distribution $f(\nu)$ for multiple-q modulated I phases in the plane wave and multisoliton lattice ($n_s = 0.6$) limits. (Reproduced by permission of Elsevier from R. Blinc, P. Prelovšek, V. Rutar, J. Seliger, and S. Žumer, in 'Incommensurate Phases in Dielectrics', eds. R. Blinc and A. P. Levanyuk, 1986, Vols. I and II)

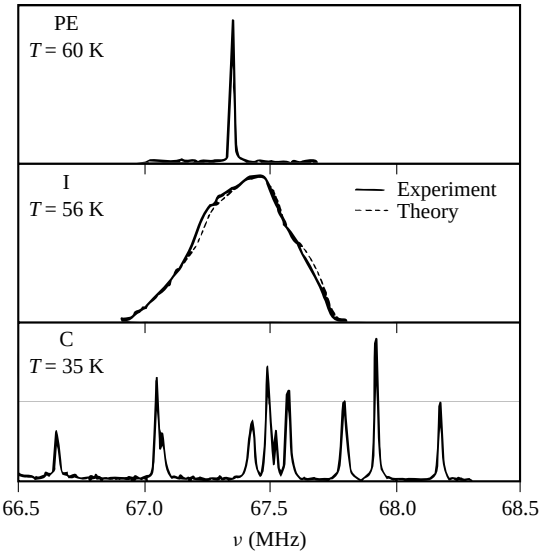

Figure 14 Comparison between the experimental and theoretical ^{75}As NQR lineshapes in the 3-***q*** modulated I phase of proustite

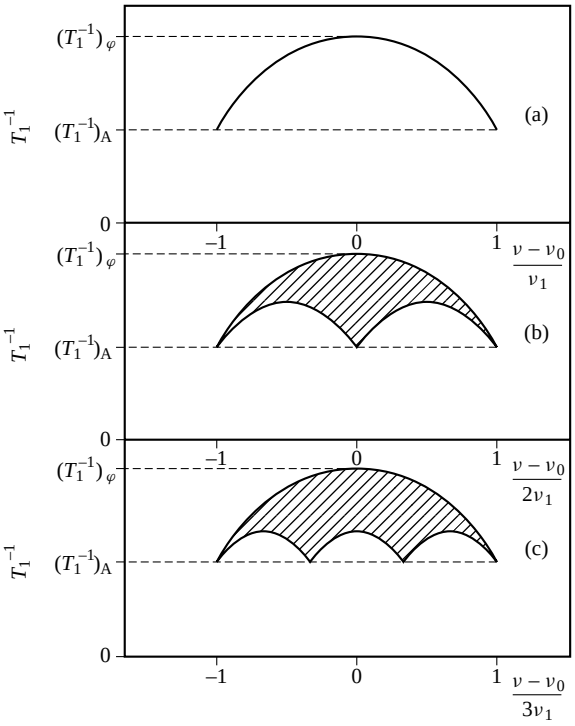

Figure 15 Relation between $T - 1/1$ and frequency shift $\nu - \nu_0$ for (a) 1-***q***, (b) 2-***q***, and (c) 3-***q***, I modulation. The shaded area designates the distribution of $T - 1/1$ values. (Reproduced by permission of The American Physical Society from R. Blinc and S. Žumer[15])

3.2 Lineshapes in 3-*q* Modulated Systems

For three independent I modulation waves, $f(\nu)$ is given by a double convolution

$$f(\nu) = \int_{-\infty}^{+\infty} \int_{-\infty}^{+\infty} f_1(\nu_1') f_2(\nu_2') f_3(\nu - (\nu_1' + \nu_2'))\, \mathrm{d}\nu_1'\, \mathrm{d}\nu_2' \tag{39d}$$

The frequency distribution function (Figure 13) has no singularities, but the derivatives have singular points. In the general case where not only linear but also higher order terms contribute as well, a bell-shaped curve is expected for $f(\nu)$.

Such a bell-shaped curve has indeed been observed[17,18] in the ^{75}As NQR of proustite, Ag_3AsS_3. It can be described[18] (Figure 14) by

$$\begin{aligned}\nu = \nu_0 &+ \nu_1[\cos(\boldsymbol{q}_1 \cdot \boldsymbol{r}) + \cos(\boldsymbol{q}_2 \cdot \boldsymbol{r}) + \cos(\boldsymbol{q}_3 \cdot \boldsymbol{r})] \\ &+ \nu_{21}[\cos(2\boldsymbol{q}_1 \cdot \boldsymbol{r} + \beta) + \cos(2\boldsymbol{q}_2 \cdot \boldsymbol{r} + \beta) + \cos(2\boldsymbol{q}_3 \cdot \boldsymbol{r} + \beta)] \\ &+ \nu_{22}\{\cos[(\boldsymbol{q}_1 - \boldsymbol{q}_2) \cdot \boldsymbol{r}] + \cos[(\boldsymbol{q}_2 - \boldsymbol{q}_3) \cdot \boldsymbol{r}] \\ &+ \cos[(\boldsymbol{q}_3 - \boldsymbol{q}_1) \cdot \boldsymbol{r}]\} + \nu_{23}\{\cos[(\boldsymbol{q}_1 + \boldsymbol{q}_2) \cdot \boldsymbol{r} + \gamma] \\ &+ \cos[(\boldsymbol{q}_2 + \boldsymbol{q}_3) \cdot \boldsymbol{r} + \gamma] + \cos[(\boldsymbol{q}_3 + \boldsymbol{q}_1) \cdot \boldsymbol{r} + \gamma]\}\end{aligned} \tag{40}$$

3.3 T_1 Effects in Multiple-*q* Modulated Incommensurate Systems

For a system with n modulation waves linearly and locally related to the NMR frequency [equation (32a)] the spin–lattice relaxation rate for one-phonon processes can be expressed as

$$\frac{1}{T_1}(\Phi_1, \Phi_2, \ldots, \Phi_n) = K \sum_{i=1}^{n} (\cos^2 \Phi_i J_{\mathrm{A},i} + \sin^2 \Phi_i J_{\Phi,i}) \tag{41}$$

where $J_{\mathrm{A},i}$ and $J_{\Phi,i}$ are local spectral densities of the amplitudon and phason order parameter fluctuation modes. Even though there is a simple relation between the effective spin–lattice relaxation rate $1/T_1$ and the NMR frequency in

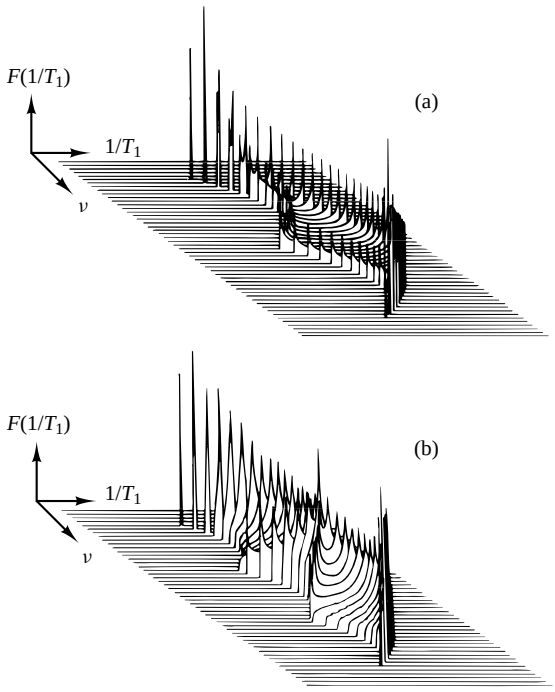

Figure 16 Distributions of relaxation rates $F(T_1{}^{-1})$ for (a) 2-*q*, and (b) 3-*q*, I modulations. (Reproduced by permission of The American Physical Society from R. Blinc and S. Žumer[15])

1-***q*** modulated systems,[1,2] this is not the case in multiple-***q*** systems. At any given frequency there is now a distribution of spin–lattice relaxation rates:[15]

$$F(T_1^{-1}, \nu) = \int \cdots \int \mathrm{d}\Phi_1\, \mathrm{d}\Phi_2 \cdots \mathrm{d}\Phi_n \delta[\nu - \nu(\Phi_1, \Phi_2, \ldots, \Phi_n)] \times \delta[T_1^{-1} - T_1'^{-1}(\Phi_1, \Phi_2, \ldots, \Phi_n)] \quad (42)$$

The relationship between T_1^{-1} and the frequency shift $\nu - \nu_0$ for multiple-***q*** modulations are illustrated in Figure 15, and the corresponding relaxation rate distributions $F(T_1^{-1})$ are shown[15] in Figure 16.

4 RELATED ARTICLES

Ferroelectrics and Proton Glasses; Quadrupolar Interactions; Quadrupolar Nuclei in Solids; Relaxation Theory for Quadrupolar Nuclei; Selective Excitation Methods: Artifacts.

5 REFERENCES

1. R. Blinc, *Phys. Rep.*, 1981, **79**, 331 and references therein.
2. eds. R. Blinc and A. P. Levanyuk, *Incommensurate Phases in Dielectrics*, Elsevier, Amsterdam, 1986 Vols. I and II. For NMR see Vol. I, Chap. 4
3. A. M. Fajdiga, T. Apih, J. Dolinsek, R. Blinc, A. P. Levanyuk, S. A. Minyukov, and D. C. Ailion, *Phys. Rev. Lett.*, 1992, **69**, 2721.
4. J. H. Ross, Z. Wang, and C. P. Slichter, *Phys. Rev. Lett.*, 1986, **56**, 663; P. Segransan, A. Janossy, C. Berthier, J. Marcus, and P. Butaud, *Phys. Rev. Lett.*, 1986, **56**, 1854.
5. M. Kogoj, S. Žumer, and R. Blinc, *J. Phys. C.*, 1984, **17**, 2415.
6. P. Bak, *Rep. Prog. Phys.*, 1982, **45**, 587 and references therein.
7. R. Blinc and J. Seliger, *Solid State Commun.*, 1985, **56**, 295.
8. S. Aubry, *Ferroelectrics*, 1980, **24**, 53; S. Aubry, *J. Phys. (France)*, 1983, **44**, 147; see also P. Bak and V. L. Pokrovsky, *Phys. Rev. Lett.*, 1981, **47**, 958.
9. F. Denoyer, A. H. Mondaten, and M. Lambert, *Ferroelectrics*, 1980, **24**, 43.
10. R. Blinc, S. Žumer, D. C. Ailion, and J. Nicponski, *J. Phys. (France)*, 1985, **46**, 1205.
11. S. Žumer and R. Blinc, *J. Phys. C*, 1981, **14**, 465.
12. S.-B. Liu and M. S. Conradi, *Phys. Rev. Lett.*, 1985, **54**, 1287.
13. R. Blinc, F. Milia, V. Rutar, and S. Žumer, *Phys. Rev. Lett.*, 1982, **48**, 47.
14. S. Chen and D. C. Ailion, *Phys. Rev. B*, 1989, **40**, 2332.
15. R. Blinc and S. Žumer, *Phys. Rev. B*, 1990, **41**, 11 314.
16. S. Žumer and J. Seliger, *Ferroelectrics*, 1981, **36**, 301.
17. A. V. Bondar, V. S. Vikhnin, S. M. Ryabchenko, and V. E. Yachmenev, *Sov. Phys. Solid State*, 1983, **25**, 1497.
18. U. Mikac, T. Apih, J. Seliger, and R. Blinc, *paper presented at the MECO meeting, 1994*; J. Norcross, D. C. Ailion, T. Apih, U. Mikac, J. Dolinsek, and R. Blinc, *Bull. Am. Phys. Soc.*, 1994, **39**, 312.

Biographical Sketches

Robert Blinc. *b* 1933. Ph.D., 1959, Physics, University of Ljubljana, Postdoctoral work with J. S. Waugh, MIT, Cambridge, Mass. Faculty member (currently Professor of Physics), University of Ljubljana, J. Stefan Institute, 1969–present. President of AMPERE Society 1988–94. Member of Slovenian, Croatian, Polish, Saxon and European Academies of Sciences. Member of Academy of Athens and Academia Europea. Approx. 450 publications and, with B. Žekš, the book 'Soft Modes in Ferroelectrics and Antiferroelectrics'. ISMAR prize 1977. Research interests include NMR of phase transitions and disordered condensed matter.

David C. Ailion. *b* 1937. A.B., 1956, M.S., 1958, Ph.D., 1964, Physics, University of Illinois, under supervision of C.P. Slichter. Faculty member (currently Professor of Physics) University of Utah, 1964–present. Fellow of American Physical Society, Humboldt Research Award (1994–5), NIH Special Fellow (1971–2), Guest Member of AMPERE Committee. Approx. 130 publications. Current research specialties: magnetic resonance imaging of lungs, NMR of partially disordered systems (incommensurate insulators and glasses).

Quasicrystalline Compounds: Metallic Glasses

Xiaoping Tang and Yue Wu

University of North Carolina, Chapel Hill, NC, USA

1 Introduction 1
2 Basic NMR Characteristics in Quasicrystalline Alloys 1
3 Probing Electronic Structures of Quasicrystalline Alloys by NMR 2
4 The Alignment Echo Technique for $I \geq 1$ 5
5 Detection of Slow Atomic Motion in Bulk Metallic Glasses by NMR of ^{9}Be 7
6 Related Articles in Volumes 1–8 8
7 References 8

1 INTRODUCTION

Two recent important developments of metallic alloys are the discoveries of quasicrystalline (QC) alloys and bulk metallic glasses (BMGs). In both cases, NMR studies have obtained crucial information that is important for the understanding of the novel properties of these systems. Discovered in 1984, QC alloys possess long-range translational and orientational orders, which lead to sharp Bragg diffraction peaks.[1] However, the diffraction patterns display point-group symmetry, such as icosahedral (i) symmetry, incompatible with periodicity.[1] Thus, QC alloys belong to a new class of solids unlike crystalline and glassy materials. In addition to their fascinating structure, QC alloys also possess novel physical properties such as the extremely low electric conductivity.[2] In this article we will focus on how NMR provides crucial information on the electronic structures of these QC alloys. Unlike crystalline and QC solids, glasses lack both long-range translational and orientational orders. Conventional metallic glasses are produced by rapid quenching of melts at cooling rates larger than $10^5\,\mathrm{K\,s^{-1}}$. In contrast, the newly discovered BMGs can be produced at a typical cooling rate of $1\,\mathrm{K\,s^{-1}}$ such that large pieces of glassy materials can be obtained. Examples of such BMGs are the Zr-based and Pd-based quaternary and quintary alloys.[3,4] Such BMGs exhibit excellent thermal stability making it experimentally possible to access the metallic supercooled liquid state down to the glass transition temperature (T_g). Clearly, BMGs possess unique thermodynamic and kinetic properties that hinder nucleation and growth in the supercooled liquid state. We will show how NMR can be used to obtain crucial information on the nature of atomic motions in the glassy and the supercooled liquid state of BMGs. Despite their different long-range orders, metallic glasses and QC alloys could share some similarities in local structures. For instance, icosahedral clusters were proposed to be the local structure in some metallic glasses and supercooled liquids. Experimentally, upon thermal annealing BMGs were observed to form QC phases prior to crystallization.[5]

2 BASIC NMR CHARACTERISTICS IN QUASICRYSTALLINE ALLOYS

NMR studies of QC alloys were carried out immediately after the initial discovery.[6] Structure, atomic motion, and electronic structures are the three main themes of most NMR studies of QC alloys. Lacking periodicity, the local environments in QC alloys are highly diversified despite the long-range translational and orientational orders. There exist a large number of nonequivalent atomic sites in QC alloys. As a result, the ^{27}Al NMR and NQR spectra measured in icosahedral Al-based QC alloys are broad and featureless. Based on ^{27}Al NQR spectra of i-$Al_{65}Cu_{23}Fe_{12}$ and i-$Al_{70}Cu_{15}Ru_{15}$ it was inferred that there exists a broad distribution of the magnitude of the EFG tensors associated with chemically nonequivalent Al sites.[7,8] On single-grain i-AlPdMn samples, the angular dependence of ^{27}Al NMR spectra was investigated.[8,9] In i-$Al_{70}Pd_{21.5}Mn_{8.5}$, the ^{27}Al NMR spectrum was found to be independent of the relative orientation between the static magnetic field (B_0) and the twofold rotation axis of the sample indicating a quasi-continuous distribution of structural environments.[8] In i-$Al_{72.4}Pd_{20.5}Mn_{7.1}$, the ^{27}Al NMR spectrum was found to be slightly different at parallel and perpendicular orientations between B_0 and the five-fold rotation axis suggesting a large but finite number of physically nonequivalent atomic sites.[9] A typical ^{27}Al NMR spectrum of Al-based QC alloys measured by the Hahn echo pulse sequence is shown in Figure 1. Powder pattern simulation of the $1/2 \leftrightarrow -1/2$ central transition at $B_0 = 9.4\,\mathrm{T}$ shows that the quadrupole frequency $\nu_Q = 3\chi/2I(2I-1)$ is on the order of 1.7 MHz in i-$Al_{65}Cu_{20}Ru_{15}$ (Figure 1),[10] consistent with the NQR measurements.[8] The isotropic shift is on the order of 150 ppm. Since the estimated second-order isotropic quadrupole shift $\delta_{\mathrm{iso}}^{(2)}$ is around –70 ppm and the typical ^{27}Al chemical shift is between 0 and 200 ppm, the Knight shift K is on the order of 200 ppm or less which is much smaller than $K^{^{27}\mathrm{Al}}$ of 1600 ppm observed in Al metal.

NMR was used to study atomic motion in QC alloys. In i-$Al_{65}Cu_{20}Ru_{15}$, a sharp increase of $1/T_1^{^{27}\mathrm{Al}}$ was measured above 673 K due to motion-induced quadrupole relaxation.[10] The Arrhenius plot indicated a thermally activated process with activation energy of 0.48 eV. It is about three times smaller than that in corresponding crystalline alloys where vacancy-assisted diffusion dominates. This suggests that a different atomic transport process is at work in QC alloys at high temperature. ^{27}Al two-dimensional exchange NMR has been employed to measure atomic motion in i-$Al_{70}Pd_{21.4}Re_{8.6}$ below 130 K.[11] The mixing time dependence of the two-dimensional exchange spectrum suggests that the detected atomic motion is spatially confined in this temperature range, extending over only several inter-atomic distances and is attributed to a mode of local motion specifically related to quasicrystallinity.[11]

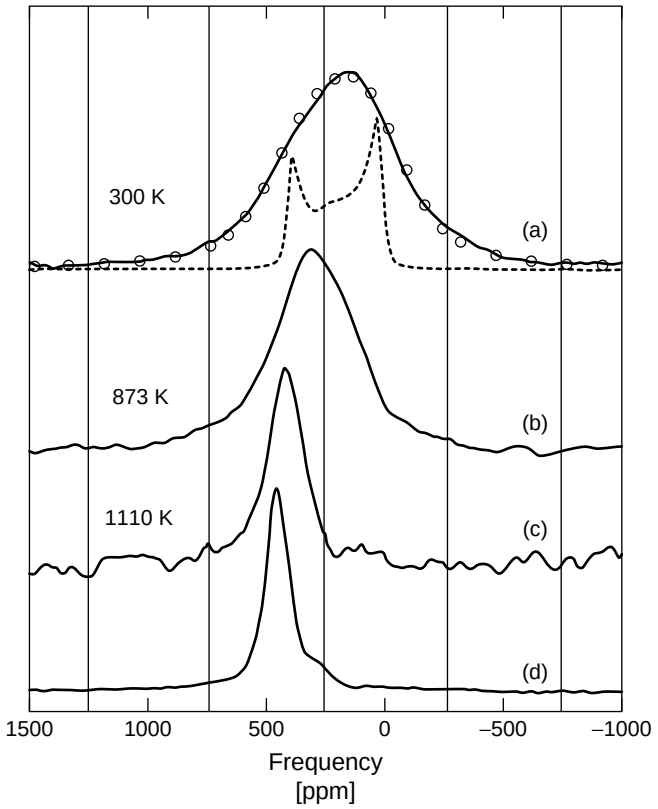

Figure 1 (a), (b), and (c) are the ^{27}Al spectra of i-$Al_{65}Cu_{20}Ru_{15}$ at various temperatures. The circles are the simulated spectrum of a powder-pattern of the anisotropic second-order quadrupole interaction convoluted with linewidth broadening. The dashed line is the quadrupole powder pattern ($\nu_Q = 1.7$ MHz, $\eta = 0$). (d) ^{27}Al spectrum of crystalline Al_7Cu_2Fe at 973 K

3 PROBING ELECTRONIC STRUCTURES OF QUASICRYSTALLINE ALLOYS BY NMR

High-quality QC alloys exhibit remarkably different physical properties than typical metals, with poor electric and thermal conductivity and very small electric heat capacity.[2] The electric resistivity of a QC alloy increases as structural order increases in contrast to typical metals.[2] Furthermore, the electric resistivity increases with decreasing temperature.[2] In fact, some of the high-quality QC alloys were found to be in the proximity of metal-insulator transition.[12] These unusual physical properties are related to novel structures of the electronic density-of-states (DOS). It is well-established both theoretically and experimentally that a broad DOS pseudogap at E_F of about 0.5–1 eV in width exists in QC alloys caused by electron scattering at the almost spherical pseudo-Brillouin zone at the Fermi surface. The pseudogap was predicted to be enhanced[13] by sp-d hybridization in Al-based QC alloys containing intermediate transition metals and plays a crucial role in the thermodynamic stability of QC phases. In addition, it was also predicted theoretically that a set of spiky DOS peaks of about 10 meV in width exist within the pseudogap as a result of strong hybridization between atomic orbits in the presence of high local symmetry[14] and hierarchical packing of icosahedral clusters.[1] The presence of such sharp feature at E_F will have a strong influence on the electric and thermal properties of QC alloys. We will show how NMR can be used to detect and characterize such sharp DOS features at E_F.

3.1 Unusual Temperature Dependence of Nuclear Spin-Lattice Relaxation

Unlike in typical metallic alloys, the measured K and $1/T_1$ in QC alloys are very small. It indicates that the DOS at E_F, $g(E_F)$, of QC alloys is small compared to the calculated value based on free-electron model. However, some earlier NMR studies did not find evidence of sharp DOS features.[15,16] Sharp features become noticeable as the quality of QC alloys improves. The NMR evidence of sharp DOS features is the unusual temperature dependence of $1/T_1$ that deviates substantially from the relation $1/T_1 \propto T$ observed in typical metallic systems. Figure 2 shows the nuclear spin-lattice relaxation (NSLR) curves of ^{27}Al measured in i-$Al_{70}Pd_{20}Re_{10}$.[17] Here, $M^*(t) = [M_0 - M(t)]/[M_0 - M(0)]$ is plotted[17] as a function of the recovery time t scaled by T^2. The NSLR curves measured between 100 and 600 K collapse into a single curve indicating that $1/T_1 \propto T^2$ (Figure 2). As discussed later, this novel temperature dependence is the signature of the sharp DOS valley at E_F. Similar temperature dependence of $1/T_1$ was also observed in other QC alloys including i-$Al_{65}Cu_{20}Ru_{15}$ and i-$Al_{62.5}Cu_{24.5}Fe_{13}$,[17] i-$Al_{70}Pd_{8.6}Re_{21.4}$,[18] i-$Al_{70.5}Pd_{21}Re_{8.5}$, i-$Al_{62}Cu_{25.5}Fe_{12.5}$ and i-$Al_{72.4}Pd_{20.5}Mn_{7.1}$.[19] At higher temperature above 600 K, $1/T_1$ is dominated by atomic motion-induced quadrupole relaxation.[10] At low temperature below 20 K, $1/T_1^{^{27}\mathrm{Al}}T \propto T^{-0.69}$ was observed in i-$Al_{70}Pd_{8.6}Re_{21.4}$.[18] This power law was described as a result of gradual real-space localization of the itinerant charge carriers. Similar low-temperature $1/T_1$ behaviors were also observed in i-$Al_{70.5}Pd_{21}Re_{8.5}$, i-$Al_{62}Cu_{25.5}Fe_{12.5}$, and i-$Al_{72.4}Pd_{20.5}Mn_{7.1}$.[19] The low-temperature NMR results, consistent with the low-temperature electric conductivity, magnetoresistivity,[12] and magnetic susceptibility[20] measurements, indicate a strong effect of the weak localization and electron-electron interaction in high-quality QC alloys at low temperature.

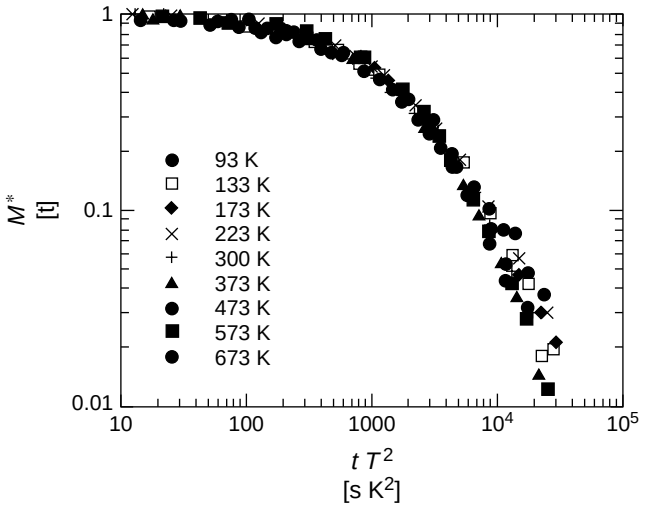

Figure 2 The inversion recovery curves of the ^{27}Al nuclear magnetization M versus τ which is scaled by T^2 in i-$Al_{70}Pd_{20}Re_{10}$. It shows that $1/T_1 \propto T^2$

3.2 The Mechanism of the Nuclear Spin-lattice Relaxation

In NMR studies of QC alloys, ^{27}Al, ^{63}Cu, and ^{63}Cu are the most frequently used isotopes. Two mechanisms can induce NSLR for these quadrupolar nuclei. One mechanism is the coupling between the nuclear spin and the unpaired conduction electron spins (magnetic relaxation). The second mechanism is the coupling of the nuclear electric quadrupole moment with the fluctuating EFG induced by atomic motions (quadrupolar relaxation). For magnetic relaxation, $1/T_1 \propto \gamma_n^2$; for quadrupolar relaxation, $1/T_1 \propto Q^2$. The relative contributions of the two mechanisms can be determined by measuring $1/T_1$ of a pair of proper isotopes. For i-AlCuRu and i-AlCuFe, ^{63}Cu and ^{65}Cu is such an excellent pair:[17] $T_1^{^{65}\mathrm{Cu}}/T_1^{^{63}\mathrm{Cu}} = (\gamma_{^{63}\mathrm{Cu}}/\gamma_{^{65}\mathrm{Cu}})^2 = 0.87$ for magnetic relaxation and $T_1^{^{65}\mathrm{Cu}}/T_1^{^{63}\mathrm{Cu}} = (Q_{^{63}\mathrm{Cu}}/Q_{^{65}\mathrm{Cu}})^2 = 1.14$ for quadrupole relaxation. Figure 3 shows the ^{63}Cu and ^{65}Cu NSLR curves measured in i-$Al_{65}Cu_{20}Ru_{15}$ at 300 K and 9.4 T where $T_1^{^{65}\mathrm{Cu}}/T_1^{^{63}\mathrm{Cu}}$ was measured to be 0.83–0.90. In i-$Al_{62.5}Cu_{24.5}Fe_{13}$ $T_1^{^{65}\mathrm{Cu}}/T_1^{^{63}\mathrm{Cu}}$ was also measured to be 0.80–0.87.[17] Thus, $1/T_1^{^{63}\mathrm{Cu}}$ and $1/T_1^{^{65}\mathrm{Cu}}$ in i-$Al_{65}Cu_{20}Ru_{15}$ and i-$Al_{62.5}Cu_{24.5}Fe_{13}$ are dominated by magnetic relaxation.[17] In i-$Al_{65}Cu_{20}Ru_{15}$ $1/T_1^{^{27}\mathrm{Al}}$ was found[17] to follow almost the same temperature dependence as $1/T_1^{^{63}\mathrm{Cu}}$. It suggests that the observed unusual temperature dependences of $1/T_1^{^{27}\mathrm{Al}}$, $1/T_1^{^{63}\mathrm{Cu}}$, and $1/T_1^{^{65}\mathrm{Cu}}$ are originated from the same mechanism through the coupling between the nuclear spins and unpaired conduction electron spins.

A strong field dependence of $1/T_1^{^{27}\mathrm{Al}}$ was observed in i-$Al_{72.4}Pd_{20.5}Mn_{7.1}$.[21] The measured $1/T_1^{^{27}\mathrm{Al}}$ was ascribed to two components; one is independent of B_0 dominating at low temperature while the other is inversely proportional to B_0 dominating at high temperature.[21] The origin of the second component remains unexplained.[21] The nature of $1/T_1^{^{27}\mathrm{Al}}$ in other QCs were shown to be different. In i-$Al_{70}Pd_{20}Re_{10}$ and i-$Al_{65}Cu_{20}Ru_{15}$, $1/T_1^{^{27}\mathrm{Al}}$ was measured to be field independent;[20] in i-$Al_{70}Pd_{21.4}Re_{8.6}$ $1/T_1^{^{27}\mathrm{Al}}$ was measured to be field independent as well.[18] Thus, the observed field dependence of $1/T_1^{^{27}\mathrm{Al}}$ in i-$Al_{72.4}Pd_{20.5}Mn_{7.1}$ is not intrinsic to QC alloys. In Al-based QC alloys with intermediate transition metals, NMR results could be complicated by possible localized magnetic moments at the atomic sites of the transition metals. Thus, the field dependence of $1/T_1^{^{27}\mathrm{Al}}$ in i-AlPdMn might be related to localized magnetic moments since the magnetic moment concentration in i-AlPdMn is several orders of magnitude larger than in i-AlPdRe and i-AlCuRu according to magnetic susceptibility measurement.[20] In view of this, i-AlPdRe and i-AlCuRu are more appropriate systems for NMR study of the intrinsic electronic properties of QC alloys.

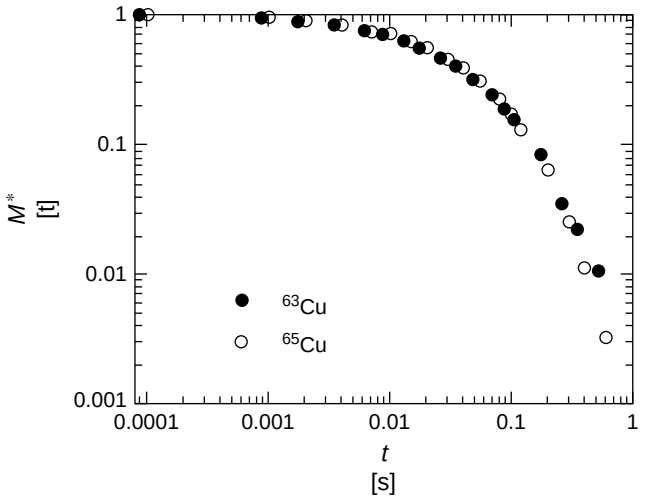

Figure 3 The ^{63}Cu and ^{65}Cu NSLR curves in i-$Al_{65}Cu_{20}Ru_{15}$ at 300 K and 9.4 T. The curve for ^{63}Cu is plotted as $M^*(0.87\,\mathrm{t})$. It shows that $T_1^{^{65}\mathrm{Cu}}/T_1^{^{63}\mathrm{Cu}}$ is 0.83–0.90

3.3 The Sharp DOS Feature

As discussed in Section 3.1, below 20 K the measured T_1 in i-$Al_{70}Pd_{8.6}Re_{21.4}$ are found to be associated with the electron-electron interaction and weak localization. Above 600 K, T_1 is dominated by the contribution of atomic motion. Therefore, only T_1 measured in the intermediate temperature range, which is governed by the coupling between the nuclear spins and the unpaired independent conduction electron spins, will be used to extract the sharp DOS feature at E_F. In this section, we discuss the derivation of the sharp DOS feature by analyzing the NMR results measured in this temperature range.

In Al-based QCs with intermediate transition metals such as i-AlPdRe and i-AlCuRu, the Al 3s and 3p-bands are strongly hybridized with the Re 5d-band and the Ru 4d-band, respectively. The K and $1/T_1$ of ^{27}Al, ^{63}Cu and ^{65}Cu are dominated by the Fermi-contact interaction with the conduction 3s-electron spins and the core-polarization induced by the conduction d electron spins. Denoting the partial DOS of the 3s and d-bands as $g_s(E)$ and $g_d(E)$, respectively, K is described by

$$K = \frac{1}{k_B T}\int [\alpha_s g_s(E) + \alpha_d g_d(E)] f(E)[1 - f(E)]\mathrm{d}E, \qquad (1)$$

where $f(E)$ is the Fermi-Dirac distribution function, $\alpha_s = \frac{4\pi}{3}\hbar^2\gamma_e^2\langle|u_k^2(0)|\rangle_{E_F}$ where γ_e is the electronic gyromagnetic ratio and $\langle|u_k^2(0)|\rangle_{E_F}$ is the density of the 3s-band wave function at the Al nucleus averaged over the Fermi surface, α_d is associated with the core-polarization by the d-bands and is negative. $1/T_1$ is described by

$$\frac{1}{T_1} = \int [\beta_s g_s^2(E) + \beta_d g_d^2(E)] f(E)[1 - f(E)]\mathrm{d}E, \qquad (2)$$

where $\beta_s = 4\pi\hbar\gamma_n^2\alpha_s^2$ and $\beta_d = 4\pi p\hbar\gamma_n^2\alpha_d^2$ (p is a factor related to the local symmetry and degeneration of the d-bands).[22]

Since $f(E)[1 - f(E)]$ vanishes quickly as E deviates from E_F by a few $k_B T$, the temperature dependence of K and $1/T_1$ are determined by DOS near E_F. In typical metallic systems, since the DOS variation over several $k_B T$ is small near E_F, K is temperature independent and $1/T_1 \propto T$. In high quality QC alloys, however, novel temperature dependences of K and $1/T_1$ were observed inferring a sharp DOS feature near E_F. For Al-based QC alloys containing intermediate transition metals,

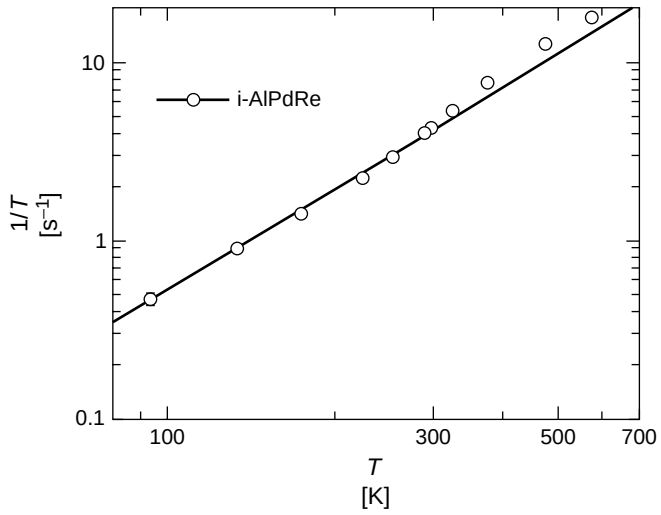

Figure 4 $1/T_1^{^{27}\mathrm{Al}}$ versus T in i-$Al_{70}Pd_{20}Re_{10}$. The solid line is a fit with equation (5)

the theoretical calculations indicated[13] an enhanced pseudogap at E_F by sp-d hybridization leading to a sharp DOS valley. The structures of the partial DOS $g_s(E)$ and $g_d(E)$ within the sharp DOS valley near E_F can be assumed as

$$g_s(E) = g_{0s} + g_{1s}|E - E_F|^{\varepsilon},$$
$$g_d(E) = g_{0d} + g_{1d}|E - E_F|^{\varepsilon} \tag{3}$$

with g_{0s} and g_{0d} as the residual DOS at E_F for 3s-band and d-bands, respectively.

K is obtained from equations (1) and (3) as

$$K = (\alpha_s g_{0s} + \alpha_d g_{0d}) + 2C(\varepsilon)(\alpha_s g_{1s} + \alpha_d g_{1d})(k_B T)^{\varepsilon}, \tag{4}$$

where $C(\varepsilon) = \int_0^{\infty} x^{\varepsilon} e^x/(1+e^x)^2 dx$. Using equations (2) and (3), $1/T_1$ is obtained as

$$\frac{1}{T_1} = k_B T[(\beta_s g_{0s}^2 + \beta_{ds} g_{0d}^2) + 4C(\varepsilon)(\beta_s g_{0s} g_{1s} + \beta_d g_{0d} g_{1d})(k_B T)^{\varepsilon}$$
$$+ 2C(2\varepsilon)(\beta_s g_{1s}^2 + \beta_{ds} g_{1d}^2)(k_B T)^{2\varepsilon}]. \tag{5}$$

At low temperature, equations (4) and (5) lead to the conventional temperature dependences where K is temperature independent and $1/T_1 \propto T$. As discussed above, however, equations (4) and (5) are not suitable for analyzing the low temperature K and $1/T_1$ data in QC alloys since the electron – electron interaction and weak localization are not included. At higher temperatures, equations (4) and (5) lead to $K \propto T^{\varepsilon}$ and $1/T_1 \propto T^{1+2\varepsilon}$. The power law $1/T_1 \propto T^2$ was observed in i-$Al_{70}Pd_{20}Re_{10}$ and i-$Al_{65}Cu_{20}Ru_{15}$ above 100 K suggesting that $\varepsilon = 1/2$.[17] Indeed, the fit of $1/T_1^{^{27}\mathrm{Al}}$ by equation (5) shows that $\varepsilon \approx 1/2$ (Figure 4). Since $1/T_1 \propto T^2$ is induced by the sharp DOS valley and is clearly obeyed up to 400 K, the width of the $\varepsilon = 1/2$ region in the sharp DOS valley should be at least as large as 25 meV.[17] The measured small residual $g(E)$ at E_F in i-$Al_{70}Pd_{20}Re_{10}$ and i-$Al_{65}Cu_{20}Ru_{15}$ agrees with the heat capacity measurements.[17] Since the NMR results at much higher temperature are complicated by atomic motion,[10] the DOS shape further away from E_F cannot be determined by NMR.

For $\varepsilon = 1/2$, equation (4) leads to a weak temperature dependence of K at high temperature. Indeed, $K^{^{27}\mathrm{Al}}$ was measured to follow such a weak temperature dependence in i-$Al_{70}Pd_{20}Re_{10}$ and i-$Al_{65}Cu_{20}Ru_{15}$.[10,17] Moreover, the measured temperature dependence of $K^{^{27}\mathrm{Al}}$ was found[17] to be correlated with that of $1/T_1^{^{27}\mathrm{Al}}$ as described by equations (4) and (5). The analysis of the temperature dependences of $K^{^{27}\mathrm{Al}}$ and $1/T_1^{^{27}\mathrm{Al}}$ indicate a strong effect of the core-polarization at Al sites that is consistent with the theoretical prediction of the strong sp-d hybridization in Al-based QC alloys containing intermediate transition metals.[12]

3.4 Comments on the Approximation Method Based on Taylor Expansion

An approximation method was used to describe the DOS variation near E_F for narrow d-bands and analyze the nonlinear temperature dependence of $1/T_1$ and the temperature dependence of K such as in Pt metal.[22] A similar approximation was used to analyze the nonlinear temperature dependence of $1/T_1$ in QC alloys.[10,19,21] Here we show that such approximation can often be insufficient and misleading in analyzing the effect of the DOS variation near E_F.

The approximation is based on the Taylor expansion of $g(E)$ at E_F^0 (E_F at $T = 0$) as

$$g(E) = g(E_F^0) + (E - E_F^0)g'(E_F^0) + \tfrac{1}{2}(E - E_F^0)^2 g''(E_F^0), \tag{6}$$

with $g'(E_F^0)$ and $g''(E_F^0)$ as the first and second derivatives of $g(E)$ to E at E_F^0, respectively. Because of the second term in equation (6), E_F could be temperature dependent if $g(E)$ is not symmetric about E_F^0. Define $\Delta E_F = E_F - E_F^0$, equation (6) can be rewritten as

$$g(E) = [g(E_F^0) + \Delta E_F g'(E_F^0) + \tfrac{1}{2}(\Delta E_F)^2 g''(E_F^0)] + (E - E_F)[g'(E_F^0) + \Delta E_F g''(E_F^0)] + \tfrac{1}{2}(E - E_F)^2 g''(E_F^0). \tag{7}$$

Using equation (7) and the conservation of electron density described by $\frac{d}{dT}[\int g(E) f(E) dE] = 0$, it is straightforward to obtain

$$\frac{d(\Delta E_F)}{dT}\left[g(E_F^0) + \Delta E_F g'(E_F^0) + \frac{1}{2}(\Delta E_F)^2 g''(E_F^0) + \frac{\pi^2}{6} g''(E_F^0)(k_B T)^2\right] = -\frac{\pi^2}{3}[g'(E_F^0) + \Delta E_F g''(E_F^0)]k_B^2\, T. \tag{8}$$

The derivatives of ΔE_F with T can be derived from equation (8) and the Taylor expansion of E_F can be calculated at $T = 0$ as

$$E_F = E_F^0 - \frac{\pi^2}{6}(k_B T)^2 \frac{g'(E_F^0)}{g(E_F^0)} + \frac{\pi^4}{72}(k_B T)^4 \frac{g'(E_F^0)}{g(E_F^0)} \times \left[2\frac{g''(E_F^0)}{g(E_F^0)} - \left(\frac{g'(E_F^0)}{g(E_F^0)}\right)^2\right] + 0(T^6). \tag{9}$$

For a symmetric $g(E)$ about $E = E_F^0$, $g'(E_F^0) = 0$ and E_F is temperature independent.

Using equations (1), (7), and (9), K can be calculated to the order of T^5 as

$$K \propto g(E_F^0)\left\{1 + \frac{\pi^2}{6}(k_BT)^2\left[\frac{g''(E_F^0)}{g(E_F^0)} - \left(\frac{g'(E_F^0)}{g(E_F^0)}\right)^2\right] + \frac{\pi^6}{60}(k_BT)^4\left(\frac{g'(E_F^0)}{g(E_F^0)}\right)^2\left[3\frac{g''(E_F^0)}{g(E_F^0)} - \left(\frac{g'(E_F^0)}{g(E_F^0)}\right)^2\right]\right\} + 0(T^6). \tag{10}$$

Using equations (2), (7), and (9), the calculated $1/T_1$ is given by

$$\frac{1}{T_1} \propto g^2(E_F^0)\left\{k_BT + \frac{\pi^2}{3}(k_BT)^3\frac{g''(E_F^0)}{g(E_F^0)} + \frac{\pi^6}{60}(k_BT)^5\frac{g''(E_F^0)}{g(E_F^0)}\left[7\frac{g''(E_F^0)}{g(E_F^0)} - 5\left(\frac{g'(E_F^0)}{g(E_F^0)}\right)^2\right]\right\} + 0(T^7). \tag{11}$$

As an approximation, equations (9), (10), and (11) are valid only if the second terms on the right hand side of these equations are much smaller than the corresponding first terms. This is exactly what was assumed in Refs.[10,19,21,22] in which only the first and second terms of these equations were included in the approximation. There, the measured $1/T_1$ in QC alloys were fitted with only the T and T^3 terms.[10,19,21] However, the fits of the $1/T_1$ data indicated that the contribution of the T^3 term is comparable or even larger than that of the T term within the investigated temperature range. In this case, equation (11) shows that the contribution of the T^5 term cannot be neglected and the expansion itself may not converge. Moreover, K should be dominated by the contribution of the T^2 and T^4 terms. Thus, the approximation implies a strong temperature dependence of K, in contrast to the observation of a weak temperature dependence of K.[10,17] Thus, the approximation is not valid for analyzing the measured $1/T_1$ in QC alloys. In general, it is not valid to use this approximation method to analyze $1/T_1$ that deviates significantly from $1/T_1 \propto T$.

4 THE ALIGNMENT ECHO TECHNIQUE FOR $I \geq 1$

NMR has made important contributions to the study of atomic and molecular motion in amorphous systems. However, NMR was rarely used to measure atomic motion in metallic glasses and metallic supercooled liquids, especially slow atomic motion. The reasons are twofold. First, the fast rate of crystallization upon heating in conventional metallic glasses and supercooled liquids does not allow sufficient time for most experimental approaches including NMR. Secondly, the longest timescale of atomic motion detectable by NMR is intrinsically limited by T_1 that is very short in typical metallic systems. Since BMGs exhibit excellent glass formability and remarkable thermal stability, a large temperature range becomes accessible for NMR up to temperatures significantly above T_g. This allows the experimental studies of the nature of glass transition and the nature of atomic motion in the supercooled liquid state near T_g. It was fortunate for NMR studies that the representative BMGs, $Zr_{41.5}Ti_{22.5}Cu_{22.5}Ni_{10}Be_{22.5}$ (vit1) and $Zr_{41.5}Ti_{22.5}Cu_{22.5}Ni_{10}$ $Be_{27.5}$ (vit4), contain Be where $T_1^{^9Be}$ is very long. This makes NMR detection of slow atomic motion feasible in both the glassy and deeply supercooled liquid states.[23–25]

The nuclear spin alignment echo technique (SAE) of ^{2}H ($I = 1$) has been used extensively for studying motion in polymers.[26] This technique was extended to the case of $I = 3/2$ in the study of translational atomic motion in BMGs using ^{9}Be NMR.[23–25] Later, ^{7}Li SAE was used in measuring ionic motion in electrolyte materials.[27] The ^{2}H SAE technique was described extensively in the literature.[26] A general treatment was given recently for $I = 1$ to 9/2.[23] Following the latter, assume that the truncated Hamiltonian of a nuclear spin system in the rotating frame consists of the Zeeman interaction (due to resonance off-set) and first-order electric quadrupole interaction given by

$$\hat{H} = \beta\hat{I}_z + \alpha\ (3\hat{I}_z^2 - \hat{I}^2) \tag{12}$$

where β is the shift relative to the rf frequency, α is proportional to the quadrupole resonance frequency.

The pulse sequence of SAE, $90^0 - \tau_1 - \theta_\phi - t - \theta'_{\phi'} - \tau_2-$, is applied with nonselective RF pulses with the time parameters chosen such that $\tau_1 < T_2 < t$. θ and θ' are the flipping angles of the second and third pulses, respectively, with ϕ and ϕ' as the corresponding phases with respect to the first pulse. Since atomic motion could occur during the diffusion time t, the values of α and β associated with a given nuclear spin during the time interval τ_1 are denoted as α_1 and β_1, respectively, and as α_2 and β_2, respectively, during the time interval τ_2. Since $t > T_2$, the spin density operator during t evolves into a diagonal density operator ($\hat{\rho}(t)$) represented by a linear combination of various nuclear spin orders (from the Zeeman order to $2I$th-rank spin order). The kth-rank spin order is proportional to the kth-rank zeroth-order irreducible tensor $A^{(k,0)}$ (see Table 1 in Ref.[23] for the explicit expressions of $A^{(k,0)}$ for $I = 1/2$ to 9/2). The signal appearing after the third pulse is given by[23]

$$S(\tau) = -\cos\phi_{\text{eff1}}e^{i\phi_{\text{eff2}}}\sum_{\text{odd}k} f_k(\theta, \alpha_1\tau_1)\, f_k(\theta', -\alpha_2\tau_2) + i\sin\phi_{\text{eff1}}e^{i\phi_{\text{eff2}}}\sum_{\text{even}k} f_k(\theta, \alpha_1\tau_1)\, f_k(\theta', -\alpha_2\tau_2), \tag{13}$$

where $\phi_{\text{eff1}} = \phi + \beta_1\tau_1$, $\phi_{\text{eff2}} = \phi' + \beta_2\tau_2$, and $f_k(\theta, \alpha\tau)$ is the coefficient given by

$$f_k(\theta, \alpha\tau) = \text{Trace}(e^{-i\theta I_y}e^{-3i\alpha I_z^2\tau}\hat{I}_x e^{3i\alpha I_z^2\tau}e^{i\theta I_y}A^{(k,0)}) \quad (\text{odd } k)$$
$$f_k(\theta, \alpha\tau) = \text{Trace}(e^{-i\theta I_y}e^{-3i\alpha I_z^2\tau}\hat{I}_y e^{3i\alpha I_z^2\tau}e^{i\theta I_y}A^{(k,0)}) \quad (\text{even } k). \tag{14}$$

Thus, $f_k(\theta, \alpha_1\tau_1)$ is the coefficient of the kth-rank nuclear spin order during t. For example, $f_1(\theta, \alpha_1\tau_1)$ and $f_2(\theta, \alpha_1\tau_1)$ correspond to the Zeeman and quadrupole order, respectively. It is of note that $\cos\phi_{\text{eff1}}e^{i\phi_{\text{eff2}}}f_k(\theta, \alpha_1\tau_1)\, f_k(\theta', -\alpha_2\tau_2)$ (odd k) and $\sin\phi_{\text{eff1}}e^{i\phi_{\text{eff2}}}f_k(\theta, \alpha_1\tau_1)\, f_k(\theta', -\alpha_2\tau_2)$ (even k) are single-particle correlation functions connecting the local environments experienced by a nuclear spin during τ_1 and τ_2.

For an ensemble of nuclear spins, an alignment echo forms at $\tau_2 = \tau_1$ if no motion occurs during t. On the other hand, atomic motion may induce the change of the local environments and destroy the single-particle correlation leading to the alignment echo decay. The kth-rank nuclear spin order created during t could decay as well during t with a decay rate of W_k induced by the NSLR mechanisms. Thus, following equation (13) the SAE echo height is described by

$$S_{\text{echo}}(t) = -\sum_{\text{odd}k} \mathrm{e}^{-W_k t}\langle \cos\phi_{\text{eff1}} \mathrm{e}^{i\phi_{\text{eff2}}} f_k(\theta, \alpha_1\tau_1) f_k(\theta', -\alpha_2\tau_2)\rangle + i\sum_{\text{even}k} \mathrm{e}^{-W_k t}\langle \sin\phi_{\text{eff1}} \mathrm{e}^{i\phi_{\text{eff2}}} f_k(\theta, \alpha_1\tau_1) f_k(\theta', -\alpha_2\tau_2)\rangle \tag{15}$$

with $\langle\rangle$ denoting the ensemble average. In metallic glasses, NSLR is usually dominated by the coupling between the nuclear spins and unpaired conduction electron spins. In this case, the evolution of $\hat{\rho}(t)$ can be described by:

$$\frac{d\hat{\rho}(t)}{dt} = J_1[[\hat{\rho}(t) - \hat{\rho}_0, \hat{I}_+], \hat{I}_-], \tag{16}$$

with J_1 as a constant related to the magnetic properties of the spin system and $\hat{\rho}_0$ as the density operator at thermal equilibrium. Using the following identity

$$[[A^{(k,0)}, \hat{I}_+], \hat{I}_-] = k(k+1)A^{(k,0)}, \tag{17}$$

it is straightforward to obtain $\hat{\rho}(t)$ as

$$\hat{\rho}(t) = \hat{\rho}_0 + \sum_{k=0}^{2I} C_k \mathrm{e}^{-k(k+1)t/2T_1} A^{(k,0)} \tag{18}$$

with C_k as the coefficients. Thus, $W_k = k(k+1)/2T_1$ which is true for other magnetic relaxation mechanisms as well. Since W_k varies with k, it is easier to extract the information about motion when only singular rank of nuclear spin order is created during t. In this case the $\mathrm{e}^{-W_k t}$ factor of the chosen rank can be easily separated from the motion-related single-particle correlation functions by measuring T_1.

In the presence of both a α distribution $\delta\alpha$ and a β distribution $\delta\beta$, it is in general difficult to produce a singular rank of spin order. If $\delta\beta \ll \delta\alpha$, τ_1 can be chosen such that $\delta\beta\tau_1 \ll \pi/2 \ll \delta\alpha\tau_1$. Then, odd-ranked spin orders can be created separately from even-ranked spin orders by choosing $\phi = 0°$ (180°) for creating odd-ranked spin orders and $\phi = 90°$ (270°) for creating even-ranked spin orders. Therefore, by selecting proper ϕ it is possible to produce pure Zeeman order or quadrupole order for $I = 1$. For $I = 3/2$, pure quadrupole order can be produced by choosing $\phi = 90°$ (270°). On the other hand, the Zeeman order and octupole order cannot be separated. Equation (15) shows that the contribution of certain undesired nuclear spin orders can be suppressed also by the choice of the θ or θ' values based on the value of $f_k(\theta, \alpha\tau)$.

In Ref.[23] $f_k(\theta, \alpha\tau)(k = 1, 2, \ldots, 2I)$ were derived explicitly based on the equation

$$\begin{aligned}\mathrm{e}^{-i\alpha\hat{I}_z^2}\hat{I}_\pm \mathrm{e}^{i\alpha\hat{I}_z^2} = \hat{I}_\pm[1 \quad \cos 2\alpha \quad \cdots \quad \cos(2I-1)\alpha] \\ \times \begin{bmatrix} 1 & 1 & \cdots & 1 \\ 0 & 2^2 & \cdots & (2I-1)^2 \\ \vdots & \vdots & \vdots & \vdots \\ 0 & 2^{2I-1} & \cdots & (2I-1)^{2I-1} \end{bmatrix} \begin{bmatrix} 1 \\ (1 \pm 2\hat{I}_z)^2 \\ \vdots \\ (1 \pm 2\hat{I}_z)^{2I-1} \end{bmatrix} \\ - i\hat{I}_\pm[\sin 2\alpha \quad \sin 4\alpha \quad \cdots \quad \sin\ (2I-1)\alpha] \\ \times \begin{bmatrix} 2 & 4 & \cdots & (2I-1) \\ 2^3 & 4^3 & \cdots & (2I-1)^3 \\ \vdots & \vdots & \vdots & \vdots \\ 2^{2I-2} & 4^{2I-2} & \cdots & (2I-1)^{2I-2} \end{bmatrix} \begin{bmatrix} (1 \pm 2\hat{I}_z) \\ (1 \pm 2\hat{I}_z)^3 \\ \vdots \\ (1 \pm 2\hat{I}_z)^{2I-2} \end{bmatrix}\end{aligned} \tag{19}$$

for half-integer I ($I = 3/2$, 5/2, 7/2, 9/2) and on the equation

$$\begin{aligned}\mathrm{e}^{-i\alpha\hat{I}_z^2}\hat{I}_\pm \mathrm{e}^{i\alpha\hat{I}_z^2} = \hat{I}_\pm[\cos\alpha \quad \cos 3\alpha \quad \cdots \quad \cos\ (2I-1)\alpha] \\ \times \begin{bmatrix} 1 & 1 & \cdots & 1 \\ 1 & 3^2 & \cdots & (2I-1)^2 \\ \vdots & \vdots & \vdots & \vdots \\ 1 & 3^{2I-2} & \cdots & (2I-1)^{2I-2} \end{bmatrix} \\ \times \begin{bmatrix} 1 \\ (1 \pm 2\hat{I}_z)^2 \\ \vdots \\ (1 \pm 2\hat{I}_z)^{2I-2} \end{bmatrix} \\ - i\hat{I}_\pm[\sin\alpha \quad \sin 3\alpha \quad \cdots \quad \sin\ (2I-1)\alpha] \\ \times \begin{bmatrix} 1 & 3 & \cdots & (2I-1) \\ 1 & 3^3 & \cdots & (2I-1)^3 \\ \vdots & \vdots & \vdots & \vdots \\ 1 & 3^{2I-1} & \cdots & (2I-1)^{2I-1} \end{bmatrix} \begin{bmatrix} (1 \pm 2\hat{I}_z) \\ (1 \pm 2\hat{I}_z)^3 \\ \vdots \\ (1 \pm 2\hat{I}_z)^{2I-1} \end{bmatrix}\end{aligned} \tag{20}$$

for integer I ($I = 1$, 3). It is interesting to note that by using

$$\mathrm{e}^{-i\alpha\hat{I}_z^2}\hat{I}_\pm^n \mathrm{e}^{i\alpha\hat{I}_z^2} = \mathrm{e}^{-in(n-1)\alpha} I_\pm^{n-1}(\mathrm{e}^{-in\alpha\hat{I}_z^2}\hat{I}_\pm \mathrm{e}^{in\alpha\hat{I}_z^2}) \tag{21}$$

and equations (19) and (20), a general formula for $\mathrm{e}^{-i\alpha\hat{I}_z^2}\hat{I}_\pm^n \mathrm{e}^{i\alpha\hat{I}_z^2}$ can be easily obtained.

For $I = 1$, $f_k(\theta, \alpha\tau)$ are given by

$$\begin{aligned} f_1(\theta, \alpha\tau) &= -\sqrt{2}\sin\theta\cos 3\alpha\tau; \\ f_2(\theta, \alpha\tau) &= \sqrt{\frac{3}{2}}\sin 2\theta \sin 3\alpha\tau. \end{aligned} \tag{22}$$

Both $f_1(\theta, \alpha\tau)$ and $f_2(\theta, \alpha\tau)$ are suitable for detecting motion, although the maximized signal from $f_1(\theta, \alpha\tau)$ (Zeeman order) is larger. For $I = 3/2$,

$$\begin{aligned} f_1(\theta, \alpha\tau) &= -\frac{1}{\sqrt{5}}\sin\theta(2 + 3\cos 6\alpha\tau); \\ f_2(\theta, \alpha\tau) &= -\frac{3}{2}\sin 2\theta \sin 6\alpha\tau; \\ f_3(\theta, \alpha\tau) &= -\frac{3}{2\sqrt{5}}\sin\theta\ (5\cos^2\theta - 1)(1 - \cos 6\alpha\tau). \end{aligned} \tag{23}$$

It is possible to create a pure Zeeman order by choosing $\phi = 0°$ (180°) and $5\cos^2\theta = 1$ or $5\cos^2\theta' = 1$. In this case

$$S_{\text{echo}}(t) \propto \mathrm{e}^{-t/T_1}\langle f_1(\theta, \alpha_1\tau_1) f_1(\theta', -\alpha_2\tau_2)\rangle \propto 4\mathrm{e}^{-t/T_1} + \frac{9}{2}\mathrm{e}^{-t/T_1}\langle\cos 6(\alpha_1 - \alpha_2)\tau_1\rangle \quad (24)$$

Since motion affects the second term but not the first, almost half the resonance signal does not change after motion. Thus, the existence of two terms with different decay rates complicates the analysis. On the other hand, a pure quadrupole order can be created by choosing $\phi = 90°$ (270°). Then, the SAE echo height is given by

$$S_{\text{echo}}(t) \propto \frac{9}{8}\mathrm{e}^{i\phi'}\mathrm{e}^{-W_2 t}\sin 2\theta \sin 2\theta' \langle\cos 6(\alpha_1 - \alpha_2)\tau_1\rangle. \quad (25)$$

The signal is maximized at $\theta = \theta' = 45°$. For $I = 5/2$,

$$f_1(\theta, \alpha\tau) = -\frac{1}{\sqrt{70}}(9 + 16\cos 6\alpha\tau + 10\cos 12\alpha\tau)\sin\theta;$$

$$f_2(\theta, \alpha\tau) = \frac{\sqrt{3}}{2\sqrt{7}}(4\sin 6\alpha\tau + 5\sin 12\alpha\tau)\sin 2\theta;$$

$$f_3(\theta, \alpha\tau) = -\frac{1}{2\sqrt{5}}(-3 - 2\cos 6\alpha\tau + 5\cos 12\alpha\tau) \times \sin\theta\ (5\cos^2\theta - 1);$$

$$f_4(\theta, \alpha\tau) = \frac{5}{8\sqrt{7}}(-2\sin 6\alpha\tau + \sin 12\alpha\tau)\sin 2\theta\ (1 + 7\cos 2\theta);$$

$$f_5(\theta, \alpha\tau) = -\frac{5}{64\sqrt{7}}(3 - 4\cos 6\alpha\tau + 12\cos 12\alpha\tau) \times \sin\theta(15 + 28\cos\theta + 21\cos 4\theta). \quad (26)$$

All $f_k(\theta, \alpha\tau)$ associated with odd-ranked nuclear spin orders contain a constant term as well as motion-related terms. As discussed above, this complicates the analysis when measuring the single-particle correlation functions of these spin orders. On the other hand, by choosing $\phi = 90°$ (270°) and $1 + 7\cos 2\theta = 0$ or $1 + 7\cos 2\theta' = 0$, a pure quadrupole order can be created. The SAE echo height is then given by

$$S_{\text{echo}}(t) \propto \frac{6}{7}\mathrm{e}^{i\phi'}\mathrm{e}^{-W_2 t}\sin 2\theta' \sin 2\theta' \times \left\langle\cos 6(\alpha_1 - \alpha_2)\tau_1 + \frac{25}{16}\cos 12(\alpha_1 - \alpha_2)\tau_1\right\rangle \quad (27)$$

5 DETECTION OF SLOW ATOMIC MOTION IN BULK METALLIC GLASSES BY NMR OF ^{9}BE

The ^{9}Be spectra of vit1 and vit4 consist of a narrow central line and a broad line (Figure 5). The broad line, with a field-independent $\Delta\nu_{1/2}$ of (100 ± 10) kHz, is associated with the satellite transitions ($3/2 \leftrightarrow 1/2$ and $-1/2 \leftrightarrow -3/2$) broadened by the first order quadrupole interaction. The central line, with $\Delta\nu_{1/2}$ as (6.1 ± 0.2) kHz at 9.4 T and (3.6 ± 0.1) kHz at 4.7 T, is associated with the central transition ($1/2 \leftrightarrow -1/2$) broadened by the Zeeman interaction distribution. The $K^{^9\text{Be}}$ is negligible and $T_2^{^9\text{Be}}$ about 1.5 ms.[24] Dominated by Korringa relaxation, $1/T_1^{^9\text{Be}}$ is[24] proportional to T with

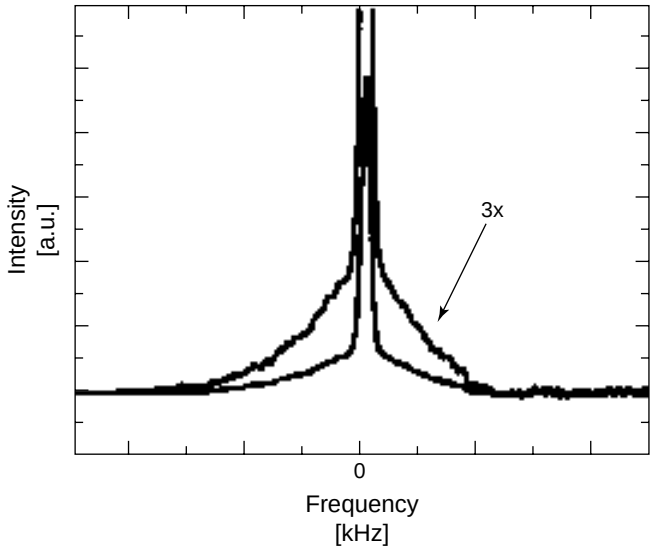

Figure 5 The ^{9}Be spectra of vit1 at 9.4 T. The broad line is shown more clearly by expanding the vertical scale by a factor of 3

$(TT_1)^{-1} = 0.00105\,\text{K}^{-1}\,\text{s}^{-1}$. According to equation (18), the decay rate of the ^{9}Be quadrupole order is $3/T_1$ as demonstrated experimentally.[23]

The ^{9}Be SAE pulse sequence is: $90^0_x - \tau_1 - 45^0_{\pm y} - t - 45^0_{\phi'} - \tau_2 -$ with a short τ_1 $(6 - 15\,\mu\text{s})$ to create a pure quadrupole order. Following equation (26), the SAE echo height is proportional to $f(t) =< \cos(\omega_1 - \omega_2)\tau_1 > \mathrm{e}^{-3t/T_1}$. $\omega_1 = 6\alpha_1$ and $\omega_2 = 6\alpha_2$, varying over a range of $2\pi \times 100$ kHz in vit1 and vit4, are determined by the truncated quadrupole interactions experienced by the spin during τ_1 and τ_2, respectively. The featureless broad line shown in Figure 5 indicates that the characteristic powder pattern of the observed ^{9}Be spectrum in Be metal is smeared out in vit1 and vit4. It suggests a random distribution of quadrupole interaction, which is crucial for SAE to be effective in detecting motion. In glasses and supercooled liquids, the quadrupole interaction with respect to B_0 differs from site to site because of the disordered structure. Thus, single-atom jumps are expected to change ω randomly within its range which induces a reduction of $f(t)$. On the other hand, SAE is not sensitive to collective motion since the quadrupole interactions at Be sites change very little under collective translational motion involving Be atoms and most of their nearest neighbors. Also, SAE is not sensitive to restricted collective rotational motion with small rotation angle because $|(\omega_1 - \omega_2)|\tau_1 \ll 1$.

Fast data acquisition is crucial for studying thermal dynamics in metastable materials such as metallic supercooled liquids. In Refs.[24,25] the pulse-spin locking technique was used to improve S/N. Following the ^{9}Be SAE pulse sequence, a train of 90° pulses are applied; the full sequence is $90^0_x - \tau_1 - 45^0_{\pm y} - t - 45^0_{\phi'} - 2\tau_1 - 90^0_{\phi'} - 2\tau_1 - 90^0_{\phi'} - \cdots - 90^0_{\phi'} -$. Here, a train of echoes with the same origin and feature as the first alignment echo are detected and all echoes are accordingly summed up. The full sequence for measuring $1/T_1$, using the saturation recovery method with a comb and quadrupole echo detection sequence, is '*comb*' $- t - 90^0_x - \tau - 90^0_{\pm y} - 2\tau - 90^0_{\pm y} - 2\tau - 90^0_{\pm y} \cdots - 90^0_{\pm y} -$. Using pulse-spin locking,

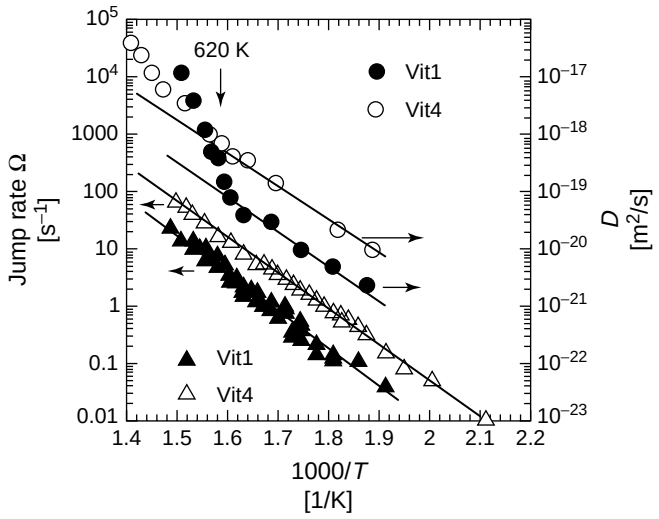

Figure 6 The temperature dependence of the atomic jump rate Ω and the diffusivity D in vit1 and vit4. D (scale on the right) and Ω (scale on the left) are plotted versus $1000/T$. A kink at 620 K, which is around T_g, is observed in the $D(T)$ curves in both vit1 and vit4. This kink is absent in the $\Omega(T)$ curves that follow the same Arrhenius behavior in both the supercooled liquid and glassy state

each ^{9}Be SAE decay curve and $1/T_1$ can be measured in several minutes. This enables the isothermal annealing study and the first NMR study in supercooled metallic liquids.

The ^{9}Be SAE echo decay curve measured at 620 K is shown in Figure 6 that is fitted by a single-exponential function $f(t) = e^{-t/T_{QE}}$. Such behavior is expected for atomic motion causing random changes of ω, where $1/T_{QE} = 3/T_1 + \Omega$ with Ω as the atomic jump rate. The observed single-exponential decay is inconsistent with constrained jumps between neighboring sites such as double-well potentials. It is consistent with unconstrained Be hopping assisted by thermal fluctuation of spread-out free volume.[24] In vit1 and vit4, the measured Ω follows Arrhenius behavior $\Omega(T) = \Omega_0 e^{-E_a/k_B T}$ with the fitted activation energy $E_a = (1.2 \pm 0.15)$ eV. Below 620 K, no annealing-time dependence of Ω is observed by SAE indicating that the measured Ω is intrinsic for the glassy state. The SAE measurements inferred that the Be diffusion process is via single-atom hopping.[24] In deeply supercooled liquids, the combine SAE and diffusion measurements indicated that two diffusion processes contribute to the long-range Be transport.[25] One is single-atom hopping. The other process is collective motion involving most of the nearest neighbors of Be atoms.

6 RELATED ARTICLES IN VOLUMES 1–8

Amorphous Materials, Volume 2; Deuterium NMR in Solids, Volume 3; Diffusion in Solids, Volume 3; Incommensurate Systems, Volume 4; Metals: Pure & Alloyed, Volume 5; Quadrupolar Nuclei in Glasses, Volume 6; Quadrupolar Nuclei in Solids, Volume 6; Quadrupolar Transition Metal & Lanthanide Nuclei, Volume 6; Relaxation Theory for Quadrupolar Nuclei, Volume 6; Slow & Ultraslow Motions in Biology, Volume 7; Ultraslow Motions in Solids, Volume 8.

7 REFERENCES

1. C. Janot, 'Quasicrystals: A Primer', 2nd edn., University Press: Oxford, 1994.
2. S. J. Poon, *Adv. Phys.*, 1992, **41**, 303.
3. A. L. Greer, *Science*, 1995, **267**, 1974.
4. W. L. Johnson, *Mat. Sci. Forum*, 1996, **225**, 35.
5. C. Li, J. Saida, M. Matsushita, and A. Inoue, *Phil. Mag. Lett.*, 2000, **80**, 621.
6. W. W. Warren, Jr., H. S. Chen, and J. J. Hauser, *Phys. Rev. B*, 1985, **32**, 7614.
7. A. Shastri, F. Borsa, D. R. Torgeson, J. E. Shield, and A. I. Goldman, *Phys. Rev. B*, 1994, **50**, 4224.
8. A. Shastri, F. Borsa, D. R. Torgeson, and A. I. Goldman, *Phys. Rev. B*, 1994, **50**, 15 651.
9. J. Apih, M. Klanjšek, D. Rau, and J. Dolinšek, *Phys. Rev. B*, 2000, **61**, 11 213.
10. E. A. Hill, T. C. Chang, Y. Wu, S. J. Poon, F. S. Pierce, and Z. M. Stadnik, *Phys. Rev. B*, 1994, **49**, 8615.
11. J. Dolinšek, B. Ambrosini, P. Vonlanthen, J. L. Gavilano, M. A. Chernikov, and R. Ott, *Phys. Rev. Lett.*, 1998, **81**, 3671.
12. J. Delahaye, J. P. Brison, and C. Berger, *Phys. Rev. Lett.*, 1998, **81**, 4204.
13. G. T. de Laissardière, D. Mayou, and D. N. Manh, *Europhys. Lett.*, 1993, **21**, 25.
14. G. T. de Laissardière and T. Fujiwara, *Phys. Rev. B*, 1994, **50**, 5999.
15. F. Hippert, L. Kandel, Y. Calvayrac, and B. Dubost, *Phys. Rev. Lett.*, 1992, **69**, 2086.
16. A. Shastri, D. B. Baker, M. S. Conradi, F. Borsa, and D. R. Torgeson, *Phys. Rev. B*, 1995, **52**, 12 681.
17. X.-P. Tang, E. A. Hill, S. K. Wonnell, S. J. Poon, and Y. Wu, *Phys. Rev. Lett.*, 1997, **79**, 1070.
18. J. L. Gavilano, B. Ambrosini, P. Vonlanthen, M. A. Chernikov, and H. R. Ott, *Phys. Rev. Lett.*, 1997, **79**, 3058.
19. J. Dolinšek, M. Klanjšek, J. Apih, A. Smontara, J. C. Lasjaunias, J. M. Dubois, and S. J. Poon, *Phys. Rev. B*, 2000, **62**, 8862.
20. X.-P. Tang, L. Wu, P. Ryan, F. Tsui, and Y. Wu, *Phys. Rev. B.*, submitted.
21. J. Apih, O. Plyushch, M. Klanjšek, and J. Dolinšek, *Phys. Rev. B*, 1999, **60**, 14 695.
22. Y. Yafet and V. Jaccarino, *Phys. Rev. A*, 1964, **133**, 1630.
23. X.-P. Tang and Y. Wu, *J. Magn. Reson.*, 1998, **133**, 155.
24. X.-P. Tang, R. Busch, W. L. Johnson, and Y. Wu, *Phys. Rev. Lett.*, 1998, **81**, 5358.
25. X.-P. Tang, U. Geyer, R. Busch, W. L. Johnson, and Y. Wu, *Nature*, 1999, **402**, 160.
26. H. W. Spiess, *J. Chem. Phys.*, 1980, **72**, 6755.
27. R. Bohmer, T. Jorg, F. Qi, and A. Titze, *Chem. Phys. Lett.*, 2000, **316**, 419.

Biographical Sketches

Xiaoping Tang, *b* 1966. B.Sc., Beijing University, PRC, 1987, Ph.D., 1996, Physics, Northwestern University, USA. Introduced to NMR by William P. Halperin studying vortex dynamics of high-T_c superconductors and ferroelectricity. Since 1996, worked on quasicrystals, metallic glasses, and carbon nanotubes with Yue Wu at UNC-Chapel Hill.

Yue Wu, *b* 1959. B.Sc., 1983, Ph.D., 1987, Physics, University of Leuven, Belgium. Postdoctoral research with Alexander Pines at Berkeley 1988–l991. Faculty in the Department of Physics and Astronomy at University of North Carolina in Chapel Hill 1991-present. Research interests: carbon nanotubes, metallic glasses, quasicrystals, and amorphous silicon.

Ferroelectrics and Proton Glasses

Robert Blinc

University of Ljubljana, Ljubljana, Slovenia

1	Introduction	1
2	Inhomogeneous Ferroelectrics and Proton Glasses	1
3	NMR in Homogeneous Ferroelectrics and Antiferroelectrics in the Fast Motion Regime	3
4	NMR in the Slow and Intermediate Motion Regime	8
5	NMR in Proton and Deuteron Glasses	9
6	NMR Determination of Order Parameters in Inhomogeneous Ferroelectrics	12
7	Related Articles	13
8	References	13

1 INTRODUCTION

Conventional methods of crystal structure determination such as X-ray and neutron scattering yield the unit cell structure averaged over space and time. While the knowledge of such a space and time averaged structure is sufficient in most systems this is not the case in inhomogeneous- or order–disorder-type ferroelectrics and proton glasses where local deviations from the averaged structure determine the specific properties of these systems. 1D and 2D NMR of nuclei with a nonzero quadrupole coupling or chemical shift tensor interaction as well as NQR provide here a unique tool for the determination of the local atomic structure and dynamics which is unobtainable by other techniques.

In the fast motion regime, $\omega\tau \ll 1$, the nucleus at site i 'sees' the time averaged value of the quadrupole coupling or chemical shift tensor interaction so that[1]

$$\omega_i = \omega_0 + \omega_1\langle\eta_i\rangle;\ \langle\eta_i\rangle \neq 0 \quad T < T_c \tag{1a}$$

whereas

$$\omega_i = \omega_0;\ \langle\eta_i\rangle = 0 \quad T > T_c \tag{1b}$$

Here $\langle\eta_i\rangle$ is the time averaged value of the long-range order parameter at site i. It is $\langle\eta_i\rangle$ which is zero above T_c and non-zero below T_c.

Close to the phase transition temperature T_c, the spin-lattice relaxation rate will be determined by the order parameter fluctuations[1]

$$T_1^{-1} \propto \sum_{\boldsymbol{q}} \int_{-\infty}^{\infty} \langle\delta\eta(\boldsymbol{q}, 0)\delta\eta(\boldsymbol{q}, t)e^{i\omega t}\, dt \tag{2a}$$

where $\delta\eta(\boldsymbol{q}, t) = \eta(\boldsymbol{q}, t) - \langle\eta(\boldsymbol{q}, t)\rangle$ and $\langle \ldots \rangle$ denotes the ensemble average.

Applying the fluctuation dissipation theorem, equation (3) can be rewritten as[1]

$$T_1^{-1} \propto \sum_{\boldsymbol{q}} \frac{\chi(\boldsymbol{q}, 0)\tau(\boldsymbol{q})}{1 + \omega^2\tau(\boldsymbol{q})^2} \tag{2b}$$

where $\chi(\boldsymbol{q}, 0)$ is the wave vector dependent static susceptibility of the order parameter and $\tau(\boldsymbol{q})$ is the corresponding wave vector dependent correlation time.[1] For the Ising model one finds

$$\chi(\boldsymbol{q}) = \frac{\chi(\boldsymbol{q} = 0, 0)}{1 + \boldsymbol{q}^2\xi^2} \tag{3a}$$

and

$$\tau(\boldsymbol{q}) = \frac{\tau(\boldsymbol{q} = 0)}{1 + \boldsymbol{q}^2\xi^2} \tag{3b}$$

where

$$\tau(\boldsymbol{q} = 0) \propto \chi(\boldsymbol{q} = 0) \propto \frac{C}{T - T_c}; \quad T > T_c \tag{3c}$$

and ξ is the correlation length, which diverges at T_c. In the limit $\omega\tau \ll 1$ T_1^{-1} thus exhibits a critical behavior near T_c, while for $\omega\tau \gg 1$ T_1^{-1} should stay nearly constant. Another point to be stressed is that in the slow motion regime the nucleus 'sees' the instantaneous value of the order parameter and not the time averaged value.

2 INHOMOGENEOUS FERROELECTRICS AND PROTON GLASSES

Ferroelectric and antiferroelectric phase transitions[1] are characterized by:

1. the breaking of a discrete symmetry group at the paraelectric to ferroelectric or antiferroelectric transition;
2. the appearance of a long-range order parameter below T_c—the spontaneous polarization P in ferroelectrics or the sublattice polarization $P_a = -P_b$ in antiferroelectrics;
3. the critical slowing down of the order parameter dynamics $\tau(\boldsymbol{q}_{crit}) \to \infty$ as $T \to T_c$ from above or below.

The breaking of the symmetry of the high temperature paraelectric phase is the result of the condensation of a polar soft phonon or a—usually overdamped—soft pseudospin wave mode, the frequency of which increases with decreasing temperature in the high-temperature phase and vanishes at T_c. The frozen out eigenvector of the soft mode represents the order parameter of the transition. In ferroelectrics the condensation of the soft mode occurs at the Brillouin zone center, whereas it occurs in antiferroelectrics at the Brillouin zone boundary.

The free energy of a ferroelectric with a one-component order parameter has a single minimum at $P = 0$ at $T > T_c$ and two minima at $+P$ and $-P$ below T_c corresponding to oppositely polarized domains [Figure 1(a)].

Solid solutions of ferroelectric (FE) and antiferroelectric (AFE) crystals form in the intermediate concentration range $x_{FE} \leq x \leq x_{AFE}$ (Figure 2) a pseudospin-like dipolar glassy phase where no macroscopic symmetry breaking takes place

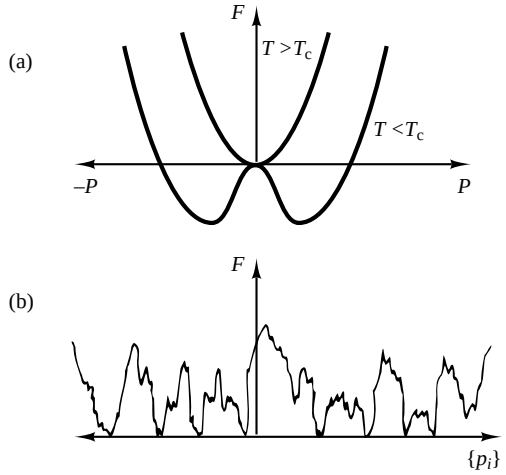

Figure 1 Free energy surface in (a) a homogeneous ferroelectric and (b) a deuteron pseudospin glass

at any temperature and no long range order parameter appears. Instead we have a random local freeze-out of the dipoles and possibly an ergodic–nonergodic transition. The existence of the glassy phase is due to randomly competing ferroelectric and antiferroelectric interactions and the resulting random frustration of the system. The free energy surface of such a system is rough and fractal-like and exhibits a large number of nearly degenerate minima separated by high potential barriers[2] [Figure 1(b)]

In the concentration range $0 \leq x \leq x_{\mathrm{FE}}$ and $x_{\mathrm{AFE}} \leq x \leq 1$ (Figure 2) we have an inhomogeneous ferroelectric and antiferroelectric phase, respectively, where long range order and glassy order coexist at $T \neq 0$.

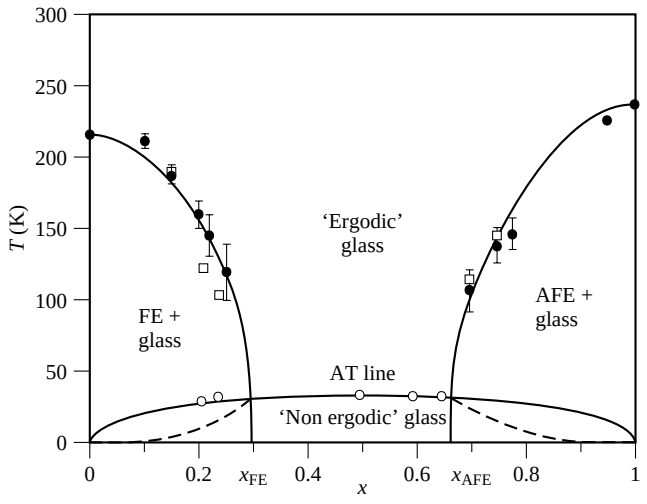

Figure 2 Phase diagram[5] of the ferroelectric solid solution $Rb_{1-x}(ND_4)_xD_2PO_4$ which forms a deuteron glass in the intermediate concentration range $x_{\mathrm{FE}} \leq x \leq x_{\mathrm{AFE}}$. Also shown are the inhomogeneous ferroelectric and inhomogeneous antiferroelectric regions for $0 \leq x \leq x_{\mathrm{FE}}$ and $x_{\mathrm{AFE}} \leq x \leq 1$. The solid lines are calculated from the random bond–random field pseudospin Ising model. Also shown is the Almeida–Thouless (AT) line separating the ergodic from the nonergodic glassy phase

The local dipolar structure of the above phases can be characterized by a local polarization distribution function,[3]

$$W(p) = \frac{1}{N}\sum_i \delta(p - \langle S^z\rangle_i) \tag{4}$$

where the pseudospin $S_i^z = \pm 1$ describes the two orientational states of the dipole at site i, and the brackets $\langle \ldots \rangle$ stand for the thermal average. In a homogeneous ferroelectric the first moment of $W(p)$,

$$P = \int W(p)p\,\mathrm{d}p \neq 0 \quad T < T_{\mathrm{c}} \tag{5a}$$

$$P = 0 \quad T > T_{\mathrm{c}} \tag{5b}$$

is the spontaneous polarization

$$P = \frac{1}{N}\sum_i \langle S_i^z\rangle \tag{5c}$$

which is different from zero for $T < T_{\mathrm{c}}$ and zero for $T > T_{\mathrm{c}}$.

In a homogeneous ferroelectric

$$W(p) = \delta(p - P) \tag{5d}$$

and the second moment of $W(p)$ is zero,

$$\tilde{q} = q - P^2 = \int W(p)p^2\,\mathrm{d}p - P^2 = 0 \tag{5e}$$

In a proton or deuteron dipolar glass the first moment of $W(p)$ is zero as there is no long range order,

$$P = \int W(p)p\,\mathrm{d}p = 0 \tag{6a}$$

but the second moment of $W(p)$ is different from zero,

$$q = \int W(p)p^2\,\mathrm{d}p \neq 0 \tag{6b}$$

Here, q is just the well known Edwards–Anderson glass order parameter which is also defined[2] as

$$q = \lim_{t\to\infty}\lim_{N\to\infty}\frac{1}{N}\sum_i \langle S_i^z(0)S_i^z(t)\rangle \tag{6c}$$

If there are no random fields present, we have a paraelectric–glass transition[3] at T_{g}:

$$q = 0 \quad T > T_{\mathrm{g}} \tag{7a}$$

$$q \neq 0 \quad T < T_{\mathrm{g}} \tag{7b}$$

In the presence of a random field, which is conjugate to this glass order parameter, $q \neq 0$ at all temperatures.[3,4] We have, however, at lower temperatures an ergodic–nonergodic transition below the Almeida–Thouless line in the random field variance–temperature plane where the pseudospin glass susceptibility, as well as the longest glass relaxation time,

diverge.[2,5] Here the replica symmetry of the 'ergodic' glassy phase is broken[2] and instead of a single order parameter q we have an infinite number of order parameters represented by the order parameter function[2] $q(x)$.

In an inhomogeneous ferroelectric, on the other hand, both

$$P \neq 0 \tag{8a}$$

and

$$\tilde{q} = q - P^2 \neq 0 \tag{8b}$$

The local polarization distribution function $W(p)$ is reflected in the inhomogeneous NMR frequency spectrum $f(\omega)$ via

$$f(\omega)\,\mathrm{d}\omega = W(p)\,\mathrm{d}p \tag{9}$$

A knowledge of the inhomogeneous NMR frequency spectrum $f(\omega)$, obtainable by 2D 'separation of interactions' NMR, and the relationship $\omega = \omega(p)$ thus enables one to determine $W(p)$ and all its moments. This is of crucial importance in glasses and inhomogeneous ferroelectrics and antiferroelectrics.

3 NMR IN HOMOGENEOUS FERROELECTRICS AND ANTIFERROELECTRICS IN THE FAST MOTION REGIME

3.1 Deuteron NMR and Relaxation

In hydrogen-bonded ferroelectrics and antiferroelectrics the O–H···O bonds are of the double-well type (Figure 3) and are the main reversible dipoles in the structure. The two positions of the proton ($I = \frac{1}{2}$) or respectively deuteron ($I = 1$) in this limit can be represented by a pseudospin $S^z = \pm 1$. The quadrupole perturbed NMR frequency of the deuteron ω_i changes when the deuteron is transferred from the 'left' to the 'right' position, O–H···O ↔ O···H–O, in the double-well potential:

$$\omega_i = \omega_0 + \omega_1 S_i^z(t) \tag{10a}$$

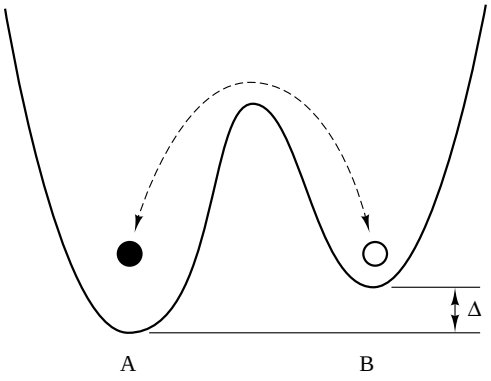

Figure 3 Double-well O–H···O hydrogen bond potential in hydrogen-bonded ferroelectrics. The two positions of the proton or deuteron in this potential can be described by a pseudospin $S^z = \pm 1$

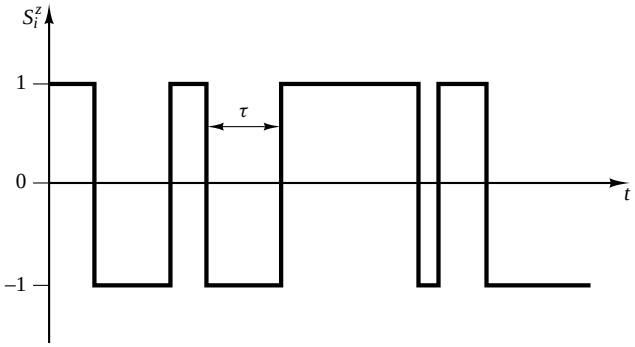

Figure 4 Time dependence of the pseudospin variable $S^z(t)$ reflecting the deuteron motion between the two equilibrium sites in the O–H···O bond

In the 'fast motion' limit, where $\tau \ll \tau_{\mathrm{NMR}} = 1/2\omega_1$ (Figure 4) the nucleus 'sees' just the time averaged value of $S_i^z(t)$ so that equation (10a) becomes

$$\omega_i = \omega_0 + \omega_1 p_i \tag{10b}$$

where $p_i = \langle S_i^z(t) \rangle$ is the local polarization. In a homogeneous ferroelectric, where equation (5d) holds, $p_i = p_j = p = P$, so that ^{2}H NMR provides a method for a microscopic measurement of the long range order parameter P as well as yielding direct information about the deuteron order–disorder transition at T_c in KD_2PO_4-type crystals.[1] As it can be seen from Figure 5, $\langle S^z(t) \rangle = 0$ above T_c and $\langle S^z(t) \rangle \neq 0$ below T_c. The deuterons are dynamically disordered between the two equilibrium sites above T_c and order into one of the two positions below T_c.[6] The T dependence of $p = P$ is equal to the one determined by macroscopic polarization measurements.

The fluctuating part of the local polarization $p_i = p + \delta p_i(t)$ and the related part of the quadrupole coupling Hamiltonian $\hat{\mathcal{H}}_{\mathrm{Q}}^{(1)}(t)$,

$$\hat{\mathcal{H}}_{\mathrm{Q}}(t) = \langle \hat{\mathcal{H}}_{\mathrm{Q}} \rangle + \hat{\mathcal{H}}_{\mathrm{Q}}^{(1)}(t) \tag{11a}$$

produces, in agreement with equations (2) and (3), a characteristic dip in T_1 at T_c (Figure 6). The form of the T_1^{-1} anomaly

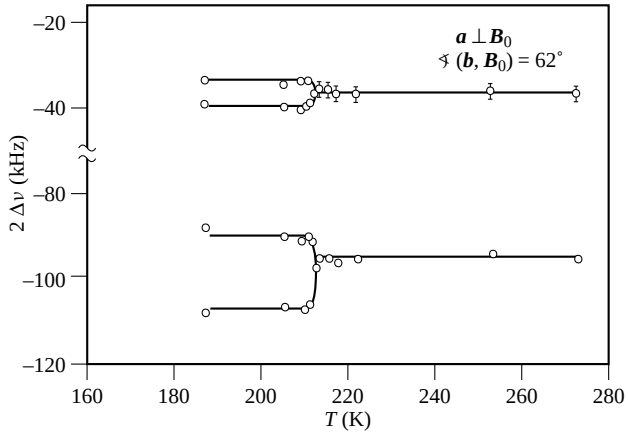

Figure 5 Temperature dependence of the quadrupole splitting of the deuteron NMR lines in CsD_2AsO_4

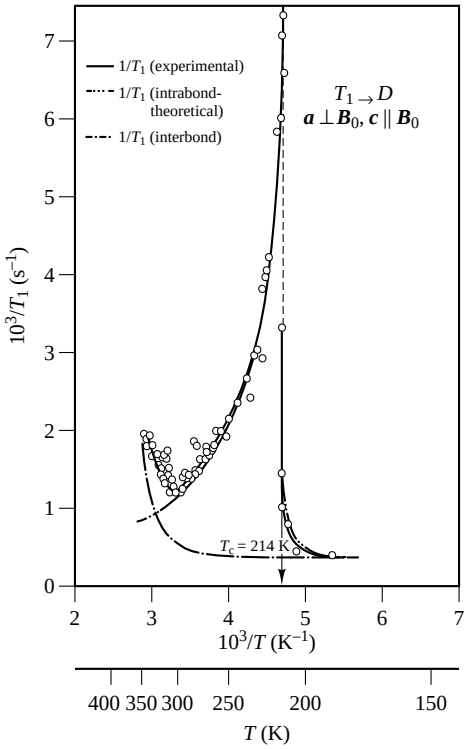

Figure 6 Temperature dependence of the deuteron spin–lattice relaxation rate in KD_2PO_4 at $\boldsymbol{B}_0$ = 1.65 T

is the one expected[1] for the condensation of an overdamped soft pseudospin wave mode:

$$T_1^{-1} \propto \ln \frac{T - T_c}{T_c} + \text{constant} \quad T > T_c \tag{11b}$$

$$T_1^{-1} \propto 1 - p^2 \quad T < T_c \tag{11c}$$

From the above data the noninteracting deuteron correlation time, i.e. the time the deuteron stays at a given site before it jumps to the other site in the O–D$\cdots$O potential, is determined as $\tau_0 = 2.7 \times 10^{-13}$ s at room temperature. This justifies the fast motion approximation. Similar results were obtained in other hydrogen bonded ferroelectrics.[1,7]

3.2 Oxygen-17–Proton Nuclear Quadrupole Double Resonance

In view of the 'geometrical' isotope effect[8] and the resulting expansion and changes in the shape of the hydrogen bond potential on deuteration one cannot simply transfer the conclusions obtained for deuterated crystals to the undeuterated ones. Since the distance between the two equilibrium sites of the hydrogen in short O–H$\cdots$O bonds ($R_{O-O} \leq 2.49$ Å) may be 0.35 Å or less, it is difficult to determine by neutron diffraction whether the proton is located in the center of the hydrogen bond or dynamically disordered between two separate, off-center equilibrium sites. For $T > T_c$ a single peaked proton density distribution in the center of the hydrogen bond is usually observed by neutron scattering. Below T_c the diffraction data show an off-center position of the proton.

The answer is provided by ^{17}O–^{1}H quadrupole double resonance spectroscopy and the direct determination of the ^{17}O–^{1}H distance from the magnetic dipole–dipole fine structure of the ^{17}O NQR lines.[9]

As an example let us consider[7] RbH_2PO_4, which is isomorphous with KH_2PO_4 and has all O–H$\cdots$O bonds equivalent. In this system the PO_4 groups are linked by O–H$\cdots$O bonds. In view of the low natural abundance of ^{17}O (0.037%) there is at most one ^{17}O nucleus ($I = \frac{5}{2}$) per O–H$\cdots$O bond.

The energies of the three doubly degenerate ($|\pm\frac{1}{2}\rangle, |\pm\frac{3}{2}\rangle, |\pm\frac{5}{2}\rangle$) ^{17}O quadrupole energy levels $E = x\,A$, $A = e^2qQ/4I(2I-1)$, $eq = V_{zz}$ can be obtained from

$$x^3 - 7(3+\eta^2)x - 20(1-\eta^2) = 0 \tag{12}$$

where $\eta = (V_{xx} - V_{zz})/V_{zz}$ is the asymmetry parameter of the EFG tensor and where $V_{zz} \geq V_{yy} \geq V_{xx}$. For small η we have

$$\nu_{1/2\rightarrow 3/2} = \frac{3e^2qQ}{20h}\left(1 + \frac{59}{54}\eta^2\right) \tag{13a}$$

$$\nu_{1/2\rightarrow 5/2} = \frac{3e^2qQ}{10h}\left(1 - \frac{11}{54}\eta^2\right) \tag{13b}$$

and $\nu_{1/2\rightarrow 5/2} = \nu_{1/2\rightarrow 3/2} + \nu_{3/2\rightarrow 5/2}$.

If the proton is centrally located we expect just one set of ^{17}O NQR lines ($\nu_{1/2\rightarrow 3/2}$, $\nu_{3/2\rightarrow 5/2}$, $\nu_{1/2\rightarrow 5/2}$) per ^{17}O–H$\cdots$O bond. If the proton is located in an 'off-center' site we expect, in view of the random occurrence of the ^{17}O isotope, two sets of ^{17}O NQR lines per O–H$\cdots$O bond. One of them would correspond to the proton in the 'close' position, i.e. ^{17}O–H$\cdots$O, and the other to the proton in the 'far' position, i.e. ^{17}O$\cdots$H–O. If the protons are dynamically disordered between the two 'off'-center sites, the observed ^{17}O EFG tensor should be an average of the tensors for the two separate 'off'-center sites, the 'far' and the 'close' one. It should be noted that the ^{17}O quadrupole coupling constant increases with decreasing O–H bond distance,[8] thus allowing for a discrimination between 'close' and 'far' sites.

The ^{17}O nuclear quadrupole double resonance results for RbH_2PO_4 are shown in Figure 7. Above T_c only three ^{17}O lines ($\nu_{1/2\rightarrow 3/2}$, $\nu_{3/2\rightarrow 5/2}$, $\nu_{1/2\rightarrow 5/2}$) are observed, demonstrating that all PO_4 oxygen sites are equivalent on the NQR timescale. Below T_c each line splits symmetrically into two components, demonstrating that we are dealing with dynamic disorder between two equivalent sites above T_c. The average value of the two components is constant while the difference is proportional to the order parameter p and measures the time averaged asymmetry in the hydrogen bond potential below T_c. We thus have

$$\begin{aligned}\langle \boldsymbol{\nu}\,(^{17}\text{O-H})\rangle &= \langle \boldsymbol{\nu}\,(^{17}\text{O}\cdots\text{H})\rangle \\ &= \tfrac{1}{2}[\boldsymbol{\nu}\,(^{17}\text{O-H}) \\ &\quad + \boldsymbol{\nu}\,(^{17}\text{O}\cdots\text{H})] \quad T > T_c\end{aligned} \tag{14a}$$

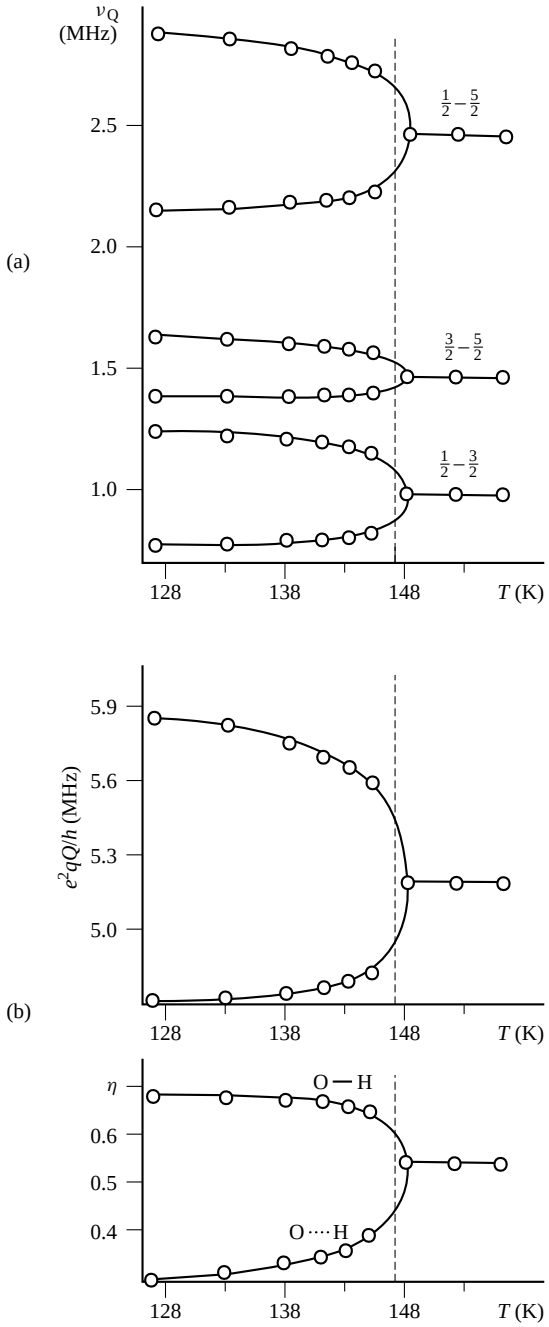

Figure 7 Temperature dependence of (a) the ^{17}O NQR transition frequencies in RbH_2PO_4 and (b) the quadrupole coupling constant and asymmetry parameter

and

$$\langle \boldsymbol{\nu}\,(^{17}\text{O-H})\rangle = \frac{1+p}{2}\boldsymbol{\nu}\,(^{17}\text{O-H}) + \frac{1-p}{2}\boldsymbol{\nu}\,(^{17}\text{O}\cdots\text{H}) \quad T < T_c \quad (14b)$$

$$\langle \boldsymbol{\nu}\,(^{17}\text{O}\cdot\text{H})\rangle = \frac{1-p}{2}\boldsymbol{\nu}\,(^{17}\text{O-H}) + \frac{1+p}{2}\boldsymbol{\nu}\,(^{17}\text{O}\cdots\text{H}) \quad T < T_c \quad (14c)$$

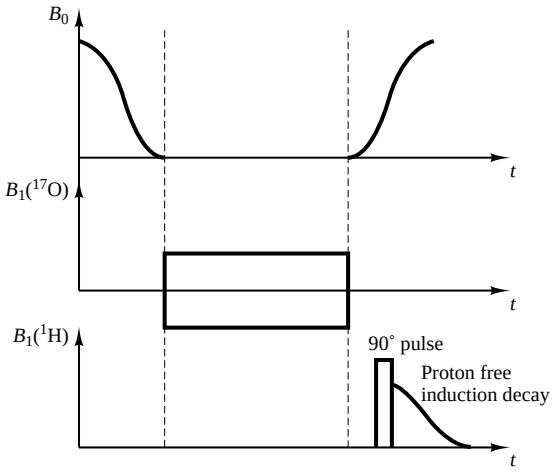

Figure 8 Field sequence for the ^{17}O–H double resonance in the laboratory frame experiment

The difference

$$\langle \boldsymbol{\nu}\,(^{17}\text{O-H})\rangle - \langle \boldsymbol{\nu}\,(^{17}\text{O..H})\rangle = p[\boldsymbol{\nu}\,(^{17}\text{O-H}) \times -\boldsymbol{\nu}\,(^{17}\text{O}\cdots\text{H})] \quad (14d)$$

is here indeed proportional to p and allows for a measurement of the local asymmetry of the hydrogen bond potential in frequency units.

The corresponding measuring sequence for the ^{17}O–^{1}H double resonance experiment in the laboratory frame is schematically shown in Figure 8.

An independent confirmation of the above results is provided by the proton magnetic dipolar fine structure of the ^{17}O lines obtained with a double frequency irradiation technique.[9] For $\eta = 0$, $E_{\pm 5/2}$ and $E_{\pm 3/2}$ split up into two doubly degenerate energy levels,

$$E_{\pm 5/2} = \frac{e^2qQ}{4} \pm \tfrac{5}{2}K\sqrt{1+3\cos^2\theta} \quad (15a)$$

$$E_{\pm 3/2} = -\frac{e^2qQ}{20} \pm \tfrac{3}{2}K\sqrt{1+3\cos^2\theta} \quad (15b)$$

whereas $E_{\pm 1/2}$ splits into four levels,

$$E_{\pm 1/2} = -\frac{e^2qQ}{5} + \frac{K}{2}[3 \pm \sqrt{37-12\cos 2\theta}] \quad (15c)$$

$$E_{\pm 1/2} = -\frac{e^2qQ}{5} + \frac{K}{2}[-3 \pm \sqrt{13-12\cos 2\theta}] \quad (15d)$$

Here $K/\hbar = 8.16\,\text{kHz}/R_{0-H}^3$ (angstroms), $\hbar$ is Planck's constant, and θ is the angle between the largest principal axis of the axially symmetric ($\eta = 0$) ^{17}O EFG tensor and the ^{17}O–H bond direction.

The effective dipolar splitting of the ^{17}O NQR lines is determined by

$$\langle R^{-3}\rangle = \frac{1+p}{2}R_{\text{O-H}}^{-3} + \frac{1-p}{2}R_{\text{O}\cdots\text{H}}^{-3} \quad T < T_c \quad (16a)$$

where p can be determined from the temperature dependence of the ^{17}O lines. The ^{17}O–H distance for the 'close' proton

site is here obtained as $R_{O-H} = 1.06 \pm 0.01$ Å at $T = 138$ K, i.e. well below T_c. The result agrees with the one obtained by neutron scattering.

Above T_c the proton spends an equal amount of time at the 'close' ($R_{O-H} = 1.06$ Å) and 'far' ($R_{O\cdots H} = 1.45$ Å) equilibrium site so that the dipolar splitting is characterized by an 'apparent' $^{17}O-H$ distance

$$\langle R^{-3} \rangle = \tfrac{1}{2}[R_{O-H}^{-3} + R_{O\cdots H}^{-3}] \quad T > T_c \tag{16b}$$

yielding $R = 1.18$ Å. If, on the other hand, the proton is above T_c, situated in the center of the O–H–O bond, the effective O–H distance obtained from the dipolar fine structure would be

$$R_{\text{symm}}(\text{O-H}) = 1.225\text{Å} \quad T > T_c \tag{16c}$$

which would contradict the experimental data. The ^{17}O quadrupole coupling as well as the $^{17}O-H$ magnetic dipolar fine structure thus provide direct evidence for the proton intra-$^{17}O-H\cdots O \leftrightarrow {}^{17}O\cdots H-O$ motion between the two sites and the dynamic order–disorder nature of the phase transition in RbH_2PO_4.

Similar results were obtained for KH_2PO_4, CsH_2PO_4, TlH_2PO_4, $PbHPO_4$, as well as squaric acid ($C_4H_2O_2$) and $KH_3(SeO_3)_2$.[7,10] In partially deuterated $RbH_{2x}D_{2(1-x)}PO_4$ the results show that the O–H$\cdots$O bonds are practically identical to the ones in pure RbH_2PO_4 whereas the O–D$\cdots$O bonds expand and show a nearly 25% higher spontaneous asymmetry below T_c than the O–H$\cdots$O bonds.[7]

3.3 Proton Chemical Shift Tensors

For protons ($I = \frac{1}{2}$) in solids, the chemical shift term $\hat{\mathcal{H}}_\sigma$ in the spin Hamiltonian

$$\hat{\mathcal{H}} = \hat{\mathcal{H}}_Z + \hat{\mathcal{H}}_D + \hat{\mathcal{H}}_\sigma \tag{17a}$$

$$\hat{\mathcal{H}}_\sigma = \gamma \sum_i \hat{\boldsymbol{I}}_i \cdot \boldsymbol{\sigma}_i \cdot \boldsymbol{B}_0 \tag{17b}$$

is usually much smaller than the dipolar term so that proton chemical shifts are lost in the dipolar width of the NMR line. Using high-resolution NMR-in-solids techniques like the WAHUHA sequence,[11]

$$(\tau, P_x, 2\tau, P_{-x}, \tau, P_y, 2\tau, P_{-y})$$

the homonuclear dipolar broadening can be eliminated while the chemical shifts are reduced by $\sqrt{3}$. This allows for a determination of the proton chemical shift tensors $\boldsymbol{\sigma}$ from the angular dependence of the spectra. Such measurements were performed in KH_2PO_4 and other hydrogen bonded systems.[12] The information obtained is in principle similar to that obtained from the deuteron quadrupole coupling data but the experiments are more tedious and the resolution is lower.

3.4 Phosphorus-31 Chemical Shift Tensors

Whereas ^{17}O NQR and deuteron quadrupole perturbed NMR measure the single-particle intra-hydrogen bond dynamics, the ^{31}P chemical shift tensor $\boldsymbol{\sigma}$ interaction in KH_2PO_4-type crystals measures the local arrangement of the four O–H$\cdots$O bonded protons in the hydrogen bonds linking a given PO_4 group to its neighbors. The chemical shift term is

$$\hat{\mathcal{H}}_\sigma = \gamma \sum_i \hat{\boldsymbol{I}}_i \cdot \boldsymbol{\sigma}_i \cdot \boldsymbol{B}_0 \tag{18a}$$

where

$$\boldsymbol{\sigma} = \boldsymbol{\sigma}(p_1, p_2, p_3, p_4) \tag{18b}$$

The temperature dependence of the ^{31}P chemical shift on going through T_c in KD_2PO_4 is shown[7,10] in Figure 9(a). There are four ^{31}P nuclei per unit cell of KH_2PO_4 both above and below T_c. The edges of two PO_4 tetrahedra are rotated by $+13^\circ$ with respect to the orthorhombic a, b axes (A sites) whereas the other two are rotated by -13° (B sites). Above T_c all ^{31}P sites in the unit cell are chemically and physically equivalent due to dynamic proton disorder in the O–H$\cdots$O bonds. The ^{31}P chemical shift tensor is axially symmetric around the fourfold c axis which passes through

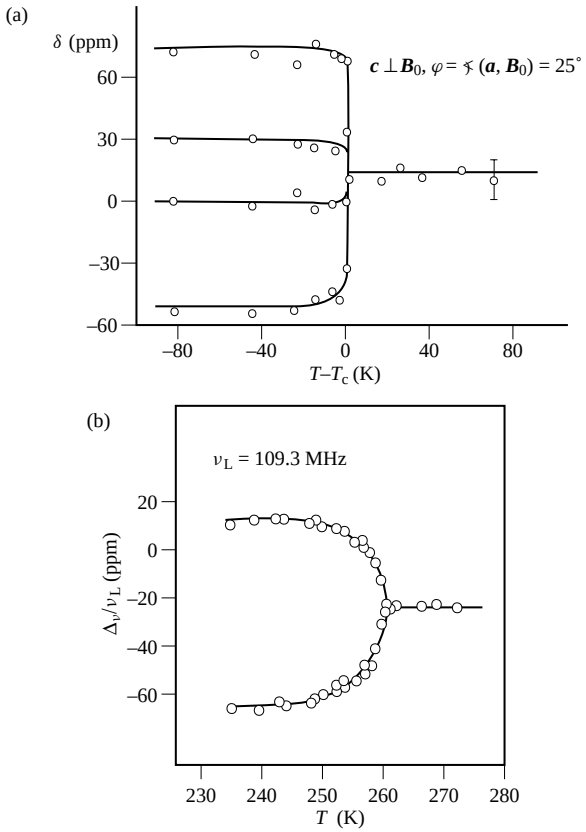

Figure 9 (a) Temperature dependence of the ^{31}P chemical shift on cooling through T_c in KD_2PO_4. (b) Splitting of the ^{31}P NMR line[11] in pseudo-1D CsD_2PO_4 where the O–H(1)$\cdots$O bonds are ordered above and below T_c whereas the O–H(2)$\cdots$O bonds are disordered above T_c and ordered below T_c and where $\sigma_{T>Tc} = \frac{1}{2}(\sigma_1+\sigma_2)_{T<Tc}$

the phosphorus sites. Below T_c there are four physically nonequivalent ^{31}P sites, which are all chemically equivalent and which reflect the ordering of the four protons into two 'close' and two 'far' sites in the O–H···O bonds: $\boldsymbol{\sigma}_1 = \boldsymbol{\sigma}_A(+\boldsymbol{P})$, $\sigma_2 = \sigma_A(-\boldsymbol{P})$, $\sigma_3 = \sigma_B(+\boldsymbol{P})$, $\sigma_4 = \sigma_B(-\boldsymbol{P})$. The paraelectric σ tensor is the average of the four ferroelectric ones.[7,10] This confirms that the phase transition in KH_2PO_4 is a protonic order–disorder one and is not driven by electronic instabilities.

The largest principal axes of the ^{31}P chemical shift tensor is nearly exactly parallel to the line connecting the two PO_4 oxygens to which the protons are directly attached. A change in the H_2PO_4 proton 'arrangement' from the 'top' to the 'bottom' oxygens, as viewed along the c axis, results in a polarization reversal ($\boldsymbol{P} \rightarrow -\boldsymbol{P}$) and in a rotation of the two largest principal axes of the ^{31}P $\boldsymbol{\sigma}$ tensor by 90°. The ^{31}P $\boldsymbol{\sigma}$ tensor is thus a very sensitive indicator of the arrangement of the four protons around a given PO_4 group in KH_2PO_4 crystals.

Similar results were also obtained in pseudo-1D CsD_2PO_4[13] [Figure 9(b)] and $PbHPO_4$[14] using high-resolution NMR-in-solids techniques.

3.5 Arsenic-75 Quadrupolar Coupling

Information similar to that from the ^{31}P chemical shift tensor can be obtained from the ^{75}As quadrupole coupling tensor in KH_2AsO_4-type arsenates.

Here, however, the resolution of the experiment is much larger as the ^{75}As NQR frequency changes[10] from ≈3.5 MHz at $T > T_c$ to ≈35 MHz at $T < T_c$ (Figure 10). The ^{75}As EFG tensor as well depends on the arrangement of the four protons around a given AsO_4 group:

$$\boldsymbol{V} = \boldsymbol{V}(p_1, p_2, p_3, p_4) \tag{19}$$

The direction of the largest principal axis (V_{zz}) of this tensor is parallel to the line connecting the two oxygens in the AsO_4 group to which the two protons are directly attached, whereas the smallest principal axis (V_{xx}) is parallel to the direction of the electric dipole moment of the H_2AsO_4 group.

The ^{75}As EFG tensors determined[1,7,10,15] in ferroelectric KH_2AsO_4 and antiferroelectric $NH_4H_2AsO_4$ could be thus assigned to the six Slater[16] H_2AsO_4 configurations predicted by the Slater–Nagamiya model[16] of the phase transition in KH_2PO_4. In ferroelectric KH_2AsO_4 both 'close' hydrogens are either attached to the 'upper' ($\boldsymbol{V}^{(1)}$) or to the 'lower' two H_2AsO_4 oxygens ($\boldsymbol{V}^{(2)}$) as viewed along the c axis,

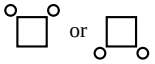

so that the dipole moment points along $\pm c$. In antiferroelectric $NH_4H_2AsO_4$ on the other hand, one hydrogen is attached to the 'upper' and one to the 'lower' oxygen,

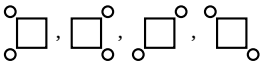

resulting in four 'antiferroelectric' H_2AsO_4 arrangements—($\boldsymbol{V}^{(3)}$, $\boldsymbol{V}^{(4)}$, $\boldsymbol{V}^{(5)}$, $\boldsymbol{V}^{(6)}$)—with dipole moments along the $\pm b$ and $\pm a$ crystal axes. In the antiferroelectric domain, where the sublattice polarization $\overleftrightarrow{P}$ ∥[100] is along the $\pm a$ axis, one sublattice corresponds to $\boldsymbol{V}^{(3)}$ and the other to $\boldsymbol{V}^{(4)}$, whereas for $\overleftrightarrow{P}$ ∥[010] the corresponding EFG tensors are $\boldsymbol{V}^{(5)}$ and $\boldsymbol{V}^{(6)}$. These results represented the first direct proof that the antiferroelectric proton ordering suggested by Nagamiya[16] is correct.

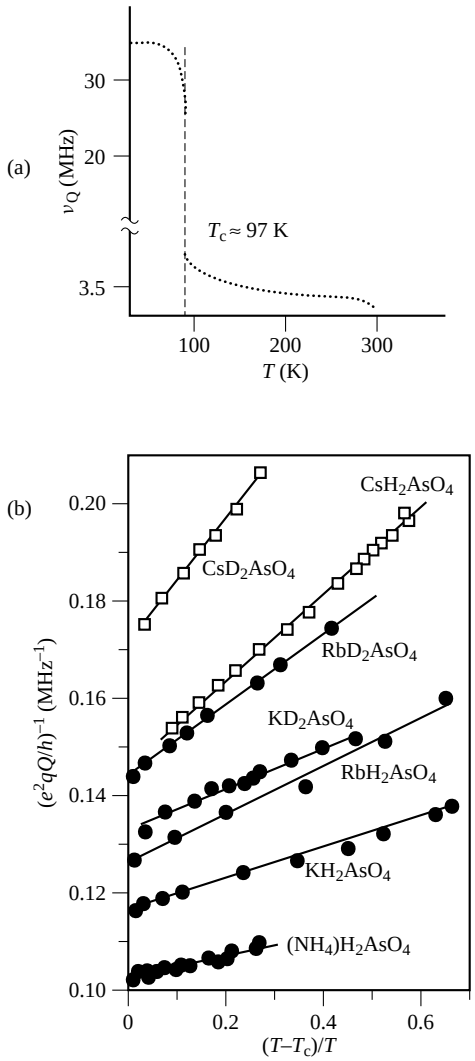

Figure 10 (a) Temperature dependence of the ^{75}As NQR frequency ν_Q in KH_2AsO_4 on cooling through T_c. (b) Dependence of the inverse ^{75}As quadrupole coupling constant $(e^2qQ/h)^{-1}$ on $(T - T_c)/T_c$ in KH_2AsO_4-type crystals above T_c

In the paraelectric phase each H_2AsO_4 group fluctuates between the six Slater configurations. The fluctuations result in a time averaging of the EFG tensors and in an anomalous increase in the ^{75}As spin–lattice relaxation rate as $T \rightarrow T_c$[19] (Figure 11). The ^{75}As T_1^{-1} has been measured by the proton–arsenic cross-relaxation technique in the dipolar frame.[17]

3.6 Fluctuations at Cationic Sites

In contrast to the nuclei discussed so far which were all covalently bonded, the EFG tensor at the K, Cs or Rb sites in

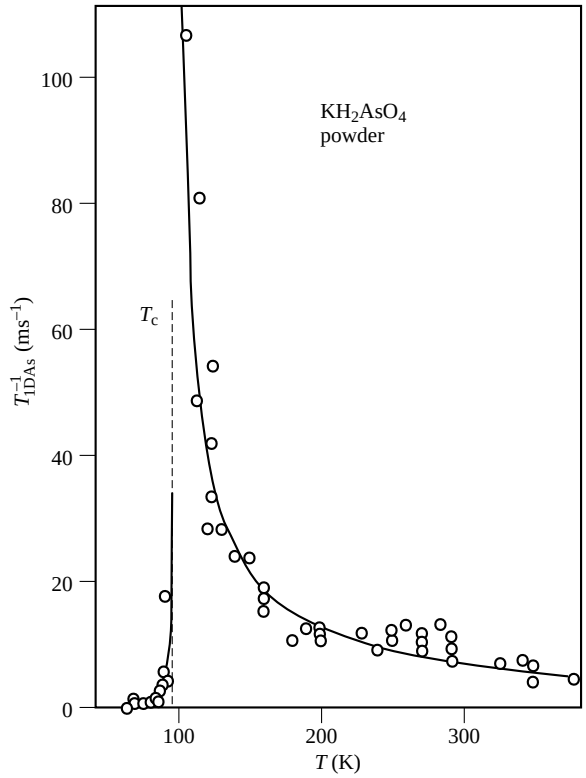

Figure 11 Temperature dependence of the arsenic spin–lattice relaxation rate in the dipolar (rotating) frame as determined by proton–arsenic cross relaxation

KH_2PO_4-type ferroelectrics is of ionic character. These nuclei are thus nonlocal probes which measure the charge distribution and order on a scale of 40–50 unit cells (i.e. more than 10^2 O–H$\cdots$O bonds). Here

$$\boldsymbol{V}_i = \boldsymbol{V}_i(p_1, p_2, \ldots, p_L) \tag{20a}$$

The temperature dependence of the ^{133}Cs ($I = \frac{7}{2}$) quadrupole coupling constant in CsH_2AsO_4, for instance[7] can be described above T_c by

$$\langle \boldsymbol{V}_i \rangle = \boldsymbol{V}_0 \quad T > T_c \tag{20b}$$

if the mean square fluctuations in the order parameter can be neglected. Below T_c, on the other hand, one finds

$$\langle \boldsymbol{V}_i \rangle = \boldsymbol{V}_0 + \boldsymbol{A}p + \boldsymbol{B}p^2 \quad T < T_c \tag{20c}$$

where the forms of the $\boldsymbol{V}_0$, $\boldsymbol{A}$, and $\boldsymbol{B}$ tensors are determined by crystal symmetry.[7,18] Similar results are obtained for the ^{39}K and ^{87}Rb quadrupole coupling tensors in other KH_2PO_4-type crystals.[1]

3.7 NMR in Perovskite Ferroelectrics

The local properties of phase transitions in perovskite-type ferroelectrics and antiferroelectrics have been extensively studied by NMR.[21] Cotts and Knight[21] and Hewitt[21] were the first to study electric quadrupole interactions in perovskites. Hewitt[21] in particular measured the temperature dependence of the EFG tensor at the ^{93}Nb sites in $KNbO_3$. The spin–lattice relaxation studies of $NaNbO_3$[21] gave important information on the softening of the collective rotations of the oxygen tetrahedra at the M point, $\boldsymbol{q} = (\frac{1}{2}, \frac{1}{2}, 0)$—of the Brillouin zone.

4 NMR IN THE SLOW AND INTERMEDIATE MOTION REGIME

4.1 Dynamic Symmetry Breaking and NMR in KSCN, RbSCN, and NH_4SCN Antiferroelectrics

The second-order quadrupole shifts[19] of the ^{39}K or ^{87}Rb $\frac{1}{2} \rightarrow -\frac{1}{2}$ NMR transitions in tetragonal KSCN and RbSCN show the effects of dynamic symmetry breaking on the NMR timescale.[19,20] The symmetry of the angular rotation pattern in the high-temperature paraelectric tetragonal phase is lower than the K or Rb site symmetry as determined by X-ray scattering[19] [Figure 12(a) and (b)]. At the same time the ^{39}K and ^{87}Rb 'site' and '90° domain' doublet splittings which are proportional to the long range order parameter vanish above T_c [Figure 12(c)] as expected from equations (1a) and (1b).

The above systems undergo at T_c antiferroelectric–paraelectric phase transitions connected with a head–tail ordering of the SCN^- groups. These groups are dynamically disordered above T_c and order in an antiparallel arrangement below T_c, resulting in a doubling of the unit cell size and the formation of 0, 90, 180, and 270° orthorhombic domains. The shift of the K^+ or Rb^+ ions from their position on the fourfold rotation axis is linearly coupled to the orientational degrees of freedom of the SCN^- ions.

The NMR results[19] show that for the second-order shifts and corresponding lineshapes the time fluctuating quadrupolar perturbation $\hat{\mathcal{H}}_Q^{(1)}(t)$, connected with the flipping of the SCN^- groups, averages out in two steps.[20] This is because both diagonal and off-diagonal matrix elements—in the representation of eigenstates of the main Hamiltonian—are important. A resonance line is a doublet with a splitting $4A$ at very long correlation times ($A\tau \gg 1$) where the spectrum is the same as in the case of two static Hamiltonians

$$\hat{\mathcal{H}}_A = \hat{\mathcal{H}}_Z + \langle \hat{\mathcal{H}}_Q^{(0)} \rangle + \hat{\mathcal{H}}_Q^{(1)} \tag{21a}$$

and

$$\hat{\mathcal{H}}_B = \hat{\mathcal{H}}_Z + \langle \hat{\mathcal{H}}_Q^{(0)} \rangle - \hat{\mathcal{H}}_Q^{(1)} \tag{21b}$$

It becomes a singlet when τ^{-1} exceeds the doublet splitting, i.e. when $A\tau \ll 1$. The second-order shift of the resonance line caused by the off-diagonal matrix element of the quadrupolar perturbation $\hat{\mathcal{H}}_Q^{(1)}(t)$ vanishes, however, only when τ^{-1} exceeds the resonance frequencies ω_L of the main Hamiltonian, $\hat{\mathcal{H}}_Z + \langle \hat{\mathcal{H}}_Q^{(0)} \rangle$. For $A\tau \ll 1$, $\omega_L\tau \gg 1$ we are thus in the intermediate motion limit and have a partial motional averaging. The doublet splitting induced by $\hat{\mathcal{H}}_Q^{(1)}(t)$ is averaged

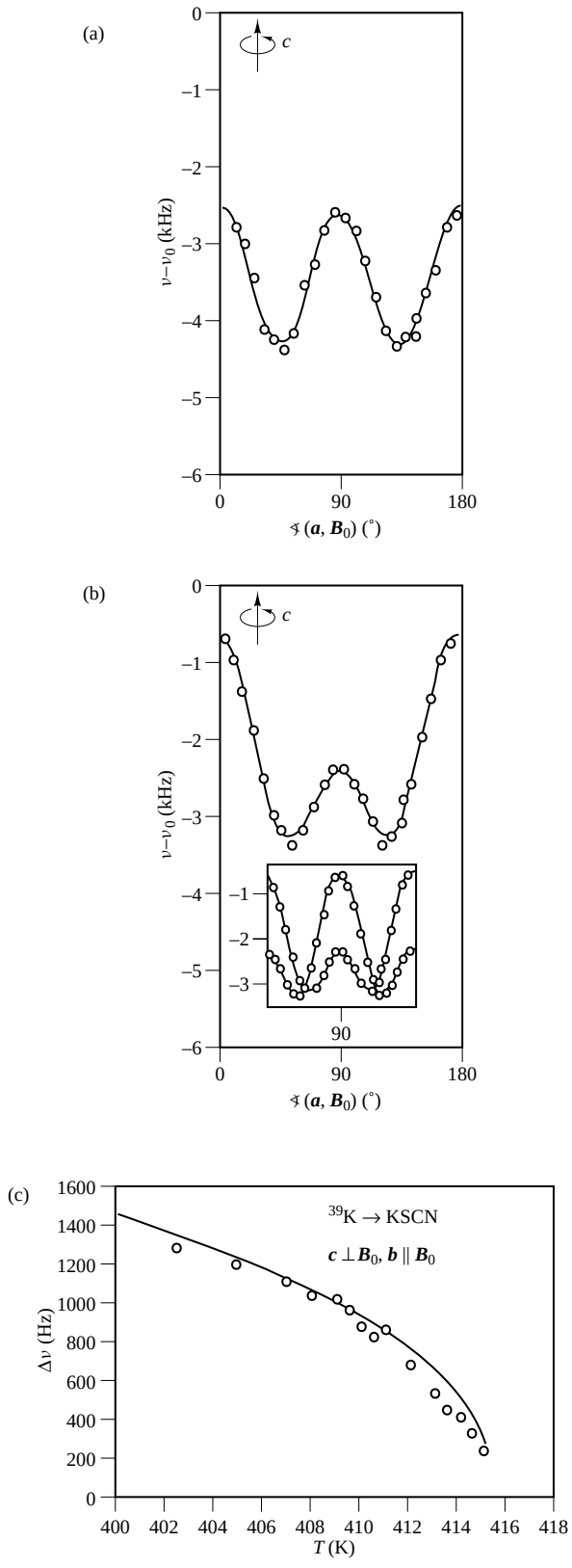

Figure 12 (a) Temperature dependence of the ^{39}K angular rotation pattern in KSCN for the c rotation above T_c and (b) below T_c. The domain splitting seen below T_c [inset to (b)] disappears above T_c whereas the angular dependence observed above T_c is incompatible with the tetragonal symmetry of the phase. (c) Temperature dependence of domain splitting

out, but the second-order quadrupolar shift induced by $\hat{\mathcal{H}}_Q^{(1)}(t)$ is still nonzero:

$$\Delta\omega_{1/2\rightarrow -1/2}(\tau) = \Delta\omega^{(0)}_{1/2\rightarrow -1/2} + \Delta\omega^{(1)}_{1/2\rightarrow -1/2}(\tau) \qquad (22a)$$

where

$$\Delta\omega^{(1)}_{1/2\rightarrow -1/2}(\tau) \propto \frac{(\omega_L\tau)^2}{1+(\omega_L\tau)^2} \qquad (22b)$$

It is only in the fast motion limit, $\omega_L\tau \ll 1$, that $\Delta\omega_{1/2\rightarrow -1/2}{}^{(1)}(\tau) \rightarrow 0$ and the angular dependence of the second-order quadrupolar shift is $\Delta\omega_{1/2\rightarrow -1/2}{}^{(0)}$, i.e. it is determined by the time averaged Hamiltonian $\langle\hat{\mathcal{H}}_Q^{(0)}\rangle$.

In agreement with this model and equations (2a)–(3c), the ^{39}K and ^{87}Rb spin–lattice relaxation rates show no anomaly at T_c as all critical factors in equation (2b) cancel (Figure 13). T_1 is proportional to $\omega_L{}^2\tau_0$, and continues to decrease with increasing temperature as the crystal is heated above T_c since τ_0 is thermally activated.

The dynamic symmetry breaking effects are not seen in the ^{14}N (I = 1) NMR in NH_4SCN,[19] as here first-order quadrupole splittings were studied where off-diagonal matrix elements are not important.

4.2 Dynamic Symmetry Breaking in KH_2AsO_4

In addition to the broad paraelectric arsenic lines, sharp 'ferroelectric' arsenic $\frac{1}{2} \rightarrow -\frac{1}{2}$ lines have been observed in KH_2AsO_4 well above T_c.[15] The angular dependence of these lines shows that here the symmetry of the paraelectric phase is also broken on the timescale of the NMR Larmor frequency. In contrast to KSCN and RbSCN where—in view of the large moment of inertia of the SCN group and the correlations between the flips of different SCN^- groups induced by the small available space for single ion reorientations—the intrinsic dynamics are very slow, we have in KH_2AsO_4 a high frequency soft mode similarly as in KH_2PO_4. The formation of nearly static polar clusters above T_c and the resulting dynamic symmetry breaking may thus be, in contrast to KSCN and RbSCN, induced here by defects.

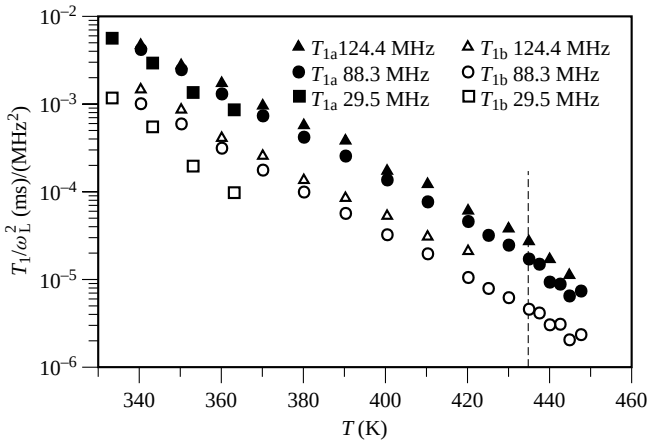

Figure 13 Temperature dependence of the normalized ^{87}Rb NMR T_1 components in RbSCN

5 NMR IN PROTON AND DEUTERON GLASSES

5.1 Determination of the Edwards–Anderson Order Parameter q_{EA} in the Fast Motion Limit

Solid solutions $Rb_{1-x}(ND_4)_xD_2PO_4$ (RADP) of ferroelectric RbH_2PO_4 and antiferroelectric $ND_4D_2PO_4$ represent a randomly frustrated hydrogen-bonded system with competing ferroelectric and antiferroelectric interactions. For $0.22 \leq x \leq 0.78$ the system forms a deuteron glass[21] with no macroscopic symmetry breaking and no spontaneous polarization at any temperature. Here too the O–D$\cdots$O bond represents a two-position reorientable dipole (see Figure 3) which can be described by an Ising pseudospin, $S^z = \pm 1$. In contrast to magnetic spin glasses where we deal with random bond interactions, proton and deuteron glasses are characterized by the presence of both random bonds and random fields[22]

$$\hat{\mathcal{H}} = -\sum_{i<j} J_{ij} S_i^z S_j^z - \sum_i f_i S_i^z \tag{23}$$

Here the J_{ij} are quenched random interactions and f_i are quenched random fields characterized by their second cumulants $[J_{ij}^2]_{AV} = J^2/N$ and $[f_i f_j]_{AV} = \delta_{ij}\Delta$. The random bond distribution is assumed to be Gaussian and centered around a mean value $J_0 = J_{AFE}x + J_{FE}(1-x)$ where x represents the NH_4 concentration. J^2 and Δ, on the other hand, are proportional to $x(1-x)$ and vanish for $x \to 0$ and $x \to 1$. For $|J_0| < J$ the system forms a glass phase without long range order whereas for $|J_0| > J$ a long range ordered inhomogeneous ferroelectric or antiferroelectric phase is predicted to occur.

The basic question in deuteron glasses is how to measure the Edwards–Anderson order parameter[2]

$$q_{EA} = \frac{1}{N}\sum_i \langle S_i^z \rangle^2 \tag{24}$$

as there is no macroscopic conjugate field attached to it. The answer is provided by NMR. In the fast motion limit NMR also allows for a direct determination of the local polarization distribution function $W(p)$, the second moment of which is q_{EA}.

In the simplest case the local NMR frequency ω_i of the deuteron in an O–D$\cdots$O bond is in the fast motion limit $[\omega_{AB}\tau \ll 1, \omega_{AB} = \omega_A - \omega_B]$ linearly related to the pseudospin polarization $\langle S_i^z \rangle = p_i$ of this bond:

$$\omega_i = \omega_0 + \omega_1 \langle S_i^z \rangle = \omega_0 + \omega_1 p_i \tag{25}$$

O–D$\cdots$O bonds with different local polarizations p_i will thus have different NMR frequencies resulting in an inhomogeneous broadening of the NMR line. The resulting frequency distribution,

$$f(\omega) = \frac{1}{N}\sum_i \delta(\omega - \omega_i) = [\delta(\omega - \omega_i)]_{AV} \tag{26}$$

is related to the local polarization distribution $W(p)$ [equation (4)] via

$$f(\omega)\,\mathrm{d}\omega = W(p)\,\mathrm{d}p \tag{27}$$

A measurement of $f(\omega)$ thus allows for a determination of $W(p)$ and its second moment q_{EA} if the relation between ω_i and p_i [equation (25)] is known from experiments on pure systems. q_{EA} in particular is obtained from

$$M_2[f(\omega)] = \int \mathrm{d}\omega\, f(\omega)(\omega - \omega_0)^2 = \omega_1^2 q_{EA} \tag{28}$$

Such experiments have been indeed performed,[4] and the results can be well described by the random bond–random field model.[4,22] The temperature dependence of q_{EA} (Figure 14) in particular demonstrates that in contrast to magnetic spin glass, random fields are present in addition to random bonds. From the shape of the deuteron NMR spectrum [Figure 15(a)] the temperature dependence of $W(p)$ can be determined [Figure 15(b)]. $W(p)$ is here symmetric around $p = 0$ and changes from a single-peaked to double-peaked form with decreasing temperature.

At lower temperatures where the pseudospin fluctuations are no longer very fast as compared to the rigid lattice quadrupole splittings ω_{AB}, we have to take into account the additional broadening due to the slowing down of the fluctuations by convoluting $W(p)$ with the well known dynamic lineshape $I(\omega, p, \tau)$ for exchange in an asymmetric two-site potential. Equation (26) now becomes

$$f(\omega) = \int I(\omega, p, \tau) W(p)\,\mathrm{d}p \tag{29}$$

When the fluctuations become too slow, $\omega_{AB}\tau \geq 1$, the second moment of the lineshape is no longer proportional to q_{EA} but

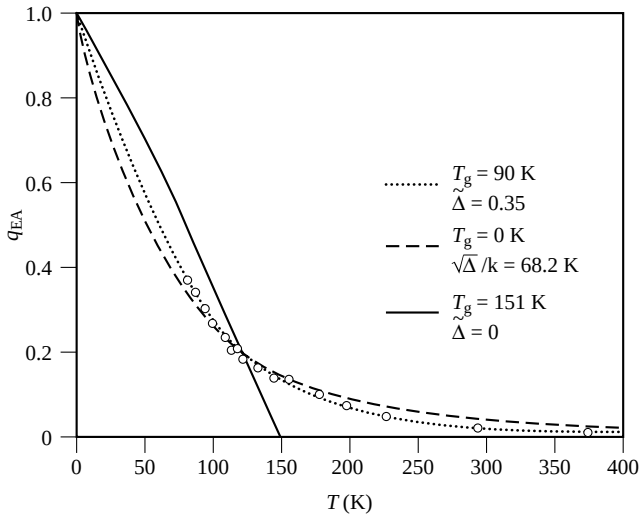

Figure 14 Temperature dependence of q_{EA} as determined from the second moment of the ^{87}Rb $\frac{1}{2} \to -\frac{1}{2}$ NMR spectra in $Rb_{0.56}(ND_4)_{0.44}D_2PO_4$. The dotted line represents the fit to the random bond–random field model with $\Delta/J^2 = 0.35$, $T_g = J/k = 90$ K, whereas the dashed line represents the best fit for the pure random field model where $T_g = 0$ K and $\sqrt{\Delta}/k = 68$ K. The solid line represents the fit to the pure random bond model with $T_g = 151$ K and $\sqrt{\Delta}/k = 0$ K

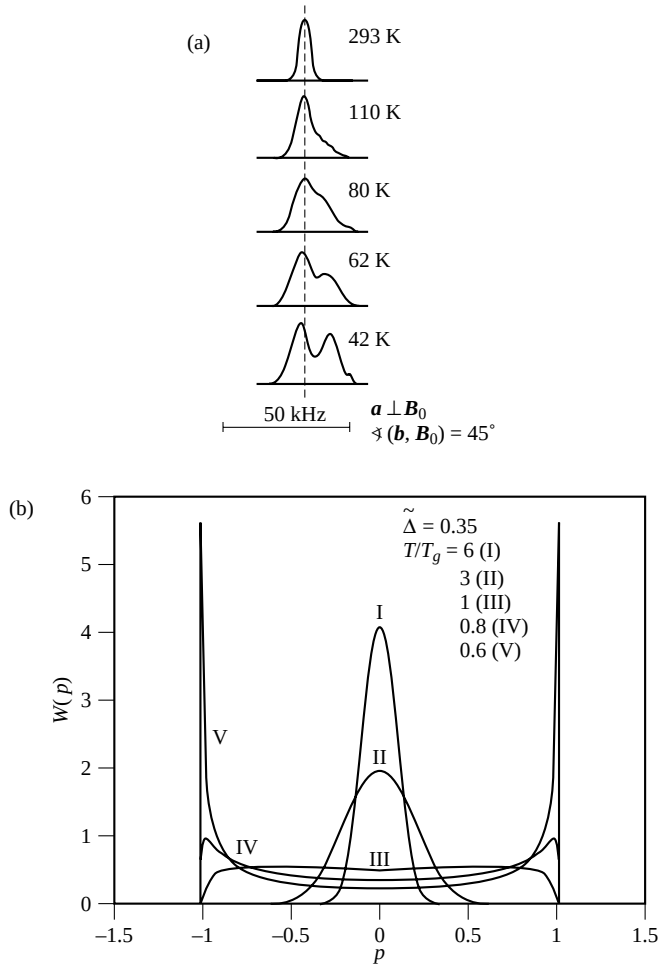

Figure 15 (a) O–D···O deuteron NMR spectrum in $Rb_{0.56}(ND_4)_{0.44}D_2PO_4$ at various temperatures. (b) Temperature dependence of the local polarization distribution function W(p) for $Rb_{0.56}(ND_4)_{0.44}D_2PO_4$ where $\Delta/J^2 = 0.35$

approaches a constant value determined by $I(\omega, p, \tau = \infty)$. Here 1D NMR cannot be used for a determination of q.

5.2 Determination of the Glass Order Parameter q in the Slow Motion Limit

In the slow motion limit where $\omega_{AB}\tau \gg 1$ the nucleus 'sees' the instantaneous value of the Hamiltonian corresponding to $S^z = \pm 1$. The NMR spectrum of the O–D···O bond deuteron will thus consist of two lines,

$$\omega_A = \omega_0 + \omega_1 \tag{30a}$$

and

$$\omega_B = \omega_0 - \omega_1 \tag{30b}$$

corresponding to the 'left' and 'right' position of the deuterons in the double-minimum hydrogen bond potentials. 2D 'exchange' NMR spectroscopy[23] can be used here to determine the glass order parameter q as well as the intrabond deuteron jump rate. The corresponding pulse sequence

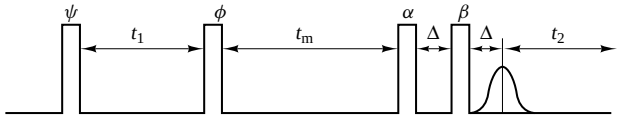

Figure 16 2D exchange NMR pulse sequence[24]

(Figure 16) developed by Spiess et al.[24] selects the signal of the form

$$\begin{aligned} F(t_1, t_2, t_m) = \exp(-t_m/T_1)\exp[-(t_1+t_2)/T_2] \\ \times[a_{AA}(t_m)\cos(\omega_A t_1)\cos(\omega_A t_2) \\ + a_{BB}(t_m)\cos(\omega_B t_1)\cos(\omega_B t_2) \\ + a_{AB}(t_m)\cos(\omega_A t_1)\cos(\omega_B t_2) \\ + a_{BA}(t_m)\cos(\omega_B t_1)\cos(\omega_A t_2)] \end{aligned} \tag{31}$$

After a Fourier transformation with respect to t_1 and t_2 the results are presented in the $\omega_1 - \omega_2$ plane. If no intrabond deuteron exchange, A $\leftrightarrow$ B, has taken place the absorption peaks lie on the diagonal of the $\omega_1 - \omega_2$ plane at (ω_A, ω_A) and (ω_B, ω_B). If intrabond deuteron transfer has taken place between the two physically nonequivalent sites A and B, we also find cross peaks at (ω_A, ω_B) and (ω_B, ω_A). The intensities of the cross peaks (Figure 17) are proportional to the fraction of nuclei that have undergone exchange in the time t_m. Since

$$a_{AA}(\infty) = \frac{1}{N}\sum_i W_{Ai}^2 \tag{32a}$$

$$a_{BB}(\infty) = \frac{1}{N}\sum_i W_{Bi}^2 \tag{32b}$$

and

$$a_{AB}(\infty) = a_{BA}(\infty) = \frac{1}{N}\sum_i W_{Ai} W_{Bi} \tag{32c}$$

where W_{Ai} is the probability of finding the deuteron of the i th O–D···O bond in site A, etc., we get for the ratio of the intensities of the cross peaks to the diagonal peaks in the limit $t_m \to \infty$ the expression

$$R(t_m \to \infty) = \frac{a_{AB}(\infty)}{a_{AA}(\infty)} = \frac{\sum_i W_{Ai} W_{Bi}}{\sum_i W_{Ai}^2} \tag{33a}$$

Using $\langle S_i^z \rangle = W_{Ai} - W_{Bi}$ and

$$q = \frac{1}{N}\sum_i \langle S_i^z \rangle^2 = \frac{1}{N}\sum_i (W_{Ai} - W_{Bi})^2 \tag{33b}$$

as well as

$$\frac{1}{N}\sum_i \langle W_{Ai} + W_{Bi})^2 = 1 \tag{33c}$$

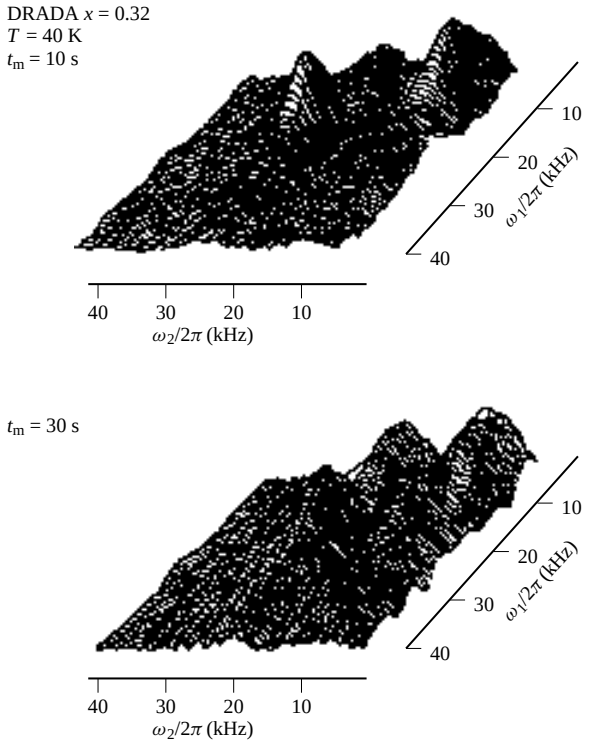

Figure 17 2D O–D···O intrabond deuteron 'exchange' NMR spectra of $Rb_{0.68}(ND_4)_{0.32}D_2AsO_4$ for $\boldsymbol{a} \perp \boldsymbol{B}_0, \sphericalangle\ (\boldsymbol{b}, \boldsymbol{B}_0) = 45^\circ$ at T = 40 K showing the gradual appearance of cross peaks with increasing mixing time

and $a_{AA} = a_{BB}$, equation (33a) can be rewritten as

$$R(t_m \to \infty) = \frac{1-q}{1+q} \tag{34}$$

A measurement of $R(t_m \to \infty)$ thus allows for a determination of q in the slow motion limit.[23]

The time evolution of $R(t_m) = a_{BA} / a_{AA}$, on the other hand (Figure 18), allows for a direct site specific measurement of

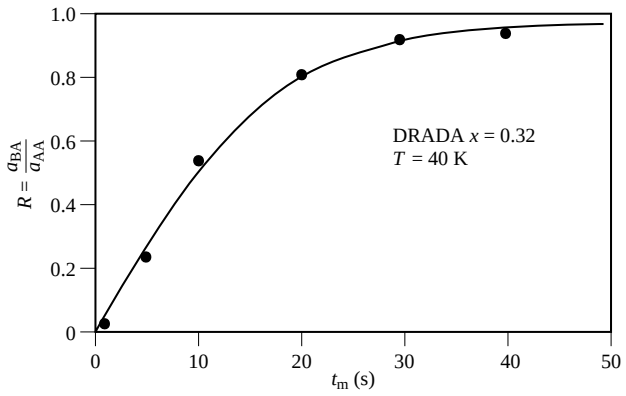

Figure 18 Ratio of cross peak to diagonal peak intensity R as a function of the mixing time t_m at T = 40 K. The same curve is obtained for different crystal orientations with different ω_{AB} splittings so that spin diffusion is excluded

the deuteron intra-hydrogen bond exchange rates, A → B:

$$R(x) = \tanh x \quad x = t_m/\tau \tag{35}$$

The observed intra-hydrogen bond deuteron exchange times[23] vary from 14.4 s at T = 45 K to 235 s at T = 24 K. The motion is thermally activated with E_a = 12.8 meV and τ_0 = 0.43 *s*, showing that phonon assisted deuteron tunneling may be important.

6 NMR DETERMINATION OF ORDER PARAMETERS IN INHOMOGENEOUS FERROELECTRICS

For $0 \le x < x_{FE}$ or $x_{AFE} \le x \le 1$ (see Figure 2) where $|J_0| > J$ a long-range ordered inhomogeneous ferroelectric or antiferroelectric phase exists below T_c. Here long-range and glassy order should coexist below T_c. Above T_c, long-range order vanishes whereas glassy order should persist. The glassy state is characterized above T_c by the Edwards–Andersson parameter q_{EA} and below T_c by $\tilde{q}_{EA} = q_{EA} - P^2$, i.e. by the difference between the EA order parameter and the square of spontaneous polarization P^2. Both $\tilde{q}_{EA}$ and q_{EA} have been determined[25] by ^{75}As NQR ($T < T_c$) and quadrupole perturbed NMR ($T > T_c$) in $Rb_{1-x}(NH_4)_xH_2AsO_4$ for x = 0.01 and x = 0.02.

In pure RbH_2AsO_4 the experimentally measured temperature dependences of the spontaneous polarization $P = P(T)$ and the ^{75}As NQR frequency $\nu_Q(T)$ determine the relationship $\nu_Q = \nu_Q(P)$. In a mixed crystal in the weak disorder limit $x \to 0$ the $\nu_Q = \nu_Q(P)$ relation for the mean NQR frequency is the same as in the pure crystal. In the general case we replace the reduced spontaneous polarization $\tilde{P} = P/P(T=0)$ by the local polarization p. We thus have

$$\omega_Q = \omega_0 + \omega_2 p^2 + \omega_4 p^4 \tag{36}$$

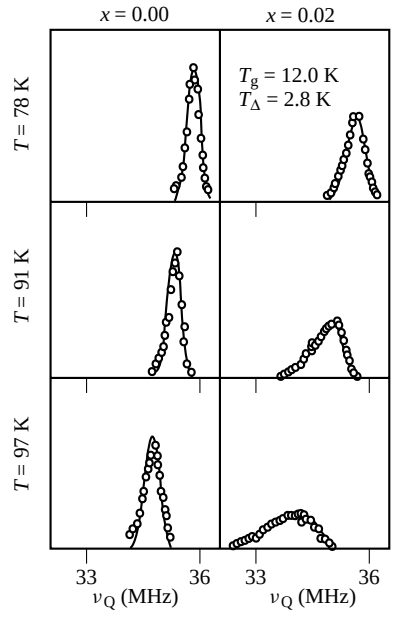

Figure 19 Experimental and theoretical ^{75}As NQR lineshapes[25] in $Rb_{1-x}(NH_4)_xH_2PO_4$ for x = 0.00 and x = 0.02 for $T < T_c$

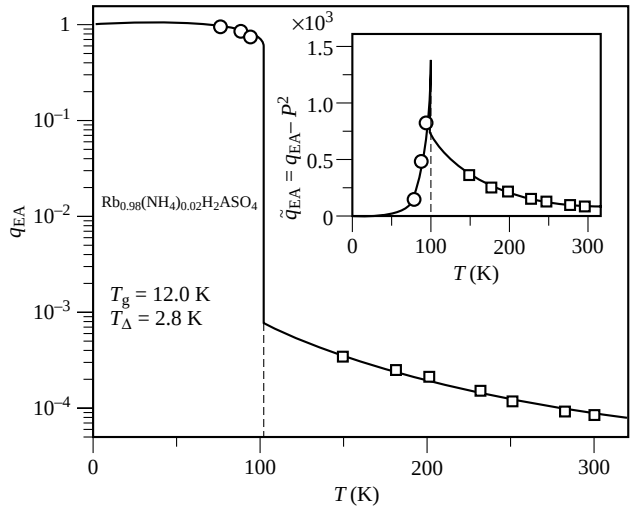

Figure 20 Temperature dependence[25] of q_{EA} and $\tilde{q}_{EA} = q_{EA} - P^2$ in $Rb_{1-x}(NH_4)_xH_2AsO_4$ for x = 0.02. Theoretical fits are shown as solid lines

as the ^{75}As NQR frequency is invariant with respect to the sign reversal of p. The temperature dependence of the mean ^{75}As NQR frequency thus yields the long-range order parameter P whereas the inhomogeneous ^{75}As NQR lineshape yields the local polarization distribution function $W(p)$, and its second moment q_{EA}, via

$$f(\omega) = W(p)|\mathrm{d}\omega/\mathrm{d}p|^{-1} \tag{37}$$

The ^{75}As pure NQR lineshapes of $Rb_{1-x}(NH_4)_xH_2AsO_4$ for $T < T_c$ are shown in Figure 19 for x = 0.00 and x = 0.02 together with the theoretical fits obtained from the compressible random bond–random field pseudospin Ising model.[25] In contrast to the case of proton and deuteron glasses ($| J_0 | < J$) the local polarization distribution function $W(p)$ is asymmetric with respect to p = 0 here.

The temperature dependence of q_{EA} and $\tilde{q}_{EA} = q_{EA} - P^2$ for x = 0.02 is shown in Figure 20. The theoretical fits are shown as solid lines. The jump in q_{EA} at T_c demonstrates the occurrence of a first-order phase transition.

Theoretical fits demonstrate that random bond effects dominate random field effects thus proving the existence of a collective glassy state in inhomogeneous ferroelectrics even in the weak substitutional disorder limit.

7 RELATED ARTICLES

Incommensurate Systems; Phase Transitions and Critical Phenomena in Solids.

8 REFERENCES

1. R. Blinc and B. Zeks, *Soft Modes in Ferroelectrics and Antiferroelectrics*, North Holland, Amsterdam, 1974.
2. K. Binder and A. P. Young, *Rev. Mod. Phys.*, 1986, **58**, 801 and R. Pirc, B. Tadić, and R. Blinc, *Physica A*, 1992, **185**, 322.
3. R. Pirc, B. Tadić, and R. Blinc, *Phys. Rev. B*, 1987, **36**, 8607.
4. R. Blinc, J. Dolinsek, R. Pirc, B. Tadić, B. Zalar, R. Kind, and O. Liechti, *Phys. Rev. Lett.*, 1989, **63**, 2248; J. Dolinšek, *J. Magn. Reson*, 1991, **92**, 312.
5. A. Levstik, C. Filipic, Z. Kutnjak, I. Levstik, R. Pirc, B. Tadić, and R. Blinc, *Phys. Rev. Lett.*, 1991, **66**, 2368.
6. J. L. Bjorkstam, *Adv. Magn. Reson.*, 1974, **7**, 1; J. L. Bjorkstam and E. A. Uehling, *Phys. Rev.*, 1959, **114**, 961; V. H. Schmidt and E. A. Uehling, *Phys. Rev.*, 1962, **126**, 447.
7. R. Blinc, in *Magnetic Resonance of Phase Transitions*, ed. F. J. Owens, C. P. Poole, and H. A. Farach, Academic Press, London, 1979, p. 247.
8. E. Matsushita and T. Matsubara, *Prog. Theor. Phys.*, 1982, **67**, 1.
9. J. Seliger, V. Žagar, R. Blinc, and V. H. Schmidt, *Phys. Rev. B*, 1990, **42**, 3881; S. G. P. Brosnan and D. T. Edmonds, *J. Magn. Reson.*, 1980, **38**, 47; D. T. Edmonds, *Phys. Rep.*, 1977, **29**, 233.
10. R. Blinc, *Ferroelectrics*, 1977, **16**, 33.
11. J. S. Waugh, L. Huber, and U. Haeberlen, *Phys. Rev. Lett.*, 1968, **20**, 180.
12. B. Schröter, H. Rosenberger, and D. Hadži, *J. Mol. Struct.*, 1983, **96**, 301.
13. R. Blinc, I. Zupančič, G. Lahajnar, J. Slak, V. Rutar, M. Verbec, and S. Žumer, *J. Chem. Phys.*, 1980, **72**, 3626.
14. F. Ermark, B. Topić, U. Haeberlen, and R. Blinc, *J. Phys.: Cond. Matter*, 1989, **1**, 5489.
15. R. Blinc and J. L. Bjorkstam, *Phys. Rev. Lett.*, 1969, **23**, 788; J. L. Bjorkstam, *J. Phys. Soc. Jpn. Suppl.*, 1970, **28**, S101.
16. J. C. Slater, *J. Chem. Phys.*, 1941, **9**, 16; *Phys. Rev.*, 1950, **78**, 748; T. Nagamiya, *Prog. Theor. Phys.*, 1952, **7**, 275.
17. R. Blinc and S. Žumer, *J. Chem. Phys.*, 1975, **62**, 3118; R. Blinc, in *Nuclear Magnetic Resonance in Solids*, ed. L. Van Gerven, Plenum, New York, 1977, p. 303.
18. R. Blinc, M. Mali, J. Slak, J. Stepišnik, and S. Žumer, *J. Chem. Phys.*, 1972, **56**, 3566.
19. R. Blinc, J. Seliger, T. Apih, J. Dolinšek, I. Zupančič, O. Plyush, A. Fuith, W. Schranz, and H. Warhanek, *Phys. Rev. B*, 1991, **43**, 569; R. Blinc, J. Seliger, V. Žagar, T. Apih, J. Dolinšek, H. Warhanek, A. Fuith, and W. Schranz, *Phys. Rev. B*, 1990, **42**, 8125; B. Topić, U. Haeberlen, R. Blinc, A. Fuith, and H. Warhanek, *Solid State Commun.*, 1989, **72**, 151.
20. J. Seliger, *J. Magn. Reson. A*, 1993, **103**, 175; J. L. Bjorkstam and M. Villa, *Phys. Rev. B*, 1980, **22**, 5025.
21. K. A. Müller (ed.), *Local Properties at Phase Transitions*, North Holland, Amsterdam, 1976; R. M. Cotts and N. D. Knight, *Phys. Rev.*, 1954, **96**, 1285; R. R. Hewitt, *Phys. Rev.*, 1961, **121**, 45; G. F. Bonera, F. Borsa, and A. Rigamonti, *Rev. Nuovo Cim.*, 1972, **2**, 325.
22. E. Courtens, *J. Phys. (Paris) Lett.*, 1982, **43**, 199; R. Blinc, J. Dolinšek, and S. Žumer, *J. Non-Crystalline Solids*, 1991, **131–133**, 125.
23. J. Dolinšek, B. Zalar, and R. Blinc, *Europhys. Lett.*, 1993, **23**, 289.
24. K. Schmidt-Rohr and H. W. Spiess, *Phys. Rev. Lett.*, 1991, **66**, 3020.
25. G. Papantopoulos, G. Papavassiliou, F. Milia, V. H. Schmidt, J. E. Drumheller, N. J. Pinto, R. Blinc, and B. Zalar, *Phys. Rev. Lett.*, 194, **73**, 276.

Biographical Sketch

Robert Blinc. *b* 1933. Ph.D., 1959, Physics, University of Ljubljana, Postdoctoral work with J. S. Waugh, MIT, Cambridge, Mass. Faculty

member (currently Professor of Physics), University of Ljubljana, J. Stefan Institute, 1969–present. President of AMPERE Society 1988–94. Member of Slovenian, Croatian, Polish, Saxon and European Academies of Sciences. Member of Academy of Athens and Academia Europea. Approx. 450 publications and, with B. Zeks, the book 'Soft Modes in Ferroelectrics and Antiferroelectrics'. ISMAR prize 1977. Research interests include NMR of phase transitions and disordered condensed matter.

Nuclear Ferromagnetism and Antiferromagnetism

Anatole Abragam
Collège de France, Paris, France

1 Introduction 1
2 Dynamic Nuclear Polarization 2
3 The Keys to the Problem 2
4 The Rotating Frame and the Refrigerator Lamp 3
5 Antiferromagnetism in Calcium Fluoride 3
6 Ferromagnetism in Calcium Fluoride 4
7 Calling up Neutrons 4
8 Related Articles 7

1 INTRODUCTION

I believe it was in 1950, when I first met Ed Purcell at the Amsterdam conference on rf spectroscopy, that I heard him mentioning nuclear ferromagnetism as a very interesting phenomenon, but inaccessible in the present state of cryogenic techniques. Since then I had been thinking about it from time to time but it was only after I discovered dynamic nuclear polarization (DNP) in solids, a method that I shall describe shortly, that I had an inkling of the key to the problem.

To understand what nuclear ferromagnetism, or more generally, any long-range nuclear order, is like, one should first recall the nature of the external order introduced in a system of nuclear spins by an external magnetic field—the so-called Zeeman order. This is the kind of order which exists in the classical nuclear magnetic resonance (NMR) experiments. A nuclear spin placed in a magnetic field tends to align the magnetic moment that it carries along that field, that is into a position of lowest energy. However, when embedded into a piece of bulk matter, the nuclear spins are continually disoriented through thermal agitation. Between the orientation caused by the magnetic field and the disorientation due to thermal agitation, a compromise is reached where the nuclear polarization is of the order of the ratio $\boldsymbol{\mu}\cdot\boldsymbol{H}/kT$ of the magnetic energy of a nuclear magnetic moment $\boldsymbol{\mu}$ in a field $\boldsymbol{H}$ to the thermal energy kT. For protons at room temperature, this ratio is on the order of a few parts in a million in a field of 1×10^4 Oe which, however, is quite adequate for classical NMR (and of the order of a few parts in a billion in the Earth's magnetic field), but it is possible, using DNP, to reach polarizations close to unity.

If there is no external field, what are the conditions for the existence of a long-range order—say, ferromagnetic—of nuclear spins? It should occur when the energy of a single spin, resulting from its interaction with the surrounding spins, is not small compared with the thermal energy kT. A crude estimate can be made as follows: at the site of each nucleus exists a local magnetic field $\boldsymbol{H}_\mathrm{L}$, produced by its neighbors. It is on the order of a few gauss for protons and smaller for other nuclear species. One can guess that, for a long-range order to exist, the ratio $\boldsymbol{\mu}\cdot\boldsymbol{H}_\mathrm{L}/kT$ of the magnetic energy of each spin in the local field $\boldsymbol{H}_\mathrm{L}$ to the thermal energy kT should be at least of order unity. With a local field $\boldsymbol{H}_\mathrm{L}$ of a few gauss and the $\boldsymbol{\mu}$ of the proton, this yields temperatures below $1\,\mu$K—no wonder that Purcell considered it to be below the cryogenic possibilities of the day.

Before discussing the means for reaching this goal, I would like to illustrate the difference between a Zeeman order—induced by an external field—and an *internal* order—induced by interactions between the spins, through an image, suggested perhaps by my acquaintance with two learned societies, the Royal Society of London and the Pontifical Academy of the Vatican.

Imagine a Roman crowd massed in St Peter's Square, being addressed by the Supreme Pontiff from a window in the Vatican. All eyes in this crowd are turned towards that window and also, inevitably, all the noses which we shall choose as vector models of the spins. All the noses are therefore parallel to each other (neglecting the small effect of parallax). We have here a Zeeman order of noses, induced by the external 'pontifical field' which is the pontifical presence at the window.

Now imagine the same Roman crowd, already massed in the square half an hour before the Pope is due to appear at his window. They have no particular reason to look towards a window where the Pope will not appear for another half an hour, and one might think that their noses are orientated entirely at random. To see how an internal order of the noses may conceivably appear, we have to make a few plausible assumptions about interactions. We shall assume (not an unrealistic assumption) that these Romans are fond of eating garlic, which they consume in large quantities, but that they relish the taste of the garlic in their own mouths more than its smell on their neighbor's breath. There will be, for each Roman nose, a trend towards avoiding his neighbor's face and turning preferentially towards his back, which makes this nose parallel to his neighbor's nose. There is a 'ferromagnetic' coupling between their orientations. Does it mean that all the noses in the square will be parallel to each other? Not quite.

This, as I said, is a Roman crowd, warm and lively. They exchange jokes and comments, they fidget, they jostle each other, and no nose keeps the same orientation for any length of time. Furthermore their dislike of the smell of garlic exhaled by their neighbors is slight. It is a case of a weak interaction and a high temperature. There will be a short-range order where two neighboring noses tend to be parallel, but this order will not spread over a large distance, and there will be no correlation between the orientation of two noses, say 20 ft apart.

Now picture a crowd of English gentlemen (an endangered species, I was told but a recent stay in an Oxford college has convinced me that this is not so; the species is thriving) *unacquainted with each other*, who naturally would not dream of eating garlic. They are, however, mortally afraid of being spoken to by people to whom they have not been introduced. There will be a strong incentive for each of them to stare at a neighboring back, with again a ferromagnetic arrangement of the noses, caused by a ferromagnetic interaction which is much stronger than with my Romans. Furthermore, this is a *cold* crowd. They do not fidget and jostle each other, and every English nose keeps the same orientation for a long time. There is a strong interaction and a low temperature; there will be a long-range order, and two English noses many yards apart will be parallel to each other.

The ferromagnetic order of spins is not the only one which exists in nature: with electronic spins, an antiferromagnetic order was observed more than half a century ago; this is where the two nearest neighbors are antiparallel. (The reader may, if he or she so wishes, imagine what kind of food would induce an antiferromagnetic arrangement in the model of the Roman crowd.)

The frivolous analogy between an assembly of spins and the Roman crowd can be pushed a little further. In the Zeeman order, the external 'pontifical field' acts on the eyes rather than on the noses of the Romans and, if it orients the noses, it is indirectly because they are anatomically parallel to the direction of the eyes. On the other hand, in the internal order it is the noses themselves which are responsible for the orientation in the 'garlic' model.

The same thing happens in ferromagnetic ordering of electronic spins. Each spin carries a magnetic moment collinear with it, which is the analog of the parallelism between the eyes and the noses of the Romans. In the Zeeman order, an external magnetic field applied to a ferromagnetic substance will act on the *magnetic moments* rather than on the spins, and the spins will follow because they are collinear with the magnetic moments. On the other hand in the internal order it is the spins themselves which are responsible for the ferromagnetic ordering through a nonmagnetic quantum-mechanical exchange coupling and it is the magnetic moments which follow suit.

In nuclear ordering, the exchange coupling between spins does not exist (with the exception only of ^{3}He which is not considered here). There is no other coupling between nuclear spins but magnetic, and at least for light nuclei it has a well-defined mathematical form—the so-called dipolar form—and a magnitude which is entirely determined from the values of the magnetic moments and the interatomic distances, all of which is very well known. Everything in nuclear dipolar order can thus be calculated entirely, at least in principle if not in practice; it is a 'clean' problem. It was these twin aspects, the cleanliness and the arduousness (something like the snowy purity of a Himalayan summit), which for many years attracted me and my co-workers in this quest. But before going any further it is necessary to explain the means which made this quest possible, namely the DNP.

2 DYNAMIC NUCLEAR POLARIZATION

Consider a solid insulator containing nuclear spins I and at a much smaller concentration, say one part in a few thousands, electronic spins S. Assume conditions of field and temperature, say 2.5×10^4 Oe and 1 K, such that the spins S are completely polarized, say all pointing 'up', and the nuclear spins, with their magnetic moments thousands of times smaller, almost completely unpolarized, as many 'up' as 'down'.

Assume also that the spin–lattice relaxation time of the spins S is very short so that, if through any circumstance a spin S happens to flip to the 'down' position away from equilibrium, its relaxation mechanism will bring it very rapidly back to the 'up' position. All these assumptions are quite realistic. The DNP problem is to bring all the nuclear spins to the 'up' position.

Consider a nuclear spin which is 'down'. It could come 'up' by making a flip-flop with an electronic spin which is 'up'. This requires an energy $\Omega = \Omega_S - \Omega_I$ which in a liquid could be borrowed from the kinetic energy of the relative motion of the two spins, but which is lacking in a rigid lattice. This energy can be provided to the spins by means of an external microwave source of frequency Ω, driving a flip-flop which brings the spin I 'up' and the spin S 'down'. However, the spin S which has come 'down' returns immediately to its equilibrium 'up' position because of its fast relaxation time. The spin I, which has come 'up', 'sees' around it only spins S also pointing 'up' with which it cannot flip-flop. It might flip-flip, however, if the energy for it ($\Omega_S + \Omega_I$) were available, but it is not, and so the spin I stays 'up'. All the spins I are thus, one by one, brought into the 'up' position.

The extreme assumption of a 100% polarization of the spins S, made for simplicity, is by no means necessary; it can be shown that, whatever the electronic polarization, this method in principle permits nuclear polarization to become equal to it.

An identical argument shows that, if the sample is irradiated with the flip-flip frequency $\Omega = \Omega_S + \Omega_I$, this will impart a polarization to the nuclear spins which is equal but opposite to the electronic polarization.

One should stress the importance of the fast relaxation of the spins S. Each of the spins S has to 'service' thousands of spins I. No sooner has it flip-flopped with a spin I than it has to come back into the position 'up' to 'service' another spin I. This fast relaxation calls for qualities, whose human analog led me sometimes to call this effect the 'King Solomon method'.

3 THE KEYS TO THE PROBLEM

The keys to the problem are DNP and the spin temperature. The first produces an almost perfect Zeeman order of the nuclear spins, and the second a 'cooling' of the nuclear spins to temperatures required for the production of a long-range order—a microkelvin or less—replacing the 'external' Zeeman order by an 'internal' dipolar order.

In fact the concept of spin temperature can advantageously be replaced by that of entropy, for which it is enough to remember here that it is a quantitative measure of the order existing within a system. The entropy is zero if the order is perfect and has its maximum value in a situation of complete chaos. By producing an almost perfect Zeeman order, one reduces the system's entropy to nearly zero, or at least to a value lower than the critical entropy, which is the value below which long-range order appears. The next step is to suppress the applied field very slowly and reversibly (adiabatically is the technical term), taking care to introduce as little new disorder as possible in the process, that is an increase in entropy which is as small as possible. During this 'adiabatic demagnetization' as it is called, the external Zeeman order turns progressively into an internal dipolar order. (The Roman analog of adiabatic demagnetization would be the disappearance of the Pope from his window, very gradually and very slowly, something like the Cheshire cat.) There is one practical difficulty connected with adiabatic demagnetization. Considering the weakness of nuclear magnetic moments, NMR is still to a large extent the only method for observing their behavior, but NMR is only observable in a high magnetic field. By reducing this field to zero in an adiabatic demagnetization, one may perhaps be creating an ordered state of the spins but, in the same move,

one deprives oneself of the possibility of making sure of its existence. It is not unlike trying to find out whether the lamp in a refrigerator goes off when one closes the door. I am now going to digress to explain the nature of the rotating frame, a concept familiar to NMR users, and how it may solve what I call the problem of the 'refrigerator lamp'.

4 THE ROTATING FRAME AND THE REFRIGERATOR LAMP

Use of the rotating frame makes it possible to '*have your cake and eat it*', that is to transfer the Zeeman order which has been created by DNP in a high field $\boldsymbol{H}$ to the dipolar spin–spin interaction, while keeping on that high field for observing the state of the spins by NMR.

The difficulty resides in the fact that the Zeeman energy is quantized in quanta of the order of, say, a hundred megahertz, whereas the energy spectrum of the dipolar energy does not extend beyond some hundred kilohertz. In high fields the two systems are not 'on speaking terms'. It is, however, possible to ensure a flow of energy and thus also of entropy between them, by providing the dipolar system with the energy that it lacks to 'speak' to the Zeeman system in the form of rf quanta which are brought in by an rf field, rotating at a frequency Ω near the Zeeman frequency Ω_0.

One of the two frequencies (the Zeeman frequency Ω_0 in general) is swept slowly (adiabatically), from a value distant from Ω all the way to Ω, that is to resonance. At resonance most of the entropy contained in the disordered dipolar system passes on into the Zeeman system or, in other words, most of the Zeeman order passes on into the dipolar system. Then, after the rf field is cut off, the two systems are again isolated from each other. One might think that the presence of the high magnetic field can be forgotten. Not quite. Although the cutting off of the rf field suppresses the flow of energy (and entropy) between the Zeeman and the dipolar system, it can be shown (we shall not do so here) that, simply by being present, the high magnetic field splits the dipolar spin–spin interaction into two parts. Only one of them, the so-called 'truncated' part, is effective in the presence of the high applied field.

The form of this truncated part depends on the orientation of the applied magnetic field with respect to the crystalline axes of the sample—which is a very essential fact.

The above presentation can be put on a more quantitative basis by introducing the concept of the 'rotating frame'. To describe the behavior of the spins in the presence of a rotating field, it is convenient to choose as a frame of reference, one which rotates with the angular velocity of Ω of the field; this is the 'rotating frame'. In that frame the rotating field of amplitude $\boldsymbol{H}_1$ orthogonal to the applied field $\boldsymbol{H}$ appears as a static field of magnitude H_1, which is much simpler. On the other hand, since the new frame is rotating, it is not an inertial frame any longer, and an inertial force must be brought in. It can be shown that this is equivalent to replacing the large applied field $\boldsymbol{H}$ by a fictitious field $\Delta\boldsymbol{H} = \boldsymbol{H} - \boldsymbol{H}^*$, where $\boldsymbol{H}^*$ is the value of $\boldsymbol{H}$ at exact resonance, when the Zeeman frequency Ω_0 has been made equal to Ω. In the rotating frame the spins 'think' that they 'feel' an effective field $\boldsymbol{H}_e$ which is the geometrical sum of the two static fields $\Delta\boldsymbol{H}$ and $\boldsymbol{H}_1$ orthogonal to each other.

The opening of the flow of entropy between the Zeeman and the dipolar systems is called adiabatic demagnetization in the rotating frame (ADRF). Far from resonance, $\Delta\boldsymbol{H}$ is much larger than $\boldsymbol{H}_1$ and the effective field $\boldsymbol{H}_e$ is almost parallel to the applied field $\boldsymbol{H}$, and thus also to the equilibrium magnetization $\boldsymbol{M}$. In the course of the ADRF this magnetization 'follows' the effective field which moves increasingly farther away from the direction of $\boldsymbol{H}$ until, at exact resonance, where $\Delta\boldsymbol{H}$ vanishes, $\boldsymbol{H}_e$ reduces to the rf field $\boldsymbol{H}_1$. The ADRF is then brought to an end by removing the field $\boldsymbol{H}_1$.

One should note that, if the ADRF is started from the other end of the resonance where $\Delta\boldsymbol{H} = \boldsymbol{H} - \boldsymbol{H}^*$ is *antiparallel* to $\boldsymbol{H}$, one starts from a situation where the equilibrium magnetization $\boldsymbol{M}$ is *antiparallel* to the effective field $\boldsymbol{H}_e$, that is from a state of *negative* temperature. This sign does not change as the ADRF proceeds and leads to a dipolar state of negative temperature.

Besides solving the problem of the 'refrigerator lamp', ADRF brings new and fascinating variations on the conventional theme of dipolar order. Two different orientations of the applied field with respect to the crystalline axes correspond to two different ways of truncating the dipolar interaction and two, qualitatively different ordered structures. Furthermore, for a given orientation of the field, the two signs of the spin temperature must correspond to quite different structures since at negative temperatures a stable structure of the spins is one which *maximizes* the energy. The nuclear magnetic order is thus very much richer than the classical electronic order. As an example, we shall single out for description, in the following, two such ordered states.

Naturally the lifetime of a state where the spins are at a positive or negative temperature, whose absolute value is millions of times lower than the lattice temperature, is limited by the spin–lattice relaxation time T_d (the subscript d referring to dipolar) which, for reasons that would be too long to discuss here, is shorter by several orders of magnitude than the Zeeman relaxation time T_1. Yet these times T_d may sometimes reach values of the order of 1 h, making the study of such ordered states possible.

5 ANTIFERROMAGNETISM IN CALCIUM FLUORIDE

The first substance chosen for the observation of nuclear magnetic order was a single crystal of calcium fluoride (CaF_2) where the nuclei of ^{19}F which have a spin-$\frac{1}{2}$ form a simple cubic lattice and the calcium nuclei, apart from a rare isotope ^{43}Ca, have zero spin. Since the ordered structures obtained by ADRF depend on the orientation of the magnetic field with respect to the crystalline axes, it is imperative to use single crystals. I pass over the different difficulties encountered in building the equipment, choosing the adequate impurities for doping the crystal, and, on the theoretical side, calculating the structures to be expected and the critical nuclear polarizations to be obtained before ADRF.

The first observation of an antiferromagnetic nuclear state was made in CaF_2 with an initial polarization higher than 60%, a negative temperature, and a field $\boldsymbol{H}$ applied along a *fourfold* axis of the cube. As predicted by theory, one observed a characteristic plateau in the transverse magnetic susceptibility

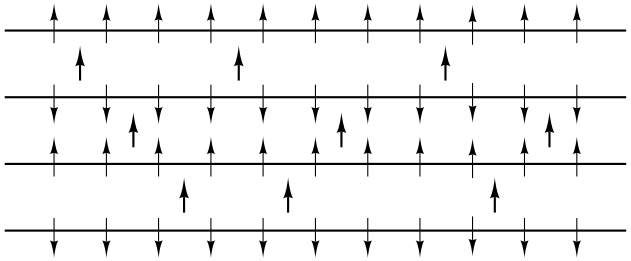

Figure 1 Antiferromagnetic ordered structure of the ^{19}F spins in CaF_2 with the field along the (001) axis and with a temperature less than 0 K. The ^{43}Ca spins all 'see' the same local field produced by the fluorines. (Light arrows for the spins of ^{19}F, heavy arrows for the spins of ^{43}Ca which act as probes)

as a function of the dipolar energy of the fluorine spins. The structure is the Néel two-sublattices model, where the nuclear spins of the successive atomic planes are alternately parallel and antiparallel to the field. The structure is shown in Figure 1. The spins of the sublattice A, which are parallel to the field, yield a positive signal, and those of the second sublattice B a negative signal. They do not cancel each other because they are displaced with respect to each other by internal mean fields which have opposite signs in the two sublattices, as shown below in Figure 3(a). (For the reader familiar with NMR techniques, this is not the *derivative* of the resonance curve!)

6 FERROMAGNETISM IN CALCIUM FLUORIDE

Theory predicts a ferromagnetic state in the same crystal, again at negative temperature, for a field applied along a *threefold* axis of the cube. This ferromagnetic structure is made up of ferromagnetic domains, which are slabs perpendicular to the applied field, each some hundred atomic planes thick, where nuclear spins in the successive *slabs* are alternately parallel and antiparallel to the field, as shown in Figure 2. It is easy to convince oneself that the NMR signal of the fluorine spins [see Figure 4(a)] should look very much the same as in the antiferromagnetic structure in Figure 3(a).

The problem of discriminating between the two structures where the fluorine spin signals are almost indistinguishable from each other, can be solved because of the existence of ^{43}Ca, a rare (0.13%) isotope of calcium with a small magnetic moment, which serves as a probe. In the antiferromagnetic structure of the fluorine spins, all the positions of a calcium nucleus are equivalent (Figure 1) and all the spins of ^{43}Ca 'see' the same mean field produced by the fluorine atoms whereas, in the ferromagnetic domain structure, spins of ^{43}Ca, situated in domains of opposite signs, 'see' opposite mean fluorine fields (Figure 2). The Zeeman NMR signal of ^{43}Ca is thus a single line in the antiferromagnetic structure and a double line in the ferromagnetic case (Figure 4)—indisputable experimental evidence of the difference between the two structures. (This, in my view, is still one of the cutest experiments in NMR.)

7 CALLING UP NEUTRONS

For many years, neutron diffraction has been a valuable tool in the study of *electronic* antiferromagnetism. This can

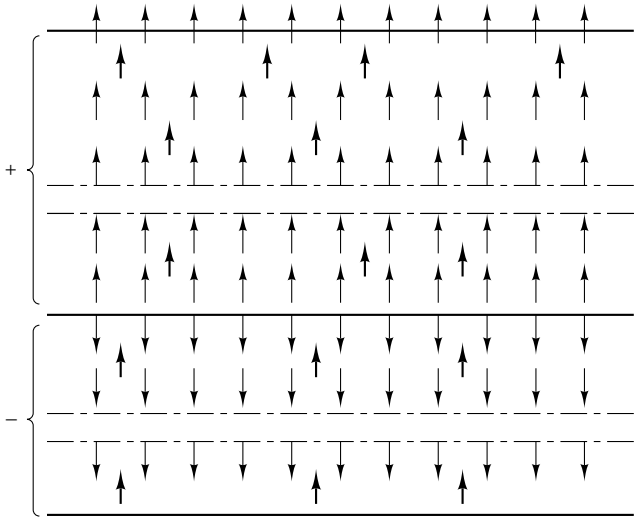

Figure 2 Domain ferromagnetic structure with the field along the (111) axis and with a temperature less than 0 K. The ^{43}Ca spins in opposite domains (heavy arrows) 'see' local fields of opposite signs

be understood by comparison with X-ray diffraction. When an X-ray beam impinges on a crystal, for certain orientations of the beam with respect to the atomic planes of the crystal, there is constructive interference between the X-photons scattered by the different atoms of the crystal, and sharp maxima of diffracted radiation, called Bragg peaks, are observed in certain well-defined directions. If the crystal is antiferromagnetic, the magnetic moments of its atoms will have opposite orientations in two neighboring atomic planes. The scattering amplitude of an X-photon on a magnetic atom is independent (almost) of the orientation of its atomic moment and the X-photon is unable to 'distinguish between' two such planes.

On the contrary, the neutron which carries a magnetic moment will have different scattering amplitudes on two magnetic atoms with opposite moments. It will 'see' two neighboring atomic planes of an antiferromagnet as being different, and it will 'deduce' a lattice period twice as large as the crystalline period. The Bragg condition applied to this new period will give rise to new Bragg peaks when an antiferromagnetic state sets in (Figure 5).

It was naturally tempting to seek from neutrons the same tangible evidence for the existence of *nuclear* antiferromagnetism. This was even more tempting because reports of the antiferromagnetic structure described in Figure 1 were, at first, met with incredulity. The objection offered to me when I first reported it at an international conference was that the structure that I described could not exist because it *maximized* the energy of the spins, and my reply that this was indeed expected of a system at a negative temperature, did not convince everybody.

The objection to the use of neutrons for studying nuclear antiferromagnetism (which was also offered to me when I first made this suggestion) was the smallness of the nuclear magnetic moments which would prevent the observation of antiferromagnetic Bragg peaks. There is, however, a way out. The scattering of a neutron by a nucleus is due to a *nuclear* force and its amplitude depends on the relative orientation of the spin of the neutron and the spin of the nucleus. The scattering amplitude will be different for

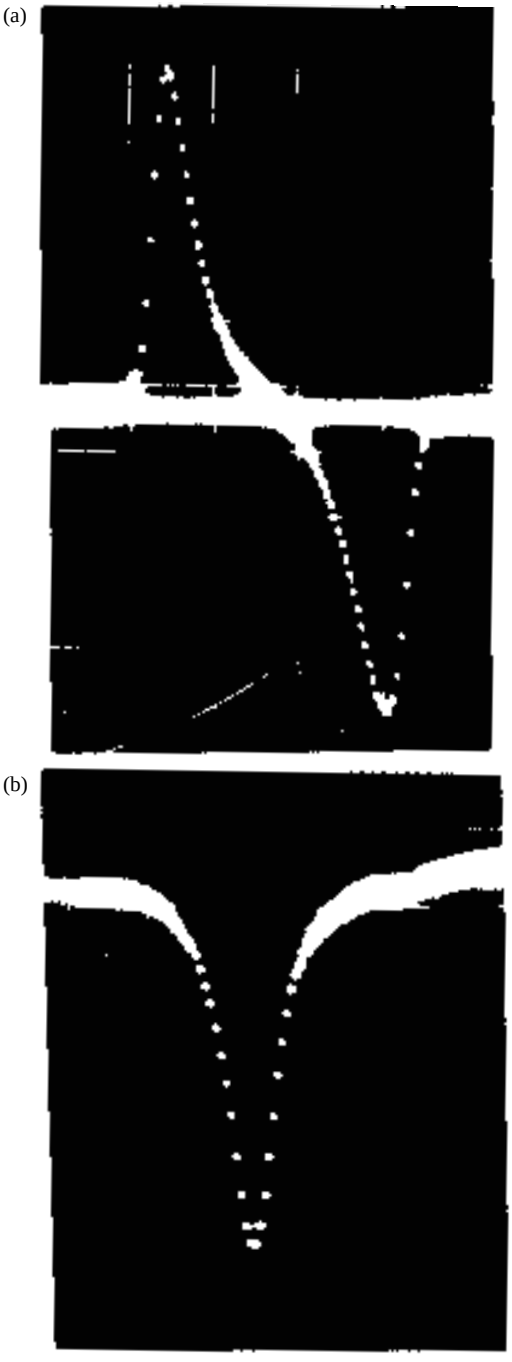

Figure 3 Antiferromagnetic structure: (a) NMR line of ^{19}F; (b) a single Zeeman NMR line of ^{43}Ca as explained in the text

two nuclei with opposite spins. The neutron spin is thus capable of distinguishing between two nuclear spins with opposite orientations, not through a magnetic interaction with their magnetic moments but through a *nuclear* interaction with their spins. The neutron is therefore able to recognize the difference between two planes with opposite nuclear orientations and is thus capable in principle of detecting nuclear antiferromagnetism. It is convenient to pretend that this 'recognition' is of a *magnetic* nature by assigning to each nuclear species a fictitious magnetic moment which is called its 'pseudomagnetic' moment and is represented by the symbol

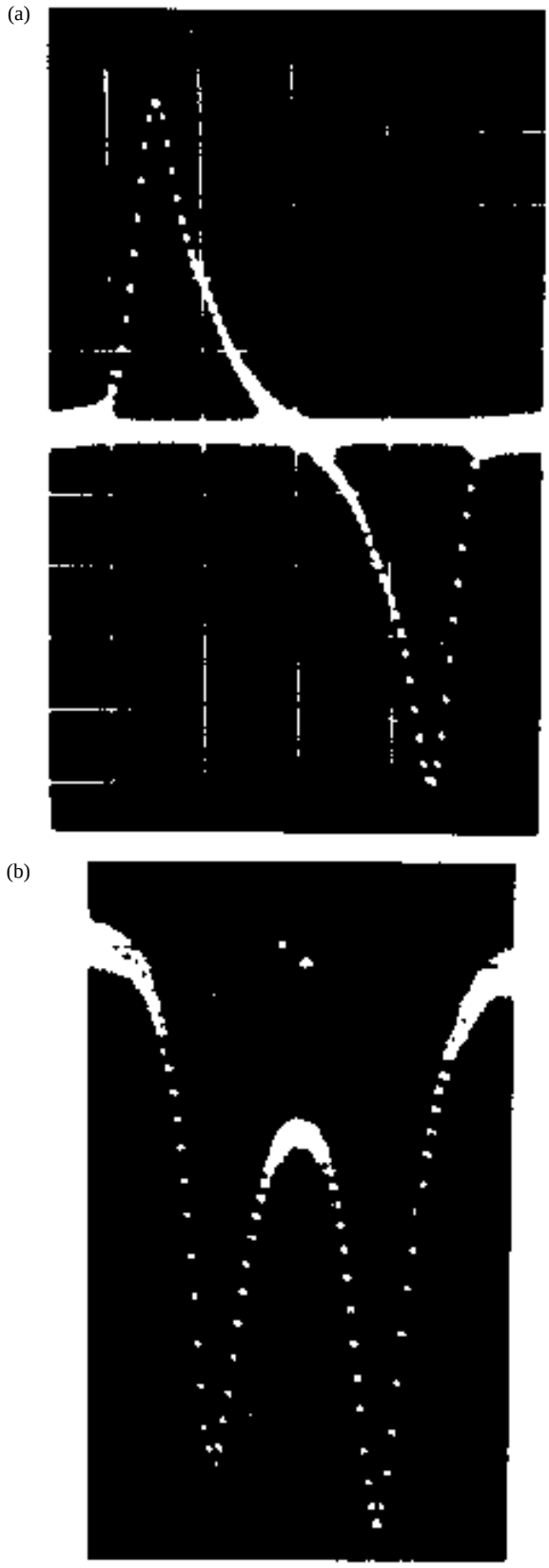

Figure 4 Domain ferromagnetic structure: (a) NMR line of ^{19}F, indistinguishable from the NMR line in Figure 3(a); (b) a Zeeman line of ^{43}Ca with two peaks, as explained in the text

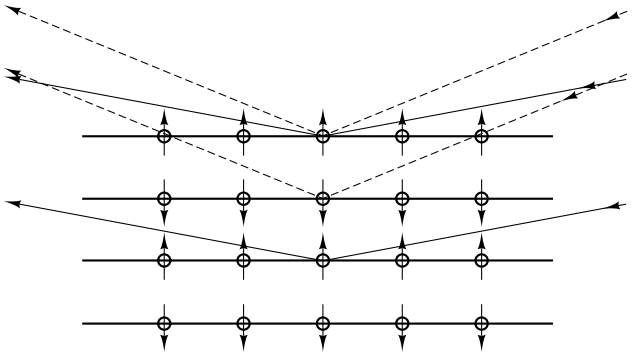

Figure 5 Normal and antiferromagnetic scattering of a neutron by an antiferromagnetic lattice (schematic). Dashed lines refer to normal scattering, full lines to antiferromagnetic scattering

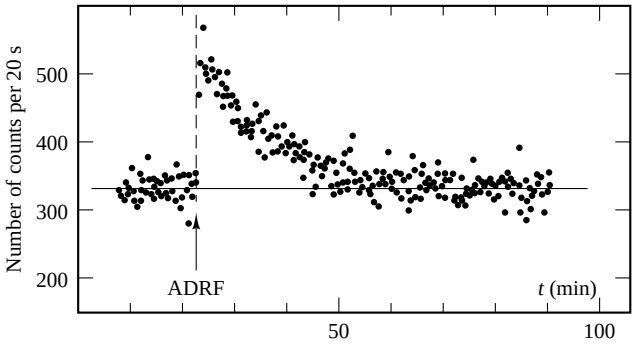

Figure 6 Sudden surge of an antiferromagnetic Bragg line, just after adiabatic demagnetization in the rotating frame, and its slow decay with the lifetime of an antiferromagnetic state. Produced in LiH, at $T < 0\,\mathrm{K}$, with the field along the (001) axis

μ^*. By definition, this pseudomagnetic moment is equal to the magnetic moment that a nucleus should possess in order that its *magnetic* coupling with the *magnetic* moment of the neutron be equal to the actual nuclear coupling, which exists between the spin of the neutron and the spin of the nucleus.

Nuclear forces are much stronger than magnetic forces, and there is reason to believe that a nuclear pseudomagnetic moment of the nucleus would be much larger than its true magnetic moment. It is certainly so for the proton whose pseudomagnetic moment $\mu^*(^1\mathrm{H})$ is 3500 times larger than its real magnetic moment. Unfortunately $\mu^*(^{19}\mathrm{F})$, once measured, turned out to be only 15-times larger than its true magnetic moment (and of opposite sign). This was far too small to observe the antiferromagnetic structure of CaF_2 and we decided to move on to a crystal containing protons, namely lithium hydride (LiH). It was not an easy task since it was only after four years of work that we were able to observe for the first time by neutron diffraction our first antiferromagnetic Bragg peak in LiH.

I shall omit here all the difficulties that we ran into during these four years, not the least of which was the fact that, unlike CaF_2, LiH is a nasty crystal, hard to grow, to dope in a reproducible way and to handle. I shall be content to describe briefly the decisive experiment where the antiferromagnetic neutron Bragg peak was first seen.

The neutron counter for diffracted neutrons had been placed in the position where the antiferromagnetic Bragg peak was expected and the nuclei of the sample were dynamically polarized above the calculated critical polarization. The counter started to count background neutrons, as expected, since the sample was not *antiferromagnetic yet*. Then the ADRF was performed. The counting rate made a jump which corresponded to the expected antiferromagnetic peak and then decreased slowly to background level with a time constant of the order of an hour, while the entropy of the nuclear spins slowly grew as a result of relaxation until it reached the critical value above which the antiferromagnetic order disappears (Figure 6). It was one of the finest hours in our laboratory.

Need I add that diffraction experiments with LiH were pursued, improved, amplified, compared with theoretical predictions, and reported at numerous international conferences. Figure 7 shows one such result. I last spoke of it in 1986 at the Royal Society in my Claude Bernard Lecture (from which the figures are taken).

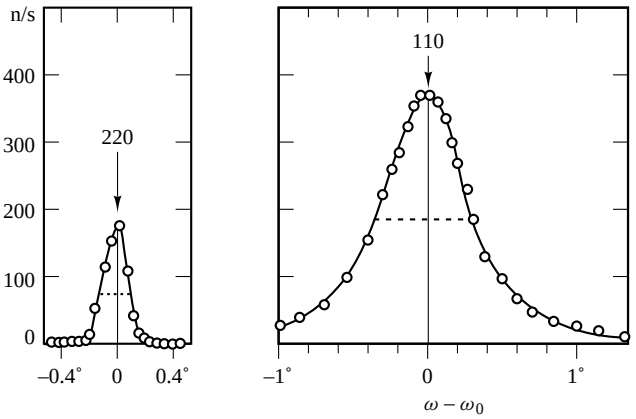

Figure 7 Normal Bragg reflection line in LiH (left) with unpolarized spins and antiferromagnetic reflection line (right) at negative temperature with the field along (001). Scattering angle along the x axis, neutron counts along the y axis

Lest the reader should be led to conclude from the examples offered so far that *positive* temperatures have no physical existence, Figure 8 shows the same type of experiment as in Figure 6, but with a positive spin temperature.

An amusing contrast can be drawn between electronic and nuclear antiferromagnetism and their study with neutrons. It is well known that electronic antiferromagnetism is caused by exchange interactions between electronic *spins* which are

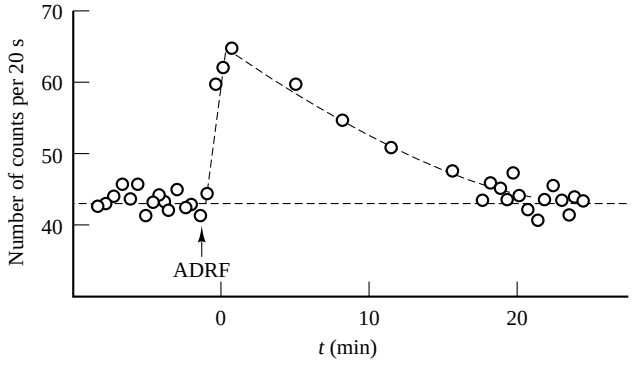

Figure 8 Same as Figure 6 but at a *positive* temperature $T > 0\,\mathrm{K}$

of a *nonmagnetic* nature. On the other hand its observation by neutron diffraction rests on the existence of *magnetic* interaction between the *magnetic* moments of the neutrons and the electrons. To sum up, we have a *nonmagnetic* phenomenon detected by *magnetic* means.

On the other hand, nuclear antiferromagnetism is a purely *magnetic* phenomenon due to *magnetic* interactions between nuclear *magnetic* moments, but its detection by neutrons rests on a nuclear, and therefore *nonmagnetic* interaction (termed for that reason pseudomagnetic) between nuclear spins and neutron spins. This is a purely magnetic phenomenon, detected by nonmagnetic means. 'So what?', one may ask. 'So nothing; it's an amusing contrast, that's all.'

At the end of a lecture on nuclear magnetic order (I have given more than one), I used to speculate on the question: 'What future for nuclear magnetic order?' I would not do this any longer. But it has a nice past.

I cannot conclude without mentioning that the Finnish school headed by Professor Lounasmaa has worked for many years on the production and observation of nuclear magnetic order in metallic copper. Their approach and their methods were very different from ours. They worked on a metal (copper) and used 'brute-force' polarization and demagnetization in the laboratory frame. We worked on insulators and used dynamic polarization and demagnetization in the rotating frame. Whichever method is better, one thing is certain: we got there first.

8 RELATED ARTICLES

Dynamic Nuclear Polarization and High-Resolution NMR of Solids; Ferroelectrics and Proton Glasses; Low Spin Temperature NMR; Thermodynamics of Nuclear Magnetic Ordering.

Biographical Sketch

Anatole Abragam. *b* 1914. Graduate of the Sorbonne, Member of the French Academy of Sciences, Foreign Member of the Royal Society of London, Foreign Associate of the US National Academy of Science. D.Phil., 1950, Oxford, UK, Hon.D.Sc., 1972, Oxford, UK, and others. Professor of Nuclear Magnetism at the Collège de France, 1960–85; Director of Physics, French Atomic Energy (CEA), 1965–70, Director of Research, 1970–80. Approx. 100 Publications. Research interests: nuclear and particle physics, solid state physics, atomic physics, muon physics, and particle accelerators.

Fast Ion Conductors

Thomas K. Halstead
York University, York, UK

1	Introduction	1
2	Ionic Transport	1
3	NMR Methods	2
4	Correlation Functions	3
5	Examples of NMR Studies	4
6	Related Articles	6
7	References	6

1 INTRODUCTION

Fast ion conductors (FICs) are generally defined as solids with ionic conductivity comparable to that found in liquids, typically 1–10 S m^{-1}, with often an unusually low activation energy for ionic motion, $E \propto 10$ kJ mol^{-1}.[1] The terms 'solid electrolyte' and 'superionic conductor' are also widely used, and the related field of interdisciplinary research is known as 'solid state ionics'. Concerns about environmental pollution and depletion of oil resources stimulated interest in FICs because of their potential use in rechargeable batteries. Interest has been sustained by the promise of other practical applications including fuel cells, chemical sensors and electrochromic displays, and by a desire to gain a better fundamental understanding of the unusual dynamic properties of these materials.

FICs are very diverse but can be divided roughly into two groups: crystalline and amorphous.[2] The crystalline materials include ionic crystals, e.g. AgI, $RbAg_4I_5$, and PbF_2, and covalent, layer- and tunnel-structured crystals, usually oxides, e.g. β-aluminas, Li_3N, and $LiAlSiO_4$. The amorphous materials include organic polymers, e.g. poly(ethylene oxide) doped with lithium triflate, and inorganic glassy systems, e.g. $AgI–Ag_2O–B_2O_3$ and $Li_2S–SiS_2$.

X-ray and neutron diffraction are the primary tools used in structural determinations of FICs. Conductivity measurements are routinely made to investigate the mechanisms of ion transport. Tracer diffusion is of very limited applicability, owing to the high diffusion coefficients of FICs, but quasielastic neutron scattering and NMR have provided experimental information about the ionic motion at a microscopic level (see also ***Diffusion in Solids***). The motion of the ions can be simulated using computer modeling techniques such as molecular dynamics (MD).

NMR has always played an important role in solid state ionics, contributing considerably to the understanding of several FICs.[3–9] NMR parameters that are used to probe the dynamic properties of FICs include linewidths and lineshapes and their temperature-dependent narrowing, nuclear spin–lattice and spin–spin relaxation times, and direct measurement of the diffusion coefficient by the pulsed field gradient technique and solid state NMR imaging. Protons, ^{7}Li, ^{19}F and ^{23}Na have been the most popular NMR probes. The information available from these studies includes the type and number of mobile ions, the prefactor, activation energy and activation volume of these motions, and dimensionality, correlation and cooperative effects. Some of the most useful information comes from relaxation time measurements because these studies provide correlation times and, in favorable cases, correlation functions that can be related to microscopic processes.

Relaxation data for FICs often deviate strongly from the well known Bloembergen–Purcell–Pound (BPP) model. The most obvious difference is that the ln T_1 vs $1/T$ plot is not symmetrical about the T_1 minimum, suggesting that the correlation function is not a single exponential function of time. Taking into account that the ions hop over a discrete one-, two-, or three-dimensional lattice, or may experience short-range interactions with each other, results in only small changes to the shape of the relaxation curve.

The simplest of several phenomenological approaches is to assume a distribution of relaxation rates with a distribution of activation energies for ionic motion. On the other hand, a homogeneous model with a single, but nonexponential, correlation function, such as the Kohlrausch–Williams–Watt (KWW) function (stretched exponential), can often fit the same observations. There have been several attempts to derive the KWW equation from first principles.

2 IONIC TRANSPORT

According to the classical model of atomic diffusion in solids, a mobile ion jumps over a potential barrier of height E (the activation energy) at a rate

$$\nu = \nu_0 \exp(-E/kT) \tag{1}$$

called the jump frequency.[5] The 'attempt' frequency ν_0 is typically related to a vibrational frequency of the ion about its equilibrium position and comparable to a phonon frequency. By assuming that the ion undergoes uncorrelated jumps of length l at a rate ν, the diffusion coefficient can be expressed as

$$D = \nu l^2/2d \tag{2}$$

where d is the dimensionality of the system (d = 1, 2, 3). The hopping (or mean residence, or dwell) time $\tau_d = 1/\nu$ is assumed to be long compared with the transit (or flight time). The Nernst–Einstein equation gives the dc ionic conductivity as

$$\sigma = cq^2 D/kT \tag{3}$$

where c is the density of mobile ions carrying charge q. In FICs, in contrast to normal ionic solids, c is usually taken to be temperature-independent and equal to the mobile ion concentration.

The ratio of the directly determined diffusion coefficient (usually from tracer measurements) to that calculated from the conductivity, σ, via equation (3) is called the Haven ratio, H_R. H_R is not necessarily unity and is sensitive to the details of the diffusion mechanism. For a typical FIC, $\sigma \approx 10$ S m^{-1} at 300 K, $c \approx 10^{28}$ m^{-3}, therefore $D \approx 1.6 \times 10^{-2}$ m^2 s^{-1}.

A typical jump distance, $l \approx 0.3\,\text{nm}$, gives $\tau_d \approx 10^{-10}\,\text{s}$. c and l must be known before ν can be calculated from the conductivity. One advantage of NMR is that it can often provide a direct estimate of ν.

3 NMR METHODS

NMR is particularly valuable in the field of FICs because of the information it can provide about ionic diffusion.[3–7] The range of diffusion coefficients that are accessible to NMR methods is 10^{-20}–$10^{-8}\,\text{m}^2\,\text{s}^{-1}$, corresponding to hopping times in the range 1–10^{-12} s. A distinct advantage of NMR over some types of diffusion experiments, such as ionic conductivity or creep, is that the mobile ions in a multicomponent system are readily identifiable. It is possible to study materials in which the same ion diffuses by more than one process, and to distinguish between localized and long-range motion, and between bulk and surface effects. Low sensitivity is one disadvantage and another is that it cannot be used to study diffusion in paramagnetic systems, and even quite low levels of paramagnetic impurities can mask the effects of diffusion. NMR has been used to study atomic diffusion in other solids (see ***Diffusion in Porous Media***; ***Diffusion in Rare Gas Solids***; ***Hydrogen–Metal Systems***; ***Intercalation Compounds*** and ***Ultraslow Motions in Solids***).

3.1 Line Narrowing

At low temperatures where the ionic hopping time, τ_d, is long, the NMR lineshapes characteristic of the rigid lattice are observed. When τ_d becomes comparable to the inverse of the characteristic linewidth, $1/\delta\omega$, the linewidth narrows. For nuclei with spin of $\frac{1}{2}$, e.g. ^{1}H, for which the nuclear dipole–dipole interaction usually dominates, the rigid-lattice lineshape is a featureless bell shape, and appreciable narrowing occurs when $\tau_d < 10^{-4}$ s. For quadrupolar nuclei, e.g. ^{2}H, for which the nuclear electric quadrupole interaction dominates, spectra may exhibit a series of well defined time-averaged lineshapes, with strongly distorted and attenuated spectra in intermediate regimes, before narrowing completely. Hopping times as short as the order of 10^{-7} s can be extracted from ^{2}H NMR lineshape studies.

3.2 Nuclear Spin Relaxation

Nuclear spin relaxation (NSR) is caused by the time dependence of the spatial part of the Hamiltonian describing the spin–lattice interaction (see ***Dipolar and Indirect Coupling Tensors in Solids***, ***Internal Spin Interactions and Rotations in Solids*** and ***Relaxation: An Introduction***).[3–5,10] The Hamiltonian is the product of a spin operator part and a 'lattice' function $F(\boldsymbol{r}(t))$. The spin operator part is treated quantum mechanically, while the lattice function is assumed to form a classical autocorrelation function (CF)

$$g(t) = \langle F(t)F^*(0)\rangle / \langle FF^*\rangle \tag{4}$$

The nuclear spin–lattice relaxation rate is given by

$$\frac{1}{T_1} = A\{j(\omega_0) + 4j(2\omega_0)\} \tag{5}$$

where $\omega_0 = -\gamma B_0$ is the resonance frequency.

A is proportional to the mean square interaction Ω_{SL}^2, describing the strength of the coupling between the spin system acting as a probe for the motion of the ions and the 'lattice'. In the case of the dipole–dipole interaction between two diffusing spins, $\Omega_{SL}^2 \propto M_2$, the Van Vleck second moment. For quadrupolar nuclei, e.g. ^{7}Li, ^{23}Na, and ^{2}H, if quadrupolar relaxation is dominant, $\Omega_{SL}^2 \propto \chi^2$, the square of the quadrupole coupling constant (***Relaxation Theory for Quadrupolar Nuclei***). In the case of heavy nuclei, e.g. ^{109}Ag, chemical shielding anisotropy is the dominant interaction; consequently $\Omega_{SL}^2 \propto \omega_0^2$. The spectral densities $j(\omega)$ are the real parts of the Fourier transforms of the CFs,

$$j(\omega) = \int_0^\infty g(t)\cos(\omega t)\,\mathrm{d}t \tag{6}$$

The spin–spin relaxation time, T_2, is given by

$$\frac{1}{T_2} = A\{\tfrac{3}{2}j(0) + \tfrac{5}{2}j(\omega_0) + j(2\omega_0)\} \tag{7}$$

This equation is valid only in the motionally narrowed regime when $T_2 \gg (\gamma B_{loc})^{-1}$, where B_{loc} is the local dipolar field. If spin–lattice relaxation occurs in the presence of a resonant rf field, B_1, and $B_0 \gg B_1 > B_{loc}$, then its characteristic time, $T_{1\rho}$, is called the spin–lattice relaxation time in the rotating frame,

$$\frac{1}{T_{1\rho}} = A\{\tfrac{3}{2}j(2\omega_1) + \tfrac{5}{2}j(\omega_0) + j(2\omega_0)\} \tag{8}$$

where $\omega_1 = -\gamma B_1$.

In order to relate $j(\omega)$ to ionic diffusion, $g(t)$ must be calculated for a given mechanism of motion. In a rough approximation it is quite reasonable for a motional process to let $g(t)$ have the functional form

$$g(t) = \exp(-|t|/\tau_c) \tag{9}$$

where τ_c is the 'NMR correlation time' (***Brownian Motion and Correlation Times***). In general, τ_c differs from the mean residence time, τ_d, of the mobile ion. In the case of the motion of a spin pair, $\tau_c = \tau_d/2$. Furthermore, spatial and temporal correlation effects in the motion process influence the relationship between τ_c and τ_d. After carrying out the Fourier transform of equation (9), the NSR rate may be expressed as

$$\frac{1}{T_1} = A\left(\frac{\tau_c}{1+\omega_0^2\tau_c^2} + \frac{4\tau_c}{1+4\omega_0^2\tau_c^2}\right) \tag{10}$$

Equation (10) is usually referred to as the 'BPP' equation, and similar expressions for T_2 and $T_{1\rho}$ may be obtained from equations (7) and (8), respectively. Although equation (10) is only an approximation, it provides a fair basis for describing the important general trends in a motion-induced relaxation

process. The main feature of the relaxation rates is that they peak at different correlation times. $1/T_{1\rho}$ has a maximum when $\omega_1\tau_c \approx 1$, so it is most sensitive to hopping rates $1/\tau_c \approx \omega_1 \approx 10^5\,s^{-1}$. On the other hand, $1/T_1$ peaks near $\omega_0\tau_c \approx 1$, i.e. for $1/\tau_c \approx \omega_0 \approx 10^9\,s^{-1}$. So the various relaxation rates can be measured to probe a wide range of ion hopping rates. Since $1/T_1$ is becoming small for $1/\tau_c \gg 10^9\,s^{-1}$ the maximum hopping rate that can be measured by NMR is determined by the point at which relaxation processes other than diffusion began to dominate. This is often determined by the level of paramagnetic impurities in the sample. The limiting forms of the BPP equation, for dipolar and quadrupolar relaxation, are

$$\frac{1}{T_1} = \begin{cases} \tau_c, & \omega_0\tau_c \ll 1 \\ (\tau_c\omega_0^2)^{-1}, & \omega_0\tau_c \gg 1 \end{cases} \tag{11}$$

If the temperature changes of τ_c can be described by a simple activation law, analogous to equation (1), both above and below the T_1 minimum, the slope of ln T_1 vs $1/T$ yields the activation energy of the motion.

3.3 PFG Method

When diffusion is sufficiently fast ($D > 10^{-13}\,m^2\,s^{-1}$), the diffusion coefficient can be measured by the PFG method.[11] This method is equivalent to a tracer experiment where the nuclear spin is used as a 'label' on the mobile ion. The position of a nuclear spin in a magnetic field gradient is 'labeled' by its Larmor frequency, $\omega_0(\boldsymbol{r})$. The method involves a modified Hahn spin echo experiment, in which the sample is subjected to a $\pi/2-\tau-\pi$ pulse sequence with intense magnetic field gradient pulses applied between the two rf pulses and between the π pulse and the echo. If the spins move their positions during the interval between the two field gradient pulses, the echo is attenuated. The method provides a direct, model-independent measurement of D, and the measurement can be calibrated by determining the attenuation in systems with known diffusion coefficients. Compared with relaxation measurements, the PFG method is relatively unaffected by the presence of paramagnetic impurities.

3.4 NMR Imaging

In NMR imaging, images of the nuclear spin density or NSR rates are reconstructed from spectra recorded in the presence of magnetic field gradients.[12] The broad lines usually encountered in solid state NMR present considerable difficulties for imaging, especially for proton-containing solids, e.g. polymers. One successful approach to the problem is to narrow the lines artificially by multiple pulse narrowing or magic angle sample spinning (see also ***Line Narrowing Methods in Solids***). For half-integral spins, such as ^{23}Na, the central, $\frac{1}{2} \rightarrow -\frac{1}{2}$, transition is relatively narrow, and the technique has been successfully used to image ^{23}Na diffusion in Na β-alumina (see also ***Ceramics Imaging*** and ***Imaging Techniques for Solids and Quasi-Solids***).

4 CORRELATION FUNCTIONS

In many FICs the BPP model [equation (10)] is inadequate, as demonstrated by the following failures: (i) the ln T_1 vs. $1/T$ plot is not symmetrical with respect to the temperature at which the T_1 minimum occurs; (ii) the value of E deduced from this plot does not agree with values obtained from conductivity data; (iii) the values of $1/\tau_c$ are not in the range of an optical phonon frequency; and (iv) on the low-temperature side, T_1 is not proportional to ω_0^2.[6] A great deal of effort has been expended over the past 20 years in trying to find better correlation functions.

4.1 Dimensionality of Motion

For both dipole–dipole and quadrupolar relaxation, $(1/T_1 \propto \omega_0^2\tau_c)^{-1}$ when $\omega_0\tau_c \gg 1$, independent of dimensionality. A dimensionality effect is expected in one- and two-dimensional systems at long times when the correlation functions decay more slowly.[4,5] Thus for $\omega_0\tau_c \ll 1$

$$\frac{1}{T_1} \propto \begin{cases} (\tau_c/\omega_0)^{1/2}, & \text{for 1D} \\ \tau_c \ln(1/\omega_0\tau_c), & \text{for 2D} \\ \tau_c, & \text{for 3D} \end{cases} \tag{12}$$

4.2 Microscopic Correlation Functions

The first improvements were achieved by explicitly taking into account the discrete character of the crystal lattice and correlations between the motion of the ions. These and other three-dimensional models of hopping diffusion, which include short-range repulsions between the mobile ions, predict only small differences in the shape and width of the T_1 minimum compared with the predictions of the BPP model.[4,5]

4.3 Phenomenological Correlation Functions

An obvious extension of the BPP model is to assume independent ionic hops over a distribution of barriers $f(E)$:

$$\frac{1}{T_1} = A\int_0^\infty \{j(\omega_0) + 4j(2\omega_0)\}\, f(E)\, dE \tag{13}$$

A Gaussian distribution often works well. This model is widely used to account for the asymmetry of the ln T_1 vs $1/T$ curves.[6]

An alternative approach is to assume a stretched exponential, or Kohlrausch–Williams–Watts (KWW) function, for the correlation function of the form

$$g(t) = \exp[-(t/\tau_c)]^\beta \tag{14}$$

with $0 < \beta \leq 1$. The corresponding limiting T_1 behavior is

$$\frac{1}{T_1} = \begin{cases} \tau_c, & \omega_0\tau_c \ll 1 \\ \tau_c^{-\beta}(\omega_0)^{-\beta-1}, & \omega_0\tau_c \gg 1 \end{cases} \tag{15}$$

There have been several attempts to derive equation (14) from first principles. These include[7] the 'jump relaxation' model, the 'two-level system' model, and the 'diffusion-controlled relaxation' model.

4.4 Graphical Determination of Spectral Density Functions

A graphical, temperature–frequency superposition technique, which is independent of any model of the motion, has been described for extracting the spectral density function, $j(\omega)$, and its temperature dependence from measurements of T_1, T_2, and $T_{1\rho}$.[13] Using a simple, iterative tracing procedure, the results of relaxation measurements at different frequencies (ω_0, ω_1, 0, etc.) and different temperatures are superimposed to form a master curve, $j(\omega\tau_c)/j(0)$ vs. $\omega\tau_c$, a datum line, $j(0)$ vs. τ_c, and an Arrhenius plot, ln τ_c vs. $1/T$. These graphs display all the statistical mechanical information contained in the data. The characteristic time, τ_c, is determined from the shape of the master curve.

5 EXAMPLES OF NMR STUDIES

5.1 Crystalline FICs

5.1.1 Solids with Phase Transitions

Relatively soft crystals, often containing large, polarizable, heavy mobile ions such as Ag^+, Cu^+, Hg^{+2}, Pb^{+2}, or Tl^+, are members of this group.[14] The transitions may be first order as in, for example, AgI, or diffuse, as in PbF_2, and apparently all fluorite-structured compounds.

A good example is α-$RbAg_4I_5$, which has the highest conductivity at room temperature, 27 S m^{-1}, of any FIC. The rubidium ions are immobile, and the 16 mobile silver ions per unit cell are disordered over 56 sites. The ^{87}Rb relaxation rate exhibits a critical behavior which is already present above the critical temperature T_c. In contrast, the ^{109}Ag relaxation rate shows only a small step-like increase in rate at T_c and indicates thermally activated hopping.[15] PFG measurements, combined with measurements of electrical conductivity, show that the Haven ratio decreases from 0.52 to 0.39 at the $\alpha \rightarrow \beta$ transition, suggesting some type of cooperative mechanism for silver diffusion. The pressure independence of E for silver relaxation shows that the activation volume is about zero, in agreement with conductivity data.

There has been considerable debate on the nature of F^-[16] transport in fluorite-structured FICs. An early model was the molten sublattice concept. β-PbF_2 is best suited for study because it has the highest σ and lowest T_c of all the fluorides. The results of a relaxation study are shown in Figure 1. Values of the Haven ratio H_R deduced from studies of PFG and σ approach unity at the highest temperatures.[17] The form of the spectral density function extracted from measurements of T_1, $T_{1\rho}$, and T_2 by the graphical temperature–frequency superposition technique shows (Figure 2) only minor deviations from an exponential correlation function and good agreement with numerical calculations of $j(\omega)$ carried out assuming hopping over a face centered cubic lattice.[13] Neither these results nor MD simulations support the molten sublattice model.

5.1.2 Heavily Doped and Massively Disordered Solids

High concentrations of dopants, typically 10–20 mol%, can produce high concentrations of mobile defects, as in Y^{3+}-doped CeO_2, where the mobile defects are oxygen vacancies.

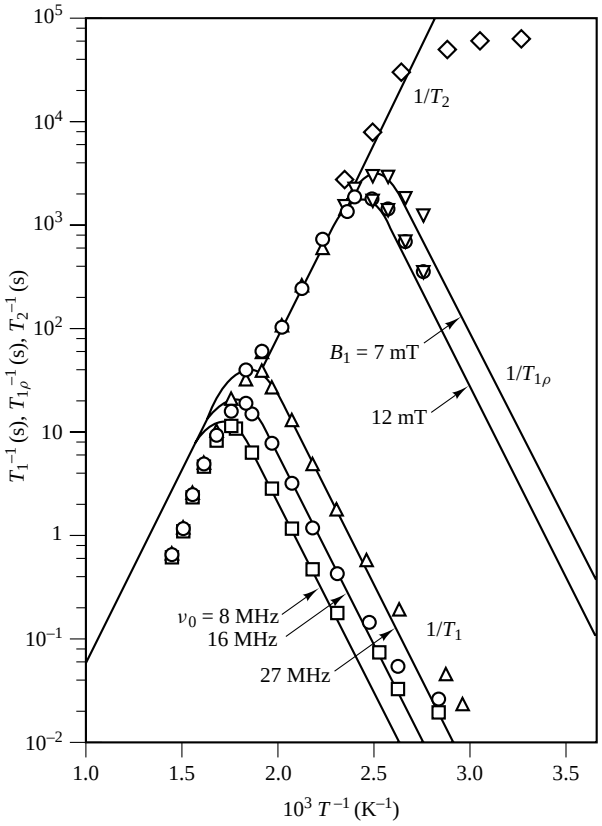

Figure 1 Relaxation rates of ^{19}F in pure polycrystalline β-PbF_2 as a function of reciprocal temperature. ν_0 is the Larmor frequency and B_1 is the rf field strength. (Reproduced by permission of Elsevier from Boyce et al.[16])

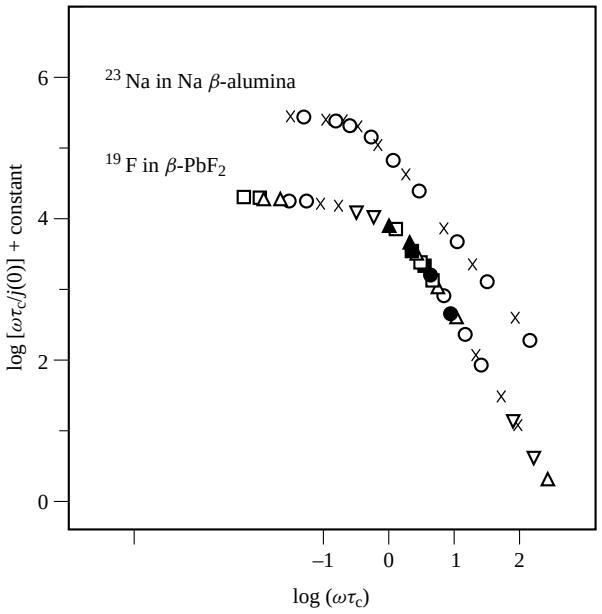

Figure 2 Spectral density functions determined using the temperature–frequency superposition method[13]. The curve for β-PbF_2 was derived from the ^{19}F relaxation rates shown in Figure 1. The curve for Na β-alumina was derived from the ^{23}Na T_1 data shown in Figure 3

In a study of T_1 and T_2 in a ^{17}O-enriched sample, the non-BPP asymmetry of the T_1 minimum was well fitted by a model based on a wide distribution of activation energies for hopping.[18]

A study of T_1, $T_{1\rho}$, and T_2 of ^{19}F has been carried out on $RbBiF_4$.[19] This massively disordered compound has a fluorite structure with a disordered distribution of rubidium and bismuth atoms over the cation sites and high levels of F^- interstitials. The fluoride ions migrate by the interstitialcy mechanism, and the NMR results show that there is fast exchange between the two fluoride sites.

5.1.3 Layer- and Tunnel-Structured Materials

The celebrated ceramic materials β- and β''-Al_2O_3 have mobile cations located in conduction planes between spinel-structured alumina blocks (see also ***Ceramics***).[7] Sodium-23 spectra[20] recorded at low temperatures show evidence of the multiple sites for sodium ions thought to be present from X-ray diffraction studies. Diffusion is sufficiently fast to average these lines to a single peak at only 100 K. The lineshape is characteristic of an asymmetric time average electric quadrupole coupling tensor up to at least 500 K, which is consistent with the motion of the sodium ions being restricted to two dimensions. Measurements of T_1 (Figure 3) show a highly asymmetric minimum, which was analyzed assuming a distribution of activation energies.[21] On the other hand, the spectral density function obtained from the same data by the temperature–frequency superposition method (Figure 2) is consistent with a single activation energy.[13] Below the T_1 minimum, $j(\omega) \propto \omega^{-1.4}$, which is similar to the behavior found for other two-dimensional systems (***Intercalation Compounds***).

Li_3N is possibly the best known lithium ion conductor, with $\sigma = 10^{-1}$ S m^{-1} at 320 K. The Li_3N structure consists of pure Li(1) layers alternating along the hexagonal c axis linked by layers of Li_2N in which Li(2) is hexagonally coordinated to N^{3-}. As might be expected, σ is anisotropic. The intralayer and slower interlayer diffusion was investigated by ^{7}Li and ^{6}Li NSR and by the PFG method.[6]

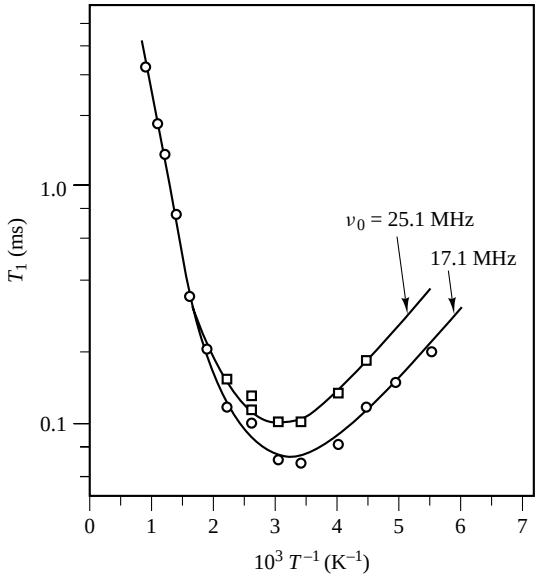

Figure 3 Spin–lattice relaxation T_1 of ^{23}Na in crystals of Na β-alumina as a function of reciprocal temperature. The fit using equation (13) with a bimodal distribution of activation energies is shown as a solid line. (Reproduced by permission of the American Institute of Physics from Walstedt et al.[21])

The mineral β-eucryptite, $LiAlSiO_4$, and materials of the hollandite type have fractionally occupied one-dimensional tunnels. T_1 measurements on ^{7}Li, ^{6}Li, and ^{27}Al are consistent with one-dimensional intratunnel and interchannel diffusion processes.[6]

5.1.4 Proton Conductors

Hydrogen uranyl phosphate hydrate, $HUO_2PO_4.4H_2O$ (HUP), is one of the best examples of the hydrated proton conductors, with $\sigma = 4 \times 10^{-1}$ S m^{-1} at room temperature. It undergoes a transition at 274 K to a low-temperature, poorly conducting phase. Planar acidic, hydrogen-bonded networks containing equal numbers of H_4O_2 and $H_5O_2^+$ dimers are located between $(UO_2PO_4)_n^{n-}$ layers.[2] Whether the protons move by a Grotthus-type mechanism in which protons move by a combination of reorientations of H_4O_2 dimers and hopping between H_4O_2 and $H_5O_2^+$, or by a 'vehicle' mechanism in which the hydrogens and oxygens move together as H_3O^+, is a matter of debate.

The spectral density function deduced by the method of temperature–frequency superposition from the temperature dependences of the ^{1}H T_1, $T_{1\rho}$, and T_2 was found to be consistent with theoretical models of two-dimensional diffusion.[22] Analysis of the ^{31}P solid echo shapes indicated that all the hydrogens are rapidly exchanging. The ^{2}H spectrum (see also ***Deuterium NMR in Solids***) has an axially symmetric lineshape. This also is consistent with fast, discrete jumps of deuterium between the sites located by neutron diffraction studies. The conclusions of PFG studies are in good agreement with the NSR studies.

5.2 Amorphous FICs

5.2.1 Polymer Electrolytes

These are formed by dissolving ionic salts, e.g. $LiClO_4$, in polymers that contain polar groups, e.g. polyethers such as poly(ethylene oxide) (PEO).[23] The proposal that thin, flexible films of these materials could be used as battery electrolytes excited considerable interest (***Conducting Polymers***). Because of complications associated with cross relaxation-effects, the interpretation of NSR data is not easy, but PFG methods have been used successfully for rubbery phases. Diffusion coefficients of ^{7}Li and ^{19}F have been measured for $(PEO)_8LiCF_3SO_3$, showing that the anion $CF_3SO_3^-$ is surprisingly more mobile than the lithium ion.

5.2.2 Glassy FICs

Fast ion conducting glasses typically consist of an oxide network former, e.g. B_2O_3, GeO_2, SiO_2, or P_2O_5, which together with a network modifier, e.g. Ag_2O_3 or Li_2O, can dissolve a salt, such as AgI or LiI, as a dopant. Highly conducting glasses are also based on sulfide and selenide

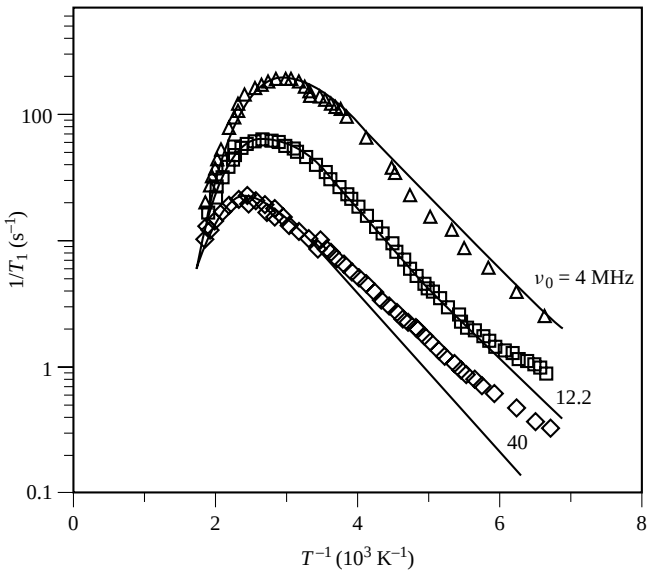

Figure 4 Spin–lattice relaxation $1/T_1$ of ^{7}Li in $(Li_2S)_{0.56}(SiS_2)_{0.44}$ as a function of reciprocal temperature. Fits using equation (13) with a Gaussian distribution of activation energies are shown as solid lines. (Reproduced by permission of the American Institute of Physics from Svare et al.[24])

network formers, e.g. SiS_2 and $GeSe_2$ (see also ***Quadrupolar Nuclei in Glasses***).[7]

The non-BPP $1/T_1$ vs. $1/T$ curves for ^{7}Li (Figure 4) and the anomalous conductivity, $\sigma(\omega, T)$, for the glassy FIC $(Li_2S)_{0.56}(SiS_2)_{0.44}$ were fitted most satisfactorily by a model of lithium ion motion using a Gaussian distribution of activation energies [equation (13)].[24] The measured values of τ_c from the two effects differ by two orders of magnitude and this difference is explained by percolation around the high barriers in the distribution. The differences between the correlation function derived from NMR and that from conductivity is intimately related to the local versus macroscopic character of the two correlation functions, which becomes important in the presence of disorder. The data can also be fitted to stretched-exponential (KWW) correlation functions [equation (14)]. Neither the 'diffusion-controlled relaxation' model nor the 'jump relaxation' model, which incorporate ionic correlations to explain non-Debye-like relaxation in conductivity and non-BPP-like NMR relaxation, predict the differences between the correlation functions for T_1 and σ found experimentally.

6 RELATED ARTICLES

Adsorbed Species: Spectroscopy and Dynamics; Amorphous Materials; Brownian Motion and Correlation Times; Ceramics; Chemical Exchange on Solid Metal Surfaces; Conducting Polymers; Diffusion in Porous Media; Diffusion in Rare Gas Solids; Diffusion in Solids; Hydrogen–Metal Systems; Inorganic Solids; Intercalation Compounds; Microporous Materials and Xenon-129 NMR; Ultraslow Motions in Solids.

7 REFERENCES

1. A. Laskar and S. Chandra (eds.), *Superionic Solids and Solid Electrolytes—Recent Trends*, Academic Press, New York, 1987.
2. C. R. A. Catlow, *J. Chem. Soc., Faraday Trans.*, 1990, **86**, 1167.
3. J. B. Boyce and B. H. Huberman, *Phys. Rep.*, 1979, **51**, 189.
4. P. M. Richards, *Top. Curr. Phys.*, 1979, **15**.
5. J. L. Bjorkstam and M. Villa, *Magn. Reson. Rev.*, 1980, **6**, 1.
6. D. Brinkmann, *Magn. Reson. Rev.*, 1989, **14**, 101.
7. D. Brinkmann, *Progr. Nucl. Magn. Reson. Spectrosc.*, 1992, **24**, 527.
8. A. V. Chadwick, *J. Chem. Soc., Faraday Trans.*, 1990, **86**, 1157.
9. J. F. Stebbins, *Chem. Rev.*, 1991, **91**, 1353.
10. P. A. Beckman, *Phys. Rep.*, 1988, **171**, 85.
11. P. Stilbs, *Prog. Nucl. Magn. Reson. Spectrosc.*, 1987, **19**, 1.
12. D. G. Cory, *Annu. Rep. NMR Spectrosc.*, 1992, **24**, 87.
13. T. K. Halstead and W. L. Roth, *J. Magn. Reson.*, 1982, **47**, 292.
14. M. A. Ratner and A. Nitzan, *Solid State Ionics*, 1988, **28–30**, 3.
15. H. Looser, D. Brinkmann, M. Mali, and J. Roos, *Solid State Ionics*, 1981, **5**, 485.
16. J. B. Boyce, J. C. Mikkelsen Jr., and M. O'Keefe, *Solid State Commun.*, 1977, **21**, 955.
17. R. E. Gordon and J. H. Strange, *J. Phys. C*, 1978, **11**, 3213.
18. K. Fuda, K. Kishio, S. Yamachi, S. Fueki, and Y. Onoda, *J. Phys. Chem. Solids*, 1985, **46**, 1141.
19. J. M. Reau, S. Matar, G. Villeneuve, and J. L. Soubeyroux, *Solid State Ionics*, 1983, **9–10**, 563.
20. I. Chung, H. S. Story, K. Metcalfe, and T. C. Jones, *J. Chem. Phys.*, 1975, **63**, 4903.
21. R. E. Walstedt, R. Dupree, J. P. Remieka, and A. Rodriguez, *Phys. Rev. B*, 1977, **15**, 3442.
22. K. Metcalfe, T. K. Halstead, and R. C. T. Slade, *Solid State Ionics*, 1988, **26**, 209.
23. C. A. Vincent, *Progr. Solid State Chem.*, 1987, **17**, 145.
24. I. Svare, F. Borsa, D. R. Torgeson, and S. W. Martin, *Phys. Rev. B*, 1993, **48**, 9336.

Biographical Sketch

Thomas K. Halstead. *b* 1937. B.A. (Chemistry), Oxford, 1962. D.Phil. Oxford, 1965 (supervisor P. G. Dickens), Research Associate, Center for Materials Research, Stanford, 1965–6 (with R. A. Huggins). Lecturer, and senior lecturer, University of York, UK, 1966–present. View of NMR influenced by U. Haeberlen and I. J. Lowe. Approx. 50 publications. Research interests include solid state NMR and its application to materials chemistry and laser-pumped xenon NMR.

Hydrogen–Metal Systems

David R. Torgeson
Iowa State University, Ames, IA, USA

1	Introduction to NMR of Hydrogen–Metal Systems	1
2	Hydrogen Motion in Metals Detected by NMR	2
3	Dynamic Studies of Hydrogen Motion in a Metal	2
4	Deuteron Lineshape for Combined Electric Quadrupole and Knight Shifts	5
5	Low Temperature Local Hydrogen Motion and Hydrogen Tunneling in HMSs	7
6	Spin–Lattice Relaxation in Amorphous Hydrogen–Metal Systems	8
7	Related Articles	9
8	References	9

1 INTRODUCTION TO NMR OF HYDROGEN–METAL SYSTEMS

The exposure of hydrogen to metals often produces significant changes in the physical properties of those metals. The absorption of hydrogen into interstitial lattice sites between metal atoms causes metallic materials to expand their volume, changes the crystal structure, and may change the electronic structure or electrical character of the material. Unable to withstand the strain, some metals fracture into powder, sometimes a useful method of producing powder of ductile metals, but at other times a possibly disastrous result as in the case of hydrogen embrittlement of steels. All the materials included in hydrogen–metal systems (HMSs) are occasionally incorrectly referred to as metal hydrides. As we will see below, metal hydrides do make up the majority of materials in HMSs. Metal hydrides can be either covalent, ionic, or metallic[1] in nature. We will confine our attention to metallic hydride materials.

One of the earliest NMR studies of hydrogen in metals was done some 40 years ago by R. E. Norberg,[2] who applied hydrogen to the palladium metal wires which made up the rf coil of his NMR probe. Linewidth, Knight shift, and relaxation times of the hydrogen in the rf skin depth of the palladium wires were studied by continuous wave and spin echo techniques.

Some of the most basic NMR studies of HMSs have been the investigation of the underlying physical principles governing hydrogen location and motion at the atomic or 'microscopic' level. Long-range hopping or diffusion of hydrogen is currently understood in terms of thermally activated, over the barrier hopping between interstitial lattice sites, which will be discussed, in part, below. Pulse magnetic field gradient NMR to measure hydrogen (and other atomic) diffusivities is discussed elsewhere (see ***Diffusion in Solids***). Attempts to characterize tunneling of hydrogen at low temperatures between interstitial vacancies in metals at low temperatures by NMR will be discussed briefly here.

Although NMR is a powerful tool for observing hydrogen interactions in HMSs, interpretation of NMR data cannot be done properly without other knowledge of the materials. Crystal structure and phase diagram results from X-ray, neutron diffraction,[3] and detailed magnetic information from susceptibility measurements are often crucial to the interpretation of NMR results of HMS.

Many of the applied NMR studies of hydrogen, deuterium, and tritium in HMSs have been undertaken to determine the location and motions of hydrogen within the metallic materials in efforts to characterize and improve the hydrogen–metal materials for applications such as purification of hydrogen, hydrogen isotope separation, and hydrogen storage for fuel or energy storage (batteries); or closed cycle, metal hydride refrigerators for remote or applications to vehicles in space.[4]

HMSs include elemental metals, MH_x, with small concentrations of hydrogen, e.g. $x < 0.01$, dissolved in the host material with hydrogen located in interstitial vacancies without significant change in the crystal structure of the metal host, M. These materials are referred to as hydrogen (metal) solid solution (α) phases. The solubility of hydrogen in metal solid solutions often diminishes rapidly with decreasing temperature, forming metal hydride precipitates at lower temperatures. High hydrogen concentrations, x = H/M, often extend to x = 3 or 4 for metal hydrides, e.g. LaH_3, SnH_4, and PbH_4, where the crystal structure of the hydride (β or γ) phase, e.g. face centered cubic (fcc) (or CaF_2 structure) for YH_2, is usually quite different from the parent metal, e.g. hexagonal close packed (hcp) for Y, and the density of the metal hydride typically is less than the parent metal density. Intermediate hydrogen concentration samples may be mixed hydrogen–metal solid solution α and metal hydride β phases. The observed NMR spectra and nuclear spin–lattice, R_1, and spin–spin, R_2, relaxation rates as functions of temperature may give evidence of the mixed phases (see ***Phase Transitions and Critical Phenomena in Solids***).

HMSs include hydrogen solid solutions of elemental metals, binary metal alloys, and intermetallic compounds, and also hydrides of metals, alloys, and intermetallic compounds. In addition, metallic halide compounds[5] and metal sulfides[6] adsorb hydrogen to significant degrees and should be included in HMSs. Some alloys and intermetallic compounds do not survive the hydriding process, but will disproportionate into hydrides of one or more of the metals and other compounds. In these cases, the hydride of the constituent metal is more stable than the hydride of the parent material.

Most NMR hydrogen–metal studies are made with samples sealed in quartz tubes to prevent loss of hydrogen upon heating the samples and to prevent oxidation or other contamination. Generally, the metallic nature of the materials requires powdered samples (particle size $\leq 100\,\mu$m) to permit the $\boldsymbol{B}_1$ rf magnetic field to penetrate the metallic particle's 'rf skin depth' uniformly. The spaces between powder particles contain hydrogen gas molecules which represent a characteristic hydrogen over pressure of the particles typical for that material, nominal hydrogen concentration, and sample temperature. The hydrogen gas molecules between particles are in constant exchange with the hydrogen atoms or ions within the metallic particles. The hydrogen exchange rate is often quite low for room temperature, but may be many orders of magnitude greater for $T > 700$ K.

The density of the hydrogen inside some hydrogen storage materials, e.g. $LaNi_5H_6$, is greater than the hydrogen density in liquid hydrogen by a factor of two or three. Generally, the

hydrogen density in the metallic powders is many orders of magnitude greater than the density of gas molecules between powder particles. Thus, the observed hydrogen spectrum is typically the spectrum of the hydrogen in the metal only. Recently, anomalously high proton spin–lattice relaxation rates, R_1, observed for $T > 700\,\mathrm{K}$ within the metal particles[7] have been understood in terms of exchange between bulk hydrogen atoms in the metallic powder and the much faster relaxing hydrogen gas molecules between the metallic powder particles[8] (see ***Hydrogen Molecules***).

2 HYDROGEN MOTION IN METALS DETECTED BY NMR

The early measurements of Norberg[2] demonstrated the motion of hydrogen in palladium. HMSs have been studied by NMR beginning with wideline CW methods measuring rigid lattice or low temperature linewidths and lineshapes. The low temperature or rigid lattice hydrogen linewidth originates from the magnetic interactions of the nuclear dipoles in the solid HMSs. Narrowing of the spectral lines with increasing temperatures gave clear evidence of hydrogen motion or hopping into interstitial vacancies within the solid.[9] This rapid hopping of hydrogen results in a simple averaging of the local magnetic field $\boldsymbol{B}_\mathrm{L}$ or the distribution of magnetic fields 'seen' by the hopping proton magnetic dipole moment. These motional narrowing studies yielded activation E_a energies of diffusion and moderately precise estimates of hydrogen jump frequencies, $\nu_\mathrm{j}(T)$, or alternately, of hydrogen 'dwell times' or mean residence time, $\tau_\mathrm{D}(T) = 1/\nu_\mathrm{j}(T)$, and hydrogen correlation times, $\tau_\mathrm{c}(T)$. With increasing T, when the average hydrogen jump frequencies exceeded the rigid lattice linewidth, the observed spectral lines narrowed. The temperature range for line-narrowing measurements was generally less than 100 K; Figure 1 from Schreiber and Cotts[10] shows multiple line-narrowing graphs of LaH_{2+x} against temperature. Lanthanum hydride shows the unusual ability to absorb hydrogen between compositions LaH_2 and LaH_3, maintains an fcc structure, and with each additional hydrogen, every hydrogen atom jumps more rapidly. In most HMSs, with increasing temperature, the average hydrogen jump frequency can easily exceed the proton resonance frequency.

The proton linewidths versus temperature[11] in zirconium chloride hemihydride ($ZrClH_{0.5}$) and zirconium chloride monohydride (ZrClH) are shown in Figure 2. This transition metal halide structure consists of two zirconium metal layers sandwiched between two chlorine layers. Hydrogen is known to reside in interstitial tetrahedral sites between the two zirconium metal layers. In addition, the crystal structures for the hemi- and monohydrides are know to be slightly different, due to the presence of the hydrogen in the material.[12]

Indirect evidence of hydrogen (deuterium) hopping was also observed on studying the ^{93}Nb electric quadrupole perturbed, NMR satellite line narrowing in $NbH_{0.73}$ and $NbD_{0.82}$ with increasing temperature.[13] Figure 3 shows the narrowing of the inhomogeneously broadened ^{93}Nb NMR satellite linewidth. This narrowing can be understood in terms of reducing the randomness (inhomogeneity) of the average value at the niobium ion sites due to the increased rapidity of the hopping motion of the hydrogen (deuterium) ions with temperature and their associated electrical charges in the vicinity of the niobium ion sites. The reduced average EFG at the ^{93}Nb site yielded a narrower NMR satellite linewidth. Thus, the stationary niobium NMR showed evidence of the mobile hydrogen (deuteron) ions hopping.

3 DYNAMIC STUDIES OF HYDROGEN MOTION IN A METAL

The magnetic dipole interactions of hydrogen with other hydrogen magnetic moments, with the host metal nuclear

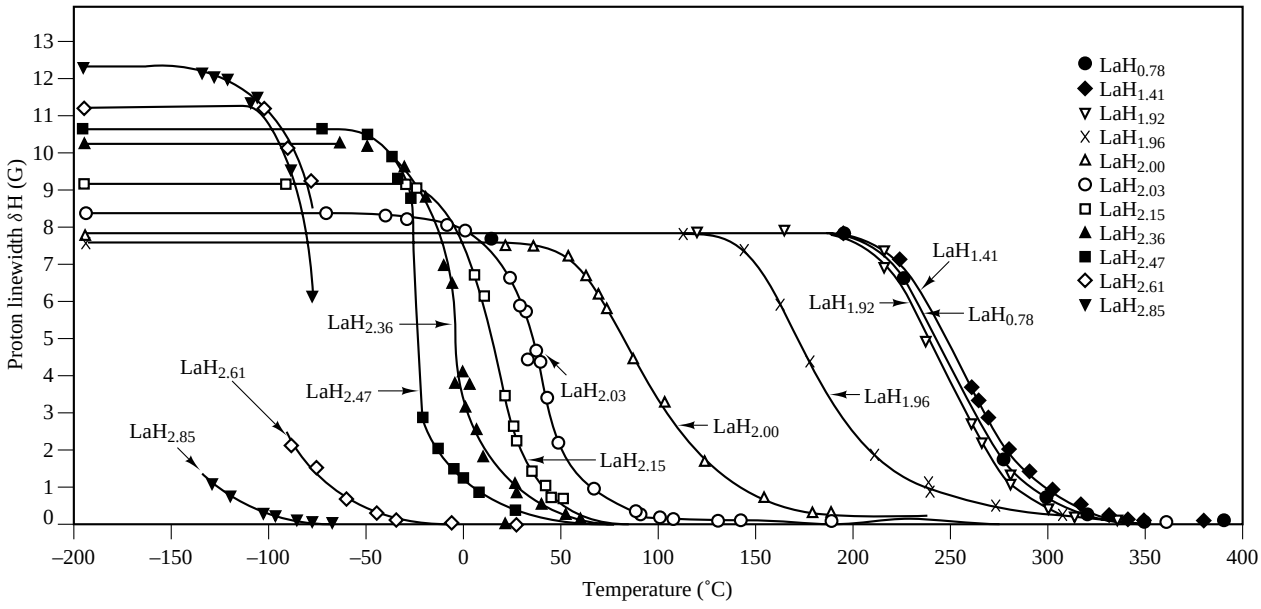

Figure 1 Proton linewidths (1G = 10^{-4} T) plotted against T for different x values. (Reproduced by permission of the American Physical Society from Schreiber and Cotts[10])

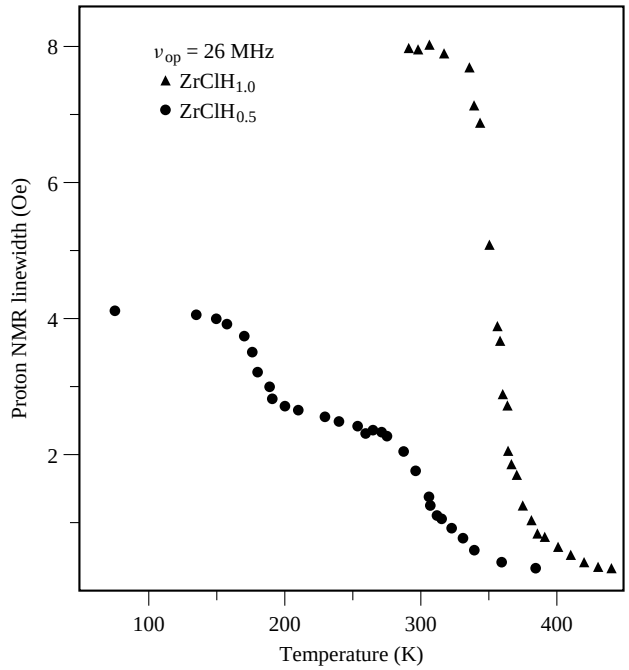

Figure 2 Temperature dependence of the proton linewidth in the two hydride phases of ZrCl, measured at nominal resonance frequency of 26 MHz. (Reproduced by permission of Elsevier Science Publishers B.V. from Hwang et al.[11])

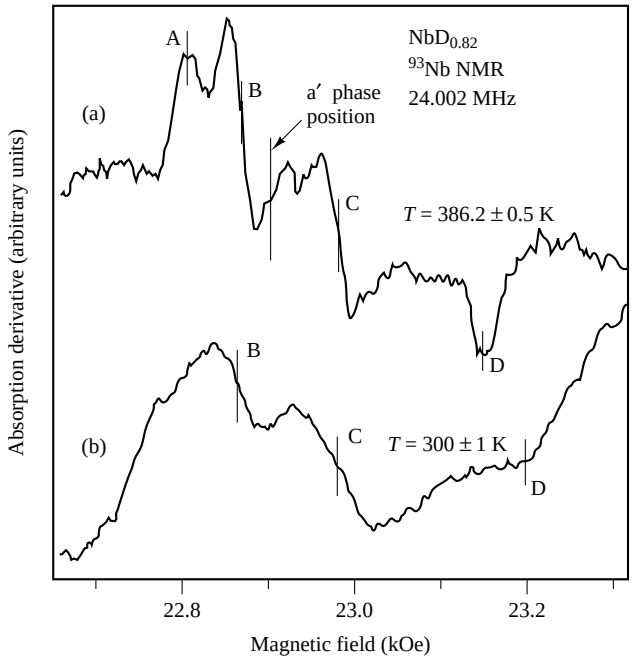

Figure 3 Wide line absorption derivative spectra of ^{93}Nb for 300 and 386 K. At 386 K hydrogen jumping rates are sufficiently fast to produce a spatial average of the electric field gradient at the Nb metal sites which narrows the spectra. (Reproduced by permission of Elsevier Science, Inc., from Hwang et al.[13])

moments, paramagnetic impurity moments, and with conduction electron magnetic moments generally govern the flow of spin energy within HMSs. Cross relaxation of protons and host metal nuclei having large nuclear electric quadrupole interactions has been observed. Also, as shown below, the hopping deuteron can be relaxed by interactions of its electric quadrupole moment with fluctuating EFGs within the material.

The observed hydrogen spin–lattice relaxation rate $R_1(\omega, T)$ varies greatly with temperature in HMSs, and is often the sum of several independent $R_1(T)$ rates, each due to separate physical relaxation mechanisms active in the material. Fortunately, these several R_1 rates have different resonance frequency and/or temperature dependences. With this fact in mind, we shall see how one can separate these spin–lattice relaxation mechanisms and thereby begin to characterize the materials.

The observed hydrogen spin–lattice relaxation rate (HSLR) R_1, in general, may be the sum of several of the following rates:[14]

$$R_1 = R_{1d} + R_{1e} + R_{1p} + R_{1CR} \tag{1}$$

where R_{1d} is the magnetic dipole–dipole relaxation of the hydrogen due to other hopping hydrogen. Bloembergen, Purcell and Pound[15] (BPP) were first to suggest the form of relaxation

$$R_{1d} = \frac{1}{T_{1d}} = M_2(T)J(\omega_0, T) \tag{2}$$

where M_2 is a mean-square fluctuating field most commonly thought to be related to the magnetic dipole–dipole interaction of the hydrogen with other magnetic moments. However, in the case of the deuteron, this formalism can also be expressed in terms of the fluctuations of the EFG about the deuteron electric quadrupole moment.[16] In this case, R_{1d} is then written R_{1q} (q denoting quadrupolar relaxation). ω_0 is the spin precession frequency in angular frequency units. $J(\omega_0)$ is the power spectrum or spectral density function of the fluctuation magnetic fields (or fluctuating EFGs) within the sample. The simplest form of $J(\omega)$ is the Lorentzian

$$J(\omega) = \frac{\tau_c}{1 + \omega^2\tau_c^2} \tag{3}$$

where τ_c is the correlation time and is strongly temperature dependent. Often τ_c varies exponentially with temperature, where $\tau_c = \tau_0 \exp(-E_a/kT)$ and where $1/\tau_0$ is thought to be the attempt frequency of hydrogen jumping or the high temperature 'rattling' frequency of hydrogen within the interstitial site.

Equation (2) is often written with an additional Lorentzian term, including dipolar interaction terms at 2ω, as

$$R_{1d} = M_2(T)\left(\frac{\tau_c}{1 + \omega^2\tau_c^2} + \frac{4\tau_c}{1 + (4\omega^2\tau_c^2)}\right) \tag{4}$$

This simple description includes no details of the hydrogen interactions with metal nuclear moments or structure considerations of the HMS. It also ignores any orientation dependence of the crystal (sample) with the magnetic field $\boldsymbol{B}_0$ direction. Nonetheless, this BPP description is quite a good characterization of the hydrogen relaxation in many simple HMSs.

In a detailed description of hydrogen relaxation anisotropy in single crystal HMSs, Hoke et al.[17] gave the relaxation rate

of protons in an hcp single crystal of $ScH_{0.25}$ as

$$R_1 = \left(\frac{\mu_0}{4\pi}\right)^2 \gamma_H^2 \gamma_S^2 \left(\frac{h}{2\pi}\right)^2 S(S+1)\left(\tfrac{1}{12}J^{(0)}(\omega_H - \omega_S) + \tfrac{3}{2}J^{(1)}(\omega_H) + \tfrac{3}{4}J^{(2)}(\omega_H + \omega_S)\right) \quad (5)$$

following Abragam[18] where γ_H and γ_S are the gyromagnetic ratios of the hydrogen and metal, S is the spin (in this case, ^{45}Sc $S = \frac{7}{2}$), and $J^{(q)}(\omega)$ are spectral density functions which depend on the diffusion model chosen and on the orientation of the crystal in the magnetic field. Within the three spectral density functions $J^{(0)}$, $J^{(1)}$, and $J^{(2)}$ the frequencies $\omega_H - \omega_S$, ω_H, and $\omega_H + \omega_S$ are the difference between hydrogen and metal frequencies, the hydrogen frequency, and the sum of hydrogen and metal frequencies, respectively.

Interestingly, the anisotropy in R_1 originates in the anisotropy of $J^{(q)}(\omega)$, written by Sholl[19] as

$$J_{qq'} = \sum_{\alpha,\beta} \frac{Y_{2q}(\Omega_\alpha)}{r_\beta^3} \frac{Y_{2q'}(\Omega_\beta)}{r_\beta^3} P(r_\alpha, r_\beta, \omega) \quad (6)$$

where Y_{2q} are spherical harmonics, r_α is the distance between the proton and metal spin at time zero, and r_β is the distance between the proton and metal spin at time t. $P(r_\alpha, r_\beta)$ is the Fourier transform of the probability function for the diffusion model chosen.[17]

The conduction electron moments in the HMS relax the hydrogen moment through a contact hyperfine interaction the same as is associated with the Knight shift.[18,20] The relaxation rate R_{1e} is proportional to the temperature and the square of the Knight shift (see Section 4 for a simple description of the Knight shift) and the square of the density of unpaired electronic (moment) states at the Fermi energy $N(E_F)$. Generally, the better the conductivity of the metallic material the greater the electronic relaxation rate R_{1e}:

$$R_{1e} = \frac{1}{T_{1e}} \propto N^2(E_F)T \quad (7)$$

For a simple metallic material, combining the Knight shift with relaxation rate,

$$T_{1e}TK^2 = \frac{T}{R_{1e}}K^2 = \frac{h/2\pi}{4\pi k}\frac{\gamma_e^2}{\gamma_n^2} \quad (8)$$

where γ_e and γ_n are the electron and nuclear (hydrogen) gyromagnetic ratios. This equation is known as the Korringa or Heitler–Teller–Korringa (HTK) relation,[21] where the Knight shift and R_{1e}/T are theoretically constant in temperature and R_{1e}/T or $1/T_{1e}T$ is often used to characterize the electronic relaxation in HMSs.

Unwanted paramagnetic ion concentrations, ignored in several NMR studies of HMSs, have shown unusual, anomalous relaxation rates and 'extra features' in the measured HSLR which have been attributed to a fictitious complex or additional diffusion mechanism. Phua et al.[22] showed that many such unusual or extra relaxation mechanisms were most likely due to the existence of residual paramagnetic impurities (dirt) in the host metals present at the time of the formation of the HMS. That study showed, generally, that the extra spin–lattice relaxation rates, R_{1p}, were linearly proportional to the concentration of paramagnetic impurities present. In addition, extra minima in $\log(T_1)$ versus $1/T$ were a direct result of the impurity relaxation; see Figure 4 for evidence of the suppression of $\log(T_1)$ versus $1/T$ and 'extra minima'. The paramagnetic moments produce a relaxation rate R_{1p} in HMS and can relax hydrogen by spin diffusion at low temperature in the low hydrogen diffusion regime. At higher temperatures, in the fast diffusion regime, hydrogens approach the stationary paramagnetic ions by rapid hopping within the sample and are relaxed via direct dipolar interactions with the paramagnetic impurity ions.

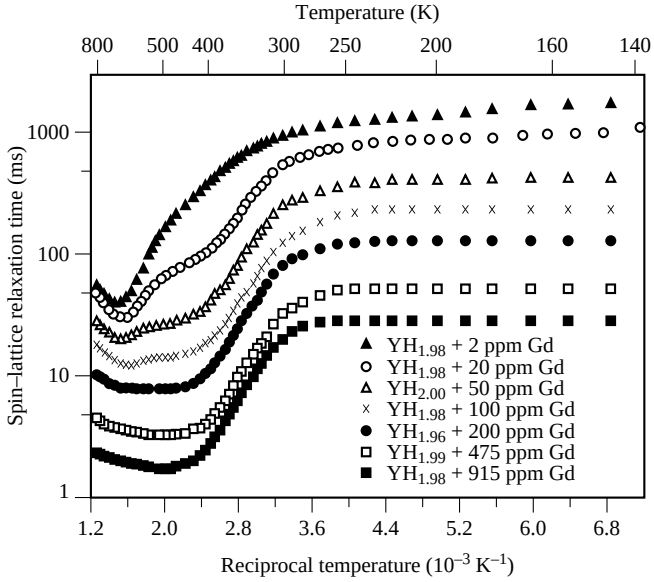

Figure 4 Proton spin–lattice relaxation time T_1 vs. $1000/T$ in YH_2 vs. Gd impurity concentration. (Reproduced by permission of American Physical Society from Phua et al.[22])

The cross relaxation of the proton, R_{1cr}, with certain host metal nuclei which have large electric quadrupole moments and subsequently large quadrupole interactions was recognized for protons in HMS at low temperatures (see Figure 5) where hydrogen hopping rates are slow. The strong nuclear electric quadrupole interactions of the metal nuclei, e.g. ^{175}Lu in $LuH_{0.20}$[23] and ^{181}Ta in Ta_2H[24] are many tens of megahertz in extent (width) and are only perturbed by the static magnetic field $\boldsymbol{B}_0$ required for proton resonance. Although the ^{93}Nb quadrupole moment and interaction in $V_xNb_{1-x}H_y$, for example, is weaker than ^{181}Ta in Ta_2H and ^{175}Lu in $LuH_{0.20}$, for frequencies $f_{max} < 24$ MHz, protons also cross relax to ^{93}Nb. When the proton resonance frequency matches one of the many spectral features of the metal NQR, spin polarization energy is transferred from the proton to the metal nucleus. The spin polarization energy is taken from the metal nucleus by the conduction electron interaction to the lattice because the contact hyperfine interaction is much stronger and thus faster (or higher rate) for the metal nucleus than for the proton. Figure 6 shows the proton cross relaxation to ^{181}Ta in $TaH_{0.32}$ as a function of proton resonance frequencies[24] (for a series of magnetic field values) while at $T = 130$ K. The calculation of the cross relaxation as a function of proton frequencies is described by Lichty et al.[24]

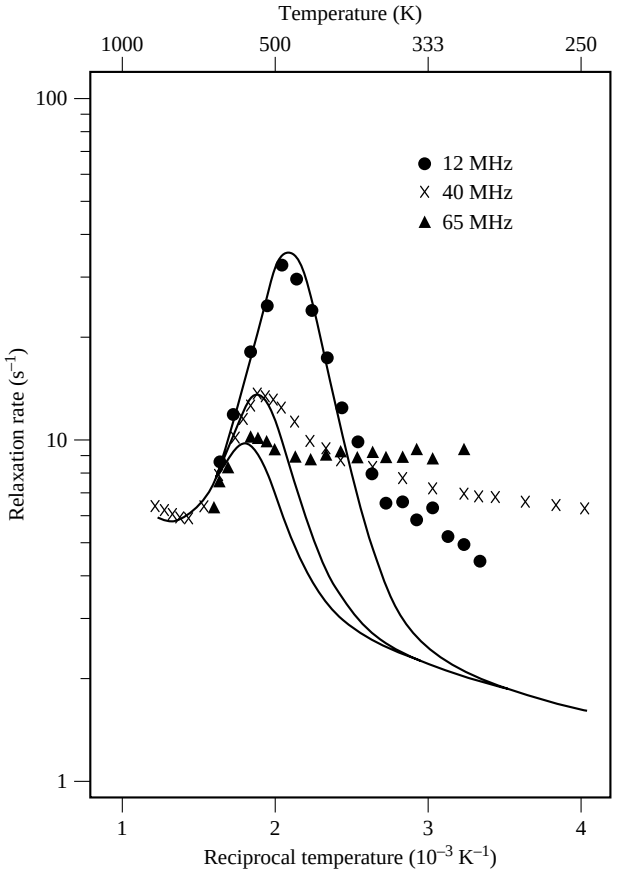

Figure 5 Proton spin–lattice relaxation rates R_1 vs. $1000/T$ in LuH_x at 12, 40 and 65 MHz. Cross relaxation between the protons and the ^{175}Lu nuclear electric quadrupole broadened NMR lines can be seen at low temperatures in the loss of temperature dependence for $T \leq 400$ K. (Reproduced by permission of R. Oldenbourg Verlag from Torgeson et al.[23])

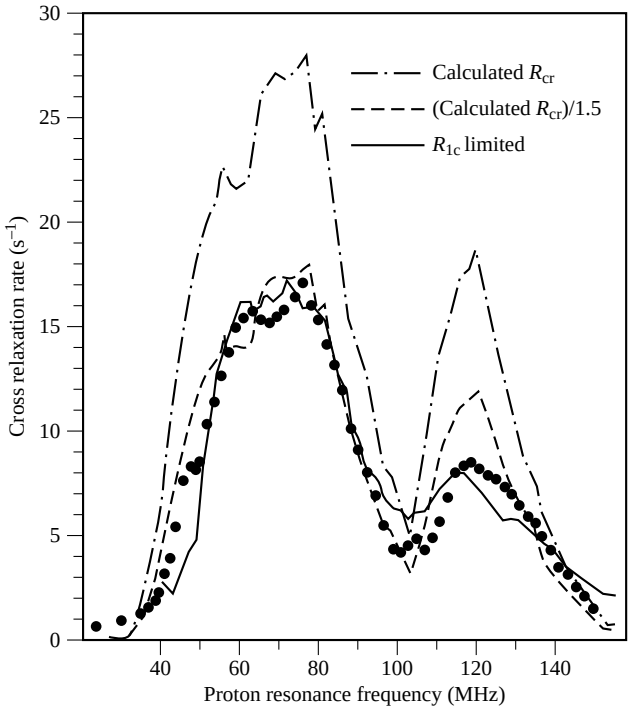

Figure 6 Proton cross-relaxation data (•) to ^{181}Ta nuclear electric quadrupole broadened NMR lines in Ta $H_{0.32}$ as a function of a series of proton resonance frequencies at 130 K. See Lichty et al.[24] for details of the theoretical calculations and the three curves presented. The analysis yielded a ^{181}Ta nuclear electric quadrupole frequency γ_Q = 43 MHz and electric field gradient asymmetry parameter η = 0.35. (Reproduced by permission of American Physical Society)

Figure 7 shows the total spin–lattice relaxation rate versus reciprocal temperature in schematic form, typical of many HMSs with the several component relaxation rates identified.

4 DEUTERON LINESHAPE FOR COMBINED ELECTRIC QUADRUPOLE AND KNIGHT SHIFTS

The Knight shift of hydrogen results from a small magnetic field at the hydrogen nucleus in an HMS from the conduction electron wave function $|\psi(0)|^2 \neq 0$ for the s electron character of the conduction electrons. This is often called the 'contact hyperfine interaction' or Fermi contact term. The application of the $\boldsymbol{B}_0$ field causes a small paramagnetic polarization of the conduction electrons, called the Pauli paramagnetism, where $M_s = \chi_s B_0$ and χ_s is the Pauli spin susceptibility. χ_s can be related to the density $N(E_F)$ of unpaired conduction electron states at the top of the conduction electron distribution or at the Fermi energy via the Pauli susceptibility $\chi_s = \frac{1}{2}(\gamma_e h)^2 N(E_F)$. The Knight shift can be written simply as $K \approx \chi_s |\psi(0)|^2/N$. The Knight shift causes a fractional change in the proton (deuteron) gyromagnetic ratio, that is, a small shift in position of the hydrogen resonance ΔH for fixed frequency or $\Delta\nu$ for fixed field measurements

$$K = \frac{\Delta H}{H} = \frac{H_R - H_M}{H_R} = \frac{\Delta\nu}{\nu} = \frac{\nu_M - \nu_R}{\nu_R} \qquad (9)$$

where subscript M refers to the metal field or frequency and R refers to the reference (solution or free ion) field or frequency. These fractional shifts are generally independent of the field or frequency.

Knight shifts of hydrogen in HMSs are generally quite small in magnitude compared with Knight shift values of metals, and often smaller in field shift magnitude ΔH than the dipolar broadened width or the $\boldsymbol{B}_L$ local magnetic field in the solid. However, the magnetic moment of the deuteron is smaller than the proton by a factor of 3.3, and effects of local magnetic fields are correspondingly smaller than for the proton. Figure 8 shows the combined effects of ^{2}D nuclear electric quadrupole interaction and Knight shifts[25] in a sample of $NbD_{0.76}$. The general subject of combined nuclear electric quadrupole interactions and Knight shift interactions in metals was first presented by Jones et al.[26] Since the ^{2}D spin I = 1, there are $2I$ + 1 or 3 levels and two transitions and no 'central line'. These two transitions for spin I = 1 are commonly referred to as the Pake doublet,[27] following the terminology established by George Pake in 1948 for the interaction of two coupled protons of combined spin I = 1 in the water of hydration in gypsum.

$NbD_{0.76}$ is orthorhombic in structure and thus the EFG and the Knight shifts must be described by tensors. The principal

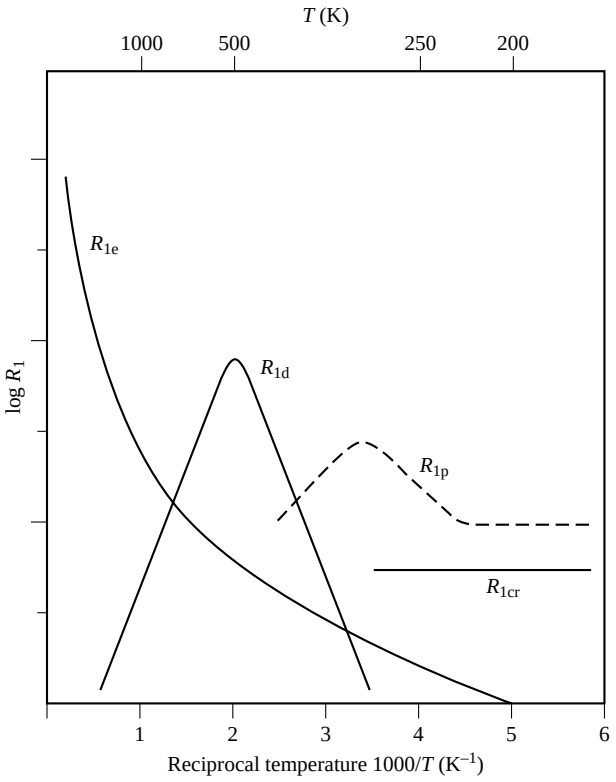

Figure 7 Generalized proton spin–lattice relaxation rate R_1 contributions vs 1000/T. These relaxation rates are: conduction electron, R_{1e}; long range diffusion/dipole–dipole, R_{1d}; paramagnetic impurity ion, R_{1p}; and cross-relaxation to quadrupole (metal) nucleus, R_{1cr}. The relative weighting of these mechanisms depends on the purity and physical details of the HMS sample studied

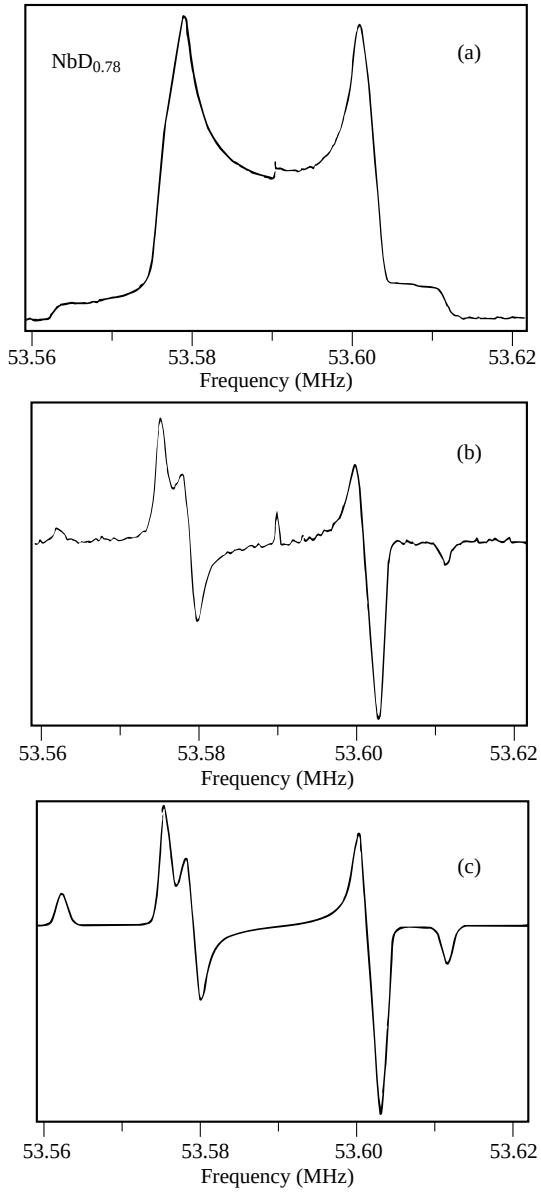

Figure 8 (a) Deuteron absorption curve vs. frequency for $NbD_{0.56}$, (b) derivative of observed deuteron absorption curve, and (c) calculated deuteron absorption derivative curve lineshape. (Reproduced by permission of Academic Press from Torgeson et al.[25])

axis system of the EFG has three separate components V_{xx}, V_{yy}, and V_{zz}, the second derivatives of the crystalline potential with respect to the coordinates x, y, and z. Note that $\nabla^2 V = V_{xx} + V_{yy} + V_{zz} = 0$ is Laplace's (electrical) equation. In the principal axis system, $|V_{xx}| < |V_{yy}| < |V_{zz}|$. The EFG asymmetry parameter for $NbD_{0.76}$ is $\eta = (V_{xx} - V_{yy})/V_{zz} = 0.11$. If η were equal to 0, then $V_{xx} = V_{yy}$ would require axial symmetry, i.e. at least three-fold rotational symmetry about the z axis. $\eta \neq 0$ implies the $\Delta m = \pm 1$ transitions $-1 \leftrightarrow 0$ and $0 \leftrightarrow +1$ in combination with the K_x, K_y, and K_z Knight shift components will produce different frequency dependences for the two transitions or ^{2}D 'powder' lineshapes.[25] The width of the pattern essentially measures the strength of the deuteron electric quadrupole interaction described by the lowest pure quadrupole frequency $\nu_Q = 3eQV_{zz}/2h = 49.3$ kHz, where eQ is the deuteron quadrupole moment, V_{zz} is the principal component of the EFG tensor and h is Planck's constant. Incidentally, $\nu_Q = 3eQV_{zz}/[2I(2I-1)h]$ is the best measure of the strength of the quadrupole interaction relative to the strength of the NMR interaction characterized by ν_0, the Larmor frequency.[28]

For powdered metal hydrides with less than cubic crystal symmetry, the single grain particles' major symmetry axes will simply point in random directions in space. However, with an applied magnetic field switched on, the majority of particles' major symmetry axes will be nearly perpendicular to the field direction and a small minority of crystal symmetry directions will point along the field direction. This produces the well known sin θ dependence of the distribution of powder particle orientations with respect to the magnetic field direction. As pointed out by Jones et al.[26] the major peaks of the absorption spectrum are due to 'singularities' at the perpendicular ($\theta = 90^\circ$) powder grains, and the smaller 'steps' at the extremes of the spectrum are due to those particle crystallites nearly parallel ($\theta = 0^\circ$) to the magnetic field.

The deuteron Knight shift, as for all hydrogen Knight shifts, originates from the contact hyperfine interaction of the conduction electrons at the deuteron (hydrogen) nucleus. In the HMS, the conduction electrons are attracted or 'cored' to the hydrogens in the same way conduction electrons are attracted to the metal nuclei. This, of course, makes the conduction electron wave functions more complex than in the pure metal, alloy, or intermetallic compound. The presence of

the hydrogen may actually change the electronic character of the HMS by changing the conduction electron wave functions and by the hydrogen donating an electron to the conduction band when hydrogen is absorbed, which may greatly modify the electronic band structure of the HMS.

The effect of the Knight shifts on the observed lineshape is simply a small displacement of the resonance position due to an additional magnetic field at the nucleus from the contact hyperfine interaction. For a non-cubic metal or HMS, the magnitude of the shift of the resonance is dependent upon orientation of the crystalline axes of the grain with respect to the field direction. Figure 8 (a) shows the observed absorption curve, (b) a derivative of the observed absorption and (c) a calculated absorption derivative with appropriate Knight shift and EFG components included. Absorption derivative lineshapes actually show more subtle lineshape features than do the absorption curves. Absorption derivatives lineshapes were commonly recorded in field or frequency scanned CW wideline studies in past years because of the use of lock-in amplifiers and small amplitude magnetic field or frequency modulation to record spectra.

5 LOW TEMPERATURE LOCAL HYDROGEN MOTION AND HYDROGEN TUNNELING IN HMSs

Scandium, yttrium, and lutetium plus other rare earth hcp metals provide a nearly unique opportunity to observe hydrogen dissolved in metals and measure hydrogen motions in metals at temperatures below 150 K. Unlike many transition metals, scandium, yttrium, and lutetium can maintain up to 30 at% hydrogen in solution without precipitating any of the hydride phase[29] down to 4 K or without transforming to another crystal structure.

Lichty et al.[30] measured proton R_1s in $ScH_{0.27}$ ($H_{0.18}$) and found both an electronic relaxation R_{1e} and a weak low temperature motional relaxation peak R_{1L} near 60 K (105 K). That peak moved with the proton resonance frequency in a manner similar to the movement of R_{1d}, the over the barrier hopping, long range diffusion relaxation rate peak at much higher temperatures. In Figure 9 we see these low temperature data for two proton frequencies. The R_{1L} motional relaxation peak is superimposed on the R_{1e} electronic relaxation, which is linear in temperature T ($R_{1L} = R_1 - R_{1e}$; R_{1L} will be discussed below).

The location of hydrogen (deuterons) in the scandium hcp lattice was studied by neutron scattering.[29] Deuterons were found to prefer to form pairs with a scandium atom between. From these neutron scattering studies, models of hydrogen ordering in chains of paired hydrogens in scandium were proposed.

The pairing of hydrogen with a scandium metal between is an interesting and unusual ordering. However, not all hydrogens are paired with a metal between. Some of the hydrogens are unpaired and thus occupy vacant tetrahedral (T) sites in a random or inhomogeneous manner. The random occupation of hydrogen in metal–solid solutions has been referred to by Barnes[14] as a proton glass. The result of an inhomogeneous hydrogen occupation can be seen in the proton spin–lattice relaxation rate data and will be explained below.

The scandium hcp lattice has two adjacent, closely spaced interstitial T sites along the c axis where hydrogen is known[29]

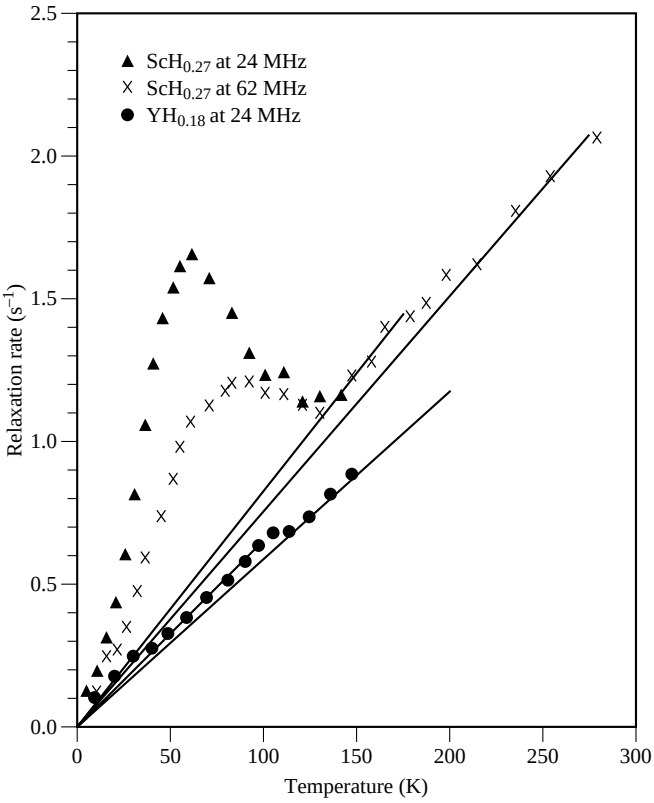

Figure 9 Proton spin–lattice relaxation rate (R_1) in $ScH_{0.27}$ as a function of temperature at 24 and 62 MHz. Proton R_1 in $YH_{0.18}$ at 24 MHz (●) shows a weak peak at ~105 K. The peak heights are due to the relaxation of the proton's tunneling motion and proton dipole 'collisions' with fixed (^{45}Sc or ^{89}Y) metal nuclear magnetic moments. Note the ^{89}Y moment is <1/20 of the ^{45}Sc moment. (Reproduced by permission of the American Physical Society from Lichty et al.[30])

to sit in one of the sites. These two sites are too closely spaced to permit two hydrogens to occupy both sites simultaneously.[31] The local motion is understood to be one hydrogen moving between these two closely spaced T sites. Activation energies derived from a 'local over a small barrier' hopping model were found to be $E_a \approx 50$ meV, much smaller than the nominal 500 meV activation energies typical of long-range hopping over a barrier found for activation energies in higher temperature hydrogen diffusion. Lichty et al.[30] were able to fit the proton spin–lattice relaxation rates versus 1000/T with two separate and quite different models for hydrogen hopping over an energy barrier. As can be seen from Figure 10, the data are not symmetrical about the peaks of the three relaxation curves. The slope of the three curves on the high temperature (low 1/T values) side of the peak is much greater than the low temperature (higher 1/T values) slopes. Symmetrical log R_1 versus 1/T curves in HMSs is a signature of hydrogen hopping where there is one unique activation energy typifying a simple hopping process and/or a simple and often cubic solid. Symmetrical log R_1 or log T_1 vs 1/T curves are often referred to as BPP type behavior. The relaxation rate curves in Figure 10 show the signature of hydrogen motion in a disordered solid with a distribution of activation energies. This subject will be discussed at length below. Lichty et al.[30] were able to fit the data with two hopping models, one assuming a distribution of activation energies and a second model with a correlation

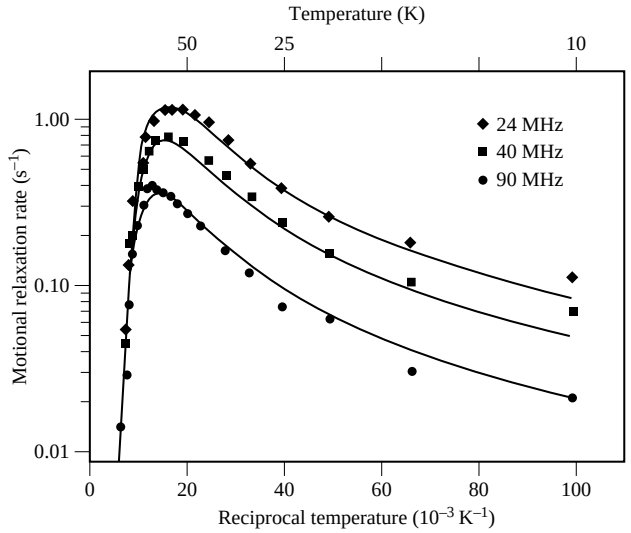

Figure 10 Proton spin–lattice relaxation rate in $ScH_{0.27}$ vs. 1000/T for proton resonance frequencies 12, 40, and 90 MHz fitted with a thermally activated over the barrier hopping model and a distribution of activation energies. (Reproduced by permission of the American Physical Society from Lichty et al.[30])

function having a stretched exponential character. Localized hydrogen motion has also been found by Skripov et al.[32] in TaV_2H_x in the temperature range 10–100 K.

Tunneling of hydrogen from one tetrahedral interstitial site to an adjacent empty T site at low temperature is an alternate mechanism rather than hydrogen thermally activated hopping over a low energy barrier. Svare et al.[33] suggested that the same proton spin–lattice relaxation data of Lichty et al.[30] in $ScH_{0.27}$ could also be described by hydrogen tunneling between adjacent T sites in the Sc hexagonal close packed lattice. The potential wells for the two sites were thought to have sinusoidal curvature near the bottoms. The two wells of the adjacent T sites were also thought to have different minimum energies, that is, the wells were asymmetric. In fact, Svare et al.[33] suggested the asymmetry, A, for the hydrogen–scandium metal solid solution would have a distribution of minimum energy difference values typical of an inhomogeneous hydrogen solid solution or proton glass. With increasing temperature, the tunneling model must include a tunneling mechanism not appropriate (or yet thermally switched on) at lower temperature. Figure 11 shows the proton spin–lattice relaxation data of Lichty et al.[30] fit with this tunneling model. The data fit adequately this tunneling theory and support the proposition that hydrogen tunneling exists in scandium at low temperatures. Hydrogen tunneling in scandium was also found by Leisure et al.[34] in a resonant ultrasound spectroscopy (not an NMR technique) study of $ScH_{0.25}$ and $ScD_{0.18}$ employing small scandium single crystals.

6 SPIN–LATTICE RELAXATION IN AMORPHOUS HYDROGEN–METAL SYSTEMS

An amorphous metal alloy may be formed by extremely rapid cooling of the molten metal alloy. Such materials are often referred to as metallic glasses. An amorphous alloy is a

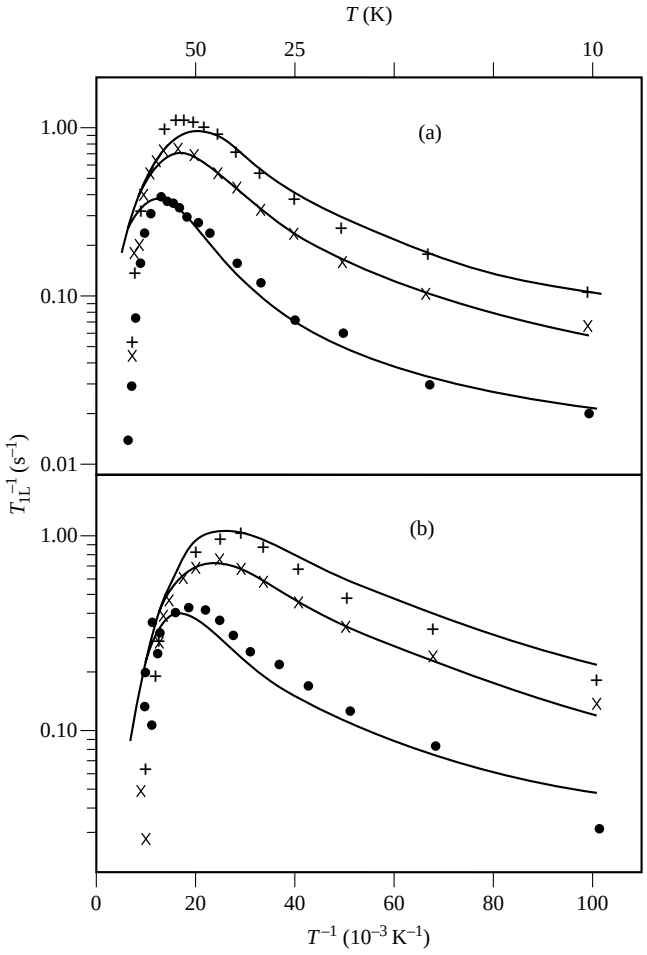

Figure 11 Low temperature proton spin-lattice relaxation rates $R_{1L} \equiv T_{1L}^{-1}$ versus reciprocal temperature in two hcp scandium–hydrogen solid solution compositions. (a) $ScH_{0.27}$ and (b) $ScH_{0.11}$ at 24 MHz (+), 40 MHz (×), and 90 MHz (•), respectively. The curves represent the fits of the tunneling model with a distribution of asymmetric energy well minima for hydrogen tunneling between adjacent tetrahedrally coordinated interstitial (T) sites. Data are from Lichty et al.[30] and tunneling model can be found in Svare et al.[33]

disordered metal and is without long range topological order. There may be short range or compositional order in amorphous alloys. These amorphous materials are then hydrided by more or less conventional means, but care must be taken not to heat the material high enough to 'recrystallize' the amorphous sample. This may be somewhat difficult as the absorption of hydrogen by metals is generally an exothermic reaction.

Bowman[35] points out that metallic alloy glasses must contain one of certain metals, i.e. titanium, zirconium, hafnium, palladium, or a rare earth metal, for the glass to be able to hold hydrogen, H/M > 0.1, where M is the total metal content. Even with one of these metals in the alloy, an alloy glass may not be formed upon quenching.

Hydrides of metallic glasses generally have quite different hydrogen motions, with lower hydrogen diffusion activation energies and spin–lattice relaxation rates than do hydrides of the crystalline HMSs of similar composition as we shall see below. In the case of crystalline and amorphous Zr_2PdH_x, Bowman et al.[36] point out the log T_1 versus 1000/T plots for $Zr_2PdH_{2.90}$ and amorphous a-$Zr_2PdH_{2.90}$ are noticeably

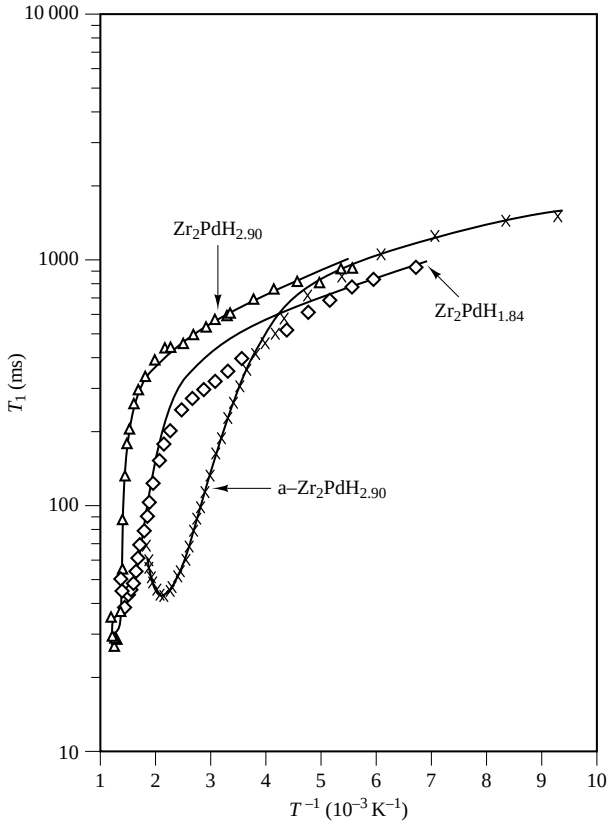

Figure 12 Proton spin–lattice relaxation times vs. 1000/T for crystalline $Zr_2PdH_{1.84}$ and $Zr_2PdH_{2.90}$ at 40 MHz and amorphous $Zr_2PdH_{2.90}$ at 34.5 MHz, and proton relaxation times for crystalline and amorphous $Zr_2PdH_{2.90}$ vs 1000/T. The latter curve shows hydrogen diffusion at lower temperatures and with lower activation energy (slope of T_1 vs. 1000/T curve) than the crystalline $Zr_2PdH_{2.90}$. (Reproduced by permission of R. Oldenbourg Verlag from Bowman et al.[36])

different. The crystalline and amorphous curves have minima at different temperatures and have different slopes or diffusion activation energies. Generally, the amorphous samples display more rapid hydrogen diffusion at lower temperatures and have lower activation energies for diffusion than do the crystalline equivalents. This can be seen in Figure 12. A simplistic explanation of this effect may relate in part to the fact that the glassy HMSs have a somewhat lower density and have more 'open' paths for hydrogen to hop through than the crystalline equivalents. A more complete description of hydrogen motion must also include the differences in electronic character known to exist between the glassy and crystalline HMSs.

7 RELATED ARTICLES

Amorphous Materials; Deuterium NMR in Solids; Diffusion in Solids; Electron–Nuclear Hyperfine Interactions; Knight Shift; Spin Diffusion in Solids.

8 REFERENCES

1. W. H. Mueller, J. P. Blackledge, and G. C. Libowitz. *Metal Hydrides*, Academic Press, New York, 1968.
2. R. E. Norberg, *Phys. Rev.*, 1952, **86**, 745.
3. D. Khatamin, W. A. Karmatakahara, R. G. Barnes, and D. T. Peterson, *Phys. Rev. B*, 1980, **21**, 2622.
4. R. C. Bowman, Jr., B. D. Freeman, and J. R. Phillips, *Cryogenics*, 1992, **32**, 127.
5. A. Struss and J. D. Corbett, *Inorg. Chem.*, 1977, **38**, 612.
6. Y. S. Hwang, D. R. Torgeson, A. S. Khan, and R. G. Barnes, *Phys. Rev. B*, 1977, **15**, 4564.
7. R. G. Barnes, M. Jerosch-Herold, J. Shinar, F. Borsa, D. R. Torgeson, D. T. Peterson, A. J. Lucas, G. A. Styles, and E. F. W. Seymour, *Phys. Rev. B*, 1987, **35**, 890.
8. D. B. Baker, N. Adolphi, M. S. Conradi, P. A. Fedders, R. E. Norberg, R. G. Barnes, and D. R. Torgeson, *Phys. Rev. B*, 1992, **46**, 184.
9. E. F. W. Seymour, *J. Less-Common Met.*, 1982, **88**, 323.
10. D. S. Schreiber and R. M. Cotts, *Phys. Rev.*, 1963, **131**, 1118.
11. T. Y. Hwang, D. R. Torgeson, and R. G. Barnes, *Phys. Lett.*, 1978, **66A**, 137.
12. H. S. Marek, J. D. Corbett, and R. L. Daake, *J. Less-Common Met.*, 1983, **89**, 249.
13. Y. S. Hwang, D. R. Torgeson, and R. G. Barnes, *Solid State Commun.* 1977, **24**, 773.
14. R. Barnes, *J. Less-Common Met.*, 1991, **172–174**, 509.
15. N. Bloembergen, E. M. Purcell, and R. V. Pound, *Phys. Rev.*, 1948, **73**, 679.
16. F. Borsa, R. G. Barnes, B. J. Beaudry and D. R. Torgeson, *Phys. Rev. B*, 1982, **26**, 1471.
17. H. C. Hoke, H. E. Schone, C. A. Sholl, S. P. Usher, R. G. Barnes, D. R. Torgeson, R. Hempelmann, and G. A. Styles, *J. Less-Common Met.*, 1991, **172–174**, 603.
18. A. Abragam, *The Principles of Nuclear Magnetism*, Oxford Press, 1961.
19. C. A. Sholl, *J. Phys. C: Solid State Phys.*, 1986, **19**, 2547.
20. C. P. Slichter, *Principles of Magnetic Resonance*, Springer-Verlag, 3rd ed, 1990.
21. W. Heitler and E. Teller, *Proc. R. Soc. London*, 1936, **A155**, 637; and J. Korringa, *Physica*, 1950, **88**, 323.
22. T.-T. Phua, B. J. Beaudry, D. T. Peterson, D. R. Torgeson, R. G. Barnes, M. Belhoul, G. A. Styles, and E. F. W. Seymour, *Phys. Rev. B*, 1983, **28**, 6227.
23. D. R. Torgeson, J.-W. Han, P.C-T. Chang, L. R. Lichty, R. G. Barnes, E. F. W. Seymour, and G. W. West, *Z. Phys. Chem. NF*, 1989, **164**, 853.
24. L. R. Lichty, J.-W. Han, D. R. Torgeson, R. G. Barnes, and E. W. F. Seymour, *Phys. Rev. B*, 1990, **42**, 7734.
25. D. R. Torgeson, R. J. Schoenberger, and R. G. Barnes, *J. Mag. Reson.*, 1986, **68**, 85.
26. W. H. Jones, Jr., T. P. Graham, and R. G. Barnes, *Phys. Rev.*, 1963, **132**, 1898.
27. G. Pake, *J. Chem. Phys.*, 1948, **16**, 327.
28. D. R. Torgeson and R. G. Barnes, *Phys. Rev. Lett.*, 1962, **9**, 255.
29. O. Blaschko, G. Krexner, J. N. Daou, and P. Vajda, *Phys. Rev. Lett.*, 1985, **55**, 2876.
30. L. R. Lichty, J.-W. Han, R. Ibanez-Meier, D. R. Torgeson, R. G. Barnes, E. F. W. Seymour, and C. A. Sholl, *Phys. Rev. B*, 1989, **39**, 2012.
31. L. R. Lichty, R. J. Schoenberger, D. R. Torgeson, and R. G. Barnes, *J. Less-Common Met.*, 1987, **129**, 31.
32. A. V. Skripov, M. Yu Belyaev, S. V. Rychkova, and A. P. Stepanov, *J. Phys. Condens. Matter*, 1989, **1**, 2121.
33. I. Svare, D. R. Torgeson, and F. Borsa, *Phys. Rev. B*, 1991, **43**, 7448.

34. R. G. Leisure, R. B. Schwarz, A. Migliori, D. R. Torgeson, and I. Svare, *Phys. Rev. B*, 1993, **48**, 893.
35. R. C. Bowman, Jr., *Mater. Sci. Forum*, 1988, **31**, 197.
36. R. C. Bowman, Jr., D. R. Torgeson, R. G. Barnes, A. J. Maeland, and J. J. Rush, *Z. Phys. Chem., NF*, 1989, **163**, 425.

Biographical Sketch

David R. Torgeson. *b* 1936. B.A., 1958, Luther College. M.S., 1960, Iowa State University. Introduced to NMR by R. G. Barnes. Basic physics research utilizing nuclear and electron resonance techniques, Ames Laboratory, Iowa State University, 1960–present. Assistant Professor of Physics, Luther College, 1967–68, and ISU, 1972. Physicist, Ames Laboratory, 1982–present. Adjunct Assistant Research Professor of Physics, Iowa State University, 1993–present. Approx. 120 publications. Research interests include: application of NMR for materials characterization of hydrogen–metal systems, fast ion conductors, high temperature superconductors, and quasicrystals; and instrumentation for solid state NMR.

Knight Shift

Walter D. Knight
University of California, Berkeley, CA, USA

and

Shun-Ichi Kobayashi
University of Tokyo, Tokyo, Japan

1	Introduction—NMR and Structure of Metals	1
2	Lattice Structure and Dynamics	1
3	Orbital and Core Polarization Shifts, Spin Relaxation	2
4	Structures of Alloys	3
5	Electronic Structure of Mesoscopic Particles[20]	3
6	Knight Shift in Superconductors	5
7	Related Articles	6
8	References	6

1 INTRODUCTION—NMR AND STRUCTURE OF METALS

The Knight shift refers to the relative shift K in NMR frequency for atoms in a metal (e.g. sodium) compared with the same atoms in a nonmetallic environment (e.g. sodium chloride). The observed shift reflects the local magnetic field produced at the sodium nucleus by the magnetization of the conduction electrons. The average local field in sodium augments the applied resonance field by approximately one part per 1000. In nonmetallic sodium chloride the local field is negligible in comparison.

Conduction electrons[1] in a metal are delocalized, meaning that no electron is uniquely associated with any particular atom more than another but all exist in eigenstates within an energy band, whose highest occupied state lies at an energy E_F, the Fermi energy. At lower energies the electron wave functions tend to be mainly s states, while at higher energies there are increasing admixtures of higher (p, d, ...) states. For s states the probability density at the nucleus ($R = 0$) is high, and since each electron carries a spin and magnetic moment μ_B, the contact interaction momentarily produces a local magnetic field at the nuclei, as the electron moves through the lattice.

The local hyperfine field in atomic sodium is approximately 39 T. This is an atomic property, independent of external fields. The average contact hyperfine field in a metal is zero, in zero applied field, because the nucleus is exposed to equal numbers of spin-up and spin-down electrons. In an externally applied magnetic field the conduction electron system acquires a magnetization proportional to the magnetic susceptibility of the conduction electron system. The appropriate susceptibility χ_p is the temperature independent Pauli paramagnetism. Because the electron magnetic moments parallel to the applied field have the lower energies, the parallel orientation is more favorable than the antiparallel, and consequently the number of parallel moments is greater, hence the paramagnetism. The fractional change in field, or observed resonance frequency, is[2]

$$K = \Delta B/B = \Delta\nu/\nu = (8\pi/3)\chi_p V_0 P_F \qquad (1)$$

where χ_p is the Pauli susceptibility per unit volume, V_0 is the volume per atom in the metal, P_F is the average value of the s electron probability density at $R = 0$, B is the applied magnetic field, and ν is the observed resonance frequency. The average P_F is taken for electrons at the Fermi energy E_F. The local field of p electrons is usually 10% or less of the contact interaction, and produces small anisotropic shifts in noncubic metals (c.f. Section 2.3). The anisotropic effects vanish in cubic metals. In noncubic metals the effects are relatively small, but yield valuable information concerning electronic and crystal structures.

To summarize some typical parameters: the hyperfine field per electron in a free sodium atom is 39 T; the corresponding contact hyperfine field in metallic sodium is smaller, ~30 T, mainly because of p admixtures in the wave functions at the Fermi surface; the small Pauli susceptibility reflects the small number of unpaired spins; the average local field is 1.1×10^{-3} T for an applied field of 1 T; and equation (1) gives $K = 0.11\%$.

Values of K have been measured for most of the metallic elements, and recorded results range approximately from $K = 0.026\%$ (Li) to 2.7% (Hg). The measurement of K is a sensitive means for probing, noninvasively, electronic and geometric structures of metallic systems in solids and liquids, and has been of value in studying phase transitions in metals, alloys, intermetallic compounds, and superconductors.[3]

2 LATTICE STRUCTURE AND DYNAMICS

2.1 Effects of Pressure, Volume, and Temperature

It is evident from equation (1) that insofar as the parameters χ_p, V_0, and P_F depend on pressure, volume, or temperature, K is affected by, and is a measure of, these variables. Compressing a specimen effectively changes the volume per atom and P_F, while heating affects the volume, the lattice dynamics, and electron–phonon interactions as well. Although the Pauli susceptibility is essentially independent of temperature, other contributions to the susceptibility are temperature dependent, and NMR shifts have corresponding temperature dependences (c.f. Sections 3.1 and 3.2).

In order to find the intrinsic temperature dependence, one can measure K versus T at constant P, and K versus V at constant T, also knowing the thermal expansion coefficient and compressibility. With so many variables, the end results are useful, but may not be as precise as one would wish. Bloembergen has pointed out[4] that P_F is nonlinear with respect to volume, and χ_p depends on lattice vibration frequency via spin–lattice relaxation.

Recently, Götz and Winter[5] have considered the volume dependence of K for the alkali metals lithium and sodium, for which many experimental data exist. They pointed out that the theoretical analysis requires the inclusion of orbital plus exchange and correlation terms (c.f. Sections 3.1 and 3.2). While they were able to arrive at good agreement with the experimental results for lithium, the result for sodium is less clear. The work serves to illustrate the fact that the theoretical problems are more elaborate than was believed at first.

2.2 Anisotropic Shift

For noncubic crystals K becomes a function of crystal orientation with respect to the applied field.[6] We can perform and analyze NMR shift experiments in crystals with axial symmetry, for example, introducing the axial shift K_{ax}, which depends on hyperfine magnetic fields at the nucleus generated by p electrons. These fields are generally 10% or less of the contact hyperfine fields, but valuable structural information may be obtained.[6]

For crystals of axial symmetry, the anisotropic part of the NMR shift is a function of the angle θ between the principal symmetry axis and the applied magnetic field.

$$K_{ax} = q_F \chi_p (3\cos^2\theta - 1) \tag{2}$$

The shape of the p electron charge distribution and its dipole field at $R = 0$ are included in the function q_F in equation (2). For an axially symmetric crystal the total NMR shift is the sum of equations (1) and (2).

For a single crystal specimen the NMR appears at frequencies varying between extremes at $\theta = 0^\circ$ and 90°. A polycrystalline sample shows a broadened lineshape between the above extremes, with the largest intensity near $\theta = 90^\circ$, and the frequency of minimum intensity appears at higher frequency for positive q_F. For nonaxial symmetry, the corresponding extended analysis is straightforward.[6] Experimental results are also interpreted in terms of crystal structure and electronic band structure (s–p admixture).

2.3 Quadrupole Coupling

An analysis similar to the above can be made for nuclei with the quadrupole moment Q in a noncubic environment. The first-order quadrupole interaction frequency is

$$\nu = e^2 q Q / h \tag{3}$$

where q is the local electric field gradient at the nucleus, which depends on crystal structure ($q = 0$ in cubic symmetry). For a first-order interaction in a specimen with nuclear $spin - \frac{3}{2}$ the spectrum consists of a pair of satellites astride the central NMR resonance and split by $\pm e^2 qQ/4h$. More complete discussions, including second-order quadrupole effects, are available.[6]

3 ORBITAL AND CORE POLARIZATION SHIFTS, SPIN RELAXATION

3.1 Orbital Paramagnetism

Several other factors contribute to the total NMR shift in metals. Beyond the Pauli term in equation (1), there is the orbital (Van Vleck) paramagnetism, and also the core polarization by d electrons. Each of the above effects is associated with a respective magnetic susceptibility, and may be summed as follows:

$$\chi = \chi_p + \chi_v + \chi_d \tag{4}$$

The Pauli term χ_p predominates in light monovalent metals, while the second and third terms generally make large contributions in heavy and transition metals. The first two are nearly independent of temperature in the normal state. The last tends to be paramagnetic and temperature dependent for transition metals with narrow d bands and low Fermi temperatures.

The orbital paramagnetism χ_v is a second-order effect in solids analogous to the Van Vleck temperature independent paramagnetism in molecules.[7,8] It arises because of the mixing of filled and unfilled orbitals in the same band. It appears that the contact term χ_p for vanadium is approximately cancelled by the negative χ_d term, and small compared with the orbital χ_v term.[9] This conclusion is consistent with the fact that the NMR shift in vanadium is minimally affected by the transition to the superconducting state (the predominant orbital hyperfine field is not related to electron spin pairing—see Sections 3.2, 4.3, and 6.1).

The orbital susceptibility can be estimated[8] in several ways, one of which can be expressed as

$$\chi_v \sim 2\mu_B^2 N/E \tag{5}$$

where N is the number of d electrons per unit volume, and E is the average energy separation of the mixed states.

3.2 Core Polarization

The third term in equation (4) represents the temperature dependent paramagnetic d states. Although the direct hyperfine interaction of d electrons is small, s electrons (either in a filled shell or in an s band) couple[10] with the paramagnetic d electrons and produce hyperfine fields which can be comparable (or of opposite sign) to the direct s electron contact interaction. For example, in platinum the predominant contribution[11] to K derives from core polarization, which is calculated to be negative, resulting in a large observed negative shift, $K_{Pt} = -3.5\%$.

A recent band structure Green's function analysis[12] points out that equation (4) implies independence among the several terms, while in fact the terms are not strictly independent, and it is in principle necessary to include spin–orbit and exchange correlation effects in the calculations. It is also clear from their results and comparison of several calculations with equation (5) that the latter provides useful but imprecise estimates for susceptibilities and shifts. The theoretical results support the previous interpretations for the observed shifts in vanadium[9] and platinum.[11]

3.3 Diamagnetism of Conduction Electrons

In addition to the terms in equations (1) and (4), the contribution of the Landau diamagnetism by the conduction electrons is significant. When a magnetic field is applied to the conduction electron system, the levels split so that the average energy of the system increases, corresponding to a diamagnetism of one-third χ_p,[13] with a correction factor involving the electron effective mass:

$$\chi_L = -(\chi_p/3)(m/m^*)^2 \tag{6}$$

This χ_L term appears to be significant but relatively small in most metals, and is believed to be mainly responsible for the large negative $K = -1.25\%$ in solid bismuth, which is characterized by a very small effective mass. By contrast, liquid bismuth behaves more like an ordinary metal, since $K = +1.4\%$ in the liquid. A further interesting observation is the oscillation of K as a function of applied magnetic field, in analogy to the de Haas–van Alphen effect.

3.4 Korringa Relation

An important means of directly relating metallic properties to NMR experiments depends on the Korringa relation,[4] which is based on the fact that the nuclear spin relaxation rate $1/T_1$ varies directly as temperature T and the square of the density of states $[N(E_F)]^2$ at the Fermi surface, while K is simply proportional to $N(E_F)$. In abbreviated form the Korringa relation is expressed

$$K^2 T_1 T \sim S \tag{7}$$

The Korringa product factor S on the right-hand side of equation (7) includes the magnetogyric ratios of the electron and nucleus. Equation (7) permits an independent evaluation of K in cases where χ is uncertain. The order of magnitude of S is generally unity when K is dominated by the contact interaction, as is true for the alkali and simple metals. For transition metals, where $S \gg 1$, equation (7) must be used with caution, noting also that the measured T_1 may include a contribution produced by fluctuating nuclear quadrupole interactions. The orbital paramagnetism χ_v depends on the average density of states over the conduction band and should not be included in a calculation involving equation (7), since χ_p and K depend simply on $N(E_F)$.

3.5 Overhauser Effect

The contact hyperfine interaction which produces the Knight shift, as well as relaxing the nuclear spins, acts reciprocally to produce a magnetic field on the conduction electrons because of the large nuclear polarization. This interaction produces a shift in the ESR, and a large enhancement of the NMR intensity, the Overhauser effect.[14] The magnitude of the intensity enhancement is easily a factor of 10 or more. Under conditions of maximum NMR intensity enhancement, the ESR is saturated, and the frequency of the ESR is shifted (the Day shift).

4 STRUCTURES OF ALLOYS

4.1 Metallurgical Phases in Simple Binary Alloys

The classical treatment of alloys was based on thermodynamic analysis, crystal structures, and the average electron–atom ratios. Further local information is obtained by measurements of the Knight shift. Alloys of cadmium in silver include an α phase (face-centered cubic) with up to ~40% cadmium, followed by a mixed α and β phase (41–49% cadmium), then a β phase (body-centered cubic) (49–51% cadmium), followed by the phases γ, ϵ, η (pure Cd). The mixed phases are characterized by two NMR lines with K values appropriate to the respective adjacent pure phases.[6,15]

In the α phase of silver–cadmium alloy, K_{Cd} decreases linearly from 0.59 to 0.53% at the β phase boundary. The silver shift drops linearly from 0.52 to 0.46% in the α phase, as predicted,[16] but was not observed at higher concentrations because of low signal strength.

Analysis of the local electronic structure, as seen by the solute atom in the alpha phase may proceed on the basis of equation (1), using χ_p (solvent), and P_F (solute, modified to include s–p character of the solvent).

The average electron density is reduced by long range charge density oscillations in space, which are induced by the perturbing solute atoms.[16] The net result is a decreasing average charge density at solvent atoms with increasing solute concentration. Since the charge density oscillates with relative positions of solute and solvent atoms, the average reduction of the K shift is accompanied by a resonance line broadening.

4.2 Intermetallic Compounds

These are alloys with definite stoichiometries. Depending on the constituents and temperature, intermetallic compounds may be metallic conductors, semiconductors, or superconductors (c.f. Section 6). It was found[9] that K for vanadium is strongly dependent on temperature in the superconducting intermetallic compound V_3Ga. Just above the transition temperature T_c the vanadium shift $K_V = +0.45\%$, changing to +0.65% for $T \ll T_c$. Correspondingly, the gallium shift K_{Ga} changes from -0.8 to -0.2%. In both cases the average hyperfine field becomes more positive as the negative core polarization shift decreases. These results raise a number of interesting questions, such as what are the charge density patterns of the band electrons.

4.3 Alloys with Dilute Magnetic Impurities

The scattering of conduction electrons by impurity atoms is considered in Sections 4.1 and 5.3. Long range spatial charge oscillations and indirect spin couplings[17] between distant electrons and nuclei result in long-range variations in local fields, and polarizations which couple with host atoms as well as other impurities. NMR shifts and line broadenings are observed, in addition to resolved satellites for the NMR resonance lines.[18]

4.4 Muon Spin Resonance

Just as the conduction electrons probe the atom cores, the muon spin rotations, prior to their decay, provide signals measuring the local magnetic fields near the decay sites.[19] Knight shifts of from 10 to 100 ppm are observed for $\mu+$ at frequencies of a few megahertz in fields of a few kilogauss. Muon spin resonance techniques have the advantages of fast timescales and no complications by quadrupole interactions.

5 ELECTRONIC STRUCTURE OF MESOSCOPIC PARTICLES

5.1 Energy Levels

The energy spectrum of electrons confined in a finite volume is, in principle, discrete. In macroscopic metals, however, the spacing of the energy levels is very much smaller than the lifetime broadening of the levels, and, therefore, the continuous energy spectrum is a good approximation. The broadening caused by electron–phonon interactions and/or electron–electron interactions diminishes as the temperature is lowered, and typically becomes of the same order as thermal energy at 1 K. Thus, in small particles with an energy spacing larger than 1 K we would expect anomalies in electronic properties at temperatures below 1 K. The spacing is evaluated as

$$\delta = [N(E_F)\Omega]^{-1} \tag{8}$$

where $N(E_F)$ is the density of states at the Fermi level and Ω is the sample volume. In ordinary metals, Ω is $(10^4\ \text{pm})^3$ for δ to be 1 K.

Fröhlich was the first to point out anomalies in the thermodynamic properties in particles, assuming that the levels are equally spaced.[21] Kubo took a more realistic level distribution, i.e. a random distribution. Kubo also put emphasis on the charge neutrality of particles because a single electron imbalance brings a large charging energy.[22] Shortly after, Gorkov and Eliashberg suggested that the level distribution is not random but has statistical correlations, in analogy to the level distribution in heavy nuclei.[23] These correlations are the results of the symmetries of Hamiltonians governing the system.

Let $P(E)\ \mathrm{d}E$ be the probability of finding the next level between E and E + dE. It can be shown that, in the limit of small E,

$$P(E) = E^{n-1}/\delta^n \tag{9}$$

where n is the number of random variables. Four cases are possible:

1. case 1, n = 2: elements of the Hamiltonian matrix are real.
2. case 2, n = 3: in high magnetic fields where the elements are complex.
3. case 3, n = 5: with a strong spin–orbit interaction, where spin and orbital states are not separable.
4. case 4, n = 1: with a large Zeeman energy, where the levels of up and down spins are no longer correlated.

These discrete and correlated levels modify the electronic quantities such as spin paramagnetism, nuclear spin–lattice relaxation time, orbital diamagnetism, and specific heat. So far, the first two have been investigated both theoretically and experimentally. The specific heat is very difficult to measure accurately. There is a prediction that the orbital magnetization can be both positive and negative, and will fluctuate with a large amplitude when a magnetic field is swept,[24] but no experiment has been reported.

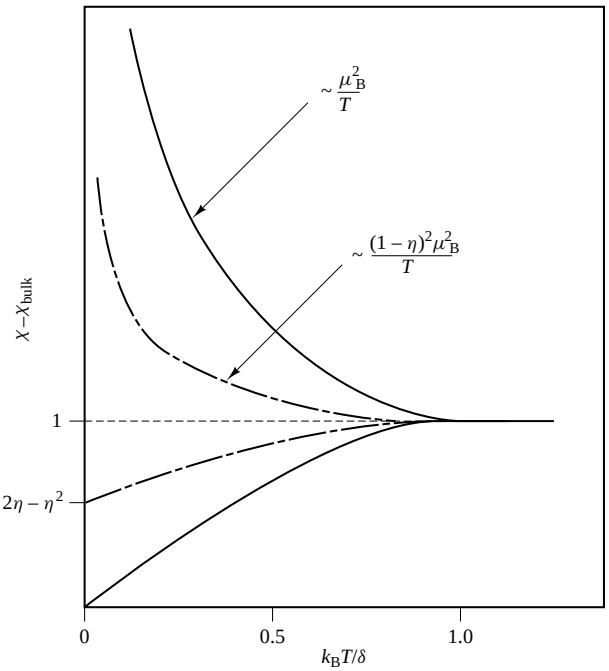

Figure 1 Temperature dependence of χ_{even} and χ_{odd}, with $\eta = (h/\tau_{so})$[27]

5.2 Magnetism

The spin paramagnetism of small particles shows characteristic behaviors. For case 1, the spin susceptibility of a particle with an odd number of electrons, χ_{odd}, is Curie-like as $T \to 0$ because there is an electron that has no partner with opposite spin. The susceptibility of a particle with an even number of electrons, χ_{even}, tends to zero as $T \to 0$, as all the spins are paired with opposite ones. In case 2, χ_{even} revives because of the mixing of up- and down-spin states. The behaviors of χ_{even} and χ_{odd} are calculated with a finite strength of the spin–orbit interaction. The results are shown schematically in Figure 1. All anomalies in susceptibility vanish when $k_B T > \delta$.

The spin magnetization is nonlinear when the magnetic field is as high as $2\mu_B H \geq \delta$, because the level correlation is diminished.[25] Thus, when $2\mu_B H \geq \delta$, the spin magnetization will take a normal Pauli value.

Nuclear spin–lattice relaxation in metals is governed by the Korringa process, the relaxation time, T_1, being inversely proportional to the temperature, reflecting the continuous energy spectrum of electrons. In small particles this process is strongly suppressed, because it is not always possible to conserve the energy through the process which involves a mutual flip of electron and nuclear spins and a change in electron orbital state.

5.3 Small Particles and Alloys

The first quantitative experiment of the Knight shift in small copper particles was reported by Yee and Knight.[26] The samples were particles that are formed on substrates at early stages of vacuum deposition. This method has been used for all the experiments described in this article. The distribution width of linear sizes of particles in each sample is about 20%

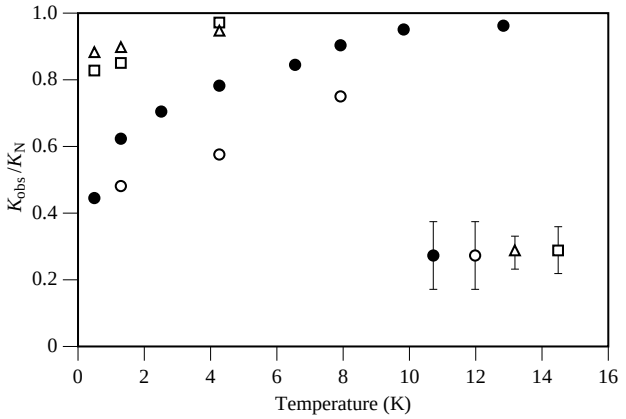

Figure 2 Temperature dependence of shifts in copper particles.[26] Particle diameters: ○, 2.5 nm; ●, 4.0 nm; □, 10.0 nm; △, 11.0 nm

of its mean value. In Figure 2 the results of the Knight shift are shown for several samples. The temperature dependence and the size dependence of the residual shifts at $T = 0$ agree quantitatively with theory.[27]

The spin–lattice relaxation time in copper particles was measured, and extraordinarily enhanced T_1 values were observed, as expected.[28]

The suppression of the Knight shift anomaly in high magnetic fields (case 4) was confirmed in 10.0 and 6.0 nm copper particles.[29] The suppression was observed when $2\mu_B H \geq \delta$.

The spin scattering by magnetic impurities destroys the effects of level discreteness. To establish a kinetic energy level in a particle, an electron has to 'see' all the boundary conditions, i.e. it has to 'sweep' the whole volume of the particle. It can be shown that the time necessary for this travel is $\tau = \Omega/\pi v_F \lambda_F{}^2$, where v_F and λ_F are the Fermi velocity and the Fermi wavelength, respectively. If an inelastic scattering takes place before τ, the level cannot be sharp. The above expression for τ is equivalent to $\tau\delta = h$. This consideration can help interpret the results of the Knight shift of ^{63}Cu in particles of copper–manganese alloys.[30] The suppression of spin paramagnetic susceptibility disappeared when the manganese concentration was increased so that the spin scattering time is shorter than h/δ. The anomaly in T_1 also vanished.[31]

The strength of the spin–orbit interaction can be modified by alloying a heavy element in particles. The Knight shift was measured in copper particles alloyed with gold.[32] As the concentration of gold increased, the Knight shift recovered the bulk value. Although this change is the same as that in copper–manganese, a substantial difference was observed in T_1. The value of T_1 stayed very long even after the shift was completely recovered. This is because the spin scattering is inelastic while the spin–orbit scattering is elastic, the phase memory being retained in the latter.[31]

6 KNIGHT SHIFT IN SUPERCONDUCTORS

6.1 Spin Pairing

According to the BCS theory of superconductivity, the Knight shift quickly vanishes below the transition temperature, because of spin–singlet pairing.[33] NMR experiments were intensively carried out to check the validity of the theory. However, in some superconductors of heavy metals the shift did not vanish but stayed finite when $T \to 0$. Soon after, it was recognized that this was a size effect. To measure the shift, samples of reduced dimension (thin films or fine powders) were used, in order to increase critical fields of superconductors of the first kind and to let the rf field penetrate the samples. The reduced dimension makes the mean free path shorter, and enhances mixing of up- and down-spin states due to spin–orbit interactions. Thus, for the same reason as for the residual Knight shift in normal heavy metal particles, the shift remains finite even when $T \to 0$.[34]

6.2 Contributions to Shift

In transition metal superconductors the Knight shift consists of three contributions: the s band spin polarization, the orbital (Van Vleck) polarization, and the core polarization induced by non-s spin polarization. The first two are positive in sign, and the last is experimentally negative, although it can take both signs in principle. The three contributions can be resolved by observing the temperature dependence of the shift in the normal state. What is suppressed in the superconducting state is the first and the last polarization, while the orbital part does not change (cf. Section 3). A great deal of data has been accumulated for various superconductors.[35]

6.3 How Small is a Superconductor

In the 1970s, the order parameter fluctuation in superconductors with reduced dimensions was exhaustively studied. Measured Knight shifts in aluminum particles smaller than the coherence length and penetration depth[36] agreed with microscopic theories for the critical region of temperature.[37] The result for aluminum particles is shown in Figure 3.[36] The theories were based on a grand canonical treatment, which is hardly applicable to small particles with a large charging energy, and does not take the discreteness of energy levels into account. As expected, substantial deviation takes place when the particles are smaller than 10.0 nm, in which δ is larger than the superconducting energy gap, Δ.[38]

The residual Knight shift in tin particles as a function of particle size demonstrates the competition among three energy parameters, i.e. δ, Δ, and h/τ_{so}, where τ_{so} is the time within which the spin direction diffuses by an angle π due to spin–orbit interactions.[39] These energies are proportional to d^{-3}, d^0 and d^{-1}, respectively, d being a linear size. Therefore, Δ dominates in the bulk, and the shift vanishes. As the size is reduced, h/τ_{so} surpasses δ, and the shift (of particles with even number electrons) revives. With a further reduction, δ becomes the largest, and the shift disappears again. The experiment in tin particles with d ranging from 2.5 to 60.0 nm[38] clearly demonstrates this competition (Figure 4). The shift exhibits a peak at around 10.0 nm which corresponds to $\delta \sim \Delta$.

It is interesting to know how many atoms are necessary in small particles for superconductivity. Unfortunately, the level discreteness and the superconductivity modify the Knight shift (in particles with an even number of electrons) and T_1 in the same direction. A reliable way to judge the superconductivity

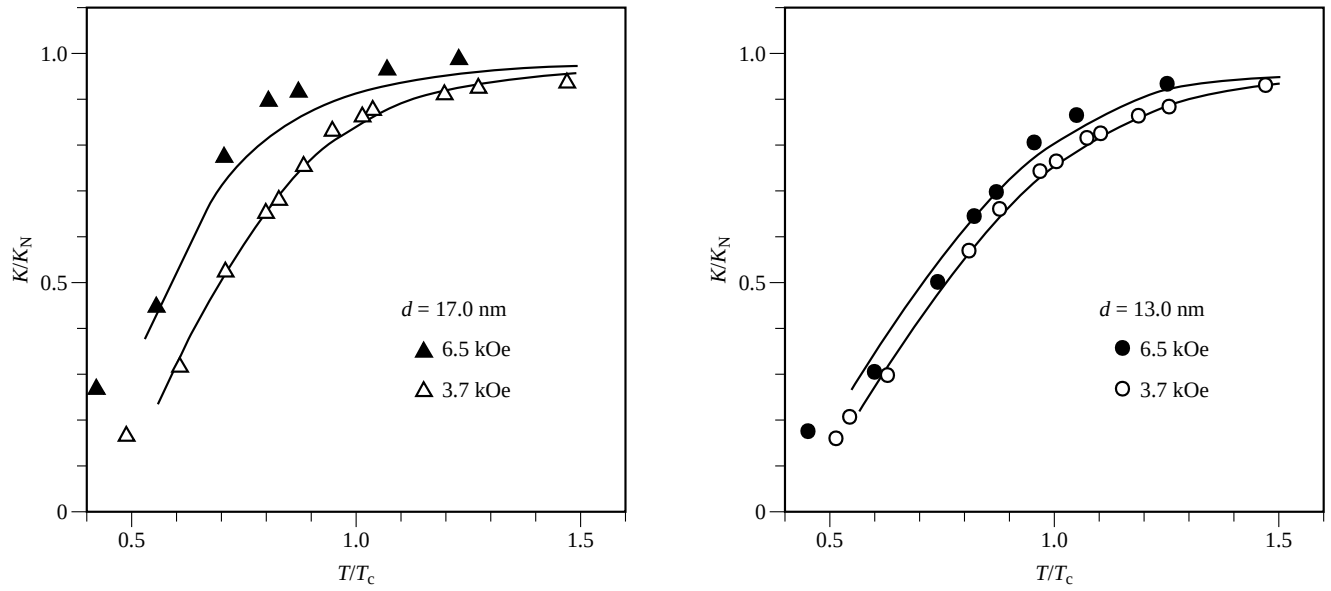

Figure 3 Temperature dependence of shifts in aluminum particles[36]

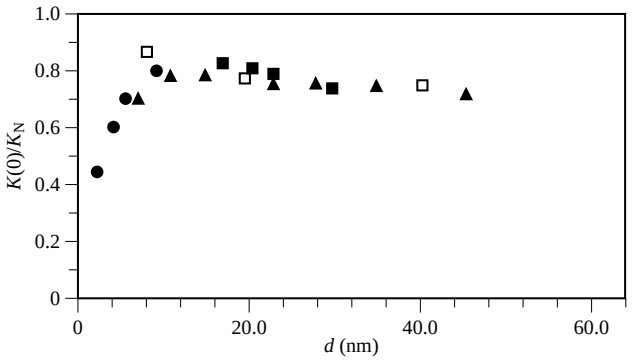

Figure 4 Size dependence of residual shifts in tin particles[38]

is to see if there is a sharp decrease in T_1 at an expected critical magnetic field for superconductivity. The results show that particles are superconductive even when $\delta \geq \Delta$. The observed critical fields support microscopic theories of pair breaking.[39,40] Much smaller particles of aluminum with $\delta \sim 65\,\mathrm{K}$ still exhibit superconducting features as long as T_1 is involved.[41]

6.4 High T_c

Since the discovery of high-T_c oxide superconductors, NMR has been used extensively to clarify the mechanism. The Knight shifts and relaxation times were measured for most of the constituent elements, such as ^{89}Y, ^{137}Ba, ^{63}Cu, and ^{17}O, in 'YBCO', yttrium barium copper oxide.

The main interest is to identify the nature of pairing, i.e. s wave or d wave pairing.[42] Recently, there has been considerable debate on this question, which appears not to be settled as of March 1994. A complete understanding of the mechanisms operating in high-T_c materials still seems remote.

7 RELATED ARTICLES

Electron–Nuclear Hyperfine Interactions; High Temperature Superconductors; Nuclear Overhauser Effect; Quadrupolar Nuclei in Solids; Relaxation of Quadrupolar Nuclei Measured via Multiple Quantum Filtration.

8 REFERENCES

1. C. Kittel, *Introduction to Solid State Physics*, Wiley, New York, Chap. 18
2. C. H. Townes, C. Herring, and W. D. Knight, *Phys. Rev.*, 1950, **77**, 852.
3. G. C. Carter, L. H. Bennett, and D. J. Kahan, *Metallic Shifts in NMR*, Part I, Pergamon Press, Oxford, 1977.
4. N. Bloembergen, *Can. J. Phys.*, 1956, **34**, 1299.
5. W. Götz and H. Winter, *J. Phys. F.*, 1991, **3**, 8931.
6. T. J. Rowland., *Progr. Metal Phys.*, 1961, **9**.
7. N. F. Ramsey, *Nuclear Moments*, Wiley, New York, 1953.
8. R. Kubo and Y. Obata, *J. Phys. Soc. Jpn.*, 1956, **11**, 547.
9. A. M. Clogston, A. C. Gossard, V. Jaccarino, and Y. Yafet, *Phys. Rev. Lett.*, 1966, **9**, 262.
10. M. H. Cohen, D. A. Goodings, and V. Heine, *Proc. Phys. Soc. (London)*, 1959, **A73**, 811.
11. A. M. Clogston, V. Jaccarino, and Y. Yafet, *Phys. Rev.*, 1964, **134**, A650.
12. H. Ebert, H. Winter, and J. Voitländer, *J. Phys F.*, 1986, **16**, 1133.
13. R. E. Peierls, *Quantum Theory of Solids*, Oxford University Press, Oxford, 1955, p. 144.
14. A. W. Overhauser, *Phys. Rev.*, 1953, **92**, 411.
15. L. E. Drain, *Phil. Mag.*, 1959, **4**, 444.
16. J. Friedel, *Phil. Mag.*, 1952, **43**, 153.
17. C. Kittel, *Quantum Theory of Solids*, Wiley, New York, 1963.
18. J. B. Boyce and C. P. Slichter, *Phys. Rev.*, 1976, **13**, 379.
19. A. Schenk, *μSR Spectroscopy, Principles and Applications in Solid State Physics*, Adam Hilger, Bristol, 1985.

20. W. P. Halperin, *Rev. Mod. Phys.*, 1986, **58**, 533; S. Kobayashi, *Phase Transitions*, 1990, **24**, 463.
21. H. Fröhlich, *Physica*, 1937, **6**, 406.
22. R. Kubo, *J. Phys. Soc. Jpn.*, 1962, **17**, 975.
23. L. P. Gorkov and G. M. Eliashberg, *JETP*, 1965, **21**, 940.
24. D. Yoshioka and H. Fukuyama, *J. Phys. Soc. Jpn.*, 1992, **61**, 2368.
25. K. B. Efetov, *JETP*, 1982, **56**, 467.
26. P. Yee and W. D. Knight, *Phys. Rev. B*, 1975, **11**, 3261.
27. J. Sone, *J. Phys. Soc. Jpn.*, 1977, **42**, 1457.
28. T. Goto, F. Komori, and S. Kobayashi, *J. Phys. Soc. Jpn.*, 1989, **58**, 3788.
29. S. Kobayashi and S. Katsumoto, *J. Phys. Soc. Jpn.*, 1987, **56**, 2256.
30. S. Kobayashi, H. Goto, and S. Katsumoto, *J. Phys. Soc. Jpn.*, 1992, **61**, 762.
31. H. Goto, S. Katsumoto, and S. Kobayashi, *J. Phys. Soc. Jpn.*, 1993, **62**, 1439.
32. S. Kobayashi, H. Goto, and S. Katsumoto, *J. Phys. Soc. Jpn.*, 1992, **61**, 1856.
33. K. Yosida, *Phys. Rev.*, 1958, **110**, 769.
34. R. A. Ferrell, *Phys. Rev.*, 1959, **3**, 262; P. W. Anderson, *Phys. Rev. Lett.*, 1959, **3**, 325; F. Reif., *Phys. Rev.*, 1957, **61**, 208; F. Wright, Jr., W. A. Hines, and W. D. Knight, *Phys. Rev. Lett.*, 1967, **18**, 115.
35. D. E. MacLaughlin, in *Solid State Physics*, ed. F. Seitz, D. Turnbull, and H. Ehrenreich, Academic Press, New York, 1976, pp. 1–69.
36. S. Kobayashi, T. Takahashi, and W. Sasaki, *J. Phys. Soc. Jpn.*, 1975, **38**, 559; M. Ido and R. Hoshino, *J. Phys. Soc. Jpn.*, 1975, **38**, 897.
37. H. Shiba, *J. Low Temp. Phys.*, 1976, **22**, 105; J. Sone, *J. Low Temp. Phys.*, 1976, **23**, 699.
38. Y. Fukagawa, S. Kobayashi, and W. Sasaki, *J. Phys. Soc. Jpn.*, 1982, **51**, 1095.
39. J. Sone, *J. Phys. Soc. Jpn.*, 1977, **41**, 1457.
40. K. Nomura, S. Kobayashi, and W. Sasaki, *J. Phys. Soc. Jpn.*, 1980, **48**, 37.
41. F. Komori, T. Goto, K. Wago, and S. Kobayashi, *J. Phys. Soc. Jpn.*, 1988, **57**, 3868.
42. C. P. Slichter, S. E. Barrett, J. A. Martindale, D. J. Durand, C. H. Pennington, C. A. Klug, K. E. O'Hara, S. M. DeSoto, T. Imai, J. P. Rice, T. A. Friedman, and D. M. Ginsberg, *Appl. Magn. Res.*, 1992, **3**, 423.

Biographical Sketches

Walter D. Knight. *b* 1919. A.B., 1941, Physics, Middlebury College, M.A., 1943, Ph.D., 1950, Physics, Duke University, NC (informal supervisor, Charles H. Townes). Instructor in physics, Trinity College, Hartford, 1946–50. Assistant, associate, and professor, Physics Department, University of California, Berkeley, 1950–90, Dean, College of Letters and Science, 1967–72, Professor Emeritus, 1990–present. Member, National Academy of Sciences, American Academy of Arts and Sciences. Approx. 90 publications. Research specialties: NMR in metals, properties of metal clusters.

Shun-ichi Kobayashi. *b* 1938. B.S., 1962, Ph.D., 1967, Physics, Osaka University, Japan; introduced to NMR by Junkichi Itoh. Postdoctoral work at Orsay, Université de Paris, 1967–68. Successively research associate, lecturer, associate professor, and professor, University of Tokyo, Japan, 1968–present. Approx. 120 publications. Research specialties: NMR in small particles of metals, the Anderson localization, quantum transport in mesoscopic systems.

Metallic Superconductors

Yoshika Masuda

Aichi Gakuin University, Aichi, Japan

1	Introduction	1
2	Knight Shift in the Superconducting State	1
3	Nuclear Spin–Lattice Relaxation in BCS Superconductors	2
4	NMR in Type-II Superconductors	6
5	Related Articles	9
6	References	9

1 INTRODUCTION

Nuclear magnetic resonance is a useful tool with which to investigate certain important aspects of superconductivity. It has played an historic role in understanding the properties of superconductors. The environment of nuclear spins in a metal is greatly modified when a metal makes the transition into the superconducting state. The nuclear spins are sensitive to this variation, leading NMR to be an important technique as a probe of the superconducting state.

In a metal, the static response to an external magnetic field in the normal state is generally expressed by a bulk diamagnetic susceptibility. The same mechanism also contributes to the Knight shift of the NMR frequency in a metal.

The dynamic coupling between a spin system and its surroundings (the lattice) gives rise to lattice-induced transitions between spin states. The nuclear spin–lattice relaxation time T_1 is a measure of the rate of exchange of energy between a spin system and the rest of the lattice. It is most generally defined as the ratio of the deviation of spin energy from its equilibrium value to the time rate of change of spin energy.

The Knight shift and T_1 are two important quantities which give much information about the properties of conduction electrons. In particular, T_1 provides information on the density of states near the Fermi surface. Accordingly, it is expected that both effects provide a test of any theory of superconductivity.

Hebel and Slichter[1] first measured T_1 in aluminum, which was believed to be a well-behaved superconductor, in parallel with the development of the Bardeen, Cooper, and Schrieffer[2] (henceforth referred to as BCS) theory in 1957, which gave a microscopic understanding of superconductivity. They calculated the relaxation time predicted by the BCS theory, and found that their experimental T_1 data were consistent with the theory. In fact, T_1 measurements together with measurements of acoustic absorption provide an important confirmation of the choice of spin pairing of the BCS wavefunctions (the so-called 'coherence effect'). The agreement of the nuclear relaxation time with theory is in contradiction to the behavior of the Knight shift, which remains finite in the superconducting state at absolute zero,[3,4] a result that was difficult to explain in any simple way.

Independently, Redfield[5] and later Masuda and Redfield[6] measured T_1 in superconducting aluminum with greater accuracy and over a wider temperature range, from which important information on the existence of an energy gap can be obtained. It was obvious that the nuclear T_1 values would be worth knowing, but these measurements were even more interesting than had been anticipated; they were in striking contrast to any two-fluid model of superconductivity, but could be easily explained by the BCS theory, assuming an energy gap at temperature $T = 0$ of $2\epsilon_0(0) = 3.2k_{\mathrm{B}}T_{\mathrm{c}}$ and a constant relative anisotropy of the energy gap, where T_{c} is the critical temperature. Studies of the superconducting state by NMR are summarized in detail elsewhere.[7]

2 KNIGHT SHIFT IN THE SUPERCONDUCTING STATE

2.1 Experiments on Elemental Superconductors

Soon after the appearance of the BCS theory, experiments on the ^{199}Hg Knight shift in mercury colloids[3] and the ^{119}Sn Knight shift in tin platelets were performed.[4] The results for both Hg and Sn metals indicated the existence of a residual Knight shift at $T = 0$. These experiments seemed to contradict the BCS hypothesis of singlet spin pairing in the superconducting ground state. A number of explanations appeared to find a way out of this dilemma, involving ideas such as modified pairing criteria and even triplet spin pairing. To explain the experiments, however, a serious modification of the BCS picture was unnecessary.

In nontransition metals the Knight shift is due mainly to the hyperfine contact interaction, and is proportional to the normal state Pauli spin susceptibility χ_{n}. By making use of the BCS theory, Yosida[8] calculated the spin susceptibility in the superconducting state and derived an expression for the Knight shift in the superconducting state.

In the superconducting state all ground state pairs are either occupied or unoccupied, and therefore the contribution to the spin susceptibility will only come from excited states, the populations of which are given by a Fermi function $f(E_k)$ of the excited state energy E_k. Accordingly, the spin susceptibility in the superconducting state is given by

$$\chi_{\mathrm{s}} = -2\mu_{\mathrm{B}}^2 \sum_k \mathrm{d}f/\mathrm{d}E_k \tag{1}$$

where μ_{B} is the Bohr magneton and k the wavevector. By making use of the BCS energy density of excited states $N_{\mathrm{BCS}}(E, T)$, the sums in equation (1) can be converted to integrals as follows,

$$\chi_{\mathrm{s}} = -4\mu_{\mathrm{B}}^2 \int_{\epsilon_0(T)}^{\infty} N_{\mathrm{BCS}}(E, T)(\mathrm{d}f/\mathrm{d}E)\,\mathrm{d}E \tag{2}$$

Here $N_{\mathrm{BCS}}(E, T)$ is given by

$$N_{\mathrm{BCS}}(E, T) = \begin{cases} 0 & \text{for } |E| < \epsilon_0(T) \\ N(0)|E|/[E^2 - \epsilon_0^2(T)]^{1/2} & \text{for } |E| > \epsilon_0(T) \end{cases} \tag{3}$$

where $N(0)$ is the normal state density of states at the Fermi level. The χ_{n} value is obtained by taking $\epsilon_0(T) = 0$.

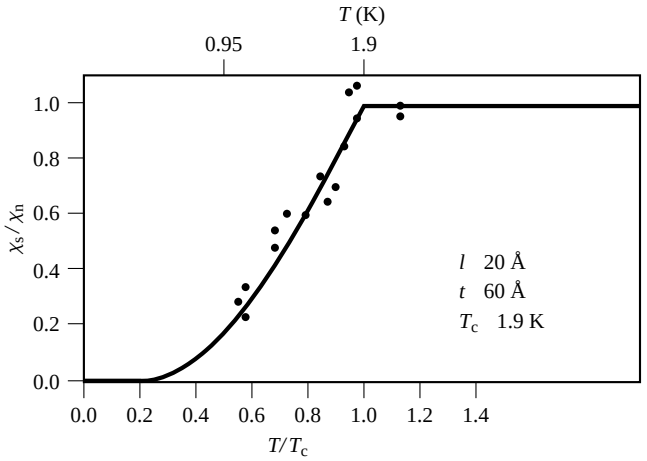

Figure 1 Spin susceptibility in pure superconducting aluminum. Filled circles: data of Fine et al.[10] Solid curve: calculated from the theory of Yosida,[8] l is the electron mean free path, and t is the average thickness of a single substrate

The early experiments of the ^{27}Al Knight shift showed that the Knight shift in the superconducting state at temperature $T = 0$, $K_s(T = 0)$ decreases to about 75% of its values in the normal state, K_n. This result suggested that a residual spin susceptibility, was conceivably due to an inclusion of paramagnetic impurities, since no other mechanism suggested itself. Hammond and Kelly[9] repeated the measurement of the ^{27}Al Knight shift on stacked Al films, taking care to eliminate paramagnetic oxygen impurities in the film. The experimental result of $K_s(T)/K_n$ extrapolated to zero at $T = 0$, as shown in Figure 1,[10] and the longstanding discrepancy between experiment and the prediction of singlet spin pairing, was thereby finally removed. Further experiments on the residual Knight shift in both tin and lead revealed that the spin–orbit coupling is induced in the conduction-electron gas by the boundary in small particles as well as imperfections, and the generalized pairing condition between time-reversed eigenstates might account for the small change of the Knight shift in the superconducting state.

2.2 Various Contributions to the Knight Shift

The conduction-electron susceptibility in the normal state of a metal consists of three important contributions: the s-band Pauli susceptibility in the case of a simple metal; the Van Vleck orbital susceptibility in transition metals with partly filled non-s bands; and the Pauli susceptibility of the non-s (usually d) bands in the case of transition metals. Each mechanism produces a shift component proportional to the corresponding susceptibility. The orbital shift is independent of the spin state of the conduction electrons, and hence does not change by spin pairing in the superconducting state. The contribution of the exchange interaction between non-s itinerant electrons and local s core electrons to the Knight shift should cancel each other out in the superconducting state if the d-band electrons take part in the formation of Cooper pairs.

The residual ^{51}V Knight shift in superconducting vanadium films is found to be intrinsically 100% of the normal state shift. This result indicates that the Knight shift due to the s-band Pauli susceptibility and the Pauli susceptibility of the non-s bands must cancel each other, so that even if spin pairing is complete in the superconducting state, the effect on the measured Knight shift is small; the orbital shift is the principal contribution in both normal and superconducting states.

Susceptibility and Knight shift measurements on the intermetallic compounds V_3Si and V_3Ga show that an increase of the ^{51}V and ^{71}Ga Knight shifts seen in the superconducting state can be attributed to a decrease of the d-band spin susceptibility at $T = 0$ to about 25% of its value at the critical temperature. V_3Si has the A15 crystal structure, in which an extremely narrow d-band exists. This crystal structure enhances the d-band susceptibility, which increases the Knight shift to well above its value in pure vanadium.

3 NUCLEAR SPIN–LATTICE RELAXATION IN BCS SUPERCONDUCTORS

3.1 Spin Relaxation due to the BCS Mechanism

The nuclear spin–lattice relaxation rate $R = 1/T_1$ in a type-I superconductor can be calculated within the framework of the BCS theory. The dominant mechanism for this relaxation process arises from the coupling of the nuclear spins I to the conduction electron spins σ, which are in equilibrium with the lattice, and the hyperfine contact interaction.

The matrix elements between excited states of the system are given by a single particle operator of the form

$$\hat{\mathcal{H}}_1 = \sum_{k\sigma,k'\sigma'} M_{k\sigma,k'\sigma'} \hat{a}^*_{k'\sigma'} \hat{a}_{k\sigma} \tag{4}$$

where $M_{k\sigma,k'\sigma'}$ is the matrix element corresponding to scattering from $k\sigma$ to $k'\sigma'$ and $\hat{\alpha}^*_{k\sigma}$ and $\hat{\alpha}_{k'\sigma'}$ are creation and destruction operators for quasiparticle excitations in the normal state. In the Bloch approximation, individual particle wavefunctions, $\phi_{k\sigma}(x)$, are defined for a self-consistent field. In this situation, therefore,

$$M_{k\sigma,k'\sigma'} = \int \phi^*_{k'\sigma'}(x) \hat{\mathcal{H}}_1(x) \phi_{k\sigma}(x)\, \mathrm{d}x \tag{5}$$

in which x is defined to include the spin variable.

The significant feature of the BCS picture is the condensation of conduction electrons into a single, occupied ground state. In a pure metal this state corresponds to a pair occupation of the Bloch states $k\sigma$, such that if $k\sigma$ is occupied, so is $-k$, $-\sigma$ in the pair. At $T = 0$ all electrons occupy pair states; at finite temperature some pairs are broken up to form single-particle excitations. Nevertheless the coherent occupation of the condensed state restricts the scattering processes, and in addition alters the number of excited state electrons that can participate in scattering. Both these effects disappear in the normal state.

A remarkable difference between the superconducting and normal states arises from coherent effects associated with the paired wavefunctions. In the normal state scattering from $k\sigma$ to $k'\sigma'$ is completely independent of scattering from $-k'$, $-\sigma'$ to $-k$, $-\sigma$, as well as of all other transitions. The probability of the former is proportional to $|M_{k\sigma,k'\sigma'}|^2$, and

the latter is $|M_{-k',-\sigma',-k,-\sigma}|^2$. Because of the nature of the paired wavefunction in a superconducting state, these two contributions to the matrix elements for transition probabilities in a superconducting state are coherent and therefore may add destructively or constructively.

The ground-state occupation changes the transition rate for scattering, in such a way that the transition rate in the normal state is modified by the factor

$$C_{\pm}(E_k, E_{k'}, T) = \tfrac{1}{2}[1 \pm (\epsilon_0^2(T)/E_k E_{k'})] \tag{6}$$

where E_k and $E_{k'}$ are the initial and final excited state energies, respectively. $C_{\pm}(E_k,E_{k'},T)$ is the coherence factor, as it represents concretely the coherent nature of the population of pair states in the formation of the condensed phase. The sign of the second term in equation (6) depends on the nature of the perturbation which induces the transition. If the interaction is invariant under time reversal applied to the conduction-electron system, the minus sign is appropriate, namely $C_{-}(E_k,E_{k'},T)$. This is the case for phonons; in the case of ultrasonic attenuation, there is a very rapid drop in attenuation versus temperature at T_c, followed by a more gradual decrease. If the perturbation is not time-reversal invariant, $C_{+}(E_k,E_{k'},T)$ is appropriate. The nuclear spin relaxation rate exhibits an increase by a factor of 2 just below T_c which gives an indication of coherence effects arising from constructive interference.

Consider, for simplicity, that $I = \frac{1}{2}$, and that an experiment is performed in a magnetic field with nuclear Zeeman energy $\hbar\omega_{\text{nuc}}$. Then the relaxation rate is given by $W_+ + W_-$, where W_+ is the transition rate from spin-up to spin-down nuclear states induced by the entire conduction-electron system, and W_- is the rate for spin-down to spin-up transitions. The relaxation rates are given by

$$W_{\pm} = \frac{\pi}{2\hbar}|M_{k\sigma,k'\sigma'}|^2 \sum_{k,k'} C_{+}(E_k, E_{k'}, T) f(E_k, T) \times [1 - f(E_{k'}, T)]\delta(E_{k'} - E_k \mp \hbar\omega_{\text{nuc}}) \tag{7}$$

where the Fermi distribution function $f(E_k,T)$ accounts for the thermal population of excited initial states, and $[1 - f(E_{k'},T)]$ gives the thermal depopulation of final states required by the Pauli principle. The delta function insures the conservation of total energy in the scattering process.

By making use of the density of states in the superconducting state $N_s(E_k,T)$, the sums in equation (7) can be converted to integrals. The relaxation rate in the superconducting state R_s is given by

$$R_s \propto \int_0^{\infty} N_s(E_k, T) N_s(E_{k'}, T)[1 + \epsilon_0^2(T)/E_k E_{k'}]\, f(E_k, T) \times [1 - f(E_{k'}, T)]\, \mathrm{d}E_k \tag{8}$$

The BCS theory shows that the superconductor has a temperature-dependent gap of halfwidth $\epsilon_0(T)$ centered about the Fermi energy E_F. If the difference in energy between final and initial electron states is ignored, then the ratio of relaxation rates in superconducting to normal states, R_s/R_n, is given by

$$R_s/R_n = 2\int [N_s(E, T)]^2[1 + \epsilon_0^2(T)/E^2]\, f(E, T) \times [1 - f(E, T)]\, \mathrm{d}E \tag{9}$$

There is actually a logarithmic divergence of the integral in the limit $\hbar\omega_{\text{nuc}} \to 0$. This divergence comes from the singularity in the BCS density of states at the edge of the energy gap. The values of T_1 in the superconducting state predicted directly by the BCS theory are thus much shorter than those observed, and much shorter than T_1 in the normal state, near T_c. In comparing the theory with experiment it is necessary to take some sort of width for the electronic levels. It is reasonable that in actual metals the singularity will be removed by some mechanisms, and it is possible to see that spin–lattice relaxation measurements can yield information on the nature of such mechanisms.

Hebel and Slichter[1] obtained N_s by weighting the BCS density of states, N_{BCS}, with a function that characterizes the breadth of the energy levels. If an energy level breadth function is assumed to be a rectangle of width 2Δ and height $\frac{1}{2}\Delta$, then

$$N_s(E, T) = (2\Delta)^{-1} \int_{E-\Delta}^{E+\Delta} N_{\text{BCS}}(E', T)\, \mathrm{d}E' \tag{10}$$

Using equation (9), we can calculate the temperature dependence of T_1 for various values of $r = \epsilon_0(0)/\Delta$. Actually, of course, the parameter Δ might be temperature dependent. Now, as T approaches T_c the gap $2\epsilon_0(T)$ decreases, and it would be natural to assume that the anisotropy decreases and is perhaps proportional to the gap, as pointed out by Masuda and Redfield.[6] In that case we would have $\Delta(T)$ proportional to $\epsilon_0(T)$.

A field cycling method was used to measure T_1. In this method a large field is applied across the sample to polarize the nuclei (about 0.4 T in this case) for a time long compared with T_1. The field is then reduced to zero in a time that is short compared with T_1, and the spins begin to relax at zero field in the superconducting state with a relaxation time characteristic of the superconducting state. After a variable time τ, the field is then turned on again (to about 0.1 T) and immediately swept past the present resonance field of 0.1045 T to observe the spin polarization in the normal state by nuclear resonance. The resonance intensity is proportional to the spin polarization at that time and from its variation of the resonance signal intensity with τ, the relaxation time can be determined.

The nuclear resonance signal obtained in this way is much smaller than that observed above T_c because the nuclei are partially irreversibly demagnetized by the sudden change in magnetic field to which they are subjected when the transition takes place between the normal and superconducting states. For the sample used in most of these measurements, the signal was reduced to less than 5% of the value it would have had in a similar nonsuperconductor after the same sequence of field cycling.

The data for the relaxation time in both normal and superconducting states are shown in Figure 2 as a function of T_c/T.[6] The fact that T_1 decreases markedly just below T_c, and then increases as $\exp[\epsilon_0(0)/k_B T]$ for $T \ll T_c$ is a rather general consequence of any gap model. As can be seen from Figure 2, superconducting aluminum has an energy gap at $T = 0$ of $2\epsilon_0(0) = 3.2k_B T_c$, assuming that the BCS density of states function is smeared over a range of about $\Delta(T) = \epsilon_0(T)/10$, or $r(T) = 10\epsilon_0(0)/\epsilon_0(T)$. The BCS theory applies to the homogeneous, pure, and isotropic electron gas with a simplified interaction term and pure plane wavefunctions. If,

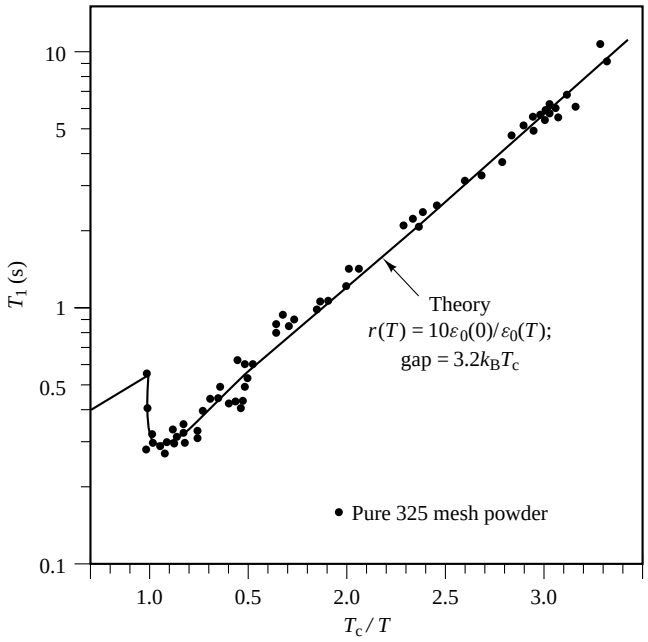

Figure 2 Measured values of T_1 in a powdered, pure aluminum sample.[6] T_c was taken to be 1.178 K. The solid line was calculated using the BCS density of states smeared over a range of 1/10 of the energy gap, assuming a smearing proportional to the energy gap

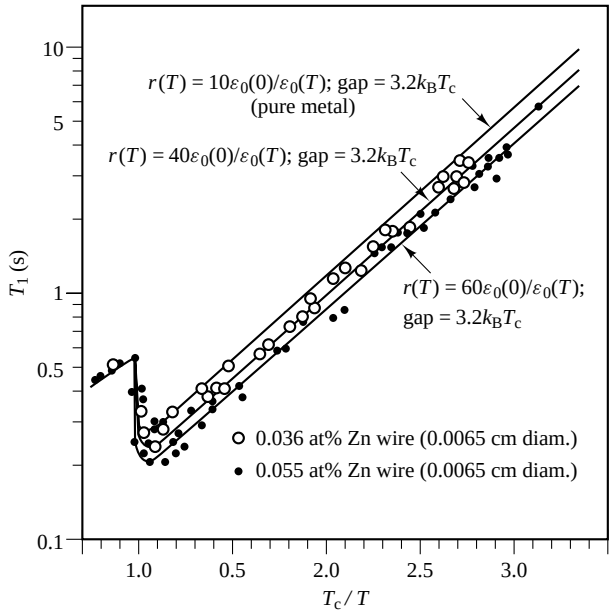

Figure 3 Measured values of T_1 in Al–Zn alloys.[12] T_c was taken to be 1.178 K. The solid lines are calculated using the BCS density of states smeared over a range of 1/10, 1/40, and 1/60 of the energy gap, assuming a smearing proportional to the energy gap

instead of the constant electron–electron interaction, one were to use wavefunctions and an electron–electron interaction that is nonconstant and anisotropic (as might be expected in actual metals), one would expect to find that the energy gap is a function of momentum vector, as well as temperature. Thus, the energy gap of a single particle excitation would depend upon the direction, as well as the magnitude, of its momentum vector. But nuclear spin relaxation has no momentum selection rule for the initial and final states of the transition, so the average density of states determines T_1, not the density of states in any particular k direction. Thus, as far as spin relaxation is concerned, the effect of anisotropy is to smear the BCS density of states by an amount equal to the anisotropy.

These experimental data are regarded as evidence for the existence of an anisotropy in the energy gap which, at any temperature, is of the order of one-tenth of the gap itself. The quantity $\Delta(T)$ could be interpreted in some other way, such as an inverse lifetime for scattering by imperfections or electrons. However, the temperature dependence of Δ or r is most naturally explained in terms of anisotropy. The anisotropy interpretation is also supported by the results described in the next section.

Measurements of T_1 in superconductors were extended to cadmium,[11] for which the behavior is practically identical with that of aluminum.

3.2 Impurity Effects: Anisotropy of the Energy Gap

The T_1 data of both superconducting aluminum and superconducting cadmium were explained very well by assuming a smearing of the anisotropy of the gap as mentioned above. To confirm this assumption experimentally, T_1 in superconducting aluminum alloys was measured.[12]

In a dilute alloy, plane-wave states with fixed spin are no longer good one-electron wavefunctions. Anderson[13] developed a BCS type of theory for dirty superconductors, in which elastic scattering from physical and chemical impurities is large compared with the energy gap. He argued that a ground-state pair should be formed by pairing a one-electron state with its exact time reversed. This state is a generalization of the k up, $-k$ down pairing of the BCS theory, which is independent of impurity scattering. If the electronic mean free path is large compared with the coherence length, the impurities will mix plane-wave states weakly as the electron moves through a coherence length. However, when the mean free path is small compared with the coherence length, the wavefunction can no longer be approximated by a single plane wave. Thus, the states are taken more or less randomly from all parts of the Fermi surface, thereby removing this source of anisotropy in the energy gap.

The experimental data on Al–Zn alloys are shown in Figure 3. The data on the 0.036 at% Zn alloy agree well with theory, assuming $r(T) = 40\epsilon_0(0)/\epsilon_0(T)$ and using the same energy gap $2\epsilon_0(0) = 3.2k_BT_c$ as that used in pure bulk aluminum (solid line). Data on the 0.055 at% Zn alloy show that a numerical factor in $r(T)$ increases from 40 to 60 but the energy gap remains the same. Roughly speaking, the increase of the numerical factor is proportional to the inverse mean free path $1/l$.

As we add impurities, the individual momentum states are scattered around the Fermi surface. Therefore, the angular dependence of the energy gap is removed from the individual excitation energy gap. If Δ represents an anisotropy of the energy gap present in pure aluminum, Δ decreases (or r increases) as the impurity concentration increases. For sufficiently small concentrations of impurities, the experimental data indicate that r increases linearly with increasing reciprocal mean free path. This apparent linear increase of r with l^{-1}

may be fortuitous, since the accuracy of the present determination of r is poor. Presumably the quantity r^{-1} is a measure of the anisotropy.

Data on a 0.16 at% Ge alloy indicate that the width of the energy gap will be close to the value predicted by BCS theory in the case of constant interaction. Once the mixing is complete, the effect on superconductivity should saturate. If we could measure T_1 in very impure samples without quadrupolar effects, the saturation value of r might be observed. But, as T_1 is proportional to log r for $T \ll T_c$, it would be hard to determine r correctly.

The theory of energy gap anisotropy in dirty superconductors was given by Clem.[14] The gap parameter in the direction θ can be defined as

$$\epsilon_0(\theta) = \langle\epsilon_0\rangle[1 + a(\theta)] \tag{11}$$

where $a(\theta)$ is the anisotropy function which describes the variation of the gap over the Fermi surface due to anisotropy in the phonon spectrum or the band structure, and $\langle a(\theta)\rangle = 0$. The density of excited states is calculated as a function of the impurity scattering mean free path, or specifically of the 'dirtiness' parameter

$$y_D = [2\epsilon_0(0)\tau]^{-1} = 1.57\xi_0/l \tag{12}$$

where τ^{-1} is the mean frequency of scattering processes and ξ_0 the coherence length. In the dirty limit, $y_D \gg 1$, the density of states approaches the singular BCS form, and by making use of the mean square anisotropy $\langle a^2\rangle$, becomes a universal function of the parameter $\eta_s = y_D/\langle a^2\rangle$. The anisotropy-induced structure in the density of states will disappear in the dirty limit.

3.3 Size Effect: Fluctuations in the Order Parameter

Measurements of the Knight shift in superconductors must, of necessity, be made on samples that are small compared with the penetration depth in order that variations in the Knight shift will not be confused with the shift due to the Meissner effect. In contrast to the Knight shift, measurements of T_1 are in good agreement with the BCS theory; these measurements have been made on 'bulk' samples, that is, powders with individual particles that are large compared with the coherence length. In view of the disagreement between the Knight shift measurements and the BCS theory, it seemed interesting to see if there is an anomaly in the relaxation time as well, when the particle size becomes small compared with the coherence length or the penetration depth. This was the motivation for performing experiments on the size effect.[15] However, the experimental results obtained surpassed our expectations and suggested an important and interesting fact of superconductivity, which is yet to be theoretically understood.

Particles of aluminum having diameters of less than 2000 Å were prepared by vaporizing aluminum in an atmosphere of argon at a pressure of a few hectopascals. Then the relaxation time T_1 was measured by using the field cycling method in the normal and superconducting states between 0.36 and 1.3 K. In the normal state, and near T_c, the relaxation time was nearly the same as for bulk aluminum, which is evidence that the particles are indeed metallic.

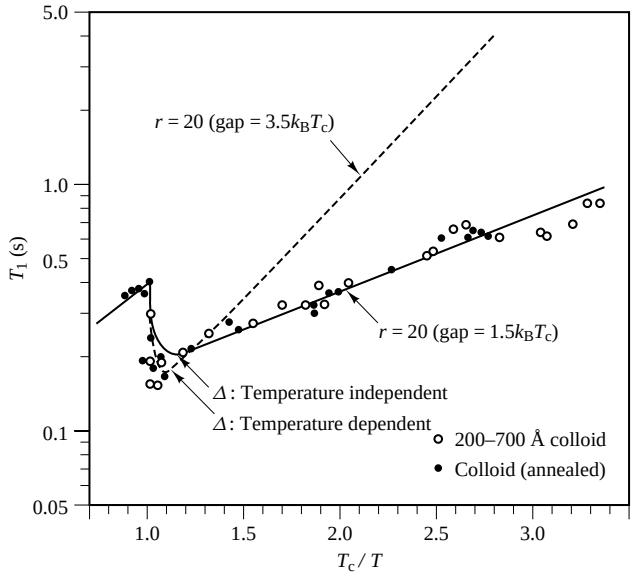

Figure 4 Measured relaxation times T_1 in pure aluminum colloid, the diameter of which ranges from 200 to 700 Å[15]

Typical T_1 results for the sample with the most uniform particle size distribution (200–700 Å) are shown in Figure 4.[15] The relatively small change in T_1 in the normal state, compared with the bulk sample, may be the result of an imperfection-induced quadrupole interaction. However, such a change was not observed when small amounts of impurities were added to bulk samples, so the change may be a true size effect.

Kubo[16] discussed the specific heat and spin susceptibility of small particles, but probably his conclusions did not apply to particles as large as those used here. It is interesting to note that the electronic level spacing in the particles is large compared with $\hbar/T_1$, in violation of the condition for the validity of time-dependent perturbation theory. This difficulty can probably be ignored since the electronic levels are broadened by interaction with lattice vibrations, so that the system, electrons plus lattice, has a higher density of states than the electrons alone.

Turning to the superconducting state, the zero field measurements can be fitted to a theoretical curve according to the procedures applied to the bulk metal described before. Well below T_c, the zero field relaxation time is shorter than that of bulk aluminum, being less than one-fifth the bulk value at 0.4 K, and indicates a gap of the order of one-half the BCS value. Thus, an important size-dependence of T_1 was found, but these results could not be explained in a satisfactory way at that time, and were forgotten. About 10 years later, this relaxation behavior was explained by considering the effects of fluctuations of the order parameter in small specimens. The first observation, made in 1967,[17] attributed to fluctuations, was an increase in conductivity just above T_c in thin films. A theoretical explanation of the observation was given in 1968.[18] A reduction in the size of specimens should increase the effect of fluctuations in the order parameter. Therefore, the most suitable specimens for the observation of the size effect are small isolated particles.

Maki et al.[19] first considered the effect of fluctuations on nuclear spin–lattice relaxation in superconductors in the mean field regime. They found an expression for the relaxation rate

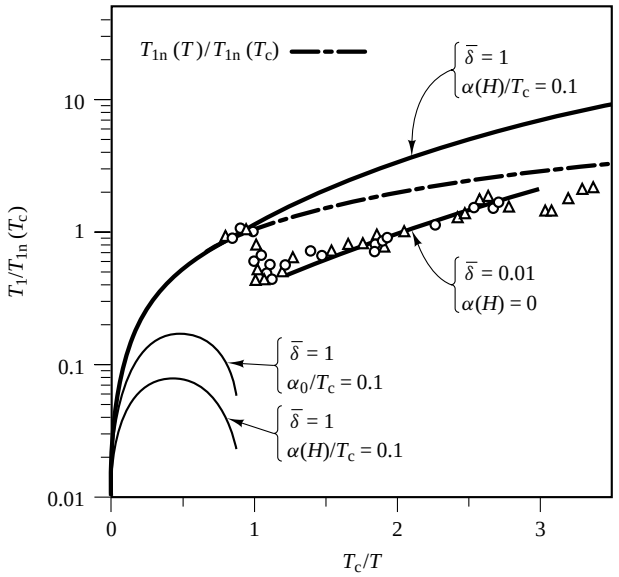

Figure 5 Reduced relaxation time $T_1/T_{1n}(T_c)$ as a function of inverse reduced temperature, reduced pair-breaking parameter α/T_c, and particle size parameter $\bar{\delta}$. Light solid curves: unrenormalized theory of Maki et al.[19] Heavy solid curves: renormalized dirty-limit theory of Simánek et al.[21] Open circles and triangles: experimental results of Masuda and Redfield (annealed and unannealed aluminum colloids, respectively. The diameter ranges from 200 to 700 Å)[15]

above T_c in the presence of fluctuations given by,

$$R_s/R_n = 1 + [\pi T_c/4N(0)v\alpha(H)(T - T_c)] \qquad (13)$$

where v is the particle volume and $\alpha(H)$ a pair-breaking parameter. Pair-breaking may be due to paramagnetic impurities, an applied magnetic field, or, in the absence of external perturbations, the small, spatial variation of the order parameter near the particle surface. According to equation (13), the relaxation rate diverges as $(T - T_c)^{-1}$ at $T = T_c$ as shown in Figure 5. This divergence is removed by allowing the normal electrons to be dressed with fluctuation-induced Cooper pairs. Using this picture, the spin–lattice relaxation rate was calculated.[20] The effect of renormalization of the normal electrons by fluctuations extended over a much wider temperature range than interactions between fluctuations themselves. Thus, the divergent behavior was removed.

The temperature dependence of R_s shows a smooth behavior in the region of T_c for all values of v and $\alpha(H)$. The size parameter is defined as $\bar{\delta} = 1/N(0)\, vT_c$. For small $\bar{\delta}$ a characteristic peak is obtained in the relaxation rate just below T_c. As $\bar{\delta}$ is increased, this peak is smeared out, and the rate decreases monotonically with decreasing temperature for $\bar{\delta} \lesssim 1$. For $\alpha(H) \neq 0$, the position of the peak is depressed to lower temperatures if $\bar{\delta} \ll 1$, and for $\bar{\delta} \lesssim 1$ the effect of additional pair breaking is a small increase in R_s. These results are shown in Figure 5.[21]

This theory is not appropriate for very small particles ($\bar{\delta} \gtrsim 1$), since here the level quantization imposed by the boundary conditions on the electronic wavefunctions at the particle surfaces splits the electronic energy levels by an amount comparable to T_c. This effect is important for Al and Sn particles of less than 50 Å in diameter.[22,23] The theory, in which the combined effect of fluctuations and level quantization are taken into account, is quite complicated.[24]

4 NMR IN TYPE-II SUPERCONDUCTORS

4.1 Magnetic Field Distribution in the Mixed State

A change in NMR properties in the mixed state is caused by the penetration of a magnetic field into a type-II superconductor by means of a periodic lattice of fluxoids, or vortices. Conventional NMR studies of the field distribution are difficult because of the large resonance linewidths, baseline drift, and noise due to vortex motion. To avoid these difficulties the same field cycling method as that used in superconducting aluminum was used. This method has the advantage that the signal can be observed in the normal state with less noise and baseline drift.[25] In the case of type-II superconductors the magnetic field was not reduced to zero but switched to a value below H_{c2} during a time τ which was fixed at about 0.1 s. During the time τ a transverse rf field $H_p \cos(2\pi\nu_p t)$, the probe field, was applied perpendicular to $\boldsymbol{H}_e$. In order to measure the effect of the probe field, the decrease in this subsequent signal reflecting the NMR absorption was measured as a function of the probe frequency ν_p. Typical subsequent signals are shown in Figure 6.

The original calculation on the vortex lattice structure performed by Abrikosov assumed a square lattice. The first direct evidence for the vortex lattice was a neutron diffraction experiment and it was concluded that the lattice must be

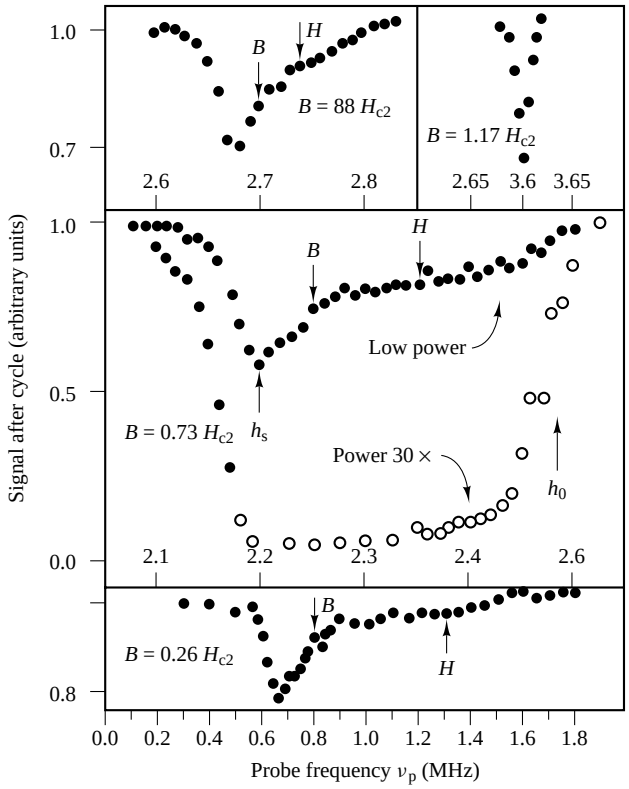

Figure 6 Raw lineshape data at various fields and power levels in type-II superconducting vanadium[25]

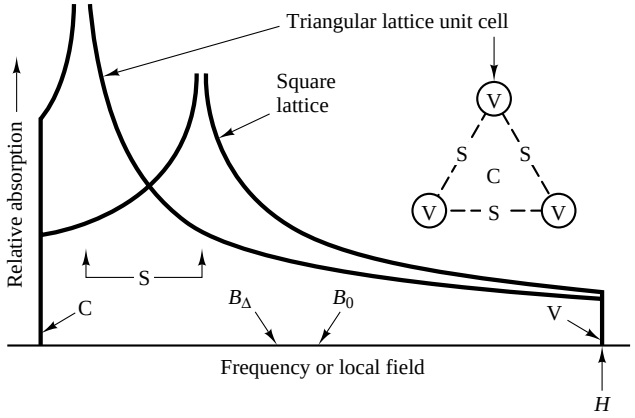

Figure 7 Theoretical resonance lineshapes.[25] The inset shows a unit cell of the triangular vortex lattice, showing points of maximum field (V), minimum field (C), and the saddle point (S)

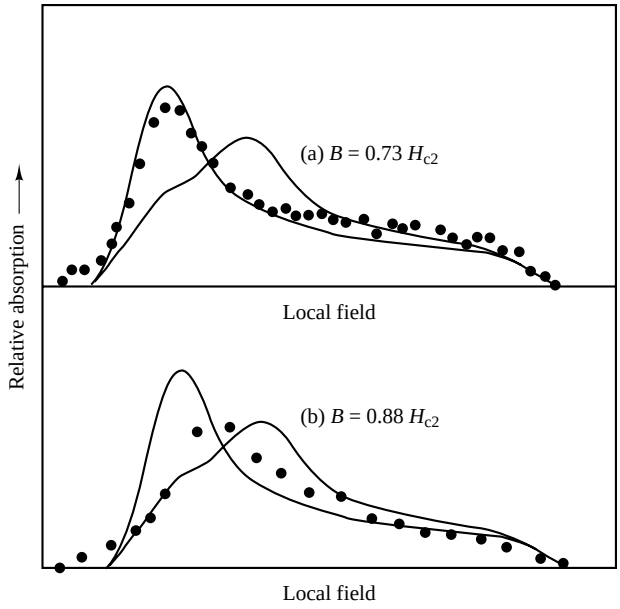

Figure 8 Comparison between theoretical lineshapes obtained by smearing the shapes of Figure 7, with the absorption lineshape deduced from the data of Figure 6[25]

triangular. The first calculation of the NMR lineshape was performed for a square fluxoid lattice and appeared to conflict with the NMR data. The theoretical resonance lineshapes for the triangular and square lattice are shown in Figure 7. The calculation was performed on the basis of a solution to the Ginzburg–Landau equation in the Abrikosov limit. The difference between the positions of the singularity for the square and triangular lattice is a general result of geometry plus the assumption that field and current cannot vary in space over a coherence length. The inset shows a unit cell of the triangular vortex lattice, showing points of maximum field (V), minimum field (C) and the saddle point (S). For the square lattice, the saddle point in real space is equidistant from the nearest vortex and the nearest minimum point. For the triangular lattice, in real space, the saddle–vortex distance (S–V) is $\sqrt{3}$ times greater than the saddle–minimum distance (S–M). Thus the saddle point field also tends to be closer to the minimum field, an effect that is much greater than the real space distance ratio suggests, because the field and current must vary smoothly in space.

The theoretical lineshapes in Figure 7 were convoluted with a Gaussian function to smear out the lineshapes by about 10%, in order to agree with the width of the end of the line at high field, and then normalized to obtain good agreement with experiment for the triangular lattice, as shown in Figure 8. The experimental points are proportional to $-\ln \{[S(H_p) - S(\infty)]/[S(0) - S(\infty)]\}$, where $S(H_p)$ is the signal observed when the probe field equals H_p, $S(0)$ is that with no probe field, and $S(\infty)$ is the signal at very high probe power, which is mostly due to repolarization of the spin system during the time the field is turned on, just before observation, at 0.6 T. If one makes a simple spin-temperature assumption about the rate of energy absorption, then one concludes that this transformation of the data should give the absorption lineshape that would be observed in conventional NMR. The excellent agreement between these points and the triangular lineshape should not be taken too seriously, since there were three parameters varied to fit the data (width, height, smearing), but it would not be possible to change these parameters to get nearly as good agreement with the square lattice curve. Closer to H_{c2} it would be harder to make this distinction. For very low magnetic field, however, one has essentially an array of nearly isolated vortices, and the peak is expected to move toward the lower end of the line for any arrangement.

Similar work using a standard continuous-absorption technique was performed by Delrieu and Winter.[26] They observed the ^{73}Nb resonance in superconducting niobium near H_{c2}, directly, and found a field distribution with the singularity near the minimum field value, as predicted for the triangular lattice, which agrees well with the conclusion by Redfield.

4.2 Nuclear Magnetic Relaxation in Type-II Superconductors

The nuclear spin–lattice relaxation time, T_1, in a type-I superconductor in zero magnetic field is determined mainly by the high density of states above the energy gap. For a type-II superconductor, the energy dependence of the density of states in the mixed state slightly below the upper critical field H_{c2} differs considerably from that in the BCS state. In the Abrikosov description of type-II superconductors in the mixed state, an external magnetic field penetrates into the specimen as quantized flux, called fluxoids or vortices. In the region of a fluxoid, the order parameter is appreciably reduced from its zero field value, approaching zero at the flux center. This reduction in the order parameter may be reflected in the density of states near the Fermi surface and hence the behavior of the nuclear spin relaxation rate.

Measurements of T_1 in a type-II superconductor were expected to add information to the picture of the mixed state. In earlier studies in the mixed state, most T_1 measurements were made far below H_{c2} and T_c.[27] This situation corresponds to the case of well-separated vortices. In the absence of vortex motion and spin diffusion, the nuclear spins located far from vortex lines certainly see quasiparticle excitation in a superconductor, and at low temperatures will show BCS behavior. Spins within the coherence length ξ_0 of a vortex

line relax rapidly with a rate comparable to the normal state value. When both spins contribute significantly to the signal, nonexponential decays will be observed. Experiments on Nb–Zr alloys indicate that the slow decay component of the signal, which is attributed to the spins located far from vortices, shows BCS behavior. In this case, the spatial fluctuations of the energy gap are considered to be localized near the flux center and most of the sample has an energy gap which is essentially equal to that in zero external field. As the temperature decreases T_1 begins to deviate from the BCS value appreciably. The field-dependent deviation from the BCS theory was attributed to a relaxation mechanism involving spin diffusion to the vortex cores. In the subcritical region slightly below H_{c2}, the distance between vortices becomes comparable to the coherence length ξ_0. In this region, the order parameter $\epsilon_0(r)$ is small and a gapless excitation spectrum is expected to appear. It is therefore likely that the nuclear relaxation in this region will show interesting features.

The T_1 of ^{51}V in an intermetallic compound V_3Sn was measured by pulsed NMR in the temperature range 1.2–77 K.[28] The measurements were carried out at the center of the resonance from 0.4470 to 1.3410 T for frequencies of 5, 10, and 15 MHz. The Korringa relationship T_1T = 420 ms·K was well fitted by the experimental points taken in the normal state over the temperature range 1.8–77 K for a magnetic field of 1.3410 T. At the critical temperature corresponding to this field (1.8 K), T_1 showed no minimum as the temperature decreased but it increased monotonically compared with the Korringa time.

The experimental results in the range 1.2–4.2 K are shown in Figure 9 in the form of the ratio R_s/R_n as a function of $T/T_c(H)$, at a fixed magnetic field. $T_c(H)$ is the critical temperature corresponding to the resonance field H. As can be seen from Figure 9 in the case of $T_c(0) > T_c(\boldsymbol{H}) > 0.6T_c(0)$, a maximum in $R_s(T)/R_n(T)$ appears at $T/T_c(\boldsymbol{H})$ = 0.9 in both cases of 0.4470 and 0.8940 T, but the magnitude of this maximum is dependent on the applied field strength. However, in the case of $T_c(\boldsymbol{H}) < 0.6T_c(0)$, $R_s(T)/R_n(T)$ shows no maximum as the temperature decreases, but it decreases exponentially. This effect of magnetic field on the relaxation behavior suggests that a pair-breaking mechanism due to magnetic field enters into the coherence factor.

Griffin and Ambegaokar[29] have extended the calculation of the nuclear spin relaxation rate to a superconductor in the presence of magnetic impurities. The conclusion that the coherence factor is due to the nature of the magnetic hyperfine coupling between the electrons and the nuclear spins is important. The superconductor containing magnetic impurities is a perfect diamagnet in an external magnetic field even in the gapless region. The fundamental property of superconductivity is thus the existence of a pair correlation rather than that of an energy gap. The most important effect of superconductivity appears only through the coherence factors. It is known that paramagnetic impurities and magnetic fields have similar effects on many physical quantities in superconductors. In these two situations the coherence factors are equivalent. This equivalence is established only for the second-order term in $\epsilon_0(r)$ and significant deviations are expected to arise in the fourth order terms. The depairing by the magnetic field or by impurities enters into the coherence factors and these pair-breaking mechanisms are equivalent in both cases. Starting

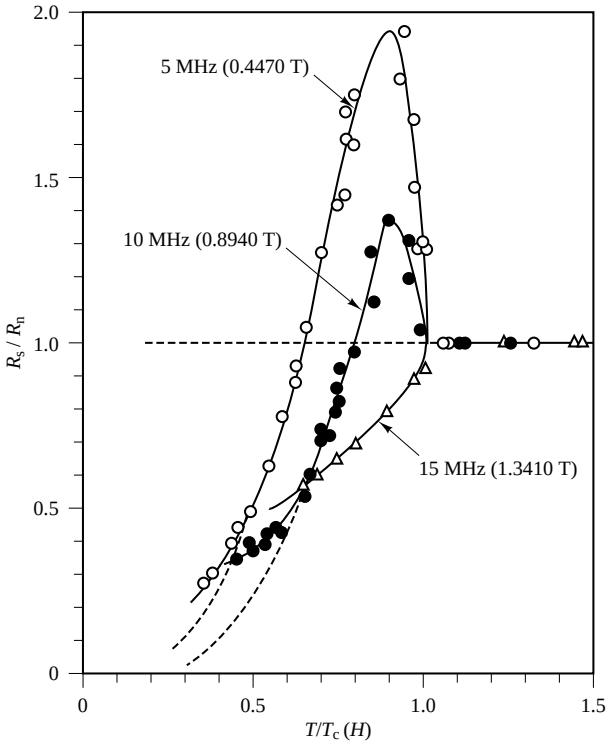

Figure 9 Reduced ^{51}V relaxation rate in the superconducting mixed state of V_3Sn. The relaxation rate for a magnetic field of 1.3410 T decreases monotonically with temperature[28]

from this point of view, Maki and Fulde[30] obtained the results equivalent to those derived by Griffin and Ambegaokar.[29]

The ratio of the nuclear spin relaxation rates in a dirty type-II superconductor in the gapless region to those in the normal state were obtained by Cyrot[31] using a perturbation calculation in powers of $\epsilon_0(r)$. He obtained the following result,

$$\frac{R_s}{R_n} = 1 + \frac{\langle|\epsilon_0(r)|^2\rangle}{2(2\pi k_B T)^2}[\rho^{-1}\phi^{(1)}(\tfrac{1}{2}+\rho) + 3\phi^{(2)}(\tfrac{1}{2}+\rho)] \quad (14)$$

where $\rho = D_e H/(2\pi k_B T)$, D is the diffusion coefficient, and $\phi^n(\rho)$ is the nth derivative of the digamma function. If we substitute the expression for $\langle|\epsilon_0|^2\rangle$, following Abrikosov, equation (14) in the case of spherical samples can be represented as follows:

$$\frac{R_s}{R_n} = 1 + \frac{ec}{8\pi^2\sigma k_B T_c(0)} - \frac{H_{c2} - H}{[2\kappa_2^2(t) - 1]\beta_A + \frac{1}{3}}C(t) \quad (15)$$

where σ is the normal state conductivity, c the velocity of light, $\kappa_2(t)$ the temperature-dependent parameter which appears in the expression for the magnetization, β_A = 1.16, and $C(t)$ is a dimensionless function of reduced temperature $t = T/T_c(0)$ given by

$$C(t) = (\rho t)^{-1}\left[1 + 3\rho\frac{\phi^{(2)}\left(\frac{1}{2}+\rho\right)}{\phi^{(1)}\left(\frac{1}{2}+\rho\right)}\right] \quad (16)$$

The temperature dependence of $C(t)$ was numerically calculated, and depicted in Figure 10. In the range of t = 0 to 0.6, $C(t)$ has a negative value and crosses zero at t = 0.6. As the

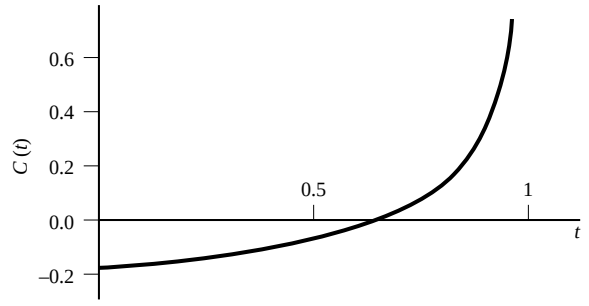

Figure 10 Dependence of the universal function $C(t)$ on the reduced temperature $t=T/T_c$. The gradient dR_s/dH of the relaxation rate at H_{c2} is proportional to $C(t)$ in the mixed state of dirty type-II superconductors[31]

temperature increases above $t = 0.6$, $C(t)$ becomes positive, and then diverges near $T_c(0)$.

As can be understood from equation (16), in the range of $H_{c2} - H \ll H_{c2}$ and for temperatures close to $T_c(H)$, the relaxation rate in the superconducting state is larger than that in the normal state. For temperatures far below $T_c(H)$, the relaxation rate in the superconducting state becomes smaller than R_n. At $0.6T_c(0)$ both rates have the same value. This behavior agrees with the experimental result that at about $T = 0.6T_c(0)$ the slope of the relaxation rate passes through zero.

The theoretical prediction of the initial slope of the relaxation rate at $T_c(H)$ for the magnetic field, in which the relaxation rate is measured, is given by the following equation:

$$\frac{1}{R_n}\frac{\partial R_s}{\partial T}\bigg|_{T=T_c(H)} = \frac{ec}{8\pi^2\sigma k_B T_c(0)} \frac{\left.\dfrac{\partial H_{c2}(T)}{\partial T}\right|_{T=T_c(H)}}{[2\kappa_2^2(t)-1]\beta_A + \frac{1}{3}} C(t) \quad (17)$$

The calculated result described above agrees with experiment quite well at low temperatures. However, a deviation appears near $T_c(0)$. One of the reasons for this deviation may be the broadening of the BCS state due to energy gap anisotropy.

4.3 Magnetic Impurity Effects in Type-II Superconductors

Magnetic impurity effects, studied by NMR in metals and alloys, give much information about the electronic states of conduction electrons. In normal metals and alloys, various paramagnetic impurity-induced relaxation mechanisms exist, in addition to the usual Korringa process. They are the relaxation due to the fluctuating local dipole fields associated with the longitudinal and transverse fluctuations of the localized magnetic impurity dipole moment (the LD and TD mechanisms); and the indirect Rudermann–Kittel–Kasuya–Yosida coupling between the localized magnetic impurity moment and nuclear spins via conduction-electron systems. The latter relaxation mechanism is associated with the real or virtual excitation of the localized magnetic impurity moment (the RE and VE mechanisms), respectively.

Superconductivity is strongly affected by the presence of magnetic impurities. The Korringa mechanism in superconductors has been investigated theoretically within the framework of the Abrikosov and Gor'kov (AG's) depairing theory by Griffin and Ambegaokar.[29] The LD, TD, RE and VE mechanisms also play an important role in the superconducting state.[32]

According to the observed macroscopic properties, Gd impurity possesses a well-defined spin and affects the superconducting properties in the way expected by the AG theory. Cerium impurity, however, shows the anomalies associated with the Kondo effect. In particular it seems very interesting to investigate microscopically by NMR the differences of the pair-breaking effects between the Gd and Ce impurities.

The relaxation rate R_s in a Kondo superconductor has been calculated numerically in the framework of the Müller–Hartmann–Zittartz depairing theory.[33] The theoretical temperature variation of R_s is expected to show very interesting behavior, corresponding to the reentrance behavior of superconductivity.

The host ^{27}Al nuclear spin–lattice relaxation in the normal and superconducting states of the $(La_{1-n}Gd_n)_3Al$ and $(La_{1-n}Ce_n)_3Al$ systems has been studied in detail.[34] The conclusions obtained are: (1) the impurity-induced relaxation rates play an important role in ^{27}Al relaxation and can be well interpreted by the LD mechanism for both the Gd and Ce doped systems; (2) the measured relaxation rates show large enhancement in the superconducting state. This seems to arise from the change of the impurity spin relaxation time. Quantitative analysis shows that the impurity spin dynamics is determined by the relaxation mechanism arising from the s–f exchange interaction between impurity spin and conduction electrons even in the superconducting state; and (3) in the vicinity of the transition temperature the observed temperature variation of T_1 seems to show a large discrepancy in comparison with the prediction of the impurity pair-breaking theory both in the Gd and Ce doped systems.

5 RELATED ARTICLES

Electron–Nuclear Hyperfine Interactions; Field Cycling Experiments; Knight Shift; Metals: Pure and Alloyed; Relaxation Theory: Density Matrix Formulation.

6 REFERENCES

1. L. C. Hebel and C. P. Slichter, *Phys. Rev.*, 1959, **113**, 1504.
2. J. Bardeen, L. N. Cooper, and J. N. Schrieffer, *Phys. Rev.*, 1957, **108**, 1175.
3. F. Reif, *Phys. Rev.*, 1956, **102**, 1417; 1957, **106**, 208.
4. G. M. Androes and W. D. Knight, *Phys. Rev.*, 1961, **121**, 779.
5. A. G. Redfield, *Phys. Rev. Lett.*, 1959, **3**, 85.
6. Y. Masuda and A. G. Redfield, *Phys. Rev.*, 1962, **125**, 159.
7. D. E. MacLaughlin, *Solid State Phys.*, 1976, **31**, 1.
8. K. Yosida, *Phys. Rev.*, 1958, **110**, 769.
9. R. H. Hammond and G. M. Kelly, *Rev. Mod. Phys.*, 1964, **36**, 185.
10. H. L. Fine, M. Lipsicas, and M. Strongin, *Phys. Lett.*, 1969, **29A**, 366.
11. Y. Masuda, *IBM J. Res. Dev.*, 1962, **6**, 24.
12. Y. Masuda, *Phys. Rev.*, 1962, **126**, 1271.
13. P. W. Anderson, *J. Phys. Chem. Solids*, 1959, **11**, 26.
14. J. R. Clem, *Phys. Rev.*, 1966, **143**, 392; *Ann. Phys. (N.Y.)*, 1966, **40**, 268.
15. Y. Masuda and A. G. Redfield, *Phys. Rev. A*, 1964, **133**, 944.
16. R. Kubo, *J. Phys. Soc. Jpn.*, 1962, **17**, 975.

17. R. E. Glover, *Phys. Lett.*, 1967, **25A**, 542.
18. L. G. Aslamazov and A. I. Larkin, *Phys. Lett.*, 1968, **26A**, 238.
19. K. Maki, J. P. Hurault, and M. T. Beal-Monod, *Phys. Lett.*, 1970, **31A**, 526; J. P. Hurault, K. Maki, and M. T. Beal-Monod, *Phys. Rev. B*, 1971, **3**, 752.
20. E. Simánek, D. E. MacLaughlin, and D. Imbro, *Phys. Lett.*, 1973, **42A**, 357.
21. E. Simánek, D. Imbro, and D. E. MacLaughlin, *J. Low Temp. Phys.*, 1973, **11**, 787.
22. S. Kobayashi, T. Takahashi, and W. Sasaki, *J. Phys. Soc. Jpn.*, 1971, **31**, 1442.
23. S. Kobayashi, T. Takahashi, and W. Sasaki, *J. Phys. Soc. Jpn.*, 1974, **36**, 714; 1975, **38**, 599.
24. J. Sone, *J. Low Temp. Phys.*, 1976, **23**, 699; 1983, **50**, 559.
25. A. G. Redfield, *Phys. Rev.*, 1967, **162**, 367.
26. J. M. Delrieu and J. M. Winter, *Solid State Commun.*, 1966, **4**, 545.
27. K. Asayama and Y. Masuda, *J. Phys. Soc. Jpn.*, 1965, **29**, 1290; 1969, **26**, 206.
28. Y. Masuda and N. Okubo, *Phys. Rev. Lett.*, 1968, **20**, 1475; *J. Phys. Soc. Jpn.*, 1969, **26**, 309.
29. A. Griffin and V. Ambegaokar: *Proc. 9th Int. Conf. on Low Temperature Physics, Columbus, OH, 1964*, Plenum, New York, 1965, p. 542.
30. K. Maki and P. Fulde, *Phys. Rev. A*, 1965, **140**, 1586; *Solid State Commun.*, 1967, **5**, 21.
31. P. M. Cyrot, *J. Phys. (Paris)*, 1966, **27**, 283.
32. K. Matsui and Y. Masuda, *J. Phys. Soc. Jpn.*, 1977, **43**, 437.
33. K. Matsui and Y. Masuda, *J. Low Temp. Phys.*, 1978, **31**, 101.
34. K. Matsui and Y. Masuda, *J. Phys. Soc. Jpn.*, 1977, **43**, 1169.

Biographical Sketch

Yoshika Masuda. *b* 1922. B.Sc., 1949; D.Sc., 1958, Osaka University. Member of the Physical Society of Japan and Fellow of the American Physical Society. Constructed NMR Laboratories at Kobe University, 1953–65. Fulbright and Q. W. Boese Fellow at Columbia University, and worked with A. G. Redfield at the IBM Watson Laboratories at Columbia University, 1959–61. Established ULT Physics Laboratories in Nagoya University, 1965–85. Emeritus Professor at Nagoya University, 1985. Professor at Aichi Gakuin University, 1985–present. Approx. 200 publications. Research interests include theory and experiment on quantum solids.

Metals: Pure and Alloyed

Theodore J. Rowland
University of Illinois, Urbana, IL, USA

1	Introduction and Background	1
2	Experimental Details	2
3	Principal Theoretical Concepts	3
4	Pure Metals with Nonzero μ_I	5
5	Alloys	6
6	Nuclear Relaxation and Atomic Diffusion: Nuclear Relaxation in $I = 1/2$ Systems	7
7	Related Articles	8
8	References	8

1 INTRODUCTION AND BACKGROUND

1.1 The Beginning of NMR in Metals: Investigators and Material

The discovery of the resonance of nuclei is so recent that the number of subspecialties that have developed is astounding. In large part it represents the number of working scientists during the intervening years. In addition, the time period is one during which solid state physics, polymer physics, and more recently the biological sciences have seen unprecedented advance.

The discovery of the fact that proton resonance could be observed with relative ease if the required conditions were understood led two independent groups to construct apparatus to search for, and to find, the phenomenon in the same year. Fortunately, nuclear physics had a long history of research culminating in a burst of activity in the early 1940s. Tables of nuclear moments were available and there was an immediate spread of NMR to a host of elements in the Periodic Table. Pound saw the Cu metal resonance from the wire of his rf spectrometer[1] and Knight[2] soon after found that Cu metal and the corresponding isotopes in CuCl were at different frequencies in the same external magnetic field. Nuclear magnetic resonance in metals was thus launched only two years after the first nuclear resonance observation of hydrogen. The latter required the knowledge and skill of brilliant scientists, each of whom received a (shared) Nobel prize. Reading the Nobel prize acceptance speeches is rewarding, as is the study of the papers of Purcell et al. and Bloch et al. published in *Physical Review* in 1946.

Workers in the field of NMR in metals require an interdisciplinary background strong in physics, especially the theory of the solid state, and also well-developed in metallurgy. The latter subject remains one in which few phenomena are derived a priori, and the words 'experience' and 'art' are sometimes necessary to describe the methods successfully used in specimen preparation. Complex studies that purport to demonstrate a correlation between an NMR result and a particular aspect of the behavior of a metal or alloy should assume from the outset that the physical property under investigation must be measured on a batch of material prepared for the study, and that the NMR must be conducted on samples from the same batch. An example study might be the rate of internal oxidation measured using resistivity or susceptibility together with NMR absorption line parameters. Correlation of NMR results with mechanical properties (rather than electrical) is usually more difficult.

1.2 Metals and Nuclei

The metallic state has several familiar but different characteristic mechanical and electrical properties when compared with other solid types. If we consider the four classic types of solids, metallic, ionic, covalent, and molecular (or van der Waals),[3] the metals are known to be highly ductile, good electrical and thermal conductors, and different in their magnetic properties from ionic and covalent solids. The underlying reasons for the physical properties of metals lies almost entirely in their electronic structure. In solids which are primarily ionic or covalent the bonding potentials are largely central or directional, respectively. Metals by contrast are held together by nondirectional atomic potentials. Nearly all metals have one atom per lattice site, and thus have structures in which the atoms lie on the points of a Bravais lattice.[4] Not surprisingly most metals have lattice structures in which the atoms are arranged as closely packed spheres [face centered cubic (fcc) and hexagonal close packed (hcp)]. The next most common structure among metals is body centered cubic (bcc). Of the roughly 50 metals in the Periodic Table about 36 are close packed and 14 bcc. Nearly *all* of these metals have at least one isotope which is useful for NMR, i.e., it has nonzero nuclear spin I, and thus a nonzero nuclear magnetic moment $\mu = \gamma_I \hbar I$, where γ_I is the nuclear gyromagnetic ratio and $\hbar$ = Planck's constant divided by 2π. The majority of metals have more than one isotope of $I > 0$ (i.e., from among $I = \frac{1}{2}, 1, \frac{3}{2}, 2, \ldots$). Isotopic abundance is a crucial factor in considering the feasibility of observing the nuclear resonance of a particular metal.

In addition to a magnetic dipole moment μ, a majority of nuclei have an observable electric quadrupole moment Q. In brief form there are two restrictions that limit the observability of electrical multipole moments:[5] (a) No odd (l odd) electrical multipole (2^l-pole) moments can exist, and (b) for a nuclear spin I, it is impossible to observe a nuclear multipole moment of order 2^l greater than that corresponding to $l = 2I$. (The result of these restrictions is that we can expect to observe no dipole, octupole, ... electrical moments; and that for $I = \frac{1}{2}$ we can observe no multipole greater than dipole, for $I = 1$ we can observe no multipole greater than quadrupole, for $I = \frac{3}{2}$ we can observe no multipole greater than octupole, for $I = 2$ we can observe no multipole greater than hexadecapole, and so on.) We distill from these statements that $Q = 0$ when $I = \frac{1}{2}$ and that for $I \geq 1$, Q may be and usually is nonzero. The hexadecapole and higher existing moments have not been observed, probably because of their minute interaction energies. These conditions apply to all nuclei; however we enumerate them here because, since metals constitute over half of the Periodic Table, it is prudent as a first step for the experimentalist to ensure that a suitable isotope is available for any projected study. Usually tables list all relevant data.[6] An additional useful fact is that the nuclear spin I is half integral

if the nuclear mass number is odd, and integral if its mass number is even.[5]

The above fundamental nuclear properties must be known if a metal is to be usefully probed. The observed magnetic dipole and electric quadrupole interaction energies are vector and tensor products, respectively, of the moments and the corresponding interaction parameters.

2 EXPERIMENTAL DETAILS

2.1 Specimen Preparation

Sample preparation is unquestionably one of the most important steps in any experimental study of metals or alloys. The metallurgical techniques necessary to prepare an alloy in a well-known state must be known and used. The characterization of metallic specimens after they are made is literally impossible. The only hope of understanding the NMR results is to have complete knowledge of the history of the alloy. The final step in preparation is usually reducing at least one and sometimes two or three dimensions of the sample to a size smaller than the skin-depth of the rf field in the specimen. At this point the metal is usually heavily cold worked and to some extent oxidized. A protective oxide layer may be very thin; a nonprotective oxide layer continues to grow if oxygen is present. The quantity of specimen in one powder particle of the total specimen is small (approx. $10-100\,\mu$g). The question of whether to anneal the specimen or not depends on having knowledge of the consequences of each alternative; there is no general answer and the choice depends upon the nuclear resonance and the materials aspects of the situation. Even the considerations involved are too numerous to introduce here. The nuclear spin, the annealing temperature of the metal or alloy, and the diffusivity of oxygen (or nitrogen, ...) at a proposed temperature are usually dominant factors.

The need to subdivide the metal was understood from the beginning; the *skin depth* or *depth of penetration* δ of the rf field into the metal depends on the frequency ν, and the resistivity ρ of the metal. The quantity δ plays a dual role in the experimental results; not only is it the distance into the metal at which the rf field strength falls to e^{-1} of its value at the surface, but a phase shift is introduced which mixes the absorption (imaginary or χ'') and dispersion (real or χ') components of the nuclear susceptibility χ.[7] If the rf field does not penetrate the metal then it is the outer layer only (measured by δ) that contributes to the magnitude of χ. The *filling factor*, which is the ratio of the volume of sample in which the rf field energy is stored, to the total volume in which the rf field energy is stored, can also be greatly decreased. The ideal situation for nonspinning samples is to have the detector (receiver) coil just full of subdivided specimen, no particles of which are in electrical contact with any other and all of which are roughly of dimension $\delta \approx 5 \times 10^{-3}(\rho/\nu)^{\frac{1}{2}}$ where δ is in centimeters, ρ is in microhm centimeters, and ν is the frequency in megahertz.

The method of separation of the particles of specimen is chosen entirely on the basis of appropriateness. The temperature, state of the sample, and composition of sample often suggest materials such as mineral oil, any inert inorganic compound containing no active nuclei, e.g. Al_2O_3 when NMR of V is observed, sheet mica, and so on. A minimum of 'filler' should be used to accomplish the particle separation; beyond that there is simply a loss of sample, filling factor, and signal.

The specimen may be either a pure metal or alloy. It is exceedingly difficult to handle metals of 99.9999% purity (usually called 'six 9s pure') or greater, without decreasing their purity. Fortunately the impurity is often on the surface only and it can be tolerated, or in some circumstances and with some risk, etched away. If during the preparation, a mechanical process such as filing, rolling, drawing, or swaging is used, the sample will be work hardened (cold worked) in addition to being contaminated. Work hardening is caused by mechanical imperfections in the lattice, primarily high densities of dislocations that comprise a three-dimensional 'forest'. The effects of mechanical and chemical imperfections will be discussed below.

2.2 Sample Containment and Conditions Used

Preparation of specimens for use at low temperature depends upon the detection technique being employed. Commonly a small thin-walled glass vial will be used to confine the specimen. For various reasons it is advisable to seal (tip off) the vial leaving the specimen under vacuum or an inert gas. Some of the same considerations apply to high-temperature NMR. A large number of experiments have been done on liquid metals.[8] The separation of particles (spheres) and the choice of filler material is more difficult because of the likelihood of increased reactivity of sample with filler.

Finally it is interesting to note that many studies of the temperature dependence of the Knight shift were done in the solid state with the thought that the results would be approximations to volume-dependence measurements. Certainly the change in volume with temperature is a straightforward concept, but the intrinsic temperature dependence is less easily measured. The exact equation,

$$\left.\frac{\partial \ln K}{\partial T}\right|_p = \left(\frac{\partial \ln K}{\partial \ln V}\right)_T \left(\frac{\partial \ln V}{\partial T}\right)_p + \left.\frac{\partial \ln K}{\partial T}\right|_V \qquad (1)$$

shows that obtaining the explicit temperature dependence of K on T at constant V requires use of the first term on the right, obtained from the pressure dependence of K at constant T and the compressibility $(\partial \ln V/\partial p)_T$, together with the coefficient of thermal expansion $(\partial \ln V/\partial T)_p$.[9]

2.3 Experimental Apparatus and Data

Early workers in the field usually used one of two or three types of nuclear resonance detection. A single-coil technique introduced by Pound[10] was used almost exclusively by those working with or near him. Bloch used a cross-coil apparatus; students and others in his laboratory favored it. The 'Pound box' (a marginal oscillator) detected only the nuclear absorption χ'', and was capable of sweeping over wide frequency regions with ease. The crossed coils, transmitter, and receiver, were constructed and adjusted in a way that made frequency change infeasible. An rf bridge technique was favored by many for its single coil capability and ease of use. For each method mentioned the rf field was applied

continuously so these were all used for steady-state NMR detection.[11] Audiofrequency modulation of the magnetic field B_0 and phase sensitive detection of the demodulated rf were commonly used to detect and display the derivative of χ'' or, for crossed coils, of a mixed χ'',χ' signal. For metals the separation of χ'' and χ' into pure components of χ is not straightforward. A bulk (1.27 cm × 1.9 cm) Al single crystal study illustrates the procedure under ideal circumstances.[12]

Pulsed nuclear resonance apparatus[13] has proved to be almost universally superior to the steady-state methods. There remain pitfalls when the samples are metallic, and these are compounded if sample spinning is introduced. The skin effect and classical Eddy currents[14] must be taken into account, or conversely, the sample prepared so as to make their effects negligible.

The data obtained from most magnetic resonance experiments eventually emerge in the form of absorption lineshape, width, amplitude (relative to a reference), and position (with respect to a reference). These are the quantities from which physical information, the goal of the work, is extracted. The interaction between the conduction electrons and the nuclei allows us to use the nuclear resonance as a probe of the charge density distribution. The association is not easy because of the complexity of the electron–nuclear, and electron–electron interactions; however problems with the theory are revealed as concepts of the electronic structure of the metal are refined. The number of locations in the lattice that can be probed are few, but when NMR is compared with other experimental approaches used to obtain data on this scale it has achieved a very impressive record.

2.4 NMR Lineshape in Powdered Metal Samples

In view of the fact that most NMR in metals is done on particles (or filings, foils, thin wires) with individual external dimensions of about 0.001″ (0.0025 cm) it is clear that the sample comprises crystallites of at most that size or smaller. The results obtained from algebraic solutions of nuclear interactions are for single crystals and include the crystal orientation, as necessary, in keeping with the crystal symmetry. A number of such averaging calculations can be handled using no more than cylindrical symmetry and an average over all angles θ of the symmetry axis with respect to the magnetic field. This procedure is sufficient to treat hexagonal and tetragonal metal lattice structures as well as a large number of cubic, hexagonal, and tetragonal alloys. The absorption distribution $I(\nu)$ for an isotropic orientation distribution of crystals having axial symmetry is obtained by a transformation from crystallite orientation density to resonance amplitude at frequency ν (B_0 = constant). The calculation entails deriving $I(\nu)$ using $I(\nu)\,\mathrm{d}\nu = \sin\theta\,\mathrm{d}\theta$,[15] and thus $I(\nu) \propto \sin\theta\,(\partial\nu/\partial\theta)^{-1}$. Derivations of NMR lineshapes (powder patterns) and the phenomena associated with structures of lower symmetry or causing low symmetry have been published.[6,15]

2.5 Some Sources of Line Broadening in Stationary Samples

The implicit assumption has been made that the NMR resembles a Dirac δ function $\delta(\nu - \nu_0)$. There are at least three sources of broadening in a stationary sample that contribute to the *linewidth* independently of its definition. The applied magnetic field is always inhomogeneous; the sample has nuclear dipoles and in the absence of atomic diffusion nuclear dipole–dipole interactions are a source of broadening; an internal field of totally classical origin is present because each metal particle has an internal field $B_{\mathrm{int}} = \chi_{\mathrm{m}}B_0$, where χ_{m} is the magnetic susceptibility of the metal. (This source can be significant in transition elements with large χ_{m}.) Lifetime or T_1 broadening is seldom a contributing factor to the linewidth of metals. T_1 and T_2 are the longitudinal and transverse relaxation times, respectively of the vector nuclear magnetization $\boldsymbol{M}$ in the stationary reference frame. M_z approaches its maximum equilibrium value in the direction of the external polarizing field; M_x and M_y decay toward zero through dephasing. These relaxation times appeared in Bloch's phenomenological equations describing the behavior of steady-state nuclear magnetization. The Bloch equations do not apply to solids in general, but the nomenclature has been carried over to the parallel quantities describing the behavior of $\boldsymbol{M}$. A brief, qualitative discussion of this topic appears in Schumacher.[11]

3 PRINCIPAL THEORETICAL CONCEPTS

3.1 Introduction

The theory of NMR per se is presented in many books and papers. The interpretation of NMR in metals has been an especially active field because of the continuing interest in understanding the electron–electron interactions, which ultimately determine our understanding of the metallic state. Although high-temperature superconductors now attract much research (including NMR), for decades metals displayed properties and posed puzzles that were unique. Both type I and type II superconductivity and ferromagnetism have been thought to have their origin in the electron–electron and electron–phonon interactions in metals.

One of the tools that confirmed the Bardeen–Cooper–Schrieffer theory of superconductivity was NMR,[6] and repeatedly it has shown its ability to reveal, on the atomic scale, electron distributions that cannot be otherwise obtained or can be obtained only with greater difficulty using another technique.

3.2 Electron–Nucleus Interactions

The topic of NMR in metals is one that can appear to lead to such complexity that it is intractable. Fortunately, however, all of the electron–nuclear interactions encountered can be formulated within the framework of quantum mechanics. It is helpful to understand the elements of the problem and the barriers to obtaining solutions in agreement with observation. Many of the difficulties can be identified in one statement: the potentials are not accurately known. The dense electron plasma is not completely understood; the chemical and other point imperfections (e.g. substitutional solutes, foreign atoms, vacancies and interstitial solutes) distort the lattice so that the positions of the surrounding atoms are not accurately known, and the potentials of the imperfections themselves are

perturbed self-consistently; higher dimensional imperfections such as dislocations (one-dimensional, 1D), grain boundaries, twin planes, and stacking faults (two-dimensional, 2D) are difficult to characterize in the metal and have received less attention than impurities and vacancies.

The above group of chemical and mechanical imperfections scatter conduction electrons and generate charge density fluctuations $\rho(\boldsymbol{r})$, which produce or perturb the following interactions: (a) hyperfine, (b) the electron–dipole nuclear–dipole, (c) indirect nuclear-spin exchange coupling via the conduction electrons, and (d) nuclear quadrupole. The magnitudes of the energy level shifts to which these give rise are usually related to the magnitudes of the nuclear dipole and/or electric quadrupole moments, and the external magnetic field. The derivation of all of the concepts to be included below and many more are explained in rigorous and elegant form by Slichter.[14] A brief introduction to the application of NMR to pure metals and to alloys follows. Examples are offered of the way such studies are approached in terms of the information it is reasonable to expect. They are presented as models to help associate the atomic structure of a metal to the fundamental properties of a nucleus, which make it useful as a probe of that structure. Atomic structure includes lattice structure with imperfections and the total electronic structure. Nuclear properties include γ, I and Q as well as the mass and charge. Such quantities as isotopic abundance, and the bulk properties of the metal, both liquid and solid, are known.

3.3 Conduction Electrons and Scattering

The electronic structure of metals in its most exact form is responsible for the distinctive character of their NMR spectra. The electron energy levels of agglomerated metal atoms resemble those of any other solid when there is no overlap between wavefunctions, i.e. the inner levels are atomic in nature. The outer (conduction) electron orbitals of metals have significant overlap and the free atom energy levels are broadened into bands that may be 1–10 eV wide. Since each atom of a pure metal is identical to each other atom, and is neutral, no shift of charge from one atomic cell to another is expected. Rather, all conduction-electron wavefunctions are delocalized and exist over the volume of the bulk metal. For the alkali metals, which have highly s-like outer electrons; the valence bands are half-full. All metals in fact have only partially filled conduction (valence) bands and thus at T = 0 K have empty states within about 10^{-21} eV of the topmost filled energy level. Presentations of band theory (i.e. the energy distribution of electrons in solids and metals in particular) appear in the solid state literature.[16] Of special interest are the transition metals in which s–d interactions are prominent; the s- and d-bands at the Fermi surface overlap and are partially full. Throughout the Periodic Table admixed orbitals can be expected for the conduction band. The greatest opportunity for systematic study is within the rows.

The s wavefunctions ψ_s play a crucial role in one of the useful applications of NMR in metals. The outer s radial wavefunctions $\psi_s(r)$ have the form $R_{n,s}(r)\,e^{-Zr/n\sigma}$, where $R_{n,s}$ is a polynomial in r, n is the principle quantum number ($n \geq 1$), Z is the screened nuclear charge,[17] r is the distance from the center of the nucleus, and σ is the screening radius. Since $\psi_s(r)$ is finite at the nucleus there is a magnetic interaction between the nuclear magnetic dipole moment μ_I and the electrons in the metal. The magnetic field at the nucleus is $B = B_0 + \Delta B$, where B_0 is the field that would exist at the site of the nucleus in the absence of the metal (the 'external' or 'applied' field) and ΔB is the difference found by measuring $B - B_0$. The quantity of interest $\Delta B/B$ is known as the Knight shift K.[2] The quantity B_0 is usually obtained by using identical nuclei in an insulating diamagnetic solid, from a solution containing the isotope of interest, or the application of any other method by which it can be accurately measured. The medium used becomes the *reference*. The Fermi contact interaction in an atom has the form $E_a = a\,\boldsymbol{I}\cdot\boldsymbol{S}$ where a, the hyperfine coupling constant, is $(16\pi/3)\gamma_I\hbar\mu_B|\psi_s(0)|^2$. Here γ_I is the nuclear gyromagnetic ratio, μ_B is the Bohr magneton, and $|\psi_s(0)|^2$ is the outer s-electron concentration at the nucleus. In a simplified discussion[4] it is found that $\Delta B = (a\chi_s M/g\mu_B\hbar\gamma_1)B_0$. A form more often used is

$$K = \Delta B/B = (8\pi/3)\chi_s\langle|\psi_A(0)|^2\rangle_{FS}M \qquad (2)$$

where χ_s is the conduction-electron spin susceptibility per unit mass (also called the Pauli paramagnetism), M is the mass of the atom, and $\langle|\psi_A(0)|^2\rangle_{FS}$ is the probability density at the nucleus of the metal A atom of those electrons at the Fermi surface (FS) averaged over the FS. Earlier in this paragraph it was shown that $|\psi_s(0)|^2 \approx R_{nl}^2(0)$. The Knight shift can, in principle, be used to measure the conduction-electron density for FS electrons at the nucleus, but the value of the s conduction-electron susceptibility χ_s is extremely difficult to measure accurately, and the experiment has been accomplished only rarely.[18] The experimental determination of $\langle|\psi_A(0)|^2\rangle_{FS}$ and its comparison with calculated values is of fundamental interest; however, many applications of NMR to metals do not require knowledge of χ_s. There are experiments in which it can be made to 'cancel out' or in which relative differences in ΔB are important in themselves.

The conduction electron component χ_s of the magnetic susceptibility is assumed to be a bulk electronic property. According to equation (2) the Knight shift at the solvent lattice sites *around* an isolated solute atom at the origin will be different from the Knight shift K_0 of the pure solvent if the charge density is changed by the solute. The value of the quantity $\langle|\psi_A(0)|^2\rangle_{FS}$ is different in pure A than it is if a B atom is in a neighboring site. The perturbation caused by B of the charge density in A is effective over several lattice spacings and is spherical; consequently the n_i atoms in shell i at distance r_i from the B nucleus all experience the same change. The word 'shell' is used in the sense that the ith shell contains n_i atoms all at r_i. (Note that the solute atoms in a dilute alloy are often referred to as 'impurity' or 'foreign' atoms.)

The above physical description of a solute atom B located on a lattice site of the solvent A suggests treating the system from the point of view of scattering on an atomic scale. Conduction electrons with velocities ranging from near zero to the Fermi velocity v_F at the top of the band impinge on the B atom and are scattered by it. The scattering potential $V_B(r)$ can be computed using atomic wavefunctions, but a simple approach that demonstrates the effect is to use the spherical square well. Electrons in states below the Fermi surface cannot be scattered because all nearby momentum states are filled. Only electrons at the FS can be scattered: an integral of the scattered charge

over all states in the band shows that the only contribution is from electrons at the FS, and that the scattered electrons produce an oscillatory charge-density wave $\delta\rho(r_i)$ around the solute.[19]

The conduction-electron density at nuclei surrounding the scattering center is $\rho(r_i)$, the sum of ρ_0 ($\langle|\psi_A(0)|^2\rangle_{FS}$ for the pure solvent) and the spherical wave $\delta\rho(r_i)$. An expression for $\delta\rho(r_i)$ is derived using the method of partial waves found in most standard texts on quantum mechanics.[20] Since $\delta\rho(r_i)$ is oscillatory and has a complicated dependence on r at short distances (several lattice spacings) expressions for it must be evaluated using the complete solution without simplification.[21] An asymptotic approximation valid as $r \to \infty$ is $\delta\rho(r) \propto r^{-3}$ $\cos(2k_F r + \theta)$, where θ is a function of the phase shifts η_l determined by the scattering potential. The asymptotic value for $\delta\rho(r)$ is never of use because: (a) even for a low solute concentration ($C_B \approx 0.01$) there is significant overlap among the charge density waves from the randomly distributed solutes and (b) the value of $\delta\rho(r)$ at large r is very small compared with other sources of linewidth. In summary, the effect of foreign atoms in a solvent matrix when the solvent nuclear spin I is $\frac{1}{2}$ is to cause a spectrum of resonance lines. Each line derives from the n_i solvent atoms in shell i. An example of such a study employing silver as the solvent and Group I, II, III, IV and V solute atoms demonstrated the presence of charge density waves.[22]

4 PURE METALS WITH NONZERO μ_I

4.1 Initial Considerations: Lattice Symmetry and Nuclear Properties of Isotope(s)

The primary concern is the point symmetry at each lattice site, assuming an imperfection-free lattice. Of the 14 space lattices only three are cubic (yet these include many metals), four (trigonal, tetragonal and hcp) have three, four and sixfold axial symmetry respectively, and the balance have lower symmetry. There are thus three possible types of lattice symmetry to be combined with the nuclear and electron moments and the electron charge distribution; this is a closed set of possible combinations.

4.2 Pure Metals with I = 1/2

For nuclei of spin $I = \frac{1}{2}$ energy level changes are caused by the contact interaction and the nuclear–dipole electron–dipole interaction at a distance.[15,23] The former has been discussed above (Section 3.3), the latter results from the non-s spin distribution in lattices with axial or lower symmetry. If for example a p_z orbital in a tetragonal lattice contained more charge than the $p_x = p_y$, then in the presence of a magnetic field the electrons near the top of the Fermi sea would produce a magnetic field at the nucleus with the axial symmetry of the spatial electron distribution. This *anisotropic Knight shift* has been observed in several metals with noncubic symmetry.[6] The resulting powder pattern lineshape (because of the polycrystalline sample) is peaked by an integrable infinity at one end and falls off abruptly at the other, since the range of symmetry axis orientation (with respect to $\boldsymbol{B}_0$) is from 0 to 180°, with the usual weighting factor of $\sin\theta$ for an isotropic orientation distribution. The number of crystallite orientations near $\theta = 90°$ is infinitely greater than those near zero degrees. Since this anisotropy gives rise to a broadening mechanism proportional to the external field it is clearly linked to the electron polarization via the Pauli susceptibility; equation (3) gives the shift for a single crystal orientation θ; it is

$$\frac{\Delta B}{B} = \mu_B^2 V_0 N(E_F) Q_K (3\cos^2\theta - 1) \tag{3}$$

where

$$Q_K = \int \psi (3\cos^2\theta - 1) r^{-3} \psi \, dV \tag{4}$$

The distribution of electron dipoles is contained in the conduction band wavefunctions ψ and the band structure determines $N(E_F)$. An s wavefunction would cause the integral to vanish so we have secondary evidence for the mixing of orbitals at the FS. Other factors important in pure metals with nuclei of $I = \frac{1}{2}$ are the *core polarization* (the polarization of inner s electrons simply because of the necessity of orthogonalizing all electrons in the atomic cell) and the *orbital* contribution.[23] The average value of the orbital magnetic moments is nonzero because currents are produced in the inner shells by the static magnetic field.

Another interaction depends upon the conduction-electron spins to couple nuclei. *Indirect coupling* describes the indirect spin–spin interaction between two nuclei i, j via the electron gas.[23] The wavefunction is in contact with both nuclei through their hyperfine interactions. This indirect exchange would be zero in the absence of s electrons; however it can be a dominant source of line broadening (and is expected to be if the hyperfine interaction is large). Large hyperfine interactions accompany large (massive) nuclei, and it is roughly true that the Knight shift and indirect nuclear coupling increase with increasing nuclear mass. The relationship is only approximate because of the many other contributing factors, not the least being the fraction of $\langle|\psi_A(0)|^2\rangle_{FS}$, which is s-like.

Pure metals with $I = \frac{1}{2}$ but which are highly paramagnetic, may exhibit nuclear linewidths reflecting (i.e. increased by) the inhomogeneity δB_0 of the static field B_0 within the particle (unless the particles are all shaped and oriented so as to ensure that the demagnetizing factor is identical in each). The additional field is of the order of $\chi_m B_0$, where χ_m is the bulk measured volume magnetic susceptibility of the metal.[6] A further contribution to the susceptibility, small in the simple metals but significant in transition metals, is the Van Vleck contribution χ_{VV}.[23] Shifts and linewidths found under the conditions of this section are of the order 0.1–1 mT.

4.3 Pure Metals with $I \geq 1$

The magnitudes of shifts and contributions to the absorption linewidth considered in Section 4.2 are likely to be totally overwhelmed by quadrupole splitting of the magnetic resonance if the lattice symmetry is other than cubic. The nuclear electric quadrupole moment Q is a measure of the shape of the nucleus and thus its charge distribution. Since magnetic resonance is the topic of interest we assume a high (1–10 T) magnetic field is present and the quadrupole perturbation is said

to take place in the high-field regime; the electric quadrupole interaction energy is much smaller than the nuclear magnetic dipole resonance energy $h\nu_0$. The magnitudes of the electric field gradient, the quadrupole moment, and $h\nu_0$ can vary over a sufficiently large range for both first- and second-order quadrupole perturbation to be frequently required in analyzing data. A comprehensive and authoritative monograph on this topic has been published.[24] In addition, the subject is covered in all works on NMR in metals and in the 'high-resolution' literature.[25] The information gained is interesting and useful, and there are more nuclei with $I \geq 1$ than with $I = \frac{1}{2}$ by almost a factor of 3. A concise yet moderately transparent expression for the quadrupole energy is the Hamiltonian,

$$\hat{\mathcal{H}}_{\mathrm{Q}} = \frac{1}{6} \sum_{j,k} V_{jk} Q_{jk} \tag{5}$$

The way in which the field gradients $V_{jk} = (\partial^2 V/\partial x_j \partial x_k)$ multiply the second rank tensor components Q_{jk} is reminiscent of other stress tensor–matter tensor interactions. The quantity Q, a scalar, is defined as the quadrupole moment of the nucleus, and is determined in the standard way of evaluating n-pole moments through knowledge of the charge distribution. By convention, the charge e is not included, and $Q = \frac{1}{2}\int(3z^2 - r^2)\rho(\boldsymbol{r})\mathrm{d}^3\boldsymbol{r}$, where $\rho(\boldsymbol{r})$ is the expectation value of the nuclear charge density for the state $m = I$. The expression requires knowledge of the probability density of the protons in the nucleus: Q is in fact a measured quantity, tabulated for many nuclei. (The accuracy to which Q is known is generally much lower than for the nuclear gyromagnetic ratio γ; however, it should also be admitted that the reason nuclear scientists began to study shieldings, electron–nuclear interactions, and so on, was because they were a nuisance in accurately determining γ.) An extensive literature has developed in the pure metal, $I \geq 1$ subset;[26] there is opportunity for systematic study because so many transition and rare earth (f shell) metals are hcp.

Early in the work on quadrupole interactions it was pointed out by Sternheimer (cf. Ref.[24] p. 341) that a factor contributing to V_{ij} is $-\gamma_\infty V^*_{ij}$. The charge distribution of an atom is distorted by the quadrupolar field of its nucleus and by the electric field gradient caused by the other atoms in the lattice. Surrounding atomic cells appear to be ionic because the mobile charge tends to distribute uniformly over the lattice; the remaining ionic lattice should be summed to derive the $V^l_{ij} \rightarrow q_{\mathrm{latt}}$ contribution to q from the lattice. The literature frequently uses a standard notation that incorporates these and other factors into the expression for the total field gradient q, given by

$$q = q_{\mathrm{latt}}(1 - \gamma_\infty) + q_{\mathrm{loc}}(1 - R_{\mathrm{Q}}) \tag{6}$$

Here q_{latt} is discussed above, $-\gamma_\infty$ is the Sternheimer factor (which may be as large as 100 in heavy atoms) required to correct for the charge redistribution in the atoms caused by q_{latt}. The local field gradient from sources inside the atomic cell q_{loc} is also a sum of terms. Schumacher[27] provides a particularly good introductory treatment of the basic features of this topic.

4.4 Pure Metals with $I \geq 1$, and Mechanical Imperfections

The majority of the strain in a metallic lattice is the result of dislocations. An early experiment[15] in which the resonance intensity of the untreated filings of Cu was compared with the intensity of annealed filings showed the effect of lattice distortion dramatically, since the satellite lines from the first order broadening were almost totally removed from the region of the central $I = \frac{1}{2} \rightarrow -\frac{1}{2}$ line; the intensity of the latter was decreased to about one-half of the absorption intensity in annealed Cu. A more careful analysis showed the slight narrowing of the Cu absorption line caused by the elimination of the contribution of the group of 'like' spins in regions of high lattice distortion. Dislocation pinning is very strongly dependent upon other imperfections, including grain boundaries and dislocations on other slip systems which cross the primary. When we use the concept of 'annealing temperature', for which there is a clear definition, the impurity content is the greatest unknown. By producing fine filings or heavily rolled or drawn Cu the dislocation density may be as high as $10^{12}\,\mathrm{cm}^{-2}$. This may be reduced to 10^6–$10^8\,\mathrm{cm}^{-2}$ upon annealing. Even at $10^{12}\,\mathrm{cm}^{-2}$ the majority of nuclei are not within several lattice spacings of a dislocation core.

5 ALLOYS

5.1 Solvent Nuclear Spin $I = 1/2$

5.1.1 Alloy Types and NMR

An alloy ordinarily is assumed to be any number of metals put into a perfectly inert container and melted under a vacuum or inert gas, then solidified under equilibrium conditions. The alloy specimens used for NMR should be very thoughtfully made; if called 'dilute' they usually consist of at most one or two elements present in minor concentration (0.1–10 at.%) in addition to the solvent. These are called binary or ternary alloys and may or may not be single phase.

Several compilations of phase (or equilibrium, or constitution) diagrams exist, and journals publish newly determined diagrams, updates, and extended work.[28] For elements and compounds of more than passing commercial or academic interest, individual monographs are devoted to the binary alloys of a single element. A four-volume work published by ASM characterizes intermetallic compounds, classifies them by structure type, and incorporates all dimensions and atom locations within the unit cell.[29] Similar collections of the literature of ternary alloys are available.

There are instances of the application of NMR to concentrated binary alloys with compositions ranging from 0 to 100 at.%B in an A–B alloy. Over this composition range, at room temperature, one can expect to encounter several solid solutions and/or intermetallic compounds with two phase regions separating them.[6] The results obtained resemble those of an X-ray study of a binary system. It is seen, however, that X-ray diffraction studies are better in almost every way, when they are feasible. (For metals this means essentially always.) However, NMR is not a universal approach, but is useful

only for special felicitous choices of nuclei. Important factors include the spin and the magnitude of the dipole moment.

5.1.2 Solvent NMR in Dilute Substitutional Random Solid Solution (DSRSS)

This subject has been discussed above in the context of Section 3.3 for simple metal A–B alloys. The substitution of a paramagnetic species causes very long range spin density waves around the magnetic site acting as a scatterer.

5.1.3 Solute NMR in DSRSS

Many references have been made to the charge density waves scattered from a solute atom. If the solute B nucleus has spin $\frac{1}{2}$ it is possible (other conditions being favorable) that the solute resonance absorption will be observable. The B site is a center of symmetry, and it is possible to evaluate $\langle|\psi_s(0)|^2\rangle_{B,FS}$ with the wavefunctions, theoretical techniques, and computing capabilities available.

5.2 Solvent Nuclear Spin $I \geq 1$

5.2.1 Solvent NMR in DSRSS

For DSRSS the scattering of electrons from solute atoms is unchanged from the foregoing description. Each impurity atom is imagined to be isolated and, by definition, *on* a site of the solvent crystal lattice. The solvent band structure and scattering process are unchanged. Here the similarity in treatment ends. Surrounding the solute are spherical charge density waves; these cause potential waves and electric field gradients that ripple out from the solute. Consider the $n_1 = 8$ nearest neighbors of a solute in a bcc lattice: Over the volume of a near neighbor (nn) cell the electric field changes and the quantity $V_{ij}^s(r_1)$ results at the nucleus. In addition, because of the presence of $V_{ij}^s(r_1)$, the electron orbitals in the nn cell are polarized. Crudely, this latter effect is the Sternheimer factor introduced earlier.

If the magnitude of V_{ij} at $r_1 = \sqrt{3}\,a_0/2$, where a_0 is the bcc lattice constant, is such that the quadrupole interaction energy, $\chi = e^2qQ/h$, is roughly equal to or within an order of magnitude greater than the unperturbed ($q = 0$) linewidth, a set of first-order satellite lines would in principle appear in the powder pattern of the NMR of the powdered DSRSS alloy.[6] In practice, the distribution of both shifts and symmetries leads to a broad distribution of absorption at the solute concentrations used. A large number of measurements of q_i at several r_i have been done using more dilute solutions.

Because of the number of energy levels associated with the nuclear spin I, for integral I (i.e., $I = 1, 2, \ldots$) there is no $m = \frac{1}{2} \leftrightarrow -\frac{1}{2}$ transition. For half-integral spin ($I = \frac{3}{2}, \frac{5}{2}, \ldots$) the $m = \frac{1}{2} \leftrightarrow -\frac{1}{2}$ transition is unperturbed and becomes the *central* $m = \frac{1}{2} \leftrightarrow -\frac{1}{2}$ line of the first order quadrupole split line structure. Carter et al.[6] illustrate the various patterns.

In second-order perturbation the remaining central ($m = \frac{1}{2} \leftrightarrow -\frac{1}{2}$) transition is shifted with respect to the unperturbed ($q = 0$) absorption. (Since first-order perturbation theory is no longer valid, but the higher $m \leftrightarrow m - 1$, $m \neq \frac{1}{2}$ transitions are very far removed, there are no longer observable satellites.)

The digression into high-field quadrupole perturbation was necessary to complete even a brief description of the many experiments in which q is the primary quantitative information obtained. A rather sweeping summation of the topic would state that in a large majority of DSRSS studies, the NMR absorption of an $I \geq 1$ solvent is either broadened, decreased in magnitude to an asymptotic limit, or decreased in magnitude to a very small value near zero. There is so little absorption left in the region of the original line that it can no longer be detected.

5.2.2 Solute Nuclei of $I \geq 1$ in DSRSS

Although many such studies exist, the principal interest in the results and the way in which the electronic structure interacts with the nuclei have been described. A study that involves the combined effects of nuclear quadrupole interaction, anisotropic Knight shift, dipolar broadening, and an inhomogeneous Knight shift distribution at the solute sites,[30] can serve as an example of a more complex system; the solutes Al and V were dissolved in hcp Ti in concentrations of 1 at.% and 2 at.%. A semiquantitative analysis of the Ti lattice wavefunction as it joins the localized orbitals in the Al and V cells is carried out. The substitution of Al on an hcp Ti site decreases the Knight shift of Al to near zero. The $3s^2$ orbitals probably lie below the Fermi surface of Ti.

5.2.3 Further Considerations

Very large segments of material have been omitted from this entry. Each is as significant as the material included, and the choice of topics presented is merely slanted toward the most basic considerations of nuclear interaction and the simplest aspects of metals and alloys, stressing their electronic structure in real space. It is clear that other electronic properties are very closely related to this area. For example, the electronic specific heat is directly proportional to $N(E_F)$, a factor in $(\Delta B/B)$. The residual resistivity (that part related to solutes in DSRSS) involves electron scattering processes, one aspect of which invokes the same phase shifts as appear in the evaluation of the solvent Knight shift in DSRSS using the method of partial waves.

6 NUCLEAR RELAXATION AND ATOMIC DIFFUSION: NUCLEAR RELAXATION IN I = 1/2 SYSTEMS

The discoverers of NMR worried about this topic. It is easy to see that in order to absorb net energy, a spin in a lower level must be excited into an upper level. How long can this go on? Experience shows that if the incoming photon density is not too large, it can go on forever, but if the magnitude goes beyond some critical level, the net photon absorption decreases, the populations of the upper and lower level approach equality and net absorption approaches zero. The strong implication is that there exists a mechanism by which nuclei in the upper energy state return to the lower state and lose the required energy to the lattice, a passing electron, a paramagnetic impurity, or by another process that can absorb the required energy $h\nu_0$. The spontaneous loss of energy to a large reservoir is described by

the relaxation time T_1. In metals T_1 is determined most often by collisions with passing conduction electrons; the calculation of T_1 was done by Korringa who found that the temperature $\times$ T_1 product is a constant in this case. Since nuclei relax via the contact interaction, T_1 is found to be directly related to the Knight shift.[23]

Another type of relaxation occurs because of the static dipole–dipole interactions among the nuclei. The transverse dipolar relaxation time T_2'' is calculated from the nuclear moments and their lattice locations in terms of the second moment of the dipolar field.[31] (If all lattice sites are occupied by nuclei with magnetic dipole moments then a field caused by all of the other dipoles is present at each site.) If the nuclei move through the lattice the average field at any nucleus will decrease and the more rapid the motion the narrower the resonance line. Accurate measurement of the linewidth as a function of temperature measures the activation energy of diffusion for this motional narrowing.[14] The mean time between atomic jumps has also been measured for Al using a pulse technique.[32]

7 RELATED ARTICLES

Chemical Exchange on Solid Metal Surfaces; Germanium, Tin, and Lead NMR; Hydrogen–Metal Systems; Lithium NMR; Metallic Superconductors; Quadrupolar Transition Metal and Lanthanide Nuclei; Supported Metal Catalysts; Thallium NMR.

8 REFERENCES

1. R. V. Pound, *Phys. Rev.*, 1948, **73**, 1112.
2. W. D. Knight, *Phys. Rev.*, 1949, **76**, 1259.
3. For simplicity models that represent the 'pure' elementary bond types will be used. Solids generally have charge distribution, which can be represented by a mixture of these types.
4. C. Kittel, *Introduction to Solid State Physics*, 5th edn., Wiley, New York, 1976, Chap. 1 (Also, any book on Solid State Physics which includes metals.)
5. N. Ramsey, *Nuclear Moments*, Wiley, New York, 1953.
6. G. C. Carter, L. H. Bennett, and D. J. Kahan, *Prog. Mater. Sci.*, 1977, **20**, Part 1, 123.
7. N. Bloembergen, *J. Appl. Phys.*, 1952, **23**, 1383.
8. R. Dupree and E. F. W. Seymour, in *Liquid Metals*, ed. S. Z. Beer, Marcel Dekker, New York, 1972, Chap. 11, p. 461; M. Shimoji, *Liquid Metals*, Academic Press, New York, 1977.
9. G. B. Benedek, *Magnetic Resonance at High Pressure*, Interscience, New York, 1963.
10. R. V. Pound and W. D. Knight, *Rev. Sci. Instrum.*, 1950, **21**, 219.
11. R. T. Schumacher, *Introduction to Magnetic Resonance*, Benjamin, New York, 1970, p. 43.
12. P. L. Sagalyn and A. Hofmann, *Phys. Rev.*, 1962, **127**, 68.
13. E. L. Hahn, *Phys. Rev.*, 1950, **80**, 580; ed. D. M. S. Bagguley, *Pulsed Magnetic Resonance: NMR, ESR and Optics*, Clarendon, Oxford, 1992.
14. C. P. Slichter, *Principles of Magnetic Resonance*, 3rd edn., Springer, New York, 1989.
15. N. Bloembergen and T. J. Rowland, *Acta Metall.*, 1953, **1**, 731.
16. M. A. Omar, *Elementary Solid State Physics*, Addison-Wesley, Reading, MA, 1975, Chaps. 4 and 5; C. Kittel, *op. cit.*, Chaps. 7 and 9.
17. W. A. Harrison, *Solid State Theory*, McGraw-Hill, New York, 1970, Chap. 3, Sect. 4.
18. R. T. Schumacher and C. P. Slichter, *Phys. Rev.*, 1956, **101**, 58.
19. A. Blandin and E. Daniel, *J. Phys. Chem. Solids*, 1959, **10**, 126.
20. A. Messiah, *Quantum Mechanics*, Wiley, New York, 1962; L. I. Schiff, *Quantum Mechanics*, McGraw-Hill, New York, 1949.
21. L. E. Drain, *Metall. Rev.*, 1967, **119**, 195; A. Blandin and E. Daniel, *J. Phys. Chem. Solids*, 1959, **10**, 126.
22. T. J. Rowland, *Phys. Rev.*, 1962, **125**, 459.
23. J. Winter, *Magnetic Resonance in Metals*, Clarendon, Oxford, 1971.
24. M. H. Cohen and F. Reif, *Solid State Phys.*, 1957, **5**, 321.
25. B. C. Gerstein and C. R. Dybowski, *Transient Techniques in NMR of Solids*, Academic Press, Orlando, FL, 1985, p. 121. (Highly recommended: proper presentation of many interactions included in this article.)
26. A. Maio, L. Hermans, M. Rots, G. N. Rao, and R. Coussement, *Hyperfine Interactions*, 1981, **11**, 239.
27. R. T. Schumacher, *Introduction to Magnetic Resonance*, Benjamin, New York, 1970, p. 110.
28. The Journal of Phase Equilibrium (formerly *Bulletin of Alloy Phase Digrams*), American Society for Metals, Materials Park, OH.
29. *Pearson's Handbook of Crystallographic Data for Intermetallic Phases*, 2nd edn., American Society for Metals, Materials Park, OH, 1991.
30. L. H. Chou and T. J. Rowland, *Phys. Rev. B.*, 1992, **45**, 11580.
31. T. J. Rowland, *Prog. Mater. Sci.*, 1961, **9**, 1.
32. F. Y. Fradin and T. J. Rowland, *Appl. Phys. Lett.*, 1967, **11**, 207.

Biographical Sketch

Theodore J. Rowland. *b* 1927. B.S., 1948, Western Reserve University; A.M., Ph.D., Applied Physics, Harvard University, USA. First student of Nicolaas Bloembergen (also vividly recalls R. V. Pound, J. H. Van Vleck, Leon Brillouin, E. M. Purcell). Research physicist, Metallurgical Laboratory, Union Carbide Corp., 1954–61; Professor of Physical Metallurgy, Metallurgy Department (now Materials Science and Engineering), University of Illinois (Urbana-Champaign) 1961–92. Research interests: NMR in metals, physics of solids, electrical and mechanical properties of metals.

Geometric Phases

Josef W. Zwanziger
Indiana University, Bloomington, IN, USA

1	Introduction	1
2	The Geometry of Quantum Evolution	1
3	Experimental Consequences of Geometric Phases	3
4	Summary	4
5	Related Articles	4
6	References	4

1 INTRODUCTION

The geometric phase of a quantum system is that portion of its total phase that is independent of the details of the system's temporal evolution. Thus, consider a quantum system prepared in an eigenstate $|\phi\rangle$ with energy E. The evolution of this system is just the familiar exp $(-\mathrm{i}Et/\hbar)|\phi\rangle$. The phase of the eigenstate, $-Et/\hbar$, is purely dynamic because it depends on the length of time t for which the system has evolved. It turns out, perhaps surprisingly, that in systems with sufficiently complex geometry there is an additional contribution to the total phase that is independent of time, but that does depend on the shape of the space through which the system evolves. This component of phase is thus termed geometric. As we illustrate below, even as simple a system as a spin in a moving magnetic field can acquire a geometric phase. Nevertheless, the existence of this effect was largely overlooked until Berry's seminal paper,[1] with some notable exceptions.[2,3] The history of the geometric phase has been outlined by Berry.[4] Since the publication of Berry's initial paper,[1] a wealth of primary and secondary literature has appeared (see, for example, Shapere and Wilczek[5] and Zwanziger et al.,[6] and references therein).

The geometric phase is a general phenomenon, and has been shown to be significant in a wide range of applications.[5,6] The exquisite control that magnetic resonance experiments can achieve has proven crucial in providing unambiguous tests of its existence and geometric properties.[7–10] Moreover, its description has stimulated a new way of thinking about a variety of NMR experiments that has led to the prediction of new phenomena.[8–11] Below we will briefly outline both the general theory of geometric phases, and NMR experiments that have verified the theory.

2 THE GEOMETRY OF QUANTUM EVOLUTION

2.1 The Aharonov–Anandan Phase

The geometric treatment of the general case of quantum evolution is due to Aharonov and Anandan,[12] and we follow their discussion here. Consider, for simplicity, a two-level system, assumed to be in a pure state. The state is completely characterized by its density operator $\hat{\rho}$, which is Hermitian ($\hat{\rho}^\dagger = \hat{\rho}$), idempotent ($\hat{\rho}^2 = \hat{\rho}$), and normalized such that it has unit trace. The set of all such operators spans a two-dimensional space that has the geometry of a sphere. The evolution of the two-level system can be viewed as a path on this sphere. We associate a wavefunction $|\psi\rangle$ with each density operator in this space, through $\hat{\rho} = |\psi\rangle\langle\psi|$; in fact, we can associate an infinite set of wavefunctions with each $\hat{\rho}$, since the overall phase of the wavefunction is irrelevant. Now suppose that the system is prepared initially in the state $|\psi(0)\rangle$, and that the system evolves along some closed path in the space of density operators during a time T. The system must return to its initial state, up to a phase, as shown in equation (1).

$$|\psi(T)\rangle = \mathrm{e}^{\mathrm{i}\alpha}|\psi(0)\rangle \tag{1}$$

In general, the phase α includes contributions from both the dynamic and geometric phases. Using $|\psi\rangle$, we define the ket $|\tilde{\psi}\rangle$ through equation (2).

$$|\tilde{\psi}(t)\rangle = \mathrm{e}^{-\mathrm{i}\phi(t)}|\psi(t)\rangle \tag{2}$$

Here ϕ is determined by the condition in equation (3)

$$\phi(T) - \phi(0) = \alpha \tag{3}$$

The reason for making this definition is that we have obtained a ket such that $|\tilde{\psi}(T)\rangle = |\tilde{\psi}(0)\rangle$. The original state $|\psi(t)\rangle$ obeys the Schrödinger equation

$$\mathrm{i}\hbar\frac{\mathrm{d}|\psi(t)\rangle}{\mathrm{d}t} = \hat{\mathcal{H}}(t)|\psi(t)\rangle \tag{4}$$

where $\hat{\mathcal{H}}(t)$ is the Hamiltonian of the system. By substituting the definition of $|\tilde{\psi}\rangle$ into equation (4), a differential equation for $\phi(t)$ can be obtained:

$$-\frac{\mathrm{d}\phi(t)}{\mathrm{d}t} = \frac{1}{\hbar}\langle\psi(t)|\hat{\mathcal{H}}(t)|\psi(t)\rangle - \langle\tilde{\psi}(t)|\mathrm{i}\frac{\mathrm{d}}{\mathrm{d}t}|\tilde{\psi}(t)\rangle \tag{5}$$

Integrating equation (5) shows that the total phase acquired by the system can be expressed in two parts. One part is dynamic, in the sense of depending in detail on the Hamiltonian, and is given in equation (6).

$$\alpha_{\mathrm{D}} = \frac{1}{\hbar}\int_0^T \langle\psi(t)|\hat{\mathcal{H}}(t)|\psi(t)\rangle\,\mathrm{d}t \tag{6}$$

The other portion of the phase is given in equation (7).

$$\gamma = \int_0^T \langle\tilde{\psi}(t)|\mathrm{i}\frac{\mathrm{d}}{\mathrm{d}t}|\tilde{\psi}(t)\rangle\,\mathrm{d}t \tag{7}$$

The phase γ is independent of the Hamiltonian, and in fact depends only on the path through the space of $\hat{\rho}$, and not at all on the mechanism that forces the system to traverse that particular path. Note that γ depends on $|\tilde{\psi}(t)\rangle$, not $|\psi(t)\rangle$. The functions $|\tilde{\psi}(t)\rangle$ were explicitly constructed to be free of phase factors, and so we can be sure that a phase generated by integrating the form $\mathrm{i}\langle\tilde{\psi}(t)|\mathrm{d}/\mathrm{d}t|\tilde{\psi}(t)\rangle$ is free of trivial (in the present context) contributions from energy factors and so forth.

Having derived a component of the overall phase of the system that depends only on the geometry and not the Hamiltonian, we can ask under what conditions this term is nonzero. Of particular interest is equation (7), evaluated along a closed loop in the space of density operators. Recognizing that the time t merely parameterizes the path (call the path C), we can rewrite the integral in terms of the path itself, as shown in equation (8).

$$\gamma(C) = \mathrm{i} \oint_C \langle \tilde{\psi} | \mathrm{d} | \tilde{\psi} \rangle \tag{8}$$

The phase $\gamma(C)$ is often called the Aharonov–Anandan phase (AA phase). Now at any given point on the path one could pick kets such that the integrand of equation (8) is zero there (this is probably why the geometric phase was overlooked for so long). But what is important is the integral around a finite path; it turns out that for spaces that are curved, such as spheres, or spaces with holes, such as the punctured plane, it is impossible to pick kets for which the integrand is *globally* zero. Then $\gamma(C)$ is, in general, nonzero. In NMR the experimentally relevant case is a spherical geometry, this being the shape of the space of density operators of a two-level system. The phase $\gamma(C)$ can be evaluated exactly in this case, yielding the beautifully compact formula shown in equation (9).

$$\gamma(C) = m\Omega(C) \tag{9}$$

Here m is the magnetic quantum number of the state being propagated, and $\Omega(C)$ is the solid angle subtended at the origin of the sphere by the path C. Examples of the geometric phase for different paths are shown in Figure 1.

2.2 The Adiabatic Limit: The Berry Phase

The AA phase described above arises from the geometry of the space of density operators; its generality is due to its independence of the details of the Hamiltonian associated with a given system. The discovery of the AA phase was actually preceded by the discovery by Berry of a geometric phase associated with adiabatic evolution;[1] this so-called Berry phase is a special case of the AA phase. The Berry phase arises from the geometry of the set of Hamiltonians associated with the slowly changing system; we sketch its derivation in this section.

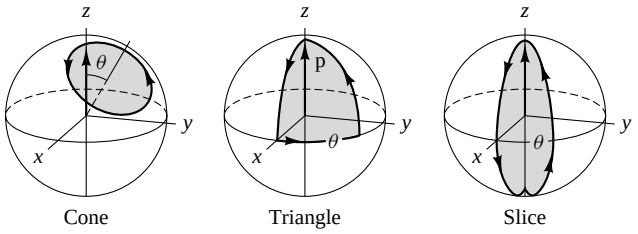

Figure 1 Paths in the space of density operators of a two-level system. The solid angle subtended at the origin is $2\pi(1 - \cos\theta)$ for the cone, θ for the triangle, and 2θ for the slice. (Reproduced by permission of the American Physical Society, from D. Suter, K. T. Mueller, and A. Pines, *Phys. Rev. Lett.*, 1988, **60**, 1218)

The calculation of the Berry phase begins by considering a Hamiltonian that depends on some set of parameters $\boldsymbol{R}$; for any given set $\boldsymbol{R}$ we solve the associated Schrödinger equation to find the energies and states of the system, conventionally indexed by the quantum number n, as shown in equation (10).

$$\hat{\mathcal{H}}(\boldsymbol{R})|n(\boldsymbol{R})\rangle = E_n(\boldsymbol{R})|n(\boldsymbol{R})\rangle \tag{10}$$

The time dependence of the problem is due to the time dependence of the parameters. If the Hamiltonian that drives the system varies slowly in time, compared with the natural precession period of the system, then the evolution can be accurately described in the adiabatic approximation.[13] In the adiabatic approximation, the state of the system at time t is

$$|\psi(t)\rangle = \mathrm{e}^{\mathrm{i}\gamma}\mathrm{e}^{-\mathrm{i}\int_0^t E_n[\boldsymbol{R}(t')]\,\mathrm{d}t'/\hbar}|n[\boldsymbol{R}(t)]\rangle \tag{11}$$

Here it is assumed that $|\psi(0)\rangle = |n[\boldsymbol{R}(0)]\rangle$. A differential equation for the phase γ can be obtained by using $|\psi(t)\rangle$ in the time-dependent Schrödinger equation, and acting with $\langle n(\boldsymbol{R})|$ on the left. The (integrated) result is summarized in equations (12) and (13).

$$\gamma = \mathrm{i}\int_0^T \langle n(\boldsymbol{R})|\frac{\mathrm{d}}{\mathrm{d}t}|n(\boldsymbol{R})\rangle\,\mathrm{d}t \tag{12}$$

$$= \mathrm{i}\oint_C \langle n(\boldsymbol{R})|\nabla_{\boldsymbol{R}}|n(\boldsymbol{R})\rangle\,\mathrm{d}\boldsymbol{R} \tag{13}$$

This phase is a special case of equation (8) above; we need merely to identify $|n(\boldsymbol{R})\rangle$ in the present case with $|\tilde{\psi}\rangle$. The natural interpretation is slightly different between the two cases; whereas we interpret the AA phase as arising from the geometry of the space of density operators, the Berry phase, equation (13), arises from the geometry of the parameter space as determined by the set $\boldsymbol{R}$.

A simple example of a nonzero Berry phase arises for a spin-J particle in a magnetic field of constant magnitude and time-dependent direction. The parameter space $\boldsymbol{R}$, here just the three components of the magnetic field, has again the geometry of a sphere. If the rate of change of the direction of the field is small compared with the precession rate of the spin around the field, then the adiabatic treatment outlined above holds, and we can expect the Berry phase shown in equation (14).

$$\gamma_n(C) = n\Omega(C) \tag{14}$$

This result is analogous to equation (9) above. This example appears in Berry's original paper,[1] and in more detail in the book by Bohm;[14] a rotating frame analog has been studied experimentally by Suter et al., and equation (14) verified.[15]

Although the Berry phase is a special case of the AA phase, more applications in NMR have made use of it, probably because the language describing it is somewhat more familiar. As noted above, whereas the AA phase arises from paths in density operator space, the Berry phase is best viewed as arising from the path followed by the Hamiltonian itself, or, more to the point, of the quantization axis of the system. A slowly varying quantization axis should always be suspected of giving rise to a Berry phase, which in many cases of interest is fairly simple to compute. The simplicity arises from the spherical geometry of the standard parameter space. For the

AA phase, however, while the two-level system yields a simple result, generalization to even a three-level system becomes significantly more complex.[16] The experimental examples of these phases to be discussed below also highlight the subtly different ways they affect real measurements.

3 EXPERIMENTAL CONSEQUENCES OF GEOMETRIC PHASES

3.1 Measurement of the Aharonov–Anandan Phase

A thorough investigation of the phase $\gamma(C)$ [equation (8)] has been carried out by Suter, Mueller, and Pines.[7] The primary obstacle that any experimental study of such a phase must overcome is that global phases associated with the density operator of an *isolated* system are in principle immeasurable. To see this, recall the invariance of $\hat{\rho}$ to phase changes; the density operator conveys all the information about the system, and the global phase is irrelevant. To measure the phase it is necessary to couple the system to its environment; since this is precisely what is done in any experiment, we see that phase shifts, even of density operators, can be expected to be important not only in theory but in practice as well.

The maximum amount of information about the phase of a system coupled to an environment is provided by an interferometric experiment, and this was the strategy pursued by Suter et al.[7] Using an approach similar to that employed by Vaughan and colleagues in a study of spinor behavior,[17] a pair of levels in a three-level system was used to provide the two-level density operator to be manipulated. Coherence to the third level provided the phase reference.

Call the phase reference level one and the two-level subsystem levels two and three. The experiment proceeds by applying a selective $\pi/2$ pulse to the $1-2$ transition, producing coherence. A time τ later a π pulse is applied to these levels, which will generate an echo. The phase of this echo provides the phase reference; it also has the advantage of refocusing all the dynamic evolution during the time τ. In a second experiment, during the refocusing period pulses are applied to the $2-3$ subsystem to drive the associated density operator through a cycle such as those shown in Figure 1. Because this subsystem has a level in common with the $1-2$ transition, the phase of the refocused $1-2$ coherence is sensitive to the phase of the $2-3$ state. In the work of Suter et al.,[7] this sequence was carried out for a variety of paths C of the $2-3$ subsystem, and the phase of the $1-2$ echo measured. The predicted phase shifts of these experiments are $\frac{1}{2}\Omega(C)$ [see equation (9)]; the experimental results and the theory are given in Figure 2. These results show that the phase $\gamma(C)$ does indeed depend on the solid angle in the way predicted; this experiment represents a complete and thorough test of the geometric evolution predicted in equation (8).

3.2 Measurement of the Berry Phase

Because any adiabatic reorientation of the quantization axis of a system can yield a geometric phase, there are a number of examples from NMR of this kind of geometric evolution. The most commonly occurring case is in solid state NMR at intermediate to low fields, where the spin degrees of freedom of the nuclei are not completely decoupled from the spatial degrees of freedom. In such a case, sample reorientations (for example, rotation) yield a slowly changing quantization axis, and hence a geometric phase.[8,9,11] The experiment of Tycko[8] is a particularly vivid example of this behavior.

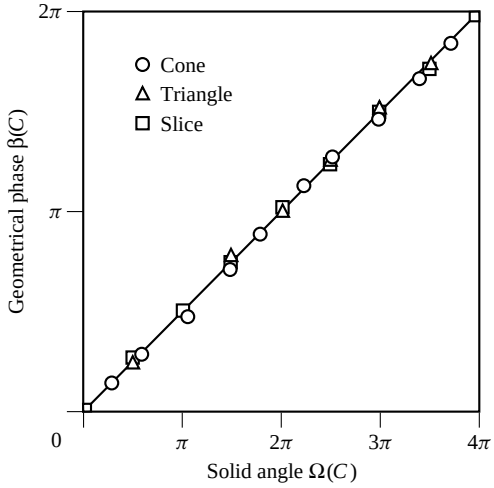

Figure 2 Experimentally determined values of $\gamma(C)$ as a function of solid angle $\Omega(C)$. The paths used are those shown in Figure 1. The solid line is theory [equation 9]. (Reproduced by permission of the American Physical Society, from D. Suter, K. T. Mueller, and A. Pines, *Phys. Rev. Lett.*, 1988, **60**, 1218)

Tycko performed a pure nuclear quadrupole resonance (NQR) experiment on the ^{35}Cl nuclei in a rotating single crystal of sodium chlorate ($NaClO_3$). In this material the quadrupolar interaction is dominant for the chlorine spins, yielding a transition frequency (in zero field) of some 30 MHz. The quantization axis for the chlorine is determined by the quadrupole principal axis system (PAS). By placing a single crystal of $NaClO_3$ in the tuned NQR detection coil, with the crystal c axis collinear with the coil axis, all four chlorine nuclei in the unit cell have equivalent orientations because the principal axis of each is at an angle of 54.74° with respect to the coil axis, and the quadrupolar interaction is axially symmetric ($\eta = 0$). Such an orientation, like any other, gives a single sharp NQR line. When the sample is made to rotate, however, the spectrum changes qualitatively. Rotating around the crystal c axis preserves the equivalence of the chlorine nuclei in the unit cell, but now the quantization axis of each one is time-dependent, tracing a circle around the coil axis (Figure 3).

Each spin state $|n\rangle$ acquires a geometric phase γ_n [see equation (13)] at a constant rate, and since the coupled partners in observable transitions ($|\frac{3}{2}\rangle \leftrightarrow |\frac{1}{2}\rangle$ and $|-\frac{3}{2}\rangle \leftrightarrow |-\frac{1}{2}\rangle$) pick up different phases, shifts of the resonance lines are observed in the spectrum. There is a subtlety in defining the spin states due to their degeneracy in zero field;[8,18,19] suffice it to say that the $|\pm\frac{3}{2}\rangle$ pair are unmixed by the rotation, and so yield good basis states, and that the superposition of the $|\pm\frac{1}{2}\rangle$ states with mixing angle arctan (2 tan θ), with θ being the angle between the quadrupole PAS and the coil axis, form good basis states. These states can be used in equation (13) to calculate the phase shift. The phase differences, modulo 2π, for the observable transitions are 0 and $\pm 2\sqrt{3}\pi$, which translate, in the frequency

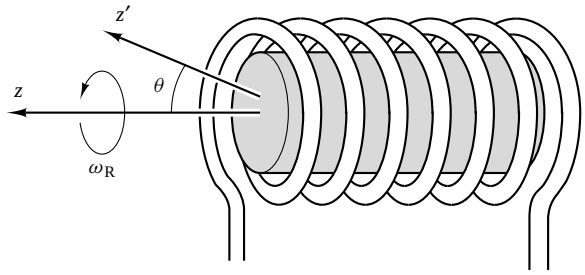

Figure 3 The experimental arrangement used in the pure NQR experiment of Tycko. The crystal *c* axis of $NaClO_3$ is oriented along the coil axis; the sample can be rotated around this axis. (Reproduced by permission of the American Physical Society, from R. Tycko, *Phys. Rev. Lett.*, 1987, **58**, 2281)

domain, into shifts at 0 and $\pm\sqrt{3}\omega_R/2\pi$ Hz (with $\omega_R/2\pi$ the rotation frequency). Note the difference between this result and the usual spinning sidebands of high field solid state NMR: here there are always four lines of constant relative intensity (two are degenerate at zero frequency shift) for all rotation speeds, and the splittings are irrationally related to the rotation frequency. Spectra, at different rotation frequencies, are shown in Figure 4. This very clean result clearly demonstrates the Berry phase, and also illustrates the primary regime in which geometric phases are important in NMR: intermediate to low field experiments, in which the quantization axis is time-dependent.

4 SUMMARY

While geometric methods have been important in relativistic quantum mechanics for some time, it is only recently that they have become used in the nonrelativistic case. The geometric phases discussed here are concrete realizations of the importance of geometry in even simple systems such as spins in magnetic fields. NMR has played a major role in demonstrating their properties, and in turn, geometric approaches are providing new insights and new predictive power into the design of magnetic resonance experiments.

5 RELATED ARTICLES

Phase Cycling; Quadrupolar Nuclei in Solids; Rotating Solids.

6 REFERENCES

1. M. V. Berry, *Proc. R. Soc. London, Ser. A*, 1984, **392**, 45.
2. S. Pancharatnam, *Proc. Indian Acad. Sci., Sect A*, 1956, **44**, 247 (reprinted in Ref. 5).
3. C. A. Mead and D. G. Truhlar, *J. Chem. Phys.*, 1979, **70**, 2284.
4. M. Berry, *Phys. Today*, 1990, **43**, 34.
5. A. Shapere and F. Wilczek (eds.), *Geometric Phases in Physics*, World Scientific, Singapore, 1989.
6. J. W. Zwanziger, M. Koenig, and A. Pines, *Annu. Rev. Phys. Chem.*, 1990, **41**, 601.

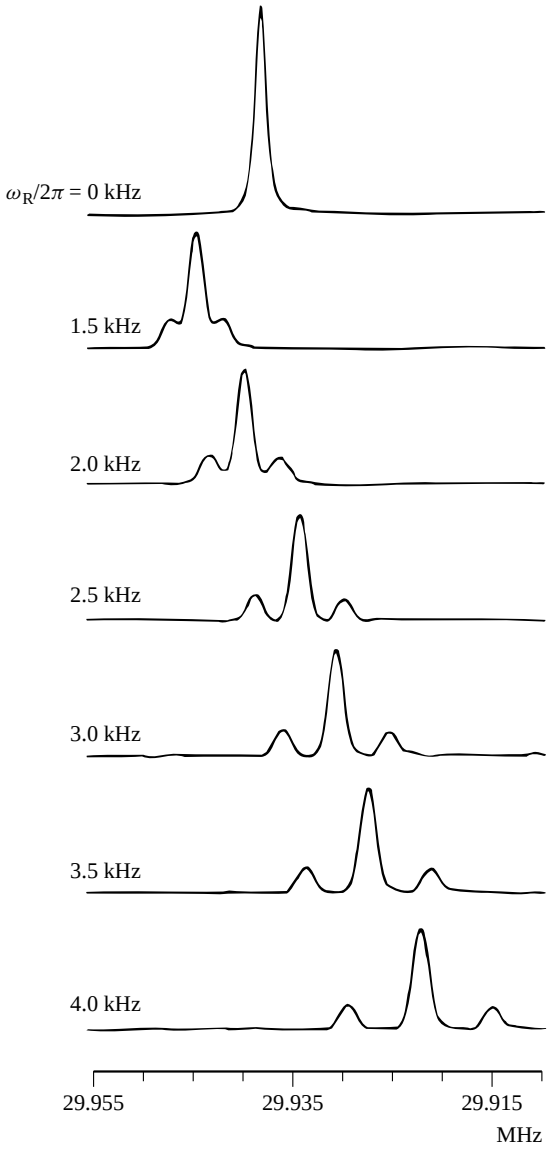

Figure 4 ^{35}Cl NQR spectra of a $NaClO_3$ single crystal in zero magnetic field at different rotation frequencies. The shift in the center of gravity is due to changing temperature. (Reproduced by permission of the American Physical Society, from R. Tycko, *Phys. Rev. Lett.*, 1987, **58**, 2281)

7. D. Suter, K. T. Mueller, and A. Pines, *Phys. Rev. Lett.*, 1988, **60**, 1218.
8. R. Tycko, *Phys. Rev. Lett.*, 1987, **58**, 2281.
9. J. W. Zwanziger, M. Koenig, and A. Pines, *Phys. Rev. A*, 1990, **42**, 1990, 3107.
10. J. W. Zwanziger, S. P. Rucker, and G. C. Chingas, *Phys. Rev. A*, 1991, **43**, 3232.
11. M. Goldman, P. J. Grandinetti, A. Llor, J. Sachleben, Z. Olejniczak, and J. W. Zwanziger, *J. Chem. Phys.*, 1992, **97**, 8947.
12. Y. Aharonov and J. Anandan, *Phys. Rev. Lett.*, 1987, **58**, 1593.
13. A. Messiah, *Quantum Mechanics*, Wiley, New York, 1958.
14. A. Bohm, *Quantum Mechanics: Foundations and Applications*, 3rd edn., Springer-Verlag, New York, 1993.

15. D. Suter, G. C. Chingas, R. Harris, and A. Pines, *Mol. Phys.*, 1987, **61**, 1327.
16. C. Bouchiat and G. W. Gibbons, *J. Phys. Paris*, 1988, **49**, 187.
17. M. E. Stoll, A. J. Vega, and R. W. Vaughan, *Phys. Rev. A*, 1977, **16**, 1521.
18. A. Zee, *Phys. Rev. A*, 1988, **38**, 1.
19. J. E. Avron, L. Sadun, J. Segert, and B. Simon, *Commun. Math. Phys.*, 1989, **124**, 595.

Biographical Sketches

Josef W. Zwanziger. *b* 1961. B.A., 1983, University of Chicago, M.S., 1985, Ph.D., 1988, Cornell University. Introduced to NMR as a postdoctoral associate with A. Pines. Faculty in Chemistry at Indiana, 1990–present. Approximately 35 publications. Research interests include the study of disordered solids with magnetic resonance, and the application of geometric methods to quantum mechanics.

Molten Salts

W. Robert Carper
Wichita State University, KS, USA

1	Introduction	1
2	Microdynamics	1
3	Chemical Shifts	2
4	Chemical Exchange	3
5	Diffusion Coefficients	3
6	Related Articles	4
7	References	4

1 INTRODUCTION

Molten salts represent an interesting class of liquids possessing unique ionic interactions. In this type of liquid, the usual ion–solvent forces are replaced by ion–ion interactions and possess Lewis acid–base properties. Molten salts may be classified according to either composition and/or temperature range: (1) high temperature molten salts which generally contain only inorganic salts, and (2) room temperature molten salts which contain both organic and inorganic components. There are numerous excellent books and reviews of molten salt chemistry, however only a few contain references to NMR studies of these highly ionic liquids.[1–5]

NMR studies of high-temperature molten salts often require special equipment (high-temperature probes, etc.), as described in a recent review article.[3] Room temperature molten salts need special treatment only in the preparation of the sample itself (usually in a drybox, followed by sealing with a torch immediately after removing the sample from the drybox). Both types of molten salt have been used as the subject of basic studies by NMR over a wide range of nuclei including ^{1}H, ^{2}H, ^{7}Li, ^{13}C, ^{17}O, ^{19}F, ^{23}Na, ^{27}Al, ^{39}K, ^{81}Br, ^{87}Rb, ^{127}I, and ^{205}Tl.

2 MICRODYNAMICS

2.1 Spin State Population

The distribution of nuclear spin states is affected by the application of low intensity radiation, resulting in a net absorption of energy and a redistribution of spin states. Removal of the source of radiation results in a return (relaxation) of the excited nuclei to ground state conditions. The rate of this relaxation process in the liquid state is controlled by rapidly fluctuating magnetic fields associated with rotational and translational motion. Theoretical models typically describe relaxation processes in terms of either rotational and/or translational correlation times. The correlation time τ_c typically represents the time taken by the involved nuclei to rotate, translate or be involved in such events as phase changes (see ***Brownian Motion and Correlation Times***).

2.2 Relaxation and Correlation Times

Relaxation times are designated as either spin–lattice (T_1) or spin–spin (T_2), depending upon the type of interaction and the method used to obtain them. Relaxation rates are simply the inversion of relaxation times ($R = 1/T$). Spin–lattice (longitudinal) relaxation times (T_1) are obtained by the inversion–recovery method and spin–spin (transverse) relaxation times are obtained from either linewidth ($T_2^* \approx T_2$) or spin echo (T_2) measurements (see ***Relaxation: An Introduction***). The theoretical equations that define relaxation times (rates) as a function of correlation time are relatively simple in the 'extreme narrowing region' where $\omega\tau_c \ll 1$ ($\omega = 2\pi\nu$). At low temperatures (approaching the solid or glassy state) where $\omega\tau_c \approx 1$, the equations become increasingly complex. In this region (T_1 minimum), one can still solve the correlation equations by assuming that $\omega\tau_c = 1$.

2.3 Relaxation Mechanisms

Relaxation studies of molten salts provide an excellent source of structural information which is difficult or impossible to obtain by other physical methods. Much useful information can be obtained from knowledge of spin–lattice (longitudinal) and/or spin–spin (transverse) relaxation times (see ***Relaxation Processes: Cross Correlation and Interference Terms***). The relaxation mechanisms that may be observed include dipolar, quadrupolar, spin–rotation, chemical shift anisotropy, scalar, and paramagnetic (see ***Relaxation Theory for Quadrupolar Nuclei*** and ***Carbon-13 Relaxation Measurements: Organic Chemistry Applications***). Of these mechanisms, paramagnetic relaxation is often the most effective. Consequently, one must be careful to exclude paramagnetic impurities from the melts under observation.

2.4 Relaxation Studies

The first significant papers on molten salt relaxation studies dealt with ^{1}H linewidth studies of potassium stearate.[6,7] These early investigations demonstrate the usefulness of this technique by correlating large changes in R_2 (= $1/T_2$) with phase transitions. A recent ^{1}H relaxation study[8] of the *N*-(1-butyl)pyridinium chloride–aluminum chloride system compares intramolecular rotational correlation times with melt viscosities. The data obtained in the acidic melt[8] region ($AlCl_3$ in excess) where $Al_2Cl_7^-$ is present, indicates that the extreme narrowing condition ($\omega\tau \ll 1$) is not met in these highly viscous melts. In the basic or neutral melts, where $AlCl_4^-$ is the primary anionic species, the extreme narrowing condition is apparently upheld.

In the initial studies of group I cations in high temperature molten salts[9,10] the spin–lattice relaxation times (T_1) of ^{23}Na and ^{7}Li in molten $NaNO_3$ and $LiNO_3/KNO_3$ mixtures are reported and the relationships between quadrupolar relaxation, diffusion and ionic radii carefully analyzed (see ***Relaxation Theory for Quadrupolar Nuclei***). The conclusion[10] that long-range order in the melt no longer exists as it does in the solid is supported by the fact that the largest part of the electric field gradient comes from only one neighboring anion and, therefore, models of ionic interactions in the melt should

involve only nearest neighbors. It should be pointed out, however, that the author[10] assumes that ^{7}Li relaxes by a purely quadrupolar relaxation mechanism, although it is likely that dipolar effects are also present as is often the case for ^{7}Li relaxation.

This type of high-temperature study is extended[11] to ^{23}Na and ^{87}Rb in molten $NaNO_3$ and $RbNO_3$. The authors[11] calculate field gradients around the cations using results from X-ray diffraction studies to test various models and conclude that relaxation processes from translational motion are more important than those from rotational motion. In a following report, they[12] study the relaxation of ^{81}Br and ^{127}I in molten LiBr and LiI. As is often the case, the NMR relaxation correlation times[12] differ by several orders of magnitude from those obtained from viscosity measurements of the same systems.

Chloroaluminate room temperature melts have been the focus of a number of relaxation studies (^{1}H, ^{13}C, ^{23}Na, and ^{27}Al).[8,13–16] Attempts by investigators[8,13] using viscosity to calculate correlation times from

$$\tau_c = \eta V/kT = 4\pi a^3 \eta/3kT \tag{1}$$

and to determine adequately molecular size from this equation have generally been unsuccessful. The correlation times determined from viscosity are typically two orders of magnitude larger than those determined from NMR.[8] Use of equation (1) to calculate ionic radii a from NMR correlation times also provides unrealistic values. The use of the Stokes–Einstein equation

$$D = kT/6\pi\eta a \tag{2}$$

with diffusion coefficients to obtain complex radii is more promising.[13]

Another use of relaxation measurements involves the dual spin probe (DSP) method.[14,15] The DSP method requires that neighboring nuclei form a chemical bond or complex, which implies that these nuclei undergo simultaneous rotation and therefore have the same correlation time (assuming that a rotational model is appropriate). In the case of ^{13}C and ^{27}Al, this leads to approximate equality between the ^{13}C dipolar correlation time τ_{eff} and the ^{27}Al quadrupolar correlation time τ_Q:

$$R_1^{\text{dipolar}}(^{13}\text{C}) = N_H(\hbar\gamma_C\gamma_H)^2 r_{CH}^{-6}\tau_{eff} \tag{3}$$

$$R_1^{Q} = [(3/10)\pi^2(2I+3)/I^2(2I-1)][1+(z^2/3)]\chi^2\tau_Q \tag{4}$$

$$\chi[e^2Qq/h] = \text{QCC} \tag{5}$$

The DSP assumptions include: (1) the asymmetry factor z is zero; (2) the intramolecular dipolar relaxation model (^{13}C) is adequate; and (3) the system is within the boundary of the extreme narrowing condition ($\omega\tau < 1$). If all these conditions are met, a plot of $R_1{}^{\text{dipolar}}(^{13}\text{C})$ versus $R_1{}^{Q}$ will be linear and pass through the origin.[14,15] An important result of this analysis is that it provides a method for determining quadrupolar coupling constants (QCCs) in the liquid state.[14,15]

An alternative method for determining QCC values is to lower the melt temperature until a T_1 minimum is observed. At this point, $\omega\tau_c \approx 1$ and the correlation equation can be solved exactly.[16] This same approach can be used in all melts for ^{13}C, ^{1}H, and other nuclei. Solution of the correlation equations is readily accomplished using a desktop computer system.

3 CHEMICAL SHIFTS

3.1 Physical Interpretation

Chemical shift studies[17,18] of a series of molten thallium salts are able to relate the ^{205}Tl chemical shift to the square of the overlap integral giving a measure of the degree of covalency. In these studies, ^{205}Tl chemical shifts in Tl(I) and Tl(III) salts are reported relative to $TlNO_3$ as a function of temperature. The observation that $TlCl_3$ has a large chemical shift relative to $TlNO_3$ and that it undergoes a very small change upon melting leads to the conclusion that the Tl(III) atoms are deshielded by the chlorine atoms within the molecule and yet are strongly shielded from neighboring molecules within the melt. The authors[17,18] also conclude that Coulombic forces predominate in molten halides while in covalent species ($AlCl_3$) intermediate forces such as ionic, covalent, dipolar, and van der Waals forces must play roles of varying importance.

3.2 Equilibrium Constants

Chemical shift values are often used to calculate equilibrium constants of molecular and ionic complexes. The basic assumption is that the observed chemical shift is the sum of the concentration-weighted chemical shifts of the free and complexed nuclei. One can usually solve these equations using either mole fraction or molar concentration terms. The resulting information is extremely useful and relatively easy to interpret compared with attempts to analyze chemical shifts of individual species which, by definition, contain a number of complex terms (see ***Shielding Calculations: LORG and SOLO Approaches***).[17,18] The following is a typical derivation[19] of the equations necessary for equilibrium analysis given the system, A + B $\rightleftharpoons$ C, where (a) B > A, (b) one assumes that A and C have characteristic chemical shifts δ_A and δ_C, and (c) the observed chemical shift δ_{obs} is the weighted arithmetic mean of δ_A and δ_C:

$$K = C/B_0(A_0 - C) \tag{6}$$

$$\delta_{obs} = [C/A_0]\delta_C + [(A_0 - C)/A_0]\delta_A \tag{7}$$

If we let $\Delta = \delta_{obs} - \delta_A$ and $\Delta_0 = \delta_C - \delta_A$, then

$$\Delta/B_0 = -K(\Delta - \Delta_0) \tag{8}$$

The major advantage of equation (8) is that a plot of Δ/B_0 versus Δ will give a straight line with a slope equal to $-K$ and an intercept of $K\Delta_0$. This avoids the inherent errors produced from a plot that gives the equilibrium constant as the reciprocal of the intercept (this often results in $1/K$ values close to the origin, producing a considerable error in the value of K). There still remains, however, the problem of determining δ_A.

In molten salts, it may be necessary to plot δ_A (observed) versus $1/A$ and extrapolate to the y intercept ($A = \infty$) by the use of a polynomial fit to obtain a value of δ_A(free). Interative methods can also be used to solve equations (6)–(8).

Examples of equilibrium constant determination include studies of tetrachloroaluminate melts[20–22] in which the cationic source is either 1-ethyl-3-methylimidazolium chloride[20,22] or *n*-butylpyridinium chloride.[21] The first of these studies[20] used ^{13}C NMR chemical shifts to establish which anionic species were present as a function of melt composition. The second study[21] identified and analyzed the equilibrium between $LiCl_2^-$ and the $LiCl_2^-$ dimer using ^{7}Li NMR. The last report[22] examined the equilibrium between HCl, Cl^-, and HCl_2^-

$$Cl^- + HCl \rightleftharpoons HCl_2^- \quad (9)$$

using ^{2}H NMR and provides an excellent example of the use of the iterative method.

3.3 Contaminant Species

A problem that always exists in molten salt studies is the possible presence of water (and similar contaminants) resulting in the formation of various oxides. The presence of these impurities have led to several honest misinterpretations of NMR spectra in the literature. An important ^{17}O NMR study of chloroaluminate melts containing water has analyzed this problem in careful detail.[23]

4 CHEMICAL EXCHANGE

4.1 Categories of Molecular Events Based on Rate of Occurrence

These categories include: (a) equilibrium species whose interconversion is slow relative to the NMR timescale, thus providing specific chemical shifts for each species; (b) species whose interconversion is extremely rapid relative to the NMR timescale, resulting in an average chemical shift which includes all equilibrium components commensurate with their relative concentration; and (c) species whose interconversion is intermediate on the NMR timescale. In the case of (c), one may observe a 'coalescence' of NMR signals which collapse into a single broad signal as the temperature is raised. The existence of such a 'coalescence' is necessary evidence that a dynamic chemical exchange process is actually occurring [species whose chemical shifts are similar undergo changes in T_2 (line broadening) as a function of temperature, producing spectra that give the false appearance of chemical exchange]. Furthermore, the analysis of such an exchange is best accomplished when the chemical shifts of the individual species are cleanly separated. Attempts to separate peaks that overlap severely can only result in significant errors (see ***Chemical Exchange Effects on Spectra***; ***Relaxation Effects of Chemical Exchange***).

4.2 Examples of Chemical Exchange

The most obvious examples of chemical exchange to be studied involve room temperature chloroaluminate melts and ^{27}Al NMR. The primary species expected to undergo exchange are included in the equilibrium

$$AlCl_3 + Al^*Cl_4^- \rightleftharpoons Al_2^*Cl_7^- \quad (10)$$

The ^{27}Al chemical shifts of the tetrachloro- and heptachloroaluminate anions given above are similar, creating a large error in any attempted mathematical analysis based on lineshapes alone. Unfortunately, studies of the chemical exchange (^{27}Al) of molten salts, where the authors have attempted to analyze equation (10), either deal with an impurity in the form of an oxide or else fail to provide examples of 'clean' reversible coalescence, as suggested earlier. The questionable use of preacquisition delay[5] is also present in a number of the aforementioned analyses. A comprehensive review[5] of ^{27}Al NMR is highly recommended, as it points out some of the many discrepancies in the few ^{27}Al chemical exchange papers in the literature.

5 DIFFUSION COEFFICIENTS

5.1 Introduction

The latest NMR method for determining self-diffusion coefficients involves the use of pulsed field gradients, as first demonstration by Stejskal and Tanner.[24] The recent availability of field gradient coils for all high-field NMR spectrometers guarantees that this technique[24] will replace various other methods (gravimetric, electrical, optical, radioactive, and stable tracers) that have been used to obtain diffusion data in molten salts (see ***Diffusion Measurements by Magnetic Field Gradient Methods***).

5.2 Experimental Description

The pulsed field gradient experiment[24] is based on the use of two identical magnetic field pulses of duration t_1 and strength g inserted into the basic $90^\circ-\tau-180^\circ$ spin echo sequence (see ***Diffusion Measurements by Magnetic Field Gradient Methods*** and ***Field Gradients and Their Application***). The first gradient pulse is applied between the 90° and 180° rf pulses, effectively 'labeling' the position of individual nuclei in the sample. The second field gradient pulse is applied between the 180° pulse and the echo after a time t_2. This second field gradient pulse monitors the movement (observation of the diffusion process) of any nuclear spins during t_2. The effect of diffusion on the spin echo appearing at time 2τ is to decrease the echo amplitude relative to that observed in absence of gradient pulses. The echo attenuation is a quantitative measure for the precession frequency changes of diffusing nuclei during t_2 and allows the evaluation of the self-diffusion coefficient for the observed nucleus. The spin echo amplitude $M(2\tau,g)$ is given by

$$M(2\tau, g) = M(2\tau, 0)\exp\{-\gamma^2 D g^2 t_1^2[t_2 - (t_1/3)]\} \quad (11)$$

5.3 Diffusion Coefficients

The spin echo method using pulsed field gradients was first used[25] successfully to determine a value of 2.30×10^{-9} m^2 s^{-1}

for the self-diffusion coefficient D of Na^+ in molten $NaNO_3$, which is in excellent agreement with values obtained using other methods.

6 RELATED ARTICLES

Chemical Shift Tensors; Carbon-13 Relaxation Measurements: Organic Chemistry Applications; Relaxation Processes: Cross Correlation and Interference Terms.

7 REFERENCES

1. S. V. Volkov, *Pure Appl. Chem.*, 1987, **59**, 1151.
2. J. S. Wilkes, *NATO ASI Ser.* C, 1987, 202, 217.
3. W. E. Warren, in *Magnetic Measurement Techniques in Molten Salt Techniques*, ed. R. J. Gale and D. G. Lovering, Plenum, New York, 1991, Vol. 4, p. 111.
4. J. F. Stebbins, *Chem. Revs.*, 1991, **91**, 1353.
5. J. W. Akitt, *Prog. NMR Spectrosc.*, 1989, **21**, 1.
6. R. F. Grant and B. A. Dunell, *Can. J. Chem.*, 1960, **38**, 1951.
7. R. F. Grant and B. A. Dunell, *Can. J. Chem.*, 1961, **39**, 359.
8. T. A. Zawodzinski, R. Kurland, and R. A. Osteryoung, *J. Phys. Chem.*, 1987, **91**, 962.
9. D. Harold-Smith, *J. Chem. Phys.*, 1973, **59**, 4771.
10. D. Harold-Smith, *J. Chem. Phys.*, 1974, **60**, 1405.
11. W. W. Filho, R. L. Havill, and J. M. Titman, *J. Magn. Reson.*, 1982, **49**, 296.
12. W. W. Filho, R. L. Havill, and J. M. Titman, *J. Phys. C.: Solid State Phys.*, 1982, **15**, 3617.
13. W. R. Carper, J. L. Pflug, A. M. Elias, and J. S. Wilkes, *J. Phys. Chem.*, 1992, **96**, 3828.
14. W. R. Carper, J. L. Pflug, and J. S. Wilkes, *Inorg. Chim. Acta*, 1992, **193**, 201.
15. W. R. Carper, J. L. Pflug, and J. S. Wilkes, *Inorg. Chim. Acta*, 1992, **202**, 89.
16. C. E. Keller and W. R. Carper, *Inorg. Chim. Acta*, 1993, **210**, 203.
17. S. Hafner and N. H. Nachtrieb, *J. Chem. Phys.*, 1964, **40**, 2891.
18. S. Hafner and N. H. Nachtrieb, *J. Chem. Phys.*, 1965, **42**, 631.
19. W. R. Carper, C. M. Buess, and G. R. Hipp, *J. Phys. Chem.*, 1970, **74**, 4229.
20. J. S. Wilkes, J. S. Frye, and G. F. Reynolds, *Inorg. Chem.*, 1983, **22**, 3870.
21. R. R. Rhinebarger, J. W. Rovang, and A. I. Popov, *Inorg. Chem.*, 1986, **25**, 4430.
22. P. C. Trulove, D. K. Sukumaran, and R. A. Osteryoung, *Inorg. Chem.*, 1993, **32**, 4396.
23. T. A. Zawodzinski and R. A. Osteryoung, *Inorg. Chem.*, 1990, **29**, 2842.
24. E. O. Stejskal and J. E. Tanner, *J. Chem. Phys.*, 1965, **42**, 288.
25. C. Herdlicka, J. Richter, and M. D. Zeidler, *Z. Naturforsch., Teil a*, 1988, **43**, 1075.

Biographical Sketch

W. Robert Carper. *b* 1935. B.S. SUNY at Albany, 1960; Ph.D., University of Mississippi, 1963. Introduced to NMR by M. Eisner. Faculty in Chemistry, Wichita State University, 1967–present. Approx. 90 publications. Research interests include the theory and application of NMR relaxation methods to molten salts, enzyme structure and function, metal ion–sugar complexes, and metal ion–humic acid complexes.

Nuclear Spin Superradiance

V. I. Yukalov

Bogolubov Laboratory of Theoretical Physics, Joint Institute for Nuclear Research, Dubna, Russia

1 Introduction 1
2 Experimental Observation 2
3 Basic Model 3
4 Evolution Equations 5
5 Nyquist Noise 7
6 Incoherent Stage 8
7 Transient Superradiance 9
8 Pulsing Superradiance 10
9 Hyperfine Interactions 12
10 Radiation Intensity 13
11 Applications 13
12 Related Articles in Volumes 1–8 14
13 References 14

1 INTRODUCTION

Nuclear spins may exhibit several coherent phenomena occurring at nuclear magnetic resonance frequencies, which have their direct counterparts in resonant atomic systems.[1] For instance, nuclear free induction is an analog of atomic free induction and the spin echo is an analog of the photon echo. These analogies are due to the fact that an ensemble of identical spins forms a collective of finite-level objects, similar to a resonant system of atoms or molecules. Such a finite-level nonequilibrium system can, under special conditions, behave as a collection of coherent radiators.

Similar to the case of resonant atoms, one may distinguish two principally different ways of dealing with spin assemblies. One situation would be when spins are near their equilibrium state, with a nonequilibrium perturbation produced by a resonant alternating field. This is a situation typical of nuclear magnetic resonance.[2] Another possibility could be if spins are initially prepared in a strongly nonequilibrium state, e.g., being polarized against a constant external magnetic field. In the latter case, the polarized spins resemble a system of inverted resonant atoms.

One of the most interesting effects exhibited by a system of inverted atoms is superradiance, when the radiation intensity is approximately proportional to the number of atoms squared, while the duration of a superradiant pulse is inversely proportional to this number. The possibility of *atomic superradiance* was predicted by Dicke,[3] and nowadays it is well studied both theoretically and experimentally. There exists a vast literature on the subject; a description can be found in recent books.[4,5] A natural question that arises is: if atomic and spin systems are so similar, then could a kind of *spin superradiance* be realized?

For spins to behave coherently, there must exist a cause correlating their motion. In the case of atoms, such a correlating mechanism is caused by the photon exchange through the common radiation field. This exchange results in the formation of effective interatomic correlations collectivizing atomic radiation. For spins, however, their magneto-dipole radiation is too weak to develop noticeable spin correlations. This concerns both nuclear as well as electron spins. Such photon-exchange interactions are negligible as compared to disordering dipolar spin interactions. How then might the spin motion be collectivized?

It is, of course, possible to force an ensemble of spins to develop coherence by imposing an initial condition of longitudinal magnetization, and using an rf pulse to produce a macroscopic transverse magnetization. But this would result in standard free nuclear induction, with the coherence being lost during the dephasing time T_2. However, free nuclear induction, although it is a coherent process, is not superradiance with one of the main characteristic features of a short radiation time of a superradiant pulse $\tau_p \ll T_2$, shorter than the transverse dephasing time. To make the superradiant pulse time τ_p so short, some internal nonlinear correlating mechanism has to be involved.

Mutual spin correlations can arise owing to a feedback field formed by a resonant electric circuit coupled to the spin system and tuned to the Zeeman transition frequency of spins. The role of such a coupling in magnetic resonance experiments has been analyzed by Bloembergen and Pound.[6] They showed that, in the presence of an electric resonant circuit, coupled to a spin system, the signal of nuclear induction can be damped in a time much smaller than T_2. Since this shortening of the induction damping time is due to collective effects, caused by the spin coupling through the resonator feedback field, the resulting process may be termed *collective induction*. This effect has been observed in a number of substances.[7] The process already possesses one of the prerequisites of superradiance, i.e., a short radiation time $\tau_p < T_2$. Usually, the induction signal starts at $t = 0$, at maximum intensity, while a superradiant pulse is always separated from the time origin by a delay time $t_0 > 0$. The signal of collective induction can also be peaked at a delay time well separated from $t = 0$. However, there is a principal difference between collective induction and superradiance: in collective induction, coherence is induced by external sources, while in superradiance coherence develops in a self-organized way due to internal correlations. The *self-organized*, *spontaneous*, nature of superradiance is one of its most important features.[3–5] In general, one includes into the class of superradiant, the processes that are triggered by initial external pulses, but with a compulsory requirement that the imposed initial coherence be very weak, playing just the role of a trigger. Thus, collective induction, although it is a collective coherent process, is not yet superradiance.

The principal characteristics of superradiance, which apply both to atomic as well as to spin systems, can be summarized as follows:

1. Superradiance is collective, coherent radiation by an ensemble of radiators.
2. It is a spontaneous process developing in a self-organized way.

3. The maximal intensity of a superradiant burst is proportional to the number of radiators in the power larger than one.
4. The duration of a superradiant pulse is essentially shorter than the dephasing time T_2.
5. A superradiant pulse has a peak at a finite delay time.

In atomic systems, one may distinguish different types of superradiance, all having the same characteristic features, including a short pulse time $\tau_p < T_2$ and finite delay time $t_0 > 0$. First, superradiance can occur as a transient process or as a lasting repeated effect, depending on whether there is no external nonresonant pumping permanently applied to the system or, respectively, there exists such a pumping supporting atomic inversion. In the first case, the system is prepared in an inverted state, after which no nonresonant pumping is involved. Then, if the relaxation process is gently promoted at $t = 0$ by an external pulse imposing weak initial coherence on the system, *triggered superradiance* may develop. When no initial coherence is thrust on the system, but superradiance appears as a completely self-organized effect starting from a purely incoherent state, then this is named *pure superradiance*. When the system is subject to the action of a nonresonant pumping constantly supporting atomic inversion, the regime of *pulsing superradiance* may arise, with a long series of superradiant bursts.

It has been of great interest to find out if a kind of spin superradiance, occurring in spin systems similarly to this phenomenon in atomic assemblies, could be realized experimentally and, if so, how should it be described theoretically. Despite several similarities between spin and atomic ensembles, they are, nevertheless, rather different. For example, spontaneous radiation, starting the process of pure atomic superradiance, is absent in spin assemblies. Therefore, one of the most intriguing questions has been if pure spin superradiance can exist and, if so, what would be its origin.

The phenomenon of spin superradiance is itself interesting and, in addition, it could be employed for several applications, as is discussed in Section 11. These applications could include:

1. *Investigation of materials characteristics* by measuring the relaxation parameters that are specific for spin superradiance and do not arise in other types of spin relaxation.
2. *Fast repolarization of targets* used in various scattering experiments of high-energy physics.
3. *Construction of spin masers* producing coherent radiation at radiofrequencies.
4. *Creation of sensitive detectors* of weak external pulses, based on the mechanism of triggered spin superradiance.
5. *Method of information processing*, derived from the feasibility of regulating the number of and the intervals between superradiant bursts in the regime of punctuated spin superradiance.

2 EXPERIMENTAL OBSERVATION

Historically, the regime of *pulsing spin superradiance* was observed first.[8–10] This was done for a ruby crystal Al_2O_3, with the Cr^{3+} paramagnetic admixture. The active nuclei were ^{27}Al, with spins $I = 5/2$. If the ruby crystal is oriented in an external magnetic field such that a fully resolved quadrupole structure of its five $\Delta m = \pm 1$ NMR transitions can be observed, and a resonant circuit is tuned to a selected NMR line, then ^{27}Al spins form a fictitious two-level system. In experiments, the resonant circuit was tuned to the central $\{-1/2, 1/2\}$ line. The density of ^{27}Al nuclei was $\rho_{Al} = 4.4 \times 10^{22}\,\mathrm{cm}^{-3}$ and that of Cr^{3+}, $\rho_{Cr} = 8.6 \times 10^{18}\,\mathrm{cm}^{-3}$. The measurements were performed in a static magnetic field of about $B_0 = 1.1\,\mathrm{T}$, which for the ^{27}Al magnetogyric ratio $7 \times 10^7\,\mathrm{s}^{-1}\,\mathrm{T}^{-1}$ makes the NMR frequency $8 \times 10^7\,\mathrm{Hz}$. The temperature range was from 1.6 to 4.2 K. The ringing time of the resonant circuit was $\tau = 10^{-6}\,\mathrm{s}$, and the quality factor Q was varied between 60 and 200. The coil filling factor was $\eta = 0.55$. The transverse spin damping time was $T_2 = 3 \times 10^{-5}\,\mathrm{s}$. The spin population inversion of the ^{27}Al nuclear spins was achieved by dynamic nuclear polarization, by means of powerful microwave radiation supplied to the sample in the vicinity of a selected Cr^{3+} electron spin resonance line. The corresponding longitudinal spin pumping time was $T_1^* = 0.1\,\mathrm{s}$. The emission of a long train of superradiant bursts was observed, with the delay time of the first pulse being $t_0 = 2 \times 10^{-3}\,\mathrm{s}$ and its duration being $\tau_p = 2.6 \times 10^{-5}\,\mathrm{s}$ in the case of the quality factor $Q = 60$, while $\tau_p = 8 \times 10^{-6}\,\mathrm{s}$ for $Q = 200$.

The first observation of *pure spin superradiance* was accomplished in Dubna.[11,12] A dielectric propanediol $C_3H_8O_2$, with a paramagnetic admixture of Cr^{5+}, was used as an active substance. This material possesses a high concentration of protons, with density $\rho_H = 4 \times 10^{22}\,\mathrm{cm}^{-3}$. The proton spins $I = 1/2$ played the role of radiators. The admixture of Cr^{5+}, with the density $\rho_{Cr} = 1.8 \times 10^{20}\,\mathrm{cm}^{-3}$, was employed for the purpose of dynamic nuclear polarization of proton spins. Experiments with the same material propanediol were repeated in Saint Petersburg.[13] In all these experiments,[11–13] electric circuits were used as resonators, with quality factors Q between 100 and 600. The filling factor was $\eta = 0.6$. The volume of samples varied from $0.5\,\mathrm{cm}^3$ to $12\,\mathrm{cm}^3$. For external static magnetic fields B_0 in the interval between 0.5 T and 2.64 T, with the proton magnetogyric ratio $2.675 \times 10^8\,\mathrm{s}^{-1}\,\mathrm{T}^{-1}$, the NMR proton frequencies were between $1.3 \times 10^8\,\mathrm{Hz}$ and $7.1 \times 10^8\,\mathrm{Hz}$. The experiments were carried out at low temperatures of 0.05–0.1 K. The inverted proton polarization reached 90%. Cooling of the sample resulted in strong suppression of the nuclear spin-lattice relaxation. The related longitudinal relaxation time was $T_1 = 1.8 \times 10^5\,\mathrm{s}$ at $B_0 = 0.5\,\mathrm{T}$ and $T_1 = 1.8 \times 10^6\,\mathrm{s}$ at $B_0 = 2.64\,\mathrm{T}$. The transverse dephasing time was $T_2 = 0.85 \times 10^{-5}\,\mathrm{s}$. After preparing an inverted sample, with the proton polarization directed against an external static magnetic field B_0, the latter was scanned with the velocity about $5 \times 10^{-3}\,\mathrm{T\,s}^{-1}$. When in the process of this slow adiabatic scanning, the field value B_0 reached the value for which the proton NMR frequency coincided with the circuit natural frequency, the resonance condition was met. Then a powerful superradiant burst was produced, with the duration time about $\tau_p = 1.3 \times 10^{-6}\,\mathrm{s}$.

Similar experiments, observing pure spin superradiance, were accomplished in Bonn,[14] with the target materials butanol (C_4H_9OH) and ammonia (NH_3). These materials are also rich with protons, with density $\rho_H \approx 3 \times 10^{23}\,\mathrm{cm}^{-3}$. By means of dynamic nuclear polarization, proton polarizations of up to 99% were achieved. The samples were cooled to low temperatures, the spin-lattice relaxation time was $T_1 \approx 3.6 \times 10^4\,\mathrm{s}$ for protons in butanol and $T_1 \approx 10^5\,\mathrm{s}$ for protons in ammonia.

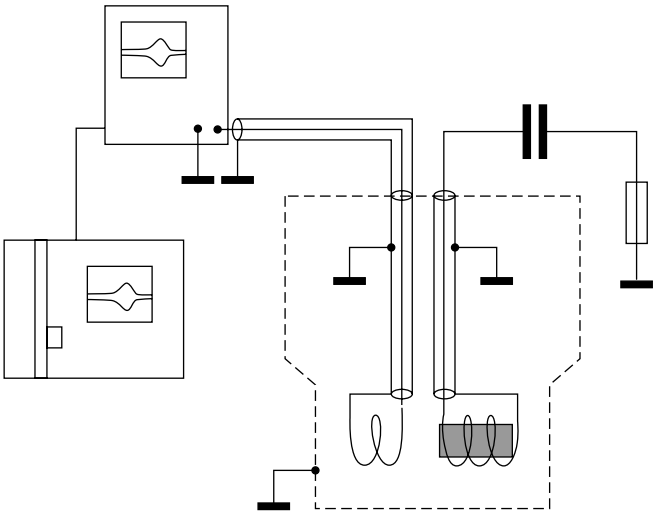

Figure 1 Typical experimental setup for detecting spin superradiance. Of the two coils below, the left one plays the role of antenna, and the right one is part of the resonant electric circuit. The sample studied is shown as a dark bar inside the resonant coil. The upper left block is an oscilloscope, and the lower one is a plotter

The resonant electric circuit, with the quality factor $Q = 33$, had a resonance frequency of 1.6×10^8 Hz.

In different experiments, slightly different setups were employed. A typical arrangement[11,12] is shown in Figure 1. The characteristic superradiant pulse[11,12] is presented in Figure 2.

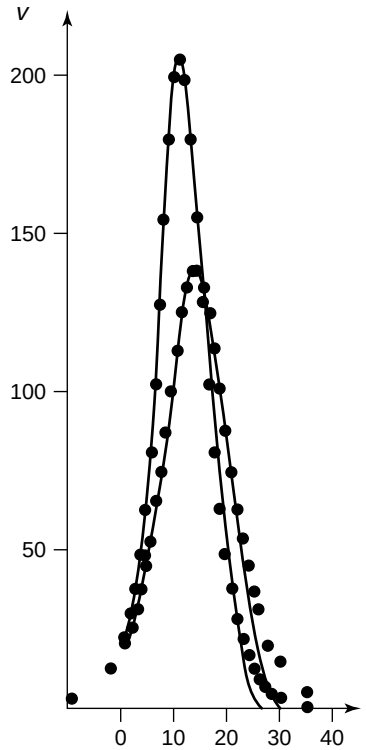

Figure 2 Voltage signal corresponding to a superradiant pulse as a function of time, measured in units of 10^{-7} s, for two initial spin polarizations, $s_0 = 0.52$ (lower curve) and $s_0 = 0.57$ (upper curve)

A series of numerical simulations were accomplished,[15,16] which could be considered as computer experiments modeling the behavior of spins in conditions typical of experimental observations. These computer simulations confirmed the existence of both pure as well as triggered spin superradiance, and are in good agreement with experiments.

3 BASIC MODEL

Since the phenomenon of spin superradiance exists in nature, it is necessary to develop its theoretical description. The simplest idea would be to invoke the Bloch equations for this purpose. However, these are designed so that they treat the magnetization of a sample as a macroscopic vector, which presupposes the existing coherence from the very beginning. If at the initial time, coherence of spins is absent, the Bloch equations would never display it. Therefore, these equations can describe only triggered spin superradiance, when coherence is thrust upon spins at the initial time by assuming the presence of nonzero transverse magnetization. But pure spin superradiance, being a self-organized coherent process, cannot in principle be treated by the Bloch equations. A discussion of this problem as well as the related references can be found in a review.[17] In order to be able to describe all possible regimes of spin dynamics, it is necessary to resort to microscopic models. A theory of *nuclear spin superradiance*, based on realistic Hamiltonians typical of nuclear spin assemblies in condensed matter[1,2,18] has been previously developed.[19–24]

A system of N nuclear spins, enumerated by an index $i = 1, 2, \ldots, N$, is characterized by their spin operators $\hat{\mathbf{I}}_i$. The Hamiltonian of nuclear spins in a solid can be written as a sum

$$\hat{H}_{\rm nuc} = \sum_i \hat{H}_i + \frac{1}{2} \sum_{i \neq j} \hat{H}_{ij} \tag{1}$$

of the Zeeman term and of a part due to many-body spin interactions. The Zeeman term contains

$$\hat{H}_i = -\hbar \gamma_n \mathbf{B} \cdot \hat{\mathbf{I}}_i \tag{2}$$

where $\mathbf{B}$ is the total magnetic field and γ_n is the nuclear magnetogyric ratio. The total magnetic field

$$\mathbf{B} = B_0 \mathbf{e}_z + (B_1 + H)\mathbf{e}_x \tag{3}$$

consists of a static magnetic field B_0 along the z-axis and of a transverse field being a sum of an external field B_1 and of a field H produced by an electric coil into which the sample is immersed. The corresponding orientation of the coordinate axes with respect to the sample is explained in Figure 3. The static magnetic field is directed so that

$$\gamma_n B_0 < 0 \tag{4}$$

In general, the nuclear magnetogyric ratio can be positive as well as negative. If it is positive, then inequality (4) states that the static field is negative. In this case, the initial polarization

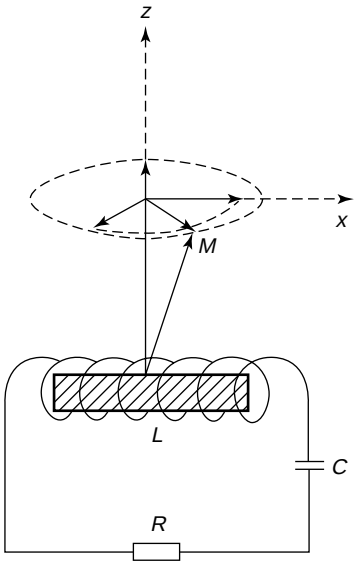

Figure 3 Orientation of the coordinate axes with respect to the sample that is inserted into the coil of a resonant electric circuit

of the sample nuclei is called inverted if it is positive, i.e., directed against the static magnetic field.

The basic force acting between nuclear spins is due to the dipolar interactions which may be described by the Hamiltonian

$$\widehat{H}_{ij} = \sum_{\alpha\beta} D_{ij}^{\alpha\beta} \hat{I}_i^{\alpha} \hat{I}_j^{\beta} \tag{5}$$

where the upper indices α and β denote the coordinate components $\alpha, \beta = x, y, z$, while

$$D_{ij}^{\alpha\beta} = \frac{\hbar^2 \gamma_n^2}{r_{ij}^3} (\delta_{\alpha\beta} - 3 n_{ij}^{\alpha} n_{ij}^{\beta}) \tag{6}$$

is the dipolar tensor, in which

$$r_{ij} \equiv |\mathbf{r}_{ij}|, \qquad n_{ij} \equiv \frac{\mathbf{r}_{ij}}{r_{ij}}, \qquad \mathbf{r}_{ij} \equiv \mathbf{r}_i - \mathbf{r}_j$$

The dipolar tensor satisfies the equalities

$$\sum_{\alpha} D_{ij}^{\alpha\alpha} = 0, \qquad \sum_{j(\neq i)} D_{ij}^{\alpha\beta} = 0 \tag{7}$$

of which the first is exact and the second is asymptotically valid for a macroscopic sample.

For practical purpose, it is convenient to work with the ladder spin operators $\hat{I}_j^{\pm} \equiv \hat{I}_j^x \pm \hat{I}_j^y$, called the raising and lowering spin operators, respectively. Then, with the help of the notation

$$a_{ij} \equiv D_{ij}^{zz}, \qquad b_{ij} \equiv \frac{1}{4}(D_{ij}^{xx} - 2i\, D_{ij}^{xy} - D_{ij}^{yy})$$
$$c_{ij} \equiv \frac{1}{2}(D_{ij}^{xz} - i\, D_{ij}^{yz}) \tag{8}$$

the Zeeman term (2), for the total field (3), becomes

$$\widehat{H}_i = -\hbar\gamma_n B_0 \hat{I}_i^z - \frac{1}{2}\hbar\gamma_n (B_1 + H)(\hat{I}_i^+ + \hat{I}_i^-) \tag{9}$$

and the dipolar interaction (5) takes the form

$$\widehat{H}_{ij} = a_{ij}\left(\hat{I}_i^z \hat{I}_j^z - \frac{1}{2}\hat{I}_i^+ \hat{I}_j^-\right) + b_{ij}\hat{I}_i^+ \hat{I}_j^+ + b_{ij}^* \hat{I}_i^- \hat{I}_j^- + 2c_{ij}\hat{I}_i^+ \hat{I}_j^z + 2c_{ij}^* \hat{I}_i^- \hat{I}_j^z \tag{10}$$

Equations (9) and (10) will be used below to derive the evolution equations.

The electric circuit, coupled with the spin sample, is characterized by resistance R, inductance L, and capacity C. The coil, surrounding the sample, has n turns of cross-section area A_c over a length l. The electric current j of the circuit is given by the Kirchhoff equation

$$L\frac{dj}{dt} + Rj + \frac{1}{C}\int_0^t j(t')dt' = \tilde{E} - \frac{d\Phi}{dt} \tag{11}$$

in which $\tilde{E}$ is an electromotive force, if any, and Φ is a magnetic flux

$$\Phi = \frac{4\pi}{c} n A_c \eta M_x \tag{12}$$

formed by the x-component of the magnetization density

$$M_x = \frac{\hbar\gamma_n}{V}\sum_i \langle \hat{I}_i^x \rangle \tag{13}$$

Here the brackets $\langle \ldots \rangle$ imply statistical averaging. The filling factor η is approximately equal to $\eta \approx V/V_c$, where V is the sample volume, while $V_c \equiv A_c l$ is the coil volume.

The electric current in the circuit is formed by moving transverse spins. In its turn, the current, circulating over the coil, produces a feedback magnetic field

$$H = 4\pi \frac{nj}{cl} \tag{14}$$

Hence, the Kirchhoff equation (11) can be rewritten for the feedback field (14). To this end, it is useful to employ the notation for the natural circuit frequency

$$\omega \equiv \frac{1}{\sqrt{LC}} \qquad \left(L \equiv 4\pi \frac{n^2 A_c}{c^2 l}\right) \tag{15}$$

and for the circuit ringing time

$$\tau \equiv \frac{1}{\gamma} \qquad \left(\gamma \equiv \frac{R}{2L}\right) \tag{16}$$

The related circuit damping

$$\gamma = \frac{\omega}{2Q} \qquad \left(Q \equiv \frac{\omega L}{R}\right) \tag{17}$$

is connected with the quality factor Q. Employing this notation, together with that for the reduced electromotive force

$$h \equiv \frac{c\tilde{E}}{nA_c\gamma} \tag{18}$$

from the Kirchhoff equation (11), one obtains the result

$$\frac{dH}{dt} + 2\gamma H + \omega^2 \int_0^t H(t')dt' = \gamma h - 4\pi\eta \frac{dM_x}{dt} \tag{19}$$

for the feedback magnetic field (14).

The feedback equation (19) can be presented in a form that is extremely useful to exploit for analysing the evolution equations.[20] By involving the method of Laplace transforms and introducing the transfer function

$$G(t) = \left(\cos\tilde{\omega}t - \frac{\gamma}{\tilde{\omega}}\sin\tilde{\omega}t\right) e^{-\gamma t}$$

with $\tilde{\omega} \equiv \sqrt{\omega^2 - \gamma^2}$, equation (19) can be presented as the integral

$$H = \int_0^t G(t-t')\left[\gamma h(t') - 4\pi\eta\dot{M}_x(t')\right] dt' \tag{20}$$

where the dot over $\dot{M}_x$ means, as usual, time derivative.

4 EVOLUTION EQUATIONS

The equations of motion for the nuclear spin operators are given by the corresponding Heisenberg equations. From these we can derive the equations for the following statistical averages. The function

$$u \equiv \frac{1}{I}\langle \hat{I}_i^- \rangle \tag{21}$$

defines the rotation of transverse spin components. The degree of coherence in this rotation is described by

$$w \equiv \frac{1}{I^2}\langle \hat{I}_i^+ \rangle \langle \hat{I}_i^- \rangle = |u|^2 \tag{22}$$

The average

$$s \equiv \frac{1}{I}\langle \hat{I}_i^z \rangle \tag{23}$$

gives the longitudinal spin polarization, which is analogous to the population difference in optic systems. Keeping in mind that wavelengths at radio frequencies are much larger than mean distances between spins and usually even essentially larger than linear sizes of a sample, one may employ the uniform approximation, assuming that the functions (21)–(23) do not depend on spatial variables.

In order to obtain the evolution equations for the quantities (21)–(23), the Heisenberg equations are averaged for the corresponding spin operators. In doing so, one encounters the known problem of the resulting equations being not closed but containing, in addition to u, w, and s, binary averages of spin operators. The standard way of closing these equations would be to employ mean-field decoupling, when the binary average $\langle \hat{I}_i^\alpha \hat{I}_j^\beta \rangle$, with $i \neq j$, is factorized onto the product $\langle \hat{I}_i^\alpha \rangle \langle \hat{I}_j^\beta \rangle$. Such a decoupling, however, ends with Bloch-type equations having the same deficiency of never exhibiting coherence if at the initial time $w(0) = 0$. This is because the mean-field decoupling completely neglects spin correlations leading to local spin fluctuations. Taking account of such fluctuations is a necessary prerequisite for describing pure spin superradiance.

Another possibility for closing the hierarchy of spin evolution equations could be by writing additional equations for the binary correlators $\langle \hat{I}_i^\alpha \hat{I}_j^\beta \rangle$ and by decoupling only the higher-order correlators, retaining the binary ones untouched. Unfortunately, this drastically increases the number of equations and so complicates the problem that it becomes practically untreatable even for equilibrium magnets;[25] the more so for nonequilibrium systems presented by nonlinear differential equations.

To render the set of spin evolution equations closed in order to keep the problem treatable and, at the same time, to take into account local spin fluctuations, one can apply the *method of stochastic decoupling*.[19–21,24] The main idea of the latter is to separate in the evolution equations the terms describing long-range correlations from the terms related to short-range fluctuations. Employing the method of restricted traces, one may define two types of statistical averages, one incorporating only long-range correlations and another involving short-range fields that are treated as stochastic variables. In what follows, the first type of averaging is denoted by the single angle brackets $\langle \ldots \rangle$, while the second type, by the double brackets $\langle\langle \ldots \rangle\rangle$. Then, the binary spin correlators are presented as

$$\langle \hat{I}_i^\alpha \hat{I}_j^\beta \rangle = \langle \hat{I}_i^\alpha \rangle \langle \hat{I}_j^\beta \rangle \qquad (i \neq j) \tag{24}$$

where the averaging does not touch stochastic variables which enter the evolution equations in the following linear combinations:

$$\xi_0 \equiv \frac{1}{\hbar}\sum_{j(\neq i)} (a_{ij}\hat{I}_j^z + c_{ij}\hat{I}_j^+ + c_{ij}^*\hat{I}_j^-)$$

$$\xi \equiv -\frac{i}{\hbar}\sum_{j(\neq i)} \left(\frac{1}{2}a_{ij}\hat{I}_j^- - 2b_{ij}\hat{I}_j^+ - 2c_{ij}\hat{I}_j^z\right) \tag{25}$$

with the coefficients defined in equation (8). Stochastic variables (25) describe local fluctuating fields which act on neighbor spins forcing them to move. The existence of such fluctuating fields should lead to the appearance of dipolar dynamic broadening.[26] To completely define the problem, it is necessary to prescribe the rules for calculating stochastic averages over the random variables (25). This can be done by considering the stochastic variables (25) as a white-noise process characterized by the stochastic averages

$$\langle\langle \xi_0(t) \rangle\rangle = \langle\langle \xi(t) \rangle\rangle = 0, \quad \langle\langle \xi_0(t)\xi_0(t') \rangle\rangle = 2\Gamma_3\delta(t-t')$$

$$\langle\langle \xi_0(t)\xi(t') \rangle\rangle = \langle\langle \xi(t)\xi(t') \rangle\rangle = 0, \quad \langle\langle \xi^*(t)\xi(t') \rangle\rangle = 2\Gamma_3\delta(t-t') \tag{26}$$

where Γ_3 is the width of *dynamic broadening* due to local dipole interactions of nuclei. This is a sort of inhomogeneous broadening existing in addition to the homogeneous broadening yielding the longitudinal, $\Gamma_1 \equiv T_1^{-1}$, and transverse, $\Gamma_2 \equiv T_2^{-1}$, relaxation widths.

To obtain the resulting evolution equations in a compact form, it is convenient to introduce the notation

$$f \equiv -i\gamma_n (B_1 + H) + \xi \tag{27}$$

for an effective force acting on a spin. The transverse external magnetic field B_1 may, in general, contain a static as well as an alternating term, as

$$B_1 = h_1 + h_2 \cos \omega t \tag{28}$$

where, for simplicity, the frequency of the alternating field is assumed to be in resonance with the frequency of the electric circuit. Recall that the magnetic field H, produced by the coil, is caused by a feedback field and, possibly, by a field of an electromotive force, which may be presented as

$$h(t) = h_0 \cos \omega t \tag{29}$$

Finally, the NMR frequency is denoted by

$$\omega_0 \equiv |\gamma_n B_0| \tag{30}$$

Then the evolution equations for the functions (21) to (23) acquire the form

$$\frac{du}{dt} = -i(\omega_0 + \xi_0 - i\Gamma_2)u + fs \tag{31}$$

$$\frac{dw}{dt} = -2\Gamma_2 w + (u^* f + f^* u)s \tag{32}$$

$$\frac{ds}{dt} = -\frac{1}{2}(u^* f + f^* u) - \Gamma_1(s - \zeta) \tag{33}$$

where ζ is an average stationary value for a z-component of a spin. Generally, $-1 \leq \zeta \leq 1$. When there is no external pumping, then $\zeta = -1$. In the presence of pumping, e.g., by means of dynamic nuclear polarization, the pumping parameter $\zeta > -1$ and can reach the value $\zeta = 1$. Equations (31)–(33) compose a nonlinear system of stochastic differential equations describing all dynamic properties of nuclear spins.

The system of evolution equations (31)–(33) still looks rather complicated. Fortunately, there are several small parameters that allow one to simplify the situation by employing the *scale separation approach*[19–21,27] which is a generalization of the Krylov–Bogolubov averaging technique[28] to stochastic and partial differential equations. The existing small parameters are connected with the relatively small values of the relaxation widths Γ_1 and Γ_2 as compared to the NMR frequency (30), so that

$$\frac{\Gamma_1}{\omega_0} \ll 1, \qquad \frac{\Gamma_2}{\omega_0} \ll 1 \tag{34}$$

Clearly, the quantity

$$\Gamma_0 \equiv \pi \eta \rho_n \gamma_n^2 \hbar I \qquad \left(\rho_n \equiv \frac{N}{V}\right) \tag{35}$$

is also small with respect to ω_0, as well as the dynamic broadening width Γ_3, that is

$$\frac{\Gamma_0}{\omega_0} \ll 1, \qquad \frac{\Gamma_3}{\omega_0} \ll 1 \tag{36}$$

All amplitudes of the applied transverse fields are also assumed to be small, which implies that the values

$$\nu_0 \equiv \gamma_n h_0, \qquad \nu_1 \equiv \gamma_n h_1, \qquad \nu_2 \equiv \gamma_n h_2 \tag{37}$$

satisfy the inequalities

$$\frac{|\nu_0|}{\omega_0} \ll 1, \qquad \frac{|\nu_1|}{\omega_0} \ll 1, \qquad \frac{|\nu_2|}{\omega_0} \ll 1 \tag{38}$$

The electric circuit, coupled to the spin system, is supposed to be of good quality, having a high quality factor, which means that the ringing width is small compared to the natural circuit frequency,

$$\frac{\gamma}{\omega} \ll 1 \qquad (Q \gg 1) \tag{39}$$

The last parameter, though not the least, is that the electric circuit has to be tuned to the NMR frequency (30), hence the resonance condition for the detuning Δ must be valid:

$$\frac{|\Delta|}{\omega_0} \ll 1 \qquad (\Delta \equiv \omega - \omega_0) \tag{40}$$

In this way, the circuit plays the role of a resonator.

The existence of the small parameters makes it possible, by analyzing the right-hand sides of the evolution equations (31)–(33), to conclude that the function u has to be classified as fast, as compared to the slow functions w and s. Conversely, the functions w and s are quasi-invariants with respect to u. In addition, one may derive an explicit expression for the resonator magnetic field H by iterating its integral representation with the solution of equation (31), where only the main term in the right-hand side is retained. This iteration gives

$$\gamma_n H = i\alpha(u - u^*) + \beta \cos \omega t \tag{41}$$

where the first term, with the coupling function

$$\alpha \equiv \frac{\Gamma_0 \omega_0}{\gamma}(1 - e^{-\gamma t}) \tag{42}$$

is caused by the feedback coupling of spins with the resonator, and the second term, with the coupling

$$\beta \equiv \frac{\nu_0}{2}(1 - e^{-\gamma t}) \tag{43}$$

is due to an electromotive force. The time dependence of the coupling functions (42) and (43) describes the retardation in the resonator action on spins. Expressions (42) and (43) are written here for the case of small detuning, such that $|\Delta| \ll \gamma$. The latter assumption is not critical but is employed solely for the simplification of formulas. Relation (41) holds true for any detuning satisfying the resonance condition (40).

Substituting relation (41) in equations (31)–(33) and using the notation

$$f_1 \equiv -i\nu_1 - i(\nu_2 + \beta)\cos \omega t + \xi \tag{44}$$

one comes to the evolution equations

$$\frac{du}{dt} = -[i(\omega_0 + \xi_0) + \Gamma_2 - \alpha s]u + f_1 s - \alpha s u^* \tag{45}$$

$$\frac{dw}{dt} = -2(\Gamma_2 - \alpha s)w + (u^* f_1 + f_1^* u)s - \alpha s[(u^*)^2 + u^2] \tag{46}$$

$$\frac{ds}{dt} = -\alpha w - \frac{1}{2}(u^* f_1 + f_1^* u) - \Gamma_1(s - \zeta) + \frac{1}{2}\alpha[(u^*)^2 + u^2] \tag{47}$$

Following the scale separation approach further, equation (45) for the fast function u can be solved, with w and s being quasi-invariants. The solution obtained is substituted in the right-hand sides of equations (46) and (47), which are averaged over the period $2\pi/\omega_0$ of fast oscillations as well as over stochastic variables defined in equation (25). Then, introducing the effective attenuation width

$$\Gamma_{\rm eff} \equiv \Gamma_3 - \alpha \frac{\nu_1^2}{\omega_0^2} s - \frac{\nu_1(\nu_2 + \beta)\Gamma}{2\omega_0^2} e^{-\Gamma t} + \frac{(\nu_2 + \beta)^2}{4\Gamma}\left(1 - e^{-\Gamma t}\right) \tag{48}$$

where

$$\Gamma \equiv \Gamma_2 - \alpha s + \Gamma_3$$

reduces equations (46) and (47) for slow functions to the evolution equations

$$\frac{dw}{dt} = -2(\Gamma_2 - \alpha s)w + 2\Gamma_{\rm eff} s^2 \tag{49}$$

$$\frac{ds}{dt} = -\alpha w - \Gamma_{\rm eff} s - \Gamma_1(s - \zeta) \tag{50}$$

In the form of the widths (48), it is again assumed that the detuning is small, such that $|\Delta| \ll |\gamma| \ll \omega_0$, which is not critical but just simplifies cumbersome expressions.

The evolution equations (49) and (50) are the main equations describing the dynamics of strongly nonequilibrium nuclear spins. The analysis of these equations makes it possible to study various regimes of spin motion.

5 NYQUIST NOISE

The main problem is: What is the origin of pure spin superradiance? In other words, what initiates the motion of spins when no coherence is thrust upon the system at $t = 0$ and there are no external fields pushing spins in the transverse direction?

Keeping in mind the analogy with atomic assemblies, one may remember that in an inverted system of atoms the relaxation process begins with atomic spontaneous radiation, which is a quantum process. After the seed radiation field appears in the system, atomic correlations start arising through the interatomic photon exchange. As soon as these correlations become sufficiently intensive, coherence develops. Then, the quantum stage of spontaneous emission changes for the coherent stage, when atoms are correlated and emit coherently, which results in superradiance.

The collectivization of spins can be produced by means of the resonator feedback field. But for this field to arise, the spins first have to start their motion. Spontaneous emission for spins is absent. Then, what could initiate the motion of spins? What mechanism would be the origin of pure spin superradiance?

There existed a widespread delusion that the thermal Nyquist noise of the resonant electric circuit could be the initiating cause of spin rotation. At this point, it is necessary to stress that the role of the thermal Nyquist noise in producing a fluctuating torque on the magnetization was discussed in detail by Bloembergen and Pound in their classic paper.[6] They showed that the average thermal damping is inversely proportional to the sample volume; thus this damping is noticeable only for a single spin. For a macroscopic sample of many spins $N \gg 1$ the coil thermal damping should be negligibly small. This analysis seems to have been completely forgotten by later workers who have proclaimed the leading role of the coil thermal noise in initiating spin rotation.

To explicitly illustrate the role of the thermal Nyquist noise, one has to consider the effective attenuation width (48), including the influence of the electromotive force related to the resonance mode of the thermal noise.[19–21] When there are no external transverse magnetic fields, that is when $\nu_1 = \nu_2 = 0$, the effective width (48) reads

$$\Gamma_{\rm eff} = \Gamma_3 + \frac{\nu_0^2}{16\Gamma}\left(1 - e^{-\Gamma t}\right)\left(1 - e^{-\gamma t}\right)^2 \tag{51}$$

The electromotive force, corresponding to the resonator thermal noise, can be written as

$$\tilde{E} = \tilde{E}_0 \cos \omega t \tag{52}$$

The related magnetic field, defined in equations (18) and (29), has the amplitude

$$h_0 = \frac{c\tilde{E}_0}{nA_c\gamma} \tag{53}$$

From here, it follows that

$$h_0^2 = 8\pi \frac{\eta\rho_n \tilde{E}_0^2}{\gamma RN} \tag{54}$$

With the definition (37), one gets the quantity

$$\nu_0^2 = \frac{8\Gamma_0 \tilde{E}_0^2}{\hbar\gamma I RN} \tag{55}$$

which characterizes in equation (51) the average thermal damping due to the Nyquist noise.

First, equation (51) shows that the thermal damping at $t = 0$ is exactly zero because of the temporal factors. The latter become essential only for $t > T_2, \tau$. Therefore, the influence of the thermal noise at short times should be suppressed by these temporal factors.

Moreover, the quantity (55) is inversely proportional to the number of spins. That is, the thermal damping is inversely proportional to N, and thus it should be negligibly small for a macroscopic sample with $N \gg 1$. This is in complete agreement with the conclusion of Bloembergen and Pound.[6]

To be more precise, it is possible to explicitly calculate the quantity (55) by substituting the square amplitude of the electromotive force due to the thermal noise,[7] which is

$$\tilde{E}_0^2 = \frac{\hbar\omega}{2\pi}\gamma R \coth\frac{\hbar\omega}{2k_B T} \tag{56}$$

At radio frequencies, the inequality

$$\frac{\omega}{\omega_T} \ll 1 \qquad \left(\omega_T \equiv \frac{k_B T}{\hbar}\right) \tag{57}$$

is valid. As a result, equation (56) simplifies to

$$\tilde{E}_0^2 \simeq \frac{\hbar}{\pi}\gamma R\omega_T \tag{58}$$

Thence, equation (55) becomes

$$\nu_0^2 = \frac{8\Gamma_0\omega_T}{\pi I N} \tag{59}$$

Expression (51) shows that the thermal damping has to be compared to the dynamic broadening width Γ_3, which can be of order of Γ_2. When the inequality

$$\frac{\nu_0^2}{\Gamma_2^2} \ll 1 \tag{60}$$

holds true, the thermal damping can be safely neglected, playing no role in spin relaxation, as compared to the dynamic broadening.

To estimate the factor (59) and, respectively, to check the inequality (60), one can accept the values typical of experiments on proton spin superradiance.[11–13] Then, for the filling factor $\eta = 0.6$, proton density $\rho_n = 4 \times 10^{22}\,\mathrm{cm}^{-3}$, and the proton magnetogyric ratio $\gamma_n = 2.675 \times 10^8\,\mathrm{s}^{-1}\,\mathrm{T}^{-1}$, the linewidth (35) is $\Gamma_0 = 2.846 \times 10^4\,\mathrm{Hz}$. At temperature $T = 0.1\,\mathrm{K}$, the thermal frequency is $\omega_T = 1.309 \times 10^{11}\,\mathrm{Hz}$. Under the static magnetic field $B_0 = 1\,\mathrm{T}$, the proton NMR frequency is $\omega_0 = 2.675 \times 10^8\,\mathrm{Hz}$. The ratio $\omega/\omega_T \sim 10^{-3}$ is small. With the transverse relaxation width $\Gamma_2 = 1.176 \times 10^5\,\mathrm{Hz}$, one obtains

$$\frac{\nu_0^2}{\Gamma_2^2} = \frac{1.37}{N} \times 10^6$$

For a sample volume of about $1\,\mathrm{cm}^3$ and $N \sim 10^{23}$, one has $\nu_0^2/\Gamma_2^2 \sim 10^{-17}$. This ratio is so small that, clearly, the thermal Nyquist noise is not able to play any role in spin relaxation in a macroscopic sample. It is only for the number of spins $N \leq 10^6$, when the thermal noise becomes noticeable. When considering macroscopic samples, with $N \gg 10^6$, the resonator thermal noise can be neglected.

6 INCOHERENT STAGE

At the initial stage, the main role in starting spin relaxation is played by the dynamic broadening due to local spin fluctuations. Omitting in the effective width, (48), the terms of second order with respect to small parameters and neglecting the resonator thermal noise by setting $\beta \to 0$, one has

$$\Gamma_{\mathrm{eff}} = \Gamma_3 + \frac{\nu_2^2}{4\Gamma}(1 - e^{-\Gamma t}) \tag{61}$$

This equation shows that at the very beginning of the process, when $t \to 0$, then $\Gamma_{\mathrm{eff}} \to \Gamma_3$. That is, the dynamic broadening width Γ_3 makes the major contribution to the effective relaxation width, equation (61).

For asymptotically small times $t \to 0$, the coupling function (42) is close to zero, $\alpha \to 0$. Then the evolution equations (49) and (50) can be reduced to the form

$$\frac{dw}{dt} = -2\Gamma_2 w + 2\Gamma_3 s^2, \qquad \frac{ds}{dt} = -\Gamma_1^*(s - \zeta^*) \tag{62}$$

in which

$$\Gamma_1^* \equiv \Gamma_1 + \Gamma_3, \qquad \zeta^* \equiv \frac{\Gamma_1}{\Gamma_1^*}\zeta \tag{63}$$

The solutions to equations (62) are

$$w = w_0 e^{-2\Gamma_2 t} + 2\Gamma_3 \int_0^t s^2(t') e^{-2\Gamma_2(t-t')}\,dt',$$
$$s = \zeta^* + (s_0 - \zeta^*)e^{-\Gamma_1^* t} \tag{64}$$

which demonstrates the character of spin motion at short times $t \to 0$. At this stage, the motion of spins is still completely incoherent, since, because of retardation, the coupling with the resonator has not yet been switched on. Assuming that $\Gamma_1 \ll \Gamma_3$, hence $\zeta^* \ll 1$, one may simplify the solution (64) as

$$w \simeq w_0 e^{-2\Gamma_2 t} + \frac{\Gamma_3 s_0^2}{\Gamma_2 - \Gamma_3}\left(e^{-2\Gamma_3 t} - e^{-2\Gamma_2 t}\right), \qquad s \simeq s_0 e^{-\Gamma_3 t}$$

The initial *incoherent stage* of spin relaxation can also be called the *quantum stage*, as long as the relaxation is caused by quantum effects of spin-spin interactions and there are yet no collective effects that could lead to the development of coherence.

The duration of the incoherent quantum stage lasts until the *quantum time* t_q, when the coupling function (42) reaches the value Γ_2, so that

$$\alpha(t_q) = \Gamma_2 \tag{65}$$

and when taking account of collective effects, due to the coupling with the resonator, becomes important. It is also easy to notice that the difference $\Gamma_2 - \alpha s$ in equation (49) may change its sign at the quantum time t_q, which means that the generation of coherent radiation would begin. Combining equations (42) and (65) for the quantum time gives

$$t_q = \tau \ln \frac{g}{g-1} \tag{66}$$

where the notation of the effective coupling parameter

$$g \equiv \frac{\Gamma_0\omega_0}{\Gamma_2\gamma} = 2Q\frac{\Gamma_0}{\Gamma_2} \tag{67}$$

is introduced. The quantum time (66) is positive only for $g > 1$. If $g = 1$, then $t_q \to \infty$. This indicates that the quantum stage is finite and may change to a collective stage only if the coupling parameter (67) is $g > 1$. If the spin-resonator coupling is weak, and $g \leq 1$, only the quantum stage exists, and the collective stage never comes into being. For sufficiently strong coupling, equation (66) gives

$$t_q \simeq \frac{\tau}{g} \qquad (g \gg 1) \tag{68}$$

The values of solutions (64) at the end of the quantum stage, i.e., at t_q, can be estimated assuming that $t_q \ll T_2$ and $t_q \ll T_3 \equiv \Gamma_3^{-1}$. Then equation (64) yields

$$w(t_q) \simeq w_0 + 2\delta_3 s^2, \qquad s(t_q) \simeq s_0 \tag{69}$$

where

$$\delta_3 \equiv \frac{\Gamma_3}{g\gamma} = \frac{\Gamma_2\Gamma_3}{\Gamma_0\omega_0} \tag{70}$$

This is a small parameter, since $\Gamma_0 \sim \Gamma_3$ while $\Gamma_2 \ll \omega$. But, no matter how small δ_3 is, it can be important if $w_0 = 0$.

7 TRANSIENT SUPERRADIANCE

After the incoherent quantum stage, the coupling function (42) increases, switching on collective effects resulting in the appearance of spin superradiance.[19–21] An accurate description of this process can be made by solving the evolution equations (49) and (50) numerically. It is also possible to present an explicit analytical description of how superradiance develops for the transient stage, when the time is larger than the quantum time t_q but yet much smaller than the spin-lattice relaxation time T_1. Then, the term with Γ_1 in equation (50) can be omitted. If there are no strong external transverse fields, then one should set $\nu_1 \to 0$ and $\nu_2 \to 0$. Assuming that the coupling function (42) has reached its maximal value, one gets $\alpha \approx g\Gamma_2$. The dynamic broadening width Γ_3 is not larger than Γ_2. Hence, for a sufficiently large coupling parameter g, one may neglect Γ_3 as compared to $g\Gamma_2 \gg \Gamma_3$. Under these conditions, equations (49) and (50) read

$$\frac{dw}{dt} = -2\Gamma_2(1 - gs)w, \qquad \frac{ds}{dt} = -g\Gamma_2 w \tag{71}$$

Initial conditions for equation (71) should be taken at $t = t_q$.

Equations (71) can be solved exactly[19–21] yielding

$$w = \left(\frac{\Gamma_p}{g\Gamma_2}\right)^2 \operatorname{sech}^2\left(\frac{t - t_0}{\tau_p}\right),$$
$$s = -\frac{\Gamma_p}{g\Gamma_2}\tanh\left(\frac{t - t_0}{\tau_p}\right) + \frac{1}{g} \tag{72}$$

Here Γ_p is a pulse width, $\tau_p = \Gamma_p^{-1}$ is a pulse time, and t_0 is a delay time. These parameters are the integration constants that are to be defined from initial conditions $w(t_q)$ and $s(t_q)$ taken at the boundary of the transient stage, that is at the quantum time t_q. Employing equations (69) results in

$$\Gamma_p^2 = \Gamma_g^2 + (g\Gamma_2)^2(w_0 + 2\delta_3 s_0^2), \quad \Gamma_g \equiv \Gamma_2(1 - gs_0), \quad \Gamma_p\tau_p = 1 \tag{73}$$

while the delay time is

$$t_0 = t_q + \frac{\tau_p}{2}\ln\left|\frac{\Gamma_p - \Gamma_g}{\Gamma_p + \Gamma_g}\right| \tag{74}$$

Solutions (72) demonstrate that the coherence intensity $w(t)$ has the shape of a burst of width τ_p and peaked at the delay time t_0.

If the spin-resonator coupling g is sufficiently weak or the initial spin polarization s_0 is sufficiently small, so that $gs_0 \leq 1$, then the value of the delay time (74) shifts to the quantum region, becoming $t_0 \leq t_q$. This means that the radiation intensity would not have the shape of a coherent burst, but is rather a decreasing function of time, typical of nuclear induction. In the case of an external pulse thrusting an essential initial coherence onto the spins, such that $g^2 w_0 > 1$, the radiation time τ_p is small, $\tau_p < T_2$, which is characteristic of collective induction. When $gs_0 > 1$ and $g^2 w_0 > 1$, the signal of collective induction is peaked at a finite delay time $t_0 > 0$. As is explained in the introduction, collective induction, with coherence induced by an initial external source, is in principle different from superradiance that is a process of spontaneously arising coherence.

For solutions (72) to describe a superradiant burst, the requirements discussed in the introduction must be satisfied. In order that the initial coherence, given by w_0, does not essentially influence the pulse width Γ_p,

$$g^2 w_0 < 1 \tag{75}$$

This guarantees a basically spontaneous character of the process. Then, the pulse time τ_p is to be sufficiently short and the delay time finite,

$$\tau_p < T_2, \qquad t_q < t_0 < \infty \tag{76}$$

The second of these inequalities yields

$$gs_0 > 1, \qquad w_0 + 2\delta_3 s_0^2 > 0 \tag{77}$$

Combining all conditions (75)–(77), one sees that there exist two types of transient spin superradiance, whose classification, taking account of the smallness of the parameter $\delta_3 \ll 1$, can be accomplished as follows:

1. *Triggered superradiance*, when

$$gs_0 > 1 + \sqrt{1 - g^2 w_0}, \qquad w_0 \neq 0$$

Here, a weak external pulse imposes an initial coherence on spins, but, being rather weak, this pulse plays just the role of a trigger, while the following development of coherence is mainly governed by internal properties.

2. *Pure superradiance*, when

$$gs_0 > 2, \qquad w_0 = 0$$

This is a purely self-organized process, with no coherence prescribed from external sources.

In the case of pure spin superradiance, the characteristic quantities (73) and (74), having regard to $\delta_3 \ll 1$, become

$$\Gamma_p \simeq (gs_0 - 1)\Gamma_2 \left[1 + \left(\frac{gs_0}{gs_0 - 1} \right)^2 \delta_3 \right]$$

$$\tau_p \simeq \frac{T_2}{gs_0 - 1} \left[1 - \left(\frac{gs_0}{gs_0 - 1} \right)^2 \delta_3 \right]$$

$$t_0 \simeq \frac{\tau}{g} + \frac{T_2}{2(gs_0 - 1)} \ln \left| \frac{2}{\delta_3} \left(1 - \frac{1}{gs_0} \right)^2 \right| \qquad (78)$$

Although the parameter δ_3 is small, it cannot be neglected, since its value is crucial for defining the delay time t_0. If $\delta_3 \to 0$, then $t_0 \to \infty$. The parameter δ_3, according to the notation (70), is proportional to the dynamic broadening width Γ_3 due to local spin fluctuations. As far as the latter fluctuations are the main cause of starting spin relaxation, it is not surprising that the related broadening defines the delay time.

From equation (72) it follows that the maximum of the coherent burst occurs at $t = t_0$, when

$$w(t_0) = \left(s_0 - \frac{1}{g} \right)^2, \qquad s(t_0) = \frac{1}{g} \qquad (79)$$

For longer times $t \gg t_0$, the superradiant signal exponentially diminishes, and the spin polarization returns to an almost inverted value,

$$w \simeq 4w(t_0)e^{-2\Gamma_p t}, \qquad s \simeq -s_0 + \frac{2}{g} \qquad (80)$$

The larger the spin-resonator coupling g, the more complete is the spin inversion. The effect of superradiant spin inversion can be employed for the ultrafast repolarization of nuclear targets used in scattering experiments.[14,29]

The shape of a superradiant pulse, described by $w(t)$ in equation (72), is in very good agreement with experiments.[11–13] Thus, the measured signal, presented in Figure 2, ideally fits the calculated function $w(t)$, as is discussed in the papers.[11,12] A concrete relation between the measured intensity of the signal and $w(t)$ is explained in Section 10.

It is worth emphasizing that the radiation intensity and radiation time of the studied pulse have the properties typical of a superradiant burst. To illustrate this, it is sufficient to recall that the initial inverted spin polarization $s_0 = N_+/N$ is the ratio of the number of inverted spins to their total number in the sample. Inverted spins play the role of radiators, whose number is N_+. For large spin-resonator coupling $g \gg 1$, one has $w(t_0) \sim s_0^2$ and $\tau_p \sim 1/s_0$, which is clear from the consideration above. Therefore

$$w(t_0) \sim N_+^2, \qquad \tau_p \sim N_+^{-1}$$

which is characteristic of superradiance.

When there is no constant pumping by means of dynamic nuclear polarization, there appears one dominant superradiant burst given by equation (72). In an inhomogeneous sample, after the first burst, secondary maser oscillations can arise, whose accurate description requires numerical investigation.[15–17,30–32]

It is interesting to mention that the signals of nuclear spin echo can also be essentially amplified by the presence of a resonant electric circuit coupled with a spin system, which has been observed in experiment.[33]

8 PULSING SUPERRADIANCE

Another regime of spin superradiance can be achieved if the inversion of nuclear spins is constantly supported by a pumping mechanism, for instance, by dynamic nuclear polarization. Then, a series of superradiant bursts can be produced, as is experimentally observed.[8–10] Such a regime, with a series of superradiant pulses that may repeatedly arise during a rather long time, can be termed pulsing superradiance. The theoretical description of this regime is based on the evolution equations (49) and (50), which require numerical computations.[17,22,24] However, for the late stage, when $t \gg T_2, \tau$, and the system is close to a stationary state, it is possible to solve the problem analytically.

At the late stage, when $t \gg \tau$, the coupling function (42) becomes $\alpha = g\Gamma_2$. As is explained in Section 5, the resonator thermal noise can always be neglected, i.e., $\beta \to 0$. When there are no strong external transverse fields, then $v_1 \to 0$ and $v_2 \to 0$. For simplicity, the dynamic broadening width Γ_3 can also be neglected as compared to a large $g\Gamma_2$. Then the evolution equations (49) and (50) can be written as a two-dimensional dynamical system

$$\frac{dw}{dt} = v_1, \qquad \frac{ds}{dt} = v_2 \qquad (81)$$

with the velocity fields

$$v_1 = -2\Gamma_2(1 - gs)w, \qquad v_2 = -g\Gamma_2 w - \Gamma_1^*(s - \zeta) \qquad (82)$$

In the presence of dynamic nuclear polarization, Γ_1^* is a pumping rate and $\zeta > 0$ is a pumping parameter.

An accurate theoretical analysis of (81) is given below. The velocity fields are taken in the simplified form (82). This is done for pedagogical reasons, in order not to become entangled in cumbersome formulas, but for emphasizing the principal ideas and techniques on which such an analysis is based. Using the same methods, one could accomplish an analysis of the evolution equations (49) and (50), including the dynamic broadening and external transverse fields, which would result in much more intricate equations.

An important quantity characterizing local stability of motion is the local expansion rate[34]

$$\Lambda(t) \equiv \frac{1}{t} \mathrm{Re} \int_0^t \mathrm{Tr}\widehat{X}(t')dt' \qquad (83)$$

whose definition involves the Jacobian expansion matrix $\widehat{X}$ which in this case is

$$\widehat{X}(t) \equiv \begin{bmatrix} \dfrac{\partial v_1}{\partial w} & \dfrac{\partial v_1}{\partial s} \\ \dfrac{\partial v_2}{\partial w} & \dfrac{\partial v_2}{\partial s} \end{bmatrix}$$

If, at the moment t, the rate (83) is positive, $\Lambda(t) > 0$; this means that the phase volume of the dynamical system

expands, while if $\Lambda(t) < 0$, then the phase volume contracts. The eigenvalues of the expansion matrix $\widehat{X}$ are the local characteristic exponents

$$X^{\pm} = -\frac{1}{2}\left\{\Gamma_1^* + 2\Gamma_2(1 - gs) \pm \sqrt{\left[\Gamma_1^* - 2\Gamma_2(1 - gs)\right]^2 - 8g^2\Gamma_2^2 w}\right\}$$

whose real parts define the local Lyapunov exponents

$$\lambda^{\pm}(t) \equiv \mathrm{Re}X^{\pm}(t)$$

The signs of the latter show whether the motion at the moment t is stable or not.

In the theory of dynamical systems,[35] one usually considers asymptotic stability related to the limit $t \to \infty$. The stationary, or fixed, points are given by the zeros of the velocity fields. The equations $v_1 = v_2 = 0$, with the velocities (82), yield two stationary solutions; one fixed point is

$$w_1^* = 0, \qquad s_1^* = \zeta \tag{84}$$

and another is

$$w_2^* = \frac{\Gamma_1^*}{g^2\Gamma_2}(g\zeta - 1), \qquad s_2^* = \frac{1}{g} \tag{85}$$

As is clear, among several solutions, the only values that make sense are in the region of validity of the considered functions. This region, as follows from equations (22) and (23), is limited by the inequalities

$$0 \le w \le 1, \qquad -1 \le s \le 1$$

Thence, it is evident that the fixed point (85) may make sense only if $g\zeta \ge 1$. When $g\zeta = 1$, both fixed points (84) and (85) coincide. On the manifold of system parameters, the value $g\zeta = 1$ is termed a bifurcation point.

Because of the existence of two stationary solutions, the limit

$$\Lambda^* \equiv \lim_{t\to\infty}\Lambda(t) = \mathrm{Re}\lim_{t\to\infty}\mathrm{Tr}\widehat{X}(t)$$

of the local expansion rate (83), for which $\Lambda^* = \lambda^+ + \lambda^-$, with the Lyapunov exponents

$$\lambda^{\pm} \equiv \mathrm{Re}\lim_{t\to\infty} X^{\pm}(t)$$

possesses two different values. The local expansion rates at the first and second fixed points, respectively, are

$$\Lambda_1^* = -\Gamma_1^* - 2\Gamma_2(1 - g\zeta), \qquad \Lambda_2^* = -\Gamma_1^* \tag{86}$$

According to the principle of minimal expansion,[34] the smaller the local expansion rate, the more stable is a dynamic state. The values (86) show that when $g\zeta < 1$, the fixed point (84) is more stable, while when $g\zeta > 1$, the stationary solution (85) becomes more stable.

The limits $X^{\pm} \equiv \lim_{t\to\infty} X^{\pm}(t)$ of the characteristic exponents, at the corresponding fixed points, are

$$X_1^+ = -\Gamma_1^*, \qquad X_1^- = -2\Gamma_2(1 - g\zeta)$$

$$X_2^{\pm} = -\frac{\Gamma_1^*}{2}\left[1 \pm \sqrt{1 - 8\frac{\Gamma_2}{\Gamma_1^*}(g\zeta - 1)}\right] \tag{87}$$

The related real parts $\lambda^{\pm} = \mathrm{Re}X^{\pm}$ define the Lyapunov exponents. Analyzing equation (87) yields the following classification of the fixed points (84) and (85).

When $g\zeta < 1$, then the Lyapunov exponents for the stationary solution (84) are negative, $\lambda_1^{\pm} < 0$. This says that the fixed point (84) is a stable node. For the stationary solution (85), one has $\lambda_2^+ < 0$ but $\lambda_2^- > 0$, which means that the fixed point (85) is a saddle. Hence, for $g\zeta < 1$, spin dynamics tends to the stationary solution (84). The relaxation rates are given by $\lambda_1^{\pm} = X_1^{\pm}$ defined in equation (87), from which it follows that the spin motion is incoherent.

In the case $g\zeta = 1$, the stationary solution is unique, since the fixed points (84) and (85) coincide. The related Lyapunov exponents are also the same: $\lambda_1^+ = \lambda_2^+ < 0$, $\lambda_1^- = \lambda_2^- = 0$. The value $g\zeta = 1$ is associated with a bifurcation point.

With the increasing pumping, when

$$1 < g\zeta < 1 + \frac{\Gamma_1^*}{8\Gamma_2},$$

one gets $\lambda_1^+ < 0$, $\lambda_1^- > 0$, while $\lambda_2^{\pm} < 0$. This indicates that the features of the fixed points have been changed − the fixed point (84) is now a saddle, while that of equation (85) has turned to a stable node. For realistic nuclear spins, $\Gamma_1^* \ll \Gamma_2$. Therefore, the considered region of $g\zeta$ is very narrow. The relaxation rates are close to $\lambda_2^{\pm} \approx -\frac{1}{2}\Gamma_1^*$; hence the spin motion is incoherent. The coherence intensity w_2^*, given in equation (85), although not zero exactly, but, since $\Gamma_1^* \ll \Gamma_2$ and $g > 1$, is very small (not much differing from zero).

Increasing the pumping further, so that

$$g\zeta > 1 + \frac{\Gamma_1^*}{8\Gamma_2}$$

changes the picture qualitatively. Then the fixed point (84) continues to be a saddle, since $\lambda_1^+ < 0$, $\lambda_1^- > 0$, but the fixed point (85) turns into a stable focus, as far as its characteristic exponents become complex,

$$X_2^{\pm} = -\frac{\Gamma_1^*}{2} \pm i\omega_{\infty} \tag{88}$$

with the asymptotic frequency

$$\omega_{\infty} \equiv \frac{\Gamma_1^*}{2}\sqrt{8\frac{\Gamma_2}{\Gamma_1^*}(g\zeta - 1) - 1} \tag{89}$$

This is the regime of pulsing spin superradiance, when there appears a long series of superradiant bursts lasting about the time $T_1^* = (\Gamma_1^*)^{-1}$. At the intermediate stage, this pulsing is not periodic, but becomes approximately periodic as time increases. The asymptotic frequency (89) defines the time interval $T_{\infty} \equiv 2\pi/\omega_{\infty}$ between superradiant pulses at the late stage, when the spin evolution is close to the stationary solution (85). This interpulse time for sufficiently strong pumping, with $g\zeta \gg 1$, is

$$T_{\infty} \equiv \frac{2\pi}{\omega_{\infty}} \simeq \pi\sqrt{\frac{2T_1^* T_2}{g\zeta}} \tag{90}$$

The time (90), by varying the related parameters, can be varied widely. For example, keeping in mind the parameters

typical of the proton spins,[11–13] one has $\Gamma_0 = 2.85 \times 10^4$ Hz, $\omega_0 = 2.675 \times 10^8$ Hz, $\Gamma_2 = 1.18 \times 10^5$ Hz. With the quality factor $Q = 100$, the ringing width is $\gamma = 1.34 \times 10^6$ Hz. The spin-resonator coupling (67) is $g = 48$. For the pumping characteristics $\zeta = 1$ and $\Gamma_1^* = 10$ Hz, the interpulse time (90) is $T_\infty = 0.59 \times 10^{-3}$ s. The number of pulses can be estimated as $T_1^*/T_\infty \sim 100$. A detailed description of the regime of pulsing spin superradiance, for arbitrary times $t > 0$, can be accomplished with the help of numerical calculations.[17,22,24] The phenomenon of pulsing spin superradiance may be employed for creating pulsing spin masers.[22]

A regime, similar to pulsing spin superradiance, can also be realized without dynamic nuclear polarization. For this purpose, one could change the experimental setup used for realizing the transient spin superradiance as follows. In the latter regime, as is described in Section 7, if the spin-resonator coupling g is sufficiently strong, a sharp superradiant burst occurs at the delay time t_0. After the time $t_0 + \tau_p$, the spin polarization, according to equation (80), becomes practically inverted, provided $g \gg 1$. If at this moment, one inverts the static magnetic field B_0 or acts on spins by a resonant π-pulse, or just turns the sample 180° about an axis perpendicular to B_0, then again a strongly nonequilibrium state of almost completely inverted spins is prepared. After the time t_0, counted from the moment when the newly inverted state is created, another superradiant burst will arise. Then, one could again either invert the static magnetic field or invert the magnetization by a resonant π-pulse, or turn the sample to arrange a novel nonequilibrium inverted state of spins. After this, one more superradiant burst will appear. Such a procedure can be repeated as many times as necessary for producing a required number of sharp superradiant pulses. The regime achieved may be named *punctuated spin superradiance*. The principal difference of this regime from the pulsing spin superradiance is the possibility of controlling the number of pulses as well as the interpulse time. The term *punctuation* here implies the possibility of varying the time intervals between pulses and to form groups of pulses, containing different numbers of the latter. In that way, it is feasible to compose a code, similar to the Morse alphabet. Hence, punctuated spin superradiance can be used for processing information, which may be employed, for instance, in quantum computers.

9 HYPERFINE INTERACTIONS

Real solids, in addition to nuclei, always contain electrons. It is therefore important to understand the influence of hyperfine spin-spin interactions between nuclei and electrons on nuclear spin superradiance.

A system of nuclear and electronic spins is described by the Hamiltonian

$$\widehat{H} = \widehat{H}_{\rm nuc} + \widehat{H}_{\rm ele} + \widehat{H}_{\rm hyp} \tag{91}$$

in which the nuclear term $\widehat{H}_{\rm nuc}$ is given by equation (1). The electronic spin Hamiltonian is

$$\widehat{H}_{\rm ele} = -\frac{1}{2}\sum_{i\neq j} J_{ij}\hat{\mathbf{S}}_i \cdot \hat{\mathbf{S}}_j + \hbar\gamma_e \sum_i \mathbf{B}\cdot\hat{\mathbf{S}}_i \tag{92}$$

where J_{ij} is an exchange interaction potential, $\hat{\mathbf{S}}_i$ is an electron spin, and γ_e is the electron magnetogyric ratio. The part of the Hamiltonian (91) describing hyperfine interactions is

$$\widehat{H}_{\rm hyp} = A\sum_i \hat{\mathbf{S}}_i \cdot \hat{\mathbf{I}}_i + \frac{1}{2}\sum_{i\neq j}\sum_{\alpha\beta} A_{ij}^{\alpha\beta}\hat{S}_i^\alpha \hat{I}_j^\beta \tag{93}$$

Here the first term is the Fermi contact hyperfine interaction of nuclei with s-electrons, characterized by the energy

$$A = \frac{8\pi}{3}\hbar^2\gamma_e\gamma_n|\psi(0)|^2 \tag{94}$$

where $\psi(\mathbf{r})$ is the electron wave function. The second term in equation (93) presents the dipolar hyperfine interactions, with

$$A_{ij}^{\alpha\beta} = -\hbar^2\frac{\gamma_e\gamma_n}{r_{ij}^3}(\delta_{\alpha\beta} - 3n_{ij}^\alpha n_{ij}^\beta) \tag{95}$$

Consideration of the problem with the Hamiltonian (91) can be accomplished by employing the same methods detailed in the previous sections. The main technical difference is that the consideration becomes more cumbersome, as now it is necessary to deal with six evolution equations for spins, three of which are nuclear spins and three are electronic spins.[23,24] The seventh equation is the Kirchhoff equation (19), in which the magnetization density is now a sum

$$M_x = \frac{\hbar}{V}\sum_i\left(\gamma_n\langle\hat{I}_i^x\rangle - \gamma_e\langle\hat{S}_i^x\rangle\right) \tag{96}$$

of the terms due to nuclear and electronic spins. The evolution equations can be again solved by invoking the scale separation approach.[19–21,24,27] The most important conclusions resulting from the presence of hyperfine interactions are as follows.

Local spin fluctuations of electrons lead to the increase of the nuclear dynamic broadening, which results in the sum

$$\tilde{\Gamma}_3 = \Gamma_3 + \Gamma_3' \tag{97}$$

of the widths caused by nuclear dipolar interactions, Γ_3, and by electron-nuclear hyperfine interactions, Γ_3'. The relation between these widths is given by the ratio

$$\frac{\Gamma_3'}{\Gamma_3} = \frac{\rho_e\mu_e}{\rho_n\mu_n} \tag{98}$$

in which ρ_e and ρ_n are the electron and nuclear densities, while $\mu_e \equiv \hbar\gamma_e S$ and $\mu_n \equiv \hbar\gamma_n I$ are the electron and nuclear magnetic moments, respectively. When the electron and nuclear densities are close to each other, then, because $\mu_e/\mu_n \sim 10^3$, the ratio (98) can be large compared to unity. Therefore, the width (97) can be essentially increased by the hyperfine interactions. This results in the shortening of the delay time t_0 of a superradiant burst, as well as in shortening the pulse time τ_p.

In the electronic subsystem, long-range magnetic order may appear due to the exchange interaction of electronic spins. If so, the NMR frequency shifts to the value

$$\omega_n = \omega_0 + \frac{A}{\hbar}Sm_z \tag{99}$$

where m_z is the z-projection of the average electronic magnetization normalized to unity and A is the parameter (94). Then, the frequency (99) will enter all formulas instead of ω_0.

Long-range magnetic order of electrons leads to the renormalization of the coupling with the resonator according to the rule

$$\tilde{g} = g\left(1 + \frac{\rho_e \mu_e A}{\rho_n \mu_n \hbar \omega_n} m_z\right) \tag{100}$$

This may result because of the large ratio $\mu_e/\mu_n \sim 10^3$ in an essential increase of the coupling (100), as compared to g. The electronic subsystem plays the role of an additional resonator, which enhances the effective coupling of nuclear spins with the resonant electric circuit.[24]

10 RADIATION INTENSITY

To complete the treatment, it is worth emphasizing once again why this phenomenon can be called spin superradiance. An ensemble of coherently moving nuclear spins, as is clear, generates magnetodipole radiation with total intensity

$$I(t) = \frac{2}{3c^3} \left|\ddot{\mathbf{M}}(t)\right|^2 \tag{101}$$

where

$$\mathbf{M}(t) = \hbar \gamma_n \sum_i \langle \mathbf{I}_i(t) \rangle$$

is the total magnetization of nuclei. The quantity of interest is the radiation intensity averaged over fast oscillations. For the intensity (101), this yields

$$\overline{I}(t) = \frac{2}{3c^3} \mu_n^2 \omega_0^4 N^2 w(t) \tag{102}$$

where, as always, $\mu_n \equiv \hbar \gamma_n I$ is the nuclear magnetic moment. As is seen, the radiation intensity is proportional to the number of spins squared, which is characteristic of superradiance.

Although coherently moving spins do produce superradiance, the radiation intensity (102) is not high. At the peak of a superradiant burst, $w(t_0)$ is given by equation (79). For $g \gg 1$ and $s_0 \approx 1$, one has $w(t_0) \approx 1$. Then the maximal radiation intensity, for proton spins, with $\mu_n = 1.411 \times 10^{-26}\,\mathrm{J\,T^{-1}}$, $\omega_0 = 2.675 \times 10^8\,\mathrm{Hz}$, and $N \approx 10^{23}$, is $\overline{I}(t_0) \approx 2.5 \times 10^{-5}\,\mathrm{W}$.

Despite such weak radiation intensity, it can be easily detected. This is because what is directly measured is the power of the current

$$P(t) = R j^2(t) \tag{103}$$

which is generated in a coil by the radiating spins. Using the relation of the induced current with the resonator magnetic field (14), one gets

$$j^2(t) = \frac{V_c}{4\pi L} H^2(t)$$

The field H can be found from equation (41). Setting $\beta = 0$ in this equation, i.e., neglecting thermal noise, and averaging over fast oscillations gives

$$\overline{H^2(t)} = \frac{2}{\gamma_n^2} \alpha^2(t) w(t)$$

Then, for the averaged current power (103), one finds

$$\overline{P}(t) = g \Gamma_2 I \hbar \omega N (1 - e^{-\gamma t})^2 w(t) \tag{104}$$

This expression contains, as compared to equation (102), an additional dependence on the feedback retardation. But for $t \gg \tau$, the radiation intensity (102) and the current power (104) differ one from another only by a numerical factor

$$\frac{\overline{P}(t)}{\overline{I}(t)} \simeq \frac{3 g \Gamma_2 \lambda^3}{16 \pi^2 \Gamma_0 V_c} = \frac{3 Q \lambda^3}{8 \pi^2 V_c} \tag{105}$$

in which $\lambda = 2\pi c/\omega$ is the radiation wavelength. For an NMR frequency $\omega = 2.675 \times 10^8\,\mathrm{Hz}$, one has $\lambda = 0.71 \times 10^3\,\mathrm{cm}$. The factor (105) can reach rather large values. Thus, if $Q = 100$ and $V_c = 10\,\mathrm{cm}^3$, this factor is of the order of 10^8. This is why even a low radiation intensity can be easily measured.

11 APPLICATIONS

Nuclear spin superradiance is collective spontaneous radiation by nuclear spins at the frequency of nuclear magnetic resonance. This phenomenon is an analog of atomic superradiance occurring at optical frequencies. Being a novel coherent phenomenon at NMR frequencies, it may find various applications.

1. *Investigation of materials characteristics*. Spin relaxation in materials is commonly employed for studying relaxation parameters describing intrinsic properties of matter. Nuclear spin superradiance is accomplished by a self-organized coherent spin relaxation, which is drastically different from other types of spin relaxation. Another kind of relaxation may provide additional information on the properties of materials. Thus, the main mechanism originating pure spin superradiance is the existence of local spin fluctuations caused by the interaction of nuclear spins with each other, by means of dipolar forces, and with electronic spins, through hyperfine forces. Therefore, studying specific features of pure spin superradiance provides information about these local fluctuations.
2. *Fast repolarization of targets*. The relaxation of nuclear spins, in the process of superradiance, happens much faster than the usual spin-dephasing time T_2. If the initial spin polarization is sufficiently high and the spin-resonator coupling is sufficiently strong, spins, after a superradiant burst, change their orientation becoming almost completely inverted. Such an ultrafast inversion of spins can be employed for quick repolarization of polarized solid-state targets used is scattering experiments.
3. *Construction of spin masers*. A superradiant spin system is a source of coherent radiation at radio frequencies. Being a source of coherent radiation, it is analogous to

lasers operating at optical frequencies. Spin masers could find applications similar to those of optical lasers. A spin maser can function in a transient regime, emitting a single burst typical of pure or triggered spin superradiance, and it can also work in a lasting regime based on pulsing spin superradiance.

4. *Creation of sensitive detectors*. Spin superradiance can be triggered by a very weak external pulse of intensity corresponding to w_0. The latter depends exponentially on the delay time t_0. Therefore, measuring the delay time of a superradiant burst provides an accurate evaluation of the triggering intensity. Then, triggered spin superradiance may serve as a sensitive mechanism for detecting weak external signals.
5. *Methods of information processing*. In the regime of punctuated superradiance, the intervals between superradiant bursts as well as the number of pulses can be regulated. This makes it feasible to compose a kind of Morse Code alphabet and then to develop a technique of processing information. Such a method of information processing could be used in quantum computers.

In conclusion, it is necessary to note that the developed theory, as well as possible applications, are appropriate not only for nuclear spins but, in general, for any spin system. For instance, all this can be immediately extended to electronic spins. A related phenomenon is *electron spin superradiance*. Other types of materials could be the so-called molecular magnets formed of magnetic molecules. The latter often have high spins, thus possessing several quantum transitions. In that case, the resonant electric circuit has to be tuned to one of the admissible transition frequencies. The resulting effect would be *molecular spin superradiance*, whose intensity could be much higher than that of nuclear spins. Nuclear spin superradiance is just a representative from a class of phenomena called *spin superradiance*. These phenomena, being realized with different materials, should exhibit a rich variety of specific features that could be not only interesting but also useful for various applications.

12 RELATED ARTICLES IN VOLUMES 1–8

Dynamic Frequency Shift, Volume 3; Dynamic Nuclear Polarization & High-Resolution NMR of Solids, Volume 3; Echoes in Solids, Volume 3; Electron-Nuclear Hyperfine Interactions, Volume 3; Laser Devices in NMR: Routes to Chaos, Volume 4; Low Spin Temperature NMR, Volume 5; Nuclear Ferromagnetism & Antiferromagnetism, Volume 5; Nuclear Overhauser Effect, Volume 5; Nuclear Spin Properties & Notation, Volume 5; Quantum Optics: Concepts of NMR, Volume 6; Radiofrequency Pulses: Response of Nuclear Spins, Volume 6; Relaxation: An Introduction, Volume 6; Relaxation Theory: Density Matrix Formulation, Volume 6; Ruby NMR Laser, Volume 7; Rudimentary NMR: The Classical Picture, Volume 7.

13 REFERENCES

1. A. Abragam, 'Principles of Nuclear Magnetism', Clarendon: Oxford, 1961.
2. C. P. Slichter, 'Principles of Magnetic Resonance', Springer: Berlin, 1978.
3. R. H. Dicke, *Phys. Rev.*, 1954, **93**, 99.
4. A. V. Andreev, V. I. Emelyanov, and Y. A. Ilinski, 'Cooperative Effects in Optics', Institute of Physics: Bristol, 1993.
5. M. G. Benedict, A. M. Ermolaev, V. A. Malyshev, I. V. Sokolov, and E. D. Trifonov, 'Superradiance-Multiatomic Coherent Emission', Institute of Physics: Bristol, 1996.
6. N. Bloembergen and R. V. Pound, *Phys. Rev.*, 1954, **95**, 8.
7. V. M. Fain and Y. I. Khanin, 'Quantum Electronics', Pergamon: Oxford, 1969.
8. P. Bösiger, E. Brun, and D. Meier, *Phys. Rev. A*, 1978, **18**, 671.
9. P. Bösiger, E. Brun, and D. Meier, *Phys. Rev. A*, 1979, **20**, 1073.
10. R. Holzner, B. Derighetti, M. Ravani, and E. Brun, *Phys. Rev. A*, 1987, **36**, 1280.
11. J. F. Kiselev, A. F. Prudkoglyad, A. S. Shumovsky, and V. I. Yukalov, *Mod. Phys. Lett. B*, 1988, **1**, 409.
12. Y. F. Kiselev, A. F. Prudkoglyad, A. S. Shumovsky, and V. I. Yukalov, *J. Exp. Theor. Phys.*, 1988, **67**, 413.
13. N. A. Bazhanov, D. S. Bulyanitsa, A. I. Zaitsev, A. I. Kovalyov, V. A. Malyshev, and E. D. Trifonov, *J. Exp. Theor. Phys.*, 1990, **70**, 1128.
14. L. A. Reichertz, H. Dutz, S. Goertz, D. Krämer, W. Meyer, G. Reicherz, W. Thiel, and A. Thomas, *Nucl. Instrum. Methods Phys. Res. A*, 1994, **340**, 278.
15. T. S. Belozerova, V. K. Henner, and V. I. Yukalov, *Phys. Rev. B*, 1992, **46**, 682.
16. T. S. Belozerova, V. K. Henner, and V. I. Yukalov, *Laser Phys.*, 1992, **2**, 545.
17. V. I. Yukalov and E. P. Yukalova, *Phys. Part. Nucl.*, 2000, **31**, 561.
18. A. Abragam and M. Goldman, 'Nuclear Magnetism: Order and Disorder', Clarendon: Oxford, 1982.
19. V. I. Yukalov, *Phys. Rev. Lett.*, 1995, **75**, 3000.
20. V. I. Yukalov, *Laser Phys.*, 1995, **5**, 970.
21. V. I. Yukalov, *Phys. Rev. B*, 1996, **53**, 9232.
22. V. I. Yukalov and E. P. Yukalova, *Laser Phys.*, 1998, **85**, 1029.
23. V. I. Yukalov, M. G. Cottam, and M. R. Singh, *Phys. Rev. B*, 1999, **60**, 1227.
24. V. I. Yukalov and E. P. Yukalova, *Laser Phys.*, 2001, **11**, 546.
25. D. Ter Haar, 'Lectures on Selected Topics in Statistical Mechanics', Pergamon: Oxford, 1977.
26. A. E. Seigman, 'Microwave Solid-State Masers', McGraw-Hill: New York, 1964.
27. V. I. Yukalov, *Laser Phys.*, 1993, **3**, 870.
28. N. N. Bogolubov and Y. A. Mitropolsky, 'Asymptotic Methods in the Theory of Nonlinear Oscillations', Gordon and Breach: New York, 1961.
29. V. I. Yukalov, *Nucl. Instrum. Methods Phys. Res. A*, 1996, **370**, 345.
30. T. S. Belozerova, C. L. Davis, and V. K. Henner, *Phys. Rev. B*, 1998, **58**, 3111.
31. M. V. Romalis and W. Happer, *Phys. Rev. A*, 1999, **60**, 1385.
32. D. S. Bulyanitsa, A. V. Druzhin, and E. D. Trifonov, *J. Exp. Theor. Phys.*, 2000, **118**, 273.
33. N. P. Fokina and K. O. Khutsishvili, *Phys. Met. Metallogr.*, 1990, **69**, 65.
34. V. I. Yukalov, *Phys. Lett. A*, 2001, **284**, 91.
35. C. Robinson, 'Dynamical Systems', CRC Press: Boca Raton, FL, 1995.

Biographical Sketch

Vyacheslav I. Yukalov, *b* 1946. M.Sc., 1970, Ph.D., 1974, Moscow, Dr.Hab., 1999, Poznan, Dr.Sci., 2001, Moscow. First involved with NMR related research in 1984, after starting his work

at JINR in Dubna, where together with an experimental group he took part in the first observation of pure nuclear spin superradiance. Then developed a microscopic theory of this phenomenon. Received the First Prize of Joint Institute for Nuclear Research for the discovery and theory of nuclear spin superradiance in 2001. Published 250 papers and 4 books. Current research interests: developing the theory of spin superradiance for including novel materials, and for finding new applications.

Ortho–Para Hydrogen at Low Temperature

Neil S. Sullivan

University of Florida, Gainesville, FL, USA

1	Introduction	1
2	Orientational Parameters and NMR Spectra	1
3	Phase Diagram of Solid *Ortho–Para* Hydrogen Mixtures	4
4	Molecular Dynamics and Low Energy Excitations	5
5	Related Articles	6
6	References	6

1 INTRODUCTION

The solid hydrogens (H_2 and D_2) are the simplest molecular solids that exist in Nature, and a detailed understanding of their many body properties is of special interest because the rotational degrees of freedom are those of quantum rotors and their behavior at low temperatures can be understood from considerations of first principles. The interaction Hamiltonians are well known and studies of the ordering of the molecular orientations have revealed interesting new regimes of collective phenomena. NMR has provided one of the most sensitive tools for probing the orientational degrees of freedom of the quantum rotors because of the intimate relationship between the constraints on the molecular nuclear spin wave function and the rotational (or orbital) degrees of freedom that results in the existence of distinct molecular species: the *ortho* and *para* modifications.

All the homonuclear isotopes of molecular hydrogen (H_2, D_2, and T_2) have distinct molecular species;[1] i.e. *ortho* and *para* modifications, resulting from the requirements of symmetry considerations that apply to the molecular wave function. For H_2 and T_2, the nuclei are fermions with nuclear spin $I = \frac{1}{2}$, and the requirement that the total molecular wave function be antisymmetric can be satisfied in two ways: (1) *ortho*-H_2 (or T_2) for which the nuclear spin wave function for the molecule is symmetric with total nuclear spin $I_T = 1$ and for which the molecular orbital angular wave function is antisymmetric with orbital angular momentum J odd ($J = 1, 3, 5, \ldots$); and (2) *para*-H_2 (or T_2) for which the nuclear spin wave function is antisymmetric ($I_T = 0$) with J even ($J = 0, 2, 4, \ldots$). For D_2, the nuclei are bosons with nuclear spin $I = 1$, and the requirement that the total molecular wave function be symmetric can also be satisfied in two distinct ways: (1) *para*-D_2 with total nuclear spin $I_T = 1$ and orbital angular momentum J odd; (2) *ortho*-D_2 with the nuclear spin wave function symmetric ($I_T = 0$ or 2) and with orbital angular momentum J even. Table 1 summarizes the symmetry properties of these different molecular species.

The aspect of the molecular species of the hydrogens that make them unique compared with other (heavier) homonuclear diatomic molecules (such as N_2) is that the separation of the rotational energy levels is very large compared with the anisotropic interactions between the molecules. The rotational kinetic energies are given by $E_J = B_J J(J + 1)$ with $B_J = \hbar^2/(2mr^2)$, where r is the intermolecular separation and $B_J = 85.6\,\mathrm{K}$ for H_2 (43.2 K for D_2), and the $J = 1$ and $J = 2$ rotational states are 171 K and 510 K above the $J = 0$ ground state, respectively, for H_2 (and 86 K and 257 K, respectively, for D_2). We therefore only need to consider the lowest rotational states $J = 1$ and $J = 0$ in the solid hydrogens. Furthermore, the anisotropic interactions between the molecules that can admix different J states are very weak ($V_{\mathrm{aniso}} \simeq 1\,\mathrm{K}$). J is therefore a good quantum number to first order and we may consider the $J = 1$ species (*ortho*-H_2 (or T_2) and *para*-D_2) as quantum rotors.

The conversion of $J = 1$ molecular species to the ground state ($J = 0$) is very slow because it is doubly forbidden; two symmetries need to be broken simultaneously, the symmetry of the nuclear wave function and that of the orbital wave function, in order to convert a $J = 1$ *ortho* molecule into a $J = 0$ molecule. In the pure solid this conversion is induced by the intermolecular magnetic interactions, and leads to a bimolecular rate constant of 1.9% per hour for H_2 (and 0.06% per hour for D_2). This rate is sufficiently slow that we may consider the *ortho* species as stable on the timescale of ordinary experiments. On the other hand, over a few weeks or months, the experimenter may explore a wide range of *ortho* concentrations continuously, simply by allowing a sample to age at constant low pressure. Alternatively, samples of essentially pure $J = 0$ species or pure $J = 1$ species can be prepared by special techniques, and solid mixtures of the full range of *ortho*/*para* concentrations studied by mixing the appropriate amounts of $J = 0$ species and $J = 1$ species in the gaseous state and solidifying the mixture. Pure $J = 0$ species are prepared by conversion on paramagnetic surfaces[2] (e.g. zeolites saturated with chromic oxide), and $J = 1$ species by selective adsorption on alumina.[3]

The behavior of the $J = 1$ quantum rotors (*ortho*-H_2 and *para*-D_2) can be studied directly by NMR.[4,5] The total nuclear spin of these molecules is $I_T = 1$ and the intramolecular interactions do not average to zero if the molecules have a preferred orientation in space. A fine structure is observed in the absorption spectrum and this can be used to determine the quantum mechanical order parameters. Furthermore, the nuclear spin–lattice (T_1) and nuclear spin–spin (T_2) relaxation times depend on the fluctuation spectrum of the molecular orientations, and measurements of T_1 and T_2 can be used to determine the fundamental rotational excitations of the molecular rotors.

2 ORIENTATIONAL PARAMETERS AND NMR SPECTRA

The $J = 1$ molecules are not spherically symmetric; they have end-on symmetry and hence no permanent electric dipole moment, but they do have a small axial electric quadrupole moment Q. There is therefore a weak electrostatic quadrupole–quadrupole (EQQ) interaction between the molecules that depends on their relative orientations.[6] At high temperatures the molecules are free to rotate, but at low temperatures the $J = 1$ molecules adopt mutual orientations to minimize their EQQ interactions. The EQQ interaction is short

Table 1 Molecular Species of Hydrogen Isotopes[a]

	ortho-H_2 (or T_2)	(*para*-D_2)	*para*-H_2 (or T_2)	(*ortho*-D_2)
Angular momentum[b]	Odd $J = 1$	(Odd) ($J = 1$)	Even $J = 0$	(Even) ($J = 0$)
Total nuclear spin	Even $I_T = 1$	(Odd) ($I_T = 1$)	Odd $I_T = 0$	(Even) ($I_T = 0$ and 2)

[a]The terminology *ortho–para* refers to the total nuclear spin symmetry. The full molecular wave function must be odd (even) for molecular H_2 and T_2 (D_2), respectively. The total nuclear spin wave function: $|I_T m_T\rangle = \sum_{m_1 m_2} C^{I_1 I_2 I_T}_{m_1 m_2 m_T} |I_1 m_1\rangle\ |I_2 m_2\rangle$ where the $C^{I_1 I_2 I_T}_{m_1 m_2 m_T}$ are the Clebsch–Gordan coefficients, e.g. for *para*-H_2,$|\mathrm{OO}\rangle = 2^{-\frac{1}{2}}\{|\frac{1}{2}, \frac{1}{2}\rangle\ |\frac{1}{2}, -\frac{1}{2}\rangle - |\frac{1}{2}, -\frac{1}{2}\rangle\ |\frac{1}{2}, \frac{1}{2}\rangle\}$.
[b]Higher J states need not be considered for normal densities at low temperatures.

range and only nearest neighbor interactions need be considered. For an isolated pair the minimum energy configuration is a 'T' orientation (Figure 1) with the quadrupoles mutually perpendicular.

For a simple two-dimensional square lattice, a simple antiferro-orientational array is the minimum energy configuration [Figure 2(a)] and this is stable with respect to substitution by a spherical ($J = 0$) molecule. For other lattices, however, the molecules cannot all be oriented so that each neighboring pair is in the 'T' configuration. This is illustrated in Figure 2(b) for a triangular lattice for which the lowest total energy configuration is a herring-bone arrangement. This arrangement is not stable with respect to substitution by 'inert' $J = 0$ molecules. This topological incompatibility between the configuration of the lowest energy pair and the geometry of the crystal lattice structure is a particularly striking example of the phenomenon of 'frustration' that is a key feature of the spin glasses and many other glass formers. The effect of substitutional disorder on frustrated systems can be studied in depth using *ortho–para* mixtures because the substitution is close to ideal (a $J = 1$ molecular species being replaced by a $J = 0$ species, with no other change) and the order parameters and the molecular dynamics can be determined directly from NMR studies.

The distinction between the ordering in the familiar magnetic systems and the diatomic molecular systems is that for the former one needs in most cases to consider only the dipole moments $\langle S_x\rangle_k$, $\langle S_y\rangle_k$, and $\langle S_z\rangle_k$ of a spin S at lattice site k, whereas for the $J = 1$ rotors we need in general to specify the quadrupole moments $\langle J_\epsilon J_\phi\rangle_k$ as well as the vectorial moments $\langle J_\epsilon\rangle_k$. Only five of the quadrupole moments are independent variables; ϵ and ϕ represent one of the Cartesian components (x,y,z) of a local reference frame.

In the absence of any interactions that break time-reversal symmetry, the orbital angular momentum is quenched, i.e. the $\langle J_\epsilon\rangle_k$ vanish for all ϵ. Five parameters are needed to describe fully the rotational degrees of freedom, and the natural choice is to select as local reference axes (x, y, z) the principal axes

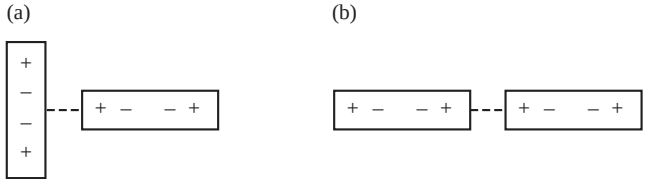

Figure 1 Configurations of a pair of interacting axial quadrupoles for (a) minimum, and (b) maximum energy

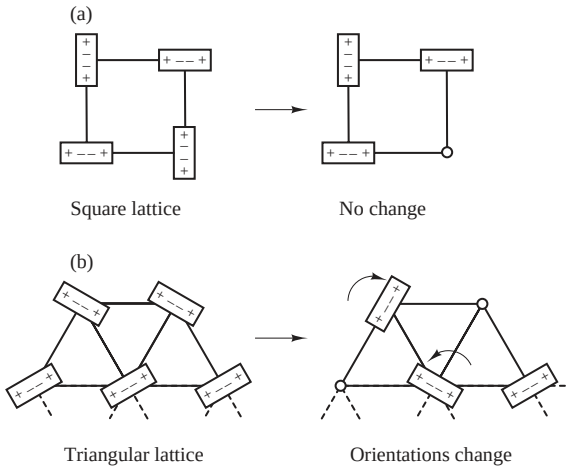

Figure 2 Schematic representation of the effect of substitutional disorder on quadrupolar arrays for (a) nonfrustrated, and (b) frustrated configurations

of the quadrupolar tensor with elements:

$$q_{\epsilon\phi} = \langle \tfrac{1}{2} J^2 \delta_{\epsilon\phi} - \tfrac{3}{4}(J_\epsilon J_\phi + J_\phi J_\epsilon)\rangle \tag{1}$$

In the local principal axes frame, the off-diagonal elements, $q_{xy} = q_{yz} = \ldots = q_{zx} = 0$, and the only intrinsic quadrupolar order parameters are: (1) the *alignment*

$$\sigma_k = Q_{zz} = \langle 1 - \tfrac{3}{2} J_z^2\rangle_k \tag{2}$$

and (2) the *eccentricity*

$$\eta_k = \langle J_x^2 - J_y^2\rangle_k \tag{3}$$

The five order parameters are the three local reference axes (specifying the direction of the molecular orientation), and the two quadrupolar order parameters σ and η (which describe the degree of alignment along those axes).

The strong positivity conditions on the single particle density matrix (i.e. that the eigenvalues be positive definite) limit the allowed values of σ and η to the bounds defined by

$$\tfrac{1}{3} + \tfrac{2}{3}\sigma \geq 0; \quad \tfrac{1}{3} - \tfrac{1}{3}\sigma \pm \tfrac{1}{2}\eta > 0 \tag{4}$$

Not all the allowed pairs (σ,η) in this range are physically distinguishable, however, since we are free to relabel the axes,

and by convention we choose axes such that $\sigma \geq \frac{1}{2}\eta > 0$. There are two single particle 'pure' states: ($\sigma = 1$, $\eta = 0$), corresponding to a ground state $|J_z = 0\rangle$ and ($\sigma = \frac{1}{2}$, $\eta = \pm 1$), corresponding to the ground state $|J_z = \pm 1\rangle$. States intermediate between these 'pure' states can be realized in the many-particle system; this feature was first observed in NMR studies of *ortho–para* hydrogen mixtures.[4,7]

The ability to study the orientational order parameters by NMR arises from the fact that the intramolecular nuclear dipole–dipole interaction $\hat{\mathcal{H}}_{\mathrm{DD}}$ between the two nuclei of a given molecule depends directly on the order parameters. This can be seen by expressing $\hat{\mathcal{H}}_{\mathrm{DD}}$ in terms of products of irreducible tensorial operators $\hat{T}_{LM}$ in the manifold $J = 1$ with the corresponding nuclear spin operators $\hat{N}_{LM}$ in the manifold $I = 1$:

$$\hat{\mathcal{H}}_{\mathrm{DD}} = \hbar D \sum_{M} \hat{T}_{LM} \hat{N}^{\dagger}_{2M} \tag{5}$$

The $\hat{T}_{LM}$ and $\hat{N}_{LM}$ transform in the same manner as the spherical harmonics Y_{LM} and are given in Table 2, with $D = 173.06\,\mathrm{kHz}$ for H_2 (2.74 kHz for D_2). [For D_2 there is an additional intramolecular term arising from the interaction of the nuclear electric quadrupole moment with the local electric field gradient. This interaction Hamiltonian transforms identically to the form given by equation (5) but with D replaced by $D_{\mathrm{Q}} = 22.50\,\mathrm{kHz}$.]

The dipolar interaction term given by equation (5) results in a small perturbation of the nuclear Zeeman energy levels. For high magnetic fields $\boldsymbol{B}_0$ lies along the z axis, and the nuclear Zeeman interaction

$$\hat{\mathcal{H}}_{\mathrm{Z}} = \gamma \hbar \hat{\boldsymbol{I}} \cdot \boldsymbol{B}_0 \tag{6}$$

results in three equally spaced Zeeman levels for $I_z = 1$, 0, -1 (Figure 3) with energy spacings $\Delta E_{10} = \Delta E_{-10} = \hbar\omega_{\mathrm{L}}$, where ω_{L} is the nuclear Larmor frequency. If $\hat{\mathcal{H}}_{\mathrm{DD}}$ is motionally averaged to zero (corresponding to isotropic molecular reorientation on a timescale that is short compared to D^{-1}), only a single NMR absorption line is observed at the Larmor frequency. If the molecule has a preferred orientation, $\hat{\mathcal{H}}_{\mathrm{DD}}$ does not average to zero and the transitions ΔE_{10} and ΔE_{-10} are no longer equal. $\hat{\mathcal{H}}_{\mathrm{DD}}$ is treated as a perturbation of

Table 2 Irreducible Angular Momentum Operators $\hat{T}_{LM}$ (in manifold $J = 1$) and Nuclear Spin Operators $\hat{N}_{LM}$ (in the manifold $I = 1$)[a]

	Tensorial operator, $\hat{T}_{LM}$	Tensorial operator, $\hat{N}_{LM}$
$L = 1$		
	$\hat{T}_{1,0} = 2^{-\frac{1}{2}}\hat{J}_z$	$\hat{N}_{1,0} = 2^{-\frac{1}{2}}\hat{I}_z$
	$\hat{T}_{1,\pm1} = \mp\frac{1}{2}(\hat{J}_x \pm \mathrm{i}\hat{J}_y)$	$\hat{N}_{1,\pm1} = \mp\frac{1}{2}(\hat{I}_x \pm \mathrm{i}\hat{I}_y)$
$L = 2$		
	$\hat{T}_{2,0} = 6^{-\frac{1}{2}}(3\hat{J}_z^2 - \hat{J}^2)$	$\hat{N}_{2,0} = 6^{-\frac{1}{2}}(3\hat{I}_z^2 - \hat{I}^2)$
	$\hat{T}_{2,\pm1} = \mp\frac{1}{2}(\hat{J}_\pm\hat{J}_z + \hat{J}_z\hat{J}_\pm)$	$\hat{N}_{2,\pm1} = \mp\frac{1}{2}(\hat{I}_\pm\hat{I}_z + \hat{I}_z\hat{I}_\pm)$
	$\hat{T}_{2,\pm2} = \frac{1}{2}(\hat{J}_\pm)^2$	$\hat{N}_{2,\pm2} = \frac{1}{2}(\hat{I}_\pm)^2$

[a] $\hat{T}_{LM} = (-)^M \hat{T}^{+}_{L,-M}$ and $\mathrm{Tr}(\hat{T}_{LM}\hat{T}^{+}_{L'M'}) = \delta_{LL'}\delta'_{MM}$; and similarly for the $\hat{N}_{LM}$.

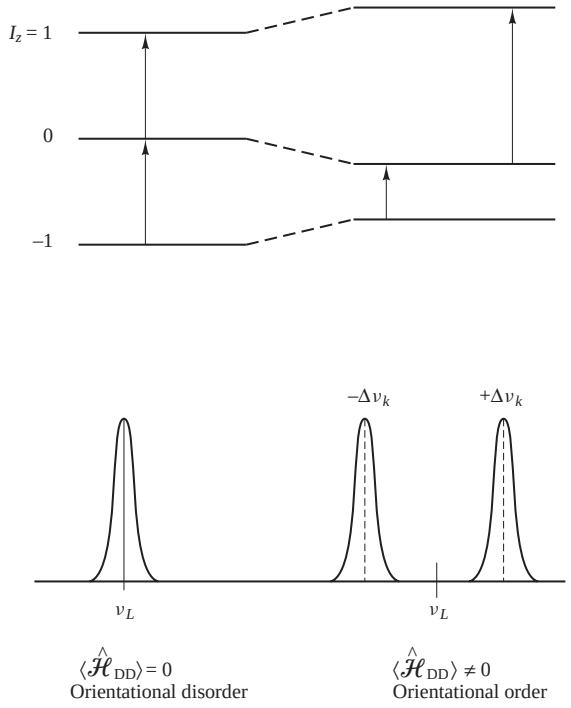

Figure 3 Splitting of the NMR absorption line at ν_L into a doublet with $|\Delta\nu_k| = D\langle 1 - \frac{3}{2}J_z^2\rangle_k$ for each molecule that is orientationally ordered

$\hat{\mathcal{H}}_z$ and each molecule now contributes a doublet to the NMR spectrum with components at frequencies

$$\Delta\nu_k = \mp D\langle 1 - \tfrac{3}{2}J_z^2\rangle_k \tag{7}$$

on either side of the Larmor frequency. Here, the brackets $\langle\ \rangle$ indicate averaging over all crystallite orientations with respect to the static field $\boldsymbol{B}$.

The average $\langle 1 - \frac{3}{2}J_z^2\rangle_k$ is valid for a timescale that is long compared with D^{-1}, and the expectation value is evaluated with respect to the magnetic field axis and not the local symmetry axis with respect to which the local molecular order parameters are defined. Transforming to the local molecular frame, we find that

$$\Delta\nu_k = \mp D[-\sigma_k P_2(\cos\alpha_k) + \tfrac{3}{4}\nu_k \sin 2\alpha_k \cos 2\beta_k] \tag{8}$$

where (α_k, β_k) are the polar angles defining the orientation of the applied magnetic field with respect to the local molecular axes. The analysis of the spectra has been carried out assuming local axial symmetry $\eta = 0$ for the molecular ordering, and while no inconsistency has been demonstrated for this assumption, it has not been established rigorously.

The majority of NMR experiments are carried out using powder samples, and the lineshapes calculated for a powder distribution with a fixed value of σ at each site yields the familiar Pake doublet lineshape (Figure 4). The intensities $I_{\pm1,0}$ for the transitions ΔE_{10} and ΔE_{-10} are given by

$$I_{\pm1,0}(\Delta\nu, \sigma) = \left[2\sqrt{3}D\sigma\left(1 \mp \frac{2\Delta\nu}{D\sigma}\right)^{1/2}\right]^{-1} \tag{9}$$

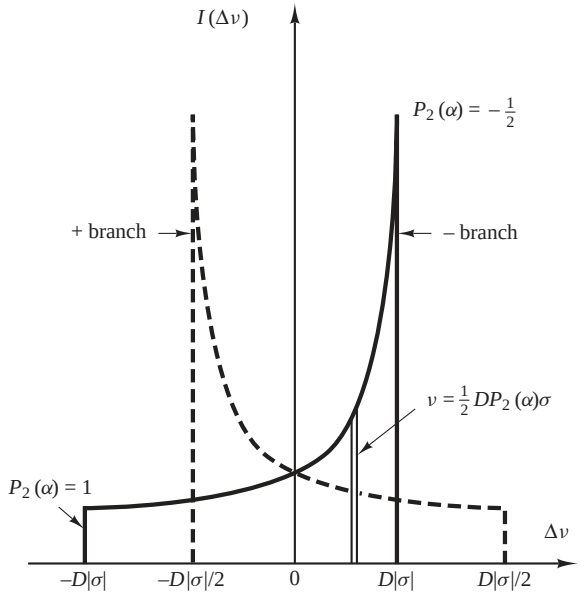

Figure 4 Pake doublet NMR absorption spectrum for the fixed value of molecular order parameter σ

The cusp singularities at $\Delta\nu = \mp \frac{1}{2}D\sigma$ correspond to molecules with $\alpha = \pi/2$, i.e. those molecules aligned in a plane normal to the applied magnetic field. The separation of the cusps provides a direct measure of the local molecular order parameters, and is thus used to study the collective ordering of the molecules as a function of temperature.

3 PHASE DIAGRAM OF SOLID *ORTHO–PARA* HYDROGEN MIXTURES

If the concentration of quadrupolar species ($J = 1$ molecules) is sufficiently high (>55% for H_2 and >59% for D_2), a long range periodic ordering of the molecular orientations is observed. At low temperatures the molecular alignments are ordered in a four-sublattice Pa_3 configuration on a fcc lattice (Figure 5), with the molecules aligned parallel to one of the four body diagonals in each sublattice. The local order parameters have the values $\sigma = 1$ at each site (when evaluated with respect to the local principal orientation axis in each sublattice). The transition to the ordered phase is first order (with a jump in the value of σ at the transition), and the transition triggers a lattice change from a hcp structure (the high-temperature phase) to a fcc lattice. Subsequent small thermal cycles above and below the transition temperature stabilize the cubic lattice, and one can observe the purely orientational order–disorder transitions on the fcc lattice. As the $J = 1$ concentration is lowered, the transition temperature is reduced, and the phase diagram calculated from first principles is in good qualitative agreement with experimental observations, but the theoretical values are consistently higher than the observed values by about 17%.[8,9]

Below the critical concentration of $J = 1$ species (approximately 55% for H_2 and 59% for D_2), the long-range periodic ordering is lost. At low concentrations a new quadrupolar glass structure is observed. Experimental observations (NMR studies and heat capacity measurements) all indicate that the molecules

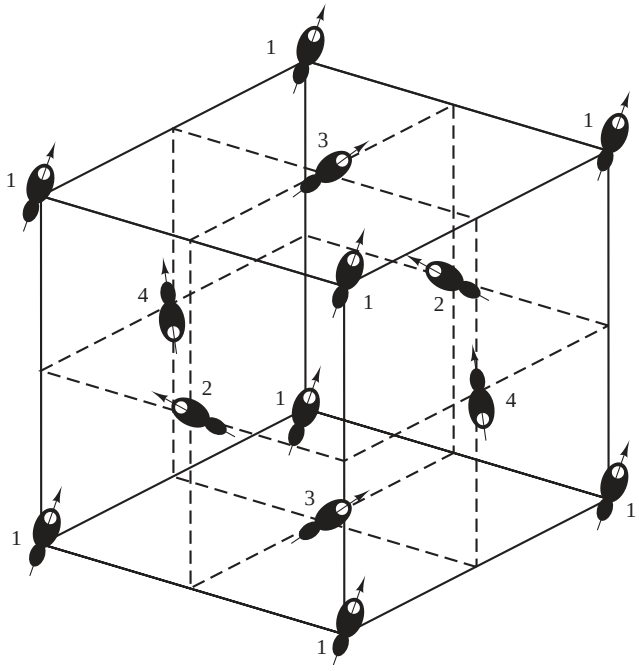

Figure 5 Pa_3 structure for molecular alignments in the fcc lattice

become frozen in a random configuration, with both the local molecular symmetry axes and the local alignments (the values of σ_k at each site) varying at random throughout the crystal. The tensorial order varies randomly from site to site in the glass state, as illustrated in Figure 6. The NMR spectra provide the strongest evidence for a glass phase from the appearance of a broad bell-shaped absorption line (Figure 7) rather than the Pake doublet lineshape which characterizes the periodic ordering.

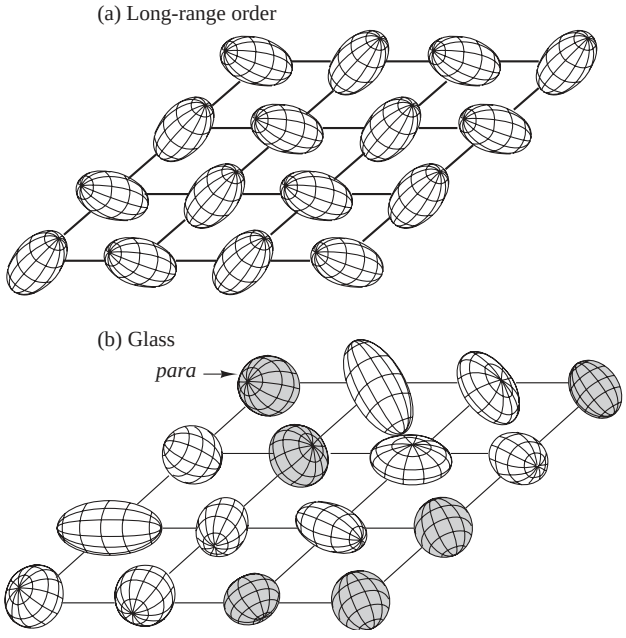

Figure 6 Schematic representation of molecular ordering for (a) a planar section of the Pa_3 structure, and (b) the quadrupolar glass phase

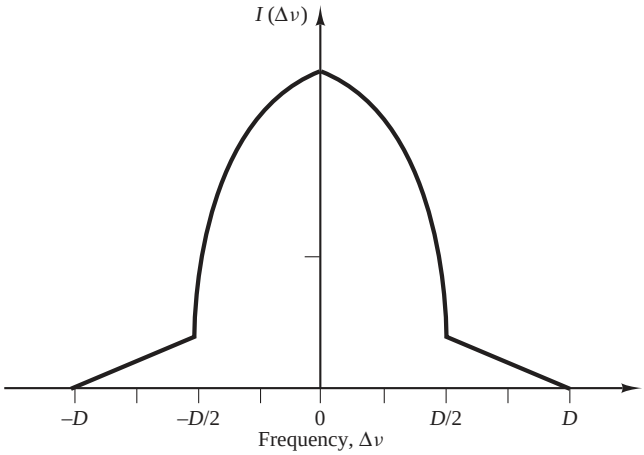

Figure 7 Bell-shaped NMR absorption line in the quadrupolar glass phase calculated for a linear distribution of order parameters

The loss of periodic order in the dilute *ortho–para* mixtures is attributed to the introduction of disorder in a highly frustrated system. The combined effects of frustration and disorder are believed to be universal features of magnetic spin glasses, and the quantum rotor glasses provide a particularly interesting example for probing the properties of these systems. The interactions are short range and well understood, the introduction of the disorder is especially clean, and the local order parameters and molecular dynamics can be studied directly by NMR.

The transitions from the high-temperature phase to the glass state are not abrupt. The molecular rotational fluctuations have been determined from measurements of the nuclear spin–lattice relaxation rates,[10–12] showing that the characteristic molecular fluctuation rates increase continuously but rapidly over a relatively small temperature range (Figure 8).

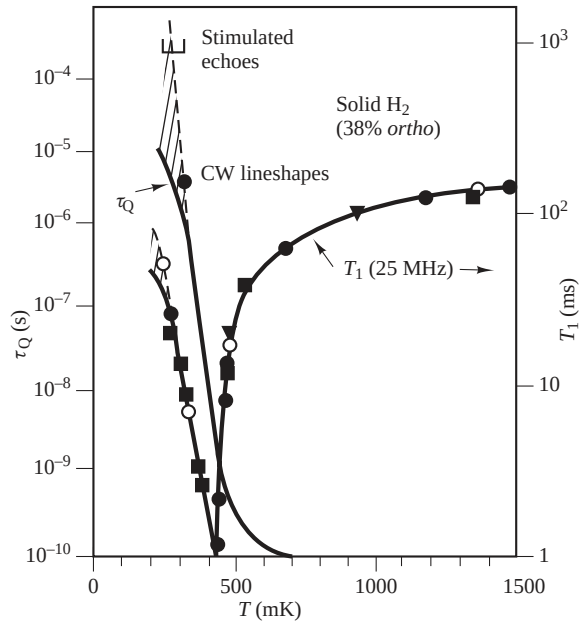

Figure 8 Temperature dependence of the nuclear spin–lattice relaxation times T_1 in the glass phase. τ_Q are the characteristic molecular reorientational times deduced from T_1

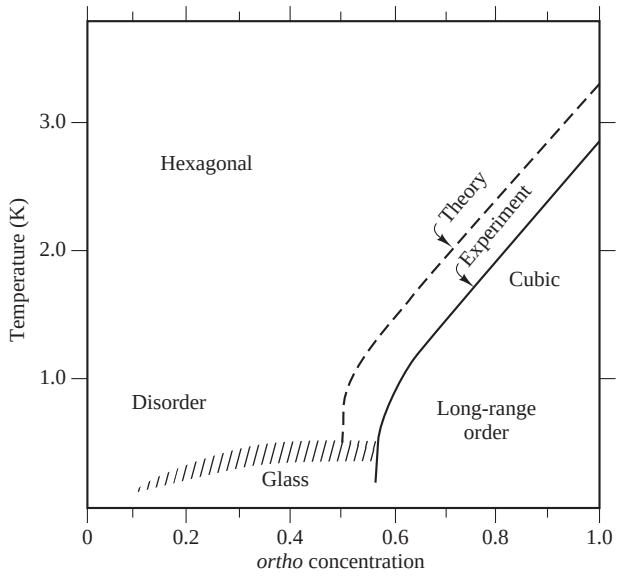

Figure 9 Phase diagram for orientationally ordered phases of solid hydrogen

The phase diagram for *ortho–para* H_2 mixtures deduced from NMR studies is shown in Figure 9. The solid and broken lines indicate first-order transitions to the periodic antiferro-orientational Pa_3 structure, and the hatched region corresponds to the continuous transition to the glass state. The behavior of the molecular orientations at very low temperatures below the percolation concentration (15%) has not been explored in detail. At very low $J = 1$ concentrations, indirect anisotropic long-range interactions are expected to dominate, and could lead to new behaviors.

4 MOLECULAR DYNAMICS AND LOW ENERGY EXCITATIONS

The molecular dynamics in the quadrupolar glass phase have been studied at low temperatures using stimulated echo techniques.[13–15] A preparatory two pulse sequence is used to store both nuclear polarizations $\langle I_z \rangle$ and nuclear spin alignments $\langle I_z^2 \rangle$ in a given initial state. After a waiting period, a third pulse is used to determine the changes in the molecular orientations during the waiting time. The intramolecular nuclear spin–spin interactions $\hat{\mathcal{H}}_{DD}$ determine the evolution during the waiting period, and because $\hat{\mathcal{H}}_{DD}$ depends directly on the order parameters σ_k, slowly varying changes in the molecular orientations can be detected using this method.

A logarithmic decay is observed for the stimulated echoes over a wide range of conditions, and this decay has been analyzed quantitatively in terms of a spectrum of low energy excitations corresponding to reorientations of clusters of molecules in the glass state. The spectrum of excitations deduced from the NMR measurements has been used to analyze the temperature dependence of the heat capacities determined from independent thermodynamic measurements.[16,17] An excellent fit to the thermodynamic data was obtained without any adjustable parameters, providing one of the most convincing demonstrations of the fundamental

nature of the glass state: a freezing of the molecular alignments in local short-range ordered clusters with a broad spectrum of collective excitations corresponding to molecular reorientations in the clusters.

The systematic NMR studies of solid *ortho*/*para* mixtures of hydrogen and deuterium have established the existence of a new quadrupolar glass state for dilute samples of quantum rotors. The local order parameters are tensorial rather than vectorial as in the conventional orientational glass and spin glass systems. The *ortho*/*para* mixtures have served as a test case for the study of glass formers in general because the interactions are well understood and the order parameters can be studied directly using NMR. Further studies on two-dimensional films and monolayers will provide new information about the effect of dimensionality on highly frustrated systems, and could reveal new collective behaviors for two-dimensional assemblies of quantum rotors at low temperatures.

5 RELATED ARTICLES

Amorphous Materials; Deuterium NMR in Solids; Hydrogen Molecules.

6 REFERENCES

1. A. Farkas, *Orthohydrogen, Parahydrogen and Heavy Hydrogen*, Cambridge University, Cambridge, 1935.
2. N. S. Sullivan, D. Zhou, and C. M. Edwards, *Cryogenics*, 1990, **30**, 734.
3. N. S. Sullivan, C. M. Edwards, M. Rall, and D. Zhou, *Cryogenics*, 1993, **33**, 1008.
4. A. B. Harris and H. Meyer, *Can. J. Phys.*, 1985, **63**, 3.
5. N. S. Sullivan, C. M. Edwards, Y. Lin, and D. Zhou, *Can. J. Phys.*, 1987, **65**, 1463.
6. A. B. Harris, *Phys. Rev. B*, 1970, **1**, 1881.
7. N. S. Sullivan, M. Devoret, B. P. Cowan, and C. Urbina, *Phys. Rev. B*, 1978, **17**, 5016.
8. J. C. Raich, *Phys. Rev.*, 1968, **168**, 425.
9. N. S. Sullivan, *J. Phys. Paris*, 1976, **37**, 981.
10. S. Washburn, M. Calkins, H. Meyer, and A. B. Harris, *J. Low Temp. Phys.*, 1982, **49**, 101.
11. W. T. Cochran, J. R. Gaines, R. P. McCall, P. E. Sokol, and B. R. Patton, *Phys. Rev. Lett.*, 1980, **45**, 1576.
12. N. S. Sullivan and D. Esteve, *Physica B*, 1981, **107**, 189.
13. I. Yu, S. Washburn, M. Calkins, and H. Meyer, *J. Low Temp. Phys.*, 1983, **51**, 401.
14. N. S. Sullivan, D. Esteve, and M. Devoret, *J. Phys. C*, 1982, **15**, 4895.
15. Y. Lin and N. S. Sullivan, *J. Magn. Reson.*, 1990, **86**, 319.
16. D. G. Haase, L. R. Perrell, and A. M. Saleh, *J. Low Temp. Phys.*, 1984, **55**, 283.
17. J. F. Jarvis, H. Meyer, and D. Ramm, *Phys. Rev.*, 1969, **178**, 1461.

Biographical Sketch

Neil Sullivan *b* 1942. B.Sc., 1964, M.Sc., 1965, Otago, New Zealand; Ph.D., 1972, Harvard, USA. Introduced to NMR by R. V. Pound. Staff physicist, C. E. N.-Saclay, 1972–82; Faculty in Physics, University of Florida, 1982–present; Chair Physics, University of Florida 1989–present. Approx. 180 publications. Research interests: NMR studies of quantum solids, ultralow temperature techniques, ultrahigh magnetic fields (coprincipal investigator at National High Magnetic Field Laboratory).

Optically Pumped NMR of Semiconductors and Two-Dimensional Electron Systems

Robert Tycko

National Institutes of Health, Bethesda, MD, USA

&

Sean E. Barrett

Department of Physics, Yale University, New Haven, CT, USA

1 Introduction 1
2 Directly Detected vs. Optically Detected 1
3 Mechanism of Optical Pumping 2
4 Application to Two-Dimensional Electron Systems in the Quantum Hall Regime 4
5 Concluding Remarks 7
6 Related Articles in this Volume 7
7 Related Articles in Volumes 1–8 7
8 References 7

1 INTRODUCTION

In the context of this article, the term 'optical pumping' refers to the creation of large, nonequilibrium nuclear spin polarizations by irradiation of a sample at optical wavelengths. Significant optical pumping effects have been reported in several classes of samples, including organic molecular crystals,[1] mixtures of noble gases and alkali metal vapors,[2] biological photosynthetic systems,[3–5] and inorganic semiconductors.[6,7] Optical pumping of nuclear spin polarization in a semiconductor was first described by George Lampel in 1968, for the case of crystalline Si.[6] In Lampel's original experiments, Si samples were irradiated with an arc lamp at 77 K and fields of 0.16 T or less, and ^{29}Si polarization was measured by direct NMR detection. Optical pumping was observed with both circularly polarized and unpolarized light. Lampel's observations were explained in terms of photoexcitation of conduction electrons with nonequilibrium electron spin polarization and subsequent dynamic polarization of hyperfine-coupled nuclear spins. Although the magnitude of the ^{29}Si polarizations in Lampel's experiments were only of order 10^{-5}, these experiments set the stage for later optical pumping experiments in which polarizations of order 10% have been achieved.[8,9]

Following Lampel's experiments and other optical pumping experiments on Si,[10–12] attention shifted to III–V semiconductors, principally GaAs and AlGaAs, and to optical detection of the NMR spectra.[13–17] These and other recent experiments have been performed at temperatures on the order of 10 K or lower. In optically detected NMR (ODNMR) experiments, the large nuclear spin polarization created by optical pumping exerts a strong average hyperfine field on the photoexcited electrons, which can then affect the evolution or steady-state of the photoexcited electron spin polarization. In analogy to the Hanle effect,[18,19] the optically pumped nuclear hyperfine field can be made to reduce the degree of circular polarization of the photoluminescence that accompanies electron-hole recombination when radio-frequency (rf) fields are applied near the NMR lines. The original ODNMR experiments on semiconductors[13–17] were carried out on bulk materials and with continuous wave (cw) rf irradiation (i.e., frequency domain ODNMR). Recent ODNMR experiments have focussed on semiconductor thin films and heterostructures[20–23] and on the development of time-domain variants that lead to dramatic improvements in NMR resolution.[9,24,25] Simultaneously, there has been a revival of interest in directly detected, optically pumped NMR (OPNMR).[8,26–33] OPNMR measurements with direct detection have been used to investigate the properties of quantum confined conduction electrons in two-dimensional systems at low temperatures and high fields,[34–38] a topic of considerable interest to condensed matter physicists.[39–41] Notably, OPNMR measurements have provided the first evidence for and characterization of novel electron states called skyrmions in two-dimensional electron systems (2DES).[34,35]

2 DIRECTLY DETECTED VS. OPTICALLY DETECTED

An important advantage of both time-domain and frequency-domain ODNMR methods is their extremely high sensitivity. Because of the high efficiency for detection of optical photons, it is possible in principle to detect the NMR spectrum of nuclei in the vicinity of single luminescent defect or impurity site in a semiconductor sample, comprising roughly 10^5 nuclei. In fact, ODNMR spectra of single GaAs quantum dots containing approximately this number of nuclei have been reported,[42–44] although in these experiments the NMR spectra were detected through modulation of the photoluminescence energy, rather than polarization, by manipulation of the optically pumped nuclear polarization. In ODNMR experiments in which photoluminescence polarization was monitored, NMR spectra of less than 10^{11} nuclei have been detected.[16,21]

An apparent limitation on ODNMR techniques based on photoluminescence polarization is that they can only be applied when the nuclear hyperfine field is a significant fraction of the external magnetic field. In practice, such ODNMR experiments are typically performed at magnetic field strengths below 1 T.

Advantageous features of directly detected OPNMR include: (1) compatibility with high fields (to the extent that the optical pumping effect itself occurs at high field);[31,33] (2) absence of photoluminescence requirements; (3) ability to detect NMR spectra of both the ground state and the photoexcited state of the sample; (4) ability to detect NMR spectra of sample regions that are spatially distinct from the optically absorbing regions, through nuclear spin diffusion;[34,35]

(5) full compatibility with pulsed NMR methodology, including multiple pulse line-narrowing techniques, heteronuclear decoupling, multidimensional spectroscopy, and nuclear spin relaxation measurements. Some of these advantages are shared by time-domain or time-sequenced ODNMR techniques.[9,24,25] In principle, because optical pumping can produce nuclear spin polarizations of order 10%,[8,9] the sensitivity of directly detected OPNMR is sufficient for the observation of roughly 10^{14} nuclei (with signal averaging), or the number of nuclei in a semiconductor monolayer with a surface area of approximately 0.2 cm.[2]

Examples of OPNMR spectra of bulk GaAs and InP are shown in Figures 1 and 2. Spectra of semiconductor quantum well samples are discussed in Section 4.

Very recently, all-optical NMR experiments on semiconductors, i.e., experiments in which nuclear spin transitions are detected with only optical irradiation of a sample, have been reported.[45–47] In these experiments, a near-infrared pump laser tuned near the semiconductor absorption band edge and propagating in a direction not parallel to the applied static magnetic field is pulsed[45,46] or modulated in amplitude or phase[47] at radio frequencies, but no rf irradiation or pulses are applied. A plot of the Faraday rotation of a weaker probe laser[45,46] or of photoluminescence polarization[47] versus the modulation frequency of the pump laser shows discontinuities at the NMR frequencies. Such experiments have been reported both for bulk GaAs[45,46] and for GaAs quantum wells.[46,47] Both single-quantum ($|\Delta m| = 1$) and overtone ($|\Delta m| = 2$) NMR transitions have been detected. Single-quantum transitions are attributed to modulation of electron-nucleus magnetic hyperfine couplings at the laser modulation frequency,[45–47] while overtone transitions are attributed to modulation of nuclear electric quadrupole couplings at the laser modulation frequency.[46,47] Observation of both types of NMR transitions is dependent upon optical pumping of nuclear spin polarizations away from resonance and subsequent destruction of the nuclear spin polarization at the resonant conditions. Further exploration and exploitation of all-optical NMR effects in semiconductors, and possibly other materials, is likely in the near future.

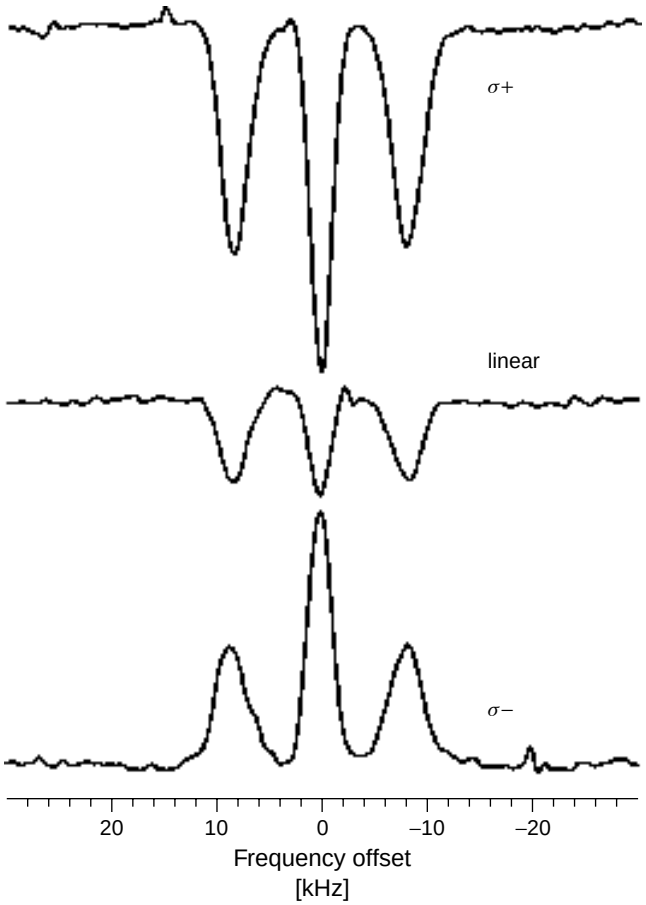

Figure 1 Optically pumped ^{71}Ga NMR spectra of a semi-insulating GaAs wafer at 4.3 K in a 9.39-T field, obtained with an optical pumping time of 10 s, a photon energy of 1.49 eV (831 nm wavelength), and the indicated light polarizations. The laser power was 240 mW in a 5-mm diameter spot. Emissive OPNMR signals are observed with linear and $\sigma+$ polarization. Under the conditions of these experiments, the optically pumped nuclear spin polarizations are of order 1%, but larger polarizations are created with longer pumping times. No NMR signals are detectable when the laser light is blocked, because of both the smaller nuclear spin polarization at equilibrium and the very long spin-lattice relaxation times in the dark ($>10^3$ s). Quadrupole splittings of the NMR lines arise from strain due to thermal contraction of the GaAs wafer, which was glued to a sapphire block in the low-temperature NMR probe

3 MECHANISM OF OPTICAL PUMPING

The general features of the physical mechanism of optical pumping in semiconductors have been described.[7] Briefly, photoexcitation of a direct-gap, ZnS-structure, bulk semiconductor at the band edge (Γ point) in zero magnetic field creates conduction electrons with spin polarization $\langle S_z \rangle = \pm(1/4)\sigma$, where the light helicity σ is $+1$ for left-circular-polarized light, -1 for right-circular-polarized light, and 0 for unpolarized light. Provided that the spin-lattice relaxation time of photoexcited electrons is not much less than the photoexcitation lifetime, a net nonequilibrium electron spin polarization is created. The electrons couple to nuclei by Fermi contact hyperfine interactions. If the hyperfine interactions fluctuate with a sufficiently short correlation time, flip–flop transitions efficiently transfer electron spin polarization to the nuclei. At steady state, the nuclear spin temperature T_n is related to the electron spin temperature T_e and lattice temperature T by the expression $(T_n^{-1} - T^{-1}) = \gamma_e/\gamma_n(T^{-1} - T_e^{-1})$, where γ_e and γ_n are the electronic and nuclear magnetogyric ratios. Since $\gamma_e/\gamma_n \sim 10^3$, a small deviation of the electron spin polarization from thermal equilibrium produces a very low (positive or negative) nuclear spin temperature, i.e., a large nuclear spin polarization.

It is commonly assumed that optical pumping is driven primarily by localized electron states (e.g., electrons trapped at defect or shallow donor sites), rather than delocalized, Bloch-function states. This is because the rate of flip–flop transitions depends on the square of the hyperfine couplings, and therefore on the square of the electron probability density at the nuclei. Because the total electron probability density (not squared) is normalized, electron states that concentrate the probability density in a smaller volume can produce a greater net flip–flop rate.

Despite this general understanding of optical pumping, nearly all details of the mechanism remain mysterious. For example:

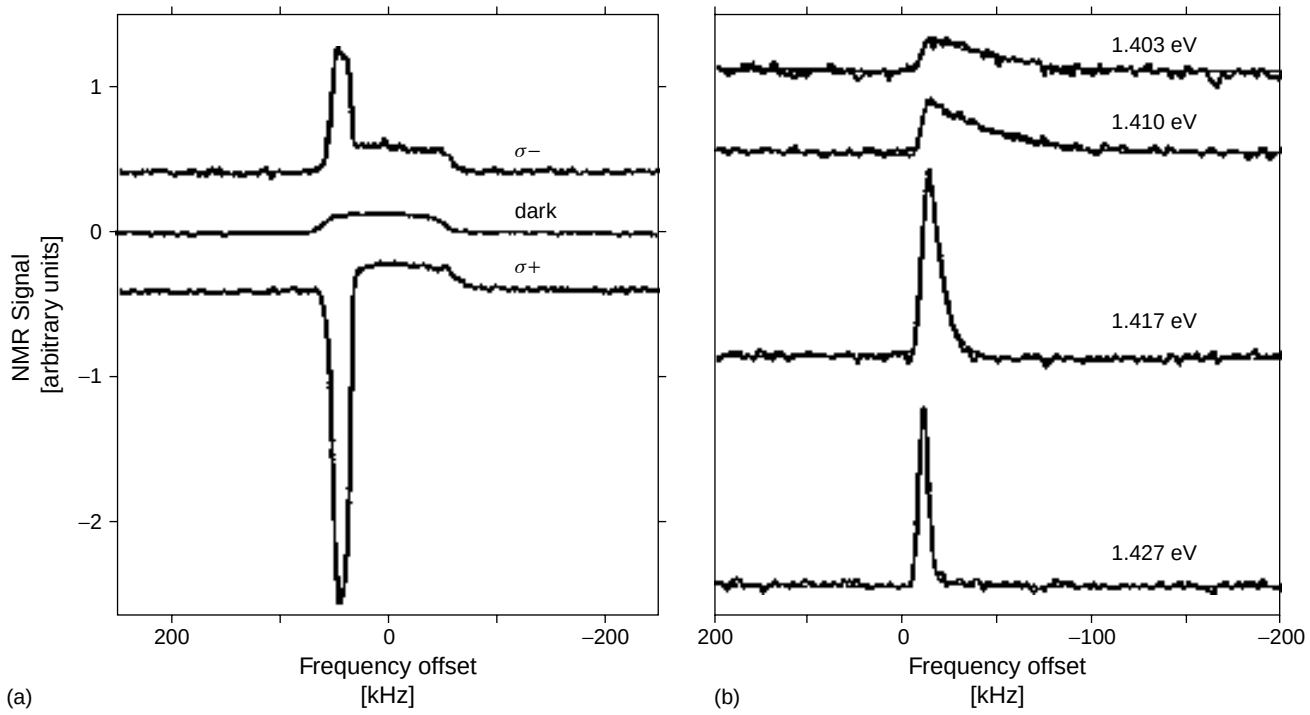

Figure 2 Optically pumped ^{13}P NMR spectra of a 348-μm thick Fe-doped semi-insulating InP wafer at 6 K, obtained in a superconducting magnet with a central field of 9.39 T. The InP wafer was located outside the homogeneous region of the magnet, producing a strong field gradient perpendicular to the surface of the wafer. The spectra then represent one-dimensional images of the nuclear spin polarization.[8] (a) Low resolution images. The InP wafer is situated in a 0.195 T/cm gradient, with an optical pumping time of 600 s at 1.412 eV, or 878 nm wavelength. Spectra were obtained with $\sigma+$ and $\sigma-$ polarized light, at a power of 200 mW in a 3.7-mm diameter spot, and in the dark. The wafer thickness corresponds to an NMR frequency range of 116 kHz. With optical pumping, ^{31}P nuclei near the laser-irradiated surface acquire either positive or negative nonequilibrium spin polarizations, depending on the direction of light polarization. (b) High resolution images. The InP wafer is situated in a 0.453 T/cm gradient, with an optical pumping time of 120 s at the indicated photon energies. Spectra were obtained with $\sigma+$ polarized light, at a power of 25 mW in a 0.45-mm diameter spot. Vertical axis is reversed relative to (a). The absorption band edge for InP at low temperatures occurs at approximately 1.427 eV, where the light penetration depth is approximately 2 μm. As the laser is tuned to lower energies, the pumping light penetrates deeper into the wafer, producing an asymmetrically broadened ^{31}P NMR lineshape. A 2-μm distance corresponds to an NMR frequency shift of 1.6 kHz. (Adapted from Ref.[8])

1. The identity of the localized states that produce optical pumping is not firmly established in any specific sample, either bulk or heterostructure.
2. The source of hyperfine fluctuations has not yet been identified conclusively. The classic Overhauser effect in a *metal* depends on hyperfine fluctuations due to translational motion of delocalized electrons near the Fermi surface. In optically pumped semiconductors, this contribution is considered negligible. Recent studies of the field dependence of optical pumping in GaAs and InP suggest that the relevant fluctuations have time scales of order 10 ps.[31,33,48]
3. Possible effects of high fields on the band structure, optical selection rules, electron-hole pairing and localization, or other aspects of the photophysics relevant to optical pumping have not been explored in theory or experiment.
4. Possible contributions to the optical pumping process from hyperfine couplings to photoexcited valence band holes and effects of spin-selective electron-hole recombination[49] on the electron spin polarization have not been analyzed in detail.
5. The signs of optically pumped ^{31}P polarizations in undoped InP[27,33] (but not Fe-doped, semi-insulating InP[8,28]) have been found to be opposite to expectations based on the simple theory outlined above, i.e., $\sigma-$ and linearly polarized light produce negative ^{31}P polarization, while $\sigma+$ light produces positive polarization. In GaAs, the signs of optically pumped nuclear spin polarizations are in accord with expectations.
6. The dependences of nuclear spin polarization on the optical photon energy in bulk GaAs and InP are not well understood. In bulk GaAs, a strong maximum in the nuclear spin polarization is observed at photon energies approximately 20 meV below the band edge, and little or no polarization is created at higher energies.[29] This observation has been attributed tentatively to direct pumping of shallow traps or excitons.[29] In bulk InP, a similar maximum has been shown by stray-field NMR imaging to be due primarily to the increased optical absorption length (i.e., greater optically pumped volume) below the band edge.[8] In bulk InP, substantial nuclear spin polarizations are generated with photon energies up to at least 60 meV above the band edge.[8,27]
7. In GaAs/AlGaAs quantum well samples at high field, optical pumping effects saturate at very low photon flux,[26] of order 60 mW cm^{-2}, while photoluminescence does not saturate up to at least 3 W cm^{-2}. This observation suggests a 'phase-space filling' phenomenon in which a rather

low density of photoexcitations is sufficient to occupy all electronic states that play a role in optical pumping.

8. Recent OPNMR experiments on bulk InP have revealed that optical pumping creates nuclear spin dipolar order in addition to the Zeeman order predicted by the simple theory outlined above.[28] Possible explanations for optical pumping of dipolar order include direct generation through electron-nuclear cross relaxation, dependent on dipolar hyperfine interactions and nuclear dipole-dipole couplings,[50] and indirect generation through diffusion of Zeeman order in the presence of spatial gradients of NMR frequencies.[28] The dominant mechanism for optical pumping of dipolar order has not been established experimentally.

Obviously, there is a great deal of room for further research into the fundamental aspects of optical pumping in semiconductors. Nonetheless, even in the absence of a detailed understanding of the mechanism, the optical pumping effect can be useful both for sensitivity enhancement and for spatial localization of NMR signals. The utility of optical pumping is exemplified by OPNMR studies of 2DES in GaAs/AlGaAs quantum wells, as described below.

4 APPLICATION TO TWO-DIMENSIONAL ELECTRON SYSTEMS IN THE QUANTUM HALL REGIME

A 2DES, cooled to extremely low temperatures in a strong magnetic field, exhibits many exotic phenomena, including the integer[51] and fractional[52] quantum Hall effects that are the subject of a large body of experimental and theoretical studies by condensed matter physicists. Transport and optical studies of the 2DES have shown that the low-energy physics in these extreme conditions is driven by the electron–electron Coulomb interaction,[53] making this 'simple' system one of the hardest to understand theoretically. OPNMR studies have contributed to the recent progress on this problem by providing important new insights into the electron spin degree of freedom, which helps to shed light on the low-lying many-body states that exist in a real 2DES.[39–41]

For these OPNMR experiments, samples typically contain multiple copies (up to forty) of a fundamental unit: a GaAs quantum well (i.e., a GaAs layer approximately 300 Å thick) doped with electrons ($n \sim 1 \times 10^{11}\,cm^{-2}$), sandwiched between $Al_{0.1}Ga_{0.9}As$ barriers (i.e., $Al_{0.1}Ga_{0.9}As$ layers approximately 1500 Å thick).[54–56] At low temperatures, all conduction electrons are confined to the quantum wells and are in the same '2D state' (i.e., the lowest electronic subband of the well). The normal component of a strong magnetic field ($B\cos\theta$, where θ is the angle between the external field **B** and the direction normal to the plane of the quantum well) quantizes the 2D motion into spin–split Landau levels.[54,55] In this regime, the many-body states and thus the physical properties of the 2DES are determined by the Landau level filling factor $\nu = (nhc/eB\cos\theta)$, where h, c, and e are Planck's constant, the velocity of light, and the electron charge. By varying n, B, or θ, ν may be tuned to reach integral[51] (e.g., $\nu = 1$) or fractional[52] (e.g., $\nu = 1/3$) quantum Hall ground states.[39–41,53] These are states in which the longitudinal resistivity ρ_{xx} of the 2DES vanishes and the transverse (or Hall) resistivity ρ_{xy} plateaus at the values $(hc/\nu e^2)$. In OPNMR experiments on 2DES in GaAs quantum wells,[34–38,57,58] ν is varied for a sample with given n by varying θ and by performing experiments at several values of B.

Figure 3 shows ^{71}Ga OPNMR spectra of a multiple quantum well sample, acquired using the timing sequence SAT – τ_L – τ_D – DET.[26,34,35,57] SAT represents an rf pulse train that saturates nuclear spin polarization. During τ_L, a near-infrared laser optically pumps the quantum well, using a photon energy above the band edge of the well and below that of the barrier. Because the laser is tuned to be absorbed only in the quantum well layers, only nuclear spins in the quantum wells, and not in the barrier, become strongly polarized. The enhanced NMR signal observed after a short illumination period (e.g., $\tau_L \sim 5$ s) is due to nuclei in the quantum wells ('W' signals in Figure 3). Eventually (e.g., as $\tau_L \to 200$ s), the optically pumped nuclear polarization spreads into the barrier regions

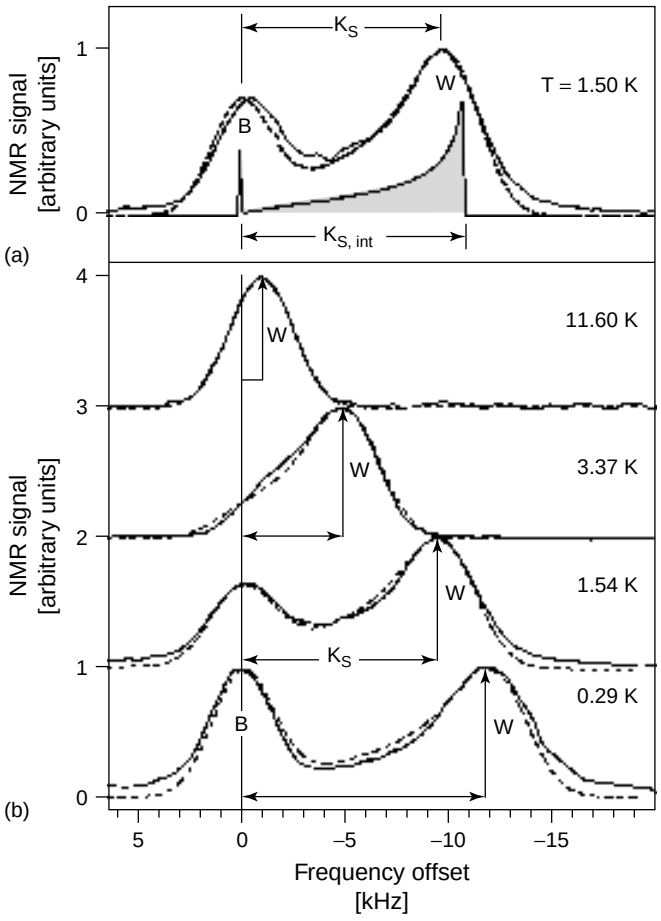

Figure 3 ^{71}Ga NMR lineshapes of an optically pumped GaAs multiple quantum well sample, obtained in a 12 T field at the indicated temperatures.[37] (a) Spectrum at Landau level filling factor $\nu = 1/3$ after approximately 60 s of optical pumping. Peak labeled W arises from nuclei in the 26-nm thick GaAs wells. Peak labeled B arises from the 312-nm thick $Al_{0.1}Ga_{0.9}As$ barriers between wells. The Knight shift K_S is defined empirically as the splitting between the peaks. The shaded lineshape is a simulation of the intrinsic Knight shift lineshape, with maximum shift $K_{S,int}$. The dashed line is a fit to the experimental lineshape obtained by convoluting the intrinsic lineshape with a Gaussian lineshape attributable to nuclear magnetic dipole-dipole couplings. (b) Temperature dependence of the optically pumped ^{71}Ga NMR lineshape at $\nu = 0.267$. (Reprinted from Ref.[37])

by nuclear spin diffusion. A second NMR signal due to nuclei in the barriers then appears ('B' signals in Figure 3). After a period τ_D in the dark ($\tau_D \geq 1$ s), nuclear free induction decay signals are recorded in the period DET. These signals probe the equilibrium properties of the 2DES as functions of ν and temperature. Nuclear spin-lattice relaxation rates R_1 at thermal equilibrium can be determined from the dependence of OPNMR signal amplitudes on τ_D[35].

The Knight shift (K_S) of quantum well signals may be defined[26,34,35] as the peak-to-peak splitting between quantum well and barrier signals (see Figure 3). K_S is due to Fermi contact hyperfine couplings between nuclei and doped (not photoexcited, because the OPNMR signals are observed in the dark after τ_D) conduction electrons confined in the quantum wells and is proportional to the spin polarization of the 2DES. The temperature dependence of K_S [Figure 3(b)] reveals the increasing spin polarization of the electrons[36] as they are cooled into a ferromagnetic ground state[59] [see Figure 4(a)]. As shown in Figure 3(a) (dashed line), a more quantitative determination of K_S[37] is achieved by fitting the experimental OPNMR lineshape to the convolution of the intrinsic hyperfine lineshape of the well and barrier [Figure 3(a), shaded] with a 3.5 kHz FWHM Gaussian lineshape due to nuclear magnetic dipole–dipole couplings. The central assumption of this model of the lineshape is that nuclei in the quantum well experience a hyperfine magnetic field that scales with the electron probability density in the direction perpendicular to the plane of the well but is uniform in the plane of the well. This model requires that any reversed electron spins [e.g., thermally excited spin waves, see Figure 4(b)] are delocalized within the plane of the quantum well, such that the electron spin polarization appears spatially homogeneous when averaged over the time scale of the NMR experiment, which is of order 40 μs. Simulated OPNMR lineshapes in this motionally-narrowed limit fit the experimental spectra at $\nu = 1/3$ and $\nu = 1$ over the observed temperature range.

The experimentally determined $K_S(T, \nu)$ represents a direct and calibrated measure[34,36] of the 2DES spin polarization $P(T, \nu) \equiv \langle S_z(T, \nu)\rangle / \max\langle S_z\rangle$. Figure 5 shows P(T, ν) measured by OPNMR at three important filling factors, $\nu = 1$,[60] $\nu = 1/3$,[36] and $\nu = 1/2$.[38] Both the $\nu = 1$ and the $\nu = 1/3$ electronic states become fully polarized in the low temperature limit [see Figure 4(a)], in agreement with theoretical predictions[59,61–63] that these integer and fractional ground states are quantum Hall ferromagnets (QHFM). P(T, ν) decreases with increasing temperature due to thermally excited spin-waves [see Figure 4(b)]. Data at $\nu = 1$ were obtained at B $\approx$ 7 T, where the electron Zeeman energy corresponds to a temperature $T_Z \approx 2.1$ K, whereas data at $\nu = 1/3$ were obtained at B $\approx$ 12 T, where $T_Z \approx 3.5$ K. The more rapid drop-off of P(T,$\nu = 1/3$) shows the dominant role that the electron–electron Coulomb interaction plays in the spectrum of excited states.[61] Specifically, the 'spin stiffness' at $\nu = 1$ is expected[64] to be much higher than at $\nu = 1/3$, which means that the number of spin waves present at low temperature is much less for $\nu = 1$, consistent with the data (Figure 5). OPNMR measurements of P(T,$\nu = 1$) have stimulated additional progress on the theoretical description of QHFM,[65–68] since the conventional assumption of dilute spin waves can not describe the experiments once the temperature exceeds T_Z.

Figure 5 also shows OPNMR measurements of P(T,$\nu = 1/2$), which appear to indicate a partially polarized 2DES state in the low-temperature limit.[38] These data also drop off more rapidly with increasing temperature than data taken in either the integral ($\nu = 1$) or the fractional ($\nu = 1/3$) quantum Hall regimes. Both observations are qualitatively consistent with the emerging picture that the $\nu = 1/2$ state is best described as a compressible (i.e., gapless) state of composite fermions.[69–77] OPNMR measurements of P(T,$\nu = 1/2$) and of the temperature dependence of the nuclear spin-lattice relaxation rate $R_1(T,\nu = 1/2)$ provide important constraints[38,78] on the theoretical description of the $\nu = 1/2$ state and shed new light on the nature of the composite fermion.[79,80]

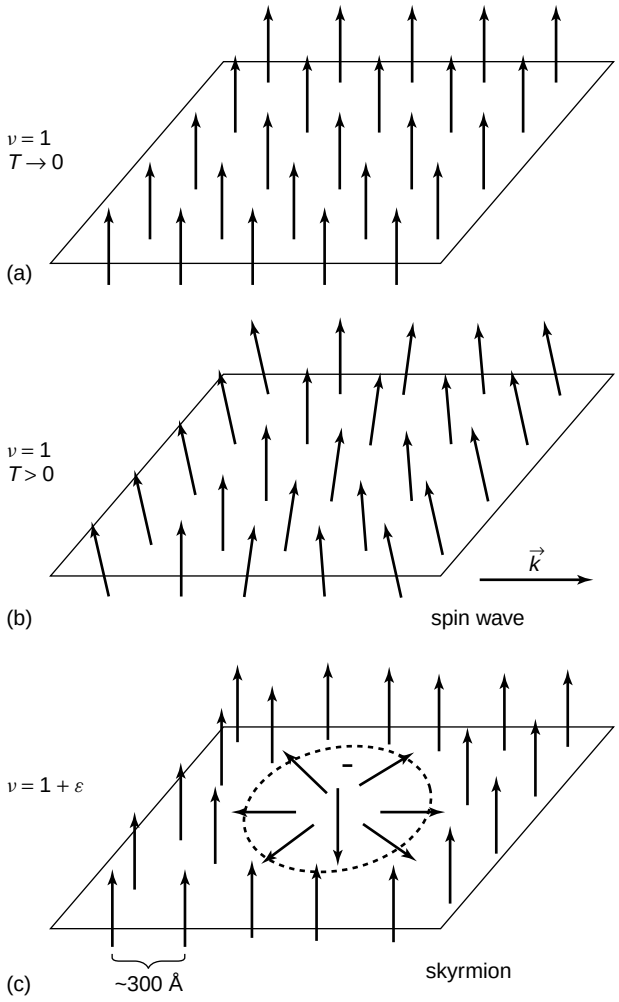

Figure 4 Illustration of electronic states in a two-dimensional system at low temperatures and high magnetic fields, as for conduction electrons in a OPNMR experiments on GaAs quantum wells. (a) At very low temperatures and Landau level filling factor $\nu = 1$, the electrons fill the lowest state of translational energy with maximum spin polarization, producing the maximum Knight shift in an OPNMR measurement. (b) At somewhat higher temperatures, thermally excited electron spin waves reduce the electron spin polarization, thereby reducing the Knight shift. (c) At very low temperatures and filling factors slightly above one, additional electrons must occupy spin-reversed states. Electron–electron interaction energies are minimized by tilting the spins of neighboring electrons, resulting in a more rapid destruction of the electron spin polarization and Knight shift than expected in the non-interacting limit. The electronic ground state contains skyrmions

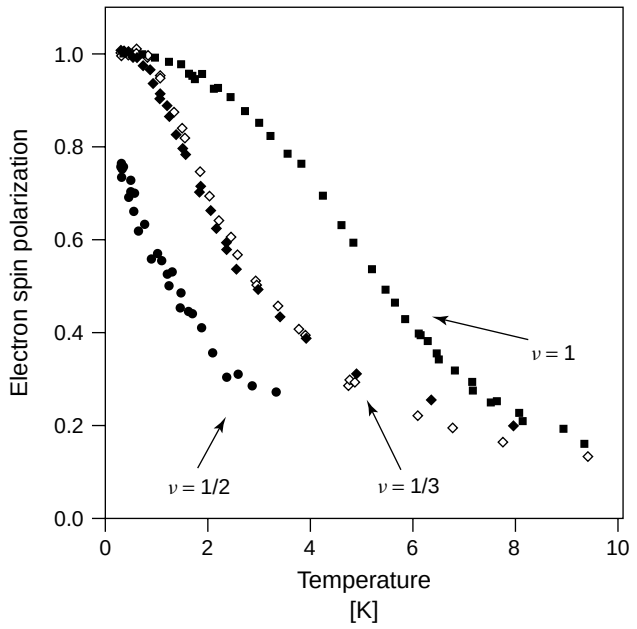

Figure 5 Temperature dependence of the electron spin polarization of a GaAs quantum well at integral ($\nu = 1$) and fractional ($\nu = 1/2$, $\nu = 1/3$) filling factors, determined from Knight shifts in OPNMR spectra. Two-dimensional electron systems at $\nu = 1$ and $\nu = 1/3$ exhibit the integer and fractional quantum Hall effects, respectively. The electronic ground state at $\nu = 1/2$ is described theoretically as a compressible (i.e., gapless) state of composite fermions

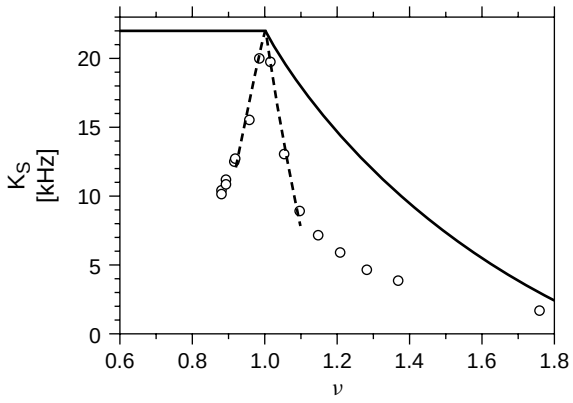

Figure 6 Dependence of the ^{71}Ga Knight shift on filling factor (open circles), obtained from OPNMR measurements on a multiple quantum well sample with 30-nm thick GaAs wells and 180-nm thick $Al_{0.1}Ga_{0.9}As$ barriers at a field of 7.05 T and 1.55 K. The filling factor was varied by tilting the sample in the field. The solid line is the theoretical curve for noninteracting electrons in a two-dimensional system. The dashed lines are fits to the data, assuming a skyrmion model in which each skyrmion carries an effective spin of 1.8, or 3.6 times the spin of a single electron. Data of this type provided the first experimental evidence for skyrmions in two-dimensional electron systems. (Reprinted from Ref.[34])

OPNMR data on GaAs quantum wells, such as the data in Figure 6, also provided the initial experimental evidence[34,35] for novel charged spin-texture excitations[62,63] called skyrmions in 2DES. To understand the meaning of a skyrmion state, consider the ground state of the QHFM at $\nu = 1$ (Figure 4(a)), and then add one electron (at fixed temperature), to move to $\nu = 1 + \varepsilon$. By the Pauli exclusion principle, the spin of the additional electron must be reversed with respect to the electron spins at $\nu = 1$. However, theory predicts a more dramatic effect: to minimize electrostatic repulsions, nearby electron spins will twist as well, making nearest neighbors more nearly parallel, until the reduction in Coulomb energy is balanced by the higher Zeeman energy of multiple reversed electron spins.[59] The resulting many-body state, a skyrmion, has one more electron but many more net reversed spins ($\sim$3 per additional electron in most experiments), relative to the $\nu = 1$ ground state. As shown in Figure 6, $K_S(\nu)$ at low temperature, and thus $P(\nu)$, drops rapidly[34] as more skyrmions (or antiskyrmions, corresponding to $\nu = 1 - \varepsilon$) are added to the system[63,81] by moving farther above or below $\nu = 1$. A similar drop has been reported[82] near $\nu = 3$. The presence of many skyrmions also leads to a strong dependence of R_1 on ν near the integral quantum Hall condition.[35] From a purely phenomenological standpoint, the effects of varying ν can be quite dramatic: at 2.1 K and 7.05 T, the spin-lattice relaxation rate of ^{71}Ga nuclei in a GaAs quantum well near $\nu = 1$ changes by a factor of 20 when the sample is rotated by only 3°! Similar effects have subsequently been observed in specific heat measurements.[83,84]

As Figure 4(c) shows, the size of the skyrmion is expected to be much less than that of spin waves [which are extended objects, Figure 4(b)], but also much greater than the internuclear spacing of roughly 3 Å. The spatial extent of the skyrmion is relatively unimportant at temperatures where skyrmions are delocalized and the OPNMR spectra are motionally narrowed[37] (i.e., the time-averaged value of $P(T,\nu)$ is invariant to translation in the plane of the quantum well).

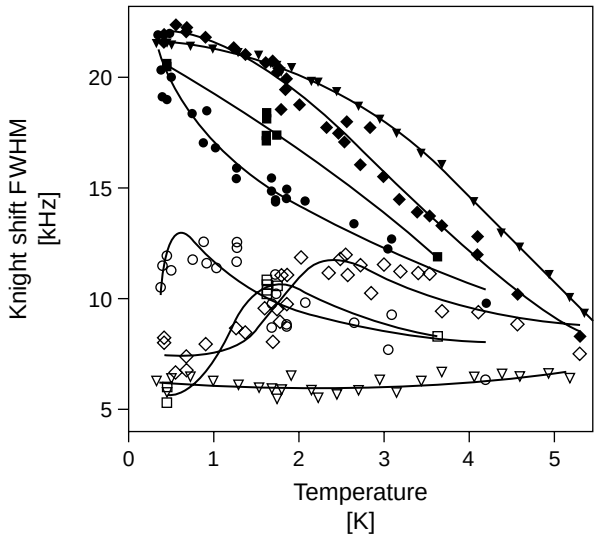

Figure 7 Dependences of the Knight shift (filled symbols) and quantum well NMR linewidth (open circles) on temperature, from ^{71}Ga OPNMR measurements on GaAs quantum wells at filling factors $\nu = 1.00$ (triangles), 0.969 (diamonds), 1.045 (squares), and 0.949 (circles). Lines are guides to the eye. The non-monotonic temperature dependence of the linewidth indicates a transition from the motionally narrowed limit at higher temperatures towards the static limit at lower temperatures, where the motion in question is translation of skyrmions in the plane of the quantum well

However, for $\nu \neq 1$, Figure 7 shows that lowering the temperature causes the width of the quantum well lineshape (open symbols) first to increase and then to decrease,[85] in stark contrast with the temperature independence of the quantum well linewidth at $\nu = 1$. Similar trends were uncovered in earlier measurements[37] near $\nu = 1/3$. The non-monotonic temperature dependence of the linewidth in Figure 7 is consistent with the evolution of the quantum well OPNMR lineshape from the motionally narrowed regime to the static regime as the temperature is lowered. Specifically, the motion at higher temperatures is that of delocalized skyrmions. As the temperature is lowered, fluctuations in local hyperfine fields freeze out as the skyrmions become localized. With spectra approaching the frozen limit, future OPNMR measurements should provide new details about the spatial distribution of skyrmions in a 2DES and the nature of the many-skyrmion ground state, which may possess unusual order.[86–92]

5 CONCLUDING REMARKS

More than three decades have passed since the first demonstration by Lampel[6] of optical pumping of nuclear spins in a semiconductor and of directly detected, optically pumped NMR. As described in this chapter, Lampel's early work has been followed by a large number of interesting methodological extensions, including the development of ODNMR techniques, time-domain ODNMR, and high-field OPNMR, and important applications, most notably the use of OPNMR as a probe of the properties of conduction electrons in two-dimensional systems in the quantum Hall regime of low temperatures and high magnetic fields. Because of the practical importance of sensitivity enhancement in all areas of NMR and the commercial and scientific importance of semiconductor devices, investigations and applications of optical pumping effects in semiconductors are certain to continue. Likely areas for future research include clarifications of the physical mechanism of optical pumping in semiconductors, investigations of optical pumping effects in other semiconductor materials and other quantum-confined structures (e.g., quantum dots), further development of all-optical NMR methods, and possibly the use of optically pumped semiconductor wafers as sources of nuclear spin polarization for sensitivity enhancement in NMR measurements on organic or biological materials deposited on the semiconductor surface.[27]

6 RELATED ARTICLES IN THIS VOLUME

Stray Field (STRAFI) NMR: Imaging in Large Field-Gradients.

7 RELATED ARTICLES IN VOLUMES 1–8

Dynamic Nuclear Polarization & High-Resolution NMR of Solids, Volume 3; Electron-Nuclear Hyperfine Interactions, Volume 3; Knight Shift, Volume 4; Optically Enhanced Magnetic Resonance, Volume 5; Quadrupolar Nuclei in Solids, Volume 6.

8 REFERENCES

1. J. Allgeier, V. Macho, D. Stehlik, H. M. Vieth, W. Auch, and J. U. Vonschutz, *Chem. Phys. Lett.*, 1982, **86**, 522.
2. T. G. Walker and W. Happer, *Rev. Mod. Phys.*, 1997, **69**, 629.
3. M. G. Zysmilich and A. McDermott, *J. Am. Chem. Soc.*, 1994, **116**, 8362.
4. M. G. Zysmilich and A. McDermott, *Proc. Natl. Acad. Sci. USA*, 1996, **93**, 6857.
5. T. Polenova and A. E. McDermott, *J. Phys. Chem. B*, 1999, **103**, 535.
6. G. Lampel, *Phys. Rev. Lett.*, 1968, **20**, 491.
7. F. Meier and B. P. Zakharchenya, 'Optical Orientation', Elsevier: Amsterdam, 1984.
8. C. A. Michal and R. Tycko, *Phys. Rev. B*, 1999, **60**, 8672.
9. J. A. Marohn, P. J. Carson, J. Y. Hwang, M. A. Miller, D. N. Shykind, and D. P. Weitekamp, *Phys. Rev. Lett.*, 1995, **75**, 1364.
10. N. T. Bagraev and L. S. Vlasenko, *Sov. Phys. Solid State*, 1979, **21**, 70.
11. N. T. Bagraev and L. S. Vlasenko, *Sov. Phys. JETP*, 1978, **48**, 878.
12. N. T. Bagraev, L. S. Vlasenko, and R. A. Zhitnikov, *Sov. Phys. Solid State*, 1977, **19**, 1467.
13. A. I. Ekimov and V. I. Safarov, *JETP Lett.*, 1972, **15**, 319.
14. D. Paget, G. Lampel, B. Sapoval, and V.I. Safarov, *Phys. Rev. B*, 1977, **15**, 5780.
15. D. Paget, *Phys. Rev. B*, 1981, **24**, 3776.
16. D. Paget, *Phys. Rev. B*, 1982, **25**, 4444.
17. D. Paget, *Phys. Rev. B*, 1984, **30**, 931.
18. W. Hanle, *Z. Phys.*, 1924, **30**, 93.
19. R. R. Parsons, *Phys. Rev. Lett.*, 1969, **23**, 1132.
20. G. P. Flinn, R. T. Harley, M. J. Snelling, A. C. Tropper, and T. M. Kerr, *Semicond. Sci. Technol.*, 1990, **5**, 533.
21. G. P. Flinn, R. T. Harley, M. J. Snelling, A. C. Tropper, and T. M. Kerr, *J. Lumines.*, 1990, **45**, 218.
22. V. K. Kalevich, V. L. Korenev, and O. M. Fedorova, *JETP Lett.*, 1990, **52**, 349.
23. M. Krapf, G. Denninger, H. Pascher, G. Weimann, and W. Schlapp, *Solid State Commun.*, 1991, **78**, 459.
24. S. K. Buratto, D. N. Shykind, and D. P. Weitekamp, *Phys. Rev. B*, 1991, **44**, 9035.
25. S. K. Buratto, D. N. Shykind, and D. P. Weitekamp, *J. Vac. Sci. Technol. B*, 1992, **10**, 1740.
26. S. E. Barrett, R. Tycko, L. N. Pfeiffer, and K. W. West, *Phys. Rev. Lett.*, 1994, **72**, 1368.
27. R. Tycko, *Solid State Nucl. Magn. Reson.*, 1998, **11**, 1.
28. C. A. Michal and R. Tycko, *Phys. Rev. Lett.*, 1998, **81**, 3988.
29. T. Pietrass, A. Bifone, T. Room, and E. L. Hahn, *Phys. Rev. B*, 1996, **53**, 4428.
30. T. Pietrass, A. Bifone, J. Kruger, and J. A. Reimer, *Phys. Rev. B*, 1997, **55**, 4050.
31. P. L. Kuhns, A. Kleinhammes, T. Schmiedel, W. G. Moulton, P. Chabrier, S. Sloan, E. Hughes, and C. R. Bowers, *Phys. Rev. B*, 1997, **55**, 7824.
32. T. Pietrass and M. Tomaselli, *Phys. Rev. B*, 1999, **59**, 1986.
33. A. Patel, O. Pasquet, J. Bharatam, E. Hughes, and C. R. Bowers, *Phys. Rev. B*, 1999, **60**, R5105.
34. S. E. Barrett, G. Dabbagh, L. N. Pfeiffer, K. W. West, and R. Tycko, *Phys. Rev. Lett.*, 1995, **74**, 5112.
35. R. Tycko, S. E. Barrett, G. Dabbagh, L. N. Pfeiffer, and K. W. West, *Science*, 1995, **268**, 1460.
36. P. Khandelwal, N. N. Kuzma, S. E. Barrett, L. N. Pfeiffer, and K. W. West, *Phys. Rev. Lett.*, 1998, **81**, 673.
37. N. N. Kuzma, P. Khandelwal, S. E. Barrett, L. N. Pfeiffer, and K. W. West, *Science*, 1998, **281**, 686.
38. A. E. Dementyev, N. N. Kuzma, P. Khandelwal, S. E. Barrett, L. N. Pfeiffer, and K. W. West, *Phys. Rev. Lett.*, 1999, **83**, 5074.
39. T. Chakraborty and P. Pietilainen, 'The Quantum Hall Effects: Integral and Fractional', 2nd edn., Springer: Berlin, 1995.

40. R. E. Prange and S. M. Girvin, 'The Quantum Hall Effect', 2nd edn., Springer: New York, 1990.
41. S. Das Sarma and A. Pinczuk, 'Perspectives in Quantum Hall Effects: Novel Quantum Liquids in Low-Dimensional Semiconductor Structures', Wiley: New York, 1997.
42. S. W. Brown, T. A. Kennedy, D. Gammon, and E. S. Snow, *Phys. Rev. B*, 1996, **54**, 17 339.
43. D. Gammon, S. W. Brown, E. S. Snow, T. A. Kennedy, D. S. Katzer, and D. Park, *Science*, 1997, **277**, 85.
44. S. W. Brown, T. A. Kennedy, and D. Gammon, *Solid State Nucl. Magn. Reson.*, 1998, **11**, 49.
45. J. M. Kikkawa and D. D. Awschalom, *Science*, 2000, **287**, 473.
46. G. Salis, D. T. Fuchs, J. M. Kikkawa, D. D. Awschalom, Y. Ohno, and H. Ohno, *Phys. Rev. Lett.*, 2001, **86**, 2677.
47. M. Eickhoff, B. Lenzman, G. Glinn, and D. Suter, *Phys. Rev. B*, in press.
48. C. R. Bowers, *Solid State Nucl. Magn. Reson.*, 1998, **11**, 11.
49. D. Mao, P. C. Taylor, and W. D. Ohlsen, *Phys. Rev. B*, 1994, **49**, 7952.
50. R. Tycko, *Mol. Phys.*, 1998, **95**, 1169.
51. K. von Klitzing, G. Dorda, and M. Pepper, *Phys. Rev. Lett.*, 1980, **45**, 494.
52. D. C. Tsui, H. L. Stormer, and A. C. Gossard, *Phys. Rev. Lett.*, 1982, **48**, 1559.
53. R. B. Laughlin, *Phys. Rev. Lett.*, 1983, **50**, 1395.
54. C. Weisbuch and B. Vinter, 'Quantum Semiconductor Structures: Fundamentals and Applications', Academic Press: San Diego, 1991.
55. D. Heiman, in 'Semiconductors and Semimetals', eds D. G. Seiler and C. L. Littler, Academic Press: London, 1992, Vol. 36.
56. L. N. Pfeiffer, K. W. West, J. P. Eisenstein, K. W. Baldwin, and P. Gammel, *Appl. Phys. Lett.*, 1992, **61**, 1211.
57. P. Khandelwal, N. N. Kuzma, S. E. Barrett, L. N. Pfeiffer, and K. W. West, *Physica B*, 1998, **256–258**, 113.
58. N. N. Kuzma, P. Khandelwal, S. E. Barrett, L. N. Pfeiffer, and K. W. West, *Physica B*, 1998, **256–258**, 121.
59. S. M. Girvin and A. H. MacDonald, in 'Perspectives in Quantum Hall Effects', eds S. Das Sarma and A. Pinczuk, Wiley: New York, 1997.
60. A. E. Dementyev, N. N. Kuzma, P. Khandelwal, S. E. Barrett, L. N. Pfeiffer, and K. W. West, submitted.
61. B. I. Halperin, *Helv. Phys. Acta*, 1983, **56**, 75.
62. S. L. Sondhi, A. Karlhede, S. A. Kivelson, and E. H. Rezayi, *Phys. Rev. B*, 1993, **47**, 16 419.
63. H. A. Fertig, L. Brey, R. Cote, and A. H. MacDonald, *Phys. Rev. B*, 1994, **50**, 11 018.
64. K. Moon, H. Mori, K. Yang, S. M. Girvin, A. H. MacDonald, L. Zheng, D. Yoshioka, and S. C. Zhang, *Phys. Rev. B*, 1995, **51**, 5138.
65. N. Read and S. Sachdev, *Phys. Rev. Lett.*, 1995, **75**, 3509.
66. M. Kasner and A. H. MacDonald, *Phys. Rev. Lett.*, 1996, **76**, 3204.
67. R. Haussmann, *Phys. Rev. B*, 1997, **56**, 9684.
68. C. Timm, S. M. Girvin, P. Henelius, and A. W. Sandvik, *Phys. Rev. B*, 1998, **58**, 1464.
69. B. I. Halperin, P. A. Lee, and N. Read, *Phys. Rev. B*, 1993, **47**, 7312.
70. R. L. Willett, K. W. West, and L. N. Pfeiffer, *Phys. Rev. Lett.*, 1995, **75**, 2988.
71. R. L. Willett, R. R. Ruel, K. W. West, and L. N. Pfeiffer, *Phys. Rev. Lett.*, 1993, **71**, 3846.
72. W. Kang, H. L. Stormer, L. N. Pfeiffer, K. W. Baldwin, and K. W. West, *Phys. Rev. Lett.*, 1993, **71**, 3850.
73. V. J. Goldman, B. Su, and J. K. Jain, *Phys. Rev. Lett.*, 1994, **72**, 2065.
74. J. H. Smet, D. Weiss, R. H. Blick, G. Lutjering, K. von Klitzing, R. Fleischmann, R. Ketzmerick, T. Geisel, and G. Weimann, *Phys. Rev. Lett.*, 1996, **77**, 2272.
75. R. R. Du, A. S. Yeh, H. L. Stormer, D. C. Tsui, L. N. Pfeiffer, and K. W. West, *Phys. Rev. Lett.*, 1995, **75**, 3926.
76. I. V. Kukushkin, K. von Klitzing, and K. Eberl, *Phys. Rev. Lett.*, 1999, **82**, 3665.
77. K. Park and J. K. Jain, *Phys. Rev. Lett.*, 1998, **80**, 4237.
78. S. Melinte, N. Freytag, M. Horvatic, C. Berthier, L. P. Levy, V. Bayot, and M. Shayegan, *Phys. Rev. Lett.*, 2000, **84**, 354.
79. R. Shankar, *Phys. Rev. Lett.*, 2000, **84**, 3946.
80. R. Shankar, *Phys. Rev. B*, 2001, **63**, 5322.
81. E. H. Aifer, B. B. Goldberg, and D. A. Broido, *Phys. Rev. Lett.*, 1996, **76**, 680.
82. Y. Q. Song, B. M. Goodson, K. Maranowski, and A. C. Gossard, *Phys. Rev. Lett.*, 1999, **82**, 2768.
83. V. Bayot, E. Grivei, S. Melinte, M. B. Santos, and M. Shayegan, *Phys. Rev. Lett.*, 1996, **76**, 4584.
84. V. Bayot, E. Grivei, J. M. Beuken, S. Melinte, and M. Shayegan, *Phys. Rev. Lett.*, 1997, **79**, 1718.
85. P. Khandelwal, A. E. Dementyev, N. N. Kuzma, S. E. Barrett, L. N. Pfeiffer, and K. W. West, *Phys. Rev. Lett.*, 2001, **86**, 5353.
86. L. Brey, H. A. Fertig, R. Cote, and A. H. MacDonald, *Phys. Rev. Lett.*, 1995, **75**, 2562.
87. A. G. Green, I. I. Kogan, and A. M. Tsvelik, *Phys. Rev. B*, 1996, **54**, 16 838.
88. R. Cote, A. H. MacDonald, L. Brey, H. A. Fertig, S. M. Girvin, and H. T. C. Stoof, *Phys. Rev. Lett.*, 1997, **78**, 4825.
89. M. Rao, S. Sengupta, and R. Shankar, *Phys. Rev. Lett.*, 1997, **79**, 3998.
90. M. Abolfath and M. R. Ejtehadi, *Phys. Rev. B*, 1998, **58**, 10 665.
91. Y. V. Nazarov and A. V. Khaetskii, *Phys. Rev. Lett.*, 1998, **80**, 576.
92. A. J. Nederveen and Y. V. Nazarov, *Phys. Rev. Lett.*, 1999, **82**, 406.

Biographical Sketches

Robert Tycko, *b* 1959. A.B., 1980, Princeton University. Ph.D., 1984, University of California at Berkeley. Began his career at AT&T Bell Laboratories, where he developed new solid state NMR methods, such as zero-field NMR in high field, and applied solid state NMR to problems in condensed matter physics. Moved to the National Institutes of Health in 1994, and now develops and applies solid state NMR methods for structural studies of biopolymers. Approx. 100 papers on all areas of magnetic resonance. Research interests: optical pumping, NMR theory and methodology, structure of proteins and amyloid fibrils.

Sean E. Barrett, *b* 1965. A.B., 1987, Princeton University. Ph.D., 1992, University of Illinois at Urbana-Champaign. Recipient of the 1995 William L. McMillan Award for outstanding contributions to condensed matter physics, in particular the development at AT&T Bell Laboratories of optically pumped NMR as a probe of two-dimensional electron systems. Approx. 25 papers on NMR in condensed matter physics. Research interests: optical pumping, two-dimensional electron systems, high-temperature superconductivity.

Quantum Tunneling Spectroscopy

Stan Clough

Department of Physics, University of Nottingham, Nottingham, UK

1	Introduction	1
2	The Rotational Spectrum of a Triangular Rotor	1
3	Fundamental Considerations	3
4	Experiments and Techniques	3
5	Related Articles	4
6	References	4

1 INTRODUCTION

Low-temperature molecular tunneling spectroscopy is of interest for four reasons: it continues into the quantum domain the study of molecular motion, it provides an outstanding example of a classical to quantum transition, it extends NMR and spin thermodynamics into the adjacent domain of coherent molecular dynamics, and finally it clarifies historical conceptual problems concerning particle indistinguishability and the topology of rotation space. The main results have recently been surveyed.[1]

The rotations of hindered symmetrical groups like CH_3 and NH_4 in solids persist to helium temperatures where the motion of hindered triangular rotors like CH_3 is characterized by a discrete frequency, the tunnel frequency ω_t, derived from the overlap of ground state librational oscillator wavefunctions localized in adjacent wells of a three-well potential. A typical low-temperature CH_3 spectrum consists of three frequencies: $\pm\omega_t$ and 0. The quantum motion of tetrahedral rotors like NH_4 and ND_4 is more complicated,[2] with several tunnel frequencies associated with rotation about the different symmetry axes. The structured spectrum changes with increasing temperature towards a Lorentzian peak with a halfwidth $1/\tau_c$, where τ_c is an orientational correlation time. This spectrum is explained by a quasi-classical hopping model. The transition, which has been studied by both magnetic resonance and neutron scattering,[3] is illustrated in Figure 1.

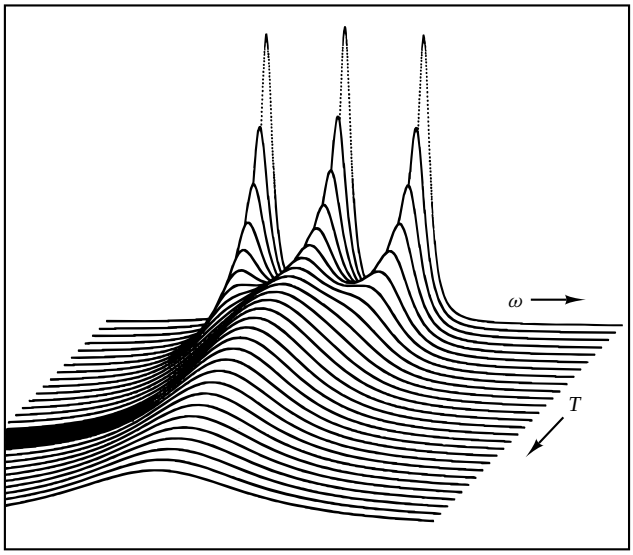

Figure 1 The rotational spectrum of a hindered CH_3 group changes from three frequencies $\pm\omega_t$ and 0 at low temperature to a Lorentzian spectrum of rotational hopping motion at high temperature. The figure is a model with a single temperature-dependent parameter that gives a good representation of observations in many materials. The temperature and frequency scales depend on the height of the hindering barrier

2 THE ROTATIONAL SPECTRUM OF A TRIANGULAR ROTOR

2.1 Stationary States

Low-temperature states have well-defined wavenumbers k. The change from well-defined orientation at high temperatures is similar to the change from hopping conduction to band conduction of polarons and excitons. Like these phenomena, molecular rotation is modeled by a particle in a periodic potential with an orientation coordinate ϕ and a hindering potential $V\cos 3\phi$. Special features are due to the finite extent, 2π, of the rotational coordinate space. For stationary states, we assume a cyclic boundary condition $\psi(\phi + 2\pi) = \psi(\phi)$ and the Hamiltonian

$$\hat{\mathcal{H}} = -\frac{\hbar^2}{2I}\frac{\partial^2}{\partial\phi^2} - V\cos 3\phi \qquad (1)$$

whose eigenvalues for the lowest band are

$$\hbar\omega(k) = -\tfrac{2}{3}\hbar\omega_t \cos\tfrac{2}{3}\pi k \qquad (2)$$

The eigenfunctions are Bloch waves with k lying between $\frac{3}{2}$ and $-\frac{3}{2}$. The boundary condition selects $k = \pm 1$ or 0. The energies are thus $-\frac{2}{3}\hbar\omega_t$ and $\frac{1}{3}\hbar\omega_t$, the latter being doubly degenerate. The three frequencies derived from the energy differences are $\pm\omega_t$ and 0, the low-temperature spectrum.

2.2 Excitations and Dynamics

When dynamical interaction with the environment is included, the space ϕ is open and may be envisaged as a helix upon which wavepackets rotate.[4] A wavepacket confined to one turn of the helix is single-valued within a range 2π and is formed by superposing two of the eigenfunctions of equation (1). Two nodes separated by 2π form the leading and trailing edges of the wavepacket. Three elemental wavepackets rotate with the angular velocities $\pm\omega_t$ and 0. Generation of wavepackets from the stationary states and their subsequent evolution in time can be compared with a 90° pulse and subsequent free induction decay in NMR. The rotation is observable, because it modulates spin-dependent interactions so that molecular rotation and NMR are intimately linked. Thermal excitation results in a transfer of angular momentum, which changes the average wavenumber, $k_a = \pm\frac{1}{2}$ or 0 to

$k_a + \sigma$, $\hbar d\sigma/dt$ being the torque. The general rotation frequency derived from equation (2) is

$$\omega_{k_a,\sigma} = (\tfrac{3}{4})^{-1/2}\omega_t \sin[\tfrac{2}{3}\pi(\sigma + k_a)] \quad (3)$$

A distribution of σ explains the broad rotational spectra of Figure 1. Relaxation to stationary states with integer k causes σ to approach zero as the temperature falls.

A wavepacket only has large amplitudes in the potential wells, and can be represented by three complex amplitudes. The three elementary wavepackets can be superposed by adding their amplitudes to form a more general wavepacket whose evolution involves all three frequencies $\omega_{k_a,\sigma}$. This complex wavepacket rotates and oscillates in shape. At low temperature, the frequency 0 is the rotation frequency and the frequencies $\pm\omega_t$ are shape oscillations. Thus the rotor comes to orientational rest, but continues its internal oscillations. This character changes smoothly into one of rotation as σ grows in absolute value. When $\sigma = \frac{3}{4}$, the complex wavepacket rotates clockwise, moving smoothly through each of the three wells in turn. To accomplish the passage between wells, the shape of the wavepacket oscillates in sympathy with the rotation. The coherent evolution of wavepackets for $\sigma = 0$ and $\sigma = \frac{3}{4}$ is compared in Figure 2.

2.3 Combined Spin and Rotational Dynamics

As an alternative to a reference frame in which the lattice is stationary, it is useful to use a frame in which the wavepacket is stationary. In this frame, σ appears as a vector potential in the angular momentum operator and the wavenumbers remain integers. Observables are the same whichever frame is used. The vector potential can be incorporated into a spin Hamiltonian to combine quantum rotation and spin dynamics. In the case of a methyl group,

$$\hat{\mathcal{H}} = \hat{\mathcal{H}}_Z + \hat{\mathcal{H}}_{DD} + \hat{\mathcal{H}}_R \quad (4)$$

$$\hat{\mathcal{H}}_R = -\tfrac{1}{3}\hbar\omega_t(\hat{R}\, e^{i2\pi\sigma/3} + \hat{R}^{-1}e^{-i2\pi\sigma/3}) \quad (5)$$

where $\hat{\mathcal{H}}_Z, \hat{\mathcal{H}}_{DD}$, and $\hat{\mathcal{H}}_R$ are the Zeeman, dipole–dipole, and rotation Hamiltonians. The basis functions are the eight product spin states of three protons at the three lattice sites. These states can be regarded as shorthand for Slater determinants. The operator $\hat{R}$ cyclically permutes the three spin states round the lattice sites. Rotation clockwise through $\frac{2}{3}\pi$ introduces the phase change $\frac{2}{3}\pi\sigma$ and rotation anticlockwise the reverse phase change. Changes in σ arise owing to collisions between one of the methyl protons and a neighboring atom. This formalism can be extended to tetrahedral molecules.

A spin state is propagated by equation (4). The new feature compared with ordinary spin dynamics is inertia. Whereas the precession frequency of a spin depends only on the instantaneous magnetic field, the rotation frequency of a methyl group depends on the previous dynamical history. The evolution involves two coupled equations: the time-dependent Schrödinger equation and the differential equation for σ. For thermal excitations, some stochastic assumption concerning $d\sigma/dt$ must be made. Another torque is due to the angular dependence of the dipole–dipole energy. This can be obtained by rotating the state slightly using $\lambda\hat{R}$, where λ is small, and finding the rate of change of dipolar energy. The change in the dipole–dipole energy due to rotation, familiar at high temperatures, has a low-temperature counterpart in which molecular rotation changes owing to the angular dependence of the dipole–dipole energy.

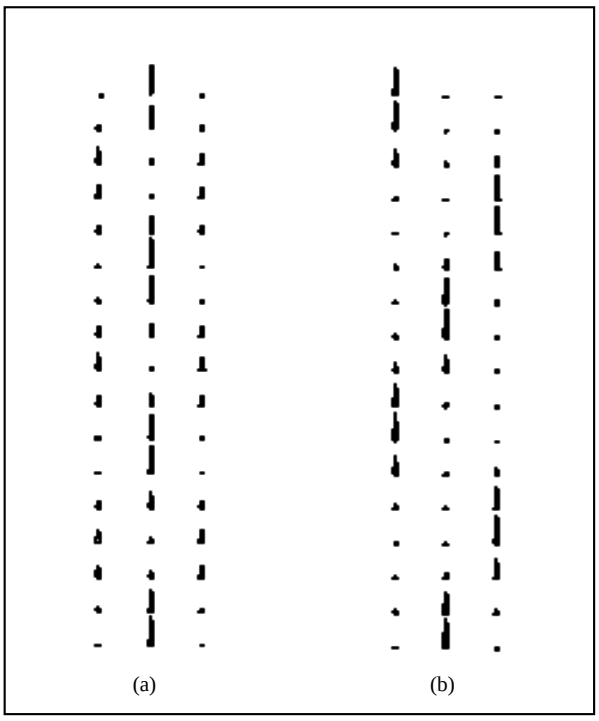

Figure 2 A methyl group wavepacket is described by three intensities in three potential wells on a circle. At low temperature (a), the wavepacket oscillates in shape without rotating. A rotational impulse changes the motion to one of coherent rotation (b), the correlated shape oscillations now assisting the passage from well to well

2.4 The Quantum-to-Classical Transition

The temperature dependence of the rotational spectrum is remarkably similar for all materials except for the scaling of temperature with barrier height. The host lattice serves as a heat bath, destroying coherence and exerting a fluctuating torque. The notable feature is that the outer (shape oscillation) peaks of the low-temperature rotational spectrum move inward with increasing temperature. There have been many theories of this,[3] which can be divided (see Section 3) into those that attribute the reduction to properties of the host lattice and those that regard it as an essential feature of the quantum-to-classical transition. The latter view is that the wavepacket shape oscillations slow down to meet the rising rotation rate in order to play their new role of assisting rotation, while fluctuations in the rotation rate broaden the spectrum. The simplest idea[4] is that the slowing can be described as a spectral averaging process. Orientational hopping is assumed to be accompanied by hopping in k-space. In this way, increasing localization in space is compensated by delocalization in k-space. The frequencies of the low-temperature spectrum are assumed to hop between $\pm\omega_t$ and 0 owing to k modulation,

while each is also subject to random phase modulation due to the changes in orientation. The spectrum is obtained by summing the elements of a matrix $\mathbf{M}^{-1}$, where

$$\mathbf{M}=\begin{bmatrix} \mathrm{i}(\omega_t-\omega)-2\rho-\delta & \rho & \rho \\ \rho & \mathrm{i}(-\omega_t-\omega)-2\rho-\delta & \rho \\ \rho & \rho & -\mathrm{i}\omega-2\rho-\delta \end{bmatrix} \quad (6)$$

Here ρ represents the rate of k hopping and δ the rate of orientational hopping. Both are identified with $1/\tau_c$. At low temperatures, $1/\tau_c \ll \omega_t$, and the frequencies and halfwidths $3/\tau_c$ of the three peaks are obtained from the diagonal elements of equation (6). At high temperatures, ω_t may be neglected. The spectrum is centered at $\omega = 0$, and the halfwidth is $1/\tau_c$. The classical hopping model is thus extended to the quantum regime. Figure 1 is calculated in this way. The parameter $1/\tau_c$ typically obeys an Arrhenius law, and can be roughly equated with a thermal average of the bandwidths of occupied excited librational states. The temperature dependence of the rotational spectrum is thus obtainable from the tunneling frequency without adjustable parameters.

3 FUNDAMENTAL CONSIDERATIONS

3.1 Indistinguishability

Particle indistinguishability has a crucial role in the theory. According to an argument from early quantum theory,[5] the hindering potential for symmetric molecules must be invariant to the interchange of the space and spin coordinates of the protons. For a methyl group, this means a threefold symmetry,[6] which prevents excitation of wavepackets and is inconsistent with the high-temperature hopping model. Though the symmetry constraint correctly identifies the stationary states of a hindered methyl group by excluding nonintegral k, it is incompatible with wavepacket dynamics. The reason is that wavepackets and stationary states have different topologies. Consider the evolution from one to the other. A superposition of two similar wavepackets $\psi(\omega t)$ and $\psi(\omega t - \gamma)\exp(\frac{1}{2}\mathrm{i}\gamma)$ is a stationary state if $\gamma = (2n + 1)\pi$. As a stationary state is approached, the helical space–time path of the wavepacket broadens, and turns of the helix overlap. The number n of rotations in a time $2\pi/\omega$ becomes ambiguous. Destructive interference between paths of different n restricts k to integral values. When the coordinate ωt disappears, the labels that in wavepacket states refer to nonidentical proton trajectories refer to identical indistinguishable particles. The symmetry constraints with antisymmetrization ensure that the phase is continuous and the Pauli principle is satisfied. Excitations restore the helical space–time topology and the proton trajectories. The constraints no longer strictly apply, but quantum behavior results while wavepackets imperfectly reflect the topology of neighboring stationary states.

3.2 The Topology of Rotation Space

The identification of labels with particles also leads to the identification of molecular rotation with the symmetry operation of permutation. This is only possible if the rotation space ϕ is closed. Symmetry-constrained theories consequently allow only integral wavenumbers and limit dynamics to transitions that conserve the wavenumber. This makes them completely different from other transport theories, and gives rise to the view that rotation is fundamentally different from translation. The unconstrained theory of Section 2 has affinities with superconductivity, SQUIDs and quantum transport phenomena in general, besides linking with the hopping model of transport.

4 EXPERIMENTS AND TECHNIQUES

The first effect of tunneling rotation to be observed was that motionally narrowed NMR lines of methyl-containing compounds often fail to broaden when the temperature is reduced to 4 K. With falling temperature, the frequency of components of the dipole–dipole interaction converge on $\pm\omega_t$, as in Figure 1, giving rise to discrete sidebands of the NMR spectrum. The total second moment of the NMR spectrum is conserved, so the sidebands are very weak if the tunnel frequency is large. The failure to broaden demonstrates that $\omega_t/2\pi$ exceeds a few tens of kilohertz. ESR studies of free radicals containing rotating methyl groups in the fragment $C-CH_3$ display more detail. At high temperature, the hyperfine spectrum is a 1 : 3 : 3 : 1 quartet, indicating equal interaction of the electron spin with the three protons. When the temperature is reduced, the spectrum changes to a seven-line pattern 1 : 1 : 1 : 2 : 1 : 1 : 1 with half the spacing of the quartet, the two inner peaks of the quartet having split into 1 : 1 : 1 triplets.[6] The splitting is due to two of the three methyl states with magnetic quantum number $\frac{1}{2}$ forming stationary wavepackets—one in the orientation that minimizes the hyperfine energy and one in the orientation that maximizes it. The energy difference is the separation of the outer members of the triplet. The central member of the triplet has $k = 0$. The collapse of the outer members of each triplet on to the central member is due to the two wavepackets hopping between the two orientations and averaging the orientationally dependent energy. As the rate of rotation increases, the tunnel frequency falls to join it, as in Figure 1. The effect is that all three members of the triplet are involved in the motional averaging process. This is observed through the fact that the central member of the triplet does not remain narrow, while the outer pair merges with it.

The main ESR transitions correspond to flips of the electron spin, while the nuclear quantum number m remains unchanged. Transitions in which m also changes give rise to weak sideband transitions, which enable the tunnel frequency to be measured with precision. The detection of such transitions, their approximate location having been previously deduced by ENDOR, marked the true beginning of tunneling spectroscopy, the motional spectrum being clearly separate from the pure magnetic transitions. Similar tunneling sidebands of NMR spectra open a frequency window in the region of 200 kHz, rather than the 100 MHz range of ESR. Level crossing or tunnel resonance techniques[7] greatly aid the detection of weak sideband transitions and extend the range of accessible tunnel frequencies. A magnetic field is chosen such that the molecular tunnel frequency is equal to a Larmor frequency—either the electron Larmor frequency for free radicals or the nuclear Larmor frequency in ordinary materials. At these internal resonances, transfer of energy between magnetic and rotational

energy occurs through a resonant relaxation process. Energy is exchanged between a Zeeman reservoir and a tunneling reservoir, each of which relaxes to the lattice by its own relaxation process. The ideas of spin thermodynamics are extended, and the process provides an extremely sensitive way of detecting tunnel frequencies. It requires the ability to vary the magnetic field. This is done either by changing the NMR measurement frequency or by using field cycling. There are two versions of the technique. In one, the sample is doped with paramagnetic impurities, often by γ irradiation, and the tunnel frequency is tuned to the electron Larmor frequency. In the other, the tunnel frequency is tuned to the nuclear Larmor frequency. Together, these cover the range from a few megahertz to 50 GHz. With paramagnetic impurities, what is observed is a dynamic polarization effect at the magnetic field of the internal resonance. Energy is transferred between the electron Zeeman and tunneling reservoirs when there is a small mismatch in their frequencies, the energy balance being made up by the nuclear Zeeman system, which is heated or cooled according to the sign of the mismatch.

The direct observation of tunneling sideband transitions is generally difficult, because they must be driven with a field that is nonuniform across the molecule. It is the dipole–dipole interaction, mixed into the magnetic states, that drives the transitions. This effect is naturally stronger at low fields. Low-field dipole–dipole driven NMR has consequently proved to be a powerful way of studying tunneling. Either a true low field[8] using field cycling or a low effective field in the rotating frame[9] may be employed, and both have given good results. They cover the frequency range from 60 kHz to 1 MHz, and thus link with tunnel resonance methods to provide a spectroscopy covering six decades of frequency. An example of a low-field spectrum is shown in Figure 3. Double resonance techniques can be employed to increase population differences and enhance transitions. The next frontier to still lower frequencies has recently been breached by the use of the Lee–Golburg method of line narrowing. Low-field Fourier transform tunnel spectroscopy is conducted slightly off-resonance in the rotating frame.[10] Another recent development in low-field spectroscopy is the use of SQUID detection.[11] It seems likely that developments in the future will come from the increasing exploitation of NMR time domain techniques to interchange magnetic and rotational order, using the spins to monitor the coherent tunneling motion.

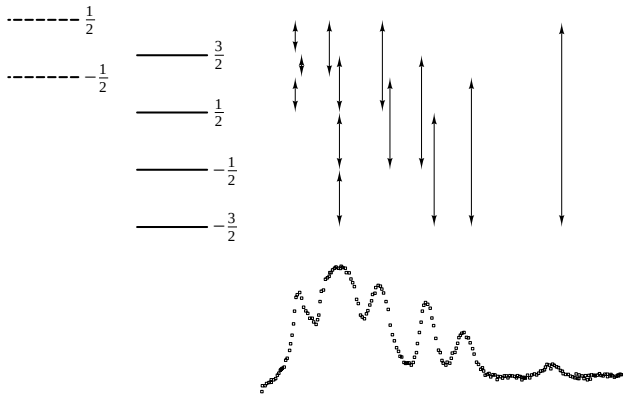

Figure 3 The low-field dipole–dipole driven NMR spectrum of dimethylmalonic acid obtained at 4.2 K. The proton Larmor frequency is 210 kHz and the tunnel frequency that splits $m = \frac{1}{2}$ and $-\frac{1}{2}$ levels is 330 kHz

There are many other phenomena associated with tunneling rotation that a brief review cannot cover, but two observations connected with nearly free rotors should be mentioned. The Haupt effect[12] is a spectacular nuclear dynamic polarization effect that occurs when the temperature of 4-methylpyridine is changed at fairly low temperatures as the slow evolution in the rotational states of the nearly free methyl group drives a large change in the dipole–dipole temperature. The second effect[13] is the optical observation of fractional quantization of the rotation of nonequilateral triangles of nitrogen atoms in molecular beams. Molecular quantum rotation covers a very wide range of phenomena. Because of its dynamical simplicity, it very clearly exhibits features that are common to all quantum systems.

5 RELATED ARTICLES

Brownian Motion and Correlation Times; Field Cycling Experiments; Geometric Phases; Low Spin Temperature NMR; Ortho–Para Hydrogen at Low Temperature; Quantum Exchange; SQUIDs.

6 REFERENCES

1. A. J. Horsewill, *Spectrochim. Acta, Part A*, 1992, **48**, 379.
2. Z. T. Lalowicz, U. Werner, and W. Muller-Warmuth, *Z. Naturforsch. A*, 1988, **43**, 219.
3. A. Heidemann, M. Prager, and M. Monkenbusch, *Z. Phys. B, Condensed Matter*, 1989, **76**, 77.
4. S. Clough, A. J. Horsewill, A. M. Alsanoosi, M. J. Barlow, and M. R. Johnson, *Chem. Phys. Lett.*, 1993, **211**, 637.
5. P. A. M. Dirac, *The Principles of Quantum Mechanics*, 2nd edn., Oxford, University Press, Oxford, 1935, Chap. 10
6. J. H. Freed, *J. Chem. Phys.*, 1965, **43**, 1710.
7. H. Glattli, A. Sentz, and M. Eisenkremer, *Phys. Rev. Lett.*, 1972, **28**, 871.
8. S. Clough, A. J. Horsewill, P. J. McDonald, and F. O. Zelaya, *Phys. Rev. Lett.*, 1985, **55**, 1794.
9. D. W. Nicoll and M. M. Pintar, *Phys. Rev. B*, 1981, **23**, 1064.
10. A. Z. Danyanovich, J. Peternelj, and M. M. Pintar, *Physica B*, 1994, **202**, 273.
11. C. Connor, J. Chang, and A. Pines, *Rev. Sci. Instrum.*, 1990, **61**, 1059.
12. J. Haupt, *Z. Naturforsch. A*, 1968, **23**, 208.
13. G. Delacretaz, E. R. Grant, R. L. Whetten, L. Woste, and J. W. Zwanziger, *Phys. Rev. Lett.*, 1986, **56**, 2598.

Biographical Sketch

Stan Clough. *b* 1932. B.Sc., 1952, Ph.D., 1963, Bangor, Wales. Industrial scientist 1952–59. Started ESR and NMR at ICI. Faculty member, Bangor, 1959–63; Nottingham, 1963–present. Approx. 150 papers. Research specialties: use of ESR, ENDOR, NMR and neutron scattering to develop molecular tunneling spectroscopy, study the quantum-to-classical transition, and extend the concepts and techniques of coherent NMR spectroscopy to particle dynamics.

Ruby NMR Laser

Ernst. Brun

University of Zürich, Zürich, Switzerland

1	Introduction	1
2	Spin Dynamical Aspects of Ruby	2
3	Conventional Bloch-Type Laser Equations	3
4	Extended Bloch-Type Laser Equations	4
5	Basic Test of the EBL Model	5
6	The NMR Laser as a Small Signal Detector	6
7	Related Articles	7
8	References	7

1 INTRODUCTION

Problems of collective ordering have fascinated scientists as well as laymen for many years, and have brought a growing, interdisciplinary community together where mathematicians, physicists, chemists, meteorologists, biologists, engineers, and sociologists—to name but a few—try to reach a common understanding of the dynamics of complex physical or mathematical nonlinear systems. A new branch of scientific life has thus evolved, which has been named 'synergetics' by its founder, Hermann Haken.[1] Its subjects are many body systems with nonlinear interactions among the individuals—'social systems' so to speak—which are in contact with their surroundings (reservoirs of heat, mass, food, or information), and further with pumping devices, feedback systems, forcing fields, modulators, control devices, and so on.

An outgrowth of synergetics has been the discovery that the nonlinear response of a self-ordered many body system can often be drastically reduced to that of a low-dimensional system by Haken's slaving principle. There, only a few relevant macroscopic variables, the order parameters, play the role of masters. A typical representative thereof is the laser, with its large number of radiating entities and field quanta. However, owing to cooperative interactions, most degrees of freedom are frozen in—only a few survive slaving and determine the laser activity. This then allows a quantitative comparison of experimental observations with low-dimensional differential models in an appropriate phase space.[2]

A laser consists typically of two main components: the radiating particles (atoms, molecules, electrons, nuclei, etc.) and the radiation field produced by them. An external pump causes population inversion, where the higher energy states are more strongly populated than the lower ones. A resonant structure (cavity), which encloses the particles, provides feedback for the radiation field, thus causing above laser threshold coherent excitation and radiation of the particles.

In the ruby NMR laser (Figure 1), the lasing 'particles' are the nuclear spins of the ^{27}Al in Al_2O_3:Cr^{3+}, and the radiation field is a magnetic radiofrequency field sustained by the tuned NMR coil that forms the cavity of the laser. Spin inversion beyond the first laser threshold is obtained by means of dynamic nuclear polarization (DNP) at the ruby lattice temperature of 4.2 K. DNP is achieved by shining microwaves at Cr^{3+}, thus causing electronic transitions that pump the nuclear spins to the lasing state. The NMR cavity is normally tuned to ν_a. The NMR laser thus acts as a tuned, single mode, homogeneously broadened, unidirectional laser. The NMR laser field induces a voltage in the receiver coil L, which can be tapped at the tuning capacitor C_T. The NMR laser signal thus is a voltage $V(t)$ across C_T that oscillates at ν_a. Since the laser dynamics involves primarily regular variations of the amplitude of V, the rf laser signal is demodulated, and its envelope $v(t)$ only is recorded. We call $v(t)$ the laser output.

The ruby NMR laser, a solid state nuclear spin flip laser, operates typically at the central NMR frequency ν_a = 12.3 MHz of ^{27}Al in a static magnetic field B_0 = 1.1 T. Therefore it may also be called a RASER, since it is a generator of coherent radiowaves rather than light, but having many of the virtues of a generic laser.

Ever since the discovery of radio wave amplification by stimulated emission of radiation in ruby (Al_2O_3:Cr^{+3}) by Bösiger,[3] we have been intrigued by the question of how to describe quantitatively the physics of the collective ordering of the ^{27}Al nuclear spins in that solid. In particular, with the discovery of laser chaos (see ***Laser Devices in NMR: Routes to Chaos***), the central problem in investigations of chaotic behavior has been to construct realistic models and relate them to a wide as possible spectrum of observations from different modes of operation. A general theory that treats the ruby NMR laser has not yet been formulated, and we still have to limit ourselves to grossly simplified models. They are derived from the famous Bloch equations and Kirchhoff rules, which describe classically the collective dynamics of the ^{27}Al spins and the electronic circuitry that provides the laser field.[4] Nuclear spin relaxation is introduced phenomenologically by the use of relaxation times or relaxation rates; DNP is expressed by a pumping rate and a pumping level. These quantities enter the model as system parameters that reflect in an average sense the exceedingly complicated interactions among the nuclear and electronic spins and their coupling to

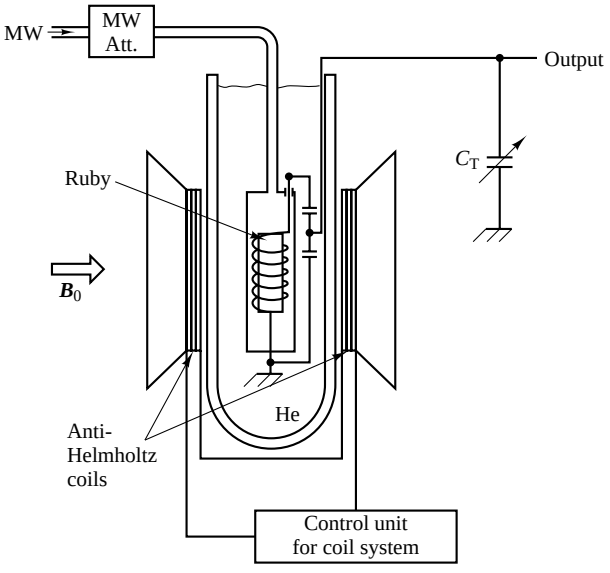

Figure 1 The basic components of the NMR laser. The anti-Helmholtz coils are used for linewidth modulation. In the case of Q modulation, the resistance of a pin diode in parallel to C_T is varied sinusoidally

the crystal electric field and to the external microwave field that ultimately pumps the ^{27}Al. Spin–spin interactions mediate the energy transfer from the lasing spins to the pumping field as well as to the lattice. Spin–spin interactions are also responsible for the irreversible dephasing of the radiating ^{27}Al nuclei.

2 SPIN DYNAMICAL ASPECTS OF RUBY

The performance of the ruby NMR laser depends strongly on the coupling of the nuclear ^{27}Al and electronic Cr^{+3} spins with magnetic and electric fields and among themselves.[5] The Hamiltonian of the combined nuclear and electronic spin system can be separated into terms that reflect magnetic (Zeeman), electric (crystal field), and spin–spin (dipole–dipole) interactions. There appear mutually commuting and noncommuting terms, $\hat{\mathcal{H}}_i$ and $\hat{\mathcal{H}}_{ik}$, respectively. Each of the commuting operators characterizes an energy reservoir of many degrees of freedom. Since the crystal field effects are small compared with the Zeeman interaction, we speak somewhat loosely of the nuclear and electronic Zeeman reservoirs, which are coupled to dipole–dipole interaction reservoirs. In thermal equilibrium, a spin temperature θ_i may be assigned to each of these subsystems.

The noncommuting operators describe internal couplings (spin–spin and spin–lattice) or interactions with time-dependent external fields, and are treated as perturbations. They are responsible for the energy flow between the reservoirs. The internal couplings tend to equalize the temperatures with time constants τ_{ik} (dephasing or relaxation and cross-relaxation times): they reflect dissipation. In contrast, the interactions with coherent radiation fields tend to offset the overall thermal equilibrium: they may produce spin order—for example, by pumping of spin states or phasing of otherwise randomly oriented single spins.

2.1 Bulk ^{27}Al and Impurity Cr^{+3}

The lasing 'particles' in ruby are the magnetic dipole moments of the 100% abundant ^{27}Al nuclei, which interact with the static magnetic field $\boldsymbol{B}_0$ and the radiation field $\boldsymbol{B}(t)$ by the magnetic dipole interaction. ^{27}Al has spin-$\frac{5}{2}$, the gyromagnetic ratio $g = 6.97 \times 10^7\ \mathrm{s^{-1}\,T^{-1}}$ (we use the symbol g instead of γ, which is reserved for relaxation rates; in so doing, we follow the notation of quantum optics), and an electric quadrupole moment. In ruby, ^{27}Al occupies equivalent sites. The nuclear Zeeman levels $E_m = -mg\hbar B_0$ ($m = \pm\frac{5}{2}, \pm\frac{3}{2}, \pm\frac{1}{2}$) are thus uniquely shifted by the quadrupolar interaction of ^{27}Al with the crystal electric field. This amounts to five, in general different, resonance frequencies $\omega_{\mathrm{a}}^{(i)}$ for the $\Delta m = \pm 1$ spin flip transitions. Since the LC circuit that forms the laser cavity has only one resonance frequency, $\omega_{\mathrm{c}} = 1/\sqrt{LC}$, the NMR laser has at most five modes. However, single mode NMR laser activity is possible when the coil is tuned to a selected NMR transition. In this case, the spin inversion should not exceed a value at which multimode excitation occurs. Unless stated otherwise, we restrict ourselves to the single mode activity of the strongest $(\frac{1}{2}, -\frac{1}{2})$ NMR transition of frequency $\omega_{\mathrm{a}} = gB_0$: the central NMR mode.

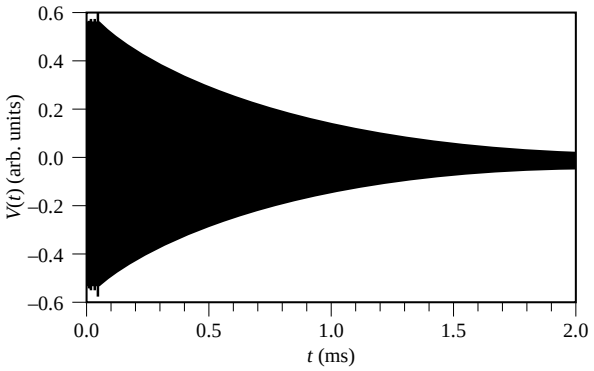

Figure 2 FID below laser threshold. Note the exponential decay and its slowing down due to the radiative feedback of the inverted spin system in the NMR coil

The Cr^{3+} impurity ions that replace Al^{3+} ions in ruby, on the one hand, shorten the spin–lattice relaxation time T_1 for ^{27}Al and, on the other, provide a mechanism to polarize the ^{27}Al positively or negatively with respect to the direction of the strong magnetic field $\boldsymbol{B}_0$. The experimental optimum for short relaxation and strong polarization was found in a specimen cut from a single crystal with a Cr^{3+} concentration of nominally 0.02%. The efficiency of the DNP technique has been tested by comparing enhanced NMR signals with those taken at the lattice temperature θ_{L}.[6] The largest enhancement of about 400, corresponding to a nuclear spin polarization of about 17%, has been observed at $\theta_{\mathrm{L}} = 1.9\,\mathrm{K}$ for a crystal orientation of about 61° between the c axis and $\boldsymbol{B}_0$. This is the standard orientation with which all our NMR laser experiments have been performed. At this angle, the two strongest ESR transitions coincide: the laser behavior is optimal. In addition, this particular crystal orientation yields an almost exponential FID below the laser threshold, as shown in Figure 2. This experimental fact reflects the anticipated Bloch dynamics in ruby under standard conditions.

In order to reach the NMR laser threshold, the nuclear spins have to be polarized in the direction opposite to $\boldsymbol{B}_0$. A negative spin polarization of the order of 10% is required, which corresponds to a negative spin temperature of some millikelvins. This condition is easily met at the lattice temperature of liquid helium when microwaves of frequency ω are supplied to the sample with ω near an ESR transition frequency ω_{e} of the Cr^{3+} impurity ions. Setting ω slightly above ω_{e} then leads to the required low, negative spin temperature. Thereby, microwave energy is absorbed and delivered to the Cr^{3+}–Cr^{3+} spin–spin system. Its spin temperature θ_{ss} rises to negative values: spin–spin order is thus greatly enhanced. Furthermore, since the ^{27}Al Zeeman splitting is smaller than the Cr^{3+} linewidth, the coupling of nuclear and electronic spins now allows exchange of energy between the electronic spin–spin and the nuclear Zeeman system. The nuclear Zeeman system is therefore effectively pumped by DNP to a negative spin temperature.

2.2 Dynamical Variables and Time Constants

In the single mode NMR laser, the active ^{27}Al spins may be considered as being members of a two-level system to which an averaged Bloch vector $\boldsymbol{M} = (M_x, M_y, M_z)$ can generally

be assigned.[7] The three macroscopic variables (M_x, M_y, M_z) are the Cartesian components of the nuclear magnetization $\boldsymbol{M}$ characterizing the active spins. They refer to a coordinate system that is fixed in the laboratory, with z parallel to $\boldsymbol{B}_0$ and x parallel to the axis of the NMR coil. The vector (M_x, M_y, 0) represents the transverse component $\boldsymbol{M}_t$ of $\boldsymbol{M}$, which, in the radiating state, precesses about $\boldsymbol{B}_0$. The vector (0, 0, M_z) is the longitudinal component of $\boldsymbol{M}$. Its value is proportional to the population difference of the two Zeeman levels that are engaged in the radiative process.

Those nuclear Zeeman levels that are not involved in the single mode behavior play an important role in the storage of nuclear Zeeman energy that can be delivered to the active spins. These inactive spins form a separate energy reservoir, whose content is also controlled by the DNP pump. It acts as a buffer, thereby drastically reducing the fluctuations of the microwave pump. For our purposes, we can lump the microwave pump and the reservoir spins together. Thus we form an effective DNP pump system, to which we assign an operationally defined pump magnetization M_e. Here we imply that the effective DNP pump tends to equalize M_z and M_e.

We now assume that the dynamics of the three macroscopic variables (M_x, M_y, M_z) are governed by two characteristic time constants T_2 and T_e. There exist spin–spin interactions in ruby that dephase the collective motion of the nuclear spins. Thus the transverse nuclear magnetization M_t tends to decay with a characteristic dephasing time equal to the transverse relaxation time T_2. The corresponding decay rate is $\gamma_\perp = 1/T_2$. However, spin–spin interactions among the nuclear ^{27}Al and the electronic Cr^{3+} spins in ruby also furnish a mechanism to transfer Zeeman energy among the spins, in particular, from the effective DNP pump system to the lasing spins. We have shown that a characteristic time constant T_e, the pump time, can be assigned to the effective DNP pump system.[4] Hence the pump speed or pump rate is $\gamma_\parallel = 1/T_e$. One should note that this drastic simplification of the complicated spin and DNP pump dynamics in ruby is only justified for the special running conditions of the NMR laser when the variations of M_z are small—typically less than a few percent. In that situation, the pumping conditions remain stable; hence M_e is approximately constant. Under these circumstances, the relatively slow spin–lattice relaxation and DNP processes can be ignored: T_e then plays the role of an effective longitudinal relaxation time.

Two further macroscopic variables of the NMR laser are amplitude and phase of the coherent radiation field $\boldsymbol{B}(t)$, which is proportional to the current $J_L(t)$ in the NMR coil. The corresponding time constant is the ringing time T_R of the LC circuit. Its decay constant is $x = 1/T_R = \omega_c/2Q$, where $Q = R_p/\omega_c L$ is the quality factor of the NMR coil.

3 CONVENTIONAL BLOCH-TYPE LASER EQUATIONS

The dynamic equations for the macroscopic variables of the NMR laser are analogous to the Maxwell–Bloch equations of quantum optics. In order to obtain them, consider the oscillating radiation field $\boldsymbol{B}(t)$ acting on the nuclear spins. We retain only those components that rotate in the same sense as the precessing spins, and introduce a reference frame (u, v, z) that similarly rotates around $\boldsymbol{B}_0$ with frequency ω. Accordingly, $\Delta\omega_a = \omega_a - \omega$ is called the NMR detuning, and $\Delta\omega_c = \omega_c - \omega$ represents the coil or cavity detuning. Although ω may be freely chosen, it is convenient to set $\omega = \omega_a = \omega_c$ for the tuned, free-running NMR laser. In the case of an externally driven NMR laser, we may set $\omega = \omega_d$, with ω_d the frequency of the injected field. The phase of the rotating frame is still free: we fix it by letting the u and x axes coincide at $t = 0$. Hence, we assume that the five macroscopic variables (M_u, M_v, M_z) and (B_u, B_v) of the single mode NMR system obey, in the rotating-frame representation, the conventional Bloch equations:[8]

$$\left.\begin{aligned} \dot{M}_u &= -\gamma_\perp M_u + \Delta\omega_a M_v - s^2 g B_v M_z \\ \dot{M}_v &= -\gamma_\perp M_v - \Delta\omega_a M_u + s^2 g B_u M_z \\ \dot{M}_z &= -\gamma_\parallel (M_z - M_e) + g(B_v M_u - B_u M_v) \end{aligned}\right\} \tag{1}$$

where $\gamma_\perp$ and $\gamma_\parallel$ are suitable decay and pumping constants that have been defined before, and s is a spin factor that has been introduced to account for the fictitious spin-$\frac{1}{2}$ nature of the ruby NMR laser when it is interpreted as a two-level system. Indeed, only two of the $2I + 1$ levels of the real system are relevant. For the special case $I = \frac{1}{2}$, we have $s = 1$. In general, s must be calculated from quantum mechanical rules.[7] For the single mode ruby laser with ^{27}Al as a spin-$\frac{5}{2}$ system, s^2 takes the values 9, 8, or 5, depending on the chosen NMR mode ($\frac{1}{2}$, $-\frac{1}{2}$), ($\frac{1}{2}$, $\frac{3}{2}$) or ($\frac{3}{2}$, $\frac{5}{2}$), respectively. For our standard NMR mode, we have $s = 3$.

In order to complete the laser equations, the components $B_u(t)$ and $B_v(t)$ of the self-induced transverse radiation field $\boldsymbol{B}_t(t)$ must be expressed in terms of the parameters of the NMR LC circuit.[4] To this end, we observe that

$$B_t(t) = \frac{\mu_0 N I(t)}{l} \tag{2}$$

with $B_t(t) = |\boldsymbol{B}_t(t)|$, where $I(t)$ is the current flowing in the NMR coil, which has length l and N windings. The relationship between the induced emf V_{ind} and the current I is given by Kirchhoff's law:

$$\ddot{I} + \frac{\omega_c}{Q}\dot{I} + \omega_c^2 I = \frac{1}{L}\dot{V}_{ind} \tag{3}$$

where $Q = R_p/\omega_c L$ is the quality factor of the coil and R_p is the effective Ohmic parallel resistance. From Faraday's induction law, we further have

$$V_{ind} = -\mu_0 \eta S N \frac{d}{dt}(M_u \cos\omega t + M_v \sin\omega t) \tag{4}$$

under the assumption that the nuclear magnetization inside the coil is homogeneous. The parameters η and S are the filling factor and the cross-section of the NMR coil, respectively.

Substituting equations (4) and (2) into equation (3) and assuming that our system satisfies the conditions

$$\dot{M}_t \ll \omega M_t, \qquad \max\{|\Delta\omega_c|, |\Delta\omega_a|\} \ll \min\{\omega_a, \omega_c, \omega\}$$
$$\omega_c^2 \gg \frac{\omega_c}{Q} \gg 1 \tag{5}$$

the second derivative in equation (3) can be dropped. The laser field equations thus become

$$\left.\begin{aligned} \dot{B}_u &= -\kappa B_u + \Delta\omega_c B_v - \chi M_v \\ \dot{B}_v &= -\kappa B_v - \Delta\omega_c B_u + \chi M_u \end{aligned}\right\} \tag{6}$$

where the field decay constant $x = 1/T_R$ and the coupling constant

$$\chi = \tfrac{1}{2}\mu_0 \eta Q \kappa \tag{7}$$

have been introduced. The expression for χ has been obtained from the well-known relation $L = \mu_0 N^2 S/l$.

Equations (1) and (5) together constitute the conventional Bloch-type laser (CBL) model. In the standard case of single mode operation involving the levels $(-\frac{1}{2}, \frac{1}{2})$ with perfect tuning $\Delta\omega_c = \Delta\omega_a = 0$, they read

$$\left.\begin{aligned} \dot{M}_u &= -\gamma_\perp M_u - 9g M_z B_v \\ \dot{M}_v &= -\gamma_\perp M_v + 9g M_z B_u \\ \dot{M}_z &= -\gamma_\parallel (M_z - M_e) + g(B_v M_u - B_u M_v) \\ \dot{B}_u &= -\kappa B_u - \chi M_v \\ \dot{B}_v &= -\kappa B_v + \chi M_u \end{aligned}\right\} \tag{8}$$

4 EXTENDED BLOCH-TYPE LASER EQUATIONS

The CBL equations, equation (8), describe the behaviors of both the amplitude and phase of the transverse magnetization $\boldsymbol{M}_t$ and of the field $\boldsymbol{B}_t$ through their (u, v) components. If one is interested only in the amplitude dynamics, as in the forthcoming examples, the CBL model, equation (8), can be reduced to a set of only three differential equations by choosing a convenient phase of the rotating frame. For this purpose, we retain only the variables M_v, M_z, and B_u (notice that the discarded M_u and B_v behave exactly as $-M_v$ and B_u, respectively, apart from the initial condition) to obtain

$$\left.\begin{aligned} \dot{M}_v &= -\gamma_\perp M_v + 9g M_z B_u \\ \dot{M}_z &= -\gamma_\parallel (M_z - M_e) - g M_v B_u \\ \dot{B}_u &= -\kappa B_u - \chi M_v \end{aligned}\right\} \tag{9}$$

This three-dimensional system can be further written in the form of the Lorenz equations:[9]

$$\left.\begin{aligned} \dot{x} &= -\sigma(x - y) \\ \dot{y} &= -y + rx - xz \\ \dot{z} &= -bz + xy \end{aligned}\right\} \tag{10}$$

by introducing the dimensionless variables

$$x = \frac{3g}{\gamma_\perp} B_u, \quad y = -\frac{3g\chi}{\kappa\gamma_\perp} M_v, \quad z = \frac{9g\chi}{\kappa\gamma_\perp}(M_z - M_e) \tag{11}$$

The derivatives are taken with respect to the dimensionless time $\tau = t\gamma_\perp$. The parameters

$$\sigma = \kappa\gamma_\perp^{-1}, \quad r = \frac{9g\chi}{\kappa\gamma_\perp}|M_e|, \quad b = \gamma_\parallel \gamma_\perp^{-1} \tag{12}$$

have the values $\sigma = 4.875$, $r = 1.807$, and $b = 2 \times 10^{-4}$ (see Table 1), which do not allow for any chaotic behavior. The system always relaxes to one of the two asymptotically stable fixed points

$$x = y = x_0 = \pm\sqrt{b(r-1)}, \quad z = z_0 = r - 1 \tag{13}$$

with a decay constant $\gamma_{rel} = \frac{1}{2}b$ and a frequency $\omega_{rel} = \sqrt{2x_0^2 - \frac{1}{4}b^2} = 1.797 \times 10^{-2}$. In physical units, they correspond to $\frac{1}{2}\gamma_\parallel \approx 2.4\,s^{-1}$ and $\nu_{rel} \approx 67.7\,Hz$.

Table 1 Experimentally Determined NMR Laser Properties for Standard Running Conditions; the Numerical Values are Used to Calculate the System Parameters of the EBL Model

Gyromagnetic ratio	g	$6.97 \times 10^7\,s^{-1}\,T^{-1}$
Lattice temperature	T	4.2 K
Quality factor	Q	330
Static NMR field	B_0	1.109 T
Laser frequency	ν	12.3×10^6 Hz
Pump magnetization	M_e	$-0.78\,A\,m^{-1}$
Threshold magnetization	M_k	$0.436\,A\,m^{-1}$
Pump factor	r	1.79
Longitudinal pump rate	$\gamma_\parallel$	$4.76\,s^{-1}$
Transverse decay rate	$\gamma_\perp$	$2.38 \times 10^4\,s^{-1}$
Nonexponential damping	α	$0.607\,m\,A^{-1}$
Filling factor	η	0.42
Coupling constant	χ	$10.19\,T\,m\,A^{-1}\,s^{-1}$
LC ringing constant	x	$1.17 \times 10^5\,s^{-1}$
Relaxation frequency	ν_{relax}	60.5 ± 0.5 Hz
Relaxation rate	γ_{relax}	$29.5 \pm 0.5\,s^{-1}$
Noise field	B_n	1.2×10^{-12} T
Bandwidth	$\Delta\nu$	37.2×10^3 Hz
Length of wire	l	1.30×10^{-2} m
Radius of wire	R	0.17×10^{-3} m
Number of turns	N	30

Early investigations have shown that the CBL model reproduces only qualitatively the behavior of the real system. Therefore, we reconsidered critically the various steps of its derivation. The crucial modification has been suggested by the observation of laser transients towards the stable state after an external perturbation. Indeed, equation (1) accounts for just the exponential decay of the transverse nuclear magnetization $\boldsymbol{M}_t$ in the absence of the radiation field (FID), with the phenomenological relaxation time $T_2 = 1/\gamma_\perp$. Although deviations from this simple behavior are common in solids with complex spin–spin and spin–lattice interactions, the single ruby crystal of the NMR laser at standard orientation exhibits an FID that comes close to an exponential decay if the radiative feedback is small. However, the CBL model does not appropriately describe transients occurring after a perturbation of the free running laser conditions. Since this appears to be the effect of a nonlinearity in the relaxation mechanism, we assume the following extended Bloch equation to hold for the FID of the ruby NMR laser:[10,11]

$$\dot{M}_t = -\gamma_\perp \left(1 + \frac{\alpha}{s} M_t\right) M_t \tag{14}$$

with $M_t = |\boldsymbol{M}_t|$. Here, α is an a priori unknown fit parameter, which can be considered as the coefficient of the lowest order term in a Taylor expansion modeling a nonexponential spin dephasing. Although the correction term $\alpha M_t/s$ is of the order of 10^{-3}, the new relaxation rule dramatically improves the accuracy of the model. It has to be remarked that there exists at present no quantitative theory that could explain the assumption in equation (14). Corrections of this type remain heuristic for the time being. However, since $\boldsymbol{M}_t$ is closely related to $\boldsymbol{B}_t$, the new contribution might be interpreted as a dephasing effect caused by the radiation field.

The complete extended Bloch-type laser (EBL) model, in the rescaled variables of Equation (11), takes the form

$$\left.\begin{aligned} \dot{x} &= -\sigma(x - y) \\ \dot{y} &= -y(1 + ay) + rx - xz \\ \dot{z} &= -bz + xy \end{aligned}\right\} \tag{15}$$

where

$$a = \frac{\alpha\kappa\gamma_\perp}{9g\chi} \approx 0.262 \tag{16}$$

Finally, by further introducing the variables

$$X = \frac{x}{x_0}, \quad Y = \frac{y}{x_0}, \quad Z = \frac{z - z_0}{x_0} \tag{17}$$

and the new time $\tau' = \tau x_0$, we obtain

$$\left.\begin{aligned} \dot{X} &= -\sigma'(X - Y) \\ \dot{Y} &= -Y(c + aY) + X(c - Z) \\ \dot{Z} &= -\beta Z - 1 + XY \end{aligned}\right\} \tag{18}$$

where $\sigma' = \sigma/x_0 \approx 384 \gg 1$, $c = 1/x_0 \approx 79$, and $\beta = b/x_0 \approx 1.57 \times 10^{-2}$. The values of X, Y, and $|Z|$ remain in the range [0, 3] under all conditions, including chaotic behavior. Hence, the term aY is clearly small compared with c. Moreover, the large value of σ' renders the adiabatic elimination of X possible, yielding

$$\left.\begin{aligned} \dot{Y} &= -Y(aY + Z) \\ \dot{Z} &= -\beta Z - 1 + Y^2 \end{aligned}\right\} \tag{19}$$

Notice that the variable Y never changes sign, since its derivative $\dot{Y}$ is proportional to Y itself: this is in agreement with the fact that Y represents the modulus of the transverse magnetization vector $\boldsymbol{M}_t$.

5 BASIC TEST OF THE EBL MODEL

In order to test the efficiency of the two available models for the NMR laser, it is necessary to have good knowledge and control of the system parameters. Fortunately, the NMR laser is one of the rare nontrivial many body systems where all relevant parameters can be determined with good accuracy. Some of them may be measured directly (Q factor and laser frequency); the others (filling factor, decay and pumping constants, etc.) can be obtained indirectly, either by fitting the laser response after a suitable perturbation, or by performing appropriate supplementary NMR measurements. Table 1 displays the parameter values that characterize the ruby NMR laser at the temperature of liquid helium. Owing to the reliability of these measurements, any discrepancy between the CBL and EBL models that lies within the experimental resolution is to be attributed to qualitative differences in the dynamics.

We first discuss the effect of the inclusion of the new parameter α in the EBL model on the relaxation of the transverse magnetization by means of a controlled Q switching technique. The laser is first allowed to relax to M_t^s with an initial quality factor Q. Then, at some later time, the quality factor is abruptly lowered to a value Q_e (Q quenching), which is kept constant for a time T_q until the original value Q is restored. The output voltage $v(t) \propto M_v(t)$ is recorded thereafter.

If the laser action is completely quenched in the interval T_q (i.e., $Y \approx 0$), the subsequent laser pulses, followed by the relaxation to the fixed point M_t^s, are triggered by the noise fluctuations of the field in the NMR coil. This observation shows that a quantitative test of the model can be made only by taking noise explicitly into account. It is assumed that the major source is due to the thermal noise current in the coil. Its rms contribution $\bar{B}_n$ to the field at the absolute temperature T is given by

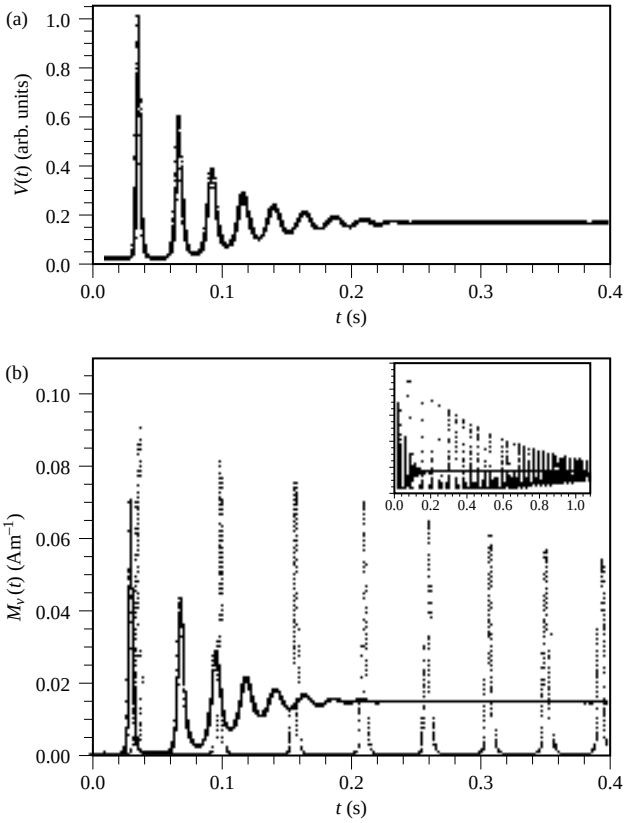

Figure 3 Laser transients $v(t)$ as obtained from experiment (a) and from numerical simulations (b), after Q quenching. The quenching time was $T_q = 2$ ms. In (b), the outcome of the EBL model (solid line, $\alpha = 0.607$ m A^{-1}) may be compared with that of the CBL model (dotted, $\alpha = 0$). Notice the striking similarity between the EBL result and experiment

$$\bar{B}_n = \sqrt{\frac{\mu_0 k_B T Q \Delta\nu}{l R^2 2\pi^2 \nu_a}} \tag{20}$$

where k_B is Boltzmann's constant, $\Delta\nu$ the LC circuit bandwidth, ν_a its resonance frequency, and R the radius of the wire. Inserting realistic numbers yields $\bar{B}_n \approx 4.7 \times 10^{-12}$ T. Hence, the transients can be numerically generated by turning equation (6) into Langevin equations with two additive Gaussian noise terms with amplitude $\bar{B}_n$. Experimental and computed transient signals are reported in Figure 3(a) and (b), respectively. The numerical simulation has been performed with the CBL (dotted line) and EBL (solid line) models, the latter yielding the best fit with the real data for $\alpha \approx 0.607$ m A^{-1}. The quenching time was $T_q = 20$ ms. The agreement with experiment is evident for the EBL model, whereas the CBL model grossly fails to reproduce both the amplitude decay and the oscillation frequency (given by γ_{rel} and ν_{rel}, respectively). These results illustrate the enormous effect of the small correction term $\alpha M_v/3 \approx 3 \times 10^{-3}$ on the laser dynamics. That observation is in great contrast to the behavior way below the laser threshold, as depicted in Figure 4, showing an FID and its fit with the CBL and EBL models. The

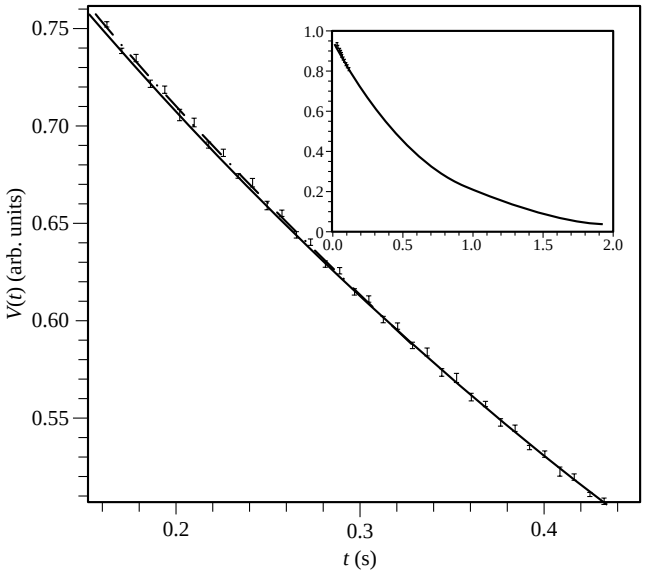

Figure 4 Amplitude of the FID below laser threshold and its fit with the EBL (solid line, $\alpha = 0.607\,\mathrm{m\ A^{-1}}$) and CBL (dash-dotted line, $\alpha = 0$) models; error bars experimental results. Note the extremely weak dependence on α

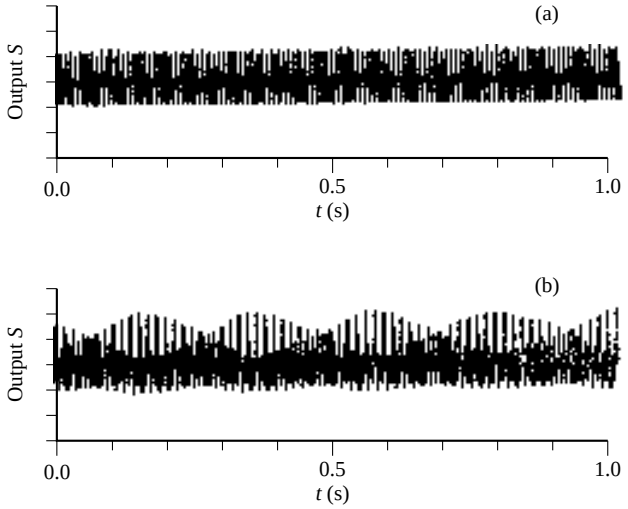

Figure 5 Experimental oscillations of the NMR laser output: (a) with the pump signal S_p on (PML), and A_p below but near $A(1)/c$; (b) with the pump and the input signal s_i on (PDML), and $\omega_\mathrm{i} \approx 1/2\omega_\mathrm{p}$. Note the strong amplification of the input signal where $a_\mathrm{i} \ll A_\mathrm{p}$

correction term α has a negligible effect on dephasing during the FID.

6 THE NMR LASER AS A SMALL SIGNAL DETECTOR

The preceding sections have shown that the NMR laser under standard conditions is restricted to a two-dimensional phase space. Within its accessible parameter space, the dynamics are governed by an attracting fixed point (constant amplitude). However, if an external drive is applied, for example in the form of a sinuosidal modulation of a system parameter, the additional degree of freedom induces bifurcations in the forced limit cycle behavior that may even lead to chaos. Experimentally, this has been realized by varying a system parameter p in time according to $p(t) = p_0(1 + A_\mathrm{p} \cos \omega_\mathrm{p} t)$, where the modulation frequency $\nu_\mathrm{p} = \omega_\mathrm{p}/2\pi$ is chosen in the range [20, 150] Hz, i.e., close to the relaxation frequency $\nu_\mathrm{rel} \approx 67.7\,\mathrm{Hz}$ of the free running laser. For a fixed value of ω_p, bifurcations occur at the critical amplitudes $A_\mathrm{c}^{(n)}, n = 1, 2, 3 \ldots$.

We now want to discuss the remarkable amplification properties of the parametrically modulated laser (PML) near one of its bifurcation points when an additional external signal is injected. This very general feature of nonlinear systems may then be used to detect small external signals.[12,13] In order to apply this small-signal detection method, we may start from the PML with a modulation signal $S_\mathrm{p} = A_\mathrm{p} \sin \omega_\mathrm{p} t$. Then, we supply a second, but small, signal $s_\mathrm{i} = \alpha_\mathrm{i} \sin \omega_\mathrm{i} t$ to the PML in order to generate an additional frequency in the system. For selected values of A_p, ω_p, and ω_i, we observe a strong nonlinear coupling of s_i with S_p, thus providing a mechanism for a frequency-selective small-signal detection scheme. We call S_p and s_i the parametric pump and input signals of this parametrically double modulated laser (PDML).

In the PML mode ($s_\mathrm{i} = 0$), A_p and ω_p are adjusted such that a sequence of period-doubling bifurcations occurs. In keeping ω_p fixed, A_p is set close to, but below, one of the observed critical values $A_\mathrm{c}^{(n)}, n = 1, 2, 3, \ldots$, for the instabilities. The PML output oscillates under the forcing signal S_p with constant amplitude and the fundamental frequency $\omega_\mathrm{p}/2^{n-1}$, as shown in Figure 5(a), for $n = 1$. Thus, we have a stable limit cycle behavior. When s_i is switched on, the output will change its amplitude periodically, as depicted in Figure 5(b). This characteristic form of the time behavior suggests the following procedure to define an operational response function for the PDML as a small-signal detector near a period-doubling bifurcation: first, measure the differences between the heights of consecutive peaks (high−low); second, determine the average amplitude ΔS of these time-dependent differences. Since ΔS is obviously a measure of the strength of the dynamical precursor of the nearby bifurcation ($\omega_\mathrm{p} \rightarrow \frac{1}{2}\omega_\mathrm{p}$), one may call ΔS the experimental sensitivity of the system to the input $s_\mathrm{i} = a_\mathrm{i} \sin \omega_\mathrm{i} t$ and $\Delta S(\omega_\mathrm{i})$ the corresponding experimental response function. That definition then can readily be extended to higher bifurcations ($\omega_\mathrm{p}/2^{n-1} \rightarrow \omega_\mathrm{p}/2^n$), where ΔS refers to peaks that differ in time by $2^{n-1}T_\mathrm{p}$, the period of the pump signal $S_\mathrm{p} = A_\mathrm{p} \sin \omega_\mathrm{p} t$. Typically, $\Delta S(\omega_\mathrm{i})$ peaks at certain frequencies, the lowest being the fractional frequency $\omega_\mathrm{p}/2^n$. A strong peaking, and therefore a high detection sensitivity for s_i, requires a pump frequency ω_p of the order of ω_relax and a pump amplitude A_p as close as possible to one of the instability points $A_\mathrm{c}^{(n)}$.

To demonstrate PDML characteristics, one measures $\Delta S(\omega_\mathrm{i})$ by means of a strobing technique for the proper testing of the PDML output. There, the signal is stroboscopically sampled at times that differ by $2^{n-1}T_\mathrm{p}$. The phase of the discrete timing is adjusted to render maximum sensitivity for $\omega_\mathrm{i} = \omega_\mathrm{p}/2^n$. The discrete output values are digitized and stored in a computer; ΔS is then calculated and displayed. In a run, the computer is used also to control the scan of ω_i in small quasi-adiabatic steps. In Figure 6, we depict the outcome of two typical runs to measure $\Delta S(\omega_\mathrm{i})$. The two cases correspond to the frequency setting $\omega_\mathrm{p} \approx 2\omega_\mathrm{relax}$. In

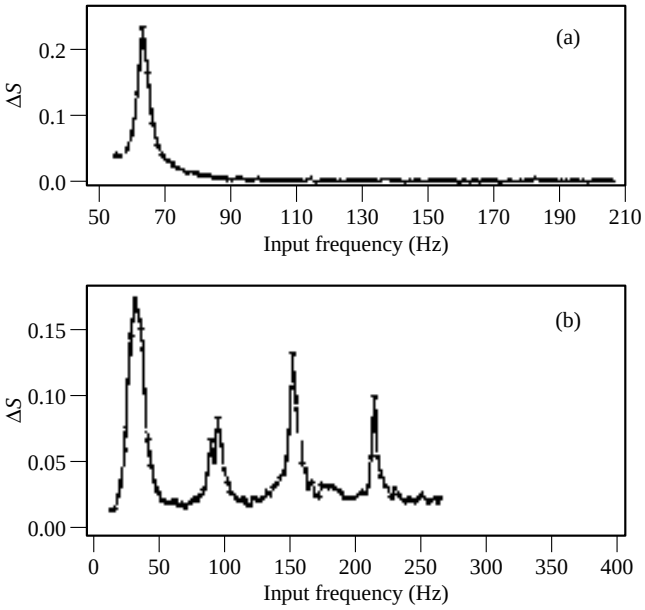

Figure 6 Stroboscopically measured small-signal detection sensitivity, showing strong maxima at defined input frequencies ω_i

run (a), A_p was set below the instability point $A_c^{(1)}$, where the first experimental period-doubling ($\omega_p \rightarrow \frac{1}{2}\omega_p$) occurs. In run (b), A_p was increased to almost $A_c^{(2)}$, where the second period-doubling ($\frac{1}{2}\omega_p \rightarrow \frac{1}{4}\omega_p$) sets in. There is a remarkable difference between runs (a) and (b). Whereas (b) yields distinct peaks at

$$\omega_i \rightarrow \tfrac{1}{4}\omega_p, \quad \tfrac{3}{4}\omega_p, \quad \tfrac{5}{4}\omega_p, \quad \ldots, \tag{21}$$

(a) yields a single peak at $\omega_i \rightarrow \frac{1}{2}\omega_p$ only. The results of run (b) indicate the presence of a true period-doubling bifurcation at $A_c^{(2)}$ with a typical response function $\Delta S(\omega_i)$ as predicted. In contrast to run (b), run (a) leads to the conclusion that the instability at $A_c^{(1)}$ does not reflect a bifurcation. More likely, the PML at $A_c^{(1)}$ jumps discontinuously from one stable attractor to another that has twice that period. In this view, the different results of Figure 6 suggest the use of the PDML scheme to study also the nature of instabilities in nonlinear systems.

Extensive numerical simulations of the PDML response are in good agreement with observations. The PDML has been used to observe weak NMR signals from an external source. Its potential as an NMR detector has yet to be exploited.

7 RELATED ARTICLES

Laser Devices in NMR: Routes to Chaos; Quantum Optics: Concepts of NMR.

8 REFERENCES

1. H. Haken, *Synergetics: An Introduction*, 3rd edn, Springer-Verlag, Berlin, 1985.
2. C. O. Weiss and R. Vilaseca, *Dynamics of Lasers*, VCH, Weinheim, 1991.
3. P. Bösiger, E. Brun, and D. Meier, *Phys. Rev. Lett.*, 1977, **52**, 602.
4. E. Brun, B. Derighetti, D. Meier, R. Holzner, and M. Ravani, *J. Opt. Soc. Am. B*, 1985, **2**, 156.
5. P. Bösiger, E. Brun, and D. Meier, *Phys. Rev. A*, 1978, **18**, 671.
6. H. H. Niebuhr, E. E. Hundt, and E. Brun, *Helv. Phys. Acta*, 1970, **43**, 777.
7. A. Abragam, *The Principles of Nuclear Magnetism*, Oxford University Press, Oxford, 1961.
8. F. Bloch, W. W. Hansen, and M. Packard, *Phys. Rev.*, 1946, **70**, 474.
9. E. N. Lorenz, *J. Atmos. Sci.*, 1963, **20**, 130.
10. L. Flepp, Ph.D. Thesis, Zürich University, 1991.
11. L. Flepp, R. Holzner, E. Brun, M. Finardi, and R. Badii, *Phys. Rev. Lett.*, 1991, **67**, 2244.
12. K. Wiesenfeld and B. McNamara, *Phys. Rev. Lett.*, 1985, **55**, 13.
13. B. Derighetti, M. Ravani, R. Stoop, P. F. Meier, E. Brun, and R. Badii, *Phys. Rev. Lett.*, 1985, **55**, 1746.

Biographical Sketch

Ernst Brun. *b* 1927. Diploma in physics, 1952. Ph.D., 1954, University of Zürich. Introduced to NMR by H. H. Staub and C. D. Jeffries. Research associate, W. E. Meierhof, Stanford University, 1955–56. Privatdozent, 1957. Extraordinarius, University of Zürich, 1958. Guest professor, University of Colorado, 1961–62. Full Professor for Experimental Physics, University of Zürich, 1963–present. Dean of faculty, 1970–72. Director of the Physics Institute, 1973–92. Retirement, 1993. Research interests include nuclear magnetism and its applications to solid state physics, spin dynamics at low temperature, nonlinear dynamics, synergetics, order and disorder in lasers, and the transitions to chaos.

Liquid-state Quantum Computing

Lieven M. K. Vandersypen, Costantino S. Yannoni, and Isaac L. Chuang

Department of Applied Physics, Selft University of Ledmology, Selft, The Netherlands

1 Introduction 1
2 Quantum Computation 1
3 NMR Quantum Computers 4
4 Summary and Conclusions 9
5 References 9

1 INTRODUCTION

Since its invention, NMR spectroscopy has developed from a technique for studying physical phenomena such as magnetism into a tool for acquiring information about molecules in chemistry and biology. Furthermore, it was pointed out early on in 1955, almost as an anecdote, that nuclear spins could also be used for storing information using spin echoes.[1]

This insight beautifully illustrated a notion that was developed in a very different context: information is physical and cannot exist without a physical representation.[2] In recent decades, the relationship between physics and information has been revisited from a new perspective: could the laws of physics play a role in *how* information is processed? The answer appears to be yes. If information is represented by systems such as nuclear spins governed by the laws of quantum mechanics, an entirely new way of doing computation, quantum computation (QC), becomes possible. Quantum computing is not just different or new; it offers an extraordinary promise, the capability of solving certain problems which are beyond the reach of any machine relying on the classical laws of physics.

The practical realization of quantum computers is still in its infancy. Interestingly, over 40 years after the initial suggestion of using spins to represent (classical) information, NMR spectroscopy has become the workhorse for experimental explorations of quantum information processing.

In this article, we first explain how quantum computers work and why they could solve certain problems so much faster than any classical computer. Next, we describe how quantum computers can be implemented using nuclear magnetic resonance (NMR) techniques and what is involved in designing and implementing QC pulse sequences, preparing a suitable initial state and interpreting the output spectra. We close with an overview of the state of the art and the prospects for NMRQC and other QC implementations.

Good reviews of quantum computation and information can be found in Refs.[3–5] A specialized review of and a good introduction to NMRQC are given in Refs.[6,7] respectively.

2 QUANTUM COMPUTATION

2.1 INEPT as a Computation

We start from a familiar place for many NMR spectroscopists, the INEPT pulse sequence (see **INEPT,** Volume 4). This sequence was designed to transfer polarization from a high γ nucleus to a low γ nucleus. However, it can also be viewed as a *logic gate* (Figure 1) which flips one spin conditioned upon the orientation of a neighboring spin.

If we arbitrarily assign "0" to a spin up and "1" to a spin down, we can think of spin-1/2 nuclei as bits in a digital computer. We remind the reader that bits ("0" or "1") can be used to represent numbers in a similar way to decimal numbers ("0" through "9"). In decimal representation, 503 means $3 \times 10^0 + 0 \times 10^1 + 5 \times 10^2$; similarly, in binary representation, 1101 means $1 \times 2^0 + 0 \times 2^1 + 1 \times 2^2 + 1 \times 2^3$ (which corresponds to the number 13 in decimal representation). All computers today process information in binary representation, and are able to rapidly perform multiplication and division (repeated addition and subtraction) as well as the most complex computations, via a sequence of very simple, elementary operations, called logic gates, acting on just one or two bits at a time.

In this binary framework, the INEPT sequence corresponds to an elementary two-bit operation known as the controlled-NOT or for short CNOT gate within the phase corrections discussed in Section 3.1. The CNOT gate performs a NOT operation on a second bit, flipping it from "0" to "1" or from "1" to "0", if and only if the value of a first bit is "1". The input to the logic gate is the initial state of the spins, and the output is the final state of the spins. The four possible input values and the corresponding output values are tabulated in Figure 2.

The CNOT combined with single-spin rotations provides for a *universal* set of logic gates. This means that *any* computational task can be implemented using a sufficiently large number of nuclear spins simply by concatenating CNOTs and single-spin rotations in the proper way.[8–10] In summary, spin-1/2 nuclei in a molecule can serve as bits in a computer, while pulses and delay times provide universal logic gates.

2.2 Quantum Parallellism

Everything we have discussed so far has been purely classical. The Bloch sphere picture of Figure 1 reinforces this

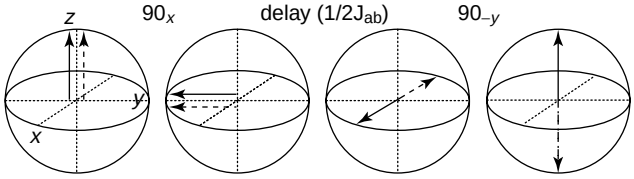

Figure 1 The evolution of one of two coupled heteronuclear spins during an INEPT type pulse sequence, when the other spin is up (solid line) or down (dashed line). The rotating frame is set on resonance with the first spin so there is no need to refocus chemical shift. The usual read-out pulse is left out. The same pulse sequence can be applied to two homonuclear spins using spin-selective pulses

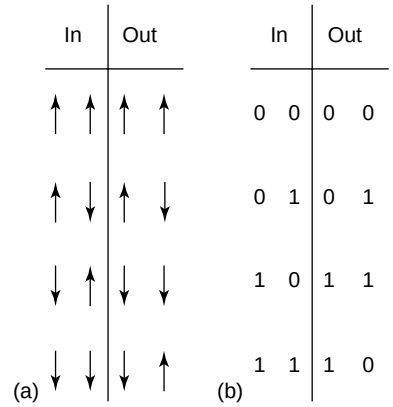

Figure 2 (a) Input and output states for the INEPT pulse sequence and (b) for the corresponding CNOT gate

classical view of the spins; however, nuclear spins are quantum objects. In Dirac notation, the state of a spin can be denoted $|0\rangle$ for a spin in the ground state (along z), and $|1\rangle$ for a spin in the excited state (along $-z$), corresponding to the two classical values for a bit ("0" and "1"). Now, a spin along the x axis is in reality in a coherent superposition state of spin up and spin down, written as $(|0\rangle + |1\rangle)/\sqrt{2}$, while a spin along the y axis is in the state $(|0\rangle + i|1\rangle)/\sqrt{2}$, etc. A spin-1/2 particle is thus more complex than a classical bit. Any two-level quantum system, such as a spin-1/2 particle, can serve as a quantum bit (qubit).

The difference between the quantum and classical descriptions becomes clear as soon as more than one quantum particle is considered. For example, it is well known that the state of n interacting spin-1/2 cannot be described simply by n sets of coordinates on the Bloch sphere. In order to include phenomena such as multiple-quantum coherence, we need recourse to $4^n - 1$ real numbers in the product operator expansion or equivalently to density matrices of dimension $2^n \times 2^n$. Furthermore, the evolution of a closed system of n spins can only be described by $2^n \times 2^n$ unitary matrices (see **Liouville Equation of Motion,** Volume 4). The number of degrees of freedom that need to be specified in a classical description of the state and dynamics of n coupled spins thus increases exponentially with the number of spins.

Richard Feynman proposed in 1982 that the exponential complexity of quantum systems might be put to good use in simulating the dynamics of another quantum system,[11] a task which requires exponential effort on a classical computer. David Deutsch extended and formalized this idea in 1985, and introduced the notion of "quantum parallellism".[12]

Consider a (classical) logic gate which implements a function f with one input bit x and one output bit $f(x)$. If $x = 0$, the gate will output $f(0)$; if $x = 1$, the output will be $f(1)$. The analogous quantum logic gate is described by a unitary operation which transforms a qubit as

$$|0\rangle \mapsto |f(0)\rangle \quad \text{and} \quad |1\rangle \mapsto |f(1)\rangle$$

However, due to the possibility of preparing coherent superposition states and to the linearity of quantum mechanics, the same gate also performs the transformation

$$\frac{|0\rangle + |1\rangle}{\sqrt{2}} \mapsto \frac{|f(0)\rangle + |f(1)\rangle}{\sqrt{2}}$$

In this sense, it is possible to evaluate $f(x)$ for both input values in one step. Next consider a different logic gate which implements a function $g(x)$ with two input bits. We can prepare each qubit in a superposition of "0" and "1". Formally, the state of the joint system is then written as $(|0\rangle + |1\rangle) \otimes (|0\rangle + |1\rangle)/2$. Leaving out the tensor product symbol as well as any normalization factors, the state can be written as $(|0\rangle + |1\rangle)(|0\rangle + |1\rangle)$, or $|0\rangle|0\rangle + |0\rangle|1\rangle + |1\rangle|0\rangle + |1\rangle|1\rangle$, which is further abbreviated to $|00\rangle + |01\rangle + |10\rangle + |11\rangle$. Therefore, a set of two spins can be in a superposition of the four states "00", "01", "10" and "11". A quantum logic gate implementing $g(x)$ then transforms this state as

$$|00\rangle + |01\rangle + |10\rangle + |11\rangle \mapsto |g(00)\rangle + |g(01)\rangle + |g(10)\rangle + |g(11)\rangle$$

Thus the function has been evaluated for the four possible input values in parallel. In general, a function of n qubits implemented on a quantum computer can be evaluated for all 2^n input values in parallel. In contrast to classical computers, for which the number of parallel function evaluations increases at best linearly with their size, the number of parallel function evaluations grows exponentially with the size of a quantum computer (the number of qubits).

Obviously, this is true only so long as the coherent superposition states are preserved throughout the computation. This means that the computation should be completed before quantum coherence is lost due to "decoherence" processes (in NMR, spin–spin and spin-lattice relaxation; see **Relaxation: An Introduction,** Volume 6). Since some degree of decoherence is unavoidable, practical quantum computers appeared virtually impossible to build, until quantum error correction was conceived, as discussed in Section 2.4.

Even if the coherence time is long compared to the duration of a typical logic gate and quantum error correction is employed, can we really access the exponential power exhibited by quantum systems? The postulates of quantum mechanics dictate that a measurement – which induces instantaneous and complete decoherence – of a qubit in a superposition state $|f(0)\rangle + |f(1)\rangle$ will give either "$f(0)$" or "$f(1)$", with equal probabilities. Similarly, after doing 2^n computations all at once, resulting in a superposition of 2^n output values, measurement of the quantum bits randomly returns a single output value. A more clever approach is thus needed exploiting quantum parallellism requires the use of quantum algorithms.

2.3 Quantum Algorithms

Special quantum algorithms allow one to take advantage of quantum parallellism in order to solve certain problems in far fewer steps than is possible classically. When comparing the capability of two computers to solve a certain type of problem, the relevant criterion is not so much what resources (time, size, signal-to-noise ratio, ...) are required to solve the problem but rather how quickly the required resources grow with the problem size.

A particularly important criterion is whether the required resources increase exponentially or polynomially with the problem size. Exponentially difficult problems are considered intractable; they become impossible to solve when the problem size is large. In contrast, polynomially difficult problems are considered tractable. The interest in quantum computing is based on the fact that certain problems which

appear intractable (resources grow exponentially with problem size) on any classical computer are tractable on a quantum computer.

This was shown in 1994 by Peter Shor, almost 10 years after Deutsch introduced quantum parallellism. Shor's quantum algorithm[13] allows one to find the period of a function exponentially faster than any classical algorithm. The importance of period-finding lies in that it can be translated, using some results from number theory, to finding the prime factors of integer numbers, and thus also to breaking widely used cryptographic codes. These codes are based precisely on the fact that no *efficient* classical algorithm is known for period-finding or factoring, i.e., the effort required to factor a number on classical computers increases exponentially with the number of digits of the integer to be factored. In contrast, Shor's algorithm is efficient: on a quantum computer, the effort to factor an integer increases only polynomially (to be precise, the third power) with the number of digits of the integer. As a result, while factoring a 1000-digit number is believed to be beyond the reach of any machine relying on the classical laws of physics, such a feat could be accomplished on a quantum computer.

The first quantum algorithm was invented by Deutsch and Jozsa[14] in 1992. This algorithm allows a quantum computer to solve with certainty an artificial mathematical problem known as Deutsch's problem. Even though this algorithm does not have much application, it is historically significant as it provided the first steps towards Shor's algorithm, and because it is a simple quantum algorithm that can be experimentally tested.

Another class of quantum algorithms was discovered in 1996 by Lov Grover. These algorithms[15] allow quadratic speed-ups of certain search problems, for which there is no better approach classically than to try all L candidate solutions one at a time. A quantum computer using Grover's algorithm needs to make only $\sqrt{L}$ such trials. Even though this speed-up is only quadratic rather than exponential, it is still significant.

The last currently known application of quantum computers lies in simulating other quantum systems,[16] as Feynman conjectured. Even a computer consisting of no more than a few dozen quantum bits could outperform the fastest classical computers in solving important physics problems, such as calculating the energy levels of an atom.[17]

In the remainder of this section, we briefly review the structure of Shor's algorithm, because it is so important and at the same time gives good insight into how quantum computing works (for a more detailed explanation, see Refs.[4,13]). The crucial step in Shor's factoring algorithm is the use of the quantum Fourier transform (QFT) to find the period r of the function $f(x) = a^x \bmod M$, which means $f(x)$ is the remainder after division of a^x by M, where M is the integer to be factored, and a is an integer which is more or less randomly chosen.[4,13]

The QFT performs the same transformation as the (classical) fast Fourier transform (FFT), but can be computed exponentially faster. As always, we do not have access to all the individual output values; the QFT merely allows us to *sample* the FFT but we will see that this suffices for period-finding. The FFT_N takes as input a string of N complex numbers x_j and produces as output another string of N complex numbers y_k, such that

$$y_k = \frac{1}{\sqrt{N}} \sum_{j=0}^{N-1} x_j e^{2\pi i jk/N} \tag{1}$$

For an input string with numbers which repeat themselves with period r, the FFT_N produces an output string with period N/r, as illustrated in the following four examples for $N = 8$ (the output strings have been rescaled for clarity)

r	input string		output string	N/r	
8	1 0 0 0 0 0 0 0	$\mapsto$	1 1 1 1 1 1 1 1	1	(a)
4	1 0 0 0 1 0 0 0	$\mapsto$	1 0 1 0 1 0 1 0	2	(b)
2	1 0 1 0 1 0 1 0	$\mapsto$	1 0 0 0 1 0 0 0	4	(c)
1	1 1 1 1 1 1 1 1	$\mapsto$	1 0 0 0 0 0 0 0	8	(d)

If r does not divide into N, the inversion of the period is approximate. Furthermore, the FFT turns shifts in the locations of the numbers in the input string into phase factors in front of the numbers in the output string:

1 0 0 0 1 0 0 0	$\mapsto$	1 0 1 0 1 0 1 0		(e)
0 1 0 0 0 1 0 0	$\mapsto$	1 0 $-i$ 0 -1 0 i 0		(f)
0 0 1 0 0 0 1 0	$\mapsto$	1 0 -1 0 1 0 -1 0		(g)
0 0 0 1 0 0 0 1	$\mapsto$	1 0 i 0 -1 0 $-i$ 0		(h)

The QFT performs exactly the same transformation, but differs from the FFT in that the complex numbers are stored in the amplitude and phase of the terms in a superposition state. The amplitude of the $|000\rangle$ term represents the first complex number, the amplitude of the $|001\rangle$ term the second number and so forth. For clarity, we will label the states $|000\rangle, |001\rangle, \ldots |111\rangle$ as $|0\rangle, |1\rangle, \ldots |7\rangle$. As an example, we see from (f) that the QFT transforms the state $|1\rangle + |5\rangle$ to the state $|0\rangle - i|2\rangle - |4\rangle + i|6\rangle$.

The QFT is incorporated in actual quantum algorithms as outlined in Figure 3. A first register (group of qubits) is prepared in a superposition of all its possible states. A second register is initialized to the ground state (for factoring a number M, the size of the second register must generally be at least $\log_2 M$ and the first register must be at least twice as large). For example, if register 1 has three qubits and register 2 has two qubits, the state of the system is prepared in

$$(|0\rangle + |1\rangle + |2\rangle + |3\rangle + |4\rangle + |5\rangle + |6\rangle + |7\rangle)|0\rangle \tag{2}$$

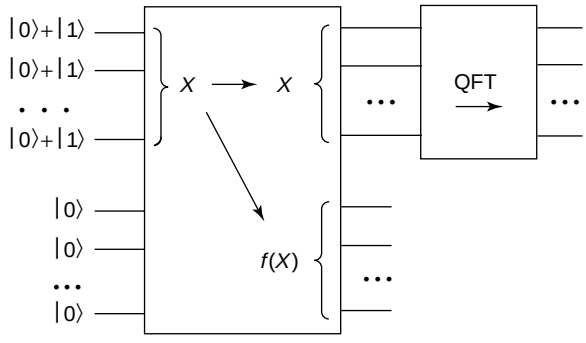

Figure 3 Schematic diagram of the main steps in quantum algorithms for period-finding

Then the function $f(x)$ is evaluated (in NMR by applying a pulse sequence, as discussed in Sections 2.1 and 3.1), where x is the value of the first register, and the output value $f(x)$ is stored in the second register. Since the first register is in an equal superposition of all $|x\rangle$, the function is evaluated for all values of x from 0 to 7 in parallel. For example, let $f(x) = 3$ for even x and $f(x) = 1$ for odd x, which means the period r is 2 (in real applications, we have a description of f but do not know r in advance). Evaluation of $f(x)$ then transforms the state of equation (2) to the state

$$|0\rangle|3\rangle + |1\rangle|1\rangle + |2\rangle|3\rangle + |3\rangle|1\rangle + |4\rangle|3\rangle + |5\rangle|1\rangle + |6\rangle|3\rangle + |7\rangle|1\rangle \quad (3)$$

$$= (|0\rangle + |2\rangle + |4\rangle + |6\rangle)|3\rangle + (|1\rangle + |3\rangle + |5\rangle + |7\rangle)|1\rangle \quad (4)$$

We pause to point out that this state is *entangled*, which means that it cannot be written as a product of single-qubit states. The state $|00\rangle + |01\rangle + |10\rangle + |11\rangle$ is an example of an unentangled state, because it can be written as $(|0\rangle + |1\rangle)(|0\rangle + |1\rangle)$, a product of single-qubit states. In contrast, $|00\rangle + |11\rangle$ is a simple example of an entangled state. Entanglement has no classical analogue and is believed to lie at the heart of the exponential speed-up offered by quantum computation.

In order to appreciate the role of the QFT, suppose we now measure the second register in equation (4) (this measurement can be left out but simplifies the explanation). The state of the first register will collapse to either

$$|0\rangle + |2\rangle + |4\rangle + |6\rangle \quad \text{or} \quad |1\rangle + |3\rangle + |5\rangle + |7\rangle \quad (5)$$

depending on whether the measurement of register 2 gave "3" or "1". We see that all eight possible outcomes are still equally likely, so the result of a measurement does not give us any useful information. But if we apply the QFT, the first register will be transformed to

$$|0\rangle + |4\rangle \quad \text{or} \quad |0\rangle - |4\rangle \quad (6)$$

Now a measurement of the first register does give useful information, because only multiples of N/r are possible outcomes, in this example "0" and "4".

This concludes the quantum part of the computation. From the measurement result, a classical computer can efficiently calculate the inverted period N/r, and thus also r, with high probability of success using results from number theory. Now that r is known, the factors of the integer M can be quickly computed from number theory as well, with high probability (the probability of success can be further increased by repeating the whole procedure a few times).

We close with two final remarks on quantum algorithms: (1) quantum computing cannot offer any speed-up for many common tasks, such as adding up two numbers or word processing, which can already be completed efficiently on a classical computer; and (2) there are many problems which take exponential effort on both quantum and classical computers. It would be somewhat disappointing from a practical viewpoint if no other applications were found; however, our understanding of the connection between physics and information and computation has already changed dramatically.

2.4 Quantum Error Correction

Any quantum computation must be completed within the coherence time, T_2 and T_1 in NMR, as pointed out in Section 2.2. T_1 and T_2 processes alter the state of the qubits and are therefore a source of errors. For many years, this requirement led to widespread pessimism about the practicality of quantum computers. In 1995, however, Peter Shor and Andrew Steane independently discovered quantum error correction[46,47] and showed that it is possible to correct for truly random errors caused by decoherence.

This came as quite a surprise, because quantum error correction had to overcome three important obstacles: (1) the no-cloning theorem, which states that it is not possible to copy unknown quantum states;[5] (2) measuring a quantum system affects its state; and (3) errors on qubits can be arbitrary rotations in Hilbert space, compared with simple bit flips for classical bits. Quantum error correction requires many extra operations and extra qubits (ancillae), however, which might introduce more errors than are corrected, especially because the effect of decoherence increases exponentially with the number of entangled qubits, in much the same manner that multiple quantum coherences decay exponentially faster than single quantum coherences. Therefore, a second surprising result[48] was that provided the error rate (probability of error per elementary operation) is below a certain threshold, and given a fresh supply of ancilla qubits in the ground state, it is possible to perform arbitrarily long quantum computations.

The threshold error rate is currently estimated[48] to be about 0.001%. The actual error rate in NMRQC is approximated by $1/2JT_2$, where $2JT_2$ is roughly the number of operations that can be computed within the coherence time. For small molecules the error rate is typically on the order of 0.1–1%, two to three orders of magnitude too high. A remarkable implication of quantum error correction, however, is that if (1) a molecule is found which achieves the threshold error rate; and (2) select spins can be fully polarized, both T_1 and T_2 could in principle be infinitely lengthened by applying an error correction pulse sequence.

3 NMR QUANTUM COMPUTERS

3.1 Pulse Sequence Design

At first sight, the translation of abstract quantum algorithms or function evaluations into actual pulse sequences may appear obscure: However, systematic techniques[18,19] exist to make pulse sequence design relatively straightforward. The starting point is that: each quantum algorithm can be described by a sequence of transformations under unitary operators.

Such unitary transformations represent rotations in Hilbert space (a multidimensional extension of the Bloch sphere). Examples of unitary transformations are evolution during RF pulses and free evolution under the system Hamiltonian; relaxation processes give rise to nonunitary transformations. Once the desired unitary operators have been identified, arbitrary unitary operators can be translated into sequences of single-qubit rotations and CNOT gates.

These building blocks can be readily implemented in NMR (see Section 3.2). Decompositions into other sets of elementary gates are also possible, and can be helpful in simplifying the pulse sequences.[20,38] In any case, it is crucial that the duration

of the pulse sequence design process as well as the length of the resulting pulse sequence do not increase exponentially with the problem size.

We now point out two important distinctions between QC and conventional pulse sequences. On the one hand, QC sequences must be more general: QC sequences must perform the desired transformation for arbitrary input states. In contrast, conventional sequences are often designed assuming a particular input state. As a first example of this difference, the sequence of Figure 1 assumes that both spins are in Zeeman states, i.e., aligned along $\pm z$. It implements the unitary operator

$$\widehat{U}_{\text{INEPT}} = \begin{pmatrix} 1 & 0 & 0 & 0 \\ 0 & i & 0 & 0 \\ 0 & 0 & 0 & 1 \\ 0 & 0 & -i & 0 \end{pmatrix} \tag{7}$$

which is similar to but different from the unitary operator for the CNOT gate, defined as

$$\widehat{U}_{\text{CNOT}} = \begin{pmatrix} 1 & 0 & 0 & 0 \\ 0 & 1 & 0 & 0 \\ 0 & 0 & 0 & 1 \\ 0 & 0 & 1 & 0 \end{pmatrix} \tag{8}$$

implemented, for example, by $90^a_z\, 90^b_{-z}\, 90^b_x\, 1/2J_{ab}\, 90^b_{-y}$.

As a second example, consider the so-called Hadamard gate, defined as

$$\widehat{U}_{\text{Had}} = \frac{1}{\sqrt{2}} \begin{pmatrix} 1 & 1 \\ 1 & -1 \end{pmatrix} \tag{9}$$

This gate creates a superposition state starting from a basis state: it transforms $|0\rangle$ to $|0\rangle + |1\rangle$ (z to x in the Bloch sphere) and $|1\rangle$ to $|0\rangle - |1\rangle$ ($-z$ to $-x$). At first sight, this transformation could be done simply via a 90_y pulse. However, the unitary operator for 90_y

$$\widehat{U}_{90_y} = \frac{1}{\sqrt{2}} \begin{pmatrix} 1 & -1 \\ 1 & 1 \end{pmatrix} \tag{10}$$

is different from $\widehat{U}_{\text{Had}}$; e.g., applying $\widehat{U}_{\text{Had}}$ twice has no net effect, but applying $\widehat{U}_{90_y}$ twice produces U_{180_y}. A possible sequence to implement $\widehat{U}_{\text{Had}}$ exactly is $90_y 180_x$.

On the other hand, QC sequences can be more specific: QC sequences can be specialized for a specific molecule using full knowledge of its spectral properties. In contrast, conventional sequences must work for any molecule, because the spectral properties of the molecule are usually not known in advance. Exact knowledge of the chemical shifts and J-coupling constants allows one not only to greatly simplify the pulse sequences, but also to achieve much more accurate unitary transformations than would otherwise be possible.

Finally, while systematic procedures exist to design a pulse sequence, there is a need to develop tools to find the pulse sequence of the shortest duration and with the fewest RF pulses. Even small-scale quantum computations easily involve tens to hundreds of gates acting on multiple spins and precise control of the spin dynamics is difficult to maintain throughout such long sequences of operations, as shown in the next section.

3.2 Implementation of Computations

The implementation of quantum computations with NMR can be based on single-spin rotations and CNOT gates, since any quantum algorithm can be translated into these building blocks. Although these elementary operations appear quite easy to implement, the requirements for precision in QC experiments are unusually high, due to the large number of pulses and the quantitative nature of the information contained in the output spectra.

Implementation of accurate *single-spin rotations* about an axis in the $x-y$ plane is relatively easy in heteronuclear molecules; yet, it can be very demanding for homonuclear spin systems because spin selectivity requires longer pulses resulting in considerable coupled evolution of the spins during the pulses.[21] Clearly, some degree of homonuclear dynamics is unavoidable when more than a handful of qubits are involved.

We therefore begin by reviewing the requirements for pulse shaping[22] (see **Selective Pulses,** Volume 7; **Shaped Pulses,** Volume 7). First, the magnetization corresponding to each of the lines in a multiplet must be rotated about exactly the same axis and over exactly the same angle, i.e., off-resonance effects due to line splitting must be removed. This requires self-refocusing shaped pulses or tailored composite pulses[23] (see **Composite Pulses,** Volume 2). Second, the effect of J-coupling between unselected spins must be removed, either during the pulse or later in the pulse sequence. Third, all pulses must be universal rotors, i.e., the rotation must be independent of the initial state of the spin. Fourth, the unselected spins must not be affected by the RF irradiation. This last requirement is difficult to satisfy because of transient Bloch–Siegert effects[24] which can result in substantial (tens of degrees) phase shifts of nearby unselected spins. However, it is possible to estimate and compensate for the Bloch–Siegert shift.[25,26] Finally, simultaneous (as opposed to consecutive) pulses at two or more nearby frequencies are desirable in order to keep pulse sequences short, but transient Bloch–Siegert shifts greatly deteriorate such simultaneous rotations.[27,28] Accurate simultaneous rotations at nearby frequencies can be achieved using a special correction technique.[29] Even then, simultaneous pulses on well-coupled spins may excite multiple quantum coherences.[30]

There are a number of hardware requirements for successful execution of QC experiments. Good RF coil homogeneity is crucial in avoiding excessive signal attenuation and related errors. Furthermore, it is desirable that one frequency source and transmitter board per qubit be available. If there are more qubits than spectrometer channels, the carrier frequency must be jumped to the appropriate frequencies throughout the pulse sequence, or phase ramping techniques must be employed.[31] A dedicated frequency source for each qubit also makes it easy to keep track of the rotating frame of each spin and apply all the pulses on any given spin with the correct relative phase. This removes the need for extra pulses to refocus chemical shift evolution.[22] Alternatively, software rotating frames can be created by detailed bookkeeping of the time elapsed since the beginning of the pulse sequence such that the evolution of the rotating frame of any given spin with respect to the carrier reference frame can be calculated. The phases of the pulses throughout the pulse sequence, as well as the receiver phase, can then be adjusted accordingly.[25,36] The same technique can be used to implicitly realize single-spin rotations about z.

Alternatively, z-rotations can be implemented using resonance offsets or composite pulses.[22]

Two strategies exist for implementing CNOT gates (both assume first order spectra). If all the spins are mutually coupled, CNOT's can be realized via line-selective pulses which invert specific lines within a multiplet.[10] In practice, it is usually more convenient to use pulse sequences such as the one demonstrated in Figure 1.[8,10] For molecules with several coupled spins, the sequence of Figure 1 must be expanded with extra pulses to refocus undesired J-couplings; systematic methods exist to design efficient refocusing schemes.[28,33,34] A CNOT between two uncoupled spins can be realized by swapping qubit states.[32,35] For example, for a CNOT between two spins a and c which are not mutually coupled but which are both coupled to a third spin b, the procedure is as follows: apply a pulse sequence which swaps the state of a and b (via CNOT_{ab} CNOT_{ba} CNOT_{ab}), then perform a CNOT between b and c, and then swap a and b again. The net result is CNOT_{ac}; spin b is unaffected. It is thus not necessary that all spins be pairwise coupled as long as the network of couplings includes all n spins.

An alternative to imposing the correct evolution on all the spins at all times, both for RF pulses and for CNOT-type gates, is to allow erroneous evolutions which will later be reversed. Such techniques have been highly successful in certain standard pulse sequences (see **Decoupling Methods,** Volume 3), but are much harder to develop for the nonintuitive and nontransparent QC pulse sequences. Nevertheless, it has been shown experimentally that a large degree of cancellation of erroneous evolutions is possible even in QC experiments: about 300 two-qubit gates involving over 1350 90° RF pulses have been successfully concatenated.[36] A general methodology designed to take advantage of this possibility has yet to be developed.

From this discussion, it will be clear that the selection of a suitable molecule is crucial for NMRQC. The desired properties are (1) sufficiently large chemical shifts for good addressability, (2) large coupling constants, while maintaining first-order spectra, for fast two-qubit gates (or a coupling network that matches the pattern of connectivities needed for the algorithm), and (3) long T_2 and T_1 in order to allow time to execute many logic gates. Furthermore, high γ nuclei are desirable for good sensitivity. More mundane but equally important requirements are that the molecule be stable, synthesizable, soluble and safe.

3.3 State Initialization

Apart from experiments designed to produce nonthermal spin polarizations, setting up a proper initial state for the nuclear spins is a concept worth revisiting for NMR spectroscopists. Since it is such a crucial step in quantum computing, this entire section is therefore devoted to state initialization.

Most quantum computations require a *pure* initial state, for example a set of fully polarized spins, in the state $|00\ldots0\rangle$. However, nuclear spins in thermal equilibrium at room temperature are in an almost totally random state: for typical magnetic field strengths, the ground ($|0\rangle$) and excited ($|1\rangle$) state probabilities differ by only about 1 part in 10^5. The spins are then said to be in a *mixed* (nonpure) state. The polarization could be increased using hyperpolarization techniques (see **Optically Enhanced Magnetic Resonance,** Volume 5) but the state of the art is still very far from cooling nuclear spins into the ground state.

The conceptional breakthrough which made NMR quantum computation possible at room temperature was the concept of *effective pure* or *pseudo-pure* states:[8–10] effective pure states are mixed states which produce the same signal as a pure state to within a scaling factor.

The signature of an effective pure state for n spins is that all but one of the 2^n populations are equal, and that no coherences are present. The density matrix then consists of an identity component and a pure state component. The identity density matrix is not observable in NMR since only population differences are observed, and furthermore does not transform under unitary evolutions ($UIU^\dagger = I$). Thus the visible signal is produced solely by the one distinct population, corresponding to a pure state. In product operator notation,[37] the effective pure ground state is proportional to $\widehat{I}_z + \widehat{S}_z + 2\widehat{I}_z\widehat{S}_z$ for two spins, to $\widehat{I}_z + \widehat{S}_z + \widehat{R}_z + 2\widehat{I}_z\widehat{S}_z + 2\widehat{I}_z\widehat{R}_z + 2\widehat{S}_z\widehat{R}_z + 4\widehat{I}_z\widehat{S}_z\widehat{R}_z$ for three spins, and so forth. Figure 4 shows how the effective pure state preparation is manifest in the spectrum of one of five coupled spins. A characteristic of effective pure (basis) states is that only one line survives in each multiplet.

Three methods are known for preparing effective pure states starting from thermal equilibrium.

(1) *Logical labeling*[8,38] consists of applying a pulse sequence which rearranges the thermal populations such that a subset of the spins is in an effective pure state, conditioned upon the state of the remaining spins. Then the computation is carried out within this embedded subsystem.[39]

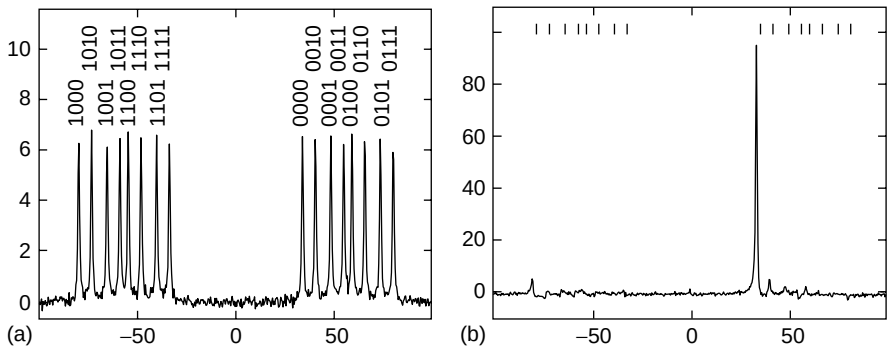

Figure 4 (a) Spectrum of pentafluorobutadienyl cyclopentadienyldicarbonyliron complex in thermal equilibrium. (b) The same spectrum after preparing an effective pure state $|00\,000\rangle$. (Reproduced from Ref.[26] by permission of the American Physical Society)

For example, the Boltzman populations for the states $\{|000\rangle, |001\rangle, |010\rangle, |011\rangle, |100\rangle, |101\rangle, |110\rangle, |111\rangle\}$ for a homonuclear three-spin system deviate from the uniform background by $\{3a, a, a, -a, a, -a, -a, -3a\}$ respectively, where

$$a = \frac{1}{2^3}\frac{\hbar\omega}{2k_BT} \ll 1$$

After rearranging the populations for the eight spin states as $\{3a, -a, -a, -a, a, a, a, -3a\}$, the last two qubits are in an effective pure state conditioned upon the first qubit being $|0\rangle$. As the total number of qubits n in the molecule increases, the relative fraction of effective pure qubits goes to 1, but the preparation sequence becomes complex quite rapidly for large n and the signal strength scales as $n/2^n$.

(2) *Temporal averaging*[40] is similar to phase cycling (see **Phase Cycling,** Volume 6), since it consists of adding up the spectra of multiple experiments. However, instead of changing just the phase of some pulses, each experiment starts off with a different state preparation sequence which permutes the populations. For two heteronuclear spins, adding together three experiments which yield respective population deviations $\{a, b, -b, -a\}$, $\{a, -b, -a, b\}$ and $\{a, -a, b, -b\}$ is equivalent to performing an experiment with population deviations $\{3a, -a, -a, -a\}$. For arbitrary n, at least $(2^n - 1)/n$ experiments are needed,[26] since the effective pure state is made up of $2^n - 1$ product operator terms and the starting state, thermal equilibrium, contains n terms.

(3) *Spatial averaging*[10] uses a pulse sequence containing magnetic field gradients (see **Field Gradients & Their Application,** Volume 3) to equalize all the populations but the ground state population. Only one experiment is involved, but the preparation sequence quickly becomes unwieldy for large spin systems and the signal strength decreases exponentially with n.

To date, temporal and spatial averaging have been the most popular choices for preparing effective pure states. Several hybrid schemes[25,40] have also been developed which trade off complexity of the preparation steps for the number of experiments. Nonetheless, all these state preparation schemes have in common that creating effective pure states incurs an exponential cost either in the signal strength or in the number of experiments involved.

Such an exponential overhead is of course not tolerable for quantum computations. The reason for this cost is that effective state preparation techniques simply select out the signal from the ground state population present in thermal equilibrium, and the fraction of molecules in the ground state is proportional to $n/2^n$.

A significant breakthrough by Schulman and Vazirani resulted in a method to cool a subset of the spins in a molecule down to the ground state without any exponential overhead.[41,42] The idea is to redistribute the entropy of the spins so that some have zero entropy (pure state) while the entropy of the remaining spins increases. In a sense, this method is simply a polarization transfer scheme. Surprisingly, both the length of the cooling pulse sequence and the number of spins that must be sacrificed increase only about linearly with the number of pure spins desired. Furthermore, the cooling algorithm approaches the entropic bound in the limit of large numbers of spins. However, with initial polarization $\alpha \ll 1$, a molecule with at least k/α^2 spins is needed to obtain k pure spins. This method is therefore impractical when starting from equilibrium at room temperature, with $\alpha \approx 10^{-5}$. Nevertheless, a combination of hyperpolarization techniques and the Schulman–Vazirani scheme may some day become practical. In any case, despite the exponential cost incurred when preparing effective pure states, the highly random initial state represents *no fundamental* obstacle to scalable quantum computation.

3.4 Read-out

In NMR spectroscopy, only one nucleus is traditionally observed. In QC, however, the concept of a single observe channel and one or more decoupler channels does not apply: the output of a quantum computation is the final state of one or several spins. The final states of each of the output spins must thus be read out.

If each of the output spins ends up in $|0\rangle$ or $|1\rangle$ (or in reality in the effective pure state corresponding to $|0\rangle$ or $|1\rangle$), the answer can be read-out directly by applying a pulse which rotates the spin from $\pm z$ to $\pm x$. With properly referenced receiver phase settings, the spectrum for each output spin then consists of either absorption or emission lines, indicating whether the output value of the corresponding bit is "0" or "1" (Figure 5).

If the output state is a superposition state, the situation is a bit more complicated. For a single quantum computer subject to a "hard" measurement (assumed in Section 2.2), the superposition "collapses" to one of the terms in the superposition, with probabilities given by the square of the amplitude of each term. In contrast, NMR spectra result from averaging over a large number of independently operating quantum computers (molecules), and for each spin the area under the spectral lines is proportional to the $|0\rangle - |1\rangle$ probability difference.

The output state of equation (6) serves as an example: half of the molecules in the ensemble collapse to $|0\rangle$ ($|000\rangle$), while the other half collapses to $|4\rangle$ ($|100\rangle$). In other words, spins 2 and 3 always end up in "0" so their spectral lines are absorptive; in contrast, the signal of spin 1 averages to zero because there are equally many molecules in which spin 1 ends up in "0" as in "1". It is not clear that such bit-wise averages of probabilistic output states are generally sufficient to solve the problem of interest. For Shor's period-finding algorithm, this problem can be circumvented[8] by performing the classical post-processing steps (Section 2.3) on the quantum computer using ancillae qubits; any classical computation can also be done on a quantum computer.[5] In this way, the output state becomes the period r for all the molecules in the ensemble (as opposed to an average over all the multiples of N/r) and the measurement result becomes deterministic.

Instead of recording the signal of each of the output spins, it is sometimes possible to use the extra information provided by the line splittings due to J couplings to derive the output state of several qubits from the spectrum of a single spin. Since each of the lines in the multiplet can be identified with specific states of the other spins (as in Figure 4), the presence or absence of each line in the multiplet gives information about the state of the other spins (Figure 5).

Finally, while the spectra of a few select spins suffice to obtain the answer to a computation, the full density matrix

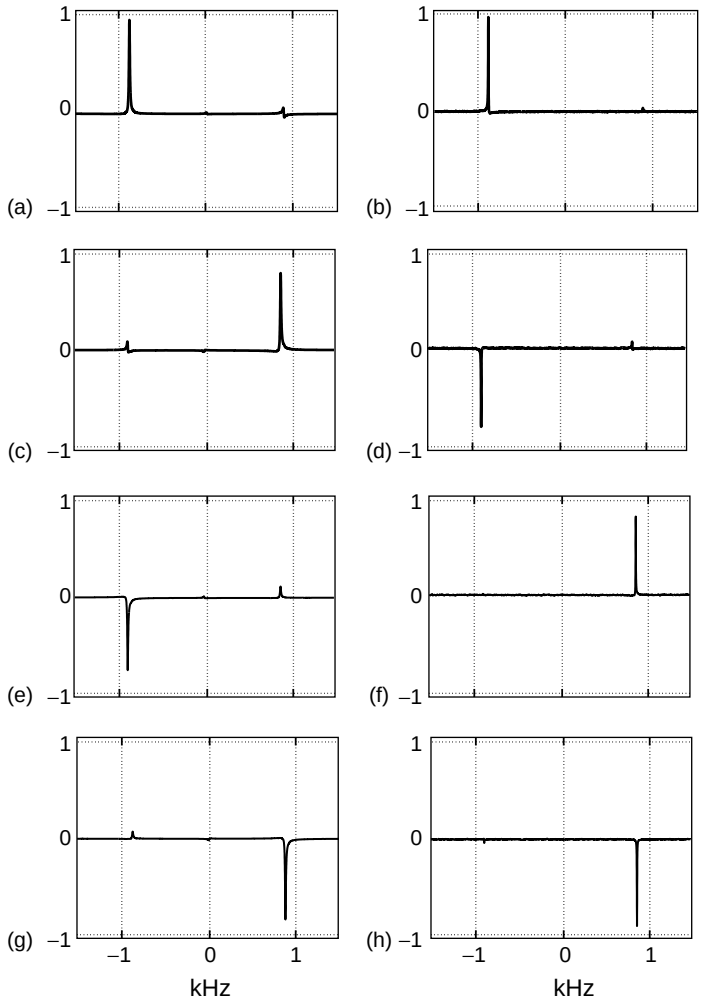

Figure 5 Output spectra of the proton (a) and carbon (b) spins of $^{13}CHCl_3$ (dissolved in a liquid crystal solution) for four different executions of Grover's search algorithm. Only the real part of the spectra is shown, and frequencies are relative to ν_H and ν_C. A positive or negative line in the spectrum indicates that the corresponding spin was in $|0\rangle$ or $|1\rangle$ before the read-out pulse. Furthermore, the position of the line in the spectrum of one spin also reveals the state of the other spin. For example, if the ^1H line is at $\nu_H - J_{CH}/2$, the ^{13}C spin is in $|0\rangle$; a ^1H line at $\nu_H + J_{CH}/2$ indicates the ^{13}C spin is in $|1\rangle$. Thus, the state of the two qubits for each of the four cases is (from top to bottom) $|00\rangle$, $|01\rangle$, $|10\rangle$ and $|11\rangle$. (Reproduced from Ref.[61] by permission of the American Institute of Physics)

conveys much more information. This extra information can be used to expose the presence of errors such as multiple quantum coherences not visible in the single output spectra and furthermore is a useful tool for debugging pulse sequences. The procedure for reconstructing the density matrix is called quantum state tomography.[43–45] It consists of repeating the computation multiple times, each time looking at the final state of the spins after applying different sets of read-out pulses which rotate different elements of the density matrix to observable positions. However, since this procedure involves on the order of 4^n experiments, it is practical only for experiments involving a few spins.

3.5 State of the art and Outlook

To date, only very simple demonstrations of quantum algorithms, all using liquid-state NMR techniques, have been carried out. Variations of Grover's algorithm have been demonstrated with two[44,49,50] and three qubits,[36] the Deutsch–Jozsa algorithm with two,[43,51] three[52] and five[53] qubits, and the period-finding algorithm with five qubits.[26] Most recently, a seven-qubit quantum computer has been used to factor the number 15 using Shor's algorithm.[67] A quantum simulation has been implemented with two[54] and three[55] qubits, and quantum error detection and correction with two,[56] three[57] and five[68] qubits. Finally, a 7-spin coherence has been created and observed[25] (see Ref.[6] for additional references). While these experiments indeed demonstrate the principles of quantum information processing, they all involve far fewer qubits than would be needed to solve a problem beyond the reach of classical machines.

Despite the rapid progress in recent years, scaling liquid state NMRQC to tens or hundreds of qubits may be impractical for several reasons, although none of them appear fundamental. In particular, as the number of qubits increases: (1) the strength of the signal selected with current state initialization techniques decreases exponentially,[8,9,58] but Schulman–Vazirani cooling[41] does not suffer any such exponential overhead (Section 3.2); (2) the chemical shift separations unavoidably become smaller,

but Lloyd[32] showed that for universal quantum computation it suffices to have a linear chain $d - abc - abc - \cdots - abc$, in which only nearest neighbour spins are coupled and with only four distinct chemical shifts δ_a, δ_b, δ_c and δ_d; (3) J-couplings become smaller or even unresolved, but this can be circumvented by swapping spin states (Section 3.2).[32] While these obstacles are not fundamental, the solutions all make the pulse sequences, very likely impractically, much longer. This would require increasingly longer T_2 and T_1 for larger molecules, while in practice the T_2 and T_1 tend to become shorter (see **Relaxation: An Introduction,** Volume 6).

NMRQC has also brought up new theoretical issues: (1) since only ensemble averaged results are available because of the large number of molecules in a sample tube, some information is lost that would be available in an idealized quantum computer such as a single molecule at zero degrees Kelvin. For the known quantum algorithms, this information can be retrieved by performing classical post-processing steps on the quantum computer (Section 2.3); and (2) since the density matrix of nuclear spins at room temperature is very close to the identity matrix, it is not possible to produce genuinely entangled states between the nuclear spins in small thermally polarized molecules in liquid solution.[59] This observation has sparked a stimulating debate about the "quantumness" of NMR, because it implies that each of the states produced in NMRQC experiments so far is classical. However, all attempts to describe the dynamics of a set of coupled spins by an efficient classical model have been unsuccessful. It is thus conjectured that even though the states show no entanglement, the dynamics of the spins is truly quantum mechanical,[60] a proposition which will appear obvious to most NMR spectroscopists. In fact, it has also been the starting point of this introduction to NMR quantum computing.

4 SUMMARY AND CONCLUSIONS

In many respects, liquid state NMR provides an ideal test bed for elementary quantum computations. The degree of control over the evolution of multiple coupled qubits – the result of 50 years of technology development – the long relaxation times of nuclear spins and a set of new insights[8,9] made it possible to perform certain computations in *fewer steps* than is possible using any classical machine. This is in itself a remarkable achievement.

It is unlikely that liquid state NMR could ever be used to solve problems *faster* than any classical machine, but it has already inspired many other NMR based proposals for quantum computing. Liquid-crystal solvents have been used to partly reintroduce dipole-dipole couplings (see **Liquid Crystals: General Considerations,** Volume 4) to speed up the gate time and increase the number of gates possible within the coherence time.[61] New molecular architectures based on liquid crystal solutions are now being investigated. Solid-state NMR near 0 K could circumvent the state initialization problem, but also poses new questions in terms of addressability and coherence times (see **Internal Spin Interactions & Rotations in Solids,** Volume 4). Several approaches to solve these issues have been proposed.[62,63] Another proposal which received much attention consists of doing NMR on impurity atoms placed in a linear or two-dimensional array, with chemical shifts and couplings controlled by electrodes placed on top of and in between the impurity atoms.[64]

Furthermore, there is a plethora of very different experimental approaches to building quantum computers (for an extensive review, see Ref.[65]). Four trapped ions have recently been entangled[66] and a single quantum logic gate has been implemented between two photons coupled with each other via interactions with an atom in a cavity.[69] In the long run, the most scalable approaches may be those based on solid-state technology, such as electron spins in quantum dots or magnetic fluxes in SQUIDs.[65]

It is clear that none of these proposals will be easy to implement since they all require substantial and innovative development of technology. The success of any approach will depend on the ratio of the coherence time to the gate duration, i.e., how many gates can be completed within the coherence time, and on the achievable degree of quantum control.

Many of the problems in quantum control are similar for different experimental systems, and we therefore expect that other quantum computer implementations will benefit from the ideas, concepts and solutions which arise from liquid state NMR experiments. In addition, we hope that some of the techniques developed within the context of quantum computation may find more general application in NMR.

The possible payoff for successful quantum computing is tremendous: to solve problems beyond the reach of any classical computer. It is not clear at this point whether quantum computers will fulfill this promise, but in any case quantum computing has already provided an exciting new perspective on NMR and, more broadly, on the connection between physics, information and computation.

5 REFERENCES

1. A. G. Anderson, R. L. Garwin, E. L. Hahn, J. W. Horton, G. L. Tucker, and R. M. Walker, *J. Appl Phys.*, 1955, **26**, 1324.
2. R. Landauer, *Phys. Today*, 1991, **44**, 5, 22.
3. C. Bennett and D. P. DiVincenzo, *Nature*, 2000, **404**, 247.
4. A. Ekert and R. Jozsa, *Rev. Mod. Phys.*, 1996, **68**, 733.
5. M. A. Nielsen and I. L. Chuang, 'Quantum Computation and Quantum Information', Cambridge University Press: Cambridge, 2000.
6. J. A. Jones, *Fortschr. Phys.*, 2000, **48**, 909.
7. N. Gershenfeld and I. L. Chuang, *Sci. Am.*, 1998, June.
8. N. Gershenfeld and I. L. Chuang, *Science*, 1997, **275**, 350.
9. D. G. Cory, M. D. Price, and T. F. Havel, *Physica D*, 1998, **81**, 2152.
10. D. G. Cory, A. F. Fahmy, and T. F. Havel, *Proc. Natl. Acad. Sci. USA*, 1997, **94**, 1634.
11. R. P. Feynman, *Int. J. Theor. Phys.*, 1982, **21**, 467.
12. D. Deutsch, *Proc. R. Soc. Lond. A*, 1885, **400**, 97.
13. P. Shor, in 'Proc. 35th Annual Symposium on the Foundations of Computer Science', IEEE Comp. Soc. Press: Los Alamitos, CA, 1994, 124.
14. D. Deutsch and R. Jozsa, *Proc. R. Soc. Lond. A*, 1992, **439**, 553.
15. L. Grover, *Phys. Rev. Lett.*, 1997, **79**, 4709.
16. S. Lloyd, *Science*, 1996, **273**, 1073.
17. D. S. Abrams and S. Lloyd, *Phys. Rev. Lett.*, 1999, **83**, 5162.
18. A. Barenco, C. Bennett, R. Cleve, D. P. Divincenzo, N. H. Margolus, P. W. Shor, T. Sleator, J. A. Smolin, and M. Weinfurter, *Phys. Rev. A*, 1995, **52**, 3457.
19. M. D. Price, S. S. Somaroo, A. E. Dunlop, T. F. Havel, and D. G. Cory, *Phys. Rev. A*, 1999, **60**, 2777.

20. J. A. Jones, R. H. Hansen, and M. Mosca, *J. Magn. Reson.*, 1998, **135**, 353.
21. N. Linden, H. Barjat, R. J. Carbajo, and R. Freeman, *Chem. Phys. Lett.*, 1999, **305**, 28.
22. R. Freeman, 'Spin Choreography', Spektrum: Oxford, 1997.
23. H. K. Cummins and J. A. Jones, *New J. Phys.*, 2000, **2**, 6.
24. L. Emsley and G. Bodenhausen, *Chem. Phys. Lett.*, 1990, **168**, 297.
25. E. Knill, R. Laflamme, R. Martinez, and C.-H. Tseng, *Nature*, 2000, **404**, 368.
26. L. Vandersypen, M. Steffen, G. Breyta, C. Yannoni, R. Cleve, and I. Chuang, *Phys. Rev. Lett.*, 2000, **85**, 5452.
27. E̅. Kupče and R. Freeman, *J. Magn. Reson. A*, 1995, **112**, 261.
28. N. Linden, E̅. Kupče, and R. Freeman, *Chem. Phys. Lett.*, 1999, **311**, 321.
29. M. Steffen, L. M. K. Vandersypen, and I. L. Chuang, *J. Magn. Reson.*, 2000, **146**, 369.
30. E̅. Kupče, J. M. Nuzillard, V. S. Dimitrov, and R. Freeman, *J. Magn. Reson. A*, 1994, **107**, 246.
31. S. L. Patt, *J. Magn. Reson.*, 1992, **96**, 94.
32. S. Lloyd, *Science*, 1993, **261**, 1569.
33. D. W. Leung, I. L. Chuang, F. Yamaguchi, and Y. Yamamoto, *Phys. Rev. A*, 2000, **61**, 042 310.
34. J. A. Jones and E. Knill, *J. Magn. Reson.*, 1999, **141**, 322.
35. D. Collins, K. W. Kim, W. C. Holton, H. Sierzputowska-Gracz, and E. O. Stejskal, *Phys. Rev. A*, 2000, **62**, 022 304.
36. L. M. K. Vandersypen, M. Steffen, M. H. Sherwood, C. S. Yannoni, G. Breyta, and I. L. Chuang, *Appl. Phys. Lett.*, 2000, **76**, 648.
37. O. W. Sorenson, G. W. Eich, M. H. Levitt, J. Bodenhausen, and R. R. Ernst, *Prog. NMR Spectrosc.*, 1983, **16**, 163.
38. L. M. K. Vandersypen, C. S. Yannoni, M. H. Sherwood, and I. L. Chuang, *Phys. Rev. Lett.*, 1999, **83**, 3085.
39. D. Suter, A. Pines, and M. Mehring, *Phys. Rev. Lett.*, 1986, **57**, 242.
40. E. Knill, I. L. Chuang, and R. Laflamme, *Phys. Rev. A*, 1998, **81**, 5672.
41. L. J. Schulman and U. Vazirani, 'Proc. 31st Ann. Symp. on Theory of Comp. Science', 1998, p. 322.
42. D. Chang, L. M. K. Vandersypen, and M. Steffen, see http://xxx.lanl.gov/abs/quant-ph/0011055.
43. I. L. Chuang, N. Gershenfeld, M. Kubinec, and D. Leung, *Proc. R. Soc. Lond. A*, 1998, **454**, 447.
44. I. L. Chuang, N. Gershenfeld, and M. Kubinec, *Phys. Rev. Lett.*, 1998, **80**, 3408.
45. I. L. Chuang, L. M. K. Vandersypen, X. Zhou, D. W. Leung, and S. Lloyd, *Nature*, 1998, **393**, 143.
46. P. W. Shor, *Phys. Rev. A*, 1995, **52**, 2493.
47. A. Steane, *Phys. Rev. Lett.*, 1996, **77**, 793.
48. D. Aharonov and M. Ben-Or, see http://xxx.lanl.gov/abs/quant-ph/9906129.
49. J. A. Jones, M. Mosca, and R. H. Hansen, *Nature*, 1998, **393**, 344.
50. J. A. Jones and M. Mosca, *Phys. Rev. Lett.*, 1999, **83**, 1050.
51. J. A. Jones and M. Mosca, *J. Chem. Phys.*, 1998, **109**, 1648.
52. N. Linden, H. Barjat, and R. Freeman, *Chem. Phys. Lett.*, 1998, **296**, 61.
53. R. Marx, A. F. Fahmy, J. M. Myers, W. Bermel, and S. J. Glaser, *Phys. Rev. A*, 2000, **62**, 012 310.
54. S. Somaroo, C.-H. Tseng, T. F. Havel, R. Laflamme, and D. G. Cory, *Phys. Rev. Lett.*, 1999, **82**, 5381.
55. C.-H. Tseng, S. Somaroo, Y. Sharf, E. Knill, R. Laflamme, T. F. Havel, and D. G. Cory, *Phys. Rev. A*, 2000, **61**, 012 302.
56. D. Leung, L. Vandersypen, X. Zhou, M. Sherwood, C. Yannoni, M. Kubinec, and I. Chuang, *Phys. Rev. A*, 1999, **60**, 1924.
57. D. G. Cory, W. Maas, E. Knill, R. Laflamme, W. H. Zurek, T. F. Havel, and S. S. Somaroo, *Phys. Rev. Lett.*, 1998, **81**, 2152.
58. W. S. Warren, *Science*, 1997, **277**, 1688.
59. S. L. Braunstein,C. M. Caves, R. Jozsa, N. Linden, S. Popescu, and R. Schack, *Phys. Rev. Lett.*, 1999, **83**, 1054.
60. R. Schack and C. Caves, *Phys. Rev. A*, 1999, **60**, 4354.
61. C. S. Yannoni, M. H. Sherwood, D. C. Miller, I. L. Chuang, L. M. K. Vandersypen, and M. G. Kubinec, *Appl. Phys. Lett.*, 1999, **75**, 3563.
62. D. G. Cory, R. Laflamme, E. Knill, L. Viola, T. F. Havel, N. Boulant, G. Boutis, E. Fortunato, S. Lloyd, R. Martinez, C. Negrevergne, M. Pravia, Y. Sharf, G. Teklemariam, Y. S. Weinstein, and W. H. Zurek, *Fortschr. Phys.*, 2000, **48**, 875.
63. F. Yamaguchi and Y. Yamamoto, *Appl. Phys. A*, 1999, **68**, 1.
64. B. E. Kane, *Nature*, 1998, **393**, 133.
65. Special Issue, *Fortschr. Phys.*, 2000, **48**, 9–11.
66. C. A. Sackett, D. Kielpinski, B. E. King, C. Langer, V. Meyer, C. J. Myatt, M. Rowe, Q. A. Turchette, W. M. Itano, D. J. Wineland, and C. Monroe, *Nature*, 2000, **404**, 256.
67. L. M. K. Vandersypen, M. Steffen, G. Breyta, C. S. Yannoni, M. H. Sherwood, and I. L. Chuang, *Nature*, 2001, **414**, 883.
68. E. Knill, R. Laflamme, R. Martinez, and C. Negrevergne, *Phys. Rev. Lett.*, 2001, **86**, 5811.
69. Q. A. Turchette, C. J. Hood, W. Lange, H. Mabuchi, and H. J. Kimble, *Phys. Rev. Lett.*, 1995, **75**, 4710.

Quantum Exchange

Kurt W. Zilm
Yale University, New Haven, CT, USA

1	Introduction	1
2	Experimental Observations	1
3	Theory	1
4	Examples	7
5	Summary	8
6	References	9

1 INTRODUCTION

By the late 1950s, all of the physics important to high-resolution solution NMR seemed to have been identified. The basic interactions of chemical shift and scalar or J couplings, as well as the dynamics leading to spin relaxation and chemical exchange, were understood—at least in principle. It seemed that all of the relevant terms in the Hamiltonian that applied to NMR in isotropic solutions were known. Advances in NMR theory focused on the details of dealing with complex spin systems and their manipulation by pulse trains, or how the spins reflected molecular dynamics, as exemplified in this Encyclopedia. This article deals with the recent recognition of an additional term in the solution NMR Hamiltonian, namely, that for nuclear–nuclear exchange coupling, and the dramatic effects it can have on solution NMR spectra. The purpose is to provide the reader with as intuitive and physical a picture of this purely quantum mechanical effect as possible. More rigorous treatments of the details of the underlying physics may be found in the references.

2 EXPERIMENTAL OBSERVATIONS

The discovery of nuclear–nuclear exchange couplings or quantum exchange couplings in solution NMR spectroscopy[1–3] grew out of NMR studies of transition metal polyhydrides in the 1980s. Kubas at Los Alamos National Laboratory had discovered a class of transition metal complexes that bind H_2 as an intact ligand, rather than oxidatively adding the H_2 to the metal center.[4] This prompted a great deal of activity among inorganic chemists in the synthesis of new hydride and dihydrogen complexes, as well as the reinvestigation of many previously known systems. At the time, the synthetic chemists also postulated that species such as H_3^+ might also be stabilized as ligands in transition metal complexes. Solution NMR spectroscopy of ^{1}H was usually the structural method of choice in these investigations, and the classic signature of an H_2 complex became a measurable value for $^1J(^1\mathrm{H}, ^2\mathrm{D})$ in the HD isotopomer, usually of the order of 20–35 Hz. It was widely assumed that a large value of $^1J(^1\mathrm{H}, ^1\mathrm{H})$ would be found in any H_3 complex.

In the late 1980s, Heinekey at Yale and Chaudret at Toulouse independently[5,6] made some somewhat startling observations in the ^{1}H NMR of several transition metal trihydrides. In these systems, the spectra indicated that $^1J(^1\mathrm{H}, ^1\mathrm{H})$ could be over 200 Hz. Since the coupling in molecular H_2 itself is only 280 Hz as inferred from the NMR of HD, these large values for ^1J were at first glance evidence for the putative H_3^+ complexes. However, it soon became clear that these systems were not to be explained so simply. During the next few years, Heinekey carried out a set of classic experiments that formed the basis on which it is now accepted that these splittings are exchange couplings.

One of the first indications that the observed splittings were not due to the usual Fermi-contact mediated scalar coupling mechanism was their extreme sensitivity to temperature. Early on, the apparent J couplings seemed to be field-dependent. However, careful experiments by Heinekey showed that this apparent B_0 dependence arose from slight variations in the probe temperature on different instruments. The splittings in fact did not depend upon field, but instead were hypersensitive to temperature. Many alternate models were considered for explaining these observations at the time. Some invoked chemical equilibria involving an unusual thermally accessible state that would have unprecedently large J couplings. Several tunneling-type mechanisms were also considered, but these seemed difficult to resolve with the observation of these splittings in fluid media at close to ambient temperatures. (For a review of previous experimental observations, other models eliminated, and pertinent references, see Zilm and Miller.[7]) Heinekey then carried out some very important experiments employing ^{2}D substitution. The resulting pattern of isotope shifts and the isotopic variations on the apparent values of $^1J(^1\mathrm{H}, ^1\mathrm{H})$ in the remaining protons ruled out any sensible model involving chemical equilibrium.[2] Unfortunately, the spectra of the partially deuterated isotopomers themselves did not provide convincing evidence for the involvement of tunneling. While no $^1J(^1\mathrm{H}, ^2\mathrm{D})$ couplings were observed, this observation could be explained just as convincingly by self-decoupling due to the rapid ^{2}D relaxation in concert with chemical exchange as by a tunneling mechanism. The key experiment to perform became clear. The NMR of a partially tritiated isotopomer would have none of the complications encountered with deuterium. Given the difficulties in handling radioactive samples, this experiment was more than difficult to perform. The results were well worth Heinekey's efforts: a coupling that started as over 500 Hz in a perprotio molecule was reduced to a $^1J(^1\mathrm{H}, ^3\mathrm{T})$ of less than 30 Hz at the same temperature.[1] This was the first conclusive evidence obtained in favor of the exchange coupling mechanism for these large temperature dependent couplings. The initial report[1] of this result and a theoretical framework for quantitatively accounting for these couplings and their temperature dependence was soon published. Simultaneously with this report, Jones and Weitekamp[8] also proposed an exchange coupling mechanism in these systems, which utilized symmetry arguments, but with no additional experimental data.

3 THEORY

Exchange interactions among electrons are familiar to any student of solid state physics or quantum chemistry. They are central to the quantum mechanical description of bonding in

molecules and the mechanism of phenomena such as high-temperature superconductivity. The appearance of $J\boldsymbol{I}_1\cdot\boldsymbol{I}_2$ type couplings in ESR spectra of triplet biradicals is a well-known spectroscopic manifestation of the electron–electron exchange interaction. For nuclei, quantum mechanical exchange interactions are less familiar, and until recently they were not known to affect high-resolution magnetic resonance spectra in any manner. (For references on quantum exchange in solid ^{3}He and in related electronic structure problems, see Zilm and Miller.[7]) The best-known example of heavy particle quantum exchange is in solid ^{3}He. In this system, diffusion rates and other properties are known in large part to be determined by ^{3}He–^{3}He exchange interactions. NMR spectra of tunneling methyl groups at low temperature also display features related to rotational tunnel splittings, but these have not usually been considered as manifestations of an exchange interaction per se. Given that quantum effects such as these have typically been considered as purely low-temperature phenomena, it is not surprising that quantum exchange involving nuclei has not until recently been recognized as having any role in solution NMR spectroscopy.

Any theory accounting for quantum exchange must consider the total wavefunctions for the nuclei being observed, spanning both spin and spatial coordinates. In this respect, quantum exchange is quite distinct from the other terms in the NMR Hamiltonian. A typical NMR interaction can usually be written as a product of a spin operator and an interaction constant or tensor, which is an expectation value of the rest of the system Hamiltonian over all coordinates except spin. In quantum exchange, however, the spin coordinate and the spatial coordinate are correlated, and such a separation is not possible. To illustrate this, we shall consider a simple two-spin system where the spins occupy chemically inequivalent sites.

3.1 Molecular Dynamics

To understand quantum exchange in the context of NMR spectroscopy, we must first consider the quantum mechanics governing the Cartesian displacements of the NMR active nuclei, i.e., their orbital wavefunctions, and then see how this is coupled to their spin coordinates, i.e., the spin functions. For a start, we shall consider a simple two-particle quantum mechanics problem that is often somewhat misunderstood. Although our treatment will be quite similar to a number of familiar problems in tunneling (see, e.g., Atkins[9]), we should like to emphasize now that quantum exchange does not in fact imply that tunneling motions occur. This point will be clarified in the following discussion.

The molecular systems in which quantum exchange has been observed by NMR all are of the form (**1**)

(1)

where the other ligands collectively denoted by L_3 are typically another hydride, a cyclopentadienyl, and a phosphine. Single crystal neutron diffraction studies[3] indicate that the hydrides are typical terminal hydrides having a single bond to the central transition metal atom M. Although the M–H linkages are significantly more 'floppy' than C–H bonds, these hydrides are basically localized at their binding sites. To a very good approximation, the potential well that each of these hydrides experiences can be approximated by the harmonic oscillator potential as depicted in Figure 1(a).

A complete quantum mechanical treatment of the pair of hydrides under consideration would involve a six-dimensional potential energy surface describing the energy of all configurations of the two hydrides as they are moved relative to each other and to the metal center. As long as the hydrides remain outside each other's van der Waals radii, the potential experienced by either is still roughly harmonic. If the hydrides do not have any appreciable interaction with one another, the problem reduces to that of two uncoupled harmonic oscillators.[7]

As a simple model for this system, consider two hydrides bound to a surface, each in locally harmonic single particle potentials, (**2**) and (**3**).

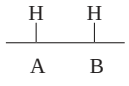

(2)

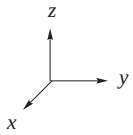

(3)

If the interaction between the two protons is sufficiently weak, their displacements are approximately harmonic except for the symmetric displacement towards one another. In this instance, each hydride feels a repulsive force, which rises rapidly as they near one another. The hydrides are also attracted to the potential minimum at the other binding site. It is the displacement of the hydrides along this type of coordinate that we shall focus upon.

A good model potential for displacements along this exchange coordinate is a double well potential such as that in Figure 1(b). Movement along this coordinate exchanges the two hydrides between the two wells. The reaction coordinate is a two-particle potential, and is necessarily somewhat complicated. If the hydrides simply each moved along the y axis towards one another, there would be an essentially infinite barrier separating the two configurations. The model we want to consider instead takes the coordinate to be a minimum energy type of path along which exchange is possible. At the barrier the two particles must move out of each other's way along a path that takes them out of the (y, z) plane.

It worthwhile to note what is, and what is not, important in the choice of this potential energy curve. The double well model is only one approach to connecting the two different possible ground state configurations of the hydrides. Displacement on a periodic rotational coordinate would also produce the type of effects to be discussed.[10] The required features are only that the potential has two wells representing two distinct configurations and that there be a finite barrier separating them.

Having reduced the two-particle problem to a single internal reaction coordinate in a double well makes the problem fairly simple. We shall only consider the vibrational ground state in this potential, since we know that the hydrides are basically bound fairly tightly to their binding sites. This places them in one of the two configurations representing the double well minima. Near the bottom of either well, the potential is close to harmonic, and a good approximate two-particle ground state

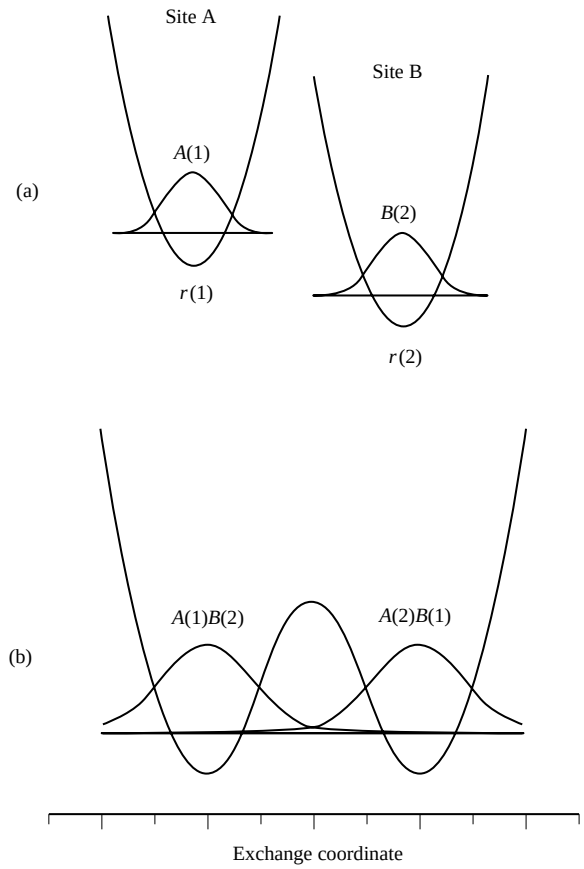

Figure 1 (a) Depiction of two harmonic potentials at two different sites, with vibrational ground state wavefunctions. This is a reasonable description of two largely uncoupled M–H vibrators in a transition metal hydride. The coordinates are the displacements of the individual hydrides. (b) A model two-particle potential describing the change in potential energy as the two hydrides in the two sites shown in (a) are exchanged between the two sites. The coordinate is the reaction coordinate along which the exchange takes place. The wavefunctions shown are two-particle wavefunctions for the two degenerate configurations

wavefunction would be a Gaussian centered in either of the two wells. We define $\psi(\mathrm{L})$ as the configuration where the protons 1 and 2 were at sites A and B, respectively. This configuration can be written as a product of one-particle wavefunctions, i.e., $A(1)B(2)$, where $A(1)$ and $B(2)$ are the Gaussians representing the one-particle ground state vibrational wavefunctions in the single particle potentials representing the two binding sites. The other side of the double well would then be represented by the two-particle wavefunction $\psi(\mathrm{R})$=$A(2)B(1)$ [see Figure 1(b)].

It is tempting to apply what we know about the quantum mechanics of a single particle in a double well directly to this two-particle problem, since the mathematical formulation is now the same at this point (see, e.g., Atkins[9]). Because the wells are a finite distance apart, the wavefunctions for the two ground state basis configurations we have chosen overlap each well. This produces an off-diagonal element in the matrix for the system Hamiltonian $\hat{\mathcal{H}}_{\mathrm{L}}$ that includes the interaction of the particles with both wells and each other. To get the best possible description of the ground state within this restricted basis set, we must diagonalize this matrix. If

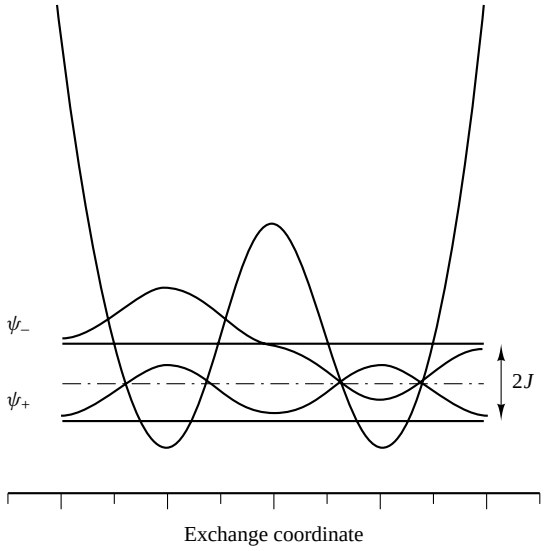

Figure 2 Model double well exchange potential showing the two lowest energy eigenfunctions ψ_+ and ψ_-. The energies of these two states are split by $2J$ symmetrically about the energy of the two degenerate localized basis states

the two sides of the double well have the same depth, the basis states are degenerate. No matter how small the off-diagonal term, the two basis set wavefunctions will be mixed. As every student of quantum mechanics knows, in the single particle case the symmetric and antisymmetric combinations of the two Gaussians are then good approximations to the proper wavefunctions. The eigenenergies of the two eigenstates $\psi_\pm = \frac{1}{2}[\psi(\mathrm{L}) \pm \psi(\mathrm{R})]$ for the symmetrical potential are $E_\pm = E \pm J$ (see Figure 2). E is the unperturbed energy of either of the degenerate configurations given by

$$\int\int [A(1)B(2)]^* \hat{\mathcal{H}}_{\mathrm{L}} A(1)B(2)\,\mathrm{d}\tau_1\,\mathrm{d}\tau_2 \qquad (1)$$

and J is the value of the off-diagonal matrix element

$$\int\int [A(1)B(2)]^* \hat{\mathcal{H}}_{\mathrm{L}} A(2)B(1)\,\mathrm{d}\tau_1\,\mathrm{d}\tau_2 \qquad (2)$$

In the case of a single particle in the double well, the energy difference $2J$ is a tunnel splitting. The wavefunctions indicate that the particle is equally likely to be in either well. This is interpreted to mean that the particle is 'delocalized' over both sides of the potential. If a localized state is prepared by a superposition of ψ_+ and ψ_-, it will evolve in time according to the usual rules of time-dependent quantum mechanics. The picture that emerges is one of the maximum in the probability density oscillating between the two wells at a frequency $2J/h$. One usually describes the particle as coherently tunneling from one well to the other at this rate. On the other hand, when the two wells are of differing depths, the particle quickly becomes localized. As long as the difference in the energies of the two states $\psi(\mathrm{L})$ and $\psi(\mathrm{R})$ is larger than the off-diagonal term J, these remain good states to first order in the perturbation treatment.

The mapping of the two-particle case onto this reduced one-particle description contains some subtleties. If the two

sites are energetically the same, i.e. the one-particle potentials at the two binding sites are identical, the configurations $A(1)B(2)$ and $A(2)B(1)$ will clearly have the same energies. The degeneracy will again be lifted by any finite matrix element connecting the functions $A(1)B(2)$ and $A(2)B(1)$, and there will be two states separated by a tunnel splitting. In the molecules we are considering, however, the hydrides are chemically inequivalent. This means that the local one-particle potentials are different, if only slightly so on a cm^{-1} scale. However, this does necessarily break the symmetry of the two-particle potential along the exchange coordinate. If the two particles are identical, the basis configurations $A(1)B(2)$ and $A(2)B(1)$ representing $\psi(\mathrm{L})$ and $\psi(\mathrm{R})$ will still have the same energies. Exchange of identical particles can then be described by a mirror-symmetric two-particle potential in the exchange coordinate. If the hydrides are not identical (e.g., a proton and a triton), this symmetry will be broken, since the two basis configurations will have different energies. The eigenstates will then be localized, and no tunneling will occur. In this case of two distinguishable particles, the two sites would have to be identical for the exchange potential to remain symmetric.

The appearance of a potential for particle exchange with mirror symmetry is then a prerequisite for exchange splittings to appear in the energy level diagram for this two-particle system. Many familiar systems have this type of symmetry, but not all can display quantum exchange. For example, consider the umbrella mode of ammonia, or the chair-to-chair inversion of cyclohexane. In the gas phase, both displacements can be described by mirror-symmetric double wells. Placing these molecules into a condensed phase, however, breaks this symmetry. When either molecule inverts, it moves from one region of space to another. The presence of an anisotropic solvent shell around each site gives the configurations distinct energies. This is not the case for the transition metal polyhydrides we are considering, or other systems such as rotating methyl groups. In the transition metal hydrides, the configuration before and after the exchange of two hydrides occupies the same region of space. Rotation of a methyl group by 120° likewise results in a new configuration that occupies the same space as before the rotation. These displacements are then always instantaneously described by mirror-symmetric potentials, and thus will have exchange-type splittings appearing in their energy level structure. It should be emphasized that whether particles are identical or not depends only on the nature of the particles and not on their location in the molecule or lattice. However, whether a molecular rearrangement that exchanges identical particles is a truly degenerate rearrangement energetically depends on the relation of the molecule to the lattice at the beginning and the end of the rearrangement.

The above treatment of the two-particle exchange problem as a single pseudoparticle in a double well is only partially correct. This is because the two-particle wavefunctions have additional constraints. One must remember that the spatial portion of a wavefunction describes the probability of a particle's location. When several particles are described by a single wavefunction, the probabilities can only be ascribed individually to particles that are distinguishable. For indistinguishable particles, the identity (e.g., particle number) is irrelevant.[11] The wavefunction for a pair of identical particles can then only give the probability of finding a particle of that type at any position. It cannot tell us the probability for finding a particular particle there.

Our interpretation of $\psi_\pm$ in the one- and two-particle cases, then, is somewhat different. For the single particle in the double well, the equal probability amplitudes on the left and right sides is taken as an indication that the particle is 'delocalized' over both sides. This notion is reinforced by the time-dependent behavior of a single particle in this potential if the initial state is localized as just discussed. On the other hand, the two-particle wavefunctions $\psi_\pm$ do not imply delocalization of the two particles, or of the configuration. These functions now simply state that the system is most likely in a configuration with one particle on the left and one on the right, but the identity of the configuration is indeterminate. We may not ask about the location of individual particles, since they are identical, and as such their labels are simply irrelevant. Thus, we see in the two-particle case that the indeterminacy as to which particle is on the left or on the right has replaced the delocalization that arises in the one-particle problem.

This statistical interpretation of the two-particle wavefunctions requires that any relabeling of the particle identities must leave the probability densities unchanged. Thus, the wavefunction must be the same, or at most change sign, when the particle labels are permuted. In accord with the well-known symmetrization postulate, wavefunctions for identical bosons are symmetric or remain the same, while those for identical fermions are antisymmetric or change sign, under particle label exchange. With this in mind, we return to the problem of two particles in the double well. Consider the case where the particles are of zero spin and are therefore bosons. The function ψ_+ has the proper symmetry, while ψ_- does not. The ground state can then only exist as ψ_+, since ψ_- is an unacceptable wavefunction. The consequence of this is that a 'localized' state cannot be constructed by combining ψ_+ and ψ_-. The picture we arrived at in the one-particle state of an initially localized state periodically moving between the two wells is then inappropriate. The system can only remain in the ground state ψ_+. This is most easily interpreted as the system being localized in one of the two possible indistinguishable configurations.

3.2 Including the Spin Coordinate

When the spin functions are included in the two-particle problem, the symmetry of the total wavefunction including spin must be considered. One place to start is to write the individual spatial and spin functions as separate symmetrized sets. For a pair of spin-$\frac{1}{2}$ nuclei the symmetrized functions are the symmetric triplet functions T_0, T_{-1}, T_{+1}, and the antisymmetric singlet spin function S_0. The total wavefunction for identical fermions must be antisymmetric with respect to exchange, and therefore ψ_+S_0, ψ_-T_0, ψ_-T_{-1}, and ψ_-T_{+1} are the only acceptable combinations. Now that spin has been introduced, the system can have an energy of either $E + J$ or $E - J$, depending upon the spin state of the nuclei. Any additional small interaction of the magnetic field would not be expected to change the situation with respect to the energy associated with the orbital or lattice terms of the Hamiltonian. On the other hand, magnetic interactions will mix the singlet and triplet spin manifolds. Any spin flip that occurs must also make up any difference in lattice energy accompanying the transition. The appearance of the exchange energy in an

NMR transition is then a consequence of the correlation of the spin states with the orbital energies associated with the displacements of the NMR active nuclei.

In general, the above type of prescription for determining properly symmetrized total spin + spatial wavefunctions is cumbersome. The resulting functions can be recast in a more physical and convenient basis, which we call the site spin basis.[11] Rather than deriving the site spin basis, we shall develop it directly from some basic symmetry considerations. Let us start by considering a pair of protons in chemically equivalent sites that comprise an AX spin system. Normally we ignore the complications brought on by the coordinate or orbital part of the wavefunction, and simply write the spin eigenfunctions as $|+\ +\rangle$, $|+\ -\rangle$, $|-\ +\rangle$, and $|-\ -\rangle$, where the labels refer to m_S for particles 1 and 2 in that order. These two-particle product basis spin functions themselves, however, do not have the proper symmetry with respect to particle exchange, i.e., $|+\ -\rangle \neq \pm|-\ +\rangle$. This at first sight seems perplexing, since every NMR spectroscopist knows that these wavefunctions are what are always used for an AX spin system. The answer is that in actuality the spin labels do not refer to the particle identities. Instead, the functions are of the form $|m_S(\mathrm{A}), m_S(\mathrm{B})\rangle$, i.e., the labels are according to the site identity, not the particle numbers. The function $|+\ -\rangle$ says the particle in site A is in the + state, and the particle in site B is in the − state. What the function does not tell us is which particle is in which site. Therefore, the spin functions labeled according to the m_S in each site are automatically symmetric with respect to particle exchange. To differentiate the product basis labeled according to sites, we shall write these kets as $[+\ -\rangle'$.

In using this site labeling convention, we must also relabel our spin Hamiltonian.[11] For instance, the Zeeman plus chemical shift term in frequency units for two spins would be written as

$$\hat{\mathcal{H}}_{\mathrm{cs}} = -\nu_{\mathrm{A}}\hat{I}_{z\mathrm{A}} - \nu_{\mathrm{B}}\hat{I}_{z\mathrm{B}} \tag{3}$$

The resonance frequencies and spin operators are thus identified with the molecular site instead of a particle number. In most instances, this is in fact how NMR problems are typically handled, even though one may have the impression that one is using particle labels instead of site labels.

The overall symmetry of the total site spin basis function $\psi_{\mathrm{site}} = \psi_{\mathrm{orbital}}\psi_{\mathrm{spin}}$ is then determined solely by the symmetry of the orbital wavefunction. For this pair of spin-$\frac{1}{2}$ nuclei, ψ_{orbital} must always be the antisymmetric function ψ_-, since ψ_{spin} is always symmetric with this site labeling convention. The total wavefunction for the $[+\ -\rangle'$ spin state is then $\sqrt{\frac{1}{2}}[A(1)B(2) - A(2)B(1)][+\ -\rangle'$ (the normalization is only approximate, since we have ignored the small overlap term). As a shorthand, these site spin basis functions will be written as $[m_S(\mathrm{A}), m_S(\mathrm{B})\rangle$, dropping the prime notation to imply the inclusion of the orbital portion. Remember that the labeling of the spin portion is according to site A and B, not particle 1 and 2, in these functions with the '[' notation. In order to calculate a spectrum, it is instructive first to explicitly calculate a few matrix elements. We shall use the sum of the coordinate Hamiltonian for the particles, $\hat{\mathcal{H}}_{\mathrm{L}}$, and $\hat{\mathcal{H}}_{\mathrm{cs}}$ as an example.

First consider $\langle+-]\hat{\mathcal{H}}_{\mathrm{cs}}[+-\rangle$. Using the site labeling convention, this is evaluated as $\frac{1}{2}(\nu_{\mathrm{B}} - \nu_{\mathrm{A}})$ in the usual fashion. The integral over the particle coordinates is unity, since the orbital function is normalized. To calculate $\langle-]\hat{\mathcal{H}}_{\mathrm{L}}[+-\rangle$, we must expand $[+\ -\rangle$ in terms of functions with particle labels:

$$[+-\rangle = \tfrac{1}{2}[A(1)B(2)|+-\rangle - A(2)B(1)|-+\rangle] \tag{4}$$

Since the spins have particle number designations on the right-hand side, the + and − labels have been arranged to keep the + spin in the A site and the − spin in the B site. The quantity $\langle+-]\hat{\mathcal{H}}_{\mathrm{L}}[+-\rangle$ can be written as a sum of products of integrals over spin and space separately:

$$\begin{aligned}
&\langle+-]\hat{\mathcal{H}}_{\mathrm{L}}[+-\rangle \\
&= \tfrac{1}{2}\langle+-\,|\,+-\rangle \int\int [A(1)B(2)]^*\hat{\mathcal{H}}_{\mathrm{L}}A(1)B(2)\,\mathrm{d}\tau_1\,\mathrm{d}\tau_2 \\
&\quad +\tfrac{1}{2}\langle-+\,|\,-+\rangle \int\int [A(2)B(1)]^*\hat{\mathcal{H}}_{\mathrm{L}}A(2)B(1)\,\mathrm{d}\tau_1\,\mathrm{d}\tau_2 \\
&\quad -\tfrac{1}{2}\langle-+\,|\,+-\rangle \int\int [A(2)B(1)]^*\hat{\mathcal{H}}_{\mathrm{L}}A(1)B(2)\,\mathrm{d}\tau_1\,\mathrm{d}\tau_2 \\
&\quad -\tfrac{1}{2}\langle+-\,|\,-+\rangle \int\int [A(1)B(2)]^*\hat{\mathcal{H}}_{\mathrm{L}}A(2)B(1)\,\mathrm{d}\tau_1\,\mathrm{d}\tau_2
\end{aligned} \tag{5}$$

Note again that the spin labels on the left refer to sites A and B, while those on the right refer to particle numbers 1 and 2. The first two integrals each give $\frac{1}{2}E$, and the last two are zero because of the vanishing integral over the spin coordinate. The net value of the element $\langle+-]\hat{\mathcal{H}}_{\mathrm{L}}[+-\rangle$ is then the lattice energy E. Now consider the element $\langle-+]\hat{\mathcal{H}}_{\mathrm{L}}[+-\rangle$. In a similar fashion, the integral can be expanded as

$$\begin{aligned}
&\langle-+]\hat{\mathcal{H}}_{\mathrm{L}}[+-\rangle \\
&= \tfrac{1}{2}\langle-+\,|\,+-\rangle \int\int [A(1)B(2)]^*\hat{\mathcal{H}}_{\mathrm{L}}A(1)B(2)\,\mathrm{d}\tau_1\,\mathrm{d}\tau_2 \\
&\quad +\tfrac{1}{2}\langle+-\,|\,-+\rangle \int\int [A(2)B(1)]^*\hat{\mathcal{H}}_{\mathrm{L}}A(2)B(1)\,\mathrm{d}\tau_1\,\mathrm{d}\tau_2 \\
&\quad -\tfrac{1}{2}\langle+-\,|\,+-\rangle \int\int [A(2)B(1)]^*\hat{\mathcal{H}}_{\mathrm{L}}A(1)B(2)\,\mathrm{d}\tau_1\,\mathrm{d}\tau_2 \\
&\quad -\tfrac{1}{2}\langle-+\,|\,-+\rangle \int\int [A(1)B(2)]^*\hat{\mathcal{H}}_{\mathrm{L}}A(2)B(1)\,\mathrm{d}\tau_1\,\mathrm{d}\tau_2
\end{aligned} \tag{6}$$

In this case, the first two integrals are zero, and the second pair give contributions of $-\frac{1}{2}J$ for a total value of $-J$.

The reader may already see that these matrix elements can be evaluated on inspection following a few simple rules. When dealing with the NMR or spin Hamiltonian, we proceed as normally, using spin operators, interaction coefficients, and spin functions labeled according to site. The coordinate part seems trickier, but can be simply treated as a permutation operator over the spin. For a term $\langle ij]\hat{\mathcal{H}}_{\mathrm{L}}[kl\rangle$, a value of E is returned if $i = k$ and $j = l$. If $i = l$ and $j = k$, a contribution of $-J$ is obtained. The additional terms that the exchange interaction brings to the NMR Hamiltonian can then be recognized as having the same form as the classical exchange matrix familiar to students of dynamic NMR lineshape analysis.

Table 1 Hamiltonian Matrix in the Site Spin Basis for a Simple AX Spin System

	$\|+\,+\rangle$	$\|+\,-\rangle$	$\|-\,+\rangle$	$\|-\,-\rangle$
$\langle++\|$	$-\frac{1}{2}\nu_A - \frac{1}{2}\nu_B + E - J$	0	0	0
$\langle+-\|$	0	$-\frac{1}{2}\nu_A + \frac{1}{2}\nu_B + E$	$-J$	0
$\langle-+\|$	0	$-J$	$+\frac{1}{2}\nu_A - \frac{1}{2}\nu_B + E$	0
$\langle--\|$	0	0	0	$+\frac{1}{2}\nu_A + \frac{1}{2}\nu_B + E - J$

For our simple AX spin system, the full Hamiltonian matrix in the site spin basis can then be written on inspection as in Table 1. Since the orbital energy E only adds to the diagonal, it just represents a shift of the energy scale and can arbitrarily be set to zero. If the chemical shift difference $|\nu_A - \nu_B| \gg |J|$ then the off-diagonal terms will be truncated, and the NMR transitions will give two doublets centered at ν_A and ν_B with splittings of $-2J$. This Hamiltonian then gives the same spectrum as that for an AX spin system with an effective J coupling of $-2J$. Since the matrix element that J represents is inherently negative, the apparent coupling in the spectrum is positive. For spin-$\frac{1}{2}$ nuclei, it can be shown that any pairwise exchange interaction gives rise to a term that behaves just as if there were a scalar coupling $-2J$ between those two sites. Higher-spin systems, however, cannot be described by such a simple effective spin Hamiltonian.[11]

One could incorrectly infer from the energy level structure of this simple example that the identity of the particles can somehow be made known by the fact that they experience different chemical shifts at the two different sites. A question that might be asked is how often the spins can change places by tunneling. The answer turns out to be that one cannot tell. The probability that a spin in site A has exchanged with a spin in site B becomes a maximum when their spin quantum numbers are identical. In other words, the spins can tunnel when one cannot tell them apart, even by their spin. Therefore, the most straightforward interpretation is that the spins remain localized, but which spin is localized where is something that cannot be known, since the particles are indistinguishable.

The advantage of the site spin basis approach to treating exchange coupling in NMR spectroscopy is that it is very easily extended to more complicated permutations or exchanges of spins, and is easily applied to problems involving nuclei of arbitrarily large I. The general form of the exchange Hamiltonian in the site spin basis can be shown[11] to be

$$\hat{\mathcal{H}}_{ex} = \sum_i \xi^{p(i)} J_i \hat{\mathcal{P}}_i(k, l, m, \ldots) \tag{7}$$

where $\xi = e^{2\pi i I}$ and I is the spin quantum number of the nucleus in question. The permutation of the spins among the sites k, l, m, ... is represented by the operator $\hat{\mathcal{P}}_i(k, l, m, \ldots)$, which acts on the spin labels within the site spin basis functions. Each site spin basis function has the same orbital function implied. For fermions, this is formed using a Slater determinant for the orbital states for each site. If the nuclei are bosons, an antideterminant is used instead. The exchange matrix element is given by J_i. It is calculated by taking the matrix element of $\hat{\mathcal{H}}_L$ between an orbital state for one configuration and that of the configuration resulting from the permutation. For example, consider a three-site problem (e.g., a methyl group). A starting configuration would be $A(1)B(2)C(3)$. If the three particles are subjected to a cyclic permutation, this state would become $A(3)B(1)C(2)$. The value of J_c would be

$$J_c = \int\int\int [A(1)B(2)C(3)]^* \hat{\mathcal{H}}_L A(3)B(1)C(2)\, d\tau_1\, d\tau_2\, d\tau_3 \tag{8}$$

Different permutations have different parities. For bosons, this is irrelevant. However, for fermions, permutations of even parity produce negative elements, and those of odd parity give positive exchange integrals. This is handled by the $\xi^{p(i)}$ term. If the nuclei are fermions with spin $I = n + \frac{1}{2}$ then $\xi = -1$. If they are bosons then $\xi = +1$. For fermions, a single pairwise permutation has odd parity, and $p(i) = 1$, which produces a negative sign for the exchange matrix element. On the other hand, a permutation that can be written as the product of two pairwise permutations has even parity, and $p(i) = 2$. These permutations give positive exchange coupling elements in the Hamiltonian matrix. One can show by straightforward but tedious calculations that the results of this prescription are to reproduce the matrix elements that would be obtained by expanding the site spin basis functions as products of properly symmetrized orbital functions and spin functions with particle labels, and performing the integration explicitly.

In practice, one simply associates a different J value with each particular topological rearrangement or permutation of the nuclei between the different locations in a molecule. High barrier permutations give low J values, and facile permutations give larger ones. The states that are connected are those where the permutation operation shuffles the spin labels so that they match those of the state to which it is coupled. The procedure is exactly the same as filling an exchange matrix for a classical chemical exchange lineshape problem. The signs of the elements are determined by whether the spins are fermions or bosons, and whether the permutation has even or odd parity. These elements are added to the rest of the standard NMR Hamiltonian, and the spectrum is determined by finding the eigenstates and determining the transition moments in the usual fashion.

A convenient starting point for computer simulation of exchange-coupled spectra in the presence of chemical exchange is to start with any of the many programs for dynamic NMR lineshape simulation. One simply duplicates the code for calculating the elements of the classical exchange matrix, and uses it to add exchange coupling elements to the Hamiltonian matrix. In this manner, we have been able to computer-simulate exchange-coupled NMR spectra for systems of up to four chemically exchanging protons or deuterons.

3.3 Temperature Dependence

Our main purpose so far has been to provide a physical picture of how exchange interactions produce splittings in

NMR spectra. The theory accounts for the disappearance of exchange couplings between different isotopes of the same element, for the persistence at ambient temperatures of an effect that is similar to tunneling, and for the different spectral patterns that are observed for spin-$\frac{1}{2}$ and spin-1 systems (see below). Accounting for the size of these splittings and their temperature dependence is another matter. Several models have been proposed, and probably all are correct to some extent. A definitive calculation of the exchange coupling would require an accurate $3N$-dimensional potential energy surface for N identical nuclei. This is at present out of reach, so the models are either approximate analytical or computational attempts to focus on key features of the exchange process.

The model we have favored most is based on a treatment of exchange in solid ^{3}He by Landesmann.[2,7] Landesmann has analytically calculated the ground state exchange splitting for two atoms in harmonic wells and repelled by a hard sphere potential. To account for the temperature dependence, thermal excitations that place the molecules in higher vibrational states are involved. Since these vibrationally excited states are more delocalized, there is more overlap of the individual particles with the neighboring sites, and the size of J goes up with vibrational quantum number. In the double well description, the splittings of the higher states increase exponentially as one moves beyond the ground state. In solution, the vibrational states are short-lived, and the NMR experiment measures a Boltzmann population weighted average of the splittings over the vibrational ladder. The spin state is conserved in these transitions, and the sign of J remains the same; therefore, the weighted average of J increases with temperature. We have shown that the sum over vibrational states can be effectively accomplished by first calculating a Boltzmann population weighted overlap function.[7] This can be shown to be approximated by a Gaussian of increasing width with increasing temperature. As Landesmann's ground state calculation used a Gaussian basis set, this result can then be applied to the averaged splitting as a function of temperature also. The final expression obtained is

$$J(T) = \frac{-3\hbar a}{8\pi m\delta(T)^3}\sqrt{\frac{3}{\pi}}\exp\left[-\frac{3}{4}\frac{a^2+\lambda^2}{\delta(T)^2}\right] \qquad (9a)$$

where

$$\delta(T)^2 = \frac{3h}{4\pi m\nu}\coth\left(\frac{h\nu}{2kT}\right) \qquad (9b)$$

Here a is the inter-hydride equilibrium distance, λ is a hard sphere radius (usually taken as 10 nm), ν is the bending frequency of the M–H bonds, and m is the proton mass. When deuterium or tritium is involved, the mass and bending frequency are adjusted accordingly.

Equation (9a) can be used to fit J versus T data, and both a and ν determined. The values found in a large number of fits are quite close to the distances a found by single crystal neutron diffraction and the few ν bending frequencies that have been measured.[2] For systems with very large ^{1}H–^{1}H exchange interactions, this equation has correctly predicted the size of the ^{2}D–^{2}D exchange couplings when they can be measured. This equation also explains why exchange couplings are not observed in organic molecules. The exchange coupling decreases about two orders of magnitude for every 100 cm^{-1} increase in ν. Since C–H bends are of the order of 600 cm^{-1} higher than M–H bends, the exchange couplings in organic systems are about 10^{12} smaller and thus unobservable.

Jones and Weitekamp have developed a similar model using numerical diagonalization of model double well potentials.[12] The behavior of J versus T is calculated by a sum over the thermally populated states. One difficulty with this approach is making a connection between the model reaction coordinate and the molecular structure. Harris and co-workers[13] have studied exchange using muffin-tin-type potentials. They are also able to account for the observed data, and have offered some insight into the types of reaction coordinates that may play an important role.

Limbach[10] has proposed an alternative model to these that is most different in the assumed exchange coordinate. This is a rotational model that produces an exchange splitting from a periodic exchange potential. In the rotational tunneling problem, the tunnel splittings alternate in sign with increasing rotational quantum number. One might then expect that the exchange coupling would have to decrease with temperature in this model instead of increasing as is observed. To circumvent this problem, Limbach proposes that in the ground state the hydrides have no appreciable rotational tunnel splitting. Thermal excitations then allow the system to access a state that is a nascent H_2 complex. The H_2 ligand in this state has a substantial tunnel splitting, which produces the appearance of the exchange coupling. The temperature dependence arises from the thermal population of essentially just the lowest rotational state of the H_2 complex. Such a model can also be used to fit all of the experimental data collected on perprotio systems to date. The main difficulty with this model is rationalizing the existence of an H_2 complex that must lie only 4–8 kJ mol^{-1} above the ground state trihydride structure. In addition, the barrier to rotation of the H_2 ligand in the thermally excited state must be well over 40 kJ mol^{-1} to properly account for the apparent tunnel splitting in the lowest rotational state of this nascent H_2 complex.

Differentiation of how well these and other models describe these systems is being tested by several computational groups at present.[14,15] Potential energy surfaces are calculated for a model system, and the Hamiltonian is then numerically diagonalized. A Boltzmann population-weighted average over the calculated exchange splittings is computed for comparison to the experimentally observed variation of J with temperature. Such calculations can be made to reproduce the trends observed experimentally. However, it remains to be seen how high a level of calculation will be needed to do a better job than the approximate analytical theories.

4 EXAMPLES

A large number of transition metal hydride systems that display exchange couplings have been discovered or rediscovered. One of the most striking is the $Cp^*(CO)IrH_3^+$ cation. At 500 MHz, spectra similar to the simulations shown in Figure 3 are observed.[16] This is a deceptively simple AB_2 spectrum, which at first glance is a single line. On closer inspection, one sees that the central line is flanked by two broader lines with integrated intensities of approx. one-tenth of the central peak. This is an example of a dynamically broadened spectrum with a very large $J(^1H,^1H)$. The apparent

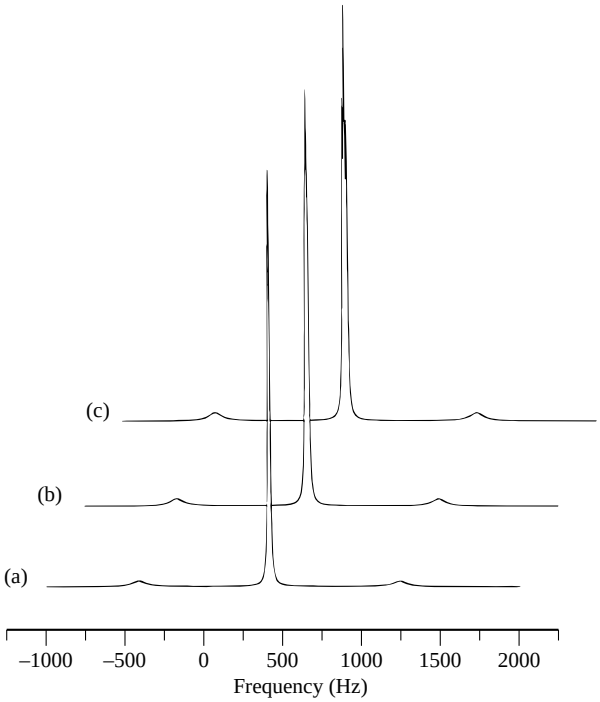

Figure 3 Simulated AB_2 dynamic ^1H NMR spectra similar to what are observed at 500 MHz and about 140 K for the $Cp^*(CO)IrH_3^+$ cation.[16] $J = -2J$ in these simulations is (a) 50 kHz, (b) 25 kHz, and (c) 18 kHz. The central line appears at the weighted average of the A and B chemical shifts. One of the dynamically broadened wings appears at the A-site chemical shift. In comparison with the experimental spectra, only simulations with $J = -2J > 50$ kHz produce a narrow enough central peak. In such cases where $|\nu_A - \nu_B| \ll J$, the central line does not broaden as the decoalescence temperature is reached—rather, only the outer wings narrow. This can lead to the impression that such a molecule is fluxional when in fact it is not

$J = -2J$ must be over 50 kHz as judged from comparison of these simulations with the experimental spectra. This large J lead us to predict that the exchange interaction in the perdeutero system would be of the order of 30–60 Hz and thus observable. Figure 4 shows an example of ^2D–^2D exchange coupling observed in this molecule. Simulation of this spectrum requires an exchange coupling. This is because, for spin $I = 1$, the Hamiltonian no longer has the same symmetry as a scalar coupling; therefore, these data cannot be simulated using a scalar coupling network. From the dependence of J on T, one can extract the parameters a and ν, which predict that $J(^1H,^1H)$ should be approx. 75 kHz, in accordance with the observed ^1H spectra. In future, it will be important to find systems in which both the ^1H and ^2D exchange interactions can be accurately measured as a test of exchange coupling theories.

As a final example, Figure 5 displays some calculated ^2D exchange-coupled spectra for AB_2 spin systems with various ratios of exchange coupling to the chemical shift difference. A D_B–D_B scalar coupling has also been included. Note that the scalar coupling between two magnetically equivalent nuclei is now seen to have an effect upon the spectrum! This result is expected, since the D_A–D_B exchange interactions do not commute with the D_B–D_B scalar coupling Hamiltonian, making it possible now to observe it in the spectra.

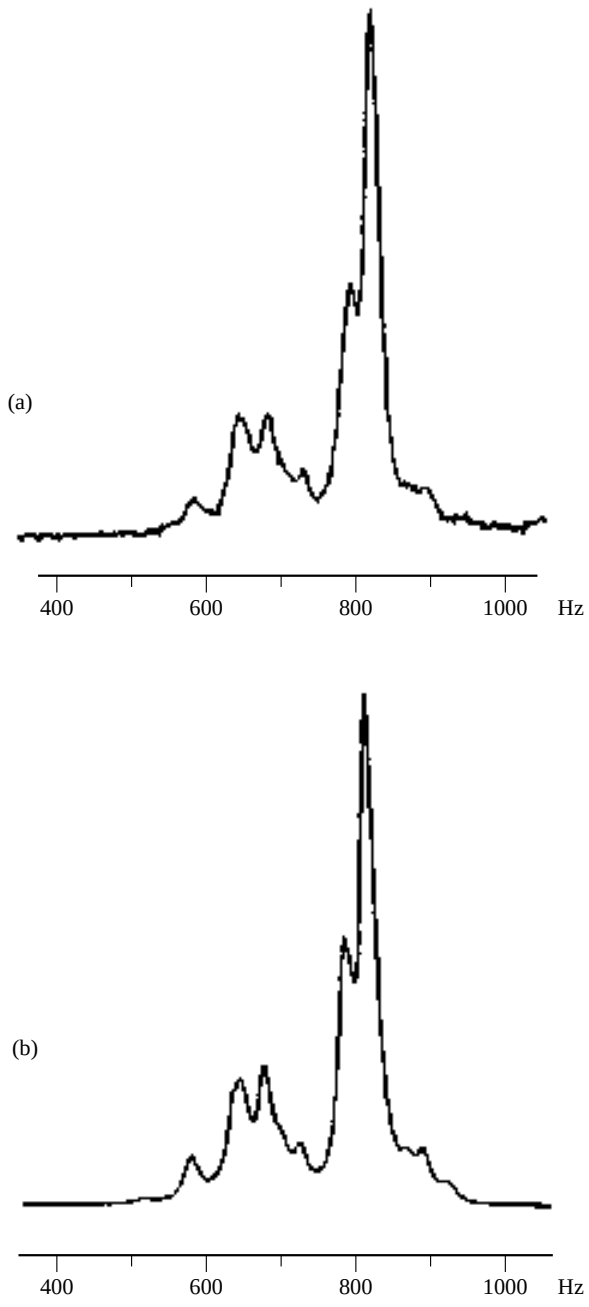

Figure 4 (a)Experimental ^2D NMR spectrum of a mixture of deuterated isotopomers of the $Cp^*(CO)IrH_3^+$ cation (approx. 60% D) at about 145 K. (b) Simulated spectrum giving a D–D exchange coupling between the A and B sites of approx. 40 Hz. Such spectra cannot be fitted using a scalar coupling network

5 SUMMARY

Exchange couplings in solution NMR spectra are manifestations of a purely quantum mechanical effect on the energy levels of sets of identical nuclei in molecules. These effects are related to rotational tunnel splittings in systems such as H_2 or methyl groups, and have the same origins as quantum exchange in solid ^3He. The unique feature of exchange coupling in transition metal polyhydride systems is that it persists to relatively high temperatures in the solution phase, making it possible to observe very small exchange splittings by

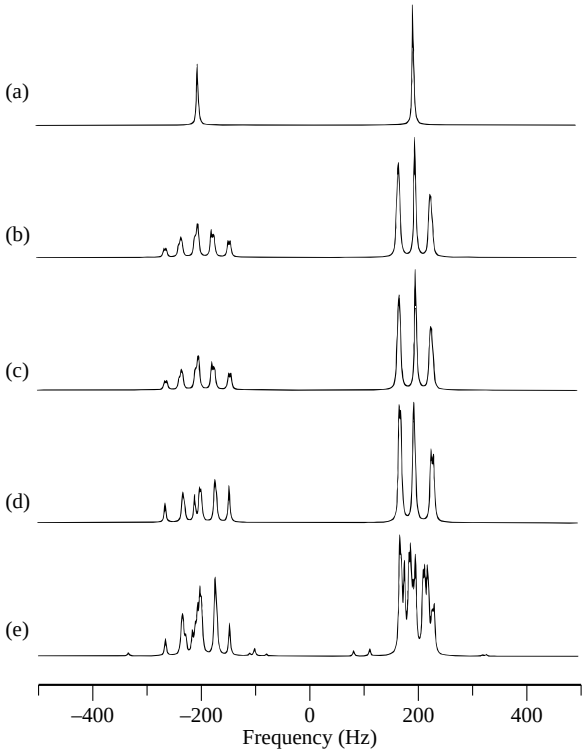

Figure 5 Calculated ^{2}D NMR spectra for an AB_2 spin system with scalar and exchange couplings (the chemical shift difference has been set at 400 Hz): (a) no couplings; (b) scalar couplings J(A, B) = 30 Hz, J(B, B) = 0; (c) scalar couplings J(A, B) = 30 Hz, J(B, B) = 100 Hz; (d) AB exchange coupling $|-2J|$ = 30 Hz, scalar J(B, B) = 0; (e) AB exchange coupling $|-2J|$ = 30 Hz, scalar J(B, B) = 100 Hz. Note that in (c) the inclusion of J(B, B) = 100 Hz has no visible effect, while the spectrum in (e) is dramatically different from that in (d) when J(B, B) is introduced

high-resolution NMR. While these splittings are related to tunnel splittings, they do not imply that coherent tunneling motions occur. Rather, they are a consequence of shifts in the orbital energies of the nuclei that are correlated with their spin states. This correlation of spatial and spin variables results in the exchange energy appearing in the transition frequencies observed in NMR spectra.

6 REFERENCES

1. K. W. Zilm, D. M. Heinekey, J. M. Millar, N. G. Payne, and P. G. Demou, *J. Am. Chem. Soc.*, 1989, **111**, 3088.
2. K. W. Zilm, D. M. Heinekey, J. M. Millar, N. G. Payne, S. P. Neshyba, J. C. Duchamp, and J. Szczyrba, *J. Am. Chem. Soc.*, 1990, **112**, 920.
3. D. M. Heinekey, J. M. Millar, T. F. Koetzle, N. G. Payne, and K. W. Zilm, *J. Am. Chem. Soc.*, 1990, **112**, 909.
4. G. J. Kubas, *Acc. Chem. Res.*, 1988, **21**, 120.
5. D. M. Heinekey, N. G. Payne, and G. K. Schulte, *J. Am. Chem. Soc.*, 1988, **110**, 2302.
6. T. Arliguie, B. Chaudret, J. Devillers, and R. Poilblanc, *C. R. Hebd. Seances Acad. Sci., Ser. 2*, 1987, **305**, 1523.
7. K. W. Zilm and J. M. Millar, *Adv. Magn. Opt. Reson.*, 1990, **15**, 163.
8. D. H. Jones, J. A. Labinger, and D. P. Weitekamp, *J. Am. Chem. Soc.*, 1989, **111**, 3087.
9. P. W. Atkins, *Molecular Quantum Mechanics*, 2nd edn., Oxford University Press, Oxford, 1983, pp. 314–316.
10. H. Limbach and B. Chaudret, *Angew. Chem., Int. Ed. Engl.*, 1992, **31**, 1369.
11. S. J. Inati and K. W. Zilm, *Phys. Rev. Lett.*, 1992, **68**, 3273.
12. C. R. Bowers, D. H. Jones, N. D. Kurur, J. A. Labinger, M. G. Pravica, and D. P. Weitekamp, *Adv. Magn. Opt. Reson.*, 1990, **14**, 269.
13. E. M. Hiller and R. A. Harris, *J. Chem. Phys.*, 1993, **98**, 2077.
14. A. Jarid, M. Moreno, A. Lledos, J. M. Lluch, and J. Bertran, *J. Am. Chem. Soc.*, 1993, **115**, 5861.
15. O. Eisenstein and P. Daudey, to appear.
16. D. M. Heinekey, personal communication.

Acknowledgments

My work in this area has benefited from many interactions with NMR spectroscopists, inorganic chemists, and theoreticians interested in transition metal hydride chemistry. Especially important to me has been my close and very enjoyable collaboration with Professor D. Michael Heinekey and his group. Without his careful attention to experimental detail, the phenomenon of exchange coupling in solution NMR spectra would probably still remain undiscovered.

Biographical Sketch

Kurt Z. Zilm. *b* 1955. B.S., 1976, Ph.D., 1981, University of Utah, USA. Introduced to NMR by D. M. Grant. Faculty in Chemistry Yale University, 1983–present. Approx. 80 publications. Research interests: theory and development of NMR techniques for solving problems of chemical interest, studies of transition metal polyhydrides, supported metal catalysts, matrix-isolated organic intermediates and metal clusters, applications of optical pumping in gas phase NMR, tunneling in NMR, dipolar demagnetizing field effects in NMR and development of new solids NMR techniques for structural studies in polymers and organic geochemistry.

Quantum Tunneling Spectroscopy

Stan Clough

Department of Physics, University of Nottingham, Nottingham, UK

1	Introduction	1
2	The Rotational Spectrum of a Triangular Rotor	1
3	Fundamental Considerations	3
4	Experiments and Techniques	3
5	Related Articles	4
6	References	4

1 INTRODUCTION

Low-temperature molecular tunneling spectroscopy is of interest for four reasons: it continues into the quantum domain the study of molecular motion, it provides an outstanding example of a classical to quantum transition, it extends NMR and spin thermodynamics into the adjacent domain of coherent molecular dynamics, and finally it clarifies historical conceptual problems concerning particle indistinguishability and the topology of rotation space. The main results have recently been surveyed.[1]

The rotations of hindered symmetrical groups like CH_3 and NH_4 in solids persist to helium temperatures where the motion of hindered triangular rotors like CH_3 is characterized by a discrete frequency, the tunnel frequency ω_t, derived from the overlap of ground state librational oscillator wavefunctions localized in adjacent wells of a three-well potential. A typical low-temperature CH_3 spectrum consists of three frequencies: $\pm\omega_t$ and 0. The quantum motion of tetrahedral rotors like NH_4 and ND_4 is more complicated,[2] with several tunnel frequencies associated with rotation about the different symmetry axes. The structured spectrum changes with increasing temperature towards a Lorentzian peak with a halfwidth $1/\tau_c$, where τ_c is an orientational correlation time. This spectrum is explained by a quasi-classical hopping model. The transition, which has been studied by both magnetic resonance and neutron scattering,[3] is illustrated in Figure 1.

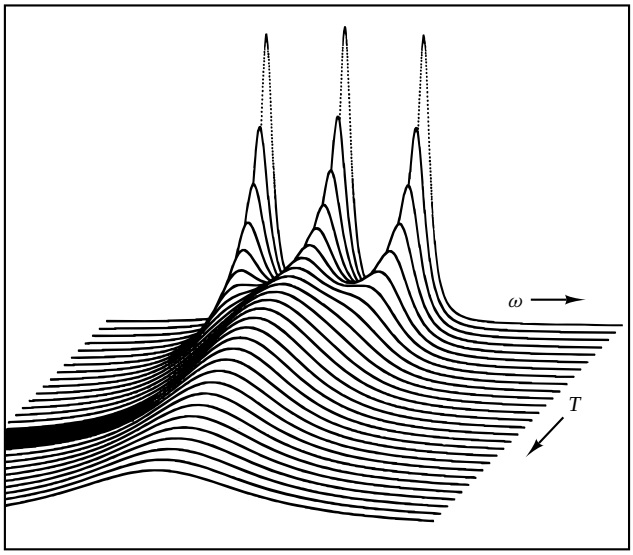

Figure 1 The rotational spectrum of a hindered CH_3 group changes from three frequencies $\pm\omega_t$ and 0 at low temperature to a Lorentzian spectrum of rotational hopping motion at high temperature. The figure is a model with a single temperature-dependent parameter that gives a good representation of observations in many materials. The temperature and frequency scales depend on the height of the hindering barrier

2 THE ROTATIONAL SPECTRUM OF A TRIANGULAR ROTOR

2.1 Stationary States

Low-temperature states have well-defined wavenumbers k. The change from well-defined orientation at high temperatures is similar to the change from hopping conduction to band conduction of polarons and excitons. Like these phenomena, molecular rotation is modeled by a particle in a periodic potential with an orientation coordinate ϕ and a hindering potential $V\cos 3\phi$. Special features are due to the finite extent, 2π, of the rotational coordinate space. For stationary states, we assume a cyclic boundary condition $\psi(\phi + 2\pi) = \psi(\phi)$ and the Hamiltonian

$$\hat{\mathcal{H}} = -\frac{\hbar^2}{2I}\frac{\partial^2}{\partial\phi^2} - V\cos 3\phi \qquad (1)$$

whose eigenvalues for the lowest band are

$$\hbar\omega(k) = -\tfrac{2}{3}\hbar\omega_t \cos\tfrac{2}{3}\pi k \qquad (2)$$

The eigenfunctions are Bloch waves with k lying between $\frac{3}{2}$ and $-\frac{3}{2}$. The boundary condition selects $k = \pm 1$ or 0. The energies are thus $-\frac{2}{3}\hbar\omega_t$ and $\frac{1}{3}\hbar\omega_t$, the latter being doubly degenerate. The three frequencies derived from the energy differences are $\pm\omega_t$ and 0, the low-temperature spectrum.

2.2 Excitations and Dynamics

When dynamical interaction with the environment is included, the space ϕ is open and may be envisaged as a helix upon which wavepackets rotate.[4] A wavepacket confined to one turn of the helix is single-valued within a range 2π and is formed by superposing two of the eigenfunctions of equation (1). Two nodes separated by 2π form the leading and trailing edges of the wavepacket. Three elemental wavepackets rotate with the angular velocities $\pm\omega_t$ and 0. Generation of wavepackets from the stationary states and their subsequent evolution in time can be compared with a 90° pulse and subsequent free induction decay in NMR. The rotation is observable, because it modulates spin-dependent interactions so that molecular rotation and NMR are intimately linked. Thermal excitation results in a transfer of angular momentum, which changes the average wavenumber, $k_a = \pm\frac{1}{2}$ or 0 to

$k_a + \sigma$, $\hbar d\sigma/dt$ being the torque. The general rotation frequency derived from equation (2) is

$$\omega_{k_a,\sigma} = (\tfrac{3}{4})^{-1/2}\omega_t \sin[\tfrac{2}{3}\pi(\sigma + k_a)] \quad (3)$$

A distribution of σ explains the broad rotational spectra of Figure 1. Relaxation to stationary states with integer k causes σ to approach zero as the temperature falls.

A wavepacket only has large amplitudes in the potential wells, and can be represented by three complex amplitudes. The three elementary wavepackets can be superposed by adding their amplitudes to form a more general wavepacket whose evolution involves all three frequencies $\omega_{k_a,\sigma}$. This complex wavepacket rotates and oscillates in shape. At low temperature, the frequency 0 is the rotation frequency and the frequencies $\pm\omega_t$ are shape oscillations. Thus the rotor comes to orientational rest, but continues its internal oscillations. This character changes smoothly into one of rotation as σ grows in absolute value. When $\sigma = \frac{3}{4}$, the complex wavepacket rotates clockwise, moving smoothly through each of the three wells in turn. To accomplish the passage between wells, the shape of the wavepacket oscillates in sympathy with the rotation. The coherent evolution of wavepackets for $\sigma = 0$ and $\sigma = \frac{3}{4}$ is compared in Figure 2.

2.3 Combined Spin and Rotational Dynamics

As an alternative to a reference frame in which the lattice is stationary, it is useful to use a frame in which the wavepacket is stationary. In this frame, σ appears as a vector potential in the angular momentum operator and the wavenumbers remain integers. Observables are the same whichever frame is used. The vector potential can be incorporated into a spin Hamiltonian to combine quantum rotation and spin dynamics. In the case of a methyl group,

$$\hat{\mathcal{H}} = \hat{\mathcal{H}}_Z + \hat{\mathcal{H}}_{DD} + \hat{\mathcal{H}}_R \quad (4)$$

$$\hat{\mathcal{H}}_R = -\tfrac{1}{3}\hbar\omega_t(\hat{R}\, e^{i2\pi\sigma/3} + \hat{R}^{-1}e^{-i2\pi\sigma/3}) \quad (5)$$

where $\hat{\mathcal{H}}_Z, \hat{\mathcal{H}}_{DD}$, and $\hat{\mathcal{H}}_R$ are the Zeeman, dipole–dipole, and rotation Hamiltonians. The basis functions are the eight product spin states of three protons at the three lattice sites. These states can be regarded as shorthand for Slater determinants. The operator $\hat{R}$ cyclically permutes the three spin states round the lattice sites. Rotation clockwise through $\frac{2}{3}\pi$ introduces the phase change $\frac{2}{3}\pi\sigma$ and rotation anticlockwise the reverse phase change. Changes in σ arise owing to collisions between one of the methyl protons and a neighboring atom. This formalism can be extended to tetrahedral molecules.

A spin state is propagated by equation (4). The new feature compared with ordinary spin dynamics is inertia. Whereas the precession frequency of a spin depends only on the instantaneous magnetic field, the rotation frequency of a methyl group depends on the previous dynamical history. The evolution involves two coupled equations: the time-dependent Schrödinger equation and the differential equation for σ. For thermal excitations, some stochastic assumption concerning $d\sigma/dt$ must be made. Another torque is due to the angular dependence of the dipole–dipole energy. This can be obtained by rotating the state slightly using $\lambda\hat{R}$, where λ is small, and finding the rate of change of dipolar energy. The change in the dipole–dipole energy due to rotation, familiar at high temperatures, has a low-temperature counterpart in which molecular rotation changes owing to the angular dependence of the dipole–dipole energy.

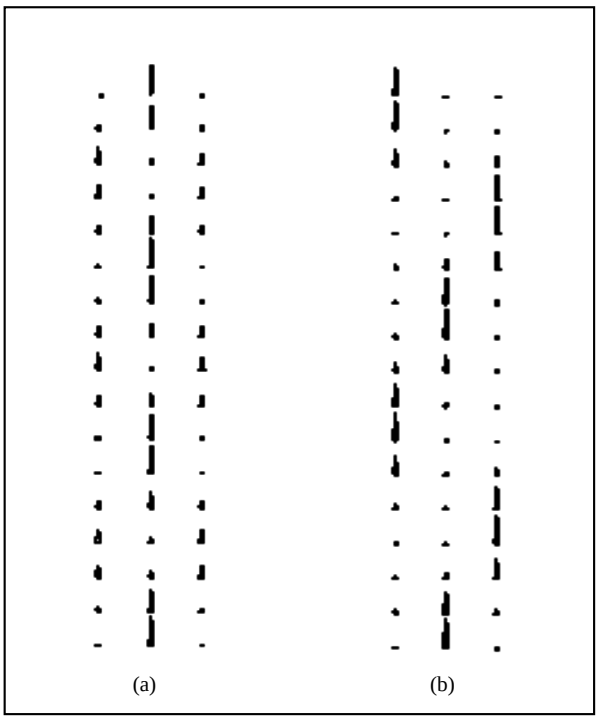

Figure 2 A methyl group wavepacket is described by three intensities in three potential wells on a circle. At low temperature (a), the wavepacket oscillates in shape without rotating. A rotational impulse changes the motion to one of coherent rotation (b), the correlated shape oscillations now assisting the passage from well to well

2.4 The Quantum-to-Classical Transition

The temperature dependence of the rotational spectrum is remarkably similar for all materials except for the scaling of temperature with barrier height. The host lattice serves as a heat bath, destroying coherence and exerting a fluctuating torque. The notable feature is that the outer (shape oscillation) peaks of the low-temperature rotational spectrum move inward with increasing temperature. There have been many theories of this,[3] which can be divided (see Section 3) into those that attribute the reduction to properties of the host lattice and those that regard it as an essential feature of the quantum-to-classical transition. The latter view is that the wavepacket shape oscillations slow down to meet the rising rotation rate in order to play their new role of assisting rotation, while fluctuations in the rotation rate broaden the spectrum. The simplest idea[4] is that the slowing can be described as a spectral averaging process. Orientational hopping is assumed to be accompanied by hopping in k-space. In this way, increasing localization in space is compensated by delocalization in k-space. The frequencies of the low-temperature spectrum are assumed to hop between $\pm\omega_t$ and 0 owing to k modulation,

while each is also subject to random phase modulation due to the changes in orientation. The spectrum is obtained by summing the elements of a matrix $\mathbf{M}^{-1}$, where

$$\mathbf{M}=\begin{bmatrix} \mathrm{i}(\omega_t-\omega)-2\rho-\delta & \rho & \rho \\ \rho & \mathrm{i}(-\omega_t-\omega)-2\rho-\delta & \rho \\ \rho & \rho & -\mathrm{i}\omega-2\rho-\delta \end{bmatrix} \quad (6)$$

Here ρ represents the rate of k hopping and δ the rate of orientational hopping. Both are identified with $1/\tau_c$. At low temperatures, $1/\tau_c \ll \omega_t$, and the frequencies and halfwidths $3/\tau_c$ of the three peaks are obtained from the diagonal elements of equation (6). At high temperatures, ω_t may be neglected. The spectrum is centered at $\omega = 0$, and the halfwidth is $1/\tau_c$. The classical hopping model is thus extended to the quantum regime. Figure 1 is calculated in this way. The parameter $1/\tau_c$ typically obeys an Arrhenius law, and can be roughly equated with a thermal average of the bandwidths of occupied excited librational states. The temperature dependence of the rotational spectrum is thus obtainable from the tunneling frequency without adjustable parameters.

3 FUNDAMENTAL CONSIDERATIONS

3.1 Indistinguishability

Particle indistinguishability has a crucial role in the theory. According to an argument from early quantum theory,[5] the hindering potential for symmetric molecules must be invariant to the interchange of the space and spin coordinates of the protons. For a methyl group, this means a threefold symmetry,[6] which prevents excitation of wavepackets and is inconsistent with the high-temperature hopping model. Though the symmetry constraint correctly identifies the stationary states of a hindered methyl group by excluding nonintegral k, it is incompatible with wavepacket dynamics. The reason is that wavepackets and stationary states have different topologies. Consider the evolution from one to the other. A superposition of two similar wavepackets $\psi(\omega t)$ and $\psi(\omega t - \gamma)\exp(\frac{1}{2}\mathrm{i}\gamma)$ is a stationary state if $\gamma = (2n + 1)\pi$. As a stationary state is approached, the helical space–time path of the wavepacket broadens, and turns of the helix overlap. The number n of rotations in a time $2\pi/\omega$ becomes ambiguous. Destructive interference between paths of different n restricts k to integral values. When the coordinate ωt disappears, the labels that in wavepacket states refer to nonidentical proton trajectories refer to identical indistinguishable particles. The symmetry constraints with antisymmetrization ensure that the phase is continuous and the Pauli principle is satisfied. Excitations restore the helical space–time topology and the proton trajectories. The constraints no longer strictly apply, but quantum behavior results while wavepackets imperfectly reflect the topology of neighboring stationary states.

3.2 The Topology of Rotation Space

The identification of labels with particles also leads to the identification of molecular rotation with the symmetry operation of permutation. This is only possible if the rotation space ϕ is closed. Symmetry-constrained theories consequently allow only integral wavenumbers and limit dynamics to transitions that conserve the wavenumber. This makes them completely different from other transport theories, and gives rise to the view that rotation is fundamentally different from translation. The unconstrained theory of Section 2 has affinities with superconductivity, SQUIDs and quantum transport phenomena in general, besides linking with the hopping model of transport.

4 EXPERIMENTS AND TECHNIQUES

The first effect of tunneling rotation to be observed was that motionally narrowed NMR lines of methyl-containing compounds often fail to broaden when the temperature is reduced to 4 K. With falling temperature, the frequency of components of the dipole–dipole interaction converge on $\pm\omega_t$, as in Figure 1, giving rise to discrete sidebands of the NMR spectrum. The total second moment of the NMR spectrum is conserved, so the sidebands are very weak if the tunnel frequency is large. The failure to broaden demonstrates that $\omega_t/2\pi$ exceeds a few tens of kilohertz. ESR studies of free radicals containing rotating methyl groups in the fragment $C-CH_3$ display more detail. At high temperature, the hyperfine spectrum is a 1 : 3 : 3 : 1 quartet, indicating equal interaction of the electron spin with the three protons. When the temperature is reduced, the spectrum changes to a seven-line pattern 1 : 1 : 1 : 2 : 1 : 1 : 1 with half the spacing of the quartet, the two inner peaks of the quartet having split into 1 : 1 : 1 triplets.[6] The splitting is due to two of the three methyl states with magnetic quantum number $\frac{1}{2}$ forming stationary wavepackets—one in the orientation that minimizes the hyperfine energy and one in the orientation that maximizes it. The energy difference is the separation of the outer members of the triplet. The central member of the triplet has $k = 0$. The collapse of the outer members of each triplet on to the central member is due to the two wavepackets hopping between the two orientations and averaging the orientationally dependent energy. As the rate of rotation increases, the tunnel frequency falls to join it, as in Figure 1. The effect is that all three members of the triplet are involved in the motional averaging process. This is observed through the fact that the central member of the triplet does not remain narrow, while the outer pair merges with it.

The main ESR transitions correspond to flips of the electron spin, while the nuclear quantum number m remains unchanged. Transitions in which m also changes give rise to weak sideband transitions, which enable the tunnel frequency to be measured with precision. The detection of such transitions, their approximate location having been previously deduced by ENDOR, marked the true beginning of tunneling spectroscopy, the motional spectrum being clearly separate from the pure magnetic transitions. Similar tunneling sidebands of NMR spectra open a frequency window in the region of 200 kHz, rather than the 100 MHz range of ESR. Level crossing or tunnel resonance techniques[7] greatly aid the detection of weak sideband transitions and extend the range of accessible tunnel frequencies. A magnetic field is chosen such that the molecular tunnel frequency is equal to a Larmor frequency—either the electron Larmor frequency for free radicals or the nuclear Larmor frequency in ordinary materials. At these internal resonances, transfer of energy between magnetic and rotational

energy occurs through a resonant relaxation process. Energy is exchanged between a Zeeman reservoir and a tunneling reservoir, each of which relaxes to the lattice by its own relaxation process. The ideas of spin thermodynamics are extended, and the process provides an extremely sensitive way of detecting tunnel frequencies. It requires the ability to vary the magnetic field. This is done either by changing the NMR measurement frequency or by using field cycling. There are two versions of the technique. In one, the sample is doped with paramagnetic impurities, often by γ irradiation, and the tunnel frequency is tuned to the electron Larmor frequency. In the other, the tunnel frequency is tuned to the nuclear Larmor frequency. Together, these cover the range from a few megahertz to 50 GHz. With paramagnetic impurities, what is observed is a dynamic polarization effect at the magnetic field of the internal resonance. Energy is transferred between the electron Zeeman and tunneling reservoirs when there is a small mismatch in their frequencies, the energy balance being made up by the nuclear Zeeman system, which is heated or cooled according to the sign of the mismatch.

The direct observation of tunneling sideband transitions is generally difficult, because they must be driven with a field that is nonuniform across the molecule. It is the dipole–dipole interaction, mixed into the magnetic states, that drives the transitions. This effect is naturally stronger at low fields. Low-field dipole–dipole driven NMR has consequently proved to be a powerful way of studying tunneling. Either a true low field[8] using field cycling or a low effective field in the rotating frame[9] may be employed, and both have given good results. They cover the frequency range from 60 kHz to 1 MHz, and thus link with tunnel resonance methods to provide a spectroscopy covering six decades of frequency. An example of a low-field spectrum is shown in Figure 3. Double resonance techniques can be employed to increase population differences and enhance transitions. The next frontier to still lower frequencies has recently been breached by the use of the Lee–Golburg method of line narrowing. Low-field Fourier transform tunnel spectroscopy is conducted slightly off-resonance in the rotating frame.[10] Another recent development in low-field spectroscopy is the use of SQUID detection.[11] It seems likely that developments in the future will come from the increasing exploitation of NMR time domain techniques to interchange magnetic and rotational order, using the spins to monitor the coherent tunneling motion.

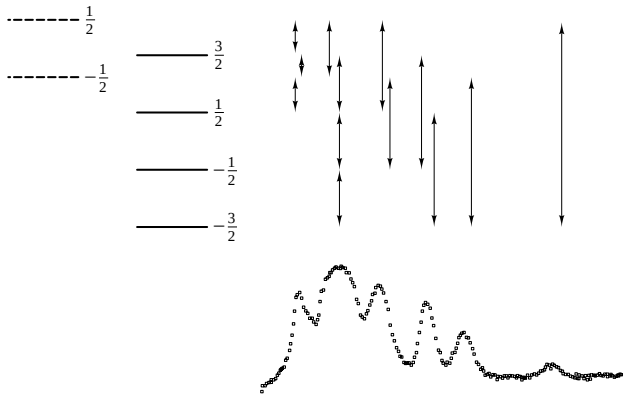

Figure 3 The low-field dipole–dipole driven NMR spectrum of dimethylmalonic acid obtained at 4.2 K. The proton Larmor frequency is 210 kHz and the tunnel frequency that splits $m = \frac{1}{2}$ and $-\frac{1}{2}$ levels is 330 kHz

There are many other phenomena associated with tunneling rotation that a brief review cannot cover, but two observations connected with nearly free rotors should be mentioned. The Haupt effect[12] is a spectacular nuclear dynamic polarization effect that occurs when the temperature of 4-methylpyridine is changed at fairly low temperatures as the slow evolution in the rotational states of the nearly free methyl group drives a large change in the dipole–dipole temperature. The second effect[13] is the optical observation of fractional quantization of the rotation of nonequilateral triangles of nitrogen atoms in molecular beams. Molecular quantum rotation covers a very wide range of phenomena. Because of its dynamical simplicity, it very clearly exhibits features that are common to all quantum systems.

5 RELATED ARTICLES

Brownian Motion and Correlation Times; Field Cycling Experiments; Geometric Phases; Low Spin Temperature NMR; Ortho–Para Hydrogen at Low Temperature; Quantum Exchange; SQUIDs.

6 REFERENCES

1. A. J. Horsewill, *Spectrochim. Acta, Part A*, 1992, **48**, 379.
2. Z. T. Lalowicz, U. Werner, and W. Muller-Warmuth, *Z. Naturforsch. A*, 1988, **43**, 219.
3. A. Heidemann, M. Prager, and M. Monkenbusch, *Z. Phys. B, Condensed Matter*, 1989, **76**, 77.
4. S. Clough, A. J. Horsewill, A. M. Alsanoosi, M. J. Barlow, and M. R. Johnson, *Chem. Phys. Lett.*, 1993, **211**, 637.
5. P. A. M. Dirac, *The Principles of Quantum Mechanics*, 2nd edn., Oxford, University Press, Oxford, 1935, Chap. 10
6. J. H. Freed, *J. Chem. Phys.*, 1965, **43**, 1710.
7. H. Glattli, A. Sentz, and M. Eisenkremer, *Phys. Rev. Lett.*, 1972, **28**, 871.
8. S. Clough, A. J. Horsewill, P. J. McDonald, and F. O. Zelaya, *Phys. Rev. Lett.*, 1985, **55**, 1794.
9. D. W. Nicoll and M. M. Pintar, *Phys. Rev. B*, 1981, **23**, 1064.
10. A. Z. Danyanovich, J. Peternelj, and M. M. Pintar, *Physica B*, 1994, **202**, 273.
11. C. Connor, J. Chang, and A. Pines, *Rev. Sci. Instrum.*, 1990, **61**, 1059.
12. J. Haupt, *Z. Naturforsch. A*, 1968, **23**, 208.
13. G. Delacretaz, E. R. Grant, R. L. Whetten, L. Woste, and J. W. Zwanziger, *Phys. Rev. Lett.*, 1986, **56**, 2598.

Biographical Sketch

Stan Clough. *b* 1932. B.Sc., 1952, Ph.D., 1963, Bangor, Wales. Industrial scientist 1952–59. Started ESR and NMR at ICI. Faculty member, Bangor, 1959–63; Nottingham, 1963–present. Approx. 150 papers. Research specialties: use of ESR, ENDOR, NMR and neutron scattering to develop molecular tunneling spectroscopy, study the quantum-to-classical transition, and extend the concepts and techniques of coherent NMR spectroscopy to particle dynamics.

High Temperature Superconductors

Sean E. Barrett
Yale University, New Haven, CT, USA
and
Charles P. Slichter
University of Illinois, Urbana, IL, USA

1	Introduction	1
2	Physical Properties of the High-Temperature Superconductors	1
3	Solid State NMR Investigation of Metals and Superconductors	3
4	NMR Studies of the HTS in the Normal State	4
5	NMR Studies of the HTS in the Superconducting State	8
6	Summary and Future Directions	11
7	Related Article	11
8	References	11

1 INTRODUCTION

The discovery of the high-temperature superconductors (HTS) in 1986 by Bednorz and Müller[1] unleashed a flurry of scientific activity aimed at understanding and exploiting the novel properties of these materials. Nuclear magnetic resonance has emerged as one of the most important probes of these compounds. NMR studies of the HTS were first motivated by the successful application of NMR to the study of conventional superconductors such as aluminum. In fact, NMR played a central role in the experimental confirmation of the Bardeen–Cooper–Schrieffer (BCS) theory of conventional superconductivity (see the Nobel Prize Lectures by Bardeen, Cooper, and Schreiffer[2]).

The nature of the HTS heightened the importance of NMR studies. These novel compounds possess extremely complicated unit cells and are very anisotropic. This complicates the analysis of results obtained with nonlocal probes of materials such as specific heat and transport measurements. On the other hand, NMR could be used as a local probe of the electronic properties, since almost every atomic species in the HTS has an isotope with a nuclear magnetic moment. The HTS are also notoriously difficult to grow as a single crystalline phase, and their surfaces are easily modified when exposed to moderate humidity or a vacuum. As a result, surface-sensitive experiments such as tunneling or light scattering frequently gave contradictory results on nominally identical samples in the early years. In contrast, NMR experiments performed around the world yielded results that were in remarkable agreement with one another. The information content and the apparent reliability of the NMR data led many theorists to concentrate on understanding the implications of the NMR results.

In order to understand the origin of the term 'HTS', we list the defining characteristics of conventional superconductors (see, e.g. Tinkham[3]).

1. T_c: Above this critical transition temperature, a metal (e.g., aluminum) is in the normal state and has all of the properties associated with a normal conductor. When $T < T_c$, the metal is in the superconducting state. The HTS have critical temperatures ranging up to about 125 K—much higher than the conventional superconductor record of $T_c \approx 20$ K.
2. *Perfect conductivity*: below T_c, in the absence of a magnetic field, the resistivity of a superconductor drops to zero, for currents less than a critical current I_c. The HTS also exhibit this effect.
3. *Perfect diamagnetism*: as the temperature is lowered below T_c, weak magnetic fields are expelled from the interior of a superconductor (the Meissner effect). In Type I superconductors, this effect continues until the applied magnetic field exceeds a critical field ($B > B_c$), at which point the sample reverts to the normal state. Type II superconductors exhibit the Meissner effect for $B < B_{c1}$. In the mixed state ($B_{c1} < B < B_{c2}$), the applied field penetrates the sample through a lattice of fluxoids (also known as vortices). When $B > B_{c2}$, the sample is in the normal state. The HTS are extreme Type II superconductors (the coherence length is of order 1 nm and the penetration depth of order 100 nm).
4. *Pairing*: the BCS theory explains conventional superconductivity as a macroscopic quantum state of the electrons in a metal that is brought about by an attractive electron pairing interaction mediated by phonons. Pairing is also found in the superconducting state of the HTS, although the microscopic mechanism for the pairing is not known.

The space limitations and format of this Encyclopedia preclude a comprehensive review of the many NMR studies that have been carried out on the HTS. Instead, this article will describe several representative experiments, which will illustrate the broad range of information that NMR measurements have revealed about the HTS. Several excellent review articles on NMR studies of the HTS may be consulted if the reader wishes to pursue this subject in more detail.[4–7]

2 PHYSICAL PROPERTIES OF THE HIGH-TEMPERATURE SUPERCONDUCTORS

For a comprehensive review of the physical properties of the HTS, see the three volumes edited by Ginsberg.[8]

2.1 Crystal Structure

The crystal structures of $YBa_2Cu_3O_{7-y}$ (1–2–3) and $La_{2-x}Sr_xCuO_4$ (2–1–4) are shown in Figure 1. $YBa_2Cu_3O_7$ has $T_c \approx 93$ K, the highest of the 1–2–3 family. Two-dimensional copper oxide planes containing the Cu(2), O(2), and O(3) sites appear in all of the HTS, and it is generally agreed that they are the source of the superconductivity. $YBa_2Cu_3O_7$ has two of these CuO_2 planes separated by the

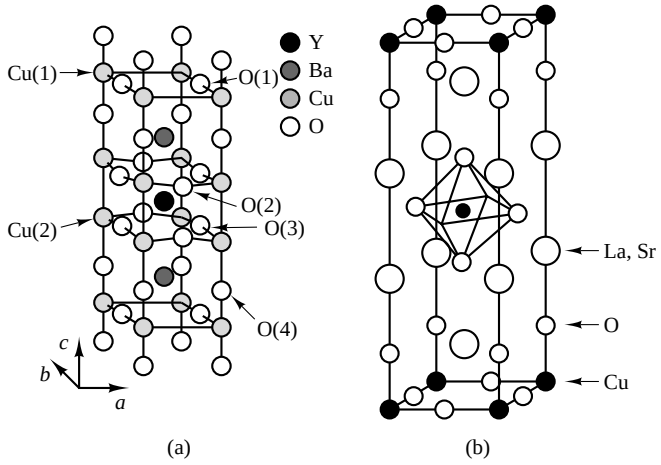

Figure 1 Crystal structures of (a) $YBa_2Cu_3O_{7-y}$;[9] (b) $La_{2-x}Sr_xCuO_4$[10]

yttrium atom. Below the CuO_2 plane is a layer containing the Ba and O(4) sites, and below that is a layer of one-dimensional CuO chains, which lie along the $\hat{\boldsymbol{B}}$ axis. The Cu(1) and O(1) sites make up these CuO chains. The assignment of the single crystal NMR lines with their respective crystallographic sites was accomplished using this crystal structure. For example, the local environment of the Cu(2) (Cu(1)) site is fourfold symmetric about the $\hat{c}$ axis ($\hat{a}$ axis), which is reflected in the magnetic shift tensor of the site.

$La_{1.85}Sr_{0.15}CuO_4$ has the highest T_c of the 2−1−4 family, $T_c \approx 38$ K. This material is considered by many to be the simplest HTS, since there is only one CuO_2 plane and no CuO chains per unit cell. Unfortunately, it is not easy to perform clean NMR experiments on this compound, since the disorder introduced by the strontium substitution greatly increases the inhomogeneous broadening of the NMR lines.

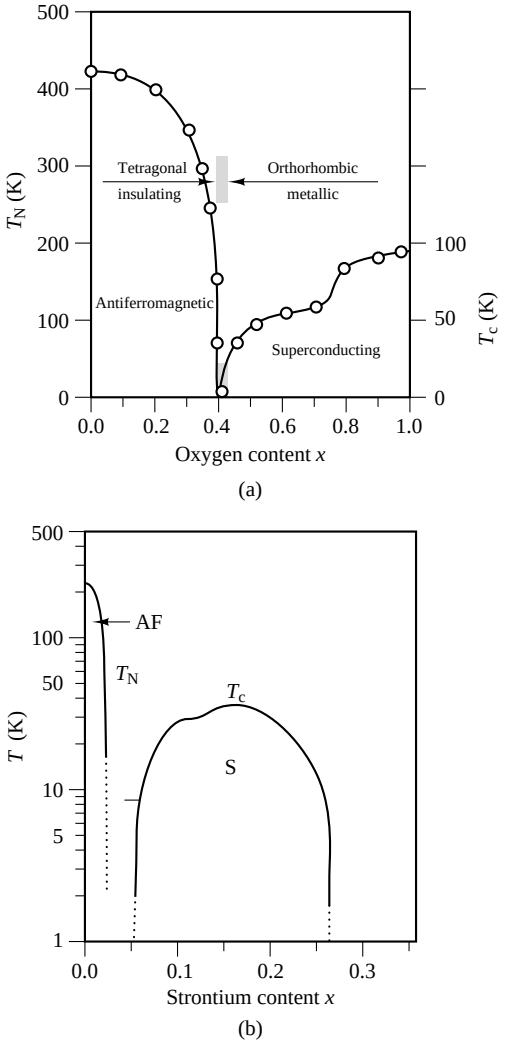

Figure 2 Phase diagrams of (a) $YBa_2Cu_3O_{6+x}$;[11] (b) $La_{2-x}Sr_xCuO_4$ (adopted from Figure 2 of Iye[12])

2.2 Parent Compounds and Doping

All of the HTS are closely related to antiferromagnetic insulators, known as *parent compounds*. For example, $YBa_2Cu_3O_6$, which is obtained by removing all of the oxygen from the O(1) sites in $YBa_2Cu_3O_7$, has a Néel temperature of 400 K. La_2CuO_4, the parent compound of the 2−1−4 family, has a Néel temperature of 300 K. In these parent compounds, the planar Cu(2) atoms are believed to be Cu^{2+}, with a hole in the $3d_{x^2-y^2}$ state (where $x,y,z = a,b,c$). Each Cu(2) site has a spin-$\frac{1}{2}$, which experiences a strong intraplane antiferromagnetic coupling, along with a much weaker interplane coupling. The parent compounds appear to be two-dimensional Heisenberg antiferromagnets.

As the stochiometry of these materials is altered, their properties change dramatically. For $YBa_2Cu_3O_6$, this change is effected by adding oxygen in the O(1) site, while for La_2CuO_4, this change may be accomplished either by adding oxygen ($La_2CuO_{4+\delta}$) or by substituting Sr for La ($La_{2-x}Sr_xCuO_4$). These chemical substitutions are thought to add holes to the oxygen 2p orbitals of the CuO_2 planes, which destroy the long-range order and cause the materials to become superconductors. One simple picture of the doped compounds is that the oxygen holes form a conduction band in which the Cu(2) moments are imbedded. Alternatively, strong hybridization of the Cu(2) and O(2,3) orbitals might create a single electronic system, with no memory of the magnetic state of the Cu(2) sites in the parent compounds. The NMR data support a picture that is a compromise between these two extremes.

The phase diagrams for 1−2−3 and 2−1−4 are shown in Figure 2. The unusual proximity of the antiferromagnetic phase to the superconducting phase is not yet understood.

2.3 HTS in the Normal and Superconducting States

It is now well established that the HTS are not simple metals. All of the HTS have a strong anisotropy of the normal state conductivity ($\rho_c/\rho_{ab} \approx 10^2-10^5$), so that currents prefer to flow along the CuO_2 planes rather than perpendicular to them. Although angle-resolved photoemission spectroscopy (ARPES) data indicate that a Fermi surface is present, the quasiparticle lifetime does not have the energy dependence expected for a Fermi liquid. The isotropic resistivity of copper metal at room temperature is $\rho_{copper} = 1.8\,\mu\Omega$ cm, while the

smallest component of the anisotropic resistivity tensor of the ceramic $YBa_2Cu_3O_7$ is $\rho_b = 70\,\mu\Omega$ cm. $YBa_2Cu_3O_7$ also has unusual temperature dependences of both the resistivity ($\rho_{ab} \propto T$, $\rho_c \propto 1/T$) and the Hall effect constant ($R_H \propto 1/T$).

A generalized BCS theory, which allows for a novel pairing mechanism and an unconventional pairing state, describes the superconducting state of the HTS. Measurements of the flux quantum and of Andreev reflection have indicated that the superconductivity involves hole (or electron) pairing. All of the HTS are extreme Type II superconductors, with large anisotropies in the coherence length and the penetration depth.

3 SOLID STATE NMR INVESTIGATION OF METALS AND SUPERCONDUCTORS

3.1 Electric Field Gradient, Magnetic Shift, and Spin–Lattice and Spin–Spin Relaxation Times

Three basic NMR measurements have been used to characterize the HTS. They are measurements of the absorption spectrum, the spin–lattice relaxation time T_1, and the spin–spin relaxation time T_2.

The absorption spectrum is a fingerprint of the chemical environment of a nucleus. More explicitly, the energy levels of the nuclei are determined by the following general nuclear spin Hamiltonian,[13] ignoring nuclear spin–spin couplings:

$$\begin{aligned}\hat{\mathcal{H}} = &-\gamma_n\hbar \sum_{\alpha=x,y,z} \hat{I}_\alpha(1+K_{\alpha\alpha})B_{0\alpha} \\ &+\frac{h}{2I(I-1)}[\nu_{zz}(3\hat{I}_z^2-\hat{I}^2) \\ &+(\nu_{xx}-\nu_{yy})(\hat{I}_x^2-\hat{I}_y^2)] \end{aligned} \tag{1}$$

The first term is the Zeeman energy of the nuclear magnetic moment ($\hat{I}$ is a dimensionless operator), in the presence of the applied field $\boldsymbol{B}_0 \parallel \boldsymbol{\alpha}$, where $\boldsymbol{\alpha}$ is one of the unit vectors along the x, y, or z axes. $K_{\alpha\alpha}$ is the magnetic shift tensor, and represents the extra fields produced at the nucleus by the electrons. $|K_{\alpha\alpha}|$ is usually small (typically $< 2\%$). The magnetic shift tensor contains several parts:

$$K_{\alpha\alpha} = K^S_{\alpha\alpha} + K^L_{\alpha\alpha} + \sigma_{\alpha\alpha} \tag{2}$$

The tensor $\sigma_{\alpha\alpha}$ is the shift due to all the closed shell electrons of an atom. Since one usually measures $K_{\alpha\alpha}$ relative to a closed shell reference, we can take $\sigma_{\alpha\alpha}$ to be zero. The tensor $K^L_{\alpha\alpha}$ is called the *chemical shift*, and is due to the extra field at the nucleus contributed by the electronic orbital susceptibility of both the valence electrons of an atom and the closed shell electrons of its neighbors. Thus, the chemical shift is directly proportional to the Van Vleck susceptibility χ^L. The tensor $K^S_{\alpha\alpha}$ is the *Knight shift*, and represents the extra field at the nucleus due to the electronic spin susceptibility χ^S (the Pauli susceptibility in metals). Thus, if one knows or can calculate the constants of proportionality (hyperfine coupling constants), a measurement of $K_{\alpha\alpha}$ yields the values of χ^L and χ^S.[14]

The second term in the above static spin Hamiltonian is the quadrupolar interaction. The electric quadrupole moment of the nucleus couples to the electric field gradient present at the nucleus. Only nuclei with spins $I > \frac{1}{2}$ (e.g. ^{63}Cu, ^{65}Cu, and ^{17}O) can have this term. The tensor $\nu_{\alpha\alpha}$ gives the $\alpha\alpha$ component of the electric field gradient (in megahertz) at the nucleus due to the electrons in the same atom and the surrounding ions.

We have ignored the nuclear dipole–dipole coupling in this Hamiltonian, because this term is mainly a source of linebreadth for the fields and nuclei in question, and is relatively unimportant for determining the line position or the magnitude of the spin–lattice relaxation.

The above spin Hamiltonian completely determines the NMR absorption spectrum. Once the resonance frequencies are measured, knowledge of the applied field $\boldsymbol{B}$ and the nuclear spin eigenstates allows one to determine the tensors $K_{\alpha\alpha}$ and $\nu_{\alpha\alpha}$. For nuclei that have a large quadrupolar term in their Hamiltonian (e.g. copper nuclei in the HTS), a zero field absorption spectrum may be measured using nuclear quadrupole resonance (NQR).

Another informative NMR experiment is a spin–lattice relaxation time T_1 measurement. In the HTS, the nuclear spin–lattice relaxation process is magnetic, so T_1 is determined by the fluctuating magnetic fields at the nucleus, which are perpendicular to the applied field. In these materials, the fluctuating fields are produced by electronic spins that have the periodicity of a Bravais lattice. Thus, following Moriya,[15] the relaxation rate of nucleus i measured with the applied field $\boldsymbol{B}_0 \parallel \boldsymbol{\alpha}$ is

$$^i\left(\frac{1}{T_1}\right)_\alpha = \frac{^i\gamma_n^2 k_B T}{2\mu_\beta^2} \lim_{\omega\to 0} \sum_{\boldsymbol{q},\alpha'\neq\alpha} |\,^iA_{\alpha'\alpha'}(\boldsymbol{q})|^2 \frac{\chi''_{\alpha'\alpha'}(\boldsymbol{q},\omega)}{\omega} \tag{3}$$

$\chi''_{\alpha\alpha}(\boldsymbol{q},\omega)$ is the imaginary part of the $\boldsymbol{q}$- and ω-dependent electronic spin susceptibility tensor (taken to be isotropic in our case), and $\boldsymbol{\alpha}$ are the principal crystalline axes (a,b,c). The limit as $\omega \to 0$ is taken, because this expression is evaluated at the Larmor frequency of the nucleus, typically around 10 mK, a very small energy on the scale of the electronic spin fluctuations. Note that $(1/T_1)_\alpha$ may be anisotropic if the hyperfine form factors $^iA_{\alpha\alpha}(\boldsymbol{q})$ are anisotropic. These form factors are completely determined by the real space hyperfine coupling Hamiltonian, which we shall discuss in Section 4.4. The Knight shift is proportional to the real part of the static electronic spin susceptibility, $\chi'_{\alpha\alpha}(\boldsymbol{q}, \omega = 0)$:

$$^iK^S_{\alpha\alpha} = \lim_{\boldsymbol{q}\to 0}[\,^iA_{\alpha\alpha}(\boldsymbol{q})\chi'_{\alpha\alpha}(\boldsymbol{q},\omega=0)] \tag{4}$$

Since the copper nuclei are spin-$\frac{3}{2}$, the recovery of the longitudinal magnetization of a particular resonance line is not, in general, exponential. Nevertheless, the recovery yields a fundamental relaxation rate $W_{1\alpha} \equiv \frac{2}{3}(1/T_1)_\alpha$.

Finally, measurement of the spin–spin relaxation time T_2 may also provide information about the electronic system. Pennington et al.[16] discovered that the decay of the transverse magnetization of the planar copper sites in $YBa_2Cu_3O_7$ is the product of an exponential (arising from T_1) and a Gaussian. The Gaussian component (T_{2G}) is an order of magnitude faster than expected for direct nuclear spin–spin coupling. Pennington et al. postulated that T_{2G} is instead due to an

indirect coupling mediated by the electronic background. Pennington and Slichter[17] showed that T_{2G} may be expressed as a function of $\chi'_{\alpha\alpha}(\boldsymbol{q}, \omega = 0)$.

3.2 NMR Studies of Metals

In a metal, the nuclear spin–lattice relaxation rate is due to the scattering of conduction electrons by the nuclear spins. The rate is then

$$\frac{1}{T_1} \propto \int_0^\infty |\langle V_{\text{en}}\rangle|^2 \rho^2(E) f(E)[1 - f(E)]\,\mathrm{d}E \propto T\rho^2(E_\text{F}) \tag{5}$$

$\langle V_{\text{en}}\rangle$ is the matrix element for the electron–nuclear interaction, $\rho(E)$ is the one-electron density of states, and $f(E)$ is the Fermi function. In this notation, the Knight shift can be written as

$$K^\text{S} \propto \int_0^\infty \rho(E) \frac{\mathrm{d}f(E)}{\mathrm{d}E}\,\mathrm{d}E \propto \rho(E_\text{F}) \tag{6}$$

Thus, the Knight shift and spin–lattice relaxation time in a normal metal are related:

$$\frac{1}{T_1 T} = \text{const} \times (K^\text{S})^2 \tag{7}$$

This is the *Korringa law*, which has been verified experimentally from 1 K to 930 K in aluminum. The constant is determined by the relevant electron–nuclear couplings, with a small correction of order unity when electron–electron interactions are included.

3.3 NMR Studies of Conventional Superconductors

For a review of this topic, see MacLaughlin.[18]

In the BCS theory, for a spin-singlet, orbital s-wave pairing state, the density of excited quasiparticle states is given by

$$\rho_\text{BCS}(E - E_\text{F}) = \rho(E_\text{F}) \frac{|E - E_\text{F}|}{\sqrt{(E - E_\text{F})^2 - \Delta^2}} \tag{8}$$

where Δ is an isotropic energy gap which opens up at T_c and is essentially temperature independent for $T/T_\text{c} \leq 0.2$. The opening of the gap freezes out thermal excitations, causing $K^\text{S} \propto \chi^\text{S} \to 0$ as $T \to 0$. The temperature dependence of the Knight shift for this pairing state, namely

$$\frac{K^\text{S}(T < T_\text{c})}{K^\text{S}(T = T_\text{c})} = \int_{-\infty}^{\infty} \frac{|E - E_\text{F}|}{\sqrt{(E - E_\text{F})^2 - \Delta^2}} \left[-\frac{\mathrm{d}f(E)}{\mathrm{d}E}\right] \mathrm{d}E = Y_0(T/T_\text{c}) \tag{9}$$

is conventionally referred to as the *Yosida function*, $Y_0(T/T_\text{c})$.

The T_1 data also show a dramatic deviation from the Korringa law for $T < T_\text{c}$. The BCS theory of superconductivity explains that the observed increase in $1/T_1$ just below T_c (the so-called *Hebel–Slichter coherence peak*) is due to both the logarithmic singularity in $\rho_\text{BCS}(E - E_\text{F})$ at the edge of the gap and to the BCS coherence factor, which modifies $|\langle V_{\text{en}}\rangle|^2$. The coherence factor reflects the correlated nature of the superconducting ground state, and its experimental confirmation established the validity of the BCS theory.

At low temperatures, when the gap is large and almost independent of temperature, the unpaired electrons that relax the nuclei need to be excited across the energy gap, so

$$1/T_1 \propto \exp(-\Delta/k_\text{B}T) \tag{10}$$

Conventional superconductors exhibit a spin-singlet, orbital s-wave pairing state. More generally, the BCS theory could also accommodate a spin-triplet pairing state, which would imply a nonzero trace of the spin susceptibility tensor at $T = 0$. It is also possible to have higher orbital angular momentum pairing states (d-wave, p-wave, etc.), which implies a superconducting energy gap with a lower symmetry than the crystal. Both of these possibilities would be reflected in the temperature dependence of the Knight shift and T_1 below T_c.[19]

NMR studies of the mixed state ($T < T_\text{c}$, $B_{\text{c1}} < B_0 < B_{\text{c2}}$) have been carried out in Type II superconductors. The applied field penetrates the interior of the sample through a lattice of fluxoids, which can affect both lineshapes and relaxation rates.

4 NMR STUDIES OF THE HTS IN THE NORMAL STATE

4.1 Sample Characterization Using the Absorption Spectra

Much of the earliest NMR and NQR work focused on determining $K_{\alpha\alpha}$ and $\nu_{\alpha\alpha}$ for the various sites. Pennington et al.[20] measured $K_{\alpha\alpha}$ and $\nu_{\alpha\alpha}$ for the Cu(2) and Cu(1) sites in $YBa_2Cu_3O_7$, using a 1 mg single crystal. Their results, shown in Table 1, permitted an unambiguous assignment of the NQR lines. Spin echo pulse sequences with phase cycling were used to acquire spectra and measure relaxation times. The importance of phase cycling is shown in Figure 3.

The electric field gradient at the Cu(2) site is axially symmetric about the $\hat{\boldsymbol{c}}$ axis. Therefore, the nuclear spin eigenstates in an NQR experiment are identical to those in an NMR experiment with $\boldsymbol{B}_0 \parallel \hat{\boldsymbol{c}}$. The Cu(2) relaxation rate $^{63}W_{1c}$ may be measured with either experiment.

To explain their shift data, Pennington et al.[20] proposed a model that is essentially the permanent moment limit. The copper atom is $Cu^{2+}(3\,d^9)$, and the spin-$\frac{1}{2}$ associated with the atom is due to a hole in the $x^2 - y^2$ ($y^2 - z^2$) state for

Table 1 Magnetic Shift and Electric Field Gradient Tensors for the ^{63}Cu(1) and ^{63}Cu(2) sites in $YBa_2Cu_3O_7$ at T = 100 K[20]

	^{63}Cu(1)	^{63}Cu(2)
$100\,K_{aa}$	1.323	0.580
$100\,K_{bb}$	0.561	0.580
$100\,K_{cc}$	0.588	1.267
ν_{aa} (MHz)	−19.01	+15.95
ν_{bb} (MHz)	+19.18	+15.54
ν_{cc} (MHz)	−0.17	−31.49

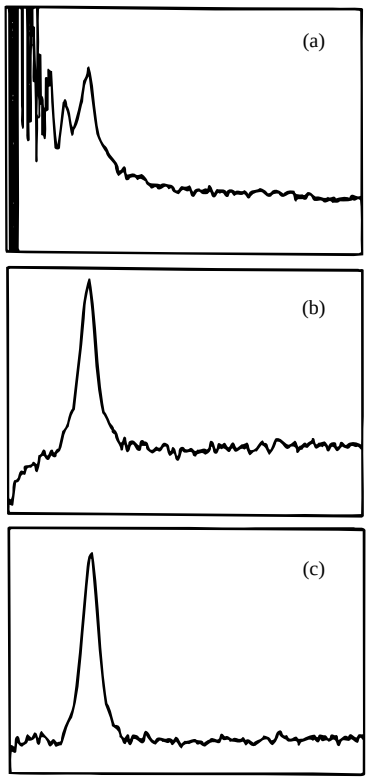

Figure 3 The average of 500 000 ^{63}Cu(2) spin echoes from a $YBa_2Cu_3O_7$ sample, showing the importance of phase cycling. The sequences are (a) a single phase Hahn echo, (b) a Hahn echo with add–subtract phase cycling, and (c) a four-phase Hahn echo cycle[21]

the plane (chain) site. The orbital susceptibility of that hole determines the chemical shift K^{L}, and the Knight shift arises from the hyperfine coupling of the nuclear spin to the Cu^{2+} spin-$\frac{1}{2}$.

A small single crystal sample is difficult to study at high temperatures or in the superconducting state. In these conditions, copper NQR measurements using large (approx. 5 g) powder samples are preferable. The NQR frequency is sensitive to the local environment of the copper sites.

Farrell et al.,[22] taking advantage of the anisotropy of the HTS, were the first to make a $\hat{\boldsymbol{c}}$-axis aligned powder sample. The $\boldsymbol{B}_0 \parallel \hat{\boldsymbol{c}}$ and $\boldsymbol{B}_0 \| \hat{\boldsymbol{a}}/\hat{\boldsymbol{b}}$ resonances are distinguishable in both aligned powder and single crystal samples, but the large mass of the former results in a superior signal-to-noise ratio. Aligned powder samples have been an absolute necessity in many experiments, such as the measurement of $K_{\alpha\alpha}$ and $\nu_{\alpha\alpha}$ for the ^{17}O(1), ^{17}O(2,3), and ^{17}O(4) sites in $YBa_2Cu_3O_7$ by Takigawa et al.[23]

Recently, ^{139}La NMR reported by Hammel et al.[24] revealed an interesting phase separation that occurs in $La_2CuO_{4+\delta}$. As the single crystal is cooled below T = 265 K, the sample develops an antiferromagnetic (oxygen-poor) phase and a metallic (oxygen-rich) phase.

4.2 Magnetic Shift

The magnetic shifts of the Cu, O, and Y nuclei in $YBa_2Cu_3O_7$ are essentially temperature independent in the

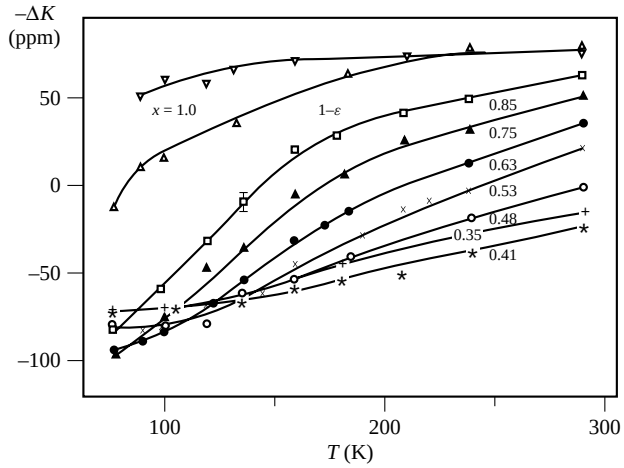

Figure 4 The shift ΔK of the ^{89}Y line of $YBa_2Cu_3O_{6+x}$, referenced to YCl_3 (ν_0= 15.64 MHz), plotted versus T, from 77 K to 300 K. The lines through the data for each value of x are guides for the eye[25]

normal state, as one expects for metals. In general, however, the magnetic shifts of the HTS vary with doping and temperature. Yttrium measurements by Alloul et al.[25] in a series of $YBa_2Cu_3O_{6+x}$ samples showed that the magnetic shift is strongly temperature dependent in the normal state for $x \approx 0.4-0.9$, as is shown in Figure 4. In fact, the ^{89}Y magnetic shift is a linear function of the bulk magnetic susceptibility. Alloul et al. inferred that the yttrium nuclei were coupled to the spins associated with the Cu(2) atoms.

Since the energy scale relevant for the orbital susceptibility is several electron volts, it is thought that the temperature dependence of the bulk susceptibility arises from the electron spin susceptibility. This temperature dependence is referred to as the 'spin gap' phenomenon. The name is derived from its two principal manifestations. First, while the spin susceptibility drops dramatically below room temperature, there is no corresponding decrease in the number of charge carriers observed in optical conductivity [$\sigma(\omega)$] measurements. Second, the decrease in the static susceptibility may be parameterized using a simple model with low-lying magnetically inert states separated from excited magnetically active states by a spin gap Δ_{SG}. The magnitude of this gap is $\Delta_{\mathrm{SG}} \approx 200$ K, a very small energy scale compared with the intraplanar exchange coupling $J \approx 1500$ K. The origin of this spin gap behavior is not yet understood theoretically.

Takigawa et al.[26] measured the ^{63}Cu and ^{17}O magnetic shifts in a sample of $YBa_2Cu_3O_{6.63}$ with a T_{c} = 62 K. The isotropic magnetic shifts for the Cu(2) and the O(2,3) are directly proportional to one another, tracking the temperature-dependent bulk susceptibility, as is shown in Figure 5. This is strong evidence that the O(2,3) nuclei couple to the same spin susceptibility as the Cu(2) nuclei. All three planar nuclei apparently couple to a single spin degree of freedom per CuO_2 unit cell, which is associated with the Cu^{2+} hole spin. This is a single component model of the CuO_2 planes.

The lack of evidence for two distinct contributions to the electron spin susceptibility of the CuO_2 planes, one associated with Cu^{2+} spins and one arising from holes doped into the oxygen 2p orbitals, is a puzzle. There are, however, theoretical arguments that the oxygen and copper holes are so strongly

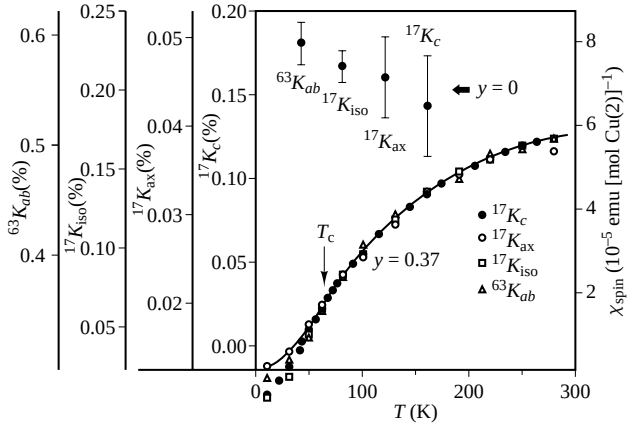

Figure 5 Various components of the ^{63}Cu(2) and ^{17}O(2,3) Knight shifts in $YBa_2Cu_3O_{7-y}$ versus temperature with different vertical scales and origins. The curve is the bulk spin susceptibility for the y = 0.37 sample[26]

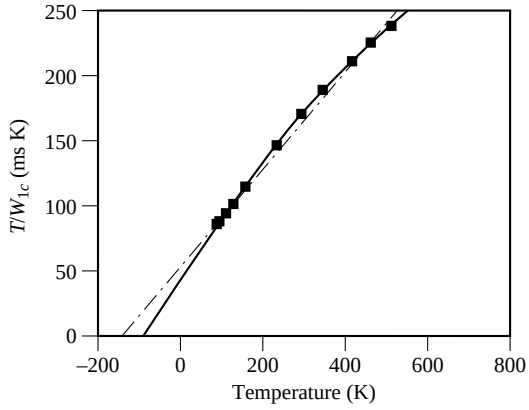

Figure 6 Temperature divided by the relaxation rate $^{63}W_{1c}$ measured in $YBa_2Cu_3O_7$, plotted versus temperature. The dotted line is a linear fit to the data, confirming equation (13)[29]

coupled that they behave as a single spin degree of freedom at low energies.[27]

4.3 Spin–Lattice Relaxation Time T_1

Many groups have studied the spin–lattice relaxation times of the Cu(1) and Cu(2) sites in $YBa_2Cu_3O_7$. Comparison of the ^{63}Cu and ^{65}Cu relaxation rates confirms the magnetic origin of the relaxation. The measured rates are surprisingly fast, not only surpassing the expected magnitude of an orbital relaxation rate, but also exceeding the room temperature relaxation rate of copper metal by an order of magnitude.[28] The anisotropy of the Cu(2) relaxation rate tensor was measured using single crystal and aligned powder samples. $^{63}W_{1a}$, the relaxation rate measured with the magnetic field applied along the CuO_2 planes, is about four times $^{63}W_{1c}$, the relaxation rate measured with the field along the $\hat{\boldsymbol{c}}$ axis.

The planar nuclei in $YBa_2Cu_3O_7$ do not share a common temperature dependence. The ^{89}Y and ^{17}O(2,3) relaxation rates are directly proportional to the temperature, as one expects for a simple metal, but the ^{63}Cu(2) rate is not. Figure 6 shows Pennington's NQR measurement of the ^{63}Cu(2) relaxation rate, plotted as T/W_{1c} versus T.[29] The straight line fit of the data shows that the $1/T_1T$ obeys a Curie–Weiss law rather than the Korringa law. At T = 100 K, $(^{63}W_{1c}) \approx 10^2 \times (^{17}W_{1c}) \approx 10^4 \times (^{89}W_{1c})$. Imai et al.[30] proposed that the anomalously fast Cu(2) relaxation rate reflects the build-up of antiferromagnetic correlations of the Cu(2) spins as the temperature is lowered. In summary, for the planar nuclei in $YBa_2Cu_3O_7$,

$$^{89}W_{1c}/T = A \tag{11}$$

$$^{17}W_{1c}/T = B \tag{12}$$

$$^{63}W_{1c}/T = C/(T + T_\theta) \tag{13}$$

where A,B,C, and T_θ are constants.

The doping dependence is quite complicated at first glance, since the above equations fail to describe the data for any material other than $YBa_2Cu_3O_7$. This is another manifestation of the spin gap phenomenon. Modified versions of equations (11)–(13) can describe the generic behavior of the HTS.[7] The new expressions for the relaxation rates of the planar nuclei are

$$^{89}W_{1c}/T = A'\chi_0^S(T) \tag{14}$$

$$^{17}W_{1c}/T = B'\chi_0^S(T) \tag{15}$$

$$^{63}W_{1c}/T = C'\chi_0^S(T)/(T + T_\theta) \tag{16}$$

where A',B',C', and T_θ are constants, and $\chi_0^S(T) = \chi^S(\boldsymbol{q} = 0, \omega = 0, T)$. For $YBa_2Cu_3O_7$, χ_0^S is independent of temperature, so we recover equations (11)–(13). For $YBa_2Cu_3O_{6.63}$, equations (14)–(16) are appropriate, as we see in Figure 7.[31]

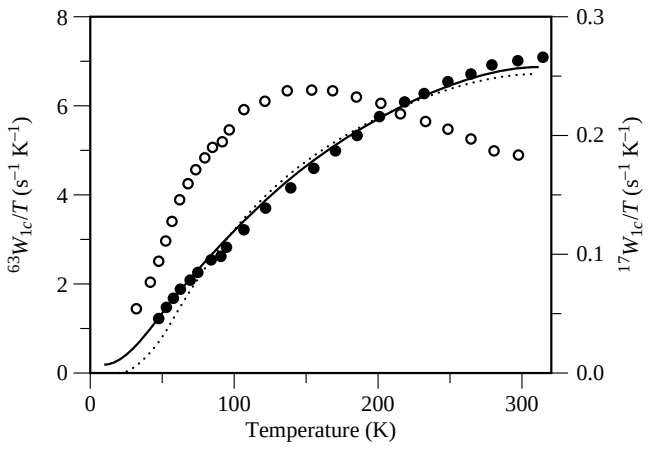

Figure 7 Temperature dependence of $^{63}W_{1c}/T$(•) and $^{17}W_{1c}/T$(○) in $YBa_2Cu_3O_{6.63}$ (taken from Figure 4 of Takigawa[31]). The solid line shows the temperature dependence of the spin susceptibility for this material, confirming (15) and (16)

4.4 Single Component Model for the CuO_2 Planes

Consideration of the shift and relaxation rate data presented in Sections 4.1–4.3 led to the creation of a single component model for the CuO_2 planes. In $YBa_2Cu_3O_7$, the hyperfine coupling Hamiltonian for the ^{63}Cu(2), ^{17}O(2,3), and ^{89}Y is

$$\hat{\mathcal{H}} = \sum_{\alpha=a,b,c} \left(A_{\alpha\alpha}\, {}^{63}\hat{I}^i_\alpha \hat{S}^{\,i}_\alpha + \sum_j B\, {}^{63}\hat{I}^i_\alpha \hat{S}^{\,i}_\alpha + \sum_l C\, {}^{17}\hat{I}^k_\alpha \hat{S}^{\,l}_\alpha + \sum_n D\, {}^{89}\hat{I}^m_\alpha \hat{S}^{\,n}_\alpha \right) \tag{17}$$

The first term is the anisotropic on-site coupling of the ith ^{63}Cu(2) nucleus to the Cu^{2+} hole spin in the $3d^9_{x^2-y^2}$ orbital, proposed by Pennington et al.[20] to explain the anisotropic tensors $^{63}W_{1a}$ and $^{63}K_{\alpha\alpha}$. The hyperfine tensor $A_{\alpha\alpha}$ includes both the magnetic dipolar and core polarization coupling. Takigawa et al.[32] showed that an additional term is required for the ^{63}Cu(2), because the isotropic Knight shift is positive. To explain this observation, Mila and Rice[33] proposed that the ith ^{63}Cu(2) nucleus experiences a large, isotropic transferred hyperfine coupling B to the four nearest neighbor Cu^{2+} spins in the same plane (the j sites). B arises from the overlap of the nearest neighbor copper spin ($x^2 - y^2$) orbital with the unfilled 4s orbital of the on-site Cu(2) atom, mediated by the intervening O(2,3) 2pσ orbitals. When $\boldsymbol{B}_0 \parallel \hat{\boldsymbol{c}}$ the ^{63}Cu(2) magnetic shift in the HTS is temperature independent, even when the spin susceptibility is temperature dependent, implying that $A_{cc} + 4B \approx 0$.

The third term in the Hamiltonian, equation (17) is the transferred hyperfine coupling C of the kth ^{17}O(2,3) nucleus to the two nearest neighbor Cu spins (the l sites). The fourth term is the hyperfine coupling of the mth ^{89}Y nucleus to its eight nearest neighbor Cu^{2+} spins (the n sites): four in the plane above and four in the plane below. In this *single* component model, there is no coupling to an electronic spin associated with holes doped into the planar oxygen orbitals.

The spin–lattice relaxation of the planar nuclei is due to fluctuations of the Cu^{2+} spins. Shastry[34] and Hammel et al.[35] pointed out that the symmetry of the hyperfine Hamiltonian in equation (17) can explain the different temperature dependences of the Cu(2), O(2,3), and Y relaxation rates. For example, antiferromagnetic alignment of the Cu^{2+} spins results in a nonzero hyperfine field at the ^{63}Cu(2) site, while the field at the ^{17}O(2,3) or ^{89}Y sites vanishes. Thus, antiferromagnetic spin fluctuations may contribute quite strongly to the relaxation rate of the Cu(2), but not to the relaxation rate of the O(2,3) or Y. In this model, the relaxation rate for each site is[15]

$$ {}^{i}\left(\frac{1}{T_1}\right)_\alpha = \frac{{}^{i}\gamma_n^2 k_B T}{2\mu_\beta^2} \lim_{\omega\to 0} \sum_{\boldsymbol{q},\alpha'=\alpha} |\,{}^{i}A_{\alpha'\alpha'}(\boldsymbol{q})|^2 \frac{\chi''_{\alpha'\alpha'}(\boldsymbol{q},\omega)}{\omega} \tag{18}$$

This expression is valid for i = 63, 17, and 89 [Cu(2), O(2,3), and Y], the only difference being the quantity $|^iA_{\alpha\alpha}(\boldsymbol{q})|$, which is the $\boldsymbol{q}$-space Fourier transform of the real space hyperfine coupling constants. This form factor $|^iA_{\alpha\alpha}(\boldsymbol{q})|$ acts as a filter, determining which spin fluctuation wavelengths contribute to the relaxation rate.

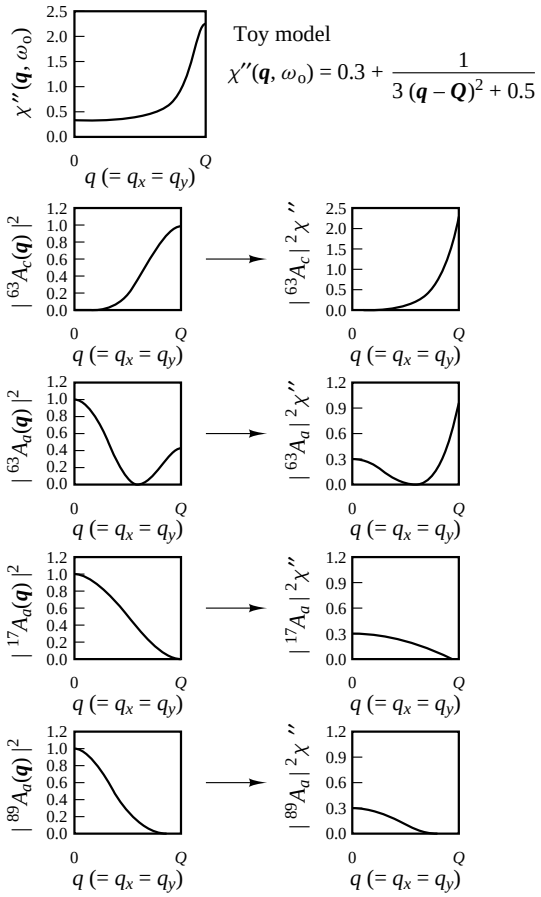

Figure 8 Each hyperfine form factor (left side) multiplied by $\chi''(\boldsymbol{q},\omega)$ (top) yields a uniquely $\boldsymbol{q}$-dependent product (right side). These products, plotted here along the Brillouin zone diagonal [q (= q_x=q_y)] enter into the expression for the relaxation rate, equation (18)[36]

The differences between the various $|^iA_{\alpha\alpha}(\boldsymbol{q})|^2$ are shown in Figure 8. For our purposes, the most important regions of the two-dimensional Brillouin zone are large $\boldsymbol{q}$ [$\boldsymbol{q} \approx \boldsymbol{Q} = (\pi/a,\pi/a)$, corresponding to antiferromagnetic fluctuations], and small $\boldsymbol{q}$ ($\boldsymbol{q} \approx 0$, corresponding to long-wavelength fluctuations). The relaxation rates, in order of decreasing sensitivity to the $\boldsymbol{q} \approx \boldsymbol{Q}$ region of $\chi''(\boldsymbol{q},\omega)$, are $^{63}W_{1a}$, $^{63}W_{1c}$, $^{17}W_{1c}$, and $^{89}W_{1c}$. To illustrate this, we show the products $|^iA_{\alpha'\alpha'}(\boldsymbol{q})|^2\chi''_{\alpha'\alpha'}(\boldsymbol{q},\omega)$ in Figure 8 for $\boldsymbol{q}$ along the zone diagonal, using a generic form for $\chi''(\boldsymbol{q},\omega)$, which has a big peak at $\boldsymbol{q} = \boldsymbol{Q}$ [due to antiferromagnetic correlations of the Cu(2) electronic spins]. If this big peak had a different temperature dependence from the $\boldsymbol{q}$ = 0 region, the Cu(2) relaxation rates would have a different temperature dependence from the O(2,3) and Y relaxation rates, as is experimentally observed.

The hyperfine couplings we have discussed so far and their implications within a one-component model are widely accepted concepts. However, the actual form chosen for $\chi''(\boldsymbol{q},\omega)$ and the microscopic justification for that form is a much more controversial issue. One particular model, proposed by Millis, Monien, and Pines (MMP),[37] achieved great success in quantitatively fitting the normal state data (K^S and T_1). An acknowledged problem with this successful model is the reconciliation of the MMP $\chi(\boldsymbol{q},\omega)$ with inelastic neutron scattering measurements. It is important to note

that the neutron scattering measurements probe $\chi''(\boldsymbol{q},\omega)$ at finite ω, while the NMR experiments are only sensitive to $\chi''(\boldsymbol{q},\omega \approx 0)$.

Although the single component model works very well, two recent experiments have concluded that the model is not complete. Takigawa et al.[38] measured the ^{89}Y relaxation rate in $YBa_2Cu_3O_{6.63}$, which deviates slightly from equation (14). Their results are consistent with the build-up of antiferromagnetic correlations between adjacent CuO_2 layers as the temperature is lowered. In another experiment, Walstedt et al.[39] have measured the planar copper and oxygen relaxation rates in $La_{1.86}Sr_{0.14}CuO_4$. They compared these data with rates calculated using the single component model and the $\chi''(\boldsymbol{q},\omega)$ measured in neutron scattering. While there is rough agreement with the copper data, they are unable to fit the planar oxygen data. They suggest that the assumptions of the single component model need to be reexamined.

4.5 The Gaussian Contribution to T_2

Pennington et al.[16] discovered that the Cu(2) transverse magnetization decay was the product of an exponential and a Gaussian, for $\boldsymbol{B}_0 \parallel \hat{\boldsymbol{c}}$. A ^{63}Cu(2)–^{65}Cu(2) SEDOR experiment was used to isolate the Gaussian contribution cleanly, as is shown in Figure 9. In order to characterize the temperature dependence of $\chi(\boldsymbol{q},\omega)$, Imai et al.[40] measured T_{2G} along with T_1 as a function of temperature in $YBa_2Cu_3O_7$.

Imai et al.[41] also measured T_{2G} and T_1 of the Cu(2) site in La_2CuO_4 from T = 450 K to 900 K. These measurements confirm that La_2CuO_4 is a two-dimensional Heisenberg antiferromagnet. When Imai et al.[42] extended their T_1 measurements of $La_{2-x}Sr_xCuO_4$ to high temperatures, they found that both the superconductor (x = 0.15) and the antiferromagnet (x = 0) exhibited the same temperature-independent T_1, as is seen in Figure 10. This surprising result shows that doped holes are clearly not determining the spin dynamics at high temperatures.

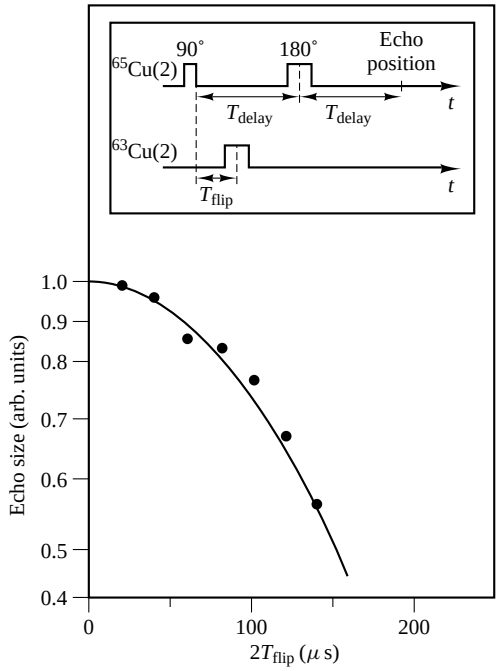

Figure 9 The ^{63}Cu(2)–^{65}Cu(2) SEDOR (spin echo double resonance) pulse sequence (inset) and data (main figure). The echo size is plotted versus $2T_{flip}$. The solid line is a Gaussian with τ_{SEDOR} = 130 μs[16]

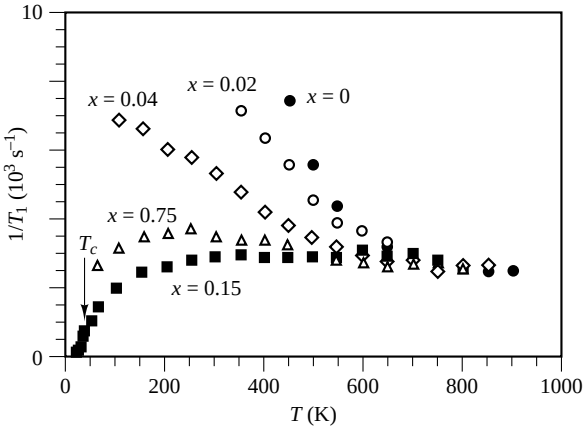

Figure 10 Temperature dependence of $1/^{63}T_1$ for various doping levels of $La_{2-x}Sr_xCuO_4$[42]

5 NMR STUDIES OF THE HTS IN THE SUPERCONDUCTING STATE

5.1 Test of the Pairing State

Given the unusual properties of the HTS in the normal state, it is reasonable to question whether a generalized BCS pairing state provides an appropriate description of the superconducting state. At present, no alternative theory has been developed to the point where its predictions may be compared with the NMR data. Comparisons of superconducting state data with the predictions of a generalized BCS theory have led to the conclusion that the pairing state is a spin singlet, and that the orbital pairing state is not conventional s-wave. Determining the pairing state symmetry is important, because the answer is linked to the microscopic mechanism for the pairing (for example, phonon-mediated pairing is usually associated with an isotropic s-wave state, while pairing mediated by antiferromagnetic spin fluctuations is usually associated with an orbital d-wave state.)

5.1.1 Knight Shift

The temperature dependence of the ^{63}Cu Knight shift $K^S(T)$ in $YBa_2Cu_3O_7$ below T_c is the most direct evidence that the pairing state is a spin singlet.[43] The experiment involves a measurement of the temperature-dependent line positions $\nu_{Cu}(T)$. Recall that the positions of the ^{63}Cu NMR resonance lines are given by

$$\nu_{Cu}(T) = \text{const} \times [1 - K^L + K^S(T)]B_{int}(T) + \nu_Q(T) \quad (19)$$

An accurate measurement of $K^S(T)$ therefore requires knowledge of the internal field $B_{int}(T)$ and the quadrupolar contribution to the resonance frequency, $\nu_Q(T)$. The uncertainty in

$B_{\rm int}(T)$ has been the traditional weakness of Knight shift measurements. In the mixed state ($B_{c1} < B_0 < B_{c2}$), $B_{\rm int} \neq B_0$ because of superconducting diamagnetic screening currents. Indeed, there will be a spread in the values of $B_{\rm int}$, which will cause an inhomogeneous broadening of the NMR line.

Fortunately, $B_{\rm int}(T)$ may be determined quite accurately in $YBa_2Cu_3O_7$ using the ^{89}Y NMR as an internal field marker. Since ^{89}Y is spin-$\frac{1}{2}$, and its shift is known to be small compared with that of the copper ($K_Y < \frac{1}{10}K_{Cu}$), the line position of the ^{89}Y is

$$\nu_Y(T) = \frac{\gamma_Y}{2\pi}[1 + K_Y(T)]B_{\rm int}(T) \approx \frac{\gamma_Y}{2\pi}B_{\rm int}(T) \qquad (20)$$

The problem with this approach is that the yttrium signal in this material is quite weak because the gyromagnetic ratio γ_Y is small and because the low temperature yttrium relaxation time is extremely long (approx. 10 min at 4.2 K). Barrett et al.[43] used a Carr–Purcell–Meiboom–Gill pulse sequence to speed up data acquisition by a factor of 6, making the experiment feasible. Their results for the temperature-dependent magnetic shift tensor of the Cu(2) and Cu(1) are shown in Figure 11.

The Knight shift tensor $K^S_{\alpha\alpha}(T)$ is related to the magnetic shift tensor $K_{\alpha\alpha}(T)$ by

$$K_{\alpha\alpha}(T) = K^L_{\alpha\alpha} + K^S_{\alpha\alpha}(T) \qquad (21)$$

If the pairing state is a spin singlet then $K^S_{\alpha\alpha}(T = 0) = 0$. The low temperature magnetic shift values are then just the chemical shift values $K_{\alpha\alpha}(T = 4.2\,\text{K}) = K^L_{\alpha\alpha}$. The chemical shift is given by

$$K^L_{\alpha\alpha} = 2\beta^2\left[\sum_n \frac{\langle 0|\hat{L}_\alpha|n\rangle\langle n|\hat{L}_\alpha/r^3|0\rangle}{E_n - E_0} + \text{c.c.}\right] \qquad (22)$$

Thus, the normal state result that the electronic state of the Cu(2) (Cu(1)) is very close to Cu^{2+} with a single d-shell hole in the $x^2 - y^2$ ($y^2 - z^2$) state predicts that[20]

$$K^L_{cc} \geq 4K^L_{aa} = 4K^L_{bb} \quad \text{for the Cu(2)} \qquad (23)$$

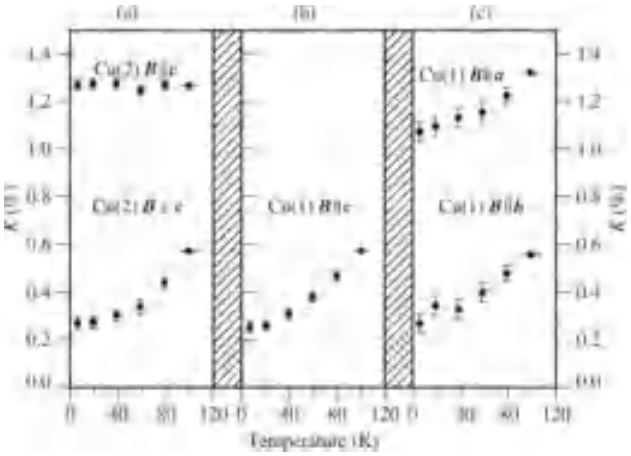

Figure 11 The total ^{63}Cu magnetic shift as a function of temperature for (a) the Cu(2), and (b),(c) the Cu(1) sites in $YBa_2Cu_3O_7$[43]

Table 2 Comparison of the Theoretical Chemical Shift Anisotropy in $YBa_2Cu_3O_7$ with the Experimental Anisotropy Implied by Spin-Singlet Pairing[20]

		Theory	Experiment
^{63}Cu(1)	K^L_{aa}/K^L_{bb}	≥4	4.00
	K^L_{aa}/K^L_{cc}	≥4	4.32
^{63}Cu(2)	K^L_{cc}/K^L_{aa}	≥4	4.57
	K^L_{cc}/K^L_{bb}	≥4	4.57

$$K^L_{aa} \geq 4K^L_{bb} = 4K^L_{cc} \quad \text{for the Cu(1)} \qquad (24)$$

From Table 2, we see that the experimental results assuming spin-singlet pairing are in quite good agreement with these predictions.

On the other hand, if the pairing state is a spin triplet then some components of the Knight shift tensor will not vanish when $T = 0$. In particular, if the trace of the spin susceptibility tensor is $3\chi^S_n$ at $T = T_c$ then it is $2\chi^S_n$ at $T = 0$.[19] Therefore, $K_{\alpha\alpha}(T = 4.2\,\text{K})$ would have a large contribution from $K^S_{\alpha\alpha}$ ($T = 4.2$ K), which would imply unphysical values for $K^L_{\alpha\alpha}$. This analysis leads to the conclusion that the pairing state is a spin singlet, and $K_{\alpha\alpha}(T = 4.2\,\text{K}) = K^L_{\alpha\alpha}$.

The temperature dependence of the Knight shift is also informative. For the Cu(2) sites, the rapid drop in $K^S_{bb}(T)$ just below T_c together with its weak temperature dependence below $T \approx 30$ K imply a strong-coupling energy gap, i.e., the gap opens up faster and goes to a larger value than predicted by the original BCS weak-coupling theory. The Knight shift temperature dependence does not rule out either orbital s-wave or orbital d-wave pairing.[43]

5.1.2 Spin–Lattice Relaxation Time T_1

For every nucleus investigated in the HTS, there is no coherence peak in the NMR (or NQR) relaxation rate below T_c. In addition, $1/T_1$ does not follow equation (10), as expected for a BCS spin-singlet, orbital s-wave pairing state. Instead, Imai et al.[44] fit their $(1/T_1)_{\rm NQR}$ data to a T^3 form over two decades (see Figure 12). Several groups suggested that these results implied either a strong pair breaking mechanism or an unconventional superconducting state.

Another probe of the pairing state is the temperature dependence of the Cu(2) relaxation rate anisotropy ratio, $^{63}W_{1a}/^{63}W_{1c}$. In the normal state, this ratio is about 3.7 in $YBa_2Cu_3O_7$, independent of temperature. This result arises from the different form factors for $^{63}W_{1a}$ and $^{63}W_{1c}$, as described in Section 4.4. Barrett et al.[29] showed that $^{63}W_{1a}/^{63}W_{1c}$ dropped suddenly below T_c. Figure 13 compares the low field $^{63}W_{1a}/^{63}W_{1c}$ measurements of Martindale et al.[45] and Takigawa et al.[46] with calculations by Bulut and Scalapino.[47] Bulut and Scalapino conclude that the Cu(2) anisotropy ratio favors an orbital d-wave pairing state over an isotropic s-wave state. The anisotropy ratio is sensitive to the orbital symmetry of the pairing state (i.e., the $\boldsymbol{q}$ dependence of the superconducting energy gap) because of the $\boldsymbol{q}$-dependent form factors $|^iA_{\alpha\alpha}(\boldsymbol{q})|$. Similarly, $^{63}W_{1c}$ and $^{17}W_{1c}$ have been measured in weak fields by Martindale et al.[48] (see Figure 14), and the observed temperature dependence has been explained

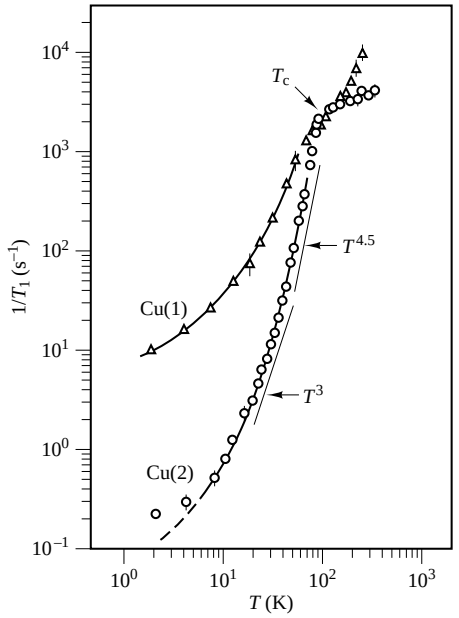

Figure 12 ^{63}Cu NQR spin–lattice relaxation rate data plotted versus temperature on a log–log scale.[44] For a BCS d-wave pairing state, one expects that $1/T_1 \propto T^3$ as $T \rightarrow 0$

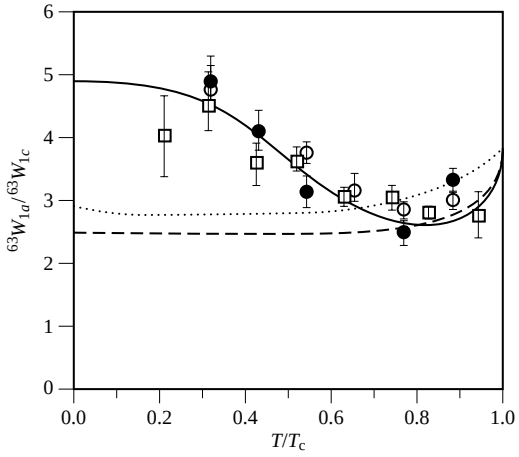

Figure 13 Plot of $^{63}W_{1a}/^{63}W_{1c}$ in $YBa_2Cu_3O_7$ versus T/T_c. The open squares are the weak-field data of Martindale et al.,[45] and the open and filled circles are the data of Takigawa et al.[46] The solid curve is Bulut and Scalapino's[47] d-wave calculation with $2\Delta_{max}(0) = 8k_BT_c$, the dotted curve is their s-wave calculation with $2\Delta(0) = 4k_BT_c$, and the dashed curve is their s-wave calculation with $2\Delta(0) = 8k_BT_c$

by Thelen et al.[49] using a $d_{x^2-y^2}$ orbital pairing state and a Fermi surface consistent with photoemission data.

5.1.3 The Gaussian Contribution to T_2

Itoh et al.[50] have measured T_{2G} in the normal and superconducting states of $YBa_2Cu_4O_8$. Their results, shown in Figure 15, compare favorably with the predictions of Bulut and Scalapiro[51] for orbital d-wave pairing.

It is important to point out that the T_1 and T_{2G} measurements do not require that the orbital symmetry of the pairing state must be $d_{x^2-y^2}$. For example, an extremely anisotropic

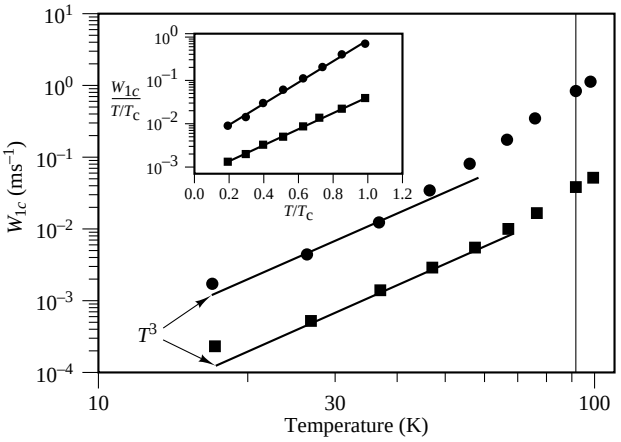

Figure 14 W_{1c} measured in a 0.67 T field versus temperature on a log–log scale.[48] The ^{63}Cu(2) and ^{17}O(2,3) data in $YBa_2Cu_3O_7$ are shown as circles and squares, respectively. The inset contains the same data plotted in an alternate form

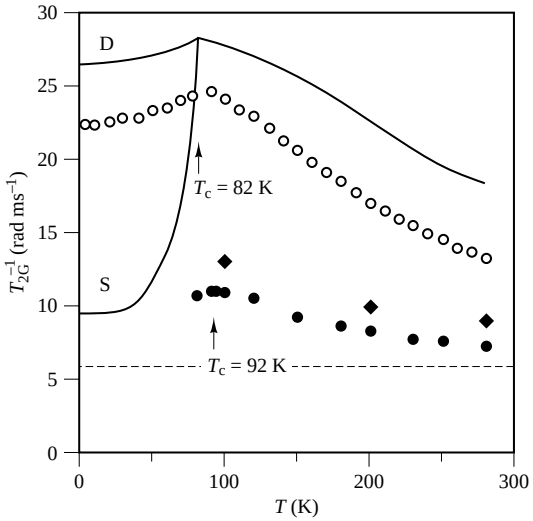

Figure 15 Plot of the Gaussian contribution to the spin–spin relaxation rate $1/T_{2G}$ versus temperature. The open circles are the data for $YBa_2Cu_4O_8$.[50] The solid curves are the calculations of Bulut and Scalapino,[51] assuming s-wave (S) and d-wave (D) pairing states

s-wave state may also account for the temperature dependence of the NMR data. Rather, the NMR results show that the pairing state is a spin singlet, with a highly anisotropic energy gap.

5.2 Studies of the 'Mixed State'

Mehring et al.[52] have observed the fluxoid-induced broadening of the ^{205}Tl NMR line in $Tl_2Ba_2CuO_6$ (T_c = 85 K), which they use to infer the low-temperature penetration depth. Several groups have used ^{89}Y and ^{205}Tl NMR measurements to study fluxoid dynamics in the HTS.

Martindale et al.[45,48] discovered that $^{63}W_{1c}$ and $^{17}W_{1c}$ are field dependent at low temperatures in $YBa_2Cu_3O_7$. The field dependence of $^{63}W_{1a}$ is much weaker. Martindale et al. suggested that fluxoids may be responsible for the field

dependence of the relaxation rates. Corey et al. (R. Corey, personal communication) studied the angular dependence of these rates, concluding that fluxoids do contribute to the relaxation at low temperatures.

6 SUMMARY AND FUTURE DIRECTIONS

NMR and NQR studies of the HTS continue to provide important information about the normal and superconducting states. Experimentalists and theorists from around the world have contributed to our current deep understanding of the wide range of behavior exhibited by these compounds. Nevertheless, there are many important open questions.

In the normal state, both the NMR and neutron scattering measurements confirm the presence of short-range antiferromagnetic spin correlations, even in the superconducting compounds. However, the detailed shape of $\chi''(\boldsymbol{q},\omega)$ that gives the best fit to the NMR experiments is not consistent with the $\chi''(\boldsymbol{q},\omega)$ measured by inelastic neutron scattering.

In the superconducting state, the pairing state seems to be a generalized BCS spin singlet, with a highly anisotropic energy gap. This conclusion, however, is based primarily upon measurements of $YBa_2Cu_3O_7$ and $YBa_2Cu_4O_8$, which are quite similar to one another. Superconducting state NMR measurements should be carried out in additional compounds, to refine our knowledge of the superconducting pairing state.

7 RELATED ARTICLES

Metallic Superconductors.

8 REFERENCES

1. J. G. Bednorz and K. A. Müller, *Z. Phys. B*, 1986, **64**, 189.
2. J. Bardeen, L. N. Cooper, and J. R. Schrieffer, *Phys. Today*, 1973, **26**, 23.
3. M. Tinkham, *Introduction to Superconductivity*, McGraw-Hill, New York, 1975.
4. C. H. Pennington and C. P. Slichter, in *Physical Properties of High Temperature Superconductors, II*, ed. D. M. Ginsberg, World Scientific, Singapore, 1990, Chap. 5
5. R. E. Walstedt and W. W. Warren, Jr., *Science (Washington, DC)*, 1990, **248**, 1082.
6. D. M. Brinkmann and M. Mali, in *NMR Basic Principles and Progress*, eds. P. Diehl, E. Fluck, and R. Kosfeld, Springer-Verlag, Berlin, 1994, Vol. 31.
7. C. P. Slichter, in *Proceedings of Symposium on Strongly Correlated Electronic Materials, Los Alamos, NM, 1993*, Addison-Wesley, Reading, MA.
8. D. M. Ginsberg, ed., *Physical Properties of High Temperature Superconductors I, II, and III*, World Scientific, Singapore, 1989, 1990, and 1992.
9. J. B. Boyce, F. Bridges, T. Claeson, and M. Nygren, *Phys. Rev. B*, 1989, **39**, 6555.
10. S.-W. Cheong, Ph.D. thesis, The University of California at Los Angeles, 1989.
11. J. Rossat-Mignod, L. P. Renault, C. Vettier, P. Burlet, J. Y. Henry, and G. Lapertot, *Physica B*, 1991, **169**, 58.
12. Y. Iye, in *Physical Properties of High Temperature Superconductors, III*, ed. D. M. Ginsberg, World Scientific, Singapore, 1992, Chap. 4
13. C. P. Slichter, *Principles of Magnetic Resonance*, 3rd edn., Springer-Verlag, Berlin, 1989.
14. J. Winter, *Magnetic Resonance in Metals*, Clarendon Press, Oxford, 1971.
15. T. Moriya, *J. Phys. Soc. Jpn.*, 1963, **18**, 516.
16. C. H. Pennington, D. J. Durand, C. P. Slichter, J. P. Rice, E. D. Bukowski, and D. M. Ginsberg, *Phys. Rev. B*, 1989, **39**, 274.
17. C. H. Pennington and C. P. Slichter, *Phys. Rev. Lett.*, 1991, **66**, 381.
18. D. E. MacLaughlin, in *Solid State Physics*, eds. H. Ehrenreich, F. Seitz, and D. Turnbull, Academic, Press, New York, 1976, Vol. 31, pp. 1–69.
19. A. J. Leggett, *Rev. Mod. Phys.*, 1975, **47**, 331.
20. C. H. Pennington, D. J. Durand, C. P. Slichter, J. P. Rice, E. D. Bukowski, and D. M. Ginsberg, *Phys. Rev. B*, 1989, **39**, 2902.
21. J. A. Martindale, Ph.D. thesis, University of Illinois at Urbana–Champaign, 1993.
22. D. E. Farrell, B. S. Chandrasekhar, M. R. DeGuire, M. M. Fang, V. G. Kogan, J. R. Clem, and D. K. Finnemore, *Phys. Rev. B*, 1987, **36**, 4025.
23. M. Takigawa, P. C. Hammel, R. H. Heffner, Z. Fisk, K. C. Ott, and J. D. Thompson, *Phys. Rev. Lett.*, 1989, **63**, 1865.
24. P. C. Hammel, A. P. Reyes, S.-W. Cheong, Z. Fisk, and J. E. Schriber, *Phys. Rev. Lett.*, 1993, **71**, 4401.
25. H. Alloul, T. Ohno, and P. Mondels, *Phys. Rev. Lett.*, 1989, **63**, 1700.
26. M. Takigawa, A. P. Reyes, P. C. Hammel, J. D. Thompson, R. H. Heffner, Z. Fisk, and K. C. Ott, *Phys. Rev. B*, 1991, **43**, 247.
27. F. C. Zhang and T. M. Rice, *Phys. Rev. B*, 1988, **37**, 3759.
28. R. E. Walstedt, W. W. Warren, Jr., R. F. Bell, G. F. Brennert, G. P. Espinosa, J. P. Remeika, R. J. Cava, and E. A. Reitman, *Phys. Rev. B*, 1987, **36**, 5727 [when reading this early paper, Cu(2) should replace the authors' Cu(1), and Cu(1) should replace the authors' Cu(2)].
29. S. E. Barrett, J. A. Martindale, D. J. Durand, C. H. Pennington, C. P. Slichter, T. A. Friedmann, J. P. Rice, and D. M. Ginsberg, *Phys. Rev. Lett.*, 1991, **66**, 108.
30. T. Imai, Ph.D. thesis, Institute for Solid State Physics, The University of Tokyo, 1991.
31. M. Takigawa, *Appl. Magn. Reson.*, 1992, **3**, 495.
32. M. Takigawa, P. C. Hammel, R. H. Heffner, and Z. Fisk, *Phys. Rev. B*, 1989, **39**, 7371.
33. F. Mila and T. M. Rice, *Physica C*, 1989, **157**, 56.
34. B. S. Shastry, *Phys. Rev. Lett.*, 1989, **63**, 1288.
35. P. C. Hammel, M. Takigawa, R. H. Heffner, Z. Fisk, and K. C. Ott, *Phys. Rev. Lett.*, 1989, **63**, 1992.
36. S. E. Barrett, Ph.D. thesis, University of Illinois at Urbana–Champaign, 1992.
37. A. J. Millis, H. Monien, and D. Pines, *Phys. Rev. B*, 1990, **42**, 167.
38. M. Takigawa, W. L. Hults, and J. L. Smith, *Phys. Rev. Lett.*, 1993, **71**, 2650.
39. R. E. Walstedt, B. S. Shastry, and S.-W. Cheong, *Phys. Rev. Lett.*, 1994, **72**, 3610.
40. T. Imai, C. P. Slichter, A. P. Paulikas, and B. Veal, *Appl. Mag. Reson.*, 1992, **3**, 729.
41. T. Imai, C. P. Slichter, K. Yoshimura, M. Katoh, and K. Kosuge, *Phys. Rev. Lett.*, 1993, **71**, 1254.

42. T. Imai, C. P. Slichter, K. Yoshimura, and K. Kosuge, *Phys. Rev. Lett.*, 1993, **70**, 1002.
43. S. E. Barrett, D. J. Durand, C. H. Pennington, C. P. Slichter, T. A. Friedmann, J. P. Rice, and D. M. Ginsberg, *Phys. Rev. B*, 1990, **41**, 6283.
44. T. Imai, T. Shimizu, H. Yasuoka, Y. Ueda, and K. Kosuge, *J. Phys. Soc. Jpn.*, 1988, **57**, 2280.
45. J. A. Martindale, S. E. Barrett, C. A. Klug, K. E. O'Hara, S. M. DeSoto, C. P. Slichter, T. A. Friedmann, and D. M. Ginsberg, *Phys. Rev. Lett.*, 1992, **68**, 702.
46. M. Takigawa, J. L. Smith, and W. L. Hults, *Phys. Rev. B*, 1991, **44**, 7764.
47. N. Bulut and D. J. Scalapino, *Phys. Rev. Lett.*, 1992, **68**, 706.
48. J. A. Martindale, S. E. Barrett, K. E. O'Hara, C. P. Slichter, W. C. Lee, and D. M. Ginsberg, *Phys. Rev. B*, 1993, **47**, 9155.
49. D. Thelen, D. Pines, and J. P. Lu, *Phys. Rev. B*, 1993, **47**, 9151.
50. Y. Itoh, H. Yasuoka, Y. Fujiwara, Y. Ueda, T. Machi, I. Tomeno, K. Tai, N. Koshizuka, and S. Tanaka, *J. Phys. Soc. Jpn.*, 1992, **61**, 1287.
51. N. Bulut and D. J. Scalapino, *Phys. Rev. Lett.*, 1991, **67**, 2898.
52. M. Mehring, F. Hentsh, H. Mattausch, and S. Simon, *Z. Phys. B*, 1989, **77**, 355.

Biographical Sketches

Sean E. Barrett. *b* 1965. A.B., Princeton University, 1987; Ph.D., 1992, University of Illinois at Urbana–Champaign (advisor C. P. Slichter). Postdoctoral member of the technical staff (with R. Tycko), AT&T Bell Laboratories, Murray Hill, NJ, 1992–1994, Assistant Professor of Physics, Yale University, 1994–present. Approx. 10 publications. Research interests: applications of NMR and optically pumped NMR to the study of correlated electron systems.

C. P. Slichter. *b* 1924. A.B., 1946, Ph.D., Harvard, 1949 (advisor E. M. Purcell). University of Illinois at Urbana-Champaign, 1949–present, currently Center for Advanced Study Professor of Physics and Chemistry. Approx. 160 publications. Author of the textbook 'Principles of Magnetic Resonance.' Research interests: applications of NMR and ESR to problems of condensed matter physics, chemistry, and surface science.

Metallic Superconductors

Yoshika Masuda

Aichi Gakuin University, Aichi, Japan

1	Introduction	1
2	Knight Shift in the Superconducting State	1
3	Nuclear Spin–Lattice Relaxation in BCS Superconductors	2
4	NMR in Type-II Superconductors	6
5	Related Articles	9
6	References	9

1 INTRODUCTION

Nuclear magnetic resonance is a useful tool with which to investigate certain important aspects of superconductivity. It has played an historic role in understanding the properties of superconductors. The environment of nuclear spins in a metal is greatly modified when a metal makes the transition into the superconducting state. The nuclear spins are sensitive to this variation, leading NMR to be an important technique as a probe of the superconducting state.

In a metal, the static response to an external magnetic field in the normal state is generally expressed by a bulk diamagnetic susceptibility. The same mechanism also contributes to the Knight shift of the NMR frequency in a metal.

The dynamic coupling between a spin system and its surroundings (the lattice) gives rise to lattice-induced transitions between spin states. The nuclear spin–lattice relaxation time T_1 is a measure of the rate of exchange of energy between a spin system and the rest of the lattice. It is most generally defined as the ratio of the deviation of spin energy from its equilibrium value to the time rate of change of spin energy.

The Knight shift and T_1 are two important quantities which give much information about the properties of conduction electrons. In particular, T_1 provides information on the density of states near the Fermi surface. Accordingly, it is expected that both effects provide a test of any theory of superconductivity.

Hebel and Slichter[1] first measured T_1 in aluminum, which was believed to be a well-behaved superconductor, in parallel with the development of the Bardeen, Cooper, and Schrieffer[2] (henceforth referred to as BCS) theory in 1957, which gave a microscopic understanding of superconductivity. They calculated the relaxation time predicted by the BCS theory, and found that their experimental T_1 data were consistent with the theory. In fact, T_1 measurements together with measurements of acoustic absorption provide an important confirmation of the choice of spin pairing of the BCS wavefunctions (the so-called 'coherence effect'). The agreement of the nuclear relaxation time with theory is in contradiction to the behavior of the Knight shift, which remains finite in the superconducting state at absolute zero,[3,4] a result that was difficult to explain in any simple way.

Independently, Redfield[5] and later Masuda and Redfield[6] measured T_1 in superconducting aluminum with greater accuracy and over a wider temperature range, from which important information on the existence of an energy gap can be obtained. It was obvious that the nuclear T_1 values would be worth knowing, but these measurements were even more interesting than had been anticipated; they were in striking contrast to any two-fluid model of superconductivity, but could be easily explained by the BCS theory, assuming an energy gap at temperature $T = 0$ of $2\epsilon_0(0) = 3.2k_{\mathrm{B}}T_{\mathrm{c}}$ and a constant relative anisotropy of the energy gap, where T_{c} is the critical temperature. Studies of the superconducting state by NMR are summarized in detail elsewhere.[7]

2 KNIGHT SHIFT IN THE SUPERCONDUCTING STATE

2.1 Experiments on Elemental Superconductors

Soon after the appearance of the BCS theory, experiments on the ^{199}Hg Knight shift in mercury colloids[3] and the ^{119}Sn Knight shift in tin platelets were performed.[4] The results for both Hg and Sn metals indicated the existence of a residual Knight shift at $T = 0$. These experiments seemed to contradict the BCS hypothesis of singlet spin pairing in the superconducting ground state. A number of explanations appeared to find a way out of this dilemma, involving ideas such as modified pairing criteria and even triplet spin pairing. To explain the experiments, however, a serious modification of the BCS picture was unnecessary.

In nontransition metals the Knight shift is due mainly to the hyperfine contact interaction, and is proportional to the normal state Pauli spin susceptibility χ_{n}. By making use of the BCS theory, Yosida[8] calculated the spin susceptibility in the superconducting state and derived an expression for the Knight shift in the superconducting state.

In the superconducting state all ground state pairs are either occupied or unoccupied, and therefore the contribution to the spin susceptibility will only come from excited states, the populations of which are given by a Fermi function $f(E_k)$ of the excited state energy E_k. Accordingly, the spin susceptibility in the superconducting state is given by

$$\chi_{\mathrm{s}} = -2\mu_{\mathrm{B}}^2 \sum_k \mathrm{d}f/\mathrm{d}E_k \tag{1}$$

where μ_{B} is the Bohr magneton and k the wavevector. By making use of the BCS energy density of excited states $N_{\mathrm{BCS}}(E, T)$, the sums in equation (1) can be converted to integrals as follows,

$$\chi_{\mathrm{s}} = -4\mu_{\mathrm{B}}^2 \int_{\epsilon_0(T)}^{\infty} N_{\mathrm{BCS}}(E, T)(\mathrm{d}f/\mathrm{d}E)\,\mathrm{d}E \tag{2}$$

Here $N_{\mathrm{BCS}}(E, T)$ is given by

$$N_{\mathrm{BCS}}(E, T) = \begin{cases} 0 & \text{for } |E| < \epsilon_0(T) \\ N(0)|E|/[E^2 - \epsilon_0^2(T)]^{1/2} & \text{for } |E| > \epsilon_0(T) \end{cases} \tag{3}$$

where $N(0)$ is the normal state density of states at the Fermi level. The χ_{n} value is obtained by taking $\epsilon_0(T) = 0$.

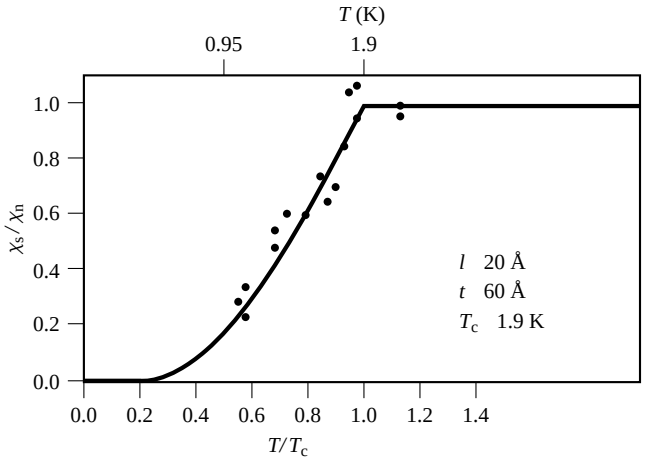

Figure 1 Spin susceptibility in pure superconducting aluminum. Filled circles: data of Fine et al.[10] Solid curve: calculated from the theory of Yosida,[8] l is the electron mean free path, and t is the average thickness of a single substrate

The early experiments of the ^{27}Al Knight shift showed that the Knight shift in the superconducting state at temperature $T = 0$, $K_s(T = 0)$ decreases to about 75% of its values in the normal state, K_n. This result suggested that a residual spin susceptibility, was conceivably due to an inclusion of paramagnetic impurities, since no other mechanism suggested itself. Hammond and Kelly[9] repeated the measurement of the ^{27}Al Knight shift on stacked Al films, taking care to eliminate paramagnetic oxygen impurities in the film. The experimental result of $K_s(T)/K_n$ extrapolated to zero at $T = 0$, as shown in Figure 1,[10] and the longstanding discrepancy between experiment and the prediction of singlet spin pairing, was thereby finally removed. Further experiments on the residual Knight shift in both tin and lead revealed that the spin–orbit coupling is induced in the conduction-electron gas by the boundary in small particles as well as imperfections, and the generalized pairing condition between time-reversed eigenstates might account for the small change of the Knight shift in the superconducting state.

2.2 Various Contributions to the Knight Shift

The conduction-electron susceptibility in the normal state of a metal consists of three important contributions: the s-band Pauli susceptibility in the case of a simple metal; the Van Vleck orbital susceptibility in transition metals with partly filled non-s bands; and the Pauli susceptibility of the non-s (usually d) bands in the case of transition metals. Each mechanism produces a shift component proportional to the corresponding susceptibility. The orbital shift is independent of the spin state of the conduction electrons, and hence does not change by spin pairing in the superconducting state. The contribution of the exchange interaction between non-s itinerant electrons and local s core electrons to the Knight shift should cancel each other out in the superconducting state if the d-band electrons take part in the formation of Cooper pairs.

The residual ^{51}V Knight shift in superconducting vanadium films is found to be intrinsically 100% of the normal state shift. This result indicates that the Knight shift due to the s-band Pauli susceptibility and the Pauli susceptibility of the non-s bands must cancel each other, so that even if spin pairing is complete in the superconducting state, the effect on the measured Knight shift is small; the orbital shift is the principal contribution in both normal and superconducting states.

Susceptibility and Knight shift measurements on the intermetallic compounds V_3Si and V_3Ga show that an increase of the ^{51}V and ^{71}Ga Knight shifts seen in the superconducting state can be attributed to a decrease of the d-band spin susceptibility at $T = 0$ to about 25% of its value at the critical temperature. V_3Si has the A15 crystal structure, in which an extremely narrow d-band exists. This crystal structure enhances the d-band susceptibility, which increases the Knight shift to well above its value in pure vanadium.

3 NUCLEAR SPIN–LATTICE RELAXATION IN BCS SUPERCONDUCTORS

3.1 Spin Relaxation due to the BCS Mechanism

The nuclear spin–lattice relaxation rate $R = 1/T_1$ in a type-I superconductor can be calculated within the framework of the BCS theory. The dominant mechanism for this relaxation process arises from the coupling of the nuclear spins I to the conduction electron spins σ, which are in equilibrium with the lattice, and the hyperfine contact interaction.

The matrix elements between excited states of the system are given by a single particle operator of the form

$$\hat{\mathcal{H}}_1 = \sum_{k\sigma,k'\sigma'} M_{k\sigma,k'\sigma'} \hat{a}^*_{k'\sigma'} \hat{a}_{k\sigma} \tag{4}$$

where $M_{k\sigma,k'\sigma'}$ is the matrix element corresponding to scattering from $k\sigma$ to $k'\sigma'$ and $\hat{\alpha}^*_{k\sigma}$ and $\hat{\alpha}_{k'\sigma'}$ are creation and destruction operators for quasiparticle excitations in the normal state. In the Bloch approximation, individual particle wavefunctions, $\phi_{k\sigma}(x)$, are defined for a self-consistent field. In this situation, therefore,

$$M_{k\sigma,k'\sigma'} = \int \phi^*_{k'\sigma'}(x) \hat{\mathcal{H}}_1(x) \phi_{k\sigma}(x)\, \mathrm{d}x \tag{5}$$

in which x is defined to include the spin variable.

The significant feature of the BCS picture is the condensation of conduction electrons into a single, occupied ground state. In a pure metal this state corresponds to a pair occupation of the Bloch states $k\sigma$, such that if $k\sigma$ is occupied, so is $-k$, $-\sigma$ in the pair. At $T = 0$ all electrons occupy pair states; at finite temperature some pairs are broken up to form single-particle excitations. Nevertheless the coherent occupation of the condensed state restricts the scattering processes, and in addition alters the number of excited state electrons that can participate in scattering. Both these effects disappear in the normal state.

A remarkable difference between the superconducting and normal states arises from coherent effects associated with the paired wavefunctions. In the normal state scattering from $k\sigma$ to $k'\sigma'$ is completely independent of scattering from $-k'$, $-\sigma'$ to $-k$, $-\sigma$, as well as of all other transitions. The probability of the former is proportional to $|M_{k\sigma,k'\sigma'}|^2$, and

the latter is $|M_{-k',-\sigma',-k,-\sigma}|^2$. Because of the nature of the paired wavefunction in a superconducting state, these two contributions to the matrix elements for transition probabilities in a superconducting state are coherent and therefore may add destructively or constructively.

The ground-state occupation changes the transition rate for scattering, in such a way that the transition rate in the normal state is modified by the factor

$$C_{\pm}(E_k, E_{k'}, T) = \tfrac{1}{2}[1 \pm (\epsilon_0^2(T)/E_k E_{k'})] \tag{6}$$

where E_k and $E_{k'}$ are the initial and final excited state energies, respectively. $C_{\pm}(E_k,E_{k'},T)$ is the coherence factor, as it represents concretely the coherent nature of the population of pair states in the formation of the condensed phase. The sign of the second term in equation (6) depends on the nature of the perturbation which induces the transition. If the interaction is invariant under time reversal applied to the conduction-electron system, the minus sign is appropriate, namely $C_{-}(E_k,E_{k'},T)$. This is the case for phonons; in the case of ultrasonic attenuation, there is a very rapid drop in attenuation versus temperature at T_c, followed by a more gradual decrease. If the perturbation is not time-reversal invariant, $C_{+}(E_k,E_{k'},T)$ is appropriate. The nuclear spin relaxation rate exhibits an increase by a factor of 2 just below T_c which gives an indication of coherence effects arising from constructive interference.

Consider, for simplicity, that $I = \frac{1}{2}$, and that an experiment is performed in a magnetic field with nuclear Zeeman energy $\hbar\omega_{\text{nuc}}$. Then the relaxation rate is given by $W_+ + W_-$, where W_+ is the transition rate from spin-up to spin-down nuclear states induced by the entire conduction-electron system, and W_- is the rate for spin-down to spin-up transitions. The relaxation rates are given by

$$W_{\pm} = \frac{\pi}{2\hbar}|M_{k\sigma,k'\sigma'}|^2 \sum_{k,k'} C_{+}(E_k, E_{k'}, T) f(E_k, T) \times [1 - f(E_{k'}, T)]\delta(E_{k'} - E_k \mp \hbar\omega_{\text{nuc}}) \tag{7}$$

where the Fermi distribution function $f(E_k,T)$ accounts for the thermal population of excited initial states, and $[1 - f(E_{k'},T)]$ gives the thermal depopulation of final states required by the Pauli principle. The delta function insures the conservation of total energy in the scattering process.

By making use of the density of states in the superconducting state $N_s(E_k,T)$, the sums in equation (7) can be converted to integrals. The relaxation rate in the superconducting state R_s is given by

$$R_s \propto \int_0^{\infty} N_s(E_k, T) N_s(E_{k'}, T)[1 + \epsilon_0^2(T)/E_k E_{k'}]\, f(E_k, T) \times [1 - f(E_{k'}, T)]\, \mathrm{d}E_k \tag{8}$$

The BCS theory shows that the superconductor has a temperature-dependent gap of halfwidth $\epsilon_0(T)$ centered about the Fermi energy E_F. If the difference in energy between final and initial electron states is ignored, then the ratio of relaxation rates in superconducting to normal states, R_s/R_n, is given by

$$R_s/R_n = 2\int [N_s(E, T)]^2[1 + \epsilon_0^2(T)/E^2]\, f(E, T) \times [1 - f(E, T)]\, \mathrm{d}E \tag{9}$$

There is actually a logarithmic divergence of the integral in the limit $\hbar\omega_{\text{nuc}} \to 0$. This divergence comes from the singularity in the BCS density of states at the edge of the energy gap. The values of T_1 in the superconducting state predicted directly by the BCS theory are thus much shorter than those observed, and much shorter than T_1 in the normal state, near T_c. In comparing the theory with experiment it is necessary to take some sort of width for the electronic levels. It is reasonable that in actual metals the singularity will be removed by some mechanisms, and it is possible to see that spin–lattice relaxation measurements can yield information on the nature of such mechanisms.

Hebel and Slichter[1] obtained N_s by weighting the BCS density of states, N_{BCS}, with a function that characterizes the breadth of the energy levels. If an energy level breadth function is assumed to be a rectangle of width 2Δ and height $\frac{1}{2}\Delta$, then

$$N_s(E, T) = (2\Delta)^{-1} \int_{E-\Delta}^{E+\Delta} N_{\text{BCS}}(E', T)\, \mathrm{d}E' \tag{10}$$

Using equation (9), we can calculate the temperature dependence of T_1 for various values of $r = \epsilon_0(0)/\Delta$. Actually, of course, the parameter Δ might be temperature dependent. Now, as T approaches T_c the gap $2\epsilon_0(T)$ decreases, and it would be natural to assume that the anisotropy decreases and is perhaps proportional to the gap, as pointed out by Masuda and Redfield.[6] In that case we would have $\Delta(T)$ proportional to $\epsilon_0(T)$.

A field cycling method was used to measure T_1. In this method a large field is applied across the sample to polarize the nuclei (about 0.4 T in this case) for a time long compared with T_1. The field is then reduced to zero in a time that is short compared with T_1, and the spins begin to relax at zero field in the superconducting state with a relaxation time characteristic of the superconducting state. After a variable time τ, the field is then turned on again (to about 0.1 T) and immediately swept past the present resonance field of 0.1045 T to observe the spin polarization in the normal state by nuclear resonance. The resonance intensity is proportional to the spin polarization at that time and from its variation of the resonance signal intensity with τ, the relaxation time can be determined.

The nuclear resonance signal obtained in this way is much smaller than that observed above T_c because the nuclei are partially irreversibly demagnetized by the sudden change in magnetic field to which they are subjected when the transition takes place between the normal and superconducting states. For the sample used in most of these measurements, the signal was reduced to less than 5% of the value it would have had in a similar nonsuperconductor after the same sequence of field cycling.

The data for the relaxation time in both normal and superconducting states are shown in Figure 2 as a function of T_c/T.[6] The fact that T_1 decreases markedly just below T_c, and then increases as $\exp[\epsilon_0(0)/k_B T]$ for $T \ll T_c$ is a rather general consequence of any gap model. As can be seen from Figure 2, superconducting aluminum has an energy gap at $T = 0$ of $2\epsilon_0(0) = 3.2k_B T_c$, assuming that the BCS density of states function is smeared over a range of about $\Delta(T) = \epsilon_0(T)/10$, or $r(T) = 10\epsilon_0(0)/\epsilon_0(T)$. The BCS theory applies to the homogeneous, pure, and isotropic electron gas with a simplified interaction term and pure plane wavefunctions. If,

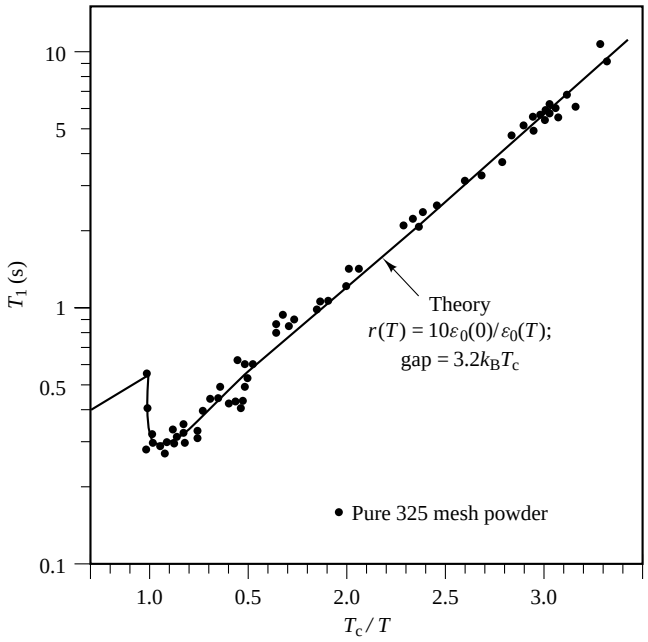

Figure 2 Measured values of T_1 in a powdered, pure aluminum sample.[6] T_c was taken to be 1.178 K. The solid line was calculated using the BCS density of states smeared over a range of 1/10 of the energy gap, assuming a smearing proportional to the energy gap

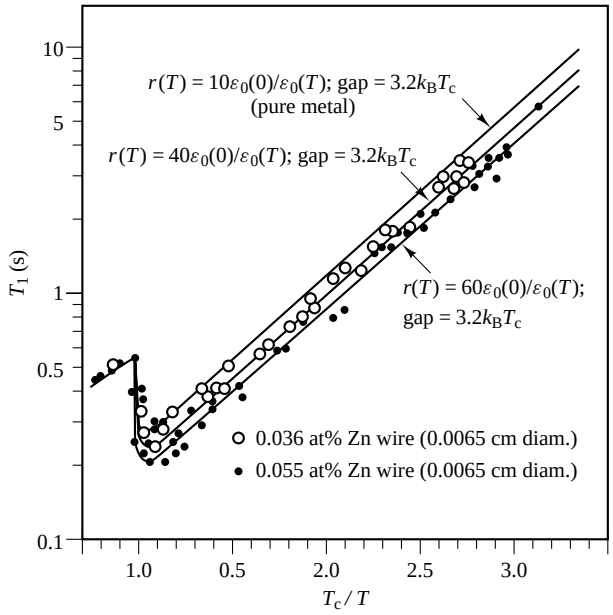

Figure 3 Measured values of T_1 in Al–Zn alloys.[12] T_c was taken to be 1.178 K. The solid lines are calculated using the BCS density of states smeared over a range of 1/10, 1/40, and 1/60 of the energy gap, assuming a smearing proportional to the energy gap

instead of the constant electron–electron interaction, one were to use wavefunctions and an electron–electron interaction that is nonconstant and anisotropic (as might be expected in actual metals), one would expect to find that the energy gap is a function of momentum vector, as well as temperature. Thus, the energy gap of a single particle excitation would depend upon the direction, as well as the magnitude, of its momentum vector. But nuclear spin relaxation has no momentum selection rule for the initial and final states of the transition, so the average density of states determines T_1, not the density of states in any particular k direction. Thus, as far as spin relaxation is concerned, the effect of anisotropy is to smear the BCS density of states by an amount equal to the anisotropy.

These experimental data are regarded as evidence for the existence of an anisotropy in the energy gap which, at any temperature, is of the order of one-tenth of the gap itself. The quantity $\Delta(T)$ could be interpreted in some other way, such as an inverse lifetime for scattering by imperfections or electrons. However, the temperature dependence of Δ or r is most naturally explained in terms of anisotropy. The anisotropy interpretation is also supported by the results described in the next section.

Measurements of T_1 in superconductors were extended to cadmium,[11] for which the behavior is practically identical with that of aluminum.

3.2 Impurity Effects: Anisotropy of the Energy Gap

The T_1 data of both superconducting aluminum and superconducting cadmium were explained very well by assuming a smearing of the anisotropy of the gap as mentioned above. To confirm this assumption experimentally, T_1 in superconducting aluminum alloys was measured.[12]

In a dilute alloy, plane-wave states with fixed spin are no longer good one-electron wavefunctions. Anderson[13] developed a BCS type of theory for dirty superconductors, in which elastic scattering from physical and chemical impurities is large compared with the energy gap. He argued that a ground-state pair should be formed by pairing a one-electron state with its exact time reversed. This state is a generalization of the k up, $-k$ down pairing of the BCS theory, which is independent of impurity scattering. If the electronic mean free path is large compared with the coherence length, the impurities will mix plane-wave states weakly as the electron moves through a coherence length. However, when the mean free path is small compared with the coherence length, the wavefunction can no longer be approximated by a single plane wave. Thus, the states are taken more or less randomly from all parts of the Fermi surface, thereby removing this source of anisotropy in the energy gap.

The experimental data on Al–Zn alloys are shown in Figure 3. The data on the 0.036 at% Zn alloy agree well with theory, assuming $r(T) = 40\epsilon_0(0)/\epsilon_0(T)$ and using the same energy gap $2\epsilon_0(0) = 3.2k_BT_c$ as that used in pure bulk aluminum (solid line). Data on the 0.055 at% Zn alloy show that a numerical factor in $r(T)$ increases from 40 to 60 but the energy gap remains the same. Roughly speaking, the increase of the numerical factor is proportional to the inverse mean free path $1/l$.

As we add impurities, the individual momentum states are scattered around the Fermi surface. Therefore, the angular dependence of the energy gap is removed from the individual excitation energy gap. If Δ represents an anisotropy of the energy gap present in pure aluminum, Δ decreases (or r increases) as the impurity concentration increases. For sufficiently small concentrations of impurities, the experimental data indicate that r increases linearly with increasing reciprocal mean free path. This apparent linear increase of r with l^{-1}

may be fortuitous, since the accuracy of the present determination of r is poor. Presumably the quantity r^{-1} is a measure of the anisotropy.

Data on a 0.16 at% Ge alloy indicate that the width of the energy gap will be close to the value predicted by BCS theory in the case of constant interaction. Once the mixing is complete, the effect on superconductivity should saturate. If we could measure T_1 in very impure samples without quadrupolar effects, the saturation value of r might be observed. But, as T_1 is proportional to log r for $T \ll T_c$, it would be hard to determine r correctly.

The theory of energy gap anisotropy in dirty superconductors was given by Clem.[14] The gap parameter in the direction θ can be defined as

$$\epsilon_0(\theta) = \langle\epsilon_0\rangle[1 + a(\theta)] \tag{11}$$

where $a(\theta)$ is the anisotropy function which describes the variation of the gap over the Fermi surface due to anisotropy in the phonon spectrum or the band structure, and $\langle a(\theta)\rangle = 0$. The density of excited states is calculated as a function of the impurity scattering mean free path, or specifically of the 'dirtiness' parameter

$$y_D = [2\epsilon_0(0)\tau]^{-1} = 1.57\xi_0/l \tag{12}$$

where τ^{-1} is the mean frequency of scattering processes and ξ_0 the coherence length. In the dirty limit, $y_D \gg 1$, the density of states approaches the singular BCS form, and by making use of the mean square anisotropy $\langle a^2\rangle$, becomes a universal function of the parameter $\eta_s = y_D/\langle a^2\rangle$. The anisotropy-induced structure in the density of states will disappear in the dirty limit.

3.3 Size Effect: Fluctuations in the Order Parameter

Measurements of the Knight shift in superconductors must, of necessity, be made on samples that are small compared with the penetration depth in order that variations in the Knight shift will not be confused with the shift due to the Meissner effect. In contrast to the Knight shift, measurements of T_1 are in good agreement with the BCS theory; these measurements have been made on 'bulk' samples, that is, powders with individual particles that are large compared with the coherence length. In view of the disagreement between the Knight shift measurements and the BCS theory, it seemed interesting to see if there is an anomaly in the relaxation time as well, when the particle size becomes small compared with the coherence length or the penetration depth. This was the motivation for performing experiments on the size effect.[15] However, the experimental results obtained surpassed our expectations and suggested an important and interesting fact of superconductivity, which is yet to be theoretically understood.

Particles of aluminum having diameters of less than 2000 Å were prepared by vaporizing aluminum in an atmosphere of argon at a pressure of a few hectopascals. Then the relaxation time T_1 was measured by using the field cycling method in the normal and superconducting states between 0.36 and 1.3 K. In the normal state, and near T_c, the relaxation time was nearly the same as for bulk aluminum, which is evidence that the particles are indeed metallic.

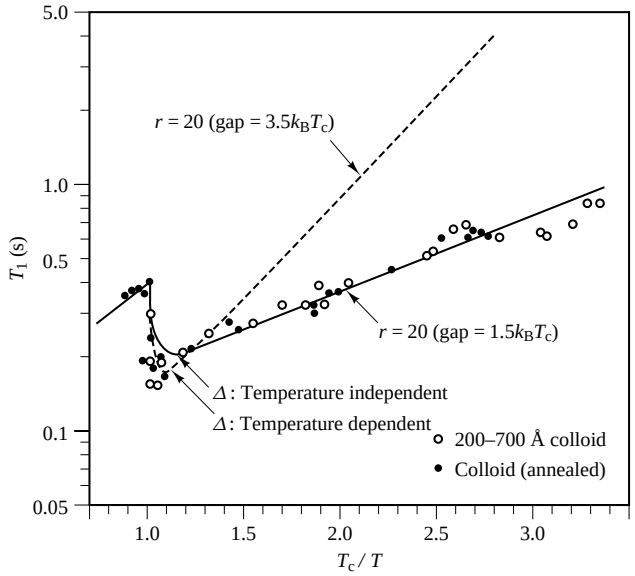

Figure 4 Measured relaxation times T_1 in pure aluminum colloid, the diameter of which ranges from 200 to 700 Å[15]

Typical T_1 results for the sample with the most uniform particle size distribution (200–700 Å) are shown in Figure 4.[15] The relatively small change in T_1 in the normal state, compared with the bulk sample, may be the result of an imperfection-induced quadrupole interaction. However, such a change was not observed when small amounts of impurities were added to bulk samples, so the change may be a true size effect.

Kubo[16] discussed the specific heat and spin susceptibility of small particles, but probably his conclusions did not apply to particles as large as those used here. It is interesting to note that the electronic level spacing in the particles is large compared with $\hbar/T_1$, in violation of the condition for the validity of time-dependent perturbation theory. This difficulty can probably be ignored since the electronic levels are broadened by interaction with lattice vibrations, so that the system, electrons plus lattice, has a higher density of states than the electrons alone.

Turning to the superconducting state, the zero field measurements can be fitted to a theoretical curve according to the procedures applied to the bulk metal described before. Well below T_c, the zero field relaxation time is shorter than that of bulk aluminum, being less than one-fifth the bulk value at 0.4 K, and indicates a gap of the order of one-half the BCS value. Thus, an important size-dependence of T_1 was found, but these results could not be explained in a satisfactory way at that time, and were forgotten. About 10 years later, this relaxation behavior was explained by considering the effects of fluctuations of the order parameter in small specimens. The first observation, made in 1967,[17] attributed to fluctuations, was an increase in conductivity just above T_c in thin films. A theoretical explanation of the observation was given in 1968.[18] A reduction in the size of specimens should increase the effect of fluctuations in the order parameter. Therefore, the most suitable specimens for the observation of the size effect are small isolated particles.

Maki et al.[19] first considered the effect of fluctuations on nuclear spin–lattice relaxation in superconductors in the mean field regime. They found an expression for the relaxation rate

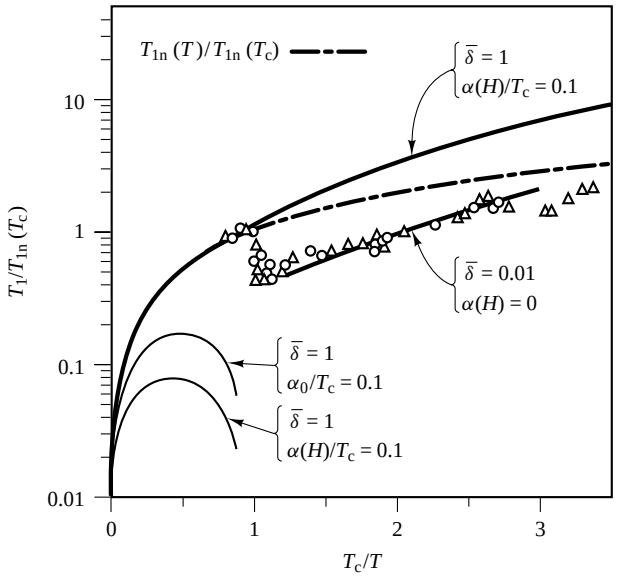

Figure 5 Reduced relaxation time $T_1/T_{1n}(T_c)$ as a function of inverse reduced temperature, reduced pair-breaking parameter α/T_c, and particle size parameter $\bar{\delta}$. Light solid curves: unrenormalized theory of Maki et al.[19] Heavy solid curves: renormalized dirty-limit theory of Simánek et al.[21] Open circles and triangles: experimental results of Masuda and Redfield (annealed and unannealed aluminum colloids, respectively. The diameter ranges from 200 to 700 Å)[15]

above T_c in the presence of fluctuations given by,

$$R_s/R_n = 1 + [\pi T_c/4N(0)v\alpha(H)(T - T_c)] \qquad (13)$$

where v is the particle volume and $\alpha(H)$ a pair-breaking parameter. Pair-breaking may be due to paramagnetic impurities, an applied magnetic field, or, in the absence of external perturbations, the small, spatial variation of the order parameter near the particle surface. According to equation (13), the relaxation rate diverges as $(T - T_c)^{-1}$ at $T = T_c$ as shown in Figure 5. This divergence is removed by allowing the normal electrons to be dressed with fluctuation-induced Cooper pairs. Using this picture, the spin–lattice relaxation rate was calculated.[20] The effect of renormalization of the normal electrons by fluctuations extended over a much wider temperature range than interactions between fluctuations themselves. Thus, the divergent behavior was removed.

The temperature dependence of R_s shows a smooth behavior in the region of T_c for all values of v and $\alpha(H)$. The size parameter is defined as $\bar{\delta} = 1/N(0)\, vT_c$. For small $\bar{\delta}$ a characteristic peak is obtained in the relaxation rate just below T_c. As $\bar{\delta}$ is increased, this peak is smeared out, and the rate decreases monotonically with decreasing temperature for $\bar{\delta} \lesssim 1$. For $\alpha(H) \neq 0$, the position of the peak is depressed to lower temperatures if $\bar{\delta} \ll 1$, and for $\bar{\delta} \lesssim 1$ the effect of additional pair breaking is a small increase in R_s. These results are shown in Figure 5.[21]

This theory is not appropriate for very small particles ($\bar{\delta} \gtrsim 1$), since here the level quantization imposed by the boundary conditions on the electronic wavefunctions at the particle surfaces splits the electronic energy levels by an amount comparable to T_c. This effect is important for Al and Sn particles of less than 50 Å in diameter.[22,23] The theory, in which the combined effect of fluctuations and level quantization are taken into account, is quite complicated.[24]

4 NMR IN TYPE-II SUPERCONDUCTORS

4.1 Magnetic Field Distribution in the Mixed State

A change in NMR properties in the mixed state is caused by the penetration of a magnetic field into a type-II superconductor by means of a periodic lattice of fluxoids, or vortices. Conventional NMR studies of the field distribution are difficult because of the large resonance linewidths, baseline drift, and noise due to vortex motion. To avoid these difficulties the same field cycling method as that used in superconducting aluminum was used. This method has the advantage that the signal can be observed in the normal state with less noise and baseline drift.[25] In the case of type-II superconductors the magnetic field was not reduced to zero but switched to a value below H_{c2} during a time τ which was fixed at about 0.1 s. During the time τ a transverse rf field $H_p \cos(2\pi\nu_p t)$, the probe field, was applied perpendicular to $\boldsymbol{H}_e$. In order to measure the effect of the probe field, the decrease in this subsequent signal reflecting the NMR absorption was measured as a function of the probe frequency ν_p. Typical subsequent signals are shown in Figure 6.

The original calculation on the vortex lattice structure performed by Abrikosov assumed a square lattice. The first direct evidence for the vortex lattice was a neutron diffraction experiment and it was concluded that the lattice must be

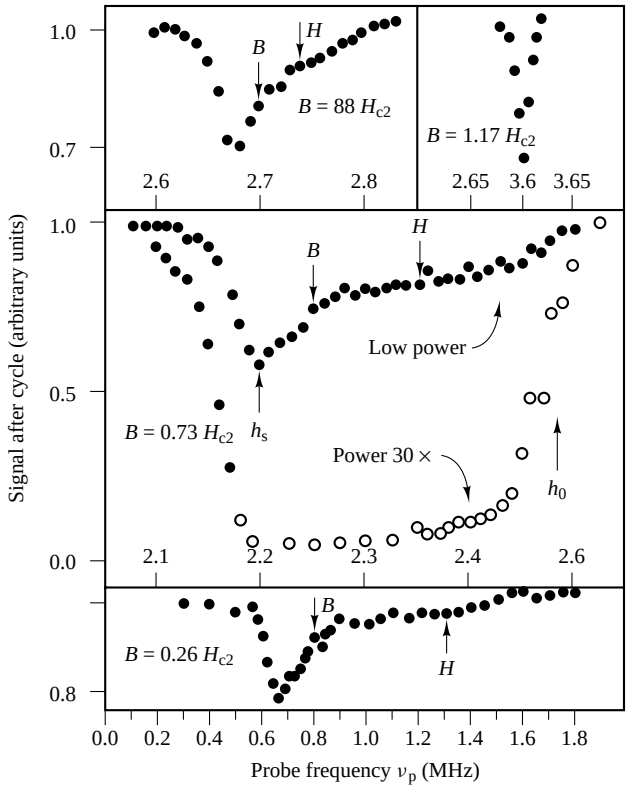

Figure 6 Raw lineshape data at various fields and power levels in type-II superconducting vanadium[25]

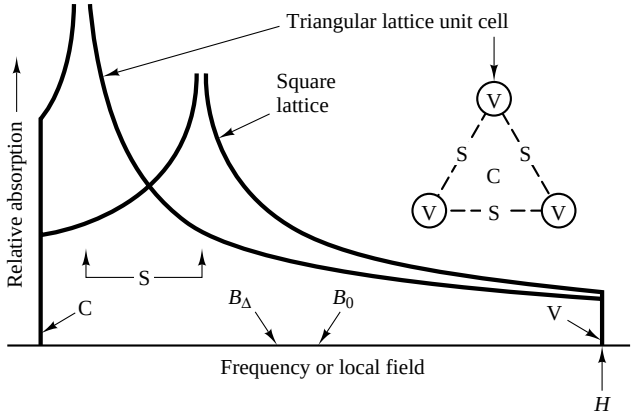

Figure 7 Theoretical resonance lineshapes.[25] The inset shows a unit cell of the triangular vortex lattice, showing points of maximum field (V), minimum field (C), and the saddle point (S)

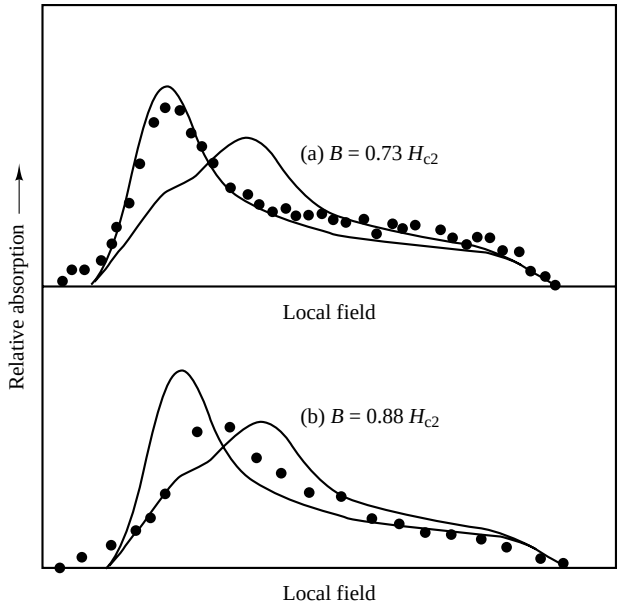

Figure 8 Comparison between theoretical lineshapes obtained by smearing the shapes of Figure 7, with the absorption lineshape deduced from the data of Figure 6[25]

triangular. The first calculation of the NMR lineshape was performed for a square fluxoid lattice and appeared to conflict with the NMR data. The theoretical resonance lineshapes for the triangular and square lattice are shown in Figure 7. The calculation was performed on the basis of a solution to the Ginzburg–Landau equation in the Abrikosov limit. The difference between the positions of the singularity for the square and triangular lattice is a general result of geometry plus the assumption that field and current cannot vary in space over a coherence length. The inset shows a unit cell of the triangular vortex lattice, showing points of maximum field (V), minimum field (C) and the saddle point (S). For the square lattice, the saddle point in real space is equidistant from the nearest vortex and the nearest minimum point. For the triangular lattice, in real space, the saddle–vortex distance (S–V) is $\sqrt{3}$ times greater than the saddle–minimum distance (S–M). Thus the saddle point field also tends to be closer to the minimum field, an effect that is much greater than the real space distance ratio suggests, because the field and current must vary smoothly in space.

The theoretical lineshapes in Figure 7 were convoluted with a Gaussian function to smear out the lineshapes by about 10%, in order to agree with the width of the end of the line at high field, and then normalized to obtain good agreement with experiment for the triangular lattice, as shown in Figure 8. The experimental points are proportional to $-\ln \{[S(H_p) - S(\infty)]/[S(0) - S(\infty)]\}$, where $S(H_p)$ is the signal observed when the probe field equals H_p, $S(0)$ is that with no probe field, and $S(\infty)$ is the signal at very high probe power, which is mostly due to repolarization of the spin system during the time the field is turned on, just before observation, at 0.6 T. If one makes a simple spin-temperature assumption about the rate of energy absorption, then one concludes that this transformation of the data should give the absorption lineshape that would be observed in conventional NMR. The excellent agreement between these points and the triangular lineshape should not be taken too seriously, since there were three parameters varied to fit the data (width, height, smearing), but it would not be possible to change these parameters to get nearly as good agreement with the square lattice curve. Closer to H_{c2} it would be harder to make this distinction. For very low magnetic field, however, one has essentially an array of nearly isolated vortices, and the peak is expected to move toward the lower end of the line for any arrangement.

Similar work using a standard continuous-absorption technique was performed by Delrieu and Winter.[26] They observed the ^{73}Nb resonance in superconducting niobium near H_{c2}, directly, and found a field distribution with the singularity near the minimum field value, as predicted for the triangular lattice, which agrees well with the conclusion by Redfield.

4.2 Nuclear Magnetic Relaxation in Type-II Superconductors

The nuclear spin–lattice relaxation time, T_1, in a type-I superconductor in zero magnetic field is determined mainly by the high density of states above the energy gap. For a type-II superconductor, the energy dependence of the density of states in the mixed state slightly below the upper critical field H_{c2} differs considerably from that in the BCS state. In the Abrikosov description of type-II superconductors in the mixed state, an external magnetic field penetrates into the specimen as quantized flux, called fluxoids or vortices. In the region of a fluxoid, the order parameter is appreciably reduced from its zero field value, approaching zero at the flux center. This reduction in the order parameter may be reflected in the density of states near the Fermi surface and hence the behavior of the nuclear spin relaxation rate.

Measurements of T_1 in a type-II superconductor were expected to add information to the picture of the mixed state. In earlier studies in the mixed state, most T_1 measurements were made far below H_{c2} and T_c.[27] This situation corresponds to the case of well-separated vortices. In the absence of vortex motion and spin diffusion, the nuclear spins located far from vortex lines certainly see quasiparticle excitation in a superconductor, and at low temperatures will show BCS behavior. Spins within the coherence length ξ_0 of a vortex

line relax rapidly with a rate comparable to the normal state value. When both spins contribute significantly to the signal, nonexponential decays will be observed. Experiments on Nb–Zr alloys indicate that the slow decay component of the signal, which is attributed to the spins located far from vortices, shows BCS behavior. In this case, the spatial fluctuations of the energy gap are considered to be localized near the flux center and most of the sample has an energy gap which is essentially equal to that in zero external field. As the temperature decreases T_1 begins to deviate from the BCS value appreciably. The field-dependent deviation from the BCS theory was attributed to a relaxation mechanism involving spin diffusion to the vortex cores. In the subcritical region slightly below H_{c2}, the distance between vortices becomes comparable to the coherence length ξ_0. In this region, the order parameter $\epsilon_0(r)$ is small and a gapless excitation spectrum is expected to appear. It is therefore likely that the nuclear relaxation in this region will show interesting features.

The T_1 of ^{51}V in an intermetallic compound V_3Sn was measured by pulsed NMR in the temperature range 1.2–77 K.[28] The measurements were carried out at the center of the resonance from 0.4470 to 1.3410 T for frequencies of 5, 10, and 15 MHz. The Korringa relationship T_1T = 420 ms·K was well fitted by the experimental points taken in the normal state over the temperature range 1.8–77 K for a magnetic field of 1.3410 T. At the critical temperature corresponding to this field (1.8 K), T_1 showed no minimum as the temperature decreased but it increased monotonically compared with the Korringa time.

The experimental results in the range 1.2–4.2 K are shown in Figure 9 in the form of the ratio R_s/R_n as a function of $T/T_c(H)$, at a fixed magnetic field. $T_c(H)$ is the critical temperature corresponding to the resonance field H. As can be seen from Figure 9 in the case of $T_c(0) > T_c(\boldsymbol{H}) > 0.6T_c(0)$, a maximum in $R_s(T)/R_n(T)$ appears at $T/T_c(\boldsymbol{H})$ = 0.9 in both cases of 0.4470 and 0.8940 T, but the magnitude of this maximum is dependent on the applied field strength. However, in the case of $T_c(\boldsymbol{H}) < 0.6T_c(0)$, $R_s(T)/R_n(T)$ shows no maximum as the temperature decreases, but it decreases exponentially. This effect of magnetic field on the relaxation behavior suggests that a pair-breaking mechanism due to magnetic field enters into the coherence factor.

Griffin and Ambegaokar[29] have extended the calculation of the nuclear spin relaxation rate to a superconductor in the presence of magnetic impurities. The conclusion that the coherence factor is due to the nature of the magnetic hyperfine coupling between the electrons and the nuclear spins is important. The superconductor containing magnetic impurities is a perfect diamagnet in an external magnetic field even in the gapless region. The fundamental property of superconductivity is thus the existence of a pair correlation rather than that of an energy gap. The most important effect of superconductivity appears only through the coherence factors. It is known that paramagnetic impurities and magnetic fields have similar effects on many physical quantities in superconductors. In these two situations the coherence factors are equivalent. This equivalence is established only for the second-order term in $\epsilon_0(r)$ and significant deviations are expected to arise in the fourth order terms. The depairing by the magnetic field or by impurities enters into the coherence factors and these pair-breaking mechanisms are equivalent in both cases. Starting

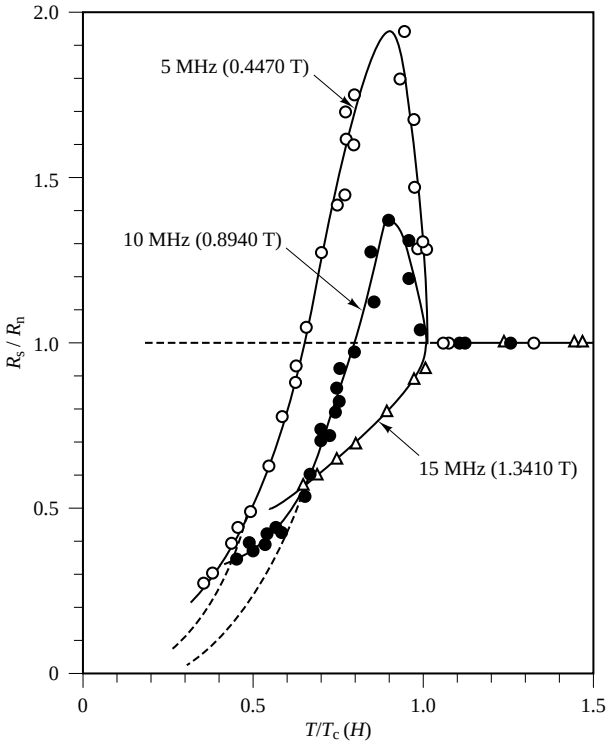

Figure 9 Reduced ^{51}V relaxation rate in the superconducting mixed state of V_3Sn. The relaxation rate for a magnetic field of 1.3410 T decreases monotonically with temperature[28]

from this point of view, Maki and Fulde[30] obtained the results equivalent to those derived by Griffin and Ambegaokar.[29]

The ratio of the nuclear spin relaxation rates in a dirty type-II superconductor in the gapless region to those in the normal state were obtained by Cyrot[31] using a perturbation calculation in powers of $\epsilon_0(r)$. He obtained the following result,

$$\frac{R_s}{R_n} = 1 + \frac{\langle|\epsilon_0(r)|^2\rangle}{2(2\pi k_B T)^2}[\rho^{-1}\phi^{(1)}(\tfrac{1}{2}+\rho) + 3\phi^{(2)}(\tfrac{1}{2}+\rho)] \quad (14)$$

where $\rho = D_e H/(2\pi k_B T)$, D is the diffusion coefficient, and $\phi^n(\rho)$ is the nth derivative of the digamma function. If we substitute the expression for $\langle|\epsilon_0|^2\rangle$, following Abrikosov, equation (14) in the case of spherical samples can be represented as follows:

$$\frac{R_s}{R_n} = 1 + \frac{ec}{8\pi^2\sigma k_B T_c(0)} - \frac{H_{c2} - H}{[2\kappa_2^2(t) - 1]\beta_A + \frac{1}{3}}C(t) \quad (15)$$

where σ is the normal state conductivity, c the velocity of light, $\kappa_2(t)$ the temperature-dependent parameter which appears in the expression for the magnetization, β_A = 1.16, and $C(t)$ is a dimensionless function of reduced temperature $t = T/T_c(0)$ given by

$$C(t) = (\rho t)^{-1}\left[1 + 3\rho\frac{\phi^{(2)}\left(\frac{1}{2}+\rho\right)}{\phi^{(1)}\left(\frac{1}{2}+\rho\right)}\right] \quad (16)$$

The temperature dependence of $C(t)$ was numerically calculated, and depicted in Figure 10. In the range of t = 0 to 0.6, $C(t)$ has a negative value and crosses zero at t = 0.6. As the

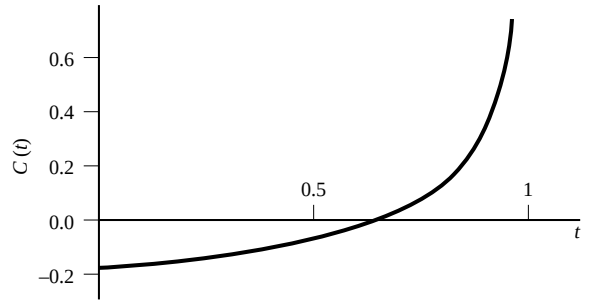

Figure 10 Dependence of the universal function $C(t)$ on the reduced temperature $t=T/T_c$. The gradient dR_s/dH of the relaxation rate at H_{c2} is proportional to $C(t)$ in the mixed state of dirty type-II superconductors[31]

temperature increases above $t = 0.6$, $C(t)$ becomes positive, and then diverges near $T_c(0)$.

As can be understood from equation (16), in the range of $H_{c2} - H \ll H_{c2}$ and for temperatures close to $T_c(H)$, the relaxation rate in the superconducting state is larger than that in the normal state. For temperatures far below $T_c(H)$, the relaxation rate in the superconducting state becomes smaller than R_n. At $0.6T_c(0)$ both rates have the same value. This behavior agrees with the experimental result that at about $T = 0.6T_c(0)$ the slope of the relaxation rate passes through zero.

The theoretical prediction of the initial slope of the relaxation rate at $T_c(H)$ for the magnetic field, in which the relaxation rate is measured, is given by the following equation:

$$\frac{1}{R_n}\frac{\partial R_s}{\partial T}\bigg|_{T=T_c(H)} = \frac{ec}{8\pi^2\sigma k_B T_c(0)} \frac{\left.\dfrac{\partial H_{c2}(T)}{\partial T}\right|_{T=T_c(H)}}{[2\kappa_2^2(t)-1]\beta_A + \frac{1}{3}} C(t) \quad (17)$$

The calculated result described above agrees with experiment quite well at low temperatures. However, a deviation appears near $T_c(0)$. One of the reasons for this deviation may be the broadening of the BCS state due to energy gap anisotropy.

4.3 Magnetic Impurity Effects in Type-II Superconductors

Magnetic impurity effects, studied by NMR in metals and alloys, give much information about the electronic states of conduction electrons. In normal metals and alloys, various paramagnetic impurity-induced relaxation mechanisms exist, in addition to the usual Korringa process. They are the relaxation due to the fluctuating local dipole fields associated with the longitudinal and transverse fluctuations of the localized magnetic impurity dipole moment (the LD and TD mechanisms); and the indirect Rudermann–Kittel–Kasuya–Yosida coupling between the localized magnetic impurity moment and nuclear spins via conduction-electron systems. The latter relaxation mechanism is associated with the real or virtual excitation of the localized magnetic impurity moment (the RE and VE mechanisms), respectively.

Superconductivity is strongly affected by the presence of magnetic impurities. The Korringa mechanism in superconductors has been investigated theoretically within the framework of the Abrikosov and Gor'kov (AG's) depairing theory by Griffin and Ambegaokar.[29] The LD, TD, RE and VE mechanisms also play an important role in the superconducting state.[32]

According to the observed macroscopic properties, Gd impurity possesses a well-defined spin and affects the superconducting properties in the way expected by the AG theory. Cerium impurity, however, shows the anomalies associated with the Kondo effect. In particular it seems very interesting to investigate microscopically by NMR the differences of the pair-breaking effects between the Gd and Ce impurities.

The relaxation rate R_s in a Kondo superconductor has been calculated numerically in the framework of the Müller–Hartmann–Zittartz depairing theory.[33] The theoretical temperature variation of R_s is expected to show very interesting behavior, corresponding to the reentrance behavior of superconductivity.

The host ^{27}Al nuclear spin–lattice relaxation in the normal and superconducting states of the $(La_{1-n}Gd_n)_3Al$ and $(La_{1-n}Ce_n)_3Al$ systems has been studied in detail.[34] The conclusions obtained are: (1) the impurity-induced relaxation rates play an important role in ^{27}Al relaxation and can be well interpreted by the LD mechanism for both the Gd and Ce doped systems; (2) the measured relaxation rates show large enhancement in the superconducting state. This seems to arise from the change of the impurity spin relaxation time. Quantitative analysis shows that the impurity spin dynamics is determined by the relaxation mechanism arising from the s–f exchange interaction between impurity spin and conduction electrons even in the superconducting state; and (3) in the vicinity of the transition temperature the observed temperature variation of T_1 seems to show a large discrepancy in comparison with the prediction of the impurity pair-breaking theory both in the Gd and Ce doped systems.

5 RELATED ARTICLES

Electron–Nuclear Hyperfine Interactions; Field Cycling Experiments; Knight Shift; Metals: Pure and Alloyed; Relaxation Theory: Density Matrix Formulation.

6 REFERENCES

1. L. C. Hebel and C. P. Slichter, *Phys. Rev.*, 1959, **113**, 1504.
2. J. Bardeen, L. N. Cooper, and J. N. Schrieffer, *Phys. Rev.*, 1957, **108**, 1175.
3. F. Reif, *Phys. Rev.*, 1956, **102**, 1417; 1957, **106**, 208.
4. G. M. Androes and W. D. Knight, *Phys. Rev.*, 1961, **121**, 779.
5. A. G. Redfield, *Phys. Rev. Lett.*, 1959, **3**, 85.
6. Y. Masuda and A. G. Redfield, *Phys. Rev.*, 1962, **125**, 159.
7. D. E. MacLaughlin, *Solid State Phys.*, 1976, **31**, 1.
8. K. Yosida, *Phys. Rev.*, 1958, **110**, 769.
9. R. H. Hammond and G. M. Kelly, *Rev. Mod. Phys.*, 1964, **36**, 185.
10. H. L. Fine, M. Lipsicas, and M. Strongin, *Phys. Lett.*, 1969, **29A**, 366.
11. Y. Masuda, *IBM J. Res. Dev.*, 1962, **6**, 24.
12. Y. Masuda, *Phys. Rev.*, 1962, **126**, 1271.
13. P. W. Anderson, *J. Phys. Chem. Solids*, 1959, **11**, 26.
14. J. R. Clem, *Phys. Rev.*, 1966, **143**, 392; *Ann. Phys. (N.Y.)*, 1966, **40**, 268.
15. Y. Masuda and A. G. Redfield, *Phys. Rev. A*, 1964, **133**, 944.
16. R. Kubo, *J. Phys. Soc. Jpn.*, 1962, **17**, 975.

17. R. E. Glover, *Phys. Lett.*, 1967, **25A**, 542.
18. L. G. Aslamazov and A. I. Larkin, *Phys. Lett.*, 1968, **26A**, 238.
19. K. Maki, J. P. Hurault, and M. T. Beal-Monod, *Phys. Lett.*, 1970, **31A**, 526; J. P. Hurault, K. Maki, and M. T. Beal-Monod, *Phys. Rev. B*, 1971, **3**, 752.
20. E. Simánek, D. E. MacLaughlin, and D. Imbro, *Phys. Lett.*, 1973, **42A**, 357.
21. E. Simánek, D. Imbro, and D. E. MacLaughlin, *J. Low Temp. Phys.*, 1973, **11**, 787.
22. S. Kobayashi, T. Takahashi, and W. Sasaki, *J. Phys. Soc. Jpn.*, 1971, **31**, 1442.
23. S. Kobayashi, T. Takahashi, and W. Sasaki, *J. Phys. Soc. Jpn.*, 1974, **36**, 714; 1975, **38**, 599.
24. J. Sone, *J. Low Temp. Phys.*, 1976, **23**, 699; 1983, **50**, 559.
25. A. G. Redfield, *Phys. Rev.*, 1967, **162**, 367.
26. J. M. Delrieu and J. M. Winter, *Solid State Commun.*, 1966, **4**, 545.
27. K. Asayama and Y. Masuda, *J. Phys. Soc. Jpn.*, 1965, **29**, 1290; 1969, **26**, 206.
28. Y. Masuda and N. Okubo, *Phys. Rev. Lett.*, 1968, **20**, 1475; *J. Phys. Soc. Jpn.*, 1969, **26**, 309.
29. A. Griffin and V. Ambegaokar: *Proc. 9th Int. Conf. on Low Temperature Physics, Columbus, OH, 1964*, Plenum, New York, 1965, p. 542.
30. K. Maki and P. Fulde, *Phys. Rev. A*, 1965, **140**, 1586; *Solid State Commun.*, 1967, **5**, 21.
31. P. M. Cyrot, *J. Phys. (Paris)*, 1966, **27**, 283.
32. K. Matsui and Y. Masuda, *J. Phys. Soc. Jpn.*, 1977, **43**, 437.
33. K. Matsui and Y. Masuda, *J. Low Temp. Phys.*, 1978, **31**, 101.
34. K. Matsui and Y. Masuda, *J. Phys. Soc. Jpn.*, 1977, **43**, 1169.

Biographical Sketch

Yoshika Masuda. *b* 1922. B.Sc., 1949; D.Sc., 1958, Osaka University. Member of the Physical Society of Japan and Fellow of the American Physical Society. Constructed NMR Laboratories at Kobe University, 1953–65. Fulbright and Q. W. Boese Fellow at Columbia University, and worked with A. G. Redfield at the IBM Watson Laboratories at Columbia University, 1959–61. Established ULT Physics Laboratories in Nagoya University, 1965–85. Emeritus Professor at Nagoya University, 1985. Professor at Aichi Gakuin University, 1985–present. Approx. 200 publications. Research interests include theory and experiment on quantum solids.

Adsorbed Species: Spectroscopy and Dynamics

Ian D. Gay
Department of Chemistry, Simon Fraser University, Burnaby, B.C., Canada

1	Introduction	1
2	Early Results	2
3	Multinuclear Magnetic Resonance	2
4	High-Resolution Solid State Techniques	3
5	Adsorbates on Metals	3
6	Adsorption Probes of Surface Sites	3
7	Surface Hydroxyl Groups	4
8	Chemical Reaction in Adsorbed Layers	4
9	Structure of Adsorbed Species	4
10	Motion in Adsorbed Layers	4
11	Related Articles	5
12	References	5

1 INTRODUCTION

The term 'adsorbed' implies concentrated at an interface. This article deals with the NMR of small molecules adsorbed, i.e. bound, to solid sufaces. (For a general introduction to adsorption and the properties of surfaces, see Adamson[1] or Somorjai.[2]) In addition to being of intrinsic scientific interest, adsorbed layers are of great practical importance in the areas of heterogeneous catalysis, separation science, and chromatography.

Molecules may bind to surfaces by any type of interaction, ranging from chemical bonding to van der Waals interaction. The case of chemical bonding is often called 'chemisorption', while the term 'physisorption' is sometimes used for weaker interactions. An adsorbed layer one molecule thick is called a 'monolayer' and thicker adsorbed deposits are called 'multilayers'. Clearly temperature is a major factor in determining the extent of adsorption, and appreciable adsorption will only be found when the interaction energy is greater in magnitude than *kT*.

NMR is the least sensitive of the common spectroscopic techniques, and thus the observation of adsorbed monolayers is dependent upon having a large amount of surface area in the NMR sample. The surfaces of highest specific area are those of activated carbon, and refractory oxides such as SiO_2 and Al_2O_3. Because of their great importance as adsorbents, catalysts, and catalyst supports, the preparation of these has been much studied.[3,4] These substances are readily prepared with specific surface areas of the order of hundreds of square meters per gram ($m^2\ g^{-1}$). Their densities as powders are typically about $1\ g\ cm^{-3}$, so an NMR sample may contain hundreds of $m^2\ cm^{-3}$. A monolayer of moderate sized molecules might contain 5 μmol m^{-2}, so that the bulk concentration of an adsorbed monolayer can be of the order of 0.5 M. Such concentrations of sensitive high-abundance nuclei, e.g. ^1H, ^{19}F, and ^{31}P, can be observed in a single scan with modern instrumentation. Those familiar with liquid NMR will find the effective sensitivity for adsorbed species to be considerably less, due to the much broader lines which arise for reasons noted below. None the less, high sensitivity nuclei are easily observed on such solids, and more difficult nuclei such as natural abundance ^{13}C can typically be observed in thousands or tens of thousands of scans. Often spin–lattice relaxation times for adsorbed molecules are appreciably shorter than for the same molecules in the liquid phase. This can make the signal averaging of large numbers of scans more feasible than might have been expected.

Another family of high area solids is the zeolites,[5] crystals with internal pores of molecular size. The interior of these pores is equivalent to a high surface area, again typically of the order of hundreds of $m^2\ g^{-1}$. Whether guest molecules inhabiting these pores can be said to be adsorbed is a matter of semantic convention. In this article the NMR of such guest molecules will be only briefly touched upon.

A large number of substances can be prepared in the $10\ m^2\ g^{-1}$ range, and almost any solid can be prepared with $1\ m^2\ g^{-1}$. Whether a high area preparation is stable with respect to loss of area by sintering depends mainly on the temperature. Typically the temperature must be kept below about one-half of the melting point to prevent substantial loss of area. A system of great practical interest is the supported metal catalyst.[6] These catalysts consist of metal crystallites dispersed on a refractory oxide, such as silica or alumina. This technique permits a very high dispersion of the metal, with reduced tendency to sinter, and makes the most effective use of expensive platinum group metals. While the metal dispersion is extremely high, such catalysts typically contain a few per cent of metal by mass and have metal areas of 1 to $10\ m^2\ g^{-1}$ of catalyst. Monolayers of high sensitivity nuclei are straightforward even at $1\ m^2\ g^{-1}$; however, if one wishes to explore nuclei of low sensitivity, or small fractions of a monolayer, severe sensitivity problems eventually arise. One possible approach to this problem is to use the Curie law enhancement of NMR sensitivity at extremely low temperatures in the millikelvin range.[7]

In general, the preparation of high-area solids will result in an aggregate of randomly oriented crystallites. Some preparations, e.g. silica gels, will lack long-range order entirely. In a few favorable cases, high-area oriented samples can be prepared, e.g. in the case of lamellar clay particles by sedimentation.[8]

If one imagines a surface prepared by the sudden cleavage of a solid, it is evident that the surface may be viewed as a macroscopic radical with large numbers of 'dangling bonds', resulting from the disruption of the chemical bonds responsible for the integrity of the solid. Such a surface will be a very reactive entity and will be subject to structural rearrangement, which can lower its free energy, and to chemical reaction with its environment. Thus all metal surfaces (with the possible exception of Au) that have been in contact with the atmosphere will be covered by a layer of oxide. This layer may be a monolayer, or may be many layers thick. Similarly, oxide surfaces that have been exposed to the atmosphere normally have a monolayer of –OH groups, resulting from their reaction with H_2O. This surface OH may be regarded either as the result of chemisorption of H_2O or as a normal constituent of oxide surface.

A 'clean' surface is one whose properties approximate the idealized cleaved crystal, at least as regards chemical

composition. (Many clean surfaces undergo rearrangement of their atoms to positions different from the bulk crystal.[2]) Clean surfaces are of much interest in fundamental surface science studies. In general, really clean surfaces are achieved only under ultrahigh vacuum conditions on areas of the order of 1 cm^2; adsorption on such surfaces is inaccessible to conventional NMR study at the present time. A possible exception to this statement is scattering experiments involving polarized atomic beams,[9,10] which can yield nuclear relaxation data and possibly other NMR-like parameters. For the most part, however, present NMR studies involve surfaces that are at best partially clean. Thus, surface oxide can be removed from the noble metals by H_2 reduction, followed by thermal desorption of the resulting adsorbed H; surface OH can be largely removed from oxide surfaces by thermal treatment under vacuum. While not too attractive from the point of view of fundamental studies, the surfaces studied by NMR can easily be kept in a state similar to those used in practical applications for adsorption and catalysis, and NMR has substantial contributions to make to these fields.

The main features of the NMR of any sample will be determined by the mobility of the molecules studied. In this context, adsorbed layers are somewhat intermediate between liquid and solid samples. For many strongly chemisorbed samples, the adsorbed species are held in place by strong chemical bonds and are solids for NMR purposes. However, strong bonding to the surface does not necessarily imply localized bonding. For example, H atoms bind to most metal surfaces with an energy in excess of 200 kJ mol^{-1}, but in the case of the platinum group metals at room temperature they are mobile parallel to the surface on the NMR timescale, and are in some sense a two-dimensional fluid. Rotational motion of adsorbed molecules is also common, but the presence of the surface is likely to introduce greater anisotropy in this motion than would be observed in a liquid. Weakly bound physisorbed molecules are typically in rapid exchange with the gas phase, and average NMR properties will be observed. For high-area solids it will usually be the case that the adsorbed population is much larger than the gas-phase population, so that properties like chemical shifts will be dominated by those of the adsorbed phase, while the rapid exchange ensures that the motional properties of the layer appear liquid-like, both translationally and rotationally.

2 EARLY RESULTS

Not surprisingly, the first NMR studies of adsorbed species involved proton NMR[11,12]. Since these predated high resolution solid state techniques, the possible experiments were broadline studies of immobile species, 'high-resolution' studies of mobile adsorbates, relaxation/linewidth measurements, and diffusion measurements by field gradient techniques. Examples of most of these exist from before 1960. For example, O'Reilly et al.[13] observed that surface OH on silica and silica–alumina is chemically shifted with respect to liquid H_2O, and inferred from the temperature-independent Lorentzian lineshape that the OH forms a dilute randomly populated dipolar coupled system. Hickmott and Selwood[14] studied the relaxation of water and several organics on various oxides, and showed the importance of surface paramagnetic species as relaxation agents. Fuschillo and Renton[15] studied the linewidth of methane on TiO_2 at low temperatures, and demonstrated the now well-known result that submonolayer amounts of physisorbed species do not become immobile until the temperature is well below the bulk freezing point.

In spite of these early successes, surface NMR in succeeding years proved somewhat disappointing. In general, very few chemical shifts proved to be measurable because of the large linewidths found for proton resonances. The sources of these linewidths were eventually realized to be rapid relaxation, especially by surface paramagnetic species, exchange with surface protons, heterogeneity of surface with respect to adsorption energetics, and inhomogeneous broadening from the nonzero magnetic susceptibility of irregular adsorbent particles; no proton linewidths less than 1 ppm were observed and much larger linewidths were common. Given the limited range of proton shifts, little of interest was shown regarding the structure and bonding of adsorbed molecules. Furthermore, with some notable exceptions,[16] it turned out to be difficult to obtain information regarding molecular motion from relaxation studies. This was largely because of the difficulties of disentangling different relaxation processes, and the often dominant effect of paramagnetic surface species, in the presence of which correlation times may be determined more by electron relaxation than by adsorbate motions. The results of this early period are well summarized in the reviews by Packer[17] and Pfeifer.[18] Diffusion measurements, particularly in the context of guest molecules in zeolites, have recently been reviewed by Kärger et al.[19]

3 MULTINUCLEAR MAGNETIC RESONANCE

More possibilities were opened by the increasing availability of multinuclear and Fourier transform NMR equipment beginning in the 1970s. If, as it turns out, lines from adsorbed species will be at least a few ppm in width, chemical shifts should be observable for nuclei whose shift range is of the order of hundreds of ppm or more. An extreme example of this is the observation[20] of an 80 ppm shift for Tl^+ adsorbed from H_2O onto silica. In a more practical vein, the early 1970s saw the first natural abundance ^{13}C spectra of molecules in zeolites[21] and physisorbed on silica[22]. Linewidths were a few ppm and it was possible to observe chemical shifts due, for example, to the hydrogen-bonding interaction of adsorbed acetone with surface hydroxyls. These works also demonstrated the possibility of measuring relaxation times separately for chemically different groups within a molecule. This could lead to simpler analysis of relaxation experiments for rigid molecules and the study of internal motions for others. In the early 1980s spectra were obtained for ^{15}N in a variety of molecules in zeolites[23] and adsorbed on SiO_2,[24] showing the advantages of studying the NMR of the atom which is the site of interaction between adsorbate and adsorbent. Relaxation studies of ^{17}O in H_2O on montmorillonite and kaolinite were performed.[25] These showed the desirability of measuring adsorbate correlation times in a system where strong quadrupolar interaction dominates the relaxation, and yielded surprisingly short correlation times for water in these systems, on the order of 10^{-11} s. Results to 1985 on multinuclear spectroscopy and relaxation measurements on adsorbed mobile molecules are comprehensively reviewed by Nagy, Engelhardt, and Michel.[26]

4 HIGH-RESOLUTION SOLID STATE TECHNIQUES

The advent of high-resolution solid state NMR techniques in the 1960s and 1970s opened up new possibilities for the study of adsorbate systems. The most obvious of these is the identification of immobile chemisorbed species. The first use of these techniques by Kaplan et al.[27] was however a CP study of physisorbed benzene and toluene at low temperatures. Observation of an axially symmetric CSA powder pattern showed that benzene undergoes rapid rotation about the hexad axis, even at 77 K. Further experiments demonstrated that rapid cooling can trap molecules in a metastable isotropically rotating state at this temperature.

Magic angle spinning was first applied to surface problems by Stejskal et al.[28] in their study of CO_2 in zeolites. This showed that substantial line broadening which may arise from microscopic susceptibility variations in the adsorbate can be removed by MAS. Use of MAS in surface problems suffers from the conflicting requirements of atmospheric integrity, best achieved with sealed samples, and of excellent mechanical balance, which is likely to be degraded by the sealing process. This conflict was resolved in a semisatisfactory way in 1984.[29]

The first use of multiple pulse line narrowing in surface studies was by Schreiber and Vaughan.[30] This permitted the measurement of the shielding anisotropy of surface protons on SiO_2; strong dipolar coupling to ^{27}Al prevented similar measurements on Al_2O_3. The combination of multiple pulse narrowing with MAS (CRAMPS), together with the use of higher magnetic fields, has recently been leading to growing success in the proton spectroscopy of adsorbed species.

5 ADSORBATES ON METALS

The resonance of hydrogen chemisorbed on platinum was first observed by Ito et al.[31] Subsequently, the resonance of hydrogen has been observed on Cu, W, Ru, Rh, Pd, Os, Ir, and a few alloys, by these and other workers. (In the case of W, the cleanliness of the surface is questionable.) For all of the metals, large shifts are observed which cannot reasonably be chemical shifts and must therefore be Knight shifts. For Cu the shift is to high frequency, for the others to low frequency. With Ru–Cu bimetallic clusters[32] the Knight shift of H on Ru decreases steadily as the Cu content is increased.

Platinum has been the most studied of these metals and it has been established that there is little difference between metallic powders and supported Pt catalysts. It has also been found that Knight shifts are smaller when the Pt particles are very small and when the adsorbed H covers a large fraction of the metal surface. As yet these trends have not received a satisfactory quantitative explanation in terms of the bonding between H and the metal surface. For all of the above metals the linewidth of the H resonance indicates that the hydrogen is mobile at room temperature. For those which have been studied to lower temperatures, motion generally ceases before liquid nitrogen temperature is reached.

^{13}C NMR of CO chemisorbed on a metal was first studied by Duncan et al. on Rh.[33] Since then it has been studied on the remaining noble metals, and on bimetallic Pt–Rh particles. Much of this work is described in the reviews by Slichter[34] and Duncan.[35] On Ru and Rh an average shift is observed that corresponds to the known shifts of metal carbonyl complexes. In static samples a broad powder pattern is observed with an anisotropy of some 400 ppm, corresponding to a linear carbonyl. On Rh, bridging carbonyl has also been observed. At room temperature, with the highest CO loadings, a narrow line appears from CO that is rotating isotropically on the NMR timescale. Thus the NMR of CO on Rh and Ru can be interpreted in terms of chemical shifts which are completely analogous to those observed in diamagnetic metal carbonyl complexes.

On the other hand, CO on supported Pt and Pd shows large high-frequency Knight shifts. Knight shifts are not observed for CO on colloidal platinum,[36] but it is not clear whether this is due to loss of metallic properties in the smaller particles or to interactions with the reagents used to stabilize the colloid. Supported Os and Ir show smaller high-frequency shifts and it is hard to be certain whether these are chemical or Knight shifts. Observations on Pt–Rh clusters[37] show that the Knight shift disappears above about 50% Rh, even though SEDOR measurements clearly show the presence of Pt in the surface layer of the particles.

The above results indicate that one must proceed with caution in interpreting the observed line positions of chemisorbed species on metals. For example, the metal (Rh) giving the largest Knight shift for adsorbed H gives no Knight shift for adsorbed CO. Thus in the absence of a reliable and comprehensive theory for Knight shifts of adsorbed species, every adsorption system must be examined carefully on its own merits.

6 ADSORPTION PROBES OF SURFACE SITES

The nature and concentration of specific types of site on solid surfaces has long been an area of interest, especially from the point of view of catalytic activity. These features can be probed spectroscopically by observing changes in the spectrum of a small molecule upon its binding to the surface. The archetypal example is the study of acid sites on oxide surfaces by IR spectroscopy of adsorbed amines;[38] pyridine, for example, gives distinct lines when physisorbed, protonated by a surface Brønsted acid, or coordinated to a surface Lewis acid.

This type of probing can obviously be done by NMR, which has the advantage that quantitative accuracy is in principle better. With IR spectroscopy it is generally difficult to be confident regarding the extinction coefficient of chemisorbed species, and there are often considerable uncertainties regarding path length and adsorbate concentration. Surface acids have thus been probed by direct proton NMR and by ^{13}C, ^{15}N, and ^{31}P NMR of adsorbed amines and phosphines. Such attempts have been generally successful and are complementary to IR studies. Much of the work in this area has been reviewed by Freude.[39]

Proton NMR cannot of course detect Lewis acids directly. For quantitative assessment of differing types of acid, ^{31}P spectroscopy seems the most desirable. The high sensitivity of this nucleus permits spectra to be obtained in reasonable time periods by 90° pulse excitation, avoiding the need for cross polarization which may compromise quantitative accuracy. Most results have so far been obtained with trimethylphosphine as a probe; studies of a wider range of phosphorus bases seem likely in the future.

Solid surfaces may also contain basic sites; indeed, the same surface may simultaneously contain both strong acid and strong base sites. Probing these surfaces by NMR is less well developed, but a few results are available. For example, ^{13}C spectroscopy has been used to demonstrate, through the formation of surface bicarbonate from CO_2, the unsurprising result that surface OH on MgO is basic.

7 SURFACE HYDROXYL GROUPS

As mentioned above, all oxides are covered with a layer of –OH groups, which may in a formal sense be regarded as the result of water chemisorption on an ideal oxide surface. The surface chemistry of oxides in their normal state is largely determined by the properties of these hydroxyl groups. The properties of these hydroxyl groups vary from one oxide to another, and the same oxide may show differing types of –OH groups, reflecting different exposed crystal planes, or different structural arrangements. Many of the classic NMR investigations[13,30] have dealt with these groups, and the literature of studies by IR spectroscopy is particularly voluminous. Much of the IR literauture and some of the NMR investigations have been reviewed by Morrow.[40] A recent review by Mastikhin et al.[41] is devoted to NMR studies, particularly of recent results obtained through magic angle spinning.

8 CHEMICAL REACTION IN ADSORBED LAYERS

Adsorbed layers are the site of heterogeneous catalysis and hence reaction in these layers is a topic of immense scientific, technical, and economic interest. NMR studies of such reactions may proceed in two rather different ways. For reasonably rapid reactions of systems that are in equilibrium under NMR conditions, the familiar methods of shift, relaxation, and lineshape analysis may be employed, as in solution NMR. The possibilities for this type of study of adsorbed systems have been reviewed by Resing.[42] On the other hand, slow reactions may easily be studied by recording NMR spectra as a function of time. A sealed NMR tube is in many ways an ideal contamination-free reactor. Reaction studies have been greatly advanced by CP MAS techniques, which permit the potential observation of a wide range of reaction products and intermediates.

For species reacting at a convenient rate at room temperature, e.g. the reaction of trimethyl phosphite with the silica surface,[43] straightforward MAS spectroscopy as a function of time can provide kinetic data for the surface reaction processes. For systems that are only reactive above room temperature, a ‘quick and dirty’ technique is to heat samples for controlled periods of time at the reaction temperature, and then cool to room temperature for NMR observation.[44] While this method provides useful insights, it suffers from uncontrolled conditions during the heating and cooling phases, together with uncertainties about desorption.

Clearly this type of study awaits the development of reliable high-temperature sealable MAS equipment, and recent progress has been made in this direction by Haw and coworkers.[45] Unfortunately, sealed-sample MAS is always open to uncertainties arising from the possibility of desorption when the sample is heated above its preparation temperature. There seems no obvious way of combining the traditional catalytic flow reactor with MAS NMR. For the case of static samples, an NMR-compatible flow reactor has been designed by Reimer and co-workers.[46]

9 STRUCTURE OF ADSORBED SPECIES

NMR of solids has the possibility of yielding direct structural information through measurement of dipolar interactions. Since the structures of chemisorbed species are in general not readily determined, this is a powerful possibility. The fundamental problem is that the motional state of observed species is not known a priori, and it will be unclear whether an observed dipolar coupling should be corrected for motional averaging. Thus, early observations of Pake doublets from adsorbed water[8] (see also bibliography in Pfeifer[18]) generally gave splittings much too small to correspond to static H_2O molecules. These results were therefore not used to infer structural information, but were instead interpreted to give motional information based on the assumption of the known structure of isolated water molecules. In a system where significant structural changes have occurred due to chemical reaction, it seems necessary to demonstrate that observed dipole couplings are independent of temperature, or to give some other evidence for lack of motion, before inferring structural parameters.

Duncan and Vaughan[47] were among the first to use modern solid state methods to determine dipolar couplings in adsorbed layers. Their H–C dipolar modulation studies of adsorbed formic acid gave essentially the same coupling as observed in crystalline formates. A deviation from the expected bond length based on X-ray measurements of calcium formate was attributed to motion, even though the couplings in the adsorbed layer appeared temperature independent.

More recently, Slichter and co-workers[34] have applied spin echoes and SEDOR to measure homonuclear and heteronuclear dipole couplings in adsorbed layers, and to attempt to measure the bond length between adsorbate and surface. The latter endeavor is complicated by the possibility, with heavy nuclei such as ^{195}Pt, of indirect (‘scalar’) couplings of magnitudes comparable to the dipolar couplings.

In principle, dipolar couplings could be estimated from relaxation or NOE measurements. In practice, the often dominant effects of surface paramagnetic impurities, and the general anisotropy of motion in adsorbed layers, render this a complicated and unattractive prospect.

A less direct way of obtaining structural information from dipolar couplings is by the observation of multiple quantum coherence, from which the size of coupled spin aggregations may be inferred. This was first applied to surface problems by Slichter and co-workers,[48] and has recently been reviewed by Hwang and Gerstein.[49]

10 MOTION IN ADSORBED LAYERS

As mentioned in the previous section, structural and motional determinations are a coupled problem pair. In general

the study of motions is simpler, because for many adsorbed systems the assumption of known structures in the adsorbed layer will be chemically tenable.

As indicated above, interpretation of relaxation is difficult in adsorbed systems. More reliable motional information is likely to be obtained by the observation of approximately local molecular properties, such as chemical shift anisotropies, dipolar splittings, and quadrupolar couplings. Thus the first CP study[27] of an adsorbed layer revealed an axially symmetric CSA powder pattern for physisorbed benzene at 77 K. This indicated rapid rotation about the sixfold axis at a temperature well below that at which such rotation occurs in the solid.

Subsequently, Resing and co-workers used analysis of CSA powder patterns to determine the motions of various adsorbed species, such as anchored phenyl groups.[50] Sindorf and Maciel[51] used cross polarization rates as an indicator of average C–H dipolar coupling to study the dynamics of long alkyl chains bound to silica surfaces. Yannoni et al.[52] observed C–C dipolar splittings in doubly-labeled benzene to study its structure and motions on a $Pt–Al_2O_3$ catalyst. The use of deuterium quadrupolar powder patterns to study motions in adsorbed phases is exemplified by the elegant studies of Luz et al.[53] on methyl amines sorbed in zeolites.

11 RELATED ARTICLES

CRAMPS; Cross Polarization in Solids; Deuterium NMR in Solids; Diffusion in Porous Media; Knight Shift; Line Narrowing Methods in Solids; Magic Angle Spinning: Effects of Quadrupolar Nuclei on Spin-1/2 Spectra; Multiple Quantum NMR in Solids; Reactions in Zeolites; Silica Surfaces: Characterization; Supported Metal Catalysts.

12 REFERENCES

1. A. W. Adamson, *Physical Chemistry of Surfaces*, 5th edn., Wiley, New York, 1990.
2. G. A. Somorjai, *Chemistry in Two Dimensions: Surfaces*, Cornell University Press, Ithaca, N.Y., 1981.
3. *Physical and Chemical Aspects of Adsorbents and Catalysts*, ed. B. G. Linsen, Academic, London, 1970.
4. A. B. Stiles, *Catalyst Supports and Supported Catalysts*, Butterworths, Boston, 1987.
5. R. M. Barrer, *Zeolites and Clay Minerals as Sorbents and Molecular Sieves*, Academic, London, 1978.
6. J. R. Anderson, *Structure of Metallic Catalysts*, Academic, London, 1975.
7. Q. Geng, O. Gonen, P. Kuhns, C. Zuo, and J. Waugh, *Bull. Magn. Reson.*, 1989, **11**, 154.
8. D. E. Woessner, in *Mass Spectrometry and NMR Spectroscopy in Pesticide Chemistry*, eds. R. Haque and F. J. Biros, Plenum, New York, 1974, p. 279.
9. B. Horn, E. Koch, and D. Fick, *Phys. Rev. Lett.*, 1984, **53**, 364.
10. R. F. Haglund, Jr., *Chem. Rev.*, 1988, **88**, 697.
11. T. M. Shaw and R. H. Elsken, *J. Chem. Phys.*, 1953, **21**, 565.
12. N. Fuschillo and J. G. Aston, *J. Chem. Phys.*, 1956, **24**, 1277.
13. D. E. O'Reilly, H. P. Leftin, and W. K. Hall, *J. Chem. Phys.*, 1958, **29**, 970.
14. T. W. Hickmott and P. W. Selwood, *J. Phys. Chem.*, 1956, **60**, 452.
15. N. Fuschillo and C. A. Renton, *Nature (London)*, 1957, **180**, 1063.
16. D. Michel and H. Pfeifer, *Z. Naturforsch.*, 1968, **23a**, 339.
17. K. J. Packer, *Prog. Nucl. Magn. Reson. Spectrosc.*, 1967, **3**, 87.
18. H. Pfeifer, *NMR Basic Principles and Progress*, Springer, New York, 1972, Vol. 7, p. 53.
19. J. Caro, M. Bülow, H. Jobic, J. Käger, and B. Zibrowius, *Adv. Catal.*, 1993, **39**, 351.
20. V. V. Morariu, *Chem. Phys. Lett.*, 1978, **56**, 272.
21. D. Michel, *Z. Phys. Chem. (Leipzig)*, 1973, **252**, 263.
22. I. D. Gay, *J. Phys. Chem.*, 1974, **78**, 38.
23. D. Michel, A. Germanus, and H. Pfeifer, *J. Chem. Soc., Faraday Trans. 1*, 1982, **78**, 237.
24. T. Bernstein, L. Kitaev, D. Michel, H. Pfeifer, and P. Fink, *J. Chem. Soc., Faraday Trans. 1*, 1982, **78**, 761.
25. V. I. Kvlividze and A. V. Krasnushkin, *Dokl. Akad. Nauk SSSR, Ser. Khim.*, 1975, **222**, 388.
26. J. B. Nagy, G. Engelhardt, and D. Michel, *Adv. Colloid Interface Sci.*, 1985, **23**, 67.
27. S. Kaplan, H. A. Resing, and J. S. Waugh, *J. Chem. Phys.*, 1973, **59**, 5681.
28. E. O. Stejskal, J. Schaefer, J. M. S. Henis, and M. K. Tripodi, *J. Chem. Phys.*, 1974, **61**, 2351.
29. I. D. Gay, *J. Magn. Reson.*, 1984, **58**, 413.
30. L. B. Schreiber and R. W. Vaughan, *J. Catal.*, 1975, **40**, 226.
31. T. Ito, T. Kadowaki, and T. Toya, *Jpn. J. Appl. Phys. Suppl. 2*, **1974**, 257.
32. X. Wu, B. C. Gerstein, and T. S. King, *J. Catal.*, 1990, **121**, 271.
33. T. M. Duncan, J. T. Yates, Jr., and R. W. Vaughan, *J. Phys. Chem.*, 1979, **71**, 3129.
34. C. P. Slichter, *Annu. Rev. Phys. Chem.*, 1986, **37**, 25.
35. T. M. Duncan, *Colloid Surf.*, 1990, **45**, 11.
36. J. S. Bradley, J. M. Millar, E. W. Hill, and S. Behal, *J. Catal.*, 1991, **129**, 530.
37. Z. Wang, J.-P. Ansermet, and C. P. Slichter, *J. Chem. Soc., Faraday Trans. 1*, 1988, **84**, 3785.
38. A. Zecchina, S. Coluccia, and C. Morterra, *Appl. Spectrosc. Rev.*, 1985, **21**, 259.
39. D. Freude, *Adv. Colloid Interface Sci.*, 1985, **23**, 21.
40. B. A. Morrow, *Stud. Surf. Sci. Catal.*, 1990, **57A**, 161.
41. V. M. Mastikhin, I. L. Mudrakovsky, and A. V. Nosov, *Prog. Nucl. Magn. Reson. Spectrosc.*, 1991, **23**, 259.
42. H. A. Resing, in *Magnetic Resonance in Colloid and Interface Science, Int. Symp. Menton, 1979, Reidel, Dordrecht*, 1980, p. 219.
43. I. D. Gay, A. J. McFarlan, and B. A. Morrow, *J. Phys. Chem.*, 1991, **95**, 1360.
44. S. H. C. Liang and I. D. Gay, *J. Catal.*, 1986, **101**, 293.
45. F. G. Oliver, E. J. Munson, and J. F. Haw, *J. Phys. Chem.*, 1992, **96**, 8106.
46. G. W. Haddix, J. A. Reimer, and A. T. Bell, *J. Catal.*, 1987, **106**, 111.
47. T. M. Duncan and R. W. Vaughan, *J. Catal.*, 1981, **67**, 49.
48. P.-K. Wang, C. P. Slichter, and J. H. Sinfelt, *Phys. Rev. Lett.*, 1984, **53**, 82.
49. S.-J. Hwang and B. C. Gerstein, *Bull. Magn. Reson.*, 1993, **15**, 211.
50. D. Slotfeldt-Ellingsen and H. A. Resing, *J. Phys. Chem.*, 1980, **84**, 2204.

51. D. W. Sindorf and G. E. Maciel, *J. Am. Chem. Soc.*, 1983, **105**, 1848.
52. M. Engelsberg, C. S. Yannoni, M. A. Jacintha, and C. Dybowski, *J. Am. Chem. Soc.*, 1992, **114**, 8319.
53. I. Kustanovich, Z. Luz, S. Vega, and A. J. Vega, *J. Phys. Chem.*, 1990, **94**, 3138.

Biographical Sketches

Ian D. Gay, *b* 1939, B.Sc., 1959, M.Sc., 1960 Dalhousie; Ph.D., D.I.C., 1964, London. Member of Faculty, Simon Fraser University, 1966–present. Research specialties: application of NMR to surface chemical problems.

Chemical Exchange on Solid Metal Surfaces

Frank Engelke
Ames Laboratory, Ames, IA, USA

1	Introduction	1
2	Theory of Magnetization Exchange	1
3	Advanced NMR Techniques to Monitor Exchange	2
4	Chemical Exchange of Adsorbed Species on Metal Surfaces: Examples	3
5	Related Articles	4
6	References	4

1 INTRODUCTION

Chemical exchange, i.e. the transfer of atoms, molecules or molecular groups between two or more different environments or regions, is a phenomenon encountered frequently in studies by NMR of a wide variety of chemical, physical and biological systems. Different environments are usually revealed in NMR experiments through distinct resonance frequencies, spin–spin coupling constants, or relaxation times characteristic of the regions between which chemical exchange takes place. The types of atomic or molecular motion most often investigated on metal surfaces include surface diffusion, adsorption and desorption, exchange between different surface sites or different types of adsorbed species, molecular reorientation, and reorientation of molecular groups.

Because NMR requires at least ca. 10^{18} spins at the surface to be able to detect a signal, single crystal surfaces cannot be studied (10^{15} spins). However, introducing the metal in the form of small particles with diameters in the order of nanometers into porous materials, provides a sufficiently high number of surface sites for adsorption to be studied by NMR. These support materials are mostly oxide compounds like silica, alumina, titania, or zeolites with high internal surfaces of several hundred square meters. At the same time, highly dispersed supported metals, e.g. group VIII elements like ruthenium, rhodium, palladium, osmium, iridium, and platinum, are very often of interest in basic and applied research in catalysis (see also ***Supported Metal Catalysts***, and ***Adsorbed Species: Spectroscopy and Dynamics***).

Several NMR techniques are available to study exchange phenomena of adsorbed species. Spin–lattice relaxation[1] measurements are useful if chemical exchange dominates as a source for relaxation, or can be separated from other relaxation mechanisms, e.g. relaxation via the conduction electrons of the metal, called Korringa relaxation (see ***Electron–Nuclear Hyperfine Interactions***). To be investigated by relaxation measurements, the characteristic time constants of exchange τ_{ex} have to be in the order of 10^{-9} s for spin–lattice relaxation in the laboratory frame to 10^{-5} s for spin–lattice relaxation in the rotating frame.[1] For a review of the relaxation method used to study the dynamics on surfaces we refer the reader to the literature.[2–4] The analysis of lineshapes or resonance shifts obtained by conventional NMR techniques are sensitive in the dynamic range of $10^{-6} \leq \tau_{ex} \leq 10^{-3}$ s. Spin labeling methods extend this range up to more than 10^{-1} s. Two-dimensional NMR techniques, applicable in approximately the same slow dynamic range, are most effective if the exchanging species exhibit separate NMR peaks or if well-defined lineshapes due to anisotropic interactions can be observed.[5]

In the present article the theoretical basis necessary to understand the evolution of nuclear spin magnetization influenced by chemical exchange is outlined briefly. The reader is introduced to spin-labeling and two-dimensional (2D) NMR techniques, which are frequently used to monitor exchange. Finally, experimental examples regarding chemical exchange on metal surfaces are discussed.

2 THEORY OF MAGNETIZATION EXCHANGE

In the following it is assumed that the spatial motion of molecules or atoms can be described classically. If all spin interactions are secular with respect to the Zeeman interaction, i.e., the corresponding interaction Hamiltonians commute with the Zeeman Hamiltonian, then each spin can be considered as being subjected to a local field arising from the environment, superimposed on the external static field. Chemical exchange has the effect of causing random fluctuations of the local field. For example, a nuclear spin situated in a molecule or atom, which jumps randomly between two regions on a surface, such that each region gives rise to a different isotropic resonance shift, experiences a random modulation of its resonance frequency. The influence of such frequency fluctuations upon the NMR lineshape was first treated by Hahn, Maxwell, Gutowsky, McCall, and Slichter.[6]

If the spin Hamiltonian contains nonsecular terms, arising, for example, from J couplings observed commonly in liquids, a quantum-mechanical treatment (spin density matrix formalism) is required.[7] Splittings due to J couplings are often difficult to detect in NMR studies of adsorbates on metal surfaces because of insufficient spectral resolution, caused by the heterogeneity of the system, leading to distributions of isotropic chemical or Knight shifts, and/or the presence of 'solid-like' spin interactions much stronger than J coupling, like chemical shift anisotropy (see ***Internal Spin Interactions and Rotations in Solids***) and paramagnetic shifts.

We confine ourselves here exclusively to the case of secular spin interactions, leading to a classical probabilistic model for the magnetization exchange originating from chemical exchange processes. The probabilistic model is commonly represented by a stationary Markov process,[8,9] allowing the derivation of equations of motion for the nuclear spin magnetization in the form of generalized Bloch equations.[9–11] The evolution of longitudinal and transversal magnetization components for all regions, between which exchange takes place, are given as a system of coupled differential equations with rate coefficients describing the magnetization exchange process. Solving these equations is a standard problem of analysis and matrix algebra (see Ernst et al.[11] and Jeener et al.[13]) and enables explicit calculation of NMR lineshapes.

Figure 1 illustrates the principal effects on the NMR lineshapes originating from magnetization exchange between two regions or sites. Regions A and B, populated by N_A and N_B spins, respectively, are characterized by distinct resonance

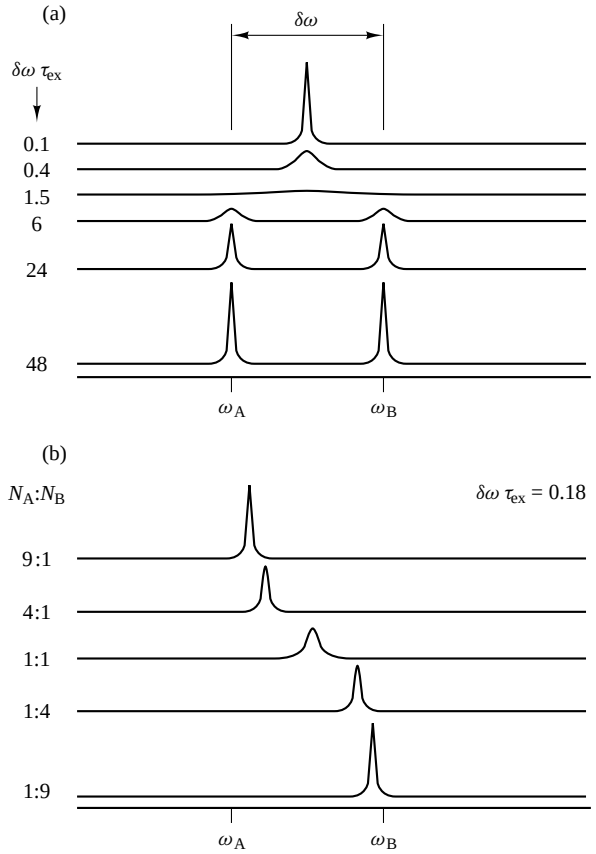

Figure 1 (a) NMR lineshape versus $\delta\omega\tau_{ex}$ for symmetric two-site exchange ($N_A = N_B$). (b) Variation of the resonance frequency in the fast exchange limit as a function of N_A:N_B

frequencies ω_A and ω_B, $\delta\omega = \omega_B - \omega_A$. This difference of resonance freqencies may be caused by different isotropic chemical or Knight shifts. In the slow exchange limit, $\delta\omega\tau_{ex} \gg 1$, where τ_{ex} is a characteristic time constant for the exchange process, two separate lines appear in the NMR spectrum [Figure 1(a)], which become broadened with decreasing $\delta\omega\tau_{ex}$, and coalesce to a single broad line at $\delta\omega\tau_{ex} \approx 1$. With $\delta\omega\tau_{ex}$ decreasing further, only one single 'exchange-averaged' narrow line is observed (fast exchange limit, $\delta\omega\tau_{ex} \ll 1$). The spectra in Figure 1(b) were calculated for the fast exchange limit varying the ratio N_A:N_B of spin numbers in regions A and B, leading to a variation in the resonance frequency of the exchange averaged resonance line as well as to a broadening for values of N_A:N_B near unity. The dependence of the resonance shift δ on N_A and N_B can be expressed for the fast exchange limit as the weighted average:

$$\delta = \frac{N_A}{N_A + N_B} + \delta_A \frac{N_B}{N_A + N_B}\delta_B \qquad (1)$$

of the individual resonance shifts δ_A and δ_B. The mathematical formalism to calculate the above lineshapes is still applicable if anisotropic interactions, to be described by interaction tensors, e.g. chemical shift anisotropy, are present. However, because of the random spatial orientations of the principal tensor axes in a powder sample, the resulting orientation dependence of the resonance frequencies has to be taken into account to obtain the lineshape.[10]

3 ADVANCED NMR TECHNIQUES TO MONITOR EXCHANGE

As shown above, no significant changes of the one-dimensional NMR lineshapes or frequencies occur in the slow exchange limit. More advanced NMR techniques are available to detect such slow exchange processes.

3.1 Spin Labeling by Selective Excitation

The idea of spin labeling is based on the fact that the actual chemical exchange process, being in thermal equilibrium, causes an exchange of spin magnetization.[12] The latter is initially prepared by irradiation of rf pulses to be in nonequilibrium. The irradiation of an rf pulse, or a sequence of rf pulses affects only spins resonating within the spectral excitation window defined by the Fourier transform of the pulse sequence [Figure 2(a) and (b)]. Although this Fourier picture is only an approximation when selective saturation or inversion is considered,[12] it is a useful qualitative description. Denoting the length of a single rf pulse or the total duration of a pulse sequence by τ_p, the excitation width in the frequency domain is proportional to $1/\tau_p$, with the rf carrier frequency in the center of the excitation window. The irradiation of either a long pulse of low rf power or a sequence of strong, but very short pulses, as indicated in Figure 2(a), allows selective excitation of spins. The pulse sequence can be adjusted to act in total like a 90° pulse (selective saturation) or a 180° pulse [selective inversion, illustrated in Figure 2(c)]. Therefore, spins within the spectral window can be labeled, for example, by inversion of their magnetization, while spins which resonate outside the window remain unaffected. If a pulse sequence is used, excitation sidebands also occur [Figure 2(b)]. During a subsequent time interval τ_m [Figure 2(a)] the spin system is allowed to undergo free time evolution. The NMR signal is detected finally by a short (nonselective) 90° pulse. Selective excitation (saturation or inversion) of a narrow frequency band within a broad NMR line, for example, caused by chemical shift anisotropy, is called 'spectral hole-burning'. If chemical exchange is present, the labeled spins may change their resonance frequencies resulting in a redistribution of spin

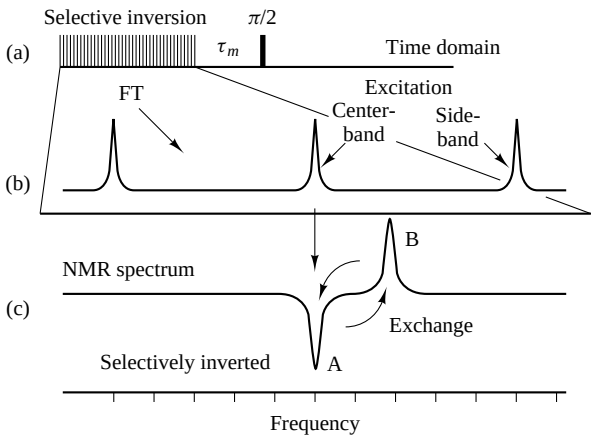

Figure 2 Spin labeling by selective excitation: (a) pulse sequence, (b) Fourier transformation of the train of equidistant pulses, and (c) NMR spectrum showing a selectively inverted line

magnetization toward spectral regions outside of the selected window. The recovery of the spectral hole, or of the intensity of an inverted single resonance line, can be measured as a function of the recovery time τ_m to reveal the kinetics of a chemical exchange process.

Magnetization recovery is also caused by spin–lattice relaxation of the spin magnetization. Only exchange processes with a characteristic time τ_{ex} shorter than the spin–lattice relaxation time T_1 can be observed. Spin-labeling becomes ineffective if the chemical exchange process is faster than the spin-labeling process itself (characteristic time constant τ_p). Thus accessible by spin-labeling techniques are exchange processes within a timescale $\tau_p < \tau_{ex} < T_1$.

3.2 Two-Dimensional Exchange NMR

Two-dimensional exchange NMR techniques[13] are based on the idea of measuring the frequency of spin magnetization components at two different times during the NMR experiment. After the initial preparation period, which consists of a waiting period to allow equilibration of the longitudinal magnetization and irradiating the first $\pi/2$ pulse, transversal magnetizations are present, oscillating with frequencies ω_A and ω_B during the time t_1 [evolution period, Figure 3(a)] corresponding to spins located in regions A and B. A second $\pi/2$ pulse converts the magnetization present at time t_1 into longitudinal magnetization. During the mixing time τ_m (usually much longer than the time t_1) slow chemical exchange leads to a random modulation of the precession frequencies of the two magnetization components M_{zA} and M_{zB}. Spins which were resonating at ω_A at the end of the period t_1 may resonate at either ω_A or ω_B at the end of the mixing period τ_m (and vice versa). The NMR signal is detected after the final $\pi/2$ pulse during the time period t_2. Repeating the experiment by incrementing the time t_1 in small steps, yields a two-dimensional time-domain interferogram which after 2D Fourier transformation[11] with respect to t_1 and t_2 gives the 2D NMR spectrum $S(\omega_1,\omega_2)$. If exchange occurs between A and B, cross peaks are observed, labeled A → B and B → A in Figure 3(b), in addition to main peaks A and B located along the principal diagonal.[14]

4 CHEMICAL EXCHANGE OF ADSORBED SPECIES ON METAL SURFACES: EXAMPLES

Chemical exchange phenomena at or near metal surfaces observed by NMR encompass a wide dynamical range extending from the fast exchange limit ($\tau_{ex} < 10^{-5}$ s) to extremely slow processes ($\tau_{ex} > 1$ s). The details of the chemical exchange processes might be quite different, originating, for example, from adsorption or desorption, exchange between different surface sites, exchange between different populations of adsorbed species or surface diffusion.[15]

4.1 Exchange Dynamics of CO Adsorbed on Metals

Carbon-13 spin labeling techniques have been applied by Duncan, et al.[16] to elucidate in detail surface diffusion of CO and slow exchange between different carbonyl species adsorbed on rhodium. Molitor and Apple[17] performed ^{13}C NMR powder lineshape calculations for reorientating dicarbonyl groups bonded to rhodium. Surface diffusion of CO chemisorbed on palladium has been investigated by means of ^{13}C relaxation measurements and lineshape analysis.[18]

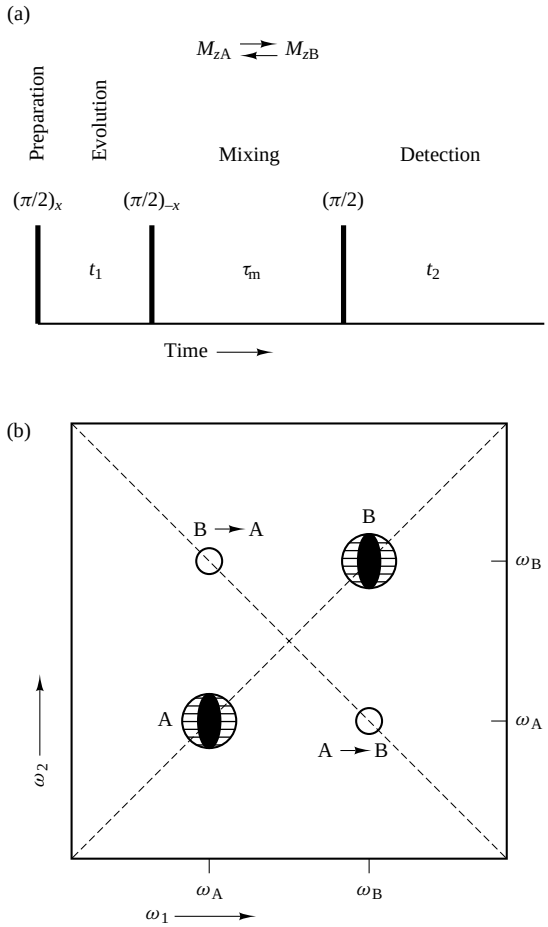

Figure 3 (a) Basic 2D NMR pulse sequence to monitor exchange. (b) Schematic representation of a 2D NMR spectrum for exchange between two sites A and B

4.2 Fast Exchange of Hydrogen on Metal Surfaces

Proton NMR peaks of hydrogen interacting with metal surfaces are commonly shifted to lower frequency (i.e. upfield) due to the Knight shift interaction and reveal relatively small linewidths, especially at elevated external H_2 pressures and temperatures above room temperature, indicating high intrinsic mobility. Variations of the resonance frequency of ^1H NMR peaks, attributed to hydrogen on the metal surface, versus pressure (i.e. changing the number of hydrogen atoms or molecules on the surface) may be caused by at least two different mechanisms: (i) fast exchange between surface environments with different Knight shifts [as illustrated in Figure 1(b)]; and (ii) by a variation of the Knight shift interaction itself, because the latter may be a function of the surface coverage. As pointed out above, fast exchange between two regions leads to an averaged NMR line representing hydrogen in both regions. Variation of the resonance shift

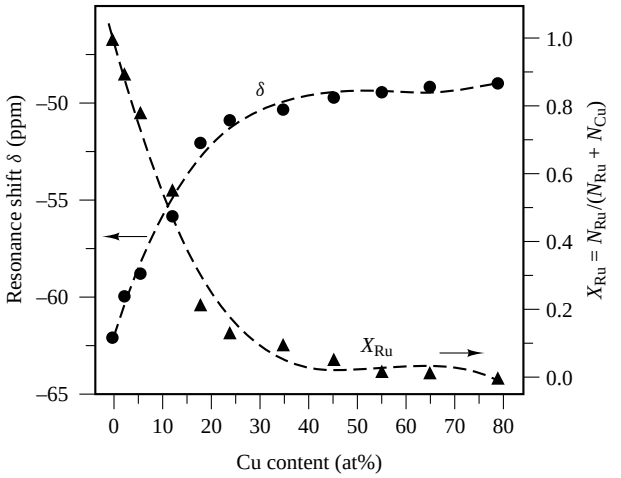

Figure 4 ^{1}NMR resonance shift δ for hydrogen adsorbed on ruthenium–copper bimetallic particles and fraction X_{Ru} of surface ruthenium as a function of the copper content

with pressure, or coverage, has been observed quite frequently by ^{1}H NMR[19] or ^{2}H NMR[20] for hydrogen adsorbed on various metals like platinum, rhodium, and ruthenium (see also refs. [18–20] and 23–24 given in Wu et al.[19]). The resonance shift variation of hydrogen due to fast exchange between different surfaced regions has been used to monitor the surface composition of bimetallic particles.[21] In this case hydrogen atoms are rapidly exchanging between sites on the bimetallic particle surface, composed of sites with different Knight shifts for adsorbed hydrogen. As shown in Figure 4, on particles consisting of pure ruthenium, hydrogen resonates at −62 ppm [to low frequency relative to tetramethylsilane (TMS)]. Increasing the total copper content of the sample leads to a systematic decrease of the ^{1}H resonance shift δ, approaching asymptotically the value of −49 ppm for a copper content near 80 at%. This shift value is regarded as the resonance shift for hydrogen adsorbed on copper sites of ruthenium–copper bimetallic particles. Applying equation (1) inserting $\delta_{Cu} = -49$ ppm and $\delta_{Ru} = -62$ ppm, the fraction $X_{Ru} = N_{Ru}/(N_{Ru} + N_{Cu})$ of ruthenium atoms exposed at the particle surface can be determined (see Figure 4). Therefore, in this example the ^{1}H NMR resonance shift provides a sensitive measure for the composition of the surface.

4.3 Slow Exchange Between Different Hydrogen Populations on the Metal Surface

Figure 5(a) shows an in situ ^{1}H NMR spectrum of silica supported ruthenium, obtained at T = 400 K and at an external H_2 pressure of 300 Torr.[22] Two distinct resonance lines (denoted as α and β) are observed, originating from two different hydrogen species, characterized by different heats of adsorption. The 2D exchange NMR spectrum [Figure 5(b)] was obtained by the pulse sequence illustrated in Figure 3(a). The cross peaks reveal a slow exchange process within the timescale of the experiment, given by the mixing time τ_{mix} = 2 ms, occurring between α and β hydrogen, but there is no exchange within this timescale between the α or β species and the hydrogen residing on the silica support. Spin

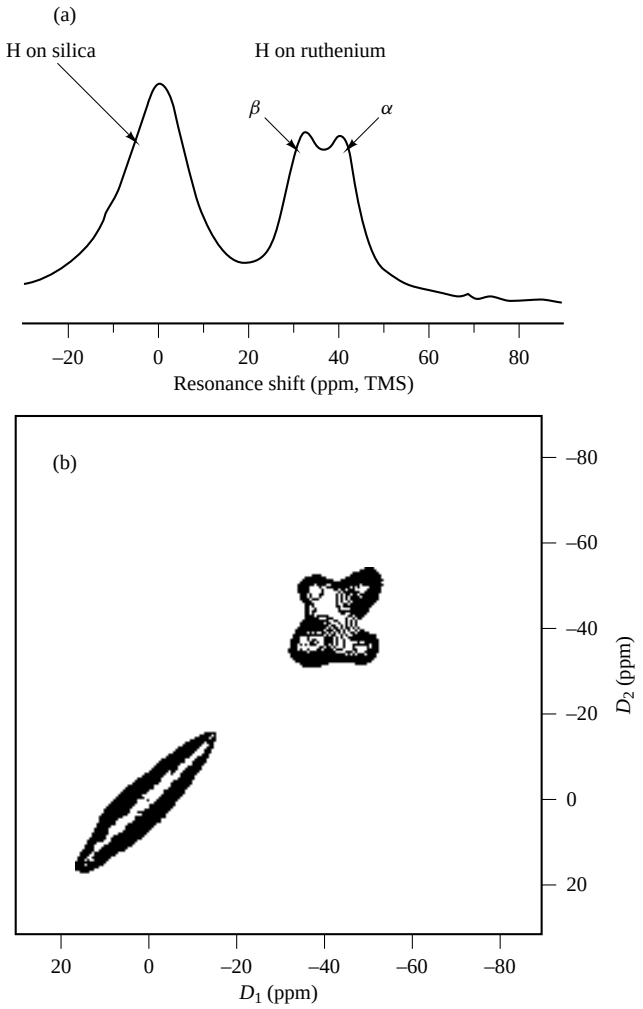

Figure 5 (a) Conventional ^{1}H NMR spectrum of silica supported ruthenium. (b) 2D exchange NMR spectrum at T = 400 K and external H_2 pressure p = 300 Torr

labeling of one of the two spin species, α or β, by selective excitation (Figure 2) allows the determination of the average time constant, τ_{ex} = 700 μs, for the magnetization exchange between α and β hydrogen.

5 RELATED ARTICLES

Adsorbed Species: Spectroscopy and Dynamics; Brønsted Acidity of Solids; Diffusion in Porous Media; Electron–Nuclear Hyperfine Interactions; Internal Spin Interactions and Rotations in Solids; Microporous Materials and Xenon-129 NMR; Silica Surfaces: Characterization; Spin Diffusion in Solids; Supported Metal Catalysts

6 REFERENCES

1. C. P. Slichter, *Principles of Magnetic Resonance*, 3rd edn., Springer, Berlin 1990, Chaps. 4–6.
2. H. Pfeifer, in *NMR Basic Principles and Progress*, eds. P. Diehl, E. Fluck, and R. Kosfeld, Springer, Berlin, 1972, Vol. 7, p. 53.

3. H. Winkler and D. Michel, *Adv. Colloid Interface Sci.*, 1985, **23**, 149.
4. C. P. Slichter, *Ann. Rev. Phys. Chem.*, 1986, **37**, 25.
5. H.-W. Spiess, *Chem. Rev.*, 1991, **91**, 1321.
6. E. L. Hahn and D. E. Maxwell, *Phys. Rev.*, 1952, **88**, 1070; H. S. Gutowsky, D. W. McCall, and C. P. Slichter, *J. Chem. Phys.*, 1953, **21**, 279.
7. J. I. Kaplan and G. Fraenkel, *NMR of Chemically Exchanging Systems*, Academic, New York, 1980.
8. A. Abragam, *The Principles of Nuclear Magnetism*, Clarendon, Oxford, 1961, Chap. X.
9. C. S. Johnson, Jr., in *Advances in Magnetic Resonance*, ed. J. S. Waugh, Academic, New York, 1965, Vol. 1, p. 33.
10. M. Mehring, *Principles of High Resolution NMR in Solids*, 2nd edn., Springer, Berlin, 1983, Chap. 28.
11. R. R. Ernst, G. Bodenhausen, and A. Wokaun, *Principles of Nuclear Magnetic Resonance in One and Two Dimensions*, Clarendon, Oxford, 1987, Chaps. 2.4, 4.6, 6.4 and 9.
12. G. A. Morris and R. Freeman, *J. Magn. Reson.*, 1978, **29**, 433; R. Freeman, *Chem. Rev.*, 1991, **91**, 1397.
13. J. Jeener, B. H. Meier, P. Bachmann, and R. R. Ernst, *J. Chem. Phys.*, 1979, **71**, 4546.
14. If direct dipolar spin–spin couplings are present, spin diffusion (a process to be distinguished from chemical exchange) may also lead to cross peaks (see Jeener et al.[13] and ***Spin Diffusion in Solids***).
15. Spin labeling is well suited to monitor surface diffusion. However, the theoretical treatment of surface diffusion is based on the diffusion equation, and not on Bloch-type equations to describe exchange as discrete jumps between distinct environments.
16. T. M. Duncan, A. M. Thayer, and T. W. Root, *Phys. Rev. Lett.*, 1989, **63**, 62. See also: T. M. Cuncan, *Colloids Surfaces*, 1990, **45**, 11, and references therein.
17. P. Molitor and T. Apple, *J. Phys. Chem.*, 1989, **93**, 7055.
18. S. E. Shore, J.-P. Ansermet, C. P. Slichter, and J. H. Sinfelt, *Phys. Rev. Lett.*, 1987, **58**, 953.
19. X. Wu, B. C. Gerstein, and T. S. King, *J. Catal.*, 1989, **118**, 238.
20. T. Chang, C. P. Cheng, and C. Yeh, *J. Phys. Chem.*, 1991, **95**, 5239.
21. X. Wu, B. C. Gerstein, and T. S. King, *J. Catal.*, 1990, **121**, 271.
22. F. Engelke, S. Bhatia, T. S. King, and M. Pruski, *Phys. Rev. B*, 1994, **49**, 2730; F. Engelke, R. Vincent, T. S. King, and M. Pruski, *J. Chem. Phys.*, 1994, **101**, 7262.

Biographical Sketch

Frank Engelke. *b* 1955. M.Sc. (physics), Ph.D. (supervisor Dieter Michel) 1985, habilitation, University of Leipzig, Germany. Postdoctoral work at Saarbruecken University, Germany (with Jörn Petersson), and since 1992–1994 at Ames Laboratory, USA (with Bernie Gerstein, Marek Pruski and Terry King). Since 1994 affiliated with Bruker Analytische Messtechnik. Approx. 20 publications. Current research specialties: solid state NMR in rotating solids, solid state NMR applications on metal surfaces, NMR probe development.

Diamond Thin Films

Karen K. Gleason

Massachusetts Institute of Technology, Cambridge, MA, USA

1	Introduction	1
2	Carbon-13	1
3	Proton NMR	4
4	Fluorine-19 NMR	5
5	Spin–Lattice Relaxation	5
6	Related Articles	6
7	References	6

1 INTRODUCTION

The unique properties of diamond, such as its high thermal conductivity, mechanical characteristics, optical transparency, and semiconductor characteristics, make it an attractive material for many applications.[1] Synthetic diamond powders and single crystals were first made in high-pressure/high-temperature (HPHT) processes in the 1950s. More recently, diamond films have been grown at technologically significant rates using a variety of subatmospheric chemical vapor deposition (CVD) processes. The primary distinction between these CVD techniques is the method by which energy is introduced in order to dissociate and excite the gas phase reactants.[2] Activation of the gas phase diamond precursors has been achieved by direct current (DC) plasmas, microwave (MW) plasmas, hot filaments, and combustion flames. Although significant variations in growth rates exist between these methods, all seem capable of producing highly faceted polycrystalline films with little evidence of nondiamond carbon and with low hydrogen concentrations ($<$0.5 at.%). Thus, diamond films are distinctly different from diamond-like carbon (DLC) films, which are amorphous, can have a significant fraction of sp^2-bonded carbon, and can have $>$30 at.% hydrogen.[3]

The deposition of diamond at low pressures, where it is metastable, appears to involve a kinetic competition between the growth and etching of various forms of carbon ranging from diamond (tetrahedral sp^3 bonded), through amorphous sp^3 and sp^2 configurations, to graphic carbon (sp^2). The range of successful reactant compositions is surprisingly similar for the various types of CVD processes.[3] Diamond films are most commonly deposited from a dilute mixture of hydrocarbons (0.5–2.0%), such as methane or acetylene, in hydrogen. However, studies of carbon sources containing oxygen (e.g. acetone, ethanol, and carbon monoxide) and halogens (fluorine and chlorine) have also shown promising results. The energy introduced into the gas phase produces molecular fragments and excited species which react on the surface of the substrate which is generally maintained at 800–1000 °C.

The hydrogen which is often predominant in the gas phase has been proposed both to stabilize the growing diamond surface and to etch graphitic carbon.[1–3] The electrical resistivity of diamond has been proposed to depend on hydrogen incorporation.[4] Also, increased hydrogen contents correlate with decreased transparency in the 8–10 μm wavelength region, degrading the performance of diamond as an infrared window.[5,6] Thus, the location and distribution of hydrogen can provide insight into diamond deposition chemistry and structure–property relationships in these films.

The commercial exploitation of CVD diamond requires consistent high-quality production, and defect-free films and coatings. While many techniques have been used to evaluate diamond film quality, most provide only qualitative information on which to evaluate differences in deposition conditions. Hydrogen is particularly difficult to measure in solid thin films.[7] The primary advantage of NMR measurements is their quantitative nature. In addition, the low-energy radiofrequency irradiation used in NMR is unlikely to result in chemical alteration of the diamond samples, unlike some higher-energy spectroscopic techniques. To date, diamond has been studied by ^{1}H,[5–10] ^{13}C,[11–22] and ^{19}F[23] NMR, often providing information which is unattainable by other techniques.

For static NMR measurements, one or more sections of a free-standing diamond film, generally $>10\,\mu$m thick, may be inserted directly into the NMR sample coil.[5] By not using a conventional NMR tube or rotor, a potential source of background signal is eliminated.[7] This is a particularly important consideration when studying thin films, since sample sizes are generally limited and the concentration of NMR active nuclei is often low. In addition, the macroscopic integrity of the film is maintained. Similarly, laser-cut disks of free-standing diamond can be stacked into MAS rotors if examination of intact films is desired.[22] Alternatively, powder, formed by crushing a film or removing a very thin film from its substrate, can be packed into an NMR tube or rotor.

In some instances, NMR spectra of films can also be acquired without removing their growth substrates.[17] For such experiments, the substrate must be nonmagnetic, have a low conductivity, have a similar magnetic susceptibility to the diamond film, and must contribute little background signal for the nuclei to be observed. These conditions can be met by using high-resistivity silicon wafers manufactured by the float zone process. The use of thin wafers ($\leq$75 mm in thickness) maximizes the number of film sections which can be inserted into the NMR coil.

2 CARBON-13

The isotropic chemical shift can resolve sp^2- from sp^3-bonded carbon. Bulk diamond is characterized by a single resonance at 36 ± 2 ppm[11] relative to tetramethylsilane (Figure 1).[13] The sp^2 carbon peak generally appears between 120 and 200 ppm, with the lower values observed for amorphous carbon films,[4] while soot gives a peak centered at 189 ppm.[18] The ratio of sp^2/sp^3 bonded carbon is quantitatively determined from the ratio of the integrated area under the peaks corresponding to these respective environments and has been experimentally demonstrated for diamond powder and soot mixture of known weight fraction.[18]

The linewidth of the sp^3 peak of natural diamond in the static ^{13}C spectra is dominated by homonuclear dipole

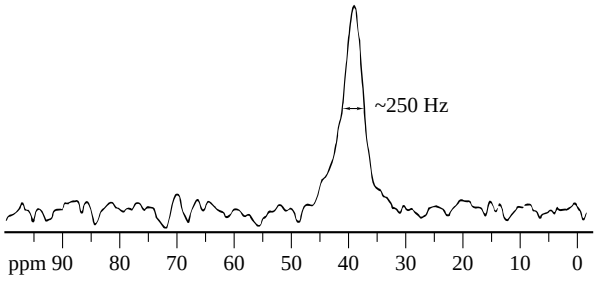

Figure 1 Static direct polarization (DP) ^{13}C NMR at 67.9 MHz of 3 carats of gemstone natural diamonds. The $\Delta\nu_{\frac{1}{2}}$ of 250 Hz includes 50 Hz added Lorentzian broadening. (Adapted from Henrichs et al.)[13]

broadening. The second moment of this interaction can be calculated via the Van Vleck equation:[12,25]

$$M_2 = \tfrac{3}{4}\gamma^4\hbar^2 I(I+1) f \sum_k \frac{(1-3\cos^2\theta_{jk})^2}{r_{jk}^6} \qquad (1)$$

where r_{jk} is the distance between two sites, and f is the fraction of these sites randomly occupied by the NMR-active nuclei of interest. The dependence on θ_{jk}, the angle the intersite vector makes with the external magnetic field, causes M_2 for a powdered sample to differ from that of a single crystal having an identical chemical structure. When active nuclear spins are dilute ($f < 0.01$), a truncated Lorentzian lineshape results, with a full width given by

$$\Delta\nu_{1/2} = \frac{\pi}{\sqrt{3}}\left(\frac{M_2^2}{M_4}\right)^{1/2}(M_2)^{1/2} \qquad (2)$$

Note that the point chosen for truncation influences the ratio $M_2{}^2/M_4$. For higher spin densities, a Gaussian lineshape is observed, with a linewidth of

$$\Delta\nu_{1/2} = 2.35(M_2)^{1/2} \qquad (3)$$

These linewidths are independent of the applied magnetic field; hence, chemical shift resolution can be improved at higher fields.

Using equation (1) for a diamond lattice with a natural abundance of ^{13}C (f = 0.011) yields M_2 = 0.037 kHz^2 for a single crystal oriented with its (014) axis parallel to the external magnetic field, which compares favorably with the measured value of M_2 = 0.041 kHz^2, confirming that homonuclear dipolar interactions are the dominant source of broadening in this environment.[12] The corresponding observed lineshape is a truncated Lorentzian with $\Delta\nu_{\frac{1}{2}}$ = 200 Hz,[12] similar to that shown in Figure 1.[13]

In materials with high hydrogen concentrations, like polymers and DLC films,[24] CP can be used to enhance the ^{13}C spectrum. However, variations in CP dynamics can cause the quantitative character of the NMR experiment to be lost. The low hydrogen concentrations found in polycrystalline diamond films make CP difficult, although achievable.[14] In the vicinity of hydrogen, where CP is most efficient, only sp^3-bonded carbon nuclei were detected. Also, because ^{1}H–^{13}C heteronuclear dipole couplings are generally negligible in diamond films, proton decoupling is often not required. Direct polarization (DP) ^{13}C NMR, while requiring larger samples, is a means of obtaining quantitative sp^2/sp^3 ratios. Typically, $>5 \times 10^{18}$ ^{13}C nuclei are required,[18] corresponding to ~10 mg of a natural abundance diamond, which is equivalent to a 10 μm thick film over an area of 2.8 cm^2.

In samples which are free of paramagnetic defects, DP NMR experiments are quantitative in that each ^{13}C nucleus gives rise to the same integrated signal intensity, regardless of its bonding environment. In samples containing paramagnetic impurities, a small fraction of nuclei in close proximity to such defects will remain undetected as a result of extreme line broadening due to interaction with the unpaired electron of the paramagnetic impurity.[12,13] However, only a small fraction of nuclei should be affected by the paramagnetic densities (10^{17}–10^{18} g^{-1}) in diamond films.[20,21] This assumption can be verified by comparing the experimental signal intensity to the expected intensity based on mass and ^{13}C enrichment in the sample and response of the spectrometer to standards of known ^{13}C content. Fortunately, these experiments show that the effects of broadening by paramagnetic centers are often below the NMR detection limit.[18] For quantitative measurements, it is also important to insure that a sufficient delay ($\geq 5T_1$) is used between signal acquisitions.

Isotopic enrichment can be used to decrease sample size requirements.[17–19,21] The spin–lattice relaxation rate will also increase as a result of enhanced spin diffusion in the ^{13}C-enriched samples. Both factors lead to increased sensitivity and/or decreased acquisition times. The concentration of ^{13}C in the solid film can be determined via the second moment of the homonuclear dipole couplings [see equation (1)]. The degree of enrichment determined in this manner is in excellent agreement with measurements of the isotopic shift of the diamond one-phonon absorption in the Raman spectra.[19] However, enrichments >25% will limit spectral resolution of sp^2 versus sp^3 carbon due to homonuclear dipolar line broadening [see equation (1)]. Resolution may be restored by MAS at speeds greater than the ^{13}C–^{13}C homonuclear dipole broadening in hertz, i.e. spinning frequencies of more than 4 kHz.

Selective isotopic labeling can be used to gain insight into the chemistry of diamond formation when more than one chemically distinct carbon is present in the gas phase reactant mixture.[17–19] For instance, films have been grown using acetone, selectively ^{13}C labeled at either the methyl or carbonyl site, as the reactive carbon source. Measuring the resulting ^{13}C concentration in a pair of otherwise identical films determines the relative efficiency at which the methyl and carbonyl sites from the selectively labeled acetone are incorporated into diamond. When such experiments are carried out in a hot filament reactor, both labels are incorporated equally when a tantalum filament is used.[17,18] In contrast, diamond deposits preferentially from the methyl site when a rhenium filament is employed.[19] However, some growth from the carbonyl site is still observed when rhenium is used. Such experiments demonstrate the importance of heterogeneous chemistry at the filament in this type of CVD reactor.

In polycrystalline CVD films, the diamond peak is nearly symmetric, revealing little CSA, as expected for a tetrahedrally symmetric bonding environment. For static spectra, the $\Delta\nu_{\frac{1}{2}}$ ranges from 310 to 500 Hz in unenriched films,[18,21] indicating broadening in addition to homonuclear dipole interactions. MAS at sufficient speeds can average broadening due

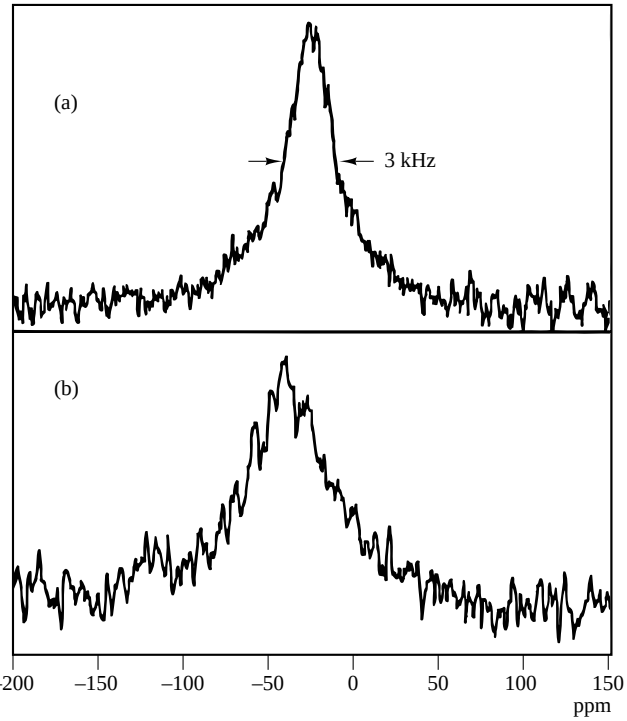

Figure 2 Static DP ^{13}C NMR at 75 MHz of two CVD diamond films, enriched to 22% ^{13}C. (a) The highly faceted film shows only the 36 ppm resonance characteristic of sp^3 bonding environments. (b) A broader sp^3 peak and a second peak at ~120 ppm due to sp^2 carbon are seen in the second film, which also has much poorer morphology. (Adapted from McNamara et al.)[18]

to dipolar interactions, CSA, and variations in magnetic susceptibility. Thus, any remaining broadening can be attributed to a wider distribution of bond angles and lengths in the film. A highly faceted hot filament film on its substrate, with 22% ^{13}C enrichment, produces a symmetric Gaussian lineshape with $\Delta\nu_{\frac{1}{2}} \sim 3$ kHz [Figure 2(a)],[17] in reasonable agreement with equations (1) and (3). Upon crushing this sample and performing MAS, the $\Delta\nu_{\frac{1}{2}}$ was reduced to 150 Hz. Variations in MAS $\Delta\nu_{\frac{1}{2}}$ from 6 to 55 Hz in natural abundance samples have been linearly correlated to increases in Raman one-phonon linewidth, which is also associated with increasing disorder of the diamond phase.[21]

Asymmetry in the sp^2 peak is expected as a result of CSA and/or bond angle disorder. Unfortunately, sp^2-bonded carbon in visibly faceted films produced via hot filament, DC arc jet, or MW plasma CVD is generally below the ^{13}C NMR detection limit.[18] An sp^2 resonance has been observed in a film of poor morphology and no detectable diamond one-phonon Raman absorption.[17] This film was prepared under identical conditions to the highly faceted hot filament film discussed above [Figure 2(a)], with the sole exception that the C/H ratio in gas feed was increased, resulting in poorer film quality. The static NMR spectra of this 22% enriched film, intact on its substrate, resolves both broad sp^2 and sp^3 peaks at ~120 and ~38 ppm, respectively [Figure 2(b)]. The ratio of the areas of these two peaks gives a quantitative sp^2/sp^3 ratio of 0.11 ± 0.2, indicating that ~10% of the carbon in this film is bonded in an sp^2 configuration. The MAS linewidth of the sp^3 peak narrows to only $\Delta\nu_{\frac{1}{2}} = 690$ Hz, indicating some disorder in the sp^3 environment, while the lineshape of the sp^2 peak remains relatively unaltered, indicating a high degree of disorder in this phase.

Quantitative sp^2/sp^3 ratios measured by solid state ^{13}C NMR have been compared with qualitative results of Raman spectroscopy,[18] one of the most widely used techniques for characterizing diamond thin films. Raman is sensitive to both the sp^2 and sp^3 bonding environments but is difficult to quantify since the scattering efficiency of sp^2-bonded carbon differs from sp^3-bonded material, and each may vary from film to film. In addition, the sp^2- and sp^3-bonded carbons may have different absorptivities, which can lead to nonuniform sampling as a function of depth in the film.

As expected, Raman spectroscopy is extremely sensitive to sp^2-bonded carbon, identifying small amounts below the detection limit of the NMR spectrometer. Comparison of the two techniques, however, indicates that Raman spectroscopy may be so sensitive to sp^2-bonded carbon that sp^3-bonded carbon in films containing as much as 90% sp^3-bonded material may remain undetected. This is undesirable when new deposition conditions are being explored, since conditions which yield a majority of sp^3-bonded sites can be overlooked by the Raman analysis.

These two techniques also differ in that NMR spectroscopy is sensitive to short-range order, while Raman spectroscopy probes order over a longer range. NMR provides only information averaged over the entire sample volume and requires relatively large samples and long acquisition times. Raman spectroscopy has the advantage of giving fast, spatially resolved information. A combination of the two techniques is desirable for obtaining reliable information for all types of diamond.

Another method for enhancing the sensitivity of NMR for characterizing diamond films is DNP.[20,21] The work on diamond films builds upon earlier DNP investigations of natural and HPHT diamond.[15,16] Polarization from paramagnetic defects is transferred to the nuclear spin reservoir by simultaneous irradiation at the electron spin and ^{13}C Larmor frequencies. The ^{13}C nuclei close to paramagnetic sites polarize most quickly. Thus, the local composition can be investigated as a function of distance from the paramagnetic sites using variable contact time experiments. Often DNP is combined with MAS in order to suppress spin diffusion.[16] When DNP is combined with CP from ^{1}H nuclei, hydrogenated regions can be selectively probed.[20,21]

The 1.4 T ^{13}C DNP MAS spectra of CVD diamond have been published for an 83 mg natural abundance sample (Figure 3) and for two ~14% enriched samples of 20 and 29 mg, respectively. Although acquisition time is reduced by using DNP, this advantage is somewhat offset by the use of high magnetic fields by the more commonly available conventional NMR spectrometers.[20] The ^{13}C DP MAS spectra of the enriched samples was also acquired on a conventional NMR spectrometer, using a 14 T magnet.[21] In addition, the static DP spectra of the same three samples had previously been reported using a 7 T NMR spectrometer.[18]

The main feature of the three DNP MAS spectra is a characteristic line at 36 ppm (Figure 3), which is also observed for bulk diamond. In some cases, a small, broad shoulder on this peak at ~45 ppm has been identified as hydrogenated sp^3-bonded carbon through its response to both $^{1}H-^{13}C$ variable CP contact times and dipolar dephasing experiments.[21] This

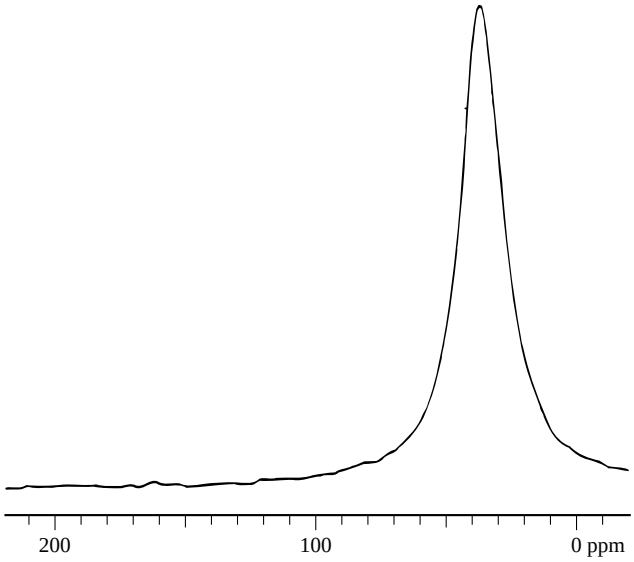

Figure 3 Static DP–DNP ^{13}C NMR at 15 MHz of natural isotopic abundance CVD diamond film, showing only the characteristic peak for diamond. (Adapted from Lock and Maciel[20])

position falls in the calculated chemical shift range of 25–54 ppm for saturated hydrocarbons with an underlying diamond skeleton. These calculations start with adamantane and progress through fully hydrogen-terminated diamond surfaces, and are compared to experimental measurements where possible.[21] A sharp peak centered at 28 ppm, observed only in DP MAS experiments may indicate freely rotating methyl groups. Only when intermediate $^{1}H-^{13}C$ CP contact times were employed with the DNP MAS experiments was a broad, weak resonance observed at ~140 ppm in one of the enriched films. This peak was not observed using DNP MAS in the absence of CP, suggesting this sp^2-bonded carbon is localized near hydrogenated sites. Unfortunately, the sp^2/sp^3 ratio could not be quantified because the polarization dynamics from both the paramagnetic defects and the proton reservoir are not well known in these samples.

3 PROTON NMR

Figure 4 shows representative ^{1}H NMR spectra, taken at a Larmor frequency of 270 MHz.[5–10] Approximately 1500 signal transients were acquired at a repetition rate of 5 s, in accordance with typical proton T_1s of less than 1 s in these samples, which contained $>10^{17}$ total proton spins. By not using an NMR sample tube and purging the NMR probe with dry nitrogen, the need for background subtraction was eliminated. Integrating such spectra yields concentrations ranging from <0.017 to ~0.5 at.% hydrogen, depending upon the exact film growth conditions used. The concentrations of hydrogen determined by NMR were used to quantify the CH_x stretching absorption in the infrared spectra of the same films. The infrared spectra reveal that the hydrogen is bonded covalently to the diamond lattice primarily as CH, CH_2, and CH_3 groups,[5,6] with some $-OCH_3$ and $-NCH_3$ moieties also possible.[10]

The ^{1}H spectra in Figure 4 are well represented by two components, a narrow Lorentzian and a broad Gaussian,[5] as shown

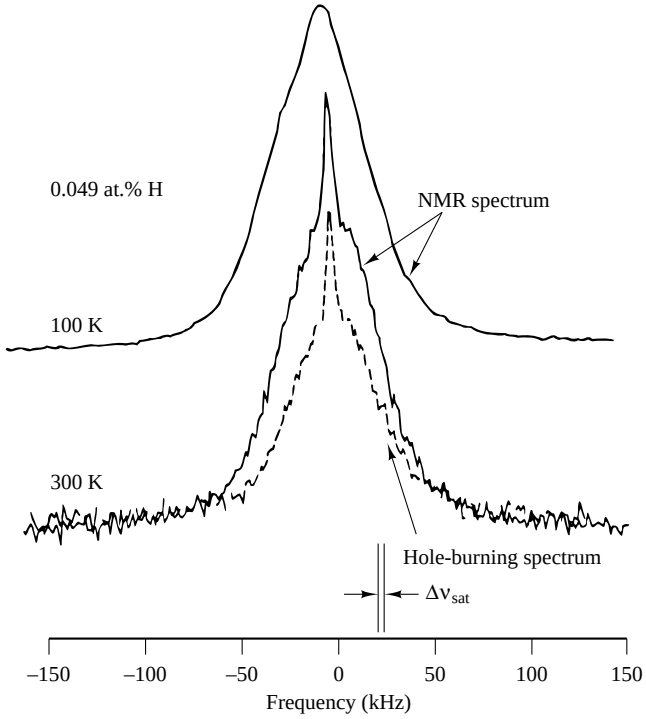

Figure 4 Static ^{1}H NMR spectra at 270 MHz of a free-standing diamond film (solid lines). Two components are resolved at 300 K (middle), but the sharp Lorentzian is broadened when the temperature is decreased to 100 K (top). A 300 K 'hole-burning' experiment (bottom, dashed line) shows uniform attenuation of both components after selective irradiation of the small band, $\Delta\nu_{sat}$, indicating dipolar communication among the two resolved proton environments

by the solid line representing a least squares fit to the data, indicating at least two different bonding configurations for hydrogen in polycrystalline diamond. Similar two-component proton lineshapes, with different narrow to broad ratios, have been observed from films deposited by a variety of CVD processes.[9,10] However, in CVD diamond with relatively high hydrogen concentrations, often only the broad feature can be resolved.[21]

A 'hole-burning' NMR experiment shows that these two resolved hydrogen environments are in close proximity.[5] When a 1 kHz-wide region, 20 kHz from the center of the lineshape, was selectively saturated, uniform attenuation of both components is observed after a 2 ms delay (Figure 4). This indicates that rapid dipolar communication occurs between protons in the two environments, requiring internuclear distances of less than 50 nm. Figure 4 also shows that at 100 K the Lorentzian component is broadened, while the Gaussian component is not significantly affected.[5] Thus, at room temperature, the narrow Lorentzian lineshape results from motional averaging, while the broad Gaussian line indicates rigidly held hydrogen. The CRAMPS ^{1}H spectra show an unresolved peak centered at ~2 ppm.[20]

The homonuclear broadening resulting from static distributions of hydrogen bonded in a rigid polycrystalline lattice can be calculated by the van Vleck equation [see equation (1)]. For polycrystalline diamond samples, if all the hydrogen in the Gaussian component were randomly distributed as CH, the resulting $\Delta\nu_{\frac{1}{2}}$ range would be more than

two orders of magnitude smaller than typically observed values of ∼60 kHz. Randomly dispersed CH_2 groups also provide too little homonuclear broadening. These discrepancies indicate locally high hydrogen concentrations, requiring significant segregation of hydrogen in polycrystalline diamond.[5,6] However, this analysis cannot distinguish between isolated small clusters and larger groupings of spins.

Possible locations for segregation are hydrogen-decorated defects and voids within the crystal, a heavily hydrogenated phase stable at the deposition temperature or at the grain boundaries in polycrystalline diamond.[5] If hydrogen was uniformly distributed on a surface, a density of 3×10^{15} H cm^{-2} would be required to give the observed $\Delta\nu_{\frac{1}{2}} = 60$ kHz. This compares favorably with areal densities of 3.1×10^{15}, 2.2×10^{15}, and 1.8×10^{15} H cm^{-2} for fully hydrogen passivated, unreconstructed ⟨100⟩, ⟨110⟩, and ⟨111⟩ diamond surfaces, respectively. In order to account for the NMR-observed bulk hydrogen incorporation of 0.01–0.22 at.%, monolayer hydrogen coverage of films composed of 0.5–150 μm cubes is required, dimensions which compare favorably to observed crystallite sizes in CVD films.[6] The structure of hydrogenated surfaces present during growth may resemble those preserved at grain boundaries, which would allow these ^{1}H NMR measurements to act as a potential test of surface chemistry models of diamond growth.

The assumption of a surface distribution of hydrogen in polycrystalline diamond films is also supported by multiple quantum (MQ) NMR studies.[8] Figure 5 shows the rate at which groups of protons are effectively correlated with increasing dimensionless MQ excitation time, $M_2^{\frac{1}{2}}\tau$, for two hot filament diamond films (CVD-1 and CVD-2) and one DC arc jet film (CVD-3). Initially, the data for the films are coincident with a known surface distribution of protons, hydrogenated diamond powder, and slower than that of known bulk hydrogen distributions, such as exist in CaH_2. Up to 20 spins were correlated in the films despite the very low (<0.1 at.%) bulk concentrations, confirming the large-scale clustering of hydrogen, most likely in a two-dimensional distribution. The morphology of hydrogen incorporated into these films, as determined by MQ NMR, depends only weakly on the manufacturing process, suggesting that similar surface chemistry has occurred in both types of reactors.

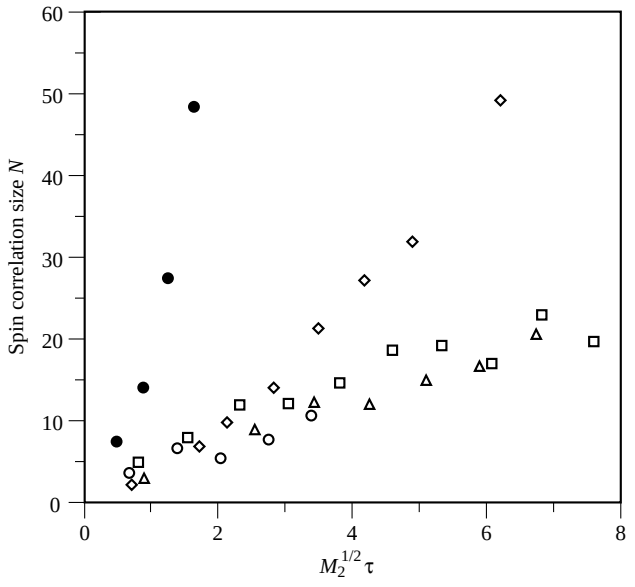

Figure 5 The number of effectively correlated protons (N) versus the dimensionless MQ excitation time, $M_2{}^{1/2}\tau$. The CaH_2 data (•) fall on the universal curve for MQ growth of three-dimensional proton distributions. This growth is faster than for two-dimensional systems, represented by the hydrogenated diamond powder data (◊). The MQ growth of the three different CVD samples (□, CVD-1; △, CVD-2; ○, CVD-3) is similar to that of the hydrogenated diamond powder at early excitation times. Nearly 20 protons are correlated in these films which have <0.5 at.% hydrogen, confirming the presence of large-scale hydrogen segregation. (Adapted from Levy and Gleason[8])

4 FLUORINE-19 NMR

The lower substrate temperatures which have been achieved using fluorine-containing CVD reactants[26] opens the possibility of depositing diamond onto materials of low thermal stability, such as organic polymers. In addition, fluorination has been proposed to enhance the chemical inertness and lower the coefficient of friction of diamond surfaces.[27] Thus, knowledge of surface passivation of diamond by fluorine is desirable.

Solid state ^{19}F NMR has been used to characterize the surfaces of diamond powder after 100% CF_4 and 98% CF_4/2% O_2 radiofrequency plasma treatments.[23] The pure CF_4 plasma results in 7.1×10^{14} F cm^{-2}, a coverage equivalent to approximately half of the available surface bond density. With the addition of 2% O_2, the equivalent coverage is reduced by roughly an order of magnitude, to 7.4×10^{13} F cm^{-2}. MQ NMR reveals that ^{19}F is not distributed uniformly on either surface.

High-speed MAS was used to average the effects of chemical shift anisotropy (Figure 6). On both surfaces, only CF_x (x = 1–3) functionalities were observed, with the predominant species being carbon monofluoride. Only 5–10% of the fluorine was bonded as CF_3. The isotropic chemical shifts were resolved and assigned relative to $CFCl_3$ as follows: CF = 148 ± 1 ppm; CF_2 = 106 ± 2 and 123 ppm; CF_3 = 78 ± 1 ppm. The peak at 123 ppm was only observed in the CF_4/O_2 plasma-treated sample, and is speculated to be the result of atomic fluorine etching of diamond.

5 SPIN–LATTICE RELAXATION

Paramagnetic defects facilitate spin–lattice relaxation in both natural and synthetic diamond.[12,13] At a fixed degree of enrichment, an increase in the ^{13}C T_1 qualitatively indicates a lower relaxation center density, hence an increase in crystal quality. The T_1s of commercial natural diamond powder are on the order of tens of seconds, while significantly longer time constants, on the order of a few hours, can be observed for large, gem-quality natural diamonds. An increase in T_1 has also been observed within a series of CVD diamond films as the morphology, observed by scanning electron microscopy, improved.[17] However, detailed quantitative studies of T_1 behavior, analogous to those on single crystal diamond,[12] are often hindered by the higher complexity of defect distributions in the polycrystalline films.

Paramagnetic defects in diamond result from either unsatisfied bonding arrangements, so-called dangling bonds, present

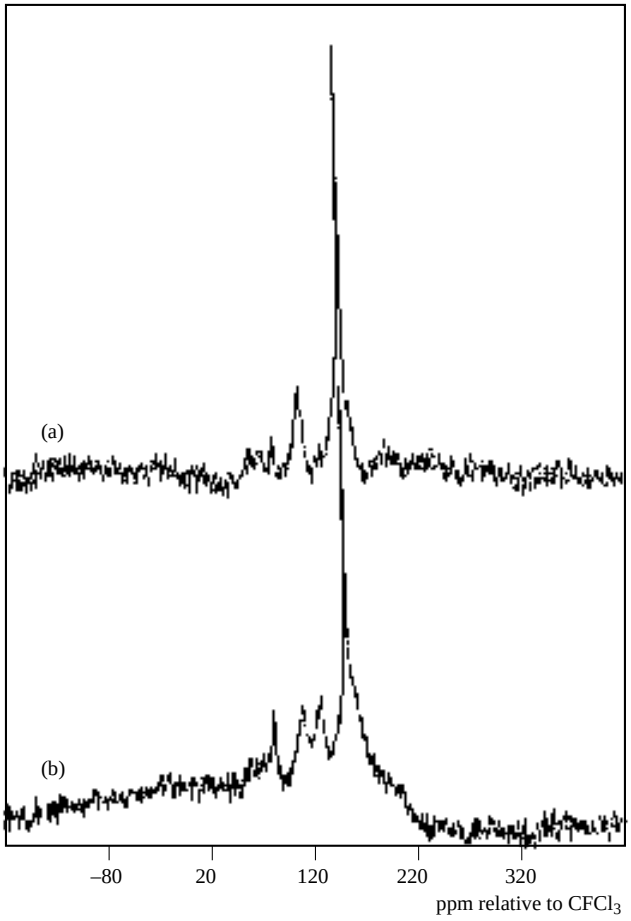

Figure 6 Room-temperature, high-speed (15 kHz) MAS ^{19}F NMR spectra at 376.5 MHz of diamond powder surfaces, fluorinated by two different methods. (Adapted from Scruggs and Gleason[23])

either internally or at the surface of a crystal or from impurity incorporation. Nitrogen is a common impurity that gives rise to a variety of ESR-active centers.[28] Often these sites act as color centers, providing a visible manifestation of their presence. Boron incorporation imparts a blue color, and is sometimes intentionally used to produce p-type semiconducting diamond (type IIb).[12] However, most impurities are unintentionally introduced. For example, ferromagnetic impurities originating from the catalyst are common in HPHT synthetic diamond, and metallic impurities from the hot filament used are common in this variety of CVD film.

The ^{13}C spin–lattice relaxation of diamond can be described by[21]

$$M(t) = M_0\{1 - \exp[-(t/T_1)^x]\} \quad (4)$$

where x is constrained by the limits, $0.5 \leq x \leq 1.0$, and M_0 is the equilibrium magnetization. For the upper bound, x = 1.0, equation (4) represents simple exponential relaxation, as predicted from the Bloch equations. In this case, every ^{13}C site has the same relaxation rate. In diamond, this limit occurs if spin diffusion among the ^{13}C nuclei is fast compared with the rate at which an individual ^{13}C nucleus relaxes as a result of a neighboring paramagnetic site. If the situation is reversed, poor communication among the ^{13}C nuclei requires that each relaxes directly with a neighboring paramagnetic site. Since there is a distribution of ^{13}C to paramagnetic site distances, a dispersion of spin–lattice relaxation rates results. Fortunately, integration over all possible rates, with appropriate assumptions, simplifies to equation (4) with x = 0.5.[13]

An excellent consideration of influence of direct ^{13}C relaxation to paramagnetic defects in comparison to spin diffusion rates in diamond is provided by Hoch et al.[12] Unfortunately, both limits as well as mixed behavior are possible. Spin diffusion is slowed when no ^{13}C enrichment is employed and MAS is used. Thus, behavior approaching the x = 0.5 limit has been observed for MAS spectra of samples having natural abundance or a 14% ^{13}C enrichment.[20,21] In contrast, pure exponential behavior (x = 1.0) is observed in static spectra of more highly enriched (22%) samples.[16] Analysis of spin diffusion rates as a function of enrichment suggests that paramagnetic centers are distributed uniformly in polycrystalline CVD diamond films, rather than being localized at grain boundaries.[14]

Short spin–lattice relaxation time constants have been reported for of both ^{1}H and ^{19}F bonded to diamond. These fast rates suggest paramagnetic centers contribute to spin–lattice relaxation and are further enhanced by rapid spin diffusion among these clustered, high-gyromagnetic ratio nuclei. For ^{1}H, room temperature T_1 values are in the range of 5 ms to 1 s.[8,9,21] These values increase after annealing CVD diamond at 500–750 °C suggesting passivation of paramagnetic centers.[9] The relaxation appears nonexponential, but exact determination of x [see equation (4)], involves a large degree of uncertainty due to the low signal levels available.[9,21,23] Also, caution must be applied in directly interpreting x, since multicomponent relaxation, motion, and, in the case of ^{19}F, CSA can also lead to nonexponential relaxation. For ^{19}F, nonexponential spin–lattice relaxation with a time constant of ~0.5 s has been observed for two samples at room temperature.[23] The ^{19}F T_1 increases as the temperature is lowered to 150 K, but remains fixed upon further decreasing the temperature to 100 K. This behavior is consistent with changes in the static ^{19}F lineshape, indicating motion is occurring at room temperature.

6 RELATED ARTICLES

Amorphous Silicon Alloys; Chemical Shift Tensors; Coal Structure from Solid State NMR; Cokes; Cross Polarization in Solids; Dynamic Nuclear Polarization and High-Resolution NMR of Solids; Fluorine-19 NMR; Fossil Fuels; Magic Angle Spinning; Multiple Quantum NMR in Solids; Silica Surfaces: Characterization; Spectral Editing Techniques: Hydrocarbon Solids.

7 REFERENCES

1. (a) R. C. DeVries, *Am. Rev. Mater. Sci.*, 1987, **17**, 161. (b) F. G. Celii and J. E. Butler, *Ann. Rev. Phys. Chem.*, 1991, **42**, 64.
2. P. K. Bachmann, D. Leers, and H. Lydtin, *Diamond Rel. Mater.*, 1991, **1**, 1.
3. M. I. Landstrass and K. V. Ravi, *Appl. Phys. Lett.*, 1989, **55**, 1391.

4. M. A. Petrich, *Mater. Sci. Forum*, 1989, **52–53**, 387.
5. K. M. McNamara, D. H. Levy, K. K. Gleason, and C. J. Robinson, *Appl. Phys. Letts.*, 1992, **60**, 580.
6. K. M. McNamara, K. K. Gleason, and C. J. Robinson, *J. Vac. Sci. Technol. A.*, 1992, **10**, 3143.
7. D. H. Levy and K. K. Gleason, *J. Vac. Sci. Technol. A.*, 1993, **11**, 195.
8. D. H. Levy and K. K. Gleason, *J. Phys. Chem.*, 1992, **31**, 8125.
9. S. Mitra and K. K. Gleason, *Diamond Rel. Mater.*, 1993, **2**, 1145.
10. K. M. McNamara and K. K. Gleason, *Chem. Mater.*, 1994, **6**, 39.
11. (a) H. L. Retcofsky and R. A. Friedel, *J. Phys. Chem.*, 1973, **77**, 68. (b) C. A. Wilkie, T. C. Ehlert, and D. T. Haworth, *J. Inorg. Nucl. Chem.*, 1978, **40**, 1983.
12. M. J. R. Hoch and E. C. Reynhardt, *Phys. Rev. B*, 1988, **37**, 9222.
13. P. M. Henrichs, M. L. Cofield, R. H. Young, and J. M. Hewitt, *J. Magn. Reson.*, 1984, **58**, 85.
14. M. Pruski, D. P. Lang, S-J. Hwang, H. Jia, and J. Shinar, *Phys. Rev. B*, 1994, **49**, 10635.
15. M. J. Duijvestijn, C. van der Lugt, J. Smidt, R. A. Wind, K. W. Zilm, and D. C. Staplen, *Chem. Phys. Lett.*, 1983, **102**, 25.
16. R. A. Wind, M. J. Duijvestijn, C. van der Lugt, A. Manenschijn, and J. Vriend, *Prog. NMR Spectrosc.*, 1985, **17**, 33.
17. K. M. McNamara and K. K. Gleason, *J. Appl. Phys.*, 1992, **71**, 2884.
18. K. M. McNamara, K. K. Gleason, D. J. Vestyck and J. Butler, *Diamond Rel. Mater.*, 1992, **1**, 1145.
19. K. M. McNamara and K. K. Gleason, *J. Electrochem. Soc.*, 1993, **140**, L22.
20. H. Lock and G. E. Maciel, *J. Mater. Res.*, 1992, **7**, 1291.
21. H. Lock, R. A. Wind, G. E. Maciel, and C. E. Johnson, *J. Chem. Phys.*, 1993, **99**, 3363.
22. L. H. Merwin, C. E. Johnson, and W. A. Weimer, *J. Mater. Res.*, 1994, **9**, 631.
23. B. E. Scruggs and K. K. Gleason, *J. Phys. Chem.*, 1993, **97**, 9187.
24. S. Kaplan, F. Jansen, and M. Machonkin, *Appl. Phys. Lett.*, 1985, **47**, 750.
25. A. Abragam, *Principles of Nuclear Magnetism*, Oxford University Press, Oxford, 1961, pp. 112–126.
26. D. E. Patterson, B. J. Bai, C. J. Chu, R. H. Hauge, and J. L. Margrave, *Proceedings of the Second International Conference on New Diamond Science and Technology, Materials Research Society, Pittsburgh, 1990*, p. 433.
27. R. A. Rudder, G. C. Hudson, J. B. Posthill, R. E. Thomas, and R. Markunas, *J. Appl. Phys. Lett.*, 1991, **59**, 791.
28. J. H. N. Loubser and J. A. van Wyk, *Rep. Prog. Phys.*, 1978, **41**, 1201.

Biographical Sketch

Karen K. Gleason. *b*. 1960 B.S., 1982, M.S., 1982, Massachusetts Institute of Technology, USA. Ph.D., University of California Berkeley, USA, 1987. Introduced to NMR by J. A. Reimer. Faculty in Chemical Engineering, Massachusetts Institute of Technology, 1987–present. Approx. 50 publications. Research interests include applying NMR to thin films and interfaces, particularly for detecting low concentrations of hydrogen, and development of multiple quantum NMR spectroscopy.

Hydrogen–Metal Systems

David R. Torgeson
Iowa State University, Ames, IA, USA

1	Introduction to NMR of Hydrogen–Metal Systems	1
2	Hydrogen Motion in Metals Detected by NMR	2
3	Dynamic Studies of Hydrogen Motion in a Metal	2
4	Deuteron Lineshape for Combined Electric Quadrupole and Knight Shifts	5
5	Low Temperature Local Hydrogen Motion and Hydrogen Tunneling in HMSs	7
6	Spin–Lattice Relaxation in Amorphous Hydrogen–Metal Systems	8
7	Related Articles	9
8	References	9

1 INTRODUCTION TO NMR OF HYDROGEN–METAL SYSTEMS

The exposure of hydrogen to metals often produces significant changes in the physical properties of those metals. The absorption of hydrogen into interstitial lattice sites between metal atoms causes metallic materials to expand their volume, changes the crystal structure, and may change the electronic structure or electrical character of the material. Unable to withstand the strain, some metals fracture into powder, sometimes a useful method of producing powder of ductile metals, but at other times a possibly disastrous result as in the case of hydrogen embrittlement of steels. All the materials included in hydrogen–metal systems (HMSs) are occasionally incorrectly referred to as metal hydrides. As we will see below, metal hydrides do make up the majority of materials in HMSs. Metal hydrides can be either covalent, ionic, or metallic[1] in nature. We will confine our attention to metallic hydride materials.

One of the earliest NMR studies of hydrogen in metals was done some 40 years ago by R. E. Norberg,[2] who applied hydrogen to the palladium metal wires which made up the rf coil of his NMR probe. Linewidth, Knight shift, and relaxation times of the hydrogen in the rf skin depth of the palladium wires were studied by continuous wave and spin echo techniques.

Some of the most basic NMR studies of HMSs have been the investigation of the underlying physical principles governing hydrogen location and motion at the atomic or 'microscopic' level. Long-range hopping or diffusion of hydrogen is currently understood in terms of thermally activated, over the barrier hopping between interstitial lattice sites, which will be discussed, in part, below. Pulse magnetic field gradient NMR to measure hydrogen (and other atomic) diffusivities is discussed elsewhere (see ***Diffusion in Solids***). Attempts to characterize tunneling of hydrogen at low temperatures between interstitial vacancies in metals at low temperatures by NMR will be discussed briefly here.

Although NMR is a powerful tool for observing hydrogen interactions in HMSs, interpretation of NMR data cannot be done properly without other knowledge of the materials. Crystal structure and phase diagram results from X-ray, neutron diffraction,[3] and detailed magnetic information from susceptibility measurements are often crucial to the interpretation of NMR results of HMS.

Many of the applied NMR studies of hydrogen, deuterium, and tritium in HMSs have been undertaken to determine the location and motions of hydrogen within the metallic materials in efforts to characterize and improve the hydrogen–metal materials for applications such as purification of hydrogen, hydrogen isotope separation, and hydrogen storage for fuel or energy storage (batteries); or closed cycle, metal hydride refrigerators for remote or applications to vehicles in space.[4]

HMSs include elemental metals, MH_x, with small concentrations of hydrogen, e.g. $x < 0.01$, dissolved in the host material with hydrogen located in interstitial vacancies without significant change in the crystal structure of the metal host, M. These materials are referred to as hydrogen (metal) solid solution (α) phases. The solubility of hydrogen in metal solid solutions often diminishes rapidly with decreasing temperature, forming metal hydride precipitates at lower temperatures. High hydrogen concentrations, x = H/M, often extend to x = 3 or 4 for metal hydrides, e.g. LaH_3, SnH_4, and PbH_4, where the crystal structure of the hydride (β or γ) phase, e.g. face centered cubic (fcc) (or CaF_2 structure) for YH_2, is usually quite different from the parent metal, e.g. hexagonal close packed (hcp) for Y, and the density of the metal hydride typically is less than the parent metal density. Intermediate hydrogen concentration samples may be mixed hydrogen–metal solid solution α and metal hydride β phases. The observed NMR spectra and nuclear spin–lattice, R_1, and spin–spin, R_2, relaxation rates as functions of temperature may give evidence of the mixed phases (see ***Phase Transitions and Critical Phenomena in Solids***).

HMSs include hydrogen solid solutions of elemental metals, binary metal alloys, and intermetallic compounds, and also hydrides of metals, alloys, and intermetallic compounds. In addition, metallic halide compounds[5] and metal sulfides[6] adsorb hydrogen to significant degrees and should be included in HMSs. Some alloys and intermetallic compounds do not survive the hydriding process, but will disproportionate into hydrides of one or more of the metals and other compounds. In these cases, the hydride of the constituent metal is more stable than the hydride of the parent material.

Most NMR hydrogen–metal studies are made with samples sealed in quartz tubes to prevent loss of hydrogen upon heating the samples and to prevent oxidation or other contamination. Generally, the metallic nature of the materials requires powdered samples (particle size $\leq 100\,\mu$m) to permit the $\boldsymbol{B}_1$ rf magnetic field to penetrate the metallic particle's 'rf skin depth' uniformly. The spaces between powder particles contain hydrogen gas molecules which represent a characteristic hydrogen over pressure of the particles typical for that material, nominal hydrogen concentration, and sample temperature. The hydrogen gas molecules between particles are in constant exchange with the hydrogen atoms or ions within the metallic particles. The hydrogen exchange rate is often quite low for room temperature, but may be many orders of magnitude greater for $T > 700$ K.

The density of the hydrogen inside some hydrogen storage materials, e.g. $LaNi_5H_6$, is greater than the hydrogen density in liquid hydrogen by a factor of two or three. Generally, the

hydrogen density in the metallic powders is many orders of magnitude greater than the density of gas molecules between powder particles. Thus, the observed hydrogen spectrum is typically the spectrum of the hydrogen in the metal only. Recently, anomalously high proton spin–lattice relaxation rates, R_1, observed for $T > 700\,\mathrm{K}$ within the metal particles[7] have been understood in terms of exchange between bulk hydrogen atoms in the metallic powder and the much faster relaxing hydrogen gas molecules between the metallic powder particles[8] (see ***Hydrogen Molecules***).

2 HYDROGEN MOTION IN METALS DETECTED BY NMR

The early measurements of Norberg[2] demonstrated the motion of hydrogen in palladium. HMSs have been studied by NMR beginning with wideline CW methods measuring rigid lattice or low temperature linewidths and lineshapes. The low temperature or rigid lattice hydrogen linewidth originates from the magnetic interactions of the nuclear dipoles in the solid HMSs. Narrowing of the spectral lines with increasing temperatures gave clear evidence of hydrogen motion or hopping into interstitial vacancies within the solid.[9] This rapid hopping of hydrogen results in a simple averaging of the local magnetic field $\boldsymbol{B}_\mathrm{L}$ or the distribution of magnetic fields 'seen' by the hopping proton magnetic dipole moment. These motional narrowing studies yielded activation E_a energies of diffusion and moderately precise estimates of hydrogen jump frequencies, $\nu_\mathrm{j}(T)$, or alternately, of hydrogen 'dwell times' or mean residence time, $\tau_\mathrm{D}(T) = 1/\nu_\mathrm{j}(T)$, and hydrogen correlation times, $\tau_\mathrm{c}(T)$. With increasing T, when the average hydrogen jump frequencies exceeded the rigid lattice linewidth, the observed spectral lines narrowed. The temperature range for line-narrowing measurements was generally less than 100 K; Figure 1 from Schreiber and Cotts[10] shows multiple line-narrowing graphs of LaH_{2+x} against temperature. Lanthanum hydride shows the unusual ability to absorb hydrogen between compositions LaH_2 and LaH_3, maintains an fcc structure, and with each additional hydrogen, every hydrogen atom jumps more rapidly. In most HMSs, with increasing temperature, the average hydrogen jump frequency can easily exceed the proton resonance frequency.

The proton linewidths versus temperature[11] in zirconium chloride hemihydride ($ZrClH_{0.5}$) and zirconium chloride monohydride (ZrClH) are shown in Figure 2. This transition metal halide structure consists of two zirconium metal layers sandwiched between two chlorine layers. Hydrogen is known to reside in interstitial tetrahedral sites between the two zirconium metal layers. In addition, the crystal structures for the hemi- and monohydrides are know to be slightly different, due to the presence of the hydrogen in the material.[12]

Indirect evidence of hydrogen (deuterium) hopping was also observed on studying the ^{93}Nb electric quadrupole perturbed, NMR satellite line narrowing in $NbH_{0.73}$ and $NbD_{0.82}$ with increasing temperature.[13] Figure 3 shows the narrowing of the inhomogeneously broadened ^{93}Nb NMR satellite linewidth. This narrowing can be understood in terms of reducing the randomness (inhomogeneity) of the average value at the niobium ion sites due to the increased rapidity of the hopping motion of the hydrogen (deuterium) ions with temperature and their associated electrical charges in the vicinity of the niobium ion sites. The reduced average EFG at the ^{93}Nb site yielded a narrower NMR satellite linewidth. Thus, the stationary niobium NMR showed evidence of the mobile hydrogen (deuteron) ions hopping.

3 DYNAMIC STUDIES OF HYDROGEN MOTION IN A METAL

The magnetic dipole interactions of hydrogen with other hydrogen magnetic moments, with the host metal nuclear

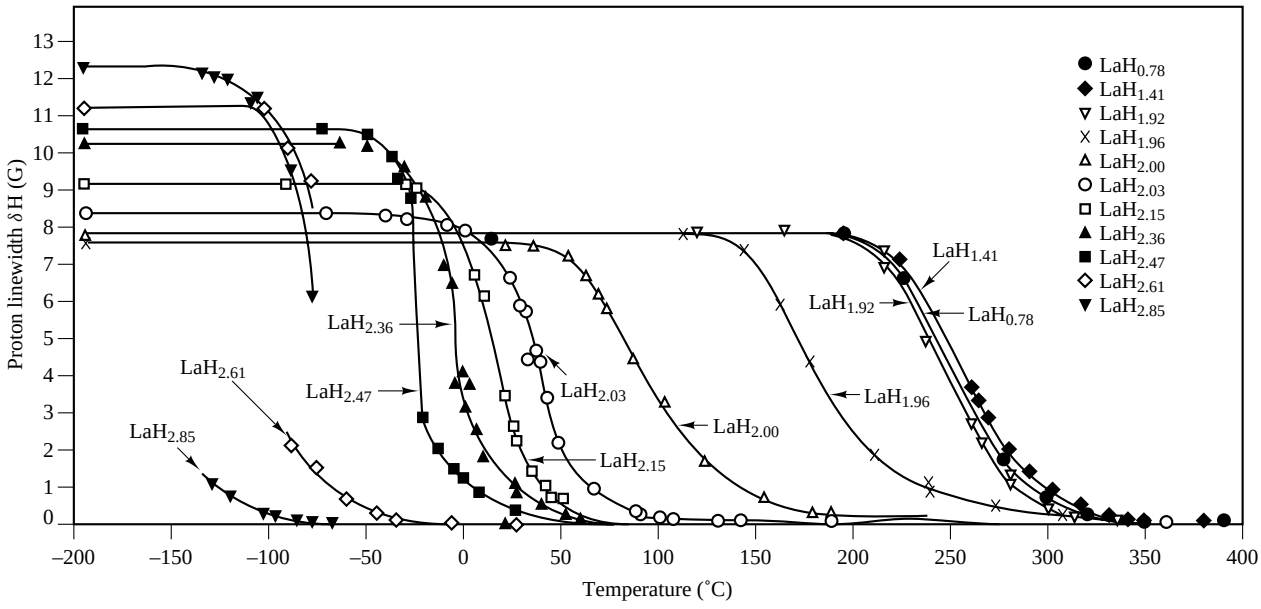

Figure 1 Proton linewidths (1G = 10^{-4} T) plotted against T for different x values. (Reproduced by permission of the American Physical Society from Schreiber and Cotts[10])

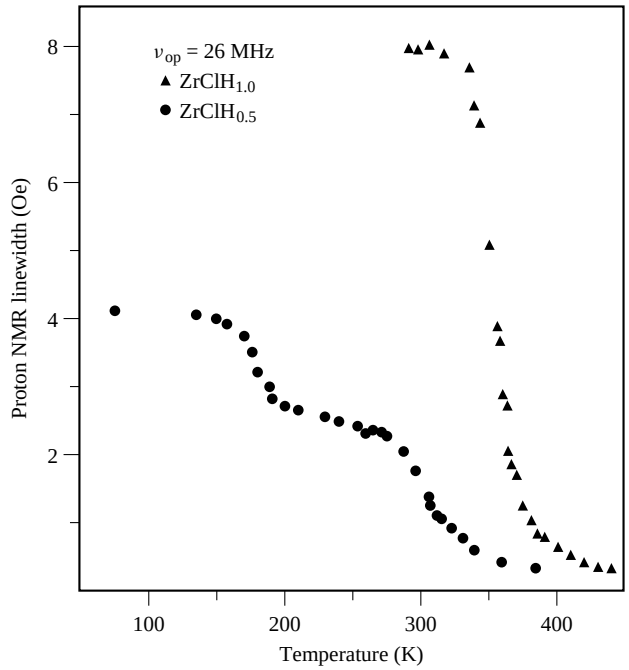

Figure 2 Temperature dependence of the proton linewidth in the two hydride phases of ZrCl, measured at nominal resonance frequency of 26 MHz. (Reproduced by permission of Elsevier Science Publishers B.V. from Hwang et al.[11])

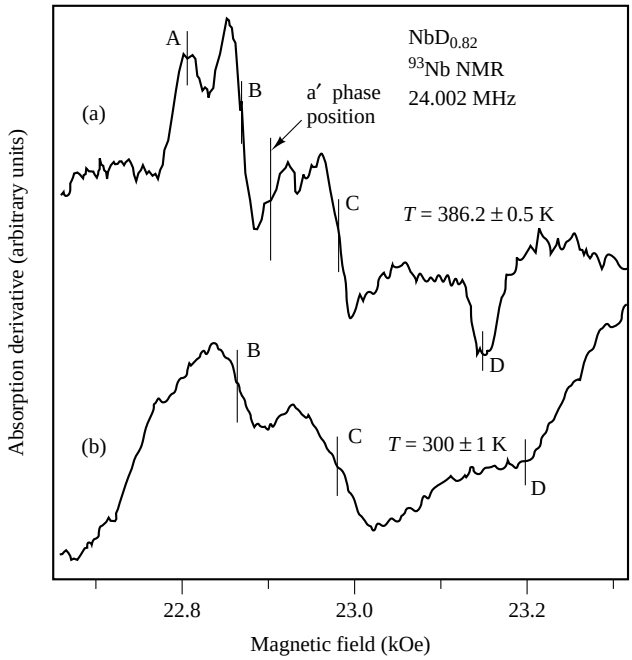

Figure 3 Wide line absorption derivative spectra of ^{93}Nb for 300 and 386 K. At 386 K hydrogen jumping rates are sufficiently fast to produce a spatial average of the electric field gradient at the Nb metal sites which narrows the spectra. (Reproduced by permission of Elsevier Science, Inc., from Hwang et al.[13])

moments, paramagnetic impurity moments, and with conduction electron magnetic moments generally govern the flow of spin energy within HMSs. Cross relaxation of protons and host metal nuclei having large nuclear electric quadrupole interactions has been observed. Also, as shown below, the hopping deuteron can be relaxed by interactions of its electric quadrupole moment with fluctuating EFGs within the material.

The observed hydrogen spin–lattice relaxation rate $R_1(\omega, T)$ varies greatly with temperature in HMSs, and is often the sum of several independent $R_1(T)$ rates, each due to separate physical relaxation mechanisms active in the material. Fortunately, these several R_1 rates have different resonance frequency and/or temperature dependences. With this fact in mind, we shall see how one can separate these spin–lattice relaxation mechanisms and thereby begin to characterize the materials.

The observed hydrogen spin–lattice relaxation rate (HSLR) R_1, in general, may be the sum of several of the following rates:[14]

$$R_1 = R_{1d} + R_{1e} + R_{1p} + R_{1CR} \tag{1}$$

where R_{1d} is the magnetic dipole–dipole relaxation of the hydrogen due to other hopping hydrogen. Bloembergen, Purcell and Pound[15] (BPP) were first to suggest the form of relaxation

$$R_{1d} = \frac{1}{T_{1d}} = M_2(T)J(\omega_0, T) \tag{2}$$

where M_2 is a mean-square fluctuating field most commonly thought to be related to the magnetic dipole–dipole interaction of the hydrogen with other magnetic moments. However, in the case of the deuteron, this formalism can also be expressed in terms of the fluctuations of the EFG about the deuteron electric quadrupole moment.[16] In this case, R_{1d} is then written R_{1q} (q denoting quadrupolar relaxation). ω_0 is the spin precession frequency in angular frequency units. $J(\omega_0)$ is the power spectrum or spectral density function of the fluctuation magnetic fields (or fluctuating EFGs) within the sample. The simplest form of $J(\omega)$ is the Lorentzian

$$J(\omega) = \frac{\tau_c}{1 + \omega^2\tau_c^2} \tag{3}$$

where τ_c is the correlation time and is strongly temperature dependent. Often τ_c varies exponentially with temperature, where $\tau_c = \tau_0 \exp(-E_a/kT)$ and where $1/\tau_0$ is thought to be the attempt frequency of hydrogen jumping or the high temperature 'rattling' frequency of hydrogen within the interstitial site.

Equation (2) is often written with an additional Lorentzian term, including dipolar interaction terms at 2ω, as

$$R_{1d} = M_2(T)\left(\frac{\tau_c}{1 + \omega^2\tau_c^2} + \frac{4\tau_c}{1 + (4\omega^2\tau_c^2)}\right) \tag{4}$$

This simple description includes no details of the hydrogen interactions with metal nuclear moments or structure considerations of the HMS. It also ignores any orientation dependence of the crystal (sample) with the magnetic field $\boldsymbol{B}_0$ direction. Nonetheless, this BPP description is quite a good characterization of the hydrogen relaxation in many simple HMSs.

In a detailed description of hydrogen relaxation anisotropy in single crystal HMSs, Hoke et al.[17] gave the relaxation rate

of protons in an hcp single crystal of $ScH_{0.25}$ as

$$R_1 = \left(\frac{\mu_0}{4\pi}\right)^2 \gamma_H^2 \gamma_S^2 \left(\frac{h}{2\pi}\right)^2 S(S+1)\left(\tfrac{1}{12}J^{(0)}(\omega_H - \omega_S) + \tfrac{3}{2}J^{(1)}(\omega_H) + \tfrac{3}{4}J^{(2)}(\omega_H + \omega_S)\right) \quad (5)$$

following Abragam[18] where γ_H and γ_S are the gyromagnetic ratios of the hydrogen and metal, S is the spin (in this case, ^{45}Sc $S = \frac{7}{2}$), and $J^{(q)}(\omega)$ are spectral density functions which depend on the diffusion model chosen and on the orientation of the crystal in the magnetic field. Within the three spectral density functions $J^{(0)}$, $J^{(1)}$, and $J^{(2)}$ the frequencies $\omega_H - \omega_S$, ω_H, and $\omega_H + \omega_S$ are the difference between hydrogen and metal frequencies, the hydrogen frequency, and the sum of hydrogen and metal frequencies, respectively.

Interestingly, the anisotropy in R_1 originates in the anisotropy of $J^{(q)}(\omega)$, written by Sholl[19] as

$$J_{qq'} = \sum_{\alpha,\beta} \frac{Y_{2q}(\Omega_\alpha)}{r_\beta^3} \frac{Y_{2q'}(\Omega_\beta)}{r_\beta^3} P(r_\alpha, r_\beta, \omega) \quad (6)$$

where Y_{2q} are spherical harmonics, r_α is the distance between the proton and metal spin at time zero, and r_β is the distance between the proton and metal spin at time t. $P(r_\alpha, r_\beta)$ is the Fourier transform of the probability function for the diffusion model chosen.[17]

The conduction electron moments in the HMS relax the hydrogen moment through a contact hyperfine interaction the same as is associated with the Knight shift.[18,20] The relaxation rate R_{1e} is proportional to the temperature and the square of the Knight shift (see Section 4 for a simple description of the Knight shift) and the square of the density of unpaired electronic (moment) states at the Fermi energy $N(E_F)$. Generally, the better the conductivity of the metallic material the greater the electronic relaxation rate R_{1e}:

$$R_{1e} = \frac{1}{T_{1e}} \propto N^2(E_F)T \quad (7)$$

For a simple metallic material, combining the Knight shift with relaxation rate,

$$T_{1e}TK^2 = \frac{T}{R_{1e}}K^2 = \frac{h/2\pi}{4\pi k}\frac{\gamma_e^2}{\gamma_n^2} \quad (8)$$

where γ_e and γ_n are the electron and nuclear (hydrogen) gyromagnetic ratios. This equation is known as the Korringa or Heitler–Teller–Korringa (HTK) relation,[21] where the Knight shift and R_{1e}/T are theoretically constant in temperature and R_{1e}/T or $1/T_{1e}T$ is often used to characterize the electronic relaxation in HMSs.

Unwanted paramagnetic ion concentrations, ignored in several NMR studies of HMSs, have shown unusual, anomalous relaxation rates and 'extra features' in the measured HSLR which have been attributed to a fictitious complex or additional diffusion mechanism. Phua et al.[22] showed that many such unusual or extra relaxation mechanisms were most likely due to the existence of residual paramagnetic impurities (dirt) in the host metals present at the time of the formation of the HMS. That study showed, generally, that the extra spin–lattice relaxation rates, R_{1p}, were linearly proportional to the concentration of paramagnetic impurities present. In addition, extra minima in $\log(T_1)$ versus $1/T$ were a direct result of the impurity relaxation; see Figure 4 for evidence of the suppression of $\log(T_1)$ versus $1/T$ and 'extra minima'. The paramagnetic moments produce a relaxation rate R_{1p} in HMS and can relax hydrogen by spin diffusion at low temperature in the low hydrogen diffusion regime. At higher temperatures, in the fast diffusion regime, hydrogens approach the stationary paramagnetic ions by rapid hopping within the sample and are relaxed via direct dipolar interactions with the paramagnetic impurity ions.

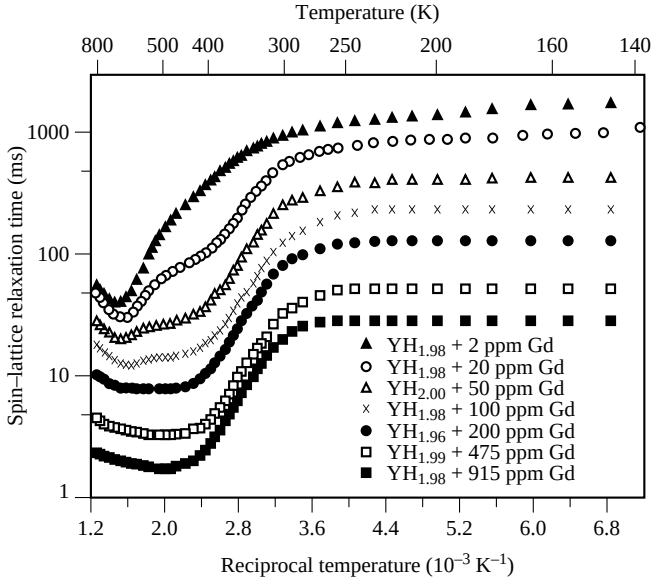

Figure 4 Proton spin–lattice relaxation time T_1 vs. $1000/T$ in YH_2 vs. Gd impurity concentration. (Reproduced by permission of American Physical Society from Phua et al.[22])

The cross relaxation of the proton, R_{1cr}, with certain host metal nuclei which have large electric quadrupole moments and subsequently large quadrupole interactions was recognized for protons in HMS at low temperatures (see Figure 5) where hydrogen hopping rates are slow. The strong nuclear electric quadrupole interactions of the metal nuclei, e.g. ^{175}Lu in $LuH_{0.20}$[23] and ^{181}Ta in Ta_2H[24] are many tens of megahertz in extent (width) and are only perturbed by the static magnetic field $\boldsymbol{B}_0$ required for proton resonance. Although the ^{93}Nb quadrupole moment and interaction in $V_xNb_{1-x}H_y$, for example, is weaker than ^{181}Ta in Ta_2H and ^{175}Lu in $LuH_{0.20}$, for frequencies $f_{max} < 24$ MHz, protons also cross relax to ^{93}Nb. When the proton resonance frequency matches one of the many spectral features of the metal NQR, spin polarization energy is transferred from the proton to the metal nucleus. The spin polarization energy is taken from the metal nucleus by the conduction electron interaction to the lattice because the contact hyperfine interaction is much stronger and thus faster (or higher rate) for the metal nucleus than for the proton. Figure 6 shows the proton cross relaxation to ^{181}Ta in $TaH_{0.32}$ as a function of proton resonance frequencies[24] (for a series of magnetic field values) while at $T = 130$ K. The calculation of the cross relaxation as a function of proton frequencies is described by Lichty et al.[24]

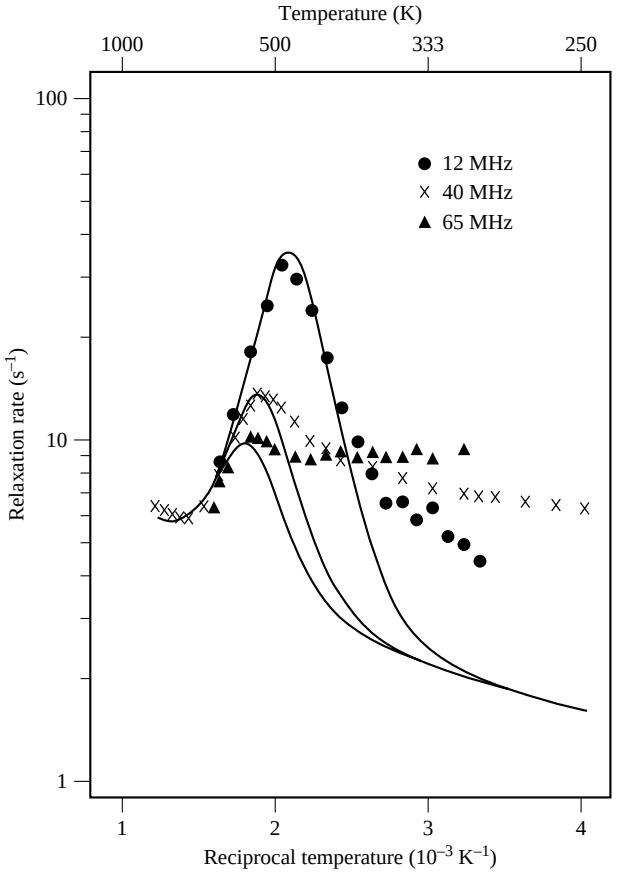

Figure 5 Proton spin–lattice relaxation rates R_1 vs. $1000/T$ in LuH_x at 12, 40 and 65 MHz. Cross relaxation between the protons and the ^{175}Lu nuclear electric quadrupole broadened NMR lines can be seen at low temperatures in the loss of temperature dependence for $T \leq 400$ K. (Reproduced by permission of R. Oldenbourg Verlag from Torgeson et al.[23])

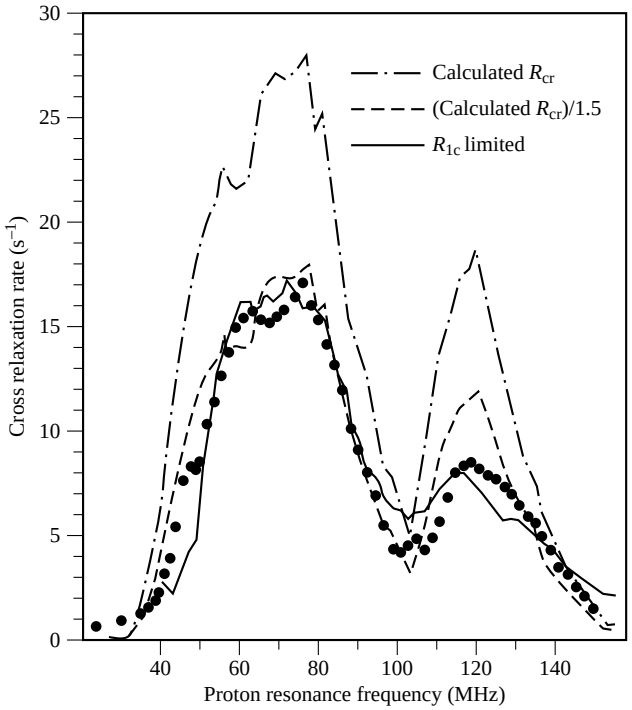

Figure 6 Proton cross-relaxation data (•) to ^{181}Ta nuclear electric quadrupole broadened NMR lines in Ta $H_{0.32}$ as a function of a series of proton resonance frequencies at 130 K. See Lichty et al.[24] for details of the theoretical calculations and the three curves presented. The analysis yielded a ^{181}Ta nuclear electric quadrupole frequency γ_Q = 43 MHz and electric field gradient asymmetry parameter η = 0.35. (Reproduced by permission of American Physical Society)

Figure 7 shows the total spin–lattice relaxation rate versus reciprocal temperature in schematic form, typical of many HMSs with the several component relaxation rates identified.

4 DEUTERON LINESHAPE FOR COMBINED ELECTRIC QUADRUPOLE AND KNIGHT SHIFTS

The Knight shift of hydrogen results from a small magnetic field at the hydrogen nucleus in an HMS from the conduction electron wave function $|\psi(0)|^2 \neq 0$ for the s electron character of the conduction electrons. This is often called the 'contact hyperfine interaction' or Fermi contact term. The application of the $\boldsymbol{B}_0$ field causes a small paramagnetic polarization of the conduction electrons, called the Pauli paramagnetism, where $M_s = \chi_s B_0$ and χ_s is the Pauli spin susceptibility. χ_s can be related to the density $N(E_F)$ of unpaired conduction electron states at the top of the conduction electron distribution or at the Fermi energy via the Pauli susceptibility $\chi_s = \frac{1}{2}(\gamma_e h)^2 N(E_F)$. The Knight shift can be written simply as $K \approx \chi_s |\psi(0)|^2/N$. The Knight shift causes a fractional change in the proton (deuteron) gyromagnetic ratio, that is, a small shift in position of the hydrogen resonance ΔH for fixed frequency or $\Delta\nu$ for fixed field measurements

$$K = \frac{\Delta H}{H} = \frac{H_R - H_M}{H_R} = \frac{\Delta\nu}{\nu} = \frac{\nu_M - \nu_R}{\nu_R} \qquad (9)$$

where subscript M refers to the metal field or frequency and R refers to the reference (solution or free ion) field or frequency. These fractional shifts are generally independent of the field or frequency.

Knight shifts of hydrogen in HMSs are generally quite small in magnitude compared with Knight shift values of metals, and often smaller in field shift magnitude ΔH than the dipolar broadened width or the $\boldsymbol{B}_L$ local magnetic field in the solid. However, the magnetic moment of the deuteron is smaller than the proton by a factor of 3.3, and effects of local magnetic fields are correspondingly smaller than for the proton. Figure 8 shows the combined effects of ^{2}D nuclear electric quadrupole interaction and Knight shifts[25] in a sample of $NbD_{0.76}$. The general subject of combined nuclear electric quadrupole interactions and Knight shift interactions in metals was first presented by Jones et al.[26] Since the ^{2}D spin I = 1, there are $2I$ + 1 or 3 levels and two transitions and no 'central line'. These two transitions for spin I = 1 are commonly referred to as the Pake doublet,[27] following the terminology established by George Pake in 1948 for the interaction of two coupled protons of combined spin I = 1 in the water of hydration in gypsum.

$NbD_{0.76}$ is orthorhombic in structure and thus the EFG and the Knight shifts must be described by tensors. The principal

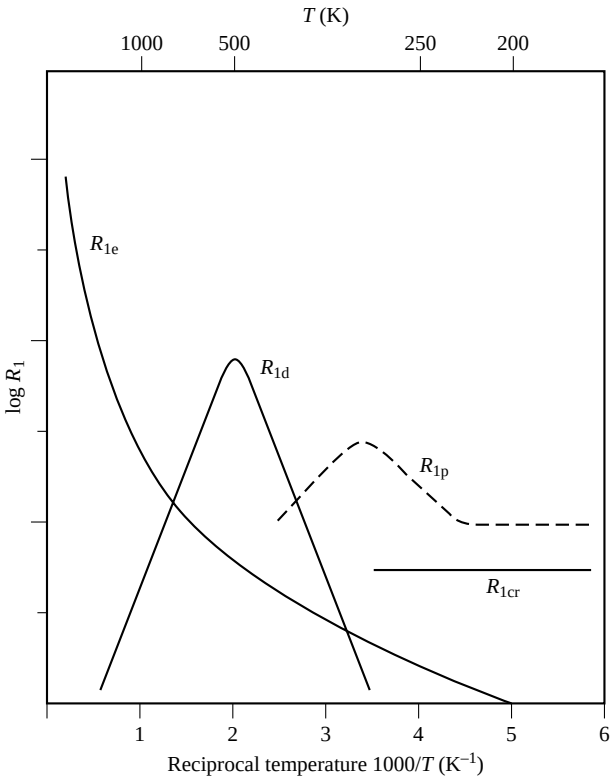

Figure 7 Generalized proton spin–lattice relaxation rate R_1 contributions vs 1000/T. These relaxation rates are: conduction electron, R_{1e}; long range diffusion/dipole–dipole, R_{1d}; paramagnetic impurity ion, R_{1p}; and cross-relaxation to quadrupole (metal) nucleus, R_{1cr}. The relative weighting of these mechanisms depends on the purity and physical details of the HMS sample studied

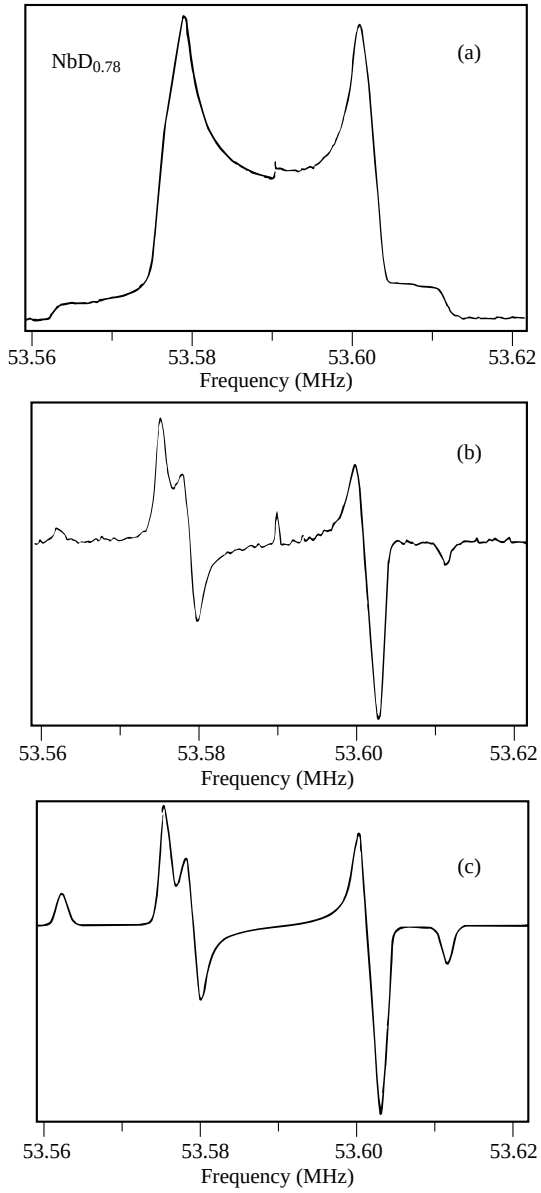

Figure 8 (a) Deuteron absorption curve vs. frequency for $NbD_{0.56}$, (b) derivative of observed deuteron absorption curve, and (c) calculated deuteron absorption derivative curve lineshape. (Reproduced by permission of Academic Press from Torgeson et al.[25])

axis system of the EFG has three separate components V_{xx}, V_{yy}, and V_{zz}, the second derivatives of the crystalline potential with respect to the coordinates x, y, and z. Note that $\nabla^2 V = V_{xx} + V_{yy} + V_{zz} = 0$ is Laplace's (electrical) equation. In the principal axis system, $|V_{xx}| < |V_{yy}| < |V_{zz}|$. The EFG asymmetry parameter for $NbD_{0.76}$ is $\eta = (V_{xx} - V_{yy})/V_{zz} = 0.11$. If η were equal to 0, then $V_{xx} = V_{yy}$ would require axial symmetry, i.e. at least three-fold rotational symmetry about the z axis. $\eta \neq 0$ implies the $\Delta m = \pm 1$ transitions $-1 \leftrightarrow 0$ and $0 \leftrightarrow +1$ in combination with the K_x, K_y, and K_z Knight shift components will produce different frequency dependences for the two transitions or ^{2}D 'powder' lineshapes.[25] The width of the pattern essentially measures the strength of the deuteron electric quadrupole interaction described by the lowest pure quadrupole frequency $\nu_Q = 3eQV_{zz}/2h = 49.3$ kHz, where eQ is the deuteron quadrupole moment, V_{zz} is the principal component of the EFG tensor and h is Planck's constant. Incidentally, $\nu_Q = 3eQV_{zz}/[2I(2I-1)h]$ is the best measure of the strength of the quadrupole interaction relative to the strength of the NMR interaction characterized by ν_0, the Larmor frequency.[28]

For powdered metal hydrides with less than cubic crystal symmetry, the single grain particles' major symmetry axes will simply point in random directions in space. However, with an applied magnetic field switched on, the majority of particles' major symmetry axes will be nearly perpendicular to the field direction and a small minority of crystal symmetry directions will point along the field direction. This produces the well known sin θ dependence of the distribution of powder particle orientations with respect to the magnetic field direction. As pointed out by Jones et al.[26] the major peaks of the absorption spectrum are due to 'singularities' at the perpendicular ($\theta = 90^\circ$) powder grains, and the smaller 'steps' at the extremes of the spectrum are due to those particle crystallites nearly parallel ($\theta = 0^\circ$) to the magnetic field.

The deuteron Knight shift, as for all hydrogen Knight shifts, originates from the contact hyperfine interaction of the conduction electrons at the deuteron (hydrogen) nucleus. In the HMS, the conduction electrons are attracted or 'cored' to the hydrogens in the same way conduction electrons are attracted to the metal nuclei. This, of course, makes the conduction electron wave functions more complex than in the pure metal, alloy, or intermetallic compound. The presence of

the hydrogen may actually change the electronic character of the HMS by changing the conduction electron wave functions and by the hydrogen donating an electron to the conduction band when hydrogen is absorbed, which may greatly modify the electronic band structure of the HMS.

The effect of the Knight shifts on the observed lineshape is simply a small displacement of the resonance position due to an additional magnetic field at the nucleus from the contact hyperfine interaction. For a non-cubic metal or HMS, the magnitude of the shift of the resonance is dependent upon orientation of the crystalline axes of the grain with respect to the field direction. Figure 8 (a) shows the observed absorption curve, (b) a derivative of the observed absorption and (c) a calculated absorption derivative with appropriate Knight shift and EFG components included. Absorption derivative lineshapes actually show more subtle lineshape features than do the absorption curves. Absorption derivatives lineshapes were commonly recorded in field or frequency scanned CW wideline studies in past years because of the use of lock-in amplifiers and small amplitude magnetic field or frequency modulation to record spectra.

5 LOW TEMPERATURE LOCAL HYDROGEN MOTION AND HYDROGEN TUNNELING IN HMSs

Scandium, yttrium, and lutetium plus other rare earth hcp metals provide a nearly unique opportunity to observe hydrogen dissolved in metals and measure hydrogen motions in metals at temperatures below 150 K. Unlike many transition metals, scandium, yttrium, and lutetium can maintain up to 30 at% hydrogen in solution without precipitating any of the hydride phase[29] down to 4 K or without transforming to another crystal structure.

Lichty et al.[30] measured proton R_1s in $ScH_{0.27}$ ($H_{0.18}$) and found both an electronic relaxation R_{1e} and a weak low temperature motional relaxation peak R_{1L} near 60 K (105 K). That peak moved with the proton resonance frequency in a manner similar to the movement of R_{1d}, the over the barrier hopping, long range diffusion relaxation rate peak at much higher temperatures. In Figure 9 we see these low temperature data for two proton frequencies. The R_{1L} motional relaxation peak is superimposed on the R_{1e} electronic relaxation, which is linear in temperature T ($R_{1L} = R_1 - R_{1e}$; R_{1L} will be discussed below).

The location of hydrogen (deuterons) in the scandium hcp lattice was studied by neutron scattering.[29] Deuterons were found to prefer to form pairs with a scandium atom between. From these neutron scattering studies, models of hydrogen ordering in chains of paired hydrogens in scandium were proposed.

The pairing of hydrogen with a scandium metal between is an interesting and unusual ordering. However, not all hydrogens are paired with a metal between. Some of the hydrogens are unpaired and thus occupy vacant tetrahedral (T) sites in a random or inhomogeneous manner. The random occupation of hydrogen in metal–solid solutions has been referred to by Barnes[14] as a proton glass. The result of an inhomogeneous hydrogen occupation can be seen in the proton spin–lattice relaxation rate data and will be explained below.

The scandium hcp lattice has two adjacent, closely spaced interstitial T sites along the c axis where hydrogen is known[29]

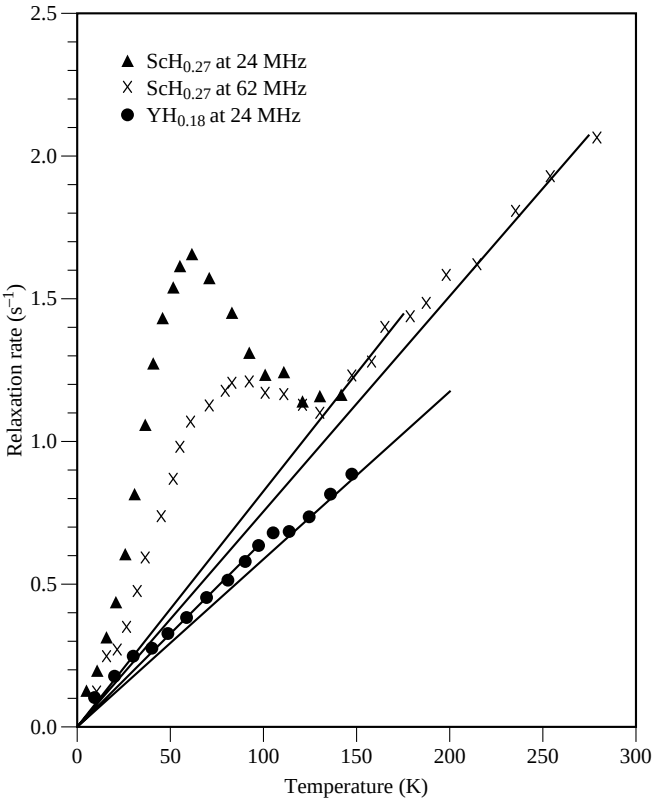

Figure 9 Proton spin–lattice relaxation rate (R_1) in $ScH_{0.27}$ as a function of temperature at 24 and 62 MHz. Proton R_1 in $YH_{0.18}$ at 24 MHz (●) shows a weak peak at ~105 K. The peak heights are due to the relaxation of the proton's tunneling motion and proton dipole 'collisions' with fixed (^{45}Sc or ^{89}Y) metal nuclear magnetic moments. Note the ^{89}Y moment is <1/20 of the ^{45}Sc moment. (Reproduced by permission of the American Physical Society from Lichty et al.[30])

to sit in one of the sites. These two sites are too closely spaced to permit two hydrogens to occupy both sites simultaneously.[31] The local motion is understood to be one hydrogen moving between these two closely spaced T sites. Activation energies derived from a 'local over a small barrier' hopping model were found to be $E_a \approx 50$ meV, much smaller than the nominal 500 meV activation energies typical of long-range hopping over a barrier found for activation energies in higher temperature hydrogen diffusion. Lichty et al.[30] were able to fit the proton spin–lattice relaxation rates versus 1000/T with two separate and quite different models for hydrogen hopping over an energy barrier. As can be seen from Figure 10, the data are not symmetrical about the peaks of the three relaxation curves. The slope of the three curves on the high temperature (low 1/T values) side of the peak is much greater than the low temperature (higher 1/T values) slopes. Symmetrical log R_1 versus 1/T curves in HMSs is a signature of hydrogen hopping where there is one unique activation energy typifying a simple hopping process and/or a simple and often cubic solid. Symmetrical log R_1 or log T_1 vs 1/T curves are often referred to as BPP type behavior. The relaxation rate curves in Figure 10 show the signature of hydrogen motion in a disordered solid with a distribution of activation energies. This subject will be discussed at length below. Lichty et al.[30] were able to fit the data with two hopping models, one assuming a distribution of activation energies and a second model with a correlation

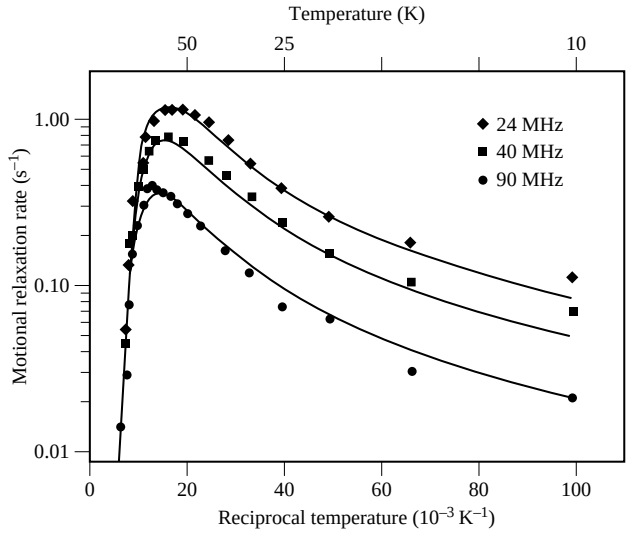

Figure 10 Proton spin–lattice relaxation rate in $ScH_{0.27}$ vs. 1000/T for proton resonance frequencies 12, 40, and 90 MHz fitted with a thermally activated over the barrier hopping model and a distribution of activation energies. (Reproduced by permission of the American Physical Society from Lichty et al.[30])

function having a stretched exponential character. Localized hydrogen motion has also been found by Skripov et al.[32] in TaV_2H_x in the temperature range 10–100 K.

Tunneling of hydrogen from one tetrahedral interstitial site to an adjacent empty T site at low temperature is an alternate mechanism rather than hydrogen thermally activated hopping over a low energy barrier. Svare et al.[33] suggested that the same proton spin–lattice relaxation data of Lichty et al.[30] in $ScH_{0.27}$ could also be described by hydrogen tunneling between adjacent T sites in the Sc hexagonal close packed lattice. The potential wells for the two sites were thought to have sinusoidal curvature near the bottoms. The two wells of the adjacent T sites were also thought to have different minimum energies, that is, the wells were asymmetric. In fact, Svare et al.[33] suggested the asymmetry, A, for the hydrogen–scandium metal solid solution would have a distribution of minimum energy difference values typical of an inhomogeneous hydrogen solid solution or proton glass. With increasing temperature, the tunneling model must include a tunneling mechanism not appropriate (or yet thermally switched on) at lower temperature. Figure 11 shows the proton spin–lattice relaxation data of Lichty et al.[30] fit with this tunneling model. The data fit adequately this tunneling theory and support the proposition that hydrogen tunneling exists in scandium at low temperatures. Hydrogen tunneling in scandium was also found by Leisure et al.[34] in a resonant ultrasound spectroscopy (not an NMR technique) study of $ScH_{0.25}$ and $ScD_{0.18}$ employing small scandium single crystals.

6 SPIN–LATTICE RELAXATION IN AMORPHOUS HYDROGEN–METAL SYSTEMS

An amorphous metal alloy may be formed by extremely rapid cooling of the molten metal alloy. Such materials are often referred to as metallic glasses. An amorphous alloy is a

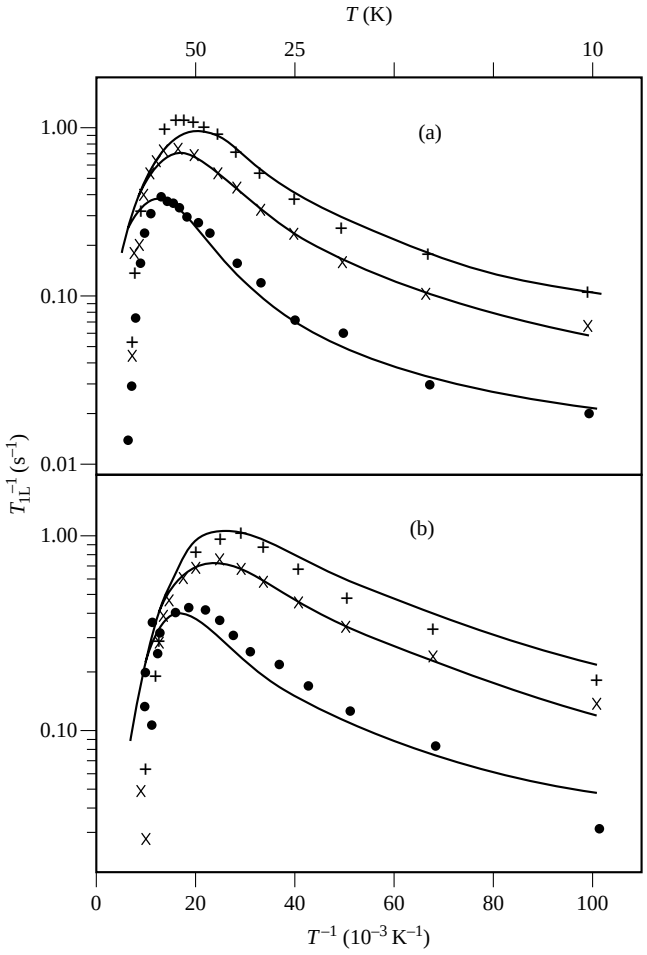

Figure 11 Low temperature proton spin-lattice relaxation rates $R_{1L} \equiv T_{1L}^{-1}$ versus reciprocal temperature in two hcp scandium–hydrogen solid solution compositions. (a) $ScH_{0.27}$ and (b) $ScH_{0.11}$ at 24 MHz (+), 40 MHz (×), and 90 MHz (•), respectively. The curves represent the fits of the tunneling model with a distribution of asymmetric energy well minima for hydrogen tunneling between adjacent tetrahedrally coordinated interstitial (T) sites. Data are from Lichty et al.[30] and tunneling model can be found in Svare et al.[33]

disordered metal and is without long range topological order. There may be short range or compositional order in amorphous alloys. These amorphous materials are then hydrided by more or less conventional means, but care must be taken not to heat the material high enough to 'recrystallize' the amorphous sample. This may be somewhat difficult as the absorption of hydrogen by metals is generally an exothermic reaction.

Bowman[35] points out that metallic alloy glasses must contain one of certain metals, i.e. titanium, zirconium, hafnium, palladium, or a rare earth metal, for the glass to be able to hold hydrogen, H/M > 0.1, where M is the total metal content. Even with one of these metals in the alloy, an alloy glass may not be formed upon quenching.

Hydrides of metallic glasses generally have quite different hydrogen motions, with lower hydrogen diffusion activation energies and spin–lattice relaxation rates than do hydrides of the crystalline HMSs of similar composition as we shall see below. In the case of crystalline and amorphous Zr_2PdH_x, Bowman et al.[36] point out the log T_1 versus 1000/T plots for $Zr_2PdH_{2.90}$ and amorphous a-$Zr_2PdH_{2.90}$ are noticeably

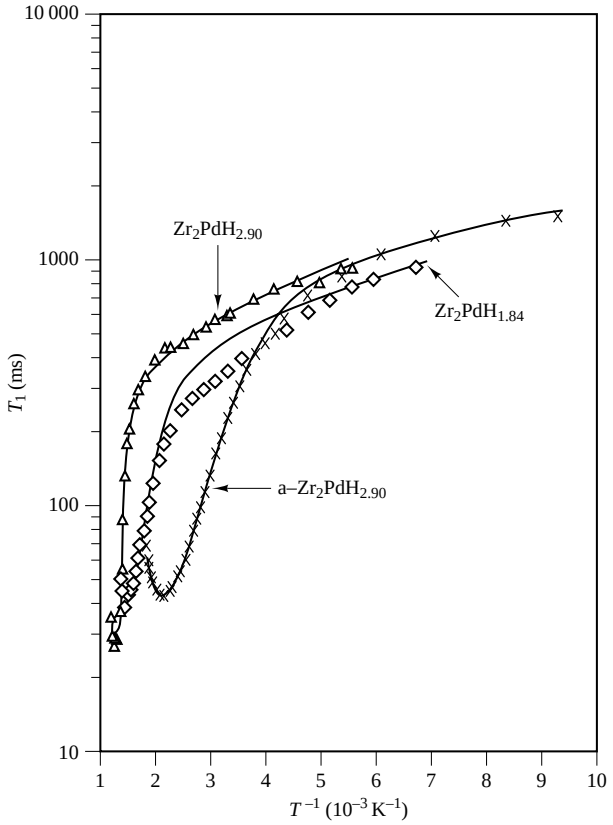

Figure 12 Proton spin–lattice relaxation times vs. 1000/T for crystalline $Zr_2PdH_{1.84}$ and $Zr_2PdH_{2.90}$ at 40 MHz and amorphous $Zr_2PdH_{2.90}$ at 34.5 MHz, and proton relaxation times for crystalline and amorphous $Zr_2PdH_{2.90}$ vs 1000/T. The latter curve shows hydrogen diffusion at lower temperatures and with lower activation energy (slope of T_1 vs. 1000/T curve) than the crystalline $Zr_2PdH_{2.90}$. (Reproduced by permission of R. Oldenbourg Verlag from Bowman et al.[36])

different. The crystalline and amorphous curves have minima at different temperatures and have different slopes or diffusion activation energies. Generally, the amorphous samples display more rapid hydrogen diffusion at lower temperatures and have lower activation energies for diffusion than do the crystalline equivalents. This can be seen in Figure 12. A simplistic explanation of this effect may relate in part to the fact that the glassy HMSs have a somewhat lower density and have more 'open' paths for hydrogen to hop through than the crystalline equivalents. A more complete description of hydrogen motion must also include the differences in electronic character known to exist between the glassy and crystalline HMSs.

7 RELATED ARTICLES

Amorphous Materials; Deuterium NMR in Solids; Diffusion in Solids; Electron–Nuclear Hyperfine Interactions; Knight Shift; Spin Diffusion in Solids.

8 REFERENCES

1. W. H. Mueller, J. P. Blackledge, and G. C. Libowitz. *Metal Hydrides*, Academic Press, New York, 1968.
2. R. E. Norberg, *Phys. Rev.*, 1952, **86**, 745.
3. D. Khatamin, W. A. Karmatakahara, R. G. Barnes, and D. T. Peterson, *Phys. Rev. B*, 1980, **21**, 2622.
4. R. C. Bowman, Jr., B. D. Freeman, and J. R. Phillips, *Cryogenics*, 1992, **32**, 127.
5. A. Struss and J. D. Corbett, *Inorg. Chem.*, 1977, **38**, 612.
6. Y. S. Hwang, D. R. Torgeson, A. S. Khan, and R. G. Barnes, *Phys. Rev. B*, 1977, **15**, 4564.
7. R. G. Barnes, M. Jerosch-Herold, J. Shinar, F. Borsa, D. R. Torgeson, D. T. Peterson, A. J. Lucas, G. A. Styles, and E. F. W. Seymour, *Phys. Rev. B*, 1987, **35**, 890.
8. D. B. Baker, N. Adolphi, M. S. Conradi, P. A. Fedders, R. E. Norberg, R. G. Barnes, and D. R. Torgeson, *Phys. Rev. B*, 1992, **46**, 184.
9. E. F. W. Seymour, *J. Less-Common Met.*, 1982, **88**, 323.
10. D. S. Schreiber and R. M. Cotts, *Phys. Rev.*, 1963, **131**, 1118.
11. T. Y. Hwang, D. R. Torgeson, and R. G. Barnes, *Phys. Lett.*, 1978, **66A**, 137.
12. H. S. Marek, J. D. Corbett, and R. L. Daake, *J. Less-Common Met.*, 1983, **89**, 249.
13. Y. S. Hwang, D. R. Torgeson, and R. G. Barnes, *Solid State Commun.* 1977, **24**, 773.
14. R. Barnes, *J. Less-Common Met.*, 1991, **172–174**, 509.
15. N. Bloembergen, E. M. Purcell, and R. V. Pound, *Phys. Rev.*, 1948, **73**, 679.
16. F. Borsa, R. G. Barnes, B. J. Beaudry and D. R. Torgeson, *Phys. Rev. B*, 1982, **26**, 1471.
17. H. C. Hoke, H. E. Schone, C. A. Sholl, S. P. Usher, R. G. Barnes, D. R. Torgeson, R. Hempelmann, and G. A. Styles, *J. Less-Common Met.*, 1991, **172–174**, 603.
18. A. Abragam, *The Principles of Nuclear Magnetism*, Oxford Press, 1961.
19. C. A. Sholl, *J. Phys. C: Solid State Phys.*, 1986, **19**, 2547.
20. C. P. Slichter, *Principles of Magnetic Resonance*, Springer-Verlag, 3rd ed, 1990.
21. W. Heitler and E. Teller, *Proc. R. Soc. London*, 1936, **A155**, 637; and J. Korringa, *Physica*, 1950, **88**, 323.
22. T.-T. Phua, B. J. Beaudry, D. T. Peterson, D. R. Torgeson, R. G. Barnes, M. Belhoul, G. A. Styles, and E. F. W. Seymour, *Phys. Rev. B*, 1983, **28**, 6227.
23. D. R. Torgeson, J.-W. Han, P.C-T. Chang, L. R. Lichty, R. G. Barnes, E. F. W. Seymour, and G. W. West, *Z. Phys. Chem. NF*, 1989, **164**, 853.
24. L. R. Lichty, J.-W. Han, D. R. Torgeson, R. G. Barnes, and E. W. F. Seymour, *Phys. Rev. B*, 1990, **42**, 7734.
25. D. R. Torgeson, R. J. Schoenberger, and R. G. Barnes, *J. Mag. Reson.*, 1986, **68**, 85.
26. W. H. Jones, Jr., T. P. Graham, and R. G. Barnes, *Phys. Rev.*, 1963, **132**, 1898.
27. G. Pake, *J. Chem. Phys.*, 1948, **16**, 327.
28. D. R. Torgeson and R. G. Barnes, *Phys. Rev. Lett.*, 1962, **9**, 255.
29. O. Blaschko, G. Krexner, J. N. Daou, and P. Vajda, *Phys. Rev. Lett.*, 1985, **55**, 2876.
30. L. R. Lichty, J.-W. Han, R. Ibanez-Meier, D. R. Torgeson, R. G. Barnes, E. F. W. Seymour, and C. A. Sholl, *Phys. Rev. B*, 1989, **39**, 2012.
31. L. R. Lichty, R. J. Schoenberger, D. R. Torgeson, and R. G. Barnes, *J. Less-Common Met.*, 1987, **129**, 31.
32. A. V. Skripov, M. Yu Belyaev, S. V. Rychkova, and A. P. Stepanov, *J. Phys. Condens. Matter*, 1989, **1**, 2121.
33. I. Svare, D. R. Torgeson, and F. Borsa, *Phys. Rev. B*, 1991, **43**, 7448.

34. R. G. Leisure, R. B. Schwarz, A. Migliori, D. R. Torgeson, and I. Svare, *Phys. Rev. B*, 1993, **48**, 893.
35. R. C. Bowman, Jr., *Mater. Sci. Forum*, 1988, **31**, 197.
36. R. C. Bowman, Jr., D. R. Torgeson, R. G. Barnes, A. J. Maeland, and J. J. Rush, *Z. Phys. Chem., NF*, 1989, **163**, 425.

Biographical Sketch

David R. Torgeson. *b* 1936. B.A., 1958, Luther College. M.S., 1960, Iowa State University. Introduced to NMR by R. G. Barnes. Basic physics research utilizing nuclear and electron resonance techniques, Ames Laboratory, Iowa State University, 1960–present. Assistant Professor of Physics, Luther College, 1967–68, and ISU, 1972. Physicist, Ames Laboratory, 1982–present. Adjunct Assistant Research Professor of Physics, Iowa State University, 1993–present. Approx. 120 publications. Research interests include: application of NMR for materials characterization of hydrogen–metal systems, fast ion conductors, high temperature superconductors, and quasicrystals; and instrumentation for solid state NMR.

Silica Surfaces: Characterization

Gary E. Maciel
Colorado State University, Fort Collins, CO, USA

1	Introduction	1
2	NMR Strategies for Silica Surface Selectivity	1
3	$^{1}H \rightarrow {}^{29}Si$ CP in Silicas	2
4	$^{1}H \rightarrow {}^{17}O$ Cross Polarization	5
5	Proton NMR Approaches	5
6	Correlating ^{1}H-based and ^{29}Si-based Information	11
7	Subsurface Silanols	14
8	Summary and Conclusions	14
9	Related Articles	15
10	References	15

1 INTRODUCTION

Silica (SiO_2) is one of the most abundant materials on Earth.[1] If the wide range of silicate minerals in which silica 'formally' occurs is included, one can account for more than 60% of the Earth's crust in terms of silica. From the industrial point of view, the number of applications of silica is enormous, and we make no attempt to represent them all here. These technological applications of silica include its use in separations (e.g. column chromatography), in composite materials, in consumer products (e.g. as thickening agents), in immobilized reagents (e.g. heterogeneous catalysts), and even in foods. Although a variety of high-surface-area forms of silica are important, including precipitated and fumed silicas, in this article we will focus mainly on samples originating as *silica gels*, i.e. silica samples precipitated from the products of reactions such as:

$$Si(OCH_2CH_3)_4(aq.) + 2H_2O(l) \rightarrow SiO_2(s) + 4CH_3CH_2OH(aq.) \qquad (1)$$

The materials prepared in this manner tend to have high surface areas and high porosities, although these properties depend substantially on details of the preparation conditions. Most of the technologically important properties of silica depend substantially on the characteristics of the silica *surface*, e.g. the numbers, types, distributions, and reactivities of silanols, i.e. ≡Si-OH groups, at the silica surface.

A priori, it would appear that the spin-$\frac{1}{2}$ nuclides ^{29}Si (4.7% natural abundance) and ^{1}H (∼100% natural abundance) should be useful for characterizing the silica surface, and possibly also the quadrupolar nuclides ^{17}O ($I = \frac{5}{2}$, 0.04% natural abundance) and ^{2}H (I = 1, 0.02% natural abundance). Clearly, for these quadrupolar nuclides to be useful, isotopic enrichment is required, but that has not been a major difficulty. Indeed, there has been a great deal of NMR work done on silicas and silica-based systems,[2–5] and it would be impossible to review it all comprehensively here, because of reasonable space limitations. Furthermore, because of restrictions on space, it will not be possible to list all of the worthwhile studies in this research area. For these reasons, the convenient approach of emphasizing studies from our own laboratory is adopted, with apologies to those who feel their work may have been neglected.

2 NMR STRATEGIES FOR SILICA SURFACE SELECTIVITY

2.1 The Need

With any NMR experiment on a solid, a technique that provides no major detection advantage to nuclei at the surface will generate spectra that are dominated by peaks due to nuclei that are in positions in the interior (bulk) of a particle, because the number of nuclei that constitute the bulk of a particle will typically be much larger than the number of corresponding nuclei in analogous structural sites at the surface (unless the surface area is very large, say, $\gg 100\,m^2\ g^{-1}$). This intensity dominance by peaks due to bulk sites can be overcome if (1) the nuclei being observed are located only (or largely) at the surface or (2) the method of generating the polarization to be observed discriminates strongly in favor of nuclei at the surface. The former situation often obtains for protons in a typical silica, because most of the protons in such systems exist at the surface as covalently attached −OH groups (vide infra), as physisorbed H_2O, or as covalently attached structures that result from derivatization processes.

Perhaps the most obvious strategy for preferentially or selectively polarizing surface nuclei in the presence of an overwhelmingly larger number of nuclei in analogous structural sites in the interior would be to use a relaxation reagent that can, at least briefly, interact with the surface and thereby relax the surface nuclei. Although surprisingly little effort seems to have been expended in this direction, one must note the elegant ultra-low-temperature (∼10 mK) NMR studies of Waugh and co-workers,[6] who have used the relaxation effects of ^{3}He impinging on a surface for the selective relaxation of nuclei at the surface. Other surface-selective (or preferential) relaxation mechanisms would seem possible via the dipolar mechanism of impinging species with large nuclear magnetic moments (say, ^{1}H or ^{19}F) or even the electron spin magnetic moments of paramagnetic relaxation agents. In the case of paramagnetic surface relaxants, the possibility of dynamic nuclear polarization (DNP)[7] of surface nuclei from adsorbed paramagnetic species seems attractive, possibly with the Overhauser mechanism operating if the adsorption is rapidly reversible, or the solid state mechanism if the adsorption/desorption process is very slow. Possibilities would also appear to exist for surface-selective relaxation mechanisms based on quadrupolar relaxation of a nuclide with $I > \frac{1}{2}$ (e.g. ^{2}H or ^{17}O) due to rapid, reversible adsorption/desorption causing a modulation of the local electric field gradient. Recent progress in the surface transfer of ^{129}Xe polarization that has been dramatically enhanced via electron → nuclear polarization transfer (e.g. from optically pumped rubidium) is promising for not only providing a surface-selective NMR strategy, but also for providing huge enhancements in the effective sensitivity of NMR detection at surfaces.[8]

2.2 Cross Polarization

To date, the most popular and generally successful surface-selective polarization strategies have been based on $^{1}H \rightarrow X$ cross polarization (CP),[9] where X is a nucleus present at the surface (and presumably also with the bulk).[10,11] These strategies are often based on the assumption that essentially all

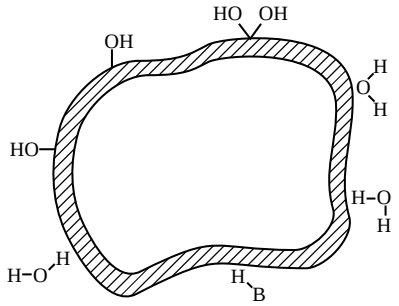

Figure 1 Cross polarization as a surface-selective strategy, showing only protons near the (hatched) surface region, as covalently attached hydroxyls, physisorbed water, or physisorbed acids (B–H) of some other type. (Taken from Maciel and Ellis[4])

(or, at least, most) of the protons in the system are present at the surface and on the fact that cross polarization depends upon a static component of the $^{1}H–X$ dipolar interaction, which has an inverse cube dependence on the $^{1}H–X$ internuclear distance (in many cases the cross polarization rate appears to have an essentially r^{-6} dependence). Cross polarization was developed during the early 1970s by Pines, Gibby, and Waugh.[9] Its early impact was primarily the dramatic increase in ^{13}C signal-to-noise ratio in NMR experiments on organic solids, which rendered such experiments especially attractive when carrried out with magic angle spinning (MAS), as demonstrated first by Schaefer and Stejskal.[12] From the point of view of surface applications, at least as important as the effective increase in sensitivity is the above-mentioned dependence of the cross-polarization rate on internuclear distances. Figure 1 displays the essence of a surface-selective CP strategy, in which only those X nuclei that are close enough to the surface (within, say, 5–6 Å, as represented by the 'cross-hatched' area) can be cross polarized by surface protons. The more remote X nuclei in the 'interior' or 'bulk' of the material are not cross polarized efficiently. Hence, the efficiency, or dynamics, of cross polarization can be used to discriminate in favor of the surface nuclei.

3 $^{1}H \rightarrow {}^{29}Si$ CP IN SILICAS

3.1 Silica Gels and Derivatized Silica Gels

In 1980, Sindorf and Maciel[10,11] published the first high-resolution example of the use of $^{1}H \rightarrow X$ cross polarization for surface-selective X detection in a demonstration of $^{1}H–{}^{29}Si$ CP in silica gel. Since that time $^{1}H \rightarrow {}^{29}Si$ CP has remained the most popular application of this strategy, although there has been significant success with applications to other types of systems. Figure 2 shows typical ^{29}Si spectra of silica gel and related samples obtained by CP MAS (cross polarization and magic angle spinning) and DP MAS (direct polarization, based on ^{29}Si spin–lattice relaxation, not CP). The DP MAS spectrum [Figure 2(a)] of an undried silica gel is dominated by the peak due to $(\equiv SiO)_4\mathbf{Si}(Q_4)$ sites, which represent the bulk (nonsurface regions) of silica particles. The ^{29}Si CP MAS spectrum of an undried silica gel [Figure 2(b)] selects primarily surface sites and shows the following three peaks: a peak at −89 ppm (relative to liquid TMS) due to

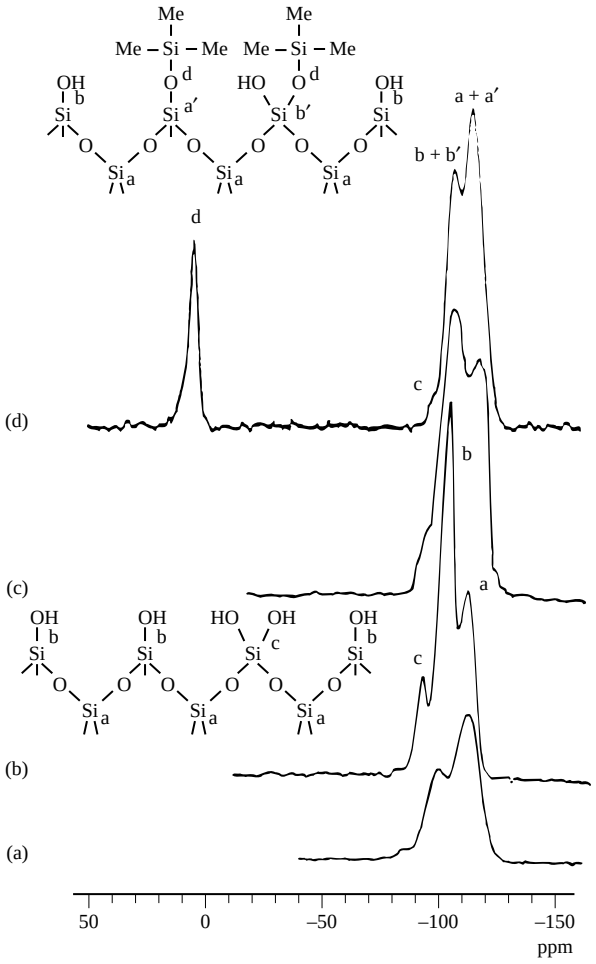

Figure 2 ^{29}Si MAS spectra of silica gel samples. (a) DP MAS spectrum of an undried sample. (b) CP MAS spectrum of the same sample as in (a). (c) CP MAS spectrum of a sample dehydrated under vacuum at 209 °C. (d) Sample derivatized with $(CH_3)_3SiCl$. (Taken from Maciel[5])

$(\equiv SiO)_2\mathbf{Si}(OH)_2$ (geminal, Q_2) sites; a peak at −99 ppm arising from $(\equiv SiO)_3\mathbf{Si}OH$ (single silanol, Q_3) sites; and a peak at −109 ppm from the Q_4 (siloxane) sites near the surface. These peak assignments can be made on the basis of the usual kinds of empirical chemical shift correlations with structure from liquid sample data on silicic acid solutions. However, the dynamics of the $^{1}H–{}^{29}Si$ CP process can also be used to make these assignments.

Figure 3 shows the results of a variable contact time CP experiment, in which the $^{1}H \rightarrow {}^{29}Si$ CP contact period (t_{cp}) is varied in order to elucidate the $^{1}H \rightarrow {}^{29}Si$ CP (relaxation) time constant (T_{HSi}) for each ^{29}Si peak. The early (small t_{cp}) part of such curves is typically dominated by the rate of CP transfer, as characterized by the rate constant $T_{HSi}{}^{-1}$, and the latter part of such curves is usually determined by the rate constant of the rotating frame spin–lattice relaxation of the protons responsible for polarization transfer to the observed silicons, as characterized by the time constant, $T_{1\rho}^{H}$ (assuming $T_{1\rho}^{H} \rangle T_{HSi}$). These curves can be analyzed mathematically in terms of equation (1),[13]

$$M(t_{cp})/M^{*} = \frac{1}{1 - T_{HSi}/T_{1\rho}^{H}}(e^{-t_{cp}/T_{1\rho}^{H}} - e^{-t_{cp}/T_{HSi}}) \qquad (2)$$

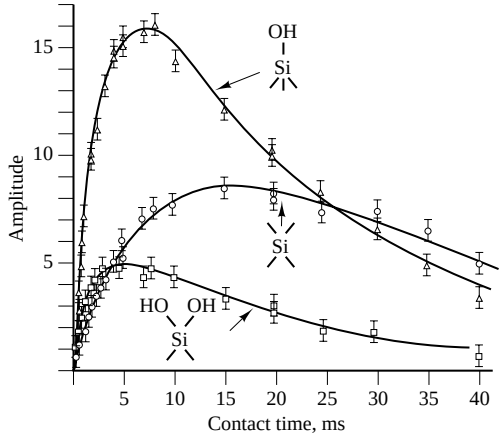

Figure 3 Variable contact time ^{29}Si CP MAS plots for silica. (Taken from Maciel and Sindorf[10])

where $M(t_{cp})$ is the ^{29}Si magnetization generated by ^{1}H–^{29}Si CP as a result of a CP contact period t_{cp}, and M^* is the 'ideal' maximum ^{29}Si magnetization that would be generated if $T_{1\rho}^{H}$ and $T_{HSi}{}^{-1}$ were both infinite. This analysis shows that $T_{HSi}{}^{-1}$ for the -89 ppm peak is roughly twice that of the -99 ppm peak, which in turn is an order of magnitude larger than the $T_{HSi}{}^{-1}$ value for the -109 ppm peak. In terms of the number and distances of nearby protons, the ^{29}Si chemical shift assignments given above in terms of Q_2, Q_3, and Q_4 sites are entirely consistent with these T_{HSi} determinations.

3.2 Dehydration of Silica

The ^{29}Si CP MAS spectra collected in Figure 2 also represent two important classes of chemical transformations of silica surfaces that were studied by ^{29}Si CP MAS spectra by Sindorf and Maciel.[10,11,14–18] Figure 2(c) shows a spectrum obtained on a silica gel sample that has been dehydrated under vacuum at 209 °C. One can see in this spectrum the subtle redistribution of peak intensity and the dramatic line broadening relative to the spectrum observed on an 'air hydrated' silica gel sample. These changes, especially the line broadening, are presumably due to a redistribution of hydrogen bonding patterns, and perhaps bond angles and bond lengths (and strains) introduced with the removal of the (predominantly physically) adsorbed water of the 'hydrated' and essentially 'annealed' silica surface represented in Figure 2(b). Such experiments carried out over a wide range of dehydration temperatures, and corresponding rehydration experiments, have revealed valuable information on the effects of dehydration and rehydration on the silica gel surface.

3.3 Silylation of Silica

The ^{29}Si CP MAS spectrum shown in Figure 2(d) represents a sample prepared by the silylation of a silica gel by $(CH_3)_3SiCl$. This silylation reaction is a member of an important class of derivatizations of the silica surface, represented by the following chemical equation:

(3)

where X represents a labile leaving group (e.g. Cl or OCH_2CH_3) and Si represents a silanol site on the reactant silica surface or a corresponding derivatized silica site in the reacted sample. Such reactions are important, or potentially important, technologically—for the preparation of stationary phases for chromatographic separations, as a means of immobilizing reactive chemical centers (e.g. catalytic sites), in coupling agents for composite materials, and for a wide range of other applications in which it is desired to anchor or 'immobilize' a chemically important moiety. Peak d in the spectrum of Figure 2(d), at ca. 10 ppm, is assigned to the trimethylsilyl group covalently attached to the silica surface. Clearly the silylation process has brought about a change of intensities of peaks a, b, and c in Figure 2(b), corresponding to the $(\equiv SiO)_2\mathbf{Si}(OH)_2$ or Q_2 sites, the $(\equiv SiO)_3\mathbf{Si}OH$ or Q_3 sites, and $(\equiv SiO)_4\mathbf{Si}$ or Q_4 sites, at the underivatized surface. At the relatively low level of structural detail represented by the Q_2, Q_3, Q_4 notation, the silylation process transforms Q_2 sites into Q_3 sites, and Q_3 sites into Q_4 sites, and these changes are seen by comparing the spectra in Figure 2(b) and (d). By examining such intensity changes systematically, it has been possible to elucidate important reactivity patterns in these systems.[10,11,14–18] Indeed, ^{29}Si CP MAS NMR, along with supporting data from ^{13}C CP MAS experiments, can serve as an analytical technique for monitoring chemical reactivity

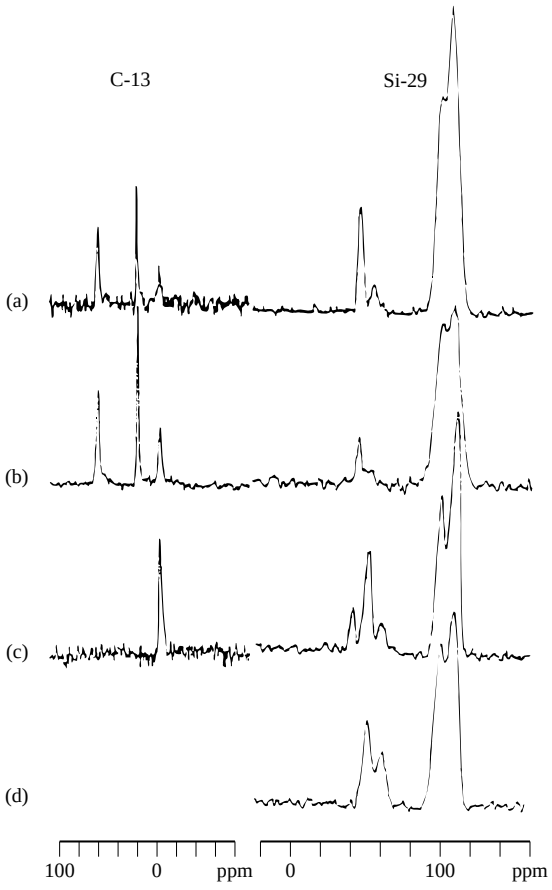

Figure 4 ^{29}Si (right) and ^{13}C (left) CP MAS spectra of silica gel derivatized with $(CH_3)_2Si(OCH_2CH_3)_2$. (a) Product of reaction with predried silica at 138 °C. (b) Product of reaction with predried silica at 240 °C. (c) Product of reaction with undried silica at 115 °C. (d) Sample (c) heated in air at 150 °C. (Taken from Sindorf and Maciel[17])

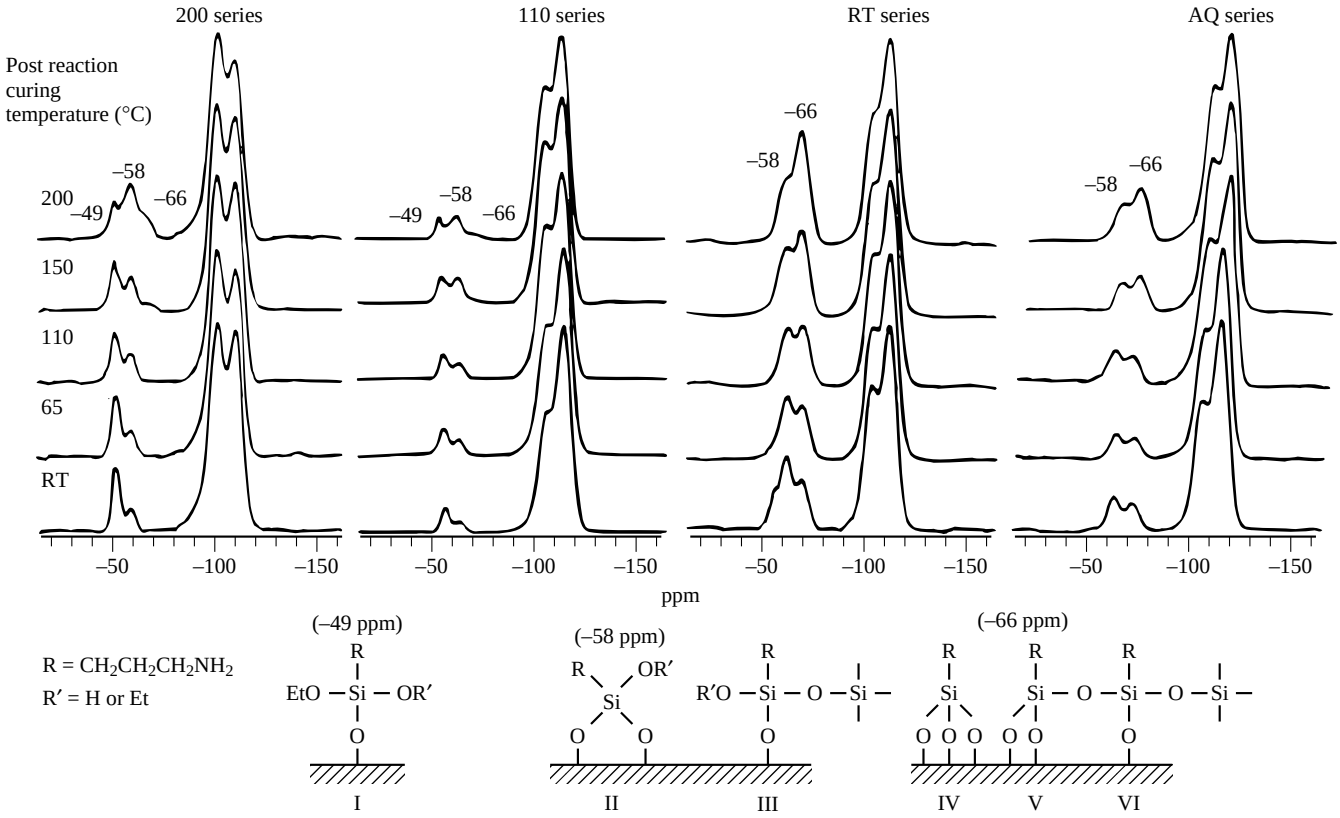

Figure 5 ^{29}Si CP MAS spectra of APTS-modified silica gels. Each column of spectra corresponds to the drying temperature of silica gel (°C; RT = room temperature) under vacuum prior to reaction in dry toluene, or aqueous reaction conditions (AQ). Postreaction treatment (curing) temperature shown on the left. Structural assignments given at the bottom. (Taken from Caravajal et al.[19])

patterns, e.g. the relative reactivities of the various types of silanols on a silica surface.

The complex chemistry that can occur on a silica surface after silylation by a reagent with more than one leaving group (X), e.g. $RR'SiX_2$ or $RSiX_3$, is also amenable to study by CP MAS NMR.[17] In the ^{29}Si CP MAS spectra shown in Figure 4 one sees that the product formed initially from the reaction of silica with $(CH_3)_2Si(OCH_2CH_3)_2$ depends on the reaction conditions and predrying of the silica, and can be converted by the moisture in air [Figure 4(c), (d)] to products in which ≻**Si**-OCH_2CH_3 moieties are replaced by ≻**Si**-OH and ultimately ≻**Si**-OSi- moieties. In this case, ^{13}C CP MAS spectra are also useful, because they detect the presence and amount of residual ≻Si-OCH_2CH_3 moieties.

The ^{29}Si CP MAS spectra shown in Figure 5 represent an even more complex derivatized silica system, a series of samples prepared by the silylation of silica with 3-aminopropyltriethoxysilane (APTS) under a variety of conditions (pretreatment temperature = 200 °C for 200 series, or 110 °C for 110 series, 25 °C for RT series, or with silylation carried out in an aqueous slurry, AQ series).[19] APTS-derivatization of the silica surface is of interest for such diverse applications as a variety of composite materials (in which APTS serves as a coupling agent between a silica-like component and, usually, an organic polymer) and for metal complexation agents. One sees from the spectra of Figure 5 that increasing the amount of water in the silylation process or increasing the postsilylation 'curing' temperature brings about changes in attached silane populations from species with one **Si**-OSi attachment (−49 ppm) to species with two such attachments (−58 ppm) to three such attachments (−66 ppm). Although ^{13}C spectra are primarily useful for monitoring the residual ≻Si-OCH_2CH_3 moieties in this system, a careful analysis of the ^{13}C CP MAS spectra of samples corresponding to those represented in Figure 5 reveals that the ^{13}C chemical shift of the central carbon of the pendant $-(CH_2)_3-$group originating from APTS is sensitive to protonation or hydrogen bonding of the amino group. ^{1}H CRAMP spectra (vide infra) and ^{15}N CP MAS spectra are also useful for studying this important issue.

3.4 Fumed Silica

Other types of silicas (and derivatized silicas), besides those based on silica gels, have also been studied by ^{29}Si CP MAS (and DP MAS) experiments, e.g. by Brinker and co-workers[20,21] and by Legrand and co-workers.[22,23] Figure 6 shows a comparison of ^{29}Si CP MAS spectra of a fumed silica (a Cab-O-Sil, formed by the vapor-phase combustion of $SiCl_4$) and a silica gel equilibrated to about the same H_2O vapor pressure.[24] The same peaks are present, but they are broader in the case of the fumed silica, and the percentage of surface silica sites that are single silanols is seen to be smaller for the fumed silica than for silica gel. The greater linewidth presumably relates to the greater dispersion of local surface geometries (and chemical shifts) in the Cab-O-Sil structure, which is formed at a higher temperature, and possibly to

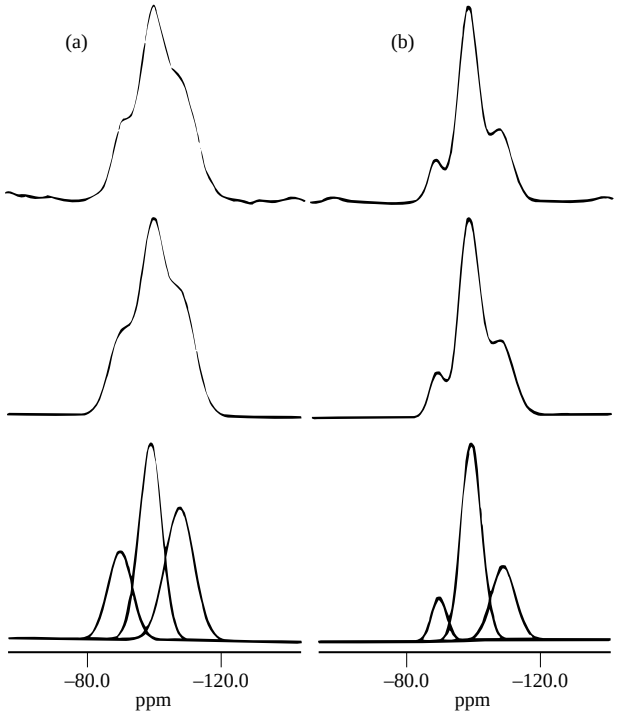

Figure 6 ^{29}Si CP MAS spectra of (a) Cab-O-Sil fumed silica and (b) silica gel. Top: experimental spectra. Bottom: individual Q_2, Q_3, and Q_4 peaks by deconvolution. Middle: computer sum of the contributions shown at the bottom. (Taken from Liu and Maciel[24])

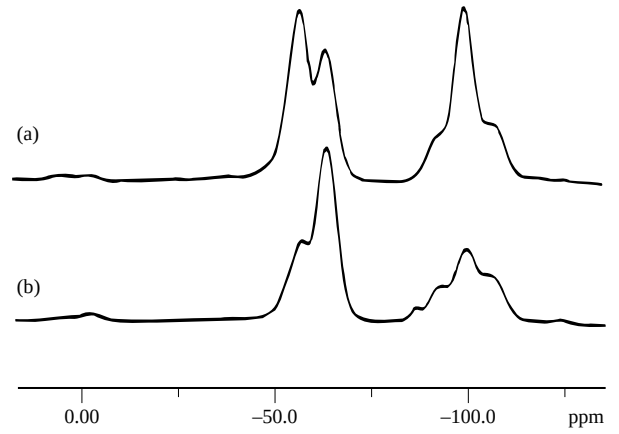

Figure 7 ^{29}Si CP MAS spectra of polysiloxane polymer prepared from $Si(OEt)_4$ and $(CH_3O)_3SiCH_2CH_2CH_2Cl$ with (a) $Bu_2Sn(OAc)_2$ or (b) 0.1 M HCl as catalyst. (Taken from Elnahhal et al.[26])

the potential effects of so-called 'interparticle sites' at the junctures of the primary particles that contribute to the overall topography of a fumed silica.[23] Detailed studies of ^{29}Si CP MAS spin dynamics of fumed silicas, especially when viewed in relationship to analogous silica gel results, appear promising for identifying the main similarities and differences between these two types of silica surfaces.[24]

3.5 Polysiloxane Systems

There has been a great deal of interest recently in a class of polysiloxane polymers prepared by the hydrolysis and gelation of mixtures of reagents of the types, $Si(OR')_4$ and $RSi(OR'')_3$, where R′ and R″ are typically methyl or ethyl and R is a 'pendant' group that contains some desired chemical moiety, e.g. a specific ligand.[25] By varying the nature of R and the ratios of the two types of starting reagents, a wide range of polysiloxane materials, with a broad variety of potentially useful properties, can be prepared. These polysiloxane materials bear a substantial similarity to derivatized (silylated) silicas, with a silica-like three-dimensional network to which the pendant (R) groups are attached. Hence, the NMR techniques that are useful for characterizing derivatized silicas are also useful for these polysiloxane systems.

Figure 7 shows ^{29}Si CP MAS spectra of polysiloxane systems with $-CH_2CH_2CH_2Cl$ as the pendant group, prepared by the reaction of $Si(OEt)_4$ with $(MeO)_3SiCH_2CH_2CH_2Cl$, using two different catalysts.[26] One notes substantially different intensity ratios for the Q_2, Q_3, and Q_4 peaks in the two spectra [and possibly a Q_1 peak at about −82 ppm in Figure 7(b)], and for the peaks due to the pendant groups (at about 60 and 65 ppm), as well as a dramatic difference in intensities between the 60 and 65 ppm peaks relative to the Q_2, Q_3, Q_4 peaks, for the products from the two catalyst systems employed.

4 ^{1}H → ^{17}O CROSS POLARIZATION

In addition to cross polarization to ^{29}Si in silica, or to ^{13}C (or ^{15}N, ^{31}P, etc.) in derivatized silicas, cross polarization to ^{17}O in isotopically-enriched silicas has also been illuminating. Oldfield and co-workers have during the past several years made significant progress in the application of solid state ^{17}O NMR techniques for the characterization of inorganic materials. Walter, Turner, and Oldfield[27] have demonstrated that ^{1}H → ^{17}O CP experiments are not only feasible, but they are also very informative from the point of view of *editing* ^{17}O spectra, by discriminating against ^{17}O signals from oxygen sites with no directly bonded hydrogen. Figure 8 shows ^{1}H → ^{17}O CP spectra of amorphous silica and a model SiOH system. From a comparison of the spectra obtained from static samples and by MAS, with and without CP, it was possible to assign the ^{17}O signal due to SiOH groups at the surface.

5 PROTON NMR APPROACHES

5.1 Dipole–Dipole Broadening

High-resolution ^{1}H NMR spectroscopy has proved to be highly useful in studying the surfaces of silicas and a variety of other solids. In order to obtain high-resolution ^{1}H NMR spectra of solids (including their surfaces), it is necessary to average not only the chemical shift anisotropy (easily done by MAS), but also ^{1}H–^{1}H dipolar interactions.[28,29] The latter can be very large (tens of kHz). Magnetic dipole–dipole interactions manifest an inverse cube dependence on internuclear distance. Therefore such interactions, and the ^{1}H–^{1}H spin–spin flip-flops that they can generate, are especially strong if the protons are situated in close proximity to each other, e.g. in a typical organic solid, but also perhaps in hydrogen-bonded clusters of hydroxy groups on a surface. Hence, a priori one can feel confident that moderate-speed MAS experiments (say, less

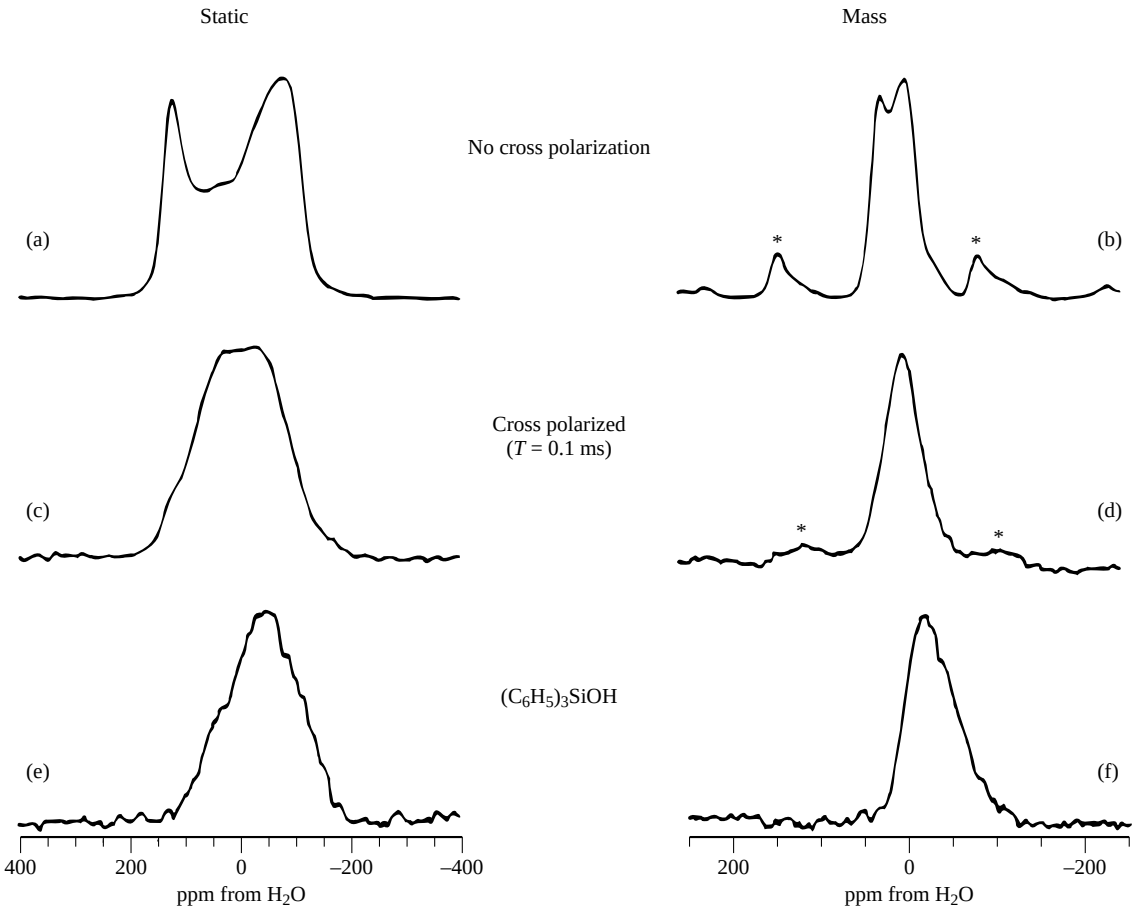

Figure 8 Static and MAS ^{17}O spectra of amorphous SiO_2 and polycrystalline $(C_6H_5)_3SiOH$ obtained at 67.8 MHz. (a) ^1H-decoupled static spectrum of SiO_2 without CP: 108 scans. (b) ^1H-decoupled MAS spectrum: 100 scans, 7.6 kHz spinning speed (*indicates spinning sidebands). (c) $^1H \rightarrow {}^{17}O$ static spectrum of SiO_2, 200 scans, 0.1 ms contact time. (d) $^1H \rightarrow {}^{17}O$ MAS spectrum of SiO_2, 200 scans, 0.1 ms contact time. (e) ^1H-decoupled static spectrum of $(C_6H_5)_3SiOH$ without CP: 500 scans. (f) ^1H-decoupled MAS spectrum of $(C_6H_5)_3SiOH$: 800 scans, 4.0 kHz spinning speed. All spectra were obtained using a 2 s recycle time. (Taken from Walter et al.[27])

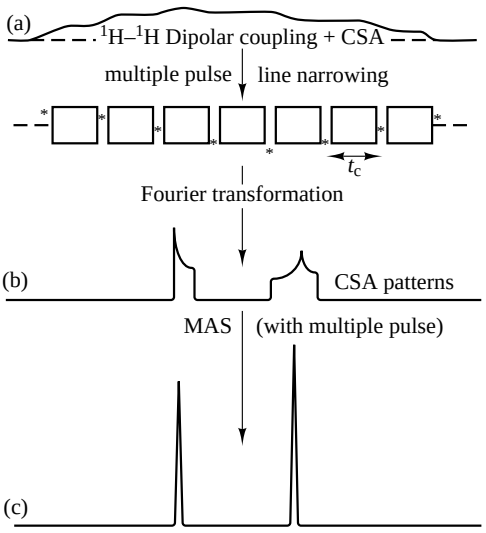

Figure 9 The multiple pulse line-narrowing strategy for averaging homonuclear dipolar interactions. Each rectangle [between (a) and (b)] represents one multiple pulse cycle (e.g. four pulses for WAHUHA, eight for MREV-8 or 24 for BR-24). There is one data acquisition point for each cycle (e.g. between each rectangle). (Taken from Maciel[5])

than 20 kHz) are adequate for studying silica surfaces only for substantially dehydrated samples. For nondehydrated or nondeuterated samples, in which the *local* surface density of protons can be substantial, multiple pulse techniques may be required for eliminating the line-broadening effects of ^1H–^1H dipolar interactions. Alternatively, a useful strategy employed by Vega and co-workers is to ensure that the ^1H concentration is small by exchanging protons at the surface with deuterons.[30]

5.2 Multiple Pulse Line Narrowing: CRAMPS

In 1968, Waugh and co-workers[31] introduced a *multiple pulse* approach for averaging strong homonuclear dipolar interactions. The strategy of this kind of approach is that, over the *entire* period of each individual multiple pulse cycle (four 90° pulses in the original work), the average Hamiltonian that governs the evolution of the spins over the entire cycle does not include the homonuclear dipolar interaction. A nonvanishing chemical shift effect, albeit scaled down, is present in the average Hamiltonian. Hence, if one acquires one data point stroboscopically between each adjacent pair of multiple pulse cycles in a long string of such cycles, the resulting time-dependent signal (analogous to a free induction decay) is

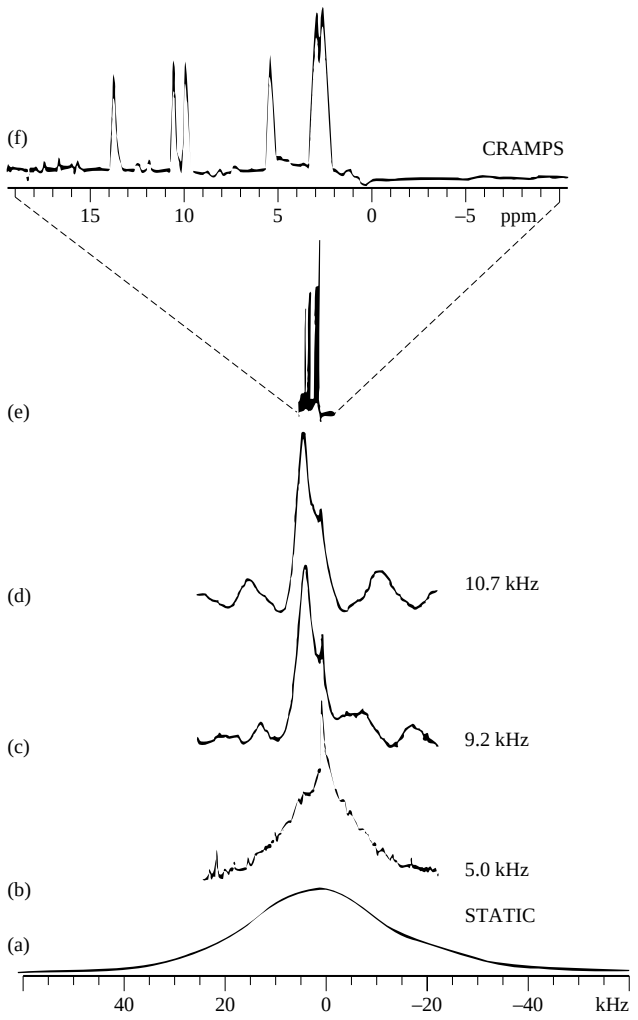

Figure 10 ^{1}H NMR spectra of citric acid. (a) Static sample, single pulse, (b),(c),(d) MAS-only with indicated MAS speed. (e) and (f) CRAMPS. (Taken from Dec et al.[35])

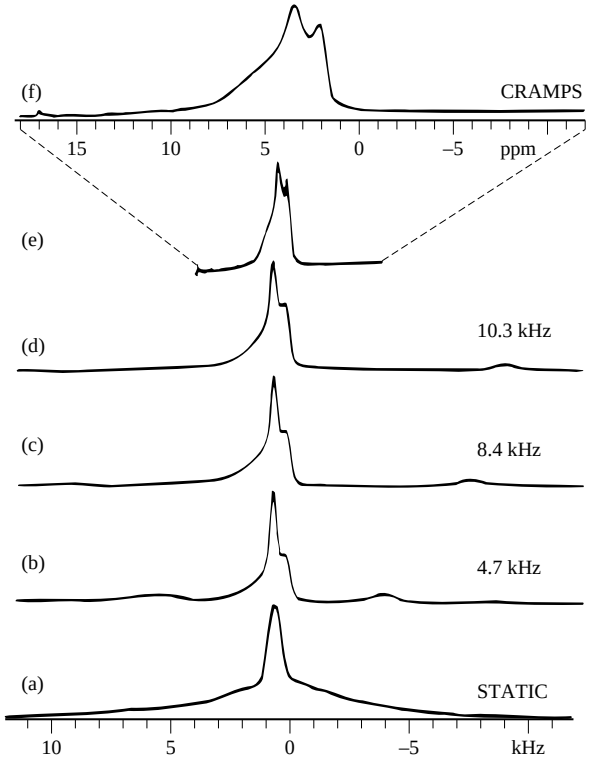

Figure 11 ^{1}H NMR spectra of untreated silica gel. (a) Static sample, single pulse. (b),(c),(d) MAS-only with indicated MAS speed. (e) CRAMPS. (f) CRAMPS on an expanded scale. (Taken from Dec et al.[35])

modulated by chemical shift effects, but not by homonuclear dipolar effects. The strategy is outlined in Figure 9 in which each rectangle represents a multiple pulse cycle and each asterisk represents a data acquisition point. The bandwidth of the experiment depends on $1/t_c$, the inverse of the multiple pulse cycle time.

The original homonuclear line-narrowing pulse sequence (WAHUHA)[31] was a four pulse sequence; later elaborations involve more pulses in the total cycle and offer compensation for pulse imperfections and/or higher order averaging of the homonuclear dipolar interaction.[32,33] In general, this class of experiments requires short ($<1.5\,\mu$s), powerful 90° pulses with precisely defined phases and until recently has been technically one of the most difficult experiments in the solid state NMR laboratory. Currently, the most popular multiple pulse sequences are the eight pulse MREV-8 sequence[32] and the 24 pulse BR-24 sequence.[33]

For powdered or amorphous samples, in order to avoid line broadening due to chemical shift anisotropy, magic angle spinning is employed (which also averages various heteronuclear dipolar couplings). Gerstein and co-workers[34] were the first to combine a multiple pulse homonuclear line-narrowing technique with magic angle spinning, and introduced the acronymn CRAMPS for Combined Rotation And Multiple-Pulse Spectroscopy.[28,29]

5.3 ^{1}H CRAMPS Studies of Silicas

Figures 10 and 11 show the difference in ^{1}H line-narrowing capabilities between CRAMPS and MAS-only (no multiple pulse sequence) with a modestly high MAS speed (10–11 kHz).[35] For powdered crystalline citric acid (Figure 10), one sees six distinctly resolved ^{1}H CRAMPS peaks, but essentially no resolution in the 10.7 kHz MAS-only ^{1}H spectrum. This difference reflects the high proton concentration (∼29 atom %) and molecular rigidity of crystalline citric acid. For the more proton-dilute (∼2.5 atom %) silica gel system (Figure 11), the ^{1}H NMR experiment yields a modestly narrowed ^{1}H spectrum even on a static sample, and 4.7 kHz MAS yields a spectrum that is superficially similar to that obtained by CRAMPS. However, close inspection reveals important details that differentiate the ^{1}H spectra obtained by these two techniques [Figure 11(d) and (e)]. All of the remaining ^{1}H spectra discussed in this article were obtained by the CRAMPS technique.

One should note that the CRAMPS technique is not necessarily a panacea for ^{1}H NMR studies on surfaces, or for any other type of sample. Dynamics associated with motion and/or chemical reactions with a time constant that is comparable to the cycle time (t_c) of the multiple pulse sequence interferes with the multiple pulse averaging of

$^1H-^1H$ dipolar interactions.[29,36] Of course, an analogous problem can also arise with magic angle spinning, for which the critical period is $\nu_{MAS}{}^{-1}$, where ν_{MAS} is the MAS frequency.[37] To quench this kind of dynamic interference with the line-narrowing efficiency of any cyclic technique, like MAS and/or a multiple pulse sequence, one can try to alter the dynamics, e.g. by changing (usually lowering) the sample temperature.

As an example of the application of the ^1H CRAMPS technique to the study of silica surfaces,[38] Figure 12 shows the ^1H CRAMPS spectra obtained on untreated [Figure 12(a), (a′), (a″)] and dried [Figure 12(b), (c), (d)] silica gel samples. Comparison of spectra (a) and (b) show that the relatively sharp peak at about 3 ppm in the spectrum of an untreated silica is removed by moderate dehydration; this peak is therefore identified as physisorbed water. The broad nonsymmetrical peak that is largely to the left of the sharp 1.9 ppm peak is unaffected by sample evacuation at 200 °C, but removed by evacuation at 500 °C; this behavior suggests that this peak can be identified tentatively with clustered (or hydrogen bonded) silanols, which are close enough together that suitable dehydration pathways are available. The sharp peak at 1.9 ppm remains after evacuation at 500 °C; this behavior implies that the silanol groups represented by this peak are sufficiently far from each other to make dehydration difficult, so it is assigned to isolated (non-hydrogen-bonded) silanols. These assignments are consistent with 35 years of literature results on liquid solution samples, which show that hydrogen bonding typically reduces proton shielding, and with the reasonable point of view that a wide range of hydrogen-bonding structures exist on a silica surface (chemical shift dispersion:broad peak). These assignments are also consistent with the results of proton dipolar-dephasing experiments, as shown in Figure 13.

5.4 CRAMPS-Based Time Domain Studies of Silicas

Figure 13(a) shows a ^1H CRAMPS version[38] of the popular 'dipolar-dephasing' experiment used routinely in ^{13}C CP MAS NMR. In this ^1H CRAMPS version, a 'dephasing period' 2τ is inserted between the initial $\pi/2$ pulse that generates transverse magnetization and the multiple pulse line-narrowing pulse train that detects the transverse magnetization. During the dephasing period, those proton magnetic moments that experience strong dipolar interactions undergo a corresponding degree of dephasing, and the resulting detected signal will be accordingly attenuated. Figure 13(b) and (c) show the results of applying the dipolar-dephasing CRAMPS experiment to untreated silica gel [Figure 13(b)] and to a silica gel sample evacuated at 200 °C [Figure 13(c)]; in both cases one sees that the broad (3.0 ppm) peak is attenuated by a dephasing period (2τ) of 160 μs, whereas the sharp (1.7 ppm) peak is largely unattenuated. From the relationship between hydrogen bonding and proximity (between atoms that participate in a hydrogen bond) and the r^{-3} dependence of dipolar interactions, this dipolar-dephasing behavior provides strong support for identifying the 1.7 ppm peak as arising from isolated (non-hydrogen-bonded) silanols and the broad 3.0 ppm peak as clustered (hydrogen bonded) silanols. This is the same conclusion regarding proximity (and hydrogen bonding) that one would reach from the dehydration behavior shown in Figure 12. It would be difficult to rationalize the elimination

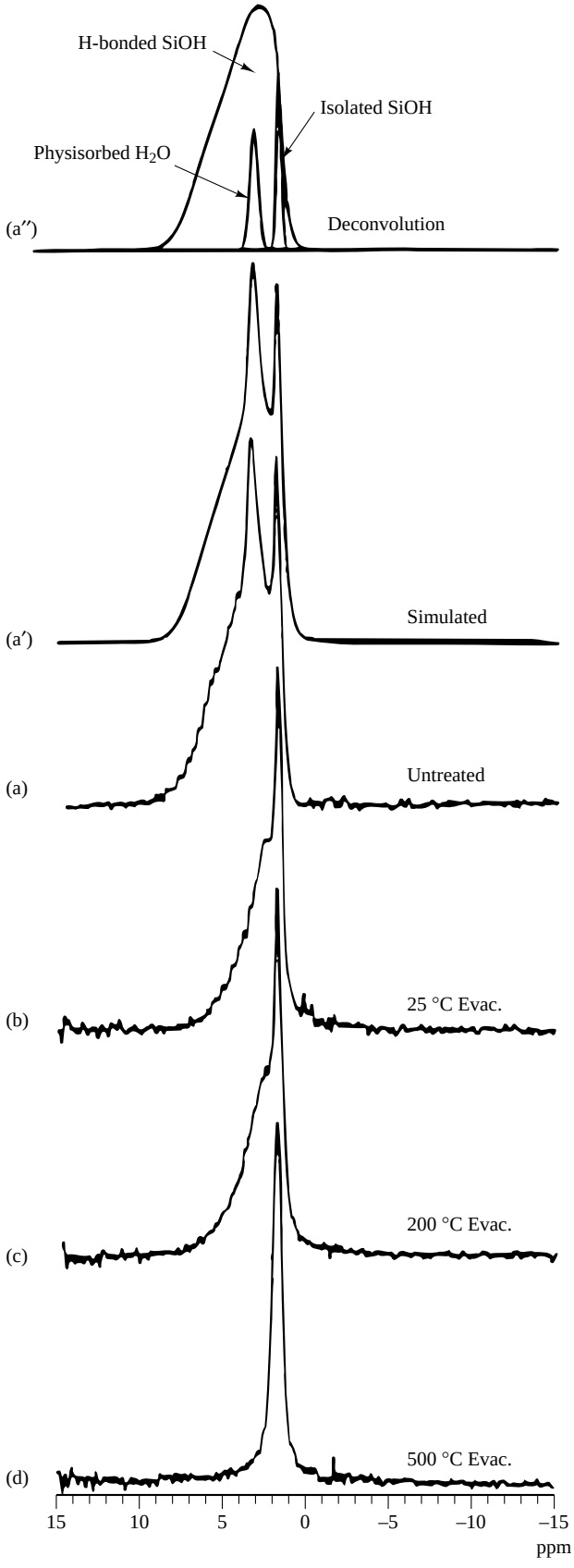

Figure 12 187-MHz ^1H CRAMPS spectra of Fisher S-679 silica gel. (a) untreated; (b) evacuated at 25 °C; (c) evacuated at 200 °C; (d) evacuated at 500 °C; (a″) deconvolution of spectrum (a); (a′) computer simulation based on (a″). (Taken from Bronnimann et al.[38])

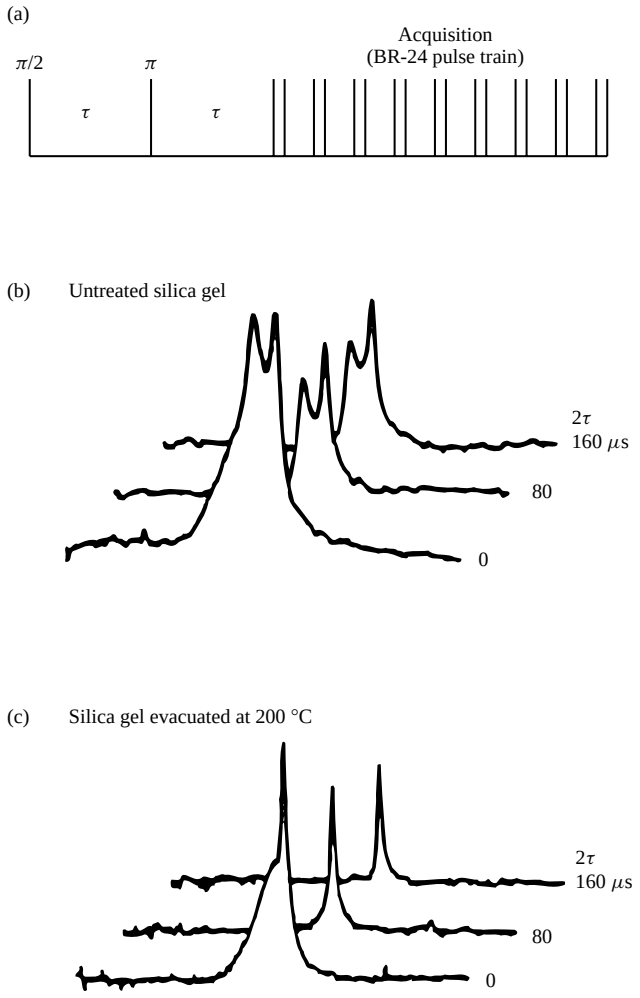

Figure 13 ^{1}H CRAMPS dipolar-dephasing experiment. (a) Pulse sequence. (b) results for untreated silica gel (showing τ values). (c) Results for sample evacuated at 200 °C (showing τ values). (Taken from Bronnimann et al.[38])

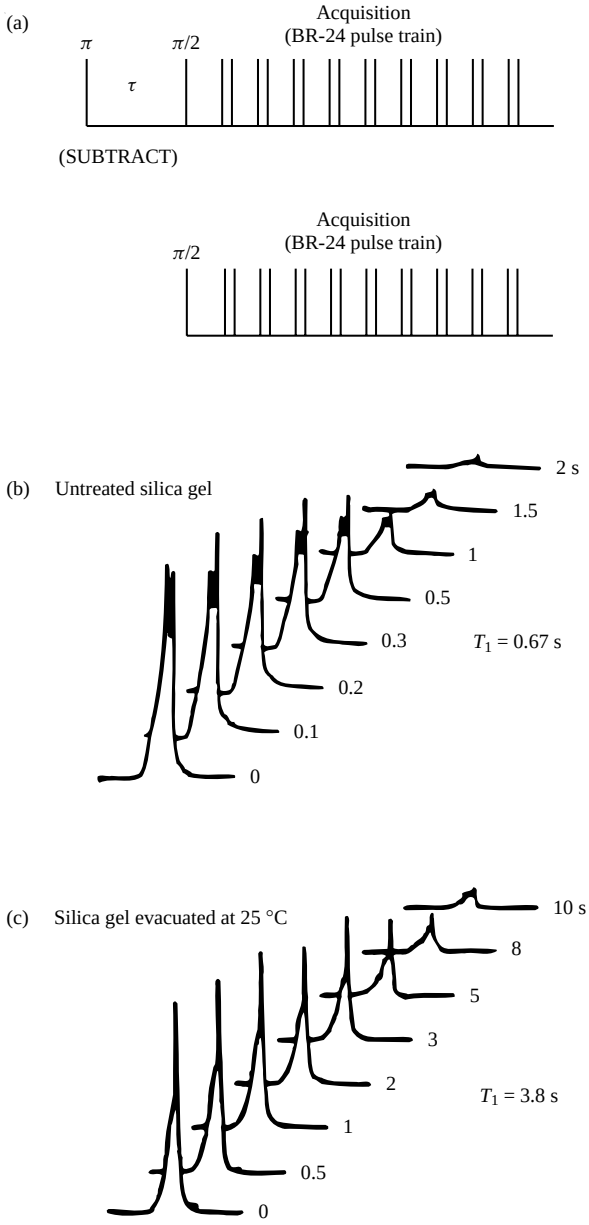

Figure 14 ^{1}H CRAMPS T_1 determination. (a) Pulse sequence, showing individual sequences employed in alternate scans (lower case subtracted from upper case in computer memory). (b) Results for untreated silica gel (showing τ values). (c) Results for sample evacuated at 25 °C. (Taken from Bronnimann et al.[38])

of water via the 'dehydration' of silanols that are *isolated* from each other. Since the physisorbed water peak (3.5 ppm) is only slightly attenuated by the 160 μs dephasing period [Figure 13(b)], one can conclude that water protons experience only weak resultant dipolar interactions, the result of efficient motional averaging.

Other CRAMPS-based ^{1}H time domain approaches have also been useful in studying silica surfaces. Figure 14 summarizes a CRAMPS-detected T_1^H determination on silica gel samples, based on an alternating, two-sequence scheme of the Freeman–Hill type.[39] One sees that for each of the two silica samples, untreated (b) and dried (c), all components of proton magnetization relax essentially homogeneously, which suggests that proton spin diffusion among the different spin isochromats is much more efficient that spin–lattice relaxation, which is characterized overall by T_1^H values of 0.7–4 s. Furthermore, the marked increase in T_1^H that results from sample drying indicates that the physisorbed water in the sample of Figure 14(b) provides an important relaxation source, and is presumably in a rapid state of motion at room temperature.[36] Having the ability to establish, via dipolar dephasing, different spin polarizations for hydrogen bonded and isolated silanols, one can explore spin exchange between these two spin sets by an experiment of the type shown in Figure 15(a).[38] One sees for the untreated silica [Figure 15(b)] that in a mixing time of a few ms after eliminating ^{1}H magnetization due to hydrogen-bonded silanols there is a substantial transfer of magnetization (spin exchange) from the isolated silanol reservoir to the hydrogen-bonded silanol protons. In any attempt to interpret or model the structure of the silica surface, the rate of this spin exchange places constraints on the spatial proximities of these two proton spin sets in terms of the dipole–dipole interactions that can be responsible for ^{1}H–^{1}H flip-flops, and/or chemical (H^+) exchange.

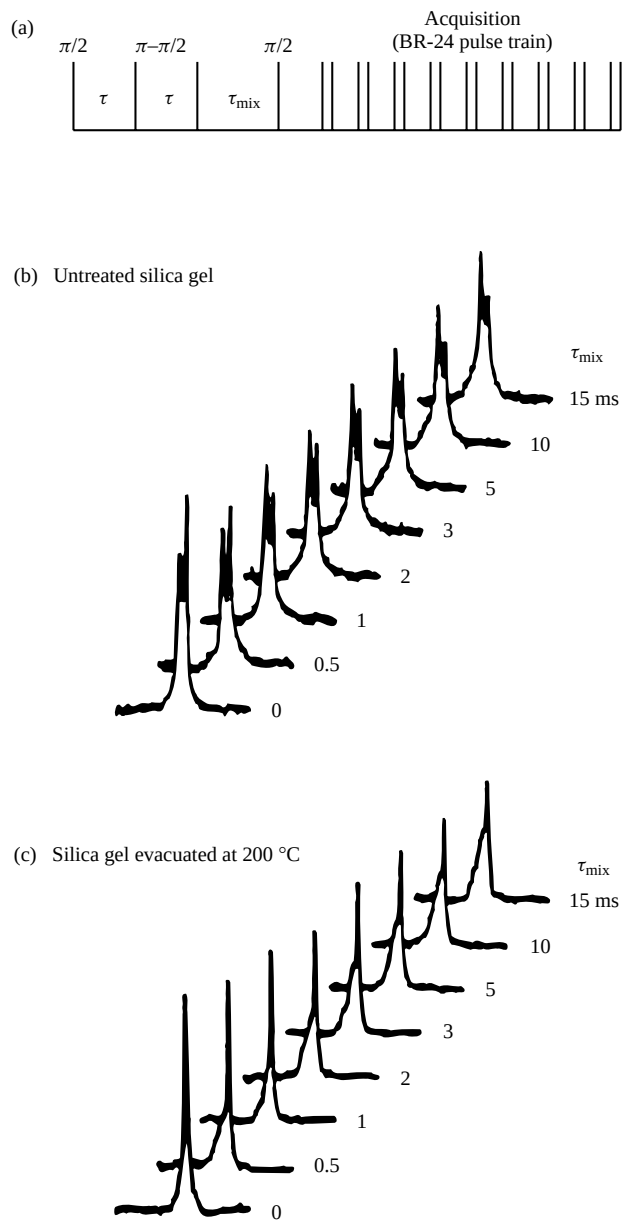

Figure 15 ^{1}H CRAMPS spin exchange experiment. (a) Pulse sequence. (b) Results for untreated silica gel (showing τ_{mix} values). (c) Results for sample evacuated at 200 °C (showing τ_{mix} values). (Taken from Bronnimann et al.[38])

A variety of CRAMPS-based ^{1}H NMR experiments of the types represented in Figures 12, 13, 14, and 15 have been carried out on silica samples in which there have been systematic variations of physisorbed water content or dehydration, and often temperature. Figure 16 shows ^{1}H CRAMPS dipolar-dephasing results obtained at room temperature on three different silica gels.[36] The behavior shown is consistent with the ideas described above. Figure 17 shows ^{1}H CRAMPS spectra of a hydrated (exposed to air) silica gel over a temperature range from 138 K to 298 K.[36] An effective freezing point depression of about 45 K can be noted from these kinds of measurements; this result is consistent with previous reports based on other types of experiments.[41]

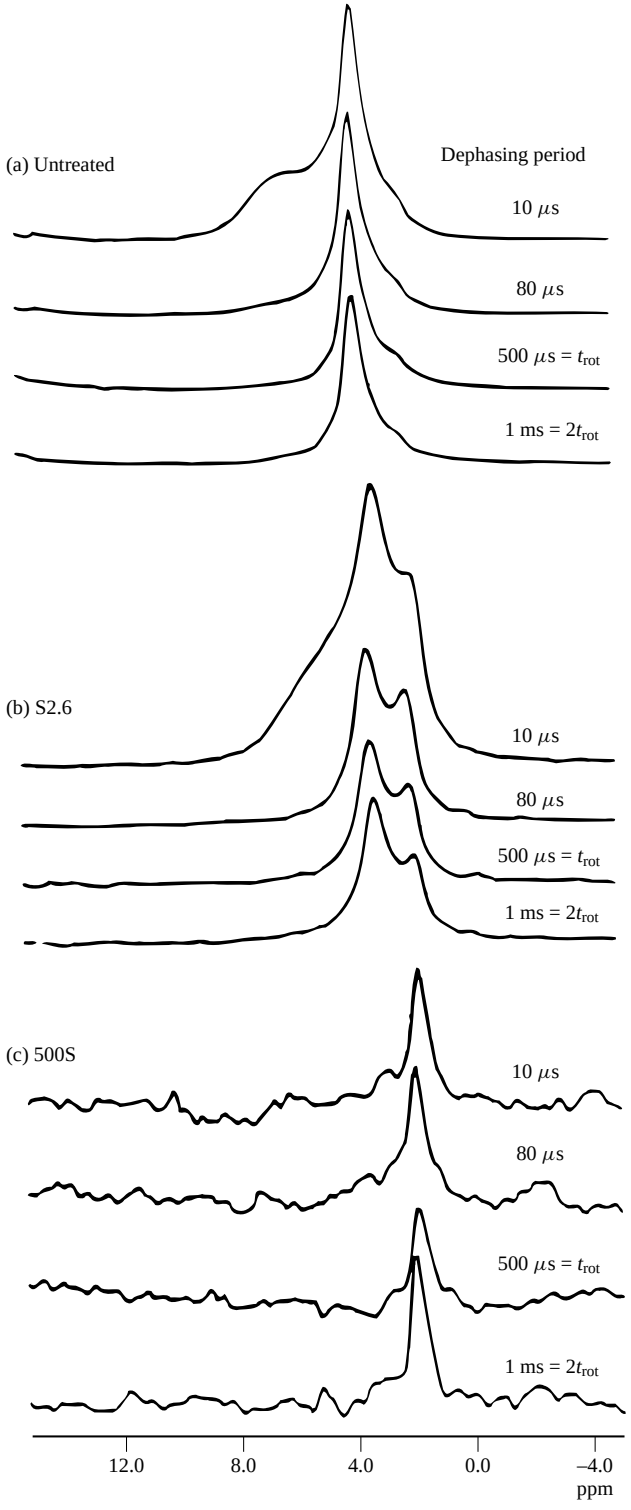

Figure 16 ^{1}H CRAMPS dipolar-dephasing spectra of three different silica gels. (a) Untreated. (b) Modestly dehydrated (2.6% weight loss). (c) Drastically dehydrated (at 500 °C)

5.5 Derivatized Silicas

Figures 18 and 19 show ^{1}H CRAMPS spectra of silica surfaces that have been derivatized with $(CH_3)_3SiCl$ and

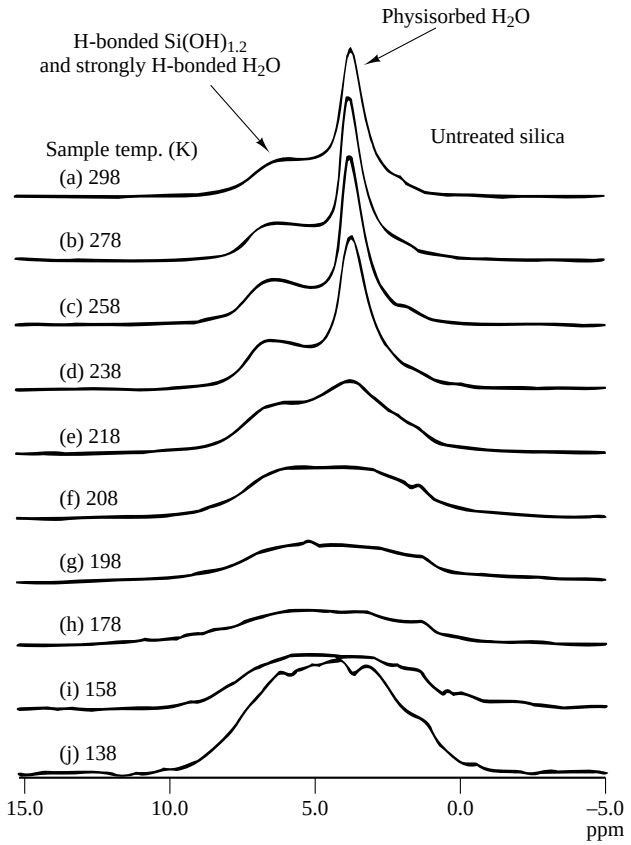

Figure 17 ^{1}H CRAMPS spectrum of an untreated silica gel as a function of temperature, as shown

$(CH_3CH_2O)_3SiCH_2CH_2CH_2NH_2$ (APTS), respectively. These spectra show that this technique can provide a rich level of structural detail on derivatized silica samples. The difference between the spectra of unprotonated and protonated APTS-derivatized samples (Figure 19) is the absence and presence, respectively, of a clearly distinct peak corresponding to the amino group of APTS.[29] This difference reflects, at least in part, the interference of ^{14}N quadrupole effects of the $-NH_2$ group with MAS averaging of $^{1}H-^{14}N$ dipolar interactions. Calculations on $=N-H$ groups show that, because of the small internuclear N–H distances for directly bonded pairs, very high NMR fields (>1000 MHz) would be required to reduce this broadening to an acceptable level by the 'brute force' approach of simply going to a higher field.[42]

6 CORRELATING ^{1}H-BASED AND ^{29}Si-BASED INFORMATION

6.1 Complementary Results

While one can distinguish between hydrogen bonded and isolated silanols by ^{1}H CRAMPS experiments and between single silanols and geminal silanols by ^{29}Si CP MAS experiments, it is important to correlate these two types of information. Ideally, one would base such a correlation on two-dimensional (2D) $^{1}H-^{29}Si$ heteronuclear chemical shift

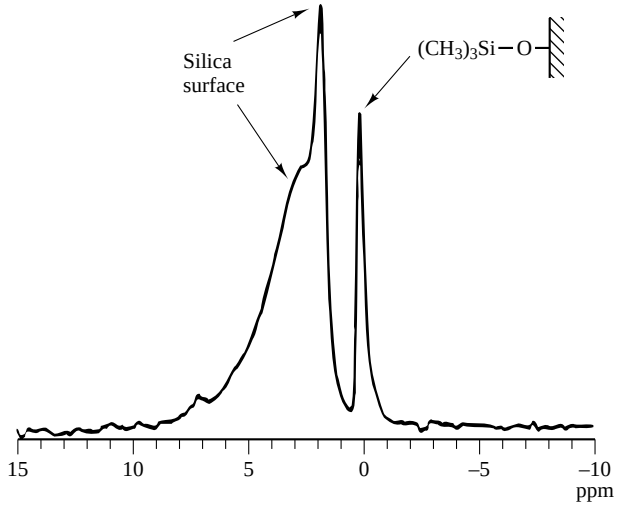

Figure 18 ^{1}H CRAMPS spectrum of trimethylsilyl-derivatized silica gel

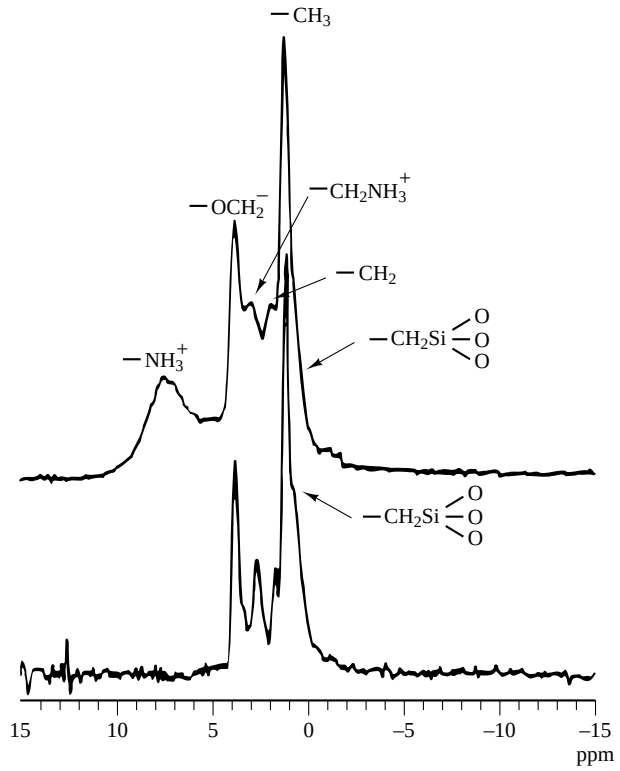

Figure 19 ^{1}H CRAMPS spectra of APTS-modified silica gel. Lower, untreated. Upper, treated with HCl. (Taken from Maciel et al.[29])

correlation (HETCOR) experiments of the general type that are employed routinely for $^{1}H-^{13}C$ correlation in liquids and more recently in solids.[43,44] Indeed, Vega has reported such experiments based on $^{1}H \rightarrow {}^{29}Si$ CP for the polarization transfer step.[45] However, as is seen below, rotating frame ^{1}H spin diffusion among the protons in a typical silica gel during the spin lock state in a $^{1}H \rightarrow {}^{29}Si$ CP experiment can substantially scramble what one would hope are discrete H $\leftrightarrow {}^{29}Si$ CP correlations in the time frame (>200 μs) required for relatively efficient CP transfer. Furthermore, the multiple

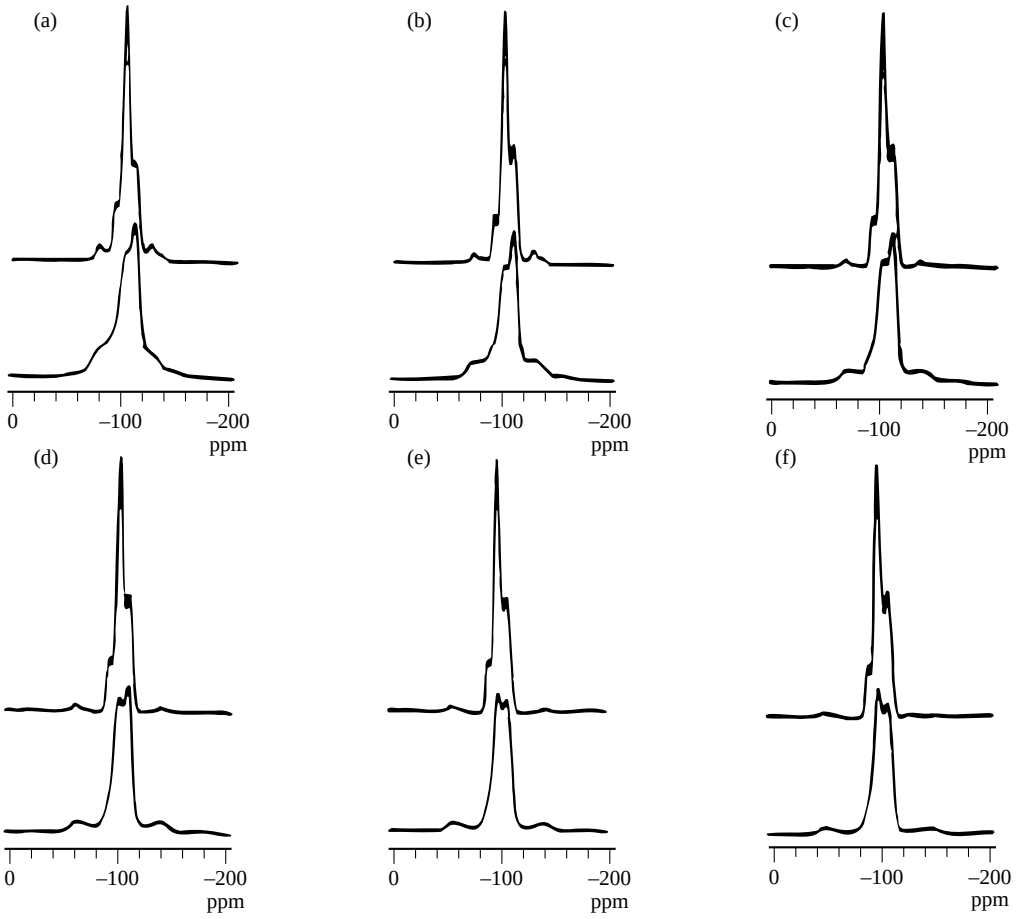

Figure 20 Proton-decoupled (top spectrum of each set) and proton-coupled (bottom spectrum of each set) 39.75 MHz ^{29}Si CP MAS NMR spectra of Fisher S-679 silica gel at six different magic angle spinning speeds. Cross polarization time, 5 ms. (a) 1.0 kHz, 1096 accumulations (b) 1.1 kHz, 3000 accumulations (c) 1.4 kHz, 720 accumulations (d) 1.6 kHz, 2000 accumulations (e) 1.8 kHz, 2000 accumulations (f) 2.0 kHz, 2000 accumulations. (Taken from Chuang et al.[47])

pulse approaches used in ^{1}H–^{13}C HETCOR experiments on solids are not very efficient in these ^{1}H–O–^{29}Si systems, although recently reported successes in ^{1}H–^{31}P 2D HETCOR experiments on P–O–H systems[46] indicate that ^{1}H–^{29}Si HETCOR in silica may be attractive. In any case, as an alternative to the 2D HETCOR approach, a variety of ^{29}Si-detected ^{1}H–^{29}Si CP experiments have been carried out, in which the behavior of protons is monitored by ^{29}Si, establishing the correlation.[47]

6.2 ^{29}Si Detection of Proton Spin Behavior

The simplest such experiment is a ^{29}Si CP MAS experiment in which ^{29}Si detection is carried out *without* proton decoupling. MAS should still average the ^{1}H–^{29}Si dipolar interaction during detection, yielding a corresponding sideband pattern to the extent that this interaction behaves inhomogeneously, i.e. to the extent that the ^{1}H–^{29}Si dipolar interaction is not altered (by chemical reaction, motion, or ^{1}H–^{1}H flip-flops) during a MAS rotor period.[47] Figure 20 shows a comparison of spectra obtained with and without ^{1}H decoupling; it is clear that the geminal silanol peak suffers most dramatically from the absence of high-power ^{1}H decoupling, implying that ^{1}H spin exchange is most efficient in the protons of geminal silanols.

Another ^{29}Si CP MAS experiment useful for correlating ^{1}H and ^{29}Si spin behaviors is the ^{1}H–^{29}Si analog of the common ^{1}H–^{13}C dipolar-dephasing experiment. In this technique, rotational and Hahn echo formation occur for a dephasing period (2τ) corresponding to two MAS rotor periods ($2\tau_{rot}$) for the isotropic ^{29}Si chemical shift, the ^{29}Si chemical shift anisotropy, and the ^{1}H–^{29}Si dipolar interaction (to the extent that it behaves inhomogenously).[47] Figure 21 shows results of the ^{1}H–^{29}Si dipolar-dephasing ^{29}Si CP MAS experiment with the dephasing period ranging over more than $4t_{rot}$. Focusing on the points at $2\tau = 0$, $2t_{rot}$ and $4t_{rot}$, one sees very little dephasing decay for the Q_4 (siloxane) signal, and more efficient decay for the Q_2 (geminal silanol) signal than for the Q_3 (single silanol) signal. This again suggests more efficient ^{1}H–^{1}H spin diffusion among the $=Si(OH)_2$ protons than among $\equiv$SiOH protons.

A very direct correlation of ^{1}H CRAMPS dipolar-dephasing behavior with ^{29}Si CP MAS signals is obtained in the experiment shown in Figure 22, in which there is a 2τ ^{1}H–^{1}H

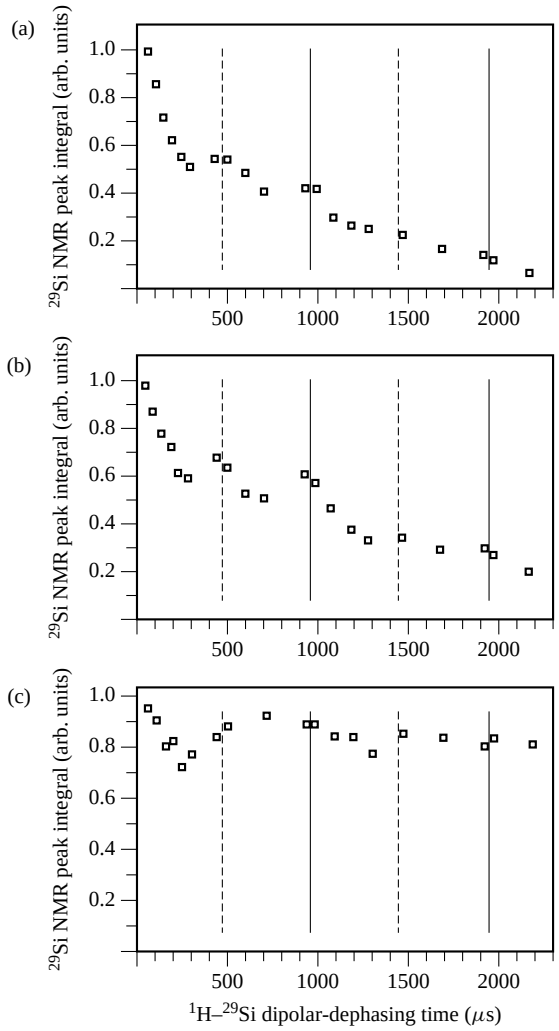

Figure 21 Plots of deconvoluted peak integrals of the 39.75-MHz ^{29}Si CP MAS NMR spectra of Fisher S-679 silica gel versus ^{1}H–^{29}Si dipolar-dephasing time up to four rotor periods. CP contact time, 5 ms; magic angle spinning speed, 2.0 kHz. Vertical dashed lines show odd numbers of rotor periods and vertical solid lines show even numbers of rotor periods. (a) −89 ppm peak (geminal silanols); (b) −99 ppm peak (single silanols); (c) −109 ppm peak (siloxane silicons). (Taken from Chuang et al.[47])

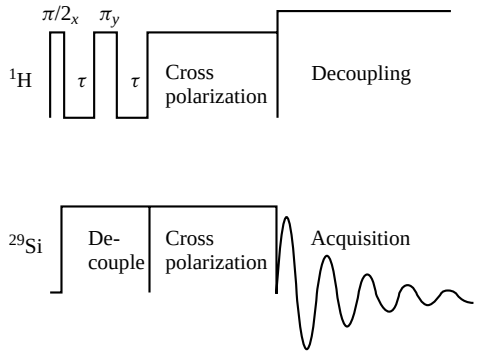

Figure 22 ^{29}Si CP MAS NMR experiment with ^{1}H–^{1}H dipolar-dephasing prior to ^{1}H → ^{29}Si cross polarization. (Taken from Chuang et al.[47])

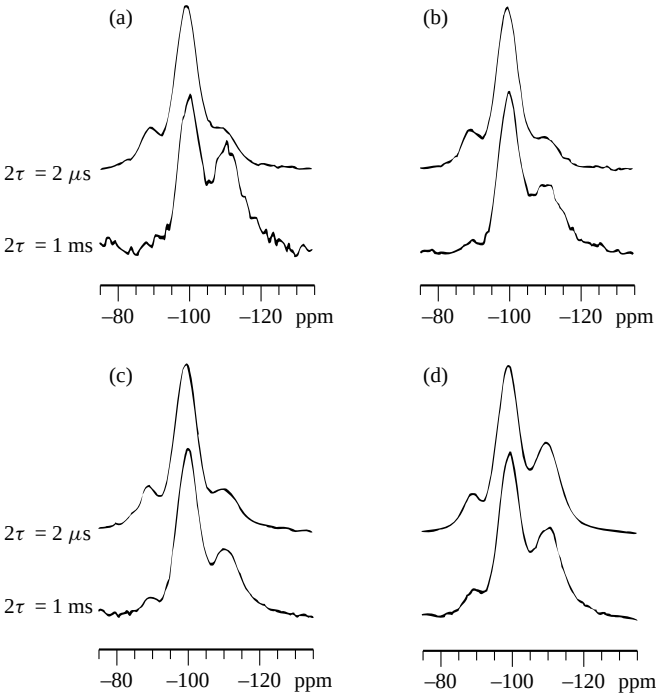

Figure 23 ^{29}Si CP MAS NMR spectra of Fisher S-679 silica gel obtained with 2 μs (top spectrum of each set) and two rotor periods (1.04 ms; bottom spectrum of each set) of ^{1}H–^{1}H dipolar-dephasing prior to four different ^{1}H–^{29}Si CP contact times. Magic angle spinning speed, 1.9 kHz. (a) t_{cp} = 100 μs (top spectrum, 7376 accumulations; bottom spectrum, 82 504 accumulations); (b) t_{cp} = 300 μs (top spectrum, 2400 accumulations; bottom spectrum, 46 200 accumulations); (c) t_{cp} = 1 ms (top spectrum, 432 accumulations; bottom spectrum, 21 232 accumulations); (d) t_{cp} = 5 ms (top spectrum, 600 accumulations; bottom spectrum, 8320 accumulations). (Taken from Chuang et al.[47])

dipolar-dephasing period *before* CP transfer to ^{29}Si.[47] Taking account of the rotational echo behavior of ^{1}H magnetization, for $2\tau = 2nt_{rot}$ essentially all relevant proton interactions refocus except the ^{1}H–^{1}H dipolar interaction. Hence, the magnetization of those protons involved in the strongest (shortest, least mobile) hydrogen bonds is most effectively dephased during $2\tau = 2nt_{rot}$ and unavailable for CP transfer to ^{29}Si. Figure 23 shows the results obtained on a silica gel sample. For a CP contact time (t_{cp}) that is small enough (100 μs) to avoid the rotating frame spin diffusion that scrambles the desired ^{1}H–^{29}Si correlation (vide supra), the geminal silanol peak at −89 ppm is the one that suffers most from ^{1}H–^{1}H dipolar dephasing for a $2t_{rot}$ period. The effect of rotating frame proton spin diffusion is also clear from the spectra in Figure 23: if a long CP contact period (e.g. 1–5 ms) is employed, essentially the same relative peak intensities are obtained whether or not the $2t_{rot}$ ^{1}H–^{1}H dipolar-dephasing period is included in the experimental sequence.

One overriding theme emerges from all the results embodied in Figures 20–23: the protons that are primarily responsible for cross polarization to geminal silanol silicons are much more extensively involved in hydrogen bonding than are the protons primarily responsible for cross polarization to single silanol silicons. This theme is consistent with structural models of the

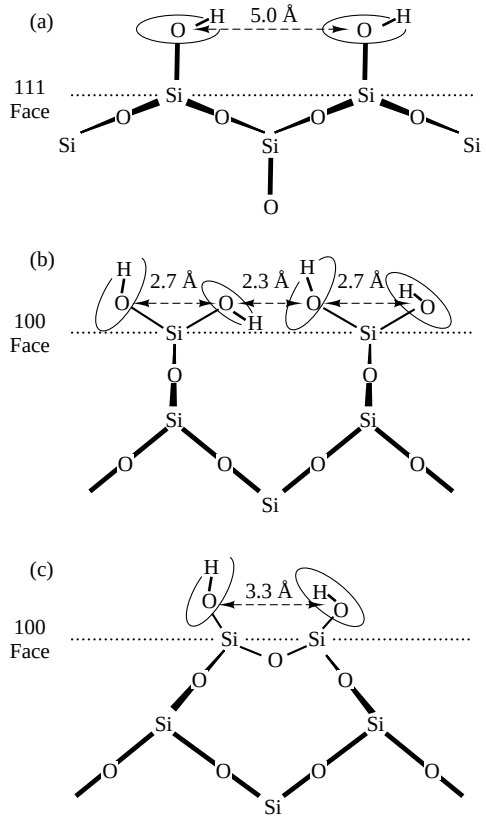

Figure 24 Side views of specific silicon planes (dashed line representing an edge of such a plane) of β-cristobalite. Drawing approximately to scale: (a) 111 face; (b) 100 face; (c) vicinal sites from dehydration of the 100 face. (Taken from Chuang et al.[47])

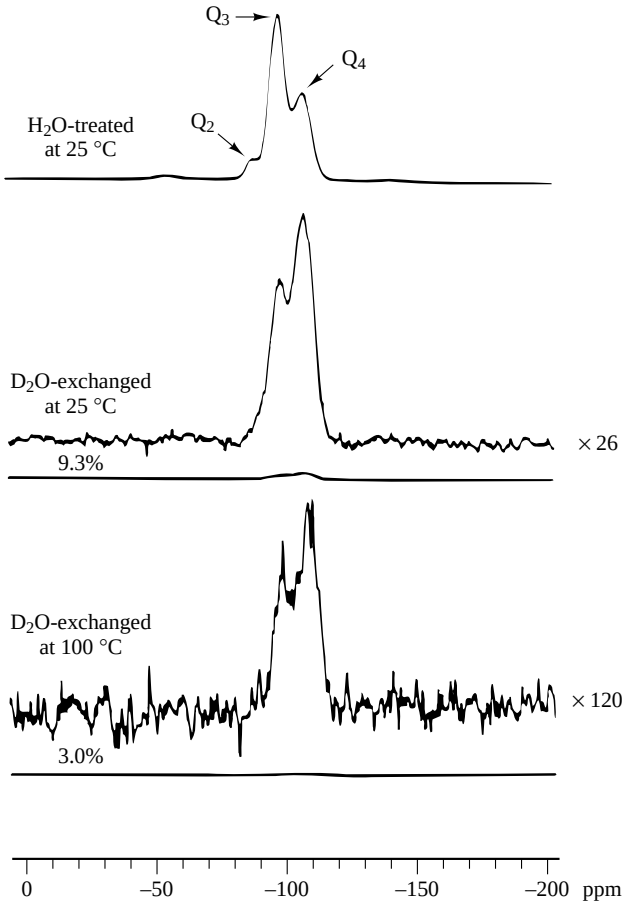

Figure 25 ^{29}Si CP MAS spectra of silica gels stirred in H_2O or D_2O at 25 °C or 100 °C, as indicated

silica surface (or, at least fragments of it) that correspond to specific faces of a β-cristobalite crystal.[47,48]

Figure 24 shows views looking 'into' the 111 and 100 faces, which contain single silanols (Q_3) and geminal silanols (Q_2), respectively. From the O–O distances between hydroxyl oxygens of these surfaces, we see that one should expect hydrogen bonding between adjacent geminal silanols, but not between adjacent single silanols; this is in agreement with the NMR results summarized above. Of course, the silica surface is not a homogeneous one, and may be describable as a composite of these two types of surfaces, with suitable interfaces. The geometrical relationship between silanols that are adjacent *across* these interfaces is important in the overall hydrogen-bonding patterns at silica surfaces. Furthermore, the presence of water on the surface dramatically changes the pattern of hydrogen bonding, including the establishment of hydrogen-bonding networks among the single silanols.

7 SUBSURFACE SILANOLS

An implicit assumption on which the use of ^{29}Si CP MAS as a kind of surface-selective technique is based is the following: essentially all (or at least most) of the protons of a sample like SiO_2 are at the surface. This assumption has been tested in a variety of ways, including ^{29}Si NMR. One NMR avenue for testing this assumption is to examine the ^{1}H and/or ^{29}Si NMR spectra of samples that have been subjected to repeated exchanges with D_2O. Figure 25 shows the ^{29}Si CP MAS spectra of silica gel samples that have been treated in this way.[40] From such studies, it has been determined that for a typical silica gel, 91–97% of the silanols are exchangeable with D_2O, the exact percentage depending on the time and temperature of the exchange. The geminal silanol signal is completely depleted by D_2O exchange, and Figure 26 shows that this signal is immediately restored to its equilibrium intensity shortly after a D_2O-exchanged silica is exposed to the moisture in air. Hence, none of the inaccessible or subsurface silanols are of the Q_2 type.

Extensive studies of spin dynamics in D_2O-exchanged samples have revealed a substantial amount of detail about the local environment and motional dynamics of 'internal' silanols in silica gel.[40] The T_{HSi} values indicate that the hydroxy groups of 'internal' silanols rotate freely about the Si–O axis in a manner similar to the rotation of non-hydrogen-bonded silanols on a dehydrated silica surface. Analogous studies have also been carried out on a fumed silica Cab-O-Sil.[24] While the D_2O-exchange behavior and various features of ^{1}H and ^{29}Si spin dynamics in Cab-O-Sil are qualitatively similar to what is discussed above for silica gel, some significant and possibly important differences are observed,[24] perhaps because of interparticle (particle bridging) silanols that have been suggested by some authors for fumed silicas.

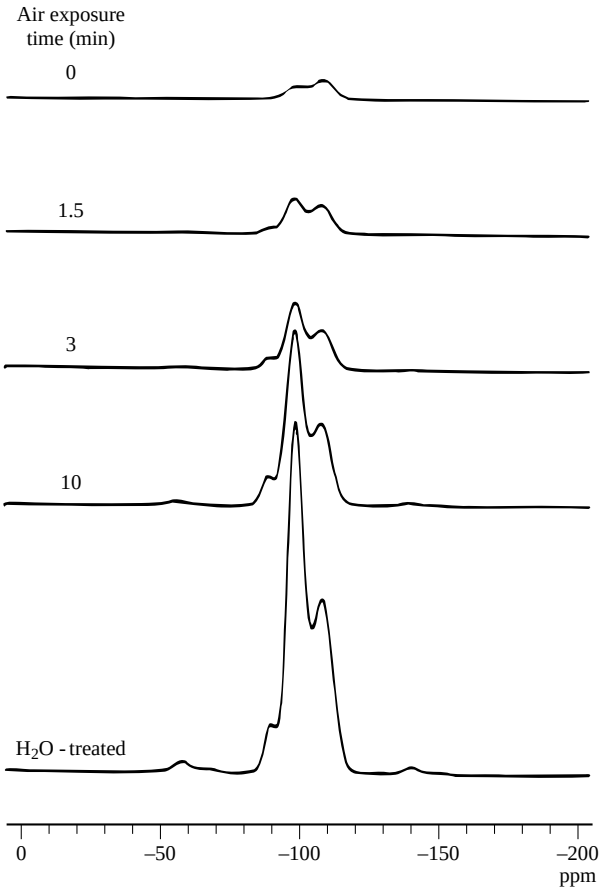

Figure 26 ^{29}Si CP MAS spectra of a D_2O-exchanged silica gel, after air exposure for the indicated times, or (bottom) stirred in H_2O

8 SUMMARY AND CONCLUSIONS

MAS NMR approaches based on ^{1}H and ^{29}Si are enormously useful in the characterization of silica surfaces, including derivatized silica surfaces. The CRAMPS technique, and especially dipolar-dephasing elaborations, provide a powerful way to distinguish between hydrogen bonding and isolated silanols. Silicon-29 CP MAS spectra clearly distinguish between Q_2, Q_3, and Q_4 sites at the surface. Via $^{1}H \rightarrow {}^{29}Si$ cross polarization, the ^{29}Si CP MAS technique provides avenues for projecting ^{1}H spin behavior onto a ^{29}Si NMR spectrum. D_2O-exchange approaches allow the use of ^{1}H and ^{29}Si NMR behavior to examine subsurface or trapped silanols.

9 RELATED ARTICLES

CRAMPS; Silicon-29 NMR of Solid Silicates.

10 REFERENCES

1. R. K. Iler, *The Chemistry of Silica. Solubility, Polymerization, Colloid and Surface Properties, and Biochemistry*, Wiley-Interscience, New York, 1979.
2. G. Engelhardt and D. Michel, *High Resolution Solid-State NMR of Silicates and Zeolites*, Wiley, New York, 1987.
3. G. E. Maciel, C. E. Bronnimann, R. C. Zeigler, I.-S. Chuang, D. R. Kinney, and E. A. Keiter, in *The Colloid Chemistry of Silica. Adv. Chem. Ser. No. 234*, ed. H. Bergna, Am. Chem. Soc., Washington, DC, 1994, p. 269.
4. G. E. Maciel and P. D. Ellis, in *NMR Techniques in Catalysis*, eds. A. T. Bell and A. Pines, Marcel Dekker, New York, 1994, pp. 231–310.
5. G. E. Maciel, in *Nuclear Magnetic Resonance in Modern Technology, NATO ASI Series C* ed. G. E. Maciel, Kluwer, Amsterdam, 1994, p. 225.
6. P. C. Hammel, P. L. Kuhns, O. Gonen, and J. S. Waugh, *Phys. Rev. B*, 1986, **34**, 6543.
7. R. A. Wind, M. J. Duijvestijn, C. Van Der Lugt, A. Manenschijn, and J. Vriend, *Prog. NMR Spectrosc.*, 1985, **17**, 33.
8. D. Raftery, H. Long, T. Meersmann, P. J. Grandinetti, L. Reven, and A. Pines, *Phys. Rev. Lett.*, 1991, **66**, 584.
9. A. Pines, W. G. Gibby, and J. S. Waugh, *J. Chem. Phys.*, 1973, **59**, 569.
10. G. E. Maciel and D. W. Sindorf, *J. Am. Chem. Soc.*, 1980, **102**, 7606.
11. D. W. Sindorf and G. E. Maciel, *J. Phys. Chem.*, 1982, **86**, 5208.
12. J. Schaefer and E. O. Stejskal, *J. Am. Chem. Soc.*, 1976, **98**, 1031.
13. M. Mehring, *High Resolution NMR in Solids*, Springer, Berlin, 1983, p. 135.
14. D. W. Sindorf and G. E. Maciel, *J. Am. Chem. Soc.*, 1983, **105**, 1487.
15. G. E. Maciel, D. W. Sindorf, and V. J. Bartuska, *J. Chromatogr.*, 1981, **205**, 438.
16. D. W. Sindorf and G. E. Maciel, *J. Am. Chem. Soc.*, 1981, **103**, 4263.
17. D. W. Sindorf and G. E. Maciel, *J. Am. Chem. Soc.*, 1983, **105**, 3767.
18. D. W. Sindorf and G. E. Maciel, *J. Phys. Chem.*, 1983, **87**, 5516.
19. G. S. Caravajal, D. E. Leyden, G. R. Quinting, and G. E. Maciel, *Anal. Chem.*, 1988, **60**, 1776.
20. C. J. Brinker, R. J. Kirkpatrick, D. R. Tallant, B. C. Bunker, and B. Montez, *J. Non-Cryst. Solids*, 1988, **99**, 418.
21. C. J. Brinker, R. K. Brow, D. R. Tallant, and R. J. Kirkpatrick, *J. Non-Cryst. Solids*, 1990, **120**, 26.
22. S. Léonardelli, L. Facchini, C. Fretigny, P. Tougne, and A. P. Legrand, *J. Am. Chem. Soc.*, 1992, **114**, 6412.
23. A. Tuel, H. Hommel, A. P. Legrand, Y. Chevallier, and J. C. Morawski, *Colloid Surf.*, 1990, **45**, 413.
24. C. Liu and G. E. Maciel, unpublished results.
25. L. L. Hench and J. K. West, *Chem. Rev.*, 1990, **90**, 33.
26. I. Elnahhal, J. Yang, I.-S. Chuang, S. F. Dec, and G. E. Maciel, *J. Non-Cryst. Solids*, submitted.
27. T. H. Walter, G. L. Turner, and E. Oldfield, *J. Magn. Reson.*, 1988, **76**, 106.
28. C. E. Bronnimann, B. L. Hawkins, M. Zhang, and G. E. Maciel, *Anal. Chem.*, 1988, **60**, 1743.
29. G. E. Maciel, C. E. Bronnimann, and B. L. Hawkins, in *Advances in Magnetic Resonance: The Waugh Symposium*, ed. W. S. Warren, Academic Press, San Diego, CA, 1990, Vol. 14, pp. 125–150.
30. Z. Luz and A. J. Vega, *J. Phys. Chem.*, 1987, **91**, 374.
31. J. S. Waugh, L. M. Huber, and V. Haeberlen, *Phys. Rev. Lett.*, 1968, **20**, 180.
32. W.-K. Rhim, D. D. Elleman, and R. W. Vaughan, *J. Chem. Phys.*, 1973, **58**, 1772.
33. D. P. Burum and W. K. Rhim, *J. Chem. Phys.*, 1979, **71**, 944.
34. B. C. Gerstein, R. G. Pembleton, R. C. Wilson, and L. M. Ryan, *J. Chem. Phys.*, 1977, **66**, 361.

35. S. F. Dec, C. E. Bronnimann, R. A. Wind, and G. E. Maciel, *J. Magn. Reson.*, 1989, **82**, 454.
36. D. R. Kinney, I.-S. Chuang, and G. E. Maciel, *J. Am. Chem. Soc.*, 1993, **115**, 6786.
37. D. Suwelack, W. P. Rothwell, and J. S. Waugh, *J. Chem. Phys.*, 1980, **73**, 2559.
38. C. E. Bronnimann, R. C. Zeigler, and G. E. Maciel, *J. Am. Chem. Soc.*, 1988, **110**, 2023.
39. R. Freeman and H. D. Hill, *J. Chem. Phys.*, 1971, **54**, 3367.
40. I.-S. Chuang, D. R. Kinney, and G. E. Maciel, *J. Am. Chem. Soc.*, 1993, **115**, 8695.
41. R. J. Wittebort, M. G. Usha, D. J. Ruben, D. E. Wemmer, and A. Pines, *J. Am. Chem. Soc.*, 1988, **110**, 5668.
42. R. A. Lewis, Ph.D. Dissertation, Colorado State University, 1994.
43. D. P. Burum and A. Bielecki, *J. Magn. Reson.*, 1991, **94**, 645.
44. C. E. Bronnimann, C. Ridenour, D. R. Kinney, and G. E. Maciel, *J. Magn. Reson.*, 1992, **97**, 522.
45. A. J. Vega, *J. Am. Chem. Soc.*, 1988, **110**, 1049.
46. R. A. Santos, R. A. Wind, and C. E. Bronnimann, *35th Exp. NMR Conf., Asilomar, CA, April 14, 1994*.
47. I.-S. Chuang, D. R. Kinney, C. E. Bronnimann, R. C. Zeigler, and G. E. Maciel, *J. Phys. Chem.*, 1992, **96**, 4027.
48. D. W. Sindorf, Ph.D. Dissertation, Colorado State University, 1982.

Acknowledgments

For that portion of the research described in this paper that was carried out at Colorado State University, the author gratefully acknowledges partial support by National Science Foundation grants during the past few years. He also acknowledges the invaluable assistance over many years of Dr. I.-Ssuer Chuang.

Biographical Sketch

Gary E. Maciel. *b* 1935. B.S., 1956, chemistry, University of California, Berkeley, Ph.D., 1960, Massachusetts Institute of Technology (MIT). Postdoctoral work at MIT (with John S. Waugh), 1960–61 which provided first hands-on experience with NMR. Assistant professor, associate professor, professor at the University of California, Davis, 1961–70. Professor of Chemistry, Colorado State University, 1971–present. Approx. 320 publications. Research specialties: development and application of NMR techniques, especially for solids and surfaces, and currently for environmental studies.

Structure and Dynamics of Proteins Adsorbed at Biomaterial Interfaces

Gary P. Drobny, Joanna R. Long, Wendy J. Shaw, Myriam Cotten, and Patrick S. Stayton

University of Washington, Seattle, WA, USA

1 Introduction 1
2 NMR Strategies for Studying Surface-Adsorbed Proteins 2
3 A Solid-State NMR Study of Salivary Statherin Adsorbed onto Hydroxyapatite (HAP) Crystals 6
4 Related Articles in Volumes 1–8 9
5 References 9

1 INTRODUCTION

1.1 Biomineralization: Background and Significance

Biomineralization, defined as the organized deposition of inorganic materials in the cellular or extracellular matrix, may be as simple a process as the formation of an iron oxide crystal in the vesicle of a magnetobacterium, or as complex a process as the formation of the intricate calcium carbonate and calcium phosphate structures found in marine coccoliths, invertebrate shells, vertebrate skeletons and teeth. The phenomenon of biomineralization has attracted a great deal of attention recently from the materials science community, which seeks to understand the way in which inorganic biological composites are synthesized and processed in nature.[1–8]

An extremely important problem in the field of biomineralization is understanding the manner in which mineral deposition is controlled in vivo. The crystal engineering processes necessary to achieve the controlled deposition of minerals at physiological temperatures and in aqueous solutions are directly provided by proteins in most known examples.[7,9–17] In particular, the deposition of minerals in most hard tissues in higher organisms is controlled by a class of unusually acidic, non-collagenous proteins and glycoproteins.[9,10,17,21–28] These acidic proteins typically comprise only about 1% of the mass of the organic matrix, and are frequently found sandwiched between crystal surfaces and major framework molecules like collagen or chitin. They are rich in acidic amino acids including aspartic and glutamic acid, and contain large numbers of phosphorylated amino acids, especially phosphoserine.

In the specific case of hydroxyapatite ($Ca_{10}(PO_4)_6(OH)_2$), the principal mineral component of bone and dental enamel, extra-cellular, acidic, non-collagenous proteins include apatite nucleators like bone sialoprotein, osteonectin, and dentin phosphoryn, while osteocalcin, osteopontin, and salivary statherin inhibit apatite formation and growth. In some cases (e.g., osteonectin, bone sialoprotein, and dentin phosphoryn) apatite formation is inhibited at high protein concentration while nucleation of apatite occurs at low protein concentration.

Substantial progress has been made in recent years in characterizing, at the macroscopic level, the structural properties of biological composites,[1,18–20] but there is still a significant gap in our understanding of the molecular recognition processes underlying acidic protein-calcium composite interactions. In particular, while protein model structures have been proposed which hypothesize the involvement of protein secondary structure motifs for presentation of carboxylate residues,[10,13,26,28,29] the lack of high resolution structural data for proteins on surfaces precluded any molecular structure vs. function studies.

The acquisition of molecular-level structural information for proteins on surfaces is not only important to the field of biomineralization but has broad applicability in a number of important fields. For example, there is currently a great deal of effort in the fields of drug delivery, implant design, tissue engineering, and diagnostics directed toward developing polymeric surfaces for immobilization and controlled release of peptides and proteins. Detailed structural information about proteins bound to material surfaces will provide important new design criteria from the perspective of peptide/protein structure, dynamics, and assembly at polymeric biomaterial surfaces.

1.2 The Role of Protein-Crystal Interactions in Biomineralization

Understanding the function of a biomineralization protein requires that the secondary and tertiary structure of the molecule be defined within its biological context, i.e. the protein in contact with the crystal. In addition, the precise nature of the interactions between the protein and the crystal which underlie the recognition process must be understood. This requires a knowledge of the contacts formed between the amino acid side chains of the protein and the ions in the crystal faces. The involvement of water molecules in these interactions must be understood as well.

Current investigations of protein-mineral interactions are commonly conducted with techniques that characterize the macroscopic behavior of proteins in the presence of mineral crystals. Equilibrium properties such as protein-crystal binding constants are derived via adsorption isotherm measurements, where data are analyzed usually by assuming a simple Langmuir model of protein adsorption onto the crystal faces. But the most commonly-used approach for determining protein-crystal interactions in vitro are kinetic experiments in which a small amount of protein is dissolved in a saturated solution of a particular inorganic salt and the time required for crystals to form is compared to a control solution in which no protein is present. Assays also exist for determining selective binding of a particular crystal face by a protein as well as oriented nucleation of crystals in the presence of acidic proteins.[30]

However, to move beyond macroscopic aspects of protein-crystal interactions, what is clearly needed are high resolution spectroscopic methods that can provide information about the atomic level structure of the protein on the crystal face, under physical conditions that are biologically relevant (physiological levels of hydration and pH). Information about the secondary structural motifs that occur in the adsorbed protein together with information on the exposure of protein

side chains to the crystal face, may lead to an understanding of how particular proteins promote or inhibit nucleation. Analytical techniques currently used to probe protein-crystal interactions at the atomic and molecular levels and the advantages that solid state NMR bring to the field will be briefly reviewed in the next section.

2 NMR STRATEGIES FOR STUDYING SURFACE-ADSORBED PROTEINS

The lack of high resolution structural data for proteins on surfaces is the result of a lack of high resolution structural methods that can be brought to bear on relevant problems. The conventional methods of high resolution structural biology, X-ray crystallography and solution nuclear magnetic resonance (NMR) spectroscopy have provided information on a few biomineralization proteins in the pure crystalline and solution states,[31–33] but both techniques are severely limited in their abilities to elucidate the structures of proteins on biomineral surfaces. Although traditional surface science methods like photo-electron spectroscopy and NEXAFS have provided important information on protein adsorbed onto planar surfaces, and, in particular, may be used to characterize the degree of long range ordering in systems of adsorbed proteins on polymer surfaces as well as average structural properties, these techniques have yet to provide detailed atomic-level structural information for surface-adsorbed proteins. In addition surface diffraction methods and many optical techniques are not applicable to proteins adsorbed onto porous surfaces (e.g., porous plastics) or to other surfaces which preclude long-range ordering.

To fully appreciate the utility of solid state NMR in the study of protein structure at biomaterial interfaces, it is first important to recognize the dual nature of the protein-surface problem. There is first the familiar structural aspect, alluded to briefly in the prior section, which includes defining the secondary and tertiary structures of the adsorbed protein and by implication any structural changes which occur upon binding to the surface. The structure and chemical composition of the crystal surface in contact with the protein side chains must also be understood. In addition, a less familiar but no less important aspect is the dynamics of the adsorbed protein. It is desirable that the protein be observed on the surface under biologically relevant conditions, i.e., fully hydrated. Dehydration of the sample may alter not only the structure of the protein from its biologically relevant form but may quench the dynamics of the protein on the surface. Here we refer to both whole-molecule dynamics describing the protein's rigid body kinematics on the surface and to internal dynamics wherein the protein's conformation may be labile on the NMR time scale. In the following section we will review how solid state NMR can be used to probe both molecular structure and dynamics on surfaces.

2.1 NMR Structural Methods for the Study of Protein Structure at Biomaterial Interfaces

Solid state NMR has long been used to identify and characterize the structures of small organic molecules adsorbed onto catalytic surfaces,[34–36] argon matrices,[37] and silica surfaces.[38–40] There similarly exist a number of solid state NMR pulse techniques capable in principle of reporting the structures of surface-adsorbed proteins. The most straightforward approach is to evaluate the secondary structure of surface-adsorbed proteins from the chemical shifts of ^{13}C spins located in the protein backbone. This approach basically exploits the fact that the isotropic chemical shifts of the backbone carbonyl, alpha, and beta ^{13}C spins of each amino acid residue are to varying extents sensitive to the local secondary structure of the protein. Although recent work by Oldfield and coworkers has placed structural interpretation of isotropic ^{13}C chemical shifts of proteins on a quantitative basis,[41–43] in the past analyses of structures using chemical shift data have been applied empirically, i.e., by comparing experimentally observed ^{13}C chemical shifts for backbone ^{13}C spins to a large body of data, derived via ^{13}C Cross Polarization/Magic Angle Spinning (CPMAS) experiments from polypeptides of known secondary structure in the condensed state. An excellent example of this type of analysis is the seminal work by Fernandez et al.[44] who studied the structures of polyglutamic acid and polylysine adsorbed to hydroxyapatite and silica using ^{13}C CPMAS. In addition to studies of the conformations of polypeptides on apatite and silica surfaces, ^{13}C MAS has been used to study the incorporation of carbonate ions in bone and synthetic apatites,[45] and ^{31}P MAS has been used to characterize the structures of various calcium phosphates found in biological systems.[46–48]

Isotropic chemical shift data can be supplemented by quantitative structural data obtained via orientational constraints and/or distance/torsion angle constraints. The best examples that illustrate the use of orientational constraints and distance/torsion angle constraints come from the membrane protein literature. Structural data on membrane-associated proteins have been acquired by two general types of solid state NMR data: (1) orientational constraints, usually obtained from magnetic interaction tensors located in the backbone of proteins oriented in mono-domain lipid bilayers; and (2) distance and torsion angle constraints acquired from proteins associated with unaligned lipid vesicles. The former class of experiment requires the application of local field spectroscopy techniques (e.g., PISEMA) to oriented samples.[49] Although possible to achieve with lipids, there is no general analog in biomaterial interfaces to the mono-domain bilayer construct, so the orientational constraint approach has yet to be applied to biomaterials. Because distance and torsion angle constraints are generally acquired from unoriented samples via homo- and heteronuclear dipolar recoupling experiments, this approach shows the greatest promise in studies of surface-adsorbed biopolymers.

There are a number of dipolar recoupling experiments currently used to address a variety of problems in the material and biological sciences. No attempt will be made here to comprehensively cover all the alternative methods, their relative advantages and disadvantages. The reader is referred to general review articles on the subject of dipolar recoupling for more extensive treatments of dipolar recoupling.[50,51] The following discussion is provided simply to clarify some general properties of dipolar recoupling sequence referred to in descriptions of studies of surface-adsorbed proteins.

Solid state NMR spectra of spin 1/2 nuclei are dominated by two magnetic interactions, the chemical shift anisotropy (CSA) and the direct nuclear dipole-dipole interaction (Figure 1). As discussed above, the former interaction is valuable as a qualitative probe of protein structure. The dipole-dipole interaction

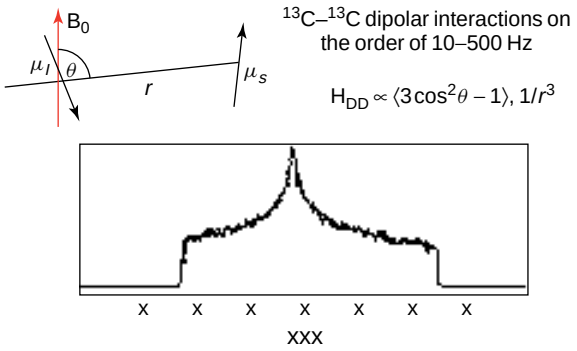

Figure 1 The dipolar coupling tensor is a uniaxial tensor. The principal axis frame of this dipolar tensor has a z axis parallel to the internuclear vector. The dipolar coupling is proportional to the inverse cube of the internuclear distance $\langle 1/r^3 \rangle$, and the second order Legendre polynomial $\langle (3/2)\cos^2\theta - (1/2) \rangle$, where θ is the angle between the internuclear vector and the magnetic field. The solid state NMR spectrum of a pair of dipolar-coupled spin 1/2 nuclei with negligible CSA's should be a Pake powder pattern, from which the dipolar coupling constant may be easily extracted. However, if the coupled spin 1/2 nuclei have CSA's much larger than the dipolar coupling it will be difficult to extract the dipolar coupling constant from the NMR powder spectrum. The figure shows the powder spectrum of two dipolar coupled ^{13}C spins, each with a CSA on the order of 20 kHz; and with dipolar coupling of 500 Hz, corresponding to a ^{13}C pair separated by 2.5 Å. The spectrum is clearly dominated by the CSA and it is very difficult to discern the presence of a dipolar coupling in the spectral data

has a straightforward structural interpretation because the dipolar coupling constant is proportional to the inverse cube of the internuclear distance. However, in many systems composed of coupled spin 1/2 nuclei, the magnitude of the CSA may exceed the magnitude of the dipole-dipole interaction. For example, for two sp^2 hybridized, directly bonded ^{13}C spins the CSA's may approach 200 ppm, corresponding to over 20 000 Hz in a 9.4 Tesla magnetic field. On the other hand, the dipole-dipole interaction for this directly bonded spin pair will not exceed 2300 Hz. and may be even smaller for non-bonded ^{13}C spins. Therefore the dipolar coupling constant may not be easily discerned in spectral data when the CSA exceeds the dipolar interactions by orders of magnitude so it is necessary to use NMR methods which suppress one of these interactions thus enabling straightforward detection of the other.

In the late 1960s NMR coherent averaging experiments were introduced to remove the dipolar coupling between spin 1/2 nuclei (^{19}F, ^{1}H, etc.) in crystalline solids, while simultaneously preserving the chemical shift anisotropy (CSA).[52,53] The spin dynamics that underlie these experiments have been thoroughly quantified with Average Hamiltonian Theory (AHT).[54,55] Basically, homonuclear dipolar decoupling sequences like WHH-4,[53] MREV-8,[56] BR-24,[57] MSHOT-3[58] etc. exploit the different transformational properties of the chemical shift anisotropy (CSA) and the dipolar interaction in spin space to remove the homonuclear dipolar interaction while preserving a scaled CSA.

Physical rotation of the sample (i.e., Magic Angle Spinning,[59] MAS) coherently averages spatial parts spin interaction Hamiltonian that transform as second rank tensors. However, both the dipolar and the chemical shift Hamiltonians transform as second rank tensors in Cartesian space, so MAS removes the effect of both interactions from solid-state NMR spectra. The objective of dipolar recoupling is to use MAS and radio frequency (rf) irradiation in synchrony, with the ultimate objective of suppressing the chemical shift while preserving the dipolar coupling. Because information on internuclear distances can be recovered using dipolar recoupling techniques, these pulse sequences are widely used in structural studies of molecular solids.

The two dipolar recoupling pulse sequences that will be discussed in the context of structural studies of proteins adsorbed at biomaterial interfaces are the heteronuclear recoupling experiment Rotational Echo Double Resonance (REDOR) and the homonuclear recoupling experiment Dipolar Recoupling with a Windowless Sequence[60] (DRAWS). REDOR, developed by Schaefer and coworkers has been reviewed elsewhere.[61] We confine our remarks to stating that in studies of surface-adsorbed biopolymers REDOR has a number of uses including: (1) Direct characterization of the surface, as was done by Pan[62] who used ^{31}P–^{19}F REDOR to study the distribution of ^{19}F in fluoroapatite; (2) ^{13}C–^{15}N REDOR to confirm helical secondary structures in surface-adsorbed proteins by measuring hydrogen bond lengths between the ^{13}C carbonyl spin of the i residue to the ^{15}N amide spin of the $i+4$ residue; and (3) probing dipolar interactions from ^{13}C and ^{15}N spins in protein side chains to NMR-active spins in the surface, ^{31}P spins in hydroxyapatite and ^{19}F spins in fluoropolymers, for example.

DRAWS is well suited to measuring distances between backbone carbonyl carbons in peptides and proteins.[63–66] Dipolar couplings of less than 40 Hz between carbonyl ^{13}C spins have been detected in biopolymers at high magnetic fields,[67–70] attesting to the ability of DRAWS to suppress large CSAs and at the same time detect small dipolar couplings between non-bonded ^{13}C spins. Figure 2 shows three forms of the DRAWS dipolar recoupling pulse sequence. In the DRAWS experiment, the unit pulse cycle (Figure 2a) is applied synchronously with the sample spinning and thus the duration of the unit cycle is exactly equal to one rotor period τ_{rotor}. The DRAWS experiment, which utilizes a four step supercycle, shown in Figure 2(a), is commonly employed in the context of a CPMAS experiment, see Figure 2(a). The basic strategy is to detect the amplitude of transverse magnetization that remains after an integral number of DRAWS super-cycles. Repeating this measurement as a function of the number of DRAWS supercycles results in a "dephasing" curve (Figure 3). Simulation of this dephasing curve results in a value for the internuclear distance.

The DRAWS dephasing curve is a useful measurement for determining protein secondary structure because, as shown in Figure 3, the carbonyl-carbonyl distance is directly related to the Ramachandran torsion angle φ. Therefore, using DRAWS distance measurements, the torsion angle φ may be determined at several positions in a peptide in a model-independent fashion. An example of a DRAWS experiment applied to a crystalline tripeptide alanylglycylglycine (AGG), labeled at both carbonyl positions with ^{13}C, is shown in Figure 4. Agreement with the crystallographically determined φ of -83° is excellent. Additionally, DRAWS can also measure conformational heterogeneity since the dipolar recoupling efficiency is independent of any correlation between chemical shift and peptide secondary structure. This allows the determination of the distribution of peptide conformers in a given sample.

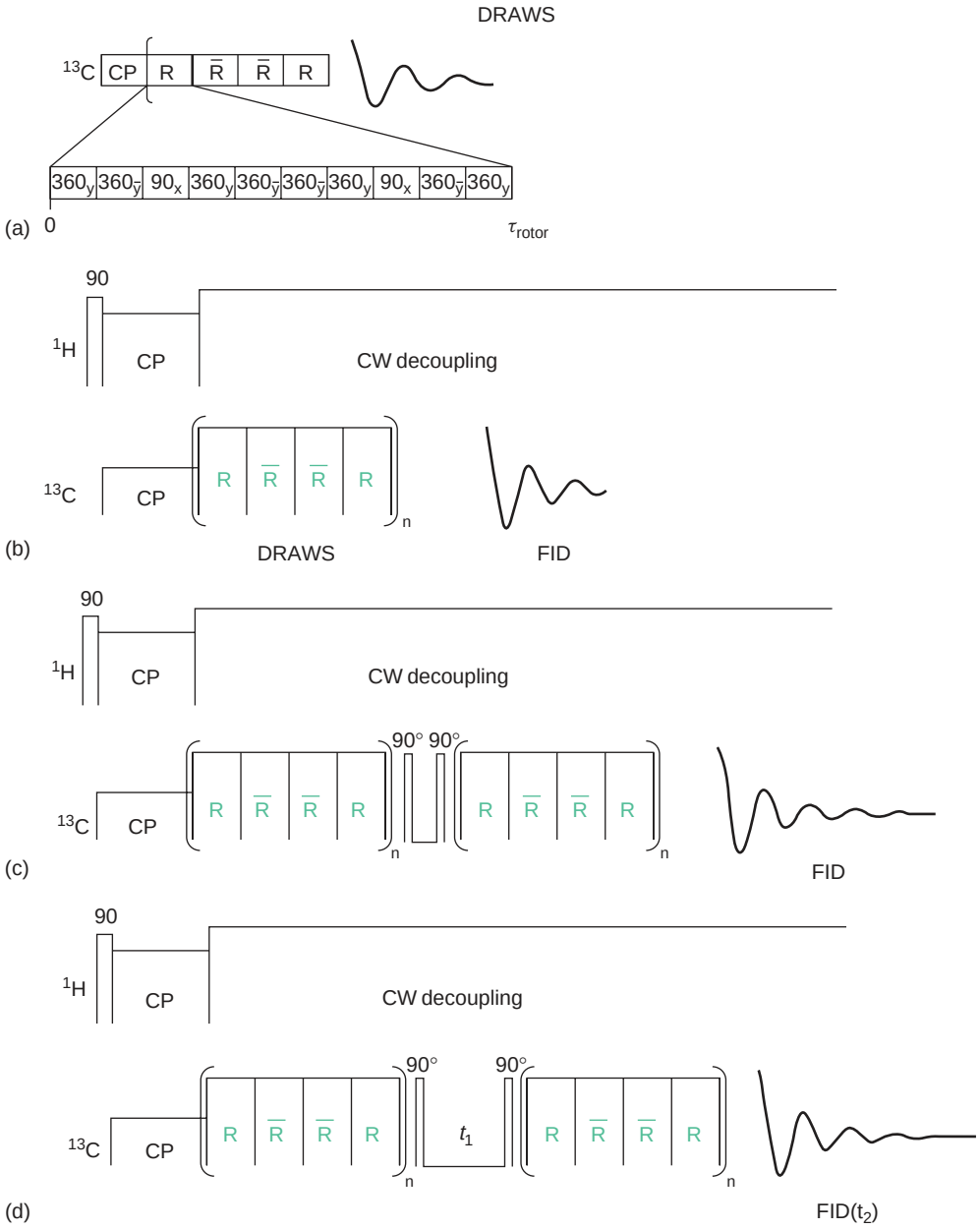

Figure 2 In most dipolar recoupling pulse sequences, pulsed irradiations are applied synchronously with the sample rotation. In DRAWS, the eight 360° pulses (alternating Y and −Y phases) and two ninety degree pulses (X phases) that constitute the unit pulse cycle (R) are applied within a single period of the rotor (τ_{rotor}). (a) The unit pulse cycle for DRAWS (Dipolar Recoupling with a Windowless Sequence) is supercycled as $R\overline{R}\overline{R}R$, where $\overline{R}$ indicates a unit cycle phase-shifted by 180°. (b) DRAWS applied in the context of a CPMAS experiment. (c) Pulse Sequence for Doubled Quantum-filtered DRAWS. (d) Two dimensional pulse sequence for double quantum DRAWS (DQDRAWS)

DRAWS dephasing curve data may be difficult to quantify in terms of an internuclear distance if a large background signal occurs from ^{13}C spins at natural abundance. The ^{13}C background arises from portions of the protein that are not enriched with ^{13}C or may come from the surface itself if the mineral contains carbon (e.g., calcite) or if the mineral contains organic impurities (e.g., carbonate incorporated into apatite crystals). In such cases NMR signals arising from dipolar coupled spin pairs are separated from the natural abundance signal, which arises mainly from isolated spins, by filtering the DRAWS signal through a double quantum state. The preparation of double quantum coherence using DRAWS dipolar recoupling is called DQDRAWS. The DQDRAWS filtering experiment is shown in Figure 2(c). Applying a DRAWS pulse sequence for a preparation time τ (typically 3–6 ms for carbonyl ^{13}C spins in the backbone of a surface-adsorbed protein) generates dipolar-correlated spin coherence (also called anti-phase magnetization). Applying a 90° pulse then generates double quantum coherence. In the double quantum buildup experiment, this coherence is immediately transferred back to anti-phase magnetization by a second 90° pulse and then to observable magnetization by reapplying the DRAWS mixing sequence for the same amount of time. The buildup of double quantum coherence is then monitored

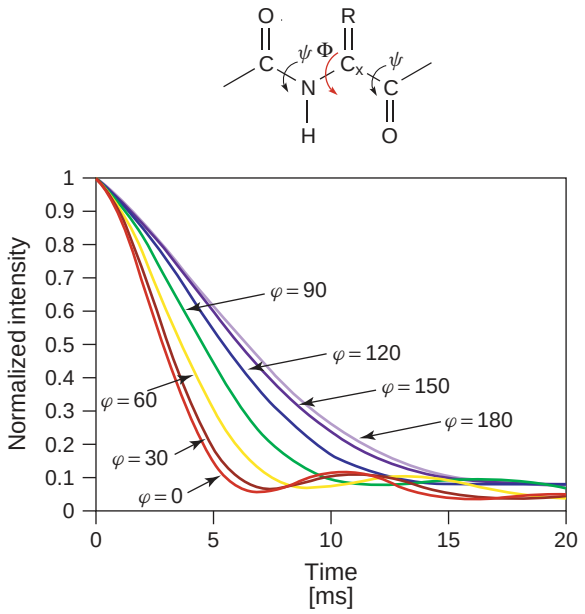

Figure 3 Simulated DRAWS decay curves for dipolar-coupled ^{13}C–^{13}C carbonyl spin pairs in the backbone of a polypeptide. The carbonyl-carbonyl distance is directly related to the Ramachandran angle φ

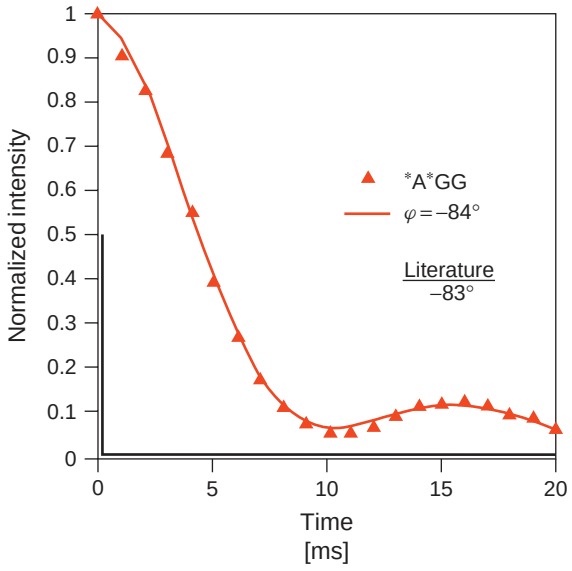

Figure 4 Experimental DRAWS dipolar dephasing curve obtained for the doubly carbonyl ^{13}C labeled crystalline tri-peptide alanyl-glycylglycine (AGG). The solid line is the simulation assuming a Ramachandran angle of −84°

as a function of the DRAWS mixing time to determine dipolar couplings and hence the inter-nuclear distance. As in the simple DRAWS experiment, the DQDRAWS filtering experiment can quantify the carbonyl-carbonyl distance and hence the Ramachandran angle φ.

Direct detection of a double quantum coherent state results in a simultaneous measurement of the (φ, ψ) Ramachandran angles.[64,71] As in other multiple quantum experiments, a double quantum state is detected via a two dimensional experiment, the pulse sequence is shown in Figure 2(d). In the 2-dimensional DQDRAWS experiment, the DRAWS pulse sequence is again applied for a preparation time τ to generate the antiphase state. After the magnetization is transferred to the double quantum state by a 90° pulse it is allowed to evolve under the chemical shift and dipolar interactions for a time t_1. The magnetization is then transferred back to observable by a second 90° pulse and reapplying the DRAWS mixing sequence for the same amount of time. Monitoring the free induction decay (FID) during the detection time t_2 as a function of double quantum evolution time t_1 yields a two dimensional interferogram. Two dimensional Fourier transformation of the time domain data followed by projection onto the ω_1 axis (i.e. the double quantum frequency axis) yields the double quantum spectrum, see Figure 5. The double quantum spectrum consists of a "fundamental" frequency, which occurs at the sum of the isotropic chemical shift frequencies of the coupled ^{13}C spins, together with side bands at integral multiples of the spinning frequency. The double quantum spinning side band intensities are dependent on the principal values of the *sum* chemical shift tensor. Because the individual chemical shift tensors add as second order tensors, the sum tensor is sensitive to the mutual orientation of the principal axis systems of the CSA tensors of the coupled ^{13}C spins.

Since carbonyl carbons in peptides possess highly anisotropic CSAs, they are particularly sensitive to the DQDRAWS approach. The relative orientations of the carbonyl carbon CSAs to the peptide amide bonds are well-studied,[72] and thus the torsion angles (φ, ψ) can be extracted by simulating the DQ spectrum. Determining (φ, ψ) with this level of accuracy not only yields secondary structure, but also gives some indication of helical pitch or twist and long range order.

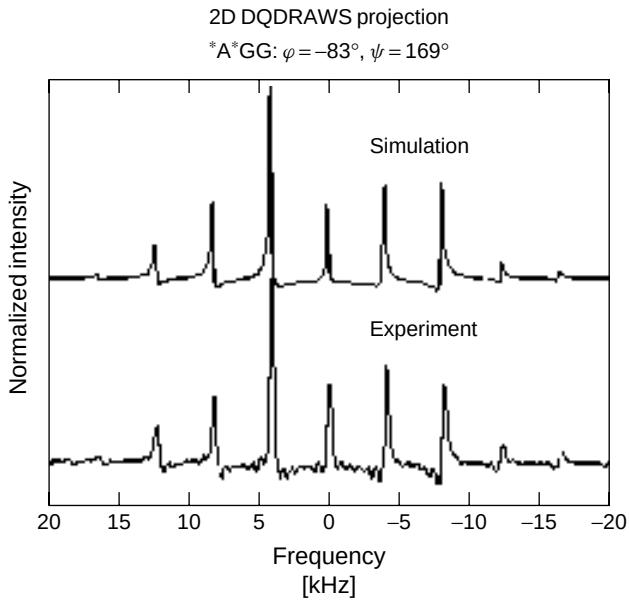

Figure 5 Simulated and experimental projections of the two dimensional double quantum DRAWS (DQDRAWS) spectra of the doubly carbonyl ^{13}C labeled crystalline tri-peptide alanylglycylglycine (AGG). The simulation assumes $\varphi = -83°$ and $\psi = 169°$

2.2 The Effect of Dynamics on the Solid State NMR Spectrum of Surface-Adsorbed Proteins

A common property of polymers is structural deformability. Polymeric molecular systems may display structural heterogeneity, meaning the polymeric system may display a distribution of static structures. In addition, the polymer may display structural lability, meaning that the molecular system cannot be described as strictly confined to one or a small number of equilibrium states, but rather possesses a kinetic aspect wherein the structure of each molecule changes in time. In such cases important properties of the polymer include the time scale and amplitude of the internal molecular motions.

The interaction between two nuclear magnetic dipoles, the interaction between the nuclear quadrupole moment and surrounding electric field gradients, and the chemical shift, are inherently tensorial quantities. In addition, these interactions detectable by NMR have sufficient anisotropy to dominate the solid state NMR spectral line shape. If internal motions modulate the orientation of magnetic interaction tensors relative to the static magnetic field direction, the solid state NMR line shape will be averaged in a way that reflects both the amplitude and the time scale of the internal motions. In addition, the relaxation of the nuclear system will be described by the time-dependent part of the spin interaction Hamiltonian. For these reasons the dynamic properties of solid polymers are frequently probed through measurements of NMR relaxation and line shapes.

Solid state NMR studies of polymer dynamics constitute an extensive literature, which cannot be summarized here in any thorough way. However, it is useful to briefly review some of the important NMR methods used in the past to characterize polymer dynamics, including surface-adsorbed polymers, in order to appreciate how these methods may or may not suffice to characterize surfaced-adsorbed proteins.

The most extensive class of polymers studied to date by solid state NMR methods are synthetic, organic polymers common examples being polystyrene,[73] polycarbonate,[74–76] polystyrene–polybutadiene blends,[77] poly(ethylene-terephthalate),[78,79] to name just a very few. In addition there are numerous reports on liquid crystal polymers,[80,81] polymers tethered to silica surfaces,[39] and polylysine and polyglutamic adsorbed to silica and hydroxyapatite surfaces.[44] In the case of hydrocarbon-based polymers the NMR dynamic probes are ^{13}C relaxation and line shape studies, proton relaxation and spin diffusion studies. In cases where protons can be replaced by deuterium, deuterium line shape and relaxation studies may be used to probe polymer motions. Because synthetic polymers are composed of regularly repeating, largely identical subunits, isotopic enrichment usually cannot be performed in a site selective manner. This means that NMR studies of polymer dynamics reflect motions that are associated with a repeating unit, or a part of the repeating unit.

Many of the problems and questions in biomineralization are similar to the structure/function issues familiar in structural biology and concentrate on specific domains within the protein: e.g., what is the identity, structure and dynamics of the mineral binding surface of the protein, what is the relationship of this binding domain to the rest of the protein, and how are the structure and dynamics of this domain related to the function? This latter question can only be answered if the orientation of the protein relative to the surface is known. These questions can only be addressed by studying the NMR line shapes and relaxation of specific sites within the protein, before and after adsorption.

3 A SOLID-STATE NMR STUDY OF SALIVARY STATHERIN ADSORBED ONTO HYDROXYAPATITE (HAP) CRYSTALS

Salivary statherin is a particularly well studied acidic phosphoprotein that inhibits the nucleation and growth of calcium phosphate minerals in the oral environment, and acts as a boundary lubricant.[82–87] The N-terminus of statherin is highly charged, with the first five amino acids containing one aspartic acid, two phosphorylated serines, and two glutamic acids that have been shown to be important in the recognition of HAP[83] (Figure 6). A solution NMR study of statherin,[87] acquired in a water/TFE solvent mixture, found the N-terminus to be alpha helical and the C-terminus was judged to be a 3_{10} helix, although the relative paucity of NOE's in the C-terminus was interpreted as indicating non-rigidity. Recent solid state NMR studies have shown that the N-terminal 15 amino acid peptide derived from statherin (called SN-15), which is believed to constitute the bulk of the HAP binding site, is partly helical on the HAP surface.[88] Also, while the N-terminal 3–6 amino acids are immobilized on the surface, the remaining portion of the peptide toward the C-terminus show increased mobility.[89]

However, to conclusively define the structure of the HAP-binding domain, the full-length protein must be studied on the mineral surface. In this section, we show how solid state NMR techniques have been applied to full length phosphorylated statherin on the hydroxyapatite crystal surface to characterize the high-resolution structure and dynamics of the N-terminal binding domain under hydrated and lyophilized conditions.

Site-specific isotopic labeling of statherin allowed structural determinations to be made unambiguously using the dipolar recoupling techniques DQDRAWS[90,91] and REDOR. DQDRAWS, a double-quantum variant of the DRAWS homonuclear recoupling technique, was applied to measure the distance between adjacent backbone carbonyl carbons and thus yield model-free determination of the backbone torsion angle φ. Determination of individual torsion angles yields insights into local secondary structure as well as structural heterogeneity. Typically α-helices are indicated by torsion angle values in the range of $-45°$ to $-80°$ with a mean of $-63°$ (Figure 7). The average values of β-sheets are somewhat larger, varying from $-80°$ to $-150°$ with a mean of

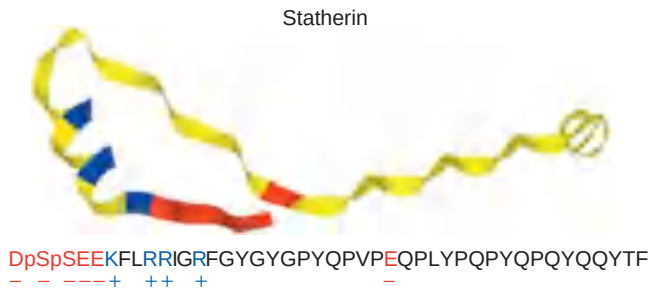

Figure 6 The primary sequence of the 43 amino acid protein salivary statherin and a possible structure based on solution and solid state NMR data

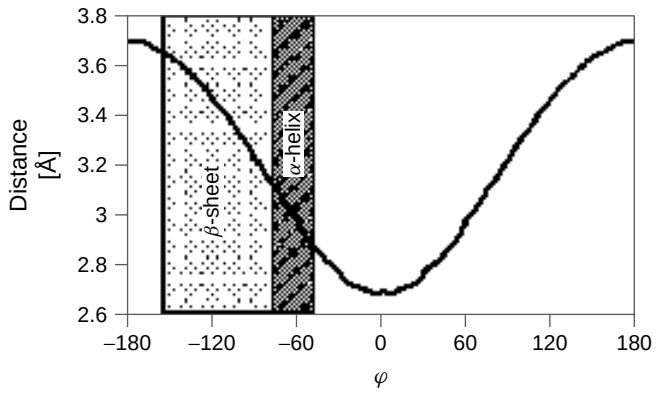

Figure 7 The carbonyl-carbonyl distance in the backbone of a polypeptide for various secondary structure motifs

−130°. REDOR, a heteronuclear recoupling technique, was used to measure the distance between the backbone carbonyl carbon and the backbone nitrogen involved in the hydrogen bond of a putative α-helical domain. This measurement is very sensitive to global secondary structure since theoretical distances expected for classical secondary structures vary from 4.2 Å for an α-helix to 10.6 Å for a β-sheet. Although isotropic chemical shifts of proteins can give qualitative indications of secondary structure in homogeneous systems, their values can be influenced by the bulk magnetic susceptibility of the support in heterogeneous systems. This makes them unreliable for structural determination in proteins closely associated with or adsorbed on inorganic surfaces such as HAP. Solid state NMR of ^{13}C nuclei is also very sensitive to dynamics, which can be probed over several order of magnitude by measuring chemical shift anisotropies (CSAs), relaxation constants including carbon T_1's and $T_{1\rho}$'s, and proton $T_{1\rho}$'s.

The structure and dynamics of salivary statherin were analyzed at the pS_2, pS_3, F_7, L_8, I_{11} and G_{12} residues. Pairs of backbone carbonyl carbons were enriched at the pS_2pS_3, F_7L_8, and $I_{11}G_{12}$ positions in separate samples and probed using DRAWS and DQDRAWS. A ^{13}C enriched carbonyl carbon was introduced at the (i) position with an ^{15}N enriched amide nitrogen at the (i + 4) position in $pS_3F_7$and L_8G_{12} samples and probed using REDOR to verify the presence or absence of hydrogen bonding. The dipolar recoupling data for the pS_2pS_3 and pS_3F_7 samples are shown in Figure 8. All 5 samples were characterized using standard ^{13}C CPMAS and $T_{1\rho}$ relaxation sequences to measure any averaging of carbonyl carbon CSAs, cross polarization efficiencies, or relaxation due to the presence of motion. Measurements on all samples were performed under in situ conditions (i.e. buffered and hydrated) as well as after lyophilization. These results are summarized in Table 1.

Both the single torsion angle measurements and the distances between putative hydrogen bond donors and acceptors indicate the N-terminal 12 residues in statherin are in an α-helical conformation when adsorbed to HAP under biologically relevant conditions. Removal of water via lyophilization under low vacuum (i.e. 100 mTorr) results in loss of this structure in the highly acidic N-terminal 6 residues. The extension of the helix during lyophilization suggests a significant role for water in stabilizing the binding domain. Water may mediate the interaction of the acidic sidechains with the HAP surface. The α-helix has been previously suggested as a general structural mechanism for aligning acidic side-chain residues with HAP,[92] either through lattice matching or through more general electrostatic complementarily. While our data support the presence of this secondary structure, they also point to the possible importance of water in HAP binding.

The dynamic properties of the immobilized protein are a critical aspect of molecular recognition at the

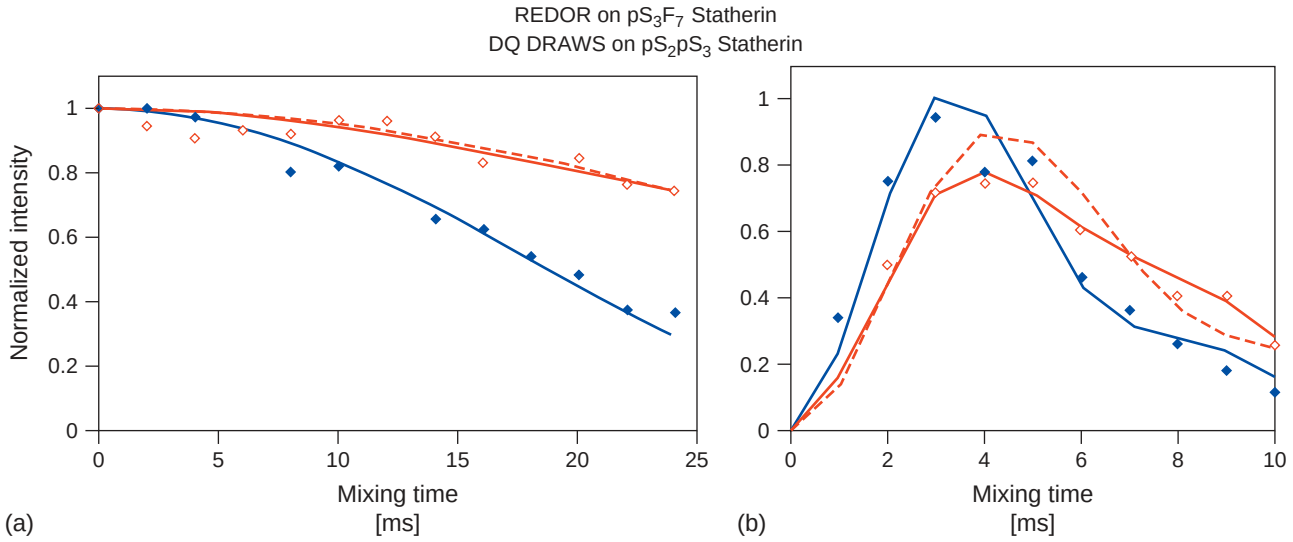

Figure 8 (a) REDOR dephasing curves for hydrated, surface adsorbed pS_3F_7 Statherin (♦), lyophilized, bound pS_3F_7 statherin (◊), and simulations for 4.2 Å (unbroken blue line), 5.2 Å (dashed red line) and a combination of 45% a-helix (4.2 Å) and 65% b-sheet (>8 Å) (unbroken red line). The hydrated pS_3F_7 distance across the hydrogen bond fits best to a distance of 4.3 Å, indicating that the region is well described by an ideal α-helix. Data for the lyophilized sample is best simulated by 5.2 Å or a combination of 35% α-helix and 65% β-sheet, indicating a loss in α-helical secondary structure upon lyophilization. (b) DQDRAWS buildup curves for hydrated, surface adsorbed pS_2pS_3 statherin (♦), lyophilized, bound pS_2pS_3 Statherin (◊), and simulations for φ torsion angles of −60° (unbroken blue line), −85° (dashed red line) and a combination of 45% α-helix (−57°) and 65% β-sheet (−120°) (unbroken red line). The increase in torsion angle on lyophilization correlates well with the loss of α-helical secondary structure

Table 1 Values for the anisotropy ($\Delta\sigma$) and asymmetry (η) of the CSA, average values of the torsion angle (φ), distance measurements across putative hydrogen bonds and ^{13}C $T_{1\rho}$ relaxation constants measured for indicated residues of salivary statherin bound to HAP in the presence and absence of water

	$\Delta\sigma$ (ppm)		η		φ/distance		$T_{1\rho}$ (ms)	
Isotopic label	Lyo.	Hyd.	Lyo.	Hyd.	Lyo.	Hyd.	Lyo.	Hyd.
pS_2	114	105	0.96	0.74			>20	18.2
pS_3	109	104	0.81	0.79	−85°(11)	−60°(10)		
pS_3F_7					5.2(0.6) Å	4.3(0.2) Å		
F_7	103	99	0.73	0.61			>20	7.5
L_8	103	98	0.72	0.69	−77°(20)			
L_8G_{12}					4.8(0.4) Å	4.8(0.4) Å		
$I_{11}G_{12}$	103	103	0.75	0.83	−65°(13)		>20	2.5

protein-biomineral interface, and relatedly to the function of proteins once adsorbed. Measurements of the dynamic properties of statherin in the presence and absence of water show a striking difference from the structural data. The ^{13}C $T_{1\rho}$ values remain largely unchanged for the phosphoserines, indicating little or no motion is present in both the lyophilized and hydrated states. However, the $T_{1\rho}$ relaxation constants are considerably shorter in the hydrated samples at the F_7, L_8, I_{11} and G_{12} positions, indicating motion on the kHz timescale when water is present. Figure 9 shows CPMAS spectra for each of the doubly carbon-labeled statherin samples under hydrated conditions, normalized to the natural abundance methyl region to account for any differences in the amounts of bound protein. A representative spectrum of a lyophilized, surface bound sample labeled at the pS_2 and pS_3 positions is also shown for comparison. The significant loss in CP efficiency at the F_7, L_8, I_{11} and G_{12} positions in the hydrated samples is also characteristic of mobility. These measurements bracket the timescale of the motion in this region to 10^{-3}–10^{-5} s. In contrast, the hydrated, surface bound pS_2pS_3 region does not display a loss in CP efficiency, indicating there is very little motion in that region on the timescale of the cross polarization experiment. The CSAs were found to narrow very little, with spans ($\Omega = |\sigma_{11} - \sigma_{33}|$) of approximately 140–150 ppm in the hydrated samples, as compared to 145–155 ppm for their lyophilized counterparts. The small change in the CSA under hydrated conditions indicates that the motion observed in the cross polarization experiments and supported by the $T_{1\rho}$ relaxation measurements somewhat restricted. Motion was observed in analogous regions for the isolated SN15 peptide, but significant narrowing of the CSA was observed at the C-terminal residues of the peptide (I_{11} and G_{12}). The nearly unchanging CSA observed for the entire N-terminus of statherin indicates a different motional mode present in the full protein. The $T_{1\rho}$ relaxation parameters for both protein and peptide are nearly the same, which would support a motion of similar frequency, but different amplitude than that observed in the SN15 peptide. The change in mobility could be due to one of several factors, including motional limitations due to the larger size of the protein, stabilization of the peptide backbone by tertiary structure, or potentially due to more substantial protein interactions with the surface at the C-terminal end of full statherin.

To explore the latter possibility, the only negatively charged residue outside of the N-terminus was replaced with its uncharged counterpart ($Glu_{26} \rightarrow Gln_{26}$). This site-directed statherin mutant displayed a $T_{1\rho}$ value at $I_{11}G_{12}$ of 2.9 msec, identical to the $T_{1\rho}$ value at the same positions of the unmodified protein (2.5 ms) within experimental uncertainty. This indicates that Glu_{26} is not involved in HAP recognition to an extent that prevents kHz frequency motions in the N-terminal region. The simplest explanation of the results is that either the larger size of full-length statherin or tertiary structural interaction is causing the lower amplitude dynamics compared to the isolated SN15 peptide, rather than being due to a different type of interaction with the HAP surface. However, the dynamics data could also be explained by more complicated models that do include protein interactions

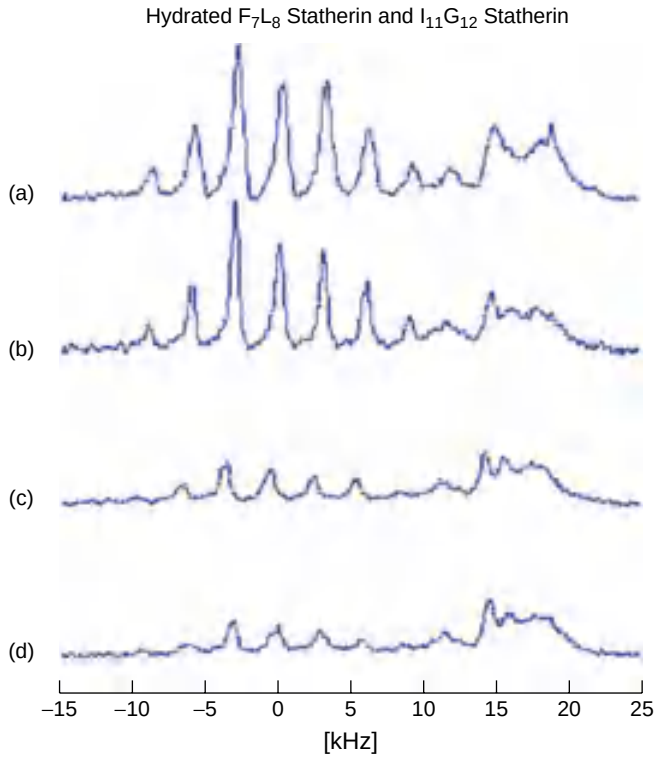

Figure 9 CPMAS spectra of (a) pS_2pS_3 Statherin bound to the surface and lyophilized, (b) hydrated, surface-adsorbed pS_2pS_3 Statherin (c) hydrated, surface-adsorbed F_7L_8 Statherin and (d) hydrated, surface-adsorbed $I_{11}G_{12}$ Statherin. Each hydrated spectrum is normalized to the natural abundance methyl region. The significant decrease in the carbonyl signal for the F_7L_8 and $I_{11}G_{12}$ hydrated spectra is indicative of molecular motion. $T_{1\rho}$ relaxation measurements support the interpretation of minimal mobility at the pS_2pS_3 region and increased mobility for the F_7L_8 and $I_{11}G_{12}$ regions

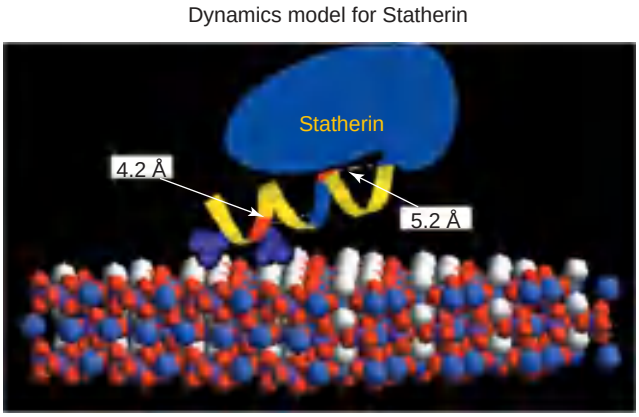

Figure 10 Schematic model showing statherin interacting with the 001 face of HAP, with calcium ions in white and phosphoserines in purple. The protein colors represent backbone $^{13}C =$ O-enriched (red), ^{15}N-enriched (blue), and unenriched (yellow) residues. The REDOR-measured hydrogen bonding distances are indicated for the hydrated N-terminal binding domain, while the remaining portion of the protein (blue) is shown as a nondescript shape to indicate unknown surface adsorbed structure (hydrogen bonds in white). The strong interaction of the N-terminus through the immobile phosphoserines is indicated, and the more mobile, non-interacting C-terminus of the pentadecyl domain is shown oriented away from the HAP surface

with the surface outside of the N-terminal domain. It is clear, however, that both the protein and peptide are only loosely associating with HAP outside of the anionic N-terminal pentapeptide region. The pentapeptide sequence is a common motif in many bone and tooth-associated proteins. It is also a recognition sequence for phosphorylation. The importance of the phosphorylated serines in statherin in binding to HAP indicates a possible regulatory mechanism for multifunctional proteins, such as osteopontin, which are found to be important in regulating mineralization in some settings, but are found in other tissues as well.

A molecular model consistent with the current structural and dynamic studies is shown in Figure 10. The N-terminal domain from residues 2 to 12 is helical on the surface. The strong interaction of statherin with HAP is mediated by the acidic N-terminus, where two phosphoserines and three carboxylate-containing side-chains are located. The dynamics studies suggest that the remainder of the helix is much more weakly interacting with HAP. The more weakly interacting residues in this domain could be viewed as a flexible rod, with torsional motions increasing with increasing distance from the highly immobile N-terminal pentapeptide sequence. The presence of a highly mobile protein segment could explain functional observations made previously by others in the field. Moreno et al.[93] found that statherin inhibited secondary crystal growth at a higher level than that expected based on coverage size, assuming a fixed, globular protein. The mobility of statherin could allow it to effectively block more nucleation sites than a completely rigid protein. The mobility of statherin on the surface may also play a significant role in the lubricating properties of the protein. To adequately model the observed motions at the molecular level, further details of the surface bound tertiary structure and experimental elucidation of the side-chain interactions with HAP will be required to orient statherin at the surface. Solid-state NMR does provide a direct route to this information, and we are currently probing the tertiary structure and the interactions of side chains with the surface to further elucidate binding mechanisms.

4 RELATED ARTICLES IN VOLUMES 1–8

Dipolar & Indirect Coupling Tensors in Solids, Volume 3; Homonuclear Recoupling Schemes in MAS NMR, Volume 4, Magic Angle Spinning, Volume 5, Polymer Dynamics & Order from Multidimensional Solid State NMR, Volume 6, REDOR & TEDOR, Volume 6.

5 REFERENCES

1. A. H. Heuer, D. J. Fink, V. J. Laraia, J. L. Arias, P. D. Calvert, K. Kendall, G. L. Messing, J. Blackwell, P. C. Rieke, D. H. Thompson, A. P. Wheeler, A. Veis, and A. I. Caplan, *Science*, 1992, **255**, 1098–1105.
2. S. Mann, D. D. Archibald, J. M. Didymus, B. R. Heywood, F. C. Meldrum, and V. J. Wade, *MRS Bull.*, 1992, **17**, 32–36.
3. S. Mann, *Nature*, 1993, **365**, 499–505.
4. B. C. Bunker, P. C. Rieke, B. J. Tarasevich, A. A. Campbell, G. E. Fryxwell, G. L. Graff, L. Song, J. Liu, J. W. Virden, and G. L. McVay, *Science*, 1994, **264**, 48–55.
5. S. Mann and S. Weiner, *J. Struct. Biol.*, 1999, **126**, 179–181.
6. A. L. Bosky, *J. Cell. Biochem. Suppl.*, 1998, **30/31**, 83–91.
7. A. G. Fincham, J. Mordian-Oldak, and J. P. Simmer, *J. Struct. Biol.*, 1999, **126**, 270–299.
8. P. Calvert, *MRS Bull.*, 1992, **17**, 37–47.
9. L. Cohen-Solal, P. Maroteaux, and M. J. Glimer, 'Presence of Gamma-Glutamyl Phosphate in the Collagens of Bone and other Calicified Tissue and its Absence in the Collagens of Unmineralized Tissues', Elsevier: Amsterdam, 1982, Vol. 7.
10. L. Addadi and S. Weiner, *Proc. Natl. Acad. Sci. USA*, 1985, **82**, 4110–4114.
11. S. Albeck, J. Aizenberg, L. Addadi, and S. Weiner, *J. Am. Chem. Soc.*, 1993, **115**, 11691–11697.
12. D. Deutsch, *Anat. Rec.*, 1989, **224**, 189–210.
13. S. Weiner and L. Addadi, *Trends Biochem. Sci.*, 1991, **16**, 252–256.
14. S. Weiner and L. Addadi, *J. Mat. Chem.*, 1997, **7**, 689.
15. P. V. Hauschka and F. H. Wians, *Anat. Rec.*, 1989, **224**, 180–188.
16. R. Fuijisawa and Y. Kuboki, *Eur. J. Oral Biol.*, 1998, **106**, 249–253.
17. R. Fujisawa, Y. Wada, Y. Nodasaka, and Y. Kuboki, *Biochim. Biophys. Acta*, 1996, **1292**, 53–60.
18. Z. Amjad, 'Calcium Phosphates in Biological and Industrial Systems', Kluwer: Boston, MA, 1998.
19. D. J. Fink, *MRS Bull.*, 1992, **17**, 27–31.
20. M. Sarikaya and I. A. Aksay, *Results Problems Cell Diff.*, 1992, **19**, 1–26.
21. J. Menanteau, W. F. Neuman, and M. W. Neuman, *Metabol. Bone Dis. Related Res.*, 1982, **4**, 157–162.
22. A. A. Campbell, A. Ebrahimpour, L. Perez, S. A. Smesko, and G. H. Nancollas, *Calc. Tissue Int.*, 1989, **45**, 122–128.
23. J. P. Gorski, *Calc. Tissue Int.*, 1992, **50**, 391–396.
24. G. K. Hunter and H. A. Goldberg, *Biochem. J.*, 1994, **302**, 175–179.
25. D. N. Misra, *J. Colloid Interface Sci.*, 1997, **194**, 249–255.
26. P. A. Raj, M. Johnsson, M. J. Levine, and G. H. Nancollas, *J. Biol. Chem.* 1992, **267**, 5968.
27. R. W. Romberg, P. G. Werness, B. L. Riggs, and K. G. Mann, *Biochemistry*, 1986, **25**, 1176.

28. K. Wikiel, E. M. Burke, J. W. Perich, E. C. Reynolds, and G. H. Nancollas, *Arch. Oral Biol.*, 1994, **39**, 715–721.
29. N. Ramasubbu, L. M. Thomas, K. Bhandary, and M. J. Levine, *Crit. Rev. Oral Biol. Med.*, 1993, **4**, 363–370.
30. S. Weiner and L. Addadi, *Trends Biochem. Sci.*, 1991, 252–256.
31. J. S. Evans, T. Chiu, and S. I. Chan, *Biopolymers*, 1994, **34**, 1359–1375.
32. W. H. Braunlin, H. J. Vogel, T. Drakenburg, and A. Bennick, *Biochemistry*, 1986, **25**, 584–589.
33. V. Gerbaud, D. Pignoli, E. Loret, J. A. Bertrand, Y. Berland, J.-C. Fontecilla-Camps, J.-P. Canselier, N. Gabas, and J.-M. Verdier *J. Biol. Chem.*, 2000, **275**, 1057–1064.
34. P.-K. Wang and C. Slichter, *Phys. Rev. Lett.*, 1984, **53**, 82–85.
35. S.-J. Hwang, C. Petucci, and D. Raftery, *J. Am. Chem. Soc.*, 1998, **120**, 4388–4397.
36. Y. Y. Tong, C. Rice, A. Wieckowski, and E. Oldfield, *J. Am. Chem. Soc.*, 2000, **122**, 11921–11924.
37. K. W. Zilm and D. W. Grant, *J. Am. Chem. Soc.*, 1981, **103**, 2913–2922.
38. V. H. Pan, T. Tao, J. W. Zhou, and G. E. Maciel, *J. Phys. Chem. B*, 1999, **103**, 6930–6943.
39. D. W. Sindorf and G. E. Maciel, *J. Am. Chem. Soc.*, 1983, **105**, 1848–1851.
40. E. Brunner, R. Seydoux, M. Haake, A. Pines, and J. A. Reimer, *J. Magn. Reson.*, 1998, **130**, 145–148.
41. L. K. Sanders, W. D. Arnold, and E. Oldfield. *J. Porphyrins Phthalocyanines*, 2001, **5**, 323–333.
42. R. Salzmann, M. Kaupp, M. T. McMahon, and E. Oldfield, *J. Am. Chem. Soc.*, 1998, **120**, 4771–4783.
43. J. Heller, D. D. Laws, M. Tomaselli, D. S. King, D. E. Wemmer, A. Pines, R. H. Havlin, and E. Oldfield, *J. Am. Chem. Soc.*, 1997, **119**, 7827–7831.
44. V. L. Fernandez, J. A. Reimer, and M. M. Denn, *J. Am. Chem. Soc.* 1992, **114**, 9634–9642.
45. K. Beshah, C. Rey, M. J. Glimcher, M. Schimizu, and R. G. Griffin, *J. Magn. Reson.*, 1990, **84**, 17–81.
46. J. P. Yesinowski, in 'Calcium Phosphates in Biological and Industrial Systems', ed Z. Amjad, Kluwer: Boston, MA, 1998.
47. J. R. Moore, L. Garrido, and J. L. Ackerman, *Magn. Reson. Med.*, 1995, **33**, 293–299.
48. M. Bak, J. K. Thomsen, H. J. Jakobsen, S. E. Petersen, T. E. Petersen, and N. C. Nielsen, *J. Urol.*, 2000, **164**, 856–863.
49. J. K. Denny, J. F. Wang, T. A. Cross, and J. R. Quine, *Biophys. J.*, 2001, **80**, 1555, Part 2.
50. R. G. Griffin, *Nature Struct. Biol.*, 1998, **5**(Suppl. S), 508–512.
51. R. Tycko, *Annu. Rev. Phys. Chem.*, 2001, **52**, 575–606.
52. M. M. Lee and W. I. Goldberg, *Phys. Rev.*, 1965, **140**, A1261.
53. J. S. Waugh, L. M. Huber, and U. Haeberlen, *Phys. Rev. Lett.*, 1968, **20**, 5.
54. U. Haeberlen, 'High Resolution NMR in Solids: Selective Averaging', Academic Press: New York, 1976.
55. M. Mehring, 'Principles of High Resolution NMR in Solids', Springer-Verlag: New York, 1983.
56. W. K. Rhim, D. D. Elleman, and R. W. Vaughn, *J. Chem. Phys.*, 1973, **59**, 3740–3749.
57. D. K. Burum and W. K. Rhim, *J. Chem. Phys.*, 1979, **7**, 944–956.
58. M. Hohwy, P. V. Bower, H. J. Jakobsen, and N. C. Nielsen, *Chem. Phys. Lett.*, 1997, **273**, 297–303.
59. E. R. Andrew, A. Bradbury, and R. B. Eades, *Nature*, 1958, **182**, 1969.
60. D. Gregory, D. Mitchell, J. A. Stringer, S. Kühne, J. C. Shiels, J. Callahan, M. A. Mehta, and G. P. Drobny, *Chem. Phys. Lett.*, 1995, **246**, 654–663.
61. J. Schaefer, in 'Encyclopedia of NMR', eds D. M. Grant and R. K. Harris, Wiley: Chichester, 1996, pp. 3977–3983.
62. Y. Pan, *Solid State Magn. Reson.*, 1995, **5**, 263–268.
63. J. R. Long, J. L. Dindot, H. Zebroski, S. Kühne, R. H. Clark, A. A. Campbell, P. S. Stayton, and G. P. Drobny, *Proc. Natl. Acad. Sci. USA*, 1998, **95**, 12 083–12 087.
64. P. V. Bower, N. Oyler, M. A. Mehta, J. R. Long, P. S. Stayton, and G. P. Drobny, *J. Am. Chem. Soc.*, 1999, **121**, 8373–8375.
65. W. J. Shaw, J. R. Long, J. L. Dindot, A. A. Campbell, P. S. Stayton, and G. P. Drobny, *J. Am. Chem. Soc.*, 2000, **122**, 1709–1716.
66. J. R. Long, W. J. Shaw, P. S. Stayton, and G. P. Drobny, *Biochemistry*, 2001, **40**: 15 451–15 455.
67. T. S. Burkoth, T. L. S. Benzinger, V. Urban, D. M. Morgan, D. M. Gregory, P. Thiyagarajan, and R. E. Botto, *J. Am. Chem. Soc.*, 2000, **122**: 7883–7889.
68. T. L. S. Benzinger, D. M. Gregory, T. S. Burkoth, H. Miller-Auer, D. G. Lynn, R. E. Botto, and S. C. Meredith, *Biochemistry USA*, 2000, **39**, 3491–3499.
69. D. M. Gregory, T. L. S. Benzinger, T. S. Burkoth, H. Miller-Auer, D. G. Lynn, S. C. Meredith, and R. E. Botto, *Solid State Magn. Reson.*, 1998, **13**, 149–166.
70. T. L. S. Benzinger, D. M. Gregory, T. S. Burkoth, H. Miller-Auer, D. G. Lynn, R. E. Botto, and S. C. Meredith, *Proc. Natl. Acad. Sci. USA*, 1998, **95**, 13 407–13 412.
71. F. J. Blanco and R. Tycko, *J. Magn. Reson.*, 2001, **149**, 131–138.
72. T. M. Duncan, 'Chemical Shift Tensors', 2nd edn., Farragut Press: Madison, WI, 1997.
73. J. Schaefer, M. D. Sefcik, E. O. Stejskal, R. A. McKay, W. T. Dixon, and R. E. Cais, *Macromolecules*, 1984, **17**, 1107–1124.
74. C. Schmidt, K. J. Kuhn, and H. W. Spiess, *Prog. Colloid Polymer. Sci.*, 1985, **71**, 71–76.
75. J. Schaefer, E. O. Stejskal, D. Perchak, J. Skolnick, and R. Yaris, *Macromolecules*, 1985, **18**, 368–373.
76. P. M. Henrichs, M. Linder, J. M. Hewitt, D. Massa, and H. V. Isaacson, *Macromolecules*, 1984, **17**, 2412–2416.
77. J. Schaefer, M. D. Sefcik, E. O. Stejskal, and R. A. McKay, *Macromolecules*, 1981, **14**, 188–192.
78. P. M. Henrichs, *Macromolecules*, 1987, **20**, 2099–2112.
79. K. Schmidt-Rohr, W. Hu, and N. Zumbulyadis, *Science*, 1998, **280**, 714–717.
80. A. F. Martins, A. E. Gomes, A. Polimeno, and L. Orian, *Phys. Rev. E*, 2000, **62**, 2301–2309.
81. R. Baxmann, M. Hess, R. Woelke, and W. Veeman, *Macromol. Symp.*, 1999, **148**, 157–177.
82. D. Schlesinger and D. I. Hay, *J. Biol. Chem.*, 1977, **252**, 1689–1695.
83. P. A. Raj, M. Johnsson, M. J. Levine, and G. H. Nancollas, *J. Biol. Chem.*, 1992, **267**, 5968–5976.
84. S. S. Schwartz, D. I. Hay, and S. K. Schluckebier, *Calc. Tissue Int.*, 1992, **50**, 511–517.
85. N. Ramasubbu, L. M. Thomas, K. K. Bhandary, and M. J. Levine, *Crit. Rev. Oral Biol. Med.*, 1993, **4**, 363–370.
86. T. L. Gururaja and M. J. Levine, *Peptide Res.*, 1996, **9**, 283–289.
87. G. A. Naganagowda, T. L. Gururaja, and M. J. Levine, *J. Biomol. Struct. Dyn.*, 1998, **16**, 91–107.
88. W. J. Shaw, J. R. Long, J. L. Dindot, A. A. Campbell, P. S. Stayton, and G. P. Drobny, *J. Am. Chem. Soc.*, 2000, **122**, 1709–1716.
89. W. J. Shaw, P. S. Long, P. S. Stayton, and G. P. Drobny, *J. Am. Chem. Soc.*, 2000, **122**, 7118–7119.
90. D. M. Gregory, M. Mehta, J. Shiels, and G. P. Drobny, *J. Chem. Phys.*, 1997, **106**, 23.
91. J. R. Long, W. J. Shaw, G. P. Drobny, and P. S. Stayton, *Biochemistry*, 2002, in press.
92. P. A. Raj, M. Johnsson, M. J. Levine, and G. H. Nancollas, *J. Biol. Chem.*, 1992, **267**, 5968–5976.
93. E. C. Moreno, K. Varughese, and D. I. Hay, *Calc. Tissue Int.* 1979, **28**, 7–16.

Acknowledgements

We acknowledge the support of the National Institute of Dental Research (DE 12554-01), the National Science Foundation

(EEC-9529161 and DMR-9616212), the Department of Energy (DE-AC06-76RL0 1830) and the Office of Science, Office of Basic Energy Sciences, Department of Energy, through Associated Western Universities (WJS).

Biographical Sketches

Gary P. Drobny, *b* 1951. Ph.D. 1981 Chemistry, University of California, Berkeley, Research Assistant, University of California, 1976–1981; with A. Pines; Research Scientist III, University of Washington, Chemistry, 1981–1982; Research Associate, University of Washington, Chemistry 1982–1985; Research Asst. Professor, University of Washington, Chemistry, 1985; Assistant Professor, University of Washington, Chemistry, 1985–1989; Associate Professor, University of Washington, Chemistry, 1989–1991; Professor, University of Washington, Chemistry, 1991–2002; Adjunct Professor of Physics, University of Washington, 1995–2002. Current research interests: solid state NMR methods applied to problems in biomineralization, biomaterials, biomolecular dynamics, dynamic aspects of DNA recognition, membrane proteins. Design and development of NMR technology.

Patrick S. Stayton, *b* 1961. Ph.D. 1989 Biochemistry, University of Illinois, USA. Research assistant, University of Illinois, 1984–89; with S. Sligar, 1984–89; Postdoctoral research associate, Beckman Institute for Advanced Science and Technology, University of Illinois, 1989–1992. Assistant Professor at University of Washington, 1992–97, Associate Professor at University of Washington, 1997–2001, Professor at University of Washington 2001–present. Approx. 120 publications. Current research interests: biomineralization, biomaterials, tissue engineering, smart molecular materials, drug delivery.

Joanna R. Long, *b* 1968. PhD. 1997 Physical Chemistry, Massachusetts Institute of Technology, USA. Research associate, University of Washington, with P.S. Stayton 1997–2000; Scientist, University of Washington, since 2000. 12 publications. Current research interests: solid state NMR and its application to biophysical and biomaterial problems.

Myriam L. Cotten, *b* 1971. Ph.D. 1999 Chemistry, Florida State University, Tallahassee, Florida, USA. Research associate, University of Washington, 1999–present. 11 publications. Current research interests: solid state NMR and its applications in biological sciences, biomaterials, and the studies of interfacial phenomena.

Wendy J. Shaw, *b* 1972. Ph.D. 2000 Physical Chemistry, University of Washington. Senior Research Scientist, Battelle Pacific Northwest National Labs, 2000–present. 6 publications. Recent research interests include using solid state NMR to study biomineralization proteins.

Accuracy Limitations on Internuclear Distances Measured by REDOR

Akira Naito

Yokohama National University, Yokohama, Japan

&

Hazime Saitô

Himeji Institute of Technology, Kamigori, Japan

1	Introduction	1
2	Theoretical Background of the REDOR Experiment	1
3	Rotational Echo Amplitude Calculated by the Density Operator Approach	2
4	Separation of S–I Distances from a S_m–I_n Multiple Spin System	2
5	Tips for Obtaining Accurate Interatomic Distances by REDOR Experiment	4
6	Natural Abundance ^{13}C REDOR Experiment	5
7	Accuracy Limit for REDOR Structure of Peptide and Proteins	6
8	Conclusions	8
9	Related Articles in Volumes 1–8	9
10	References	9

1 INTRODUCTION

In principle, accurate interatomic distances can be evaluated from careful analysis of specific dipolar interactions that were normally sacrificed under the condition of high power decoupling and magic angle spinning (MAS) techniques. A number of methods to recouple a single pair of dipolar interaction among homo and hetero nuclear spin pairs under the magic angle spinning condition have been proposed for determining the interatomic distances.[1–10] These distances have been used as constraints to determine the three-dimensional (3D) structure of peptides and proteins.[11–16] Rotational Echo DOuble Resonance (REDOR) was explored to recouple the relatively weak heteronuclear dipolar interactions under the MAS condition by applying a π pulse synchronously with the rotor period.[8,9] Consequently, the transverse magnetization cannot be refocused completely at the end of the rotor cycle, leading to a reduction of the echo amplitude. The extent of the reduction of the echo amplitude as a function of the number of rotor periods depends on the strength of the heteronuclear dipolar interaction. This method is extensively used to determine the relatively remote interatomic distance of 2–8 Å. When a number of isolated pairs are involved in a REDOR dephasing, the REDOR transformation could be useful in determining interatomic distances because it yields single peaks against distance axis for each heteronuclear coupling strength.[17,18] This approach is, however, not applicable for the case where the observed nuclei in REDOR are coupled with multiple nuclei.

It turned out that determination of accurate interatomic distances ($\pm$0.1 Å) is a prerequisite to arrive at a unique 3D structure of peptides and proteins.[15,16] It is emphasized that the distance measurement by REDOR is the only available means to satisfy this condition among the many kinds of proposed procedures mentioned above in view of the achieved accuracy and precision. Nevertheless, it is important to bear in mind that every possible effort to achieve the distance measurement with ultimate accuracy is essential to any possible applications. This is because any measurement based on the peak-intensity is susceptible to unexpected errors, which are not easy to check. After brief survey, tips to avoid this problem will be discussed in detail.

2 THEORETICAL BACKGROUND OF THE REDOR EXPERIMENT[8]

Transverse magnetization that precesses about the static magnetic field due to the dipolar interaction under the MAS condition moves back to the same direction at every rotor period because the integration of ω_D over one rotor period is zero. Consequently, the rotational echo signals are refocused at every rotor period. When a π pulse is applied to the I nucleus (Figure 1), which is coupled with the S nucleus, in one rotor period, this pulse plays a role to invert the precession direction of the magnetization of the observed S nucleus. Consequently, the magnetization vector of the S nucleus cannot move back to the same direction after one rotor period. Therefore the amplitude of the echo intensity decreases.

The extent of the reduction of the rotational echo amplitude yields the interatomic distances. To evaluate the REDOR echo amplitude theoretically, one has to consider the average precession frequency in the presence of the π pulse at the center of the rotor period over one rotor cycle as follows:

$$\overline{\omega_D(\alpha,\beta)} = \pm\frac{1}{Tr}\left[\int_0^{Tr/2}\omega_D dt - \int_{Tr/2}^{Tr}\omega_D dt\right] = \pm\frac{D}{\pi}\sqrt{2}\sin 2\beta\sin\alpha \quad (1)$$

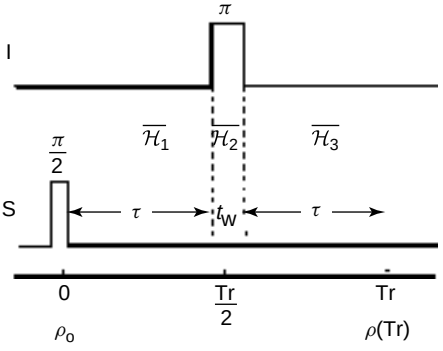

Figure 1 Pulse sequence and timing chart of REDOR experiment

where α is the azimuthal angle and β is the polar angle defined by the internuclear vector with respect to the rotor axis. Therefore, the phase angle, $\Delta\Phi(\alpha, \beta)$ for the Nc rotor cycle can be given by

$$\Delta\Phi(\alpha, \beta) = \overline{\omega_{\mathrm{D}}(\alpha, \beta)}\mathrm{NcTr} \tag{2}$$

where Tr is the rotor period. Finally, the echo amplitude can be obtained by averaging over every orientations as follows

$$S_{\mathrm{f}} = \frac{1}{4\pi}\int_{\alpha}\int_{\beta} cos[\Delta\varphi(\alpha, \beta)]\,\mathrm{d}\alpha \sin\beta\,\mathrm{d}\beta \tag{3}$$

Therefore, the normalized echo difference, $\Delta S/S_{\mathrm{o}}$, can be given by

$$\frac{\Delta S}{S_{\mathrm{o}}} = \frac{S_{\mathrm{o}} - S_{\mathrm{f}}}{S_{\mathrm{o}}} = 1 - S_{\mathrm{f}} \tag{4}$$

Experimentally, REDOR and full echo spectra are acquired for a variety of NcTr values and the respective REDOR (S_{f}) and full echo (S_{o}) amplitudes are evaluated.

3 ROTATIONAL ECHO AMPLITUDE CALCULATED BY THE DENSITY OPERATOR APPROACH[15]

The REDOR echo amplitude can be evaluated more rigorously by using density matrix operators and for the REDOR experiment. The time evolution of density operator, ρ_{o}, under the heteronuclear dipolar interaction during one rotor period, can be considered by taking the pulse length into account. The average Hamiltonian in the rotating frame over one rotor period can be given by

$$\begin{aligned}
\overline{\mathcal{H}} &= \frac{1}{\mathrm{Tr}}\left[\overline{\mathcal{H}_1(t)}\tau + \overline{\mathcal{H}_2(t)}\tau + \overline{\mathcal{H}_3(t)}\tau\right] \\
&= \frac{\mathrm{D}}{4\pi}\Big\{\sin^2\beta[\sin(2\alpha + \omega_{\mathrm{r}}t_{\mathrm{w}}) + \sin(2\alpha - \omega_{\mathrm{r}}t_{\mathrm{w}}) - 2\sin 2\alpha] \\
&\quad - 2\sqrt{2}\sin 2\beta\left[\sin\left(\alpha + \frac{1}{2}\omega_{\mathrm{r}}t_{\mathrm{w}}\right) + \sin\left(\alpha - \frac{1}{2}\omega_{\mathrm{r}}t_{\mathrm{w}}\right) + 2\sin 2\alpha\right] \\
&\quad - \sin^2\beta\,[\sin(2\alpha + \omega_{\mathrm{r}}t_{\mathrm{w}}) + \sin(2\alpha - \omega_{\mathrm{r}}t_{\mathrm{w}})]\,\frac{4\omega_{\mathrm{r}}^2 t_{\mathrm{w}}^2}{4\omega_{\mathrm{r}}^2 t_{\mathrm{w}}^2 - \pi^2} \\
&\quad + \sqrt{2}\sin 2\beta\left[\sin\left(\alpha + \frac{1}{2}\omega_{\mathrm{r}}t_{\mathrm{w}}\right) + \sin\left(\alpha - \frac{1}{2}\omega_{\mathrm{r}}t_{\mathrm{w}}\right)\right] \\
&\quad \times \frac{2\omega_{\mathrm{r}}^2 t_{\mathrm{w}}^2}{\omega_{\mathrm{r}}^2 t_{\mathrm{w}}^2 - \pi^2}\Big\}\hat{I}_Z\hat{S}_Z \\
&\quad + \frac{\mathrm{D}}{4\pi}\Big\{\sin^2\beta[\cos(2\alpha + \omega_{\mathrm{r}}t_{\mathrm{w}}) + \cos(2\alpha - \omega_{\mathrm{r}}t_{\mathrm{w}})] \\
&\quad \times \frac{2\pi\omega_{\mathrm{r}}t_{\mathrm{w}}}{4\omega_{\mathrm{r}}^2 t_{\mathrm{w}}^2 - \pi^2} \\
&\quad - \sqrt{2}\sin 2\beta\left[\cos\left(\alpha + \frac{1}{2}\omega_{\mathrm{r}}t_{\mathrm{w}}\right) + \cos\left(\alpha - \frac{1}{2}\omega_{\mathrm{r}}t_{\mathrm{w}}\right)\right] \\
&\quad \times \frac{2\pi\omega_{\mathrm{r}}t_{\mathrm{w}}}{\omega_{\mathrm{r}}^2 t_{\mathrm{w}}^2 - \pi^2}\Big\}\hat{I}_Z\hat{S}_Y \\
&= a\hat{I}_Z\hat{S}_Z + b\hat{I}_Z\hat{S}_Y
\end{aligned} \tag{5}$$

where ω_{r} is the angular velocity of the rotor and t_{w} is the duration of π pulse. $\overline{\mathcal{H}_1(t)}$, $\overline{\mathcal{H}_2(t)}$, and $\overline{\mathcal{H}_3(t)}$ are the average Hamiltonians corresponding to the period shown in Figure 1. Pulse length, t_{w}, is also considered in the calculations for the analysis of the REDOR results. The density operator, ρ (Tr), at Tr after evolution under the average Hamiltonian can be calculated as

$$\rho(\mathrm{Tr}) = \exp(-i\overline{\mathcal{H}}\mathrm{Tr})\rho_{\mathrm{o}}\exp(i\overline{\mathcal{H}}\mathrm{Tr}) \tag{6}$$

where ρ_{o} is considered to be $\hat{I}y$ after the contact pulse. Then finally the transverse magnetization at Tr can be given by

$$\begin{aligned}
\langle\hat{I}y(\mathrm{Tr})\rangle &= \mathrm{Tr}\{\rho(\mathrm{Tr})\hat{I}y\} \\
&= \cos\left(\frac{1}{2}\sqrt{a^2 + b^2}\mathrm{Tr}\right)
\end{aligned} \tag{7}$$

Echo amplitude in the powder sample can be calculated by averaging over every orientation as follows

$$S_{\mathrm{f}} = \frac{1}{4\pi}\int_{\alpha}\int_{\beta}\langle\hat{I}y(\mathrm{Tr})\rangle\sin\beta\,\mathrm{d}\beta\,\mathrm{d}\alpha \tag{8}$$

Therefore, the normalized echo difference, $\Delta S/S_{\mathrm{o}}$, can be given by equation (4). When the length of t_{w} is zero, equation (7) can be simplified as follows:

$$\langle\hat{I}y(\mathrm{Tr})\rangle = \cos\left(\frac{D}{\pi}\sqrt{2}\sin 2\beta\sin\alpha\mathrm{Tr}\right) \tag{9}$$

In this case, equation (8) is equivalent to equation (3) in the case of $\mathrm{Nc} = 1$.

4 SEPARATION OF S–I DISTANCES FROM A S_m–I_n MULTIPLE SPIN SYSTEM

It should be taken into account that a spin system for a doubly labeled sample should be generally treated as a multiple spin system ($S–I_n$ system) as shown in Figure 2(a) in which S^* is the observed nuclei and the recoupling pulse is applied to the I^* nuclei. The ideal S–I system is available only when the doubly labeled preparation is infinitely diluted with unlabeled preparation. In contrast, uniformly and singly labeled preparations are treated as $S_m–I_n$ and $S–I_n$ systems, respectively (Figure 2b,c), although S^* in the latter is S nuclei of natural abundance. For this reason, it is advisable to utilize a variety of isotopically doubly labeled samples in order to obtain respective interatomic distances, although it is too laborious to make so many kinds of preparations. In fact, we made six kinds of doubly labeled preparations to determine the 3D structure of the pentapeptide, Leu-enkephalin.[16] In addition, it is essential to make certain that all such preparations take the same polymorphic structure, because crystalline peptides or proteins under consideration may take different kinds of polymorphs depending on condition for crystallization, pH, temperature, etc.[15,16] The most convenient way to check this problem is to use the conformation-dependent ^{13}C chemical shifts,

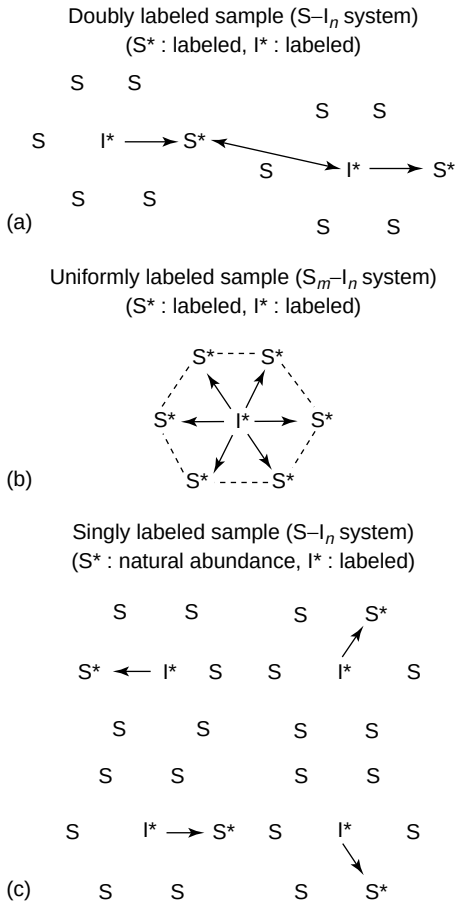

Figure 2 Schematic representation of multiple spin systems for (a) doubly labeled, (b) uniformly labeled and (c) singly labeled samples

which are very sensitive to the presence of such polymorphic structure.[15,16,19]

In this connection, use of a uniformly labeled sample seems to be more attractive both for the sample preparation and also to avoid the problem of polymorphs.[20] This view turned out to be not always true, however, because separation of a particular S–I interaction from S$_m$–I$_n$ spin systems, consisting of many homo- and heteronuclear dipolar and scalar interactions, is not always as straightforward as anticipated. In practice, all of the following conditions should be taken into account to determine the accurate interatomic distances of a particular spin pair from the uniformly labeled samples. First, J coupling among the observed S nuclei should be removed to reduce the phase twist due to the coherent evolution by J coupling, when its magnitude is comparable to the dipolar coupling, as illustrated for uniformly [^{15}N, ^{13}C]-labeled ammonium L-glutamate monohydrate at NcTr = 8 ms (Figure 3).[21,28] This phase twist can be removed by using a shaped pulse as a Z-filter instead of a π pulse at the center position of the REDOR evolution period.[21] Second, the linewidths of individual signals might be broadened due to strong homonuclear dipolar interaction with neighboring S nuclei, which should be eliminated by homonuclear decoupling pulses.[22] Thus, in the case of a uniformly labeled sample, combination of both homonuclear dipolar and scalar decoupling is required to simplify the S$_m$–I$_n$ to S–I$_n$ spin system. Third, relatively shortened transverse relaxation times (T_2), due to residual dipolar interactions, reduce the

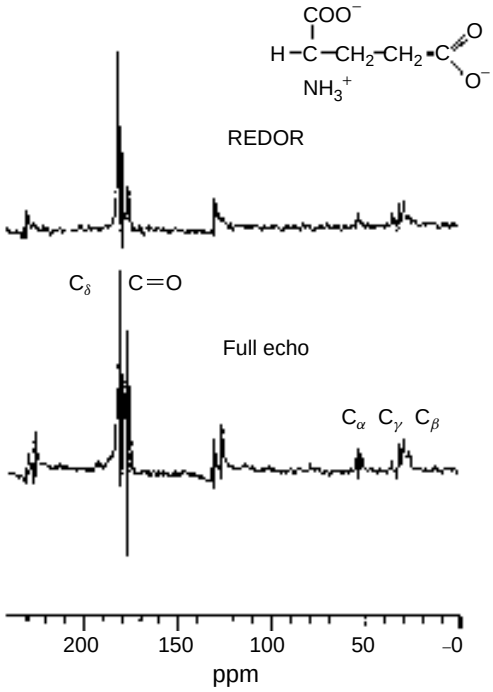

Figure 3 ^{13}C-REDOR and full echo spectra at NcTr = 8 ms for crystalline uniformly labeled ammonium [^{15}N]L-glutamate monohydrate

transverse magnetization during the dipolar recoupling period in REDOR experiments. This makes it difficult to observe the REDOR effect for the nuclei with relatively long internuclear distances, because it is required to measure relatively long evolution times to observe slow dephasing of the REDOR signals. Fourth, REDOR factors against the dipolar evolution time should be analyzed using multiply coupled S–I$_n$ spin systems rather than an isolated two-spin system under the condition of homonuclear decoupling.[23–26] Accordingly, the four kinds of obstacles mentioned above should be removed to determine a set of accurate interatomic distances simultaneously for a uniformly labeled sample.

Gullion et al.[27] proposed a θ-REDOR as an approach to determine the individual interatomic distance in a uniformly labeled sample by dividing S–I$_n$ spin system into 'n' number of isolated S–I two-spin systems. This makes the REDOR analysis simple and allows one to use the REDOR transformation to obtain the dipolar coupling frequencies of individual S–I spin couplings, although this method is not always easy to apply for measurement of a relatively long interatomic distance. Alternatively, homonuclear and scalar interactions are completely removed when natural abundant ^{13}C REDOR experiments were performed.[28] This approach provides an excellent means to determine the interatomic distances for a number of isolated spin pairs simultaneously under condition of high resolution (Figure 2c). Further, it is emphasized that this approach is free from the problem of the above-mentioned shortened T_2 values due to homonuclear ^{13}C spin interactions. However, a multiple coupled spin system, ^{13}C–^{15}N$_n$, has still to be explicitly considered, because the intermolecular dipolar interactions cannot be neglected for a small molecule. In practice, we have recently demonstrated that accurate interatomic distances can be determined by analyzing intramolecular and

intermolecular dipolar contributions based on root mean square deviation (RMSD) between the theoretically and experimentally obtained REDOR factors.[28]

5 TIPS FOR OBTAINING ACCURATE INTERATOMIC DISTANCES BY REDOR EXPERIMENT

It is emphasized that determination of interatomic distances accurate to 0.1 Å is a prerequisite to arrive at a unique solution of the three-dimensional structure of peptides, proteins, etc. A careful evaluation of the following points are the most important steps to obtain reliable interatomic distances by the REDOR experiment, although they have not always been seriously taken into account in a number of papers so far published.

5.1 The Finite Pulse Length and Fluctuation of RF Power

This effect is experimentally observed and calculated using equation (8) as shown in Figure 4. The REDOR parameter, $\Delta S/S_o$, as measured for 20% [1 − ^{13}C, ^{15}N]Gly($r_{CN} = 2.48$ Å) is plotted for the lengths of the ^{15}N π pulse of 13.0 μs for the experiment and 24.6 μs (chosen to satisfy 10% rotor cycle) as a function of NcTr with the calculated lines using the π pulse

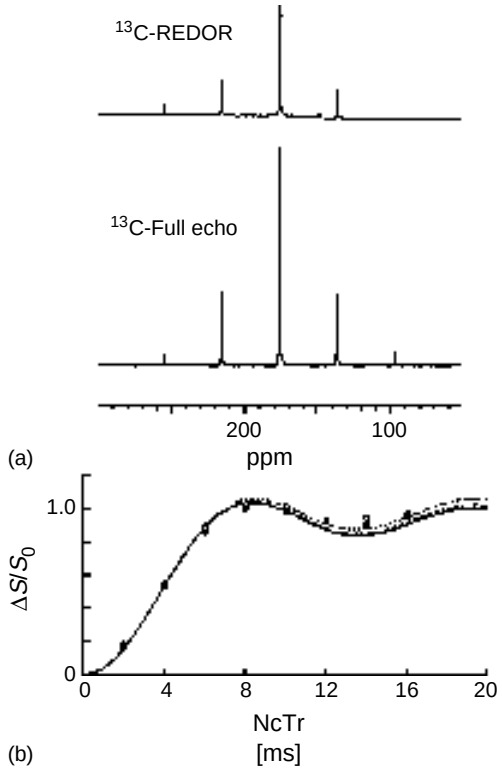

Figure 4 ^{13}C REDOR and full echo spectra of [1-^{13}C, ^{15}N]glycine as recorded by the rotor frequency of 4000 Hz and NcTr of 4 ms (a) and plots of the $\Delta S/S_o$ vs. NcTr (b). Solid and open circles denote the experimental points recorded using a ^{15}N π-pulse of 13.0 and 24.6 μs, respectively. Solid, broken and dotted lines are calculated using the π-pulses of δ, 13.0 and 24.6 μs, respectively, together with the C–N interatomic distance of 2.48 Å[15]

length and finite lengths (13.0 and 24.6 μs) of the π pulse. It turns out, however, that the finite length of the ^{15}N π pulse does not significantly affect the REDOR effect provided that the pulse length is less than 10% of the rotor cycle at the rotor frequency of 4000 Hz. This effect, however, should be seriously taken into account if fast MAS, e.g., 40 kHz is used.

For most spectrometers, it is difficult to be free from fluctuations of RF power during the acquisition of REDOR experiments. It is, therefore, critical that RF power be stabilized. If not, the π pulse will vary in length. Consequently, the REDOR factor is greatly decreased to yield relatively longer interatomic distances. Compensation of instability of such RF power, e.g., by approximate pulse sequence is, therefore, necessary to be free from long term fluctuations of amplifiers. xy-4 and xy-8 pulse sequences have been developed for this purpose. The xy-8 pulse is known to be the best sequence to compensate for the fluctuation of the RF power.[29]

5.2 Contribution from Natural Abundance Nuclei

Since the early stages of the REDOR experiment, contributions from natural abundance nuclei have been seriously considered as a major source of error in the distance measurement.[30] It appears that the observed dipolar interaction can be modified by the presence of such neighboring naturally abundant nuclei. This effect was originally taken into account by simply calculating the $\Delta S/S_o$ value for two isolated pairs and adding proportionally to the natural abundant fraction.[30] Careful analysis of the three-spin system, however, indicates that this sort of simple addition of the fraction of the two-spin system may result in a serious overestimate of the natural abundance effect, to yield shorter distances.[23] The most accurate way to consider the natural abundance effect is, therefore, to treat the whole spin system as a three-spin system by taking into account the neighboring carbons in addition to the labeled pair. In practice, contributions from naturally abundant nuclei can be ignored for ^{13}C REDOR but not for ^{15}N REDOR, because the proportion of naturally abundant ^{13}C nuclei is much higher than that of the ^{15}N nuclei.[23]

5.3 Sample Dilution

^{13}C, ^{15}N-doubly labeled samples are usually used in the REDOR experiment to determine the interatomic distances between the labeled nuclei. More importantly, the dipolar interaction with the labeled ^{15}N nuclei for the neighboring molecules should be taken into account as an additional factor to contribute to the dipolar interaction of the observed pair under consideration. This contribution could be serious when the observed distance is quite remote, because there are many contributions from nearby nuclei. This effect can be completely removed by diluting the labeled sample with a sample of naturally abundant molecules.[23] The sensitivity of the signals, however, has to be sacrificed if one wants to remove the effect completely as the sample must be diluted to 1/49 so that the signal intensity is reduced by a factor roughly 0.02.[11] Instead, it is advised to evaluate the REDOR factors at the infinitely diluted condition by extrapolating the data by stepwise dilution of the sample (i.e., 60%, 30%, etc.) without losing sensitivity, because a linear relationship between the REDOR factor and the dilution is ascertained by a theoretical consideration.[23] Alternatively, the observed plots of $\Delta S/S_o$ values against the

corresponding NcTr values for the sample without dilution can be fitted by a theoretical curve obtained from the dipolar interactions among three-spin systems, although the accuracy is not always improved to the level of the dilution experiment.

5.4 T_2 Effect

The transverse magnetization of the REDOR experiment decays as a function of the ^{1}H decoupling field.[31,32] Under appropriate conditions, molecular motion may interfere with dipolar decoupling. This occurs when molecular motion, if any, exists when the motional frequency is of the same order of magnitude as the decoupling field, and hence the transverse relaxation times (T_2) are significantly shortened. In fact, it was found that the T_2 values of the carbonyl carbons in crystalline Leu-enkephalin are relatively short because of the presence of backbone motion.[33] This is a serious problem for the REDOR experiment, especially for the long distance pairs, because the S/N ratio is significantly deteriorated. In this case, it is required to measure the ^{13}C REDOR signal under a sufficiently strong decoupling field to elongate the transverse relaxation times. It is also useful to perform measurements at low temperature so as to reduce the motional frequency. Note, however, that crystalline phase transitions might be associated together with the freezing of the solvent molecules. This effect has been observed in a variety of enkephalin samples.[34,35]

5.5 RF Inhomogeneity and Confinement of the Sample within RF Coil

In the commercial spectrometer, the rotor is designed to allow the sample volume to be as large as possible in order to gain better sensitivity. Obviously, this arrangement causes H_1 inhomogeneity, which results in a broad distribution of the lengths of the 90° pulses. This problem is serious for the REDOR experiment in which a number of π pulses are applied. As a result, the pulse error can accumulate during the acquisition to give serious error in the measurements of internuclear distances. Particularly, the samples located at the top or bottom part of the sample rotor feel quite a weak RF field. This causes a great reduction of the REDOR factor for a sample that is filled all the way along the sample rotor.[15] This effect should be seriously taken into account prior to experiments with a commercial spectrometer. It is, therefore, strongly recommended to fill the sample only in the central part of the coil just like a multiple pulse experiment to be able to acquire as accurate interatomic distances as possible in the REDOR experiment.

5.6 Standard Sample

All of the considerations mentioned above are essential to achieve accurate interatomic distances. Nevertheless, it is also possible that accuracy may deteriorate even if one of the conditions is not satisfied for every possible measurement. It is therefore advisable to determine the interatomic distances from a standard sample, in order to check that all the conditions are satisfied. More preferentially, use of two standard samples for short and long distances is recommended. In practice, it is recommended to use [1-^{13}C, ^{15}N]glycine as the former standard sample whose C–N interatomic distance is determined as 2.48 Å by a neutron diffraction study, and to check that all the instrumental conditions of a given spectrometer are satisfied prior to every new experiment. As a second standard sample for long distance, it is recommended to use [^{13}C, ^{15}N]*N*-acetyl-Pro-Gly-Phe (Table 1). This crystalline peptide is very stable with relatively long T_2 values, because it does not contain solvent molecules, and the presence of two polymorphic structures is well characterized.[15]

6 NATURAL ABUNDANCE ^{13}C REDOR EXPERIMENT[28]

As mentioned already, it is impossible to obtain meaningful interatomic distances from a uniformly labeled sample as far as the standard REDOR procedure is concerned. Instead, the natural abundance REDOR experiment is more preferable as a means free from both homonuclear dipolar and scalar interactions (Figure 3). This approach provides the interatomic distances for a number of isolated spin pairs simultaneously under high resolution conditions. Further, this approach is free from the problem of the shortened T_2 values due to homonuclear ^{13}C spin interactions. Figure 5 shows the REDOR and full echo spectra of natural abundance ^{13}C nuclei of singly ^{15}N labeled crystalline ammonium [^{15}N]L-glutamate monohydrate (I) at NcTr = 8 ms, in contrast to the twisted spectra from the same sample uniformly labeled (Figure 3). The assignment of peaks to the C_β, $C\gamma$, C_α, C=O and C_δ carbon nuclei, from high to low field, is also shown in Figure 5. The C=O (176.6 ppm) peak was distinguished from the C_δ (179.5 ppm) peak as a peak yielding a stronger REDOR effect as shown in Figure 5. Similarly, the peak at 56.0 ppm was assigned to the C_α carbon nucleus that give the strongest REDOR effect among the three aliphatic ^{13}C peaks. In a similar manner, the peak at 30.5 ppm showed a stronger REDOR effect compared

Table 1 C–N interatomic distances (Å) determined from REDOR experiments as compared with those by X-ray diffraction and MD[15]

Labeled peptides	Experimental			Calculated		
	REDOR	X-Ray		Energy-minimized[a]	MD	
	Orthorhombic	Orthorhombic	Monoclinic[b]		Orthorhombic	Monoclinic
I	3.24 ± 0.05 (3.43 ± 0.05)[c]	3.19	3.76	3.17	3.22 ± 0.10	3.63 ± 0.10
II	3.43 ± 0.05 (3.66 ± 0.05)	3.35	3.21	3.57	3.32 ± 0.10	3.33 ± 0.10
III	4.07 ± 0.05 (4.45 ± 0.05)	3.99	3.91	4.17	3.92 ± 0.10	3.83 ± 0.10

[a]Energy-minimized structure based on REDOR data.
[b]Ref.[36]
[c]Data from Ref.[23] based on fully packed 7.5 mm rotor systems.

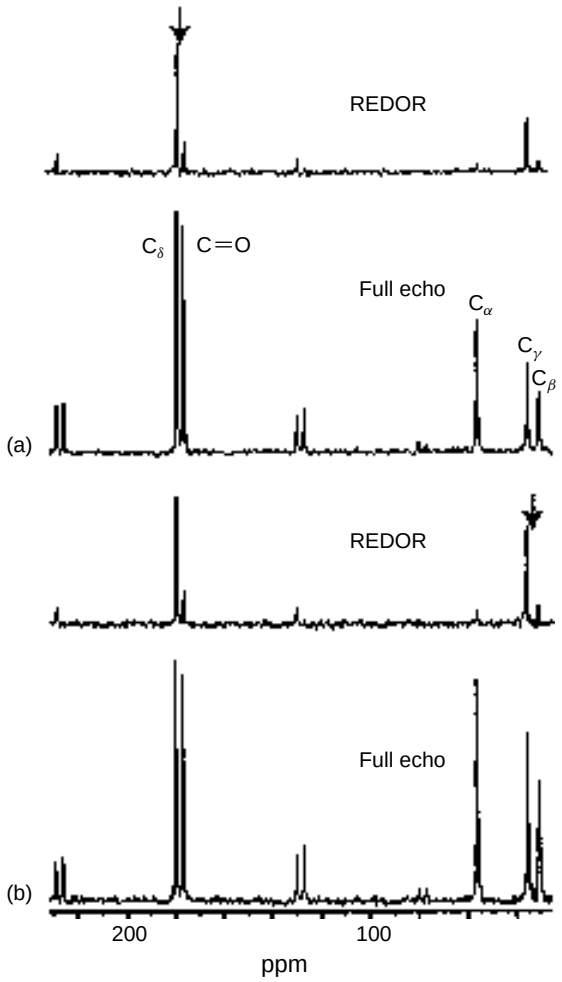

Figure 5 Naturally abundant ^{13}C-REDOR and full echo spectra at NcTr = 8 ms with two different carrier frequencies for crystalline ammonium [^{15}N]L-glutamate monohydrate. Arrows indicate carrier frequency positions at the center of (a) C=O and C_δ resonances; and (b) Cβ and C_γ resonances

with that at 35.2 ppm. Thus, the peaks at 35.2 and 30.5 ppm were assigned to the C_γ and C_β carbon nuclei, respectively.

The interatomic C–N distances between ^{15}N and ^{13}C=O, $^{13}C_\alpha$, $^{13}C_\beta$, $^{13}C_\gamma$, and $^{13}C_\delta$ carbon nuclei were determined with accuracy of 0.15 Å, after experimental conditions were carefully optimized. ^{13}C-REDOR factors for a three-spin system, $(\Delta S/S_o)_{CN1N2}$, and the sum of two isolated two-spin systems, $(\Delta S/S_o)^* = (\Delta S/S_o)_{CN1} + (\Delta S/S_o)_{CN2}$, were further evaluated by the REDOR measurements on isotopically diluted I in a controlled manner. Subsequently, the intramolecular and intermolecular C–N distances were separated by searching the minimum in the contour map of the root mean square deviation (RMSD) between the theoretically and experimentally obtained $(\Delta S/S_o)^*$ values against two interatomic distances, r_{C-N1} and r_{C-N2}. When the intramolecular C–N distance (r_{C-N1}) of the particular carbon nucleus is substantially shorter than the intermolecular distance (r_{C-N2}), C–N distances between the molecule in question and the nearest neighboring molecules can also be obtained, although accuracy is inevitably deteriorated. On the other hand, it was difficult to determine the interatomic distances in the same molecule when the intermolecular dipolar contribution is larger than the intramolecular one as in the case of the C_δ carbon nucleus.

7 ACCURACY LIMIT FOR REDOR STRUCTURE OF PEPTIDE AND PROTEINS

Naito et al.[15] systematically applied this technique to elucidate the three-dimensional structure of *N*-acetyl-Pro-Gly-Phe. They proposed that the carbonyl carbon of the (i-1)th residue and the amino nitrogen of the (i+1)th residue should be labeled with ^{13}C and ^{15}N, respectively. Namely, [1-^{13}C]*N*-acetyl-Pro-[^{15}N]Gly-Phe(I), *N*-acetyl-[1-^{13}C]Pro-Gly-[^{15}N]Phe(II) and [1-^{13}C]*N*-acetyl-Pro-Gly-[^{15}N]Phe(III) were synthesized and the resulting distances were determined to be 3.24 ± 0.05, 3.43 ± 0.05, and 4.07 ± 0.05 Å respectively, utilizing the REDOR factor obtained for the infinitely diluted state to prevent errors from the contributions of the neighboring labeled nuclei. No correction from the contribution of the naturally abundant nuclei turned out to be necessary. Surprisingly, these distances do not agree well with the values obtained from an X-ray diffraction study available when the initial part of this experiment was performed, showing the maximum discrepancy between them to be 0.5 Å.[36] This value seems to be much larger than the expected error as estimated from the precision of the REDOR experiment (±0.05 Å). The reason why the discrepancy is unexpectedly larger was explained by the fact that the crystal (orthorhombic) used for the REDOR experiments is different from that used in the X-ray diffraction study (monoclinic). To check the accuracy of the REDOR experiment, an X-ray diffraction study was performed on the same crystals used for the REDOR experiment. It was found that the distances from the new crystalline polymorph (orthorhombic) agree well between REDOR and X-ray diffraction, within an accuracy of 0.05 Å as shown in Table 1.

Conformational maps based on the possible combinations of the torsion angles of the Pro and Gly residues are calculated on the basis of the distance constraints thus obtained. Further, the difference of the chemical shifts between the C_β and C_γ carbons of the Pro residues $\Delta\beta\gamma$ was used as a constraint to determine the ψ value (−13°).[37] The φ angle of the Pro residue is in many instances restricted to −75° which shows the minimum energy in the residue. Therefore, the torsion angles of the Pro residue are uniquely determined to be (−75°, −28°). Using these torsion angles, conformational maps were again calculated. Finally two pairs of torsion angles were selected as (−112°, 48°) and (−112°, −48°). Minimization by a molecular mechanics calculation yielded the structure of the β-turn I structure, as shown in Figure 6(a). It is found that the three-dimensional structure of this peptide is well reproduced by a molecular dynamics simulation by taking into account all of the intermolecular interactions in the crystals, although a molecular dynamics calculation treating *single* molecular system does not always yield a correct picture as illustrated in Figure 6(b), unless otherwise all the molecules in a unit cell are correctly taken into account.[15,38]

Elucidation of the three dimensional structure of an opioid peptide Leu-enkephalin crystal, Tyr-Gly-Gly-Phe-Leu grown from MeOH/H_2O mixed solvent was performed by the REDOR method alone.[16] This seems to be an additional challenge for this technique to reveal the three-dimensional structure of more complicated systems. Six differently labeled

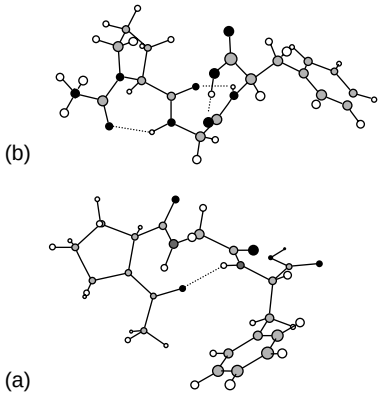

Figure 6 Optimized conformation of *N*-acetyl-Pro-Gly-Phe as obtained by the minimization of energy from the initial form as deduced from the REDOR experiment (a) and a snapshot of the conformation deduced by MD simulation in vacuo (at 100 K) (b)[15]

Leu-enkephaline molecules were synthesized and the resulting interatomic distances (Figure 7a) are accurately determined. It turns out, however, that an extremely careful experiment is required to avoid unexpected crystalline conversion among polymorphs either by dehydration from a tightly sealed rotor or a phase transition occurring at ambient temperature. In principle, pressure under MAS may shift a temperature of phase transition to some extent, because centrifugal force is proportional to the square of the spinning frequency. No significant effect, however, has been noted so far as a sample is spun at relatively low frequency such as 2−4 kHz but care might be taken when rotor is spun at a frequency one order of magnitude high as in 40 kHz.

This may be the reason why final refinement of X-ray diffraction data was abandoned in spite of the pioneering X-ray diffraction data as to the similarity of the tertiary structure between this opioid peptide and morphine.[39] Therefore, it is necessary to check whether the six differently labeled samples are all in the same crystalline polymorph by means of the ^{13}C chemical shifts. Otherwise, meaningless data can be obtained without this precaution. When the distance data are converted to yield the necessary numbers of torsion angles, a unique combination of torsion angles in the corresponding conformational map is determined sequentially as shown in Figure 7(b). It is emphasized that accuracy within 0.1 Å is essential to select unique torsion angles for each amino acid residue. Namely, if the error is larger than 0.41 Å, torsion angles can no longer be selected as shown in Figure 8.

It is also important to point out that the chemical shift data can be used as additional constraints. A three dimensional structure was thus determined as shown in Figure 9. However, this structure is not the same as that previously determined

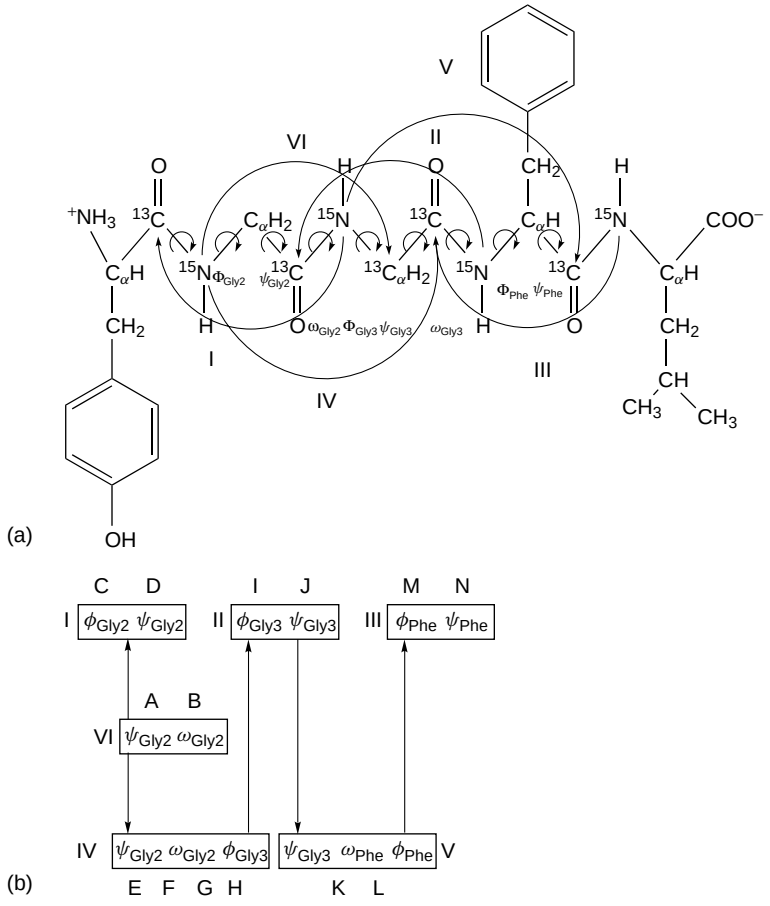

Figure 7 (a) Schematic representation between the sites of a variety of [^{13}C, ^{15}N]-doubly-labeled Leu-enkephalin dehydrates and their related torsion angles. (b) Block diagram to show how respective torsion angles are uniquely determined by the combined examinations of the conformation maps based on the distances of four-bonds apart (I, II, III and VI) and five-bonds apart (IV and V)[16]

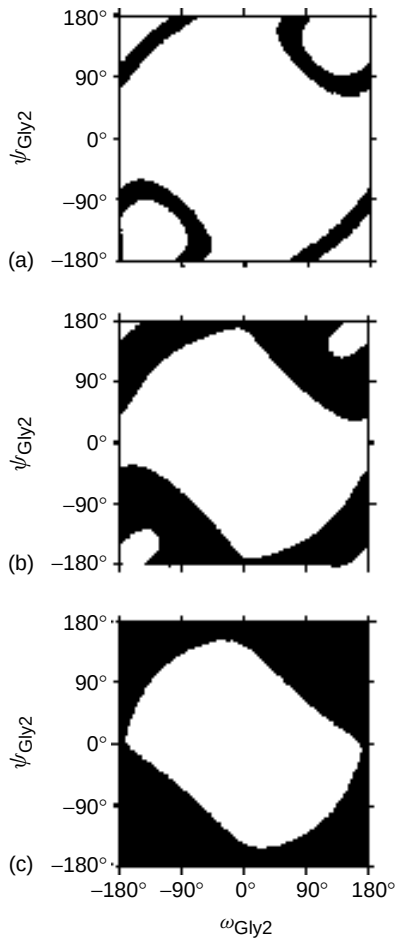

Figure 8 Conformation maps for (Ψ_{Gly2}, ω_{Gly2}) based on the interatomic distance of 4.55 Å with increased experimental errors: (a) ±0.10 Å, (b) ±0.20 Å, and (c) ±0.41 Å[16]

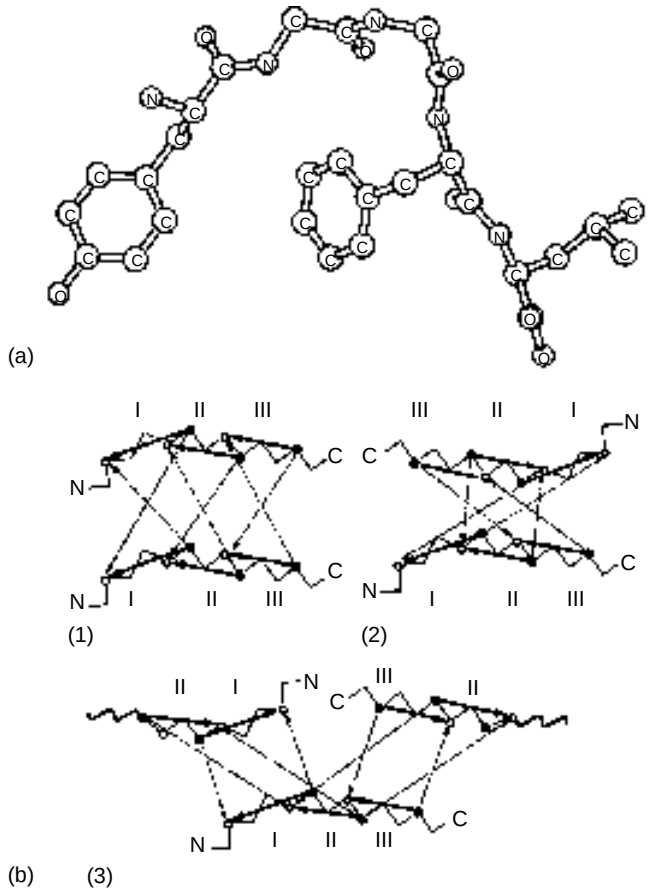

Figure 9 (a) Three-dimensional structure of Leu-enkephalin dihydrate determined uniquely by the successive application of the conformation maps as well as additional constraints of the conformation-dependent ^{13}C chemical shifts. (b) Three kinds of models for putative intermolecular packing as illustrated in the cartoons: (1) interaction through parallel β-sheet form; (2) interaction through an antiparallel β-sheet; and (3) interaction through interaction of three molecules. Solid and dotted arrows correspond with the dipolar interactions between intramolecular and intermolecular $^{13}C-^{15}N$ pairs, respectively[16]

by X-ray diffraction because one is dealing with a crystalline polymorph that is not fully explored. It is possible to figure out the molecular packing in the crystals by looking at the intermolecular dipolar contribution. Since the intermolecular dipolar contributions in I and III are larger than that of II, a β-sheet is formed as one peptide interacts with two peptides as an antiparallel β-sheet as shown in Figure 9(b).

Finally, it should be pointed out that, in order to isolate an S–I spin pair, it is essential to avoid any unnecessary errors from dipolar contributions of neighboring molecules from the overall $S-I_n$ spin system. This is generally encountered for a variety of peptides and the aforementioned dilution procedure turned out to be not required in the case of α-helical polypeptides as far as the measurement of the interatomic distance for $^{15}NH(i)\cdots O = {}^{13}C(i+4)$ is concerned.[40] This is because the interhelical dipolar contribution is found to be negligible in view of the mutual packing of α-helical chains or random mutual orientation between isotopically labeled atoms. Further, it was found that in helical peptides, due to the manner of chain packing, this kind of measurement is feasible to yield 4.5 ± 0.1 Å, without any assumptions, for a variety of transmembrane α-helical peptides in lipid bilayers to mimic a biomembrane at a temperature below liquid crystalline-gel phase transition at which rotation of such peptides about the α-helical axis turns out to be frozen, in spite of the presence of rotational motions of lipid molecules, as viewed from the observation of three principal components of ^{13}C and ^{31}P chemical shift tensors.[41] As is shown in this example, it is essential to ensure that molecular motion is reasonably ceased.

8 CONCLUSIONS

REDOR is one of the most powerful methods to determine accurate interatomic distances after taking into account a number of points in applying the method to a practical sample. Simultaneous measurement of interatomic distances using uniformly labeled samples can only be achieved by removing the homonuclear dipolar and scalar interactions. Alternatively, natural abundance ^{13}C REDOR measurements provide interatomic distances simultaneously free from homonuclear dipolar and scalar interactions. These accurate interatomic distances obtained from REDOR experiments can provide important information on structure and molecular packing of solid peptides and proteins.

9 RELATED ARTICLES IN VOLUMES 1–8

REDOR & TEDOR, Volume 6.

10 REFERENCES

1. D. P. Raleigh, M. H. Levitt, and R. G. Griffin, *Chem. Phys. Lett.*, 1988, **146**, 71.
2. M. H. Levitt, D. P. Raleigh, F. Creuzet, and R. G. Griffin, *J. Chem. Phys.*, 1990, **92**, 6347.
3. R. Tycko and G. Dabbagh, *Chem. Phys. Lett.*, 1990, **173**, 461.
4. B. -Q. Sun, P. R. Costa, D. Kocisko, P. T. Lansbury Jr., and R. G. Griffin, *J. Chem. Phys.*, 1995, **102**, 702.
5. T. Gullion and S. Vega, *Chem. Phys. Lett.*, 1992, **194**, 423.
6. A. E. Bennett, J. H. Ok, R. G. Griffin, and S. Vega, *J. Chem. Phys.*, 1992, **96**, 8624.
7. D. M. Gregory, D. J. Mitchell, J. A. Stringer, S. Kiihne, J. C. Shiels, J. Callahan, M. A. Mehta, and G. P. Drobny, *Chem. Phys. Lett.*, 1995, **246**, 654.
8. T. Gullion and J. Schaefer, *Adv. Magn. Reson.*, 1989, **13**, 57.
9. T. Gullion and J. Schaefer, *J. Magn. Reson.*, 1989, **81**, 196.
10. A. W. Hing, S. Vega, and J. Schaefer, *J. Magn. Reson.*, 1992, **96**, 205.
11. J. R. Garbow and C. A. McWherter, *J. Am. Chem. Soc.*, 1993, **115**, 238.
12. J. R. Garbow, M. Breslav, O. Antohi, and F. Naider, *Biochemistry*, 1994, **33**, 10 094.
13. A. W. Hing, N. Tjandra, P. F. Cottam, J. Schaefer, and C. Ho, *Biochemistry*, 1994, **33**, 8651.
14. R. C. Anderson, T. Gullion, J. M. Joers, M. Shapiro, E. B. Villhauer, and H. P. Weber, *J. Am. Chem. Soc.*, 1995, **117**, 10 546.
15. A. Naito, K. Nishimura, S. Kimura, S. Tuzi, M. Aida, N. Yasuoka, and H. Saitô, *J. Phys. Chem.*, 1996, **100**, 14 995.
16. K. Nishimura, A. Naito, S. Tuzi, H. Saitô, C. Hashimoto, and M. Aida, *J. Phys. Chem. B*, 1998, **102**, 7476.
17. K. T. Mueller, T. P. Jarvie, D. J. Aurentz, and B. W. Roberts, *Chem. Phys. Lett.*, 1995, **242**, 535.
18. T. P. Jarvie, G. T. Went, and K. T. Mueller, *J. Am. Chem. Soc.*, 1996, **118**, 5330.
19. H. Saitô, S. Tuzi, and A. Naito, *Annu. Rep. NMR Spectrosc.*, 1998, **38**, 79.
20. C. A. Michal and L. W. Jelinski, *J. Am Chem. Soc.*, 1997, **119**, 9059.
21. C. P. Jaroniec, B. A. Tounge, C. M. Rienstra, J. Herzfeld, and R. G. Griffin, *J. Am. Chem. Soc.*, 1999, **121**, 100–237.
22. J. Schaefer, *J. Magn. Reson.*, 1999, **137**, 272.
23. A. Naito, K. Nishimura, S. Tuzi, and H. Saitô, *Chem. Phys. Lett.*, 1994, **229**, 506.
24. K. Nishimura, A. Naito, S. Tuzi, and H. Saitô, *J. Phys. Chem. B*, 1999, **103**, 8398.
25. L. M. McDowell, C. A. Klug, D. D. Beusen, and J. Shaefer, *Biochemistry*, 1996, **35**, 5395.
26. J. M. Goetz and J. Schaefer, *J. Magn. Reson.*, 1997, **127**, 147.
27. T. Gullion and C. H. Pennington, *Chem. Phys. Lett.*, 1998, **290**, 88.
28. K. Nishimura, K. Ebisawa, E. Suzuki, H. Saito, and A. Naito, *J. Mol. Struct.*, 2001, **560**, 29.
29. T. Gullion and J. Schaefer, *J. Magn. Reson.*, 1991, **92**, 439.
30. Y. Pan, T. Gullion, and J. Schaefer, *J. Magn. Reson.*, 1990, **90**, 330.
31. D. Suwelack, W. P. Rothwell, and J. S. Waugh, *J. Chem. Phys.*, 1980, **73**, 2559.
32. W. P. Rothwell and J. S. Waugh, *J. Chem. Phys.*, 1981, **74**, 2721.
33. A. Naito, A. Fukutani, M. Uitdehaag, S. Tuzi, and H. Saitô, *J. Mol. Struct.*, 1998, **441**, 231.
34. M. Kamihira, A. Naito, K. Nishimura, S. Tuzi, and H. Saitô, *J. Phys. Chem. A*, 1998, **102**, 2826.
35. M. Kamihira, A. Naito, S. Tuzi, and H. Saitô, *J. Phys. Chem.*, 1999, **103**, 3356.
36. S. K. Brahmachari, T. N. Bhat, V. Sudhakar, M. Vijayan, R. S. Rapaka, R. S. Bhatnagar, and V. S. Aranthanarayanan, *J. Am. Chem. Soc.*, 1981, **103**, 1703.
37. von I. Z. Siemion, T. Wieland, and K. -H. Pook, *Angew. Chem.*, 1975, **87**, 712.
38. M. Aida, A. Naito, and H. Saitô, *J. Mol. Struct. Theochem.*, 1996, **388**, 187.
39. G. D. Smith and T. Blundel, *Science*, 1978, **199**, 1214.
40. S. Kimura, A. Naito, H. Saitô, K. Ogawa, and A. Shoji, *J. Mol. Struct.*, 2001, **157**, 562.
41. S. Kimura, A. Naito, S. Tuzi, and H. Saitô, *J. Mol. Struct.*, 2002, **125**, 602–603.

Biographical Sketches

Akira Naito, *b* 1949. B.Eng., 1973, Nagoya Institute of Technology. Ph.D., 1978, Kyoto University. Post Doctoral Fellow, University of British Columbia, 1978–1984. Assistant Professor, Kyoto University, 1984–1990. Associate Professor, Himeji Institute of Technology, 1990–2001. Professor, Yokohama National University, 2001–present. Approx. 110 publications. Current research specialty: development of solid-state NMR technique and its application to biological systems.

Hazime Saitô, *b* 1937. B.Sc., 1961, Ph.D., 1968, Kyoto University. Research Scientist, Basic Research Laboratories, Toray Industries, Inc., 1963–1975, Section head, Biophysics Division, National Cancer Center Research Institute, Tokyo, 1975–1990. Professor, Himeji Institute of Technology, 1990–present. Approx. 250 publications. Current research specialty: solid state NMR and its application to structural biology with emphasis on membrane proteins.

Bacteriorhodopsin and Rhodopsin

Judith Herzfeld and Jingui G. Hu
Brandeis University, Waltham, MA, USA

1	Introduction	1
2	NMR Strategies	2
3	Structure	3
4	Protonation and Hydrogen Bonding	7
5	Proton Diffusion	8
6	Related Articles	8
7	References	9

1 INTRODUCTION

Situated at the barrier between the interior and exterior of a cell or organelle, membrane proteins execute a variety of vital functions, including energy transduction (i.e. conversion of energy between different forms) and signal transduction (i.e. triggering a cascade of events in response to an environmental effector). The rhodopsins are light-transducing membrane proteins with a chromophore formed by a retinal molecule linked to the protein (known as the opsin) via a Schiff base with a lysine residue (Figure 1). Most rhodopsins are signal transducers: absorption of a proton induces a change in the rhodopsin that activates a primed system, leading to a visual response (e.g. in mammals) or phototactic response (e.g. in algae and archaeobacteria). However, two energy-transducing rhodopsins have been found in halophilic archaeobacteria: in these cases, absorption of a photon results in transport of an ion across the membrane, against its gradient, resulting in conversion of radiant energy into electrochemical energy which can be stored. One of these energy-transducing rhodopsins, known as bacteriorhodopsin because it was the first rhodopsin discovered in a unicellular organism, pumps protons and the other, known as halorhodopsin, pumps halide ions.

Bacteriorhodopsin (248 amino acids, 26 kDa) is the most thoroughly studied membrane protein. This is because it is a major product of *Halobacterium salinarium* (previously also known as *Halobacterium halobium*), and crystallizes in the plane of the membrane to form patches with 2D hexagonal order, from which all other proteins are excluded.[1] These patches (known as 'purple membranes' due to the color of the pigment) are readily separated from the rest of the cell membrane and are stable and functional over an exceptionally wide range of conditions (including pH values, ionic strengths, and temperatures). Thus, it is relatively easy to prepare large samples of the protein in its native form. Due to the 2D crystalline order in the membranes, it has been possible to construct 3D electron density maps from electron micrographs taken over a range of tilt angles.[2] These studies show that the protein folds into a bundle of seven transmembrane helices that encapsulates the retinal chromophore. Chemical studies have shown that the retinal Schiff base is formed with Lys216.[3] Neutron diffraction studies find that the retinal is located near the center of the membrane with the ionone ring closer to the extracellular side than the Schiff base.

Figure 2 shows the relationships between the functionally important forms of bacteriorhodopsin. In the dark, there is a thermal equilibrium between bR_{555} and bR_{568}, where the subscript indicates the wavelength of maximum visible absorbance. The photoproducts of bR_{555} (not shown) decay to bR_{568}, so that bR_{555} disappears upon light adaptation. The photocycle of bR_{568} is responsible for proton transport. The initial photoreaction is the isomerization of the chromophore from all-*trans* in bR_{568} to 13-*cis* in J_{625}. The proton on the Schiff base is lost in the $L_{550}-M_{412}$ transition, and restored in the $M_{412}-N_{520}$ transition. FTIR and kinetic studies, of wild-type and mutant samples, indicate that the immediate proton acceptor is Asp85, and the immediate proton donor is Asp96. However, the proton pathway traverses the entire membrane, and pumping occurs because a proton is released into the extracellular medium in the first half of the photocycle and taken up from the cytoplasm in the second half of the photocycle. The central question regarding the mechanism of bacteriorhodopsin is how this switch occurs: what prevents the system from being reprotonated from the extracellular side? For *Halobacterium*, bacteriorhodopsin

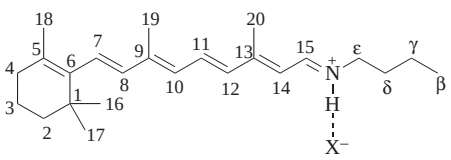

Figure 1 Protonated Schiff base of all-*trans*-retinal with a Lys side chain. X^- is the Schiff base counterion. The carbons atoms are identified according to convention by numbers on the retinal and Greek letters on the Lys residue

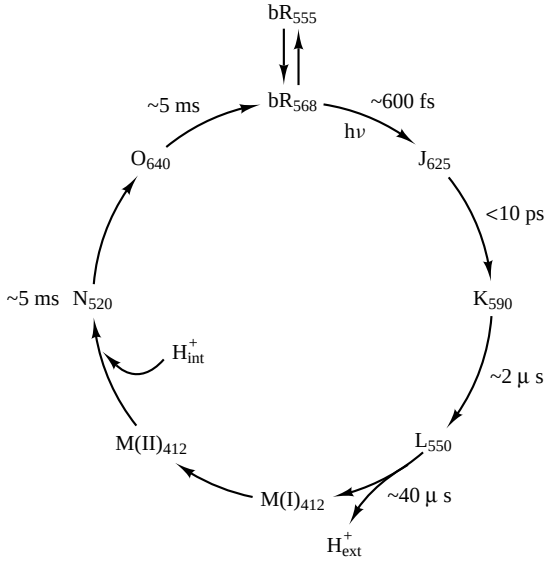

Figure 2 Relationships among the functionally important forms of bacteriorhodopsin. Subscripts indicate the wavelength of maximum visible absorbance. The chromophore is photoisomerized from all-*trans* to 13-*cis* in the bR_{568} to L_{625} photoreaction. The Schiff base is protonated in all but the M-states

provides a solar-powered alternative to respiration for creating the proton electrochemical potential gradient that is required for regeneration of ATP from ADP (the 'proton motive' force of the chemiosmotic mechanism).

Bovine rhodopsin (348 amino acids, 40 kDa) is the most thoroughly studied visual pigment, due to Western dietary habits. Rhodopsin is solubilized and purified from the rod cells of the retina, and then reconstituted into lipid bilayers. Although it does not naturally form a crystalline lattice, it can be induced to do so, and electron cryomicroscopy of such preparations indicates that rhodopsin also forms a bundle of seven transmembrane helices.[4] The retinal Schiff base is formed with Lys296,[5] and the Schiff base counterion is Glu113.[6,7] Figure 3 shows the photointermediates of rhodopsin. In the initial photoreaction, the 11-*cis*-retinal in rhodopsin is isomerized to the all-*trans* form. The following thermal steps lead to the release of the retinal from the protein. Photoactivation of rhodopsin leads to interaction with a heterotrimeric guanine nucleotide-binding protein (G-protein) on the intracellular side of the membrane. The activated G-protein then triggers the further steps that ultimately lead to the hyperpolarization of the plasma membrane that initiates a nerve impulse. In its seven-helix structure and embedded ligand, rhodopsin is believed to be representative of G-protein-coupled receptors generally, a class which includes the signal transducers for acetylcholine, dopamine, glycoprotein hormones, and peptides.[8] While rhodopsin is the rod cell pigment responsible for low-light vision, other retinal proteins in the cone cells are responsible for color vision. For these pigments the action spectrum is of obvious functional importance. In general, the visible spectra of rhodopsins are red shifted relative to the 440 nm absorption maximum of protonated retinal Schiff bases in methanol. Because this bathochromic shift is due to the protein environment, it is known as the 'opsin shift'.[9] The mechanisms by which the opsins 'tune' the chromophore has been one of the central issues in research on retinal proteins. The particularly large opsin shift in bacteriorhodopsin (to 568 nm) has made it a particularly interesting case even though it is not a visual pigment.

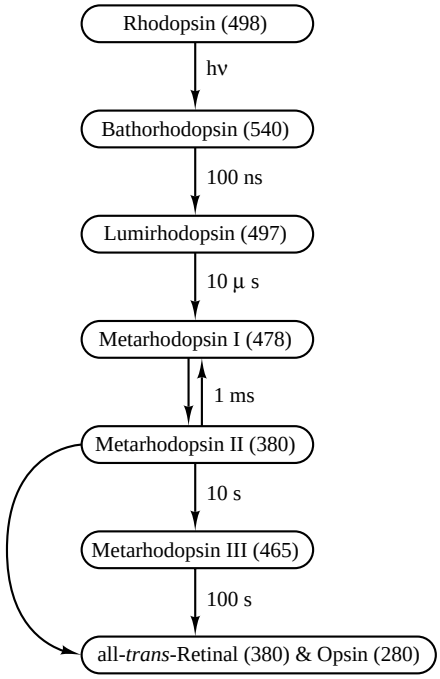

Figure 3 Photoproducts of bovine rhodopsin and their wavelengths of maximum visible absorbance. The chromophore is isomerized from 11-*cis* to all-*trans* in the initial photoreaction. Metarhodopsin II is the form that activates the G-protein. The isomerized chromophore is subsequently released and recycled by the cell

2 NMR STRATEGIES

Although NMR studies have also been made of fragments, here we will focus on studies of intact retinal proteins. These large integral membrane proteins are amenable to different NMR approaches depending on their manner of preparation. In solubilized form, they can be studied by solution techniques, with the caveats that the large protein–detergent complexes have relatively long rotational correlation times and that functional integrity cannot be assayed in the absence of a membrane. For membrane preparations, solid state techniques are required and have the potential of providing additional information from anisotropic interactions. In the crystalline native membrane, bacteriorhodopsin does not diffuse, which is ideal for solid state spectroscopy. With the exception of a few initial studies of lyophilized samples, purple membranes are normally studied as wet ultracentrifuge pellets which are frozen as needed to trap photointermediates (see below) or improve the signal-to-noise ratio. Rhodopsin, reconstituted in lipids after purification, undergoes slow rotational diffusion about an axis perpendicular to the plane of the bilayer. Since such motion interferes with cross polarization and decoupling, it is quenched for solid state NMR studies by lyophilization or freezing.

The large size of these systems makes selective isotopic labeling essential. For studies of the chromophore, the native retinal can be replaced by a synthetic isotopomer:[10] the sample is bleached by treatment with hydroxylamine (which breaks the Schiff base linkage and releases retinal oxime) and then the pigment is regenerated by incubation of the sample with synthetic retinal in the appropriate conformation. Labeling of the opsins relies on bacterial or in vitro expression systems. In the case of bacteriorhodopsin, biosynthetic labeling is practical for those amino acids that the *Halobacteria* do not synthesize in excess. Attempts to isolate auxotrophic strains for the other amino acids have been successful only for arginine.[11] In one NMR study, an auxotroph of *Escherichia coil* was used to express selectively labeled bacteriorhodopsin, which was then purified and reconstituted in lipids.[12] So far, in vitro expression of bacteriorhodopsin[13] has not been achieved on a scale relevant for NMR. For rhodopsin, it has so far proved impossible to prepare NMR quantities of properly folded protein either in cultures or in vitro. NMR studies of rhodopsin have therefore been restricted to the chromophore, with the exception of a recent study of a labeled fragment of G-protein bound to rhodopsin.[14]

For the most part, isotopic labeling of retinal proteins has taken the form of selective enrichment of naturally rare isotopes. This has the advantage of minimizing perturbation of the molecule. Thus, most NMR studies have made use of selective substitution of ^{13}C for ^{12}C, ^{15}N for ^{14}N, and ^{2}H for ^{1}H. However, NMR nuclei have occasionally been

introduced less conservatively, by substitution of ^{19}F for ^{1}H.[15] Most studies up to this point have made use of dilute spin systems; however, increasing attention is now being given to measurements of dipolar interactions between spin pairs to obtain internuclear distances. In ^{13}C studies the large natural-abundance signal generally makes the spectrum difficult to interpret, even with selective isotopic enrichment. Thus, in ^{13}C studies, it has become routine to subtract the spectrum of a natural-abundance sample from the spectrum of the labeled sample obtained under the same conditions (particularly spinning speed).[16]

In order to understand the molecular mechanisms of light transduction in retinal proteins, it is necessary to study their photointermediates. Time-resolved NMR studies have not been possible because of the very high optical density of the large samples required. Thus, NMR studies of photointermediates have relied on cryotrapping. In bacteriorhodopsin, pure bR_{568} obtained by light adaptation can be stabilized for the duration of an NMR experiment by cooling to $-5^{\circ}C$. The only intermediates of the bR_{568} photocycle that have so far proven accessible are one of the M-intermediates and the N-intermediate. The M-intermediate is trapped alone in guanidinium hydrochloride at pH 10, which slows the M to N transition of the photocycle. These conditions are justified by the fact that the proton pump, which is the focus of interest, still functions, albeit relatively slowly. In NaCl at pH 10, the N-intermediate accumulates along with the M-intermediate. In both of these preparations, cooling to $-40^{\circ}C$ suffices to stabilize the intermediates for the duration of an NMR experiment. In rhodopsin, NMR studies have been conducted on the bathorhodopsin[17] and metarhodopsin II[18] intermediates, by cooling below 120 and 130 K, respectively.

3 STRUCTURE

3.1 Chromophore

In the earliest studies, retinal conformations were determined by analysis after chemical extraction. Although this procedure is relatively safe for the C=C configurations, it is not useful for single bonds, which are free to rotate when the chromophore is liberated from its binding pocket. It is also not useful for the C=N bond, which is broken on extraction. In situ studies have made use of resonance Raman spectroscopy and NMR spectroscopy. Of these, NMR has the advantage of avoiding any possible perturbation by light.

Initial NMR studies made use of the sensitivity of ^{13}C chemical shifts to steric interactions of directly bonded protons: electron density driven from the proton produces a low-frequency shift at the carbon. This effect was first identified for a retinal pigment in [12-^{13}C] retinal-labeled bacteriorhodopsin. In the dark-adapted state, the spectrum showed a doublet with a low-frequency:high-frequency stoichiometry similar to the accepted 60:40 stoichiometry of bR_{555}:bR_{568}.[19] Upon light adaptation to form pure bR_{568}, the low-frequency signal disappeared, confirming the assignment of signals originally made by stoichiometry.[20] These observations supported previous evidence for 13-*cis* and all-*trans* chromophores in bR_{555} and bR_{568}, respectively. However, a doublet with similar stoichiometry was also seen in dark-adapted [14-^{13}C]retinal-labeled bacteriorhodopsin.[21] Again, the low-frequency signal disappeared on light adaptation.[20] These observations suggested that the chromophores of bR_{555} and bR_{568} are 13-*cis*,15-*syn* and all-*trans*,15-*anti*, respectively. According to this interpretation, a corresponding steric effect should also be seen at C-ϵ of Lys216. These expectations have recently been confirmed in studies of [ϵ-^{13}C]Lys-labeled bacteriorhodopsin, with a doublet in the dark-adapted state and disappearance of the low-frequency signal on light adaptation.[22] Although the chemical shift data are thoroughly self-consistent, the most unambiguous determination of the C=N configuration has been made by rotational resonance studies of [14-^{13}C]retinal,[ϵ-^{13}C]Lys-labeled bacteriorhodopsin. The rate of magnetization exchange between the two carbons indicated an internuclear distance of 0.3 ± 0.02 nm in bR_{555} and 0.41 ± 0.03 nm in bR_{568}, as expected for C=N *syn* and *anti* configurations, respectively.[23] This spin pair has also been revisited recently in a 2D rf-driven recoupling (RFDR) experiment in which the interactions can be observed in bR_{555} and bR_{568} simultaneously.[24] In this case, the more rapid development of cross-peak intensity for the low-frequency signals clearly demonstrates that these are associated with the shorter internuclear distance and steric interaction.

Steric interactions also play an important role at the other end of the chromophore. Retinal in solution comprises a rapidly exchanging mixture of the skewed 6-*s*-*cis* and planar 6-*s*-*trans* conformations, with the former dominating. The planar 6-*s*-*trans* conformation (shown in Figure 1) has the advantage of the extended planar π-system, but it has two methyl groups in close proximity to C-8. In the skewed 6-*s*-*cis* conformation the planar π-system is truncated, but only one methyl group is near C-8. Since the length of the π-system is an important factor for color discrimination, the 6-*s* conformation of the bound chromophore has received considerable attention. Studies of the 6-*s*-*cis* and 6-*s*-*trans* crystal forms of retinoic acid demonstrated that the ^{13}C-5 shift is sensitive to isomerization of the 6-*s* bond, as expected given the changes in steric interactions.[25] Interestingly the effect is entirely in the most high-frequency tensor element which moves 20 ppm to high frequency on 6-*s*-*cis* to 6-*s*-*trans* isomerization.

In [5-^{13}C]retinal-labeled bacteriorhodopsin, the most high-frequency and most low-frequency tensor elements were found to correspond exactly to that of 6-*s*-*trans*-retinoic acid, suggesting that the chromophore in bacteriorhodopsin is the 6-*s*-*trans* form.[26] (The middle tensor element will be discussed in Section 4.1.) Complementary evidence for a 6-*s*-*trans* conformation in bacteriorhodopsin was obtained from the ^{13}C-8 chemical shift, which is also affected by the changes in steric interactions.[26] Steric interactions also influence the dynamics of the methyl groups, and the ^{13}C-18 longitudinal relaxation time in bacteriorhodopsin was found to be more typical of a 6-*s*-*trans* chromophore than a 6-*s*-*cis* conformation.[26] More recent ^{2}H NMR measurements of the activation energy for threefold hopping of the C-18 methyl group are also consistent with a 6-*s*-*trans* chromophore and inconsistent with a 6-*s*-*cis* chromophore.[27] Again, however, the most unambiguous determination of the 6-*s* conformation has been made by rotational resonance studies of doubly labeled bacteriorhodopsin. In [8,18-^{13}C]retinal-labeled bacteriorhodopsin, the slow rate of magnetization exchange indicated a 6-*s*-*trans*

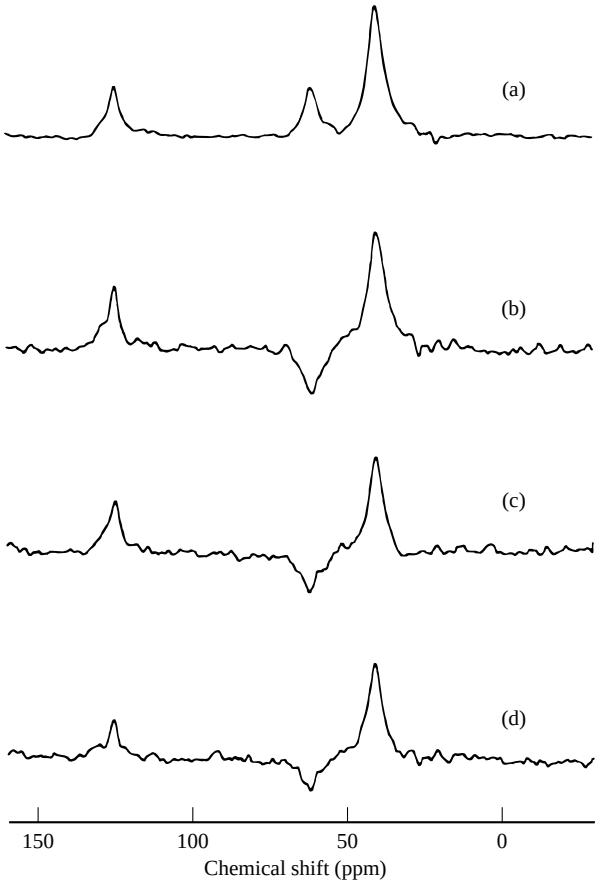

Figure 4 Solid state ^{13}C MAS difference spectra obtained by subtraction of a spectrum of natural-abundance bacteriorhodopsin from spectra of [ϵ-^{13}C]Lys[14-^{13}C]retinal-labeled bacteriorhodopsin in the M-state.[31] (a) The CP MAS difference spectrum. The ^{13}C-14 signal is to high frequency. There are two ^{13}C-ϵ signals, the stronger low-frequency signal is from the six free lysine residues. The smaller signal is from Lys216, which forms the Schiff base with the retinal. (b)–(d) The n = 1 rotational resonance difference spectra for magnetization exchange between [ϵ-^{13}C]Lys216 and [14-^{13}C]retinal at mixing times of 0.2, 5.0 and 20.0 ms, respectively

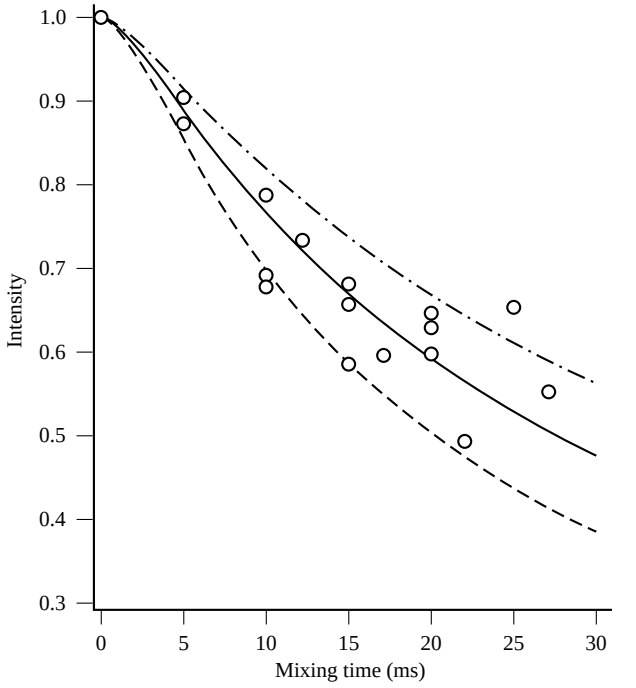

Figure 5 The observed and simulated magnetization exchange between [ϵ-^{13}C]Lys216 and [14-^{13}C]retinal in the M-state, under the n = 1 rotational resonance condition.[31] - - - -, 0.38 nm; ——, 0.39 nm; —·—, 0.40 nm

conformation[28] with an internuclear distance of 0.41 nm.[29] In [8,16/17-^{13}C]retinal-labeled bacteriorhodopsin the average internuclear distance was found to be 0.33–0.35 nm, also consistent with a 6-*s*-*trans* conformation.[29]

Analogous studies have been conducted of the M-state that is trapped at pH 10, in 0.3–0.5 M guanidinium hydrochloride or 0.1 M NaCl, when bR_{568} is illuminated with light of wavelengths > 540 nm, at low temperatures.[22,30,31] The ^{13}C-5 chemical shift indicates that the 6-*s* bond is still *trans*.[30] The ^{13}C-12 chemical shift confirms that the chromophore is 13-*cis*. The ^{13}C-14 and [ϵ-^{13}C]Lys216 chemical shifts indicate that the Schiff base configuration is still *anti*.[22,30] This was confirmed by rotational resonance (Figures 4 and 5), which gave a 14-ϵ internuclear distance of 0.39 ± 0.01 nm, as expected for a C=N *anti* configuration and 0.1 nm larger than expected for a *syn* configuration.[31] These results are consistent with interpretations made of resonance Raman spectra.[32]

Similar studies have been made of the N-intermediate, cryotrapped with the M-intermediate in 0.1 M NaCl at pH 10.[33] The 6-*s* conformation was not investigated, but the ^{13}C-12 chemical shift showed that the chromophore is still 13-*cis*, and the ^{13}C-14 and [ϵ-^{13}C]Lys216 chemical shifts showed that the Schiff base remains in the C=N *anti* configuration. These results agree with the conclusions of time-resolved resonance Raman studies of the N-intermediate at room temperature.[34]

Carbon-13 chemical shifts have also been used to characterize the rhodopsin chromophore. As in bacteriorhodopsin, the ^{13}C-14 chemical shift indicates that the Schiff base is C=N *anti* in rhodopsin[35] and bathorhodopsin.[17] Whereas the bacteriorhodopsin chromophore has been found to be 6-*s*-*trans*, a 6-*s*-*cis* conformation is indicated by the ^{13}C-5 chemical shift in rhodopsin,[35–37] and the ^{13}C-8 chemical shift in bathorhodopsin.[17] Other ^{13}C chemical shifts are generally similar to those in the corresponding retinal Schiff base model compounds (11-*cis* for rhodopsin and all-*trans* for bathorhodopsin). Interestingly, those deviations that are observed are localized in the region of the chromophore that was identified in retinal analog studies as interacting with a protein charge.[17,36,37] Perturbations in this region have also been detected by ^{19}F NMR of rhodopsin-containing fluorinated retinals.[15]

While bond isomerization determines the orientations of different parts of the chromophore relative to each other, it is also important to determine absolute orientations, especially for vectorial transport. Ulrich et al.[38] have used the quadrupole splittings of ^{2}H labels in uniaxially oriented films of bacteriorhodopsin to examine the orientation of the ionone ring relative to the membrane normal. Using the ^{31}P NMR spectral lineshape to determine the mosaic spread of the sample, and treating the ionone ring as a rigid unit, ^{2}H spectral lineshapes of oriented [2,4,4,16,16,16,17,17,17,18,18-$^{2}H_{11}$] retinal-labeled bacteriorhodopsin, at various inclinations to the magnetic field,

were simulated for various ionone ring orientations. The fit to the experimental series of ^{2}H spectra was optimal for an ionone ring orientation that places the methyl groups on C-16, C-17, and C-18 at angles of 94, 75, and 46°, respectively, relative to the membrane normal. Given the known tilt of the chromophore, with the Schiff base closer to the cytoplasmic side and the ionone ring closer to the extracellular side, the ^{2}H analysis indicates that the C-18 methyl group points toward the cytoplasmic side of the membrane. This means that, for a fully planar all-*trans*,15-*anti* or 13-*cis*,15-*syn* chromophore the Schiff base proton or lone pair points toward the extracellular surface (as found for bR_{568} in linear dichroism experiments[39]), while for a fully planar 13-*cis*,15-*anti* chromophore the Schiff base proton or lone pair points toward the cytoplasmic surface.

3.2 Protein

Isotopic labeling of the opsin in NMR quantities has so far only been possible for bacteriorhodopsin. In this system, both secondary structure and tertiary structure have been addressed in a variety of ways.

The peptide backbone was first labeled by Lewis et al.,[40] in the carbonyls of the leucine residues, because these hydrophobic residues were expected to be buried in the membrane on the basis of their location in the hydrophobic stretches of the peptide sequence that were expected to form the transmembrane segments. The spectrum of intact [1-^{13}C]Leu-labeled purple membrane showed a rigid-lattice carbonyl powder pattern which indicated that, at the Leu residues, the peptide backbone was immobile on the ^{13}C NMR timescale even at 40°C. When the labeled bacteriorhodopsin was solubilized and reconstituted in DMPC (dimyristoyl phosphatidylcholine) vesicles above the lipid phase transition temperature, the spectrum was narrowed by fast rotational diffusion. Analysis of the motionally averaged lineshape was used to determine the possible orientations of the Leu peptide bonds relative to the diffusion axis. The data were found to be consistent with α_I helices tilted at 20° from the membrane normal, a model that is congruent with electron density information.[2]

Bowers and Oldfield[41] also studied [1-^{13}C]Leu-labeled purple membrane, and found a mobile component. Mobile components were also found for purple membranes 1-^{13}C labeled in Gly, Ile, Lys, Phe, and Val residues. For each amino acid except Val, the proportion of mobile residues was correlated with the proportion of residues in the C-terminus, suggesting that the C-terminus is mobile on the ^{13}C NMR timescale. Since the C-terminus does not contain any Val residues, it was suggested that the observation of mobile Val residues indicates another mobile region in protein. The discrepancy between these results for Leu and those of Lewis et al., described above, has not been solved.

Helgerson et al.[42] have considered the chemical shifts of peptide carbonyl atoms. Based on homopolymers, in which the carbonyl carbon resonance is found at 176 ± 1 ppm for helical structures and 171 ± 1.5 ppm for nonhelical structures, they concluded that about 85% of Leu, 75% of Val, and 80% of Lys residues in bacteriorhodopsin are in helical regions. Less quantitatively, but more generally, Engelhard et al.[43] have noted that the chemical shift of the peak of the natural-abundance peptide signal in bacteriorhodopsin suggests a largely α-helical secondary structure. These results are consistent with the electron density distribution in bacteriorhodopsin.[2]

Seigneuret and co-workers have labeled the peptide backbone at the carbonyl carbons of the Phe[44] and Met[45] residues. Narrow, well-resolved signals were obtained by solubilizing in *n*-dodecylmaltoside. For the [1-^{13}C]Met-labeled bacteriorhodopsin, sequence specific assignments were obtained by selective colabeling of neighboring amino acid residues with ^{15}N and by papain proteolysis. Using these assignments, it was determined that, of the nine Met residues, only Met32, Met68, and Met163 are water exposed (as reflected in susceptibility to H_2O_2 oxidation) and weakly hydrogen bonded (as indicated by deuterium exchange from ^2H_2O). These results are also consistent with the current structural model of bacteriorhodopsin.[2]

Deber et al.[46] focused on the secondary structure at proline peptide bonds, which are thought to play an important role in transport proteins. [γ-^{13}C]Pro-labeled bacteriorhodopsin was solubilized in $CHCl_3$:CD_3OD (1:1) with 0.1 M $LiClO_4$. Sufficient resolution was achieved to distinguish the 2 ppm difference in ^{13}C chemical shift between a *cis* and a *trans* X-Pro peptide bond. No *cis* signal was observed, and it was concluded that all 11 X-Pro peptide bonds in the solubilized bacteriorhodopsin are in the *trans* conformation. Further evidence has been supplied by an analogous solid state NMR study.[47] The chemical shift difference between C-β and C-γ of a proline residue is 7−11 and 3−5 ppm when the X−Pro peptide bond is *cis* and *trans*, respectively. The MAS spectrum of [β,γ-^{13}C]Pro-labeled bacteriorhodopsin showed only *trans*-configured X−Pro peptide bonds.

The Pro peptide bonds have also been studied by ^{15}N solid state NMR of [^{15}N]Pro-labeled purple membranes. Five well-resolved peaks are obtained at room temperature for the 11 Pro residues.[48] Less resolution is obtained at lower temperatures, suggesting that disorder is being frozen in. In order to assign the Pro91 signal, a REDOR experiment was carried out on a [1-^{13}C]Thr,[^{15}N]Pro-labeled sample, which has only one ^{13}C−^{15}N spin pair, between Thr90 and Pro91.[49] As shown in Figure 6, a single signal is obtained for Pro91 in bR_{568}. Figure 6 also shows a REDOR difference spectrum for a mixture of the bR_{568} and M forms of bacteriorhodopsin. The spectrum clearly reveals a difference in the Pro91 ^{15}N chemical shift, providing direct evidence for a structural change in that part of the protein.

Nitrogen-15-labeled bacteriorhodopsin was also studied by heteronuclear ^{1}H−^{15}N coherence spectroscopy in methanol/chloroform (1:1) solution with 0.1 M NH_4CHO_2.[50] In a uniformly ^{15}N-enriched sample, less than half of the cross peaks expected from the amino acid sequence were observed. By selective labeling and proteolytic cleavage, it was determined that the ^{1}H−^{15}N cross peaks were exclusively from the first two and the last helices in the sequence. Dynamic processes were inferred in the other four helices of the solubilized protein.

The protein structure has also been studied from the vantage point of the amino acid side chains. Initial studies of the mobilities of different side chains using ^{2}H NMR found a significant proportion of mobile residues that were attributed to surface groups.[51−54] However, other investigations suggested that the mobile residues were largely due to contamination by residual plasma membrane.[55] More direct measures of surface exposure have made use of paramagnetic broadening in solubilized [^{13}C]methyl-labeled bacteriorhodopsin[56] and photochemically induced dynamic nuclear polarization of aromatic signals in ^{1}H NMR studies of solubilized natural-abundance

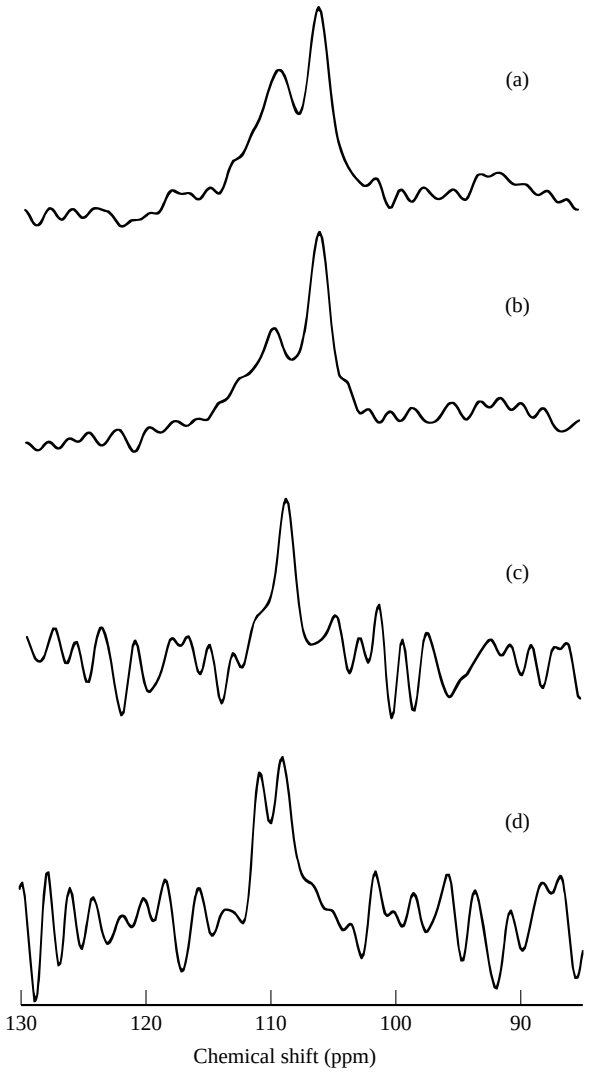

Figure 6 Nitrogen-15 MAS spectra for [1-^{13}C]Thr,[^{15}N]Pro-labeled bacteriorhodopsin.[49] (a) CP MAS spectrum in the light-adapted state. (b) REDOR MAS spectrum in the light-adapted state. (c) The difference between spectra (a) and (b), showing only the signal from Pro91 (the only Pro bound to Thr) in the light-adapted state. (d) REDOR difference spectrum as in part (c) but for a mixture of the light-adapted and M states to show the change in the Pro91 chemical shift

bacteriorhodopsin.[57] Arseniev et al.[58] attempted to detect interactions between tryptophan residues in [5-^{19}F]Trp-labeled bacteriorhodopsin solubilized in $CD_3OH//CHCl_3$ (1:1) with 0.1 M $LiClO_4$. No such interactions were observed, but effects on different signals in the ^{19}F spectrum were noted upon addition of formic acid, reduction of the Schiff base, and modification of the retinal ionone ring. In similar studies of [3-^{19}F]Phe-labeled bacteriorhodopsin, a distance of 1.3 $\pm$ 0.1 nm was measured between Phe230 and a spin label introduced at Met163.[59]

4 PROTONATION AND HYDROGEN BONDING

Changes in protonation are obviously critical along the proton transport pathway in bacteriorhodopsin. As it happens, a protonation change is also at the heart of signal transduction in rhodopsin.[60] Chemical shifts are excellent probes of protonation, and have been used to good advantage in studies of both bacteriorhodopsin and rhodopsin.

4.1 Schiff Base

Model compound studies show that chemical shifts of the odd-numbered carbon atoms of a retinal Schiff base are sensitive to the protonation of the Schiff base,[25] as expected based on the resonance structures which redistribute the positive charge from the Schiff base to the odd-numbered carbon atoms. The sensitivity is greatest at the C-13 position and, for rhodopsin studies which are so far limited to labels on the retinal, the ^{13}C-13 chemical shift is the clearest indicator of the protonation of the Schiff base. After some early false starts due to difficulties in replacing natural-abundance retinal with labeled retinal,[61–63] Mateescu obtained the first ^{13}C NMR spectra for [13-^{13}C]retinal-labeled samples of rhodopsin and bacteriorhodopsin.[64,65] In both proteins, the ^{13}C-13 chemical shift indicated a protonated Schiff base. The ^{13}C-11 chemical shift also provided evidence for a protonated Schiff base in bacteriorhodopsin.[19] In more recent work, the ^{13}C-13 and ^{13}C-15 chemical shifts obtained for bathorhodopsin are consistent with a protonated Schiff base in this photointermediate,[17] and those obtained for metarhodopsin II indicate a deprotonated Schiff base in this activated state.[18] In bacteriorhodopsin, the ^{13}C-13 chemical shifts correspond to a deprotonated Schiff base in the M-state[30] and a reprotonated Schiff base in the N-state.[33]

However, the ^{15}N chemical shift of the Schiff base is by far the most sensitive probe of protonation,[66] and in bacteriorhodopsin, where it is possible to label the protein, the solid state ^{15}N NMR spectrum of [ϵ-^{15}N]Lys-labeled bacteriorhodopsin provides the definitive determination of the protonation state of the Schiff base. Such spectra for dark-adapted bacteriorhodopsin were reported independently by Mateescu et al.[65] and by Harbison and co-workers.[66–69] With a good signal-to-noise ratio, the spectrum shows a doublet due to the coexistence of bR_{568} and bR_{555} in a dark-adapted sample.[66–69] Solid state ^{15}N NMR spectra have also been obtained for [ϵ-^{15}N]Lys-labeled bacteriorhodopsin cryotrapped in the M- and N-states. The [ϵ-^{15}N]Lys chemical shifts indicate that the Schiff base is deprotonated in the M-state and reprotonated in the N-state.[33]

From the start, it was noted that the ^{15}N chemical shifts in bR_{568} and bR_{555} are still further to low frequency than normal for protonated retinal Schiff bases, and it was suggested that this is due to an unusually weak counterion.[66] Comparison of the shift tensor elements for different retinylidenebutylimine salts[70] and retinylideneanilinimine salts[71] has shown that the lowest-frequency element is insensitive to counterion strength, and the two high-frequency elements vary proportionately. The same relationship is observed between the tensor elements for bacteriorhodopsin, strengthening the association of the ^{15}N chemical shift with counterion strength.[70] However, the effect is more extreme in bacteriorhodopsin, indicating a counterion that is weaker than any halide, carboxylate, or phenolate moiety that might be available as a simple counterion in a protein. In order to explain the data it became necessary to postulate a complex counterion, involving water-mediated hydrogen bonding between the Schiff base and protic amino

acid residues.[70] Such a hydrogen-bonded complex would diffuse the counterion charge over several bonds. The complex counterion is consistent with the current structural model of bacteriorhodopsin, which locates water, two Asp residues and one Arg residue in the vicinity of the Schiff base.[2]

Interestingly, weakening the strength of the Schiff base counterion also affects the ^{13}C-5 chemical shift at the other end of the polyene chain.[71,72] In the retinylideneanilinimine salts, which crystallize in the planar 6-*s*-*trans* conformation, the effect shows up essentially exclusively in the middle element of the ^{13}C-5 chemical shift tensor, and the unusually weak Schiff base counterion in bacteriorhodopsin completely explains the unusual value of the middle element of the ^{13}C-5 chemical shift tensor in bacteriorhodopsin.[71] A weak Schiff base counterion also destabilizes the ground electronic state of the chromophore relative to the excited state, and thereby constitutes an important mechanism for the bathochromic opsin shift. This effect is larger in the retinylideneanilinimine salts, which crystallize in the planar 6-*s*-*trans* conformation, than in the retinylidenebutylimine salts, which crystallize in the skewed 6-*s*-*cis* conformation.[71] This enhancement is also seen in solution in 1,1-didemethylretinal Schiff bases, which adopt a planar 6-*s*-*trans* conformation, compared with retinal Schiff bases in which the planar 6-*s*-*trans* conformation is sterically disfavored.[72] The synergistic effects of the extended π system, due to ring–chain planarization, and the weak Schiff base hydrogen bonding, due to the complex counterion, are sufficient to explain completely the very large opsin shift in bacteriorhodopsin.[71]

With HCl titration, the visible absorption maximum of bacteriorhodopsin shifts from 568 nm (at pH ~7) to 605 nm (at pH ~2), and then reverts to 565 nm (at pH ~0). Spectra of [ϵ-^{15}N]Lys-labeled samples indicated that the ^{15}N chemical shift is closely correlated with the color.[73] A 16 ppm low-frequency shift in the blue species indicates an even weaker Schiff base counterion than in the two purple species. This is consistent with the expected protonation of an acidic residue in the complex counterion at low pH. The recovery of the color and ^{15}N chemical shift at still lower pH is thought to be due to the replacement of a water molecule in the complex counterion by chloride from the bulk acid. Carbon-13 NMR results for selectively enriched polyene carbons in bR_{605} revealed that the chromophore conformation is generally not very different from that of bR_{568}, although the spectrum of [14-^{13}C]retinal bR_{605} showed doublets for the 15-*syn* and 15-*anti* forms that may reflect the coexistence of 13-*cis* and all-*trans* conformers in each case.[73]

4.2 Polar Amino Acid Residues

Amino acids capable of ionization or hydrogen bonding could participate in proton transport in bacteriorhodopsin. Roles proposed for Tyr and Asp residues have motivated NMR studies of these groups.

Tyrosinate is an unusual species, but FTIR and UV studies suggested that it existed in bacteriorhodopsin. Since the [4′-^{13}C]Tyr chemical shift is sensitive to deprotonation of the adjoining oxygen, it provides an unambiguous probe for long-lived tyrosinate. However, MAS NMR spectra of [4′-^{13}C]Tyr-labeled bacteriorhodopsin showed no detectable long-lived tyrosinate in dark-adapted bacteriorhodopsin at pH bulk values below 13,[74] light-adapted bacteriorhodopsin at pH = 7 or 10,[75] or the M-state at pH = 10.[75] It was concluded that the changes in Tyr residues detected by FTIR and UV spectroscopy represented changes in hydrogen bonding rather than deprotonation.

Internal Asp residues certainly do play a direct role in proton transport. Engelhard et al.[43] biosynthetically labeled bacteriorhodopsin with [4-^{13}C]Asp. Unexpected scrambling of the label to Trp was found, but this signal causes no problem because it appears in a distinct region of the spectrum. On the other hand, the signals of the nine labeled Asp residues and the three labeled Asn residues are superimposed on peptide backbone signals due to natural-abundance ^{13}C and some scrambling through the tricarboxylic acid cycle to [1-^{13}C]Glu. Nevertheless, six resonances were resolved. These were considered in terms of five categories: exposed Asp residues which must be deprotonated, buried Asp residues that are not protonated, buried Asp residues that are protonated, Asn residues in polar environments, and Asn residues in nonpolar environments. The signals due to surface Asp residues were assigned to high-frequency resonances by comparison of the spectrum of the native membrane with that obtained after 'deionization' (ion exchange chromatography to replace the intrinsic cations of the purple membrane with protons). Based initially on chemical shifts and ^{14}N line-broadening effects in model compounds, the two most narrow, lowest frequency lines were assigned to protonated Asp residues which must be buried. The protonated state of these low-frequency resonances was later confirmed by estimation of the middle chemical shift tensor element from sideband intensities.[76] Specific assignments for the Asp96 and Asp85 signals were subsequently obtained by studies of site-specific mutants.[77] By elimination, based on the current structural model of bacteriorhodopsin and FTIR studies of Asp residues, the other narrow low-frequency signal was assigned to Asp115.[76] Based on the current structural model of bacteriorhodopsin and the functional properties of site-specific mutants, Asp85 and Asp212 are expected to be influenced by light adaptation. This prediction was borne out: two signals shifted on light adaptation, including the previously assigned Asp85 signal and a signal further to high frequency which was assigned to Asp212 by elimination.[76] The signals of all four internal Asp residues have thus been assigned in bR_{555} and bR_{568}. Using these assignments to interpret the spectrum of the M-intermediate in the D96 N mutant, deprotonation of the Schiff base is seen to lead to protonation of Asp85 while Asp212 remains protonated.[78] Deionization of the membranes was also found to induce protonation of Asp85.[78]

5 PROTON DIFFUSION

Among the various forms of spectroscopy that have been applied to bacteriorhodopsin, NMR has the unique potential to chart the movement of protons, which is central to the energy transduction process. One approach makes use of the relatively fast relaxation of the immobile protons of the protein.[79] In this CP MAS experiment, cross polarization is delayed until ^{1}H magnetization remains only in the bulk water. Under these circumstances, the only nuclei that are cross polarized effectively are those that exchange protons with bulk water on the submillisecond timescale. Using this

selection technique for [ϵ-^{15}N]Lys-labeled bacteriorhodopsin, Harbison et al.[79] observed cross polarization of the Schiff base and the six free Lys residues, although there was no longer any cross polarization of the natural-abundance ^{15}N in the peptide backbone. By varying the delay, it was demonstrated that proton exchange between the Schiff base and bulk water is essentially complete in about 0.5 ms. Delayed cross polarization has also been applied to [^{15}N]Arg-labeled bacteriorhodopsin.[80,81] In this case, rapid proton exchange was only observed at high pH.[81]

Proton NMR provides a more direct means of following proton movement. Zheng et al.[82] have shown that high-resolution 2D ^{1}H MAS NMR spectra can be obtained by using ^{2}H to dilute and cross polarize the protons. This approach was used to obtain 2D ^{1}H NOESY spectra of chemically exchanging solids, and the development of cross-peak intensities was analyzed to extract the kinetic constants for exchange. Proton exchange was found to occur preferentially along hydrogen bonds. Initial 2D ^{1}H NOESY spectra have also been obtained for perdeuterated bacteriorhodopsin.[83] Signal intensity from the residual nonexchanging protons on the protein prevents detailed examination of the signals of the exchanging protons. However, the 2D spectrum shows the expected exchange among high-frequency absorbing protons and, on a somewhat longer timescale, unexpected exchange between high-frequency and low-frequency protons. The latter are believed to be water molecules in nonpolar pockets. This interpretation is supported by parallel ^{2}H studies of water dynamics, which show a small population of freely rotating water molecules even at very low temperatures where hydrogen bonding would inhibit rotation.[83] Although these experiments are the first to find evidence for water in hydrophobic regions of purple membranes, such water has been suggested to fill gaps between polar amino acids along the proton transport pathway.

6 RELATED ARTICLES

Amino Acids, Peptides and Proteins: Chemical Shifts; Carbon and Nitrogen Chemical Shifts of Solid State Enzymes; Cross Polarization in Rotating Solids: Spin-1/2 Nuclei; Chemical Exchange on Solid Metal Surfaces; Deuterium NMR in Solids; Dipolar and Indirect Coupling Tensors in Solids; Homonuclear Recoupling Schemes in MAS NMR; Hydrogen Bonding; Magic Angle Spinning; Membrane Proteins; Membranes: Carbon-13 NMR; Protein Dynamics from Solid State NMR; REDOR and TEDOR; Rotational Resonance in Biology.

7 REFERENCES

1. W. Stoeckenius, *Sci. Am.*, 1976, **234**(6), 38.
2. R. Henderson, J. M. Baldwin, T. A. Ceska, F. Zemlin, E. Beckmann, and K. H. Downing, *J. Mol. Biol.*, 1990, **213**, 899.
3. H. Bayley, K.-S. Huang, R. Radharkrishnan, A. H. Ross, Y. Takayaki, and H. G. Khorana, *Proc. Natl. Acad. Sci. USA*, 1981, **78**, 2225.
4. G. F. X. Schertler, C. Villa, and R. Henderson, *Nature*, 1993, **362**, 770
5. M. L. Applebury and P. A. Hargrave, *Vision Res.*, 1986, **26**, 1881.
6. E. A. Zhukovsky and D. D. Oprian, *Science*, 1989, **246**, 928.
7. T. P. Sakmar, R. R. Franke, and H. G. Khorana, *Proc. Natl. Acad. Sci. USA*, 1989, **86**, 8309.
8. J. M. Baldwin, *EMBO J.*, 1993, **12**, 1693.
9. K. Nakanishi, V. Balogh-Nair, M. Arnabaldi, K. Tsujimoto, and B. Honig, *J. Am. Chem. Soc.*, 1980, **102**, 7945.
10. J. Lugtenburg, *Pure Appl. Chem.*, 1985, **57**, 753.
11. M. B. Bizounok, M. M. Simpson, and J. Herzfeld, To be submitted.
12. M. Auger, K. V. Lakshmi, E. van den Berg, S. Roesselet, H. G. Khorana, S. K. Das Gupta, W. B. D. van Liemt, J. Raap, J. Lugtenburg, J. Herzfeld, and R. G. Griffin, *Biophys. J.*, 1992, **61**, A532.
13. S. Sonar, N. Patel, W. Fischer, and K. J. Rothschild, *Biochemistry*, 1993, **32**, 13 777.
14. E. A. Dratz, J. E. Furstenau, C. G. Lambert, D. L. Thireault, H. Rarick, T. Schepers, S. Pakhlevaniants, and H. E. Hamm, *Nature*, 1993, **363**, 276.
15. L. U. Colmenares, A. E. Asato, M. Denny, D. Mead, J. P. Zingoni, and R. S. H. Liu, *Biochem. Biophys. Res. Commun.*, 1991, **179**, 1337.
16. H. J. M. de Groot, V. Copié, S. O. Smith, P. J. Allen, C. Winkel, J. Lugtenburg, J. Herzfeld, and R. G. Griffin, *J. Magn. Reson.*, 1988, **77**, 251.
17. S. O. Smith, J. Courtin, H. De Groot, R. Gebhard, and J. Lugtenburg, *Biochemistry*, 1991, **30**, 7409.
18. S. O. Smith, H. J. M. de Groot, R. Gebhard, and J. Lugtenburg, *Photochem. Photobiol.*, 1992, **56**, 1035.
19. G. S. Harbison, S. O. Smith, J. A. Pardoen, P. P. J. Mulder, J. Lugtenburg, J. Herzfeld, R. Mathies, and R. G. Griffin, *Biochemistry*, 1984, **23**, 2662.
20. S. O. Smith, H. J. M. de Groot, R. Gebhard, J. M. L. Courtin, J. Lugtenburg, J. Herzfeld, and R. G. Griffin, *Biochemistry*, 1989, **28**, 8897.
21. G. S. Harbison, S. O. Smith, J. A. Pardoen, C. Winkel, J. Lugtenburg, J. Herzfeld, R. Mathies, and R. G. Griffin, *Proc. Natl. Acad. Sci. USA*, 1984, **81**, 1706.
22. M. R. Farrar, K. V. Lakshmi, S. O. Smith, R. S. Brown, J. Rapp, J. Lugtenburg, R. G. Griffin, and J. Herzfeld, *Biophys. J*, 1993, **65**, 310.
23. L. K. Thompson, A. E. McDermott, J. Raap, C. M. van der Wielen, J Lugtenburg, J. Herzfeld, and R. G. Griffin, *Biochemistry*, 1992, **31**, 7931.
24. J. M. Griffiths, K. V. Lakshmi, A. E. Bennett, J. Raap, C. M. van der Wielen, J. Lugtenburg, J. Herzfeld, and R. G. Griffin, *J. Am. Chem. Soc.*, 1994, **116**, 10 178.
25. G. S. Harbison, P. P. J. Mulder, H. Pardoen, J. Lugtenburg, J. Herzfeld, and R. G. Griffin, *J. Am. Chem. Soc.*, 1985, **107**, 4809.
26. G. S. Harbison, S. O. Smith, J. A. Pardoen, J. M. L. Courtin, J. Lugtenburg, J. Herzfeld, R. A. Mathies, and R. G. Griffin, *Biochemistry*, 1985, **24**, 6955.
27. V. Copié, A. E. McDermott, K. Beshah, J. C. Williams, M. Spijker-Assink, R. Gebhard, J. Lugtenburg, J. Herzfeld, and R. G. Griffin, *Biochemistry*, 1994, **33**, 3280.
28. F. Creuzet, A. McDermott, R. Gebhard, K. van der Hoef, M. B. Spijker-Assin, J. Herzfeld, J. Lugtenburg, M. H. Levitt, and R. G. Griffin, *Science*, 1991, **251**, 783.
29. A. E. McDermott, F. Creuzet, R. Gebhard, K. van der Hoef, M. H. Levitt, J. Herzfeld, J. Lugtenburg, and R. G. Griffin, *Biochemistry*, 1994, **33**, 6129.

30. S. O. Smith, J. Courtin, E. van den Berg, C. Winkel, J. Lugtenburg, J. Herzfeld, and R. G. Griffin, *Biochemistry*, 1989, **28**, 237.
31. K. V. Lakshmi, M. Auger, J. Raap, J. Lugtenburg, R. G. Griffin, and J. Herzfeld, *J. Am. Chem. Soc.*, 1993, **115**, 8515.
32. J. B. Ames, S. P. A. Fodor, R. Gebhard, J. Raap, E. M. M. van den Berg, J. Lugtenburg, and R. A. Mathies, *Biochemistry*, 1989, **28**, 3681.
33. K. V. Lakshmi, M. R. Farrar, J. Raap, J. Lugtenburg, R. G. Griffin, and J. Herzfeld, *Biochemistry*, 1994, **33**, 8853.
34. S. P. A. Fodor, J. B. Ames, R. Gebhard, E. M. M. van den Berg, W. Stoeckenius, J. Lugtenburg, and R. A. Mathies, *Biochemistry*, 1988, **27**, 7097.
35. S. O. Smith, I. Palings, V. Copie, D. P. Raleigh, J. Courtin, J. A. Pardoen, J. Lugtenburg, R. A. Mathies, and R. G. Griffin, *Biochemistry*, 1987, **26**, 1606.
36. L. C. P. J. Mollevanger, A. P. M. Kentgens, J. A. Pardoen, J. M. L. Courtin, W. S. Veeman, J. Lugtenburg, and W. J. De Grip, *Eur. J. Biochem.*, 1987, **163**, 9.
37. S. O. Smith, I. Palings, M. E. Miley, J. Courtin, H. J. M. de Groot, J. Lugtenburg, R. A. Mathies, and R. G. Griffin, *Biochemistry*, 1990, **29**, 8158.
38. A. S. Ulrich, M. P. Heyn, and A. Watts, *Biochemistry*, 1992, **31**, 10 390.
39. S. W. Lin and R. A. Mathies, *Biophys. J.*, 1989, **56**, 653.
40. B. A. Lewis, G. S. Harbison, J. Herzfeld, and R. G. Griffin, *Biochemistry*, 1985, **24**, 4671.
41. J. L. Bowers and E. Oldfield, *Biochemistry*, 1988, **27**, 5156.
42. S. L. Helgerson, S. L. Slemson, E. A. Adams, R. D. Renthal, and E. A. Dratz, *Biophys. J.*, 1991, **59**, 475 a.
43. M. Engelhard, B. Hess, D. Emeis, G. Metz, W. Kreutz, and F. Siebert, *Biochemistry*, 1989, **28**, 3967.
44. M. Seigneuret, J. M. Neumann, and J. L. Rigaud, *J. Biol. Chem*., 1991, **266**, 10 066.
45. M. Seigneuret and M. Kainosho, *FEBS Lett.*, 1993, **327**, 7.
46. C. M. Deber, B. J. Sorrell, and G. Y. Xu, *Biochem. Biophys. Res. Commun.*, 1990, **172**, 862.
47. M. Engelhard, S. Finkler, G. Metz, and F. Siebert, *Biophys. J.*, 1992, **61**, A532.
48. M. R. Farrar, L. K. Thompson, R. S. Brown, R. G. Griffin, and J. Herzfeld, *Biophys. J.*, 1991, **59**, 326a.
49. J. G. Hu, B. Q. Sun, M. B. Bizounok, R. G. Griffin, and J. Herzfeld, To be submitted.
50. V. Yu. Orekhov, G. V. Abdulaeva, L. Yu. Musina, and A. S. Arseniev, *Eur. J. Biochem.*, 1992, **210**, 223.
51. R. A. Kinsey, A. Kintanar, and E. Oldfield, *J. Biol. Chem.*, 1981, **256**, 9028.
52. R. A. Kinsey, A. Kintanar, M. D. Tsai, R. L. Smith, N. Janes, and E. Oldfield, *J. Biol. Chem.*, 1981, **256**, 4146.
53. M. A. Keniry, H. S. Gutowsky, and E. Oldfield, *Nature (London)*, 1984, **307**, 383.
54. I. C. Baianu, H. S. Gutowsky, E. Oldfield, *Biochemistry*, 1984, **23**, 3105.
55. J. Herzfeld, C. M. Mulliken, D. J. Siminovitch, and R. G. Griffin, *Biophys. J.*, 1987, **52**, 855.
56. M. Seigneuret, J. M. Neumann, D. Levy, and J. L. Rigaud, *Biochemistry*, 1991, **30**, 3885.
57. K. H. Mayo, A. Schussheim, G. W. Vuiter, R. Boelens, R. Kaptein, M. Engelhard, and B. Hess, *FEBS Lett.*, 1988, **235**, 163.
58. A. S. Arseniev, A. B. Kuryatov, V. I. Tsetlin, V. F. Bystrov, V. T. Ivanov, and Yu. A. Ovchinnikov, *FEBS Lett.*, 1987, **213**, 283.
59. G. V. Abdulaeva, A. G. Sobol, A. S. Arseniev, V. I. Tsetlin, and V. F. Bystrov, *Biol. Membr.*, 1991, **8**, 30.
60. G. B. Cohen, D. D. Oprian, and P. R. Robinson, *Biochemistry*, 1992, **31**, 12 592.
61. J. Shriver, G. Mateescu, R. Fager, D. Torchia, and E. W. Abrahamson, *Nature (London)*, 1977, **270**, 271.
62. J. Shriver, G. D. Mateescu, and E. W. Abrahamson, *Methods Enzymol.*, 1982, **81**, 698.
63. A. Yamaguchi, T. Unemoto, and A. Ikegami, *Photochem. Photobiol.*, 1981, **33**, 511.
64. G. D. Mateescu, W. G. Copan, D. D. Muccio, D. V. Waterhous, and E. W. Abrahamson, in *Synthesis and Applications of Isotopically Labeled Compounds: Proceedings of the First International Symposium*, ed. W. P. Duncan and A. B. Susan, Elsevier, Amsterdam, 1982, p. 123.
65. G. D. Mateescu, E. W. Abrahamson, J. W. Shriver, W. Copan, D. Muccio, M. Iqbal, and D. V. Waterhous, *NATO ASI Ser., Ser. C.*, 1984, **139**, 257.
66. G. S. Harbison, J. Herzfeld, and R. G. Griffin, *Biochemistry*, 1983, **22**, 1.
67. S. O. Smith, G. S. Harbison, D. P. Raleigh, J. E. Roberts, J. A. Pardoen, S. K. Das Gupta, C. Mulliken, R. A. Mathies, J. Lugtenburg, J. Herzfeld, and R. G. Griffin, in *Biomolecular Stereodynamics: Proceedings of the Fourth Conversation in the Discipline Biomolecular Stereodynamics*, 4th edn., ed. R. H. Sarma and M. H. Sarma, Adenine Press, Guilderland, NY, 1986, Vol. 3, p. 159.
68. S. O. Smith, G. S. Harbison, D. P. Raleigh, J. E. Roberts, J. A. Pardoen, S. K. Das Gupta, R. A. Mathies, J. Lugtenburg, J. Herzfeld, and R. G. Griffin, in *Synthesis and Applications of Isotopically Labeled Compounds: Proceedings of the Second International Symposium*, ed. R. R. Muccino, Elsevier, Amsterdam, 1985, p. 239.
69. G. S. Harbison, J. Herzfeld, S. O. Smith, R. Mathies, J. A. Pardoen, P. P. J. Mulder, C. Winkel, J. Lugtenburg, and R. G. Griffin, In *XXIInd Congress AMPERE Magnetic Resonance and Related Phenomena, Proceedings*, ed. K. A. Mueller, R. Kind, and J. Roos, 22nd Zurich AMPERE Commun., Zurich, 1984, p. 461.
70. H. J. M. de Groot, G. S. Harbison, J. Herzfeld, and R. G. Griffin, *Biochemistry*, 1989, **28**, 3346.
71. J. G. Hu, R. G. Griffin, and J. Herzfeld, *Proc. Natl. Acad. Sci. USA*, in press.
72. A. Albeck, N. Livnah, H. Gottlieb, and M. Sheves, *J. Am. Chem. Soc.*, 1992, **114**, 2400.
73. H. J. M. de Groot, S. O. Smith, J. Courtin, E. Van den Berg, C. Winkel, J. Lugtenburg, R. G. Griffin, and J. Herzfeld, *Biochemistry*, 1990, **29**, 6873.
74. J. Herzfeld, S. K. Das Gupta, M. R. Farrar, G. S. Harbison, A. E. McDermott, S. L. Pelletier, D. P. Raleigh, S. O. Smith, C. Winkel, J. Lugtenburg, and R. G. Griffin, *Biochemistry*, 1990, **29**, 5567.
75. A. E. McDermott, L. K. Thompson, C. Winkel, M. R. Farrar, S. Pelletier, J. Lugtenburg, J. Herzfeld, and R. G. Griffin, *Biochemistry*, 1991, **30**, 8366.
76. G. Metz, F. Siebert, and M. Engelhard, *Biochemistry*, 1992, **31**, 455.
77. M. Engelhard, B. Hess, G. Metz, W. Kreutz, F. Siebert, J. Soppa, and D. Oesterhelt, *Eur. Biophys. J.*, 1990, **18**, 17.
78. G. Metz, F. Siebert, and M. Engelhard, *FEBS Lett.*, 1992, **303**, 237.
79. G. S. Harbison, J. E. Roberts, J. Herzfeld, and R. G. Griffin, *J. Am. Chem. Soc.*, 1988, **110**, 7221.
80. M. Engelhard, B. Hess, G. Metz, and F. Siebert, *Biophys. J.*, 1990, **57**, 361a.

81. K. V. Lakshmi, A. E. McDermott, J. Herzfeld, and R. G. Griffin, *Biophys. J.*, 1991, **59**, 327a.
82. L. Zheng, K. W. Fishbein, R. G. Griffin, and J. Herzfeld, *J. Am. Chem. Soc.*, 1993, **115**, 6254.
83. L. L. Z. Cheng, R. G. Griffin, and J. Herzfeld, Submitted.

Biographical Sketches

Judith Herzfeld. *b* 1948. A.B. 1967, Barnard College, Columbia University, USA, Ph.D., 1972, Massachusetts Institute of Technology, USA, M.P.P., 1973, John F. Kennedy School of Government, Harvard University, USA, Faculty in Chemistry, Amherst College, USA, 1973–74, Faculty in Physiology and Biophysics, Harvard Medical School USA, 1975–85, Faculty in Chemistry, Brandeis University, USA, 1985–present. Currently Professor of Biophysical Chemistry and Chair of the Department of Chemistry. Approx. 115 publications. Research specialties: solid state NMR studies of the structure and function of membrane proteins, statistical mechanical studies of entropically driven long-range order in crowded solutions of self-assembling amphiphiles.Jingui G. Hu. *b* 1962. B.S., 1984, M.S. 1987, Tsinghua University, People's Republic of China. Assistant Professor, Tsinghua University, 1987–90. As a Ph.D. candidate in chemistry at Brandeis University, USA, he is conducting solid state NMR studies of bacteriorhodopsin and related model compounds.

Biological Systems: Spin-3/2 Nuclei

Charles S. Springer Jr.
Brookhaven National Laboratory, Upton, NY, and State University of New York, Stony Brook, NY, USA,

1	Introduction	1
2	Types of Spin-3/2 Spectra	1
3	The Debye Model	1
4	Discrete Exchange Models	2
5	The Berendsen Model	3
6	Experimental Discrimination of Spectral Types	5
7	Experimental Discrimination of Signals from Physiological Compartments	8
8	^{23}Na MR Imaging	11
9	Related Articles	11
10	References	11

1 INTRODUCTION

In biological systems, there are three species of significance that have major isotopes with nuclear spin-$\frac{3}{2}$. These are mainly present as monovalent aquo ions. They are $^{23}Na^{+}$ and $^{35}Cl^{-}$, which are mostly extracellular, and $^{39}K^{+}$, which is concentrated in the cytoplasm. The NMR signal from the first is much stronger than those from the other two. In fact, it is weaker than only the $^{1}H_2O$ resonance and, in some regions, the ^{1}H signal from fat.[1] We have recently reviewed the study of these ionic resonances,[2] and have cited 20 other reviews of this much investigated subject. The great interest stems from two tantalizing possibilities. The first is that the dominance of the quadrupolar relaxation mechanism for the NMR signals of these spins can allow a sensitive characterization of the molecular environments in which they find themselves. The second is that NMR could offer a noninvasive way of monitoring the transcytolemmal concentration gradients of these species, the energies of which are the sources of their main biochemical roles.[1] The facts that the compartmental resonances of each of these species are isochronous have hindered realization of both of these goals.

2 TYPES OF SPIN-3/2 SPECTRA

The isolated spin-$\frac{3}{2}$ nucleus provides for a one-spin, four-level system. This can manifest itself in four different types of spectra, depending on the nature of the spin dynamics and the nature of the molecular environment. Figure 1 shows rotating frame energy level diagrams and actual one-pulse single quantum (SQ) ^{23}Na spectra exemplifying each of these four types. The classification is one we proposed in 1988.[3] Thus, the *type-a spectrum* (on the right in Figure 1) is a single-crystal-like spectrum. There is at least a *residual* EFG projection present at the nucleus that causes shifts in the level energies and the average spectroscopic splitting factor, $\bar{\omega}_Q$, to be nonzero. The areas of each of the two satellite peaks is 0.3, relative to that of the center peak of 0.4. Even though the three population differences (between states with adjacent levels) are essentially equal at Boltzmann equilibrium, the NMR signal intensity measures this difference as weighted by the magnetic moment *projection* of the state.[4] This is the lowest spin quantum number for which unequal peaks areas are manifest. Although the type-a spectrum in Figure 1 looks like that of a true single crystal, the value of $\bar{\nu}_Q$ ($\sim$17 kHz) is one or two orders of magnitude smaller. It is actually the motionally narrowed spectrum from an oriented liquid crystal. The same relationship is true for the *type-b spectrum* in Figure 1, which looks like that of a true microcrystalline powder, but is actually that of an unoriented liquid crystal. It is, nonetheless, an inhomogeneous spectrum, as far as the satellite transitions are concerned. The *type-c spectrum* is a 'homogeneous' ('biexponential, super-Lorentzian') spectrum, in which the satellite peaks have essentially coalesced into a single, broad, homogeneous peak which is effectively isochronous with the narrower center peak.[2] Again, $\frac{3}{2}$ is the lowest spin quantum number for which this kind of spectrum can occur. Finally, the *type-d spectrum* is the extreme narrowed case, represented in Figure 1 by a ^{23}Na spectrum from an aqueous solution of NaCl.

3 THE DEBYE MODEL

One can understand the progression from a type-d spectrum to a type-a spectrum in terms of a random fluctuation of the EFG tensor strength and/or orientation that can be described with a single correlation time, τ_c—this is the Debye model.[2] Thus, the type d spectrum obtains when τ_c is much smaller than the Larmor period, ${\omega_L}^{-1}$ (ω_L is the Larmor frequency), usually of the order of nanoseconds. In this case, $\bar{\omega}_Q$ is zero, even if the fluctuations of the EFG projection are quite large (for the ^{23}Na aquo ion itself, ${\nu_Q}^{rms}$ is about 1 MHz but τ_c is less than picosecond[2]). As τ_c increases and passes through ${\omega_L}^{-1}$, the spectrum changes from type d to type c. In this case, however, $\bar{\omega}_Q$ remains zero. If τ_c continues to increase, the fluctuation becomes slower, and passes through $({\omega_Q}^{rms})^{-1}$, the value of $\bar{\omega}_Q$ becomes nonzero and the spectrum changes from type-c to type-b or type-a, depending on the macroscopic order of the sample. If the sample is disordered, say a powder with a random distribution of the orientations of the EFG tensor, then a type-b spectrum emerges. A simulation of a spectrum evolving from type-c to type-b with the lengthening of a single τ_c is shown in Figure 2 (Figure 1 of Eliav et al.[5]). The values of τ_c are: 10^4 ns, 10^3 ns, 80 ns, and 20 ns [panels (a)–(d), respectively]. A clear type-b spectrum is seen in panel (a). Because the value of ν_Q is so (unrealistically) large (12.5 MHz), a clear type-c spectrum is observed only for the case when τ_c is 20 ns [panel (d)], and a second-order frequency shift of the center peak is seen in the insets in Figure 2. If the simulation had been for a completely ordered sample, say a single crystal with a unique site, then a type-a spectrum would have emerged in panel (a).

The Debye model is conceptually the simplest for the quadrupolar relaxation mechanism. It has been found, however, that it is inconsistent with experimental observations on the ^{23}Na resonances from such seemingly simple systems as

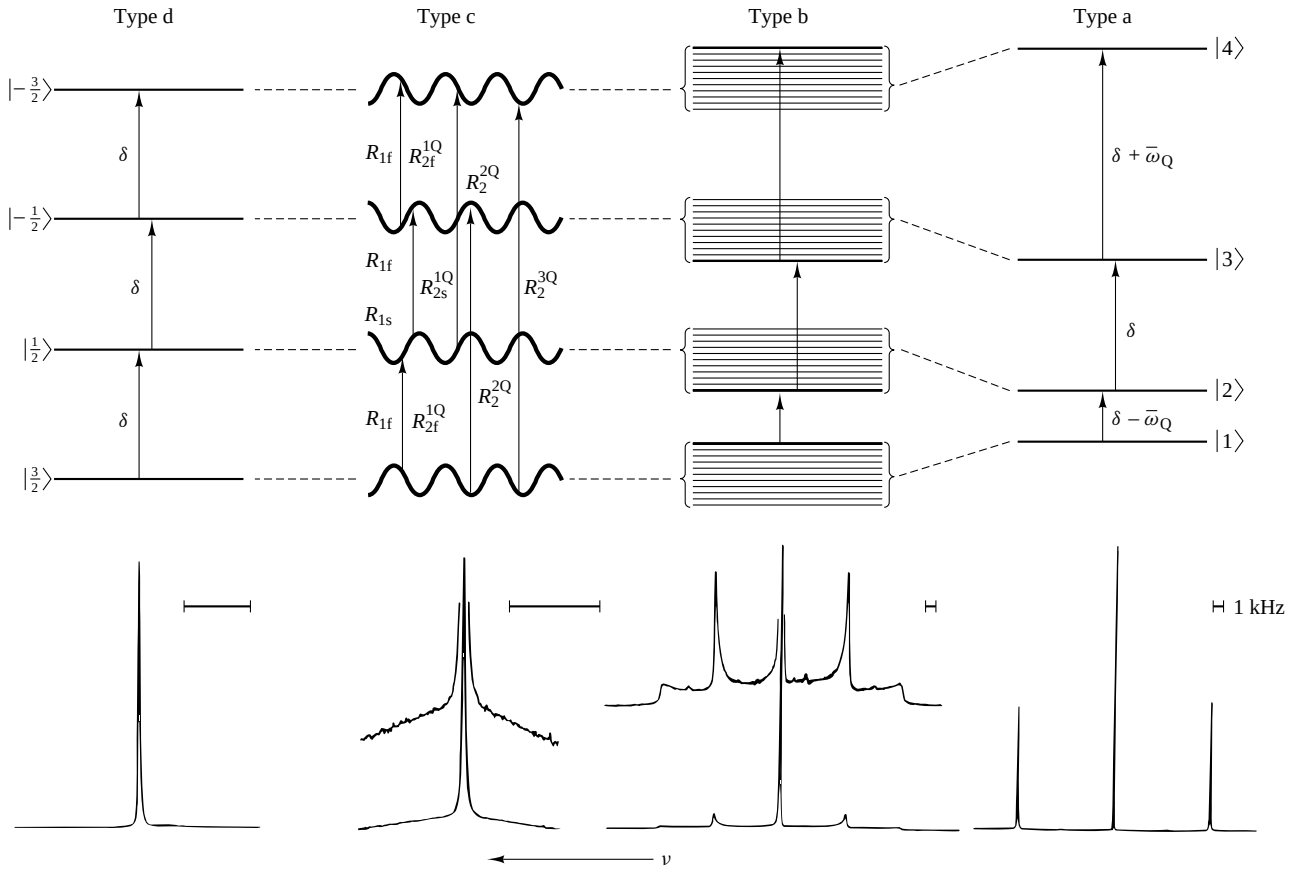

Figure 1 Rotating frame energy level diagrams for isolated $I = \frac{3}{2}$ systems. Four types of motionally narrowed SQ spectra are possible (a, b, c, and d). Representative ^{23}Na spectra are seen below each of the energy level diagrams. The type-d spectrum is that of NaCl in H_2O. The type-c spectrum is that of Na^+ in an aqueous solution that has a high concentration of micelle-solubilized gramicidin channels. The type-b and type-a spectra are of Na^+ in aqueous suspensions of unoriented and oriented dodecyl sulfate micelles, respectively. (Reproduced from W. D. Rooney and C. S. Springer, Jr., *NMR Biomed.*, 1991, **4**, 209)

suspensions of pure bovine serum albumin in saline solution[6] and agarose gel soaked in saline solution (see ***Relaxation of Quadrupolar Nuclei Measured via Multiple Quantum Filtration***.). Thus, it is not surprising that it also does not apply to the intracellular or extracellular ^{23}Na signals from suspensions of yeast cells.[6]

4 DISCRETE EXCHANGE MODELS

Very popular models that can sustain more complexity than the Debye picture have invoked equilibrium chemical exchange between two distinct sites that have different quadrupolar properties. These sites can be characterized by their location in the Debye continuum.[2] Thus, *James–Noggle exchange*[7] is that between two different type-d sites and can yield only a type-d spectrum as a resultant. *Bull exchange*[8] is that between a type-d site and a type-c site and can yield either type of resultant spectrum, depending on the lability of the exchange on the timescale determined by the properties of the two sites. *Chan exchange*[9] is that between a type-d site and a type-a site. It can produce a type-c resultant spectrum, as well as a type-d or a type-a spectrum, depending on the lability of the exchange, or a type-b spectrum if there is a random orientation distribution of the type-a sites, which are otherwise identical. A very informative simulation of a Chan exchange equilibrium, showing all three resultant spectra that appear as a function of the exchange lifetime, is shown in Figure 3. (Figure 2 in Eliav et al.[5]). Here, there are equal populations of a Debye type-d site (with ν_Q = 0.3 MHz and τ_c = 0.1 ns) and a Debye type-a site [with (again) ν_Q = 12.5 MHz and $\tau_c = 4 \times 10^3$ ns]. Since there is a random distribution of the orientations of the latter, a clear type-b spectrum of this population is observed at the longest exchange time, 5×10^4 ns (bottom). The exchange time shortens on going up Figure 3. When τ_{ex} = 10 ns, a type-c resultant spectrum is seen. When τ_{ex} = 0.001 ns (top), a type-d resultant spectrum is manifest. It is important to note, however, that the isothermal James–Noggle, Bull, or Chan two-site exchange models each have six independent parameters (the relative population of one site, the values of ω_Q^{rms} for each site, the values of τ_c for each site, and the preexchange lifetime in one site). If temperature-dependent data are fitted, the number of parameters rises to at least eight.

Interpretations using discrete exchange models (DEMs) are always couched in terms of true chemical 'binding' of the ion in the more severe (in the quadrupolar sense) site; that which is type-c or type-a. This is true whether the exchange is fast or relatively slow. This may be realistic in some model situations, in which a characterized, real binding site is present

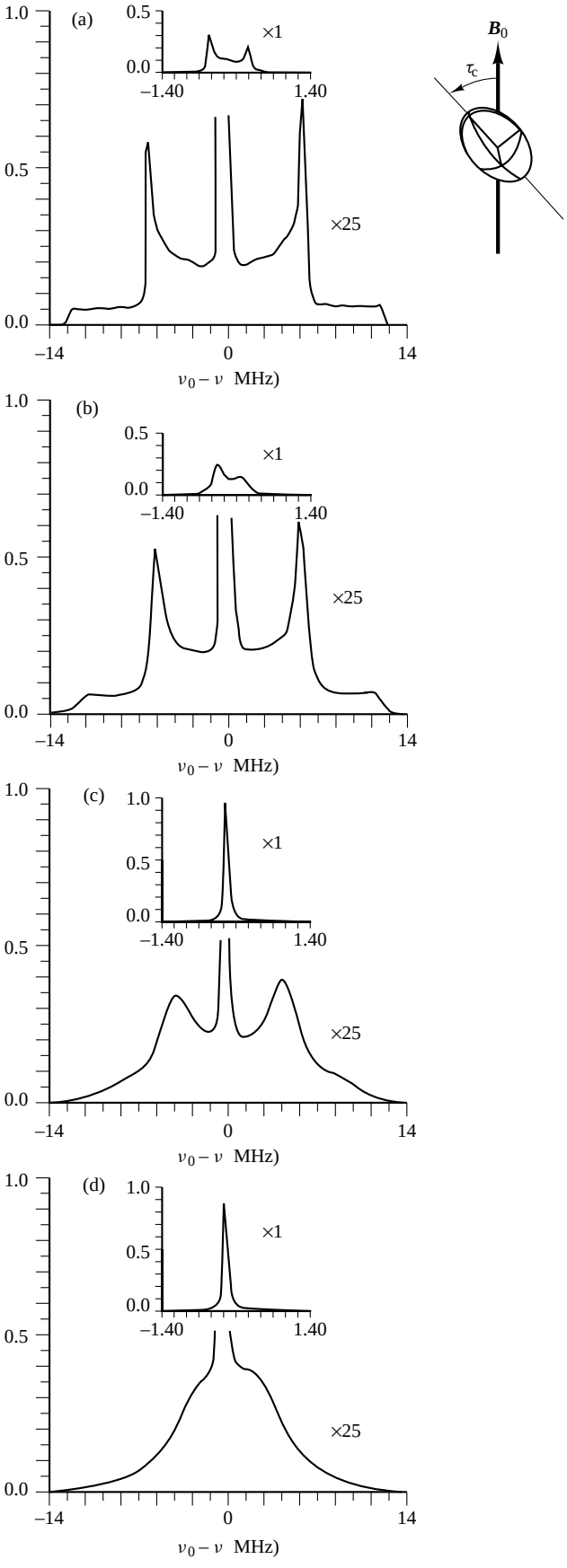

in some quantity. For example, the type-c spectrum in Figure 1 is that of Na^+ in an aqueous solution that has a high concentration of micelle-solubilized gramicidin channels.[10] However, in tissue, the concentration of well-defined binding sites is much, much less than the concentration of ions.[2] This is why DEM fittings of tissue data always result in a very small population in the bound site (1% or less) but with very severe quadrupolar properties (large ν_Q^{rms} and/or τ_c) required to achieve agreement. An additional problem for tissue is that though the concentration of known binding sites for these ions is tiny, the kinds of binding sites are varied. A three-site exchange model[11] requires at least 13 independent parameters. Analyzing the tissue situation with a realistic DEM is rather untenable.

It would be fortunate if some other mechanism dominated. Thus, it is significant that residual quadrupolar splitting has been observed for systems (co-ions and noble gases)[2] in which it is highly unlikely that there can be discrete binding sites.

5 THE BERENDSEN MODEL

In 1973, Berendsen and Edzes[12] described a model that seems to us to be much more realistic. We have elaborated on it.[2,6] If focuses first on the EFG tensor projection fluctuations caused by motions of the inner hydration shell of the ion. As pointed out above, for the $^{23}Na^+$(aq) ion, these are very powerful and very rapid. Superimposed on these are slower modulations, usually also of lower amplitudes, which are generated as the aquo ion diffuses about and encounters macromolecules and/or lipid assemblies. These low-frequency modulations could simply be due to distortions of the inner hydration shell during outer-sphere collisions with the macromolecules. These would surely be more frequent than occurrences of actual inner-sphere binding to macromolecular loci, though the latter would also modulate the EFG. The preponderance of negative fixed charges found on natural macromolecules and lipid assemblies could serve to increase the occurrence of inner sphere complexation in the cases of Na^+(aq) and K^+(aq), but it could just as well increase the frequency of outer-sphere collisions by increasing the effective concentrations of the mobile cations in the diffuse double layers. The very rapid inner-sphere fluctuations are ignored in Figure 1, but the slow modulation of the level energies is suggested for the type-c diagram.

To complete the picture of the Berendsen mechanism, one needs the concept of a sample *domain*, as experienced by a diffusing aquo ion. A domain must be at least as large as the average volume sampled by the diffusional excursions during the lifetime of an NMR coherence. The RMS three-dimensional random walk distance can be estimated [$r^{rms} = (6Dt)^{\frac{1}{2}}$] if a value for the diffusion coefficient, D, is assumed. The diffusion time, t, might be taken to be the time for the

Figure 2 A spectral simulation of the Debye model. There is only one site, with ν_Q = 12.5 MHz, but with a random distribution of orientations. The values of τ_c are: 10^4 ns (a), 10^3 ns (b), 80 ns (c), and 20 ns (d). A type-b spectrum is seen in (a) and a type-c spectrum is seen in (d). The value of ν_L is 94.5 MHz. The insets depict the center peak. (Adapted from Figure 1 of U. Eliav, A. Baram, and G. Navon, *J. Chem. Phys.*, 1988, **89**, 5584)

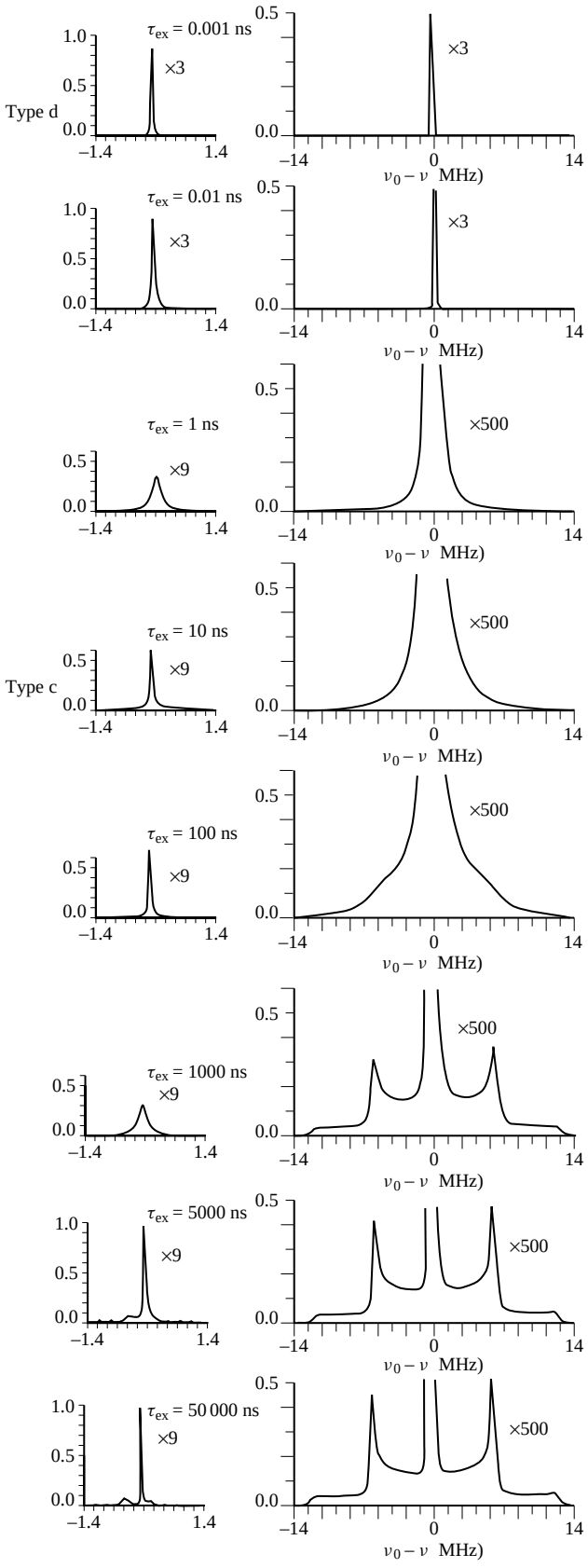

coherence to fall to 10% of its initial value (i.e. t = 2.3 T_2). If the diffusion is isotropic, then the minimum domain is a sphere with a radius of r^{rms}. Now, the fluctuations of the inner hydration sphere are certainly isotropic. However, a macromolecule appears as a more or less two-dimensional surface to a diffusing ion. The distortion caused by its encounter is not isotropic but has a direction; the normal to the surface in the simplest picture. If the surface normals encountered in the average NMR diffusional volume of an ion are not randomly oriented (relative to $\boldsymbol{B}_0$), then the slow fluctuation will be anisotropic, and will not average to zero.

The type-a and type-b spectra shown in Figure 1 were obtained from suspensions of cylindrical dodecyl sulfate micellar liquid crystals.[2,3,6] Figure 4 illustrates the Berendsen model for these situations. A sample domain is suggested as a region enclosed by heavy lines. Within each domain in these liquid crystalline samples, the micelle cylinders are shown as being completely parallel. In Figure 4(a), the cylindrical axes in all domains are parallel to each other, and to $\boldsymbol{B}_0$, in this case. Although a Na^+(aq) ion is free to diffuse in the aqueous space between the cylinders (an average NMR diffusion volume is less than the size of a domain), the micellar surfaces it encounters all have their normals perpendicular to $\boldsymbol{B}_0$. Thus, the slow modulation is never averaged to zero. Although the diffusional motion considerably narrows the spectrum from what it would be for a single crystal with Na^+ bound to a dodecyl sulfate head-group (splitting, probably of the order of megahertz), it remains perfectly single-crystal like. This is because the sample of oriented liquid crystals has macroscopic order as well as microscopic order. Berendsen and coworkers first reported this in 1971 with oriented, hydrated DNA fibers (ref. 3 in Berendsen and Edzes[12]). Figure 4(b) depicts a similar situation, except that the liquid crystalline domains are no longer oriented. Although there remains microscopic order within a domain [it is identical to that in Figure 4(a)], and thus each domain is of type-a, the viewer is to imagine a random distribution of the cylindrical axes from different domains, i.e. macroscopic disorder. This would give rise to the inhomogeneous broadening of the satellite peaks seen in the type-b spectrum in Figure 1, provided the true sample domains are large enough relative to the average NMR diffusion volume that interdomain exchange is sufficiently slow. The ensemble of these domains should still be considered a single population, in the chemical sense. In this picture, there is really no such thing as a type-b domain; if there is intradomain disorder, a type-c spectrum results.

What about the Berendsen model for the type-c spectrum? Figure 4(c) illustrates a small region of human blood at one million times magnification (for the original), such that only macromolecules are shown. The water and monovalent aquo ion molecules are omitted for clarity. Let us concentrate initially on the extracellular (plasma) space [top of Figure 4(c)] where Na^+ is concentrated. For a $^{23}Na^+$ spin out in the bulk

Figure 3 A spectral simulation of the Chan discrete exchange model. There are equal populations of a Debye type-d site (ν_Q = 0.3 MHz, τ_c = 0.1 ns) and a Debye type-a site (ν_Q = 12.5 MHz, τ_c = 4 × 10^3 ns). There is a random distribution of orientations of the latter. Thus, it gives rise to a type-b spectrum at the longest exchange time (5 × 10^4 ns; bottom). The value of the exchange time τ_{ex} is given for each spectrum. The left panels show the center peak(s). (Adapted from Figure 2 of Eliav et al.[5])

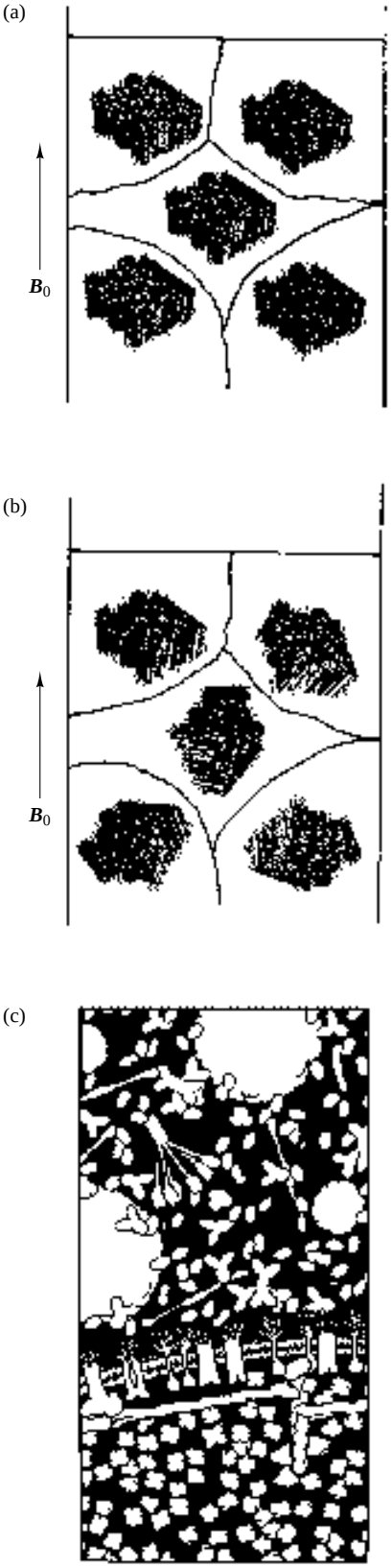

of the plasma well away from the external erythrocyte surface, the macromolecular surfaces it may encounter in its diffusional excursions are apt to have randomly oriented normals. The average distance between these surfaces is about 10 nm (100 Å). It has been demonstrated that ^{23}Na spectra from dense suspensions of more or less globular proteins and polymeric gels in saline are of type-c.[6,15,16] (See also ***Relaxation of Quadrupolar Nuclei Measured via Multiple Quantum Filtration***.) Thus, in addition to the rapid modulations of the inner hydration sphere, the slow fluctuation of the EFG by diffusion is also isotropic, and averages to zero.

It is much more difficult to make an explicit statement of the Berendsen model than of a DEM. Nevertheless, this has been done in the form of continuous diffusion models (reviewed by Rooney and coworkers[2,6]), models with distributions of τ_c values,[2,6,17] and what appears to be a Debye model with a distribution of ω_Q^{rms} values.[18]

6 EXPERIMENTAL DISCRIMINATION OF SPECTRAL TYPES

Step 2 of the comprehensive approach we suggested in 1991[2] was the determination of the *spectral type* of each resonance. Inspection of the one-pulse SQ spectra displayed in 1 would lead one to imagine that this is straightforward. Such is rarely the case, however, for at least two reasons. First, the extremely high signal-to-noise (S/N) values evident in Figure 1 are really quite necessary for the discrimination of the type-b, -c, and -d spectra seen there. The second reason is that the inhomogeneous width of the type-b spectrum shown in Figure 1 is quite large compared with the intrinsic linewidths for the spectral peaks of those liquid crystalline samples (see the type-a spectrum). Recently, it has been found that some more-biological systems, and some human tissues in vivo yield type-b spectra with very small inhomogeneous widths, which are quite similar to the intrinsic spectral linewidths.[15,16,18–20] (A DEM interpretation of these results would require the existence of at least one Chan exchange equilibrium.) Effecting this determination requires the creation of the double- or triple-quantum (DQ or TQ) coherences (denoted by 2Q and 3Q on the type-c diagram in Figure 1), which are (indirectly) detectable for all but the type-d spectra.

The description of multiple quantum coherence experiments on these single (isolated) spin, four-level systems with spherical (irreducible) tensor bases for the density matrix operators has proved to be most informative (see ***Relaxation of Quadrupolar Nuclei Measured via Multiple Quantum Filtration***). These tensor operators are often represented by

Figure 4 Illustrations depicting sample domains that give rise to the various spectral types according to the Berendsen model. (a, b) Domains in liquid crystalline samples comprising cylindrical micelles. In (a), the domains are all oriented, parallel to $\boldsymbol{B}_0$, in this case, and, in fact, *by* $\boldsymbol{B}_0$ for the micelles giving rise to the type-a spectrum in Figure 1. In (b) the domains are to be considered as randomly oriented. This would give rise to a type-b spectrum. (c) A small portion of human blood, 118 nm × 228 nm (1180 Å × 2280 Å), containing a region of plasma (top) and erythrocyte cytoplasm (bottom), separated by a section of cytolemma and cytoskeletal network (middle). [(a,b) Modified from Khetrapal et al.[13]; (c) reproduced from D. S. Goodsell,[14] *Am. Sci.*, 1992, **80**, 457]

Table 1 Spectral Types and Spherical Tensor Representations

	Type			
Tensor	d	c	b	a
$\boldsymbol{T}_{00}$	A	A	A	A
$\boldsymbol{T}_{10}$	A	A	A	A
$\boldsymbol{T}_{20}$	–	–	A	A
$\boldsymbol{T}_{30}$	–	A	A	A
$\boldsymbol{T}_{11}$	D	D	D	D
$\boldsymbol{T}_{21}$	–	–	I	I
$\boldsymbol{T}_{31}$	–	I	I	I
$\boldsymbol{T}_{22}$	–	–	I	I
$\boldsymbol{T}_{32}$	–	I	I	I
$\boldsymbol{T}_{33}$	–	I	I	I

[a]A, accessible; D, directly detectable; I, indirectly detectable.

the symbols, $\boldsymbol{T}_{li}$, where l is the rank (statistical multipolar order) and i is the component (coherence order).[2] The rank index, l, conveys information about the eigenstate populations,[21] while the order index, i, describes the coherent superpositions of eigenstates. In the present case, the l index can take all integral values from 0 to 3 and the i index can take all integral values from 0 to $\pm l$. In this article, when we give an i value we mean it to represent $\pm i$. Table 1 indicates which eigenstate populations are accessible and which coherences are directly and indirectly observable for the four spectral types. Figure 5 depicts the eigenstate populations $\boldsymbol{T}_{00}$, $\boldsymbol{T}_{10}$, $\boldsymbol{T}_{20}$, and $\boldsymbol{T}_{30}$, the type-a and type-b single quantum spectra that are detected when $\boldsymbol{T}_{11}$ evolves from the $\boldsymbol{T}_{21}$ coherence, and the type-a, type-b, and type-c single quantum spectra that are detected when $\boldsymbol{T}_{11}$ evolves from the $\boldsymbol{T}_{31}$ coherence.

Jaccard et al.[23] were the first to point out that, though the third rank tensors are accessible to $I = \frac{3}{2}$ spins displaying type-a, -b, or -c spectra, the second-rank tensors are not accessible to type-c spins (Table 1, Figure 5) Thus, they suggested the demonstration of $\boldsymbol{T}_{21}$ as a clear proof of type-a or type-b. They proposed editing the spectrum by passage of the magnetization through a DQ filter designed to annihilate all but that from the $\boldsymbol{T}_{21}$ coherence. The absence in $\boldsymbol{T}_{11}$ from $\boldsymbol{T}_{21}$ (Figure 5) of the center peak present in $\boldsymbol{T}_{11}$ (Figure 1) aids in the inference that $\boldsymbol{T}_{21}$ existed.

Kemp-Harper and Wimperis[19a] have argued in favor of displaying the absorption/emission singly antiphase mode of $\boldsymbol{T}_{11}$ from $\boldsymbol{T}_{21}$ shown in Figure 5, because of the resemblance the dispersion mode type-b spectrum from singly antiphase $\boldsymbol{T}_{21}$ (see 1 in Eliav and Navon[18]) can bear to the absorption/emission mode spectrum arising from doubly antiphase $\boldsymbol{T}_{31}$ for either type-c or type-b (Figure 5) when the inhomogeneous width is similar to the intrinsic linewidth, apparently a common situation. However, when one has the superposition of spectra from both the $\boldsymbol{T}_{21}$ and $\boldsymbol{T}_{31}$ representations of a single population of type-b or type-a spins, the two spectral components cannot be simultaneously phased in their absorption/emission modes. They are shown this way in Figure 5 primarily for their pedagogical value in reflecting the relative eigenstate populations.

Employing experiments of this kind, Navon and coworkers[18,20] and Kemp-Harper and Wimperis[19a] have examined ^{23}Na spectra from bovine cartilage, which may serve as a model for interstitial extracellular space, the primary locus of tissue Na^+. These two groups each find that there is at least one population of Na^+ giving rise to a type-b spectrum, although the experimental results depend on the exact nature of the cartilage. Nasal cartilage gives rise to a residual splitting $2\bar{\nu}_Q$ of 550 ($\pm$76) Hz,[18] while the articular leg or ligament cartilage yields a value almost an order of magnitude greater.[19a] The major macromolecular constituents of cartilage are proteoglycan and collagen fiber polymers, the former bearing a significant net negative fixed charge.[20] Eliav and Navon found that hydrated collagen fiber powder could yield a broader type-b spectrum than their cartilage sample.[18] The fact that a 'soluble form of denatured collagen' (gelatin) does not give a type-b spectrum[18] suggests that the microscopic order experienced by the ^{23}Na spins is 'associated with the helical structure of the collagen fiber'. It is possible that the cylindrical liquid crystalline micelles suggested in Figure 4(b) model this situation. In the actual liquid crystals represented in Figure 4(b), however, the parallel cylinders within a domain can be as close as 10 nm (100 Å),[6] depending on the extent of hydration, and thus can give rise to such values of $2\bar{\nu}_Q$ as the 34000 Hz observed the type-b spectrum in Figure 1. It seems most likely that the residual splitting produced by microscopic order in a Berendsen domain is proportional to the degree of *parallelity* (to coin a new word) in the macromolecular structure and inversely proportional to the *spacing* of the more or less parallel surfaces. Thus, one may expect very large splitting from the extracellular Na^+ in cell junction gaps, where the degree of parallelity is very high and the adjacent exterior cell surfaces can come within 2.7 nm (27 Å) of each other, over an area very large on the microscopic scale.[24]

Although there is less Na^+ inside cells, the intracellular ^{23}Na (Na_i) signal has also been studied with DQ and TQ filtering techniques. Shinar et al.[15] and Tauskela and Shoubridge[16] have each found at least one population of Na^+ inside human erythrocytes that gives rise to a type-b spectrum. The two laboratories agree that the residual splitting is very small: $2\bar{\nu}_Q$ is 40–50 Hz; the spectrum is almost type-c. From various ancillary experiments, they also agree in the suspicion that the type-b spectrum arises from the interaction of Na^+ with the intact cytoskeletal network comprising the spectrin and actin proteins. A portion of this network is seen just inside the section of cytoplasmic membrane depicted in Figure 4(c). Of course, the cytoskeletal network also gives rise to the unusual biconcave discoid shape of the erythrocyte, which brings the internal faces of the cytolemma, and the network, to within about 1500 nm (15000 Å) of one another at the closest point—the disk diameter is about 7700 nm (77000 Å).[25a] Thus, it is not clear whether it is simply the shape of the cells or direct interaction with the network that is the source of the type-b spectrum. The fact that there is at least one population of extracellular Na^+ (Na_o) in the erythrocyte pellet that also exhibits a type-b spectrum ($2\bar{\nu}_Q \approx 25$ Hz) argues in favor of the former.[16] The interior of each cell could be considered as one, large type-a domain. If it were possible to orient the cells all in one direction, and thus to produce macroscopic order, the spectra of these Na_i populations should become type-a. This still would not completely settle the issue, however, because the cytoskeletal networks from all the cells would also have been macroscopically ordered. Experiments have not yet ruled out the existence of an additional Na_i population, in

slow exchange, that exhibits a type-c spectrum. Such studies constitute step 3 of our comprehensive approach.[2]

Disk-shaped and rod-shaped cells have some degree of parallelity, which they impose on their intracellular and extracellular (in a pellet) spaces, though the spacing may be quite large on the microscopic scale. What about the situation for spherically shaped cells? If the cell is large enough such that the curvature of the surface is small relative to the average NMR diffusional volume, a Na_i^+ aquo ion near the cytolemma would sense a distinct orientation of the surface normal, as if it were in a type-a domain. However, there is absolutely no parallelity and the residual EFG dies away as the spin wanders away from the surface. It seems quite clear that out in the bulk of the cytoplasmic soup, the ^{23}Na nucleus experiences a microscopically disordered (isotropic) macromolecular environment. Figure 4(c) depicts a portion of the erythrocyte cytoplasm—the surfaces of the hemoglobin molecules, which constitute the vast majority, are about 5 nm (50 Å) apart, on average. The cytoplasms of other cells are quite similar, if one disregards the macromolecule variety.[14] Recall the determinations of type-c spectra reported above for dense protein solutions not contained by a cytolemma. However, recent results suggest that the macromolecular variety can be quite important.[25b]

Although we did not conduct the most sensitive test for type b (the DQ filter for $\boldsymbol{T}_{11}$ from $\boldsymbol{T}_{21}$ described above), we have studied the $^{23}Na_i$ signal from the yeast cell fairly exhaustively.[2,6] Our results are quite consistent with a single population of Na^+ exhibiting a type-c spectrum. *S. cerevisiae* yeast cells are spherical with an internal diameter of about 5000 nm (50 000 Å).[6] In the lifetime of the shortest transverse coherence for the $^{23}Na_i$ resonance, we estimated that the Na^+ aquo ion could sample an average NMR diffusion volume represented by a sphere with diameter of about 3400 nm (34 000 Å); i.e. less than the entire intracellular space.[6] Since we do not see evidence of significant amounts of different populations of Na_i in slow exchange, the conclusion is that the microscopic environment is rather uniform throughout the cell. The huge ribosomal molecules[14] are crucial in determining the type-c character of the $^{39}K_i$ resonance in *Escherichia coli*[25b] and other 'viable' cells such as yeast.

The family of multiple quantum filtering techniques (reviewed in Rooney and Springer;[2] see also ***Relaxation of Quadrupolar Nuclei Measured via Multiple Quantum Filtration***) are most elegant for discriminating the spectral type and accurately measuring the relaxation rate constant (R; there are six such constants and they are indicated on the energy level diagram for the type-c spectrum in Figure 1) values

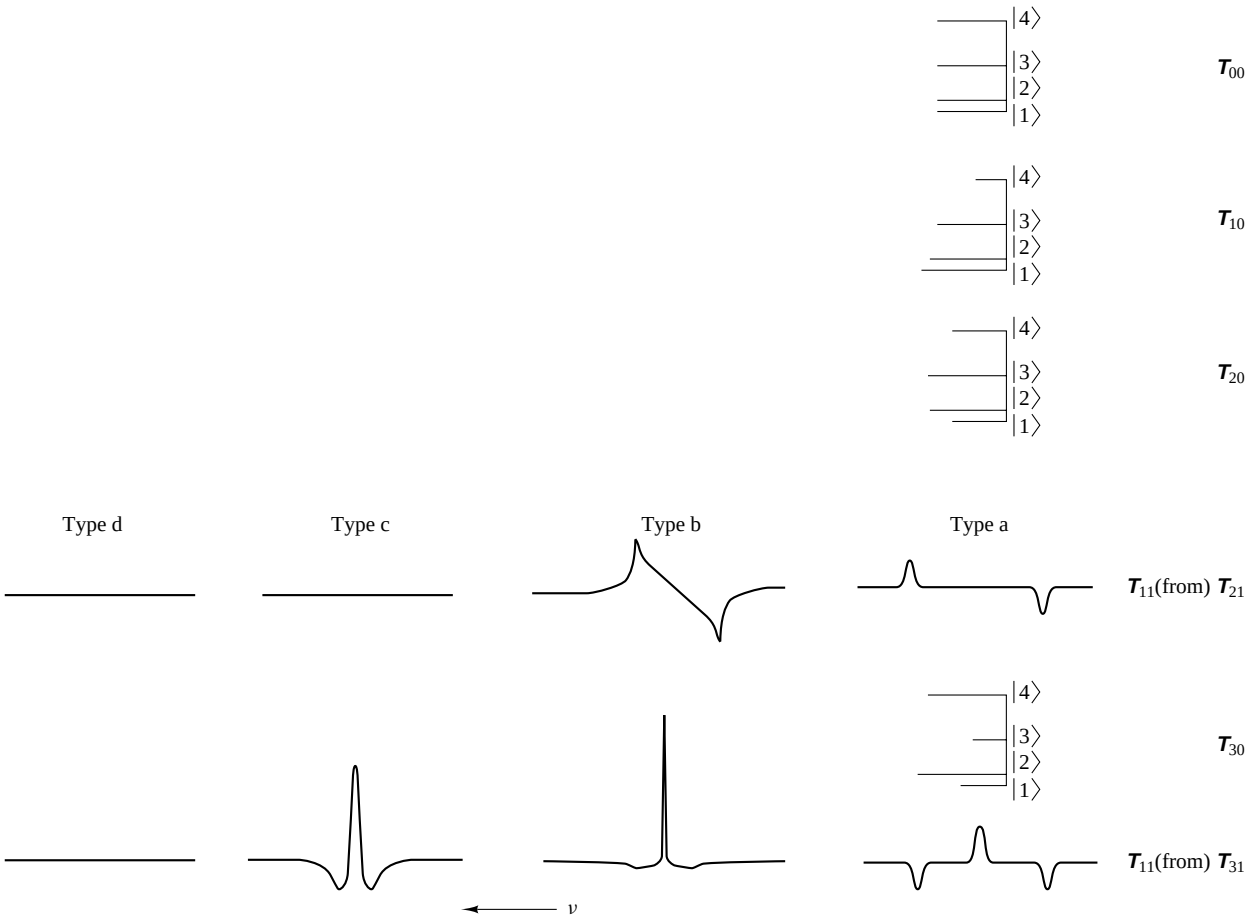

Figure 5 Depictions of eigenstate populations ($\boldsymbol{T}_{00}$, $\boldsymbol{T}_{10}$, $\boldsymbol{T}_{20}$, and $\boldsymbol{T}_{30}$), and observable SQ coherences ($\boldsymbol{T}_{11}$) that evolve exclusively from higher rank spherical tensor representations of the density matrix ($\boldsymbol{T}_{21}$ and $\boldsymbol{T}_{31}$). For $\boldsymbol{T}_{00}$, $\boldsymbol{T}_{10}$, $\boldsymbol{T}_{20}$, and $\boldsymbol{T}_{30}$, the level splitting is analogous to that in Figure 1. The lengths of the horizontal lines represent the relative eigenstate populations. Adapted from Fig. 4. Halstead et al.[21] The type-a coherences are adapted from 1 Sanctuary[22]. For the simulations of type-b coherences, that from $\boldsymbol{T}_{21}$ is reproduced with permission of S. Wimperis from Kemp-Harper et al.,[19b] and that from $\boldsymbol{T}_{31}$ is reproduced with permission of G. Navon from U. Eliav and G. Navon[18]

necessary for the molecular interpretation of the resonance. However, since the multiple quantum coherences are formally forbidden, and must be detected indirectly, there is a signal intensity penalty associated with their use. The maximum intensity for the DQ-filtered T_1 experiment is 8% (measured by peak areas) while that for the DQ-filtered T_2 experiment is 15%, relative to the one-pulse SQ signal intensity acquired in the same time.[2] The DQ-filtered experiment for $\boldsymbol{T}_{21}$ described above has a maximum intensity of 10–12%.[19] The TQ-filtered T_2 experiment has a maximum intensity of 22% (see ***Relaxation of Quadrupolar Nuclei Measured via Multiple Quantum Filtration***), but it does not discriminate type-b spectra from type-c ones (Table 1).[19a] A Jeener–Broekaert experiment (which filters for $\boldsymbol{T}_{20}$, just as diagnostic for type-b spectra, Table 1) is a little more sensitive than the $\boldsymbol{T}_{21}$ experiment.[19a,b] The use of gradients for multiple quantum filtering (instead of phase cycling) is expected to yield even lower intensities.[26] Of course, these are *maximum* intensities. The results obtained in actual practice are even smaller.[16,27] For example, Tauskela and Shoubridge[16] found that the DQ-filtered T_2 intensity never rose above 2.5% in their studies of erythrocyte suspensions.

Following Pekar et al.,[28] there have been a number of schemes suggested for the use of multiple quantum filter experiments to discriminate compartmental signals from tissue samples. There are two aspects that make them less than ideal, however. The first is their reduced sensitivity. One hates to dispense with one order of magnitude of an already weak signal, especially in an in vivo and/or imaging situation; though this has been tried for the latter.[29,30] The second aspect is that they do not quantitatively discriminate the compartments—because of the significant overlap of compartmental spectral types (see ***Relaxation of Quadrupolar Nuclei Measured via Multiple Quantum Filtration***)—and end up requiring some shift or relaxation reagent anyway.

7 EXPERIMENTAL DISCRIMINATION OF SIGNALS FROM PHYSIOLOGICAL COMPARTMENTS

We now turn to step 1 of the comprehensive approach that we suggested in 1991.[2] It is interesting that the most recent developments in the oldest method make it the most sensitive and the most quantitative, if it can be conducted properly. This is the acquisition of one-pulse SQ spectra in the presence of a shift reagent (SR), a paramagnetic molecular anion. The membrane-impermeant SR species can enter only certain compartments and shift the resonance frequency of only the $^{23}Na^+$ and $^{39}K^+$ ions contained in those compartments. It does this due to a rapid chemical binding equilibrium with the monovalent cation. The SR approach was introduced, independently, by our laboratory[31] and another[32] in 1982. We reviewed the development of SRs in 1990.[33] Shachar-Hill and Shulman[34] as well as ourselves[35a] have recently considered the difficult possibilities with regard to SRs for the resonance of the mostly extracellular $^{35}Cl^-$ aquo anion.

The initial demonstrations of the utility of SRs were with lipid vesicle and cell suspensions, and allowed monitoring of the transcytolemmal Na^+ gradient, in particular. We reviewed the literature of such studies in 1987.[1,36] In 1985, we introduced the use of SRs for perfused ex vivo tissue, with the beating rat heart preparation.[37] Since that time, there have been many semiquantitative studies of transmembrane Na^+ (and, to a lesser extent, K^+) transport. These have been reviewed in 1987[36] and 1989.[38] Important qualitative observations of fundamental aspects have been made using this approach. One is the discovery that extracellular Mg^{2+} blocks Na^+ influx into myocardial cells during Ca^{2+}-free perfusion of the rat heart.[39] Another is that the accumulation of $Na_i{}^+$ during global ischemia of the rat heart occurs via the Na^+/H^+ exchange transporter.[40] Moreover, the level of Na_i is a reasonable predictor of whether the heart will go into ventricular fibrillation during ischemia.[41] An example from this latter work is shown in Figure 6 (M. M. Pike, personal communication). Figure 6(a) shows one-pulse SQ ^{23}Na spectra acquired in 50 s each from a heart perfused with 4 mM of the SR $TmDOTP^{5-}$ before (control), and after 51 min of low-flow ischemia (during which beating was maintained). The unshifted resonance at zero ppm represents $Na_i{}^+$. The large peak shifted 2.5 ppm to higher frequency by $TmDOTP^{5-}$ represents $Na_o{}^+$ and, in this case, includes the large contribution from the effluent perfusate surrounding the heart in the NMR tube. The peak at about 8 ppm is that of Na^+ in a reference balloon, contained in the left ventricle and filled with 4 mM $TmDOTP^{5-}$ in a Ca^{2+}-free saline solution. The Na_i level clearly increases during ischemia. The spectra in Figure 6(b) were obtained before, and after 51 min of ischemia in a heart that experienced ventricular fibrillation during the ischemia. Not only was the Na_i level higher just before ventricular fibrillation began (not shown), but it rises to a very high value during the ischemic period.

In 1986, Ingwall's laboratory introduced the study of localized in vivo ^{23}Na spectra obtained from a rat infused with SR.[42] We reviewed such reports in 1993.[43a] The Dallas group of Sherry and Malloy[44] has developed the $TmDOTP^{5-}$ SR mentioned above [$DOTP^{8-}$ represents 1,4,7,10-tetraazacyclododecane-*N*,*N*′,*N*″,*N*‴-tetra(methylenephosphonate)], shown it to be the most effective, and demonstrated its potential for in vivo use. Figure 6(c) (similar to 2 in Bansal et al.[44a]) shows the time dependence of interleaved in vivo one-pulse SQ $^{23}Na/^{31}P$ spectra obtained from the liver of a rat during a programmed, varied infusion of $TmDOTP^{5-}$. The ^{31}P spectra demonstrate the maintenance of the energy state of the liver. The infusion time is shown in the left column and the cumulative SR dose in the next column. The ^{23}Na spectra, typically acquired in about 1 min each, show the development of a shift to high frequency of a portion of the resonance as the SR enters the liver. If the infusion is stopped, the spectrum will slowly revert to the preinfusion form as the SR is eliminated through the kidney and washed out of the liver.[42b] The conventional wisdom is that the SR enters the entire extracellular space of the liver, where Na^+ is concentrated, and that the shifted peak represents Na_o, while the unshifted peak represents Na_i. Figure 6(d) shows localized ^{23}Na spectra from regions of interest in different organs, after infusion of $TmDOTP^{5-}$.[44b] The kidney shows an additional broad peak at very high frequency (about 32 ppm) due to Na^+ in the tubular filtrate, where the SR is concentrated in the process of its elimination. It appears that the SR enters the extracellular interstitial space in every major organ except the healthy brain, where it is constrained to the plasma space by the intact blood–brain barrier.[35b] This is most important because it is the monitoring of the status of the transcytolemmal Na^+ gradient that is desired.

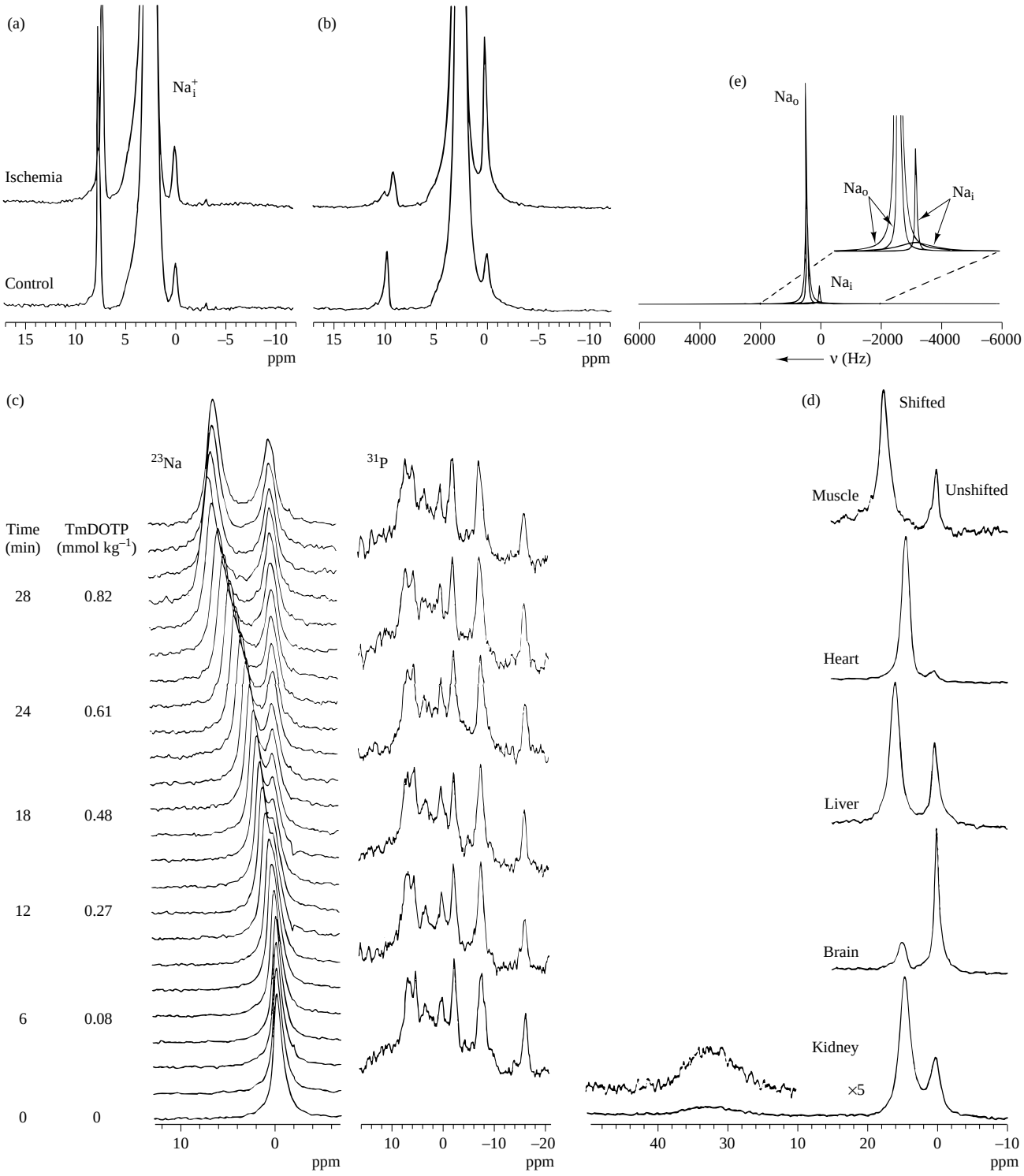

Figure 6 One-pulse SQ ^{23}Na spectra obtained from samples treated with a shift reagent (SR). (a,b) Spectra from ex vivo beating rat hearts perfused with TmDOTP^{5-} (M. M. Pike, personal communication). They are similar to 4 in Pike et al.[41] (a) Spectra of a normal heart before (bottom) and after (top) a period of global ischemia. (b) As (a), except for a heart that experienced ventricular fibrillation during ischemia. (c, d) In vivo spectra (A. D. Sherry, personal communication). (c) Localized spectra from a region of interest in the liver, as a rat is infused with TmDOTP^{5-} beginning at time zero. SQ ^{31}P spectra, obtained with interleaved acquisition, are also presented. It is similar to 2 in Bansal et al.[44a] (d) Spectra from regions of interest in various organs after a period of SR infusion (Reproduced from N. Bansal, in 'MR Pulse', Society of Magnetic Resonance, Berkeley, CA, 1994, 2.). (e) A simulation of SQ spectra obtained from nonbrain tissue containing SR. (Reproduced from W. D. Rooney and C. S. Springer, *NMR Biomed.*, 1991, **4**, 209)

Although qualitative assessment of changes in this gradient is extremely useful, the possibility of quantifying it is so tantalizing that it has generated much effort. Unfortunately, the issue is not simple. Figure 6(e) is a simulation of an in vivo one-pulse SQ ^{23}Na spectrum from nonbrain tissue,[2] where each compartment is pictured as giving rise to a type-c spectrum and the component linewidths are estimated using transverse relaxation data from yeast cell suspensions.[6] One must realize that the broad components correspond to small T_2 [$(R_{2f}^{1Q})^{-1}$, in Figure 1] values. These can be in the submillisecond range. If a T_2 value is sufficiently small compared to the receiver 'dead-time' in a one-pulse experiment, some of the signal has vanished even before the receiver has turned on. The situation is even worse for the delay in an echo-based experiment. This is the main source of the famous ^{23}Na 'visibility' problem.[2] For ^{23}Na in most cases, the T_2 of the center peak [$(R_{2s}^{1Q})^{-1}$, in Figure 1] is sufficiently large that it is always detected, and the visibility never falls below 0.40. For ^{35}Cl[9,34,35] and ^{39}K,[25b,45] which have been much less studied, it is not clear if this remains the case. Obviously, it is best to employ the smallest dead-time or echo delay that is experimentally possible.

Even if one succeeds in acquiring the entire signal, it is clear in Figure 6(e) that there is extensive overlap of the compartmental peaks, particularly their broad, coalesced satellite components. The accurate curve resolution of these from experimental spectra is an almost impossible task. Figure 6(e) suggests that one should fit only the upper portions of the sharp features with Lorentzian lineshapes, and then assume that these represent 0.4 of the intensities, respectively, from the Na^+ in those compartments.[2] It is important to note from Figure 1 that this assumption will be a good one whether a compartmental spectrum is type-c or type-b. It seems to us that this approach is the most sensitive and the most accurate for the tissue signal situation.

We have pointed out another quantitative feature of the SR approach.[43a] With a relevant calibration curve, one can use the resonance frequency of the Na_o peak to estimate the instantaneous thermodynamic concentration of the SR; that in its actual volume of distribution. For example, using the appropriate calibration curve (of those in Figure 7 Albert et al.[43a]), we estimate [$TmDOTP_o^{5-}$] to be about 9 mM in the liver giving rise to the spectrum in Figure 6(d).

A qualitative advantage of the SR technique is that it can be used in combined spectroscopy and imaging experiments.[46–48] In principle, one can resolve subvoxel Na_i and Na_o signals[49] and produce Na_i and Na_o maps (for all tissues except the brain) by spectroscopic imaging.

Thus, it is clear that the SR approach has many advantages. However, it also has problems, some of which almost certainly preclude its use in larger animals or humans. We mention five of these. (1) In cell suspension and perfused tissue studies, each $TmDOTP^{5-}$ anion usually replaces five Cl^- anions (normally about 110 mM) in extracellular fluids. This could cause small perturbations in transmembrane Donnan potentials. (2) For in vivo experiments, $Na_5TmDOTP$ is usually added to the blood. Thus, in the case above where $TmDOTP_o^{5-}$ is 9 mM in the liver, there is an additional burden of 45 mM Na^+ in the extracellular space (an increase of about 30%). (3) The SR $TmDOTP^{5-}$ has been found to extract Ca^{2+} from the body and into the blood (and the urine?),[44b,c] since it interacts with Ca^{2+}, in addition to Na^+.[43a,b] Extra Ca^{2+} is added to $TmDOTP^{5-}$-containing perfusion medium for beating rat hearts.[44a] (4) Even if there were not toxicity concerns arising from the above facts, the amount of SR required makes it probably prohibitively expensive for use with large animals or humans. The maximum cumulative dose of SR shown in Figure 6(c) corresponds to 10 g of thallium (and 7 g of sodium) for a 75-kg human. (5) Finally, it would be particularly interesting to monitor the transcytolemmal gradient in the brain. However, the SR is denied access to the extracellular interstitium in the healthy brain by the intact blood–brain barrier [Figure 6(d)].[35b]

We have recently considered an approach that may allow SR-free discrimination of compartmental ^{23}Na resonances.[50] This is to obtain the *relaxogram*, or distribution of relaxation times, that describes a relaxation decay data set; a study we refer to as *relaxography*.[49] Figure 7 shows a stacked plot of transverse relaxograms obtained from ^{23}Na FIDs of suspensions of canine erythrocytes at different hematocrit (hct) values acquired by our colleagues (Drs Y. Seo and M. Murakami), with a dead-time of 25 μs.[50b] The abscissa is log T_2* (T_2* in milliseconds) and the oblique axis is hct. Although the erythrocyte Na_i signal may be slightly type-b (see above), it appears as effective type-c in these relaxograms. Two Na_i peaks are seen, with the area under the one at the larger T_2* value averaging 0.67 of that of the one at the smaller T_2* value.[50b] The total area of these increases with increasing hct. Although the Na_o signal can become type-c or even slightly type-b at elevated hct values (see above), it appears as effective type-d (one peak) in the relaxograms shown in Figure 7, at least in those from lower hct values. The single Na_o resonance appears between the Na_i peaks, where they coexist, and its area decreases with increasing hct. It may have turned into effective type-c at hct = 0.66, just before it disappears, and may be incompletely resolved from the Na_i resonances. The signal-averaged FIDs for Figure 7 were acquired in about 5 min each. However, other results lead us to expect that FIDs of sufficient quality could be obtained in slightly less than 1 min each. The total area under all of the peaks in each relaxogram in Figure 7 is proportional to the amount of Na^+ within the

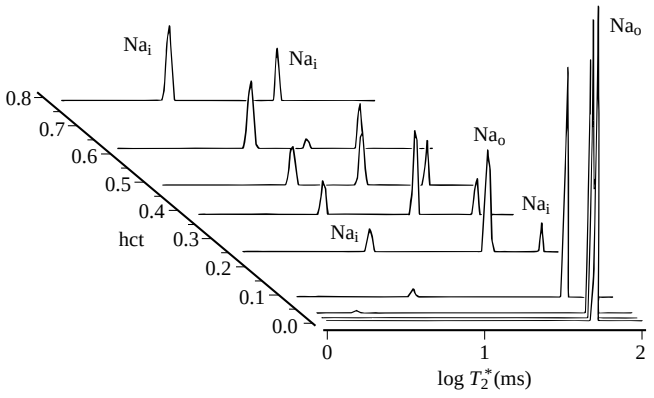

Figure 7 A stacked plot of transverse ^{23}Na relaxograms obtained from suspensions of canine erythrocytes at different hematocrit values. (Reproduced from J. H. Lee, Y. Seo, M. Murakami, C. Labadie, and C. S. Springer, in Abstracts of the 11th Annual Meeting of the Society of Magnetic Resonance Medicine, Society of Magnetic Resonance Medicine, Berkeley, CA, 1992, p. 2222)

NMR sensitive volume. It is in excellent agreement with an independent analysis for Na^+.[50b]

It remains to be seen whether ^{23}Na relaxography will be successful with true in vivo experiments. Relaxographic analysis involves the formal inverse Laplace transformation of the relaxation decay data set. This is a notoriously 'ill-posed' problem,[49] and it is not clear if the tissue situation produces parameters such that the transformation can be effectively carried out with the quality of data that can be obtained from the living organism.

8 ^{23}Na MR IMAGING

Although the ^{23}Na signal is the second strongest from tissue[1], it is still 4–5 orders of magnitude weaker than that of ^1H_2O.[1] The small values of T_1 for ^{23}Na, due to the quadrupolar relaxation mechanism, allow more frequent excitation and ameliorate this problem, but only to a modest extent. Nevertheless, there has been persistent interest in producing images from the ^{23}Na resonance, even though an imaging protocol is always longer than a spectroscopic one.

All of the considerations given above are, of course, also important when generating and interpreting ^{23}Na images. For example, Thulborn and coworkers[51] have found that significant intensity from the rat brain is lost if the dead-time (echo time, in this case) is increased from 0.5 to 2 ms. In accurate quantitative work, Thulborn's group[52] has shown how to use the ratios of ^{23}Na to ^1H_2O voxel intensities to generate *concentration maps*. They find values narrowly centered about 45 mM in the normal rat brain. This is in good agreement with what is expected.[1] It is important to note, however, that this is a volume-weighted average value—as if Na^+ was uniformly distributed throughout the voxel. Of course, Na^+ is concentrated in the extracellular space (about 150 mM) and mostly excluded (about 10 mM) from the millions of cells in a voxel. Since it is this transcytolemmal gradient that is the main biological role for Na^+, an important goal would be to map the gradient itself. This may be possible. We have shown above that the use of SRs allows the discrimination of Na_o and Na_i signals in most tissues of small animals, except the brain. Relaxographic analysis may allow SR-free discrimination, even in the brain, and in larger animals. In other work, we have shown that, at least with the use of a relaxation-catalyzing contrast agent in the extracellular space, relaxographic analysis also allows the discrimination and imaging of subvoxel $^1H_2O_o$ and $^1H_2O_i$ signals.[49] In principle, taking the corresponding ^{23}Na to ^1H_2O signal intensity ratios would allow the mapping of the thermodynamic values, $[Na_o{}^+]$ and $[Na_i{}^+]$. A map of the ratios of these quantities would be a concentration gradient map, and, with a reasonable assumption of activity coefficients, even an activity gradient map.

9 RELATED ARTICLES

Cation Movements Across Cell Walls of Intact Tissues using MRS; DNA–Cation Interactions: Quadrupolar Studies; Double Quantum Coherence; Dynamics of Water in Biological Systems: Inferences from Relaxometry; Electrolytes; High Speed MAS of Half-Integer Quadrupolar Nuclei in Solids; Liquid Crystalline Samples: Diffusion; Lithium NMR; Lyotropic Liquid Crystalline Samples; Multiple Quantum Coherence Imaging; Multiple Quantum Spectroscopy in Liquid Crystalline Solvents; Nutation Spectroscopy of Quadrupolar Nuclei; Overtone Spectroscopy of Quadrupolar Nuclei; Quadrupolar Interactions; Quadrupolar Nuclei in Glasses; Quadrupolar Nuclei in Liquid Samples; Quadrupolar Nuclei in Solids; Relaxation of Quadrupolar Nuclei Measured via Multiple Quantum Filtration; Relaxation Theory for Quadrupolar Nuclei; Sodium-23 Magnetic Resonance of Human Subjects; Sodium-23 NMR.

10 REFERENCES

1. C. S. Springer, Jr., *Annu. Rev. Biophys. Biophys. Chem.*, 1987, **16**, 375.
2. W. D. Rooney and C. S. Springer, Jr., *NMR Biomed.*, 1991, **4**, 209.
3. W. D. Rooney, T. M. Barbara, and C. S. Springer, Jr., *J. Am. Chem. Soc.*, 1988, **110**, 674.
4. L. G. Werbelow and A. G. Marshall, *J. Magn. Reson.* 1981, **43**, 443.
5. U. Eliav, A. Baram, and G. Navon, *J. Chem. Phys.*, 1988, **89**, 5584.
6. W. D. Rooney and C. S. Springer, *NMR Biomed.*, 1991, **4**, 227.
7. T. L. James and J. H. Noggle, *J. Am. Chem. Soc.*, 1969, **91**, 3424.
8. T. E. Bull, *J. Magn. Reson.*, 1972, **8**, 344.
9. J. J. Falke, R. J. Pace, and S. I. Chan, *J. Biol. Chem.*, 1984, **259**, 6472.
10. D. W. Urry, T. L. Trapane, C. M. Venkatachalam, and R. B. McMichens, *Methods Enzymol.*, 1989, **171**, 286.
11. E. Berggren and P.-O. Westlund, *Chem. Scr.*, 1989, **29**, 1.
12. H. J. C. Berendsen and H. T. Edzes, *Ann. NY Acad. Sci.*, 1973, **204**, 459.
13. C. L. Khetrapal, A. C. Kunwar, A. S. Tracey, and P. Diehl, *Nuclear Magnetic Resonance Studies in Lyotropic Liquid Crystals*, Springer-Verlag, New York, 1975, p. 6.
14. D. S. Goodsell, *Am. Sci.*, 1992, **80**, 457.
15. H. Shinar, T. Knubovets, and G. Navon, *Biophys. J.*, 1993, **64**, 1273.
16. J. S. Tauskela and E. A. Shoubridge, *Biochim. Biophys. Acta*, 1993, **1158**, 155.
17. A. Stevens, P. Paschalis, and T. Schleich, *Biophys. J.*, 1992, **61**, 1061.
18. U. Eliav and G. Navon, *J. Magn. Reson., Ser. B*, 1994, **103**, 19.
19. (a) R. Kemp-Harper and S. Wimperis, *J. Magn. Reson., Ser. B*, 1993, **102**, 326; (b) R. Kemp-Harper, S. P. Brown, P. Styles, and S. Wimperis, *J. Magn. Reson. Ser. B*, 1994, **105**, 199; (c) R. Reddy, L. Bolinger, M. Shinnar, E. Noyszewski and J. S. Leigh, *Magn. Reson. Med.*, 1995, **33**, 134.
20. U. Eliav, H. Shinar, and G. Navon, *J. Magn. Reson.*, 1992, **98**, 223.
21. T. K. Halstead, P. A. Osment, and B. C. Sanctuary, *J. Magn. Reson.*, 1984, **60**, 382.
22. B. C. Sanctuary, *Mol. Phys.*, 1983, **49**, 785.
23. G. Jaccard, S. Wimperis, and G. Bodenhausen, *J. Chem. Phys.*, 1986, **85**, 6282.
24. L. Makowski, D. L. D. Caspar, W. C. Phillips, and D. A. Goodenough, *J. Cell Biol.*, 1977, **74**, 629.

25. (a) Yu. A. Plyavin', and E. 'Ya. Blum, *Magnetohydrodynamics*, 1984, **19**, 349; (b) H. J. Guttman, S. Cayley, M. Li, C. F. Anderson, and M. T. Record, *Biochemistry*, 1995, **34**, 1393.
26. J. W. C. van der Veen, S. Slegt, J. H. N. Creyghton, A. F. Mehlkopf, and W. M. M. J. Bovée, *J. Magn. Reson., Ser. B*, 1993, **101**, 87.
27. R. B. Hutchison, D. Malhotra, R. E. Hendrick, L. Chan, and J. I. Shapiro, *J. Biol. Chem.*, 1990, **265**, 15506.
28. J. Pekar, P. F. Renshaw, and J. S. Leigh, Jr., *J. Magn. Reson.*, 1987, **72**, 159.
29. R. H. Griffey, B. V. Griffey, and N. A. Matwiyoff, *Magn. Reson. Med.*, 1990, **13**, 305.
30. M. D. Cockman, L. W. Jelinski, J. Katz, D. J. Sorce, L. M. Boxt, and P. J. Cannon, *J. Magn. Reson.*, 1990, **90**, 9.
31. (a) M. M. Pike and C. S. Springer, Jr., *J. Magn. Reson.*, 1982, **46**, 348; (b) M. M. Pike, S. R. Simon, J. A. Balschi, and C. S. Springer, Jr., *Proc. Natl. Acad. Sci. USA*, 1982, **79**, 810; (c) J. A. Balschi, V. P. Cirillo, and C. S. Springer, *Biophys. J.*, 1982, **38**, 323.
32. R. K. Gupta and P. Gupta, *J. Magn. Reson.*, 1982, **47**, 344.
33. J. Szklaruk, J. F. Marecek, A. L. Springer, and C. S. Springer, Jr., *Inorg. Chem.*, 1990, **29**, 660.
34. Y. Shachar-Hill and R. G. Shulman, *Biochemistry*, 1992, **31**, 6272.
35. (a) Y. Xu, T. M. Barbara, W. D. Rooney, and C. S. Springer, Jr., *J. Magn. Reson.*, 1989, **83**, 279; (b) E. Preston and D. O. Foster, *NMR Biomed.*, 1993, **6**, 339.
36. C. S. Springer, Jr., *Ann. NY Acad. Sci.*, 1987, **508**, 130.
37. M. M. Pike, J. C. Frazer, D. F. Dedrick, J. S. Ingwall, P. D. Allen, C. S. Springer, Jr., and T. W. Smith, *Biophys. J.*, 1985, **48**, 159.
38. B. P. Hills and P. S. Belton, *Ann. Rep. NMR Spectrosc.*, 1989, **21**, 99.
39. C. J. A. van Echteld, J. H. Kirkels, M. H. J. Eijgelshoven, P. van der Meer, and T. J. C. Ruigrok, *J. Mol. Cell Cardiol.*, 1991, **23**, 297.
40. M. M. Pike, C. S. Luo, M. D. Clark, K. A. Kirk, M. Kitakaze, M. C. Madden, E. J. Cragoe, and G. M. Pohost, *Am. J. Physiol.*, 1993, **265**, H2017.
41. M. M. Pike, C. S. Luo, S. Yanagida, G. R. Hageman, and P. G. Anderson, *Circ. Res.*, 1995, **77**, 394.
42. (a) J. A. Balschi, J. A. Bittl, and J. S. Ingwall, *Magn. Reson. Med.*, **1986**, 343; (b) J. A. Balschi, J. A. Bittl, C. S. Springer, Jr., and J. S. Ingwall, *NMR Biomed.*, 1990, **3**, 47.
43. (a) M. S. Albert, W. Huang, J.-H. Lee, J. A. Balschi, and C. S. Springer, Jr., *NMR Biomed.*, 1993, **6**, 7; (b) S. C.-K. Chu, H. Z.-H. Qiu, C. S. Springer, Jr., and A. Wishnia, *J. Magn. Reson.*, 1990, **87**, 287.
44. (a) N. Bansal, M. J. German, V. Seshan, G. T. Shires, III, C. R. Malloy, and A. D. Sherry, *Biochem.*, 1993, **32**, 5638; (b) N. Bansal, in *MR Pulse*, Society of Magnetic Resonance, Berkeley, CA, 1994, Vol. 1, p. 18; (c) N. Bansal, M. J. German, I. Lazar, C. R. Malloy, and A. D. Sherry, *J. Magn. Reson. Imaging*, 1992, **2**, 385.
45. R. M. Wellard, B. P. Shehan, W. R. Adam, and D. J. Craik, *Magn. Reson. Med.*, 1993, **29**, 68.
46. C. T. W. Moonen, S. E. Anderson, and S. Unger, *Magn. Reson. Med.*, 1987, **5**, 296.
47. D. Burstein and M. Mattingly, *J. Magn. Reson.*, 1989, **83**, 197.
48. S. J. Kohler, N. H. Kolodny, A. C. Celi, T. A. Burr, D. Weinberg, D. J. D'Amico, and E. S. Gragoudas, *Magn. Reson. Med.*, 1992, **23**, 77.
49. C. Labadie, J.-H. Lee, G. Vétek, and C. S. Springer, Jr. *J. Magn. Reson., Ser. B.*, 1994, **105**, 99.
50. (a) J. H. Lee, C. Labadie, and C. S. Springer, Jr., *Magn. Reson. Med.*, **1992**, 2214; (b) J.-H. Lee, Y. Seo, M. Murakami, C. Labadie, and C. S. Springer, Jr., *Magn. Reson. Med.*, **1992**, 2222.
51. (a) F. E. Boada, J. D. Christensen, F. R. Huang-Hellinger, and K. R. Thulborn, *Magn. Reson. Med.*, **1993**, 960; (b) F. E. Boada, J. D. Christensen, F. R. Huang-Hellinger, T. G. Reese, and K. R. Thulborn, *Magn. Reson. Med.*, 1994, **32**, 219.
52. (a) B. J. Barrère, J. D. Christensen, F. E. Boada, J. X. Yu, T. G. Reese, D. A. Chesler, J. M. Vevea, J. M. Kosewski, C. M. Mills, M. Troca, and K. R. Thulborn, *Magn. Reson. Med.*, **1993**, 400; (b) J. D. Christensen, B. J. Barrère, F. E. Boada, J. M. Vevea, J. M. Kosewski, C. M. Mills, and K. R. Thulborn, *Magn. Reson. Med.*, **1993**, 978.

Acknowledgments

I thank my present and former graduate and undergraduate students as well as my collaborators (their names appear frequently in the references): they have made what I consider to be outstanding contributions to this subject. I also thank Ms Marie Dippolito for processing this manuscript and, in fact, almost all of our spin-$\frac{3}{2}$ papers. I thank Professors Gil Navon, Martin Pike, Dean Sherry, Keith Thulborn, Cees van Echteld, and Steve Wimperis, as well as Drs Hadassah Shinar, Uzi Eliav, and Joe Tauskela for sending reprints and preprints describing the most impressive work of their groups. Many of these individuals also provided critical readings of a draft of this article. I also thank the National Institutes of Health (Grant GM 32125) and Brookhaven National Laboratory (Laboratory Directed Research and Development Program Grant/co-PI, Joanna Fowler) for support during the preparation of this contribution.

Biographical Sketch

Charles Sinclair Springer, Jr. *b* 1940. B.S. (Chemistry), St. Louis University, 1962; M.S., 1964; Ph.D. 1967 (Chemistry), The Ohio State University (supervisors, Devon W. Meek and Robert E. Sievers). Chemistry faculty, State University of New York at Stony Brook, 1968–present; Chemistry faculty, Brookhaven National Laboratory; 1994–present. Approximately 60 publications. Current research interests: in vivo NMR; particularly quadrupolar nuclei, principles and effects of bulk magnetic susceptibility, and the uses of the formal inverse Laplace transform.

Double-quantum Filtered NMR of Ordered Biological Tissues

Gil Navon, Hadassah Shinar, and Uzi Eliav

Tel Aviv University, Tel Aviv, Israel

1 Introduction 1
2 Theoretical Background 1
3 ^{2}H DQF NMR Study of Water Compartmentation and Diffusion in Rat Sciatic Nerve 3
4 ^{2}H DQF NMR of Cartilage 4
5 ^{2}H DQF NMR of Blood Vessels 5
6 ^{1}H DQF NMR: An Application to the Study of Connective Tissues 6
7 References 10

1 INTRODUCTION

In molecules that experience anisotropic motion, the dipolar and quadrupolar interactions are not averaged to zero, resulting in residual splittings in their NMR spectrum. The best example of this phenomenon is of molecules dissolved in liquid crystals.

Most biological tissues, with the exception of body fluids, contain ordered structures such as membranes, fibrous proteins and nerve fibers. These structures can induce anisotropic motion to water and other molecules interacting with them, which is expressed in residual dipolar or quadrupolar interactions. In the single quantum (SQ) spectra of water molecules in biological tissues the splitting resulting from these interactions is masked by the strong isotropic signal of the bulk media. The advantage of the double quantum filtered (DQF) NMR is that it detects only molecules with residual quadrupolar or dipolar interactions and J couplings. Thus, the strong signal of the isotropic water molecules that do not have J splitting is filtered out.

The first application of DQF to the study of ordered biological systems was performed on ^{23}Na of sodium ions.[1] This topic, which was reviewed in the previous volumes of the Encyclopedia[2] as well as in some recent reviews,[3] will not be dealt with in the present study. This article will concentrate on the applications of ^{1}H and ^{2}H DQF NMR to water molecules in biological systems.

2 THEORETICAL BACKGROUND

The basic double quantum filtered (DQF) pulse sequence is

$$90^\circ - \frac{\tau}{2} - 180^\circ - \frac{\tau}{2} - 90^\circ - t_{\mathrm{DQ}} - 90^\circ - t_2\ (\mathrm{Acq}) \qquad (1)$$

We use the notation of the irreducible spherical tensor operator $T_{l,p}$, where l is the rank and p is the coherence of the tensor with $|p| \leq l$. These tensors are composed of combinations of the more familiar spin operators I_z and $I_\pm = I_X \pm i I_y$. By using this representation the processes that take place during the pulse sequence are easily understood, while keeping in mind the following two simple rules: (a) a radiofrequency pulse can change the coherence p within the limits of $|p| \leq l$; (b) changes in the rank l can occur by relaxation and by quadrupolar, dipolar or J couplings, keeping the same value of p. Thus, in the DQF pulse sequence (equation 1), the first 90° pulse generates SQ coherences ($T_{1,\pm1}$). During the time interval τ, denoted as the creation time, second rank tensors $T_{2,\pm1}$ are formed by the residual dipolar or quadrupolar interactions. The 180° pulse in the middle of the creation time τ serves to refocus the chemical shifts and magnetic field inhomogeneities. The second 90° pulse converts the SQ coherences of the second rank tensors, $T_{2,\pm1}$, into double quantum coherences ($T_{2,\pm2}$), which evolve during the double quantum evolution time, t_1. The last 90° pulse transfers the magnetization back to $T_{2,-1}$, which evolves into the detectable $T_{1,-1}$. The selection of the double quantum coherence pathway is accomplished by either a proper phase cycling[4] or by the application of field gradients.[5]

For spin $I = 1$ nuclei or for a pair of dipolar coupled protons, with the residual interaction (quadrupolar or dipolar) being much greater than the relaxation rate (and the exchange rate for protons), the DQF free induction decay (FID) is given by:[6–8]

$$\mathrm{FID} \propto \sin(\omega_i^{\mathrm{L}}\tau)\, e^{-R_2\tau} \sin(\omega_i^{\mathrm{L}} t_2)\, e^{-R_2 t_2} \qquad (2)$$

where ω_i^{L} is either the quadrupolar ($\omega_{\mathrm{Q}}^{\mathrm{L}}$) or the dipolar ($\omega_{\mathrm{D}}^{\mathrm{L}}$) residual interaction in the laboratory frame of reference (with the Z direction along the magnetic field) $R_2 = 1/T_2$ for $I = 1$ nuclei, and $R_2 = k/2 + 1/T_2$ (where k is the proton exchange rate) for protons. ω_i^{L} is given in terms of its value in the local director frame of reference ω_i^{loc} by the following transformation:

$$\omega_i^{\mathrm{L}} = \alpha \omega_i^{\mathrm{loc}} \frac{(3\cos^2\theta_{\mathrm{LD}} - 1)}{2} \qquad (3)$$

where θ_{LD} is the angle between the local director and the magnetic field, and $\alpha = 1$ for $I = 1$ and $\alpha = 3/2$ for a pair of protons.

As expected from a Fourier transform of $\sin(\omega_i^{\mathrm{L}} t_2)$ the lineshape of the DQF spectra is composed of an antiphase pair of lines separated by $2\omega_i^{\mathrm{L}}$ (Figure 1). The antiphase presentation of the DQF spectra is sometimes inconvenient. In order to obtain a presentation where all the peaks have the same phase, the pulse sequence denoted as IP-DQF[8] (Figure 2), where a reconversion process is introduced after the DQF step, can be used.

In biological tissues we frequently encounter situations with a distribution of the residual interactions. From equation (2) one can predict that the DQF spectra will show an increasing number of peaks ('wiggles') when the creation time τ is increased. The splitting between those peaks, in completely

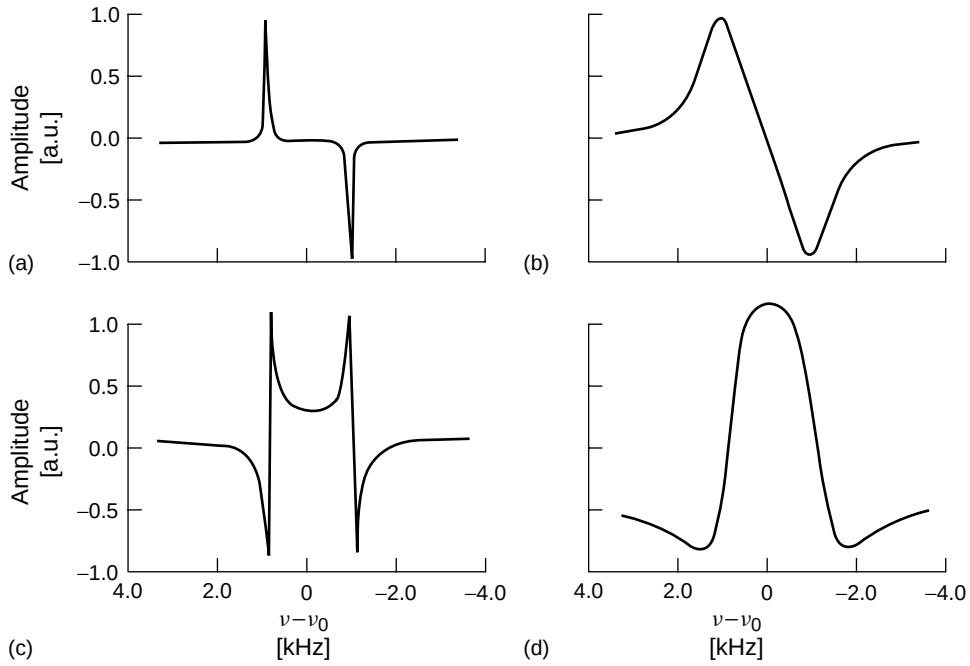

Figure 1 Calculated DQF spectral lineshapes as a function of $R = \omega_i^{\mathrm{L}} T_2$. (a, c) $R = 40.0$; (b, d) $R = 3.0$; (a, b) are given in a absorption mode; (c, d) are given in a dispersion mode

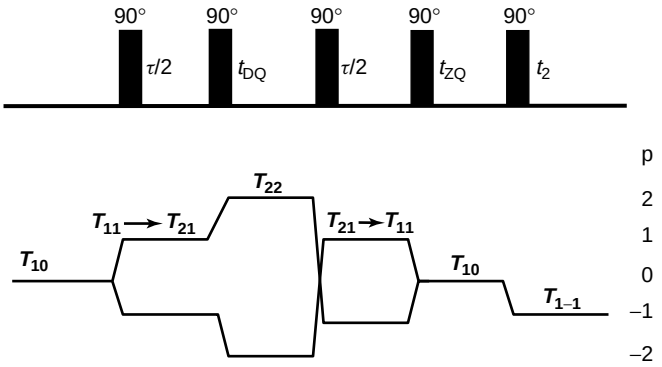

Figure 2 The in-phase DQF (IP-DQF) pulse sequence. (Reproduced from Ref.[8])

disordered tissue, is only a function of τ and is given by $1/\tau$ (Hz).[7]

^{1}H NMR spectra of water in ordered biological tissues differ from those of ^{2}H spectra due to the effect of proton chemical exchange. This effect is responsible for the coalescence of the dipolar-split proton spectrum into a single line upon raising the temperature.[9,10] This is in contrast with the ^{2}H spectrum, whose splitting is not sensitive to temperature.

The dependence of the DQF signal on the residual dipolar interaction and proton exchange rate has recently been calculated.[8] For the two cases of (a) $k < 2\omega_{\mathrm{D}}^{\mathrm{L}}$, and (b) $k > 2\omega_{\mathrm{D}}^{\mathrm{L}}$, the expressions for the DQF signal are given by:

$$\mathrm{FID} \propto \frac{2\omega_{\mathrm{D}}^2}{r^2} e^{-R_2\tau} \sin r\tau e^{-R_2\tau_2} \sin rt_2 \quad (k < 2\omega_{\mathrm{D}}^{\mathrm{L}}) \tag{4a}$$

$$\mathrm{FID} \propto \frac{2\omega_{\mathrm{D}}^2}{\rho^2} e^{-R_2\tau} \sinh \rho\tau e^{-R_2\tau_2} \sinh \rho t_2 \quad (k > 2\omega_{\mathrm{D}}^{\mathrm{L}}) \tag{4b}$$

where

$$\rho = \frac{\sqrt{k^2 - 4\omega_{\mathrm{D}}^2}}{2}, \quad r = \frac{\sqrt{4\omega_{\mathrm{D}}^2 - k^2}}{2}$$

Clearly for very slow proton exchange ($k \ll 2\omega_{\mathrm{D}}^{\mathrm{L}}$) the expression in equation (4a) converges into equation (2). On the other hand for very fast exchange ($k \gg 2\omega_{\mathrm{D}}^{\mathrm{L}}$) provided that $\tau, t_2 \gg 1/k$, one obtains:

$$\mathrm{FID} \propto \left(\frac{\omega_{\mathrm{D}}^{\mathrm{L}}}{k}\right)^2 e^{-\tau/T_2^e} e^{-t_2/T_2^e}$$

$$\frac{1}{T_2^e} = \frac{(\omega_{\mathrm{D}}^{\mathrm{L}})^2}{k} + \frac{1}{T_2} \tag{5}$$

Equation (5) clearly shows that $1/T_2^e$ is orientation dependent and that the intensity of the DQF spectra decreases as $(\omega_{\mathrm{D}}^{\mathrm{L}}/k^2)$. As the water proton exchange rate is similar in the different tissues, the main reason for the contrast between them is the differences in the values of $\omega_{\mathrm{D}}^{\mathrm{L}}$.

Warren et al.[11] have shown that DQF and zero quantum filtered (ZQF) NMR signals can also be formed by intermolecular dipolar interaction between very distant protons. This effect depends on two factors. (a) A large magnetization that results in non-negligible contributions to the equilibrium density matrix of tensors with ranks higher than one (for instance $T_{2,0}$). Such large magnetization can result from either high concentrations of the spins or from a high magnetic field. (b) A mechanism for the conversion of high-rank, single quantum tensors (such as $T_{2,-1}$) to the observable $T_{1,-1}$. The last process is enabled by the presence of field gradients or by a non-spherical geometry of the vessel. Intermolecular DQF and ZQF have been used to obtain a new contrast in MR images of the brain.[12] Typically, the time scale of these processes is

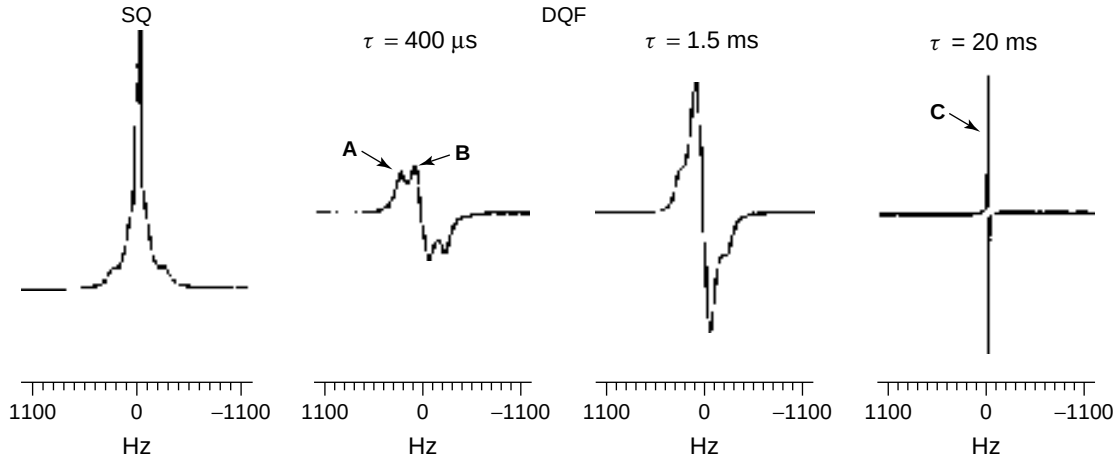

Figure 3 SQ and DQF ^{2}H NMR spectra at 76.8 MHz of rat sciatic nerve equilibrated in deuterated saline. (Adapted from Ref.[13])

tens of milliseconds, depending on the gradient strength. Thus, it can be neglected in tissues where the intramolecular dipolar interaction causes relaxation on a much shorter time scale, such as tendon and cartilage.

3 ^{2}H DQF NMR STUDY OF WATER COMPARTMENTATION AND DIFFUSION IN RAT SCIATIC NERVE

Peripheral nerves comprise three types of tissues: the endoneurium, the epineurium and axons. The first two tissues contain collagen fibers, while axons are thin tubes with an inner diameter of a few micrometers, wrapped in many layers of myelin sheath. The ^{2}H single pulse spectrum of a rat sciatic nerve equilibrated in deuterated saline[13] (Figure 3) consists of a very strong peak and two pairs of satellite transitions, which can be observed upon magnification of the spectrum. The central transition is mostly due to free D_2O molecules. The satellites represent D_2O molecules in anisotropic environment having a non-zero residual quadrupolar splitting. The ^{2}H DQF NMR spectrum of the same nerve is composed of three quadrupolar-split water signals. The signal of the isotropic water, which is most pronounced in the single pulse spectrum, is eliminated by the DQF pulse sequence and a very narrow signal, which evolves at longer creation times, is revealed. On the basis of the time course of the shifts of the different water signals caused by the addition of $CoEDTA^{2-}$ or $CoCl_2$ and on the basis of the action of collagenase, the signals with peak to peak splittings of about 470 (A), 120 (B) and 9 (C) Hz were assigned to water in the endoneurium, epineurium, and the intra-axonal compartment, respectively.[13] Each of the satellite signals has a characteristic dependence on the creation time τ (Figure 4). Fitting this dependence to equation (2) indicates that the contribution of the quadrupolar splitting to the peak to peak separation in the narrow intra-axonal signal, is only 6 Hz, and the rest is due to T_2 relaxation rate.

By performing the DQF experiment at different values of τ, the properties of the water in each compartment can be studied independently. One such property is the water diffusion in nerves. It has attracted a lot of attention since the development of diffusion weighted imaging of the brain.

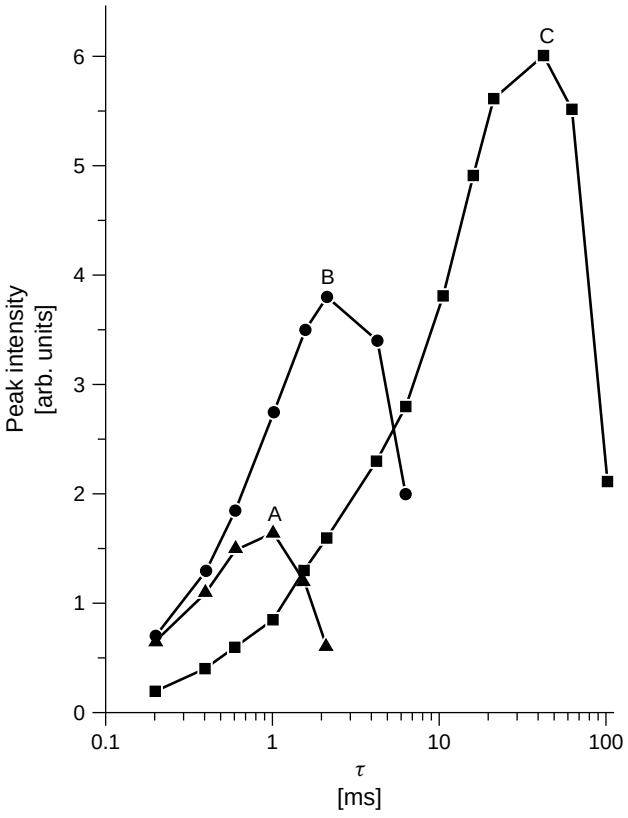

Figure 4 Peak intensity of the three different signals shown in Figure 3, as a function of the creation time, τ. (Reproduced from Ref.[13] by permission of Academic Press)

^{2}H diffusion measurements for water in the rat sciatic nerve was performed[14] by the DQF pulsed gradient spin echo (DQF-PGSE) sequence:[15]

$$90^\circ - \frac{\tau}{2} - 180^\circ - \frac{\tau}{2} - 90^\circ - t_3 - \delta - t_4 - 180^\circ - t_3 - \delta - t_4 - 90^\circ - \text{Acq} \qquad (6)$$

In this pulse sequence the two gradient pulses of duration δ are applied during the DQ evolution time, and thus the

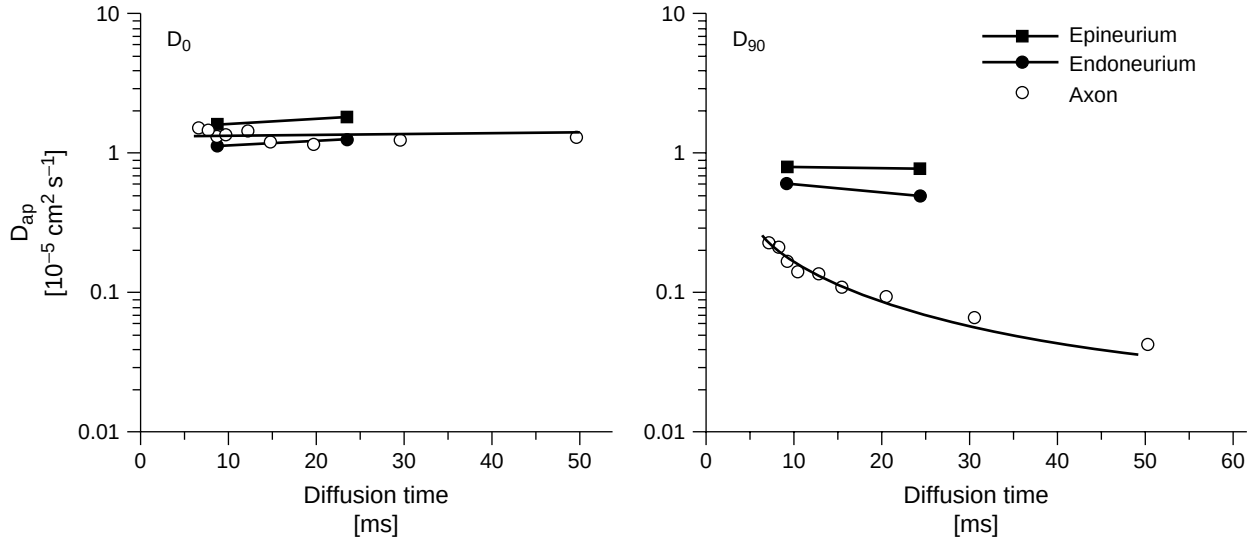

Figure 5 Diffusion coefficients, D_{app}, of deuterated water in an excised rat sciatic nerve equilibrated in deuterated saline measured at 46.0 MHz as a function of the diffusion time Δ. D_0, diffusion gradients parallel to the nerve axis and D_{90}, perpendicular to the nerve axis. For the axon, creation time $\tau = 30$ ms and time to echo $TE = 60$ ms. For the endoneurium and epineurium, $\tau = 0.6$ ms and $TE = 16$ ms. The D_{90} solid line for the axon is a fitted curve based on Ref.[16] with a diameter of 6.0 μm and $D_0 = 1.20 \times 10^{-5}$ cm^2 s^{-1}. (Reproduced from Ref.[14] by permission of Wiley InterScience)

effective gradient strength is doubled. Also, since the ^{2}H DQ relaxation time of water molecules is much longer than T_2, the measurements can be performed at longer diffusion times and smaller gradient strengths.

The apparent diffusion coefficients at each diffusion time were calculated from the attenuation of the echo as a function of the gradient strength.[14] The water diffusion coefficients in all three compartments were found to be anisotropic. Anisotropic diffusion of water in the endoneurium and epineurium may result from the thick collagen fibers. These structures reduce the effective diffusion distance of the water perpendicular to the axis of the fibers. For the intra-axonal compartment, the apparent diffusion coefficient perpendicular to the nerve axis is strongly dependent on the diffusion time (Figure 5). A model for restricted diffusion in cylinders,[16] was used to interpret the results. In this way the intra-axonal inner diameter of the axon was estimated at 7.5 ± 1.5 μm ($n = 3$). This value is in agreement with the known mean inner diameter of the rat sciatic nerve axons of 6 ± 1 μm.[17] For the measurement of diffusion in multi-compartment systems the ^{2}H DQF technique is unique, since it enables the observation of each compartment independently and avoids multi-parameter fitting of the experimental data.

4 ^{2}H DQF NMR OF CARTILAGE

Cartilage is composed of a solid matrix of collagen fibrils, proteoglycans and water. The collagen fibrils are arranged in fibers and bundles, which may have random orientations or may be aligned along a major axis. In both cases ^{2}H DQF spectra are observed, yet only in the latter case the lineshape depends on the orientation of the sample in the magnetic field.

For nasal cartilage the DQF spectra did not change as a function of the orientation of the sample in the magnetic field, indicating local order.[7] A representative set of lineshapes obtained at different τ values is given in Figure 6. Both the intensity and the shape of the spectra vary considerably for

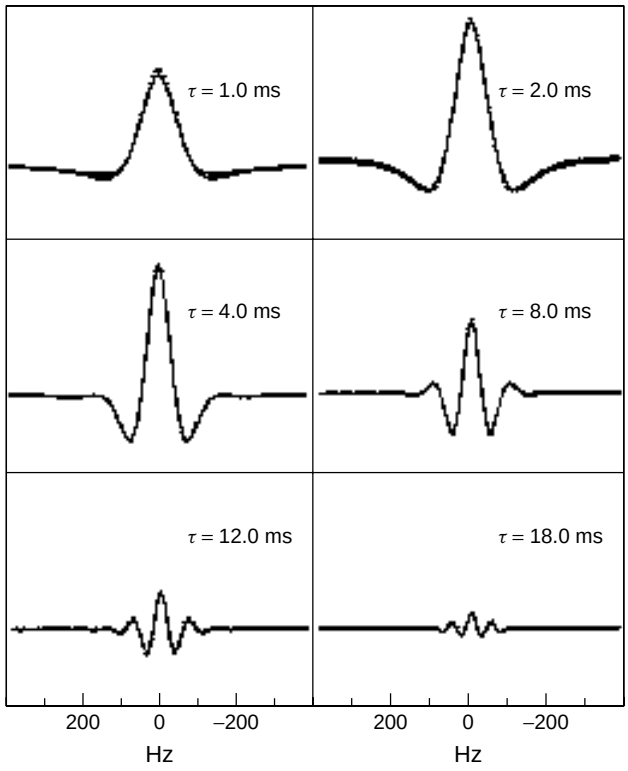

Figure 6 A representative set of observed (dotted line) and calculated (solid line) ^{2}H DQF spectra of bovine nasal cartilage immersed in D_2O. For the calculated spectra a single set of parameters was used: $\langle\omega_Q^{loc}\rangle/2\pi = 110$ Hz, $\Delta\omega_Q^{loc}/2\pi = 73$ Hz and $R_2 = 63$ s^{-1}. (Reproduced from Ref.[7] by permission of Academic Press)

the different τ values. For longer values of τ, the formation of 'wiggles' is apparent. As was mentioned in the Theoretical Introduction, these oscillations have intervals of $1/\tau$ and are due to the heterogeneity of the system.

The series of DQF lineshapes obtained for different creation times was fitted using a set of three parameters: the average residual quadrupolar interaction $\langle\omega_Q^{loc}\rangle/2\pi = 110\,\text{Hz}$, its standard deviation $\Delta\omega_Q^{loc}/2\pi = 73\,\text{Hz}$ and a transverse relaxation rate of $63\,\text{s}^{-1}$. The large standard deviation indicates that we are indeed dealing with a heterogenous system.

In articular cartilage the DQF lineshape is orientation dependent, indicating macroscopic order in the tissue. In order to obtain the detailed distribution of the fiber orientations, an image that contains the spectroscopic information has to be obtained. The pulse sequence for one-dimensional (1D) ^{2}H DQF spectroscopic imaging is identical to equation (1), with phase encoding gradients being applied during the DQ evolution time, t_{DQ} thus taking advantage of the relatively long ^{2}H DQ relaxation time and the doubling of the effect of the gradients applied during this period. The image obtained, together with some individual spectra, is given in Figure 7.[18] Near the bone, the quadrupolar splitting is of the order of 1500 Hz. A smaller splitting (~400 Hz) is detected in the radial zone. This splitting decreases gradually towards the cartilage surface, is lost in the intermediate zone, and is then again observed at the surface. Upon 90° rotation of the plug, the splitting of the calcified and radial zones is halved, while the splitting of the surface zone is slightly increased. This is an indication that the fibers align perpendicular to the bone at the calcified and radial zones and at the cartilage surface become parallel to the bone. In the intermediate zone there is a distribution of orientations around the magic angle and therefore no splitting is observed. These results are well correlated with the known histology of the collagen fibers in articular cartilage, namely they are oriented perpendicular to the bone in the deep areas of the cartilage, then they bend and align parallel to the bone at the surface.[19]

5 ^{2}H DQF NMR OF BLOOD VESSELS

The mechanical properties of blood vessel walls play a central role in cardiovascular function. The wall of the blood vessel has remarkable elasticity and fatigue resistance. At normal blood pressure the length of the vessel is as much as 40% longer and its circumference is about 30% greater than in the unstressed condition. The blood vessel wall is composed of three layers: the outer layer (the tunica adventitia), the intermediate layer (the tunica media), and the inner layer (the tunica intima). All three layers consist of different proportions of collagen, elastin and smooth muscle fibers, which are responsible for their mechanical properties.

In 2D ^{2}H DQF spectroscopic MRI a spectrum for each pixel is obtained, thus enabling the mapping of the distribution of the residual quadrupole interaction $\langle\upsilon_Q\rangle = \langle\omega_Q^L\rangle/2\pi$ within the blood vessel wall.[20] Since this property, as well as the τ dependence of the DQF signal intensity, is related to the composition of the tissue, the results can be interpreted as 'histological' images. A comparison between the conventional gradient echo image (Figure 8a) and the DQF images (Figure 8b–d) clearly demonstrates the suppression of the free water signal. Furthermore, the ability of the method to selectively display each of the tissue layers allows convenient measurements of the luminal area as well as of the thickness of the layers.

^{2}H DQF NMR spectroscopy was used to monitor structural changes following the application of strain.[21] The spectrum of water in the outer layer (adventitia) of coronary and carotid arteries was found to be highly sensitive to the strain exerted

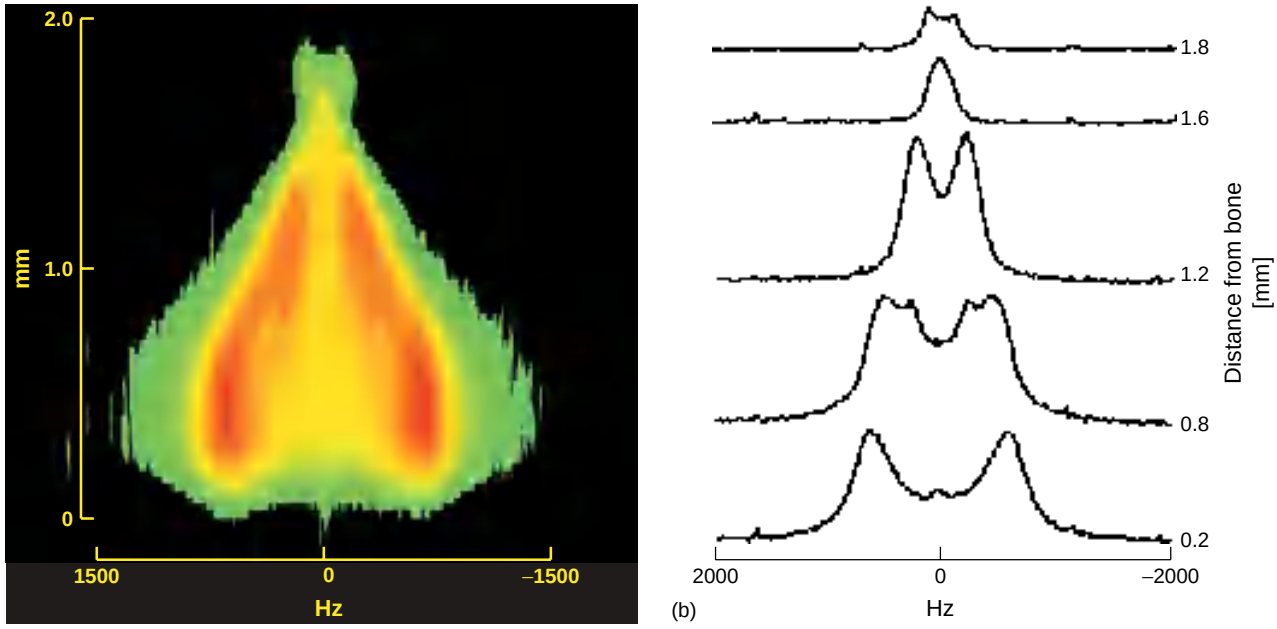

Figure 7 (a) 1D ^{2}H DQF spectroscopic image of bovine articular cartilage and bone plug, equilibrated with deuterated saline. The plug was measured with the magnetic field perpendicular to the surface. (b) ^{2}H DQF spectra extracted from the image, at various distances from the cartilage surface

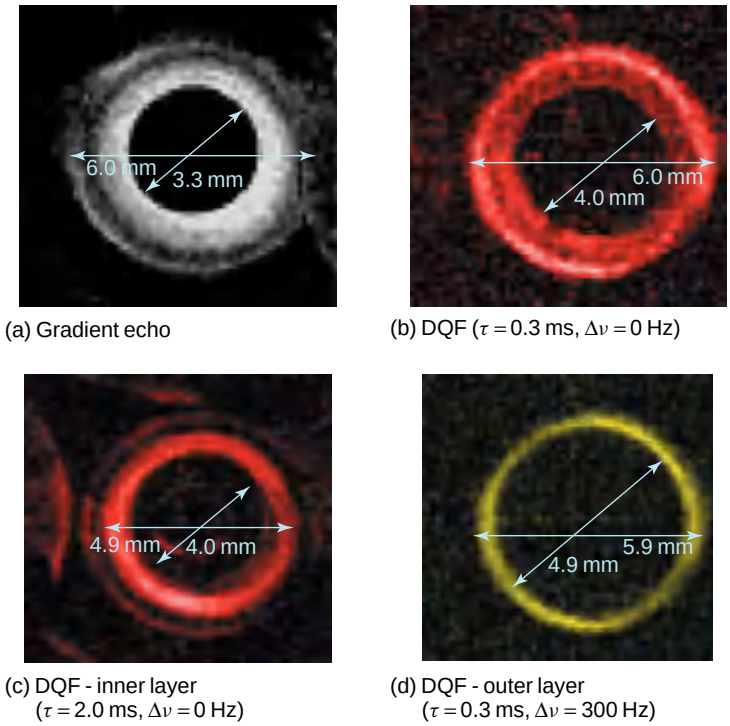

(a) Gradient echo

(b) DQF ($\tau = 0.3$ ms, $\Delta\nu = 0$ Hz)

(c) DQF - inner layer ($\tau = 2.0$ ms, $\Delta\nu = 0$ Hz)

(d) DQF - outer layer ($\tau = 0.3$ ms, $\Delta\nu = 300$ Hz)

Figure 8 Histological images of a cross section bovine coronary artery. A piece of coronary artery was equilibrated in D_2O saline. A polyacrilamide rod (3.3 mm diameter) was inserted in the vascular lumen and both ends of the artery were tied with silk threads. The axis of the artery was set parallel to the magnetic field. (a) A 2D ^{2}H GRE image of the artery. The image mostly corresponds to the free water in the space between the rod and the tissue, which remained to prevent magnetic susceptibility artifacts. (b–d) 2D ^{2}H DQF spectroscopic images constructed for a width of 100 Hz in the spectroscopic dimension. The use of different colors (yellow for $\nu = 0$ Hz and red for $\nu = 300$ Hz) emphasizes the fact that the images were taken from different frequency regions. (b) 2D ^{2}H DQF image measured at $\tau = 0.3$ ms and frequency of 0 Hz in the spectroscopic dimension. The image consists of water in all layers of artery, but water in the lumen is completely suppressed. (c) 2D ^{2}H DQF spectroscopic image measured at $\tau = 2.0$ ms and $\nu = 0$ Hz in the spectroscopic dimension. Only the water in the inner layer (tunica media) is depicted, and the thickness of the inner layer is 0.9 mm. (d) 2D ^{2}H DQF spectroscopic image measured at $\tau = 0.3$ ms and $\nu = 300$ Hz in the spectroscopic dimension. Only the water in the outer layer (tunica adventitia) is depicted, and the thickness of the layer is 1.0 mm. (Reproduced from Ref.[20] by permission of National Academy of Science USA)

on the vessel wall (Figure 9). The average residual quadrupolar interaction $\langle\nu_Q\rangle$ was calculated for each spectrum[20] and is given as a function of elongation in Figure 10. The strain sensitivity of $\langle\nu_Q\rangle$ provides us with the possibility to obtain a strain map for intact blood vessels. This is accomplished by the measurement of 2D spectroscopic ^{2}H DQF MRI. An example of such a measurement is given for a fully relaxed and a 55% elongated sample of a bovine coronary artery (Figure 11). In this experiment the average residual quadrupole interaction $\langle\nu_Q\rangle$ was calculated for each pixel and an image was constructed with a color code which represents the value of $\langle\nu_Q\rangle$ for each pixel rather than the usual signal intensity. The blue color in both images demonstrates the relatively narrow spectrum of the tunica media, which is insensitive to strain. In the left image, the green color that dominates the outer layer, the tunica adventitia, corresponds to $\langle\nu_Q\rangle$ values of 350–450 Hz for the unstressed vessel. In the right image the variety of red and yellow colors in the outer layer of the stretched sample reflects larger values of the residual quadrupolar interaction ($\langle\nu_Q\rangle$ ranges between 550 and 800 Hz) associated with regions with higher strain. Apparently, the broad distribution of $\langle\nu_Q\rangle$ is caused by non-uniform strain in the sample. Using a calibration of $\langle\nu_Q\rangle$ vs. the elongation, these images can be interpreted as strain maps.

6 ^{1}H DQF NMR: AN APPLICATION TO THE STUDY OF CONNECTIVE TISSUES

The natural abundance of ^{1}H and its superior S/N ratio make it the nucleus of choice for in vivo measurements. As was discussed in the theoretical background section, anisotropic motion of water molecules leads to a non-vanishing ^{1}H dipolar interaction. Water proton dipolar splitting has already been observed in water molecules adsorbed on oriented collagen fibers, and in partially dried tendon at low temperatures.[9] In intact tissues, owing to exchange between adsorbed and bulk water molecules and proton exchange between water molecules, the residual dipolar interaction is smaller and the large signal of the isotropic water masks the split signal.[9] In the case of ^{1}H DQF spectroscopy, like in the case of ^{2}H, the isotropic water signal is filtered out, enabling the observation of partially oriented water even at high temperatures when the doublet has already coalesced. There are, however, a few important differences between ^{1}H and ^{2}H DQF spectra. (a) While the ^{2}H spectrum consists only of water signals, that of ^{1}H also exhibits signals from non-exchanging protons of proteins and lipids.[22] (b) The ratio between the ^{1}H residual dipolar interaction and the T_2 relaxation rate is considerably smaller than the corresponding ratio of the ^{2}H

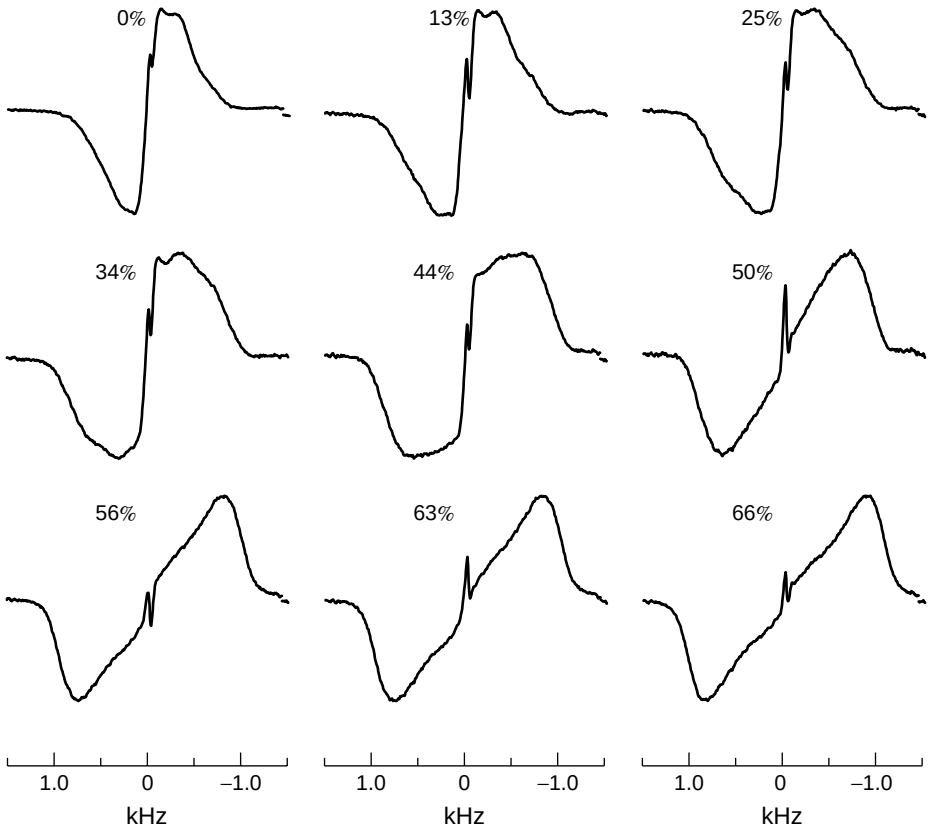

Figure 9 ^{2}H DQF spectra of the outer layer of bovine coronary artery as a function of elongation. The spectra were obtained by subtracting the contributions of the isolated inner layers from that of the intact tissue. (Reproduced from Ref.[21] by permission of Wiley InterScience)

residual quadrupolar interaction. Thus the resolution obtained in the ^{2}H DQF is better. (c) The ^{1}H DQ relaxation time is much shorter than the corresponding value for ^{2}H, due to ^{1}H magnetization transfer from the macromolecules. This fact influences the design of the pulse sequences for spectroscopy and imaging. (d) The water ^{1}H DQF signal intensity is sensitive to the degree of order of the tissue and it rapidly decreases with the temperature due to proton exchange. One should note that for molecules that do not exhibit proton exchange one can see dipolar splitting even in the presence of a small degree of order. An example is the splitting observed in SQ and DQF spectra of phosphocreatine in muscles in vivo.[23]

Water ^{1}H DQF spectra have been measured for various connective tissues.[22] For bovine Achilles tendon (Figure 12),[8] when the tendon's long axis is parallel to the magnetic field, the spectrum consists of a well resolved doublet at low temperatures, with a splitting of about 900 Hz, which coalesces at room temperatures. Fitting the results to equations (4a) and (4b) gave a temperature independent residual dipolar interaction (ν_D) of 300 Hz, and proton exchange rates of $k = 1.75 \times 10^3$, 3.5×10^3 and $6.0 \times 10^3\,s^{-1}$, at 1.5°, 24° and 41 °C, respectively. In the perpendicular orientation, ν_D is reduced by about a factor of 2. Performing the same analysis for articular cartilage,[22] with the magnetic field perpendicular to the bone surface, ν_D of 40 Hz is obtained.

In standard imaging techniques connective tissues appear with a very low S/N ratio, due to the short T_2 associated with

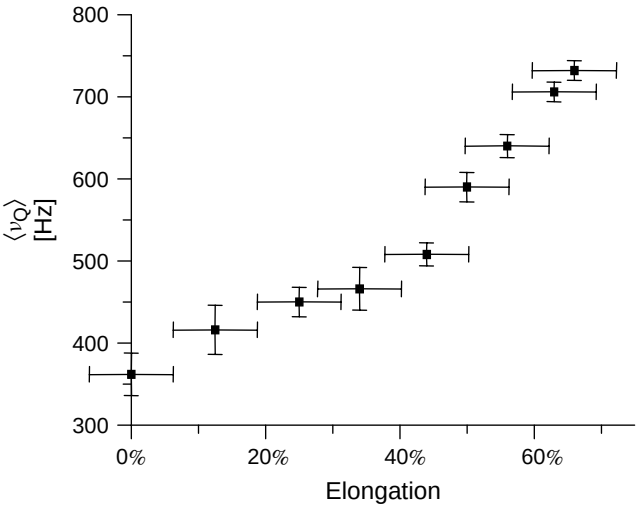

Figure 10 The average quadrupolar interaction $\langle \nu_Q \rangle$ as a function of elongation. The calculation was performed on the full set of spectra shown in Figure 9. (Reproduced from[21] by permission of Wiley InterScience)

these tissues. As the DQF method exclusively detects ordered structures, it is suitable for selectively imaging these tissues. A pulse sequence, which is suitable for the ^{1}H DQF MRI experiment, is illustrated in Figure 13.[24] Unlike in the case of ^{2}H DQF imaging, because of the short ^{1}H DQ relaxation

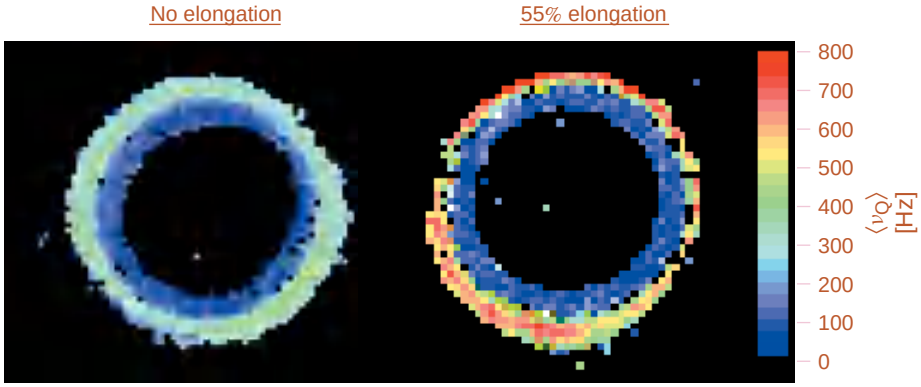

Figure 11 Two images that display a 2D map of the average ^{2}H quadrupolar splitting, $\langle \nu_Q \rangle$ of a bovine coronary artery, unstressed (left) and 55% elongated (right). In the magnet the artery, equilibrated in D_2O, was aligned with the external magnetic field. The field of view of both images was 0.75 cm. (Reproduced from Ref.[20] by permission of National Academy of Science USA)

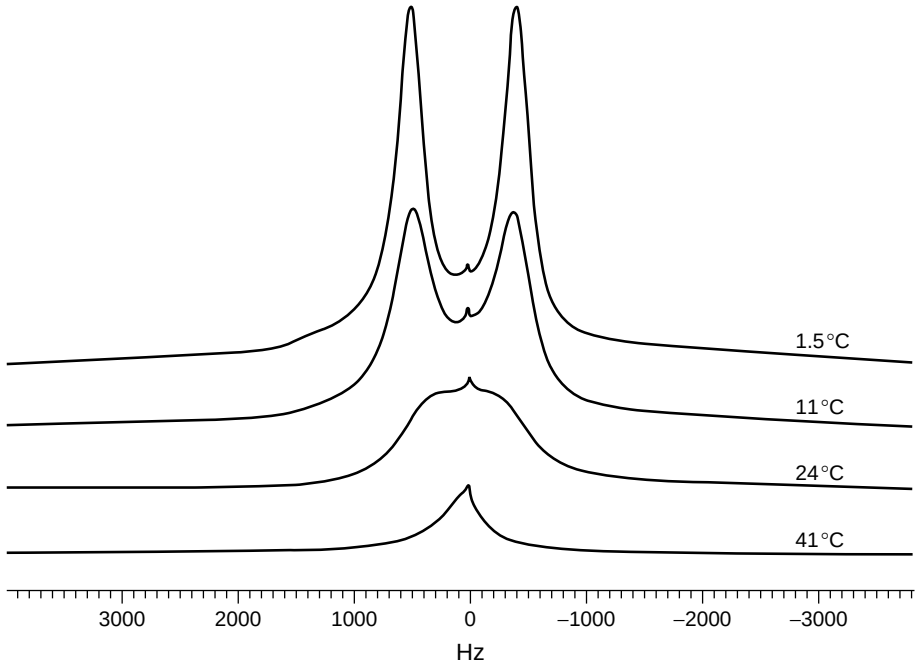

Figure 12 The temperature dependence of the ^{1}H IP-DQF spectra of a bovine Achilles tendon. (Reproduced from Ref.[8] by permission of Academic Press)

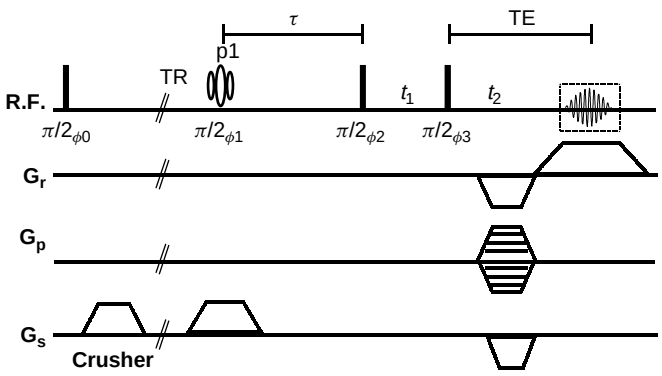

Figure 13 Slice selective ^{1}H DQF pulse sequence for very short τ values. (Reproduced from Ref.[24] by permission of Wiley InterScience)

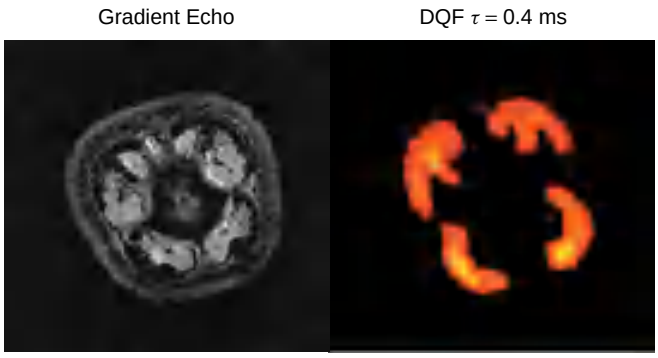

Figure 14 GRE and DQF ^{1}H images of intact rat tail. The long axis of the tail was parallel to the magnetic field. (Reproduced from Ref.[26] by permission of Wiley InterScience)

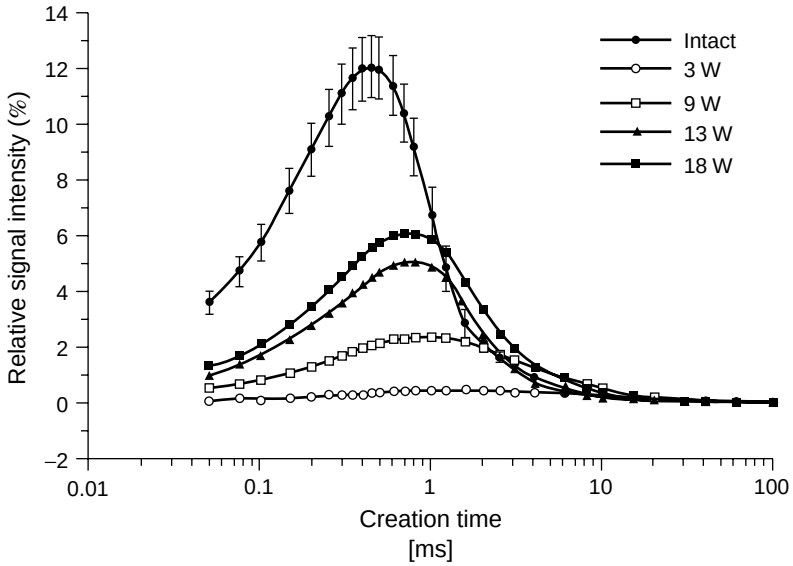

Figure 15 ^{1}H DQF signal intensity of the intact and the regenerated parts of rabbit Achilles tendons as a function of the creation time τ. Means and standard errors are shown for the intact tendon ($n = 6$). Typical results of 3, 9, 13 and 18 weeks after the tenotomy are shown from three experiments in each. Reproducibility of measurement is similar to that of the intact tendon (ca. $\pm$10% of the mean). (Reproduced from Ref.[27] by permission of Wiley InterScience)

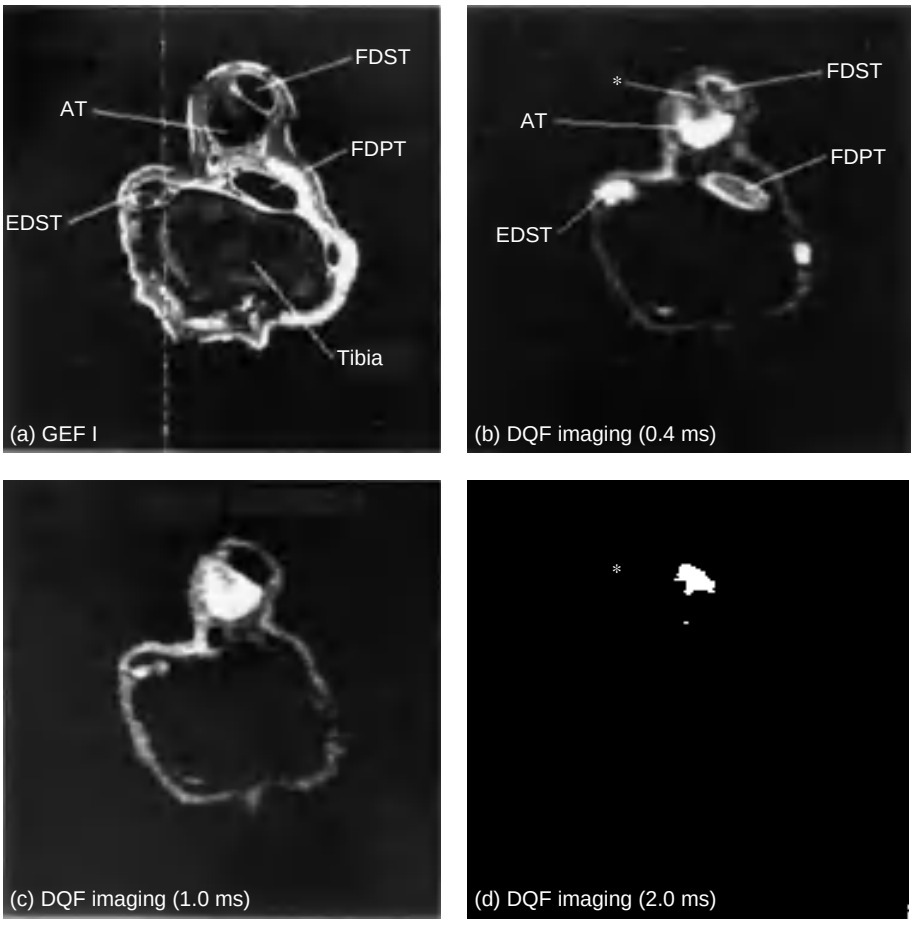

Figure 16 Images of a regenerated rabbit leg measured 18 weeks after tenotomy. (a) Transverse GRE T_2-weighted image. (b–d) Transverse DQF images obtained at: (b) $\tau = 0.4$ ms; (c) $\tau = 1.0$ ms; (d) $\tau = 2.0$ ms. (Reproduced from Ref.[27] by permission of Wiley InterScience)

time, the imaging gradients are applied during t_2,[25] and the DQ evolution time is kept as short as possible.

A comparison between standard ^{1}H gradient-echo (GRE) MRI and ^{1}H DQF MRI of an isolated rat tail is shown in Figure 14.[26] The rat tail is composed of a central spinal bone, four tendons, muscle, adipose and subcutaneous tissue, surrounded by skin. In the GRE image the muscle, as well as the subcutaneous and adipose tissues, is bright while the skin surrounding the tail has a lower intensity. The four tendons and the bone are black. Inside the tendons, some loose connective tissue appears as thin bright lines. In the ^{1}H DQF image, measured at $\tau = 0.4$ ms, only the tendons are depicted with a good positive contrast to the surrounding tissues. When the measurement is repeated at a much longer creation time, the tendons disappear and the skin is depicted. This is in accordance with the spectroscopic result and is a demonstration of the τ contrast mechanism.

In order to assess the application of ^{1}H DQF MRI to medically relevant problems, a follow up of the healing process of ruptured tendons was undertaken.[27] The rupture of the Achilles tendon is a common incident in daily and sport activities. Rehabilitation is a long process and MRI and ultrasonography do not supply enough information regarding the state of the tendon. The experiment presented here was performed on tenotomized (ruptured) rabbit Achilles tendons. After tenotomy, the animals were allowed unrestricted activity in the cage. At different times both the ruptured leg as well as the healthy one, which serves as a reference, were dissected en bloc. After imaging the Achilles tendons were excised and spectroscopic measurements were performed.

The dependence of the DQF spectrum on the creation time was measured for intact tendons as well as for tendons during the healing process. The results are given in Figure 15. Three weeks after tenotomy, hardly any DQF signal is detected from the tendon. The signal gradually regains its intensity but is still far from normal even 18 weeks after the rupture. Moreover, τ_{max}, the creation time where a maximum intensity is observed, is prolonged from 0.4 ms for intact tendons to 1.0 ms at 9 weeks. Concomitantly with the increase of the ^{1}H DQF signal intensity, τ_{max} is shortened, and like the intensity, it does not reach its original value even after 18 weeks.

In the conventional GRE T_2 weighted image of the ruptured lower leg, 18 weeks after the tenotomy of the Achilles tendon, all the tendons have very low signal intensity (Figure 16). In the DQF image measured at $\tau_{max} = 0.4$ ms the intact tendons as well as the ruptured Achilles tendon appear with a positive contrast. On the other hand, in the DQF image measured at τ of 1.0 ms, only the Achilles tendon is depicted. This is in line with the spectroscopic results obtained for τ_{max} during the healing process. At a creation time of 2 ms, only part of the Achilles tendon is observed. We assume that not all parts of the tendon have healed to the same degree and the technique is sensitive enough to depict such differences.

The ^{1}H DQF imaging method was recently applied to the study of human joints on a clinical MRI scanner.[28] Although these results are very preliminary they indicate that the method has a potential for clinical applications.

7 REFERENCES

1. U. Eliav, H. Shinar, and G. Navon, *J. Magn. Reson.*, 1992, **98**, 223.
2. C. S. Springer, Jr., in 'Encyclopedia of Nuclear Magnetic Resonance', eds D. M. Grant and R. K. Harris, Wiley: Chichester, 1996, p 940; S. Wimperis, in 'Encyclopedia of Nuclear Magnetic Resonance', eds D. M. Grant and R. K. Harris, Wiley: Chichester, 1996, p 4078.
3. W. D. Rooney and C. S. Springer, Jr., *NMR Biomed.*, 1991, **4**, 209, 227; S. Wimperis, *Prog. NMR*, 1997, **30**, 157; G. Navon, H. Shinar, U. Eliav, and Y. Seo, *NMR Biomed.*, 2001, **14**, 112.
4. G. Bodenhausen, H. Kogler, and R. R. Ernst, *J. Magn. Reson.*, 1984, **58**, 370.
5. A. Bax, P. G. de Jong, A. F. Mehlkopf, and J. Smidt, *Chem. Phys. Lett.*, 1980, **69**, 567; P. Barker and R. Freeman, *J. Magn. Reson.*, 1985, **64**, 334; R. E. Hurd, *J. Magn. Reson.*, 1990, **87**, 422.
6. G. Bodenhausen, R. L. Vold, and R. R. Vold, *J. Magn. Reson.*, 1980, **37**, 93.
7. Y. Sharf, U. Eliav, H. Shinar, and G. Navon, *J. Magn. Reson. B*, 1994, **107**, 60.
8. U. Eliav and G. Navon, *J. Magn. Reson.*, 1999, **137**, 295.
9. H. J. C. Berensden, *J. Chem. Phys.*, 1962, **36**, 3297; C. Migchelsen and H. J. C. Berensden, *J. Chem. Phys.*, 1973, **59**, 296; B. E. Chapman and K. A. McLauchlan, *Proc. R. Soc. B*, 1969, **173**, 223; B. E. Chapman, S. S. Danyluk, and K. A. McLauchlan, *Proc. R. Soc. B*, 1971, **178**, 465.
10. R. E. Dehl and C. A. J. Hoeve, *J. Chem. Phys.*, 1969, **50**, 3245.
11. W. S. Warren, W. Richter, A. H. Andreotti, and B. T. Farmer, *Science*, 1993, **262**, 2005; S. Lee, W. Richter, S. Vathyam, and W. S. Warren, *J. Chem. Phys.*, 1996, **105**, 874.
12. W. S. Warren, S. Ahn, M. Mescher, M. Garwood, K. Ugrubil, W. Richter, R. R. Rizi, J. Hopkins, and J. S. Leigh, *Science*, 1998, **281**, 247.
13. H. Shinar, Y. Seo, and G. Navon, *J. Magn. Reson.*, 1997, **129**, 98.
14. Y. Seo, H. Shinar, Y. Morita, and G. Navon, *Magn. Reson. Med.*, 1999, **42**, 461.
15. J. F. Martin, L. S. Selwyn, R. R. Vold, and R. L. Vold, *J. Chem. Phys.*, 1982, **76**, 2632.
16. P. van Gelderen, D. DesPres, P. C. M. van Zijl, and C. T. W. Moonen, *J. Magn. Reson., B*, 1994, **103**, 255.
17. T. Ushiki and C. Ide, *J. Neurocytol.*, 1987, **16**, 737.
18. H. Shinar, L. Tsoref, U. Eliav, K. Ikoma, Y. Seo, and G. Navon, In *Proceedings of the ISMRM 8th Annual Meeting*, Denver, CO, 2000, p 2117; H. Shinar, Y. Seo, K. Ikoma, Y. Kusaka, U. Eliav, and G. Navon, *Magn. Reson. Med.*, in press.
19. J. M. Clark, *J. Orthop. Res.*, 1991, **9**, 246.
20. Y. Sharf, Y. Seo, U. Eliav, S. Akselrod, and G. Navon, *Proc. Natl. Acad. Sci. USA*, 1998, **95**, 4108.
21. Y. Sharf, S. Akselrod, and G. Navon, *Magn. Reson. Med.*, 1997, **37**, 69.
22. L. Tsoref, H. Shinar, and G. Navon, *Magn. Reson. Med.*, 1998, **39**, 11.
23. R. Kreis and C. Boesch, *J. Magn. Reson. B*, 1994, **104**, 189.
24. L. Tsoref, U. Eliav, Y. Seo, H. Shinar, and G. Navon, *J. Magn. Reson. Imag.*, 2000, **11**, 336.
25. M. D. Cockman and L. W. Jelinski, *J. Magn. Reson.*, 1990, **90**, 9.
26. L. Tsoref, H. Shinar, Y. Seo, U. Eliav, and G. Navon, *Magn. Reson. Med.*, 1998, **40**, 720.
27. Y. Seo, K. Ikoma, H. Takamiya, Y. Kusaka, L. Tsoref, U. Eliav, H. Shinar, and G. Navon, *Magn. Reson. Med.*, 1999, **42**, 884.
28. A. Alteras, L. Tsoref, and G. Navon, *Magn. Reson. Med.*, 2000, **43**, 640.

Biographical Sketches

Gil Navon, *b* 1936. M.Sc., 1961, Hebrew University, Jerusalem; Ph.D. (Physical Chemistry), 1965, Hebrew University, Jerusalem; Postdoctoral work with R. G. Shulman, 1965–1967, Bell Labs, Murray Hill. Tel Aviv University, 1968–present. Since 1980 Full

Professor. Approx. 220 publications. Principal research interest: biomedical NMR and MRI.

Hadassah Shinar, *b* 1947. MSc, 1974, Tel Aviv University; Ph.D 1985, Tel Aviv University. 1985–present: head of the NMR and MRI laboratory at the Tel Aviv University. Principle research interest: biological NMR and MRI. Approx. 30 publications.

Uzi Eliav, *b* 1948; M.Sc., 1975, Hebrew University, Jerusalem (Physics); Ph.D. 1983, Hebrew University, Jerusalem (Physical Chemistry); Postdoctoral work with J. H. Freed, 1981–1984, Baker Lab. Cornell University; 1986–present, Tel Aviv University. Approx. 30 publications. Research interest: physical and chemical properties of biological tissues as measured by NMR and MRI.

Filamentous Bacteriophage Coat Protein

Stanley J. Opella

University of Pennsylvania, Philadelphia, PA, USA

1	Introduction	1
2	Structural Form of Coat Protein in Virus Particles	1
3	Membrane-Bound Form of Coat Protein	2
4	Procoat Protein	4
5	Comparisons Among the Various Forms of Coat Protein	4
6	Related Articles	5
7	References	5

1 INTRODUCTION

NMR studies of filamentous bacteriophage coat protein have been technically challenging and scientifically fruitful; they have provided many opportunities to develop new NMR methodology as well as to learn about structural and membrane proteins, classes of proteins which differ substantially from the globular proteins that receive the vast majority of attention in structural studies by multidimensional solution NMR spectroscopy and X-ray crystallography. The structural biology of coat protein is complex, especially considering that the protein has only 45–50 residues. It is the most abundant product of the small viral genome and, perhaps because of that, it expresses several distinct biological functions.[1,2] The polypeptide actually encoded by the viral gene VIII, procoat protein, inserts into the cell membrane,[3] where processing by bacterial leader peptidase removes the leader sequence from the N-terminus of the protein.[4] Many copies of the membrane-bound form of the coat protein accumulate within the cell membrane prior to their assembly into the outer coat of the virus particles as they are extruded through the cell membrane. During the course of the viral life cycle the product of gene VIII goes from a preprotein, to a membrane protein, to a DNA-binding structural protein.

Class I filamentous bacteriophages (fd, M13, f1) have important roles that extend beyond their own life cycle, because they are widely used in molecular biology as essential components of experimental methods for DNA sequencing, site-directed mutagenesis, and other procedures. A major new application to biotechnology results from the display of foreign peptides and proteins over the surface of the virus particle by inserting their sequences near the N-terminus of the coat protein.[5]

Comparisons among all of the various coat protein species have been made in the course of the NMR studies, especially between the structural form in the virus and the membrane-bound form, between procoat protein and mature coat protein, and between the proteins from class I and class II bacteriophages (e.g. Pf1). The flexibility of NMR spectroscopy is demonstrated by its ability to show how differences between the membrane-bound form of coat protein and the structural form of coat protein in the virus reflect the structure and dynamics of the protein, and these are directly related to its biological roles. Although neutron[6] and X-ray fiber[7,8] diffraction have played important roles in describing the structure of coat protein and the packing of coat protein and DNA in the virus particles, none of the forms of coat protein have been crystallized. Also, none of the forms in aqueous solution are suitable for multidimensional solution NMR experiments. The difficulties encountered in studying the various coat protein samples by the conventional methods of structural biology provide a great deal of motivation for the development of NMR methods suitable for proteins in supramolecular structures, including DNA–protein and membrane–protein complexes. The NMR studies are feasible even though some forms of the protein exist only transiently in vivo, because all of them can be prepared in vitro as isotopically labeled samples suitable for investigation by NMR spectroscopy, by utilizing solid phase peptide synthesis, isolation from virus particles, and expression in plasmid-containing bacteria.

2 STRUCTURAL FORM OF COAT PROTEIN IN VIRUS PARTICLES

Filamentous bacteriophage particles reorient neither rapidly nor isotropically in solution because of their large size (10^7 Da) and highly elongated shape (9×900 nm). The NMR spectra in Figure 1(a) and (c) demonstrate that conventional high-resolution solution NMR methods are not applicable to proteins, no matter how small, that are immobile on NMR timescales because they are constituents of supramolecular structures.[9] However, the ^{13}C and ^{15}N NMR spectra of coat protein in fd bacteriophage in Figure 1(b) and (d) demonstrate that the combination of selective isotopic labeling of dilute nuclei and high-resolution solid state NMR methods can successfully replace rapid molecular reorientation as a line-narrowing mechanism. Although magic angle spinning in combination with cross polarization and proton decoupling[10]

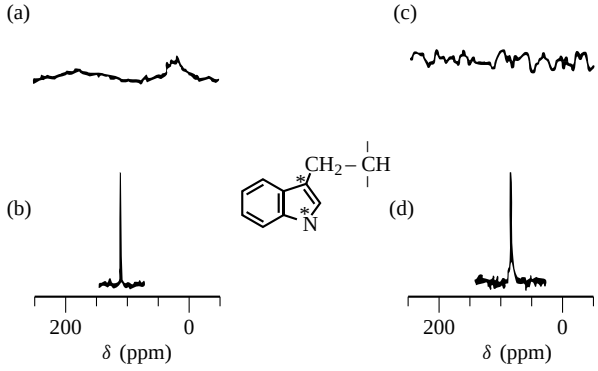

Figure 1 Experimental NMR spectra of fd bacteriophage in solution. (a), (c) Conventional solution NMR spectra on a natural-abundance sample. Only very broad and weak ^{13}C or ^{15}N signals are observable even after extensive signal averaging. (b), (d) Solid state NMR spectra on samples labeled in the single tryptophan residue with either [^{13}C]-γ or [^{15}N]indole obtained with cross polarization, proton decoupling, and magic angle sample spinning. (Reproduced by permission of the American Chemical society from Gall et al.[9])

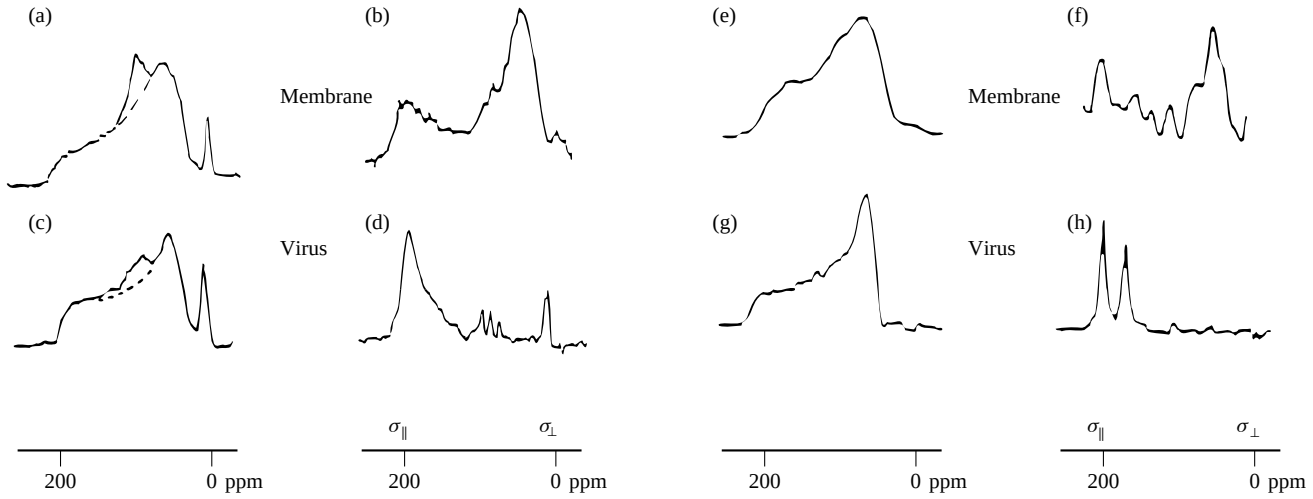

Figure 2 Solid state ^{15}N NMR spectra of fd coat protein. (a)–(d) Uniformly ^{15}N-labeled protein. (e)–(h) Selectively [^{15}N]Leu-14,41-labeled protein. (a), (b), (e), and (f) are of the membrane-bound form of the protein in lipid bilayers. (c), (d), (g), and (h) are of the structural form of the protein in virus particles. (a), (c), (e), and (g) are unoriented samples. (b), (d), (f), and (h) are oriented samples. (Reproduced by permission of Academic Press from McDonnell et al.[16] and Cross and Opella[17])

gives narrow single-line spectra, it is at the expense of the considerable information in the anisotropic chemical shift and dipolar interactions. Nonetheless, the finding that each of the tryptophan (Trp)-26-labeled samples have a single resonance line in Figure 1(b) and (d) provides strong evidence that all coat protein subunits have the same conformation and orientation in the virus particles.

Uniaxial sample orientation is an alternative to magic angle sample spinning as a way to obtain single-line resonances in solid state NMR spectra of polymers,[11] with the important advantage that the anisotropic information present in the nuclear spin interactions is retained and expressed in the observable spectral parameters. It is suitable for proteins that are immobile and oriented along the direction of the applied magnetic field.[12,13] Coat proteins in filamentous bacteriophages are very well suited for this approach, since their structured residues are immobilized by interactions among the protein subunits, and the virus particles behave as rigid cylinders that orient spontaneously with their filament axis aligned with the direction of the applied magnetic field. Peptides and proteins in lipid bilayers can be macroscopically oriented between glass plates for NMR studies,[14] and these samples have been valuable in characterizing the membrane-bound forms of Pf1[15] and fd[16] coat proteins.

The ^{15}N spectra from oriented bacteriophage samples in Figure 2(d) and (h) have resonances with frequencies that reflect the orientations of the amide nitrogens, and hence the peptide bonds, with respect to the direction of the applied magnetic field. Nearly all of the amide resonances in the uniformly ^{15}N-labeled sample of oriented fd [Figure 2(d)] have frequencies near that of the principal element of the chemical shift tensor aligned approximately along the N–H bond.[17] The helical protein subunits are arranged along the filament axis, therefore the N–H bonds of the peptide groups are approximately parallel to the helix axis. There is some spread among the overlapping chemical shift frequencies because of variation and tilt of the α-helix[13] In the spectrum of the selectively [^{15}N]Leu-labeled virus sample in Figure 2(h), the two resonances are well resolved without interference from the overlapping resonances from the rest of the protein; their resonance frequencies reflect the two distinct orientations for these residues, although both have their N–H bonds approximately parallel in the virus particle. The dramatic effects of sample orientation on solid state NMR spectra can be seen by comparing the spectra in Figure 2(c) and (d) for uniformly ^{15}N-labeled coat protein and those in Figure 2(g) and Figure 2(h) for selectively [^{15}N]Leu-labeled coat protein. The chemical shift powder patterns in Figure 2(c) and (g) show that most, but not all, of the residues in coat protein are immobile in the virus particles. With only two ^{15}N amide sites contributing to the powder pattern in Figure 2(g) there can be little doubt that both Leu-14 and Leu-41 have immobile peptide bonds. The situation for the entire protein, as seen in the uniformly labeled sample, is more complex, since the narrow resonance intensity near the isotropic position in Figure 2(c) indicates that some of the residues other than Leu-14 and Leu-41 are mobile on the timescale of the chemical shift anisotropy interaction, which is 10^4 Hz. There are a few mobile residues near the N-terminus of coat protein in the virus particles.[13]

Data derived from oriented spectra, such as those in Figure 2, provide the spectral parameters used to determine the orientation of each peptide plane of the protein relative to the axis defined by the direction of orientation of the sample and the applied magnetic field. These spectral parameters, which can be chemical shift frequencies, dipolar couplings, quadrupolar couplings, or others, define restrictions on the orientations of the spin interaction tensor, and its associated bond or molecular grouping, consistent with the experimental data. It is possible to determine the orientations of peptide planes to within a few degrees by solid state NMR spectroscopy and, therefore, to determine the three-dimensional structure of a protein in this way. Complete polypeptide backbone structures require that several spectral parameters be measured to characterize the angles between each of the peptide planes and the direction of sample orientation. These measurements have been used to derive the model for coat protein in fd virus shown in Figure 3.[13]

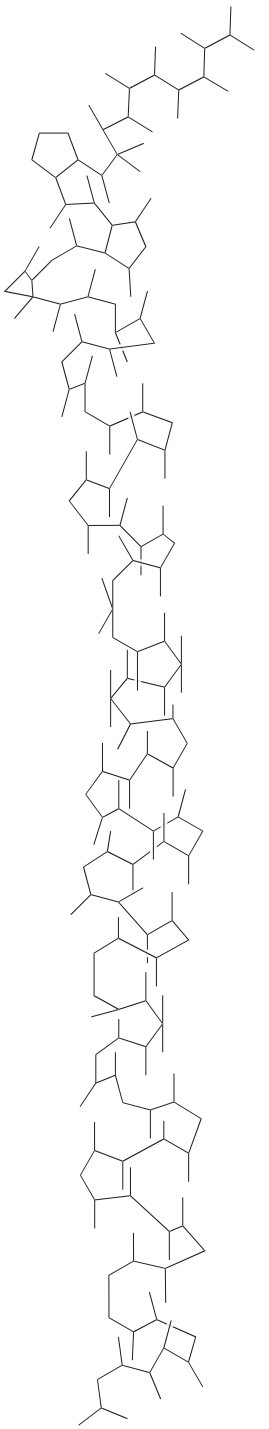

Figure 3 Structural model of fd coat protein in virus particles based on solid state NMR data. (Reproduced by permission of Academic Press from Opella et al.[13])

3 MEMBRANE-BOUND FORM OF COAT PROTEIN

Many of the difficulties associated with NMR studies of membrane proteins can be overcome with a concerted approach that combines the methods of high-resolution solid state NMR spectroscopy on samples of membrane proteins in bilayers with those of multidimensional solution NMR spectroscopy on samples of membrane proteins in micelles.[18,19] fd and Pf1 coat proteins have had important roles in the development of this methodology.[15,16] In this approach, the secondary structure of the protein is determined on the basis of internuclear distance measurements in micelle samples, and the arrangement of the major elements of secondary structure is derived from measurements of angular parameters in oriented bilayer samples.

Membrane proteins display a wide variety of intramolecular dynamics. fd coat protein in micelles was the first system to display heterogeneous backbone dynamics where the resonances from mobile residues could be clearly distinguished from the rigid residues on the basis of multiple relaxation parameters,[20] most dramatically with ^{15}N-labeled samples in micelles by the observation of large negative heteronuclear ^{1}H/^{15}N NOEs,[21] as well as in bilayers with the observation of narrow isotropic resonance intensity in ^{15}N solid state NMR spectra.[22] The comparisons between solid state NMR and solution NMR results can be particularly revealing, since there are residues that are mobile on the slow timescales of solid state NMR powder pattern lineshapes but are immobile on the rapid timescales of solution NMR relaxation measurements. These results have been supplemented by measurements of amide N–H exchange rates throughout the polypeptide in micelles.[23]

A fairly complete picture of the dynamics of the membrane-bound form of coat protein has emerged from the NMR studies. Residues 1–5 at the N-terminus are mobile on the 10^{-9} s timescale of NMR relaxation measurements as well as the 10^{-4} s timescale of solid state NMR lineshapes. Proline-6 is immobile in all forms of the protein on timescales as slow as 10^{-4} s, and the structured portion of the protein begins at this residue. Solid state NMR lineshapes show that Tyr-21 has some mobility, even though homonuclear ^{1}H NOEs indicate that it is part of a stable structure. The two helical segments, residues 7–20 and residues 23 and 42, appear to be rigidly structured on all timescales. The C-terminal residues 44 through 50 show evidence of mobility on various timescales, depending on the temperature.

Multidimensional solution NMR methods can be applied to the membrane-bound form of coat protein in micelles in aqueous solution.[15,16,20,24,25] Isotopic labeling is especially important for a slowly reorienting protein in micelles, and this need led to coat protein being the first uniformly ^{15}N-labeled[26] and uniformly ^{15}N/^{2}H-labeled[27] protein for multidimensional NMR experiments. The choice of detergent and its concentration are crucial aspects of sample preparation, and have been problematic for solution NMR studies of fd coat protein in micelles.[28] The spectrum in Figure 4 shows that single correlation peaks can be resolved and assigned for fd coat protein in micelles. Three-dimensional spectra show backbone NOEs that are consistent with extensive helical secondary structure in the protein.[19,25] This can be demonstrated with the leucine residues, Leu-14 and Leu-41, the same residues labeled selectively to obtain the data in Figure 2. ^{1}H/^{1}H strips at ^{15}N chemical shifts corresponding to Ser-13, Leu-14 and Gln-15 show the presence of NOEs between resonances from hydrogens on adjacent amide nitrogens, α-carbons, and β-carbons; these residues are part of an amphipathic helix that lies in the plane of the lipid bilayer. Lys-40, Leu-41 and Phe-42 also exhibit these characteristic NOEs and are a part of the hydrophobic transmembrane helix. Numerous other NOEs observed for residues 13–15 and

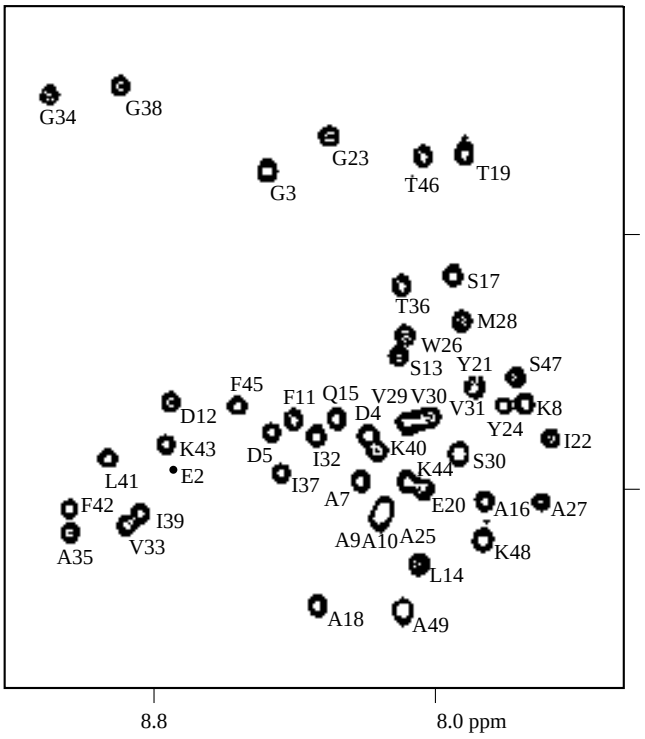

Figure 4 Two-dimensional $^{1}H/^{15}N$ heteronuclear multiple quantum correlation spectrum of uniformly ^{15}N-labeled fd coat protein in micelles. (Reproduced by permission from McDonnell et al.[16])

40−42 are between $NHC_{\alpha}H(i, i + 3)$ and $NHC_{\alpha}H(i, i + 4)$ sites, strongly supporting the presence of helical secondary structure for both Leu-14 and Leu-41 of fd coat protein in micelles.

Since it is possible to prepare both oriented and unoriented samples of proteins in fully hydrated phospholipid bilayers, a wide variety of spectral parameters can be resolved and measured from single-line and powder pattern spectra obtained on these samples.[16] The ^{15}N chemical shift powder patterns from unoriented samples of uniformly [Figure 2(a)] and selectively ^{15}N-labeled fd coat protein in lipid bilayers [Figure 2(e)] indicate that the membrane-bound form of the protein has both mobile and rigid backbone sites. The amide groups of both Leu-14 and Leu-41 are immobile in membrane bilayers because the powder pattern spectrum in Figure 2(e) shows little evidence of motional averaging. However, the spectrum in Figure 3(a) from the uniformly ^{15}N-labeled coat protein in bilayers has substantially more isotropic resonance intensity than the same protein in virus particles [Figure 2(c)], which indicates that there is a difference in dynamics between these two forms of the protein.

The resonance bands in the spectrum of an oriented bilayer sample of uniformly ^{15}N-labeled fd coat protein [Figure 2(b)] occur near the positions expected for transmembrane and in-plane helices. Better spectral resolution is available from selectively labeled samples. Since the secondary structure for the two leucine residues is established as helical by NOE data as discussed above, the resonance frequency of each nitrogen site can be used to establish the orientations of the two helices relative to the plane of the bilayer. The spectrum in Figure 2(f) of [^{15}N]Leu-labeled coat protein in oriented bilayers has one line with a resonance frequency near the parallel orientation for the N−H bond and a second line with a resonance frequency near the perpendicular orientation for the N−H bond, indicating that the hydrophobic helix spans the bilayer because the N−H bond of one of the leucine residues is parallel to the direction of orientation and that the amphipathic helix is in the plane of the bilayer because the N−H bond of the other leucine residue is perpendicular to the direction of orientation.

4 PROCOAT PROTEIN

The 73-residue procoat protein, which includes the 23-residue N-terminal leader sequence, was prepared by solid phase peptide synthesis with two ^{15}N-labeled residues, one in the leader sequence and one as a control in the rigid hydrophobic helix found in the mature protein.[29] Spectra from these labeled species in micelles and bilayers qualitatively characterized the dynamics of these proteins. Ser-20- a residue near the N-terminus of the leader sequence, was found to be mobile on both the 10^{-4} and 10^{-9} s timescales, while residues −13 through −10, all of which are in the midsection of the leader sequence, were found to be rigidly held on all timescales. Residues at or near the cleavage site of leader peptidase are mobile, in particular Ala-1− and Gly-3+ are mobile on the basis of both solution and solid state NMR data. The mobile region of procoat protein near the cleavage site may be necessary for removal of the leader sequence to form the mature protein. In separate solid state NMR experiments on an oriented sample of procoat protein in lipid bilayers, the ^{15}N resonance frequencies for labels in the leader sequence are shown to be in the plane of the bilayer.

5 COMPARISONS AMONG THE VARIOUS FORMS OF COAT PROTEIN

The major stages of the filamentous bacteriophage life cycle are associated with distinct forms of coat protein. Comparisons among these forms are highly suggestive of the molecular events that accompany the transitions of coat protein and the virus. The results of the NMR experiments on the various forms of fd coat protein are summarized in Figure 5. As shown in the model for procoat protein, the leader sequence has a mobile N-terminus, a structured section, and then a mobile area near the cleavage site. Both procoat protein and the membrane-bound form of coat protein are monomers, since each amide site gives a single resonance in micelles. The features of the model of the membrane-bound form of fd coat protein are similar to those found for the membrane-bound form of Pf1 coat protein,[15] in spite of the absence of sequence homology between these proteins. Both proteins consist of helical secondary structure intermixed with mobile termini and loop regions. The helical regions in fd and Pf1 coat protein consist of two segments, with hydrophobic residues forming a transmembrane helix, and amphipathic residues forming a helix parallel to the bilayer plane. The two proteins differ most in the extent of mobility of the segment connecting the two helices. The connecting loop residues in Pf1 are highly mobile on both slow (10^{-4} s) and fast (10^{-9} s) timescales with an absence of homonuclear ^{1}H NOE cross peaks involving the

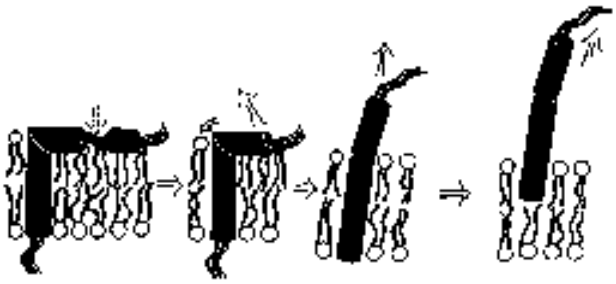

Figure 5 NMR-based models of fd coat protein throughout the viral life cycle

amide resonances for these residues. In contrast, fd coat protein has homonuclear NOE cross peaks throughout the sequence, including the residues involved in the turn connecting the two helices, although there is evidence of limited motional averaging for Tyr-21 – .[16]

The structural elements found in the membrane-bound forms of fd and Pf1 coat proteins are similar to those in other membrane proteins, such as bacteriorhodopsin and the photosynthetic reaction center. The dynamic profiles of both coat proteins are also similar to those found in other membrane proteins, since mobile N- and C-terminal residues and a mobile loop connecting rigidly structured helices have been found. The NMR studies show that both fd and Pf1 coat proteins are typical membrane proteins.

Coat protein undergoes minor changes in secondary structure but major changes in tertiary structure upon assembly into the virus particles. A few residues at the C-terminus that are mobile in the membrane-bound form become structural in the virus particles, and some rearrangement of the conformations of the residues in the turn connecting the two helices occurs. However, the protein undergoes a dramatic change in tertiary structure as the two helical segments go from approximately perpendicular, as shown in Figure 5, to approximately collinear in the virus particles. This change demonstrates why there are mobile residues in the turn region between the two helices. This is a very clear example of why it is essential to analyze protein structure and dynamics in concert. It could only have been discovered by NMR spectroscopy.

6 RELATED ARTICLES

Membrane Proteins; Protein Dynamics from Solid State NMR; Structures of Larger Proteins, Protein-Ligand, and Protein-DNA Complexes by Multi-Dimensional Heteronuclear NMR.

7 REFERENCES

1. D. A. Marvin and B. Hohn, *Bacteriol. Rev.*, 1969, **33**, 172.
2. M. Russel, *Mol. Microbiol.*, 1991, **5**, 1607.
3. C. N. Chang, G. Blobel, and P. Model, *Proc. Nal. Acad. Sci. U.S.A.*, 1978, **75**, 361.
4. R. Zimmerman, C. Watts, and W. Wickner, *J. Biol. Chem.*, 1982, **257**, 6529.
5. J. Greenwood, A. E. Willis, and R. N. Perham, *J. Mol. Biol.*, 1991, **220**, 821.
6. R. Nambudripad, W. Stark, S. J. Opella, and L. Makowski, *Science*, 1991, **252**, 1305.
7. L. Makowski, in *Biological Macromolecules and Assemblies*, ed. A. McPherson, Wiley, New York, 1984, Vol. 1, p. 203.
8. D. A. Marvin, R. D. Hale, C. Nave, and M. H. Citterich, *J. Mol. Biol.*, 1994, **235**, 260.
9. C. M. Gall, T. A. Cross, J. A. DiVerdi, and S. J. Opella, *Proc. Natl. Acad. Sci. U.S.A.*, 1982, **79**, 101.
10. J. Schaefer and E. O. Stiejskal, *J. Am. Chem. Soc.*, 1976, **98**, 1031.
11. S. J. Opella and J. S. Waugh, *J. Chem. Phys.*, 1977, **66**, 4919.
12. T. A. Cross and S. J. Opella, *J. Am. Chem. Soc.*, 1983, **105**, 306.
13. S. J. Opella, P. L. Stewart, and K. G. Valentine, *Q. Rev. Biophys.*, 1987, **19**, 7.
14. B. Bechinger, Y. Kim. L. E. Chirlian, J. Gesell, J.-M. Neumann, M. Montal, J. Tomich, M. Zasloff, and S. J. Opella, *J. Biomol. NMR*, 1991, **1**, 167.
15. K. Shon, Y. Kim, L. A. Colnago, and S. J. Opella, *Science*, 1991, **252**, 1303.
16. P. A. McDonnell, K. Shon, Y. Kim, and S. J. Opella, *J. Mol. Biol.*, 1993, **233**, 447.
17. T. A. Cross and S. J. Opella, *J. Mol. Biol.*, 1985, **182**, 367.
18. S. J. Opella and P. A. McDonnell, in *NMR of Proteins*, eds. A. M. Gronenborn and G. M. Clore, MacMillan Press, 1993, p. 159.
19. S. J. Opella, Y. Kim, and P. McDonnell, *Methods Enzymol.*, 1994, in press.
20. T. A. Cross and S. J. Opella, *Biochem. Biophys. Res. Commun.*, 1980, **92**, 478.
21. M. J. Bogusky, R. A. Schiksnis, G. C. Leo, and S. J. Opella, *J. Magn. Reson.*, 1987, **72**, 186.
22. G. C. Leo, L. A. Colnago, K. G. Valentine, and S. J. Opella, *Biochemistry*, 1987, **26**, 854.
23. J. D. J. O'Neil and B. D. Sykes, *Biochemistry*, 1988, **27**, 2753.
24. G. D. Henry and B. D. Sykes, *Biochemistry*, 1992, **31**, 5284.
25. F. J. M. van de Ven, J. W. M. van Os, J. M. A. Aelen, S. S. Wymenga, M. L. Remerowski, R. N. H. Konigs, and C. W. Hilbers, *Biochemistry*, 1993, **32**, 14 275.
26. M. J. Bogusky, P. Tsang, and S. J. Opella, *Biochem. Biophys. Res. Commun.*, 1985, **127**, 540.
27. K. Shon and S. J. Opella, *J. Magn. Reson.*, 1989, **82**, 193.
28. P. A. McDonnell and S. J. Opella, *J. Magn. Reson., Ser. B*, 1993, **102**, 120.
29. P. A. McDonnell, Y. Kim, J. H. Tomich, J. H. Richards, and S. J. Opella, unpublished results.

Acknowledgments

The research on filamentous bacteriophages has been supported by National Institutes of Health grants GM24266 and AI20770.

Biographical Sketch

Stanley J. Opella. *b* 1947. B.S., Chemistry, University of Kentucky (undergraduate research with S. L. Smith), 1969. Ph.D., Chemistry, Stanford University (with O. Jardetzky and H. McConnell), 1974. Postdoctoral fellow, Massachusetts Institute of Technology (with J. S. Waugh), 1975–76. Currently Professor of Chemistry at the University of Pennsylvania. Approx. 125 publications. Research interests: development and application of NMR spectroscopy for the study of proteins, especially protein structure determination by solid state NMR spectroscopy.

Glycolipids

Harold C. Jarrell

National Research Council, Ottawa, Ontario, Canada

1	Introduction	1
2	Glycolipid Headgroup Structure	1
3	Glycolipid Dynamics	5
4	^{1}H and ^{13}C Magic Angle Spinning	7
5	Related Articles	7
6	References	7

1 INTRODUCTION

Glycolipids are amphiphilic molecules which are anchored in the cell membrane by a hydrophobic tail. They may be divided, although not exclusively, into two broad categories: those based on diacyl- (or dialkyl-)glycerol [Figure 1(a)], and those based on sphingosine [Figure 1(b)]. Glycoglycerolipids represent the most abundant lipid in nature constituting the dominant membrane lipid in some microorganisms and in plant cells. The relationship between the nature of the glycolipid headgroup and the physical–chemical properties of membranes containing these lipids has been the focus of many studies.[1] It is recognized that biological membranes normally contain lipids that form nonlamellar structures, and that their amounts are actively regulated to maintain proper membrane function. The preference of a lipid to form different aggregate structures (lamellar, hexagonal, etc.) in aqueous dispersions has been related to its 'molecular shape' which is intimately connected to the nature and structure of the lipid headgroup (see ***Lipid Polymorphism***).[2]

Glycosphingolipids typically represent minor membrane lipid components, but they play important roles as antibody recognition sites, as toxin receptors, and as elements of cell adhesion.[3] This diverse functionality involves biomolecular recognition and, as a result, has motivated structural studies which are directed at defining the conformation(s) of the carbohydrate region.

Since biomolecular recognition of glycolipids takes place within the reference frame of the membrane, the orientation of the lipid headgroup relative to the membrane surface is thought to be important.[4] Figure 2 compares the isolated glycosphingolipid GM_1 with the molecule in a membrane environment. The important difference between the two systems is that in a membrane the carbohydrate region is proximal to a lipid/water interface. This interfacial environment may have significant impact not only on the carbohydrate conformation but also on how it is presented to the outside world.

2 GLYCOLIPID HEADGROUP STRUCTURE

Given the potential for interplay between membrane environment and the structure–function relationship of these biomolecules, there is widespread interest to probe molecular

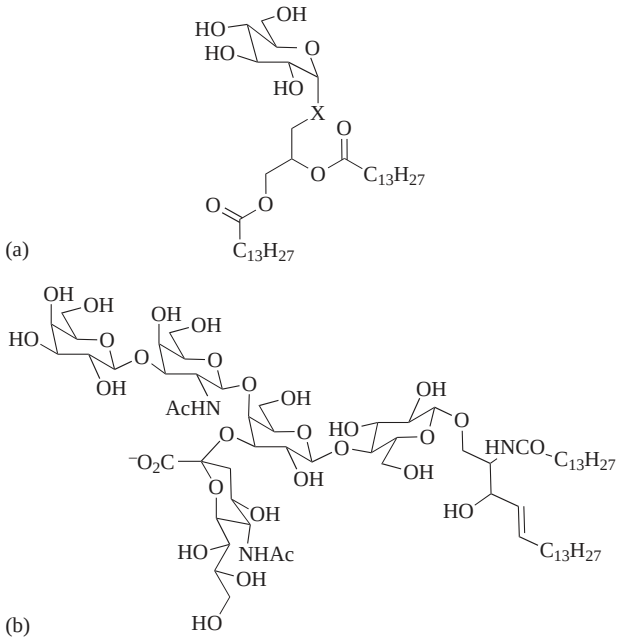

Figure 1 Structures of the two classes of glycolipids: (a) X = C glycoglycerolipids (most frequently glucosyl or galactosyl residues) which may have saturated or unsaturated fatty acyl or alkyl chains; (b) glycosphingolipids in which mono- to oligosaccharides are attached to an acylsphingosine residue

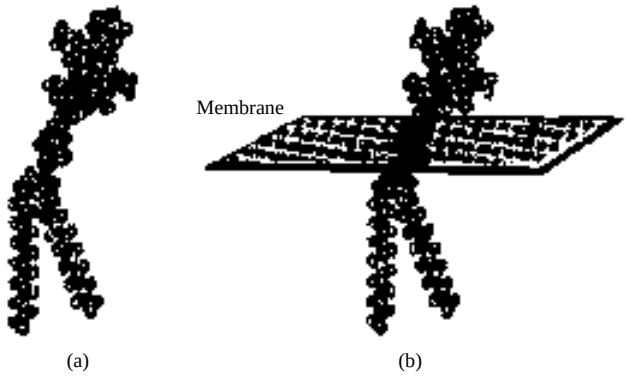

Figure 2 Comparison of possible situations for a glycolipid headgroup of GM_1: (a) intact lipid as a monomer as may occur in organic solvents such as dimethyl sulfoxide; (b) lipid embedded in a bilayer membrane. Note that in (b) the headgroup 3D structure is the same as in (a) but is referenced not only to the rest of the lipid molecule but also to the bilayer plane. The orientation of the carbohydrate headgroup [having the same three-dimensional structure in (a) and (b)] relative to the lipid/water interface may influence the recognition process and 'molecular shape'

structure in macromolecular assemblies, such as lipid bilayer membranes. In general, glycolipids are not readily crystallized and, as a result, the number of X-ray crystallographic studies is small.[5] For this reason much of the structural information has come from NMR studies. This article will focus on the glycolipid headgroup region. The reader is referred to other articles in this volume for discussion of the acyl chain region (see ***Membranes: Deuterium NMR*** and ***Membrane Lipids of Acholeplasma laidlawii***).

2.1 Glycolipid Solution State NMR

Due to their amphiphilic character, glycolipids form micelles or liposomes when they are dispersed in water, which makes high-resolution NMR studies either impractical or of reduced utility in structural studies. This difficulty has been overcome by two approaches that have found frequent use. The first is to cleave the headgroup from the hydrophobic tail and perform conformational studies in aqueous solution. The second approach is to study the lipid in an organic solvent such as dimethyl sulfoxide (DMSO) in which the lipid does not form large aggregates.[6] Under these conditions, standard high-resolution 1D and 2D NMR techniques for resonance assignment and 3D structure determination have found widespread use.[7]

Much of the glycolipid structural work has focused on glycosphingolipids, in particular gangliosides. Such studies mainly rely on the nuclear Overhauser effect (NOE) to obtain the spatial proximities between protons. This distance map is used in conjunction with molecular mechanics or dynamics calculations to deduce headgroup conformation. However, unlike proteins and oligonucleotides,[8] oligosaccharides frequently show very few structurally relevant NOE constraints so that three-dimensional structure analysis is dominated by theoretical calculations. Recently, Dabrowski and co-workers have shown that in DMSO protons of hydroxyl and amido groups may be used to obtain additional NOE contacts and thereby extend the experimental basis with which to verify theoretically calculated conformations.[5,9] The latter approach has been used with the glycolipids globoside[5] and with gangliosides.[9–13]

Internal flexibility in glycolipid headgroups indicates that there is an ensemble of structures present. Both ^{1}H and ^{13}C relaxation studies have been used to probe for carbohydrate segmental motion.[6,10] Although a number of studies have shown that the oligosaccharide is relatively rigid, some oligosaccharides appear to have limited motion about the glycosidic bonds. Recent ^{1}H $T_{1\rho}$ measurements have shown a pronounced flexibility in globoside and in the ganglioside GM_3.[5,10]

In a few studies the natural cell surface environment has been approached by incorporating glycolipids at low concentration in aqueous mixed micelles of dodecylphosphocholine under which conditions solution state NMR techniques are still viable. Little difference was seen between solution and micelle associated headgroup conformations.[9,10]

2.2 Membrane Glycolipid Headgroup Conformation and Orientation

While isotropic solution and micelle studies provide insight into the 3D structural preferences of isolated glycolipids, the results may not be transferable to the membrane situation. Molecular mechanics calculations have shown that in a bilayer arrangement the range of possible conformations is considerably reduced.[14,15] NMR studies of glycolipids in lipid bilayer environments probe more directly the influence of the membrane environment on carbohydrate structure, surface presentation, and dynamics.

Above the gel to liquid crystal phase transition temperatures, aqueous lipid systems behave spectroscopically as uniaxial nematic liquid crystals. Thus they represent partially ordered systems, wherein molecular motion is anisotropic covering timescales from picoseconds to seconds. NMR spectra of such systems are dominated by tensorial spin interactions which are only partially averaged. The strategies for structural and motional studies in such systems are similar to those used for organic liquid crystals.[16]

To date, $^{13}C-^{13}C$ and $^{13}C-^{1}H$ dipolar and ^{2}H quadrupolar interactions have been used successfully to probe glycolipid systems. In lipid bilayer systems the dipolar and quadrupolar spectral splittings are given by:

$$\Delta\nu = \Lambda \cdot [A_{zz}S_{zz} + 1/3(A_{xx} - A_{yy})(S_{xx} - S_{yy}) + 4/3A_{xy}S_{xy} + 4/3A_{xz}S_{xz} + 4/3A_{yz}S_{yz}] \quad (1)$$

where

$$\Lambda = 3/2 \cdot \chi \cdot 3(\cos^2\beta - 1)/2 \quad \text{(quadrupolar)} \quad (2)$$

or

$$\Lambda = -\gamma_1\gamma_2/\pi^2 r_{12}^3 \cdot 3(\cos^2\beta - 1)/2 \quad \text{(dipolar)} \quad (3)$$

and

$$A_{p,q} = (3\cos\alpha_p \cos\alpha_q - \delta_{pq})/2 \quad (4)$$

and

$$S_{p,q} = \langle 3\cos\theta_p \cos\theta_q - \delta_{pq}\rangle/2 \quad (5)$$

The angle β is the angle the bilayer normal makes with the magnetic field direction. The $\cos\alpha_p$ terms are the direction cosines defining the orientation of the $C-^{2}H$ bond direction (quadrupolar interaction) or of the internuclear vector (dipolar interaction, where here the internuclear distance, r_{12}, is not conformation-dependent) to a molecule-fixed frame, and the $S_{p,q}$ terms are orientational order parameters describing the average orientation of the molecular axes p,q with respect to the director of motional averaging, the bilayer normal. The $S_{p,q}$ terms are the elements of a 3×3 order matrix having five independent elements. The order matrix may be diagonalized to give the principal axes of order in the molecular frame. The latter transformation establishes the average orientation of the molecular frame relative to the bilayer normal. If there were no reorientation of the molecule away from the membrane director, then S_{zz} would have a value of 1.0 (completely ordered). If the molecule reorients isotropically about the bilayer normal, then the lipid shows no orientational order and S_{zz} would be 0. Inspection of equations (1)–(5) reveals that the quadrupolar and dipolar splittings depend upon the orientation of the labeled molecular segment through the geometric terms $\alpha_{p,q}$. Structure determination is essentially a matter of obtaining enough geometric constraints to define the structure. For a rigid deuterated or ^{13}C-labeled sugar ring, each $C-^{2}H$ bond, $^{13}C-^{13}C$ or $^{1}H-^{13}C$ internuclear vector in the ring has a well-defined orientation within the molecular frame and all sites in the residue have the same order parameters. Thus labeling the carbohydrate with ^{2}H or ^{13}C at several positions allows one to determine $\alpha_{p,q}$ for each site, which may be used to define the average orientation of the sugar

ring, relative to the bilayer normal. If orientational ordering is axially symmetric then equation (1) reduces to:

$$\Delta\nu = \Lambda \cdot [(3\cos^2\alpha_{zz} - 1)/2] \cdot S_{zz} \qquad (6)$$

and at least three quadrupolar (or dipolar) splittings are required (i.e. three or more labeled positions). In general, at least five splittings are required to determine the order matrix and the geometrical terms. To determine the 3D structure of an oligosaccharide chain having no internal flexibility (on the timescale shorter than ms) about the interresidue glycosidic linkages, spin interactions for as many sites as possible need to be measured, preferably at least three splittings for each residue.

A similar strategy has been exploited for peptide structure determination in solid state and membrane samples.[17,18] Structure determination requires a search over all possible structures wherein direction cosines for the ^{2}H–C bonds (and/or internuclear dipolar vectors in the molecular frame) and an order matrix (reflecting the restriction of orientational averaging) best fit the NMR results. This is analogous to methods of high-resolution NMR structure determination in which distance constraints obtained from NOE measurements and geometry derived from scalar couplings help to define structure. The two approaches differ in that unlike solution studies, the membrane related 3D structures are spatially referenced to the molecular environment which is the membrane plane. It is this latter aspect that is important in a discussion of recognition-site presentation.

It has been possible to study biological membranes containing glycolipids with isotopically labeled acyl chains by NMR.[19] The difficulty in introducing isotopic labels specifically into glycolipid headgroups in biological membranes has necessitated the use of model membrane systems to examine specific features of interest. Two approaches to modeling the bilayer membrane environment have been used for such NMR studies. The first uses multilamellar liposomes formed by dispersing lipids or lipid mixtures in water or buffer. Such systems give rise to 'powder spectra' such as shown in Figure 3(a) and have been shown to reproduce NMR spectral characteristics obtained with intact biological membranes. The second approach uses glycolipids incorporated into micelle-forming lipid mixtures that orient in the magnetic field[20] which give rise to spectra such as shown in Figure 3(b). Spectroscopy in such systems shares strong similarities with that in nematic liquid crystals for which there is a vast literature.[16] These micellar systems may be a poorer model of bilayer membranes than liposomes but they have proven to be useful.

2.2.1 *Multilamellar Liposomes*

The first use of ^{2}H NMR to determine the surface orientation of a membrane glycolipid headgroup was reported by Skarjune and Oldfield for galactosylceramide in a phospholipid membrane.[21] The surface orientation of the monosaccharide headgroup was sensitive to the type of phospholipid present and to other membrane components. A series of simple glycoglycerolipids have been studied to investigate systematically the dependence of glycolipid headgroup orientation on the carbohydrate moiety. A comparison of three lipids having α-glucosyl, β-glucosyl (β-DTGL), and α-mannosyl residues

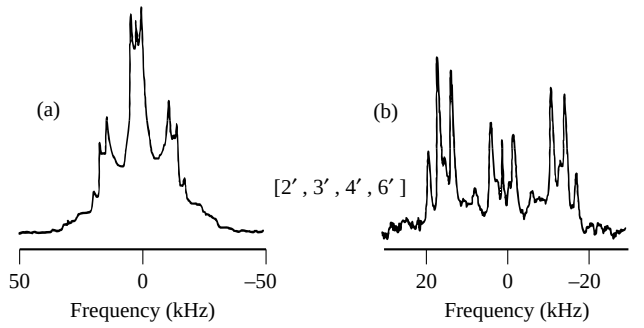

Figure 3 ^{2}H NMR of the glycolipid DTLL in: (a) multilamellar liposomes randomly dispersed (β is random, powder spectrum) with respect to the magnetic field direction (from Renou et al.[25] with permission); (b) discoidal micelles (sodium glycocholate-dipalmitoylphosphatidylcholine) which are oriented (oriented spectrum) with the micelle surface at 90° (β = 90°) relative to the magnetic field

attached to a dialkylglycerol anchor showed that both headgroup orientation and ordering were very sensitive to the nature of the carbohydrate residue.[22,23] A typical ^{2}H NMR spectrum of β-DTGL labeled at several positions in the glucose ring is shown in Figure 4(a). Position-dependent splittings are readily seen with resonance assignments made by controlling the degree to which each position was labeled. In these studies it was assumed that orientational ordering was axially symmetric and equation (6) was used to extract the order parameter and orientational information from the ^{2}H quadrupolar splittings. Headgroup order parameters ranged from 0.45 to 0.8 for the three glycolipids. Since dialkyl- and diacylglycoglycerolipids constitute major components of membranes in plants and a number of microorganisms, the three lipids served as a means of examining how glycolipid headgroup properties influence the biophysical properties of membranes. In the case of the lipid β-DTGL, both the headgroup and the glycerol were labeled. Analysis of the glycerol segment alone gave an order parameter of 0.65 whereas that of the glucose ring was 0.45, indicating the presence of segmental motion about the glucose–glycerol linkage. The average structure and bilayer orientation of the glucose–glycerol segment was determined as shown in Figure 5 (left).[24] Interestingly, β-DTGL was found to

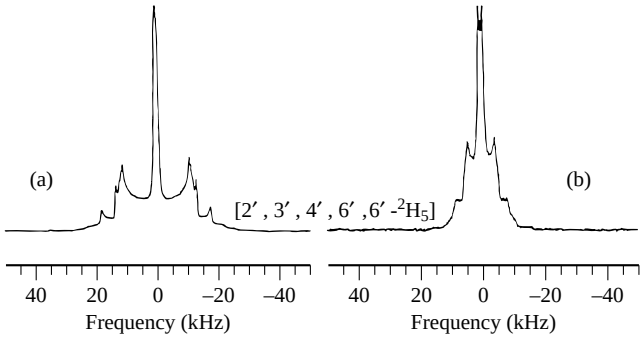

Figure 4 Typical ^{2}H NMR spectra of the glycolipid β-DTGL: (a) in the lamellar (bilayer) phase; (b) inverted hexagonal phase. The lipid has been ^{2}H-labeled to differing degrees at the indicated sugar ring positions. Note that each position gives rise to a separate quadrupolar splitting indicative of the site dependent geometric (structural) terms α_p in equation (4). (From Jarrell et al.[22] with permission)

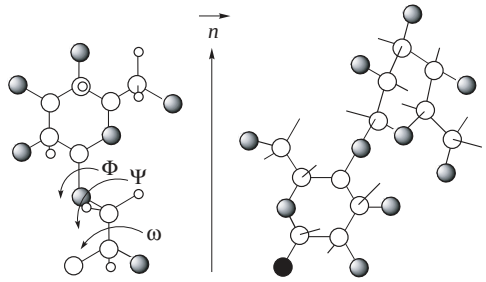

Figure 5 Average structure and orientation of (left) the glucosyl–glycerol region of the glycolipid β-DTGL in a bilayer lipid membrane as determined by ^{2}H NMR (from Jarrell et al.[24] with permission). Note that since the structure is not rigid, there is some motion about the glycosidic linkage, i.e. there is conformational equilibrium representing a range of ϕ, ψ, and ω angles; (right) the lactosyl residue in the membrane-associated glycolipid DTLL, where the headgroup is presented with the average orientation relative to the surface as determined by ^{2}H NMR (from Renou et al.[25] with permission). The membrane surface extends into and out of the plane of the page, and the views are shown along the membrane surface

have a headgroup orientation and orientational ordering similar to that of galactosylceramide, with the sugar ring essentially fully extended away from the membrane surface into the aqueous medium.

Hydrated lipids may exhibit phase polymorphism when the temperature is varied. Aqueous dispersions of pure β-DTGL above its gel to liquid crystalline transition temperature (52 °C) form bilayer structures, which on heating to 56 °C form an inverted hexagonal structure. This phase transition leads to dramatic NMR spectral changes such as are shown in Figure 4(b). The formation of nonlamellar phases is a result of the small surface area occupied by the lipid headgroup, arising from its surface orientation and relatively high ordering. The headgroup orientation of lipid in a bilayer structure was shown to differ significantly from that of lipid in the hexagonal phase. Such studies indicate that it is now possible to evaluate more rigorously the suggestion that lipid 'molecular shape' influences the physical–chemical properties of biological membranes.[1]

^{2}H NMR studies of disaccharide glycolipids have been reported.[25,26] A dialkylglycoglycerolipid, DTLL, containing the lactosyl ($Gal_p\beta$ (1 → 4) Glc_p) residue was ^{2}H-labeled in each of the two sugar rings affording six quadrupolar splittings and thus six geometrical structural constraints.[25] ^{2}H longitudinal relaxation measurements showed that there was no motion about the galactose–glucose glycosidic linkage, suggesting a relatively rigid headgroup. The ^{2}H quadrupolar splittings were analyzed according to equation (1) to obtain the order matrix and the disaccharide orientation. Since the signs of the quadrupolar splittings were not known and the splitting values depend upon geometric terms having the functional form in equation (4), a number of headgroup conformations were consistent with the geometric constraints. To evaluate further the structures that were consistent with the NMR data required additional information obtained from conformational potential energy calculations. A search over all possible conformations for the NMR-consistent lactolipid structures gave the lowest energy structure, shown in Figure 5 (right). This structure differs considerably from that of crystalline lactose and that of methyl lactoside in solution, suggesting that the membrane surface has an influence on the headgroup structure. The headgroup on average was determined to be extended away from the surface and as having nearly axially symmetric ordering with an order parameter of 0.51.

The glycolipid systems studied in detail to date are relatively simple, but such studies demonstrate the potential of the experimental approach. Recently, studies on more complex glycosphingolipids have been initiated. EPR spin label studies have suggested that the oligosaccharide chains of gangliosides in membranes exhibit substantial motion, possibly as a result of segmental motion within the carbohydrate moiety.[27] A ^{2}H NMR study of the ganglioside GM_1 (Figure 2), labeled in the terminal galactosyl residue and incorporated into phospholipid liposomes, has revealed substantial motional restriction.[28] GM_1 (five sugar residues) exhibited orientational ordering similar to that of the monosaccharide lipid galactosylceramide, indicating that if there is segmental motion in the oligosaccharide chain it must be of small amplitude.

2.2.2 Molecular Modeling and Liposomal NMR Data

Structure prediction via molecular mechanics/dynamics procedures is a frequently used approach in evaluating the range of conformational structures that a molecule may have. Such methods have found widespread use in carbohydrate structure analysis.[6] For membrane-associated glycolipids these calculations offer a means of gaining insight into segmental fluctuations in the headgroup region. In comparison with prediction in isotropic solution, the methodology for molecules at membrane surfaces is not as well developed.

The surface-bound blood group A-active glycosphingolipids[14] and a disaccharide lipid[25] have been modeled by a modified HSEA (Hard Sphere ExoAnomeric) analysis in which conformations were discarded if any part of the headgroup protruded below the membrane surface. Prestegard and coworkers have used an NMR pseudoenergy approach with AMBER in which ^{2}H quadrupolar and ^{13}C dipolar splitting data were used as a pseudoenergy term which directed the conformational energy minimization calculations to identify the favored conformation of membrane surface glycolipid analogs in oriented systems.[20,29–31]

A somewhat different approach has been used with the glycolipid β-DTGL where PFOS (Potential Functions of OligoSaccharides) conformational energy calculations were used to evaluate the conformational potential energy over the ϕ, ψ, and ω angles [see Figure 5 (left) for definitions of the angles ϕ, ψ, and ω].[32] The membrane situation was modeled by surrounding a central β-DTGL molecule with an annulus of six static lipid molecules with the distance r between the central molecule and the surrounding lipids as a variable. The sensitivity of the structure to the local environment is seen in a comparison of the ϕ, ψ energy contours for the membrane-embedded molecule [r = 9.5 Å, Figure 6 (top)] with that of the isolated molecule [Figure 6 (bottom)]. Such maps clearly show the most likely range of conformational fluctuations that the 'averaged glycolipid headgroup structure' can undergo.

The conformations that are potentially allowed for the isolated molecule have a very broad distribution in comparison with those of the membrane-associated molecule. Such theoretical calculations were linked with experiment by estimating quadrupolar splitting values by a Boltzmann-weighted average of quadrupolar splittings calculated for the

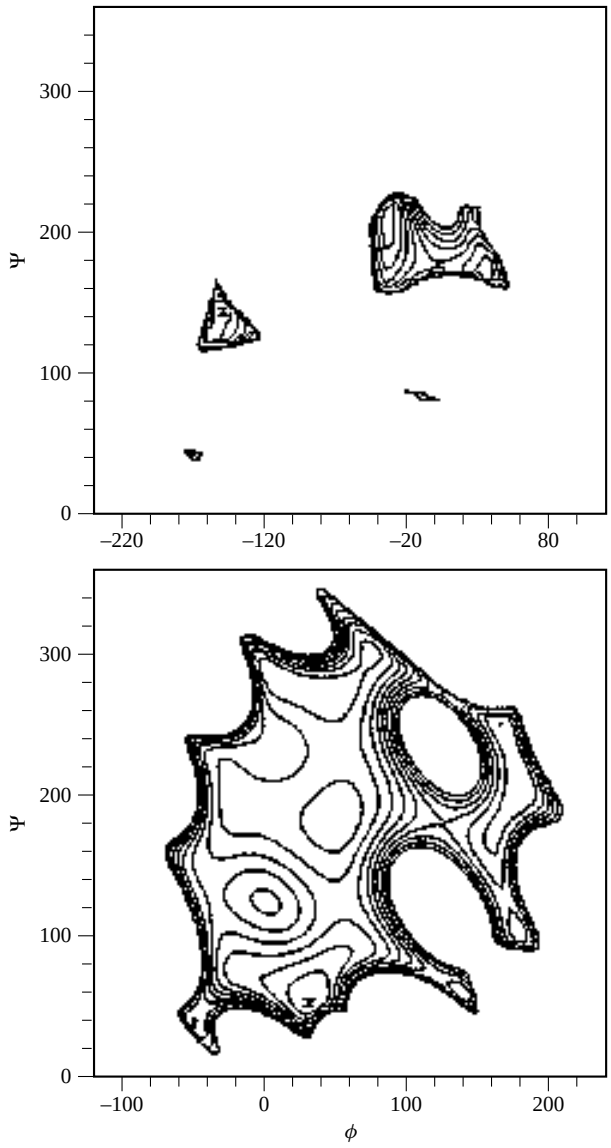

Figure 6 Influence of headgroup surface area on conformational energy. Conformational energy as a function of the angles ϕ and ψ for the β-DTGL analog molecule surrounded by an annulus of six surface analog molecules at a distance of (top) 9.5 Å and (bottom) molecule in vacuo. There are 10 contours, each contour is 4.18 kJ mol^{-1}; X represents the global minimum. (From Winsborrow et al.[32] with permission)

glucose deuterons (^{2}H-1, ^{2}H-2, ^{3}H-3, and ^{2}H-4) of β-DTGL for each ϕ, ψ, ω conformation. The calculated ^{2}H NMR quadrupolar splittings were found to agree well with those observed experimentally, within the range of intermolecular separations from 9.5 to 10.5 Å (Table 1). The intermolecular separations which gave the best fit were in good agreement with those values determined from monolayer and calorimetric studies which estimated the cross-sectional area occupied by β-DTGL in the liquid crystalline phase to be 102 ± 4 Å^2 per molecule, giving an intermolecular separation of about 11 Å.[33] In cases where there is evidence of headgroup flexibility, such calculations appear to offer some insight into the degree of conformational averaging involved in the 'average structure' and in the segmental order parameters.

Table 1 Experimental and Calculated ^{2}H Quadrupolar Splittings for β-DTGL Glucose Headgroups for Different Surface Constraints

Glucose deuteron quadrupolar splittings (kHz)		
	Experimental	Calculated[a] (r = 9.34–10 Å)
^{2}H-1	22.9	20.1–25.1
^{2}H-2	22.8	17.7–23.9
^{2}H-3	24.0	20.5–26.6
^{2}H-4	26.0	21.4–33.3

[a]Weighted average of splittings calculated for each allowed ϕ, ψ, ω combination [Figure 6 (top)].[32]

2.2.3 *Oriented Micelles*

An alternative to multilamellar systems which give rise to powder NMR spectra are micellar systems that orient in the magnetic field. Such systems have a single (or a very narrow distribution of) bilayer orientation, β in equation (1), and give NMR spectra of higher resolution than is achievable with unoriented samples. They also generally require less labeled material than liposomal systems. This is illustrated in Figure 3(b) which compares spectra of the disaccharide lipid, DTLL, in a liposomal system and in oriented micelles. In addition to ^{2}H NMR studies, such systems are amenable to measuring ^{13}C–^{13}C and ^{13}C–^{1}H dipolar couplings for ^{13}C-labeled glycolipids. Prestegard and co-workers have exploited such systems to elucidate the structure of a glycolipid as well as of glycolipid analogs by ^{2}H and ^{13}C NMR techniques.[20,29–31] In these studies, a molecular mechanics program appropriately modified for carbohydrates was used to calculate minimum energy structures, and the NMR data were added as a pseudoenergy term to the empirical description of molecular energies. The NMR data guided the structure calculations amongst a potentially large number of structures having similar energies. Using this approach, Prestegard and co-workers have deduced the average membrane orientation of the sialic acid residue of GM_3 and presented a model of the binding of the sphingolipid GM_3 to wheat germ agglutinin as shown in Figure 7.[31] Of particular interest in this study is that the sialyl residue's orientational order parameter S_{33} was found to be 0.73. This order parameter has a value comparable with molecular order parameters reported for other glycolipids and for phospholipids, suggesting that the entire GM_3 molecule may be fluctuating essentially as a single unit. This is particularly interesting since a solution NMR study of GM_3 concluded that a marked flexibility existed for the carbohydrate region.[10]

3 GLYCOLIPID DYNAMICS

In solution, it has become increasingly important to probe internal molecular dynamics in order to assess whether a molecular structure is unique or, in fact, an equilibrium of closely related structures. This is also true for membrane associated molecules where an 'average structure' may be elucidated. The presence of a hierarchy of internal or segmental motion is frequently encountered with lipid systems. This is true of glycolipids and has led to a number of studies directed toward characterizing the nature and timescales of molecular motion.

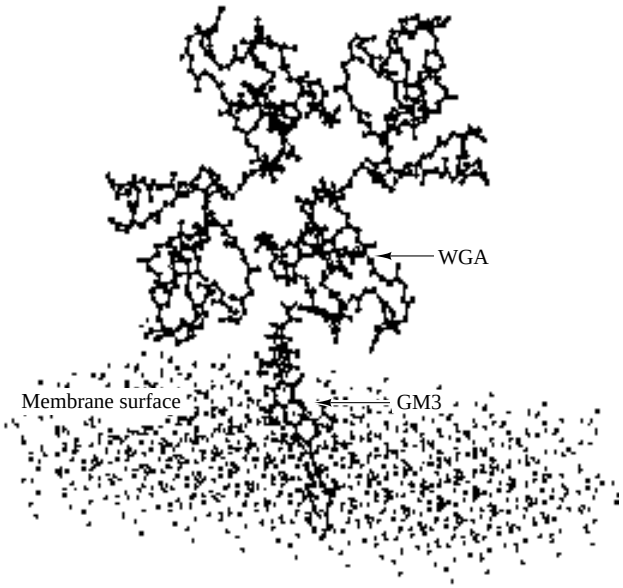

Figure 7 Model of membrane-bound GM_3 bound to wheat germ agglutinin (WGA). The 3D membrane structure and orientation of GM_3 was calculated from $^{13}C-^{13}C$ and $^{1}H-^{13}C$ dipolar splittings in oriented micelles. (From Aubin et al.[31] with permission)

3.1 Elucidating the Types and Rates of Molecular Motion—General Considerations

Deuterium NMR lineshape and relaxation time analysis has become the technique of choice for probing dynamic disorder and molecular mobility in these systems. Through such measurements, molecular dynamics can be followed over at least 10 decades in motional frequencies in a range (10^0-10^{10} Hz) where molecular motions in lipid bilayers are concentrated. Lineshape analysis of quadrupolar echo spectra provides information on the rates and mechanism of reorientation in the range of 10^3-10^6 Hz. Access to shorter timescales is provided by longitudinal relaxation measurements which probe motions occurring on the timescale of the Larmor frequency (10^8-10^{12} Hz). Studies of glycolipid motion have exploited the two longitudinal relaxation times, T_{1Z} and T_{1Q}, and their differing dependences on the orientation of the bilayer normal with respect to the magnetic field (T_1 anisotropy). Since the T_1 anisotropy is sensitive to both the rate and type of motion, it affords a powerful means of distinguishing between physically reasonable motional descriptions. Such measurements augment the usual studies of temperature and magnetic field strength dependence of T_1. The application of anisotropic relaxation has found extensive use with protein systems but has only recently been exploited in lipid membranes.[34] Unambiguous measurement of relaxation anisotropies have been best made by aligning the bilayers of model lipid membranes between glass plates, which can then be precisely oriented within the magnetic field.[34] Measurement of the dependence of relaxation rates on sample orientation maps out the orientation dependence. Longer timescales are accessible through two-dimensional chemical exchange experiments which extend the frequency range to include motions $<10^3$ Hz.[35]

3.2 Membrane Glycolipid Motion

There have been relatively few detailed motional studies of glycolipids in membrane systems. Deuterium lineshape studies of lipids labeled at the C-3 position of the glycerol residue have shown that as the temperature is lowered below the gel–liquid crystalline phase transition, reorientation about the molecular long axis slows. The lineshape changes from one characteristic of axially symmetric motion to one representative of motion having lower than threefold symmetry [Figure 8 (top left)].[36] This spectral behavior has been seen in a number of glycolipid systems and has been reproduced in lineshape simulations by a *gauche*(+)–*trans*–*gauche*(−) equilibrium about the C-2–C-3 glycerol bond.

Additional support for such segmental reorientation about the glycerol C-2–C-3 bond has been obtained through ^2H T_{1Z} relaxation. Partially-recovered spectra [Figure 8 (left)] of an inversion–recovery experiment for a multilamellar dispersion of the glycolipid β-DTGL labeled at the C-3 glycerol region show complex changes in lineshape as a function

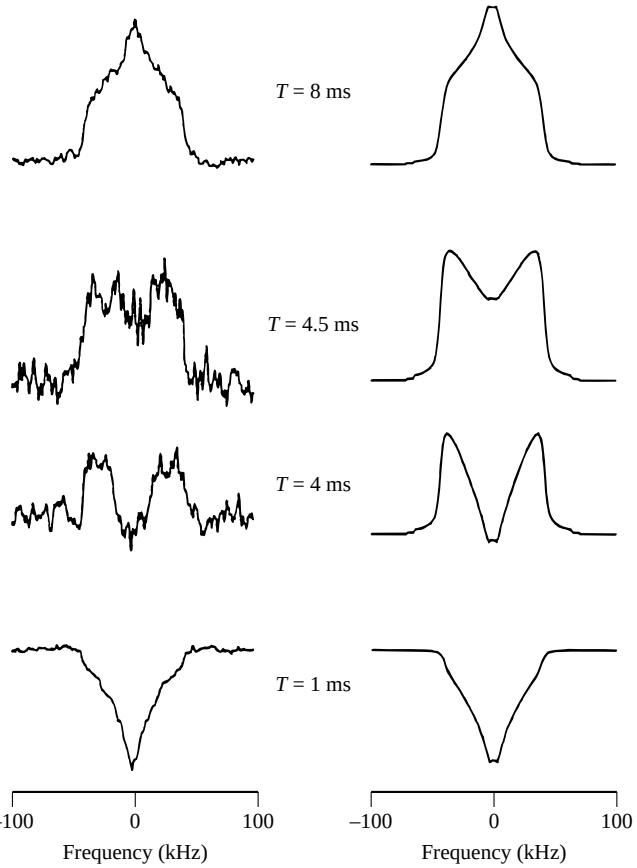

Figure 8 Partially-relaxed ^2H spectra of multilamellar dispersions of the β-glucosyl lipid, β-DTGL, labeled at the C-3 position of glycerol at 25 °C. Note that the equilibrium spectrum (top left) has a shape consistent with motion having less than threefold symmetry. The intermediate spectra (left) show lineshape changes which reflect anisotropic relaxation. The precise details of the spectral changes depend upon the nature and rate of motion. The spectral changes may be reproduced by theoretical calculations (right) in which a specific motion model is used. In this case the motion was 120° jumps between three unequally populated conformers about the glycerol C-2–C-3 bond. (From Auger et al.[36] with permission)

of the relaxation delay.[36] Using the motional model that reproduced the low-temperature quadrupolar echo lineshape, the relaxation experiment was simulated and the resulting theoretical lineshape reproduced the experimental spectra very well [Figure 8 (right)].

Another common observation with glycolipids is that at temperatures just below the gel–liquid crystalline phase transition, the ^{2}H NMR lineshape and intensity (only a few per cent of the original intensity remains) indicate motion is occurring on the 10^{-3}–10^{-5} s timescale. The nature of the additional motion involved was shown by lineshape simulations to be rotation about the molecular long axis. This was confirmed by two-dimensional chemical exchange experiments.[35] When molecular motion is slow ($<10^3\ s^{-1}$), reorientation of the molecule will cause the ^{2}H NMR quadrupolar splitting at one particular time to differ a short time later. In simple cases, a change in splitting corresponds to a change in the angle the C–^{2}H bond makes with the magnetic field direction—it is possible to measure directly the angle through which a molecule has jumped. If there is no frequency change a diagonal two-dimensional spectrum is observed, whereas frequency changes resulting from the motion lead to off-diagonal peaks or ridges, revealing the frequency correlations. Figure 9 illustrates what happens as β-DTGL is heated from the gel state to the liquid crystalline state. At low temperature the spectrum shows no frequency changes. At 40 °C, within the gel state, cross-ridges reveal that molecular motion has occurred during the mixing time. Spectral simulations indicate that the lipid reorients slowly about its long axis, most likely via large angle jumps. It has been suggested that this is a common feature of glycolipid motion in membrane systems.

The elucidation of glycolipid headgroup motion is difficult because of the motional hierarchy: glycolipid headgroup motion would be a combination of the lipid backbone (glycerol or ceramide) motions and rotation about the various glycosidic linkages, the latter representing conformational equilibria. In the case of β-DTGL labeled at the C-1 position of the glucose ring, the experimental T_{1Z} orientation dependence was well simulated for the average structure and the bilayer orientation shown in Figure 4, and assuming the glycerol isomerization and molecular long-axis reorientation discussed above.[37] Quantitative differences between the simulated and experimental spectral lineshapes of relaxation experiments were attributed to the conformational equilibrium about the carbohydrate–glycerol linkage. This equilibrium may involve the range of possible conformations shown in Figure 6 (top).

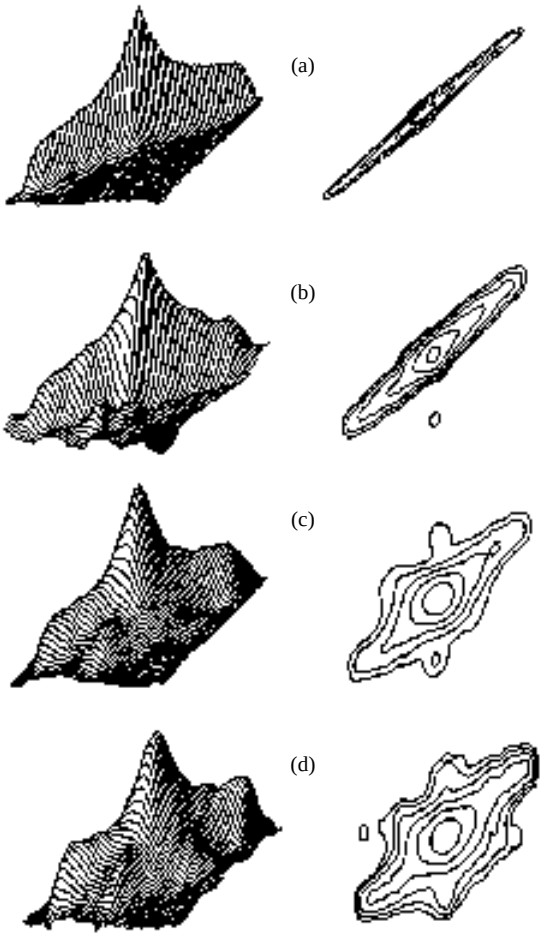

Figure 9 ^{2}H 2D exchange NMR spectra (left) and contour plots (right) of gel state β-DTGL labeled at the glycerol C-3 position. (a) 25 °C, t_{mix} = 1 ms; (b) 35 °C, t_{mix} = 0.5 ms; (c) 35 °C, t_{mix} = 2 ms; (d) 40 °C, t_{mix} = 2 ms. The cross-ridges seen at 40 °C are indicative of reorientation about the molecular long axis. (From Auger et al.[35] with permission)

4 ^{1}H AND ^{13}C MAGIC ANGLE SPINNING

The methodologies developed for liposomes or oriented micelles require isotopic labeling, a not inconsequential effort. To overcome this difficulty partially and to provide some structural insight into such systems, Oldfield and co-workers have recently used natural abundance ^{13}C and ^{1}H MAS techniques to study glycoglycerolipid–water systems.[38] In the liquid crystalline phase the lipids gave well resolved spectra for which resonance assignments could be made. Carbon-13 spin–lattice relaxation times indicated that the glycosyl headgroups and glycerol backbone have similar high-frequency motions. This together with temperature-dependent line broadening suggested that the glycerol backbone together with the mono- and disaccharide headgroups behave as a single 'rigid body'. These findings are in general agreement with results from more detailed ^{2}H NMR studies. Such an approach offers some promise for investigating a larger range of systems without the need for isotopic labeling.

5 RELATED ARTICLES

Bilayer Membranes: Deuterium and Carbon-13 NMR; Carbohydrates and Glycoconjugates; Lipid Polymorphism; Membrane Lipids of Acholeplasma laidlawii; Membranes: Deuterium NMR.

6 REFERENCES

1. W. Curatolo, *Biochim. Biophys. Acta*, 1987, **906**, 111.
2. L. Rilfors, Å. Wieslander, and G. Lindblom, in *Subcellular Biochemistry*, ed. S. Rottem and I. Kahane, Plenum Press, New York, 1993, Vol. 20, Chap. 4

3. S. K. Kundu, in *Glycoconjugates*, ed. H. J. Allen and E. C. Kasailus, Marcel Dekker, New York, 1992, Chap. 8
4. S. L. Hakomori, *Chem. Phys. Lipids*, 1986, **42**, 209.
5. I. Pascher and S. Sundell, *Chem. Phys. Lipids*, 1977, **20**, 175.
6. L. Poppe, C.-W. von der Lieth, and J. Dabrowski, *J. Am. Chem. Soc.*, 1990, **112**, 7762.
7. A. S. Serianni, in *Glycoconjugates*, ed. H. J. Allen and E. C. Kasailus, Marcel Dekker, New York, 1992, Chap. 4 See also ***Carbohydrates and Glycoconjugates***.
8. K. Wüthrich, *NMR of Proteins and Nucleic Acids*, Wiley, New York; 1986. See also ***Biological Macromolecules: Structure Determination in Solution***.
9. D. Acquotti, L. Poppe, J. Dabrowski, C.-W. von der Lieth, S. Sonnino, and G. Tettamanti, *J. Am. Chem. Soc.*, 1990, **112**, 7772.
10. H.-C. Siebert, G. Reuter, R. Schauer, C.-W. von der Lieth, and J. Dabrowski, *Biochemistry*, 1992, **31**, 6962.
11. S. Sabesan, J. Ø. Duus, T. Fukunaga, K. Bock, and S. Ludvigsen, *J. Am. Chem. Soc.*, 1991, **113**, 3236.
12. J. N. Scarsdale, R. K. Yu, and J. H. Prestegard, *J. Am. Chem. Soc.*, 1986, **108**, 6778.
13. J. N. Scarsdale, J. H. Prestegard, and R. K. Yu, *Biochemistry*, 1990, **29**, 9843.
14. P.-G. Nyholm, B. E. Samuelsson, M. Breimer, and I. Pascher, *J. Mol. Rec.*, 1989, **2**, 103.
15. P.-G. Nyholm and I. Pascher, *Biochemistry*, 1993, **32**, 1225.
16. J. W. Emsley and J. C. Lindon, *NMR Spectroscopy Using Liquid Crystal Solvents*, Pergamon Press, New York, 1975; a good summary of many aspects of NMR spectroscopy in liquid crystal systems is given in *Nuclear Magnetic Resonance of Liquid Crystals*, ed. J. W. Emsley, D. Reidel Publishing Company, Boston, 1985.
17. P. L. Stewart, K. G. Valentine, and S. J. Opella, *J. Magn. Reson.*, 1987, **71**, 45.
18. L. K. Nicholson and T. A. Cross, *Biochemistry*, 1989, **28**, 9379.
19. I. C. P. Smith, in *NMR: Principles and Applications to Biomedical Research*, ed. J. W. Pettegrew, Springer-Verlag, New York, 1989.
20. C. R. Sanders, II and J. H. Prestegard, *J. Am. Chem. Soc.*, 1991, **113**, 1987.
21. R. Skarjune and E. Oldfield, *Biochemistry*, 1982, **21**, 3154.
22. H. C. Jarrell, J. B. Giziewicz, and I. C. P. Smith, *Biochemistry*, 1986, **25**, 3950.
23. H. C. Jarrell, A. J. Wand, J. B. Giziewicz, and I. C. P. Smith, *Biochim. Biophys. Acta*, 1987, **897**, 69.
24. H. C. Jarrell, P. A. Jovall, J. B. Giziewicz, L. A. Turner, and I. C. P. Smith, *Biochemistry*, 1987, **26**, 1805.
25. J. P. Renou, J. B. Giziewicz, I. C. P. Smith, and H. C. Jarrell, *Biochemistry*, 1989, **28**, 1804.
26. D. Carrier, J. B. Giziewicz, D. M. Moir, I. C. P. Smith, and H. C. Jarrell, *Biochim. Biophys. Acta*, 1989, **983**, 100.
27. P. M. Lee, N. V. Ketis, K. R. Barber, and C. W. M. Grant, *Biochim. Biophys. Acta*, 1980, **601**, 302.
28. H. C. Jarrell, D. Singh, and C. W. M. Grant, *Biochim. Biophys. Acta*, 1992, **1103**, 331.
29. P. Ram, L. Mazzola, and J. H. Prestegard, *J. Am. Chem. Soc.*, 1989, **111**, 3176.
30. P. Ram and J. H. Prestegard, *J. Am. Chem. Soc.*, 1988, **110**, 2383.
31. Y. Aubin, Y. Ito, J. C. Paulson, and J. H. Prestegard, *Biochemistry*, 1993, **32**, 13 405.
32. B. G. Winsborrow, J.-R. Brisson, I. C. P. Smith, and H. C. Jarrell, *Biophys. J.*, 1992, **63**, 428.
33. H.-J. Hinz, L. Six, K.-P. Ruess, and M. Liefländer, *Biochemistry*, 1985, **24**, 806.
34. J. M. Bonmatin, I. C. P. Smith, H. C. Jarrell, and D. S. Siminovitch, *J. Am. Chem. Soc.*, 1990, **112**, 1697. See also the many references on anisotropic relaxation and spectral simulations cited therein.
35. M. Auger, I. C. P. Smith, and H. C. Jarrell, *Biophys. J.*, 1991, **59**, 31.
36. M. Auger, D. Carrier, I. C. P. Smith, and H. C. Jarrell, *J. Am. Chem. Soc.*, 1990, **112**, 1373.
37. B. G. Winsborrow, I. C. P. Smith, and H. C. Jarrell, *Biophys. J.*, 1991, **59**, 729.
38. F. Adebodun, J. Chung, B. Montez, E. Oldfield, and X. Shan, *Biochemistry*, 1992, **31**, 4502.

Biographical Sketch

Harold C. Jarrell. *b* 1949. B.Sc. (Hons.), 1972, M.Sc., 1974, Ph.D., 1977, Chemistry, Queen's University, Canada. Research associate at National Research Council, 1977–82, where he was introduced to NMR by Ian C. P. Smith. Senior Research Officer, National Research Council, and adjunct Professor of Biochemistry, University of Ottawa, Canada, 1982–present. Approx. 100 publications. Research specialties: solid state NMR and its applications to biomolecular systems.

Gramicidin Channels: Orientational Constraints for Defining High-Resolution Structures

Timothy A. Cross

Florida State University, Tallahassee, FL, USA

1	Introduction	1
2	Observation and Quality of Orientational Constraints	1
3	From Constraints to Molecular Structure	2
4	From Initial to Refined Structure	3
5	Structural Quality	3
6	Related Articles	4
7	References	4

1 INTRODUCTION

The native environment of most proteins is anisotropic, compromising both crystallographic and solution NMR methods for structure determination. Advantage can be taken of the anisotropy to obtain orientational constraints by solid state NMR.[1–4] There are inherent advantages and disadvantages associated with these constraints and their use for defining three-dimensional macromolecular structure.

There are two challenges before high quality constraints can be obtained. First, unique spin interactions must be resolved and assigned and, secondly, the samples must be uniformly aligned with respect to a single axis, i.e. three-dimensional or even two-dimensional order is not required, but very high quality one-dimensional order is necessary. For the initial development of orientational constraints as high quality structural constraints specific isotopic labeling of polypeptides has been utilized to achieve resolution and assignments. This is, however, not a fundamental requirement of this structural approach. There have been numerous approaches developed for achieving one-dimensional alignment for many different spectroscopies. NMR has a great advantage in that the experiments are performed in the presence of a strong magnetic field. Provided that the sample is in a liquid crystalline phase the magnetic field can be used to align the bulk phase as in the studies of viruses.[5,6] In this way it has been possible to achieve uniform alignment of most molecules in a sample relative to a single axis.

The observation of a nuclear spin interaction from such a sample can be used to constrain the orientation of the spin interaction tensor with respect to the magnetic field of the NMR spectrometer. This leads to two conclusions. First, if structural information is to be gained from these data the orientation of the spin interaction tensor with respect to the molecular frame must be known. Secondly, if a structural solution is achieved by this method, then a determination of how the molecule is aligned with respect to the liquid crystalline plane will also be achieved.

Fundamentally, the quality of the structure achieved by orientational constraints is dependent on both the inherent quality of the constraints and on how effectively these constraints can be used. It is difficult to predict analytically the errors in the structure determined by any of the current structural approaches. Similarly, it is difficult for this approach; however, considerable insight into these errors can be gleaned from both the initial and refined structures.

The model system that has been chosen for demonstrating the use of orientational constraints for structure determination is gramicidin A, a 15 amino acid polypeptide that, as a dimer, forms a monovalent cation selective channel across membranes and synthetic lipid bilayers. While it has been known for many years that this peptide forms a channel, and a reasonable model for the folding motif of this polypeptide has existed since 1971,[7] still there has been no high-resolution structure determination for this peptide in a lipid environment prior to this effort.[8] However, a solution NMR structure in a detergent environment was achieved in the 1980s and makes for an interesting comparison now that the structure in a lipid environment has been achieved from orientational constraints.[9]

2 OBSERVATION AND QUALITY OF ORIENTATIONAL CONSTRAINTS

A wide variety of orientational constraints can be achieved. In Figure 1 spectra of $^{15}N_{\epsilon 1}$ Trp9-labeled gramicidin are shown. In Figure 1(a) a single sharp line results from the spin-$\frac{1}{2}$ chemical shift interaction for which the $^{15}N{-}^{1}H$ dipolar interaction has been decoupled. However, in Figure 1(b) the uniformly aligned sample that gave rise to the spectrum in Figure 1(a) was incubated in a D_2O saturated environment. The resulting spectrum shows the superposition of the chemical shift and the $^{15}N{-}^{2}H$ dipolar interactions. The 1940 Hz splitting has an error of approximately ± 100 Hz, corresponding to a maximum orientational error of $\pm 1.4^{\circ}$. Consequently, well aligned samples can be prepared, and observations of both the ^{15}N chemical shift and $^{15}N{-}^{2}H$ dipolar interactions are shown as orientational constraints. The orientation of the dipolar interaction with respect to the molecular frame is well accepted, in having the unique interaction axis parallel with the internuclear vector. The orientation of the axially asymmetric chemical shift tensor is less certain.

In Figure 2(a) the static magnitudes of ^{15}N chemical shift tensors are shown. These data were obtained on a sample that had been mixed with lipid, hydrated to form bilayers and the channel state of the polypeptide, and then rapidly frozen to generate a static sample without severe distortion due to ice crystal formation.[10–12] The importance of determining the tensor element magnitudes for the site of interest and in the conformation of interest has been elegantly shown by Hiyama et al.,[13] who reported on work in which a dipeptide crystallized in two different forms and gave rise to very different chemical shift tensors for the same site in the two different crystals. Not only is it important to determine the magnitudes of the tensor elements, but also to determine how the tensor is oriented with respect to the molecular frame. This can be achieved by orienting the chemical shift tensor with respect to an internuclear vector.[14] Here the ^{15}N chemical shift tensor is aligned with respect to the $N{-}C_1$ bond axis via the $^{15}N{-}^{13}C$

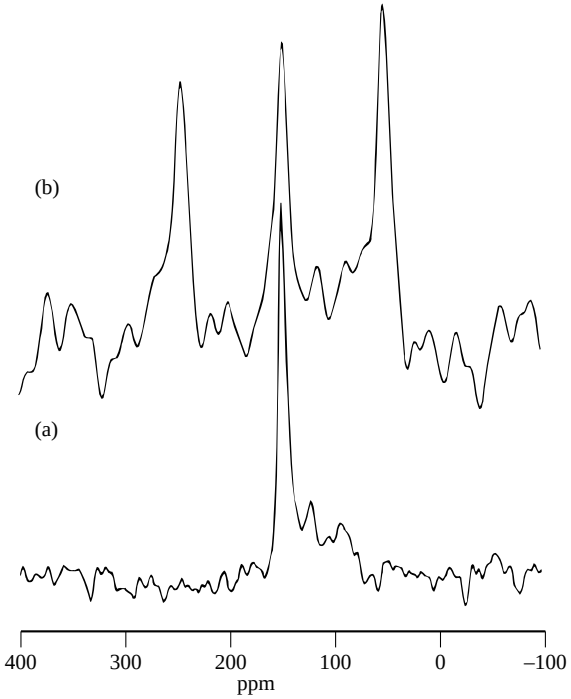

Figure 1 Nitrogen-15 chemical shift spectra of $^{15}N_{\epsilon 1}$ Trp9-labeled gramicidin in uniformly aligned lipid (dimyristoylphosphatidylcholine) bilayers with the bilayer normal parallel to the magnetic field. (a) Sample hydrated with H_2O. The spectrum was recorded at 40 MHz on an Oxford Instruments 400/89 magnet using a Chemagnetics data acquisition system. The radiofrequency electronics were home assembled. All ^{15}N spectra were cross-polarized with high power ^{1}H decoupling. (b) Sample in (a) that has been opened and exposed to a D_2O atmosphere for 2 days and the loss of moisture replaced with D_2O. The spectrum was recorded at 20 MHz in a narrow bore system, using an IBM/Bruker console with a heavily modified Doty solid state NMR package. Isotopically labeled gramicidin A was synthesized by solid phase peptide synthesis using fluorenylmethoxycarbonyl blocking (Fmoc) chemistry[18]

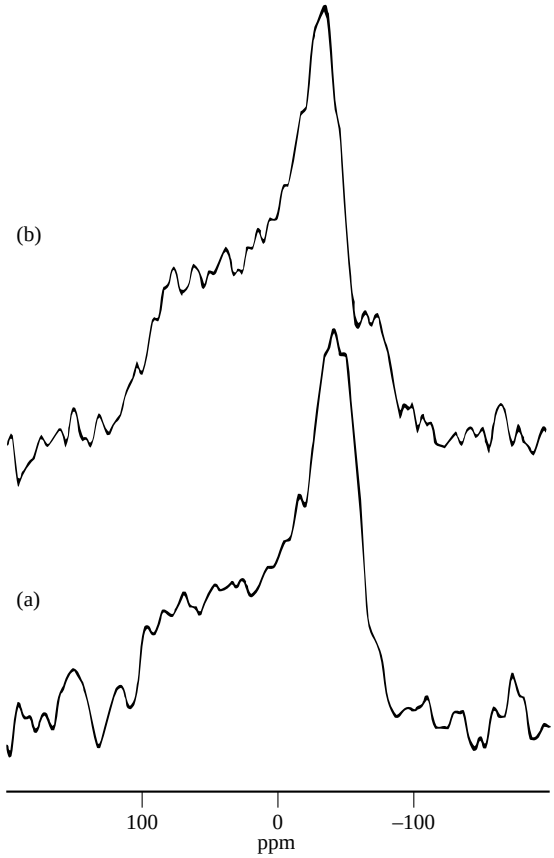

Figure 2 Nitrogen-15 chemical shift powder pattern spectra of ^{15}N Val8-labeled gramicidin. Samples in hydrated lipid bilayers were rapidly cooled by plunging thin films into liquid propane. The sample was then stored at liquid nitrogen temperatures before transfer to the precooled NMR probe.[15] (a) The single-site isotopically labeled preparation providing the static chemical shift tensor for the site of interest in the conformation and environment of interest. (b) Spectrum of gramicidin that is also $^{13}C_1$ Val7-labeled. The powder pattern also displays the $^{15}N-^{13}C$ dipolar interaction. From the spectral analysis the relative orientation of the dipolar and chemical shift interactions can be achieved

dipolar interaction in a sample that has also been rapidly frozen. The superposition of these two interactions is shown in Figure 2(b).

Not only are the static tensor element magnitudes important, but the spin interaction data need to be interpreted in light of the motionally averaged tensors. Such information can be obtained from the temperature dependence of the chemical shift powder patterns. There are two important features observed from sites in the polypeptide backbone between 200 K and room temperature. First, there is considerable averaging of the tensor elements and, secondly, the asymmetry of the tensor changes with temperature. This latter result means that the librational averaging is anisotropic. In fact, the averaging is consistent with a motional axis described by the axis joining successive α carbons.[15]

3 FROM CONSTRAINTS TO MOLECULAR STRUCTURE

An initial structure of the gramicidin backbone can be assembled from N–H and $N-C_1$ dipolar constraints for each peptide plane. However, each constraint has ambiguities associated with its interpretation. For each constraint the spin interaction frequency is related to an angle through a $\cos^2 \theta$ term and, therefore, the sign of $\cos \theta$ is undetermined. Furthermore, the sign of the dipolar coupling is also unknown except for those cases where the splitting is greater than half-maximal. These ambiguities would accumulate to a plethora of structural possibilities except that most combinations are not consistent with the known bond angles of the polypeptide backbone. Other combinations are not consistent with the observed ^{15}N chemical shift. For an initial structure the peptide planes are assumed to be planar (i.e. the ω torsion angle is assumed to be 180°). By taking advantage of the tetrahedral geometry and the orientation of adjacent planes relative to a common axis it is possible to achieve the relative orientation of the peptide planes (i.e. the ϕ, ψ torsion angles). Such a structural unit, known as a diplane unit, can then be combined with the adjacent diplane which shares a common plane. Only those common planes having an identical orientation can be combined. The result for gramicidin is two closely related conformers (1 and 2 in Figure 3). Interestingly, as the structure

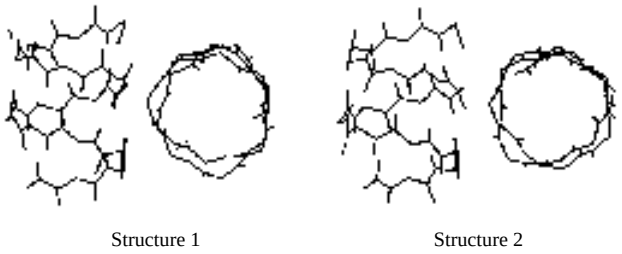

Figure 3 Two initial structures have been achieved from orientational constraints. Only half of the symmetric dimeric channel structure is shown. Both structures have the same folding motif: 6–7 residues per turn, a β-sheet type structure, and a right-handed helix. However, significant structural differences exist

was assembled from the original combination of two diplanes the structural ambiguities did not increase, but remained as just two possibilities. This is because the data for each additional peptide plane is unique and independent of the data used previously. Furthermore, the constraints are all relative to a single common axis, the magnetic field direction and channel axis of the polypeptide dimer.

Both of the initial structures have the same folding motif: 6–7 residues per turn, a β-sheet type of hydrogen-bonding pattern and a right-handed helical sense. Both structures also have an uninterrupted pattern of alternating peptide plane orientations. This is clearly seen in Figure 4, where each peptide plane is shown edge on with the vertical axis being the channel axis with the channel center to the left of each frame. For both structures the peptide planes alternate between being approximately parallel to the channel axis (the even–odd planes) and being tipped by approximately 20° with respect to the channel axis (the odd–even planes). The fundamental difference between these two structures is that conformer 1 has the carbonyl oxygens oriented in toward the channel center for those planes having a significant tilt and conformer 2 has these planes oriented with the carbonyl oxygen away from the channel center. Considering that this channel is a cation selective channel it is unrealistic to think that carbonyl oxygens would be preferentially turned away from the channel axis. Consequently, conformer 1 is the favored possibility.

4 FROM INITIAL TO REFINED STRUCTURE

For these initial structures not all of the orientational constraints have been optimally utilized. Nitrogen-15 and ^{13}C chemical shifts, ^{2}H quadrupolar interactions, and, now that the hydrogen-bonding pattern has been identified, ideal N–O and H–O distances can be used as structural constraints. A refinement protocol has been developed in which slight changes to the torsion angles, including the ω torsion angle which had been fixed at 180°, are made followed by a calculation of the observables. The difference between calculated and experimental values generates a penalty function which is minimized through numerous cycles of torsion angle modifications in this simulated annealing approach to refinement. Although the torsion angles for the refined structures are typically very close to the initial structure, there are significant differences. The refinement has also adjusted the residues per turn of the helix and the pitch as seen in Figure 5.

5 STRUCTURAL QUALITY

The inherent quality of these orientational constraints has been clearly demonstrated through the achieved structure. The errors associated with each observed constraint can be reasonably estimated. Accumulated structural errors can be estimated from the comparison of initial and refined structures. These latter errors were small enough so that the complete hydrogen-bonding pattern was defined by the initial structure. And yet it is clear that significant improvements or minimization of the errors can be achieved through experimental procedures designed to minimize conformational heterogeneity. Also, more accurate characterization of the local dynamics will improve the accuracy of the structural analysis. Not only can the structure be improved with better constraints but the quantity of the constraints can be used to great advantage through a refinement protocol. The primary advantage that the orientational constraints have over other structural constraints is that each constraint is absolute, i.e. it is relative to the fixed laboratory frame of reference. Unlike solution NMR and solid state NMR distance constraints which

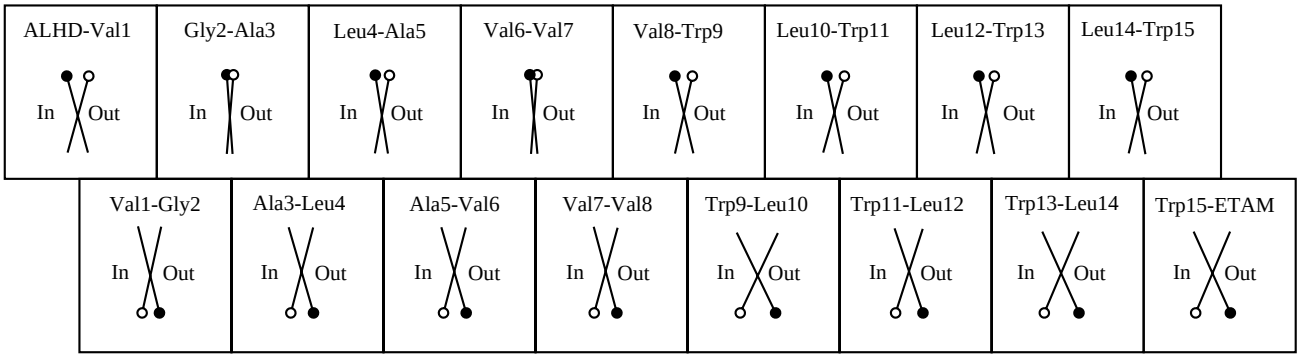

Figure 4 A view of each peptide plane in the two initial gramicidin structures displayed in Figure 3, as viewed along an axis defined as perpendicular to the channel axis in the peptide plane. The channel axis is vertical, and the circles represent the carbonyl oxygen atom. The inside of the channel is displayed on the left side of each frame. Each pair of orientations is symmetric because of the symmetry of the orientational constraints. There is an alternating pattern for the orientation of the carbonyl groups between large and small angles to the channel axis. The structure (1) with open circles that has the carbonyl oxygens tipped furthest into the channel and least to the membrane environment is considered the likely structural conformer. ALHD represents the formyl blocking group of the amino terminus and ETAM represents the ethanolamine

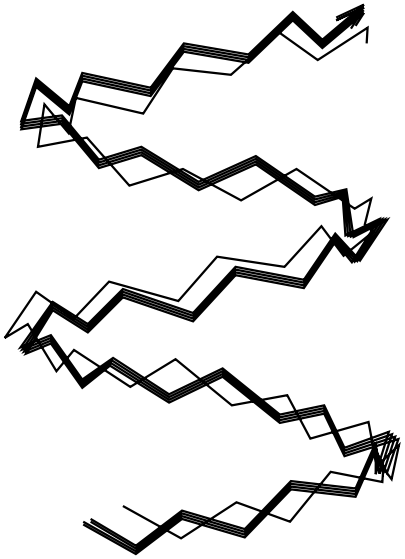

Figure 5 The refinement process against all of the experimental data and ideal hydrogen-bonding distances yields a very consistent set of structures that differs significantly from the initial structure shown as the fine line. Only the backbone atoms of C_α, N, and C_1 are displayed for the monomer in this figure, since the dimer is symmetric

relate the position of one site relative to another in the molecule, here the orientation of one site in the molecule is related to a fixed frame of reference that is the same for each constraint.

There have been few occasions when a structure of a polypeptide or protein has been determined in a lipid environment. Here the lipid bilayer generates an environment that strengthens electrostatic interactions, thereby minimizing large amplitude motions induced by hydrogen bond exchange. Through a high resolution structure and dynamics characterization details of how cation passage through this channel is facilitated by this polypeptide will be elucidated. Not only are the carbonyl oxygens oriented in toward the channel axis, but local motions of the backbone occur on the nanosecond timescale.[16] Such overdamped motions could result from correlated motions or coherence that propagates through the channel and bilayer at a rate coincident with the kinetic rate for cation translocation. In fact, the 10 ns timescale that has been determined for the molecular motions is also the kinetically estimated rate for the cation to move from one carbonyl binding group to another. Furthermore, the motions of the single file of water molecules must be correlated since the cations cannot pass around these molecules in the channel. Therefore, if the water molecules have correlated motions then the motions of the carbonyl groups that surround this column of water molecules must also be correlated.

Such structure–dynamics–function correlations can be achieved with the high-resolution characterization possible from solid state NMR and orientational constraints. While isotopic labeling and solid phase synthesis have been used to generate resolution and assignments, approaches with ^{1}H and ^{14}N NMR[17] have been described which could yield numerous constraints in a single spectrum without isotopic labeling or with uniform ^{15}N labeling. Although the complete structure determination of sizeable proteins may remain a monumental task for this approach the determination of a domain or structural subunit to high resolution is feasible, as is the high-resolution structure of a ligand bound to a uniformly aligned receptor.

6 RELATED ARTICLES

Filamentous Bacteriophage Coat Protein; Homonuclear Recoupling Schemes in MAS NMR; Membrane Proteins; Membranes: Carbon-13 NMR; REDOR and TEDOR; Time-Resolved Solid State NMR of Enzyme–Substrate Interactions.

7 REFERENCES

1. T. A. Cross and S. J. Opella, *J. Am. Chem. Soc.*, 1983, **105**, 306.
2. R. Smith and B. A. Cornell, *Biophys. J.*, 1986, **49**, 117.
3. A. W. Hing, S. P. Adams, D. F. Silbert, and R. E. Norberg, *Biochemistry*, 1990, **29**, 4144.
4. R. S. Prosser, J. H. Davis, F. W. Dahlquist, and M. A. Lindorfer, *Biochemistry*, 1991, **30**, 4687.
5. S. J. Opella, P. L. Stewart, and K. G. Valentine, *Quart. Rev. Biophys.*, 1987, **19**, 7.
6. T. A. Cross, S. J. Opella, G. Stubbs, and D. L. D. Caspar, *J. Mol. Biol.*, 1983, **170**, 1037.
7. D. W. Urry, *Proc. Natl. Acad. Sci. USA*, 1971, **68**, 672.
8. R. R. Ketchem, W. Hu, and T. A. Cross, *Science*, 1993, **261**, 1457.
9. A. L. Lomize, V. Yu. Orechov, and A. S. Arseniev, *Bioorg. Khim.*, 1992, **18**, 182.
10. N. D. Lazo, W. Hu, and T. A. Cross, *J. Chem. Soc., Chem. Commun.*, 1992, 1529.
11. A. M. Christensen and J. Schaefer, *Biochemistry*, 1993, **32**, 2868.
12. J. N. S. Evans, R. J. Appleyard, and W. A. Shuttleworth, *J. Am. Chem. Soc.*, 1993, **115**, 1588.
13. Y. Hiyama, C.-H. Niu, J. V. Silverton, A. Bavoso, and D. A. Torchia, *J. Am. Chem. Soc.*, 1988, **110**, 2378.
14. M. Linder, A. Hohener, and R. R. Ernst, *J. Chem. Phys.*, 1980, **73**, 4959.
15. N. D. Lazo, W. Hu, K.-C. Lee, and T. A. Cross, *Biochem. Biophys. Res. Commun.*, 1993, **197**, 904.
16. C. L. North and T. A. Cross, *J. Magn. Reson. B*, 1993, **101**, 35.
17. R. Tycko, P. L. Stewart, and S. J. Opella, *J. Am. Chem. Soc.*, 1986, **108**, 5419.
18. C. G. Fields, G. B. Fields, R. L. Noble, and T. A. Cross, *Int. J. Peptide Protein Res.*, 1989, **33**, 298.

Acknowledgments

For support of this research the author wishes to thank the Biophysics Program of the National Science Foundation through grants DMB-9005938 and MCB-9317111.

Biographical Sketch

Timothy A. Cross. *b* 1953. B.S., 1976, Trinity College. Ph.D., 1981, University of Pennsylvania (with Stanley J. Opella). Postdoctoral work at the Biozentrum, University of Basel with Joachim Seelig. Currently Professor of Chemistry at Florida State University and Deputy Director of the NMR Program in the National High Magnetic Field Laboratory. Approx. 75 publications. Research interests: biological solid state NMR and the development of very high field NMR instrumentation and applications.

Lipid Polymorphism

David B. Fenske and Pieter R. Cullis

University of British Columbia, Vancouver, Canada

1	Introduction	1
2	Lipid Polymorphism and NMR	1
3	Biological Implications of Lipid Polymorphism	4
4	Related Articles	5
5	References	5

1 INTRODUCTION

Lipids are a structurally diverse class of biological molecules that are defined on the basis of their solubility in organic solvents. Lipids are involved in numerous metabolic processes including energy metabolism and hormone biosynthesis. They are also important structural components of biological membranes. Biological membranes are fluid, noncovalent assemblies of lipid and protein which form the external boundary and internal compartments of eukaryotic cells, thereby allowing local environments appropriate to particular functions. Membranes are also selective permeability barriers which provide a means of regulating cellular concentrations of ions and metabolites. The essential structural features of membranes are described by the fluid mosaic model, which was proposed by Singer and Nicholson over 20 years ago.[1] In this model, the lipid components are arranged in lamellar sheets with a thickness of two molecules (about 4 nm), providing a fluid matrix into which proteins can insert or associate at the surface. The lipid bilayers form spontaneously in water, as a result of the amphipathic nature of the lipid molecules.

Membranes contain a remarkable diversity of lipids which exceed the requirements for basic structural functions. For example, although a single lipid such as phosphatidylcholine can form fluid semipermeable bilayers, biological membranes typically contain over 100 lipid components. That the synthesis and transport of these lipids requires significant metabolic expenditure suggests specific biochemical or physicochemical roles for the individual components of membranes. Efforts to clarify these roles have been a focus of membrane biology for over three decades, with the task still ongoing. Much insight has been gained through investigations of the physicochemical properties of model systems formed from different membrane lipids. The pioneering X-ray diffraction studies of Luzzati et al. revealed that isolated membrane lipids could, upon hydration, adopt fluid phases (known as mesophases) other than the bilayer, a phenomenon referred to as lipid polymorphism.[2] While elucidation of the structure of many of these mesophases was accomplished using X-ray diffraction, a great deal of information pertaining to the phase behavior and physical properties of different lipid mesophases, for both pure and mixed lipid assemblies, has come from solid state ^{31}P and ^{2}H NMR.[3–7] This review will discuss the information provided by magnetic resonance techniques, and attempt to place these data within a biological framework. The importance of lipid polymorphism stems not only from the interesting biophysics of lipid–water assemblies, but from the insight which it provides into many aspects of membrane function.

2 LIPID POLYMORPHISM AND NMR

2.1 Lipid Structure and Diversity

The main classes of lipids found in eukaryotic membranes include the glycerophospholipids, the sphingolipids, and cholesterol.[8] Lipids found in the former group include phosphatidylcholine (PC), phosphatidylethanolamine (PE), phosphatidylserine (PS), phosphatidylinositol (PI), and cardiolipin (CL). The type of phospholipid is determined by the polar headgroup, which is attached to position 3 of the glycerol backbone; fatty acyl chains occupy the other two positions. The structures of a representative PC and PE are shown in Figure 1 (see legend for details). The two lipids differ only at the headgroup nitrogen, which is protonated in PE and trimethylated in PC. The sphingolipids are derivatives of the long-chain base sphingosine. The headgroup can be the same as that of PC (giving sphingomyelin), or a hydroxyl group (giving ceramide), or can contain a variety of sugars (giving the glycosphingolipids). A single fatty acyl chain attaches to sphingosine via an amide bond. Cholesterol is a sterol; a hydroxyl group is found at one end of its rigid ring system and a branched hydrocarbon chain at the other.

This brief summary of the main lipid groups illustrates the heterogeneous nature of biological membranes. This is

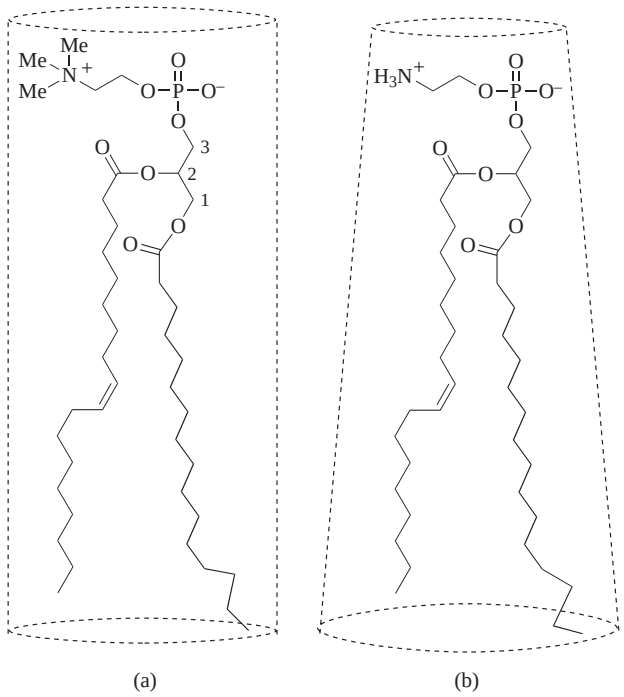

Figure 1 Chemical structures of representative phospholipids: (a) 1-palmitoyl-2-oleoyl-*sn*-glycero-3-phosphocholine (POPC) and (b) 1-palmitoyl-2-oleoyl-*sn*-glycero-3-phosphoethanolamine (POPE). The stereospecific numbering of the glycerol backbone is shown in (a). POPC has a cylindrical shape which favors the bilayer phase, whereas POPE has a cone shape which favors the H_{II} phase

further compounded by variation in fatty acid chain length and degree of unsaturation, as well as the presence of minor lipid components.

2.2 Lipid Polymorphic Phases

Lipids pack within a bilayer such that the headgroups form the aqueous interface of the membrane surface, while the fatty acyl chains form the hydrophobic membrane interior [Figure 2(a)].[1] Lipid bilayer models include multilamellar vesicles (MLVs), oriented multibilayers, and large and small unilamellar vesicles (LUVs and SUVs, respectively).[9] For NMR studies of polymorphism, MLVs have been utilized almost exclusively. These large quasispherical structures ($1-10\,\mu$m diameter) are easily formed by dispersing lipid in water with vortexing and (often) several cycles of freezing and thawing. In addition, they are large enough so that tumbling of the MLV, or lateral diffusion of lipids around the MLV do not result in significant motional averaging effects. As a result, broadline ^{31}P and ^{2}H spectra are observed.

Some membrane lipids, PE in particular, adopt the hexagonal H_{II} phase in isolation [Figure 2(b)].[3,10] This nonbilayer phase is composed of hexagonally packed lipid cylinders, where the phospholipid headgroup points towards the center of the cylinder, forming an aqueous channel with a diameter of approximately 2 nm. Most lipids that adopt the H_{II} phase can also adopt the bilayer phase if the temperature is low enough; transitions between the two phases are rapid and reversible, although little exchange of lipid between these phases appears to occur when they coexist.[11]

Other nonbilayer phases include micellar structures and cubic phases, in which the lipid aggregate forms a three-dimensional lattice.[12] The structures of the cubic phases are quite complex, and will not be described here. In general, neither the H_{II} nor cubic phases are observed as long-lived structures in vivo. The reason these phases are of interest in a biological context stems from evidence suggesting that some of the intermediates of bilayer to nonbilayer transitions are involved in processes such as membrane fusion (see Section 3).[3,13,14]

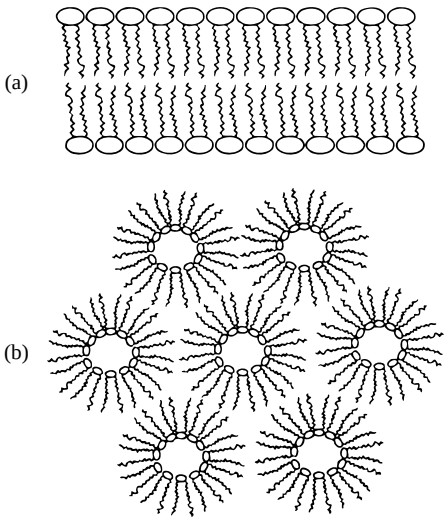

Figure 2 Schematic cross-sectional representation of (a) the liquid crystalline bilayer and (b) hexagonal H_{II} phases, showing how these phases favor the packing of cylindrical and cone shaped lipids, respectively. The H_{II} cylinder axis is normal to the plane of the paper

2.3 Phosphorus-31 NMR

Phosphorus-31 NMR has been widely used in the study of membrane structure and lipid polymorphism.[3,4] Phosphorus-31 is a spin-$\frac{1}{2}$ nucleus with a natural abundance of 100%, found in membranes only in the headgroups of phospholipids and sphingolipids. All of the common phospholipids give rise to broad ^{31}P NMR spectra, where the spectral width can range from 20 to 200 ppm depending on the mesophase being examined and the extent of hydration. Because ^{31}P NMR spectra are almost always acquired with broadband decoupling (to remove ^{1}H–^{31}P dipolar interactions), the observed lineshape depends on the types of motions which average the shielding anisotropy of the phosphate group. The nonaxially symmetric shielding tensor gives rise to three principal components, which are observed in spectra of anhydrous lipid, having widths of the order of 200 ppm.[4] In liquid crystalline MLVs, rapid axial rotation averages the components of the shielding tensor in the plane of the membrane, giving rise to the classic 'powder pattern' lineshape [Figure 3(a)] with a width of 40–50 ppm.[3] The origin of this lineshape is discussed by Cullis and DeKruijff and by Seelig.[4,15]

In the H_{II} phase, rapid diffusion of lipid about the cylinder long axis provides an additional mechanism of motional averaging.[3,4,10,15] The result is a powder pattern which, compared with that of the bilayer, is reduced by a factor of two and has the opposite sign [Figure 3(b)]. This allows transitions between the two phases to be conveniently and accurately monitored. The correlation between phase determinations by

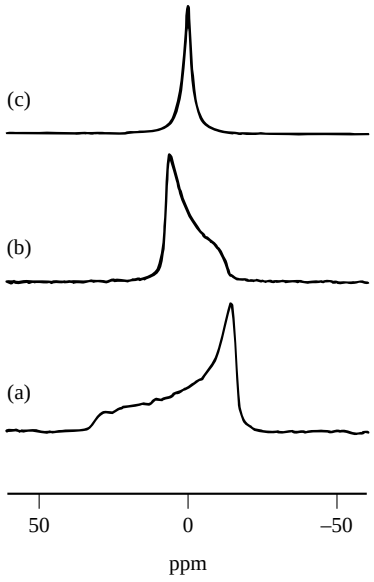

Figure 3 Phosphorus-31 NMR spectra of different liquid crystalline polymorphic phases: (a) multilamellar dispersions of dimyristoyl-PC (DMPC) at 30 °C (b) hexagonal phase dioleoyl-PE:cholesterol (1:1) at 20 °C (c) LUVs of dioleoyl-PC containing 20 mol% phosphatidic acid at 20°C

^{31}P NMR and small-angle X-ray diffraction has been shown to be excellent.[16]

The cubic phases, although structurally diverse, allow the phospholipid molecules to sample all angles in a period short on the NMR timescale, i.e. they allow isotropic averaging of the powder lineshape.[3,12] This results in a narrow peak at the isotropic chemical shift, which is difficult to differentiate from that produced by micelles, SUVs, or some LUVs [Figure 3(c)]. Lipid mixtures containing nonbilayer lipids often exhibit isotropic peaks,[12] which are said to originate from 'isotropic phase' lipid.

Phosphorus-31 NMR is clearly a convenient tool for monitoring the polymorphic phase preferences of pure and mixed lipid assemblies. Although techniques such as X-ray diffraction and freeze–fracture electron microscopy have arguably been of equal importance,[2,17] the advantages of NMR, primarily in convenience and rapidity, have made it the technique of choice for characterizing a variety of different lipids and their response to variation in parameters such as pH, temperature, and ion concentrations. These results are summarized in the next section.

2.4 Lipid Polymorphic Phase Preferences

A comprehensive tabulation of the polymorphic phase preferences of a large variety of pure and mixed lipid systems is given in Cullis et al.[18] A number of interesting observations have emerged from these data. In single-component systems, a few lipids favor the bilayer phase almost exclusively: these include the PCs, PI, sphingomyelin, diglucosyldiglyceride (DGlcDG), and digalactosyldiglyceride (DGalDG). Other lipids can adopt either the lamellar or H_{II} phase depending on the conditions; these include PE, PS, phosphatidic (PA), phosphatidylglycerol (PG), and CL. Two of the glycolipids [monoglucosyldiglyceride (MGlcDG) and monogalactosyldiglyceride (MGalDG)] adopt the H_{II} phase exclusively.

Of the nonbilayer phase lipids, PE has been most extensively studied.[3,10,14,18] PEs form stable bilayers at sufficiently low temperatures, undergoing a transition to the H_{II} phase as the temperature is raised above some critical value. Increasing the level of acyl chain unsaturation favors the formation of the H_{II} phase. Other lipids, such as PS and phosphatidic acid, will only form the H_{II} phase below pH 3.5, where the negative charge on the headgroup is neutralized. Similarly, phosphatidic acid and CL will adopt the H_{II} phase in the presence of Ca^{2+}, which neutralizes the negative surface charge. These observations have biological relevance, as they indicate possible mechanisms (control of pH and divalent ion concentration) available to the cell to regulate bilayer–nonbilayer transitions in an isothermal environment.

Phosphorus-31 NMR has also proven useful in characterizing the polymorphism of multicomponent systems, which bear a greater resemblance to biological membranes than pure lipid systems. This has resulted in two important observations. Firstly, mixtures of bilayer and nonbilayer lipids will progressively favor the bilayer phase as the proportion of bilayer forming lipids is increased; sometimes as little as 20 mol% of the bilayer lipid will completely stabilize the lamellar phase.[3,14] Secondly, cholesterol may play a role in regulating bilayer to nonbilayer transitions in complex systems. Cholesterol can induce the formation of H_{II} phase in PE-containing bilayer systems that have been stabilized by PC.[14]

The substantial body of data on lipid polymorphic behavior has led to theoretical insight into the factors which determine the phase preference of a given lipid system. One of the most successful approaches, developed by Israelachvili et al.,[19] involves consideration of the molecular shapes of individual lipid molecules. The basic idea is that molecules with different shapes will preferentially pack in phases of different symmetry. As illustrated in Figure 1, lipids such as PC which favor the lamellar phase have similar average cross-sectional areas in the headgroup and acyl chain regions, and are thus said to be 'cylindrical'. Lipids such as PE have a cone shape, where the headgroup occupies a smaller cross-sectional area than the acyl chains, thereby imparting a curvature to the assembly that favors the H_{II} phase (see Figure 2). For detergent-like lipids which form micellar structures the geometry is reversed, giving an inverted cone where the headgroup cross-sectional area is greater than that of the chains. To see how this can provide insight into polymorphic phase transitions, consider the lamellar to hexagonal transition of dioleoyl-PE (DOPE). At temperatures less than 10 °C the lipid chains are sufficiently ordered to impart a cylindrical molecular geometry [see Figure 1(a)] that favors the bilayer phase [see Figure 2(a)]. Elevating the temperature increases the extent of acyl chain molecular motion, resulting in a greater cross-sectional area of the hydrocarbon chains relative to the headgroup. This results in a cone geometry [see Figure 1(b)] that favors the H_{II} phase at room temperature [see Figure 2(b)]. Similar considerations explain why neutralizing the charge of the headgroup, either via pH or divalent cations, leads to the formation of the H_{II} phase in other lipids. Charged headgroups repel and are therefore larger; neutralizing the charge reduces their effective size thereby imparting cone geometry to the lipid.

A more quantitative approach to understanding the factors involved in the formation of nonbilayer phases has come from the 'curvature' concept introduced by Gruner.[20] In this model, the lamellar to hexagonal transition is described as a tendency for nonbilayer lipids to force a monolayer to curl into cylinders with a spontaneous radius of curvature R_0; the magnitude of this parameter, which can be measured by X-ray diffraction, provides a measure of the polymorphic tendencies of a lipid system. A lipid with a strong tendency to form the H_{II} phase will have a small radius of curvature, whereas a system with less tendency, such as a PC/PE mixture, will have a larger radius of curvature. Studies on DOPE and its methylated derivatives reveal that while systems with small and large R_0 form hexagonal and lamellar phases, respectively, those with intermediate values have a strong tendency to form cubic phases.[21]

2.5 Deuterium NMR

Deuterium NMR is a powerful technique for the study of molecular order and dynamics in model and biological membranes.[5–7] The theory and application of ^{2}H NMR have been extensively reviewed; we will summarize only those aspects relevant to the study of polymorphism. Deuterium is a quadrupolar nucleus (I = 1) whose behavior is dominated by the quadrupolar interaction, and is therefore sensitive primarily to intramolecular motions of the C–^{2}H bond. In anisotropic

dispersions such as MLVs, each C–^{2}H bond gives rise to a 'powder pattern' lineshape, also known as a 'Pake doublet'. The separation between the two maxima is the quadrupolar splitting $\Delta\nu_Q$, which, for deuterons on the acyl chain carbons, is related to the carbon–deuterium bond order parameter S_{CD} by

$$\Delta\nu_Q = \frac{3}{4}\chi S_{CD} \quad (1)$$

where χ is the quadrupolar coupling constant. The order parameter provides a measure of the angular excursions of the acyl chains about the surface normal. For lipids containing several deuterons, a superposition of Pake doublets is obtained [Figure 4(a)]. This is problematic for measurements of S_{CD} only if the splittings cannot be assigned.

Deuterium NMR can be used to assess lipid polymorphic preferences, and in this way provides analogous information to ^{31}P NMR. In addition, the use of selectively deuterated lipids allows monitoring of the phase behavior of individual components of mixed phospholipid systems, as exemplified by the Ca^{2+} triggered lamellar to H_{II} transition for [^{2}H]dioleoyl-PS ([^{2}H]DOPS) in DOPE/dioleoyl-PC/[^{2}H]DOPS/cholesterol (1:1:1:3).[22]

A fascinating polymorphic system recently investigated by ^{2}H NMR models the intercellular lipid lamellae of mammalian stratum corneum, the uppermost layer of skin.[23] The model, composed of ceramide, cholesterol, and perdeuterated palmitic acid (1:1:1), displays a complex polymorphism, with the palmitic acid partitioning into solid, gel, liquid ordered, hexagonal, and isotropic phases depending on the temperature and pH.[23] The ^{2}H NMR spectrum obtained at 50 °C and pH 5.2, where the palmitic acid is neutral, reveals liquid ordered membranes (plateau S_{CD} = 0.4), which are significantly more ordered than liquid crystalline bilayers but have the same lineshape [Figure 4(a)]. Heating to 75 °C induces an isotropic phase [Figure 4(c)]. However, if the pH is adjusted to 7.4, where the palmitic acid is negatively charged, the same temperature increase triggers a transition to the H_{II} phase [Figure 4(b)]. In this case the charge on the palmitic acid (i.e. size of the headgroup) regulates the phase induced at elevated temperatures. Furthermore, if the system is prepared with sphingomyelin instead of ceramide (where the former contains a phosphocholine headgroup compared with the hydroxyl group of the latter), then at low pH the membranes are liquid ordered over a wide temperature range and no polymorphism is observed.[23]

In addition to phase preferences, ^{2}H NMR can provide information concerning variation in orientational order in the hydrocarbon region of lamellar and hexagonal phases. For lipids containing a perdeuterated acyl chain, dePaking and integration methodology allows the complete order profile to be derived from a single spectrum.[24] This has been applied to dispersions of 1-[$^2H_{31}$]palmitoyl-2-oleoyl-*sn*-glycero-3-phosphocholine (POPC-d_{31}) and POPE-d_{31}, and mixtures there- of.[25–27] Significant differences are observed in the lamellar and H_{II} phases (Figure 5). The variation of S_{CD} in bilayers shows little change from carbons 2 to 10 (the plateau region), followed by a rapid drop in order toward the center of the bilayer. In the inverted hexagonal phase, the magnitude of the order parameters is decreased by at least a factor of two, and the plateau region is essentially nonexistent, giving a relatively linear decrease in order down the length of the chain. This results from looser packing of carbons 2 through 8 in the H_{II} phase.[25,26] The results indicate that order parameters are sensitive to the lipid phase symmetry, suggesting a relationship between the order profile and lipid polymorphic tendencies. This is further supported by the ability of nonbilayer lipids to modulate the order profile of a lamellar matrix. The introduction of POPE into POPC (or DOPE into DOPC) increases the order of the bilayer lipid.[25,27,28] Whether the changes in order parameters are as predictive of polymorphic preferences as changes in parameters such as R_0 remains to be seen.

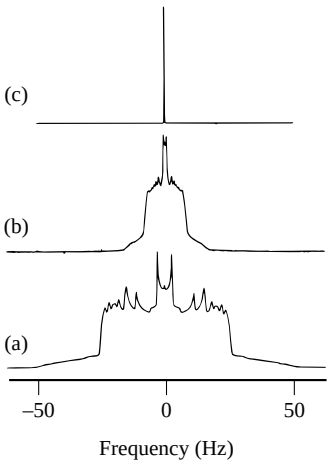

Figure 4 Deuterium NMR as a technique for assessing lipid polymorphic preferences. All of the spectra are equimolar dispersions of ceramide:cholesterol:palmitic acid-d_{31}, which approximates the composition of mammalian stratum corneum. (a) Liquid ordered membranes (maximum S_{CD} = 0.4) acquired at pH 5.2 and 50°C. (b) Hexagonal H_{II} phase at 75°C, acquired after adjustment of the pH to 7.4. (c) Isotropic phase at 75°C and pH 5.2. (We thank Dr Jennifer L. Thewalt and Dr Neil Kitson for providing the spectra)

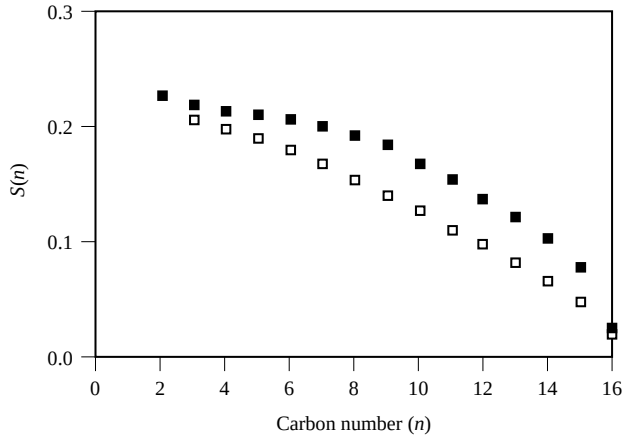

Figure 5 Smoothed order parameter profile of bilayer phase POPC-d_{31} (■) and hexagonal phase POPE-d_{31} (□), obtained by integration of dePaked spectra acquired at 30 and 70°C, respectively. The two profiles are normalized, but the absolute order parameters of the H_{II} phase at C-2 are approximately half those of the bilayer phase. (We thank Dr M. A. Monck for providing the data)

3 BIOLOGICAL IMPLICATIONS OF LIPID POLYMORPHISM

Although nonbilayer lipids are constrained to the lamellar phase in biological membranes, the study of lipid polymorphism has provided insight into several aspects of membrane function. Nonbilayer lipids may be involved in the regulation of certain membrane enzymes, and in some cases this regulation may involve modulation of membrane order, which can be achieved by controlling the ratio of bilayer to nonbilayer lipids. One example comes from ^{2}H NMR studies on the microorganism *Acholeplasma laidlawii* strain B, where perdeuterated palmitic acid was biosynthetically incorporated into the cell membrane. Growth of the microorganism could only occur over a fairly narrow range of order ($0.14 < S_{CD} < 0.18$).[29] Maintenance of the order profile was attributed to the ratio of MGlcDG to DGlcDG, which in isolation prefer the H_{II} and bilayer phases, respectively. The failure of the organism to thrive outside this range of order suggests an order requirement for optimum membrane protein function.

Nonbilayer lipids may play an important role in membrane fusion. LUVs made of charged and nonbilayer lipids (such as PE and PS) can often be induced to fuse in the presence of Ca^{2+} to form larger lamellar structures which then rearrange to the H_{II} phase.[14] When these same systems are studied as MLVs, they undergo lamellar to H_{II} transitions. Certain lipid soluble fusogens, such as monoolein, are capable of inducing H_{II} or cubic phase structure in model and biological membranes.[12,14] Clearly, membrane fusion cannot occur without local, transient departures from bilayer morphology at the fusion interface. These observations provide strong evidence that fusion proceeds via nonbilayer intermediates.[13]

Our understanding of the link between lipid polymorphism and membrane fusion owes much to the work of Siegel,[13] who has developed a unified description of both lamellar to hexagonal and lamellar to cubic transitions. Siegel has proposed that the first fusion intermediates are either inverted micellar intermediates (IMIs) or stalk structures, which form between apposed bilayers at appropriate temperatures, and then assemble into either H_{II} phase or cubic phase precursors [the latter are also referred to as interlamellar attachments (ILAs)]. The particular path chosen is a function of the spontaneous radius of curvature of the membrane,[30] but only the latter path (ILAs) leads to membrane fusion. The highly curved ILA structure explains the narrow 'isotropic' resonances often observed in lipid mixtures by ^{31}P NMR. Liposome fusion has been observed to occur only over the same narrow temperature range where isotropic ^{31}P NMR resonances are observed.[30]

4 RELATED ARTICLES

Bilayer Membranes: Deuterium and Carbon-13 NMR; Glycolipids; Membrane Lipids of Acholeplasma laidlawii; Membranes: Carbon-13 NMR; Membranes: Deuterium NMR; Membranes: Phosphorus-31 NMR; Molecular Motions: T_1 Frequency Dispersion in Biological Systems.

5 REFERENCES

1. S. J. Singer and G. L. Nicholson, *Science*, 1972, **175**, 720.
2. V. Luzzatti, T. Gulik-Kryzwicki, and A. Tardieu, *Nature (London)*, 1968, **255**, 684.
3. P. R. Cullis and B. de Kruijff, *Biochim. Biophys. Acta*, 1979, **559**, 399.
4. J. Seelig, *Biochim. Biophys. Acta*, 1978, **515**, 105.
5. J. Seelig, *Q. Rev. Biophys.*, 1977, **10**, 353.
6. J. H. Davis, *Biochim. Biophys. Acta*, 1983, **737**, 117.
7. M. Bloom, E. Evans, and O. G. Mouritsen, *Q. Rev. Biophys.*, 1991, **24**, 293.
8. P. R. Cullis and M. J. Hope, in *Biochemistry of Lipids, Lipoproteins, and Membranes*, ed. D. E. Vance and J. Vance, Elsevier, Amsterdam, 1991, p. 1.
9. M. J. Hope, M. B. Bally, L. D. Mayer, A. S. Janoff, and P. R. Cullis, *Chem. Phys. Lipids*, 1986, **40**, 89.
10. J. M. Seddon, *Biochim. Biophys. Acta*, 1990, **1031**, 1.
11. D. B. Fenske and P. R. Cullis, *Biochim. Biophys. Acta*, 1992, **1108**, 201.
12. G. Lindblom and L. Rilfors, *Biochim. Biophys. Acta*, 1989, **988**, 221.
13. D. P. Siegel, *Biophys J.*, 1993, **65**, 2124.
14. P. R. Cullis, M. J. Hope, B. de Kruijff, A. J. Verkleij, and C. P. S. Tilcock, in *Phospholipids and Cellular Regulation*, ed. J. F. Kuo, CRC Press, Boca Raton, FL, 1985, p. 1.
15. P. R. Cullis and B. DeKruijff, *Biochim. Biophys. Acta*, 1976, **436**, 523.
16. C. P. S. Tilcock, P. R. Cullis, and S. M. Gruner, *Chem. Phys. Lipids*, 1986, **40**, 47.
17. M. J. Hope, K. F. Wong, and P. R. Cullis, *J. Electron Microsc. Techniques*, 1989, **13**, 277.
18. P. R. Cullis, C. P. Tilcock, and M. J. Hope, in *Membrane Fusion*, ed. J. Wilschut and D. Hoekstra, Dekker, New York, 1990, p. 35.
19. J. N. Israelachvili, S. Marcelja, and R. G. Horn, *Q. Rev. Biophys.*, 1980, **13**, 121.
20. S. M. Gruner, *Proc. Natl. Acad. Sci. USA*, 1985, **82**, 3665.
21. S. M. Gruner, M. W. Tate, G. L. Kirk, P. T. C. So, D. C. Turner, D. T. Keane, C. P. S. Tilcock, and P. R. Cullis, *Biochemistry*, 1988, **27**, 2853.
22. C. P. S. Tilcock, P. R. Cullis, and S. M. Gruner, *Biochemistry*, 1988, **27**, 1415.
23. J. Thewalt, N. Kitson, C. Araujo, A. MacKay, and M. Bloom, *Biochem. Biophys. Res. Commun.*, 1992, **188**, 1247.
24. M. Lafleur, B. Fine, E. Sternin, P. R. Cullis, and M. Bloom, *Biophys. J.*, 1989, **56**, 1037.
25. M. Lafleur, M. Bloom, and P. R. Cullis, *Biochem. Cell Biol.*, 1990, **68**, 1.
26. M. Lafleur, P. R. Cullis, B. Fine, and M. Bloom, *Biochemistry*, 1990, **29**, 8325.
27. M. Lafleur, P. R. Cullis, and M. Bloom, *Eur. Biophys. J.*, 1990, **19**, 55.
28. D. B. Fenske, H. C. Jarrell, Y. Guo, and S. W. Hui, *Biochemistry*, 1990, **29**, 11 222.
29. M. A. Monck, M. Bloom, M. Lafleur, R. N. A. H. Lewis, R. N. McElhaney, and P. R. Cullis, *Biochemistry*, 1992, **31**, 10 037.
30. H. Ellens, D. P. Siegel, D. Alford, P. L. Yeagle, L. Boni, L. J. Lis, P. J. Quinn, and J. Bentz, *Biochemistry*, 1989, **28**, 3692.

Biographical Sketches

Pieter R. Cullis. *b* 1946. B.Sc., 1967, Ph.D., 1972, University of British Columbia. Introduced to NMR by Sir R. E. Richards. Postdoctoral fellow, Oxford, UK, 1973–76, and University of Utrecht,

Holland, 1977. Faculty in Biochemistry, University of British Columbia, 1978–present. Approx. 180 publications. Research interests include the study of lipid polymorphism and the functional roles of lipids in membranes, the generation of model membrane systems which more accurately model biological systems, and the use of liposomes for in vivo targeted delivery of biologically active materials.

David B. Fenske. *b* 1958. B.Sc., 1980, Ph.D., 1988, Simon Fraser University. Visiting fellow, National Research Council of Canada, 1988–90. Postdoctoral fellow, University of British Columbia, 1991. Research associate, Biochemistry, University of British Columbia, 1992–present. Approx. 19 publications. Research interests include the study of membrane structure and dynamics using ^{2}H and ^{31}P NMR.

Membrane Proteins

Stanley J. Opella and Francesca M. Marassi
University of Pennsylvania, Philadelphia, PA, USA

1	Introduction	1
2	Early NMR Studies of Membranes	1
3	Applications to Membrane Proteins in Micelles	2
4	Solid state NMR Spectroscopy of Membrane Proteins in Lipid Bilayers	3
5	NMR Studies of the Membrane Bound Form of Filamentous Bacteriophage Coat Protein	6
6	Prospects for NMR Studies of Membrane Proteins	8
7	Related Articles	8
8	References	8

1 INTRODUCTION

Membrane proteins are responsible for many important biological functions, including some that are unique, such as those of receptors and ion channels, as well as some that overlap with those of soluble proteins, such as enzymes. Even though more than half of all proteins are associated with membranes, and there are many additional reasons to be interested in their structural biology, only a few high-resolution structural studies of membrane proteins have been reported.[1–4] This is largely because samples of membrane proteins are problematic for the most commonly used methods of structural biology. Proteins complexed with lipids are difficult to crystallize in forms suitable for X-ray diffraction and conventional multidimensional solution NMR methods are hampered by their slow overall reorientation rates. However, in spite of its limitations, NMR spectroscopy has played an important role in the characterization of membrane proteins and, more importantly, it has the potential to play a dominant role in future studies. The development of high-resolution solid state NMR methods gives NMR spectroscopy sufficient versatility to determine the structures and describe the dynamics of proteins in bilayer samples. Further development of the instrumentation and methods for multidimensional solution NMR spectroscopy will also improve its effectiveness in studies of membrane proteins in micelle samples.

The key to NMR studies of membrane proteins is sample preparation.[5] Figure 1 illustrates the molecular arrangements in phospholipid bilayers and detergent micelles, the two well-characterized model membrane systems used in a wide variety of biophysical investigations including NMR spectroscopy. Each micelle, of detergents most commonly used in NMR studies, contains approximately 50–60 single chain lipid molecules and a single polypeptide. In contrast, lipid bilayers are very large supramolecular structures with many phospholipid and polypeptide molecules in extended two-dimensional arrays. Proteins in micelles reorient relatively slowly, although rapidly enough to be suitable for most heteronuclear multidimensional solution NMR experiments in high-field spectrometers, while those in bilayers are immobile on the relevant

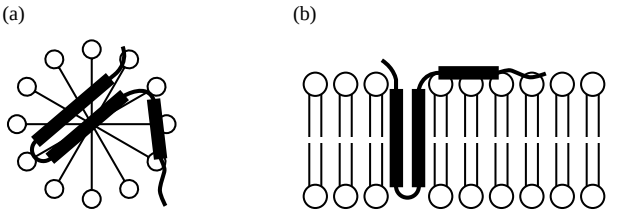

Figure 1 Schematic drawings of a protein in membrane environments: (a) detergent micelle; (b) phospholipid bilayer

NMR timescales, enabling them to be treated spectroscopically as solids. Therefore, the most important advantage of utilizing these two different types of model membrane is that they permit the use of both high-resolution solid state NMR and multidimensional solution NMR methods with membrane proteins. The results from these two essentially independent spectroscopic approaches can be combined to describe structural features of membrane proteins that are otherwise inaccessible to any single method of structure determination. Solid state NMR spectroscopy of oriented and unoriented bilayer samples and multidimensional solution NMR spectroscopy of micelle samples are most effective when the proteins are suitably labeled with stable isotopes and the samples are carefully prepared. The dynamics of backbone and side-chain sites can be described over a wide range of timescales through the analysis of nuclear spin relaxation in both micelle and bilayer samples, and motionally averaged powder pattern lineshapes in bilayer samples.[6] Local protein motions have a dramatic effect on many spectral parameters; therefore mobile residues in loop and terminal segments can be readily identified in both types of sample.[7,8]

2 EARLY NMR STUDIES OF MEMBRANES

NMR spectroscopy was applied to proteins within a decade of its initial demonstration. The first NMR spectrum of a protein reported in 1957 was that of a small globular protein, ribonuclease, in aqueous solution.[9] This spectrum, despite its low sensitivity and limited resolution, encouraged additional development by demonstrating the basic feasibility of NMR spectroscopy for the study of proteins in aqueous solution. However, the development and application of NMR spectroscopy has been conspicuously focused on soluble proteins that do not aggregate and reorient rapidly in solution. Technical advances, especially high-field magnets and small, fast computers, and methodological advances, especially multidimensional experiments utilizing pulsed irradiation at several rf frequencies, led to the development and implementation of approaches to structure determination of globular proteins in solution by the mid-1980s.[10,11]

The immediate application of NMR to the study of membrane proteins was precluded by the difficulty of identifying resonances that could be attributed to the relatively small amounts of protein in spectra dominated by resonances from the highly abundant lipids and by the broad lines and hence, poor sensitivity and resolution obtained from proteins bound to native membranes, or multilamellar liposomes or sonicated vesicles in reconstituted systems. For these reasons the majority of the early NMR studies of membrane systems was

devoted to dynamics and organization of the lipids in bilayers, and to some extent the influence of proteins and peptides on the properties of the lipids. Nevertheless, the results of NMR experiments, especially in combination with those from contemporary ESR experiments, strongly influenced the understanding of biological membranes as dynamic entities. The NMR studies gave a picture of protein–lipid interaction where the proteins generally have a disordering effect on the membrane lipids; there is little evidence of selectivity in the interaction between proteins and lipids, with the exception of some charged species; and there is a fast exchange between protein-associated and bulk lipid, on the NMR timescale. There are a number of thorough review articles on these subjects.[12,13]

A substantial amount of the early research on membranes was devoted to conformational studies of small membrane active polypeptide antibiotics and their interactions with phospholipids. Certain such peptides are known to induce cation permeation across cells and artificial membranes, and to form lipid soluble complexes. Early NMR studies of peptides such as alamethicin and gramicidin[14,15] set the stage for later detailed investigations of peptide ion channels and their interaction with membranes.

The initial studies of native and reconstituted membranes demonstrated that high-resolution NMR spectra suitable for detailed structural analysis of membrane proteins could not be readily obtained.[16] Sonicated vesicle samples have the advantage of being bilayers, albeit highly curved, and sealed chambers suitable for transport studies. Although spectra obtained from lipids in sonicated vesicles are considerably narrower than those in multilamellar bilayers, the overall correlation time (approximately 10^{-6} s) of the vesicles is extremely inconvenient. This means that any resonances from protein, or other molecular constituents immobilized within the vesicle are very broad because of efficient relaxation.[17] These resonances do not respond to solid state NMR procedures because their breadth is due to relaxation rather than powder pattern characteristics. Therefore there have been very few ^{1}H or ^{13}C NMR studies of proteins in vesicles. However, some results have been obtained with ^{19}F-labeled proteins, since the number of resonances is greatly reduced and there is no interference from lipid resonances. For example, the motional properties of the M13 major coat protein, fluorinated at its two tyrosyl residues, have been examined in this manner.[18,19] The filamentous bacteriophage coat proteins have turned out to be very valuable model systems for many types of NMR study of membrane proteins.

In 1968, Kamat and Chapman[20] showed that the resolution and sensitivity of ^{1}H NMR spectra could be substantially improved by solubilizing native membranes in lysolipid or detergent micelles. Around 1979, the first high-resolution NMR studies of membrane associated peptides in small perdeuterated micelles were reported.[21,22] The relatively well-resolved spectra, and the observation of homonuclear NOEs in well-behaved and stable samples set the stage for many fruitful multidimensional solution NMR studies of membrane associated peptides and proteins.

3 APPLICATIONS TO MEMBRANE PROTEINS IN MICELLES

Multidimensional solution NMR methods can be applied to peptides and proteins in micelles because the reorientation of the protein–micelle complex in solution is rapid enough to average the spectral parameters from the various nuclear spin interactions to their isotropic values. This enables the indirect effects of their fluctuations, as monitored by relaxation phenomena, to describe local dynamics as well as provide spatial information in the form of relative proximities. However, the methods of solution NMR spectroscopy are somewhat limited, at least compared with what can be done with well-behaved globular proteins in solution, by the broad linewidths and efficient spin diffusion that accompany the relatively slow reorientation of protein–micelle complexes in solution. These limitations can be minimized with careful sample preparation, especially through specific, selective, and uniform isotopic labeling of the protein, and through careful preparation of the micelles by ensuring sufficient detergent and salt concentrations to form uniform, small micelles.[23] Some membrane proteins are soluble in organic solvents or mixed aqueous solvents without lipids, and these preparations have been used in NMR studies. While well-resolved protein resonances can be observed in many cases, there is always considerable concern about the status of the protein in these solvents, especially in the popular trifluoroethanol because of its helix forming propensity. However, as the methods for studying proteins in micelles improve, there is less need to rely on solubilizing membrane proteins in organic solvents.

Protein structure determination by multidimensional NMR spectroscopy is straightforward for relatively small globular proteins in solution, especially when uniformly ^{15}N and ^{13}C labeled samples are available. There are several basic steps in protein structure determination, as widely utilized with globular proteins in aqueous solution, including: the resolution and assignment of backbone and side-chain resonances based on through-bond and through-space interactions observed in multidimensional NMR spectra; the measurement of many homonuclear ^{1}H–^{1}H NOEs among the assigned resonances, supplementing these short range distances with other structural constraints including spin–spin coupling constants; the interpretation of all structural constraints in terms of secondary structure; and the generation of a family of three-dimensional protein structures using distance geometry, molecular dynamics, and other calculations.

Melittin has been studied extensively by NMR spectroscopy after its initial use as an example to show the feasibility of micelle samples.[24,25] This 26-residue peptide disrupts membranes. Solution NMR studies of melittin in detergent micelles show that the amino terminal and carboxyl terminal regions are α-helical and separated by a kink. The NMR data from melittin have been subjected to considerable refinement, and provide a model for other amphipathic helical peptides that interact with membranes. The bombolitins are another class of peptides isolated from the venom of bees, whose functions include the lysis of erythrocytes and liposomes. The structures of bombolitin I and III have been investigated by ^{1}H NMR both in sodium dodecyl sulfate (SDS) micelles and in aqueous solution.[26] In micelles the presence of strong NH(i)–NH(i + 1) NOEs over the full range of the molecules is indicative of helical structures. In water, bombolitin I lacks any observable secondary structure, while bombolitin III adopts a highly helical structure which is believed to arise from extensive peptide aggregation.

Membrane modifying channel-forming peptides of fungal origin, that are rich in hydrophobic amino acids including α-aminoisobutyric acid (Aib), have been the focus of many NMR investigations. Alamethicin is a 20 amino acid peptide known to induce voltage gated conductance in bilayers. This peptide has been studied extensively by solution NMR, both in organic solvents and, more definitively, in SDS micelles.[27] Interproton distances obtained from the NOE data suggest a structure for alamethicin where the amino terminus is predominantly α-helical while the carboxyl terminus is less regular and more flexible.

δ-Hemolysin is another 26 residue peptide that interacts with membranes. NMR studies of the peptide in micelles indicate that it forms an extended helix.[28] Typical of many membrane bound amphipathic helical peptides, δ-hemolysin gives a quite well-resolved one-dimensional ^{1}H NMR spectrum, with some limitations in the two-dimensional spectrum, resulting from the broad resonance linewidths and efficient spin diffusion. The 32 residue polypeptide hormone calcitonin was characterized in SDS micelles and found to have an amphipathic helix running into the amino terminal disulfide bridged loop.[29]

The major functional channels in membranes, such as the nicotinic acetylcholine receptor and cation channels, are large oligomeric proteins. Structural studies of these proteins are limited by their overall size and the difficulty in crystallizing them. A promising approach to their analysis is to synthesize and study peptide sequences corresponding to segments of the proteins. We have studied the peptide M2 selected from the δ subunit of the torpedo acetylcholine receptor, because homology and model studies suggest that this sequence-specific motif is responsible for specific functions in the channel activity of the receptor and the 23 residue M2 δ peptide forms channels by self-association when added to membranes. Solution NMR experiments demonstrate that there is substantial helical secondary structure in the M2 δ peptide in micelles.[30]

Many membrane interactive peptides have antibiotic activities. Cecropin A, a 37 residue peptide found in *Hyalophora cecropia* and other insects, is part of their defense mechanism against bacteria. NMR studies show that this peptide is essentially a random coil in aqueous solution. This peptide has also been studied in hexafluoroisopropyl alcohol solutions by NMR spectroscopy.[31,32] Interproton distance restraints determined by nuclear Overhauser enhancement measurements and distance restraints hydrogen bonds were used as a basis for three-dimensional structure determination by simulated annealing. The resulting converged structures indicate that there are two α-helical regions extending from residues 5–21 and 24–37. Magainins are a family of 21–26 residue peptides that protect frogs from infections, even after severe injury, with a broad spectrum of antibacterial and antifungal activities. These peptides interact strongly with bacterial and model membranes. Their antibiotic activity appears to be associated with the disruption of the electrochemical ionic gradient across cell membranes. Multidimensional solution NMR spectra, as shown in Figure 2, indicate that magainins are unstructured in aqueous solution, but completely α-helical in detergent micelles[33] and trifluoroethanol/water solutions.[34]

Adenosine 5′-triphosphate (ATP) synthase consists of two main components; the water soluble complex F_1, and the membrane-bound complex F_0. The latter, in turn, consists of three subunits (a, b and c), all of which are needed

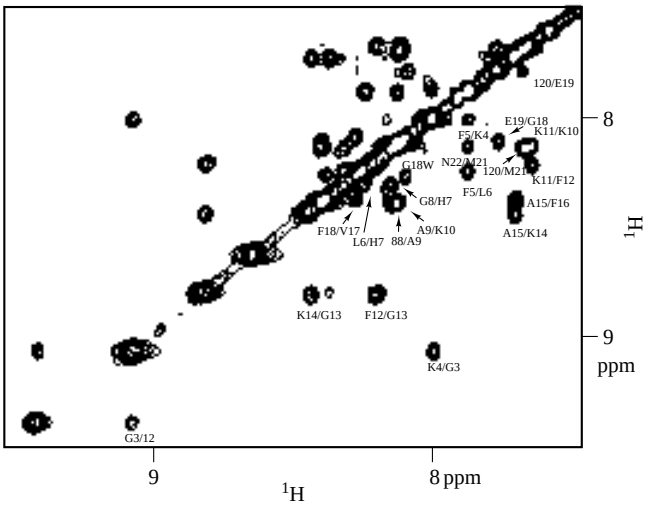

Figure 2 Amide region of two-dimensional ^{1}H/^{1}H NOE spectrum of magainin-2 in micelles

for the maintenance of proton pumping. Subunit c is the smallest (79 amino acids) and most abundant subunit. The structure of subunit c dissolved in mixed organic solvents has been investigated by multidimensional solution NMR spectroscopy. The secondary structure was determined from a combination of homonuclear NOE connectivities, and coupling constant measurements. The protein consists of two long and predominantly helical segments separated by a mobile, unstructured, eight residue stretch. The amino and carboxyl termini are close together, such that the molecule is folded in a hairpin arrangement.[35–37]

Bacteriorhodopsin, the principal component of the outer membrane of *Halobacterium halobium*, where it serves as a light-driven proton pump, is one of the most intensively studied membrane proteins. It consists of 248 amino acids and its structure is dominated by seven transmembrane hydrophobic helices. The protein binds a retinal chromophore to absorb light and translocate protons across the membrane. Solution NMR spectroscopy has been useful in characterizing the structure of bacteriorhodopsin. Fragments corresponding to several of the transmembrane helical sections have been obtained by proteolytic cleavage or peptide synthesis, and have been studied in both organic solvents and detergent micelles. For example, the 34–65 fragment peptide, corresponding to the membrane spanning segment B, was investigated in SDS micelles where it was found to adopt a right-handed helix from residues 41 to 62 with a kink at residue 50, and a disordered amino terminus from residues 34 to 40.[38] The longer 163–231 fragment peptide, corresponding to the transmembrane segments F and G, was also investigated in a similar fashion and found to contain extensive regions of right-handed helix and a flexible amino terminus.[39]

4 SOLID STATE NMR SPECTROSCOPY OF MEMBRANE PROTEINS IN LIPID BILAYERS

Polypeptides that are strongly associated with phospholipids are well suited for solid state NMR spectroscopy,[30,40,41] because their structured regions are essentially completely

immobilized on the timescales defined by the spectral ranges (10^3-10^6 Hz) of the chemical shift, dipolar, and quadrupolar spin-interactions of the nuclei present in proteins. This immobilization preserves the anisotropic characteristics of the nuclear spin interactions averaged out by the rapid isotropic reorientation that occurs in solution, including proteins in micelles. Since it is possible to prepare both oriented and unoriented samples of proteins in fully hydrated phospholipid bilayers, many different parameters can be resolved and measured from single line and powder pattern spectra.

In solid state NMR spectroscopy rf irradiation supplemented by mechanical sample spinning or orientation replace molecular motions as line-narrowing mechanisms. Not only do solid state NMR methods give spectra with high-resolution and sensitivity, they also enable measurements of distance and orientational parameters. There are two complementary methods for protein structure determination by solid state NMR spectroscopy. In one approach, orientational constraints for bonds and chemical groups are derived from spectral parameters observed in samples of peptides and proteins embedded in lipid bilayers oriented between glass plates.[42] In the other approach, unoriented or powder samples examined in the presence of magic angle sample spinning employ procedures to preserve the dipolar couplings so they can be used for distance measurements.[43,44]

Very favorable spectroscopic properties are associated with uniaxially oriented samples where the axis of molecular orientation lies parallel to the direction of the applied magnetic field.[45] Spectra from these samples consist of single line resonances (or multiplets) rather than powder patterns from each isotopically labeled site. Since the observed resonance frequencies (or splittings) are directly related to the orientations of individual atoms or bonds relative to the axis defined by the direction of the applied magnetic field, spectroscopic measurements on oriented samples provide the basis for protein structure determination. The nuclear spin interactions provide spectral parameters that vary as a function of the angle between a bond (or a chemical group) and the direction of the applied magnetic field.

High-resolution structures can be determined with two or more spectroscopic measurements for each structural element, such as a peptide plane or indole ring, since each orientation can be related to a common axis defined by the direction of macroscopic molecular orientation and the applied magnetic field.[46] The orientational constraints together with the established covalent geometry of the molecule are sufficient to define the complete three-dimensional structure. Limited but worthwhile orientational information can be derived from single spectroscopic measurements on oriented samples.[42] Once the secondary structure of a polypeptide segment is established, for example from multidimensional solution NMR experiments on samples in micelles, a single spectral parameter is often sufficient to establish the orientation of a helix relative to the plane of the bilayer, which is especially valuable in studies of membrane proteins where helices are often the dominant secondary structural feature.

The structure of a protein can be determined from the measurement of many short-range distances. Distances can be measured quantitatively between pairs of nuclei with solid state NMR experiments. Magic angle sample spinning enables high resolution spectra to be obtained from unoriented samples; however, since the spinning averages out both the unwanted broadening from the chemical shift anisotropy as well as the dipolar couplings essential for the measurements, it is necessary to cancel out selectively the effects of the spinning on the dipolar interactions. Different experimental approaches are used depending on whether homo- or heteronuclear dipole–dipole couplings are the source of distance information. This application of solid state NMR spectroscopy is rapidly increasing in popularity for structural studies of a variety of biopolymers, including peptides and proteins in lipid bilayers.[47]

It is possible to arrange for heteronuclear dipole–dipole interactions to be present at locations throughout polypeptides by isotopic labeling, enabling distance measurements between specific sites of interest. Rotational echo double-resonance (REDOR) NMR spectroscopy is a general method for measuring internuclear distances between two different nuclei that utilizes rf pulses at the resonance frequency for one of the types of coupled spins to interfere with the averaging of the dipole–dipole interactions.[43] Rotational resonance spectroscopy is also used with magic angle sample spinning to measure weak dipole–dipole couplings,[44] although, unlike REDOR, it is a homonuclear method measuring distances between the same kind of nuclei. The method depends on special effects that occur when the spinning frequency is an integral multiple of the chemical shift difference between the two labeled sites.

Helical peptides are of interest in studies of membrane proteins because they serve as independent structural or functional entities of monomers, oligomers, or domains of larger proteins associated with membranes. Helical peptides, whether hydrophobic or amphipathic, have been found to adopt either transmembrane or in-plane orientations in bilayers, and solid state NMR experiments on oriented samples are adept at differentiating between these two situations. Once the secondary structure is established as helical, then a single solid state NMR measurement is generally sufficient to determine the orientation of the helix in the bilayer. Both qualitative and quantitative analyses of the orientational parameters have given consistent results in determining transmembrane and in-plane orientations of helices. The ^{15}N chemical shift for labeled amide sites is particularly useful for distinguishing between transmembrane and in-plane orientations of helices because of the convenient orientation of the chemical shift tensor in the molecular frame.[42] A conformation with the N–H bond approximately parallel to the field, which occurs for a transmembrane helix in oriented bilayers, has a ^{15}N chemical shift with a frequency near $\sigma_{\parallel}$, while a conformation with the N–H bond approximately perpendicular to the field, which occurs for an in-plane helix in oriented bilayers, has a ^{15}N chemical shift with a frequency near $\sigma_{\perp}$. These frequencies are separated by the full breadth of the chemical shift anisotropy powder pattern illustrated with the spectra in Figure 3. For example, the spectrum in Figure 3(c) is from a single ^{15}N labeled amide site in a 23 residue peptide with the sequence corresponding to the M2 helical segment of the δ subunit of the acetylcholine receptor, which has been shown to be helical.[30] The M2 peptide is shown to have a transmembrane orientation (Figure 4) because its ^{15}N resonance frequency is near the low frequency (high field) ($\sigma_{\parallel}$) edge of the powder pattern. This orientation is consistent with the model for its functioning as a channel by oligomerization within the bilayers.

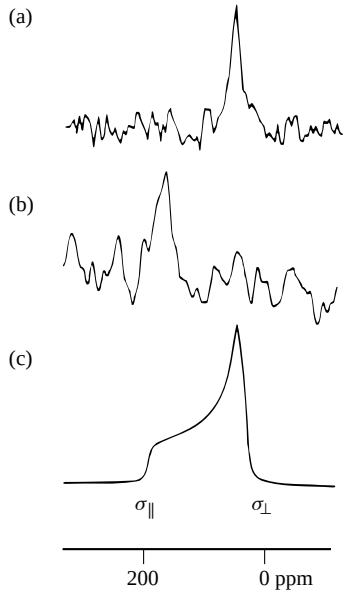

Figure 3 (a,b) Experimental solid state ^{15}N NMR spectra of 23 residue amphipathic peptides in oriented bilayers. (a) [^{15}N]Ala-labeled magainin-2. (b) [^{15}N]Ala-12-labeled M2 δ peptide. (c) Simulation of the powder pattern for an immobile ^{15}N amide site

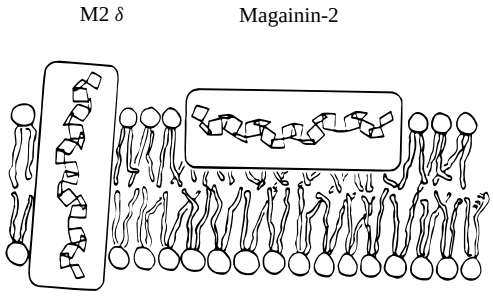

Figure 4 Schematic drawing of in-plane (magainin-2) and transmembrane (M2 δ) orientations of 23-residue amphipathic helical peptides in lipid bilayers. The helical backbones are represented by their 22 peptide bond planes, whereas the white boxes indicate the extending side chains

Contrast the position of the ^{15}N resonance from the M2 transmembrane peptide in Figure 3(b) to that from the magainin-2 peptide in Figure 3(a), which has a ^{15}N resonance frequency near the high frequency ($\sigma_{\perp}$) edge of the powder pattern. This large 170 ppm difference in resonance frequencies is due solely to the difference in orientations of the peptides in the bilayer. Magainin antibiotic peptides from frog skin have been investigated by solid state NMR spectroscopy in lipid bilayers. Their secondary structure has been demonstrated to be a helical by a variety of methods, including solid state NMR spectroscopy.[48] Spectra, such as that shown in Figure 3(b), from many labeled sites indicate that these peptides are oriented through their entire length in the plane of the bilayers, as shown in Figure 4. In other experiments the heteronuclear dipole–dipole splittings associated with the labeled sites have been measured, providing a second spectral parameter for each site. This enabled the structural determination of four contiguous residues of magainin-2 based only on solid state NMR experiments of oriented samples. The α-helical secondary structure is in complete agreement with that determined by a variety of other methods, including multidimensional solution NMR spectroscopy in micelles. However, solid state NMR spectroscopy of oriented bilayer samples is unique in being able to determine the in-plane orientation of the helix in the bilayer.

Rotational resonance spectroscopy has been used to measure the distances between ^{13}C labeled sites in peptides with sequences corresponding to the transmembrane domain of glycophorin A protein in lipid bilayers.[49] These measurements indicate a helical geometry throughout the peptide, with some evidence of unraveling of the helix near the membrane surface. Measurements have also been made of the distances between sites on the lipids and on the peptides, indicating the feasibility for using these methods to characterize fundamental peptide–membrane interactions.[50]

Gramicidin A is a linear polypeptide of 15 amino acid residues having alternating D and L stereochemistry. As an amino terminus to amino terminus dimer, gramicidin forms a monovalent cation selective channel across lipid bilayers and natural membranes. The channel conformation is a β-strand that forms a helix with 6.3 residues per turn. Solid state NMR spectra of oriented samples provide very high resolution constraints, making it possible to define each peptide plane orientation with respect to the magnetic field. By combining data from adjacent planes and the tetrahedral geometry of the C-α atom, the $\Phi\Psi$ torsion angles can be determined.[51] Considerable effort has been devoted to a characterization of the gramicidin side-chain conformation and dynamics,[52,53] in particular to the four indole groups per monomer.[54,55] The orientation for each indole ring with respect to the channel axis and bilayer normal has been determined. This information contributes to models for the roles of indoles in channel conductance. REDOR has been used to measure the dipolar coupling between the Gly-2 ^{13}C-1 carbon and Ala-3 [^{15}N]amide nitrogen atom in a sample of gramicidin where the peptide was in lipid bilayers.[56] This effective coupling was used to determine the orientation of this bond with respect to the bilayer normal. A significant feature of these measurements is that they give the magnitude and sign of the dipolar coupling, enabling the angle to be reduced to a single value and its supplement. This information about the Gly-2-Ala-3 ^{13}C–^{15}N peptide bond angle was consistent with the data obtained from orientational constraints, showing that gramicidin is a right-handed, single-stranded β-helical dimer in lipid bilayers.

Bacteriorhodopsin has been used in the development of many methods, including solid state NMR spectroscopy,[57] for probing the structures of membrane proteins. The configuration of the single molecule of retinal bound to bacteriorhodopsin and involved in its mechanism of action is the key to understanding its chemical mechanism. Watts and co-workers have labeled both ring[58] and individual methyl groups[59] along the retinal moiety with ^{2}H. From oriented preparations and the resulting orientational constraints a detailed picture of the bound chromophore conformation has been established. These results add to the large number of prior studies of the retinal with rotational resonance methods. Rotational resonance methods have also been used to measure distances between sites on the retinal chromophore and protein residues.[60] By utilizing the ^{13}C-labeled retinals and ^{13}C-ϵ lysine labeled bacteriorhodopsin, it was possible to take advantage of the

unique chemical shift of the C-ϵ atom of the lysine involved in the Schiff base.

5 NMR STUDIES OF THE MEMBRANE BOUND FORM OF FILAMENTOUS BACTERIOPHAGE COAT PROTEIN

The membrane bound filamentous bacteriophage coat protein is a small, but typical membrane protein with both amphipathic and hydrophobic helices. It has been the subject of extensive NMR studies in both micelle and bilayer samples and provides an excellent system to illustrate what can be done by combining results from both of these methods. fd is a filamentous bacteriophage that infects *Escherichia coli* and has approximately 2700 copies of a 50 residue major coat protein surrounding its DNA. The viral coat protein is synthesized with an amino terminal signal sequence which directs it to the bacterial inner membrane before being removed by cleavage with leader peptidase. The coat protein becomes the most abundant membrane in infected cells, and then subunits assemble to form the outer coat of the virus particles as they are extruded through the membrane.

fd coat protein in micelles was the first protein shown to have such heterogeneous backbone dynamics that resonances from mobile residues could be clearly distinguished from the rigid residues on the basis of multiple relaxation parameters. Initially, about eight of the backbone C-α resonances were observed to have much narrower linewidths, longer T_1 values, and larger heteronuclear NOEs than the rest of the C-α resonances in natural abundance ^{13}C NMR spectra of fd coat protein in SDS micelles.[61] The presence of mobile amide backbone sites near the amino and carboxyl termini in the membrane bound form of fd coat protein was also shown with ^{15}N-labeled samples in micelles by the observation of large negative heteronuclear ^{1}H/^{15}N NOEs and in bilayers with the observation of narrow isotropic resonance intensity in ^{15}N solid state NMR spectra.[8] The observation of narrow ^{13}C resonance linewidths for some carbonyl sites confirmed that the coat protein had mobile backbone sites in micelle samples.[62] Additional evidence for mobile residues comes from labeled side-chain sites with the observation of isotropic resonance intensity in ^{2}H solid state NMR spectra of samples in bilayers[63] and with the analysis of the relaxation properties of $^{13}CH_3$ labeled alanine residues.[64]

Additional evidence concerning protein backbone dynamics comes from the kinetics of hydrogen exchange at amide sites; however, these data are more difficult to interpret directly in terms of protein structure and fluctuations. There are substantial qualitative differences in the exchange rates of amides in different parts of the protein.[61,65] The exchange rates of individual amide sites throughout the protein have been measured;[66] the finding was that residues 28 and 45 undergo very slow exchange, while residues 7 and 20 exchange more rapidly, although not nearly as fast as for unstructured solvent exposed sites.

The determination of the secondary structure of fd coat protein in SDS micelles utilizes multidimensional NMR spectroscopy.[66–68] The majority of the sequential assignments of the amide resonances were made using homonuclear ^{1}H NOE data from two- and three-dimensional NOE/HMQC

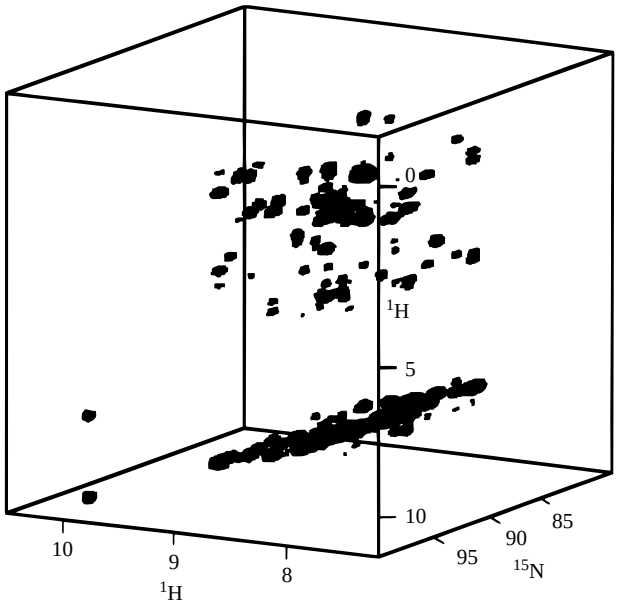

Figure 5 Three-dimensional (^{1}H/^{15}N HMQC/^{1}H/^{1}H NOE) solution spectrum of uniformly ^{15}N labeled fd coat protein in SDS micelles in solution

experiments as shown in Figure 5, supplemented with information from TOCSY/HMQC experiments, and spectra of selectively ^{15}N-labeled samples.[67] All the NOE data are consistent with extensive helical secondary structure in the protein; in particular, NOEs are observed between NH–NH(i, i + 1), NH–C-αH(i, i + 1), NH–C-βH(i, i + 1), NH–C-αH(i, i + 3), and NH–C-αH(i, i + 4) for many residues determined to have helical secondary structure. The ^{1}H/^{1}H strips in Figure 6 at ^{15}N chemical shifts corresponding to S13, L14, and Q15 show the presence of NOEs between resonances from hydrogen atoms on adjacent amide nitrogens, and α- and β-carbon atoms; these residues are part of an amphipathic helix that lies in the plane of the lipid bilayer. K40, L41, and F42 also exhibit these characteristic NOEs and are a part of

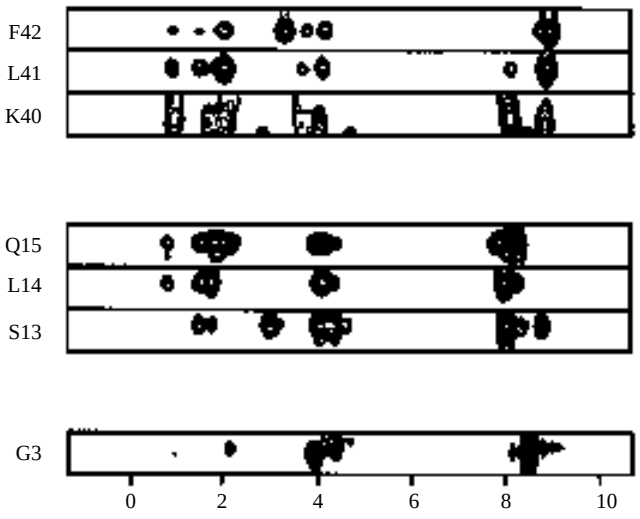

Figure 6 Strips taken from the three-dimensional spectrum shown in Figure 5

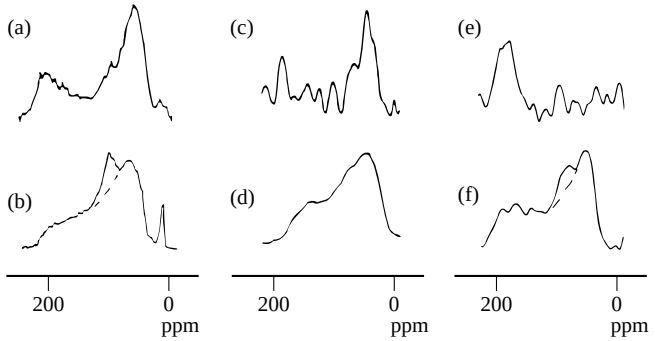

Figure 7 Solid state ^{15}N NMR spectra of uniformly and selectively ^{15}N-labeled fd coat protein in phospholipid bilayer samples. (a) Uniformly ^{15}N-labeled fd coat protein in bilayers oriented between glass plates. (b) Uniformly ^{15}N-labeled fd coat protein in unoriented bilayers. (c) Selectively [^{15}N]leucine-labeled fd coat protein in bilayers oriented between glass plates. (d) Selectively [^{15}N]leucine-labeled fd coat protein in unoriented bilayers. (e) Selectively [^{15}N]tyrosine-labeled fd coat protein in bilayers oriented between glass plates. (f) Selectively [^{15}N]tyrosine-labeled fd coat protein in unoriented bilayers

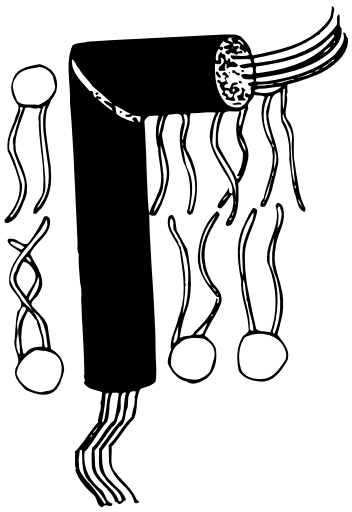

Figure 8 Model of the membrane-bound form of fd coat protein. The amphipathic helix is parallel to the plane of the bilayer, the hydrophobic helix spans the membrane, and the terminal residues and bend are mobile

the hydrophobic transmembrane helix. The numerous NOEs observed for residues 13−15 and 40−42 are between NH−C-αH(i, i + 3) and NH−C-αH(i, i + 4) sites, and strongly support the presence of helical secondary structure for these residues. The absence of NOEs for residues 1−5 at the amino terminus of the coat protein indicates that these residues do not participate in stable secondary structure, and the strip from the NOE/HMQC experiment (corresponding to G3 in Figure 8 below) has no NOEs to any other residue. Residues 1−5 are highly mobile, as seen in relaxation data of the coat protein in micelle samples.[8]

The ^{15}N chemical shift powder patterns from unoriented samples of uniformly [Figure 7(b)] and selectively ^{15}N-labeled fd coat protein in lipid bilayers [Figure 7(d)] establish that the membrane bound form of the protein has both mobile and rigid backbone sites. The amide groups of both L14 and L41 are immobile in membrane bilayers because the powder pattern spectrum in Figure 7(d) shows little evidence of motional averaging. However, the spectrum in Figure 7(b) from the uniformly ^{15}N-labeled sample has substantial isotropic intensity from the mobile amino and carboxyl terminal residues.

^{15}N solid state NMR spectra of selectively [^{15}N]leucine-labeled coat proteins in unoriented phospholipid bilayers and in oriented phospholipid bilayers are shown in Figure 7(d) and (c), respectively. The comparison of these spectra shows the effect of sample orientation; the two ^{15}N resonances go from a broad, characteristically shaped powder pattern to narrow, single lines with frequencies determined by the orientation of the peptide planes with respect to the direction of the magnetic field. Comparison of the spectra in Figure 7(a) and (b) also shows the effect of sample orientation, although at lower resolution because of multiple overlapping resonances in the uniformly ^{15}N-labeled samples. However, the resonance bands occur at the positions expected for transmembrane and in-plane helices. Since the secondary structure for the two leucine residues is established as helix by the NOE data in Figure 6, the resonance frequency of each nitrogen site can be used to establish the orientations of the helices relative to the plane of the bilayer. The spectrum of [^{15}N]leucine-labeled coat protein in oriented bilayers [Figure 7(c)] has one line with a resonance frequency near $\sigma_{\parallel}$ and a second line with a resonance frequency near $\sigma_{\perp}$, indicating that the hydrophobic helix spans the bilayer because the N−H bond of one of the leucine residues is parallel to the direction of orientation and that the amphipathic helix is in the plane of the bilayer because the N−H bond of the other leucine residue is perpendicular to the direction of orientation.

Figure 8 summarizes the results of the NMR experiments.[67] The structure and dynamics of the membrane bound form of fd coat protein were determined by combining results from solid state NMR experiments of the coat protein in bilayers with solution NMR results of the coat protein in micelles. The secondary structure of the protein is almost entirely helical, based on the observation of NOEs among all amide resonances from adjacent residues 7−50 and the NOEs between hydrogen atoms on the nitrogen amide and the α-carbon atoms three and four residues away. The orientation of the helical segments were determined by solid state NMR experiments that showed residues in the amphipathic helix lying parallel to the plane of the bilayer and residues in the hydrophobic helix spanning the bilayer. Tyr-21 is located between the two helices; it is structured on short timescales but shows evidence of mobility on the slower solid state NMR timescale, as shown in Figure 7(f). The presence of strong NH−NH(i, i + 1) and NH−C-αH(i, i + 2) NOEs, and the mobility of Y21 on slow timescales suggest that it participates in a turn that connects the two helical regions. Residues 1−5 at the amino terminus of the protein are highly mobile based on a variety of relaxation data in micelle samples and motional averaging of lineshapes in bilayer samples. Residues at the carboxyl terminus are also mobile in both bilayer and micelle samples; however, the observation of homonuclear NOEs indicates that helical secondary structure extends through to the carboxyl terminal on some timescales.

The features of the model of the membrane bound form of fd coat protein are similar to those found for the membrane bound form of Pf1 coat protein,[69] in spite of the absence of sequence homology between these proteins. The structure and dynamics

of the membrane bound forms of both fd and Pf1 coat proteins were characterized by combining the results of solution and solid state NMR spectroscopies. Both proteins consist of helical secondary structure intermixed with mobile termini and loop regions. The helical regions in fd and Pf1 coat protein consist of two segments, with hydrophobic residues forming a transmembrane helix and amphipathic residues forming a helix parallel to the bilayer plane. The two proteins differ most in the extent of mobility of the segment connecting the two helices. The connecting loop residues in Pf1 are highly mobile on both slow (10^{-4} s) and fast (10^{-9} s) timescales with an absence of homonuclear ^{1}H NOE cross peaks involving the amide resonances for these residues. In contrast, fd coat protein has homonuclear NOE cross peaks throughout the sequence, including the residues involved in the turn connecting the two helices; there is evidence of limited motional averaging for Tyr-21.

6 PROSPECTS FOR NMR STUDIES OF MEMBRANE PROTEINS

Structural studies devoted to membrane proteins seek to determine their three-dimensional structure and dynamics, with the ultimate aim of integrating these properties into models for their mechanism of action within the natural environment of the biological membrane. Since the structure and function of membrane proteins are intimately related to their hydrophobic membrane environment, serious investigations of these species must, at some stage, focus on the entire supramolecular assembly. NMR spectroscopy has proved itself to be a well suited and sufficiently versatile technique for this purpose, with the micelle and the bilayer samples providing excellent supramolecular model systems for multidimensional NMR solution and solid state NMR studies, respectively. Thus, considering the already large impact of NMR spectroscopy in the membrane protein field, there is good reason to be optimistic that, as the sample preparation and spectroscopic methods are improved, NMR spectroscopy will become generally applicable to the study of membrane proteins.

The development of multidimensional solution NMR spectroscopy of membrane proteins in micelles will be similar to that for larger globular proteins, since the limiting factor, the rotational correlation time, is the same in both cases. The solid state NMR methods that utilize uniaxially oriented samples or implement magic angle sample spinning to achieve resolution, provide measurements of angles and distances between bonds and chemical groups which can be interpreted in terms of structures. The former method has the added advantage of providing details about the orientation of the protein structural elements with respect to the plane of the lipid bilayer. Thus, by using macroscopically and uniaxially oriented membrane samples it becomes possible to distinguish between the case where the protein is membrane spanning and that where the protein associates only superficially with the membrane, or, yet again, where the protein interacts with the bilayer in a wedge-like manner. This is important for understanding the functions of membrane proteins, since they interact asymmetrically with the membrane, imparting different properties to its inner and outer leaflets. The situation is a very different from the more or less isotropic environment of the cell cytoplasm and periplasm occupied by globular proteins. As a result, NMR spectroscopy has the potential of opening up an entire area of structural biology by providing an added dimension for membrane protein studies.

7 RELATED ARTICLES

Bacteriorhodopsin and Rhodopsin; Bilayer Membranes: Deuterium and Carbon-13 NMR; Bilayer Membranes: Proton and Fluorine-19 NMR; Gramicidin Channels: Orientational Constraints for Defining High-Resolution Structures; Membranes: Carbon-13 NMR; Membranes: Phosphorus-31 NMR; Protein Dynamics from Solid State NMR; Structures of Larger Proteins, Protein-Ligand, and Protein-DNA Complexes by Multi-Dimensional Heteronuclear NMR.

8 REFERENCES

1. J. Deisenhofer, O. Epp, K. Miki, R. Huber, and H. Michel, *Nature*, 1985, **318**, 618.
2. D. Rees, H. Komiga, T. Yeates, J. Allen, and G. Feher, *Ann. Rev. Biochem.*, 1989, **58**, 607.
3. R. Henderson, J. Baldwin, T. Cesko, F. Zemlin, E. Beckmann, and K. Downing, *J. Mol. Biol.*, 1990, **213**, 899.
4. M. Weiss, U. Abele, J. Weckesser, W. Welte, E. Schiltz, and G. Schulz, *Science*, 1991, **254**, 1627.
5. S. J. Opella, Y. Kim, and P. McDonnell, *Methods Enzymol.*, 1994, **239**, 536.
6. S. J. Opella, *Methods Enzymol.*, 1985, **131**, 327.
7. M. A. Keniry, H. S. Gutowsky, and E. Oldfield, *Nature*, 1984, **307**, 383.
8. M. J. Bogusky, G. C. Leo, and S. J. Opella, *Proteins: Structure, Function, Genet.*, 1988, **4**, 123.
9. M. Saunders, A. Wishnia, and J. G. Kirkwood, *J. Am. Chem. Soc.*, 1957, **79**, 3289.
10. G. Clore and A. Gronenborn, *CRC Crit. Rev. Biochem. Mol. Biol.*, 1989, **24**, 479.
11. K. Wüthrich, *NMR of Proteins and Nucleic Acids*, Wiley, New York, 1986.
12. A. Watts, in *Phospholipids Handbook*, ed G. Cevc, Dekker, New York, 1993, p. 687.
13. J. H. Davis, *Chem. Phys. Lipids*, 1986, **40**, 223.
14. H. Hauser, E. G. Finer, and D. Chapman, *J. Mol. Biol.*, 1970, **53**, 419.
15. D. W. Urry, *Proc. Natl. Acad. Sci. USA*, 1971, **68**, 672.
16. D. Chapman, V. B. Kamat, J. Degier, and S. A. Penkett, *Nature*, 1967, **213**, 74.
17. S. I. Chan, M. P. Sheetz, C. H. A. Seiter, G. W. Feigenson, M. C. Hsu, A. Lau, and A. Yan, *Ann. NY Acad. Sci.*, 1973, **222**, 499.
18. D. S. Hagen, J. H. Weiner, and B. D. Sykes, *Biochemistry*, 1978, **17**, 3860.
19. M. L. Wilson and F. W. Dahlquist, *Biochemistry*, 1985, **24**, 1920.
20. V. B. Kamat and D. Chapman, *Biochim. Biophys. Acta*, 1968, **163**, 411.
21. L. R. Brown, *Biochim. Biophys. Acta*, 1979, **557**, 135.
22. J. Lauterwein, Ch. Boesch, L. R. Brown, and K. Wüthrich, *Biochim. Biophys. Acta*, 1979, **163**, 411.

23. P. A. McDonnell and S. J. Opella, *J. Magn. Reson. B*, 1993, **102**, 120.
24. C. E. Dempsey, R. Bazzo, T. S. Harvey, I. Syperek, G. Boheim, and I. D. Campbell, *FEBS Lett.*, 1991, **281**, 240.
25. T. Ikura, N. Go, and F. Inagaki, *Proteins*, 1991, **9**, 81.
26. E. Bairaktari, D. F. Mierke, S. Mammi, and E. Peggion, *Biochemistry*, 1990, **29**, 10 090.
27. J. C. Franklin, J. F. Ellena, S. Jayasinghe, L. P. Kelsh, and D. S. Cafiso, *Biochemistry*, 1994, **33**, 4036.
28. K. H. Lee, J. E. Fitton, and K. Wüthrich, *Biochim. Biophys. Acta*, 1987, **911**, 144.
29. A. Motta, A. Pastore, N. A. Goud, and M. A. C. Morelli, *Biochemistry*, 1991, **30**, 10 444.
30. S. J. Opella, J. Gesell, and B. Bechinger, in *The Amphipathic Helix*, ed. R. Epand, CRC Press, Boca Raton, 1993, pp. 87–106.
31. T. Holak, A. Engstrom, P. Kraulis, G. Lindeberg, H. Bennich, T. Jones, A. Gronenborn, and G. M. Clore, *Biochemistry*, 1988, **27**, 7620.
32. D. Sipos, M. Andersson, and A. Ehrenberg, *Eur. J. Biochem.*, 1992, **209**, 163.
33. J. Gesell, M. Zasloff, and S. J. Opella, unpublished results.
34. D. Marion, M. Zasloff, and A. Bax, *FEBS Lett.*, 1989, **227**, 21.
35. M. F. Moody, P. T. Jones, J. A. Carver, J. Boyd, and I. D. Campbell, *J. Mol. Biol.*, 1987, **193**, 759.
36. T. J. Norwood, D. A. Crawford, M. E. Steventon, P. C. Driscoll, and I. D. Campbell, *Biochemistry*, 1992, **31**, 6285.
37. M. E. Girvin and R. H. Fillingame, *Biochemistry*, 1993, **32**, 12 167.
38. K. V. Pervushin, A. S. Arseniev, A. T. Kozhich, and V. T. Ivanov, *J. Biomol. NMR*, 1991, **1**, 313.
39. I. L. Barsukov, G. V. Abdulaeva, A. S. Arseniev, and V. F. Bystrov, *Eur. J. Biochem.*, 1990, **192**, 321.
40. S. J. Opella, and P. A. McDonnell, in *NMR of Proteins*, ed. A. M. Gronenborn and G. M. Clore, MacMillan, 1993, pp. 159–189.
41. S. J. Opella, in *Membrane Protein Structure: Experimental Approaches*, ed. S. H. White, Oxford, 1994, in press.
42. B. Bechinger, Y. Kim, L. E. Chirlian, J. Gesell, J.-M. Neumann, M. Montal, J. Tomich, M. Zasloff, and S. J. Opella, *Biomol. NMR*, 1991, **1**, 167.
43. T. Gullion and J. Schaefer, *J. Magn. Reson.*, 1989, **81**, 196.
44. D. P. Raleigh, M. H. Levitt, and R. G. Griffin, *Chem. Phys. Lett.*, 1988, **146**, 71.
45. S. J. Opella, and J. S. Waugh, *J. Chem. Phys.*, 1977, **66**, 4919.
46. S. J. Opella, P. L. Stewart, and K. G. Valentine, *Q. Rev. Biophys.*, 1987, **19**, 7.
47. S. O. Smith, *Curr. Opinion Struct. Biol.*, 1993, **3**, 755.
48. B. Bechinger, M. Zasloff, and S. J. Opella, *Protein Sci.*, 1993, **2**, 2077.
49. S. O. Smith, R. Jonas, M. Braiman, and B. J. Bormann, *Biochemistry*, 1994, **33**, 6334.
50. S. O. Smith, J. Hamilton, A. Salmon, and B. J. Bormann, *Biochemistry*, 1994, **33**, 6327.
51. R. R. Ketchem, W. Hu, and T. A. Cross, *Science*, 1993, **261**, 1457.
52. J. A. Killian, M. J. Taylor, and R. E. Koeppe II, *Biochemistry*, 1992, **31**, 11 283.
53. K.-C. Lee and T. A. Cross, *Biophys. J.*, 1994, **66**, 1380.
54. W. Hu, K.-C. Lee, and T. A. Cross, *Biochemistry*, 1993, **32**, 7035.
55. R. R. Koeppe II, J. A. Killian, and D. V. Greathouse, *Biophys. J.*, 1994, **66**, 14.
56. A. W. Hing and J. Schaefer, *Biochemistry*, 1993, **32**, 7593.
57. S. O. Smith and R. G. Griffin, *Ann. Rev. Phys. Chem.*, 1968, **39**, 511.
58. A. S. Ulrich, M. P. Heyn, and A. S. Watts, *Biochemistry*, 1992, **31**, 10 390.
59. A. S. Ulrich, A. Watts, I. Wallat, and M. P. Heyn, *Biochemistry*, 1994, **33**, 5370.
60. L. K. Thompson, A. E. McDermott, J. Raap, C. M. Van der Wielen, J. Lugtenburg, J. Herzfeld, and R. G. Griffin, *Biochemistry*, 1992, **31**, 7931.
61. T. A. Cross and S. J. Opella, *Biochem. Biophys. Res. Commun.*, 1980, **92**, 478.
62. G. D. Henry, J. H. Weiner, and B. D. Sykes, *Biochemistry*, 1987, **26**, 3619.
63. G. C. Leo, L. A. Colnago, K. G. Valentine, and S. J. Opella, *Biochemistry*, 1987, **26**, 854.
64. G. D. Henry, J. H. Weiner, and B. D. Sykes, *Biochemistry*, 1986, **25**, 590.
65. J. D. J. O'Neil and B. D. Sykes, *Biochemistry*, 1988, **27**, 2753.
66. G. D. Henry and B. D. Sykes, *Biochem. Cell. Biol.*, 1990, **68**, 318.
67. P. A. McDonnell, K. Shon, Y. Kim, and S. J. Opella, *J. Mol. Biol.*, 1993, **233**, 447.
68. F. J. M. van de Ven, J. W. M. van Os, J. M. A. Aelen, S. S. Wymenga, M. L. Remerowski, R. N. H. Konings, and C. W. Hilbers, *Biochemistry*, 1993, **32**, 8322.
69. K. Shon, Y. Kim, L. A. Colnago, and S. J. Opella, *Science*, 1991, **252**, 1303.

Biographical Sketches

Stanley J. Opella. *b* 1947. B.S., 1969, chemistry, University of Kentucky (undergraduate research with S. L. Smith); Ph.D., 1974 chemistry, Stanford University, (with O. Jardetzky and H. McConnell). Postdoctoral fellow, 1975–76, M.I.T. (with J. S. Waugh). Professor of Chemistry, University of Pennsylvania, 1976–present. Approx. 125 publications. Research interests: development and application of NMR spectroscopy for the study of proteins, especially protein structure determination by solid state NMR spectroscopy.

Francesca M. Marassi. *b* 1963. B.Sc., 1987, chemistry (undergraduate research with J. C. Rucklidge), M.Sc., 1989, chemistry (with M. Thompson), Ph.D., 1993, chemistry, (with P. M. Macdonald), University of Toronto, Natural Sciences and Engineering Research Council postdoctoral fellow, University of Pennsylvania, 1993–present. Approx. 8 publications. Research interests: structural investigation of membrane proteins, and protein–lipid interactions by means of solid state NMR spectroscopy.

Multiple-Resonance Multi-Dimensional Solid-State NMR of Proteins

Stanley J. Opella

Department of Chemistry and Biochemistry, University of California, San Diego, La Jolla, CA, USA

1	Introduction	1
2	Local Field	1
3	Separation of Local Fields	3
4	Multidimensional Solid-State NMR Correlation Spectroscopy	4
5	PISA Wheels	5
6	Calculations for Protein Structure Determination from Solid-State NMR Data	6
7	Application to the Three-Dimensional Structure of the Acetylcholine M2 Peptide in Lipid Bilayers	7
8	Summary	8
9	References	9

1 INTRODUCTION

Solid-state NMR spectroscopy is much more than a method for obtaining high resolution NMR spectra of materials that are crystalline, polymeric, aggregated, or otherwise ill-suited for more generally applicable and available solution NMR methods. It is a method for determining the structures of molecules, including those as large and complex as proteins, under the most appropriate conditions, including those where the molecular correlation times are slow. Advances in selective averaging and the measurement of local fields resulting from heteronuclear dipolar couplings were needed to transform this branch of spectroscopy into a full-blown method for structure determination. The local field, which results from the interactions of two or more proximate nuclei, provides a particularly direct source of structural information. Other nuclear spin interactions, especially the chemical shift, also provide valuable structural information, although, their interpretation is generally more complicated and somewhat less firmly grounded. Taken together, the structural constraints resulting from measurements of spectral parameters from several spin-interactions, where at least one of them is a local field, are more than sufficient to determine the three-dimensional structures of complex molecules including proteins.

The experimental demonstration of the local field by Pake in 1948 means that solid-state NMR spectroscopy has been recognized as a method for determining molecular structures for more than 50 years;[1] however, it took until the mid-1970s to develop the methods and instrumentation for structure determination of small organic molecules[2,3] and simple polymers.[4] And only recently has it become feasible to determine the structures of proteins by solid-state NMR spectroscopy. This article discusses the crucial roles of the local field in structural studies of systems that range in complexity from waters of hydration in gypsum[1] and crystalline trichloroacetate[5] to uniformly isotopically labeled membrane proteins in lipid bilayers.[6] The combination of heteronuclear dipolar coupling and chemical shift frequencies is shown to be sufficient for characterizing the structures of membrane proteins as a qualitative index[7,8] as well as through direct calculations of structures from the NMR data.[9] The approach is illustrated with an example of structure determination of a polypeptide corresponding to a transmembrane helix of the acetylcholine receptor that functions in membrane bilayers as an ion channel.[10]

2 LOCAL FIELD

"The interaction between two nuclear spins depends on the magnitude and orientation of their magnetic moments and also the length and orientation of the vector describing their relative positions."[11] As shown in Figure 1, the local magnetic field resulting from the interactions between two nuclear spins is described in a strikingly simple way. With its explicit dependence on a distance and an angle, it provides access to geometrical parameters that can be directly translated into molecular structures. It is also important for experimental spectroscopy, and many of the developments in solid-state NMR spectroscopy have been concerned with the selective averaging of dipolar couplings so that the chemical shift and other spectroscopic parameters can be observed.[12–16]

The attenuation of dipolar couplings is essential because solid-state NMR spectra are typically very broad and overlapped as a consequence of the cumulative effect of the many different local fields. Only in exceptional cases does the material of interest provide sufficient isolation among pairs of spins so that the effects of a single local field can be observed. A doublet with properties described in Figure 1 from the waters of hydration in samples of gypsum was observed by Pake.[1] While the Pake doublet from a polycrystalline sample shown in Figure 2 can be used to determine the internuclear distance between the two hydrogens, the rotation patterns from single crystals enabled the angular dependence to be confirmed and, indeed, for the distance to be measured with greater precision.

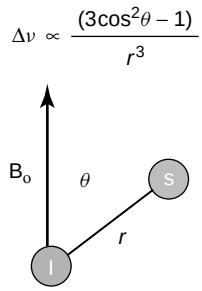

Figure 1 The principal factors that affect the splittings observed in solid-state NMR spectra from the dipole–dipole interaction between two nuclei. θ is the angle between the internuclear vector and the direction of the applied magnetic field and r is the distance between the two nuclei

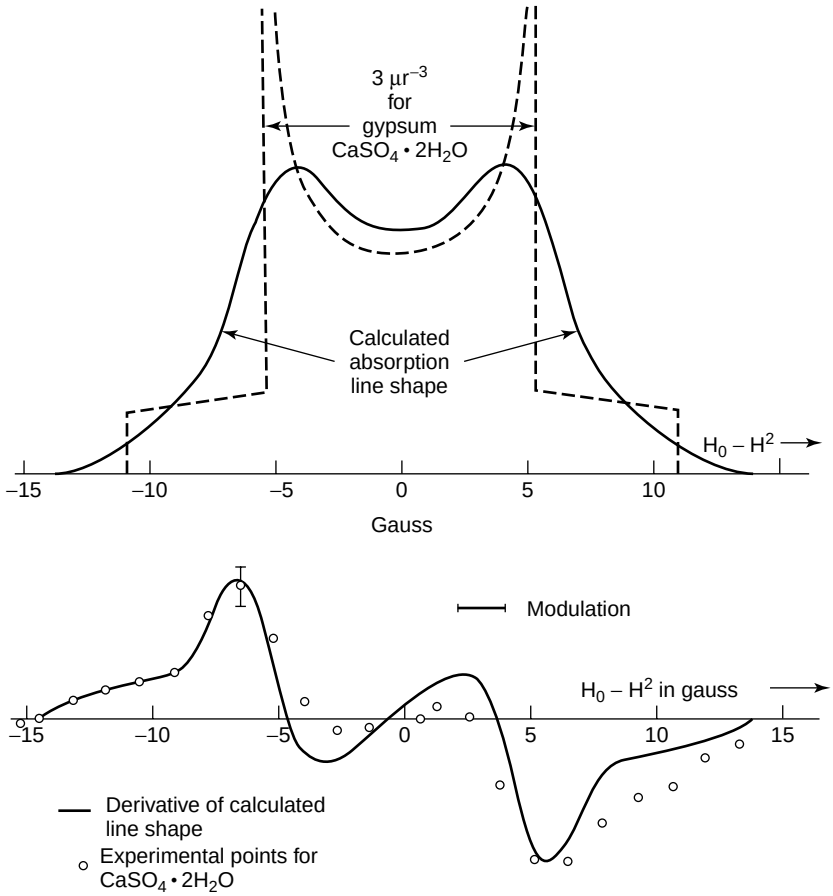

Figure 2 This is Figure 8 from the paper by Pake.[1] The broken line in the upper curve shows the calculated distribution of component line centers for the proton resonance in powdered $CaSO_4 \cdot H_2O$. The continuous line on the same plot is the calculated line shape obtained by superposing Gaussians of width 1.54 gauss according to this distribution function. The lower plot contains experimental points for powdered $CaSO_4 \cdot H_2O$, and a curve which is the derivative of the calculated line shape

Other important topics discussed in this seminal contribution on the local field include the effects of motional averaging and the dominance of homo-nuclear over hetero-nuclear couplings.

Twenty-years after Pake[1] showed that solid-state NMR spectra from samples with chemically isolated pairs of spins could be used to determine molecular structures and Van Vleck[17] discussed the consequences of truncation in NMR experiments, Waugh et al.[15] demonstrated that the severe line-broadening present in chemical samples with normally abundant collections of spins could be selectively averaged with multiple-pulse sequences that could be analyzed in terms of coherent averaging theory.[18] In particular, a pulse sequence was employed that removed the effects of homo-nuclear dipolar couplings while largely preserving the chemical shift effects. Significant parallel developments involved the application of magic angle sample spinning[12,13] and the demonstration of line narrowing by irradiation arranged by choice of amplitude and frequency-offset to place the magnetization at the magic angle with respect to the magnet field.[14,19] Thorough analysis of multiple-pulse and other line-narrowing procedures led to a thorough understanding in terms of coherent averaging theory as well as improvements in the sequences themselves.[18,20–24] Multiple-pulse sequences offer the important advantage of being able to sample the magnetization in the windows between the pulses. The high duty cycle of the Lee-Goldburg procedures, especially when implemented with phase- and frequency-alternation[25–27] has led to its use in many multi-dimensional hetero-nuclear experiments where the signals from the dilute rather than the abundant spins are observed.[28]

The development of double-resonance cross-polarization methods[16,29] enabled solid-state NMR spectroscopy to shift its emphasis to the "dilute" spins, such as ^{13}C and ^{15}N. Heteronuclear decoupling is easier to implement experimentally and can be accomplished without the scaling (reduction) of chemical shift frequencies that accompanies multiple-pulse line narrowing of ^{1}H resonances. It is possible to study polycrystalline samples with the use of magic angle sample spinning.[30] However, there is a second way to obtain high resolution chemical shift spectra of solid samples that involves the use of single crystals where the molecules have only one or a few orientations relative to each other and the applied magnetic field. Fortunately, it is not necessary to have a single crystal sample. One direction of molecular orientation is sufficient, as long as it is parallel to the magnetic field, to give all of the spectroscopic benefits of sample orientation.[4] Typically, it is much easier to prepare uniaxially oriented samples of many materials, including proteins in biological supramolecular structures like membrane bilayers, than single crystals for X-ray diffraction or even rapidly reorienting solutions for NMR spectroscopy.

The samples can take the form of drawn fibers, magnetically oriented liquid crystals, or phospholipid bilayers mechanically oriented between glass plates. In uniaxially oriented samples, each site on one molecule can be transformed into the identical site on another molecule through a combination of translation, inversion, and rotation operations about an axis parallel to the direction of the applied magnetic field. Just as observed for single crystals, the spectra of oriented protein samples are characterized by narrow single line resonances rather than powder patterns. The resonance frequencies reflect the orientations of the individual groups, and the geometrical dependencies of the chemical shift, heteronuclear dipolar, and quadrupolar interactions are well characterized. As a result, the solid-state NMR spectra of oriented samples are a rich source of structural information.

3 SEPARATION OF LOCAL FIELDS

The spectroscopic separation of effects from the chemical shift and heteronuclear dipolar interactions are manifested in several different ways in solid-state NMR experiments. This can be appreciated by considering that both the build-up of signal intensity through cross-polarization and the observation of decoupled signals depend on quite different manipulations of the heteronuclear dipolar couplings. There are additional opportunities to observe the effects of heteronuclear dipolar couplings in more complex experiments.

Transient oscillations are observed in the rates of build-up of the intensities of the dilute spin signals as they are developed through spin-lock cross-polarization.[31] These oscillations have characteristic frequencies that reflect the magnitude of the heteronuclear dipolar coupling that provides the mechanism for transfer of magnetization from the abundant ^{1}H spin to the dilute ^{13}C or ^{15}N spin.[32] Since the dilute spin signals are detected under high-resolution conditions, the signals from individual molecular sites are resolved. This is most obvious in the spectra of single crystal samples. However, it is also the case for polycrystalline samples where the chemical shift powder pattern discriminates among spins with different orientations with respect to the applied magnetic field, consistent with the representation in Figure 1. Vaughan and coworkers[5] utilized the modulation of chemical shift spectra by the effects of heteronuclear dipolar interactions of polycrystalline solids.

While most attention has been paid to heteronuclear couplings, as described above, there are situations when the homonuclear couplings are of interest. This is the case for both abundant and dilute spins, and their definitions can overlap with the use of uniformly ^{13}C and ^{15}N labeled proteins. The original work of Pake demonstrated the value of the homonuclear dipolar coupling and that it was spectroscopically accessible with a chemically dilute sample. Stoll et al.[5] demonstrated a multiple pulse experiment that incorporated two separate time incrementations. This experiment is quite interesting in that it is basically the reverse of what would be used in many subsequent multi-dimensional experiment involving heteronuclear dipolar couplings. Here the first interval is used for the evolution of the homonuclear dipolar interaction, and then the multiple-pulse sequence is applied and data acquired in the usual way in the windows. In this study, the dipolar modulated chemical shift powder patterns were analyzed by comparison to calculations based on the established properties of the molecule. As suggested by the one-dimensional ^{1}H NMR spectrum with great similarity to the Pake doublet in Figure 2, the Fourier transformation of signals in both time dimensions was about to have its enormous impact on all types of spectra, including those that separate the homonuclear dipolar Pake doublet from the chemical shift powder pattern in polycrystalline samples. Since both the chemical shift and dipolar coupling frequencies depend on orientation, hydrogens with different chemical shifts have different dipolar couplings. The first use of the Fourier transform to analyze the frequencies of the dipolar oscillations during cross-polarization

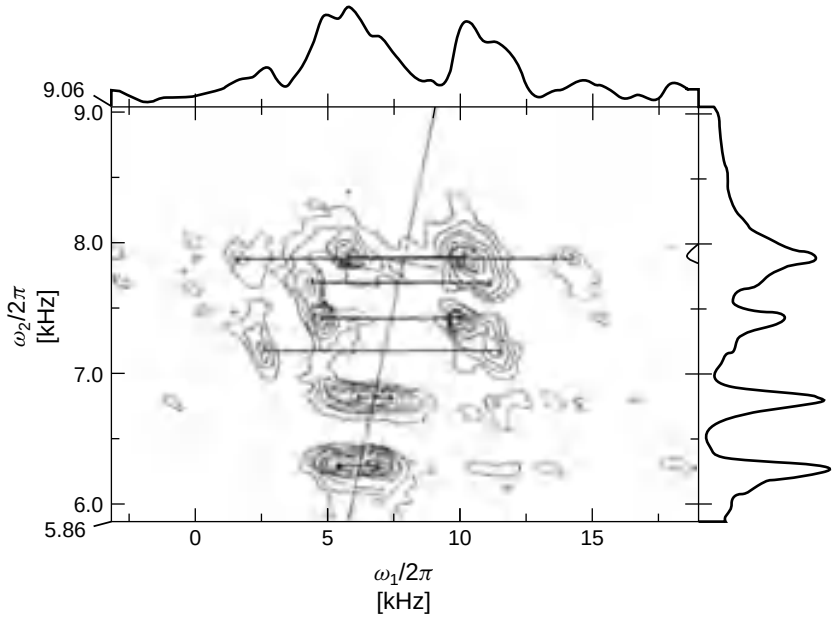

Figure 3 This is Figure 2 from the paper by Hester et al.[2] Contour plot of function f(ω1, ω2). Dipolar splittings for each of the observed seven lines are indicated by the heavy lines. The line bisecting the splittings is the locus $\omega 1 = \omega 2 = \Delta$n

was demonstrated by Hester et al.[32] However, this experiment was soon replaced by separated local field spectroscopy, which yielded direct measurements of dipolar coupling and chemical shift frequencies.[2,33]

As proposed[33] and demonstrated[2] by Waugh and coworkers, the separate lines of spectroscopic development described above could be consolidated within the domain of two-dimensional spectroscopy.[34] Separated-local-field spectroscopy elegantly incorporates radio frequency irradiations in the form of multiple-pulse sequences to average out homonuclear dipole–dipole couplings and double-resonance procedures to average out heteronuclear dipole–dipole couplings. The chemical-shift dimension in separated-local-field spectra has intrinsically high resolution because continuous on-resonance ^{1}H irradiation decouples the heteronuclear dipolar interactions during the t_2 interval when data are acquired; however, even with the use of homonuclear multiple-pulse decoupling, the doublets (or multiplets) in the dipolar frequency dimension are generally quite broad due to the rapid decay of the *S*-spin signals from incomplete decoupling of the homonuclear dipole–dipole interactions, short T_2 and cumulative effects of longer-range heteronuclear dipole–dipole interactions. The two-dimensional separated local field spectrum in Figure 3 illustrates the ability of this approach to associate a single dipolar coupling with each resolved dilute spin resonance.[2]

PISEMA (polarization inversion spin-exchange at the magic angle)[28] is a high-resolution version of separated local field spectroscopy. By combining polarization inversion with flip–flop Lee–Goldburg homonuclear decoupling on the abundant *I* spins following spin-lock cross polarization to the dilute *S* spin during the t_1 interval of the pulse sequence, very high resolution two-dimension heteronuclear $I-S$ dipolar spectra of solid samples can be obtained. Line widths in the dipolar dimension are reduced by more than an order of magnitude compared to a conventional separated local field spectrum obtained without homonuclear decoupling during the t_1 interval. The combination of narrow lines and favorable scaling factor has such a dramatic effect on the appearance of the spectra that it is now feasible to formulate solid-state NMR experiments where heteronuclear dipolar coupling frequencies provide a mechanism for resolution among similar chemical sites. Even more interestingly, dipolar coupling and chemical shift frequencies can be used in a number of complementary ways to enhance resolution in reduced or maximum dimensional experiments, and to provide qualitative and quantitative indications of molecular structure. Two-dimensional ^{1}H/^{15}N and ^{1}H/^{13}C PISEMA spectra have narrow line widths in both the heteronuclear dipolar coupling and chemical shift frequency dimensions, enabling dipolar couplings to complement chemical shifts as a mechanism for spectroscopic resolution as well as the measurement of readily interpretable orientationally dependent frequencies for individual molecular sites.

4 MULTIDIMENSIONAL SOLID-STATE NMR CORRELATION SPECTROSCOPY

The two-dimensional PISEMA experiment provides a fundamental building-block for multidimensional solid-state NMR experiments on proteins in oriented samples. The pulse sequence for three-dimensional ^{1}H shift/^{1}H–^{15}N dipolar coupling/^{15}N shift correlation spectroscopy shown in Figure 4[35] enabled the first fully resolved spectra of uniformly ^{15}N labeled proteins to be obtained for membrane proteins in lipid bilayers.[6,10,36] Further, many individual resonances could be resolved in a membrane protein with 190 residues,[37] and it is clear that with further development substantially larger membrane proteins can be studied.

The ^{1}H chemical shift, ^{1}H–^{15}N dipolar coupling, and ^{15}N chemical shift interactions at amide sites are of particular interest because of their important roles in both solution and solid-state NMR studies of ^{15}N-labeled proteins. The three-dimensional powder pattern in Figure 5(A)[35] encompasses all frequencies available to the three spin interactions present in a ^{15}N labeled amide group of a peptide. Since the $I-S$ dipolar interaction is symmetric about zero, the unique spectral information from the ^{1}H–^{15}N couplings is contained in the positive frequencies. When the spectrum in Figure 5(A)

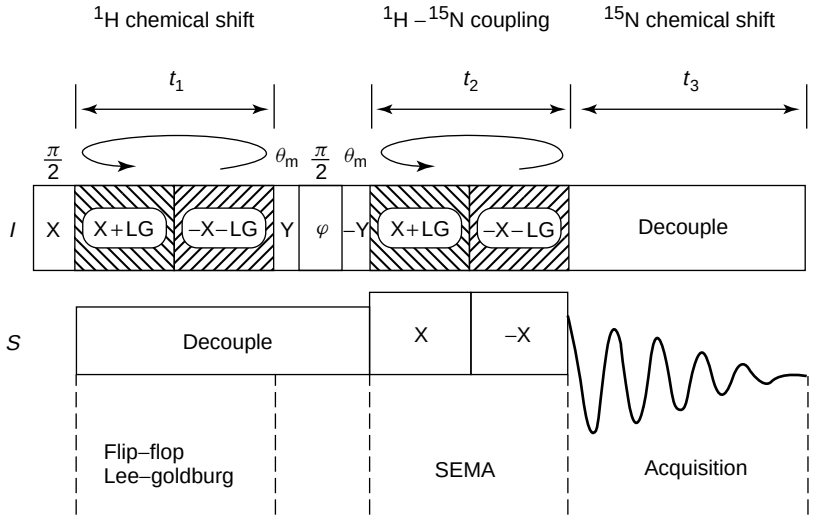

Figure 4 This is Figure 1 from the paper by Ramamoorthy et al.[35] Pulse sequence for three-dimensional $I-$spin chemical shift, $I-S$ dipolar coupling, and *S*-spin chemical-shift correlation spectroscopy

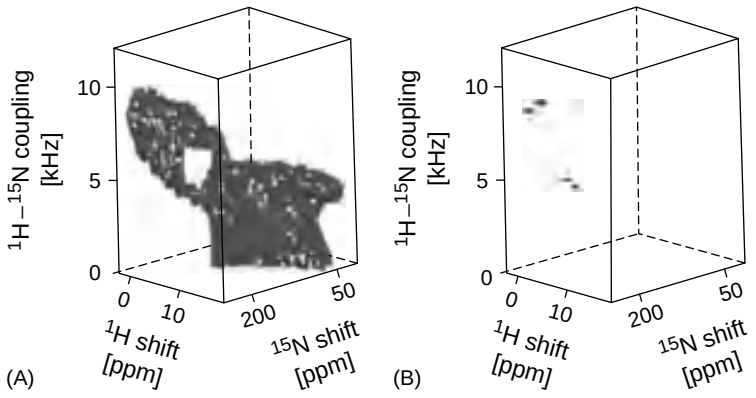

Figure 5 This is Figure 2 from the paper by Ramamoorthy et al.[35] Experimental three-dimensional ^{1}H chemical shift/^{15}N–^{1}H heteronuclear dipolar coupling/^{15}N chemical-shift correlation spectra of ^{15}N-acetyl-leucine. (A) Polycrystalline sample. (B) Single-crystal sample

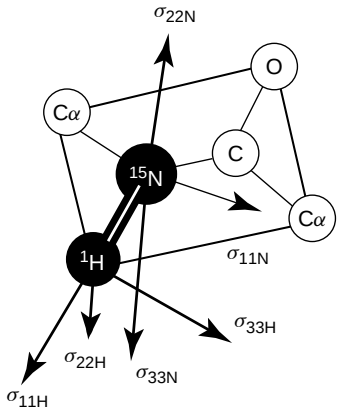

Figure 6 This is Figure 3 from the paper by Wu et al.[28] Orientation of the principal axes of the amide 1H chemical shift, ^{1}H–^{15}N dipolar, and ^{15}N chemical shift interaction tensors in a peptide bond

is viewed from the ^{15}N chemical shift/^{1}H–^{15}N dipolar coupling plane it has a characteristic low-intensity "hole" that is a consequence of the marked noncolinarity of the ^{15}N chemical-shift tensor and the N–H bond axis, as shown in Figure 6.[28]

The resolution available by applying the three-dimensional pulse sequence diagrammed in Figure 4 to the most crowded spectral regions of a protein is illustrated in Figure 7.[36] The sample is uniformly ^{15}N labeled fd coat protein in oriented lipid bilayers. This polypeptide has two major classes of resonances because it has a *trans*-membrane helix and a shorter in-plane helix that resolute in the vast majority of residues having similar backbone orientations with their N–H bonds either parallel or perpendicular to the field. However, the ^{1}H chemical shift separated two-dimensional ^{1}H–^{15}N dipolar coupling/^{15}N chemical shift planes display excellent resolution.

5 PISA WHEELS

On the path toward three-dimensional structure determination, the secondary structure and topology of membrane proteins can be described by inspection of the two-dimensional ^{1}H/^{15}N PISEMA spectra of uniformly ^{15}N-labeled samples in oriented bilayers. The characteristic 'wheel-like' patterns of resonances observed in these spectra reflect helical wheel projection of residues in both transmembrane and in-plane helices and hence provide direct indices of secondary structure and topology of membrane proteins in phospholipid bilayers. We refer to these patterns as PISA (polarity index slant angle) wheels.[7,8] The resonance frequencies in PISEMA spectra of oriented samples or membrane proteins depend on helix orientation, as well as on the backbone dihedral angles, the magnitudes and orientations of the principal elements of the amide ^{15}N chemical shift tensor, and the NH bond length. Therefore, it is possible to calculate solid-state NMR spectra for specific structural models of proteins, as shown in Figure 8.

When the helix axis is parallel to the bilayer normal all of the amide sites have an identical orientation relative to the direction of the applied magnetic field, and therefore all of the resonances overlap with the same dipolar coupling and chemical shift frequencies. Tilting the helix away from the membrane normal breaks the symmetry, introducing variations in the orientations of the amide NH bond vectors relative to the field. This is manifest in the spectra as dispersions of both the ^{1}H–^{15}N dipolar coupling and the ^{15}N chemical shift frequencies. Since a modest helix tilt of about 10° aligns the NH bond form one amide site and the σ_{33} amide ^{15}N chemical shift tensor element of another amide site with the magnetic field, the maximum values of both of these frequencies are observed in the spectrum, albeit from different amide resonances because σ_{33} of the shift tensor is rotated approximately 17° from the NH bond vector, as shown by the low-intensity region of the spectrum in Figure 6. Nearly all transmembrane helices are tilted with respect to the bilayer normal, and it is the combination of the tilt and the 17° difference between the direction of σ_{33} and the NH bond vector that makes it possible to resolve many resonances from residues in otherwise uniform helices and is responsible for the 'wheel-like' pattern in PISEMA spectra. For all helix orientations other than parallel to the field (0°), the spectra have 'wheel-like' patterns whose frequency breadths, especially in the dipolar coupling dimension, reflect the extent of helix tilt. For helices with tilts greater than 40° some amide NH bonds adopt orientations near the magic angle (55°) with respect to the direction of the magnetic field and have resonances with dipolar couplings of close to 0 kHz. Other

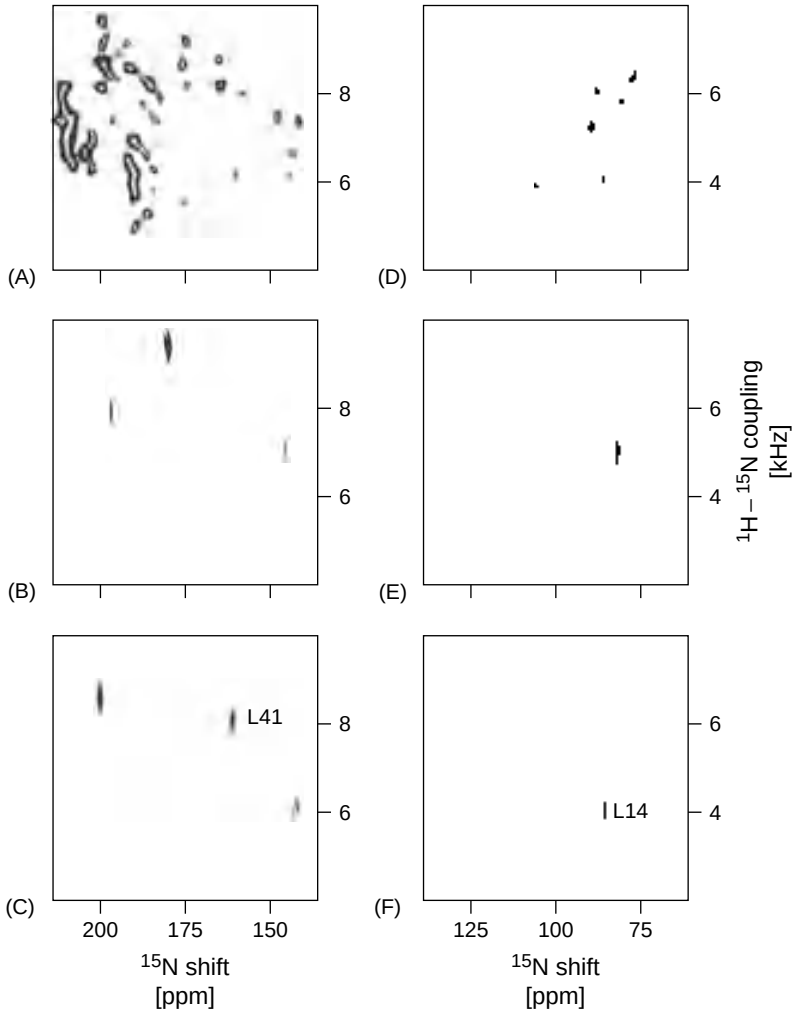

Figure 7 This is Figure 3 from the paper by Marassi et al.[6] Two-dimensional ^{1}H–^{15}N heteronuclear dipolar coupling/^{15}N chemical shift spectral planes from spectra of an oriented sample of uniformly ^{15}N-labeled fd coat protein in phospholipid bilayers. (A. and D.) expansion of the complete two-dimensional PISEMA spectrum of the protein. A is the trans-membrane helix region and D is the in-plane helix region. (B) Plane extracted from the three-dimensional correlation spectrum at ^{1}H chemical shift 7.4 ppm. (C) Plane extracted from a three-dimensional correlation spectrum at ^{1}H chemical shift 11.0 ppm; the resonance assigned to Leu-41 is marked. (E) Plane extracted from a three-dimensional correlation spectrum at ^{1}H chemical shift 12.5 ppm. (F) Plane extracted from a three-dimensional correlation spectrum at ^{1}H chemical shift 11.6 ppm; the resonance assigned to Leu-14 in the amphipathic in-plane helix is marked

amide NH bonds are oriented with angle greater than 55° and have resonances with dipolar couplings of opposite sign, which results in a portion of the 'wheel-like' PISEMA spectrum being reflected through the 0 kHz axis. Figure 8 shows that helices oriented parallel to the membrane surface have their amide NH bonds and σ_{33} of the ^{15}N chemical shift tensor nearly orthogonal to the field and give highly overlapped spectra with all of the resonance frequencies around 5 kHz and 75 ppm. The spectra in Figure 8 demonstrate that it is possible to determine the tilt of a helix in lipid bilayers without resonance assignments.

In the experimental PISEMA spectrum of AchR M2 shown in Figure 9(B), the order of resonances in the 'wheel-like' pattern follows that of the helical wheel projection shown in Figure 9(A). The helical wheel is arranged so that the residues align with their corresponding amide resonances, as predicted by the simulated spectrum in Figure 9(C). The polarity of the ordering of resonances in the 'wheel-like' pattern in a PISEMA spectrum provides a direct measure of the angle of helix rotation (polarity index) about its long axis within the membrane. In principle, only a single assignment is needed to determine the polarity of a helix in the membrane. This example is based on an ideal helix. Deviations from ideal Ramachandran angles that result in local kinks or long-range bends can be readily accommodated within this framework.

6 CALCULATIONS FOR PROTEIN STRUCTURE DETERMINATION FROM SOLID-STATE NMR DATA

In principle, a single three-dimensional correlation spectrum of an oriented sample of a uniformly ^{15}N labeled protein provides sufficient information for complete structure determination. The three frequencies, ^{1}H chemical shift, ^{15}N chemical

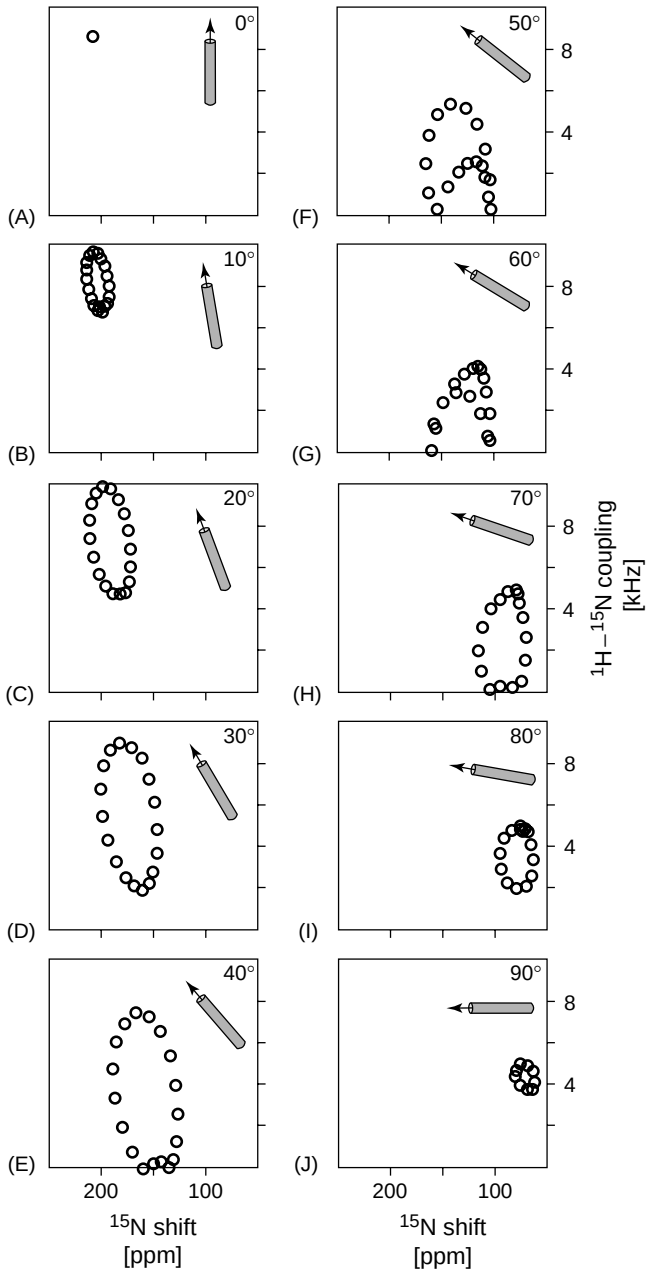

Figure 8 This is Figure 1 from the paper by Marassi and Opella.[7] PISEMA spectra calculated for a 19-residue α-helix with 3.6 residues per turn and uniform dihedral angles ($\phi = -65°$, $\psi = -40°$) at various helix tilt angles relative to the bilayer normal

shift, and ^{1}H/^{15}N dipolar coupling, measured for each resonance depend on the magnitudes and orientations of the principal elements of the spin-interaction tensors in the molecule, and on the orientation of the molecular site with respect to the direction of the applied magnetic field. Because the orientation of the bilayer is fixed by the method of sample preparation, each frequency reflects the orientation of a specific site in the protein with respect to the bilayer. Structures are calculated using the angular constraints extracted from the measured spectral frequencies. Using this approach determined the three-dimensional structure of the M2 transmembrane segment from the acetylcholine receptor, as described below.[10] The ^{13}C chemical shift and the ^{2}H quadrupolar coupling frequencies, measured from selectively or specifically labeled samples in separate experiments, also provide valuable structural information, and have been used together with the ^{15}N chemical shift and the ^{1}H/^{15}N dipolar coupling, to determine the structure of the gramicidin channel at high resolution.[38]

The backbone structure of a protein is defined by the planes formed by the individual rigid peptide bonds and their directly bonded atoms. This is equivalent to the conventional description by vectors representing bonds between non-hydrogen atoms. A standard planar peptide geometry serves as the building block for the structure assembly process. The orientation of a peptide plane consistent with the measured NMR frequencies is defined in terms of polar angles relative to the magnetic field. The inputs to the computer program are the NMR frequencies measured from a three-dimensional correlation spectrum, and the values of the amide ^{15}N and ^{1}H chemical shift tensors. Once the orientations of all the peptide planes in the protein are calculated, neighboring planes of fixed orientation are connected through their common α-carbon atom, with the only constraint of a fixed tetrahedral angle of 110°. Another program calculates the phi and psi dihedral angles for the two contiguous peptide plane combinations that satisfy tetrahedral angle geometry at the α-carbon. The advantage of this direct mathematical analysis is that it is possible to determine the standard deviations in phi and psi based on uncertainties in the experimentally determined angles. Another important advantage of the method is that is results in the 'piece-wise' assembly of structures. Different parts of the protein structure can be determined independently of the rest. This is not possible in methods where distance constraints between different regions of the protein must be established for three-dimensional structure determination. Because the orientation of individual peptide planes is determined relative to a unique external reference the corresponding errors are not cumulative.

7 APPLICATION TO THE THREE-DIMENSIONAL STRUCTURE OF THE ACETYLCHOLINE M2 PEPTIDE IN LIPID BILAYERS

The three-dimensional structures of functional peptides corresponding to the M2 segments from the α-subunit of the Acetylcholine receptor (AchR) and the NR1 subunit of the NMDA subtype glutamate receptors were determined by solution and solid-state NMR spectroscopy in membrane environments.[10] The relatively large quantities of isotopically labeled M2 peptides required for NMR spectroscopy were prepared by expression of recombinant peptides in *E. coli*, for selective or uniform isotopic labeling, and by solid-phase synthesis, for specifically labeled samples.

The incorporation of the M2 peptides into lipid bilayers reconstitutes functional, cation-selective channels. The single channel currents recorded from AchR M2 in lipid bilayers, under voltage clamp conditions have heterogeneous conductances and lifetimes, as expected for monomeric peptides that self-assemble into conductive oligomers of discrete yet variable size, and display a linear current-voltage relationship. The channels that occur most frequently exhibit a single-channel conductance of about 38 pS in both NaCl and KCl. Significantly, the channel properties of peptides prepared by solid-phase synthesis and by expression in bacteria are nearly

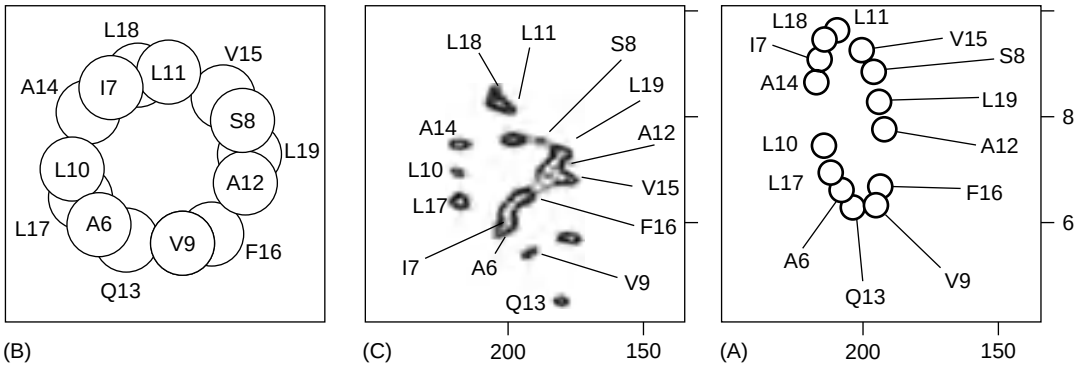

Figure 9 This is taken from Figure 2 from the paper by Marassi and Opella.[7] Helical wheel projection and two-dimensional PISEMA spectra of the uniformly ^{15}N-labeled acetylcholine receptor M2 polypeptide in oriented lipid bilayers. (A) Helical wheel projection of the amide N atoms of the polypeptide. (B) Experimental PISEMA wheel spectrum of the polypeptide, which provided most of the orientational constraints used for structure determination. (C) Spectrum calculated for an a-helix with 3.6 residues per turn, identical dihedral angles (phi $= -65\,°$, psi $= -40\,°$), and a tilt of 12° relative to the membrane normal

identical. Furthermore, peptides with the same amino acid composition as the M2 but with scrambled sequences do not form channels, nor do peptides patterned after the sequences of the predicted M1, M3 or M4 helices. Taken together, these results indicate that both the recombinant and synthetic M2 peptides used in the NMR experiments are functional, and form sequence-specific, discrete ion-channels in lipid bilayers.

The two-dimensional solid-state ^{1}H/^{15}N PISEMA spectrum of the peptide in oriented bilayers (Figure 9B) has excellent resolution, with each amide resonance characterized by ^{15}N chemical shift and ^{1}H$-^{15}$N dipolar coupling frequencies. The ^{15}N chemical shift and ^{1}H$-^{15}$N dipolar coupling frequencies provide orientational constraints for structure determination of ^{15}N labeled peptides in lipid bilayer membranes, and can be measured directly from the two-dimensional PISEMA spectrum shown in Figure 7(B) for AchR M2. The backbone structure of AchR M2, determined from ^{15}N chemical shift, ^{1}H$-^{15}$N dipolar coupling, and some ^{1}H chemical shift constraints, is shown in Figure 10. Solid-state NMR on oriented lipid bilayer samples is unique in determining the complete topology, including three-dimensional structure and orientation, of the peptide in the membrane, at high resolution. This is a crucial element of membrane protein structure, and in the case of AchR M2, sheds light on the details of supramolecular channel architecture. The AchR M2 peptide is a transmembrane α-helix with its long helix axis tilted 12° relative to the lipid bilayer normal (88° from the lipid bilayer plane).

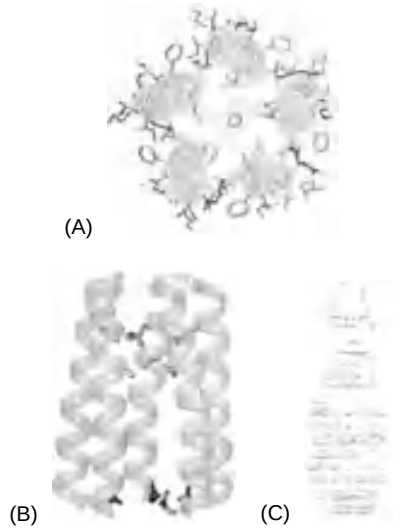

Figure 10 This is taken from Figure 5 from the paper by Opella et al.[10] Top (A) and side (B, C) views of a model of the acetylcholine receptor M2 funnel-like pentameric bundle. The channel architecture was calculated using the three-dimensional coordinates of the M2 helix in the lipid bilayer determined by solid-state NMR spectroscopy, and by imposing a symmetric pentameric organization. (C) is the pore profile

Figure 10 shows a model of the AchR channel pore. It was constructed from the three-dimensional structure of the AchR M2 helix derived from solid-state NMR data and the pentameric organization of the channel in lipid bilayers. The optimized pentameric bundle has a right-handed, inter-helical twist with an orientation angle of 12°. A central narrow pore has a diameter ranging from about 3.0 Å to 8.6 Å. Nonpolar residues are predominantly on the exterior of the bundle, while polar residues line the pore. The residues exposed to the pore lumen are Glu-1, Ser-4, Ser-8, Val-15, Leu-18 and Gln-22, which is in agreement with evidence collected from mutagenesis, affinity labeling and cysteine accessibility measurements. A side view shows a funnel-shaped bundle, 33 Å in length, with the wide mouth at the N-terminus. A dotted contour depicting the profile of the ion-conduction pore calculated from the structure is shown. The channel lining hydroxyl residues are in agreement with the expectations of a water-filled pore, and the constrictions are compatible with the permeation of both Na and K ions.

8 SUMMARY

The structure of the polypeptide shown in Figure 10 was determined using solid-state NMR methods that were direct descendents of the initial observations of doublets due to local fields in 1948. The advances required to transform solid-state NMR from a spectroscopic technique to a generally applicable method for determining molecular structures included

multiple-pulse sequences, double-resonance methods, and separated local field spectroscopy. It also required improvements in instrumentation, especially the use of high-field magnets. The pace of development is accelerating, and the local field is being utilized in an increasing number of ways in spectroscopic investigations of molecular structure and dynamics.

9 REFERENCES

1. G. E. Pake, *J. Chem. Phys.*, 1948, **16**, 327.
2. R. K. Hester, J. L. Ackerman, B. L. Neff, and J. S. Waugh, *Phys. Rev. Lett.*, 1976, **36**, 1081.
3. E. F. Rybaczewski, B. L. Neff, J. S. Waugh, and J. S. Sheerfinski, *J. Chem. Phys.*, 1976, **67**, 1232.
4. S. J. Opella and J. S. Waugh, *J. Chem. Phys.*, 1977, **66**, 4919.
5. M. E. Stull, A. J. Vega, and R. W. Vaughan, *J. Chem. Phys.*, 1978, **69**, 5458.
6. F. M. Marassi, A. Ramamoorthy, and S. J. Opella, *Proc. Natl. Acad. Sci. USA*, 1997, **94**, 8551.
7. F. M. Marassi and S. J. Opella, *J. Magn. Reson.*, 2000, **144**, 150.
8. J. Wang, J. Denny, C. Tian, S. Kim, Y. Mo, F. Kovacs, Z. Song, K. Nishimura, Z. Gan, R. Fu, J. R. Quine, and T. A. Cross, *J. Mag. Reson.*, 2000, **144**, 162.
9. S. J. Opella, P. L. Stewart, and K. G. Valentine, *Q. Rev. Biophys.*, 1987, **19**, 7.
10. S. J. Opella, F. M. Marassi, J. J. Gesell, A. P. Valente, Y. Kim, M. Oblatt-Montal, and M. Montal, *Nature Struct. Biol.*, 1999, **6**, 374.
11. A. Abragam, 'The Principles of Nuclear Magnetism', Clarendon Press: Oxford, 1961.
12. E. R. Andrew, A. Bradbury, and R. G. Eades, *Arch. Sci.*, 1958, **11**, 223.
13. I. J. Lowe, *Phys. Rev. Lett.*, 1959, **2**, 28.
14. W. J. Goldburg and M. Lee, *Phys. Rev. Lett.*, 1963, **11**, 255.
15. J. S. Waugh, L. M. Huber, and U. Haeberlen, *Phys. Rev. Lett.*, 1968, **20**, 180.
16. A. Pines, M. G. Gibby, and J. S. Waugh, *J. Chem. Phys.*, 1972, **56**, 1776.
17. J. H. VanVleck, *Phys. Rev.*, 1948, **74**, 1168.
18. U. Haeberlen and J. S. Waugh, *Phys. Rev. Lett.*, 1968, **175**, 453.
19. M. Lee and W. J. Goldburg, *Phys. Rev.*, 1965, **140**, A1261.
20. P. Mansfield, *Phys. Lett.*, 1970, **A32**, 485.
21. W.-K. Rhim, D. D. Elleman, and R. W. Vaughan, *J. Chem. Phys.*, 1973, **58**, 1772.
22. W.-K. Rhim, D. D. Elleman, and R. W. Vaughan, *J. Chem. Phys.*, 1973, **59**, 3740.
23. W.-K. Rhim, D. D. Elleman, L. B. Schreiber, and R. W. Vaughan, *J. Chem. Phys.*, 1974, **60**, 4595.
24. U. Haeberlen, 'High Resolution NMR in Solids', Academic Press: New York, 1976.
25. M. Mehring and J. S. Waugh, *Phys. Rev. B*, 1972, **5**, 3459.
26. A. Bielecki, A. C. Kolbert, and M. H. Levitt, *Chem. Phys. Lett.*, 1989, **155**, 341.
27. A. Bielecki, A. C. Kolbert, H. J. M. de Groot, R. G. Griffin, and M. H. Levitt, *Adv. Mag. Reson.*, 1990, **14**, 111.
28. C. H. Wu, A. Ramamoorthy, and S. J. Opella, *J. Mag. Reson.*, 1994, **A109**, 270.
29. A. Pines, M. G. Gibby, and J. S. Waugh, *J. Chem. Phys.*, 1973, **59**, 569.
30. J. Schaefer and E. O. Stejskal, *J. Am. Chem. Soc.*, 1976, **98**, 1031.
31. L. Muller, A. Kumar, T. Baumann, and R. R. Ernst, *Phys. Rev. Lett.*, 1974, **32**, 1402.
32. R. K. Hester, J. L. Ackerman, V. R. Cross, and J. S. Waugh, *Phys. Rev. Lett.*, 1975, **34**, 993.
33. J. S. Waugh, *Proc. Nat. Acad. Sci. USA*, 1976, **73**, 1394.
34. W. P. Ave, E. Bartholdi, and R. R. Ernst, *J. Chem. Phys.*, 1976, **64**, 2229.
35. A. Ramamoorthy, C. H. Wu, and S. J. Opella, *J. Mag. Reson.*, 1995, **B107**, 88.
36. F. M. Marassi, C. Ma, J. J. Gesell, and S. J. Opella, *J. Magn. Reson.*, 2000, **144**, 156.
37. Y. Kim, K. Valentine, S. J. Opella, S. L. Schendel, and W. A. Cramer, *Protein Sci.*, 1998, **7**, 342.
38. R. R. Ketchem, W. Hu, and T. A. Cross, *Science*, 1993, **261**, 1457.

Acknowledgements

The research on solid-state NMR of proteins was supported by grants R37GM24266, RO1GM29754, and PO1GM56538 from the National Institute of General Medical Sciences and utilized the Resource for Solid-State NMR of Proteins supported by grant P41RR09731 from the Biomedical Research Technology Program, National Center for Research Resources.

Biographical Sketch

Stanley Joseph Opella, *b* 1947. Ph.D. 1974 Physical Chemistry, Stanford University. Postdoctoral fellow, M.I.T., 1975–76; Professor of Chemistry at the University of Pennsylvania, 1976–2000. Professor of Chemistry and Biochemistry at the University of California, San Diego, 2000-present. Approx. 200 publications. Current research interests: development and application of NMR for the study of proteins.

Phospholipid–Cholesterol Bilayers

Kevin M. W. Keough and Michael R. Morrow
Memorial University of Newfoundland, St. John's, NF, Canada

and

Robert Bittman
Queens College of The City University of New York, Flushing, NY, USA

1	Introduction: Cholesterol and Model Membranes	1
2	Early Work on Cholesterol–Phospholipid Interactions	1
3	Refinement of Phospholipid–Cholesterol NMR Studies	2
4	Other Recent Phospholipid–Cholesterol Phase Diagram Studies	6
5	Concluding Remarks	6
6	Related Articles	6
7	References	6

1 INTRODUCTION: CHOLESTEROL AND MODEL MEMBRANES

Cholesterol and related structures are distributed ubiquitously in the membranes of living organisms. Cholesterol is a major component of mammalian plasma membranes and plasma lipoproteins. Cell surface membranes, some viral membranes, and specialized cell membranes such as myelin contain large amounts of cholesterol, having as much as equimolar amounts of cholesterol and phospholipids. On the other hand, subcellular membranes tend to have less cholesterol, with the inner mitochondrial membrane having a very low cholesterol content.[1,2] Cholesterol levels are altered in the membranes of some pathophysiological states such as malignant lymphoid cells.[3] Cholesterol plays many important roles in membranes, including modulation of phospholipid packing density, separation of phospholipid headgroups and disruption of interactions between neighboring headgroups, alteration of membrane permeability behavior, and regulation of membrane-bound enzyme activities. Therefore, studies of the interactions between cholesterol and phospholipids and their consequences with respect to membrane structure and function have been the subject of intense scrutiny for more than three decades.[4–7]

Much of the current understanding of the effects of cholesterol in membranes has come from studies of model bilayer membranes, which are formed by simply dispersing phospholipids, cholesterol, and other compounds in aqueous media. Since the composition of these aqueous dispersions is easily controlled, bilayers prepared from fully hydrated phospholipids have been used extensively in physicochemical studies. This review of the use of NMR for the study of phospholipid–sterol interactions places special emphasis on ^{2}H NMR. The principal topic in this review is the use of NMR to obtain information about the equilibrium phase behavior of cholesterol–phospholipid mixtures, as expressed in phase diagrams and measurements of the order of the hydrocarbon region of membranes. We also present here a brief review of selected NMR literature on methods employing several nuclei that has led to our current understanding of sterol–phospholipid interactions, together with an overview of differential interactions of cholesterol with a variety of phospholipid subclasses such as ester- and ether-linked phosphatidylcholines (PCs).

2 EARLY WORK ON CHOLESTEROL–PHOSPHOLIPID INTERACTIONS

Some of the earliest work on cholesterol–phospholipid mixtures in model bilayer membranes was carried out using X-ray diffraction and differential scanning calorimetry (DSC) techniques, which produced phase diagrams that were refined as discussed below.[4,8] These studies led to the concept that cholesterol produces a state of 'intermediate fluidity' in a phospholipid by decreasing hydrocarbon chain motion in the liquid crystalline state and increasing the hydrocarbon chain motion in the gel state.[4] These properties of bilayers were consistent with earlier observations in monolayers that showed that cholesterol 'condensed' phospholipids in which there was freedom of chain motion[9] and expanded phospholipids in which chain motion was restricted.[10] More precise DSC studies led to a partial phase diagram of the dipalmitoylphosphatidylcholine (DPPC)–cholesterol system,[11] and partitioning experiments with the spin probe Tempo (2,2,6,6-tetramethylpiperidine-*N*-oxyl) resulted in partial phase diagrams of dimyristoylphosphatidylcholine (DMPC)–DPPC mixtures with parts of the boundaries of the L_α, or liquid-disordered (*ld*) and liquid-ordered (*lo*), delineated.[12] Similarly, a partial phase diagram was constructed for DMPC–cholesterol mixtures which included the gel or solid-ordered (*so*), *ld*, and *lo* regions (see below).[13]

The first use of NMR to investigate phospholipid–cholesterol interactions was carried out by Chapman and Penkett,[14] who used continuous wave ^{1}H NMR to show that cholesterol broadened the resonances of the fatty acyl chains and headgroup of egg PC bilayers above the phospholipid phase transition temperature. Similar information was obtained from other early ^{1}H and ^{13}C NMR studies of various phospholipid–cholesterol mixtures.[15] The first application of ^{2}H NMR to the investigation of model membranes was a study of the effects of cholesterol and temperature on dual-chain perdeuterated DMPC-d_{54} bilayers.[16] Above the phase transition temperature (T_m), cholesterol caused the quadrupole splitting of the methylene deuterons to increase, indicative of increased order and reduced motion in the presence of cholesterol. Use of PCs and cholesterol, specifically deuterated at selected sites, provided a wealth of information about the PC–cholesterol system; for references to early ^{2}H NMR studies, see Davis[17] and Vist and Davis.[18] Many of these studies suffered from the drawback that it was not possible to reproduce faithfully the ^{2}H NMR lineshapes, particularly in the gel phase, with the pulsed Fourier transform methods then in use. The introduction of quadrupole echo Fourier transform NMR[19] overcame

this problem and allowed essentially undistorted ^{2}H NMR spectra to be recorded and detailed phase diagrams to be produced. Application of this technique to examine order and dynamics in deuterated DMPC–cholesterol mixtures[20] and other bilayer-forming phospholipids (reviewed in Davis[17]) followed quickly. Proton magic angle sample spinning NMR has also been applied to the study of phospholipid–cholesterol interactions.[21] Recently, ^{2}H NMR was used to carry out a comprehensive examination of molecular order and dynamics in DMPC–cholesterol mixtures.[22]

3 REFINEMENT OF PHOSPHOLIPID–CHOLESTEROL NMR STUDIES

3.1 The Effect of Cholesterol on Phospholipid Acyl Chain Order

The ^{2}H NMR spectrum of a deuteron on the acyl chain of a phospholipid in the liquid crystalline state of a bilayer with random orientation is an axially symmetric Pake doublet. The sharp edges of the doublet arise from molecules undergoing reorientation about an axis that is perpendicular to the applied magnetic field. The quadrupolar splitting of these 90° edges is

$$\Delta\nu_Q = \frac{3}{4}\frac{e^2qQ}{h}S_{CD} \quad (1)$$

where S_{CD}, the orientational order parameter of the carbon–deuterium bond, is given by

$$S_{CD} = \tfrac{1}{2}\langle 3\cos^2\theta_{CD} - 1\rangle \quad (2)$$

In equation (2), θ_{CD} is the angle between the carbon–deuterium bond and the applied magnetic field, and the average is over the motions of the bond. In the gel phase, the chains are more highly ordered, so their slower, asymmetric motion results in a broad spectrum with no sharp features. The ^{2}H NMR spectra of deuterated lipids have been reviewed in Davis.[17]

The ^{2}H NMR spectrum of perdeuterated phospholipids in the liquid crystalline phase of bilayers is a superposition of doublets with a range of splittings reflecting the decrease in orientational order toward the bilayer center. The effect of cholesterol on the chains is illustrated in Figure 1. Above T_m, which is about 38 °C for DPPC-d_{62}, addition of cholesterol increases the doublet splittings, indicative of an increase in acyl chain order and bilayer thickness. Below T_m, the spectrum in the presence of cholesterol indicates that the chains are ordered but undergoing axially symmetric reorientation. The result is a superposition of axially symmetric doublets with large splittings.

Incorporation of DPPC-d_{62} (at 25 mol%) into undeuterated egg PC liposomes resulted in the appearance of a plateau region (which reflects the superposition of the quadrupole splittings of the seven or eight CD_2 groups nearest to the glycerol backbone) and a series of peaks for the more motionally disordered segments between the middle of the chain and the terminal CD_3 group.[23] Incorporation of cholesterol (at 50 mol%) increased the peak-to-peak quadrupole splittings by 75–140%, indicative of a more ordered system.

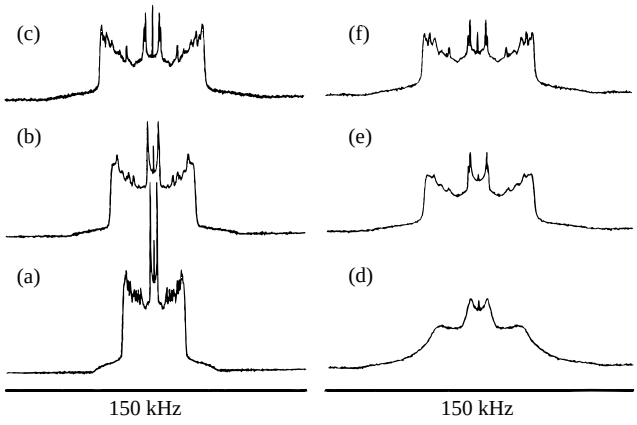

Figure 1 ^{2}H NMR spectra of DPPC-d_{62} in DPPC-d_{62}–cholesterol (chol) bilayers. Spectra were collected at 23.2 MHz using the quadrupole echo sequence with a pulse separation of 40 μs. (a) x_{chol} = 0.035, T = 40 °C; (b) x_{chol} = 0.16, T = 40 °C; (c) x_{chol} = 0.285, T = 40 °C; (d) x_{chol} = 0.035; T = 35 °C; (e) x_{chol} = 0.16; T = 35 °C; (f) x_{chol} = 0.285, T = 35 °C

3.2 The Effect of Analogs of Cholesterol on Phospholipid Acyl Chain Order

3.2.1 ^{2}H and ^{13}C NMR Studies of the Interaction of Epicholesterol (5-Cholesten-3α-ol) with PC

NMR and other physical studies have shown that the molecular features required in a sterol for the ability to moderate the angular fluctuations of phospholipids in bilayers are a planar steroid nucleus, a 3β-hydroxy group, and a long apolar side chain at C-17. Deletion of any of these features results in failure of cholesterol to reduce membrane permeability, broaden the gel-to-liquid-cystalline phase transition, or reduce the mean molecular area of phospholipids in monolayers. Sterols with a planar α face interact principally by van der Waals interactions with the phospholipid acyl chains. Lanosterol, which lacks a planar α face since its 14α-methyl group protrudes from this surface, has considerably more mobility than cholesterol in PC vesicles as judged by ^{13}C NMR.[24]

The relative mobilities of cholesterol and epicholesterol have also been compared in bilayers. The rotational freedom of cholesterol molecules in sonicated phospholipid vesicles can be estimated from spin–lattice relaxation (T_1) and linewidth ($\Delta\nu_{1/2}$) measurements of selected carbon resonances. A comparison of the rotational freedom of cholesterol and epicholesterol in egg PC vesicles was made by ^{13}C NMR as a function of temperature.[25] Below 32 °C epicholesterol has a broad C-6 resonance of about the same linewidth as the C-6 nucleus of cholesterol, and both sterols have a similar effect on PC dynamics as estimated from their ability to cause similar broadening of the *sn*-1 carbon but not of the *sn*-3 carbon. At 41–42 °C, however, the motion of epicholesterol is less restricted than that of cholesterol in egg PC vesicles, as judged by the observation of resonances from C-9 and C-14,17. These studies provide additional proof that the dynamics of component lipids are relevant to membrane function.

Models have been proposed to explain the molecular basis of the differential effects of epicholesterol and cholesterol on the packing of phospholipids in bilayers. Although both

sterols are oriented with the long axis normal to the bilayer surface, a collinear hydrogen bond may be formed with the 3β-hydroxy group of cholesterol and an acceptor such as one of the carbonyl oxygen atoms of the phospholipid;[26] alternatively, the 3β-hydroxy group of cholesterol may be more extensively hydrated than the 3α-hydroxy group of epicholesterol.[27] On the basis of ^{2}H NMR studies with specifically deuterated cholesterol and epicholesterol in DMPC or DMPC-d_{27} bilayers between 10 and 65 °C, a pronounced tilt of epicholesterol with respect to the bilayer normal was evident at physiological temperatures.[28] Furthermore, the isooctyl side chain of cholesterol was found to be as ordered as the steroid nucleus. The quadrupolar splittings of epicholesterol and cholesterol deuterated at C-3 in DPPC bilayers suggested that the angle of tilt of the sterol nucleus relative to the bilayer normal is different in the two sterols.[29] Cholesterol was estimated to be inclined at an angle of 16–19° at 24 °C and 60 °C, which is similar to the tilt of the fatty acyl chains in bilayers; thus, the steroid nucleus and the phospholipid fatty acyl chains have a nearly parallel alignment, with the 3β-hydroxy group projecting toward the water and fully accessible for hydrogen bonding. In contrast, the steroid nucleus of epicholesterol was proposed to lie nonparallel to the phospholipid fatty acyl chains at 24 °C. The 3α-hydroxy group was postulated to lie essentially perpendicular to the bilayer normal, accessible to interaction with water, but positioned at an angle that increases the distance between the steroid nucleus and fatty acyl chains, thus diminishing the extent of lipid–lipid interactions and perturbing the packing of the lipid chains. These studies make clear the reason why epicholesterol is not a naturally occurring membrane component; its presence would destabilize bilayers by disturbing close packing of lipid chains.

3.2.2 ^{2}H NMR Studies of the Interaction of Terpene Alcohols ('Cholesterol Ancestors') with PC

Many polyterpenoid 'ancestors' of cholesterol, although they resemble cholesterol in their rigidity, overall cylindrical shape, and amphiphilic character, generally fail to increase the acyl chain order of phospholipids in fluid phase oriented multilayers, as probed by the increase in mean order parameter using single chain perdeuterated phospholipids such as DMPC-d_{27} and DPPC-d_{31}.[30] Thus the molecular dimensions of cholesterol have apparently evolved in a manner that permits this sterol to play an important role in modulating membrane structure, and this sterol became ubiquitous in most eukaryotic cell membranes. Incorporation of cholesterol at 30 mol% increases the order parameter of the plateau region and terminal methyl region by 78% and 130%, respectively.[31] The extent to which a cholesterol surrogate has the capacity to increase the mean order parameter of oriented bilayers represents a measure of its resemblance to cholesterol.

3.3 Interaction of Cholesterol with Sphingomyelin

There is considerable evidence that the lateral packing density of cholesterol with sphingomyelin is higher than that with PCs (for references, see Bittman[32]). However, ^{13}C NMR studies of [4-^{13}C]cholesterol did not reveal a significant difference in the rotational freedom of cholesterol molecules in PC and sphingomyelin sonicated vesicles, as estimated by $\Delta\nu_{1/2}$ and T_1 measurements.[33] There is substantial evidence that sphingomyelin bilayers are packed more tightly than PC bilayers of similar degree of acyl saturation. Early ^{2}H NMR studies of unsonicated bilayers showed that a semisynthetic sphingomyelin labeled with deuterium at C-10 of the amide-linked chain had significantly higher quadrupole splitting ($\Delta\nu_Q$) than DPPC labeled with deuterium at C-10 of the *sn*-2 palmitoyl chain.[34] More detailed studies of this system are required with specifically labeled, chemically defined sphingomyelins in order to examine whether the mode of packing of cholesterol differs in sphingomyelin and PC bilayers.

3.4 Interaction of Cholesterol with Ether-Linked Phosphocholines

3.4.1 ^{1}H NMR Studies with Plasmenylcholine and PC Vesicles

It is of interest to examine the possibility that cholesterol modulates the motional characteristics of the major mammalian choline glycerophospholipids' subclasses in a differential manner. Proton spin–lattice relaxation times and apparent activation energies of T_1 relaxation times for vinyl and bisallylic methylene protons in liquid crystalline bilayers of a diacyl-PC (1-palmitoyl-2-arachidonoyl-3-PC) were higher than that of a plasmenylcholine, 1-*O*-(*Z*)-hexadec-1′-enyl-2-arachidonyl-3-PC.[35] Incorporation of cholesterol resulted in substantial decreases in the proton spin–lattice (T_1) relaxation times in the interior regions of plasmenylcholine bilayers, and this decrease was larger than that in PC bilayers. On the other hand, the T_1 values of the choline methylene protons of plasmenylcholine bilayers were increased on introduction of cholesterol, and this increase was larger than that found in diacyl-PC bilayers.

Although ^{2}H and ^{13}C NMR studies have shown that polar headgroup motion of phospholipids in multilamellar vesicles is not significantly altered by incorporation of cholesterol,[13,36] the spin–spin relaxation times (T_2) of CH_2N and $N{-}CH_3$ of both PC and plasmenylcholine sonicated vesicles were decreased by cholesterol (at 30 mol%): also, the T_2 values of the bis-allylic protons of arachidonic acid in PC or plasmenylcholine vesicles were decreased by cholesterol (at 30 mol%).[37] These proton spin–spin relaxation time measurements indicate that introduction of cholesterol results in slower motion of the polar headgroup of plasmenylcholine and PC vesicles. Since plasmenylcholine lacks an ester linkage at the *sn*-1 position, yet still has its motional properties altered by cholesterol, these results suggest that hydrogen bonding to an *sn*-1 carbonyl group of diacyl-PC is not required for interaction of phospholipids with cholesterol.

3.4.2 ^{13}C NMR Studies of Saturated Ether–PC and Ester–PC Vesicles

The conclusion stated above is consistent with previous ^{13}C NMR studies of cholesterol enriched with ^{13}C at the 4-position, in which ^{13}C NMR relaxation measurements indicated that no significant relocation of the 4-^{13}C atom of cholesterol took place when a methylene group was substituted for a carbonyl

group in PC sonicated vesicles.[38] The apparent spin–spin relaxation time $T_2[= (\pi \cdot \Delta\nu_{1/2})^{-1}]$, which reflects mainly slower motions involving reorientation of local segments, for the 4-^{13}C atom of cholesterol was shorter in bilayers prepared with 1-ester-2-ether-PC or 1,2-diether-PC than in those prepared with 1,2-diester-PC. Thus, the presence of an *sn*-2 *O*-alkyl linkage in PC rather than an *sn*-2 ester linkage appears to result in a relatively restricted motion of cholesterol (present at 10 mol%). In a diester-PC, the arrangement of the *sn*-1 and *sn*-2 chains is different near the lipid–water interface; the ester linkage at *sn*-2 lies at the interface, whereas the *sn*-1 ester linkage penetrates into the bilayer. In PCs having an *sn*-2 *O*-alkyl linkage, the absence of a bend results in tighter packing of PC molecules in this region of the membrane interface, which is reflected in the shorter apparent T_2 values for [4-^{13}C]cholesterol in dihexadecyl- and 1-palmitoyl-2-*O*-hexadecyl-PC vesicles. This difference in lipid packing property does not require that formation of a hydrogen bond be postulated between cholesterol and the phospholipid. Indeed, no evidence for such a hydrogen bond was found in recent ^{2}H NMR studies of 3-[^{2}H]-cholesterol in DMPC vesicles.[39] However, evidence for a putative hydrogen bond between the 3β-hydroxy group of cholesterol and the *sn*-2 carbonyl of DPPC has been suggested from a high-frequency shift in the ^{13}C NMR spectrum of DPPC carbonyl carbon atoms in the presence of cholesterol.[40,41]

3.5 Use of Spectral Subtraction for Phase Diagram Determination

Many studies have been directed toward the refinement of phase diagrams of a variety of phospholipid–cholesterol systems by application of a wide range of physical techniques (see, for example, references cited in Vist and Davis[18] and Blume and Griffin[42]).

In excess water, a system containing two bilayer-forming components can be treated as a binary mixture. It can be shown that along a line of constant temperature in a binary phase diagram, regions corresponding to different homogeneous phases must be separated by regions in which the free energy of the system is lowered by separation into coexisting domains of the adjacent homogeneous phases. One approach to determining the boundaries of such regions of two-phase coexistence is to scan the temperature through the two-phase region, while observing some property that is sensitive to the thermodynamic phase of the sample, such as excess specific heat in a DSC experiment or lineshape in an NMR experiment. When carried out for a series of sample concentrations, this type of experiment indicates the upper and lower temperature limits of two-phase coexistence for a particular composition.

In order to describe the way in which spectral differences are used in phase diagram studies, we consider here a two-component bilayer system with a temperature and composition that falls within a region of two-phase coexistence in the binary phase diagram. We will use x to denote the mole fraction of component 2 in the bilayer. For the purpose of this discussion, we will take the coexisting phases to be a phase G with a lower concentration of component 2 and a phase F, which is richer in component 2. If, at a particular temperature T, the composition x falls within the two-phase region, the mixture will separate into domains of G and F, with compositions that correspond to the points at which an isotherm at temperature T intersects the boundaries of the two-phase region. These points are referred to as endpoints. For the example described here, the gel-phase boundary composition at temperature T is labeled $x_G(T)$, and the fluid-phase boundary composition is labeled $x_F(T)$. If component 2 lowers the $G \rightarrow F$ transition temperature, then we have $x_F(T) > x_G(T)$. The partitioning of the sample between the coexisting phases is determined by the lever rule. For example, the fraction of the sample in the F phase will be given by

$$f_F(x, T) = \frac{x - x_G(T)}{x_F(T) - x_G(T)} \tag{3}$$

Consider the situation where one of the components is deuterated. We will take component 1 to be the labeled component. The endpoint concentrations can be determined if exchange between domains of the coexisting phases is slow on the ^{2}H NMR timescale.[43] Under these circumstances, the observed spectrum $S(x)$ for a sample of composition x in the two-phase coexistence region, at a particular temperature, will be a superposition of spectra S_G and S_F, corresponding to the endpoint compositions at that temperature. If $S(x)$, S_G, and S_F are normalized to a constant area, then the observed spectrum is given by

$$S(x) = \frac{(1 - x_G)(x - x_F)}{(1 - x)(x_G - x_F)} S_G + \frac{(1 - x_F)(x_G - x)}{(1 - x)(x_G - x_F)} S_F \tag{4}$$

The factor multiplying $S_G(S_F)$ in equation (4) is the number of labeled molecules in phase $G(F)$ divided by the total number of labeled molecules in the sample. Under some circumstances, it may be necessary to apply a correction to account for different transverse relaxation rates in the coexisting phases.

Consider two spectra, $S(x_A)$ and $S(x_B)$, obtained for sample compositions x_A and x_B on the same tie line within a two-phase region. They should consist of the same pair of endpoint spectra superimposed in differing proportions. If $x_A > x_B$, then $S(x_A)$ will contain a higher proportion of S_G than will $S(x_B)$. By subtracting one observed spectrum from the other, one can obtain a spectrum that is exclusively characteristic of one or the other endpoints. K is defined as the fraction of $S(x_B)$ that must be subtracted from $S(x_A)$ to yield S_G. Similarly, K' is the fraction of $S(x_A)$ that must be subtracted from $S(x_B)$ to yield S_F. The endpoint compositions are given by

$$x_G = \frac{x_A(1 - x_B) - K x_B(1 - x_A)}{(1 - x_B) - K(1 - x_A)} \tag{5}$$

and

$$x_F = \frac{x_B(1 - x_A) - K y' x_A(1 - x_B)}{(1 - x_A) - K'(1 - x_B)} \tag{6}$$

For locating phase boundaries, spectral subtraction complements other methods in which properties are observed as sample temperatures are scanned through the region of interest. If several spectra are available along a tie line, a consistent result obtained from a series of different pairwise subtractions provides evidence that the system obeys the lever rule and that the observed spectral changes do indeed reflect two-phase coexistence. Scanning techniques such as DSC depend on the

identification of a threshold temperature at which a property, such as excess heat capacity, exhibits departures from baseline behavior. As such, they are sensitive to the way in which the baseline is extrapolated into the coexistence temperature range. It is significant that the spectral difference approach is based on equilibrium partitioning of the sample.

In practice, K or K' is varied until features characteristic of one or the other coexisting phases are eliminated. The ease with which the appropriate values of K and K' are assigned is very sensitive to the distinctness of the spectra corresponding to the two endpoints. The DPPC-d_{62}–cholesterol system presented a particular challenge to the spectral subtraction technique. Figure 2 shows the form of the phase diagram obtained by Vist and Davis.[18] The labels *ld* and *so* correspond to the liquid-disordered (or liquid crystal) and solid-ordered (or gel) phases, respectively. The *ld*–*so* coexistence region below 7.5 mol% cholesterol was less than 1 °C wide. The nearly horizontal boundaries of this region were determined by inspection of spectra for samples with cholesterol concentration below 7.5 mol% under the assumption that spectral subtraction in this region would be overly sensitive to uncertainty in the sample temperature. Figures 1(a) and 1(d) are characteristic of the *ld* and *so* spectra above and below this two-phase region. The spectra in the *lo* phase beyond about 20 mol%, which Vist and Davis[18] labeled the 'β' phase, are axially symmetric but with a greater average splitting than in the liquid crystalline phase. Figures 1(c) and 1(f) are characteristic of this phase. Within the *ld*–*lo* coexistence region, there was evidence that fast exchange between domains of the two phases caused averaging of the spectra, and spectral differences again were not used. The boundary between *ld* and the *ld*–*lo* coexistence region was determined from DSC studies. Figure 1(b) corresponds to a point inside the two-phase region close to the boundary. Below 20 mol% cholesterol, the lower boundary of this region is a three-phase line at which the *so* phase melts into the *ld* phase. This line was primarily identified from a sharp transition observed calorimetrically. The boundary between the *ld*–*lo* coexistence region and the *lo* region was assigned at the point where the sharp doublets of the *lo* phase broadened as the sample temperature was increased. This was taken to indicate the onset of spectral averaging due to fast exchange with domains of liquid crystal. Determining the exact location of this boundary remains somewhat problematic.

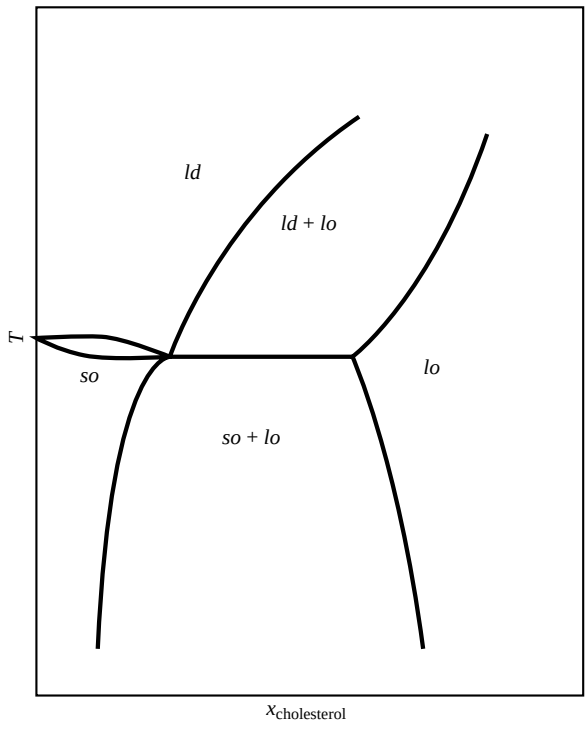

Figure 2 A schematic drawing of the PC–cholesterol phase diagrams. For DPPC-d_{62}, the three-phase line (separating *so* + *lo* from *ld* + *lo*) is at 37 °C and extends from about 7 mol% to 20 mol% cholesterol.[18] For POPC-d_{31}–cholesterol, the three-phase line is at about −7 °C and extends from 7 mol% to about 20 mol% cholesterol.[45] For stearoyl-elaidoyl-PC-d_{35}–cholesterol, the three-phase line is at about 31 °C and extends from about 10 to 25 mol% cholesterol,[46] *ld* is the liquid-disordered phase (also called liquid crystal or L_α). *lo* is the liquid-ordered phase (called β by Vist and Davis[18]), *so* is the solid-ordered phase (also called gel or L_β). (Adapted from Vist and Davis[18])

Within the *so*–*lo* region, spectral subtraction provided important evidence of predominantly vertical boundaries. Figure 1(e) is characteristic of spectra in this region. Such spectra are not obvious superpositions of spectra from two coexisting phases. However, spectral subtraction did give rise to endpoints that were characteristic of the *so* phase and axially symmetric endpoint spectra with large quadrupole splittings that were identified as arising from the *lo* phase. That these were indeed true endpoint spectra was confirmed by comparison with spectra obtained from samples having cholesterol concentrations close to the endpoint concentrations determined by spectral subtraction.

The doublet with the smallest splitting in the axially symmetric spectra arises from the methyl deuterons at the ends of the acyl chains. At high cholesterol concentration, the methyl doublet was split, indicating a slight difference in ordering of the two chains near the bilayer center (see Figure 1).[18] The temperature dependence of the splitting was examined,[44] and a correspondence was noted between the temperature at which the inequivalence of the methyl deuterons disappears and the boundary of the *ld*–*lo* coexistence region reported by Vist and Davis.[18] Partial orientation of DPPC-d_{62} vesicles containing 25 mol% cholesterol was found between 36 and 42 °C, which was attributed to a change in the mechanical properties of the bilayer. The temperature dependence of these effects in the *lo* phase may reflect a reorganization of cholesterol from a position near the bilayer center to one closer to the headgroup region with increasing temperature.

Spectral differences were also used to determine the phase diagrams of mixtures of cholesterol with two unsaturated PCs.[45] Although the phase diagrams were shifted to lower temperatures, in accordance with the T_m values of the phospholipids, remarkable similarities with the DPPC–cholesterol phase diagrams are apparent. A universal shape for the PC–cholesterol phase diagram was postulated, and it was suggested that the β or *lo* phase is probably common to cholesterol-rich biological membranes. No attempt was made to define the *ld*–*lo* coexistence region. Recently, the comparison was extended to mixtures of stearoyl-elaidoyl-PC and cholesterol, which were also found to resemble the DPPC–cholesterol phase diagram.[46] In each binary mixture, the shift on temperature of the three-phase line, relative to that for DPPC–cholesterol, is approximately the same as the shift in the pure phospholipid transition temperature relative to

that for DPPC. Theoretical efforts to model the DPPC phase diagram have been reviewed.[47,48]

4 OTHER RECENT PHOSPHOLIPID–CHOLESTEROL PHASE DIAGRAM STUDIES

The determination of phospholipid–cholesterol phase diagrams by using neutron scattering has been reviewed.[49] Electron spin resonance studies generated phospholipid–cholesterol phase diagrams in which a phase boundary was detected that appears to correspond to the boundary between the *ld*–*lo* coexistence region and the *lo* region beyond 20 mol% cholesterol.[50]

The phospholipid–cholesterol phase diagram has also been studied by Griffin and co-workers using a variety of techniques, including ^{13}C NMR. A region of two-phase coexistence below T_m was found in the phase diagram for dipalmitoylphosphatidylethanolamine–cholesterol mixtures by using ^{2}H and ^{13}C NMR.[42] In a similar study with distearoyl-PC (DSPC)–cholesterol and DPPC–cholesterol systems, the ^{13}C NMR spectrum of the *sn*-2 carbonyl was found to be an axially symmetric powder pattern with a width of about 100 ppm in the gel phase.[42,51] In the liquid crystalline phase, the spectrum is a narrow line (5–10 ppm in width), suggestive of isotropic motion. This behavior is attributed to a conformational change in which the unique axis of the chemical shift tensor orients close to the magic angle. In the $P_{\beta'}$ phase, a superposition of the powder pattern and narrow line spectra is seen. As cholesterol is added, the temperature at which the narrow component first appears is lowered. Where the narrow and powder pattern components are superimposed, the narrow component is broadened. The presence of the narrow and powder pattern spectral components together was taken to indicate the coexistence of a cholesterol-rich phase (LG_I or *lo*) and the gel phase (L_β or *so*). The broadening of the narrow component was simulated by assuming exchange between domains of the two phases. In this way, estimates of domain size have been obtained. The boundary of the LG_I or *lo* region above the temperature of the three-phase line was determined by ^{2}H NMR. The boundary of the *lo* region below the temperature of the three-phase line was found to be shifted to higher cholesterol concentration in mixtures containing the longer chain DSPC compared with DPPC.

The boundary of the DPPC–cholesterol *so*–*lo* region determined by ^{2}H NMR appears to be rather different from that determined by ^{13}C NMR. Carbon-13 NMR measurements indicated that the boundaries of this region curve toward higher cholesterol concentration as the temperature is lowered,[51] whereas ^{2}H NMR measurements showed the corresponding boundaries to be nearly vertical.[18] Similar results were obtained in mixtures of cholesterol with some unsaturated phospholipids.[45,46] However, the temperature ranges over which these boundaries have been determined by ^{2}H NMR are limited.[51] Whether there is really a discrepancy between the findings of the two techniques regarding these boundaries is not clear at this time.

A variety of techniques, including ^{2}H NMR, electron spin resonance, and fluorescence recovery after photobleaching, have been applied to the construction of phospholipid–cholesterol phase diagrams[52] that are qualitatively similar to the one reported by Vist and Davis.[18] Based on ^{2}H NMR studies of bilayer thickness in a series of PCs with increasing chain length, it was suggested that cholesterol spans the bilayer in the *ld* phase and that, with increasing cholesterol concentration and increasing order, the bilayer becomes partially interdigitated in the *lo* phase.[53] The fluid phase immiscibility represented by the *ld*–*lo* region was attributed to this behavior.

5 CONCLUDING REMARKS

What are the implications of these findings for biological membranes? There are common features for each of the lipid–cholesterol phase diagrams, with three phases, *so*, *lo*, and *ld*, plus the corresponding two-phase regions appearing for each phospholipid–cholesterol combination. The phase boundaries show similar, although not identical, properties with respect to cholesterol concentration, with their positions being dependent on the specific phospholipid involved.

At their physiological temperature(s), the lipids of most membranes will be above T_m and above the three phase lines in the phase diagrams. Plasma membranes, therefore, will be in the *lo* or, at elevated temperatures, in the *ld* state. Under equilibrium conditions, these are continuous phases, although interaction energies might vary between cholesterol and individual, specific phospholipids. (Indeed, such comparisons should be made with full knowledge of the phase diagrams, so that cholesterol–phospholipid interactions in comparable phases can be compared.) Subcellular membranes and other membranes having low cholesterol content, on the other hand, while possibly being in the phases just mentioned, might also exist in the *ld*–*lo* two-phase region above the three-phase line. Thus, cholesterol-enriched and cholesterol-poor regions could coexist in membranes, and these domains might have important consequences for insertion and regionalization of proteins, and for modulation of protein functions.

6 RELATED ARTICLES

Bilayer Membranes: Deuterium and Carbon-13 NMR; Bilayer Membranes: Proton and Fluorine-19 NMR; Biosynthesis and Metabolic Pathways: Deuterium NMR; Deuteron Relaxation Rates in Liquid Crystalline Samples: Experimental Methods; Lipid Polymorphism; Lipoproteins; Liquid Crystalline Samples: Carbon-13 NMR; Liquid Crystalline Samples: Deuterium NMR; Membrane Lipids of Acholeplasma laidlawii; Membranes: Carbon-13 NMR; Membranes: Deuterium NMR; Sonicated Membrane Vesicles.

7 REFERENCES

1. D. F. H. Wallach, *Membrane Molecular Biology of Neoplastic Cells*, Elsevier, Amsterdam, 1975, pp. 217–241.
2. G. Rouser, in *Membrane Fluidity in Biology*, ed. R. C. Aloia, Academic Press, New York, 1983, Vol. 1, pp. 235–289.
3. W. J. Van Blitterswijk, in *Membrane Fluidity in Biology*, eds. R. C. Aloia and J. M. Boggs, Academic Press, New York, 1985, Vol. 3, pp. 85–159.

4. R. D. Ladbrooke, R. M. Williams, and D. Chapman, *Biochim. Biophys. Acta*, 1968, **150**, 333.
5. K. E. Bloch, *CRC Crit. Rev. Biochem.*, 1983, **14**, 47.
6. F. T. Presti, in *Membrane Fluidity in Biology*, eds. R. C. Aloia and J. M. Boggs, Academic Press, New York, 1985, Vol. 3, pp. 97–146.
7. P. L. Yeagle, *Biochim. Biophys. Acta*, 1985, **822**, 267.
8. M. C. Bourgès, D. M. Small, and D. G. Dervichian, *Biochim. Biophys. Acta*, 1967, **137**, 157.
9. J. B. Leathes, *Lancet*, 1925, **208**, 853.
10. D. O. Shah and J. H. Schulman, *J. Lipid Res.*, 1967, **8**, 215.
11. S. Mabrey, P. L. Mateo, and J. M. Sturtevant, *Biochemistry*, 1978, **17**, 2464.
12. E. J. Shimshick and H. M. McConnell, *Biochem. Biophys. Res. Commun.*, 1973, **53**, 446.
13. D. J. Recktenwald and H. M. McConnell, *Biochemistry*, 1981, **20**, 4505.
14. D. Chapman and S. A. Penkett, *Nature (London)*, 1966, **211**, 1304.
15. K. M. Keough, E. Oldfield, D. Chapman, and P. Benyon, *Chem. Phys. Lipids*, 1973, **10**, 37.
16. E. Oldfield, D. Chapman, and W. Derbyshire, *FEBS Lett.*, 1971, **16**, 102.
17. J. H. Davis, in *Cholesterol in Membrane Models*, ed. L. Finegold, CRC Press, Boca Raton, FL, 1993, pp. 67–135.
18. M. R. Vist and J. H. Davis, *Biochemistry*, 1990, **29**, 451.
19. J. H. Davis, K. R. Jeffrey, M. Bloom, M. I. Valic, and T. P. Higgs, *Chem. Phys. Lett.*, 1976, **42**, 390.
20. R. Jacobs and E. Oldfield, *Biochemistry*, 1979, **18**, 3280.
21. J. Forbes, C. Husted, and E. Oldfield, *J. Am. Chem. Soc.*, 1988, **110**, 1059.
22. K. Weisz, G. Gröbner, C. Mayer, J. Stohrer, and G. Kothe, *Biochemistry*, 1992, **31**, 1100.
23. D. A. Johnson, C. F. Valenzuela, and R. Zidovetzki, *Biochem. Pharmacol.*, 1992, **44**, 769.
24. P. L. Yeagle, R. B. Martin, A. K. Lala, H.-K. Lin, and K. Bloch, *Proc. Natl. Acad. Sci. USA*, 1977, **74**, 4924.
25. J. R. Brainard and E. H. Cordes, *Biochemistry*, 1981, **20**, 4607.
26. C.-H. Huang, *Lipids*, 1977, **12**, 348.
27. B. DeKruyff, R. A. Demel, A. J. Slotboom, L. L. M. Van Deenen, and A. F. Rosenthal, *Biochim. Biophys. Acta*, 1973, **307**, 1.
28. E. J. Dufourc, E. J. Parish, S. Chitrakorn, and I. C. P. Smith, *Biochemistry*, 1984, **23**, 6062.
29. R. Murari, M. P. Murari, and W. J. Baumann, *Biochemistry*, 1986, **25**, 1062.
30. M.-A. Krajewski-Bertrand, A. Milon, Y. Nakatani, and G. Ourisson, *Biochim. Biophys. Acta*, 1992, **1105**, 213.
31. E. Oldfield, M. Meadows, D. Rice, and R. Jacobs, *Biochemistry*, 1978, **17**, 2727.
32. R. Bittman, in *Cholesterol in Membrane Models*, ed. L. Finegold, CRC Press, Boca Raton, FL, 1993, pp. 45–65.
33. S. Lund-Katz, H. M. Laboda, L. R. McLean, and M. C. Phillips, *Biochemistry*, 1988, **27**, 3416.
34. L. J. Neuringer, B. Sears, F. B. Jungalwala, and E. K. Shriver, *FEBS Lett.*, 1979, **104**, 173.
35. X. Han and R. W. Gross, *Biochim. Biophys. Acta*, 1991, **1063**, 129.
36. H.-U. Gally, A. Seelig, and J. Seelig, *Hoppe-Seyler's Z. Physiol. Chem.*, 1976, **357**, 1447.
37. X. Chen, X. Han, and R. W. Gross, *Biochim. Biophys. Acta*, 1993, **1149**, 241.
38. R. Bittman, S. Clejan, S. Lund-Katz, and M. C. Phillips, *Biochim. Biophys. Acta*, 1984, **772**, 117.
39. J. Higinbotham, P. H. Beswick, R. J. Malcolmson, D. Reed, J. A. Parkinson, and I. H. Sadler, *Chem. Phys. Lipids*, 1993, **66**, 1.
40. J. Forbes, J. Bowers, X. Shan, L. Moran, E. Oldfield, and M. A. Moscarello, *J. Chem. Soc., Faraday Trans. 1*, 1988, **84**, 3821.
41. M. B. Sankaram and T. E. Thompson, *Proc. Natl. Acad. Sci. USA*, 1991, **88**, 8686.
42. A. Blume and R. G. Griffin, *Biochemistry*, 1982, **21**, 6230.
43. J. C. Huschilt, R. S. Hodges, and J. H. Davis, *Biochemistry*, 1985, **24**, 1377.
44. H. Reinl, T. Brumm, and T. M. Bayerl, *Biophys. J.*, 1992, **61**, 1025.
45. J. L. Thewalt and M. Bloom, *Biophys. J.*, 1992, **63**, 1176.
46. F. M. Linseisen, J. L. Thewalt, M. Bloom, and T. M. Bayerl, *Chem. Phys. Lipids*, 1993, **65**, 141.
47. H. L. Scott, in *Cholesterol in Membrane Models*, ed. L. Finegold, CRC Press, Boca Raton, FL, 1993, pp. 197–221.
48. M. J. Zuckermann, J. H. Ipsen, and O. G. Mouritsen, in *Cholesterol in Membrane Models*, ed. L. Finegold, CRC Press, Boca Raton, FL, 1993, pp. 223–257.
49. T. M. Bayerl and E. Sackmann, in *Cholesterol in Membrane Models*, ed. L. Finegold, CRC Press, Boca Raton, Fl, 1993, pp. 13–43.
50. Y.-K. Shin and J. H. Freed, *Biophys. J.*, 1989, **56**, 1093.
51. T.-H. Huang, C. W. B. Lee, S. K. Das Gupta, A. Blume, and R. G. Griffin, *Biochemistry*, 1993, **32**, 13277.
52. P. F. F. Almeida, W. L. C. Vaz, and T. E. Thompson, *Biophys. J.*, 1993, **64**, 399.
53. M. B. Sankaram and T. E. Thompson, *Biochemistry*, 1990, **29**, 10670.

Biographical Sketches

Kevin M. W. Keough. *b* 1943. B.Sc., 1965, M.Sc., 1967, Ph.D., 1971, biochemistry, University of Toronto, Canada. Postdoctoral work at the University of Sheffield (with Dennis Chapman, F.R.S.). Successively assistant professor, associate professor, professor and Head of Biochemistry; currently Vice-President (Research), Memorial University of Newfoundland. Approx. 80 publications. Current research: lipid–protein, and lipid–cholesterol interactions in membranes and pulmonary surfactant.

Michael R. Morrow. *b* 1955. B.Sc., 1977, M.Sc., 1979, Ph.D., 1983, (Supervised by Walter Hardy) physics, University of British Columbia, Canada. Postdoctoral work at the University of Guelph (with James H. Davis). Successively assistant professor, associate professor, Memorial University of Newfoundland. Approx. 30 publications. Current research: solid-state NMR studies of phase behavior and interactions in membranes and pulmonary surfactant.

Robert Bittman. *b* 1942. B.S., 1962, Ph.D., 1965 (supervisor Andrew J. Streitwieser, Jr.), chemistry, University of California at Berkeley, USA. Postdoctoral work at Max-Planck-Institute for Biophysical Chemistry, Göttingen, Germany (with Manfred Eigen). Successively assistant professor, associate professor, professor, and distinguished professor, Queens College of The City University of New York, Flushing, NY, USA, 1966–present. Approx. 200 publications. Current research specialties: lipid–lipid interactions, sterol movement between membranes, new methods for chemical synthesis of glycero- and sphingolipids, lipids as second messengers, antitumor phospholipids.

Polysaccharide Solid State NMR

Hazime Saitô

Himeji Institute of Technology, Kamigori, Hyogo, Japan

1	Introduction	1
2	Conformation-Dependent ^{13}C Chemical Shifts	1
3	Secondary Structure of Gel-Forming Polysaccharides	1
4	Dynamic Aspects of Polysaccharide Gels	4
5	Concluding Remarks	5
6	Related Article	5
7	References	5

1 INTRODUCTION

A variety of polysaccharides are known to play essential roles as the structural components in the cell walls of plant and microorganisms, in insect cuticles, as storage polysaccharides, as matrix components in animal fluids and connective tissues, and as molecular signals for biological recognition. These functions are strongly related to their respective secondary structures, taking in the solid, gel, or solution states. Nevertheless, it is not easy to reveal the secondary structures of these polysaccharides either in the solid or in solution, as compared with those of globular proteins or nucleic acids which have been extensively studied by X-ray diffraction or multidimensional NMR spectroscopy. This is mainly because the crystallization of polysaccharides for an X-ray diffraction study is extremely difficult and the number of interresidual nuclear Overhauser enhancements in solution NMR is not sufficient for the purpose of model building. Moreover, it should be emphasized that the secondary structures of polysaccharides are generally very heterogeneous, especially in the gel state in which several different kinds of domain are simultaneously present.

Conformational elucidation by solid state NMR spectroscopy as a means for in situ structural analysis is especially important for a number of polysaccharides, because they are in many instances not soluble in mild solvent systems (such as aqueous solution) and other spectroscopic means for this purpose are virtually unavailable. It should be anticipated that solubilization in either alkaline or DMSO solution can usually be associated with a conformational change. In addition, too much reliance should not be laid on a secondary structure as deduced by fiber X-ray diffraction studies, because any physical treatment to improve the crystallinity (such as thermal treatment) may cause a conformational change. There remains an ambiguity about secondary structure owing to the limited number of diffraction data available. In this respect solid state NMR is invaluable as a complement to fiber X-ray diffraction as well as a means to gain insight into the dynamic aspects of polysaccharides, especially in relation to a study of gel networks.

2 CONFORMATION-DEPENDENT ^{13}C CHEMICAL SHIFTS

We have previously shown that the ^{13}C chemical shifts of a variety of molecular systems, including polypeptides and proteins, carbohydrates and polysaccharides, ionophores, etc., vary by as much as 8 ppm depending on their conformations.[1,2] In principle, such a conformation-dependent change in polysaccharides is observable either in the solid state or in solution when rapid conformational isomerism about the glycosidic linkages is frozen. However, there are a limited number of examples which exhibit the existence of conformation-dependent ^{13}C chemical shifts: ^{13}C chemical shifts recorded in solution are generally identical, within experimental error, to those observed in the solid state, as in higher molecular weight (1 → 3)-β-D-glucans and α-cycloamylose. The situation arose when rapid rotational motion about the glycosidic linkages was frozen (even in solution) due to the formation of cross-links or to the presence of cyclic structures for the (1 → 3)-β-D-glucans and α-cycloamylose, respectively.

The existence of conformation-dependent ^{13}C chemical shifts, however, is more clearly visualized by an examination of the ^{13}C chemical shifts of solid polysaccharides which have a variety of polymorphs. It is also useful to examine the ^{13}C NMR spectra of crystalline cycloamyloses enclosing a variety of guest molecules, because detailed conformational data for such complexes are available from single crystal X-ray diffraction studies. We previously demonstrated that the C-1 and C-4 ^{13}C chemical shifts of crystalline cycloamyloses enclosing various types of guest molecules could be well related to a set of torsion angles about the glycosidic linkages (ϕ, ψ).[3] Later, similar but slightly different relationships[4,5] were proposed. Therefore, conformational elucidation by means of solid state NMR is feasible on the basis of the concept of conformation-dependent ^{13}C chemical shifts.[1,2]

3 SECONDARY STRUCTURE OF GEL-FORMING POLYSACCHARIDES

It is well recognized that cross-links of polysaccharide gels are formed via several degrees of molecular association of the ordered polysaccharide chains. It is thus important to obtain the detailed in situ secondary structure of various polymorphs of polysaccharides by solid state NMR as reference data useful for conformational studies of gel samples.

3.1 (1 → 3)-β-D-Glucans

As an illustrative example, we first demonstrate comparative ^{13}C NMR studies on linear and branched (1 → 3)-β-D-glucans isolated from bacteria and reserve polysaccharide, and fungi (edible mushrooms), respectively.[6,7] Curdlan [(**1**), Figure 1], a bacterial linear (1 → 3)-β-D-glucan from *Alcaligenes faecalis* (Wako Pure Chemicals, Osaka, Japan) is able to form a firm elastic gel when its aqueous suspension is heated at a temperature above 54 °C. On the other hand, several branched glucans such as lentinan (Ajinomoto Co. Japan), schizophyllan (Taito, Japan), etc. (**2**) from various types of mushrooms are able to form gels of a rather brittle type at higher

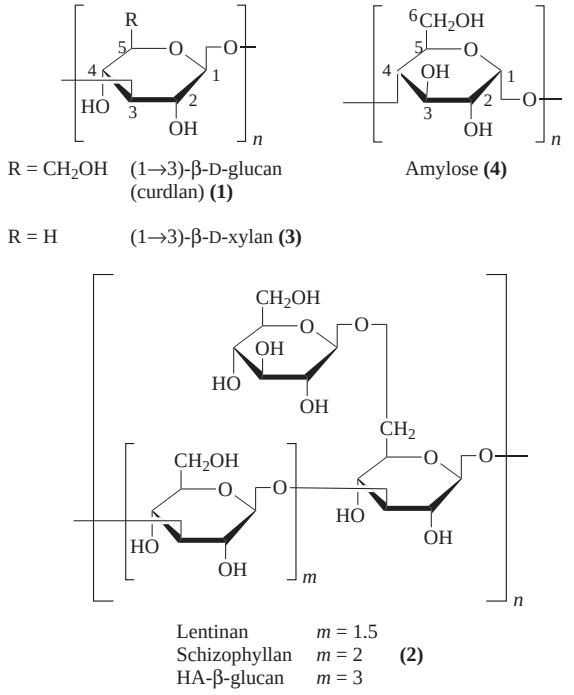

Figure 1 Primary structures of a variety of polysaccharides

concentrations (>10%). Such a difference in macroscopic texture of these gel samples is closely related to a different architecture of the network structure between the two types of gels, as will be discussed later in more detail. In fact, rather sharp ^{13}C NMR signals (about 40% of the total NMR spectrum) are visible from curdlan gel using conventional liquid state NMR with broadband decoupling.[8] The C-1 and C-3 ^{13}C chemical shifts from the elastic gel were displaced to high frequency by 2.8 and 3.2 ppm, respectively, as compared with those of a lower molecular weight glucan with a random coil conformation. As pointed out in the previous section, such a conformation-dependent ^{13}C chemical shift of (1 → 3)-β-D-glucans arises from the fact that the rotational motions of the polysaccharide backbone about the glycosidic linkages are frozen due to the formation of an ordered helical conformation. The polysaccharide chain in this case must be a *single* helical species in spite of the existence of a triple helical model, based on fiber X-ray diffraction studies,[9,10] because the molecular chain is found to be rather flexible, as demonstrated by relaxation parameters such as the spin–lattice relaxation times and the NOE.[6] In contrast, all of the ^{13}C NMR signals of the branched glucans were found to be completely suppressed in the gel state as recorded on a traditional solution state NMR spectrometer.[11] This finding implies that the molecular conformations of these two types of polysaccharides are different from each other. It is essential for this reason to examine the solid state ^{13}C NMR spectra of various types of polymorphs in (1 → 3)-β-D-glucans for use as reference data.

Figure 2 illustrates the ^{13}C NMR spectrum of a hydrated sample of curdlan (b) obtained by placing it in a desiccator at 96% relative humidity for 8 h compared with that of the anhydrous powder as received from the manufacturer (a)[12] and annealed curdlan[13] prepared by heating an aqueous suspension at 150 °C followed by slow cooling (c). It is noteworthy

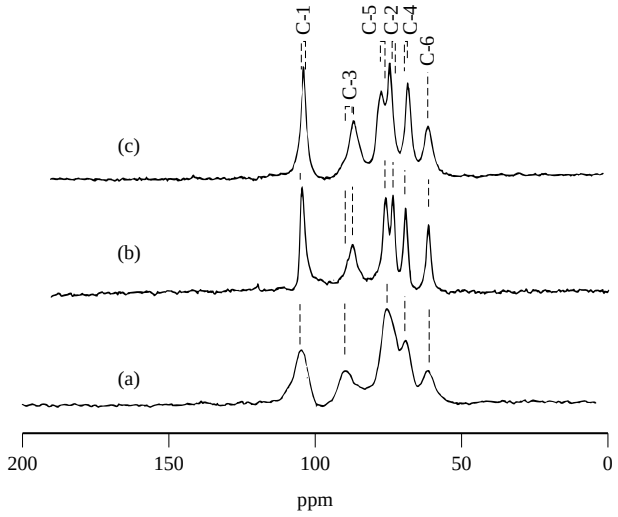

Figure 2 ^{13}C CP MAS NMR spectra of curdlan in the solid state: (a) anhydrous; (b) hydrated; and (c) annealed[12]

that the ^{13}C NMR linewidths of the hydrated sample are considerably narrowed in comparison to those of the anhydrous sample and are comparable to those of the annealed curdlan [Figure 2(c)]. The C-3 ^{13}C chemical shift of curdlan hydrate is displaced to low frequency by 2.5 ppm with respect to that of the anhydrous state. Distinction between the hydrated and annealed curdlan is straightforward by means of the C-5 chemical shifts (75.8 ppm and 77.5 ppm for the former and latter, respectively) and the peak separation between the C-5 and C-2 signals (2.0 and 3.2 ppm, respectively). Lyophilized curdlan from DMSO solution gave rise to narrower spectra but the peak positions were exactly the same as those for the anhydrous sample.[14] Annealed curdlan may be related straightforwardly to the triple-helix form on the basis of its powder X-ray diffraction by reference to previous fiber diffraction data.[9,10]

Hydrated curdlan gave rise to ^{13}C NMR signals which were identical to those observed in the gel state. Hence, this form was ascribed to the flexible single helix already mentioned. Consistent with this view, a recent fiber X-ray diffraction[15] study showed the presence of a 6/1 single helix conformation for the curdlan gel prepared by heating an aqueous suspension at 70 °C for 10 min, although Fulton and Atkins previously ascribed a similar diffraction pattern to a 7/1 triple helix conformation.[16] It is surprising that the C-1 and C-3 chemical shifts of the single helical curdlan hydrate are very similar to those of the triple helical annealed curdlan, although distinction between the two forms is possible from the C-2 and C-5 peaks. This is because the two pairs of the torsion angles about the glycosidic linkages (ϕ, ψ) are very similar, as revealed by X-ray diffraction studies.[10,15] The anhydrous form, on the other hand, is ascribed to a single-chain form whose torsion angles vary to some extent from those of the single helix form owing to loss of hydrated water molecules (which are essential for stability in the single helix conformation). In a similar manner, DMSO molecules in the single-chain form are complexed with the polysaccharide chains (ca. 0.5 DMSO molecules per residue)[14] and may play an important role for the conformational stabilization, although they are readily replaced by water molecules on hydration

to yield the single helix form.[12,14] This situation is very similar to the case of DMSO molecules complexed with V-amylose, which are very easily replaced by water molecules by hydration, leading to the conversion to the B- form, as will be described later.

Linear (1 → 3)-β-D-glucans of low molecular weight oligomers such as laminariheptaose and acid-degraded curdlan with a degree of polymerisation (*DP*) of 14 can adopt neither the single helix nor triple helix form, as judged from the characteristic ^{13}C signals.[12,13,17] Interestingly, glucans of either short-chain (*DP* < 14) or longer-chain species are incapable of forming triple helices by lyophilization from aqueous solution. Laminaran from *Laminaria* species (*DP* 39) turned out to be able to exist in the triple helix form by lyophilization from aqueous solution, although this polysaccharide adopts a random coil form in aqueous solution.[13] In contrast, triple helix conformations were achieved when high molecular weight branched (1 → 3)-β-D-glucans such as schizophyllan or HA-β-glucan were lyophilized from their aqueous solution, although the single-chain form was available from an aqueous solution of lentinan.[17] It is now clear that the obvious preponderance of the single helix conformation for the linear (1 → 3)-β-D-glucans of high molecular weight arises mainly from insufficient hydration. Once this molecule is completely dissolved in an aqueous solution at a temperature above 150 °C, it is able to refold to yield the triple helical conformation when cooled slowly to ambient temperature.[13] It is thus expected that such a conversion is inefficient when heated samples are cooled rapidly (at most 50%).[13] It is noteworthy that conversion of the single helix to the triple helix by annealing at 150 °C is accompanied by fragmentation of the polymer chain due to thermal degradation from an initial *DP* of 3930 to a final *DP* of 110.[18] Such an annealing is not necessary in the case of the branched glucans, because these molecules are well hydrated in aqueous media at ambient temperature. It appears that rather weak intermolecular association of the branched glucan (as compared with that of the linear glucan) arises from the presence of a pendant glucose moiety (Figure 1) for every two or three glucose residues. This is the reason why the branched (1 → 3)-β-D-glucans and laminaran have a preponderance of the triple helix over the single helix conformations.

In general, several types of polysaccharides including (1 → 3)-β-D-glucans can acquire the double or triple stranded form as the most energetically stable, as expected from a molecular mechanics calculation.[19] Nevertheless, any given polysaccharide sample does not always take the energetically most stable conformation, because of different sample histories. Distinction between the single and multiple helical chains, however, is not always straightforward to obtain by X-ray diffraction, because distinguishing multiple stranded coaxial helices and nested single helices is one of the most difficult problems encountered in interpreting fiber diffraction data.[20] It should be emphasized that this problem is readily solved by examination of the conversion diagram of these polysaccharides after a series of physical treatments, as summarized in Figure 3. The present approach can be further extended to any types of polysaccharide. In fact, a very similar conversion diagram was recently obtained for (1 → 3)-β-D-xylan (**3**), which is also found to acquire the three above-mentioned types of conformation, as may be expected from its structural similarity with (1 → 3)-β-D-glucans.[21] The

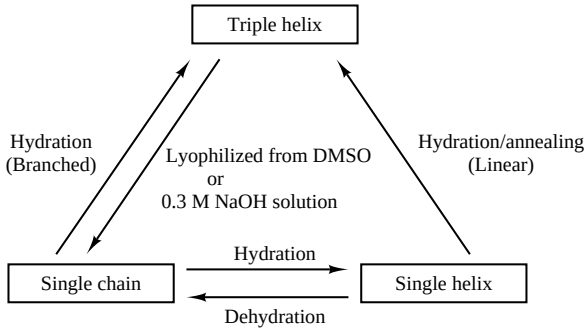

Figure 3 Conversion diagram for (1 → 3)-β-D-glucans by various physical treatments (based on Saitô et al.[12,13])

triple helical conformation was initially proposed for (1 → 3)-β-D-xylan[22] and then adopted for (1 → 3)-β-D-glucan, because the C-6 hydroxymethyl group of the latter is located outside the helical chains. It turned out that the triple helix conformation of the former is more stable than that of the latter because of the greater hydrophobic character in the polymer chain and it cannot be readily converted to the single chain form even if dissolved in DMSO. This type of conversion was made possible by dissolution of the sample in aqueous zinc chloride solution in place of the more common DMSO solution.[21]

3.2 Amylose and Starch

Amylose (**4**) has a common feature with (1 → 3)-β-D-glucans as viewed from the presence of the single helical conformation, which is stabilized by DMSO molecules, and also from its gel-forming ability. Amylose and starch are known to have the following four kinds of polymorphs: V-, A-, B-, and C-forms.[23,24] The V form exists as a complex with a variety of small organic molecules and has a left-handed single helical conformation. The A- and B-forms are found in cereal and tuber starches, respectively, and can be distinguished by the splittings of the C-1 peaks as triplet and doublet peaks, respectively.[25–27] In contrast, V-amylose gives rise to single lines.[28] The C-4 peak of V-amylose is particularly displaced to high frequency by ca. 4–5 ppm from that of the B form. These amylose polymorphs can also be mutually interconverted by a series of physical treatments in a similar manner to (1 → 3)-β-D-glucan, as demonstrated for amylose of low molecular weight (*DP* 17, Figure 4).[29] Obviously, anhydrous amylose lyophilized from a DMSO solution [Figure 4(b)] gave rise to a spectral pattern of the V form. The anhydrous powder as received, however, has an amorphous structure distorted from the B form, as judged from the broad envelope of the ^{13}C NMR signal in the C-1 region and the absence of the C-4 peak at 81 ppm [Figure 4(a)]. Furthermore, hydration of the anhydrous powder or V-amylose resulted in conversion to the B-amylose as judged from the ^{13}C NMR spectra [Figure 4(c)]. It is interesting that such conversion occurs efficiently for amylose of either low (*DP* 17) or high (*DP* 1000) molecular weight but was incomplete for amylose of intermediate molecular weight (*DP* 100).[29]

The secondary structure of the B form was initially considered to be the single helical conformation,[30] since the conversion of the V- to the B-form amylose takes place on humidification.[31] Later, however, the structure was refined as

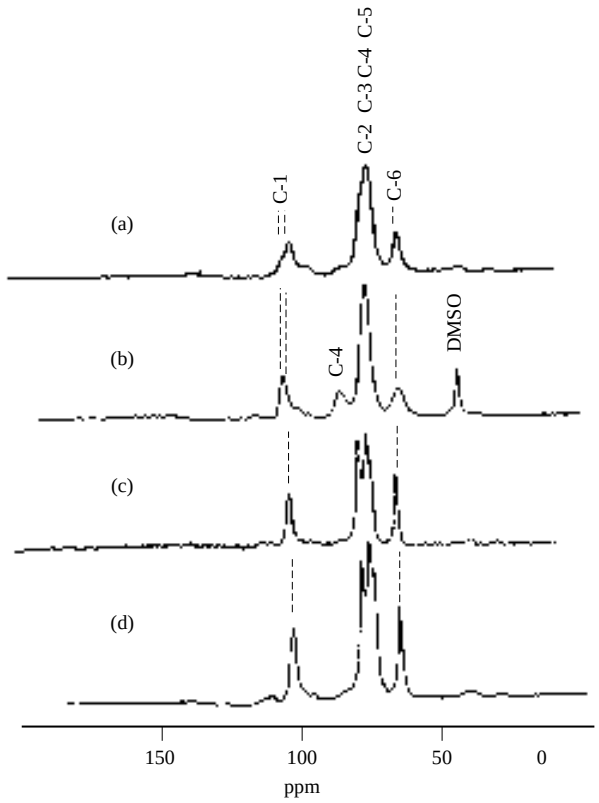

Figure 4 ^{13}C CP MAS NMR spectra of low molecular weight amylose (*DP* 17): (a) anhydrous powder; (b) anhydrous lyophilized sample from DMSO solution; (c) hydrated amylose power; and (d) hydrated iodine complex[29]

a right-handed double helix in an antiparallel fashion.[32] The handedness of the double helix form, however, was recently revised as a left-handed double helix.[33] Nevertheless, it is hardly likely that simple humidification of amylose by placing it in a desiccator at a relative humidity of 96% causes such a drastic conformational change. In this connection, it is crucially important to clarify whether the secondary structure of B-amylose is a left-handed single helix as suggested from solid state NMR or a left-handed double helix as suggested from fiber X-ray diffraction study.

It was expected that ^{2}H NMR spectra of ^2H_2O or DMSO-d_6 complexed to amylose by forming the B- or V-form would be split into a doublet pattern, with the separation of peaks being about 100–200 kHz and 40 kHz (with C_3 rotation of the methyl group), respectively, if they are tightly bound to the polymer chains (static). It emerged, however, that only a singlet was visible as a result of rapid isotropic averaging of the quadrupole interaction in the solid state, with correlation times on the order of 10^{-6} s. The correlation times of isotropic tumbling of ^2H_2O and DMSO-d_6 as estimated from ^{2}H spin–lattice relaxation times are found to be in the vicinity of the T_1 minimum and on the high-temperature side of the T_1 minimum, respectively.[29]

4 DYNAMIC ASPECTS OF POLYSACCHARIDE GELS

Network structures of gel samples should be highly heterogeneous from the conformational and dynamic point of view. Any single NMR measurement, however, does not give rise to such information, because the correlation times of the molecular motions may be broadly distributed from the liquid- to solid-like domains. We have already demonstrated that ^{13}C NMR signals from the liquid-like domains are easily visible with a conventional solution state spectrometer but those of the solid-like domains are not.[5,6] It is therefore necessary to record NMR signals from these solid-like domains in order to gain some insight into the gel structure and dynamics. It is accordingly a major advantage of the NMR approach that it is able to select a particular domain from a variety of motionally different domains.

We have recorded ^{13}C NMR spectra of curdlan gels (Figure 5) by various methods including broadband decoupling for the liquid-like domain as discussed above (b), high-power dipolar decoupling with magic angle spinning (MAS) for intermediate domains between the liquid- and solid-like domains (c), and cross-polarization magic angle spinning (CP MAS) for the solid-like domains (d), and have compared these with the ^{13}C NMR spectrum of hydrated curdlan (a).[34] Such comparison indicated that the single helix form is dominant for all of the motionally different domains of an elastic curdlan gel, although a low intensity peak arising from the contribution from the triple helix is visible in the solid-like domains as shown by the arrowed peak in the CP MAS NMR spectrum. It is worthwhile to relate here the present view of the gel structure with the data for gel strength as a function of heating temperature:[35] the gel strength is almost the same at temperatures between 60–80 °C (low-set gel) and thereafter increases with heating temperature together with the development of turbidity and shrinkage of the gel (high-set gel). The first step of gelation thus corresponds to the formation of pseudo cross-links by hydrophobic association of

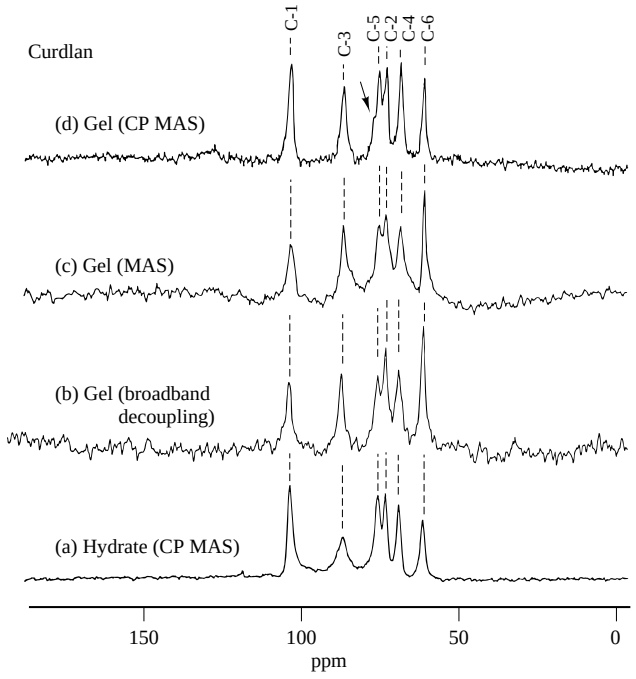

Figure 5 ^{13}C NMR spectra of curdlan gel (b–d) and curdlan hydrate (a) recorded by various types of NMR measurements: (a) and (d) by CP MAS; (b) by broadband decoupling; and (c) by MAS experiments[34]

the single helical chain. The increased gel strength in the high-set gel is well explained in terms of an increased proportion of the triple helical conformation.[5,6]

On the other hand, we found that ^{13}C NMR spectra of branched glucans such as lentinan, schizophyllan, and HA-β-glucan exhibited characteristic peaks of the triple helix conformation.[34] As pointed out, such a preponderance of the triple helix forms resulted in the complete absence of the peaks from the liquid-like domains.[5,6] In this connection, Yanaki and co-workers[36] showed that the triple helical chain of (1 → 3)-β-D-glucans is stiffer than that of native collagen, as manifested from the measurements of persistent chain length for schizophyllan (2000 ± 300 Å). This means that the resulting slow tumbling motion of the stiff rod-like triple helices is not sufficient to average out the dipolar or chemical shift anisotropy interactions in the gel state. Thus, it follows that the major gelation mechanism for the branched (1 → 3)-β-D-glucans proceeds from partial association of the triple helical chains. It appears that the absence of the flexible molecular chain is consistent with the property of a brittle gel. Here we point out that the linear and branched (1 → 3)-β-D-glucans so far discussed are involved in a variety of host-defence biological responses such as antitumor activity, activation of the coagulation system of horseshoe crab amebocyte lysate (LAL), etc. It is interesting that such biological response is initiated by recognition of the molecular chains of the single helical conformations.[18,37,38]

Gidley[39] showed that amylose gel exhibits two kinds of ^{13}C NMR signals: B type signals from motionally restricted regions as recorded by the CP MAS technique and signals identical to those found in aqueous solution. Obviously the latter signals can be ascribed to the presence of a mobile region (liquid-like domain) in the network whose conformation is random coil. The former peaks are naturally ascribed to the solid-like domain with cross-links, either consisting of double helical junction zones,[39] or aggregated regions of the single helical chains[29] as discussed in the previous section. To date, two different views have been presented for the gelation mechanism of amylose: Miles et al.[40] have suggested that gels are formed upon cooling molecularly entangled solutions as a result of phase separation of the polymer-rich phase, whereas Wu and Sarko[33] proposed that gelation occurs through cross-linking by double helical junction zones. Recently, we measured the ^{13}C spin−lattice relaxation times of the liquid- and solid-like domains of starch gel by means of dipolar decoupled single pulse MAS and CP MAS, respectively.[41] It turned out that the T_1 of the C-6 carbon is 0.16 s and 2.1 s for the former and latter, respectively. It appears that such a long T_1 for the latter as compared with that of other types of swollen gels (<0.5 s) arises mainly from motionally restricted crystalline portions consisting of aggregated molecular species such as single helical chains. In any case, it is crucially important to distinguish single helical chains from double helical chains by means of solid state NMR spectroscopy.

5 CONCLUDING REMARKS

It has been demonstrated that the solid state NMR approach is a very powerful means of clarifying conformational features of a variety of polysaccharides in an empirical manner based on the concept of the conformation-dependent displacements of ^{13}C chemical shifts. Careful examination of an NMR-based conversion diagram by a series of physical treatments has proved to be a very useful means for the distinction of single-chain/multiple helices. The application of a modern methodology is urgently required to determine the secondary structure in a nonempirical manner, such as rotational echo double resonance or rotational resonance as currently being applied to a variety of peptides or proteins in the solid state.

6 RELATED ARTICLES

Solid Biopolymers.

7 REFERENCES

1. H. Saitô, *Magn. Reson. Chem.*, 1986, **24**, 835.
2. H. Saitô and I. Ando, *Annu. Rep. NMR Spectrosc.*, 1989, **21**, 209.
3. H. Saitô, G. Izumi, T. Mamizuka, S. Suzuki, and R. Tabeta, *J. Chem. Soc., Chem. Commun.*, 1982, 1386.
4. J. A. Ripmeester, *J. Inclusion Phenom.*, 1985, **4**, 179.
5. R. G. Veregin, C. A. Fyfe, R. H. Marchessault, and M. G. Taylor, *Carbohydr. Res.*, 1987, **160**, 41.
6. H. Saitô, *ACS Symp. Ser.*, 1981, **150**, 125.
7. H. Saitô, *ACS Symp. Ser.*, 1992, **489**, 296.
8. H. Saitô, T. Ohki, and T. Sasaki, *Biochemistry*, 1977, **16**, 908.
9. R. H. Marchessault, Y. Deslandes, K. Ogawa, and P. R. Sundarajan, *Can. J. Chem.*, 1977, **55**, 300.
10. C. T. Chuah, A. Sarko, Y. Deslandes, and R. H. Marchessault, *Macromolecules*, 1983, **16**, 1375.
11. H. Saitô, T. Ohki, and T. Sasaki, *Carbohydr. Res.*, 1979, **74**, 227.
12. H. Saitô, M. Yokoi, and Y. Yoshioka, *Macromolecules*, 1989, **22**, 3892.
13. H. Saitô, R. Tabeta, M. Yokoi, and T. Erata, *Bull. Chem. Soc. Jpn.*, 1987, **60**, 4259.
14. H. Saitô and M. Yokoi, *Bull. Chem. Soc. Jpn.*, 1989, **62**, 392.
15. K. Okuyama, A. Otsubo, Y. Fukuzawa, M. Ozawa, T. Harada, and N. Kasai, *J. Carbohyr. Chem.*, 1991, **10**, 645.
16. W. S. Fulton and E. D. T. Atkins, *ACS Symp. Ser.*, 1980, **141**, 385.
17. H. Saitô, R. Tabeta, T. Sasaki, and Y. Yoshioka, *Bull. Chem. Soc. Jpn.*, 1986, **59**, 2093.
18. Y. Yoshioka, N. Uehara, and H. Saitô, *Chem. Pharm. Bull.*, 1992, **40**, 1221.
19. T. L. Bluhm and A. Sarko, *Can. J. Chem.*, 1977, **55**, 293.
20. T. A. Foord and E. D. T. Atkins, *Biopolymers*, 1987, **28**, 1345.
21. H. Saitô, J. Yamada, Y. Yoshioka, Y. Shibata and T. Erata, *Biopolymers*, 1991, **31**, 933.
22. E. D. T. Atkins, K. D. Parker, and R. D. Preston, *Proc. R. Soc. London, Ser. B.*, 1969, **173**, 209.
23. A. Sarko and P. Zugenmaier, *ACS Symp. Ser.*, 1980, **141**, 459.
24. D. French, *Starch: Chemistry and Technology*, ed. R. L. Whistler and E. D. Pascal, 2nd edn., Academic Press, New York, 1984, p. 183.
25. R. P. Veregin, C. A. Fyfe, R. H. Marchessault, and M. G. Taylor, *Macromolecules*, 1986, **19**, 1030.
26. M. J. Gidley and S. M. Bociek, *J. Am. Chem. Soc.*, 1985, **107**, 7040.
27. F. Horii, H. Yamamoto, A. Hirai, and R. Kitamaru, *Carbohydr. Res.*, 1987, **160**, 29.

28. H. Saitô and R. Tabeta, *Chem. Lett.*, 1981, 713.
29. H. Saitô, J. Yamada, T. Yukumoto, H. Yajima, and R. Endo, *Bull. Chem. Soc. Jpn.*, 1991, **64**, 3528.
30. J. B. Blackwell, A. Sarko, and R. H. Marchessault, *J. Mol. Biol.*, 1969, **42**, 379.
31. F. R. Senti and L. P. Witnauer, *J. Am. Chem. Soc.*, 1948, **70**, 1438.
32. H. C. H. Wu and A. Sarko, *Carbohydr. Res.*, 1978, **61**, 7.
33. A. Imberty and S. Perez, *Biopolymers*, 1988, **27**, 1205.
34. H. Saitô, Y. Yoshioka, M. Yokoi, and J. Yamada, *Biopolymers*, 1990, **29**, 1689.
35. T. Harada, *ACS Symp. Ser.*, 1977, **45**, 265.
36. T. Yanaki, T. Norisue, and H. Fujita, *Macromolecules*, 1980, **13**, 1462.
37. H. Saitô, Y. Yoshioka, N. Uehara, J. Aketagawa, S. Tanaka, and Y. Shibata, *Carbohydr. Res.*, 1991, **217**, 181.
38. J. Aketagawa, S. Tanaka, H. Tamura, Y. Shibata, and H. Saito, *J. Biochem (Tokyo)*, 1993, **113**, 683.
39. M. J. Gidley, *Macromolecules*, 1989, **22**, 351.
40. M. J. Miles, V. J. Morris, and S. G. Ring, *Carbohydr. Res.*, 1985, **135**, 257.
41. H. Saitô, H. Shimizu, T. Sakagami, A. Tuzi, and A. Naito, in *Magnetic Resonance in Food Science*, ed. P. S. Bolton, I. Delgadillo, A. M. Gil, and G. A. Webb, Royal Society of Chemistry, London, 1995, p. 257.

Biographical Sketch

Hazime Saitô. *b* 1937. B.S., 1961, Ph.D., 1968 (supervisor Teijiro Yonezawa), applied chemistry, Kyoto University, Japan. Postdoctoral work at The National Research Council, Canada (with Ian C. P. Smith). Research chemist, Toray Industries, 1963–75, section head, Biophysics Division, National Cancer Center Research Institute, Tokyo, 1975–90, Professor, Himeji Institute of Technology, 1990–present. Approx. 200 publications. Current research specialty: solid state NMR and its application to biophysical chemistry/structural biology.

Proton Chemical Shift Measurements in Biological Solids

Ann McDermott
Columbia University, New York, NY, USA

and

Cynthia F. Ridenour
Otsuka Electronics, Inc., Fort Collins, CO, USA

1 Introduction 1
2 Approaches to Narrowing Proton Resonances 1
3 Information From the Lineshape 2
4 Hydrogen Bonding: Chemical Shift and Hydrogen Exchange 2
5 2D Correlation with Carbon 3
6 Conclusions 4
7 Related Articles 4
8 References 4

1 INTRODUCTION

There are strong motivations for pursuing solid state NMR of protons, namely the inherently good sensitivity and the possibilities for study of hydrogen bonding via chemical shifts. Despite its enormous potential, solid state NMR of protons in biomolecules has had surprisingly few applications in comparison with other high-resolution NMR methods for studying biological macromolecules. In this article we discuss experimental solutions to the problem of spectral resolution and the analysis of spectra for chemical information. Although essentially all of the successful measurements of chemical shift and shift anisotropy were obtained on simple crystalline solids we also discuss possible future applications in structural biology.

2 APPROACHES TO NARROWING PROTON RESONANCES

Producing narrow proton linewidths is the most significant challenge to solid state proton NMR. For the case of a typical rigid organic solid, ^{1}H NMR spectra obtained without sample spinning or with moderate speed sample spinning show very broad lines, on the order of a few tens of kilohertz. Narrowing of these lines by the technique of combined rotation and multiple pulse spectroscopy, CRAMPS,[1–4] or by dilution of the protons[5–7] has been demonstrated in crystalline small molecules. These methods have provided the means to study hydrogen bonding and proton exchange in solids, but practically no high-resolution solid state ^{1}H NMR applications to macromolecules have been reported. In contrast to rigid organic solids, solids with high molecular mobility such as lipids and membrane structures often provide well-resolved ^{1}H NMR simply by Bloch decay acquisition with slow magic angle spinning.[8–11]

The CRAMPS method is the most common experimental approach to achieving high-resolution ^{1}H spectra of materials in the solid state. It has been used in interesting applications of chemical analysis,[12–15] and probably has the most potential for general studies of amorphous biological solids. Proton NMR linewidths obtained by CRAMPS or magnetic dilution can be as low as 0.2 ppm, which could be sufficient to separate the typical functional groups found in a protein but of course would never be adequate for site-specific assignments of even a small peptide. Highly crystalline compounds typically produce the narrowest lines, while compounds with some amorphous character produce somewhat broader lines.[14] Macroscopic susceptibility due to the shape of the microcrystal presumably contributes to the linewidth, and specific anisotropic bulk susceptibility effects in aromatic systems have been discussed.[14]

An alternative method that has been little pursued to date is the detection of deuterons during magic angle spinning (MAS). With this approach resolution comparable to that of CRAMPS or dilution can often be obtained without special effort,[16,17] and spectral overlap can be avoided by utilizing selective labeling. Considerable spectral intensity is squandered into spinning sidebands, so application of methods to fold the sidebands together is important. On the other hand, the quadrupolar constants and dynamic information normally obtained from static ^{2}H NMR can be derived from the sideband patterns in these spectra. Several reports of cross polarization between deuterium and protons have appeared.[16,18]

In the following discussion we will focus more on CRAMPS than the other two approaches because of the much larger existing literature and the far fewer complications with sample preparation. We illustrate the typical appearance of CRAMPS spectra of simple organic biological solids with a series of CRAMPS spectra of amino acids and dipeptides in Figure 1; some of these samples have also been characterized by measurement of dilute protons[6] or by spinning ^{2}H spectra.[17] It is apparent from Figure 1 that the linewidths are significantly below 1 ppm in every case and the spectra allow resolution

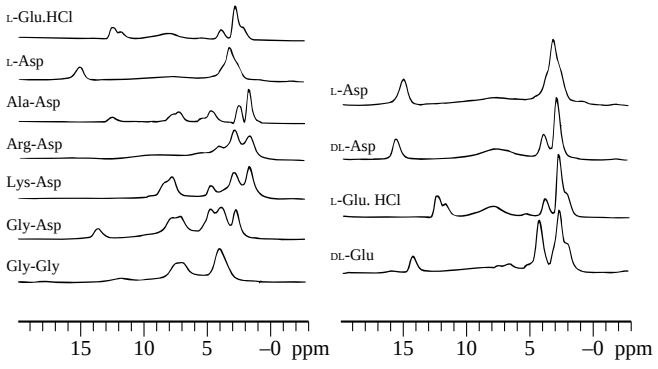

Figure 1 The 200 MHz BR-24 spectra of crystalline amino acids (as indicated). Pulse length was 1.3 μs with a τ value of 2.3–3.0 μs and spinning speeds of 1.0–1.5 kHz. Sixteen transients were accumulated. Glu = glutamic acid, Asp = aspartic acid, Ala = alanine, Arg = arginine, Lys = lysine, Gly = glycine

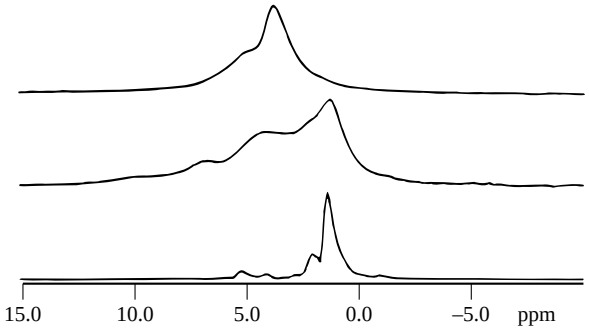

Figure 2 Typical CRAMPS spectra of biological molecules, measured at 187 MHz with the BR-24 pulse sequence.[19] Top: amylopectin; middle: γ-globulin; bottom: coconut oil. Spectra were acquired with MAS spinning speed of 1–2 kHz, pulse width = 1.0–1.2 μs, τ = 3.0 μs, repetition time 1.7 s

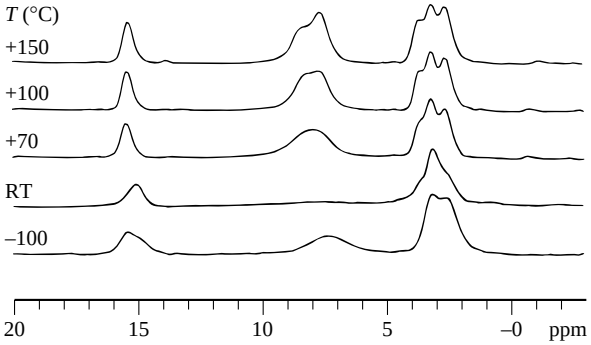

Figure 3 The 200 MHz BR-24 spectrum of l-aspartic acid at various temperatures. Note that the amine resonance at 7.7 ppm disappears near room temperature (RT) due to the microsecond correlation time for the amine's threefold hopping rate. This behavior is quite common for amine groups although the critical temperature is variable

of one chemical classification from another. For aliphatic or aromatic protons the chemical shifts are comparable to those known from solution state experiments, that is −1 to 2 ppm for methyl groups, 1–3 ppm for methylene, 3–5 ppm for methine, and 6–8 ppm for aromatic protons. Unlike solution spectroscopy, in solid state experiments observing acid and other exchangeable protons is possible, and in particular for the case of carboxylic acids the range in typical shifts is quite a lot broader than the linewidths. The amine and many of the other N–H functionalities are often around 7–8 ppm, while imidazole protons and structural water protons and carboxylic acids can be found at a broad range of shift values depending on hydrogen bonding, with strongly hydrogen-bonded groups being significantly deshielded (10–20 ppm). The chemical shifts and lineshapes for resonances in hydrogen bonding groups are discussed in detail in the following sections.

Typical ^{1}H CRAMPS spectra of other biological materials are also exhibited in Figure 2.[19] The carbohydrate spectrum (top) is dominated by methine and hydroxyl protons. The protein spectrum (middle) shows contributions from methyl, methylene, methine, amine, and other groups but is largely unresolved. A methylene resonance at 1.3 ppm dominates the lipid spectrum (bottom). As noted above, MAS-only spectra of lipids provide good ^{1}H resolution. Proton linewidths of lipids and highly mobile materials are often narrower in MAS-only spectra than in CRAMPS spectra[19] due to pulse imperfections in the multiple pulse sequence.

3 INFORMATION FROM THE LINESHAPE

All three detection methods show certain potentially confusing effects that deserve special comment. As has been reported previously[1,20] dynamic processes can interfere with the CRAMPS detection of groups undergoing motion if the correlation times are comparable to the pulse width, the multiple pulse cycle time, or to the sample spinning speed. This effect is often seen at room temperature in the form of missing amine resonances. Amine groups enact a three-site hopping motion on the microsecond timescale near room temperature since they have activated barriers in the range of 30 kJ mol^{-1}. This motion has been previously characterized by wideline ^{1}H T_1 measurements[21] but not by lineshape methods. Such amine lines that are broad or undetected near room temperature are readily detected at temperatures above 70 °C or below −100 °C in typical cases. Figure 3 shows variable temperature ^{1}H CRAMPS spectra of L-aspartic acid in which the amine line at 7.7 ppm illustrates this effect. Other effects on the lineshapes as a function of temperature are often observed, and analysis of these lineshapes by explicit simulation would be informative but has not yet been accomplished. Other than the amine rotation, common local motions in proteins rarely result in loss of signal because the rates are not on the microsecond timescale near room temperature. The ^{2}H MAS spectra exhibit lineshape and intensity effects for amines in a comparable temperature range: here the sampling rate of data collection is usually in the submegahertz range so again motions in the microsecond range interfere with detection. Proton spectra of magnetically diluted (deuterated) samples detected using Bloch decay during MAS would presumably show lineshape effects due to much slower motions, approximately on the millisecond timescale. Hence detection of sharp spectra due to the amine peaks is usually straightforward by ^{1}H MAS spectra. In all three methods interpretation of line intensities is quite unreliable because of all of these lineshape effects and/or the uncertainties involved in the extent of chemical incorporation of deuterium.

Protons that are directly bound to nitrogens often exhibit a lineshape that is obviously affected by the incomplete averaging of dipolar coupling to the ^{14}N resulting from the fact that the strongly quadrupolar ^{14}N is not in the high-field limit. These effects are most clear in lower field spectra[22] and can be seen in the 200 MHz high-temperature CRAMPS spectrum of aspartic acid (Figure 3) but also have been seen in well-resolved high field spectra.[5] They offer the possibility of characterization of the bonding geometry and the quadrupole parameters for the nitrogen from the ^{1}H lineshapes[22] as has been done for ^{13}C lineshapes for ^{13}C^{14}N pairs.[23–26]

4 HYDROGEN BONDING: CHEMICAL SHIFT AND HYDROGEN EXCHANGE

For protons that participate in hydrogen bonding, there are well-known correlations between the shielding of the ^{1}H isotropic chemical shift, the ^{1}H shielding anisotropy, the ^{2}H coupling constant, and hydrogen bonding distances[1,27–29] for

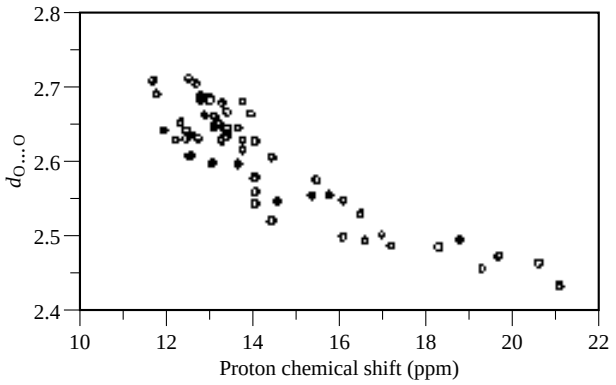

Figure 4 The ^{1}H chemical shifts of the amino acids in Figure 1 plotted against their O ... O distances as indicated by crystallography. Filled circles show proton chemical shifts derived from our data, as shown in Figure 1; crystal structures for these compounds can be found in Rao,[40] Eggleston and Hodgson,[41–43] Derissen et al.,[44] Bhat and Vijayan,[45] Sequeira et al.,[46] and Hamilton and Parthasarathy.[47] The open circles are from previous measurements in Harris et al.[1]

small crystalline compounds. Quantification of hydrogen bonding is of great interest for studies in structural biology because of the role in recognition and conformational preferences. Solid state NMR could potentially be far more sensitive to details of hydrogen bonding and ionization states than crystallography. The chemical shifts for the acid protons for carboxyl groups in amino acids (shown in Figure 1) correlate with hydrogen-bonding length and this plot is shown in Figure 4 in filled circles. In comparison with previous measurements[1] which are entered here as open circles, our data encompass a rather restricted range because of the limited scope of compounds that are both relevant as model systems for proteins and sufficiently characterized. Clearly there is some scatter in the data but there is also a general trend that reproduces previous correlations.

Anisotropy of the proton shielding has been reported in a variety of solids with very simple structures; a thorough compilation and reviews are available.[30–32] Many of these values were obtained from static multiple pulse measurements on either single crystals or powders or from rotation plots of the deuterium signal of a single crystal. The shielding anisotropy, $|\Delta\sigma| = |(\sigma_\perp - \sigma_\parallel)|$, is quite narrow (about 4–7 ppm) for alkyl or aromatic protons (except for methyl groups which are 1–2 ppm), but for some ionizable protons the anisotropy is more pronounced, with values of approximately 17 ppm for amides and 16–30 ppm for acids, alcohols, and water, but only about 5 ppm for amines. A detailed analysis of tensor values and orientations would presumably be useful in studying nonbonded interactions but is probably not possible in biological solids in the near future. Many complications affect the CSA measurements by CRAMPS, such as residual homonuclear and heteronuclear dipolar interactions, molecular motion, and chemical shift scaling. Magnetically dilute protons in organic solids give rise to spinning sidebands during low-speed MAS, and when the percentage of hydrogens that are replaced with deuterons is approximately 99% or larger these sidebands appear to be dominated by CSA effects (A. McDermott, unpublished).

A point of specific interest in solid state studies of hydrogen bonding is the fact that hydrogen bonds can have profound effects upon reactivity in biological catalysis. For example, acid–base chemistry or proton mobility in the solid state is presumably strongly affected by local nonbonded interactions, a point which is relevant in many enzyme mechanisms. The geometric preferences of hydrogen bonds and the specific control of reactivity can be probed in the solid state studies since particular networks are arrested on an experimentally accessible timescale. Protons that participate in typical thermally driven and near-reversible exchange processes in proteins are found on the 'ionizable' hydrogen bonded groups such as carboxyl, imidazole, water, amine, alcohol, and guanidinium. The typical exchange timescales of microseconds to hours are presumably sensitive to the specific hydrogen-bonding geometry in a way that might be predicted by ab initio[33] or semiempirical methods. A systematic study of chemical exchange processes as a function of geometry in structurally characterized solids by NMR would help to clarify the theory of proton exchange.

Recent advances in ^{1}H NMR of deuterated simple model compounds for proteins show that such measurements of exchange processes are possible. Variable temperature two-dimensional (2D) methods applied to one example of a low symmetry hydrogen-bonded network of carboxylic acids and crystallographic water molecules demonstrated unambiguously that a proton is transferred between water and a carboxyl group[6] in an activated process with a barrier of 37 kJ mol^{-1}. Additional measurements will be necessary for the purpose of creating a database that correlates rates of exchange with structural features.

5 2D CORRELATION WITH CARBON

The more ambitious goal of utilizing ^{1}H NMR for detailed structural analyses of amorphous solid materials or complex solid state macromolecules is not practical without addressing the problem of resolution of one ^{1}H resonance from the others of the same chemical functional group. The approach taken by solution NMR spectroscopy to correlate the ^{1}H resonance with nearby or attached heteronuclei is applicable in solids as well. The ^{15}N or ^{13}C NMR spectra in the solid state are considerably broader than solution spectra but nonetheless often allow distinction of a handful of selectively labeled residues. Two important classes of 2D H–X experiments for solid state NMR of H–X pairs are dipolar chemical shift correlation methods or 'DIPSHIFT'[34] for determination of the bond distance to a great accuracy in a spin pair and heteronuclear correlation methods or 'HETCOR',[35–37] which maps the chemical shifts of the X nucleus to nearby protons via the dipolar coupling. The latter is clearly the experiment of choice when more than one proton connected with the heteronucleus of interest should be resolved and rather approximate distance information will suffice. Our recent work with HETCOR and modified versions of the pulse sequence demonstrate the observation of longer H–X distances including C–O ... H hydrogen bonds which appear as weak cross peaks. Rotor-synchronized transfer sequences have been used to increase the range of H–X distances probed by this method.[38] As an example, the HETCOR spectrum of alanyl aspartic acid is shown in Figure 5. In particular the ^{1}H–^{13}C correlation peaks between the carboxyl groups around 170 ppm in the ^{13}C dimension and the acid proton near 12.5 ppm in the

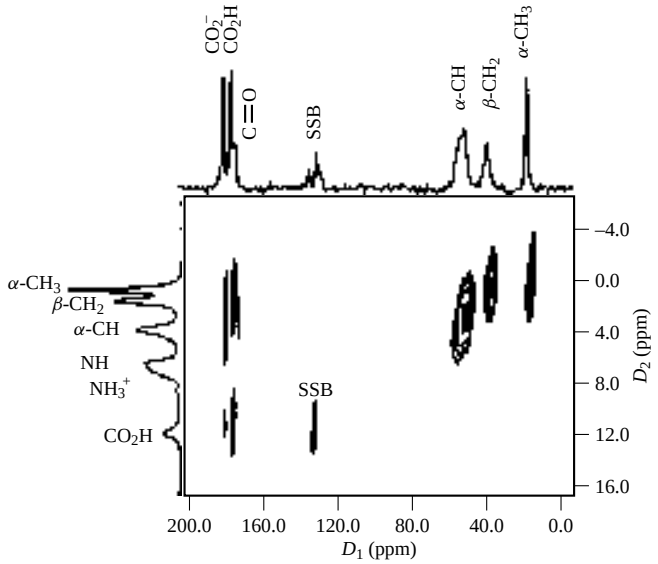

Figure 5 Rotor-synchronized HETCOR spectrum of alanyl aspartic acid at 200 MHz and room temperature. Magnetization transfer was accomplished by 2.5 WIM-24 cycles per rotor period during four sequential rotor periods. The 90° pulse lengths were 3.2 μs for both channels. Experimental repetition time was 1.7 s. Data matrix was 80 × 512 points zero-filled to 512 × 512 with 20 Hz linebroadening in D_2 and a Kaiser window applied to D_1. SSB = spinning sidebands

^{1}H dimension are indirectly connected pairs; several of the ^{13}C resonances show more than one ^{1}H cross peak.

Since essentially all of the resolution in the HETCOR experiment comes from the heteronuclear dimension, it is probably worthwhile to reiterate the virtues of such a 2D experiment in comparison with a one-dimensional (1D) heteronuclear measurement. Although detailed information about hydrogen bonding is available from heteronuclear NMR, the information from the ^{1}H shifts is often independent of that obtained from the heteronuclear shift. A case in point is the carboxylate group: the ^{1}H shift depends on the interaction of the detected acid proton with the nearest hydrogen bond acceptor, while σ_{22} of the ^{13}C shift depends on the distance between the carboxyl oxygen, which acts as a hydrogen bond acceptor, and the nearest proton.[39] The 2D HETCOR experiment provides the possibility of identifying the chemical nature of the hydrogen bonding partners to a carbon-containing functional group, even if the partners are water molecules. In a more practical light, we have found the HETCOR experiment to be quite useful in determining or confirming ^{13}C assignments for larger peptides and pharmaceuticals. As for disadvantages, obviously the time investment in such an experiment is enormously greater than that necessary for a 1D heteronuclear experiment. In the 2D spectra interpretation of the proton dimension is subject to similar complications as the CRAMPS experiment. In particular the intensities of the lines depend strongly on the presence or absence of mid-kHz motions.

Some of these issues are well illustrated with the spectrum of natural abundance alanyl aspartic acid. The three carbonyl-type carbons are readily identified by the HETCOR spectrum with one being a protonated carboxyl, one being deprotonated but hydrogen bonded to the protonated carbonyl, and the third being an amide carbonyl with no cross peak to the acid proton. A strong hydrogen bond between the two carboxyl groups is indicated by both the deshielded acid proton (14 ppm) that was detected in the HETCOR spectrum and the σ_{22} value for the deprotonated carboxyl group (184 ppm) that was determined in 1D low-spinning CP MAS sideband analysis. Moreover the assignment of both the ^{13}C and ^{1}H dimensions can be verified by comparison of the ^{1}H shifts in the cross peaks of the carbonyl resonances with those in the methylene/methine region. From such a comparison one could have identified, for example, that the protonated carboxyl is alpha to a methylene while the deprotonated carboxyl is alpha to a methine. The fact that good sensitivity was obtained for a naturally abundant dipeptide implies that moderate-sized proteins can be studied by this approach if they are selectively labeled.

6 CONCLUSIONS

The long-established relationships between proton shift and hydrogen-bonding distances were confirmed in the more restricted data base of amino acids and peptides. Utilization of these 1D CRAMPS methods for proteins is unlikely because of the 0.3–1 ppm linewidths. These measurements might be of use in more complex solids if the spectrum is separated into two dimensions using correlations to attached heteronuclei in the HETCOR experiment. Demonstrations of HETCOR spectra on small peptides with naturally abundant ^{13}C demonstrate the requisite sensitivity for biological work and indicate the potential for measuring hydrogen bonding parameters and confirming assignments.

7 RELATED ARTICLES

HETCOR in Organic Solids; Hydrogen Bonding; Line Narrowing Methods in Solids; Magic Angle Spinning Carbon-13 Lineshapes: Effect of Nitrogen-14.

8 REFERENCES

1. R. K. Harris, P. Jackson, L. H. Merwin, B. J. Say, and G. Hagele, *J. Chem. Soc., Faraday Trans. 1*, 1988, **84**, 3649.
2. B. C. Gerstein, R. G. Pembleton, R. C. Wilson, and L. M. Ryan, *J. Chem. Phys.*, 1977, **66**, 361.
3. D. P. Burum and W. K. Rhim, *J. Chem. Phys.*, 1979, **71**, 944.
4. B. C. Gerstein, *Philos. Trans. R. Soc. London, Ser. A*, 1981, **299**, 521.
5. A. E. McDermott, F. J. Creuzet, A. C. Kolbert, and R. G. Griffin, *J. Magn. Reson.*, 1992, **98**, 408.
6. L. Zheng, K. Fishbein, R. Griffin, and J. Herzfeld, *J. Am. Chem. Soc.*, 1993, **115**, 6254.
7. J. Yesinowski, H. Eckart, and G. Rossman, *J. Am. Chem. Soc.*, 1988, **110**, 1367.
8. S. Un, Ph.D. Dissertation, University of California, Berkeley, 1987.
9. C. Lee and R. G. Griffin, *Biophys. J.*, 1989, **55**, 355.
10. J. Forbes, C. Husted, and E. Oldfield *J. Am. Chem. Soc.*, 1988, **110**, 1059.
11. V. Rutar, *J. Agric. Food Chem.*, 1989, **37**, 67.

12. G. Maciel, C. Bronniman, and B. Hawkins, *Adv. Magn. Reson.*, 1990, **14**, 125.
13. C. E. Bronnimann, R. C. Zeigler, and G. E. Maciel, *J. Am. Chem. Soc.*, 1988, **110**, 2023.
14. C. E. Bronnimann, B. L. Hawkins, M. Zhang, and G. E. Maciel, *Anal. Chem.*, 1988, **60**, 1743.
15. P.-J. Chu, M. J. Potrzebowski, Y. Gao, and A. I. Scott, *J. Am. Chem. Soc.*, 1990, **112**, 881.
16. L. Muller, *Chem. Phys.*, 1981, **61**, 235.
17. L. Zheng, Ph.D. Dissertation, Brandeis University, Waltham, MA, 1993.
18. A. J. Kim and L. G. Butler, *J. Magn. Reson.*, 1992, **99**, 292.
19. C. F. Ridenour, Ph.D. Dissertation, Colorado State University, Fort Collins, CO, 1992.
20. U. Haeberlin and J. Waugh, *Phys. Rev.*, 1969, **185**, 420.
21. E. R. Andrew, *Mol. Phys.*, 1976, **31**, 1479.
22. A. Naito, A. Root, and C. A. McDowell, *J. Phys. Chem.*, 1991, **95**, 3578.
23. A. C. Olivieri, L. Frydman, and L. E. Diaz, *J. Magn. Reson.*, 1987, **75**, 50.
24. J. W. Diesveld, E. M. Menger, H. T. Edjes, and W. S. Veeman, *J. Am. Chem. Soc.*, 1980, **102**, 7935.
25. J. G. Hexem, M. Frey, and S. J. Opella, *J. Chem. Phys.*, 1982, **77**, 3847.
26. N. Zumbulyadis, P. M. Henrichs, and R. H. Young, *J. Chem. Phys.*, 1981, **75**, 1603.
27. B. Berglund and R. W. Vaughan, *J. Chem. Phys.*, 1980, **73**, 2037.
28. G. A. Jeffrey and Y. Yeon, *Acta Crystallogr., Sect. B*, 1986, **42**, 410.
29. M. C. Etter and G. M. Vojta, *J. Magn. Reson.*, 1991, **93**, 609.
30. T. M. Duncan, *A Compilation of Chemical Shift Anisotropies*, Farragut Press, Chicago, 1990, pp. H-1–H-12.
31. U. Haeberlin, *High Resolution NMR in Solids; Selective Averaging*, Academic Press, New York, 1976.
32. M. Mehring, *Principles of High Resolution NMR in Solids*, 2nd edn., Springer, New York, 1983.
33. K. Luth and S. Scheiner, *Int. J. Quantum Chem., Quantum Chem. Symp.*, 1992, **26**, 817.
34. M. G. Munowitz and R. G. Griffin, *J. Chem. Phys.*, 1982, **76**, 2848.
35. P. Caravatti, G. Bodenhausen, and R. R. Ernst, *Chem. Phys. Lett.*, 1982, **89**, 363.
36. J. E. Roberts, S. Vega, and R. G. Griffin, *J. Am. Chem. Soc.*, 1984, **106**, 2506.
37. D. P. Burum and A. Bieleski *J. Magn. Reson.*, 1991, **94**, 645.
38. C. E. Bronnimann, R. A. Santos, and R. A. Wind, *J. Magn. Reson.*, 1994, **105**, 183.
39. Z. Gu and A. McDermott, *J. Am. Chem. Soc.*, 1993, **115**, 4282.
40. S. T. Rao, *Acta Crystallogr., Sect. B*, 1973, **29**, 1718.
41. D. S. Eggleston and D. J. Hodgson, *Int. J. Peptide Protein Res.*, 1985, **25**, 242.
42. D. S. Eggleston and D. J. Hodgson, *Int. J. Peptide Protein Res.*, 1983, **21**, 288.
43. D. S. Eggleston and D. J. Hodgson, *Int. J. Peptide Protein Res.*, 1982, **19**, 206.
44. J. L. Derissen, H. J. Endeman, and A. F. Peerdman, *Acta Crystallogr., Sect. B*, 1968, **24**, 1349.
45. T. N. Bhat and M. Vijayan, *Acta Crystallogr., Sect. B*, 1976, **32**, 891.
46. A. Sequeira, H. Rajagopal, and R. Chidambaram, *Acta Crystallogr., Sect. B*, 1972, **28**, 2514.
47. T. F. W. C. Hamilton and R. Parthasarathy, *Acta Crystallogr., Sect. B*, 1972, **28**, 2083.

Biographical Sketches

Ann McDermott. *b* 1960. B.S., 1981, Harvey Mudd College; Ph.D., 1987, University of California, Berkeley, with Professor Ken Sauer and Dr. Melvin Klein; postdoctoral research, 1988–1990, MIT and Francis Bitter National Magnet Laboratory with Professor Robert Griffin, postdoctoral research 1990–1991, Université Catholique de Louvain, Institute for Clinical Pathology, Tropical Diseases Unit; Assistant Professor of Chemistry, Columbia University, 1991–present.

Cynthia F. Ridenour. *b* 1962. B.A., 1984, University of Colorado, Boulder; Ph.D., 1992, Colorado State University, with Professor Gary E. Maciel, applications scientist, Otsuka Electronics (USA), Inc., 1992–present.

Rotational Resonance in Biology

Steven O. Smith

Yale University, New Haven, CT, USA

1	Introduction	1
2	Methods	1
3	Biological Applications	3
4	Related Articles	4
5	References	4

1 INTRODUCTION

Rotational resonance (RR) dates back to the early 1960s when Andrew and co-workers found that in magic angle spinning (MAS) experiments the T_1 relaxation times of the ^{31}P resonances from phosphous pentachloride, which normally differed by an order of magnitude, were identical when the spinning speed was set equal to the frequency difference between two ^{31}P resonances in the sample.[1] An enhancement of the relaxation rates also occurred when the MAS speed was set to one-half or one-third of the frequency difference,[2] or more generally when the chemical shift difference between the two resonances ($\Delta\omega$) equaled an integral multiple of the MAS frequency (ω_r), namely $\Delta\omega = n\omega_r$. Since 1988, RR has been incorporated into a magnetization exchange experiment for measuring homonuclear dipolar couplings.[3–6] In this article, I describe the RR magnetization exchange experiment and its application to biological systems.

Rotational resonance NMR is one of several solid state NMR approaches that have been developed recently for determining weak dipolar couplings under conditions of MAS.[7] There are also MAS experiments for measuring homonuclear dipolar interactions that do not require RR, but restore the dipolar coupling through sequences of rf pulses (see ***Homonuclear Recoupling Schemes in MAS NMR***). For measuring heteronuclear dipolar interactions, such as between ^{13}C and ^{15}N, Schaefer and co-workers have developed REDOR and TEDOR NMR (see ***REDOR and TEDOR***).

The measurement of weak dipolar couplings in MAS experiments using any of these methods greatly enhances solid state NMR for studying biological systems since the dipolar couplings are directly related to internuclear distances which in turn provide constraints for the determination of molecular structure. The RR NMR and REDOR/TEDOR approaches have been shown to yield accurate measurements of internuclear distances. The distance limits that are accessible scale with the gyromagnetic ratios of the dipole-coupled spins. The upper limit for ^{13}C–^{13}C measurements is ∼6.5 Å and for ^{31}P–^{31}P measurements is ∼10.5 Å. Structural studies can be designed where the measurement of only a few accurate distances can establish the conformation of an enzyme-bound substrate/inhibitor, or the local secondary structure and tertiary contacts in biological macromolecules.

2 METHODS

The RR NMR experiment targets isolated homonuclear spin pairs in which the two spins have different chemical shifts. The most commonly observed spins in biological systems are ^{13}C, ^{15}N, and ^{31}P. Specific isotope labeling is needed for ^{13}C and ^{15}N to enhance sensitivity and target selected sites. In order to measure the dipolar coupling between two labeled sites, such as an amino acid side-chain $^{13}CH_3$ group and peptide backbone $^{13}C{=}O$ group, and thereby estimate their internuclear separation, a magnetization exchange experiment is performed in which one of the ^{13}C resonances are selectively inverted while spinning at RR with a second ^{13}C resonance. The intensities of both ^{13}C resonances is then monitored as a function of a mixing time during which Zeeman magnetization is exchanged between the two sites. The rate of magnetization exchange is used to determine the internuclear distance.

2.1 Pulse Sequence

The RR NMR pulse sequence [Figure 1(a)] begins with proton cross polarization (CP; see ***Cross Polarization in Solids***). Variable amplitude cross polarization (VACP) greatly facilitates the RR experiment.[8] With conventional CP, the signal generated by CP is extremely sensitive to the exact amplitudes of the spin lock pulses at the high MAS rates often required for RR experiments. Under these conditions, the Hartmann–Hahn matching profiles are transformed into a series of sharp peaks separated by the MAS frequency and can exhibit resonance offsets such that CP from the two spins cannot be simultaneously optimized. A direct consequence of the CP amplitude sensitivity is that the absolute intensities of the resonances being monitored in the RR experiment can change substantially with small changes in the amplifier output or probe tuning. The VACP sequence solves this problem by producing stable intensities over a large range of Hartmann–Hahn mismatches.

After CP, the ^{13}C magnetization generated by the CP pulses is stored along the Z axis with a ^{13}C flip-back pulse. One of the two ^{13}C resonances is selectively inverted and magnetization is allowed to exchange between the two sites for a variable mixing period (τ_m). The distribution of ^{13}C signal at the end of this period is detected with a 90° pulse that flips the magnetization into the transverse plane for acquisition of the NMR signal. Strong proton decoupling is essential during the exchange time. Incomplete decoupling leads to a decrease in the observed magnetization exchange rate.[6]

2.2 RR NMR Spectra

Figure 1(b) illustrates magnetization exchange in a RR experiment with ^{13}C NMR spectra of a crystalline undecapeptide bearing ^{13}C labels at a side-chain methyl group (20 ppm) and backbone carbonyl (175 ppm) separated by 3.7 Å.[9] The MAS rate has been set to the n = 1 RR condition where it exactly matches the 14 413 Hz frequency difference between the carbonyl and methyl carbon resonances at a carbon Larmor frequency of 90.4 MHz. The MAS speed must be regulated to within about ±5 Hz in order to maintain the rotational resonance condition. The $^{13}C{=}O$ resonance has been selectively

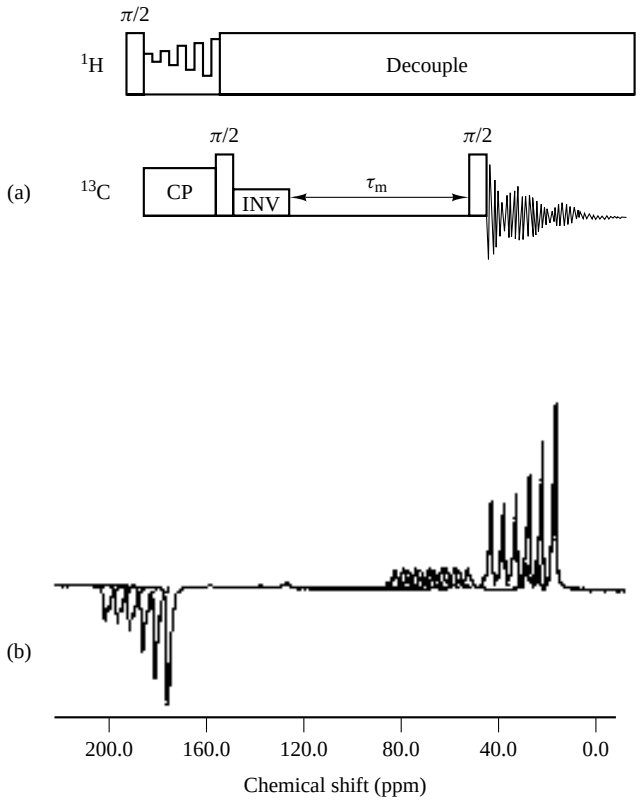

Figure 1 (a) The pulse sequence for RR NMR experiments incorporating variable amplitude cross polarization (CP) on the proton channel. Magnetization generated by CP is stored on the Z axis with a 90° pulse and one of the two spins being studied is then selectively inverted. The spins are then allowed to exchange Zeeman magnetization during a variable mixing time (τ_m) and the distribution of signal at the end of this period is sampled with a 90° read pulse. (b) Carbon-13 RR NMR spectra of a crystalline undecapeptide at the n = 1 resonance condition. The carbonyl resonance has been selectively inverted with a low-intensity pulse while spinning at RR with a $^{13}CH_3$ resonance. The full spectrum using a 1 ms mixing time is shown together with inserts (offset for clarity) from spectra obtained at mixing times of 3, 5, 7, 9, and 11 ms. The internuclear distance, determined from the X-ray crystal structure of the peptide, is 3.7 Å, and the ^{13}C labeled peptide has been diluted ~1:7 with unlabeled peptide to prevent intermolecular transfer between the labeled sites. The MAS frequency of 14 413 Hz was regulated to within ±5 Hz for the duration of the experiment

inverted with a low-power 500 μs pulse and the full spectrum was obtained with a short mixing time (1 ms) such that magnetization exchange has not had time to occur. As the mixing time is increased, the $^{13}C{=}O$ resonance returns to equilibrium and the coupled $^{13}CH_3$ resonance drops in intensity due to RR-driven exchange of magnetization between the two spins. The intensity changes are clearly seen in the offset plots taken from spectra at the longer mixing times. As an internal control, those peaks that are not at rotational resonance do not change in intensity during the experiment.

2.3 Generation and Interpretation of Magnetization Exchange Curves

The intensity changes observed in the RR experiment are translated into an internuclear distance by first generating a magnetization exchange curve. This is a plot of the net signal from the two exchanging resonances as a function of the mixing time. The signal is calculated as the intensity difference between the noninverted and inverted resonances to account for magnetization present in both of the exchanging spin populations. Two considerations that are crucial in calculating these curves are (1) establishing an accurate intensity for the first time point that is used to normalize the curve to an initial value of 1.0 and (2) accounting for natural abundance background signals and exchange.

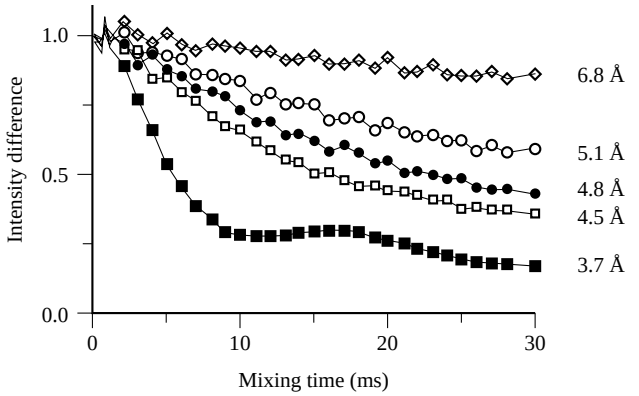

Figure 2 Magnetization exchange curves for $^{13}CH_3{-}^{13}C{=}O$ pairs showing the correlation between internuclear distance and the rate of magnetization exchange. The data have been obtained from five crystalline peptides bearing pairs of specific ^{13}C labels separated by 3.7, 4.5, 4.8, 5.1, and 6.8 Å. The distances are known independently from the X-ray structure of the peptide. The curves have been normalized to an initial value of 1.0 and have been corrected for natural abundance contributions

Figure 2 presents a set of n = 1 magnetization exchange curves for $^{13}CH_3{-}^{13}C{=}O$ pairs separated by 3.7, 4.5, 4.8, 5.1, and 6.8 Å.[9] These data were obtained on the crystalline undecapeptide described above where the internuclear distances are known independently from a high-resolution crystal structure. The magnetization exchange rates scale with internuclear distance, with the largest changes in intensity observed with the shortest distance. The resolution of the experiment is in the range of 0.1–0.2 Å (below about 5 Å) and the upper limit for observing RR-driven magnetization exchange is on the order of 6.5 Å. These 'standard' curves provide one way of determining unknown distances between similar functional groups.

A second approach for determining internuclear distances from the magnetization exchange curves is by computer simulations.[5] Simulations of the RR process reveal that the rate of magnetization exchange depends on several parameters in addition to the internuclear distance. These include the orientation and chemical shift anisotropy (CSA) of each spin as well as the zero quantum T_2 relaxation which accounts in a global way for several processes influencing magnetization exchange that are not driven by rotational resonance. The size and orientation of the chemical shift tensor for each site can often be based on model compound data. Importantly, the dependence of magnetization exchange on both the CSA and the tensor orientations is minor when spinning at the n = 1 RR condition. The zero quantum T_2 relaxation, however, has a considerable influence on the exchange rate, especially for weak dipolar couplings. A major contribution to this term can come from residual proton coupling. A lower limit for

the zero quantum T_2, corresponding to a lower limit for the distance estimate, can be based on the observed linewidths of the exchanging resonances. Inhomogeneous line broadening leads to an underestimate of the internuclear distance if the observed linewidth is used to estimate the zero quantum T_2.[10] An upper limit on the zero quantum T_2, and a corresponding upper limit on the distance estimate, can be taken from the linewidths observed for similar functional groups in model compounds.

3 BIOLOGICAL APPLICATIONS

Rotational resonance measurements have been most effective for studying the structure of enzyme-bound substrates and inhibitors and for characterizing specific internuclear distances in membrane systems. The studies on enzyme complexes are often motivated by the lack of a high-resolution crystal structure or by high molecular weights which limit the application of solution NMR approaches. These experiments are facilitated in many cases by the relative ease of specific isotope labeling of a small substrate or inhibitor molecule. In a similar fashion, biological membranes are large heterogeneous systems that are not well suited for study by single crystal diffraction and solution NMR methods. Rotational resonance NMR has been used increasingly for structural studies on membrane proteins and lipids. We discuss below several examples that illustrate these applications.

3.1 Inhibitors and Substrates

The conformation of enzyme-bound substrates and inhibitors can be determined by measurements of both internuclear distances and molecular orientations using RR methods. Rotational resonance measurements have been used to establish the mechanism of inactivation of D-alanyl-D-alanine ligase by an aminoalkyl dipeptide phosphinate inhibitor.[11] The enzyme normally catalyzes ligation of D-alanine to form a dipeptide using ATP-dependent phosphorylation in the first step of the reaction. The peptide inhibitor is thought to become phosphorylated in the active site of the protein producing an enzyme complex containing ADP and a phosphoryl phosphinate inhibitor. The dipolar coupling measured between the ^{31}P site on the inhibitor and the ^{31}P group of a phosphate ester corresponded to a ^{31}P–^{31}P distance of 2.7 $\pm$ 0.2 Å. This strongly implied that the two species were bridged in a P–O–P linkage. Two other resonances in the ^{31}P spectrum assigned to ADP did not exhibit intensity changes when placed on RR with the inhibitor, indicating that these ^{31}P atoms were more than 5 Å from the phosphinate.

The RR-driven magnetization exchange is largely insensitive to the orientation and CSA of the two exchanging sites at the $n = 1$ condition.[5] However, the exchange rates become increasingly sensitive to these parameters with higher RR orders ($n > 2$). Recently, this orientation dependence has been exploited to determine the conformation of transition state analogs bound to triose phosphate isomerase.[12] It was found that the phosphate of phosphoglycolic acid had an inplane orientation relative to the carboxyl group when bound to the enzyme, providing an explanation for the lack of phosphate elimination during catalysis.

3.2 Membrane Proteins

Solid state NMR has been applied extensively to study membrane systems, particularly lipid dynamics (see ***Bilayer Membranes: Deuterium and Carbon-13 NMR*** and ***Bilayer Membranes: Proton and Fluorine-19 NMR***). Rotational resonance NMR provides one of the only approaches for generating high-resolution distance constraints in these systems. The conformation about several bonds in the retinal prosthetic group of bacteriorhodopsin (see ***Bacteriorhodopsin and Rhodopsin***), a 26 kDa protein, has been determined by RR methods [Figure 3(a)]. These studies are conceptually similar to those of enzyme-bound inhibitors where the conformation of a specifically labeled molecule is studied complexed to a large protein. The conformation of the C-6–C-7 bond connecting the β-ionone ring to the conjugated retinal chain was determined to be *s-trans* and the configuration of the C=N bond linking the retinal chromophore to a lysine side chain in the interior of the protein was determined to be *trans* in bR_{568} and *cis* in bR_{548}.[13] Rotational resonance measurements have further established that the C=N bond has an *anti* configuration in an M form of the protein.[14]

Rotational resonance experiments can also be designed to establish the secondary structure and tertiary interactions of the protein components in membranes [Figure 3(b)].[6] Most proteins span membrane bilayers in α-helical secondary structures. Interactions between helices serve to stabilize the protein tertiary structure or drive protein dimerization. Furthermore, the transmembrane regions of membrane proteins can form separate folded and interacting domains, and can be studied independently of the soluble extramembranous domains. Internuclear distance measurements between ^{13}C sites that are separated by 2–4 residues in the amino acid sequence can be used to probe local secondary structure. The distance between a C=O backbone carbonyl and the α-carbon of a residue separated by 2–3 residues is ~4.6–5.2 Å in a helical geometry, but greater than 8 Å in an extended β-conformation. These intrahelical distances are well within the distance limits of RR measurements.

Similarly, the contacts between interacting helices can be established using RR NMR. The backbone to backbone separation of interacting helices is roughly 5 Å. The side chains of opposing helices are in van der Waals contact within this region. Rotational resonance measurements on peptides corresponding to the transmembrane domain of glycophorin A have demonstrated that RR can be used to probe both local secondary structure and helix interactions.[6,15] Glycophorin is an integral membrane protein that spans the cell membrane of erythrocytes in a single helical stretch of ~23 hydrophobic amino acids. Interactions between helices stabilize a protein dimer. Intramolecular RR measurements have shown that the transmembrane domain of glycophorin forms a helix in membranes. Intermolecular RR measurements have suggested that the side-chain valines of residues 80 and 84 are packed in the helix interface near glycine residues 79 and 83 suggesting that these residues are packed in the interface in a 'knobs-in-holes' arrangement.

3.3 Other Systems

Rotational resonance NMR has also been used to study the conformation of lipids in membranes[6,10] and the local

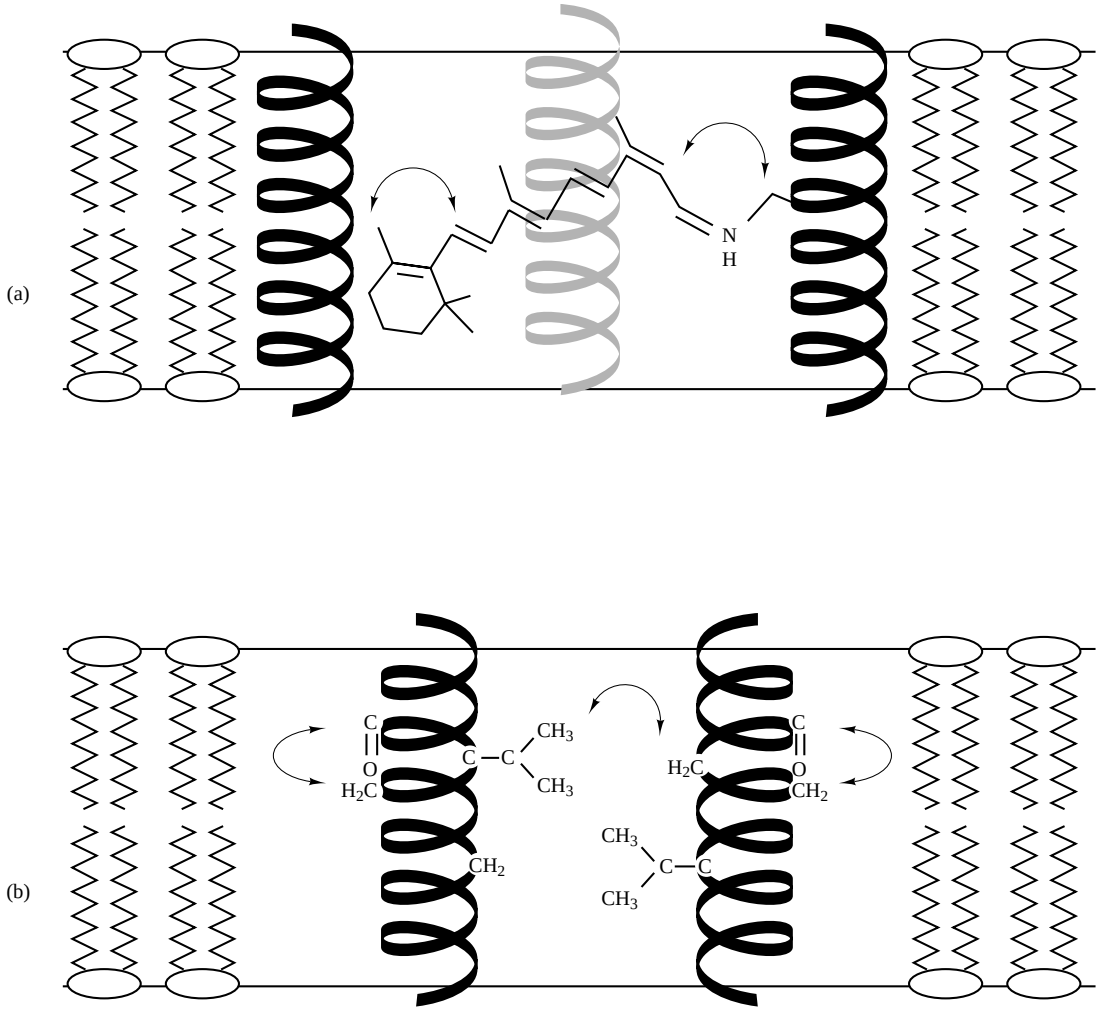

Figure 3 Models of membrane proteins illustrating internuclear distances that have been measured using RR NMR. (a) Schematic representation of bacteriorhodopsin, a 26 kDa integral membrane protein that spans the cell membrane with seven α-helical transmembrane domains (only three helices depicted). The retinal chromophore is buried in the hydrophobic interior of the protein. Rotational resonance NMR has been used to establish the conformation of the C-6–C-7 single bond and the configuration of the C=N double bond by measuring the distances between specific ^{13}C labels introduced into the retinal chromophore and lysine side chain of the protein. (b) Schematic representation of the transmembrane domain of glycophorin A. Rotational resonance NMR has been used to establish the local secondary structure and tertiary contacts in 29-residue peptides corresponding to the transmembrane sequence of the protein. Magnetization exchange rates were measured between [^{13}C]methyl groups in the targeted hydrophobic sequence -G_{79}-V_{80}-M_{81}-A_{82}-G_{83}-V_{84}- (G = glycine, V = valine, M = methionine, A = alanine) located in the middle of the transmembrane domain and specific [^{13}C]carbonyl labels along the peptide backbone across the dimer interface

secondary structure of amyloid peptides in fibrillar aggregates.[16] In both cases, specific ^{13}C labels were incorporated into a low molecular weight component of a much larger complex. These studies, together with those on the enzyme complexes and membrane proteins discussed above, illustrate the range of problems that can be addressed using RR NMR. Future prospects for RR NMR lie in the further development of both NMR and biochemical methods for targeting specific sites in biological macromolecules.

4 RELATED ARTICLES

Bacteriorhodopsin and Rhodopsin; Bilayer Membranes: Deuterium and Carbon-13 NMR; Bilayer Membranes: Proton and Fluorine-19 NMR; Cross Polarization in Solids; Homonuclear Recoupling Schemes in MAS NMR; Magic Angle Spinning; Membrane Lipids of Acholeplasma laidlawii; Membrane Proteins; Membranes: Carbon-13 NMR; REDOR and TEDOR; Rotating Solids.

5 REFERENCES

1. E. R. Andrew, A. Bradbury, R. G. Eades, and V. T. Wynn, *Phys. Lett.*, 1963, **4**, 99.
2. E. R. Andrew, S. Clough, L. F. Farnell, T. D. Gledhill, and I. Roberts, *Phys. Lett.*, 1966, **21**, 505.
3. D. P. Raleigh, M. H. Levitt, and R. G. Griffin, *Chem. Phys. Lett.*, 1988, **146**, 71.
4. M. G. Colombo, B. H. Meier, and R. R. Ernst, *Chem. Phys. Lett.*, 1988, **146**, 189.
5. M. H. Levitt, D. P. Raleigh, F. Creuzet, and R. G. Griffin, *J. Chem. Phys.*, 1990, **92**, 6347.

6. O. B. Peersen and S. O. Smith, *Concepts Magn. Reson.*, 1993, **5**, 303.
7. S. O. Smith, *Curr. Opin. Struct. Biol.*, 1993, **3**, 755.
8. O. B. Peersen, X. Wu, I. Kustanovich, and S. O. Smith, *J. Magn. Reson.*, 1993, **104**, 334.
9. O. B. Peersen, S. Yoshimura, H. Hojo, S. Aimoto, and S. O. Smith, *J. Am. Chem. Soc.*, 1992, **114**, 4332.
10. S. O. Smith, J. Hamilton, A. Salmon, and B. J. Bormann, *Biochemistry*, 1994, **33**, 6327.
11. A. E. McDermott, F. Creuzet, R. G. Griffin, L. E. Zawadzke, Q. Ye, and C. T. Walsh, *Biochemistry*, 1990, **29**, 5767.
12. Y. Tomita, E. O'Connor, and A. E. McDermott, *Experimental Nuclear Magnetic Resonance Conference Abstracts, St Louis, MO, 1993*, P31, 88.
13. F. Creuzet, A. McDermott, R. Gebhard, K. van der Hoef, M. B. Spijker-Assink, J. Herzfeld, J. Lugtenburg, M. H. Levitt, and R. G. Griffin, *Science*, 1991, **251**, 783.
14. K. V. Lakshmi, M. Auger, J. Raap, J. Lugtenburg, R. G. Griffin, and J. Herzfeld, *J. Am. Chem. Soc.*, 1993, **115**, 8515.
15. S. O. Smith, R. Jonas, M. Braiman, and B. J. Bormann, *Biochemistry*, 1994, **33**, 6334.
16. R. G. S. Spencer, K. J. Halverson, M. Auger, A. E. McDermott, R. G. Griffin, and P. T. Lansbury, Jr., *Biochemistry*, 1991, **30**, 10 382.

Biographical Sketch

Steven O. Smith. *b* 1956. B.A., 1979, Humboldt State University; Ph.D., 1985, University of California, Berkeley. Postdoctoral research with R. G. Griffin, MIT, 1986–1988. Faculty, Department of Molecular Biophysics and Biochemistry, Yale University, 1988–present. Approx. 40 publications. Research interests; the structure and mechanism of membrane proteins.

Solid Biopolymers

Isao Ando and Shigeki Kuroki

Tokyo Institute of Technology, Japan

1	Introduction	1
2	Solid State ^{13}C NMR of Polypeptides and Proteins	1
3	Solid State NMR Studies of ^{15}N in Synthetic Polypeptides	6
4	Solid State ^{17}O NMR of Synthetic Polypeptides	7
5	Related Articles	9
6	References	9

1 INTRODUCTION

The structural investigation of peptides, polypeptides, proteins, and other biopolymers in the solid state is being pursued increasingly by means of high-resolution solid state NMR.[1–8] Most of the biopolymers considered here consist of repeating sequences of peptide bonds with 20 different types of substituent at the α carbon. The secondary structures of these biopolymers are classified as α-helix, β-sheet, ω-helix, and so on, by means of a set of dihedral angles (ϕ, ψ).

In the solution state, the NMR chemical shifts of biopolymers with internal rotations are often the averaged values for all internal rotations because of rapid interconversion by rotation about peptide bonds. In the solid state, however, chemical shifts are often characteristic of specific conformations because of highly restricted rotation about the peptide bonds. The NMR chemical shift is affected by a change in the electronic state arising from the conformational change.[9] NMR chemical shifts in the solid state, therefore, provide useful information about the electronic state and conformation of a biopolymer with a fixed structure.[10]

The present article concentrates on the use of solid state ^{13}C, ^{15}N, and ^{17}O NMR studies in the structural investigation of biopolymers such as polypeptides, proteins, and similar compounds.

2 SOLID STATE ^{13}C NMR OF POLYPEPTIDES AND PROTEINS

2.1 Synthetic Polypeptides

Synthetic polypeptides consist of repeating sequences of certain amino acids and their structures are not as complicated as those of proteins. For this reason, synthetic polypeptides are sometimes used as model compounds for proteins. Their conformations are classified as α-helix, β-sheet, ω-helix, and so on. High-resolution solid state ^{13}C NMR spectroscopy has proved to be a very powerful tool for determining the structure of polypeptides in the crystalline state.[1,5–8] It has been demonstrated that the ^{13}C chemical shifts are related to particular conformations. Carbon-13 CP MAS NMR spectra of solid poly(L-alanine) ([Ala]$_n$) show the C-α, C-β, and C=O carbon signals to be well resolved between the α-helix and β-sheet forms.[11] The ^{13}C chemical shifts are plotted against the number-average degree of polymerization in Figure 1. Clearly, ^{13}C chemical shifts of [Ala]$_n$ ($n > 16$) are unchanged for the peptides of various molecular weights within experimental error, and thus can serve to characterize the α-helix form. The chemical shifts of the C-α and carbonyl carbons of the α-helix are displaced significantly to high frequency (downfield) by 4.2 and 4.6 ppm, respectively relative to those of the β-sheet form, while the chemical shift of the C-β carbon of the α-helix is displaced to low frequency by about 5 ppm with respect to that of the β-sheet (−5.0 ppm). For this reason, the value of the ^{13}C chemical shift can be used to describe the local conformation.[12] In addition, the ^{13}C chemical shifts of randomly coiled poly(L-alanine) in trifluoroacetic acid solution have values between those of the α-helix and β-sheet forms.

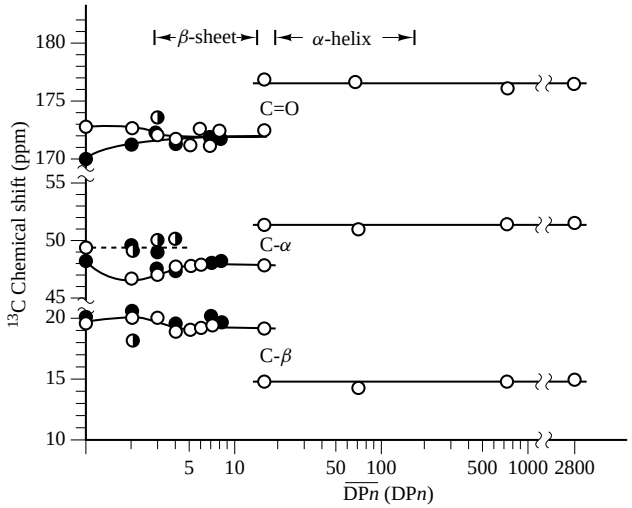

Figure 1 Plots of the ^{13}C chemical shifts of oligo-L-Ala and poly-L-Ala against the number-average degree of polymerization ($\overline{DP_n}$)

The existence of such characteristic displacements of ^{13}C chemical shifts is not limited to the Ala residue. In Table 1 are summarized the ^{13}C chemical shift values of various amino acid residues in the α-helix and β-sheet forms.[5,6] Here it is seen that the C-α and C=O peaks of the α-helix form are all displaced to high frequency with respect to those of the β-sheet form, which is consistent with the data of poly(L-alanine). The absolute ^{13}C chemical shifts of the C-α and C-β carbons are affected by the chemical structure of the individual amino acid residues and can be used effectively for conformational studies of particular amino acid residues in polypeptides and proteins. On the other hand, the C=O chemical shifts do not seem to be affected by residue structure and can be used for diagnosing the main chain conformation.

Poly(β-benzyl L-aspartate) (PBLA) in the solid state adopts various conformations such as a right-handed $\alpha(\alpha_R)$-helix, a left-handed $\alpha(\alpha_L)$-helix, a left-handed $\omega(\omega_L)$-helix, and a β-sheet form depending upon the temperature. The measured values for the ^{13}C chemical shifts depend significantly on the conformations of the peptide as shown in Table 2.[13] Variable temperature ^{13}C CP MAS NMR spectra of PBLA are shown in Figure 2.[14] The temperatures of the conformational changes of PBLA are indicated in the Figure. From this, it is clear that

Table 1 Carbon-13 Chemical Shift Characteristics of the α-helix and β-Sheet Forms (±0.5 ppm; from TMS)

	C-α			C-β			C=O		
Polypeptides[a]	α-Helix	β-Sheet	Δ[b]	α-Helix	β-Sheet	Δ[b]	α-Helix	β-Sheet	Δ[b]
$(Ala)_n$	52.4	48.2	4.2	14.9	19.9	−5.0	176.4	171.8	4.6
	52.3	48.7	3.6	14.8	20.0	−5.2	176.2	171.6	4.6
	52.8	49.3	3.5	15.5	20.3	−4.8	176.8	172.2	4.6
$(Leu)_n$	55.7	50.5	5.2	39.5	43.3	−3.8	175.7	170.5	5.2
	55.8	51.2	4.6	43.7[c]	39.6[c]	(4.1)	175.8	171.3	4.5
$[(Glu(OBzl)]_n$	56.4	51.2	5.2	25.6	29.0	−3.4	175.6	171.0	4.6
	56.8	51.1	5.7	25.9	29.7	−3.8	175.4	172.2	3.2
$[(Asp(OBzl)]_n$	53.4	49.2	4.2	33.8	38.1	−4.3	174.9	169.8	5.1
	53.6[d]			34.2[d]			174.9[d]		
$(Val)_n$	65.5	58.4	7.1	28.7	32.4	−3.7	174.9	171.8	3.1
		58.2			32.4			171.5	
$(Ile)_n$	63.9	57.8	6.1	34.8	39.4	−4.6	174.9	172.7	2.2
		57.1			33.1			171.0	
$(Lys)_n$[e]	57.4			29.9			176.5		
$[(Lys(Z))]_n$	57.6	51.4	6.2	29.3	28.5	−0.8	175.7	170.4	5.3
$(Arg)_n$[e]	57.1			28.9			176.8		
$(Phe)_n$	61.3	53.2	8.1	35.0	39.3	−4.3	175.2	169.0	6.2
$(Met)_n$	57.2	52.2	5.0	30.2	34.8	−4.6	175.1	170.6	4.5
$(Gly)_n$		43.2						168.4	
		44.3						169.2	
			5.1 ± 1.0[f]			−4.1 ± 0.7	175.8 ± 0.8	170.9 ± 1.2	4.9 ± 1.1

[a]Ala = alanine, Leu = leucine, Glu = glutamic acid, Asp = aspartic acid, Val = valine, Ile = isoleucine, Lys = lysine, Arg = arginine, Phe = phenylalanine, Met = methionine, Gly = glycine.
[b]Difference of the ^{13}C chemical shifts of the α-helix relative to those of the β-sheet form.
[c]Mistyping or erroneous assignment.
[d]Erroneously assigned to the left-handed α-helix.
[e]Data taken in neutral aqueous solution.
[f]Average values.

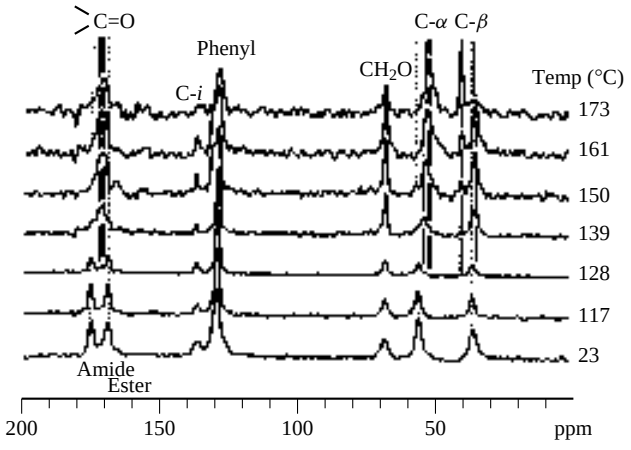

Figure 2 Variable temperature ^{13}C CP MAS TOSS NMR spectrum of poly(β-benzyl L-aspartate) in the solid state at various temperatures: *dashed line*, α_R-helix form; *light solid line*, ω_L-helix form; *bold solid line*; β-sheet form

the conformational changes α_R-helix → ω_L-helix → β-sheet occur with increasing temperature.

The conformations of polypeptides such as poly(L-alanine), polyglycine, and so on in the solid state are in many instances quite fixed. However, additional types of conformation can be formed when a small amount of guest glycine[15] or L-Ala[16] residues are incorporated into the host polypeptides. For example, solid state ^{13}C CP MAS NMR spectra of PBLA containing [3-^{13}C]L-Ala residues have been measured. The Ala C-β carbon shows significant displacements of the ^{13}C chemical shift depending on the conformational change.

Using the reference data, the helical sense of the ω-helix of poly(L-phenylalanine) has been shown to be right-handed, and this could not have been determined absolutely by X-ray diffraction. Furthermore, the side-chain conformation-dependent ^{13}C chemical shifts of this polymer and the L-phenylalanine residue in oligopeptides have been determined.[17]

The principal values of the ^{13}C chemical shift tensors (σ_{11}, σ_{22}, and σ_{33}) determined from the ^{13}C powder pattern spectrum are valuable as parameters for obtaining structural information which can be related to the electronic state more directly than the isotropically averaged value [$\sigma_{iso} = (\sigma_{11} + \sigma_{22} + \sigma_{33})/3$].[10] Nevertheless, very few data are available for the ^{13}C chemical shift tensor for carbon atoms in peptides. There have been a few studies of conformation using ^{13}C chemical shift tensors of polypeptides in the solid state. Solid state ^{13}C CP MAS NMR spectra of a variety of polypeptides containing [1-^{13}C]glycine residues as a minor component (<8%) have also been recorded. This was to obtain the ^{13}C isotropic average chemical shifts, and the principal values of the chemical shift tensors of the glycine (Gly) carbonyl carbon in β-sheet, α-helix, ω-helix, and 3_1-helix forms.[15] The last two conformations were obtained only when Gly residues were incorporated into the homopolypeptides. It was found that the magnitudes of displacements of chemical shifts upon conformational changes are larger for σ_{22} and σ_{33} than the

Table 2 Carbon-13 Chemical Shifts of Various Conformations of Poly(β-benzyl L-aspartate) in the Solid State (ppm from TMS; $\pm$0.5 ppm)

Sample	Conformation	C-α	C-β	C=O(amide)	C=O(ester)	Phenyl	CH_2O
Polymer	α_R-helix	53.4	33.8	174.9	167.0	129.8	65.7
	α_L-helix	50.9	33.8	171.1	169.0	129.2	66.1
	ω-helix	50.5	32.9	171.3	167.8	129.0	65.3
	β-sheet	49.2	38.2; 35.1	169.6	169.5	129.2	65.9
Oligomers							
DP_n5[a]	β-sheet	49.1	38.0	169.8	168.2	129.0	65.5
DP_n10	β-sheet	49.5	36.8	169.6	168.0	128.4	65.9

[a]DP = degree of polymerization.

isotropic chemical shift values, while σ_{11} is almost unaffected by any conformational change.

A solid state ^{13}C NMR study of some polypeptides containing [2-^{13}C]glycine residues has been carried out in order to clarify a conformational effect on the ^{13}C chemical shift tensors. It was found that the isotropic chemical shifts and principal values of the chemical shift tensor of Gly C-α incorporated in some homopolypeptides are displaced.

Hydrogen bonding plays an important role in the adoption of any specific conformation in peptides and polypeptides in the solid state. The effect of hydrogen bonding on the solid state ^{13}C chemical shifts of carbonyl carbons in peptides has been examined. Carbon-13 chemical shifts were determined for a series of oligopeptides containing glycine (Gly), L-Ala, L-valine, and L-leucine residues, for which the crystal structures were already available from X-ray diffraction studies. It was found that the ^{13}C chemical shifts of the carbonyl carbons in the $-C{=}O\cdots H-N-$type of hydrogen bond move linearly to high frequency with a decrease in the hydrogen bond length (R_{N-O}) as $\delta = a\ R_{N-O} + b$ (ppm). For the Gly, L-Ala, L-valine, and L-leucine residues, a and b are -12.4 and 206, -21.7 and 237.5, -14.2 and 215.4 and -10.0 and 202.2 ppm, respectively.[18,19] Using these relations, the hydrogen-bond length can be determined from the observed ^{13}C chemical shift values for the carbonyl carbons. These experimental results were explained by using ^{13}C chemical shift calculations based on the finite perturbation theory (FPT) intermediate neglect of differential overlap (INDO) method.

The conformational structures of poly(α-L-glutamic acid) [poly(Glu)], poly(α-L-aspartic acid) [poly(Asp)] and irregular poly(α,β-D,L-Asp) in the solid state have been studied by means of ^{13}C CP MAS NMR in conjunction with results from X-ray diffraction and infrared spectroscopy studies.[20] From these, it has been shown that poly(Glu) and poly(Asp) in the free acid form exhibit both α-helical and β-sheet forms, whereas the random coil form predominates in their sodium salts. Both the free acid and sodium salt of poly(α,β-Asp) exist predominantly in the random coil form. It turns out that the sodium salts are especially suitable for determining the NMR characteristics of the random coil conformation in the solid state.

2.2 Proteins

2.2.1 Fibrous Proteins

Since fibrous proteins generally have periodic amino acid sequence and higher order structures, the clarification of their fine structure in the solid state becomes very important not only when discussing the physical and chemical properties, but also when obtaining information about the molecular design of synthetic polypeptides. Indeed, a comparison of some fibrous proteins and their model synthetic polypeptides has been carried out. The conformation-dependent ^{13}C chemical shifts are useful for the determination of the conformational features of fibrous proteins.

Silk fibroin is one of the fibrous proteins having a simple amino acid composition, and isotopic enrichment can be performed easily. More detailed analyses of static or dynamic structures have been made by solid state NMR.[1,21,22] The amino acid composition of silk varies with the species of silkworm. In reflecting the higher Ala content of *Phylosamia cynthia ricini* fibroin it has been shown that the ^{13}C chemical shifts of the Ala residues of a dried sample, taken from the silk gland of *P.c. ricini*, are identical to those of the α-helical $[Ala]_n$. In contrast, the cocoon of *P.c. ricini* was found to have an antiparallel β-sheet form, as determined from the ^{13}C chemical shifts of the Ala and serine (Ser) residues. On the other hand, the ^{13}C peaks of the Ala and Gly residues of the silk II form of *Bombyx mori* silk fibroin are in good agreement with those of $[Ala\text{-}Gly]_n$ II as well as $[Gly]_n$ II and $[Ala]_n$ in the β-sheet form. The ^{13}C chemical shifts of samples taking the silk I form are significantly displaced from those of the silk II form. Models for the silk I structure of *B. mori* silk fibroin have been proposed on the basis of ^{13}C NMR data, X-ray diffraction data, and conformational energy calculations.

Collagen is composed of a triple-stranded helix. The individual triple chains are composed of the repeating pattern, $[Gly\text{-}X\text{-}Y]_n$, where X and Y are frequently occupied by proline (Pro) and hydroxyproline residues, respectively. Torchia and co-workers[23,24] have reported substantial work on the molecular dynamics of collagens by means of multinuclear solid state MR, using isotopically labeled samples which were obtained by cultivation techniques. Saito et al.[25] have found that most of the ^{13}C signals of collagen fibrils from bovine tendon and skin are in good agreement with those of $[Pro\text{-}Gly\text{-}Pro]_n$, although some peaks characteristic of the collagen are slightly displaced from those of the model polypeptides. All of the peaks of collagen fibrils have been assigned on the basis of computer simulation by utilizing amino acid composition and chemical shift data from the solid state and solution.

Carbon-13 CP MAS NMR spectra of tropomyosin, one of the muscle proteins, were measured in the solid state, in order to elucidate the higher order structure of the protein via the observation of the ^{13}C chemical shifts of the amino acid residues and their mobility. The higher order structure of tropomyosin is a right-handed α-helix coiled-coil structure,

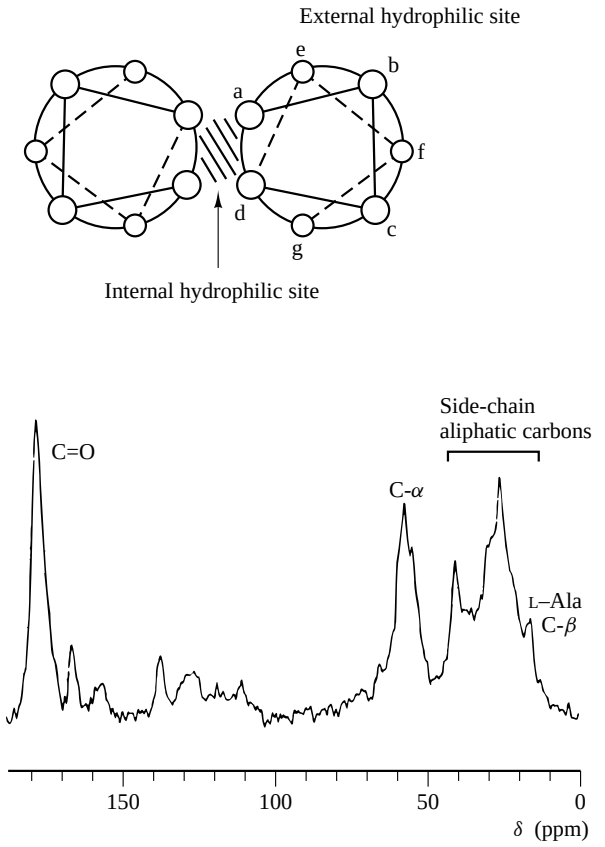

Figure 3 A schematic picture of the cross-section of the coiled-coil structure in tropomyosin (top), and the typical ^{13}C CP MAS NMR spectrum of tropomyosin at room temperature (bottom)

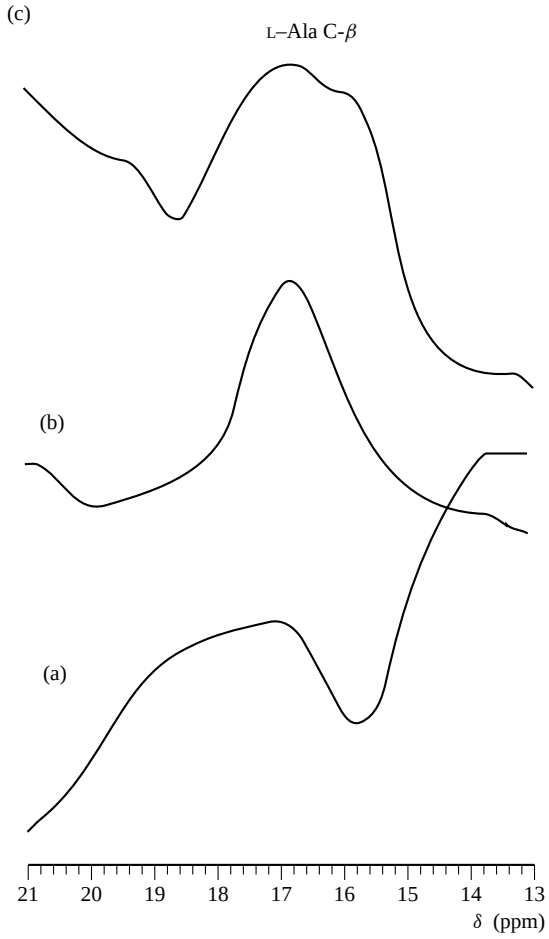

Figure 4 The expanded ^{13}C NMR spectra of the Ala C-β carbon atoms of tropomyosin, measured using the inversion–recovery method at room temperature. Recovery time, t: (a) 10 ms; (b) 500 ms; (c) 3500 ms

which contains two different sites. These are characterized by an internal hydrophobic site and an external hydrophilic site (Figure 3). A typical ^{13}C CP MAS NMR spectrum for tropomyosin in the solid state is shown in Figure 3.[26] Since the Ala residue is one of the major components, the ^{13}C signal which appears at 15–17 ppm can be assigned readily to the Ala C-β carbons, and it is seen that this signal consists of two peaks. Figure 4 shows the expanded Ala C-β signal, measured using the inversion–recovery method. These peaks indicated that there are at least two kinds of Ala C-β carbons. Furthermore, the carbon atoms contributing to the peak at 15.8 ppm have a larger value of T_1 than those at 16.7 ppm. This indicates that the former carbons are more mobile than the latter carbons, because the Ala C-β carbons in tropomyosin have correlation times with values appearing in an extremely narrow region at room temperature. The distance between the two α-helical axes in the coiled-coil structure is shorter than in coiled-coil helices which are packed in parallel in native muscle, as shown from X-ray studies. Therefore, it can be argued that the mobility of the Ala C-β carbon atoms in the internal site is expected to be more restricted than that in the external site. The two peaks at 15.8 and 16.7 ppm therefore are assigned to the Ala C-β carbons in the external and internal sites of the coiled-coil structure, respectively.

Native wool fiber consists of intermediate filaments composed of low-sulfur-containing proteins which are embedded in a nonfilamentous matrix. The nonfilamentous matrix usually consists of two classes of proteins; one is a high-sulfur-containing protein and the other is a protein containing Gly and tyrosine (Tyr) residues. Wool keratin can be divided into three main fractions after reducing the disulfide bonds and protection of the resulting thiol groups with iodoacetic acid to form *S*-carboxymethylkerateine (SCMK). The solid state ^{13}C CP MAS TOSS NMR spectra of wool and four kinds of SCMKs extracted from low-sulfur fractions (SCMKA), helix-rich fragments (SCMKA-hf), high-sulfur fractions (SCMKB), and high-Gly-Tyr fractions (HGT) are shown in Figure 5.[27,28] For characterization of the main-chain conformation of polypeptides and proteins in the solid state, it is very useful to use the ^{13}C chemical shift value of the main-chain carbonyl carbon, because it is strongly influenced by the conformation of the main chain but not by the type of amino acids and/or a specific amino acid sequence. Hence, it can be argued that the lineshape of the ^{13}C signals in the carbonyl region for proteins reflects the main-chain conformation.

The carbonyl ^{13}C signal can be resolved into four peaks by computer fitting. The relative intensity of the high-frequency peak at about 176 ppm corresponds to the proportion of the α-helix component, because this peak comes from the main-chain carbonyl carbons in the α-helix form. The proportion of

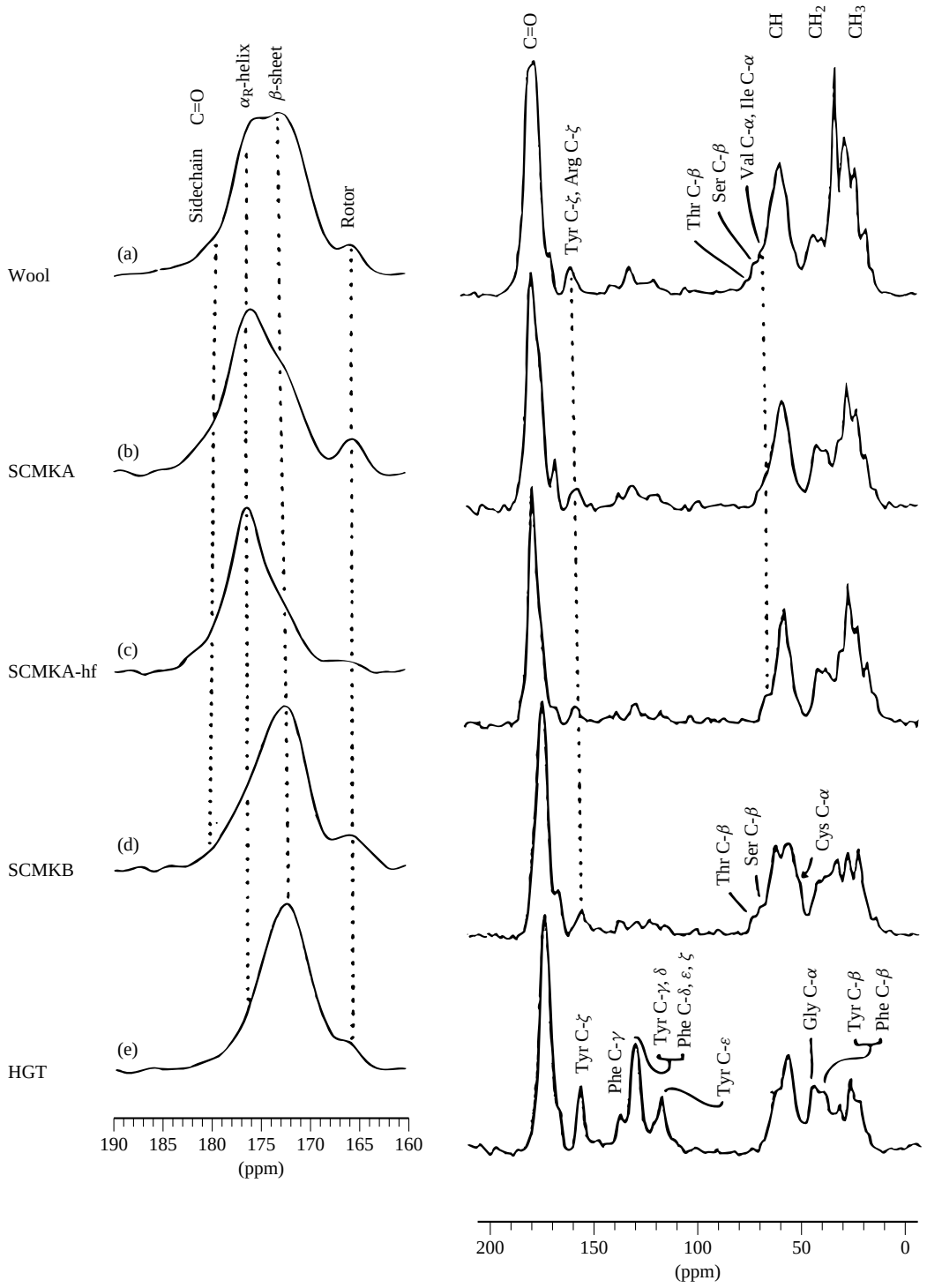

Figure 5 ^{13}C CP MAS TOSS NMR spectra of (a) wool, (b) SCMKA, (c) SCMKA-hf, (d) SCMKB, and (e) HGT, and their expanded spectra of the carbonyl carbon region. Arg = arginine, Thr = threonine, Val = valine, Ile = isoleucine, Cys = cysteine, Phe = phenylalanine

the α-helix component increases in the order: wool, SCMKA, SCMKA-hf. On the other hand, the low-frequency peak at 172 ppm is characteristic of the main-chain carbonyl carbons in the β-sheet form. On the basis of the above assignment, it can be said that the β-sheet form is predominant in SCMKB and HGT. These findings are also confirmed from the peaks in other carbon regions. Furthermore, it is suggested that the coiled-coil structure exists in wool, SCMKA, and SCMKA-hf, because the ^{13}C chemical shift values of the Ala C-β carbons in these samples coincide, within experimental error, with that of the Ala residue located in the internal site of the coiled-coil structure in tropomyosin.

This conformational analysis, using conformation-dependent ^{13}C chemical shifts, has been applied to investigate the conformational transition of SCMKA induced by stretching, heating, or steam-treating. The β-sheet form appears and the proportion

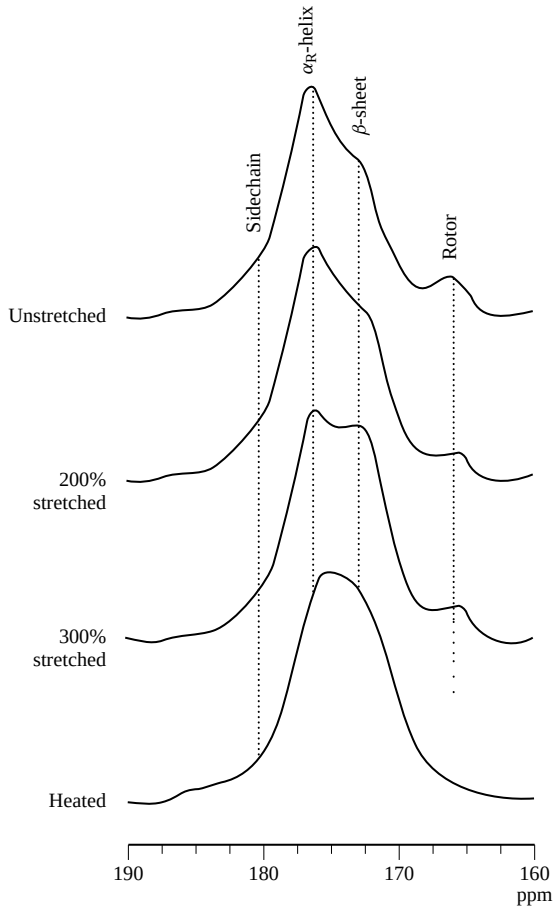

Figure 6 Expanded ^{13}C CP MAS TOSS NMR spectra for the carbonyl carbon region in SCMKA films cast from aqueous solution

of the α-helix form decreases upon stretching and steam-treating as shown in Figure 6.[28] For the SCMKA heated at 200 °C for 3 h in vacuo, the ^{13}C CP MAS spectrum shows that each peak is broader than those of other treated specimens. This indicates the existence of various conformations and/or different microenvironments in the heated SCMKA. Thus, it can be said that the random coil form appears by heating. From X-ray diffraction measurements, the α-helix form completely vanishes in SCMKA heated under the same conditions. However, Figure 6 shows that the α-helix form remains to an appreciable extent in the heated sample, although the random coil form also appears. The difference between the results from X-ray diffraction and NMR spectroscopy studies suggests that only the packing of the ordered structure (the α-helix form) in SCMKA is disrupted by heating, but that the secondary structure is retained. On the other hand, in the case of the structural transition for the same protein, the change of the lineshape for the α-methine carbons can be attributed mainly to the conformational change.

The dynamics and structure of mouse keratin intermediate filaments has been investigated by solid state ^{13}C and ^{2}H NMR spectroscopy, using isotopically labeled samples.[29]

2.2.2 Membrane Proteins

The structural and dynamic analysis of membrane proteins is readily achieved by solid state ^{13}C NMR. The reasons are as follows: firstly, biological membranes greatly restrict the motion of embedded proteins and consequently are difficult to study by solution NMR methods; secondly, only a few membrane proteins have been crystallized and studied by X-ray diffraction methods; thirdly, if the membrane protein is uniaxially oriented in the lipid, there is the advantage of being able to determine the structure at the atomic level by NMR as well as X-ray crystallography. Further, since phospholipids coexist in many cases in membranes, the NMR method is still suitable because of its ability to observe selectively by means of isotopic labeling, multinuclear MR, and utilizing the differences of relaxation times. Thus phospholipids, for example, are readily and selectively studied by solid state NMR methods using specifically ^{31}P NMR.[30]

The ^{13}C CP MAS spectra of ^{13}C-labeled gramicidin A (GA) were measured to determine directly the structure of this peptide in a lipid membrane.[31] The seven GA analogs, each labeled at a single carbonyl group of each of some amino acid residues, were synthesized by the solid phase method. These ^{13}C-labeled GAs were incorporated into aligned multilayers of dimyristoylphosphatidylcholine or diether lipid bearing 14- or 16-carbon chains, at a 1:15 peptide:lipid molar ratio. Carbon-13 CP NMR spectra were obtained at several temperatures and over a range of sample orientations with respect to the spectrometer magnetic field. The observed chemical shielding anisotropies indicate that all of the labeled carbonyl bonds are oriented almost parallel to the molecular long axis and perpendicular to the lipid bilayer plane. These orientations are consistent with GA forming a β6.3 single-strand helix that is oriented parallel to the methylene chains of the lipid molecules. Comparison of the linewidths from labeled residues that are in the innermost turn of the helix, and in the turn nearest the lipid bilayer surface suggests that although the peptide behaves largely as a right-handed barrel, segments of the peptide close to the membrane surface possess greater motional freedom.

Bacteriorhodopsin and rhodopsin are integral membrane proteins that contain the vitamin A aldehyde, retinal, as a photoreactive chromophore. Many solid state NMR studies on the structure and environment of the retinal chromophore in these proteins have been reported, using mainly specifically ^{13}C-labeled retinals.[2,32,33] It may reasonably be said that the structure of retinal in bacteriorhodopsin and rhodopsin has been determined by solid state NMR. Hence, solid state NMR is an extremely important experimental procedure in investigating the mechanism of sight. Most recently, the spectrum of ^{13}C-labeled bacteriorhodopsin in purple membranes was recorded. On the basis of the ^{13}C CP MAS NMR experiments, a discussion has been presented of the change of the manner of mutual orientation between α-helices as induced by hydration/dehydration.

Also, soluble proteins such as enzymes, conjugated proteins such as glycoproteins, and proteins which are in more complex systems have been investigated by solid state NMR.[34–36]

3 SOLID STATE NMR STUDIES OF ^{15}N IN SYNTHETIC POLYPEPTIDES

It has been demonstrated that the isotropic ^{15}N chemical shifts of systems such as poly(Gly) (PG), poly(L-Ala), poly(L-leucine), poly(L-isoleucine) poly(L-valine), poly

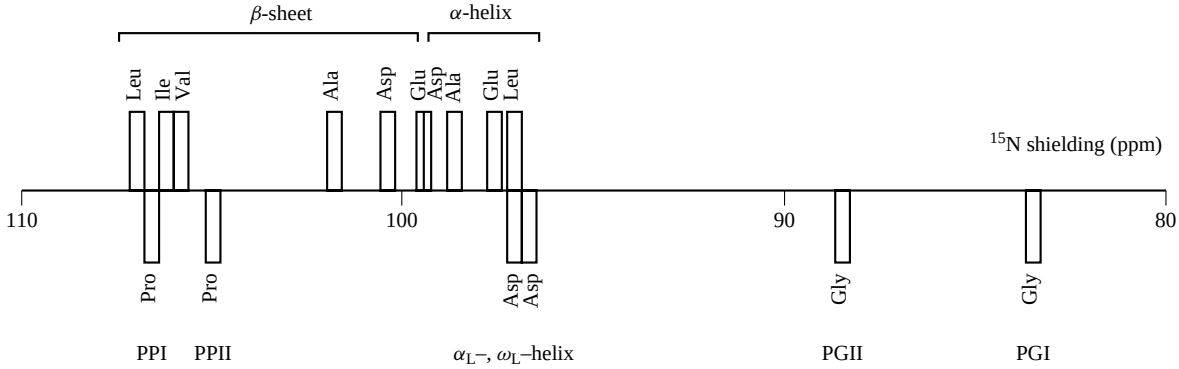

Figure 7 Diagram of the observed isotropic ^{15}N shielding of some homopolypeptides $[X]_n$ with various conformations (α-helix, β-sheet, α_L-helix, ω_L-helix, PG I, PG II, PP I, and PP II forms). Leu = leucine, Ile = isoleucine, Val = valine, Glu = glutamic acid

(L-phenylalanine), poly(γ-methyl L-glutamate), poly(β-benzyl L-aspartate) and poly(L-Pro) (PP) in the peptide backbone of polypeptides in the solid state exhibit a significant conformation-dependent change. Both experimental observation and theoretical calculation confirm this.[37–39] The σ_{iso} for the α-helix form (97.0−99.2 ppm) appears to low frequency by about 1.2−10.0 ppm with respect to that for the β-sheet form (99.5−107.0 ppm) of polypeptides, which obviously depends on the structure of the individual amino acid residue, as shown in Figure 7 (relative to $^{15}NH_4NO_3$). Some ^{15}N chemical shift differences are rather small, but are meaningful in the context of polypeptides. The variations of the σ_{iso} for various kinds of polypeptides are about 2.5 ppm in the α-helix form and about 7.5 ppm in the β-sheet form. In addition, the σ_{iso} of the β-sheet form of the L-leucine, L-valine, and L-isoleucine residues, which possess alkyl side chains, appear to high frequency with respect to that of the L-Ala residue. In contrast, the σ_{iso} value for the β-sheet form of the L-Asp(OBzl), L-Glu(OBzl), and L-Glu(OMe) residues (where Glu = glutamic acid), which possess a side-chain ester, is to low frequency with respect to that of the L-Ala residue. These results indicate that the ^{15}N chemical shift difference between the α-helix and β-sheet forms depends on the side-chain structure of individual amino acid residues.

Further, σ_{iso} gives information about the helix sense (α_R-helix or α_L-helix) of poly(β-benzyl L-aspartate) (ω-helix: 99.2 ppm; α_L-helix: 97.0 ppm).[40] In addition, the ^{15}N chemical shift value of PBLA with low molecular weight (β-sheet form) is identical with that of PBLA with high molecular weight (β-sheet form), indicating that the ^{15}N chemical shift of solid polypeptides is independent of the chain length, if no conformational changes occur. Accordingly, the ^{15}N chemical shift depends mainly on the conformation and side-chain structure of individual amino acid residues. In order to support this view theoretical calculations of ^{15}N chemical shifts are required, using the electronic states derived by quantum chemical methods. The relative ^{15}N NMR chemical shift of a dipeptide fragment forming hydrogen bonds with two formamide molecules has been calculated using the FPT INDO theory.[37]

The relation between the isotropic ^{15}N chemical shift or chemical shift tensor and the structures of various kinds of synthetic copolypeptides in the solid state have been studied.[38–40] It was found that the ^{15}N chemical shifts indicate strong neighboring sequence effects.

An analytical method for the determination of dihedral angles of the GA backbone from solid state ^{15}N NMR spectroscopic data has been demonstrated.[31,41] Advantage is taken of the ^{15}N−^{1}H and ^{15}N−^{13}C dipolar interactions as well as the ^{15}N chemical shift interaction in the oriented samples. The dihedral angles for the L-Ala$_3$ site are determined by obtaining the NMR data for both the Gly$_2$-L-Ala$_3$ and L-Ala$_3$-D-leucine$_4$ peptide linkages. Two possible sets of torsion angles for the L-Ala$_3$ site are obtained (ϕ,ψ = − 129°, 153° and − 129°, 122°), both of which are consistent with a right-handed α-helix. In addition, the dynamics of the backbone of GA in dimyristoylphosphatidylcholine bilayers have been investigated using solid state ^{15}N NMR.[41] Nitrogen-15 CP NMR spectra of single-site ^{15}N-labeled GA at 8 °C were analyzed to yield a spatial model for local backbone motion. This model includes the axis of motion, the mean orientation, and the maximum amplitude of displacement for individual peptide planes. Specific sites in the first turn of the amino terminus were investigated, with emphasis on the L-Ala$_3$ and D-leucine$_4$ linkages, for which the orientation of the ^{15}N chemical shift tensor with respect to the molecular frame has been determined.

4 SOLID STATE ^{17}O NMR OF SYNTHETIC POLYPEPTIDES

The oxygen atom is an important atom in the hydrogen bonding structure in peptides and polypeptides. Nevertheless, a solid state ^{17}O NMR study of peptides and polypeptides has never been carried out, to our knowledge. This is due to the very low sensitivity of solid state ^{17}O NMR measurements which arises for two reasons. One is that the ^{17}O nucleus is in very low natural abundance, 0.037%. The other is that the ^{17}O nuclear spin quantum number (I) is $\frac{5}{2}$, which is a quadrupolar nucleus, and so the ^{17}O signal is broadened by nuclear quadrupolar effects in the solid. On the other hand, solution state ^{17}O NMR spectroscopy has been employed successfully to elucidate a number of structural problems in organic chemistry,[42] because the ^{17}O signal becomes very sharp due to the removal of quadrupolar interaction by isotropic fast reorientation in solution. For example, as the oxygen atom is directly associated with the formation of hydrogen bonds, hydrogen bonding for the carbonyl group

in various compounds often results in large low-frequency shifts of the carbonyl ^{17}O NMR signal.[43] From these results, solution state ^{17}O NMR has been established as a means of investigating structural characterizations.

Clearly therefore, solid state ^{17}O NMR does offer a unique opportunity for understanding the hydrogen-bonding structure in solid peptides and polypeptides. Kuroki et al.[44] have observed high-resolution ^{17}O NMR spectra of systems with a wide range of hydrogen bond length, of PG I, PG II, glycylglycine (GlyGly) and glycylglycine nitrate (GlyGly·HNO_3) in the solid state, in order to obtain three kinds of NMR parameters: chemical shift, the quadrupolar coupling constant (e^2qQ/h) and the asymmetric parameter (η_Q), and to understand the relationship between the hydrogen bonding structure and these NMR parameters.

Static ^{17}O CP NMR spectra of GlyGly were observed at 36.6, 54.2, and 67.8 MHz. The spectra at 36.6 and 54.2 MHz consist of two major split signals, but that at 67.8 MHz becomes one major signal. Such splitting comes from the quadrupolar interaction. By computer simulation, the quadrupolar coupling constant e^2qQ/h was determined to be 8.55 MHz. This value is much larger than that for the amide ^{14}N nitrogen nucleus (1.11 MHz). It is seen that the NMR spectra depend strongly on the measurement frequency because the quadrupolar effect depends on the measurement frequency, and the broadening of the ^{17}O NMR signal is further increased by the quadrupolar effect as the measurement frequency is decreased. Thus, it is clear that high-frequency measurements are needed for quadrupolar nuclei such as ^{17}O.

Figure 8 shows 67.8 MHz static ^{17}O CP NMR spectra of PG I, PG II, GlyGly, and GlyGly·HNO_3 (points), compared with the computer simulations (continuous lines). The ^{17}O NMR parameters of PG I, PG II, GlyGly, and GlyGly·HNO_3 obtained by computer simulations are shown in Table 3. From these results, the δ_{11}, δ_{22}, and δ_{33} values of the samples were found to change from 546 to 574 ppm, 382 to 425 ppm, and − 132 to − 101 ppm, respectively. The magnitude of the chemical shift change is much larger than that of the carbonyl

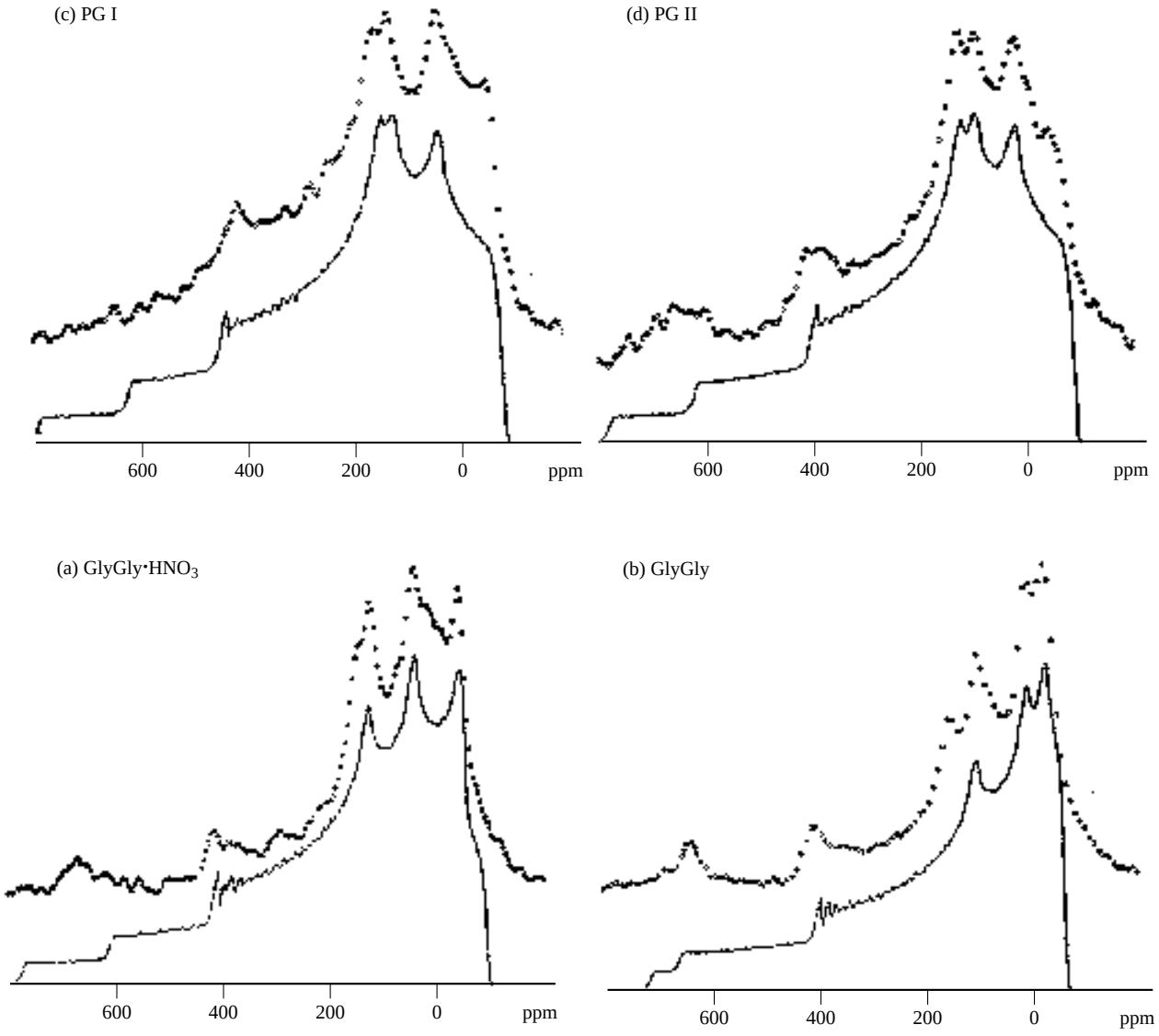

Figure 8 ^{17}O 67.8 MHz CP static NMR spectra of GlyGly·HNO_3 (a), GlyGly (b), PG I (c), and PG II (d), together with theoretically simulated spectra

Table 3 Determined ^{17}O NMR Parameters of Solid Peptides and Polypeptides Containing a Gly Residue

Sample	e^2qQ/h (MHz)	η_Q	Chemical shift tensor (ppm)						Angle Δ[a] (deg)		
			δ_{11}	δ_{22}	δ_{33}	δ_{iso}	$\Delta\delta$[b]	η[c]	α	β	γ
Polypeptides											
PG II	8.30	0.29	562	410	−108	288	396	0.38	92	89	−81
PG I	8.55	0.26	574	425	−101	299	400	0.37	100	91	−79
Oligopeptides											
GlyGly	8.55	0.45	546	382	−132	265	397	0.41	94	90	−87
GlyGly·HNO_3	8.75	0.47	559	408	−127	280	407	0.37	94	89	−81

[a]Angle Δ indicates the Euler angles between the principal axes of the quadrupolar tensor and the chemical shift tensor.
[b]$\Delta\delta = \delta_{iso} - \delta_{33}$.
[c]$\eta = (\delta_{11} - \delta_{22})/\Delta\delta$.

^{13}C and amide ^{15}N chemical shift. Every $\Delta\delta$ defined by $\Delta\delta = \delta_{33} - \delta_{iso}$, is about 400 ppm, which is much larger than that of the carbonyl ^{13}C and amide ^{15}N chemical shifts by about 170, 100 ppm, respectively. Every η value, defined by $\eta = (\delta_{22} - \delta_{11})/\Delta\delta$, is roughly 0.4. These values are common to the carbonyl oxygen in peptides. Although the chemical shift tensor is axially symmetric ($\delta_{11} = \delta_{22}$) for the case of the carbonyl oxygen of L-Ala as reported by Fiat and co-workers,[45,46] the chemical shift tensor of the carbonyl oxygen in the peptides considered here is not axially symmetric.

The e^2qQ/h values change from 8.30 to 8.75 MHz. These values are larger than the e^2qQ/h value of χ for L-leucine, which is 8.0 MHz at 190 K.[46] The η_Q values of polypeptides such as PG I and II are 0.26 and 0.29, and the η_Q values of oligopeptides such as GlyGly and GlyGly·HNO_3 are 0.45 and 0.47, respectively. The difference may come from a difference in molecular packing between them. Further, it is found that the principal axis of the quadrupolar tensor and the principal axis of the ^{17}O chemical shielding tensor for the carbonyl oxygen of the peptides and polypeptides are not coincident with each other. From these experimental results it can be said that each of the above NMR parameters is strongly influenced by the electronic structure of molecules.

So far, there has been little study aimed at determining the direction of the principal axes of the electric field gradient tensor and the chemical shielding of carbonyl oxygen of peptides and polypeptides from NMR experiments. The direction of the principal axes of the chemical shielding of the carbonyl oxygen of peptides and polypeptides has been calculated using FPT-MNDO-PM3 methods. It was found that the σ_{22} component lies approximately along the C=O bond, the σ_{11} component is aligned in the direction perpendicular to the C=O bond on the peptide plane, and σ_{33} which is the most shielded component is aligned in the direction perpendicular to the peptide plane. In the case of the electric field gradient tensor of the carbonyl oxygen, it was shown that the V_{22} component lies approximately along the C=O bond, the V_{33} component is aligned in the direction perpendicular to the C=O bond on the peptide plane, and the V_{11} component is aligned in the direction perpendicular to the peptide plane. These results show that the largest component V_{33} of the electric field gradient lies along the molecular chain direction. The relationship between the electric field gradient tensor and the chemical shielding obtained by this calculation agree with the experimental results.

The plot of the observed e^2qQ/h values vs. the hydrogen bond length shows that the e^2qQ/h values decrease linearly with a decrease in the hydrogen-bond length (R_{N-O}) (in Å) as expressed by e^2qQ/h (MHz) = 5.15 + 1.16R_{N-O}. This shows that the decrease of the hydrogen-bond length leads to a decrease in electric gradient (q). The value of q is very sensitive to the hydrogen-bond-length change. From this relationship it is apparent that the hydrogen-bond length can be determined by the observation of the e^2qQ/h value. The plot of the observed isotropic ^{17}O chemical shift values (δ_{iso}) against the hydrogen-bond length (R_{N-O}) shows that the δ_{iso} values in both peptides and polypeptides move upfield with a decrease in the hydrogen-bond length (R_{N-O}). The plot of the observed principal values of ^{17}O chemical shifts against the hydrogen-bond length (R_{N-O}) also shows every principal value in both the peptides and polypeptides and moves to low frequency with a decrease in the hydrogen-bond length (R_{N-O}).

From these experimental findings, it is clear that ^{17}O NMR spectroscopy will become a powerful tool for elucidating the hydrogen-bonding structure in solid peptides and polypeptides.

5 RELATED ARTICLES

Chemical Shift Tensors; Chemical Shifts in Biochemical Systems; Membrane Proteins; Oxygen-17 NMR; Protein Dynamics from Solid State NMR; Quadrupolar Nuclei in Solids.

6 REFERENCES

1. H. Saito, T. Tabeta, A. Shoji, I. Ando, and T. Asakura, in *Magnetic Resonance in Biology and Medicine*, eds. G. Govil, C. L. Kheterapal, and A. Saran, Tata McGraw-Hill, New Delhi, 1985, p. 195
2. S. O. Smith and R. G. Griffin, *Annu. Rev. Phys. Chem.*, 1988, **39**, 511.
3. G. A. Hartfield and G. E. Maciel, *Methods Protein Anal.*, **1988**, 214.
4. S. J. Opella and P. L. Stewart, *Methods Enzymol.*, 1989, **176**, 242; S. J. Opella, *Biol. Magn. Reson.*, 1990, **9**, 177.
5. H. Saito and I. Ando, *Annu. Rep. NMR Spectrosc.*, 1989, **21**, 210.
6. I. Ando, T. Yamanobe, and T. Asakura, *Prog. NMR Spectrosc.*, 1990, **22**, 349.
7. A. Shoji, S. Ando, S. Kuroki, I. Ando, and G. A. Webb, *Annu. Rep. NMR Spectrosc.*, 1993, **26**, 55.

8. H. Kurosu, S. Ando, H. Yoshimizu, and I. Ando, *Annu. Rep. NMR Spectrosc.*, 1994, **28**, 189.
9. I. Ando and G. A. Webb, *Theory of NMR Parameters*, Academic Press, London, 1983.
10. I. Ando, T. Yamanobe, H. Kurosu, and G. A. Webb, *Annu. Rep. NMR Spectrosc.*, 1989, **22**, 205.
11. H. Saito, R. Tabeta, A. Shoji, T. Ozaki, and I. Ando, *Macromolecules*, 1983, **16**, 1050.
12. I. Ando, H. Saito, R. Tabeta, A. Shoji, and T. Ozaki, *Macromolecules*, 1984, **17**, 457.
13. H. Saito, R. Tabeta, I. Ando, T. Ozaki, and A. Shoji, *Chem. Lett.*, 1983, 1437.
14. T. Akieda, H. Mimura, S. Kuroki, H. Kurosu, and I. Ando, *Macromolecules*, 1992, **25**, 5794.
15. S. Ando, T. Yamanobe, I. Ando, A. Shoji, T. Ozaki, R. Tabeta, and H. Saito, *J. Am. Chem. Soc.*, 1985, **107**, 7648.
16. S. Tuzi, T. Komoto, I. Ando, H. Saito, A. Shoji, and T. Ozaki, *Biopolymers*, 1987, **26**, 1983.
17. H. Miyamoto, T. Komoto, H. Kurosu, I. Ando, T. Ozaki, and A. Shoji, *J. Mol. Struct.*, 1990, **220**, 251.
18. S. Ando, I. Ando, A. Shoji, and T. Ozaki, *J. Am. Chem. Soc.*, 1988, **110**, 3380.
19. N. Asakawa, S. Kuroki, H. Kurosu, I. Ando, A. Shoji, and T. Ozaki, *J. Am. Chem. Soc.*, 1992, **114**, 326.
20. H. Piocova, V. Sasudek, P. Schmidt, D. Hlavata, J. Plestill, and F. Lauprette, *Polymer*, 1987, **28**, 1991.
21. H. Saito, R. Tabeta, T. Asakura, Y. Iwanaga, A. Shoji, T. Ozaki, and I. Ando, *Macromolecules*, 1984, **17**, 1405.
22. T. Asakura, M. Demura, Y. Watanabe, and K. Sata, *J. Polym. Sci., Polym. Phys. Ed.*, 1992, **30**, 693.
23. D. A. Torchia and D. L. VanderHart, *J. Mol. Biol.*, 1976, **104**, 315.
24. Y. Hiyama and D. A. Torchia, *Basic Life Sci.*, 1990, **56**, 273.
25. H. Saito, R. Tabeta, A. Shoji, T. Ozaki, I. Ando, and T. Miyata, *Biopolymers*, 1984, **23**, 2279.
26. S. Tuzi, S. Sakamaki, and I. Ando, *J. Mol. Struct.*, 1990, **221**, 289.
27. H. Yoshimizu and I. Ando, *Macromolecules*, 1990, **23**, 2908.
28. H. Yoshimizu, H. Mimura, and I. Ando, *Macromolecules*, 1991, **24**, 862.
29. J. W. Mack, D. A. Torchia, and M. Steinert, *Biochemistry*, 1988, **27**, 5418.
30. H. Tournois, J. L. Bijvelt, C. W. M. Haest, J. Ier, and B. Kruiff, *Biochemistry*, 1987, **26**, 6613.
31. L. K. Nicholson, F. Moll, T. E. Mixon, P. V. LoGrasse, J. C. Lay, and T. A. Cross, *Biochemistry*, 1987, **26**, 6621.
32. G. S. Harbison, J. Herzfeld, and R. G. Griffin, *Biochemistry*, 1983, **22**, 1.
33. S. O. Smith, H. J. M. De Groot, R. Gebhard, J. M. L. Courtin, J. Lugtenburg, J. Herzfeld, and R. G. Griffin, *Biochemistry*, 1989, **28**, 8897.
34. R. A. Santos, E. S. Gruff, S. A. Koch, and G. S. Harbison, *J. Am. Chem. Soc.*, 1991, **113**, 469.
35. J. R. Garbow, H. Fujiwara, C. R. Sharp, and E. W. Logusch, *Biochemistry*, 1991, **30**, 7057.
36. J. Schaefer, K. J. Kramer, J. R. Garbow, G. S. Jacob, E. O. Stejskal, T. L. Hopkins, and R. D. Speirs, *Science*, 1987, **235**, 1200.
37. A. Shoji, T. Ozaki, T. Fujito, K. Deguchi, and I. Ando, *Macromolecules*, 1987, **20**, 2441.
38. A. Shoji, T. Ozaki, T. Fujito, K. Deguchi, S. Ando, and I. Ando, *Macromolecules*, 1989, **22**, 2860.
39. A. Shoji, T. Ozaki, T. Fujito, K. Deguchi, S. Ando, and I. Ando, *J. Am. Chem. Soc.*, 1990, **112**, 4693.
40. A. Shoji, T. Ozaki, T. Fujito, K. Deguchi, and I. Ando, in preparation.
41. L. K. Nicholson and T. A. Cross, *Biochemistry*, 1991, **28**, 607.
42. ed. D. W. Boykin, *^{17}O NMR Spectroscopy in Organic Chemistry*, CRC Press, Boca Raton, FL, 1991.
43. D. W. Boykin and A. L. Baumstark, *New J. Chem.*, 1992, **16**, 357.
44. S. Kuroki, A. Takahashi, I. Ando, A. Shoji, and T. Ozaki, *J. Mol. Struct.*, 1994, **323**, 197.
45. R. Goc, E. Ponnusomy, J. Tritt-Goc, and D. Fiat, *Int. J. Pept. Protein Res.*, 1988, **31**, 130.
46. R. Goc, J. Tritt-Goc, and D. Fiat, *Bull. Magn. Reson.*, 1989, **11**, 238.

Biographical Sketches

Isao Ando. *b* 1941. Ph.D., 1972 (supervisor Atsuo Nishioka), polymer chemistry, Tokyo Institute of Technology, Japan. Postdoctoral work at University of Illinois, Urbana (with Herb Gutowsky). Successively research associate, associate professor, and professor, Tokyo Institute of Technology. Approx. 250 publications. Research specialties: structures and electronic states of solid polymers and biopolymers, solid state NMR, and nuclear shielding calculation.

Shigeki Kuroki. *b* 1965. Ph.D., 1994 (supervisor Isao Ando), polymer chemistry; postdoctoral fellowship, 1994–present, Tokyo Institute of Technology. Approx. 15 publications. Research specialties: structures of solid biopolymers, and solid state NMR.

Structure and Dynamics of Proteins Adsorbed at Biomaterial Interfaces

Gary P. Drobny, Joanna R. Long, Wendy J. Shaw, Myriam Cotten, and Patrick S. Stayton

University of Washington, Seattle, WA, USA

1 Introduction 1
2 NMR Strategies for Studying Surface-Adsorbed Proteins 2
3 A Solid-State NMR Study of Salivary Statherin Adsorbed onto Hydroxyapatite (HAP) Crystals 6
4 Related Articles in Volumes 1–8 9
5 References 9

1 INTRODUCTION

1.1 Biomineralization: Background and Significance

Biomineralization, defined as the organized deposition of inorganic materials in the cellular or extracellular matrix, may be as simple a process as the formation of an iron oxide crystal in the vesicle of a magnetobacterium, or as complex a process as the formation of the intricate calcium carbonate and calcium phosphate structures found in marine coccoliths, invertebrate shells, vertebrate skeletons and teeth. The phenomenon of biomineralization has attracted a great deal of attention recently from the materials science community, which seeks to understand the way in which inorganic biological composites are synthesized and processed in nature.[1–8]

An extremely important problem in the field of biomineralization is understanding the manner in which mineral deposition is controlled in vivo. The crystal engineering processes necessary to achieve the controlled deposition of minerals at physiological temperatures and in aqueous solutions are directly provided by proteins in most known examples.[7,9–17] In particular, the deposition of minerals in most hard tissues in higher organisms is controlled by a class of unusually acidic, non-collagenous proteins and glycoproteins.[9,10,17,21–28] These acidic proteins typically comprise only about 1% of the mass of the organic matrix, and are frequently found sandwiched between crystal surfaces and major framework molecules like collagen or chitin. They are rich in acidic amino acids including aspartic and glutamic acid, and contain large numbers of phosphorylated amino acids, especially phosphoserine.

In the specific case of hydroxyapatite ($Ca_{10}(PO_4)_6(OH)_2$), the principal mineral component of bone and dental enamel, extra-cellular, acidic, non-collagenous proteins include apatite nucleators like bone sialoprotein, osteonectin, and dentin phosphoryn, while osteocalcin, osteopontin, and salivary statherin inhibit apatite formation and growth. In some cases (e.g., osteonectin, bone sialoprotein, and dentin phosphoryn) apatite formation is inhibited at high protein concentration while nucleation of apatite occurs at low protein concentration.

Substantial progress has been made in recent years in characterizing, at the macroscopic level, the structural properties of biological composites,[1,18–20] but there is still a significant gap in our understanding of the molecular recognition processes underlying acidic protein-calcium composite interactions. In particular, while protein model structures have been proposed which hypothesize the involvement of protein secondary structure motifs for presentation of carboxylate residues,[10,13,26,28,29] the lack of high resolution structural data for proteins on surfaces precluded any molecular structure vs. function studies.

The acquisition of molecular-level structural information for proteins on surfaces is not only important to the field of biomineralization but has broad applicability in a number of important fields. For example, there is currently a great deal of effort in the fields of drug delivery, implant design, tissue engineering, and diagnostics directed toward developing polymeric surfaces for immobilization and controlled release of peptides and proteins. Detailed structural information about proteins bound to material surfaces will provide important new design criteria from the perspective of peptide/protein structure, dynamics, and assembly at polymeric biomaterial surfaces.

1.2 The Role of Protein-Crystal Interactions in Biomineralization

Understanding the function of a biomineralization protein requires that the secondary and tertiary structure of the molecule be defined within its biological context, i.e. the protein in contact with the crystal. In addition, the precise nature of the interactions between the protein and the crystal which underlie the recognition process must be understood. This requires a knowledge of the contacts formed between the amino acid side chains of the protein and the ions in the crystal faces. The involvement of water molecules in these interactions must be understood as well.

Current investigations of protein-mineral interactions are commonly conducted with techniques that characterize the macroscopic behavior of proteins in the presence of mineral crystals. Equilibrium properties such as protein-crystal binding constants are derived via adsorption isotherm measurements, where data are analyzed usually by assuming a simple Langmuir model of protein adsorption onto the crystal faces. But the most commonly-used approach for determining protein-crystal interactions in vitro are kinetic experiments in which a small amount of protein is dissolved in a saturated solution of a particular inorganic salt and the time required for crystals to form is compared to a control solution in which no protein is present. Assays also exist for determining selective binding of a particular crystal face by a protein as well as oriented nucleation of crystals in the presence of acidic proteins.[30]

However, to move beyond macroscopic aspects of protein-crystal interactions, what is clearly needed are high resolution spectroscopic methods that can provide information about the atomic level structure of the protein on the crystal face, under physical conditions that are biologically relevant (physiological levels of hydration and pH). Information about the secondary structural motifs that occur in the adsorbed protein together with information on the exposure of protein

side chains to the crystal face, may lead to an understanding of how particular proteins promote or inhibit nucleation. Analytical techniques currently used to probe protein-crystal interactions at the atomic and molecular levels and the advantages that solid state NMR bring to the field will be briefly reviewed in the next section.

2 NMR STRATEGIES FOR STUDYING SURFACE-ADSORBED PROTEINS

The lack of high resolution structural data for proteins on surfaces is the result of a lack of high resolution structural methods that can be brought to bear on relevant problems. The conventional methods of high resolution structural biology, X-ray crystallography and solution nuclear magnetic resonance (NMR) spectroscopy have provided information on a few biomineralization proteins in the pure crystalline and solution states,[31–33] but both techniques are severely limited in their abilities to elucidate the structures of proteins on biomineral surfaces. Although traditional surface science methods like photo-electron spectroscopy and NEXAFS have provided important information on protein adsorbed onto planar surfaces, and, in particular, may be used to characterize the degree of long range ordering in systems of adsorbed proteins on polymer surfaces as well as average structural properties, these techniques have yet to provide detailed atomic-level structural information for surface-adsorbed proteins. In addition surface diffraction methods and many optical techniques are not applicable to proteins adsorbed onto porous surfaces (e.g., porous plastics) or to other surfaces which preclude long-range ordering.

To fully appreciate the utility of solid state NMR in the study of protein structure at biomaterial interfaces, it is first important to recognize the dual nature of the protein-surface problem. There is first the familiar structural aspect, alluded to briefly in the prior section, which includes defining the secondary and tertiary structures of the adsorbed protein and by implication any structural changes which occur upon binding to the surface. The structure and chemical composition of the crystal surface in contact with the protein side chains must also be understood. In addition, a less familiar but no less important aspect is the dynamics of the adsorbed protein. It is desirable that the protein be observed on the surface under biologically relevant conditions, i.e., fully hydrated. Dehydration of the sample may alter not only the structure of the protein from its biologically relevant form but may quench the dynamics of the protein on the surface. Here we refer to both whole-molecule dynamics describing the protein's rigid body kinematics on the surface and to internal dynamics wherein the protein's conformation may be labile on the NMR time scale. In the following section we will review how solid state NMR can be used to probe both molecular structure and dynamics on surfaces.

2.1 NMR Structural Methods for the Study of Protein Structure at Biomaterial Interfaces

Solid state NMR has long been used to identify and characterize the structures of small organic molecules adsorbed onto catalytic surfaces,[34–36] argon matrices,[37] and silica surfaces.[38–40] There similarly exist a number of solid state NMR pulse techniques capable in principle of reporting the structures of surface-adsorbed proteins. The most straightforward approach is to evaluate the secondary structure of surface-adsorbed proteins from the chemical shifts of ^{13}C spins located in the protein backbone. This approach basically exploits the fact that the isotropic chemical shifts of the backbone carbonyl, alpha, and beta ^{13}C spins of each amino acid residue are to varying extents sensitive to the local secondary structure of the protein. Although recent work by Oldfield and coworkers has placed structural interpretation of isotropic ^{13}C chemical shifts of proteins on a quantitative basis,[41–43] in the past analyses of structures using chemical shift data have been applied empirically, i.e., by comparing experimentally observed ^{13}C chemical shifts for backbone ^{13}C spins to a large body of data, derived via ^{13}C Cross Polarization/Magic Angle Spinning (CPMAS) experiments from polypeptides of known secondary structure in the condensed state. An excellent example of this type of analysis is the seminal work by Fernandez et al.[44] who studied the structures of polyglutamic acid and polylysine adsorbed to hydroxyapatite and silica using ^{13}C CPMAS. In addition to studies of the conformations of polypeptides on apatite and silica surfaces, ^{13}C MAS has been used to study the incorporation of carbonate ions in bone and synthetic apatites,[45] and ^{31}P MAS has been used to characterize the structures of various calcium phosphates found in biological systems.[46–48]

Isotropic chemical shift data can be supplemented by quantitative structural data obtained via orientational constraints and/or distance/torsion angle constraints. The best examples that illustrate the use of orientational constraints and distance/torsion angle constraints come from the membrane protein literature. Structural data on membrane-associated proteins have been acquired by two general types of solid state NMR data: (1) orientational constraints, usually obtained from magnetic interaction tensors located in the backbone of proteins oriented in mono-domain lipid bilayers; and (2) distance and torsion angle constraints acquired from proteins associated with unaligned lipid vesicles. The former class of experiment requires the application of local field spectroscopy techniques (e.g., PISEMA) to oriented samples.[49] Although possible to achieve with lipids, there is no general analog in biomaterial interfaces to the mono-domain bilayer construct, so the orientational constraint approach has yet to be applied to biomaterials. Because distance and torsion angle constraints are generally acquired from unoriented samples via homo- and heteronuclear dipolar recoupling experiments, this approach shows the greatest promise in studies of surface-adsorbed biopolymers.

There are a number of dipolar recoupling experiments currently used to address a variety of problems in the material and biological sciences. No attempt will be made here to comprehensively cover all the alternative methods, their relative advantages and disadvantages. The reader is referred to general review articles on the subject of dipolar recoupling for more extensive treatments of dipolar recoupling.[50,51] The following discussion is provided simply to clarify some general properties of dipolar recoupling sequence referred to in descriptions of studies of surface-adsorbed proteins.

Solid state NMR spectra of spin 1/2 nuclei are dominated by two magnetic interactions, the chemical shift anisotropy (CSA) and the direct nuclear dipole-dipole interaction (Figure 1). As discussed above, the former interaction is valuable as a qualitative probe of protein structure. The dipole-dipole interaction

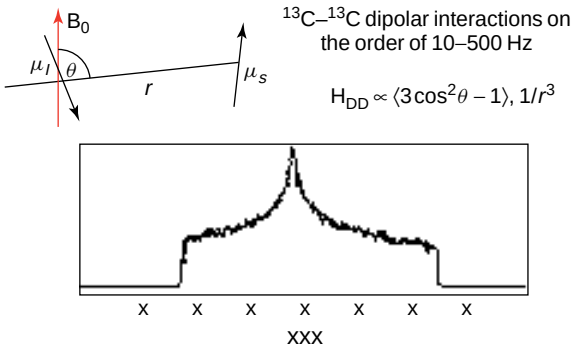

Figure 1 The dipolar coupling tensor is a uniaxial tensor. The principal axis frame of this dipolar tensor has a z axis parallel to the internuclear vector. The dipolar coupling is proportional to the inverse cube of the internuclear distance $\langle 1/r^3 \rangle$, and the second order Legendre polynomial $\langle (3/2)\cos^2\theta - (1/2) \rangle$, where θ is the angle between the internuclear vector and the magnetic field. The solid state NMR spectrum of a pair of dipolar-coupled spin 1/2 nuclei with negligible CSA's should be a Pake powder pattern, from which the dipolar coupling constant may be easily extracted. However, if the coupled spin 1/2 nuclei have CSA's much larger than the dipolar coupling it will be difficult to extract the dipolar coupling constant from the NMR powder spectrum. The figure shows the powder spectrum of two dipolar coupled ^{13}C spins, each with a CSA on the order of 20 kHz; and with dipolar coupling of 500 Hz, corresponding to a ^{13}C pair separated by 2.5 Å. The spectrum is clearly dominated by the CSA and it is very difficult to discern the presence of a dipolar coupling in the spectral data

has a straightforward structural interpretation because the dipolar coupling constant is proportional to the inverse cube of the internuclear distance. However, in many systems composed of coupled spin 1/2 nuclei, the magnitude of the CSA may exceed the magnitude of the dipole-dipole interaction. For example, for two sp^2 hybridized, directly bonded ^{13}C spins the CSA's may approach 200 ppm, corresponding to over 20 000 Hz in a 9.4 Tesla magnetic field. On the other hand, the dipole-dipole interaction for this directly bonded spin pair will not exceed 2300 Hz. and may be even smaller for non-bonded ^{13}C spins. Therefore the dipolar coupling constant may not be easily discerned in spectral data when the CSA exceeds the dipolar interactions by orders of magnitude so it is necessary to use NMR methods which suppress one of these interactions thus enabling straightforward detection of the other.

In the late 1960s NMR coherent averaging experiments were introduced to remove the dipolar coupling between spin 1/2 nuclei (^{19}F, ^{1}H, etc.) in crystalline solids, while simultaneously preserving the chemical shift anisotropy (CSA).[52,53] The spin dynamics that underlie these experiments have been thoroughly quantified with Average Hamiltonian Theory (AHT).[54,55] Basically, homonuclear dipolar decoupling sequences like WHH-4,[53] MREV-8,[56] BR-24,[57] MSHOT-3[58] etc. exploit the different transformational properties of the chemical shift anisotropy (CSA) and the dipolar interaction in spin space to remove the homonuclear dipolar interaction while preserving a scaled CSA.

Physical rotation of the sample (i.e., Magic Angle Spinning,[59] MAS) coherently averages spatial parts spin interaction Hamiltonian that transform as second rank tensors. However, both the dipolar and the chemical shift Hamiltonians transform as second rank tensors in Cartesian space, so MAS removes the effect of both interactions from solid-state NMR spectra. The objective of dipolar recoupling is to use MAS and radio frequency (rf) irradiation in synchrony, with the ultimate objective of suppressing the chemical shift while preserving the dipolar coupling. Because information on internuclear distances can be recovered using dipolar recoupling techniques, these pulse sequences are widely used in structural studies of molecular solids.

The two dipolar recoupling pulse sequences that will be discussed in the context of structural studies of proteins adsorbed at biomaterial interfaces are the heteronuclear recoupling experiment Rotational Echo Double Resonance (REDOR) and the homonuclear recoupling experiment Dipolar Recoupling with a Windowless Sequence[60] (DRAWS). REDOR, developed by Schaefer and coworkers has been reviewed elsewhere.[61] We confine our remarks to stating that in studies of surface-adsorbed biopolymers REDOR has a number of uses including: (1) Direct characterization of the surface, as was done by Pan[62] who used ^{31}P–^{19}F REDOR to study the distribution of ^{19}F in fluoroapatite; (2) ^{13}C–^{15}N REDOR to confirm helical secondary structures in surface-adsorbed proteins by measuring hydrogen bond lengths between the ^{13}C carbonyl spin of the i residue to the ^{15}N amide spin of the $i+4$ residue; and (3) probing dipolar interactions from ^{13}C and ^{15}N spins in protein side chains to NMR-active spins in the surface, ^{31}P spins in hydroxyapatite and ^{19}F spins in fluoropolymers, for example.

DRAWS is well suited to measuring distances between backbone carbonyl carbons in peptides and proteins.[63–66] Dipolar couplings of less than 40 Hz between carbonyl ^{13}C spins have been detected in biopolymers at high magnetic fields,[67–70] attesting to the ability of DRAWS to suppress large CSAs and at the same time detect small dipolar couplings between non-bonded ^{13}C spins. Figure 2 shows three forms of the DRAWS dipolar recoupling pulse sequence. In the DRAWS experiment, the unit pulse cycle (Figure 2a) is applied synchronously with the sample spinning and thus the duration of the unit cycle is exactly equal to one rotor period τ_{rotor}. The DRAWS experiment, which utilizes a four step supercycle, shown in Figure 2(a), is commonly employed in the context of a CPMAS experiment, see Figure 2(a). The basic strategy is to detect the amplitude of transverse magnetization that remains after an integral number of DRAWS super-cycles. Repeating this measurement as a function of the number of DRAWS supercycles results in a "dephasing" curve (Figure 3). Simulation of this dephasing curve results in a value for the internuclear distance.

The DRAWS dephasing curve is a useful measurement for determining protein secondary structure because, as shown in Figure 3, the carbonyl-carbonyl distance is directly related to the Ramachandran torsion angle φ. Therefore, using DRAWS distance measurements, the torsion angle φ may be determined at several positions in a peptide in a model-independent fashion. An example of a DRAWS experiment applied to a crystalline tripeptide alanylglycylglycine (AGG), labeled at both carbonyl positions with ^{13}C, is shown in Figure 4. Agreement with the crystallographically determined φ of -83° is excellent. Additionally, DRAWS can also measure conformational heterogeneity since the dipolar recoupling efficiency is independent of any correlation between chemical shift and peptide secondary structure. This allows the determination of the distribution of peptide conformers in a given sample.

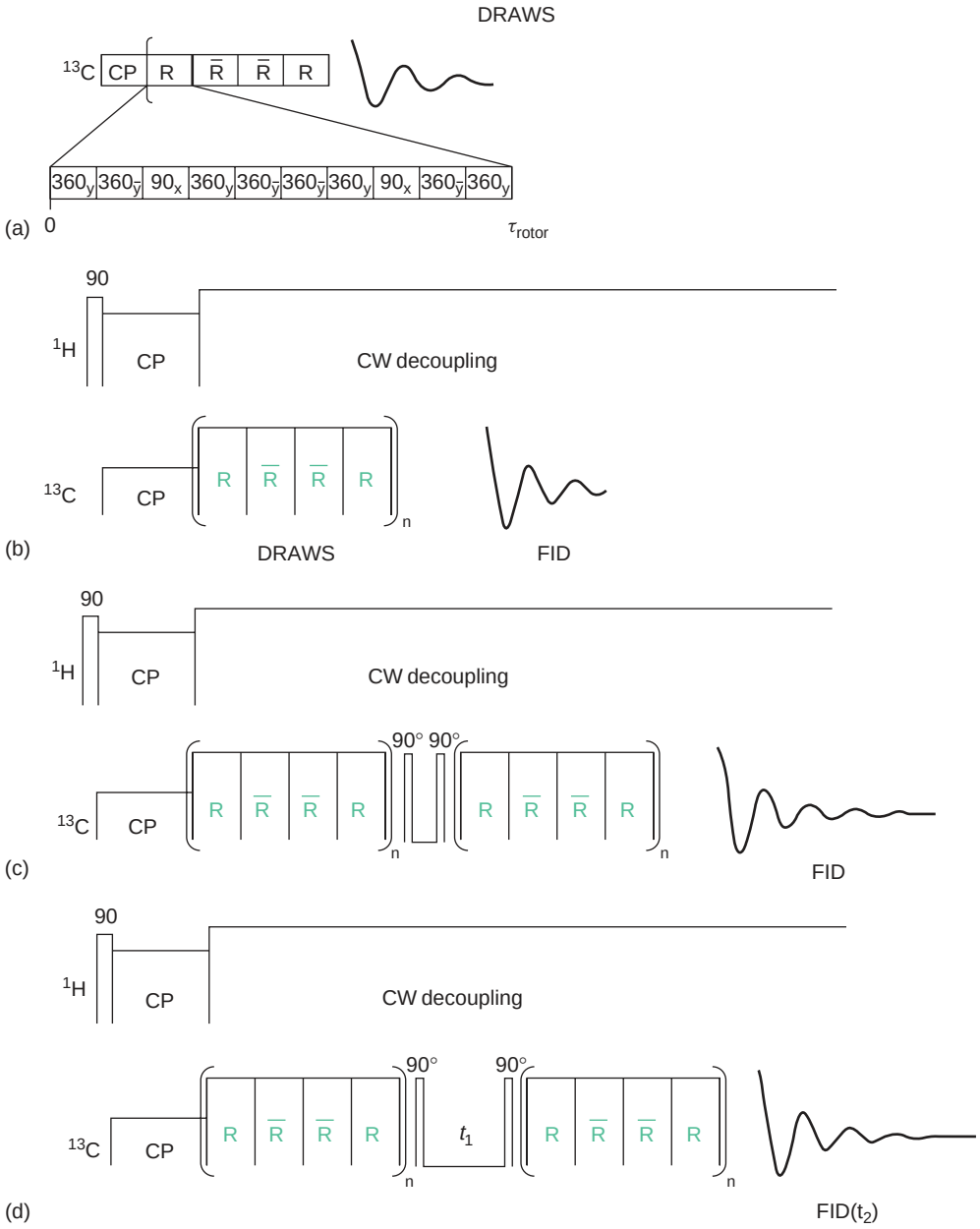

Figure 2 In most dipolar recoupling pulse sequences, pulsed irradiations are applied synchronously with the sample rotation. In DRAWS, the eight 360° pulses (alternating Y and −Y phases) and two ninety degree pulses (X phases) that constitute the unit pulse cycle (R) are applied within a single period of the rotor (τ_{rotor}). (a) The unit pulse cycle for DRAWS (Dipolar Recoupling with a Windowless Sequence) is supercycled as $R\overline{R}\overline{R}R$, where $\overline{R}$ indicates a unit cycle phase-shifted by 180°. (b) DRAWS applied in the context of a CPMAS experiment. (c) Pulse Sequence for Doubled Quantum-filtered DRAWS. (d) Two dimensional pulse sequence for double quantum DRAWS (DQDRAWS)

DRAWS dephasing curve data may be difficult to quantify in terms of an internuclear distance if a large background signal occurs from ^{13}C spins at natural abundance. The ^{13}C background arises from portions of the protein that are not enriched with ^{13}C or may come from the surface itself if the mineral contains carbon (e.g., calcite) or if the mineral contains organic impurities (e.g., carbonate incorporated into apatite crystals). In such cases NMR signals arising from dipolar coupled spin pairs are separated from the natural abundance signal, which arises mainly from isolated spins, by filtering the DRAWS signal through a double quantum state. The preparation of double quantum coherence using DRAWS dipolar recoupling is called DQDRAWS. The DQDRAWS filtering experiment is shown in Figure 2(c). Applying a DRAWS pulse sequence for a preparation time τ (typically 3–6 ms for carbonyl ^{13}C spins in the backbone of a surface-adsorbed protein) generates dipolar-correlated spin coherence (also called anti-phase magnetization). Applying a 90° pulse then generates double quantum coherence. In the double quantum buildup experiment, this coherence is immediately transferred back to anti-phase magnetization by a second 90° pulse and then to observable magnetization by reapplying the DRAWS mixing sequence for the same amount of time. The buildup of double quantum coherence is then monitored

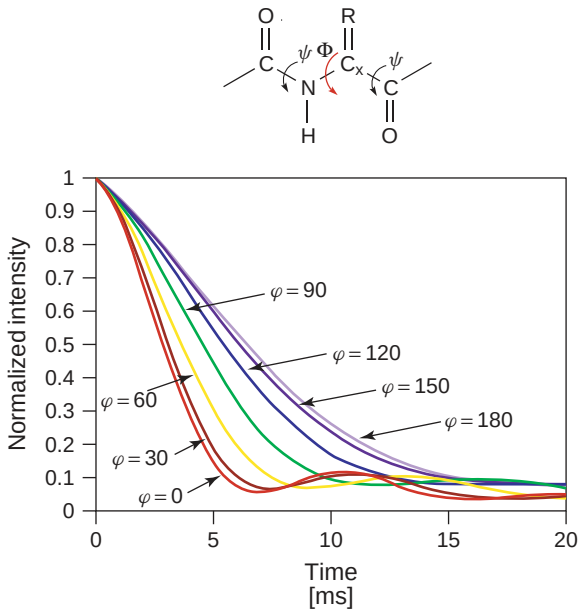

Figure 3 Simulated DRAWS decay curves for dipolar-coupled ^{13}C–^{13}C carbonyl spin pairs in the backbone of a polypeptide. The carbonyl-carbonyl distance is directly related to the Ramachandran angle φ

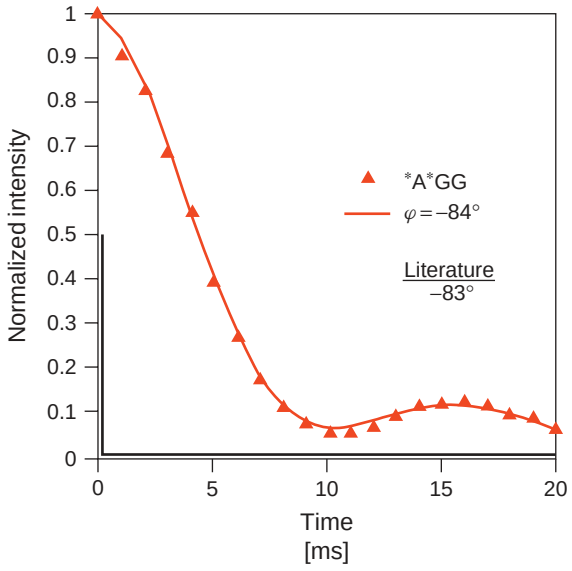

Figure 4 Experimental DRAWS dipolar dephasing curve obtained for the doubly carbonyl ^{13}C labeled crystalline tri-peptide alanyl-glycylglycine (AGG). The solid line is the simulation assuming a Ramachandran angle of −84°

as a function of the DRAWS mixing time to determine dipolar couplings and hence the inter-nuclear distance. As in the simple DRAWS experiment, the DQDRAWS filtering experiment can quantify the carbonyl-carbonyl distance and hence the Ramachandran angle φ.

Direct detection of a double quantum coherent state results in a simultaneous measurement of the (φ, ψ) Ramachandran angles.[64,71] As in other multiple quantum experiments, a double quantum state is detected via a two dimensional experiment, the pulse sequence is shown in Figure 2(d). In the 2-dimensional DQDRAWS experiment, the DRAWS pulse sequence is again applied for a preparation time τ to generate the antiphase state. After the magnetization is transferred to the double quantum state by a 90° pulse it is allowed to evolve under the chemical shift and dipolar interactions for a time t_1. The magnetization is then transferred back to observable by a second 90° pulse and reapplying the DRAWS mixing sequence for the same amount of time. Monitoring the free induction decay (FID) during the detection time t_2 as a function of double quantum evolution time t_1 yields a two dimensional interferogram. Two dimensional Fourier transformation of the time domain data followed by projection onto the ω_1 axis (i.e. the double quantum frequency axis) yields the double quantum spectrum, see Figure 5. The double quantum spectrum consists of a "fundamental" frequency, which occurs at the sum of the isotropic chemical shift frequencies of the coupled ^{13}C spins, together with side bands at integral multiples of the spinning frequency. The double quantum spinning side band intensities are dependent on the principal values of the *sum* chemical shift tensor. Because the individual chemical shift tensors add as second order tensors, the sum tensor is sensitive to the mutual orientation of the principal axis systems of the CSA tensors of the coupled ^{13}C spins.

Since carbonyl carbons in peptides possess highly anisotropic CSAs, they are particularly sensitive to the DQDRAWS approach. The relative orientations of the carbonyl carbon CSAs to the peptide amide bonds are well-studied,[72] and thus the torsion angles (φ, ψ) can be extracted by simulating the DQ spectrum. Determining (φ, ψ) with this level of accuracy not only yields secondary structure, but also gives some indication of helical pitch or twist and long range order.

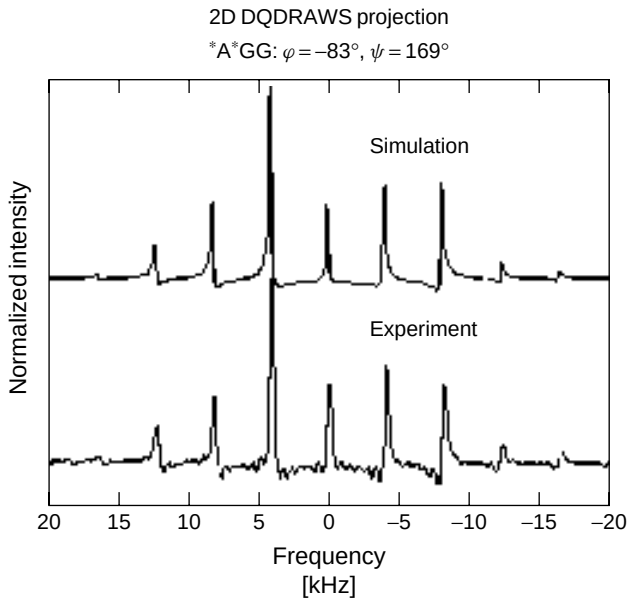

Figure 5 Simulated and experimental projections of the two dimensional double quantum DRAWS (DQDRAWS) spectra of the doubly carbonyl ^{13}C labeled crystalline tri-peptide alanylglycylglycine (AGG). The simulation assumes $\varphi = -83°$ and $\psi = 169°$

2.2 The Effect of Dynamics on the Solid State NMR Spectrum of Surface-Adsorbed Proteins

A common property of polymers is structural deformability. Polymeric molecular systems may display structural heterogeneity, meaning the polymeric system may display a distribution of static structures. In addition, the polymer may display structural lability, meaning that the molecular system cannot be described as strictly confined to one or a small number of equilibrium states, but rather possesses a kinetic aspect wherein the structure of each molecule changes in time. In such cases important properties of the polymer include the time scale and amplitude of the internal molecular motions.

The interaction between two nuclear magnetic dipoles, the interaction between the nuclear quadrupole moment and surrounding electric field gradients, and the chemical shift, are inherently tensorial quantities. In addition, these interactions detectable by NMR have sufficient anisotropy to dominate the solid state NMR spectral line shape. If internal motions modulate the orientation of magnetic interaction tensors relative to the static magnetic field direction, the solid state NMR line shape will be averaged in a way that reflects both the amplitude and the time scale of the internal motions. In addition, the relaxation of the nuclear system will be described by the time-dependent part of the spin interaction Hamiltonian. For these reasons the dynamic properties of solid polymers are frequently probed through measurements of NMR relaxation and line shapes.

Solid state NMR studies of polymer dynamics constitute an extensive literature, which cannot be summarized here in any thorough way. However, it is useful to briefly review some of the important NMR methods used in the past to characterize polymer dynamics, including surface-adsorbed polymers, in order to appreciate how these methods may or may not suffice to characterize surfaced-adsorbed proteins.

The most extensive class of polymers studied to date by solid state NMR methods are synthetic, organic polymers common examples being polystyrene,[73] polycarbonate,[74–76] polystyrene–polybutadiene blends,[77] poly(ethylene-terephthalate),[78,79] to name just a very few. In addition there are numerous reports on liquid crystal polymers,[80,81] polymers tethered to silica surfaces,[39] and polylysine and polyglutamic adsorbed to silica and hydroxyapatite surfaces.[44] In the case of hydrocarbon-based polymers the NMR dynamic probes are ^{13}C relaxation and line shape studies, proton relaxation and spin diffusion studies. In cases where protons can be replaced by deuterium, deuterium line shape and relaxation studies may be used to probe polymer motions. Because synthetic polymers are composed of regularly repeating, largely identical subunits, isotopic enrichment usually cannot be performed in a site selective manner. This means that NMR studies of polymer dynamics reflect motions that are associated with a repeating unit, or a part of the repeating unit.

Many of the problems and questions in biomineralization are similar to the structure/function issues familiar in structural biology and concentrate on specific domains within the protein: e.g., what is the identity, structure and dynamics of the mineral binding surface of the protein, what is the relationship of this binding domain to the rest of the protein, and how are the structure and dynamics of this domain related to the function? This latter question can only be answered if the orientation of the protein relative to the surface is known. These questions can only be addressed by studying the NMR line shapes and relaxation of specific sites within the protein, before and after adsorption.

3 A SOLID-STATE NMR STUDY OF SALIVARY STATHERIN ADSORBED ONTO HYDROXYAPATITE (HAP) CRYSTALS

Salivary statherin is a particularly well studied acidic phosphoprotein that inhibits the nucleation and growth of calcium phosphate minerals in the oral environment, and acts as a boundary lubricant.[82–87] The N-terminus of statherin is highly charged, with the first five amino acids containing one aspartic acid, two phosphorylated serines, and two glutamic acids that have been shown to be important in the recognition of HAP[83] (Figure 6). A solution NMR study of statherin,[87] acquired in a water/TFE solvent mixture, found the N-terminus to be alpha helical and the C-terminus was judged to be a 3_{10} helix, although the relative paucity of NOE's in the C-terminus was interpreted as indicating non-rigidity. Recent solid state NMR studies have shown that the N-terminal 15 amino acid peptide derived from statherin (called SN-15), which is believed to constitute the bulk of the HAP binding site, is partly helical on the HAP surface.[88] Also, while the N-terminal 3–6 amino acids are immobilized on the surface, the remaining portion of the peptide toward the C-terminus show increased mobility.[89]

However, to conclusively define the structure of the HAP-binding domain, the full-length protein must be studied on the mineral surface. In this section, we show how solid state NMR techniques have been applied to full length phosphorylated statherin on the hydroxyapatite crystal surface to characterize the high-resolution structure and dynamics of the N-terminal binding domain under hydrated and lyophilized conditions.

Site-specific isotopic labeling of statherin allowed structural determinations to be made unambiguously using the dipolar recoupling techniques DQDRAWS[90,91] and REDOR. DQDRAWS, a double-quantum variant of the DRAWS homonuclear recoupling technique, was applied to measure the distance between adjacent backbone carbonyl carbons and thus yield model-free determination of the backbone torsion angle φ. Determination of individual torsion angles yields insights into local secondary structure as well as structural heterogeneity. Typically α-helices are indicated by torsion angle values in the range of $-45°$ to $-80°$ with a mean of $-63°$ (Figure 7). The average values of β-sheets are somewhat larger, varying from $-80°$ to $-150°$ with a mean of

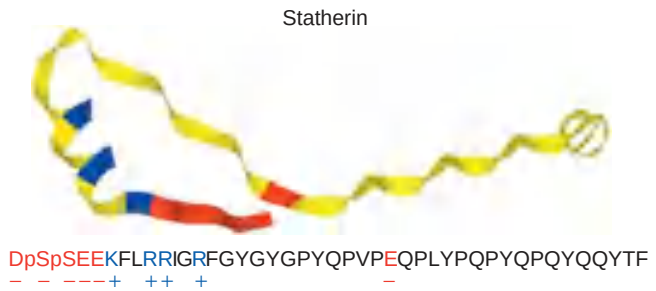

Figure 6 The primary sequence of the 43 amino acid protein salivary statherin and a possible structure based on solution and solid state NMR data

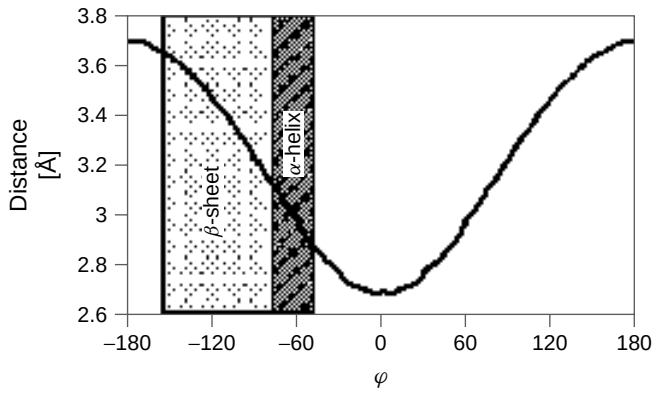

Figure 7 The carbonyl-carbonyl distance in the backbone of a polypeptide for various secondary structure motifs

−130°. REDOR, a heteronuclear recoupling technique, was used to measure the distance between the backbone carbonyl carbon and the backbone nitrogen involved in the hydrogen bond of a putative α-helical domain. This measurement is very sensitive to global secondary structure since theoretical distances expected for classical secondary structures vary from 4.2 Å for an α-helix to 10.6 Å for a β-sheet. Although isotropic chemical shifts of proteins can give qualitative indications of secondary structure in homogeneous systems, their values can be influenced by the bulk magnetic susceptibility of the support in heterogeneous systems. This makes them unreliable for structural determination in proteins closely associated with or adsorbed on inorganic surfaces such as HAP. Solid state NMR of ^{13}C nuclei is also very sensitive to dynamics, which can be probed over several order of magnitude by measuring chemical shift anisotropies (CSAs), relaxation constants including carbon T_1's and $T_{1\rho}$'s, and proton $T_{1\rho}$'s.

The structure and dynamics of salivary statherin were analyzed at the pS_2, pS_3, F_7, L_8, I_{11} and G_{12} residues. Pairs of backbone carbonyl carbons were enriched at the pS_2pS_3, F_7L_8, and $I_{11}G_{12}$ positions in separate samples and probed using DRAWS and DQDRAWS. A ^{13}C enriched carbonyl carbon was introduced at the (i) position with an ^{15}N enriched amide nitrogen at the (i + 4) position in $pS_3F_7$and L_8G_{12} samples and probed using REDOR to verify the presence or absence of hydrogen bonding. The dipolar recoupling data for the pS_2pS_3 and pS_3F_7 samples are shown in Figure 8. All 5 samples were characterized using standard ^{13}C CPMAS and $T_{1\rho}$ relaxation sequences to measure any averaging of carbonyl carbon CSAs, cross polarization efficiencies, or relaxation due to the presence of motion. Measurements on all samples were performed under in situ conditions (i.e. buffered and hydrated) as well as after lyophilization. These results are summarized in Table 1.

Both the single torsion angle measurements and the distances between putative hydrogen bond donors and acceptors indicate the N-terminal 12 residues in statherin are in an α-helical conformation when adsorbed to HAP under biologically relevant conditions. Removal of water via lyophilization under low vacuum (i.e. 100 mTorr) results in loss of this structure in the highly acidic N-terminal 6 residues. The extension of the helix during lyophilization suggests a significant role for water in stabilizing the binding domain. Water may mediate the interaction of the acidic sidechains with the HAP surface. The α-helix has been previously suggested as a general structural mechanism for aligning acidic side-chain residues with HAP,[92] either through lattice matching or through more general electrostatic complementarily. While our data support the presence of this secondary structure, they also point to the possible importance of water in HAP binding.

The dynamic properties of the immobilized protein are a critical aspect of molecular recognition at the

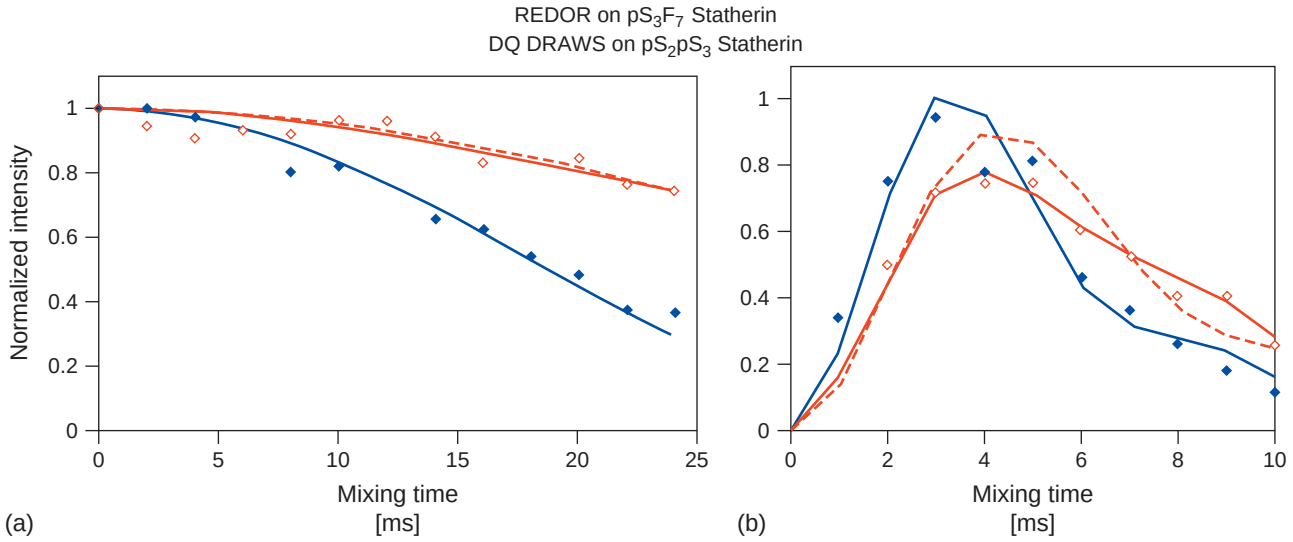

Figure 8 (a) REDOR dephasing curves for hydrated, surface adsorbed pS_3F_7 Statherin (♦), lyophilized, bound pS_3F_7 statherin (◊), and simulations for 4.2 Å (unbroken blue line), 5.2 Å (dashed red line) and a combination of 45% a-helix (4.2 Å) and 65% b-sheet (>8 Å) (unbroken red line). The hydrated pS_3F_7 distance across the hydrogen bond fits best to a distance of 4.3 Å, indicating that the region is well described by an ideal α-helix. Data for the lyophilized sample is best simulated by 5.2 Å or a combination of 35% α-helix and 65% β-sheet, indicating a loss in α-helical secondary structure upon lyophilization. (b) DQDRAWS buildup curves for hydrated, surface adsorbed pS_2pS_3 statherin (♦), lyophilized, bound pS_2pS_3 Statherin (◊), and simulations for φ torsion angles of −60° (unbroken blue line), −85° (dashed red line) and a combination of 45% α-helix (−57°) and 65% β-sheet (−120°) (unbroken red line). The increase in torsion angle on lyophilization correlates well with the loss of α-helical secondary structure

Table 1 Values for the anisotropy ($\Delta\sigma$) and asymmetry (η) of the CSA, average values of the torsion angle (φ), distance measurements across putative hydrogen bonds and ^{13}C $T_{1\rho}$ relaxation constants measured for indicated residues of salivary statherin bound to HAP in the presence and absence of water

	$\Delta\sigma$ (ppm)		η		φ/distance		$T_{1\rho}$ (ms)	
Isotopic label	Lyo.	Hyd.	Lyo.	Hyd.	Lyo.	Hyd.	Lyo.	Hyd.
pS_2	114	105	0.96	0.74			>20	18.2
pS_3	109	104	0.81	0.79	−85°(11)	−60°(10)		
pS_3F_7					5.2(0.6) Å	4.3(0.2) Å		
F_7	103	99	0.73	0.61			>20	7.5
L_8	103	98	0.72	0.69	−77°(20)			
L_8G_{12}					4.8(0.4) Å	4.8(0.4) Å		
$I_{11}G_{12}$	103	103	0.75	0.83	−65°(13)		>20	2.5

protein-biomineral interface, and relatedly to the function of proteins once adsorbed. Measurements of the dynamic properties of statherin in the presence and absence of water show a striking difference from the structural data. The ^{13}C $T_{1\rho}$ values remain largely unchanged for the phosphoserines, indicating little or no motion is present in both the lyophilized and hydrated states. However, the $T_{1\rho}$ relaxation constants are considerably shorter in the hydrated samples at the F_7, L_8, I_{11} and G_{12} positions, indicating motion on the kHz timescale when water is present. Figure 9 shows CPMAS spectra for each of the doubly carbon-labeled statherin samples under hydrated conditions, normalized to the natural abundance methyl region to account for any differences in the amounts of bound protein. A representative spectrum of a lyophilized, surface bound sample labeled at the pS_2 and pS_3 positions is also shown for comparison. The significant loss in CP efficiency at the F_7, L_8, I_{11} and G_{12} positions in the hydrated samples is also characteristic of mobility. These measurements bracket the timescale of the motion in this region to 10^{-3}–10^{-5} s. In contrast, the hydrated, surface bound pS_2pS_3 region does not display a loss in CP efficiency, indicating there is very little motion in that region on the timescale of the cross polarization experiment. The CSAs were found to narrow very little, with spans ($\Omega = |\sigma_{11} - \sigma_{33}|$) of approximately 140–150 ppm in the hydrated samples, as compared to 145–155 ppm for their lyophilized counterparts. The small change in the CSA under hydrated conditions indicates that the motion observed in the cross polarization experiments and supported by the $T_{1\rho}$ relaxation measurements somewhat restricted. Motion was observed in analogous regions for the isolated SN15 peptide, but significant narrowing of the CSA was observed at the C-terminal residues of the peptide (I_{11} and G_{12}). The nearly unchanging CSA observed for the entire N-terminus of statherin indicates a different motional mode present in the full protein. The $T_{1\rho}$ relaxation parameters for both protein and peptide are nearly the same, which would support a motion of similar frequency, but different amplitude than that observed in the SN15 peptide. The change in mobility could be due to one of several factors, including motional limitations due to the larger size of the protein, stabilization of the peptide backbone by tertiary structure, or potentially due to more substantial protein interactions with the surface at the C-terminal end of full statherin.

To explore the latter possibility, the only negatively charged residue outside of the N-terminus was replaced with its uncharged counterpart ($Glu_{26} \rightarrow Gln_{26}$). This site-directed statherin mutant displayed a $T_{1\rho}$ value at $I_{11}G_{12}$ of 2.9 msec, identical to the $T_{1\rho}$ value at the same positions of the unmodified protein (2.5 ms) within experimental uncertainty. This indicates that Glu_{26} is not involved in HAP recognition to an extent that prevents kHz frequency motions in the N-terminal region. The simplest explanation of the results is that either the larger size of full-length statherin or tertiary structural interaction is causing the lower amplitude dynamics compared to the isolated SN15 peptide, rather than being due to a different type of interaction with the HAP surface. However, the dynamics data could also be explained by more complicated models that do include protein interactions

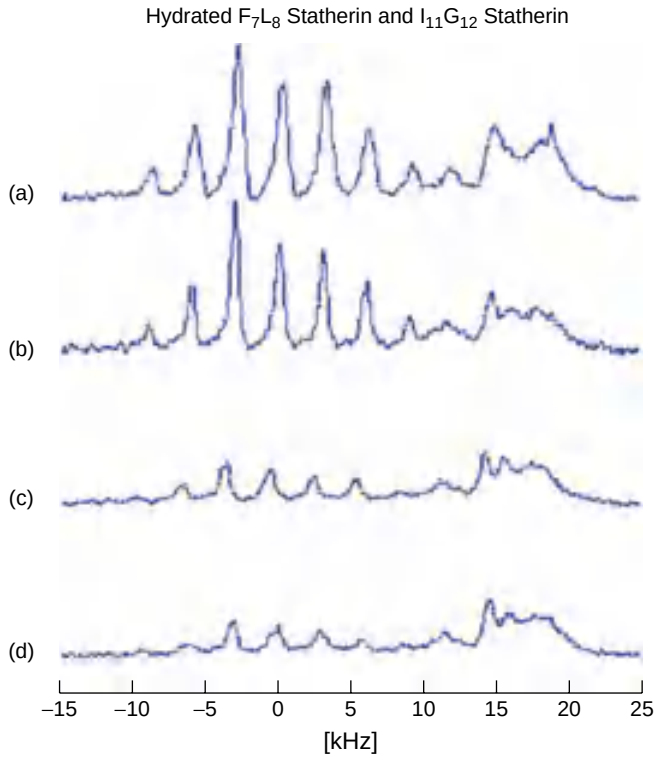

Figure 9 CPMAS spectra of (a) pS_2pS_3 Statherin bound to the surface and lyophilized, (b) hydrated, surface-adsorbed pS_2pS_3 Statherin (c) hydrated, surface-adsorbed F_7L_8 Statherin and (d) hydrated, surface-adsorbed $I_{11}G_{12}$ Statherin. Each hydrated spectrum is normalized to the natural abundance methyl region. The significant decrease in the carbonyl signal for the F_7L_8 and $I_{11}G_{12}$ hydrated spectra is indicative of molecular motion. $T_{1\rho}$ relaxation measurements support the interpretation of minimal mobility at the pS_2pS_3 region and increased mobility for the F_7L_8 and $I_{11}G_{12}$ regions

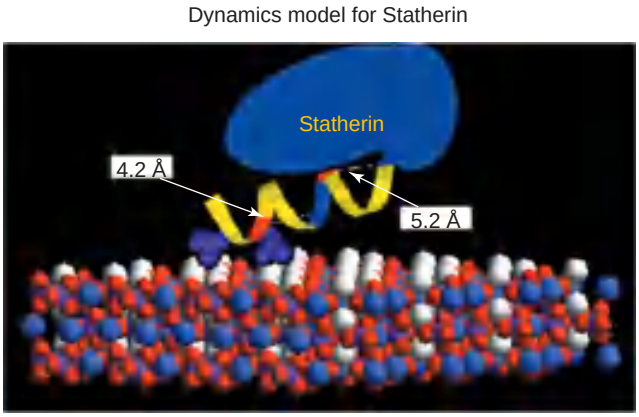

Figure 10 Schematic model showing statherin interacting with the 001 face of HAP, with calcium ions in white and phosphoserines in purple. The protein colors represent backbone $^{13}C =$ O-enriched (red), ^{15}N-enriched (blue), and unenriched (yellow) residues. The REDOR-measured hydrogen bonding distances are indicated for the hydrated N-terminal binding domain, while the remaining portion of the protein (blue) is shown as a nondescript shape to indicate unknown surface adsorbed structure (hydrogen bonds in white). The strong interaction of the N-terminus through the immobile phosphoserines is indicated, and the more mobile, non-interacting C-terminus of the pentadecyl domain is shown oriented away from the HAP surface

with the surface outside of the N-terminal domain. It is clear, however, that both the protein and peptide are only loosely associating with HAP outside of the anionic N-terminal pentapeptide region. The pentapeptide sequence is a common motif in many bone and tooth-associated proteins. It is also a recognition sequence for phosphorylation. The importance of the phosphorylated serines in statherin in binding to HAP indicates a possible regulatory mechanism for multifunctional proteins, such as osteopontin, which are found to be important in regulating mineralization in some settings, but are found in other tissues as well.

A molecular model consistent with the current structural and dynamic studies is shown in Figure 10. The N-terminal domain from residues 2 to 12 is helical on the surface. The strong interaction of statherin with HAP is mediated by the acidic N-terminus, where two phosphoserines and three carboxylate-containing side-chains are located. The dynamics studies suggest that the remainder of the helix is much more weakly interacting with HAP. The more weakly interacting residues in this domain could be viewed as a flexible rod, with torsional motions increasing with increasing distance from the highly immobile N-terminal pentapeptide sequence. The presence of a highly mobile protein segment could explain functional observations made previously by others in the field. Moreno et al.[93] found that statherin inhibited secondary crystal growth at a higher level than that expected based on coverage size, assuming a fixed, globular protein. The mobility of statherin could allow it to effectively block more nucleation sites than a completely rigid protein. The mobility of statherin on the surface may also play a significant role in the lubricating properties of the protein. To adequately model the observed motions at the molecular level, further details of the surface bound tertiary structure and experimental elucidation of the side-chain interactions with HAP will be required to orient statherin at the surface. Solid-state NMR does provide a direct route to this information, and we are currently probing the tertiary structure and the interactions of side chains with the surface to further elucidate binding mechanisms.

4 RELATED ARTICLES IN VOLUMES 1–8

Dipolar & Indirect Coupling Tensors in Solids, Volume 3; Homonuclear Recoupling Schemes in MAS NMR, Volume 4, Magic Angle Spinning, Volume 5, Polymer Dynamics & Order from Multidimensional Solid State NMR, Volume 6, REDOR & TEDOR, Volume 6.

5 REFERENCES

1. A. H. Heuer, D. J. Fink, V. J. Laraia, J. L. Arias, P. D. Calvert, K. Kendall, G. L. Messing, J. Blackwell, P. C. Rieke, D. H. Thompson, A. P. Wheeler, A. Veis, and A. I. Caplan, *Science*, 1992, **255**, 1098–1105.
2. S. Mann, D. D. Archibald, J. M. Didymus, B. R. Heywood, F. C. Meldrum, and V. J. Wade, *MRS Bull.*, 1992, **17**, 32–36.
3. S. Mann, *Nature*, 1993, **365**, 499–505.
4. B. C. Bunker, P. C. Rieke, B. J. Tarasevich, A. A. Campbell, G. E. Fryxwell, G. L. Graff, L. Song, J. Liu, J. W. Virden, and G. L. McVay, *Science*, 1994, **264**, 48–55.
5. S. Mann and S. Weiner, *J. Struct. Biol.*, 1999, **126**, 179–181.
6. A. L. Bosky, *J. Cell. Biochem. Suppl.*, 1998, **30/31**, 83–91.
7. A. G. Fincham, J. Mordian-Oldak, and J. P. Simmer, *J. Struct. Biol.*, 1999, **126**, 270–299.
8. P. Calvert, *MRS Bull.*, 1992, **17**, 37–47.
9. L. Cohen-Solal, P. Maroteaux, and M. J. Glimer, 'Presence of Gamma-Glutamyl Phosphate in the Collagens of Bone and other Calicified Tissue and its Absence in the Collagens of Unmineralized Tissues', Elsevier: Amsterdam, 1982, Vol. 7.
10. L. Addadi and S. Weiner, *Proc. Natl. Acad. Sci. USA*, 1985, **82**, 4110–4114.
11. S. Albeck, J. Aizenberg, L. Addadi, and S. Weiner, *J. Am. Chem. Soc.*, 1993, **115**, 11691–11697.
12. D. Deutsch, *Anat. Rec.*, 1989, **224**, 189–210.
13. S. Weiner and L. Addadi, *Trends Biochem. Sci.*, 1991, **16**, 252–256.
14. S. Weiner and L. Addadi, *J. Mat. Chem.*, 1997, **7**, 689.
15. P. V. Hauschka and F. H. Wians, *Anat. Rec.*, 1989, **224**, 180–188.
16. R. Fuijisawa and Y. Kuboki, *Eur. J. Oral Biol.*, 1998, **106**, 249–253.
17. R. Fujisawa, Y. Wada, Y. Nodasaka, and Y. Kuboki, *Biochim. Biophys. Acta*, 1996, **1292**, 53–60.
18. Z. Amjad, 'Calcium Phosphates in Biological and Industrial Systems', Kluwer: Boston, MA, 1998.
19. D. J. Fink, *MRS Bull.*, 1992, **17**, 27–31.
20. M. Sarikaya and I. A. Aksay, *Results Problems Cell Diff.*, 1992, **19**, 1–26.
21. J. Menanteau, W. F. Neuman, and M. W. Neuman, *Metabol. Bone Dis. Related Res.*, 1982, **4**, 157–162.
22. A. A. Campbell, A. Ebrahimpour, L. Perez, S. A. Smesko, and G. H. Nancollas, *Calc. Tissue Int.*, 1989, **45**, 122–128.
23. J. P. Gorski, *Calc. Tissue Int.*, 1992, **50**, 391–396.
24. G. K. Hunter and H. A. Goldberg, *Biochem. J.*, 1994, **302**, 175–179.
25. D. N. Misra, *J. Colloid Interface Sci.*, 1997, **194**, 249–255.
26. P. A. Raj, M. Johnsson, M. J. Levine, and G. H. Nancollas, *J. Biol. Chem.* 1992, **267**, 5968.
27. R. W. Romberg, P. G. Werness, B. L. Riggs, and K. G. Mann, *Biochemistry*, 1986, **25**, 1176.

28. K. Wikiel, E. M. Burke, J. W. Perich, E. C. Reynolds, and G. H. Nancollas, *Arch. Oral Biol.*, 1994, **39**, 715–721.
29. N. Ramasubbu, L. M. Thomas, K. Bhandary, and M. J. Levine, *Crit. Rev. Oral Biol. Med.*, 1993, **4**, 363–370.
30. S. Weiner and L. Addadi, *Trends Biochem. Sci.*, 1991, 252–256.
31. J. S. Evans, T. Chiu, and S. I. Chan, *Biopolymers*, 1994, **34**, 1359–1375.
32. W. H. Braunlin, H. J. Vogel, T. Drakenburg, and A. Bennick, *Biochemistry*, 1986, **25**, 584–589.
33. V. Gerbaud, D. Pignoli, E. Loret, J. A. Bertrand, Y. Berland, J.-C. Fontecilla-Camps, J.-P. Canselier, N. Gabas, and J.-M. Verdier *J. Biol. Chem.*, 2000, **275**, 1057–1064.
34. P.-K. Wang and C. Slichter, *Phys. Rev. Lett.*, 1984, **53**, 82–85.
35. S.-J. Hwang, C. Petucci, and D. Raftery, *J. Am. Chem. Soc.*, 1998, **120**, 4388–4397.
36. Y. Y. Tong, C. Rice, A. Wieckowski, and E. Oldfield, *J. Am. Chem. Soc.*, 2000, **122**, 11921–11924.
37. K. W. Zilm and D. W. Grant, *J. Am. Chem. Soc.*, 1981, **103**, 2913–2922.
38. V. H. Pan, T. Tao, J. W. Zhou, and G. E. Maciel, *J. Phys. Chem. B*, 1999, **103**, 6930–6943.
39. D. W. Sindorf and G. E. Maciel, *J. Am. Chem. Soc.*, 1983, **105**, 1848–1851.
40. E. Brunner, R. Seydoux, M. Haake, A. Pines, and J. A. Reimer, *J. Magn. Reson.*, 1998, **130**, 145–148.
41. L. K. Sanders, W. D. Arnold, and E. Oldfield. *J. Porphyrins Phthalocyanines*, 2001, **5**, 323–333.
42. R. Salzmann, M. Kaupp, M. T. McMahon, and E. Oldfield, *J. Am. Chem. Soc.*, 1998, **120**, 4771–4783.
43. J. Heller, D. D. Laws, M. Tomaselli, D. S. King, D. E. Wemmer, A. Pines, R. H. Havlin, and E. Oldfield, *J. Am. Chem. Soc.*, 1997, **119**, 7827–7831.
44. V. L. Fernandez, J. A. Reimer, and M. M. Denn, *J. Am. Chem. Soc.* 1992, **114**, 9634–9642.
45. K. Beshah, C. Rey, M. J. Glimcher, M. Schimizu, and R. G. Griffin, *J. Magn. Reson.*, 1990, **84**, 17–81.
46. J. P. Yesinowski, in 'Calcium Phosphates in Biological and Industrial Systems', ed Z. Amjad, Kluwer: Boston, MA, 1998.
47. J. R. Moore, L. Garrido, and J. L. Ackerman, *Magn. Reson. Med.*, 1995, **33**, 293–299.
48. M. Bak, J. K. Thomsen, H. J. Jakobsen, S. E. Petersen, T. E. Petersen, and N. C. Nielsen, *J. Urol.*, 2000, **164**, 856–863.
49. J. K. Denny, J. F. Wang, T. A. Cross, and J. R. Quine, *Biophys. J.*, 2001, **80**, 1555, Part 2.
50. R. G. Griffin, *Nature Struct. Biol.*, 1998, **5**(Suppl. S), 508–512.
51. R. Tycko, *Annu. Rev. Phys. Chem.*, 2001, **52**, 575–606.
52. M. M. Lee and W. I. Goldberg, *Phys. Rev.*, 1965, **140**, A1261.
53. J. S. Waugh, L. M. Huber, and U. Haeberlen, *Phys. Rev. Lett.*, 1968, **20**, 5.
54. U. Haeberlen, 'High Resolution NMR in Solids: Selective Averaging', Academic Press: New York, 1976.
55. M. Mehring, 'Principles of High Resolution NMR in Solids', Springer-Verlag: New York, 1983.
56. W. K. Rhim, D. D. Elleman, and R. W. Vaughn, *J. Chem. Phys.*, 1973, **59**, 3740–3749.
57. D. K. Burum and W. K. Rhim, *J. Chem. Phys.*, 1979, **7**, 944–956.
58. M. Hohwy, P. V. Bower, H. J. Jakobsen, and N. C. Nielsen, *Chem. Phys. Lett.*, 1997, **273**, 297–303.
59. E. R. Andrew, A. Bradbury, and R. B. Eades, *Nature*, 1958, **182**, 1969.
60. D. Gregory, D. Mitchell, J. A. Stringer, S. Kühne, J. C. Shiels, J. Callahan, M. A. Mehta, and G. P. Drobny, *Chem. Phys. Lett.*, 1995, **246**, 654–663.
61. J. Schaefer, in 'Encyclopedia of NMR', eds D. M. Grant and R. K. Harris, Wiley: Chichester, 1996, pp. 3977–3983.
62. Y. Pan, *Solid State Magn. Reson.*, 1995, **5**, 263–268.
63. J. R. Long, J. L. Dindot, H. Zebroski, S. Kühne, R. H. Clark, A. A. Campbell, P. S. Stayton, and G. P. Drobny, *Proc. Natl. Acad. Sci. USA*, 1998, **95**, 12 083–12 087.
64. P. V. Bower, N. Oyler, M. A. Mehta, J. R. Long, P. S. Stayton, and G. P. Drobny, *J. Am. Chem. Soc.*, 1999, **121**, 8373–8375.
65. W. J. Shaw, J. R. Long, J. L. Dindot, A. A. Campbell, P. S. Stayton, and G. P. Drobny, *J. Am. Chem. Soc.*, 2000, **122**, 1709–1716.
66. J. R. Long, W. J. Shaw, P. S. Stayton, and G. P. Drobny, *Biochemistry*, 2001, **40**: 15 451–15 455.
67. T. S. Burkoth, T. L. S. Benzinger, V. Urban, D. M. Morgan, D. M. Gregory, P. Thiyagarajan, and R. E. Botto, *J. Am. Chem. Soc.*, 2000, **122**: 7883–7889.
68. T. L. S. Benzinger, D. M. Gregory, T. S. Burkoth, H. Miller-Auer, D. G. Lynn, R. E. Botto, and S. C. Meredith, *Biochemistry USA*, 2000, **39**, 3491–3499.
69. D. M. Gregory, T. L. S. Benzinger, T. S. Burkoth, H. Miller-Auer, D. G. Lynn, S. C. Meredith, and R. E. Botto, *Solid State Magn. Reson.*, 1998, **13**, 149–166.
70. T. L. S. Benzinger, D. M. Gregory, T. S. Burkoth, H. Miller-Auer, D. G. Lynn, R. E. Botto, and S. C. Meredith, *Proc. Natl. Acad. Sci. USA*, 1998, **95**, 13 407–13 412.
71. F. J. Blanco and R. Tycko, *J. Magn. Reson.*, 2001, **149**, 131–138.
72. T. M. Duncan, 'Chemical Shift Tensors', 2nd edn., Farragut Press: Madison, WI, 1997.
73. J. Schaefer, M. D. Sefcik, E. O. Stejskal, R. A. McKay, W. T. Dixon, and R. E. Cais, *Macromolecules*, 1984, **17**, 1107–1124.
74. C. Schmidt, K. J. Kuhn, and H. W. Spiess, *Prog. Colloid Polymer. Sci.*, 1985, **71**, 71–76.
75. J. Schaefer, E. O. Stejskal, D. Perchak, J. Skolnick, and R. Yaris, *Macromolecules*, 1985, **18**, 368–373.
76. P. M. Henrichs, M. Linder, J. M. Hewitt, D. Massa, and H. V. Isaacson, *Macromolecules*, 1984, **17**, 2412–2416.
77. J. Schaefer, M. D. Sefcik, E. O. Stejskal, and R. A. McKay, *Macromolecules*, 1981, **14**, 188–192.
78. P. M. Henrichs, *Macromolecules*, 1987, **20**, 2099–2112.
79. K. Schmidt-Rohr, W. Hu, and N. Zumbulyadis, *Science*, 1998, **280**, 714–717.
80. A. F. Martins, A. E. Gomes, A. Polimeno, and L. Orian, *Phys. Rev. E*, 2000, **62**, 2301–2309.
81. R. Baxmann, M. Hess, R. Woelke, and W. Veeman, *Macromol. Symp.*, 1999, **148**, 157–177.
82. D. Schlesinger and D. I. Hay, *J. Biol. Chem.*, 1977, **252**, 1689–1695.
83. P. A. Raj, M. Johnsson, M. J. Levine, and G. H. Nancollas, *J. Biol. Chem.*, 1992, **267**, 5968–5976.
84. S. S. Schwartz, D. I. Hay, and S. K. Schluckebier, *Calc. Tissue Int.*, 1992, **50**, 511–517.
85. N. Ramasubbu, L. M. Thomas, K. K. Bhandary, and M. J. Levine, *Crit. Rev. Oral Biol. Med.*, 1993, **4**, 363–370.
86. T. L. Gururaja and M. J. Levine, *Peptide Res.*, 1996, **9**, 283–289.
87. G. A. Naganagowda, T. L. Gururaja, and M. J. Levine, *J. Biomol. Struct. Dyn.*, 1998, **16**, 91–107.
88. W. J. Shaw, J. R. Long, J. L. Dindot, A. A. Campbell, P. S. Stayton, and G. P. Drobny, *J. Am. Chem. Soc.*, 2000, **122**, 1709–1716.
89. W. J. Shaw, P. S. Long, P. S. Stayton, and G. P. Drobny, *J. Am. Chem. Soc.*, 2000, **122**, 7118–7119.
90. D. M. Gregory, M. Mehta, J. Shiels, and G. P. Drobny, *J. Chem. Phys.*, 1997, **106**, 23.
91. J. R. Long, W. J. Shaw, G. P. Drobny, and P. S. Stayton, *Biochemistry*, 2002, in press.
92. P. A. Raj, M. Johnsson, M. J. Levine, and G. H. Nancollas, *J. Biol. Chem.*, 1992, **267**, 5968–5976.
93. E. C. Moreno, K. Varughese, and D. I. Hay, *Calc. Tissue Int.* 1979, **28**, 7–16.

Acknowledgements

We acknowledge the support of the National Institute of Dental Research (DE 12554-01), the National Science Foundation

(EEC-9529161 and DMR-9616212), the Department of Energy (DE-AC06-76RL0 1830) and the Office of Science, Office of Basic Energy Sciences, Department of Energy, through Associated Western Universities (WJS).

Biographical Sketches

Gary P. Drobny, *b* 1951. Ph.D. 1981 Chemistry, University of California, Berkeley, Research Assistant, University of California, 1976–1981; with A. Pines; Research Scientist III, University of Washington, Chemistry, 1981–1982; Research Associate, University of Washington, Chemistry 1982–1985; Research Asst. Professor, University of Washington, Chemistry, 1985; Assistant Professor, University of Washington, Chemistry, 1985–1989; Associate Professor, University of Washington, Chemistry, 1989–1991; Professor, University of Washington, Chemistry, 1991–2002; Adjunct Professor of Physics, University of Washington, 1995–2002. Current research interests: solid state NMR methods applied to problems in biomineralization, biomaterials, biomolecular dynamics, dynamic aspects of DNA recognition, membrane proteins. Design and development of NMR technology.

Patrick S. Stayton, *b* 1961. Ph.D. 1989 Biochemistry, University of Illinois, USA. Research assistant, University of Illinois, 1984–89; with S. Sligar, 1984–89; Postdoctoral research associate, Beckman Institute for Advanced Science and Technology, University of Illinois, 1989–1992. Assistant Professor at University of Washington, 1992–97, Associate Professor at University of Washington, 1997–2001, Professor at University of Washington 2001–present. Approx. 120 publications. Current research interests: biomineralization, biomaterials, tissue engineering, smart molecular materials, drug delivery.

Joanna R. Long, *b* 1968. PhD. 1997 Physical Chemistry, Massachusetts Institute of Technology, USA. Research associate, University of Washington, with P.S. Stayton 1997–2000; Scientist, University of Washington, since 2000. 12 publications. Current research interests: solid state NMR and its application to biophysical and biomaterial problems.

Myriam L. Cotten, *b* 1971. Ph.D. 1999 Chemistry, Florida State University, Tallahassee, Florida, USA. Research associate, University of Washington, 1999–present. 11 publications. Current research interests: solid state NMR and its applications in biological sciences, biomaterials, and the studies of interfacial phenomena.

Wendy J. Shaw, *b* 1972. Ph.D. 2000 Physical Chemistry, University of Washington. Senior Research Scientist, Battelle Pacific Northwest National Labs, 2000–present. 6 publications. Recent research interests include using solid state NMR to study biomineralization proteins.

Structure Determination of Solid Proteins Using MAS and Isotopic Enrichment

Ann E. McDermott

Department of Chemistry, Columbia University, New York, NY, USA

&

Anja Böckmann

Centre National de la Recherche Scientifique, Lyon, France

1 Assigning High Resolution Spectra of Biological Solids 1
2 Experimental Structural Constraints 4
3 Structure Calculations 6
4 References 7

1 ASSIGNING HIGH RESOLUTION SPECTRA OF BIOLOGICAL SOLIDS

Numerous important proteins are not studied by X-ray or solution nuclear magnetic resonance methods because of size or insolubility. Solid-like systems, proteins for which the whole-body hydrodynamic tumbling is insignificant on the millisecond timescale, can be studied by high resolution solid state nuclear magnetic resonance (SSNMR), formulated as raw membranes or native multi-enzyme complexes, micelle-protein suspensions, frozen glasses, or hydrated microcrystals. One important application area of solid proteins is the study of cryogenically trapped species in proteins. Another is the problem of non-soluble misfolded systems; this field continues to increase in its medical and biophysical impact. Many of these systems have been extensively elucidated by SSNMR because of their insolubility, including the β-amyloid peptides.[1,2] Another very important application area is the structural biology of intrinsic membrane proteins; these proteins are key players supervising cell–cell communication and making energy available to the cell. Exciting studies of membrane systems by solid state NMR are underway and partial structures at atomic detail are forthcoming for many fragments of membrane systems and fragments of insoluble proteins, including: gramicidin A,[3,4] a fragment M2 of the acetylcholine receptor,[5] phospholamban,[6] aspartate chemotaxis receptor,[7] viral fusion peptides,[8] rhodopsin,[9] and bacteriorhodopsin.[10]

Solid state NMR studies of these systems offer similar kinds of information as solution NMR studies offer for soluble proteins. For example the chemical structure, the conformation, the conformational dynamics, and the pK_a values for ionizable residues are among the types of characterization that can be carried out. On the other hand, there are important differences between solid state and solution NMR, both technical and scientific. Principally the differences are related to the fact that all of the fine structure information (chemical, quadrupolar coupling, dipolar couplings) are anisotropic. While the anisotropy can be a source of spectral complexity and line broadening, these anisotropic interactions are also the principal source of structural and chemical information in a NMR spectrum. Dipolar couplings offer a direct probe of internuclear distances. Anisotropic shielding terms and quadrupolar splittings offer information on local electronic structure. All anisotropic interactions can in principle offer an angular constraint on a functional group with respect to an external coordinate system. Usually the nucleus has several local interactions (all tensorial). Some pulse sequences aim to isolate and measure one interaction. Other experiments depend on the sum of two interactions, and these allow one to probe the relative orientations of two anisotropic interactions and thereby potentially probe torsion angles. Any anisotropic interaction provides a basis for orientational labeling thereby offering an avenue for probing dynamics: hole burning recovery experiments, lineshape experiments and relaxation based experiments all typically operate on the basis of anisotropic local interactions and the effects of motion on the energy levels. The biophysical information provided through tensorial interactions is indeed very broad, and the need for a quantitative understanding of them is clear.

The impact of the anisotropy of these interactions for solution NMR is very different from that for solid state NMR. The tumbling of small molecules on a picosecond timescale or of macromolecules on a nanosecond timescale leads to narrowed spectra that report the weighted angular average of the values. The tumbling also leads to relaxation phenomena that are dominated by overall molecular tumbling; the relaxation rates are largely predictable from Stokes–Einstein type relations. Recent developments in solution NMR make additional creative use of the tensorial interactions. For example, small dipolar-based splittings for weakly macroscopically aligned samples can offer useful structural constraints (see **Liquid Crystalline Samples: Application to Macromolecular Structure Determination**). If two tensors of comparable size and spatial direction, but of opposite sign, dominate the local field, then the local field can be quite small, and therefore relaxation rates and linewidths are minimized for macromolecules (see **Transverse Relaxation-optimized NMR Spectroscopy with Biomacromolecular Structures in Solution**). Probably the future will bring ever more clever use of anisotropic interactions in solution NMR spectroscopy.

In contrast, for solids the anisotropy is manifest in the spectra. For single crystals, the anisotropy is studied through rotation plots, where the rotation of a sample leads to large changes in the NMR shift. This relation between functional group orientation and NMR frequency has formed the basis of structural studies of uniaxially aligned intrinsic membrane proteins by solid state NMR (see **Multiple-Resonance Multi-Dimensional Solid-State NMR of Proteins**). For powdered static solid samples the anisotropy results in inhomogeneously broadened lines wherein the resonance frequency is analytically related to the rotational orientation of the parent functional group. The experiments described in this review are

based on yet another scheme, magic angle spinning (MAS), in which polycrystalline solids are rotated mechanically at an axis of 55.7° with respect to the applied magnetic field. During MAS all first order interactions (i.e., interactions that are much weaker than the applied field) will refocus at the end of every full turn of the rotor. In this case the spectra contain a comb of narrow lines for each chemically distinct site, with a 'center band' at the isotropic shift and spinning sidebands flanking this center band, spaced by integral numbers of the rotation frequency. These spectra can, in favorable cases, exhibit resolution and sensitivity approaching that of solution NMR. On the other hand, the anisotropic interactions remain measurable or amenable to manipulations by the experimentalists. Since the tensor is not averaged by random molecular motion but rather by systematic magic angle spinning, powerful probes of dipolar couplings, of shielding anisotropy, of local torsional states and of local molecular motion on the microsecond and millisecond timescale are still available. Interactions that are comparable to or stronger than the spinning speed are sometimes probed through the amplitudes of the spinning sidebands, or equivalently through the dephasing and refocusing of the magnetization during each rotor period. Alternatively, weaker interactions can be probed through cumulative dephasing or evolution over several rotor periods when the RF pulses, synchronized with the rotor cycle, interfere with the formation of rotor echoes. Clever utilization of this fact has allowed experimentalists to select the terms in the Hamiltonian that should remain active and quench those that are not wanted.

For solid samples, relaxation is driven purely by local molecular motions; the lack of overall molecular tumbling has significant potential advantages for studies of conformational dynamics by NMR. Changes in the orientation of a functional group often result in very large changes in frequency, typically much larger than they would in solution. Although the relaxation rates are frank probes of local conformational motions, and sound theoretical tools exist for predicting relaxation rates from motional models, interpretation of experimental relaxation rates for solid proteins is nonetheless a muddy topic, needing much development.

MAS NMR has been used for the purpose of confirming the presence of a chemical species in an enzyme active site, or measurement of an internuclear distance to confirm the conformation of an important functional group in a protein. Site-specific isotopic enrichment with 'heteronuclei' (^{13}C or ^{15}N) at strategically selected sites has been a key ingredient in most of these biophysical solid state NMR studies.[11] The use of engineered isotopes obviates the need for peak assignments and allows one to utilize one-dimensional broadline methods. Because the labeling site(s) must of course be selected in advance, experiments with site specific labels often test a specific hypothesis, involving a particular set of atoms of interest in the macromolecule. These methods are useful for focusing on specific ligands or domains in very large structures, for example in the case of taxol conformational studies on tubulin,[12] or the case of chemotaxis receptors.[7] The strength in many of these studies is the unique ability to probe a system under highly biologically relevant conditions or in a chemically unusual state, regardless of the intrinsic linewidth and dispersion; the weakness is the inefficient rate at which structural information is gathered.

Recently, efforts to study uniformly or extensively isotopically enriched biological solids including assignment of the spectra have met with an encouraging level of success in several laboratories. The objectives in these experiments are to study simultaneously an entire protein or an entire domain of a protein, and probe such issues as conformation, dynamics and ligand binding. The use of uniform enrichment represents an important change in experimental planning; optimal conditions for resolving the hundreds of ^{13}C and ^{15}N lines must be found, and strategies are needed for determining peak assignments. These issues have been, to some degree, tackled in the recent past. Partial assignment of ^{13}C and ^{15}N resonances for protein solid state NMR spectra have recently been shown to be feasible for small globular proteins[13,14] through multi-dimensional correlation of the backbone nitrogen and the side-chain Cα and Cβ isotropic shifts. Homonuclear ^{13}C shift correlation spectra during magic angle spinning was used to identify sidechains on the basis of isotropic carbon chemical shifts, while heteronuclear ^{15}N–^{13}C chemical shift correlation spectra during magic angle spinning was used to provide site specific assignments for these spin systems. Thus far proton spectroscopy has not been extensively used in this context. Once site specific assignments are determined, a broad range of biophysical characterization can be carried out using solid state NMR. ^{13}Cα and ^{13}Cβ isotropic shifts provide information on the secondary structure context.[15,16] The shifts are sensitive probes of ligand binding and can be used to locate the important cavities in the protein. It is possible that complete 3D structures of proteins will be soon determined using these spectra. It is likely that characterization of conformational changes, ionization states and proton transfer and other chemical reactions will be possible using these spectra. This review will attempt to offer a summary of the prospects for these studies, including some speculation about the near term future (Figure 1).

The chemical shift correlation experiments require the ability to 'turn on' and 'turn off' dipolar couplings during

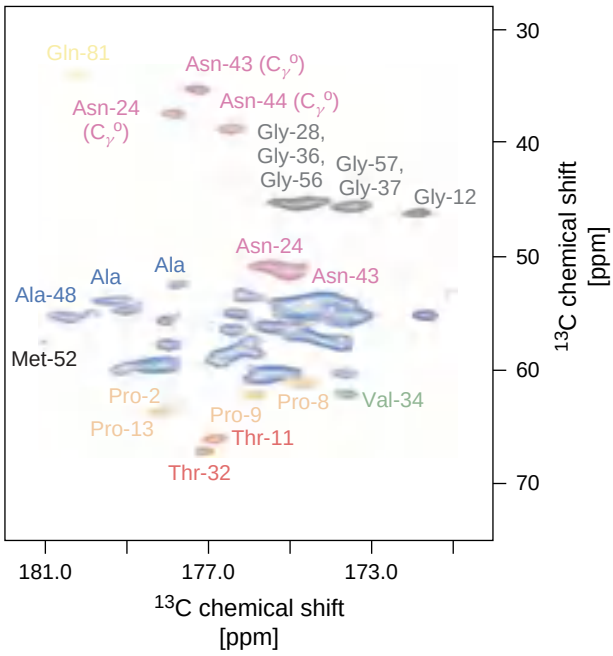

Figure 1 Backbone Cα–CO correlation spectra of microcrystalline BPTI, measured at 800 MHz as described in Ref.[13]. Many peaks were assignable based on 1-bond and 2-bond homonuclear correlations

a pulse sequence. During the indirect and direct detection periods, magic angle spinning and RF decoupling conditions can be combined such a way that the internuclear couplings are essentially ineffective and negligible. The linewidths typically seen in MAS spectra (0.5–2 ppm) indeed allow many residues to be resolved and assigned. On the other hand, during mixing periods the dipolar couplings can become effective for polarization transfer due to the use of other types of RF pulses that are synchronized with the rotor rotation. Advances in MAS based magnetization transfer allow for directed, highly efficient homonuclear ($^{13}C-^{13}C$) or heteronuclear ($^{13}C-^{15}N$) transfers during the mixing times.

The main ingredient providing narrow lines for measurement of chemical shifts during the detection periods is magic angle spinning. The selection of the spinning rate is important, and is typically in the range 5–30 kHz for applied field strengths in the range 400–800 MHz. In a practical sense it is crucial that the angle is set accurately (within 0.05°) for high field work, and is maintained stably. It is also crucial that the proteins survive long signal acquisition times in these conditions. Protein samples experience forces comparable to those in an ultracentrifuge, and care must be taken that the formulation of the sample (e.g., crystallinity) is not changed during the experiment. Furthermore, it is important that the large volumes of dry gas used in this protocol not accidentally dehydrate the sample. In order to achieve acceptable linewidths for ^{13}C or ^{15}N NMR peaks, strong proton decoupling must be applied throughout all direct and indirect detection periods; typically decoupling strengths of 80–125 kHz are used. If these MAS and proton decoupling techniques are applied, then linewidths of the order of 0.2–0.5 ppm can be expected for isolated spins in crystalline materials.

There are other central points influencing the quality of the spectra of uniformly isotopically enriched biological macromolecules, and therefore influencing the likelihood of succeeding in an assignment protocol. Of course, the applied field strength, homogeneity, and stability remain among the most important variables in the quality of any high resolution NMR spectrum. However, the need for high fields for proteins in solution is not fully analogous to the need for solid proteins. The linewidths and transverse relaxation rates for proteins in solution have a formal dependence upon molecular weight as governed by the Stokes–Einstein relation; this of course has no relevance for solid state samples. For solid state uniformly labeled samples, the most important reason that high field NMR improves spectra is related to internuclear homonuclear ^{13}C couplings, and the use of direct ^{13}C detection. Assuming that there is little inhomogeneous dispersion, homonuclear spin couplings can have a dominant effect on the linewidths of uniformly enriched materials. J values of 35 Hz for $^{13}C\alpha-^{13}C\beta$ and 55 for Hz $^{13}C\alpha-^{13}CO$ coupling are expected to add significant apparent width and there is substantial merit in refocusing these interactions to achieve a homogeneous underlying linewidth. Of course these splittings are fixed with respect to variations in the applied field, and have a more important effect on the resolution at low field than at high field. In solution NMR of uniformly labeled materials, ^{13}C shifts are often measured during constant time indirect evolution periods, thereby removing this source of broadening. Due to the relatively shorter expected dephasing times in solids, selective decoupling pulses have been proposed for removing these J couplings from indirect evolution periods of solid state spectra.[17] Such a technique is only recently under consideration, and will probably be very useful for indirect dimensions. No such remedy has been demonstrated for direct detection periods. For solid state ^{13}C NMR spectra, homonuclear dipolar couplings can also add significant linewidth. In this regard the selection of magic angle spinning speed is very important. 'Rotational resonance' conditions, conditions wherein spinning sidebands of one carbon spectrally overlap the center band or isotropic shift of a strongly coupled (directly bonded) neighboring site, must be avoided. When overlap of this type occurs, the spectra become much more congested, and dipolar interactions cause significant line broadening. For moderate applied magnetic field strengths, significant linewidth is added also when the peaks are close to, but not exactly at, a rotational resonance condition. Therefore very low and very high spinning speeds often offer the best linewidths. As stronger magnets are utilized, this effect becomes less important; at high fields, the rotational resonance conditions occur in more sharply defined ranges of speeds, whereas for lower field strengths the conditions are quite broad. Strongly coupled ^{13}C pairs with similar chemical shifts and large chemical anisotropy tensors, such as neighboring aromatic carbons, also exhibit a significant degree of dipolar linewidth during MAS experiments, which can resist even moderately high spinning speeds and applied field strengths. Thus the aromatic groups in uniformly enriched proteins present a specific spectroscopic challenge.

For some experiments, the homonuclear couplings, both J and D, can be removed or reduced through selective isotopic labeling. Labeling strategies[18] involve use of 1,3-^{13}C or 2-^{13}C glycerol[19] or 3-^{13}C-pyruvate[20] media to derive 'even-odd' or 'checkerboard' labeling schemes. These approaches might have important impact for directly detected carbon spectra, especially for cases with small chemical shift differences in between neighboring nuclei such as aromatic systems and neighboring methylene groups.

Additional effects of applied field strength on the linewidth and resolution can be expected but are not well documented at present. An underlying apparently homogeneous linewidth would presumably be associated with the residual proton couplings during moderate proton decoupling irradiation, while other contributions to the transverse relaxation rate might be expected from fast-limit motions. It is expected that these sources of transverse relaxation would become less important with increasing field, but the extent of improvement is not yet well characterized.

Finally, the sample's physical formulation is simply the most significant consideration; a structurally and physically homogeneous sample is required for high resolution multidimensional work, no matter what field strength is available. Benchmark linewidths have never been achieved using dehydrated or lyophilized materials. While crystalline materials satisfy this requirement they are probably not the only way in which this can be achieved. Raw biological membranes have shown very good linewidths in several cases. No matter what linewidth is achieved, of course the dispersion of the protein is equally important as the linewidth in determining the likelihood of resolving lines. This can be expected to be strongly influenced by the secondary structure content, by whether the protein is well folded or not, and by many other factors.

It is not possible to close this discussion of the achievements and benchmarks and likely future for assignment work by solid

state NMR without mentioning the expected effects of protein conformational change. Like the case for solution NMR, conformational exchange in proteins is expected to broaden the line and to reduce the efficiency of many of the polarization transfer sequences. Both effects are much more pronounced for proteins in the solid state; both effects involve a much broader range of timescales than they do for solution NMR. For a solid state protein, the conformation exchange causes a modulation in the frequency governed by the breadth of the anisotropic interaction; for solution NMR the effect mainly involves the difference in chemical shift. In solid state NMR experiments motions can also interfere with the two central tools for sharpening the spectra, namely MAS and proton decoupling. Thus motions on timescales from seconds to microseconds can contribute to chemical exchange, and the expected result is a reduced line intensity. The lack of peaks for many of the important lines is a 'half-empty cup'; the many opportunities, including lineshape analysis and relaxation rate measurements, for experimentally probing conformational exchange during biochemical function is a 'half-full cup'. Experimental control of the sample and thereby the motion is expected to be a very important tool in understanding these exchange effects. For example, variable temperature experiments or titration of the sample to control the rates and populations involved in the motion may serve as important throttles on the exchange effects. To the extent that the peaks can be recovered at lower temperatures or altered conditions, and the underlying spectroscopic constants can be determined, then one can hope that these interference effects could be useful for characterizing conformational exchange.

The restoration of dipolar couplings during MAS for the purpose of distance measurements has been accomplished in many ways. The effective average dipolar coupling for a spin pair undergoing MAS is zero, and no population transfer is expected after a full rotor period. Most methods to effect population transfer within the pair involve RF pulses with cycle times that are related to the spinning speed. For example, in one implementation, the specific CP sequence utilizes a condition in which the difference in RF field strength for the two spins is equal to the rotor frequency. In this case, the average Hamiltonian for the internuclear dipolar coupling, averaged over a full rotor period, can be shown to be non-zero. While these sequences have their historical origin in the study of site specific pairs of labels, most of them work well for detecting strongly coupled pairs such as directly bound pairs in uniformly labeled samples.

What sequences were actually used for population transfer during the mixing time of the chemical shift correlations of proteins? In some assignment efforts reported to date, adiabatic homonuclear transfer sequences at moderate field strengths were featured,[14] such as dipolar recoupling enhancement through amplitude modulation (DREAM),[21] an adiabatic version of the homonuclear rotary resonance (HORROR) condition, which involves rather mild RF field strengths conditions. Alternatively, homonuclear recoupling has been achieved using simpler sequences such as spin diffusion and RFDR sequences.[13] The selection of these sequences rather than the many others in the literature partly reflects practical considerations of instrument stability, the ease of 'set-up' and minimization of RF strength and attendant sample heating. With respect to heteronuclear $^{13}C-^{15}N$ correlation spectra, selective cross polarization has been most often used for protein assignment.[22–24] Transfer efficiencies of 25–50% on model systems and proteins have been reported. 3D $^{15}N-^{13}C-^{13}C$ correlation spectra have been reported for simple systems but not yet for large proteins.[25–29]

While the benchmarks for linewidths continue to drop, and the benchmarks for polarization transfer efficiency continue to rise, it is already clear that assignments of protein MAS spectra can be achieved, and that other aspects of the NMR studies such as structure determination and biophysical characterization are therefore ripe for pursuit.

2 EXPERIMENTAL STRUCTURAL CONSTRAINTS

With the recent accomplishments of partial assignments of several proteins, one issue lying ahead is the question of whether it is possible to solve the three-dimensional structure of a protein. Prospects for structure calculations based on distance and torsion constraints from solid state NMR experiments appear to be promising, although demonstrations are still at an early stage. It is useful to divide this process into characterization of secondary structure, determination of the fold and refinement to produce high quality structures. Many measurements are sensitive to backbone torsional states and can be used to characterize secondary structure. Chemical shift measurements are known to correlate with torsional states of the backbone.[16,30] A variety of computational strategies have been developed to take advantage of the growing database of chemical shifts for proteins. Isotropic shifts can be analyzed using the chemical shift index, a well calibrated indicator of secondary structure, which is likely to work as well for microcrystalline proteins as it does for proteins in solution. Chemical shifts have been included in a refinement algorithm to effectively restrain the ϕ and ψ torsional angles and predict secondary structure with an accuracy of approximately 85%. Chemical shift surfaces could also be used to utilize the torsional information in the shift and shift anisotropy more quantitatively.[31]

Alternatively, the torsion angles in the backbone (or side chain) can be directly measured; many solid state NMR methods for torsion angle measurements have appeared recently.[32–34] Heteronuclear local field spectroscopy is the underlying tool for most of these methods. In these experiments, the relative orientations of two tensors are measured in an unoriented sample. To probe X–Y bond torsions, one generates double quantum coherences for neighboring nuclei X and Y. Subsequently one probes the sum dipolar tensors for adjacent sites $D_{P-X}+D_{B-Y}$, using a dephasing pulse sequence that simultaneously excites both passively coupled spins P and B and simultaneously both dipolar couplings are re-introduced. The double quantum coherence for each crystallite will evolve under the sum of both local fields, and the angular relationship between the two dipolar tensors D_{P-X} and D_{B-Y} has a strong effect on the sum dipolar tensor. For example, if the dipolar tensors are collinear, the tensors are added 'in line', i.e., if for one particular crystal at one orientation the dipolar coupling for P–X is positive, then that for B–Y is also positive; more rapid dephasing is expected for each crystallite and broader dipolar tensors are expected. Alternatively, if the tensor orientations are at right angles to one another the shifts work in opposite directions and cancel each other; in this case a more slowly dephasing spin evolution and a narrower tensor is expected.

The relative orientation of the two tensors can also be probed without actually generating a multiple quantum coherence; if the dipolar dephasing for P−X and B−Y can be measured at separate times in the sequence, but if the two dephasing intervals are rotor synchronized, and if the evolution periods are incremented in a coordinated fashion, then the experiment will also probe the relative orientations of the two tensors. All of these separated local field based methods are expected to be well suited for uniformly enriched proteins. Backbone torsion angles could be measured with these methods; ϕ can be measured using the $^{1}H^{15}N^{13}C^{1}H$ spin system,[34] and ψ can be measured using $^{15}N^{13}C^{13}C^{15}N$ systems,[32] thus providing another reliable method for recognition of secondary structures. Side chain torsion angles involving $^{1}H^{13}C^{13}C^{1}H$ spin systems can be similarly measured.[33] Although for many of these methods multiple conformers are expected to be compatible with the same spectra, distinct patterns are generally expected for α-helical or β-sheet conformations.

For tertiary structure determination, or fold definition, long range constraints serve a critical role. By far the most commonly used type of long range information for protein structure determination has been the distance measurement between nuclei from residues far separated in the primary sequence (more than five residues apart). Therefore we focus on the question of the number of potentially useful long range distance constraints in solid state NMR spectra of uniformly or extensively labeled systems.

What tertiary structural constraints can be measured in uniformly labeled systems? This important question is largely open at present. At first glance, it appears that the common nuclei in isotopically labeled proteins, ^{1}H, ^{15}N and ^{13}C, provide many opportunities for measuring long range distances. Poor spectral resolution and dense networks of multi-spin couplings, however, make the protons a complicated reservoir for measurement or for relaying structural information. This situation is likely to change in the near future; preliminary efforts for distance and torsion angle measurements based on direct detection of protons in extensively deuterated peptides look quite promising, and perhaps these nuclei will ultimately be an important component of a protein structural protocol.[35,36] Carbon nuclei are numerous in the side chains of the protein, and are reasonably well resolved. Tertiary $^{13}C-^{15}N$ or $^{13}C-^{13}C$ contacts typically involve internuclear distances longer than 3.3 Å. The carbon pair distribution for nearest neighbors peaks at longer distances (4−5 Å) than for protons (near 3 Å). Thus tertiary heteronuclear contacts typically involve weak couplings in the range 30−150 Hz. Distance measurements in the order of 5 Å or longer in isolated pairs can be measured either homonuclear[37−39] or heteronuclear.[40] The principal fundamental limitation for measurements in specifically labeled samples is related to the comparison of the coupling strength with dephasing rates for the transverse coherences involved in the coherent transfer processes or in the evolution of the detected spin (probably of the order of 10−100 Hz).

Measurements of tertiary $^{13}C-^{15}N$ or $^{13}C-^{13}C$ contacts encounter additional obstacles for application in uniformly labeled samples, however, if not applied with some thoughtful strategy. $^{13}C-^{13}C$ and $^{13}C-^{15}N$ long range contacts in uniformly labeled samples would be difficult to measure with broadbanded recoupling methods, because each ^{13}C is coupled to many directly neighboring ^{13}C nuclei. Firstly, spectra involving mixing times long enough to achieve extensive population transfer to distant sites are expected to be very congested and poorly resolved, and cross peak intensities might not be related to distance in any simple way because of indirect coherence transfer pathways. More importantly, because the population transfers for solid state NMR typically occur through coherent evolution, the weaker couplings can become 'truncated' by the stronger couplings and ineffective for population transfer. Essentially every carbon in the protein has strongly bound neighbors. Measurements of weak couplings associated with bond lengths of 3−5 Å (ca. 50−250 Hz) in the presence of one bond couplings (ca. 2100 Hz) and several two bond couplings (ca. 500 Hz) is not straightforward. If a non-selective recoupling sequence is used with a uniformly labeled sample, then each carbon evolves coherently under the joint effect of several strong couplings and many weak couplings simultaneously. Such experiments would be expected to fail completely in the sense that very little magnetization is expected to reach long range tertiary contacts under a 'total recoupling' scheme.

The problem of detecting weak dipolar couplings can be met with two kinds of solutions. Introduction of 'odd-alternate' or 'checkerboard' labeling schemes, for example based on growth from 2-^{13}C glycerol or 1−3-^{13}C glycerol and use of specific bacterial strains,[19] largely eliminates directly neighboring spins, making the detection of tertiary contacts possibly with simple non-selective recoupling protocols such as spin diffusion. These protocols can be used to provide dilute ^{13}C spins propitious for high resolution MAS spectroscopy and useful distance measurements.[41] These schemes were used in the analysis of tertiary contacts in α-spectrin (Oshkinat et al., unpublished). Introduction of 2-^{13}C-glycerol while supplementing the growth medium with unlabeled amino acids, results in ^{13}C labels on the His C^{δ}, C^{α} of Ser Gly and Cys C^{α}, Trp (C^{α}, $C^{\zeta 2}$, $C^{\zeta 3}$, $C^{\delta 2}$), Phe (C^{α}, C^{γ}, $C^{\epsilon 1}$), Tyr (C^{α}, C^{γ}, $C^{\epsilon 1}$), Ala C^{α}, Val C^{α}, and Leu (C', C^{β}, C^{γ}). Because of the sparse nature of the labels in this particular scheme, relatively few long range constraints are expected. Roughly 0.3−0.5 tertiary constraints per residue are expected from these schemes.

Alternatively, a uniformly enriched sample can be characterized using tailored sequences based on selective recoupling of non-bonded functional groups. Spectrally selective sequences are analogous to non-selective recoupling sequences in that RF cycle times relate to the spatial (MAS) averaging in such a way that the net effect of the dipolar coupling is non-zero. They differ from non-selective sequences partly in that weak RF fields are used so that a dipolar matching condition may be met for one spectral band corresponding to carbons of one class of functional groups, but the dipolar recoupling condition is not met for most other functional groups. The recoupling conditions can therefore be established for tertiary but not primary contacts. For example, amide nitrogen and carbon methyl moieties are never in direct contact in proteins and only for alanine are they in a 'two-bond' arrangement. Therefore, tertiary contacts of this type will not usually be in competition with strong couplings in the same spectral band. These groups can be selectively recoupled using the selective CP experiment[42] with the nitrogen carrier non-selectively covering all amides while the carbon selectively sweeps the methyl region. This approach was used to detect numerous tertiary contacts in ubiquitin (Rienstra et al., in preparation). Analogously, REDOR experiments that selectively probe long

range contacts have also been demonstrated in tripeptides.[43] On the other hand, band-selective homonuclear sequences also have a lot of promise for detecting relatively long range correlations, for example couplings between methyl and carbonyl ^{13}C nuclei. These include rotational resonance tickling,[44] or DREAM.[45]

How many tertiary contacts of this type are expected in a protein structure? A cursory count of heteroatom pairs (i.e., pairs involving ^{13}C and ^{15}N rather than ^{1}H), at moderate distances (up to 5 Å), involving distant amino acids in the primary sequence (separated by more than four residues) indicates that several contacts per residue are expected. Which can practically be measured? Spectral overlap of the weakly bound pair of nuclei with strongly coupled neighbors should be avoided. Experiments are likely to work well for tertiary contacts involving the following kinds of functional groups: methyl–N, methyl–CO, aromatic–N aromatic–CO, methyl–methyl, CO–CO and methyl aromatic. Back-bone methyl contacts are both numerous (ca. 0.3–1 tertiary contact per residue in a typical protein) and practical to measure with the pulse sequences listed above. Backbone aromatic contacts require full assignments of the congested aromatic spin systems, and require decoupling of the neighboring aromatic carbons so that the long range contact can be developed. These are formidable tasks, which will require development of new pulse sequences. Long-range contacts between pairs of backbone sites, i.e., CO–CO or Cα – Cα constraints, are numerous (0.5–1 per residue); these contacts will primarily report on backbone–backbone hydrogen bonds and provide constraints for the secondary structure. Side chain–side chain contacts include methyl–methyl and aromatic–methyl contacts. These are typically few in number (<0.3 per residue) but are located in the hydrophobic core and can provide crucial information on tertiary contacts. The combination of these tertiary constraints (backbone–backbone, backbone–side chain and side chain–side chain) might result in more than one long-range constraint per residue, which will be practically measurable with a handful of multi-dimensional experiments. As conceived above, each experiment would have to be set up and run separately, which would be rather time intensive.

Dipolar splittings in aligned liquids also provide constraints on torsion angles.[46] These splittings offer a relationship between the direction of a local functional group and a fixed global axis system, and are independent from the local torsional constraints or the tertiary contacts. It is clear that these measurements have significantly sharpened solution NMR structures, and have provided the main constraint for solid NMR structures of aligned static samples. The role that such constraints might play for solid state studies, i.e., utilization of aligned microcrystals or membranes, remains to be investigated, but also appears to be quite promising.[47]

In summary, data from many experiments would be combined in order to have a large number of structural constraints: 1–2 tertiary contacts per residue in aggregate from separate selective recoupling experiments involving the pairs. N amide–Me, N amide–aromatic, CO–Me, CO–CO, Me–aromatic, and Me–Me. Proteins labeled in an odd-alternate pattern using specific metabolic pathways that might also provide constraints would be useful complements to the selective recoupling data. Additional data could be available from the use of ordered samples and torsion measurements.

3 STRUCTURE CALCULATIONS

How many contacts are needed to define the tertiary structure, and, procedurally, how can these structural constraints be used to compute structures? Protocols for analysis of tertiary constraints to define a three-dimensional structure are expected to be highly analogous to those used for solution NMR-derived nuclear Overhauser effects (NOEs).[48] Recently, we simulated carbon homonuclear structural constraints corresponding to both approaches, using known protein structures and simple assumptions about information that may be potentially accessible using selective labeling or selective recoupling schemes and knowledge of the ψ or ϕ torsional angles. Constraint lists for bovine pancreatic trypsin inhibitor (BPTI) were generated from the crystal structure (PDB entry 5pti.pdb)[49] (using the program 'ANALOGY', available from C. Geourjon, c.geourjon@ibcp.fr). Ensembles of 50 structures were calculated using X-PLOR; the 10 best structures were chosen on the criteria of minimum energy and violations, and the root mean squared deviation (RMSD) with respect to the crystal structure was calculated using the program MOLMOL.[50] A constraint set corresponding to all carbon–carbon contacts up to 5 Å can be used to determine high quality structures, i.e., with <1 Å RMSD; a variety of subsets of these contacts produced acceptable structures so long as more than one long range contact per residue was included. Combinations of the constraints discussed in the previous section offer a robust basis for structure; even if incomplete (<50%) data sets are assumed, high quality structures result (RMSD 1–2 Å). Correlations between backbone carbonyl and side chain carbons are of particular significance because they are numerous (>1 per residue), in many cases practically reasonable to measure, and appear to provide key information to constrain the tertiary structure. For example, 44 tertiary constraints from among the 86 that would result from selective recoupling of carbonyl methyl and aromatic carbons, result in a well-defined structure with an RMS of 1.9 Å. While a more honest assessment of the capability of solid state NMR derived structural parameters to constrain structures awaits actual data sets, these calculations are encouraging; they show that tertiary contacts derived from solid state NMR experiments may be sufficient to determine the correct fold.

Membrane proteins are among the most important targets for structural studies by solid state NMR due to their insolubility and the difficulties encountered in crystallization. The statistical distributions of distances typically encountered in membrane proteins such as bacteriorhodopsin and porin is somewhat different as contrasted with globular proteins. The percentage of amino acids with methyl bearing side-chains groups, and the related constraints, is typically much higher than for BPTI. Interhelical contacts in helical membrane proteins are mainly established through the methyl and aromatic groups of hydrophobic residues. The number of backbone–backbone tertiary contacts was negligible and not of practical importance for helical secondary structure, while for beta sheet structures these are of course more important. Many membrane proteins are ring-like oligomeric structures, which pose additional problems in interpretation. Clearly some fundamental issues for the study of these proteins will be the extent of resolution among the aliphatic side chains, which provide many of the long

range contacts, and the use of ambiguous restraints (i.e., restraints involving unidentified residues) in structure determination.

In conclusion, the past few years have seen rapid growth in the success of solid state NMR to study uniformly or extensively labeled proteins. Assignments of many proteins will clearly be within reach, and structural constraints are forthcoming as well. Protein constraint sets, analyzed with distance geometry simulated annealing protocols, appear to be capable of generating high resolution structures. Selective recoupling techniques among hydrophobic side chains and the carbonyl of the backbone appear to be especially promising, particularly if accompanied with measurements of torsional constraints. Alternative computational methods, such as methods for using ambiguous constraints[51] and knowledge-based methods involving sparse data sets, might also be important for long term success.

4 REFERENCES

1. P. T. Lansbury, P. R. Costa, J. M. Griffiths, E. J. Simon, M. Auger, K. J. Halverson, D. A. Kocisko, Z. S. Hendsch, T. T. Ashburn, R. G. S. Spencer, B. Tidor, and R. G. Griffin, *Nature Struct. Biol.*, 1995, **2**, 990–998.
2. T. L. S. Benzinger, D. M. Gregory, T. S. Burkoth, H. Miller-Auer, D. G. Lynn, R. E. Botto, and S. C. Meredith, *Proc. Natl. Acad. Sci. USA*, 1998, **95**, 13 407–13 412.
3. T. A. Cross and J. R. Quine, *Concepts Magn. Reson.*, 2000, **12**, 55–70.
4. R. Q. Fu, M. Cotton, and T. A. Cross, *J. Biomol. NMR*, 2000, **16**, 261–268.
5. F. A. Kovacs et al., *Biophys. J.*, 1998, **74**, A388.
6. W. W. Ying, S. E. Irvine, R. A. Beekman, D. J. Siminovitch, and S. O. Smith, *J. Am. Chem. Soc.*, 2000, **122**, 11 125–11 128.
7. O. J. Murphy, F. A. Kovacs, E. Sicard, and L. K. Thompson, *Biochemistry*, 2001, **40**, 1358–1366.
8. J. Yang et al., *J. Mol. Graph. Model.*, 2001, **19**, 129–135.
9. X. Feng, P. J. E. Verdegem, Y. K. Lee, D. Sandström, M. Edén, P. Bovée-Geurts, W. J. de Grip, J. Lugtenburg, H. J. M. de Groot, and M. H. Levitt, *J. Am. Chem. Soc.*, 1997, **119**, 6853–6857.
10. L. K. Thompson, A. E. McDermott, J. Raap, C. M. van der Wielen, J. Lugtenburg, J. Herzfeld, and R. G. Griffin, *Biochemistry*, 1992, **31**, 7931–7938.
11. J. Schaefer, *J. Magn. Reson.*, 1999, **137**, 272–275.
12. Y. K. Li, B. Poliks, L. Cegelski, M. Poliks, Z. Cryczynski, G. Piszczek, P. G. Jagtap, D. J. Studelska, D. G. I. Kingston, J. Schaefer, and S. Bane, *Biochemistry*, 2000, **39**, 281–291.
13. A. McDermott, T. Polenova, A. Bockmann, K. W. Zilm, E. K. Paulson, R. W. Marin, and G. T. Montelione, *J. Biomol. NMR*, 2000, **16**, 209–219.
14. J. Pauli et al., *Chembiochem*, 2001, **2**, 272–281.
15. W. M. Westler, B. J. Stockman, and J. L. Markley, *J. Am. Chem. Soc.*, 1988, **110**, 6256–6258.
16. D. S. Wishart and B. D. Sykes, *J. Biomol. NMR*, 1994, **4**, 171–180.
17. S. K. Straus, T. Bremi, and R. R. Ernst, *Chem. Phys. Lett.*, 1996, **262**, 709–715.
18. D. M. LeMaster, *Prog. NMR Spectrosc.*, 1994, **26**, 371–419.
19. D. M. LeMaster, *J. Am. Chem. Soc.*, 1996, **118**, 9255–9264.
20. M. K. Rosen, K. H. Gardner, R. C. Willis, W. E. Parris, T. Pawson, and L. E. Kay, *J. Mol. Biol.*, 1996, **263**, 627–636.
21. R. Verel, M. Ernst, and B. H. Meier, *J. Magn. Reson.*, 2001, **150**, 81–99.
22. S. Hediger, B. H. Meier, N. D. Kurur, G. Bodenhausen, and R. R. Ernst, *Chem. Phys. Lett.*, 1994, **223**, 283–288.
23. S. Hediger, B. H. Meier, and R. R. Ernst, *Chem. Phys. Lett.*, 1995, **240**, 449–456.
24. M. Baldus, D. G. Geurts, S. Hediger, and B. H. Meier, *J. Magn. Reson. Ser. A*, 1996, **118**, 140–144.
25. B. Q. Sun, C. M. Rienstra, P. R. Costa, J. Herzfeld, J. Williamson, and R. G. Griffin, *J. Am. Chem. Soc.*, 1997, **119**, 8540–8546.
26. M. Hong and R. G. Griffin, *J. Am. Chem. Soc.*, 1998, **120**, 7113–7114.
27. T. Fujiwara, K. Sugase, M. Kainosho, A. Ono, A. Ono, and H. Akutsu, *J. Am. Chem. Soc.*, 1995, **117**, 11 351–11 352.
28. C. A. Michal and L. W. Jelinski, *J. Am. Chem. Soc.*, 1997, **119**, 9059–9060.
29. C. M. Rienstra, M. Hohwy, M. Hong, and R. G. Griffin, *J. Am. Chem. Soc.*, 2000, **122**, 10 979–10 990.
30. D. S. Wishart and A. M. Nip, *Biochem. Cell Biol.*, 1998, **76**, 153–163.
31. J. Heller, D. D. Laws, M. Tomaselli, D. S. King, D. E. Wemmer, A. Pines, R. H. Havlin, and E. Oldfield, *J. Am. Chem. Soc.*, 1997, **119**, 7827–7831.
32. P. R. Costa, D. A. Kocisko, B. Q. Sun, P. T. Lansbury, and R. G. Griffin, *J. Am. Chem. Soc.*, 1997, **119**, 10 487–10 493.
33. X. Feng, M. Eden, A. Brinkmann, H. Luthman, L. Eriksson, A. Graslund, O. N. Antzutkin, and M. H. Levitt, *J. Am. Chem. Soc.*, 1997, **119**, 12 006–12 007.
34. M. Hong, J. D. Gross, C. M. Rienstra, R. G. Griffin, K. K. Kumashiro, and K. Schmidt-Rohr, *J. Magn. Reson.*, 1997, **129**, 85–92.
35. B. Reif, M. Hennig, and C. Griesinger, *Science*, 1997, **276**, 1230–1233.
36. Y. Ishii, J. P. Yesinowski, and R. Tycko, *J. Am. Chem. Soc.*, 2001, **123**, 2921–2922.
37. M. H. Levitt, T. G. Oas, and R. G. Griffin, *Isr. J. Chem.*, 1988, **28**, 271–282.
38. D. P. Raleigh, M. H. Levitt, and R. G. Griffin, *Chem. Phys. Lett.*, 1988, **146**, 71–76.
39. D. M. Gregory, D. J. Mitchell, J. A. Stringer, S. Kiihne, J. C. Shiels, J. Callahan, M. A. Mehta, and G. P. Drobny, *Chem. Phys. Lett.*, 1995, **246**, 654.
40. T. Gullion and J. Schaefer, *J. Magn. Reson.*, 1989. **81**, 196–200.
41. M. Hong and K. Jakes, *J. Biomol. NMR*, 1999, **14**, 71–74.
42. M. Baldus, A. T. Petkova, J. Herzfeld, and R. G. Griffin, *Mol. Phys.*, 1998, **95**, 1197–1207.
43. C. P. Jaroniec, B. A. Tounge, J. Herzfeld, and R. G. Griffin, *J. Am. Chem. Soc.*, 2001, **123**, 3507–3519.
44. P. R. Costa, B. Q. Sun, and R. G. Griffin, *J. Am. Chem. Soc.*, 1997, **119**, 10 821–10 830.
45. R. Verel, M. Ernst, and B. H. Meier, *J. Magn. Reson.*, 2001, **150**, 81–99.
46. N. Tjandra and A. Bax, *Science*, 1997, **278**, 1111–1114.
47. D. A. Middleton et al., *J. Magn. Reson.*, 2000, **147**, 366–370.
48. A. T. Brunger, P. D. Adams, G. M. Clore, W. L. DeLano, P. Gros, R. W. Grosse-Kunstleve, J. S. Jiang, J. Kuszewski, M. Nilges, N. S. Pannu, R. J. Read, L. M. Rice, T. Simonson, and G. L. Warren, *Acta Crystallogr. D*, 1998, **54**, 905–921.
49. A. Wlodawer, J. Walter, R. Huber, and L. Sjolin, *J. Mol. Biol.*, 1984. **180**, 301–329.
50. R. Konradi, M. Billeter, and K. Wuthrich, *J. Mol. Graph.*, 1996, **14**, 51–55.
51. J. P. Linge, S. I. O'Donoghue, and M. Nilges, *Methods Enzymol.*, 2001, **339**, 71–90.

Acknowledgements

The authors acknowledge support from NSF Molecular Biophysics grant MCB 9983581.

Biographical Sketches

Anja Böckmann, *b*. 1966. Dipl.-Chem., 1993, Technische Universität Berlin; Ph.D. 1996, Université Paris VI, France with E. Guittet; postdoctoral research, 1996–1997, Columbia University with Professor Ann McDermott; affiliated with the Centre National de la Recherche Scientifique as Chargée de Recherche at the Institut de Biologie et de Chimie de Protéines, Lyon, France, 1998–present.

Ann McDermott, *b*. 1960. B.Sc. Harvey Mudd College 1981, Ph.D. University of California at Berkeley, 1987, postdoctoral research MIT 1988–1991 and Université Catholique de Louvain; Columbia University 1991–present. Approx 70 publications. Research Specialties: solid state NMR studies of enzyme catalytic function.

Structures of Larger Proteins, Protein–Ligand, and Protein–DNA Complexes by Multidimensional Heteronuclear NMR

G. Marius Clore and Angela M. Gronenborn
National Institutes of Health, Bethesda, MD, USA

1 Introduction 1
2 General Strategy for the Determination of Three-dimensional Structures of Larger Proteins and Protein Complexes by NMR 1
3 Application of Three- and Four-dimensional NMR to Structure Determination of Larger Proteins: the Structure of Interleukin-1β 5
4 Combining Experimental Information from Crystal and Solution Studies: Joint X-ray and NMR Refinement 7
5 Structure Determination of Protein–Peptide and Protein–DNA Complexes 9
6 Concluding Remarks 18
7 Related Articles 19
8 References 19

1 INTRODUCTION

The last few years have seen a quantum jump in both the accuracy of the determination and in the size of protein structures that can be determined by NMR.[1] Thus it is now possible to determine the structures of proteins in the 15–25 kDa range at a resolution comparable to 0.2 nm resolution for crystal structures.[2] This advance is attributable to the development of three- and four-dimensional heteronuclear NMR techniques which circumvent problems associated with chemical shift overlap and degeneracy, on the one hand, and large linewidths on the other.[1,3–5] In this article, we summarize some of these developments and illustrate their application to the structure determination of interleukin-1β (IL-1β),[6] a complex of calmodulin with a target peptide,[7] and a complex of the DNA binding domain of the transcription factor GATA-1 with its cognate DNA target site.[8]

2 GENERAL STRATEGY FOR THE DETERMINATION OF THREE-DIMENSIONAL STRUCTURES OF LARGER PROTEINS AND PROTEIN COMPLEXES BY NMR

The main source of geometric information used in protein structure determination lies in the nuclear Overhauser effect (NOE) which can be used to identify protons separated by less than 0.5 nm.[9] This distance limit arises from the fact that the NOE is proportional to the inverse sixth power of the distance between the protons. Hence the NOE intensity falls off very rapidly with increasing distance between proton pairs. Despite the short range nature of the observed interactions, the short approximate interproton distance restraints derived from the NOE measurements can be highly conformationally restrictive, particularly when they involve residues that are far apart in the sequence but close together in space.

The power of NMR over other spectroscopic techniques results from the fact that every proton gives rise to an individual resonance in the spectrum which can be resolved by higher (i.e. two, three and four) dimensional techniques. Bearing this in mind, the principles of structure determination by NMR can be summarized very simply by the scheme depicted in Figure 1. The first step is to obtain sequential resonance assignments using a combination of through-bond and through-space correlations; the second step is to obtain stereospecific assignments at chiral centers and torsion angle restraints using three-bond scalar couplings combined with intraresidue and sequential interresidue NOE data; the third step is to identify through-space connectivities between protons separated by less than 0.5 nm and, finally, the fourth step involves calculating three-dimensional structures on the basis of the amassed interproton distance and torsion angle restraints using one or more of a number of algorithms[10–12] such as distance geometry and/or simulated annealing. It is not essential to assign all the NOEs initially. Indeed, many may be ambiguous and several possibilities may exist for their assignments. However, once a low-resolution structure has been calculated from a subset of the NOE data which can be interpreted unambiguously, it is then possible to employ iterative methods to resolve the vast majority of ambiguities. Consider, for example, an NOE cross peak which could be attributable to a through-space interaction between either protons A and B or between protons A and C. Once a low-resolution structure is available it is usually possible to discriminate between these two possibilities. Thus, if protons A and C are significantly greater than 0.5 nm apart while protons A and B are less than 0.5 nm apart, it is clear that the cross peak must arise from an NOE between protons A and B.

The quality of an NMR protein structure determination increases as the number of restraints increase.[1,4,13–15] This progression in coordinate precision is illustrated in Figure 2 which shows four generations of structures, ranging from the first generation which simply provides a picture of the polypeptide fold with little detail, to the fourth generation which is broadly equivalent to a 0.2 nm resolution X-ray structure.

2.1 Sequential Resonance Assignment

Conventional sequential resonance assignment relies on two-dimensional homonuclear $^1H-^1H$ correlation experiments to identify amino acid spin systems coupled with two-dimensional $^1H-^1H$ NOE experiments to identify sequential connectivities along the backbone of the type $C^\alpha H(i)$–$NH(i + 1, 2, 3, 4)$, $NH(i)$–$NH(i \pm 2)$ and $C^\alpha H(i)$–$C^\beta H(i + 3)$.[16,17] This methodology has been successfully applied to proteins of less than 100 residues. For larger proteins, the

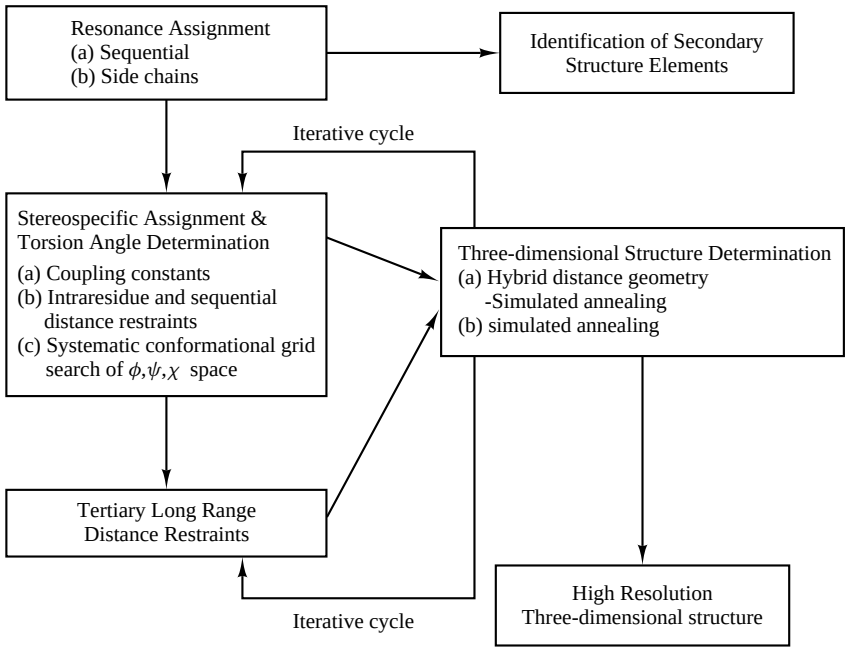

Figure 1 Summary of the general strategy employed to solve three-dimensional structures of macromolecules by NMR. (Adapted from G. M. Clore and A. M. Gronenborn, *Science*, 1991, **252**, 1390)

spectral complexity is such that two-dimensional experiments no longer suffice, and it is essential to increase the spectral resolution by increasing the dimensionality of the spectra.[18] In some cases it is still possible to apply the same strategy by making use of three-dimensional heteronuclear (^{15}N or ^{13}C) edited experiments to increase the spectral resolution, as illustrated in Figure 3.[19–22] In many cases, however, numerous ambiguities still remain and it is advisable to adopt a sequential assignment strategy based solely on well defined heteronuclear scalar couplings.[3,5,23–25] The double and triple resonance experiments that we currently use, and the correlations that they demonstrate, are summarized in Table 1. With the advent of pulse field gradients to eliminate undesired coherence transfer pathways,[26] it is now possible to employ only two-step phase cycles without any loss in sensitivity (other than that due to the reduction in measurement time) such that each three-dimensional experiment can be recorded in as little as 7 h. In most cases, however, signal-to-noise ratio requirements necessitate 1–3 days of measuring time, depending on the experiment.

2.2 Stereospecific Assignments and Torsion Angle Restraints

It is often possible to obtain stereospecific assignments of β-methylene protons on the basis of a qualitative interpretation of the homonuclear $^3J(\alpha,\beta)$ coupling constants and the intraresidue NOE data involving the NH, C$^\alpha$H and C$^\beta$H protons.[27,28] A more rigorous approach, which also permits one to obtain ϕ, ψ, and χ_1 restraints, involves the application of a conformational grid search of ϕ,ψ,χ_1 space on the basis of the homonuclear ^3J(N-α,H) and $^3J(\alpha,\beta)$ coupling constants (which are related to ϕ and χ_1, respectively), and the intraresidue and sequential ($i \pm 1$) interresidue NOEs involving the NH, C$^\alpha$H and C$^\beta$H protons.[29,30] This information can be supplemented by the measurement of heteronuclear ^3J(N,H-β) and ^3J(CO,H-β) couplings which are also related to χ_1.[31] Stereospecific assignment of valine methyl groups can be made on the basis of ^3J(C-γ,CO) and ^3J(N,C-γ) couplings,[31] as well as on the basis of the pattern of intraresidue NOEs involving the NH, C$^\alpha$H and C$^\gamma$H protons.[32] Finally, stereospecific assignments of leucine methyl groups can be made on the basis of heteronuclear ^3J(C-δ,C-α) and ^3J(C-δ,H-β) couplings[31] in combination with the pattern of intraresidue NOEs, provided that the stereospecific assignment of the β-methylene protons and the χ_1 rotamer have been previously determined.[33]

2.3 Assignment of Through-space Proton–Proton Interactions within a Protein

While the panoply of three-dimensional heteronuclear experiments is sufficient for the purposes of spectral assignment, yet further increases in resolution are required for the reliable identification of NOE through space interactions. This can be achieved by extending the dimensionality still further to four dimensions.[34] This is illustrated in Figure 4. Consider a simple two-dimensional spectrum demonstrating 11 cross peaks from aliphatic resonances to a single NH resonance position. In the two-dimensional spectrum it is impossible to ascertain whether this involves one NH proton or many. Extending the spectrum to three dimensions by separating the NOE interactions according to the ^{15}N chemical shift of the nitrogen attached to each amide proton reveals that there are three NH protons involved. The identity of the originating aliphatic protons, however, is only specified by their proton chemical shifts. Yet the extent of spectral overlap in the aliphatic region of the spectrum vastly exceeds that in the amide region. This can be resolved by adding a further dimension in which each plane of the three-dimensional spectrum now constitutes a cube in the

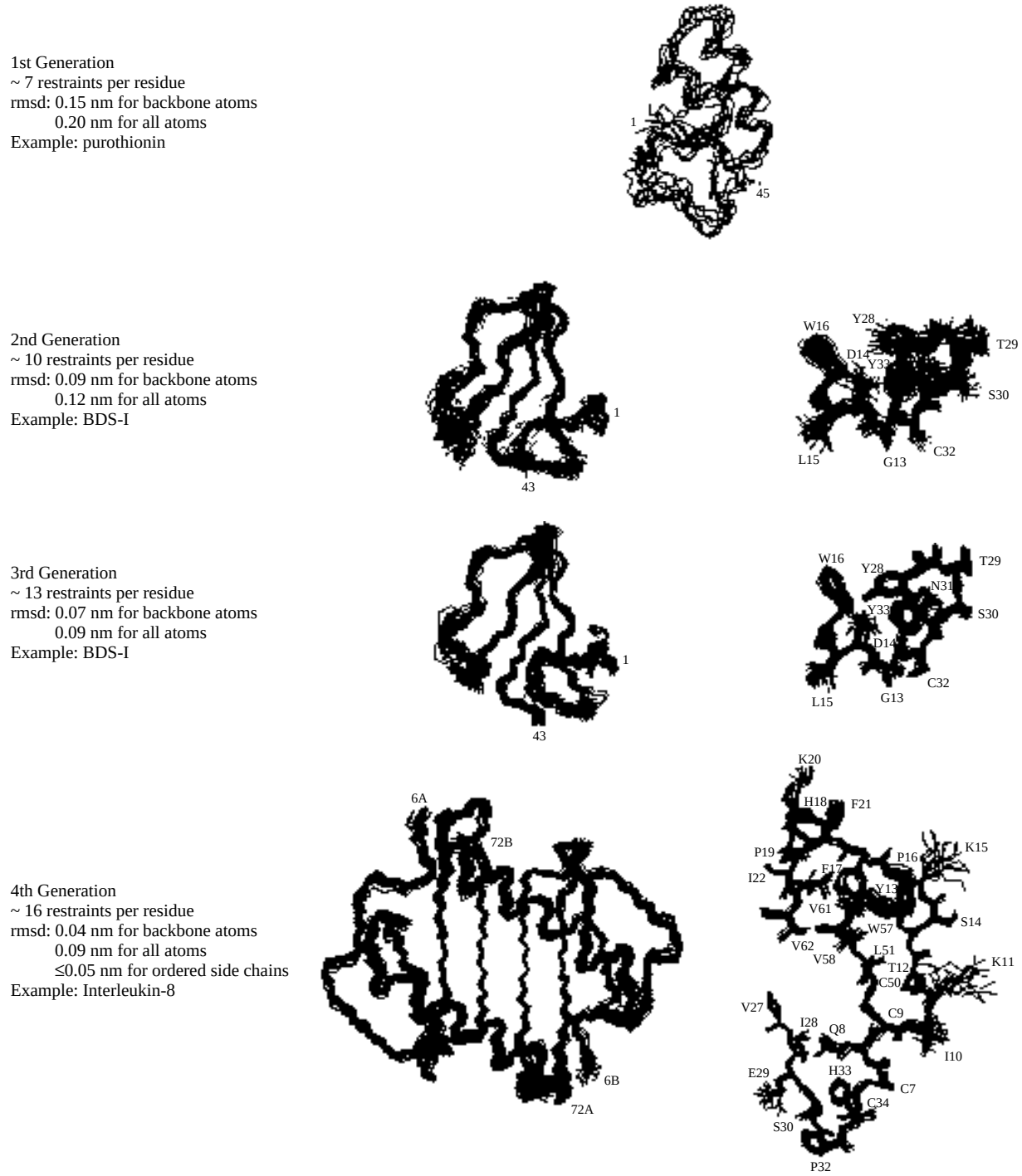

Figure 2 Illustration of the progressive improvement in the precision and accuracy of NMR structure determinations with increasing number of experimental restraints. All the structures have been calculated using the hybrid distance geometry, simulated annealing method, and in each case the NOE derived interproton distance restraints have been grouped into the three broad ranges: 0.18–0.27, 0.18–0.33, and 0.18–0.5 nm, corresponding to strong, medium and weak NOEs, respectively. (Adapted from G. M. Clore and A. M. Gronenborn, *Science*, 1991, **252**, 1390)

four-dimensional spectrum edited by the ^{13}C shift of the carbon atom attached to each aliphatic proton. In this manner, each $^{1}H-^{1}H$ NOE interaction is specified by four chemical shift coordinates, the two protons giving rise to the NOE and the heavy atoms to which they are attached. The resolving power of four-dimensional heteronuclear-edited NOE spectroscopy is illustrated in Figure 5.

Because the number of NOE interactions present in each two-dimensional plane of a four-dimensional $^{13}C/^{15}N$ or $^{13}C/^{13}C$ edited NOESY spectrum is so small, the inherent resolution in a four-dimensional spectrum is extremely high, despite the low level of digitization. Indeed, spectra with equivalent resolution can be recorded at magnetic field strengths considerably lower than 600 MHz, although this

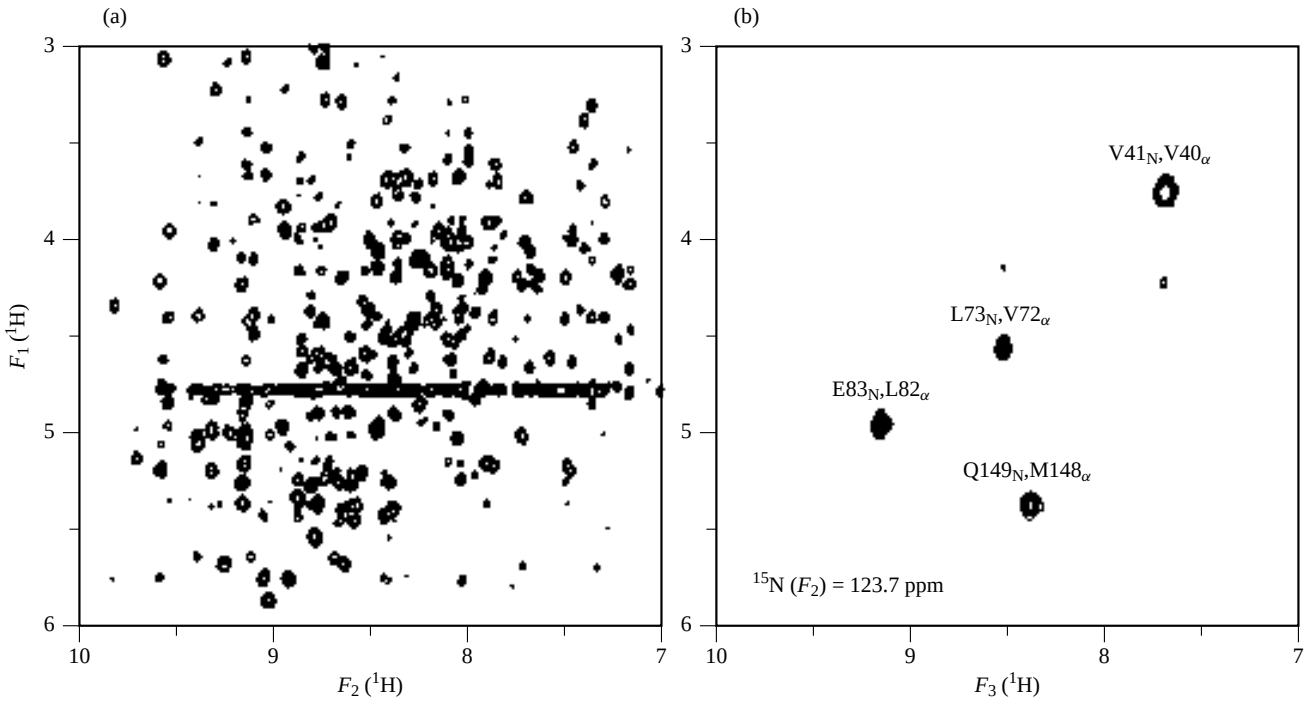

Figure 3 Comparison of the NH–C$^\alpha$H/C$^\beta$H region of a two-dimensional ^{15}N-edited NOESY spectrum (a) with that of a single plane taken from the three-dimensional ^{15}N-edited NOESY spectrum of interleukin-1β (b), illustrating the increase in spectral resolution afforded by increasing the dimensionality from two to three. (Adapted from D. Marion, P. C. Driscoll, L. E. Kay, P. T. Wingfield, A. Bax, A. M. Gronenborn, and G. M. Clore, *Biochemistry*, 1989, **28**, 6150)

Table 1 Summary of Correlations Observed in the Three-dimensional Double and Triple Resonance Experiments used for Sequential and Side-Chain Assignments in our Laboratory

Experiment	Correlation	J Coupling[a]
^{15}N edited HOHAHA	C$^\alpha$H(i)–^{15}N(i)–NH(i)	^3J(N-α,H)
	C$^\beta$H(i)–^{15}N(i)–NH(i)	^3J(N-α,H) and ^3J(α,β)
HNHA	C$^\alpha$H(i)–^{15}N(i)–NH(i)	^3J(N,H)
H(CA)NH	C$^\alpha$H(i)–^{15}N(i)–NH(i)	^1J(N,C-α)
	C$^\alpha$H($i-1$)–^{15}N(i)–NH(i)	^2J(N,C-α)
HNCA	^{13}C$^\alpha$(i)–^{15}N(i)–NH(i)	^1J(N,C-α)
	^{13}C$^\alpha$($i-1$)–^{15}N(i)–NH(i)	^2J(N,C-α)
HN(CO)CA	^{13}C$^\alpha$($i-1$)–^{15}N(i)–NH(i)	^1J(N,CO) and ^1J(C-α,CO)
HNCO	^{13}CO($i-1$)–^{15}N(i)–NH(i)	^1J(N,CO)
HCACO	C$^\alpha$H(i)–^{13}C$^\alpha$(i)–^{13}CO(i)	^{1}J(C-α,CO)
HCA(CO)N	C$^\alpha$H(i)–^{13}C$^\alpha$(i)–^{15}N($i+1$)	^1J(C-α,CO) and ^1J(N,CO)
CBCA(CO)NH	^{13}C$^\beta$($i-1$)/^{13}C$^\alpha$($i-1$)–^{15}N(i)–NH(i)	^1J(C-α,CO), ^1J(N,CO) and ^1J(C,C)
CBCANH	^{13}C$^\beta$(i)/^{13}C$^\alpha$(i)–^{15}N(i)–NH(i)	^1J(N,C-α) and ^1J(C,C)
	^{13}C$^\beta$($i-1$)/^{13}C$^\alpha$($i-1$)–^{15}N(i)–NH(i)	^2J(N,C-α) and ^1J(C,C)
HBHA(CO)NH	C$^\beta$H($i-1$)/C$^\alpha$H($i-1$)–^{15}N(i)–NH(i)	^1J(C-α,CO), ^1J(N,CO) and ^1J(C,C)
HBHANH	C$^\beta$H(i)/C$^\alpha$H(i)–^{15}N(i)–NH(i)	^1J(N,C-α) and ^1J(C,C)
	C$^\beta$H($i-1$)/C$^\alpha$H($i-1$)–^{15}N(i)–NH(i)	^2J(N,C-α) and ^1J(C,C)
C(CO)NH	^{13}C^j($i-1$)–^{15}N(i)–NH(i)	^1J(C-α,CO), ^1J(N,CO) and ^1J(C,C)
H(CCO)NH	H^j($i-1$)–^{15}N(i)–NH(i)	^1J(C-α,CO), ^1J(N,CO) and ^1J(C,C)
HCCH-COSY	H^j–^{13}C^j–^{13}C$^{j\pm1}$–H$^{j\pm1}$	^1J(C,C)
HCCH-TOCSY	H^j–^{13}C^j ... ^{13}C$^{j\pm n}$–H$^{j\pm n}$	^1J(C,C)

[a]In addition to the couplings indicated, all the experiments make use of the ^1J(C,H) ($\approx$140 Hz) and/or ^1J(N,H) ($\approx$ 95 Hz) couplings. The values of the couplings employed are as follows: ^3J(N-α,H) $\approx$ 3–10 Hz, ^1J(C,C) $\approx$ 35 Hz, ^1J(C-α,CO) $\approx$ 55 Hz, ^1J(N,CO) $\approx$ 15 Hz, ^1J(N,C-α) $\approx$ 11 Hz, ^2J(N,C-α) $\approx$ 7 Hz.

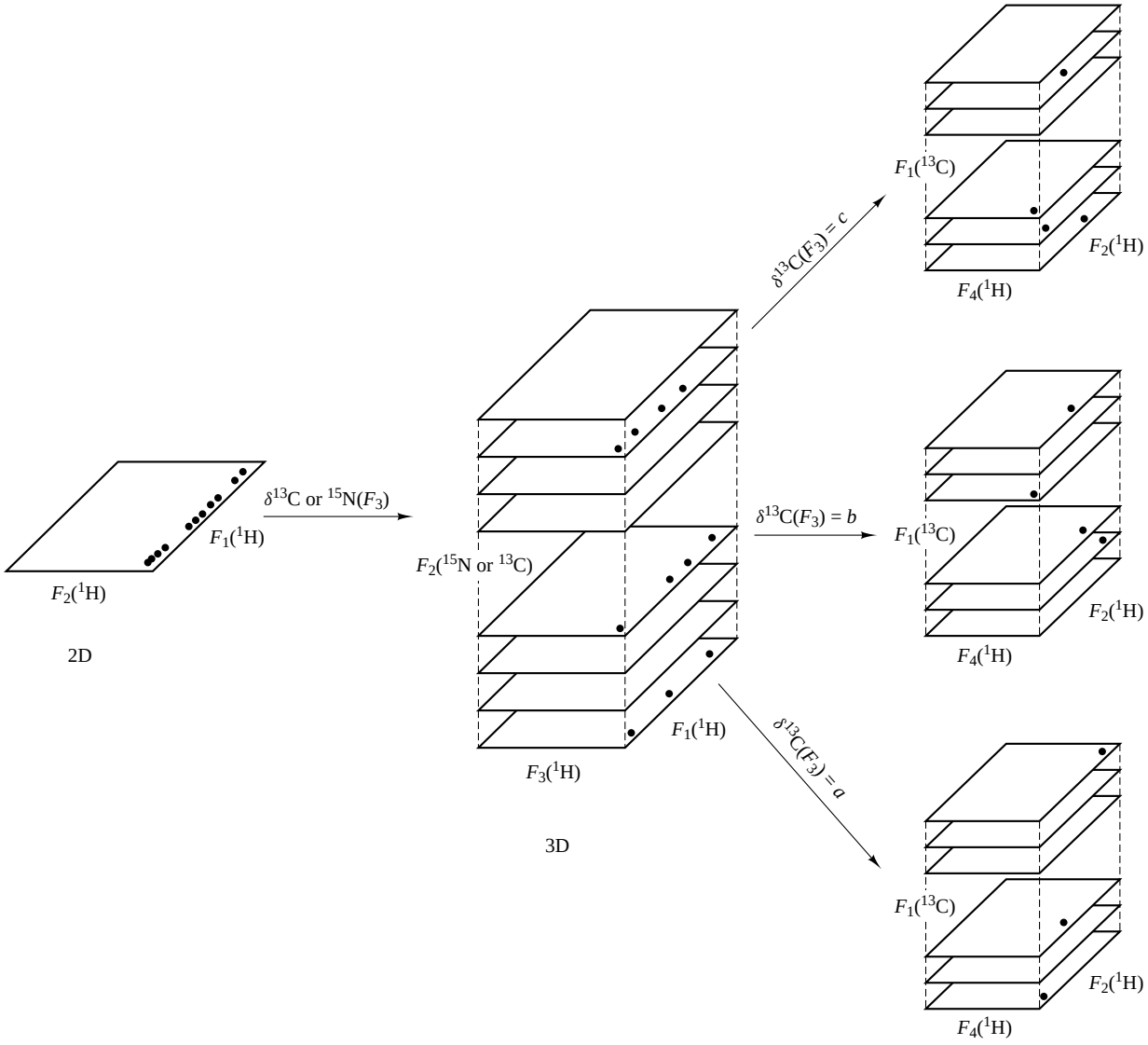

Figure 4 Schematic illustration of the progression and relationship between two-, three-, and four-dimensional heteronuclear-edited NMR spectroscopy. (Adapted from G. M. Clore and A. M. Gronenborn, *Science*, 1991, **252**, 1390)

would obviously lead to a reduction in sensitivity. Furthermore, it can be calculated that four-dimensional spectra with virtual lack of resonance overlap and good sensitivity can be obtained on proteins with as many as 400 residues. Thus, once complete ^{1}H, ^{15}N, and ^{13}C assignments are obtained, analysis of four-dimensional ^{15}N/^{13}C and ^{13}C/^{13}C edited NOE spectra[34–37] should permit the automated assignment of almost all NOE interactions.

3 APPLICATION OF THREE- AND FOUR-DIMENSIONAL NMR TO STRUCTURE DETERMINATION OF LARGER PROTEINS: THE STRUCTURE OF INTERLEUKIN-1β

While the potential of heteronuclear three- and four-dimensional NMR methods in resolving problems associated with both extensive resonance overlap and large linewidths is obvious, how does this new approach fare in practice? In this regard it should be borne in mind that resonance assignments are only a means to an end, and the true test of multidimensional NMR lies in examining its success in solving the problem which it was originally designed to tackle, namely the determination of high-resolution three-dimensional structures of larger proteins in solution.

The first successful demonstration of these new methods was the determination of the high-resolution solution structure of interleukin-1β (IL-1β), a cytokine of 153 residues and molecular weight 17.4 kDa, which plays a key role in the immune and inflammatory responses.[6] At the time IL-1β was 50% larger, in terms of the number of residues, than the previously largest protein structures solved by NMR, namely human[38] and *Escherichia coli*[39] thioredoxin which have 105 and 108 residues, respectively. Moreover, IL-1β still represents one of the most highly refined and precise structures for proteins of this size solved by NMR.

Despite extensive analysis of two-dimensional spectra obtained at different pH values and temperatures, as well as

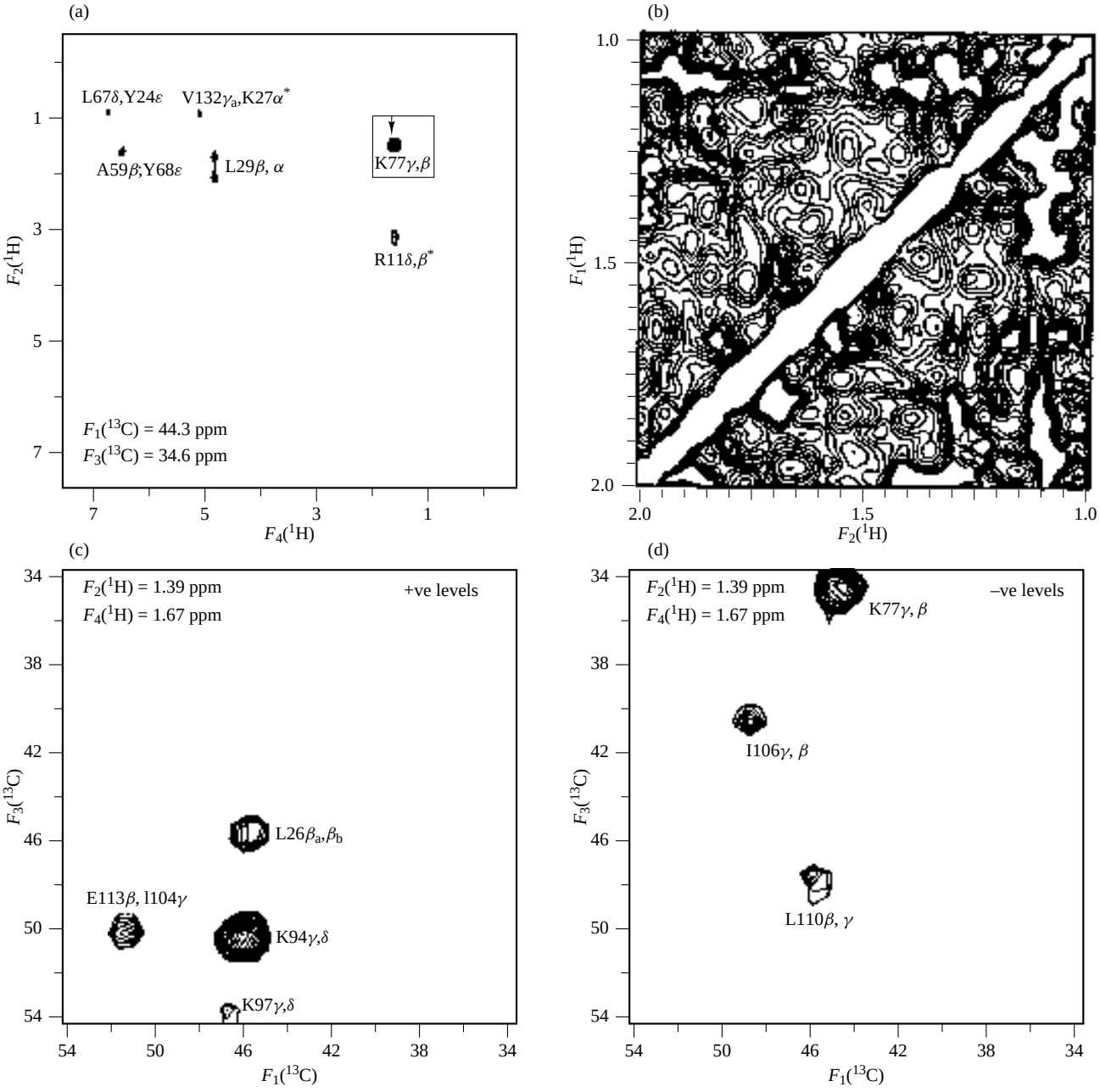

Figure 5 Example of the increase in spectral resolution afforded by four-dimensional $^{13}C/^{13}C$-edited NOE spectroscopy, illustrated with IL-1β. (a) $^{1}H(F_2)-^{1}H(F_4)$ plane of the four-dimensional spectrum at $\delta^{13}C(F_1)$ = 44.3 ppm and $\delta^{13}C(F_3)$ = 34.6 ppm; the region between 1 and 2 ppm is boxed in and the arrow indicates the position of the Lys77 $C^{\gamma}H-C^{\beta}H$ NOE cross peak. (b) Two-dimensional $^{1}H-^{1}H$ NOE spectrum between 1 and 2 ppm; the X marks the chemical shift position of the Lys77 $C^{\gamma}H-C^{\beta}H$ NOE cross peak seen in (a). (c, d) Positive and negative contours in the $^{13}C(F_1)-^{13}C(F_3)$ plane of the four-dimensional spectrum at the ^{1}H chemical shift coordinates $\delta^{1}H(F_2)$ = 1.39 ppm and $\delta^{1}H(F_4)$ = 1.67 ppm corresponding to the Lys77 $C^{\gamma}H-C^{\beta}H$ NOE cross peak seen in (a) and the X mark shown in (b). Because extensive folding is employed, the ^{13}C chemical shifts are given by $x \pm n$SW, where x is the ppm value listed in the figure, n is an integer, and SW is the spectral width (20.71 ppm). Peaks folded an even number of times are of opposite sign to those folded an odd number of times. All the peaks in (a) are positive, except for the two indicated by an asterisk which are negative. (Adapted from G. M. Clore and A. M. Gronenborn, *Science*, 1991, **252**, 1390)

examination of two-dimensional spectra of mutant proteins, it did not prove feasible to obtain unambiguous ^{1}H assignment for more than about 30% of the residues of interleukin-1β.[22] Thus, any further progress could only be made by resorting to higher dimensionality heteronuclear NMR. The initial step involved the complete assignment of the ^{1}H, ^{15}N, and ^{13}C resonances of the backbone and side chains using many of the double and triple resonance three-dimensional experiments listed in Table 1.[22,40,41] In the second step, backbone and side-chain torsion angle restraints, as well as stereospecific assignments for β-methylene protons, were obtained by means of a three-dimensional systematic grid search of ϕ,ψ,χ_1 space.[30] In the third step, approximate interproton distance restraints between nonadjacent residues

were derived from analysis of three- and four-dimensional heteronuclear-edited NOE spectra. Analysis of the three-dimensional heteronuclear-edited NOE spectra alone was sufficient to derive a low-resolution structure on the basis of a small number of NOEs involving solely NH, $C^{\alpha}H$ and $C^{\beta}H$ protons.[42] However, further progress using three-dimensional NMR was severely hindered by the numerous ambiguities still present in these spectra, in particular for NOEs arising from the large number of aliphatic protons. Thus, the four-dimensional heteronuclear-edited NOE spectra proved to be absolutely essential for the successful completion of this task. In addition, the proximity of backbone NH protons to bound structural water molecules was ascertained from a three-dimensional ^{15}N-separated ROESY spectrum which permits one to distinguish specific protein–water NOE interactions from chemical exchange with bulk solvent.[43] In this regard it should be emphasized that all the NOE data were interpreted in as conservative a manner as possible, and were simply classified into three distance ranges: 0.18–0.27, 0.18–0.33, and 0.18–0.50 nm, corresponding to strong, medium, and weak intensity NOEs, respectively.

With an initial set of experimental restraints in hand, three-dimensional structure calculations were initiated using the hybrid distance geometry–dynamical simulated annealing method.[44] A key aspect of the overall strategy lies in the use of an iterative approach whereby the experimental data are reexamined in the light of the initial set of calculated structures in order to resolve ambiguities in NOE assignments, to obtain more stereospecific assignments (e.g. the α-methylene protons of glycine and the methyl groups of valine and leucine) and torsion angle restraints, and to assign backbone hydrogen bonds associated with slowly exchanging NH protons as well as with bound water molecules. The iterative cycle comes to an end when all the experimental data have been interpreted.

The final experimental data set for IL-1β comprised a total of 3146 approximate and loose experimental restraints made up of 2780 distance and 366 torsion angle restraints.[6] This represents an average of about 21 experimental restraints per residue. If one takes into account that interresidue NOEs affect two residues, while intraresidue NOE and torsion angle restraints only affect individual residues, the average number of restraints influencing the conformation of each residue is approximately 33. Superpositions of the backbone atoms and selected side chains for 32 independently calculated structures are shown in Figures 6(b) and 6(d). All 32 structures satisfy the experimental restraints within their specified errors, display very small deviations from idealized covalent geometry, and have good nonbonded contacts. It can be seen that both the backbone and ordered side chains are exceptionally well defined. Indeed, the atomic root-mean-square (rms) distribution about the mean coordinate positions is 0.04 nm for the backbone atoms, 0.08 nm for all atoms, and 0.05 nm for side chains with $\leq$40% of their surface (relative to that in a tripeptide Gly-X-Gly) accessible to solvent.[6]

The structure of IL-1β itself resembles a tetrahedron and displays three-fold internal pseudosymmetry. There are 12 β-strands arranged in an exclusively antiparallel β-structure, and six of the strands form a β-barrel [seen in the front of Figure 6(a)] which is closed off at the back of the molecule by the other six strands. Each repeating topological unit is composed of 5 strands arranged in an antiparallel manner with respect to each other, and one of these units is shown in Figure 6(c). Water molecules occupy very similar positions in all three topological units, as well as at the the interface of the three units, and are involved in bridging backbone hydrogen bonds. Thus, in the case of the topological unit shown in Figure 6(c), the water molecule labeled W5 accepts a hydrogen bond from the NH of Phe112 in strand IX and donates two hydrogen bonds to the backbone carbonyls of Ile122 in strand X and Thr144 in strand XII. The packing of some internal residues with respect to one another, as well as the excellent definition of internal side chains, is illustrated in Figure 6(d). Because of the high resolution of the IL-1β structure it was possible to analyze in detail side-chain–side-chain interactions involved in stabilizing the structure. In addition, examination of the structure in the light of mutational data permitted us to propose the presence of three distinct sites involved in the binding of IL-1β to its cell surface receptor.[6]

4 COMBINING EXPERIMENTAL INFORMATION FROM CRYSTAL AND SOLUTION STUDIES: JOINT X-RAY AND NMR REFINEMENT

It is clear from the preceding discussion that NMR is a valid method, alongside X-ray crystallography, for determining high-resolution structures of small to medium sized proteins of less than about 35 kDa. IL-1β offers an ideal system for comparing the results of NMR and X-ray crystallography as, in addition to the solution structure, there are three independently solved X-ray structures at 0.2 nm resolution of the same crystal form.[45–47] The backbone atomic rms difference between the NMR and the X-ray structures is about 0.1 nm, with the largest differences being confined to some of the loops and turns connecting the β-strands.[2] Interestingly, however, the atomic rms distribution of the 32 calculated solution structures about their mean coordinate positions (about 0.04 nm for the backbone atoms, about 0.08 nm for all atoms, and about 0.05 nm for all atoms of internal residues) is approximately the same as the atomic rms differences between the three X-ray structures, indicating that the positional errors in the atomic coordinates determined by the two methods are similar.[2] Upon initial inspection, the X-ray structures appear to be incompatible with the NMR data, as manifested by a relatively large number of NOE and torsion angle violations and, conversely, the NMR structure fits the X-ray data poorly with an R factor of 40–50%. Because of the very different nature of the two methods, it is not immediately apparent that these discrepancies reflect genuine differences between the solution and X-ray structures or whether they reflect differences in the computational procedures employed. To analyze this in more detail we have developed a new method of structure determination in which the NMR and X-ray data are combined and used simultaneously in the structure refinement.[48] Using this approach we have shown that a model can readily be generated from a joint NMR/X-ray refinement which is compatible with the data from both techniques. Thus, there are only minimal violations of the NMR restraints (NOEs and torsion angles), the value of the crystallographic R factor is comparable to, if not better than, that derived from refinement against the crystallographic data alone, and the deviations from idealized covalent geometry are small. In addition, the R free[49] for the model refined with the NMR and

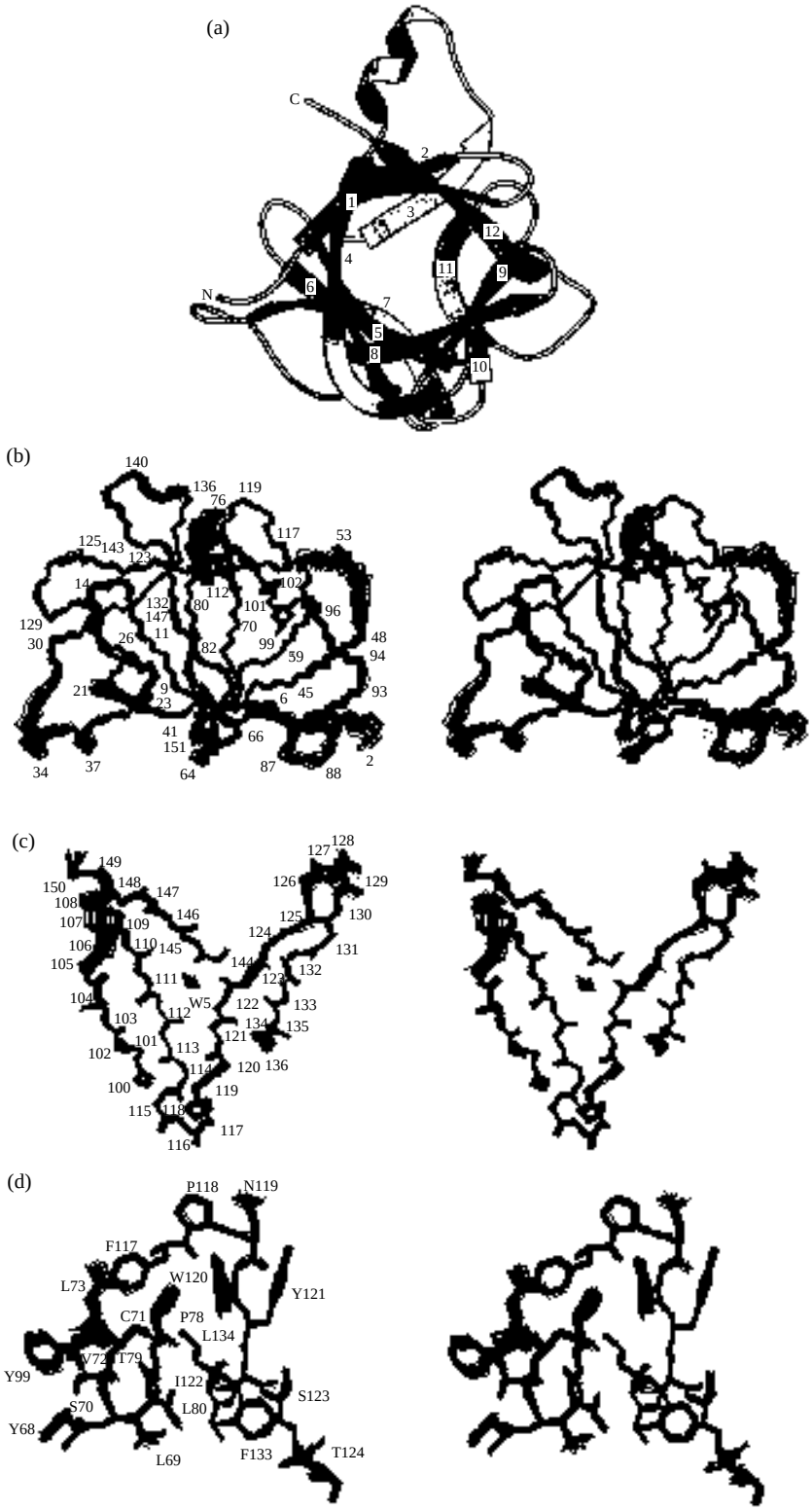

Figure 6 Solution structure of IL-1β determined by three- and four-dimensional heteronuclear NMR spectroscopy. (a) Ribbon diagram of the polypeptide fold. (b) Superposition of the backbone (N, C^{α}, and C) atoms of 32 simulated annealing structures calculated from the experimental NMR data. (c) Superposition of the backbone (N, C^{α}, C, and O) atoms of one of the three repeating topological units, illustrating the position of tightly bound water at the interface of the three central strands of the unit. (d) Superposition of all atoms (excluding protons) for selected side chains. The diagram in (a) was made using the program MOLSCRIPT.[102] The coordinates are from Clore et al.[6] (PDB accession code 6I1B). (Adapted from G. M. Clore, P. T. Wingfield, and A. M. Gronenborn, *Biochemistry*, 1991, **30**, 2315)

X-ray restraints is smaller than that of the model obtained by conventional crystallographic refinement, indicating that the crystallographic phases obtained by the joint NMR/X-ray refinement are more accurate. Moreover, the few NMR observations that are still violated by the model serve as an indicator for genuine differences between the crystal and solution structures.

The implications of the joint NMR/X-ray refinement method to structural biology are of considerable significance. In particular, the full potential and future use of the method will be for structure determinations of multidomain proteins, for which only low-resolution X-ray data for the entire protein are available but for which detailed structural information may be obtained by NMR on the individual domains. Using the joint X-ray/NMR refinement approach in such cases will open the way to the study of proteins which may otherwise never be structurally accessible by either of the two methods alone.

5 STRUCTURE DETERMINATION OF PROTEIN–PEPTIDE AND PROTEIN–DNA COMPLEXES

Provided the ligand (e.g. a peptide, an oligonucleotide, or a drug) presents a relatively simple spectrum that can be assigned by two-dimensional methods, the most convenient strategy for dealing with protein–ligand complexes involves one in which the protein is labeled with ^{15}N and ^{13}C and the ligand is unlabeled (i.e. at natural isotopic abundance).[50] It is then possible to use a combination of heteronuclear filtering and editing to design experiments in which correlations involving only protein resonances, only ligand resonances, or only through-space interactions between ligand and protein are observed. These experiments are summarized in Table 2 and were first applied successfully to a complex of calmodulin with a target peptide from skeletal muscle myosin light chain kinase,[7] and subsequently to the specific complex of the DNA binding domain of the transcription factor GATA-1 with its cognate DNA target site.[8]

5.1 The Structure of the Calmodulin–Target Peptide Complex

Calmodulin (CaM) is a ubiquitous Ca^{2+} binding protein of 148 residues which is involved in a wide range of cellular Ca^{2+}-dependent signaling pathways, thereby regulating the activity of a large number of proteins.[51] The crystal structure of Ca^{2+}-CaM was solved a number of years ago.[52] It is a dumb-bell shaped molecule with an overall length of about 6.5 nm and consisting of two globular domains, each of which contains two Ca^{2+} binding sites of the helix–loop–helix type, connected by a long, solvent exposed, rigid central helix some eight turns in length (residues 66–92). In solution, on the other hand, $^{1}H-^{15}N$ NMR relaxation measurements have demonstrated unambiguously that the central helix is disrupted near its midpoint, with residues 78–81 adopting an essentially unstructured 'random coil' conformation which is so flexible that the N- and C-terminal domains of Ca^{2+}-CaM effectively tumble independently of each other.[58] Thus, in solution, the so-called 'central helix' is not a helix at all but is a 'flexible tether' the purpose of which is to keep the two domains in close proximity for binding to their target.

In order to understand the way in which Ca^{2+}-CaM recognizes its target sites, we set out to solve, in collaboration with Ad Bax, the solution structure of a complex of Ca^{2+}-CaM with a 26 residue peptide (known as M13) comprising residues 577–602 of the calmodulin binding domain of skeletal muscle myosin light chain kinase. The solution structure was determined on the basis of 1995 experimental NMR restraints including 133 interproton distance restraints between the peptide and the protein. The N-terminus (residues 1–5) and C-terminus (residues 147–148) of CaM, the tether connecting the two domains of CaM (residues 74–82), and the N-terminus (residues 1–2) and C-terminus (residues 22–26) of M13 were ill-defined by the NMR data and appear to be disordered in solution. The atomic rms distribution about the mean coordinate positions for the rest of the structure (i.e. residues 6–73 and 83–146 of CaM, and residues 3–21 of M13) is 0.1 nm for the backbone atoms and 0.14 nm for all atoms. Thus this structure represents a second generation

Table 2 Summary of Heteronuclear-filtered and -edited NOE Experiments used to Study Protein–Ligand Complexes Comprising a Uniformly $^{15}N/^{13}C$ Labeled Protein and an Unlabeled Ligand

Type of contact	Connectivity
A Intramolecular protein contacts	
4D $^{13}C/^{13}C$-edited NOE in D_2O	$H(j)-^{13}C(j)\text{---}H(i)-^{13}C(i)$
4D $^{15}N/^{13}C$-edited NOE in H_2O	$H(j)-^{15}N(j)\text{---}H(i)-^{13}C(i)$
3D $^{15}N/^{15}N$-edited NOE in H_2O	$H(j)-^{15}N(j)\text{---}H(i)-^{15}N(i)$
B Intramolecular ligand contacts	
2D $^{12}C,^{14}N(F_1)/^{12}C,^{14}N(F_2)$ filtered NOE in H_2O[a]	$H(j)-^{12}C(j)\text{---}H(i)-^{12}C(i)$
	$H(j)-^{14}N(j)\text{---}H(i)-^{12}C(i)$
	$H(j)-^{12}C(j)\text{---}H(i)-^{14}N(i)$
	$H(j)-^{14}N(j)\text{---}H(i)-^{14}N(i)$
2D $^{12}C(F_1)/^{12}C(F_2)$ filtered NOE in D_2O[a]	$H(j)-^{12}C(j)\text{---}H(i)-^{12}C(i)$
C Intramolecular protein–ligand contacts	
3D ^{15}N-edited $(F_1)/^{14}N,^{12}C(F_3)$ filtered NOE in H_2O	$H(j)-^{15}N(j)\text{---}H(i)-^{12}C(i)$
	$H(j)-^{15}N(j)\text{---}H(i)-^{14}N(i)$
3D ^{13}C-edited $(F_1)/^{12}C(F_3)$ filtered NOE in D_2O	$H(j)-^{13}C(j)\text{---}H(i)-^{12}C(i)$

[a]Similar heteronuclear filtered two-dimensional correlation and Hartmann–Hahn spectra can also be recorded to assign the spin systems of the ligand.

structure in the classification of Clore and Gronenborn.[1] A stereoview showing a best fit superposition of the 24 calculated structures is shown in Figure 7(a).

The major conformational change in Ca^{2+}-CaM that occurs upon binding M13 involves an extension of the flexible tether (residues 78–81) in the middle of the 'central' helix of the solution structure of free Ca^{2+}-CaM to a long flexible loop extending from residues 74–81, flanked by two helices (residues 65–73 and 83–93), thereby enabling the two domains to come together, gripping the peptide rather like two hands capturing a rope. The hydrophobic channel formed by the two domains is complementary in shape to that of the peptide helix. This is clearly illustrated by the schematic ribbon drawings shown in Figures 7(b) and 7(c) which also serve to highlight the approximate two-fold pseudosymmetry of the complex. Thus, whereas the two domains of CaM are arranged in an approximately orthogonal manner to each other in the crystal structure of Ca^{2+}-CaM,[52] in the Ca^{2+}-CaM–M13 complex they are almost symmetrically related by a 180° rotation about a two-fold axis. A large conformational change also occurs in the M13 peptide upon complexation from a random coil state to a well defined helical conformation. Indeed, the helix involves all the residues (3–21) of M13 that interact with CaM, while the N-terminus (residues 1–2) and C-terminus (residues 22–26) of the peptide which do not interact with CaM, remain disordered.

Upon complexation there is a decrease in the accessible surface area of CaM and M13 of 18.48 and 14.77 nm^2, respectively, which corresponds to a decrease in the calculated solvation free energy of folding[53] of 18 and 20 kcal mol^{-1} (75–83 kJ mol^{-1}), respectively. This large decrease in solvation free energy would account for the very tight binding ($K_{ass} \approx 10^9\ M^{-1}$) of M13 to calmodulin. In addition, the accessible surface area of the portion of M13 (residues 3–21) in direct contact with CaM in the complex is only 4.94 nm^2 compared with an accessible surface of area 31.23 nm^2 for a random coil and 22.50 nm^2 for a helix. Thus, over 80% of the surface of the peptide in contact with CaM is buried.

In the view shown in Figure 7(b), the roof of the channel is formed by helices II (residues 29–38) and VI (residues 102–111) of the N- and C-terminal domains, respectively, which run antiparallel to each other; and the floor is formed by the flexible loop (residues 74–82) connecting the two domains and by helix VIII (residues 138–146) of the C-terminal domain. The front of the channel in Figure 7(b) and the left wall of the channel in Figure 7(c) are formed by helices I (residues 7–19) and IV (residues 65–73) and the mini-antiparallel β-sheet comprising residues 26–28 and 62–64, all from the N-terminal domain; the back of the channel in Figure 7(b) and the right wall of the channel in Figure 7(c) are formed by helices V (residues 83–93) and VIII (residues 138–146) and the miniantiparallel β-sheet comprising residues 99–101 and 135–137, all from the C-terminal domain. The two domains of CaM are staggered with a small degree of overlap such that the hydrophobic face of the N-terminal domain mainly contacts the C-terminal half of the M13 peptide, while the C-terminal domain principally interacts with the N-terminal half of M13 (Figure 7(b)).

The overall Ca^{2+}-CaM–M13 complex has a compact globular shape approximating to an ellipsoid with dimensions 4.7 × 3.2 × 3.0 nm. The helical M13 peptide passes through the center of the ellipsoid at an angle of about 45° to its long axis. By way of contrast, the approximate dimensions of the Ca^{2+}-CaM X-ray structure are 6.5 × 3.0 × 3.0 nm.[52] In addition, the calculated radius of gyration for Ca^{2+}-CaM–M13 is about 1.7 nm which is completely consistent with the decrease in the radius of gyration from about 2.1 to about 1.6 nm observed by both small angle X-ray and neutron scattering upon complexation of Ca^{2+}-CaM with M13.[54]

The Ca^{2+}-CaM–M13 complex is stabilized by numerous hydrophobic interactions which are summarized in Figure 8. Particularly striking are the interactions of Trp4 and Phe17 of the peptide which serve to anchor the N- and C-terminal halves of M13 to the C-terminal and N-terminal hydrophobic patches of CaM, respectively [Figure 7(c)]. These interactions also involve a large number of methionine residues which are unusually abundant in CaM, in particular four methionine residues in the C-terminal domain (Met109, Met124, Met144, and Met145) and three methionine residues in the N-terminal domain (Met36, Met51, and Met71). As methionine is an unbranched hydrophobic residue extending over four heavy atoms (C-β, C-γ, S-δ, and C-ϵ), the abundance of methionine residues can generate a hydrophobic surface the detailed topology of which is readily adjusted by minor changes in side-chain conformation, thereby providing a mechanism to accommodate and recognize different bound peptides.[55]

In addition to hydrophobic interactions, there are a number of possible electrostatic interactions that can be deduced from the calculated NMR structures. Putative interactions exist between the Arg and Lys residues of M13 and the Glu residues of CaM, and these are also included in Figure 8. Glu11 and Glu14 in helix I are within 0.5 nm of Lys5 and Lys6 of M13; Glu83, Glu84, and Glu87 in helix V of CaM are close to Lys19, Arg16, and Lys18, respectively, of M13; and Glu127 in helix VII of CaM is close to Arg3 of M13.

The solution structure of the Ca^{2+}-CaM–M13 complex explains a number of interesting observations. Studies of backbone amide exchange behavior have shown that upon complexation with M13, the amide exchange rates of residues 75–79 are substantially increased.[56] Prior NMR studies on Ca^{2+}-CaM indicated that the long central helix is already disrupted near its middle (from Asp78 to Ser81) in solution[57] and that large variations in the orientation of one domain relative to the other occur randomly with time.[58] The further disruption of the central helix upon complexation seen in the structure of the complex is manifested by the increased amide exchange rates, and supports the view of the central helix serving as a flexible linker between the two domains. Similarly, the structure of the complex explains the finding that as many as four residues can be deleted from the middle of the central helix without dramatically altering the stability or shape of the Ca^{2+}-CaM–M13 complex,[59,60] as the long flexible loop connecting the two domains can readily be shortened without causing any alteration in the structure (see Figure 7). The observation from photoaffinity labeling studies that the two domains of CaM interact simultaneously with opposite ends of the peptide such that residue 4 of the peptide (numbering for M13) can be cross-linked to Met124 or Met144 of the C-terminal domain and that residue 13 of the peptide can be cross linked to Met71 of the N-terminal domain,[61] is readily explained by the structural finding that the N-terminal half of the peptide interacts predominantly with the C-terminal domain, while the C-terminal half of the peptide interacts predominantly with the N-terminal domain (Figures 7 and 8).

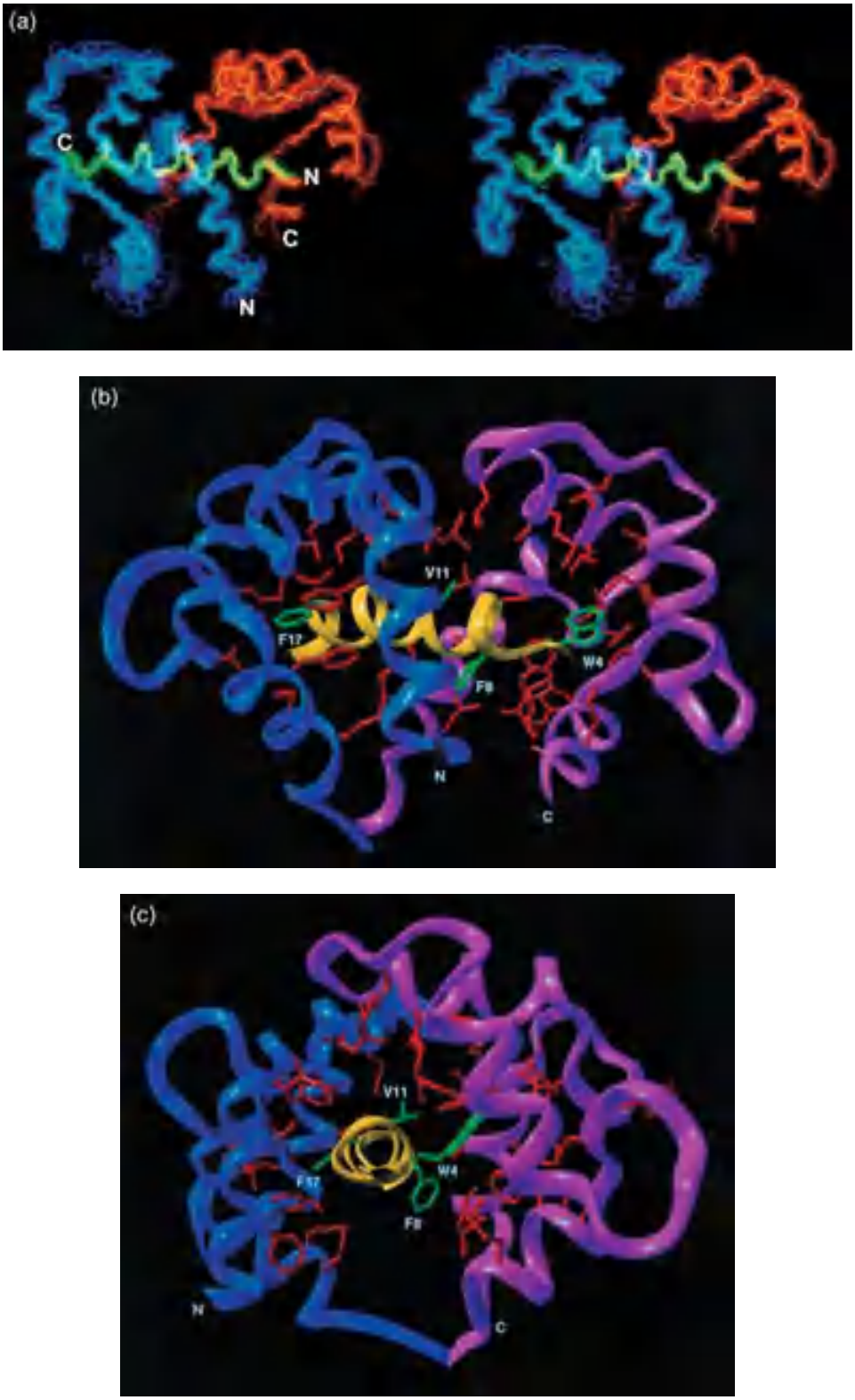

Figure 7 Solution structure of the Ca^{2+}–CaM–M13 peptide complex determined by three- and four-dimensional heteronuclear NMR spectroscopy. (a) Superposition of the backbone (N, C^{α}, and C) atoms of 24 simulated annealing structures calculated from the experimental NMR data; the N- and C-terminal domains of calmodulin are shown in blue and red, respectively, and the M13 peptide is in green; the restrained regularized average structure is highlighted. (b, c) Two orthogonal views of a schematic ribbon drawing representation of the structure with the N- and C-terminal domains of CaM in blue and purple, respectively, the M13 peptide in yellow, the hydrophobic side chains of the protein in red, and Trp4, Phe8, Va111, and Phe17 side chains of the peptide in green. The diagrams in (b) and (c) were generated using the program VISP.[103] The coordinates are from Ikura et al.[7] (PDB accession code 1BBM). (Adapted from M. Ikura, G. M. Clore, A. M. Gronenborn, G. Zhu, C. B. Klee, and A. Bax, *Science*, 1992, **256**, 632)

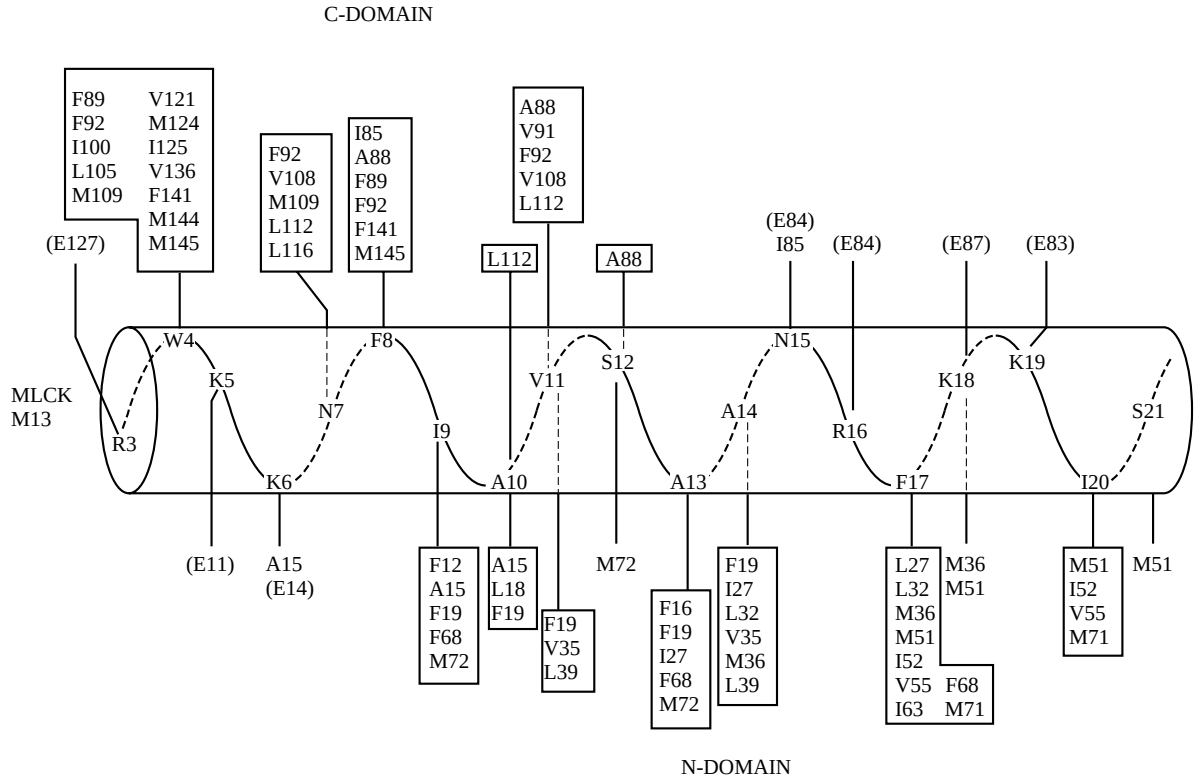

Figure 8 Summary of residue pairs for which intermolecular NOEs between CaM and M13 are observed. CaM residues involved in hydrophobic interactions are boxed. Also included are potential electrostatic interactions between negatively charged Glu residues of CaM (shown in parentheses) and positively charged Lys and Arg residues of M13. (Adapted from M. Ikura, G. M. Clore, A. M. Gronenborn, G. Zhu, C. B. Klee, and A. Bax, *Science*, 1992, **256**, 632)

The observation that at least 17 residues of the M13 peptide from either skeletal muscle or smooth muscle are necessary for high affinity binding[62,63] is readily explained by the intimate interactions of the C-terminal hydrophobic residue (i.e. Phe17) with the N-terminal domain of CaM by which the peptide is anchored. Finally, the structure accounts for experiments in which cross-linking of residues 3 and 146 of CaM, mutated to Cys, has no effect on the activation of myosin light chain kinase, even if the central helix is cleaved proteolytically at Lys77 by trypsin.[64] Thus, while the atoms of the residues 3 and 146 are 3.7 nm apart in the X-ray structure of Ca^{2+}-CaM, they are only about 2.0 nm apart in the solution structure of the Ca^{2+}-CaM–M13 complex, which is close enough to permit cross-linking to occur.

A large body of experimental data shows that CaM binds to numerous proteins whose binding domains exhibit a propensity for α-helix formation.[51] A comparison of these sequences reveals little homology. Nevertheless, many of the very tightly binding peptides ($K_{ass} \geq 5 \times 10^7\ M^{-1}$) have the common property of containing either aromatic residues or long-chain hydrophobic residues (Leu, Ile, or Val) separated by 12 residues, as summarized in Figure 9. In the case of M13, these two residues are Trp4 and Phe17 which are exclusively in contact with the C- and N-terminal domains, respectively,

		1							5							10							15							20							25			
SK-MLCK	M13							K	R	R	W	K	K	N	F	I	A	V	S	A	A	N	R	F	K	K	I	S	S	S	G	A	L	M			
SM-MLCK	M13							R	R	K	W	Q	K	T	G	H	A	V	R	A	I	G	R	L	S	S	S											
Ca pump	C24W							Q	I	L	W	F	R	G	L	N	R	I	Q	T	Q	I	R	V	V	N	A	F	R	S	S							
	C20W	L	R	R	G	Q	I	L	W	F	R	G	L	N	R	I	Q	T	Q	I	K																		
Calspermin					A	R	R	K	L	K	A	A	V	K	A	V	V	A	S	S	R	L	G	S															
Calcineurin				A	R	K	E	V	I	R	W	K	I	R	A	I	G	K	M	A	R	V	S	F	V	L													
Mastaporan									I	N	L	K	A	L	A	A	L	A	K	K	I	L																	
Mastaporan	X								I	N	W	K	G	I	A	A	M	A	K	K	L	L																	
Mellitin				G	I	G	A	V	L	K	V	L	T	T	G	L	P	A	L	I	S	W	I	K	R	K	R	Q	Q									
Interacting domain of CaM									C				C			C						N																
																N																							

Figure 9 Alignment of tightly binding ($K_{ass} \geq 5 \times 10^7\ M^{-1}$) CaM binding sequences based on the structural role of Trp4 and Phe17 in anchoring the M13 peptide to the C- and N-terminal domains, respectively, of CaM. (Adapted from M. Ikura, G. M. Clore, A. M. Gronenborn, G. Zhu, C. B. Klee, and A. Bax, *Science*, 1992, **256**, 632)

of CaM, (Figure 7 and Figure 8). Given that these two residues are involved in more hydrophobic interactions with CaM than any other residues of the peptide (see Figure 8), it seems likely that this feature of the sequence can be used to align the CaM binding sequences listed in Figure 9, thereby permitting one to predict their interaction with CaM. It is clear from this alignment that the pattern of hydrophobic and hydrophilic residues is, in general, comparable for the various peptides, suggesting that the mode of binding and the structure of the corresponding complexes with Ca^{2+}-CaM are also likely to be similar. For example, there is, in general, conservation of hydrophobic residues at the positions equivalent to Phe8 which interacts with the C-terminal domain and Val11 which interacts with both domains (see Figures 7 and 8). In addition, there are no acidic residues present which would result in unfavorable electrostatic interactions with the negatively charged Glu residues on the surface of CaM (see Figure 7). The minimum length of peptide required for high affinity binding to Ca^{2+}-CaM is defined by the 14 residue mastaporans which comprise the two hydrophobic residues at the N- and C-termini (Figure 9) and have approximately the same equilibrium association constant ($K_{ass} \approx 1-3 \times 10^9\ M^{-1}$) as M13.[65] This structural alignment also predicts that a peptide stopping just short of the second hydrophobic residue of the pair (i.e. the residue equivalent to Phe17) would only bind to the C-terminal domain and that the resulting complex would therefore retain the dumb-bell shape of Ca^{2+}-CaM. This is exactly what has been observed by small angle X-ray scattering using two synthetic peptides, C24 W and C20 W (Figure 9), comprising different portions of the CaM binding domain of the plasma membrane Ca^{2+} pump.[66] The complex with the C24 W peptide which corresponds to residues 1–24 of M13 and contains a Trp at position 4 and a Val at position 17, has a globular shape similar to that of Ca^{2+}-CaM–M13. The complex with the C20 W peptide, on the other hand, which corresponds to residues −4 to 16 of M13 and therefore lacks the C-terminal hydrophobic residue of the pair, retains the dumb-bell shape of Ca^{2+}-CaM, suggesting that the peptide only binds to the C-terminal domain.

Thus the solution structure of the complex of Ca^{2+}-CaM with M13 reveals an unusual binding mode in which the target peptide is sequestrated into a hydrophobic channel formed by the two domains of CaM with interactions involving 19 residues of the target peptide (i.e. residues 3–21 of M13). In addition, a key requirement appears to be the presence of two long-chain hydrophobic or aromatic residues separated by 12 residues in order to anchor the peptide to the two domains of CaM (Figure 7). By analogy, the rope (i.e. the CaM binding domain of the target) has to be long enough and have two knots at each end for the two hands (i.e. domains) of CaM to grip it. This particular mode of binding is therefore only likely to occur if the CaM binding site is located either at an easily accessible C- or N-terminus or in a long exposed surface loop of the target protein. An example of the former is myosin light chain kinase and of the latter is calcineurin, and, in accordance with their location, the CaM binding sites are susceptible to proteolysis.[63,67] Clearly, other types of complex between Ca^{2+}-CaM and its target proteins are possible, given the inherent flexibility of the central helix. For example, in the case of the γ-subunit of phosphorylase kinase, it appears that there are two discontinuous CaM binding sites which are capable of binding to Ca^{2+}-CaM simultaneously,[68] and binding of a peptide derived from one of these sites causes elongation rather than contraction of Ca^{2+}-CaM,[69] indicating that the complex is of a quite different structural nature. Similarly, in the case of cyclic nucleotide phosphodiesterase[70] and CaM kinase II,[71] the CaM binding sequences do not have the same spacing of hydrophobic residues seen in M13 and the other sequences listed in Figure 13 (see below) and, in addition, CaM kinase II is not susceptible to proteolysis in the absence of phosphorylation,[72] suggesting that the mode of binding is different again. Thus, in all likelihood, the complexes of Ca^{2+}-CaM with target peptides from skeletal and smooth muscle myosin light chain kinase represent one of a range of Ca^{2+}-CaM binding modes achieving CaM–target protein interactions in an efficient and elegant manner.

5.2 The Structure of the Specific Complex of the Transcription Factor GATA-1 with DNA

The erythroid specific transcription factor GATA-1 is responsible for the regulation of transcription of erythroid-expressed genes and is an essential component required for the generation of the erythroid lineage.[73] GATA-1 binds specifically as a monomer to the asymmetric consensus target sequence (T/A)GATA(A/G) found in the *cis*-regulatory elements of all globin genes and most other erythroid specific genes that have been examined.[74] GATA-1 was the first member of a family of proteins, which now includes regulatory proteins expressed in other cell lineages, characterized by their recognition of the GATA DNA sequence and by the presence of two metal binding regions of the form Cys-X-X-Cys-$(X)_{17}$-Cys-X-X-Cys separated by 29 residues. Mutation and deletion studies on GATA-1 have indicated that the N-terminal metal binding region is not required for specific DNA binding,[75] and studies with synthetic peptides have demonstrated conclusively that a 59 residue fragment (residues 158–216 of chicken GATA-1) comprising the C-terminal metal binding region complexed to zinc and 28 residues C-terminal to the last Cys constitutes the minimal unit required for specific binding ($K_{ass} \approx 1.2 \times 10^8\ M^{-1}$).[76] In order to understand the mechanism of specific DNA recognition by GATA-1 we set out to solve the solution structure of the specific complex of a 66 residue fragment (residues 158–223) comprising the DNA binding domain of chicken GATA-1 (cGATA-1) with a 16 base pair oligonucleotide containing the target sequence AGATAA, by means of multidimensional heteronuclear filtered and separated NMR spectroscopy.[8]

The structure calculations were based on a total of 1772 experimental NMR restraints, including 117 intermolecular interproton distance restraints between the protein and the DNA. A stereoview of a best-fit superposition of 30 calculated structures (residues 2–59 of the protein and base pairs 6 to 13 of the DNA) is shown in Figure 10. The N-terminus (residue 1) and C-terminus (residues 60–66) of the protein are disordered. Base pairs 6 to 13 of the DNA are in contact with the cGATA-1 DNA binding domain and are well defined both locally and globally. The orientation, however, of the first five and last three base pairs of the DNA, which are not in contact with the protein, is poorly defined with respect to the core of the complex, although the conformation of each of these bases at a local level is reasonably well defined. This is due to the fact that, in addition to their approximate

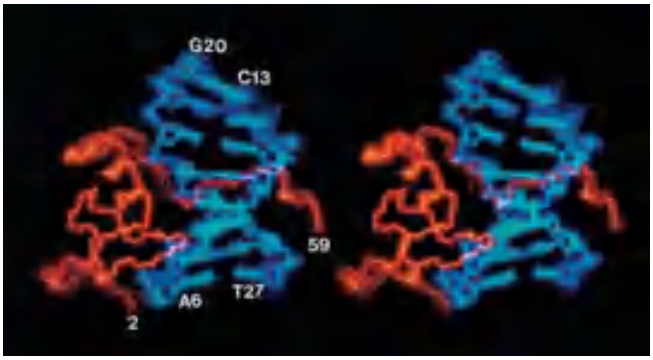

Figure 10 Stereoview showing a superposition of the 30 simulated annealing structures of the specific complex of the DNA binding domain of cGATA-1 with DNA calculated on the basis of the experimental NMR data derived from three- and four-dimensional heteronuclear NMR spectroscopy. The backbone (N, C^{α}, and C) atoms of cGATA-1 are shown in red and all the non-hydrogen atoms of the DNA in blue. The restrained regularized mean structure of the complex is highlighted. The coordinates are from Omichinski et al.[8] (PDB accession code 1GAT). (Adapted from J. G. Omichinski, G. M. Clore, O. Schaad, G. Felsenfeld, C. Trainor, E. Appella, S. J. Stahl, and A. M. Gronenborn, *Science*, 1993, **261**, 438)

nature, the interproton distance restraints within the DNA are solely sequential. Hence, they are inadequate to ascertain the relative orientation of base pairs separated by more than 5–6 steps with any great degree of precision and accuracy. The global conformation of the central eight base pairs, on the other hand, is determined not only by the restraints within the DNA, but more importantly by the large number of intermolecular interproton distance restraints between the protein and DNA. The atomic rms distribution of the 30 SA structures about the mean coordinate positions for the complex proper (i.e. residues 2–59 of the protein and base pairs 6–13 of the DNA) is 0.070 $\pm$ 0.013 and 0.113 $\pm$ 0.008 nm for protein backbone plus DNA and all protein atoms plus DNA, respectively.

The protein can be divided into two modules: the protein core which consists of residues 2–51 and contains the zinc coordination site, and an extended C-terminal tail (residues 52–59).

A schematic ribbon drawing of the core is presented in Figure 11(a). The core starts out with a turn (residues 2–5), followed by two short irregular antiparallel β-sheets, a helix (residues 28–38) and a long loop (residues 39–51) which includes a helical turn (residues 44–47), as well as an Ω like loop (residues 47–51). β-strands 1 (residues 5–7) and 2 (residues 11–14) form the first β-sheet, while β-strands 3 (residues 18–21) and 4 (residues 24–27) form the second β-sheet.

Part of the core of the cGATA-1 DNA binding domain is structurally similar to that of the N-terminal zinc containing module of the DNA binding domain of the glucocorticoid receptor.[77] Thus the C^{α} atoms of 30 residues of these two proteins can be superimposed with an rms difference of only 0.14 nm Figure 11(b). Apart from the four Cys residues that coordinate the zinc atom, only 1 residue (Lys36 in the cGATA-1 DNA binding domain and Lys465 in the glucocorticoid receptor) is conserved between the two proteins. The structural similarity extends from the N-terminus up to the end of the helix (residues 3–39 of the cGATA-1 DNA binding domain and residues 436 to 468 of the glucocorticoid receptor), and the Zn–Sγ geometry, as well as the side-chain conformations of the four coordinating cysteines, are identical. The loop between strands β2 and β3 has three deletions, and the turn between strands β3 and β4 has one deletion in the glucocorticoid receptor with respect to cGATA-1. The topology and polypeptide trace following the carboxyl end of the helix, however, are entirely different in the two proteins. Thus, in the DNA binding domain of the glucocorticoid receptor there is a second compact zinc containing module (residues 470–514) made up of two strands and two helices, while in the cGATA-1 DNA binding domain there is a long loop (residues 38–51) and extended strand (residues 52–59).

The overall topology and structural organization of the complex is shown in Figures 12(a) and 12(b). The conformation of the oligonucleotide is of B type. The helix and the loop connecting strands β2 and β3 (which is located directly beneath the helix) are located in the major groove, while the C-terminal tail wraps around the DNA and lies in the minor groove, directly opposite the helix. The overall appearance is analogous to that of a right hand holding a rope, with the rope representing the DNA, the palm and fingers of the hand the core of the protein, and the thumb the C-terminal tail. It is this pincer-like configuration of the protein that causes a small 10° kink in the DNA. The long axis of the helix lies at an angle of about 40° to the base planes of the DNA [Figure 12(a)], while the C-terminal tail is approximately parallel to the base planes [Figure 12(b)].

Views of side-chain contacts with the DNA in the major and minor grooves are shown in Figures 12(c) and 12(d), respectively, while a schematic representation of all the contacts is provided in Figure 13. The cGATA-1 DNA binding domain makes specific contacts with eight bases, seven in the major groove (A6, G7, A8, T25, A24, T23, and T22) and one in the minor groove (T9). All the base contacts in the major groove involve the helix and the loop connecting β-strands 2 and 3. In contrast to other DNA binding proteins, the majority of base contacts involve hydrophobic interactions. Thus, Leu17 interacts with A6, G7, and T25; Thr16 with A24 and T25; Leu33 with A24 and T23; and Leu37 with T23 and T22. This accounts for the predominance of thymidines in the DNA target site. Indeed, there are only three hydrogen-bonding interactions: namely, between the side chain of Asn29 and the N-6 atoms of A24 and A8 in the major groove, and between the $N\zeta H_3^+$ of Lys57 and the O-2 atom of T9 in the minor groove. In this regard, it is interesting to note that there is a reduction of 11.27 nm^2 in the surface accessible area of the cGATA-1 DNA binding domain in the presence of DNA (corresponding to a 20% decrease in the accessible surface), and a decrease in the calculated solvation free energy of folding[53] of 13 kcal mol^{-1} (54 kJ mol^{-1}). This latter effect can clearly make a sizable contribution to the specific binding constant ($K_{ass} \approx 1.2 \times 10^8\ M^{-1}$).

The remaining contacts involve the sugar–phosphate backbone, the majority of which are located on the second strand (that is G20 to T27). Salt bridges and/or hydrogen bonds with the phosphates of G7, A24, and T22 are made by Arg19, Arg47, and His38, respectively, in the major groove, and with the phosphates of C13, T25, C26 and T27 by Arg54, Thr53, Arg56, and Ser59, respectively, in the minor groove. The interactions of Arg54, and Arg56 above and below the polypeptide chain span the full length of the target site and are probably responsible for the bending of the DNA in the direction of the

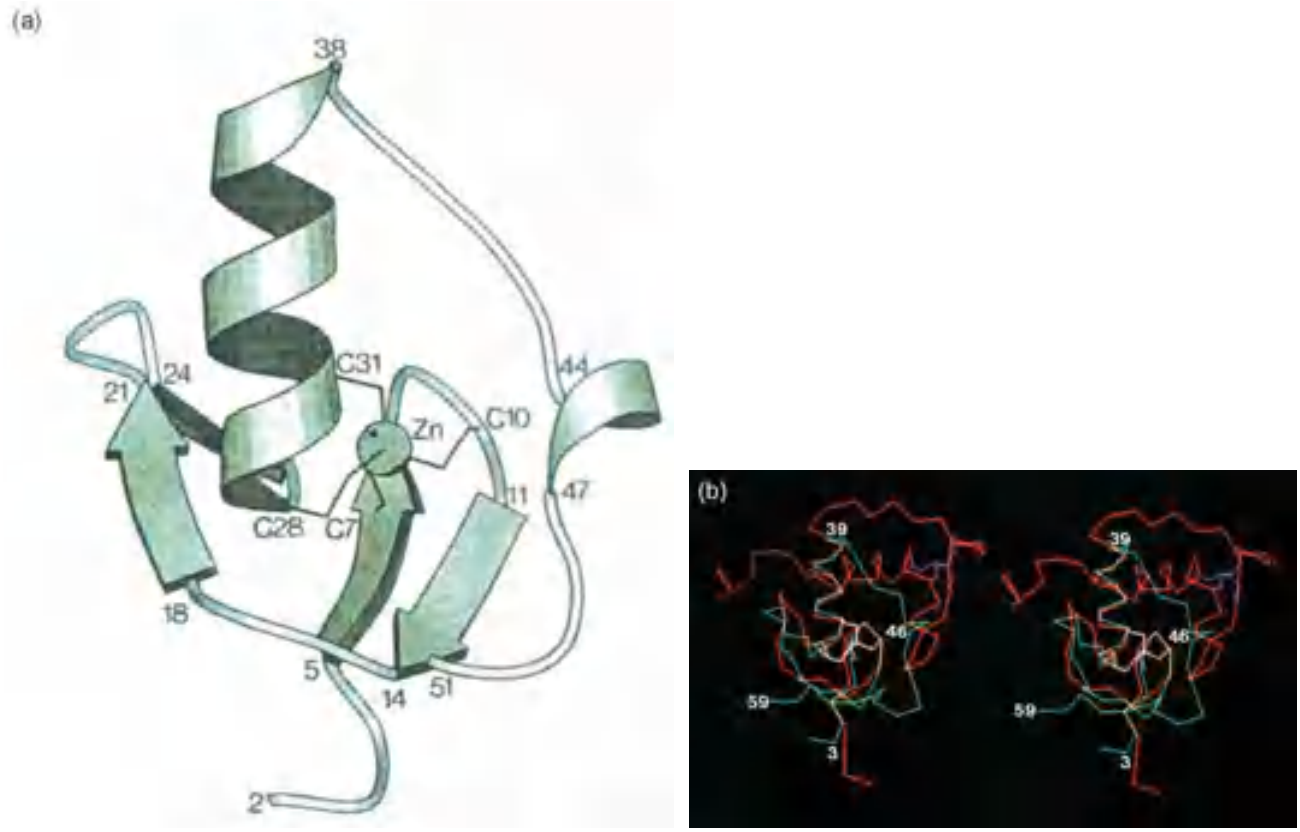

Figure 11 (a) Schematic ribbon drawing of the core of the cGATA-1 DNA binding domain. (b) Superposition of the C^{α} atoms of the cGATA-1 (green) and glucocorticoid receptor (red) DNA binding domains. The zinc and coordinating cysteines are shown in yellow for cGATA-1 and in purple for the glucocorticoid receptor; the residues are labeled according to the numbering in cGATA-1. The alignment of cGATA-1 with the glucocorticoid receptor is as follows: residues 3–13, 18–21, 25–39, and 46 of cGATA-1 are superimposed on residues 436–446, 448–451, 454–468, and 490, respectively, of the glucocorticoid receptor with a C^{α} atomic rms of 0.14 nm. The diagram in (a) was made using the program MOLSCRIPT.[102] The coordinates of the glucocorticoid receptor DNA binding domain shown in (b) are taken from Luisi et al.[79] The cGATA-1 coordinates are from Omichinski et al.[8] (PDB accession code 1GAT). (Adapted from J. G. Omichinski, G. M. Clore, O. Schaad, G. Felsenfeld, C. Trainor, E. Appella, S.J. Stahl, and A. M. Gronenborn, *Science*, 1993, **261**, 438)

minor groove. Likewise, all the sugar contacts involve the second strand. In the major groove they are hydrophobic in nature, and involve contacts between the sugars of T22, T23 and A24 with Tyr34, Leu33 and Ala30, and Ile51 and Thr16, respectively. In the minor groove, hydrophobic sugar DNA–protein interactions are made by C-13 with the aliphatic portion of the side chain of Arg54, T23 and T24 with Gln52, T25 and C26 with the aliphatic portion of the side chain of Arg 56, and C26 with Ser59. In addition, there is a hydrogen bond between the side-chain amide of Gln52 and the sugar O-3′ atom of T23.

The mode of specific DNA binding protein that is revealed in this structure is distinct from that observed for the other three classes of zinc containing DNA binding domains whose structures have previously been solved.[77–82] Features specific to the complex with the DNA binding domain of cGATA-1 include: the relatively small size of the DNA target site (eight base pairs of which only a contiguous stretch of six is involved in specific contacts); the monomeric nature of the complex in which only a single zinc binding module is required for specific binding; the predominance of hydrophobic interactions involved in specific base contacts in the major groove; the presence of a basic C-terminal tail which interacts with the DNA in the minor groove and constitutes a key component of specificity; and, finally, the pincer-like nature of the complex in which the core and tail subdomains are opposed and surround the DNA just like a hand gripping a rope. The structure of the cGATA-1 DNA binding domain reveals a modular design. The fold of residues 3–39 is similar to that of the N-terminal zinc binding module of the DNA binding domain of the glucocorticoid receptor, although, with the exception of the four Cys residues that coordinate zinc, there is no significant sequence identity between these regions of the two proteins. Residues 40–66 are part of a separate structural motif. In this regard it is interesting to note that, in addition to both zinc binding modules being encoded on separate exons in the cGATA-1 gene (exons 4 and 5), the next intron/exon boundary lies between amino acids 39 and 40 (current numbering scheme) of the DNA binding domain, thereby separating the C-terminal zinc binding domain from the basic tail[83].

5.3 Hydration of the Specific Complex of the Transcription Factor GATA-1 with DNA

A number of recent high resolution crystal structures of protein–DNA complexes have suggested that bound water may play an important role in the recognition process in the

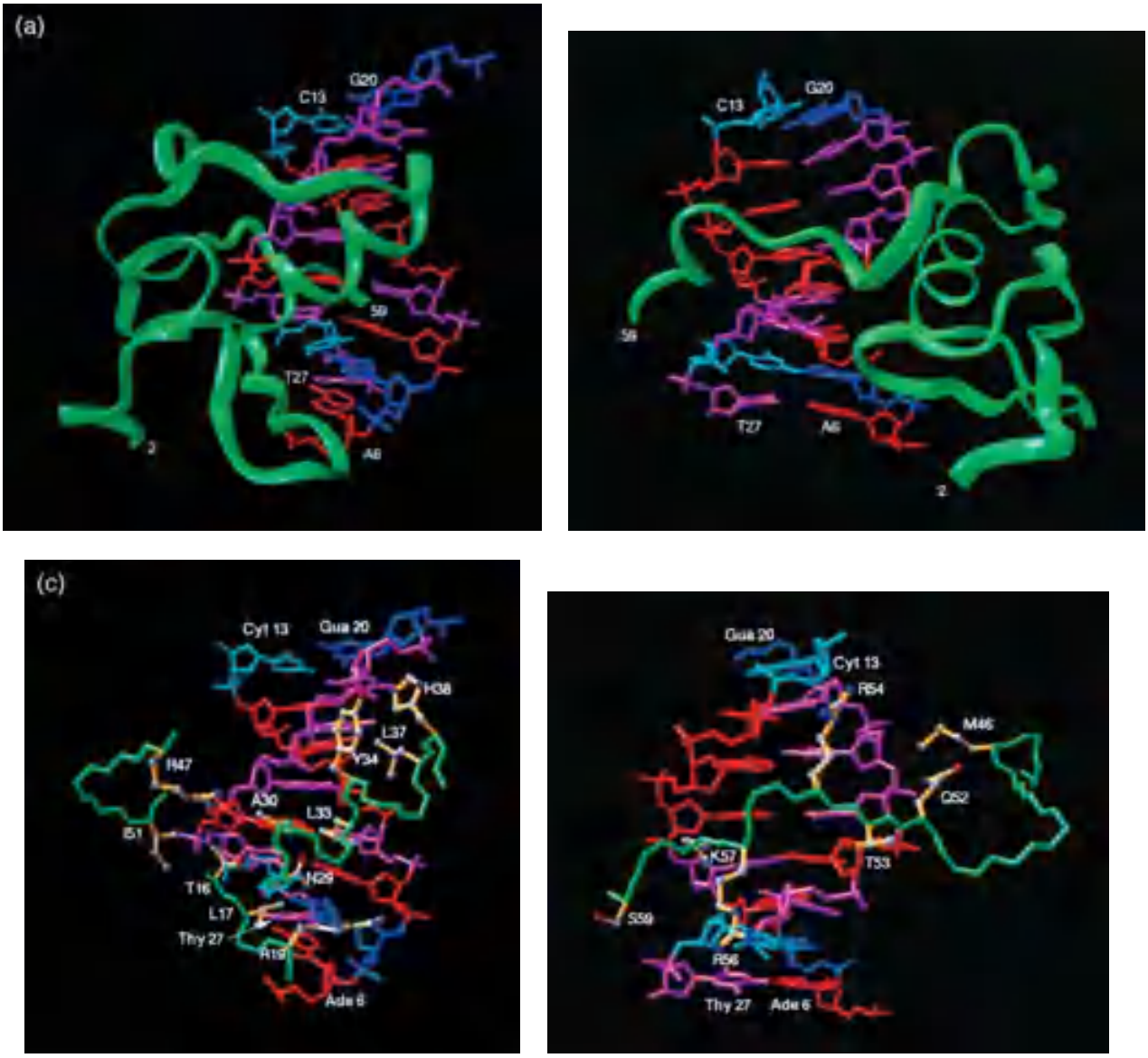

Figure 12 (a, b) Schematic ribbon drawings illustrating the interactions of cGATA-1 with DNA. (c, d) Side-chain interactions between cGATA-1 and the DNA in the major and minor grooves, respectively. The protein backbone is shown in green and the protein side chains in yellow; the color code for the DNA bases is as follows: red for A, lilac for T, dark blue for G, and light blue for C. The diagrams were made using the program VISP.[103] The coordinates of the cGATA-1–DNA complex are from Omichinski et al.[8] (PDB accession code 1GAT). (Adapted from J. G. Omichinski, G. M. Clore, O. Schaad, G. Felsenfeld, C. Trainor, E. Appella, S. J. Stahl, and A. M. Gronenborn, *Science*, 1993, **261**, 438)

form of indirect read-out in which the bound water molecules serve to bridge hydrogen bonds between functional groups on the protein and the DNA bases.[84–86] In addition, a bound water molecule has been detected at the interface of the complex between the *Antp*(C39 S) homeodomain and a 14-base pair duplex in solution using NMR spectroscopy.[87] In contrast to other protein–DNA complexes, in which the majority of specific interactions involve hydrogen bonds between the protein and the DNA bases, the structure of the specific complex of GATA-1 with DNA, as indicated in the previous section, suggests that hydrophobic effects constitute a large proportion of the specific binding energy.[8] This would predict that water of hydration would be excluded from the interface between GATA-1 and the DNA bases in the major groove, but would be present at the interface between GATA-1 and the sugar–phosphate backbone, as well as at the solvent exposed surface of the protein. To test this hypothesis we carried out selective two-dimensional H_2O NOE and H_2O rotating frame Overhauser effect (ROE) $^1H-^{15}N$ and $^1H-^{13}C$ heteronuclear single quantum correlation experiments[88] to detect through space (<0.4 nm) contacts between bound water and protons of the protein, thereby identifying the location of bound water molecules in the specific complex of chicken GATA-1 with DNA.[89]

A number of water molecules could be detected between the protein and the phosphate backbone, as well as at the solvent exposed surface of the protein. However, no water molecules could be observed at the interface of the protein with the bases of the DNA. With only one exception, the bound water molecules have a residency time greater than 200–300 ps. On

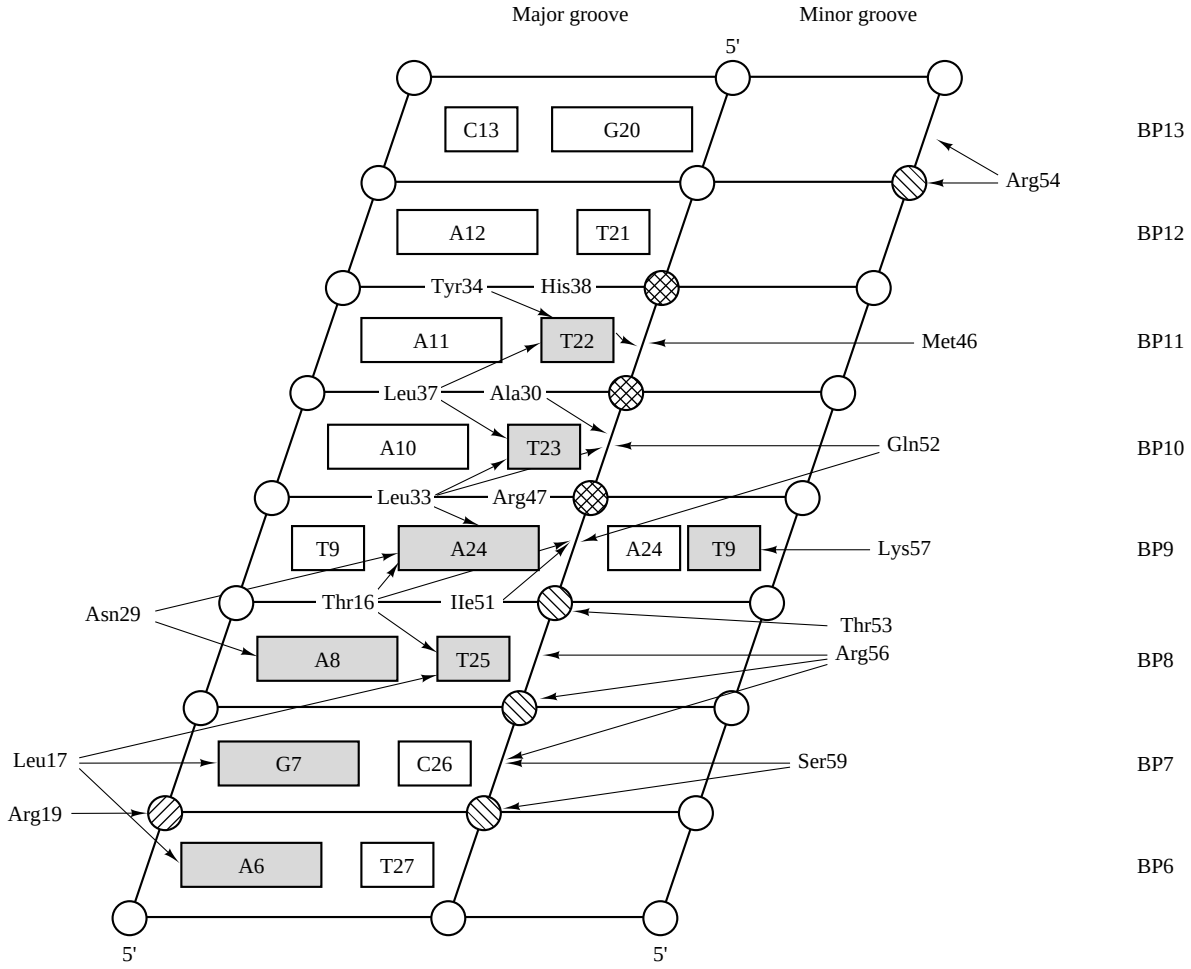

Figure 13 Schematic diagram summarizing the contacts between cGATA-1 and DNA. The DNA is represented as a cylindrical projection. Bases interacting with the protein are shaded; phosphates are represented as circles; cicles with hatches directed towards the right and left indicate sites of interaction with sugar or phosphate or both in the major and minor grooves, respectively. (Adapted from J. G. Omichinski, G. M. Clore, O. Schaad, G. Felsenfeld, C. Trainor, E. Appella, S. J. Stahl, and A. M. Gronenborn, *Science*, 1993, **261**, 438)

the basis of the structure of the complex of GATA-1 with DNA,[8] we were able to identify unambiguously 17 methyl protons and 3 backbone NH protons in close proximity to bound water.[89] The location of the protein residues near bound water are indicated in the structure of the complex of GATA-1 with DNA shown in Figure 14.

An approximate estimate of the residency times of these bound water molecules can be obtained from the sign of the NOE.[9,90] If a water molecule is bound to a macromolecule with a correlation time in the spin diffusion limit (i.e. greater than about 2 ns), the NOE between water and a protein proton will be zero for a residency time of about 300 ps, while for residency times smaller and longer than 300 ps the NOE will be positive and negative, respectively. In contrast, the ROE remains positive for all residency and correlation times. The NH protons of Ala30, Tyr34, and Tyr35 and the methyl goups of Ala3, Ala30, Met46, and Ile51 (γ_m and δ_m) exhibited negative NOEs to water, indicating a residency time greater than about 500 ps. The methyl protons of Met23 exhibited a positive NOE to water, indicative of a residency time of 100–300 ps. For the remaining surface methyl protons, the NOEs (at a mixing time of 60 ms) to water were too weak to observe and only ROEs were seen, indicating residency times in the range 200–500 ps.

All methyl groups that are exposed to solvent are associated with bound water molecules. These include Ala3, Val6 (γ_1 and γ_2), Leu17 (δ_2 only), Met23, Val40 (γ_1 and γ_2), Leu44 (δ_1 and δ_2), and Val58 (γ_1 and γ_2). Bound water molecules in contact with exposed hydrophobic surfaces are rarely seen in protein crystal structures as the water molecules are only well ordered (high occupancy and low thermal factor) if the protein donates anchor points in suitable hydrogen-bonding positions.[91] In the absence of hydrogen bonding, low occupancies and high thermal *B* factors render such water molecules unobservable.[91] Indeed, there is only one crystallographic example where water surrounding an exposed hydrophobic group has been seen in the absence of hydrogen bonding, namely the water pentagons surrounding Leu18 in the 0.088 nm resolution crystal structure of crambin.[92] In contrast to the crystallographic case, bound water can be readily detected by NMR over a very wide range of residency times (with a lower limit of 50–100 ps) and is not eliminated by rapid independent rotation of a water pentagon around a rotating methyl group. Moreover, the NMR experiment is not dependent on uniform ordering insofar as the bound water could be in somewhat different positions

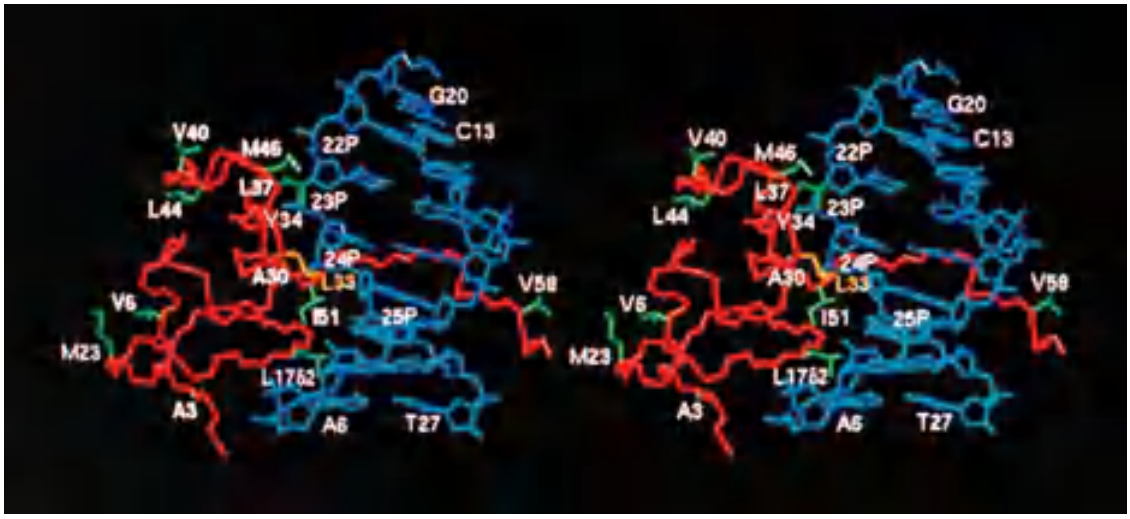

Figure 14 Stereoview of the solution structure of the specific complex of GATA-1 and DNA, illustrating the location of groups in close proximity to bound water. The DNA is displayed in blue, the protein backbone in red, and the side chains in close proximity to bound water detected in the H_2O ROE/NOE HSQC (heteronuclear single quantum correlation) experiments in green. The side chain of Leu33 which interacts directly with the bases of the DNA in the major groove and is not close to bound water is shown in orange. In the case of Leu17, only the surface exposed $C^{\delta 2}H_3$ methyl group gives rise to a ROE with bound water; the $C^{\delta 1}H_3$ methyl group which interacts directly with the DNA bases is not close to bound water. The model is taken from the solution NMR structure given by Omichinski et al.[8] (PDB accession number 1GAT) and was generated using the program VISP.[103] (Adapted from G. M. Clore, A. Bax, J. G. Omichinski, and A. M. Gronenborn, *Structure*, 1994, **2**, 89)

in different molecules. In the X-ray diffraction experiment, on the other hand, bound water could only be detected if it occupied the same position in different protein molecules; that is to say there has to be uniform ordering of the bound water throughout the protein molecules of the crystal. Consequently, rapid rotation of a water pentagon about a methyl group, in the absence of discrete hopping, would result in smearing of the electron density beyond the limit of detectability.

The ubiquitous presence of bound water molecules close to exposed hydrophobic groups observed by NMR is completely consistent with the thermodynamic results of Privalov and Makhatadze,[93,94] who showed that the hydration of methyl groups is associated with a large negative entropy ($-40.3\,J\,mol^{-1}\,K^{-1}$), a negative enthalpy ($-8.28\,kJ\,mol^{-1}$) and only a small positive Gibbs free energy ($3.72\,kJ\,mol^{-1}$). Indeed, the entropy of hydration of methyl groups is comparable to that of polar groups (-41 to $-50\,J\,mol^{-1}\,K^{-1}$), indicating that their ordering power for water is comparable.

All methyl groups that are in close proximity to the phosphodiester backbone but do not interact with the bases are also associated with bound water molecules. In these cases, it is clear that the water is stabilized by hydrogen bonding interactions with either the phosphate group or the O-5′ and O-3′ oxygen atoms. Interestingly, similarly located water molecules have also been observed in crystal structures of DNA–protein complexes.[95,96] The results on the specific complex of GATA-1 with DNA indicate the presence of a cluster of water molecules in the vicinity of the sugar–phosphate backbone of T22, T23, A24, and T25. It is important to note, however, that these interactions do not confer specificity. In the minor groove there is a bound water molecule(s) between the $C^{\epsilon}H_3$ of Met46, the sugar of T22 and the phosphate of T23. In the major groove, four clusters of bound water molecules are observed: namely between the $C^{\delta 2}H_3$ methyl group of Leu37 and the sugar and phosphate of T22; between the $C^{\delta 1}H_3$ of Leu37, the backbone NH protons of Tyr34 and Ty35, and the phosphate of T23; between the methyl group of Ala30, the NH proton of Ala30, and the phosphate of A24; and finally between the $C^{\gamma}H_3$ and $C^{\delta}H_3$ methyl groups of Ile51, the sugar of A24 and the phosphate of T25. In all likelihood, the water molecule(s) associated with the NH protons Tyr34 and Tyr35, and with the NH proton of Ala30, participate in bridging hydrogen bonds between the relevant amide group of the protein and the sugar–phosphate backbone of the DNA.

In contrast to the above methyl groups, no NOEs or ROEs to water were observed for either of the two Leu33 methyl groups or the $C^{\delta 1}H_3$ methyl group of Leu17, all of which are involved in hydrophobic interactions with the bases.[8] This indicates that water is excluded from the interface between the protein and the DNA bases in the major groove. In addition, complementary conventional two-dimensional $^1H-^1H$ NOE experiments with ^{12}C filtering failed to detect any bound water close to the thymine methyl groups of the DNA, providing further evidence for the exclusion of water at the interface of the protein and the DNA bases. The absence of water at the interface between the protein and the DNA bases in the major groove lends further credence to the importance of hydrophobic interactions in stabilizing the specific interaction between chicken GATA-1 and DNA, and indicates that hydrophobic interactions can play an important role in protein–DNA recognition and specificity.

6 CONCLUDING REMARKS

From the examples presented in this article it should be clear that the recent development of a whole range of highly sensitive multidimensional heteronuclear edited and filtered NMR experiments has revolutionized the field of protein structure determination by NMR. Proteins and protein–ligand complexes in the 15–25 kDa range are now amenable to detailed

structure analysis in solution. Moreover, the potential of the current methods can probably be extended to systems even up to 40 kDa, providing that they are very well behaved from an NMR perspective. Nevertheless, despite these advances, it should always be borne in mind that there are a number of key requirements that have to be satisfied to permit a successful structure determination of larger proteins and protein complexes by NMR. The protein in hand must be soluble and should not aggregate up to concentrations of about 1 mM, it must be stable at room temperature or slightly higher for many weeks, it should not exhibit significant conformational heterogeneity that could result in extensive line broadening, and finally it must be amenable to uniform ^{15}N and ^{13}C labeling. At the present time there are only a few examples in the literature of proteins in the 15–25 kDa range that have been solved by means of multidimensional heteronuclear NMR spectroscopy. In addition to the three examples presented here, only the structures of interleukin-4,[33,97,98] glucose permease IIA,[99] the complex of cyclophilin with cyclosporin,[100] and the *Antennapedia* homeodomain–DNA complex[101] have been published. It is hoped that over the next few years, the widespread use of these multidimensional heteronuclear experiments coupled with semiautomated assignment procedures will result in many more NMR structures of such larger proteins and protein–ligand complexes.

7 RELATED ARTICLES

Distance Geometry; DNA: A-, B-, and Z-; Peptide and Protein Secondary Structural Elements; Peptides and Polypeptides; Protein Dynamics from NMR Relaxation; Protein Hydration; Protein Structures: Relaxation Matrix Refinement.

8 REFERENCES

1. G. M. Clore and A. M. Gronenborn, *Science*, 1991, **252**, 1390.
2. G. M. Clore and A. M. Gronenborn, *J. Mol. Biol.*, 1991, **221**, 47
3. G. M. Clore and A. M. Gronenborn, *Prog. Nucl. Magn. Reson. Spectrosc.*, 1991, **23**, 43.
4. G. M. Clore and A. M. Gronenborn, *Annu. Rev. Biophys. Biophys. Chem.*, 1991, **20**, 29.
5. A. Bax and S. Grzesiek, *Acc. Chem. Res.*, 1993, **26**, 131.
6. G. M. Clore, P. T. Wingfield, and A. M. Gronenborn, *Biochemistry*, 1991, **30**, 2315.
7. M. Ikura, G. M. Clore, A. M. Gronenborn, G. Zhu, C. B. Klee, and A. Bax, *Science*, 1992, **256**, 632.
8. J. G. Omichinski, G. M. Clore, O. Schaad, G. Felsenfeld, C. Trainor, E. Appella, S. J. Stahl, and A. M. Gronenborn, *Science*, 1993, **261**, 438.
9. R. R. Ernst, G. Bodenhausen, and A. Wokaun, *Principles of Nuclear Magnetic Resonance in One and Two Dimensions*, Clarendon, Oxford, 1987.
10. T. F. Havel, I. D. Kuntz, and G. M. Crippen, *Bull. Math. Biol.*, 1983, **45**, 665.
11. W. Braun, *Q. Rev. Biophys.*, 1987, **19**, 115.
12. G. M. Clore and A. M. Gronenborn, *CRC Crit. Rev. Biochem. Mol. Biol.*, 1989, **24**, 479.
13. T. F. Havel and K. Wüthrich, *J. Mol. Biol.*, 1985, **182**, 281.
14. T. F. Havel, *Prog. Biophys. Mol. Biol.*, 1991, **56**, 43.
15. G. M. Clore, M. A. Robien, and A. M. Gronenborn, *J. Mol. Biol.*, 1993, **231**, 82.
16. G. M. Clore and A. M. Gronenborn, *Protein Eng.*, 1987, **1**, 275.
17. K. Wüthrich, *NMR of Proteins and Nucleic Acids*, Wiley, New York, 1986.
18. H. Oschkinat, C. Griesinger, P. J. Kraulis, O. W. Sørensen, R. R. Ernst, A. M. Gronenborn, and G. M. Clore, *Nature*, 1998, **332**, 374.
19. D. Marion, P. C. Driscoll, L. E. Kay, P. T. Wingfield, A. Bax, A. M. Gronenborn, and G. M. Clore, *Biochemistry*, 1989, **28**, 6150.
20. S. W. Fesik and E. R. P. Zuiderweg, *J. Magn. Reson.*, 1988, **78**, 588.
21. S. W. Fesik and E. R. P. Zuiderweg, *Q. Rev. Biophys.*, 1990, **23**, 97.
22. P. C. Driscoll, G. M. Clore, D. Marion, P. T. Wingfield, and A. M. Gronenborn, *Biochemistry*, 1990, **29**, 3542.
23. G. T. Montelione and G. Wagner, *J. Am. Chem. Soc.*, 1989, **111**, 5474
24. G. T. Montelione and G. Wagner, *J. Magn. Reson.*, 1990, **87**, 183.
25. M. Ikura, L. E. Kay, and A. Bax, *Biochemistry*, 1990, **29**, 4659.
26. A. Bax and S. S. Pochapsky, *J. Magn. Reson.*, 1992, **99**, 638.
27. G. Wagner, W. Braun, T. F. Havel, T. Schaumann, N. Go, and K. Wüthrich, *J. Mol. Biol.*, 1987, **196**, 611.
28. S. G. Hyberts, W. Märki, and G. Wagner, *Eur. J. Biochem.*, 1987, **164**, 625.
29. P. Güntert, W. Braun, M. Billeter, and K. Wüthrich, *J. Am. Chem. Soc.*, 1989, **111**, 3997.
30. M. Nilges, G. M. Clore, and A. M. Gronenborn, *Biopolymers*, 1990, **29**, 813.
31. A. Bax, G. W. Vuister, S. Grzesiek, F. Delaglio, A. C. Wang, R. Tschudin, and G. Zhu, *Methods Enzymol.*, 1994, **239**, 79.
32. E. R. P. Zuiderweg, R. Boelens, and R. Kaptein, *Biopolymers*, 1985, **24**, 601.
33. R. Powers, D. S. Garrett, C. J. March, E. A. Frieden, A. M. Gronenborn, and G. M. Clore, *Biochemistry*, 1993, **32**, 6744.
34. L. E. Kay, G. M. Clore, A. Bax, and A. M. Gronenborn, *Science*, 1990, **249**, 411.
35. G. M. Clore, L. E. Kay, A. Bax, and A. M. Gronenborn, *Biochemistry*, **30**, 1991, 12.
36. E. R. P. Zuiderweg, A. M. Petros, S. W. Fesik, and E. T. Olejniczak, *J. Am. Chem. Soc.*, 1991, **113**, 370.
37. G. W. Vuister, G. M. Clore, A. M. Gronenborn, R. Powers, D. S. Garrett, R. Tschudin, and A. Bax, *J. Magn. Reson., Ser. B*, 1993, **101**, 210.
38. J. D. Forman-Kay, G. M. Clore, P. T. Wingfield, and A. M. Gronenborn, *Biochemistry*, 1991, **30**, 2685.
39. H. J. Dyson, G. P. Gippert, D. A. Case, A. Holmgren, and P. E. Wright, *Biochemistry*, 1990, **29**, 4129.
40. P. C. Driscoll, A. M. Gronenborn, P. T. Wingfield, and G. M. Clore, *Biochemistry*, 1990, **29**, 4668.
41. G. M. Clore, A. Bax, P. C. Driscoll, P. T. Wingfield, and A. M. Gronenborn, *Biochemistry*, 1990, **29**, 8172.
42. G. M. Clore, P. C. Driscoll, P. T. Wingfield, and A. M. Gronenborn, *J. Mol. Biol.*, 1990, **214**, 811.
43. G. M. Clore, A. Bax, P. T. Wingfield, and A. M. Gronenborn, *Biochemistry*, 1990, **29**, 5671.
44. M. Nilges, G. M. Clore, and A. M. Gronenborn, *FEBS Lett.*, 1988, **229**, 317.

45. B. C. Finzel, L. L. Clancy, D. R. Holland, S. W. Muchmore, K. D. Watenpaugh, and H. M. Einspahr, *J. Mol. Biol.*, 1989, **209**, 779.
46. J. P. Priestle, H. P. Schär, and M. G. Grütter, *Proc. Natl. Acad. Sci. USA*, 1989, **86**, 9667.
47. B. Veerapandian, G. L. Gilliland, R. Raag, A. L. Svensson, Y. Masui, Y. Hirai, and T. L. Poulos, *Protein Struct. Function Genet.*, 1991, **12**, 10.
48. B. Shaanan, A. M. Gronenborn, G. H. Cohen, G. L. Gilliland, B. Veerapandian, D. R. Davies, and G. M. Clore, *Science*, 1992, **257**, 961.
49. A. T. Brünger, *Nature*, 1992, **355**, 472.
50. M. Ikura and A. Bax, *J. Am. Chem. Soc.*, 1992, **114**, 2433.
51. P. Cohen and C. B. Klee, *Molecular Aspects of Cellular Regulation*, Elsevier, New York, 1988, Vol. 5.
52. Y. S. Babu, J. S. Sack, T. J. Greenhough, C. E. Bugg, A. R. Means, and W. J. Cook, *Nature*, 1985, **315**, 37.
53. D. Eisenberg and A. D. McLachlan, *Nature*, 1986, **319**, 199.
54. D. B. Heidorn, P. A. Seeger, S. E. Rokop, D. K. Blumenthal, A. R. Means, H. Crespi, and J. Trewhella, *Biochemistry*, 1989, **28**, 6757.
55. K. T. O'Neil and W. F. DeGrado, *Trends Biochem.* 1990, **15**, 59.
56. S. Spera, M. Ikura, and A. Bax, *J. Biomol. NMR*, 1991, **1**, 155.
57. M. Ikura, L. E. Kay, M. Krinks, and A. Bax, *Biochemistry*, 1991, **30**, 5498.
58. G. Barbato, M. Ikura, L. E. Kay, R. W. Pastor, and A. Bax, *Biochemistry*, 1992, **31**, 5269.
59. A. Persechini, D. K. Blumenthal, H. W. Jarrett, C. B. Klee, D. O. Hardy, and R. H. Kretsinger, *J. Biol. Chem.*, 1989, **264**, 8052.
60. M. Kataoka, J. F. Head, A. Persechini, H. Kretsinger, and D. M. Engelman, *Biochemistry*, 1991, **30**, 1188.
61. K. T. O'Neil, S. Erickson-Viitanen, and W. F. DeGrado, *J. Biol. Chem.*, 1989, **264**, 14 571.
62. T. J. Lukas, W. H. Burgess, F. G. Prendergast, W. Lau, and D. M. Watterson, *Biochemistry*, 1986, **25**, 1458.
63. D. K. Blumenthal and E. G. Krebs, *Methods Enzymol.*, 1987, **139**, 115.
64. A. Persechini and R. H. Kretsinger, *J. Biol. Chem.*, 1988, **263**, 12175.
65. J. A. Cox, M. Comte, J. E. Fitton, and W. F. DeGrado, *J. Biol. Chem.*, 1985, **260**, 2527.
66. M. Kataoka, J. F. Head, T. Vorherr, J. Krebs, and E. Carafoli, *Biochemistry*, 1991, **30**, 6247.
67. D. Guerini and C. B. Klee, *Adv. Protein Phosphatases*, 1991, **6**, 391.
68. M. Dasgupta, T. Honeycutt, and D. K. Blumenthal, *J. Biol. Chem.*, 1989, **264**, 17 156.
69. J. Trewhella, D. K. Blumenthal, S. E. Rokup, and P. A. Seeger, *Biochemistry*, 1990, **29**, 9316.
70. H. Charbonneau, S. Kumar, J. P. Novack, D. K. Blumenthal, P. R. Griffin, J. Shabanowitz, D. F. Hunt, J. A. Beavo, and K. A. Walsh, *Biochemistry*, 1991, **30**, 7931.
71. M. K. Bennett and M. B. Kennedy, *Proc. Natl. Acad. Sci. USA*, 1987, **84**, 1794.
72. A. P. Kwiatkowski and M. M. King, *Biochemistry*, 1989, **28**, 5380.
73. S. H. Orkin, *Blood*, 1992, **80**, 575.
74. T. Evans, and G. Felsenfeld, *Cell*, 1989, **58**, 877.
75. D. I. K. Markin and S. H. Orkin, *Genes Dev.*, 1986, **4**, 1886.
76. J. G. Omichinski, C. Trainor, T. Evans, A. M. Gronenborn, G. M. Clore, and G. Felsenfeld, *Proc. Natl. Acad. Sci. USA*, 1993, **90**, 1676.
77. B. F. Luisi, W. X. Xu, Z. Otwinowski, L. P. Freedman, K. R. Yamamoto, and P. B. Sigler, *Nature*, 1991, **352**, 497.
78. N. P. Pavletich and C. O. Pabo, *Science*, 1991, **252**, 809.
79. N. P. Pavletich and C. O. Pabo, *Science*, 1993, **261**, 1701.
80. R. Mamorstein, M. Carey, M. Ptashne, and S. C. Harrison, *Nature*, 1992, **356**, 408.
81. J. W. R. Schwabe, L. Chapman, J. T. Finch, and D. Rhodes, *Cell*, 1993, **75**, 567.
82. L. Fairall, J. W. R. Schwabe, L. Chapman, J. T. Finch, and D. Rhodes, *Nature*, 1993, **366**, 483.
83. R. Hannon, T. Evans, G. Felsenfeld, and H. Gould, *Proc. Natl. Acad. Sci. USA*, 1991, **88**, 3004.
84. Z. Otwinowski, R. W. Schevitz, R.-G. Zhang, C. I. Lawson, A. Joachimiak, E. Q. Mamorstein, B. F. Luisi, and P. B. Sigler, *Nature*, 1988, **335**, 321.
85. C. L. Lawson and J. Carey, *Nature*, 1993, **366**, 178.
86. K. L. Clark, E. D. Halay, E. Lai, and S. K. Burley, *Nature*, 1993, **364**, 412.
87. Y. Q. Qian, G. Otting, and K. Wüthrich, *J. Am. Chem. Soc.*, 1993, **115**, 1189.
88. S. Grzesiek and A. Bax, *J. Biomol. NMR.*, 1993, **3**, 627.
89. G. M. Clore, A. Bax, J. G. Omichinski, and A. M. Gronenborn, *Structure*, 1994, **2**, 89.
90. G. Otting, E. Liepinsh, and K. Wüthrich, *Science*, 1991, **254**, 974.
91. G. A. Jeffrey and W. Saenger, *Hydrogen Bonding in Biological Structures*, Springer, Berlin, 1991.
92. M. M. Teeter, *Proc. Natl. Acad. Sci. USA*, 1984, **81**, 6014.
93. G. I. Makhatadze and P. L. Privalov, *J. Mol. Biol.*, 1993, **232**, 639.
94. P. I. Privalov and G. I. Makhatadze, *J. Mol. Biol.*, 1993, **232**, 660.
95. A. K. Aggarwal, D. W. Rodgers, M. Drottar, M. Ptashne, and S. C. Harrison, *Science*, 1998, **242**, 899.
96. R. S. Hegde, S. R. Grossman, L. A. Laimins, and P. B. Sigler, *Nature*, 1992, **359**, 505.
97. R. Powers, D. S. Garrett, C. J. March, E. A. Frieden, A. M. Gronenborn, and G. M. Clore, *Science*, 1992, **256**, 1673.
98. L. J. Smith, C. Redfield, J. Boyd, G. M. P. Lawrence, R. G. Edwards, R. A. G. Smith, and C. M. Dobson, *J. Mol. Biol.*, 1992, **224**, 899.
99. W. J. Fairbrother, G. P. Gippert, J. Reizer, M. J. Saier, Jr., and P. E. Wright, *FEBS Lett.*, 1992, **296**, 148.
100. Y. Théuriault, T. M. Logan, R. Meadows, L. Yu, E. T. Olejniczak, T. F. Holzman, R. L. Simmer, and S. W. Fesik, *Nature*, 1993, **361**, 88.
101. M. Billeter, Y. Q. Qian, G. Otting, M. Müller, W. Gehring, and K. Wüthrich, *J. Mol. Biol.*, 1993, **234**, 1084.
102. P. J. Kraulis, *J. Appl. Crystallogr.*, 1991, **24**, 946.
103. E. de Castro and S. Edelstein, *VISP 1.0 User's Guide*, University of Geneva, 1992.

Acknowledgments

We thank our many colleagues, past and present, who have contributed to the work carried out in our laboratory. Above all, we thank Ad Bax with whom we have shared numerous stimulating discussions, fruitful experiments, and a continuous and most enjoyable collaboration in the best of scientific spirits. This work was supported in part by

the AIDS Targeted Anti-Viral Program of the Office of the Director of the National Institutes of Health. This article is adapted from two reviews: *Protein Science*, 1994, **3**, 372, and *Progress in Biophysical and Molecular Biology*, 1994, **62**, 153..

Biographical Sketches

G. Marius Clore. *b* 1955. B.Sc. University College London, 1976; M.D., University College Hospital Medical School, London, 1979; Ph.D., National Institute for Medical Research, London, 1982. Scientific staff, National Institute for Medical Research, London, 1980–1984; Joint Head, Biological NMR Group, Max-Planck Institute for Biochemistry, Martinsried, West Germany 1984–1988; Chief, Section of Protein NMR, Laboratory of Chemical Physics, National Institutes of Health 1988 – present. Approx. 260 publications, and with A. M. Gronenborn the book 'NMR of Proteins'. Research interests include biological NMR spectroscopy and structural biology.

Angela M. Gronenborn. *b* 1950. Dipl. Chem., 1975; Ph.D., 1978, University of Cologne; Scientific staff, National Institute for Medical Research, London, 1979–1984; Joint Head, Biological NMR Group, Max-Planck Institute for Biochemistry, Martinsried, West Germany 1984–1988; Chief, Section of Structural Biology, Laboratory of Chemical Physics, National Institutes of Health, 1988 – present. Approx. 250 publications, and with G. M. Clore the book 'NMR of Proteins'. Research interests include biological NMR spectroscopy and structural biology.

Calmodulin

Mitsuhiko Ikura

University of Toronto, Canada

1	Introduction	1
2	Interactions with Metal Ions and Drugs	2
3	Calcium–Calmodulin Complex	4
4	Calcium–Calmodulin–Peptide Ternary Complexes	4
5	Related Articles	6
6	References	6

1 INTRODUCTION

Calmodulin (CaM) was discovered as an activator of cyclic nucleotide phosphodiesterase in brain by Cheung[1] and by Kakiuchi and Yamazaki[2] in 1970. Since then, it has became clear that CaM is a ubiquitous intracellular calcium receptor present in eukaryotic cells and that its structure has been highly conserved during evolution.[3] The amino acid and gene sequences of CaM from various species have been determined.[4–6] Figure 1 shows the amino acid sequence of bovine brain CaM.[4] The molecular weight of CaM is ca. 16 700. The amino terminal is acetylated and lysine-115 is trimethylated at the ϵ position. CaM consists of four repeated sequences of about 35 amino acid residues, each of which forms a helix–loop–helix Ca^{2+}-binding motif of the EF-hand type, first discovered in parvalbumin by Kretsinger and co-workers.[7] The biophysical properties of CaM have been extensively studied (for reviews, see Cohen and Klee[5]). CaM is an acidic (pI = 4.3) and heat stable protein which binds four Ca^{2+} ions. The four Ca^{2+}-binding motifs can be classified into the high affinity sites III and IV in the C-terminal region ($K_d \approx 10^{-6}$ M) and the low affinity sites I and II in the N-terminal region ($K_d \approx 10^{-5}$ M).[8]

A number of enzymes and proteins have been reported to date to be stimulated by CaM.[4] These include myosin light chain kinase (MLCK), CaM kinase II, phosphorylase kinase, calcineurin, myristoylated alanine-rich C kinase substrate (MARCKS), and many others (for reviews, see Cohen and Klee[5] and Crivici and Ikura[6]). Thus, CaM plays a role as a multifunctional activator or regulator in various Ca^{2+}-dependent cellular processes. CaM-binding regions in many target enzymes and proteins have been mapped. These regions are generally small (14–27 amino acid residues) and rich in basic and hydrophobic residues. Most of the CaM-binding sequences identified so far appear to have a propensity for helix formation. A number of naturally occurring peptides are also known to bind CaM in a Ca^{2+}-dependent manner.[9] These peptides include insect venom peptides such as mastoparans and melittin, and certain hormones and opioids such as ACTH, VIP, glucagon, and substance P. In addition, phenothiazines and other hydrophobic drugs including trifluroperazine (TFP), chlorpromazine, and W-7, bind CaM and inhibit the CaM-mediated activation of enzymes.[10] Proteolytic fragments and synthetic peptides comprising the CaM-binding regions of target proteins, as well as the insect and hormone peptides and the hydrophobic drugs, have been extensively used to study the structural and biochemical properties of the interaction of CaM with targets.

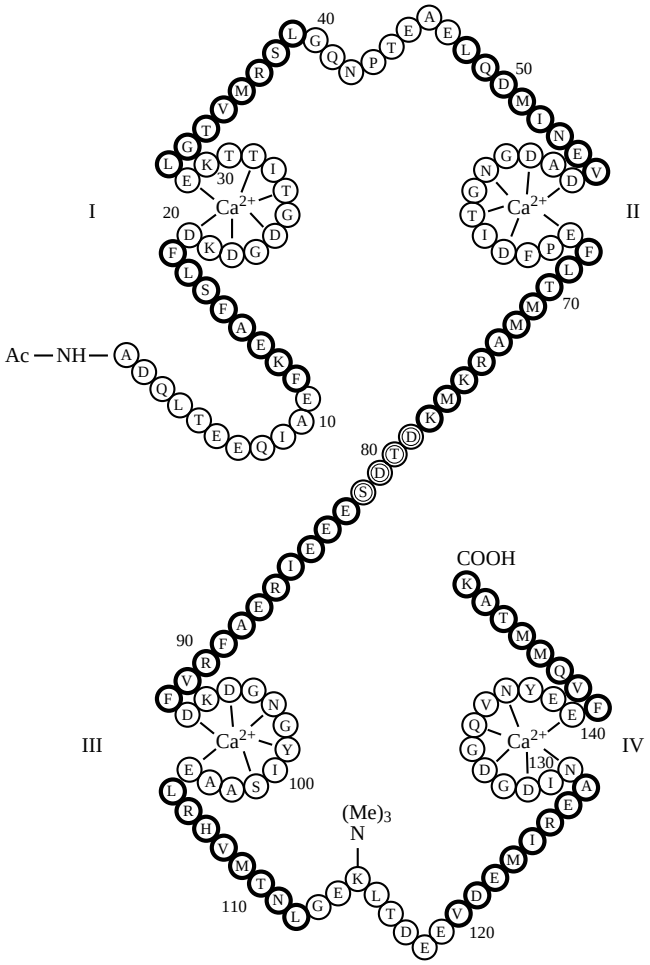

Figure 1 The amino acid sequence of bovine brain calmodulin[4] [Courtesy of C. B. Klee]

The crystal structures of Ca^{2+}-loaded CaM were reported by Babu et al.[11] in 1985 and by Kretsinger et al.[12] in 1986. The structures have an unusual dumbbell shape [Figure 2(a)] in which the N- and C-terminal globular domains are connected by a long α-helix. The length of the molecule is about 65 Å, with each lobe having approximate dimensions of 25 × 20 × 20 Å.[3] Each domain possesses a hydrophobic patch, which is considered to be responsible for target binding. Similar structural features were found in the crystal structure of a homologous Ca^{2+}-binding protein, skeletal muscle troponin C[13] (see ***Calcium-Binding Proteins*** and ***Muscle Proteins***). In 1992, an NMR structure of CaM complexed with a 26-residue CaM-binding peptide derived from skeletal muscle MLCK was determined[14] [Figure 2(b)]. Subsequently, a crystal structure of CaM complexed with a smooth muscle MLCK peptide was also solved at 2.4 Å. More recently, a crystal structure of CaM complexed with a CaM kinase II peptide has been reported.[16]

Detailed mechanisms by which CaM regulates the activity of target enzymes and proteins are still not yet fully understood even for a single case. Nevertheless, NMR spectroscopy has contributed tremendously to our understanding of the structural basis of the action of CaM in the context of interactions with

Ca^{2+}, and peptides and drugs. In the following discussion NMR studies on CaM reported during the period of 1979–93 will be summarized.

2 INTERACTIONS WITH METAL IONS AND DRUGS

The first 250- and 360-MHz ^{1}H NMR spectra of bovine brain CaM were reported by Seamon[17,18] in 1979 and 1980, who demonstrated that dramatic Ca^{2+}-dependent spectral changes could be monitored by ^{1}H NMR. Aromatic proton resonances of Tyr-99, His-107, and Tyr-138, and a unique trimethyl group of ϵ-trimethylated Lys-115 were identified. Klevit et al.[19] and Krebs and Carafoli[20] studied the interaction of bovine brain CaM with TFP using ^{1}H NMR. Shimizu et al.[21,22] used ^{19}F NMR to study the interactions of porcine brain and *Tetraphymena pyriformis* CaM with TFP. All these studies indicate that one CaM molecule binds two TFP molecules.

More detailed assignments for aromatic ring and methyl protons in scallop testis CaM were reported by Ikura et al.[23] in 1983. Using those resonance assignments, Ca^{2+}-induced conformational changes have been examined.[24] Figure 3 illustrates Ca^{2+}-induced changes in the aromatic region of the ^{1}H NMR spectra. The results show that many resonances C-terminal domain (Phe-99, His-107, trimethyl Lys-115, and Tyr-138) are shifted in an early stage of Ca^{2+} titration (0–2 mol Ca^{2+} per mol of CaM), thus concluding that the C-terminal domain contains the high affinity sites for Ca^{2+}. Forsén and co-workers independently reached the same conclusion from ^{43}Ca and ^{113}Cd NMR studies[25,26] using two tryptic fragments

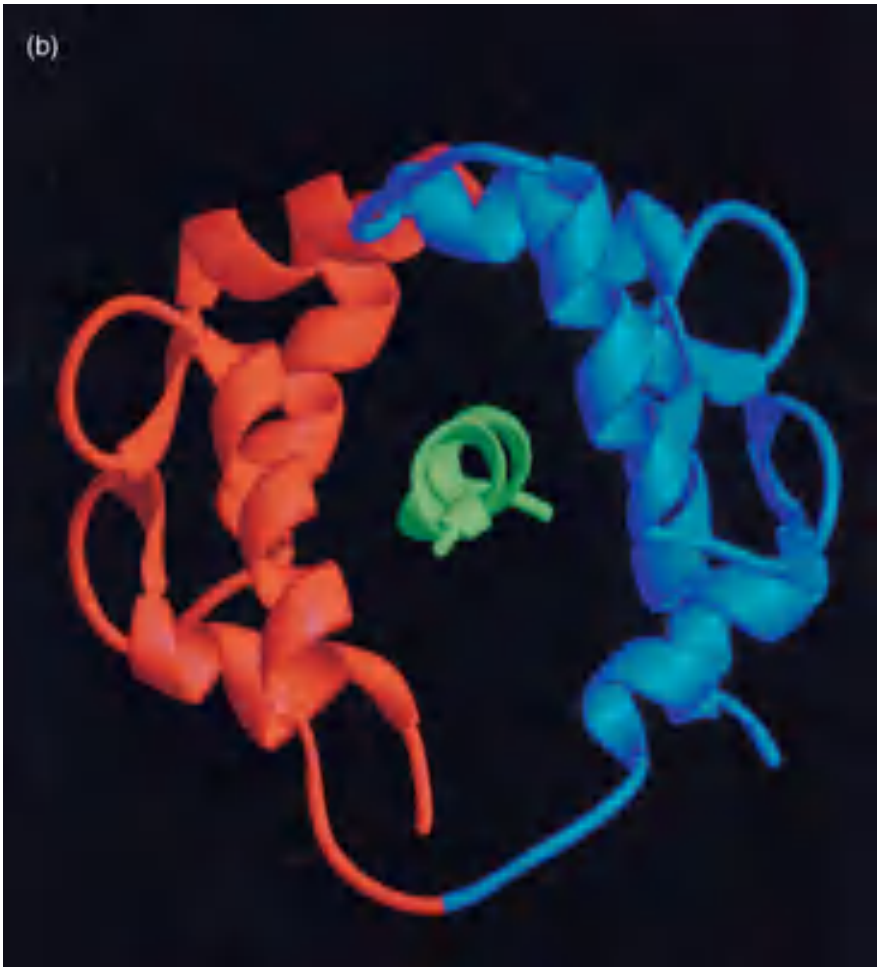

Figure 2 Ribbon diagram representations of (a) Ca^{2+}–CaM[11] and (b) the Ca^{2+}–CaM–M13 complex[14] as generated by the program ribbons. The CaM N-terminal domain is shown in blue and the C-terminal domain in red. In Figure 2(b), the structure is viewed parallel to the M13 peptide helix axis

of CaM (TR_1C, fragment 1–75; TR_2C, fragment 78–148). These half-fragments were found to be extremely useful for NMR studies of CaM. In 1984, ^1H NMR studies on the half-fragments were reported by three groups[27–30] almost at the same time. Two uniquely low-frequency shifted ring proton resonances at 6.46 and 6.50 ppm of apo-CaM were assigned to phenylalanines in the N-terminal domain. All these studies provided further evidence for the order of Ca^{2+} binding to four sites in CaM. Together with ^{43}Ca and ^{113}Cd NMR[25,26] and other biophysical studies,[4,5,8] it became clear that the two tryptic half-fragments retain the conformations which they assume in whole CaM. The property was shown for both the Ca^{2+}-free and Ca^{2+}-bound forms.

Because of the complexity of the ^1H NMR spectra of whole CaM, several groups used the tryptic half-fragments to elucidate the structural details of CaM. In 1984, Aulabaugh et al.[31] applied 2D ^1H NMR at 600 MHz to fragment TR_2C in the absence of Ca^{2+} and obtained assignments for many side-chain proton resonances to particular amino acid types. In 1985, Ikura et al.[32] applied 2D ^1H NMR techniques to the TR_2C fragment both in the presence and the absence of Ca^{2+}, and obtained about 30% backbone and side-chain proton assignments in each state using the sequential assignment procedure proposed by Wüthrich and co-workers (see ***Biological Macromolecules: Structure Determination in Solution*** and ***Structures of Larger Proteins, Protein-Ligand, and Protein-DNA Complexes by Multi-Dimensional Heteronuclear NMR***). Extremely high-frequency shifted amide proton resonances (10.0–11.0 ppm) were assigned to the glycine residues at the fifth position of the Ca^{2+}-binding loops. These uniquely shifted glycine amide resonances were further characterized using both TR_1C and TR_2C fragments.[33] Such large shifts of the amide protons of this conserved glycine residues in EF-hand Ca^{2+}-binding loops were also found in troponin C[34] and calbindin[35] (see ***Calcium-Binding Proteins***), suggesting that this feature is universal among the members of the EF-hand superfamily. Hoffman and Klevit[36] reported 2D ^1H NMR analysis of the Ca^{2+}-free TR_1C fragment in the absence of Ca^{2+}, indicating hydrophobic contacts between Phe-16 and Val-35 which are absent in the Ca^{2+}-bound form of the crystal structure.[11,12] More recently, Finn et al.[37] obtained the complete backbone ^1H resonance assignments of the Ca^{2+}-free TRC fragment, indicating that the Ca^{2+}-free state retains the helix–loop–helix secondary structure similar to that observed in the Ca^{2+}-bound form.[11,12,38]

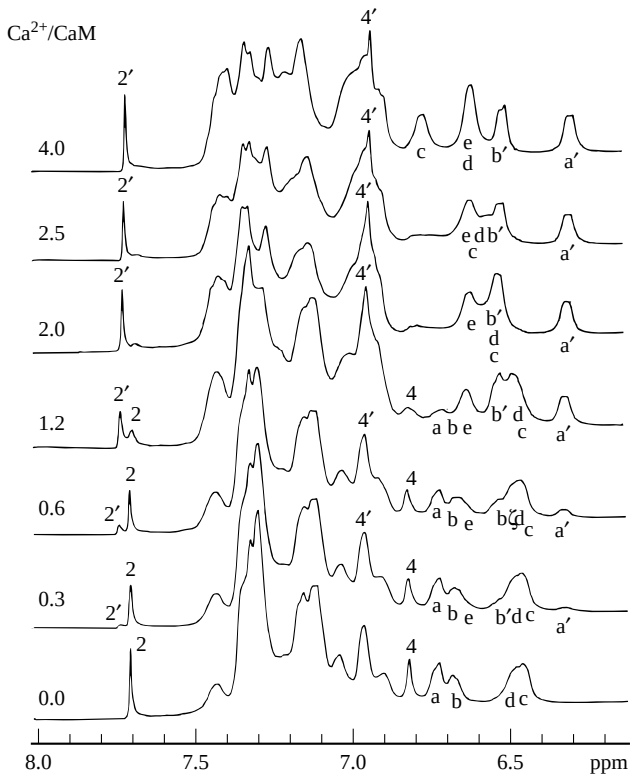

Figure 3 The aromatic region of the 400 MHz ^{1}H NMR spectra of scallop testis calmodulin at various Ca^{2+} concentrations. (Reproduced by permission of the American Chemical Society from Ikura et al.[24])

Several different NMR techniques were used to study the kinetics of Ca^{2+} binding to CaM and its fragments. Calcium-43 and ^{113}Cd NMR studies[25,26] indicate that the resonances from metal ions bound to sites III and IV show much slower exchange on the NMR timescale than those from metal ions bound to sites I and II. ^{1}H NMR saturation transfer and spectral simulation methods were employed to obtain the exchange rate constants and activation parameters between Ca^{2+}-free and Ca^{2+}-bound forms of two half-fragments.[39] Two distinct rate constants of $3-10\,s^{-1}$ and $300-500\,s^{-1}$ were found at 22 °C for the C-terminal and the N-terminal fragments, respectively. All these results confirm the identification of sites III and IV as being the high affinity sites.

Starovasnik et al[40] studied the Ca^{2+} binding and structural properties of CaM from the yeast *Saccharomyces cerevisiae* using flow dialysis and ^{1}H NMR. The amino acid sequence of yeast CaM is 60% identical to that of vertebrate CaM, whereas all known vertebrate CaM sequences are totally identical. The results indicate that, unlike vertebrate CaM, yeast CaM binds only three Ca^{2+} ions and that all three sites exhibit slow-exchange behavior upon Ca^{2+} binding. Thermal denaturation properties of yeast CaM as well as of its half-fragments were also studied. Starovasnik et al.[41] studied a series of four site-directed mutants using the same techniques, demonstrating interactions between the Ca^{2+}-binding sites in CaM.

Vogel and co-workers have extensively studied lysine residues in CaM using ^{1}H and ^{13}C NMR. The pK_a values of *N*-dimethylated lysine residues were obtained both in apo and Ca^{2+}-bound forms, as well as in a complex with a 22-residue peptide comprising the CaM-binding region of skeletal muscle MLCK.[42,43] Zhang et al.[44] applied ^{14}N NMR to ϵ-trimethyl Lys-115 in both vertebrate and yeast CaMs. The ϵ-trimethyl group of this posttranslated lysine gives rise to a sharp ^{14}N NMR resonance because of its unique tetrahedral symmetry. Selenium-77 NMR was used to study the microenvironments of the nine methionine residues in CaM, all of which were biosynthetically substituted with selenomethionine.[45]

3 CALCIUM–CALMODULIN COMPLEX

During the period 1989–93, CaM was extensively used by Bax's group at the NIH to develop multidimensional heteronuclear MR methods (see ***Multidimensional Spectroscopy: Concepts***, and ***Three- and Four-Dimensional Heteronuclear Magnetic Resonance***). This methodology requires isotope enrichment of proteins with ^{15}N and ^{13}C. Uniformly ^{15}N- and ^{13}C-labeled CaM was obtained using an *E. coli* expression system.[46] Figure 4 shows a ^{1}H–^{15}N heteronuclear single quantum coherence (HSQC) spectrum of Ca^{2+}-loaded recombinant CaM labeled uniformly with ^{15}N, illustrating that a high-quality ^{1}H–^{15}N shift correlation spectrum can be obtained at 1 mM protein concentration. Ikura et al.[38,47] reported complete backbone and side-chain ^{1}H, ^{13}C, and ^{15}N assignments of Ca^{2+}-loaded recombinant *Drosophila* CaM using a series of triple- and double-resonance 3D and 4D experiments. The secondary structure in solution was then characterized using NOE, $^3J_{NH\alpha}$ coupling constants, and ^{13}C chemical shift data.[38] These results confirm the crystal structure[11,12] in that both the N- and C-terminal globular domains assume a pair of the EF-hand type helix–loop–helix motifs. However, the central helix portion (residues 65–92), found in the crystal structure, appears to contain a nonhelical region at residues 78–81 in solution. Nitrogen-15 relaxation studies reported by Barbato et al.[48] further indicate that this nonhelical portion has considerable flexibility, consistent with other studies using solution techniques such as small angle X-ray or neutron scattering.[49] The ^{15}N relaxation studies[48] (see ***Protein Dynamics from NMR Relaxation***) provide additional interesting insights into the structure and dynamics of Ca^{2+}–CaM. The rotational correlation times obtained for the N- and C-terminal domain (7.1 ns and 6.3 ns, respectively) do not reflect the overall motion of a 16.7 kDa protein, but rather correspond to that of a smaller protein (ca. 12 kDa). Further, the correlation times for the individual amide bond vectors vary to a much lesser degree than predicted by hydrodynamic calculations for rigid dumbbell models. These results indicate that the two domains move independently in solution.

4 CALCIUM–CALMODULIN–PEPTIDE TERNARY COMPLEXES

In 1985, Klevit et al.[50] using ^{1}H NMR studied the interaction of CaM with a 26-residue synthetic peptide (known as M13) comprising the CaM-binding domain of skeletal muscle myosin light chain kinase. These data indicate that both the N- and C-terminal domains must participate in the interaction with the M13 peptide. The ^{113}Cd NMR studies of mastoparan binding to Cd_4CaM have shown that both the N- and C-terminal domains undergo conformational

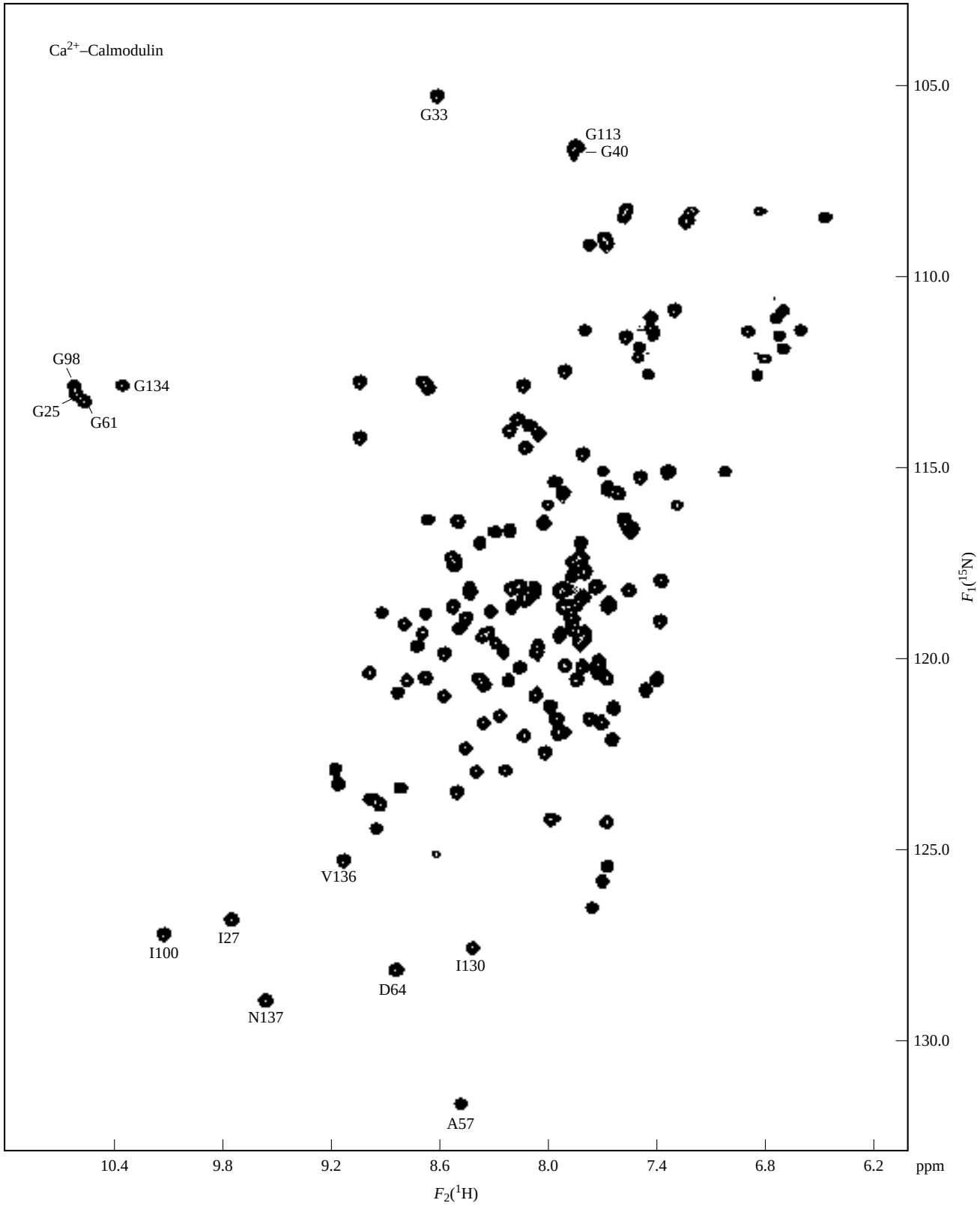

Figure 4 The 500 MHz $^{1}H-^{15}N$ HSQC shift correlation spectrum of *Xenopus laevis* calmodulin. The spectrum was recorded using a pulse sequence combined with the pulse field gradient technique described by Kay et al.[66] The full backbone amide assignment of *Xenopus* calmodulin is available from the author

changes upon binding of the peptide (see ***Calcium-Binding Proteins***). Seeholzer et al.[51] also used ^{1}H NMR to study the interaction of melittin with [^{1}H]- and [^{2}H]-CaM, suggesting that melittin assumes an α-helical conformation upon binding CaM, consistent with earlier conclusions based on circular dichroism spectra. Yazawa et al.,[52] using the ^{1}H NMR signal of His-107, showed that in the presence of M13 the Ca^{2+}-dependent conformational change becomes completely cooperative between the N- and C-terminal domains. Ikura et al.[53] studied the Cd^{2+} dependence of the interactions of CaM with M13 and mastoparan using ^{113}Cd NMR, supporting the notion of the higher cooperativity of metal binding in the presence of these peptides. Ohki et al.[54,55] studied the interaction of mastoparan with CaM under various solution conditions using ^{1}H NMR. It was shown that the N-terminal domain may interact with a second mastoparan molecule with a lower affinity, and that Mg^{2+} reduces the cooperative Ca^{2+} binding to CaM in the presence of mastoparan.

In 1991, Ikura et al.[56] completed ^{1}H, ^{13}C, and ^{15}N backbone assignments of Ca^{2+}–CaM complexed with M13 by using multidimensional heteronuclear MR methods. Proton assignments of M13 in the complex were also obtained using ^{15}N/^{13}C-filtered techniques[57] (see ***Half-Filter Experiments: Proton–Carbon-13***). Based on these assignments, the three-dimensional NMR structure of the Ca^{2+}–CaM–M13 ternary complex was determined.[14] Figure 2(b) shows a schematic ribbon model of the restrained minimized mean structure. A striking difference in conformation can be seen as compared with the crystal structure of Ca^{2+}–CaM[11] [Figure 2(a)]. The N- and C-terminal domains of CaM (residues 6–73 and 83–146) remain essentially unchanged upon complexation. The long central helix, (residues 65–93), however, which connects the two domains in the crystal structure of Ca^{2+}–CaM [Figure 4(a)], is disrupted into two helices connected by a long flexible loop (residues 74–82), thereby enabling the two domains to clamp residues 3–21 of the bound peptide which adopt a helical conformation. Key residues of the peptide are Trp-4 and Phe-17, which serve to anchor the N- and C-terminal halves of the peptide to the C- and N-terminal domains of CaM, respectively. This characteristic structure of Ca^{2+}–CaM complexed with the M13 peptide was confirmed by a crystallographic study on Ca^{2+}–CaM complexed with a similar peptide derived from smooth muscle MLCK.[15] Based on the knowledge of the structural features of these Ca^{2+}–CaM–peptide complexes, Prumb et al.[58] produced a hybrid CaM–peptide molecule and characterized the structural and Ca^{2+}-binding properties using ^{1}H–^{15}N HSQC and flow dialysis experiments.

Roth et al.[59,60] revealed the secondary structure of a 19-residue smooth muscle MLCK peptide and CaM in their complex using heteronuclear multidimensional NMR techniques. Most of the backbone amide nitrogen nuclei in the MLCK peptide were labeled with ^{15}N, which allowed the characterization of the α-helix structure of the peptide. Precheur et al.[61] also used a similar labeling technique on a 17-residue model peptide proposed by DeGrado et al.,[62] and showed a stable α-helical structure in the N-terminal 11 residues of the complex. Zhang et al.,[63,64] using 2D ^{1}H NMR, studied three synthetic CaM binding peptides which are derived from skeletal muscle MLCK, rat cerebellar nitric oxide synthase, and smooth muscle caldesmon. The MLCK[63] and caldesmon[64] peptides were found to assume an α-helical conformation in an aqueous trifluoroethanol mixture (75%/25%) The nitric oxide synthase peptide[66] also adopts an α-helical structure in aqueous solution at pH 5.5 and 5 °C.

In summary, CaM has provided an excellent example of the power of the high-resolution multinuclear magnetic resonance approach. Various NMR studies have provided valuable information on the structural and physical properties of CaM as a Ca^{2+}-sensitive molecular switch in cells. Yet, further studies have to come in order to elucidate secrets involved in multitarget recognition of this amazing molecule.

5 RELATED ARTICLES

Biological Macromolecules; Biological Macromolecules: NMR Parameters; Calcium-Binding Proteins; Half-Filter Experiments: Proton–Carbon-13; Multidimensional Spectroscopy: Concepts; Muscle Proteins; Protein Dynamics from NMR Relaxation; Structures of Larger Proteins, Protein-Ligand, and Protein-DNA Complexes by Multi-Dimensional Heteronuclear NMR; Three- and Four-Dimensional Heteronuclear Magnetic Resonance

6 REFERENCES

1. W. Y. Cheung, *Biochem. Biophys. Res. Commun.*, 1970, **38**, 533.
2. S. Kakiuchi and R. Yamazaki, *Biochem. Biophys. Res. Commun.*, 1970, **41**, 1104.
3. A. R. Means, J. S. Tash, and J. G. Chafouleas, *Physiol. Rev.*, 1982, **62**, 1.
4. D. M. Watterson, F. Sharief, and T. Vanaman, *J. Biol. Chem.*, 1980, **255**, 962.
5. P. Cohen and C. B. Klee (eds.), *Calmodulin*, Elsevier, Amsterdam, 1988.
6. A. Crivici and M. Ikura, *Annu. Rev. Biophys. Biomol. Struct.*, 1995, **24**, 85.
7. P. C. Moews and R. H. Kretsinger, *J. Mol. Biol.*, 1975, **91**, 201; *Cell Calcium*, 1992, **13**, 353.
8. O. Minowa and K. Yagi, *J. Biochem. (Tokyo)*, 1984, **96**, 1175.
9. S. R. Anderson and D. A. Malencik, in *Calcium and Cell Function*, Academic Press, New York, 1986, Vol. 6, pp. 1–42.
10. H. Hidaka, T. Yamaki, T. Totsuka, and M. Asano, *Mol. Pharmacol.*, 1979, **15**, 49.
11. Y. S. Babu, J. S. Sack, T. J. Greenhough, C. E. Bugg, A. R. Means, and W. J. Cook, *Nature (London)*, 1985, **315**, 37.
12. R. H. Kretsinger, S. E. Rudnick, and L. J. Weissman, *J. Inorg. Biochem.*, 1986, **28**, 289.
13. O. Herzberg and M. N. G. James, *Nature (London)*, 1985, **313**, 653.
14. M. Ikura, G. M. Clore, A. M. Gronenborn, G. Zhu, C. B. Klee, and A. Bax, *Science*, 1992, **256**, 632.
15. W. E. Meador, A. R. Means, and F. A. Quiocho, *Science*, 1992, **257**, 1251.
16. W. E. Meador, A. R. Means, and F. A. Quiocho, *Nature*, **262**, 1718.
17. K. B. Seamon, *Biochem. Biophys. Res. Commun.*, 1979, **86**, 1256.
18. K. B. Seamon, *Biochemistry*, 1980, **19**, 207.
19. R. E. Klevit, B. A. Levine, and R. J. P. Williams, *FEBS Lett.*, 1981, **123**, 25.
20. J. Krebs and E. Carafoli, *Eur. J. Biochem*, 1982, **124**, 619.

21. T. Shimizu and M Hatano, *FEBS Lett.*, 1983, **160**, 182.
22. T. Shimizu, M. Hatano, S. Nagao, and Y. Nozawa, *Biochem. Biophys. Res.* Commun., 1982, **106**, 1112.
23. M. Ikura, T. Hiraoki, K. Hikichi, T. Mikuni, M. Yazawa, and K. Yagi, *Biochemistry*, 1983, **22**, 2568.
24. M. Ikura, T. Hiraoki, K. Hikichi, T. Mikuni, M. Yazawa, and K. Yagi, *Biochemistry*, 1983, **22**, 2573.
25. S. Forsén A. Andersson, T. Drakenberg, O. Teleman, E. Thulin, and H. J. Vogel, *Calcium-Binding Proteins* Elsevier, Amsterdam, 1983, p.# 121.
26. A. Andersson, S. Forsén, E. Thulin, and H. J. Vogel, *Biochemistry*, 1983, **22**, 2309.
27. E. Thulin, A. Andersson, T. Drakenberg, S. Forsen, and H. J. Vogel, *Biochemistry*, 1984, **23**, 1862.
28. M. Ikura, T. Hiraoki, K. Hikichi, O. Minowa, H. Yamaguchi, M. Yazawa, and K. Yagi, *Biochemistry*, 1984, **23**, 3124.
29. D. C. Dalgarno, B. A. Levine, R. J. P. Williams, C. S. Fullmer, and R. H. Wasserman, *Eur. J. Biochem.*, 1983, **137**, 523.
30. R. E. Klevit, D. C. Dalgarno, B. A. Levine, and R. J. P. Williams, *Eur. J. Biochem.*, 1984, **139**, 109.
31. A. Aulabaugh, W. P. Niemczura, T. L. Blundell, and W. A. Gibbons, *Eur. J. Biochem.*, 1984, **143**, 409.
32. M. Ikura, O. Minowa, and K. Hikichi, *Biochemistry*, 1985, **24**, 4264.
33. M. Ikura, O. Minowa, M. Yazawa, K. Yagi, and K. Hikichi, *FEBS Lett.*, 1987, **219**, 17.
34. S. Tsuda, K. Ogura, Y. Hasegawa, K. Yagi, and K. Hikichi, *Biochemistry*, 1990, **29**, 4951.
35. J. Kördel, S. Forsén, T. Drakenberg, and W. J. Chazin, *Biochemistry*, 1990, **29**, 4400.
36. R. Hoffman and R. E. Klevit, in *Techniques in Protein Chemistry II*, Academic Press, New York, 1991, p. 383.
37. B. E. Finn, T. Drakenberg, and S. Forsén, *FEBS Lett.*, 1994, **336**, 368.
38. M. Ikura, S. Spera, G. Barbato, L. E. Kay, M. Krinks, and A. Bax, *Biochemistry*, 1991, **30**, 9216.
39. M. Ikura, *Biochem. Biophys. Acta*, 1986, **872**, 195.
40. M. A. Starovasnik, T. N. Davis, and R. E. Klevit, *Biochemistry*, 1993, **32**, 3261.
41. M. A. Starovasnik, D.-R. Su, K. Beckingham, and R. E. Klevit, *Protein Sci.*, 1992, **1**, 245.
42. M. E. Huque and H. J. Vogel, *J. Protein Chem.*, 1993, **12**, 693.
43. M. Zhang and H. J. Vogel, *J. Biol. Chem.*, 1993, **268**, 22420.
44. M. Zhang, M. E. Huque, and H. Vogel, *J. Biol. Chem.*, 1994, **269**, 5099.
45. M. Zhang and H. J. Vogel, *J. Mol. Biol.*, submitted for publication.
46. M. Ikura, D. Marion, L. E. Kay, H. Shih, M. Krinks, C. B. Klee, and A. Bax, *Biochem. Pharmacol.*, 1990, **40**, 153.
47. M. Ikura, L. E. Kay, and A. Bax, *Biochemistry*, 1990, **29**, 4659.
48. G. Barbato, M. Ikura, L. E. Kay, R. W. Pastor, and A. Bax, *Biochemistry*, 1992, **31**, 5269.
49. T. Trewhella, *Cell Calcium*, 1992, **13**, 377, and references cited therein.
50. R. E. Klevit, D. K. Blumenthal, D. E. Wemmer, and E. G. Krebs, *Biochemistry*, 1985, **24**, 8152.
51. S. H. Seeholzer, M. Cohn, J. A. Putkey, A. R. Means, and H. L. Crespi, *Proc. Natl. Acad. Sci. USA*, 1986, **83**, 3634.
52. M. Yazawa, M. Ikura, K. Hikichi, L. Ying. and K. Yagi, *J. Biol. Chem.*, 1987, **262**, 10 951.
53. M. Ikura, N. Hasegawa, S. Aimoto, M. Yazawa, and K. Yagi, and K. Hikichi, *Biochem. Biophys. Res. Commun.*, 1989, **161**, 1233.
54. S. Ohki, M. Yazawa, K. Yagi, and K. Hikichi, *J. Biochem.*, 1991, **110**, 737.
55. S. Ohki, U. Iwamoto, S. Aimoto, M. Yazawa, and K. Hikichi, *J. Biol. Chem.*, 1993, **268**, 12 388.
56. M. Ikura, L. E. Kay, M. Krinks, and A. Bax, *Biochemistry*, 1991, **30**, 5498.
57. M. Ikura and A. Bax. *J. Am. Chem. Soc.*, 1992, **114**, 2433.
58. T. Prumb, P. Yau, T. S. Harvey, and M. Ikura, *Protein Eng.*, 1994, **7**, 109.
59. S. M. Roth, D. M. Schneider, L. A. Strobel, M. F. A. van Berkum, A. R. Means, and A. J. Wand, *Biochemistry*, 1991, **30**, 10 078.
60. S. M. Roth, D. M. Schneider, L. A. Strobel, M. F. A. van Berkum, A. R. Means, and A. J. Wand, *Biochemistry*, 1992, **31**, 1443.
61. B. Precheur, H. Munier, J. Mispelter, O. Barzu, and C. T. Craescu, *Biochemistry*, 1992, **31**, 229.
62. W. F. DeGrado, F. G. Prendergast, H. R. Wolfe, Jr., and J. A. Cox, *J. Cell. Biochem.*, 1985, **29**, 83.
63. M. Zhang, T. Yuan, and H. J. Vogel, *Protein Sci.*, 1993, **2**, 1931.
64. M. Zhang and H. J. Vogel, *Biochemistry*, 1994, **33**, 1163.
65. M. Zhang and H. J. Vogel, *J. Biol. Chem.*, 1994, **269**, 981.
66. L. E. Kay, P. Keifer, and T. Saarinen, *J. Am. Chem. Soc.*, 1992, **114**, 10 663.

Biographical Sketches

Mitsuhiko Ikura. *b* 1956. B.S., 1979, Ph.D., 1986, Hokkaido University, Japan, where he was introduced to NMR by Kunio Hikichi. Postdoctoral work with Ad Bax at National Institutes of Health, USA, 1988–91. Senior scientist, Ontario Cancer Institute University of Toronto, Canada, 1991–present. Approx. 80 publications. Current research specialty: structural biology of calcium binding proteins and other biological macromolecules.

Chemical Exchange Effects in Biological Macromolecules

Arthur G. Palmer, III

Department of Biochemistry and Molecular Biophysics, Columbia University, New York, NY, USA

1 Introduction 1
2 Two-site Chemical Exchange 1
3 Identifying Spins Affected by Chemical Exchange 2
4 ZZ-Exchange Spectroscopy 3
5 Lineshape Analysis 4
6 $R_{1\rho}$ Rotating Frame Relaxation Methods 5
7 CPMG Relaxation Methods 7
8 Chemical Exchange in Multiple Quantum Spectroscopy 8
9 Conclusions 9
10 Related Articles in this Volume 9
11 Related Articles in Volumes 1–8 9
12 References 9

1 INTRODUCTION

The effects of chemical exchange, including transverse relaxation and magnetization transfer, have long been of interest in NMR spectroscopy (see **Chemical Exchange Effects on Spectra,** Volume 2 and **Relaxation Effects of Chemical Exchange,** Volume 6). Exchange phenomena in solution NMR spectroscopy arise when chemical or conformational kinetic processes render the isotropic chemical shifts of nuclear spins time-dependent, either by transferring the spins between distinct chemical sites or by altering the local magnetic environment of the spins. Kinetic processes on times scales ranging from μs to s are effective in causing chemical exchange effects. Many biological processes occur with time constants within this range, and numerous applications have been reported that utilize chemical exchange effects to characterize time-dependent processes in biological macromolecules.[1–20]

The present article describes a subset of ZZ-exchange,[21,22] lineshape,[23,24] Carr–Purcell–Meiboom–Gill (CPMG),[25,26] and $R_{1\rho}$[27,28] relaxation techniques that are sensitive to molecular motions or chemical kinetic processes on μs–s time scales in biological macromolecules. The experimental techniques, rather than specific applications, will be emphasized. In most cases, pulse sequences suitable for application to isolated I_nS ($I = {}^1H$; $X = {}^{15}N$ or ${}^{13}C$; $n = 1, 2,$ or 3) spin systems are presented. The pulse sequences shown do not include details of solvent suppression techniques because different approaches are used for ${}^1H$, ${}^{13}C$, and ${}^{15}N$.[29,30] Compensatory rf fields should be applied during the recycle delay to ensure that the same average rf power is deposited into the sample for all values of the relaxation period.[31] The pulse sequences illustrated use INEPT elements for polarization transfer; in some cases, increased sensitivity can be obtained by replacing the INEPT transfers with heteronuclear cross polarization or CPMG-INEPT methods with large effective fields.[32–34]

2 TWO-SITE CHEMICAL EXCHANGE

For simplicity, only two-site exchange will be considered. The nucleus of interest is assumed to exchange between two magnetically distinct environments A and B while the system remains at chemical equilibrium throughout the NMR experiment. Furthermore, the present article focuses on situations in which scalar coupling constants are not perturbed by the exchange process (see **Chemical Exchange Effects on Spectra,** Volume 2); consequently, the modified Bloch or McConnell equations are sufficient to describe the effect of exchange (see **Relaxation Effects of Chemical Exchange,** Volume 6). The kinetic scheme is:

$$A \underset{k_{-1}}{\overset{k_1}{\rightleftharpoons}} B \tag{1}$$

in which k_1 and k_{-1} are forward and reverse rate constants and the chemical exchange rate constant, k_{ex}, is given by,

$$k_{ex} = k_1 + k_{-1} = \frac{k_1}{p_B} = \frac{k_{-1}}{p_A} \tag{2}$$

$p_A \geq 0.5$ and $p_B = 1 - p_A$ denote the equilibrium populations of equivalent nuclear spins in species A and B. Higher order chemical reactions, such as ligand binding or oligomerization, are treated by defining k_1 and k_{-1} as pseudo-first-order rate constants. The resonance frequencies in the rotating frame for spins in site A and B are Ω_A and Ω_B, respectively, in units of angular frequency, and the chemical shift difference between the two sites is $\Delta\omega = \Omega_B - \Omega_A$. The total equilibrium magnetization is M^0, and the equilibrium longitudinal magnetization at each site is $M_A^0 = p_A M^0$ and $M_B^0 = p_B M^0$. The longitudinal relaxation rate constants of the sites in the absence of exchange (resulting from dipolar, shielding anisotropy (CSA), and quadrupolar relaxation) are R_{1A}^0 and R_{1B}^0. The transverse relaxation rate constants of the sites in the absence of exchange are R_{2A}^0 and R_{2B}^0.

The effect of exchange on free-precession lineshapes has been discussed in **Relaxation Effects of Chemical Exchange,** Volume 6. The relative values of k_{ex} and $\Delta\omega$ define the limits of what is commonly referred to as "fast" and "slow" exchange on the chemical shift time scale:

$$\begin{aligned} k_{ex} &< \Delta\omega \quad \text{Slow exchange} \\ k_{ex} &\approx \Delta\omega \quad \text{Intermediate exchange} \\ k_{ex} &> \Delta\omega \quad \text{Fast exchange} \end{aligned} \tag{3}$$

In the slow exchange limit, resolved lines are observed for the two sites with resonance frequencies Ω_A and Ω_B. The effect of exchange is to shift the resonance positions and broaden the lines until the lines coalesce in the intermediate exchange regime (a more exact analysis yields the result that coalescence occurs when $2(p_A p_B)^{1/2}\Delta\omega \approx k_{ex}$). In the fast exchange limit, a single averaged resonance line is observed at the population-weighted average shift, $\Omega = p_A\Omega_A + p_B\Omega$.

3 IDENTIFYING SPINS AFFECTED BY CHEMICAL EXCHANGE

The initial step in characterizing a kinetic process by NMR spectroscopy is identifying spins subject to chemical exchange. If p_B is sufficiently large and exchange is slow on the chemical shift time scale, then additional resonances arising from the second species are observed in the NMR spectra. These resonances usually are identified during initial efforts to obtain sequence specific resonance assignments. NOESY, ROESY, and ZZ-exchange spectroscopy, discussed below, are used to confirm that the additional resonances arise from chemical exchange processes. However, only a single set of resonances are observed in the NMR spectra if exchange is fast on the chemical shift time scale or if p_B is sufficiently low that the minor component is not observable in the slow exchange limit. In such circumstances, exchange effects are recognized by an increase in the transverse relaxation rate constant relative to the value expected for dipolar, quadrupolar and CSA interactions for the observed resonance signals:

$$R_2 = R_2^0 + R_{ex} \tag{4}$$

in which R_2^0 refers to either the relaxation rate constant for an individual site (for slow exchange) or to the population averaged relaxation rate constant (for fast exchange) and R_{ex} is the excess contribution to R_2 due to exchange.

R_2 in equation (4) can be approximated either by R_2*, the free-precession damping constant including effects of magnetic field inhomogeneity, or by $R_{2\text{echo}}$, the damping constant observed for a Hahn spin echo experiment. The value of R_2* is obtained from the resonance full-width at half-height linewidth, $\Delta\nu_{1/2}$, using $R_2^* = \Delta\nu_{1/2}/\pi$ or equivalently, from the decay of the time domain free induction decay or interferogram (in multidimensional NMR spectra).[35] The size of the inhomogeneity contribution to R_2* can be estimated using spins not affected by the exchange process. The value of $R_{2\text{echo}}$ is obtained using the sequence $t - 180^\circ - t$ incorporated into either a one-dimensional or multidimensional NMR experiment.[36] The 180° pulse must be selective to refocus scalar coupling interactions. If spectra are recorded for $t = 0$ and $t = \tau$, then $R_{2\text{echo}} = (2\tau)^{-1}\ln[I(0)/I(\tau)]$, in which $I(t)$ is the intensity of the resonance measured for an echo time t. The echo time, τ, should be long enough that $\tau k_{ex} \gg 1$; otherwise, the effects of exchange on the echo decay are partially suppressed. Complete expressions for the echo decay are given in **Relaxation Effects of Chemical Exchange,** Volume 6. In either approach, additional decoupling sequences may need to be applied during the free-precession evolution period or during the spin-echo delay to prevent evolution into antiphase coherences subject to additional relaxation mechanisms.[37,38]

The value of R_2^0 is obtained by one of the following approaches: (1) analysis of R_1, R_2 and NOE data for ^{13}C or ^{15}N spins using the model free formalism;[39,40] (2) use of the magnetic field dependence of R_2 to determine $J(0)$, the spectral density function at zero frequency;[41–43] and (3) use of ^{1}H–X dipole/X CSA relaxation interference rate constants.[43,44]

The first method determines the rotational diffusion tensor for the molecule using R_1, R_2 and NOE relaxation rate constants for spins not subject to conformational exchange broadening (see **Protein Dynamics from NMR Relaxation,** Volume 6). Once the diffusion tensor for the molecule is known, R_2^0 for individual exchange broadened nuclear spins is approximated using the measured values of R_1 and NOE. This method is automated in software programs such as ModelFree.[39] Residues subject to exchange broadening must be carefully distinguished from residues affected by rotational diffusion anisotropy in order to obtain an accurate assessment of the diffusion tensor.[44–46]

Most investigations of molecular dynamic properties of macromolecules through spin relaxation measure R_2 using CPMG experiments with a single spin echo delay, τ_{cp}, satisfying $1/\tau_{cp} \geq 1000\,\text{s}^{-1}$ or $R_{1\rho}$ experiments with an effective field in the rotating frame, ω_e, satisfying $\omega_e \geq 12\,000\,\text{s}^{-1}$ to partially suppress exchange effects.[47] Under these conditions, the residual R_{ex} contribution to R_2 is proportional to B_0^2, in which B_0 is the static magnetic field strength, for all exchange time scales.[48] Using this result, the second approach defines:[42,43]

$$\Gamma = R_2 - \frac{1}{2}R_1 - \left(\frac{3d^2}{4}\right)J(\omega_H)$$
$$= \left(\frac{d^2}{2}\right)J(0) + \left(\frac{2}{9}\gamma_C^2\Delta\sigma^2 J(0) + \Theta_{ex}\right)B_0^2 \tag{5}$$

in which $d = (\mu_0 h\gamma_H\gamma_X)/(8\pi^2 r_{XH^3})$; μ_0 is the permeability of free space; h is Planck's constant; γ_H and γ_X are the gyromagnetic ratios for ^{1}H and X spins, respectively; r_{XH} is the distance between the two nuclei; Θ_{ex} is a constant of proportionality; $\Delta\sigma = \sigma_\parallel - \sigma_\perp$; and the principal components of the X spin CSA tensor are $\sigma_\parallel$ and $\sigma_\perp$. The value of $J(\omega_H)$ is obtained from the heteronuclear NOE by reduced spectral density mapping methods.[49] The value of $J(0)$ is obtained from the intercept of a linear least squares fit of Γ versus B_0^2. Once $J(0)$ is determined, values of R_2^0 at each value of B_0 can be obtained by setting $\Theta_{ex} = 0$ in equation (5).

The third method only is applicable to nuclear spins, such as backbone amide ^{15}N spins in proteins, with substantial CSA contributions to laboratory frame relaxation. Interference between the ^{1}H–X dipolar and X CSA interactions constitutes an additional relaxation mechanism that is unaffected by chemical exchange (see **Relaxation Effects Involving Cross Correlation in Biomolecules**). The transverse cross-correlation relaxation rate constant, η_{xy}, represents cross-relaxation between in-phase and antiphase magnetization, while the longitudinal cross-correlation relaxation rate constant, η_z, represents cross-relaxation between longitudinal magnetization and two-spin order. For an axially symmetric chemical shift tensor, the cross-correlation rate constants are:[50]

$$\eta_z = -\sqrt{3}cd\,P_2(\cos\beta)J(\omega_X)$$
$$\eta_{xy} = -\frac{\sqrt{3}}{6}cd\,P_2(\cos\beta)[4J(0) + 3J(\omega_X)] \tag{6}$$

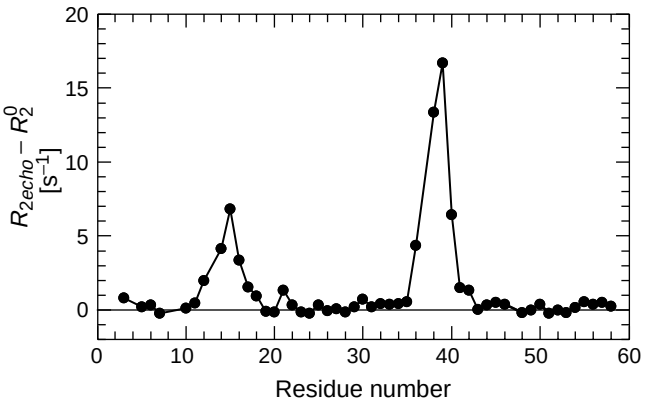

Figure 1 Identifying chemical exchange in BPTI. Shown is a graph of $R_{2echo} - R_2^0$ versus the protein sequence. Regions of pronounced chemical exchange linebroadening, for which $R_{ex} = R_{2echo} - R_2^0 \gg 0$, are evident in the vicinity of the Cys 14–Cys 38 disulfide bond

in which $c = 3^{-1/2}\gamma_X B_0 \Delta\sigma$, β is the angle between the symmetry axes of the chemical shift and dipole tensors, and $P_2(x) = (3x^2 - 1)/2$. If both η_{xy} and η_z have been measured,[44,51] then:[43]

$$R_2^0 = \left(R_1 - \frac{7}{4}J(\varepsilon\omega_H)\right)\frac{\eta_{xy}}{\eta_z} + \frac{13}{8}J(\xi\omega_H) \qquad (7)$$

which does not require assumptions about the values of $\Delta\sigma$ and β. If only η_{xy} has been measured, but $\Delta\sigma$ and β are known, then:

$$R_2^0 = \left(\frac{3d^2 + 4c^2}{4\sqrt{3}cd\,P_2(\cos\beta)}\right)\eta_{xy} + \frac{13}{8}d^2 J(\xi\omega_H) \qquad (8)$$

The value of ε is 0.92 in equation (7) and ξ is 0.96 in equations (7) and (8) for ^{15}N.

An example of the use of R_{2echo} and R_2^0 for detecting chemical exchange broadened backbone amide ^{15}N resonances is provided for basic pancreatic trypsin inhibitor (BPTI) in Figure 1. Values of R_{2echo} were measured using a Hahn spin-echo sequence incorporated into an in-phase ^{15}N–^{1}H HSQC experiment.[36,52] WALTZ-16 decoupling was used during the spin echo period to suppress evolution of the ^{15}N–^{1}H scalar coupling interaction.[53] Values of R_2^0 were obtained from η_{xy} using equation (8) and η_{xy} was measured using established techniques.[43] Significant values of $R_{ex} = R_{2echo} - R_2^0$ are observed for residues near the Cys 14 to Cys 38 disulfide linkage.[48,54]

4 ZZ-EXCHANGE SPECTROSCOPY

Slow chemical exchange processes can be studied by monitoring the exchange of longitudinal magnetization between sites if the population of the minor site B is large enough to generate observable resonance signals.[55] In addition, k_{ex} must not be much less than R_{1A} and R_{1B}; otherwise, the signals decay due to relaxation faster than population transfer. Investigations of chemical exchange using ^{1}H NMR spectroscopy are complicated by the coexisting transfer of magnetization through the nuclear Overhauser effect, although the opposite signs of the NOE and ROE for macromolecules can be used to approximately suppress magnetization transfer through dipolar relaxation.[56] Isotopic enrichment of macromolecules enables X-nucleus ZZ-exchange to be utilized instead of ^{1}H magnetization transfer. Although either exchange of longitudinal magnetization[57,58] or two-spin order[57,59] can be monitored, longitudinal relaxation is much slower for ^{15}N and ^{13}C spins than for ^{1}H spins in macromolecules; consequently, the relaxation rate constant for two-spin order is less favorable than for X-nucleus longitudinal magnetization. For biological macromolecules, X-nucleus R_1 values typically are on the order of $1\,s^{-1}$; consequently, ZZ-exchange measurements are applicable to chemical exchange processes with $k_{ex} < 10^2\,s^{-1}$.

A three-dimensional ^{1}H–X–^{1}H pulse sequence for a ZZ-exchange measurement is shown in Figure 2; as described in the figure caption, either ^{1}H–^{1}H or X–^{1}H two-dimensional pulse sequences can be derived from the three-dimensional sequence and employed if the resonances due to exchanging spins are sufficiently well-resolved.[58,60] The evolution of longitudinal magnetization during the mixing time, t, is described by the modified Bloch or McConnell equations:[61]

$$\frac{d}{dt}\begin{bmatrix}\Delta M_{zA}(t)\\ \Delta M_{zB}(t)\end{bmatrix} = \begin{bmatrix}-R_{1A}^0 - p_B k_{ex} & p_A k_{ex}\\ p_B k_{ex} & -R_{1B}^0 - p_A k_{ex}\end{bmatrix}\begin{bmatrix}\Delta M_{zA}(t)\\ \Delta M_{zB}(t)\end{bmatrix} \qquad (9)$$

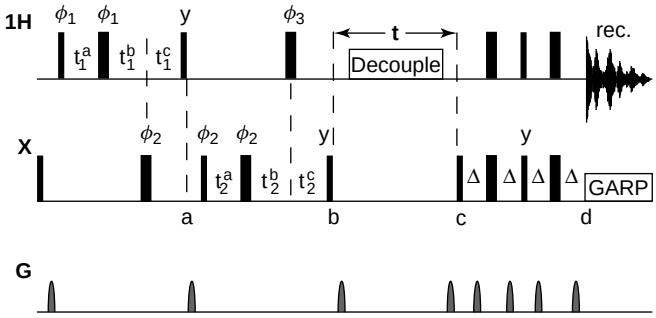

Figure 2 Three-dimensional pulse sequence for ZZ-exchange NMR spectroscopy.[58] Narrow and wide bars depict 90° and 180° pulses respectively. All pulses are x-phase unless otherwise indicated. Decoupling during the relaxation delay to suppress heteronuclear dipole–dipole cross relaxation and dipole/CSA cross correlation can be performed using WALTZ-16[53] or a train of ^{1}H 180° pulses at 5 ms intervals. Decoupling during acquisition is achieved with the GARP sequence.[92] Delays are $\Delta = 1/(4J_{XH})$, $t_1^a = (1 - t_1/t_{1max})\Delta$, $t_1^b = (1 - 2\Delta/t_{1max})t_1/2$, $t_1^c = \Delta + t_1/2$, t_{1max} is the maximum value of the t_1 labeling period, $t_2^a = (1 - t_2/t_{2max})\Delta$, $t_2^b = (1 - 2\Delta/t_{2max})t_2/2$, $t_2^c = \Delta + t_2/2$, t_{2max} is the maximum value of the t_2 labeling period, and t is the mixing time. A two-dimensional X–^{1}H correlation spectrum is obtained by setting $t_1^a = t_1^c = \Delta$ and $t_1^b = 0$; a two-dimensional ^{1}H–^{1}H correlation spectrum is obtained by setting $t_2^a = t_2^c = \Delta$ and $t_2^b = 0$. The phase cycle is $\phi_1 = x, -x$; $\phi_2 = 4(x), 4(-x)$; $\phi_3 = x, x, y, y, -x, -x, -y, -y$; and receiver $= x, -x, -x, x$. The gradients are used to suppress unwanted coherences and pulse imperfections.[93] Frequency discrimination during t_1 and t_2 is obtained by shifting the phase of ϕ_1 and ϕ_2, respectively, and the receiver according to the States-TTPI protocol.[94] As discussed in the text, magnetization transfer during the periods a-b and c-d may need to be considered in addition to the mixing time t

in which $\Delta M_{zA}(t) = M_{zA}(t) - M_A^0$ and $\Delta M_{zB}(t) = M_{zB}(t) - M_B^0$. The solution of this equation is:

$$\begin{bmatrix} \Delta M_{zA}(t) \\ \Delta M_{zB}(t) \end{bmatrix} = \begin{bmatrix} a_{AA}(t) & a_{AB}(t) \\ a_{BA}(t) & a_{BB}(t) \end{bmatrix} \begin{bmatrix} \Delta M_{zA}(0) \\ \Delta M_{zB}(0) \end{bmatrix} \tag{10}$$

in which,

$$\begin{aligned} a_{AA}(t) &= \frac{1}{2}[(1-\Lambda)\exp(-\lambda_- t) + (1+\Lambda)\exp(-\lambda_+ t)] \\ a_{BB}(t) &= \frac{1}{2}[(1+\Lambda)\exp(-\lambda_- t) + (1-\Lambda)\exp(-\lambda_+ t)] \\ a_{AB}(t) &= \frac{k_{ex}\, p_A}{\lambda_+ - \lambda_-}[(\exp(-\lambda_- t) - \exp(-\lambda_+ t))] \\ a_{BA}(t) &= \frac{k_{ex}\, p_B}{\lambda_+ - \lambda_-}[(\exp(-\lambda_- t) - \exp(-\lambda_+ t))] \end{aligned} \tag{11}$$

and,

$$\begin{aligned} \Lambda &= \frac{R_{1A}^0 - R_{1B}^0 + k_{ex}(p_B - p_A)}{\lambda_+ - \lambda_-} \\ \lambda_\pm &= \frac{1}{2}\{R_{1A}^0 + R_{1B}^0 + k_{ex} \\ &\quad \pm [(R_{1A}^0 - R_{1B}^0 + k_{ex}(p_B - p_A))^2 + 4 p_A p_B k_{ex}^2]^{1/2}\} \end{aligned} \tag{12}$$

Thus, the intensity of the autopeak for site A (site B) evolves as $a_{AA}(t)$ ($a_{BB}(t)$), and the crosspeak between A and B (B and A) evolves as $a_{AB}(t)$ ($a_{BA}(t)$).

Crosspeak intensity can be observed at $t = 0$ if exchange is fast enough to transfer magnetization between sites during the INEPT periods. If ^{1}H magnetization is frequency labeled during t_1, then exchange effects must be considered between points a-b and c-d in Figure 2. If only X magnetization is frequency labeled, during t_2, then exchange effects must be considered between points c-d in Figure 2. The effects of exchange during the INEPT periods can be approximated by including the length of the INEPT sequences, 2Δ, in the mixing time provided that $|R_{1A}^0 - R_{1B}^0| \ll k_{ex}$ and $|R_{2A}^0 - R_{2B}^0| \ll k_{ex}$ for the X nucleus and $|R_{2A}^0 - R_{2B}^0| \ll k_{ex}$ for the ^{1}H spin. If these conditions do not hold, then the effects of exchange during the INEPT periods must be analyzed numerically. If a three-dimensional experiment is performed, then exchange during the t_2 evolution period must be analyzed numerically unless $t_{2max} k_{ex} \ll 1$.

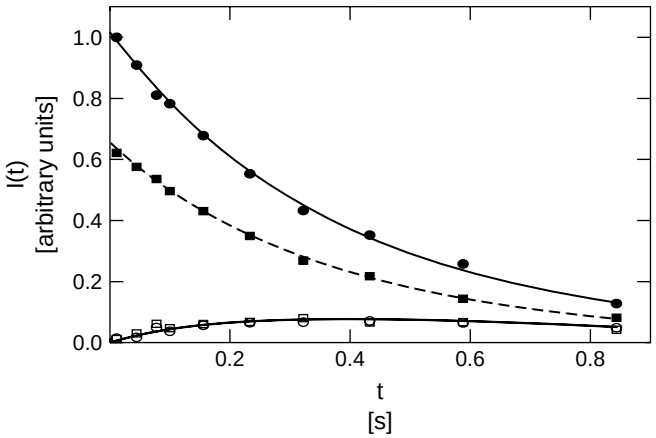

Figure 3 ^{15}N ZZ-exchange data for Thr 12 of the drk SH3 domain.[29] $I_{ij}(t)$ is the integrated peak volume as a function of the mixing time T. (●) $I_{AA}(t) = \Delta M_{zA}(0) a_{AA}(t)$ and (■) $I_{BB}(t) = \Delta M_{zB}(0) a_{BB}(t)$ are the volumes of the autocorrelation peaks and (○) $I_{BA}(t) = \Delta M_{zA}(0) a_{BA}(t)$ and (□) $I_{AB}(t) = \Delta M_{zB}(0) a_{AB}(t)$ are the volumes of the crosspeaks. The lines are the optimized fits to equations (10)–(12). The fitted results yield $R_{1A}^0 = 2.41 \pm 0.05\,\mathrm{s}^{-1}$, $R_{1B}^0 = 1.90 \pm 0.11\,\mathrm{s}^{-1}$, $k_1 = 0.86 \pm 0.06\,\mathrm{s}^{-1}$, and $k_{-1} = 0.43 \pm 0.03\,\mathrm{s}^{-1}$. (Reproduced with permission from *Biochemistry*, 1995, **34**, 868–878. Copyright 1994 Am. Chem. Soc)

Two-dimensional ^{15}N ZZ-exchange experiments have been used to quantify chemical exchange between folded and unfolded forms of the drk SH3 domain.[14,29] Typical results are shown in Figure 3. The data were analyzed using equations (10)–(12) to determine the relaxation rate constants for the folded (site A) and unfolded forms (site B) of the protein and the folding (k_{-1}) and unfolding (k_1) rate constants.

5 LINESHAPE ANALYSIS

Lineshape analysis is a classical approach for analyzing exchange processes in NMR spectroscopy.[23,24] Applications to proteins include chemical exchange arising from folding,[12,62,63] ligand binding,[64] and oligomerization.[13] In each of these applications, the lineshapes can be altered by varying experimental parameters, such as temperature, ligand concentration, denaturant concentration, or protein concentration, which enables a global analysis of lineshapes to be performed as functions of the adjustable parameters. Typically, lineshape analysis is applicable to exchange processes in biological macromolecules with $k_{ex} < 10^4\,\mathrm{s}^{-1}$.

For transverse coherence subject to free precession under the Zeeman Hamiltonian, the evolution of the magnetization is described by the modified Bloch or McConnell equations:[61]:

$$\frac{d}{dt}\begin{bmatrix} M_A^+(t) \\ M_B^+(t) \end{bmatrix} = \begin{bmatrix} -i\Omega_A - R_{2A}^0 - p_B k_{ex} & p_A k_{ex} \\ p_B k_{ex} & -i\Omega_B - R_{2B}^0 - p_A k_{ex} \end{bmatrix} \times \begin{bmatrix} M_A^+(t) \\ M_B^+(t) \end{bmatrix} \tag{13}$$

The solution of these equations is:

$$\begin{bmatrix} M_A^+(t) \\ M_B^+(t) \end{bmatrix} = \begin{bmatrix} a_{AA}(t) & a_{AB}(t) \\ a_{BA}(t) & a_{BB}(t) \end{bmatrix} \begin{bmatrix} M_A^+(0) \\ M_B^+(0) \end{bmatrix} \tag{14}$$

in which $M_A^+(t) = M_{Ax}(t) + i M_{Ay}(t)$, $M_B^+(t) = M_{Bx}(t) + i M_{By}(t)$,

$$\begin{aligned} a_{AA}(t) &= \frac{1}{2}[(1-\Lambda)\exp(-\lambda_- t) + (1+\Lambda)\exp(-\lambda_+ t)] \\ a_{BB}(t) &= \frac{1}{2}[(1+\Lambda)\exp(-\lambda_- t) + (1-\Lambda)\exp(-\lambda_+ t)] \\ a_{AB}(t) &= \frac{k_{ex}\, p_A}{\lambda_+ - \lambda_-}[(\exp(-\lambda_- t) - \exp(-\lambda_+ t))] \\ a_{BA}(t) &= \frac{k_{ex}\, p_B}{\lambda_+ - \lambda_-}[(\exp(-\lambda_- t) - \exp(-\lambda_+ t))] \end{aligned} \tag{15}$$

and,

$$\Lambda = \frac{-i\Delta\omega + R_{2A}^0 - R_{2B}^0 + k_{ex}(p_B - p_A)}{\lambda_+ - \lambda_-}$$

$$\lambda_\pm = \frac{1}{2}\{-i\Omega_A - i\Omega_B + R_{2A}^0 + R_{2B}^0 + k_{ex} \pm [(-i\Delta\omega + R_{2A}^0 - R_{2B}^0 + k_{ex}(p_B - p_A))^2 + 4p_A p_B k_{ex}^2]^{1/2}\} \quad (16)$$

The NMR spectrum is given by the Fourier transformation of $M_A^+(t) + M_B^+(t)$. Computer optimization of the parameters in equations (14)–(16) is utilized to fit the experimental lineshapes. In practical applications, particularly for ^{1}H lineshapes, the magnetization components in equations (14)–(16) should be regarded as representing individual resonance lines of scalar coupled multiplets. If scalar coupling constants are modulated by the exchange process, then the more general theoretical approach described in **Chemical Exchange Effects on Spectra,** Volume 2 is required.

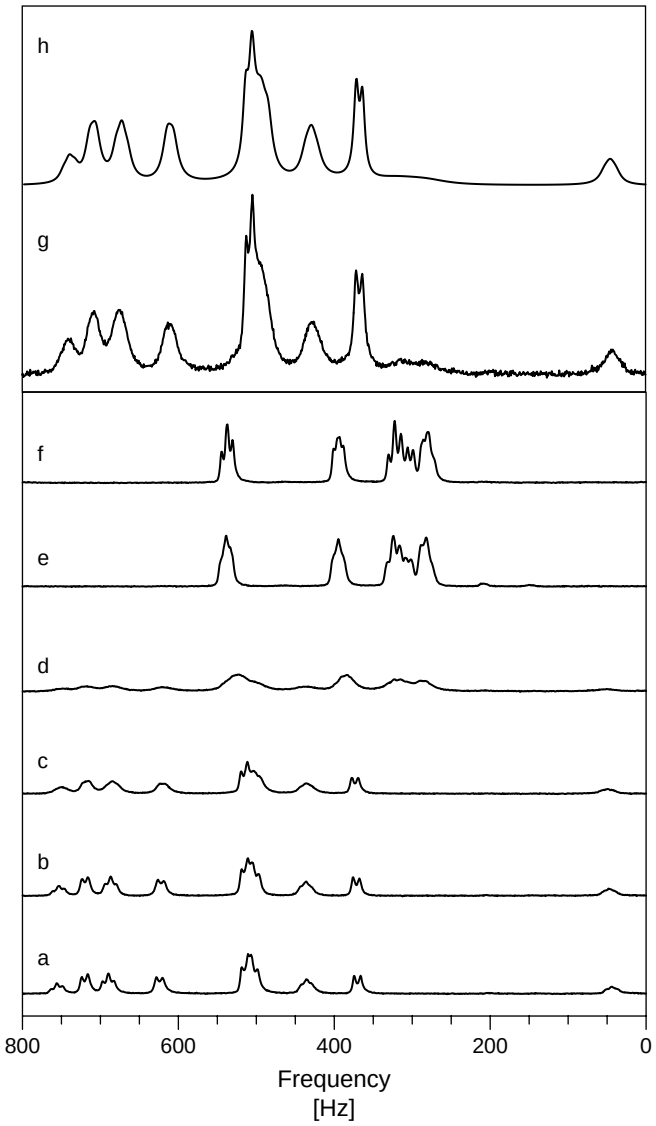

Figure 4 Lineshape analysis for folding of λ repressor. The aromatic regions of the ^{1}H NMR spectra of the monomeric Gly 46 Ala/Gly 48 Ala mutant of λ repressor (residues 6–85) at 30 °C are shown for urea denaturant concentrations of (a) 0 M, (b) 2.2 M, (c) 4.1 M, (d) 5.1 M, (e) 7.0 M, and (f) 8.9 M. Expansions of the (g) experimental and (h) fitted ^{1}H aromatic spectra also are shown for λ repressor in 4.1 M urea. (Reproduced with permission from *J. Biomol. NMR*, 1998, **11**, 355–359)

Folding of the Gly 46 Ala/Gly 48 Ala mutant of monomeric λ repressor has been investigated as a function of urea denaturant concentration by Oas and coworkers using ^{1}H one-dimensional spectroscopy.[62] The aromatic regions of a series of NMR spectra are shown in Figure 4 to illustrate the changes in lineshape observed as the urea concentration is increased from 0 to 8.9 M. Figure 4(h) and (g) compare the experimental and fitted lineshapes for a single urea concentration of 4.1 M. Data were analyzed using the program ALASKA to fit k_1 (unfolding) and k_{-1} (folding) assuming values of other spectral parameters for folded and unfolded species obtained from the spectra recorded at 0 and 8.9 M urea, respectively.[62] In most cases, lineshape analyses have been restricted to one-dimensional ^{1}H spectra; however, two-dimensional lineshape analysis using X–^{1}H heteronuclear correlation spectroscopy yields increased spectral resolution, provides lineshape information for both the ^{1}H and X spins, and exhibits simplified lineshapes in indirect frequency dimensions because heteronuclear scalar coupling interactions are easily decoupled. As an example, ^{15}N–^{1}H HSQC spectroscopy has been used in a lineshape analysis of the dimerization of the protein barstar.[13]

6 $R_{1\rho}$ ROTATING FRAME RELAXATION METHODS

In an $R_{1\rho}$ experiment, magnetization is spin-locked in the rotating frame by application of a radio-frequency field.[27,28] The relaxation rate constant for the component of the magnetization along the direction of effective field in the rotating frame is called $R_{1\rho}$ and depends on the amplitude, ω_1, and frequency, ω_{rf}, of the applied radiofrequency field. The effective field in the rotating frame is $\omega_e = (\Omega^2 + \omega_1^2)^{1/2}$ in which $\Omega = p_A\Omega_A + p_B\Omega_B$ is the population-average chemical shift, and the tilt angle of the effective field is given by $\tan\theta = \omega_1/\Omega$. $R_{1\rho}$ experiments are sensitive to chemical exchange processes if values of ω_e near k_{ex} are achievable experimentally. Typically, $R_{1\rho}$ experiments are limited to values of $k_{ex} < 10^5\,s^{-1}$. Sample heating and limitations on the maximum value of ω_1 tolerated by the spectrometer probe and amplifiers during sustained spin-locking pulses are the principal experimental constraints on ω_e. Furthermore, exchange processes with $k_{ex} > 10^5\,s^{-1}$ result in small exchange linebroadening unless $\Delta\omega$ is very large. $R_{1\rho}$ measurements on biological macromolecules can be performed using near-resonance (often called on-resonance for convenience)[65] or off-resonance[66–68] rf fields. In the former case, the rf transmitter frequency is positioned close to the resonances of interest (or in the middle of the NMR spectrum) and the minimum value of ω_1 is large enough to ensure that $\theta > 70°$ over the spectral region of interest. The relaxation dispersion curve is obtained by varying ω_1. In the latter case, the rf transmitter is positioned far enough off-resonance to ensure that $\theta < 70°$. The relaxation dispersion curve is obtained by varying ω_1 or the carrier offset or both in order to vary ω_e.

A pulse sequence for an off-resonance $R_{1\rho}$ experiment for X spins is shown in Figure 5(a)[66–68] and a pulse sequence

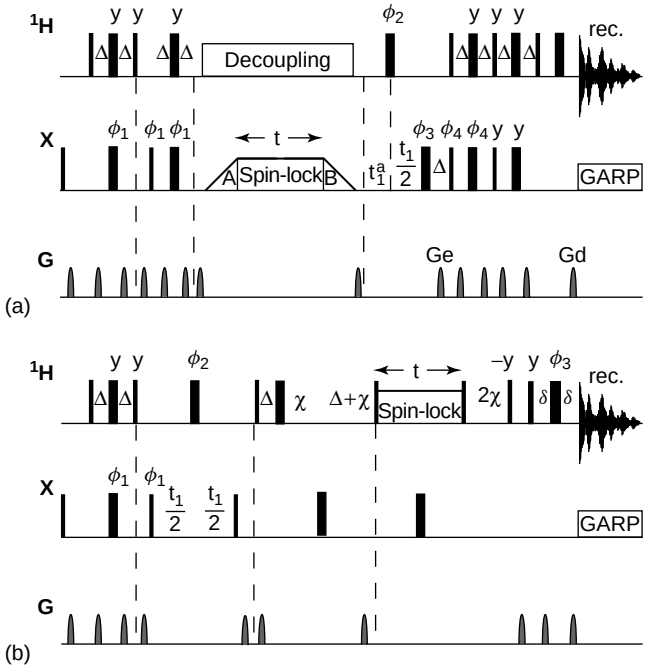

Figure 5 Pulse sequences for (a) X-nucleus and (b) ^{1}H-nucleus $R_{1\rho}$ experiments.[65–68,71] Narrow and wide bars depict 90° and 180° pulses respectively. All pulses are x-phase unless otherwise indicated. Decoupling during acquisition is achieved with the GARP sequence.[92] The unlabeled gradients are used to suppress unwanted coherences and pulse imperfections.[93] Delays are $\Delta = 1/(4J_{XH})$, $t_1^a = \Delta + t_1/2$, t is the relaxation delay, and δ is longer than the duration of the gradients applied during δ. (a) The spin-lock rf frequency is set outside the spectral region of interest. The adiabatic sweep A rotates z-magnetization to the direction of the effective field and the adiabatic sweep B rotates the spin-locked magnetization back to the z-axis.[66,68] The phase cycle is $\phi_1 = x, -x$; $\phi_2 = 4(x)$, 4(−x); $\phi_3 = x, x, y, y, -x, -x, -y, -y$; $\phi_4 = x$; receiver $= x, -x, -x, x$. Gradient coherence selection are achieved with gradients Gd and Ge. Echo/antiecho signals are recorded in separate experiments by inverting the amplitude of Gd and phase ϕ_4.[95] The ϕ_1 and the receiver phases are inverted for each t_1 increment to shift axial peaks to the edge of the spectrum.[94] (b) The spin-lock rf frequency is positioned in the center of the spectral region of interest, and $\chi = 1/(2\omega_1)$ serves to align the magnetization along the direction of the effective field.[96] The phase cycle is $\phi_1 = x, -x$; $\phi_2 = 4(x), 4(-x)$; $\phi_3 = x, x, -x, -x$; and receiver $= x, -x$. Frequency discrimination is obtained by shifting the phase of the receiver and ϕ_1 according the States-TTPI protocol[94]

for a near-resonance $R_{1\rho}$ experiment for ^{1}H spins is shown in Figure 5(b).[69,70] The pulse sequence in Figure 5(b) is applicable to ^{1}H spins that do not have significant homonuclear scalar coupling interactions; for example, the $^3J_{N\alpha}$ scalar coupling interaction is eliminated in uniformly ^{15}N/^{2}H enriched proteins.[71]

$R_{1\rho}$ experiments have been applied principally to characterize kinetic processes in the fast-exchange limit ($k_{ex}/\Delta\omega \gg 1$) using the theoretical expression:[27,28,72]

$$R_{1\rho}(\omega_e) = R_2^0 \sin^2\theta + R_1 \cos^2\theta + \sin^2\theta \frac{\Phi_{ex} k_{ex}}{k_{ex}^2 + \omega_e^2} \qquad (17)$$

in which R_2^0 and R_1 are population-averaged relaxation rate constants and $\Phi_{ex} = p_A p_B \Delta\omega^2$. Other expressions applicable outside of the fast-exchange limit have been derived, but have not been applied yet to relaxation in proteins.[72,73] The dependence of $R_{1\rho}$ on R_1 in equation (17) can be removed either by the constant-relaxation time approach[67] or by independently measuring R_1. The number of independent parameters in equation (17) can be further reduced either by measuring R_2*[35] or R_2^0.[7]

The folding equilibrium of the peripheral subunit binding domain (PSBD) from the dihydrolopoamide acetyltransferase component of the pyruvate dehydrogenase multienzyme complex from *Bacillus stearothermophilus* has been characterized using ^{15}N $R_{1\rho}$ measurements.[7] R_1 was measured independently and R_2^0 was obtained from measurements of η_{xy} using equation (8) in order to express R_{ex} as

$$R_{ex} = \frac{R_{1\rho}}{\sin^2\theta} - \frac{R_1}{\tan^2\theta} - R_2^0 = \frac{\Phi_{ex} k_{ex}}{k_{ex}^2 + \omega_e^2} \qquad (18)$$

The relaxation dispersion curve is linearized by plotting $1/R_{ex}$ versus ω_e^2, as shown in Figure 6(a). Values of $k_{ex} = (b/m)^{1/2}$ and $\Phi_{ex} = (mb)^{-1/2}$ are obtained from the slope m and intercept b.[74] In the fast-exchange limit, p_A, p_B, and $\Delta\omega$ cannot be obtained separately from Φ_{ex} by fitting the relaxation dispersion. However, Φ_{ex} and Ω are related by $\Phi_{ex} = -\Omega^2 + a\Omega - b$ in which $a = \Omega_A + \Omega_B$ and $b = \Omega_A\Omega_B$. If Φ_{ex} and Ω are measured as a function of temperature

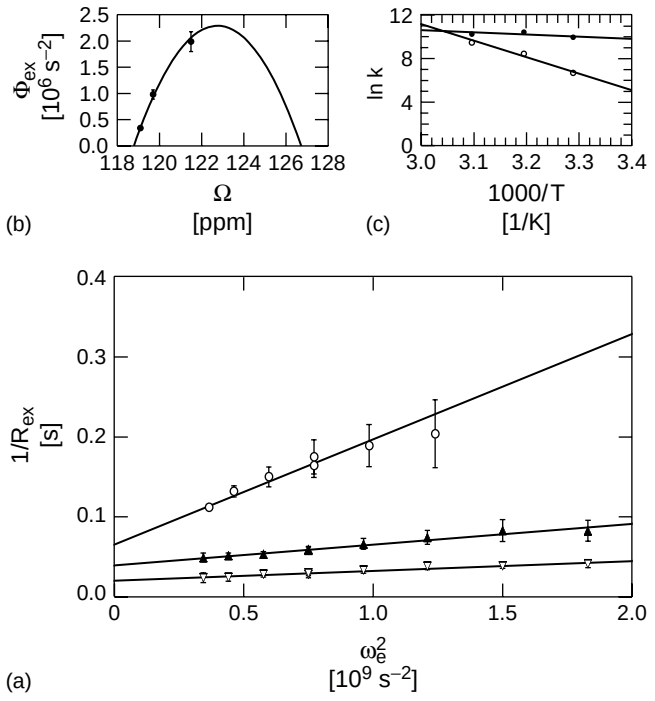

Figure 6 ^{15}N $R_{1\rho}$ relaxation dispersion for Ala 11 of PSBD. (a) Data recorded at 304 (○), 313 (▲), and 323 K (▽).[7] R_{ex} data for Ala 11 were obtained from equation (18), values of R_1 and η_{xy} were measured by conventional approaches,[29,44] and values of R_2^0 obtained from η_{xy} using equation (8). The best least squares fitted line is drawn for each data set. (b) Φ_{ex} is plotted versus the isotropic shift Ω at each temperature. The solid line is the best fit to determine the x-intercepts $\Omega_A = 118.80 \pm 0.02$ ppm and $\Omega_B = 126.7 \pm 0.4$ ppm with $\Delta\omega = 7.9 \pm 0.4$ ppm. (c) Arrhenius plot for (○) folding (k_{-1}) and (●) unfolding (k_1) rate constants. The apparent activation barriers are 17 ± 14 kJ mol^{-1} for folding and 125 ± 19 kJ mol^{-1} for unfolding

and Ω_A and Ω_B are assumed to be independent of temperature, then the coefficients a and b can be determined by least squares optimization. Subsequently, $|\Delta\omega| = (a^2 - 4b)^{1/2}$, and $\Omega_{A,B} = [a \pm (a^2 - 4b)^{1/2}]/2$. Once $\Delta\omega$ is known, p_A, p_B, k_1, and k_{-1} are obtained from Φ_{ex} and k_{ex} at each temperature. An example of this analysis is shown in Figure 6(b); the temperature dependence of the rate constants obtained from this analysis is shown in Figure 6(c). The chemical shift of the (unobserved) unfolded PSBD species is determined to be 126.7 ± 0.4 ppm; this value is in good agreement with the predicted random coil chemical shift of 126.0 ppm for an Ala residue preceded by a Tyr residue.[75]

7 CPMG RELAXATION METHODS

In a CPMG experiment, the relaxation of transverse magnetization is observed during a $(\tau - 180^\circ - 2\tau - 180^\circ - \tau)_n$ spin-echo sequence, in which $\tau_{cp} = 2\tau$ is the spacing between 180° pulses and n is an integer.[25,26] CPMG experiments are sensitive to chemical exchange processes if values of $1/\tau_{cp}$ near k_{ex} are achievable experimentally. CPMG experiments in proteins typically are applicable to chemical exchange processes with values of $k_{ex} < 10^4\,s^{-1}$ as a result of experimental constraints on the minimum value of τ_{cp}. Sample heating at high pulsing rates is a major experimental limitation. In addition, theoretical analyses of relaxation during CPMG experiments assume that the refocusing pulses have negligible duration;[76–78] at pulse duty cycles >10%, this assumption may not be valid.[66] The maximum value of τ_{cp} for CPMG experiments applied to X spins is limited by evolution under the one-bond heteronuclear scalar coupling Hamiltonian, which interconverts in-phase and antiphase magnetization during the spin-echo period. The relaxation rate constant for heteronuclear antiphase magnetization includes a contribution from longitudinal relaxation of the coupled ^{1}H spin and is greater than the rate constant for in-phase magnetization. To minimize contributions from antiphase magnetization, $\tau_{cp} < 1/(4J_{XH})$, where J_{XH} is the one-bond heteronuclear scalar coupling constant; therefore, the maximum values of τ_{cp} are 1.7 ms for ^{13}C and 2.6 ms for ^{15}N.

The range of τ_{cp} values that can be utilized is expanded by CPMG experiments designed to average in-phase and antiphase magnetization. Relaxation-compensated CPMG pulse sequences for IS,[79] I_2S,[80] and I_3S[81] are shown in Figure 7. In these experiments, in-phase and antiphase coherences are interchanged during the period U in order to eliminate any τ_{cp} -dependent effects arising from differential relaxation rates. Conventional CPMG pulse sequences for measuring R_2 are self-compensating for evolution of the scalar coupling if $\tau_{cp} = m/J_{XH}$, in which m is an integer.[48] Hahn spin echo measurements, self-compensated CPMG experiments and relaxation-compensated CPMG experiments can be used in combination to cover the widest possible range of τ_{cp} values.[48] For I_2S and I_3S spin systems, relaxation is multiexponential and constant relaxation time experiments are necessary to obtain accurate results.[80,81]

These approaches are illustrated in Figure 8 for residue Cys 38 in BPTI at temperatures of 300 and 313 K.[48] The backbone ^{15}N resonance of Cys 38 is broadened as a result of isomerization of the Cys 14–Cys 38 disulfide bond. The

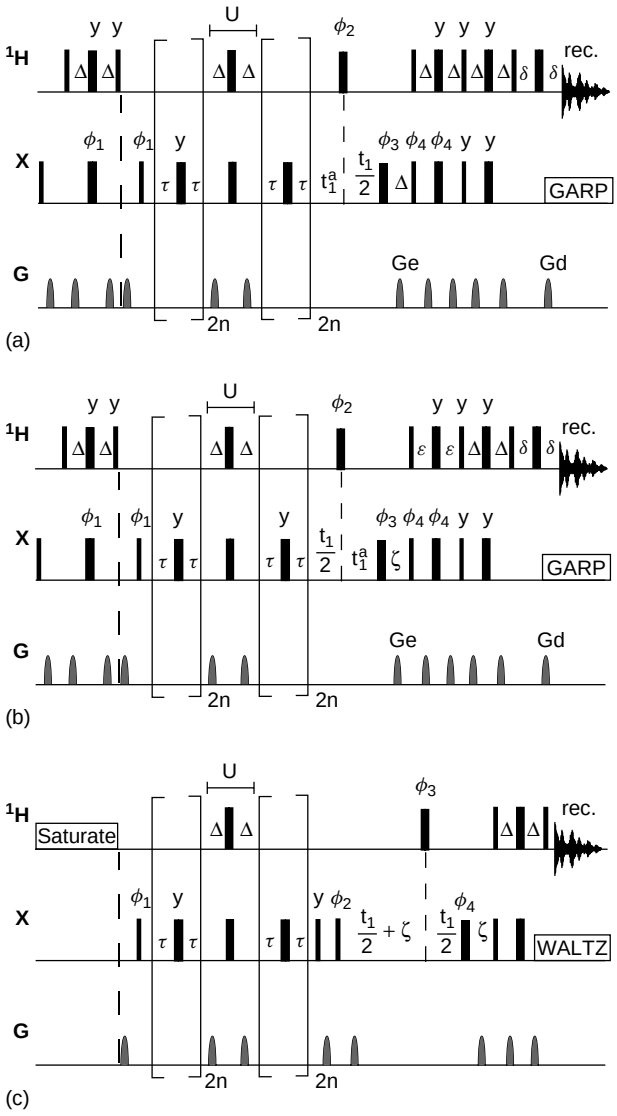

Figure 7 Pulse sequences for relaxation-compensated CPMG experiments in (a) IS, (b) I_2S, and (c) I_3S spin systems.[48,79] Narrow and wide bars depict 90° and 180° pulses respectively. All pulses are x-phase unless otherwise indicated. Decoupling during acquisition is achieved with the GARP or WALTZ-16 sequences.[53,92] Delays are $\tau = \tau_{cp}/2$, $\Delta = 1/(4J_{XH})$, and $\delta >$ Gd. In (a) $t_1^a = \Delta + t_1/2$; in (b) $\varepsilon = 1/(8J_{XH})$, $t_1^a = \zeta + t_1/2$, and $\zeta >$ Ge; and in (c) $\zeta = 1/(10J_{XH})$. In (a) and (b), the phase cycle is $\phi_1 = x, -x$; $\phi_2 = 4(x), 4(-x)$; $\phi_3 = x, x, y, y, -x, -x, -y, -y$; $\phi_4 = x$; receiver $= x, -x, -x, x$. The unlabeled gradients are used to suppress unwanted coherences and pulse imperfections.[93] Gradient coherence selection are achieved with gradients Gd and Ge. Echo/antiecho signals are recorded in separate experiments by inverting the amplitude of Gd and phase ϕ_4.[95] The ϕ_1 and the receiver phases are inverted for each t_1 increment to shift axial peaks to the edge of the spectrum.[94] In (c), the phase cycle is $\phi_1 = x, -x$; $\phi_2 = 2(x), 2(-x)$; $\phi_3 = 8(x), 8(-x)$; $\phi_4 = 4(x), 4(y), 4(-x), 4(-y)$; receiver $= x, -x, -x, x, -x, x, x, -x$. The unlabeled gradients are used to suppress unwanted coherences and pulse imperfections.[93] Frequency discrimination during t_1 is obtained by shifting the phase of ϕ_2 and the receiver according the States-TTPI protocol[94]

values of $R_2(1/\tau_{cp})$ were acquired using the pulse sequence of Figure 7(a) for values of $\tau_{cp} < 10$ ms, a self-compensated pulse sequence for $\tau_{cp} = 10.8$ and 21.5 ms, and a Hahn-echo

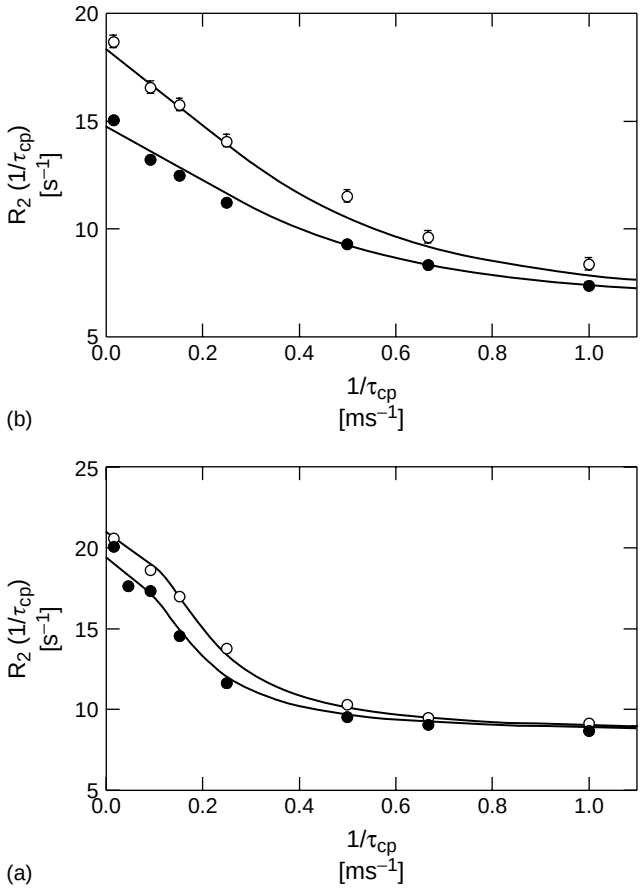

Figure 8 Global analysis of chemical exchange for the ^{15}N spin of Cys 38 in BPTI. Values of $R_2(1/\tau_{cp})$ at (●) $B_0 = 11.7$ T and (○) $B_0 = 14.1$ T are shown at temperatures of (a) 300 K and (b) 313 K. At 300 K, fitting with equation (19) yields $p_A = 0.953 \pm 0.004$, $\Delta\omega = 8.9 \pm 0.4$ ppm, $k_{ex} = 380 \pm 70\,s^{-1}$ and $R_2^0 = 8.6 \pm 0.1\,s^{-1}$. At 313 K, fitting with equation (21) yields $\Phi_{ex} = 0.108 \pm 0.024$ ppm^2, $k_{ex} = 1300 \pm 290\,s^{-1}$, and $R_2^0 = 6.4 \pm 0.7\,s^{-1}$

pulse sequence for $\tau_{cp} = 64.5$ ms.[48] Dispersion data were fit with a general expression for the transverse relaxation rate constant for site A ($p_A > p_B$), $R_2(1//\tau_{cp})$ given by,[28,77,82]

$$R_2\left(\frac{1}{\tau_{cp}}\right) = R_2^0 + \frac{k_{ex}}{2} - \frac{1}{2\tau_{cp}}\cosh^{-1}\left[D_+\cosh(\eta_+) - D_-\cos(\eta_-)\right] \tag{19}$$

in which,

$$D_\pm = \frac{1}{2}\left[\pm 1 + \frac{\Psi + 2\Delta\omega^2}{(\Psi^2 + \zeta^2)^{1/2}}\right]$$

$$\eta_\pm = \frac{\tau_{cp}}{\sqrt{2}}\left[\pm\Psi + (\Psi^2 + \zeta^2)^{1/2}\right]^{1/2} \tag{20}$$

$\Psi = k_{ex}^2 - \Delta\omega^2$ and $\zeta = 2\Delta\omega k_{ex}(p_B - p_A)$ and identical relaxation rates R_2^0 have been assumed for the two sites. In the fast-exchange limit, equation (19) is approximated by,[83]

$$R_2\left(\frac{1}{\tau_{cp}}\right) = R_2\left(\frac{1}{\tau_{cp}} \to \infty\right) + \frac{\Phi_{ex}}{k_{ex}}\left[1 - \frac{2}{k_{ex}\tau_{cp}}\tanh\left(\frac{k_{ex}\tau_{cp}}{2}\right)\right] \tag{21}$$

and R_2^0 is the population-average value. The static magnetic field dependence of exchange linebroadening indicates that the exchange time scale is intermediate at 300 K and approaches the fast limit at 313 K. Consequently, dispersion curves recorded at two static magnetic field strengths were analyzed globally using equations (19) for data acquired at 300 K and equation (21) for data acquired at 313 K. Analysis of data recorded at a single static magnetic field or data recorded for a limited range of τ_{cp} values can give substantial systematic errors.[48,79] Simultaneous analysis of both CPMG and $R_{1\rho}$ data has been proposed to increase the range of accessible effective fields and robustness of the data analysis.[5,10]

The pulse sequences shown in Figure 7 average the relaxation rate constants for in-phase and antiphase magnetization; consequently, R_2^0 in these sequences is larger than the in-phase relaxation rate constant and contains contributions from ^{1}H longitudinal relaxation. For IS spin systems, relaxation periods for two-spin order can be incorporated into the pulse sequence of Figure 5(a) to remove the contributions to $R_2(1/\tau_{cp})$ from ^{1}H longitudinal relaxation.[84] For ^{15}N spins, this method facilitates the use of relaxation interference rate constants to determine R_2^0 [equations (7) and (8)] and enables faster kinetic processes to be investigated by CPMG methods. Wüthrich and coworkers have shown that significantly narrower NMR signals can be obtained for one component of the ^{15}N–^{1}H scalar-coupled doublet from cancellation of ^{1}H–^{15}N dipole–dipole and ^{15}N CSA interactions (see **Transverse Relaxation-optimized NMR Spectroscopy with Biomacromolecular Structures in Solution**).[85] Recently, CPMG pulse sequences have been modified to select the narrow TROSY doublet component during the relaxation period, the indirect labeling period, and the detection period.[71,86,87] These modifications facilitate the quantification of exchange linebroadening contributions in larger macromolecules because the relative conformational exchange contribution to the phenomenological relaxation rate constant during the CPMG period is enhanced and the improved resolution and sensitivity of TROSY ^{1}H–^{15}N correlation spectra are obtained.

8 CHEMICAL EXCHANGE IN MULTIPLE QUANTUM SPECTROSCOPY

If two spins are affected by the same chemical exchange kinetic process, then the chemical shift changes for the two spins resulting from transitions between sites will be correlated. This correlation gives rise to exchange effects that can either broaden or narrow resonance lineshapes for multiple quantum coherences.[88] In essence, for multiple quantum coherences, the value of $\Delta\omega$ in the equations given above should be replaced by the difference in multiple quantum frequencies, $\Delta\omega_{MQ}$; thus, for double (DQ) and zero (ZQ) quantum coherences, respectively, $\Delta\omega_{DQ} = \Delta\omega_I + \Delta\omega_S$ and $\Delta\omega_{ZQ} = \Delta\omega_I - \Delta\omega_S$, in which $\Delta\omega_I$ ($\Delta\omega_S$) is the chemical shift difference between sites A and B for the I (S) spin. Hahn spin-echo pulse sequences for measuring the difference between the relaxation rate constants for DQ and ZQ quantum coherences have been developed for ^{1}H–^{15}N backbone amide moieties[89] and for $^{13}C^\alpha$–$^{13}C^\beta$ moieties[90] in proteins. The sign of the difference between DQ and ZQ relaxation rate constants gives the relative sign of the chemical shift differences for ^{1}H and ^{15}N spins. This information, which cannot be obtained

from single quantum experiments, is helpful for mechanistic interpretations of exchange phenomena. In some cases, selection of the narrower of the DQ or ZQ coherences (depending on the relative chemical shifts) results in improved resolution and sensitivity of multidimensional NMR spectra.[88,91]

9 CONCLUSIONS

Chemical exchange effects in NMR spectroscopy provide information on conformational and chemical kinetic processes occurring in biological macromolecules on biologically-relevant time scales. Experimental methods described in this article enable chemical exchange constants, k_{ex}, to be determined over a range from 0.1 to $10^5\,s^{-1}$ using ZZ-exchange, lineshape, CPMG, and $R_{1\rho}$ methods. Applications of these techniques promise to enhance understanding of the biological function of kinetic processes on μs-s time scales in proteins and other biological macromolecules.

10 RELATED ARTICLES IN THIS VOLUME

Relaxation Effects Involving Cross Correlation in Biomolecules; Transverse Relaxation-optimized NMR Spectroscopy with Biomacromolecular Structures in Solution.

11 RELATED ARTICLES IN VOLUMES 1–8

Chemical Exchange Effects on Spectra, Volume 2; Protein Dynamics from NMR Relaxation, Volume 6; Relaxation: An Introduction, Volume 6; Relaxation Effects of Chemical Exchange, Volume 6; Rotating Frame Spin-Lattice Relaxation Off-Resonance, Volume 7.

12 REFERENCES

1. J. Evenäs, A. Malmendal, and M. Akke, *Structure*, 2001, **9**, 185.
2. R. Ishima, D. Freedberg, Y.-X. Wang, J. M. Louis, and D. A. Torchia, *Structure*, 1999, **7**, 1047.
3. S. Kim, C. Bracken, and J. Baum, *J. Mol. Biol.*, 1999, **294**, 551.
4. P. B. McIntosh, I. A. Taylor, T. A. Frenkiel, S. J. Smerdon, and A. N. Lane, *J. Biomol. NMR*, 2000, **16**, 183.
5. F. A. A. Mulder, P. J. A. van Tilborg, R. Kaptein, and R. Boelens, *J. Biomol. NMR*, 1999, **13**, 275.
6. M. Pfuhl, H. A. Chen, S. M. Kristensen, and P. C. Driscoll, *J. Biomol. NMR*, 1999, **14**, 307.
7. L. Vugmeyster, C. D. Kroenke, F. Picart, A. G. Palmer, and D. P. Raleigh, *J. Am. Chem. Soc.*, 2000, **122**, 5387.
8. S. B. M. Whittaker, M. Czisch, R. Wechselberger, R. Kaptein, A. M. Hemmings, R. James, C. Kleanthous, and G. R. Moore, *Protein Sci.*, 2000, **9**, 713.
9. V. A. Feher and J. Cavanagh, *Nature*, 1999, **400**, 289.
10. A. E. Meekhof and S. M. V. Freund, *J. Biomol. NMR*, 1999, **14**, 13.
11. A. Malmendal, J. Evenas, S. Forsén, and M. Akke, *J. Mol. Biol.*, 1999, **293**, 883.
12. M. E. Holtzer, G. L. Bretthorst, D. A. d'Avignon, R. H. Angeletti, L. Mints, and A. Holtzer, *Biophys. J.*, 2001, **80**, 939.
13. D. S. Korchuganov, S. B. Nolde, M. Y. Reibarkh, V. Y. Orekhov, A. A. Schulga, Y. S. Ermolyuk, M. P. Kirpichnikov, and A. S. Arseniev, *J. Am. Chem. Soc.*, 2001, **123**, 2068.
14. M. Tollinger, N. R. Skrynnikov, F. A. A. Mulder, J. D. Foreman-Kay, and L. E. Kay, *J. Am. Chem. Soc.*, 2001, in press.
15. R. B. Hill, C. Bracken, W. F. DeGrado, and A. G. Palmer, *J. Am. Chem. Soc.*, 2000, **122**, 11 610.
16. B. F. Volkman, D. Lipson, D. E. Wemmer, and D. Kern, *Science*, 2001, **291**, 2429.
17. C. G. Hoogstraten, J. R. Wank, and A. Pardi, *Biochemistry*, 2000, **39**, 9951.
18. V. A. Feher and J. Cavanagh, *Nature*, 1999, **400**, 289.
19. F. A. A. Mulder, B. Hon, D. R. Muhandiram, F. W. Dahlquist, and L. E. Kay, *Biochemistry*, 2000, **39**, 12 614.
20. S. B. -M. Whittaker, M. Czisch, R. Wechselberger, R. Kaptein, A. M. Hemmings, R. James, C. Kleanthous, and G. R. Moore, *Protein Sci.*, 2000, **9**, 713.
21. G. Bodenhausen, G. Wagner, M. Rance, O. W. Sørensen, K. Wüthrich, and R. R. Ernst, *J. Magn. Reson.*, 1984, **59**, 542.
22. G. Wagner, G. Bodenhausen, N. Müller, M. Rance, O. Sørensen, R. R. Ernst, and K. Wüthrich, *J. Am. Chem. Soc.*, 1985, **107**, 6440.
23. B. D. N. Rao, *Meth. Enzymol.*, 1989, **176**, 279.
24. J. Sandstrom, 'Dynamic NMR Spectroscopy', Academic Press: London, 1982.
25. H. Y. Carr and E. M. Purcell, *Phys. Rev.*, 1954, **94**, 630.
26. S. Meiboom and D. Gill, *Rev. Sci. Instrum.*, 1958, **29**, 688.
27. C. Deverell, R. E. Morgan, and J. H. Strange, *Mol. Phys.*, 1970, **18**, 553.
28. D. G. Davis, M. E. Perlman, and R. E. London, *J. Magn. Reson., Ser. B*, 1994, **104**, 266.
29. N. A. Farrow, O. Zhang, J. D. Forman-Kay, and L. E. Kay, *Biochemistry*, 1995, **34**, 868.
30. S. Grzesiek and A. Bax, *J. Am. Chem. Soc.*, 1993, **115**, 12 593.
31. A. C. Wang and A. Bax, *J. Biomol. NMR*, 1993, **3**, 715.
32. V. V. Krishnan and M. Rance, *J. Magn. Reson., Ser. A*, 1995, **116**, 97.
33. L. Mueller, P. Legault, and A. Pardi, *J. Am. Chem. Soc.*, 1995, **117**, 11 043.
34. F. A. A. Mulder, C. A. E. M. Spronk, M. Slijper, R. Kaptein, and R. Boelens, *J. Biomol. NMR*, 1996, **8**, 223.
35. M. Akke, J. Liu, J. Cavanagh, H. P. Erickson, and A. G. Palmer, *Nature Struct. Biol.*, 1998, **5**, 55.
36. L. C. Wang, Y. X. Pang, T. Holder, J. R. Brender, A. V. Kurochkin, and E. R. P. Zuiderweg, *Proc. Natl. Acad. Sci. USA*, 2001, **98**, 7684.
37. E. Kay, L. K. Nicholson, F. Delagio, A. Bax, and D. A. Torchia, *J. Magn. Reson.*, 1992, **97**, 359.
38. A. G. Palmer, N. J. Skelton, W. J. Chazin, P. E. Wright, and M. Rance, *Mol. Phys.*, 1992, **75**, 699.
39. A. M. Mandel, M. Akke, and A. G. Palmer, *J. Mol. Biol.*, 1995, **246**, 144.
40. A. M. Mandel, M. Akke, and A. G. Palmer, *Biochemistry*, 1996, **35**, 16 009.
41. J. Peng and G. Wagner, *Biochemistry*, 1995, **34**, 16 733.
42. I. Q. H. Phan, J. Boyd, and I. D. Campbell, *J. Biomol. NMR*, 1996, **8**, 369.
43. C. D. Kroenke, M. Rance, and A. G. Palmer, *J. Am. Chem. Soc.*, 1999, **121**, 10 119.
44. C. D. Kroenke, J. P. Loria, L. K. Lee, M. Rance, and A. G. Palmer, *J. Am. Chem. Soc.*, 1998, **120**, 7905.
45. N. Tjandra, S. E. Feller, R. W. Pastor, and A. Bax, *J. Am. Chem. Soc.*, 1995, **117**, 12 562.
46. J. M. Schurr, H. P. Babcock, and B. S. Fujimoto, *J. Magn. Reson., Ser. B*, 1994, **105**, 211.
47. A. G. Palmer, J. Williams, and A. McDermott, *J. Phys. Chem.*, 1996, **100**, 13 293.
48. O. Millet, J. P. Loria, C. D. Kroenke, M. Pons, and A. G. Palmer, *J. Am. Chem. Soc.*, 2000, **122**, 2867.

49. N. A. Farrow, O. Zhang, A. Szabo, D. A. Torchia, and L. E. Kay, *J. Biomol. NMR*, 1995, **6**, 153.
50. M. Goldman, *J. Magn. Reson.*, 1984, **60**, 437.
51. N. Tjandra, A. Szabo, and A. Bax, *J. Am. Chem. Soc.*, 1996, **118**, 6986.
52. A. Bax, M. Ikura, L. E. Kay, D. A. Torchia, and R. Tschudin, *J. Magn. Reson.*, 1990, **86**, 304.
53. A. J. Shaka, J. Keeler, T. Frenkiel, and R. Freeman, *J. Magn. Reson.*, 1983, **52**, 334.
54. G. Otting, E. Liepinsh, and K. Wüthrich, *Biochemistry*, 1993, **32**, 3571.
55. J. J. Led, H. Gesmar, and F. Abildgaard, *Methods Enzymol.*, 1989, **176**, 311.
56. J. Fejzo, W. M. Westler, S. Macura, and J. L. Markley, *J. Am. Chem. Soc.*, 1990, **112**, 2574.
57. G. T. Montelione and G. Wagner, *J. Am. Chem. Soc.*, 1989, **111**, 3096.
58. N. Farrow, O. Zhang, J. D. Forman-Kay, and L. E. Kay, *J. Biomol. NMR*, 1994, **4**, 727.
59. G. Wider, D. Neri, and K. Wüthrich, *J. Biomol. NMR*, 1991, **1**, 93.
60. H. Wang, Y. Hea, C. D. Kroenke, S. Kodukulab, J. Storch, A. G. Palmer, and R. E. Stark, *Biochemistry*, 2002, in press.
61. H. M. McConnell, *J. Chem. Phys.*, 1958, **28**, 430.
62. R. E. Burton, R. S. Busby, and T. G. Oas, *J. Biomol. NMR*, 1998, **11**, 355.
63. B. Kuhlman, D. L. Luisi, P. A. Evans, and D. P. Raleigh, *J. Mol. Biol.*, 1998, **284**, 1661.
64. D. Kern, G. Kern, G. Scherer, G. Fischer, and T. Drakenberg, *Biochemistry*, 1995, **34**, 13 594.
65. T. Szyperski, P. Luginbühl, G. Otting, P. Güntert, and K. Wüthrich, *J. Biomol. NMR*, 1993, **3**, 151.
66. S. Zinn-Justin, P. Berthault, M. Guenneugues, and H. Desvaux, *J. Biomol. NMR*, 1997, **10**, 363.
67. M. Akke and A. G. Palmer, *J. Am. Chem. Soc.*, 1996, **118**, 911.
68. F. A. A. Mulder, R. A. de Graaf, R. Kaptein, and R. Boelens, *J. Magn. Reson.*, 1998, **131**, 351.
69. F. C. L. Almeida and S. J. Opella, *J. Magn. Reson.*, 1997, **124**, 509.
70. R. Ishima, J. M. Louis, and D. A. Torchia, *J. Magn. Reson.*, 1999, **137**, 289.
71. R. Ishima, P. T. Wingfield, S. J. Stahl, J. D. Kaufman, and D. A. Torchia, *J. Am. Chem. Soc.*, 1998, **120**, 10 534.
72. S. Meiboom, *J. Chem. Phys.*, 1961, **34**, 375.
73. O. Trott and A. G. Palmer, *J. Magn. Res.*, 2002, **154**, 157.
74. M. J. Blackledge, R. Brüschweiler, C. Griesinger, J. M. Schmidt, P. Xu, and R. R. Ernst, *Biochemistry*, 1993, **32**, 10 960.
75. D. Braun, G. Wider, and K. Wüthrich, *J. Am. Chem. Soc.*, 1994, **116**, 8466.
76. A. Allerhand and E. Thiele, *J. Chem. Phys.*, 1966, **45**, 902.
77. J. P. Carver and R. E. Richards, *J. Magn. Reson.*, 1972, **6**, 89.
78. W. T. Sobol, *Magn. Reson. Med.*, 1991, **21**, 2.
79. J. P. Loria, M. Rance, and A. G. Palmer, *J. Am. Chem. Soc.*, 1999, **121**, 2331.
80. F. A. A. Mulder, N. R. Skrynnikov, B. Hon, F. W. Dahlquist, and L. E. Kay, *J. Am. Chem. Soc.*, 2001, **123**, 967.
81. N. R. Skrynnikov, F. A. A. Mulder, B. Hon, F. W. Dahlquist, and L. E. Kay, *J. Am. Chem. Soc.*, 2001, **123**, 4556.
82. J. Jen, *J. Magn. Reson.*, 1978, **30**, 111.
83. Z. Luz and S. Meiboolm, *J. Chem. Phys.*, 1963, **39**, 366.
84. C. Wang, M. J. Grey, and A. G. Palmer, *J. Biomol. NMR*, 2001, **21**, 361.
85. K. Pervushin, R. Riek, G. Wider, and K. Wüthrich, *Proc. Natl. Acad. Sci. USA*, 1997, **94**, 12 366.
86. J. P. Loria, M. Rance, and A. G. Palmer, *J. Biomol. NMR*, 1999, **15**, 151.
87. J. Boisbouvier, B. Brutscher, J.-P. Simorre, and D. Marion, *J. Biomol. NMR*, 1999, **14**, 241.
88. M. Rance, *J. Am. Chem. Soc.*, 1988, **110**, 1973.
89. K. Kloiber and R. Konrat, *J. Biomol. NMR*, 2000, **18**, 33.
90. Früh, J. R. Tolman, G. Bodenhausen, and C. Zwahlen, *J. Am. Chem. Soc.*, 2001, **123**, 4810.
91. K. Pervushin, *J. Biomol. NMR*, 2001, **20**, 275.
92. A. J. Shaka, P. B. Barker, and R. Freeman, *J. Magn. Reson.*, 1985, **64**, 547.
93. A. Bax and S. S. Pochapsky, *J. Magn. Reson.*, 1992, **99**, 638.
94. D. Marion, M. Ikura, R. Tschudin, and A. Bax, *J. Magn. Reson.*, 1989, **85**, 393.
95. L. E. Kay, P. Keifer, and T. Saarinen, *J. Am. Chem. Soc.*, 1992, **114**, 10 663.
96. T. Yamazaki, R. Muhandiram, and L. E. Kay, *J. Am. Chem. Soc.*, 1994, **116**, 8266.

Acknowledgements

This work was supported by National Institutes of Health grant GM-59273.

Biographical Sketch

Arthur G. Palmer, III, *b* 1956. B. A., 1980, Haverford College, USA. Ph.D., 1989, Chemistry, University of North Carolina, Chapel Hill, USA (thesis advisor Nancy L. Thompson). National Science Foundation Postdoctoral Fellow, 1989–1992, The Scripps Research Institute (with Peter E. Wright). Assistant Professor, 1992–1998; Associate Professor; 1998–2001; Professor, 2001-present, Columbia University, USA. Approx. 75 publications. Research specialties: NMR relaxation and molecular motions in biological macromolecules.

Diffusion-Based Studies of Aggregation, Binding and Conformation of Biomolecules: Theory and Practice

William S. Price

Royal Institute of Technology (KTH), Stockholm, Sweden

1 Introduction 1
2 Translational Diffusion and Solute Concentration 1
3 Analysis of PGSE Diffusion Data 2
4 Applications 4
5 Practical Aspects of PGSE Measurements 6
6 Related Articles in this Volume 9
7 Related Articles in Volumes 1–8 9
8 References 9

1 INTRODUCTION

The study of tertiary and quaternary structures, binding and aggregation is of central importance in the biological, chemical and pharmaceutical sciences. For example, the homo- and hetero-associations of proteins are important in normal physiological conditions, some diseases (e.g., Alzheimer's disease), protein pharmaceutical development and crystallization. Due to its non-invasive nature and that it provides an estimate of the self-diffusion coefficient, as opposed to the mutual diffusion coefficient, pulsed-gradient spin-echo (PGSE) NMR translational diffusion measurements (also commonly referred to as DOSY or PFG NMR) provide an ideal way for studying what are generally such weakly interacting systems. Such measurements provide complementary information to traditional NMR structural studies and can provide information on conformation even when individual assignments of the resonances of a macromolecule are unknown. The basis of using diffusion measurements to probe such systems relies on the different species being able to be separated by differences in their diffusion coefficients and additionally, in the case of binding studies, the exchange between the free and bound states modulates the observed diffusion coefficient. Although the application of PGSE diffusion measurements to study conformation, binding and aggregation has a long history, it has undergone a tremendous resurgence in the last decade due to both the commercial availability of the requisite hardware for performing such measurements and also due to the realization of its applicability to a wide variety of applications.

This chapter is concerned with the applications of PGSE diffusion measurements to study conformation, binding and association. In Section 2, a few salient remarks on translational diffusion are given. In Section 3, exchange and binding are considered. Some of the recent applications are reviewed in Section 4, and finally, in Section 5 some of the practical aspects of PGSE diffusion measurements are presented. Special attention is given to developments since the publication of the main volumes of the Encyclopedia. Due to space limitations, generally only recent references, from which the history can be traced, are given. Studies involving polymers, liquid crystals, porous systems, restricted diffusion and imaging are outside the scope of the present chapter.

2 TRANSLATIONAL DIFFUSION AND SOLUTE CONCENTRATION

2.1 Diffusion at Infinite Dilution

At infinite dilution, the translational diffusion coefficient, D^0, of a solute species is often related to its friction coefficient, f, and to the solvent viscosity, η, by the Stokes–Einstein equation, which is derived assuming that the solute sees the solvent as a continuum (e.g., see Ref.[1]),

$$D^0 = \frac{kT}{f} \tag{1}$$

where k is the Boltzmann constant and T is the temperature. For the particularly simple case of a sphere under stick boundary conditions, f is given by (Stokes law)

$$f = 6\pi\eta R \tag{2}$$

where R is the effective hydrodynamic (or Stokes) radius. Exact solutions are only known for some simple geometries (e.g., see Table 1 in Ref.[2]). However, since f is determined by the overall dimensions of the diffusing species (which may include the effects of solvation and rugosity), few species are well described by a simple geometry. Consequently, f must normally be determined numerically (e.g., Ref.[3]).

The difficulty in modeling the hydrodynamics is greatly increased in associating systems. If the monomer–monomer contact in oligomeric species can be regarded as hard-sphere contact, the ratio of the diffusion coefficient at infinite dilution of an n-mer, D_n^0, to that of the monomer can be modeled as

$$\frac{D_n^0}{D_1^0} = \frac{f_1}{f_n} = F_n\, n^{-1/3} \tag{3}$$

and the values of F_n for various geometries have been determined.[4] Generally, there is but no recourse but to consider all oligomers as hydrodynamically spherical, thus, the friction coefficient increases according to the inverse cube root of the molecular weight. In defense of this simplistic assumption, the friction coefficients calculated from equation (3) for reasonable geometrical possibilities for the oligomeric shapes are all quite close to that obtained for a sphere of equivalent volume.

2.2 Diffusion at Finite Concentrations

Aggregating systems are often 'crowded' in that the average spacing between the solute molecules is much less than the

mean-squared displacement of the particles over the timescale of the PGSE diffusion experiment (i.e., Δ; vide infra). At finite solute concentrations, the diffusion coefficients of both the solute and the solvent will be affected due to the solute molecules lengthening the diffusion path of the solvent (i.e., 'obstruction'), and similarly, the solute molecules effecting the diffusion path of themselves (i.e., 'self-obstruction' or 'crowding'). Obstruction can be visualized as restriction by a complicated, and perhaps time-dependent geometry, and it has the effect of reducing the diffusion coefficient of both the solvent and solute. Since the degree of obstruction is dependent on the shapes of the obstructing particles, it provides an additional source of structural information. Calculation of the diffusion reduction factor, f_C, is exceedingly difficult and exact solutions are known only for some very simple cases, and in general, analysis is performed using various approximations or numerical simulations (see Figure 1).[5–8] The currently available models contain serious limitations, not the least being that they do not account for the presence of an aggregation process. Consequently, f_C is progressively overestimated as the concentration (and thus often the degree of aggregation) increases.

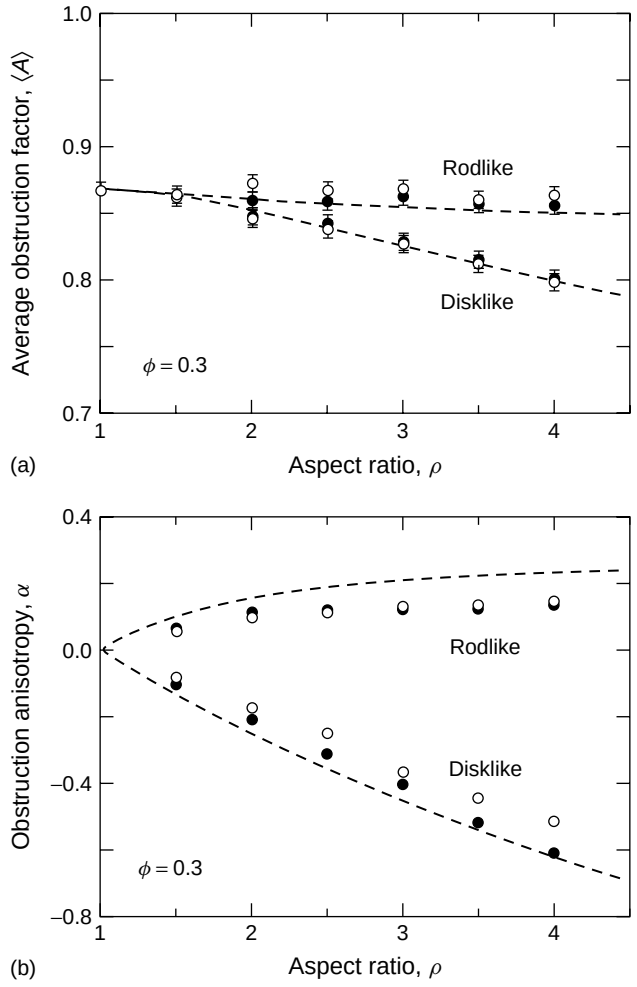

Figure 1 Off-lattice random flight simulations of (a) the isotropically averaged obstruction factor ($=f_C$) and (b) obstruction anisotropy $[=(f_{C\parallel} - f_{C\perp})/\langle f_C\rangle]$ versus the aspect ratio of spheroids (●), disks (○) and spherocylinders (○) on an expanded face centered cubic lattice at a volume fraction of 0.3. The effective cell approximation result is also given (dashed curves). (Reproduced by permission of the American Institute of Physics from H. Jóhannesson and B. Halle, *J. Chem. Phys.*, 1996, **104**, 6807)

3 ANALYSIS OF PGSE DIFFUSION DATA

3.1 PGSE Data from Multicomponent Systems

The basics of the PGSE measurements have been considered previously in this encyclopedia and elsewhere.[9,10] A further and rather obvious complication in modeling of the diffusive behavior of interacting systems is the lifetime of the individual species and this is likely to be very sample specific. In the case of aggregating protein species, the lifetime is often found to be long on the timescale of the PGSE experiment, Δ (typically tens to hundreds of milliseconds), whereas for ligand–protein interactions it is generally short.

It is commonly found that the resonances of the different species overlap, and thus, the PGSE attenuation data is the sum of all of the intensities from each of the species multiplied by their respective relaxation time(s). If the exchange between these species is slow (with respect to Δ), then the echo signal amplitude from a Hahn-echo based sequence for n different oligomeric species present (e.g., monomer, dimer...n-mer) undergoing isotropic free diffusion is given by (in the short gradient pulse limit)

$$S(g) = \sum_n M_{0,n} \exp(-\gamma^2 g^2 \delta^2 \Delta D_n) \exp\left(\frac{-2\tau}{T_{2,n}}\right) \qquad (4)$$

where $M_{0,n}$ denotes the equilibrium magnetization ($\propto Mw_n n_n$; where Mw_n is the molar mass of the nth aggregate species and n_n is the number of such molecules present), $T_{2,n}$ is the spin–spin relaxation time of the nth resonance, 2τ is the total echo time, γ is the gyromagnetic ratio, g is the magnitude and δ is the duration of the magnetic field gradient pulses and Δ is the separation between the leading edges of the gradient pulses. Modeling of the populations of the different oligomeric species is considered in Section 3.2. For a stimulated echo (STE) based sequence, relaxation weighting due to spin–lattice relaxation would also be included. Neglecting the relaxation effects, the PGSE NMR data can then be normalized,

$$E(q, \Delta) = \frac{S(q, 2\tau)}{S(0, 2\tau)} = \frac{\sum_n Mw_n n_n \exp(-4\pi^2 q^2 \Delta D_n)}{\sum_n Mw_n n_n} \qquad (5)$$

and for brevity, we have set $q = (2\pi)^{-1}\gamma g \delta (m^{-1})$. If the exchange is fast (with respect to Δ) then equation (5) reduces to a single exponential,

$$E(q, \Delta) = \exp(-4\pi^2 q^2 \Delta \langle D\rangle_w) \qquad (6)$$

where $\langle D\rangle_w$ is the mass averaged diffusion coefficient defined by

$$\langle D\rangle_w = \frac{\sum_n Mw_n n_n D_n}{\sum_n Mw_n n_n} \qquad (7)$$

For example, in the case of a two-site system, such as a ligand (e.g., a peptide) in fast exchange (with respect to Δ) between free and bound (e.g., bound to a micelle) forms with diffusion coefficients D_f and D_b, respectively, the echo attenuation would appear to be single exponential (i.e., equation (6)) with an apparent diffusion coefficient being given by

$$\langle D\rangle_w = P_\mathrm{b} D_\mathrm{b} + P_\mathrm{f} D_\mathrm{f} \tag{8}$$

where P_b and $P_\mathrm{f}\,(=1-P_\mathrm{b})$ are the populations of the bound and free forms. Hence, information on the binding isotherm can be obtained by performing experiments with different relative concentrations of the ligand to the macromolecule. If the exchange is intermediate on the timescale, the attenuation function is more complicated.[11,12] Binding studies are considered in greater detail in Section 3.3.

For only small degrees of polydispersity, the multi-exponential nature of the attenuation (i.e., equation (5)) is not apparent – especially if a microscopic averaging process exists such that the range of diffusion coefficients measured are narrower than would have been expected on the basis of the polydispersity.[13] Thus, with the exception of highly polydisperse polymer systems, only a single 'average' diffusion coefficient is normally obtained from the PGSE data.[14,15] The averaging process can be approximated by taking the cumulant expansion of equation (5) (to second order),

$$\ln(E(q,\Delta)) = -4\pi^2 q^2 \Delta \langle D\rangle_w + \frac{(4\pi^2 q^2 \Delta)^2}{2}(\langle D\rangle_w^2 - \langle D^2\rangle_w) \tag{9}$$

The second term in equation (9) (i.e., the 'variance') reflects the degree of polydispersity and may become evident as non-linearity in the attenuation plot (i.e., $\ln(E)$ vs. q^2) at larger q values. Ideally, PGSE data from a sample containing a number of species can be decomposed to obtain the individual diffusion coefficients of the species. However, the decomposition of such multi-exponential data is fraught with difficulty[16] and meaningful attempts require prior knowledge such as the number of components.[17] Results of such attempts to spectrally separate the components of a mixture on the basis of their diffusion coefficient are often displayed in a two-dimensional format generally referred to as DOSY.[18,19] However, the crowding effects that occur at finite concentrations mediate against the success of such multi-exponential decompositions.

When the measured attenuation plots appear linear, analysis proceeds by fitting equation (9) (excluding the second term) to the attenuation data. Since the diffusion coefficients of the oligomers (i.e., D_i) inherently contain the effects of crowding, analysis of the results of the PGSE experiment yields the apparent diffusion coefficient, $\langle D\rangle_w^C$, where the superscript C denotes the inclusion of crowding effects. Interestingly, equation (9) is, due to the effects of the microscopic averaging, mathematically equivalent to that for the case of fast exchange (equation (6)).

3.2 Models for Self-Associating Systems

Given the realistic limits of the sort of aggregate distributions/models that can feasibly be tested against the experimental PGSE NMR data and the effects of crowding, a practical approach to evaluating PGSE diffusion data for an aggregating protein system is outlined in Figure 2. Typically the exact populations of the n-mers are not known and instead equation (4) is expressed in terms of a discrete or continuous distribution.[15,20] For example, in the isodesmic model, aggregates grow by the addition of a monomer unit, L_1, thus,

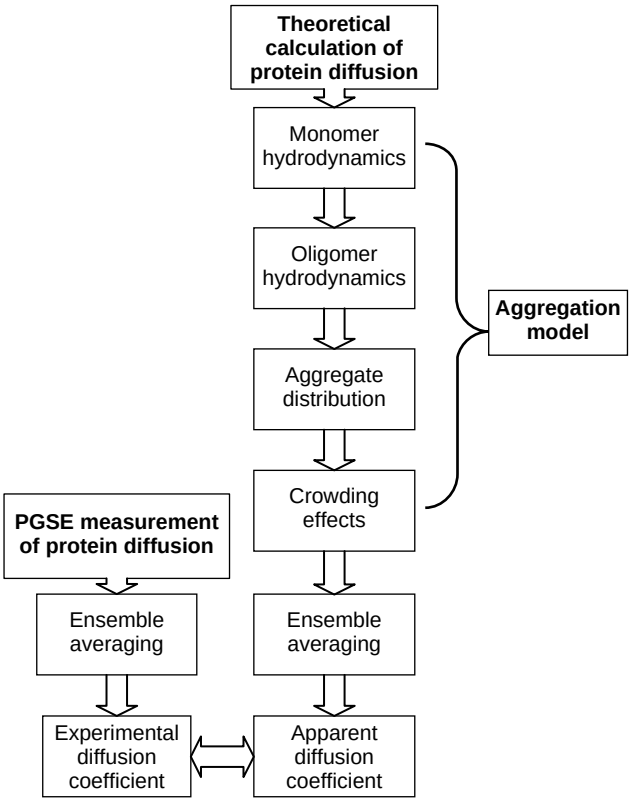

Figure 2 A schematic diagram of the steps involved in analyzing the PGSE data of an aggregating protein system. (Reproduced by permission of the American Chemical Society from W. S. Price, F. Tsuchiya, and Y. Arata, *J. Am. Chem. Soc.*, 1999, **121**, 11 503)

$$L_{n-1} + L_1 \overset{K_e}{\longleftrightarrow} L_n \quad n = 1\ldots\infty \tag{10}$$

where K_e $(= K_2 = K_3 = \cdots = K_n)$ is the equilibrium constant. From the conservation of mass equation, we have

$$C = \sum_{n=1}^{\infty} c_n\, n \tag{11}$$

Thus the mole fraction of the n-mer is given by

$$\alpha_n = n(K_e C)^{n-1}\left(\frac{2K_eC + 1 - \sqrt{1+4K_eC}}{2(K_eC)^2}\right)^n \tag{12}$$

Hence, the theoretical apparent diffusion coefficient for a polydisperse oligomeric system is given by (NB $Mw_n\, n_n \propto c_n\, n$)

$$\langle D\rangle_w^C = \langle D\rangle_w f_\mathrm{C}(C) = \frac{\sum_n c_n\, n\, D_1^0\, n^{-\frac{1}{3}}}{C} f_\mathrm{C}(C) = \sum_n \alpha_n\, D_1^0\, n^{-\frac{1}{3}}\, f_\mathrm{C}(C) \tag{13}$$

3.3 Binding Studies

Binding studies can proceed in a number of ways depending upon the sample experimental conditions: (1) If (some of) the ligand resonances are distinct from those of the protein, the ligand diffusion coefficient can be measured directly, (2) if the resonances are overlapped, it may be possible to separate the attenuation curves if the exchange rate is slow (with respect to Δ), (3) edit out signals from one of the species by applying relaxation or diffusion filters or (4) to use specific isotopic labeling in conjunction with heteronuclear filtration.[21,22]

4 APPLICATIONS

A number of reviews are either entirely devoted to or contain some coverage of diffusion-based studies of association, binding and conformation.[12,19,22–29] Some of the more interesting studies from the literature are cited in the following, somewhat loosely classified, sub-sections.

4.1 Conformation

PGSE measurements have shown that the *cis*- and *trans*-conformers of *N*-methylformamide have different diffusion coefficients.[30] On a more macroscopic scale PGSE was used to probe the conformation of amylopectin[31] and to determine the radii of dendrimers.[32]

In a pioneering study in 1968, the helix to random coil transition of poly-L-glutamic acid as a function of pH was studied using PGSE NMR.[33] Recent studies have included BPTI and unfolded variants,[34] urea-induced unfolding of lysozyme[35] and the effects of pH and NaCl concentration on the heterodimeric salt-mediated killer toxin (SMKT) from *Pichia farinosa*.[36] Both the lysozyme and SMKT studies revealed that as a protein loses its compact structure and becomes a random coil, there is a ~37% increase in effective hydrodynamic radius. PGSE measurements have even been used to study the folding process of lactalbumin in real time.[37]

Some examples of protein diffusion coefficients are given in Table 1, and also in Table 4 in Ref.[27]. Since equation (1) only rigorously applies at infinite dilution, to extract conformational information, it is generally necessary to extrapolate the results of diffusion measurements to infinite dilution (e.g., see Ref.[34]). Further, changes in solvent viscosity must be accounted for to avoid misinterpretation.[36] Experimentally, it has been found that the self-diffusion coefficients of the proteins correlate

Table 1 Selected diffusion coefficients of biological molecules derived from PGSE NMR measurements[a,b]

Protein/solute	Concentration; pH (or pD)	Solvent	T(K)	D (m^2s^{-1})	Reference
BPTI	7.5 mg/ml	CO_2/TFE/detergent	293	2.5×10^{-9}	**102**
BPTI	Infinite dilution[c] 4.5	D_2O	274	7.7×10^{-10}	**34**
Calbindin-D_{9k}	1–2 mM	90% H_2O		1.11×10^{-10}	**38**
Calcyclin	1–2 mM	90% H_2O		7.15×10^{-11}	**38**
CPA-Ca_0	1 mM; 6.5	95% H_2O	298	1.1×10^{-10}	**103**
CPA-Ca_2	1 mM; 6.5	95% H_2O	298	1.4×10^{-10}	**103**
Cyclosporin A	21 mM	$MeOD_4/CO_2$	293	14.1×10^{-9}	**102**
GVKGDKGNPGWPGAPY	7 mg/ml; 6	D_2O	297	4.2×10^{-10}	**104**
Hemoglobin	Infinite dilution[c]; 6.9	H_2O	298	6.75×10^{-11}	**105**
IL-10		90% H_2O	298	8.2×10^{-11}	**106**
Insulin dimer	0.72 mM; 9.3–9.4	D_2O	298	1.38×10^{-10}	**52**
Insulin tetramer	3 mM; 9.3–9.4	D_2O	298	1.07×10^{-10}	**52**
Lysozyme	Infinite dilution[c]; 4.6	90% H_2O	298	1.1×10^{-10}	**14**
MCP-1	1.5 mM; 3.0	90% H_2O	298	1.08×10^{-10}	**106**
MonH·H_2O	Infinite dilution[c]	$CDCl_3$	293	7.84×10^{-10}	**107**
MonNa	Infinite dilution[c]	$CDCl_3$	293	7.42×10^{-10}	**107**
Monocyte CP	1–2 mM	90% H_2O		1.08×10^{-10}	**38**
$NG_{(28-43)}$	2 mM	D_2O	298	2.5×10^{-10}	**108**
Ovalbumin	Infinite dilution[c]; 5,5	H_2O		7.92×10^{-11}	**109**
Psychosine	2.8 mM; 4.5	D_2O	298	1.16×10^{-10}	**50**
	2.8 mM; 7.0			0.77×10^{-10}	
PU − 1	1–2 mM	90% H_2O		1.09×10^{-10}	**38**
RJunLZ	5.5 mg/ml; 3.6	95% H_2O	298	1.36×10^{-10}	**40**
α-RNA	1–2 mM	90% H_2O		0.91×10^{-10}	**38**
SMKT	1 mM; <5	H_2O	298	1.15×10^{-10}	**36**
Ubiquitin	10 mg/ml; 4.0	95% H_2O	298	1.52×10^{-10}	**40**
Viomycin	50 mM	90% H_2O	303	2.73×10^{-10}	**61**

$CPA\text{-}Ca_2$ = Calcium loaded carp parvalbumin; $CPA\text{-}Ca_0$ = calcium free carp parvalbumin; MonH·H_2O = monensin free acid form; MonNa = monensin sodium salt; monocyte CP = monocyte chemotactic protein-1; $NG_{(28-43)}$ = residues 28–43 of neurogranin; rJunLZ = c-Jun leucine zipper; αRNA = α subunit of RNA polymerase; SMKT = salt-mediated killer toxin.

[a]It is possible to scale the diffusion coefficients measured at a particular temperature, T, and viscosity, η, to standard conditions (i.e., temperature T_n and solvent viscosity, η_n) using the following relation $D(T_n, \eta_n) = D(T, \eta)[T_n\eta/T\eta_n]$.

[b]Modified with Permission from the Royal Society of Chemistry from W. S. Price, in 'Annual Reports on the Progress in Chemistry Part C', ed G. A. Webb, Royal Society of Chemistry, London, 2000, **96**, Chap. 2, p. 3–53.

[c]Extrapolated to infinite dilution.

linearly with the solvent accessible surface.[38] Diffusion measurements are now commonly used to determine whether the protein or nucleic acid in a sample exists in the monomeric state (e.g., see Ref.[39]) and also to provide an independent estimate of rotational diffusion coefficients (i.e., reorientational correlation times) in NMR relaxation studies of protein backbone dynamics.[40]

4.2 Obstruction and Hydration

Obstruction effects have been observed for small molecules such as for H_2 and H_2O moving in protein solutions[41,42] and for cations in DNA solutions.[43] Accounting for the effects of obstruction on the diffusion coefficient of the unbound ligand has also been shown to be important in extracting the true free diffusion coefficient in binding studies.[44]

Protein hydration has been studied as a bulk property by measuring the obstruction effect on water diffusion[45] and by using diffusion filters to edit out bulk water, thereby allowing identification of individual hydration sites.[46]

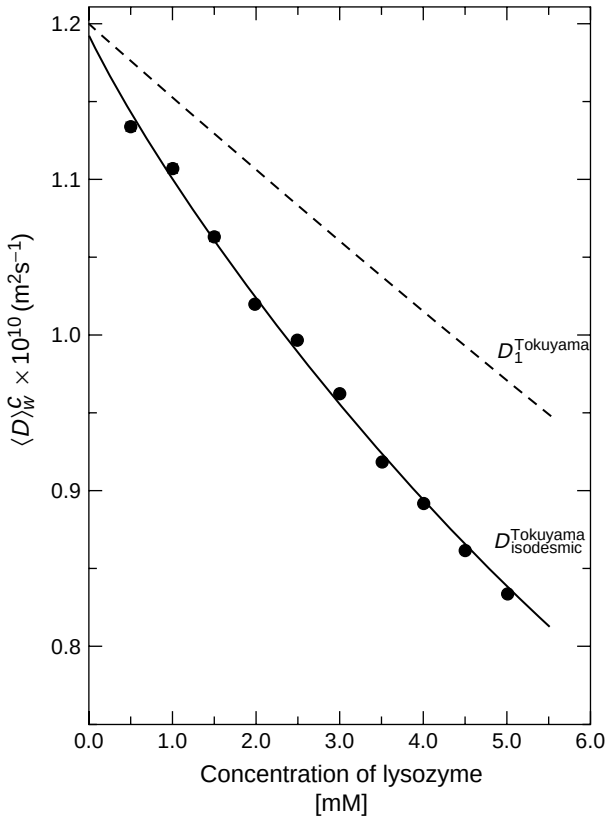

Figure 3 Change in lysozyme diffusion coefficients at 298 K and pH 4.6 in the presence of 0.5 M NaCl. The dashed line represents the monomer diffusion coefficient at infinite dilution (i.e., D_1^0) corrected for crowding using the Tokuyama and Oppenheim model.[8] The lysozyme clearly undergoes a self-association process as the experimental diffusion coefficient is considerably smaller than the crowding effect corrected (with either model) monomer diffusion coefficient. The best fit to the data was obtained using the isodesmic model in conjunction with the Tokuyama and Oppenheim correction (solid line). (Adapted by permission of the American Chemical Society from W. S. Price, F. Tsuchiya, and Y. Arata, *J. Am. Chem. Soc.*, 1999, **121**, 11 503)

4.3 Association

The ability of PGSE NMR to measure diffusion at high solute concentrations makes it a very powerful tool for studying self-association processes in alcohol solutions,[47] bile salt/phospholipid aggregation,[48] micelle–peptide association,[49] the aggregation of β-galactosylsphingosine[50] and hydrogen bonded calixarene assemblies.[51]

The last few years has seen an enormous increase in such studies, including the self-association of human insulin,[52] BPTI,[53] the Alzheimer's related βA4 peptide,[54] lysozyme[14] and others.[55] In a detailed study of lysozyme self-association,[14] it was shown that it was crucial to consider the effects of crowding in analyzing the observed diffusion coefficients – otherwise the degree of self-association was seriously overestimated (see Figure 3). Further, if aggregation proceeded to the extent that some of the lysozyme precipitated, it was observed that the measured diffusion coefficient increased since the effective solution lysozyme concentration was lowered and the larger aggregates were removed from the average in equation (7) due to the effects of relaxation-weighting (see Figure 4).[56]

4.4 Binding and Exchange

Diffusion-based binding studies have included protein–ligand interactions such as polyamine–DNA association,[57] cation–DNA interactions,[58] protein–surfactant and protein–lipid interactions,[49,59] hydration water and amide–water

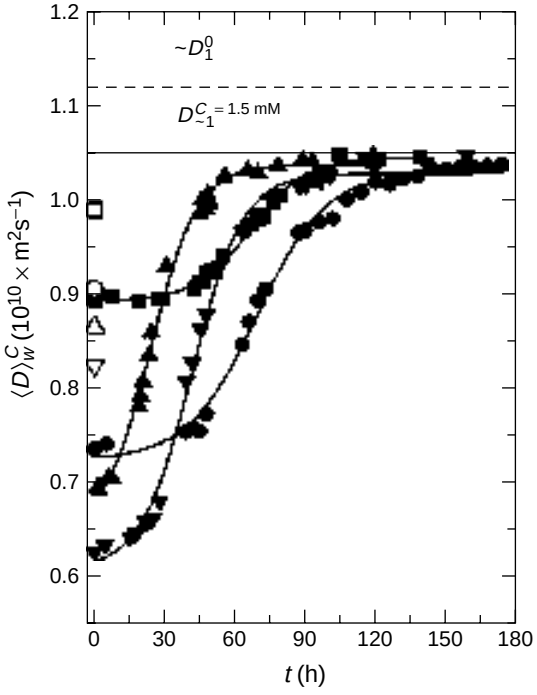

Figure 4 The change in the PGSE NMR-determined diffusion coefficients, $\langle D \rangle_w^C$, of the lysozyme samples (3 mM, ■; 5 mM, ●; 6 mM, ▲; 7 mM, ▼) with time at pH 6 and 298 K in 0.5 M NaCl. The open symbols at $t = 0$ h represent the corresponding D_1^C values for these concentrations. The horizontal solid line indicates $D_{\sim 1}^{C=1.5\text{ mM}}$ and the horizontal dashed line indicates $\sim D_1^0$ (see text). (Adapted by permission of the Biophysical Society from W. S. Price, F. Tsuchiya, and Y. Arata, *Biophys. J.*, 2001, **80**, 1585)

exchange rates,[60,61] and nucleic acid–ligand interactions such as ethidium bromide binding to DNA.[62] PGSE analysis has also been used to probe the selective complexation of the *cis*- and *trans*-isomers of phenylalanylproline by β-cyclodextrin[63] and macrocycle–guest interactions.[64]

^{1}H PFG DQ experiments can be used to determine the diffusion coefficients of unlabelled molecules by utilizing the gradient pulses at the beginning and end of the DQ excitation period.[21] Heteronuclear filtered diffusion experiments of peptide binding have also been reported.[65] X-filter ^{1}H PFG DQ can be used to identify the molecules in a mixture of unlabelled compounds in solution with a ^{15}N and/or ^{13}C-labelled protein which interact with the protein.[66]

Diffusion based editing has also found an application in characterizing biomolecules in biofluids such as blood plasma,[67] and PGSE-based binding measurements and spectral editing have now become a major tool in drug screening and combinatorial chemistry where they are often referred to as "affinity NMR".[68] Diffusion editing may be used to identify which ligands bind to macromolecules.[69] In contrast to conventional screening methods, the ligand binding is detected directly, thereby minimizing the observation of false positives. From the NMR perspective, it has the advantage that since only the signals from the ligands are observed, there is no need for isotope labeling. A diffusion-assisted NOE pumping experiment has been used to study the binding of L-ascorbic acid, glucose and salicylic acid to human serum albumin.[70]

5 PRACTICAL ASPECTS OF PGSE MEASUREMENTS

5.1 Introduction

Gradient generation hardware and the commonly used pulse sequences have been covered in the encyclopedia and elsewhere.[10,19,23,28] In this section, we focus on some recent developments and also on artifacts, how they can be diagnosed and how their effects can be avoided/minimized. With careful experimental technique, it is possible to reduce errors in the measured diffusion coefficient to less than 1%.[71]

5.2 Sample Related Problems

5.2.1 Convection

Convection is a source of insidious artifacts in PGSE experiments performed above or below ambient temperature (see Figure 5).[72,73] While a net flow of spins along the direction of the gradient is clearly indicated by the resulting net phase change, convection currents (see Figure 6),[74,75] which typically occur along the long axis of the NMR tube, do not produce a phase change since the flow of the spins along the direction of the gradient is exactly matched by the flow in the anti-parallel direction. However, convection causes a cosine modulation of the PGSE signal attenuation (for a single diffusing species),

$$E(g, \Delta) = \cos(\gamma \delta g v \Delta) \exp\left(-\gamma^2 g^2 D \delta^2 \left(\Delta - \frac{\delta}{3}\right)\right) \quad (14)$$

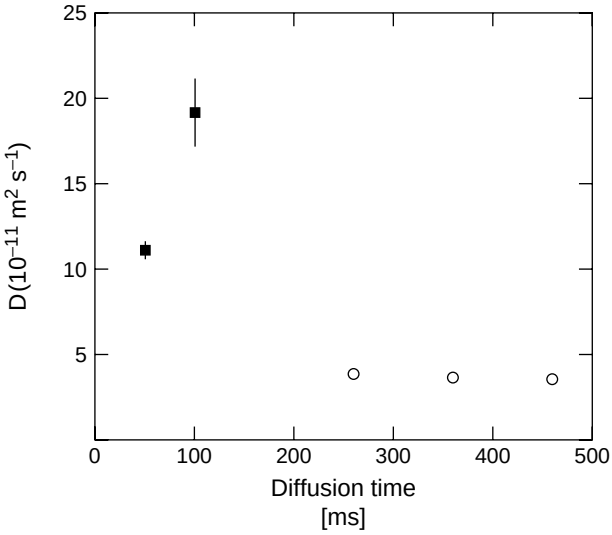

Figure 5 The change in diffusion coefficients versus diffusion time (△) for $C_{12}E_8$ micelles (5 wt%) in D_2O at 45 °C measured using the conventional ^{1}H PGSE STE sequence (■) and the convection compensated double STE sequence[76] (○). The error bars represent $\pm 2\sigma$. (Reproduced by permission of the American Chemical Society from N. Hedin, T. Y. Yu, and I. Furó, *Langmuir*, 2000, **16**, 7548)

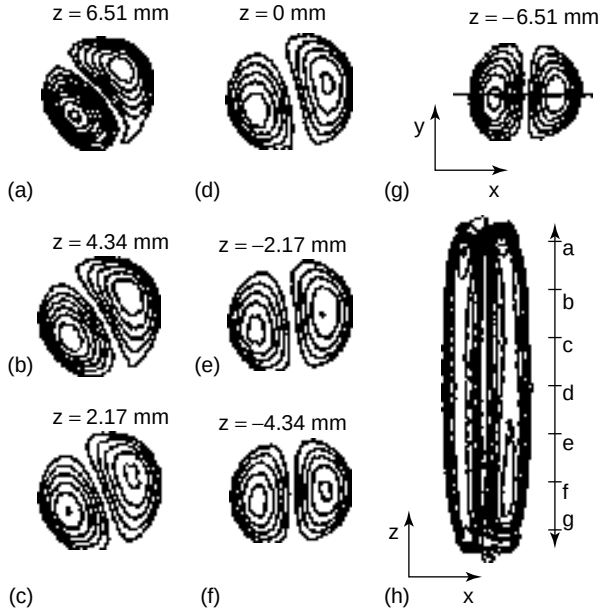

Figure 6 Observation of a twisted nodal plane (a–g) in a sample of DMSO at 311 K. The slices are acquired at different positions along the cylinder. (Reproduced by permission of Academic Press from A. Jerschow, *J. Magn. Reson.*, 2000, **145**, 125)

where v is the velocity of the flow. However, when $v^2\Delta \ll D$ and $\delta \ll \Delta$, the presence of convection is generally not apparent due to the similarity between the cosine and Gaussian functions. In such circumstances, the data appears to be well described by the usual exponential function giving, to first approximation, an apparent diffusion coefficient of

$$D_{\text{app}} = D + \frac{\Delta v^2}{2} \quad (15)$$

Thus, the presence of convection is suspected when the measured diffusion coefficient of a non-exchanging freely diffusing species increases with Δ. Importantly, whereas the diffusion coefficient depends on molecular size, the flow velocity is common to all of the species in the sample.

Apart from simply improving the temperature control to reduce any temperature gradients, convection can also be minimized or prevented by (i) using a narrower tube; (ii) in the case of some samples, glass wool can be placed in the sample; (iii) surrounding the sample with a fluid of higher heat capacity[72] or (iv) using specialized pulse sequences (e.g., Ref.[76] and see Figure 5).

5.2.2 Background Gradients and Radiation Damping

Although the effects of microscopic magnetic inhomogeneities on PGSE measurements are well known and specialized sequences have been devised to counteract the effects, the effects of macroscopic background gradients due to susceptibility differences at the sample interfaces (see Figure 7) have until recently[77] received scant attention. Similarly, the effects of radiation damping (e.g., see Ref.[78]) on strong signals in PGSE experiments have also been ignored. Both phenomena can lead to the seemingly strange effect of the echo signal growing as the gradient strength increases at low applied gradient strengths and have serious implications for accuracy in determinations of D. For a freely diffusing species, background gradients are often evident as slight concave or convex inflections in the PGSE attenuation curve – depending on the polarity of the applied gradient. The effects of radiation damping can also result in the attenuation curve being non-linear when plotted in the usual semi-log fashion but, in contradistinction to background gradients, the non-linearity is insensitive to the polarity of the applied gradient.

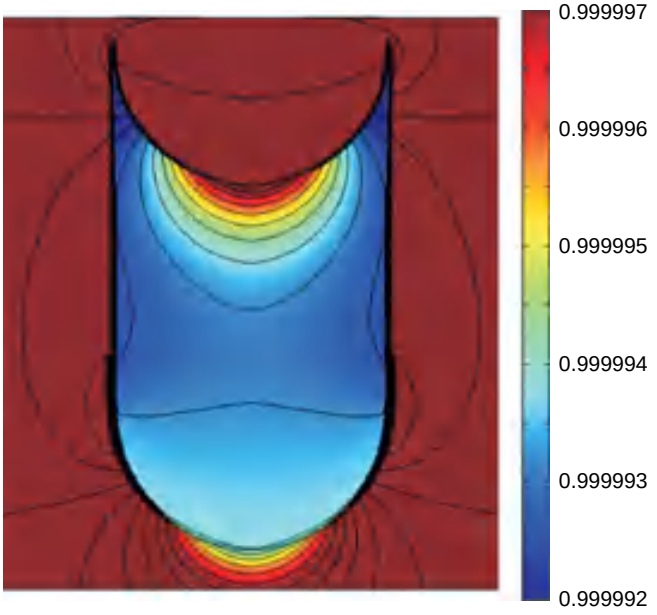

Figure 7 Simulation of the background gradients in a standard NMR tube. The simulations were performed using a radius of 4.5 mm and a length of 6.2 mm and setting $\chi_{air} = 1$ and $\chi_{water} = 0.999991$. Each contour reflects a 0.5 ppm change in the field. (Reproduced by permission of Academic Press from W. S. Price, P. Stilbs, B. Jönsson, and O. Söderman, *J. Magn. Reson.*, 2001, **150**, 49)

5.2.3 Transfer of Longitudinal Spin Polarization

The deleterious and often confusing influence of intermolecular and intramolecular transfer of longitudinal spin polarization by either chemical exchange, spin diffusion or dipolar cross relaxation in STE-based sequences has now been examined in detail.[79,80] It is noted that problems resulting from these effects can be obviated by the usage of bipolar gradient variations of the STE sequence.

5.3 Problems Related to Gradient Pulses

Five problems related to the gradient pulses that need to be considered in order to obtain accurate diffusion measurements are: (1) the constancy (although more commonly referred to as the linearity) of the applied gradient, (2) gradient pulse mismatch, (3) vibration, (4) eddy currents and (5) gradient calibration. The severity of the latter problems (2)–(4) increases with higher amplitude gradient pulses such as would be used when measuring very large (i.e., very slowly diffusing) biomolecules, solids or attempting to use a short Δ to obviate relaxation-weighting problems. Eddy currents have previously been treated in detail in the encyclopedia and elsewhere[10,81] and will not be discussed here.

5.3.1 Gradient Constancy

The analysis of the PGSE experiment is simplified if the sample volume is contained within the constant region of the gradient, although small deviations do not generally cause serious errors.[82] Gradient coils generally only produce a constant gradient over a small part of the sample volume, thus, it is necessary to restrict either the volume from which the NMR signal is acquired such as by making the first pulse in the PGSE sequence slice-selective (e.g., Ref.[83]) or by simply restricting the volume of the sample. This latter approach has been made particularly simple with the advent of susceptibility matched NMR tubes. The effective sample volume is also restricted to a significant extent by the size of the rf coils, however, this volume is often larger than the volume of constant gradient.

5.3.2 Gradient Mismatch and Vibration

Gradient pulse mismatch, vibration/sample movement with respect to the gradient coils and eddy currents can all produce confusingly similar effects.[84] Gradient pulse mismatch and vibration/sample movement in the PGSE experiment for the case of a freely diffusing species can be modeled by rewriting the PGSE attenuation equation in the short gradient pulse limit including a phase-shift, ϕ, due to the effects of a gradient (magnitude) mismatch, Δq (i.e., it is assumed that Δq is parallel to $\mathbf{q}$ which is directed along the z-axis) and sample movement, Δz, between the first and second gradient pulses (NB in Δq and Δz, 'Δ' denotes differential) thereby

obtaining[84,85]

$$E(q,\Delta) = \underbrace{\int P(Z,\Delta)\, e^{i2\pi qZ} dZ}_{E_{\text{diff}}(q,\Delta)} \underbrace{\left\{e^{i2\pi(q+\Delta q)\Delta z}\right\}}_{\exp\phi(\Delta z)} \times \underbrace{\int \rho(z_1)\, e^{i2\pi\Delta q z_1} dz_1}_{E_{\text{phase}}(\Delta q)} \quad (16)$$

where $P(Z,\Delta)$ is the average propagator,[86] $E_{\text{diff}}(q,\Delta)$ is the diffusive attenuation (i.e., equation (6)), $\exp\phi(\Delta z)$ is the residual phase-shift due to vibration/sample movement, is position independent and can be removed by individually phase-correcting each spectrum or by computing the absolute value spectrum.[85]

The third term (i.e., $E_{\text{phase}}(\Delta q)$) is the residual phase-twist resulting from the gradient pulse mismatch and is, for the case of a cylindrical sample of length l, centered in the gradient,

$$E_{\text{phase}}(\Delta q) = \frac{\int_{-l/2}^{l/2} e^{i2\pi\Delta q z_0} dz_0}{l} = \text{sinc}(\pi\Delta q l) \quad (17)$$

Even extremely small mismatches can cause a severe loss in echo signal intensity. If Δq is taken as being a fixed proportion of q (not an unreasonable assumption), then $E_{\text{phase}}(\Delta q)$ is a damped oscillation with the degree of damping and the periodicity being exquisitely sensitive to the degree of mismatch. In extreme cases, this has the potential to produce artifactual 'diffraction' peaks.

Phase-based artifacts can be detected by performing measurements on a freely diffusing sample with a very small diffusion coefficient (e.g., large polymer) using the same experimental parameters (i.e., q and Δ) to be used in the intended experiment. Their removal, however, is more troublesome. The possibilities include: (1) improving the gradient pulse generation, (2) empirically matching the gradient pulse pairs, (3) using the imaging based Modulus Addition using Spatially Separated Echo spectroscopY (MASSEY) sequence approach,[85] (4) prefixing a number of Δ-spaced gradient prepulses[87] to increase gradient pulse reproducibility or (5) using shaped gradient pulses which are easier to generate reproducibly. The last two choices are the most convenient and additionally they retain spectral information. The addition of gradient prepulses can also help to alleviate eddy current problems as they have the effect of balancing the eddy current distortions in the τ-periods. In addition to reducing both mismatch and eddy current problems, shaped gradient pulses, due to their slower rise and fall times, are also less likely to produce vibration of the sample/probe.[84]

5.3.3 Gradient Calibration

There are a number of methods for gradient calibration including: (1) theoretical coil calculation, (2) performing a measurement with a sample of known diffusion coefficient (see Ref.[88] for a list of suitable standards), (3) shape analysis of the spin-echo and one-dimensional images and (4) intentional gradient mismatch. These methods have been reviewed in detail elsewhere,[10] and methods for calibrating gradients for stray field (STRAFI also known as supercon-fringe field steady-gradient spin-echo) studies have recently been considered.[89]

In practice, calculating the gradient from the coil dimensions and the applied current results in an error of about 10%, due primarily to interactions with nearby metal in the probe. The standard sample technique is particularly useful since non-ideal gradient behavior (e.g., non-constancy) is to some degree compensated for by being incorporated into the apparent calibration value determined. It is important, however, that the experimental conditions (i.e., sample shape, delays, pulse lengths, gradient strengths, etc.) used for the calibration follow closely those used in the subsequent experiments. This method of gradient calibration requires excellent temperature control and is further limited by the need to have a compound containing a nucleus that can be observed with the probe at hand and with a similar diffusion coefficient.

Using a sample with a single resonance (e.g., H_2O), the gradient strength can also be calculated from the echo shape from a sample of known geometry since both the observed FID and spectrum will reflect both the gradient and the shape of the sample. Since the number of spins is constant along the cylinder axis, the absolute value of the Fourier transform of the signal must be rectangular with a 'line width', Δv (Hz), given by

$$\Delta v = \frac{\gamma g l}{2\pi} \quad (18)$$

If the transmitter offset is placed at the resonance frequency of the sample (i.e., in the absence of the gradient) then, if the sample is correctly centered in the gradient, the gradient broadened spectrum will expand symmetrically around the transmitter offset as the gradient strength is increased. This method requires that the length of the sample containing cell be known accurately and the final calibration will have an error of less than 5%. Two virtues of this method are that the calibration can be performed without any knowledge of the sample diffusion coefficient and, so long as the dimensions of the container holding the sample are not too temperature sensitive, it can be used to cross-check that the gradient strength is not temperature dependent. However, this method has a limited range of applications since, for anything more than modest gradients, the gradient broadened spectrum is larger than the maximum spectrometer bandwidth.

The gradient mismatch approach is based on the notion that the time displacement of the echo maximum caused by the intentional mismatch of gradient pulses shifts in a very well-defined way allowing the gradient to be calibrated (vide supra).

The large steady gradients used in STRAFI techniques can be calibrated using the separation in sensitive planes from a heteronuclear sample (e.g., ^{1}H and ^{19}F) and from field profiling by following the change in resonance frequency with position in the gradient of a single signal.

5.4 Sequence Developments

5.4.1 Solution State

Heteronuclear PGSE sequences which invoke polarization transfer from protons to the heteronuclei (e.g., ^{13}C or ^{15}N) have been developed for macromolecular studies.[65,90] and there has also been considerable interest in the development of sequences for the selective editing of spectra based on diffusion coefficient differences and for determining exchange.[21,46,68,69,91] A diffusion assisted NOE-pumping experiment has also been proposed in which a diffusion experiment

is prefixed to an NOE experiment which is useful when the difference in diffusion coefficients between the binding and non-binding ligands is insufficient to allow editing solely on the basis of the difference in diffusion coefficients.[70] There has been some interest in the use of nonlinear spin echo based diffusion measurements.[92]

Although technically more difficult, there are numerous reasons for desiring large applied gradients including being able to measure slower diffusion (i.e., in solids), but also to use shorter Δ-values to obviate the problems associated with relaxation-weighting and convection. The availability of stronger gradient pulses also increases the applicability of Hahn-echo based PGSE sequences which can be important since they obviate the problems resulting from cross-relaxation which can occur when performing measurements on macromolecular systems with STE based sequences. The larger available gradient pulses also allow diffusion measurements in liquid isotropic systems to be performed on quadrupolar nuclei with short relaxation times such as ^{17}O.[93]

5.4.2 Near Solid State and the Solid State

The applicability of standard PGSE methods to near solids and solids is severely limited due to the short relaxation times (usually less than 1 ms) which leave insufficient time for the application of the gradient pulses. True solids present additional difficulties due to the presence of (unaveraged) anisotropic interactions (e.g., dipole–dipole). Efforts to circumvent the relaxation time difficulties have proceeded along two paths: (1) Generation of larger gradient pulses with short settling times in PGSE experiments or the use of the extremely large gradients in the stray field of superconducting magnets in steady gradient diffusion experiments and (2) modifications to the PGSE sequence to average out the nuclear spin interactions and thereby lengthen the available time to perform the PGSE sequence.[94] The application of very high gradients to diffusion measurements has recently been reviewed.[95]

5.4.2.1 Large Gradient Pulses and Stray Field

Gradient coils have now been designed to generate pulsed gradients up to 52 Tm^{-1} and have allowed the study of samples with T_2s of less than 1 ms.[96] Using gradients of this magnitude, diffusion coefficients down to $7.5 \times 10^{-16}\,m^2s^{-1}$ have been measured.[97]

The available gradient strengths in STRAFI have been increased up to 180 Tm^{-1} by using superconducting coils in an anti-Helmholtz arrangement. However, STRAFI measurements suffer from poor signal-to-noise as the rf pulses can only excite a thin slice of the sample and, because the echo is acquired in the presence of the gradient, spectral information is lost. Further, since this is a steady gradient experiment, the delays in the sequence have to be lengthened to probe the diffusion process, and consequently attention must be paid to removing relaxation weighting effects[98] in addition to the problems resulting from cross relaxation, spin diffusion and chemical exchange.

5.4.2.2 Non-Vanishing Dipolar Decoupling

Early attempts to measure diffusion coefficients in samples with static dipolar couplings used PGSE sequences based on nematic and solid echoes (also relevant to quadrupole broadened spectra). During the past decade, numerous sequence modifications have been presented including dipolar decoupling (both homo and heteronuclear) which not only extends the periods in which the gradients can be applied but also prevents spin diffusion during the gradient application.[80,99–101] By combining dipolar decoupling with STRAFI, diffusion coefficients down to $3 \times 10^{-16}\,m^2s^{-1}$ have been reported.[99]

6 RELATED ARTICLES IN THIS VOLUME

Diffusion-Ordered Spectroscopy (DOSY); Stray Field (STRAFI) NMR: Imaging in Large Field-Gradients.

7 RELATED ARTICLES IN VOLUMES 1–8

Colloidal Systems, Volume 2; Diffusion & Flow in Fluids, Volume 3; Diffusion Measurements by Magnetic Field Gradient Methods, Volume 3; Diffusion in Porous Media, Volume 3; Diffusion in Solids, Volume 3; Eddy Currents & Their Control, Volume 3; Field Gradients & Their Application, Volume 3; Gradient Coil Systems, Volume 4; Liquid Crystalline Samples: Diffusion, Volume 4; Protein Hydration, Volume 6.

8 REFERENCES

1. H. J. V. Tyrrell and K. R. Harris, 'Diffusion in Liquids', Butterworths: London, 1984.
2. K. E. van Holde, W. C. Johnson, and P. S. Ho, 'Principles of Physical Biochemistry', Prentice Hall, New Jersey, 1988.
3. J. García de la Torre, M. L. Huertas, and B. Carrasco, *Biophys. J.*, 2000, **78**, 719.
4. D. C. Teller, E. Swanson, and C. De Haën, *Methods Enzymol.*, 1979, **61**, 103.
5. J. H. Wang, *J. Am. Chem. Soc.*, 1954, **76**, 4755.
6. B. Jönsson, H. Wennerström, P. G. Nilsson, and P. Linse, *Colloid Polymer Sci.*, 1986, **264**, 77.
7. H. Jóhannesson and B. Halle, *J. Chem. Phys.*, 1996, **104**, 6807.
8. M. Tokuyama and I. Oppenheim, *Phys. Rev.*, 1994, **E50**, R16.
9. W. S. Price, *Concepts Magn. Reson.*, 1997, **9**, 299.
10. W. S. Price, *Concepts Magn. Reson.*, 1998, **10**, 197.
11. J. Kärger, *Adv. Coll. Interfac. Sci.*, 1985, **23**, 129.
12. A. R. Waldeck, P. W. Kuchel, A. J. Lennon, and B. E. Chapman, *Prog. NMR Spectrosc.*, 1997, **30**, 39.
13. P. T. Callaghan and D. N. Pinder, *Macromolecules*, 1985, **18**, 373.
14. W. S. Price, F. Tsuchiya, and Y. Arata, *J. Am. Chem. Soc.*, 1999, **121**, 11 503.
15. B. Håkansson, M. Nydén, and O. Söderman, *Colloid Polymer Sci.*, 2000, **278**, 399.
16. A. I. Istratov and O. F. Vyvenko, *Rev. Sci. Instrum.*, 1999, **70**, 1233.
17. P. Stilbs, *J. Magn. Reson.*, 1998, **135**, 236.
18. P. Stilbs, *Anal. Chem.*, 1981, **53**, 2135.
19. C. S. Johnson, Jr., *Prog. NMR Spectrosc.*, 1999, **34**, 203.
20. R. B. Martin, *Chem. Rev.*, 1996, **96**, 3043.
21. C. Dalvit and J.-M. Böhlen, in 'Annual Reports on NMR Spectroscopy', ed G. A. Webb, Academic Press: London, 1999, Vol. 37, p. 203–271.
22. M. J. Shapiro and J. S. Gounarides, *Prog. NMR Spectrosc.*, 1999, **35**, 153.
23. W. S. Price, in 'Annual Reports on NMR Spectroscopy', ed G. A. Webb, Academic Press: London, 1996, Vol. 32, p. 51–142.

24. R. Kimmich, 'NMR: Tomography, Diffusometry, Relaxometry', Springer-Verlag: Berlin, 1997.
25. G. Otting, *Prog. NMR Spectrosc.*, 1997, **31**, 259.
26. J. C. Lindon, M. Liu, and J. K. Nicholson, *Rev. Anal. Chem.*, 1999, **18**, 23.
27. L. Fielding, *Tetrahedron*, 2000, **56**, 6151.
28. W. S. Price, in 'Annual Reports on the Progress in Chemistry Part C', ed G. A. Webb, Royal Society of Chemistry: London, 2000, Vol. 96, Chap. 2. p. 3–53.
29. P. Stilbs, in 'Encyclopedia of Spectroscopy and Spectrometry', eds J. C. Lindon, G. E. Tranter, and J. L. Holmes, Academic Press: London, 2000, p. 369–375.
30. L. Chen, T. Gross, H.-D. Lüdemann, H. Krienke, and R. Fischer, *Naturwissenschaften*, 2000, **87**, 225.
31. P. T. Callaghan and J. Lelievre, *Biopolymers*, 1985, **24**, 441.
32. I. B. Rietvald and D. Bedeaux, *Macromolecules*, 2000, **33**, 7912.
33. R. E. Moll, *J. Am. Chem. Soc.*, 1968, **90**, 4739.
34. H. Pan, G. Barany, and C. Woodward, *Protein Sci.*, 1997, **6**, 1985.
35. J. A. Jones, D. K. Wilkins, L. J. Smith, and C. M. Dobson, *J. Biomol. NMR*, 1997, **10**, 199.
36. W. S. Price, F. Tsuchiya, C. Suzuki, and Y. Arata, *J. Biomol. NMR*, 1999, **13**, 113.
37. J. Balbach, *J. Am. Chem. Soc.*, 2000, **122**, 5887.
38. V. V. Krishnan, *J. Magn. Reson.*, 1997, **124**, 468.
39. J. Lapham, J. P. Rife, P. B. Moore, and D. M. Crothers, *J. Biomol. NMR*, 1997, **10**, 255.
40. J. P. Mackay, G. L. Shaw, and G. F. King, *Biochemistry*, 1996, **35**, 4867.
41. P. W. Kuchel, B. E. Chapman, and A. J. Lennon, *J. Magn. Reson.*, 1993, **A103**, 329.
42. R. Knauss, G. Fleischer, W. Gründer, J. Kärger, and A. Werner, *Magn. Reson. Med.*, 1996, **36**, 241.
43. S. J. Gibbs and C. S. Johnson, Jr., *Macromolecules*, 1991, **24**, 5224.
44. X. Gao and T. C. Wong, *Biophys. J.*, 1998, **74**, 1871.
45. M. Baranowska and K. J. Olszewski, *Biochim. Biophys. Acta*, 1996, **1289**, 312.
46. G. Wider, *Prog. NMR Spectrosc.*, 1998, **32**, 193.
47. M. Mayele and M. Holz, *Phys. Chem. Chem. Phys.*, 2000, **2**, 2429.
48. C.-Y. Li and T. S. Wiedmann, *J. Phys. Chem.*, 1996, **100**, 18 464.
49. L. Orfi, M. Lin, and C. K. Larive, *Anal. Chem.*, 1998, **70**, 1339.
50. L. Orfi, C. K. Larive, and S. M. LeVine, *Lipids*, 1997, **32**, 1035.
51. P. Timmerman, J.-L. Weidmann, K. A. Jolliffe, L. J. Prins, D. N. Reinhoudt, S. Shinkai, L. Frish, and Y. Cohen, *J. Chem. Soc., Perkin Trans. 2*, 2000, 2077.
52. M. Lin and C. K. Larive, *Anal. Biochem.*, 1995, **229**, 214.
53. E. Ilyina, V. Roongta, H. Pan, C. Woodward, and K. H. Mayo, *Biochemistry*, 1997, **36**, 3383.
54. S. L. Mansfield, D. A. Jayawickrama, J. S. Timmons, and C. K. Larive, *Biochim. Biophys. Acta*, 1998, **1382**, 257.
55. J. J. Skalicky, B. R. Gibney, F. Rabanal, R. J. B. Urbauer, P. L. Dutton, and A. J. Wand, *J. Am. Chem. Soc.*, 1999, **121**, 4941.
56. W. S. Price, F. Tsuchiya, and Y. Arata, *Biophys. J.*, 2001, **80**, 1585.
57. B. Andreasson, L. Nordenskiöld, and J. Schultz, *Biophys. J.*, 1996, **70**, 2847.
58. L. van Dam, A. P. Lyubartsev, A. Laaksonen, and L. Nordenskiöld, *J. Phys. Chem.*, 1998, **B102**, 10 636.
59. P. C. Griffiths, P. Stilbs, A. M. Howe, and T. Cosgrove, *Langmuir*, 1996, **12**, 2884.
60. A. Böckmann and E. Guittet, *FEBS Lett.*, 1997, **418**, 127.
61. M. Liu, H. C. Toms, G. E. Hawkes, J. K. Nicholson, and J. C. Lindon, *J. Biomol. NMR*, 1999, **13**, 25.
62. W. H. Gmeiner, C. J. Hudalla, A. M. Soto, and L. Marky, *FEBS Lett.*, 2000, **465**, 148.
63. M. Lin, D. A. Jayawickrama, R. A. Rose, J. A. DelViscio, and C. K. Larive, *Anal. Chim. Acta*, 1995, **307**, 449.
64. A. Gafni and Y. Cohen, *J. Org. Chem.*, 1997, **62**, 120.
65. M. L. Tillett, M. A. Horsfield, L.-Y. Lian, and T. J. Norwood, *J. Biomol. NMR*, 1999, **13**, 223.
66. C. Dalvit, P. Ramage, and U. Hommel, *J. Magn. Reson.*, 1998, **131**, 148.
67. M. Liu, J. K. Nicholson, J. A. Parkinson, and J. C. Lindon, *Anal. Chem.*, 1997, **69**, 1504.
68. M. Lin, M. J. Shapiro, and J. R. Wareing, *J. Org. Chem.*, 1997, **62**, 8930.
69. P. J. Hajduk, E. T. Olejniczak, and S. W. Fesik, *J. Am. Chem. Soc.*, 1997, **119**, 12 257.
70. A. Chen and M. J. Shapiro, *J. Am. Chem. Soc.*, 1998, **120**, 10 258.
71. I. Furó and H. Jóhannesson, *J. Magn. Reson.*, 1996, **A119**, 15.
72. N. Hedin and I. Furó, *J. Magn. Reson.*, 1998, **131**, 126.
73. N. Hedin, T. Y. Yu, and I. Furó, *Langmuir*, 2000, **16**, 7548.
74. A. Jerschow, *J. Magn. Reson.*, 2000, **145**, 125.
75. A. Mohoric and J. Stepišnik, *Phys. Rev.*, 2000, **E62**, 6628.
76. A. Jerschow and N. Müller, *J. Magn. Reson.*, 1997, **125**, 372.
77. W. S. Price, P. Stilbs, B. Jönsson, and O. Söderman, *J. Magn. Reson.*, 2001, **150**, 49.
78. W. S. Price, in 'Annual Reports on NMR Spectroscopy', ed G. A. Webb, Academic Press: London, 1999, Vol. 38, p. 289–354.
79. J. C. Peschier, J. A. Bouwstra, J. De Bleyser, H. E. Junginger, and J. C. Leyte, *J. Magn. Reson.*, 1996, **B110**, 150.
80. S. V. Dvinskikh and I. Furó, *J. Magn. Reson.*, 2000, **146**, 283.
81. M. Czisch, A. Ross, C. Cieslar, and T. A. Holak, *J. Biomol. NMR*, 1996, **7**, 121.
82. B. Håkansson, B. Jönsson, P. Linse, and O. Söderman, *J. Magn. Reson.*, 1997, **124**, 343.
83. Y. Xia, *Concepts Magn. Reson.*, 1996, **8**, 205.
84. W. S. Price, K. Hayamizu, H. Ide, and Y. Arata, *J. Magn. Reson.*, 1999, **139**, 205.
85. P. T. Callaghan, *J. Magn. Reson.*, 1990, **88**, 493.
86. J. Kärger and W. Heink, *J. Magn. Reson.*, 1983, **51**, 1.
87. E. von Meerwall and M. Kamat, *J. Magn. Reson.*, 1989, **83**, 309.
88. M. Holz and H. Weingärtner, *J. Magn. Reson.*, 1991, **92**, 115.
89. A. R. Preston, P. Kinchesh, and E. W. Randall, *J. Magn. Reson.*, 2000, **146**, 359.
90. A. J. Dingley, J. P. Mackay, G. L. Shaw, B. D. Hambly, and G. F. King, *J. Biomol. NMR*, 1997, **10**, 1.
91. M. Andrec and J. H. Prestegard, *J. Biomol. NMR*, 1997, **9**, 136.
92. I. Ardelean and R. Kimmich, *J. Chem. Phys.*, 2000, **112**, 5275.
93. W. S. Price, H. Ide, and Y. Arata, *J. Chem. Phys.*, 2000, **113**, 3686.
94. M. Silva-Crawford, B. C. Gerstein, A.-L. Kuo, and C. G. Wade, *J. Am. Chem. Soc.*, 1980, **102**, 3728.
95. B. Geil, *Concepts Magn. Reson.*, 1998, **10**, 299.
96. J. E. M. Snaar, P. Robyr, and R. Bowtell, *Magn. Reson. Imaging*, 1998, **16**, 587.
97. P. T. Callaghan, M. E. Komlosh, and M. Nydén, *J. Magn. Reson.*, 1998, **133**, 177.
98. P. J. McDonald and B. Newling, *Rep. Prog. Phys.*, 1998, **61**, 1441.
99. I. Chang, G. Hinze, G. Diezemann, F. Fujura, and H. Sillescu, *Phys. Rev. Lett.*, 1996, **76**, 2523.
100. W. Zhang and D. G. Cory, *Phys. Rev. Lett.*, 1998, **80**, 1324.
101. S. V. Dvinskikh and I. Furó, *J. Magn. Reson.*, 2000, **144**, 142.
102. S. Gaemers, C. J. Elsevier, and A. D. Bax, *Chem. Phys. Lett.*, 1999, **301**, 138.
103. W. S. Price, M. Nara, and Y. Arata, *Biophys. Chem.*, 1997, **65**, 179.
104. V. A. Daragan, E. Ilyina, and K. H. Mayo, *Biopolymers*, 1993, **33**, 521.

105. C. H. Everhart and C. S. Johnson, Jr., *J. Magn. Reson.*, 1982, **48**, 466.
106. A. S. Altieri, D. P. Hinton, and R. A. Byrd, *J. Am. Chem. Soc.*, 1995, **117**, 7566.
107. K. Adachi, M. Natsuisaka, and A. Tanioka, *J. Chem. Soc., Faraday Trans.*, 1997, **93**, 3347.
108. W. J. Chien, S. F. Cheng, and D. K. Chang, *Anal. Biochem.*, 1998, **264**, 211.
109. S. J. Gibbs, A. S. Chu, E. N. Lightfoot, and T. W. Root, *J. Phys. Chem.*, 1991, **95**, 467.

Acknowledgements

WSP thanks the Swedish Council for International Cooperation in Research and Higher Education (STINT) for financial support. Dr. István Furó and Professor Olle Söderman are thanked for critically reading the manuscript.

Biographical Sketch

William S. Price, *b* 1964. B.Sc. 1986 and Ph.D. 1990 University of Sydney. Postdoctoral fellow the Institute of Atomic and Molecular Science in Taipei, Taiwan 1990–1993 (with Lian-Pin Hwang) and the National Institute of Material and Chemical Research in Tsukuba, Japan 1993–1995 (with Kikuko Hayamizu). Between 1995 and 1999, Chief Scientist, Water Research Institute in Tsukuba, Japan. More than 60 publications. Research interests include pulsed gradient spin-echo NMR, NMR microscopy, spin relaxation, water suppression and solid state ^{2}H studies.

Dynamics of Water in Biological Systems: Inferences from Relaxometry

Seymour H. Koenig
Relaxometry, Inc., Mahopac, NY, USA

1	Introduction to Relaxometry	1
2	Protein–Water Interfaces	2
3	Lipid–Water Interactions	6
4	Quantification of the Dynamics of Water on the Molecular Scale: Results from Magnetic Solutes	8
5	Water as a Viscous Vacuum	10
6	Concluding Remarks	10
7	Related Articles	11
8	References	11

1 INTRODUCTION TO RELAXOMETRY

The demonstration half a century ago of proton NMR in liquid water by Bloch et al.[1,2] and in solid paraffin by Purcell et al.[3] came one year after Rabi received the Nobel Prize (1944) 'for his discovery of a resonance method for recording the magnetic properties of atomic nuclei'; i.e., for discovering NMR. Rabi and his associates had worked with radiofrequency (rf) resonant transitions in atomic and molecular beams since the mid-1930s.[4,5] By the time of the discoveries of Bloch and Purcell, the proton g-value was known to six-figure accuracy,[6] the concept and language of rotating frames were in place,[7–9] and wartime technological advances were such that it was clear that a proton NMR signal could be seen in condensed matter well above noise at the then attainable fields 'provided that thermal equilibrium could be established in a reasonable time'.[3] The major unknown was the longitudinal relaxation time T_1 of protons, a parameter that has no relevance in beam measurements; early estimates for proton relaxation times for the condensed state were minutes to hours.[10] Bloch et al. used 'paramagnetic catalysts ... to accelerate the establishment of thermal equilibrium';[1] they added trace amounts of ferric nitrate to their water samples.[2] In addition they used the 'nuclear induction' signal generated by proton magnetization precessing in the transverse plane to help circumvent problems associated with a long T_1. Purcell et al. measured absorption using an rf bridge and a very low power level, such that 'the absorption would persist for hours regardless of the relaxation time, once thermal equilibrium had been established'.[3]

A fairly complete theory of proton relaxation in diamagnetic liquids, e.g. water and its mixtures with glycerol, and in solutions with trace millimolar amounts of small paramagnetic solutes was developed in short order.[11–14] The basic concept is that of 'motional narrowing' of the interaction ω_{int} (the intrinsic uncertainty width) that induces relaxation in liquid systems. The rapid Brownian motion of liquid molecules reduces the uncertainty width by the factor $\omega_{\text{int}}\tau_c \ll 1$, where τ_c is a correlation time that characterizes the timescale of the Brownian fluctuations. The result, in the limit of the external field B_0 approaching zero, is

$$1/T_1 = 1/T_2 \simeq 6\omega_{\text{int}}(\omega_{\text{int}}\tau_c) \quad (1)$$

for the interaction of two identical nuclei with spin of $\frac{1}{2}$. For protons of water the fluctuating interaction is a sum over the magnetic dipolar interaction of all pairs of protons (dominated by the intramolecular water proton–proton interaction of about 5 Oe). Where ω_{int} ($\sim 10^5$ s^{-1}) is the angular Larmor precession frequency ω_L of a proton in this interaction field and τ_c ($\sim 3 \times 10^{-12}$ s at 25 °C) is determined by the Brownian reorientational time of a water molecule since the magnetic interaction of two protons is a function of their spatial orientation. For water deuterons, the fluctuating interaction is that of the nuclear quadrupolar moment with the gradient of the electric field at the nucleus. For deuterons ω_{int} is three times larger than for protons, leading to intrinsic relaxation rates for deuterons that are ten times greater than for protons in analogous diamagnetic systems. The six-fold lower g-value of the deuteron makes magnetic interactions of deuterons, e.g. with proton and electronic moments, 40 times less than the analogous proton interactions and generally ignorable. However, for both protons and deuterons of solvent water, any diamagnetic solute (or other variable, such as temperature) that slows the motion of a water molecule, on average, reduces the effect of motional narrowing and thereby increases relaxation rates at low fields by comparable factors. Both $1/T_1$ and $1/T_2$ decrease with increasing B_0, with a Lorentzian dispersion centered near $\omega_L\tau_c = 1$. Hence there is a need for measurements of relaxation rates over a wide range of B_0 if relaxation mechanisms are to be studied effectively.

Early applications of proton NMR were directed towards an understanding of the molecular dynamics of water molecules in water solutions, i.e. the nature of microscopic viscosity, self-diffusion of solvent, Brownian motion of hydrated paramagnetic solutes and the lifetimes of solute–solvent complexes. The data were the relaxation rates of the majority solvent protons, as a function of temperature and, to the extent possible, as a function of the applied field B_0, since available NMR resolution and signal intensity were inadequate to resolve structure in the water line and certainly inadequate to detect solute nuclei. Hence the relaxation rates of solvent water nuclei served as indicators of solvent interactions with solute. With advances in magnet technology and electronics, 'higher resolution' NMR became possible, and research emphasis shifted to measurements of proton spectra in water solutions of relatively small solutes. Increasingly higher fields, superconducting magnets, signal averaging and Fourier transform methodologies have brought applications of high-resolution NMR to 600 MHz and beyond, with multidimensional high-field spectroscopy now routinely applied to solute polymers, polypeptides, and increasingly larger proteins.

As spectroscopy has advanced, so has 'relaxometry', the field—in analogy with spectroscopy—that includes the measurement and theory of, and instrumentation ('relaxometers') for, increasingly sophisticated investigations of relaxation rates

of (mainly) water nuclei in progressively more complex systems, both diamagnetic and paramagnetic. ('Relaxometry' and 'relaxometer' are terms coined by the author in 1983.) Initially, as noted, relaxometry was the approach of choice for the study of water dynamics in simple solute–solvent systems. When early improvements in resolution of NMR signals made possible the direct study of spectral lines of small solutes, relaxometry was applied, typically, to solutions of paramagnetic metalloproteins, including their complexes with small substrates and activators; the area now called 'bioinorganic chemistry.' With further improvements in NMR resolution, and the advent of proton spectroscopy of small protein solutes, relaxometry became the approach of choice for studying the dynamics of water in progressively more complex systems, including tissue. This was aided by the development of a field-cycling relaxometer,[15] based on the early ideas of Redfield,[16] that could record the dependence of $1/T_1$ on B_0 (called a nuclear magnetic relaxation dispersion (NMRD) profile) automatically, under computer control, over almost four decades of B_0. The discussion of the dynamics of water in biological systems presented here is based on NMRD data obtained with our field-cycling relaxometers.

In magnetic resonance imaging (MRI) in clinical diagnostic radiology, an increasingly important application of high-resolution NMR, the image generated is a three-dimensional spatial representation of tissue dependent relaxation rates of the volume of interest. Most tissues contain about the same amount of water, ostensibly for reasons of osmotic equilibrium, so MRI would be ineffectual unless signal intensity was weighted by some parameter other than (water) proton density. This has stimulated research on relaxation processes of water protons in complex systems, including several different tissues, and their model systems. We now have a relatively complete molecular theory of relaxation of water protons in tissue[17] (which is mostly water and immobile protein), as well as in solutions of proteins, both native and immobilized; the latter is an excellent model system for the relaxation behavior of water protons in most tissues. Much has been learned about the dynamics of water molecules in these macromolecular biological systems, particularly regarding the details of dynamic and magnetic protein–water interfacial interactions and, to a lesser extent, lipid–water interfacial interactions. Pertinent data, chosen to support the generalizations made here regarding water dynamics, are collected in this article. The theory and a short discussion of the instrumentation are given in another article in this Encyclopedia (***Relaxometry of Tissue***).

The emphasis throughout this article is on broad generalizations regarding the behavior of water in biological systems, concepts that have come from relaxometry investigations. In particular we argue for the view that water, even in complex tissues, is no more structured than is pure water, and that the water molecules in each have comparable mobility and diffusivity. In essence, solvent molecules, as regards their molecular dynamics—which in turn determines nuclear relaxation rates—really do not learn about the presence of small or macromolecular solute until solute and solvent molecules collide physically, essentially at their hard-core radii. The overall water dynamics are altered imperceptibly by these collisions and associations. However, relaxation rates are very sensitive to the details of these collisions—because of the possibility of massive, although momentary, lengthening of τ_c—and to the possibility of diffusion of proton magnetization in immobile macromolecules. The far-ranging result is a very rich set of phenomena that can be encompassed by a simple picture of water dynamics in biological systems.

2 PROTEIN–WATER INTERFACES

2.1 Water Deuteron $1/T_1$ NMRD Profiles in Systems of Immobile Protein

The data shown in Figure 1 are perhaps the most telling for the major generalization made here. They include $1/T_1$ NMRD profiles of deuterons in water–protein systems in which the protein is not free to rotate:[18] two samples of bovine serum albumin (BSA, 68 kDa) in water at relatively low concentrations, initially liquid, in which the solvent protein was immobilized by chemical cross linking; a third, otherwise identical sample, in which the macroscopic viscosity of the solvent was increased seven-fold by the addition of dextran before cross linking; and a sample of cross-linked bovine carbonic anhydrase (BCAB, 30 kDa), about one-half the molecular weight of BSA. (The solid curve is an empirical fit to the data for these four samples, for clarity.) A fifth sample was powder,[19] BSA hydrated to 50% by weight (corresponding to about four water hydration layers per BSA molecule). The profiles are all normalized to their low field values after

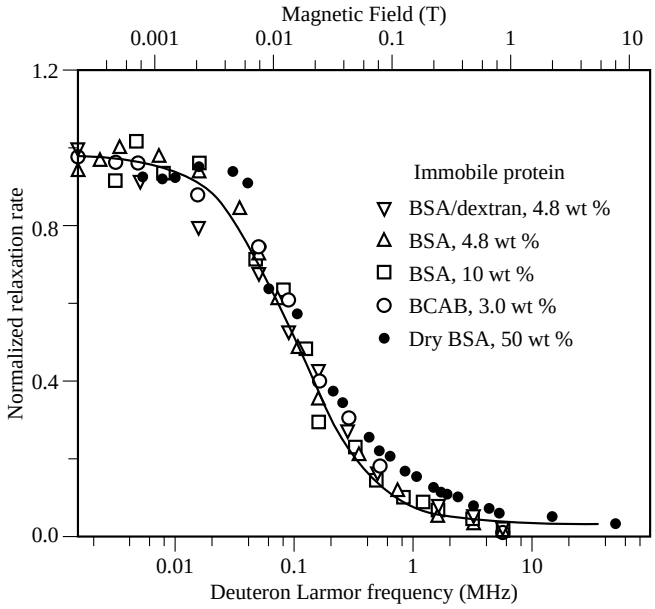

Figure 1 $1/T_1$ NMRD profiles of water deuterons for five samples of immobile proton, all normalized to the same vertical scale after subtraction of $1/T_1$ of solvent at each temperature. (∇,△) 4.8 wt %, chemically cross-linked BSA (68 kDa) at 35 °C, the first (∇) containing 70 mg ml^{-1} dextran, which increases the macroscopic solvent viscosity by a factor of 7.4. (□) As (△), but with 10% BSA. (○) 3 wt % BCAB (30 kDa) at 25 °C. The solid curve is an empirical fit to the profiles of these four samples, with ν_c = 0.097 MHz. The curve is for visual clarity, and has no theoretical importance in the present context. The low field rates, above the solvent background are, respectively, 42, 44, 75, and 24 s^{-1}. (●) Powder, dried BSA rehydrated to 50 wt % water, at 18 °C.[19] (Reproduced by permission from S. H. Koenig, R. D. Brown III, and R. Ugolini, *Biophys. J.*, 1988, **53**, 77)

subtraction of the background rate of pure water, to show that the normalized functional forms of the five profiles of these disparate samples are essentially the same. Deuterons were measured, rather than protons (although their signal is smaller than for protons and more difficult to obtain accurately), because their relaxation is predominantly electric quadrupolar. As a result, changes in their relaxation rates induced by solute arise only from (subtle) alterations of the molecular dynamics of the water solvent, uninfluenced by magnetic interactions. What do such data indicate?

The five samples all appear to be relatively solid, the cross-linking (in four of them) creating an extended network of immobile protein which entrains solvent water by capillarity. However, the proton NMR signals from the water deuterons in all the samples indicate that essentially all the water is highly liquid and mobile. That the normalized profiles of the 4.8 and 10% BSA samples have the same form, after correction for the uniform water background ($\sim 2\,s^{-1}$ at 35 °C, which is a significant fraction of the observed rates, particularly above ~ 0.5 MHz), means that the intrinsic $1/T_1$ contribution of the solvent water when not in interaction with the protein (i.e. τ_c, and therefore the Brownian rotation of the bulk water) is unaltered by the presence of solute protein. Similarly the presence of dextran in one sample, which increases solvent viscosity seven-fold, neither alters the form nor the magnitude of the NMRD profile. The correction for water background is essentially that for pure water, assumed to be unaltered by the large change in macroscopic viscosity. The data are similar for carbonic anhydrase, which shows that BSA is not unique in its surface properties. The most intriguing results are those for BSA hydrated powder. The very existence of a signal shows that most of the water in the four monolayers is highly mobile, i.e. the dynamics of a two-dimensional array of four monolayers of water molecules abutting a protein interface is very much like that of pure three-dimensional water.

The major question is what the inflection frequency ν_c (Figure 1) (at the half magnitude ~ 0.1 MHz) represents. It corresponds[20] to $\tau_c \simeq 1/11\nu_c$, or $\tau_c \simeq 1\,\mu$s because of factors of 2π and the contributions of both single- and double-quantum transitions to relaxation. We have only recently[17,18] been able to associate this correlation time with the lifetime of a class of water molecules held rigidly at two sites (rounded) per BSA molecule (one monolayer corresponds to 700 water molecules). It was argued that these two water molecules are bound in a very specific configuration by four hydrogen bonds, an accident of the geometry of protein surfaces. The conjecture is that one proton of a coordinated water binds symmetrically to the two oxygen atoms of a deprotonated surface carboxylate, attached by two hydrogen bonds. The other proton could bind similarly to a nearby carboxylate or, as found recently in a neutron diffraction study of myoglobin (B. Schoenborn, private communication), symmetrically between the deprotonated nitrogen atoms of two surface histidines. An estimate of the water lifetime, obtained from the energy required to break four such bonds (2.6 kcal mol^{-1} or ~ 5 kT each) and the infrared stretching frequency of such bonds ($\sim 3 \times 10^{12}$ s^{-1}), are consistent with the τ_c evident in Figure 1.

The foregoing leads directly to a 'two-site rapid exchange' view of relaxation in these systems, which we favor: water molecules bind at specific protein–water interfacial sites, at which the slowed motion increases their relaxation rates in situ. The resident lifetimes should be shorter than the interfacial T_1 values or the effect of binding will be limited by 'slow exchange'. Because of their quadrupolar relaxation, binding of deuterons will not alter the strength of the interaction that relaxes them, but will change the correlation time. The extent of this change for the samples (Figure 1) is known. Increases in τ_c from 3 ps in solution to $1\,\mu$s when bound leads to only two bound water molecules in rapid exchange being necessary to explain these data. It follows that all the other interfacial water molecules must have much shorter lifetimes. This view implicitly leads to an approach that readily allows—indeed requires—the various water molecules that hydrate protein to be grossly inequivalent. Some authors have taken exception to this in explaining water relaxation in protein and colloidal systems, noting without argument that the bound 'state comprises an unphysically small number of water molecules',[21] and have looked for mechanisms in which all interfacial water molecules behave identically at all interfacial locations, altered in their motion by the imposition of a very small order parameter with a long relaxation time, by unknown mechanisms. The data shown in Figure 1 and the discussion given in the next section make this view untenable; the small number of long-lived interfacial water molecules is indeed the physical reality.

2.2 Water Deuteron and Proton $1/T_1$ NMRD Profiles in Solutions of Mobile Protein

Figure 2 shows both deuteron and proton $1/T_1$ profiles of solutions of native (mobile) carbonic anhydrase for solvents of differing isotopic composition.[22] For deuterons the profiles are independent of whether water is partially or fully deuterated. This is as expected, since a deuteron is relaxed by very local interactions of its quadrupole moment with the local electric field gradient. A second point of note is that the quasi-Lorentzian form of the profile, although much like that of immobile carbonic anhydrase (Figure 1) has $\nu_c \simeq 4$ MHz, i.e. 40 times higher for mobile than immobile protein. It has been known for some time,[23,24] and demonstrated for almost three decades of molecular weight,[20] that ν_c for mobile proteins is determined in the main by the Brownian rotation of solute and is calculable from Stokes' law.

In contrast to the deuteron profiles, those for protons are dependent upon whether a water proton has another proton as its neighbor. However, this dependence is much less than the expected linear dependence on $1/T_1$ (including the solvent background) with proton dilution. This is the most direct evidence that interactions between solute and solvent protons ('cross relaxation'[22]) contribute to solvent proton relaxation. The extent of the contribution of cross relaxation to each sample can be inferred from the broken curves, which show the proton $1/T_1$ profiles predicted from the deuteron results, assuming no cross relaxation for protons. It is evident that cross relaxation and 'hydrodynamic' relaxation (for protons) are comparable for a protein of 30 kDa, even with undeuterated solvent.

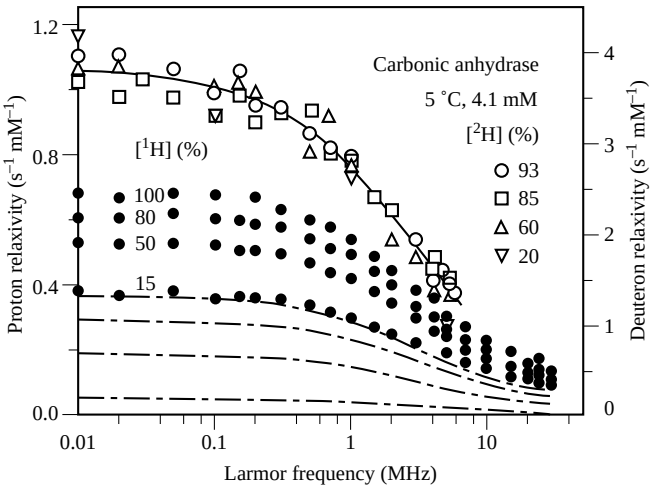

Figure 2 $1/T_1$ NMRD profiles of water deuterons (open symbols) and protons (filled symbols) for samples of 4.1 mM native (mobile) BCAB (30 kDa), at 5 °C. The data are expressed as relaxivity, the value of $1/T_1$, with the solvent contribution subtracted, per mM of solute protein. For the deuteron profiles, the water was 93% (○), 85% (□), 60% (△), and 20% (▽) deuterated. The solid curve is a fit to these profiles, which are seen to be independent of solvent isotopic composition. The broken curves are the profiles expected for protons, based on the deuteron results, taking into account only the different intrinsic relaxation rates of deuterons and protons in pure water. For the measured proton profiles, the water was 100, 80, 50, and 15% protonated. In each case, the relaxivities were significantly about the broken curves, indicating a significant contribution to the relaxivities arising from interactions between solute and solvent protons (cross relaxation). (Reproduced by permission from S. H. Koenig, R. G. Bryant, K. Hallenga, and G. S. Jacob, *Biochemistry*, 1978, **17**, 4348)

2.3 Conjectured Classes of Other Protein–Water Interfacial Binding Sites

We have argued for a class of interfacial binding sites with water molecules, held in place by four hydrogen bonds, having $\tau_M \simeq 1\,\mu$s. What then of three bonds, two bonds, etc? Table 1 gives our estimate of the interfacial lifetimes of these other configurations and the associated values of ν_c when protein rotation can be ignored. Each added bond is estimated to increase τ_M by a Boltzmann factor of about 50. What follows are data that support the table entries. The picture that emerges of the nature of the protein–water interface in solution is one of several (four) classes of water-binding site, each with a narrow and identifiable range of water lifetimes and increasing in number as the stereochemical requirements become less restrictive.

2.4 Influence of Protein Molecular Weight on Water Proton $1/T_1$ NMRD Profiles

Figure 3 shows proton $1/T_1$ profiles[24] for solutions of the same total protein content, but with molecular weights ranging from 14 to 450 kDa. For water molecules with $\tau_M \simeq 1\,\mu$s ($\nu_c \simeq 0.1$ MHz), this lifetime is sufficiently long to sense the protein rotation of all the proteins shown in the figure. It is only when the molecular weight becomes about 10 times greater than that of hemocyanin (∼5000 kDa) that Brownian

Table 1 Values of the Lifetime τ_M of a Water Molecule bound at a Protein–Water Interface when Held by n Hydrogen Bonds, Near 25°C[a]

n	τ_M	$\nu_c = \frac{1}{2}\pi(\sqrt{3})\tau_M$ (MHz)	B_0 (T)
4	1 μs	0.1	0.0024
3	20 ns	5	0.12
2	400 ps	250	6
1	8 ps	12500	300

[a]For immobile protein, τ_M becomes the correlation time for interfacial interactions, leading to an inflection in the NMRD profile at nuclear Larmor frequency ν_c, corresponding to a magnetic field B_0 for protons.

rotation is too slow to be sensed by these long-lived water molecules,[25] and so this is not a concern here. However, τ_M for three bonds was found[17] to be 23 ns in a particular case, which corresponds to $\nu_c \simeq 4$ MHz, a field well above the major dispersion of hemocyanin. A contribution from such shorter lived sites is clear in the hemocyanin data, shown here for proton profiles of a native mobile protein for the first time. The two solid lines represent true Lorentzian dispersive contributions to $1/T_1$, ostensibly the 1 μs and 20 ns sites, the latter with 5.2 times the population, and with values of ν_c of 0.4 and 4.0, respectively. For the lower field curve the dispersion relates to protein rotation, whereas for the higher field curve the dispersion arises from τ_M. The two curves sum to the open symbols (√), which clearly represent the data quite well.

The existence of three-bond sites has been argued for recently[17] (see ***Relaxometry of Tissue***), based mainly on extensive theoretical analysis of proton profiles of cross-linked BSA in highly deuterated solutions, to emphasize cross relaxation, but has also been deduced from analyses of data such as those shown in Figure 1. However, the density and lifetime of this three-bond class of sites are such that their contribution to relaxation can only be deduced with some certainty in special circumstances, including the high molecular weight hemocyanin (Figure 3), and then only if the existence of such sites is suspected.

The four- and three-bond sites still leave 97% of a hydrogen monolayer unaccounted for. Two-bond sites should have $\nu_c \simeq$ 250 MHz and $\tau_M \simeq 400$ ps, as in Table 1. Extensive arguments were given some time ago from the first NMRD profiles of protein solutions for sites with these characteristics:[23] they are ostensibly associated with water molecules surrounding polar groups at the protein–water interface, comprising about one-third of a hydration monolayer.[26] Quite recently, results of multidimensional NMR at 600 MHz were reported[27] for a very small protein (7 kDa), bovine pancreatic trypsin inhibitor—a protein too small to have any four-bond sites and few three-bond sites. The finding was that no water lifetimes were longer than about 300 ps, which is consistent with the foregoing discussion, although the fraction of interfacial water molecules that might exchange more rapidly was not determined.

The lifetime of a water molecule held by a single bond (Table 1) should be about 8 ps. This is only three times greater than the rotational relaxation time of a free water molecule at 25 °C. Even a monolayer of such bonds in a concentrated protein solution would contribute minimally to $1/T_1$, and be difficult to identify. It should be emphasized that it is very difficult to obtain an estimate of this value from the literature. An assiduous search was made earlier, when the relaxivity of

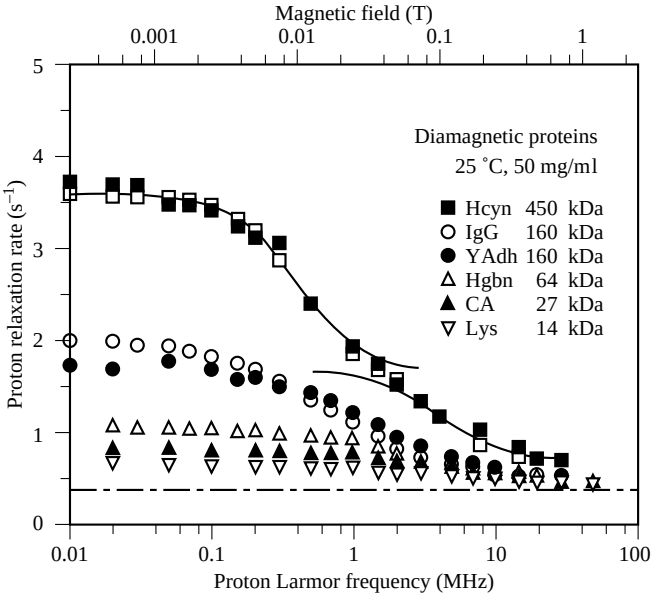

Figure 3 $1/T_1$ NMRD profiles of water protons in solutions of native proteins of various molecular weights, at a fixed concentration of 50 mg ml^{-1}, at 25 °C: (■) hemocyanin (450 kDa); (○) immunoglobulin G (160 kDa); (●) yeast alcohol dehydrogenase (160 kDa) (▲) bovine carbonic anhydrase (30 kDa); (▽) lysozyme (14 kDa). The broken horizontal line is the solvent background rate. The two solid curves associated with the hemocyanin data are Lorentzians, the sum of which (□) matches the data; they have ν_c values of 0.8 and 4.0 MHz. The lower field Lorentzian is, in our view, associated with exchange of water molecules bound at sites with lifetimes of about 1 μs, i.e. sufficiently long to sense the Brownian rotation of solute, and the higher field Lorentzian is associated with sites of lifetimes of about 20 ns, which is sufficiently short that the lifetime determines ν_c. (Reproduced by permission from K. Hallenga and S. H. Koenig, *Biochemistry*, 1976, **15**, 4255)

nitroxide radicals was studied in some detail.[28] There is clearly no formal inner coordination sphere for these solutes, but there was a question of whether they formed short-lived hydrogen-bonded complexes with solvent water. The conclusion was that any such complexes had to have lifetimes less than the rotational relaxation time of the nitroxide ($\lesssim$500 ps).

Relaxation of water deuterons by montmorillonite clays, which contain large lamellar particles with atomically smooth surfaces and oxygen atoms pointing to the water, were studied[29] in some detail to investigate interfacial interactions in these well-defined systems. Deuterons were measured to minimize artifactual contributions from possible paramagnetic impurities and interlamellar spacing was adjusted by dilution with solvent. The finding was a small contribution to $1/T_1$ that could be explained by a monolayer of water molecules being slowed in their rotation by a factor of about 5. We suggest that this could arise from the formation of a single hydrogen bond between each interfacial water proton with an uncharged surface oxygen atom. The major point is how little the motion of water is influenced by surfaces that have no special sites for enhancing solute–solvent interactions.

The power of computers and computing algorithms has advanced significantly during the last decade. Relevant interatomic and intermolecular interaction potentials are also well known, so that the molecular dynamics of water in relatively complex systems can be computed reliably to times approaching several hundred picoseconds. In a recent computation[30] of water interacting with myoglobin (15 kDa), the highly local self-diffusion constant of water was calculated near to the solute–solvent interface. The major result, as read by this author, is how little water is affected by the protein. Major questions would be whether the local diffusion constant is two- rather than three-fold different from its value in bulk water. There is no structure induced in the water, either temporal or spatial, other than that demanded by hard-sphere geometry, certainly to first order. Unfortunately, τ_M values for our three- and four-bond sites are far longer than the limits of such computations, although there are a few pockets of depressed diffusion that hint at the influence of these sites on local water dynamics.

2.5 Water Proton $1/T_1$ NMRD Profiles in Systems of Immobile Protein

The picture becomes complete when proton $1/T_1$ NMRD profiles of immobilized protein systems are also considered. Figure 4 shows[18] that, in contrast to deuterons, for protons the functional form of the profiles is dramatically altered by immobilization. Moreover, the profiles become like those of tissue, most of which have the same form but differ in magnitude.[20] Without going into details of theory and mechanism, which are covered elsewhere in this Encyclopedia (***Relaxometry of Tissue***), we note that—whether measured in a relaxometer or imager, or whether one measures $1/T_1$, $1/T_2$, or $1/T_{1\rho}$ at any field or temperature—it is not possible to

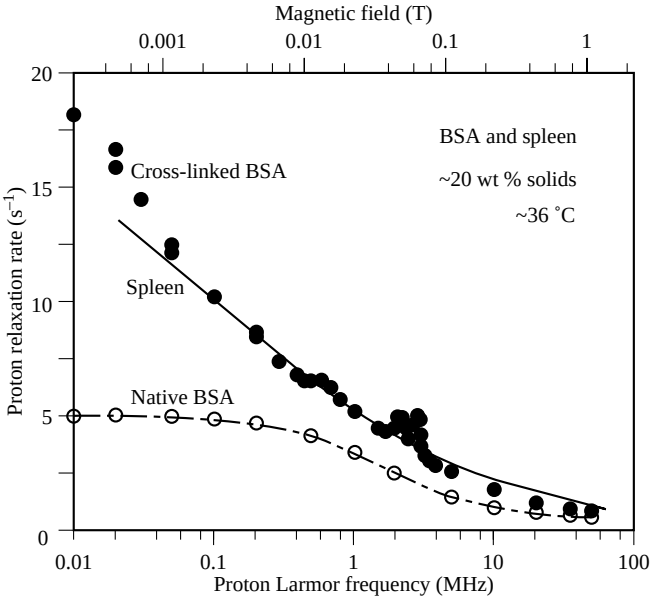

Figure 4 $1/T_1$ NMRD profiles of water protons of three samples with essentially the same (~20 wt %) solids content, at physiological temperature: human spleen (solid curve), native bovine serum albumin (○), and the same sample immobilized by chemical cross linking (●). Such cross-linked protein is an excellent model system for most tissue, so much so that the two cannot be distinguished by measurements in either a relaxometer or an imager[17] (Reproduced by permission from S. H. Koenig, R. D. Brown III, and R. Ugolini, *Magn. Reson. Med.*, 1993, **29**, 77)

distinguish a sample of, for example, cross-linked BSA from a typical tissue (exclusive of white matter and adipose tissues, both with different but significant lipid contributions). A ready inference is that water is not compartmentalized in tissue on a relaxation timescale, otherwise one would see tissue-specific effects. Most protein in tissue, which usually contains no more than protein and water, is also immobile.

The difference in functional form between proton and deuteron profiles in immobile systems (see Figures 1 and 4), but not mobile systems (Figure 2), must relate to the presence and absence, respectively, of cross relaxation for these two nuclei plus an increase in the importance of cross relaxation in immobilized systems. Briefly, the change relates to the mobility of proton magnetization in immobile systems, for which relaxation is like that in the solid state, and its absence in liquid state systems, where motional narrowing holds. For the solid state mutual spin flips of neighboring protons serve to transport Zeeman energy without loss of magnetization, since there are few fluctuations to relax the magnetization to the 'lattice'. Thus spin diffusion in the solute and chemical diffusion in the solvent generate a combined system that can be modeled as two Zeeman reservoirs. Each of these has spatially uniform magnetization which is coupled through interfacial interactions that transfer energy between the reservoirs. For protein–water systems the four-bond sites serve not only as the dominant sites for such transfer but, because of the relaxation that occurs at these sites, also serve as the major sites for relaxation of the total Zeeman energy with the thermal energy of the sample[17] (see also ***Relaxometry of Tissue***). For the liquid state, appropriate for mobile protein, the situation changes dramatically. Unlike the solid state case, for which mutual spin flips derive from the precession of a proton in the static interaction field, mutual spin flips arise from the zero quantum transitions generated by a fluctuating interaction field (ω_{int}). However these also generate single- and double-quantum transitions that relax the diffusing magnetization.[20] The net result is that the Zeeman energy of most of the solute is not in good contact with solvent and the potential amount of cross relaxation is reduced. In fact, as can be seen from Figure 2, the contributions of cross relaxation and hydrodynamic relaxation to $1/T_1$ of protons is comparable. That is, each proton of a water molecule bound at a $1\,\mu$s site is relaxed comparably by its intramolecular proton and protons of the protein. This conclusion was derived previously[17] by a quantitative analysis of the proton profile of cross-linked BSA in highly deuterated solvent. Put another way, Zeeman energy does not diffuse very far in liquids unless it is transported chemically.

2.6 Summary of the Dynamics of Water in Diamagnetic Protein–Water Systems

The picture presented so far, which derives from relaxometry measurements of deuteron and proton $1/T_1$ NMRD profiles of water in a range of protein–water systems of increasing complexity, models water as a slippery hard sphere. Despite the extended hydrogen bonding within the extended liquid, water can rotate substantially and move its own radius in times no longer than about 10 ps. These multiple bonds do not impede the rotational (or translational) motion of a water molecule; this time is 3 ps, not $1\,\mu$s. The reason for this is that rotation of a water molecule involves a concerted breaking and reforming of four bonds, which does not impose the energy requirements associated with removing a water molecule from an interfacial protein–water site, akin to evaporating it into the solvent. This is a major point, since the distinction amounts to more than six orders of magnitude difference in the relevant rate processes. (It is also not established theory, but an observation that is part of, and follows from, the larger picture of water mobility in biological systems, as discussed here.)

Macromolecular solutes (and small solutes) influence the molecular dynamics of water molecules only during physical collisions at solute–solvent interfaces. For proteins it was shown that four classes of interaction can be distinguished, corresponding to binding of water molecules to the protein by one, two, three, or four hydrogen bonds. For four bonds, the lifetime τ_{M} of the complex is about $1\,\mu$s; the lifetime is proportionately shorter for the other configurations (see Table 1). The relative densities of such sites appear to be similar for most proteins, including the proteins of most tissue, at least near physiological values of pH. The values of $1/T_1$ are very sensitive to the long values of τ_{M}, a $1\,\mu$s site generating an almost a million-fold enhancement of the magnitude of the perturbed water dynamics, making relaxometry relevant to MRI diagnostic radiology.

3 LIPID–WATER INTERACTIONS

Lipids, although minority constituents of tissue, are all important in that they form membranes which control the spatial organization of both macromolecules and small ions within and between cells. The interactions that concern us are interfacial, with the added feature that water can, and does, permeate membranes. The discussion in the earlier sections shows that, to first order, the presence of a plethora of membranes does not restrict the motion of water on a relaxation timescale (with the possible exception of organs designed to filter body fluids, such as kidney). The permeability to water of realistic biological membranes is often greater than in their analogs because of specialized pores that enhance water exchange. Nonetheless, exchange is also rapid in ideal systems, as expected from the generalizations presented above for water in protein and tissue and now extended below to water in lipid.

3.1 Myelin of White Matter

Myelin is the lipid of white matter, the membranes of specialized cells that generate a lipid–cytoplasm–lipid– ... 'jelly-roll' of electrical insulation and structural rigidity that surrounds the long axons which connect grey matter with other parts of the brain and beyond. About half the lipid includes a range of (unusual) phospholipids, with the polar and charged groups projecting into the intra- and extracellular spaces. Their contribution to the $1/T_1$ of white matter, as expected from the small contribution to the $1/T_1$ of the polar groups in the hydration layers of protein,[26] is too small to be resolved with any certainty in lipid systems[31] because of their limited solubility. On the other hand, half of the myelin lipid is cholesterol, a multiring alcohol that is highly insoluble in water and which adds to the stability of lipid–water systems by

dissolving in the lipid phase with the alcohol moiety projecting into the aqueous phases. This provides an extensive array of opportunities for interfacial hydrogen bonding. The presence of cholesterol also rigidifies the membrane, making it more like the solid state, and thereby increasing cross relaxation between water and lipid protons.[32] Studies of the NMRD profiles of white matter contain a contribution to $1/T_1$ from myelin that can be explained by assuming that each cholesterol has a hydrogen-bonded water with a lifetime of about 200 ps. (This corresponds to a continuous surface about 15 times more effective[31] at relaxing water than montmorillonite clay.[29]) From the data on interfacial interactions of water and protein (see Table 1) this suggests a geometry with two hydrogen bonds. The stereochemistry remains to be described, but the picture that emerges—particularly in the larger context—is quite satisfying. As an aside, the foregoing means that the widely known images of the adult brain in T_1-weighted MRI, in which white matter is much brighter than gray matter, is a map of the intact cholesterol-containing myelin of the white matter.[31] This relative brightness is not found in unmyelinated white matter of infants and it is altered in white matter disease by mechanisms that have yet to be quantified.

3.2 Permeability of Lipid Bilayer Membranes to Water

The water of myelin is about 15% of the water of white matter, so that unless it mixes with the majority (intra-axonal) water within the appropriate relaxation time (at physiological temperatures), myelin could not contribute to $1/T_1$ as generally measured. On a grander scale, white matter would not appear brighter than gray matter in MRI, since it is myelin that contains the needed relaxation sites. The question is what determines the permeability of lipid bilayers to water?

Here we elaborate the view that there is little that impedes the dynamics of a given water molecule in an extended solvent; water in water or water in lipid? Simply put, the molecular dynamics of water moving through an H_2O environment cannot be much different from water moving through an H_2C environment (the methylene groups that dominate lipid environments). The major difference between water and lipid environments arises from, on average, the four hydrogen bonds that a water molecule makes with its nearest water neighbors and which is absent for water in lipid.

A second difference between a water molecule in water and one in lipid is their different energies; water is highly polar (i.e. has a high dielectric constant), lipids are not. Call it image forces, electrostatics, or something more sophisticated, the extra electrostatic energy of a water molecule within a lipid reduces its probability of being there when it can be elsewhere—in particular when it can be in bulk water in contact with lipid. Thus the partition coefficient of water in water compared with water in lipid can be many orders of magnitude in favor of there being little water in the lipid. However, once there, given that the diffusion of water in lipid must be close in value to the self-diffusion of water, one can readily estimate that, for a water molecule somewhere within a (typical) 15 nm thick lipid membrane, water will escape in less than 50 ns. This view, based on the idea that it is in general very difficult to hold a water molecule chemically or physically, is the essence of the dissolve-and-diffuse theory of membrane permeability, which has been reviewed elsewhere.[33] Although not universally accepted, it is a simple and broadly applicable concept that follows from a larger picture of the dynamics of water in biological and related systems.

It is not simple to measure the permeability of bilipid layers either accurately or rapidly. An NMRD method was reported recently[34] which is rapid and accurate for those lipids that can be made to form unilamellar vesicles of relatively uniform size, something that is not too difficult to do in many instances. The technique is to entrain a chelated paramagnetic ion, of known NMRD profile, within the vesicles at a sufficiently high concentration such that $1/T_1$ within the vesicle is comparable to or less than the time it takes for a water molecule to 'escape' from the interior of the vesicle by permeation. The details are given elsewhere,[34] but typical results are shown in Figure 5. Here the influence of temperature and cholesterol on the permeability of POPC (1-palmitoyl-2-oleoyl-phosphatidylcholine) vesicles is shown for 100 nm diameter vesicles. The paramagnetic ion is Gd(DTPA) (diethylenetriaminepentaacetic acid), the relaxivity of which has been examined in great detail[20] given that it is used extensively as a contrast-enhancing agent in MRI. The accuracy or, at least the reproducibility, of the method can be gleaned from Figure 5. Data for one sample can be collected and analyzed in half a day. Interestingly, the escape time is of the order of milliseconds, which is shorter than the deadtime of earlier stopped-flow measurements that claim

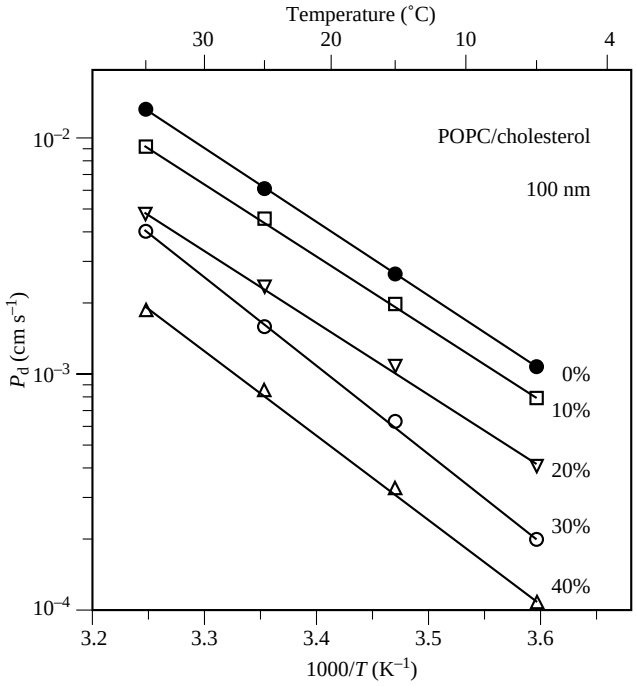

Figure 5 P_d, the permeability to water of bilayers of POPC unilamellar vesicles (100 nm diameter) as a function of temperature, for several values of cholesterol content. The vesicles, which occupy a small fraction of the total volume, contained sufficient paramagnetic ions (Gd(DTPA)) to make the $1/T_1$ of water protons within the vesicles comparable to the time required for water to 'escape' by permeation. The form of the $1/T_1$ NMRD profiles is then a function of the ratio of these two times, from which the permeability can then be calculated. (Reproduced by permission from S. H. Koenig, Q. F. Ankong, R. D. Brown III; M. Lafleur, M. Spiller, E. Unger, and C. Tilcock, *Magn. Reson. Med.*, 1992, **23**, 275)

to measure permeability by the swelling time of osmotically stressed vesicles.

3.3 Summary of the Dynamics of Water in Lipid–Water Systems

Lipid–water interfaces are quite different from their protein analogs. Unless the lipid contains components that have not only hydrophilic moieties but also, more specifically, OH (and possibly other) groups, and a surface geometry that favors extensive hydrogen bonding, the interfacial collisions are hard sphere collisions with no transient complex formation and little observable effect on $1/T_1$.

There is another major difference between lipid and protein interfaces. Proteins, because of their three-dimensional bonded structure, are not penetrable by water (on the timescales of interest here), whereas lipids have little lateral cohesion and water can readily penetrate, at least sterically. From the vesicle data (Figure 5), which gives an escape lifetime of the order of milliseconds and a transit time of about 50 ns, one can estimate that one encounter in 20 000 of a water molecule at a lipid bilayer interface will be successful in getting the water in. This makes it appropriate to consider these membranes as relatively impermeable. The kinetic factor (20 000) should (intuitively, according to the thinking here) relate directly to the equilibrium solubility of water in the lipid; in fact, it is a number that agrees well with the very low solubility of water in most lipids.[33] Nonetheless, the infrequent penetration of the membrane by water is generally sufficiently frequent to allow water to average out the intra- and extracellular environments of water within a relaxation time, thus making the NMRD profiles of tissue relatively insensitive to specific details of both the anatomical and histological morphologies of tissue, as can be observed.

4 QUANTIFICATION OF THE DYNAMICS OF WATER ON THE MOLECULAR SCALE: RESULTS FROM MAGNETIC SOLUTES

The emphasis above has been on the liquidity of water and how little its qualitative behavior is influenced by the presence of macromolecule–water interfaces and the specifics of the surface chemical composition. However, with the exception of the reference to results for clay[29] no quantitative results are presented that give values for the self-diffusion of water at this level (either translational or rotational) or the relative diffusion constants of molecular and macromolecular solute. A set of useful quantitative results can be obtained from the NMRD profiles of water protons in solutions of magnetic solutes. In the very early days of NMR such relaxometry data were used to learn about the structure of solutes,[14] with the assumptions about their influence (or lack thereof) on the solvent being left implicit. Due to the advent of MRI and the wide use of magnetic pharmaceuticals for altering contrast in MRI, enough is now known about the structure of many such solutes and the theory of their relaxivity that their presence can be used to probe the mobility of water in their vicinity. In essence, these particles produce magnetic fields that contribute to the relaxation of water protons out to a distance of about one solute diameter from the solute surface; this is called 'outer sphere' relaxation. In addition, the smaller agents (exemplified by Gd-DTPA) form a complex with a single water molecule coordinated directly to the metal ion which is in rapid exchange with solvent; this is 'inner sphere' relaxation.

4.1 Gd(DTPA)

About half of clinical MRI procedures involve magnetic agents, predominantly a commercial preparation of Gd(DTPA). Although this is often referred to as a paramagnetic agent [the magnetic susceptibility of solutions of Gd(DTPA) do exhibit classic Curie-law behavior], from the point of view of a mobile water molecule near a Gd(DTPA) solute molecule the water protons experience a fully magnetized S-state ion, spin of $\frac{7}{2}$, and a magnetic moment of 7 Bohr-magnetons from the parallel spins of the half-filled f shell. Thus, for our purposes, Gd(DTPA) can be considered as one of the smallest 'ferromagnetic' solute particles, with the seven spins of each particle permanently parallel.

Admittedly, particularly at low magnetic fields, the spatial orientation of the gadolinium moments fluctuates rapidly, corresponding to an electronic T_1 (τ_{1S}) of about 100 ps. However, this relaxation time, which affects both inner sphere and outer sphere relaxation, is field dependent[14,20] and, at typical imaging fields, τ_{1S} becomes much longer than the two other correlation times that contribute to the relaxivity of Gd(DTPA). These are τ_R, the reorientation time of the solute due to Brownian motion, which controls inner sphere relaxation and τ_D, a diffusional correlation time comparable to the time required for a water molecule to leave the solute environment, which controls outer sphere relaxation.

Figure 6 shows the measured proton $1/T_1$ NMRD profile of a solution of Gd(DTPA), together with two curves derived from theory (broken lines) for the (comparable) inner and outer sphere contributions to the relaxivity.[20] The inner sphere results assume one inner-coordinated water molecule in the usual geometry, with a lifetime of 1 ns, taken from that of the gadolinium aquoion. (Recent work has shown this time to be unexpectedly long,[35] about 250 ns, but this has little effect on the present discussion.) The zero field electronic relaxation time τ_{1S0} used is 85 ps, a correlation time τ_V of 20 ps characterizes its field dependence, and τ_R is 80 ps; this generates the inner sphere curve shown in Figure 6. Indeed, at high fields, τ_R is the only adjustable parameter that determines inner sphere relaxivity. For the outer sphere contribution, a τ_D of 41 ps and a (hard sphere) distance of closest approach a of 0.36 nm were used. Similarly, at high fields, the outer sphere contribution depends only (inversely) on a and the relative diffusion constant D of solute and solvent through the relation $\tau_D = a^2/D$. In turn, a must agree with the known crystallographic structure of Gd(DTPA). τ_R also depends on a and the applicability of Stokes' law at these molecular dimensions. Thus, there is little room to adjust the parameters that determine the relaxation at high fields. The high field data by themselves demand, in essence, that water behaves as a continuum fluid with fixed transport parameters even at solute dimensions, with a hard sphere interaction with the relatively small solute Gd(DTPA) molecules. In addition, since the inner and outer sphere contributions depend differently on field, fitting of the entire profile to theory fixes the relative amount

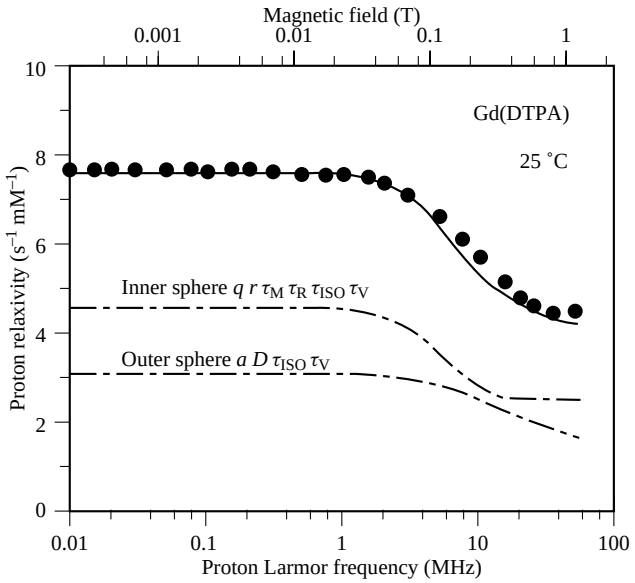

Figure 6 $1/T_1$ NMRD profile of water protons with solute Gd(DTPA) at 25 °C. The solid curve through the data is the sum of two contributions (broken lines): that of a single water molecule in rapid exchange from the inner coordination sphere of the gadolinium ion, and that of water molecules diffusing in the magnetic field of the gadolinium ion in the outer sphere environment of the chelate complex (see text). (Reproduced by permission from S. H. Koenig and R. D. Brown III, *Prog. NMR Spectrosc.*, 1990, **22**, 487)

of inner and outer sphere contributions, further constraining the values of the system parameters that describe the observed relaxivities. It is a fair estimate that small alterations (of the order of ±30%) of the parameters given would make a self-consistent fit of data and theory difficult.

4.2 Gd(DTPA) in Blood

In diagnostic radiology Gd(DTPA) is injected intravenously into the circulation where it mostly remains until excreted through the kidney. Its utility of course involves a balance of contrast enhancement versus toxicity, so that it is a realistic question as to whether NMRD data (Figure 6) can predict the behavior of Gd(DTPA) in clinical applications. Blood, like most tissues, is 20% solid, with one-third of its water in the dominant red cells. These contain the majority of blood protein (hemoglobin), although the extracellular space (plasma) contains an additional 30% of the total protein. The questions associated with Gd(DTPA) in blood are whether the agent attaches to, or enters, the cells and whether it binds to protein. Binding of small paramagnetic agents to macromolecules, which increases τ_R dramatically, can alter the NMRD profiles in the MRI field range in a particularly favorable way in a manner that is understood but not predictable.[15,20] From NMRD profiles of blood with and without added Gd(DTPA), and of the plasma that remains after the cells settle, it is readily demonstrated[36] that, from the water molecule's viewpoint, the partitioning of the blood by the cell membranes is irrelevant to relaxation, as the presence of macromolecules is to the relaxivity contribution of Gd(DTPA). All constituents—extracellular plasma protein, intracellular hemoglobin, and Gd(DTPA)—contribute independently to the NMRD profile of blood, with appropriate consideration given to excluded volume effects.

4.3 Superparamagnetic Particulates

Virus-size particles of iron oxide, predominantly magnetite, are becoming of increasing interest to the MRI community. Unlike smaller agents, these are removed from the circulation and deposited elsewhere in the body, apparently in ways that may prove useful for imaging liver, spleen, and marrow. These small 'nanoparticles,' typically in the range 5–10 nm diameter,[37] are generally protected from body fluids by attachments of polymeric sugars or starches designed to impede access of water as little as possible to the outer sphere environment of the iron oxide cores. They are termed 'superparamagnetic', a word that is ambiguous in that it can be properly applied to individual particles as well as to an ensemble of such particles in solution. In the latter case it means, as for Gd(DTPA), that the magnetic susceptibility of a solution obeys Curie's law, but now with a 'super' response. This is because the magnetic dipolar moment of each solute particle is very large and because the susceptibility of a solution containing a fixed total number of magnetic ions increases quadratically with the number of ions in each solute particle and only linearly in the total number of particles. Since a magnetite nanoparticle may contain about 5000 magnetite molecules,[38] susceptibility is enhanced by a factor of about 5000 over that of a solution of individual magnetite molecules. Ironically, the superparamagnetic aspects of the individual particles do not influence the behavior at imaging fields.[20]

Again, relaxometry studies of these particles, of which there are few—particularly on particles that are well-characterized chemically and magnetically—yield information on both solute and solvent. Here, outer sphere relaxation dominates, but the range is 10 times greater than for Gd(DTPA), which makes τ_D (which is proportional to the square of this range) very long and the intrinsic relaxivity of these particles very large. This is further enhanced because the relaxivity is also linearly proportional to the 'supersusceptibility' of the solute particles. Thus small total amounts of agent, far less on a molar basis of magnetic ion than for typical gadolinium chelate complexes, may prove adequate for diagnostic MRI. To this must be added that iron is an endogenous ion and questions of relative toxicity may favor iron over gadolinium. In any event, the increasing interest in such agents is making more relaxation data available and providing more knowledge of the behavior of water on a 10 nm scale. Again, 'water is water'. Initial results for particles with relatively narrow size distributions, measured by microscopy of one sort or another (X-ray, electron transmission, etc.) give contributions to $1/T_1$ at imaging fields[17] consistent with their size, using macroscopic values for the self-diffusion of water in microscopic environments.

4.4 Summary of Findings for Magnetic Solutes

There is a large body of literature on the influence of magnetic solutes, including metalloproteins, that has been discussed elsewhere.[15] The points considered here relate to the reality that the theory of relaxation of solvent protons

by magnetic solute has been improved remarkably within the past decade,[39] in part spurred by advances in clinical MRI and its incorporation of magnetic pharmaceuticals into its routine practice. Particularly as regards outer sphere relaxation in solutions of nanoparticles and larger particles (including paramagnetic red cells[40]), theory and data are in excellent agreement (even though the computations may be difficult). This agreement assumes the fluidity and mobility of water, often through organic binders and flagellate attachments[37] to the iron oxide cores of the nanoparticles.

There is one point that ought to be made for completeness, which relates to inhibition of inner sphere relaxation by protein-bound paramagnetic ions by the inhibition of protein function. Examples of this would be binding of sulfonamides to cobalt-substituted carbonic anhydrase and the reduction of cupric to cuprous ions in superoxide dismutase. The result is an NMRD profile like that of the diamagnetic protein, i.e., either demetalated or substituted with a diamagnetic metal ion. One might ask, on the basis of the extended diffusion of magnetization within immobilized protein considered in the sections above, whether in metalloproteins there is any contribution to the water proton relaxation by the magnetization diffusing through the protein to get around to the back of a paramagnetic ion for which water has been excluded by complex formation. The answer is that for mobile proteins no such effect has ever been reported, and for immobile proteins, that no pertinent data are available.

5 WATER AS A VISCOUS VACUUM

Important as the dynamics of water are for the proper functioning of biological systems, it is the behavior of the macromolecular solute, mainly protein, that underlies the functioning of these systems. Moreover, living systems typically contain about 20 wt % solids, mostly protein, a concentration far greater than the values of $<1\%$ that typify physico-chemical studies of protein in solution. There has been little emphasis on bridging this gap; understanding the behavior of protein at high concentration is often regarded as a hopeless activity. However, from our understanding of the dynamics of water in these systems, discussion of protein–protein interactions in solution at high concentration can be made simple. Several examples follow.

5.1 Rotational Relaxation of Solute Protein at High Concentration

For example, how free to rotate is the hemoglobin of red cells? The answer is known:[15] it is as free to rotate as in an infinite solution of hemoglobin at the same concentration, which is about 10 times slower than in the dilute limit. Is this reasonable: and what are the underlying physics? First, we remark that almost all soluble (globular) proteins have the same partial specific volume ($0.73\,\mathrm{cm}^3\,\mathrm{g}^{-1}$, with the exception of eye-lens protein, for reasons of lens transparency[25,41]), so that solute protein molecules can be regarded as relatively incompressible microsolids. As shown by Stokes in the middle of the last century, the rotational relaxation time of a sphere of radius r in an infinite viscous medium is proportional to its (macroscopic) viscosity η_0. Stokes also showed that if the sphere is at the center of a stationary larger sphere of radius R, its rotational relaxation time will increase as if the viscosity of the infinite medium were given by

$$\eta = \frac{\eta_0}{1 - [r/(R - r)]^3} \tag{2}$$

The increase in apparent viscosity is a geometric factor that is solely a function of the volume fraction occupied by the smaller sphere, i.e. the scale of the spheres is not germane (and of course should not be for a particle in a continuum fluid). For the protein–protein problem, let the outer sphere be an imaginary one defined as the largest sphere that excludes, on average, all protein neighbors of a given protein. If r is taken as the protein radius, and the radius of the imaginary sphere is taken as R in the Stokes example, then this simple model[26] affords an excellent description of the rotational mobility of hemoglobin as a function of protein concentration, up to the physiological concentrations in the red cell. Thus the interaction of proteins in solution is determined, in the main, by classical hydrodynamics, provided that there is no appreciable equilibrium association of solute.

5.2 Thermodynamics in a Viscous Vacuum

When considering the thermodynamics of an aqueous solution of protein at high concentration from the chemical viewpoint, it is usually handled as a two component system in equilibrium, with free energies being equal for the two components and for any other oligomeric forms in equilibrium with the monomer. From this viewpoint, it is difficult to address questions of, for example, osmotic pressure and possible phase separation. On the other hand, if one accepts the argument that the dynamics of water are little influenced by solute protein, then—realizing that equilibrium results derived from statistical mechanics of interacting particles are independent of the laws of motion of the particles—it becomes a powerful simplication to treat solute protein as a single system of interacting particles. The water may be considered as a vacuum in which Newton's laws are replaced by the response to a force typical of a viscous medium, and then ignored. The solute is then a hard sphere gas of identically charged particles that are weakly repulsive because of the high dielectric constant of water. Two extremely important results follow immediately, both of importance to the eye lens, in which the proteins reach uniquely high concentrations. One result is that the osmotic pressure of these proteins should be given by the results for hard spheres, as they are.[41] The second result is that, since a (three-dimensional) hard sphere gas with a repulsive interaction cannot have a first-order phase transition, the phase separation seen in one such protein, γ_{II}-crystallin, must be due to oligomerization and the creation of a multicomponent solute system.[42]

6 CONCLUDING REMARKS

Water in biological systems is in no sense innocuous. The polarity of its molecules (otherwise identical to neon) leads to a high dielectric constant, and thus water dissolves

and ionizes many salts. It also leads to extensive hydrogen bonding and the density minimum that keeps the oceans from freezing permanently. But once these effects are accounted for, which is done here by a 'renormalization' of attitude, then the molecular dynamic properties of water molecules can generally be ignored. Indeed, in order to use water in specialized ways in chemical reactions in biological systems, Nature has had to invent metalloproteins—with emphasis on the transition metals. In these compounds the water molecules can be maintained in desirable stereochemical orientations for times sufficient to allow enzymatic reactions to proceed, molecule by molecule. But this is another subject.

7 RELATED ARTICLES

Biological Macromolecules: Structure Determination in Solution; Brownian Motion and Correlation Times; Contrast Agents in MRI: Superparamagnetic Iron Oxide; Contrast Agents in Whole Body Magnetic Resonance: An Overview; Contrast Agents in Magnetic Resonance: Operating Mechanisms; Gadolinium Chelate Contrast Agents in MRI: Clinical Applications; Magnetization Transfer Contrast: Clinical Applications; Magnetization Transfer and Cross Relaxation in Tissue; Magnetization Transfer between Water and Macromolecules in Proton MRI; Molecular Motions: T_1 Frequency Dispersion in Biological Systems; Relaxometry of Tissue; Magnetic Resonance Imaging of White Matter Disease.

8 REFERENCES

1. F. Bloch, W. W. Hansen, and M. Packard, *Phys. Rev.*, 1946, **69**, 127.
2. F. Bloch, W. W. Hansen, and M. Packard, *Phys. Rev.*, 1946, **70**, 474.
3. E. M. Purcell, H. C. Torrey, and R. V. Pound, *Phys. Rev.*, 1946, **69**, 37.
4. I. I. Rabi, J. R. Zacharias, S. Millman, and P. Kusch, *Phys. Rev.*, 1938, **53**, 318.
5. I. I. Rabi, S. Millman, P. Kusch, and J. R. Zacharias, *Phys. Rev.*, 1939, **55**, 526.
6. J. M. B. Kellogg, I. I. Rabi, N. F. Ramsey, Jr., and J. R. Zacharias, *Phys. Rev.*, 1939, **56**, 728.
7. J. Schwinger, *Phys. Rev.*, 1937, **51**, 648.
8. I. I. Rabi, *Phys. Rev.*, 1937, **51**, 652.
9. F. Bloch and I. I. Rabi, *Rev. Mod. Phys.*, 1945, **17**, 237.
10. I. Waller, *Z. Phys.*, 1932, **79**, 370.
11. N. Bloembergen, E. M. Purcell, and R. V. Pound, *Phys. Rev.*, 1948, **73**, 679.
12. I. Solomon, *Phys. Rev.*, 1955, **99**, 559.
13. R. Kubo and K. Tomita, *J. Phys. Soc. Jpn*, 1954, **9**, 888.
14. N. Bloembergen and L. O. Morgan, *J. Chem. Phys.*, 1961, **34**, 842.
15. For a review and early references see: S. H. Koenig and R. D. Brown III, in *NMR Spectroscopy of Cells and Organisms*, ed. R. K. Gupta, CRC Press, Boca Raton, FL, 1987, Vol. 2.
16. A. G. Redfield, W. FiteII, and H. E. Bleich, *Rev. Sci. Instrum.*, 1968, **39**, 710.
17. S. H. Koenig and R. D. BrownIII, *Magn. Reson. Med.*, 1993, **30**, 685.
18. S. H. Koenig, R. D. BrownIII, and R. Ugolini, *Magn. Reson. Med.*, 1993, **29**, 77.
19. G. S. Schauer, R. Kimmich, and W. Nusser, *Biophys. J.*, 1988, **53**, 397.
20. S. H. Koenig and R. D. BrownIII, *Prog. NMR Spectrosc.*, 1990, **22**, 487.
21. L. Piculell and B. Halle, *J. Chem. Soc., Faraday Trans. 1*, 1986, **82**, 401.
22. S. H. Koenig, R. G. Bryant, K. Hallenga, and G. S. Jacob, *Biochemistry*, 1978, **17**, 4348.
23. S. H. Koenig and W. E. Schillinger, *J. Biol. Chem.*, 1969, **244**, 3283.
24. K. Hallenga and S. H. Koenig, *Biochemistry*, 1976, **15**, 4255.
25. S. H. Koenig, R. D. BrownIII, M. Spiller, B. Chakrabarti, and A. Pande, *Biophys. J.*, 1992, **61**, 776.
26. S. H. Koenig, in *Water in Polymers* (*ACS Symposium Series 127*), ed. S. P. Rowland, 1980, p. 23.
27. G. Otting, E. Liepinsh, and K. Wüthrich, *Science*, 1991, **254**, 974.
28. H. F. Bennett, R. D. BrownIII, S. H. Koenig, and H. M. Swartz, *Magn. Reson. Med.*, 1987, **4**, 93.
29. D. E. Woessner, *J. Magn. Reson.*, 1980, **39**, 297.
30. V. Lounnas, B. M. Pettitt, and G. N. Phillips, Jr, *Biophys. J.*, 1994, **66**, 601.
31. S. H. Koenig, R. D. BrownIII, M. Spiller, and N. Lundbom, *Magn. Reson. Med.*, 1990, **14**, 482.
32. T. A. Fralix, T. L. Ceckler, S. D. Wolff, S. A. Simon, and R. S. Balaban, *Magn. Reson. Med.*, 1991, **18**, 214.
33. A. Finkelstein, *Water Movement through Lipid Bilayers, Pores, and Plasma Membranes: Theory and Reality*, Wiley-Interscience, New York, 1987.
34. S. H. Koenig, Q. F. Ahkong, R. D. BrownIII, M. Lafleur, M. Spiller, E. Unger, and C. Tilcock, *Magn. Reson. Med.*, 1992, **23**, 275.
35. G. González, D. H. Powell, V. Tissières, and A. E. Merbach, *J. Phys. Chem.*, 1994, **98**, 53.
36. S. H. Koenig, M. Spiller, R. D. BrownIII, and G. L. Wolf, *Magn. Reson. Med.*, 1986, **3**, 791.
37. T. Shen, R. Weissleder, M. Papisov, A. Bogdanov, Jr, and T. J. Brady, *Magn. Reson. Med.*, 1993, **29**, 599.
38. S. H. Koenig, *Magn. Reson. Med.*, 1991, **22**, 183.
39. S. H. Koenig and K. Kellar, *Magn. Reson. Med.*, 1995, **34**, 227.
40. P. Gillis and S. H. Koenig, *Magn. Reson. Med.*, 1987, **5**, 323.
41. F. Vérétout, M. Delaye, and A. Tardieu, *J. Mol. Biol.*, 1989, **205**, 713.
42. S. H. Koenig, C. F. Beaulieu, R. D. BrownIII, and M. Spiller, *Biophys. J.*, 1990, **57**, 461.

Biographical Sketch

Seymour H. Koenig. *b* 1927. B.S., 1949, M.A., 1951, Ph.D., 1952, Physics, Columbia University, USA. IBM Research, 1952–93. Presently, Research Professor, Radiology, Dartmouth Medical School, Hanover, NH, USA and President, Relaxometry, Inc., Mahopac, NY, USA. Approximately 200 publications. Research specialties: atomic beams, solid state electrical transport, phonons and neutron scattering, laser-light scattering, and relaxometry, including protein structure and function, water proton relaxation in protein solutions and in tissue, and magnetic contrast-enhancing agents for MRI.

Hydrogen Exchange and Macromolecular Dynamics

S. Walter Englander

University of Pennsylvania School of Medicine, Philadelphia, PA, USA

1	Introduction	1
2	Nomenclature	1
3	HX Chemistry	1
4	HX Rate and Structural Dynamics	3
5	Applications: Macromolecular Dynamics	3
6	Applications: HX Labeling	4
7	Related Articles	5
8	References	5

1 INTRODUCTION

Proteins and nucleic acids contain many polar hydrogens that are in continual exchange with the hydrogens of a solvent. These hydrogens are distributed throughout the main chains and side chains of proteins and the nucleotides of nucleic acids. The different hydrogens in a protein molecule exchange over a vast range of rates, 10 orders of magnitude or more wide; the spread in nucleic acid rates is considerably smaller. These atoms, placed at many dozens, even hundreds, of positions throughout every macromolecule, emit a continual stream of information, in a nonperturbing way, in the coded language of hydrogen exchange (HX) rate, concerning structure, structure change, dynamics, and energetics. This is just the kind of information we need to work out the fundamental principles of structural stabilization and function. We have but to receive and decode the information in these terms.

Multidimensional NMR methods (See ***Multidimensional Spectroscopy: Concepts***.) now make it possible to resolve the signals from each exchanging hydrogen, identify its parent proton in the molecule, and measure its HX rate. Fast exchanging hydrogens can be followed by methods based on magnetization transfer and lineshape analysis. Slower hydrogens can be measured in isotopic $^1H-^2H$ exchange experiments. The literature details a variety of NMR methods for HX measurement, using both 1D and multidimensional approaches. NMR-detected HX behavior has been discussed previously.[1,2]

The present article briefly presents the conceptual and technical information necessary for the design and execution of protein and nucleic acid HX experiments and summarizes some important recent applications. HX coupled with NMR detection accesses a whole new dimension of dynamic behavior in proteins and nucleic acids and allows a direct measurement of their important thermodynamic stability parameters. Further, HX labeling experiments can provide fairly detailed structural information on protein forms that defy the usual NMR and even X-ray methodologies.

2 NOMENCLATURE

Use of the term 'proton exchange' reaches back to the early NMR literature in which protons played the predominant role. One now studies in various ways the exchange of protons, deuterons, and tritions. Thus the generic term 'hydrogen exchange' should be preferred, and is used here. Similarly, the use of the term 'amide', for the peptide group of proteins, derives from its chemical shift position in the amide region. Proteins have three kinds of amides, the primary amide side chains of asparagine and glutamine, the secondary amide or peptide group, and the tertiary amide of prolyl residues. One should specify the peptide group by its proper name.

3 HX CHEMISTRY

The HX behavior of protein and nucleic acid molecules can provide direct information on their structural dynamics and functional interactions. These effects are superimposed on the underlying HX chemistry of the exchanging groups studied. Thus, knowledge of basic HX chemistry is essential for the interpretation of HX results.

HX between water and solute molecules proceeds by way of distinct chemical reactions that involve as catalysts H_3O^+, OH^-, and general acids and bases, including H_2O itself. The primary steps in a hydrogen exchange sequence involve proton transfer reactions [equation (1)].

$$\mathrm{AH} + \mathrm{B} \underset{k_{-\mathrm{D}}}{\overset{k_{\mathrm{D}}}{\rightleftharpoons}} (\mathrm{AH}\ldots\mathrm{B} \overset{K_{\mathrm{c}}}{\rightleftharpoons} \mathrm{A}\ldots\mathrm{HB}) \underset{k_{\mathrm{D}}}{\overset{k_{-\mathrm{D}}}{\rightleftharpoons}} \mathrm{A} + \mathrm{HB} \qquad (1)$$

For unstructured polymers in free solution, diffusion-limited collision and hydrogen bond formation between a proton donor (AH) acting as an acid and a base acceptor (B) occur with the second-order rate constant, $k_{\mathrm{D}} \sim 10^{10}\,\mathrm{M}^{-1}\ \mathrm{s}^{-1}$. Within the hydrogen-bonded encounter complex thus formed, hydrogen redistribution occurs rapidly, by tunneling, and reaches an equilibrium given by $K_{\mathrm{c}} = 10^{\Delta \mathrm{p}K}$, where $\Delta \mathrm{p}K = \mathrm{p}K_{\mathrm{B}} - \mathrm{p}K_{\mathrm{A}}$. Presently the complex dissociates, either to the left of equation (1) in a wasted collision, or to the right in a fruitful one. The overall hydrogen transfer rate is given by the collisional rate times the success rate [equation (2)]

$$k_{\mathrm{tr}} = k_{\mathrm{D}}(10^{\Delta \mathrm{p}K}/(1 + 10^{\Delta \mathrm{p}K})) = k_{\mathrm{ch}} \qquad (2)$$

The rate-limiting chemical step in any HX reaction (k_{ch}) is always such a transfer sequence. When transfer is energetically downhill (stronger acid to weaker acid), $\Delta \mathrm{p}K > 0$, the success fraction is close to unity, and HX goes at k_{D}. When transfer is energetically uphill ($\Delta \mathrm{p}K < 0$), exchange can be much slower, with $k_{\mathrm{ch}} \approx k_{\mathrm{D}} 10^{\Delta \mathrm{p}K}$. For example, the ring nitrogen-bonded protons (NHs) of nucleotides and most protein polar side chains, with $\mathrm{p}K < 15$, are removed by OH^- at $k_{\mathrm{ch}} \sim 10^{10}\,\mathrm{M}^{-1}\ \mathrm{s}^{-1}$. In contrast, removal of a peptide group NH by OH^-, a transfer from donor $\mathrm{p}K \sim 18.5$ to acceptor $\mathrm{p}K$ 15.7, is slower by ~1000-fold. Similar considerations apply to catalysis by H^+ and by general acids and bases. As a result, the polar hydrogens of protein side chains exchange rapidly, and therefore are relatively useless for structural studies, and also are hard to assign. Peptide group NH exchange is more accessible, being intrinsically slower and not catalyzable by general acids and bases. The tryptophan indole NH is also

usefully slow. In nucleic acids, the ring NHs, with pK ∼ 10, can be catalyzed effectively by general bases as well as by OH^-, while the strongly basic exocyclic NH_2 hydrogens cannot. Carbon hydrogens are exceedingly slow; they do not readily form hydrogen bonds on collision, and do not transfer easily due to their high effective pK.

Most protein HX studies center on the well distributed and slowly exchanging peptide group NH. Figure 1 shows the pD dependence of its exchange, reflecting simple catalysis by OH^- above ∼pH 3 (in polypeptides) and by H^+ at lower pH. The figure shows that HX of the freely exposed NH can be sterically blocked by neighboring bulky side chains [Figure 1(a)] and can also be modified by inductive effects [Figure 1(b)] due to neighboring polar side chains. These effects along with other influences such as temperature, sequence, and isotope effects have been calibrated for all the naturally occurring amino acids.[3,4] Figure 2 shows a similar representation for some nucleotide bases. The odd behavior of the adenine NH_2 hydrogens includes catalysis by OH^- at high pH, and by H^+ at low pH. At intermediate pH, HX

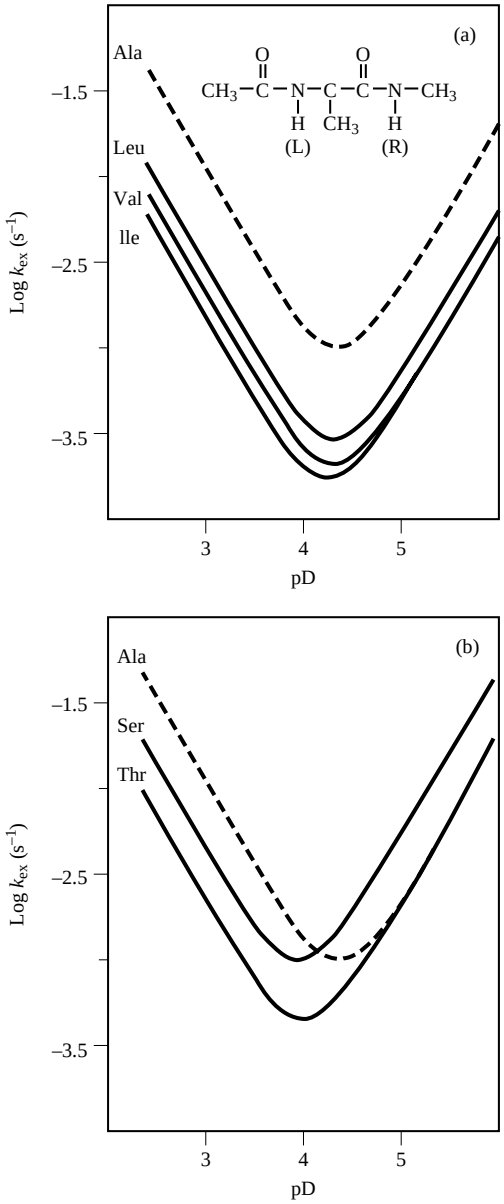

Figure 1 HX of free peptide NH in small molecule models. (a) Steric blocking effects and (b) inductive effects of neighboring amino acid side chains are illustrated. Polypeptides show pH minima between pH 2.5 to pH 3. L, left; R, right. (Reproduced by permission of John Wiley and Sons, Inc. from Bai et al.)[3]

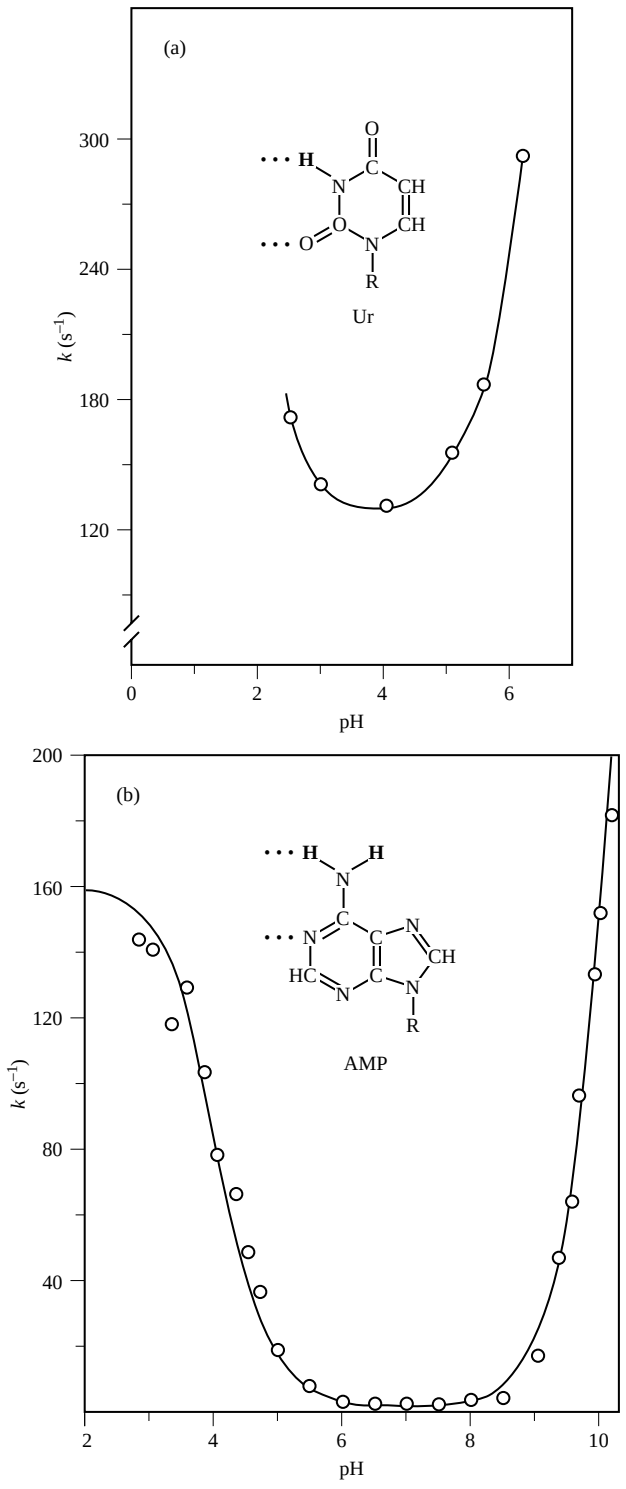

Figure 2 The pH dependence of HX for some nucleotide NHs [uracil (Ur) and AMP]. (Reproduced by permission of Cambridge University Press from Englander and Kallenbach)[6]

proceeds by a reaction that involves an initial protonation at the N-1 position (normally buried in the double helix) followed by a deprotonation either by OH^- or by a general base at sufficiently high concentration. The $H^+ \times OH^-$ reaction produces the pH-independent behavior seen in the figure.

When these groups are involved in structured macromolecules, the basic chemical exchange rate can be decreased by large factors. One commonly expresses the structural slowing or protection factor as $P = k_{rc}/k_{ex}$, where k_{rc} [equation (2)] is the computed rate for the group in a structureless random coil, dependent on the principles[5,6] just discussed and calculated from calibrations using model molecules (in peptides[5,6] and nucleotide HX chemistry).[7,8]

4 HX RATE AND STRUCTURAL DYNAMICS

HX slowing by folded structure is due to a physical blocking of the chemical steps just described. Structurally slowed hydrogens are, in the great majority of cases but not always, involved in hydrogen bonding. One assumes that exchange cannot occur unless the blocking structure is removed. Under native conditions this requires a transient opening reaction that has been modeled by various authors as a breaking of individual hydrogen bonds,[9] a local cooperative unfolding,[6] or even a gross whole molecule transient unfolding.[10] Over the years other possible mechanisms, based on various kinds of catalyst and solvent penetrational processes, have been suggested.[6,10]

Opening dependent exchange can be schematically represented as in equation (3):

$$\text{closed} \underset{k_{cl}}{\overset{k_{op}}{\rightleftharpoons}} \text{open} \xrightarrow{k_{rc}} \text{exchange}\colon\ K_{op} = k_{op}/k_{cl} \tag{3}$$

In the steady state, this reaction sequence produces HX rates given by equation (4):

$$k_{ex} = k_{op}k_{rc}/(k_{op} + k_{cl} + k_{rc}) \tag{4}$$

At the so-called EX1 limit,[9] where $k_{cl} \ll k_{rc}$, this leads to the HX rate in equation (5), which has hardly ever been seen:

$$k_{ex} = k_{op} \tag{5}$$

Equation (6) gives the HX rate at the usually observed EX2 limit, where $k_{cl} \gg k_{rc}$:

$$k_{ex} = (k_{op}/k_{cl})k_{rc} = K_{op}k_{rc} \tag{6}$$

These equations assume that structure is stable, so that $K_{op} \ll 1$. K_{op} is then essentially equal to the fraction of time the restraining structure is open [fraction open = $K_{op}/(K_{op} + 1)$]. Since values for k_{rc}, the HX rate for NHs in a random chain polypeptide, are known,[3,4] the measurement of k_{ex} leads to K_{op} [equation (6)], and thus to the free energy for the underlying structural opening reactions, according to equation (7):

$$\Delta G_{HX} = -RT\ \ln K_{op} = -RT\ \ln(k_{ex}/k_{rc}) \tag{7}$$

Measurement of the dependence on temperature can then provide ΔH and ΔS of the dynamic opening reaction. Effects of mutations, functional state, etc., on stability can similarly be studied.

NMR methods have been developed that can measure a range of dynamic structural behavior, due to dipolar relaxation in solution (<1 ns), quadrupolar relaxation in solids (<1 μs), and slower chemical shift averaging (~1 ms) and saturation transfer (~1 s) effects. The equations just described extend this capability to an entirely different class of structural events, selected by the fact that they can allow solvent catalyzed HX chemistry to proceed. The timescale of the structural events measured by HX has elicited some confusion. The underlying structural events themselves occur on a fast timescale, with k_{cl} rates between seconds and nanoseconds. Opening events are of course slower than closing when the structure is stable ($k_{cl} > k_{op}$). The HX timescale itself is far longer, in the general range between milliseconds and years. As described before, the HX rate depends on solution conditions (k_{rc}; Figure 1), which can be set at the convenience of the experimenter, and on the equilibrium structural parameter, K_{op}, which can vary from close to unity for the smallest fluctuations down to perhaps 10^{-10} for global protein unfolding reactions. To measure the structural timescale at work, in any case, one must access EX1 behavior [equation (5)]. This has hardly been possible for proteins, specifically because k_{cl} is so fast, but has been accomplished for nucleic acids.[7,8]

5 APPLICATIONS: MACROMOLECULAR DYNAMICS

5.1 Protein Structural Thermodynamics

Protein molecules spend a small fraction of the time cycling through their global unfolding transition, even under normal solution conditions, determined by their free energy for unfolding and the Boltzmann distribution. Some of the slowest protein hydrogens exchange by way of this transiently open state. Therefore, it is possible to obtain global thermodynamic parameters by HX measurements far below the melting transition [equation (7)].

Figure 3 shows simulated data for HX measurements of some of the slowest exchanging NHs in a protein and for some faster ones, calculated in terms of the ΔG of the operative unfolding reaction. At present one must study protein stability by obtaining data through the melting transition, about $\Delta G = 0$. From such measurements one hopes to obtain thermodynamic parameters, and then to extrapolate into the region of more normal conditions. HX analyzed by 1D NMR can allow the direct determination of the operative parameters at much lower temperatures or much lower denaturant concentration, under conditions where proteins are stable.[11] Similarly, hydrogens that exchange by way of more limited openings can reveal the stability parameters of these fluctuations.

Since the slowest peptide NHs in a protein can often be resolved and their H–D exchange directly measured in D_2O by simple 1D NMR spectroscopy, this approach has considerable promise for protein stability studies.

5.2 Nucleic Acid Structural Dynamics

Nucleotides have two kinds of exchangeable NHs, the exocyclic amino NH_2 hydrogens and the endocyclic imino ring

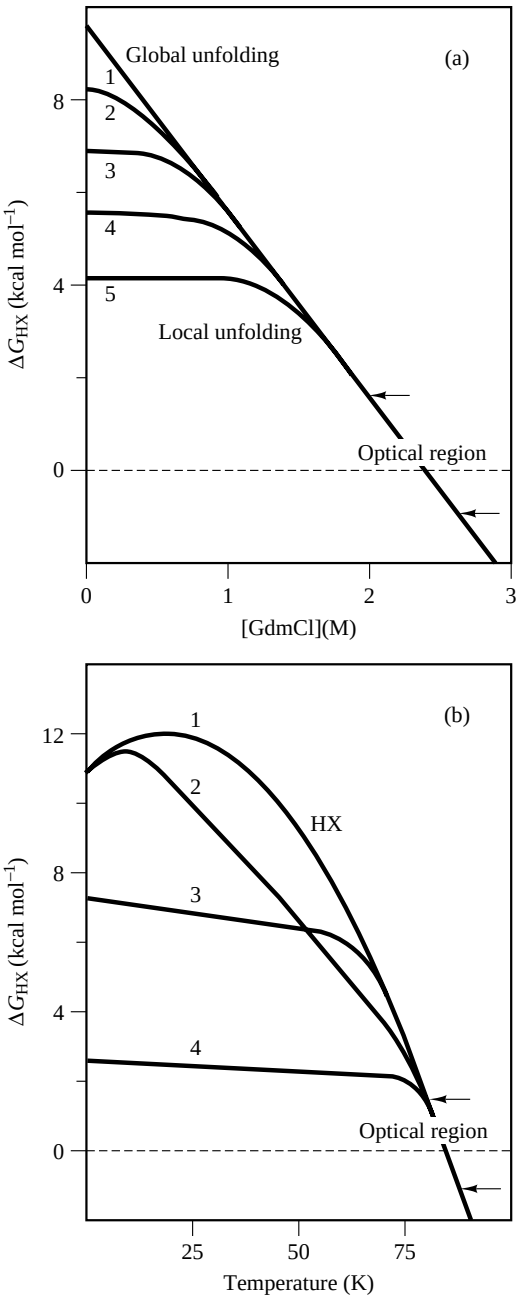

Figure 3 Simulated behavior for the HX of some protein NHs, calculated in terms of the ΔG of the operative unfolding reaction. The slowest NHs (curves 1) exchange through the global unfolding reaction, and the faster ones (curves 2–5) by way of more local unfolding reactions. (Reproduced by permission of John Wiley and Sons, Inc. from Bai et al.)[11]

NHs (see Figure 2). In the double helix, A-U and A-T base pairs trap two of their three NHs in hydrogen bonding. G-C pairs trap three of their five NHs. The other NH_2 hydrogens hydrogen bond out to water.

HX results found are contrary to all expectations. All the hydrogens in a Watson–Crick base pair exchange slowly, three for each A-T or A-U pair and five for each G-C. The most deeply buried hydrogen, the hydrogen bonded ring NH, is the fastest to exchange, while both hydrogens of a given NH_2 group, the one that is internally hydrogen bonded and the one that is exposed and hydrogen bonded to solvent, exchange at the same rate. All of this surprising behavior is due to a simple fact. In the double helix, nucleotide HX occurs from a transient base pair open form. Thus the relative rates of the different NHs are determined not by their condition in the native structure but by their chemistry in the solvent exposed state, described in a previous section. These basic ground rules were worked out in the laboratories of Englander and Kallenbach by use of tritium exchange methods and by H–D exchange measured by absorption spectroscopy, and have been reviewed by them.[6]

Since polynucleotide HX generally progresses on a timescale of minutes, NMR analysis is limited to 1D methods. Unfortunately, the amino NH_2 resonances overlap the aromatic CHs, and have been difficult to study. Therefore, NMR applications have generally focused on the imino NHs of G, T, and U, which resonate in an otherwise empty high-frequency (downfield) region at 12–15 ppm (see ***Nucleic Acids: Chemical Shifts***). Their HX behavior has been measured mainly by line broadening in a $^1H-^1H$ exchange mode, using water suppression as described by Gueron (see ***Water Signal Suppression in NMR of Biomolecules***). Spectral overlap limits the size of oligonucleotides that can be studied.

The earlier non-NMR studies developed the use of catalyzed exchange and the discrimination between EX1 and EX2 behavior based on equations (5) to (7), and concluded that base pair opening equilibria were surprisingly high, with K_{op} up to 0.01, and that opening rates, k_{op}, were in the range of $1\,s^{-1}$. Gueron and his colleagues, using similar approaches together with 1D NMR methods, have found results that point to faster base pair opening ($k_{op} \sim 10^2\,s^{-1}$) and closing ($k_{cl} \sim 10^7\,s^{-1}$) rates and correspondingly lower equilibrium opening constants.[8]

These approaches can potentially be brought to bear on a whole range of challenging issues concerning nucleic acid structure, dynamics, interactions, and function.[8]

6 APPLICATIONS: HX LABELING

The application of HX methods to protein problems gains special power when used in the labeling mode. Here H–D exchange can be done under conditions most suitable for the protein behavior to be studied. An H–D exchange pattern that depends on the behavior being measured becomes imprinted on the protein. Conditions can then be reset to make HX slow, and samples can be handled to optimize for NMR analysis.

6.1 Binding Regions in Protein Complexes

Recent experiments with protein complexes too large to study directly by NMR methods illustrate the ability of HX labeling methods to extend the scope of NMR structural investigations. If one of the proteins in the complex is sufficiently small to allow resolution of its individual peptide NHs, the interaction surface of that protein can be delineated in an HX footprinting experiment.

In these experiments, the complex is formed, and placed into D_2O under any conditions one may wish to study. H–D exchange proceeds. NHs not involved in the complex interface

generally exchange at the same rate as when free, although interesting exceptions not yet explained have been seen. NHs in the interface are slowed by varying amounts, depending on the interesting details of the interaction and the chemical and physical principles described before. Samples are taken in time and placed under slow HX conditions (lower pH and temperature). The complex is separated, and a 2D NMR spectrum of the protein to be analyzed is recorded to measure the remaining amplitude of a large number of exchangeable NH resonances. The timed samples trace out the HX kinetics of the various NHs. Comparison with similar data for the noncomplexed protein can then directly indicate which parts of the protein are involved in the binding interface and which are not, essentially to an amino acid resolved level, and can provide other details of the dynamics and thermodynamics of the interaction. The few studies so far available have dealt with some protein–monoclonal antibody complexes, an enzyme–inhibitor complex, and an electron transfer complex. In principle, many kinds of large-molecule interactions might be studied in this way.

6.2 Structure in Floppy Equilibrium Intermediates

Similar HX labeling methods can be used to obtain structural information on protein forms that resist study by the usual X-ray and NMR approaches. One such form is the so called molten globule, which most often shows exceedingly limited chemical shift resolution due to rapid conformational averaging. These forms are produced by mildly destabilizing conditions such as moderately low pH.

The molten globule forms of a few proteins have now been studied by HX labeling detected by 2D NMR. In these experiments, the disordered protein is incubated in D_2O for increasing times. Each peptide NH exchanges at a rate determined by the fact of its involvement in H-bonded structure and by the relative stability of its local structure against the dynamic opening reactions that determine HX rate [equation (6)]. Samples taken in time are returned to native conditions where the H–D pattern, produced during the HX incubation, is essentially frozen. A 2D NMR spectrum is then recorded on the native protein, where one can resolve and identify the various peptide NHs. A series of such spectra on timed samples reveal the HX rates of the various NHs. The results show directly what parts of the protein were involved in structure in the molten globule state and give semiquantitative information on the stability of the different structured segments.

6.3 Structure in Transient Folding Intermediates

The most striking example of the power of HX NMR labeling is provided by its ability to provide structural information on protein forms that exist only transiently, for less than 1 s. The HX pulse labeling experiment is designed to label a protein by H–D exchange during refolding in a structure-sensitive way on a millisecond timescale. Subsequent NMR analysis of the native protein can then provide information on the time dependence of hydrogen bond formation at many defined positions in the protein.

In these experiments, the protein is initially unfolded, for example with a concentrated denaturant such as guanidinium chloride (GdmCl) in D_2O, so that all the NHs exist as NDs. At time zero of a kinetic experiment, the solution is rapidly diluted into GdmCl-free H_2O under conditions where HX is relatively slow (e.g. pH 6 and 10 °C, where the HX half-time is seconds (Figure 1). The protein begins to refold. Deuteron to proton exchange under these conditions is relatively slow and does not yet occur. At some time during the refolding process, the solution is subjected to a brief, high pH pulse in a second mixing step in order to label NH sites that are still exposed. For example, at pH 10 and 10 °C, peptide NDs in parts of the protein that are still unfolded will exchange to NHs in ∼1 ms, while NDs that have already formed hydrogen-bonded structures will be protected from exchange. The high pH pulse is maintained for a few milliseconds while deuteron to proton exchange occurs. Then a third mix drops the pH to perhaps 5, halting all further exchange. The proteins complete their run to the native form. The H–D exchange pattern, imprinted on the partially folded intermediate, is now frozen into the native protein and can be read by a 2D ^{1}H spectrum to determine the degree of proton labeling at many positions all through the protein. A series of such experiments, with the labeling pulse imposed after different times of refolding, can then show the time-course for formation of the various hydrogen-bonded sites in the protein, and thus provide direct structural information on the folding pathway. In practice, of course, one can only detect the particular folding intermediates that happen to achieve high occupancy.

The HX pulse labeling experiment has been described in some detail by Englander and Mayne.[12]

7 RELATED ARTICLES

Multidimensional Spectroscopy: Concepts; Nucleic Acids: Base Stacking and Base Pairing Interactions; Nucleic Acids: Chemical Shifts; Water Signal Suppression in NMR of Biomolecules.

8 REFERENCES

1. G. Wagner, *Q. Rev. Biophys.*, 1983, **16**, 1.
2. H. Roder, *Meth. Enzymol.*, 1989, **176**, 446.
3. Y. Bai, J. S. Milne, L. Mayne, and S. W. Englander, *Proteins*, 1993, **17**, 75.
4. G. P. Connelly, Y. Bai, M.-F. Jeng, and S. W. Englander, *Proteins*, 1993, **17**, 87.
5. M. Eigen, *Angew. Chem. Int. Ed. Engl.*, 1964, **3**, 1.
6. S. W. Englander and N. R. Kallenbach, *Q. Rev. Biophys.*, 1983, **16**, 521.
7. H. Teitelbaum and S. W. Englander, *J. Mol. Biol.*, 1975, **92**, 55.
8. M. Gueron and J.-L. Leroy, in *Nucleic Acids and Molecular Biology*, eds. F. Eckstein and D. M. J. Lilley, Springer-Verlag, New York, 1992, vol. 6, p. 1.
9. A. Hvidt and S. O. Nielsen, *Adv. Protein Chem.*, 1966, **21**, 287.
10. C. K. Woodward, I. Simon, and E. Tuchsen, *Mol. Cell. Biochem.*, 1982, **48**, 135.
11. Y. Bai, J. S. Milne, L. Mayne, and S. W. Englander, *Proteins*, 1994, **20**, 4.
12. S. W. Englander and L. Mayne, *Annu. Rev. Biophys. Biomol. Struct.*, 1992, **21**, 243.

Biographical Sketch

S. Walter Englander. *b* 1930. B.S. M.S., Ph.D. (Biophysics), University of Pittsburgh. Instructor and Assistant Professor, Dartmouth. Associate and Full Professor, University of Pennsylvania. Over 100 publications. Research specialties: protein structure, function, dynamics, hydrogen exchange.

Oxygen-17 NMR: Applications in Biochemistry

John G. Pearson and Eric Oldfield

University of Illinois at Urbana-Champaign, IL, USA

1	Introduction	1
2	^{17}O NMR Parameters	1
3	Biophosphates	1
4	Amino Acids and Polypeptides	2
5	CO and O^2 in Hemoproteins	2
6	Summary and Prospects	2
7	Related Article	2
8	References	2

1 INTRODUCTION

^{17}O is the least utilized of the NMR active nuclei commonly found in biological systems. While oxygen atoms play an important role in the hydrogen bonding, electrostatics, and hydration of biomolecules, the very low natural abundance (0.037%) and quadrupolar nature ($I = \frac{5}{2}$) of ^{17}O nuclei have hindered the development of ^{17}O NMR as compared with ^{1}H, ^{13}C, ^{15}N, and ^{31}P NMR in biological systems. Over the last decade, however, the availability of both ^{17}O enriched materials and ever higher field FT NMR spectrometers have led to the utilization of ^{17}O nuclei as probes of biomolecular structure and function, some 40 years after the nucleus was first observed.[1]

It is the intention of this article to review the characteristic parameters governing the use of ^{17}O NMR in, and how the behavior of ^{17}O nuclear spin magnetization has been applied to, biological systems. The effects of ^{17}O quadrupolar relaxation on ^{31}P magnetization are also important, but are beyond the scope of this review.

2 ^{17}O NMR PARAMETERS

The detailed quantum chemical description of sites in biologically relevant molecules is, in general, extremely complex. The task is greatly simplified in NMR by modeling nuclear spin interactions as independent of the rest of the system, with time-dependent interactions between spins and the bulk (or lattice) being termed 'relaxation'. This, and other considerations, allows for the simplification of the ^{17}O NMR of biomolecules to the study of ^{17}O chemical shielding, ^{17}O relaxation (resulting from couplings between the nuclear quadrupole and its local environment), and ^{17}O quadrupole couplings.

The chemical shielding of a nucleus is a function of the electronic structure near the nucleus. ^{17}O nuclei are particularly sensitive to differences in chemical environment; for example, the two distinct oxygen sites in ozone are separated by 566 ppm.[2] Differences in chemical shift between sites in a molecule can be used to determine molecular structures, as well as to study dynamical processes in these structures, such as conformational changes, substrate binding, and hydrogen bonding. The ^{17}O chemical shift is commonly referenced to $H_2{}^{17}O$ in biological NMR studies.

All nuclei with $I > \frac{1}{2}$ have a nuclear quadrupole moment eQ. The interaction of eQ with an electric field gradient eq is quite strong, typically dominating the NMR spectrum of a quadrupolar nucleus. For most biomolecules, the interaction between the eQ of ^{17}O and eq is modulated by rotational motion, either molecular tumbling or internal rotations, making it an efficient relaxation mechanism. In the extreme narrowing limit (very fast motions on the NMR timescale), the nuclear quadrupole relaxation rate essentially determines the resonance linewidth L which can be expressed as

$$L \approx (12\pi/125)(1 + \eta^2/3)\chi^2\tau_r \qquad (1)$$

where $\chi = e^2qQ/h$ is the nuclear quadrupole coupling constant, η is the asymmetry parameter of the electric field gradient tensor, and τ_r is the rotational correlation time.[3] ^{17}O linewidths are therefore proportional to the square of the electric field gradient at the nucleus, and are generally inversely proportional to the molecular correlation time. This limits the applicability of ^{17}O NMR either to relatively small molecules or to sites in molecules where χ is much less than typically found for ^{17}O nuclei (about 10 MHz, see Kintzinger[4]). Within this limitation, ^{17}O relaxation can be used to measure differences in χ and τ_r for either two sites in the same molecule, or the same site under different conditions. For slow molecular motions ($\tau_r \gg 1/\nu_L$) relaxation is a weighted sum of three exponentials, resulting in deviations from Lorentzian lineshapes, and such effects have been observed experimentally for C^{17}O bound to heme proteins, where χ values are very small (about 1–2 MHz).[5]

3 BIOPHOSPHATES

Biophosphates are involved in many biological processes, such as energy transport and utilization, information storage and retrieval, and membrane structure and transport. Examples of such compounds are adenosine diphosphate (ADP), adenosine triphosphate (ATP), DNA, RNA, and phospholipids.

Tsai et al.[6] have demonstrated that bridging and phosphoryl ^{17}O resonances in biophosphates can be assigned from their relative linewidths, due to differences in χ between the various sites. Linewidths are all relatively broad, and several groups have demonstrated improved spectral resolution upon sample heating,[7–11] which decreases τ_r and thereby the ^{17}O linewidths, allowing for more accurate determination of ^{17}O chemical shifts and spin–spin coupling constants, $J(^{31}P, ^{17}O)$. Gerothanassis and Sheppard[11] also demonstrated the utility of using ^{17}O depleted water to minimize the background $H_2{}^{17}O$ solvent peak, which in aqueous samples frequently overwhelms the resonance from even an ^{17}O enriched sample.

The pH dependence of the ^{17}O chemical shift has been determined for phosphoryl oxygen atoms in several phosphates, including adenosine monophosphate (AMP), ADP, and

ATP,[9,10] demonstrating the effect of protonation upon the phosphoryl ^{17}O chemical shift.

The binding of several diamagnetic ions to ATP has been studied using ^{17}O relaxation rates.[12,13] The phosphoryl ^{17}O linewidth increases markedly upon ion binding, indicating the coordination sites for Mg(II), Co(III), Sc(III), La(III), and Lu(III) in $M \cdot ATP_n$ complexes.

The hydrogen bonding of uridine derivatives has been studied using ^{17}O NMR.[14] Equilibrium constants and interaction enthalpies of water–uridine hydrogen bond complexes were determined by observing changes in ^{17}O chemical shift as a function of water concentration, in acetonitrile.

^{17}O spectra of hemiacetal and aldehydic abasic sites in DNA of importance in DNA damage and repair have been studied,[15] demonstrating the ability to observe approximately 10 μM aldehyde signals in the presence of approximately 20 M solvent ^{17}O.

4 AMINO ACIDS AND POLYPEPTIDES

The tertiary structures of polypeptides and proteins in aqueous solution are strongly influenced by hydrogen bonding, both within the solute molecule and with the solvent, and ^{17}O NMR has been used to gain insights into these interactions.

The effects of proton exchange between peptide termini and water on ^{17}O chemical shifts have been used to probe the electronic structures of amino acids,[11,16] dipeptides,[17,18] and peptide carboxamides.[19] The ^{17}O chemical shift has also been used to monitor the presence of hydrogen bonding in peptide models,[20] dipeptides,[18] peptide carboxamide,[19] acylprolines (model β- and γ-turns),[21–23] and small polypeptides.[24]

The hydration and aggregation of peptides has been studied using ^{17}O relaxation measurements. ^{17}O linewidths of amino acids,[16,25] dipeptides,[18] peptide carboxamides,[19] and small polypeptides[24] have been determined in various solvents, locating hydration sites at carboxylate and carbonyl oxygen atoms, in addition to providing a method of monitoring peptide aggregation. In addition, a ^{17}O relaxation study of ATP binding to adenylate kinase[26] has been reported, demonstrating the feasibility of studying enzyme–substrate interactions via ^{17}O NMR, providing the ligand is not rigidly held.

^{17}O chemical shifts have also been found to be torsion-angle dependent in aryl carboxylic esters, acids, and amides,[27] and ^{17}O NMR promises to be a powerful technique for elucidating the structures of membrane peptides and proteins, using oriented samples.

5 CO AND O_2 IN HEMOPROTEINS

The nature of Fe–O_2 and Fe–CO bonding in heme proteins and model compounds has been studied using ^{17}O NMR. ^{17}O resonance frequencies and linewidths have been measured for O_2 bound to Vaska's compound,[28] O_2 bound to picket-fence and basket-handle porphyrin model compounds,[29–31] CO bound to peroxidases,[32] as well as other hemoproteins,[5,33] and O_2 bound to hemoproteins in the solid state.[31] Results were found to be in general agreement with Pauling's ideas of end-on bonding, with additional electrostatic field effects being proposed to take into account the chemical shift variation seen from protein to protein.[34] In Fe–O_2 systems, the chemical shift difference between the two oxygen nuclei has been found to be about 600 ppm,[29–31] comparable to that found in ozone, consistent with previous analogies between FeO_2 bonding and that found in O_3.

6 SUMMARY AND PROSPECTS

Given the central importance of oxygen in biochemical systems (lipids, proteins, nucleic acids and carbohydrates), there have been remarkably few studies of ^{17}O NMR chemical shifts, and even fewer studies aimed at detailed, quantum chemical analyses of chemical shifts and quadrupolar couplings. ^{17}O NMR in biochemistry is therefore still in its infancy. However, with the advent of 750 MHz spectrometers, the current development of 900–1000 MHz machines, as well as recent development in quantum chemical applications to macromolecules,[35] ^{17}O NMR can be expected to benefit enormously over the next few years. Thus, ^{17}O chemical shifts and quadrupole couplings can be exploited to analyze, for example, lipid headgroup and backbone orientations in membranes, sterol orientations and interactions, peptide/protein structures in condensed phases, carbohydrate conformations and interactions, as well as small DNA structures. For ^{17}O, only relatively low resolution magnets are required, thus the sensitivity gains possible with very high-field operation can be readily exploited. Indeed, most ^{17}O NMR studies of biochemical systems reported to date could have been obtained at about 1 ppm resolution only. With recent improvements in computer price/performance ratios, and much more efficient algorithms, theoretical analyses of ^{17}O shifts and χ values are also to be expected. Thus, ^{17}O NMR in biochemistry undoubtedly has an extremely bright future.

7 RELATED ARTICLES

Oxygen-17 NMR.

8 REFERENCES

1. F. Alder and F. C. Yu, *Phys. Rev.*, 1951, **81**, 1067.
2. I. J. Solomon, J. N. Keith, A. J. Kacmarek, and J. K. Raney, *J. Am. Chem. Soc.*, 1968, **90**, 5408.
3. A. Abragam, *The Principles of Nuclear Magnetism*, ed W. C. Marshall and D. H. Williamson, Oxford University, Oxford, 1961, pp. 297–305.
4. J.-P. Kintzinger and H. Marsmann, in *NMR Basic Principles and Progress*, ed. P. Diehl, E. Fluck, and R. Kosfeld, Springer, Berlin, 1981, Vol. 17, pp. 1–64.
5. H. C. Lee and E. Oldfield, *J. Am. Chem. Soc.*, 1989, **111**, 1584.
6. M.-D. Tsai, S. L. Huang, J. F. Kozlowski, and C. C. Chang, *Biochemistry*, 1980, **19**, 3531.
7. C. Rodger, N. Sheppard, H. C. E. McFarlane, and W. McFarlane, in *NMR and the Periodic Table*, ed. R. K. Harris and B. E. Mann, Academic, London, 1978, Chap. 12A.
8. H. M. Schwartz, M. MacCoss, and S. S. Danyluk, *Tetrahedron Lett.*, 1980, **21**, 3837.

9. J. A. Coderre, S. Mehdi, P. C. Demou, R. Weber, D. D. Traficante, and J. A. Gerlt, *J. Am. Chem. Soc.*, 1981, **103**, 1870.
10. J. A. Gerlt, P. C. Demou, and S. Mehdi, *J. Am. Chem. Soc.*, 1982, **104**, 2848.
11. I. P. Gerothanassis and N. Sheppard, *J. Magn. Res.*, 1982, **46**, 423; I. P. Gerothanassis, R. Hunston, and J. Lauterwein, *Helv. Chim. Acta*, 1982, **65**, 1764.
12. S. L. Huang and M.-D. Tsai, *Biochemistry*, 1982, **21**, 951.
13. Y.-J. Shyy, T.-C. Tsai, and M.-D. Tsai, *J. Am. Chem. Soc.*, 1985, **107**, 3478.
14. H. M. Schwartz, M. MacCoss, and S. S. Danyluk, *J. Am. Chem. Soc.*, 1983, **105**, 5901.
15. J. A. Wilde, P. H. Bolton, A. Mazumder, M. Manoharan, and J. A. Gerlt, *J. Am. Chem. Soc.*, 1989, **111**, 1894.
16. B. Valentine, T. St. Amour, R. Walter, and D. Fiat, *J. Magn. Reson.*, 1980, **38**, 413.
17. C. S. Irving and A. Lapidot, *J. Chem. Soc., Chem. Commun.*, 1976, 43.
18. B. Valentine, A. Steinschneider, D. Dhawan, M. I. Burgar, T. St. Amour, and D. Fiat, *Int. J. Peptide Protein Res.*, 1985, **25**, 56.
19. A. Steinschneider and D. Fiat, *Int. J. Peptide Protein Res.*, 1984, **23**, 591.
20. A. Steinschneider, M. I. Burgar, A. Buku, and D. Fiat, *Int. J. Peptide Protein Res.*, 1981, **18**, 324.
21. J. Lauterwein, I. P. Gerothanassis, and R. N. Hunston, *J. Chem. Soc., Chem. Commun.*, 1984, 367.
22. R. N. Hunston, I. P. Gerothanassis, and J. Lauterwein, *J. Am. Chem. Soc.*, 1985, **107**, 2654.
23. N. Birlirakis, I. P. Gerothanassis, C. Sakarellos, and M. Marraud, *J. Chem. Soc., Chem. Commun.*, 1989, 1122.
24. C. Sakarellos, I. P. Gerothanassis, N. Birlirakis, T. Karayannis, and M. Sakarellos-Daitsiotis, *Biopolymers*, 1989, **28**, 15.
25. J. Lauterwein, I. P. Gerothanassis, R. N. Hunston, and M. Schumacher, *J. Phys. Chem.*, 1991, **95**, 3804.
26. D. A. Wisner, C. A. Steginsky, Y.-J. Shyy, and M.-D. Tsai, *J. Am. Chem. Soc.*, 1985, **107**, 2814.
27. A. L. Baumstark, P. Balakrishnan, M. Dotrong, C. J. McCloskey, M. G. Oakley, and D. W. Boykin, *J. Am. Chem. Soc.*, 1987, **109**, 1059.
28. H. C. Lee and E. Oldfield, *J. Magn. Reson.*, 1986, **69**, 367.
29. I. P. Gerothanassis and M. Momenteau, *J. Am. Chem. Soc.*, 1987, **109**, 6944.
30. I. P. Gerothanassis, M. Momenteau, and B. Loock, *J. Am. Chem. Soc.*, 1989, **111**, 7006.
31. E. Oldfield, H. C. Lee, C. Coretsopoulos, F. Adebodun, K. D. Park, S. Yang, J. Chung, and B. Phillips, *J. Am. Chem. Soc.*, 1991, **113**, 8680.
32. H. C. Lee, K. Cummings, K. Hall, L. P. Hager, and E. Oldfield, *J. Biol. Chem.*, 1988, **263**, 16118.
33. K. D. Park, K. Guo, F. Adebodun, M. L. Chiu, S. G. Sligar, and E. Oldfield, *Biochemistry*, 1991, **30**, 2333.
34. J. D. Augspurger, C. E. Dykstra, and E. Oldfield, *J. Am. Chem. Soc.*, 1991, **113**, 2447.
35. A. C. de Dios, J. G. Pearson, and E. Oldfield, *Science*, 1993, **260**, 1491.

Acknowledgments

This work was supported by the United States Public Health Service (Grant HL-19481). J. G. P. was a USPHS Postdoctoral Fellow (grant GM-14545).

Biographical Sketches

John G. Pearson. *b* 1963. B.S., University of California at Santa Barbara; 1986; Ph.D., (Supervisor Alexander Pines), University of California at Berkeley, USA, 1991. Successively, postdoctoral work (with Eric Oldfield), postdoctoral research fellow, University of Illinois at Urbana–Champaign, 1991–present. Approx. 20 publications. Research specialties: protein chemical shifts and multiple quantum NMR.

Eric Oldfield. *b* 1948. B.Sc., 1969, University of Bristol, Ph.D., 1972 (supervisor Dennis Chapman), University of Sheffield, D.Sc., 1982, University of Bristol, UK. Postdoctoral work at Indiana University, Bloomington (with Adam Allerhand) and Massachusetts Institute of Technology, Cambridge (with John S. Waugh). Professor, University of Illinois at Urbana-Champaign, 1975–present. Approx. 200 publications. Research specialties: inorganic and biochemical applications, especially proteins, membranes, and heterogeneous catalysts.

Pancreatic Trypsin Inhibitor

Kurt Wüthrich

Eidgenössische Technische Hochschule Zürich, Switzerland

1	Introduction	1
2	Growing up with BPTI	2
3	Survey of Key NMR Experiments with BPTI	2
4	BPTI and NMR Spectroscopy with Proteins	3
5	BPTI and Resonance Assignments in Proteins	3
6	BPTI and Protein Structure Determination by NMR	4
7	BPTI and Amide Proton Exchange	4
8	BPTI and Internal Mobility in Proteins	5
9	BPTI and Protein Folding	5
10	Concluding Remarks	6
11	Related Article	7
12	References	7

1 INTRODUCTION

> The basic pancreatic trypsin inhibitor (BPTI) from bovine pancreas[1] has a molecular weight of 6500 and consists of 58 amino acid residues. The amino acid sequence and the molecular conformation in single crystals[2] are known, and it has been found that the solution conformation of BPTI is unusually stable towards denaturing agents and heat. Some time ago we briefly discussed proton NMR data which revealed yet another rather unexpected structural feature of BPTI, i.e. very slow exchange of some of the amide protons.[3] This paper presents new data on the denaturation of BPTI and the proton exchange in solutions of BPTI in D_2O. An obvious goal of the investigations of BPTI is to understand in more detail the mode of action of this inhibitor. In addition, since BPTI is by its small size amenable to detailed studies by different techniques, work on this molecule could on a more general basis be particularly valuable for the further development of the investigations of molecular conformations in proteins. In view of the temperature stability of BPTI, some of the data on this protein might conceivably even be relevant for the investigation of conformational features in proteins from thermophilic organisms.

This quotation represents the introduction of the first paper from my laboratory that was devoted entirely to BPTI.[4] We started work on this protein in 1972, and at the time no one could have guessed that I would some day be asked to write an article on BPTI for the *Encyclopedia of Nuclear Magnetic Resonance*. However, the prediction made lightheartedly in 1973, that work with BPTI might be 'particularly valuable' for the future development of research on protein structures, turned out to have been, if anything, an understatement. In the meantime my laboratory has published more than 70 papers on experiments with BPTI and 15 papers on work with chemical modifications and homologs of BPTI, and by now the output of NMR papers on BPTI by other groups exceeds these numbers by far. Outside of the NMR field, BPTI was one of the first proteins, in 1975, for which a refined high-resolution X-ray crystal structure became available,[5] which in turn made BPTI a preferred object for theoretical studies on protein structure and dynamics.[6] At that time BPTI was also already used for studies on protein folding.[7] In 1982, BPTI was the first protein for which the ^1H NMR spectrum was completely assigned,[8] which contributed greatly to making it a focal point for research on amide proton exchange in proteins.[9] More recently, numerous projects on protein-folding studies and amide proton exchange measurements with BPTI relied heavily on the use of NMR for characterization of molecular structures and for kinetic measurements. For the sake of completeness it should also be added that a vast body of literature on the biochemistry and physiology of BPTI provides the platform for the physicochemical and structural investigations.

Figure 1 presents a ribbon drawing of the polypeptide backbone fold in BPTI, and a stereo view of the complete NMR solution structure[10] is shown in Figure 2. The polypeptide backbone forms a 3_{10}-helix from residues 3 to 7, a β-hairpin of residues 18–35, a one-residue third antiparallel β-strand of residue 44, and an α-helix of residues 47–56. There are three disulfide bonds linking the cysteinyl residues 5–55, 14–38, and 30–51. The molecule contains four phenylalanyl residues in positions 4, 22, 23, and 45, and the four tyrosyl residues 10, 21, 23, and 35 as the only aromatic side chains. The arrangement of the polypeptide backbone and the interior side chains (green and blue in Figure 2) is nearly identical in crystals[5] and in solution.[10] The conformation of the protein surface (red in

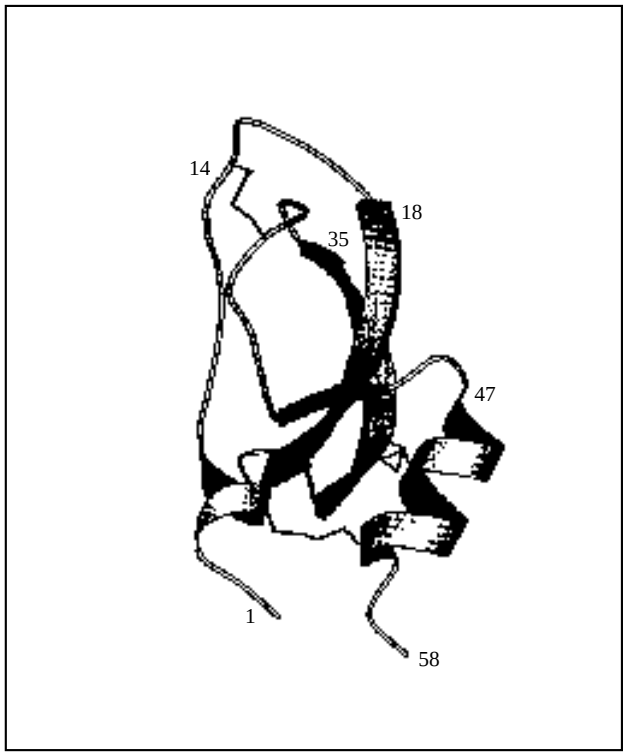

Figure 1 Ribbon drawing of the three-dimensional NMR solution structure of BPTI.[10] The three disulfide bonds 5–55, 14–38, and 30–51 are displayed as solid lines tracing the covalently linked side chains. For easy reference some residue positions have been identified. (Drawing prepared using the atom coordinates from Berndt et al.[10])

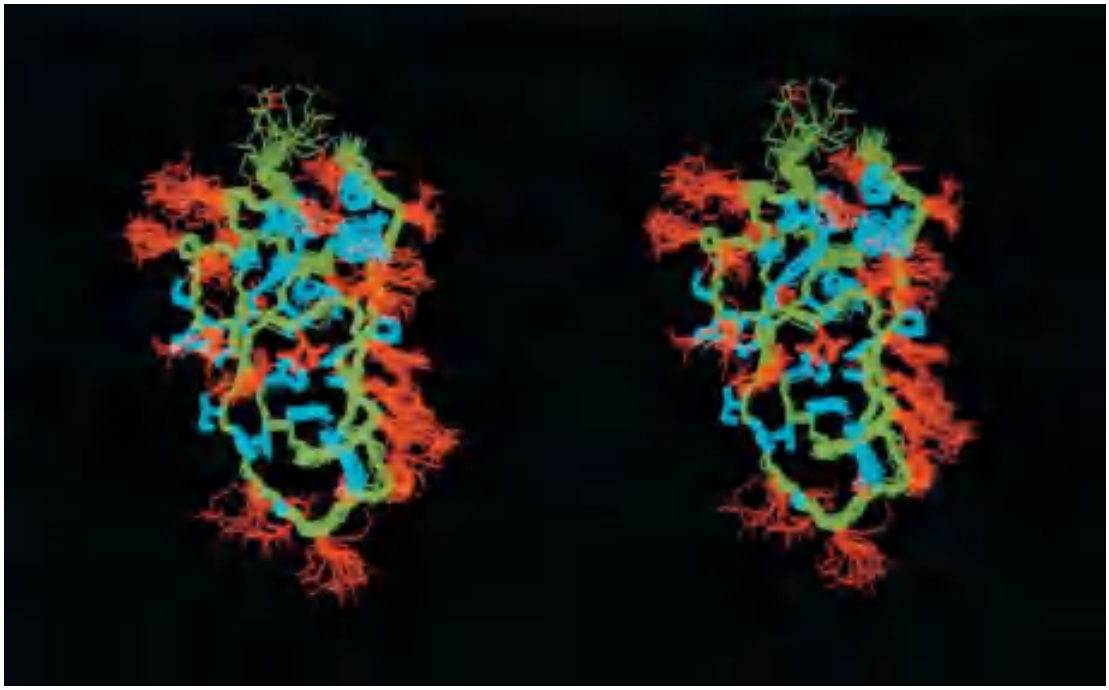

Figure 2 Stereo view of the NMR solution structure of BPTI represented as a superposition of 20 conformers. All heavy atoms are displayed. Color code: green, polypeptide backbone; blue, core side chains; red, surface side chains. A close fit among the 20 conformers indicates regions of the molecule where the structure is well defined, whereas a large dispersion implicates the presence of (dynamically) disordered structure. (Drawing prepared using the atom coordinates from Berndt et al.[10])

Figure 2) and the surface hydration[11] in solution are highly dynamic and different from the X-ray structure because of crystal lattice effects. The globular structure of BPTI is stable over the pH range 2–10 at ambient temperature, and over the temperature range 1–90 °C at neutral pH. Physicochemical studies of the folded protein can thus be performed with extensive variation of the experimental conditions.

2 GROWING UP WITH BPTI

Considering the long years of our involvement with BPTI, it is inevitable that this account has a personal note. There is only one other protein that influenced the activities of my group in a comparable way, i.e. cytochrome *c* (see ***Wüthrich, Kurt: NMR Structures of Biological Macromolecules***). However, it was with BPTI that we were introduced to protein structures and the physical chemistry of proteins. When dealing with cytochrome *c* our interest was focused on the one hand on NMR experimentation, and on the other hand on the heme group and its immediate surroundings. For example, all our theoretical work connected with cytochrome *c* and other hemoproteins related to ligand field treatments of the electronic states of the heme iron. With BPTI we became motivated to understand protein structure at a more general level, and through frequent contacts with Robert Huber's group in Munich we also learned about protein crystallography. In particular, during the first 3 years of our NMR work, when we mostly tried to rationalize NMR spectral properties on the basis of the BPTI crystal structure, Deisenhofer and Steigemann[5] refined the original BPTI structure at 0.15 nm resolution, and we got access to the improvements from the original molecular model[2] to the final refined structure in several steps. At that time, the X-ray data were visualized by physical molecular models, and the coordinates were obtained by measuring interatomic distances in these models. I remember a day when local structural features contained in a preliminary set of atom coordinates provided by the Munich group completely upset some calculations in my laboratory. A trip to Munich then revealed that there had been an impact on the BPTI model by an unidentified object (probably a broomstick in the hands of the cleaning personnel) before the atom coordinates were measured. Unimportant as this story is in perspective, it was the kind of experience we needed to develop a realistic view of experimental protein structure determination.

As happens so often with timely research projects, we were not alone in 1973 in starting publishing NMR work with BPTI. Brian Sykes and his co-workers reported studies of the amide protons and the tyrosyl rings,[12] and pursued the investigations of the tyrosyls with the use of chemical modification.[13] We thus had an opportunity to practice functioning under the pressure of direct competition. Starting around 1975, more and more theoretical work appeared that related directly to our experimental data,[6] which gave us good motivation to get more thoroughly educated in this area.

3 SURVEY OF KEY NMR EXPERIMENTS WITH BPTI

In Table 1 I have identified 19 key events which have been directly associated with BPTI during the period from the initial NMR experiments with BPTI in 1972[3,4,12] until the completion of the first NMR structure determination of a protein in

Table 1 Key NMR Experiments with BPTI, 1973–84

Year	Experiment/Observation	Ref.
1973	^{1}H NMR of individual amide protons	4, 12
1974	Ring flips of Phe and Tyr	14
1975	Theory of ring flips	6, 15
1976	Sine-bell for digital filtering	16
1977	Homonuclear 2D *J*-resolved NMR	17
1978	Quantitative NMR studies of amide proton exchange	18–20
1978	Dynamic model for globular proteins	18
1978	Sequential assignments using 1D NMR	21
1979	Mechanisms for amide proton exchange in BPTI	22, 23
1979	SECSY	24
1979	NOESY	25
1980	2D ^{1}H NMR with proteins in H_2O solution	26
1980	Sequential assignments using 2D NMR	27, 28
1981	NOE build-up measured with 2D NOESY	29
1981	Complete ^{1}H NMR assignment of a protein	8
1981	Amide proton exchange in the EX_1 regime	30, 31
1981	NH trap experiment for detection of early folding events	30, 32
1983	Phase sensitive 2QF-COSY	33
1984	Structure calculation from NMR data using the program DISGEO	34

1984.[35] These were either developments of new NMR experiments, important steps toward protein structure determination from NMR data, or NMR observations relating to novel features of protein conformation, and they will be discussed in more detail in the following sections. The selection is based on general considerations of the follow-up activities as reflected, for example, in the citation record, but also on my memory of the impact from these events on our subsequent projects. Table 1 contains mostly references to our own work, since besides several papers on amide proton exchange, mostly by Clare Woodward's group,[19, 22] only seven NMR studies with BPTI were published by others up to 1984. These are four papers by Brian Sykes's group,[12] of which three are on nitrotyrosyl derivatives of BPTI,[13] two are on refolding of heat-denatured, modified BPTI,[36] and a theoretical paper is on chemical shift averaging.[37] In addition, by 1984 BPTI was more and more widely used as a standard to check instrument performance.

In recent years in my laboratory, BPTI has lost its pivotal role of the 'heroic era' up to 1984, but elsewhere applications of NMR techniques became more and more widespread in projects on the folding, stability, and dynamics of BPTI (see Section 10 below).

4 BPTI AND NMR SPECTROSCOPY WITH PROTEINS

In the 1970s my group worked mainly with hemoproteins, oligopeptides, and BPTI (see ***Wüthrich, Kurt: NMR Structures of Biological Macromolecules***). Among the proteins studied, BPTI was the most robust (see above), and it could be dissolved in water at concentrations up to 20 mM. It is not surprising, therefore, that it was used for most of the NMR technique developments in my laboratory. The first such entry in Table 1 is the sine-bell,[16] which was of particular practical importance during all those years when absolute value presentations of the 2D NMR spectra were used.[8, 17, 24–29] It continues to be widely applied, and is a fitting tribute to the beautiful spectroscopy performed by the late Antonio DeMarco during his all too short life span.

The remaining technique entries refer to early 2D NMR experiments. 2D *J*-resolved spectroscopy had previously been developed in Richard Ernst's laboratory, but the BPTI paper in 1977[17] presents not only the first 2D NMR spectrum of a protein, but also the first 2D spectra recorded with a data size that made the technique useful for practical applications beyond observation of the classical test compounds, such as CH_3I or CH_3CH_2OH. SECSY[24] was designed as an alternative to the previously described COSY scheme to overcome limitations imposed by the then available computer capacities. For several years, until phase sensitive 2D NMR became available as a daily routine,[38, 39] the concept of delayed aquisition used in SECSY was widely propagated also by the instrument manufacturers. From our 1D experiments with BPTI[21] (see also the following section) and cytochrome *c*[40, 41] it was clear in 1978 that NOEs would be the key parameter for studies of macromolecular structures. The first 2D NOESY spectrum on record[25] was obtained with BPTI by Anil Kumar in my laboratory during the Christmas recess of 1979. Funding for this project was obtained through a grant application submitted jointly with Richard Ernst in 1978, which requested support for developing improved NOE measurements, including 2D NOESY. Within weeks after the first successful NOESY experiment we recorded homonuclear 2D NMR spectra in H_2O solutions of proteins.[26] This was an important step ahead, which enabled the extension of the NMR assignments in the protein core, where the amide protons exchange sufficiently slowly to be observed in D_2O, to the molecular surface. Although the preirradiation used to suppress the solvent line lacks the sophistication of other solvent suppression schemes, it turned out to be exactly what was needed for complete protein structure determinations by NMR. A further fundamentally important advance was to repeat the earlier 1D NMR measurements of NOE build-up curves for BPTI using 2D NOESY.[29] BPTI was also used in the first application of a two quantum filter for further improvement of the high-resolution phase sensitive COSY spectra of proteins[33] which we had obtained with the earlier implementation of time proportional phase incrementation (TPPI) by Dominique Marion.[38]

5 BPTI AND RESONANCE ASSIGNMENTS IN PROTEINS

In 1975, initial resonance assignments in BPTI were obtained for the aromatic region by Brian Sykes's group using chemical derivation of the tyrosyl rings[13] and in my laboratory using spectroscopic techniques.[42] In the following years we tried just about any available approach to add assignments for other amino acid side chains in BPTI,[43] but the decisive breakthrough that opened the way to NMR structure determination of proteins[44, 45] came in 1978 with the successful 'sequential NOE walk' by Andreas Dubs and Gerhard Wagner for obtaining sequential assignments of the

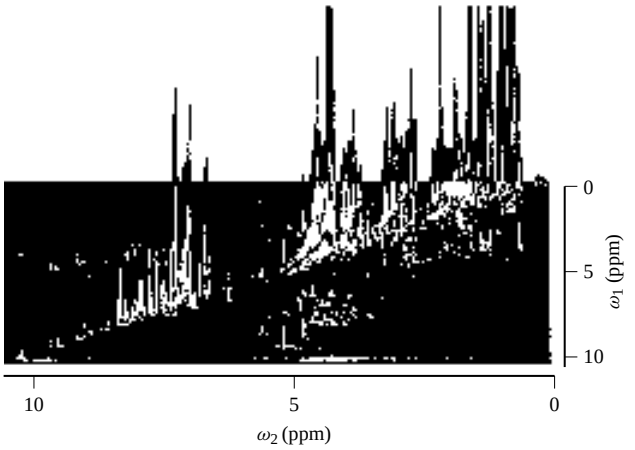

Figure 3 Stacked-plot representation of a symmetrized, absolute-value 500 MHz ^{1}H COSY spectrum of a 0.02 M solution of BPTI in a mixed solvent of 90% H_2O and 10% D_2O, pH = 4.6. T = 80°C. The spectrum was recorded in ~24 h. The digital resolution is 5.3 Hz/point. Due to the symmetrization the residual perturbations from the water suppression appear as a band of weak peaks parallel to the diagonal. (Reproduced with permission from G. Wagner and K. Wüthrich, *J. Mol. Biol.*, 1982, **155**, 347)

β-sheet in BPTI (see Figure 1).[21] This approach was based on detailed inspection of the BPTI crystal structure (see the following section) and on NMR techniques used previously in our laboratory for a similar sequential walk around the heme group in hemoproteins.[40] Once the aforementioned 2D NMR experiments were available, the assignments could be extended to other regions of BPTI,[27,28] and when we obtained a 500 MHz spectrometer in 1981 the complete polypeptide chain in BPTI was assigned.[8] Figure 3 shows a COSY spectrum from the assignment paper,[8] illustrating Gerhard Wagner's mastery of the art of NMR spectroscopy with proteins. Over the years this figure has appeared more than 10 times on the cover of books and journals, and a decade after its original publication I was quite surprised to find it also on the EENC poster.

6 BPTI AND PROTEIN STRUCTURE DETERMINATION BY NMR

From joint inspection of NMR data and the high-resolution X-ray crystal structure of BPTI, which was started in a systematic way by Andreas Dubs and Gerhard Wagner in connection with the initial sequential assignment,[21] we obtained important insights which resulted in a theoretical basis for the sequential resonance assignment technique[46] and a pattern recognition approach for the identification of secondary structures in proteins.[47,48] The crucial BPTI contribution to structure calculation from NMR data, however, was the paper with Timothy Havel listed as the last entry in Table 1.[34] Using the program DISGEO and simulated input data sets of NOE upper-distance constraints derived from the BPTI crystal structure, this paper demonstrated that complete protein structures at atomic resolution could indeed be obtained from experimental NMR data, and by extensive controlled variation of the simulated input it could also be shown that the method would be robust with respect to incomplete collection of input data as well as low precision of the individual NOE distance measurements.

Considering the extent to which our activities in the early 1980s were focused on BPTI, the questions must arise why even in 1987 only a low-resolution NMR structure had been published,[49] and why a complete high-quality structure determination was achieved only in 1992.[50] An initial BPTI structure calculation from NMR data had indeed already been performed in 1982 by Werner Braun and Gerhard Wagner (unpublished). The software used was an implementation of a metric matrix distance geometry algorithm that had the capacity of handling all-atom structures of oligopeptides with up to about 10 amino acid residues, which had been used successfully for a structure determination of the nonglobular polypeptide hormone glucagon.[51,52] For the calculations with BPTI a simplified presentation of the polypeptide chain had to be adopted, with each amino acid residue described by two spheres representing the backbone and the side chain, respectively. The fit of the resulting structure with the X-ray crystal structure[5] was not significantly better than that of model calculations done at the same time by others without use of experimental data. I accepted this outcome as a clear-cut documentation that protein structure calculations from NMR data have to be performed with the complete covalent polypeptide structure to represent properly both the van der Waals constraints and the chirality of the individual residues. We also realized, from comparison with other proteins as well as with simulated input data from the BPTI crystal structure, that we were not obtaining a good quality input of conformational NMR constraints for BPTI. Eventually it turned out that the generally available BPTI preparations contain about 10% of closely related BPTI analogs. Although this did not interfere either with the use of BPTI for the development of NMR techniques or with the resonance assignments, it made the collection of an extensive set of NOE distance constraints as input for a structure determination difficult, since the assignments of many NOESY cross peaks remained ambiguous. Furthermore, work with a recombinant isotope-labeled mutant BPTI also confirmed earlier observations by Gerhard Wagner that some resonance lines were not observed because of conformational exchange, which was now traced to a dynamic equilibrium between the two different chiral forms of the disulfide bridge 14–38 (see Figure 1).[53] Based on this information and with the use of a homogeneous protein sample, a high-quality structure determination was finally obtained in 1992.[50]

7 BPTI AND AMIDE PROTON EXCHANGE

Figure 4 shows the first BPTI spectrum published by my laboratory in 1973[3,4] (comparison with Figure 3 affords a good illustration of the progress made during the following decade), and the high-frequency region illustrates part of an early amide proton exchange measurement. The protein was dissolved in D_2O, and the replacement of individual amide protons by deuterons was followed by measurement of the decrease of the intensities of the corresponding resonance lines with time. In Figure 4, the loss of intensity between the two spectra recorded within 10 min and 170 h after sample preparation, respectively, is readily apparent. This was one of the few experiments with proteins that could be done well in 1973 (see ***Wüthrich, Kurt:***

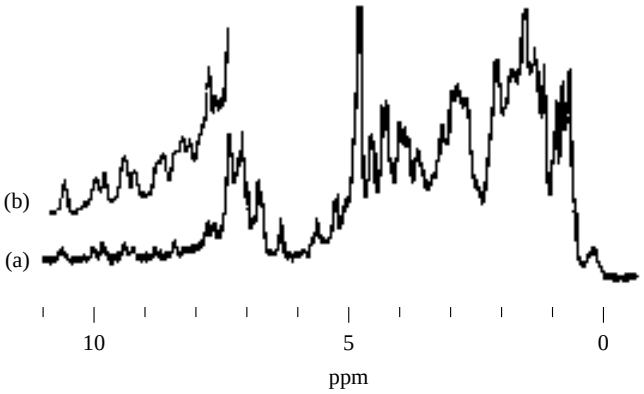

Figure 4 Proton NMR spectrum at 220 MHz of a 0.01 M solution of BPTI in D_2O, pD = 7.7, T = 20°C. Two spectra were recorded 170 h (a) and 10 min (b) after the preparation of the solution. (Reproduced with permission from A. Masson and K. Wüthrich, *FEBS Lett.*, 1973, **31**, 114)

NMR Structures of Biological Macromolecules), and so we started to collect exchange data with BPTI under a wide variety of conditions of pH, temperature, and ionic strength, and subsequently also with homologs and chemical modifications of BPTI.

Amide proton exchange measurement has been a classical approach in protein chemistry long before any such studies were started with BPTI, dating back to the days of the Linderstrøm–Lang laboratory in Copenhagen.[54] The NMR measurements with BPTI added a new element in that the exchange from individual sites in the protein could be followed, whereas earlier techniques yielded information only on the percentage of the ensemble of all amide protons that had exchanged after a certain time span.[54] The new potentialities of NMR were soon recognized by those specializing in the field of amide proton exchange,[55] and in particular Clare Woodward and her group[19,22] started to perform NMR exchange measurements with BPTI under a wide range of conditions. The follow-up to the NMR studies on amide proton exchange listed in Table 1[18–20] continues to the present, and the mechanisms for amide proton exchange in BPTI proposed in 1979[22,23] provide a much discussed background.

The next advance came with the individual assignments of amide proton NMR lines,[21] so that exchange rates could be attributed to unique sites in the BPTI crystal structure.[20,23] This step was completed in 1982, when a map of all individual exchange rates in BPTI was obtained.[56] The last entry on this topic in Table 1[30,31] covers experiments by Heinrich Roder in which experimental conditions were identified where the exchange in a chemically modified BPTI derivative proceeds via a so-called EX_1 process, so that the exchange rates are directly related to the frequencies of protein structure fluctuations.[54] This paper shows that EX_1 processes for amide proton exchange in proteins can be obtained only under extreme conditions which are not normally used for exchange measurements. Therefore, nearly all available exchange data are governed by EX_2 processes, where the exchange rates are not directly related to the frequencies of internal motions in the protein structure but rather to the acid/base-catalyzed reaction at the amide group modulated by conformational equilibria in the protein.[23]

8 BPTI AND INTERNAL MOBILITY IN PROTEINS

In the X-ray crystal structure of BPTI the aromatic rings of phenylalanine and tyrosine are among the side chains with the smallest temperature factors.[5] For each ring the relative values of the B-factors increase toward the periphery, so that the largest positional uncertainty is indicated for the C-4 position on the symmetry axis through the $C\beta-C\gamma$ bond. The observation of ring-flipping motions on the millisecond to microsecond timescale (Figure 5)[14] was therefore a genuine surprise, since it appeared to be incompatible with the crystal structure. Theoretical studies performed in a collaboration of my group with Robert Huber's laboratory,[15] and independently by Martin Karplus's group[6] then showed that the crystallographic B-factors sample multiple rotation states about the $C\alpha-C\beta$ bond, whereas the ring flips about the $C\beta-C\gamma$ bond seen by NMR are very rapid 180° rotations connecting two indistinguishable equilibrium orientations of the ring. The B-factors do not manifest these rotational motions because the populations of all nonequilibrium rotational states about the $C\beta-C\gamma$ bond are vanishingly small. The ring flip phenomenon, which turned out to be a general feature of globular proteins, thus showed that there are low-frequency internal motions in protein molecules, which have activation energies of 60–100 kJ mol^{-1} and amplitudes of $\gtrsim$0.1 nm, and involve concerted displacements of numerous groups of atoms. Ring flips have since been the subject of a long series of theoretical and experimental investigations.

Working with a series of chemical modifications of BPTI and homologous proteins, we observed in 1978[18] that amide proton exchange rates measured under conditions of EX_2 exchange are correlated with the thermal stability of the protein, i.e. corresponding protons would exchange more rapidly in the less stable proteins. In contrast, the ring flip rates, which are directly related to the frequencies of internal protein structure fluctuations, were found to be insensitive to protein stability as long as the 3D structure was preserved at the conditions of the experiment.

BPTI continues to be a source of observations on dynamic features which turn out to be common to globular proteins at large. Most important, it was with BPTI that we succeeded in 1989 in observing individual molecules of hydration water by NMR,[57] to demonstrate that internal hydration water molecules exchange with the bulk solvent on a millisecond timescale or faster,[58] and to distinguish qualitatively between interior hydration sites and surface hydration,[11] which provides a rationale for the generally observed dynamic surface disorder in NMR solution structures of globular proteins (see Figure 2). Another novel dynamic feature identified recently in BPTI is the aforementioned slow interconversion between two conformation states of the disulfide bond 14–38,[53] which was also clearly manifested in ^{15}N $T_{1\rho}$ measurements.[59]

9 BPTI AND PROTEIN FOLDING

One of the 1981 entries in Table 1 is the amide proton trap experiment for studies of early events in protein refolding, which was performed as part of Heinrich Roder's Ph.D. thesis in 1981.[30,32] This experiment and refined forms thereof became very popular in the late 1980s, and it is now one of

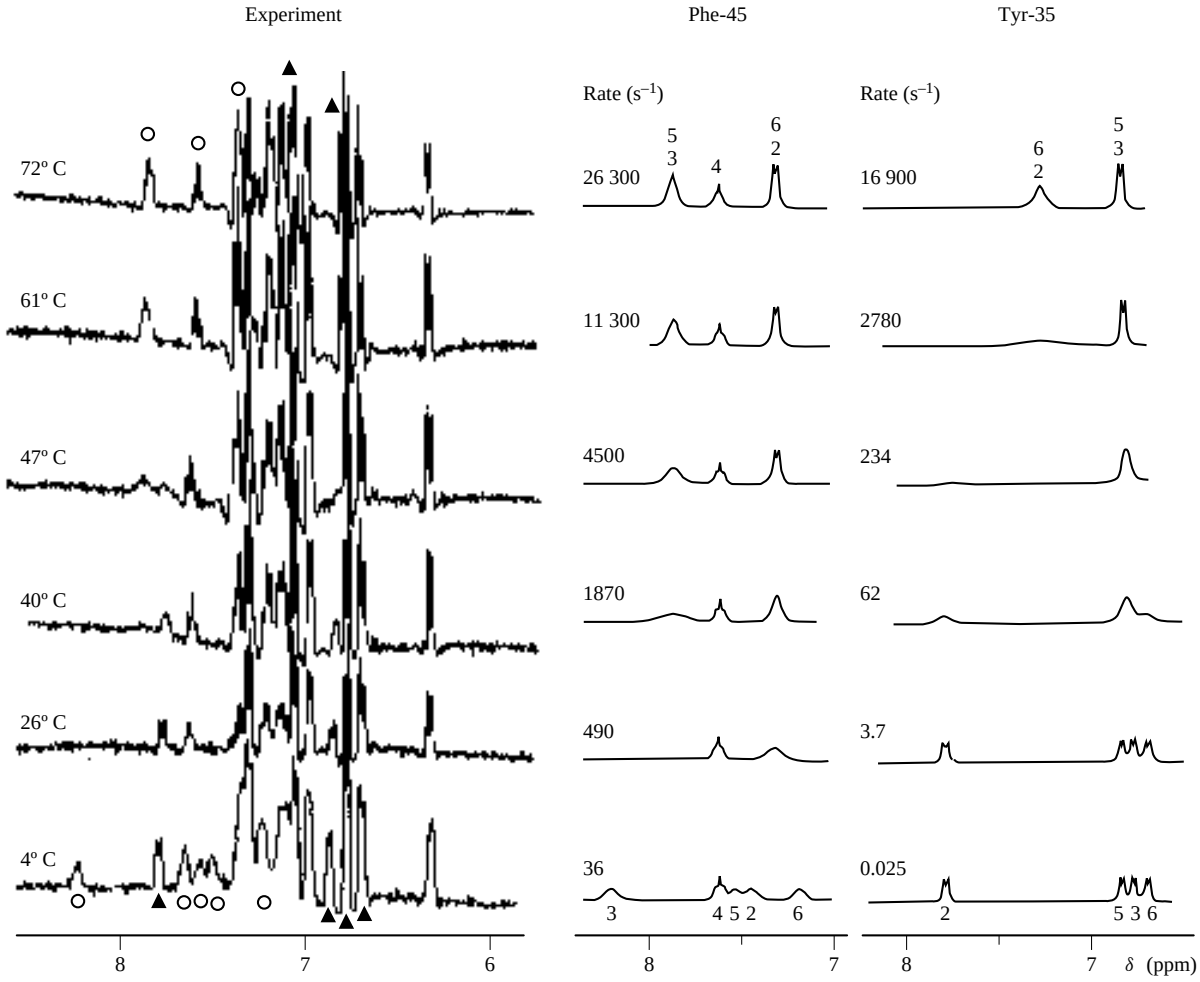

Figure 5 1D 360 MHz ^{1}H NMR spectra at variable temperature of a 0.01 M solution of BPTI in D_2O, pD = 7.8. The region from 6.0 to 8.5 ppm is shown. The resonances of the aromatic rings of Phe-45 (○) and Tyr-35 (▲) were simulated in the center and on the right, respectively, using the ring flip frequencies indicated with the individual spectra. The resonance assignments in the simulated spectra refer to the standard numeration for the aromatic rings of phenylalanine and tyrosine. (Reproduced by permission of Wiley from K. Wüthrich, 'NMR of Proteins and Nucleic Acids', 1986)

the standard techniques in laboratories working on the protein-folding problem.

As mentioned in the introduction, BPTI has long played an important role in the area of protein folding,[7] and early attempts to use NMR experiments for folding studies have already been cited.[32,36] More recently, NMR has been used extensively for structural characterization of BPTI folding intermediates containing only part of the native disulfide bonds (see Figure 1), mainly in the laboratories of Thomas Creighton[60] and Peter Kim.[61]

10 CONCLUDING REMARKS

BPTI has been a focal point for my research group from 1973 until about 1984, when our main activities shifted away from method development toward applications of NMR for protein structure determination in a variety of different systems. This article covers mainly the period of our intense involvement with this protein. Around 1985 we undoubtedly had a feeling of saturation with BPTI, which was also nurtured by referee comments on 'yet another paper on BPTI'. Things were rather quiet for several years after 1985, but in the late 1980s research with BPTI picked up momentum again, triggered primarily by the production of recombinant mutants of BPTI and the possibility of labeling the recombinant proteins with isotopes. Although crystal structures of at least 10 BPTI mutants have been described during the last few years, most of the structural work is done using NMR in connection with folding studies.[60,61] These were recently very much in the limelight due to a widely publicized controversy between Thomas Creighton and Peter Kim on certain aspects of the BPTI refolding pathway. Listening to a presentation by Clare Woodward at the 1994 Annual Meeting of the US Biophysical Society I also learned that the correlation between thermal stability of the folded protein and amide proton exchange rates[18,23] is being further investigated with the use of recombinant BPTI mutants. Overall, considering the advanced techniques now available for protein preparation and NMR investigations, we can look forward to many more years of excitement in research with BPTI.

11 RELATED ARTICLES

Biological Macromolecules: Structure Determination in Solution.

12 REFERENCES

1. M. Kunitz and J. H. Northrop, *J. Gen. Physiol.*, 1936, **19**, 991.
2. R. Huber, D. Kukla, A. Rühmann, and W. Steigemann, *Cold Spring Harbor Symp. Quant. Biol.*, 1971, **36**, 141.
3. K. Wüthrich, *Naturwissenschaften*, 1973, **60**, 221.
4. A. Masson and K. Wüthrich, *FEBS Lett.*, 1973, **31**, 114.
5. J. Deisenhofer and W. Steigemann, *Acta Crystallogr.*, 1975, **B31**, 238.
6. B. R. Gelin and M. Karplus, *Proc. Natl. Acad. Sci. USA*, 1975, **72**, 2002.
7. T. E. Creighton, *J. Mol. Biol.*, 1974, **87**, 579.
8. G. Wagner and K. Wüthrich, *J. Mol. Biol.*, 1982, **155**, 347.
9. G. Wagner, *Q. Rev. Biophys.*, 1983, **16**, 1.
10. K. D. Berndt, P. Güntert, L. P. M. Orbons, and K. Wüthrich, *J. Mol. Biol.*, 1992, **227**, 757.
11. G. Otting, E. Liepinsh, and K. Wüthrich, *Science*, 1991, **254**, 974.
12. S. Karplus, G. H. Snyder, and B. D. Sykes, *Biochemistry*, 1973, **12**, 1323.
13. G. H. Snyder, R. Rowan III, S. Karplus, and B. D. Sykes, *Biochemistry*, 1975, **14**, 3765.
14. K. Wüthrich and G. Wagner, *FEBS Lett.*, 1975, **50**, 265.
15. R. Hetzel, K. Wüthrich, J. Deisenhofer, and R. Huber, *Biophys. Struct. Mech.*, 1976, **2**, 159.
16. A. DeMarco and K. Wüthrich, *J. Magn. Reson.*, 1976, **24**, 201.
17. K. Nagayama, K. Wüthrich, P. Bachmann, and R. R. Ernst, *Biochem. Biophys. Res. Commun.* 1977, **78**, 99.
18. G. Wagner and K. Wüthrich, *Nature*, 1978, **275**, 247.
19. B. D. Hilton and C. K. Woodward, *Biochemistry*, 1978, **17**, 3325.
20. R. Richarz, P. Sehr, G. Wagner, and K. Wüthrich, *J. Mol. Biol.*, 1979, **130**, 19.
21. A. Dubs, G. Wagner, and K. Wüthrich, *Biochim. Biophys. Acta*, 1979, **577**, 177.
22. B. D. Hilton and C. K. Woodward, *Biochemistry*, 1979, **18**, 5834.
23. G. Wagner and K. Wüthrich, *J. Mol. Biol.*, 1979, **134**, 75.
24. K. Nagayama, K. Wüthrich, and R. R. Ernst, *Biochem. Biophys. Res. Commun.*, 1979, **90**, 305.
25. Anil Kumar, R. R. Ernst, and K. Wüthrich, *Biochem. Biophys. Res. Commun.*, 1980, **95**, 1.
26. Anil Kumar, G. Wagner, R. R. Ernst, and K. Wüthrich, *Biochem. Biophys. Res. Commun.*, 1980, **96**, 1156.
27. K. Nagayama and K. Wüthrich, *Eur. J. Biochem.*, 1981, **114**, 365.
28. G. Wagner, Anil Kumar, and K. Wüthrich, *Eur. J. Biochem.*, 1981, **114**, 375.
29. Anil Kumar, G. Wagner, R. R. Ernst, and K. Wüthrich, *J. Am. Chem. Soc.*, 1987, **103**, 3654.
30. H. Roder, Ph.D. Thesis 6932, Eidgenössische Technische Hochschule, Zürich, 1981.
31. H. Roder, G. Wagner, and K. Wüthrich, *Biochemistry*, 1985, **24**, 7396.
32. H. Roder and K. Wüthrich, *Proteins*, 1986, **1**, 34.
33. M. Rance, O. W. Sørensen, G. Bodenhausen, G. Wagner, R. R. Ernst, and K. Wüthrich, *Biochem. Biophys. Res. Commun.*, 1983, **117**, 479.
34. T. F. Havel and K. Wüthrich, *J. Mol. Biol.*, 1985, **182**, 281.
35. M. P. Williamson, T. F. Havel, and K. Wüthrich, *J. Mol. Biol.*, 1985, **182**, 295.
36. D. J. States, C. M. Dobson, M. Karplus, and T. E. Creighton, *J. Mol. Biol.*, 1984, **174**, 411.
37. J. C. Hoch, C. M. Dobson, and M. Karplus, *Biochemistry*, 1982, **21**, 1118.
38. D. Marion and K. Wüthrich, *Biochem. Biophys. Res. Commun.*, 1983, **113**, 967.
39. D. J. States, R. A. Haberkorn, and D. J. Ruben, *J. Magn. Reson.*, 1982, **48**, 286.
40. R. M. Keller and K. Wüthrich, *Biochim. Biophys. Acta*, 1978, **533**, 195.
41. S. L. Gordon and K. Wüthrich, *J. Am. Chem. Soc.*, 1978, **100**, 7094.
42. G. Wagner, A. DeMarco, and K. Wüthrich, *J. Magn. Reson.*, 1975, **20**, 565.
43. K. Wüthrich, G. Wagner, R. Richarz, and S. J. Perkins, *Biochemistry*, 1978, **17**, 2253.
44. K. Wüthrich, G. Wider, G. Wagner, and W. Braun, *J. Mol. Biol.*, 1982, **155**, 311.
45. K. Wüthrich, *NMR of Proteins and Nucleic Acids*, Wiley, New York, 1986.
46. M. Billeter, W. Braun, and K. Wüthrich, *J. Mol. Biol.*, 1982, **155**, 321.
47. K. Wüthrich, M. Billeter, and W. Braun, *J. Mol. Biol.*, 1984, **180**, 715.
48. A. Pardi, M. Billeter, and K. Wüthrich, *J. Mol. Biol.*, 1984, **180**, 741.
49. G. Wagner, W. Braun, T. F. Havel, T. Schaumann, N. Gō, and K. Wüthrich, *J. Mol. Biol.*, 1987, **196**, 611.
50. K. D. Berndt, P. Güntert, L. P. M. Orbons, and K. Wüthrich, *J. Mol. Biol.*, 1992, **227**, 757.
51. W. Braun, C. Bösch, L. R. Brown, N. Gō, and K. Wüthrich, *Biochim. Biophys. Acta*, 1981, **667**, 377.
52. W. Braun, G. Wider, K. H. Lee, and K. Wüthrich, *J. Mol. Biol.*, 1983, **169**, 921.
53. G. Otting, E. Liepinsh, and K. Wüthrich, *Biochemistry*, 1993, **32**, 3571.
54. A. Hvidt and S. O. Nielsen, *Adv. Protein Chem.*, 1966, **21**, 287.
55. S. W. Englander and N. R. Kallenbach, *Q. Rev. Biophys.*, 1984, **16**, 521.
56. G. Wagner and K. Wüthrich, *J. Mol. Biol.*, 1982, **160**, 343.
57. G. Otting and K. Wüthrich, *J. Am. Chem. Soc.*, 1989, **111**, 1871.
58. G. Otting, E. Liepinsh, and K. Wüthrich, *J. Am. Chem. Soc.*, 1991, **113**, 4363.
59. T. Szyperski, P. Luginbühl, G. Otting, P. Güntert, and K. Wüthrich, *J. Biomol. NMR*, 1993, **3**, 151.
60. C. P. M. van Mierlo, J. Kemmink, D. Neuhaus, N. J. Darby, and T. E. Creighton, *J. Mol. Biol.*, 1994, **235**, 1044.
61. J. P. Staley and P. S. Kim, *Proc. Natl. Acad. Sci. USA*, 1992, **89**, 1519.

Acknowledgments

Our own research covered in this article was generously supported by the ETH Zürich, the Schweizerischer Nationalfonds, the Kommission zur Förderung der wissenschaftlichen Forschung and Bruker-Spectrospin AG. I would like to thank Bayer AG for providing us with

a generous supply of BPTI (Trasylol) during more than two decades, and Mr. R. Marani for the careful processing of the manuscript.

Biographical Sketch

Kurt Wüthrich. *b* 1938. Licentiat, 1964, Physics, Mathematics, Chemistry, University of Bern, Eidgeñssisches Sportlehrerdiplom, 1964, Ph.D., 1964, Inorganic Chemistry (Prof. S. Fallab), University of Basel. Stein and Moore Award, 1989; Horwitz prize, 1991; Prix Jeantet, 1993. Postdoctoral work, University of Basel (Prof. S. Fallab), University of California, Berkeley (Prof. R. E. Connick), Bell Telephone Laboratories, Murray Hill, USA (Supervisor Dr. R. G. Shulman). Professor of Biophysics and Head of the Institute of Molecular Biology and Biophysics, ETH Zürich, 1969–present. Approx. 500 publications. Research specialties: NMR structure determination of biological macromolecules, drug design, and protein engineering.

Phage Lysozyme: Dynamics and Folding Pathway

Frederick W. Dahlquist
University of Oregon, Eugene, OR, USA

1 Introduction 1
2 Spectral Resolution and Resonance Assignment 1
3 T4 Lysozyme as a System for Studying Protein Folding 1
4 Core Packing Mutants and Dynamic Access to the Hydrophobic Core 2
5 Folding Pathway 3
6 References 4

1 INTRODUCTION

During the last several years there has been a revolution in the use of NMR to study proteins and nucleic acids in solution (see Wüthrich[1]). In principle, NMR offers the ability simultaneously to observe each hydrogen, carbon, and nitrogen atom in a protein or nucleic acid in a variety of solution environments. Very detailed structural information can be obtained by using a form of dipolar energy transfer between nuclear spins (nuclear Overhauser enhancements or NOEs) to monitor the distance between those atoms on a 1–5 Å scale. Bonding and torsion angle information can be obtained by monitoring the through-bond scalar couplings between nuclear spins. In addition, information concerning the rates of molecular fluctuations and chemical reactions can be obtained by measurement of the relaxation properties of the nuclear spins and the exchange of amide protons with solvent.

In the past, it had been difficult to gain access to this wealth of information. There are three difficulties that must be overcome. The first is spectral resolution. A typical protein of 150 amino acid residues contains about 1100 protons, 750 carbon atoms, and 180 nitrogen atoms. While ^{1}H, ^{15}N, and ^{13}C resonate at very different frequencies, the overlap of the various ^{1}H, ^{15}N, and ^{13}C resonances with others of their kind is severe. The second fundamental difficulty concerns the assignment of the large number of overlapping resonances to individual atoms in the macromolecule of interest. The third difficulty concerns the relatively low sensitivity of detection of NMR signals. This is an especially serious problem for ^{15}N and ^{13}C since these nuclei are relatively poorly detected and these isotopes are present in only about 1% natural abundance.

There have been remarkable advances in the development of new and very powerful strategies to overcome all these problems. Here we will discuss some of these approaches and their applications to problems concerning protein structure, the dynamics or 'breathing' motions of proteins, and the elucidation of the kinetic pathway by which an unfolded, random coil, linear polymer of amino acids folds to become a functional, folded molecule.

2 SPECTRAL RESOLUTION AND RESONANCE ASSIGNMENT

The development of two-dimensional (2D) ^{1}H NMR made it possible to study small proteins and oligopeptides. This greatly increases the resolution of the experiment and many individual proton resonances can be resolved. In addition, the through-space (NOE) and through-bond interactions exploited to produce the 2D spectrum provide structural information directly. However, the complexity of the ^{1}H spectra of proteins of more than 100 residues makes it very technically challenging to assign and analyze these spectra of proteins of this size or larger. Larger proteins require the increased resolution available by dispersion of the resonances in three or four dimensions. Typically this requires the biosynthetic incorporation of ^{15}N and/or ^{13}C isotopes into the protein and the use of these nuclear spins to provide the additional dimensionality required for reasonable resolution (see, for example, Fesik and Zuiderweg,[2] Marion et al.,[3,4] Ikura et al.,[5] Kay et al.,[6,7] and Boucher et al.[8]). The increased resolution and the nature of the interactions exploited in the experiments make these approaches very well suited to the assignment and analysis of proteins of 100–300 residues. The upper limit is an estimate and may be somewhat optimistic. Importantly, these approaches begin to gain access to a number of proteins with interesting and important activities.

3 T4 LYSOZYME AS A SYSTEM FOR STUDYING PROTEIN FOLDING

In general, the primary amino acid sequence of a polypeptide chain is thought to encode all the information necessary to determine the final folded structure of a protein. However, the contributions made by individual amino acid residues to the overall structure, dynamics, and stability of the folded protein as well as the role(s) of individual residues in the kinetic pathways between the unfolded and folded states remains less clear. In recent years, there has been a substantial amount of progress in addressing these questions (e.g. Bowie et al.,[9] Alber,[10] Dill,[11] Lim and Sauer,[12] Pace et al.,[13] Kim and Baldwin,[14] Goldenberg et al.,[15] and Matthews[16]). The lysozyme produced by bacteriophage T4 offers an excellent experimental system to address these important questions. In addition, the collaborative research efforts of the Matthews (crystallography, structural bases of protein stability), Schellman (thermodynamics), Hudson (nanosecond dynamics), and our laboratories at the University of Oregon offer a nearly unique environment for the investigation of these issues.

The lysozyme from bacteriophage T4 is a 164-residue (18 700 dalton), single-chain polypeptide. As shown schematically in Figure 1, the protein is folded into a bilobed structure centered on a 19-residue α-helix.[17] The protein is primarily composed of helical secondary structure, but also contains a small antiparallel β-sheet in the N-terminal lobe. Figure 2 shows the amino acid sequence of the protein with the α-helices indicated with the letters A–H. The C-terminal domain contains the first helix (helix A) of the N-terminus of the protein.

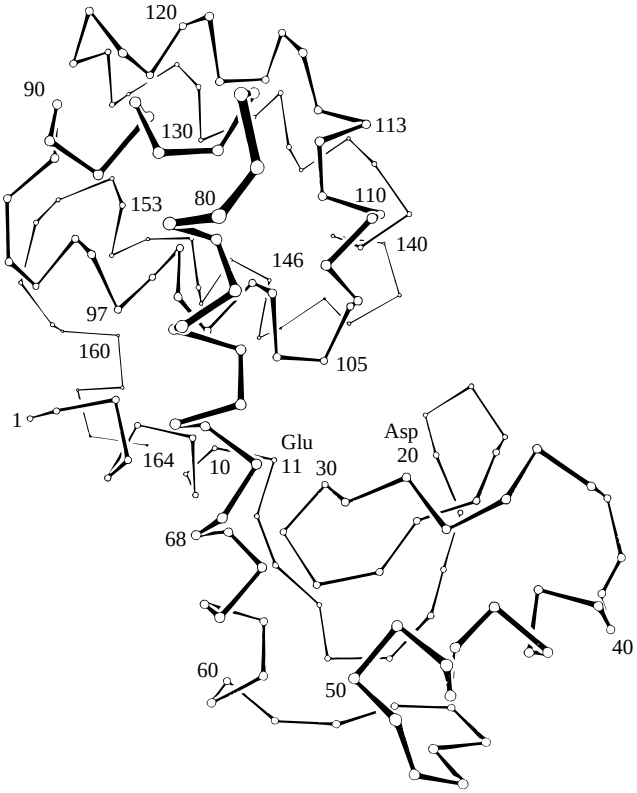

Figure 1 The α-carbon backbone of T4 lysozyme as deduced from the refined model derived from X-ray data by Brian Matthews (with permission)

```
1   MNIFEMLRIDEGLRLKIYKDTEGYYTIGIGHLLTKSPSLNAAKSELDKAI
      Helix A          β-sheet and turns          Helix B

51  GRNCNGVITKDEAEKLFNEDVDAAVRGILRNAKLKPVYDSLDAVRRCALI
                Helix C              Helix D      Helix

101 NMVFQMGETGVAGFTNSLRMLQQKRWDEAAVNLAKSRWYNQTPNRAKVI
      E          Helix F        Helix G      Helix H

151 TTFRTGTWDAYKNL
```

Figure 2 The amino acid sequence of wild-type T4 lysozyme. The α-helical regions are indicated with the letters A–H. The region H consists of two α-helices separated by threonine-141 and proline-142. In addition there are two distorted α-helical segments corresponding to residues 107–113 and the C-terminus

A wide variety of mutations have been introduced into the protein. These include the replacement of the two cysteine residues to produce a thiol-free version of the wild-type protein with nearly identical thermodynamic stability as the original,[18] introduction of new disulfides at several positions, which usually increases the thermodynamic stability of the protein,[19] and a host of systematic changes introduced at many positions to investigate hydrophobic,[20] electrostatic,[21] core packing,[22] and hydrogen-bonding interactions.[23] The great majority of these mutant proteins have been crystallized and their crystal structures have been determined in the Matthews laboratory. To date the structures of about 150 T4 lysozyme variants have been determined. Some of these involve different crystal packing arrangements,[24,25] and have allowed seven distinct views of the protein to be obtained. In addition Poteete's laboratory has recently developed a genetic system in which T4 lysozyme is used to complement a lysozyme-deficient P22 bacteriophage.[26] Using this system Poteete and co-workers have described the complementation properties of a huge collection of lysozyme variants in which residues 2–164 have each been replaced by 13 different residues using nonsense suppressors. This provides a qualitative indication of the activity and stability of these variants, which can be very useful in the design of new lysozyme variants. Finally, a very efficient bacterial expression system allows the isolation of about 50 mg of pure protein from a liter of minimal medium.[27] To date this expression system has produced proteins from about 300 lysozyme variants in quantities suitable for physical studies. Thus the T4 lysozyme system offers an excellent opportunity to examine the interrelationships of amino acid sequence, structure, stability, and dynamics.

We have published the assignments of the proton and ^{15}N magnetic resonance spectra of the backbone and about 25% of the side-chain protons of wild-type T4 lysozyme[28] and these are shown in Figure 3. The Figure shows a heteronuclear multiple quantum coherence (HMQC) spectrum[29] in which each cross peak represents an ^{15}N–H directly bonded pair in the protein. The ^{15}N and H coordinates of each cross peak correspond to the chemical shifts of the ^{15}N and proton environments of the pair.

This paper describes some of the recent work from our laboratory, which is directed toward understanding the dynamics of the folded state, and the kinetic path used by the protein while it folds. Much of this work takes advantage of some of the recent advances in high-resolution NMR as applied to biological systems. When combined with site-directed mutation, thermodynamic analysis, and rapid X-ray diffraction analysis of mutant structures, questions in these areas can often be addressed with exquisite sensitivity at atomic resolution.

4 CORE PACKING MUTANTS AND DYNAMIC ACCESS TO THE HYDROPHOBIC CORE

Recently, the Matthews laboratory has discovered that several mutations in which bulky side chains in the hydrophobic core are replaced by smaller side chains can create or expand apparent cavities in the core.[22,30] In the case of the mutation L99A, replacement of the leucine side chain by a methyl group expands an existing cavity in the core of the C-terminal domain. The mutant protein is substantially destabilized when compared with its wild-type. They found that some of these mutant proteins can bind hydrophobic compounds such as benzene in the apparent cavities.[31] This binding has been detected as a benzene-dependent stabilization of the mutant proteins toward reversible unfolding and has also been detected by the observation of bound benzene molecules in the crystal structures of these mutant proteins in the presence of benzene.

We have examined the effects of these apparent cavity mutants on the dynamic properties of T4 lysozyme in solution. Baldwin, working in the Matthews laboratory, has constructed a series of alanine substitution mutants for residues 94–106. The mutants that bind benzene in the core include L99A, F104A, M102A, and two substitutions outside the E helix, L133G and F153A. The mutations L99A, M102A, and N101A all create apparent cavities that have no static route allowing access to the cavity by a molecule of the bulk solvent.

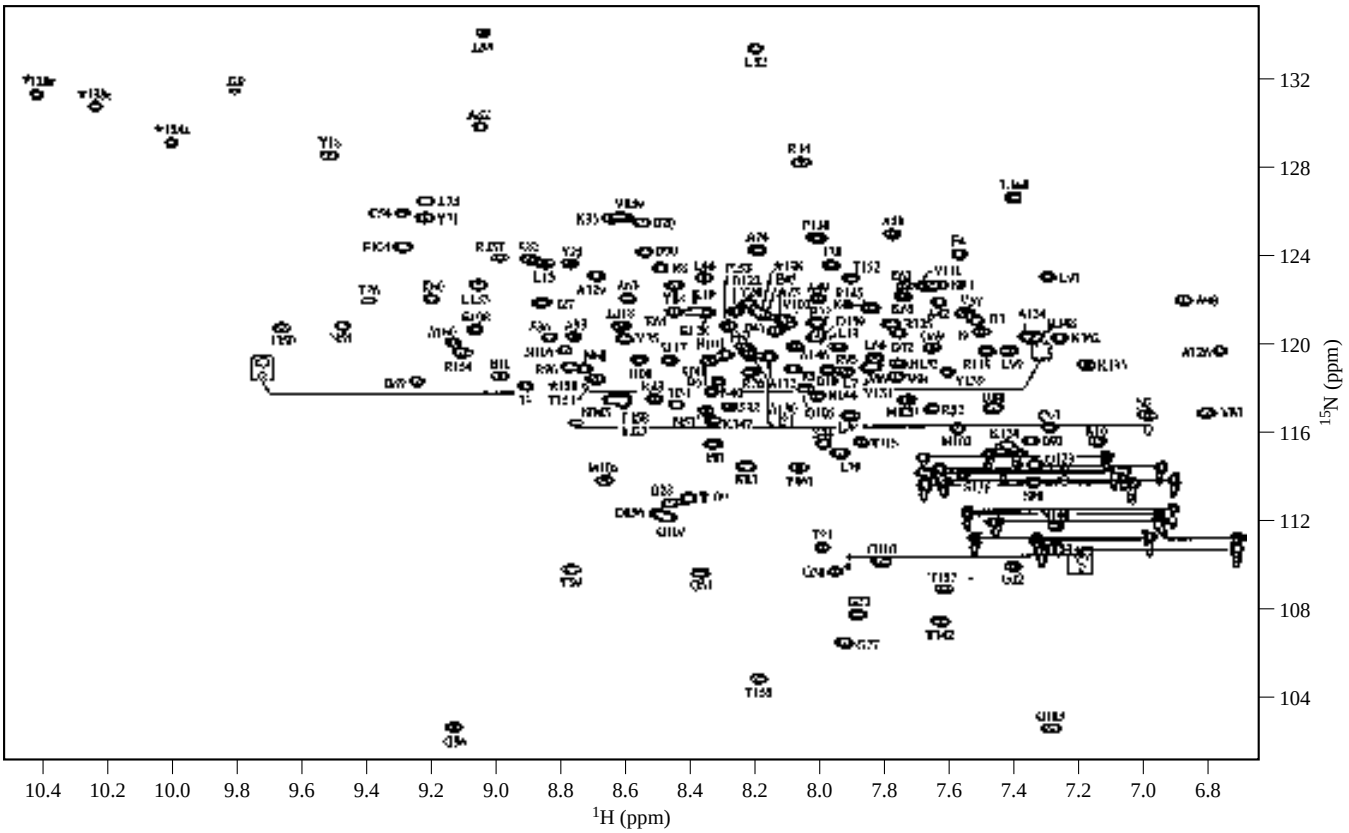

Figure 3 The $^{1}H-^{15}N$ HMQC spectrum of uniformly ^{15}N-labeled T4 lysozyme. The horizontal bars indicate the resonances of the primary amides of asparagine and glutamine residues. (Reproduced by permission from McIntosh et al.[28])

Are the cavities empty in the absence of small hydrophobic molecules? There are few, if any, hydrogen-bonding partners in the cavity to stabilize water in the cavity. The X-ray crystallographic analyses of most of these mutants do not show the presence of water in these cavities, but it is possible that the water is disordered and is not detected for that reason. The presence or absence of solvent in the cavities gives rise to different views of energetic changes associated with these types of mutations. In one view, the empty cavity results in decreased van der Waals interactions and that accounts for larger than expected destabilization of the folded state. In another view, the presence of solvent in the cavity causes a larger than anticipated destabilization due to unfavorable contacts between the remaining hydrophobic groups of the core and solvent molecules.

Examination of the crystal structure of L99A and the benzene–L99A complex shows that there is 7 Å or more between the surface and the bound benzene.[30,31] There must be a fluctuation in the structure of about 7 Å (also the van der Waals thickness of benzene) to allow the benzene to gain access to the interior of the protein. Using NMR to monitor the binding kinetics of benzene to the L99A mutant protein shows that the entry of benzene into the cavity is nearly diffusion-controlled despite the absence of a clear pathway for such entry in the static structure. This suggests that benzene can gain access to the core rather readily despite the apparent lack of a sterically allowed path.

What is the nature of the fluctuations that allow such access? We have examined the mechanism by which a molecule such as benzene gains access to the core. Feher has examined the binding kinetics of benzene and indole to the cavity mutant L99A. There are several alanine amide protein resonances that show broadenings and lineshape changes in the presence of partially saturating concentrations of benzene or indole. The exchange broadening of these resonances allows us to determine the binding kinetics for benzene to the core under a variety of conditions and in a variety of mutant proteins. These results demonstrate that the relatively large benzene and indole molecules gain access to the cavity with a bimolecular rate constant of about $10^{7}\,M^{-1}\,s^{-1}$ or only one or two orders of magnitude slower than diffusion-controlled encounter rates. This result suggests that the protein must undergo large amplitude fluctuations in its structure to allow the hydrophobic molecules into the protein core. This approach, combined with the more traditional amide hydrogen exchange rate measurements, promises to provide complementary information concerning the processes that allow small molecules into the protein core.

5 FOLDING PATHWAY

Recently, 2D NMR techniques combined with quenched flow measurements of hydrogen–deuterium exchange of amide protons have been used to detect and characterize kinetic intermediates observed during protein folding. This approach can also provide some structural information about intermediates on the folding pathway. This method has been

applied to several proteins including ribonuclease A,[32,33] egg-white lysozyme,[34] cytochrome *c*,[35] ubiquitin,[36] and barnase.[37]

Measurement of hydrogen–deuterium exchange rates of amide protons is a sensitive probe for the presence of structure in a fully or partially folded protein. The formation of hydrogen bonds such as those seen in α-helices or β-sheets dramatically reduces hydrogen–deuterium exchange rates of amide protons. In a typical pulse hydrogen-exchange experiment (see Robertson and Baldwin[38]), refolding of a deuterated protein is initiated in D_2O and a 'snapshot' of the protein is taken at different times after refolding by subjecting the sample to a proton-labeling pulse of H_2O at high pH to label rapidly those amides that remain exposed at that particular time. After allowing the protein to refold under conditions where hydrogen exchange is slow, 2D ^1H,^{15}N NMR is then used to determine which amide protons are protected at various times during the folding process.[39]

When folding is initiated, the native, folded structure is produced in about 150 ms. However, selected parts of the amino acid sequence form structure as soon as we take the first data point at 10 ms. It appears that most, if not all, of the molecules form an intermediate or a population of intermediates that is characterized by significant protection from solvent exchange. This behavior is observed at 25–30 residues with varying degrees of protection at early times.

This information is presented in Figure 4 as a plot of relative protection factor versus position. These data clearly demonstrate that three regions are protected from amide exchange within 30 ms of folding. The calculated relative protection factors are at least 20 and vary to a maximum of 300 for the residues in three regions of the sequence, corresponding to residues 5–13 (helix A), those near residue 20 of the N-terminal domain β-sheet, and residues 96–105 (helix E). The most protected residues, contained in the β-sheet in the N-terminal domain and in helix A and helix E in the C-terminal domain, are protected about 100-fold relative to free amides. Protection factors of similar magnitude were observed in the partly folded apomyoglobin structure formed under equilibrium conditions by Hughson et al.[40] Such behavior is consistent with the formation of relatively isolated regions of secondary structure.

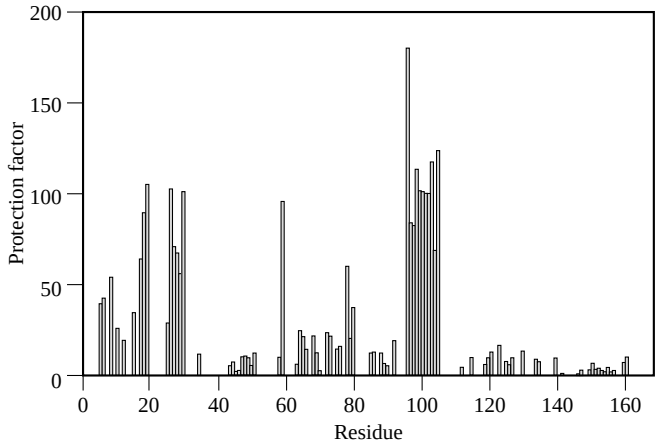

Figure 4 The amide exchange properties of the unfolded state of T4 lysozyme expressed as the calculated protection factor versus position at pH 2.4, 30 °C, and in 3.0 M urea. The protection factors are calculated as the ratio of the observed first-order rate constant for exchange for each residue as compared with a theoretical value that accounts for the pH of the sample, the presence of urea, and the effects of adjacent residues. (Reproduced by permission from Lu and Dahlquist[39])

The region of the protein that shows the highest degree of protection from hydrogen exchange corresponds to residues 95–103. This region corresponds to helix E in the native structure of the protein. The crystal structure of the native state shows that this helix is the most buried. It is reasonable that this helix forms earliest during refolding. Helix A is in close contact with helix E and amide-hydrogen exchange is also slow in helix A. It is possible that these early protected regions form a structure for the subsequent refolding of the entire protein.

The stability of the folded state of T4 lysozyme can be modified both by low pH values and by mutational substitutions of side chains. Morton has used both pH and the mutation F153A to lower the stability of the protein such that it unfolds at room temperature in the absence of denaturant. Under these conditions, the protein appears to form a 'molten globule' state in which there is still significant α-helical content, as judged by circular dichroism. The protein does not appear to have much tertiary structure, as evidenced by very little if any dispersion in side-chain chemical shift. This molten globule state bears significant similarity to the kinetic folding intermediate discussed above. This suggests that the kinetic intermediate we detect using the pulsed hydrogen-exchange approach may reflect the most stable form of the unfolded state when the protein is placed in conditions that strongly favor folding. These molten globule states are usually not seen at equilibrium because such conditions strongly favor the folded state.

If this reasoning is correct, the kinetic properties of the folding reaction should reflect the free energy differences between the molten globule, unfolded state, and the overall transition state for the folding reaction. We have used this model to interpret our recent observations involving a series of mutations in the C-terminal domain core, that all slow folding occurs by a significant amount. The side chains of these residues all appear to participate in the formation of the core during the rate-limiting step for the folding reaction. Our observations suggest that the dominant folding pathway of the wild-type protein involves the formation of this hydrophobic core in the C-terminal domain during the major rate-limiting step for folding. In mutants in which the core is destabilized by removal of hydrophobic surface area, other kinetic paths become the dominant paths. In some cases it appears that events in the N-terminal domain may become rate-limiting or co-rate-limiting. These observations argue that there are likely to be a number of competitive pathways for a given protein to fold. If one or another of these paths are made less favorable the protein still reaches its most thermodynamically favored state but uses an alternative path.

6 REFERENCES

1. Wüthrich, 1986.
2. S. W. Fesik and E. R. P. Zuiderweg, *J. Magn. Reson.*, 1988, **78**, 588.
3. D. Marion, L. E. Kay, S. W. Sparks, D. A. Torchia, and A. Bax, *J. Am. Chem. Soc.*, 1989, **111**, 1515.

4. D. Marion, P. C. Driscoll, L. E. Kay, P. T. Wingfield, A. Bax, A. M. Gronenborn, and G. M. Clore, *Biochemistry*, 1989, **28**, 6150.
5. M. Ikura, L. E. Kay, and A. Bax, *Biochemistry*, 1990, **29**, 4659.
6. L. E. Kay, M. Ikura, R. Tschudin, and A. Bax, *J. Magn. Reson.*, 1990, **89**, 496.
7. L. E. Kay, M. Ikura, G. Zhu, and A. Bax, *J. Magn. Reson.*, 1991, **91**, 422.
8. W. Boucher, E. D. Laue, S. Campbell-Burk, and P. J. Domaille, *J. Am. Chem. Soc.*, 1992, **114**, 2262.
9. J. U. Bowie, J. F. Reidhaar-Olson, W. A. Lim, and R. T. Sauer, *Science*, 1990, **247**, 3544.
10. T. Alber, *Annu. Rev. Biochem.*, 1989, **58**, 765.
11. K. A. Dill, *Biochemistry*, 1990, **29**, 7133.
12. W. A. Lim and R. T. Sauer, *Nature (London)*, 1989, **339**, 31.
13. C. N. Pace, D. V. Laurents, and J. A. Thomson, *Biochemistry*, 1990, **29**, 2564.
14. P. S. Kim and R. L. Baldwin, *Annu. Rev. Biochem.*, 1990, **59**, 631.
15. D. P. Goldenberg, R. W. Frieden, J. A. Haak, and T. B. Morrison, *Nature (London)*, 1989, **338**, 127.
16. C. R. Matthews, *Curr. Opin. Struct. Biol.*, 1991, **1**, 28.
17. B. W. Matthews and S. J. Remington, *Proc. Natl. Acad. Sci. USA*, 1974, **71**, 4178.
18. M. Matsumura and B. W. Matthews, *Science*, 1989, **243**, 792.
19. M. Matsumura, W. J. Becktel, M. Levitt, and B. W. Matthews, *Proc. Natl. Acad. Sci. USA*, 1989, **86**, 6562.
20. M. Matsumura, W. J. Becktel, and B. W. Matthews, *Nature (London)*, 1988, **334**, 406.
21. H. Nicholson, W. J. Becktel, and B. W. Matthews, *Nature (London)*, 1988, **336**, 651.
22. M. Karpusas, W. A. Baase, M. Matsumura, and B. W. Matthews, *Proc. Natl. Acad. Sci. USA*, 1989, **86**, 8237.
23. T. Alber, S. Dao-pin, K. Wilson, J. A. Wozniak, S. P. Cook, and B. W. Matthews, *Nature (London)*, 1987, **330**, 41.
24. H. R. Faber and B. W. Matthews, *Nature (London)*, 1990, **348**, 263.
25. M. M. Dixon, H. Nicholson, L. Shewchuck, W. A. Baase, and B. W. Matthews, *J. Mol. Biol.*, 1992, **227**, 917.
26. D. Rennell, S. E. Bouvier, L. W. Hardy, and A. Poteete, *J. Mol. Biol.*, 1991, **222**, 67.
27. D. C. Muchmore, L. P. McIntosh, C. B. Russell, D. E. Anderson, and F. W. Dahlquist, *Methods Enzymol.*, 1990, **177**, 44.
28. L. P. McIntosh, A. J. Wand, D. F. Lowry, A. G. Redfield, and F. W. Dahlquist, *Biochemistry*, 1990, **29**, 6341.
29. A. Bax, R. H. Griffey, and B. L. Hawkins, *J. Magn. Reson.*, 1983, **55**, 301.
30. A. E. Eriksson, W. A. Baase, J. A. Wozniak, and B. W. Matthews, *Nature (London)*, 1992, **355**, 371.
31. A. E. Eriksson, W. A. Baase, X.-J. Zhang, D. W. Heinz, M. Blaber, E. P. Baldwin, and B. W. Matthews, *Science*, 1992, **255**, 178.
32. J. B. Udgaonkar and R. L. Baldwin, *Nature (London)*, 1988, **335**, 694.
33. J. B. Udgaonkar and R. L. Baldwin, *Proc. Natl. Acad. Sci. USA*, 1990, **87**, 8197.
34. A. Miranker, S. E. Radford, M. Karplus, and C. M. Dobson, *Nature (London)*, 1991, **349**, 633.
35. H. Roder, G. A. Elöve, and W. S. Englander, *Nature (London)*, 1988, **335**, 700.
36. M. S. Briggs and H. Roder, *Proc. Natl. Acad. Sci. USA*, 1992, **89**, 2017.
37. M. Bycroft, A. Matouschek, J. T. Kellis, Jr., L. Serrano, and A. R. Fersht, *Nature (London)*, 1990, **346**, 488.
38. A. D. Robertson and R. L. Baldwin, *Biochemistry*, 1991, **30**, 9907.
39. J. Lu and F. W. Dahlquist, *Biochemistry*, 1992, **31**, 4749.
40. F. M. Hughson, P. E. Wright, and R. L. Baldwin, *Science*, 1990, **249**, 1544.

Protein Dynamics from NMR Relaxation

Dennis A. Torchia

National Institutes of Health, Bethesda, MD, USA

1	Introduction	1
2	Theoretical Considerations	1
3	Pulse Sequences and Data Analysis	2
4	Two-Dimensional Heteronuclear Relaxation Studies of Proteins	4
5	Summary of ^{15}N Work and Prospects for ^{13}C Measurements	5
6	Related Articles	5
7	References	5

1 INTRODUCTION

Triple resonance (^{1}H, ^{13}C, ^{15}N) NMR techniques[1] have greatly reduced the effort required to obtain protein signal assignments as well as interproton distance and dihedral angle restraints.[2] This development has enhanced the prospects of obtaining information about protein structure. Such information is of widespread interest because it is fundamental for understanding protein function. However, proteins are not rigid bodies, but rather execute internal motions on a wide range of timescales.[3] In order to understand important aspects of protein function such as folding, molecular recognition, and enzyme action, detailed knowledge about protein dynamics is essential. At a more fundamental physical level, experimental information about the amplitudes and rates of internal motions in proteins can be used to check the predictions of molecular dynamics trajectories. Such tests of theoretical calculations should result in improved formulas for the potential functions used in the computations.

Protein structures in solution are derived using restraints obtained almost exclusively from proton J couplings and NOEs,[4,5] whereas information about the internal motions of proteins is derived most directly from measurements of spin relaxation rates of nuclei such as ^{15}N and ^{13}C (designated A spins herein).[6–8] Although ^{13}C relaxation studies of proteins were initiated over a decade ago,[8] these early studies were limited by the lack of sequential assignments as well as by the low resolution and sensitivity afforded by one-dimensional NMR spectra recorded with A spin detection. Fortunately, triple resonance experiments[1] provide sequential assignments of ^{15}N and ^{13}C nuclei along with those of protons. Hence, proton-detected two-dimensional heteronuclear relaxation experiments[9–16] are a means of measuring A spin relaxation rates with high sensitivity and resolution.

2 THEORETICAL CONSIDERATIONS

2.1 Relaxation Equations

Elegant general formalisms relating nuclear spin relaxation to molecular motion have been provided by Abragam[17] and Redfield.[18] In the case of a spin $I = \frac{1}{2}$ A nucleus such as ^{13}C or ^{15}N directly bonded to N protons (designated X), the AX_N dipolar interactions and A-spin chemical shift anisotropy, CSA, are the significant relaxation mechanisms. Provided that cross correlations can be neglected, the A-spin longitudinal relaxation time, T_1, transverse relaxation time, T_2, and A-{X} NOE, are given by[9,17]

$$1/NT_1 = d^2[J(\omega_A - \omega_X) + 3J(\omega_A) + 6J(\omega_A + \omega_X)] + c^2 J(\omega_A) \quad (1)$$

$$1/NT_2 = 0.5d^2[4J(0) + J(\omega_A - \omega_X) + 3J(\omega_A) + 6J(\omega_X) + 6J(\omega_A + \omega_X)] + \tfrac{1}{6}c^2[4J(0) + 3J(\omega_A)] \quad (2)$$

$$\mathrm{NOE} = 1 + (\gamma_A/\gamma_X)d^2[6J(\omega_A + \omega_X) + J(\omega_A - \omega_X)]NT_1 \quad (3)$$

where ω_i is the Larmor frequency of spin i, $J(\omega)$ is the spectral density function, γ_i is the gyromagnetic ratio of spin i, $d^2 = 0.1[(\mu_0/4\pi)\gamma_A\gamma_X h/(2\pi\langle 1/r_{AX}^3\rangle)]^2$, $c^2 = \frac{2}{15}[\omega_A(\sigma_{vert} - \sigma_\perp)]^2$, h is Planck's constant, r_{AX} is the AX bond length (0.102 nm for NH and 0.109 nm for CH), and $\sigma_\parallel$ and $\sigma_\perp$ are principal components of the axially symmetric CSA tensor. For the amide ^{15}N, the CSA is about 160 ppm,[19] and at 11.7 T contributes nearly 20% to the ^{15}N relaxation rate. In contrast, the CSA contribution is much smaller in the case of aliphatic carbons. For example, the CSAs of rotating methyl and backbone α-carbons are about 25 and 35 ppm respectively, and, at 11.7 T, contribute less than 2.5% to ^{13}C spin relaxation.

As noted above, equations (1)–(3) are valid only when the effects of cross correlations are negligible. Although rf pulses can eliminate cross correlation of AX dipolar A-spin CSA interactions,[11] such pulses cannot completely eliminate the effects of dipolar cross correlations in AX_2 and AX_3 spin systems.[20] In general, A-spin magnetization relaxes in multiexponential fashion in AX_2 and AX_3 spin systems, and equations (1) and (2) yield the initial decay rates of longitudinal and transverse magnetization, respectively.[20]

2.2 The Model-Free Formulation of the Spectral Density Function

In equations (1)–(3), the spectral density function contains the information about molecular motion. However, if experiments are recorded at a single external field, only three experimental parameters are measured, and hence the data are insufficient to determine the spectral density function at five frequencies. In principle, spectral densities at 11 frequencies can be determined from the set of 12 A-spin T_1, T_2, and NOEs measured at four magnetic fields: $\gamma_A\omega$, $\gamma_H\omega$, $(\gamma_H \pm \gamma_A)\omega$, where ω is the A-spin Larmor frequency at the lowest

field employed. However, the large value of γ_H/γ_A, requires that one data set be obtained at low field (<3.5 T) where sensitivity and resolution are poor. Spectral densities have been determined for eglin c from spectra recorded at a single high field by measuring an expanded set of relaxation parameters that include the relaxation of certain two-spin coherences and the selective proton longitudinal relaxation.[16] A potential limitation of this approach is that the relaxation of the two-spin coherences contain a large contribution from the selective proton relaxation. This contribution must be subtracted from the two-spin relaxation in order to obtain reliable values of $J(\omega_i)$.

An alternative to direct determination of the spectral density functions is afforded by the model-free approach.[6,7] According to this formalism, the spectral density function is expressed in terms of three motional parameters according to

$$J(\omega) = S^2\tau_m/(1+\omega^2\tau_m^2) + (1-S^2)\tau/(1+\omega^2\tau^2) \quad (4)$$

where S is the generalized order parameter, τ_m is the overall correlation time, and $1/\tau = 1/\tau_m + 1/\tau_e$, where τ_e is an effective correlation time characterizing the internal motions of the protein. Equation (4) is an exact expression provided that (a) the overall motion of the protein is isotropic and is not correlated with the internal motions, and (b) all correlation times associated with the internal motions are in the extreme narrowing limit. When internal motions take place on two significantly different timescales, a useful, approximate, generalization of equation (4) is

$$J(\omega) = S^2\tau_m/(1+\omega^2\tau_m^2) + (1-S_f^2)\tau_1/(1+\omega^2\tau_1^2) + S_f^2(1-S_s^2)\tau_2/(1+\omega^2\tau_2^2) \quad (5)$$

where S_f, τ_1 and S_s, τ_2 are order parameters and effective correlation times associated with the 'fast' and 'slow' (outside the extreme narrowing limit) internal motions, and $S = S_fS_s$.[21]

The analysis of relaxation data using the model-free approach yields the overall correlation time of the protein as well as values of S^2 and τ_e for individual amino acid residues in the protein. Because τ_e is, in general, a complex combination of geometric factors and internal correlation times it cannot be interpreted in a quantitative manner. However, its determination does provide an estimate of the timescale of the internal motion at a particular site in the protein. In contrast, the order parameter is precisely related to the amplitude of the internal motion.[6,7] When the interaction responsible for relaxation is axially symmetric, with the symmetry axis along the AX bond, (rigorously true for the AX dipolar interaction and approximately so for the ^{15}N amide CSA interaction) S^2 is given by

$$S^2 = \int d\Omega_1\, p_{eq}(\Omega_1) \int d\Omega_2\, p_{eq}(\Omega_2) P_2(\cos\theta_{12}) \quad (6)$$

where $p_{eq}(\Omega)\, d\Omega$ is the equilibrium probability that the unit vector along the AX bond axis has orientation $d\Omega$, $\Omega = (\theta, \phi)$, in a coordinate system fixed in the protein, θ_{12} is the angle between two such vectors, and $P_2(x) = (3x^2 - 1)/2$. The advantage of the model-free approach derives from the fact that values of S^2 are obtained for numerous sites in the protein without the need to assume an explicit model of the internal motion. Using equation (6) values of S^2 can be calculated for any model of interest. Then, it can be determined if the model does indeed yield order parameters in agreement with experiment, and if the order parameters correspond to physically reasonable values of angular amplitudes of internal motion.

A useful and popular model of internal motion is diffusion in a cone, in which the AX bond axis is thought to diffuse freely in the angular region $0 \le \theta \le \theta_0$, $0 \le \phi \le 360^\circ$, where θ and ϕ are spherical, polar angles. For this model,

$$S^2 = [0.5\cos\theta_0\,(1+\cos\theta_0)]^2 \quad (7)$$

so that the cone semiangle can be derived from the order parameter. Equation (7) reveals several general features about the relationship between the amplitude of angular reorientation and S^2. S^2 equals unity when θ_0 is zero, diminishes as θ_0 increases, and vanishes when $\theta_0 = 180^\circ$, i.e., isotropic motion. Note however that S^2 is not a monotonic function of θ_0, and vanishes when motion is not isotropic, $\theta_0 = 90^\circ$. In general, S^2 is large for a small amplitude motion, but the converse need not be true; for example, S^2 equals unity if the AX bond reorients by a two-site jump of 180°. Analytical expressions for S^2 are available for other plausible models of internal motion.[6,7]

3 PULSE SEQUENCES AND DATA ANALYSIS

Two-dimensional heteronuclear pulse sequences designed to measure A-spin T_1, T_2, and NOE values in AX spin systems (A = ^{13}C or ^{15}N, X = ^{1}H) are depicted in Figure 1.[9,14] In order to maximize sensitivity, A-spin magnetization is derived from proton magnetization using an INEPT scheme in the T_1 and T_2 pulse sequences, and proton detection is employed in all three experiments. The application of 180° proton pulses during the relaxation delay period, T, suppresses cross correlation of AX dipolar and A-spin CSA interactions. The NOE experiment is the least sensitive of the three measurements because one must record spectra starting with equilibrium A-spin magnetization (in the absence and presence of proton saturation), and it is necessary to wait a long period between scans ($\ge 3T_L$, where T_L is the larger of either the proton or the A-spin T_1 value) to ensure that the A-spin magnetization attains equilibrium. Also, when the spectrum is recorded in H_2O without a NOE, water saturation must be achieved quickly in order to minimize transfer of saturation from water to protein protons. Recently it has been shown that one can avoid water saturation in the NOE experiment using pulsed field gradients and water flip-back pulses.[22]

Pulse sequences for measuring methyl ^{13}C relaxation parameters, while similar to those depicted in Figure 1, differ from them in several significant respects.[12,13,23] First, one must use magic angle delays in INEPT- or DEPT-type transfer steps in order to avoid complications that arise from dipolar cross correlations[12] and to ensure that carbon magnetization in $\frac{3}{2}$ and $\frac{1}{2}$ proton manifolds is faithfully transferred back to protons[13] in the reverse INEPT or DEPT portions of the sequences. Second, a sequence of 125° proton pulses should be applied during the CPMG period in order to eliminate dipolar cross correlations from ^{13}C transverse relaxation within the $\frac{3}{2}$ manifold. Third, the final delays, Δ, in the reverse INEPT portion of the sequence should be set to a short value, about

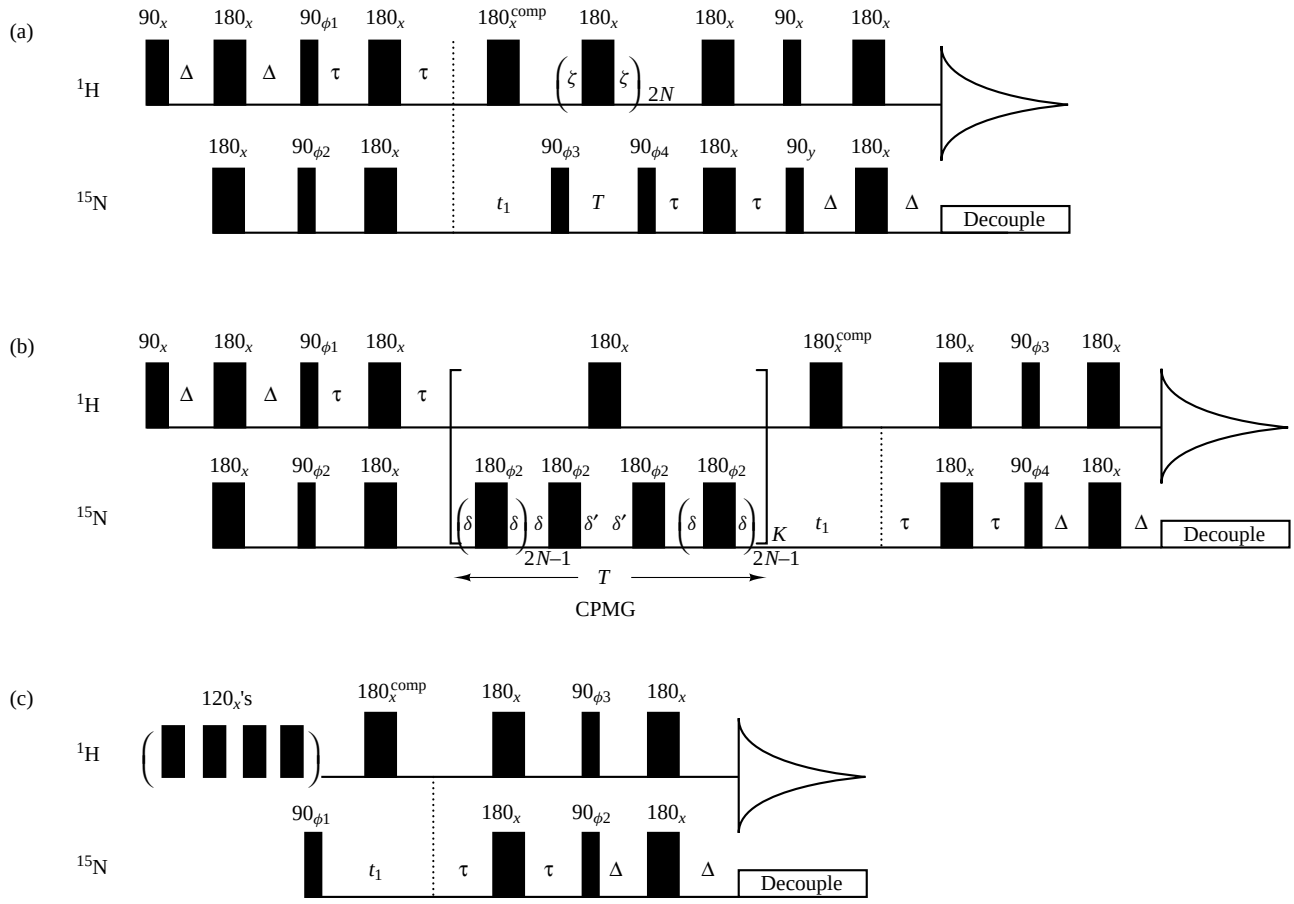

Figure 1 Pulse sequences used to measure A-spin (a) T_1, (b) T_2, and (c) A{-X} NOE in AX spin systems. The sequences are discussed in Kay et al.[14]

$1/[8J(\mathrm{C, H})]$, to minimize the effect of rapid proton relaxation upon the measurement of the ^{13}C relaxation rates. Finally, because the methyl ^{13}C NOE is large, there is no sensitivity loss in saturating the protons and initiating the T_1 and T_2 experiments with ^{13}C magnetization. Sequences for measuring methyl carbon relaxation have been discussed in detail,[12,13,23] and Kay et al.[13] have discussed the errors in T_2 measurements that are caused by (a) missetting the magic angle, and (b) rapid relaxation of proton magnetization in the $\frac{3}{2}$ manifold, when INEPT- and DEPT-type sequences are recorded without applying 125° pulses during the CPMG period. Application of 125° pulses, during the CPMG period, decreases (increases) the error in the T_2 measurement in the INEPT (DEPT)-type experiment caused by magic angle misset, and increases (decreases) error in the INEPT (DEPT) experiment caused by rapid proton relaxation.

Although the pulse schemes used to measure methyl relaxation minimize the effects of dipolar cross correlation, rf pulses cannot mix the $\frac{3}{2}$ and $\frac{1}{2}$ proton manifolds and therefore cannot completely eliminate such effects. Fortunately, dipolar cross correlations make very small contributions to T_1 and NOE of rapidly rotating methyl carbons in proteins in the 5–40 kDa molecular weight range.[24] Hence, equations (1) and (3) can be applied in the analysis of methyl carbon relaxation in proteins. However, the effects of dipolar cross correlations are significant in the case of transverse relaxation, and equation (2) provides the rate of the initial decay of the methyl carbon transverse magnetization. Finally, we note that chemical exchange often contributes to T_2 relaxation in proteins. Because accurate T_2 values are obtained by the CPMG method only when $\delta \ll 1/[2J(\mathrm{A, X})]$,[9,14,16] small δ values are employed in the CPMG sequence. For this reason, and because the maximum spin lock field that can be safely applied to protein solutions is about 10 kHz, chemical exchange often affects T_2 and $T_{1\rho}$ in a similar way. Therefore, even in the presence of chemical exchange, T_2 may be equal to $T_{1\rho}$. A significant increase in $1/T_2$, as the external field increases, is strong evidence that fast chemical exchange contributes to transverse relaxation.

In view of the large amount of data that is required to determine residue-specific relaxation parameters in proteins, surface fitting routines are an extremely useful means of determining signal positions and intensities in individual two-dimensional spectra. The derived signal intensities are fit to an equation of the form $y = A\exp(-t/T_i)$, $i = 1$, 2, using conjugate gradient minimization techniques,[25] and standard errors in A and T_i are obtained using a Monte Carlo approach.[26] The NOE values are determined by measuring the ratio of signal intensities in the presence and absence of proton saturation. The standard error in the NOE measurement is derived from the rms noise measured in a signal-free region of the spectrum.

Although the model-free approach can be applied when the overall motion of the protein is anisotropic,[6,7,27] most globular

proteins have approximately spherical shapes, and it is usually assumed that the overall motion of the protein is characterized by a single overall correlation time, τ_m. In the framework of the model-free formalism, each NMR parameter is then related to three parameters: the global parameter τ_m, and two residue-specific internal motion parameters, S^2 and τ_e. A general approach to determine the three model-free parameters consists of minimizing the function[25,28,29]

$$\chi^2 = \sum_i \{[(T_{1i}^{obs} - T_{1i}^{cal})/\sigma_{1i}]^2 + [(T_{2i}^{obs} - T_{2i}^{cal})/\sigma_{2i}]^2 + [(NOE_i^{obs} - NOE_i^{cal})/\sigma_{NOEi}]^2\} \quad (8)$$

where the summation is over the residues in the protein, the superscripts indicate observed and calculated parameters, and σ is the standard error in the measured parameter. A single value of τ_m is assigned to all residues in the protein and then the set of $\{S_i^2, \tau_{ei}\}$ values that minimize χ^2 is found using conjugate gradient minimization.[25] This process is repeated, incrementing τ_m until the minimum value of χ^2 is attained. Then, several hundred synthetic data sets are used in a Monte Carlo approach[23,26,29] to determine the uncertainties in the model-free parameters.

In analyzing relaxation data, residues that have unusually small T_2 values should be noted, because a small T_2 suggests that chemical exchange contributes to transverse relaxation. In contrast, unusually large T_2 values indicate the presence of large-amplitude, rapid internal motions that may not be well fit by a single internal correlation time. It is probably best to exclude residues with unusual T_2 values from the initial determination of τ_m using equation (8). Once the value of τ_m is determined, residues having anomalous T_2 values can be analyzed to see if an exchange term is required to account for a small T_2 or if an analysis involving more than one internal correlation time is required to account for relaxation data of residues having large T_2 values. An approach has been presented,[29] based upon statistical criteria, for systematically adding parameters to analyze relaxation data within the framework of the model-free formalism.

4 TWO-DIMENSIONAL HETERONUCLEAR RELAXATION STUDIES OF PROTEINS

4.1 Staphylococcal Nuclease (SNase)

Staphylococcal nuclease is a 17 kDa phosphodiesterase that efficiently hydrolyzes strands of both DNA and RNA. Relaxation studies of a uniformly ^{15}N-labeled protein yielded an overall correlation time of 8.3–8.5 ns,[30] while ^{13}C relaxation measurements[31] of samples labeled at alanine (Ala) C-α sites yielded a somewhat larger value of τ_m in the range 9.2–9.5 ns. The larger value of τ_m, obtained from the carbon relaxation data has been ascribed to the fact that the viscosity of the solvent (D_2O) is about 20% greater than the solvent (H_2O) used in the ^{15}N study. The residue-specific order parameters of the Ala ^{15}N amide and C-α sites were in good agreement. Moreover, values of S^2 were in the range 0.8–0.95 for nearly all amino acids in the protein. This result showed that internal motion of the SNase backbone is limited to rapid small-amplitude motions. Exceptions to this statement are (a) highly flexible residues in the N- and C-termini which have large T_2 values, and (b) several residues in the functionally important Ω loop which have unusually small T_2 values. In the X-ray structure of SNase[32] residues in the Ω loop have weak electron density and large B factors. In solution, the loop is highly flexible, as evidenced by the broad lines and missing amide signals of residues in, or adjacent to, the loop. Although the Ω loop is flexible, it has a significant role in catalysis, as constructs of SNase lacking the loop have virtually the same structure as the parent molecule, but significantly lower levels of activity.

Although the side chains of all 11 leucine (Leu) residues in SNase are in well-structured regions of the protein, the values of S^2 of the Leu methyl sites fall into two distinct classes.[23,30] In the presence of stabilizing ligands, thymidine 3′,5′-bisphosphate and Ca^{2+}, four residues have values of S^2, approx. 0.4–0.5, that are substantially less than the values of S^2, approx. 0.8–0.9, of six of the remaining residues. This result indicates that there is a significant range in the flexibility of the large, hydrophobic side chains in SNase. Furthermore, it was found that the flexibility of the Leu methyl groups was sensitive to ligand binding, with side chains in the neighborhood of the ligand binding sites increasing in flexibility in the absence of the ligands.

4.2 Calmodulin and Calbindin D_{9k}

Calmodulin is a 148-residue protein that couples fluctuations in Ca^{2+} concentration to cellular activity. In the crystalline state the protein has the shape of a dumbbell in which two globular domains are connected by a continuous 26-residue α-helix. However, a ^{15}N relaxation study has shown that residues in the center of this helix have small order parameters, in the 0.5–0.6 range.[33] In addition, the relaxation data showed that the N- and C-terminal globular domains tumble nearly isotropically with slightly different correlation times. These results are strong evidence that the central helix is flexible in solution, a result that structural studies of the calmodulin/M19 complex have confirmed.[34]

Calbindin D_{9k} is a 75-residue member of the calmodulin superfamily of calcium-binding proteins, containing two calcium binding sites. A careful comparison of ^{15}N relaxation measurements[35] made on the apo protein, the protein with Ca^{2+} in binding site II, and the protein with ions in both sites I and II, has shown that ion binding has very small effects on amide order parameters, with the notable exception of residues in binding site II. The order parameters of these residues increase from 0.6 to 0.85 when an ion is bound in site II. In contrast, residues in site I have large order parameters, S^2 approx. 0.8–0.85, in the absence and presence of bound ions. The asymmetry in the dynamic behavior of the two Ca^{2+} binding sites may be related to the fact that site I is not a typical EF hand (Ca^{2+}-binding loop), and is being characterized by further work on protein samples, half saturated with Ca^{2+}.

4.3 Interleukins, IL-1β, IL-4, and IL-8

High-resolution crystal and solution structures, as well as backbone amide order parameters are available[36] for IL-1β, IL-4, and IL-8. Analysis of these extensive data has

shown that amide nitrogen order parameters correlate with the inverse of (a) rms deviation (rmsd) values of the amide nitrogen coordinates, derived from the NMR structures, and (b) the amide nitrogen crystallographic *B* factors. While the correlations show significant scatter, this is to be expected because internal motions on a timescale slower than τ_m will not usually affect S^2 but will affect the other two parameters. Furthermore, crystal contacts may hinder motions that occur in solution. In general, it was found that amide nitrogen sites, having small *B* factors and small rmsd values in NMR structures, are strongly correlated with amide nitrogen sites that have large values of S^2.

4.4 Bovine Pancreatic Trypsin Inhibitor, BPTI

Bovine pancreatic trypsin inhibitor (BPTI) was one of the first proteins whose internal dynamics were characterized by NMR lineshape and relaxation studies. More recently, measurement of transverse relaxation rates using natural abundance two-dimensional $^1H-^{13}C$ heteronuclear techniques has provided evidence for slow internal motions involving cysteine (Cys) 14 and Cys-38.[10] A thorough investigation of this process in wild-type BPTI and in a mutant protein, BPTI(G36S), showed that the protein is an equilibrium mixture of interconverting isomers of the Cys-14–Cys-38 disulfide bond.[37] The rate of interconversion of the two isomers, as determined by measurements of the ^{15}N $T_{1\rho}$ of Cys-38 and of Arg-39, as a function of the spin lock field,[38] was in reasonable agreement with the rate of conformational exchange determined independently using two-spin-order exchange experiments and from measurements of chemical exchange line broadening. This work also demonstrates that, because of the inherent limited sensitivity of protein NMR spectra, slow dynamic processes in proteins are difficult to observe and may be more common than has been supposed.

5 SUMMARY OF ^{15}N WORK AND PROSPECTS FOR ^{13}C MEASUREMENTS

Unfortunately, space does not permit even brief individual reviews of the substantial number of other interesting proteins that have been studied using ^{15}N relaxation measurements. However, a few general comments about backbone mobility, based upon the ^{15}N relaxation work, can be made. Internal motions of the amide backbone are small in amplitude, with order parameters typically greater than 0.8 for amino acids in regions of regular secondary structure. In contrast, residues in either the terminal regions of the protein sequence or in small external loops often exhibit large amplitude, $S^2 < 0.6$, rapid internal motions, with $\tau_e \ll \tau_m$. Much slower motions, on the chemical shift timescale, are most commonly seen for large loops or segments near the protein surface, that often contain amino acid residues implicated in the function of the molecule.

While the ^{15}N studies have provided the first comprehensive view of internal dynamics of the protein backbone in solution, internal motions of protein side chains are likely to be considerably more varied and interesting. While the use of specifically ^{13}C-labeled samples is a means of studying such motions, it would be much more efficient to use uniformly ^{13}C-labeled samples, provided that the pulse sequences can be developed that suppress effects of carbon–carbon coupling. Labeling a protein with ^{13}C at alternate carbon sites has also been proposed[39] to achieve this goal. Elimination of the effects of dipolar cross correlation ^{13}C relaxation measurements is also highly desirable. This has been done for glycine (Gly) C-α H_2 sites in *Escherichia coli* thioredoxin by preparing a sample labeled with 50% [U-^2H, 2-^{13}C]Gly,[39] and recording spectra using pulse sequences that (a) select for Gly α-carbons bonded to a single proton, and (b) decouple deuterons. Deuteration also has the advantage that both carbon and proton T_2 values are significantly larger than in the protonated protein. Although it will require considerably more effort to measure relaxation parameters of protein uniformly labeled with ^{13}C than with ^{15}N, the wealth of information about protein side-chain motions that will be provided by the ^{13}C experiments should fully reward the effort required.

6 RELATED ARTICLES

Motional Effects on Protein Structure: Acyl Carriers; Protein Dynamics from Solid State NMR; Selective Relaxation Techniques in Biological NMR.

7 REFERENCES

1. A. Bax and S. Grzesiek, *Acc. Chem. Res.*, 1993, **26**, 131.
2. S. J. Archer, V. K. Vinson, T. D. Pollard, and D. A. Torchia, *Biochemistry*, 1993, **32**, 6680.
3. M. Karplus and J. A. McCammon, *Sci. Am.*, 1986, **254**, 42.
4. K. Wüthrich, *NMR of Proteins and Nucleic Acids*, Wiley, New York, 1986.
5. G. M. Clore and A. M. Gronenborn, *Crit. Rev. Biochem. Mol. Biol.*, 1989, **24**, 479.
6. G. Lipari and A. Szabo, *J. Am. Chem. Soc.*, 1982, **104**, 4546.
7. G. Lipari and A. Szabo, *J. Am. Chem. Soc.*, 1982, **104**, 4559.
8. R. E. London, *Methods Enzymol.*, 1989, **176**, 358.
9. L. E. Kay, D. A. Torchia, and A. Bax, *Biochemistry*, 1989, **28**, 8972.
10. N. R. Nirmala and G. Wagner, *J. Magn. Reson.*, 1989, **82**, 659.
11. J. Boyd, U. Hommel, and I. D. Campbell, *J. Chem. Phys.*, 1990, **175**, 477.
12. A. G. Palmer, III, P. E. Wright, and M. Rance, *Chem. Phys. Lett.*, 1991, **185**, 41.
13. L. E. Kay, T. E. Bull, L. K. Nicholson, C. Griesinger, H. Schwalbe, A. Bax, and D. A. Torchia, *J. Magn. Reson.*, 1992, **100**, 538.
14. L. E. Kay, L. K. Nicholson, F. Delaglio, A. Bax, and D. A. Torchia, *J. Magn. Reson.*, 1992, **97**, 359.
15. A. G. Palmer, N. J. Skelton, W. J. Chazin, P. E. Wright, and M. Rance, *Mol. Phys.*, 1992, **75**, 699.
16. J. W. Peng and G. Wagner, *J. Magn. Reson.*, 1992, **98**, 308.
17. A. Abragam, *The Principles of Nuclear Magnetism*, Oxford University Press, Oxford, 1961.
18. A. G. Redfield, *Adv. Magn. Reson.*, 1965, **1**, 1.
19. Y. Hiyama, C. H. Niu, J. V. Silverton, A. Bavoso, and D. A. Torchia, *J. Am. Chem. Soc.*, 1988, **110**, 2378.
20. L. G. Werbelow and D. M. Grant, *Adv. Magn. Reson.*, 1977, **9**, 189.

21. G. M. Clore, A. Szabo, A. Bax, L. E. Kay, P. C. Driscoll, and A. M. Gronenborn, *J. Am. Chem. Soc.*, 1990, **112**, 4989.
22. S. Grzesiek and A. Bax, *J. Am. Chem. Soc.*, 1993, **115**, 12 593.
23. L. K. Nicholson, L. E. Kay, D. M. Baldisseri, J. Arango, P. E. Young, A. Bax, and D. A. Torchia, *Biochemistry*, 1992, **31**, 5253.
24. L. E. Kay and D. A. Torchia, *J. Magn. Reson.*, 1991, **95**, 536.
25. W. H. Press, B. P. Flannery, S. A. Teukolsky, and W. T. Vetterling, *Numerical Recipes in C*, Cambridge University Press, Cambridge, 1988.
26. U. Kamath and J. W. Shriver, *J. Biol. Chem.*, 1989, **264**, 5586.
27. D. M. Schneider, M. J. Dellwo, and A. J. Wand, *Biochemistry*, 1992, **31**, 3645.
28. M. J. Dellwo and A. J. Wand, *J. Am. Chem. Soc.*, 1989, **111**, 4571. 4578.
29. M. J. Stone, W. J. Fairbrother, A. G. Palmer, III, J. Reizer, M. H. Saier, Jr., and P. E. Wright, *Biochemistry*, 1992, **31**, 4394.
30. D. A. Torchia, L. K. Nicholson, H. B. R. Cole, and L. E. Kay, in *NMR of Proteins*, eds. G. M. Clore and A. M. Gronenborn, Macmillan, London, 1993, pp. 190–219.
31. L. K. Nicholson, L. E. Kay, and D. A. Torchia, in *NMR Spectroscopy and its Application to Biomedical Research*, ed. S. K. Sarkar, Elsevier, Amsterdam, 1995.
32. P. J. Loll and E. E. Lattman, *Proteins Struct. Funct. Genet.*, 1989, **5**, 183.
33. G. Barbato, M. Ikura, L. E. Kay, R. W. Pastor, and A. Bax, *Biochemistry*, 1992, **31**, 5269.
34. M. Ikura, G. M. Clore, A. M. Gronenborn, G. Zhu, C. B. Klee, and A. Bax, *Science*, 1992, **256**, 632.
35. J. Kördel, N. J. Skelton, M. Akke, A. G. Palmer, III, and W. J. Chazin, *Biochemistry*, 1992, **31**, 4856.
36. R. Powers, G. M. Clore, D. S. Garrett, and A. M. Gronenborn, *J. Magn. Reson., Ser. B*, 1993, **101**, 325.
37. G. Otting, E. Liepinsh, and K. Wüthrich, *Biochemistry*, 1993, **32**, 3571.
38. T. Szyperski, P. Luginbühl, G. Otting, P. Guntert, and K. Wüthrich, *J. Biomol. NMR*, 1993, **3**, 151.
39. D. M. Kushlan and D. M. LeMaster, *J. Am. Chem. Soc.*, 1993, **115**, 11026.

Biographical Sketch

Dennis A. Torchia. *b* 1939. B.A., 1961, physics, University of California, Ph.D., 1967, Physics, Yale University. Postdoctoral fellow, Harvard Medical School, 1967–1969 with Elkan Blout; Bell Laboratories, 1969–1971, with Frank Bovey. Staff member, National Bureau of Standards, 1971–1974. Dental Institute, NIH, 1974–present. Currently, Chief, Protein Biophysics Section, Bone Research Branch. Approx. 125 publications. Current research specialty: application of solution state heteronuclear NMR techniques to study protein structure and dynamics.

Relaxation Effects Involving Cross Correlation in Biomolecules

Mark Rance

Department of Molecular Genetics, Biochemistry and Microbiology, University of Cincinnati College of Medicine, Cincinnati, OH, USA

1	Introduction	1
2	Theory	1
3	Sensitivity and Resolution Enhancement via Cross-Correlation Effects	3
4	Measurement of Angles Between Bond Vectors	4
5	Studies of Molecular Dynamics via Cross-Correlated Relaxation Effects	5
6	Cross-Correlation Effects in Paramagnetic Systems	8
7	Characterization of Hydrogen Bond Lengths	8
8	Relaxation-Induced Violations of Coherence Transfer Selection Rules in Multiple Quantum NMR Spectroscopy	8
9	Additional Cross-Correlation Effects	9
10	Elimination of Cross-Correlation Effects	9
11	Summary	9
12	Related Articles in this Volume	9
13	Related Articles in Volumes 1–8	9
14	References	9

1 INTRODUCTION

Studies of nuclear spin relaxation processes can provide invaluable information regarding the structure and dynamics of biological macromolecules. Numerous methodologies have been proposed for the measurement and interpretation of various nuclear spin relaxation rate constants. In recent years the arsenal of tools available for NMR relaxation studies has expanded rapidly, due in part to the greater appreciation and subsequent exploitation of cross-correlation effects. The presence of cross-correlation, or relaxation interference, effects in nuclear spin relaxation processes has been recognized since the early days of NMR experimentation. One of the earliest reports on this subject was the proposal by McConnell[1] that relaxation interference effects could explain the observed dependence of multiplet linewidths on the nuclear spin quantum number in paramagnetic resonance spectra of solutions of ionic salts. Another pioneering study was that by Hubbard,[2,3] concerning relaxation interference effects on the spin-lattice relaxation of three- and four-spin-1/2 systems. Despite these early reports, and with some notable exceptions, the prevailing view for many years seemed to be that cross-correlation effects were more of a theoretical curiosity than a practically useful feature of nuclear spin relaxation. This sentiment was due in part to improper extrapolations of Hubbard's results to other systems.[4] Fortunately, the rigorous theoretical treatments of cross-correlation effects by several groups, especially those of Werbelow, Grant, and Lynden-Bell,[5–7] and the development of multi-dimensional and multiple quantum NMR methodologies in the 1970s lead to a renewed interest and solid foundation for the exploitation of cross-correlated relaxation phenomena. As a result, many important and very valuable NMR techniques that rely on the measurement and/or utilization of cross-correlation effects are now available and in common use for obtaining detailed information on the structure and dynamics of a variety of systems, including biological macromolecules.

The purpose of the present article is to provide an overview of the subject of cross-correlated nuclear spin relaxation effects (see also **Relaxation Processes: Cross Correlation & Interference Terms,** Volume 6, and **Relaxation Theory: Density Matrix Formulation,** Volume 6), focusing on those areas of particular importance in studies of the structure and dynamics of proteins, nucleic acids and other biological macromolecules. The basic concepts are emphasized, rather than providing a detailed theoretical description. Readers interested in the theoretical formalism of cross-correlated relaxation and/or a more complete presentation than is possible here are directed to an excellent and comprehensive review of cross-correlations in NMR that was published recently by Kumar et al.[8] A number of other review and research articles are also highly recommended for those wishing to learn more about this fascinating field.[5–14]

2 THEORY

A number of interactions can contribute to the overall relaxation behavior of a nuclear spin, including the stochastic modulation of dipole–dipole couplings, chemical shift anisotropies, and quadrupolar couplings (for spin $>1/2$). Cross-correlation effects result from the interference of two such relaxation mechanisms, under the conditions that the time-dependent modulation of the two relaxation mechanisms arises from the same source, and that the tensors that describe the time-dependence of the interactions have the same rank. To put this in more formal terms, the stochastic Hamiltonian responsible for the relaxation behavior of a nuclear spin can be written as:[15]

$$\mathbf{H}_1(t) = \sum_m \sum_{q=-k}^{k} F_{mk}^q(t)\mathbf{A}_{mk}^q \tag{1}$$

in which the summation over the index m accounts for the different relaxation mechanisms, $F_{mk}^q(t)$ is a function of spatial variables that describes the effective motional behavior and $\mathbf{A}_{mk}^q$ is a tensor spin operator. The index k gives the rank of the tensor operators for the relevant interactions. The Liouville-von Neumann equation for the density operator is given by:

$$\frac{\mathrm{d}\sigma}{\mathrm{d}t}(t) = -i[\mathbf{H}_\mathrm{o}, \sigma(t)] - \hat{\Gamma}(\sigma(t) - \sigma_\mathrm{o}) \tag{2}$$

where $\mathbf{H}_\mathrm{o}$ is the time-independent part of the nuclear spin Hamiltonian, $\sigma(t)$ is the time-dependent density operator, σ_o is the thermal equilibrium density operator, and $\hat{\Gamma}$ is the

relaxation superoperator. If the density operator σ is expanded in terms of a set of basis spin operators $\mathbf{B}_i$, the rate constant for relaxation between the operators $\mathbf{B}_r$ and $\mathbf{B}_s$ is:

$$\begin{aligned}\Gamma_{rs} &= \frac{1}{2}\sum_m\sum_q\sum_p\{\langle\mathbf{B}_r|[\mathbf{A}^{-q}_{mkp},[\mathbf{A}^{q}_{mkp},\mathbf{B}_s]]\rangle/\langle\mathbf{B}_r|\mathbf{B}_r\rangle\}j^q(\omega_p)\\ &\cdots+\frac{1}{2}\sum_{\substack{m,n\\ m\neq n}}\sum_q\sum_p\{\langle\mathbf{B}_r|[\mathbf{A}^{-q}_{mkp},[\mathbf{A}^{q}_{nkp},\mathbf{B}_s]]\rangle/\langle\mathbf{B}_r|\mathbf{B}_r\rangle\}j^q_{mn}(\omega_p)\\ &\cdots=\sum_m\Gamma^m_{rs}+\sum_{\substack{m,n\\ m\neq n}}\Gamma^{mn}_{rs}\end{aligned}\qquad(3)$$

in which the $\mathbf{A}^q_{mkp}$ are basis operators that can be summed over index p to generate the tensor operators $\mathbf{A}^q_{mk}$ appearing in equation (1), and the cross-correlation spectral density is:

$$j^q_{mn}(\omega)=\mathrm{Re}\left\{\int_{-\infty}^{\infty}\overline{F^q_{mk}(t)F^{-q}_{nk}(t+\tau)}\exp(-i\omega\tau)\mathrm{d}\tau\right\}\qquad(4)$$

The terms Γ^{mn}_{rs} represent the contributions to the relaxation between $\mathbf{B}_r$ and $\mathbf{B}_s$ that results from the interference or cross-correlation between the m^{th} and n^{th} relaxation mechanisms. From equation (4) it is clear that if the motional processes modulating relaxation mechanisms m and n are uncorrelated, there will be no cross-correlated relaxation involving these two mechanisms. Likewise, from equation (3) it can be seen that cross-correlated relaxation requires that the double commutator involving spin operators $\mathbf{A}^{-q}_{mkp}$ and $\mathbf{A}^q_{nkp}$ be non-zero. In applications to biomolecules, the most common relaxation interference effects arise from the three cross-correlation combinations involving the dipole–dipole (DD) and chemical shift anisotropy (CSA) relaxation mechanisms.

The concept of cross-correlated nuclear spin relaxation can be illustrated by considering a simple two spin-1/2 system, a ^{15}N–^{1}H spin pair in a protein backbone, and analyzing the transverse relaxation of the ^{15}N spin.[16] The relevant cross-correlation in this example is the relaxation interference between the ^{15}N chemical shift anisotropy (CSA) and the ^{15}N–^{1}H dipole–dipole (DD) interactions. Figure 1 demonstrates the basic principle of CSA/DD cross-correlated relaxation in the ^{15}N–^{1}H system. The case of a ^{15}N spin bonded to a ^{1}H spin in the $|\alpha\rangle$ state (as indicated by the upward arrow through the ^{1}H nucleus) is shown in Figure 1(A) and (B); in Figure 1(A) the ^{15}N–^{1}H bond vector is oriented parallel to the externally applied magnetic field, whereas Figure 1(B) shows the case where the bond vector is perpendicular to the applied field. Figure 1(C) and (D) show the analogous situations where the ^{1}H spin is in the $|\beta\rangle$ state. The solid lines drawn to the right of the ^{15}N nuclei indicate the direction of the local magnetic field, arising from the ^{1}H spin, at the position of the ^{15}N spin, while the dashed lines to the left of the ^{15}N nuclei show the direction of the induced magnetic field arising from the ^{15}N CSA interaction. Relaxation of the ^{15}N spin is caused by fluctuations in the net sum of these local magnetic fields as the orientation of the bond vector is randomly modulated by motional processes. The key observation in this example is that when the ^{1}H spin is in the $|\alpha\rangle$ state, the local magnetic fields arising from the CSA and DD interactions have the same sign, regardless of the bond orientation, whereas these local fields have opposite signs when the ^{1}H spin is in the $|\beta\rangle$ state. Constructive interference of the local magnetic fields arising from the CSA and dipolar interactions will therefore result in a broadening of the ^{15}N resonance associated with the ^{1}H in the $|\alpha\rangle$ state, while destructive interference of these local fields will lead to a narrowing of the ^{15}N resonance associated with the ^{1}H in the $|\beta\rangle$ state. This type of cross-correlated relaxation effect forms the basis of TROSY, or transverse relaxation-optimized spectroscopy (see **Transverse Relaxation-optimized NMR Spectroscopy with Biomacromolecular Structures in Solution**).

The measurement of cross-correlated relaxation rate constants is greatly facilitated by the fact that the relaxation behavior can be controlled in a substantial way via the design of the pulse sequences.[17] This is quite different from the situation that exists for the measurement of auto-relaxation processes, where pulse sequence elements normally do not affect relaxation. Thus, pulse sequence design has played an essential role in allowing various cross-correlated relaxation processes to be distinguished from one another and in allowing quantitative analyses to be performed. Cross-correlated relaxation rate constants are normally measured in one of two ways. The first method is to observe changes in individual multiplet intensities after an evolution period (usually a constant-time element) during which the relaxation processes of interest have been active. The second possibility is to observe and measure the cross-correlation-induced cross-relaxation of one spin operator with another. In many cases the cross-correlated relaxation rate constants of interest are rather small, and this can present significant challenges in terms of making reliable measurements. Careful attention to experimental design can reduce some sources of uncertainty and error in cross-correlated relaxation measurements.[18]

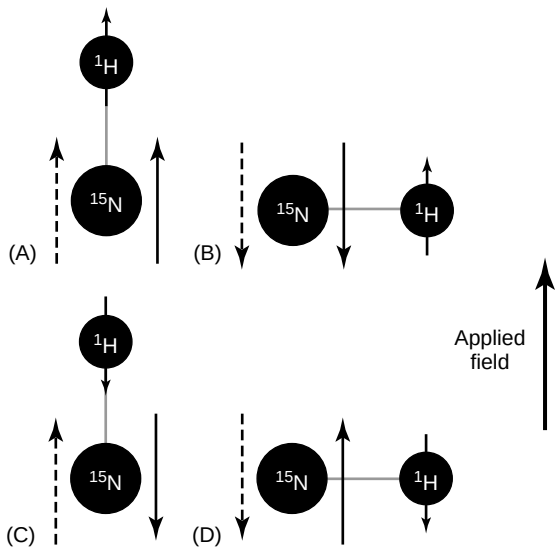

Figure 1 Schematic illustration of the origin of ^{15}N chemical shift anisotropy/^{15}N–^{1}H dipole–dipole cross-correlation effects on the relaxation of the ^{15}N spin. Arrows through the ^{1}H nuclei indicate the ^{1}H spin state $|\alpha\rangle$ (up arrow) or $|\beta\rangle$ (down arrow). Solid arrows adjacent to the ^{15}N nuclei indicate the direction of the local ^{1}H dipolar magnetic field at the site of the ^{15}N spin, while the dashed arrows indicate the direction of the induced magnetic field from the ^{15}N chemical shift interaction. In (A) and (C) the ^{15}N–^{1}H bond vector is parallel to the applied external field, while in (B) and (D) the bond vector is in the perpendicular orientation

Cross-correlation effects in nuclear spin relaxation can be exploited for a number of useful purposes in studies of biomolecules, including sensitivity and/or resolution enhancement, dynamics studies, and measurement of structural constraints. Cross-correlation contributions to relaxation can also be an undesirable feature in dynamics studies that are based on the measurement of auto-relaxation rate constants, and thus it has been necessary to devise various techniques for eliminating specific, cross-correlation-induced cross-relaxation pathways. The following sections describe examples of both the exploitation and elimination of cross-correlation effects that have been found to be of particular relevance in studies of biological macromolecules.

3 SENSITIVITY AND RESOLUTION ENHANCEMENT VIA CROSS-CORRELATION EFFECTS

3.1 TROSY

One of the most exciting and important developments in recent years in the field of solution-state NMR studies of biomolecules has been the introduction of methodologies for sensitivity and/or resolution enhancement that are based on the exploitation of cross-correlation effects. These enhancements have their origin in the differential relaxation rates of multiplet components in the presence of relaxation interference between DD and CSA interactions. Griffey and Redfield anticipated the potential advantages of DD/CSA cross-correlation, as evidenced by their statement that "In certain cases higher resolution and/or sensitivity might be achieved by operating without decoupling, perhaps using an INEPT or double-INEPT sequence".[19] Their belief was validated ten years later when Pervushin and coworkers[20] reported the development of an experimental scheme for transverse relaxation-optimized spectroscopy (TROSY). The TROSY methodology is the subject of another article in this volume, and so only a very brief discussion of the basic principles is presented here.

One of the most important and widely used NMR techniques for studies of biomolecules is the 2D HSQC experiment,[15] which provides correlation information for heteronuclear spin pairs such as ^{1}H–^{15}N or ^{1}H–^{13}C. The HSQC-type pulse scheme is an integral component in most heteronuclear, multi-dimensional NMR experiments. The sensitivity and resolution of HSQC-based experiments is dependent on the transverse relaxation rates of the spins actively involved in the coherence transfer pathway. As the molecular weight of the system under study increases, so do the transverse relaxation rate constants, and thus the sensitivity and resolution of the HSQC spectra are degraded. In the presence of significant dipole–dipole/CSA relaxation interference, the linewidths of individual spin multiplet components can be quite different. The spin decoupling normally performed during an HSQC-type experiment causes an averaging of the transverse relaxation rates of the multiplet components. However, by carefully avoiding this mixing of spin states, it is possible to take advantage of the line-narrowing of one of the multiplet components that arises due to destructive interference of the dipole–dipole and CSA interactions.[14] This forms the basis for the TROSY scheme, as was illustrated in Figure 1. In the first application reported by Pervushin et al.,[20] the TROSY scheme was incorporated into a 2D ^{1}H–^{15}N HSQC experiment. The pulse sequence was designed to select only one of the four multiplet components that would normally be observed for a ^{1}H–^{15}N spin pair correlation in an undecoupled 2D HSQC spectrum. Selecting the component with the smallest ^{15}N and ^{1}H linewidths can lead to significant improvements in sensitivity and/or resolution, under favorable conditions. Heading the list of required conditions of course is that there be a significant dipole–dipole/CSA cross-correlation effect. Thus, the TROSY scheme is most effective at ultra-high magnetic field strengths, due to the field dependence of the CSA interaction, and for heteronuclei with large chemical shift anisotropies, such as ^{15}N or aromatic ^{13}C spins. A number of other factors also affect whether the TROSY scheme will provide useful sensitivity and/or resolution enhancements. Other sources of relaxation, such as dipolar interactions with remote protons, will tend to mask the line narrowing from the DD/CSA interference, as will exchange contributions to the linewidths. Thus, TROSY-based schemes are most useful for large molecular systems that are highly deuterated and not subject to conformational exchange broadening. Even under such conditions, the maximal advantage theoretically possible for a TROSY-based pulse sequence is usually not reached, due to different data acquisition and processing parameters for TROSY and non-TROSY experiments. For example, the advantage of reduced transverse relaxation rates in the ^{15}N evolution period of a TROSY-based HSQC is most useful if relatively long evolution periods are required; such is the case for experiments used to measure small coupling constants. Implementation of the TROSY scheme is also of particular value in constant-time periods in various multi-pulse sequences to minimize relaxation-associated loss of signal intensity.

In practical applications, the TROSY scheme has been extremely useful for studies of deuterated molecules or complexes, especially those that are in excess of 50 kDa in size. The TROSY scheme has been incorporated into a large number of the standard triple resonance experiments employed for resonance assignment as well as other pulse sequences, such as those used to measure small scalar couplings across hydrogen bonds (see **Polarization Transfer Experiments via Scalar Coupling in Liquids,** Volume 6).

The TROSY scheme, as it was originally proposed, was based on the exploitation of relaxation interference between dipole–dipole and CSA interactions to achieve line narrowing of single quantum coherences. Griffey and Redfield[19] pointed out that line-narrowing could also be achieved for zero-quantum (ZQ) coherences, utilizing relaxation interference of the CSA interactions of the two spins actively involved in the ZQ coherence. Pervushin and coworkers[21] have developed a modified TROSY scheme to take advantage of this ZQ line-narrowing via the cross-correlation of ^{15}N and ^{1}H CSA interactions for ^{15}N–$^{1}H^{N}$ spin pairs. They have also incorporated this ZQ-TROSY scheme into a novel 3D ^{15}N-separated ^{1}H–^{1}H NOESY experiment. The three main features/advantages of this so-called 3D NOESY-[^{1}H, ^{15}N, ^{1}H]-ZQ-TROSY experiment are: (1) the ^{15}N CSA/$^{1}H^{N}$ CSA cross-correlation is used to reduce transverse relaxation during the ^{15}N evolution time; (2) line-narrowing is achieved in all three frequency dimensions; and (3) substantial suppression of the diagonal peaks is achieved, thereby facilitating the observation of NOESY cross-peaks that lie very close to the diagonal.

3.2 CRINEPT

Most multi-dimensional experiments applied to biomolecules employ polarization/coherence transfer steps to transfer magnetization from one nuclear species to another; in some cases this is done solely for sensitivity enhancement, and in others it is done to implement a desired coherence transfer pathway. The coherence transfer between two spins I and S normally involves the evolution of magnetization under the scalar coupling Hamiltonian according to (assuming a pulse-interrupted free precession period)

$$I_x \xrightarrow{H_J} I_x \cos(\pi J_{IS}\tau) + 2I_y S_z \sin(\pi J_{IS}\tau) \qquad (5)$$

where J_{IS} is the scalar coupling between spins I and S. Coherence is transferred from I to S by the application of 90° rf pulses to the I and S spins to convert the second term above from anti-phase I spin magnetization to anti-phase S spin magnetization. The 90° rf pulses are applied at a time τ that is chosen to optimize the efficiency of the transfer; in the absence of relaxation, exchange effects, and remote couplings to the I spin, the optimal value of τ would be $1/(2J_{IS})$. However, in the presence of significant I spin relaxation and/or exchange broadening of the I spin, the coherence transfer process is adversely affected and τ will have to be reduced in order to obtain the maximum transfer allowed by the experimental conditions. The loss of magnetization due to relaxation during the scalar coupling evolution period becomes increasingly significant as the size, and thus the rotational correlation time, of the system increases.

Another possibility exists for achieving polarization/coherence transfer between a heteronuclear spin pair. Dalvit[22] and Brüschweiler and Ernst[23] have demonstrated the possibility of employing DD/CSA cross-correlation effects to obtain a coherence transfer of the type

$$I_x \xrightarrow{\Gamma_{\mathrm{DD,CSA}}} 2I_x S_z \qquad (6)$$

In this case the relevant process is the cross-correlation of the I spin CSA and the dipolar interaction between the I and S spins. Coherence can then be transferred from the I spin to the S spin via the anti-phase term by application of 90° rf pulses to both I and S spins. Riek and coworkers[24] have coined the term CRIPT (cross relaxation-induced polarization transfer) for this process, and have discussed the sensitivity advantages achievable, relative to scalar coupling-induced coherence transfer, in applications to very large molecules. They have also developed experimental procedures for utilizing both scalar coupling-induced and cross-correlation-induced coherence transfer pathways in a methodology they have named CRINEPT. Maximum sensitivity enhancements in appropriate applications are obtained by also including the TROSY scheme in the CRINEPT pulse sequences.[25]

3.3 CSA Tensor Characterization via Cross-Correlation Effects

Accurate knowledge of CSA tensors is important for interpreting the results of many NMR experiments in order to obtain structural and motional parameters. Information concerning the magnitude and orientation of CSA tensors has most commonly been obtained from solid-state NMR studies of model compounds. However, experimental studies have demonstrated that CSA tensors are very sensitive to the local environment of a nucleus in a biomolecule, and thus the applicability of tensor parameters from small model compounds is limited. Progress has been made in the use of quantum-chemical calculations to obtain CSA tensor parameters,[26] but there clearly is still a great need to have procedures for experimentally measuring such parameters directly from the systems of interest. Such measurements are potentially a valuable source of structure and dynamics information.

Several groups have demonstrated that site-specific, quantitative information on ^{1}H, ^{13}C and ^{15}N chemical shift anisotropies can be obtained for these nuclei in biomolecules from the measurement of dipole–dipole/CSA relaxation interference effects.[8] Several related procedures have been proposed for obtaining CSA information from DD/CSA relaxation interference measurements. For a heteronuclear two spin (I, S) system, DD/CSA transverse cross-correlation rate constants can be obtained either from measurements of the differential relaxation of the individual doublet components or from measurements of the $I_x \rightarrow 2I_xS_z$ coherence transfer process. The methodology described by Kroenke and coworkers[27] also involves measurement of the longitudinal cross-correlation rate constants via the $I_z \rightarrow 2I_zS_z$ polarization transfer process. Fushman and coworkers[28] demonstrated that the magnitudes and the orientation of a CSA tensor (^{15}N in their study) can be obtained from magnetic field-dependent measurements of the ratio η/R_2, where η is the transverse DD/CSA cross-correlation rate constant and R_2 is the heteronuclear transverse relaxation rate constant. Pang and Zuiderweg[29] have proposed an elegant procedure for determining the protein backbone ^{13}C′ carbonyl CSA tensor that involves measuring the relaxation interference between the ^{13}C′ CSA transverse relaxation and three different dipole–dipole relaxation terms: ^{13}C′–^{13}C$^{\alpha}$, ^{13}C′–^{15}N, and ^{13}C′–^{1}H$^{\mathrm{N}}$.

4 MEASUREMENT OF ANGLES BETWEEN BOND VECTORS

Due to the dependence of cross-correlated relaxation effects on the relative orientation of the interaction tensors involved, the measurement of such effects can provide valuable structural information in studies of biomolecules. Considering CSA and dipolar interactions, cross-correlated relaxation can arise from the CSA of two different spins, from the CSA of spin i and the dipolar interaction between spins j and k[DD(jk)], from the CSA of spin j or k and the dipolar interaction between spins j and k affecting the relaxation of spin i, and from two pairs of dipolar interactions DD(ij) and DD(kl) with no common spin between them. In such cases the cross-correlation effects depend on the relative orientation of the relevant interaction tensors but not explicitly on distances. These types of cross-correlations are termed ‘remote’,[30] since the relaxation interference does not depend explicitly on the distance of other spins from the spin or spins of interest. For example, the CSA/CSA cross-correlation involving spins i and j does not depend explicitly on the distance between i and j. Likewise, the DD/DD cross-correlation between spin pairs i, j and k, l depends on r_{ij} (the distance between spins i and j) and

r_{kl} inter-nuclear distances but not explicitly on the distances between the spin pairs, i.e., the r_{ik}, r_{il}, r_{jk} or r_{jl} distances.

Reif and coworkers[31] introduced a strategy which utilizes remote cross-correlation effects to measure the relative orientation of bond angles; a major advantage of this strategy is the fact that there is no requirement to establish a parameterized Karplus-type relationship, as there is when scalar couplings are used to measure torsion angles. Another advantage is the fact that the cross-correlated relaxation is not limited to the analysis of local geometry, since there is no explicit distance dependence. In principle, the relative orientation of arbitrary interaction tensors within one molecule, or even between two molecules, can be measured as long as a correlation between these two can be established.[17]

An approach that has proven to be very effective for the measurement of remote cross-correlation effects is to examine the relaxation behavior of double and zero quantum coherences created between nuclei affected by the interactions of interest. In the strategy proposed by Reif et al., double quantum coherence is created involving the $^{13}C^{\alpha}$ nucleus of amino acid residue i and the backbone ^{15}N nucleus of residue $i+1$ in a protein, and the effects of relaxation interference between the $^{13}C^{\alpha}$–$^{1}H^{\alpha}$ (residue i) and the ^{15}N–$^{1}H^{N}$ (residue $i+1$) dipolar interactions on the $^{13}C^{\alpha}$–^{15}N double quantum coherence is probed. The cross-correlation effects are manifested in the differential relaxation rates of the four double quantum transitions. These rates can be determined either from the linewidths of the double quantum signals or from resonance intensities measured from a constant-time NMR experiment. For practical reasons the latter approach is normally easier to accomplish. Intensity ratios provide a measure of the desired cross-correlation relaxation rate constants. In turn, these rate constants can then be used to determine the relative orientation of the interaction tensors.[14] For the example described here, and assuming a macromolecule that tumbles slowly in solution, the cross-correlated dipolar relaxation depends on the angle θ between the $^{13}C^{\alpha}$–$^{1}H^{\alpha}$ (residue i) and ^{15}N–$^{1}H^{N}$ (residue $i+1$) bonds according to

$$\Gamma = \frac{\gamma_H \gamma_N}{(r_{NH})^3} \frac{\gamma_H \gamma_C}{(r_{CH})^3} \left(\frac{\hbar \mu_o}{4\pi}\right)^2 \frac{2}{5} (3\cos^2\theta - 1)\tau_c \qquad (7)$$

The γ_H, γ_N and γ_C are the magnetogyric ratios of the ^{1}H, ^{15}N and ^{13}C nuclei, respectively, r_{NH} and r_{CH} are the ^{15}N–$^{1}H^{N}$ and $^{13}C^{\alpha}$–$^{1}H^{\alpha}$ inter-nuclear distances, respectively, τ_c is the rotational correlation time of the molecule, and $\hbar$ and μ_o are natural constants. This expression does not take fast internal motion or anisotropic reorientation of the molecule into account. Due to the planarity of the peptide bond, the angle θ can be directly related to the dihedral angle ψ, and thus the dipole–dipole cross-correlation measurement provides information on the allowed values of ψ. Such information can provide important new structural constraints in the structure determination of proteins, due to the fact that the dihedral angle ψ is difficult to assess by other experimental means.

Since the pioneering work of Reif et al. was first reported, additional and/or improved schemes for using cross-correlation effects to assess ϕ and ψ dihedral angles in proteins and sugar puckers in nucleic acids have been proposed by several groups (see for example Kloiber and Konrat[32] and references cited therein). Almost all of these schemes have been based on the measurement of DD/DD and/or DD/CSA cross-correlation effects. However, Skrynnikov and coworkers[33] have proposed a technique for measuring CSA cross-correlated relaxation between pairs of carbonyl spins in proteins, and have demonstrated that in the case where the carbonyl spins reside on successive residues, information about the intervening (ϕ, ψ) backbone dihedral angles is obtained. They also demonstrated the possibility of observing CSA/CSA cross-correlated relaxation between carbonyl spins residing on two peptide planes linked via a hydrogen bond, which can provide information about the relative orientation of these planes. With the availability of dihedral angle information, especially for the ψ angles, from various cross-correlated relaxation measurements, it has become possible to use such structural constraints in NMR protein structure calculations. Refinement methods that have been modified to incorporate cross-correlation-based structural constraints can be used to significantly improve the quality of NMR structures and are applicable to larger proteins.[34]

5 STUDIES OF MOLECULAR DYNAMICS VIA CROSS-CORRELATED RELAXATION EFFECTS

The measurement of nuclear spin relaxation rate constants provides valuable information on motional processes occurring within biomolecules. Experiments for measuring auto-correlated relaxation rate constants for ^{1}H, ^{13}C, ^{15}N and ^{2}H are in widespread use, particularly for characterizations of the backbone dynamics and the rotational diffusion tensor of proteins and their complexes.[11] Building upon this base, there is growing interest in obtaining more detailed information on conformational dynamics within proteins. Two areas of focus are the development of more realistic models of the local motions of peptide planes in proteins and quantitative measurements of side chain dynamics. Cross-correlated relaxation experiments are proving to be particularly useful for studying the motional properties of structural elements that have a fixed geometry, such as peptide planes and CH_2, CH_3 and NH_2 groups. The motions of such moieties within proteins and similar elements within other biomolecules are expected in general to be anisotropic. Experimental NMR studies of such anisotropic motions are greatly facilitated by exploiting the sensitivity of cross-correlated relaxation rates to the direction of motion. Cross-correlated relaxation measurements are complementary to the standard auto-correlated relaxation experiments in several ways. Cross-correlation rate constants are not, or only little, affected by conformational or chemical exchange processes (see **Chemical Exchange Effects in Biological Macromolecules**), spin-rotation relaxation, or relaxation by paramagnetic oxygen;[35] such contributions can complicate the interpretation of dipolar or CSA auto-relaxation data. An additional advantage is that transverse cross-correlation effects are generally confined to subsystems containing two, three or four spins, with outside spins having little effect. On the other hand, a potential complication in the use of cross-correlation effects involving CSA interactions is that independent knowledge of the CSA tensor parameters is necessary in order to separate out the motional contributions to the cross-correlated relaxation processes. Information from other sources, such as solid-state NMR, molecular dynamics simulations, and CSA quantum chemical calculations, can be employed for characterizing the necessary CSA tensor parameters.[26,35]

A thorough description of the theory and application of cross-correlated relaxation measurements for studies of motional processes in biomolecules is beyond the scope of this article. The interested reader is directed to several excellent review articles that have appeared recently.[8–11] Instead, a very limited survey of some of the most promising uses of cross-correlation effects in biomolecular dynamics studies is presented here.

5.1 Dipole–Dipole/Dipole–Dipole Cross-Correlation Measurements

The cross-correlated relaxation measurements most commonly employed in biomolecular NMR studies involve dipole–dipole/dipole–dipole (DD/DD) and DD/CSA interactions. The measurement of DD/DD cross-correlated relaxation has the advantage that no assumptions generally need to be made about the interaction tensors, since they involve known physical constants such as the bond lengths, the orientation of the principal axis of the dipolar tensor is usually known, and the dipolar tensor is axially symmetric. There has been a long history to the use of DD/DD cross-correlated relaxation effects for characterizing molecular motions. Much of the work has focussed on the examination of relaxation effects for proton-coupled ^{13}C spins, especially for AX_2 and AX_3 groups.[7,8,10] For the ^{13}C multiplet spectra of methylene and methyl groups, the central and outer components of the multiplet exhibit different relaxation behavior as a result of DD/DD cross-correlation.[10] Differences in the high field relaxation behavior of the outer lines of the ^{13}C multiplet result from DD/CSA cross-correlation. Building upon earlier work of their own and that of other groups such as Grant, Werbelow and Bodenhausen, Daragan and Mayo have championed the use of DD/DD cross-correlated relaxation measurements for obtaining information on motional processes in biomolecules.[10,11]

A particularly useful method for measuring DD/DD cross-correlated relaxation in heteronuclear spin systems is to monitor the cross-relaxation process $S_z \rightarrow 4S_zI_{1z}I_{2z}$; this technique has been referred to as "SIIS cross relaxation".[36] This cross-relaxation process can occur only when the two heteronuclear dipolar interactions SI_1 and SI_2 are modulated in a correlated manner by the random process that causes relaxation. The SIIS-type of experiment is particularly useful for characterizing the motion of CH_2 groups about χ dihedral angles in the side chains of proteins, since the relative orientation of the two interacting dipoles is known. Measurements of scalar coupling constants can provide information concerning the relative populations of χ rotamers, but provides no information on the rate constants for the bond rotations. By measuring the cross-relaxation behavior between the S_z polarization and the three-spin order $4S_zI_{1z}I_{2z}$, Ernst and Ernst[36] demonstrated that it is possible to distinguish between equally populated three-site jump or unrestricted rotational diffusion models on the one hand and two-site or restricted rotational diffusion models on the other hand; it is often possible to make this judgement based just on the sign of the cross-relaxation peaks. The SIIS cross-relaxation process is typically measured by creating either the S_z polarization or the three-spin order $4S_zI_{1z}I_{2z}$, and then detecting the cross-relaxation partner. Due to the slow tumbling of large molecules, there is some advantage to performing the experiment in the so-called tilted rotating frame, as in the related T-ROESY experiment.[37] The reason for this is that in the laboratory frame the cross-relaxation process depends only on the spectral density function at the Larmor frequency ω_{os}, which tends towards zero as the tumbling slows. A dependence on $J(0)$ is introduced by performing the experiment in the tilted rotating frame. Yang and coworkers[38] have proposed an alternative method, using a triple resonance pulse scheme, for measuring cross-correlated dipole–dipole spin relaxation in proteins. Their experiment records $^{13}C^{\beta}$ multiplet component intensities in one of the three dimensions, and the cross-correlation relaxation rate constant for the interaction between the two ^{13}C β-methylene ^{13}C–^{1}H dipoles is obtained by taking the appropriate ratio of multiplet component intensities. Kay's group, among others, has elegantly demonstrated the usefulness of DD/DD cross-correlation measurements for assessing side-chain dynamics in folded and unfolded proteins and for selecting appropriate motional models.[10,38,39]

A number of DD/DD cross-correlations exist among the various nuclei that form the backbone of a protein, and in principle measurements of the associated cross-correlated relaxation rate constants can provide information about the dynamics of peptide planes. Carlomagno and coworkers[40] proposed a scheme for measuring the sum of the $^{13}C'$–$^{13}C^{\alpha}$/^{15}N–$^{1}H^{N}$ and $^{13}C'$–$^{1}H^{N}$/^{15}N–$^{13}C^{\alpha}$ DD/DD cross-correlated relaxation rate constants by analyzing the influence of these processes on ^{15}N–$^{13}C'$ double and zero quantum coherences. The same experiment gives access to the cross-correlated relaxation rate constants between the $^{13}C'$ CSA and the ^{15}N–$^{1}H^{N}$ or $^{13}C'$–$^{13}C^{\alpha}$ dipoles. The rate constants are very small for small proteins, and thus are difficult to interpret quantitatively. However, the rate constants are expected to increase for larger molecules, which would allow a more rigorous, quantitative analysis. Nevertheless, even a qualitative analysis of the DD/DD cross-correlation data can be helpful in identifying anisotropic motions of peptide planes. Another possible DD/DD cross-correlation involving protein backbone nuclei is the $^{1}H^{N}$–^{15}N/$^{1}H^{N}$–$^{13}C'$ dipole–dipole interaction, which has been examined by Zuiderweg's group.[41]

5.2 Dipole–Dipole/CSA Cross-Correlation Measurements

The measurement of dipole–dipole/CSA cross-correlation effects has proven to be quite valuable for studying motional processes in biomolecules. Such experiments have found important applications in characterizing motional processes occurring on both fast timescales (picosecond-nanosecond) and slower timescales (microsecond-millisecond).

Tjandra and coworkers[42] demonstrated the possibility of measuring ^{15}N–^{1}H dipolar/^{15}N CSA relaxation interference effects to obtain approximate values of the generalized order parameter S^2 that is frequently used to characterize the motional properties of bond vectors such as the backbone $^{1}H^{N}$–^{15}N amide group in proteins. They proposed a straightforward experiment for monitoring the cross-relaxation between in-phase ^{15}N coherence, S_x (or S_y), and anti-phase coherence, $2I_zS_x$ (or $2I_zS_y$), and measuring the corresponding cross-correlation rate constant η_{xy}. The theoretical expression for this transverse cross-correlation rate constant is[42,43]

$$\eta_{xy} = -\frac{\sqrt{3}}{6} cd P_2(\cos\beta)[4J(0) + 3J(\omega_N)] \qquad (8)$$

in which $d = (\mu_o h\gamma_H\gamma_N)/(8\pi^2 r_{NH}^3)$, $c = \gamma_N B_o \Delta\sigma/\sqrt{3}$, μ_o is the permeability of free space, h is Planck's constant, γ_H and γ_N are the magnetogyric ratios for ^{1}H and ^{15}N, respectively, r_{NH} is the distance between the two nuclei, B_o is the static magnetic field strength, $\Delta\sigma = \sigma_\parallel - \sigma_\perp$, the principal components of the ^{15}N CSA tensor are $\sigma_\parallel$ and $\sigma_\perp$, $P_2(x) = (3x^2 - 1)/2$, β is the angle between the symmetry axis of the ^{15}N CSA tensor and the ^{15}N–^{1}H bond vector, and $J(\omega)$ is the spectral density function. Since the cross-correlation rate constant η_{xy} is proportional to the generalized order parameter S^2 (through the dependence on the spectral density function), measurements of η_{xy} yield information on the amplitude of rapid internal motions within a biomolecule. A major advantage of utilizing measurements of η_{xy} is the fact that this cross-correlation process is not affected by line broadening caused by slow conformational exchange,[23,42] and thus the interpretation of the data is greatly simplified in that regard. A disadvantage of the method, however, is that variation in S^2 and $\Delta\sigma$ cannot be distinguished from each other in terms of their effect on η_{xy}. Thus, one must be cautious when interpreting changes in η_{xy}, due to the uncertainties there may be in knowledge of $\Delta\sigma$. On the other hand, if the generalized order parameter S^2 has been determined independently, measurement of η_{xy} can provide information on $\Delta\sigma$.[42]

Dipole–dipole/CSA cross-correlation can cause not only the transverse cross-relaxation process described above but also the longitudinal cross-relaxation process between a single spin order S_z and two-spin order $2I_zS_z$, characterized by a rate constant η_z. The theoretical expression for η_z is[43]

$$\eta_z = -\sqrt{3}cdP_2(\cos\beta)J(\omega_N) \tag{9}$$

with the various symbols having the same definitions as above in the expression for η_{xy}. Kroenke and coworkers[43] have developed a method for distinguishing the contributions of chemical exchange from the contributions due to anisotropic rotational diffusion in ^{15}N spin relaxation studies by measuring both the longitudinal and transverse relaxation interference between the ^{1}H–^{15}N dipolar and ^{15}N CSA interactions. Accurate assessment of chemical exchange contributions to transverse relaxation rate constants (R_2) is critical for a proper interpretation of both model-free and spectral density mapping results. If a biomolecule is regarded as a spherical top that rotates isotropically in solution, then the trimmed mean value of the ratio R_2/R_1 (R_1 is the spin-lattice relaxation rate constant) provides an estimate of the isotropic rotational correlation time of the molecule. Atomic sites subject to chemical or conformational exchange have significantly increased R_2/R_1 ratios. A serious complication arises if the rotational diffusion of the molecule is not isotropic. If rotational diffusion anisotropy is significant, increases in the values of R_2/R_1 for a given nucleus can result from particular orientations of the symmetry axis of the dipolar or CSA tensor in the principal axis frame of the diffusion tensor. These increases can be interpreted mistakenly as evidence of conformational exchange. At the same time, real chemical exchange contributions to R_2 interfere with measurements of the rotational diffusion anisotropy by systematically increasing the R_2/R_1 ratio for the affected nuclei. In practice, sites with large R_2/R_1 ratios are excluded from analysis, which reduces the available data and risks exclusion of data important for accurate assessment of rotational diffusion anisotropy. The basis for the methodology proposed by Kroenke et al.[43] is the fact that both η_{xy} and η_z are independent of chemical exchange and that the η_{xy}/η_z ratio is, to a good approximation, independent of the principal values and orientations of the CSA tensor, unlike the η_{xy} and η_z values separately. As a result, the η_{xy}/η_z ratio is sensitive only to internal and overall motions that contribute to dipolar and CSA relaxation mechanisms. The dependence of the η_{xy}/η_z ratio on the orientation of the ^{1}H–^{15}N bond vector in a molecular reference frame provides a robust method of determining the rotational diffusion tensor. In addition, comparison of the η_{xy}/η_z ratios to the R_2/R_1 ratios permits unequivocal identification of nuclei that are subject to chemical exchange processes, without the need for multi-field and/or rotating-frame relaxation experiments. The methodology for measuring η_z is straightforward.[43] A potential complication in the measurement of η_z is the competing cross-relaxation of the $2I_zS_z$ two-spin order ($I \equiv {}^1$H) with surrounding protons. This problem can be minimized through the use of deuteration or by more complex experimental schemes.[44,45]

Cross-correlated relaxation measurements are proving to be a rich source of information for characterizing the backbone dynamics of proteins. Such motions have commonly been studied through the use of ^{15}N, $^{13}C^\alpha$ and, more recently, ^{13}C′ carbonyl auto-correlated relaxation experiments. Several groups have demonstrated that the measurement of various relaxation interference effects, many involving the cross-correlation of dipole–dipole and CSA interactions, can provide useful insights concerning the locally anisotropic motions of peptide planes and complement the information obtained from auto-correlated relaxation experiments. A large number of relaxation interference effects are possible among the group of spin-1/2 nuclei in the protein backbone (^{13}C′, ^{15}N, $^1H^N$, $^{13}C^\alpha$, $^1H^\alpha$), and many have already been exploited. Only some of the possibilities that have been demonstrated are discussed here.

Zuiderweg's group has reported that there is a poor correlation between the generalized order parameters of the C′–C^α and the $^1H^N$–^{15}N bond vectors, as determined from auto-correlated relaxation studies.[46] They interpreted the lack of correlation as evidence of local or semi-local anisotropic motion of the peptide planes. To further their studies, they developed a new experiment to measure the relaxation interference between the carbonyl (C′) CSA and the ^{13}C′–$^{13}C^\alpha$ dipole–dipole relaxation interactions. The availability of such additional experimental data that reports on anisotropic motion is of great value for modeling such motions.[10,11,47] The Zuiderweg group has also developed a novel scheme for measuring transverse ^{13}C′–$^1H^N$ dipole–dipole/^{13}C′ CSA cross-correlated relaxation rates, using an E.COSY-type triple resonance experiment.[48] The advantage of this method for measuring the cross-correlation effects is that it by-passes the usual requirement for having a resolvable scalar coupling between, in this case, the ^{13}C′ and $^1H^N$ nuclei.

Brutscher and coworkers[49] devised a general scheme to use zero-quantum/double-quantum (ZQ/DQ) NMR experiments to measure various dipole–dipole/CSA cross-correlation rate constants. They demonstrated their methodology for the three-spin system consisting of the $^1H^N$, ^{15}N and ^{13}C′ nuclei of the peptide plane in proteins. The dipole–dipole/CSA relaxation interference effects on the zero- and double-quantum coherences formed between the ^{15}N and ^{13}C′ spins are manifested as differential relaxation in the two components of the ^{15}N–$^1H^N$ doublet. The measured relaxation rate constants include both

local and remote cross-correlation effects. There is a distinct dependence of the local and remote cross-correlation effects on internal anisotropic reorientational fluctuations of the peptide plane, providing the possibility of using such information to obtain a better understanding of local motions within a protein backbone.

5.3 CSA/CSA Cross-Correlation Measurements

Although the measurement of CSA/CSA cross-correlation effects has not yet attracted as much attention as DD/DD or DD/CSA cross-correlation measurements, the CSA/CSA-based experiments complement the other methods and can also provide valuable information for characterizing motional anisotropy within biomolecules. Vold and Vold[12] anticipated the possibility of observing CSA/CSA relaxation interference effects, which other groups subsequently have verified and elaborated upon.[8,11] In terms of applications to biomolecules, Pellecchia and coworkers[41] have demonstrated the potential usefulness of measuring the cross-correlation effects between the CSAs of the backbone amide ^{15}N and carbonyl $^{13}C'$ nuclei in proteins. Their measurement scheme is based upon the differential relaxation of double- and zero-quantum coherences formed between the backbone ^{15}N and carbonyl $^{13}C'$ spins. As it turns out, their experiment also permits the measurement of the cross-correlation between $^{1}H^{N}$–^{15}N and $^{1}H^{N}$–$^{13}C'$ dipole–dipole interactions. The ^{15}N CSA tensor is, to a good approximation, axially symmetric, which simplifies the theoretical treatment. However, the $^{13}C'$ tensor is not axially symmetric. However, it is possible to decompose the $^{13}C'$ CSA tensor into two orthogonal axially symmetric tensors and separately consider the contributions of each.[11] Interpretation of CSA/CSA cross-correlated relaxation effects is challenging since observed variations, as reported by Pellecchia et al., can depend on local internal anisotropic motion and variations of tensor parameters and of angles between tensors. However, even though much work is still required in developing a robust procedure for interpreting CSA/CSA relaxation interference effects in biomolecules, such measurements will clearly be useful in characterizing internal motional anisotropies such as that for individual peptide planes. Such studies will be greatly facilitated by developments in the understanding of structural and motional effects on CSA tensor parameters.

6 CROSS-CORRELATION EFFECTS IN PARAMAGNETIC SYSTEMS

The presence of cross-correlation effects in paramagnetic systems has been exploited for a number of useful purposes.[8] The dipolar interaction between a nucleus and the static electron magnetic moment results in the so-called Curie spin relaxation (CSR). A theoretical analysis demonstrates that, for example, the cross-correlation between the ^{1}H-Curie spin and ^{1}H–^{15}N dipolar interactions is formally identical to ^{1}H–^{15}N dipolar/^{1}H CSA cross-correlated relaxation. Boisbouvier and coworkers[50] have demonstrated that the measurement of ^{1}H–^{15}N dipole–dipole/^{1}H CSR cross-correlated relaxation rate constants can provide valuable, long-range structural constraints in NMR studies of paramagnetic molecules, due to the dependence of the rate constant on the distance between the amide proton and the electron spin and on the angle defined by the triangle ^{15}N–^{1}H–S (S is the electron spin). Madhu and coworkers[51] demonstrated that in addition to providing geometric constraints for structure refinement, the presence of cross-correlated relaxation involving the Curie spin relaxation and inter-nuclear dipolar relaxation mechanisms can also permit TROSY-type schemes to be used to obtain sensitivity and/or resolution enhancements. In this case, the enhancements can occur for any of the four components of a 2D ^{1}H–^{15}N multiplet, in contrast to the case for diamagnetic proteins and dipole–dipole/CSA cross-correlations.[8,51] Another important consequence of cross-correlation effects in paramagnetic systems is the possibility of observing 'relaxation-allowed' coherence transfer between two nuclei.[8,52]

7 CHARACTERIZATION OF HYDROGEN BOND LENGTHS

Hydrogen bond formation is an essential mechanism for the stabilization of biomolecular structures, and thus the development of experimental methods capable of directly detecting the presence of hydrogen bonds is quite valuable. Riek[53] has demonstrated that hydrogen bond lengths can be characterized by the measurement of DD/CSA cross-correlated relaxation involving the ^{1}H CSA and the dipole–dipole couplings of the ^{1}H to its hydrogen bond acceptor ^{15}N and to its hydrogen bond donor ^{15}N. The ratio of these two cross-correlation rate constants is dependent on the hydrogen bond length and on the generalized order parameter of the dipole–dipole ^{1}H–^{15}N vectors. Although the distance and motional contributions cannot be distinguished in this experiment, qualitative information is obtained concerning the characteristics of the hydrogen bond.

8 RELAXATION-INDUCED VIOLATIONS OF COHERENCE TRANSFER SELECTION RULES IN MULTIPLE QUANTUM NMR SPECTROSCOPY

Homonuclear multiple quantum and multiple quantum-filtered spectroscopy can be quite useful for resonance assignment in NMR studies of biomolecules.[54,55] The interpretation of multiple quantum and multiple quantum-filtered spectra is greatly assisted by the use of the coherence transfer selection rules given by Braunschweiler and coworkers,[56] which indicate the conditions required for transfer of multiple quantum coherence to observable single quantum transitions. While the predictions made based on these selection rules generally agree very well with experimental results, some anomalous resonances are frequently observed that violate these selection rules. In particular, multiple quantum coherence actively involving two or three methyl protons (attached to the same carbon atom) can be transferred to observable single quantum transitions of the methyl protons, in violation of the aforementioned selection rules. Such 'forbidden' peaks arise due to differential relaxation rates of degenerate single quantum transitions of magnetically equivalent nuclei.[57–59] Müller and coworkers presented a detailed analysis of the dipolar cross-correlation effects that give rise to the multi-exponential transverse relaxation of degenerate transitions. Müller has also proposed several experiments that exploit the presence of relaxation-allowed coherence transfer pathways in systems of degenerate spins.[8]

9 ADDITIONAL CROSS-CORRELATION EFFECTS

Most of the applications of cross-correlation effects in studies of biomolecules have involved the various combinations of dipole–dipole and CSA interactions and, for paramagnetic molecules, Curie spin relaxation. However, other possibilities exist as well, and a few of these are mentioned here.

Brüschweiler and Ernst[23] pointed out that cross-correlated relaxation effects can occur when a motional process simultaneously modulates a chemical shielding and a spin coupling term. For example, cross-correlated relaxation would occur for an I–S spin pair if the chemical shift of one of the spins and the isotropic scalar coupling J_{IS} were both modulated by the same motional process. Another possibility is the cross-correlation of chemical exchange effects involving multiple quantum coherences.[60] The latter effect was hypothesized to be a contributing factor in $^1H^N/^{15}N$ CSA/CSA cross-correlated relaxation measurements in proteins. Cross-correlation effects can be important in the analysis of dynamic frequency shifts.[8] For example, a dynamic frequency shift (see **Dynamic Frequency Shift,** Volume 3) can result from DD/CSA cross-correlated relaxation in a two-spin-1/2 system and is manifested as an additive contribution to the apparent scalar J coupling between the two spins.[61] This cross-correlation-induced J coupling is dependent on the motional properties of the spin system and thus can serve as a unique probe of molecular dynamics.

10 ELIMINATION OF CROSS-CORRELATION EFFECTS

The presence of cross-correlation effects can complicate the measurement of various relaxation rate constants by introducing additional terms into the rate equations that describe relaxation. In such cases it is desirable to devise methods for eliminating specific cross-correlation effects. These methods can be as simple as using non-selective 90° measuring pulses to eliminate multiplet effects in homonuclear spin systems,[8] or more elaborate procedures requiring new elements to be added to the relevant pulse sequences. Among the most common type of experiments in which the elimination of cross-correlation effects is important is the measurement of heteronuclear spin relaxation rate constants. At high magnetic fields, the magnitudes of the ^{1}H–X dipolar and X spin CSA interactions are comparable for X representing the ^{15}N in a peptide group or the aromatic ^{13}C nuclei; consequently, cross-correlation between these two relaxation mechanisms systematically affects relaxation rate constants measured using conventional experimental methods. Boyd and coworkers[62] demonstrated that unwanted dipole–dipole/CSA cross-correlation effects in ^{15}N longitudinal (T_1) relaxation measurements can be eliminated by broadband ^{1}H decoupling during the magnetization recovery period. They also proposed experimental schemes for monitoring the cross-relaxation between S_z and $2I_zS_z$ operators that results from dipole–dipole/CSA cross-correlation, and suggested that such measurements could provide information on the ^{15}N CSA tensor and on the angle θ between the principal axis of the ^{15}N CSA tensor and the ^{1}H–^{15}N inter-nuclear vector. Analogous means for suppressing dipole–dipole/CSA cross-correlation effects in CPMG experiments have been proposed,[63,64] allowing accurate measurements of spin-spin relaxation rate constants for heteronuclei with significant chemical shift anisotropies.

11 SUMMARY

Rather than being a complicating nuisance, as it was widely perceived to be in the past, cross-correlated relaxation has turned out to be extremely valuable as the basis for many new NMR tools that have been developed for probing the structure and dynamics of biomolecules. The observed effects of cross-correlated relaxation range from subtle to dramatic. The sensitivity and resolution improvements achieved in TROSY- and CRINEPT-type experiments have made it possible to study much larger systems than was previously feasible. New experiments are available for the characterization of CSA tensors, obtaining unique structural constraints, and probing motional processes within biomolecules at an unprecedented level of detail. Although much theoretical and experimental work needs to be done to fully exploit the potential of cross-correlated relaxation phenomena, the rewards are clear and undoubtedly there are many new, valuable discoveries yet to be made in this field.

12 RELATED ARTICLES IN THIS VOLUME

Chemical Exchange Effects in Biological Macromolecules; Transverse Relaxation-optimized NMR Spectroscopy with Biomacromolecular Structures in Solution.

13 RELATED ARTICLES IN VOLUMES 1–8

Dynamic Frequency Shift, Volume 3; Protein Dynamics from NMR Relaxation, Volume 6; Relaxation: An Introduction, Volume 6; Relaxation of Transverse Magnetization for Coupled Spins, Volume 6; Relaxation Processes: Cross Correlation & Interference Terms, Volume 6; Relaxation Processes in Coupled-Spin Systems, Volume 6; Relaxation Theory: Density Matrix Formulation, Volume 6.

14 REFERENCES

1. H. M. McConnell, *J. Chem. Phys.*, 1956, **25**, 709.
2. S. Hubbard, *Phys. Rev.*, 1958, **111**, 1746.
3. P. S. Hubbard, *Phys. Rev.*, 1958, **109**, 1153.
4. R. Brüschweiler, Structural Dynamics in Biomolecules Monitored by Nuclear Magnetic Resonance Relaxation, Ph.D. Diss. No. 9466, ETH Zürich, Zürich, 1991.
5. A. D. Bain and R. M. Lynden-Bell, *Mol. Phys.*, 1975, **30**, 325.
6. L. G. Werbelow and D. R. Grant, *Adv. Magn. Reson.*, 1977, **9**, 189.
7. D. M. Grant, C. L. Mayne, F. Liu, and T.-X. Xiang, *Chem. Rev.*, 1991, **91**, 1591.
8. A. Kumar, R. C. R. Grace, and P. K. Madhu, *Prog. NMR Spectrosc.*, 2000, **37**, 191.
9. B. Brutscher, *Concepts Magn. Reson.*, 2000, **12**, 207.
10. V. A. Daragan and K. H. Mayo, *Prog. NMR Spectrosc.*, 1997, **31**, 63.
11. M. W. F. Fischer, A. Majumdar, and E. R. P. Zuiderweg, *Prog. NMR Spectrosc.*, 1998, **33**, 207.

12. R. L. Vold and R. R. Vold, *Prog. NMR Spectrosc.*, 1978, **12**, 79.
13. L. G. Werbelow, in 'Nuclear Magnetic Resonance Probes of Molecular Dynamics', ed R. Tycko, Kluwer: Amsterdam, 1994, p. 223–263.
14. M. Goldman, *J. Magn. Reson.*, 1984, **60**, 437.
15. J. Cavanagh, W. J. Fairbrother, A. G. Palmer, and N. J. Skelton, 'Protein NMR Spectroscopy. Principles and Practice', Academic Press, 1996.
16. M. H. Levitt, 'Spin Dynamics. Basics of Nuclear Magnetic Resonance', Wiley, 2001.
17. B. Reif, A. Diener, M. Hennig, M. Maurer, and C. Griesinger, *J. Magn. Reson.*, 2000, **143**, 45.
18. T. Carlomagno and C. Griesinger, *J. Magn. Reson.*, 2000, **144**, 280.
19. R. H. Griffey and A. G. Redfield, *Q. Rev. Biophys.*, 1987, **19**, 51.
20. K. Pervushin, R. Riek, G. Wider, and K. Wüthrich, *Proc. Natl. Acad. Sci. USA*, 1997, **94**, 12 366.
21. K. V. Pervushin, G. Wider, R. Riek, and K. Wüthrich, *Proc. Natl. Acad. Sci. USA*, 1999, **96**, 9607.
22. C. Dalvit, *J. Magn. Reson.*, 1992, **97**, 645.
23. R. Brüschweiler and R. R. Ernst, *J. Chem. Phys.*, 1992, **96**, 1758.
24. R. Riek, G. Wider, K. Pervushin, and K. Wüthrich, *Proc. Natl. Acad. Sci. USA*, 1999, **96**, 4918.
25. R. Riek, K. Pervushin, and K. Wüthrich, *Trends Biochem. Sci.*, 2000, **25**, 462.
26. D. Sitkoff and D. A. Case, *Prog. NMR Spectrosc.*, 1998, **32**, 165.
27. C. D. Kroenke, M. Rance, and A. G. Palmer, *J. Am. Chem. Soc.*, 1999, **121**, 10 119.
28. D. Fushman, N. Tjandra, and D. Cowburn, *J. Am. Chem. Soc.*, 1998, **120**, 10 947.
29. Y. Pang and E. R. P. Zuiderweg, *J. Am. Chem. Soc.*, 2000, **122**, 4841.
30. P. Kumar and A. Kumar, *J. Magn. Reson., Ser. A*, 1996, **119**, 29.
31. B. Reif, M. Hennig, and C. Griesinger, *Science*, 1997, **276**, 1230.
32. K. Kloiber and R. Konrat, *J. Am. Chem. Soc.*, 2000, **122**, 12 033.
33. N. R. Skrynnikov, R. Konrat, D. R. Muhandiram, and L. E. Kay, *J. Am. Chem. Soc.*, 2000, **122**, 7059.
34. R. Sprangers, M. J. Bottomley, J. P. Linge, J. Schultz, M. Nilges, and M. Sattler, *J. Biomol. NMR*, 2000, **16**, 47.
35. C. Scheurer, N. R. Skrynnikov, S. F. Lienin, S. K. Straus, R. Brüschweiler, and R. R. Ernst, *J. Am. Chem. Soc.*, 1999, **121**, 4242.
36. M. Ernst and R. R. Ernst, *J. Magn. Reson. A*, 1994, **110**, 202.
37. R. Brüschweiler, C. Griesinger, and R. R. Ernst, *J. Am. Chem. Soc.*, 1989, **111**, 8034.
38. D. Yang, A. Mittermaier, Y.-K. Mok, and L. E. Kay, *J. Mol. Biol.*, 1998, **276**, 939.
39. D. Yang, Y.-K. Mok, D. R. Muhandiram, J. D. Forman-Kay, and L. E. Kay, *J. Am. Chem. Soc.*, 1999, **121**, 3555.
40. T. Carlomagno, M. Maurer, M. Hennig, and C. Griesinger, *J. Am. Chem. Soc.*, 2000, **122**, 5105.
41. M. Pellecchia, Y. Pang, L. Wang, A. V. Kurochkin, A. Kumar, and E. R. P. Zuiderweg, *J. Am. Chem. Soc.*, 1999, **121**, 9165.
42. N. Tjandra, A. Szabo, and A. Bax, *J. Am. Chem. Soc.*, 1996, **118**, 6986.
43. C. D. Kroenke, J. P. Loria, L. K. Lee, M. Rance, and A. G. Palmer, *J. Am. Chem. Soc.*, 1998, **120**, 7905.
44. I. C. Felli, H. Desvaux, and G. Bodenhausen, *J. Biomol. NMR*, 1998, **12**, 509.
45. L. Wang, A. V. Kurochkin, and E. R. P. Zuiderweg, *J. Magn. Reson.*, 2000, **144**, 175.
46. M. W. F. Fischer, L. Zeng, Y. Pang, W. Hu, A. Majumdar, and E. R. P. Zuiderweg, *J. Am. Chem. Soc.*, 1997, **119**, 12 629.
47. T. Bremi and R. Brüschweiler, *J. Am. Chem. Soc.*, 1997, **119**, 6672.
48. Y. Pang, L. Wang, M. Pellecchia, A. V. Kurochkin, and E. R. P. Zuiderweg, *J. Biomol. NMR*, 1999, **14**, 297.
49. B. Brutscher, N. R. Skrynnikov, T. Bremi, R. Brüschweiler, and R. R. Ernst, *J. Magn. Reson.*, 1998, **130**, 346.
50. J. Boisbouvier, P. Gans, M. Blackledge, B. Brutscher, and D. Marion, *J. Am. Chem. Soc.*, 1999, **121**, 7700.
51. P. K. Madhu, R. Grandori, K. Hohenthanner, P. K. Mandal, and N. Müller, *J. Biomol. NMR*, 2001, **20**, 31.
52. H. Desvaux and M. Gochin, *Mol. Phys.*, 1999, **96**, 1317.
53. R. Riek, *J. Magn. Reson.*, 2001, **149**, 149.
54. M. Rance, W. J. Chazin, C. Dalvit, and P. E. Wright, *Methods Enzymol.*, 1989, **176**, 114.
55. T. J. Norwood, *Prog. NMR Spectrosc.*, 1992, **24**, 295.
56. L. Braunschweiler, G. Bodenhausen, and R. R. Ernst, *Mol. Phys.*, 1983, **48**, 535.
57. M. Rance and P. E. Wright, *Chem. Phys. Lett.*, 1986, **124**, 572.
58. N. Müller, G. Bodenhausen, and R. R. Ernst, *J. Magn. Reson.*, 1987, **75**, 297.
59. L. E. Kay, T. A. Holak, and J. H. Prestegard, *J. Magn. Reson.*, 1988, **76**, 30.
60. M. Tessari and G. W. Vuister, *J. Biomol. NMR*, 2000, **16**, 171.
61. R. Brüschweiler, *Chem. Phys. Lett.*, 1996, **257**, 119.
62. J. Boyd, U. Hommel, and I. D. Campbell, *Chem. Phys. Lett.*, 1990, **175**, 477.
63. A. G. Palmer, N. J. Skelton, W. J. Chazin, P. E. Wright, and M. Rance, *Mol. Phys.*, 1992, **75**, 699.
64. L. E. Kay, L. K. Nicholson, F. Delaglio, A. Bax, and D. A. Torchia, *J. Magn. Reson.*, 1992, **97**, 359.

Acknowledgements

This work was supported by funding from the National Institutes of Health (GM40089).

Biographical Sketch

Mark Rance, *b* 1953. B.Sc. physics, 1976, University of Waterloo, Canada; Ph.D. physics, 1981, University of Guelph, Canada. Research associate, National Research Council of Canada, 1981–82. Postdoctoral fellow, ETH Zürich, Switzerland with Profs. Ernst and Wüthrich, 1982–84. Scripps Research Institute, La Jolla, California, 1984–95. Associate professor, University of Cincinnati, 1996–present. Principal research interests: NMR methodology development, biomolecular structure and dynamics.

Selective Relaxation Techniques in Biological NMR

Claudio Rossi
University of Siena, Siena, Italy

1	Introduction	1
2	Selective Pulse Excitation	1
3	The Dipolar Relaxation Mechanism	1
4	General Remarks on Selective Relaxation Experiments	3
5	Application of Selective Relaxation Techniques in Biological Systems	4
6	Related Articles	8
7	References	9

1 INTRODUCTION

Interest in selective relaxation experiments was aroused when it emerged that it was possible to interpret experimental selective relaxation parameters in terms of different relaxation contributions. Considering the dipole–dipole interaction between $I = \frac{1}{2}$ nuclei as the dominant relaxation contribution of biomolecules in solution, selective relaxation experiments can be used to calculate both selective 'cross-relaxation' rates σ_{ij} and individual, direct self-relaxation rates ρ_i. The observation of specific dipolar connectivities can provide useful information on several aspects of the chemical behavior of biomolecules, especially molecular structures and organization, solution dynamics, and biomolecular interactions.

2 SELECTIVE PULSE EXCITATION

Any selective relaxation experiment is performed with a specific pulse sequence which contains at least one selective excitation period. An ideal selective pulse should have the following features:[1,2]

1. good frequency selectivity (i.e. uniform excitation of a limited spectral region);
2. short duration (to avoid effects such as relaxation, chemical shift, and coupling evolution during the pulse);
3. uniform phase behavior of the magnetization.

Several approaches, recently reviewed,[1–3] have been developed, to generate excitation profiles to yield selective perturbation, starting from the pioneering work of Alexander.[4] The pulse sequences proposed for selective excitation can be regarded as belonging to the following categories:

1. rectangular sequence;
2. DANTE sequence;
3. shaped sequence.

2.1 Rectangular Sequences

Rectangular sequences are single, soft pulses obtained like an ordinary hard pulse but with low-amplitude power of the radiofrequency field and a long pulse duration. Two main disadvantages are the low-frequency selectivity and the long excitation time.[5]

2.2 DANTE Sequence[6,7]

The DANTE sequence is an ingenious system for selective excitation using high-power pulses. It consists of a sequence of 10–100 short, high-power pulses with a pulse angle $\phi < \pi/2$ and a repetition frequency $1/\tau$. The effect generated on a magnetic moment vector is similar to that of a soft rectangular pulse with a larger selectivity that improves as the number of pulses in the pulse train is increased. With respect to the soft rectangular pulse, the DANTE sequence generates a set of excitation bands at a frequency n/τ (where n is an integer 1, 2, 3, etc.) symmetrical with the transmitter frequency ω_o.

Important improvements to the original DANTE sequence have increased the frequency selectivity (reducing the effect of side lobes of the excitation function) by pulse-shaping with DANTE[8] and have enabled selective simultaneous excitation of two frequencies by double-DANTE sequences.[9]

2.3 Shaped Pulses

Selective relaxation experiments require the generation of sharp selective pulses that cannot be obtained from soft rectangular pulses. An almost ideal excitation profile requires smoothing of the side lobes in the frequency domain. This is now achieved by appropriate pulse-shaping procedures, which usually require a pulse-shaping spectrometer device.

Gaussian pulse shaping was one of the first shaping functions to be used.[5,10,11] Now a number of different shaping functions are available to generate selective soft pulses for any multidimensional relaxation experiment. Tables 1 and 2 (from Kessler et al.)[1] show the main characteristics of the different soft excitation pulses and their 'recommended' applications.

3 THE DIPOLAR RELAXATION MECHANISM

In solution the exchange of magnetic energy between excited nuclei and the lattice occurs mainly through dipole–dipole interactions between $I = \frac{1}{2}$ nuclei. The efficiency of energy diffusion from 'hot' nuclei (excited) to the 'cold' lattice is a function of internuclear distances between spin-$\frac{1}{2}$ nuclei and the modulation of these internuclear vectors by dynamic processes, typical of molecules in solution. The time evolution of the z component magnetization of two spins I and S in a dipolar interaction has the form[12,13]

$$\frac{d\langle I_z\rangle}{dt} = -\rho_I(\langle I_z\rangle - I_o) - \sigma_{IS}(\langle S_z\rangle - S_0) \quad (1)$$

$$\frac{d\langle S_z\rangle}{dt} = -\rho_S(\langle S_z\rangle - S_o) - \sigma_{SI}(\langle I_z\rangle - I_0) \quad (2)$$

where $\langle I_z\rangle$ and $\langle S_z\rangle$, and S_0 and I_0 are the z components and the equilibrium values of magnetization of spins I and S, ρ_I

Table 1 Characteristics of the Soft Excitation Forms

Form of soft excitation	Special hardware requirements[a]	Excitation function (frequency domain)		Offset-dependent phase gradient	Selectivity[b]	Side lobes	Comments
		Absorptive component	Dispersive component				
Hermite	Pulse-shaping device	Gaussian	Yes	Large, linear	Similar	No	
Rectangular	None	flattened top sinc	Yes	Large, linear	Worse	Yes	
DANTE[c]	None	sinc	Yes	Large, linear	Worse	Yes	Main band and sidebands
90° Gaussian	Pulse-shaping device	Gaussian	Yes	Large, linear		No[d]	
Half Gaussian	Pulse-shaping device	Almost Gaussian	Yes	Large, nonlinear	Worse	No	Dispersive component shows low selectivity
Purged half Gaussian	Pulse-shaping device	Almost Gaussian	No	None	Better	No	
$90° - \alpha_{sel}$	None[e]	$sinc^2$ (near resonance)	No	None	Worse Worse	Yes[e] Yes[e]	Low sensitivity to $\boldsymbol{B}_1$ inhomogeneity
270° Gaussian	Pulse-shaping device	Almost Gaussian	Yes	Small, linear[f]	Worse	Yes	Slightly higher[b] sensitivity to $\boldsymbol{B}_1$ inhomogeneity[b]
Pulse shaping by DANTE	None	Any desired function	[g]	[g]	[g]	[g]	Main band and sidebands
Tailored excitation	None None	Any desired function	[g]	[g]	[g]	[g]	[g]

[a]In general pulse shaping by DANTE possible for all of the shaped pulses.
[b]In comparison with the Gaussian.
[c]'Rectangular' without modulation.
[d]After application of phase correction.
[e]Depends on the soft pulse used.
[f]Only in a small area in the center of the excitation band.
[g]Depends on the excitation sequence.

Table 2 Recommended Applications of the Different Soft Excitation Forms

Form of soft excitation	Recommended application	Evolution of J and Ω during the pulse
Hermite	In cases where uniform excitation is needed	Yes
Rectangular	Only for experiments with low demand on selectivity	Yes
DANTE	For simultaneous excitation of two resonances; excitation of an off-resonance signal	Yes
DANTE	by a side band	Yes
90° Gaussian	Pulse sequence that requires antiphase magnetization for mixing	Yes
Half Gaussian	Pulse sequence that requires antiphase magnetization for mixing; purging of dispersive	Negligible at the end
Half Gaussian	component accomplished by mixing sequence[a]	Negligible at the end
Purged half Gaussian	As above, but experiments with need for explicit purging[b]	Negligible at the end
$90° - \alpha_{sel}$	Pulse sequence starting with antiphase magnetization for mixing	Yes
270° Gaussian	As for the purged half Gaussian in cases with no high selectivity requirements	Partially refocused
Pulse shaping by DANTE	[c]	[c]
Tailored	Solvent peak suppression; excitation of arbitrary spectral regions; hole burning	[c]

[a]E.g. TOCSY or by the phase cycling of 90° pulse before the NOESY mixing.
[b]E.g. ROESY.
[c]Depends on the excitation sequence.

and ρ_S the direct self-relaxation rates, and $\sigma_{IS} = \sigma_{SI}$ the 'cross-relaxation' rates. In this case the relaxation process assumes an exponential decay with a rate constant R_1, the spin–lattice relaxation rate:

$$R_1^i = \rho_i + \sigma_{ij} \quad (i = I, S), (j = S, I) \tag{3}$$

For multispin interaction, as occurs in complex systems of biomolecules, the 'nonselective' spin–lattice relaxation rate ${R_1}^{NS}$ of an i nucleus interacting with neighboring j nuclei can be described by a modified version of Equation (3):

$$R_1^{NS} = \sum_{i \neq j} \rho_{ij} + \sum_i \sigma_{ij} + R^* \tag{4}$$

with the approximation of independent pairwise interactions and considering the contribution of nondipolar relaxation processes R^*.

The explicit form of ρ_{ij} and σ_{ij} in the case of intramolecular dipolar interactions are:

$$\rho_{ij} = \frac{1}{10}\frac{\gamma_H^4\hbar^2}{r_{ij}^6}\left(\frac{3\tau_c}{1+\omega_H^2\tau_c^2} + \frac{6\tau_c}{1+4\omega_H^2\tau_c^2} + \tau_c\right) \quad (5)$$

$$\sigma_{ij} = \frac{1}{10}\frac{\gamma_H^4\hbar^2}{r_{ij}^6}\left(\frac{6\tau_c}{1+4\omega_H^2\tau_c^2} - \tau_c\right) \quad (6)$$

where $\hbar$ is the reduced Planck's constant, γ_H and ω_H are the proton magnetogyric ratio and Larmor frequency respectively, r_{ij} the internuclear distance, and τ_c the effective correlation time which modulates the $i-j$ magnetic interaction.

When the excited i nucleus relaxes with j nuclei at their thermal equilibrium, the 'cross-relaxation' term vanishes[14–16] [as the difference between the second terms of equations (1) and (2) becomes zero] and equation (4) becomes:

$$R_{1i}^{SE} = \sum_{i\neq j}\rho_{ij} \quad (7)$$

where R_{1i}^{SE} is the selective spin–lattice relaxation rate.

Selective excitation of two (or more) resonances adds a selective cross-relaxation term to equation (7) and the relaxation process is driven by the biselective spin–lattice relaxation rate[17] R_{1i}^{BS}:

$$R_{1i}^{BS} = \sum_{i\neq j}\rho_{ij} + \sigma_{ij} \quad (8)$$

Proton and ^{13}C nuclei can be regarded as limiting examples of complexity for dipolar relaxation analysis and, in both cases, the possibility of using spin–lattice relaxation rates for conformational investigations is based on the ability to dissect the complex relaxation process of a multispin system.

In principle, internuclear distances can be measured for biomolecules in solution provided that (1) they have a single predominant structure or a limited number of conformers and (2) a single ρ_{ij} or σ_{ij} can be experimentally measured. This can be achieved by selective spin–lattice relaxation techniques and by combining selective relaxation rates and nuclear Overhauser effects (NOEs) as described below.

As shown by equation (4) in nonselective spin–lattice relaxation experiments on proton nuclei, the measured relaxation rate is the sum of many terms related to all the direct and σ_{ij} cross-relaxation contributions. Thus, only limited information on molecular conformation and dynamics can be obtained from nonselective proton relaxation data since several different internuclear distances and correlation times determine the experiment rate. No structural information can be obtained from the conventional ^{13}C selective relaxation of protonated carbon atoms since the one-bond C–H interaction dominates the relaxation process, and conformational analysis by studying the relaxation of quaternary carbons is complicated by the multiplicity of long-range C–H interactions.[18,19]

The selective excitation of single (or double) protons simplifies the nuclear relaxation pathway and can be performed by a variety of techniques.[1,2,4,20] If the experimental conditions are such that the selective relaxation process of a nucleus involved in dipole–dipole interactions is described by the above equations, simple and reliable methods of calculation of relaxation parameters from selective relaxation measurements can be used, and structural and/or dynamic information can be obtained.

Although selective relaxation parameters can be efficiently used as tools to investigate conformational properties and biomolecular interactions in small and medium-size molecules, cross-relaxation processes may be profoundly altered under the slow motion conditions ($\omega_0\tau_c \gg 1$) typical of large biomacromolecules such as proteins, nucleic acids, and polysaccharides. When these dynamic conditions apply, the rate of transfer of spin energy between nuclei becomes much larger than the rate of transfer of energy to the lattice. The process of propagation of the magnetization in the network of dipolar-coupled spins, known as 'spin diffusion',[21] has the effect of destroying differences in spin–lattice relaxation rates in the molecules so that all tend to the same value.[22–24]

Analyzing the relaxation process on a short timescale, i.e. using the 'initial rate approximation', it has been possible to simplify the interpretation of the results on the basis of a hypothetical two-spin system, but large problems still remain due to the extensive overlapping resonances typical of biomacromolecular spectra.

Some novel one-dimensional (1D)[25–27] and two-dimensional (2D)[28–30] methods have recently eliminated the 'spin diffusion' process by exclusion of selected nuclei from the dipolar-coupled bulk proton network[29,30] or by removing the interference of all protons other than the selected pair.[25–27] In the era of 1D, 2D, three-dimensional, and multidimensional NMR these methods can open up a new age for the application of selective relaxation measurement to study large biomacromolecules.

4 GENERAL REMARKS ON SELECTIVE RELAXATION EXPERIMENTS

In order to perform selective relaxation experiments, the use of pulse sequences able to perturb the nuclear spin population is required. Initial relaxation rates can be obtained provided that the experiment is correctly carried out and that theoretical problems do not quench the dipolar relaxation strategy. As the recovery of the longitudinal component of nuclear magnetization very rarely follows a true exponential decay, it is important to analyze under what circumstances these undesired effects can be avoided. Unfortunately the main effects that alter the exponential behavior of the magnetization are intrinsic, as they arise in coupled spin systems and are due to dipole–dipole 'cross-relaxation' effects and scalar coupling.[31,32]

4.1 Cross-Relaxation Effects

As shown by equations (1) and (2), the recovery of the longitudinal component of the magnetization is usually described by two constant rates ρ and σ, and only under special conditions is this behavior a pure exponential. This is the case

for ^{13}C magnetization measured under conditions of continuous broadband proton decoupling, where proton irradiation sets up and maintains a constant spin population of allowed energy levels such that cross relaxation no longer affects the recovery curve. Similar behavior is expected for selective proton relaxation in cases of weak dipolar coupling or when the effect of cross-relaxation diffusion is truncated using the initial slope approximation. In the latter case the experimental relaxation parameter is calculated by measuring the initial rates in the semi-logarithmic plot of reduced intensity $(I_0 - I_z)/2I_0$ vs. delay times. In more general cases, especially in biological systems, the presence of a network of dipolar-coupled spins induces cross-relaxation contributions that change the pure exponential decay. Nevertheless, at least for small and medium-size biomolecules and for dipolar interactions within a 3.5 distance, the initial rate approximation can be used to interpret the data in terms of two-spin systems and to calculate by numerical simulation the direct self-relaxation rate and the 'cross-relaxation' contributions. A more complex situation occurs when the fast motion conditions $\omega_0{}^2\tau_c{}^2 \ll 1$ do not hold, as in large biomolecules. Under these conditions, due to spin diffusion, the initial slope approximation is no longer valid, especially for long-range interactions, and only recently has it been possible to determine by virtue of synchronous nutation experiments[25–27] the structural properties of proteins from cross-relaxation data obtained by selective relaxation measurements.

4.2 Scalar Coupling

In strongly coupled spin systems, the transition probabilities for the components of a spin multiplet are no longer equal. An important element of symmetry is thus lost, even though the excitation pulse acts equally on all multiplet components. Even for a single two-spin system AB, the zero quantum, single quantum and the double quantum transition probabilities do not assume the classical form,[31–33] but a mixing term W_{AB} appears. It is this last term W_{AB} that causes different recovery curves for the components of a spin multiplet with a specific deviation from pure exponential magnetization decay.

However the perturbative effect of scalar coupling on the behavior of the magnetization recovery curve can be considered a priori. Moreover the 'classical' relaxation equations are still valid when $\Delta\omega/J > 10$, where $\Delta\omega$ is the difference in chemical shift between two spins and J is their scalar coupling constant. This is a general condition met in studying biological systems. Again the synchronous nutation experiment[27] has simplified the problem of correctly calculating the relaxation parameter in the presence of strong scalar coupling, by removing all scalar interactions between spins that are irradiated (active) and at Boltzmann equilibrium (passive). Although the effect of strong scalar coupling between irradiated (active) spins can still affect the recovery curve, its contribution can be taken into account by simple numerical analysis.

5 APPLICATION OF SELECTIVE RELAXATION TECHNIQUES IN BIOLOGICAL SYSTEMS

Many papers have fairly recently been published[25,34–38] proposing the use of selective relaxation experiments to investigate biological systems. For simplicity, proton homonuclear and heteronuclear interactions and their field of application will be treated separately.

5.1 Homonuclear Selective Relaxation Experiments

In ^1H homonuclear spin systems, the nonselective inversion recovery, 180°-τ-90° pulse sequence gives partially relaxed spectra in which it is possible to follow the recovery of the Boltzmann equilibrium for each resonance by individual constant rates (R_1^{NS}) which are the sum of two contributions: the direct and the cross-relaxation terms [as described by equation (4)]. It has been shown by Freeman et al.[14] that cross relaxation may be negligible provided that the 180° pulse selectively excites single-proton resonances. In particular, if the initial relaxation is monitored after selective population inversion of proton i, i.e., short delays are used between the selective and the nonselective observing 90° pulse, the initial recovery rate of the magnetization (R_{1i}^{SE}) is described by equation (7). At longer delay times, cross relaxation becomes significant, as can be observed from the intensity changes of the resonances of protons dipolarly coupled to the excited proton. It follows that selective excitation techniques can be used to achieve a simplification of the proton relaxation process and to calculate the selective dipolar relaxation contribution to the observed spin–lattice relaxation rate.

The initial selective relaxation rate R_{1i}^{SE} is an important parameter which can be used to obtain information on: (1) relaxation mechanisms, (2) molecular dynamics, and (3) molecular conformations.

1. In molecular systems which satisfy the extreme narrowing condition $(\omega_0\tau_c)^2 \ll 1$, for proton i, the ratio between the nonselective relaxation, R_1^{NS}, and R_{1i}^{SE} is diagnostic of the efficiency of the dipole–dipole relaxation mechanism, since this ratio, F_i, is equal to 1.5 for a relaxation pathway completely dominated by the i–j proton dipolar interactions.[39]
2. As shown in Figure 1, F_i also depends on $\omega_0\tau_c$ and, hence, for rigid isotropically reorienting molecules, motions can be quantified from the latter parameter.[39]
3. The combined use of R_{1i}^{SE} and homonuclear Overhauser effects, NOEs, yields an absolute evaluation of σ_{ij} rates since, neglecting cross-polarization effects, the following relationship holds[40]

$$\mathrm{NOE} = \sigma_{ij}/R_i(\mathrm{SE}) \tag{9}$$

where NOE is the Overhauser effect on proton i upon selective excitation of proton j.

The calculation of the cross-relaxation rate relative to a single i–j dipolar interaction is also possible by the simultaneous double excitation of protons i and j. If selectivity in the double excitation can technically be achieved, the relaxation process is driven by the biselective relaxation rate, $R_{1i}{}^{BS}$, as shown by equation (8).

It should be noted that the initial conditions for the evaluation of $R_{1i}{}^{BS}$ are critically important because the peak intensities observed in the partially relaxed spectra are determined by the relaxation process and the time-dependent i–j NOE.[31,41]

Homonuclear selective relaxation experiments are widely used to investigate different properties of biological systems. The most interesting approaches are related to the analysis of:

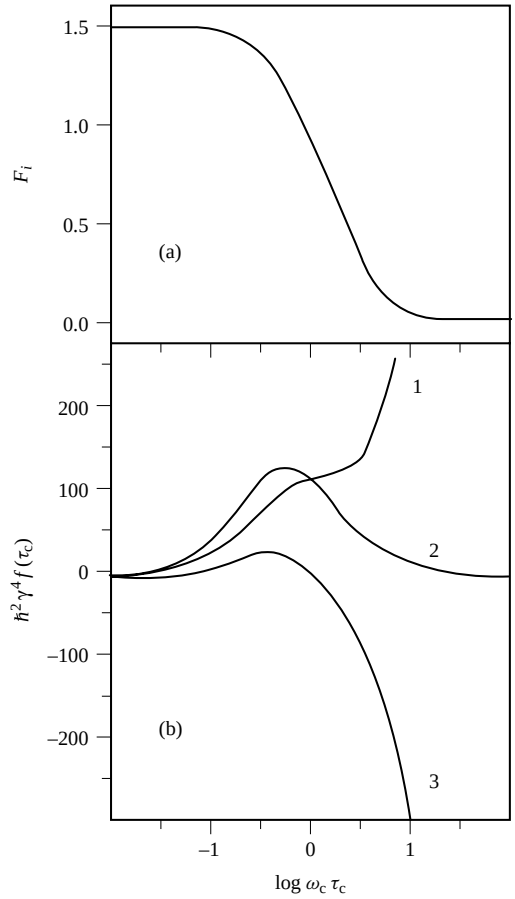

Figure 1 (a) Dependence of $F = R_i(\mathrm{NS})/R_i(i)$ versus log $\omega_0\tau_c$. (b) Behavior of *R*SE/1 (1), *R*NS/1 (2), and σ_{ij} (3) for a two-spin system under different dynamic conditions; (1), (2), and (3) are readily generalized for proton i, involved in multiple interactions with several protons, $i \neq j$. (Reproduced by permission of Academic Press from N. Niccolai et al.[39])

1. conformational and dynamic properties of biomolecules in solution;
2. the interaction process between ligand and biological receptors;
3. the behavior of water in the presence of large, organized biological systems.

5.1.1 Conformational and Dynamic Properties of Biomolecules in Solution

The network of intramolecular dipolar connectivities in small to medium-size biomolecules can be easily evaluated by selective relaxation experiments. The most suitable approach consists first of calculating the cross-relaxation rates between selective proton pairs as the difference between selective and biselective relaxation experiments:

$$\sigma_{ij} = R_{1i}^{\mathrm{BS}} - R_{1i}^{\mathrm{SE}} \tag{10}$$

$$\sigma_{ji} = R_{1j}^{\mathrm{BS}} - R_{1j}^{\mathrm{SE}} \tag{11}$$

in which $\sigma_{ij} = \sigma_{ji}$ are the cross-relaxation values obtained from analysis of the relaxation properties of the i and j nuclei, respectively. Selective homonuclear NOE experiments can also be used to evaluate σ_{ij}. Figure 2 shows an example of proton-selective and biselective experiments used for calculating σ_{ij}. The effect of the additional cross-relaxation contribution to the magnetization recovery process in the biselective experiment, is evident.

As shown by equation (6) and Figure 3, σ_{ij} contains both structural (r_{ij}) and dynamic (τ_c) information.[42] Constant calibration distances are required for the calculation of the effective correlation time τ_c. This is easily achieved by considering independent conformational distances as geminal interactions of CH_2 groups, *ortho* protons of aromatic residues, etc.

As shown in Figure 1, $F_1 = R_{1i}^{\mathrm{NS}}/R_{1i}^{\mathrm{SE}}$ can be used as a probe for molecular motion assuming as dominant the intramolecular dipolar mechanism. Carbon-13 relaxation measurements (see next section) obtained under broad-band proton decoupling can also be used to map the distribution of motions along a biomolecule or to verify isotropic tumbling in systems with restricted internal flexibility. A detailed description of the modulation of the dipole–dipole interaction allows selected interproton distances, from which the solution conformation can be derived, to be calculated with confidence. From the first papers[39,43,44] in which this approach was proposed, nearly every class of biological molecule was investigated: amino acids,[43,45] peptides,[42] carbohydrates,[46] oligosaccharides,[47,48] drugs,[49,50] natural products,[37,51,52] etc.

Recently when the 2D approach for studying dipolar networks seemed to diminish the importance of these selective relaxation studies, a new selective experiment was proposed which enabled large macromolecules such as proteins to be investigated[25] (Figure 4). According to this new approach, one or two proton resonances are simultaneously excited by an amplitude modulated radiofrequency field which forces the magnetization vectors to undergo simultaneous motion defined as 'synchronous nutation'.[25–27] Time-dependent analysis under different initial conditions allows calculation of the direct self-relaxation rate or the 'cross-relaxation' term. In the 'synchronous nutation' experiment, the neighboring spins do not affect the magnetization behavior of the selectively isolated spin system even in the presence of the spin diffusion typical of slow molecular tumbling $\omega_0\tau_c \gg 1$ conditions. Conformational studies (through selected-pair distance determination) by selective relaxation measurements in large biomacromolecules appear to be a valid alternative to the classical approach based on 2D analysis of dipolar-coupled spin systems.

5.1.2 Intermolecular Interaction: Ligand–Macromolecular Receptor

Ligand–macromolecule interactions can be detected by selective relaxation measurements. The formation of intermolecular adducts affects nonselective and selective spin–lattice relaxation rates to different extents, assuming that fast chemical exchange occurs between the bound and free environments with respect to both the chemical shift difference and the proton relaxation rate.[53]

If only two environments are considered, the relaxation parameters are expressed by:

$$R_{1\mathrm{obs}}^{\mathrm{A}} = \chi_{\mathrm{f}} R_{1\mathrm{f}}^{\mathrm{A}} + \chi_{\mathrm{b}} R_{1\mathrm{b}}^{\mathrm{A}} \tag{12}$$

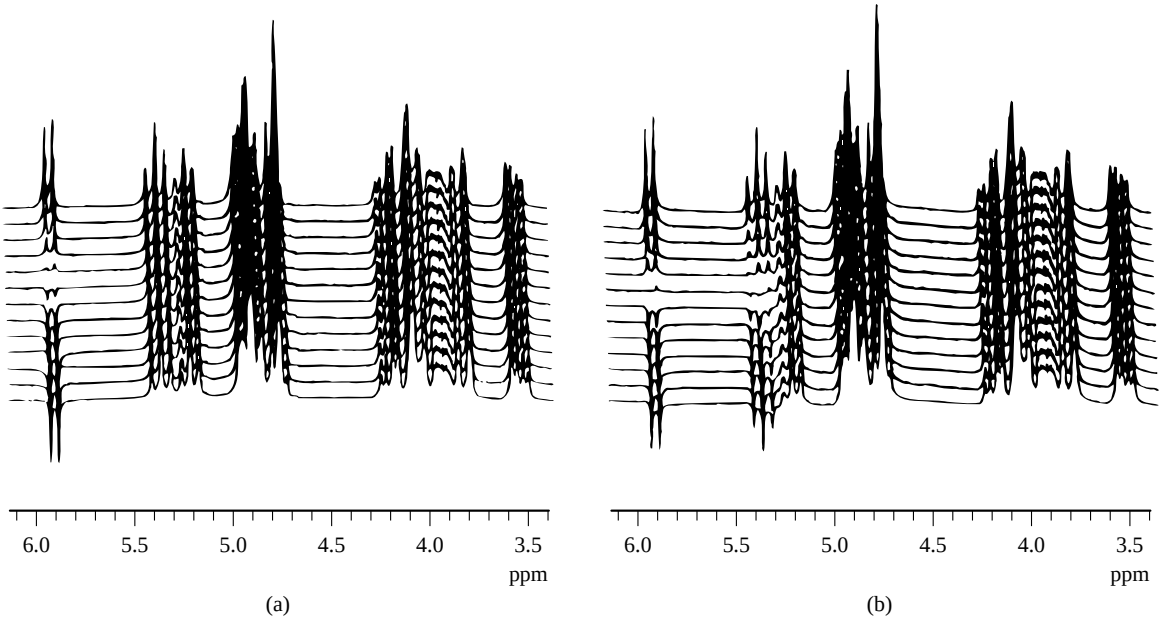

Figure 2 Proton-selective and biselective partially relaxed spectra obtained by selective inversion of the magnetization of H-1′ (a) and of both H-1′–H-3 (b) protons of a 0.15 mol dm^{-3} gentiobiose octaacetate solution in dimethyl sulfoxide-d_6. T = 300 K. The delay values between the selective and nonselective pulses were: 5, 10, 20, 40, 80, 100, 200, 400, 600, 800, 1000, 2000, and 10 000 ms

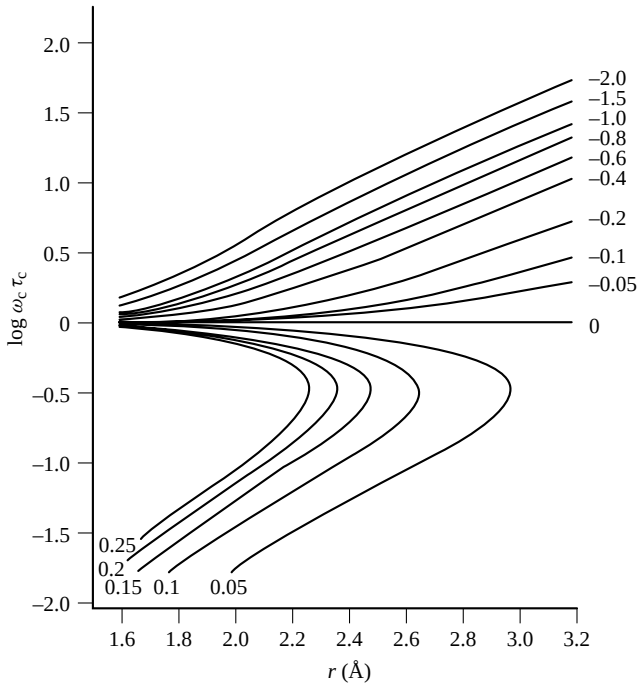

Figure 3 Isosigma contours for log $\omega_0\tau_c$ vs. interproton distances calculated from equation [6]; the selected σ values are expressed in s^{-1}. (Reproduced by permission of Elsevier from N. Niccolai, L. Pogliani, C. Rossi, P. Corti, and W. A. Gibbons, *Biophys. Chem.*, 1984, **20**, 217)

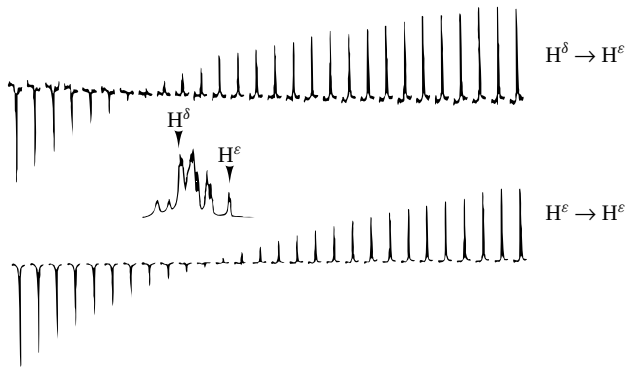

Figure 4 Selective inversion–recovery measurements of the aromatic protons H^δ and H^ε of the tyrosine (Tyr) residue in bovine pancreatic trypsin inhibitor dissolved in ^2H_2O at 327 K. The inset shows the aromatic region (between 8.2 and 5.8 ppm) of the 1D spectrum (eight scans); the arrows indicate the shifts of H^ε at 6.30 ppm and of H^δ at 7.20 ppm. Lower part: normal inversion–recovery measurement of H^ε in Tyr[23] using selective pulses and direct observation of H^ε. Upper part: inversion–recovery of H^δ using selective pulses and Hartmann–Hahn transfer from H^δ to H^ε. (Reproduced by permission of the American Chemical Society from B. Boulat, R. Konrat, I. Burghardt, and G. Bodenhausen, *J. Am. Chem. Soc.*, 1992, **114**, 5412)

where χ_f and χ_b are the ligand fractions in the free and bound environments. Since $\chi_f + \chi_b = 1$ and taking $\chi_b \ll 1$, equation (12) becomes:

$$R_{1\text{obs}}^{\text{A}} = R_{1\text{f}}^{\text{A}} + \chi_{\text{b}} R_{1\text{b}}^{\text{A}} \qquad (13)$$

where A = SE or NS. From equation (13) it emerges that only experimental parameters broadly affected by the ligand–macromolecular interaction make the second term of equation (13) significant. Binding of a ligand to a macromolecular receptor slows down its reorientation motion from $\omega_0\tau_c \ll 1$ to $\omega_0\tau_c \gg 1$. In diamagnetic systems where the dipole–dipole interaction is the dominant relaxation mechanism, entering into the slow-motion region does not significantly alter the nonselective spin–lattice relaxation rates [equation (4)]. On the contrary, the selective relaxation of the bound ligand can be expected to be quite different from that

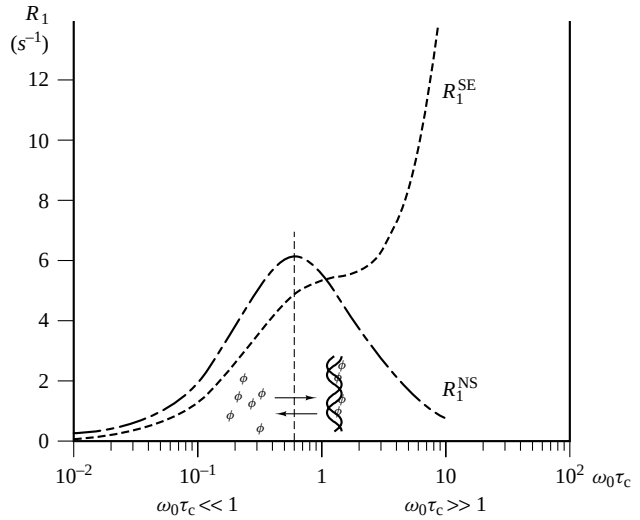

Figure 5 *R*NS/1 and *R*SE/1 of a proton pair versus $\omega_0\tau_c$ assuming a constant r_{i-j} distance (1.77 Å) for the $i-j$ dipolar interaction. The equilibrium between the ligand molecules in the bulk ($\omega_0\tau_c \ll 1$) and DNA-bonded ($\omega_0\tau_c \gg 1$) is also shown. (Reproduced by permission of Elsevier from C. Rossi, A. Donati, and M. R. Sansoni, *Chem. Phys. Lett.*, 1992, **189**, 278)

of the free ligand in solution as shown in Figure 5 for a ligand–DNA interaction.[36]

Since the study of biomolecular interactions by selective relaxation measurement is based on a slowing of ligand molecular motion, the effect of the macromolecular receptor on the viscosity of the system must be considered. Temperature-dependent analysis of R_1^{NS} can address this point. In fact as seen in Figure 5, fast-motion ($\omega_0\tau_c \ll 1$) and slow-motion ($\omega_0\tau_c \gg 1$) conditions show opposite slopes, so hypothetical, drastic changes in viscosity due to the receptor site can be monitored simply by following R_1^{NS} dependence on temperature.[36,54] This method is very powerful since is has a wide range of applications in biological systems. As the information is gained from selective relaxation rates of the ligand, ill-defined receptors in biological samples[55] such as blood whole cells etc. can be investigated and receptor purification followed.

A wide range of ligand–biomacromolecule interactions have been investigated by selective spin–lattice relaxation rate analysis;[56] these include enzyme–substrate,[53] drug–membrane interactions,[57] and recently ligand–DNA,[36] for the purpose of identifying potential mutagens and toxic compounds. This approach can also be used to calculate the association constant for the interaction processes.[58]

5.1.3 Water Selective Relaxation in Large Organized Biological Systems

Water proton relaxation rates have been found to correlate with the physiological and pathological state of the cell as well as to the conformational state of cell constituents.[59–61] Experimental evidence that water selective relaxation is faster than nonselective water relaxation rates in protein solutions and cell suspensions has focused attention on the relaxation mechanism of water protons in large organized systems.[38,62–65] The water spin–lattice relaxation (R_{1W}) may be described as the sum of two contributions:[66]

$$R_{1W} = R_{1A} + R_{1B} \tag{14}$$

where R_{1A} and R_{1B} are the intra- and inter-molecular relaxation rates. The intramolecular term is due to:

$$R_{1B} = R_{1WW} + R_{1WM} \tag{15}$$

R_{1WW} is the dipolar contribution due to intramolecular water–water interactions and R_{1WM} that arising from water–macromolecule (or cell constituent) interactions.[31] The latter interaction can yield direct ρ_{WM} and cross-relaxation σ_{WM} contributions from simultaneous water and macromolecule proton excitation:

$$R_{1WM} = \sum \rho_{WM} + \sum \sigma_{WM} \tag{16}$$

If the water relaxation rate is measured in the selective mode, only a small fraction of the macromolecule protons are excited and the σ_{WM} term disappears. It follows that in the presence of large biological surfaces:[65]

$$R_{1W}^{NS} - R_{1W}^{SE} = \sum \sigma_{WM} \tag{17}$$

where R_{1A} and R_{1WW} are constants in nonselective and selective experiments respectively. Experimental evidence obtained for protein solutions and cell culture suspensions shows that the difference between nonselective and selective relaxation rates [equation (17)] are not only due to the dynamic change in the solvent molecules but also to dipolar intermolecular connectivities between the solvent and the surface of hydrophilic regions of macromolecules. This suggests that it would be useful to use the complete set of relaxation parameters, such as $R_{1W}^{NS}R_{1W}^{SE}$, and σ_{WM} to investigate the physiological and pathological state of cells or to study drug–cell and virus–cell interactions:[67] R_{1W}^{NS} to probe essentially dynamic features of the heterogeneous systems, and R_{1W}^{SE} and σ_{WM} to study the water–macromolecule magnetic energy transfer process, which is intimately linked to the solvent exposed interface structure assumed by the biological material.

5.2 Heteronuclear Selective Relaxation Experiments

Our discussion will be limited to the ^{13}C nucleus, due to its importance for verifying dynamic and structural information on biological systems.

In spite of the low sensitivity of heteronuclei with respect to protons, several advantages exist. Carbon-13 signals are spread over a large chemical shift range (over 300 ppm). The carbon resonances can be treated as single resonances removing proton scalar coupling by a broadband decoupling pulse. Under these conditions the carbon relaxations can be regarded as pure exponential, determined by a single contribution: the direct self-relaxation term. Furthermore, relaxation contributions due to intermolecular interactions are seldom significant (as the carbons are shielded by the proton surface) and, in natural abundance experiments, homonuclear $^{13}C-^{13}C$ dipolar interactions are rare due to ^{13}C isotopic dilution. These properties make carbon relaxation a suitable parameter for investigating solution properties of biomolecules.

5.2.1 ^{13}C Selective Relaxation

In conventional ^{13}C relaxation experiments (obtained by broadband proton decoupling), cross relaxation between carbon nuclei is ignored and the measurement gives the selective, direct carbon spin–lattice relaxation rate:

$$R_{1C}^{SE} = \sum \frac{1}{10} \frac{\hbar^2 \gamma_H^2 \gamma_C^2}{r_i^6} \left[\frac{3\tau_c}{1+\omega_C^2\tau_c^2} + \frac{6\tau_c}{1+(\omega_H+\omega_C)^2\tau_c^2} + \frac{\tau_c}{1+(\omega_H-\omega_C)^2\tau_c^2} \right] \quad (18)$$

R_{1C}^{SE} of protonated carbons are dominated by the dipolar interaction between bonded proton–carbon nuclei.[17,18] In this case the internuclear proton–carbon distance can be assumed to be constant and the effective correlation time calculated. In flexible molecules, a mapping of dynamic properties may be obtained from the R_{1C}^{SE} of different carbons. If continuous broadband proton decoupling is replaced by a selective 180° proton pulse, applied to the i nucleus, with the first 180° carbon pulse the initial rate of the longitudinal magnetization of carbon is:[68–70]

$$R_{1C}^{BS} = R_{1C}^{SE} + \xi\sigma_{CH_i} \quad (19)$$

where R_{1C}^{BS} is the biselective carbon relaxation rate $\xi = \gamma_H/\gamma_C$ and σ_{CH} the single proton–carbon 'cross-relaxation' term. When the selective 180° proton pulse is replaced by a proton perturbation which can invert the spin equilibrium of the entire proton population, the carbon relaxation is described by:[69–71]

$$R_{1C}^{NS} = R_{1C}^{SE} + \xi \sum \sigma_{CH_i} \quad (20)$$

The following dynamic and structural information is obtained by comparing R_{1C}^{SE}, R_{1C}^{BS}, and R_{1C}^{NS} measurements.

5.2.1.1 Dynamic analysis. The R_{1C}^{NS}/R_{1C_i} ratio takes a value in the range 2.99–1, depending on the molecular motion. In this way the value of the R_{1C}^{NS}/R_{1C_i} ratio allows the correlation times for each molecular moiety to be determined (or at least the limit value of τ_c). The R_{1C}^{NS}/R_{1C_i} ratio in particular is a very useful parameter for evaluating the effective correlation time of nonprotonated carbon atoms.

5.2.1.2 Structural analysis. The difference between R_{1C}^{BS} and R_{1C}^{SE} gives the cross relaxation term $\sigma_{C_iH_A}$ for each $^1H-^{13}C$ magnetic interaction which contains distance information. This method has been demonstrated with different natural products, giving reliable results.[69–71]

5.2.2 Selective Proton–Carbon NOEs

Several authors have shown that selective proton–carbon NOEs, $(^1H)^{13}C$-NOE, can be generated.[72–74] When a selective pulse is used to saturate a single proton then 'cross relaxation' between the irradiated proton and the carbon microenvironment occurs. The $(^1H)^{13}C$-NOE is described by:[75,76]

$$(^1H_A)^{13}C_i - \text{NOE} = \frac{\sigma_{C_iH_A}}{R_{1C}^{SE} + R_{1C}^{*}} \quad (21)$$

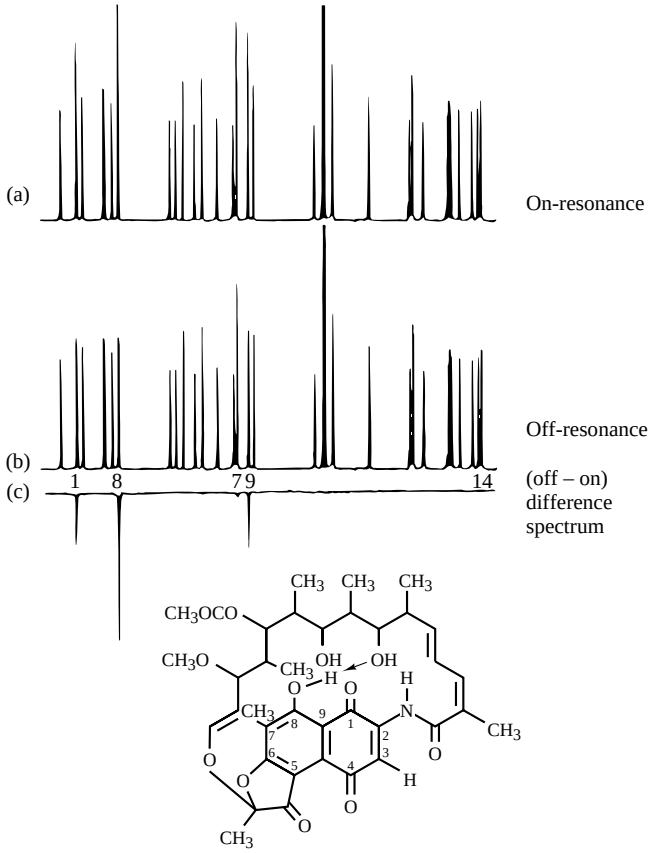

Figure 6 Carbon-13 spectra of 0.5 mol dm^{-3} rifamycin in $CDCl_3$ recorded on a Varian XL-200 spectrometer at 296 K: (a) ^{13}C spectrum after irradiation of the phenolic hydroxyl proton; (b) as (a) but with the decoupler set 'off-resonance'. (c) Difference spectrum (b)–(a). The presaturation selective pulse on the phenolic hydroxyl proton had a 10 s duration and 0.5 W power. During the acquisition of the FIDs the decoupler was on with a power of 4 W in the broadband mode. The structure of rifamycin S is shown. (Reproduced by permission of the American Chemical Society from N. Niccolai et al.[75])

where $\sigma_{C_iH_A}$ is the selective 'cross relaxation', R_{1C}^{SE} the selective carbon relaxation rate, and R_1* the relaxation contribution due to nondipolar interactions [in paramagnetic systems this term often quenches the $(^1H)^{13}C$-NOE]. Thus by combining selective NOEs with carbon relaxation rates, specific distance calculations can be obtained.

Although care must be taken in dealing with large macromolecules when magnetization diffusion occurs between spins, this method has been usefully applied to investigate the conformation of biological molecules such as antibiotics, peptides, natural components,[77–79] etc. Figure 6 illustrates the capacity of $(^1H)^{13}C$ - NOE to discriminate the carbon microenvironment by selective proton perturbation.[75]

6 RELATED ARTICLES

Biological Macromolecules: Structure Determination in Solution; Molecular Motions: T_1 Frequency Dispersion in Biological Systems; Nuclear Overhauser Effect; Relaxation: An Introduction; Relaxation Mechanisms: Magnetization Modes; Selective Pulses.

7 REFERENCES

1. H. Kessler, S. Mronga, and G. Gemmecker, *Magn. Reson. Chem.*, 1991, **29**, 527.
2. R. Freeman, *Chem. Rev.*, 1991, **91**, 1397.
3. E. Gaggelli and G. Valensin, *Concepts Magn. Reson.*, 1992, **4**, 339.
4. S. Alexander, *Rev. Sci. Instrum.*, 1961, **32**, 1066.
5. C. Bauer, R. Freeman, T. Frenkiel, J. Keeler, and A. J. Shaka, *J. Magn. Reson.*, 1984, **58**, 442.
6. G. A. Morris and R. Freeman, *J. Magn. Reson.*, 1978, **29**, 433.
7. G. Bodenhausen, R. Freeman, and G. A. Morris, *J. Magn. Reson.*, 1976, **23**, 171.
8. J. Friedrich, S. Davies, and R. Freeman, *J. Magn. Reson.*, 1987, **75**, 390.
9. H. Geen, X.-L. Wu, P. Xu, J. Friedrich, and R. Freeman, *J. Magn. Reson.*, 1989, **81**, 646.
10. R. J. Sutherland and J. M. S. Hutchinson, *J. Phys. E*, 1978, **11**, 79.
11. J. M. Hutchinson, R. J. Sutherland, and J. R. Mallard, *J. Phys. E*, 1978, **11**, 217.
12. F. Bloch, *Phys. Rev.*, 1957, **105**, 1206.
13. I. Solomon, *Phys. Rev.*, 1955, **99**, 559.
14. R. Freeman, H. D. W. Hill, B. L. Tomlinson, and L. D. Hall, *J. Chem. Phys.*, 1974, **61**, 4466.
15. J. H. Noggle and R. E. Shirmer, *The Nuclear Overhauser Effect; Chemical Applications*, Academic Press, New York, 1971.
16. D. Neuhans and M. P. Williamson, *The Nuclear Overhauser Effect in Structural and Conformational Analysis*, VCH, Berlin, 1989.
17. A. Abragam, *The Principles of Nuclear Magnetism*, Oxford University Press, London, 1961.
18. A. Allerhand, D. Doddrell, and R. Komoroski, *J. Chem. Phys.*, 1971, **55**, 189.
19. L. G. Werbelow and D. M. Grant, *J. Chem. Phys.*, 1975, **63**, 544.
20. C. J. Turner, *Prog. NMR Spectrosc.*, 1984, **16**, 311.
21. A. Kalk and H. J. C. Berendsen, *J. Magn. Reson.*, 1975, **24**, 343.
22. W. Massefski Jr. and A. G. Redfield, *J. Magn. Reson.*, 1988, **78**, 150.
23. V. V. Krishnan, N. Murali, and A. Kumar, *J. Magn. Reson.*, 1989, **84**, 255.
24. V. V. Krishnan, U. Hedge, and A. Kumar, *J. Magn. Reson.*, 1991, **94**, 605.
25. B. Boulat, R. Konrat, I. Burghardt, and G. Bodenhausen, *J. Am. Chem. Soc.*, 1992, **114**, 5412.
26. B. Boulat, I. Burghardt, and G. Bodenhausen, *J. Am. Chem. Soc.*, 1992, **114**, 10 679.
27. I. Burghardt, R. Konrat, B. Boulat, S. J. F. Vincent, and G. Bodenhausen, *J. Chem. Phys.*, 1993, **98**, 1721.
28. J. Fejzo, W. M. Westler, S. Macura, and J. L. Markley, *J. Magn. Reson.*, 1991, **92**, 195.
29. J. Fejzo, W. M. Westler, S. Macura, and J. L. Markley, *J. Magn. Reson.*, 1991, **92**, 20.
30. J. Fejzo, W. M. Westler, S. Macura, and J. L. Markley, *J. Am. Chem. Soc.*, 1992, **114**, 1523.
31. I. D. Campbell and R. Freeman, *J. Magn. Reson.*, 1973, **11**, 143.
32. I. D. Campbell, C. M. Dobson, R. G. Ratcliffe, and R. J. P. Williams, *J. Magn. Reson.*, 1978, **29**, 397.
33. R. L. Vold and R. R. Vold, *Prog. NMR Spectrosc.*, 1978, **12**, 79.
34. N. Niccolai and C. Rossi, *Methods in Enzymol.*, 1989, **176**, 184.
35. N. Marchettini and G. Valensin, *J. Phys. Chem.*, 1990, **94**, 4507.
36. C. Rossi, A. Donati, and M. R. Sansoni, *Chem. Phys. Lett.*, 1992, **189**, 278.
37. M. Sugiura, T. Sai, M. Ichimaru, A. Kato, and N. Takao, *Magn. Reson. Chem.*, 1991, **29**, 755.
38. B. P. Hills, *Mol. Phys.*, 1992, **76**, 489.
39. N. Niccolai, M. P. Miles, and W. A. Gibbons, *Biochem. Biophys. Res. Commun.*, 1979, **91**, 157.
40. C. R. Jones, C. T. Sikakana, S. Hehir, M.-C. Kuo, and W. A. Gibbons, *Biophys. J.*, 1978, **24**, 815.
41. C. Rossi and N. Niccolai, *Chem. Phys. Lett.*, 1989, **156**, 438.
42. N. Niccolai, L. Pogliani, C. Rossi, P. Corti, and W. A. Gibbons, *Biophys. Chem.*, 1984, **20**, 217.
43. N. Niccolai, M. P. de Leon de Miles, S. P. Hehir, and W. A. Gibbons, *J. Am. Chem. Soc.*, 1978, **100**, 6528.
44. N. Niccolai, A. K. Schnoes, and W. A. Gibbons, *J. Am. Chem. Soc.*, 1980, **102**, 1513.
45. C. Rossi, L. Pogliani, F. Laschi, and N. Niccolai, *J. Chem. Soc., Faraday Trans. 1*, 1983, **79**, 2955.
46. T. R. Brown and S. Ogawa, *Proc. Natl. Acad. Sci. U.S.A.*, 1977, **74**, 3627.
47. C. Rossi, L. Pogliani, S. Masi, C. Ceccarini, and N. Niccolai, *J. Biomol. Struct. Dyn.*, 1984, **2**, 481.
48. C. Rossi, S. Ulgiati, and N. Marchettini, *J. Chem. Soc., Faraday Trans. 1*, 1989, **85**, 2149.
49. T. Sai, N. Takao, and M. Sugiura, *Magn. Reson. Chem.*, 1992, **30**, 1041.
50. E. Gaggelli, N. Gaggelli, G. Valensin, and A. Vivi, *Can. J. Chem.*, 1993, **71**, 738.
51. W. Chen, X.-H. Zhu, M. J. Avison, and R. G. Shulman, *Biochemistry*, 1993, **32**, 9417.
52. C. Anselmi, M. Centini, M. Scotton, and A. Sega, *Magn. Reson. Chem.*, 1992, **30**, 994.
53. G. Valensin, T. Kushnir, and G. Navon, *J. Magn. Reson.*, 1982, **46**, 23.
54. C. Rossi, M. R. Sansoni, and A. Donati, *Trends Ecol. Phys. Chem.*, 1993, **57**.
55. I. Barni-Comparini, E. Gaggelli, N. Marchettini, and G. Valensin, *Biophys. J.*, 1985, **48**, 247.
56. G. Uccello-Barretta, C. Bertucci, E. Domenici, and P. Salvadori, *J. Am. Chem. Soc.*, 1991, **113**, 7017.
57. G. Valensin, A. Casini, A. Lepri, and E. Gaggelli, *Biophys. Chem.*, 1983, **17**, 297.
58. E. Gaggelli, G. Valensin, T. Kushnir, and G. Navon, *Magn. Reson. Chem.*, 1992, **30**, 461.
59. D. E. Woessner, *Mol. Phys.*, 1977, **34**, 899.
60. R. Damadian, *Science*, 1971, **171**, 1151.
61. P. T. Beall, C. F. Hazlewood, and P. N. Rao, *Science*, 1976, **192**, 904.
62. D. C. Chang and D. E. Waessner, *Science*, 1978, **198**, 1180.
63. G. Valensin and N. Niccolai, *Chem. Phys. Lett.*, 1981, **79**, 47.
64. N. Niccolai, C. Rossi, and E. Tiezzi, *Chem. Phys. Lett.*, 1983, **96**, 154.
65. N. Niccolai, L. Pogliani, and C. Rossi, *Chem. Phys. Lett.*, 1984, **110**, 294.
66. J. A. Glasel, *Water. A Comprehensive Treatise*, ed. F. Franks, Plenum Press, New York, 1975, Vol. 1, p. 215.
67. G. Valensin, E. Gaggelli, E. Tiezzi, P. F. Valensin, and M. L. Bianchi-Bandinelli, *Biophys. Chem.*, 1979, **10**, 143.
68. I. D. Campbell and R. Freeman, *J. Chem. Phys.*, 1973, **58**, 2666.
69. C. Rossi, *J. Chem. Phys.*, 1986, **84**, 6581.
70. K. E. Kövér and G. Batta, *Prog. NMR Spectrosc.*, 1987, **19**, 223.
71. C. Rossi, N. Marchettini, L. Pogliani, F. Laschi, and N. Niccolai, *Chem. Phys. Lett.*, 1987, **136**, 506.

72. K. F. Kuhlmann, D. M. Grant, and R. K. Harris, *J. Chem. Phys.*, 1970, **52**, 3439.
73. S. Takeuchi, J. Uzawa, H. Seto, and H. Yonehara, *Tetrahedron Lett.*, 1977, 2943.
74. J. J. Ford, W. A. Gibbons, and N. Niccolai, *J. Magn. Reson.*, 1982, **47**, 522.
75. N. Niccolai, C. Rossi, V. Brizzi, and W. A. Gibbons, *J. Am. Chem. Soc.*, 1984, **106**, 5732.
76. N. Niccolai, C. Rossi, P. Mascagni, W. A. Gibbons, and V. Brizzi, *J. Chem. Soc., Perkin Trans. 1*, 1985, 239.
77. M. F. Aldersley, F. M. Dean, and B. E. Mann, *J. Chem. Soc., Chem. Commun.*, 1983, 107.
78. N. Niccolai, C. Rossi, P. Mascagni, P. Neri, and W. A. Gibbons, *Biochem. Biophys. Res. Commun.*, 1984, **124**, 739.
79. C. Rossi, N. Niccolai, and F. Laschi, *J. Phys. Chem.*, 1987, **91**, 3903.

Biographical Sketch

Claudio Rossi. *b* 1952. Ph.D., University of Siena, Italy (Supervisor Professor Enzo Tiezzi, 1977). Postdoctoral work at the Biochemistry Department, University of Wisconsin, Madison (Prof. William A. Gibbons), 1981, and at the Pharmaceutical Chemistry Department, University of California at San Francisco (Prof. Thomas L. James), 1985–86. Successively research associate and associate professor at the University of Siena, 1987–93. Currently full Professor of Physical Chemistry, Department of Chemistry, University of Siena, 1994–present. Approx. 100 publications. Research specialities: ^{1}H and ^{13}C selective relaxation experiments and their applications to biological systems.

Slow and Ultraslow Motions in Biology

Gerd Kothe and Nicholas Heaton

Universität Stuttgart, Stuttgart, Germany

1 Introduction 1
2 Observation of Slow Motions: Pulse-Frequency-Dependent Spin Relaxation 2
3 Characterization of Slow Motions: Transverse Spin Relaxation in Biological Membranes 3
4 Evaluation of Viscoelastic Properties: Collective Orientational Fluctuations 7
5 Related Articles 8
6 References 8

1 INTRODUCTION

Many of the biologically relevant dynamic processes that take place in naturally occurring materials may be considered to be slow on the NMR timescale. This implies that the characteristic frequencies of the motions are comparable to or lower than the width of the NMR spectra that would be obtained in the absence of any molecular motion. Since virtually all nuclei commonly employed for NMR studies of biological systems yield rigid lattice spectra less than 1 MHz wide, a slow process may be defined for present purposes as one whose correlation times τ_C are longer than $(2\pi \times 10^6)^{-1}$ s. This article describes how NMR can be used to investigate such motions, with particular reference to biological studies.

There exists a wide range of NMR techniques available for probing low-frequency molecular dynamics. The methods themselves are by no means applicable only to biological systems, and indeed many of them were originally developed primarily to study synthetic materials. Most of the techniques are discussed in detail in other entries of this Encyclopedia. As far as NMR-observable nuclei are concerned, ^{1}H, ^{13}C, ^{14}N, and ^{31}P, which are, of course, abundant in biologically relevant compounds, can all be used in principle to investigate slow motions. In addition, the use of ^{2}H-labeled materials has now become almost commonplace, and has permitted highly detailed site-specific dynamic NMR studies even in extremely complex systems.

Spin–lattice relaxation rates $1/T_1$ are essentially measures of the amplitudes of motional processes occurring at the Larmor frequency ω_0 of the probe nucleus. Thus, measurement of T_1 as a function of ω_0 provides a means of determining the motional frequency spectrum. For purposes of resolution and sensitivity, commercial spectrometers employ high magnetic fields. In the case of protons, for example, $\omega_0/2\pi$ ranges between 60 and 750 MHz, so that measurement of ^{1}H T_1 on a complete range of standard spectrometers could yield dynamic information over about one order of magnitude on the frequency scale. Field cycling techniques[1,2] enable the determination of T_1 at frequencies lower than the standard high Larmor frequencies and greatly extend the range of the motional frequency spectrum that can be observed. This has particular significance for the study of slow motions in complex systems, where several processes may contribute to the overall spin relaxation mechanism. The application of field cycling for measuring ^{1}H T_1 dispersions has been instrumental in characterizing collective motions in proteins[3] and in phospholipid membranes.[4]

Whereas spin–lattice relaxation is essentially nonadiabatic and reflects exclusively those motions with frequency components at ω_0, transverse spin relaxation is affected in addition by adiabatic dephasing mechanisms due to processes with smaller rate constants, on the order of the rigid lattice linewidth. Transverse relaxation times are most commonly measured using spin echo experiments in which inhomogeneous (i.e., static) contributions to the magnetization dephasing process are refocused. The simplest spin echo experiment consists of a 90° pulse followed by a delay τ, after which a refocusing pulse (180° or 90°) is applied. An echo is formed a period τ after the second pulse, the intensity of which decreases with increasing τ.[5,6] If the dominant motional process is fast in the sense that the correlation time τ_C is shorter than τ then the echoes decay exponentially, and it is possible to extract a single transverse relaxation time T_{2E}. For slower motions, however, for which τ_C is comparable to or longer than τ, the effective relaxation rate itself depends on the value of τ,[7] and the echo decay can no longer be described by a single exponential. In fact, the precise form of the echo decay function depends sensitively on the nature of the underlying motional process.

Although this phenomenon has been understood since the early days of pulsed NMR spectroscopy,[7] its potential applications in the study of slow processes in complex phases such as biological membranes have been recognized only relatively recently.[8] In practice, rather than measure the form of the simple spin echo decay function, multipulse trains such as the Carr–Purcell–Meiboom–Gill (CPMG) sequence[9,10] and its quadrupolar analog[11] are employed. In these experiments, instead of a single refocusing pulse, a series of equally spaced refocusing pulses is applied, resulting in the formation of an echo train. For samples containing a single spin label, the echoes decay monoexponentially with a time constant $T_{2E}^{CP}g$, which depends on the pulse spacing τ. The form of the pulse spacing variation of T_{2E}^{CP} is indicative of the distribution of correlation times for the responsible motional processes, whilst the absolute values of T_{2E}^{CP} reflect their effective amplitudes.[12]

Transverse spin relaxation techniques, employing either ^{2}H or ^{31}P as the probe nuclei, have been applied to study a variety of mechanisms such as collective motions[12–15] and lateral diffusion[8] in biological membranes. An alternative but related approach for observing slow motions involves rotating frame relaxation measurements.[16] The locking-field dependence of $T_{1\rho}$ is analogous to the pulse spacing dependence of T_{2E}^{CP},[17] and has been exploited to characterize low-frequency dynamics in phospholipid membranes.[18,19]

Ultraslow exchange NMR methods directly measure the time variation of the resonance frequency as a result of molecular reorientation.[20] The basic requirement for all experiments of this type can be expressed by the relation $T_1 > \tau_C > T_{2E}$. This approach affords the possibility to study processes with effective correlation times of up to several seconds, depending on T_1 of the resonant nucleus. In the two-dimensional version of the experiment,[21] cross peaks

appear connecting the different frequencies experienced by the spins. In general, the resonance frequency of a particular spin is determined by the orientation Ω of the dominant spin interaction tensor relative to the static magnetic field. Consequently, it is rather straightforward to interpret the exchange spectra in terms of the time variation of Ω.

The choice of experiment to use for investigating a particular system will be dictated by the expected timescale of the motional process of interest and, of course, by the materials available. In the case of ultraslow motions, one of the exchange type of experiments would be most suitable, although the condition $\tau_C > T_{2E}$ is rarely fulfilled in biological systems. For complex collective and/or low-amplitude processes, one of the spin relaxation techniques (T_1, T_{2E}^{CP}, or $T_{1\rho}$) would be most appropriate. The field cycling ^{1}H T_1 approach undoubtedly offers the greatest dynamic range—typically six orders of magnitude in frequency. This is especially useful when dealing with collective motions with broad distributions of correlation times. The method is limited at low frequencies, however, by internal field effects, which render ambiguous the interpretation of any cutoffs that may appear in the T_1 dispersion profiles. The same restrictions apply to $T_{1\rho}$ measurements but not to T_{2E}^{CP} studies. This, together with the simplicity of the experimental techniques, makes pulse-frequency-dependent T_{2E}^{CP} experiments particularly attractive for characterizing slow motions in biological systems. In the following sections, frequency-dependent transverse relaxation is described in more detail, with particular reference to its application in the study of slow motions in biological membranes.

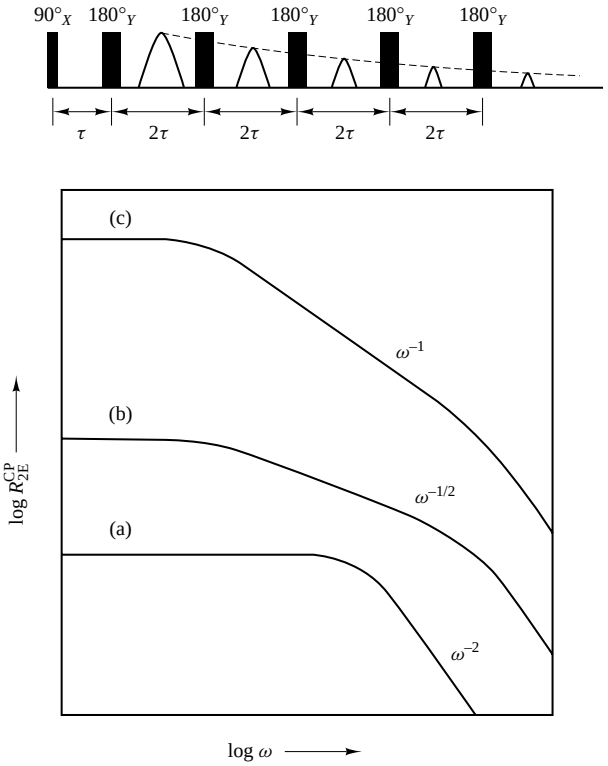

Figure 1 Top: Schematic of CPMG pulse sequence, showing echo decay. Bottom: Dependence of transverse relaxation rate RCP/2E on pulse frequency $\omega = 1/\tau$ for (a) a single Markov process, and (b) three-dimensional and (c) two-dimensional collective orientational fluctuations

2 OBSERVATION OF SLOW MOTIONS: PULSE-FREQUENCY-DEPENDENT SPIN RELAXATION

Nuclear spin relaxation times provide information regarding the timescale, symmetry and amplitude of molecular motion. In order to distinguish between different possible mechanisms, it is advisable if not essential to exploit each of these three aspects of the dynamics. A simple and effective method for achieving this in the slow motional regime involves determining the pulse spacing and orientation dependence of transverse spin relaxation times T_{2E}^{CP}.

2.1 Spin Echo Pulse Trains

The CPMG pulse sequence[9,10] and its quadrupolar equivalent[11] measures the decay of successive spin echoes as illustrated schematically in Figure 1 (top). If the motional correlation time τ_C is of the same order of magnitude as the pulse spacing τ then the echo decay rate $R_{2E}^{CP} = 1/T_{2E}^{CP}$ depends on τ. Generally, the form of the pulse spacing dependence is characteristic of the motion responsible for the relaxation. This is illustrated in Figure 1 (bottom), which shows R_{2E}^{CP} pulse frequency dispersions $[R_{2E}^{CP}(\omega), \omega = 1/\tau]$ for three different types of motion. The Markov process with a single correlation time τ_C exhibits a Lorentzian dispersion with a plateau at low frequencies ($\omega << 1/\tau_C$) and an inverse square dependence $R_{2E}^{CP} \propto \omega^{-2}$ at higher frequencies.[22] More complex processes exhibit, in addition, an intermediate dispersion regime characteristic of the motion. Thus, collective orientational fluctuations provide a $R_{2E}^{CP} \propto \omega^{-1/2}$ dispersion in 'three-dimensional' phases (e.g., nematic liquid crystals),[23] whilst in 'two-dimensional' phases (e.g., bilayer membranes), the relaxation rate is inversely proportional to the pulse frequency: $R_{2E}^{CP} \propto \omega^{-1}$.[12,15] The experimentally accessible frequency range of R_{2E}^{CP} depends, in general, on the sensitivity of the observed spin and on the form of the relaxation dispersion. For ^{31}P, in biological membranes, for example, it is possible to measure R_{2E}^{CP} at frequencies between 10^2 and 10^5 s^{-1}, which is sufficient to cover the relevant slow motional regime.[15]

There are two possible approaches to the analysis of transverse spin relaxation measurements, and some consideration should be given as to which method is most appropriate for each individual case. Motional narrowing limit expressions, which are usually adequate for the interpretation of spin–lattice relaxation experiments, cannot always be applied to transverse relaxation. In particular, for systems undergoing slow motions, it will generally be necessary to solve numerically the equations of motion for the relaxing spins.

2.2 Full Numerical Analysis

The starting point for a full numerical analysis of spin relaxation is the stochastic Liouville equation[24,25]

$$\frac{\partial}{\partial t}\hat{\rho}(\Omega,t) = -\frac{\mathrm{i}}{\hbar}\hat{\mathcal{H}}^{x}(\Omega)\hat{\rho}(\Omega,t) - \hat{\Gamma}(\Omega)[\hat{\rho}(\Omega,t) - \hat{\rho}_{\mathrm{eq}}(\Omega)] \quad (1)$$

which describes the time dependence of the spin density matrix $\hat{\rho}(\Omega, t)$ under the influence of the spin Hamiltonian $\hat{\mathcal{H}}^x(\Omega)$ and the stochastic operator $\hat{\Gamma}(\Omega)$, for the various motional processes. The Euler angles Ω define the orientation of the dominant spin interaction tensor relative to a set of laboratory axes. Fortunately, for the purposes of interpreting transverse relaxation rates due to slow motions, it is often possible to separate the coupled differential equations [see equation (1)] into independent subsets describing the time variation of specific density matrix elements. Thus, the relevant part of equation (1) can be represented by a reduced set of differential equations, written in matrix form as[26–28]

$$\frac{\partial}{\partial t}[\rho_{ij}(\Omega, t)] = -[\mathrm{i}\mathbf{W}(\Omega) + \mathbf{K}(\Omega)][\rho_{ij}(\Omega, t)] \tag{2}$$

where $\rho_{ij}(\Omega,t)$ are the single quantum coherence components of $\hat{\rho}(\Omega, t)$, with $j = i \pm 1$. $\mathbf{K}(\Omega)$ is a rate matrix with elements determined by the discretized stochastic operator $\hat{\Gamma}(\Omega)$.[26,27] Thus, $K(\Omega_{mn})$ is the rate constant for population transfer from site n to site m and $K(\Omega_{mm}) = -\sum_{n\neq m} K(\Omega_{nm})$. The diagonal matrix $\mathbf{W}(\Omega)$ contains the free precession frequencies for each site, m. In order to solve equation (2) it is convenient first to symmetrize $\mathrm{i}\mathbf{W}(\Omega) + \mathbf{K}(\Omega)$ by a similarity transformation and then apply an efficient eigenvalue method.[29,30]

Spin echo experiments can be simulated by successive application of equation (2) to describe each stage of the pulse sequence.[31,32] Refocusing pulses can be treated as ideal rotations, inducing an instantaneous 180° phase shift in $\rho_{ij}(\Omega,t)$. The transverse relaxation rate $R_{2\mathrm{E}}^{\mathrm{CP}}$ for a given pulse spacing τ is then[33]

$$R_{2\mathrm{E}}^{\mathrm{CP}} = -\ln[M(2\tau)/M(0)]/2\tau \tag{3a}$$

$$M(t) = \sum_m \sum_i \rho_{i\,i-1}(\Omega_m, t) \tag{3b}$$

Note that for a homogeneous system, it is not necessary to evaluate the entire CPMG sequence, but it suffices to calculate just the first echo and apply equations (3a) and (3b).[34]

2.3 Motional Narrowing Limit Expressions

For slow low-amplitude processes, it is conceivable that motional narrowing limit theory[35] may be applied to account for transverse spin relaxation. Exact analytical expressions for $R_{2\mathrm{E}}^{\mathrm{CP}}$ valid in this regime have been derived.[7,17,22] A useful approximate version of these derivations is[23,33]

$$R_{2\mathrm{E}}^{\mathrm{CP}} \approx \tfrac{3}{2} C\, J_0^{\mathrm{lab}}(\omega) \tag{4}$$

where $J_0^{\mathrm{lab}}(\omega)$ is the spectral density of the motion at the pulse frequency $\omega = 1/\tau$ and C is the effective interaction strength parameter (e.g., $C = \frac{2}{3}\langle\Delta\sigma^2\rangle$ for ^{31}P and $C = \frac{3}{8}\langle(e^2qQ/\hbar)^2\rangle$ for ^{2}H). For certain dynamic models, analytical expressions are available or can be derived for $J_0^{\mathrm{lab}}(\omega)$. Otherwise, they may be evaluated numerically using the same finite grid point approach[26,27] described above. In this case, we have[36,37]

$$J_{\mathrm{M}}^{\mathrm{lab}}(\omega) = (F_{20}^{\mathrm{mag}})^{-2}\Bigg[\sum_{m,n} F_{2\mathrm{M}}^{\mathrm{lab}}(\Omega_m) F_{2\mathrm{M}}^{\mathrm{lab}*}(\Omega_n) X_m^{(0)} X_n^{(0)} \times \sum_k X_m^{(k)} X_n^{(k)} j^{(k)}(\omega)\Bigg] \tag{5a}$$

$$j^{(k)}(\omega) = \frac{8}{\pi^2}\frac{\lambda^{(k)}}{(\lambda^{(k)})^2 + (\frac{1}{2}\pi\omega)^2} \tag{5b}$$

where $\lambda^{(k)}$ and $\boldsymbol{X}^{(k)}$ are the eigenvalues and corresponding eigenvectors of the stochastic operator $\boldsymbol{\Gamma}$, obtained by diagonalizing the symmetrized rate matrix $\mathbf{K}^{\mathrm{s}}$. The $F_{2\mathrm{M}}^{\mathrm{lab}}(\Omega_m)$ are the components of the magnetic interaction tensor for the mth site, expressed in the laboratory axis system (z parallel to $\boldsymbol{B}_0$). Similarly, F_{20}^{mag} is the zeroth component of the interaction tensor expressed in its principal axis system. Note that the Lorentzian reduced spectral density $j^{(k)}(\omega)$ defined above uses the inverse pulse spacing as the frequency variable, and for this reason differs from standard expressions for spectral densities in magnetic resonance, which generally involve the Larmor frequency ω_0.

Combining equations (4), (5a), and (5b), we obtain a general expression for the transverse relaxation rate:

$$R_{2\mathrm{E}}^{\mathrm{CP}} = \tfrac{3}{2} C \sum_l P(l) J_0^{(l)\mathrm{lab}}(\omega) \tag{6}$$

where the summation index l specifies the effective motional modes and $P(l)$ is the respective mode amplitude. In the case of collective motions, the spectrum of modes is expected to be continuous, and the summation in equation (6) can be replaced by an integral.

Transverse spin relaxation rates are invariably measured in the laboratory frame, and therefore depend on the spectral densities $J_{\mathrm{M}}^{\mathrm{lab}}(\omega)$ [see equation (4)]. On the other hand, dynamic models are generally defined with respect to local symmetry axes and the respective spectral density functions $J_{\mathrm{M}}^{\mathrm{loc}}(\omega)$ evaluated relative to these axes. The transformation between laboratory and local axis systems leads to a simple expression for the anisotropy of $R_{2\mathrm{E}}^{\mathrm{CP}}$:[38]

$$R_{2\mathrm{E}}^{\mathrm{CP}} = \tfrac{3}{2} C[\tfrac{1}{4}(3\cos^2\theta_{\mathrm{N}} - 1)^2 J_0^{\mathrm{loc}}(\omega) + 3\sin^2\theta_{\mathrm{N}}\cos^2\theta_{\mathrm{N}} J_1^{\mathrm{loc}}(\omega) + \tfrac{3}{4}\sin^4\theta_{\mathrm{N}} J_2^{\mathrm{loc}}(\omega)] \tag{7}$$

where θ_{N} refers to the angle between the static magnetic field and the local axis system. In a powder sample, all values of θ_{N} are observed, and the relaxation is in general multiexponential. For macroscopically aligned samples, it is possible to measure $R_{2\mathrm{E}}^{\mathrm{CP}}$ as a function of θ_{N} and hence determine each of the three $J_{\mathrm{M}}^{\mathrm{loc}}(\omega)$. With this information, it is possible to determine the overall symmetry of the motion, without recourse to any specific model.

Interestingly, equations (5) and (7), describing the dispersion and anisotropy of $R_{2\mathrm{E}}^{\mathrm{CP}}$, are qualitatively valid over a dynamic range that extends beyond the limits usually associated with motional narrowing theory.[39] However, it should be stressed that these simple expressions are not always suitable, and, when in doubt, it is advisable to use the full numerical approach discussed above.

3 CHARACTERIZATION OF SLOW MOTIONS: TRANSVERSE SPIN RELAXATION IN BIOLOGICAL MEMBRANES

The majority of NMR studies of biological membranes have employed model systems whose composition is well defined and therefore permits more detailed investigations of specific aspects of membrane behavior. In this section, we present an instructive example of the application of NMR transverse spin relaxation methods to study low-frequency molecular dynamics in a biological model membrane. The particular system studied is a dispersion of dimyristoylphosphatidylcholine (DMPC) in water. From a biological point of view, it is the liquid crystalline (L_α) phase of this system that has received most attention. In this phase, the phospholipid molecules arrange in bilayers, separated by water, with the hydrophobic carbon chains oriented towards the center of the bilayer as illustrated in Figure 2. The most commonly employed preparation methods yield dispersions of approximately spherical multilamellar vesicles (see Figure 2). The mean value and variance of the vesicle radius distribution, however, depend significantly on the method of preparation employed.[40] Alternatively, macroscopically oriented samples can be obtained by incorporating thin layers of the DMPC/water mixture between thin glass plates (see Figure 2).[41]

3.1 Multilamellar Vesicles

It was pointed out in the previous section that transverse spin relaxation rates R_{2E}^{CP} depend on the sample orientation, the pulse frequency, and the spin interaction strength. Independent measurement of these three effects, however, is complicated to some extent by the use of vesicle samples. Since multilamellar vesicles are, in effect, isotropic powders, all orientations θ_N are represented, and therefore relaxation is generally multiexponential [see equation (7)]. In principle, it is possible to determine both the anisotropy and the pulse frequency dependence by Fourier transforming the final echoes of CPMG trains for different numbers of echoes, n, at each pulse frequency. This procedure, however, is time and labor-intensive, and alternative methods have usually been employed to extract the desired information. For homogenous samples with a single effective spin label, it is possible to exploit equation (7), so that the measured amplitude $M(2n\tau)$ of the nth echo in a CPMG experiment is

$$M(2n\tau) = M_0 \int_0^1 \exp\{-[\tfrac{1}{4}(3\cos^2\theta_N - 1)^2 F_0 + 3\sin^2\theta_N \cos^2\theta_N F_1 + \tfrac{3}{4}\sin^4\theta_N F_2]2n\tau\}\, d\cos\theta_N \quad (8)$$

and the decay curve for a given pulse spacing τ may be fitted by independently varying the three parameters F_0, F_1, and F_2. Although equation (8) is strictly correct only in the motional narrowing limit, where the parameters F_M can be identified with the spectral densities $J_M^{loc}(\omega)$, it may be usefully applied in any regime provided that for each individual orientation θ_N the spins relax monoexponentially.

Figure 3, shows ^{31}P and ^{2}H scaled transverse relaxation rates, $R_{2E}^{CP}/\Delta\nu^2$ as functions of pulse frequency ω for 2-[14,14,14-d_3]DMPC (see Figure 2) multilamellar vesicles. The ^{31}P relaxation rates were measured using the standard CPMG pulse sequence with spin lock proton decoupling.[42] For ^{2}H, the quadrupolar CPMG sequence[11] was employed without proton decoupling. Results are shown for pure DMPC bilayers (open circles), DMPC/4 mol% gramicidin (filled diamonds), and DMPC/40 mol% cholesterol (open triangles), and in each case refer to the $\theta_N = 45^\circ$ orientation, extracted from CPMG echo decays using equation (8). Two important conclusions may be drawn from the results in Figure 3, independently of possible dynamic models. First, the evident frequency dependence of the rates indicates that slow motional processes are responsible for transverse relaxation. Moreover, the fact that the measured dispersion is in all cases approximately given by $R_{2E}^{CP} \propto \omega^{-1}$ suggests a superposition of different modes with frequency components in the 10^2–10^5 s^{-1} regime probed specifically in the experiments. The second notable aspect of the results in Figure 3 is that the scaled rates $R_{2E}^{CP}/\Delta\nu^2$ are, to within experimental error, the same for ^{31}P and ^{2}H. The spectral parameter $\Delta\nu$ is defined as the measured frequency difference between the 0° and 90° singularities in the powder spectra. Thus, $\Delta\nu^2 \propto C$, and we find that the spin-interaction-independent (i.e., purely dynamic) contributions to the relaxation rates for ^{31}P and ^{2}H are identical. In other words, the lipid headgroup (^{31}P) and the *sn*-2 chain methyl group (^{2}H) undergo the same low-frequency motions, despite the fact that they are located at opposite extremities of the lipid molecule (see Figure 2). This indicates that the effective dynamic processes are of a mesoscopic nature. In comparing the ^{31}P and ^{2}H results, it is also worth pointing out that ^{31}P provides markedly superior signal-to-noise ratio and a correspondingly wider dynamic range than ^{2}H, and there is a good case for proposing ^{31}P as the nucleus of choice for low-frequency dynamics studies of biological membranes.

The results in Figure 3 evaluated for the $\theta_N = 45^\circ$ orientation reflect the most rapidly relaxing component of the multiexponential decay. However, a second slowly relaxing component corresponding to the 90° orientation can also be detected in the ^{31}P CPMG experiments. The scaled ^{31}P relaxation rates are shown in Figure 4. Interestingly, at low frequencies, a plateau appears in the $R_{2E}^{CP}/\Delta\nu^2$ dispersion plot. What is more, the ratios between the plateau values for the different samples are different from the corresponding ratios found for the rapidly relaxing component.

Figure 5 shows the ^{31}P scaled transverse relaxation rates measured for pure DMPC vesicles at four different magnetic fields between 4.7 and 11.7 T. Note that in the case of ^{31}P, it is modulation of the chemical shift anisotropy that is responsible for transverse relaxation. Since the effective chemical shift anisotropy is determined by B_0 ($\Delta\nu \propto B_0$), it follows that the spin interaction strength parameter C also depends on the magnetic field ($C \propto B_0^2$). Thus, if the dynamic behavior of the membrane is unaffected by the presence of magnetic fields, the scaled relaxation rates $R_{2E}^{CP}/\Delta\nu^2$ should be independent of B_0. The results in Figure 5 show that the higher frequency processes ($\geq 10^3$ s^{-1}), monitored by the rapidly relaxing component [Figure 5(a)], are virtually unaffected by the presence of the magnetic field, whereas the low-frequency motions ($\leq 10^3$ s^{-1}), reflected by the slowly relaxing component [Figure 5(b)], are apparently suppressed at higher magnetic fields.

NMR studies of slow motions in multilamellar vesicles have focused principally on two types of process, namely lateral diffusion across a curved surface[8] and collective

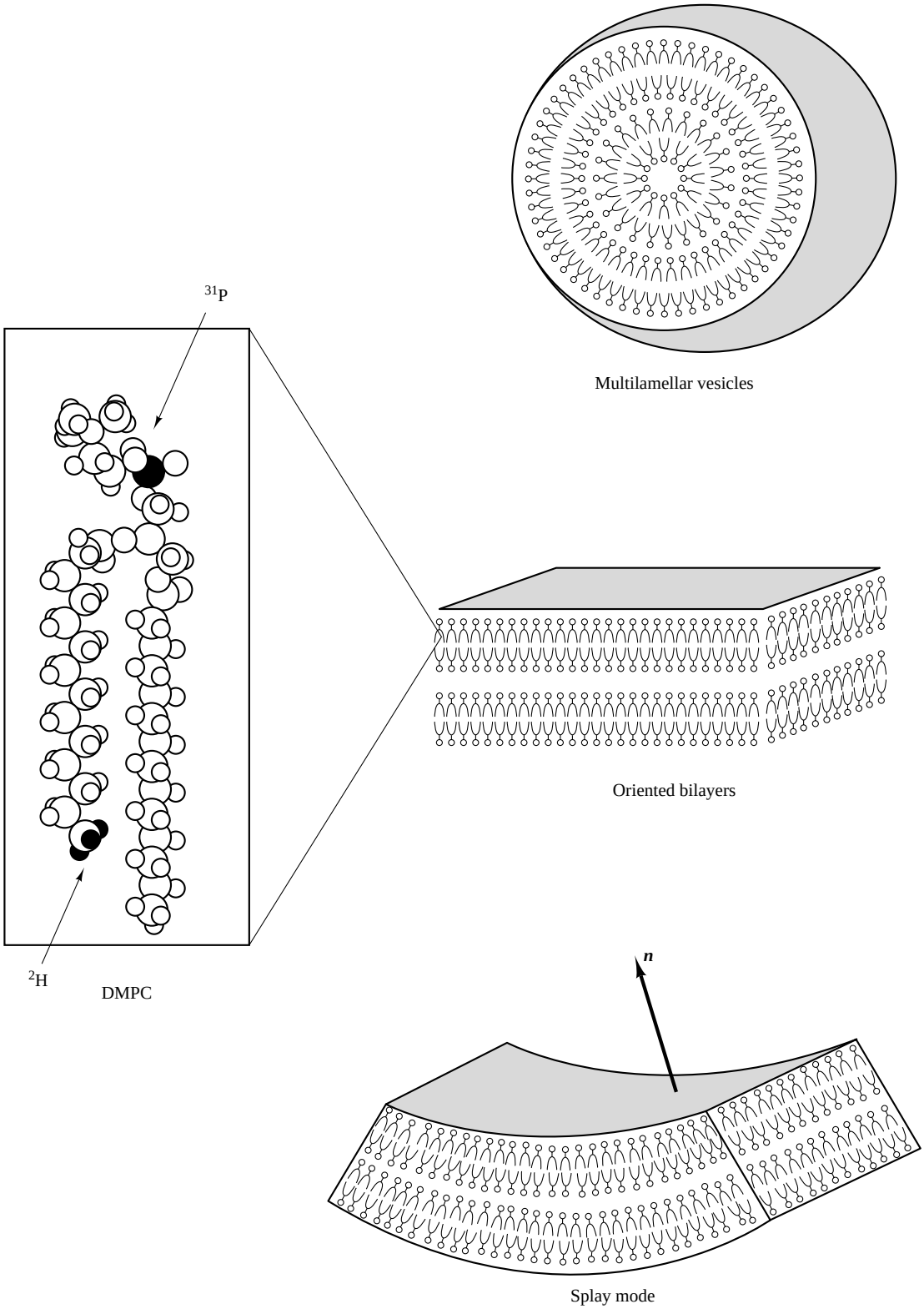

Figure 2 Dimyristoylphosphatidylcholine (DMPC) molecule with ^{2}H and ^{31}P nuclei sites indicated. Also shown are schematic representations of multilamellar vesicles, oriented bilayers, and the collective splay mode for director fluctuations in biological membranes

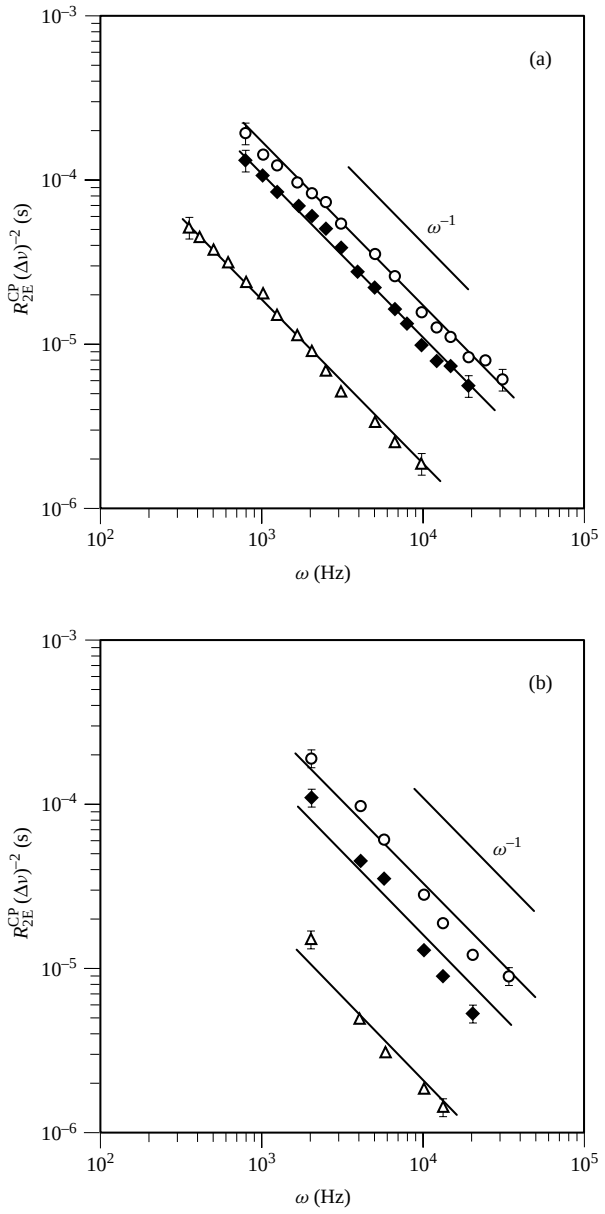

Figure 3 (a) Scaled ^{31}P transverse relaxation rates RCP/2E/$\Delta\nu^2$ measured as functions of pulse frequency ω for hydrated DMPC (open circles), DMPC/4 mol% gramicidin (filled diamonds), and DMPC/40 mol% cholesterol (open triangles) multilamellar vesicles at 313 K. Results refer to the rapidly relaxing 45° orientation. (b) Scaled ^{2}H transverse relaxation rates RCP/2E/$\Delta\nu^2$ measured for the same samples under the same conditions. Solid lines are included as guides to the eye

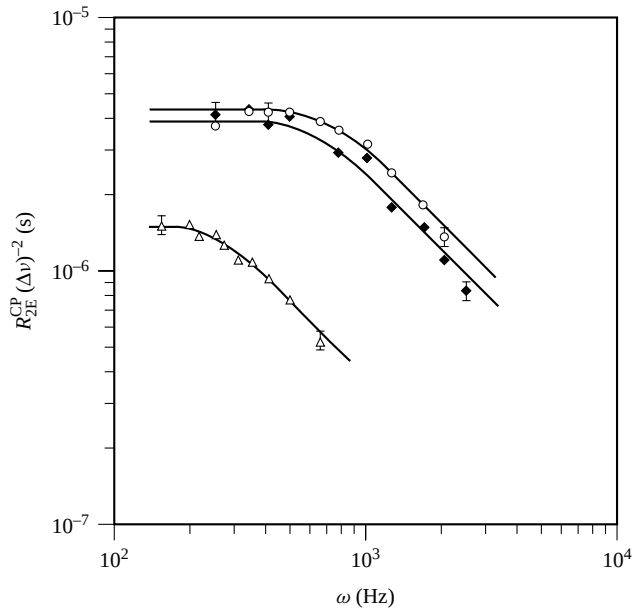

Figure 4 Scaled ^{31}P transverse relaxation rates RCP/2E/$\Delta\nu^2$ measured as functions of pulse frequency ω for hydrated DMPC (open circles), DMPC/4 mol% gramicidin (filled diamonds) and DMPC/40 mol% cholesterol (open triangles) multilamellar vesicles at 313 K. Results refer to the slowly relaxing 90° orientation. Solid lines are included as guides to the eye

orientation fluctuations.[13,15,43] Both of these mechanisms can be considered mesoscopic in that they involve long-range orientational correlations. In the case of collective motions, a low-frequency cutoff in the relaxation dispersion is expected if long-wavelength fluctuation modes are suppressed. This could arise as a result of the finite size of the particles themselves. Alternatively, magnetic damping of the low-energy modes might occur owing to coupling between the NMR static magnetic field and the anisotropic diamagnetic susceptibility of the vesicles.[44] Simple models for lateral diffusion over a curved surface do not predict such a magnetic-field-dependent low-frequency cutoff. Apparently, the measured $R_{2E}^{CP}/\Delta\nu^2$ dispersion profiles indicate that collective motions play a major role in the relaxation mechanism of multilamellar vesicles. However, the quantitative analysis of these measurements is inevitably limited by the sample heterogeneity. Indeed, it is most likely that the dominant relaxation mechanism depends on the vesicle size and that in any particular sample there may be two or more distinct processes that contribute to the overall measured echo decays.

3.2 Oriented Membrane Samples

The problems associated with the use of multilamellar vesicles for studying membrane dynamics have long been recognized, and alternative methods of sample preparation have been proposed. For example, spherical supported vesicles, prepared by condensing membrane bilayers onto spherical silica beads, have been used to measure lateral diffusion rates of lipid molecules.[45] The silica beads employed have extremely narrow distributions of radii, and therefore provide virtually monodisperse vesicles. An alternative approach that seeks to avoid the effects of lateral diffusion involves the use of oriented samples.[41] In this case, the membrane bilayers are uniaxially aligned on glass plates such that the bilayer normal and the plate normal are coincident. Lateral diffusion of the molecules no longer induces any angular reorientation of the lipid molecules, and therefore is ineffective as a spin relaxation mechanism for isolated spins such as ^{2}H or decoupled ^{31}P. Results obtained for oriented DMPC bilayers show R_{2E}^{CP} anisotropies and pulse frequency dispersions consistent with those obtained for multilamellar vesicles, and support the

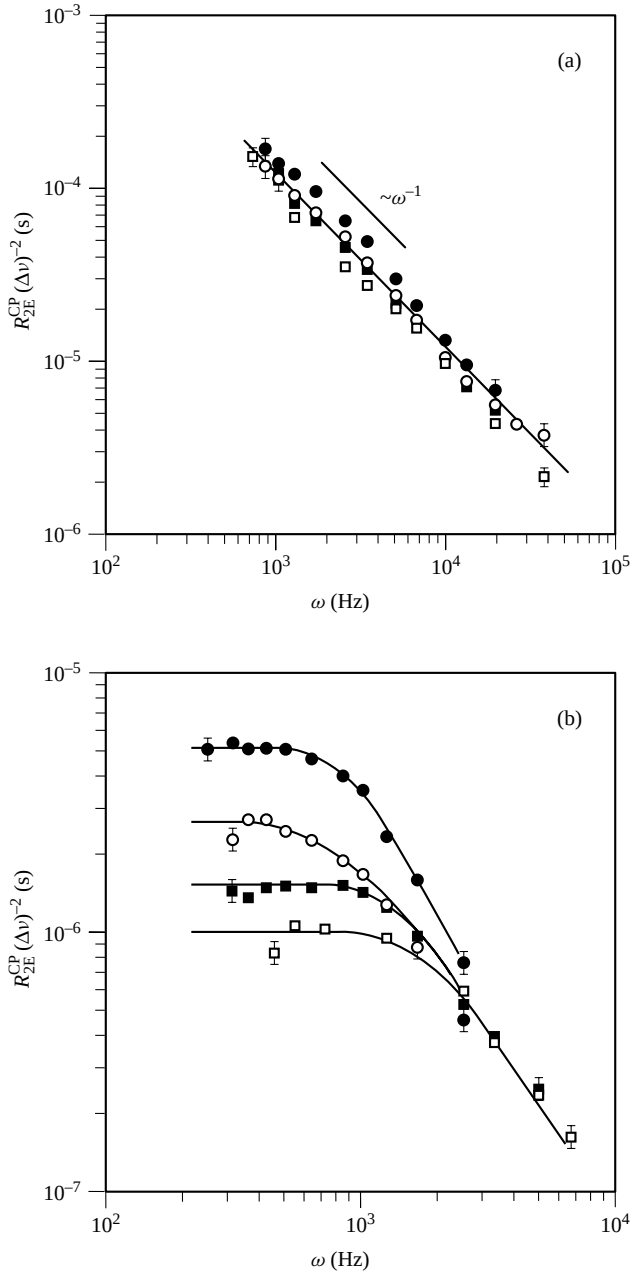

Figure 5 Scaled ^{31}P transverse relaxation rates $R\mathrm{CP/2E}/\Delta\nu^2$ measured as functions of pulse frequency ω for hydrated DMPC at magnetic fields of 4.7 T (filled circles), 7.0 T (open circles), 9.3 T (filled squares), and 11.7 T (open squares): (a) for the rapidly relaxing 45° orientation; (b) for the slowly relaxing 90° orientation. Solid lines are included as guides to the eye

conclusion that collective motions play a major role in the transverse spin relaxation.[12,46]

4 EVALUATION OF VISCOELASTIC PROPERTIES: COLLECTIVE ORIENTATIONAL FLUCTUATIONS

Having identified collective motions as a dominant transverse relaxation process, it then remains to apply a suitable model in order to evaluate the relevant viscoelastic properties. Several hydrodynamic models have been postulated to describe collective orientational fluctuations[47] and surface undulations[14] in membranes.

4.1 Director Fluctuations

One such model, which has been employed by several groups to interpret transverse relaxation, is based on the concept of director fluctuations.[12,13,47,48] In liquid crystal terminology, the director $\boldsymbol{n}$ is defined as the vector describing the orientation of the local phase symmetry axis. It represents the direction of preferred molecular orientation, and in a two-dimensional system such as a membrane may be taken to be normal to the layer surface (see Figure 2). Thermally induced deviations of the director about its average orientation occur, which necessarily modulate the spin interactions of the constituent molecules and hence effect spin relaxation. The director fluctuations may be decomposed into a set of Fourier modes of wavevector q, with mean-square amplitudes $\langle\theta_0^2(q)\rangle$ and exponential decay constants, $\tau(q)$ given by

$$\langle\theta_0^2(q)\rangle = \frac{k_\mathrm{B}T}{VKq^2} \tag{9a}$$

$$\tau(q) = \frac{\eta}{Kq^2} \tag{9b}$$

where K is an elastic constant, η is an effective viscosity, and V is the volume of the mesoscopic uniform sample. By analogy with models developed for director fluctuations in thermotropic liquid crystals,[48] K can be identified with the splay elastic constant K_1, although it has also been suggested that an appropriate quantity for membranes is the curvature elastic modulus $\kappa_\mathrm{c} = Kd$, dependent on the bilayer repeat distance d. A more general model for collective motions in membranes, considering bilayer interactions, has been presented recently.[49]

In deriving Equation (9a), it has been assumed that the director fluctuations are of low amplitude. It then follows that the corresponding spectral densities, defined in the average director or local frame, are highly anisotropic in that $J_1^{\mathrm{loc}}(\omega) \gg J_0^{\mathrm{loc}}(\omega)$, $J_2^{\mathrm{loc}}(\omega)$, and, as a first approximation, it is reasonable to retain just $J_1^{\mathrm{loc}}(\omega)$. Combining equations (6) and (7), and replacing the sum over modes l with an integral over the wavevector q, we obtain

$$R_{2\mathrm{E}}^{\mathrm{CP}} = \frac{27}{8}C\frac{k_\mathrm{B}T}{\pi Kd}\sin^2\theta_\mathrm{N}\cos^2\theta_\mathrm{N} \times \int_{q_l}^{q_\mathrm{c}} \frac{8}{\pi^2}\frac{\tau(q)}{1+\tau^2(q)(\frac{1}{2}\pi\omega)^2}\,hbox{d}\,\ln q \tag{10}$$

The short-wavelength cutoff q_c is governed principally by the molecular dimensions, while the long-wavelength cutoff q_l is related to the size of the effective uniform sample and therefore reflects mesoscopic dimensions. In the case of magnetic damping of collective modes, the long-wavelength cutoff is determined by the magnetic coherence length $\xi = 1/q_l = (K\mu_0/\Delta\chi)^{\frac{1}{2}}(1/B_0)|P_2(\cos\theta_\mathrm{N})|^{-\frac{1}{2}}$, where $\Delta\chi$ is the effective diamagnetic susceptibility anisotropy and μ_0 is the absolute magnetic permeability. The Legendre polynomial $P_2(\cos\theta_\mathrm{N})$ accounts for the orientation dependence of the

Table 1 NMR and Viscoelastic Parameters for Biological Model Membranes at $T = 313\,\mathrm{K}$

Membrane System	Spectral parameter $\Delta\nu$ (kHz)		Elastic constant[a] $K(10^{-11}\,\mathrm{N})$		Effective viscosity[b] $\eta(10^{-3}\,\mathrm{Pa\,s})$
	^{31}P	^{2}H	^{31}P	^{2}H	^{31}P
Pure DMPC	5.2	3.5	0.65	0.50	3.0
DMPC/4 mol% gramicidin	4.9	4.8	1.1	1.0	3.5
DMPC/40 mol% cholesterol	5.4	11.7	6.0	6.0	8.0

[a] K can be identified with the splay elastic constant K_1.[47] A related quantity for membranes is the curvature elastic modulus $k_c = Kd$,[14] dependent on the bilayer repeat distance d.
[b] The viscosity η estimated from the low-frequency cutoff ω_l (see text), based on a diamagnetic susceptibility anisotropy of $\Delta\chi = 1.2 \times 10^{-7}$ SI units.[51]

magnetic interaction.[44] Performing the integration in equation (10) gives

$$R_{2E}^{CP} = \begin{cases} A\omega_l^{-1} & (\omega < \omega_l) \\ A\omega^{-1} & (\omega_c \rangle \omega \rangle \omega_l) \\ A\omega_c\omega^{-2} & (\omega \rangle \omega_c) \end{cases} \tag{11}$$

with

$$A = \frac{27}{2\pi^3} C \sin^2\theta_N \cos^2\theta_N \frac{k_B T}{Kd} \tag{12}$$

where $\omega_l = Kq_l^2/\eta = \Delta\chi B_0^2 |P_2(\cos\theta_N)|/\mu_0\eta$ is the low-frequency cutoff and $\omega_c = Kq_c^2/\eta$ is the high-frequency cutoff. Thus, in the intermediate dispersion regime, we find that $R_{2E}^{CP} \propto \omega^{-1}$ and is independent of η. In the low-frequency regime, R_{2E}^{CP} depends on both K and η as well as on B_0.

4.2 Viscoelastic Parameters

The above expressions account at least qualitatively for the results presented in the previous section. The only obvious point of discrepancy between equation (11) and the experimental results is in the predicted divergence of T_{2E}^{CP} at $\theta_N = 0^\circ$ and $\theta_N = 90^\circ$, although both the oriented sample and the multilamellar vesicles were found to exhibit the correct form for the R_{2E}^{CP} anisotropy. A second-order analysis of director fluctuations[44,50] yields expressions for $J_0^{loc}(\omega)$ and $J_2^{loc}(\omega)$, and consequently predicts finite T_{2E}^{CP} values at all orientations. A slow motional approach also predicts finite T_{2E}^{CP} at 0° and 90°, and is probably more suitable in the present case. However, the detailed modeling of multiple diffusion process such as director fluctuations in the slow motional regime is far from trivial. For present purposes, we restrict our analysis to the first-order motional narrowing limit expressions. By fitting experimental results, the fast relaxation component (45°) yields values for the elastic constant K of the DMPC membranes. From the low-frequency cutoff of the slow relaxation component (90°), estimates for the effective viscosity η are obtained. The results of the analysis are given in Table 1.

The values obtained for K and η are reasonable, and indicate that transverse spin relaxation is able to provide information concerning viscoelastic properties in biological membranes. Of particular importance from a biological point of view is that the technique may be exploited to investigate modifications of membrane viscoelastic behavior caused by included sterols, peptides, or proteins. Indeed, the results presented in Table 1 suggest that these effects are by no means small, and invite speculation regarding the consequences for overall membrane function.

5 RELATED ARTICLES

Amphiphilic Liquid Crystalline Samples: Nuclear Spin Relaxation; Bilayer Membranes: Deuterium and Carbon-13 NMR; Dynamics of Water in Biological Systems: Inferences from Relaxometry; Field Cycling Experiments; Liquid Crystalline Samples: Relaxation Mechanisms; Membrane Lipids of Acholeplasma laidlawii; Membranes: Deuterium NMR; Membranes: Phosphorus-31 NMR; Molecular Motions: T_1 Frequency Dispersion in Biological Systems; Relaxation Effects of Chemical Exchange; Relaxation Theory: Density Matrix Formulation; Ultraslow Motions in Solids.

6 REFERENCES

1. A. G. Anderson and A. G. Redfield, *Phys. Rev.*, 1959, **116**, 583.
2. F. Noack, in *Progress in Nuclear Magnetic Resonance Spectroscopy*, eds. J. W. Emsley, J. Feeney, and L. H. Sutcliffe, Pergamon Press, Oxford, 1986, Vol. 18, p. 171.
3. R. Kimmich and F. Winter, *Prog. Colloid Polym. Sci.*, 1985, **71**, 66.
4. E. Rommel, F. Noack, P. Meier, and G. Kothe, *J. Phys. Chem.*, 1988, **92**, 2981.
5. E. L. Hahn, *Phys. Rev.*, 1950, **80**, 580.
6. J. H. Davis, K. R. Jeffrey, M. Bloom, M. I. Valic, and T. P. Higgs, *Chem. Phys. Lett.*, 1976, **42**, 390.
7. Z. Luz and S. Meiboom, *J. Chem. Phys.*, 1963, **39**, 366.
8. M. Bloom and E. Sternin, *Biochemistry*, 1987, **26**, 2101.
9. H. Y. Carr and E. M. Purcell, *Phys. Rev.*, 1954, **94**, 630.
10. S. Meiboom and D. Gill, *Rev. Sci. Instrum.*, 1958, **29**, 688.
11. S. B. Ahmad, K. J. Packer, and J. M. Ramsden, *Mol. Phys.*, 1977, **33**, 857.
12. J. Stohrer, G. Gröbner, D. Reimer, K. Weisz, C. Mayer, and G. Kothe, *J. Chem. Phys.*, 1991, **95**, 672.
13. P. I. Watnick, P. Dea, and S. I. Chan, *Proc. Natl. Acad. Sci. USA*, 1990, **87**, 2082.
14. M. Bloom and E. Evans, in *Biologically Inspired Physics*, ed. L. Peliti, Plenum Press, New York, 1991, p. 137.
15. E. J. Dufourc, C. Mayer, J. Stohrer, G. Althoff, and G. Kothe, *Biophys. J.*, 1992, **61**, 42.

16. C. P. Slichter and D. C. Ailion, *Phys. Rev.*, 1964, **135**, A1099.
17. A. J. Vega, R. Poupko, and Z. Luz, *J. Magn. Reson.*, 1989, **83**, 111.
18. B. A. Cornell, J. B. Davenport, and F. Separovic, *Biochim. Biophys. Acta*, 1982, **689**, 337.
19. Z.-Y. Peng, V. Simplaceaunu, I. J. Lowe, and C. Ho, *Biophys. J.*, 1988, **54**, 81.
20. H. W. Spiess, *J. Chem. Phys.*, 1980, **72**, 6755.
21. C. Schmidt, S. Wefing, B. Blümich, and H. W. Spiess, *Chem. Phys. Lett.*, 1986, **130**, 84.
22. J. S. Blicharski, *Can. J. Phys.*, 1986, **64**, 733.
23. N. Heaton, D. Reimer, and G. Kothe, *Chem. Phys. Lett.*, 1992, **195**, 448.
24. R. Kubo, in *Advances in Chemical Physics*, ed. K. Schuler, Wiley, New York, 1969, Vol. 15, p. 101.
25. J. H. Freed, G. V. Bruno, and C. F. Polnaszek, *J. Phys. Chem.*, 1971, **75**, 3385.
26. J. R. Norris and S. I. Weissman, *J. Phys. Chem.*, 1969, **73**, 3119.
27. G. Kothe, *Mol. Phys.*, 1977, **33**, 147.
28. R. R. Vold and R. L. Vold, in *Advances in Magnetic and Optical Resonance*, ed. W. S. Warren, Academic Press, San Diego, 1991, Vol. 16, p. 85.
29. R. G. Gordon and J. Messenger, in *Electron Spin Relaxation in Liquids*, eds. L. T. Muus and P. W. Atkins, Plenum Press, New York, 1972, p. 341.
30. G. Moro and J. H. Freed, *J. Chem. Phys.*, 1981, **74**, 3757.
31. H. W. Spiess and H. Sillescu, *J. Magn. Reson.*, 1981, **42**, 381.
32. P. Meier, E. Ohmes, G. Kothe, A. Blume, J. Weildner, and H.-J. Eibl, *J. Phys. Chem.*, 1983, **87**, 4904.
33. D. Reimer, N. Heaton, A. Schleicher, K. Müller, G. Kothe and M. Vilfan, *J. Chem. Phys.*, 1994, **100**, 1693.
34. K. Müller, R. Poupko, and Z. Luz, *J. Magn. Reson.*, 1990, **90**, 19.
35. A. G. Redfield, in *Advances in Magnetic Resonance*, ed. J. S. Waugh, Academic Press, New York, 1965, Vol. 1, p. 1.
36. D. A. Torchia and A. Szabo, *J. Magn. Reson.*, 1982, **49**, 107.
37. C. Mayer, G. Gröbner, K. Müller, K. Weisz, and G. Kothe, *Chem. Phys. Lett.*, 1990, **165**, 155.
38. T. M. Barbara, R. R. Vold, and R. L. Vold, *J. Chem. Phys.*, 1983, **79**, 6338.
39. A. J. Vega, *J. Magn. Reson.*, 1985, **65**, 252.
40. P. Gale, *Biophys. Biochem. Res. Commun.*, 1993, **192**, 1042.
41. H. C. Jarrell, P. Å. Jovall, J. B. Giziewicz, L. A. Turner, and I. C. P. Smith, *Biochemistry*, 1987, **26**, 1805.
42. E. J. Dufourc, C. Mayer, J. Stohrer, and G. Kothe, *J. Chim. Phys.*, 1992, **89**, 243.
43. K. Weisz, G. Gröbner, C. Mayer, J. Stohrer, and G. Kothe, *Biochemistry*, 1992, **31**, 1100.
44. B. Halle, P-O. Quist, and I. Furó, *Phys. Rev. A*, 1992, **45**, 3763.
45. C. Dolainsky, A. Möps, and T. Bayerl, *J. Chem. Phys.*, 1993, **98**, 1712.
46. G. Althoff, N. Heaton, S. Prosser, G. Gröbner, and G. Kothe, manuscript in preparation.
47. J. A. Marqusee, M. Warner, and K. A. Dill, *J. Chem. Phys.*, 1984, **81**, 6404.
48. P. G. De Gennes, *The Physics of Liquid Crystals*, Clarendon Press, Oxford, 1974.
49. B. Halle, *Phys. Rev. E*, 1994, **50**, R2415.
50. R. L. Vold, R. R. Vold, and M. Warner, *J. Chem. Soc., Faraday Trans. 2*, 1988, **84**, 997.
51. F. Scholz, E. Boroske, and W. Helfrich, *Biophys. J.*, 1984, **45**, 589.

Biographical Sketches

Gerd Kothe. *b* 1941. M.S., 1965, University of Munich; Ph.D., 1971, University of Freiburg. Introduced to magnetic resonance by S. I. Weissman. Faculty in Chemistry, University of Stuttgart, 1981–94, University of Freiburg, 1994–present. Approx 90 publications. Research interests include the theory of dynamic magnetic resonance and its application to liquid crystals, polymers, membranes and photosynthetic processes.

Nicholas Heaton. *b* 1962. B.Sc., 1983, University of Leeds; Ph.D., 1986, University of Southampton. Postdoctoral work at UCSD with Bob and Gitte Vold. From 1991–1994 postdoctoral researcher with Gerd Kothe at the University of Stuttgart. Approx. 20 publications. Research interests include application of NMR to study molecular dynamics and structure in liquid crystals and molecular solids.

Structure and Dynamics of Disordered Proteins

H. Jane Dyson and Peter E. Wright

Department of Molecular Biology MB2, The Scripps Research Institute, La Jolla, CA, USA

1 Introduction 1
2 Resonance Assignments of Disordered Proteins 1
3 Useful Diagnostic NMR Parameters 2
4 Estimation of Polypeptide Chain Dynamics 6
5 Future Prospects 8
6 References 8

1 INTRODUCTION

With the advent of high-field NMR spectrometers and the advances in spectral sensitivity and resolution afforded by the use of isotopically-labeled proteins, it has become possible to study in atomic detail the structural features of unfolded proteins. As long as resolution was limited to that of the proton spectrum, unfolded proteins remained inaccessible to study. However, the spectral dispersion of several of the heteronuclei employed in the labeling of proteins is significantly greater than that of protons, even in the absence of local perturbations caused by different local environments in the folded protein. Thus, for example, the backbone ^{15}N and ^{13}CO chemical shifts of a protein are influenced largely by the amino acid sequence, and are thus of comparable dispersion in unfolded and folded proteins. NMR methods of particular utility in the elucidation of the conformational properties of unfolded and partly folded proteins have recently been reviewed.[1]

There are two major reasons to study unfolded proteins. In the first place, a knowledge of the "structure" of the unfolded state is an important pre-requisite for the understanding of the process of protein folding. It is necessary to understand the nature of the starting species before the process can be understood. Secondly, it is becoming clear following the publication of complete genomes that the sequences of many proteins are unlikely to be folded into "normal" globular protein structures.[2] It is clear from the sequences themselves that the polypeptides must either be unfolded under normal conditions, or else fold into non-globular structures of unknown conformation. It is clear from the large number of such sequences present in the genomes studied so far that these polypeptides must have important, as yet unknown functions, and that the assumption that a folded three-dimensional structure is essential for function needs to be re-examined. The functions of many proteins are dependent on the correct folding of their three-dimensional structure, but numerous proteins, frequently involved in some of the most important regulatory functions in the cell, appear to lack well-defined structure in the absence of targets or ligands. An understanding of the properties of such proteins will clearly be important in the overall understanding of cellular metabolism.

2 RESONANCE ASSIGNMENTS OF DISORDERED PROTEINS

High-resolution NMR studies of unfolded proteins have been largely enabled by the advent of high-field spectrometers and multidimensional heteronuclear NMR experiments. High sensitivity is a critical factor in the study of unfolded and partly folded proteins, since NMR experiments must often be performed at very low concentration (of the order of 50–300 μM) to prevent protein aggregation.

Compared to the assignment process for folded proteins, resonance assignment for disordered states of proteins presents greater difficulties because of the flexibility of the polypeptide chain, which rapidly interconverts between a large number of conformations. Since the observed chemical shift for a particular resonance is an average over a large number of chemical environments, the chemical shifts of resonances belonging to nuclei in the same residue type are very similar and hard to distinguish from each other. That is, the dispersion of most resonances, especially protons, is poor, with the result that sequence-specific assignment of resonances is difficult. A major advance in the characterization of unfolded states came with the introduction of methods for uniform isotope labeling with ^{13}C and ^{15}N and the development of multidimensional triple resonance NMR methods. The backbone ^{15}N and ^{13}CO (carbonyl) resonances are influenced both by residue type and by the local amino acid sequence and therefore remain well-dispersed, even in fully unfolded states.[3,4] This is illustrated in Figure 1, which shows strips from a series of three-dimensional spectra of unfolded apomyoglobin. In the unfolded state, the dispersion of the $^{13}C^{\alpha}$, $^{13}C^{\beta}$, H^{α}, H^{β} and HN resonances of the alanine residues are virtually identical (Figure 1a and b). The ^{13}CO (Figure 1c) and ^{15}N (not shown) resonances show greater dispersion. An assignment strategy that utilizes the superior chemical shift dispersion of the ^{13}CO resonance in unfolded proteins is especially valuable, given the excellent resolution and long T_2 relaxation time of these resonances.[5] A set of high resolution constant-time triple resonance experiments utilizing magnetization transfer between sequential ^{13}CO resonances, including those of prolines, have been developed specifically for assignment of unfolded proteins.[6]

The NMR spectra of unfolded proteins have the advantage that the intrinsic flexibility of the polypeptide generally causes the resonances to be much narrower than they would be in a folded protein of similar molecular weight. This characteristic gives special advantages in the implementation of pulse sequences with a large number of delays, which can be rather insensitive for folded proteins of molecular weight greater than 15–20 kDa, due to decay of magnetization during the pulse sequence. For unfolded proteins, however, since T_2 is significantly longer, experiments such as the (HCA)CO(CA)NH[7] are extremely sensitive and can be utilized with great success.[8] Unfortunately, partly folded proteins or molten globule states are frequently extremely difficult to study by NMR because their lines are exceptionally broad due to exchange processes on intermediate time scales.

3 USEFUL DIAGNOSTIC NMR PARAMETERS

Since unfolded and partly folded proteins present a manifold of states, it is usually uninformative to attempt the calculation of a solution structure. Instead, a number of NMR parameters can be studied to give information on the relative proportions and nature of residual structure in the protein in a site-specific manner. The values of these parameters for particular residues in the polypeptide chain can build up a picture of the conformational preferences of the protein in the unfolded state. It should always be remembered that unfolded and partly folded states of proteins are highly dynamic. All parameters are a population-weighted average over all structures in the conformational ensemble. Therefore, conformational preferences must be identified by comparison of experimental NMR parameters to those expected for a random coil state.[9,10]

3.1 Chemical Shifts

The primary data obtained from resonance assignment for any biomolecule is a set of chemical shift values. Besides identifying the resonances of each amino acid residue in

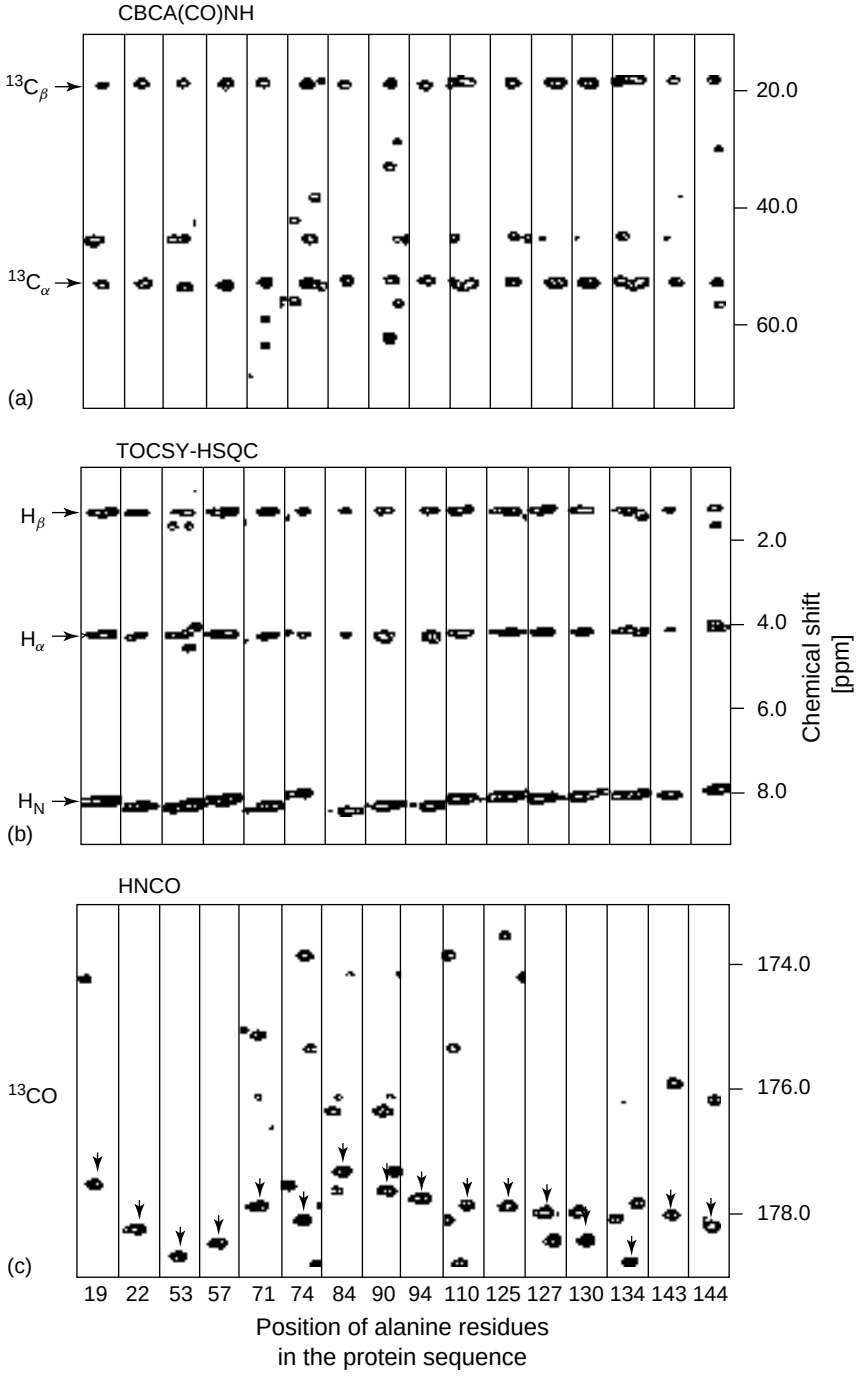

Figure 1 Comparison of the resonances of the $^{13}C^{\alpha}$, $^{13}C^{\beta}$, $^{1}H^{\alpha}$, $^{1}H^{\beta}$, ^{1}HN and ^{13}CO for the 15 alanine residues in apomyoglobin at pH 2.3, 10 mM acetate-d6 and 5 °C. (Reproduced from Ref.[5] with permission)

the polypeptide, these values can also give a great deal of information on local conformational preferences of the polypeptide. In the case of unfolded proteins, other NMR parameters may be more sensitive to averaging and less sensitive to small concentrations of structured forms (see below), with the result that the chemical shifts are frequently the best data available to make estimates of conformational preferences.

Since they are least sensitive to the local amino acid sequence, the chemical shifts of $^{13}C^{\alpha}$, $^{13}C^{\beta}$, and $^{1}H^{\alpha}$ nuclei can provide a convenient and sensitive probe of secondary structural propensities.[11,12] In addition, the ^{13}CO chemical shift can be used, provided the values are corrected for sequence dependence.[13] Residues in a completely-folded α-helix have $^{13}C^{\alpha}$ and ^{13}CO resonances shifted downfield relative to their positions in random coil states, while the $^{13}C^{\beta}$ and $^{1}H^{\alpha}$ resonances are shifted upfield. The reverse is true for residues in β-strands ($^{13}C^{\alpha}$ and ^{13}CO resonances shifted upfield, $^{13}C^{\beta}$ and $^{1}H^{\alpha}$ resonances shifted downfield). This is illustrated in Figure 2, which shows the conformational preferences for the unfolded states of two proteins, apomyoglobin at pH 2.3 and apoplastocyanin in low salt at pH 7.0. Preferences for backbone dihedral angles in the α region of (ϕ, ψ) space in some regions of the apomyoglobin sequence are revealed by the secondary chemical shifts, while those of apoplastocyanin reveal an overall propensity for β-structure formation, with a short sequence around residue 60 where (non-native) α-structure propensity is observed.

We wish to stress that these data are extremely sensitive to quite small populations of structured forms, and that the

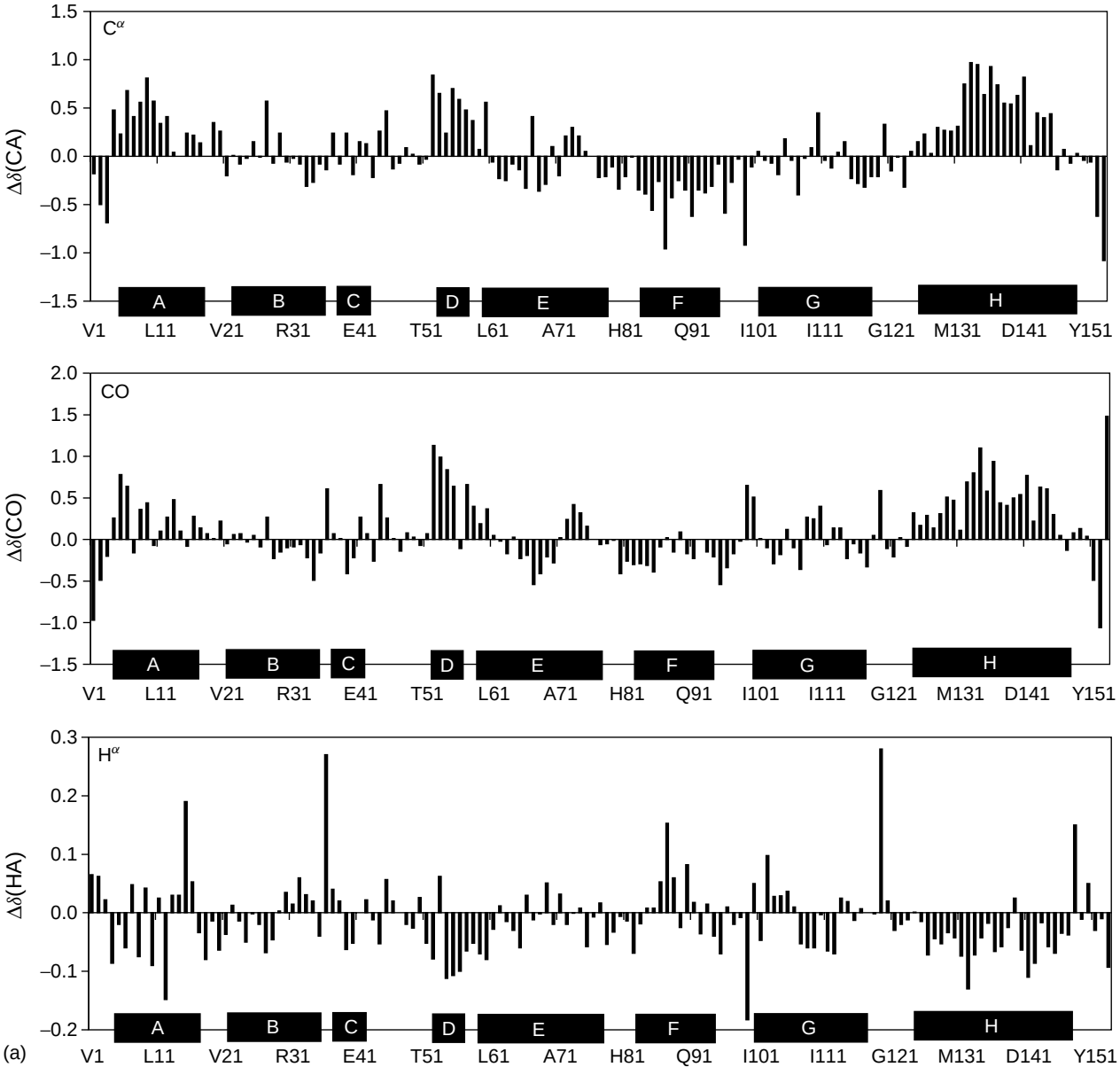

Figure 2 Secondary chemical shifts, corrected for sequence-dependent contributions, for $^{13}C^{\alpha}$, ^{13}CO and $^{1}H^{\alpha}$, for (a) apomyoglobin at pH 2.3, 10 mM acetate-d6 and 5 °C (adapted from Ref.[16] with permission) and (b) apoplastocyanin at pH 6.0, 5 mM KH_2PO_4, 5 mM β-mercaptoethanol, 35 °C. (Adapted from Ref.[17] with permission)

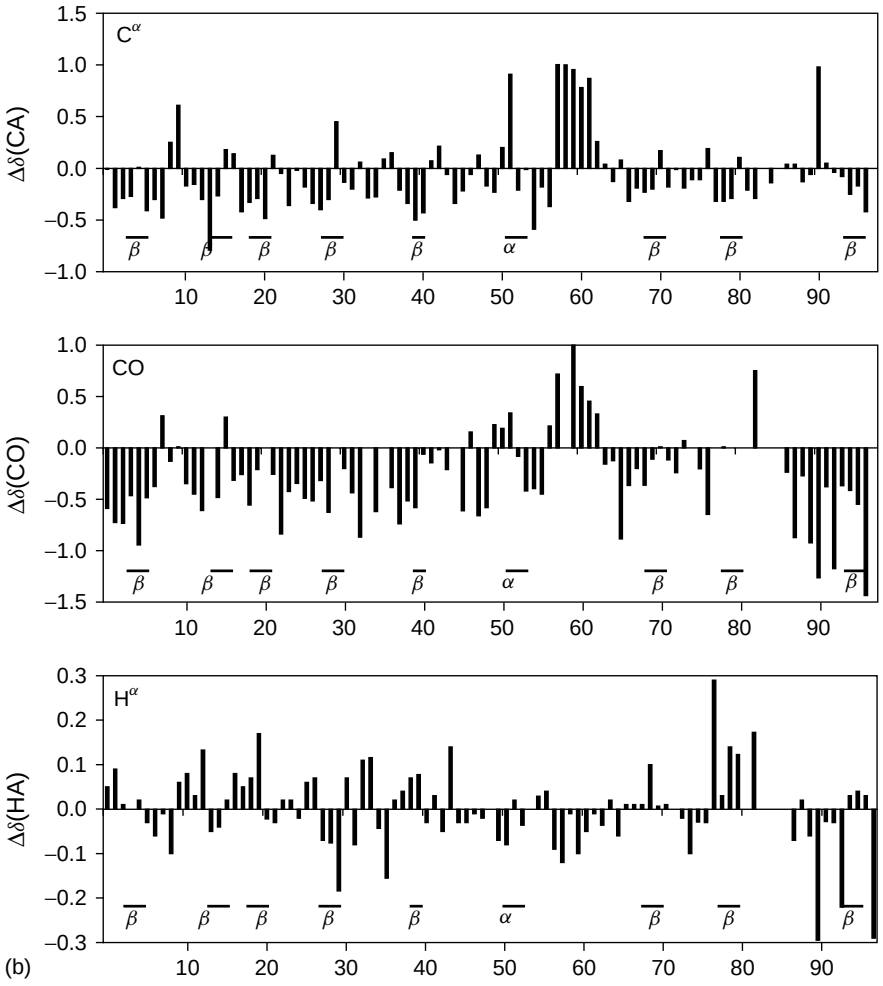

Figure 2 (*Continued*)

preferences indicated by the plots in Figure 2 are representative of preferences within a conformational ensemble only, rather than well-formed α-helix or β-sheet. This is illustrated in Figure 3, which shows the $^{13}C^{\alpha}$ secondary shifts for several different folded and partly-folded species of apomyoglobin. It is clear that, while the unfolded form at pH 2.3 shows preferences for a-structure in the sequences corresponding to the A, G and H-helix regions of the folded protein, these secondary shifts are considerably smaller than those in the partly-folded (pH 4) and fully-folded (pH 6) forms.

3.2 Coupling Constants

Coupling constants can in principle provide additional insights into backbone conformational preferences. The most commonly measured coupling constant, $^{3}J_{\mathrm{HN,H}\alpha}$, varies from about 8–10 Hz in β-strands to 4–5 Hz in helix. In disordered proteins, however, conformational fluctuations average the coupling constants and make them insensitive to local structural preferences.[9] In addition, corrections for residue type and for the nature of the preceding residue are necessary.[14,15] However, even with such corrections, the $^{3}J_{\mathrm{HN,H}\alpha}$ scalar coupling constants generally provide a very poor diagnostic of residual secondary structure propensities in unfolded proteins.[16,17]

3.3 Amide Proton Temperature Coefficients and Hydrogen Exchange Rates

Information about hydrogen bonding and solvent interactions can be provided by amide proton temperature coefficients and hydrogen exchange rates.[9] Temperature coefficients are relatively easy to measure by recording a series of NMR spectra at different temperatures. Values of temperature coefficients normally lie in the range 6–9 ppb K^{-1}. Values lower than this, relative to random coil values, can be an indication of local hydrogen bonded structure and sequestration from solvent. Amide proton exchange rates tend to be very rapid in unfolded proteins because of the presence of completely unfolded members of the conformational ensemble. However, if amide protons protected from exchange are observed, this is a good indication of the presence of structured regions, especially in partly folded proteins and molten globules.[18]

3.4 Nuclear Overhauser Effect

The nuclear Overhauser effect (NOE) is the primary source of structural information for folded proteins. It can also be a valuable resource for unfolded and partly folded proteins, but the utility of the NOE is diminished due to the conformational averaging characteristic of these states. Characteristic

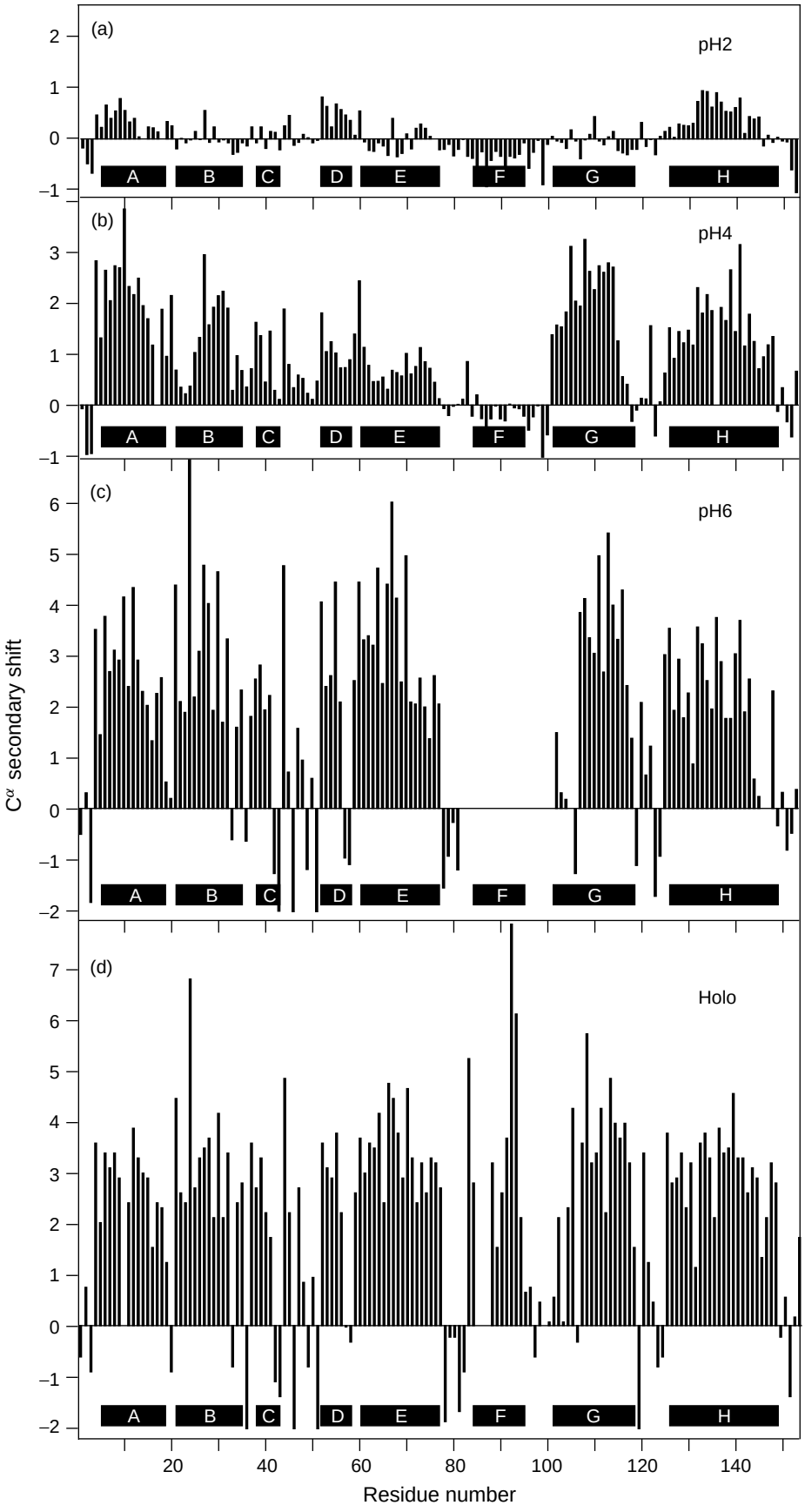

Figure 3 Summary of secondary shifts for $^{13}C^{\alpha}$ for (a) apomyoglobin at pH 2.3, (b) apomyoglobin at pH 4.1, (c) apomyoglobin at pH 6.1, and (d) holomyoglobin (with heme bound) at pH 6.1. (Adapted from Ref.[8] with permission)

short and medium-range NOEs can be used as a diagnostic of secondary structure preferences.[9] Sequential $d_{\alpha N}(i, i+1)$ NOEs are observed in virtually all unstructured states, since the majority populate the β-region of (ϕ, ψ) space.[9] A propensity for the formation of backbone dihedral angles in the α-region of (ϕ, ψ) space is indicated by the observation of $d_{NN}(i, i+1)$ NOEs, usually in addition to the $d_{\alpha N}(i, i+1)$. The observation of both NOE types for a given residue is a strong indication that conformational averaging is occurring; the relative population of dihedral angles in the α and β regions of ϕ, ψ space can be deduced from the intensity ratio of these two NOEs.[9] It is important to note that the $d_{\alpha N}(i, i+1)$ and $d_{NN}(i, i+1)$ sequential NOEs provide information only on local backbone dihedral angle preferences and do not indicate the presence of folded conformations in the absence of additional information, either from medium-range NOEs (e.g., $d_{\alpha N}(i, i+2)$, $d_{\alpha N}(i, i+3)$, $d_{\alpha\beta}(i, i+3)$ NOE connectivities) or from other forms of spectroscopy such as circular dichroism.[9]

The observation of long range NOEs is difficult either for unfolded or partly folded proteins, due to the flexibility of the polypeptide. It requires the presence of a sizeable majority population of a particular folded species before long range NOEs can be observed; so far this has been achieved in only one case.[19]

3.5 Paramagnetic Relaxation Probes

With the difficulty of observing long-range NOEs in unfolded and partly folded proteins, it has become necessary to employ a technique of greater sensitivity to detect the presence of transient contacts between distant parts of the polypeptide. This technique relies on the r^{-6} distance-dependent enhancement of nuclear spin relaxation by the unpaired electron in a paramagnetic center, where r is the distance between the unpaired electron and the nuclear spin, and the paramagnetic center is provided by an added spin label such as a nitroxide group. The paramagnetic group can be added to the protein by site-directed mutagenesis to form a cysteine residue, which can be specifically coupled to the nitroxide-bearing moiety. Care must be taken in the interpretation of the results of spin label experiments for unfolded proteins,[20] as the presence of conformational averaging is likely to introduce a bias towards those conformations with the shortest contact distances, even though their populations within the ensemble may be quite small. Nevertheless, use of paramagnetic spin label probes can provide exceptionally important insights into the global topology and long-range interactions in unstructured states and partly folded proteins.

4 ESTIMATION OF POLYPEPTIDE CHAIN DYNAMICS

NMR estimates of polypeptide chain dynamics have the potential to provide valuable insights into the internal molecular dynamics and the overall hydrodynamic behavior of unfolded and partly folded states. Local variations in backbone dynamics are correlated with constriction of backbone motions that result from propensities for local interactions of the polypeptide chain.[8,21] These interactions include formation of local hydrophobic clusters, formation of elements of secondary structure, or long-range tertiary interactions in a partly folded protein or molten globule.

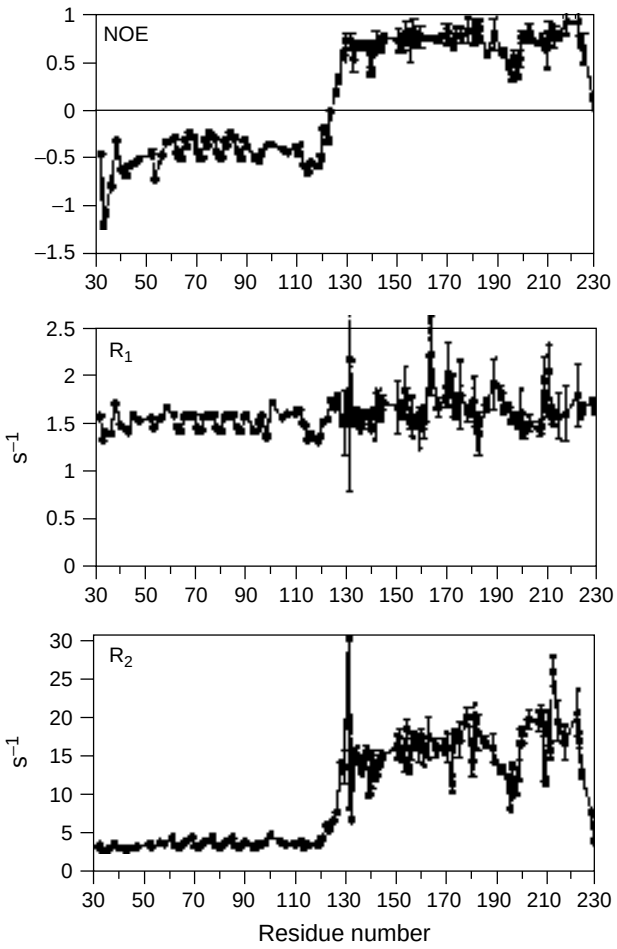

Figure 4 Relaxation rates R_1 ($= 1/T_1$) and R_2 ($= 1/T_2$) and heteronuclear NOE for PrP(29–231) at 500 MHz. Sample conditions: 30 °C, pH 5.5 and 0.1 M acetate buffer. (Adapted from Ref.[36] with permission)

4.1 Measurement of Relaxation Times

To date, the most common method of investigating backbone dynamics is by measurement of ^{15}N T_1 and T_2 relaxation times and the $\{^1H\}$-^{15}N NOE in uniformly ^{15}N-labeled protein, using 2D HSQC-based methods. Optimized pulse sequences have been described.[22] If necessary, amino acid specific labeling can be used to obtain additional data in overlapped regions of the spectrum.[21] Relaxation times and heteronuclear NOEs for unfolded proteins have characteristic values that are quite distinct from those of folded proteins. This can be used to identify regions of flexibility in folded proteins, as shown for example in Figure 4. Values in the two halves of the cellular prion protein PrP^C are quite different. In the N-terminal half of the protein, the NOE and R_2 values are significantly lower than those for the C-terminal half of the protein. In particular, the heteronuclear NOE shows a difference between negative values (N-terminal half) and positive values (C-terminal half), a diagnostic feature distinguishing unfolded protein (N-terminal) from folded (C-terminal).

4.2 Analysis of Relaxation Data

The interpretation of spin relaxation data for folded proteins is commonly performed using the model-free formalism.[23,24] The dynamics are described in terms of an overall rotational correlation time τ_m, an internal correlation time τ_e, and an order parameter S^2 describing the amplitude of the internal motions.[24] These parameters can be interpreted for folded proteins as intuitive physical parameters describing molecular motions. However, the dynamics of unfolded or partly folded proteins are difficult to describe accurately by the model-free approach, because the basic assumption of isotropic tumbling with a single molecular correlation time is not valid. Nevertheless, qualitative insights into the dynamics of unfolded states have been obtained by model-free analysis.[25–27]

An alternative approach is to undertake direct mapping of the spectral density either by measurement of additional relaxation parameters[28] or by making simplifying approximations.[29,30] Reduced spectral density mapping gives an interpretation of the dynamics information obtained that depends only upon the accuracy of the experimental relaxation data, in contrast to the assumptions made in model-free analysis, which are of dubious validity for unfolded proteins. The reduced spectral density function, $J(\omega)$, gives information on

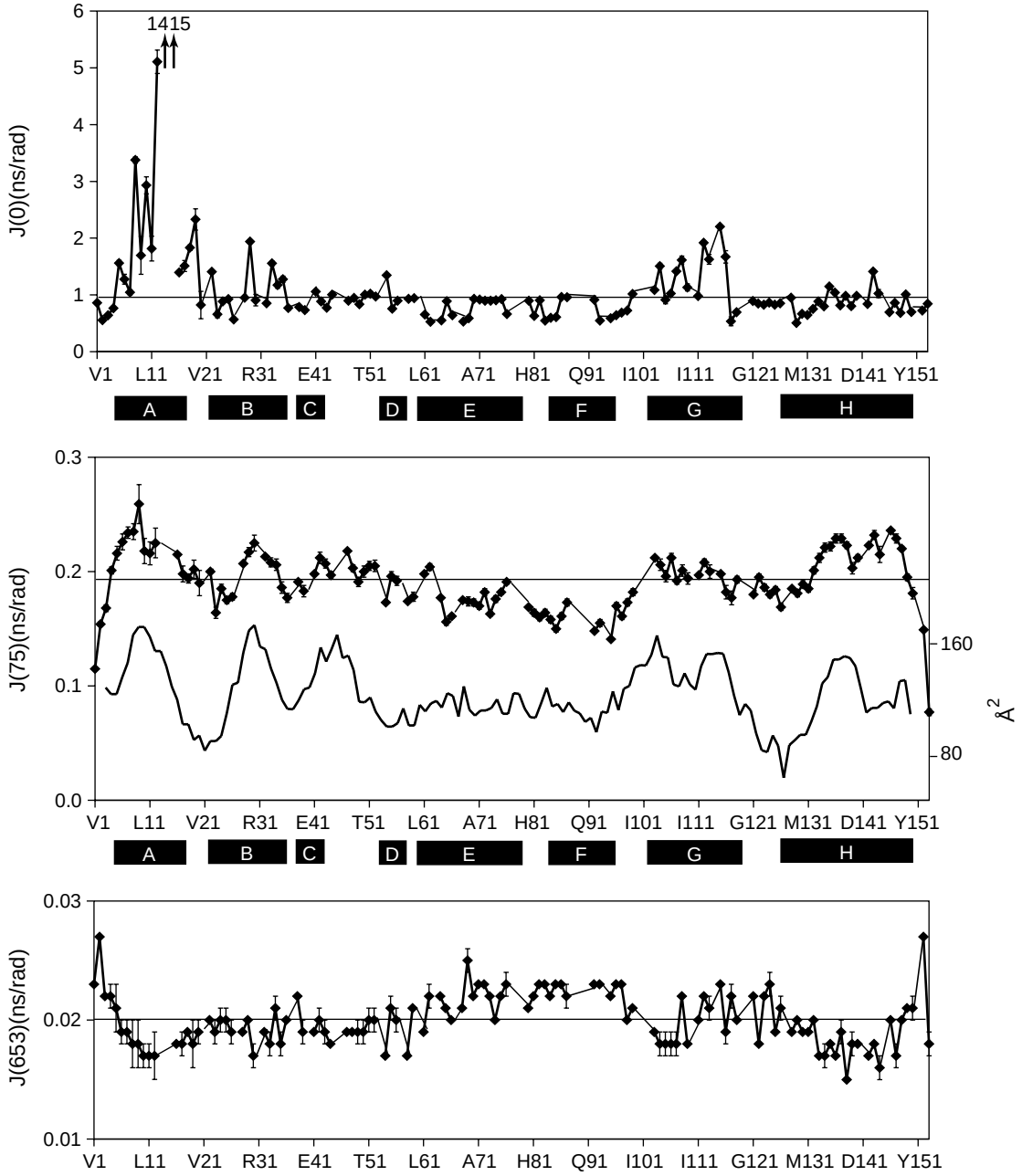

Figure 5 Calculated values of $J(0)$, $J(75)$ and $J(653)$ for apomyoglobin, pH 2.3, 25 °C. The horizontal lines show mean values of $J(75)$ (0.19 ns rad^{-1}), $J(653)$ (0.020 ns rad^{-1}), and the 10% trimmed mean value of $J(0)$ (0.97 ns rad^{-1}). Average buried surface area,[34] averaged over a seven residue window, is shown together with $J(75)$, with corresponding scale on the right of the figure. (Adapted from Ref.[16] with permission)

the motion of the NH bond vector at three frequencies ω_0, ω_N and 0.87 ω_H. The spectral density function at zero frequency is sensitive both to internal motions on the nanosecond time scale that are faster than the overall tumbling of the protein and to slow motions on the ms-μs time scale. In contrast, the high frequency spectral densities $J(0.87\ \omega_H)$ are sensitive only to fast internal motions, on a picosecond time scale. In the prion protein, nanosecond time scale motions [large $J(0)$ and low $J(0.87\ \omega_H)$ values] are dominant for residues with restricted motion, while the reverse is true for more flexible regions of the backbone. The N-terminal region is very flexible, with $J(0)$ values less than 1.5 ns for most residues in the region 29–125. The $J(\omega_N)$ values show less variation with residue number, with typical values between 0.25 and 0.35 ns, although the structured C-terminal part of the protein gives generally higher values. The higher frequency spectral density function $J(0.87\omega_H)$ has much smaller values (between 0.001 and 0.04 ns), and the trend is opposite to that of $J(0)$, with larger values in the unstructured region and smaller values in the structured region.

4.3 Translational Diffusion Analysis

Further information on the compactness of unfolded states of proteins can be obtained by measurement of the translational diffusion coefficient using the pulsed field gradient water-suppressed longitudinal encode-decode (water-sLED) experiment.[31] The method can be used to monitor unfolding transitions[32] or to measure hydrodynamic radii.[32,33] The effective dimensions of an unfolded or partly folded protein depend on the extent of local compaction, which is mediated through formation of local hydrophobic clusters or local elements of secondary structure.

4.4 Example of an Application of Spectral Density Mapping

Apomyoglobin unfolded at pH 2.3 provides a good example of the application of spectral density mapping to the elucidation of the local motions in an unfolded protein. The spectral densities of unfolded apomyoglobin[16] are shown in Figure 5. The spectral densities $J(\omega_N)$ ($J(75)$) and $J(0.87\ \omega_H)$ ($J(653)$) (Figure 5b and c) are sensitive only to fast (ps-ns) time scale motions. Larger than average values of $J(75)$ are observed in several contiguous regions of the polypeptide chain, Gly5-His12 in the A helix of native myoglobin, Ile28-Lys34 in the B helix, and residues Lys133-Glu148 in the H helix, indicating that motion is somewhat restricted on a sub-ns time scale. Restriction of motions in these regions is confirmed by the observation of lower than average values for $J(653)$. Interestingly, the principal features of the plot of $J(75)$ versus residue number correlate well with the average buried surface area calculated using the parameters of Rose et al.;[34] the correlation between $J(\omega_N)$ and hydrophobicity[35] is much poorer. Burial of hydrophobic surface area appears to be of major importance in initiation of protein folding.[34]

The most noticeable features of the $J(0)$ spectral density (Figure 5a) are the greatly increased values in two contiguous segments of the polypeptide, formed by residues Gln8-Ala19, and residues Ile112-His116. The $J(0)$ values in these regions are much larger than expected on the basis of $J(\omega_N)$ and $J(0.87\ \omega_H)$ and provide evidence for slow motional processes, on the ms-μs time scale. In addition, the NH resonances of Trp14 and Ala15 are broadened beyond detection, an indication that R_2 (and hence $J(0)$) could not be measured but must be very large. A plausible explanation for the broadening of resonances in these two highly localized regions (and nowhere else in the sequence) is that there is some transient (ms-μs time scale) contact in the acid-unfolded state between the A and G helix regions.[16] These observations provide the first evidence for transient contacts between specific segments of an unfolded polypeptide, and give an indication of the likely mechanism of the earliest collapse steps in the folding of a protein. These data are supported by studies with spin-labeled apomyoglobin (Lietzow, Jamin, Dyson, and Wright, unpublished observations).

5 FUTURE PROSPECTS

The advent of high-field NMR spectrometers and the widespread use of stable isotope labeling has led to an explosion of information on unfolded states of proteins. It is likely that further information will be forthcoming with these and additional new techniques being introduced at the present time. Given the increasing relevance of unfolded states to biologically important systems, including their implication in a number of disease states, we anticipate that the next few years will see a significant increase in the amount of experimental work in this field, and a concomitant increase in our understanding of the nature of unfolded and partly folded states of proteins, as well as of the folding process.

6 REFERENCES

1. H. J. Dyson and P. E. Wright, *Methods Enzymol.*, 2001, **339**, 258.
2. P. E. Wright and H. J. Dyson, *J. Mol. Biol.*, 1999, **293**, 321.
3. D. Braun, G. Wider, and K. Wüthrich, *J. Am. Chem. Soc.*, 1994, **116**, 8466.
4. O. Zhang, J. D. Forman-Kay, D. Shortle, and L. E. Kay, *J. Biomol. NMR*, 1997, **9**, 181.
5. J. Yao, H. J. Dyson, and P. E. Wright, *FEBS Lett.*, 1997, **419**, 285.
6. A. Liu, R. Riek, G. Wider, C. Von Schroetter, R. Zahn, and K. Wuthrich, *J. Biomol. NMR*, 2000, **16**, 127.
7. F. Löhr and H. Rüterjans, *J. Biomol. NMR*, 1995, **6**, 189.
8. D. Eliezer, J. Yao, H. J. Dyson, and P. E. Wright, *Nature Struct. Biol.*, 1998, **5**, 148.
9. H. J. Dyson and P. E. Wright, *Annu. Rev. Biophys. Biophys. Chem.*, 1991, **20**, 519.
10. L. J. Smith, K. M. Fiebig, H. Schwalbe, and C. M. Dobson, *Fold. Design*, 1996, **1**, R95.
11. S. Spera and A. Bax, *J. Am. Chem. Soc.*, 1991, **113**, 5490.
12. D. S. Wishart and B. D. Sykes, *Methods Enzymol.*, 1994, **239**, 363.
13. S. Schwarzinger, G. J. A. Kroon, T. R. Foss, J. Chung, P. E. Wright, and H. J. Dyson, *J. Am. Chem. Soc.*, 2001, **123**, 2970.
14. L. J. Smith, K. A. Bolin, H. Schwalbe, M. W. MacArthur, J. M. Thornton, and C. M. Dobson, *J. Mol. Biol.*, 1996, **255**, 494.
15. C. J. Penkett, C. Redfield, I. Dodd, J. Hubbard, D. L. McBay, D. E. Mossakowska, R. A. G. Smith, C. M. Dobson, and L. J. Smith, *J. Mol. Biol.*, 1997, **274**, 152.
16. J. Yao, J. Chung, D. Eliezer, P. E. Wright, and H. J. Dyson, *Biochemistry*, 2001, **40**, 3561.

17. Y. Bai, J. Chung, H. J. Dyson, and P. E. Wright, *Protein Sci.*, 2001, **10**, 1056.
18. F. M. Hughson, P. E. Wright, and R. L. Baldwin, *Science*, 1990, **249**, 1544.
19. Y. K. Mok, C. M. Kay, L. E. Kay, and J. Forman-Kay, *J. Mol. Biol.*, 1999, **289**, 619.
20. J. R. Gillespie and D. Shortle, *J. Mol. Biol.*, 1997, **268**, 158.
21. D. Eliezer, J. Chung, H. J. Dyson, and P. E. Wright, *Biochemistry*, 2000, **39**, 2894.
22. N. A. Farrow, R. Muhandiram, A. U. Singer, S. M. Pascal, C. M. Kay, G. Gish, S. E. Shoelson, T. Pawson, J. D. Forman-Kay, and L. E. Kay, *Biochemistry*, 1994, **33**, 5984.
23. G. Lipari and A. Szabo, *J. Am. Chem. Soc.*, 1982, **104**, 4546.
24. G. Lipari and A. Szabo, *J. Am. Chem. Soc.*, 1982, **104**, 4559.
25. N. A. Farrow, O. Zhang, J. D. Forman-Kay, and L. E. Kay, *Biochemistry*, 1995, **34**, 868.
26. A. T. Alexandrescu and D. Shortle, *J. Mol. Biol.*, 1994, **242**, 527.
27. M. Buck, H. Schwalbe, and C. M. Dobson, *J. Mol. Biol.*, 1996, **257**, 669.
28. J. W. Peng and G. Wagner, *J. Magn. Reson.*, 1992, **98**, 308.
29. N. A. Farrow, O. Zhang, A. Szabo, D. A. Torchia, and L. E. Kay, *J. Biomol. NMR*, 1995, **6**, 153.
30. R. Ishima and K. Nagayama, *J. Magn. Reson. Series B*, 1995, **108**, 73.
31. A. S. Altieri, D. P. Hinton, and R. A. Byrd, *J. Am. Chem. Soc.*, 1995, **117**, 7566.
32. J. A. Jones, D. K. Wilkins, L. J. Smith, and C. M. Dobson, *J. Biomol. NMR*, 1997, **10**, 199.
33. D. K. Wilkins, S. B. Grimshaw, V. Receveur, C. M. Dobson, J. A. Jones, and L. J. Smith, *Biochemistry*, 1999, **38**, 16 424.
34. G. D. Rose, A. R. Geselowitz, G. J. Lesser, R. H. Lee, and M. H. Zehfus, *Science*, 1985, **229**, 834.
35. J. Kyte and R. F. Doolittle, *J. Mol. Biol.*, 1982, **157**, 105.
36. J. H. Viles, D. G. Donne, G. J. A. Kroon, S. B. Prusiner, F. E. Cohen, H. J. Dyson, and P. E. Wright, *Biochemistry*, 2001, **40**, 2743.

Acknowledgements

This work was supported by grants GM57374 and DK34909 from the National Institutes of Health.

Biographical Sketches

H. Jane Dyson, *b* 1951. B.Sc. 1973; Ph.D. 1977, Sydney. Postdoctoral work M.I.T. 1977–78 with Paul Schimmel; Chemistry faculty, University of New South Wales, 1979–84. NMR work at Scripps Clinic in 1984 in collaboration with Peter Wright. Faculty at Scripps, 1984–present. Approx. 140 publications. Research interests: protein folding, structure and dynamics of proteins, structure-function relationships of proteins.

Peter E. Wright, *b* 1947. B.Sc. 1968; M.Sc., 1969; Ph.D., 1972, Auckland. Postdoctoral work: Oxford, 1972–76, with R.J.P. Williams in protein NMR; Inorganic Chemistry faculty, University of Sydney, 1976–84. Faculty at Scripps, 1984–present. Currently Chairman, Department of Molecular Biology, Cecil and Ida Green Chair in Biomedical Research, Member, Skaggs Institute of Chemical Biology. Approx. 280 publications. Research Interests: applications of NMR to protein folding and structure determination, solution structure and dynamics of proteins, DNA-protein interactions.

Amino Acids, Peptides and Proteins: Chemical Shifts

David A. Case

The Scripps Research Institute, La Jolla, CA, USA

1	Introduction	1
2	Empirical Surveys of Chemical Shifts in Peptides and Proteins	1
3	Chemical Shifts and Secondary Structure	2
4	Chemical Shifts and Tertiary Structure	3
5	Conclusions	4
6	Related Articles	4
7	References	4

1 INTRODUCTION

Perhaps the most direct observables in NMR spectra are the positions of the resonances, which are generally reported as chemical shifts relative to a standard position. The very existence of useful spectra depends upon chemical shift dispersion, so that nuclei in chemically distinct positions resonate at different frequencies. For peptides and proteins it is convenient to divide the origins of chemical shift differences into two components: the first arises from variations in the local electronic environment, so that aromatic and aliphatic protons, for example, have characteristic shifts that differ from each other and from amide protons. A second component of chemical shift dispersion occurs with nominally identical protons, such as valine Hα, due to variations in the nature of adjoining residues and especially to conformational differences in secondary and tertiary structure. While there is no sharp distinction between these two components, the 'local' effects usually arise from variations in shielding by electrons in the bonds that contain (or are adjacent to) the resonating nucleus, whereas the longer range effects are generally 'through-space' interactions involving functional groups separated by many chemical bonds from the nucleus in question.

This article surveys both empirical trends and theoretical approaches to understanding chemical shift trends in amino acids, peptides and proteins. The main emphasis is on connections between conformation (especially secondary and tertiary structure) and chemical shift. It has been clear for some time that chemical shifts in proteins and peptides depend upon structure in a reasonably regular way, so that, for example, the shifts in structurally homologous proteins are themselves homologous.[1,2] One force driving recent reexaminations of the origins of chemical shift dispersion has been the rapid growth in the number of protein and peptide assignments. Many of these are now available in a relational database that contains about 140 000 assignments.[3] While much of the 'information content' of these data remains to be discovered, the following two sections outline some of the clear trends that emerge from surveys of shift distributions

2 EMPIRICAL SURVEYS OF CHEMICAL SHIFTS IN PEPTIDES AND PROTEINS

2.1 Peptides

Short, unstructured peptides provide a useful reference point for many examinations of protein shifts, since they embody most of the local contributions that depend upon the chemical nature of the amino acid side chain, but lack the longer range contributions characteristic of folded proteins. The values most often cited are those of Bundi and Wüthrich (for protons),[4] and Richarz and Wüthrich (for ^{13}C),[5] based on the peptide H-Gly-Gly-X-Ala-OH, where X represents any of the 20 common amino acids. Table 1 lists these values for the backbone nuclei. It is common practice to define a 'structural' shift as the difference between an observed resonance position in a protein or structured peptide and these 'random coil' values.

In principle, peptide shifts like these could be computed from first principles using quantum chemistry calculations. At present such calculations are limited to relatively small molecules in the gas phase, and are generally not of routine 'chemical' accuracy, at least when one is considering nuclei in different bonding environments.[6] The situation is changing rapidly, however, and ab initio calculations with reasonable basis sets are now feasible for protein fragments such as amino acids and dipeptides.[7–11] Such calculations appear to be able to rationalize the dependence of some shifts on backbone dihedral angles, and point the way to the exploration of other effects such as hydrogen bonding and external electric fields. Because a variety of effects are important in influencing shifts, reliable computational studies on amino acids and peptides could have an important impact in the next few years.

2.2 Proteins

The primary empirical study of chemical shifts in proteins is that of Wishart et al.[12] who correlated observed chemical shifts and secondary-structure assignments in over 70 proteins, and computed averages and distributions for shifts in helix, β-strand, and coil configurations. Table 1 gives the results (not sorted by secondary structure) for a larger sample drawn from the BioMagResBank database.[3] There are only minor differences between the proton averages given in Table 1 and the earlier results; for the amide ^{15}N shifts, results for M, P and T differ by more than 1 ppm between the two compilations; for ^{13}Cα, C, M, N, Q and W differ by at least 1 ppm; the majority of values for the carbonyl ^{13}C shift differ by at least this much, perhaps reflecting the small number of available shifts even now. As might be expected, the Cα and Hα nuclei, which are closest to the side chain, show a strong correlation between the median shift observed in proteins and the 'random coil' peptide value: linear correlation coefficients are 0.95 and 0.99 for Hα and Cα respectively. On the other hand, median shifts in proteins for the amide proton and carbonyl carbon are only weakly related to the peptide random coil shifts, with correlation coefficients of 0.11, and 0.56, respectively. This suggests that longer range interactions, such as hydrogen bonding, may be important in influencing these shifts.

Table 1 Backbone Shift Distributions in protein[a]

	HN				Hα			
Res.	No.	Median	SD	rc	No.	Median	SD	rc
A	1446	8.16	0.61	8.25	1429	4.18	0.50	4.35
C	882	8.44	0.66	8.31	942	4.72	0.63	4.69
D	975	8.34	0.62	8.41	936	4.59	0.32	4.76
E	1225	8.30	0.68	8.37	1167	4.17	0.45	4.29
F	668	8.40	0.76	8.23	694	4.61	0.61	4.66
G	1485	8.33	1.31	8.39	2295	3.92	0.68	3.97
H	421	8.27	0.96	8.41	450	4.61	1.02	4.63
I	789	8.24	0.68	8.19	807	4.15	0.62	4.23
K	1593	8.17	0.75	8.41	1500	4.20	0.48	4.36
L	1447	8.19	0.73	8.42	1426	4.24	0.51	4.38
M	326	8.30	0.63	8.42	325	4.29	0.49	4.52
N	862	8.33	0.84	8.42	827	4.67	0.46	4.75
P	–	–	–	–	683	4.42	0.40	4.44
Q	730	8.16	0.65	8.41	683	4.25	0.46	4.37
R	892	8.23	0.58	8.27	848	4.25	0.46	4.38
S	1113	8.27	1.43	8.38	1118	4.45	0.44	4.50
T	1082	8.16	0.82	8.24	1087	4.40	0.57	4.35
V	1157	8.21	0.82	8.44	1202	4.08	0.86	4.18
W	227	8.26	0.86	8.09	220	4.63	0.61	4.70
Y	685	8.26	0.81	8.18	717	4.58	0.61	4.60

	N			Cα				C			
Res.	No.	Median	SD	No.	Median	SD	rc	No.	Median	SD	rc
A	335	122.8	8.7	118	52.1	2.1	50.8	40	177.8	2.4	175.8
C	62	117.8	3.7	35	55.0	3.1	53.9	40	172.2	2.0	173.9
D	216	120.3	4.1	77	53.0	2.1	52.7	31	176.9	1.4	174.2
E	258	120.9	3.2	112	56.7	2.6	55.4	42	177.2	2.1	173.7
F	136	121.3	4.4	79	56.2	2.6	56.2	38	174.7	2.5	172.9
G	277	109.1	4.0	171	44.0	1.9	43.9	52	172.7	2.1	171.8
H	59	119.5	3.5	30	53.8	5.7	53.6	6	175.8	1.8	172.2
I	169	123.6	4.6	59	60.0	3.0	59.6	22	175.8	1.9	174.2
K	364	120.7	4.0	153	56.0	2.1	54.6	30	175.7	2.2	174.5
L	289	122.0	4.4	115	53.7	1.9	53.8	26	176.5	1.8	174.7
M	79	120.9	4.8	42	54.7	2.2	54.0	19	177.4	1.8	173.4
N	172	118.9	5.1	65	52.7	1.9	53.8	26	173.7	1.9	173.1
P	34	137.7	3.8	61	62.3	1.6	61.9	19	175.0	2.1	174.1
Q	179	120.2	3.8	64	55.4	2.1	54.1	19	175.1	1.8	174.0
R	128	120.7	3.7	57	55.6	2.5	54.6	31	174.7	3.7	173.4
S	166	116.9	3.6	78	57.0	1.9	56.6	19	173.7	1.6	172.6
T	200	115.7	5.6	111	60.3	2.6	60.1	38	174.8	1.9	172.5
V	237	121.3	6.0	92	60.8	2.9	60.7	24	174.8	2.1	173.9
W	41	120.3	4.0	16	55.7	2.2	55.7	0	–	–	173.4
Y	114	121.2	5.5	69	55.7	1.7	56.3	14	173.9	1.9	172.9

[a]Data extracted from version 1.0 of the BioMagResBank database.[3] For each shift, the first three columns list the number of shifts, the median value and the standard deviation SD about the mean Column labeled 'rc' gives peptide shifts for H-Gly-Gly-X-Ala-OH from Bundi and Wüthrich[4] and Richarz and Wüthrich.[5]

3 CHEMICAL SHIFTS AND SECONDARY STRUCTURE

Considerable attention has been paid to ways in which the Hα shift reflects local secondary structure. It has been recognized for some time that β-sheet regions show high-frequency shifts for this resonance, while helical regions show low-frequency shifts. In the Wishart et al.[12] survey, the mean Hα positions in helices and sheets differ by nearly 0.8 ppm, and there is remarkably little overlap between the two distributions. The same general trend is found for amide protons, whereas Hβ shifts move in the opposite direction by a smaller amount. Amide protons at the N-terminus of helices tend to be shifted to high frequency compared with those at the C-terminus. These relationships are in many cases clear enough to drive secondary-structure assignments in proteins,[13,14] and to gain a qualitative idea of structural differences among homologous systems. It has been shown that this dependence of Hα and Hβ shifts on secondary structure can be explained in terms of peptide group contributions, as outlined below.[15]

These ideas may also be of use for linear peptides, where conformational heterogeneity hampers quantitative NOE-based structure calculations. For example, amide proton shifts in model helical peptides are often periodic (with a 3–4 residue repeat pattern);[16,17] amphipathic helices show a periodic behavior that appears to be related to curving of the helix axis;[18,19] and it may be possible to characterize helices of marginal stability through an analysis of the solvent dependence of backbone shifts.[20]

The relationship of ^{15}N and ^{13}C shifts to secondary structure is also of considerable current interest.[9–12,21] Cα and carbonyl shifts exhibit a strong correlation with secondary structure, both moving to higher frequency in helical conformations and to lower frequency in β-strand or extended configurations. As with Hα shifts, there is surprisingly little overlap between the distributions, which suggests that reliable conformational conclusions may be drawn, and the Cα shift has been used as a site-specific probe of the helix/coil transition in linear peptides.[22] There are also indications from solid state studies of peptides that the carbonyl ^{13}C resonance moves to higher frequency with decreasing CO$\cdots$HN hydrogen-bond length,[23–27] a result that is in rough accord with quantum chemical calculations.[26] Cβ shifts also show systematic differences between helices and sheets, but with much more overlap in the observed distributions.

The situation for amide ^{15}N shifts in proteins (as with amide protons) is less clear. There are general differences between shifts in helix and sheet structures of about 3 ppm, but the overlap between the two distributions is often greater than this, so that it is difficult to draw simple conclusions from a given set of shifts.[12,28,29] There is a correlation between amide proton and amide ^{15}N shifts, suggesting that similar physical effects are influencing both. There is some evidence that ^{15}N shifts may be periodic in helices, reflecting the local structure, but the relationship does not appear to be a simple one.[16,30]

4 CHEMICAL SHIFTS AND TERTIARY STRUCTURE

In both organic chemistry and biochemistry, empirical analyses of the effects of 'distant' substituents on chemical shifts have played an important role for many years.[31] There are generally two such types of interaction: magnetic fields arising from anisotropies in the magnetic susceptibilities of distant functional groups, and electric fields created by distant dipoles or charges. The former are strongest with conjugated or partially delocalized electrons (such as in aromatic rings or peptide groups) where there are significant anisotropies in group magnetic susceptibilities.[32–34] These groups then respond to an external spectrometer field $\boldsymbol{B}_0$ to create a local magnetic field which can augment or oppose $\boldsymbol{B}_0$.[35] The electrostatic fields of distant groups influence chemical shifts indirectly, by polarizing chemical bonds, and thus contributing to shielding or deshielding of the nuclei.[36] These mechanisms are considered in more detail in the following paragraphs.

4.1 Ring Current Calculations

The general form of empirical theories is $\sigma_{rc} = iBG(\boldsymbol{r})$ where $\boldsymbol{r}$ is the vector from the observed proton to the aromatic ring, $G(\boldsymbol{r})$ is a geometric factor, and i and B are constants.[31,34] It is conventional to incorporate in B those constants that would yield the expected contribution from a benzene ring, and to use i# (the 'ring current intensity' factor) to represent the ratio of the intensity expected for the ring in question to that of a benzene ring. There have been several attempts to estimate these factors, based on both quantum mechanical and empirical calculations[37,38]

Two commonly used parameterizations of the geometric factors were proposed by Johnson and Bovey[39] and by Haigh and Mallion.[34] In the latter model, which is one of the simplest to implement, the geometric factor is

$$G(\boldsymbol{r}) = \sum_{ij} s_{ij} \left\{ \frac{1}{r_i^3} + \frac{1}{r_j^3} \right\} \qquad (1)$$

Here r_i and r_j are the distances from ring atoms i and j to the proton, and s_{ij} is the area of the triangle formed by atoms i and j and the proton projected onto the plane of the aromatic ring. The sum is over the bonds in the ring. The Johnson–Bovey model sets up 'rings' of current above and below the plane of the atoms, and computes fields from this model. There appears to be very little difference between the two models, except at very short distances.

The heme group is an important special case for ring current calculations, and a variety of empirical calculations have been carried out.[40–43] A simple model that gives good results treats the heme as five rings: four for the pyrroles, and one 'macrocycle' that traverses the large conjugated ring in the canonical valence-bond structure. Cross and Wright[43] compared the results of this and other models with a dataset composed of protein and model compound shifts, and Ösapay and Case[38] used a larger heme protein database, including cytochromes c, b_5, and c_{551} and myoglobin. The empirical formulas appear to reproduce the observed behavior quite well.

4.2 Peptide Group Contributions

It has been recognized for some time that the magnetic anisotropy of the peptide group is likely to contribute significantly to chemical shifts in proteins. McConnell[35] has shown that when the observed proton and the 'source' of the magnetic anisotropy are far apart, the contribution to the local shielding tensor depends upon the magnetic anisotropy of the distant group:

$$\sigma_m = (3L_0R^3)^{-1} \sum_{i=x,y,z} \chi_{ii}(1 - 3\cos^2\theta_i) \qquad (2)$$

Here L_0 is the Avogadro constant, R is the distance from the proton to the distant group, χ_{ii} is a component of the magnetic susceptibility tensor, and θ_i is the angle between the i axis and the radius vector $\boldsymbol{R}$. Since there is no direct method for measuring the magnetic anisotropy of a peptide group within a protein, all estimates of these effects are to some extent empirical. Data for formamide[44] suggest that the peptide group is nearly axially symmetric about the out-of-plane axis, with an anisotropy $\Delta\chi$ of $-5.1 \pm 0.6 \times 10^{-6}$ erg (G^2-mol)$^{-1}$. This value is in good agreement with the one obtained using an empirical theoretical approach developed by Pauling:[33] -5.4×10^{-6} erg (G^2-mol)$^{-1}$.

Alternative models for peptide groups can be constructed by adding contributions from individual atoms[45] or bonds,[46–48] rather than using parameters for the peptide group as a whole. These alternative methods give generally similar results.[49,50]

Contributions from peptide groups calculated in this way can explain to a large extent the observed behavior of Hα chemical shifts as a function of local secondary structure.[15] Because of the R^{-3} distance dependence in equation (2), the neighboring peptide groups have the greatest influence, so that the shift depends to a large extent on the backbone dihedral angles ϕ and ψ, which determine the geometric relationship between the peptide planes and the Hα position.

4.3 Electrostatic Contributions

A significant contribution to chemical shifts can also arise from distant charges and dipoles, which can polarize the C–H bond and thereby increase or decrease the local shielding by electrons. The most significant term is expected to be proportional to the projection of the local electric field onto the C–H vector:

$$\sigma_{\mathrm{el}} = AE(\mathrm{C\text{–}H}) \qquad (3)$$

Buckingham[36] suggested that an appropriate value for A would be -2×10^{-12} esu^{-1}, but this magnitude clearly depends upon the way in which local electric fields are estimated. Most estimates to date have been based on Coulomb's law using partial charge models from molecular mechanics force fields, but this approach ignores important solvent effects that screen charge interactions, and further work in this area is needed.

The relative importance of various contributions is expected to be different for protons than for heavier nuclei. Ring current and magnetic anisotropy contributions will contribute the same absolute shift for all nuclei, and hence should be less important for nuclei like ^{13}C or ^{15}N that have large chemical shift ranges (compared with protons). These heavier nuclei, on the other hand, are more sensitive to electrostatic effects than are protons, probably because of the ability of electric fields to polarize their occupied p shells, which are unoccupied for hydrogen,[51] and some interesting attempts have been made to correlate shifts in proteins with estimates of the local electric fields.[52,53]

The analysis of chemical shift patterns using these ideas has a long history in organic chemistry.[31,34,46] Recently, several groups have shown that such calculations can explain a large portion of the chemical shift dispersion seen in globular proteins.[38,47,48,54,55] For example, Ösapay and Case[38] analyzed proton shifts from 17 proteins whose X-ray crystal structures had been determined; for 5678 protons bonded to carbon they obtained a linear correlation coefficient of 0.88 between the calculated and observed structural shifts, with an rms error of 0.23 ppm; for side-chain protons in nonheme proteins the rms error was 0.18 ppm, and for methyl groups it was 0.13 ppm. Computer codes that implement these ideas are available from the author, and equivalent code is part of the AMBER molecular modeling package, which also allows refinement of structures using penalty functions based on chemical shift formulas.[56] Initial applications to myoglobin[57] suggest that this idea may be a feasible and useful approach.

5 CONCLUSIONS

There is little doubt that the use of chemical shift information for peptides and proteins will continue to grow as a source of structural information. The Hα and Cα shifts appear to provide a reliable indicator of local secondary structure, and useful theories are available for magnetic interactions with aromatic rings and peptide groups. Electrostatic interactions (including hydrogen bonding and solvation effects) are less well understood. Ab initio electronic structure calculations are beginning to address problems of interest to peptide and protein chemists, and this, together with empirical analyses of larger numbers of shifts, should provide new insight into the origins of chemical shift dispersion.

6 RELATED ARTICLES

Carbon-13 Spectral Simulation; Shielding Calculations: LORG and SOLO Approaches; Chemical Shifts in Biochemical Systems; Shielding: Overview of Theoretical Methods; Shielding in Small Molecules.

7 REFERENCES

1. C. Redfield and J. P. Robertson, in *Computational Aspects of the Study of Biological Macromolecules by NMR Spectroscopy*, ed. J. Hoch, F. M. Poulsen, and C. Redfield, Plenum, New York, 1991, pp. 303–316.
2. B. J. Stockman, T. A. Scahill, N. A. Strakalaitis, D. P. Brunner, A. W. Yem, and M. R. Deibel, Jr., *J. Biomol. NMR*, 1992, **2**, 591.
3. B. R. Seavey, E. A. Farr, W. M. Westler, and J. L. Markley, *J. Biomol. NMR*, 1991, **1**, 217.
4. A. Bundi and K. Wüthrich, *Biopolymers*, 1979, **18**, 285.
5. R. Richarz and K. Wüthrich, *Biopolymers*, 1978, **17**, 2133.
6. G. A. Webb, in *Nuclear Magnetic Shieldings and Molecular Structure*, ed. J. A. Tossell, Kluwer, Dordrecht, 1993, pp. 1–25.
7. D. B. Chestnut and C. G. Phung, *Chem. Phys. Lett.*, 1991, **183**, 505.
8. D. B. Chestnut and C. G. Phung, in *Nuclear Magnetic Shieldings and Molecular Structure*, ed. J. A. Tossell, Kluwer, Dordrecht, 1993, pp. 221–241.
9. D. Jiao, M. Barfield, and V. J. Hruby, *J. Am. Chem. Soc.*, 1993, **115**, 10883.
10. A. C. de Dios, J. G. Pearson, and E. Oldfield, *J. Am. Chem. Soc.*, 1993, **115**, 9768.
11. A. C. de Dios, J. G. Pearson, and E. Oldfield, *Science*, 1993, **260**, 1491.
12. D. S. Wishart, B. D. Sykes, and F. M. Richards, *J. Mol. Biol.*, 1991, **222**, 311.
13. D. S. Wishart, B. D. Sykes, and F. M. Richards, *Biochemistry*, 1992, **31**, 1647.
14. N. H. Andersen, B. Cao, and C. Chen, *Biochem. Biophys. Res. Commun.*, 1992, **184**, 1008.
15. K. Ösapay and D. A. Case, *J. Biomol. NMR*, 1994, **4**, 215.
16. I. D. Kuntz, P. A. Kosen, and E. C. Craig, *J. Am. Chem. Soc.*, 1991, **113**, 1406.
17. M. A. Jiménez, F. J. Blanco, M. Rico, J. Santoro, J. Herranz, and J. L. Nieto, *Eur. J. Biochem.*, 1992, **207**, 39.

18. N. E. Zhou, B. -Y. Zhu, B. D. Sykes, and R. S. Hodges, *J. Am. Chem. Soc.*, 1992, **114**, 4320.
19. F. J. Blanco, J. Herranz, C. González, M. A. Jiménez, M. Rico, J. Santoro, and J. L. Nieto, *J. Am. Chem. Soc.*, 1992, **114**, 9676.
20. M. Bruix, M. Perello, J. Herranz, M. Rico, and J. L. Nieto, *Biochem. Biophys. Res. Commun.*, 1990, **167**, 1009.
21. S. Spera and A. Bax, *J. Am. Chem. Soc.*, 1991, **113**, 5490.
22. M. D. Reily, V. Thanabal, and D. O. Omecinsky, *J. Am. Chem. Soc.*, 1992, **114**, 6251.
23. D. W. Urry, L. W. Mitchell, and T. Ohnishi, *Proc. Natl. Acad. Sci. USA*, 1974, **71**, 3265.
24. T. Asakura, M. Kamio, and A. Nishioka, *Biopolymers*, 1979, **18**, 467.
25. S. Ando, I. Ando, A. Shoji, and T. Ozaki, *J. Am. Chem. Soc.*, 1988, **110**, 3380.
26. N. Asakawa, S. Kuroki, H. Kurosu, I. Ando, A. Shoji, and T. Ozaki, *J. Am. Chem. Soc.*, 1992, **114**, 3261.
27. E. Tüchsen and P. E. Hansen, *Int. J. Biol. Macromol.*, 1991, **13**, 2.
28. J. Glushka, M. Lee, S. Coffin, and D. Cowburn, *J. Am. Chem. Soc.*, 1989, **111**, 7716.
29. J. Glushka, M. Lee, S. Coffin, and D. Cowburn, *J. Am. Chem. Soc.*, 1990, **112**, 2843.
30. N. J. Skelton, M. Akke, J. Kördel, E. Thulin, S. Forsén, and W. J. Chazin, *FEBS Lett.*, 1992, **303**, 136.
31. R. K. Harris, *Nuclear Magnetic Resonance Spectroscopy, A Physicochemical View*, Longman, Harlow, 1986.
32. W. H. Flygare, *Chem. Rev.*, 1974, **74**, 653.
33. L. Pauling, *Proc. Natl. Acad. Sci. USA*, 1979, **76**, 2293.
34. C. W. Haigh and R. B. Mallion, *Prog. Nucl. Magn. Reson. Spectrosc.*, 1980, **13**, 303.
35. H. M. McConnell, *J. Chem. Phys.*, 1957, **27**, 226.
36. A. D. Buckingham, *Can. J. Chem.*, 1960, **38**, 300.
37. C. Giessner-Prettre and B. Pullman, *C. R. Hebd. Seances Acad., Sci., Ser. D*, 1969, **268**, 1115.
38. K. Ösapay and D. A. Case, *J. Am. Chem. Soc.*, 1991, **113**, 9436.
39. C. E. Johnson and F. A. Bovey, *J. Chem. Phys.*, 1958, **29**, 1012.
40. R. J. Abraham, *Mol. Phys.*, 1961, **4**, 145.
41. R. J. Abraham, G. R. Bedford, D. McNeillie, and B. Wright, *Org. Magn. Reson.*, 1980, **14**, 418.
42. R. J. Abraham, *J. Magn. Reson.*, 1981, **43**, 491.
43. K. J. Cross and P. E. Wright, *J. Magn. Reson.*, 1985, **64**, 220.
44. H. L. Tigelaar and W. H. Flygare, *J. Am. Chem. Soc.*, 1972, **94**, 343.
45. T. Asakura, Y. Niizawa, and M. P. Williamson, *J. Magn. Reson.*, 1992, **98**, 646.
46. R. F. Zürcher, *Prog. Nucl. Magn. Reson. Spectrosc.*, 1967, **2**, 205.
47. M. P. Williamson and T. Asakura, *J. Magn. Reson.*, 1991, **94**, 557.
48. M. P. Williamson, T. Asakura, E. Nakamura, and M. Demura, *J. Biomol. NMR*, 1992, **2**, 83.
49. J. Herranz, C. González, M. Rico, J. L. Nieto, J. Santoro, M. A. Jiménez, M. Bruix, J. L. Neira, and F. J. Blanco, *Magn. Reson. Chem.*, 1992, **30**, 1012.
50. M. P. Williamson and T. Asakura, *J. Magn. Reson., Ser. B*, 1993, **101**, 63.
51. J. Augspurger, J. G. Pearson, E. Oldfield, C. E. Dykstra, K. D. Park, and D. Schwartz, *J. Magn. Reson.*, 1992, **100**, 342.
52. J. D. Augspurger, A. C. de Dios, E. Oldfield, and C. E. Dykstra, *Chem. Phys. Lett.*, 1993, **213**, 211.
53. J. G. Pearson, E. Oldfield, F. S. Lee, and A. Warshel, *J. Am. Chem. Soc.*, 1993, **115**, 6851.
54. C. Giessner-Prettre, M. T. Cung, and M. Marraud, *Eur. J. Biochem.*, 1987, **163**, 79.
55. N. Gresh and C. Giessner-Prettre, *Biochem. Biophys. Res. Commun.*, 1990, **171**, 1211.
56. D. A. Pearlman, D. A. Case, J. C. Caldwell, G. L. Seibel, U. C. Singh, P. Weiner, and P. A. Kollman, *AMBER 4.0*, University of California, San Francisco, CA, 1991.
57. D. A. Case and P. E. Wright, in *NMR in Proteins*, ed. G. M. Clore and A. Gronenborn, MacMillan, New York, 1993, pp. 53–91.

Acknowledgments

This work was supported by NIH Grant GM45811. I thank Beverley Seavey and John Markley for providing access to the BioMagResBank database, and Gene Merutka, Jane Dyson, Peter Wright, and Klara Ösapay for helpful discussions.

Biographical Sketches

David A. Case, b 1948. B.S., 1970, Michigan State, A.M., 1972, Harvard, Ph.D., 1977, Harvard, USA. Approx. 90 publications. Research interests include modeling of proteins and nucleic acids, quantum mechanical studies of the active sites of metalloenzymes, and computational aspects of NMR.

Bilayer Membranes: Deuterium and Carbon-13 NMR

Michael F. Brown
University of Arizona, Tucson, AZ, USA
&
Sunney I. Chan
California Institute of Technology, Pasadena, CA, USA

1	Introduction	1
2	Irreducible Representation of the Nuclear Spin Hamiltonian	1
3	NMR Lineshapes for Dipolar and Quadrupolar Interactions	3
4	Nuclear Spin Relaxation	4
5	Testing of Conceptual Frameworks	9
6	Equilibrium and Dynamical Properties of Lipid Bilayers	12
7	Related Articles	14
8	References	14

1 INTRODUCTION

NMR spectroscopy affords a unique and powerful analytical tool which can be used to investigate matter in its various states, particularly inasmuch as it provides information pertinent to both average and dynamical properties. By contrast, with reference to disordered systems, X-ray and neutron-scattering techniques yield information of a relatively low-resolution nature, and atomic level data are not obtained. Because NMR spectroscopy provides knowledge at the microscopic level regarding liquid crystalline materials, it plays a unique and vital role in their investigation. The application of NMR methods to membrane bilayers builds upon the following: ^{1}H NMR studies by the groups of Bloom,[1] Chan,[2–4] and Klein;[5] the introduction of ^{2}H NMR spectroscopy by Seelig and co-workers;[6] natural abundance ^{13}C NMR studies by the group of Metcalfe;[7] and finally the ground-breaking EPR spin label work of McConnell and colleagues.[8,9]

It is known that biomembranes comprise a bilayer of lipids, containing proteins which span the bilayer or are associated with the aqueous interface. In the biologically relevant liquid crystalline phase, the constituents of membranes are highly disordered, and considerable motion occurs. The lipid bilayer represents the fundamental permeability barrier to the passage of ions and polar molecules, whereas the distinctive functions of biological membranes are carried out by proteins. In this contribution we briefly describe the advances made during the past few decades in the application of ^{2}H and ^{13}C NMR methods to the investigation of lipid bilayers in the fluid (Lα) phase. (i) First we review multinuclear MR lineshape studies of lipid bilayers; (ii) the use of ^{2}H and ^{13}C NMR relaxation methods is described as a means of obtaining information regarding the spectral densities of motion and dynamical properties of liquid crystalline materials; and, finally, (iii) we provide a summary of the application of NMR relaxation methods to lipid bilayers in the liquid crystalline phase.

2 IRREDUCIBLE REPRESENTATION OF THE NUCLEAR SPIN HAMILTONIAN

With regard to molecular solids and liquid crystalline materials, the information provided by NMR spectroscopy includes the motionally averaged NMR lineshapes due to the dipolar, quadrupolar, or chemical shift tensors, together with the relaxation rates which are due to fluctuations of the tensors about their equilibrium values. The above information is manifested in the correlation functions $G_m(t)$ corresponding to the various second-rank quantities, i.e. the dipolar, quadrupolar, or chemical shift tensors, or equivalently their Fourier transform partners, the spectral densities $J_m(\omega)$. By combining lineshape and relaxation studies one can gain considerable insight regarding equilibrium and dynamical properties of bilayers. How can liquid crystalline bilayers be investigated at the molecular and atomic levels?

In general, the coupling of a spin $I = 1$ system is described by the Hamiltonian operator[10]

$$\hat{\mathcal{H}}_\lambda = C_\lambda \sum_{m=-2}^{2} (-1)^m \hat{T}^{(2)\text{lab}}_{-m} V^{(2)\text{lab}}_m \qquad (1)$$

where C_λ is a constant and λ refers to a specific interaction, e.g. the dipolar (D) or quadrupolar (Q) coupling. All symbols have their customary meanings, where $\hat{T}^{(2)}_m$ and $V^{(2)}_m$ are second-rank irreducible spherical tensors, corresponding to the nuclear spin angular momentum operators $\hat{\boldsymbol{I}}$ and the coupling tensor $\boldsymbol{V}$, respectively. The spin angular momentum is quantized in the main external magnetic field (denoted 'lab'), where the corresponding irreducible tensor operators are defined by[11]

$$\hat{T}^{(2)\text{lab}}_0 = \sqrt{\tfrac{1}{6}}\,(3\hat{I}_Z\hat{S}_Z - \hat{\boldsymbol{I}}\cdot\hat{\boldsymbol{S}}) \qquad (2a)$$

$$\hat{T}^{(2)\text{lab}}_{\pm1} = \mp\tfrac{1}{2}(\hat{I}_Z\hat{S}_\pm + \hat{I}_\pm\hat{S}_Z) \qquad (2b)$$

$$\hat{T}^{(2)\text{lab}}_{\pm2} = \tfrac{1}{2}\hat{I}_\pm\hat{S}_\pm \qquad (2c)$$

in which $\hat{I}_\pm \equiv \hat{I}_X \pm \mathrm{i}\hat{I}_Y$ and likewise for $\hat{S}_\pm$. (For the heteronuclear magnetic dipolar coupling $\hat{\boldsymbol{I}} \neq \hat{\boldsymbol{S}}$; whereas for the homonuclear dipolar coupling or the electric quadrupolar coupling $\hat{\boldsymbol{I}} = \hat{\boldsymbol{S}}$.) By contrast, the irreducible components of the coupling tensor $V_m{}^{(2)}$ are expressed in a molecule-fixed principal axis system (PAS) as discussed by Häberlen[11] and Spiess:[10]

$$V^{(2)\text{PAS}}_0 = \sqrt{\tfrac{3}{2}}\,\delta_\lambda \qquad (3a)$$

$$V^{(2)\text{PAS}}_{\pm1} = 0 \qquad (3b)$$

$$V^{(2)\text{PAS}}_{\pm2} = -\tfrac{1}{2}\delta_\lambda\eta_\lambda \qquad (3c)$$

Here the asymmetry parameter $\eta_\lambda \equiv (V_{yy} - V_{xx})/V_{zz}$ describes the deviation of the Cartesian principal values from axial symmetry, where η_λ [0, 1], and $\delta_\lambda \equiv V_{zz}$ specifies the largest Cartesian principal component. The coupling parameters for the magnetic dipolar interaction and the electric quadrupolar interaction are summarized below:

Dipolar coupling:	Quadrupolar coupling (I=1):
$C_D = -2\gamma_I\gamma_S\hbar$	$C_Q = eQ/2\hbar$
$\delta_D = \langle r_{IS}^{-3}\rangle$	$\delta_Q = eq$
$\eta_D = 0$	η_Q

For the dipolar coupling the internuclear distance cubed is averaged over fast vibrational coordinates, such that $\langle r_{IS}^{-3}\rangle^{-1/3}$ can be greater than the equilibrium internuclear distance;[12,13] similar considerations apply to the quadrupolar coupling.[14]

Note that the above irreducible tensors are expressed in different coordinate frames; the spin operators $\hat{\boldsymbol{I}}$ and $\hat{\boldsymbol{S}}$ correspond to the laboratory frame defined by the main magnetic field, whereas the dipolar or quadrupolar couplings involve the molecule-fixed frame. To express the Hamiltonian in a single frame, e.g. that of the laboratory, one must employ the transformation properties of irreducible tensors under rotations.[15] The irreducible components of the coupling tensor in the laboratory frame and the principal axis system are related by

$$V_m^{(2)\mathrm{lab}} = \sum_{s=-2}^{2} V_s^{(2)\mathrm{PAS}} D_{sm}^{(2)}(\Omega_{\mathrm{PL}}) \tag{4}$$

In the above expression, $\Omega_{\mathrm{PL}} = (\alpha_{\mathrm{PL}}, \beta_{\mathrm{PL}}, \gamma_{\mathrm{PL}})$ are the Euler angles which describe active transformation[15] of the irreducible components from the principal axis system (P) to the laboratory frame (L). The definitions of Brink and Satchler[15] are used for the Wigner rotation matrices, $D_{m'm}^{(j)}(\Omega) = \mathrm{e}^{-\mathrm{i}m'\alpha} d_{m'm}^{(j)}(\beta) \mathrm{e}^{-\mathrm{i}m\gamma}$; where (m', m) are generalized projection indices, j is the angular momentum, $\Omega \equiv (\alpha, \beta, \gamma)$ are generalized Euler angles, and the elements of the reduced rotation matrix are indicated by $d_{m'm}^{(j)}(\beta)$. [Note that $D_{00}^{(j)}(\Omega) = d_{00}^{(j)}(\beta) = P_j(\cos\beta)$, where P_j is a Legendre polynomial of rank j.]

One can then use the closure property of the rotation group[15] to express the Wigner rotation matrix elements for the overall transformation, $D_{sm}^{(2)}(\Omega_{\mathrm{PL}})$, in terms of various intermediate frames (Figure 1). This gives

$$\begin{aligned} D_{sm}^{(2)}(\Omega_{\mathrm{PL}}; t) = \sum_r \sum_q \sum_p \sum_n & D_{sr}^{(2)}(\Omega_{\mathrm{PI}}; t) D_{rq}^{(2)}(\Omega_{\mathrm{IM}}; t) \\ & D_{qp}^{(2)}(\Omega_{\mathrm{MN}}; t) D_{pn}^{(2)}(\Omega_{\mathrm{ND}}; t) D_{nm}^{(2)}(\Omega_{\mathrm{DL}}) \end{aligned} \tag{5}$$

where all summations run from -2 to 2. The Euler angles Ω_{PI} specify active rotation of the irreducible components from the principal axis system (P) of the static tensor to the internal (I) motional frame; Ω_{IM} correspond to transformation from the internal frame to the molecular (M) axis system; Ω_{MN} to rotation from the molecular frame to the instantaneous director $\boldsymbol{n}(t)$, an axis of local cylindrical symmetry; Ω_{ND} to transformation from the instantaneous director to the average director $\boldsymbol{n}_0$, the macroscopic bilayer normal; and finally the angles Ω_{DL} describe the fixed transformation from the average director (D) to the laboratory frame (L) corresponding to the static external magnetic field. In the last transformation the spherical polar angles characterizing the orientation of the magnetic field within the frame of the bilayer are denoted by $(\alpha_{\mathrm{DL}}, \beta_{\mathrm{DL}}) \equiv (\phi, \theta)$. The Euler angles describing the various transformations may be either time-dependent as in Figure 1 or fixed; whereas the Ω_{DL} transformation is fixed. The expansion, equation (5), can be further generalized to encompass an arbitrary number of transformations; alternatively, closure enables those transformations not relevant for a given motional description to be collapsed.[16]

In the liquid crystalline state of lipid bilayers a hierarchy of motions exists as indicated by the frequency dependence of the ^{1}H, ^{2}H, and ^{13}C nuclear R_{1Z} and $R_{1\rho}$ relaxation rates.[17–21] Thus, one can expect contributions from segmental motions, as well as molecular motions and possibly collective fluctuations of the bilayer. The general types of motional models considered in this work are represented by Figure 1. In the case of segmental motions the dynamics involve the angles $\Omega_{\mathrm{PD}}(t)$ between the frame of the coupling tensor and the director; the remaining transformations are collapsed. Likewise, molecular motions are formulated in terms of the angles $\Omega_{\mathrm{MD}}(t)$ between the molecular frame and the director. Finally, collective motions involve fluctuations of the instantaneous director relative to the average director and are described by the angles $\Omega_{\mathrm{ND}}(t)$.

Now in general the transition frequencies are governed by the eigenvalues of the motionally averaged Hamiltonian, in which secular terms (m = 0) are considered. For the different models investigated, the observed lineshape is dependent on the equilibrium distribution of the tensor orientations. In the case of ^{2}H NMR the coupling is due to the quadrupolar interaction of the ^{2}H nucleus with the electric field gradient of

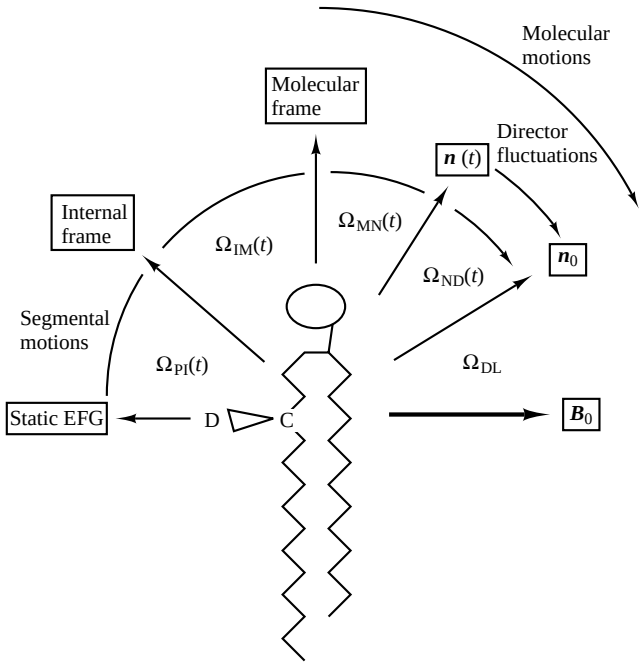

Figure 1 Schematic illustration of transformations employed in dynamical models for membrane constituents as described in the text

the chemical bond. One can then write that

$$\langle \nu_Q^{\pm} \rangle = \pm \tfrac{3}{4} \chi S_{CD} D_{00}^{(2)}(\Omega_{DL}) \quad (6)$$

where the doublet components $\nu_Q^{\pm}$ are separated by the quadrupolar splitting, $\Delta\nu_Q \equiv \nu_Q^+ - \nu_Q^-$, and the angular brackets denote a time or ensemble average. The segmental C–^{2}H order parameter is then defined by

$$S_{CD} \equiv \langle D_{00}^{(2)}(\Omega_{PD}) \rangle = \tfrac{1}{2} \langle 3\cos^2 \beta_{PD} - 1 \rangle \quad (7)$$

A similar formalism can be used for the homonuclear dipolar interaction in the case of ^{1}H NMR, and the heteronuclear ^{13}C–^{1}H dipolar interaction in the case of ^{13}C NMR spectroscopy.

3 NMR LINESHAPES FOR DIPOLAR AND QUADRUPOLAR INTERACTIONS

3.1 Proton NMR Spectroscopy

In order to obtain information about residual anisotropic interactions, e.g. dipolar interactions, it is necessary to study unsonicated bilayer systems. Perhaps the simplest approach entails investigation of the ^{1}H NMR spectral lineshapes.[1–3,22] Due to lateral self-diffusion of the lipids, the intermolecular ^{1}H–^{1}H dipolar interactions are averaged to zero,[1] and one observes the intramolecular part. However, because the motions are restricted in their angular range, one still has dipolar interactions among the different groups on the chain and between the two acyl chains, so that pairwise dipolar couplings are not resolved.[1–3,22] In this case the moments of the lineshapes contain useful information, and can be analyzed in terms of a superposition of dipolar order parameters corresponding to the various ^{1}H–^{1}H pairs.[1] (See also ***Bilayer Membranes: Proton and Fluorine-19 NMR***.)

One avenue to simplification is to study small sonicated vesicles where the rapid tumbling averages the dipolar interactions to zero. Here the lineshape is due to modulation of the residual dipolar couplings by the overall vesicle reorientation.[1,22] Alternatively, one can employ magic angle spinning (MAS) to narrow the spectral lines.[23] But in either case knowledge of the residual dipolar interactions may be difficult to extract in a model-free manner,[4,24] and there may be influences due to curvature of the interface.[2,25] Another strategy involves complete deuteration of the lipid molecule, with the exception of individual proton–proton pairs, which is a challenging synthetic task. However, a simpler alternative is to recognize that the Hamiltonian for the quadrupolar interaction of the ^{2}H nucleus is isomorphous to the pairwise dipolar interaction between like spins; both comprise spin I = 1 systems! It is synthetically much easier to incorporate deuterium into a lipid than to deuterate the entire molecule.

3.2 Deuterium NMR Spectroscopy

In discussing NMR observables in relation to the equilibrium and dynamical properties of bilayers, it is useful to focus on ^{2}H NMR spectroscopy.[6,26] Here the electric quadrupolar interaction is by far the largest coupling, and dominates over the chemical shift or homo- or heteronuclear dipolar interactions. The great value of ^{2}H NMR is that one can study the properties of an isolated spin I = 1 system without the complication of additional interactions of comparable magnitude. Moreover, as noted above, the quadrupolar interaction is isomorphous to the dipolar coupling, so that the formalism and conceptual approach can be extended to other nuclei such as ^{1}H and ^{13}C.

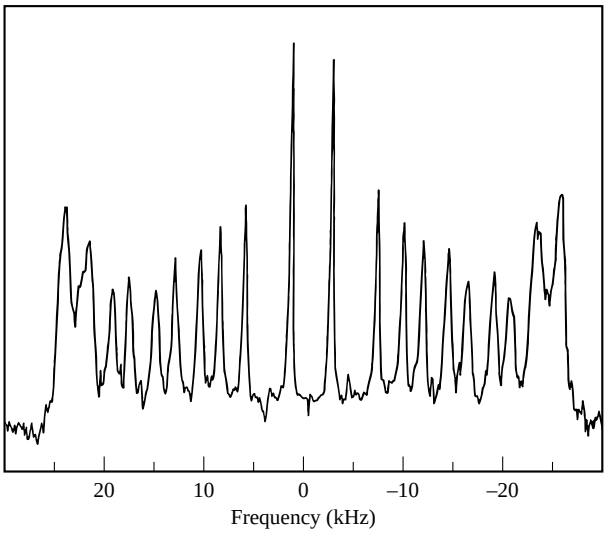

Figure 2 Representative ^{2}H NMR spectrum (de-Paked) of a multilamellar dispersion of 1-perdeuteropalmitoyl-2-docosahexaenoyl-*sn*-glycero-3-phosphocholine (PDPC) obtained at 55.4 MHz and 30 °C in the liquid crystalline (L_α) phase

Figure 2 depicts a representative ^{2}H NMR spectrum of a lipid bilayer in the fluid, liquid crystalline state.[27,28] If all the segments were equivalent then a single quadrupolar splitting would be observed. However, this is clearly not the case; rather, a family of splittings is found which indicate variations in motional averaging among the different chain segments. Although the static quadrupolar coupling is the same everywhere along the chain, the residual quadrupolar couplings of the various segments are clearly inequivalent. Now for significant motional averaging to occur the rate of the fluctuations must be greater than about $9\chi/8 = 1.9 \times 10^5$ s^{-1}, corresponding to the full angular anisotropy of the single quantum transitions of the I = 1 nucleus. It is remarkable that well-defined residual quadrupolar interactions are observed, corresponding to the order parameters S_{CD} of the various chain segments.[6] The ^{2}H NMR spectrum clearly shows that the system can be quite fluid and still give rise to distinct quadrupolar splittings. Thus, one obtains information at the atomic level in the disordered, liquid crystalline state. (See also ***Membranes: Deuterium NMR***.)

3.3 Carbon-13 NMR Spectroscopy

When the motion is restricted, so that the magnetic dipolar, chemical shift, or electric quadrupolar tensors are not averaged to their traces, then considerable broadening of the spectral lines occurs. Thus, natural-abundance ^{13}C NMR spectra of

unsonicated bilayer membranes are dominated by unresolved homo- and heteronuclear dipolar interactions, together with the anisotropic chemical shift of the ^{13}C nucleus.[20] As in the case of ^{1}H NMR, the dipolar and chemical shift tensors can be averaged to their traces by investigating small sonicated vesicles; well-resolved ^{13}C NMR spectra are then obtained.[7] However, information regarding the averaged tensors is difficult to retrieve, and one is largely confined to relaxation studies.[17,18] (See also ***Sonicated Membrane Vesicles***.)

An alternative is to remove the chemical shift anisotropy and ^{13}C–^{1}H dipolar interaction by MAS; high-power dipolar decoupling is unnecessary in the fluid, liquid crystalline phase.[20,23,29] Figure 3 shows representative natural-abundance MAS ^{13}C NMR spectra of 1,2-dilauroyl-*sn*-glycero-3-phosphocholine (DLPC) (Figure 3a) and a mixture of 1,2-dipalmitoyl-*sn*-glycero-3-phosphocholine (DPPC)/cholesterol (1:1) (Figure 3b), each in the fluid phase.[20,30] The isotropic chemical shifts of both the flexible phospholipids as well as the rigid cholesterol moiety are readily detected.[30]

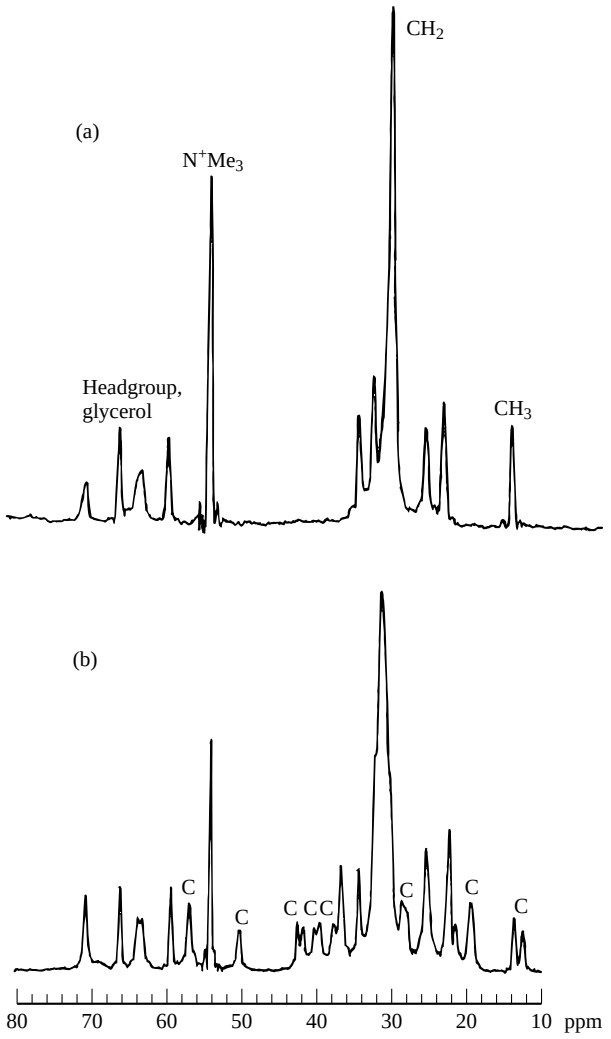

Figure 3 Magic angle spinning (MAS) natural abundance ^{13}C NMR spectra at 50 MHz of multilamellar dispersions of (a) DLPC at ambient temperature, and (b) DPPC/cholesterol (1:1) at 50 °C in the liquid crystalline phase. Resonances are denoted; C refers to cholesterol

These results clearly illustrate the utility of MAS methods for NMR studies of disordered lipid bilayer systems, as well as other liquid crystalline systems and soft matter in general. (See also ***Magic Angle Spinning***.)

One can then reintroduce the dipolar interaction[20,30] or the chemical shift anisotropy (CSA)[31] selectively by implementation of two-dimensional NMR techniques. Heteronuclear dipolar interactions can be included by applying WAHUHA[11] or other suitable pulse sequences for decoupling of the homonuclei during the evolution period t_1, with MAS during the acquisition period t_2 to obtain dipolar–chemical shift NMR spectra.[20,30] Alternatively, modulation due to the chemical shift anisotropy can be included during the evolution period t_1 by variable angle hopping, followed by MAS during t_2 to yield CSA–chemical shift ^{13}C NMR spectra.[31] These natural-abundance ^{13}C NMR methods provide a potentially rich source of knowledge about the average structural properties of lipid bilayers. Such approaches have the advantage that information regarding the entire lipid molecule is obtained without isotopic labeling, but they have the drawback that appreciable spectral overlap occurs within the acyl carbon region (Figure 3). However, by combining the results of ^{2}H NMR with ^{13}C NMR spectroscopy of lipid bilayers one can obtain considerably more information than with either technique alone! (See also ***Membranes: Carbon-13 NMR***.)

3.4 Order Profiles from Deuterium and Carbon-13 NMR Spectroscopy

In the case of ^{2}H NMR spectroscopy the information content can be reduced to a profile of the order parameters $S_{CD}^{(i)}$ as a function of chain position (index i).[6,32] Such a representative plot of the order parameters versus the chain position is shown for 1,2-diperdeuterolauroyl-*sn*-glycero-3-phosphocholine (DLPC-d_{46}) in Figure 4(a). The order profile comprises a plateau in the $S_{CD}^{(i)}$ values over the first part of the chains, followed by a decrease as the chain terminus is approached. The plateau in the order profile is associated with tethering of the acyl chains to the aqueous interface. It follows that beyond the plateau region the segments are more disordered to fill in the free volume that would otherwise be present, i.e. to maintain the density constant at essentially that of liquid hydrocarbon. Analogous ^{2}H NMR studies of phospholipids have been carried out for lipids in other physical states, including the normal hexagonal (H_I) and reverse hexagonal (H_{II}) phases.[25,33,34] (See also ***Lipid Polymorphism***.) In the case of ^{13}C NMR spectroscopy, order parameters, S_{CH}, are obtained by comparing the residual dipolar or chemical shift tensors to their static values, and yield good agreement with previous ^{2}H NMR results.[20,31]

4 NUCLEAR SPIN RELAXATION

In the fluid L_α phase, dynamical information can be obtained from measurement and interpretation of the nuclear spin relaxation rates.[14] Analysis of the relaxation enables one to disentangle the various types of motions which lead to the averaging of the dipolar, quadrupolar, or chemical shift tensors. Early ^{1}H NMR[2,5] and ^{13}C NMR[7] relaxation

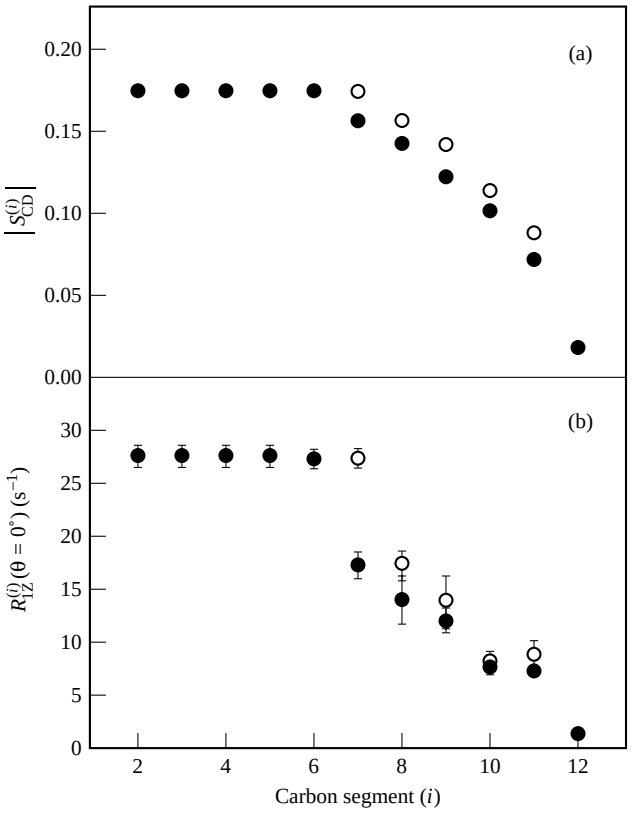

Figure 4 Profiles of (a) segmental order parameters, $S_{CD}^{(i)}$, and (b) spin–lattice relaxation rates, $R_{1Z}^{(i)}$, as functions of acyl segment position *(i)* for DLPC-d_{46} oriented on planar substrates at 46.1 MHz and 40 °C in the liquid-crystalline phase. •, *sn*-1 chain; ○, *sn*-2 chain. (Reproduced by permission of the American Institute of Physics from T. P. Touard, T. M. Alam, and M. F. Brown, *J. Chem. Phys.*, 1994, **101**, 5229)

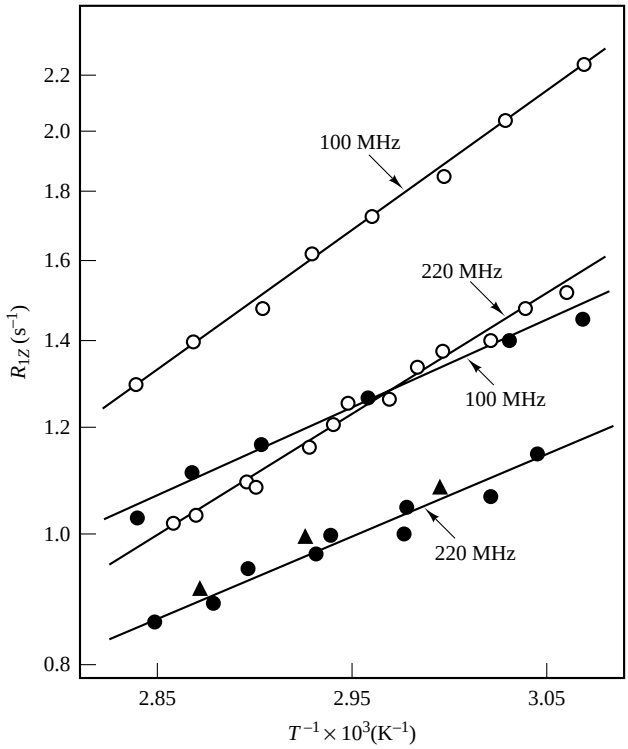

Figure 5 Proton spin–lattice relaxation rates R_{1Z} for acyl segments of DPPC vesicles in the liquid crystalline state versus reciprocal temperature at two different frequencies (magnetic field strengths); ○, DPPC; ▲, DPPC/DPPC-d_{62} (2:8); •, DPPC/DPPC-d_{62} (1:9). The results indicate the presence of both intermolecular and intramolecular contributions. (Reproduced by permission of Elsevier Science Publishers from P. A. Kroon, M. Kainosho, and S. I. Chan, *Biochim. Biophys. Acta*, 1976, **433**, 282)

rate studies provided evidence for a liquid-like mobility of the chains; however, separation of the contributions from the statistical ordering and rate of motions[2] was not always considered.

As shown by Brown, Seelig, and Häberlen,[35] a profile is seen in the ^{2}H NMR relaxation rates as a function of chain position, which is markedly reminiscent of the profile seen for the ^{2}H NMR order parameters. A representative ^{2}H NMR relaxation profile for DLPC-d_{46} is shown in Figure 4(b). As can be seen, the $R_{1Z}^{(i)}$ profile parallels the order profile in that a plateau is observed over the initial part of the chain, followed by a decrease in the $R_{1Z}^{(i)}$ relaxation rates as the acyl chain terminus is approached. Similar relaxation profiles are obtained for the ^{13}C R_{1Z} values of small vesicles,[18] as well as the R_{1Z} and $R_{1\rho}$ values of unsonicated bilayer membranes.[20] It is noteworthy that few differences exist between the R_{1Z} rates of unsonicated bilayers and small vesicles.[35] The relaxation profile can be due to a profile of the motional amplitudes along the chains, or alternatively it can represent the rate of motion along the chains, viz. as a function of depth within the bilayer hydrocarbon region. Which of the above interpretations is correct?

Moreover, an inherent feature of the nuclear spin relaxation is that there is a characteristic frequency (magnetic field strength) dependence.[17–19, 36] This was first extensively investigated by Chan and co-workers;[17] representative ^{1}H NMR data from their work for DPPC at two different frequencies are shown in Figure 5. The frequency dependence of the relaxation suggests that slow motions of the lipids occur within the bilayer, which are not found in simple fluids. These experiments paved the way for subsequent investigations of the relaxation frequency dependence using ^{13}C and ^{2}H NMR techniques.[18,19] In addition, investigations involving magnetic field cycling have provided further valuable knowledge of the relaxation frequency dependence.[21] (See also ***Field Cycling Experiments***.)

Let us take a closer look at what can be learned from combined NMR lineshape and relaxation studies. One can apply the Bloch–Wangsness–Redfield treatment of the density matrix[37] to the relaxation of lipid bilayers,[38] in which fluctuations of the nuclear coupling with its environment yield a time-dependent perturbation. (See also ***Relaxation Theory: Density Matrix Formulation***.) The residual or time-averaged Hamiltonian $\langle\hat{\mathcal{H}}_\lambda\rangle$ is subtracted from the time-dependent Hamiltonian to yield the fluctuating part $\hat{\mathcal{H}}'_\lambda(t)$, which is given by[2,35]

$$\hat{\mathcal{H}}'_\lambda(t) \equiv \hat{\mathcal{H}}_\lambda(t) - \langle\hat{\mathcal{H}}_\lambda\rangle \tag{8}$$

Correlation functions of the coupling Hamiltonian can then be written as

$$G_{\alpha\beta\alpha'\beta'}(t) = \langle(\alpha|\hat{\mathcal{H}}'_\lambda(0)|\beta)(\beta'|\hat{\mathcal{H}}'_\lambda(t)|\alpha')\rangle \tag{9}$$

The Dirac bra–ket notation (| and |) is used, where α, α', β, and β' correspond to the eigenstates of the spin system, and the angled brackets indicate a time or ensemble average. Substituting for the Hamiltonian $\hat{\mathcal{H}}'_\lambda(t)$, one obtains for the correlation functions due to the fluctuating part

$$G_{\alpha\beta\alpha'\beta'}(t) = \frac{3}{2}\delta_\lambda^2 C_\lambda^2 \sum_m (\alpha|\hat{T}^{(2)\text{lab}}_{-m}|\beta)^*(\alpha'|\hat{T}^{(2)\text{lab}}_{-m}|\beta')G_m(t) \tag{10}$$

Now according to equation (10) the correlation functions contain products of the matrix elements of the irreducible tensor operators due to the angular momentum, as well as the irreducible correlation functions $G_m(t)$ which describe fluctuations of the coupling tensor. The matrix elements encompass the selection rules and characterize the allowed transitions; whereas the correlation functions $G_m(t)$ describe the time dependence of the fluctuating irreducible components about their mean values. (It can be shown using group theoretical procedures that cross-correlation terms involving different values of the projection index m vanish rigorously for the case of cylindrical symmetry.)

The correlation functions $G_m(t)$ can be written as

$$G_m(t) = \langle [V_m^{(2)\text{lab}}(0) - \langle V_m^{(2)\text{lab}}\rangle]^*[V_m^{(2)\text{lab}}(t) - \langle V_m^{(2)\text{lab}}\rangle]\rangle / [V_0^{(2)\text{PAS}}]^2 \tag{11}$$

For $\eta_\lambda = 0$ only the $V_0^{(2)\text{PAS}}$ irreducible component is nonzero, so that one obtains[39,40]

$$G_m(t) = \langle D_{0m}^{(2)*}(\Omega_{\text{PL}}; 0) D_{0m}^{(2)}(\Omega_{\text{PL}}; t)\rangle - |\langle D_{0m}^{(2)}(\Omega_{\text{PL}})\rangle|^2 \tag{12}$$

In general, however, one needs to consider cross terms involving the symmetric (δ_λ) and asymmetric (η_λ) components of the coupling tensor.[41] The corresponding irreducible spectral densities are the Fourier transform partners of the correlation functions, $G_m(t)$, and are given by

$$J_m(\omega) = \text{Re}\int_{-\infty}^{\infty} G_m(t) e^{-i\omega t}\, dt \tag{13}$$

The spectral densities $J_m(\omega)$ describe the density of the fluctuations at the frequency ω, which produce the observed nuclear relaxation. In what follows, it is useful to introduce the following coupling constants:

$$\chi_{\text{D}} \equiv (\gamma_I \gamma_S h/2\pi^2)\langle r_{IS}^{-3}\rangle \tag{14a}$$

$$\chi_{\text{Q}} \equiv e^2 q Q/h \tag{14b}$$

4.1 Proton and Deuterium NMR Spectroscopy

For the case that $\hat{\boldsymbol{I}} = \hat{\boldsymbol{S}}$, e.g. due to the pairwise magnetic dipolar interaction between ^{1}H nuclei or the electric quadrupolar interaction of the ^{2}H nucleus, one obtains for the various relaxation rates

$$R_{1\text{Z}} \equiv \frac{1}{T_{1\text{Z}}} = \frac{3}{4}\pi^2\chi^2[J_1(\omega_I) + 4J_2(2\omega_I)] \tag{15a}$$

$$R_{1\text{D}},\, R_{1\text{Q}} \equiv \frac{1}{T_{1\text{D}}},\ \frac{1}{T_{1\text{Q}}} = \frac{9}{4}\pi^2\chi^2 J_1(\omega_I) \tag{15b}$$

$$R_2 \equiv \frac{1}{T_2} = \frac{3}{8}\pi^2\chi^2[3J_0(0) + 3J_1(\omega_I) + 2J_2(2\omega_I)] \tag{15c}$$

Here χ is the coupling constant for the dipolar or quadrupolar interaction, i.e. $\chi \equiv \chi_{\text{D}}$ or χ_{Q}; ω_I is the nuclear Larmor frequency; and $J_m(\omega_I)$ are the spectral densities of motion. The relaxation rate for the longitudinal or Zeeman magnetization (i.e. the spin–lattice relaxation rate) is denoted by $R_{1\text{Z}}$, where $T_{1\text{Z}}$ is the corresponding relaxation time. The rates for the decay of dipolar order and the decay of quadrupolar order are denoted by $R_{1\text{D}}$ and $R_{1\text{Q}}$, respectively, with relaxation times $T_{1\text{D}}$ and $T_{1\text{Q}}$. Finally, the relaxation rate for the decay of transverse single quantum coherence (i.e. the spin–spin relaxation rate) is denoted by R_2, where the relaxation time is T_2. The cylindrical symmetry about the bilayer normal (director axis) means in general that the irreducible spectral densities depend on the projection index m. In systems undergoing isotropic averaging, e.g. phospholipid vesicles, the dependence on the m index vanishes due to the spherical symmetry, such that $J_m(\omega_I) \rightarrow \langle J_m(\omega_I)\rangle \equiv J(\omega_I)$.

One should note that, as indicated above, R_2 corresponds to the transverse relaxation rate in ordered media, where the $|+1) \rightarrow |0)$ and $|0) \rightarrow |-1)$ single quantum transitions are typically nondegenerate.[38] In systems undergoing isotropic averaging, the transverse cross-relaxation rate must also be included, yielding

$$R_2 = \frac{3}{8}\pi^2\chi^2[3J(0) + 5J(\omega_I) + 2J(2\omega_I)] \tag{16}$$

(See also ***Deuteron Relaxation Rates in Liquid Crystalline Samples: Experimental Methods Liquid Crystalline Samples: Deuterium NMR***.)

4.2 Carbon-13 NMR Spectroscopy

For $\hat{\boldsymbol{I}} \neq \hat{\boldsymbol{S}}$, e.g. the ^{13}C–^{1}H direct magnetic dipolar interaction, the various observables are given by[42]

$$R_{1\text{Z}} \equiv \frac{1}{NT_{1\text{Z}}} = \frac{3}{2}\pi^2\chi_{\text{D}}^2\left[\frac{1}{6}J_0(\omega_S - \omega_I) + \frac{1}{2}J_1(\omega_I) + J_2(\omega_S + \omega_I)\right] \tag{17a}$$

$$\eta_{IS} = \left(\frac{\gamma_S}{\gamma_I}\right)\frac{-\frac{1}{6}J_0(\omega_S - \omega_I) + J_2(\omega_S + \omega_I)}{\frac{1}{6}J_0(\omega_S - \omega_I) + \frac{1}{2}J_1(\omega_I) + J_2(\omega_S + \omega_I)} \tag{17b}$$

$$R_2 \equiv \frac{1}{NT_2} = \frac{3}{4}\pi^2\chi_D^2\left[\frac{1}{6}J_0(\omega_S - \omega_I) + \frac{1}{2}J_1(\omega_I) + J_2(\omega_S + \omega_I) + \frac{2}{3}J_0(0) + J_1(\omega_S)\right] \tag{17c}$$

Here $R_{1\text{Z}}$ is the Zeeman (spin–lattice) relaxation rate with relaxation time $T_{1\text{Z}}$; η_{IS} is the heteronuclear Overhauser effect

due to the fluctuating dipolar interactions; and R_2 is the transverse (spin–spin) relaxation rate with relaxation time T_2; N is the number of directly bonded ^{1}H nuclei. For the case of orientational averaging, the m index vanishes due to the spherical symmetry as mentioned above, such that $J_m(\omega_I) \rightarrow \langle J_m(\omega_I)\rangle \equiv J(\omega_I)$. (See also ***Liquid Crystalline Samples: Carbon-13 NMR***.)

4.3 Correlation Functions and Spectral Densities for Restricted Diffusion

Generally speaking, one can employ a simple diffusion model to describe either segmental motions or molecular motions. Let us define generic Euler angles as $\Omega \equiv (\alpha, \beta, \gamma)$; i.e. $\Omega = \Omega_{\mathrm{ID}}$ for segmental diffusion or $\Omega = \Omega_{\mathrm{MD}}$ for molecular diffusion, with generalized projection indices $(m', m) \equiv (r, n)$ or (q, n). The spectral densities for rotational diffusion $F^{(2)}_{m'm}(\Omega; \omega)$ are Fourier transform partners of the correlation functions $G^{(2)}_{m'm}(\Omega; t)$, as indicated below:

$$F^{(2)}_{m'm}(\Omega; \omega) = \mathrm{Re}\int_{-\infty}^{\infty} G^{(2)}_{m'm}(\Omega; t)e^{-\mathrm{i}\omega t}\,\mathrm{d}t \tag{18a}$$

$$\equiv [\langle |D^{(2)}_{m'm}(\Omega)|^2\rangle - |\langle D^{(2)}_{m'm}(\Omega)\rangle|^2\delta_{m'0}\delta_{m0}]\, j^{(2)}_{m'm}(\Omega; \omega) \tag{18b}$$

where $G^{(2)}_{m'm}(\Omega; t) = G^{(2)}_{m'm}(\Omega; 0)g^{(2)}_{m'm}(\Omega; t)$. As a rule, $F_{rn}{}^{(2)}(\Omega_{\mathrm{ID}}; \omega)$ for segmental diffusion or $F^{(2)}_{qn}(\Omega_{\mathrm{MD}}; \omega)$ for molecular diffusion are a function of both even and odd rank order parameters.[16,41] Assuming a value of the second-rank polynomial $\langle D^{(2)}_{00}(\Omega_{\mathrm{ID}})\rangle$ for segmental motions or $\langle D^{(2)}_{00}(\Omega_{\mathrm{MD}})\rangle$ for molecular motions, the parameters of the potential of mean torque can be determined.[39,41]

One can solve the rotational diffusion equation[43] in the presence of a uniaxial potential of mean torque to give for the reduced correlation functions

$$g^{(2)}_{m'm}(\Omega; t) = \exp[-(D_{\parallel} - D_{\perp})m'^2 t] \times \sum_{k=1}^{\infty} c^{(2,k)}_{m'm}\exp(-\alpha^{(2,k)}_{m'm}D_{\perp}t) \tag{19}$$

Here $\alpha^{(2,k)}_{m'm}$ denotes the kth eigenvalue of the diffusion operator, and $c^{(2,k)}_{m'm}$ and $\tau^{(2,k)}_{m'm}$ are the relative normalized weight and correlation time for the kth relaxation component. (See also ***Liquid Crystalline Samples: Relaxation Mechanisms***.) Solutions in closed form are obtained by making a single exponential approximation in terms of a short time expansion,[44] yielding for the mean of the eigenvalues

$$\alpha^{(2)}_{m'm} = \sum_{k=1}^{\infty} c^{(2,k)}_{m'm}\alpha^{(2,k)}_{m'm} = \frac{\mu_{m'm}}{G^{(2)}_{m'm}(0)} \tag{20}$$

The moments $\mu_{m'm}$ are given by their expansions[16,44] in terms of the order parameters $\langle D^{(j)}_{00}(\Omega)\rangle$. Within the single exponential approximation, the correlation times are denoted by

$$\frac{1}{\tau^{(2)}_{m'm}} = [\alpha^{(2)}_{m'm} + (\eta_{\mathrm{diff}} - 1)m'^2]D_{\perp} \tag{21}$$

where $\eta_{\mathrm{diff}} \equiv D_{\parallel}/D_{\perp}$ and $\boldsymbol{D}$ is the rotational diffusion tensor. The reduced correlation functions are then given by

$$g^{(2)}_{m'm}(\Omega; t) = \exp(-t/\tau^{(2)}_{m'm}) \tag{22}$$

and likewise the reduced spectral densities are given by

$$j^{(2)}_{m'm}(\Omega; \omega) = \frac{2\tau^{(2)}_{m'm}}{1 + (\omega\tau^{(2)}_{m'm})^2} \tag{23}$$

4.4 Segmental Motions

In the case of segmental motions the dynamics can involve dihedral angle isomerizations together with torsional oscillations. For simplicity and generality, one can assume a diffusion model[39] in terms of the angles $\Omega_{\mathrm{PD}}(t)$ between the frame of the coupling tensor and the director; alternatively, jump models can be considered.[45–47] The result for the irreducible spectral densities $J_m(\omega)$ in the laboratory frame can be expressed in general as[41,48,49]

$$J_m(\omega) = \sum_r\sum_n |D^{(2)}_{0r}(\Omega_{\mathrm{PI}}) - \sqrt{\tfrac{1}{6}}\,\eta_{\lambda}[D^{(2)}_{-2r}(\Omega_{\mathrm{PI}}) + D^{(2)}_{2r}(\Omega_{\mathrm{PI}})]|^2 F^{(2)}_{rn}(\Omega_{\mathrm{ID}}; \omega)|D^{(2)}_{nm}(\Omega_{\mathrm{DL}})|^2 \tag{24}$$

For either the dipolar or quadrupolar interactions, the asymmetry parameter, η_{λ}, describes the deviation of the static coupling tensor from cylindrical symmetry, as noted above. The squares of the Wigner rotation matrix elements $|D^{(2)}_{m'm}(\Omega)|^2 >$ are given in terms of their Clebsch–Gordan series expansions.[15] Note that in general the orientation dependence of the relaxation is described by the factor $|D^{(2)}_{nm}(\Omega_{\mathrm{DL}})|^2$.

4.5 Molecular Motions

Likewise, one can apply a diffusion model to restricted molecular rotations within the potential of mean torque of the bilayer. Here the molecular motions are formulated in terms of reorientation of a single molecule in the mean field due to all its neighbors. The slow motions may be noncollective, i.e.'molecular' in nature, and involve wobbling or rattling of the lipid as described by the angles $\Omega_{\mathrm{MD}}(t)$ between the molecular frame and the director. It is simple to show[39] that the relaxation rates are isomorphous to those for segmental motions,[38] in which $\chi_{\lambda} \rightarrow \chi_{\lambda}{}^{\mathrm{eff}}$ and $\eta_{\lambda} \rightarrow \eta_{\lambda}{}^{\mathrm{eff}}$. The spectral densities are scaled by the local order parameter squared, which gives

$$J_m(\omega) = |\langle D^{(2)}_{00}(\Omega_{\mathrm{PI}})\rangle|^2 \sum_q\sum_n |D^{(2)}_{0q}(\Omega_{\mathrm{IM}}) - \sqrt{\tfrac{1}{6}}\,\eta^{\mathrm{eff}}_{\lambda}[D^{(2)}_{-2q}(\Omega_{\mathrm{IM}}) + D^{(2)}_{2q}(\Omega_{\mathrm{IM}})]|^2 \times F^{(2)}_{qn}(\Omega_{\mathrm{MD}}; \omega)|D^{(2)}_{nm}(\Omega_{\mathrm{DL}})|^2 \tag{25}$$

Here the two coupling parameters are $\chi_\lambda^{\text{eff}} = \chi_\lambda \langle D_{00}^{(2)}(\Omega_{\text{PI}})\rangle$ and $\eta_\lambda^{\text{eff}} = -\frac{3}{2}\langle \sin^2 \beta_{\text{PI}} \cos(2\gamma_{\text{PI}})\rangle / \langle D_{00}^{(2)}(\Omega_{\text{PI}})\rangle$. Because the spectral densities are multiplied by $|\langle D_{00}^{(2)}(\Omega_{\text{PI}})\rangle|^2$, the local order parameter squared, the static coupling constant $\chi_\lambda^2 \rightarrow (\chi_\lambda^{\text{eff}})^2$ in the relaxation rate expressions, equations (15)–(17). Now if the orientations of the residual tensor principal axes, together with the mean-squared amplitudes and reduced spectral densities of the slow motions as described by $F_{\text{qn}}^{(2)}(\Omega_{\text{MD}}; \omega)$, are nearly constant, then the dependence of the relaxation on chain position is largely governed by the two quantities $\chi_\lambda^{\text{eff}}$ and $\eta_\lambda^{\text{eff}}$. Assuming the effective asymmetry parameter $\eta_\lambda^{\text{eff}}$ is nearly zero or constant along the chain, then a square law functional dependence of the spectral densities on the observed segmental order parameter S_{CD} results.[18,39,50]

4.6 Collective Motions

As an alternative to considering distinct rotational modes, one can adopt a three-dimensional picture for the bilayer in terms of a continuum of twist, splay, and bend deformations as proposed by Brown.[39] It is assumed that the various chain segments reorient collectively, in which the key distinction from the above molecular picture is that a broad distribution of wave-like elastic modes is present.[39,51,52] Here the shorter wavelengths approach the molecular or chain diameter, where of course the continuum description breaks down; the longer wavelengths approach the macroscopic dimensions of the bilayer and for simplicity are taken as ∞. The slow motions are described by the angles $\Omega_{\text{ND}}(t)$ between the instantaneous (or local) director and the average director (the bilayer normal), where a small angle approximation is made.

For such a picture one obtains that

$$J_m(\omega) = C|\langle D_{00}^{(2)}(\Omega_{\text{PI}})\rangle|^2 |\omega|^{-1/2} |D_{\pm 1m}^{(2)}(\Omega_{\text{DL}})|^2 \qquad (26)$$

in which C is a collection of various constants (a single elastic constant approximation is made). The angular anisotropy is described by the factor $|D_{\pm 1m}^{(2)}(\Omega_{\text{DL}})|^2$ and thus reflects the assumption of small angle director fluctuations. Assuming that the amplitude of the slow motions is nearly uniform along the chain, a squared dependence on the observed order parameter results as for the molecular model (vide supra). Alternatively, a two-dimensional picture in terms of fluctuations of the lipid/water interface can be considered, in which the finite thickness of the bilayer is disregarded.[53] Such a formulation is analogous to a smectic undulation model, in which there is a large increase in the elastic constants for the twist and bend modes.[54] Hence only splay is considered in terms of a single elastic constant K_{c}; this yields

$$J_m(\omega) = C'|\langle D_{00}^{(2)}(\Omega_{\text{PI}})\rangle|^2 |\omega|^{-1} |D_{\pm 1m}^{(2)}(\Omega_{\text{DL}})|^2 \qquad (27)$$

where C′ is similarly a collection of elastic and other constants.

4.7 Observed Spectral Densities

Now the presence of a motional hierachy means that the residual interaction due to an individual component is further modulated by the slower motions of larger orientational amplitude. Let us modify our notation and denote the observed order parameter by $S^{(2)} \equiv S_{\text{CD}}$. The following product approximation can be made if the fast and slow motions are axially symmetric:[55]

$$S^{(2)} = S_{\text{f}}^{(2)} S_{\text{s}}^{(2)} \qquad (28)$$

One can then write for the spectral densities that

$$J_m(\omega) = J_m^{\text{f}}(\omega) + J_m^{\text{s}}(\omega) \qquad (29)$$

where, in principle, both the fast and slow contributions depend on the (i) degree of ordering, (ii) frequency, and (iii) orientation.[39,40]

Further simplification is possible if one assumes that orientational averaging of the relaxation occurs, e.g. as in the case of vesicles and also multilamellar dispersions.[36] We shall denote $S_{\text{f}}^{(2)} \equiv \langle D_{00}^{(2)}(\Omega_{\text{PI}})\rangle$ as the order parameter for the fast motions, and $S_{\text{s}}^{(2)} \equiv \langle D_{00}^{(2)}(\Omega_{\text{ID}})\rangle$ as the order parameter for the slow motions. The spectral density for the fast motions is given by[39]

$$J^{\text{f}}(\omega) = \frac{1}{5}[1 - S_{\text{f}}^{(2)2}]\, j_{\text{f}}^{(2)}(\omega) \qquad (30)$$

in which

$$j_{\text{f}}^{(2)}(\omega) = \frac{2\tau_{\text{f}}^{(2)}}{1 + [\omega\tau_{\text{f}}^{(2)}]^2} \qquad (31)$$

Here $\tau_{\text{f}}{}^{(2)}$ is the correlation time for the motions with respect to the local director axis (internal frame).

In the case of the spectral densities due to slow motions, a molecular model can be considered, or alternatively a collective model; the spectral densities are scaled by the fast order parameter squared, viz. $S_{\text{f}}{}^{(2)2}$. Assuming a single correlation time, one obtains for the orientationally averaged spectral density that[39]

$$J^{\text{s}}(\omega) = \frac{1}{5} S_{\text{f}}^{(2)2}[1 - S_{\text{s}}^{(2)2}]\, j_{\text{s}}^{(2)}(\omega) \qquad (32)$$

where

$$j_{\text{s}}^{(2)}(\omega) = \frac{2\tau_{\text{s}}^{(2)}}{1 + [\omega\tau_{\text{s}}^{(2)}]^2} \qquad (33)$$

Note that if the correlation time for the slow motions is sufficiently long so that $[\omega\tau_{\text{s}}^{(2)}]^2 \gg 1$, then a ω^{-2} frequency dependence results.[55] However, in general the frequency dependence is more complicated.[39]

It is worth noting that if the slow motion is unrestricted, e.g. as occurs in globular proteins[56] or detergent micelles,[57] then there is no preferred symmetry axis (corresponding to the

average director) and hence the slow order parameter $S_s^{(2)} \rightarrow 0$; this gives

$$J^s(\omega) \rightarrow \frac{1}{5} S_f^{(2)2} j_s^{(2)}(\omega) \tag{34}$$

One then immediately obtains as a limiting case the results formulated independently by Lipari and Szabo[56] as the 'model-free approach', or by Wennerström and co-workers[57] as the 'two-step model'. (See also ***Protein Dynamics from NMR Relaxation*** and ***Micellar Solutions and Microemulsions***.) Because the present treatment[38–40] is more general, it is referred to as the 'generalized approach'.[12]

For the collective model, the orientationally averaged spectral density due to the slow motions is given by

$$J^s(\omega) = \frac{1}{5} S_f^{(2)2} j_s^{(2)}(\omega) \tag{35}$$

where

$$j_s^{(2)}(\omega) = C\omega^{-1/2} \tag{36}$$

Here C is a collection of elastic and other constants; a single elastic constant approximation is made for the twist, splay, and bend modes. Alternatively, a two-dimensional smectic-like formulation can be considered.[53,54] Such a treatment in terms of splay only gives[53,54]

$$j_s^{(2)}(\omega) = C'\omega^{-1} \tag{37}$$

where C′ is similarly a collection of elastic and other constants.

5 TESTING OF CONCEPTUAL FRAMEWORKS

As indicated above, the spectral densities $J_m(\omega)$ and associated relaxation rates depend on the segmental ordering, frequency ω(magnetic field strength), temperature, and the bilayer orientation.[39] For the sake of illustration, let us again consider the order and relaxation profiles depicted in Figure 4.[16] One plausible interpretation is that the static interaction constant is modulated by the motions; here the residual or effective quadrupolar coupling (≈30–40 kHz) is smaller than the static quadrupolar coupling (170 kHz), so that the mean

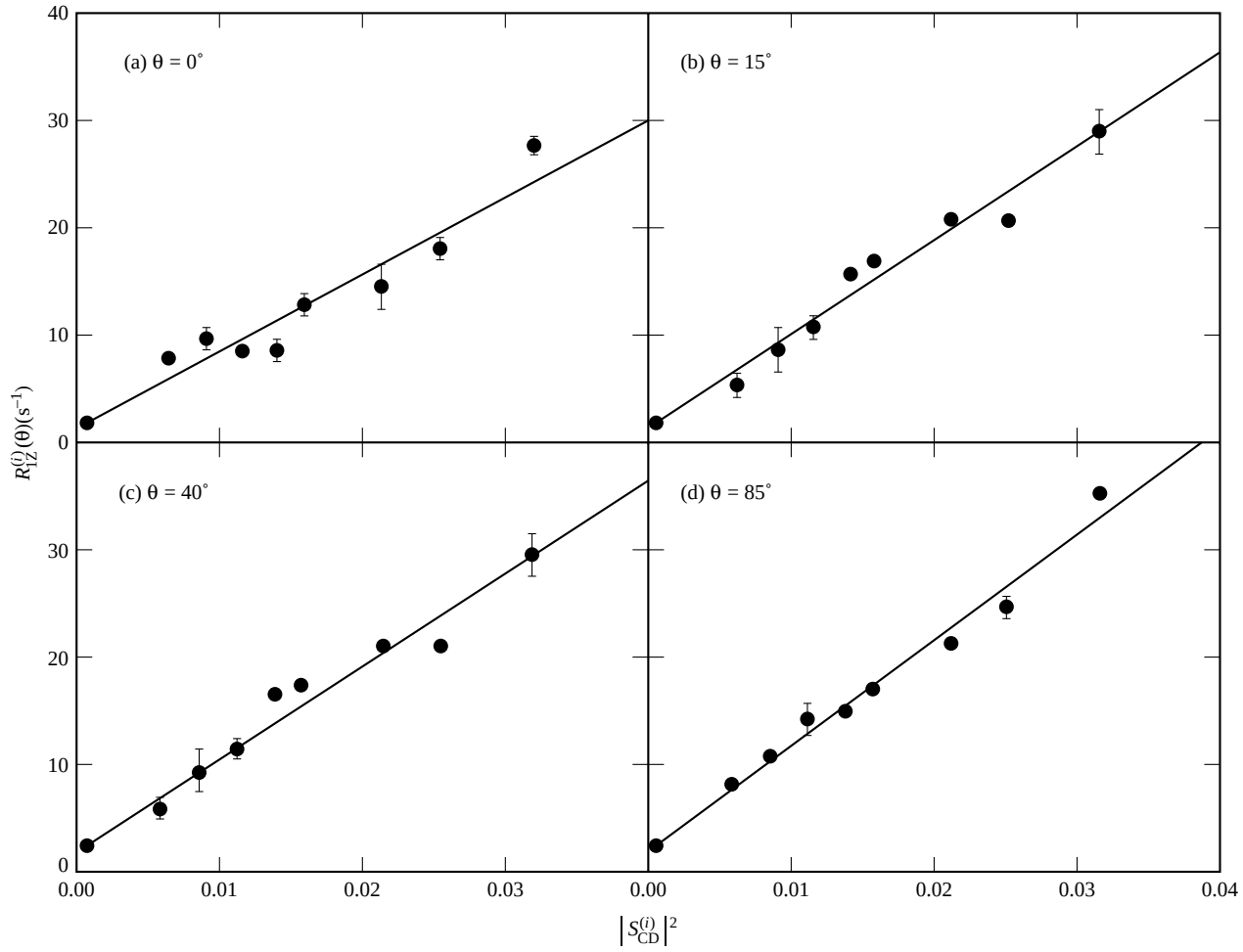

Figure 6 Plots of ^{2}H $R_{IZ}^{(i)}$ rates versus the corresponding values of $|S_{CD}^{(i)}|^2$ for acyl segments of DLPC-d_{46} in the liquid crystalline phase at 46.1 MHz and 40 °C. (a)–(d) Results for bilayers aligned on planar substrates at different angles (θ) with respect to the main magnetic field. (Reproduced by permission of the American Institute of Physics from T. P. Touard, T. M. Alam, and M. F. Brown, *J. Chem. Phys.*, 1994, **101**, 5229)

squared amplitudes provide a relatively minor influence. As a result the relaxation profile is governed by the local motional rates along the chain. Another possibility is that the interaction varies along the chain, and corresponds not to the static coupling, but rather to an effective or residual coupling that is preaveraged by faster motions of a more local nature, e.g. dihedral angle isomerizations.[48] Instead of the static coupling being constant and the dynamical parameters varying along the chain, the opposite holds. The coupling parameters as reflected in the mean-squared amplitudes vary with the chain position, and thus govern the shape and magnitude of the relaxation profile, whereas the dynamical parameters are essentially the same. What is the correspondence to equilibrium and dynamical properties of bilayers in the fluid phase?

To interpret further such relaxation profiles, it is necessary to introduce motional models which encompass the key physics of interest. As already noted, the angular anisotropy of the relaxation for $I = 1$ nuclei is related to the orientation and symmetry of the coupling tensor within the frame undergoing the fluctuations, i.e. the segment, molecule, or bilayer.[39] Fits of the angular dependence of the R_{1Z} rates of lipid bilayers in the fluid (L_α) phase to the segmental, molecular, and collective models can all explain the angular dependence for disaturated phosphatidylcholines to a greater or lesser degree of success, depending on the number of adjustable parameters.[16] How can one further distinguish among these different interpretations?

In this regard, the magnitude of the ^{2}H and ^{13}C relaxation times together with their dependence on frequency and temperature renders it unlikely that an interpretation in

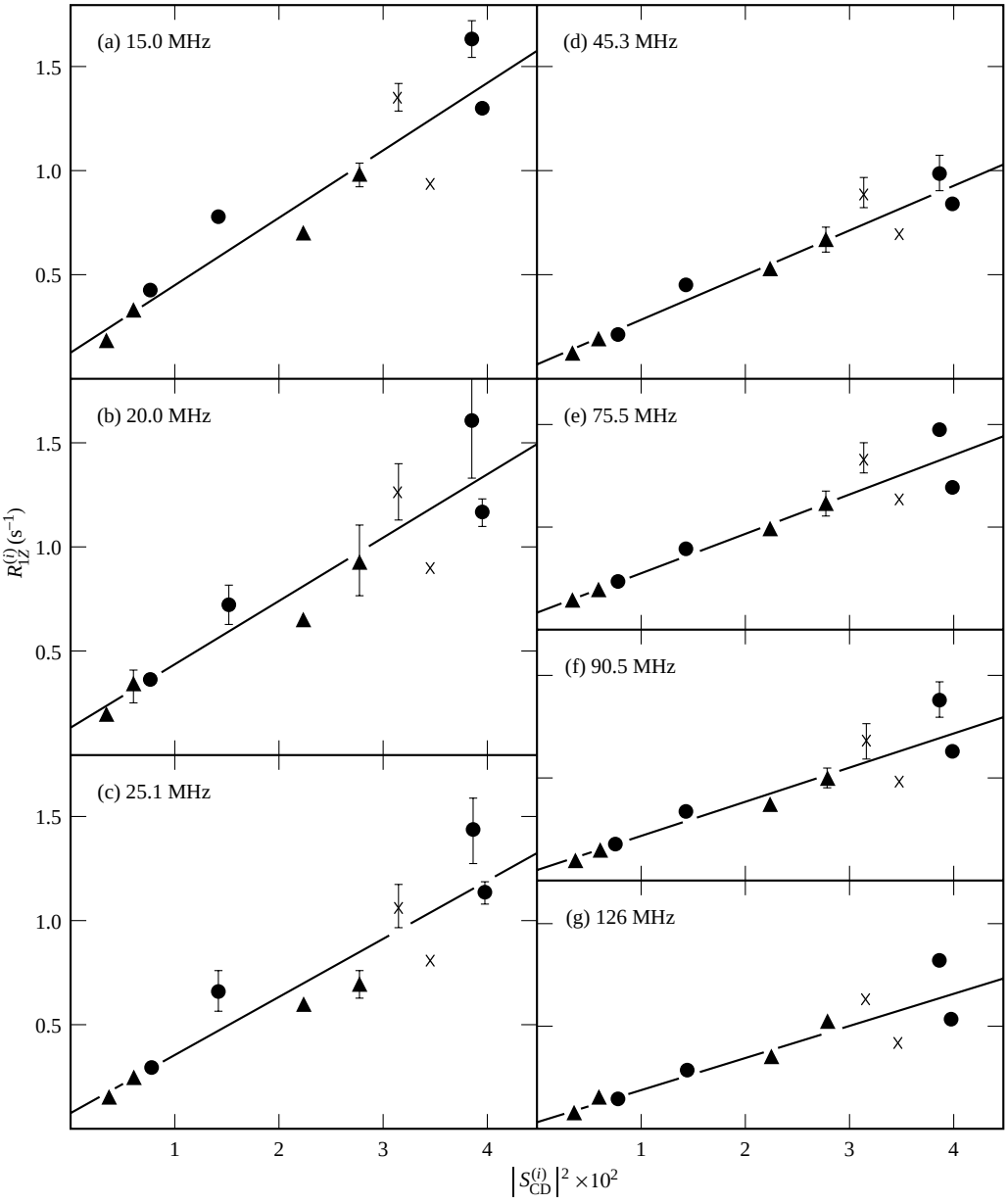

Figure 7 Plots of natural-abundance ^{13}C spin–lattice relaxation rates, $R_{IZ}^{(i)}$, for acyl chain segments of DPPC vesicles versus $|S_{CD}^{(i)}|^2$ from ^{2}H NMR studies at various temperatures in the liquid crystalline state. (a)–(g) Results obtained at different ^{13}C frequencies (magnetic field strengths). (Reproduced by permission of the American Institute of Physics from M. F. Brown, *J. Chem. Phys.*, 1984, **80**, 2808)

terms of a single type of local motion can explain the results.[39,40] Such a formulation has been suggested as a first approximation for describing the dynamics in fluid L_α phase bilayers.[35,38] However, subsequent studies have indicated that a fundamentally different physical picture may be involved.[18,19,39] As a result, the possible influences of slow motions which modulate the residual coupling left over from faster local motions must be considered. Figure 6 shows that if the ^{2}H $R_{1Z}^{(i)}$ rates are plotted versus the corresponding values of the order parameters, $S_{CD}^{(i)}$, squared, a nearly straight line results. The presence of such a square law dependence was first recognized by Brown,[39] and represents a hallmark or characteristic signature of the fluid, liquid crystalline state of disaturated lipid bilayers. The experimentally observed square law functional dependence of $R_{1Z}^{(i)}$ and $S_{CD}^{(i)}$ is independent of any motional model. It can be readily explained by Fermi's Golden Rule, in which the strength of the interaction depends on the matrix elements squared, and thus varies with the chain position; the motional parameters are largely constant. Consequently, although the slow motions provide the dominant contribution to the observed relaxation rates, the internal fast motions govern the relaxation profile along the chains.

Further information can be obtained from ^{13}C NMR studies, in which the relaxation is due to the direct magnetic dipolar interaction of the ^{13}C nucleus with the directly bonded ^{1}H atoms. By carrying out ^{13}C NMR R_{1Z} studies of small vesicles, it is possible to employ conventional high-resolution NMR spectrometers to obtain relaxation data at different magnetic field strengths. As noted above, ^{13}C R_{1Z} studies of both small vesicles of phosphatidylcholines as well as the corresponding multilamellar dispersions evince little difference in their relaxation rates.[18,20] Hence the motions governing the relaxation in the megahertz regime in both cases must be rather similar. In Figure 7 the natural-abundance ^{13}C NMR R_{1Z} relaxation rates of DPPC small vesicles obtained at seven magnetic field strengths,[18] covering a range of ^{13}C frequencies from 15.0 MHz (1.40 T) to 126 MHz (11.7 T), are plotted versus the square of the corresponding ^{2}H NMR order parameters, S_{CD}. As in the case of the ^{2}H NMR data, evidence of a square law relation is found, as discussed above. Moreover, a comparison of the data in Figure 7(a)–(g) reveals a progressive decrease in the slopes of the square law plots as the ^{13}C frequency is increased from 15.0 to 126 MHz, i.e. there is a characteristic frequency dependence of the relaxation in agreement with earlier ^{1}H NMR studies.[17]

At present, the most extensive frequency-dependent R_{1Z} relaxation data for lipid vesicles comprise ^{2}H NMR studies of specifically deuterated 1,2-dimyristoyl-*sn*-glycero-3-phosphocholine (DMPC). The results encompass nine different magnetic field strengths, ranging from 2.5 MHz (0.38 T) to 62.4 MHz (9.55 T), employing both electromagnets and superconducting NMR magnets.[19] Figure 8 summarizes the results of fitting the dispersion data for DMPC deuterated at the C-3 position to (i) the three-dimensional collective model involving twist, splay, and bend deformations, (ii) the two-dimensional interfacial collective model involving splay only, and, finally, (iii) the noncollective molecular model formulated in terms of a single Lorentzian plus a constant to account for internal motions. It is noteworthy that vesicle tumbling is too slow to influence appreciably the relaxation in the megahertz regime.[19] As can be seen, the $\omega_I^{-1/2}$ dependence[39,58] provides the best fit to the data; fits to an ω_I^{-1} dependence in terms of splay only[53] or to a Lorentzian dispersion[55] are clearly not as successful. One should also note that a different interpretation of these preliminary R_{1Z} relaxation rate data has appeared.[59]

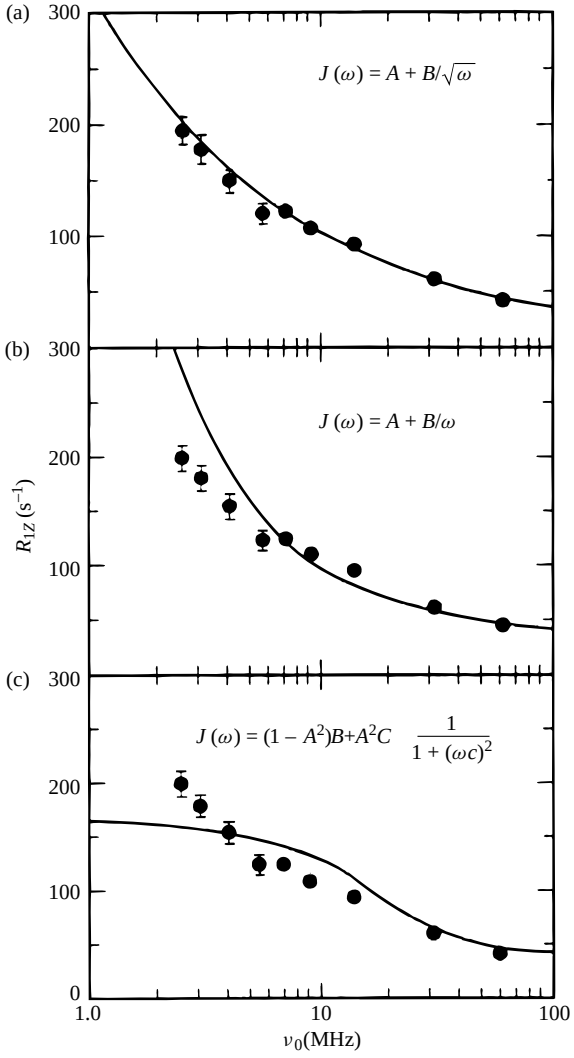

Figure 8 Deuteron R_{1Z} rates as a function of frequency for vesicles of DMPC deuterated at the C-3 acyl segment at 30 °C in the liquid crystalline state. Data are indicated at nine different frequencies (magnetic field strengths) and are fitted to the various relaxation laws described in the text. (Reproduced by permission of Taylor and Francis Ltd. from M. F. Brown, A. Salmon, U. Henriksson, and O. Söderman, *Mol. Phys.*, 1990, **69**, 379)

With regard to the various acyl chain positions, the ^{13}C NMR measurements for DPPC at the seven different magnetic field strengths are currently the most extensive data available.[18] The ^{13}C R_{1Z} rates can be plotted as a function of $\omega_C^{-1/2}$ in accord with the three-dimensional collective model; the slopes are seen in Figure 9 to decrease progressively along the chain. This is to be expected since the relaxation rates depend on the order parameter S_{CH} ($=S_{CD}$) squared. Additional information is obtained from ^{13}C–^{1}H heteronuclear Overhauser effect (NOE) studies of vesicles of disaturated phosphatidylcholines. The predicted NOE = 1 + η_{IS} of 2.34 for the collective model[40] is in good agreement with experimental data, which reveal little dependence on the magnetic field strength.[60]

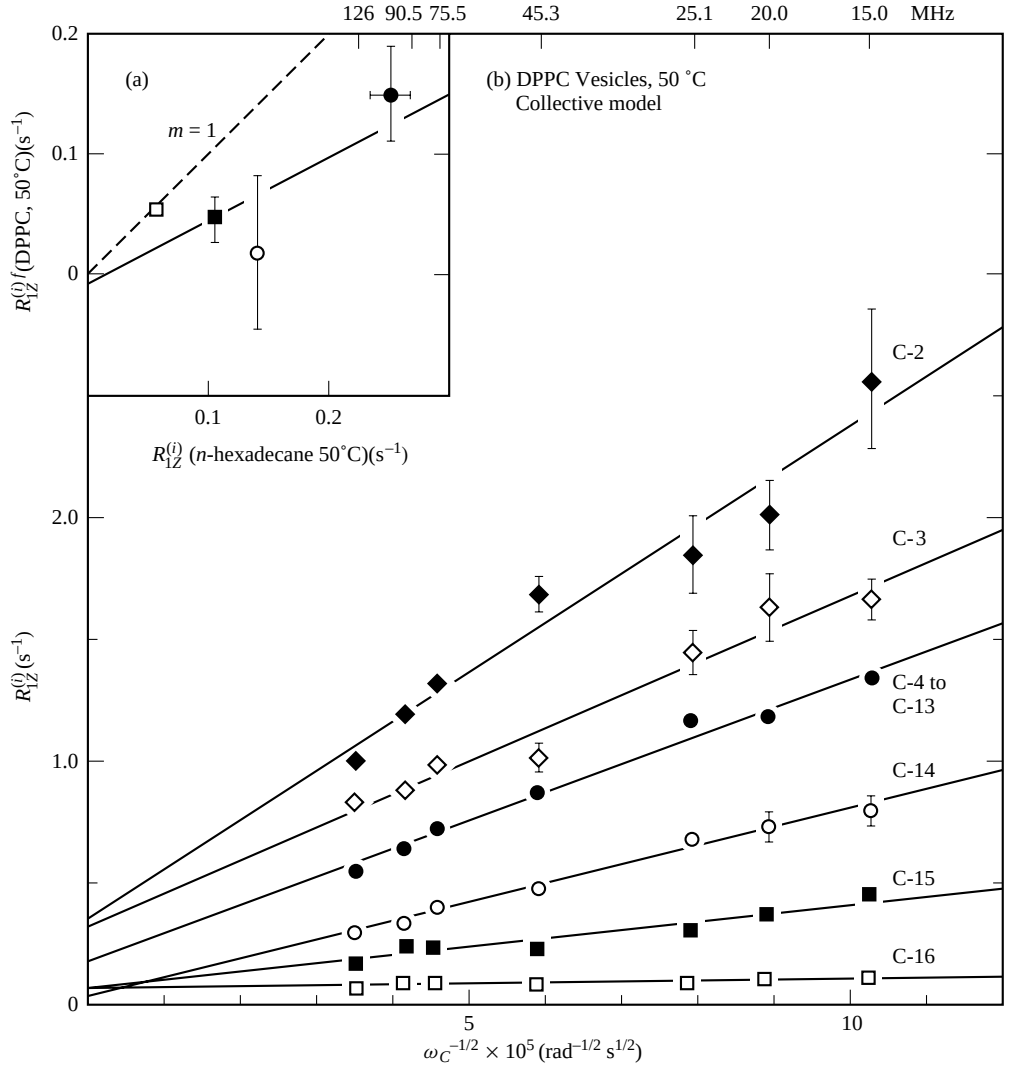

Figure 9 Plots of natural-abundance ^{13}C spin–lattice relaxation rates, R_{1Z}, for acyl chain segments of DPPC vesicles versus $\omega_C^{-1/2}$ at 50 °C in the liquid crystalline state.[40] Data are indicated at seven ^{13}C frequencies (magnetic field strengths) and are fitted to a collective relaxation law. The inset shows the contribution from fast local motions plotted against the spin–lattice relaxation rates of the corresponding segments of *n*-hexadecane, where the dashed line indicates a slope of $m = 1$. (Reproduced by permission of the American Institute of Physics from M. F. Brown, *J. Chem. Phys.*, 1984, **80**, 2808)

In fact, the entire body of ^{2}H R_{1Z} data for multilamellar dispersions and ^{13}C R_{1Z} data for vesicles of disaturated phosphatidylcholines are consistent with a relaxation law in which the spectral densities due to slow motions have the form of equation (35) and (36). Moreover, by subtracting the local contribution and normalizing the various R_{1Z} data by the square of the ^{2}H NMR order parameters, one can superimpose all of the data for all of the nuclei, viz. including ^{1}H, ^{2}H, and ^{13}C on a common plot versus $\omega_I^{-1/2}$ as indicated in Figure 10(a). Here it is necessary to assume[12] a vibrationally averaged ^{13}C–^{1}H dipolar coupling constant corresponding to $\langle r_{CH}^{-3}\rangle^{-1/3} = 0.114$ nm rather than the equilibrium bond length $r_{CH} = 0.109$ nm as in Figure 10(b). This is in agreement with independent estimates of the ^{13}C–^{1}H dipolar coupling constant and the ^{13}C–^{2}H quadrupolar coupling constant.[13]

6 EQUILIBRIUM AND DYNAMICAL PROPERTIES OF LIPID BILAYERS

A summary of the currently available NMR results for multilamellar dispersions and small vesicles of DPPC is provided in Figure 11.[18,39] The square law functional dependence of the ^{2}H R_{1Z} relaxation rates and ^{2}H NMR order parameters is illustrated in the case of DPPC multilamellar dispersions in Figure 11(a); in addition, the $\omega_C^{-1/2}$ frequency dispersion found in ^{13}CR_{1Z} relaxation studies of small DPPC vesicles is displayed in Figure 11(b). Both dependencies are characteristic signatures of the fluid L_α phase of membrane lipid bilayers.[39] By contrast, Figure 11(b) shows that the ^{13}C R_{1Z} rates of liquid alkanes such as *n*-hexadecane are essentially independent of frequency, i.e. magnetic field strength, over the range investigated.[18]

The presence of a hierarchy of motions in lipid bilayers was first recognized by the Chan[17] and Klein[5] groups, and

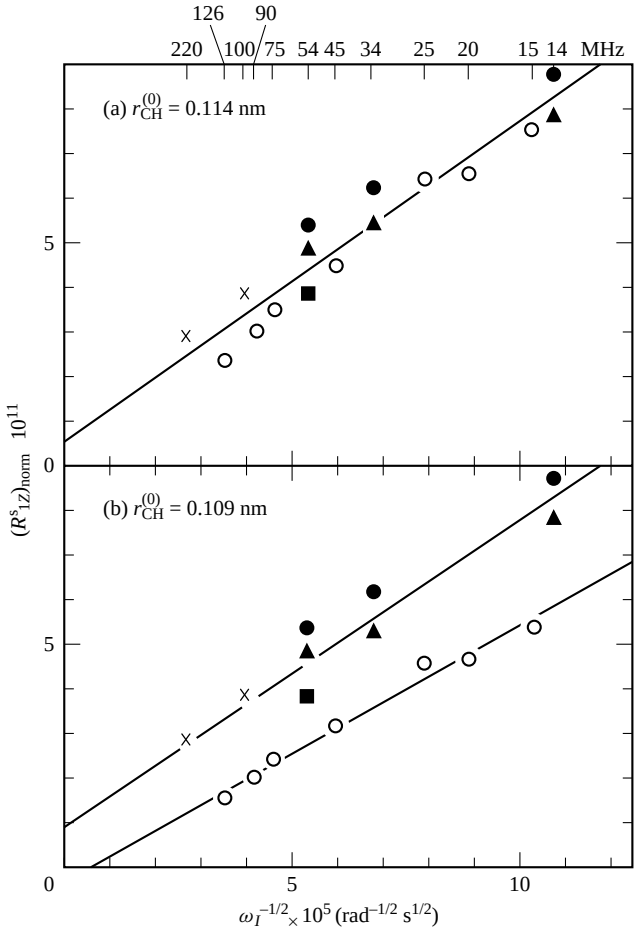

Figure 10 Plots of normalized contribution from slow motions to ^{1}H, ^{2}H, and ^{13}C R_{1Z} rates versus $\omega_I^{-1/2}$ for various acyl chain segments of DPPC at 50 °C in the liquid crystalline state ($\omega_0 \equiv \omega_I$). In (a) a vibrational averaged ^{13}C–^{1}H distance ($r_{CH}^{(0)} \equiv \langle r_{CH}^{-3} \rangle^{-1/3}$) of 0.114 nm is used; whereas in (b) the equilibrium bond length of 0.109 nm is assumed. (Reproduced by permission of the American Institute of Physics from M. F. Brown, *J. Chem. Phys.*, 1984, **80**, 2832)

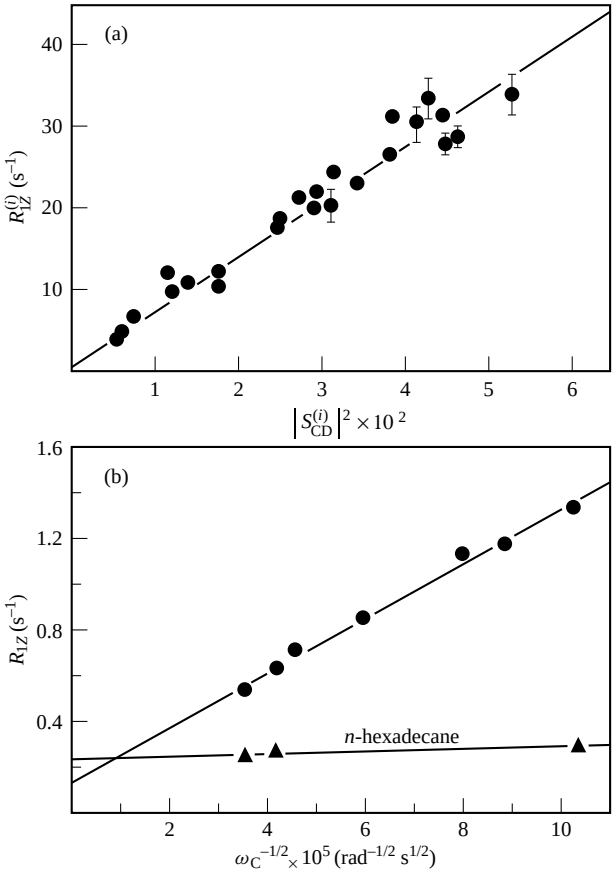

Figure 11 Summary of NMR results for DPPC at 50 °C in the liquid crystalline state. (a) Plot of ^{2}H spin–lattice relaxation rates $R_{1Z}^{(i)}$ versus $|S_{CD}^{(i)}|^2$ for acyl segments of multilamellar dispersions; (b) plot of ^{13}C spin–lattice relaxation rates, R_{1Z}, for $(CH_2)_n$ resonance versus $\omega_C^{-1/2}$ for small vesicles

subsequently interpreted in terms of collective dynamics by Brown.[39] (See also ***Slow and Ultraslow Motions in Biology***.) One can model the proposed bilayer order fluctuations in terms of twist, splay, and bend deformations in the high-frequency or free membrane limit, and possibly by smectic undulation modes involving splay only in the low-frequency or strongly coupled limit.[18] Figure 12 shows a schematic illustration from a 1979 conference at Stanford University, which indicates the types of collective excitations that can explain the frequency- and ordering-dependent relaxation enhancement of membrane bilayers.[18] For such a continuum picture, the higher-frequency modes have smaller amplitudes, whereas the lower-frequency modes have larger amplitudes; the high- and low-frequency cutoffs are neglected for simplicity. Following Blinc et al.,[54] there are two limits for a smectic A mesophase such as a bilayer dispersion, depending on the repeat distance d between the layers relative to the wavelength λ. First there is the high-frequency regime where $\lambda \ll d$, corresponding to the free membrane limit where coupling between the bilayers is negligible; in this case the relaxation is similar to the nematic phase. Secondly, there is the low-frequency regime where $\lambda \gg d$. In this case there is the possibility of smectic undulation waves having a constant interlamellar distance,[53,54] in which the restriction to splay only leads to an ω^{-1} frequency dependence over the entire range; other modes are possible.

Thus at higher frequencies in the megahertz regime, within the free membrane limit, a nematic-like behavior is found comprising relatively short-wavelength twist, splay, and bend modes, yielding the experimentally observed $\omega^{-1/2}$ dependence.[39,51,54,61] On such a length scale, no direct correspondence exists between the microscopic elastic constants and the bulk elastic constants that are experimentally measured. Because the R_{1Z} rates for vesicles and multilamellar dispersions are nearly the same,[35] the megahertz dispersion most likely does not arise from two-dimensional surface fluctuations.[53] However, at lower frequencies in the kilohertz regime, the properties of the membrane lipid/water interface become increasingly important, and a transition occurs to the strongly coupled limit involving interactions among the different layers. There may now be a correspondence with the bulk elastic constant as experimentally measured; additional research is necessary. The restriction to splay only for the lower-frequency modes leads to an ω^{-1} frequency dependence in the kilohertz regime.[54] (See also ***Molecular Motions: T_1 Frequency Dispersion in Biological Systems***.)

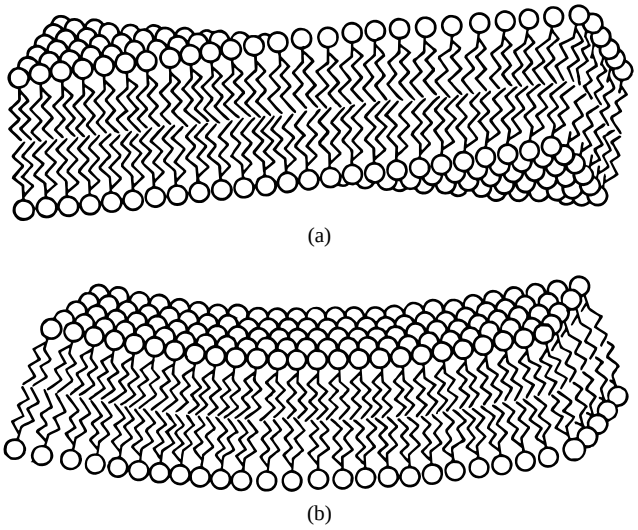

Figure 12 Examples of the types of collective bilayer excitations leading to $\omega^{-1/2}$ frequency dependence. (a) Twist. (b) Splay

Finally, the contribution from local internal motions is obtained by extrapolating the ordering- and frequency-dependent relaxation enhancement for a fluid lipid bilayer to zero ordering or infinite frequency (see Figure 11). As a result, one can conclude that the microviscosity of the bilayer hydrocarbon region, where a bulk viscosity cannot be measured, is essentially equivalent to liquid *n*-alkanes having a macroscopic viscosity on the order of a few centipoise! It follows that the membrane lipid/water interface may be very important with regard to lateral diffusion of membrane lipids and proteins. These previous conclusions[18,39] are now supported by detailed molecular mechanics studies of membrane bilayers in the fluid phase.[62,63] With the advent of more powerful computers, one can expect the availability of longer timescales, so that the motional distribution proposed on the basis of NMR spectroscopy can be further addressed.

7 RELATED ARTICLES

Amphiphilic Liquid Crystalline Samples: Nuclear Spin Relaxation; Bilayer Membranes: Proton and Fluorine-19 NMRCarbon-13 Relaxation Measurements: Organic Chemistry Applications; Deuterium NMR in Solids; Deuteron Relaxation Rates in Liquid Crystalline Samples: Experimental Methods; Field Cycling Experiments; Glycolipids; Lipid Polymorphism; Liquid Crystalline Samples: Carbon-13 NMR; Liquid Crystalline Samples: Deuterium NMR; Liquid Crystalline Samples: Relaxation Mechanisms; Magic Angle Spinning; Membrane Lipids of Acholeplasma laidlawii; Membranes: Carbon-13 NMR; Membranes: Deuterium NMR; Micellar Solutions and Microemulsions; Molecular Motions: T_1 Frequency Dispersion in Biological Systems; Protein Dynamics from NMR Relaxation; Quadrupolar Interactions; Quadrupolar Nuclei in Solids; Relaxation Theory: Density Matrix Formulation; Relaxation Theory for Quadrupolar Nuclei; Slow and Ultraslow Motions in Biology; Sonicated Membrane Vesicles

8 REFERENCES

1. M. Bloom, E. E. Burnell, A. L. MacKay, C. P. Nichol, M. I. Valic, and G. Weeks, *Biochemistry*, 1978, **17**, 5750.
2. C. H. A. Seiter and S. I. Chan, *J. Am. Chem. Soc.*, 1973, **95**, 7541.
3. G. W. Feigenson and S. I. Chan, *J. Am. Chem. Soc.*, 1974, **96**, 1312.
4. D. F. Bocian and S. I. Chan, *Annu. Rev. Phys. Chem.*, 1978, **29**, 307.
5. A. F. Horwitz, W. J. Horsley, and M. P. Klein, *Proc. Natl. Acad. Sci. USA*, 1972, **69**, 590.
6. J. Seelig, *Q. Rev. Biophys.*, 1977, **10**, 353.
7. Y. K. Levine, N. J. M. Birdsall, A. G. Lee, and J. C. Metcalfe, *Biochemistry*, 1972, **11**, 1416.
8. W. L. Hubbell and H. M. McConnell, *J. Am. Chem. Soc.*, 1971, **93**, 314.
9. B. G. McFarland and H. M. McConnell, *Proc. Natl. Acad. Sci. USA*, 1971, **68**, 1274.
10. H. W. Spiess, in *NMR Basic Principles and Progress*, ed. P. Diehl, E. Fluck, and R. Kosfeld, Springer-Verlag, Heidelberg, 1978, Vol. 15, p. 55.
11. U. Häberlen, *Adv. Magn. Reson.*, Suppl. 1, 1976.
12. M. F. Brown, *J. Chem. Phys.*, 1984, **80**, 2832.
13. O. Söderman, *J. Magn. Reson.*, 1986, **68**, 296.
14. R. R. Vold and R. L. Vold, *Adv. Magn. Opt. Reson.*, 1991, **16**, 85.
15. D. M. Brink and G. R. Satchler, *Angular Momentum*, Oxford University Press, London, 1968.
16. T. P. Trouard, T. M. Alam, and M. F. Brown, *J. Chem. Phys.*, 1994, **101**, 5229.
17. P. A. Kroon, M. Kainosho, and S. I. Chan, *Biochim. Biophys. Acta.*, 1976, **433**, 282.
18. M. F. Brown, A. A. Ribeiro, and G. D. Williams, *Proc. Natl. Acad. Sci. USA*, 1983, **80**, 4325.
19. M. F. Brown, A. Salmon, U. Henriksson, and O. Söderman, *Mol. Phys.*, 1990, **69**, 379.
20. M. D. Sefcik, J. Schaefer, E. O. Stejskal, R. A. McKay, J. F. Ellena, S. W. Dodd, and M. F. Brown, *Biochem. Biophys. Res. Commun.*, 1983, **114**, 1048.
21. E. Rommel, F. Noack, P. Meier, and G. Kothe, *J. Phys. Chem.*, 1988, **92**, 2981.
22. H. Wennerström and G. Lindblom, *Q. Rev. Biophys.*, 1977, **10**, 67.
23. E. Oldfield, J. L. Bowers, and J. Forbes, *Biochemistry*, 1987, **26**, 6919.
24. Y. I. Parmar, S. R. Wassall, and R. J. Cushley, *J. Am. Chem. Soc.*, 1984, **106**, 2434.
25. R. L. Thurmond, G. Lindblom, and M. F. Brown, *Biochemistry*, 1993, **32**, 5394.
26. J. H. Davis, *Biochim. Biophys. Acta*, 1983, **737**, 117.
27. A. Salmon, S. W. Dodd, G. D. Williams, J. M. Beach, and M. F. Brown, *J. Am. Chem. Soc.*, 1987, **109**, 2600.
28. A. Salmon and M. F. Brown, Unpublished, 1987.
29. R. A. Haberkorn, J. Herzfeld, and R. G. Griffin, *J. Am. Chem. Soc.*, 1978, **100**, 1296.
30. M. D. Sefcik, J. Schaefer, E. O. Stejskal, R. A. McKay, and M. F. Brown, Unpublished, 1983.
31. M. Hong, K. Schmidt-Rohr, Y. K. Lee, C. Husted, and A. Pines, *Proc. 35th Experimental Nuclear Magnetic Resonance Conference*, Pacific Grove, California, 1994, p. 201.
32. A. Seelig and J. Seelig, *Biochemistry*, 1974, **13**, 4839.

33. M. Lafleur, P. Cullis, B. Fine, and M. Bloom, *Biochemistry*, 1990, **29**, 8325.
34. R. L. Thurmond, D. Otten, M. F. Brown, and K. Beyer, *J. Phys. Chem.*, 1994, **98**, 972.
35. M. F. Brown, J. Seelig, and U. Häberlen, *J. Chem. Phys.*, 1979, **70**, 5045.
36. M. F. Brown and J. H. Davis, *Chem. Phys. Lett.*, 1981, **79**, 431.
37. C. P. Slichter, *Principles of Magnetic Resonance*, 3rd edn., Springer-Verlag, Heidelberg, 1990.
38. M. F. Brown, *J. Magn. Reson.*, 1979, **35**, 203.
39. M. F. Brown, *J. Chem. Phys.*, 1982, **77**, 1576.
40. M. F. Brown, *J. Chem. Phys.*, 1984, **80**, 2808.
41. T. P. Trouard, T. M. Alam, J. Zajicek, and M. F. Brown, *Chem. Phys. Lett.*, 1992, **189**, 67.
42. D. Doddrell, V. Glushko, and A. Allerhand, *J. Chem. Phys.*, 1972, **56**, 3683.
43. P. L. Nordio and U. Segre, in *The Molecular Physics of Liquid Crystals*, ed. G. R. Luckhurst and G. W. Gray, Academic Press, New York, 1979, p. 411.
44. A. Szabo, *J. Chem. Phys.*, 1984, **81**, 150.
45. D. A. Torchia and A. Szabo, *J. Magn. Reson.*, 1982, **49**, 107.
46. D. J. Siminovitch, M. J. Ruocco, E. T. Olejniczak, S. K. Das Gupta, and R. G. Griffin, *Biophys. J.*, 1988, **54**, 373.
47. M. Auger, D. Carrier, I. C. P. Smith, and H. C. Jarrell, *J. Am. Chem. Soc.*, 1990, **112**, 1373.
48. M. F. Brown and O. Söderman, *Chem. Phys. Lett.*, 1990, **167**, 158.
49. M. F. Brown, *Mol. Phys.*, 1990, **71**, 903.
50. G. D. Williams, J. M. Beach, S. W. Dodd, and M. F. Brown, *J. Am. Chem. Soc.*, 1985, **107**, 6868.
51. R. J. Pace and S. I. Chan, *J. Chem. Phys.*, 1982, **76**, 4228.
52. P. A. Watnick, P. Dea, and S. I. Chan, *Proc. Natl. Acad. Sci. USA*, 1990, **87**, 2082.
53. J. A. Marqusee, M. Warner, and K. A. Dill, *J. Chem. Phys.*, 1984, **81**, 6404.
54. R. Blinc, M. Luzar, M. Vilfan, and M. Burgar, *J. Chem. Phys.*, 1975, **63**, 3445.
55. N. O. Petersen and S. I. Chan, *Biochemistry*, 1977, **16**, 2657.
56. G. Lipari and A. Szabo, *J. Am. Chem. Soc.*, 1982, **104**, 4546.
57. H. Wennerström, B. Lindman, O. Söderman, T. Drakenberg, and J. B. Rosenholm, *J. Am. Chem. Soc.*, 1979, **101**, 6860.
58. M. F. Brown, J. F. Ellena, C. Trindle, and G. D. Williams, *J. Chem. Phys.*, 1986, **84**, 465.
59. B. Halle, *J. Phys. Chem.*, 1991, **95**, 6724.
60. M. F. Brown, J. F. Ellena, and G. D. Williams, Unpublished, 1984.
61. K. R. Jeffrey, T. C. Wong, E. E. Burnell, M. J. Thompson, T. P. Higgs, and N. R. Chapman, *J. Magn. Reson.*, 1979, **36**, 151.
62. R. W. Pastor, R. M. Venable, and M. Karplus, *Proc. Natl. Acad. Sci. USA*, 1991, **88**, 892.
63. R. M. Venable, Y. Zhang, B. J. Hardy, and R. W. Pastor, *Science*, 1993, **262**, 223.

Acknowledgments

Basic research carried out in our laboratories is sponsored by the US National Science Foundation and by the US National Institutes of Health. This work has benefited from the contributions of our previous students and colleagues, who have been a source of encouragement, criticism, and creative inspiration.

Biographical Sketches

Michael F. Brown. *b* 1948. A.B., 1970, University of California at Santa Cruz, USA, Ph.D., 1975, University of California at Santa Cruz, National Institutes of Health Postdoctoral Fellow, University of Basel, Switzerland, 1976–79, National Institutes of Health Postdoctoral Fellow, University of California at Berkeley, USA, 1979–80. Introduced to NMR by Ulrich Häberlen and Joachim Seelig. Faculty in Chemistry, University of Virginia, USA, 1980–87. Faculty in Chemistry, University of Arizona, USA, 1987–present. Present title: Professor of Chemistry and Professor of Biochemistry. Approx. 65 publications. Research specialties: the theory and application of nuclear spin relaxation to liquid crystalline materials, applications of NMR to lipid bilayers and proteins, structure and dynamics of proteins, biophysical chemistry of membranes, magnetic resonance imaging of atherosclerosis, molecular basis of visual excitation.

Sunney I. Chan. *b* 1936. B.S., 1957, University of California at Berkeley, USA, Ph.D., 1960, University of California at Berkeley, National Science Foundation Postdoctoral Fellow in Physics, Harvard University, USA, 1960–61. Introduced to NMR by Norman F. Ramsey. Faculty in Chemistry, University of California at Riverside, USA, 1961–63. Faculty in Chemistry, California Institute of Technology, USA, 1963–present. Present title: George Grant Hoag Professor of Biophysical Chemistry & Executive Officer in Chemistry. Approx. 250 publications. Research specialties: biophysical and biochemical studies of membranes (with emphasis on the structure and function of proteins involved in electron, ion, and solute transport), alkane functionalization, bioenergetics.

Bilayer Membranes: Proton and Fluorine-19 NMR

Ronald J. Pace

Australian National University, Canberra, Australia

1	Introduction	1
2	Dipolar and Chemical Shift Interactions	2
3	Spectral Shapes—Multilamellar Dispersions	2
4	^{19}F Spectra	4
5	Relaxation Data	5
6	Vesicles and High Resolution	8
7	Related Articles	10
8	References	10

1 INTRODUCTION

Because they constitute the basic structural component of biological membranes, bilayers composed of fatty acid containing amphiphiles have been the object of extensive study by NMR over the last three decades. The bulk of this work has been performed on fatty acid soaps and phosphatidyl glycerol esters of fatty acids phospholipids. Depending on water content and temperature, these substances exist in a number of well-characterized phases. The two phases of primary importance as biological membrane models are the smectic gel and liquid crystalline phases, between which there is a first-order melting transition. In both phases, the amphiphile molecules are organized as extended bilayers, separated by hydration regions in contact with the polar head groups of the amphiphile molecules. These are called multilamellar liposomes (in the case of lipids) or lyotropic liquid crystals (typically for soaps). In addition, closed single spherical bilayer structures are also possible for most lipids, termed unilamellar vesicles. These are normally generated by high-frequency agitation (ultrasonic irradiation) of lipid/water dispersions. They represent only a quasistable thermodynamic state when small (less than ∼20 nm radius). A detailed description of bilayer systems is given in Chapman and Salsbury.[1]

The first NMR studies on bilayers were performed by Lawson and Flautt,[2] who examined aqueous dispersions of fatty acid soaps. Chapman and coworkers[3] soon after performed the first NMR studies on phospholipid bilayer dispersions. These, and almost all of the other early investigations by Chan and colleagues (see, for example, Bocian and Chan[4] for a review) involved ^{1}H NMR, although the studies by Chapman et al. pioneered the use of selective deuteration to isolate contributions to the total lipid ^{1}H spectrum of different proton components of the lipid molecule.

After the proton, the ^{19}F nucleus has the next highest NMR sensitivity of any stable isotope (∼83% of the sensitivity of ^{1}H) and like ^{1}H, has essentially 100% natural abundance. In addition, due to its inertness and small size, a fluorine atom may often replace a proton, in say a C−H bond, with minimal disturbance to the biological properties and structure of the recipient molecule. Since fluorine is not normally present in biological systems, and bilayer-forming amphiphiles in particular, this offers the great potential advantage of being able to label specific portions of a molecule for study by NMR. Moreover, ^{19}F has a much higher range of chemical shifts than ^{1}H, and as such the ^{19}F shift is much more responsive to environmental perturbations than the ^{1}H shift. This allows the ^{19}F nucleus to be a very sensitive reporter of both molecular environment and motional state. There is, however, the caveat that the atom is larger, and the bond to carbon longer than the corresponding case for hydrogen. Thus ^{19}F cannot be a totally 'nonperturbing' probe of the molecular proton environment in the way that deuterium, (^{2}H) is. However, deuterium has only ∼1% of the NMR sensitivity of ^{1}H or ^{19}F and its NMR spectroscopy is somewhat more technically demanding than is that for the latter nuclei. These factors combine to make ^{19}F labeling a useful NMR tool in many instances. The balance of data at present (see below) appears to suggest that ^{19}F is a good qualitative reporter of the C−H proton environment in bilayer systems, but that there are modest quantitative differences between motional behavior of C−F and the corresponding C−H groups.

To minimize disturbance and exploit the capacity for precise label localization, essentially all ^{19}F NMR studies on bilayers have been performed on systems composed of selectively fluorinated molecules. Most commonly these have involved phospholipids, singly or doubly ^{19}F substituted at the same methylene carbon in the acyl chain region. Two groups have been prominent in this work, those of Ho (see, for example Ho et al.[5]) and McElhaney (see ***Membrane Lipids of Acholeplasma laidlawii***). When allowance is made for the moderate perturbations alluded to above, the results of these and other workers show that ^{19}F labeling provides an uniquely useful 'window' into the structural and dynamic states within bilayer membranes. The ^{19}F nucleus shares with ^{1}H its NMR sensitivity and capacity for significant internuclear dipolar interaction (see below), while possessing the strong 'bond centered' orientational properties of quadrupolar ^{2}H spectroscopy, due to the typically large chemical shift anisotropy of ^{19}F.

NMR is able to probe a wide range of molecular motional timescales through the frequency dependence of magnetization relaxation rates. Such studies have been arguably the most important and revealing applications of ^{1}H and ^{19}F NMR to bilayer systems. With current techniques, molecular motions with characteristic times in the range $\sim 10^{-5}$–10^{-11} s may be examined. The pioneering studies in this area on bilayer systems were performed by Chan and coworkers (see, for example, Feigenson and Chan[6]), who were the first to establish that a range of molecular motional timescales existed within bilayers and that the broad proton resonances seen from such systems arose from incomplete orientational averaging within an anisotropic environment (see below). This gave the first direct indication that even in the 'fluid' L_α liquid crystalline phase, the hydrocarbon interior of the bilayer was still partially ordered. An important subsequent development of this approach, certainly for ^{1}H and ^{19}F NMR studies, was the use of macroscopically aligned hydrated bilayer samples and wide-line, solid state NMR techniques to study both the frequency and angular (relative to the external field) dependences of relaxation parameters. The main contributions in these areas have come over the last decade from Cornell

and colleagues (see, for example, Pope et al.[7]) for ^{1}H and Ho et al.[8] for ^{19}F labeled systems.

Precisely because of the incomplete motional averaging which occurs in bilayers, the ^{1}H spectra of bilayer dispersions tend to be broad and relatively featureless. Small unilamellar vesicles (which tumble rapidly in solution) give moderately well-resolved ^{1}H spectra, and allow 'high-resolution', two-dimensional techniques (such as NOESY ^{1}H–^{1}H Overhauser spectroscopy) to be employed (see, for example, Ellena et al.[9]). This is particularly useful for the headgroup region resonances (e.g. the choline methyl groups in phospholipids). However, recently it has been demonstrated by Forbes et al.[10] that magic angle sample spinning techniques, which largely average out the ^{1}H–^{1}H dipolar interactions, give well-resolved ^{1}H spectra from the liquid crystalline mesophase of soap or lipid dispersions. While gel phase systems, which possess much less internal motion than L_α phase samples, still present difficulties for the technique, it is clear that this approach will find increasing applications in the future for the NMR study of bilayers (see, for example Lee and Griffin[11]).

2 DIPOLAR AND CHEMICAL SHIFT INTERACTIONS

Both ^{1}H and ^{19}F have nuclear spin, $I = \frac{1}{2}$ (no quadrupolar effects), large values of the nuclear gyromagnetic ratio γ, and relatively small atomic excluded volume radii. The latter means that internuclear separations at van der Waals contact are only ∼0.2 nm for these atoms in systems of interest here. These factors combine to ensure that after the Zeeman interaction, orientation-dependent *nonbonded* internuclear dipolar interactions are major contributors to the ^{1}H and ^{19}F spin Hamiltonian in systems such as bilayers, which lack complete motional averaging on the relevant NMR timescale. In addition, the Zeeman coupling to the external field has itself an orientation dependence, due to the variation in chemical shift screening with direction in a molecule fixed coordinate frame. For protons in C–H groups this variation is negligible (<1 ppm) and will be ignored here, but for ^{19}F in C–F groups it is substantial (∼200 ppm) and may dominate the spectrum. Both the dipolar and chemical shift interaction energies may be written in compact form using irreducible tensor formalism.[12,13] This has the virtue of emphasizing the common orientational dependence features of these basically quite different physical effects. Moreover, we will be concerned mainly with the pure 'orientation-only' component of these interactions, i.e. those that average to zero over the sphere. For the dipole–dipole term this is the total interaction itself, and for the chemical shift term it is the total interaction minus the isotropic shift, which difference we call the chemical shift anisotropy (CSA). Then either the $\hat{\mathcal{H}}_{\mathrm{D}}$ or $\hat{\mathcal{H}}_{\mathrm{CSA}}$ interaction Hamiltonians may be written:

$$\hat{\mathcal{H}}(t) = \sum_{q=-2}^{2} F_q(t)\hat{T}_q \qquad (1)$$

For dipolar interactions the $F_q(t)$ are proportional to the spherical harmonics of order 2:[12]

$$F_q[\Omega(t)] \simeq [1/r(t)^3]Y_{2,q}[\Omega(t)] \qquad (2)$$

where the internuclear separation, r, and its polar orientation, Ω, in the laboratory frame may both be functions of time. For the CSA interaction, the $F_q(t)$ are proportional to the components of the irreducible CSA tensor in the laboratory frame. The $\hat{T}_q$ are second-rank-tensor operators, formed from the relevant spin/magnetic field operators in each case (see Wennerström and Lindblom[17] for details). The utility of equations (1) and (2) is that, irrespective of their physical nature, the F_q terms have the same transformation properties under axis rotations and all of the orientation dependence of the interactions is contained in these terms.

At all normal experimental field strengths used in NMR, the Zeeman interaction totally dominates all other terms in the Hamiltonian, that is the nuclear spins are quantized along the external magnetic field at equilibrium. This means that the basic NMR spectrum shape is determined by the 'static' (motionally averaged) component of the dipolar or CSA interaction terms, and that only such effects contributing in first-order perturbation theory need be considered (i.e. only the spin components parallel to the external field contribute). The time-dependent parts of the interactions determine relaxation behavior, in a manner reflecting the amplitudes and timescales of molecular motions in the system.[13] Both the static and dynamic elements of ^{1}H and ^{19}F NMR have proved extremely valuable in 'decomposing' the molecular motions within partially ordered media, such as bilayers, and have allowed direct study of processes with timescales ranging from $\sim 10^{-6}$–10^{-11} s.

3 SPECTRAL SHAPES—MULTILAMELLAR DISPERSIONS

For simple ^{1}H NMR on bilayers, the spectral shape is governed by the only component, $\hat{\mathcal{H}}_{\mathrm{stat}}$, of equation (1) which contributes in first order. This derives from the $q = 0$ term. For any given proton, proton pair (labeled 1,2)

$$\hat{\mathcal{H}}_{\mathrm{stat}} = a\hat{I}_{z1}\hat{I}_{z2} \cdot \frac{1}{2}[\overline{(3\cos^2\beta_{1,2} - 1)/r_{1,2}^3}]\ ;\ a = \hbar^2\gamma_{\mathrm{H}}^2 \qquad (3)$$

where $\hat{I}_z$ is the nuclear spin component along the external field axis (z axis), $\beta_{1,2}$ is the angle between the internuclear vector and the external field, and $\hbar = h/2\pi$ where h is Planck's constant. The bar indicates averaging over all motions faster than the timescale set by the inverse of the typical dipole–dipole interaction (in frequency units). This latter interaction is ∼60 kHz for a pair of geminal CH_2 protons (see below).

Two distinct types of averaging are contained in equation (3), that over β and that over r. In the high temperature, fluid liquid crystalline (L_α) phase of bilayers, rapid molecular reorientation, and lateral diffusion average the r dependence of the intermolecular dipolar contribution to zero on a timescale of $\sim 10^{-8}$ s (see, for example, Pace and Chan,[14] and below). In the hexagonal intermediate ($P_{\beta'}$) and low-temperature orthorhombic ($L_{\beta'}$) phases, the hydrocarbon chains are mainly in a rigid, all-*trans* configuration, with highly restricted lateral mobility. However, relatively free rotational motion occurs about the long chain axis, especially in the $P_{\beta'}$ phase,[15] and the r^{-3} dependence then ensures that this axially symmetric

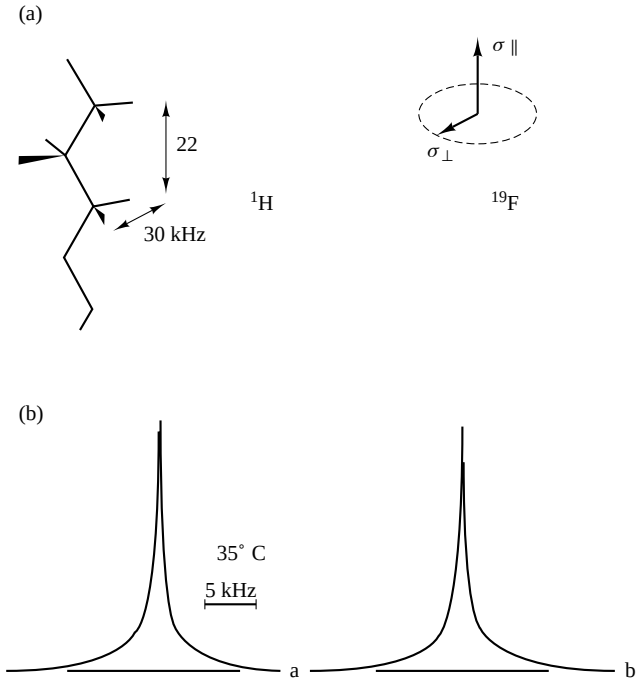

Figure 1 (a) All-*trans*-methylene chain showing the most important dipolar interactions and ^{19}F chemical shift tensor orientation which project onto the chain axis during fast axial rotation. (b) Comparison of an experimental (left) and theoretical (right) proton NMR spectrum (100 MHz) for the L_α phase of a DMPC/water dispersion as described in the text. [Data of Ulmius et al. (in Wennerström and Lindblom[17])]

motion largely eliminates intermolecular contributions to equation (3), even in the absence of lateral diffusion. Thus the proton NMR spectrum shape is dominated by purely intramolecular dipolar interactions, both above and below the main ($P_{\beta'} \leftrightarrow L_\alpha$) phase transition.

Seiter and Chan[16] showed that under such conditions of fast axial molecular averaging, the effective intramolecular dipolar interactions were 'projected' onto the local axis about which the total motion was symmetric. Under these circumstances (see also Section 5)

$$\frac{1}{2}[\overline{(3\cos^2\beta_{1,2}-1)/r_{1,2}^3}] = \frac{1}{2}[\overline{(3\cos^2\beta_b'-1)/r_b'^3}]\cdot\frac{1}{2} \times (3\cos^2\beta'-1) \qquad (4)$$

where the subscript b refers to the local molecular coordinate system and β' now refers to the orientation of the local averaging axis to the main field direction. For an all-*trans* chain rotating about the chain axis, the principal projected interactions for a given proton are shown in Figure 1(a). The strongest of these is the methylene geminal pair interaction, which is the only one for which r'_b is constant (0.182 nm) in all chain geometries. The 22 kHz β methylene interactions are substantially reduced for configurations other than all-*trans*, due to β'_b being then closer on average to the magic angle (54.7°), and r'_b being larger on average than 0.25 nm.

Figure 1(b) shows the ^{1}H spectrum for a dispersion of a C_{14} lipid [dimeristoyl phosphatidyl choline (DMPC)] in the L_α phase, together with a theoretical, simulated spectrum.[17] The broad, generally unresolved shape of the ^{1}H spectrum is typical of that seen in macroscopically unoriented bilayer systems, and has a super-Lorentzian bandshape.[4] The simulated spectrum of Wennerström et al. is based on equation (4) and assumes that the averaging results in a specific Gaussian bandshape for each class of protons, whose width is modulated by the ($3\cos^2\beta' - 1$) term. The spectrum results from appropriately summing these contributions over all orientations β'. The three classes of proton assumed were those of the main chain methylene groups (including the glycerol headgroup), the chain terminal methyl groups and the headgroup methyl groups. The use of a common bandshape for the chain methylene protons is consistent with the roughly constant order profile for the chain methylene protons seen in the ^{2}H NMR of membranes.

A major advance in the general interpretation of the NMR of bilayers came from the early recognition by Chan and coworkers (see, for example, Bocian and Chan[4]) that the axially symmetric motions, particularly of the main chain methylene groups in the L_α phase, could be further decomposed into 'fast' and 'slow' types. The fast motions correspond to the expected timescale for *trans–gauche* isomerization in the chain ($\sim 10^{-10}$ s), while the slow motions describe a restricted reorientation of the whole chain about the direction of the local bilayer normal (the local averaging axis). This picture, which supplanted a number of earlier interpretations, arose from a consideration of the very different longitudinal (T_1) and transverse (T_2) relaxation rates seen for protons in bilayers, as well as the static spectral shape. Current interpretations of molecular motions in bilayers retain this basic view. Thus Seiter and Chan[16] were able to demonstrate a reasonable simulation of the early component of the ^{1}H free induction decay from egg lecithin (mainly C_{18}, monounsaturated lipids) bilayer dispersions using this model. Only geminal proton interactions were considered, with essentially free rotation about a local chain axis, which could itself move randomly in a cone of half angle $\sim 50^\circ$ about the bilayer normal. While an evident simplification, this description is still semiquantitatively in accord with more recent interpretations (Section 5), at least in its essential statistical features. Following this, a number of detailed analyses of the general problem of dipolar interactions in systems with incomplete motional averaging have been presented, notably by Bloom and coworkers (for a review see Bocian and Chan[4]). However, the difficulty of uniquely 'deconvoluting' the ^{1}H powder pattern spectra to obtain molecular ordering information, such as is directly available from ^{2}H spectra, restricts the ultimate utility of these approaches.

A technique which addresses some of these difficulties in bilayer systems, while retaining the unique information content of ^{1}H NMR, is the use of wideline, solid state NMR spectroscopy on macroscopically aligned, hydrated lipid bilayer samples. This has been pioneered by Cornell, Pope and coworkers (see, for example, Pope et al.[18]). Figure 2(a) shows their data for aligned DMPC multilayers in the $L_{\beta'}$, $P_{\beta'}$ and L_α phases. From equations (3) and (4) one expects the contribution to the resonance from any proton pair in an aligned sample to be a doublet, whose splitting scales as $\frac{1}{2}(3\cos^2\beta' - 1)$, where β' is equal to the angle between the sample stack normal and the magnetic field, θ, in cases where the motional averaging is symmetric about the membrane normal [see Figure 2(b)]. The spectra in Figure 2 are for $\theta = 0$. Unlike the case for unoriented lipid dispersions, partially resolved

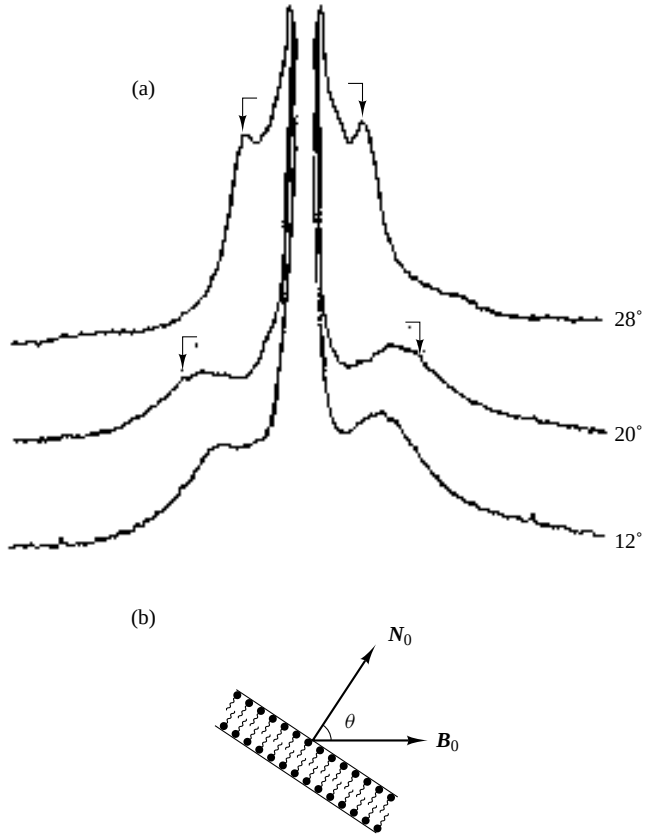

Figure 2 (a) ^{1}H NMR spectra (90 MHz) from hydrated macroscopically oriented DMPC bilayers at temperatures 12 °C ($L_{\beta'}$), 20 °C ($P_{\beta'}$) and 28 °C (L_α), showing resolved dipolar splittings (from Pope et al.[18]). Marker separations are 59 kHz (20 °C) and 30 kHz (28 °C) and the sample stack is oriented with its normal parallel to the main field $\boldsymbol{B}_0$. (b) Schematic picture (after Wennerström and Lindblom[17]) of a macroscopically aligned bilayer oriented at an angle'θ'to the main field. For the L_α phase, $\beta' = \theta$, but for gel phase lipids $\beta' \neq \theta$, due to static tilt (see text)

splittings are observed in all three phases. These arise mainly from the chain methylene protons (methyl protons are near the spectrum center). From Figure 1(a), the total ^{1}H methylene splitting, $\Delta\nu_{\text{chain}}$, for an all-*trans* chain, averaging about the chain rotation axis, is $\sim 30 + 2 \times 22 \approx 75$ kHz. Additional interactions not included in Figure 1(a) will increase this value somewhat. It is known that there is a static 'tilt' angle between the chain axis and the membrane normal in the gel phases.[1] This is greater in the $L_{\beta'}$ than the $P_{\beta'}$ phase, which is reflected in the larger pattern splitting for the $P_{\beta'}$ phase [Figure 2(a)]. Pope et al. determined this angle to be $\sim 23^\circ$ for the $P_{\beta'}$ phase, from the angular dependence of the ^{1}H free induction decay in their system. Taking $\beta' = 23^\circ$, and the above 75 kHz estimate, a pattern width of $\sim$58 kHz is expected for the $P_{\beta'}$ phase in Figure 2. This is plausibly close to the value seen, although there are clearly extra contributions in the wings of the spectrum from neglected interactions.

In the L_α phase, the spectrum narrows and sharpens dramatically. In this case the total chain motion is known to be symmetric about the bilayer normal (i.e. $\beta' = \theta$), but is composed of rapid intramolecular motions, modulated by a whole-chain 'wobble'. The spectral narrowing due to the latter motion is referred to as the molecular or chain axis order parameter, S_α (see, for example, Bocian and Chan,[4] Section 5 and Figure 7). S_α may be independently estimated from ESR studies on cholestane spin probes in bilayers and is typically $\sim$0.7 (see, for example, the discussion in Pace and Chan[19]). Since

$$\Delta\nu_{\text{obs}} = S_\alpha \Delta\nu_{\text{chain}} \tag{5}$$

where $\Delta\nu_{\text{obs}}$ and $\Delta\nu_{\text{chain}}$ are the observed and fast intramolecular-only chain averaged splittings, Figure 2(a) suggests that $\Delta\nu_{\text{chain}}$ is only $\sim$40 kHz. This is a significant conclusion, from ^{1}H NMR, and indicates a major reduction of the all-*trans* ($\Delta\nu_{\text{chain}} \approx 75$ kHz) concentration in the L_α state (resulting in substantial loss of the $\sim$44 kHz β-CH_2 interactions). Recent molecular dynamics simulation studies support this conclusion (see Section 5).

4 ^{19}F SPECTRA

Selective labeling of proton positions with ^{19}F is, in principle, a powerful tool for examining molecular processes in bilayers. Ho and colleagues (see, for example, Ho et al.[5]) have contributed substantially in this area, particularly with studies of ^{19}F labels in the acyl chains of lipids. The combination of both CSA and dipolar interaction derived information should provide a unique picture at the molecular level. The only concern is whether the larger fluorine atom perturbs the local molecular environment, either structurally or dynamically. The answer appears to be that it does quantitatively, but probably not qualitatively. In an elegant ^{2}H NMR experiment, Oldfield et al.[20] showed, by labeling lipid chains with both ^{2}H and ^{19}F, that the replacement of a CH_2 group by a CF_2 group increases the apparent disorder of neighboring CD_2 groups by $\sim$30%. Despite this, the study of ^{19}F substituted lipids in bilayers has proved very illuminating and worthwhile.

At typically used NMR field strengths (>3 T), the CSA interaction in the C–F bond dominates the ^{19}F spectrum in bilayers. Whenever axially symmetric motional averaging is present (which is essentially always the case), the first-order interaction Hamiltonian for the CSA, analogous to equations (3) and (4), is:[5]

$$\hat{\mathcal{H}}_{\text{CSA}} = \frac{3}{2} B_0 \hat{I}_z \cdot \left(\overline{\sum_i \sigma_{ii} S_{ii}} \right) \frac{1}{2} (3\cos^2 \beta' - 1) \tag{6}$$

The S_{ii} order parameters are simply the motional averages of the quantities $\frac{1}{2}(3\cos^2\theta_i - 1)$, where θ_i is the angle between the ith ($i = x, y, z$) principal axis of the CSA tensor (in the local molecule fixed frame) and the axis about which averaging occurs. At present, the individual values of the σ_{ii} for a CF_2 group in a lipid chain are not known. However, the z molecular frame axis direction is very probably as indicated in Figure 1(a) (σ_{11}), and the value of the bracketed term in equation (6) (called the effective CSA, $\Delta\sigma$) is $\sim$170 ppm for an all-*trans* chain undergoing rotational averaging about its long axis.[5]

In a CF_2 group, the F- -F separation is 0.218 nm, giving a splitting of $\sim$31 kHz, which is smaller than the geminal ^{1}H- -^{1}H value of $\sim$60 kHz or the ^{19}F CSA splitting of $\sim$50 kHz at high field ($\sim$300 MHz). Figure 3 shows ^{19}F spectra for dispersions of 2-(8,8-^{19}F)DMPC in D_2O. In Figure 3(a),

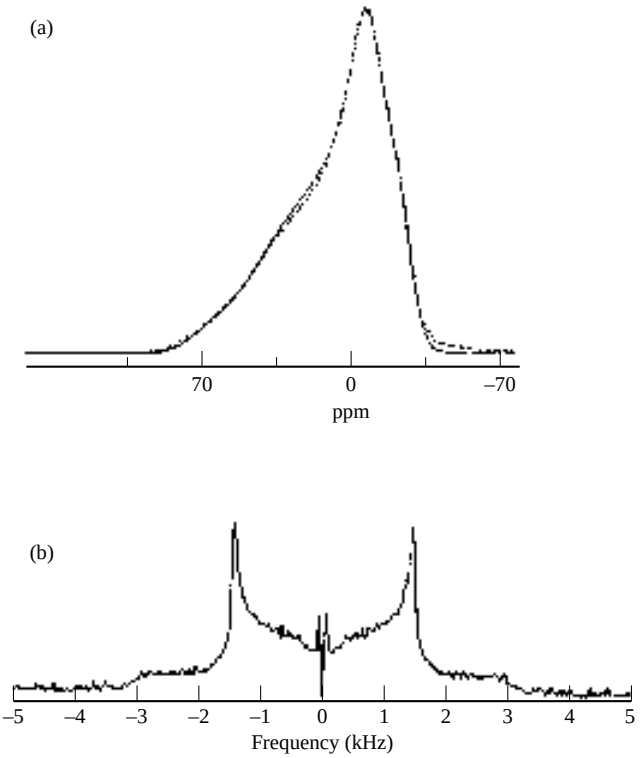

Figure 3 (a) ^{19}F spectrum (282 MHz) of 8,8-difluoro-substituted DMPC in aqueous (D_2O) dispersion at 27 °C (L_α phase): (...) experimental and (−) theoretical spectra assuming an axial CSA interaction with F−F and F−H dipolar interactions. (b) Dipolar ^{19}F NMR spectrum (40 MHz) of the same lipid obtained with CPMG pulse sequence to suppress chemical shift and heteronuclear dipolar interactions. (From Ho et al.[5])

the full high field spectrum shows the characteristic axial CSA shape, with an evident axial dipolar (geminal F−F) contribution and some H−F dipolar broadening. The estimated $\Delta\sigma$ value is ∼55 ppm. Even allowing for an S_α reduction [as in equation (5)] due to whole chain motion, this still implies a $\Delta\sigma_{\text{chain}}$ of only ∼80 ppm, which is less than half the all-*trans* value (see the discussion in Section 3). Interactions linear in the spin operators of a given spin species (here ^{19}F), such as the CSA and heteronuclear dipolar interaction (here ^{1}H−^{19}F), may be averaged to zerousing pulse sequences of the CPMG type. Figure 3(b) shows the F−F dipolar-only spectrum resulting from such suppression (taken at 40 MHz to reduce CSA interaction). This has the classical Pake doublet shape for the powder pattern arising from an axially averaged dipolar interaction. The sharp peaks correspond to orientations with $\beta' = 90°$, and their splitting gives the value of the total order parameter, $S = \frac{1}{2}[\overline{3\cos^2\beta'_b - 1}]$, for the geminal F−F internuclear vector [equation (4)]. For an all-*trans* chain, S = 0.5 S_α (in magnitude) for either the F−F or C−D (from ^{2}H NMR) bond vectors (see section 5 and Figure 7. Figure 4 shows a comparison of the S_{FF} and S_{CD} order parameters as a function of temperature for labeled DMPC in the L_α phase.[5] In general, S_{FF} is less than S_{CD} at the corresponding methylene position. Since the F−F (or H−H) and C−D vectors are geometrically inequivalent within the chain, there is no reason why their order parameters should be equal under conditions of partial motional averaging. The results of Oldfield et al.[20]

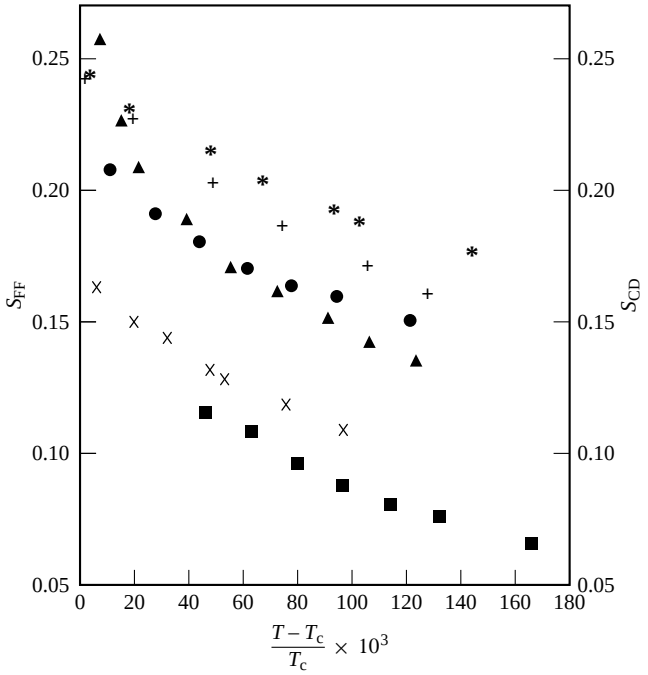

Figure 4 Comparison of S_{FF} and S_{CD} as a function of fractional temperature increase above the melting temperature, T_c, for equivalently methylene disubstituted DPMC lipids. (•, ⧫, ■) S_{FF}; (×, + , *) S_{CD}. (•*) 4,4-Disubstituted; (⧫+) 8,8-disubstituted; (■ ×) 12,12-disubstituted. All substitutions on the 2 chain. (Data from Ho et al.[5])

suggest that S_{FF} underestimates the true S_{HH} by ∼30%, and so Figure 4 implies that S_{HH} is probably larger than S_{CD}. This is consistent with other estimates of these quantities (see, for example, the discussion in Pace and Chan[21]).

5 RELAXATION DATA

Studies of the frequency and orientational dependence of the various magnetic relaxation rates have proved to be one of the most illuminating applications of ^{1}H and ^{19}F NMR to the study of bilayers. Mostly these have involved measurements of the longitudinal relaxation times in the laboratory (T_1) and rotating frame ($T_{1\rho}$). In the systems of interest here, relaxation is governed by those components of the CSA and dipolar interactions which average to zero[13] on a timescale short compared with the bulk magnetization relaxations. Generally that means time scales $\leq 10^{-4}$ s.

From Redfield theory one has[8,21] the well-known contributions to the relaxation rates at nucleus, I;

homonuclear dipolar interaction, r_{II} constant:

$$\frac{1}{T_1} = \frac{3}{4}\nu_I^2[J_1(\omega_I) + 4J_2(2\omega_I)] \tag{7a}$$

$$\frac{1}{T_{1\rho}} = \frac{3}{4}\nu_I^2\left[\frac{3}{2}J_0(\omega'_I) + \left(\text{terms} \simeq \frac{1}{T_1}\right)\right] \tag{7b}$$

CSA interaction:

$$\frac{1}{T_{1\rho}} = \nu_{\mathrm{CSA}}^2 \left[\frac{1}{3} J_0(\omega_I') + \left(\text{terms} \simeq \frac{1}{T_1} \right) \right] \qquad (7c)$$

where

$$\begin{aligned} \nu_{\mathrm{CSA}} &= \tfrac{1}{4}\sqrt{6}\gamma_I B_0 \Delta\sigma \\ \nu_{\mathrm{I}} &= (\gamma_I^2 \hbar / r_{II}^3)^2 \end{aligned} \qquad (7d)$$

The ν terms are proportional to the characteristic magnitude of the interaction in each case; ν_{H} (geminal) = 1.55×10^{10} s^{-2}, ν_{F} (geminal) = 4.11×10^9 s^{-2}. The effective CSA, $\Delta\sigma$, in equation (7d) is that arising from fast intramolecular motion, but not chain axis motion. For the order plateau region of a lipid chain $\Delta\sigma$ is ~80 ppm in the L_α phase (Section 4). The $J_q(\omega)$ are the Fourier transforms of the autocorrelation functions, $G_q(\tau)$, of the zero averaging (as $\tau \to \infty$) components of the F_q terms in equation (1), (see, for example, Pace and Chan[21]). ω_I and ω_I' are the resonant frequencies in the laboratory and rotating frames, respectively. For simple processes characterized by a single correlation time, τ_c, $G(\tau) = G(0)\exp[-|\tau|/|\tau_c|]$ and so

$$J(\omega) = \int_{-\infty}^{\infty} G(\tau)\exp(-\mathrm{i}\omega\tau)\mathrm{d}\tau = G(0)\cdot\frac{2\tau_c}{1+\omega^2\tau_c} \qquad (8)$$

Because there is a range of molecular motional timescales contributing to $G_q(\tau)$ in the bilayer, the J_q terms do not have the simple ω dependences suggested by equation (8). Feigenson and Chan[6] recognized this when they performed the first ω_{H} dependence studies of T_1 relaxation in lecithin bilayer dispersions. These data showed that at least two broad classes of motion were contributing, with τ_c values of ~10^{-10} and 10^{-7} s. The fast motions were assumed to be intrachain isomerizations and the slow motions whole-chain reorientations. A subsequent analysis of the results[21] indicated an approximate $\omega^{-\frac{1}{2}}$ dependence of T_1^{-1} for protons, and this has now been firmly established by Brown and coworkers as the dominating frequency power law for both ^{2}H and ^{13}C relaxation in bilayers (see ***Bilayer Membranes: Deuterium and Carbon-13 NMR***).

Kimmich and Voigt,[22] in an experimental tour de force, measured the ω_{H} dependence of proton T_1 in DPPC (C_{16} lipid), over the range 10^4–10^8 Hz. Figure 5 shows their data for L_α phase lipid dispersions. Not only are there extended regions showing $\omega_{\mathrm{H}}^{\frac{1}{2}}$ dependence, but there are evident transitions between these regions. Although there are several physical mechanisms that predict an $\omega^{-\frac{1}{2}}$ dependence of NMR relaxation rates, including linear defect ('kink') diffusion in ordered chains (such as seen in polyethylene[22]), the most likely basis of the $\omega^{-\frac{1}{2}}$ observation in bilayer systems is the presence of liquid-crystal-like collective order fluctuations (see, for example, de Gennes[23]). This is particularly true in the L_α phase, where, as has been shown, the intramolecular disorder is high, but kink diffusion processes may well contribute significantly below the phase transition. This matter is as yet unresolved.

Pace and Chan[19,21] proposed a simple heuristic model of molecular motion in bilayers, inspired by the observations

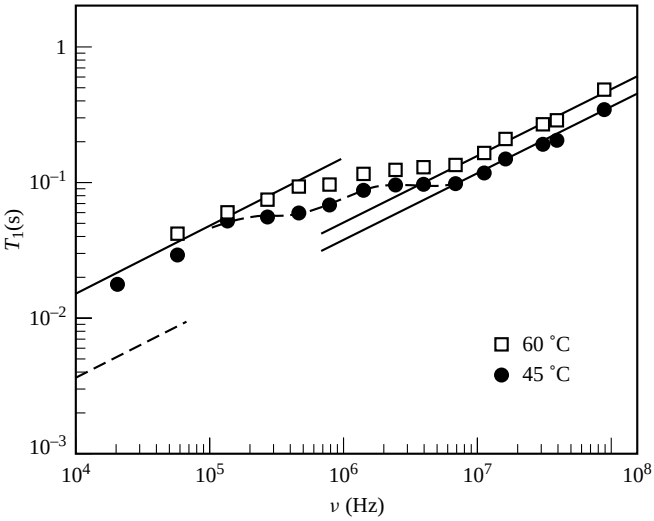

Figure 5 Frequency dependences of the proton T_1 relaxation time in L_α phase aqueous (D_2O) DPPC (dipalmitoyl phosphatidyl choline) dispersion for temperatures 45° and 60 °C. The solid lines show two regions of $\omega^{-1/2}$ relaxation rate behavior, with an evident two-step transition between these. Steps correspond to motional 'cutoffs' at $\omega_{\mathrm{H}} \approx 6 \times 10^7$ and 2×10^6 s^{-1} (see text)

from ^{2}H NMR (see ***Bilayer Membranes: Deuterium and Carbon-13 NMR***) that the L_α phase C–D order parameter profile is roughly constant over the first 10–12 chain methylene groups. This is shown in Figure 6(a) and assumes that, in the fluid state, the lipid chains adopt an alternating $tg^{\pm}tg^{\pm}$ or $g^{\pm}\,tg^{\pm}t$ conformation, with the g bonds being approximately aligned with an average chain axis. Isomerizations ('crankshaft rotations') about these bonds are allowed, as they still permit the chain to be statistically 'confined' within a roughly cylindrical region; however, isomerizations about the 'horizontal' *trans* bonds are strongly disfavored. The chain axes may then undergo angular displacements about a local average position, as in liquid crystals. Although this model is clearly a simplified 'cartoon' of the actual events in lipid bilayers, it is interesting that recent realistic molecular simulations (see, for example, Pearce and Harvey[24]) of these systems show typical chain configurations supporting the model, as well as exposing its limitations, particularly near the chain ends [Figure 6(b)]. An important feature of crankshaft-type models is that there are two disordered chain states, $g^{\pm}tg^{\pm}t\ \ldots$, or $tg^{\pm}tg^{\pm}\ \ldots$, and that interconversion between these is likely to be *slow* and proceed via an all-*trans* configuration.

Within a model like the above, it is possible systematically to decompose the relevant bond motions of the chain. This is illustrated in Figure 7. The bond vector is assumed to execute rapid, cylindrically symmetric motion about the instantaneous chain axis with order parameter, $S_\gamma = \frac{1}{2}\overline{(3\cos^2\beta_{\mathrm{b}} - 1)}$. The angle β_{b} is constant in the crankshaft geometry, but only approximately so in reality. The chain axis vector, $\boldsymbol{N}$, then executes restricted fluctuations about the local director (membrane normal) axis, $\boldsymbol{N}_0$, defined by polar angles α', β' in the laboratory frame. This motion then defines the molecular order parameter, $S_\alpha = \frac{1}{2}\overline{(3\cos^2\beta'' - 1)}$ within the model. The total order parameter is $S = S_\gamma S_\alpha$. The nonzero averaging interactions, referred to above, which do not contribute to relaxation, are simply those which remain projected along

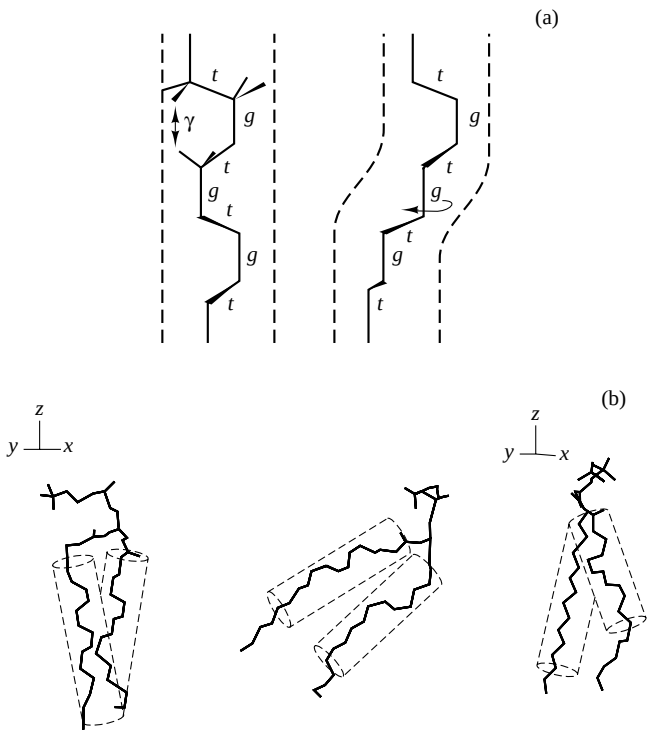

Figure 6 (a) 'Crankshaft' model of the fluid lipid acyl chain configuration. Alternating *trans–gauche* configuration confines the chain to a roughly cylindrical region, and isomerizations ($g^{\pm} \leftrightarrow t \leftrightarrow g^{\pm}$) are permitted only for chain-axis-aligned (typically *gauche*) bonds. This imposes minimal packing disturbance on neighboring chains and allows these to execute liquid-crystal-type motions. Nongeminal dipolar interaction occurs mostly with a γ-methylene proton, as shown. (b) Typical molecular configurations from Langevin dynamics simulations of C_{16} lipids in a bilayer (from Pearce and Harvey[24]). Configurations are mostly 'disordered' with some resemblance in the upper chain region to the model shown in (a). However, the simulations generally allow more types of disordered states than the crankshaft model predicts

the 'static' direction $\boldsymbol{N}_0$. In multilamellar dispersions and oriented samples, $\boldsymbol{N}_0$ may be generally regarded as static on the NMR timescale, but in small vesicles, this is not so and all interactions average to zero.

The correlation times associated with *trans–gauche* isomerization (i.e. the γ motion in Figure 7) are $\sim 10^{-10}$ s. Hence these motions are all in the extreme narrowing NMR range ($\omega\tau_c < 1$), at least for the L_α phase bilayers. Under these circumstances, one obtains for the geminal H–H contribution to the ^{1}H methylene T_1 relaxation rate:[21]

$$\frac{1}{T_1} \simeq \frac{9}{8}(\gamma_H \hbar / r_{HH}^3)^2(\tau_c + 1.02 S_\gamma^2 \cdot \zeta \omega_H^{-1/2}) \qquad (9)$$

where τ_c is the correlation time for fast isomerization motions and the ζ term arises from treating the chain axis motion within the linearized nematic order formalism for liquid crystals:

$$\zeta \simeq (3kT/2\sqrt{2\pi})\eta^{1/2} K^{-3/2} \qquad (10)$$

where K and η are average nematic elastic and viscosity constants. While the liquid crystalline phase of bilayers is not strictly a bulk nematic, an interpretation of bilayer motional behavior in these terms appears still to be quantitatively reasonable.

At high ^{1}H frequency (>200 MHz), the limiting intramolecular contribution to the ^{1}H relaxation in fluid bilayers is ~ 1 s^{-1} (see Kroon et al.[25] and the discussion in Pace and Chan[21]). This corresponds to an apparent τ_c of $\sim 7 \times 10^{-11}$ s from equation (9). Direct estimates of τ_c from ^{2}H and ^{13}C labeled lipid data give $\tau_c \approx (3–4) \times 10^{-11}$ s. Thus nongeminal interactions contribute about 50% of fast proton intramolecular T_1 relaxation in bilayers. The observed rates are essentially the average methylene values, as these groups constitute the bulk of the protons in lipids and are the principal relaxation 'sinks' due to rapid spin diffusion in the system.[21] At ^{1}H frequencies below ~100 MHz, the nematic term in equation (9) begins to dominate the relaxation. Its value depends upon $S_\gamma{}^2$, the projection of the geminal H–H bond vector motion onto the local chain axis direction. This is ~0.2 (0.25 in the crankshaft model), and a reasonable estimate for ζ is $\sim(2–3) \times 10^{-6}$ $s^{\frac{1}{2}}$ for fluid DPPC.[14,19] equation (9) then semiquantitatively predicts (within ~50%) the observed T_1 behavior for fluid DPPC (Figure 5) in the limiting low-frequency regime ($\nu < 10^5$ Hz), but underestimates the rate by a factor of ~4 at high (>10^7 Hz) frequency, although the $\omega^{\frac{1}{2}}$ power law dependence is evident in both limiting regions. An apparent 'two-step' transition occurs between these regions in Figure 5. The first, at which $\omega_H \approx 6 \times 10^7$ s^{-1} (10^7 Hz) clearly corresponds to lipid lateral diffusion (timescale $\tau_d \sim 10^{-8}$ s).[14] Over times less than τ_d (i.e. $\omega_H > 1/\tau_d$), nematic motions modulate unaveraged intermolecular dipolar interactions—which produce a total $T_1{}^{-1}$ contribution comparable to the total intramolecular processes in this region. When $\omega_H > 1/\tau_d$, the intermolecular motions contribute only a constant $T_1{}^{-1}$ component [roughly proportional to τ_d, see equation (8)], which is of diminishing relative magnitude as ω_H drops. The surprising result from Figure 5 is that there is a further distinct 'cut-off' at $\sim 4 \times 10^5$ Hz (corresponding to $\tau_c \approx 4 \times 10^{-7}$ s). This can only be of intramolecular origin, and represents a slow motion which largely averages out all remaining nongeminal dipolar interactions.

An important insight into this slow process comes from $T_{1\rho}$ measurements on oriented bilayers, both for ^{1}H and ^{19}F. Rotating frame relaxation is sensitive to molecular motions in the 10^{-5}–10^{-6} s range, as $\omega' \approx 10^5$ s^{-1}. Figure 8 shows the data of Pope et al.[18] and of Ho and co-workers[8], for the angular dependence of $T_{1\rho}$ in aligned lipid multilayers. Because of the similar forms of equations (7b) and (7c), the angular dependence of the nematic fluctuation contribution to $T_{1\rho}$ is the same for ^{1}H and ^{19}F. This is proportional to $(\sin\beta' \cos\beta')^2$, i.e. to the square of the derivative of $(3\cos^2\beta' - 1)$ [this is evident from considering Figure 7(c), but see Ho and coworkers[8] and Pace and Chan[21]]. Such a dependence is seen in liquid crystals.[26] Figures 8(a) and 8(b) show, however, that the ^{1}H and ^{19}F $T_{1\rho}$ relaxation is dominated by a component roughly proportional to $(3\cos^2\beta' - 1)^2$. Furthermore, this component was essentially absent from the ^{2}H $T_{1\rho}$ angular dependence of perdeuterated lipids.[18] Thus the relaxation mechanism must involve a modulation of the magnitude of residual nongeminal intramolecular dipolar interaction directed along the chain axis, not any large-scale angular motion of the chain itself, which would also reflect in deuterium $T_{1\rho}$. The most likely basis of this modulation is

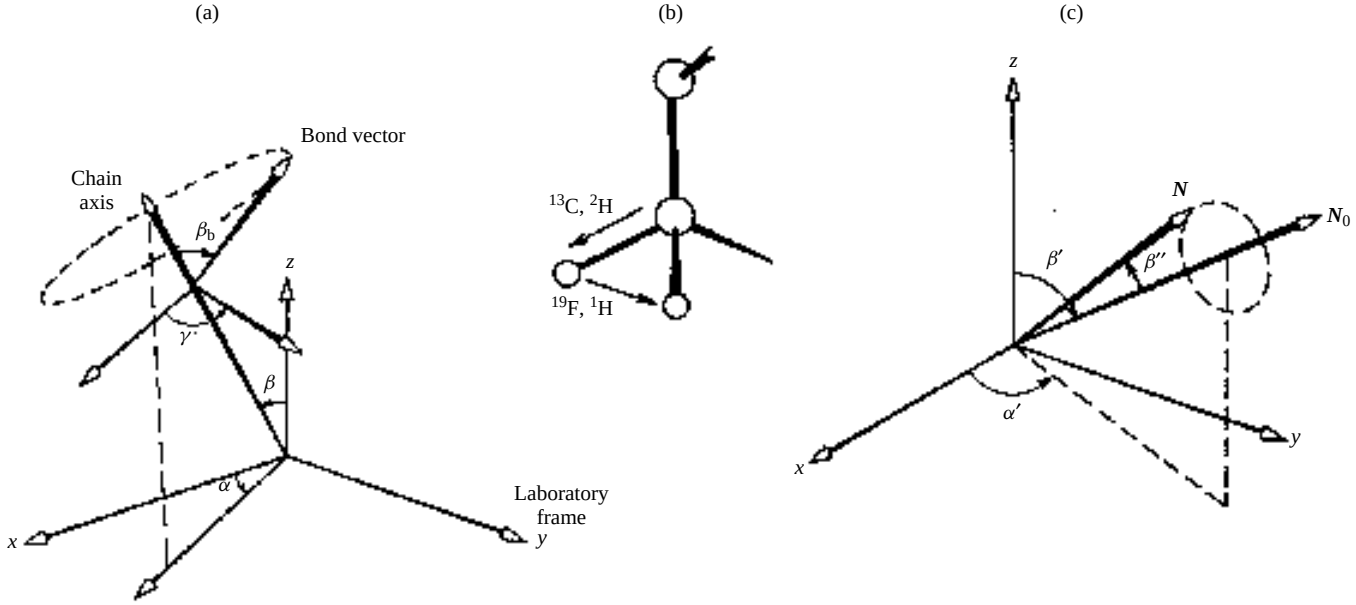

Figure 7 Decomposition of bond vector motions for methylene groups in chains. (a) Fast, symmetric axial motion of the bond vector about the instantaneous chain axis is assumed, with order parameter $S_\gamma = \frac{1}{2}\overline{(3\cos^2\beta_b - 1)}$. (b) β_b is constant in the crankshaft model for a particular intramethylene interaction. (c) The chain axis then executes limited motion (nematic fluctuation) about a local 'fixed' axis (normal to the membrane plane), $\boldsymbol{N}_0$. This latter motion defines the molecular order parameter $S_\alpha = \frac{1}{2}\overline{(3\cos^2\beta'' - 1)}$ and is associated with a wide range of motional timescales. The total order parameter is $S = S_\gamma S_\alpha$

the slow interconversion of (surprisingly) long lived average chain configurations, each possessing a distinct, residual intramolecular order. For example, the average nongeminal interactions between a particular methylene proton and its individual neighbors [particularly γ-methylene protons, see Figure 6(a)] are different in the two crankshaft states, although the actual events in the bilayer are likely to be more complex than this simple picture suggests. From measurements at several rotating frame frequencies, the correlation time, τ_i, for the relaxation was estimated as $\sim 10^{-6}$ s (protonated lipids) and $>10^{-5}$ s (difluoro-substituted lipids). The protonated lipid value is generally consistent with the above estimate from unoriented dispersions (-4×10^{-7} s), but the fluorinated lipid value is much longer, presumably reflecting a slowing of the interconversion in this system due to steric hindrance from the fluorine atoms on the chain. Although the natures of the molecular processes underlying the data given in Figure 8 are yet to be fully resolved, the results graphically demonstrate the power of ^1H and ^{19}F NMR to reveal quite unanticipated results in partially ordered systems.

6 VESICLES AND HIGH RESOLUTION

Ultrasonic irradiation (sonication) of aqueous dispersions of phospholipids produces sealed, single walled bilayer vesicles (radius, $R \approx 10.0$–15.0 nm), whose NMR spectra show medium–high resolution features (see ***Sonicated Membrane Vesicles***). In these systems nuclear dipolar and chemical shift anisotropies are averaged to zero on the timescale of vesicle tumbling, which is normally faster than $\sim 10^{-5}$ s. For this reason, most of the earlier high-resolution NMR studies on bilayers utilized vesicles as the membrane model (see, for example, Bocian and Chan[4]).

Small vesicles are kinetically but not thermodynamically stable, reverting over hours or days into larger bilayer aggregates. The high surface curvature, particularly for the inner lipid layer, raises some questions concerning their quantitative similarity to 'flat', stable bilayers. The answer appears to be that for the outer monolayer at least (which constitutes ~70% of the material), the lipids are in a similar environment to that of a flat bilayer, but with somewhat more motional disorder. The high-frequency (100 kHz) proton T_1 values are virtually the same (0.3 s) in DPPC bilayers (Figure 5) and vesicles[25] at 50 °C. By varying the suspending solution viscosity, Mackay et al.[27] showed that most of the proton linewidth for small vesicles arose from a term proportional to the net correlation time, τ_v, for vesicle tumbling, plus lateral diffusion of lipids around the vesicle surface. These and other ^2H results on vesicles (see Pace and Chan[21]) appeared to contradict the conclusions of Bocian and Chan[4] that chain disorder, arising from local processes, was greater in vesicles than in bilayers, due to the high vesicle surface curvature. However, it was subsequently shown[21] that when the chain-axis fluctuations were treated as motions in a two-dimensional nematic medium, the linewidth expression took the form:

$$\Delta\nu_H = \frac{1}{\pi T_2} \simeq \frac{9}{8\pi}\,\nu_H^2 S_\gamma^2 Z_v(0) + \left(\text{terms} \simeq \frac{1}{T_1}\right) \qquad (11)$$

where $Z_v(0)$ is given by

$$Z_v(0) = \frac{2\tau_v}{5}\left(1 - \frac{3kT}{\pi K'}\,\ln\frac{R}{d}\right) \qquad (12)$$

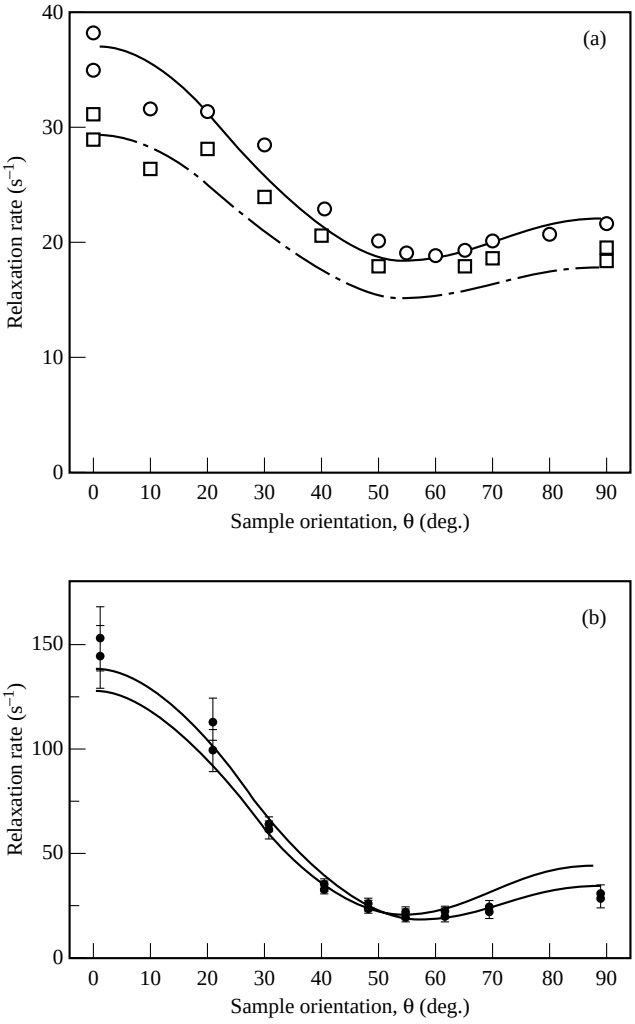

Figure 8 Angular dependence [see Figure 2(b)] of rotating frame relaxation ($T_{1\rho}$) rates in aligned fluid multilayer samples. (a) Data of Pope et al.18 for ^{1}H relaxation in egg lecithin (mostly C_{18} PC) at ω_H' values of 9.4×10^4 (○) and 3.2×10^5 (□) s^{-1}. (b) Data of Ho and coworkers8 for 8,8-difluoro-substituted DMPC, $\omega_F' = 5.1 \times 10^4$ s^{-1}. Curves are theoretical fits assuming mostly a $(3\cos^2\beta' - 1)^2$ dependence (see text). The larger magnitude of this effect in the fluorolipid arises from the ∼10-fold longer correlation time associated with the relaxation motion in this case (see text)

Here K' is the average two-dimensional nematic force constant and d is approximately equal to the lipid molecule chain diameter (∼0.5 nm). The significance of equation (11) is that essentially the *whole* interaction (tumbling plus nematic motions) scales as τ_v. This happens because the nematic fluctuations are continuously distributed on all timescales down the 'cutoff' imposed by overall vesicle motion, τ_v. The bracketed expression in equation (12) may be thought of as the square of an effective vesicle S_α term. From the observed $\Delta\nu_H$ value of ∼60 Hz for small ($R \approx 10.0$ nm, $\tau_v \approx 4.7 \times 10^{-7}$ s) C_{18} vesicles,[28] S_α is ∼0.58, which is significantly smaller than the value of >0.7 for bilayers of the same material. This also corresponds to a K' value substantially smaller than for bilayer dispersions (see Pace and Chan[19,21]). Thus the main difference revealed by these studies between the lipids in bilayers and vesicles (outer layer mostly) is that the chain

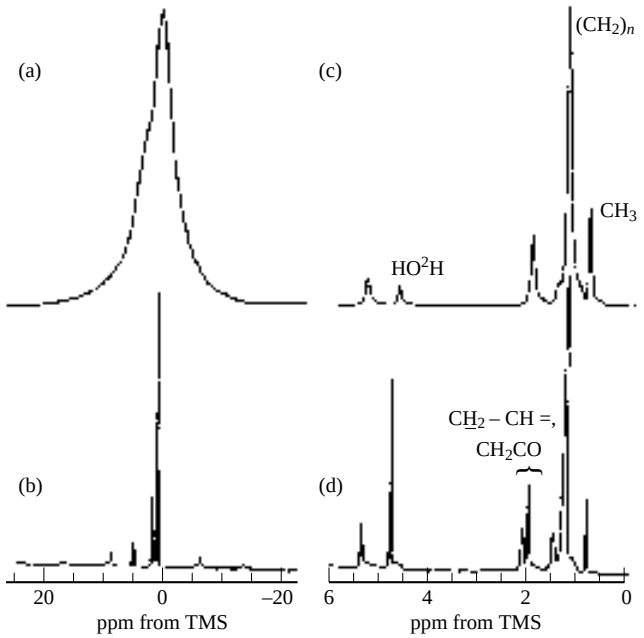

Figure 9 360 MHz static and magic angle spinning (MAS) ^{1}H Fourier transform NMR spectra of a potassium oleate (∼ 70% in D_2O) L_α phase dispersion. (a) Static spectrum at 26 °C; (b) 2.7 kHz MAS NMR spectrum; (c) expansion of the centerband region of (b);, (d) solution spectrum (micellar) of potassium oleate in D_2O. (From Forbes et al.[10])

packing is 'looser' in the vesicle, leading to larger chain-axis fluctuations, but with no evidence of a significant difference in chain internal order. For the inner layer, this is probably not so. Certainly, average chemical shift differences occur between the inner and outer monolayers in vesicles and the resonance lines from the inner monolayer are narrow.[28]

Equation (4) shows that one way to minimize dipolar broadening in bilayers is to use aligned multilamellar samples, oriented to the main field at the 'magic angle', $\beta' = 54.7°$ (whence $\frac{1}{2}[3\cos^2\beta' - 1] = 0$). This has been used (see, for example, van der Leeuw and Stulen)[29] and produces spectra with at least the resolution obtainable from vesicles. However, the technique has not been as widely employed for ^{1}H studies on bilayers, as has been the case for other nuclei (^{31}P and ^{13}C, for example). Preparation of suitably aligned sample stacks is not straightforward and special (usually solid state) NMR probes must be used. Another approach is to induce the averaging required by equation (4) using MAS. This also requires special probes, but dilute, unoriented samples may be used. This technique was first applied to ^{1}H NMR of bilayers by Chapman et al.[30] and has recently been revived by Oldfield and coworkers.[10] Figure 9 shows typical results obtained with potassium oleate, illustrating the impressive line narrowing achieved. The interesting feature here is that the sample spinning frequency is < 3 kHz, which is not technically demanding for modern instruments. Oldfield et al. demonstrated that the resolution was sufficient that two-dimensional NMR techniques, such as cross relaxation (NOESY) which has also been applied to vesicles,[9] could usefully be employed. The fact that dilute, unoriented samples may be used means that the MAS approach is likely to prove increasingly useful in the study of such areas as membrane–drug, membrane–protein, etc.,

interactions. This is the most likely future direction for ^{1}H and ^{19}F NMR applications to bilayer systems, particularly when combined with heteronuclear techniques such as chemical shift correlation spectroscopy (see, for example, Lee and Griffin[11]).

7 RELATED ARTICLES

Bilayer Membranes: Deuterium and Carbon-13 NMR; Membrane Lipids of Acholeplasma laidlawii; Membranes: Carbon-13 NMR; Molecular Motions: T_1 Frequency Dispersion in Biological Systems; Sonicated Membrane Vesicles

8 REFERENCES

1. D. Chapman and N. J. Salsbury, *Recent Prog. Surf. Sci.*, 1970, **3**, 121.
2. K. D. Lawson and T. J. Flautt, *J. Phys. Chem.*, 1965, **69**, 4256.
3. Z. Veksli, N. J. Salsbury and D. Chapman, *Biochim. Biophys. Acta*, 1969, **183**, 434.
4. D. F. Bocian and S. I. Chan, *Ann. Rev. Phys. Chem.*, 1978, **29**, 307.
5. C. Ho, S. R. Dowd, and J. F. M. Post, *Curr. Top. Bioenerget.*, 1985, **14**, 53.
6. G. W. Feigenson and S. I. Chan, *J. Am. Chem. Soc.*, 1974, **96**, 1312.
7. J. M. Pope, L. Walker, B. A. Cornell, and F. Separovic, *Mol. Cryst. Liq. Cryst.*, 1982, **89**, 137.
8. Z.-Y. Peng, V. Simplaceanu, I. J. Lowe, and C. Ho, *Biophys. J.*, 1988, **54**, 81.
9. J. F. Ellena, W. C. Hutton, and D. F. Cafiso, *J. Am. Chem. Soc.*, 1985, **107**, 1530.
10. J. Forbes, C. Husted, and E. Oldfield, *J. Am. Chem. Soc.*, 1988, **110**, 1059.
11. C. W. B. Lee and R. G. Griffin, *Biophys. J.*, 1989, **55**, 355.
12. M. E. Rose, *Elementary Theory of Angular Momentum*, Wiley, New York, 1957, Chap. 4
13. A. Abragam, *The Principles of Nuclear Magnetism*, Oxford University Press, London, 1961, Chap. 8
14. R. J. Pace and S. I. Chan, *J. Chem. Phys.*, 1982, **76**, 4241.
15. E. Boroske and L. Trahms, *Biophys. J.*, 1983, **42**, 275.
16. C. H. A. Seiter and S. I. Chan, *J. Am. Chem. Soc.*, 1973, **95**, 7541.
17. H. Wennerström and G. Lindblom, *Q. Rev. Biophys.*, 1977, **10**, 67.
18. J. M. Pope, L. Walker, B. A. Cornell, and G. W. Francis, *Biophys. J.*, 1981, **35**, 509.
19. R. J. Pace and S. I. Chan, *J. Chem. Phys.*, 1982, **76**, 4217.
20. E. Oldfield, R. W. K. Lee, M. Meadows, S. R. Dowd, and C. Ho, *J. Biol. Chem.*, 1980, **255**, 11 652.
21. R. J. Pace and S. I. Chan, *J. Chem. Phys.*, 1982, **76**, 4228.
22. R. Kimmich and G. Voigt, *Chem. Phys. Lett.*, 1979, **62**, 181.
23. P.-G. de Gennes, *The Physics of Liquid Crystals*, Clarendon, Oxford, 1975.
24. L. L. Pearce and S. C. Harvey, *Biophys. J.*, 1993, **65**, 1084.
25. P. A. Kroon, M. Kainosho, and S. I. Chan, *Biochim. Biophys. Acta*, 1976, **433**, 282.
26. J. W. Doane, C. E. Tarr, and M. A. Nickerson, *Phys. Rev. Lett.*, 1974, **33**, 620.
27. A. L. Mackay, E. E. Burnell, C. P. Nichol, G. Weeks, M. Bloom, and M. I. Valic, *FEBS Lett.*, 1978, **88**, 97.
28. J. R. Schuh, U. Banerjee, L. Mueller, and S. I. Chan, *Biochim. Biophys. Acta*, 1982, **687**, 219.
29. Y. C. W. van der Leeuw and G. Stulen, *J. Magn. Reson.*, 1981, **42**, 434.
30. D. Chapman, E. Oldfield, D. Doskočilová, and B. Schneider, *FEBS Lett.*, 1972, **25**, 261.

Biographical Sketches

R. J. Pace. *b* 1946. B.Sc. 1969, Ph.D., 1979, University of NSW, Australia. Introduced to NMR of bilayers by S. I. Chan at Caltech. Faculty, Department of Chemistry ANU, 1987–present. Research interests include relaxation processes in NMR of biological systems, but more recently ESR studies on redox active centers in photosynthetic membrane protein complexes and ion channel based biosensor systems. Approximately 40 publications and several patents.

Chemical Exchange Effects in Biological Macromolecules

Arthur G. Palmer, III

Department of Biochemistry and Molecular Biophysics, Columbia University, New York, NY, USA

1 Introduction 1
2 Two-site Chemical Exchange 1
3 Identifying Spins Affected by Chemical Exchange 2
4 ZZ-Exchange Spectroscopy 3
5 Lineshape Analysis 4
6 $R_{1\rho}$ Rotating Frame Relaxation Methods 5
7 CPMG Relaxation Methods 7
8 Chemical Exchange in Multiple Quantum Spectroscopy 8
9 Conclusions 9
10 Related Articles in this Volume 9
11 Related Articles in Volumes 1–8 9
12 References 9

1 INTRODUCTION

The effects of chemical exchange, including transverse relaxation and magnetization transfer, have long been of interest in NMR spectroscopy (see **Chemical Exchange Effects on Spectra,** Volume 2 and **Relaxation Effects of Chemical Exchange,** Volume 6). Exchange phenomena in solution NMR spectroscopy arise when chemical or conformational kinetic processes render the isotropic chemical shifts of nuclear spins time-dependent, either by transferring the spins between distinct chemical sites or by altering the local magnetic environment of the spins. Kinetic processes on times scales ranging from μs to s are effective in causing chemical exchange effects. Many biological processes occur with time constants within this range, and numerous applications have been reported that utilize chemical exchange effects to characterize time-dependent processes in biological macromolecules.[1–20]

The present article describes a subset of ZZ-exchange,[21,22] lineshape,[23,24] Carr–Purcell–Meiboom–Gill (CPMG),[25,26] and $R_{1\rho}$[27,28] relaxation techniques that are sensitive to molecular motions or chemical kinetic processes on μs–s time scales in biological macromolecules. The experimental techniques, rather than specific applications, will be emphasized. In most cases, pulse sequences suitable for application to isolated I_nS ($I = {}^1H$; $X = {}^{15}N$ or ${}^{13}C$; $n = 1, 2,$ or 3) spin systems are presented. The pulse sequences shown do not include details of solvent suppression techniques because different approaches are used for ${}^1H$, ${}^{13}C$, and ${}^{15}N$.[29,30] Compensatory rf fields should be applied during the recycle delay to ensure that the same average rf power is deposited into the sample for all values of the relaxation period.[31] The pulse sequences illustrated use INEPT elements for polarization transfer; in some cases, increased sensitivity can be obtained by replacing the INEPT transfers with heteronuclear cross polarization or CPMG-INEPT methods with large effective fields.[32–34]

2 TWO-SITE CHEMICAL EXCHANGE

For simplicity, only two-site exchange will be considered. The nucleus of interest is assumed to exchange between two magnetically distinct environments A and B while the system remains at chemical equilibrium throughout the NMR experiment. Furthermore, the present article focuses on situations in which scalar coupling constants are not perturbed by the exchange process (see **Chemical Exchange Effects on Spectra,** Volume 2); consequently, the modified Bloch or McConnell equations are sufficient to describe the effect of exchange (see **Relaxation Effects of Chemical Exchange,** Volume 6). The kinetic scheme is:

$$A \underset{k_{-1}}{\overset{k_1}{\rightleftharpoons}} B \tag{1}$$

in which k_1 and k_{-1} are forward and reverse rate constants and the chemical exchange rate constant, k_{ex}, is given by,

$$k_{ex} = k_1 + k_{-1} = \frac{k_1}{p_B} = \frac{k_{-1}}{p_A} \tag{2}$$

$p_A \geq 0.5$ and $p_B = 1 - p_A$ denote the equilibrium populations of equivalent nuclear spins in species A and B. Higher order chemical reactions, such as ligand binding or oligomerization, are treated by defining k_1 and k_{-1} as pseudo-first-order rate constants. The resonance frequencies in the rotating frame for spins in site A and B are Ω_A and Ω_B, respectively, in units of angular frequency, and the chemical shift difference between the two sites is $\Delta\omega = \Omega_B - \Omega_A$. The total equilibrium magnetization is M^0, and the equilibrium longitudinal magnetization at each site is $M_A^0 = p_A M^0$ and $M_B^0 = p_B M^0$. The longitudinal relaxation rate constants of the sites in the absence of exchange (resulting from dipolar, shielding anisotropy (CSA), and quadrupolar relaxation) are R_{1A}^0 and R_{1B}^0. The transverse relaxation rate constants of the sites in the absence of exchange are R_{2A}^0 and R_{2B}^0.

The effect of exchange on free-precession lineshapes has been discussed in **Relaxation Effects of Chemical Exchange,** Volume 6. The relative values of k_{ex} and $\Delta\omega$ define the limits of what is commonly referred to as "fast" and "slow" exchange on the chemical shift time scale:

$$\begin{aligned} k_{ex} &< \Delta\omega \quad \text{Slow exchange} \\ k_{ex} &\approx \Delta\omega \quad \text{Intermediate exchange} \\ k_{ex} &> \Delta\omega \quad \text{Fast exchange} \end{aligned} \tag{3}$$

In the slow exchange limit, resolved lines are observed for the two sites with resonance frequencies Ω_A and Ω_B. The effect of exchange is to shift the resonance positions and broaden the lines until the lines coalesce in the intermediate exchange regime (a more exact analysis yields the result that coalescence occurs when $2(p_A p_B)^{1/2}\Delta\omega \approx k_{ex}$). In the fast exchange limit, a single averaged resonance line is observed at the population-weighted average shift, $\Omega = p_A\Omega_A + p_B\Omega$.

3 IDENTIFYING SPINS AFFECTED BY CHEMICAL EXCHANGE

The initial step in characterizing a kinetic process by NMR spectroscopy is identifying spins subject to chemical exchange. If p_B is sufficiently large and exchange is slow on the chemical shift time scale, then additional resonances arising from the second species are observed in the NMR spectra. These resonances usually are identified during initial efforts to obtain sequence specific resonance assignments. NOESY, ROESY, and ZZ-exchange spectroscopy, discussed below, are used to confirm that the additional resonances arise from chemical exchange processes. However, only a single set of resonances are observed in the NMR spectra if exchange is fast on the chemical shift time scale or if p_B is sufficiently low that the minor component is not observable in the slow exchange limit. In such circumstances, exchange effects are recognized by an increase in the transverse relaxation rate constant relative to the value expected for dipolar, quadrupolar and CSA interactions for the observed resonance signals:

$$R_2 = R_2^0 + R_{ex} \tag{4}$$

in which R_2^0 refers to either the relaxation rate constant for an individual site (for slow exchange) or to the population averaged relaxation rate constant (for fast exchange) and R_{ex} is the excess contribution to R_2 due to exchange.

R_2 in equation (4) can be approximated either by R_2*, the free-precession damping constant including effects of magnetic field inhomogeneity, or by $R_{2\text{echo}}$, the damping constant observed for a Hahn spin echo experiment. The value of R_2* is obtained from the resonance full-width at half-height linewidth, $\Delta\nu_{1/2}$, using $R_2^* = \Delta\nu_{1/2}/\pi$ or equivalently, from the decay of the time domain free induction decay or interferogram (in multidimensional NMR spectra).[35] The size of the inhomogeneity contribution to R_2* can be estimated using spins not affected by the exchange process. The value of $R_{2\text{echo}}$ is obtained using the sequence $t - 180^\circ - t$ incorporated into either a one-dimensional or multidimensional NMR experiment.[36] The 180° pulse must be selective to refocus scalar coupling interactions. If spectra are recorded for $t = 0$ and $t = \tau$, then $R_{2\text{echo}} = (2\tau)^{-1}\ln[I(0)/I(\tau)]$, in which $I(t)$ is the intensity of the resonance measured for an echo time t. The echo time, τ, should be long enough that $\tau k_{ex} \gg 1$; otherwise, the effects of exchange on the echo decay are partially suppressed. Complete expressions for the echo decay are given in **Relaxation Effects of Chemical Exchange,** Volume 6. In either approach, additional decoupling sequences may need to be applied during the free-precession evolution period or during the spin-echo delay to prevent evolution into antiphase coherences subject to additional relaxation mechanisms.[37,38]

The value of R_2^0 is obtained by one of the following approaches: (1) analysis of R_1, R_2 and NOE data for ^{13}C or ^{15}N spins using the model free formalism;[39,40] (2) use of the magnetic field dependence of R_2 to determine $J(0)$, the spectral density function at zero frequency;[41–43] and (3) use of ^{1}H–X dipole/X CSA relaxation interference rate constants.[43,44]

The first method determines the rotational diffusion tensor for the molecule using R_1, R_2 and NOE relaxation rate constants for spins not subject to conformational exchange broadening (see **Protein Dynamics from NMR Relaxation,** Volume 6). Once the diffusion tensor for the molecule is known, R_2^0 for individual exchange broadened nuclear spins is approximated using the measured values of R_1 and NOE. This method is automated in software programs such as ModelFree.[39] Residues subject to exchange broadening must be carefully distinguished from residues affected by rotational diffusion anisotropy in order to obtain an accurate assessment of the diffusion tensor.[44–46]

Most investigations of molecular dynamic properties of macromolecules through spin relaxation measure R_2 using CPMG experiments with a single spin echo delay, τ_{cp}, satisfying $1/\tau_{cp} \geq 1000\,\text{s}^{-1}$ or $R_{1\rho}$ experiments with an effective field in the rotating frame, ω_e, satisfying $\omega_e \geq 12\,000\,\text{s}^{-1}$ to partially suppress exchange effects.[47] Under these conditions, the residual R_{ex} contribution to R_2 is proportional to B_0^2, in which B_0 is the static magnetic field strength, for all exchange time scales.[48] Using this result, the second approach defines:[42,43]

$$\Gamma = R_2 - \frac{1}{2}R_1 - \left(\frac{3d^2}{4}\right)J(\omega_H)$$
$$= \left(\frac{d^2}{2}\right)J(0) + \left(\frac{2}{9}\gamma_C^2\Delta\sigma^2 J(0) + \Theta_{ex}\right)B_0^2 \tag{5}$$

in which $d = (\mu_0 h\gamma_H\gamma_X)/(8\pi^2 r_{XH^3})$; μ_0 is the permeability of free space; h is Planck's constant; γ_H and γ_X are the gyromagnetic ratios for ^{1}H and X spins, respectively; r_{XH} is the distance between the two nuclei; Θ_{ex} is a constant of proportionality; $\Delta\sigma = \sigma_\parallel - \sigma_\perp$; and the principal components of the X spin CSA tensor are $\sigma_\parallel$ and $\sigma_\perp$. The value of $J(\omega_H)$ is obtained from the heteronuclear NOE by reduced spectral density mapping methods.[49] The value of $J(0)$ is obtained from the intercept of a linear least squares fit of Γ versus B_0^2. Once $J(0)$ is determined, values of R_2^0 at each value of B_0 can be obtained by setting $\Theta_{ex} = 0$ in equation (5).

The third method only is applicable to nuclear spins, such as backbone amide ^{15}N spins in proteins, with substantial CSA contributions to laboratory frame relaxation. Interference between the ^{1}H–X dipolar and X CSA interactions constitutes an additional relaxation mechanism that is unaffected by chemical exchange (see **Relaxation Effects Involving Cross Correlation in Biomolecules**). The transverse cross-correlation relaxation rate constant, η_{xy}, represents cross-relaxation between in-phase and antiphase magnetization, while the longitudinal cross-correlation relaxation rate constant, η_z, represents cross-relaxation between longitudinal magnetization and two-spin order. For an axially symmetric chemical shift tensor, the cross-correlation rate constants are:[50]

$$\eta_z = -\sqrt{3}cd\,P_2(\cos\beta)J(\omega_X)$$
$$\eta_{xy} = -\frac{\sqrt{3}}{6}cd\,P_2(\cos\beta)[4J(0) + 3J(\omega_X)] \tag{6}$$

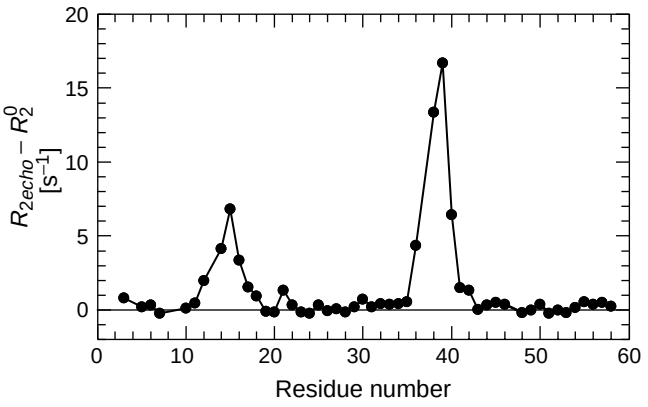

Figure 1 Identifying chemical exchange in BPTI. Shown is a graph of $R_{2echo} - R_2^0$ versus the protein sequence. Regions of pronounced chemical exchange linebroadening, for which $R_{ex} = R_{2echo} - R_2^0 \gg 0$, are evident in the vicinity of the Cys 14–Cys 38 disulfide bond

in which $c = 3^{-1/2}\gamma_X B_0 \Delta\sigma$, β is the angle between the symmetry axes of the chemical shift and dipole tensors, and $P_2(x) = (3x^2 - 1)/2$. If both η_{xy} and η_z have been measured,[44,51] then:[43]

$$R_2^0 = \left(R_1 - \frac{7}{4}J(\varepsilon\omega_H)\right)\frac{\eta_{xy}}{\eta_z} + \frac{13}{8}J(\xi\omega_H) \qquad (7)$$

which does not require assumptions about the values of $\Delta\sigma$ and β. If only η_{xy} has been measured, but $\Delta\sigma$ and β are known, then:

$$R_2^0 = \left(\frac{3d^2 + 4c^2}{4\sqrt{3}cd\,P_2(\cos\beta)}\right)\eta_{xy} + \frac{13}{8}d^2 J(\xi\omega_H) \qquad (8)$$

The value of ε is 0.92 in equation (7) and ξ is 0.96 in equations (7) and (8) for ^{15}N.

An example of the use of R_{2echo} and R_2^0 for detecting chemical exchange broadened backbone amide ^{15}N resonances is provided for basic pancreatic trypsin inhibitor (BPTI) in Figure 1. Values of R_{2echo} were measured using a Hahn spin-echo sequence incorporated into an in-phase ^{15}N–^{1}H HSQC experiment.[36,52] WALTZ-16 decoupling was used during the spin echo period to suppress evolution of the ^{15}N–^{1}H scalar coupling interaction.[53] Values of R_2^0 were obtained from η_{xy} using equation (8) and η_{xy} was measured using established techniques.[43] Significant values of $R_{ex} = R_{2echo} - R_2^0$ are observed for residues near the Cys 14 to Cys 38 disulfide linkage.[48,54]

4 ZZ-EXCHANGE SPECTROSCOPY

Slow chemical exchange processes can be studied by monitoring the exchange of longitudinal magnetization between sites if the population of the minor site B is large enough to generate observable resonance signals.[55] In addition, k_{ex} must not be much less than R_{1A} and R_{1B}; otherwise, the signals decay due to relaxation faster than population transfer. Investigations of chemical exchange using ^{1}H NMR spectroscopy are complicated by the coexisting transfer of magnetization through the nuclear Overhauser effect, although the opposite signs of the NOE and ROE for macromolecules can be used to approximately suppress magnetization transfer through dipolar relaxation.[56] Isotopic enrichment of macromolecules enables X-nucleus ZZ-exchange to be utilized instead of ^{1}H magnetization transfer. Although either exchange of longitudinal magnetization[57,58] or two-spin order[57,59] can be monitored, longitudinal relaxation is much slower for ^{15}N and ^{13}C spins than for ^{1}H spins in macromolecules; consequently, the relaxation rate constant for two-spin order is less favorable than for X-nucleus longitudinal magnetization. For biological macromolecules, X-nucleus R_1 values typically are on the order of $1\,s^{-1}$; consequently, ZZ-exchange measurements are applicable to chemical exchange processes with $k_{ex} < 10^2\,s^{-1}$.

A three-dimensional ^{1}H–X–^{1}H pulse sequence for a ZZ-exchange measurement is shown in Figure 2; as described in the figure caption, either ^{1}H–^{1}H or X–^{1}H two-dimensional pulse sequences can be derived from the three-dimensional sequence and employed if the resonances due to exchanging spins are sufficiently well-resolved.[58,60] The evolution of longitudinal magnetization during the mixing time, t, is described by the modified Bloch or McConnell equations:[61]

$$\frac{d}{dt}\begin{bmatrix}\Delta M_{zA}(t)\\ \Delta M_{zB}(t)\end{bmatrix} = \begin{bmatrix}-R_{1A}^0 - p_B k_{ex} & p_A k_{ex}\\ p_B k_{ex} & -R_{1B}^0 - p_A k_{ex}\end{bmatrix}\begin{bmatrix}\Delta M_{zA}(t)\\ \Delta M_{zB}(t)\end{bmatrix} \qquad (9)$$

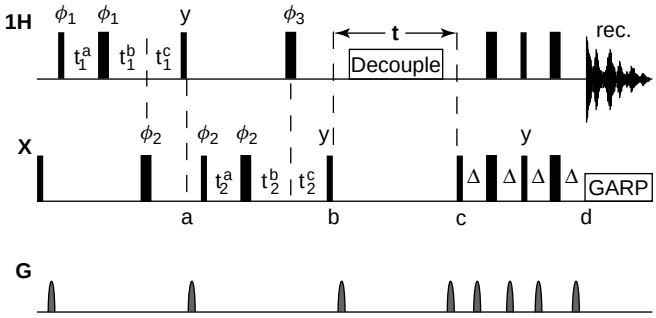

Figure 2 Three-dimensional pulse sequence for ZZ-exchange NMR spectroscopy.[58] Narrow and wide bars depict 90° and 180° pulses respectively. All pulses are x-phase unless otherwise indicated. Decoupling during the relaxation delay to suppress heteronuclear dipole–dipole cross relaxation and dipole/CSA cross correlation can be performed using WALTZ-16[53] or a train of ^{1}H 180° pulses at 5 ms intervals. Decoupling during acquisition is achieved with the GARP sequence.[92] Delays are $\Delta = 1/(4J_{XH})$, $t_1^a = (1 - t_1/t_{1max})\Delta$, $t_1^b = (1 - 2\Delta/t_{1max})t_1/2$, $t_1^c = \Delta + t_1/2$, t_{1max} is the maximum value of the t_1 labeling period, $t_2^a = (1 - t_2/t_{2max})\Delta$, $t_2^b = (1 - 2\Delta/t_{2max})t_2/2$, $t_2^c = \Delta + t_2/2$, t_{2max} is the maximum value of the t_2 labeling period, and t is the mixing time. A two-dimensional X–^{1}H correlation spectrum is obtained by setting $t_1^a = t_1^c = \Delta$ and $t_1^b = 0$; a two-dimensional ^{1}H–^{1}H correlation spectrum is obtained by setting $t_2^a = t_2^c = \Delta$ and $t_2^b = 0$. The phase cycle is $\phi_1 = x, -x$; $\phi_2 = 4(x), 4(-x)$; $\phi_3 = x, x, y, y, -x, -x, -y, -y$; and receiver $= x, -x, -x, x$. The gradients are used to suppress unwanted coherences and pulse imperfections.[93] Frequency discrimination during t_1 and t_2 is obtained by shifting the phase of ϕ_1 and ϕ_2, respectively, and the receiver according to the States-TTPI protocol.[94] As discussed in the text, magnetization transfer during the periods a-b and c-d may need to be considered in addition to the mixing time t

in which $\Delta M_{zA}(t) = M_{zA}(t) - M_A^0$ and $\Delta M_{zB}(t) = M_{zB}(t) - M_B^0$. The solution of this equation is:

$$\begin{bmatrix} \Delta M_{zA}(t) \\ \Delta M_{zB}(t) \end{bmatrix} = \begin{bmatrix} a_{AA}(t) & a_{AB}(t) \\ a_{BA}(t) & a_{BB}(t) \end{bmatrix} \begin{bmatrix} \Delta M_{zA}(0) \\ \Delta M_{zB}(0) \end{bmatrix} \tag{10}$$

in which,

$$\begin{aligned} a_{AA}(t) &= \frac{1}{2}[(1-\Lambda)\exp(-\lambda_- t) + (1+\Lambda)\exp(-\lambda_+ t)] \\ a_{BB}(t) &= \frac{1}{2}[(1+\Lambda)\exp(-\lambda_- t) + (1-\Lambda)\exp(-\lambda_+ t)] \\ a_{AB}(t) &= \frac{k_{ex}\, p_A}{\lambda_+ - \lambda_-}[(\exp(-\lambda_- t) - \exp(-\lambda_+ t))] \\ a_{BA}(t) &= \frac{k_{ex}\, p_B}{\lambda_+ - \lambda_-}[(\exp(-\lambda_- t) - \exp(-\lambda_+ t))] \end{aligned} \tag{11}$$

and,

$$\begin{aligned} \Lambda &= \frac{R_{1A}^0 - R_{1B}^0 + k_{ex}(p_B - p_A)}{\lambda_+ - \lambda_-} \\ \lambda_\pm &= \frac{1}{2}\{R_{1A}^0 + R_{1B}^0 + k_{ex} \\ &\quad \pm [(R_{1A}^0 - R_{1B}^0 + k_{ex}(p_B - p_A))^2 + 4 p_A p_B k_{ex}^2]^{1/2}\} \end{aligned} \tag{12}$$

Thus, the intensity of the autopeak for site A (site B) evolves as $a_{AA}(t)$ ($a_{BB}(t)$), and the crosspeak between A and B (B and A) evolves as $a_{AB}(t)$ ($a_{BA}(t)$).

Crosspeak intensity can be observed at $t = 0$ if exchange is fast enough to transfer magnetization between sites during the INEPT periods. If ^{1}H magnetization is frequency labeled during t_1, then exchange effects must be considered between points a-b and c-d in Figure 2. If only X magnetization is frequency labeled, during t_2, then exchange effects must be considered between points c-d in Figure 2. The effects of exchange during the INEPT periods can be approximated by including the length of the INEPT sequences, 2Δ, in the mixing time provided that $|R_{1A}^0 - R_{1B}^0| \ll k_{ex}$ and $|R_{2A}^0 - R_{2B}^0| \ll k_{ex}$ for the X nucleus and $|R_{2A}^0 - R_{2B}^0| \ll k_{ex}$ for the ^{1}H spin. If these conditions do not hold, then the effects of exchange during the INEPT periods must be analyzed numerically. If a three-dimensional experiment is performed, then exchange during the t_2 evolution period must be analyzed numerically unless $t_{2max} k_{ex} \ll 1$.

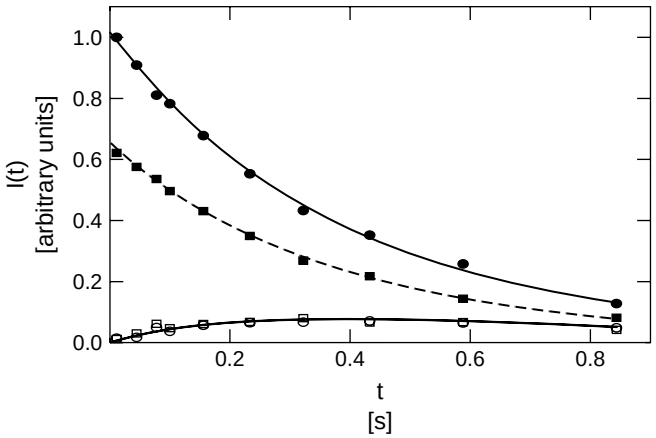

Figure 3 ^{15}N ZZ-exchange data for Thr 12 of the drk SH3 domain.[29] $I_{ij}(t)$ is the integrated peak volume as a function of the mixing time T. (●) $I_{AA}(t) = \Delta M_{zA}(0) a_{AA}(t)$ and (■) $I_{BB}(t) = \Delta M_{zB}(0) a_{BB}(t)$ are the volumes of the autocorrelation peaks and (○) $I_{BA}(t) = \Delta M_{zA}(0) a_{BA}(t)$ and (□) $I_{AB}(t) = \Delta M_{zB}(0) a_{AB}(t)$ are the volumes of the crosspeaks. The lines are the optimized fits to equations (10)–(12). The fitted results yield $R_{1A}^0 = 2.41 \pm 0.05\,\mathrm{s}^{-1}$, $R_{1B}^0 = 1.90 \pm 0.11\,\mathrm{s}^{-1}$, $k_1 = 0.86 \pm 0.06\,\mathrm{s}^{-1}$, and $k_{-1} = 0.43 \pm 0.03\,\mathrm{s}^{-1}$. (Reproduced with permission from *Biochemistry*, 1995, **34**, 868–878. Copyright 1994 Am. Chem. Soc)

Two-dimensional ^{15}N ZZ-exchange experiments have been used to quantify chemical exchange between folded and unfolded forms of the drk SH3 domain.[14,29] Typical results are shown in Figure 3. The data were analyzed using equations (10)–(12) to determine the relaxation rate constants for the folded (site A) and unfolded forms (site B) of the protein and the folding (k_{-1}) and unfolding (k_1) rate constants.

5 LINESHAPE ANALYSIS

Lineshape analysis is a classical approach for analyzing exchange processes in NMR spectroscopy.[23,24] Applications to proteins include chemical exchange arising from folding,[12,62,63] ligand binding,[64] and oligomerization.[13] In each of these applications, the lineshapes can be altered by varying experimental parameters, such as temperature, ligand concentration, denaturant concentration, or protein concentration, which enables a global analysis of lineshapes to be performed as functions of the adjustable parameters. Typically, lineshape analysis is applicable to exchange processes in biological macromolecules with $k_{ex} < 10^4\,\mathrm{s}^{-1}$.

For transverse coherence subject to free precession under the Zeeman Hamiltonian, the evolution of the magnetization is described by the modified Bloch or McConnell equations:[61]:

$$\frac{d}{dt}\begin{bmatrix} M_A^+(t) \\ M_B^+(t) \end{bmatrix} = \begin{bmatrix} -i\Omega_A - R_{2A}^0 - p_B k_{ex} & p_A k_{ex} \\ p_B k_{ex} & -i\Omega_B - R_{2B}^0 - p_A k_{ex} \end{bmatrix} \times \begin{bmatrix} M_A^+(t) \\ M_B^+(t) \end{bmatrix} \tag{13}$$

The solution of these equations is:

$$\begin{bmatrix} M_A^+(t) \\ M_B^+(t) \end{bmatrix} = \begin{bmatrix} a_{AA}(t) & a_{AB}(t) \\ a_{BA}(t) & a_{BB}(t) \end{bmatrix} \begin{bmatrix} M_A^+(0) \\ M_B^+(0) \end{bmatrix} \tag{14}$$

in which $M_A^+(t) = M_{Ax}(t) + i M_{Ay}(t)$, $M_B^+(t) = M_{Bx}(t) + i M_{By}(t)$,

$$\begin{aligned} a_{AA}(t) &= \frac{1}{2}[(1-\Lambda)\exp(-\lambda_- t) + (1+\Lambda)\exp(-\lambda_+ t)] \\ a_{BB}(t) &= \frac{1}{2}[(1+\Lambda)\exp(-\lambda_- t) + (1-\Lambda)\exp(-\lambda_+ t)] \\ a_{AB}(t) &= \frac{k_{ex}\, p_A}{\lambda_+ - \lambda_-}[(\exp(-\lambda_- t) - \exp(-\lambda_+ t))] \\ a_{BA}(t) &= \frac{k_{ex}\, p_B}{\lambda_+ - \lambda_-}[(\exp(-\lambda_- t) - \exp(-\lambda_+ t))] \end{aligned} \tag{15}$$

and,

$$\Lambda = \frac{-i\Delta\omega + R_{2A}^0 - R_{2B}^0 + k_{ex}(p_B - p_A)}{\lambda_+ - \lambda_-}$$

$$\lambda_\pm = \frac{1}{2}\{-i\Omega_A - i\Omega_B + R_{2A}^0 + R_{2B}^0 + k_{ex} \pm [(-i\Delta\omega + R_{2A}^0 - R_{2B}^0 + k_{ex}(p_B - p_A))^2 + 4p_A p_B k_{ex}^2]^{1/2}\} \quad (16)$$

The NMR spectrum is given by the Fourier transformation of $M_A^+(t) + M_B^+(t)$. Computer optimization of the parameters in equations (14)–(16) is utilized to fit the experimental lineshapes. In practical applications, particularly for ^{1}H lineshapes, the magnetization components in equations (14)–(16) should be regarded as representing individual resonance lines of scalar coupled multiplets. If scalar coupling constants are modulated by the exchange process, then the more general theoretical approach described in **Chemical Exchange Effects on Spectra,** Volume 2 is required.

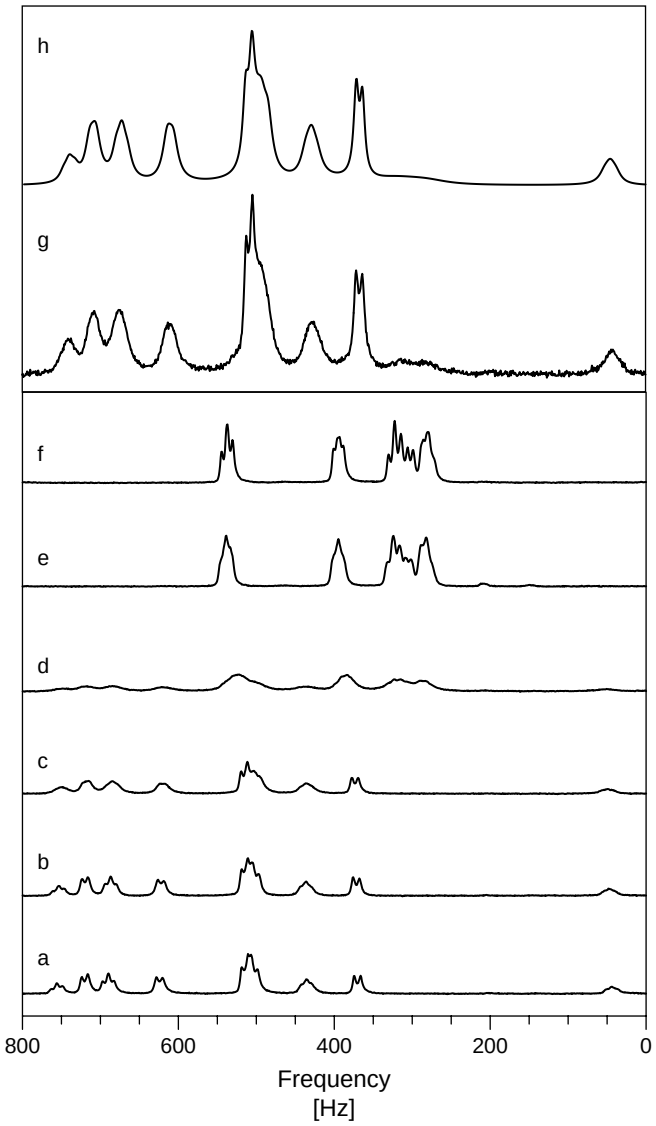

Figure 4 Lineshape analysis for folding of λ repressor. The aromatic regions of the ^{1}H NMR spectra of the monomeric Gly 46 Ala/Gly 48 Ala mutant of λ repressor (residues 6–85) at 30 °C are shown for urea denaturant concentrations of (a) 0 M, (b) 2.2 M, (c) 4.1 M, (d) 5.1 M, (e) 7.0 M, and (f) 8.9 M. Expansions of the (g) experimental and (h) fitted ^{1}H aromatic spectra also are shown for λ repressor in 4.1 M urea. (Reproduced with permission from *J. Biomol. NMR*, 1998, **11**, 355–359)

Folding of the Gly 46 Ala/Gly 48 Ala mutant of monomeric λ repressor has been investigated as a function of urea denaturant concentration by Oas and coworkers using ^{1}H one-dimensional spectroscopy.[62] The aromatic regions of a series of NMR spectra are shown in Figure 4 to illustrate the changes in lineshape observed as the urea concentration is increased from 0 to 8.9 M. Figure 4(h) and (g) compare the experimental and fitted lineshapes for a single urea concentration of 4.1 M. Data were analyzed using the program ALASKA to fit k_1 (unfolding) and k_{-1} (folding) assuming values of other spectral parameters for folded and unfolded species obtained from the spectra recorded at 0 and 8.9 M urea, respectively.[62] In most cases, lineshape analyses have been restricted to one-dimensional ^{1}H spectra; however, two-dimensional lineshape analysis using X–^{1}H heteronuclear correlation spectroscopy yields increased spectral resolution, provides lineshape information for both the ^{1}H and X spins, and exhibits simplified lineshapes in indirect frequency dimensions because heteronuclear scalar coupling interactions are easily decoupled. As an example, ^{15}N–^{1}H HSQC spectroscopy has been used in a lineshape analysis of the dimerization of the protein barstar.[13]

6 $R_{1\rho}$ ROTATING FRAME RELAXATION METHODS

In an $R_{1\rho}$ experiment, magnetization is spin-locked in the rotating frame by application of a radio-frequency field.[27,28] The relaxation rate constant for the component of the magnetization along the direction of effective field in the rotating frame is called $R_{1\rho}$ and depends on the amplitude, ω_1, and frequency, ω_{rf}, of the applied radiofrequency field. The effective field in the rotating frame is $\omega_e = (\Omega^2 + \omega_1^2)^{1/2}$ in which $\Omega = p_A\Omega_A + p_B\Omega_B$ is the population-average chemical shift, and the tilt angle of the effective field is given by $\tan\theta = \omega_1/\Omega$. $R_{1\rho}$ experiments are sensitive to chemical exchange processes if values of ω_e near k_{ex} are achievable experimentally. Typically, $R_{1\rho}$ experiments are limited to values of $k_{ex} < 10^5\,s^{-1}$. Sample heating and limitations on the maximum value of ω_1 tolerated by the spectrometer probe and amplifiers during sustained spin-locking pulses are the principal experimental constraints on ω_e. Furthermore, exchange processes with $k_{ex} > 10^5\,s^{-1}$ result in small exchange linebroadening unless $\Delta\omega$ is very large. $R_{1\rho}$ measurements on biological macromolecules can be performed using near-resonance (often called on-resonance for convenience)[65] or off-resonance[66–68] rf fields. In the former case, the rf transmitter frequency is positioned close to the resonances of interest (or in the middle of the NMR spectrum) and the minimum value of ω_1 is large enough to ensure that $\theta > 70°$ over the spectral region of interest. The relaxation dispersion curve is obtained by varying ω_1. In the latter case, the rf transmitter is positioned far enough off-resonance to ensure that $\theta < 70°$. The relaxation dispersion curve is obtained by varying ω_1 or the carrier offset or both in order to vary ω_e.

A pulse sequence for an off-resonance $R_{1\rho}$ experiment for X spins is shown in Figure 5(a)[66–68] and a pulse sequence

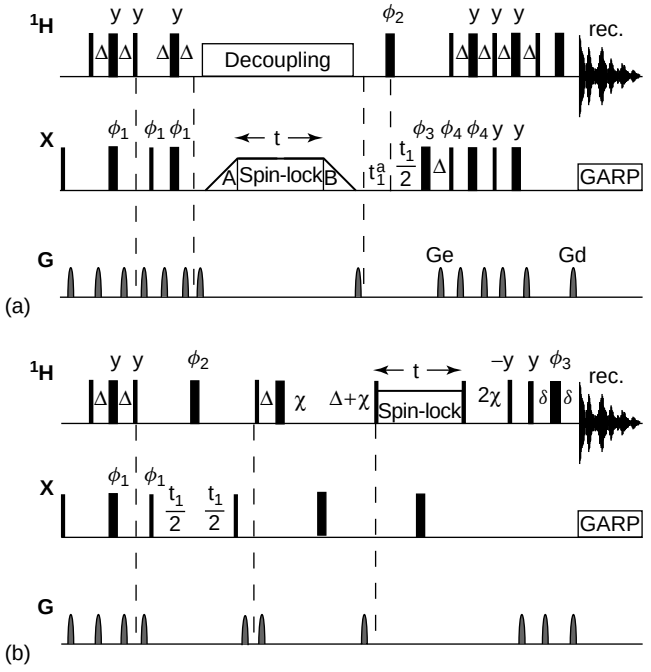

Figure 5 Pulse sequences for (a) X-nucleus and (b) ^{1}H-nucleus $R_{1\rho}$ experiments.[65–68,71] Narrow and wide bars depict 90° and 180° pulses respectively. All pulses are x-phase unless otherwise indicated. Decoupling during acquisition is achieved with the GARP sequence.[92] The unlabeled gradients are used to suppress unwanted coherences and pulse imperfections.[93] Delays are $\Delta = 1/(4J_{XH})$, $t_1^a = \Delta + t_1/2$, t is the relaxation delay, and δ is longer than the duration of the gradients applied during δ. (a) The spin-lock rf frequency is set outside the spectral region of interest. The adiabatic sweep A rotates z-magnetization to the direction of the effective field and the adiabatic sweep B rotates the spin-locked magnetization back to the z-axis.[66,68] The phase cycle is $\phi_1 = x, -x$; $\phi_2 = 4(x)$, 4(−x); $\phi_3 = x, x, y, y, -x, -x, -y, -y$; $\phi_4 = x$; receiver $= x, -x, -x, x$. Gradient coherence selection are achieved with gradients Gd and Ge. Echo/antiecho signals are recorded in separate experiments by inverting the amplitude of Gd and phase ϕ_4.[95] The ϕ_1 and the receiver phases are inverted for each t_1 increment to shift axial peaks to the edge of the spectrum.[94] (b) The spin-lock rf frequency is positioned in the center of the spectral region of interest, and $\chi = 1/(2\omega_1)$ serves to align the magnetization along the direction of the effective field.[96] The phase cycle is $\phi_1 = x, -x$; $\phi_2 = 4(x), 4(-x)$; $\phi_3 = x, x, -x, -x$; and receiver $= x, -x$. Frequency discrimination is obtained by shifting the phase of the receiver and ϕ_1 according the States-TTPI protocol[94]

for a near-resonance $R_{1\rho}$ experiment for ^{1}H spins is shown in Figure 5(b).[69,70] The pulse sequence in Figure 5(b) is applicable to ^{1}H spins that do not have significant homonuclear scalar coupling interactions; for example, the $^3J_{N\alpha}$ scalar coupling interaction is eliminated in uniformly ^{15}N/^{2}H enriched proteins.[71]

$R_{1\rho}$ experiments have been applied principally to characterize kinetic processes in the fast-exchange limit ($k_{ex}/\Delta\omega \gg 1$) using the theoretical expression:[27,28,72]

$$R_{1\rho}(\omega_e) = R_2^0 \sin^2\theta + R_1 \cos^2\theta + \sin^2\theta \frac{\Phi_{ex} k_{ex}}{k_{ex}^2 + \omega_e^2} \qquad (17)$$

in which R_2^0 and R_1 are population-averaged relaxation rate constants and $\Phi_{ex} = p_A p_B \Delta\omega^2$. Other expressions applicable outside of the fast-exchange limit have been derived, but have not been applied yet to relaxation in proteins.[72,73] The dependence of $R_{1\rho}$ on R_1 in equation (17) can be removed either by the constant-relaxation time approach[67] or by independently measuring R_1. The number of independent parameters in equation (17) can be further reduced either by measuring R_2*[35] or R_2^0.[7]

The folding equilibrium of the peripheral subunit binding domain (PSBD) from the dihydrolopoamide acetyltransferase component of the pyruvate dehydrogenase multienzyme complex from *Bacillus stearothermophilus* has been characterized using ^{15}N $R_{1\rho}$ measurements.[7] R_1 was measured independently and R_2^0 was obtained from measurements of η_{xy} using equation (8) in order to express R_{ex} as

$$R_{ex} = \frac{R_{1\rho}}{\sin^2\theta} - \frac{R_1}{\tan^2\theta} - R_2^0 = \frac{\Phi_{ex} k_{ex}}{k_{ex}^2 + \omega_e^2} \qquad (18)$$

The relaxation dispersion curve is linearized by plotting $1/R_{ex}$ versus ω_e^2, as shown in Figure 6(a). Values of $k_{ex} = (b/m)^{1/2}$ and $\Phi_{ex} = (mb)^{-1/2}$ are obtained from the slope m and intercept b.[74] In the fast-exchange limit, p_A, p_B, and $\Delta\omega$ cannot be obtained separately from Φ_{ex} by fitting the relaxation dispersion. However, Φ_{ex} and Ω are related by $\Phi_{ex} = -\Omega^2 + a\Omega - b$ in which $a = \Omega_A + \Omega_B$ and $b = \Omega_A\Omega_B$. If Φ_{ex} and Ω are measured as a function of temperature

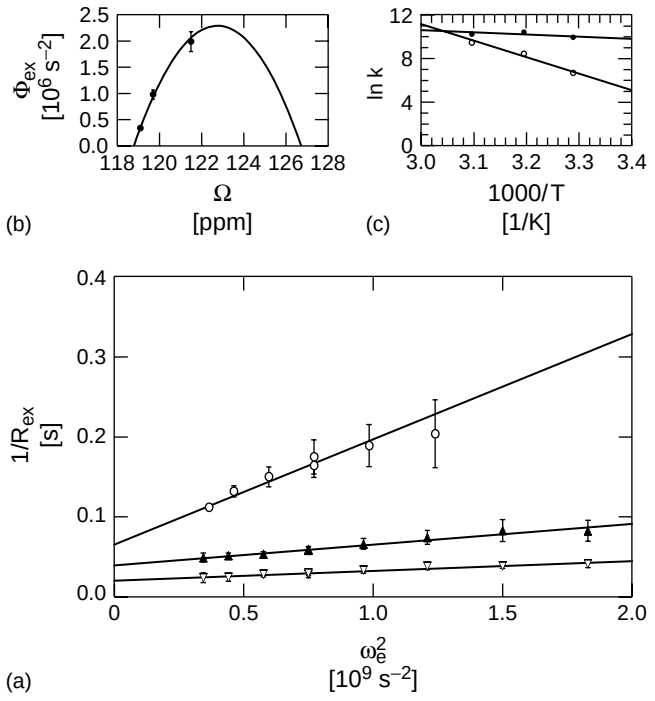

Figure 6 ^{15}N $R_{1\rho}$ relaxation dispersion for Ala 11 of PSBD. (a) Data recorded at 304 (○), 313 (▲), and 323 K (▽).[7] R_{ex} data for Ala 11 were obtained from equation (18), values of R_1 and η_{xy} were measured by conventional approaches,[29,44] and values of R_2^0 obtained from η_{xy} using equation (8). The best least squares fitted line is drawn for each data set. (b) Φ_{ex} is plotted versus the isotropic shift Ω at each temperature. The solid line is the best fit to determine the x-intercepts $\Omega_A = 118.80 \pm 0.02$ ppm and $\Omega_B = 126.7 \pm 0.4$ ppm with $\Delta\omega = 7.9 \pm 0.4$ ppm. (c) Arrhenius plot for (○) folding (k_{-1}) and (●) unfolding (k_1) rate constants. The apparent activation barriers are 17 ± 14 kJ mol^{-1} for folding and 125 ± 19 kJ mol^{-1} for unfolding

and Ω_A and Ω_B are assumed to be independent of temperature, then the coefficients a and b can be determined by least squares optimization. Subsequently, $|\Delta\omega| = (a^2 - 4b)^{1/2}$, and $\Omega_{A,B} = [a \pm (a^2 - 4b)^{1/2}]/2$. Once $\Delta\omega$ is known, p_A, p_B, k_1, and k_{-1} are obtained from Φ_{ex} and k_{ex} at each temperature. An example of this analysis is shown in Figure 6(b); the temperature dependence of the rate constants obtained from this analysis is shown in Figure 6(c). The chemical shift of the (unobserved) unfolded PSBD species is determined to be 126.7 ± 0.4 ppm; this value is in good agreement with the predicted random coil chemical shift of 126.0 ppm for an Ala residue preceded by a Tyr residue.[75]

7 CPMG RELAXATION METHODS

In a CPMG experiment, the relaxation of transverse magnetization is observed during a $(\tau - 180^\circ - 2\tau - 180^\circ - \tau)_n$ spin-echo sequence, in which $\tau_{cp} = 2\tau$ is the spacing between 180° pulses and n is an integer.[25,26] CPMG experiments are sensitive to chemical exchange processes if values of $1/\tau_{cp}$ near k_{ex} are achievable experimentally. CPMG experiments in proteins typically are applicable to chemical exchange processes with values of $k_{ex} < 10^4\,s^{-1}$ as a result of experimental constraints on the minimum value of τ_{cp}. Sample heating at high pulsing rates is a major experimental limitation. In addition, theoretical analyses of relaxation during CPMG experiments assume that the refocusing pulses have negligible duration;[76–78] at pulse duty cycles >10%, this assumption may not be valid.[66] The maximum value of τ_{cp} for CPMG experiments applied to X spins is limited by evolution under the one-bond heteronuclear scalar coupling Hamiltonian, which interconverts in-phase and antiphase magnetization during the spin-echo period. The relaxation rate constant for heteronuclear antiphase magnetization includes a contribution from longitudinal relaxation of the coupled ^{1}H spin and is greater than the rate constant for in-phase magnetization. To minimize contributions from antiphase magnetization, $\tau_{cp} < 1/(4J_{XH})$, where J_{XH} is the one-bond heteronuclear scalar coupling constant; therefore, the maximum values of τ_{cp} are 1.7 ms for ^{13}C and 2.6 ms for ^{15}N.

The range of τ_{cp} values that can be utilized is expanded by CPMG experiments designed to average in-phase and antiphase magnetization. Relaxation-compensated CPMG pulse sequences for IS,[79] I_2S,[80] and I_3S[81] are shown in Figure 7. In these experiments, in-phase and antiphase coherences are interchanged during the period U in order to eliminate any τ_{cp} -dependent effects arising from differential relaxation rates. Conventional CPMG pulse sequences for measuring R_2 are self-compensating for evolution of the scalar coupling if $\tau_{cp} = m/J_{XH}$, in which m is an integer.[48] Hahn spin echo measurements, self-compensated CPMG experiments and relaxation-compensated CPMG experiments can be used in combination to cover the widest possible range of τ_{cp} values.[48] For I_2S and I_3S spin systems, relaxation is multiexponential and constant relaxation time experiments are necessary to obtain accurate results.[80,81]

These approaches are illustrated in Figure 8 for residue Cys 38 in BPTI at temperatures of 300 and 313 K.[48] The backbone ^{15}N resonance of Cys 38 is broadened as a result of isomerization of the Cys 14–Cys 38 disulfide bond. The

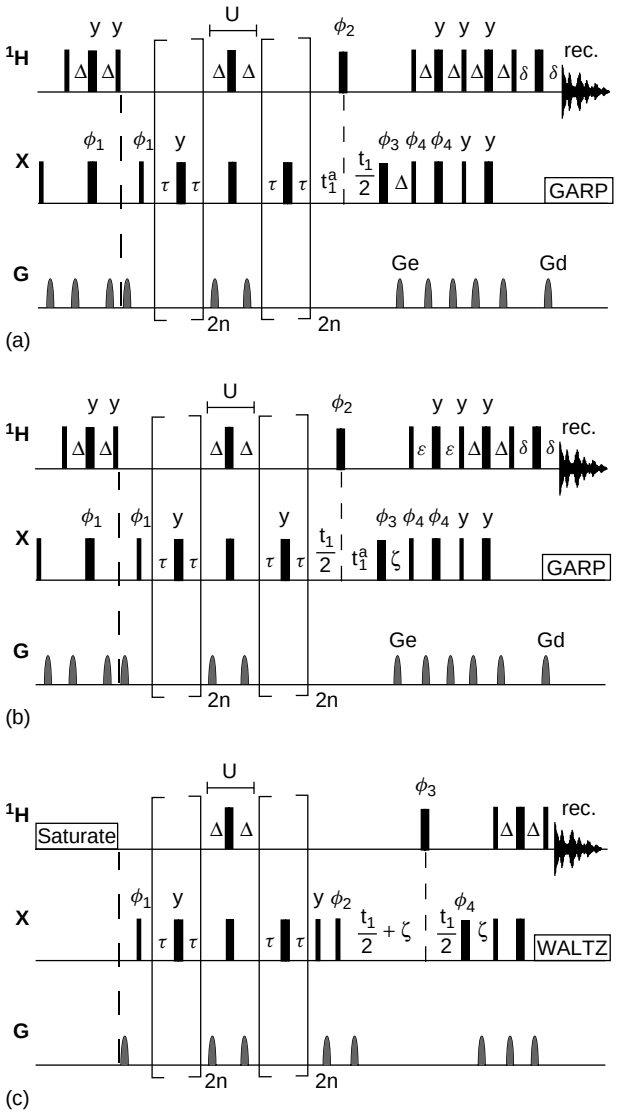

Figure 7 Pulse sequences for relaxation-compensated CPMG experiments in (a) IS, (b) I_2S, and (c) I_3S spin systems.[48,79] Narrow and wide bars depict 90° and 180° pulses respectively. All pulses are x-phase unless otherwise indicated. Decoupling during acquisition is achieved with the GARP or WALTZ-16 sequences.[53,92] Delays are $\tau = \tau_{cp}/2$, $\Delta = 1/(4J_{XH})$, and $\delta >$ Gd. In (a) $t_1^a = \Delta + t_1/2$; in (b) $\varepsilon = 1/(8J_{XH})$, $t_1^a = \zeta + t_1/2$, and $\zeta >$ Ge; and in (c) $\zeta = 1/(10J_{XH})$. In (a) and (b), the phase cycle is $\phi_1 = x, -x$; $\phi_2 = 4(x), 4(-x)$; $\phi_3 = x, x, y, y, -x, -x, -y, -y$; $\phi_4 = x$; receiver $= x, -x, -x, x$. The unlabeled gradients are used to suppress unwanted coherences and pulse imperfections.[93] Gradient coherence selection are achieved with gradients Gd and Ge. Echo/antiecho signals are recorded in separate experiments by inverting the amplitude of Gd and phase ϕ_4.[95] The ϕ_1 and the receiver phases are inverted for each t_1 increment to shift axial peaks to the edge of the spectrum.[94] In (c), the phase cycle is $\phi_1 = x, -x$; $\phi_2 = 2(x), 2(-x)$; $\phi_3 = 8(x), 8(-x)$; $\phi_4 = 4(x), 4(y), 4(-x), 4(-y)$; receiver $= x, -x, -x, x, -x, x, x, -x$. The unlabeled gradients are used to suppress unwanted coherences and pulse imperfections.[93] Frequency discrimination during t_1 is obtained by shifting the phase of ϕ_2 and the receiver according the States-TTPI protocol[94]

values of $R_2(1/\tau_{cp})$ were acquired using the pulse sequence of Figure 7(a) for values of $\tau_{cp} < 10$ ms, a self-compensated pulse sequence for $\tau_{cp} = 10.8$ and 21.5 ms, and a Hahn-echo

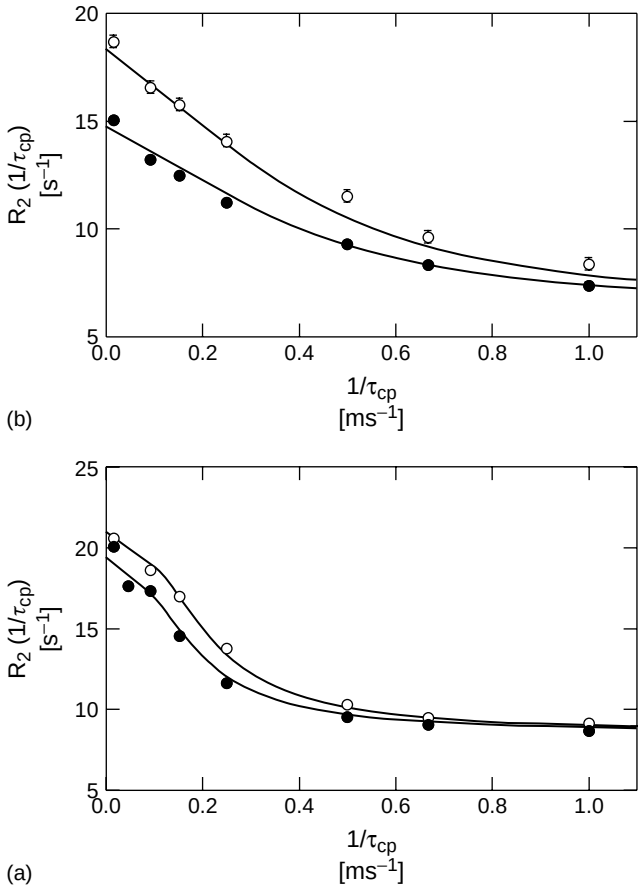

Figure 8 Global analysis of chemical exchange for the ^{15}N spin of Cys 38 in BPTI. Values of $R_2(1/\tau_{cp})$ at (●) $B_0 = 11.7$ T and (○) $B_0 = 14.1$ T are shown at temperatures of (a) 300 K and (b) 313 K. At 300 K, fitting with equation (19) yields $p_A = 0.953 \pm 0.004$, $\Delta\omega = 8.9 \pm 0.4$ ppm, $k_{ex} = 380 \pm 70\,s^{-1}$ and $R_2^0 = 8.6 \pm 0.1\,s^{-1}$. At 313 K, fitting with equation (21) yields $\Phi_{ex} = 0.108 \pm 0.024$ ppm^2, $k_{ex} = 1300 \pm 290\,s^{-1}$, and $R_2^0 = 6.4 \pm 0.7\,s^{-1}$

pulse sequence for $\tau_{cp} = 64.5$ ms.[48] Dispersion data were fit with a general expression for the transverse relaxation rate constant for site A ($p_A > p_B$), $R_2(1//\tau_{cp})$ given by,[28,77,82]

$$R_2\left(\frac{1}{\tau_{cp}}\right) = R_2^0 + \frac{k_{ex}}{2} - \frac{1}{2\tau_{cp}}\cosh^{-1}\left[D_+\cosh(\eta_+) - D_-\cos(\eta_-)\right] \tag{19}$$

in which,

$$D_\pm = \frac{1}{2}\left[\pm 1 + \frac{\Psi + 2\Delta\omega^2}{(\Psi^2 + \zeta^2)^{1/2}}\right]$$

$$\eta_\pm = \frac{\tau_{cp}}{\sqrt{2}}\left[\pm\Psi + (\Psi^2 + \zeta^2)^{1/2}\right]^{1/2} \tag{20}$$

$\Psi = k_{ex}^2 - \Delta\omega^2$ and $\zeta = 2\Delta\omega k_{ex}(p_B - p_A)$ and identical relaxation rates R_2^0 have been assumed for the two sites. In the fast-exchange limit, equation (19) is approximated by,[83]

$$R_2\left(\frac{1}{\tau_{cp}}\right) = R_2\left(\frac{1}{\tau_{cp}} \to \infty\right) + \frac{\Phi_{ex}}{k_{ex}}\left[1 - \frac{2}{k_{ex}\tau_{cp}}\tanh\left(\frac{k_{ex}\tau_{cp}}{2}\right)\right] \tag{21}$$

and R_2^0 is the population-average value. The static magnetic field dependence of exchange linebroadening indicates that the exchange time scale is intermediate at 300 K and approaches the fast limit at 313 K. Consequently, dispersion curves recorded at two static magnetic field strengths were analyzed globally using equations (19) for data acquired at 300 K and equation (21) for data acquired at 313 K. Analysis of data recorded at a single static magnetic field or data recorded for a limited range of τ_{cp} values can give substantial systematic errors.[48,79] Simultaneous analysis of both CPMG and $R_{1\rho}$ data has been proposed to increase the range of accessible effective fields and robustness of the data analysis.[5,10]

The pulse sequences shown in Figure 7 average the relaxation rate constants for in-phase and antiphase magnetization; consequently, R_2^0 in these sequences is larger than the in-phase relaxation rate constant and contains contributions from ^{1}H longitudinal relaxation. For IS spin systems, relaxation periods for two-spin order can be incorporated into the pulse sequence of Figure 5(a) to remove the contributions to $R_2(1/\tau_{cp})$ from ^{1}H longitudinal relaxation.[84] For ^{15}N spins, this method facilitates the use of relaxation interference rate constants to determine R_2^0 [equations (7) and (8)] and enables faster kinetic processes to be investigated by CPMG methods. Wüthrich and coworkers have shown that significantly narrower NMR signals can be obtained for one component of the ^{15}N–^{1}H scalar-coupled doublet from cancellation of ^{1}H–^{15}N dipole–dipole and ^{15}N CSA interactions (see **Transverse Relaxation-optimized NMR Spectroscopy with Biomacromolecular Structures in Solution**).[85] Recently, CPMG pulse sequences have been modified to select the narrow TROSY doublet component during the relaxation period, the indirect labeling period, and the detection period.[71,86,87] These modifications facilitate the quantification of exchange linebroadening contributions in larger macromolecules because the relative conformational exchange contribution to the phenomenological relaxation rate constant during the CPMG period is enhanced and the improved resolution and sensitivity of TROSY ^{1}H–^{15}N correlation spectra are obtained.

8 CHEMICAL EXCHANGE IN MULTIPLE QUANTUM SPECTROSCOPY

If two spins are affected by the same chemical exchange kinetic process, then the chemical shift changes for the two spins resulting from transitions between sites will be correlated. This correlation gives rise to exchange effects that can either broaden or narrow resonance lineshapes for multiple quantum coherences.[88] In essence, for multiple quantum coherences, the value of $\Delta\omega$ in the equations given above should be replaced by the difference in multiple quantum frequencies, $\Delta\omega_{MQ}$; thus, for double (DQ) and zero (ZQ) quantum coherences, respectively, $\Delta\omega_{DQ} = \Delta\omega_I + \Delta\omega_S$ and $\Delta\omega_{ZQ} = \Delta\omega_I - \Delta\omega_S$, in which $\Delta\omega_I$ ($\Delta\omega_S$) is the chemical shift difference between sites A and B for the I (S) spin. Hahn spin-echo pulse sequences for measuring the difference between the relaxation rate constants for DQ and ZQ quantum coherences have been developed for ^{1}H–^{15}N backbone amide moieties[89] and for $^{13}C^\alpha$–$^{13}C^\beta$ moieties[90] in proteins. The sign of the difference between DQ and ZQ relaxation rate constants gives the relative sign of the chemical shift differences for ^{1}H and ^{15}N spins. This information, which cannot be obtained

from single quantum experiments, is helpful for mechanistic interpretations of exchange phenomena. In some cases, selection of the narrower of the DQ or ZQ coherences (depending on the relative chemical shifts) results in improved resolution and sensitivity of multidimensional NMR spectra.[88,91]

9 CONCLUSIONS

Chemical exchange effects in NMR spectroscopy provide information on conformational and chemical kinetic processes occurring in biological macromolecules on biologically-relevant time scales. Experimental methods described in this article enable chemical exchange constants, k_{ex}, to be determined over a range from 0.1 to $10^5\,s^{-1}$ using ZZ-exchange, lineshape, CPMG, and $R_{1\rho}$ methods. Applications of these techniques promise to enhance understanding of the biological function of kinetic processes on μs-s time scales in proteins and other biological macromolecules.

10 RELATED ARTICLES IN THIS VOLUME

Relaxation Effects Involving Cross Correlation in Biomolecules; Transverse Relaxation-optimized NMR Spectroscopy with Biomacromolecular Structures in Solution.

11 RELATED ARTICLES IN VOLUMES 1–8

Chemical Exchange Effects on Spectra, Volume 2; Protein Dynamics from NMR Relaxation, Volume 6; Relaxation: An Introduction, Volume 6; Relaxation Effects of Chemical Exchange, Volume 6; Rotating Frame Spin-Lattice Relaxation Off-Resonance, Volume 7.

12 REFERENCES

1. J. Evenäs, A. Malmendal, and M. Akke, *Structure*, 2001, **9**, 185.
2. R. Ishima, D. Freedberg, Y.-X. Wang, J. M. Louis, and D. A. Torchia, *Structure*, 1999, **7**, 1047.
3. S. Kim, C. Bracken, and J. Baum, *J. Mol. Biol.*, 1999, **294**, 551.
4. P. B. McIntosh, I. A. Taylor, T. A. Frenkiel, S. J. Smerdon, and A. N. Lane, *J. Biomol. NMR*, 2000, **16**, 183.
5. F. A. A. Mulder, P. J. A. van Tilborg, R. Kaptein, and R. Boelens, *J. Biomol. NMR*, 1999, **13**, 275.
6. M. Pfuhl, H. A. Chen, S. M. Kristensen, and P. C. Driscoll, *J. Biomol. NMR*, 1999, **14**, 307.
7. L. Vugmeyster, C. D. Kroenke, F. Picart, A. G. Palmer, and D. P. Raleigh, *J. Am. Chem. Soc.*, 2000, **122**, 5387.
8. S. B. M. Whittaker, M. Czisch, R. Wechselberger, R. Kaptein, A. M. Hemmings, R. James, C. Kleanthous, and G. R. Moore, *Protein Sci.*, 2000, **9**, 713.
9. V. A. Feher and J. Cavanagh, *Nature*, 1999, **400**, 289.
10. A. E. Meekhof and S. M. V. Freund, *J. Biomol. NMR*, 1999, **14**, 13.
11. A. Malmendal, J. Evenas, S. Forsén, and M. Akke, *J. Mol. Biol.*, 1999, **293**, 883.
12. M. E. Holtzer, G. L. Bretthorst, D. A. d'Avignon, R. H. Angeletti, L. Mints, and A. Holtzer, *Biophys. J.*, 2001, **80**, 939.
13. D. S. Korchuganov, S. B. Nolde, M. Y. Reibarkh, V. Y. Orekhov, A. A. Schulga, Y. S. Ermolyuk, M. P. Kirpichnikov, and A. S. Arseniev, *J. Am. Chem. Soc.*, 2001, **123**, 2068.
14. M. Tollinger, N. R. Skrynnikov, F. A. A. Mulder, J. D. Foreman-Kay, and L. E. Kay, *J. Am. Chem. Soc.*, 2001, in press.
15. R. B. Hill, C. Bracken, W. F. DeGrado, and A. G. Palmer, *J. Am. Chem. Soc.*, 2000, **122**, 11 610.
16. B. F. Volkman, D. Lipson, D. E. Wemmer, and D. Kern, *Science*, 2001, **291**, 2429.
17. C. G. Hoogstraten, J. R. Wank, and A. Pardi, *Biochemistry*, 2000, **39**, 9951.
18. V. A. Feher and J. Cavanagh, *Nature*, 1999, **400**, 289.
19. F. A. A. Mulder, B. Hon, D. R. Muhandiram, F. W. Dahlquist, and L. E. Kay, *Biochemistry*, 2000, **39**, 12 614.
20. S. B. -M. Whittaker, M. Czisch, R. Wechselberger, R. Kaptein, A. M. Hemmings, R. James, C. Kleanthous, and G. R. Moore, *Protein Sci.*, 2000, **9**, 713.
21. G. Bodenhausen, G. Wagner, M. Rance, O. W. Sørensen, K. Wüthrich, and R. R. Ernst, *J. Magn. Reson.*, 1984, **59**, 542.
22. G. Wagner, G. Bodenhausen, N. Müller, M. Rance, O. Sørensen, R. R. Ernst, and K. Wüthrich, *J. Am. Chem. Soc.*, 1985, **107**, 6440.
23. B. D. N. Rao, *Meth. Enzymol.*, 1989, **176**, 279.
24. J. Sandstrom, 'Dynamic NMR Spectroscopy', Academic Press: London, 1982.
25. H. Y. Carr and E. M. Purcell, *Phys. Rev.*, 1954, **94**, 630.
26. S. Meiboom and D. Gill, *Rev. Sci. Instrum.*, 1958, **29**, 688.
27. C. Deverell, R. E. Morgan, and J. H. Strange, *Mol. Phys.*, 1970, **18**, 553.
28. D. G. Davis, M. E. Perlman, and R. E. London, *J. Magn. Reson., Ser. B*, 1994, **104**, 266.
29. N. A. Farrow, O. Zhang, J. D. Forman-Kay, and L. E. Kay, *Biochemistry*, 1995, **34**, 868.
30. S. Grzesiek and A. Bax, *J. Am. Chem. Soc.*, 1993, **115**, 12 593.
31. A. C. Wang and A. Bax, *J. Biomol. NMR*, 1993, **3**, 715.
32. V. V. Krishnan and M. Rance, *J. Magn. Reson., Ser. A*, 1995, **116**, 97.
33. L. Mueller, P. Legault, and A. Pardi, *J. Am. Chem. Soc.*, 1995, **117**, 11 043.
34. F. A. A. Mulder, C. A. E. M. Spronk, M. Slijper, R. Kaptein, and R. Boelens, *J. Biomol. NMR*, 1996, **8**, 223.
35. M. Akke, J. Liu, J. Cavanagh, H. P. Erickson, and A. G. Palmer, *Nature Struct. Biol.*, 1998, **5**, 55.
36. L. C. Wang, Y. X. Pang, T. Holder, J. R. Brender, A. V. Kurochkin, and E. R. P. Zuiderweg, *Proc. Natl. Acad. Sci. USA*, 2001, **98**, 7684.
37. E. Kay, L. K. Nicholson, F. Delagio, A. Bax, and D. A. Torchia, *J. Magn. Reson.*, 1992, **97**, 359.
38. A. G. Palmer, N. J. Skelton, W. J. Chazin, P. E. Wright, and M. Rance, *Mol. Phys.*, 1992, **75**, 699.
39. A. M. Mandel, M. Akke, and A. G. Palmer, *J. Mol. Biol.*, 1995, **246**, 144.
40. A. M. Mandel, M. Akke, and A. G. Palmer, *Biochemistry*, 1996, **35**, 16 009.
41. J. Peng and G. Wagner, *Biochemistry*, 1995, **34**, 16 733.
42. I. Q. H. Phan, J. Boyd, and I. D. Campbell, *J. Biomol. NMR*, 1996, **8**, 369.
43. C. D. Kroenke, M. Rance, and A. G. Palmer, *J. Am. Chem. Soc.*, 1999, **121**, 10 119.
44. C. D. Kroenke, J. P. Loria, L. K. Lee, M. Rance, and A. G. Palmer, *J. Am. Chem. Soc.*, 1998, **120**, 7905.
45. N. Tjandra, S. E. Feller, R. W. Pastor, and A. Bax, *J. Am. Chem. Soc.*, 1995, **117**, 12 562.
46. J. M. Schurr, H. P. Babcock, and B. S. Fujimoto, *J. Magn. Reson., Ser. B*, 1994, **105**, 211.
47. A. G. Palmer, J. Williams, and A. McDermott, *J. Phys. Chem.*, 1996, **100**, 13 293.
48. O. Millet, J. P. Loria, C. D. Kroenke, M. Pons, and A. G. Palmer, *J. Am. Chem. Soc.*, 2000, **122**, 2867.

49. N. A. Farrow, O. Zhang, A. Szabo, D. A. Torchia, and L. E. Kay, *J. Biomol. NMR*, 1995, **6**, 153.
50. M. Goldman, *J. Magn. Reson.*, 1984, **60**, 437.
51. N. Tjandra, A. Szabo, and A. Bax, *J. Am. Chem. Soc.*, 1996, **118**, 6986.
52. A. Bax, M. Ikura, L. E. Kay, D. A. Torchia, and R. Tschudin, *J. Magn. Reson.*, 1990, **86**, 304.
53. A. J. Shaka, J. Keeler, T. Frenkiel, and R. Freeman, *J. Magn. Reson.*, 1983, **52**, 334.
54. G. Otting, E. Liepinsh, and K. Wüthrich, *Biochemistry*, 1993, **32**, 3571.
55. J. J. Led, H. Gesmar, and F. Abildgaard, *Methods Enzymol.*, 1989, **176**, 311.
56. J. Fejzo, W. M. Westler, S. Macura, and J. L. Markley, *J. Am. Chem. Soc.*, 1990, **112**, 2574.
57. G. T. Montelione and G. Wagner, *J. Am. Chem. Soc.*, 1989, **111**, 3096.
58. N. Farrow, O. Zhang, J. D. Forman-Kay, and L. E. Kay, *J. Biomol. NMR*, 1994, **4**, 727.
59. G. Wider, D. Neri, and K. Wüthrich, *J. Biomol. NMR*, 1991, **1**, 93.
60. H. Wang, Y. Hea, C. D. Kroenke, S. Kodukulab, J. Storch, A. G. Palmer, and R. E. Stark, *Biochemistry*, 2002, in press.
61. H. M. McConnell, *J. Chem. Phys.*, 1958, **28**, 430.
62. R. E. Burton, R. S. Busby, and T. G. Oas, *J. Biomol. NMR*, 1998, **11**, 355.
63. B. Kuhlman, D. L. Luisi, P. A. Evans, and D. P. Raleigh, *J. Mol. Biol.*, 1998, **284**, 1661.
64. D. Kern, G. Kern, G. Scherer, G. Fischer, and T. Drakenberg, *Biochemistry*, 1995, **34**, 13 594.
65. T. Szyperski, P. Luginbühl, G. Otting, P. Güntert, and K. Wüthrich, *J. Biomol. NMR*, 1993, **3**, 151.
66. S. Zinn-Justin, P. Berthault, M. Guenneugues, and H. Desvaux, *J. Biomol. NMR*, 1997, **10**, 363.
67. M. Akke and A. G. Palmer, *J. Am. Chem. Soc.*, 1996, **118**, 911.
68. F. A. A. Mulder, R. A. de Graaf, R. Kaptein, and R. Boelens, *J. Magn. Reson.*, 1998, **131**, 351.
69. F. C. L. Almeida and S. J. Opella, *J. Magn. Reson.*, 1997, **124**, 509.
70. R. Ishima, J. M. Louis, and D. A. Torchia, *J. Magn. Reson.*, 1999, **137**, 289.
71. R. Ishima, P. T. Wingfield, S. J. Stahl, J. D. Kaufman, and D. A. Torchia, *J. Am. Chem. Soc.*, 1998, **120**, 10 534.
72. S. Meiboom, *J. Chem. Phys.*, 1961, **34**, 375.
73. O. Trott and A. G. Palmer, *J. Magn. Res.*, 2002, **154**, 157.
74. M. J. Blackledge, R. Brüschweiler, C. Griesinger, J. M. Schmidt, P. Xu, and R. R. Ernst, *Biochemistry*, 1993, **32**, 10 960.
75. D. Braun, G. Wider, and K. Wüthrich, *J. Am. Chem. Soc.*, 1994, **116**, 8466.
76. A. Allerhand and E. Thiele, *J. Chem. Phys.*, 1966, **45**, 902.
77. J. P. Carver and R. E. Richards, *J. Magn. Reson.*, 1972, **6**, 89.
78. W. T. Sobol, *Magn. Reson. Med.*, 1991, **21**, 2.
79. J. P. Loria, M. Rance, and A. G. Palmer, *J. Am. Chem. Soc.*, 1999, **121**, 2331.
80. F. A. A. Mulder, N. R. Skrynnikov, B. Hon, F. W. Dahlquist, and L. E. Kay, *J. Am. Chem. Soc.*, 2001, **123**, 967.
81. N. R. Skrynnikov, F. A. A. Mulder, B. Hon, F. W. Dahlquist, and L. E. Kay, *J. Am. Chem. Soc.*, 2001, **123**, 4556.
82. J. Jen, *J. Magn. Reson.*, 1978, **30**, 111.
83. Z. Luz and S. Meiboolm, *J. Chem. Phys.*, 1963, **39**, 366.
84. C. Wang, M. J. Grey, and A. G. Palmer, *J. Biomol. NMR*, 2001, **21**, 361.
85. K. Pervushin, R. Riek, G. Wider, and K. Wüthrich, *Proc. Natl. Acad. Sci. USA*, 1997, **94**, 12 366.
86. J. P. Loria, M. Rance, and A. G. Palmer, *J. Biomol. NMR*, 1999, **15**, 151.
87. J. Boisbouvier, B. Brutscher, J.-P. Simorre, and D. Marion, *J. Biomol. NMR*, 1999, **14**, 241.
88. M. Rance, *J. Am. Chem. Soc.*, 1988, **110**, 1973.
89. K. Kloiber and R. Konrat, *J. Biomol. NMR*, 2000, **18**, 33.
90. Früh, J. R. Tolman, G. Bodenhausen, and C. Zwahlen, *J. Am. Chem. Soc.*, 2001, **123**, 4810.
91. K. Pervushin, *J. Biomol. NMR*, 2001, **20**, 275.
92. A. J. Shaka, P. B. Barker, and R. Freeman, *J. Magn. Reson.*, 1985, **64**, 547.
93. A. Bax and S. S. Pochapsky, *J. Magn. Reson.*, 1992, **99**, 638.
94. D. Marion, M. Ikura, R. Tschudin, and A. Bax, *J. Magn. Reson.*, 1989, **85**, 393.
95. L. E. Kay, P. Keifer, and T. Saarinen, *J. Am. Chem. Soc.*, 1992, **114**, 10 663.
96. T. Yamazaki, R. Muhandiram, and L. E. Kay, *J. Am. Chem. Soc.*, 1994, **116**, 8266.

Acknowledgements

This work was supported by National Institutes of Health grant GM-59273.

Biographical Sketch

Arthur G. Palmer, III, *b* 1956. B. A., 1980, Haverford College, USA. Ph.D., 1989, Chemistry, University of North Carolina, Chapel Hill, USA (thesis advisor Nancy L. Thompson). National Science Foundation Postdoctoral Fellow, 1989–1992, The Scripps Research Institute (with Peter E. Wright). Assistant Professor, 1992–1998; Associate Professor; 1998–2001; Professor, 2001-present, Columbia University, USA. Approx. 75 publications. Research specialties: NMR relaxation and molecular motions in biological macromolecules.

Membranes: Carbon-13 NMR

Frances Separovic and Bruce A. Cornell

CSIRO Food Research Laboratory, Sydney, NSW, Australia

1	Introduction	1
2	Biomembrane and Model Membrane Studies	1
3	Membrane Protein Structure	3
4	Conclusions	4
5	Related Articles	4
6	References	4

1 INTRODUCTION

High-resolution solid state ^{13}C NMR spectroscopy has been used extensively to analyze the conformation, dynamics, and molecular order of biological and model membrane systems. With improvements in magnet technology, the mid 1970s saw ^{13}C NMR used for a broad range of studies of biological membrane systems under natural abundance conditions.[1] As a spin-$\frac{1}{2}$ nucleus of intermediate abundance (1.1%), ^{13}C is suitable for investigations employing both isotopically enriched and natural abundance samples. The large chemical shift range provided by ^{13}C NMR and the sensitivity enhancement possible from cross polarization (CP) to neighboring protons permits the acquisition of well-resolved solid state ^{13}C NMR spectra from both biomembranes and model lipid bilayer systems.

As a fundamental constituent of natural membrane bilayers, lipid dispersions have been widely studied as model membranes. From the ^{13}C static powder spectra of membrane lipids, many of the resonances in the hydrocarbon chain, the carbonyl positions, the headgroup, and the glycerol backbone regions can be resolved. Line broadening due to the dipolar interaction with the abundant protons can be overcome by decoupling. Resolution can be enhanced with magic angle spinning (MAS) and applied to both model and cell membranes. Alternatively, multibilayers may be macroscopically aligned on glass slides or magnetically oriented to improve resolution (see Figure 1). Each magnetically equivalent site gives a single resonance, and measurements taken at a range of sample orientations relative to the magnetic field direction permit the observation of the ^{13}C chemical shift anisotropy (CSA),[2,3] which is normally unresolved in the static powder pattern.

A number of physical techniques including ^{1}H and ^{13}C NMR of ultrasonically dispersed lipid vesicles, ^{2}H NMR of deuterated lipids, and ^{31}P NMR of lipid headgroups[4,5] have shown that within lipid bilayers and biological membranes, lipid molecules undergo rapid conformational and long-axis rotation reorientation. This anisotropic motion results in incomplete averaging of anisotropic nuclear interactions such as dipolar and shielding anisotropy tensors, necessitating the use of solid state NMR techniques. Since MAS can average the residual of these interactions, high-resolution ^{13}C

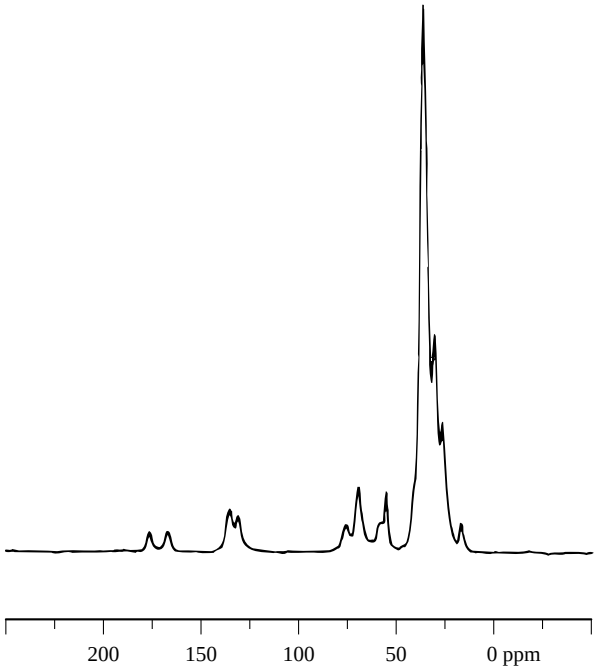

Figure 1 Natural abundance ^{13}C CP NMR spectrum of an aligned lipid bilayer, egg yolk phosphatidylcholine dispersed in water. The bilayer normal is perpendicular to the magnetic field, and the resonances from the lipid carbonyls, double bonds, glycerol region, headgroup methyls, chain methylenes, and terminal methyl are well resolved

NMR spectra can be obtained from unsonicated multibilayer dispersions[6] and intact biological membranes.[7] It has been demonstrated that the resolution of ^{13}C MAS NMR spectra of phospholipid bilayers can be equal to that of sonicated samples.[8,9] Membranes contain several components in addition to phospholipids, including proteins, peptides, and steroids. To determine structural parameters of membrane proteins and polypeptides, specific isotopic labeling is usually required.

2 BIOMEMBRANE AND MODEL MEMBRANE STUDIES

Phospholipids are the major lipid component found in biomembranes, and consequently, phospholipid bilayers are commonly used as model membranes. When dispersed in water phospholipids form multilamellar, lyotropic, liquid crystals with a random distribution of bilayer orientations. If the dispersion is subjected to ultrasonic irradiation, these structures break down into small, unilamellar vesicles. The reorientation of these vesicles in solution results in substantial cancellation of the static dipolar and anisotropic chemical shielding interactions, resulting in ^{13}C spectra that are resolved in isotropic chemical shift. The first reported observation of high-resolution NMR spectra from a model membrane was by Chapman and Penkett.[10] Early ^{13}C NMR investigations of membrane systems included studies of unsonicated multibilayers with and without cholesterol[11,12] and rat liver mitochondrial membranes.[13] Natural abundance ^{13}C relaxation rates were measured for pure phospholipid bilayers above the phase transition temperature.[14] The ^{13}C

relaxation rates were found to decrease as the terminal methyl is approached from the glycerol backbone.

2.1 CP Studies

Early ^{13}C NMR studies employing CP to study powder patterns of lipid bilayers and membranes,[15,16] showed that after the severe broadening of the $^{13}C-^{1}H$ dipole interactions was removed by decoupling, the unsonicated lipid multilayers still displayed a residual linewidth resulting from the unaveraged ^{13}C CSA. The dynamics of phospholipids has been analyzed in terms of the conformation and order at the lipid–water interface by studies of the ^{13}C CP powder pattern of the carbonyl groups at the 1 and 2 positions of phosphatidylcholine in multilamellar dispersions.[17,18] The headgroup mobility and the rotational correlation times in the acyl chain region of membrane lipids has been measured using ^{13}C NMR over a range of temperatures spanning the L_β, P_β, and the L_α phases of the lipid dispersion.[19]

The incorporation of cholesterol was found to broaden the chain resonances of phospholipids in multilamellar dispersions.[20] The interaction of phospholipids with cholesterol[21] and the membrane-bound polypeptide gramicidin A[22] was examined using CP ^{13}C NMR. These compounds were found to introduce a long correlation time component to the motion of the lipid molecules, as evident in the shortening of $T_{1\rho}^{H}$, and to order the motion, as determined from the increased CSA of the 1-carbonyl site. Carbon-13 NMR has been used in conjunction with ^{31}P NMR to gain further insight into dynamic and structural details of gramicidin–phospholipid phase formation.[23]

Cross polarization ^{13}C NMR has been used to study the motion of the carbonyl groups and the phase behavior of mixed chain phosphatidylcholines,[24] and to characterize motionally restricted molecules in normal human erythrocytes.[25] The rotating frame relaxation time, $T_{1\rho}^{H}$, of membranes appears to be dominated by contributions from cooperative molecular or segmental motions on the millisecond to microsecond timescale.[26] The effect of glycophorin from human erythrocyte membranes on the dynamics of lipids in phospholipid vesicles was found to be similar.[27,28] Subsequently, using ^{13}C relaxation measurements, the incorporation of retinal was found to result in a reduction of mobility in the lipid acyl chain[29] region. The dynamics of various chemical groups in anhydrous bacteriorhodopsin membranes was characterized using ^{13}C CP MAS spectra.[30] More recent work employing ^{13}C CP MAS has been performed using hydrated phospholipid dispersions,[31–33] and illustrates the usefulness of ^{13}C NMR for the study of model membrane systems. The interaction of cytochrome *c* with cardiolipin bilayers was investigated using ^{13}C CP NMR, natural abundance lipid, and specifically labeled protein.[34]

2.2 Non-CP Studies

Cross polarization is not always necessary in hydrated samples because the T_1^C values are sufficiently short. Carbon-13 NMR was used to measure the outside/inside bilayer distribution and translocation of phospholipids in mixed sonicated vesicles.[35] The ^{13}C chemical shifts and T_1 relaxation times of chloroplast lipid extracts were reported[36] in 1977, and later applied to the study of molecular order within chloroplast membranes.[37] Carbon-13 NMR spectroscopy has been used to determine the headgroup conformation of phospholipids.[38,39] The integrity of large unilamellar vesicles made from ^{13}C-labeled phosphatidylcholine was demonstrated using shift reagents that affected the outer lipid monolayer headgroups.[40] Using ^{13}C T_1 measurements, cholesteryl esters were shown to reduce the mobility of phospholipids.[41] In liposomes or vesicles made from polar lipid extracts of *Halobacterium halobium*,[42] a sharp change in molecular motion was detected at the lipid phase transition by ^{13}C NMR.

The mobility of ^{13}C-enriched human myelin basic protein reconstituted in multilayer liposomes[43] was reported in 1980. Specific ^{13}C labeling of the choline group of phospholipids in erythrocyte, endoplasmic, and sarcoplasmic reticulum membranes was used to study the phases of membrane lipids.[44] By employing ^{13}C-enriched enkephalin, an opioid peptide, its binding to phosphatidylserine was monitored by changes in chemical shift and T_1 measurements.[45] Evidence for lipid-associated chlorophyll in whole spinach thylakoid membranes[46] was verified with ^{13}C NMR spectroscopy. Using a simple spin echo, the powder pattern of phosphatidylcholine, ^{13}C-labeled at the 2-carbonyl, was recorded as a function of temperature, both below and above the lipid main phase transition temperature.[47] Further work has shown ^{13}C NMR to be a useful technique for defining phases in pure and mixed phospholipid systems,[24,48–50] and for studying lipid–steroid interactions.[51,52]

Carbon-13 T_1 relaxation rates and $^{13}C-^{1}H$ nuclear Overhauser effects (NOE) reported in 1992, revealed little difference in the lipid acyl chain dynamics between small and large unilamellar vesicles.[53] In addition, the lateral diffusion of lipid molecules in phospholipid vesicles has been estimated from ^{13}C spin–spin relaxation time, T_2, measurements.[54] Using magnetically aligned phosphatidylcholine–detergent mixtures, solid state ^{13}C NMR has yielded high-resolution spectra. From the measured chemical shift anisotropies and dipolar splittings in these systems structural and dynamic information has been derived, such as the headgroup orientation of alkyl glycosides at a lipid bilayer interface.[55,56]

2.3 MAS Studies

A study of the dynamics of the lipids in phospholipid–rhodopsin powders and in whole retinal rod disk membranes using ^{13}C MAS, demonstrated that rhodopsin reduces the rate of high-frequency motions.[57,58] Similar results were obtained with bacteriorhodopsin in lipid bilayers[59] using static, ^{13}C, solid state NMR and CP. High-resolution CP MAS was used to determine the dynamic behavior of the resolved ^{13}C resonances of anhydrous bacteriorhodopsin membranes,[30] and the lipid, protein, and bacteriochlorophyll *a* of intracytoplasmic membrane and the light-harvesting complex of photosynthetic bacteria.[60]

MAS techniques were employed to determine the spin–lattice relaxation times, T_1, of individual carbons in unsonicated phospholipid dispersions.[61] In addition, well-resolved ^{13}C MAS spectra have been obtained from erythrocyte ghosts[62] and intact myelin membranes.[7] CP MAS was used to determine the headgroup and hydrocarbon packing in

hydrated and dry phospholipids.[31–33,63] Subsequently, the interfacial conformation of the glycerol backbone of lipids in phospholipid bilayers[64] was characterized using specifically labeled lipids and ^{13}C MAS NMR. Two-dimensional $^{1}H-^{13}C$ heteronuclear chemical shift[65] and NOESY spectra[66] of phospholipid–water dispersions have been recorded using solid state MAS techniques. Recently, ^{13}C MAS NMR has been demonstrated as a powerful tool for examining structure and motions of cholesterol[67] and cholesteryl esters[68] in crystalline and liquid crystalline phases and the molecular organization in phospholipid-triglyceride aqueous dispersions.[69] Further, MAS ^{13}C NMR T_1 relaxation studies were used to determine the location and effects of α-tocopherol and ubiquinone in unsonicated model membranes.[70] The application of MAS techniques for the determination of the structure of integral membrane proteins will be discussed in the following section.

3 MEMBRANE PROTEIN STRUCTURE

Biological membranes greatly restrict the motion of integral proteins, and consequently solid state NMR is more suitable for structural studies of membrane proteins than solution methods. Nevertheless, conventional high-resolution NMR spectra of membrane proteins have been obtained by replacing the membrane lipids with detergents which form micelles in solution, e.g. ^{1}H spectra of gramicidin A in micelles.[71] Carbon-13 NMR studies have been performed on ^{13}C-enriched retinals embedded in bacteriorhodopsin solubilized in detergent.[72] More recently, ^{13}C spectra have provided both structural and dynamic information from hydrophobic oligopeptides,[73] the major coat protein of bacteriophage M13,[74,75] bacteriorhodopsin,[76,77] and cytochrome *c* oxidase[78] in micellar systems. Phospholipid vesicles were used to study the mobility of incorporated ^{13}C-enriched glycophorin A, a transmembrane glycoprotein,[79] using conventional solution state NMR methods. From relaxation measurements and accessibility to paramagnetic NMR probes, the ion channel gramicidin A was demonstrated to be an N-terminal to N-terminal helical dimer in phospholipid vesicles using ^{13}C-enriched gramicidin A.[80] However, vesicle systems have limited use for solution studies of membrane proteins as the small, unilamellar vesicles tend to aggregate, and solid state techniques are required.

For the study of membrane proteins, severe broadening as a result of incomplete averaging of dipolar interactions can be overcome by applying high-resolution solid state NMR techniques. The magnetically dilute spin-$\frac{1}{2}$ nuclei such as ^{13}C have had the most far-reaching application since the CSA is the dominant spin interaction in the NMR spectrum. The CSA can, in principle, be directly related to molecular structure if the axis system of the chemical shift tensor has been determined relative to a molecular fixed axis system. This directional information conveyed by the CSA is lost in solution studies that only retain the isotropic component of the shift tensor. Magic angle spinning has been widely used for resolving isotropic and anisotropic chemical shifts. A common approach for determination of membrane protein structure has been selective isotopic enrichment at specific sites and the use of MAS combined with CP and proton decoupling.

Alternative approaches, including oriented samples, have been applied to measure dipolar couplings and CSAs and these have been related to molecular structures. Hydrated dispersions of phosphatidylcholine incorporating specifically ^{13}C-labeled gramicidin A have been aligned on glass coverslips to improve spectral resolution. The experimental CSA of the ^{13}C carbonyl resonance of the labeled peptide was compared with the values calculated for various proposed models.[81] The membrane ion channel form of gramicidin A was consistent with a $\beta^{6.3}$ single helix. An accurate knowledge of the principal values and direction cosines of the CSA tensor is crucial for the interpretation of the oriented NMR spectra. These values may be determined from single crystal studies or from powder samples if the nucleus under investigation is dipole-coupled to a nearby nucleus.[82]

Solid state ^{13}C NMR spectroscopy is capable of determining the structure of membrane polypeptides to high resolution, including both backbone[83] and side-chain groups. The orientation of the tryptophan side chains was determined using gramicidin A, ^{13}C labeled at the indole C-2 of tryptophan, and macroscopically aligned in phospholipid dispersions.[84] Carbon-13 NMR was further utilized to demonstrate the Na^{+} binding site in specifically ^{13}C-labeled gramicidin A channels incorporated within model membrane systems.[85–87] Two-dimensional REDOR of $^{13}C-^{15}N$-labeled gramicidin A in multilamellar dispersions[88] further defined the ion channel form to be the $\beta^{6.3}$-helix.

The dynamics and aggregation of alamethicin, another peptide ion channel, was determined using ^{13}C NMR of spin-labeled peptides and phospholipid vesicles.[89] The results indicated that the ion-conductive aggregate represents only a minor fraction of the total membrane-bound peptide. Natural abundance T_1 measurements and $^{13}C-^{1}H$ NOEs of alamethicin in methanol suggested that the peptide is a rigid helix in the membrane.[90] Rotational resonance measurements of a ^{13}C-labeled undecapeptide, analogous to the N-terminus of alamethicin, within membrane bilayers, have shown that the peptide maintains a helical structure.[91] These studies have demonstrated that $^{13}C-^{13}C$ distances of up to 0.68 nm can be measured with an accuracy of up to 0.05 nm using rotational resonance techniques.

Melittin, a constituent of bee venom, is one of the most extensively studied membrane peptides. Carbon-13 relaxation measurements of the motion of fatty acyl chains in multibilayers of chloroplast membrane lipids and melittin,[92] were consistent with the melittin penetrating deep into the bilayer. However, ^{13}C relaxation measurements of lipids in melittin-containing vesicles[93] were interpreted as evidence for a surface rather than transmembrane orientation of the melittin helix. Solid state ^{13}C CP NMR studies of melittin in aligned lipid multilayers indicated that at higher concentrations of the peptide melittin inserted within the lipid bilayer.[94] The dynamics of tryptophan side chains and the peptide backbone has been studied using selectively ^{13}C-enriched melittin in lipid vesicles and micelles.[95] The data were found to be consistent with a transbilayer orientation of the N-terminal α-helical segment.

Information about the secondary structure of virus fd coat proteins oriented by the magnetic field has been obtained using doubly labeled $^{13}C-^{15}N$ peptides.[96,97] The protein has been studied both as an intrinsic membrane protein reconstituted into phospholipids, and as the native form found in the

virion. Spectra obtained from ^{13}C carbonyl-labeled Pf1 coat protein display motional averaging consistent with the protein being predominantly α-helical, with the helix axis aligned approximately parallel to the phage filament.[98] The C-terminal residues were found to be rigid when the protein formed the outer coat of the virus, and highly mobile when the protein was in a lipid bilayer.

A larger membrane protein, [1-^{13}C]leucine bacteriorhodopsin, incorporated within a phospholipid bilayer was shown to undergo rotational diffusion about an axis parallel to the bilayer normal, resulting in a narrowing of the peptide carbonyl lineshapes.[99] The dynamic structure of the backbone of bacteriorhodopsin in purple membranes was deduced from ^{13}C spectra obtained from samples using biosynthetically incorporated ^{13}C-labeled amino acids.[100]

Solid state NMR studies of ^{13}C-labeled retinal, the chromophore in bacteriorhodopsin and rhodopsin, have been carried out in both dry and hydrated samples.[101–103] Dark-adapted bacteriorhodopsin was shown to contain a mixture of retinal isomers from the ^{13}C peak splitting.[104] From the isotropic chemical shift and principal values of the chemical shift tensor of the ^{13}C-5 label, it was demonstrated that retinal is in a 6-*s*-*cis* conformation in rhodopsin but in the 6-*s*-*trans* form in bacteriorhodopsin.[103,104]

Rotational resonance NMR was used to measure the distance between the C-8 and C-18 carbons of retinals within bacteriorhodopsin,[105] an integral membrane protein. Further, solid state ^{13}C MAS NMR has been used to investigate light-induced and temperature-dependent changes between 215 and 260 K, in detergent-solubilized photosynthetic reaction centers of *Rhodobacter sphaeroides*,[106] selectively enriched with [4-^{13}C]tyrosine. Similarly, [4-^{13}C]aspartic acid resonances were used to study light and dark adaption of bacteriorhodopsin.[107] By ^{13}C-labeling both the retinal chromophore and the lysine side chain of the protein, rotational resonance NMR was used to measure the active site distance in a membrane protein.[108] An important aspect of these studies has been the development of ^{13}C NMR solid state techniques for investigating the tertiary structure of membrane proteins within biological systems.

4 CONCLUSIONS

The above examples have illustrated the value of ^{13}C NMR spectroscopy as a tool for the study of membrane systems. Membranes are complicated structures and in order to elucidate their organization, it has been necessary to examine model systems such as lipids and lipid–protein complexes. With the developments in pulse methods and selective enrichment, ^{13}C NMR has enabled the study of the motion and orientation of particular membrane sites, and to relate these results to the structure and function of biological membranes.

5 RELATED ARTICLES

Bacteriorhodopsin and Rhodopsin; Bilayer Membranes: Deuterium and Carbon-13 NMR; Bilayer Membranes: Proton and Fluorine-19 NMR; Cross Polarization in Solids; Glycolipids; Gramicidin Channels: Orientational Constraints for Defining High-Resolution Structures; Lipid Polymorphism; Liquid Crystalline Samples: Structure of Nonrigid Molecules; Magic Angle Spinning; Membrane Lipids of Acholeplasma laidlawii; Membrane Proteins; Membranes: Deuterium NMR; Membranes: Phosphorus-31 NMR; Molecular Motions: T_1 Frequency Dispersion in Biological Systems; Protein Dynamics from Solid State NMR; REDOR and TEDOR; Rotational Resonance in Biology; Sonicated Membrane Vesicles; Spinning Liquid Crystalline Samples.

6 REFERENCES

1. A. G. Lee, N. J. M. Birdsall, and J. C. Metcalfe, in *Methods in Membrane Biology* ed. E. D. Korn, Plenum, New York, 1974, Vol. 2.
2. R. Blinc, M. I. Burgar, V. Rutar, B. Žekš, R. Kind, H. Arend, and G. Chapius, *Phys. Rev. Lett.*, 1979, **43**, 1679.
3. V. L. B. Braach-Maksvytis and B. A. Cornell, *Biophys. J.*, 1988, **53**, 839.
4. R. G. Griffin, *Methods Enzymol.*, 1981, **72**, 108.
5. J. Seelig, *Q. Rev. Biophys.*, 1977, **10**, 353.
6. R. A. Haberkorn, J. Herzfeld, and R. G. Griffin, *J. Am. Chem. Soc.*, 1978, **100**, 1296.
7. J. Forbes, J. Bowers, X. Shan, L. Moran, E. Oldfield, and M. A. Moscarello, *J. Chem. Soc., Faraday Trans. 1*, 1988, **84**, 3821.
8. E. Oldfield, J. L. Bowers, and J. Forbes, *Biochemistry*, 1987, **26**, 6919.
9. J. Forbes, C. Husted, and E. Oldfield, *J. Am. Chem. Soc.*, 1988, **110**, 1059.
10. D. Chapman and S. A. Penkett, *Nature (London)*, 1966, **211**, 314.
11. J. C. Metcalfe, N. J. M. Birdsall, J. Feeney, A. G. Lee, Y. K. Levine, and P. Partington, *Nature (London)*, 1971, **233**, 199.
12. E. Oldfield and D. Chapman, *Biochem. Biophys. Res. Commun.*, 1971, **43**, 949.
13. K. M. Keough, E. Oldfield, D. Chapman, and P. Beynon, *Chem. Phys. Lipids*, 1973, **10**, 37.
14. Y. K. Levine, N. J. M. Birdsall, A. G. Lee, and J. C. Metcalfe, *Biochemistry*, 1972, **11**, 1416.
15. J. Urbina and J. S. Waugh, *Proc. Natl. Acad. Sci. USA*, 1974, **71**, 5062.
16. S. J. Opella, J. P. Yesinowski, and J. S. Waugh, *Proc. Natl. Acad. Sci. USA*, 1976, **73**, 3812.
17. B. A. Cornell, *Chem. Phys. Lett.*, 1980, **72**, 462.
18. B. A. Cornell, *Chem. Phys. Lipids*, 1981, **28**, 69.
19. E. Boroske and L. Trahms, *Biophys. J.*, 1983, **42**, 275.
20. A. M. W. Lancee-Hermkens and B. DeKruijff, *Biochim. Biophys. Acta*, 1977, **470**, 141.
21. B. A. Cornell, M. Keniry, R. G. Hiller, and R. Smith, *FEBS Lett.*, 1980, **115**, 134.
22. B. A. Cornell and M. Keniry, *Biochim. Biophys. Acta*, 1983, **732**, 705.
23. J. A. Killian and B. de Kruijff, *Biochemistry*, 1985, **24**, 7881.
24. B. A. Lewis, S. K. Das Gupta, and R. G. Griffin, *Biochemistry*, 1984, **23**, 1988.
25. S. K. Ackerman, C. T. Noguchi, A. N. Schechter, and D. A. Torchia, *Biochem. Biophys. Res. Commun.*, 1982, **106**, 1161.
26. B. A. Cornell, R. G. Hiller, J. Raison, F. Separovic, R. Smith, J. C. Vary, and C. Morris, *Biochim. Biophys. Acta*, 1983, **732**, 473.
27. H. Utsumi, B. D. Tunggal, and W. Stoffel, *Biochemistry*, 1980, **19**, 2385.

28. R. L. Ong and J. H. Prestegard, *Biochim. Biophys. Acta*, 1982, **692**, 252.
29. Y. Inuoe, Y. Hanafusa, M. Toda, and R. Chujo, *Bull. Chem. Soc. Jpn.*, 1982, **55**, 540.
30. K.-H. Spohn and R. Kimmich, *Biochem. Biophys. Res. Commun.*, 1983, **114**, 713.
31. K. S. Bruzik, G. M. Salamonczyk, and B. Sobon, *Biochim. Biophys. Acta*, 1990, **1023**, 143.
32. W.-G. Wu and L.-M. Chi, *Biochim. Biophys. Acta*, 1990, **1026**, 225.
33. P. J. R. Spooner, L. C. M. van Gorkom, and A. Watts, *J. Magn. Reson.*, 1990, **90**, 584.
34. P. J. R. Spooner and A. Watts, *Biochemistry*, 1992, **31**, 10129.
35. B. de Kruyff, A. M. H. P. van den Besselaar, and L. L. M. van Deenen, *Biochim. Biophys. Acta*, 1977, **465**, 443.
36. S. R. Johns, D. R. Leslie, R. I. Willing, and D. G. Bishop, *Aust. J. Chem.*, 1977, **30**, 813.
37. R. C. Yashroy, *Indian J. Biochem. Biophys.*, 1987, **24**, 177.
38. R. E. London, T. E. Walker, D. M. Wilson, and N. A. Matwiyoff, *Chem. Phys. Lipids*, 1979, **25**, 7.
39. H. Hauser, W. Guyer, I. Pascher, P. Skrabal, and S. Sundell, *Biochemistry*, 1980, **19**, 366.
40. W. J. Gerritsen, E. J. J. van Zoelen, A. J. Verkleij, B. DeKruijff, and L. L. M. van Deenen, *Biochim. Biophys. Acta*, 1979, **551**, 248.
41. R. J. Cushley and B. J. Forrest, *Can. J. Chem.*, 1979, **57**, 2364.
42. H. Degani, A. Danon, and S. R. Caplan, *Biochemistry*, 1980, **19**, 1626.
43. J. G. Stollery, J. M. Boggs, M. A. Moscarello, and C. M. Deber, *Biochemistry*, 1980, **19**, 2391.
44. B. de Kruijff, A. Rietveld, and C. J. A. van Echteld, *Biochim. Biophys. Acta*, 1980, **600**, 597.
45. H. C. Jarrell, R. Deslauriers, W. H. McGregor, and I. C. P. Smith, *Biochemistry*, 1980, **19**, 385.
46. K. E. Eigenberg, W. R. Croasmun, and S. I. Chan, *Biochim. Biophys. Acta*, 1981, **642**, 438.
47. R. J. Witterbort, C. F. Schmidt, and R. G. Griffin, *Biochemistry*, 1981, **20**, 4223.
48. R. J. Witterbort, A. Blume, T.-H. Huang, S. K. Das Gupta, and R. G. Griffin, *Biochemistry*, 1982, **21**, 3487.
49. A. Blume, R. J. Witterbort, S. K. Das Gupta, and R. G. Griffin, *Biochemistry*, 1982, **21**, 6243.
50. J. Jonas, C.-L. Xie, A. Jonas, P. J. Grandinetti, D. Campbell, and D. Driscoll, *Proc. Natl. Acad. Sci. USA*, 1988, **85**, 4115.
51. A. Blume and R. G. Griffin, *Biochemistry*, 1982, **21**, 6230.
52. A. Makriyannis, D. J. Siminovitch, S. K. Das Gupta, and R. G. Griffin, *Biochim. Biophys. Acta*, 1986, **859**, 49.
53. L. S. Lepore, J. F. Ellena, and D. S. Cafiso, *Biophys. J.*, 1992, **61**, 767.
54. J. F. Ellena, L. S. Lepore, and D. S. Cafiso, *J. Phys. Chem.*, 1993, **97**, 2952.
55. C. R. Sanders II and J. H. Prestegard, *J. Am. Chem. Soc.*, 1992, **114**, 7096.
56. C. R. Sanders II, *Biophys. J.*, 1993, **64**, 171.
57. M. F. Brown, A. J. Deese, and E. A. Dratz, *Methods Enzymol.*, 1982, **81**, 709.
58. M. D. Sefcik, J. Schaefer, E. O. Stejskal, R. A. McKay, J. F. Ellena, S. W. Dodd, and M. F. Brown, *Biochem. Biophys. Res. Commun.*, 1983, **114**, 1048.
59. B. A. Cornell, C. A. Morris, V. L. B. Braach-Maksvytis, and F. Separovic, in *Retinal Proteins*, ed. Yu. A. Ovchinnikov, VNU Science Press, Utrecht, 1987, p. 285.
60. T. Nozawa, M. Nishimura, M. Hatano, H. Hayashi, and K. Shimada, *Biochemistry*, 1985, **24**, 1890.
61. P. L. Yeagle and T. Frye, *Biochim. Biophys. Acta*, 1987, **899**, 137.
62. E. Oldfield, *Biochem. Soc. Trans.*, 1987, **16**, 1.
63. G. H. W. M. Meulendijks, J. W. de Hahn, A. H. J. A. Vos, L. J. M. van de Ven, and H. M. Buck, *J. Phys. Chem.*, 1989, **93**, 3806.
64. S. O. Smith, I. Kustanovich, S. Bhamidipati, A. Salmon, and J. A. Hamilton, *Biochemistry*, 1992, **31**, 11 660.
65. C. W. B. Lee and R. G. Griffin, *Biophys. J.*, 1989, **55**, 355.
66. H. N. Halladay, R. E. Stark, S. Ali, and R. Bittman, *Biophys. J.*, 1990, **58**, 1449.
67. T.-H. Huang, C. W. B. Lee, S. K. Das Gupta, A. Blume, and R. G. Griffin, *Biochemistry*, 1993, **32**, 13 277.
68. W. Guo and J. A. Hamilton, *Biochemistry*, 1993, **32**, 9038.
69. K.-L. Li, C. A. Tihal, M. Guo, and R. E. Stark, *Biochemistry*, 1993, **32**, 9926.
70. J. Salgado, J. Villalain, and J. C. Gomez-Fernandez, *Eur. Biophys. J.*, 1993, **22**, 151.
71. A. S. Arseniev, I. L. Barsukov, V. F. Bystrov, A. L. Lomize, and Yu. A. Ovchinnikov, *FEBS Lett.*, 1985, **186**, 168.
72. A. Yamaguchi, T. Unemoto, and A. Ikegami, *Photochem. Photobiol.*, 1981, **33**, 511.
73. A. J. Weaver, M. D. Kemple, and F. G. Prendergast, *Biophys. J.*, 1988, **54**, 1.
74. G. D. Henry, J. H. Weiner, and B. D. Sykes, *Biochemistry*, 1987, **26**, 3619.
75. F. J. M. van de Ven, J. W. M. van Os, J. M. A. Alen, S. S. Wymenga, M. L. Remerowski, R. N. H. Konings, and C. W. Hilbers, *Biochemistry*, 1993, **32**, 8322.
76. M. Seigneuret, J.-M. Neumann, D. Levy, and J.-L. Rigaud, *Biochemistry*, 1991, **30**, 3885.
77. M. Seigneuret, in *Membrane Proteins: Structures, Interactions and Models*, eds. A. Pullman, J. Jortner, and B. Pullman, Kluwer Academic, Dordrecht, 1992, p. 39.
78. S. Tuzi, K. Shinzawa-Itoh, T. Erata, A. Naito, S. Yoshikawa, and H. Saito, *Eur. Biochem. J.*, 1992, **208**, 713.
79. R. L. Batstone-Cunningham and K. Dill, *Int. J. Biol. Macromol.*, 1984, **6**, 108.
80. S. Weinstein, B. A. Wallace, J. S. Morrow, and W. R. Veatch, *J. Mol. Biol.*, 1980, **143**, 1.
81. B. Cornell, F. Separovic, A. J. Baldassi, and R. Smith, *Biophys. J.*, 1988, **53**, 67.
82. T. G. Oas, C. J. Hartzell, T. J. McMahon, G. P. Drobny, and F. W. Dahlquist, *J. Am. Chem. Soc.*, 1987, **109**, 5956.
83. R. Smith, D. E. Thomas, F. Separovic, A. R. Atkins, and B. A. Cornell, *Biophys. J.*, 1989, **56**, 307.
84. F. Separovic, K. Hayamizu, R. Smith, and B. A. Cornell, *Chem. Phys. Lett.*, 1991, **181**, 157.
85. D. W. Urry, T. L. Trapane, S. Romanowski, R. J. Bradley, and K. U. Prasad, *Int. J. Peptide Protein Res.*, 1983, **21**, 16.
86. D. W. Urry, in *Spectroscopy of Biological Molecules*, eds. C. Sandorfy and T. Theophanides, Reidel, Dordrecht, 1984, p. 511.
87. R. Smith, D. A. Thomas, A. R. Atkins, F. Separovic, and B. A. Cornell, *Biochim. Biophys. Acta*, 1990, **1026**, 161.
88. A. W. Hing and J. Schaefer, *Biochemistry*, 1993, **32**, 7593.
89. S. J. Archer, J. F. Ellena, and D. S. Cafiso, *Biophys. J.*, 1991, **60**, 389.
90. L. P. Kelsh, J. F. Ellena, and D. S. Cafiso, *Biochemistry*, 1992, **31**, 5136.

91. O. B. Peersen, S. Yoshimura, H. Hojo, S. Aimoto, and S. O. Smith, *J. Am. Chem. Soc.*, 1992, **114**, 4332.
92. J. M. Coddington, S. R. Johns, R. I. Willing, J. R. Kenrick, and D. G. Bishop, *Biochim. Biophys. Acta*, 1983, **727**, 1.
93. R. Stanislawski and H. Ruterjans, *Eur. Biophys. J.*, 1987, **15**, 1.
94. R. Smith, F. Separovic, F. C. Bennett, and B. A. Cornell, *Biophys. J.*, 1992, **63**, 469.
95. A. J. Weaver, M. D. Kemple, J. W. Brauner, R. Mendelsohn, and F. Prendergast, *Biochemistry*, 1992, **31**, 1301.
96. T. A. Cross and S. J. Opella, *J. Mol. Biol.*, 1982, **159**, 543.
97. K.-J. Shon, Y. Kim, L. A. Colnago, and S. J. Opella, *Science*, 1991, **252**, 1303.
98. P. Tsang and S. J. Opella, *Biopolymers*, 1986, **25**, 1859.
99. B. A. Lewis, G. S. Harbison, J. Herzfeld, and R. G. Griffin, *Biochemistry*, 1985, **24**, 4671.
100. J. L. Bowers and E. Oldfield, *Biochemistry*, 1988, **27**, 5156.
101. E. A. Dratz, W. Gartner, D. Oesterhelt, and W. S. Veeman, *Biophys. J.*, 1983, **41**, 12a.
102. G. S. Harbison, S. O. Smith, J. A. Pardeon, C. Winkel, J. Lugtenburg, J. Herzfeld, R. Mathies, and R. G. Griffin, *Proc. Natl. Acad. Sci. USA*, 1984, **81**, 1706.
103. L. C. P. J. Mollevanger, A. P. M. Kentgens, J. A. Pardeon, J. M. L. Courtin, W. S. Veeman, J. Lugtenburg, and W. J. de Grip, *Eur. J. Biochem.*, 1987, **163**, 9.
104. S. O. Smith, I. Palings, V. Copié, D. P. Raleigh, J. Courtin, J. A. Pardeon, J. Lugtenburg, R. A. Mathies, and R. G. Griffin, *Biochemistry*, 1987, **26**, 1606.
105. F. Creuzet, A. McDermott, R. Gebhard, K. van der Hoef, M. B. Spijker-Assink, J. Herzfeld, J. Lugtenburg, M. H. Levitt, and R. G. Griffin, *Science*, 1991, **251**, 783.
106. M. R. Fischer, H. J. M. de Groot, J. Raap, C. Winkel, A. J. Hoff, and J. Lugtenburg, *Biochemistry*, 1992, **31**, 11038.
107. G. Metz, F. Siebert, and M. Engelhard, *Biochemistry*, 1992, **31**, 455.
108. L. K. Thompson, A. E. McDermott, J. Raap, C. M. van der Wielen, J. Lugtenburg, J. Herzfeld, and R. G. Griffin, *Biochemistry*, 1992, **31**, 7931.

Biographical Sketches

Frances Separovic. *b* 1954. B.A., 1985, Mathematics and Physics, Macquarie University; Ph.D., 1992, Physics, University of New South Wales, Australia. Senior Research Scientist, CSIRO Food Science and Technology. Over 30 publications. Research interests: solid state NMR of membrane systems, NMR theory, membrane structure and dynamics.

Bruce A. Cornell. *b* 1945. B.S., Ph.D., 1974, Physics, Monash University, Australia. Postdoctoral work with Dennis Chapman. Snr. principal research scientist, CSIRO. Director Cooperative Research Centre for Molecular Engineering and Technology. Research specialties: solid state NMR, membrane biophysics.

Membranes: Deuterium NMR

James H. Davis
University of Guelph, Guelph, ON, Canada

1	Introduction	1
2	Membranes: Dynamic Anisotropy and Compositional Heterogeneity	1
3	^{2}H NMR: Probing Orientational Order, Structure, and Dynamics	2
4	Before the Quadrupolar Echo	3
5	Technical Issues and Developments	3
6	Applications	5
7	Conclusion	6
8	Related Articles	6
9	References	6

1 INTRODUCTION

Biological systems are rich in hydrogen nuclei, and the NMR of hydrogen has in many cases yielded beautifully detailed descriptions of molecular structure and dynamics in biology. The abundant isotope of hydrogen, ^{1}H, while possessing a large magnetic moment and, therefore, a significant sensitivity advantage, suffers from the lack of a quadrupolar moment, being a spin-$\frac{1}{2}$ nucleus. Deuterium, with a spin of 1, has a conveniently sized quadrupolar moment, which makes this nucleus a sensitive probe of its environment within the molecule and of the reorientational motions of the molecule in a magnetic field. This more than compensates for what is lost in intrinsic signal sensitivity relative to ^{1}H. In addition, for partially ordered systems such as solids, liquid crystals, and membranes, the high natural abundance and strong magnetic dipole–dipole interactions among ^{1}H nuclei generally result in a broad, featureless, NMR spectrum whose potentially rich information content has been lost. The quadrupolar interaction between the ^{2}H quadrupolar moment and the electric field gradient tensor at the nucleus dominates its NMR spectrum, dipole–dipole interactions even with surrounding ^{1}H nuclei often being negligible. Thus, by selective isotopic labeling with deuterium, one can probe local structural and dynamic details at virtually any site within a biological system.

2 MEMBRANES: DYNAMIC ANISOTROPY AND COMPOSITIONAL HETEROGENEITY

The membranes of living cells, although tremendously varied, show a common basic structure, that of the lipid bilayer. The amphiphilic character of lipid molecules typically results in the presence of excess water, with the formation of thin (4–6 nm) bimolecular films, which serve not only to encapsulate individual cells but also to compartmentalize the interior of the cell (in the case of eukaryotes). The lipid polar headgroups form the two surfaces of the bilayer at the lipid/water interface, while the lipid hydrocarbon chains lie at the interior of the bilayer. The physical properties of the membrane are strongly dependent on its molecular composition. Biological membranes may contain hundreds of chemically distinct lipid molecules, differing in headgroup composition, some of the different classes being phospholipids, glycolipids, sphingolipids, etc. or having different chain compositions, differing in chain length, degree of unsaturation, etc. In addition, the membranes of higher organisms are often rich in sterols, cholesterol in particular for mammalian cells. In fact, the cholesterol content can be as high as 60 mol% of the total lipid fraction of the membrane (where sterols and lipids are considered to form the lipid fraction). Into this already heterogeneous lipid matrix are inserted a wide variety of different protein molecules. Again there are perhaps hundreds of distinct proteins each with specific biochemical or structural functions to perform within the membrane. The proteins' functions are determined by the type of membrane, e.g., photosynthesis in the case of the chloroplast thylakoid membranes, oxidative phosphorylation in the mitochondrial inner membrane, gated ion channels in excitable membranes, absorption of light by rhodopsin in the retinal rod outer segment disk membranes. In addition, both glycolipids and glycoproteins determine cell type specificity and are involved in cell–cell communication and recognition in general. Innumerable biochemical processes occur at the membrane surface and even those occurring within the cell cytoplasm or within the various organelles are mediated or regulated by processes occurring within the membrane. The realization of the fundamental role of membranes in the performance and regulation of cellular biochemical processes has led to widespread interest in the biology, chemistry, and physics of natural and model membrane systems.

Under physiological conditions most natural membranes are in a 'fluid' state, characterized by rapid molecular reorientation and diffusion of both lipid and protein molecules. Due to the bilayer symmetry of the membrane these motions are anisotropic, e.g., lateral diffusion within the plane of the membrane is generally rapid, and the 'flip-flop' of a molecule from one side of the bilayer to the other is very slow. Individual molecular reorientations are also anisotropic: axial diffusion of lipids or proteins about an axis roughly aligned along the bilayer normal is often fast and relatively unrestricted while reorientation of the molecule in the directions perpendicular to the bilayer normal is highly restricted. The fluid membrane is an anisotropic fluid or liquid crystal: the molecules possess orientational order in one dimension but are positionally disordered in two dimensions.

The two characteristics of biological membranes that dominate their physical properties are their compositional heterogeneity and their dynamic anisotropy. Because of the molecular heterogeneity and the highly fluid nature of the membrane, there is an almost total lack of positional order within the bilayer plane. There are some notable exceptions, such as bacteriorhodopsin in the purple membranes of *Halobacterium halobium*,[1] where the proteins can form large two-dimensionally ordered patches. In these cases, diffraction techniques can be used to study the structure of the protein. However, for the typical membrane, diffraction experiments can at best provide only qualitative information on molecular structure, although they can provide a great deal of information

on the phase behavior and long-range structure of many model membrane systems.

The anisotropy in the molecular reorientations within the membrane presents both a challenge and an opportunity for NMR spectroscopy. Because these systems are partially ordered (which leads to the anisotropy in the motions), the second rank tensor spin interactions, such as the magnetic dipole–dipole interaction, the anisotropic part of the chemical shift, and the quadrupolar interaction, dominate the NMR spectrum. This results in broad lines, similar to those observed in solids, that often completely obscure the fine detail potentially available from the isotropic parts of the chemical shifts and the J couplings that have been so valuable in structure determinations of molecules in isotropic solutions. In the case of abundant like nuclei interacting via strong dipole–dipole interactions, as is the case with ^{1}H nuclei of lipids or proteins, the normal spectrum of a fluid membrane will be a largely featureless bump with little or no structural detail. However, the second rank tensor interactions are exquisitely sensitive to the orientation of the molecular segment relative to any local symmetry axis for the motions (typically the bilayer normal or a long molecular diffusion axis), and to the extent of motional averaging perpendicular to that axis. By specific isotopic labeling, and by removing if necessary any strong dipolar coupling to surrounding protons (by proton decoupling), it is possible to use the second rank tensor interactions to probe the local molecular structure, orientation, order, and dynamics. Thus, measurement of the residual part of the quadrupolar interaction for a ^{2}H nucleus in a C–^{2}H bond can yield valuable structural and dynamic details at the labeled position.

3 ^{2}H NMR: PROBING ORIENTATIONAL ORDER, STRUCTURE, AND DYNAMICS

It is the orientation dependence of the electric quadrupolar interaction that permits the study of molecular orientational order, structure, and dynamics by ^{2}H NMR. In the large magnetic fields commonly used in NMR laboratories (i.e., for $B_0 > 1$ T) the ^{2}H quadrupolar interaction is small relative to the Zeeman Hamiltonian. In particular, since the gyromagnetic ratio of deuterium is $\gamma = 6.536\,\text{MHz T}^{-1}$, at a field of 8.5 T the Larmor precession frequency, ν_0, is 55.26 MHz, whereas the deuterium quadrupolar coupling constant for a ^{2}H nucleus in a typical C–^{2}H bond is only 167 kHz. Thus, in the theoretical description of ^{2}H NMR we may treat the quadrupolar Hamiltonian as a small perturbation on the Zeeman Hamiltonian. Of equal importance is the fact that the nuclear dipole–dipole interactions experienced by a ^{2}H nucleus are small compared with the quadrupolar interaction, being of the order of a few kHz for ^{1}H–^{2}H dipolar coupling, and correspondingly weaker for other types of neighboring nuclei (since the ^{1}H gyromagnetic ratio is second only to that of ^{3}H). Finally, the range of ^{2}H chemical shifts is quite small, like that for ^{1}H, being only about 15–20 ppm (about 1 kHz at 8.5 T). For ^{2}H, the quadrupolar Hamiltonian dominates its NMR spectrum and its relaxation behavior, all other contributions being relatively small. Under certain circumstances the dipolar coupling with surrounding ^{1}H nuclei can significantly broaden the ^{2}H spectrum and shorten the transverse relaxation time. In these cases, ^{1}H decoupling can be used either to eliminate or to quantitate and measure this effect. For these reasons, the theoretical description of ^{2}H spectroscopy and relaxation are particularly straightforward. The detailed theoretical analysis has been presented in a number of recent review articles[2–7] and will not be repeated here. However, a brief summary of the principles is appropriate.

The quadrupolar Hamiltonian in the electric field gradient's principal axis system, which is fixed within the molecular segment, can be written

$$\hat{\mathcal{H}}_\text{Q} = \frac{eQ}{2} \sum_{m=-2}^{2} (-1)^m \hat{T}_{2m} F^\text{P}_{2-m} \tag{1}$$

where the electric field gradient (EFG) tensor in its principal axis system is defined by

$$\begin{aligned} F^\text{P}_{2,0} &= \sqrt{\tfrac{3}{2}}eq \\ F^\text{P}_{2,\pm1} &= 0 \\ F^\text{P}_{2,\pm2} &= \tfrac{1}{2}eq\eta \end{aligned} \tag{2}$$

and the second-rank spherical tensors for the spin variables are

$$\begin{aligned} \hat{T}_{2,0} &= \sqrt{\tfrac{1}{6}}[3\hat{I}_z^2 - I(I+1)] \\ \hat{T}_{2,\pm1} &= \mp\tfrac{1}{2}(\hat{I}_z\hat{I}_\pm + \hat{I}_\pm\hat{I}_z) \\ \hat{T}_{2,\pm2} &= \tfrac{1}{2}\hat{I}_\pm^2 \end{aligned} \tag{3}$$

If a transformation from the EFG tensor principal axis system to the laboratory fixed coordinate system is defined by the Euler angles (α, β, γ), then the quadrupolar Hamiltonian is written

$$\begin{aligned} \hat{\mathcal{H}}_\text{Q} = \frac{e^2qQ}{8}[3\hat{I}_z^2 - I(I+1)][(3\cos^2\beta - 1) \\ +\eta\sin^2\beta\cos 2\alpha] \end{aligned} \tag{4}$$

(The angle γ does not appear because the direction of the static laboratory field, $\boldsymbol{B}_0$, defines the z axis only and we are free to choose γ to be zero.) For ^{2}H, which has spin $I = 1$, this leads to the orientation-dependent quadrupolar splitting

$$\omega_\text{Q} = \frac{3e^2qQ}{4\hbar}[(3\cos^2\beta - 1) + \eta\sin^2\beta\cos 2\alpha] \tag{5}$$

If the structural or dynamic symmetry of the system suggests an intermediate coordinate frame, we can interpose a second transformation via a second set of Euler angles (α', β', γ'). In the case of the fluid phase of membranes, this intermediate coordinate system is defined by the local bilayer normal, which is an axis of symmetry for the motions. Because of this

symmetry, the Euler angle α may also be taken to be zero, and we obtain the expression for the average quadrupolar splitting

$$\begin{aligned}\langle\omega_{\mathrm{Q}}\rangle &= \frac{e^2qQ}{4\hbar}(3\cos^2\beta' - 1)\tfrac{1}{2}\langle(3\cos^2\beta - 1) \\ &\quad +\eta\sin^2\beta\cos 2\alpha\rangle \\ &= \frac{e^2qQ}{4\hbar}(3\cos^2\beta' - 1)\tfrac{1}{2}[S_{zz} + \tfrac{1}{3}\eta(S_{xx} - S_{yy})] \quad (6)\end{aligned}$$

where β' is the angle between the bilayer normal and the static magnetic field and where the angular brackets are averages over the molecular motions occurring on the ^{2}H NMR timescale (which is at least loosely defined by the inverse of the residual quadrupolar splitting). This expression also introduces the 'order parameter' tensor, $\mathbf{S}$, at the labeled position.

Rapid molecular reorientation decreases the sizes of the quadrupolar splittings from their static values. If the reorientation is isotropic, the averages in equation (6) are zero and the spectrum collapses to an 'isotropic' singlet. The magnitude of the residual quadrupolar splitting depends, in this fashion, on the orientational averaging present. In the case of partially ordered, anisotropic systems, and in particular for membranes, it depends also on the average orientation of the efg tensor with respect to the local bilayer normal. Since for C–^{2}H bonds the efg tensor at the ^{2}H nucleus is nearly axially symmetric (η is generally in the range 0.01–0.03), and the principal, or z axis of the efg system lies along the C–^{2}H bond, the quadrupolar splitting can be used to determine the orientation of the bond relative to the bilayer normal (there can remain some ambiguity due to the dependence on $\cos^2\beta$, which leads to two solutions with the same splitting for $35^\circ \leq \beta \leq 90^\circ$) (except at the magic angle where the splitting is 0).

Molecular reorientations also affect the 'relaxation' of the spin system to its equilibrium state after the perturbation due to the rf pulses in the NMR experiment. In fact, for ^{2}H, the fluctuations of the quadrupolar Hamiltonian dominate these relaxation processes. The time-dependent quadrupolar Hamiltonian, which can be divided into its static and fluctuating parts,

$$\hat{\mathcal{H}}_{\mathrm{Q}}(t) = \langle\hat{\mathcal{H}}_{\mathrm{Q}}\rangle + [\hat{\mathcal{H}}_{\mathrm{Q}}(t) - \langle\hat{\mathcal{H}}_{\mathrm{Q}}\rangle] \quad (7)$$

describes the recovery of all of the elements of the density operator to their equilibrium values. For ^{2}H, the density operator may be represented by a 3×3 matrix or it may be expanded in terms of a set of nine independent operators, $\hat{\mathcal{Q}}_q$, such that

$$\rho(t) = \sum_q c_q(t)\hat{\mathcal{Q}}_q \quad (8)$$

The solution of the Liouville equation gives the time evolution of the density operator (and of the spin system). For ^{2}H this leads to a set of eight coupled first-order differential equations (the ninth involves the identity operator), which can often be solved analytically. In the Redfield approximation, we can use these equations to define the spin-1 relaxation times: $T_{1\mathrm{Z}}$, for the decay of Zeeman polarization (the spin–lattice relaxation time); $T_{1\mathrm{Q}}$, for the decay of quadrupolar polarization; $T_{2\mathrm{e}}$, the decay of transverse magnetization; and T_{DQ}, the decay of double quantum coherence.[2,6,8] The decay of the fifth coherence, which is zero quantum coherence, is related to the decay of the transverse magnetization.

Careful experimental measurement of the residual quadrupolar splitting and of the relevant relaxation times can lead to an accurate description of local molecular orientation, order, and dynamics.

4 BEFORE THE QUADRUPOLAR ECHO

In 1969 Charvolin and Rigny[9] published their work on the continuous wave broadline NMR study of ^{2}H in mixtures of ^2H_2O and potassium laurate. Among the phases formed by this soap/water lyotropic liquid crystalline system is a lamellar phase which has served as a simple and useful model for the biological membrane. Two years later, Oldfield et al.,[10] applied the same technique to a phospholipid model membrane system formed from chain perdeuterated dimyristoylphosphatidylcholine (DMPC) and ^1H_2O. This study showed the influence of the gel-to-liquid-crystalline phase transition and the effect of cholesterol on lipid hydrocarbon chain mobility, and demonstrated the potential of ^{2}H NMR for the study of molecular order and dynamics in membrane systems. In 1972 the same authors[11] published the results of the first ^{2}H NMR experiments on biological membranes, studying the membranes extracted from *Acholeplasma laidlawii* grown in media supplemented with perdeuterated lauric and palmitic acids. The introduction of pulsed NMR and the Fourier transform did not have a large effect on the quality of the ^{2}H spectra obtained from membrane systems nor on the sensitivity. Nonetheless, the field developed rapidly from this point. Charvolin et al.[12] published their study of chain-perdeuterated potassium laurate in 1973 and, shortly afterwards, Seelig and Seelig[13] published the results of their experiments on a series of specifically deuterated dipalmitoylphosphatidylcholine (DPPC)/water samples. These experiments demonstrated the existence of a 'flexibility gradient' across the bilayer, the chain positions near the lipid/water interface being significantly more ordered than those near the center of the bilayer. Stockton et al.[14] studied the order and dynamics, using both $T_{1\mathrm{Z}}$ and T_2 measurements of deuterium labeled phospholipid and fatty acid probes in egg phosphatidylcholine bilayers, using both sonicated vesicles and multilamellar dispersions. By the end of 1975 numerous studies had been published on the orientational order and dynamics of model membrane systems, demonstrating among other things, the inequivalence of the two hydrocarbon chains of phospholipids,[15] the conformation and dynamics of the phospholipid headgroup,[16] and the differences between the description of chain order given by electron paramagnetic resonance (EPR) spin labels and ^{2}H NMR.[17] In addition, these early studies introduced the use of oriented samples[12,14,18] and demonstrated that the bilayer normal was an axis of symmetry for the motions.

5 TECHNICAL ISSUES AND DEVELOPMENTS

The major experimental difficulty encountered in these early experiments was the combination of the finite receiver dead time and the very broad lines, with the subsequent rapid decay

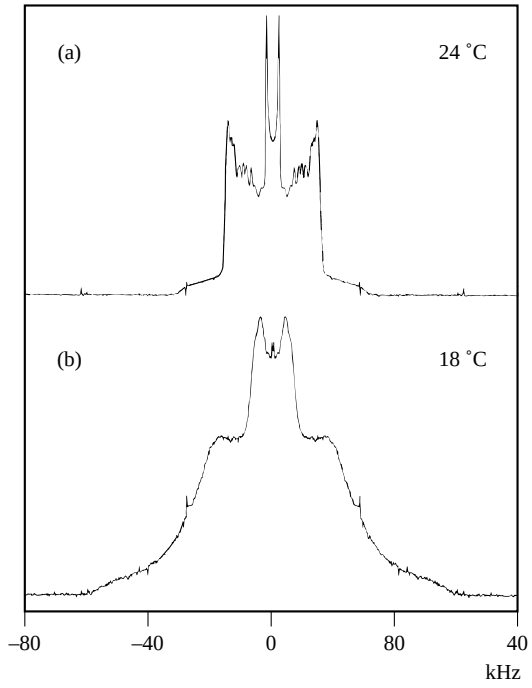

Figure 1 Deuterium NMR spectra of chain-perdeuterated DMPC/water dispersion in (a) the fluid or liquid crystalline phase, and (b) the gel phase, at the temperatures shown. Spectrometer frequency was 55.26 MHz

of the magnetization following a 90° pulse. The FID envelope of a fluid phase powder sample with a width of about 30 kHz will decay to $1\,e^{-1}$ of its initial value within 20 or 30 μs and the receiver dead time at the low frequencies then in use (typically 8–15 MHz) is about the same. This results in a serious distortion of the spectrum which cannot be corrected by phase adjustments.[19] The situation is even more serious for a sample in the gel phase where the quadrupolar splittings from C–^{2}H bonds can be as large as 126 kHz. Thus, the early studies were restricted to membranes and lyotropic liquid crystals in their fluid phases.

The introduction of the quadrupolar echo[19] solved this problem, making it possible to obtain high-quality spectra displaying the true powder pattern lineshape even for lipids in the gel phase[20] (Figure 1). Since the sign of the quadrupolar echo depends on the phase of the first pulse but not on the second, we were able to eliminate ringing from the probe by alternating the phase of the first pulse between 0 and 180°. This was later extended to more complex phase cycling schemes.[3,5] The high fidelity of the lineshapes led to the use of the moments of the spectra for the quantitative description of hydrocarbon chain order. In the fluid phase, the first moment (calculated from the upper half of the symmetrical ^{2}H spectrum) is proportional to the average quadrupolar splitting.[3,20] The liquid-crystalline-to-gel phase transition, which occurs as the sample is cooled, results in a sudden dramatic increase in the quadrupolar splittings, which is reflected in the moments of the spectrum. This led to the use of ^{2}H NMR 'calorimetry' for the study of phase transitions and phase equilibria in lipid/lipid, lipid/sterol, lipid/peptide, and lipid/protein mixtures.[5,6]

The broad lines observed in the gel phase presented two additional spectroscopic challenges. Firstly, the large quadrupolar splittings, ω_Q, were comparable to the amplitude, ω_1, of the rf pulses, leading to substantial distortion of the spectrum. The extent of this distortion can be calculated analytically,[21] and was found to vary strongly with ω_1/ω_Q and with the length of the $\pi/2$ pulse. For undistorted spectra with splittings of 126 kHz, it would be necessary to use $\pi/2$ pulses of 1 μs or less to obtain essentially undistorted spectra. However, by using shorter pulses, which may not correspond to a full $\pi/2$ rotation, it is possible to sacrifice signal-to-noise ratio for improved spectral fidelity. The second challenge arose because of the decay of transverse magnetization during the time between pulses. To avoid the preamp dead times of 20–30 μs one needs to use an echo delay, τ, which is at least of the same magnitude. If the echo decay time, T_{2e}, is comparable, and is a function of orientation (within the powder sample), then the lineshape changes with τ. However, this presents a problem since it is not possible to obtain directly the true lineshape corresponding to $\tau = 0$, but it does, however, provide a method of studying the slow molecular motions that are responsible for the rapid orientation-dependent transverse relaxation in these systems.[22]

The spectra of chain-perdeuterated lipids in the liquid crystalline phase, such as that shown in Figure 1, can provide a description of the distribution of quadrupolar splittings. These spectra consist of a superposition of overlapping powder patterns and the sharp discontinuities corresponding to the 90° orientation allows the measurement of the C–^{2}H bond 'order parameters', S_{C-D}. If the molecules undergo rapid axially symmetric reorientation, the powder pattern lineshapes can be 'de-Paked' to yield the spectrum that would have been obtained from an oriented sample.[23] This allows one to follow more easily the changes in chain order profile that occur as temperature, pressure, sample composition, etc. are varied.

If the spectra are of sufficiently high fidelity and the signal-to-noise ratio is sufficient, it is possible to study the phase behavior of mixed systems using the technique of spectral subtraction.[4,5,24,25] Since a thermodynamic mixture in a two phase coexistence region will consist of domains of different composition, it will be possible to quantitate the partitioning of the system between the different domains provided that the ^{2}H-labeled molecules do not diffuse rapidly between the two types of domains during the spectroscopic timescale, and provided that there is a significant, observable difference between the spectra characteristic of labeled molecules in the two domains. In the case of gel/fluid coexistence regions, the ^{2}H NMR spectra of lipids in fluid and gel phase are dramatically different (see Figure 1), and it is often straightforward to identify two components in the spectra. In this case, by performing pairwise spectral subtractions, one can use the lever rule to determine the end point concentrations of the two phase region.

Perhaps the major remaining experimental limitation to ^{2}H NMR is the low signal-to-noise ratio caused by the small nuclear gyromagnetic ratio of deuterium. Since the signal-to-noise ratio scales as $B_0^{3/2}$, the large superconducting magnets that have become available during the past 20 years have had a tremendous impact on the application of ^{2}H NMR to biological systems. Further increases in magnetic field strength will be especially valuable for ^{2}H NMR of membranes since the spin–lattice relaxation times are short even at high fields and the chemical shift dispersion is very small compared with the quadrupolar splittings observed in membranes. Already it

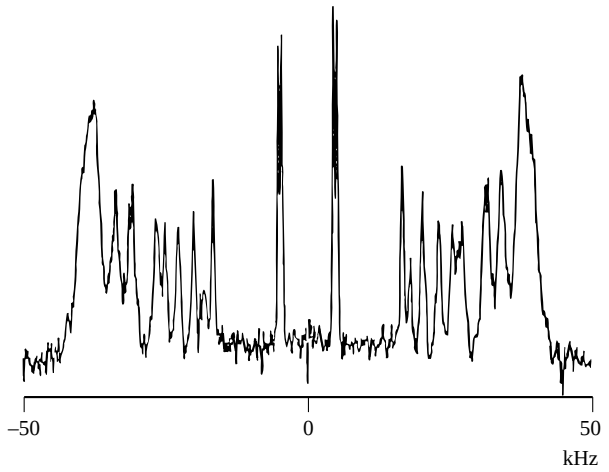

Figure 2 Deuterium NMR spectrum of a single 'sandwich' of approximately 3 mg of chain-perdeuterated dilauroylphosphatidylcholine/water between two thin glass plates with an area of about 1 cm^2. Spectrometer frequency was 55.26 MHz, temperature was 35 °C, and the spectrum was the result of 3000 acquisitions at a repetition time of 0.5 s. The glass plates were oriented with their normal parallel to the external magnetic field

is possible to obtain good spectra from as little as 1 μmol of deuterium, making it possible in some cases to study even natural abundance samples. Finally, techniques for making oriented samples with lipids or mixtures of lipids and other molecules have been perfected, and one can obtain excellent spectra from even a single 'sandwich' of lipid between glass plates, as illustrated by Figure 2.

6 APPLICATIONS

Many of the innovations in the technique of ^{2}H NMR have already been described. A review of all of its applications to membranes would be beyond the scope of this short article. However, it is important to discuss a few selected applications, some of historical significance and some very recent, to show the current state of the field. These have been grouped by system, beginning with simple lipid mixtures and ending with natural membranes.

6.1 Lipid/Water, Lipid/Sterol, and Lipid/Lipid Mixtures

The earliest applications of ^{2}H NMR to model membranes were studies of water: ^2H_2O. Perhaps surprisingly there is still a lot to be learned about the order and dynamics of water in membrane systems. Hence it is still a very active area of research.[26,27] Of particular interest are the effects at low levels of hydration where the role of water in determining lipid headgroup conformation and the overall structure of the phase becomes evident.

The influence of hydrostatic pressure on molecular order and the phase behavior of lipid/water systems has recently been investigated by ^{2}H NMR.[28] Lipid/lipid mixtures also exhibit some very interesting phase behavior. A recent study using ^{2}H NMR difference spectroscopy[29] has determined the phase diagram of mixtures of DMPC/DSPC, where the difference between chain lengths of the two lipids leads to very nonideal mixing.

One of the most important components of biological membranes is cholesterol, which can make up more than 50 mol% of the lipid content of a membrane. ^{2}H NMR difference spectroscopy, combined with other techniques, has helped to elucidate the phase equilibria of DPPC/cholesterol mixtures[25] and to describe the effects of cholesterol on lipid order and dynamics and on the physical properties of the bilayer.[25,30] At high cholesterol concentrations, the system enters a new 'liquid-ordered', or 'β', phase, which seems to be the phase characteristic of natural membranes that are rich in cholesterol, such as the cytoplasmic membranes of mammalian cells.

6.2 Peptide/Lipid Mixtures

^{2}H NMR difference spectroscopy was originally applied to mixtures of a synthetic amphiphilic bilayer spanning peptide in chain-perdeuterated DPPC[31] to determine the phase behavior. The influence of this peptide on lipid chain order and dynamics has been studied extensively by ^{2}H NMR.[32] A similar system, formed from mixtures of the natural channel-forming peptide gramicidin A, has also been investigated by ^{2}H NMR. These studies examined the effect of the peptide on lipid order and dynamics and phase equilibria,[33] and on the structure and dynamics of the peptide itself.[34–36] By exchange labeling the peptide it is possible to study the backbone structure and dynamics through the ^{2}H spectra of the amides. Figure 3 shows a spectrum of exchange-labeled gramicidin A in bilayers of dilauroylphosphatidylcholine (DLPC) oriented between glass plates. The sample contained about 20 mg of exchange-labeled gramicidin and 150 mg of lipid, and the plates were oriented with their normal perpendicular to the static magnetic field. Relaxation measurements, both T_{1Z} and T_{1Q}, were made as a function of the orientation of the glass plates (bilayer normal)

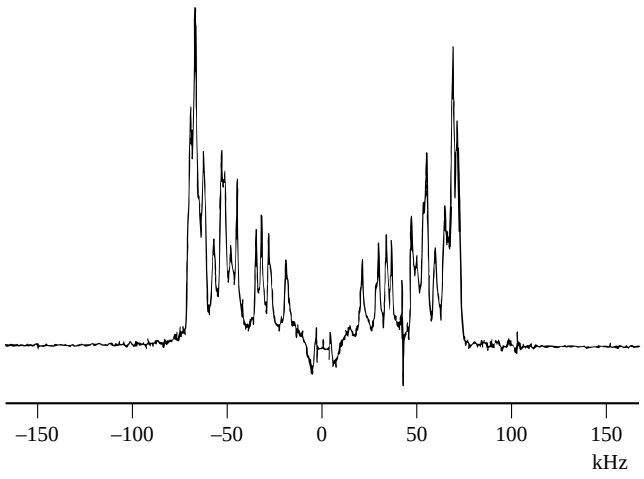

Figure 3 Deuterium NMR spectrum of exchange-deuterated gramicidin D (from *Bacillus brevis*) in DLPC/water oriented between glass plates. Each of the 15 amide positions and the indole positions of the four tryptophan residues are labeled. The spectrum is the result of about 120 000 acquisitions using a repetition time of 0.9 s at a temperature of 65 °C. The glass plates are oriented with their normal perpendicular to the applied magnetic field

with respect to the field. These results led to a model for the reorientation of the peptide within the fluid bilayer wherein gramicidin diffuses axially with a correlation time of about 7 ns and the diffusion axis diffuses perpendicular to the bilayer normal, in an orienting potential, with a correlation time of about 6 μs.[36]

6.3 Protein/Lipid Reconstitutions

The question of the role of lipid diversity in membrane function led to the study of reconstituted protein/lipid mixtures where carefully prepared and purified membrane proteins are reinserted into lipid bilayers of defined composition, often consisting of a single lipid type. The interaction between protein and lipid in these reconstituted membranes had been studied by many techniques, most notably EPR. The EPR results suggested the existence of an 'annulus' of ordered lipid surrounding a protein, and many experiments were designed to study the specificity of this protein/lipid interaction. ^{2}H NMR of labeled lipids was soon applied to these same systems,[37] and it was quickly discovered that these 'boundary' lipids did not reside on the protein surface for long periods of time, i.e., that they readily exchanged with 'bulk' lipids. The different views offered by EPR and NMR were related to the very different spectroscopic timescales of the two techniques.[38–40] An important realization arising from this work was that Nature designs membrane proteins and the lipid composition of the natural membrane to closely match each other so that the incorporation of large quantities of protein does not change dramatically the properties of the bilayer, and so that the properties of the lipid do not adversely affect the function of the protein.

^{2}H NMR studies of protein/lipid interactions and of the phase behavior of protein/lipid mixtures have continued and are qualitatively in agreement with work on the simpler peptide/lipid model systems discussed earlier.[41–43] One of the more interesting, unresolved questions is whether or not the protein/lipid or peptide/lipid mixtures at physiological concentrations are near a critical mixing point.

6.4 Natural Membranes

The ^{2}H NMR spectra of the membranes of *A. laidlawii* grown on specifically deuterated palmitic acids[44] demonstrated that natural biological membranes exhibited the same hydrocarbon chain flexibility gradient as had been observed in fluid-lamellar-phase phospholipid/water dispersions. The incorporation of cholesterol, normally absent in *A. laidlawii* membranes, had a profound influence on the lipid order and suppressed the chain melting transition,[45,46] as was later observed in human erythrocyte ghosts into which either perdeuterated palmitic acid[47] or DPPC[48] had been incorporated. These observations are in agreement with the results of studies of DPPC/cholesterol mixtures[25,30] and suggest that the 'β', or 'liquid ordered' phase is the natural state of the membranes of cells rich in cholesterol. Similar results have been recently reported in a related bacterial system, *Mycoplasma capricolum*.[49]

Comparisons of the inner and outer membranes of *Escherichia coli* grown on deuterated palmitic acids[50,51] were made as a function of temperature in order to investigate the influences of membrane composition on lipid order and dynamics. The differences observed were subtle even though the compositions of the inner and outer membrane were widely different, the most significant difference being the predominance of lipopolysaccharide on the outer leaflet of the outer membrane. The influences of membrane protein on lipid order and conformation were equally subtle, resulting only in modest changes in chain order and small decreases in spin–lattice relaxation time, in agreement with work on reconstituted systems.

These studies, and others, demonstrated that lipid/water dispersions were excellent models of natural membranes, exhibiting the same hydrocarbon chain ordering, the same gel, fluid, and 'β' phases, the same polar headgroup organization,[52] and the same sensitivity to cholesterol.

7 CONCLUSION

Over the past 25 years the application of ^{2}H NMR to membrane systems has changed and expanded dramatically. Its capabilities and potential are greater than ever, and the continued development of more powerful magnets will open up new possibilities. At the present time it is just becoming possible to study the backbone dynamics of membrane-bound peptides and proteins. Improvements in signal-to-noise ratio will make these studies routine in a few years time.

8 RELATED ARTICLES

Amphiphilic Liquid Crystalline Samples: Nuclear Spin Relaxation; Bilayer Membranes: Deuterium and Carbon-13 NMR; Bilayer Membranes: Proton and Fluorine-19 NMR; Deuterium NMR in Solids; Deuteron Relaxation Rates in Liquid Crystalline Samples: Experimental Methods; Gramicidin Channels: Orientational Constraints for Defining High-Resolution Structures; Lipid Polymorphism; Liquid Crystalline Samples: Deuterium NMR; Lyotropic Liquid Crystalline Samples; Membrane Lipids of Acholeplasma laidlawii; Membrane Proteins; Membranes: Carbon-13 NMR; Membranes: Phosphorus-31 NMR; Molecular Motions: T_1 Frequency Dispersion in Biological Systems; Phospholipid–Cholesterol Bilayers; Polymer Dynamics and Order from Multidimensional Solid State NMR; Protein Dynamics from Solid State NMR; Quadrupolar Interactions; Quadrupolar Nuclei in Solids.

9 REFERENCES

1. R. Henderson, J. M. Baldwin, T. A. Ceska, F. Zemlin, E. Beckmann, and K. H. Downing, *J. Mol. Biol.*, 1990, **213**, 899.
2. K. R. Jeffrey, *Bull. Magn. Reson.*, 1981, **3**, 69.
3. J. H. Davis, *Biochim. Biophys. Acta*, 1983, **737**, 117.
4. J. H. Davis, *Chem. Phys. Lipids*, 1986, **40**, 223.
5. J. H. Davis, in *Isotopes in the Physical and Biomedical Sciences*, eds. E. Buncel and J. R. Jones, Elsevier, Amsterdam, 1991, Vol. 2, Chap. 3, p. 199.

6. J. H. Davis, in *Cholesterol in Membrane Models*, ed. L. Finegold, CRC Press, Boca Raton, FL, 1993, Chap. 4, p. 68.
7. R. G. Vold and R. R. Vold, in *Adv. Magn. Opt. Reson.*, 1991, **16**, 85.
8. J. H. Davis, K. R. Jeffrey, and M. Bloom, *J. Magn. Reson.*, 1978, **29**, 191.
9. J. Charvolin and P. Rigny, *J. Phys. (Paris), Colloq.*, 1969, **30**, c4.
10. E. Oldfield, D. Chapman, and W. Derbyshire, *FEBS Lett.*, 1971, **16**, 102.
11. E. Oldfield, D. Chapman, and W. Derbyshire, *Chem. Phys. Lipids*, 1972, **9**, 69.
12. J. Charvolin, P. Manneville, and B. Deloche, *Chem. Phys. Lett.*, 1973, **23**, 345.
13. A. Seelig and J. Seelig, *Biochemistry*, 1974, **13**, 4839.
14. G. W. Stockton, C. F. Polnaszek, L. C. Leitch, A. P. Tulloch, and I. C. P. Smith, *Biochim. Biophys. Res. Commun.*, 1974, **60**, 844.
15. A. Seelig and J. Seelig, *Biochim. Biophys. Acta*, 1975, **406**, 1.
16. H.-U. Gally, W. Niederberger, and J. Seelig, *Biochemistry*, 1975, **14**, 3647.
17. J. Seelig and W. Niederberger, *Biochemistry*, 1974, **13**, 1585.
18. J. Seelig and W. Niederberger, *J. Am. Chem. Soc.*, 1974, **96**, 2069.
19. J. H. Davis, K. R. Jeffrey, M. Bloom, M. I. Valic, and T. P. Higgs, *Chem. Phys. Lett.*, 1976, **42**, 390.
20. J. H. Davis, *Biophys. J.*, 1979, **27**, 339.
21. M. Bloom, J. H. Davis, and M. I. Valic, *Can. J. Phys.*, 1980, **58**, 1510.
22. R. G. Griffin, *Methods Enzymol.*, 1981, **72**, 108.
23. M. Bloom, J. H. Davis, and A. L. MacKay, *Chem. Phys. Lett.*, 1981, **80**, 198.
24. J. C. Huschilt, R. S. Hodges, and J. H. Davis, *Biochemistry*, 1985, **24**, 1377.
25. M. R. Vist and J. H. Davis, *Biochemistry*, 1990, **29**, 451.
26. S. Konig, E. Sackmann, D. Richter, R. Zorn, C. Carlile, and T. M. Bayerl, *J. Chem. Phys.*, 1994, **100**, 3307.
27. F. Volke, S. Eisenblatter, and G. Klose, *Chem. Phys. Lipids*, 1994, **70**, 121.
28. D. A. Driscoll, J. Jonas, and A. Jonas, *Chem. Phys. Lipids*, 1991, **58**, 97.
29. M. R. Morrow, R. Srinivasan, and N. Grandal, *Chem. Phys. Lipids*, 1991, **58**, 63.
30. T.-H. Huang, C. W. B. Lee, S. K. Das Gupta, A. Blume, and R. G. Griffin, *Biochemistry*, 1993, **32**, 13277.
31. J. C. Huschilt, R. S. Hodges, and J. H. Davis, *Biochemistry*, 1985, **24**, 1377.
32. R. S. Prosser, J. H. Davis, C. Mayer, K. Weisz, and G. Kothe, *Biochemistry*, 1992, **31**, 9355.
33. M. R. Morrow and J. H. Davis, *Biochemistry*, 1988, **27**, 2024.
34. R. S. Prosser, J. H. Davis, F. W. Dahlquist, and M. A. Lindorfer, *Biochemistry*, 1991, **30**, 4687.
35. R. S. Prosser, S. I. Daleman, and J. H. Davis, *Biophys. J.*, 1994, **66**, 1415.
36. R. S. Prosser and J. H. Davis, *Biophys. J.*, 1994, **66**, 1429.
37. F. W. Dahlquist, D. C. Muchmore, J. H. Davis, and M. Bloom, *Proc. Natl. Acad. Sci. USA*, 1977, **74**, 5435.
38. E. Oldfield, R. Gilmore, M. Glaser, H. S. Gutowsky, J. C. Hshung, S. Y. Kang, T. E. King, M. Meadows, and D. Rice, *Proc. Natl. Acad. Sci. USA*, 1978, **75**, 4657.
39. A. Seelig and J. Seelig, *Hoppe-Seyler's Z. Physiol. Chem.*, 1978, **359**, 1747.
40. M. R. Paddy, F. W. Dahlquist, J. H. Davis, and M. Bloom, *Biochemistry*, 1981, **20**, 3152.
41. X. Shan, J. H. Davis, J. W. K. Chu, and F. J. Sharom, *Biochim. Biophys. Acta*, 1994, **1193**, 127.
42. A. S. Ulrich, M. P. Heyn and A. Watts, *Biochemistry*, 1992, **31**, 10390.
43. A. Bienvenue, M. Bloom, J. H. Davis and P. F. Devaux, *J. Biol. Chem.*, 1982, **257**, 3032.
44. G. W. Stockton, K. G. Johnson, K. W. Butler, A. P. Tulloch, Y. Boulanger, I. C. P. Smith, J. H. Davis and M. Bloom, *Nature (London)*, 1977, **269**, 267.
45. J. H. Davis, M. Bloom, K. W. Butler, and I. C. P. Smith, *Biochim. Biophys. Acta*, 1980, **597**, 477.
46. M. A. Monck, M. Bloom, M. Lafleur, R. N. A. H. Lewis, R. N. McElhaney, and P. R. Cullis, *Biochemistry*, 1992, **31**, 10037.
47. J. H. Davis, B. Maraviglia, G. Weeks, and D. V. Godin, *Biochim. Biophys. Acta*, 1979, **550**, 362.
48. B. Maraviglia, J. H. Davis, M. Bloom, J. Westerman, and K. W. A. Wirtz, *Biochim. Biophys. Acta*, 1982, **686**, 137.
49. T.-H. Huang, A. J. DeSiervo, and Q.-X. Yang, *Biophys. J.*, 1991, **59**, 691.
50. J. H. Davis, C. P. Nichol, G. Weeks, and M. Bloom, *Biochemistry*, 1979, **18**, 2103.
51. C. P. Nichol, J. H. Davis, G. Weeks, and M. Bloom, *Biochemistry*, 1980, **19**, 451.
52. H.-U. Gally, G. Pluschke, P. Overath, and J. Seelig, *Biochemistry*, 1981, **20**, 1826.

Acknowledgments

I would like to thank the many collegues with whom I have had the pleasure to work in this fascinating field. I would especially like to thank the pioneers, Jean Charvolin, Eric Oldfield, Joachim and Anna Seelig, and Ian Smith, for having opened the doors.

Biographical Sketch

James H. Davis. *b* 1946. Ph.D., 1976, Physics, University of Manitoba, Canada. Began work on deuterium NMR of membranes with Myer Bloom at the University of British Columbia in 1976. Presently Professor of Physics at the University of Guelph (since 1980). Current research interests include the application of solid state NMR—of deuterium, carbon, and protons, both static and using magic angle spinning—to membranes and model membrane systems and molecular dynamics simulations of peptides and lipids in model membranes.

Membranes: Phosphorus-31 NMR

Philip L. Yeagle
University at Buffalo, Buffalo, NY, USA

1	Introduction	1
2	^{31}P NMR in the Asymmetric Environment of Model and Biological Membranes	1
3	Membrane Asymmetry	4
4	Phospholipid Headgroup Conformation and Dynamics	4
5	Phospholipid–Protein Interactions in Membranes	5
6	Membrane Morphology	6
7	Membrane Protein Phosphorylation	7
8	Related Articles	7
9	References	7

1 INTRODUCTION

Phosphorus-31 NMR is a powerful, nonperturbing probe of membrane structure and dynamics, both for model and for biological membranes. Mammalian cell membranes, and most other cellular membranes, contain phospholipids as a major component. Phospholipids each have a phosphate group (or in some cases, more than one) so that the 100% natural abundance of the ^{31}P isotope (and its relatively high sensitivity) can be exploited to explore the properties of phospholipids in membranes from ^{31}P NMR, and, from that, extract information about the membranes themselves.

Phosphorus-31 NMR of membranes has provided considerable information on membrane structure and dynamics since the first ^{31}P NMR spectra of membranes were published.[1–4] The following will provide insight into the system, the lipid bilayer and biological membrane, and will follow with an analysis of the usage of ^{31}P NMR for problem solving. Specific problems will be used as examples of how this approach has been used. The reader is referred to the literature for more detail. Reviews (from which much of the older information in the following discussion is derived) with more extensive literature citations are available.[5–7]

2 ^{31}P NMR IN THE ASYMMETRIC ENVIRONMENT OF MODEL AND BIOLOGICAL MEMBRANES

2.1 Membrane Structure

Much of the function and structure of living cells is determined by the membranes of those cells.[8] As an example, consider the plasma membrane of mammalian cells, which determines the outer boundary of those cells, controls the permeability of solutes into and out of the cell, and pumps essential nutrients in and out of the cell. The plasma membrane contains the receptors that transduce the signals from the outer environment (outside the cell) to the interior of the cell. The plasma membrane anchors the glycoproteins that play roles in cell–cell recognition and the immune response. These and other functions echo throughout the architecture of living cells, with an incredible array of cell membranes supporting basic cell function, cell growth, and cell differentiation.

An understanding of cell membrane structure and function can be gained through a study of the structural components of the membranes. The two most important classes of membrane components are the membrane lipids and the membrane proteins. Much of the attention will be focused on the membrane lipids here because many of them (though not all) contain phosphate as part of their structure, thus making the phospholipids amenable to study by ^{31}P NMR. However, at the end, some consideration will be given to membrane proteins, since it is now possible to obtain ^{31}P NMR spectra of the phosphorylation sites of membrane proteins.

The chemical structure of a phospholipid, phosphatidylcholine, is given in Figure 1. This is an amphipathic molecule. The end consisting of the lipid hydrocarbon chains is highly hydrophobic (many different kinds of hydrocarbon chains are found in nature). The other end of the molecule, consisting of the phosphate and the alcohol (or remainder of the polar headgroup), is polar (many different kinds of headgroups are found in nature). The phosphate, with its negative charge, is located in the polar headgroup of the molecule. Phosphorus-31 NMR therefore reports, most directly, on the behavior of the polar headgroup of the phospholipid.

The lipid bilayer is the fundamental structural component of biological membranes. The lipid bilayer is also spontaneously formed by many phospholipids in aqueous suspension, including phospholipids extracted from cell membranes. In the case where the cross-sectional area of the headgroup is similar to the cross-sectional area of the hydrophobic region of the molecule (the packing ratio, $P_r = A_h/A_c$, where h refers to the headgroup and c refers to the hydrocarbon chain region) $P_r \approx 1$, and the phospholipid shape can be approximated as a cylinder. The hydrophobic effect demands that the hydrophobic region of the phospholipid be sequestered from the water. Packing of the cylinders into a bilayer satisfies the thermodynamics of the hydrophobic effect. Thus the lipid bilayer, which is the fundamental structural element of all cell membranes, is a structure that spontaneously results from the chemical structure of the phospholipid and the hydrophobic effect (see Figure 2). These factors play important roles in the shape of the ^{31}P powder patterns obtained from phospholipid assemblies.

Phosphorus-31 NMR, because of the high natural abundance of the ^{31}P isotope, has been employed to study both model

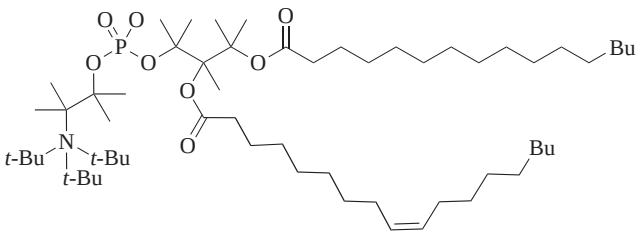

Figure 1 Structure of phosphatidylcholine, a common membrane phospholipid

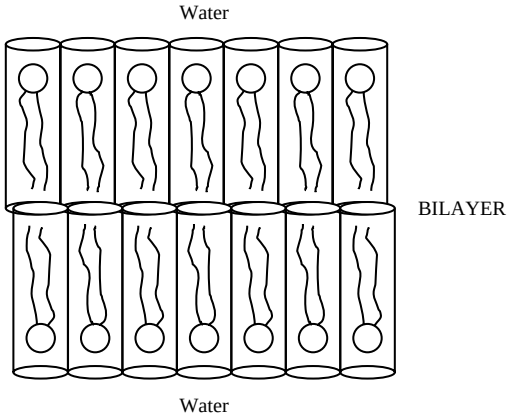

Figure 2 Schematic representation of assembly of phospholipids into bilayers when $P_r = 1$

and biological membranes. Some consideration of the physical structure of these systems is important to an understanding of the ^{31}P NMR powder patterns that are observed in the study of membranes.

The sonicated, unilamellar phospholipid vesicle (SUV) was used extensively in studies of lipid properties in bilayers.[9] The SUVs are surrounded by a single bilayer and are 210–150 Å in diameter. The rotational correlation time for SUV is close to 10^{-6} s. This correlation time is short enough to cause extensive isotropic motional averaging of the elements of the phosphorus chemical shift tensor at most field strengths, and isotropic resonances are normally observed from phospholipids in SUVs, centered on the isotropic chemical shift of the phospholipid in the vesicle.

Another system that gives rise to isotropic chemical shifts is the detergent micelle. In this case the $P_r > 1$. The result is an approximately cone-shaped molecule, which, when packing to satisfy the hydrophobic effect, forms a micelle (roughly spheroid in shape). The isotropic chemical shifts of some of the most common phospholipids (solubilized in detergent) are given in Table 1.[10]

Probably the most common model membrane system to be studied by ^{31}P NMR is the multilamellar liposome (MLV). This is a much larger (than the above mentioned structures) phospholipid assembly, consisting of concentric bilayers of phospholipid and exhibiting diameters of 10 000 Å or more. Rotational correlation times of such structures are in the seconds range. Thus these MLVs do not permit sufficient motional averaging to produce isotropic ^{31}P NMR resonances from the phospholipids.

Biological membranes are usually isolated from tissue or cell suspension and consist of vesicles that are heterogeneous in size. Usually the size of these vesicles leads to rotational correlation times long enough for isotropic motional averaging not to occur. However, it is not unusual for smaller vesicles to form during the isolation procedures. These smaller vesicles have much shorter rotational correlation times than the MLVs, for example, and may produce isotropic resonances in the ^{31}P NMR spectrum. Such vesicles could interfere with the correct interpretation of lineshapes in the ^{31}P NMR spectrum, and the researcher should always be alert to such effects. Usually, electron microscopy or gel filtration chromatography is required to distinguish between the possible interpretations in such situations.

2.2 Characteristic NMR Properties

The membranes of cells describe a largely two-dimensional world, with only a limited third dimension. This structure influences the nature of the ^{31}P NMR spectra obtained from membranes. The lipid components diffuse laterally in the plane of the membrane as long as the membrane is liquid crystalline, except when lateral diffusion is inhibited by membrane proteins. Membrane lipids undergo rapid axial diffusion, usually with the director oriented perpendicular to the membrane surface. Time dependence of the orientation of the director (or wobble) is also observed. Internal motions, associated with rotations about single bonds within the lipid molecule, can often be described by order parameters. However, it should be noted that translational diffusion in the third dimension (perpendicular to the plane of the membrane) is severely restricted by the hydrophobic effect. These properties lead to a membrane structure that is highly anisotropic.

The ^{31}P chemical shift tensor is anisotropic. Measurements of the principal elements of the chemical shift tensor have been made for both simple organic phosphodiesters and phospholipids in dry powders. The results of these measurements are given in Table 2. The full range of the chemical shift tensor is over 200 ppm ($\sigma_{33} - \sigma_{11}$) for phospholipids. In bilayers, rapid axial diffusion leads to a partial motional averaging of the ^{31}P chemical shift tensor. A pseudoaxially symmetric powder pattern is observed, characteristic of phospholipid bilayers (see Figure 3).

2.3 Technical Challenges

The powder patterns that arise from phospholipids in bilayers (that do not undergo rapid isotropic rotational diffusion) can easily be distorted due to instrumental conditions during accumulations of the FIDs. Inadequate ^{1}H decoupling is one source of such distortions that can lead to loss of the characteristic edges of the powder patterns and incorrect interpretations in static systems. The static ^{1}H–^{31}P dipolar interaction is of the order of 6 kHz.[11] However, in the liquid crystalline state, rapid axial diffusion partially motionally averages the ^{1}H–^{31}P interactions, so ^{1}H decoupling in the liquid crystalline state is rarely a serious problem.

The most common source of spectral distortions arises from instrumental artifacts common on non-solid-state spectrometers. The powder patterns obtained from model and biological membranes are broad. As a result the decay of the signal in the time domain from these powder patterns is rapid. Instrumental limitations often lead to a loss of the early portion of the FID, which contains the most crucial information for defining the spectral shape and intensity of the ^{31}P NMR powder pattern. As a result, most ^{31}P NMR powder patterns reported from membranes contain distortions. The broader the component, the more likely the 'loss' of that component from the transformed spectrum. Thus broad, motionally restricted, components in ^{31}P NMR spectra are easily missed. This problem can be rectified, at least in part, by using a fully phase-cycled Hahn echo.[12]

Another problem can arise from alteration in the T_2 relaxation in the ^{31}P powder pattern. An alteration in T_2, which is observed when the bilayer is perturbed (such as in the presence of membrane proteins)[13] will change the shape of the ^{31}P

Table 1 Principal values of the ^{31}P Shielding Tensor of Some Phospholipids and Phospholipid Constituents Relative to 85% H_3PO_4[a]

	σ_{11}	σ_{22}	σ_{33}	Temp. (°C)
A. Phospholipid constituents				
Urea phosphoric acid				
crystal	−26.6	−2.5	44.6	20
powder	−24	−5	45	20
Phosphoethanolamine				
crystal	−67	−13	69	25 ± 5
powder	−63	−8	65	25 ± 5
	−63	−8	72	−72
Serine phosphate				
crystal	−48	−2	51	25 ± 5
powder	−46	−3	52	25 ± 5
	−42	1	61	−110
Glycerol phosphate	−63	5	44	25 ± 5
	−63	5	44	−100
Barium diethylphosphate				
crystal	−75.9	−17.5	109.8	20
powder	−79	−19	113	20
	−80	−22	108	−110
B. Phospholipids				
DPPC				
anhydrous	−98	−34	134	20
monohydrate	−81	−25	108	25 ± 5
	−87	−25	119	25 ± 5
	−81	−25	110	20
50% (by wt.) H_2O	−81	−21	108	−110
DMPC				
anhydrous	−97	−34	133	20
monohydrate	−81	−22	110	20
DPLC				
anhydrous	−96	−32	133	20
monohydrate	−79	−19	108	20
DPPE				
anhydrous	−85	−14	87	25 ± 5
	−81	−20	105	25 ± 5
	−83	−21	103	20
50% (by wt.) H_2O				
pH = 5.4	−81	−22	104	−110
pH = 10.8	−80	−21	104	−110
DLPE (anhydrous)	−84	−23	100	20
DSPA (anhydrous)	−40	−4	48	25 ± 5
PS (anhydrous)	−80	−20	112	25 ± 5

[a]From Seelig.[7] DPPC = dipalmitoylphosphatidylcholine; DMPC = dimyristoylphosphatidylcholine; PS = phosphatidylserine.

Table 2 ^{31}P Chemical Shifts of Phospholipids[a]

Species	Chemical shift from external 85% H_3PO_4 (ppm) in cholate
PC	+0.65
PI	+0.40
lyso PC	+0.15
PS	+0.12
PE	+0.000
SM	+0.00
CL	−0.31
PG	−0.43
PA	−3.8

[a]From London and Feigenson.[10] PC = phosphatidylcholine; PI = phosphatidylinositol; PS = phosphatidylserine; PE = phosphatidylethanolamine; SM = sphingomyelin; CL = cardiolipin; PG = phosphatidylglycerol; PA = phosphatidic acid.

NMR powder pattern. In some cases, an idealized lineshape has been reported which is incorrect (because of alteration of T_2 by the membrane proteins), but is observed because the early portion of the FID is missed in the data collection.

In the case of large MLVs and high magnetic fields, another 'distortion' of the ^{31}P powder pattern can be observed. This is due to orientation of the MLV in the magnetic field. Under these conditions, certain orientations become favored, and thus the ^{31}P powder pattern, which is only a summation of the relative populations of the possible orientations and the chemical shifts associated with those orientations, will change, reflecting the favored orientations in the magnetic field.[14]

2.4 Relaxation

Considerable progress has been made in the understanding of relaxation in ^{31}P NMR of membranes, but that understanding

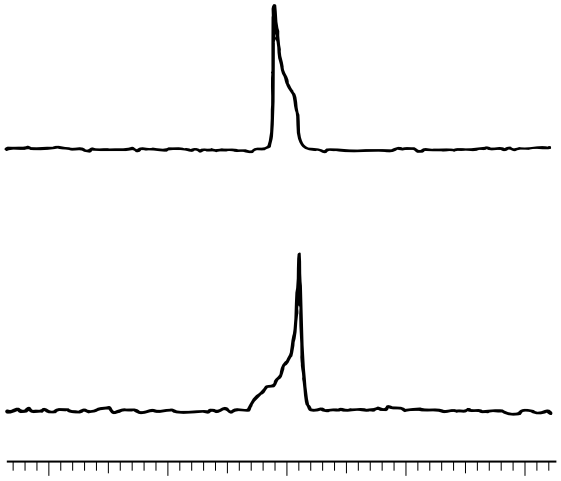

Figure 3 Phosphorus-31 NMR spectra of phospholipid assemblies. Bottom: bilayer; top: H_{II} phase

is as yet incomplete. In principle, the spin–lattice relaxation of the phosphorus can be represented as:

$$\frac{1}{T_{1(\text{obs})}} = \frac{1}{T_{1(\text{DD})}} + \frac{1}{T_{1(\text{CSA})}} \qquad (1)$$

where DD refers to dipolar interactions with protons and CSA refers to relaxation due to a time-dependent modulation of the chemical shift anisotropy. The available data suggest that at low fields, the first term is dominant[15] and at higher fields, the latter term becomes dominant.[16] As will be described below, the effective correlation times for the phosphate motion are around 1 ns. At some field strengths and temperatures, this means that T_1 relaxation is in the fast motion regime ($\omega_0\tau_c < 1$), or liquid-like when the membranes are liquid crystalline, yet the ^{31}P NMR spectra show powder patterns, which are solid-like. Thus, the researcher must carefully choose techniques from both high-resolution NMR and solid state NMR when studying ^{31}P NMR of membranes.

Given that the membranes give rise to ^{31}P powder patterns due to the ordered environment of the membrane, a valid question is whether the T_1 is anisotropic across the powder pattern. Such anisotropy has not been observed at low fields, because lateral diffusion of phospholipids through the orientations represented by the powder pattern is rapid. The latter was determined by saturation transfer experiments utilizing DANTE sequences.[17] At high fields, some anisotropy is observed, where CSA relaxation dominates.[16]

Since T_1 can be measured in both SUVs and in MLVs, the question was raised of whether relaxation was any different in these two systems. While T_2 relaxation was most assuredly different in the two membrane systems, T_1 was not found to be significantly different.

3 MEMBRANE ASYMMETRY

3.1 Phospholipid Vesicles

Because SUVs produce high-resolution ^{31}P NMR spectra, distinguishable resonances are observed for many of the phospholipids (by headgroup class) in SUVs. These vesicles are impermeable to cations. Therefore, the water-soluble shift reagent species of the lanthanide series can be selectively placed on one side of the vesicle membrane or the other. The lanthanides will alter the chemical shift of the ^{31}P NMR resonance from the phospholipid phosphates that they can contact through a scalar interaction. It is thus possible to alter selectively the isotropic chemical shift of the resonance from the phospholipids that inhabit the side of the membrane to which the lanthanide has access. With this technique, the resonance due to phospholipids in the inner leaflet of the vesicle membrane is separated from the resonance due to phospholipids in the outer leaflet of the vesicle membrane.[18] A number of such studies have been reported and in some cases the distribution of phospholipid classes across the membrane is not uniform.[19–21]

3.2 Potential Use of Magic Angle Spinning (MAS)

Magic angle spinning introduces the factor $(3\cos^2\theta - 1)$ which, when the sample is at an angle of about 54.7° with respect to the external magnetic field, leads to averaging of CSA when the spinning is rapid compared with the breadth of the chemical shift tensor. Magic angle spinning ^{31}P NMR of unsonicated MLVs leads to isotropic resonances and some ability to distinguish individual phospholipid classes based on their respective isotropic chemical shifts.[22] It is possible that this technology might be useful in the study of phospholipid asymmetry in biological membranes.

4 PHOSPHOLIPID HEADGROUP CONFORMATION AND DYNAMICS

4.1 Phospholipid Bilayers

Information on phospholipid headgroup conformation was obtained by exploiting the nuclear Overhauser effect (NOE) arising from the ^{1}H–^{31}P dipolar interactions. At low field, the ^{1}H–^{31}P dipolar interactions are relatively strong, due to the dominance of the dipolar interactions in the spin–lattice relaxation. These interactions were explored to determine which protons were most effective in relaxing the phosphorus. A pre-two-dimensional NOE study was performed with a variable frequency proton decoupling field, and the *N*-methyl protons of the phosphatidylcholine headgroup were found to be major contributors to the relaxation of the phosphorus.[23] This result led to the conclusion that the phospholipid headgroup was oriented parallel to the membrane surface. The NOE data also made clear that the phospholipid headgroups were engaging in intermolecular headgroup interactions, because, for example, the spin–lattice relaxation for the phosphate in phosphatidylethanolamine in mixed phosphatidylethanolamine/phosphatidylcholine bilayers was determined by dipolar interactions with the phosphatidylcholine *N*-methyl protons.

A combination of ^{31}P NMR and ^{2}H NMR powder pattern data were used to assign phospholipid headgroup conformation by an independent method. The conclusion was the same as in the NOE studies.[7] These intermolecular interactions could be disrupted by cholesterol.

^{31}P NMR powder patterns from membranes are a result of the anisotropic structure of the lipid bilayer. The dominant motion of the phospholipids that determine the ^{31}P lineshapes is axial diffusion in the bilayer. The director for axial diffusion is ordered. Therefore, the effect of phospholipid motion in the membrane on the ^{31}P NMR lineshape can be described, to a first approximation, by application of a rotation matrix to the chemical shift tensor of the phosphorus. Such axial rotation leads directly to the axially symmetric powder pattern observed in the ^{31}P NMR spectra from phospholipid bilayers. However, the width of the powder pattern in the liquid crystalline state is less than that predicted from simple rotation of the ^{31}P chemical shift tensor. The simplest model to explain the observed powder pattern adds a time-dependence of the director for axial diffusion, or wobble, to the motion.[24]

The NOE studies also indicated that the dominant correlation time for the phospholipid phosphate was about 1 ns, because the ^{31}P{^{1}H} NOE was motionally limited in its magnitude.[15] This evaluation of correlation time was confirmed by later studies in which the T_1 relaxation was measured as a function of temperature. It was noted that at higher temperatures the ^{31}P nuclei in the phospholipid phosphates were behaving as if they were in the fast motion regime. Temperature provided a means of varying the dynamics of the system through thermally induced motion, moving from the fast motion regime toward the slow motion regime. A plot of T_1 as a function of temperature revealed a minimum.[25] This unambiguously determined a correlation time of about 1 ns for phosphate dynamics.

4.2 Effects of Gel–Liquid-Crystalline Phase Transition

When the phospholipid bilayer undergoes a phase transition from the liquid crystalline state to the gel state, the molecular dynamics change. This change is reflected in the ^{31}P lineshapes. Predictable increases in the breadth of the powder pattern are observed due to the motional restriction in the gel state.[26] In cross-polarization ^{31}P NMR spectra, distinctive lineshape changes occur as the headgroups 'freeze' into the gel state.[27] These data show that the headgroups behave somewhat independently of the hydrocarbon chains, as the 'melting' temperatures for motion in the headgroups are different from those in the hydrocarbon chains.

4.3 Effects of Ions

Ion binding to the phospholipid headgroups can cause changes in the ^{31}P NMR spectra. Cations can cause a shift of the ^{31}P phosphate resonance.[21] Changes in headgroup conformation can also be induced by cations and are reflected in the ^{31}P powder pattern observed from negatively charged phospholipid phosphates.[28]

4.4 Effects of the Radius of Curvature

The size of the phospholipid assembly will often influence the ^{31}P NMR lineshape, since isotropic tumbling of small radii of curvature particles will lead to motional averaging of the chemical shift tensor. This has been explicitly measured using a variety of sized vesicles and measuring the lineshapes.[29] In the case of small vesicles, increasing the viscosity of the medium to reduce the tumbling rate of the vesicles can create a situation in which the motional averaging due to lateral diffusion around the surface of the vesicle can be measured. The diffusion coefficient obtained from such measurements agrees well with the diffusion coefficient obtained from measurements in MLVs by independent techniques.[30]

5 PHOSPHOLIPID–PROTEIN INTERACTIONS IN MEMBRANES

5.1 Perturbations of Membrane Bilayer Properties by Proteins

At this point it is necessary to introduce the other major component of membranes, the membrane proteins. Of particular interest here are the integral, transmembrane proteins that have a portion of their mass integrated into the lipid bilayer. The question that has been of interest for many years is whether any of the phospholipids of the bilayer have specific interactions with the membrane proteins that have functional consequences. Although this has been a field of considerable controversy in the past, today there can be little doubt that at least some proteins have phospholipid binding sites that are specific for particular phospholipid structures. Among these are glycophorin, cytochrome oxidase, adenosine 5′-triphosphate–adenosine 5′-diphosphate (ATP–ADP) exchange protein, and the phospholipases.

5.2 Motionally Restricted Phospholipid Domains

The case of glycophorin is illustrative. A component of phospholipid is found bound to glycophorin when it is isolated from the erythrocyte membrane. This phospholipid is enriched with phosphatidylinositol.[31] Other researchers have shown that the state of phosphorylation of this specifically bound phosphatidylinositol controlled the affinity of glycophorin for the membrane skeleton of the erythrocyte.[32] Since ^{31}P NMR can in principle be sensitive to all the phospholipids in a sample, ^{31}P NMR should be able to reveal something of the dynamics of the phospholipids bound to glycophorin. Recent experiments have examined the properties of the phospholipids tightly bound to glycophorin by reconstituting the glycophorin with only the tightly bound phospholipids bound into a glycolipid bilayer. The ^{31}P NMR spectrum therefore arose only from the tightly bound phospholipids. The powder pattern obtained was an axially symmetric powder pattern, but much broader than that from pure phospholipid bilayers. It was concluded that the phospholipids bound to the protein were undergoing rotational diffusion with the protein in the membrane.[33]

Another example can be found in the ATP–ADP exchange protein from mitochondria. This protein requires cardiolipin for activity. Recent ^{31}P studies revealed that cardiolipin is tightly bound to this enzyme. Only the action of a strong detergent, like sodium dodecyl sulfate is capable of disrupting these phospholipid–protein interactions.[34]

5.3 Phospholipid Exchange Between Domains

Since membrane proteins, in some cases, create a distinguishable domain of motionally restricted phospholipids in membranes, one must ask whether there is exchange between the bound phospholipids and those of the surrounding phospholipid bilayer. In the case of glycophorin, the tightly bound phospholipids apparently exchange only slowly with the glycolipids. For the calcium pump protein of sarcoplasmic reticulum, the exchange rate was measured using magnetization transfer. A rate of 1 s^{-1} was measured.[35] These exchange rates are slow, but no slower than phospholipid exchange between nonlamellar and lamellar phases in the same sample.

5.4 Reconciliation of ^{31}P NMR Data with Other Magnetic Resonance Data

Deuterium NMR experiments with deuterated phospholipids have not shown a component of motionally restricted phospholipid in the presence of membrane proteins. An important question is how to reconcile those results with the ^{31}P NMR results. This is understood in terms of protein motion in the membrane. Correlation times for protein axial diffusion in the membrane are of the order of 10^{-4} to 10^{-5} s. Motion on this timescale has been shown to cause artificial attenuation of the spectral intensity for ^{2}H NMR of deuterated lipids. This is the result of a fast decaying echo in the solid echo experiment used for the ^{2}H NMR experiments.[36] As a specific example, rhodopsin was reconstituted with a specifically deuterated phospholipid. In the ^{31}P NMR spectrum two overlapping powder patterns were observed, one due to motionally restricted phospholipid interacting with the protein. With ^{2}H NMR of the same sample, only one spectral component was observed, that due to the normal phospholipid bilayer surrounding the protein.[37] Thus ^{2}H NMR is not a good technique to probe properties of lipids interacting with membrane proteins, as any tightly bound lipids will be invisible in the ^{2}H NMR spectrum. However, at least in some cases, ^{31}P NMR is sensitive to the bound phospholipid component.

6 MEMBRANE MORPHOLOGY

As indicated above, the lamellar (bilayer) phase gives rise to characteristic ^{31}P NMR powder patterns (see Figure 3). These powder patterns are the result of motional averaging of the ^{31}P chemical shift tensor. The dominant motion in the lipid bilayer influencing the shape of the bilayer powder pattern is axial diffusion about a director approximately perpendicular to the membrane surface (which is further modulated by a wobble of the director). It would be expected that in phospholipid assemblies with different structures and different modes of motion available, that the powder patterns might be different. The hexagonal II (H_{II}) phase provides an example.

6.1 ^{31}P NMR of Hexagonal II Phase

The H_{II} phase is a nonlamellar phase that is readily formed by some biological phospholipids, including phosphatidylethanolamine. The H_{II} phase consists of tubes, each containing a small aqueous channel, with the phospholipid headgroups directed inward toward the aqueous channel. The hydrocarbon chains are directed toward the exterior of the tubes. The tubes of the H_{II} phase are stacked with the hydrocarbon surfaces of the tubes in close apposition. These cylinders are small in diameter. Typically the diameter of the aqueous channel is 20–30 Å. With a common diffusion coefficient for lateral diffusion of 10^{-8} cm^2 s^{-1}, circumnavigation of the cylinder occurs with a correlation time of about 10^{-6} s. This is sufficiently rapid to introduce an additional degree of motional averaging of the chemical shift tensor. All other things being equal, this motional averaging produces a lineshape with half the breadth of the bilayer powder pattern and with an apparent reversal of the lineshape (see Figure 3). The older literature on this subject has been reviewed.[38] Much work was done, utilizing the ability of ^{31}P NMR to determine readily the extent of lamellar and H_{II} phase structures in a sample, to characterize the factors that regulate the L_α–H_{II} phase transition.

Current interest in this subject has focused on the observation of intermediate structures on the pathway of the L_α–H_{II} phase transition (this subject has been recently reviewed[39]). These can be seen as part of the phase diagram of some mixtures of phospholipids that undergo the L_α–H_{II} phase transition. These intermediate structures appear as isotropic resonances in the ^{31}P NMR spectra and are not detected in X-ray diffraction of these samples, pointing to the usefulness of ^{31}P NMR. Freeze fracture electron microscopy of these samples reveals that the isotropic ^{31}P resonances arise from interlamellar attachments made of phospholipids. In some systems, these intermediates are the result of the initiation of membrane fusion, and thus have been studied with ^{31}P NMR to obtain clues as to the intermediates on the membrane fusion pathway.

6.2 NMR of Isotropic Phases

The above discussion has already introduced the topic of isotropic ^{31}P NMR resonances from phospholipid dispersions. One means of obtaining an isotropic ^{31}P NMR resonance is to create a phospholipid assembly sufficiently small that isotropic tumbling of the assembly can average the expression of the ^{31}P chemical shift tensor. The SUV is one example. Another example is provided by the intermediate structures just described. Here the movement of the phospholipid phosphate through an angle of 90° on the surface of the intermediate structure is sufficiently rapid to average the expression of the chemical shift tensor. Another example is provided by the cubic phase.[40] Trivial examples are seen in the case of solution phase phospholipids (such as in methanol/chloroform) and in detergent micelles.

6.3 Domains and the Exchange of Lipids between Domains

The ^{31}P NMR spectra of phospholipid dispersions with complex morphology can produce overlapping powder patterns characteristic of each of the phases present. The simultaneous observations of powder patterns from as many as three different structures (for example, lamellar, H_{II}, and isotropic) are commonly observed. These observations suggest that exchange

between these structures is slow. Using magnetization-transfer ^{31}P NMR, this question was explicitly addressed and the conclusion reached that exchange between the structures was slow on the seconds timescale.[41]

7 MEMBRANE PROTEIN PHOSPHORYLATION

All of the above discussion focused on the phospholipid component of biological membranes, exploiting the power of ^{31}P NMR and the naturally occurring phosphorus in the phosphate of every phospholipid. There is another location for phosphorus in biological membranes. Phosphorus is found on some membrane proteins when these membrane proteins have been phosphorylated by cellular kinases. Phosphates can be found on serine, threonine, and tyrosine, depending upon the particular kinase that is active. In principle, it should be possible to probe these phosphorylation sites with ^{31}P NMR. Since these sites are attached to membrane proteins, their motion would be expected to be severely restricted. Therefore MAS ^{31}P NMR was used to search for resonances due to protein phosphorylation sites. Recent experiments using this approach demonstrated the ability to visualize phosphorylation sites on the membrane protein rhodopsin.[22] Chemical shift dispersion may prove to be sufficient to distinguish different sites of phosphorylation, according to class of kinase activity.

8 RELATED ARTICLES

Chemical Shift Tensors; Glycolipids; Lipid Polymorphism; Liquid Crystalline Samples: Deuterium NMR; Liquid Crystalline Samples: Diffusion; Magic Angle Spinning; Membrane Lipids of Acholeplasma laidlawii; Membrane Proteins; Membranes: Carbon-13 NMR; Membranes: Deuterium NMR; Phospholipid–Cholesterol Bilayers; Phosphorus-31 NMR; Sideband Analysis in Magic Angle Spinning NMR of Solids; Slow and Ultraslow Motions in Biology; Sonicated Membrane Vesicles.

9 REFERENCES

1. R. W. Barker, J. D. Bell, G. K. Radda, and R. E. Richards, *Biochim. Biophys. Acta*, 1972, **260**, 161.
2. A. F. Horwitz and M. P. Klein, *J. Supramol. Struct.*, 1972, **1**, 19.
3. D. G. Davis and G. Inesi, *Biochim. Biophys. Acta*, 1972, **282**, 180.
4. M. P. Sheetz and S. I. Chan, *Biochemistry*, 1972, **11**, 4573.
5. P. L. Yeagle, in *Biological Magnetic Resonance*, eds. L. J. Berliner and J. Reuben, Plenum, New York, 1990, Vol. 9, p. 1.
6. P. L. Yeagle, *Acc. Chem. Res.*, 1978, **11**, 321.
7. J. Seelig, *Biochim. Biophys. Acta*, 1978, **515**, 105.
8. P. L. Yeagle, in *The Membranes of Cells*, 2nd edn. Academic Press, San Diego, 1993.
9. C.-H. Huang, *Biochemistry*, 1969, **8**, 344.
10. E. London and G. W. Feigenson, *J. Lipid Res.*, 1979, **20**, 408.
11. S. I. Chan, D. F. Bocian, and N. O. Peterson, in *Membrane Spectroscopy*, ed. E. Grell, Springer, New York, 1981, Vol. 31, p. 91.
12. M. Rance and R. A. Byrd, *J. Magn. Reson.*, 1983, **52**, 221.
13. P. L. Yeagle, *Biophys. J.*, 1981, **37**, 227.
14. J. Seelig, F. Borle, and T. A. Cross, *Biochim. Biophys. Acta*, 1985, **814**, 195.
15. P. L. Yeagle, W. C. Hutton, C.-H. Huang, and R. B. Martin, *Proc. Natl. Acad. Sci. USA*, 1975, **72**, 3477.
16. M. P. Milburn and K. R. Jeffrey, *Biophys. J.*, 1989, **56**, 543.
17. B. de Kruijff, P. R. Cullis, and A. J. Verkleij, *Trends Biochem. Sci.*, 1980, **5**, 79.
18. V. F. Bystrov, Y. E. Shapiro, A. V. Viktorov, L. I. Barsukov, and L. D. Bergelson, *FEBS Lett.*, 1972, **25**, 337.
19. D. M. Michaelson, A. F. Horwitz, and M. P. Klein, *Biochemistry*, 1973, **12**, 2637.
20. A. Chrzeszczyk, A. Wishnia, and C. S. Springer, Jr., *Biochim. Biophys. Acta*, 1977, **470**, 161.
21. W. C. Hutton, P. L. Yeagle, and R. B. Martin, *Chem. Phys. Lipids*, 1977, **19**, 255.
22. A. D. Albert, J. S. Frye, and P. L. Yeagle, *Biophys. Chem.*, 1990, **35**, 27.
23. P. L. Yeagle, W. C. Hutton, C.-H. Huang, and R. B. Martin, *Biochemistry*, 1977, **16**, 4344.
24. S. J. Kohler and M. P. Klein, *Biochemistry*, 1977, **16**, 519.
25. L. K. Tamm and J. Seelig, *Biochemistry*, 1983, **22**, 1474.
26. R. F. Campbell, E. Meirovitch, and J. H. Freed, *J. Phys. Chem.*, 1979, **83**, 525.
27. J. Frye, A. D. Albert, B. S. Selinsky, and P. L. Yeagle, *Biophys. J.*, 1985, **48**, 547.
28. P. R. Cullis and B. De Kruyff, *Biochim. Biophys. Acta*, 1976, **436**, 523.
29. E. E. Burnell, P. R. Cullis, and B. De Kruijff, *Biochim. Biophys. Acta*, 1980, **603**, 63.
30. P. R. Cullis, *FEBS Lett.*, 1976, **70**, 223.
31. I. M. Armitage, D. L. Shapiro, H. Furthmayr, and V. T. Marchesi, *Biochemistry*, 1983, **16**, 1317.
32. R. A. Anderson and V. T. Marchesi, *Nature (London)*, 1985, **318**, 295.
33. P. L. Yeagle and D. Kelsey, *Biochemistry*, 1989, **28**, 2210.
34. K. Beyer and M. Klingenberg, *Biochemistry*, 1985, **24**, 3821.
35. B. S. Selinsky and P. L. Yeagle, *Biochim. Biophys. Acta*, 1985, **813**, 33.
36. H. W. Spiess and H. Sillescu, *J. Magn. Reson.*, 1981, **42**, 381.
37. A. D. Albert, S. A. Lane, and P. L. Yeagle, *J. Membrane Biol.*, 1985, **87**, 211.
38. P. R. Cullis and B. De Kruijff, *Biochim. Biophys. Acta*, 1978, **507**, 207.
39. P. L. Yeagle, in *Cell Lipids: From Synthesis to Cell Biology*, ed. D. Hoekstra, Academic Press, New York, 1994, Vol. 40.
40. L. T. Boni and S. W. Hui, *Biochim. Biophys. Acta*, 1983, **731**, 177.
41. D. B. Fenske and P. R. Cullis, *Biochim. Biophys. Acta*, 1992, **1108**, 201.

Biographical Sketch

Philip L. Yeagle. *b* 1949. B.A., 1971, Ph.D., 1974, Physical Chemistry, Duke University, USA. Postdoctoral work at University of Virginia (with R. B. Martin and C. Huang). Currently Professor of Biochemistry, University at Buffalo, NY. Approx. 100 publications and five books. Current research specialties: NMR of membranes and proteins, cholesterol, membrane fusion, photoreceptor structure and function, intermediate filament structure and function.

Nucleic Acid Flexibility and Dynamics: Deuterium NMR

Regitze R. Vold

University of California, San Diego, CA, USA

1	Introduction	1
2	Deuterium Quadrupole Echo Spectra of Poly- and Oligonucleotides	2
3	Deuterium Relaxation Measurements and Rates of Internal Motion	4
4	Summary	5
5	Related Articles	5
6	References	5

1 INTRODUCTION

This article summarizes what has been learnt up to 1994 about the internal flexibility and motion of DNA and RNA from NMR studies of solid poly- and oligonucleotides. Although in vivo high molecular weight nucleic acids, such as ribosomes, nucleosomes, and viruses, are often found in environments that are more solid-like than liquid-like, relatively few—30+ at last count—NMR studies of solid nucleic acids have been published. Of these, only half are concerned with the internal dynamics, but the results accumulated so far are of basic interest as a test of theories of biopolymer motion. They are also useful to practitioners of high-resolution NMR structural studies of oligonucleotides and nucleic acid/protein complexes because they complement the structural data obtained from X-ray diffraction studies with information about rates and amplitudes of internal motion.

So far the major tools for obtaining information about the dynamics of nucleic acids have been ^{2}H and, to a lesser extent, ^{31}P NMR lineshape simulations and relaxation measurements. DiVerdi and Opella[1] reported the first deuterium quadrupole echo spectra of high molecular weight DNA. Their nearly full width powder spectra of calf thymus DNA labeled at the purine C-8 positions suggested that the base pairs are quite immobile at 20 °C, but a drop in quadrupole echo intensity at 50 °C indicated the onset of librational motion at this temperature. Subsequently James and co-workers[2,3] obtained similar wide spectra of solid poly(I)·poly(C) deuterated at inosine C-8, but a short spin–lattice relaxation time T_1 clearly indicated the presence of small angle librational motion. In addition, the quadrupole echo decay time T_{2e} was observed to drop with increasing humidity, to a point where the ^{2}H quadrupole echo spectrum would vanish completely and then reappear as a single line only after a regular solution state was achieved. Apparently, some slow, large angle dynamic process set in as the polynucleotide absorbed water.

Phosphorus solid state NMR spectroscopy was initially used for studies of DNA backbone conformation by Shindo et al.[4] and Nall et al.,[5] who observed little internal motion at moderate humidities, but the onset of large angle, slow motion above 90% relative humidity (RH). Opella and co-workers also used ^{31}P solid state NMR spectroscopy to illustrate the absence of large angle motion in chromatin,[6] in viral DNA,[7,8] and viral RNA.[9] More recently, two-dimensional ^{15}N and ^{13}C NMR spectroscopy has been used in studies of high molecular weight DNA,[10,11] but here the emphasis was solely on structural elucidation.

When most of the water bound to nucleic acids is removed, the regular helical structure distorts.[12] The resulting disorder, and its reversibility upon exposure of dry DNA to moisture, has been documented by ^{2}H NMR studies of oriented samples of Li-DNA.[13] The extent of water uptake, w, as a function of atmospheric humidity is shown in Figure 1 for both Na-DNA, which takes the A-form below 85% RH, and Li-DNA, which retains a regular B-form down to 50% RH. As also illustrated in Figure 1, the hydration of DNA has a strong effect on the ^{31}P spin–lattice relaxation times as first demonstrated in 1983 for high molecular weight calf thymus DNA. Mai et al.[14] showed that the phosphate backbone of completely dry (lyophilized) DNA is quite rigid, and that the amplitude of backbone motion increases continuously, if not uniformly, as the water content of the material is increased from 0 to 33 mol of water per nucleotide. Figure 1 shows that the ^{31}P spin–lattice relaxation rate R_1 increases by a factor of roughly 500-times as 20 mol of water is absorbed, and an R_1 maximum observed at 90% RH shows that some motional process with an *effective* correlation time of 10^{-9} s is present at this level of hydration, which corresponds to a point where Na-DNA has

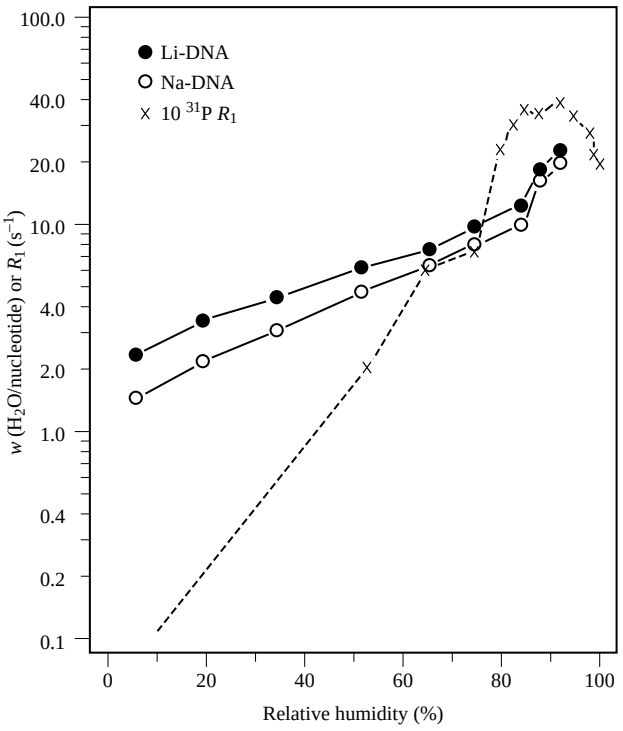

Figure 1 Water content, w, of Na-DNA (○) and Li-DNA (●) as a function of relative humidity (% RH). The water uptake by the two salts is quite similar, but Na-DNA undergoes a transition from the B- to the A-form as the humidity is reduced below 85% RH while Li-DNA retains the B-form until ca. 20% RH. The ^{31}P spin–lattice relaxation rate (×10) for calf thymus DNA (Na salt) measured by Mai et al.[14] is included to show the dramatic effect of hydration on the extent of internal motion in DNA

changed from the A- to the B-form. On the basis of the ^{31}P lineshapes, the authors concluded that this motion involved twisting of the DNA molecule by at least 30° about the helix axis, quite likely corresponding to torsional modes[15,16] observed in optical studies of DNA in solution.

A ^{31}P spectral lineshape analysis was undertaken in 1985 by Fujiwara and Shindo,[17] and their results basically agreed with the conclusions of Mai et al.[14] The mode of motion found to influence the spectra most strongly at high humidity (92% and 98% RH), was confirmed as rotation about the helix axis with a rate of $1-5 \times 10^4$ s^{-1}, and the onset of this motion presumably leads to the breakup of the fiber structure as interstitial water permits individual helices to rotate relative to one another.

Deuterium NMR studies of polynucleotides began in earnest in the mid-1980s with studies by Shindo et al.[18] and by Vold and Kearns and their co-workers,[19,20] while the Drobny group[21,22] focused on the dynamics of oligonucleotides. The deuterium work, summarized below, was aimed at elucidating the nature of the librational motion of the base pairs and the conformational flexibility of the sugar moieties at humidities below 98% RH. A review by Alam and Drobny[22] should be consulted for details. Since that review was published in 1991, two papers on deuterium relaxation and internal motion in poly- and oligoribonucleotides have appeared[23,24] which document the higher rigidity of solid RNA compared with DNA. For comparison with relaxation and molecular dynamics of nucleic acids in solution, two reviews by James[25] and Lane[26] are available.

2 DEUTERIUM QUADRUPOLE ECHO SPECTRA OF POLY- AND OLIGONUCLEOTIDES

The resonance frequency of a deuteron in a solid material is a function of the quadrupole coupling constant χ and the asymmetry parameter η of the quadrupole coupling tensor; of the orientation relative to the external magnetic field of an X–D bond (X = C, N, or O); and of the amplitude and rate of any motion of this bond. For C-8 deuterated base pairs in nucleic acids, the relevant quadrupole coupling parameters have been determined to be $\chi = 179 \pm 1$ kHz, $\eta = 0.07 \pm 0.01$ from quadrupole echo spectra of very dry DNA[19] and suitable, 'rigid' model nucleosides.[27] The principal component of the quadrupole coupling tensor, χ_{zz}, is very nearly collinear with the bond and if no motion occurs the two deuterium transitions can be observed at

$$\nu_{\pm} = \pm\tfrac{3}{4}\chi\left[\tfrac{1}{2}(3\cos^2\beta - 1) + \frac{\eta}{2}\sin^2\beta\cos\gamma\right] \qquad (1)$$

where $\beta = \beta_{lp}$ and $\gamma = \gamma_{lp}$ are the Euler angles relating the orientation of the principal axis system of the quadrupole coupling tensor (p) in a coordinate system (l) fixed in the laboratory and defined by the direction, z_l, of the magnetic field. The angles β_{lp} and γ_{lp} are illustrated in Figure 2 for a deuteron in the C-8 position of an idealized GC base pair. The lineshape of the deuterium NMR spectrum of a 'rigid' solid sample may be calculated from equation (1) by summing contributions from all possible values of β and γ.

Deuterium powder spectra of calf thymus DNA recorded as a function of humidity[2,18,19] showed that hydration results

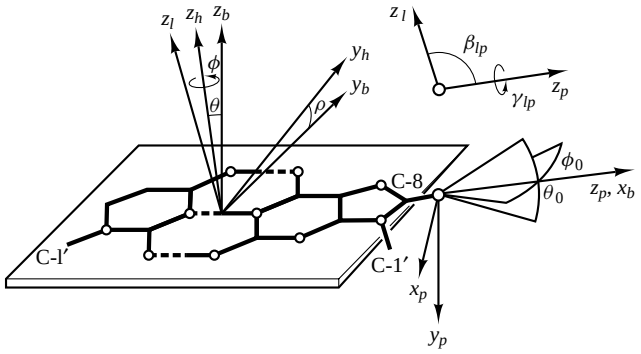

Figure 2 Four coordinate systems, l for laboratory, h for helix, b for base pair, and p for the principal axis system of the deuterium quadrupole coupling tensor, are necessary for describing the orientation and internal motion of the base pairs in nucleic acids. Specifically shown are the Euler angles relating the orientation of the deuteron quadrupole coupling tensor to the magnetic field direction along z_l. Also included are the tilt (θ), roll (ρ), and twist (ϕ) angles for the base pairs, and the amplitudes of libration, θ_0 and ϕ_0 used to model the librational motion of base pairs relative to the helix orientation

in small, but unmistakable changes in the apparent χ and η. In order to account for these changes, a model of C–D bond libration in two orthogonal planes, one containing the base pair and one containing the helix axis and the C–D bond, was introduced. With the additional assumption of uniform distribution of θ and ϕ within the ranges $-\theta_0 \leq \theta \leq \theta_0$ and $-\phi_0 \leq \phi \leq \phi_0$ (see Figure 2), the deuterium frequencies in B-form DNA with $\langle\theta\rangle = 90°$ and $\langle\theta\rangle = 0°$ is still given by equation (1), but with *effective* quadrupole coupling parameters

$$\chi_{\text{eff}} = \frac{\chi}{4}\left[1 - \eta - (3+\eta)\frac{\sin 2\theta_0}{2\theta_0}\right] \qquad (2)$$

and

$$\eta_{\text{eff}} = -\frac{\sin 2\phi_0}{2\phi_0}\cdot\frac{(\eta-1) + (3+\eta)\sin 2\theta_0/2\theta_0}{3(\eta-1) - (3+\eta)\sin 2\theta_0/2\theta_0} \qquad (3)$$

and $\beta = \beta_{lh}$ and $\gamma = \gamma_{lh}$ defining the orientation of the two planes in the laboratory frame. A typical ^{2}H quadrupole echo spectrum of partially hydrated B-form Li-DNA is presented in Figure 3 together with theoretical spectra (dashed and dotted curves) calculated[19] according to equations (1)–(3). Comparison of the experimental and calculated spectra show that the librational amplitudes at 66% RH are $\theta_0 = 8 \pm 2°$ and $\phi_0 = 12 \pm 2°$.

The librational amplitudes in purine C-8-deuterated DNA were determined more accurately as a function of humidity from ^{2}H quadrupole echo spectra of C-8-deuterated, folded, oriented films of calf thymus DNA.[13] The spectra of a 75% RH Li-DNA sample oriented with the helix axis parallel with [Figure 4(a), $\beta_{lh} = 0°$] and perpendicular to [Figure 4(b), $\beta_{lh} = 90°$] the magnetic field are shown in Figure 4. Simulations of such spectra[13] show that the purine C-8–D bond is oriented at $90 \pm 1°$ from the helix axis and that the samples are quite well ordered with a Gaussian distribution in helix and/or base pair orientation of less than 9° when $w \geq 6$. The results of fitting the spectra to yield amplitudes of motion are shown in

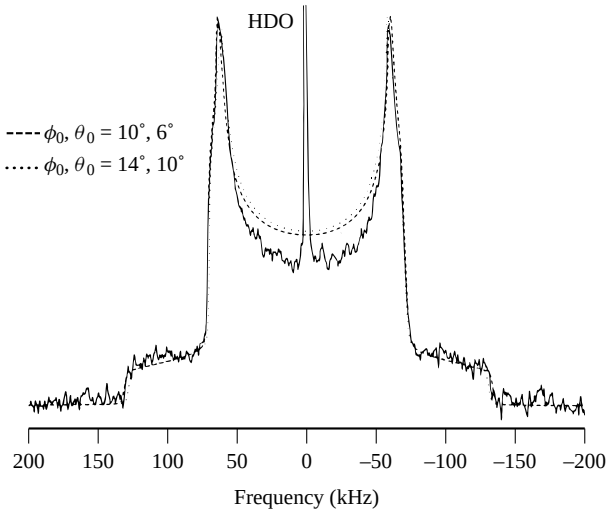

Figure 3 Deuterium quadrupole echo NMR spectrum of calf thymus Li-DNA (5.9% excess LiCl). The spectrum (with T_1 = 200 ± 10 ms, T_{2e} = 250 ± 50 μs) was obtained at 38.4 MHz, 25 °C and 66% RH[19] from 64 000 quadrupole echoes using an 8-step phase cycled sequence $\pi/2_x$, τ, $\pi/2_y$, τ, acq with a $\pi/2$ pulse length of 2.0 μs and τ = 30 μs. A 2 kHz Gaussian line-broadening function was used for signal-to-noise enhancement. Superimposed on the experimental spectrum are two simulations calculated as described in the text according to equations (2)–(4) with libration amplitudes that define the uncertainty (±2°) in fitting the experimental spectra. The discrepancy between experimental and calculated spectra intensity near the center arises because the spectra were calculated without including transverse relaxation, and the 'spike' near ν = 0 arises from natural abundance ^{2}H in normal water

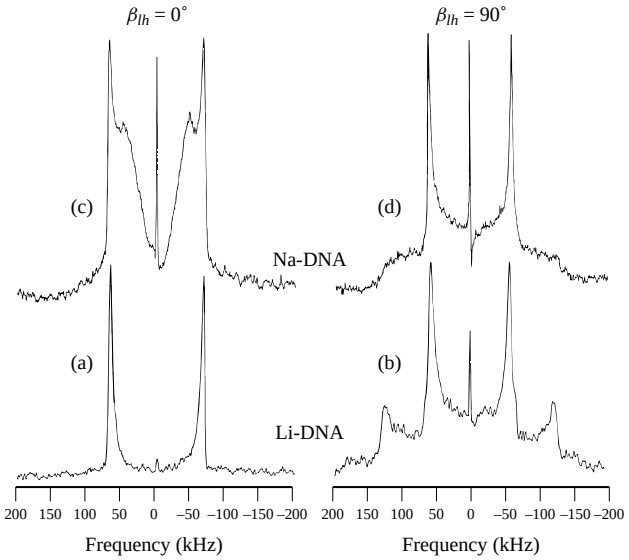

Figure 4 Deuterium quadrupole echo spectra of oriented folded films of the Li salt [(a) and (b)] and Na salt [(c) and (d)] of calf thymus DNA obtained at 75% RH and otherwise under conditions as described for Figure 3, except that 1 kHz line broadening was applied to (a), (c), and (d). Spectra (a) and (c) were recorded with the helix axis parallel to the magnetic field, while in (b) and (d) the helix axis was perpendicular to the field. The number of transients required was (a): 70 000; (b): 280 000; (c): 112 000; and (d): 190 000

Figure 5. Below w = 13 H_2O/nucleotide (84% RH) neither libration angle exceeds ±15°, and the amplitude of the twist motion is slightly larger than that of the tilt motion. Also shown in Figure 4 [(c) and (d)] are the ^{2}H spectra of oriented Na-DNA. The spectra show[28] that the bulk of the sample has the expected A-form and the angle between the C–D bond and the helix is 67 ± 1°, also with a Gaussian distribution of 9° in the helix and/or base pair orientation. However, some of the DNA is present in the B-form. This component shows up in the X-ray diffraction patterns only as diffuse background scattering, because this component is dispersed and nondiffracting.

Above 85% RH, w increases rapidly (see Figure 1), and the spectral signal-to-noise ratio worsens because the quadrupole echo dephases rapidly. This shortening of T_{2e}, from 400 μs to less than 100 μs at high humidities, shows that a slow motion with an effective correlation time $\tau_c \sim 10^{-6}$–10^{-4} s is present, in agreement with the earlier ^{31}P results.[14] Shindo et al.[18] explored the effects of higher humidity (92% RH) on the deuterium lineshapes of oriented B-form samples of Na-DNA, and established that T_{2e} is much longer at β_{lh} = 0° than at other helix orientations. This implies that the slower motion responsible for the short T_{2e} takes place in a plane perpendicular to the helix axis, and their simulations suggested that at 92% RH the amplitude of this torsional motion is on the order of 60°. As even more water is absorbed, the DNA fibers begin to dissolve and complete reorientation about the helix axis takes place.

Deuterium quadrupole echo spectra obtained by Drobny and co-workers[22] of selectively deuterated samples of the dodecamer duplex [d(CGCGAATTCGCG)]$_2$ present a similar

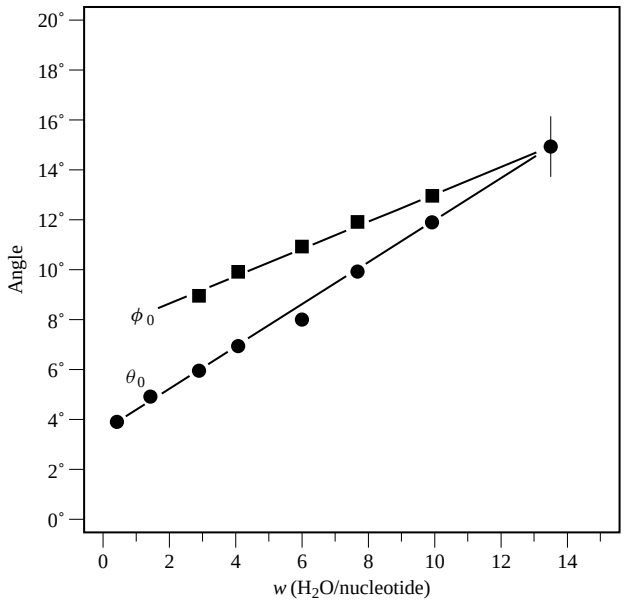

Figure 5 Amplitudes of libration θ_0 (circles) and ϕ_0 (squares) plotted as a function of water content and obtained by fitting spectra of macroscopically oriented Li-DNA fibers[13] such as those shown in Figure 4. The experimental uncertainty in the amplitudes is ≤1°

picture of the internal motion in nucleic acids. Nearly full width powder patterns were observed below $w \sim 10$ for several base labeled isotopomers and a four-site jump model, corresponding to libration with increasing amplitude in two orthogonal directions, could account for the data in the lower hydration range. Above $w \sim 10$ (>80% RH) the echo intensity

was observed to drop and the lineshapes indicated the influence of large angle restricted rotation about the helix axis with rotational correlation times on the order of 10 μs, just as was found for highly hydrated high molecular weight DNA. The spectra of a methyl deuterated dodecamer were found to be particularly informative because of the better signal-to-noise ratio associated with having six deuterons per molecule and a spectrum narrowed by rapid methyl rotation. Thus, an isotropic peak was observed in the thymidine CD_3 spectra above 90% RH, as complete, nearly isotropic reorientation of the short (aspect ratio 1.7) dodecamer set in.

Spectra obtained by Huang et al.[29] for a dodecamer sample deuterated in the C-2′ position (2″-*d*) of adenosines 5 and 6 support the analysis of the base pair data. The intrinsic asymmetry parameter η is very small for aliphatic deuterons, and since the spectra remain nearly cylindrically symmetric below 88% RH, the small angle libration of the 2″ deuteron responsible for spectral narrowing must be uniaxial as well. Lineshapes obtained between 80% and 92% RH showed that the only large angle motion was that of overall molecular reorientation about the helix axis. In particular, Huang et al.[29] found no evidence for fast ($>10^3$ s^{-1}) 2′-*endo* to 3′-*endo* conformational exchange of the furanose ring.

3 DEUTERIUM RELAXATION MEASUREMENTS AND RATES OF INTERNAL MOTION

Information about the rate of the librational motion in solid nucleic acids has been obtained from ^{2}H spin–lattice relaxation measurements on Na and Li salts of calf thymus DNA[20,30] and synthetic poly-[24] and oligo-[23] ribonucleotides. As shown in Figure 6 for the polymers, R_1 grows steeply with hydration, paralleling the increase observed for ^{31}P R_1,[14] and the motion responsible for this increased relaxation efficiency must be the small angle libration described above. It is quite clear from the data in Figure 6, and similar measurements on oligonucleotides,[23] that the internal motion in RNA provides a less efficient relaxation mechanism than in DNA. As pointed out by Wang et al.,[23] this difference is matched in the solution relaxation behavior of oligoribo- and deoxyribonucleotides. At this point it is not entirely clear whether this is due to a smaller amplitude or a lower rate of motion in RNA. The relaxation rate associated with small angle libration is roughly proportional to the square of the amplitude of the motion, and calculated relaxation rates are therefore very sensitive to small changes in spectral splittings, which are hard to detect in powder spectra with limited signal-to-noise ratios. The libration in poly(G)·poly(C) was also observed to be slightly less effective in relaxing the C-8 deuterons than in poly(A)·poly(U) and poly(I)·poly(C), possibly because of the triple hydrogen bond reducing any propeller motion of the base pairs, but the difference is barely outside the experimental uncertainty of the measurements.

The frequency dependence of the spin–lattice relaxation rate in Li-DNA illustrated in Figure 6 proves that the librational motion observed below 84% RH is characterized by effective correlation times longer than approximately 1 ns. Treating this restricted motion as a diffusional process with a Lorentzian spectral density function yields a rotational diffusion constant $D \sim 10^6$ s^{-1}. However, the ratio, R_1(38.4 MHz)/R_1(76.8 MHz)

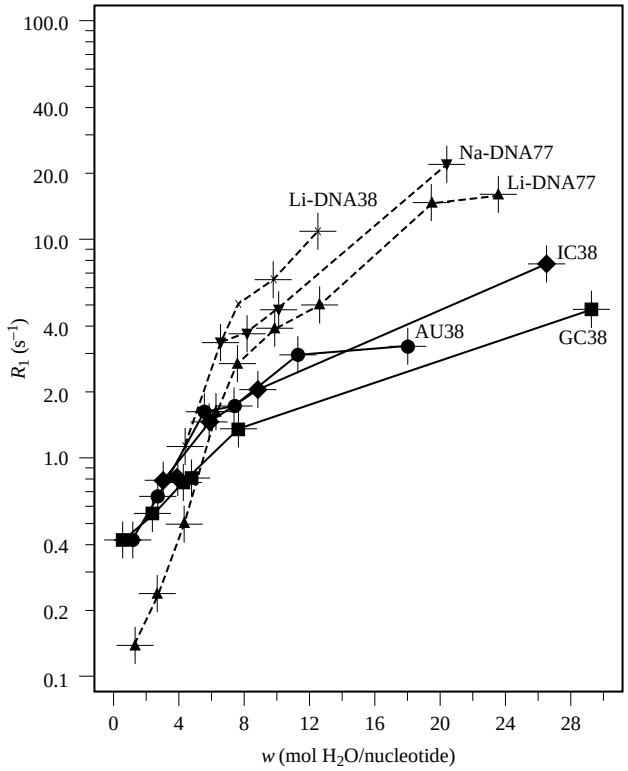

Figure 6 Spin–lattice relaxation rates R_1 of Li- and Na-DNA and three synthetic polyribonucleotides, poly(A)·poly(U), poly(G)·poly(C), and poly(I)·poly(C), measured at 76.8 and 38.4 MHz and plotted as a function of water content, w. The relaxation rates were measured at the perpendicular edges of the powder patterns by the 'saturation–recovery' method, i.e. by varying the recycling delay between individual quadrupole echo pulse sequences.[19,24] It should be noted that the recovery curves were always slightly nonexponential as expected from overlapping transitions and T_1 anisotropy. The water content was determined gravimetrically, and below w = 5–6 systematic errors in w may be present because the dehydrated polymers absorb water very quickly

~ 2 observed between data obtained at 5.9 T and 11.8 T shows that a diffusional process, which predicts a value of four for this ratio, cannot account for the relaxation data. Further insight into the nature of this motion has been gained from measurements[20] of the individual spectral densities, $J_1(\omega_0)$ and $J_2(2\omega_0)$, of the librational motion. The quantities $J_1(\omega_0)$ and $J_2(2\omega_0)$ were obtained using the Jeener–Broekaert pulse sequence[31] from measurements of the rate of recovery of Zeeman order R_{1Z} (equal to the familiar spin–lattice relaxation rate, R_1) and the rate of decay of quadrupolar order R_{1Q} according to the expressions[32]

$$R_{1Z} = \frac{3\pi^2}{2}\chi^2[J_1(\omega_0) + 4J_2(2\omega_0)] \quad (4a)$$

$$R_{1Q} = \frac{9\pi^2}{2}\chi^2 J_1(\omega_0) \quad (4b)$$

Spectral density data obtained for samples of Li-DNA oriented with the helix axis parallel to the magnetic field (β_{lh} = 0°) at 76.8 and 38.4 MHz and presented in Figure 7 show that $J_1(\omega_0)$ is consistently larger than $J_2(2\omega_0)$. This result rules out in-plane, torsional motion about the helix axis as the dominant

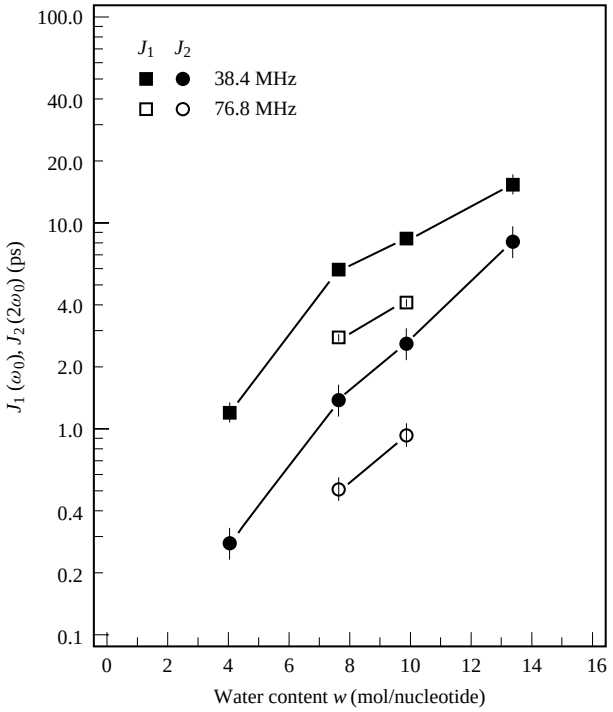

Figure 7 Spectral densities of motion for Li-DNA at 76.8 and 38.4 MHz, $\beta_{lh} = 0°$, 25 °C as a function of water content. The quantities $J_1(\omega_0)$ and $J_2(2\omega_0)$ were determined from R_{1Q} and R_{1Z} in a Jeener–Broekaert experiment

relaxation mechanism[20] below 84% RH, but as the humidity is increased the ratio $J_1(\omega_0)/J_2(2\omega_0)$ drops indicating increasing contributions from torsional motion. Both spectral densities are also seen to be frequency-dependent with $J_2(2\omega_0)$ showing the larger effect of changing field, but the frequency-dependence is too weak to reflect a diffusional process with effective correlation times longer than 1 ns. Instead, it is likely that the $\sim\omega_0{}^{-1}$ frequency-dependence is due to collective bending motions of the polymer as described by Barkley and Zimm[15] and Schurr.[33]

Brandes et al.[19] noted that the ratio of ^{31}P and ^{2}H spin–lattice relaxation times did not change as a function of hydration level in high molecular weight DNA. Similarly, Huang et al.[29] showed that the ratio between deuterium T_1 values for base pair and furanose 2″-deuterons in the oligonucleotide was constant. This strongly suggests that in both poly- and oligomers the relaxation active motions of base pair, sugar, and phosphate backbone are coupled at nearly all levels of hydration. This is an interesting observation because it agrees with a similar conclusion drawn by Holbrook and Kim[34] from a segmental motion analysis of the X-ray data for the dodecamer.

4 SUMMARY

On the basis of deuterium lineshape analysis and relaxation measurements, one can draw the following picture of the dynamics in solid DNA and RNA. In fully dehydrated poly- and oligonucleotides, all internal motion is very highly restricted, amounting to at most 4–6° of very fast libration, since full-width powder patterns are observed and the spin–lattice relaxation times are quite long. For both base pairs and sugar moieties, moderate water uptake is accompanied by librational motion of increasing amplitude, but below $w \sim 10\text{–}15 H_2O$/nucleotide the amplitude does not exceed ca. 15°. The application of different models, such as finite jumps or restricted diffusion, leads to slightly different estimates of this maximum librational excursion, but for all parts of the nucleic acid molecule—base pair, sugar, and phosphate backbone—there is no evidence for fast, large angle, local motion. The base pair motions in poly- and oligonucleotides appear to be very similar and the motion can be modeled as librations of roughly similar magnitude in two planes, parallel and perpendicular to the base pairs. The libration is fast compared to the width of the deuterium spectrum, i.e. $>10^5$ s^{-1}, with significant density near the Larmor frequency. This follows from the observation of a substantial increase in the rates of both ^{2}H and ^{31}P spin–lattice relaxation and the measurement of frequency-dependent relaxation rates for high molecular weight Li-DNA. The observation of a ratio of ca. 2 for T_1 at 38.4 MHz and T_1 at 76.8 MHz shows that this motion cannot be characterized as a simple process with an exponential correlation function. Furthermore, frequency-dependent measurements of the individual spectral densities of motion, $J_1(\omega_0)$ and $J_2(2\omega_0)$, for oriented Li-DNA has proven that the motion dominating the relaxation at humidities below ca. 80% RH is a wobble of the base pair normal, perhaps of the local helix axis, rather than torsional motion about the helix axis. A comparison of relaxation data for deoxyribo- and ribonucleotides showed that the librational motion in RNA is less relaxation-active than in DNA. Whether this is due to a difference in librational amplitude or a difference in rate of motion has yet to be ascertained.

At high humidity the deuterium lineshapes and short T_{2e} values show that a slow dynamic process sets in. The process is characterized by effective correlation times in the 1–100 μs range, and consists of torsional motion, or molecular reorientation, about the helix axis. Finally, as the humidity is increased even more to the point where the sample is a viscous gel-like material, T_{2e} is so short that no deuterium quadrupole echo spectra can be observed, except in the case of the methyl-deuterated dodecamer. The CD_3 spectrum, like the ^{31}P spectra of the polymer, is reduced to an isotropic line, which indicates the onset of large angle fluctuations in all directions as the nucleic acid dissolves. The classification of these fluctuations as either internal or overall motion has yet to be made categorically, but all experimental data obtained so far suggest that heavily hydrated DNA is highly flexible.

5 RELATED ARTICLES

Amino Acids, Peptides and Proteins: Chemical Shifts; Biological Macromolecules: NMR Parameters; Nucleic Acids: Spectra, Structures, and Dynamics.

6 REFERENCES

1. J. A. DiVerdi and S. J. Opella, *J. Mol. Biol*, 1981, **149**, 307.
2. P. Bendel, J. Murphy-Boesch, and T. L. James, *Biochim. Biophys. Acta*, 1983, **759**, 205.

3. T. L. James, P. Bendel, J. L. James, J. W. Keepers, P. A. Kollman, A. Lapidot, J. Murphy-Boesch, and J. E. Taylor, in *Nucleic Acids: The Vectors of Life*, eds. B. Pullman and J. Jortner, Reidel, Dordrecht, Holland, 1983, p. 155.
4. H. Shindo, J. B. Wooten, B. H. Pheiffer, and S. B. Zimmerman, *Biochemistry*, 1980, **19**, 518.
5. B. T. Nall, W. P. Rothwell, J. S. Waugh, and A. Rupprecht, *Biochemistry*, 1981, **20**, 1881.
6. J. A. DiVerdi, S. J. Opella, R.-T. Ma, N. R. Kallenbach, and N. C. Seeman, *Biochem. Biophys. Res. Commun.*, 1981, **102**, 885.
7. J. A. DiVerdi and S. J. Opella, *Biochemistry*, 1981, **20**, 280.
8. T. A. Cross, P. Tsang, and S. J. Opella, *Biochemistry*, 1983, **22**, 721.
9. T. A. Cross, S. J. Opella, G. Stubbs, and D. L. D. Caspar, *J. Mol. Biol.*, 1983, **170**, 1037.
10. S. J. Opella and K. M. Morden, in *Dynamic Properties of Biomolecular Assemblies*, eds. C. S. E. Harding and A. J. Rowe, The Royal Society of Chemistry, Cambridge, UK, 1989, p. 196.
11. P. Tang, R. A. Santos, and G. S. Harbison, *Adv. Magn. Reson.*, 1989, **13**, 225.
12. W. Saenger, in *Principles of Nucleic Acid Structure*, Springer-Verlag, New York, 1984.
13. R. Brandes, R. R. Vold, D. R. Kearns, and A. Rupprecht, *J. Mol. Biol.*, 1988, **202**, 321.
14. M. T. Mai, D. E. Wemmer, and O. Jardetzky, *J. Am. Chem. Soc.*, 1983, **105**, 7149.
15. M. D. Barkley and B. H. Zimm, *J. Chem. Phys.*, 1979, **70**, 2991.
16. S. A. Allison and J. M. Schurr, *Chem. Phys.*, 1979, **41**, 35.
17. T. Fujiwara and H. Shindo, *Biochemistry*, 1985, **24**, 896.
18. H. Shindo, Y. Hiyama, S. Roy, J. S. Cohen, and D. A. Torchia, *Bull. Chem. Soc. Jpn.*, 1987, **60**, 1631.
19. R. Brandes, R. R. Vold, R. L. Vold, and D. R. Kearns, *Biochemistry*, 1986, **25**, 7744.
20. R. Brandes, R. R. Vold, D. R. Kearns, and A. Rupprecht, *Biochemistry*, 1990, **29**, 1717.
21. A. Kintanar, W.-C. Huang, D. C. Schindele, D. E. Wemmer, and G. Drobny, *Biochemistry*, 1989, **28**, 282.
22. T. M. Alam and G. P. Drobny, *Chem. Rev.*, 1991, **91**, 1545.
23. A. C. Wang, M. A. Kennedy, B. R. Reid, and G. P. Drobny, *J. Am. Chem. Soc.*, 1992, **114**, 6583.
24. P. Tsang, D. R. Kearns, and R. R. Vold, *J. Am. Chem. Soc.*, 1992, **114**, 6585.
25. T. L. James, in *Phosphorus-31 NMR: Principles and Applications*, Academic Press, New York, 1984, Chap. 12, p. 349.
26. A. N. Lane, *Prog. NMR Spectrosc.*, 1993, **25**, 481.
27. P. Tsang, R. R. Vold, and R. L. Vold, *J. Magn. Reson.*, 1987, **71**, 276.
28. R. Brandes, R. R. Vold, D. R. Kearns, and A. Rupprecht, *Biopolymers*, 1988, **27**, 1159.
29. W. C. Huang, J. Orban, A. Kintanar, B. R. Reid, and G. P. Drobny, *J. Am. Chem. Soc.*, 1990, **112**, 9059.
30. J. Feigon, W. Leupin, W. A. Denny, and D. R. Kearns, *Biochemistry*, 1983, **22**, 5943.
31. J. Jeener and P. Broekaert, *Phys. Rev.*, 1967, **157**, 232.
32. R. L. Vold, W. H. Dickerson, and R. R. Vold, *J. Magn. Reson.*, 1981, **43**, 213.
33. J. M. Schurr, *J. Chem. Phys.*, 1984, **84**, 71.
34. S. R. Holbrook and S. Kim, *J. Mol. Biol.*, 1984, **173**, 361.

Biographical Sketch

Regitze R. Vold. *b* 1937, M.S. 1960, Chemical Engineering, Ph.D., 1962, Chemistry, Danmarks Tekniske Højskole, København, Danmark. Postdoctoral work at the University of New Mexico, 1962–64. Staff Fellow at the National Institutes of Health with Edwin D. Becker, 1965–71; research chemist, 1971–82, and Professor of Chemistry, 1982–present, at the University of California, San Diego, USA. Approx. 120 publications. Research specialties: relaxation in multilevel spin systems, especially of ^{2}H, and molecular motion in liquid crystals, inclusion compounds, biopolymers, and paramagnetic materials.

Phospholipid–Cholesterol Bilayers

Kevin M. W. Keough and Michael R. Morrow
Memorial University of Newfoundland, St. John's, NF, Canada

and

Robert Bittman
Queens College of The City University of New York, Flushing, NY, USA

1	Introduction: Cholesterol and Model Membranes	1
2	Early Work on Cholesterol–Phospholipid Interactions	1
3	Refinement of Phospholipid–Cholesterol NMR Studies	2
4	Other Recent Phospholipid–Cholesterol Phase Diagram Studies	6
5	Concluding Remarks	6
6	Related Articles	6
7	References	6

1 INTRODUCTION: CHOLESTEROL AND MODEL MEMBRANES

Cholesterol and related structures are distributed ubiquitously in the membranes of living organisms. Cholesterol is a major component of mammalian plasma membranes and plasma lipoproteins. Cell surface membranes, some viral membranes, and specialized cell membranes such as myelin contain large amounts of cholesterol, having as much as equimolar amounts of cholesterol and phospholipids. On the other hand, subcellular membranes tend to have less cholesterol, with the inner mitochondrial membrane having a very low cholesterol content.[1,2] Cholesterol levels are altered in the membranes of some pathophysiological states such as malignant lymphoid cells.[3] Cholesterol plays many important roles in membranes, including modulation of phospholipid packing density, separation of phospholipid headgroups and disruption of interactions between neighboring headgroups, alteration of membrane permeability behavior, and regulation of membrane-bound enzyme activities. Therefore, studies of the interactions between cholesterol and phospholipids and their consequences with respect to membrane structure and function have been the subject of intense scrutiny for more than three decades.[4–7]

Much of the current understanding of the effects of cholesterol in membranes has come from studies of model bilayer membranes, which are formed by simply dispersing phospholipids, cholesterol, and other compounds in aqueous media. Since the composition of these aqueous dispersions is easily controlled, bilayers prepared from fully hydrated phospholipids have been used extensively in physicochemical studies. This review of the use of NMR for the study of phospholipid–sterol interactions places special emphasis on ^{2}H NMR. The principal topic in this review is the use of NMR to obtain information about the equilibrium phase behavior of cholesterol–phospholipid mixtures, as expressed in phase diagrams and measurements of the order of the hydrocarbon region of membranes. We also present here a brief review of selected NMR literature on methods employing several nuclei that has led to our current understanding of sterol–phospholipid interactions, together with an overview of differential interactions of cholesterol with a variety of phospholipid subclasses such as ester- and ether-linked phosphatidylcholines (PCs).

2 EARLY WORK ON CHOLESTEROL–PHOSPHOLIPID INTERACTIONS

Some of the earliest work on cholesterol–phospholipid mixtures in model bilayer membranes was carried out using X-ray diffraction and differential scanning calorimetry (DSC) techniques, which produced phase diagrams that were refined as discussed below.[4,8] These studies led to the concept that cholesterol produces a state of 'intermediate fluidity' in a phospholipid by decreasing hydrocarbon chain motion in the liquid crystalline state and increasing the hydrocarbon chain motion in the gel state.[4] These properties of bilayers were consistent with earlier observations in monolayers that showed that cholesterol 'condensed' phospholipids in which there was freedom of chain motion[9] and expanded phospholipids in which chain motion was restricted.[10] More precise DSC studies led to a partial phase diagram of the dipalmitoylphosphatidylcholine (DPPC)–cholesterol system,[11] and partitioning experiments with the spin probe Tempo (2,2,6,6-tetramethylpiperidine-*N*-oxyl) resulted in partial phase diagrams of dimyristoylphosphatidylcholine (DMPC)–DPPC mixtures with parts of the boundaries of the L_α, or liquid-disordered (*ld*) and liquid-ordered (*lo*), delineated.[12] Similarly, a partial phase diagram was constructed for DMPC–cholesterol mixtures which included the gel or solid-ordered (*so*), *ld*, and *lo* regions (see below).[13]

The first use of NMR to investigate phospholipid–cholesterol interactions was carried out by Chapman and Penkett,[14] who used continuous wave ^{1}H NMR to show that cholesterol broadened the resonances of the fatty acyl chains and headgroup of egg PC bilayers above the phospholipid phase transition temperature. Similar information was obtained from other early ^{1}H and ^{13}C NMR studies of various phospholipid–cholesterol mixtures.[15] The first application of ^{2}H NMR to the investigation of model membranes was a study of the effects of cholesterol and temperature on dual-chain perdeuterated DMPC-d_{54} bilayers.[16] Above the phase transition temperature (T_m), cholesterol caused the quadrupole splitting of the methylene deuterons to increase, indicative of increased order and reduced motion in the presence of cholesterol. Use of PCs and cholesterol, specifically deuterated at selected sites, provided a wealth of information about the PC–cholesterol system; for references to early ^{2}H NMR studies, see Davis[17] and Vist and Davis.[18] Many of these studies suffered from the drawback that it was not possible to reproduce faithfully the ^{2}H NMR lineshapes, particularly in the gel phase, with the pulsed Fourier transform methods then in use. The introduction of quadrupole echo Fourier transform NMR[19] overcame

this problem and allowed essentially undistorted ^{2}H NMR spectra to be recorded and detailed phase diagrams to be produced. Application of this technique to examine order and dynamics in deuterated DMPC–cholesterol mixtures[20] and other bilayer-forming phospholipids (reviewed in Davis[17]) followed quickly. Proton magic angle sample spinning NMR has also been applied to the study of phospholipid–cholesterol interactions.[21] Recently, ^{2}H NMR was used to carry out a comprehensive examination of molecular order and dynamics in DMPC–cholesterol mixtures.[22]

3 REFINEMENT OF PHOSPHOLIPID–CHOLESTEROL NMR STUDIES

3.1 The Effect of Cholesterol on Phospholipid Acyl Chain Order

The ^{2}H NMR spectrum of a deuteron on the acyl chain of a phospholipid in the liquid crystalline state of a bilayer with random orientation is an axially symmetric Pake doublet. The sharp edges of the doublet arise from molecules undergoing reorientation about an axis that is perpendicular to the applied magnetic field. The quadrupolar splitting of these 90° edges is

$$\Delta\nu_Q = \frac{3}{4}\frac{e^2qQ}{h}S_{CD} \quad (1)$$

where S_{CD}, the orientational order parameter of the carbon–deuterium bond, is given by

$$S_{CD} = \tfrac{1}{2}\langle 3\cos^2\theta_{CD} - 1\rangle \quad (2)$$

In equation (2), θ_{CD} is the angle between the carbon–deuterium bond and the applied magnetic field, and the average is over the motions of the bond. In the gel phase, the chains are more highly ordered, so their slower, asymmetric motion results in a broad spectrum with no sharp features. The ^{2}H NMR spectra of deuterated lipids have been reviewed in Davis.[17]

The ^{2}H NMR spectrum of perdeuterated phospholipids in the liquid crystalline phase of bilayers is a superposition of doublets with a range of splittings reflecting the decrease in orientational order toward the bilayer center. The effect of cholesterol on the chains is illustrated in Figure 1. Above T_m, which is about 38 °C for DPPC-d_{62}, addition of cholesterol increases the doublet splittings, indicative of an increase in acyl chain order and bilayer thickness. Below T_m, the spectrum in the presence of cholesterol indicates that the chains are ordered but undergoing axially symmetric reorientation. The result is a superposition of axially symmetric doublets with large splittings.

Incorporation of DPPC-d_{62} (at 25 mol%) into undeuterated egg PC liposomes resulted in the appearance of a plateau region (which reflects the superposition of the quadrupole splittings of the seven or eight CD_2 groups nearest to the glycerol backbone) and a series of peaks for the more motionally disordered segments between the middle of the chain and the terminal CD_3 group.[23] Incorporation of cholesterol (at 50 mol%) increased the peak-to-peak quadrupole splittings by 75–140%, indicative of a more ordered system.

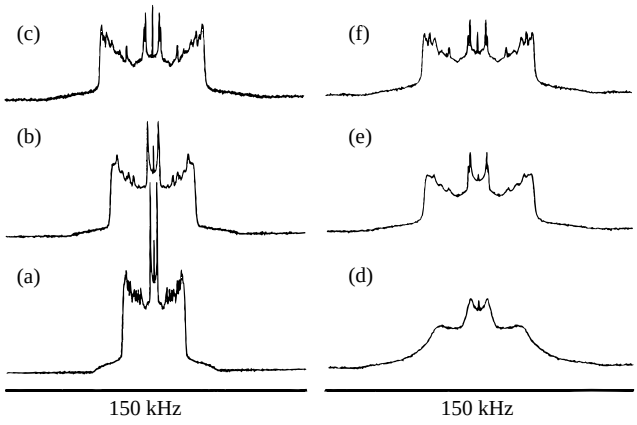

Figure 1 ^{2}H NMR spectra of DPPC-d_{62} in DPPC-d_{62}–cholesterol (chol) bilayers. Spectra were collected at 23.2 MHz using the quadrupole echo sequence with a pulse separation of 40 μs. (a) x_{chol} = 0.035, T = 40 °C; (b) x_{chol} = 0.16, T = 40 °C; (c) x_{chol} = 0.285, T = 40 °C; (d) x_{chol} = 0.035; T = 35 °C; (e) x_{chol} = 0.16; T = 35 °C; (f) x_{chol} = 0.285, T = 35 °C

3.2 The Effect of Analogs of Cholesterol on Phospholipid Acyl Chain Order

3.2.1 ^{2}H and ^{13}C NMR Studies of the Interaction of Epicholesterol (5-Cholesten-3α-ol) with PC

NMR and other physical studies have shown that the molecular features required in a sterol for the ability to moderate the angular fluctuations of phospholipids in bilayers are a planar steroid nucleus, a 3β-hydroxy group, and a long apolar side chain at C-17. Deletion of any of these features results in failure of cholesterol to reduce membrane permeability, broaden the gel-to-liquid-cystalline phase transition, or reduce the mean molecular area of phospholipids in monolayers. Sterols with a planar α face interact principally by van der Waals interactions with the phospholipid acyl chains. Lanosterol, which lacks a planar α face since its 14α-methyl group protrudes from this surface, has considerably more mobility than cholesterol in PC vesicles as judged by ^{13}C NMR.[24]

The relative mobilities of cholesterol and epicholesterol have also been compared in bilayers. The rotational freedom of cholesterol molecules in sonicated phospholipid vesicles can be estimated from spin–lattice relaxation (T_1) and linewidth ($\Delta\nu_{1/2}$) measurements of selected carbon resonances. A comparison of the rotational freedom of cholesterol and epicholesterol in egg PC vesicles was made by ^{13}C NMR as a function of temperature.[25] Below 32 °C epicholesterol has a broad C-6 resonance of about the same linewidth as the C-6 nucleus of cholesterol, and both sterols have a similar effect on PC dynamics as estimated from their ability to cause similar broadening of the *sn*-1 carbon but not of the *sn*-3 carbon. At 41–42 °C, however, the motion of epicholesterol is less restricted than that of cholesterol in egg PC vesicles, as judged by the observation of resonances from C-9 and C-14,17. These studies provide additional proof that the dynamics of component lipids are relevant to membrane function.

Models have been proposed to explain the molecular basis of the differential effects of epicholesterol and cholesterol on the packing of phospholipids in bilayers. Although both

sterols are oriented with the long axis normal to the bilayer surface, a collinear hydrogen bond may be formed with the 3β-hydroxy group of cholesterol and an acceptor such as one of the carbonyl oxygen atoms of the phospholipid;[26] alternatively, the 3β-hydroxy group of cholesterol may be more extensively hydrated than the 3α-hydroxy group of epicholesterol.[27] On the basis of ^{2}H NMR studies with specifically deuterated cholesterol and epicholesterol in DMPC or DMPC-d_{27} bilayers between 10 and 65 °C, a pronounced tilt of epicholesterol with respect to the bilayer normal was evident at physiological temperatures.[28] Furthermore, the isooctyl side chain of cholesterol was found to be as ordered as the steroid nucleus. The quadrupolar splittings of epicholesterol and cholesterol deuterated at C-3 in DPPC bilayers suggested that the angle of tilt of the sterol nucleus relative to the bilayer normal is different in the two sterols.[29] Cholesterol was estimated to be inclined at an angle of 16–19° at 24 °C and 60 °C, which is similar to the tilt of the fatty acyl chains in bilayers; thus, the steroid nucleus and the phospholipid fatty acyl chains have a nearly parallel alignment, with the 3β-hydroxy group projecting toward the water and fully accessible for hydrogen bonding. In contrast, the steroid nucleus of epicholesterol was proposed to lie nonparallel to the phospholipid fatty acyl chains at 24 °C. The 3α-hydroxy group was postulated to lie essentially perpendicular to the bilayer normal, accessible to interaction with water, but positioned at an angle that increases the distance between the steroid nucleus and fatty acyl chains, thus diminishing the extent of lipid–lipid interactions and perturbing the packing of the lipid chains. These studies make clear the reason why epicholesterol is not a naturally occurring membrane component; its presence would destabilize bilayers by disturbing close packing of lipid chains.

3.2.2 ^{2}H NMR Studies of the Interaction of Terpene Alcohols ('Cholesterol Ancestors') with PC

Many polyterpenoid 'ancestors' of cholesterol, although they resemble cholesterol in their rigidity, overall cylindrical shape, and amphiphilic character, generally fail to increase the acyl chain order of phospholipids in fluid phase oriented multilayers, as probed by the increase in mean order parameter using single chain perdeuterated phospholipids such as DMPC-d_{27} and DPPC-d_{31}.[30] Thus the molecular dimensions of cholesterol have apparently evolved in a manner that permits this sterol to play an important role in modulating membrane structure, and this sterol became ubiquitous in most eukaryotic cell membranes. Incorporation of cholesterol at 30 mol% increases the order parameter of the plateau region and terminal methyl region by 78% and 130%, respectively.[31] The extent to which a cholesterol surrogate has the capacity to increase the mean order parameter of oriented bilayers represents a measure of its resemblance to cholesterol.

3.3 Interaction of Cholesterol with Sphingomyelin

There is considerable evidence that the lateral packing density of cholesterol with sphingomyelin is higher than that with PCs (for references, see Bittman[32]). However, ^{13}C NMR studies of [4-^{13}C]cholesterol did not reveal a significant difference in the rotational freedom of cholesterol molecules in PC and sphingomyelin sonicated vesicles, as estimated by $\Delta\nu_{1/2}$ and T_1 measurements.[33] There is substantial evidence that sphingomyelin bilayers are packed more tightly than PC bilayers of similar degree of acyl saturation. Early ^{2}H NMR studies of unsonicated bilayers showed that a semisynthetic sphingomyelin labeled with deuterium at C-10 of the amide-linked chain had significantly higher quadrupole splitting ($\Delta\nu_Q$) than DPPC labeled with deuterium at C-10 of the *sn*-2 palmitoyl chain.[34] More detailed studies of this system are required with specifically labeled, chemically defined sphingomyelins in order to examine whether the mode of packing of cholesterol differs in sphingomyelin and PC bilayers.

3.4 Interaction of Cholesterol with Ether-Linked Phosphocholines

3.4.1 ^{1}H NMR Studies with Plasmenylcholine and PC Vesicles

It is of interest to examine the possibility that cholesterol modulates the motional characteristics of the major mammalian choline glycerophospholipids' subclasses in a differential manner. Proton spin–lattice relaxation times and apparent activation energies of T_1 relaxation times for vinyl and bisallylic methylene protons in liquid crystalline bilayers of a diacyl-PC (1-palmitoyl-2-arachidonoyl-3-PC) were higher than that of a plasmenylcholine, 1-*O*-(*Z*)-hexadec-1′-enyl-2-arachidonyl-3-PC.[35] Incorporation of cholesterol resulted in substantial decreases in the proton spin–lattice (T_1) relaxation times in the interior regions of plasmenylcholine bilayers, and this decrease was larger than that in PC bilayers. On the other hand, the T_1 values of the choline methylene protons of plasmenylcholine bilayers were increased on introduction of cholesterol, and this increase was larger than that found in diacyl-PC bilayers.

Although ^{2}H and ^{13}C NMR studies have shown that polar headgroup motion of phospholipids in multilamellar vesicles is not significantly altered by incorporation of cholesterol,[13,36] the spin–spin relaxation times (T_2) of CH_2N and $N{-}CH_3$ of both PC and plasmenylcholine sonicated vesicles were decreased by cholesterol (at 30 mol%): also, the T_2 values of the bis-allylic protons of arachidonic acid in PC or plasmenylcholine vesicles were decreased by cholesterol (at 30 mol%).[37] These proton spin–spin relaxation time measurements indicate that introduction of cholesterol results in slower motion of the polar headgroup of plasmenylcholine and PC vesicles. Since plasmenylcholine lacks an ester linkage at the *sn*-1 position, yet still has its motional properties altered by cholesterol, these results suggest that hydrogen bonding to an *sn*-1 carbonyl group of diacyl-PC is not required for interaction of phospholipids with cholesterol.

3.4.2 ^{13}C NMR Studies of Saturated Ether–PC and Ester–PC Vesicles

The conclusion stated above is consistent with previous ^{13}C NMR studies of cholesterol enriched with ^{13}C at the 4-position, in which ^{13}C NMR relaxation measurements indicated that no significant relocation of the 4-^{13}C atom of cholesterol took place when a methylene group was substituted for a carbonyl

group in PC sonicated vesicles.[38] The apparent spin–spin relaxation time $T_2[= (\pi \cdot \Delta\nu_{1/2})^{-1}]$, which reflects mainly slower motions involving reorientation of local segments, for the 4-^{13}C atom of cholesterol was shorter in bilayers prepared with 1-ester-2-ether-PC or 1,2-diether-PC than in those prepared with 1,2-diester-PC. Thus, the presence of an *sn*-2 *O*-alkyl linkage in PC rather than an *sn*-2 ester linkage appears to result in a relatively restricted motion of cholesterol (present at 10 mol%). In a diester-PC, the arrangement of the *sn*-1 and *sn*-2 chains is different near the lipid–water interface; the ester linkage at *sn*-2 lies at the interface, whereas the *sn*-1 ester linkage penetrates into the bilayer. In PCs having an *sn*-2 *O*-alkyl linkage, the absence of a bend results in tighter packing of PC molecules in this region of the membrane interface, which is reflected in the shorter apparent T_2 values for [4-^{13}C]cholesterol in dihexadecyl- and 1-palmitoyl-2-*O*-hexadecyl-PC vesicles. This difference in lipid packing property does not require that formation of a hydrogen bond be postulated between cholesterol and the phospholipid. Indeed, no evidence for such a hydrogen bond was found in recent ^{2}H NMR studies of 3-[^{2}H]-cholesterol in DMPC vesicles.[39] However, evidence for a putative hydrogen bond between the 3β-hydroxy group of cholesterol and the *sn*-2 carbonyl of DPPC has been suggested from a high-frequency shift in the ^{13}C NMR spectrum of DPPC carbonyl carbon atoms in the presence of cholesterol.[40,41]

3.5 Use of Spectral Subtraction for Phase Diagram Determination

Many studies have been directed toward the refinement of phase diagrams of a variety of phospholipid–cholesterol systems by application of a wide range of physical techniques (see, for example, references cited in Vist and Davis[18] and Blume and Griffin[42]).

In excess water, a system containing two bilayer-forming components can be treated as a binary mixture. It can be shown that along a line of constant temperature in a binary phase diagram, regions corresponding to different homogeneous phases must be separated by regions in which the free energy of the system is lowered by separation into coexisting domains of the adjacent homogeneous phases. One approach to determining the boundaries of such regions of two-phase coexistence is to scan the temperature through the two-phase region, while observing some property that is sensitive to the thermodynamic phase of the sample, such as excess specific heat in a DSC experiment or lineshape in an NMR experiment. When carried out for a series of sample concentrations, this type of experiment indicates the upper and lower temperature limits of two-phase coexistence for a particular composition.

In order to describe the way in which spectral differences are used in phase diagram studies, we consider here a two-component bilayer system with a temperature and composition that falls within a region of two-phase coexistence in the binary phase diagram. We will use x to denote the mole fraction of component 2 in the bilayer. For the purpose of this discussion, we will take the coexisting phases to be a phase G with a lower concentration of component 2 and a phase F, which is richer in component 2. If, at a particular temperature T, the composition x falls within the two-phase region, the mixture will separate into domains of G and F, with compositions that correspond to the points at which an isotherm at temperature T intersects the boundaries of the two-phase region. These points are referred to as endpoints. For the example described here, the gel-phase boundary composition at temperature T is labeled $x_G(T)$, and the fluid-phase boundary composition is labeled $x_F(T)$. If component 2 lowers the $G \rightarrow F$ transition temperature, then we have $x_F(T) > x_G(T)$. The partitioning of the sample between the coexisting phases is determined by the lever rule. For example, the fraction of the sample in the F phase will be given by

$$f_F(x, T) = \frac{x - x_G(T)}{x_F(T) - x_G(T)} \tag{3}$$

Consider the situation where one of the components is deuterated. We will take component 1 to be the labeled component. The endpoint concentrations can be determined if exchange between domains of the coexisting phases is slow on the ^{2}H NMR timescale.[43] Under these circumstances, the observed spectrum $S(x)$ for a sample of composition x in the two-phase coexistence region, at a particular temperature, will be a superposition of spectra S_G and S_F, corresponding to the endpoint compositions at that temperature. If $S(x)$, S_G, and S_F are normalized to a constant area, then the observed spectrum is given by

$$S(x) = \frac{(1 - x_G)(x - x_F)}{(1 - x)(x_G - x_F)} S_G + \frac{(1 - x_F)(x_G - x)}{(1 - x)(x_G - x_F)} S_F \tag{4}$$

The factor multiplying $S_G(S_F)$ in equation (4) is the number of labeled molecules in phase $G(F)$ divided by the total number of labeled molecules in the sample. Under some circumstances, it may be necessary to apply a correction to account for different transverse relaxation rates in the coexisting phases.

Consider two spectra, $S(x_A)$ and $S(x_B)$, obtained for sample compositions x_A and x_B on the same tie line within a two-phase region. They should consist of the same pair of endpoint spectra superimposed in differing proportions. If $x_A > x_B$, then $S(x_A)$ will contain a higher proportion of S_G than will $S(x_B)$. By subtracting one observed spectrum from the other, one can obtain a spectrum that is exclusively characteristic of one or the other endpoints. K is defined as the fraction of $S(x_B)$ that must be subtracted from $S(x_A)$ to yield S_G. Similarly, K' is the fraction of $S(x_A)$ that must be subtracted from $S(x_B)$ to yield S_F. The endpoint compositions are given by

$$x_G = \frac{x_A(1 - x_B) - K x_B(1 - x_A)}{(1 - x_B) - K(1 - x_A)} \tag{5}$$

and

$$x_F = \frac{x_B(1 - x_A) - K y' x_A(1 - x_B)}{(1 - x_A) - K'(1 - x_B)} \tag{6}$$

For locating phase boundaries, spectral subtraction complements other methods in which properties are observed as sample temperatures are scanned through the region of interest. If several spectra are available along a tie line, a consistent result obtained from a series of different pairwise subtractions provides evidence that the system obeys the lever rule and that the observed spectral changes do indeed reflect two-phase coexistence. Scanning techniques such as DSC depend on the

identification of a threshold temperature at which a property, such as excess heat capacity, exhibits departures from baseline behavior. As such, they are sensitive to the way in which the baseline is extrapolated into the coexistence temperature range. It is significant that the spectral difference approach is based on equilibrium partitioning of the sample.

In practice, K or K' is varied until features characteristic of one or the other coexisting phases are eliminated. The ease with which the appropriate values of K and K' are assigned is very sensitive to the distinctness of the spectra corresponding to the two endpoints. The DPPC-d_{62}–cholesterol system presented a particular challenge to the spectral subtraction technique. Figure 2 shows the form of the phase diagram obtained by Vist and Davis.[18] The labels *ld* and *so* correspond to the liquid-disordered (or liquid crystal) and solid-ordered (or gel) phases, respectively. The *ld*–*so* coexistence region below 7.5 mol% cholesterol was less than 1 °C wide. The nearly horizontal boundaries of this region were determined by inspection of spectra for samples with cholesterol concentration below 7.5 mol% under the assumption that spectral subtraction in this region would be overly sensitive to uncertainty in the sample temperature. Figures 1(a) and 1(d) are characteristic of the *ld* and *so* spectra above and below this two-phase region. The spectra in the *lo* phase beyond about 20 mol%, which Vist and Davis[18] labeled the 'β' phase, are axially symmetric but with a greater average splitting than in the liquid crystalline phase. Figures 1(c) and 1(f) are characteristic of this phase. Within the *ld*–*lo* coexistence region, there was evidence that fast exchange between domains of the two phases caused averaging of the spectra, and spectral differences again were not used. The boundary between *ld* and the *ld*–*lo* coexistence region was determined from DSC studies. Figure 1(b) corresponds to a point inside the two-phase region close to the boundary. Below 20 mol% cholesterol, the lower boundary of this region is a three-phase line at which the *so* phase melts into the *ld* phase. This line was primarily identified from a sharp transition observed calorimetrically. The boundary between the *ld*–*lo* coexistence region and the *lo* region was assigned at the point where the sharp doublets of the *lo* phase broadened as the sample temperature was increased. This was taken to indicate the onset of spectral averaging due to fast exchange with domains of liquid crystal. Determining the exact location of this boundary remains somewhat problematic.

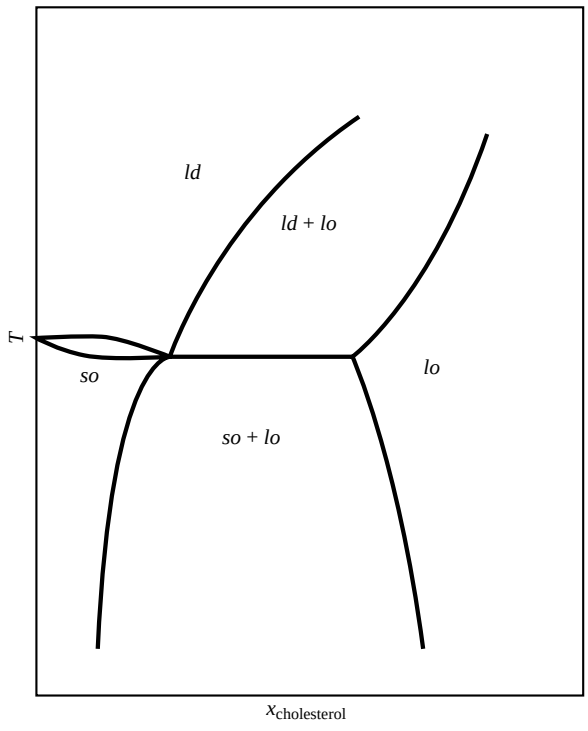

Figure 2 A schematic drawing of the PC–cholesterol phase diagrams. For DPPC-d_{62}, the three-phase line (separating *so* + *lo* from *ld* + *lo*) is at 37 °C and extends from about 7 mol% to 20 mol% cholesterol.[18] For POPC-d_{31}–cholesterol, the three-phase line is at about −7 °C and extends from 7 mol% to about 20 mol% cholesterol.[45] For stearoyl-elaidoyl-PC-d_{35}–cholesterol, the three-phase line is at about 31 °C and extends from about 10 to 25 mol% cholesterol,[46] *ld* is the liquid-disordered phase (also called liquid crystal or L_α). *lo* is the liquid-ordered phase (called β by Vist and Davis[18]), *so* is the solid-ordered phase (also called gel or L_β). (Adapted from Vist and Davis[18])

Within the *so*–*lo* region, spectral subtraction provided important evidence of predominantly vertical boundaries. Figure 1(e) is characteristic of spectra in this region. Such spectra are not obvious superpositions of spectra from two coexisting phases. However, spectral subtraction did give rise to endpoints that were characteristic of the *so* phase and axially symmetric endpoint spectra with large quadrupole splittings that were identified as arising from the *lo* phase. That these were indeed true endpoint spectra was confirmed by comparison with spectra obtained from samples having cholesterol concentrations close to the endpoint concentrations determined by spectral subtraction.

The doublet with the smallest splitting in the axially symmetric spectra arises from the methyl deuterons at the ends of the acyl chains. At high cholesterol concentration, the methyl doublet was split, indicating a slight difference in ordering of the two chains near the bilayer center (see Figure 1).[18] The temperature dependence of the splitting was examined,[44] and a correspondence was noted between the temperature at which the inequivalence of the methyl deuterons disappears and the boundary of the *ld*–*lo* coexistence region reported by Vist and Davis.[18] Partial orientation of DPPC-d_{62} vesicles containing 25 mol% cholesterol was found between 36 and 42 °C, which was attributed to a change in the mechanical properties of the bilayer. The temperature dependence of these effects in the *lo* phase may reflect a reorganization of cholesterol from a position near the bilayer center to one closer to the headgroup region with increasing temperature.

Spectral differences were also used to determine the phase diagrams of mixtures of cholesterol with two unsaturated PCs.[45] Although the phase diagrams were shifted to lower temperatures, in accordance with the T_m values of the phospholipids, remarkable similarities with the DPPC–cholesterol phase diagrams are apparent. A universal shape for the PC–cholesterol phase diagram was postulated, and it was suggested that the β or *lo* phase is probably common to cholesterol-rich biological membranes. No attempt was made to define the *ld*–*lo* coexistence region. Recently, the comparison was extended to mixtures of stearoyl-elaidoyl-PC and cholesterol, which were also found to resemble the DPPC–cholesterol phase diagram.[46] In each binary mixture, the shift on temperature of the three-phase line, relative to that for DPPC–cholesterol, is approximately the same as the shift in the pure phospholipid transition temperature relative to

that for DPPC. Theoretical efforts to model the DPPC phase diagram have been reviewed.[47,48]

4 OTHER RECENT PHOSPHOLIPID–CHOLESTEROL PHASE DIAGRAM STUDIES

The determination of phospholipid–cholesterol phase diagrams by using neutron scattering has been reviewed.[49] Electron spin resonance studies generated phospholipid–cholesterol phase diagrams in which a phase boundary was detected that appears to correspond to the boundary between the *ld*–*lo* coexistence region and the *lo* region beyond 20 mol% cholesterol.[50]

The phospholipid–cholesterol phase diagram has also been studied by Griffin and co-workers using a variety of techniques, including ^{13}C NMR. A region of two-phase coexistence below T_m was found in the phase diagram for dipalmitoylphosphatidylethanolamine–cholesterol mixtures by using ^{2}H and ^{13}C NMR.[42] In a similar study with distearoyl-PC (DSPC)–cholesterol and DPPC–cholesterol systems, the ^{13}C NMR spectrum of the *sn*-2 carbonyl was found to be an axially symmetric powder pattern with a width of about 100 ppm in the gel phase.[42,51] In the liquid crystalline phase, the spectrum is a narrow line (5–10 ppm in width), suggestive of isotropic motion. This behavior is attributed to a conformational change in which the unique axis of the chemical shift tensor orients close to the magic angle. In the $P_{\beta'}$ phase, a superposition of the powder pattern and narrow line spectra is seen. As cholesterol is added, the temperature at which the narrow component first appears is lowered. Where the narrow and powder pattern components are superimposed, the narrow component is broadened. The presence of the narrow and powder pattern spectral components together was taken to indicate the coexistence of a cholesterol-rich phase (LG_I or *lo*) and the gel phase (L_β or *so*). The broadening of the narrow component was simulated by assuming exchange between domains of the two phases. In this way, estimates of domain size have been obtained. The boundary of the LG_I or *lo* region above the temperature of the three-phase line was determined by ^{2}H NMR. The boundary of the *lo* region below the temperature of the three-phase line was found to be shifted to higher cholesterol concentration in mixtures containing the longer chain DSPC compared with DPPC.

The boundary of the DPPC–cholesterol *so*–*lo* region determined by ^{2}H NMR appears to be rather different from that determined by ^{13}C NMR. Carbon-13 NMR measurements indicated that the boundaries of this region curve toward higher cholesterol concentration as the temperature is lowered,[51] whereas ^{2}H NMR measurements showed the corresponding boundaries to be nearly vertical.[18] Similar results were obtained in mixtures of cholesterol with some unsaturated phospholipids.[45,46] However, the temperature ranges over which these boundaries have been determined by ^{2}H NMR are limited.[51] Whether there is really a discrepancy between the findings of the two techniques regarding these boundaries is not clear at this time.

A variety of techniques, including ^{2}H NMR, electron spin resonance, and fluorescence recovery after photobleaching, have been applied to the construction of phospholipid–cholesterol phase diagrams[52] that are qualitatively similar to the one reported by Vist and Davis.[18] Based on ^{2}H NMR studies of bilayer thickness in a series of PCs with increasing chain length, it was suggested that cholesterol spans the bilayer in the *ld* phase and that, with increasing cholesterol concentration and increasing order, the bilayer becomes partially interdigitated in the *lo* phase.[53] The fluid phase immiscibility represented by the *ld*–*lo* region was attributed to this behavior.

5 CONCLUDING REMARKS

What are the implications of these findings for biological membranes? There are common features for each of the lipid–cholesterol phase diagrams, with three phases, *so*, *lo*, and *ld*, plus the corresponding two-phase regions appearing for each phospholipid–cholesterol combination. The phase boundaries show similar, although not identical, properties with respect to cholesterol concentration, with their positions being dependent on the specific phospholipid involved.

At their physiological temperature(s), the lipids of most membranes will be above T_m and above the three phase lines in the phase diagrams. Plasma membranes, therefore, will be in the *lo* or, at elevated temperatures, in the *ld* state. Under equilibrium conditions, these are continuous phases, although interaction energies might vary between cholesterol and individual, specific phospholipids. (Indeed, such comparisons should be made with full knowledge of the phase diagrams, so that cholesterol–phospholipid interactions in comparable phases can be compared.) Subcellular membranes and other membranes having low cholesterol content, on the other hand, while possibly being in the phases just mentioned, might also exist in the *ld*–*lo* two-phase region above the three-phase line. Thus, cholesterol-enriched and cholesterol-poor regions could coexist in membranes, and these domains might have important consequences for insertion and regionalization of proteins, and for modulation of protein functions.

6 RELATED ARTICLES

Bilayer Membranes: Deuterium and Carbon-13 NMR; Bilayer Membranes: Proton and Fluorine-19 NMR; Biosynthesis and Metabolic Pathways: Deuterium NMR; Deuteron Relaxation Rates in Liquid Crystalline Samples: Experimental Methods; Lipid Polymorphism; Lipoproteins; Liquid Crystalline Samples: Carbon-13 NMR; Liquid Crystalline Samples: Deuterium NMR; Membrane Lipids of Acholeplasma laidlawii; Membranes: Carbon-13 NMR; Membranes: Deuterium NMR; Sonicated Membrane Vesicles.

7 REFERENCES

1. D. F. H. Wallach, *Membrane Molecular Biology of Neoplastic Cells*, Elsevier, Amsterdam, 1975, pp. 217–241.
2. G. Rouser, in *Membrane Fluidity in Biology*, ed. R. C. Aloia, Academic Press, New York, 1983, Vol. 1, pp. 235–289.
3. W. J. Van Blitterswijk, in *Membrane Fluidity in Biology*, eds. R. C. Aloia and J. M. Boggs, Academic Press, New York, 1985, Vol. 3, pp. 85–159.

4. R. D. Ladbrooke, R. M. Williams, and D. Chapman, *Biochim. Biophys. Acta*, 1968, **150**, 333.
5. K. E. Bloch, *CRC Crit. Rev. Biochem.*, 1983, **14**, 47.
6. F. T. Presti, in *Membrane Fluidity in Biology*, eds. R. C. Aloia and J. M. Boggs, Academic Press, New York, 1985, Vol. 3, pp. 97–146.
7. P. L. Yeagle, *Biochim. Biophys. Acta*, 1985, **822**, 267.
8. M. C. Bourgès, D. M. Small, and D. G. Dervichian, *Biochim. Biophys. Acta*, 1967, **137**, 157.
9. J. B. Leathes, *Lancet*, 1925, **208**, 853.
10. D. O. Shah and J. H. Schulman, *J. Lipid Res.*, 1967, **8**, 215.
11. S. Mabrey, P. L. Mateo, and J. M. Sturtevant, *Biochemistry*, 1978, **17**, 2464.
12. E. J. Shimshick and H. M. McConnell, *Biochem. Biophys. Res. Commun.*, 1973, **53**, 446.
13. D. J. Recktenwald and H. M. McConnell, *Biochemistry*, 1981, **20**, 4505.
14. D. Chapman and S. A. Penkett, *Nature (London)*, 1966, **211**, 1304.
15. K. M. Keough, E. Oldfield, D. Chapman, and P. Benyon, *Chem. Phys. Lipids*, 1973, **10**, 37.
16. E. Oldfield, D. Chapman, and W. Derbyshire, *FEBS Lett.*, 1971, **16**, 102.
17. J. H. Davis, in *Cholesterol in Membrane Models*, ed. L. Finegold, CRC Press, Boca Raton, FL, 1993, pp. 67–135.
18. M. R. Vist and J. H. Davis, *Biochemistry*, 1990, **29**, 451.
19. J. H. Davis, K. R. Jeffrey, M. Bloom, M. I. Valic, and T. P. Higgs, *Chem. Phys. Lett.*, 1976, **42**, 390.
20. R. Jacobs and E. Oldfield, *Biochemistry*, 1979, **18**, 3280.
21. J. Forbes, C. Husted, and E. Oldfield, *J. Am. Chem. Soc.*, 1988, **110**, 1059.
22. K. Weisz, G. Gröbner, C. Mayer, J. Stohrer, and G. Kothe, *Biochemistry*, 1992, **31**, 1100.
23. D. A. Johnson, C. F. Valenzuela, and R. Zidovetzki, *Biochem. Pharmacol.*, 1992, **44**, 769.
24. P. L. Yeagle, R. B. Martin, A. K. Lala, H.-K. Lin, and K. Bloch, *Proc. Natl. Acad. Sci. USA*, 1977, **74**, 4924.
25. J. R. Brainard and E. H. Cordes, *Biochemistry*, 1981, **20**, 4607.
26. C.-H. Huang, *Lipids*, 1977, **12**, 348.
27. B. DeKruyff, R. A. Demel, A. J. Slotboom, L. L. M. Van Deenen, and A. F. Rosenthal, *Biochim. Biophys. Acta*, 1973, **307**, 1.
28. E. J. Dufourc, E. J. Parish, S. Chitrakorn, and I. C. P. Smith, *Biochemistry*, 1984, **23**, 6062.
29. R. Murari, M. P. Murari, and W. J. Baumann, *Biochemistry*, 1986, **25**, 1062.
30. M.-A. Krajewski-Bertrand, A. Milon, Y. Nakatani, and G. Ourisson, *Biochim. Biophys. Acta*, 1992, **1105**, 213.
31. E. Oldfield, M. Meadows, D. Rice, and R. Jacobs, *Biochemistry*, 1978, **17**, 2727.
32. R. Bittman, in *Cholesterol in Membrane Models*, ed. L. Finegold, CRC Press, Boca Raton, FL, 1993, pp. 45–65.
33. S. Lund-Katz, H. M. Laboda, L. R. McLean, and M. C. Phillips, *Biochemistry*, 1988, **27**, 3416.
34. L. J. Neuringer, B. Sears, F. B. Jungalwala, and E. K. Shriver, *FEBS Lett.*, 1979, **104**, 173.
35. X. Han and R. W. Gross, *Biochim. Biophys. Acta*, 1991, **1063**, 129.
36. H.-U. Gally, A. Seelig, and J. Seelig, *Hoppe-Seyler's Z. Physiol. Chem.*, 1976, **357**, 1447.
37. X. Chen, X. Han, and R. W. Gross, *Biochim. Biophys. Acta*, 1993, **1149**, 241.
38. R. Bittman, S. Clejan, S. Lund-Katz, and M. C. Phillips, *Biochim. Biophys. Acta*, 1984, **772**, 117.
39. J. Higinbotham, P. H. Beswick, R. J. Malcolmson, D. Reed, J. A. Parkinson, and I. H. Sadler, *Chem. Phys. Lipids*, 1993, **66**, 1.
40. J. Forbes, J. Bowers, X. Shan, L. Moran, E. Oldfield, and M. A. Moscarello, *J. Chem. Soc., Faraday Trans. 1*, 1988, **84**, 3821.
41. M. B. Sankaram and T. E. Thompson, *Proc. Natl. Acad. Sci. USA*, 1991, **88**, 8686.
42. A. Blume and R. G. Griffin, *Biochemistry*, 1982, **21**, 6230.
43. J. C. Huschilt, R. S. Hodges, and J. H. Davis, *Biochemistry*, 1985, **24**, 1377.
44. H. Reinl, T. Brumm, and T. M. Bayerl, *Biophys. J.*, 1992, **61**, 1025.
45. J. L. Thewalt and M. Bloom, *Biophys. J.*, 1992, **63**, 1176.
46. F. M. Linseisen, J. L. Thewalt, M. Bloom, and T. M. Bayerl, *Chem. Phys. Lipids*, 1993, **65**, 141.
47. H. L. Scott, in *Cholesterol in Membrane Models*, ed. L. Finegold, CRC Press, Boca Raton, FL, 1993, pp. 197–221.
48. M. J. Zuckermann, J. H. Ipsen, and O. G. Mouritsen, in *Cholesterol in Membrane Models*, ed. L. Finegold, CRC Press, Boca Raton, FL, 1993, pp. 223–257.
49. T. M. Bayerl and E. Sackmann, in *Cholesterol in Membrane Models*, ed. L. Finegold, CRC Press, Boca Raton, Fl, 1993, pp. 13–43.
50. Y.-K. Shin and J. H. Freed, *Biophys. J.*, 1989, **56**, 1093.
51. T.-H. Huang, C. W. B. Lee, S. K. Das Gupta, A. Blume, and R. G. Griffin, *Biochemistry*, 1993, **32**, 13277.
52. P. F. F. Almeida, W. L. C. Vaz, and T. E. Thompson, *Biophys. J.*, 1993, **64**, 399.
53. M. B. Sankaram and T. E. Thompson, *Biochemistry*, 1990, **29**, 10670.

Biographical Sketches

Kevin M. W. Keough. *b* 1943. B.Sc., 1965, M.Sc., 1967, Ph.D., 1971, biochemistry, University of Toronto, Canada. Postdoctoral work at the University of Sheffield (with Dennis Chapman, F.R.S.). Successively assistant professor, associate professor, professor and Head of Biochemistry; currently Vice-President (Research), Memorial University of Newfoundland. Approx. 80 publications. Current research: lipid–protein, and lipid–cholesterol interactions in membranes and pulmonary surfactant.

Michael R. Morrow. *b* 1955. B.Sc., 1977, M.Sc., 1979, Ph.D., 1983, (Supervised by Walter Hardy) physics, University of British Columbia, Canada. Postdoctoral work at the University of Guelph (with James H. Davis). Successively assistant professor, associate professor, Memorial University of Newfoundland. Approx. 30 publications. Current research: solid-state NMR studies of phase behavior and interactions in membranes and pulmonary surfactant.

Robert Bittman. *b* 1942. B.S., 1962, Ph.D., 1965 (supervisor Andrew J. Streitwieser, Jr.), chemistry, University of California at Berkeley, USA. Postdoctoral work at Max-Planck-Institute for Biophysical Chemistry, Göttingen, Germany (with Manfred Eigen). Successively assistant professor, associate professor, professor, and distinguished professor, Queens College of The City University of New York, Flushing, NY, USA, 1966–present. Approx. 200 publications. Current research specialties: lipid–lipid interactions, sterol movement between membranes, new methods for chemical synthesis of glycero- and sphingolipids, lipids as second messengers, antitumor phospholipids.

Protein Dynamics from Solid State NMR

Stanley J. Opella

University of Pennsylvania, Philadelphia, PA, USA

1	Introduction	1
2	Solid State NMR Spectroscopy	1
3	Backbone Sites in Proteins	2
4	Aromatic Side Chains	2
5	Aliphatic Side Chains	3
6	Summary	4
7	Related Articles	4
8	References	5

1 INTRODUCTION

Solid state NMR spectroscopy is one of the premier methods for characterizing protein dynamics. It is used primarily to describe the intramolecular motions of proteins that are immobilized as part of supramolecular structures in solution, such as membrane or virus particles, or in crystalline samples. Although many different experiments and calculations reflect the internal motions in proteins, it is generally quite difficult to extract detailed information about these motions. By contrast, the effects of motional averaging on the lineshapes of solid state NMR spectra are so clear cut that their analysis has provided a very large proportion of the definitive information currently available about protein dynamics.

Spectral parameters from the nuclear spin interactions operative in both solution NMR and solid state NMR experiments are strongly affected by motion; however solid state NMR experiments have the advantages of avoiding the influences of overall reorientation and analyzing the effects of motional averaging on powder pattern lineshapes. Since the proteins themselves are immobilized by their environments, motion associated with specific backbone or side-chain sites can be readily identified. For the most part, solid state NMR studies of molecular dynamics rely on the analysis of powder patterns by comparing the experimental lineshapes with those calculated for static sites affected by specific models of motional averaging, although relaxation parameters can be analyzed in combination with the lineshapes to determine the actual frequencies of the motions. These studies typically require isotopic labeling of the protein with ^{2}H, ^{13}C, or ^{15}N.

An important benefit of solid state NMR studies is that the structure and dynamics of proteins can be considered in concert. Both orientation and distance measurements are feasible with solid state NMR experiments, and these results can be used to determine the three-dimensional structures of proteins. Of course, the results of the NMR dynamics studies are complementary to the structural information also derived from X-ray crystallography and solution NMR spectroscopy. The backbone and side-chain motions of individual residues are of considerable interest because they have a profound effect on the properties and functions of proteins, especially the structural and membrane proteins where solid state NMR spectroscopy finds its greatest applicability.

2 SOLID STATE NMR SPECTROSCOPY

The precise nature of the influence of molecular motion on spectral parameters, especially powder pattern lineshapes, depends on the spin interactions that are present at the site of interest, the frequencies, amplitudes, and directions of local and global motions, and experimental parameters such as the frequencies of the resonances and the amplitudes and timings of the irradiations. There is a comprehensive review on the subject of NMR studies of dynamics and it provides the necessary physical and mathematical detail for understanding the roles of motion in solid state NMR spectroscopy.[1] There are also reviews on the applications of solid state NMR spectroscopy to protein dynamics.[2,3]

The solid state NMR approach to studying molecular dynamics that is most successful relies on the fundamental concept of dilute spins to provide the necessary isolation of the spin interactions. The spin-$\frac{1}{2}$ nuclei of ^{13}C and ^{15}N are available in isotopically enriched sites in proteins. Although these spins interact strongly with the abundant ^{1}H spins, which can usually be decoupled with strong enough irradiation, they do not interact among themselves; therefore, the spectral parameters available for the analysis of motional averaging are heteronuclear dipolar couplings and chemical shift anisotropy. Deuterium with spin 1 is widely used in solid state NMR studies of molecular dynamics because its lineshapes are dominated by the effects of the nuclear quadrupole interaction, and ^{2}H labeling can be placed in backbone and side-chain sites.

In polycrystalline or unoriented samples, where the proteins do not undergo rapid overall reorientation, powder pattern lineshapes like those in Figure 1 are obtained.[2] The absence of motion in a molecular site must always be defined with respect to a frequency determined by the observed spectral parameter from the dominant spin interactions. Static powder pattern lineshapes are calculated from the principal values of the tensor that describes the spin interaction by taking into account the probability density of all orientations of the tensor with respect to the applied magnetic field. The frequency breadth of a powder pattern reflects the total spectral range for the resonance frequencies possible for the spin interactions at a particular site, since all possible angles are present in a powder. It is this breadth that determines the lower limit for the frequencies of motions that can influence the powder pattern lineshape.

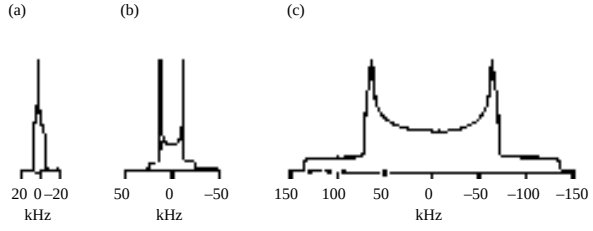

Figure 1 Calculated static powder patterns for an aromatic carbon site. (a) ^{13}C chemical shift anisotropy. (b) ^{13}C–^{1}H heteronuclear dipolar coupling. (c) ^{2}H quadrupolar coupling. (Reproduced by permission from Opella.[2])

Figure 1 presents calculated powder patterns for three spin interactions that can be arranged to be present through isotopic labeling at an aromatic carbon site with a bonded hydrogen. The ^{13}C chemical shift powder pattern from an aromatic carbon is clearly nonaxially symmetric; the $^{13}C-^{1}H$ dipolar powder pattern is axially symmetric; and the ^{2}H quadrupolar powder pattern is nearly axially symmetric. These spectra are displayed on a constant frequency scale in Figure 1 to demonstrate the range of frequencies to which the different spectral parameters are sensitive. For example, the chemical shift powder pattern is averaged by motions substantially slower than those required to average the heteronuclear dipolar and quadrupole powder patterns.

In addition to the frequencies of the motions, the lineshapes are affected by their amplitudes, directions, and other characteristics. In order to understand the influences of these factors, specific models of motions must be considered because of the intimate relationships among molecular sites, spin interactions, and the motions. There are substantial differences between how slow, large amplitude motions and rapid, small amplitude motions affect lineshapes; examples of both are seen in proteins.

3 BACKBONE SITES IN PROTEINS

The initial step in the investigation of a protein is to find out if the entire polypeptide chain is immobile. This information, by itself, is highly suggestive about general aspects of the architecture of the protein, since mobile residues do not participate in the secondary structure of the protein. This is particularly relevant for membrane proteins which characteristically have mobile loops and termini and rigid, structured helical regions. Backbone dynamics are characterized most directly by observing powder pattern lineshapes from labeled sites in unoriented samples and comparing their shape and breadth with those from rigid polycrystalline samples. Residues that undergo large-amplitude motions more often than the frequency breadth of the powder pattern are readily recognized because they have narrow resonance lines at the average, isotropic frequency. The spectra in Figure 2 demonstrate that it is possible to observe narrow, isotropic resonance intensity from the mobile sites superimposed on the broad powder pattern lineshape from the structured sites in a membrane protein.[4] The narrow resonance intensity arises from the mobile sites near the N- and C-termini, although most of the residues of the membrane-bound form of the protein are rigidly held in structured helical regions of the protein.

As shown in Figure 2, ^{15}N-labeled protein samples are very useful in describing the dynamics of proteins. However since the amide tensor in the backbone sites is nearly axially symmetric with the parallel component along the helical axis, it is necessary to observe powder patterns from other sites in order to establish if rotation about an axis coincident with transmembrane helices in the bilayer is occurring. The indole nitrogen of tryptophan side chains is ideal for this, enabling this site to be used to monitor the global motion of the protein since the bulky, asymmetric side chain is rigidly held within the framework of the protein. The results for the membrane-bound form of fd coat protein are shown in Figure 3.[5] The data from ^{15}N-labeled gramicidin in bilayers are quite different;

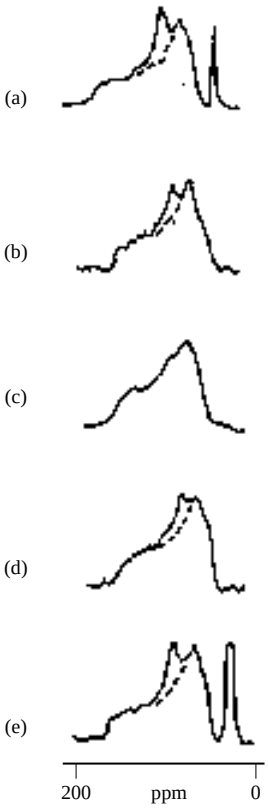

Figure 2 Experimental solid state ^{15}N NMR spectra of the membrane-bound form of fd coat protein in lipid bilayers. (a) Uniformly ^{15}N labeled. (b) Selectively [^{15}N]glycine-labeled (four residues). (c) Selectively [^{15}N]leucine-labeled (two residues). (d) Selectively [^{15}N]Phe-labeled (three residues). (e) Selectively [^{15}N]lysine-labeled (five residues). (Reproduced by permission from Bogusky et al.[4])

although at low temperatures the peptide is immobile, it rapidly rotates at higher temperatures in bilayers.[6] Experiments with other nuclei have confirmed these same results for gramicidin.[7] Global molecular reorientation about a single axis has also been observed for Pf1 virus particles[8] and bacteriorhodopsin in bilayers.[9] In addition to the global motions and large-amplitude local motions, it is possible to use solid state NMR to describe smaller fluctuations through relaxation measurements.[10]

The backbone dynamics of several membrane proteins have been analyzed in detail by solid state NMR experiments.[12–15] Dynamics studies of bacteriorhodopsin in particular have utilized spectra from both backbone and side-chain sites to monitor the motions of the backbone.[16–19] Deuterium NMR spectra of many labeled sites show narrow isotropic resonance intensity superimposed on broad powder patterns,[20] which is typically the case for membrane proteins. The results have been interpreted in terms of structural models of bacteriorhodopsin where the mobile residues are most likely associated with the mobile C-terminus or interhelical loops.[21,22]

4 AROMATIC SIDE CHAINS

The motions of the aromatic amino acid side chains have received a great deal of attention in all studies of

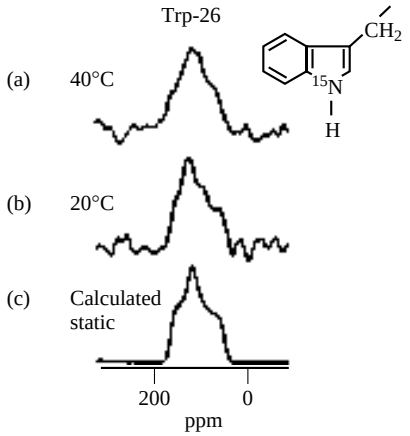

Figure 3 ^{15}N solid state NMR spectra of specifically indole-labeled Trp fd coat protein in lipid bilayers. (Reproduced by permission from Leo et al.[11])

protein dynamics. Not only are these residues important to the structure of the molecules, but also their bulk suggests that their individual motions must influence a substantial number of other residues. Phenylalanine and tyrosine rings have C_2 symmetry and an obvious path for internal motion, the $C^{\beta}-C^{\gamma}$ bond axis. In principle, there are two limiting cases for reorientation of the rings around this axis: (1) jumps (or ring flips) between two indistinguishable sites, where the residence times are long compared with the transit times; and (2) diffusional rotation, where the rings are continuously moving about the bond axis. While all of the spin interactions present in the ring can be used in these studies, the vast majority of work has utilized ^{2}H quadrupole powder patterns to provide the experimental data.[18,23–25] The calculated powder patterns shown in Figure 4 vary strongly with the types of motion.

fd is a filamentous bacteriophage consisting of about 3000 copies of its major coat protein surrounding its DNA. The virus and its coat protein are immobile on all NMR timescales analyzed. The coat protein is small, with two tyrosine residues. The lineshape of the ^{2}H NMR spectrum of [^{2}H]tyrosine (Tyr)-labeled fd virus is very similar in appearance to that calculated for the flip-averaged rings sites.[23] The protein has three phenylalanine (Phe) residues and the ^{2}H NMR spectrum of [^{2}H]Phe-labeled fd is a superposition of two different powder patterns. The inner pattern is from the δ and ϵ bonds undergoing rapid 180° ring flips; the lineshape is very similar to those observed for the Tyr-labeled sample and calculated for the flip-averaged static spectrum. The C–D bonds of the Phe rings contribute the outer discontinuities as a static powder pattern, because these deuterons are unaffected by reorientation about the $C^{\beta}-C^{\gamma}$ bond axis.[24] The lineshape of the [^{2}H]Phe-labeled ^{2}H NMR spectrum demonstrates that these rings also flip rapidly. The observed frequencies in the powder patterns are reduced slightly from those anticipated for a rigid ring only undergoing flips, indicating the presence of some small-amplitude motions. The ^{2}H NMR powder pattern from the single tryptophan (Trp) residue shows its side chain to be tightly constrained within the protein.

Solid state NMR studies on peptides and proteins lead to some general conclusions about the dynamics of aromatic side chains. In the cases examined Trp rings are rigid on NMR

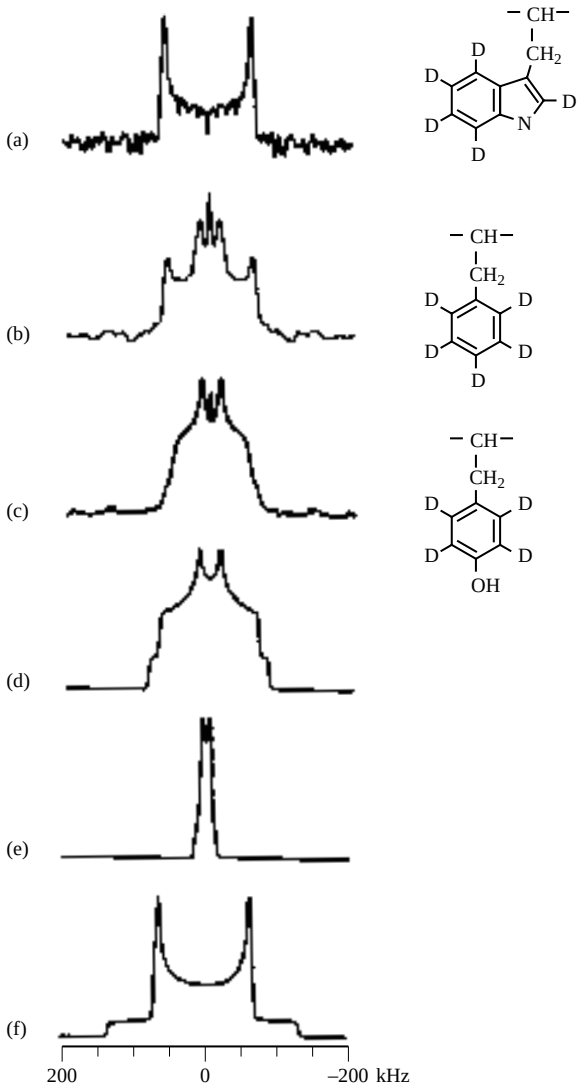

Figure 4 Solid state ^{2}H NMR spectra. (a), (b), and (c) are experimental spectra from selectively ^{2}H-labeled aromatic residues in fd bacteriophage. (d), (e), and (f) are calculated spectra for rigid C–D bonds subject to defined motional averaging. (a) Experimental spectrum from the one labeled tryptophan. (b) Experimental spectrum from the three labeled phenylalanines. (c) Experimental spectrum from the two labeled tyrosines. (d) Calculated spectrum for a C–D bond undergoing two-site hops on an aromatic ring. (e) Calculated spectrum for a C–D bond undergoing diffusional rotation on an aromatic ring. (Reproduced by permission from Gall et al.[23])

timescales, whereas many Tyr and Phe rings undergo two-site 180° hop motions. The aromatic side chains undergo both large-amplitude jump motions and small-amplitude librations in a well-defined manner. The conclusion based on the solid state NMR data is that the proteins in these side chains are both highly ordered and very mobile.

5 ALIPHATIC SIDE CHAINS

Most of the attention in solid state NMR studies of aliphatic side chains in proteins has been focused on CD_3-labeled sites. Both lineshapes and relaxation parameters can

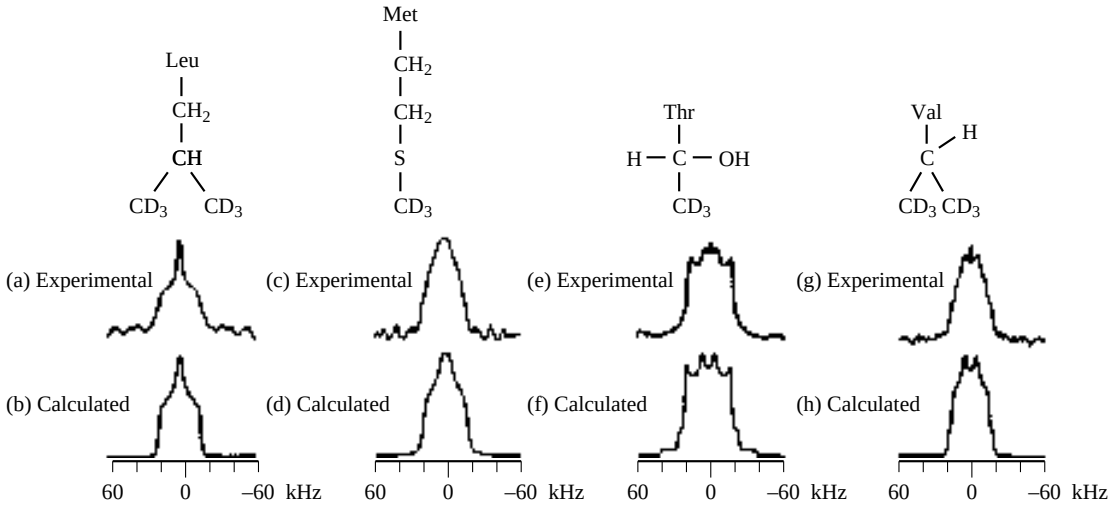

Figure 5 Comparison of experimental and calculated spectra for selectively CD_3-labeled fd virus samples. Leu = leucine, Met = methionine, Thr = threonine, Val = valine. (Reproduced by permission from Colnago et al.[5])

be analyzed. At temperatures of interest for proteins the lineshapes of deuterated methyl groups are axially symmetric powder patterns that are significantly reduced in breadth from a static pattern.[26,27] Since jumps between three or more equivalent sites and diffusional rotation affect powder pattern lineshapes in the same way, the characteristic features of the spectra are indicative of only the angles of intramolecular motion. The facile reorientation of CD_3 groups about their C_3 axis has been extensively studied in crystalline amino acids and peptides, as well as proteins.[5,11,17,19,28,29] It is relatively easy to place deuterated methyl groups in desired locations through synthesis or biosynthetic incorporation, and they have favorable properties for analysis.

The effects of the motional averaging on methyl groups have been observed in ^2H NMR experiments in many different amino acid side chains in peptides and proteins.[5,11] Figure 5 compares calculated ^2H NMR powder patterns characteristic of the methyl group motions actually observed in proteins. All methyl groups undergo rapid reorientation about the C_3 symmetry axis. In addition, many aliphatic side chains undergo rapid jump motions about tetrahedral or near-tetrahedral carbon sites. The deuterium powder pattern lineshapes resulting from two-site jump motions on top of the C_3 axis methyl group reorientation can be calculated by standard methods as two-site 'fast-exchange' processes consisting of jumps betwen two equally populated positions. This was first demonstrated for leucine residues in collagen,[29] and subsequently in a variety of proteins. Of course, large-amplitude motions that occur in all directions result in isotropic averaging of the powder pattern lineshapes to single line resonances that occur at the central frequency for the interaction. Because of the limitations imposed by the side chains, the C–D groups can undergo isotropic reorientation only if the backbone at those residues undergoes isotropic reorientation.

6 SUMMARY

The methods for solid state NMR studies of protein dynamics are well developed, especially with regard to the observation and analysis of motionally averaged powder pattern lineshapes of unoriented or polycrystalline samples. In large part, the success of the applications depends on the placement of isotopic labels in selected locations.

The main conclusion from solid state NMR studies of proteins is that their dynamics fall into three distinct categories. Sites that do not have large-amplitude motions, which occur frequently compared with the timescale of the spectral parameter measured, are categorized as 'rigid' or 'immobile', even if they have small-amplitude rapid motions that result in slight reductions of the parameters compared with static values. Some sites, especially in side chains, undergo large-amplitude jumps between several conformations with residence times that are long compared with the transit times between conformations. In addition, there are mobile sites that undergo rapid reorientation in many directions that are, by definition, unstructured.

Relaxation measurements can provide quantitative information about rates of motion. However, there are many variables that influence the interpretation of these results, and this limits the certainty of the conclusions about the amplitudes and directions of motions. Indeed, there is a tendency to reduce the detail by resorting to an order parameter analysis in order to increase the reliability of the interpretations. Optical and other methods of studying dynamics have even less detail and certainty.

Solid state NMR spectroscopy gives definitive descriptions of the most important backbone and side-chain motions of proteins. The combination of detail concerning the directions, amplitudes, and types of motions with the reliability of lineshape analysis makes this a very powerful approach for the analysis of the time-dependent behavior of proteins.

7 RELATED ARTICLES

Polymer Dynamics and Order from Multidimensional Solid State NMR; Protein Dynamics from NMR Relaxation.

8 REFERENCES

1. H. W. Spiess, *NMR Basic Principles Progr.*, 1982, **15**, 55.
2. S. J. Opella, *Methods Enzymol.*, 1986, **131**, 327.
3. D. A. Torchia, *Annu. Rev. Biophys. Bioeng.*, 1984, **13**, 125.
4. M. J. Bogusky, G. C. Leo, and S. J. Opella, *Proteins Struct. Funct. Genet.*, 1988, **4**, 123.
5. L. A. Colnago, K. G. Valentine, and S. J. Opella, *Biochemistry*, 1987, **26**, 847.
6. H. Hu, K.-C. Lee, and T. A. Cross, *Biochemistry*, 1993, **32**, 7035.
7. R. E. Koeppe, II, J. A. Killian, and D. V. Greathouse, *Biophys. J.*, 1994, **66**, 14.
8. P. Tsang and S. J. Opella, *Biopolymers*, 1986, **25**, 1859.
9. B. A. Lewis, G. S. Harbison, J. Herzfeld, and R. G. Griffin, *Biochemistry*, 1985, **24**, 4671.
10. H. B. R. Cole and D. A. Torchia, *Chem. Phys.*, 1991, **158**, 271.
11. G. C. Leo, L. A. Colnago, K. G. Valentine, and S. J. Opella, *Biochemistry*, 1987, **26**, 854.
12. T. A. Cross and S. J. Opella, *J. Mol. Biol.*, 1985, **182**, 367.
13. S. J. Opella, Y. Kim, and P. McDonnell, *Methods Enzymol.*, 1994, **239**, 536.
14. K.-J. Shon, Y. Kim, L. A. Colnago, and S. J. Opella, *Science*, 1991, **252**, 1303.
15. P. A. McDonnell, K. Shon, Y. Kim, and S. J. Opella, *J. Mol. Biol.*, 1993, **233**, 447.
16. D. M. Rice, A. Blume, J. Herzfeld, R. J. Wittebort, T. H. Huang, S. K. Das Gupta, and R. G. Griffin, *Biomol. Stereodyn.*, 1981, **11**, 255.
17. R. A. Kinsey, A. Kintanar, M.-D. Tsai, R. L. Smith, N. James, and E. Oldfield, *J. Biol. Chem.*, 1981, **256**, 4146.
18. R. A. Kinsey, A. Kintanar, and E. Oldfield, *J. Biol. Chem.*, 1981, **256**, 9028.
19. M. A. Keniry, A. Kintanar, R. L. Smith, H. S. Gutowsky, and E. Oldfield, *Biochemistry*, 1984, **23**, 288.
20. M. A. Keniry, H. S. Gutowsky, and E. Oldfield, *Nature (London)*, 1984, **307**, 383.
21. J. Herzfeld, C. M. Mulliken, D. J. Siminovitch, and R. G. Griffin, *Biophys. J.*, 1987, **52**, 855.
22. J. L. Bowers and E. Oldfield, *Biochemistry*, 1988, **27**, 5156.
23. C. M. Gall, T. A. Cross, J. A. DiVerdi, and S. J. Opella, *Proc. Natl. Acad. Sci. USA*, 1982, **79**, 101.
24. C. M. Gall, J. A. DiVerdi, and S. J. Opella, *J. Am. Chem. Soc.*, 1981, **103**, 5039.
25. D. M. Rice, R. J. Wittebort, R. G. Griffin, E. Meirovitch, E. R. Stimson, Y. C. Meinwald, J. H. Freed, and H. A. Scheraga, *J. Am. Chem. Soc.*, 1981, **103**, 7707.
26. L. S. Batchelder, C. H. Nin, and D. A. Torchia, *J. Am. Chem. Soc.*, 1983, **105**, 2228.
27. K. Beshah, E. T. Olejniczak, and R. G. Griffin, *J. Chem. Phys.*, 1987, **86**, 4730.
28. L. W. Jelinski and D. A. Torchia, *J. Mol. Biol.*, 1980, **138**, 255.
29. L. W. Jelinski, C. E. Sullivan, and D. A. Torchia, *Nature (London)*, 1980, **284**, 531.

Acknowledgments

This research performed at the University of Pennsylvania was supported by grants GM24266, GM29754, and AI20770 from the National Institutes of Health.

Biographical Sketch

Stanley J. Opella. *b* 1947. B.S., Chemistry, University of Kentucky (undergraduate research with S. L. Smith), 1969. Ph.D., Chemistry, Stanford University (with O. Jardetzky and H. McDonnell), 1974. Postdoctoral fellow, Massachusetts Institute of Technology (with J. S. Waugh), 1975–76. Currently Professor of Chemistry at the University of Pennsylvania. Approx. 125 publications. Research interests: development and application of NMR spectroscopy for the study of proteins, especially protein structure determination by solid state NMR spectroscopy.

Selective Relaxation Techniques in Biological NMR

Claudio Rossi
University of Siena, Siena, Italy

1	Introduction	1
2	Selective Pulse Excitation	1
3	The Dipolar Relaxation Mechanism	1
4	General Remarks on Selective Relaxation Experiments	3
5	Application of Selective Relaxation Techniques in Biological Systems	4
6	Related Articles	8
7	References	9

1 INTRODUCTION

Interest in selective relaxation experiments was aroused when it emerged that it was possible to interpret experimental selective relaxation parameters in terms of different relaxation contributions. Considering the dipole–dipole interaction between $I = \frac{1}{2}$ nuclei as the dominant relaxation contribution of biomolecules in solution, selective relaxation experiments can be used to calculate both selective 'cross-relaxation' rates σ_{ij} and individual, direct self-relaxation rates ρ_i. The observation of specific dipolar connectivities can provide useful information on several aspects of the chemical behavior of biomolecules, especially molecular structures and organization, solution dynamics, and biomolecular interactions.

2 SELECTIVE PULSE EXCITATION

Any selective relaxation experiment is performed with a specific pulse sequence which contains at least one selective excitation period. An ideal selective pulse should have the following features:[1,2]

1. good frequency selectivity (i.e. uniform excitation of a limited spectral region);
2. short duration (to avoid effects such as relaxation, chemical shift, and coupling evolution during the pulse);
3. uniform phase behavior of the magnetization.

Several approaches, recently reviewed,[1–3] have been developed, to generate excitation profiles to yield selective perturbation, starting from the pioneering work of Alexander.[4] The pulse sequences proposed for selective excitation can be regarded as belonging to the following categories:

1. rectangular sequence;
2. DANTE sequence;
3. shaped sequence.

2.1 Rectangular Sequences

Rectangular sequences are single, soft pulses obtained like an ordinary hard pulse but with low-amplitude power of the radiofrequency field and a long pulse duration. Two main disadvantages are the low-frequency selectivity and the long excitation time.[5]

2.2 DANTE Sequence[6,7]

The DANTE sequence is an ingenious system for selective excitation using high-power pulses. It consists of a sequence of 10–100 short, high-power pulses with a pulse angle $\phi < \pi/2$ and a repetition frequency $1/\tau$. The effect generated on a magnetic moment vector is similar to that of a soft rectangular pulse with a larger selectivity that improves as the number of pulses in the pulse train is increased. With respect to the soft rectangular pulse, the DANTE sequence generates a set of excitation bands at a frequency n/τ (where n is an integer 1, 2, 3, etc.) symmetrical with the transmitter frequency ω_o.

Important improvements to the original DANTE sequence have increased the frequency selectivity (reducing the effect of side lobes of the excitation function) by pulse-shaping with DANTE[8] and have enabled selective simultaneous excitation of two frequencies by double-DANTE sequences.[9]

2.3 Shaped Pulses

Selective relaxation experiments require the generation of sharp selective pulses that cannot be obtained from soft rectangular pulses. An almost ideal excitation profile requires smoothing of the side lobes in the frequency domain. This is now achieved by appropriate pulse-shaping procedures, which usually require a pulse-shaping spectrometer device.

Gaussian pulse shaping was one of the first shaping functions to be used.[5,10,11] Now a number of different shaping functions are available to generate selective soft pulses for any multidimensional relaxation experiment. Tables 1 and 2 (from Kessler et al.)[1] show the main characteristics of the different soft excitation pulses and their 'recommended' applications.

3 THE DIPOLAR RELAXATION MECHANISM

In solution the exchange of magnetic energy between excited nuclei and the lattice occurs mainly through dipole–dipole interactions between $I = \frac{1}{2}$ nuclei. The efficiency of energy diffusion from 'hot' nuclei (excited) to the 'cold' lattice is a function of internuclear distances between spin-$\frac{1}{2}$ nuclei and the modulation of these internuclear vectors by dynamic processes, typical of molecules in solution. The time evolution of the z component magnetization of two spins I and S in a dipolar interaction has the form[12,13]

$$\frac{d\langle I_z\rangle}{dt} = -\rho_I(\langle I_z\rangle - I_o) - \sigma_{IS}(\langle S_z\rangle - S_0) \quad (1)$$

$$\frac{d\langle S_z\rangle}{dt} = -\rho_S(\langle S_z\rangle - S_o) - \sigma_{SI}(\langle I_z\rangle - I_0) \quad (2)$$

where $\langle I_z\rangle$ and $\langle S_z\rangle$, and S_0 and I_0 are the z components and the equilibrium values of magnetization of spins I and S, ρ_I

Table 1 Characteristics of the Soft Excitation Forms

Form of soft excitation	Special hardware requirements[a]	Excitation function (frequency domain)		Offset-dependent phase gradient	Selectivity[b]	Side lobes	Comments
		Absorptive component	Dispersive component				
Hermite	Pulse-shaping device	Gaussian	Yes	Large, linear	Similar	No	
Rectangular	None	flattened top sinc	Yes	Large, linear	Worse	Yes	
DANTE[c]	None	sinc	Yes	Large, linear	Worse	Yes	Main band and sidebands
90° Gaussian	Pulse-shaping device	Gaussian	Yes	Large, linear		No[d]	
Half Gaussian	Pulse-shaping device	Almost Gaussian	Yes	Large, nonlinear	Worse	No	Dispersive component shows low selectivity
Purged half Gaussian	Pulse-shaping device	Almost Gaussian	No	None	Better	No	
$90° - \alpha_{sel}$	None[e]	$sinc^2$ (near resonance)	No	None	Worse Worse	Yes[e] Yes[e]	Low sensitivity to $\boldsymbol{B}_1$ inhomogeneity
270° Gaussian	Pulse-shaping device	Almost Gaussian	Yes	Small, linear[f]	Worse	Yes	Slightly higher[b] sensitivity to $\boldsymbol{B}_1$ inhomogeneity[b]
Pulse shaping by DANTE	None	Any desired function	[g]	[g]	[g]	[g]	Main band and sidebands
Tailored excitation	None None	Any desired function	[g]	[g]	[g]	[g]	[g]

[a]In general pulse shaping by DANTE possible for all of the shaped pulses.
[b]In comparison with the Gaussian.
[c]'Rectangular' without modulation.
[d]After application of phase correction.
[e]Depends on the soft pulse used.
[f]Only in a small area in the center of the excitation band.
[g]Depends on the excitation sequence.

Table 2 Recommended Applications of the Different Soft Excitation Forms

Form of soft excitation	Recommended application	Evolution of J and Ω during the pulse
Hermite	In cases where uniform excitation is needed	Yes
Rectangular	Only for experiments with low demand on selectivity	Yes
DANTE	For simultaneous excitation of two resonances; excitation of an off-resonance signal	Yes
DANTE	by a side band	Yes
90° Gaussian	Pulse sequence that requires antiphase magnetization for mixing	Yes
Half Gaussian	Pulse sequence that requires antiphase magnetization for mixing; purging of dispersive	Negligible at the end
Half Gaussian	component accomplished by mixing sequence[a]	Negligible at the end
Purged half Gaussian	As above, but experiments with need for explicit purging[b]	Negligible at the end
$90° - \alpha_{sel}$	Pulse sequence starting with antiphase magnetization for mixing	Yes
270° Gaussian	As for the purged half Gaussian in cases with no high selectivity requirements	Partially refocused
Pulse shaping by DANTE	[c]	[c]
Tailored	Solvent peak suppression; excitation of arbitrary spectral regions; hole burning	[c]

[a]E.g. TOCSY or by the phase cycling of 90° pulse before the NOESY mixing.
[b]E.g. ROESY.
[c]Depends on the excitation sequence.

and ρ_S the direct self-relaxation rates, and $\sigma_{IS} = \sigma_{SI}$ the 'cross-relaxation' rates. In this case the relaxation process assumes an exponential decay with a rate constant R_1, the spin–lattice relaxation rate:

$$R_1^i = \rho_i + \sigma_{ij} \quad (i = I, S), (j = S, I) \tag{3}$$

For multispin interaction, as occurs in complex systems of biomolecules, the 'nonselective' spin–lattice relaxation rate ${R_1}^{NS}$ of an i nucleus interacting with neighboring j nuclei can be described by a modified version of Equation (3):

$$R_1^{NS} = \sum_{i \neq j} \rho_{ij} + \sum_i \sigma_{ij} + R^* \tag{4}$$

with the approximation of independent pairwise interactions and considering the contribution of nondipolar relaxation processes R^*.

The explicit form of ρ_{ij} and σ_{ij} in the case of intramolecular dipolar interactions are:

$$\rho_{ij} = \frac{1}{10}\frac{\gamma_H^4\hbar^2}{r_{ij}^6}\left(\frac{3\tau_c}{1+\omega_H^2\tau_c^2} + \frac{6\tau_c}{1+4\omega_H^2\tau_c^2} + \tau_c\right) \quad (5)$$

$$\sigma_{ij} = \frac{1}{10}\frac{\gamma_H^4\hbar^2}{r_{ij}^6}\left(\frac{6\tau_c}{1+4\omega_H^2\tau_c^2} - \tau_c\right) \quad (6)$$

where $\hbar$ is the reduced Planck's constant, γ_H and ω_H are the proton magnetogyric ratio and Larmor frequency respectively, r_{ij} the internuclear distance, and τ_c the effective correlation time which modulates the $i-j$ magnetic interaction.

When the excited i nucleus relaxes with j nuclei at their thermal equilibrium, the 'cross-relaxation' term vanishes[14–16] [as the difference between the second terms of equations (1) and (2) becomes zero] and equation (4) becomes:

$$R_{1i}^{SE} = \sum_{i\neq j}\rho_{ij} \quad (7)$$

where R_{1i}^{SE} is the selective spin–lattice relaxation rate.

Selective excitation of two (or more) resonances adds a selective cross-relaxation term to equation (7) and the relaxation process is driven by the biselective spin–lattice relaxation rate[17] R_{1i}^{BS}:

$$R_{1i}^{BS} = \sum_{i\neq j}\rho_{ij} + \sigma_{ij} \quad (8)$$

Proton and ^{13}C nuclei can be regarded as limiting examples of complexity for dipolar relaxation analysis and, in both cases, the possibility of using spin–lattice relaxation rates for conformational investigations is based on the ability to dissect the complex relaxation process of a multispin system.

In principle, internuclear distances can be measured for biomolecules in solution provided that (1) they have a single predominant structure or a limited number of conformers and (2) a single ρ_{ij} or σ_{ij} can be experimentally measured. This can be achieved by selective spin–lattice relaxation techniques and by combining selective relaxation rates and nuclear Overhauser effects (NOEs) as described below.

As shown by equation (4) in nonselective spin–lattice relaxation experiments on proton nuclei, the measured relaxation rate is the sum of many terms related to all the direct and σ_{ij} cross-relaxation contributions. Thus, only limited information on molecular conformation and dynamics can be obtained from nonselective proton relaxation data since several different internuclear distances and correlation times determine the experiment rate. No structural information can be obtained from the conventional ^{13}C selective relaxation of protonated carbon atoms since the one-bond C–H interaction dominates the relaxation process, and conformational analysis by studying the relaxation of quaternary carbons is complicated by the multiplicity of long-range C–H interactions.[18,19]

The selective excitation of single (or double) protons simplifies the nuclear relaxation pathway and can be performed by a variety of techniques.[1,2,4,20] If the experimental conditions are such that the selective relaxation process of a nucleus involved in dipole–dipole interactions is described by the above equations, simple and reliable methods of calculation of relaxation parameters from selective relaxation measurements can be used, and structural and/or dynamic information can be obtained.

Although selective relaxation parameters can be efficiently used as tools to investigate conformational properties and biomolecular interactions in small and medium-size molecules, cross-relaxation processes may be profoundly altered under the slow motion conditions ($\omega_0\tau_c \gg 1$) typical of large biomacromolecules such as proteins, nucleic acids, and polysaccharides. When these dynamic conditions apply, the rate of transfer of spin energy between nuclei becomes much larger than the rate of transfer of energy to the lattice. The process of propagation of the magnetization in the network of dipolar-coupled spins, known as 'spin diffusion',[21] has the effect of destroying differences in spin–lattice relaxation rates in the molecules so that all tend to the same value.[22–24]

Analyzing the relaxation process on a short timescale, i.e. using the 'initial rate approximation', it has been possible to simplify the interpretation of the results on the basis of a hypothetical two-spin system, but large problems still remain due to the extensive overlapping resonances typical of biomacromolecular spectra.

Some novel one-dimensional (1D)[25–27] and two-dimensional (2D)[28–30] methods have recently eliminated the 'spin diffusion' process by exclusion of selected nuclei from the dipolar-coupled bulk proton network[29,30] or by removing the interference of all protons other than the selected pair.[25–27] In the era of 1D, 2D, three-dimensional, and multidimensional NMR these methods can open up a new age for the application of selective relaxation measurement to study large biomacromolecules.

4 GENERAL REMARKS ON SELECTIVE RELAXATION EXPERIMENTS

In order to perform selective relaxation experiments, the use of pulse sequences able to perturb the nuclear spin population is required. Initial relaxation rates can be obtained provided that the experiment is correctly carried out and that theoretical problems do not quench the dipolar relaxation strategy. As the recovery of the longitudinal component of nuclear magnetization very rarely follows a true exponential decay, it is important to analyze under what circumstances these undesired effects can be avoided. Unfortunately the main effects that alter the exponential behavior of the magnetization are intrinsic, as they arise in coupled spin systems and are due to dipole–dipole 'cross-relaxation' effects and scalar coupling.[31,32]

4.1 Cross-Relaxation Effects

As shown by equations (1) and (2), the recovery of the longitudinal component of the magnetization is usually described by two constant rates ρ and σ, and only under special conditions is this behavior a pure exponential. This is the case

for ^{13}C magnetization measured under conditions of continuous broadband proton decoupling, where proton irradiation sets up and maintains a constant spin population of allowed energy levels such that cross relaxation no longer affects the recovery curve. Similar behavior is expected for selective proton relaxation in cases of weak dipolar coupling or when the effect of cross-relaxation diffusion is truncated using the initial slope approximation. In the latter case the experimental relaxation parameter is calculated by measuring the initial rates in the semi-logarithmic plot of reduced intensity $(I_0 - I_z)/2I_0$ vs. delay times. In more general cases, especially in biological systems, the presence of a network of dipolar-coupled spins induces cross-relaxation contributions that change the pure exponential decay. Nevertheless, at least for small and medium-size biomolecules and for dipolar interactions within a 3.5 distance, the initial rate approximation can be used to interpret the data in terms of two-spin systems and to calculate by numerical simulation the direct self-relaxation rate and the 'cross-relaxation' contributions. A more complex situation occurs when the fast motion conditions $\omega_0{}^2\tau_c{}^2 \ll 1$ do not hold, as in large biomolecules. Under these conditions, due to spin diffusion, the initial slope approximation is no longer valid, especially for long-range interactions, and only recently has it been possible to determine by virtue of synchronous nutation experiments[25–27] the structural properties of proteins from cross-relaxation data obtained by selective relaxation measurements.

4.2 Scalar Coupling

In strongly coupled spin systems, the transition probabilities for the components of a spin multiplet are no longer equal. An important element of symmetry is thus lost, even though the excitation pulse acts equally on all multiplet components. Even for a single two-spin system AB, the zero quantum, single quantum and the double quantum transition probabilities do not assume the classical form,[31–33] but a mixing term W_{AB} appears. It is this last term W_{AB} that causes different recovery curves for the components of a spin multiplet with a specific deviation from pure exponential magnetization decay.

However the perturbative effect of scalar coupling on the behavior of the magnetization recovery curve can be considered a priori. Moreover the 'classical' relaxation equations are still valid when $\Delta\omega/J > 10$, where $\Delta\omega$ is the difference in chemical shift between two spins and J is their scalar coupling constant. This is a general condition met in studying biological systems. Again the synchronous nutation experiment[27] has simplified the problem of correctly calculating the relaxation parameter in the presence of strong scalar coupling, by removing all scalar interactions between spins that are irradiated (active) and at Boltzmann equilibrium (passive). Although the effect of strong scalar coupling between irradiated (active) spins can still affect the recovery curve, its contribution can be taken into account by simple numerical analysis.

5 APPLICATION OF SELECTIVE RELAXATION TECHNIQUES IN BIOLOGICAL SYSTEMS

Many papers have fairly recently been published[25,34–38] proposing the use of selective relaxation experiments to investigate biological systems. For simplicity, proton homonuclear and heteronuclear interactions and their field of application will be treated separately.

5.1 Homonuclear Selective Relaxation Experiments

In ^1H homonuclear spin systems, the nonselective inversion recovery, 180°-τ-90° pulse sequence gives partially relaxed spectra in which it is possible to follow the recovery of the Boltzmann equilibrium for each resonance by individual constant rates (R_1^{NS}) which are the sum of two contributions: the direct and the cross-relaxation terms [as described by equation (4)]. It has been shown by Freeman et al.[14] that cross relaxation may be negligible provided that the 180° pulse selectively excites single-proton resonances. In particular, if the initial relaxation is monitored after selective population inversion of proton i, i.e., short delays are used between the selective and the nonselective observing 90° pulse, the initial recovery rate of the magnetization (R_{1i}^{SE}) is described by equation (7). At longer delay times, cross relaxation becomes significant, as can be observed from the intensity changes of the resonances of protons dipolarly coupled to the excited proton. It follows that selective excitation techniques can be used to achieve a simplification of the proton relaxation process and to calculate the selective dipolar relaxation contribution to the observed spin–lattice relaxation rate.

The initial selective relaxation rate R_{1i}^{SE} is an important parameter which can be used to obtain information on: (1) relaxation mechanisms, (2) molecular dynamics, and (3) molecular conformations.

1. In molecular systems which satisfy the extreme narrowing condition $(\omega_0\tau_c)^2 \ll 1$, for proton i, the ratio between the nonselective relaxation, R_1^{NS}, and R_{1i}^{SE} is diagnostic of the efficiency of the dipole–dipole relaxation mechanism, since this ratio, F_i, is equal to 1.5 for a relaxation pathway completely dominated by the i–j proton dipolar interactions.[39]
2. As shown in Figure 1, F_i also depends on $\omega_0\tau_c$ and, hence, for rigid isotropically reorienting molecules, motions can be quantified from the latter parameter.[39]
3. The combined use of R_{1i}^{SE} and homonuclear Overhauser effects, NOEs, yields an absolute evaluation of σ_{ij} rates since, neglecting cross-polarization effects, the following relationship holds[40]

$$\mathrm{NOE} = \sigma_{ij}/R_i(\mathrm{SE}) \tag{9}$$

where NOE is the Overhauser effect on proton i upon selective excitation of proton j.

The calculation of the cross-relaxation rate relative to a single i–j dipolar interaction is also possible by the simultaneous double excitation of protons i and j. If selectivity in the double excitation can technically be achieved, the relaxation process is driven by the biselective relaxation rate, $R_{1i}{}^{BS}$, as shown by equation (8).

It should be noted that the initial conditions for the evaluation of $R_{1i}{}^{BS}$ are critically important because the peak intensities observed in the partially relaxed spectra are determined by the relaxation process and the time-dependent i–j NOE.[31,41]

Homonuclear selective relaxation experiments are widely used to investigate different properties of biological systems. The most interesting approaches are related to the analysis of:

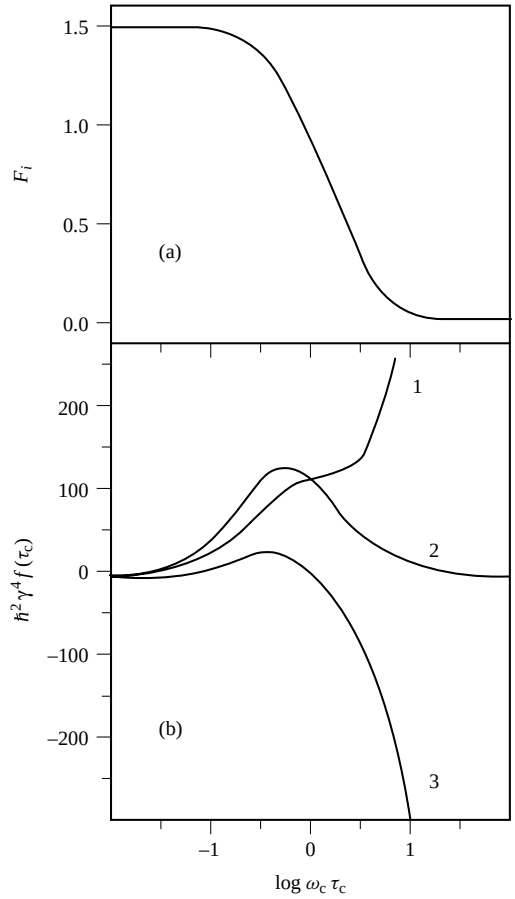

Figure 1 (a) Dependence of $F = R_i(\mathrm{NS})/R_i(i)$ versus log $\omega_0\tau_c$. (b) Behavior of *R*SE/1 (1), *R*NS/1 (2), and σ_{ij} (3) for a two-spin system under different dynamic conditions; (1), (2), and (3) are readily generalized for proton i, involved in multiple interactions with several protons, $i \neq j$. (Reproduced by permission of Academic Press from N. Niccolai et al.[39])

1. conformational and dynamic properties of biomolecules in solution;
2. the interaction process between ligand and biological receptors;
3. the behavior of water in the presence of large, organized biological systems.

5.1.1 Conformational and Dynamic Properties of Biomolecules in Solution

The network of intramolecular dipolar connectivities in small to medium-size biomolecules can be easily evaluated by selective relaxation experiments. The most suitable approach consists first of calculating the cross-relaxation rates between selective proton pairs as the difference between selective and biselective relaxation experiments:

$$\sigma_{ij} = R_{1i}^{\mathrm{BS}} - R_{1i}^{\mathrm{SE}} \tag{10}$$

$$\sigma_{ji} = R_{1j}^{\mathrm{BS}} - R_{1j}^{\mathrm{SE}} \tag{11}$$

in which $\sigma_{ij} = \sigma_{ji}$ are the cross-relaxation values obtained from analysis of the relaxation properties of the i and j nuclei, respectively. Selective homonuclear NOE experiments can also be used to evaluate σ_{ij}. Figure 2 shows an example of proton-selective and biselective experiments used for calculating σ_{ij}. The effect of the additional cross-relaxation contribution to the magnetization recovery process in the biselective experiment, is evident.

As shown by equation (6) and Figure 3, σ_{ij} contains both structural (r_{ij}) and dynamic (τ_c) information.[42] Constant calibration distances are required for the calculation of the effective correlation time τ_c. This is easily achieved by considering independent conformational distances as geminal interactions of CH_2 groups, *ortho* protons of aromatic residues, etc.

As shown in Figure 1, $F_1 = R_{1i}^{\mathrm{NS}}/R_{1i}^{\mathrm{SE}}$ can be used as a probe for molecular motion assuming as dominant the intramolecular dipolar mechanism. Carbon-13 relaxation measurements (see next section) obtained under broad-band proton decoupling can also be used to map the distribution of motions along a biomolecule or to verify isotropic tumbling in systems with restricted internal flexibility. A detailed description of the modulation of the dipole–dipole interaction allows selected interproton distances, from which the solution conformation can be derived, to be calculated with confidence. From the first papers[39,43,44] in which this approach was proposed, nearly every class of biological molecule was investigated: amino acids,[43,45] peptides,[42] carbohydrates,[46] oligosaccharides,[47,48] drugs,[49,50] natural products,[37,51,52] etc.

Recently when the 2D approach for studying dipolar networks seemed to diminish the importance of these selective relaxation studies, a new selective experiment was proposed which enabled large macromolecules such as proteins to be investigated[25] (Figure 4). According to this new approach, one or two proton resonances are simultaneously excited by an amplitude modulated radiofrequency field which forces the magnetization vectors to undergo simultaneous motion defined as 'synchronous nutation'.[25–27] Time-dependent analysis under different initial conditions allows calculation of the direct self-relaxation rate or the 'cross-relaxation' term. In the 'synchronous nutation' experiment, the neighboring spins do not affect the magnetization behavior of the selectively isolated spin system even in the presence of the spin diffusion typical of slow molecular tumbling $\omega_0\tau_c \gg 1$ conditions. Conformational studies (through selected-pair distance determination) by selective relaxation measurements in large biomacromolecules appear to be a valid alternative to the classical approach based on 2D analysis of dipolar-coupled spin systems.

5.1.2 Intermolecular Interaction: Ligand–Macromolecular Receptor

Ligand–macromolecule interactions can be detected by selective relaxation measurements. The formation of intermolecular adducts affects nonselective and selective spin–lattice relaxation rates to different extents, assuming that fast chemical exchange occurs between the bound and free environments with respect to both the chemical shift difference and the proton relaxation rate.[53]

If only two environments are considered, the relaxation parameters are expressed by:

$$R_{1\mathrm{obs}}^{\mathrm{A}} = \chi_{\mathrm{f}} R_{1\mathrm{f}}^{\mathrm{A}} + \chi_{\mathrm{b}} R_{1\mathrm{b}}^{\mathrm{A}} \tag{12}$$

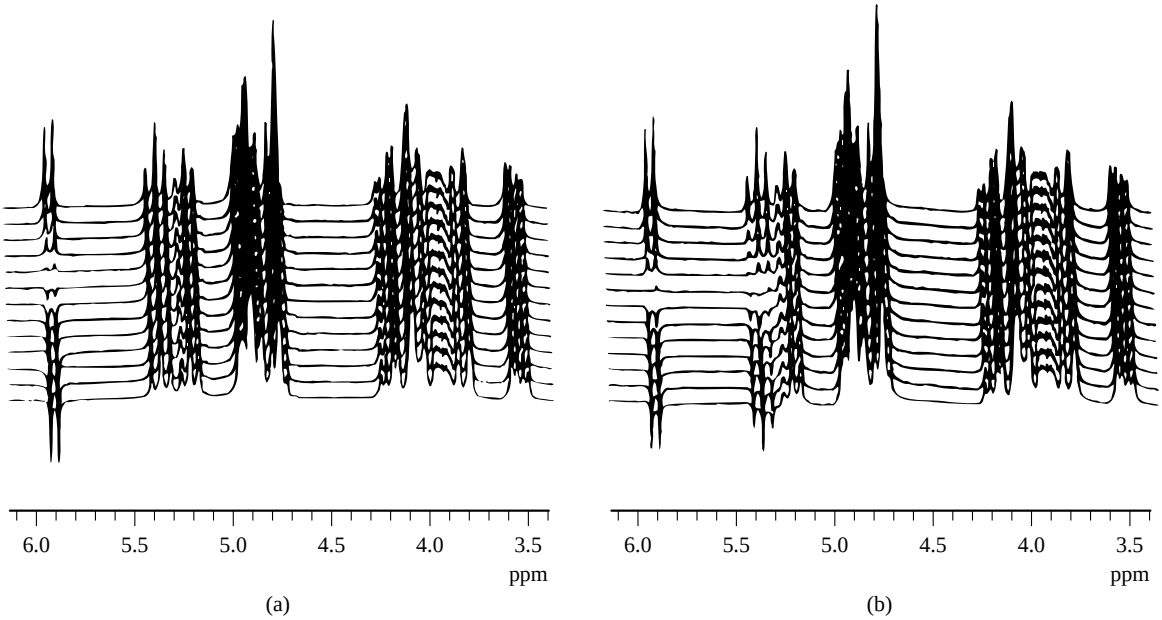

Figure 2 Proton-selective and biselective partially relaxed spectra obtained by selective inversion of the magnetization of H-1′ (a) and of both H-1′–H-3 (b) protons of a 0.15 mol dm^{-3} gentiobiose octaacetate solution in dimethyl sulfoxide-d_6. T = 300 K. The delay values between the selective and nonselective pulses were: 5, 10, 20, 40, 80, 100, 200, 400, 600, 800, 1000, 2000, and 10 000 ms

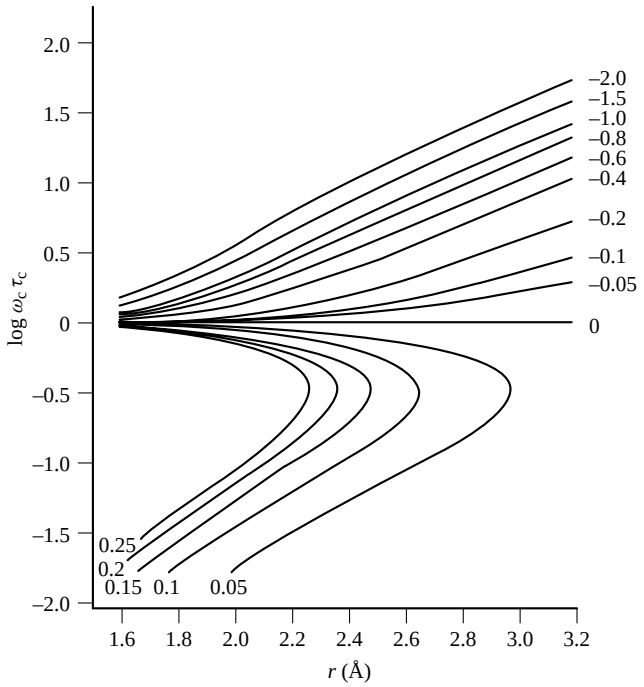

Figure 3 Isosigma contours for log $\omega_0\tau_c$ vs. interproton distances calculated from equation [6]; the selected σ values are expressed in s^{-1}. (Reproduced by permission of Elsevier from N. Niccolai, L. Pogliani, C. Rossi, P. Corti, and W. A. Gibbons, *Biophys. Chem.*, 1984, **20**, 217)

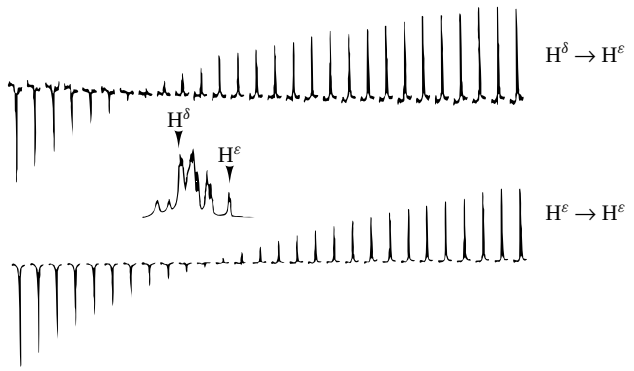

Figure 4 Selective inversion–recovery measurements of the aromatic protons H^δ and H^ε of the tyrosine (Tyr) residue in bovine pancreatic trypsin inhibitor dissolved in ^2H_2O at 327 K. The inset shows the aromatic region (between 8.2 and 5.8 ppm) of the 1D spectrum (eight scans); the arrows indicate the shifts of H^ε at 6.30 ppm and of H^δ at 7.20 ppm. Lower part: normal inversion–recovery measurement of H^ε in Tyr[23] using selective pulses and direct observation of H^ε. Upper part: inversion–recovery of H^δ using selective pulses and Hartmann–Hahn transfer from H^δ to H^ε. (Reproduced by permission of the American Chemical Society from B. Boulat, R. Konrat, I. Burghardt, and G. Bodenhausen, *J. Am. Chem. Soc.*, 1992, **114**, 5412)

where χ_f and χ_b are the ligand fractions in the free and bound environments. Since $\chi_f + \chi_b = 1$ and taking $\chi_b \ll 1$, equation (12) becomes:

$$R_{1\text{obs}}^{\text{A}} = R_{1\text{f}}^{\text{A}} + \chi_{\text{b}} R_{1\text{b}}^{\text{A}} \qquad (13)$$

where A = SE or NS. From equation (13) it emerges that only experimental parameters broadly affected by the ligand–macromolecular interaction make the second term of equation (13) significant. Binding of a ligand to a macromolecular receptor slows down its reorientation motion from $\omega_0\tau_c \ll 1$ to $\omega_0\tau_c \gg 1$. In diamagnetic systems where the dipole–dipole interaction is the dominant relaxation mechanism, entering into the slow-motion region does not significantly alter the nonselective spin–lattice relaxation rates [equation (4)]. On the contrary, the selective relaxation of the bound ligand can be expected to be quite different from that

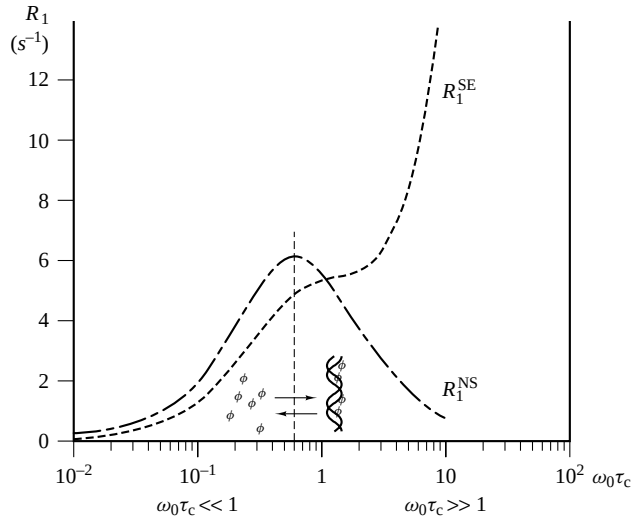

Figure 5 *R*NS/1 and *R*SE/1 of a proton pair versus $\omega_0\tau_c$ assuming a constant r_{i-j} distance (1.77 Å) for the $i-j$ dipolar interaction. The equilibrium between the ligand molecules in the bulk ($\omega_0\tau_c \ll 1$) and DNA-bonded ($\omega_0\tau_c \gg 1$) is also shown. (Reproduced by permission of Elsevier from C. Rossi, A. Donati, and M. R. Sansoni, *Chem. Phys. Lett.*, 1992, **189**, 278)

of the free ligand in solution as shown in Figure 5 for a ligand–DNA interaction.[36]

Since the study of biomolecular interactions by selective relaxation measurement is based on a slowing of ligand molecular motion, the effect of the macromolecular receptor on the viscosity of the system must be considered. Temperature-dependent analysis of R_1^{NS} can address this point. In fact as seen in Figure 5, fast-motion ($\omega_0\tau_c \ll 1$) and slow-motion ($\omega_0\tau_c \gg 1$) conditions show opposite slopes, so hypothetical, drastic changes in viscosity due to the receptor site can be monitored simply by following R_1^{NS} dependence on temperature.[36,54] This method is very powerful since is has a wide range of applications in biological systems. As the information is gained from selective relaxation rates of the ligand, ill-defined receptors in biological samples[55] such as blood whole cells etc. can be investigated and receptor purification followed.

A wide range of ligand–biomacromolecule interactions have been investigated by selective spin–lattice relaxation rate analysis;[56] these include enzyme–substrate,[53] drug–membrane interactions,[57] and recently ligand–DNA,[36] for the purpose of identifying potential mutagens and toxic compounds. This approach can also be used to calculate the association constant for the interaction processes.[58]

5.1.3 Water Selective Relaxation in Large Organized Biological Systems

Water proton relaxation rates have been found to correlate with the physiological and pathological state of the cell as well as to the conformational state of cell constituents.[59–61] Experimental evidence that water selective relaxation is faster than nonselective water relaxation rates in protein solutions and cell suspensions has focused attention on the relaxation mechanism of water protons in large organized systems.[38,62–65] The water spin–lattice relaxation (R_{1W}) may be described as the sum of two contributions:[66]

$$R_{1W} = R_{1A} + R_{1B} \tag{14}$$

where R_{1A} and R_{1B} are the intra- and inter-molecular relaxation rates. The intramolecular term is due to:

$$R_{1B} = R_{1WW} + R_{1WM} \tag{15}$$

R_{1WW} is the dipolar contribution due to intramolecular water–water interactions and R_{1WM} that arising from water–macromolecule (or cell constituent) interactions.[31] The latter interaction can yield direct ρ_{WM} and cross-relaxation σ_{WM} contributions from simultaneous water and macromolecule proton excitation:

$$R_{1WM} = \sum \rho_{WM} + \sum \sigma_{WM} \tag{16}$$

If the water relaxation rate is measured in the selective mode, only a small fraction of the macromolecule protons are excited and the σ_{WM} term disappears. It follows that in the presence of large biological surfaces:[65]

$$R_{1W}^{NS} - R_{1W}^{SE} = \sum \sigma_{WM} \tag{17}$$

where R_{1A} and R_{1WW} are constants in nonselective and selective experiments respectively. Experimental evidence obtained for protein solutions and cell culture suspensions shows that the difference between nonselective and selective relaxation rates [equation (17)] are not only due to the dynamic change in the solvent molecules but also to dipolar intermolecular connectivities between the solvent and the surface of hydrophilic regions of macromolecules. This suggests that it would be useful to use the complete set of relaxation parameters, such as $R_{1W}^{NS}R_{1W}^{SE}$, and σ_{WM} to investigate the physiological and pathological state of cells or to study drug–cell and virus–cell interactions:[67] R_{1W}^{NS} to probe essentially dynamic features of the heterogeneous systems, and R_{1W}^{SE} and σ_{WM} to study the water–macromolecule magnetic energy transfer process, which is intimately linked to the solvent exposed interface structure assumed by the biological material.

5.2 Heteronuclear Selective Relaxation Experiments

Our discussion will be limited to the ^{13}C nucleus, due to its importance for verifying dynamic and structural information on biological systems.

In spite of the low sensitivity of heteronuclei with respect to protons, several advantages exist. Carbon-13 signals are spread over a large chemical shift range (over 300 ppm). The carbon resonances can be treated as single resonances removing proton scalar coupling by a broadband decoupling pulse. Under these conditions the carbon relaxations can be regarded as pure exponential, determined by a single contribution: the direct self-relaxation term. Furthermore, relaxation contributions due to intermolecular interactions are seldom significant (as the carbons are shielded by the proton surface) and, in natural abundance experiments, homonuclear $^{13}C-^{13}C$ dipolar interactions are rare due to ^{13}C isotopic dilution. These properties make carbon relaxation a suitable parameter for investigating solution properties of biomolecules.

5.2.1 ^{13}C Selective Relaxation

In conventional ^{13}C relaxation experiments (obtained by broadband proton decoupling), cross relaxation between carbon nuclei is ignored and the measurement gives the selective, direct carbon spin–lattice relaxation rate:

$$R_{1C}^{SE} = \sum \frac{1}{10} \frac{\hbar^2 \gamma_H^2 \gamma_C^2}{r_i^6} \left[\frac{3\tau_c}{1+\omega_C^2\tau_c^2} + \frac{6\tau_c}{1+(\omega_H+\omega_C)^2\tau_c^2} + \frac{\tau_c}{1+(\omega_H-\omega_C)^2\tau_c^2} \right] \quad (18)$$

R_{1C}^{SE} of protonated carbons are dominated by the dipolar interaction between bonded proton–carbon nuclei.[17,18] In this case the internuclear proton–carbon distance can be assumed to be constant and the effective correlation time calculated. In flexible molecules, a mapping of dynamic properties may be obtained from the R_{1C}^{SE} of different carbons. If continuous broadband proton decoupling is replaced by a selective 180° proton pulse, applied to the i nucleus, with the first 180° carbon pulse the initial rate of the longitudinal magnetization of carbon is:[68–70]

$$R_{1C}^{BS} = R_{1C}^{SE} + \xi\sigma_{CH_i} \quad (19)$$

where R_{1C}^{BS} is the biselective carbon relaxation rate $\xi = \gamma_H/\gamma_C$ and σ_{CH} the single proton–carbon 'cross-relaxation' term. When the selective 180° proton pulse is replaced by a proton perturbation which can invert the spin equilibrium of the entire proton population, the carbon relaxation is described by:[69–71]

$$R_{1C}^{NS} = R_{1C}^{SE} + \xi \sum \sigma_{CH_i} \quad (20)$$

The following dynamic and structural information is obtained by comparing R_{1C}^{SE}, R_{1C}^{BS}, and R_{1C}^{NS} measurements.

5.2.1.1 Dynamic analysis. The R_{1C}^{NS}/R_{1C_i} ratio takes a value in the range 2.99–1, depending on the molecular motion. In this way the value of the R_{1C}^{NS}/R_{1C_i} ratio allows the correlation times for each molecular moiety to be determined (or at least the limit value of τ_c). The R_{1C}^{NS}/R_{1C_i} ratio in particular is a very useful parameter for evaluating the effective correlation time of nonprotonated carbon atoms.

5.2.1.2 Structural analysis. The difference between R_{1C}^{BS} and R_{1C}^{SE} gives the cross relaxation term $\sigma_{C_iH_A}$ for each $^1H-^{13}C$ magnetic interaction which contains distance information. This method has been demonstrated with different natural products, giving reliable results.[69–71]

5.2.2 Selective Proton–Carbon NOEs

Several authors have shown that selective proton–carbon NOEs, $(^1H)^{13}C$-NOE, can be generated.[72–74] When a selective pulse is used to saturate a single proton then 'cross relaxation' between the irradiated proton and the carbon microenvironment occurs. The $(^1H)^{13}C$-NOE is described by:[75,76]

$$(^1H_A)^{13}C_i - \text{NOE} = \frac{\sigma_{C_iH_A}}{R_{1C}^{SE} + R_{1C}^{*}} \quad (21)$$

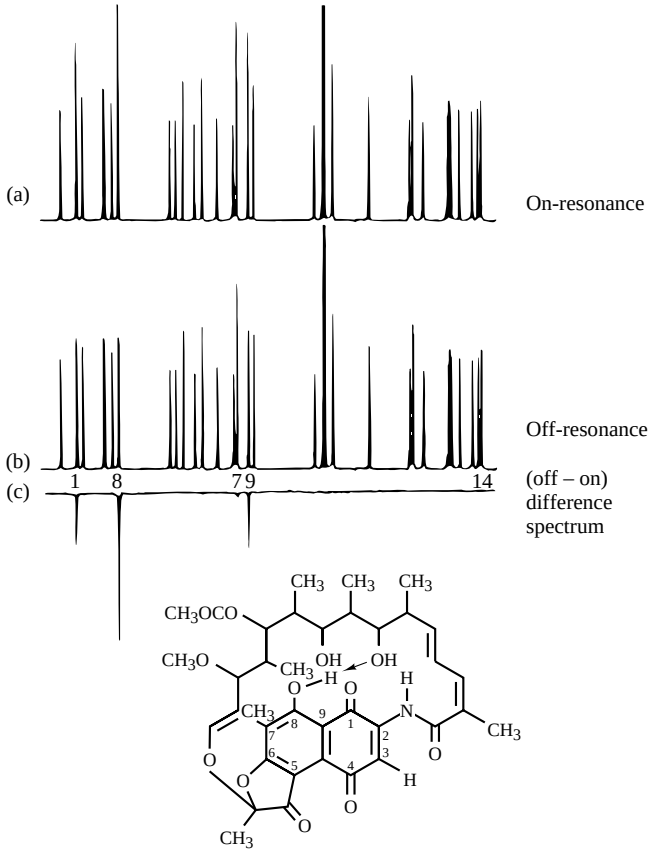

Figure 6 Carbon-13 spectra of 0.5 mol dm^{-3} rifamycin in $CDCl_3$ recorded on a Varian XL-200 spectrometer at 296 K: (a) ^{13}C spectrum after irradiation of the phenolic hydroxyl proton; (b) as (a) but with the decoupler set 'off-resonance'. (c) Difference spectrum (b)–(a). The presaturation selective pulse on the phenolic hydroxyl proton had a 10 s duration and 0.5 W power. During the acquisition of the FIDs the decoupler was on with a power of 4 W in the broadband mode. The structure of rifamycin S is shown. (Reproduced by permission of the American Chemical Society from N. Niccolai et al.[75])

where $\sigma_{C_iH_A}$ is the selective 'cross relaxation', R_{1C}^{SE} the selective carbon relaxation rate, and R_1* the relaxation contribution due to nondipolar interactions [in paramagnetic systems this term often quenches the $(^1H)^{13}C$-NOE]. Thus by combining selective NOEs with carbon relaxation rates, specific distance calculations can be obtained.

Although care must be taken in dealing with large macromolecules when magnetization diffusion occurs between spins, this method has been usefully applied to investigate the conformation of biological molecules such as antibiotics, peptides, natural components,[77–79] etc. Figure 6 illustrates the capacity of $(^1H)^{13}C$ - NOE to discriminate the carbon microenvironment by selective proton perturbation.[75]

6 RELATED ARTICLES

Biological Macromolecules: Structure Determination in Solution; Molecular Motions: T_1 Frequency Dispersion in Biological Systems; Nuclear Overhauser Effect; Relaxation: An Introduction; Relaxation Mechanisms: Magnetization Modes; Selective Pulses.

7 REFERENCES

1. H. Kessler, S. Mronga, and G. Gemmecker, *Magn. Reson. Chem.*, 1991, **29**, 527.
2. R. Freeman, *Chem. Rev.*, 1991, **91**, 1397.
3. E. Gaggelli and G. Valensin, *Concepts Magn. Reson.*, 1992, **4**, 339.
4. S. Alexander, *Rev. Sci. Instrum.*, 1961, **32**, 1066.
5. C. Bauer, R. Freeman, T. Frenkiel, J. Keeler, and A. J. Shaka, *J. Magn. Reson.*, 1984, **58**, 442.
6. G. A. Morris and R. Freeman, *J. Magn. Reson.*, 1978, **29**, 433.
7. G. Bodenhausen, R. Freeman, and G. A. Morris, *J. Magn. Reson.*, 1976, **23**, 171.
8. J. Friedrich, S. Davies, and R. Freeman, *J. Magn. Reson.*, 1987, **75**, 390.
9. H. Geen, X.-L. Wu, P. Xu, J. Friedrich, and R. Freeman, *J. Magn. Reson.*, 1989, **81**, 646.
10. R. J. Sutherland and J. M. S. Hutchinson, *J. Phys. E*, 1978, **11**, 79.
11. J. M. Hutchinson, R. J. Sutherland, and J. R. Mallard, *J. Phys. E*, 1978, **11**, 217.
12. F. Bloch, *Phys. Rev.*, 1957, **105**, 1206.
13. I. Solomon, *Phys. Rev.*, 1955, **99**, 559.
14. R. Freeman, H. D. W. Hill, B. L. Tomlinson, and L. D. Hall, *J. Chem. Phys.*, 1974, **61**, 4466.
15. J. H. Noggle and R. E. Shirmer, *The Nuclear Overhauser Effect; Chemical Applications*, Academic Press, New York, 1971.
16. D. Neuhans and M. P. Williamson, *The Nuclear Overhauser Effect in Structural and Conformational Analysis*, VCH, Berlin, 1989.
17. A. Abragam, *The Principles of Nuclear Magnetism*, Oxford University Press, London, 1961.
18. A. Allerhand, D. Doddrell, and R. Komoroski, *J. Chem. Phys.*, 1971, **55**, 189.
19. L. G. Werbelow and D. M. Grant, *J. Chem. Phys.*, 1975, **63**, 544.
20. C. J. Turner, *Prog. NMR Spectrosc.*, 1984, **16**, 311.
21. A. Kalk and H. J. C. Berendsen, *J. Magn. Reson.*, 1975, **24**, 343.
22. W. Massefski Jr. and A. G. Redfield, *J. Magn. Reson.*, 1988, **78**, 150.
23. V. V. Krishnan, N. Murali, and A. Kumar, *J. Magn. Reson.*, 1989, **84**, 255.
24. V. V. Krishnan, U. Hedge, and A. Kumar, *J. Magn. Reson.*, 1991, **94**, 605.
25. B. Boulat, R. Konrat, I. Burghardt, and G. Bodenhausen, *J. Am. Chem. Soc.*, 1992, **114**, 5412.
26. B. Boulat, I. Burghardt, and G. Bodenhausen, *J. Am. Chem. Soc.*, 1992, **114**, 10 679.
27. I. Burghardt, R. Konrat, B. Boulat, S. J. F. Vincent, and G. Bodenhausen, *J. Chem. Phys.*, 1993, **98**, 1721.
28. J. Fejzo, W. M. Westler, S. Macura, and J. L. Markley, *J. Magn. Reson.*, 1991, **92**, 195.
29. J. Fejzo, W. M. Westler, S. Macura, and J. L. Markley, *J. Magn. Reson.*, 1991, **92**, 20.
30. J. Fejzo, W. M. Westler, S. Macura, and J. L. Markley, *J. Am. Chem. Soc.*, 1992, **114**, 1523.
31. I. D. Campbell and R. Freeman, *J. Magn. Reson.*, 1973, **11**, 143.
32. I. D. Campbell, C. M. Dobson, R. G. Ratcliffe, and R. J. P. Williams, *J. Magn. Reson.*, 1978, **29**, 397.
33. R. L. Vold and R. R. Vold, *Prog. NMR Spectrosc.*, 1978, **12**, 79.
34. N. Niccolai and C. Rossi, *Methods in Enzymol.*, 1989, **176**, 184.
35. N. Marchettini and G. Valensin, *J. Phys. Chem.*, 1990, **94**, 4507.
36. C. Rossi, A. Donati, and M. R. Sansoni, *Chem. Phys. Lett.*, 1992, **189**, 278.
37. M. Sugiura, T. Sai, M. Ichimaru, A. Kato, and N. Takao, *Magn. Reson. Chem.*, 1991, **29**, 755.
38. B. P. Hills, *Mol. Phys.*, 1992, **76**, 489.
39. N. Niccolai, M. P. Miles, and W. A. Gibbons, *Biochem. Biophys. Res. Commun.*, 1979, **91**, 157.
40. C. R. Jones, C. T. Sikakana, S. Hehir, M.-C. Kuo, and W. A. Gibbons, *Biophys. J.*, 1978, **24**, 815.
41. C. Rossi and N. Niccolai, *Chem. Phys. Lett.*, 1989, **156**, 438.
42. N. Niccolai, L. Pogliani, C. Rossi, P. Corti, and W. A. Gibbons, *Biophys. Chem.*, 1984, **20**, 217.
43. N. Niccolai, M. P. de Leon de Miles, S. P. Hehir, and W. A. Gibbons, *J. Am. Chem. Soc.*, 1978, **100**, 6528.
44. N. Niccolai, A. K. Schnoes, and W. A. Gibbons, *J. Am. Chem. Soc.*, 1980, **102**, 1513.
45. C. Rossi, L. Pogliani, F. Laschi, and N. Niccolai, *J. Chem. Soc., Faraday Trans. 1*, 1983, **79**, 2955.
46. T. R. Brown and S. Ogawa, *Proc. Natl. Acad. Sci. U.S.A.*, 1977, **74**, 3627.
47. C. Rossi, L. Pogliani, S. Masi, C. Ceccarini, and N. Niccolai, *J. Biomol. Struct. Dyn.*, 1984, **2**, 481.
48. C. Rossi, S. Ulgiati, and N. Marchettini, *J. Chem. Soc., Faraday Trans. 1*, 1989, **85**, 2149.
49. T. Sai, N. Takao, and M. Sugiura, *Magn. Reson. Chem.*, 1992, **30**, 1041.
50. E. Gaggelli, N. Gaggelli, G. Valensin, and A. Vivi, *Can. J. Chem.*, 1993, **71**, 738.
51. W. Chen, X.-H. Zhu, M. J. Avison, and R. G. Shulman, *Biochemistry*, 1993, **32**, 9417.
52. C. Anselmi, M. Centini, M. Scotton, and A. Sega, *Magn. Reson. Chem.*, 1992, **30**, 994.
53. G. Valensin, T. Kushnir, and G. Navon, *J. Magn. Reson.*, 1982, **46**, 23.
54. C. Rossi, M. R. Sansoni, and A. Donati, *Trends Ecol. Phys. Chem.*, 1993, **57**.
55. I. Barni-Comparini, E. Gaggelli, N. Marchettini, and G. Valensin, *Biophys. J.*, 1985, **48**, 247.
56. G. Uccello-Barretta, C. Bertucci, E. Domenici, and P. Salvadori, *J. Am. Chem. Soc.*, 1991, **113**, 7017.
57. G. Valensin, A. Casini, A. Lepri, and E. Gaggelli, *Biophys. Chem.*, 1983, **17**, 297.
58. E. Gaggelli, G. Valensin, T. Kushnir, and G. Navon, *Magn. Reson. Chem.*, 1992, **30**, 461.
59. D. E. Woessner, *Mol. Phys.*, 1977, **34**, 899.
60. R. Damadian, *Science*, 1971, **171**, 1151.
61. P. T. Beall, C. F. Hazlewood, and P. N. Rao, *Science*, 1976, **192**, 904.
62. D. C. Chang and D. E. Waessner, *Science*, 1978, **198**, 1180.
63. G. Valensin and N. Niccolai, *Chem. Phys. Lett.*, 1981, **79**, 47.
64. N. Niccolai, C. Rossi, and E. Tiezzi, *Chem. Phys. Lett.*, 1983, **96**, 154.
65. N. Niccolai, L. Pogliani, and C. Rossi, *Chem. Phys. Lett.*, 1984, **110**, 294.
66. J. A. Glasel, *Water. A Comprehensive Treatise*, ed. F. Franks, Plenum Press, New York, 1975, Vol. 1, p. 215.
67. G. Valensin, E. Gaggelli, E. Tiezzi, P. F. Valensin, and M. L. Bianchi-Bandinelli, *Biophys. Chem.*, 1979, **10**, 143.
68. I. D. Campbell and R. Freeman, *J. Chem. Phys.*, 1973, **58**, 2666.
69. C. Rossi, *J. Chem. Phys.*, 1986, **84**, 6581.
70. K. E. Kövér and G. Batta, *Prog. NMR Spectrosc.*, 1987, **19**, 223.
71. C. Rossi, N. Marchettini, L. Pogliani, F. Laschi, and N. Niccolai, *Chem. Phys. Lett.*, 1987, **136**, 506.

72. K. F. Kuhlmann, D. M. Grant, and R. K. Harris, *J. Chem. Phys.*, 1970, **52**, 3439.
73. S. Takeuchi, J. Uzawa, H. Seto, and H. Yonehara, *Tetrahedron Lett.*, 1977, 2943.
74. J. J. Ford, W. A. Gibbons, and N. Niccolai, *J. Magn. Reson.*, 1982, **47**, 522.
75. N. Niccolai, C. Rossi, V. Brizzi, and W. A. Gibbons, *J. Am. Chem. Soc.*, 1984, **106**, 5732.
76. N. Niccolai, C. Rossi, P. Mascagni, W. A. Gibbons, and V. Brizzi, *J. Chem. Soc., Perkin Trans. 1*, 1985, 239.
77. M. F. Aldersley, F. M. Dean, and B. E. Mann, *J. Chem. Soc., Chem. Commun.*, 1983, 107.
78. N. Niccolai, C. Rossi, P. Mascagni, P. Neri, and W. A. Gibbons, *Biochem. Biophys. Res. Commun.*, 1984, **124**, 739.
79. C. Rossi, N. Niccolai, and F. Laschi, *J. Phys. Chem.*, 1987, **91**, 3903.

Biographical Sketch

Claudio Rossi. *b* 1952. Ph.D., University of Siena, Italy (Supervisor Professor Enzo Tiezzi, 1977). Postdoctoral work at the Biochemistry Department, University of Wisconsin, Madison (Prof. William A. Gibbons), 1981, and at the Pharmaceutical Chemistry Department, University of California at San Francisco (Prof. Thomas L. James), 1985–86. Successively research associate and associate professor at the University of Siena, 1987–93. Currently full Professor of Physical Chemistry, Department of Chemistry, University of Siena, 1994–present. Approx. 100 publications. Research specialities: ^{1}H and ^{13}C selective relaxation experiments and their applications to biological systems.

Slow and Ultraslow Motions in Biology

Gerd Kothe and Nicholas Heaton

Universität Stuttgart, Stuttgart, Germany

1 Introduction 1
2 Observation of Slow Motions: Pulse-Frequency-Dependent Spin Relaxation 2
3 Characterization of Slow Motions: Transverse Spin Relaxation in Biological Membranes 3
4 Evaluation of Viscoelastic Properties: Collective Orientational Fluctuations 7
5 Related Articles 8
6 References 8

1 INTRODUCTION

Many of the biologically relevant dynamic processes that take place in naturally occurring materials may be considered to be slow on the NMR timescale. This implies that the characteristic frequencies of the motions are comparable to or lower than the width of the NMR spectra that would be obtained in the absence of any molecular motion. Since virtually all nuclei commonly employed for NMR studies of biological systems yield rigid lattice spectra less than 1 MHz wide, a slow process may be defined for present purposes as one whose correlation times τ_C are longer than $(2\pi \times 10^6)^{-1}$ s. This article describes how NMR can be used to investigate such motions, with particular reference to biological studies.

There exists a wide range of NMR techniques available for probing low-frequency molecular dynamics. The methods themselves are by no means applicable only to biological systems, and indeed many of them were originally developed primarily to study synthetic materials. Most of the techniques are discussed in detail in other entries of this Encyclopedia. As far as NMR-observable nuclei are concerned, ^{1}H, ^{13}C, ^{14}N, and ^{31}P, which are, of course, abundant in biologically relevant compounds, can all be used in principle to investigate slow motions. In addition, the use of ^{2}H-labeled materials has now become almost commonplace, and has permitted highly detailed site-specific dynamic NMR studies even in extremely complex systems.

Spin–lattice relaxation rates $1/T_1$ are essentially measures of the amplitudes of motional processes occurring at the Larmor frequency ω_0 of the probe nucleus. Thus, measurement of T_1 as a function of ω_0 provides a means of determining the motional frequency spectrum. For purposes of resolution and sensitivity, commercial spectrometers employ high magnetic fields. In the case of protons, for example, $\omega_0/2\pi$ ranges between 60 and 750 MHz, so that measurement of ^{1}H T_1 on a complete range of standard spectrometers could yield dynamic information over about one order of magnitude on the frequency scale. Field cycling techniques[1,2] enable the determination of T_1 at frequencies lower than the standard high Larmor frequencies and greatly extend the range of the motional frequency spectrum that can be observed. This has particular significance for the study of slow motions in complex systems, where several processes may contribute to the overall spin relaxation mechanism. The application of field cycling for measuring ^{1}H T_1 dispersions has been instrumental in characterizing collective motions in proteins[3] and in phospholipid membranes.[4]

Whereas spin–lattice relaxation is essentially nonadiabatic and reflects exclusively those motions with frequency components at ω_0, transverse spin relaxation is affected in addition by adiabatic dephasing mechanisms due to processes with smaller rate constants, on the order of the rigid lattice linewidth. Transverse relaxation times are most commonly measured using spin echo experiments in which inhomogeneous (i.e., static) contributions to the magnetization dephasing process are refocused. The simplest spin echo experiment consists of a 90° pulse followed by a delay τ, after which a refocusing pulse (180° or 90°) is applied. An echo is formed a period τ after the second pulse, the intensity of which decreases with increasing τ.[5,6] If the dominant motional process is fast in the sense that the correlation time τ_C is shorter than τ then the echoes decay exponentially, and it is possible to extract a single transverse relaxation time T_{2E}. For slower motions, however, for which τ_C is comparable to or longer than τ, the effective relaxation rate itself depends on the value of τ,[7] and the echo decay can no longer be described by a single exponential. In fact, the precise form of the echo decay function depends sensitively on the nature of the underlying motional process.

Although this phenomenon has been understood since the early days of pulsed NMR spectroscopy,[7] its potential applications in the study of slow processes in complex phases such as biological membranes have been recognized only relatively recently.[8] In practice, rather than measure the form of the simple spin echo decay function, multipulse trains such as the Carr–Purcell–Meiboom–Gill (CPMG) sequence[9,10] and its quadrupolar analog[11] are employed. In these experiments, instead of a single refocusing pulse, a series of equally spaced refocusing pulses is applied, resulting in the formation of an echo train. For samples containing a single spin label, the echoes decay monoexponentially with a time constant $T_{2E}^{CP}g$, which depends on the pulse spacing τ. The form of the pulse spacing variation of T_{2E}^{CP} is indicative of the distribution of correlation times for the responsible motional processes, whilst the absolute values of T_{2E}^{CP} reflect their effective amplitudes.[12]

Transverse spin relaxation techniques, employing either ^{2}H or ^{31}P as the probe nuclei, have been applied to study a variety of mechanisms such as collective motions[12–15] and lateral diffusion[8] in biological membranes. An alternative but related approach for observing slow motions involves rotating frame relaxation measurements.[16] The locking-field dependence of $T_{1\rho}$ is analogous to the pulse spacing dependence of T_{2E}^{CP},[17] and has been exploited to characterize low-frequency dynamics in phospholipid membranes.[18,19]

Ultraslow exchange NMR methods directly measure the time variation of the resonance frequency as a result of molecular reorientation.[20] The basic requirement for all experiments of this type can be expressed by the relation $T_1 > \tau_C > T_{2E}$. This approach affords the possibility to study processes with effective correlation times of up to several seconds, depending on T_1 of the resonant nucleus. In the two-dimensional version of the experiment,[21] cross peaks

appear connecting the different frequencies experienced by the spins. In general, the resonance frequency of a particular spin is determined by the orientation Ω of the dominant spin interaction tensor relative to the static magnetic field. Consequently, it is rather straightforward to interpret the exchange spectra in terms of the time variation of Ω.

The choice of experiment to use for investigating a particular system will be dictated by the expected timescale of the motional process of interest and, of course, by the materials available. In the case of ultraslow motions, one of the exchange type of experiments would be most suitable, although the condition $\tau_C > T_{2E}$ is rarely fulfilled in biological systems. For complex collective and/or low-amplitude processes, one of the spin relaxation techniques (T_1, T_{2E}^{CP}, or $T_{1\rho}$) would be most appropriate. The field cycling ^{1}H T_1 approach undoubtedly offers the greatest dynamic range—typically six orders of magnitude in frequency. This is especially useful when dealing with collective motions with broad distributions of correlation times. The method is limited at low frequencies, however, by internal field effects, which render ambiguous the interpretation of any cutoffs that may appear in the T_1 dispersion profiles. The same restrictions apply to $T_{1\rho}$ measurements but not to T_{2E}^{CP} studies. This, together with the simplicity of the experimental techniques, makes pulse-frequency-dependent T_{2E}^{CP} experiments particularly attractive for characterizing slow motions in biological systems. In the following sections, frequency-dependent transverse relaxation is described in more detail, with particular reference to its application in the study of slow motions in biological membranes.

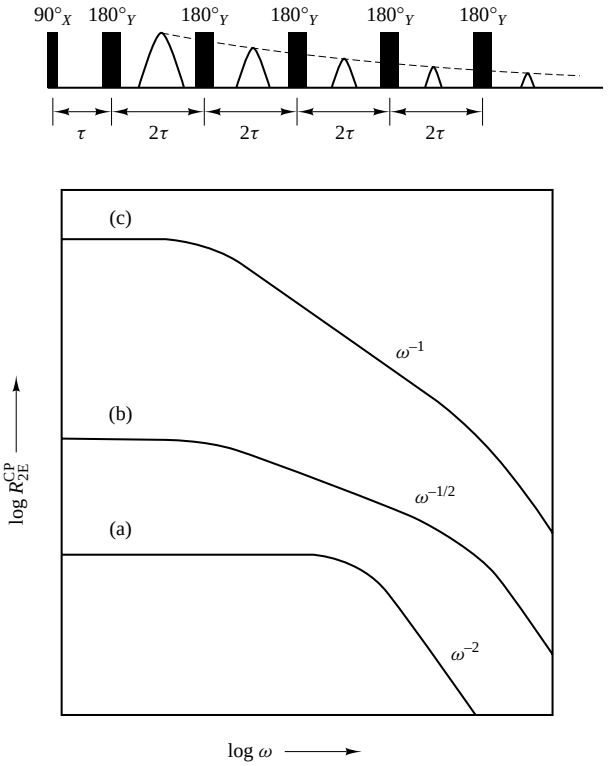

Figure 1 Top: Schematic of CPMG pulse sequence, showing echo decay. Bottom: Dependence of transverse relaxation rate RCP/2E on pulse frequency $\omega = 1/\tau$ for (a) a single Markov process, and (b) three-dimensional and (c) two-dimensional collective orientational fluctuations

2 OBSERVATION OF SLOW MOTIONS: PULSE-FREQUENCY-DEPENDENT SPIN RELAXATION

Nuclear spin relaxation times provide information regarding the timescale, symmetry and amplitude of molecular motion. In order to distinguish between different possible mechanisms, it is advisable if not essential to exploit each of these three aspects of the dynamics. A simple and effective method for achieving this in the slow motional regime involves determining the pulse spacing and orientation dependence of transverse spin relaxation times T_{2E}^{CP}.

2.1 Spin Echo Pulse Trains

The CPMG pulse sequence[9,10] and its quadrupolar equivalent[11] measures the decay of successive spin echoes as illustrated schematically in Figure 1 (top). If the motional correlation time τ_C is of the same order of magnitude as the pulse spacing τ then the echo decay rate $R_{2E}^{CP} = 1/T_{2E}^{CP}$ depends on τ. Generally, the form of the pulse spacing dependence is characteristic of the motion responsible for the relaxation. This is illustrated in Figure 1 (bottom), which shows R_{2E}^{CP} pulse frequency dispersions $[R_{2E}^{CP}(\omega), \omega = 1/\tau]$ for three different types of motion. The Markov process with a single correlation time τ_C exhibits a Lorentzian dispersion with a plateau at low frequencies ($\omega << 1/\tau_C$) and an inverse square dependence $R_{2E}^{CP} \propto \omega^{-2}$ at higher frequencies.[22] More complex processes exhibit, in addition, an intermediate dispersion regime characteristic of the motion. Thus, collective orientational fluctuations provide a $R_{2E}^{CP} \propto \omega^{-1/2}$ dispersion in 'three-dimensional' phases (e.g., nematic liquid crystals),[23] whilst in 'two-dimensional' phases (e.g., bilayer membranes), the relaxation rate is inversely proportional to the pulse frequency: $R_{2E}^{CP} \propto \omega^{-1}$.[12,15] The experimentally accessible frequency range of R_{2E}^{CP} depends, in general, on the sensitivity of the observed spin and on the form of the relaxation dispersion. For ^{31}P, in biological membranes, for example, it is possible to measure R_{2E}^{CP} at frequencies between 10^2 and 10^5 s^{-1}, which is sufficient to cover the relevant slow motional regime.[15]

There are two possible approaches to the analysis of transverse spin relaxation measurements, and some consideration should be given as to which method is most appropriate for each individual case. Motional narrowing limit expressions, which are usually adequate for the interpretation of spin–lattice relaxation experiments, cannot always be applied to transverse relaxation. In particular, for systems undergoing slow motions, it will generally be necessary to solve numerically the equations of motion for the relaxing spins.

2.2 Full Numerical Analysis

The starting point for a full numerical analysis of spin relaxation is the stochastic Liouville equation[24,25]

$$\frac{\partial}{\partial t}\hat{\rho}(\Omega,t) = -\frac{\mathrm{i}}{\hbar}\hat{\mathcal{H}}^{x}(\Omega)\hat{\rho}(\Omega,t) - \hat{\Gamma}(\Omega)[\hat{\rho}(\Omega,t) - \hat{\rho}_{\mathrm{eq}}(\Omega)] \quad (1)$$

which describes the time dependence of the spin density matrix $\hat{\rho}(\Omega, t)$ under the influence of the spin Hamiltonian $\hat{\mathcal{H}}^x(\Omega)$ and the stochastic operator $\hat{\Gamma}(\Omega)$, for the various motional processes. The Euler angles Ω define the orientation of the dominant spin interaction tensor relative to a set of laboratory axes. Fortunately, for the purposes of interpreting transverse relaxation rates due to slow motions, it is often possible to separate the coupled differential equations [see equation (1)] into independent subsets describing the time variation of specific density matrix elements. Thus, the relevant part of equation (1) can be represented by a reduced set of differential equations, written in matrix form as[26–28]

$$\frac{\partial}{\partial t}[\rho_{ij}(\Omega, t)] = -[\mathrm{i}\mathbf{W}(\Omega) + \mathbf{K}(\Omega)][\rho_{ij}(\Omega, t)] \tag{2}$$

where $\rho_{ij}(\Omega,t)$ are the single quantum coherence components of $\hat{\rho}(\Omega, t)$, with $j = i \pm 1$. $\mathbf{K}(\Omega)$ is a rate matrix with elements determined by the discretized stochastic operator $\hat{\Gamma}(\Omega)$.[26,27] Thus, $K(\Omega_{mn})$ is the rate constant for population transfer from site n to site m and $K(\Omega_{mm}) = -\sum_{n\neq m} K(\Omega_{nm})$. The diagonal matrix $\mathbf{W}(\Omega)$ contains the free precession frequencies for each site, m. In order to solve equation (2) it is convenient first to symmetrize $\mathrm{i}\mathbf{W}(\Omega) + \mathbf{K}(\Omega)$ by a similarity transformation and then apply an efficient eigenvalue method.[29,30]

Spin echo experiments can be simulated by successive application of equation (2) to describe each stage of the pulse sequence.[31,32] Refocusing pulses can be treated as ideal rotations, inducing an instantaneous 180° phase shift in $\rho_{ij}(\Omega,t)$. The transverse relaxation rate $R_{2\mathrm{E}}^{\mathrm{CP}}$ for a given pulse spacing τ is then[33]

$$R_{2\mathrm{E}}^{\mathrm{CP}} = -\ln[M(2\tau)/M(0)]/2\tau \tag{3a}$$

$$M(t) = \sum_m \sum_i \rho_{i\,i-1}(\Omega_m, t) \tag{3b}$$

Note that for a homogeneous system, it is not necessary to evaluate the entire CPMG sequence, but it suffices to calculate just the first echo and apply equations (3a) and (3b).[34]

2.3 Motional Narrowing Limit Expressions

For slow low-amplitude processes, it is conceivable that motional narrowing limit theory[35] may be applied to account for transverse spin relaxation. Exact analytical expressions for $R_{2\mathrm{E}}^{\mathrm{CP}}$ valid in this regime have been derived.[7,17,22] A useful approximate version of these derivations is[23,33]

$$R_{2\mathrm{E}}^{\mathrm{CP}} \approx \tfrac{3}{2} C\, J_0^{\mathrm{lab}}(\omega) \tag{4}$$

where $J_0^{\mathrm{lab}}(\omega)$ is the spectral density of the motion at the pulse frequency $\omega = 1/\tau$ and C is the effective interaction strength parameter (e.g., $C = \frac{2}{3}\langle\Delta\sigma^2\rangle$ for ^{31}P and $C = \frac{3}{8}\langle(e^2qQ/\hbar)^2\rangle$ for ^{2}H). For certain dynamic models, analytical expressions are available or can be derived for $J_0^{\mathrm{lab}}(\omega)$. Otherwise, they may be evaluated numerically using the same finite grid point approach[26,27] described above. In this case, we have[36,37]

$$J_{\mathrm{M}}^{\mathrm{lab}}(\omega) = (F_{20}^{\mathrm{mag}})^{-2}\Bigg[\sum_{m,n} F_{2\mathrm{M}}^{\mathrm{lab}}(\Omega_m) F_{2\mathrm{M}}^{\mathrm{lab}*}(\Omega_n) X_m^{(0)} X_n^{(0)} \times \sum_k X_m^{(k)} X_n^{(k)} j^{(k)}(\omega)\Bigg] \tag{5a}$$

$$j^{(k)}(\omega) = \frac{8}{\pi^2}\frac{\lambda^{(k)}}{(\lambda^{(k)})^2 + (\frac{1}{2}\pi\omega)^2} \tag{5b}$$

where $\lambda^{(k)}$ and $\boldsymbol{X}^{(k)}$ are the eigenvalues and corresponding eigenvectors of the stochastic operator $\boldsymbol{\Gamma}$, obtained by diagonalizing the symmetrized rate matrix $\mathbf{K}^{\mathrm{s}}$. The $F_{2\mathrm{M}}^{\mathrm{lab}}(\Omega_m)$ are the components of the magnetic interaction tensor for the mth site, expressed in the laboratory axis system (z parallel to $\boldsymbol{B}_0$). Similarly, F_{20}^{mag} is the zeroth component of the interaction tensor expressed in its principal axis system. Note that the Lorentzian reduced spectral density $j^{(k)}(\omega)$ defined above uses the inverse pulse spacing as the frequency variable, and for this reason differs from standard expressions for spectral densities in magnetic resonance, which generally involve the Larmor frequency ω_0.

Combining equations (4), (5a), and (5b), we obtain a general expression for the transverse relaxation rate:

$$R_{2\mathrm{E}}^{\mathrm{CP}} = \tfrac{3}{2} C \sum_l P(l) J_0^{(l)\mathrm{lab}}(\omega) \tag{6}$$

where the summation index l specifies the effective motional modes and $P(l)$ is the respective mode amplitude. In the case of collective motions, the spectrum of modes is expected to be continuous, and the summation in equation (6) can be replaced by an integral.

Transverse spin relaxation rates are invariably measured in the laboratory frame, and therefore depend on the spectral densities $J_{\mathrm{M}}^{\mathrm{lab}}(\omega)$ [see equation (4)]. On the other hand, dynamic models are generally defined with respect to local symmetry axes and the respective spectral density functions $J_{\mathrm{M}}^{\mathrm{loc}}(\omega)$ evaluated relative to these axes. The transformation between laboratory and local axis systems leads to a simple expression for the anisotropy of $R_{2\mathrm{E}}^{\mathrm{CP}}$:[38]

$$R_{2\mathrm{E}}^{\mathrm{CP}} = \tfrac{3}{2} C[\tfrac{1}{4}(3\cos^2\theta_{\mathrm{N}} - 1)^2 J_0^{\mathrm{loc}}(\omega) + 3\sin^2\theta_{\mathrm{N}}\cos^2\theta_{\mathrm{N}} J_1^{\mathrm{loc}}(\omega) + \tfrac{3}{4}\sin^4\theta_{\mathrm{N}} J_2^{\mathrm{loc}}(\omega)] \tag{7}$$

where θ_{N} refers to the angle between the static magnetic field and the local axis system. In a powder sample, all values of θ_{N} are observed, and the relaxation is in general multiexponential. For macroscopically aligned samples, it is possible to measure $R_{2\mathrm{E}}^{\mathrm{CP}}$ as a function of θ_{N} and hence determine each of the three $J_{\mathrm{M}}^{\mathrm{loc}}(\omega)$. With this information, it is possible to determine the overall symmetry of the motion, without recourse to any specific model.

Interestingly, equations (5) and (7), describing the dispersion and anisotropy of $R_{2\mathrm{E}}^{\mathrm{CP}}$, are qualitatively valid over a dynamic range that extends beyond the limits usually associated with motional narrowing theory.[39] However, it should be stressed that these simple expressions are not always suitable, and, when in doubt, it is advisable to use the full numerical approach discussed above.

3 CHARACTERIZATION OF SLOW MOTIONS: TRANSVERSE SPIN RELAXATION IN BIOLOGICAL MEMBRANES

The majority of NMR studies of biological membranes have employed model systems whose composition is well defined and therefore permits more detailed investigations of specific aspects of membrane behavior. In this section, we present an instructive example of the application of NMR transverse spin relaxation methods to study low-frequency molecular dynamics in a biological model membrane. The particular system studied is a dispersion of dimyristoylphosphatidylcholine (DMPC) in water. From a biological point of view, it is the liquid crystalline (L_α) phase of this system that has received most attention. In this phase, the phospholipid molecules arrange in bilayers, separated by water, with the hydrophobic carbon chains oriented towards the center of the bilayer as illustrated in Figure 2. The most commonly employed preparation methods yield dispersions of approximately spherical multilamellar vesicles (see Figure 2). The mean value and variance of the vesicle radius distribution, however, depend significantly on the method of preparation employed.[40] Alternatively, macroscopically oriented samples can be obtained by incorporating thin layers of the DMPC/water mixture between thin glass plates (see Figure 2).[41]

3.1 Multilamellar Vesicles

It was pointed out in the previous section that transverse spin relaxation rates R_{2E}^{CP} depend on the sample orientation, the pulse frequency, and the spin interaction strength. Independent measurement of these three effects, however, is complicated to some extent by the use of vesicle samples. Since multilamellar vesicles are, in effect, isotropic powders, all orientations θ_N are represented, and therefore relaxation is generally multiexponential [see equation (7)]. In principle, it is possible to determine both the anisotropy and the pulse frequency dependence by Fourier transforming the final echoes of CPMG trains for different numbers of echoes, n, at each pulse frequency. This procedure, however, is time and labor-intensive, and alternative methods have usually been employed to extract the desired information. For homogenous samples with a single effective spin label, it is possible to exploit equation (7), so that the measured amplitude $M(2n\tau)$ of the nth echo in a CPMG experiment is

$$M(2n\tau) = M_0 \int_0^1 \exp\{-[\tfrac{1}{4}(3\cos^2\theta_N - 1)^2 F_0 + 3\sin^2\theta_N \cos^2\theta_N F_1 + \tfrac{3}{4}\sin^4\theta_N F_2]2n\tau\}\, d\cos\theta_N \quad (8)$$

and the decay curve for a given pulse spacing τ may be fitted by independently varying the three parameters F_0, F_1, and F_2. Although equation (8) is strictly correct only in the motional narrowing limit, where the parameters F_M can be identified with the spectral densities $J_M^{loc}(\omega)$, it may be usefully applied in any regime provided that for each individual orientation θ_N the spins relax monoexponentially.

Figure 3, shows ^{31}P and ^{2}H scaled transverse relaxation rates, $R_{2E}^{CP}/\Delta\nu^2$ as functions of pulse frequency ω for 2-[14,14,14-d_3]DMPC (see Figure 2) multilamellar vesicles. The ^{31}P relaxation rates were measured using the standard CPMG pulse sequence with spin lock proton decoupling.[42] For ^{2}H, the quadrupolar CPMG sequence[11] was employed without proton decoupling. Results are shown for pure DMPC bilayers (open circles), DMPC/4 mol% gramicidin (filled diamonds), and DMPC/40 mol% cholesterol (open triangles), and in each case refer to the $\theta_N = 45^\circ$ orientation, extracted from CPMG echo decays using equation (8). Two important conclusions may be drawn from the results in Figure 3, independently of possible dynamic models. First, the evident frequency dependence of the rates indicates that slow motional processes are responsible for transverse relaxation. Moreover, the fact that the measured dispersion is in all cases approximately given by $R_{2E}^{CP} \propto \omega^{-1}$ suggests a superposition of different modes with frequency components in the 10^2–10^5 s^{-1} regime probed specifically in the experiments. The second notable aspect of the results in Figure 3 is that the scaled rates $R_{2E}^{CP}/\Delta\nu^2$ are, to within experimental error, the same for ^{31}P and ^{2}H. The spectral parameter $\Delta\nu$ is defined as the measured frequency difference between the 0° and 90° singularities in the powder spectra. Thus, $\Delta\nu^2 \propto C$, and we find that the spin-interaction-independent (i.e., purely dynamic) contributions to the relaxation rates for ^{31}P and ^{2}H are identical. In other words, the lipid headgroup (^{31}P) and the *sn*-2 chain methyl group (^{2}H) undergo the same low-frequency motions, despite the fact that they are located at opposite extremities of the lipid molecule (see Figure 2). This indicates that the effective dynamic processes are of a mesoscopic nature. In comparing the ^{31}P and ^{2}H results, it is also worth pointing out that ^{31}P provides markedly superior signal-to-noise ratio and a correspondingly wider dynamic range than ^{2}H, and there is a good case for proposing ^{31}P as the nucleus of choice for low-frequency dynamics studies of biological membranes.

The results in Figure 3 evaluated for the $\theta_N = 45^\circ$ orientation reflect the most rapidly relaxing component of the multiexponential decay. However, a second slowly relaxing component corresponding to the 90° orientation can also be detected in the ^{31}P CPMG experiments. The scaled ^{31}P relaxation rates are shown in Figure 4. Interestingly, at low frequencies, a plateau appears in the $R_{2E}^{CP}/\Delta\nu^2$ dispersion plot. What is more, the ratios between the plateau values for the different samples are different from the corresponding ratios found for the rapidly relaxing component.

Figure 5 shows the ^{31}P scaled transverse relaxation rates measured for pure DMPC vesicles at four different magnetic fields between 4.7 and 11.7 T. Note that in the case of ^{31}P, it is modulation of the chemical shift anisotropy that is responsible for transverse relaxation. Since the effective chemical shift anisotropy is determined by B_0 ($\Delta\nu \propto B_0$), it follows that the spin interaction strength parameter C also depends on the magnetic field ($C \propto B_0^2$). Thus, if the dynamic behavior of the membrane is unaffected by the presence of magnetic fields, the scaled relaxation rates $R_{2E}^{CP}/\Delta\nu^2$ should be independent of B_0. The results in Figure 5 show that the higher frequency processes ($\geq 10^3$ s^{-1}), monitored by the rapidly relaxing component [Figure 5(a)], are virtually unaffected by the presence of the magnetic field, whereas the low-frequency motions ($\leq 10^3$ s^{-1}), reflected by the slowly relaxing component [Figure 5(b)], are apparently suppressed at higher magnetic fields.

NMR studies of slow motions in multilamellar vesicles have focused principally on two types of process, namely lateral diffusion across a curved surface[8] and collective

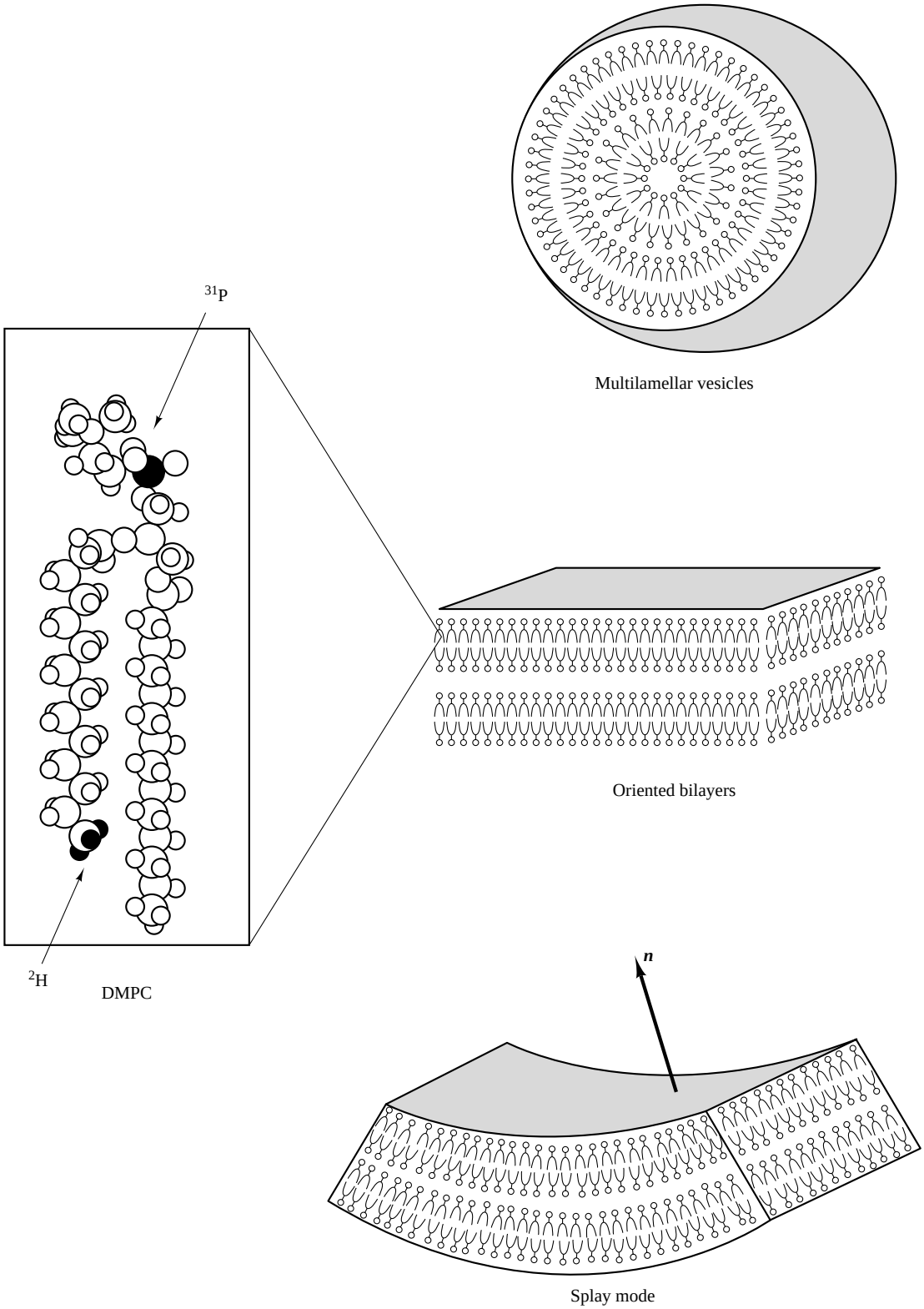

Figure 2 Dimyristoylphosphatidylcholine (DMPC) molecule with ^{2}H and ^{31}P nuclei sites indicated. Also shown are schematic representations of multilamellar vesicles, oriented bilayers, and the collective splay mode for director fluctuations in biological membranes

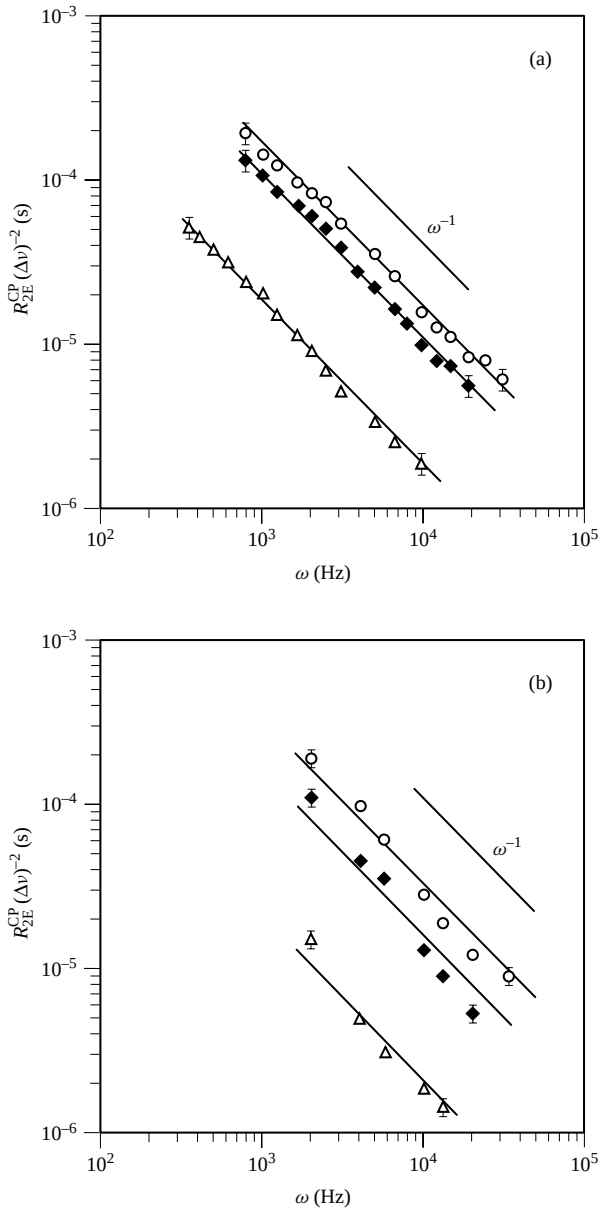

Figure 3 (a) Scaled ^{31}P transverse relaxation rates RCP/2E/$\Delta\nu^2$ measured as functions of pulse frequency ω for hydrated DMPC (open circles), DMPC/4 mol% gramicidin (filled diamonds), and DMPC/40 mol% cholesterol (open triangles) multilamellar vesicles at 313 K. Results refer to the rapidly relaxing 45° orientation. (b) Scaled ^{2}H transverse relaxation rates RCP/2E/$\Delta\nu^2$ measured for the same samples under the same conditions. Solid lines are included as guides to the eye

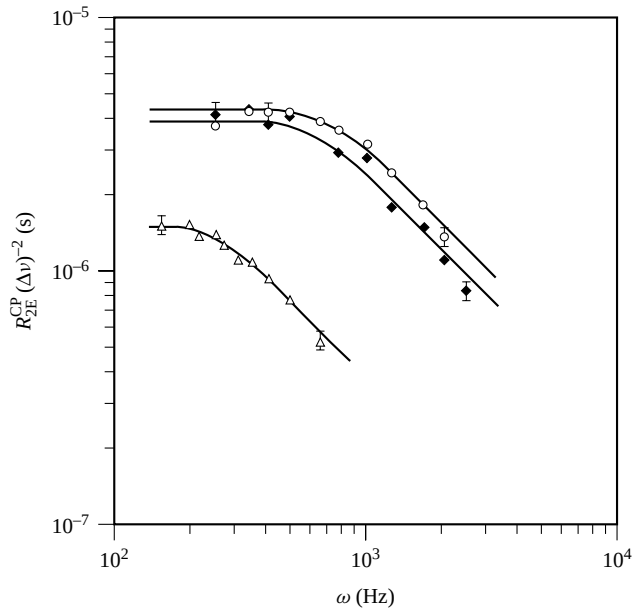

Figure 4 Scaled ^{31}P transverse relaxation rates RCP/2E/$\Delta\nu^2$ measured as functions of pulse frequency ω for hydrated DMPC (open circles), DMPC/4 mol% gramicidin (filled diamonds) and DMPC/40 mol% cholesterol (open triangles) multilamellar vesicles at 313 K. Results refer to the slowly relaxing 90° orientation. Solid lines are included as guides to the eye

orientation fluctuations.[13,15,43] Both of these mechanisms can be considered mesoscopic in that they involve long-range orientational correlations. In the case of collective motions, a low-frequency cutoff in the relaxation dispersion is expected if long-wavelength fluctuation modes are suppressed. This could arise as a result of the finite size of the particles themselves. Alternatively, magnetic damping of the low-energy modes might occur owing to coupling between the NMR static magnetic field and the anisotropic diamagnetic susceptibility of the vesicles.[44] Simple models for lateral diffusion over a curved surface do not predict such a magnetic-field-dependent low-frequency cutoff. Apparently, the measured $R_{2E}^{CP}/\Delta\nu^2$ dispersion profiles indicate that collective motions play a major role in the relaxation mechanism of multilamellar vesicles. However, the quantitative analysis of these measurements is inevitably limited by the sample heterogeneity. Indeed, it is most likely that the dominant relaxation mechanism depends on the vesicle size and that in any particular sample there may be two or more distinct processes that contribute to the overall measured echo decays.

3.2 Oriented Membrane Samples

The problems associated with the use of multilamellar vesicles for studying membrane dynamics have long been recognized, and alternative methods of sample preparation have been proposed. For example, spherical supported vesicles, prepared by condensing membrane bilayers onto spherical silica beads, have been used to measure lateral diffusion rates of lipid molecules.[45] The silica beads employed have extremely narrow distributions of radii, and therefore provide virtually monodisperse vesicles. An alternative approach that seeks to avoid the effects of lateral diffusion involves the use of oriented samples.[41] In this case, the membrane bilayers are uniaxially aligned on glass plates such that the bilayer normal and the plate normal are coincident. Lateral diffusion of the molecules no longer induces any angular reorientation of the lipid molecules, and therefore is ineffective as a spin relaxation mechanism for isolated spins such as ^{2}H or decoupled ^{31}P. Results obtained for oriented DMPC bilayers show R_{2E}^{CP} anisotropies and pulse frequency dispersions consistent with those obtained for multilamellar vesicles, and support the

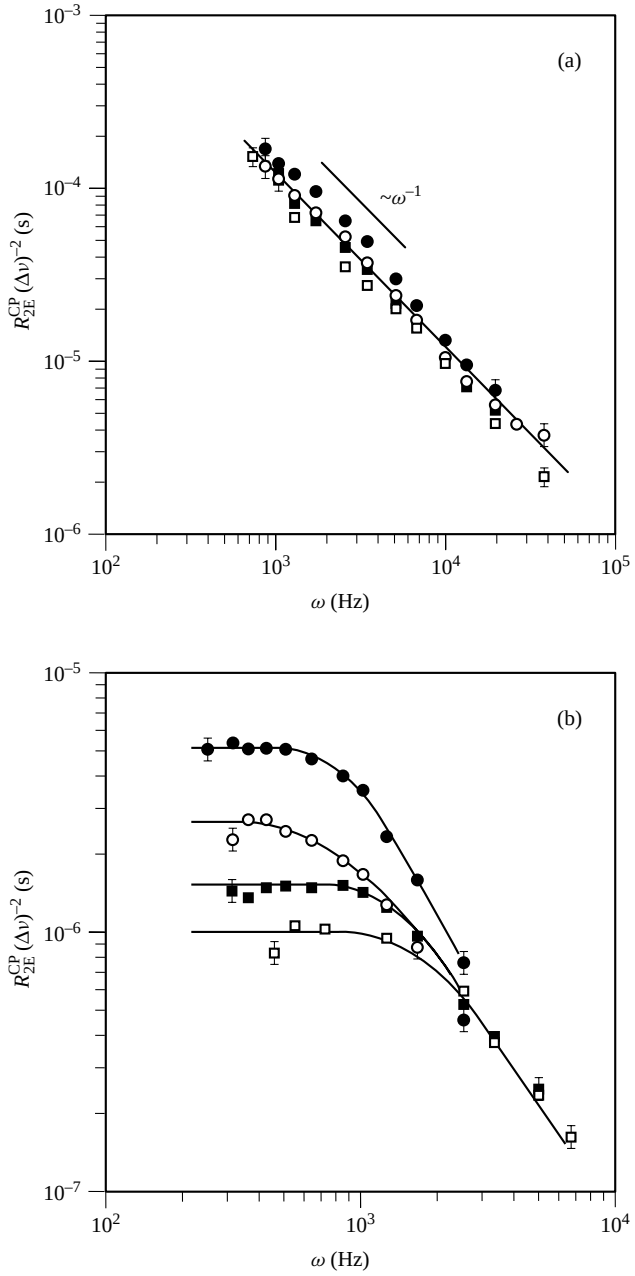

Figure 5 Scaled ^{31}P transverse relaxation rates $R\mathrm{CP/2E}/\Delta\nu^2$ measured as functions of pulse frequency ω for hydrated DMPC at magnetic fields of 4.7 T (filled circles), 7.0 T (open circles), 9.3 T (filled squares), and 11.7 T (open squares): (a) for the rapidly relaxing 45° orientation; (b) for the slowly relaxing 90° orientation. Solid lines are included as guides to the eye

conclusion that collective motions play a major role in the transverse spin relaxation.[12,46]

4 EVALUATION OF VISCOELASTIC PROPERTIES: COLLECTIVE ORIENTATIONAL FLUCTUATIONS

Having identified collective motions as a dominant transverse relaxation process, it then remains to apply a suitable model in order to evaluate the relevant viscoelastic properties. Several hydrodynamic models have been postulated to describe collective orientational fluctuations[47] and surface undulations[14] in membranes.

4.1 Director Fluctuations

One such model, which has been employed by several groups to interpret transverse relaxation, is based on the concept of director fluctuations.[12,13,47,48] In liquid crystal terminology, the director $\boldsymbol{n}$ is defined as the vector describing the orientation of the local phase symmetry axis. It represents the direction of preferred molecular orientation, and in a two-dimensional system such as a membrane may be taken to be normal to the layer surface (see Figure 2). Thermally induced deviations of the director about its average orientation occur, which necessarily modulate the spin interactions of the constituent molecules and hence effect spin relaxation. The director fluctuations may be decomposed into a set of Fourier modes of wavevector q, with mean-square amplitudes $\langle\theta_0^2(q)\rangle$ and exponential decay constants, $\tau(q)$ given by

$$\langle\theta_0^2(q)\rangle = \frac{k_\mathrm{B}T}{VKq^2} \tag{9a}$$

$$\tau(q) = \frac{\eta}{Kq^2} \tag{9b}$$

where K is an elastic constant, η is an effective viscosity, and V is the volume of the mesoscopic uniform sample. By analogy with models developed for director fluctuations in thermotropic liquid crystals,[48] K can be identified with the splay elastic constant K_1, although it has also been suggested that an appropriate quantity for membranes is the curvature elastic modulus $\kappa_\mathrm{c} = Kd$, dependent on the bilayer repeat distance d. A more general model for collective motions in membranes, considering bilayer interactions, has been presented recently.[49]

In deriving Equation (9a), it has been assumed that the director fluctuations are of low amplitude. It then follows that the corresponding spectral densities, defined in the average director or local frame, are highly anisotropic in that $J_1^{\mathrm{loc}}(\omega) \gg J_0^{\mathrm{loc}}(\omega)$, $J_2^{\mathrm{loc}}(\omega)$, and, as a first approximation, it is reasonable to retain just $J_1^{\mathrm{loc}}(\omega)$. Combining equations (6) and (7), and replacing the sum over modes l with an integral over the wavevector q, we obtain

$$R_{2\mathrm{E}}^{\mathrm{CP}} = \frac{27}{8}C\frac{k_\mathrm{B}T}{\pi Kd}\sin^2\theta_\mathrm{N}\cos^2\theta_\mathrm{N} \times \int_{q_l}^{q_\mathrm{c}} \frac{8}{\pi^2}\frac{\tau(q)}{1+\tau^2(q)(\frac{1}{2}\pi\omega)^2}\,hbox{d}\,\ln q \tag{10}$$

The short-wavelength cutoff q_c is governed principally by the molecular dimensions, while the long-wavelength cutoff q_l is related to the size of the effective uniform sample and therefore reflects mesoscopic dimensions. In the case of magnetic damping of collective modes, the long-wavelength cutoff is determined by the magnetic coherence length $\xi = 1/q_l = (K\mu_0/\Delta\chi)^{\frac{1}{2}}(1/B_0)|P_2(\cos\theta_\mathrm{N})|^{-\frac{1}{2}}$, where $\Delta\chi$ is the effective diamagnetic susceptibility anisotropy and μ_0 is the absolute magnetic permeability. The Legendre polynomial $P_2(\cos\theta_\mathrm{N})$ accounts for the orientation dependence of the

Table 1 NMR and Viscoelastic Parameters for Biological Model Membranes at $T = 313\,\mathrm{K}$

Membrane System	Spectral parameter $\Delta\nu$ (kHz)		Elastic constant[a] $K(10^{-11}\,\mathrm{N})$		Effective viscosity[b] $\eta(10^{-3}\,\mathrm{Pa\,s})$
	^{31}P	^{2}H	^{31}P	^{2}H	^{31}P
Pure DMPC	5.2	3.5	0.65	0.50	3.0
DMPC/4 mol% gramicidin	4.9	4.8	1.1	1.0	3.5
DMPC/40 mol% cholesterol	5.4	11.7	6.0	6.0	8.0

[a] K can be identified with the splay elastic constant K_1.[47] A related quantity for membranes is the curvature elastic modulus $k_c = Kd$,[14] dependent on the bilayer repeat distance d.
[b] The viscosity η estimated from the low-frequency cutoff ω_l (see text), based on a diamagnetic susceptibility anisotropy of $\Delta\chi = 1.2 \times 10^{-7}$ SI units.[51]

magnetic interaction.[44] Performing the integration in equation (10) gives

$$R_{2E}^{CP} = \begin{cases} A\omega_l^{-1} & (\omega < \omega_l) \\ A\omega^{-1} & (\omega_c \rangle \omega \rangle \omega_l) \\ A\omega_c\omega^{-2} & (\omega \rangle \omega_c) \end{cases} \tag{11}$$

with

$$A = \frac{27}{2\pi^3} C \sin^2\theta_N \cos^2\theta_N \frac{k_B T}{Kd} \tag{12}$$

where $\omega_l = Kq_l^2/\eta = \Delta\chi B_0^2 |P_2(\cos\theta_N)|/\mu_0\eta$ is the low-frequency cutoff and $\omega_c = Kq_c^2/\eta$ is the high-frequency cutoff. Thus, in the intermediate dispersion regime, we find that $R_{2E}^{CP} \propto \omega^{-1}$ and is independent of η. In the low-frequency regime, R_{2E}^{CP} depends on both K and η as well as on B_0.

4.2 Viscoelastic Parameters

The above expressions account at least qualitatively for the results presented in the previous section. The only obvious point of discrepancy between equation (11) and the experimental results is in the predicted divergence of T_{2E}^{CP} at $\theta_N = 0^\circ$ and $\theta_N = 90^\circ$, although both the oriented sample and the multilamellar vesicles were found to exhibit the correct form for the R_{2E}^{CP} anisotropy. A second-order analysis of director fluctuations[44,50] yields expressions for $J_0^{loc}(\omega)$ and $J_2^{loc}(\omega)$, and consequently predicts finite T_{2E}^{CP} values at all orientations. A slow motional approach also predicts finite T_{2E}^{CP} at 0° and 90°, and is probably more suitable in the present case. However, the detailed modeling of multiple diffusion process such as director fluctuations in the slow motional regime is far from trivial. For present purposes, we restrict our analysis to the first-order motional narrowing limit expressions. By fitting experimental results, the fast relaxation component (45°) yields values for the elastic constant K of the DMPC membranes. From the low-frequency cutoff of the slow relaxation component (90°), estimates for the effective viscosity η are obtained. The results of the analysis are given in Table 1.

The values obtained for K and η are reasonable, and indicate that transverse spin relaxation is able to provide information concerning viscoelastic properties in biological membranes. Of particular importance from a biological point of view is that the technique may be exploited to investigate modifications of membrane viscoelastic behavior caused by included sterols, peptides, or proteins. Indeed, the results presented in Table 1 suggest that these effects are by no means small, and invite speculation regarding the consequences for overall membrane function.

5 RELATED ARTICLES

Amphiphilic Liquid Crystalline Samples: Nuclear Spin Relaxation; Bilayer Membranes: Deuterium and Carbon-13 NMR; Dynamics of Water in Biological Systems: Inferences from Relaxometry; Field Cycling Experiments; Liquid Crystalline Samples: Relaxation Mechanisms; Membrane Lipids of Acholeplasma laidlawii; Membranes: Deuterium NMR; Membranes: Phosphorus-31 NMR; Molecular Motions: T_1 Frequency Dispersion in Biological Systems; Relaxation Effects of Chemical Exchange; Relaxation Theory: Density Matrix Formulation; Ultraslow Motions in Solids.

6 REFERENCES

1. A. G. Anderson and A. G. Redfield, *Phys. Rev.*, 1959, **116**, 583.
2. F. Noack, in *Progress in Nuclear Magnetic Resonance Spectroscopy*, eds. J. W. Emsley, J. Feeney, and L. H. Sutcliffe, Pergamon Press, Oxford, 1986, Vol. 18, p. 171.
3. R. Kimmich and F. Winter, *Prog. Colloid Polym. Sci.*, 1985, **71**, 66.
4. E. Rommel, F. Noack, P. Meier, and G. Kothe, *J. Phys. Chem.*, 1988, **92**, 2981.
5. E. L. Hahn, *Phys. Rev.*, 1950, **80**, 580.
6. J. H. Davis, K. R. Jeffrey, M. Bloom, M. I. Valic, and T. P. Higgs, *Chem. Phys. Lett.*, 1976, **42**, 390.
7. Z. Luz and S. Meiboom, *J. Chem. Phys.*, 1963, **39**, 366.
8. M. Bloom and E. Sternin, *Biochemistry*, 1987, **26**, 2101.
9. H. Y. Carr and E. M. Purcell, *Phys. Rev.*, 1954, **94**, 630.
10. S. Meiboom and D. Gill, *Rev. Sci. Instrum.*, 1958, **29**, 688.
11. S. B. Ahmad, K. J. Packer, and J. M. Ramsden, *Mol. Phys.*, 1977, **33**, 857.
12. J. Stohrer, G. Gröbner, D. Reimer, K. Weisz, C. Mayer, and G. Kothe, *J. Chem. Phys.*, 1991, **95**, 672.
13. P. I. Watnick, P. Dea, and S. I. Chan, *Proc. Natl. Acad. Sci. USA*, 1990, **87**, 2082.
14. M. Bloom and E. Evans, in *Biologically Inspired Physics*, ed. L. Peliti, Plenum Press, New York, 1991, p. 137.
15. E. J. Dufourc, C. Mayer, J. Stohrer, G. Althoff, and G. Kothe, *Biophys. J.*, 1992, **61**, 42.

16. C. P. Slichter and D. C. Ailion, *Phys. Rev.*, 1964, **135**, A1099.
17. A. J. Vega, R. Poupko, and Z. Luz, *J. Magn. Reson.*, 1989, **83**, 111.
18. B. A. Cornell, J. B. Davenport, and F. Separovic, *Biochim. Biophys. Acta*, 1982, **689**, 337.
19. Z.-Y. Peng, V. Simplaceaunu, I. J. Lowe, and C. Ho, *Biophys. J.*, 1988, **54**, 81.
20. H. W. Spiess, *J. Chem. Phys.*, 1980, **72**, 6755.
21. C. Schmidt, S. Wefing, B. Blümich, and H. W. Spiess, *Chem. Phys. Lett.*, 1986, **130**, 84.
22. J. S. Blicharski, *Can. J. Phys.*, 1986, **64**, 733.
23. N. Heaton, D. Reimer, and G. Kothe, *Chem. Phys. Lett.*, 1992, **195**, 448.
24. R. Kubo, in *Advances in Chemical Physics*, ed. K. Schuler, Wiley, New York, 1969, Vol. 15, p. 101.
25. J. H. Freed, G. V. Bruno, and C. F. Polnaszek, *J. Phys. Chem.*, 1971, **75**, 3385.
26. J. R. Norris and S. I. Weissman, *J. Phys. Chem.*, 1969, **73**, 3119.
27. G. Kothe, *Mol. Phys.*, 1977, **33**, 147.
28. R. R. Vold and R. L. Vold, in *Advances in Magnetic and Optical Resonance*, ed. W. S. Warren, Academic Press, San Diego, 1991, Vol. 16, p. 85.
29. R. G. Gordon and J. Messenger, in *Electron Spin Relaxation in Liquids*, eds. L. T. Muus and P. W. Atkins, Plenum Press, New York, 1972, p. 341.
30. G. Moro and J. H. Freed, *J. Chem. Phys.*, 1981, **74**, 3757.
31. H. W. Spiess and H. Sillescu, *J. Magn. Reson.*, 1981, **42**, 381.
32. P. Meier, E. Ohmes, G. Kothe, A. Blume, J. Weildner, and H.-J. Eibl, *J. Phys. Chem.*, 1983, **87**, 4904.
33. D. Reimer, N. Heaton, A. Schleicher, K. Müller, G. Kothe and M. Vilfan, *J. Chem. Phys.*, 1994, **100**, 1693.
34. K. Müller, R. Poupko, and Z. Luz, *J. Magn. Reson.*, 1990, **90**, 19.
35. A. G. Redfield, in *Advances in Magnetic Resonance*, ed. J. S. Waugh, Academic Press, New York, 1965, Vol. 1, p. 1.
36. D. A. Torchia and A. Szabo, *J. Magn. Reson.*, 1982, **49**, 107.
37. C. Mayer, G. Gröbner, K. Müller, K. Weisz, and G. Kothe, *Chem. Phys. Lett.*, 1990, **165**, 155.
38. T. M. Barbara, R. R. Vold, and R. L. Vold, *J. Chem. Phys.*, 1983, **79**, 6338.
39. A. J. Vega, *J. Magn. Reson.*, 1985, **65**, 252.
40. P. Gale, *Biophys. Biochem. Res. Commun.*, 1993, **192**, 1042.
41. H. C. Jarrell, P. Å. Jovall, J. B. Giziewicz, L. A. Turner, and I. C. P. Smith, *Biochemistry*, 1987, **26**, 1805.
42. E. J. Dufourc, C. Mayer, J. Stohrer, and G. Kothe, *J. Chim. Phys.*, 1992, **89**, 243.
43. K. Weisz, G. Gröbner, C. Mayer, J. Stohrer, and G. Kothe, *Biochemistry*, 1992, **31**, 1100.
44. B. Halle, P-O. Quist, and I. Furó, *Phys. Rev. A*, 1992, **45**, 3763.
45. C. Dolainsky, A. Möps, and T. Bayerl, *J. Chem. Phys.*, 1993, **98**, 1712.
46. G. Althoff, N. Heaton, S. Prosser, G. Gröbner, and G. Kothe, manuscript in preparation.
47. J. A. Marqusee, M. Warner, and K. A. Dill, *J. Chem. Phys.*, 1984, **81**, 6404.
48. P. G. De Gennes, *The Physics of Liquid Crystals*, Clarendon Press, Oxford, 1974.
49. B. Halle, *Phys. Rev. E*, 1994, **50**, R2415.
50. R. L. Vold, R. R. Vold, and M. Warner, *J. Chem. Soc., Faraday Trans. 2*, 1988, **84**, 997.
51. F. Scholz, E. Boroske, and W. Helfrich, *Biophys. J.*, 1984, **45**, 589.

Biographical Sketches

Gerd Kothe. *b* 1941. M.S., 1965, University of Munich; Ph.D., 1971, University of Freiburg. Introduced to magnetic resonance by S. I. Weissman. Faculty in Chemistry, University of Stuttgart, 1981–94, University of Freiburg, 1994–present. Approx 90 publications. Research interests include the theory of dynamic magnetic resonance and its application to liquid crystals, polymers, membranes and photosynthetic processes.

Nicholas Heaton. *b* 1962. B.Sc., 1983, University of Leeds; Ph.D., 1986, University of Southampton. Postdoctoral work at UCSD with Bob and Gitte Vold. From 1991–1994 postdoctoral researcher with Gerd Kothe at the University of Stuttgart. Approx. 20 publications. Research interests include application of NMR to study molecular dynamics and structure in liquid crystals and molecular solids.

Bacterial Chemotaxis Proteins: Fluorine-19 NMR

Mark A. Danielson and Joseph J. Falke
University of Colorado, Boulder, CO, USA

1	Introduction	1
2	Methods	1
3	Use of ^{19}F NMR to Probe Conformational Changes	2
4	Use of ^{19}F NMR to Probe Ligand-Binding Kinetics	6
5	Related Articles	7
6	References	7

1 INTRODUCTION

Though crystallographic techniques continue to provide a wealth of protein structural information, the study of conformational changes involved in protein function remains problematic. A protein frequently can only be crystallized in a single conformational state, crystallization may suppress essential dynamics, and crystallography may fail to resolve subtle, but important, conformational changes. Where the protein is too large or the lifetime of a conformational state (e.g. a phosphorylated intermediate) is too short, solution structure determination by multidimensional NMR is not a viable alternative. Fluorine-19 NMR can overcome these problems by providing rapid, sensitive detection of large protein resonances in solution.[1–3] The utility of ^{19}F NMR can be augmented by applying it to proteins of known crystal structure, thereby combining the advantages of high-resolution structural information and the ability to observe the behavior of the protein in solution. The ^{19}F NMR studies of the proteins of bacterial chemotaxis[4–10] represent the first such structure-based application, and the results are being used as a database for the prediction of ^{19}F chemical shifts in proteins (see also ***Chemical Shifts in Biochemical Systems***).[11,12] The power of this approach has been further enhanced by the use of genetic manipulation.

There are several factors contributing to the power of ^{19}F NMR.[4–10,13,14] (i) The ^{19}F nucleus ($S = \frac{1}{2}$) occurs with 100% natural abundance and has a high sensitivity (83% that of ^{1}H). (ii) ^{19}F does not occur naturally in proteins, thus there are no background signals with which to contend. (iii) Though the large anisotropy of the chemical shift tensor leads to broader linewidths at high field strengths, the frequency range is large (100-fold larger than ^{1}H), and individual resonances can generally be resolved. Furthermore, the chemical shift is controlled primarily by the fluorine lone pair electrons, which provide a large paramagnetic term in the shielding formula. As a result, the resonance frequency is exquisitely sensitive to changes in the local van der Waals environment as well as local electrostatic forces.[11,12] (iv) Fluorine is nearly the same size as hydrogen (covalent radius of 0.014 nm compared with 0.012 nm, respectively), and aromatic fluorine lacks the propensity to form hydrogen bonds.[13,14] Thus the substitution of fluorine for hydrogen on an aromatic ring is generally nonperturbing, as confirmed by activity assays.[3,4,9,10] (v) Fluorine can be easily incorporated biosynthetically. (vi) Fluorine resonances are often resolved in one-dimensional spectra, thus detection requires less time and lower concentrations of protein than multidimensional techniques.

Bacterial chemotaxis provides an ideal model system for conformational studies of signaling proteins. It is a simple, well-defined pathway of the two-component type widespread in prokaryotes and eukaryotes, which has many features in common with other eukaryotic signaling pathways.[15–18] Furthermore, structures have been determined for many of its components. These proteins, being in a bacterial system, are easily genetically manipulated. Chemotaxis proteins which have been studied by ^{19}F NMR include the galactose-binding protein,[4–7] the aspartate receptor,[7,10] and the response regulator, CheY.[8,9] Briefly, the galactose-binding protein is a 32 kDa periplasmic soluble receptor which binds the attractant galactose or glucose, then docks to and regulates a transmembrane chemoreceptor similar to the aspartate receptor. The transmembrane aspartate receptor is a 120 kDa dimeric protein which directly senses attractants such as aspartate or glutamate in the periplasm and, in response to changes in concentrations of these ligands, alters the activity of an associated cytoplasmic kinase. This kinase transfers a phosphate to the response regulator CheY, a 14 kDa signaling protein which binds to and regulates the flagellar motor, thereby altering the swimming behavior of the cell.

2 METHODS

The fluorine labels of choice are aromatic amino acids containing a single fluorine substituted for hydrogen at a specific ring position. A wide variety of isomers are available. One advantage of these labels is that they can be easily biosynthetically incorporated into the protein by eliminating the ability of the cell to synthesize endogenously the respective amino acid. This is accomplished by using a bacterial strain auxotrophic for the amino acid of interest[4,8] or by adding glyphosate,[10] which inhibits all three aromatic amino acid synthesis pathways. Subsequently the desired fluorine label is added to the growth medium during protein expression. Less than 100% incorporation is achieved because it is necessary to include unlabeled amino acid in order to maximize protein production. Observed incorporation levels range from 5 to 65%.[4,8,10]

It is important to determine the effect of fluorine incorporation on protein activity, to ascertain whether the fluorine label is perturbing. Two approaches are used. When high levels of incorporation are achieved, the effect of fluorine on the activity can be assayed directly.[4] When the level of incorporation is low, a mutagenic approach is required. For instance, in studies using 4-F-Phe, a specific phenylalanine may be replaced with tyrosine to determine the maximum effect of *para* substitution at that location in the protein.[9,10]

Assignment of resonances is carried out by site-directed mutagenesis. Figure 1 illustrates the two different methods utilized in assignment. The first method generates a conservative substitution at a specific labeling position (e.g. phenylalanine to tyrosine).[3,4,8,10] When a single resonance disappears, leaving those remaining unaffected, this resonance can be directly

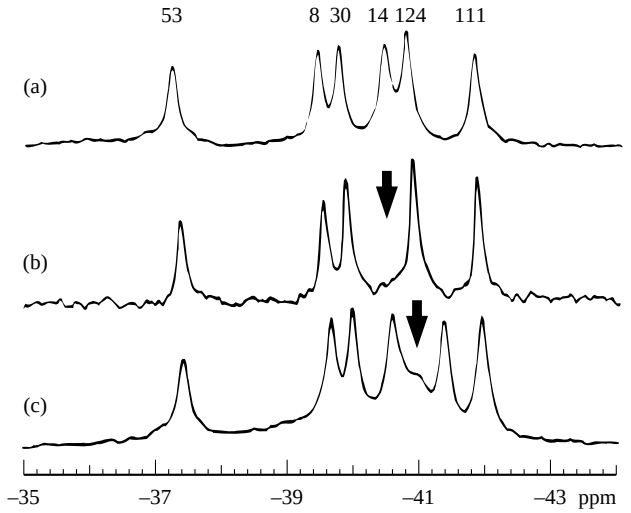

Figure 1 Assignment of 4-F-Phe resonances in CheY.[8] Shown are ^{19}F NMR spectra of (a) the wild-type protein, (b) the F14Y mutant used to assign the 4-F-Phe14 resonance by direct replacement, and (c) the N121Q mutant which assigns the 4-F-Phe124 resonance by the "nudge" method. The numbers above the spectra indicate the 4-F-Phe residue to which each resonance has been assigned. The arrows indicate the original position of each altered resonance

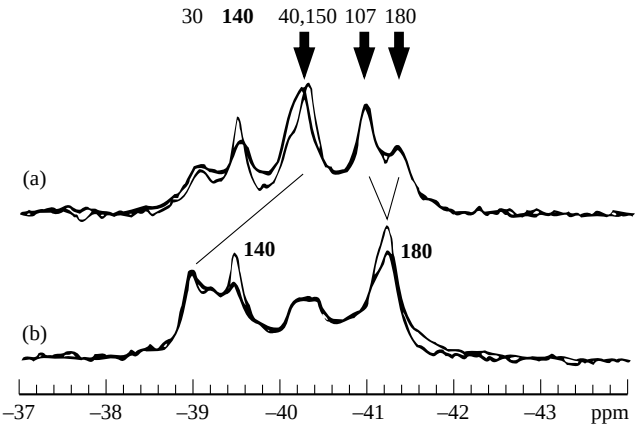

Figure 2 Paramagnetic broadening of solvent-exposed resonances by $Gd^{3+}EDTA^{4-}$. Shown are the ^{19}F NMR spectra[10] of the (a) apo and (b) aspartate-bound conformations of the 4-F-Phe-labeled aspartate receptor in the presence (bold line) and absence (fine line) of $Gd^{3+}EDTA^{4-}$. The numbers above the spectra indicate the 4-F-Phe positions to which each resonance has been assigned. Bold-face numbers indicate the resonances which have been broadened by the probe. The arrows and diagonal lines indicate resonances which are shifted by aspartate

assigned to the substituted position [Figure 1(b)]. The second approach (termed the 'nudge' method) identifies, in the crystal structure, a sidechain which is in van der Waals contact with the position of interest. The contacting side chain is then replaced with a larger or smaller side chain, and, when a single resonance is altered, it can be assigned to the 'nudged' position [Figure 1(c)].[8,10] In most cases, the assignment of a surface residue can be confirmed by paramagnetic broadening,[8,10] since the resonance of a surface residue should be broadened by an aqueous paramagnetic probe, such as chelated Gd^{3+} (Figure 2).

3 USE OF ^{19}F NMR TO PROBE CONFORMATIONAL CHANGES

3.1 Strategy

Due to the importance of aromatic side chains in many aspects of protein function, aromatic fluorine labels are often located in critical regions of the target protein, including most ligand and effector protein-binding sites, as indicated in Figure 3. Two ^{19}F NMR approaches are used to probe conformational changes. The first is to map out the regions involved in the conformational change by observing which ^{19}F NMR resonances yield chemical shift changes (e.g. Figure 4). Though neither the sign nor the magnitude of a chemical shift change is interpretable, the shift change does indicate a conformational change in the vicinity of the label. In fact, the extreme sensitivity of ^{19}F NMR resonances to their environment provides what is perhaps the most sensitive physical method available for the detection of local conformational changes. The second technique uses paramagnetic broadening to measure distances and changes in solvent exposure (e.g. Figure 2). The two techniques have been used to characterize conformational changes due to ligand binding, mutagenesis, disulfide formation, phosphorylation, and protein–protein interactions in the following chemotaxis proteins.

3.2 Galactose-Binding Protein

When the galactose-binding protein is labeled at its five tryptophan positions with 5-F-Trp, the ligands D-galactose and D-glucose are observed to induce significantly different chemical shift changes for the 5-F-Trp183 resonance from the sugar-binding site, while inducing identical shift changes for both the 5-F-Trp133 and 5-F-Trp195 resonances, as seen in Figure 4.[4] In contrast, no shift changes are observed for the 5-F-Trp127 and 5-F-Trp133 resonances from the vicinity of the Ca^{2+} binding site. The converse is observed when Ca^{2+} binds: only the nearby 5-F-Trp127 and 5-F-Trp133 resonances yield detectable shift changes [compare Figure 3(a) and Figure 3(b)].[5] Similar results are obtained when the protein is labeled at its seven phenylalanine positions with 3-F-Phe.[4,5] Together these results indicate that sugar binding triggers a long-range conformational change in both domains of the galactose-binding protein, while Ca^{2+} alters only the region near its binding site. The results are consistent with the different functions of these ligands: sugar binding must generate changes in surface structure which enable docking to a transmembrane receptor, while Ca^{2+} binding simply stabilizes the folded structure and does not have a signaling role. The results also demonstrate the ability of ^{19}F NMR to distinguish local and global conformational changes in the same signaling protein.

A key feature of the conformational change induced by sugar binding is the closure of the sugar-binding cleft, which traps the sugar inside. The minimum angle of cleft opening upon removal of sugar has been measured by paramagnetic broadening using the aqueous probe $Gd^{3+}EDTA^{4-}$. This method utilizes the inverse sixth power distance dependence of paramagnetic broadening which quantifies the separation

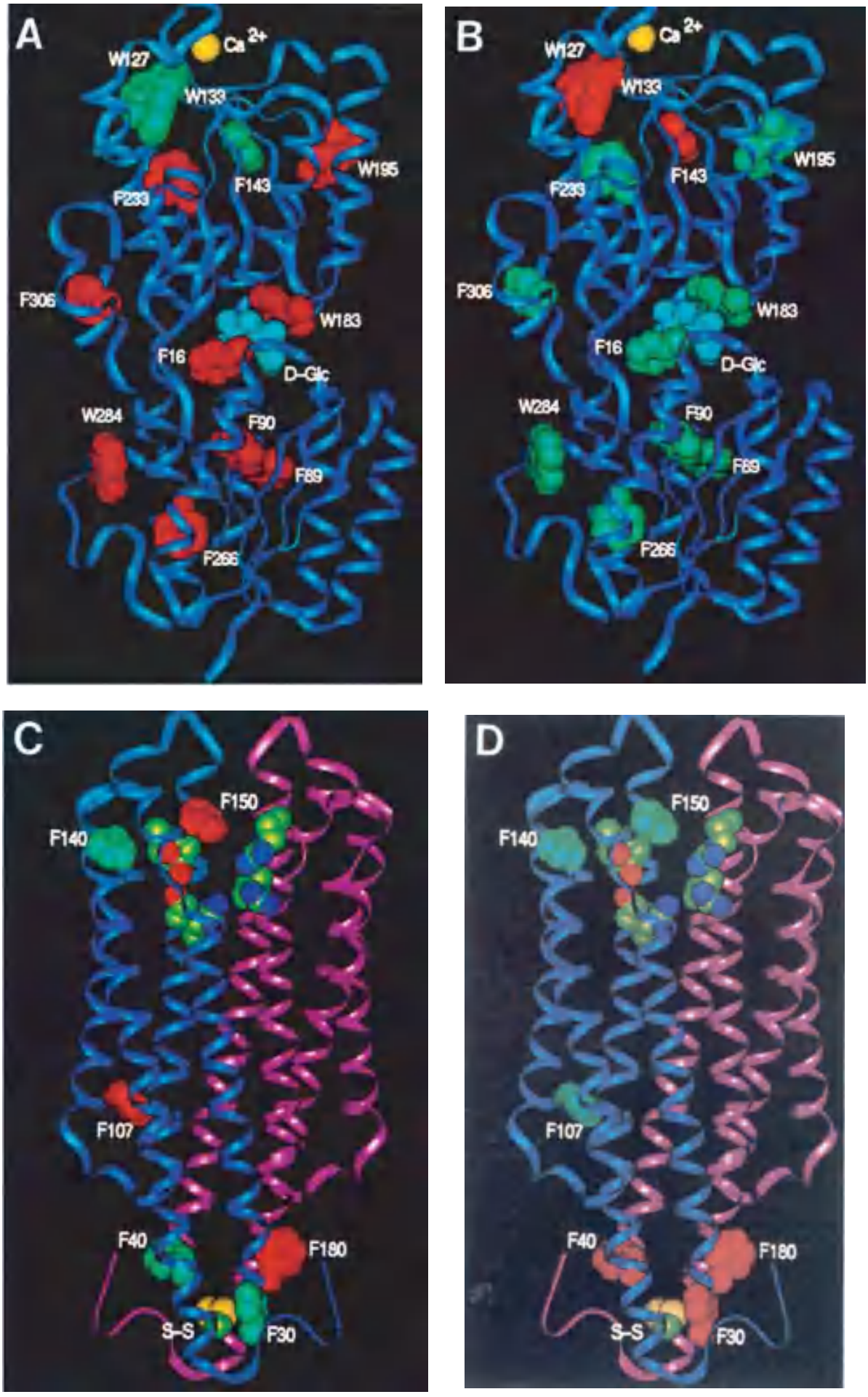
A
Ca 2+
W127
W133
W195
F143
F233
F306
W183
F16
D-Glc
W284
F90
F89
F266
B
Ca 2+
W127
W133
W195
F143
F233
F306
W183
F16
D-Glc
W284
F90
F89
F266
C
F150
F140
F107
F40
F180
S-S
F30
D
F150
F140
F107
F40
F180
S-S
F30

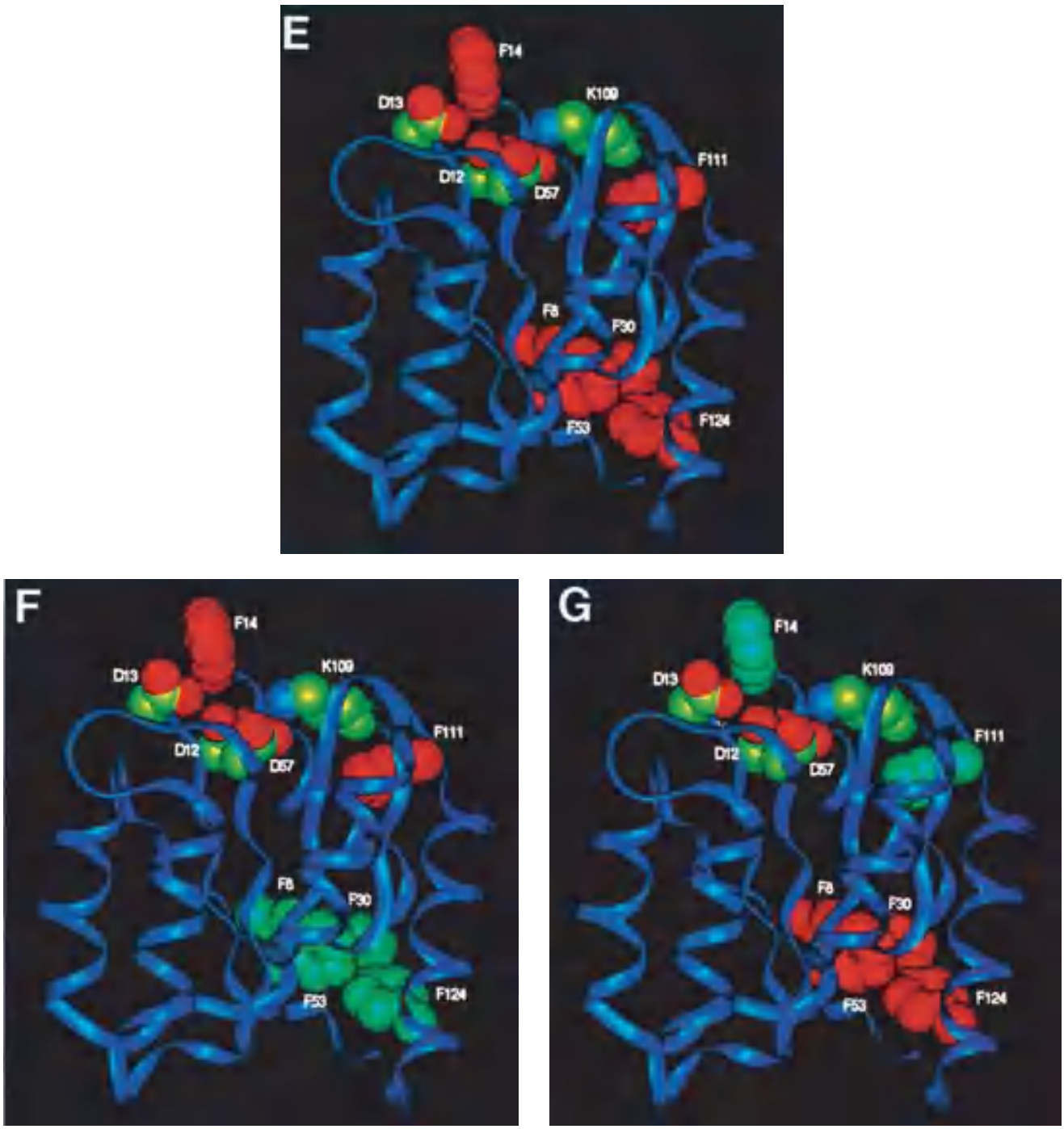

Figure 3 Use of ^{19}F NMR to map conformational changes in the crystal structures of the galactose-binding protein,[19] the ligand-binding domain of aspartate receptor,[20] and the response regulator CheY.[21] Fluorine-labeling positions are shown as CPK aromatic side chains colored green when the ^{19}F NMR chemical shift is unperturbed by the indicated conformational changes, or red when the chemical shift is perturbed. Thus the red probe residues map out the regions involved in each observed conformational change. (A),(B) Conformational effects of D-glucose (cyan CPK) and Ca^{2+} (yellow sphere) binding to the galactose-binding protein, respectively.[3,4] (C),(D) Conformational effects of aspartate binding, and either intersubunit disulfide formation or 1,10-phenanthroline binding to the ligand-binding domain of the aspartate receptor, respectively.[10] Also shown are one of the two symmetric aspartate-binding sites (CPK side-chains colored by atom type) and the intersubunit disulfide (CPK side-chain labeled S−S′). (E),(G) Conformational effects of phosphorylation, activating mutations (D13K and D13R), and kinase fragment binding [CheA(P2)] on the response regulator CheY, respectively.[8,9,24] Also displayed are the conserved active site residues Asp12, Asp13, Asp57, and Lys109 (CPK side chains colored by atom type)

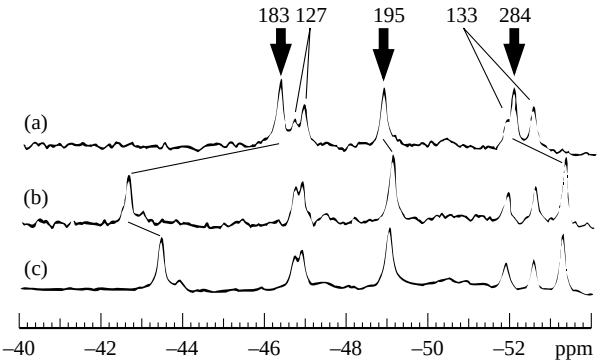

Figure 4 Effect of sugar ligands on the galactose-binding protein.[4] Shown are the ^{19}F NMR spectra of the (a) apo, (b) D-galactose-bound, and (c) D-glucose-bound conformations of the 5-F-Trp-labeled galactose-binding protein. The numbers above the spectra indicate the 5-F-Trp positions to which the resonances have been assigned. The arrows and diagonal lines indicate resonances which shift upon ligand binding

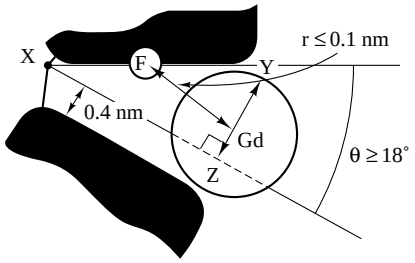

Figure 5 Determination of the extent of cleft opening in the galactose-binding protein.[6] The minimum distance (r) between the ^{19}F nucleus of 5-F-Trp183 (F) and the $Gd^{3+}EDTA^{4-}$ probe (Gd) is determined by the paramagnetic broadening of the observed NMR resonance. The known dimensions of the cleft and the probe, together with the minimum distance r, enable calculation of the cleft angle

between the paramagnet and the observed ^{19}F nucleus. Due to the mobility of the paramagnet, the linewidth cannot determine the exact separation, but it can establish an upper bound on this distance and thus a minimum angle of cleft opening. The cleft is observed to open at least 18° in the absence of sugar, enabling the paramagnetic probe to enter (Figure 5).[6]

3.3 Aspartate Receptor

In a ^{19}F NMR study of the 5-F-Trp-labeled aspartate receptor in its native membrane, the resonance of a lone, mobile 5-F-Trp residue in the cytoplasmic domain near the C-terminus is detected.[7] Aspartate binding to the periplasimic domain on the opposite side of the membrane generates a transmembrane conformational transition yielding a chemical shift change for the probe resonance. Multiple probe resonances are needed, however, to map out the regions of the protein involved in transmembrane signaling.

To probe the initiation of the transmembrane signal, the soluble ligand-binding domain of the receptor, which has been cloned and shown to retain the native conformational change,[10, 22] has been investigated. Upon labeling with 4-F-Phe at the six phenylalanine positions in each monomer, ^{19}F NMR studies of the dimeric domain reveal a broad group of unresolved resonances in the absence of ligand, indicating a dynamic or heterogenous structure.[10] Introduction of a cysteine mutation and formation of a disulfide bond (Cys36-Cys36′) between subunits of the homodimer stabilizes the apo conformation such that resonances become resolved and the effect of ligand binding can be monitored. As seen for the galactose-binding protein, different ligands generate different local conformations in the activation site but the same long-range conformational change [Figure 2 and 3(c)]. Furthermore, since the 4-F-Phe107 residue lies over 1 nm from the subunit interface the aspartate-induced chemical shift change observed for its resonance indicates that a conformational change occurs within each subunit. The 4-F-Phe180 resonance also exhibits an aspartate-induced chemical shift change, as well as an increase in solvent exposure detected by paramagnetic line broadening (see Figure 2). These results imply that the transmembrane signal may be transmitted through the C-terminal helix of the domain, which extends from the Phe180 position across the bilayer as the second transmembrane helix in the intact receptor. Finally, though the dimer contains two identical attractant binding sites, the full conformational change is observed when only one site is occupied, indicating negative cooperativity between the sites.[10]

In contrast to the long-range conformational change triggered by aspartate binding to the activation site, introduction of the Cys36-Cys36′ disulfide bond or the binding of the nonphysiological ligand 1,10-phenanthroline generates only a local conformational change [see Figure 3(d)].[10] Thus, as for the galactose-binding protein, ^{19}F NMR is able to identify the long-range conformational change specifically generated by an activating ligand.

3.4 CheY

The short lifetime of the phosphorylated state of CheY ($\tau_{\frac{1}{2}} \sim 6$ s) poses considerable difficulties in studies of the activated conformation by NMR. This problem has been overcome by chemically phosphorylating CheY with small-molecule phosphodonors such as acetyl phosphate.[23] Using excess acetyl phosphate to maintain steady state phosphorylation over a period of 10 min, a ^{19}F NMR spectrum has been obtained of 4-F-Phe-labeled CheY-phosphate.[8] The results indicate that a global conformational change is induced by phosphorylation (see Figure 3(e)).

Investigating the conformational changes induced by six single or double mutations which constitutively activate the protein allows development of a more detailed model for CheY.[9] The one consistent perturbation caused by these activating mutations is in the chemical shift of the 4-F-Phe111 resonance, which provides a sensitive probe of the salt bridge between Lys 109 and Asp57, the site of phosphorylation in the wild-type protein (see Figure 3(f)). It has been proposed that a repositioning of this salt bridge provides an on–off 'switch' during activation.[14] The chemical shift change of the 4-F-Phe111 probe suggests that the salt bridge is weakened or broken by the activating mutations, thereby supporting the idea that this ionic interaction plays a central role in activation. Other ^{19}F NMR and genetic results indicate that the activation of Che Y occurs in two conformational steps: the first generated by phosphorylation, and the second presumably

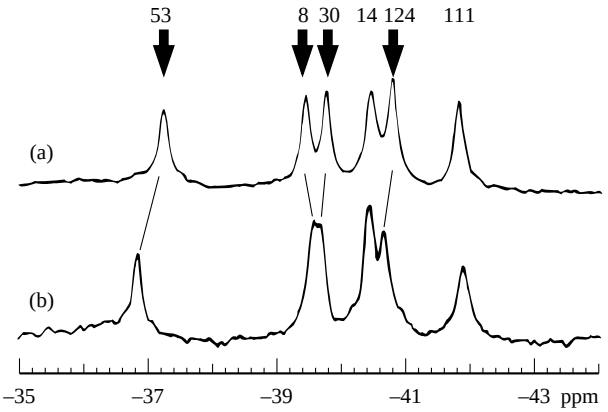

Figure 6 Effect of kinase fragment binding on CheY.[24] Shown are the ^{19}F NMR spectra of 4-F-Phe-labeled CheY in the (a) absence (apo conformation) and (b) presence of the unlabeled kinase fragment CheA(P2). The numbers above the spectra indicate the 4-F-Phe positions to which each resonance has been assigned. The arrows and diagonal lines indicate resonances which have been shifted by CheA(P2) binding. ^{19}F NMR spectra were obtained as previously described.[8] Protein concentrations were [CheY] = 4 mM and [CheA(P2)] = 6 mM

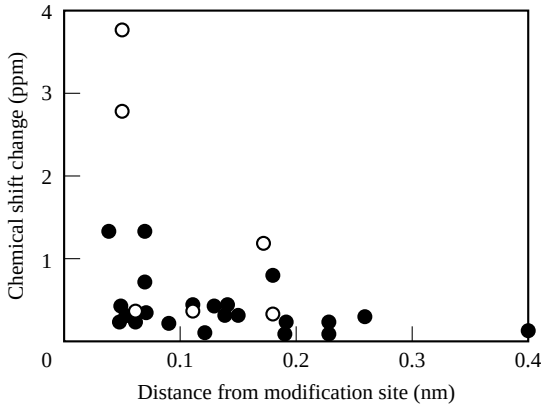

Figure 7 Distance dependence of chemical shift changes. Shown is a summary of chemical shift changes induced by ligand binding, phosphorylation, disulfide formation, and lock-on mutations in three chemotaxis proteins. Each chemical shift change is plotted according to its distance from the modification site in the known crystal structure. ○, 5-F-Trp; ●, 4-F-Phe

triggered by docking to its effector complex, the flagellar motor.

A subsequent ^{19}F NMR study of 4-F-Phe-labeled CheY has characterized the region of this protein perturbed by the binding of CheA(P2), a kinase fragment containing the CheY-binding domain (Figure 6).[24] Interestingly, the conformational change is localized on the opposite side of CheY from the site of phosphorylation [Figure 3(g)], implying that the kinase domain of CheA must reach around the CheY molecule in order to phosphorylate it.

3.5 Summary of ^{19}F NMR Chemical Shift Changes

Figure 7 summarizes the chemical shift changes triggered by ligand binding, phosphorylation, activating mutations, and disulfide formation in the galactose-binding protein, the aspartate binding domain, and CheY. The largest frequency shifts are observed for fluorine labels within 0.7 nm of the modification site. However, large shifts (>0.5 ppm) are also observed at label positions ranging up to 1.8 nm from the modification site. These results confirm the ability of ^{19}F NMR to detect both the local changes near a modification site and the long-range conformational changes which play critical roles in the functions of these signaling proteins.

4 USE OF ^{19}F NMR TO PROBE LIGAND-BINDING KINETICS

In addition to providing a spatial map of conformational changes in chemotaxis proteins, ^{19}F NMR has been used to characterize the kinetic parameters of these conformational changes. The standard relationships of NMR exchange averaging can place limits on the frequency of a conformational change, or, in favorable cases, can determine this rate directly [equations (1)–(3)].[25]

Slow exchange: distinct resonances

$$(\nu_{ic} \ll |\nu_A - \nu_B|) \quad (1)$$

Intermediate exchange: resonances disappear

$$(\nu_{ic} \sim |\nu_A - \nu_B|) \quad (2)$$

Fast exchange: single averaged resonance

$$(\nu_{ic} \gg |\nu_A - \nu_B|) \quad (3)$$

When two conformations A and B yielding NMR frequencies ν_A and ν_B interconvert over time at a frequency of ν_{ic}, two distinct resonances are observed if the interconversion is slow relative to the difference in their NMR frequencies (equation (1)). If, on the other hand, the interconversion rate is rapid relative to the NMR frequency difference, then a single exchange-averaged resonance is observed (equation (3)). In the intermediate exchange limit, where the interconversion rate approximately equals the NMR frequency difference, the two resonances disappear due to extreme broadening [equation (2)]. Observation of the latter intermediate exchange limit enables direct determination of the interconversion rate, while the slow and rapid exchange cases provide upper and lower limits, respectively, on the interconversion rate. Spectral simulations can provide further information on both interconversion kinetics and the relative populations of different conformational states.

In the case of the galactose-binding protein, ^{19}F NMR has confirmed the long lifetime of sugar bound in the cleft,[4] which enables the binding protein to trap a sugar molecule until the complex diffuses to its membrane docking site. The 5-F-Trp183 resonance shifts by 3.8 ppm (1800 Hz) upon addition of D-galactose, and by 2.8 ppm (1300 Hz) upon addition of D-glucose. In either case, addition of substoichiometric amounts of the ligand results in distinct resonances at positions corresponding to the apo and ligand-bound states, indicating

that sugar dissociation is in the slow exchange limit. Thus, from equation (1) it can be concluded that the lifetime of the galactose-bound state $\tau_{ic} \gg 0.6$ ms and the lifetime of the glucose-bound state is $\tau_{ic} \gg 0.8$ ms, consistent with direct kinetic measurements yielding bound sugar lifetimes of 220 ms for D-galactose and 710 ms for D-glucose.[26]

Turning to the ligand-binding domain of the aspartate receptor, kinetic analysis has revealed the rate constants for both aspartate association and dissociation.[10] When the ligand-binding domain is titrated with increasing concentrations of aspartate, the ^{19}F NMR resonance of 4-F-Phe150 in the aspartate-binding pocket passes from slow to intermediate to rapid exchange as the rate of aspartate binding increases, due to the interconversion of the apo and aspartate-occupied conformations. At an estimated free aspartate concentration of 0.4 μM, the intermediate exchange limit is reached and the resonance disappears. From equation (2), this aspartate concentration yields an aspartate-binding rate which matches the frequency difference ($\nu_{ic} = k_{on}\cdot[\text{Asp}] \sim |\nu_A - \nu_B|$), thereby yielding the pseudo-first order rate constant for aspartate binding, $k_{on} \sim 10^9\ M^{-1}\ s^{-1}$. Subsequently the dissociation rate can be calculated from the association rate constant and K_D ($= k_{off}/k_{on} = 10^{-6}$ M), yielding $k_{off} \sim 10^3\ s^{-1}$. (Here the frequency difference $|\nu_A - \nu_B|$ is 1.3 ppm or 610 Hz, as measured at saturating aspartate concentrations. In this example no corrections are needed for population differences, since in the intermediate exchange limit the aspartate association and dissociation rates are nearly equal, so that the apo and aspartate-occupied conformations are equally populated.) These results indicate that aspartate binding approaches the diffusion-controlled limit, placing the aspartate-binding domain in the category of the most rapid protein enzymes in its ability to bind ligands on a short timescale. Moreover, the aspartate binding and dissociation rates are fast on the timescale of the chemotactic response, indicating that subsequent phosphorylation and/or diffusion events are rate-limiting in the signaling pathway.

5 RELATED ARTICLES

Bilayer Membranes: Proton and Fluorine-19 NMR; Chemical Shifts in Biochemical Systems; Fluorine-19 NMR; D-Lactate Dehydrogenase.

6 REFERENCES

1. B. D. Sykes, H. I. Weingarten, and M. J. Schlesinger, *Proc. Natl. Acad. Sci. USA*, 1974, **71**, 469.
2. M. L. Wilson, and F. W. Dahlquist, *Biochemistry*, 1985, **24**, 1920.
3. G. S. Rule, E. A. Pratt, V. Simplaceau, and C. Ho, *Biochemistry*, 1987, **26**, 549.
4. L. A. Luck, and J. J. Falke, *Biochemistry*, 1991, **30**, 4248.
5. L. A. Luck, and J. J. Falke, *Biochemistry*, 1991, **30**, 4257.
6. L. A. Luck, and J. J. Falke, *Biochemistry*, 1991, **30**, 6484.
7. J. J. Falke, L. A. Luck, and J. Sherrer, *Biophys. J.*, 1992, **62**, 82.
8. S. K. Drake, R. B. Bourret, L. A. Luck, M. I. Simon, and J. J. Falke, *J. Biol. Chem.*, 1993, **268**, 13 081.
9. R. B. Bourret, S. K. Drake, S. A. Chervitz, M. I. Simon, and J. J. Falke, *J. Biol. Chem.*, 1993, **268**, 13 089.
10. M. A. Danielson, H.-P. Biemann, D. E. Koshland, Jr., and J. J. Falke, *Biochemistry*, 1994, **33**, 6100.
11. A. C. deDios, J. G. Pearson, and E. Oldfield, *Science*, 1993, **260**, 1491.
12. S. E. Chambers, E. Y. Lau, and J. T. Gerig, *J. Am. Chem. Soc.*, 1994, in press.
13. J. T. Gerig, *Methods Enzymol.*, 1989, **177**, 3.
14. J. T. Gerig, *Prog. Nucl. Magn. Reson. Spectrosc.*, 1994, **26**, 293.
15. J. B. Stock, and G. S. Lukat, *Annu. Rev. Biophys. Biophys. Chem.*, 1991, **20**, 109.
16. R. B. Bourret, K. A. Borkovich, and M. I. Simon, *Annu. Rev. Biochem.*, 1991, **60**, 401.
17. J. S. Parkinson, and E. C. Kofoid, *Annu. Rev. Genet.*, 1992, **26**, 71.
18. G. L. Hazelbauer, H. C. Berg, and P. Matsumura, *Cell*, 1993, **73**, 15.
19. N. K. Vyas, M. N. Vyas, and F. A. Quiocho, *Nature*, 1987, **327**, 635.
20. M. V. Milburn, G. G. Privé, D. L. Milligan, W. G. Scott, J. Yeh, J. Jancarik, D. E. Koshland, Jr., and S.-H. Kim, *Science*, 1991, **254**, 1342.
21. K. Volz, and P. Matsumura, *J. Biol. Chem.*, 1991, **266**, 15 511.
22. D. L. Milligan, and D. E. Koshland, Jr., *J. Biol. Chem.*, 1993, **268**, 19 991.
23. G. S. Lukat, W. R. McCleary, A. M. Stock, and J. B. Stock, *Proc. Natl. Acad. Sci. USA*, 1992, **89**, 718.
24. S. L. Butler, and J. J. Falke, Unpublished collaboration with J. S. Parkinson (University of Utah).
25. G. Wagner, and K. Wüthrich, *Methods Enzymol.*, 1986, **131**, 307.
26. D. M. Miller, J. S. Olson, and F. A. Quiocho, *J. Biol. Chem.*, 1980, **255**, 2465

Biographical Sketches

Mark A. Danielson. *b* 1968. B.S., 1990, University of Minnesota, USA, Ph.D., in progress, University of Colorado, USA. Introduced to NMR by Professor Falke and Professor A. Pardi. Research specialties: the mechanism of transmembrane signaling by the transmembrane aspartate receptor, application of ^{19}F NMR to the study of protein conformational changes.

Joseph J. Falke. *b* 1956. B.A. 1978, Earlham College, USA, Ph.D., 1984, California Institute of Technology, USA (introduced to NMR by doctoral advisor S. I. Chan). Postdoctoral work at the University of California at Berkeley, USA, 1984–1987 (postdoctoral advisor D. E. Koshland, Jr.). Faculty in Chemistry and Biochemistry, University of Colorado, Boulder, 1987–present. Research specialties: biophysical studies of sensory and signaling proteins, the use of NMR to probe conformational changes in large proteins.

Biological Macromolecules

Oleg Jardetzky
Stanford University, CA, USA

1 Introduction 1
2 Macromolecular Structure from NMR Data—General Strategy 1
3 Macromolecular Dynamics 13
4 Molecular Interactions 17
5 Protein Function 18
6 Conclusions 18
7 Appendix: Definition of Symbols Used in Equation (16) 18
8 References 19

1 INTRODUCTION

High-resolution NMR spectroscopy has become, alongside X-ray crystallography, one of the two most important physical methods for the study of the *structure, dynamics, interactions* and *function* of biological macromolecules—in particular proteins and nucleic acids and, to a lesser extent, polysaccharides. This article summarizes under each of these headings the general framework, the essential techniques and classical paradigms for the application of NMR in molecular biology, illustrated by the key original findings. More specialized accounts can be found under specific topics. The historical development of this field has been described in volume I of this Encyclopedia.

High-resolution NMR shares a common feature with X-ray diffraction in that both methods—in contrast to all other physical methods—permit the study of biological macromolecules at *atomic resolution*. Beyond that, the two methods are in many ways complementary. NMR offers the advantage that it allows the study of macromolecules in solution, their natural environment, while X-ray diffraction requires crystallization. Structures with molecular weights up to 37 kDa can now be determined by NMR, and the molecular weight range is likely to be soon extended upwards. Structures approaching the 1000 kDa range are already amenable to study by X-ray diffraction. Yet crystallography yields a static picture, whereas NMR provides, in addition to the structure, information on its dynamics. Such information is particularly important for the understanding of biological function. NMR is also the method of choice for the study of ligand interactions. It lends itself more easily to the determination of informative partial structures and allows estimates of ligand exchange rates, rates of structural changes in the macromolecule and observations of the modulation of macromolecular dynamics by ligand binding.

There is, however, a fundamental difference between structural information that can be derived from NMR data and that obtainable by X-ray diffraction. The experimental diffraction pattern is a simple function of geometric parameters and can be converted by Fourier transformation directly into an electron density map and hence, in principle, into a set of coordinates. In practice, for macromolecular structures, resolution is never sufficient, and model building becomes an essential part of structure determination. On the other hand, direct transformation from data to a set of coordinates is, even in principle, impossible in NMR. Measurable NMR parameters depend simultaneously on several internuclear distances, rates of motion and rates of conformational averaging. To obtain geometric parameters (internuclear distances or angles) from a set of NMR data, it is necessary to make assumptions about the dynamics and other features of the structure. To then obtain a set of coordinates, it is necessary to search the conformational space accessible to the macromolecular chain, usually adding information not obtainable directly from NMR experiments. Both the subjective judgments required and the methods of searching conformational space are important potential sources of error. These are discussed further in the sections devoted to specific methods of structure calculation.

2 MACROMOLECULAR STRUCTURE FROM NMR DATA—GENERAL STRATEGY

Defining the structure and dynamics of a biological macromolecule (protein or nucleic acid fragment) from NMR data requires four steps: (1) experimental *resolution* and (2) *assignment* of the macromolecular spectrum; (3) *interpretation* of the observed spectra in terms of *geometric parameters* and their changes in time; and (4) *structure calculation or model building*, for which a variety of computer algorithms are available.

The limiting steps are usually the resolution and the assignment of the NMR spectrum. NMR spectra of a macromolecule typically consist of a few hundred to a few thousand overlapping lines. The first experimental task is then to resolve all spectral lines and to assign each spectral line to a specific nucleus in a specific residue in the sequence. For linear polymers, such as proteins and nucleic acids (with few exceptions), the task has become manageable. The situation for polysaccharides, where branching is frequent, is more complicated, and the assignment problem has not been completely solved.

The geometric parameters necessary for building models of a macromolecular structure are[1] estimates of internuclear distances, derived from relaxation parameters, in particular from the Nuclear Overhauser Effect (NOE)[2] estimates of dihedral angles, derived from coupling constants, and auxiliary constraints,[3] which can sometimes be derived from chemical shifts (e.g. ring current shifts in nucleic acids, charateristic shifts in α-helices), proton exchange rates (slow rates are often taken to be indicative of hydrogen bonding), or other spectroscopic measure-ments. NMR spectroscopic data are by themselves never sufficient to define a macromolecular structure. Any structural interpretation of NMR data is, in practice, though not in principle, predicated on prior knowledge of the primary sequence of the macromolecule, of the covalent distances, chirality and bond angles within it and of the van der Waals radii of the constituent atoms.

Model building thus relies on the geometric parameters contained in the known primary structure and on the additional geometric constraints derived from NMR, which play a determining role in the definition of the three-dimensional

folding. It is the only one of the steps that has been largely automated, but it will always require considerable judgment. As will be discussed below, 'calculation' of NMR structures assumes that the structure is rigid. The extent to which this assumption applies varies from one macromolecule to another, and choosing the wrong assumption can lead to a wrong structure.

2.1 Solution Structures of Proteins

Resolution and assignment usually go hand in hand. The specific techniques that can be used at each step of an NMR structure determination differ, depending on the molecular weight of the protein. Simple, purely spectroscopic procedures for obtaining resolution and assignment, applicable to small structures (<10 kDa), break down at higher molecular weights, whereas the more elaborate isotope labeling techniques needed for larger structures are rarely needed for proteins of lower molecular weight.

2.1.1 Resolution

Sufficient resolution of protein NMR spectra to allow their interpretation in atomic detail has become possible by the development of three technologies: (1) high frequency NMR spectrometers, at 500–750 MHz for ^{1}H, allowing a high degree of chemical shift dispersion; (2) multidimensional (initially two-dimensional) spectroscopy, which allows further separation of lines overlapping in a one-dimensional spectrum by cross peaks to other lines representing physically interacting nuclei; and (3) isotopic spectral editing, or the simplification of protein NMR spectra by prior isotopic (^{2}H, ^{13}C or ^{15}N) labeling of the protein. As noted, purely spectroscopic methods [(1) and (2)] usually suffice to resolve the spectra of small proteins (<10 kDa). For larger proteins (>20 kDa), isotopic spectral editing is indispensable, and for the intermediate molecular weight range (10–20 kDa), the methodological requirements depend on the extent of overlap of spectral lines, which in turn depends on the specific structure.

The contributions of each of the three technologies to the resolution of protein spectra are best illustrated graphically. Figure 1 compares the one-dimensional spectra of ribonuclease at 40 MHz[1] and 750 MHz. Figure 2 shows the relationship between two-, three-, and four-dimensional spectra.[2] Figure 3 illustrates the simplification of a two-dimensional proton spectrum by selective deuteration[3] and Figure 4 shows the two-dimensional resolution of an overlapping ^{1}H spectrum by adding a heteronuclear dimension through ^{15}N labeling.[4] Many multidimensional and isotopic spectral editing schemes are now available. Inasmuch as they not only improve resolution but also allow different assignment strategies, they are discussed below under assignment.

2.1.2 Assignment. Sequential Assignment Methods

The basic idea underlying all *sequential assignment methods* is to establish a connectivity between the spectrum of an amino acid residue with that of its sequential neighbors. Two types of connectivities are generally observable in NMR spectra: (1) through-bond connectivity reflected in spin–spin coupling, possible only between covalently linked atoms;

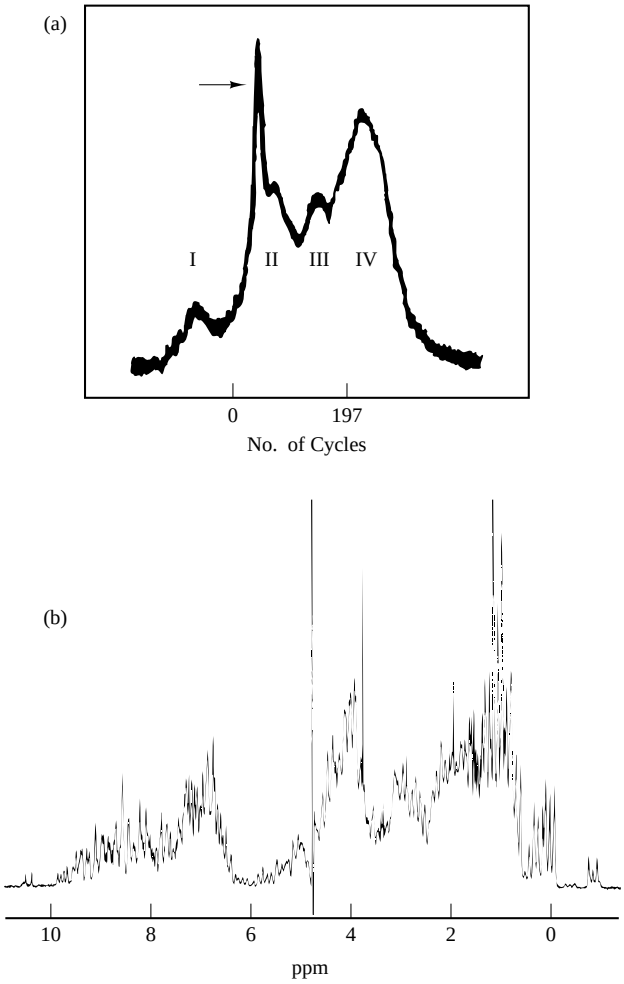

Figure 1 (a) Ribonuclease spectra taken at 40 MHz. (Reproduced from M. Saunders, A. Wishnia and J. G. Kirkwood, *J. Am. Chem. Soc.*, 1957, **79**, 3289). (b) Ribonuclease spectra (2 mmol double-labeled RNAse in 90% H_2O/10% D_2O, ^{1}H NOESY, 16 scans) taken at 750 MHz. (Courtesy of Bruker Instruments, Inc.)

and (2) through-space connectivity reflected in relaxation parameters—in particular the NOE, i.e. the connectivity between any two atoms in spatial proximity. Either can be used for sequential assignment, and different assignment strategies now use different combinations of either or both. The classical paradigm for sequential assignment emerged gradually. The use of coupling constants to identify amino acid residues in peptides by residue type was introduced in 1957 in the very first systematic study of amino acid and peptide spectra by Takeda and Jardetzky.[5] The use of relaxation parameters to evaluate distances in macromolecules was first suggested in 1964.[6] The usefulness of the combination was first demonstrated in 1976 by Gibbons[7] on one-dimensional (1D) spectra of the cyclic peptide, gramicidin S. In this paradigm the peptide NH of each residue is identified by its (small, $J \leq 10$ Hz) coupling to the α-CH of the same residue, and the connectivity between the NH group of residue i and the NH and α-CH groups of residue $i \pm 1$ by a NOE. This 'jumps' the peptide bond, across which spin–spin coupling is too small to be useful, with the help of a relaxation parameter. In this manner, it is, in principle, possible to assign the entire spectrum of a protein, beginning with a residue

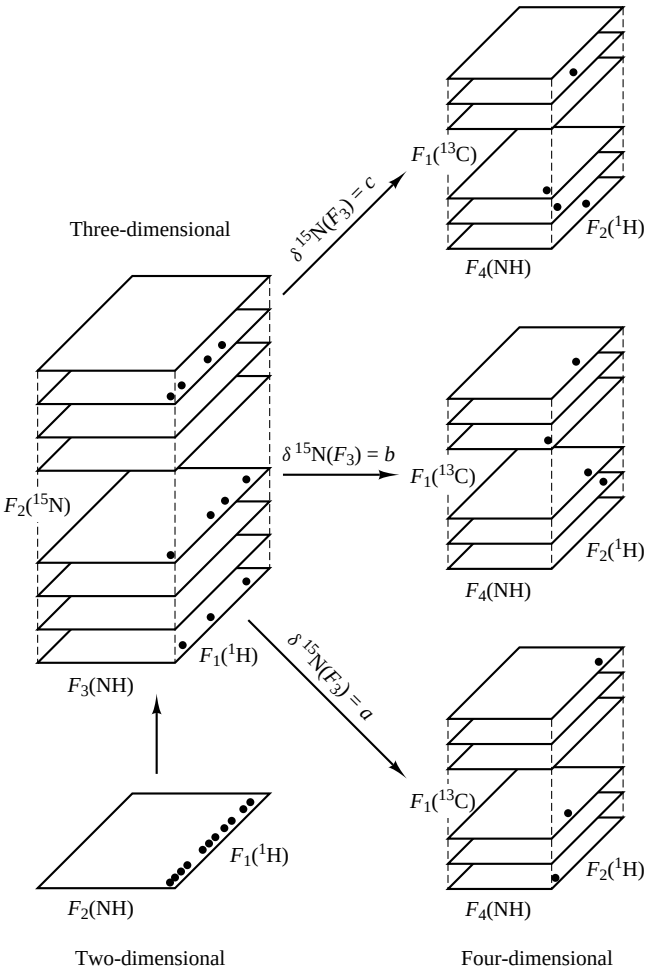

Figure 2 Illustration of relationships between heteronuclear $^{15}N/^{13}C$-edited two-, three-, and four-dimensional (^{13}C or ^{15}N) NOESY spectra. (Modified from Clore and Gronenborn[2])

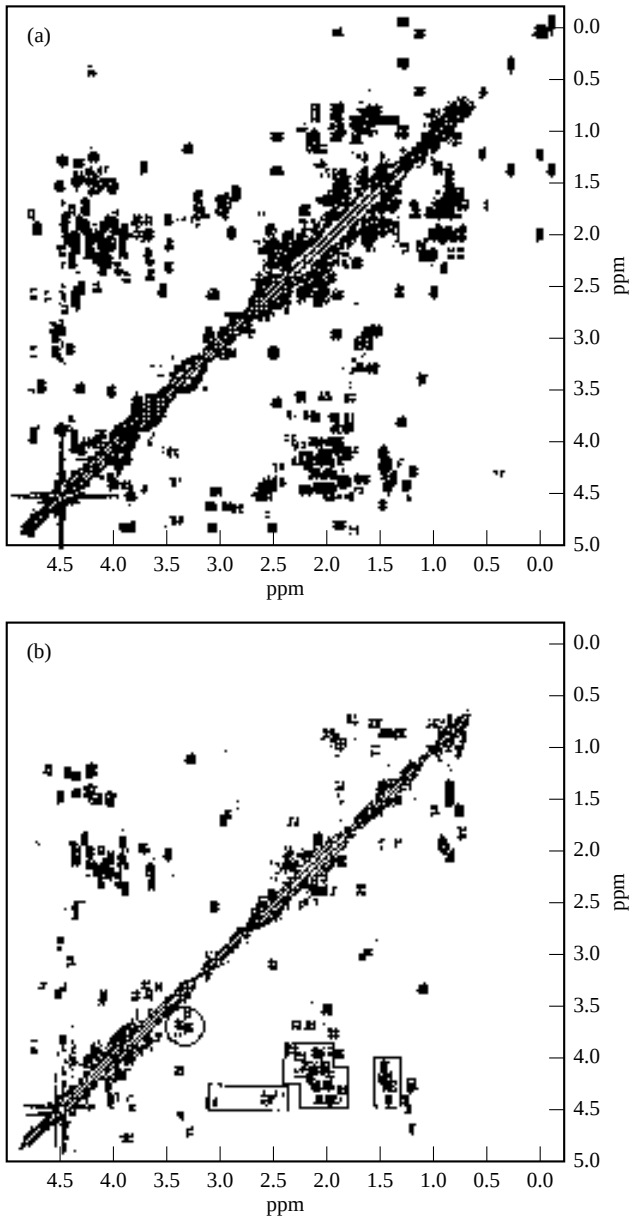

Figure 3 Comparison of the aliphatic region of (a) the natural abundance or wild-type *trp*-repressor DQF (double quantum filtered) COSY spectrum with (b) the spectrum of selectively deuterated *trp*-repressor analog (A5). (Reproduced from C. H. Arrowsmith, L. Treat Clemons, L. Szilágyi, R. Pachter and O. Jardetzky, *Makromol. Chem., Macromol. Symp.*, 1990, **34**, 33)

whose assignment is easily established (e.g. an N- or C-terminal, or with a unique residue in a protein) and then sequentially tracing all connectivities along the polypeptide chain. The Gibbons paradigm is illustrated in Figure 5. The tracing is much more easily done in 2D spectra, where the connectivities are seen directly as cross peaks in the spectrum. Two types of 2D spectra are required as a minimum for this purpose: a COSY-type spectrum to establish through-bond connectivities, thereby at least identifying the side chains; and a NOESY-type spectrum to establish through-space connectivities. For peptides and small proteins studied at 500–600 MHz, stumbling blocks are rare, and a complete assignment of the ^1H spectrum using this paradigm can, as a rule, be obtained. Since other characteristics distances can be defined for specific types of secondary structure (e.g., for the NH $i \rightarrow$ NH $i + 3$ for α-helices, or NH $i \rightarrow$ NH $i + 2$ for β-sheets), the assignment procedure simultaneously yields the secondary structure pattern of the protein.

Although the paradigm is applicable, in principle, to any polypeptide chain regardless of length, practical limitations preclude its use for larger proteins. For structures larger than 10 kDa the overlap makes it difficult to distinguish between different sequential assignment possibilities and, in addition, at higher molecular weights (15–20 kDa) line broadening is usually sufficient to obliterate most NH–α-CH couplings. A scheme based entirely on NOEs along the peptide chain and a combination of coupling constants and NOEs within side chains can sometimes be used instead.[8] However, for unedited spectra the usefulness of this technique is still limited by overlap: increasing overlap with increasing molecular weight leads to exponentially growing ambiguities in following the sequence. Therefore, for larger molecules, isotopic spectral editing is required for both resolution and assignment.

Isotopic Spectral Editing in its simplest form, as proposed by us in 1965, is achieved by selective deuteration. Biosynthesis of proteins from a mixture of deuterated and protonated amino acids allows the preparation of a series of labeled

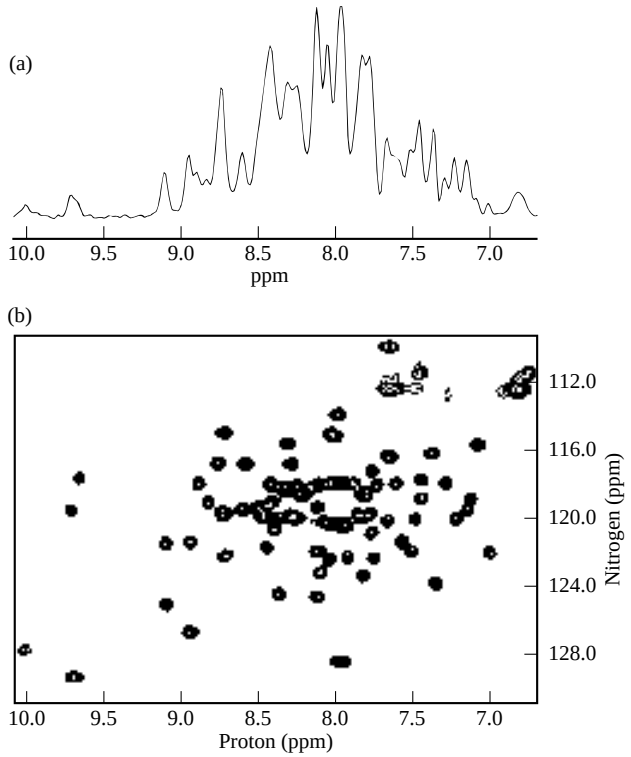

Figure 4 (a) Two-dimensional homonuclear spectrum of *trp*-repressor. (b) The ^{15}N-labeled HMQC spectrum of the same region of the *trp*-repressor

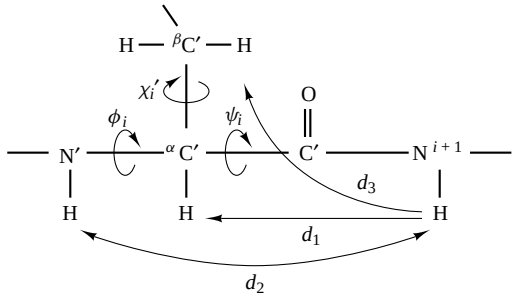

Figure 5 Gibbons's paradigm: magnetization transfer pathways and scalar connectivities in the peptide backbone. Arrows denote distances from the amide proton that can be defined. (Reproduced from O. Jardetzky, A. Lane, J.-F. Lefèvre, O. Lichtarge, B. Hayes-Roth, and B. Buchanan, in 'NMR in the Life Sciences', eds. E. M. Bradbury and C. Nicolini, Plenum, New York, 1986, pp. 49–72)

analogs in which only the desired combinations of amino acids remain visible to ^{1}H spectroscopy. Even though the labeling is by residue type (e.g. all leucines protonated, or all isoleucines deuterated), this type of editing reduces the problems of overlap sufficiently to allow, by itself, complete sequential assignment in larger proteins. Its largest drawback is the expense of preparing a sufficient number of deuterated analogs. Selective deuteration also narrows the linewidths by reducing the number of interacting neighbors and hence the number of alternative pathways for magnetization transfer or 'spin diffusion'. This may in some cases allow the observation of coupling constants not observable in a fully protonated species and the use of such constants for sequential assignment. In other cases, however, line broadening by the nearest neighbor will be sufficient to limit the assignment options to those relying on through-space (NOE) connectivities.

Heteronuclear spectral editing schemes for resolution and assignment using multidimensional spectroscopy based on uniform ^{15}N or combined ^{15}N and ^{13}C labeling have been devised, and their usefulness for assigning the spectra of proteins in the intermediate molecular weight range (20–30 kDa) has been demonstrated. The simplest among these are heteronuclear three-dimensional 3D HMQC (heteronuclear multiple quantum coherence)-NOESY or HSQC (heteronuclear single quantum coherence)-NOESY experiments on uniformly ^{15}N labeled peptide chains. In this experiment, the backbone NH resonances are spread out in two dimensions (^{1}H and ^{15}N) and their connectivities to each other and to their respective side chains are established by a NOESY experiment in an additional (^{1}H) dimension. In favorable cases the overlap is reduced sufficiently to allow a complete, or nearly complete, set of sequential assignments needed for a structure determination. At higher molecular weights, however, this is not always sufficient to eliminate overlap, and selective labeling becomes necessary.

A very general triple-resonance sequential assignment strategy based on ^{13}C and ^{15}N double labeling of the peptide chain has been developed.[9,10] The connectivities that can be established using this strategy, and the 3D experiments required for this purpose are summarized in Figure 6.[9,11] The crucial interresidue connectivity bridging the peptide bond can be obtained in several different ways, relying on each of the following correlations: (1) HNCO relying on the across-the-amide bond ^{13}CO–^{15}N coupling J(NCO) $\approx$ 15 Hz; (2) HNCA identifying each NH with the C-α of its side chain by the ^{15}N–^{13}C-α coupling constant J(NC-α) $\approx$ 7–11 Hz; (3) HCACO identifying each carbonyl with the C-α of its side chain by the large ^{13}C-α–^{13}CO coupling constant J(C-αCO) $\approx$ 55 Hz; (4) ^{15}N HOHAHA-HMQC providing the same identification of the ^{15}NH group with its side chain as (2), but relying on proton couplings, J(NC-αH) $\approx$ 5–10 Hz; and (5) HCA(CO)N, again bridging the peptide bond using the two-bond ^{13}C-$\alpha(i+1)$–^{15}N$_{(i)}$ constant J(C-αN) $\leq$ 7 Hz.

Additional and alternative correlation pathways for the triple resonance correlations can also be defined, and the technique has been successfully used to establish the structures of calmodulin and of its complex with a 2 kDa calmodulin receptor binding domain (16.7 kDa; 19.4 kDa in the complex),[12] the ribonuclease domain of HIV-reverse transcriptase (18 kDa),[13] *Escherichia coli* enzyme III(glc) (18.1 kDa),[14] and human interleukin-4 (15.4 kDa).[15] The details of these and many other possible similar experiments are described in more detail elsewhere in this Encyclopedia. Although they are very useful extensions of the existing technology for the study of intermediate-size proteins (up to 30 kDa), as a class the heteronuclear multidimensional assignment strategies do not escape the problems posed by increasing molecular weight, for two reasons. First, they require relatively long pulse sequences, which lower the sensitivity of the NMR experiment, and as the T_2 becomes shorter with increasing molecular weight, this effect becomes more prominent. Second, they rely on heteronuclear coupling constants of the order of 10–15 Hz, and in a fully protonated protein at molecular weights above the range 30–40 kDa most of these will be obliterated by line

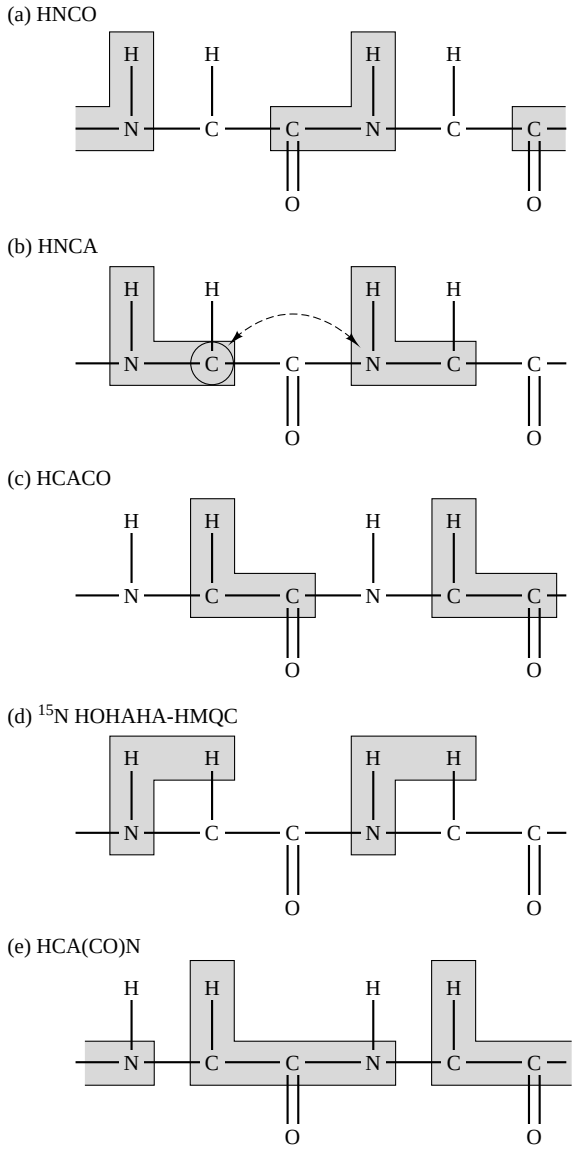

Figure 6 Connectivities observed in the five different types of three-dimensional NMR experiments. (a) The HNCO experiment correlates the peptide bond C′ and ^{15}N resonances with the NH chemical shift. (b) The HNCA experiment correlate the NH and ^{15}N shifts with the intraresidue C-α shift. For $\approx$ 60% of the residues in calmodulin, a two-bond connectivity to the C-α resonance of the preceding residue is also observed (broken line). (c) The HCACO experiment correlates intraresidue H-α, C-α, and C′ chemical shifts. (d) The ^{15}N HOHAHA-HMQC experiment correlate intraresidue ^{15}N, NH and H-α shifts. (e) The HCA(CO)N experiment correlates the H-α and C-α shifts of one residue with the ^{15}N shift of the next residue. (Reproduced from M. Ikura, L. E. Kay and A. Bax, *Biochemistry*, 1990, **29**, 4659)

broadening. Their usefulness can be extended by combination with selective deuteration, and the combination has been used successfully in the determination of the structure of the *trp*-repressor–DNA complex (37 kDa).[16] It can be expected that the very significant reduction of the relaxation rate in selectively deuterated proteins will allow even further extension of the usefulness of the combined homo/heteronuclear labeling methods to achieve complete resolution and assignment for proteins of still higher molecular weight. At the time of writing, the potential of the combined isotope editing techniques has not yet been fully realized. A more detailed discussion of the possibilities and limitations is available.[17]

2.1.3 Interpretation of NMR Data to Obtain Geometric Constraints

The conversion of the experimentally observed parameters (mostly intensities of cross peaks in multidimensional spectra) into geometric parameters that can be used for structure calculation (i.e. internuclear distances and dihedral angles) requires a series of subjective judgments.

The simplest model for obtaining a distance from cross peak intensities in a NOESY spectrum is the well known and widely used 'two-spin approximation', relating the observed cross-peak intensity (in this case equal to the cross-relaxation rate) to a single internuclear distance, r:

$$\sigma = \frac{K\tau}{r^6} \tag{1a}$$

where K is a constant and τ is the single (rigid body) correlation time. This equation holds *approximately* for small structures observed at short mixing times. For larger structures (above 15 kDa), equation (1a) does not hold even approximately. Even in the simplest case there exists an uncertainty in the relationship between distance and peak intensity, because the value of τ(the local correlation time of the internuclear vector in question) is unknown. The most commonly made assumption is that the macromolecule is rigid and that the overall rotational tumbling time can be used for all internuclear vectors. As noted, this assumption has proved very useful as a first approximation, even though it generally does not hold. The reason for the success of the assumption, even in some cases where its applicability is doubtful, is that the sixth-power relationship between peak intensity or correlation time and distance substantially reduces the error in the distance that results from an erroneous estimate of either peak intensity or correlation time: an error of a factor of 10 in either of the latter results in only a 46% error in the estimated distance. For the determination of the overall topology such errors can be tolerated. To account for them, as well as for the experimental errors of intensity measurements, it is customary to interpret each observed NOE not in terms of a single distance, but in terms of a distance range. A commonly used classification is into ranges allowed for 'strong', 'medium', and 'weak' NOEs. Many different calibrations of appropriate distance ranges, some differentiating between 'very strong' and 'strong', and 'weak' and 'very weak', have now been carried out. It can be said that for the first structure calculation, the differences between them are not significant. A set of typical values is given in Table 1, and the issues are discussed in more detail elsewhere.[18,19]

Some workers have attempted to reduce the uncertainties of relating observed intensities to distance by using an empirical calibration in the form:

$$r_{\mathrm{u}}^6 = \frac{(\mathrm{NOE})_{\mathrm{k}}}{(\mathrm{NOE})_{\mathrm{u}}} \cdot r_{\mathrm{k}}^6 \tag{1b}$$

where $(\mathrm{NOE})_{\mathrm{u}}$ is the intensity of the NOE for the spin pair at an unknown distance, r_{u}, and $(\mathrm{NOE})_{\mathrm{k}}$ is the NOE intensity

Table 1 Distance between Residues as Determined by NOE Intensity

NOE Intensity	Distance Range (nm)
Strong	0.18–0.27
Medium	0.18–0.33
Weak	0.18–0.50
Very Weak	0.30–0.60

for a spin pair for which the distance r_k is known. However, the use of this calibration implies strictly that the molecule is rigid and that the two-spin approximation applies. Use of distance *ranges* is equivalent to loosening these constraints in order to take the reality of internal flexibility in proteins at least partially into account. The precision of a calibration is therefore deceptive. Given that differences in local correlation times and the limits of the applicability of equation (1a) are now well known, it is doubtful that distances derived by calibration can be considered accurate. Better accuracy is still achieved by using a reasonable estimate of the allowed distance ranges.

A more significant source of error is the fact that equation (1a) does not hold, except for small structures and mixing times that are too short to obtain good spectra on larger molecules. Under these conditions one must take into account that magnetization transfer during the experiment is not limited to the two spins, but occurs between all neighboring spins in the structure. This phenomenon is known as spin diffusion, and the evolution of magnetization (peak intensity) in the presence of spin diffusion is given by the generalized Bloch equations:

$$\frac{dM_i}{dt} = -\rho_i[M_i - M_i(0)] - \sum_{j \neq i} \sigma_{ij}[M_j - M_j(0)]; i \neq j \quad (2)$$

where ρ_i is the spin–lattice relaxation rate of the ith nucleus, and σ_{ij} is the cross-relaxation rate between the two nuclei i and j, as defined in equation (1a).

To solve the generalized Bloch equations, one obviously has to know already the structure that one is trying to determine. The initial structure calculation therefore *always* has to rely on the assumption that equation (1a) holds as a first approximation. To compensate for the additional (and often substantial) errors resulting from spin diffusion, it is necessary to widen the limits for the distance estimates for purposes of the initial calculations on larger molecules. The effects (and errors) due to spin diffusion can be greatly reduced by selective deuteration of the protein, as noted above. The ultimate molecular weight limit for structure determination by NMR remains to be explored, but given the dramatic reduction of linewidths by selective deuteration, probably lies much higher that originally expected. Good local spectra have now been obtained for structures as large as 150 kDa.[20] It must be noted that using the solution of equation (2), or of its equivalent, the relaxation matrix equation for the back-calculation of spectra from an initial structure again usually involves the assumption that the structure is rigid and a single correlation time can be used in the structure calculation. Back-calculation based on this assumption may not significantly increase the accuracy of the structure over the crude initial model—as discussed below. The important point to bear in mind is that the geometric parameters derived from NMR experiments are always approximate, and the quality of the approximations used is an important determinant of the accuracy of the resulting structure.

The magnitude of the errors that can be introduced by neglecting spin diffusion can be well illustrated by an early model calculation on sperm whale myoglobin.[18] Distances derived from the X-ray structure and a correlation time of 8 ns were used to calculate cross-peak intensities by solving the generalized Bloch equations [equation (2)]. These intensities were then analyzed using equation (1a) and the same correlation time to estimate (apparent) 'NOE distances'. A plot of the apparent distances versus actual crystallographic distances (Figure 7),[18] indicates that the error in the distances calculated from equation (1a) depends on the details of the surrounding structure and may be as high as ±50% for distances >0.3 nm. Very precise distance calibrations of NOEs on an unknown structure [equation (1a) or equation (1b)] are apt to introduce significant distortions into the calculated structure.[21]

The dihedral angles, which can be derived from coupling constants in COSY-type spectra and used to define the conformations of both the protein backbone and of the side chains, are subject to similar uncertainties. In the presence of free rotation around side-chain bonds, the observed values

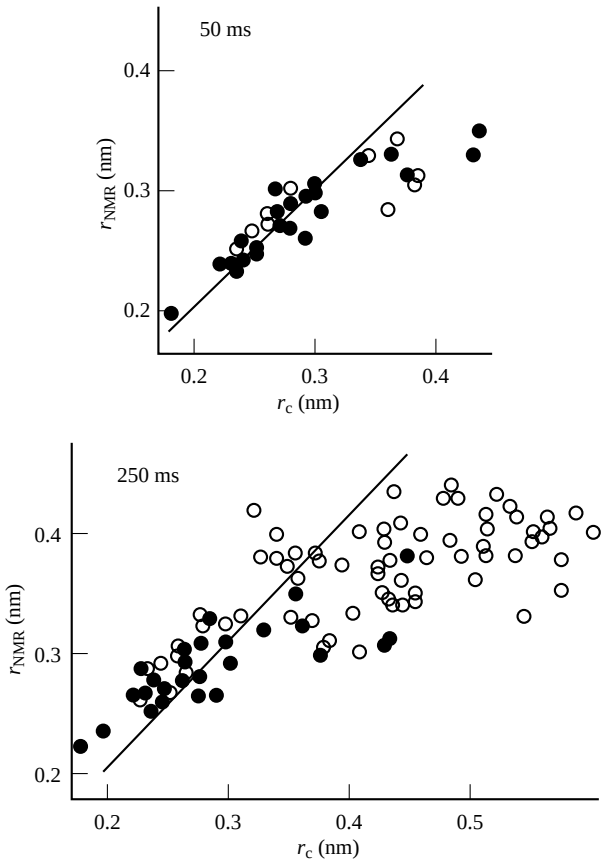

Figure 7 Apparent $^1H-^1H$ distances calculated from NOEs (r_{NMR}) plotted versus actual crystallographic distances (r_c) for helix 4 of myoglobin. NOE cut-off: 2%. (•) Intramolecular distances; (○) intermolecular distances. (Reproduced from O. Jardetzky and A. N. Lane, in 'Physics of NMR Spectroscopy in Biology and Medicine,' ed. B. Maraviglia, Italian Physical Society, North-Holland, Amsterdam, 1988, pp. 267–301)

are averages over several conformations and do not permit a unique interpretation. Dihedral angles are most useful along the backbone, where the rotation is hindered, and stereospecific assignments, e.g. those of individual methylene protons, β-CH$'$ and CH$''$, are possible. In that case, a unique value of the angle (more precisely, a narrow range of angles allowed by the coupling constant) can often be derived from the Karplus relation.[22] Since the coupling constant has a strong dependence on the dihedral angle, experimentally derived angles are powerful constraints in a structure calculation. The largest limitation to their use is the fact that the small coupling constants involved (often $<10-15$ Hz) become largely unresolvable at molecular weights above 15 kDa. For larger molecules, only broad ranges of dihedral angles, inferred from indirect evidence on the secondary structure, can be used (as relatively loose constraints) in the structure calculation.

It is still best to make the choice of assumptions explicitly, on the basis of prior experience and with additional knowledge of the specific system on which the structure is to be determined, although there is an increasing tendency to make them implicitly in an iterative back-calculation of spectral intensities using one of the several computer programs available for this purpose. The danger of such implicit decision-making is that each program has specific assumptions built into it, of which the user may or may not be aware. Almost all programs are built on the assumption that the protein is rigid (or undergoes only averaging of the first kind, i.e. in a potential well about a single energy minimum, but does not undergo any averaging of the second kind, i.e. between different metastable conformations). This assumption holds reasonably well as a zero-order approximation in many cases, especially for smaller, well chosen globular proteins, but the cases of the *trp*-repressor and several other larger proteins have clearly shown that it is not universally applicable. *There exists no general, universally applicable, set of assumptions for the exact geometric interpretation of spectroscopic parameters in macromolecular spectra.* Obviously, the calculated structure will be wrong if the assumptions made at this step are not appropriate for the molecule under study.

2.1.4 Model Building and the Calculation of Protein Structures

There are several options for defining a three-dimensional structure of a protein from the geometric constraints implied by NMR data. The basic paradigm is straightforward: given the primary sequence (with all covalent bond lengths and angles and van der Waals radii implied by it, which must be determined by other methods and known to begin with), and given a set of distance and angular constraints derived from NMR experiments, as outlined above, find the family of all three-dimensional configurations that satisfy the given set of experimental constraints. The essential step here is to search the conformational space available to the polypeptide chain, selecting only those configurations that are allowed by the NMR constraints. The first 3D structure derived from NMR data, that of the *lac*-repressor headpiece (MW $\approx$ 6 kDa) was built by hand, using Pauling-Corey space-filing models.[23] At the time of writing, several classes of search procedures have been implemented in computer programs and are generally available. A major consideration in choosing the procedure is that the search must be sufficiently representative to ascertain that alternative configurations equally compatible with the experimental data set are included in the final result. This is more easily said than done. The conformational space available to a polypeptide chain is very large (for the two Ramachandran angles, each allowed only two values, it is of the order of 2^{2N}, where N is the number of amino acid residues in the chain; i.e. for 100 residues, it is of the order of 2^{200} or 10^{60}). A systematic search of all possible configurations is therefore computationally out of the question. Even exhaustive random sampling, starting with a variety of randomly chosen arbitrary configurations, is possible only for relatively short peptide chains (up to 10–12 kDa). Consequently, all search procedures have to rely on approximations and it remains important to ascertain that the approximations made in each applicable algorithm are valid for the specific system under investigation. The derivation of three-dimensional structures from NMR data is only possible because some of the experimental distance constraints—in particular NOE constraints between residues distant in the primary sequence (e.g. between residues 6 and 42, or 24 and 98)—at once eliminate large segments of the conformational space. Furthermore, a not very large number of imprecise constraints can define the folding of a polypeptide chain rather accurately, as originally pointed out by Kuntz and coworkers.[24] The human mind remains by far the most efficient instrument for recognizing and applying this hierarchy of constraints in order to reduce the search space. For this reason, model building, which had at first been all but abandoned in favor of 'more objective' search procedures that treat all constraints alike, is again gaining in importance as the molecular size of the structures being determined increases, making 'objective' random searches computationally intractable.

Among the available algorithms for searching conformational space and selecting structures compatible with the experimental constraints, it is useful to distinguish between methods that (a) rely on geometric information alone, and (b) those that bring to bear additional information on the search in the form of energy potentials. In the first category of purely geometric methods, there are three classes of algorithms: (1) computer model building, (2) distance geometry, and (3) optimal filtering. In the second category—there is one class: (4) restrained molecular dynamics (RMD). In practice, a combination of a geometric and a dynamic method[25] is now almost universally used, and molecular dynamics can be considered indispensable for the refinement of NMR as well as of X-ray structures. At the same time, molecular dynamics is most effective if a starting structure not very far from the final structure is provided. Only for rather small structures is it practical to fold a random polypeptide chain into its final configuration by using an RMD algorithm.

(1) Computer model building programs are either entirely manual (e.g. Frodo, Quanta, and MacImDad) or have a built-in routine for conformational-space searches under geometric constraints (e.g. PROTEAN). In the manual programs, the application of covalent, bond angle and van der Waals constraints is often automated, but the application of NMR-derived distance and angular constraints is under the complete control of the experimenter. Application of constraints is usually sequential, with those deemed most constraining (i.e. those connecting two structures, as in the case of protein–DNA complexes, or two distant parts of a protein chain) being applied first. Even though the procedure is subjective, it

is generally valid because all conformations violating these key constraints can be ruled out. As in all initial model building, the assumption is made that averaging between two or more distinct conformations (averaging of the second kind) does not occur. The typical result is a topologically accurate, but imprecise, model that can be used as a starting structure for refinement by RMD. In the case of constraint satisfaction programs, such as PROTEAN, which build models automatically under a given set of constraints, a *systematic* search of the space available for the mutual positioning of units of secondary structure is possible. By considering each unit of secondary structure as a rigid entity and representing it at a higher level of geometrical abstraction (e.g. cylinders for α-helices or β-strands), the number of conformational variables is reduced to a manageable size. This makes a systematic search of the conformational space available to define the main topological features (with the reduced set of key variables) computationally tractable. Since the space to be searched grows exponentially with the number of variables (e.g. rotatable bonds), systematic sampling of conformational space using the complete set of variables is otherwise only possible for very small peptides. If the output of such a systematic search, which generally defines the overall topology rather well, is used as a set of starting structures for molecular-dynamic refinement at atomic resolution, it is possible to minimize the danger of having the refined structure represent a single local minimum. This is difficult, if not impossible, when only a smaller set of starting structures is used, whether such a set is derived from manual model building or random sampling by distance geometry. Adequate sampling of random structures is at present limited to proteins smaller than ~12 kDa. For larger structures, random sampling that could safely be considered extensive enough is prohibitively expensive in computer time, and the danger that the reported structure represents only a local minimum remains ever present. Computer model building is hardly necessary for the smaller structures where adequate random sampling is computationally feasible. For larger structures, some degree of preliminary model building is unavoidable. A typical PROTEAN output, defining the topology of the helix–turn–helix *lac*-repressor DNA binding domain (headpiece), along with the uncertainty in the positioning of the different units of secondary structure, is shown in Figure 8.[26]

(2) Distance geometry (DG)[27] is a general method for calculating the atomic coordinates of a structure from an arbitrary set of internal distance and/or angular constraints. It has two highly attractive characteristics: (1) it is a simple and rigorous mathematical theory containing the proof that if all the distances between all points within a structure are known precisely, an exact calculation of the coordinates of each point in the structure is possible; and (2) computational efficiency. In applications to NMR structure determination—where only a fraction of all distances that rigorously define the structure can be obtained experimentally—theoretical rigor is lost, but the efficiency of the method for randomly searching conformational space remains.

The input to a DG calculation is: the *distance matrix* derived from experiment—in principle the square matrix of $N(N-1)/2$ distances between all N atoms (points), in practice a (usually asymmetric) matrix of the distances available from experiment; and an *initial coordinate matrix*, preferably consisting of a random arrangement of points.

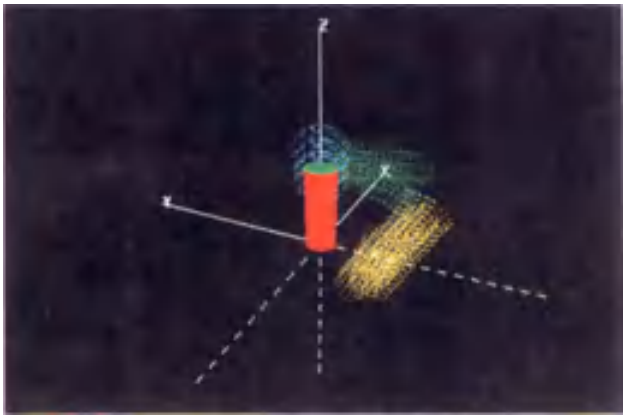

Figure 8 *Lac*-Repressor headpiece structure calculated by PROTEAN, showing the uncertainty in the positioning of the different units of secondary structure. (Reproduced from R. B. Altman and O. Jardetzky, *J. Biochem.*, 1986, **100**, 1403)

This represents the 'starting structure' for the search of the conformational space. The first step in a DG calculation, called *embedding*, calculates a set of coordinates that represents a multidimensional best fit of the coordinates to all the distances considered simultaneously. As allowed distance ranges rather than precise distances have to be used, and because the number of observable distances is too small to define the structure precisely, the resulting structures that at first seem to satisfy the constraints in fact usually contain a large number of constraint violations—and also violate constraints at first not considered, such as van der Waals radii. A second *optimization* step is therefore necessary to minimize the errors by iterative adjustments, using a scoring function that reflects the number and severity of the violations as a criterion for the goodness of fit.

There are many different algorithms for carrying out the embedding step and many different formulations of the optimization function, a detailed description of which is beyond the scope of this article, but can be found elsewhere.[28] The essential mathematical features of the two steps are given by equations (3) and (4). In the first step

$$\mathbf{S} = \boldsymbol{\lambda}\mathbf{M} \tag{3a}$$

where **S** is the coordinate matrix and **M** is the metric (distance) matrix, calculated from the initially set up distance matrix by a coordinate transformation to refer all distances to the geometric center of the structure which can be calculated from the distance matrix. The elements of **M** are:

$$M_{ij} = \frac{1}{2}(D_{io}^2 + D_{jo}^2 - D_{ij}^2) \tag{3b}$$

where D_{io} is the distance of the atom i from the origin and D_{ij} the internuclear distance between i and j. $\boldsymbol{\lambda}$ is the matrix of coefficients relating the two.

The embedding process itself is thus seen from equation (3a) to be an eigenvalue problem (finding the values of $\boldsymbol{\lambda}$ to yield the values of **S**), for the solution of which a variety of techniques is available.[29] A typical error function useful for

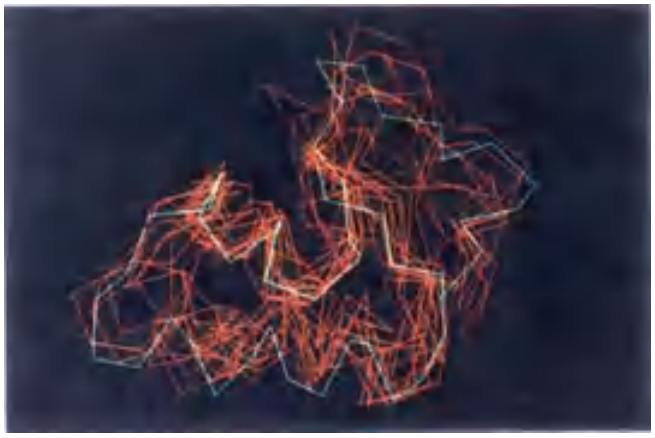

Figure 9 C-α traces of a family of crambin structures computed using the distance geometry protocol. The target structure is shown in green. (Reproduced from J. C. Hoch and A. S. Stern, *J. Biomol. NMR*, 1992, **2**, 535)

optimization in distance space is:

$$F_E(R) = \sum_{i<j}(|R_{ij}| - U_{ij})^2 + \sum_{k<l}(L_{kl} - |R_{kl}|)^2 \qquad (4)$$

where $F_E(R)$ is the distance error, L_{ij} and U_{ij} the lower and upper distance boundaries, respectively, and R_{ij} the actual distance in the proposed structure. Similar error functions can be introduced for dihedral angles and chiral constraints (to distinguish between L- and D-amino acid configurations). The result of each calculation is a single optimized structure. Experience shows that repeated calculations with the same set of initial constraints but different starting structures do not exactly reproduce the same structure. Therefore, a family of structures is usually obtained by repeated runs of the DG algorithm. Published structure determinations report anywhere from 30 to over 100 closely related but different structures, and the precision of the structure can be measured by taking the root-mean-square deviation (RMSD) of the individual atomic coordinates. A typical family of structures calculated by repeated optimization using a DG algorithm is shown in Figure 9.[30]

Important to note is that all non systematic search procedures contain several potential sources of bias. Among the most important in the case of DG are: (1) the algorithms used for the generation of starting structures; (2) the adequacy of their use in an individual case; and (3) the choice of weighting factors for the error function when forms more complex than equation (6) are chosen, as they now usually are. Comparisons of different programs are therefore of utmost importance, but thus far have been carried out only sporadically, as discussed below.

(3) Optimal filtering is a probabilistic method widely used in signal processing. Its application to the search of conformational space in the course of an NMR structure determination has the advantage that a set of coordinates, and the uncertainty limits of each coordinate, can be obtained in a single calculation from the starting set of distance and angular constraints and the estimated uncertainties of these constraints. This eliminates the need for repeated optimization runs with different starting structures and the bias potentially introduced by limiting the calculation to an inadequate number of runs. All data relevant to the uncertainty of the final structure are introduced into the calculation and used throughout the calculation at once.

The principle of the method is to represent the system (structure) by a coordinate 'state vector' of length $3N$, where N is the number of atoms in the structure, and of the form:

$$\mathbf{x} = [x_1\ y_1\ z_1\ x_2\ y_2\ z_2\ x_3\ y_3\ z_3 \ldots] \qquad (5)$$

x_1,y_1,z_1, etc., denote the x,y,z coordinates of all individual atoms. The uncertainty of the structure is contained in the covariance matrix of $\mathbf{x}$:

$$\mathbf{C}(\mathbf{x}) = \begin{bmatrix} \mathbf{C}(x_{1,1}) & \mathbf{C}(x_{1,2}) & \ldots & \mathbf{C}(x_{1,N}) \\ \mathbf{C}(x_{2,1}) & \mathbf{C}(x_{2,2}) & & \\ \vdots & & \ddots & \vdots \\ \mathbf{C}(x_{N,1}) & \ldots & & \mathbf{C}(x_{N,N}) \end{bmatrix} \qquad (6a)$$

where

$$\mathbf{C}(x_{i,j}) = \begin{bmatrix} \sigma_{x_i x_j} & \sigma_{x_i y_j} & \sigma_{x_i z_j} \\ \sigma_{y_i x_j} & \sigma_{y_i y_j} & \sigma_{y_i z_j} \\ \sigma_{z_i x_j} & \sigma_{z_i y_j} & \sigma_{z_i z_j} \end{bmatrix} \qquad (6b)$$

is the covariance matrix for an individual atom with the variance $\sigma_{xy} = E_{(xy)} - E_{(x)}E_y$ is defined as usual in terms of the expectation values. The diagonal terms of equation (6b) measure the uncertainty in each coordinate, and the off-diagonal terms determine the shape of the spatial distribution of the uncertainty. A common assumption is that this distribution is normal, in which case the uncertainty in the position is given by an ellipsoid. However, asymmetry in the uncertainty distribution of the initial constraints can be taken into account by the use of higher order moments to describe the distribution.

In the first order calculation, distance constraints are used in the form

$$z = |x_i - x_j| + v, \text{ or, generally, } z = h(\mathbf{x}) + v \qquad (7)$$

where v is the uncertainty range in the measurement of the distance. A similar equation applies to angular constraints.

The constraints are introduced to update an initial structure given by an initial state vector $\mathbf{x}_o$ to a new structure that better fits the constraints by calculating a new set of coordinates from the Kalman filter formula:

$$\mathbf{x}_{new} = \mathbf{x}_{old} + \mathbf{K}[z - h(\mathbf{x}_{old})] \qquad (8)$$

where

$$\mathbf{K} = \mathbf{C}(\mathbf{x}_{old})H^T[\mathbf{H}\mathbf{C}(\mathbf{x}_{old})\mathbf{H}^T + \mathbf{C}(v)]^{-1} \qquad (9)$$

where T denotes the transpose and $\mathbf{H}$ is given by:

$$H = \frac{\partial h(\mathbf{x})}{\partial x}|\mathbf{x}_{old} \qquad (10)$$

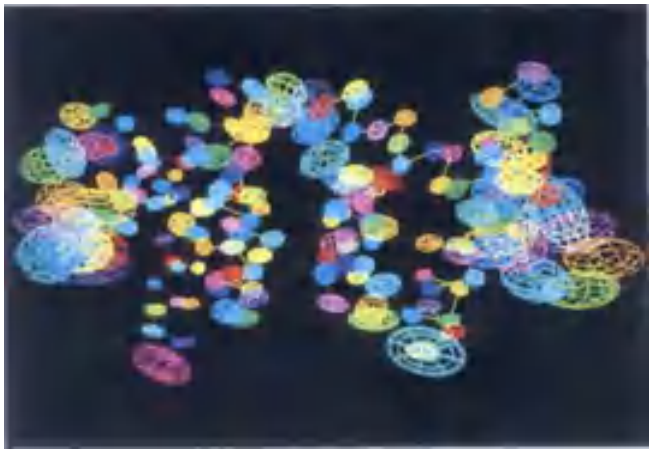

Figure 10 Tertiary structure of the *trp*-holorepressor calculated using the Kalman filter. The α-carbon trace is displayed (at 2 SD) with ellipsoids of uncertainty for each α-carbon, the larger ellipsoids at the extreme left and right indicating the larger uncertainty for region D. (Reproduced from C. Arrowsmith, R. Pachter, R. Altman and O. Jardetzky, *Eur. J. Biochem.*, 1991, **202**, 53)

The covariance matrix **C** is updated by a formula analogous to equation ((8)). Programs have been written for either a sequential or a simultaneous introduction of constraints, and for calculations in either cartesian (PROTEAN2)[31] or dihedral angle space (FILMAN).[32] The calculation must be iterated for nonlinear systems, hence the occasionally used name, 'Doubly Iterated Kalman Filter' (DIKF). As in the case of DG, for small structures the initial 'structure' can be a random distribution of points (or all points placed at the origin) with very large initial variances. In both cases, starting structures more closely resembling the final result (and obtained by initial model building) are required for larger proteins to make the structure calculation feasible computationally. Also, in both cases, the definition of the uncertainty in the distance constraints used for the conformational space search remains subjective, as discussed in the section on the conversion of spectral intensities into distances. The topology of the *trp*-repressor backbone, determined by optimal filtering, together with the uncertainty ellipsoids of the α-carbon atoms is shown in Figure 10.[33]

The model-building methods described thus far rely on purely geometric information. Because the geometric constraints derived from NMR experiments are generally imprecise and too few in number to give an exact definition of the protein structure, the resulting structures generally represent the overall topology rather well, but contain numerous energetically unfavorable, and sometimes impossible, features. For this reason, refinement of the crude structure by energy minimization is generally necessary, and molecular dynamics algorithms have become the method of choice for this purpose.

(4) Molecular dynamics, as a method for search of the conformational space under a given set of geometric constraints, differs from the purely geometric methods of model building, distance geometry and optimal filtering in that energy potentials, representing both attractive and repulsive interactions between atoms, are introduced into the calculation in addition to the experimental constraints.

The technique is based on the solution of Newton's equations of motion for all atoms in the structure simultaneously:

$$\frac{\partial^2 \boldsymbol{r}_i}{\partial t^2} = \frac{\partial \boldsymbol{v}_i}{\partial t} = \frac{\nabla E(\boldsymbol{r}_i)}{m_i} \tag{11}$$

where $\partial\ ^2\boldsymbol{r}_i/\partial\ t^2$ is the acceleration and $\boldsymbol{v}_i$ is the velocity of atom i. This mass, m_i, of each atom is known. The force is taken to be the gradient of an empirically defined set of potentials, which is the weighted sum of all relevant terms:

$$\begin{aligned} E_{(xi)\text{empirical}} = {} & \textstyle\sum_{P=1}^{N} N_1 E_{\text{bond}} + w_2^P E_{\text{angle}} + w_3^P E_{\text{dihedral}} \\ & + w_4^P E_{\text{van der Waals}} + w_5^P E_{\text{electrostatic}} \\ & + w_6^P E_{\text{H bond}} \end{aligned} \tag{12}$$

In *restrained molecular dynamics* (RMD), experimental distance and angular constraints are usually introduced as pseudopotentials of the form

$$E_{\text{NOE}} = S\frac{kT}{2d^2}(R-d)^2 \tag{13}$$

where S is a scaling factor, k is the Boltzmann constant, T is the absolute temperature, R is the averaged internuclear distance, and d is the allowed distance bounds.

The solution of Newton's equations proceeds by numerical integration over very small time steps, Δt, over which the forces are assumed to remain constant:

$$\boldsymbol{r}_{n+1} = 2\boldsymbol{r}_n - \boldsymbol{r}_{n-1} - \frac{\nabla_{\mathbf{r}_n} E(\boldsymbol{r}_n)}{m}\Delta t^2$$

$$\boldsymbol{V}_n = \frac{1}{2\Delta t}(\boldsymbol{r}_{n+1} - \boldsymbol{r}_{n-1}) \tag{14}$$

This is the so-called *Verlet algorithm*. The choice of a sufficiently small time step (by comparison to the timescale of the fastest motion in the system) is critical, and values of the order of Δt = 0.001–0.002 ps are normally used.

A large amount of literature exists on the best choice of potentials, number of terms and weighting factors,[34–36] and different programs incorporate sometimes very different sets of potentials. Similarly, the choice of initial velocities, usually based on a Maxwell distribution at a chosen temperature, can be made at will. Both an energy minimum and a trajectory for the motions of individual atoms over the period of the calculation can be calculated for any starting structure.

It is possible to use RMD as a purely geometric method for the search of the conformational space by assigning very high values to the pseudopotentials representing the experimental constraints and making all other potentials negligible by comparison. As in the case of DG and DIKF, the topology of small structures can be calculated successfully by starting with an arbitrary arrangement of atoms (usually given the correct covalent and bond angle constraints). As

the molecular size increases, it rapidly becomes necessary to start with a structure resembling the final result if the computational time is to be kept within manageable limits. This is much more important for RMD than for DG or DIKF calculations because of the larger number of arbitrarily adjustable parameters. The large number of adjustable parameters also makes the method subject to stronger built-in systematic bias. Fortunately, several programs have been tested extensively—notably X-PLOR, CHARMm, GROMOS and AMBER—and even though none of these are foolproof or free of all bias, internally consistent results can be obtained in most cases. Credible refinement of NMR structures to an 'effective resolution', i.e. precision of 0.05 nm, is possible in many cases. This 'resolution' is obtained, as in the case of DG, by calculating a family of structures, each representing a complete RMD calculation beginning with a different starting structure each time, and then determining the RMSDs of the atomic coordinates within the family. Of particular interest for structure calculations using molecular dynamics is the simulated annealing protocol (sometimes even discussed as a separate method of structure calculation). In this protocol the temperature is repeatedly raised in the course of each molecular dynamics simulation, in order to reduce systematic bias by randomizing the structure, and then allowed to converge onto a new configuration. For the largest structures refined thus far (37 kDa), the computer time required for the calculation of an RMD family by this procedure can be prohibitively long. For such structures, however, it is possible to invoke the ergodic theorem (equality of the time average to the ensemble average) and use the Sequential simulated annealing protocol[37] to obtain a family of structures from a single calculation. A typical family of structures obtained by RMD has the same appearance as a family calculated by DG (see Figure 9).

2.1.5 Back-Calculation of NMR Spectra

Back-calculation of NMR spectra from a given structure has long been recognized as a desirable step for the validation and refinement of the proposed structure,[38] regardless of the method initially used to derive the structure. The back-calculation for NOESY-type spectra is based on the numerical integration of the set of generalized Bloch equations [equation (2)] or, as an equivalent, the inversion of the relaxation matrix[37,39] using the coordinates of the proposed structure to calculate the required interproton distances.[40,41] Several programs—including BLOCH, CORMA, IRMA, MARDIGRAS—are available for this purpose. Direct refinement of the structure against experimental NOE intensities has also been developed and implemented in X-PLOR. The use of time-averaged distances, with the averaging based on a molecular dynamics trajectory, has been suggested as an improvement to the accuracy of such calculations.[42] Iterative protocols are part of most suggested procedures. Back-calculation and its applications to both protein and nucleic acid structures are described elsewhere in this Encyclopedia. Of importance in the general context is the fact that a completely correct back-calculation is not possible without detailed knowledge of the spectral density functions (correlation times) needed to describe internal motions in the protein. Good predictions of spectra from proposed structures are possible when the structure can be taken as rigid and the spectral density functions to be the same throughout the molecule. Unfortunately, spurious agreement between calculated and observed spectra can also occur. In an iterative calculation based on inaccurate (or even wrong) values of the spectral density function, the internuclear distances (and hence the coordinates) can be adjusted until 'the best fit' is obtained, even though the adjusted distances would give poor agreement, and hence be judged incorrect, if correct values of the spectral density function were known. The use of time-averaged distances in the back-calculation is also not unproblematic, since molecular dynamics simulations generate predominantly averages of the first kind (around a single major energy minimum), with major conformational averaging being largely left out. With the inherent imprecision of the data, the indeterminacy of the generalized Bloch equations, and the limitations of the proposed remedies of this indeterminacy, the observation has been made on several occasions that back-calculation with existing methods does not significantly improve the 'quality' of the reported structures.[43] Although a completely rigorous test of this observation is lacking, the observation is likely to remain correct, unless, or until, back-calculations using a correct set of spectral density functions become possible and the obtainable raw NMR data become more precise.

2.1.6 Accuracy and Precision of Protein Structures Determined by NMR

Given the uncertainties and potential sources of bias in each exploration of the conformational space, with each method and each program potentially subject to its own limitations and bias, the use of combined search methods has gained wide popularity. Particularly common are protocols combining DG and RMD into a single program package (e.g. DIANA and DADAS) and those combining either DG or RMD structure calculations with the back-calculation of spectra. It is thought that the bias of each of the constituent search methods will be canceled by the other. The possibility that the errors will be additive has, regrettably, not been properly tested.

Before it becomes possible to assess the validity of individual structures calculated by any particular method or combination of methods, it is necessary to evaluate the *accuracy*, as well as the *precision*, of NMR structure calculations by a comparison of the families of structures calculated by different methods. Accuracy, in this as in other contexts, means the faithfulness of the reproduction of the 'true' structure and is only measurable with respect to a 'gold standard', i.e. a structure independently determined by another method. Precision, in its usual definition, measures the reproducibility of repeated measurements or calculations. Most of the NMR literature published to date is confused on this issue, and all too often one sees measures of precision offered as a measure of accuracy. The 'first-order answer'—that protein structures built from NMR constraints, by whatever method, rather faithfully reproduce the main topological features of a protein molecule —can be considered to have been demonstrated beyond any doubt. An exact answer with regard to how accurate NMR structures are is more difficult to give. Only a few rigorous comparisons of the accuracy of NMR structures calculated by different methods have been made thus far.[21,44] The principal finding is that the mean

structures calculated by different methods from the same set of data differ by an RMSD of 0.1–0.2 nm from each other and from a 'true' structure independently determined by X-ray diffraction. Claims that an accuracy of 0.025 nm can be achieved for NMR structures[45] were not based on a rigorous study of accuracy, but on a comparison of the relative precision of structures calculated by the same method using two different protocols. In such a procedure, the reference ('true') structure and the test structures are subject to the same systematic error. The calculated estimates are still estimates of precision and not of accuracy, and the claim is therefore not valid. The accuracy of NMR structures determined by now existing methods cannot be taken to be higher than 0.1–0.2 nm, although the precision of the family of structures calculated by any one method can be considerably higher (of the order of 0.03–0.05 nm). If one remembers that proteins in solution are subject to Brownian and internal motions, it is not too surprising that the family of structures reflected in the NMR data may be appreciably larger than any one particular structure calculation may show.

2.2 Solution Structures of Nucleic Acids

These can be defined by using the same procedures as for the structures of proteins. The structure determination involves the same four steps: resolution and assignment of the spectrum, derivation of geometric parameters from spectroscopic data, and model building. For reasons of resolution, limited by spectral overlap, the possibilities of NMR structure determination are for the present limited to relatively short stretches of oligonucleotides (up to 20–30 mers for double-stranded DNA). For such structures an additional serious limitation comes into play in that only short-range distances, i.e. between adjacent bases and base pairs, can be found. Long range interactions, so useful in defining the tertiary fold of a polypeptide chain, are not found in the short, rod-like structures. It is conceivable that for larger circular and supercoiled DNAs, where long-range interactions occur, they could also be detected and used, as in the case of polypeptides to define the tertiary structure. However, the resolution of the spectra of larger DNA structures is beyond the limits of current methodology. Thus only local structural features in nucleic acids—for di- or trinucleotide stretches— can, for the present, be studied by NMR. An exception is the structure of DNA fragments in complexes with proteins, exemplified by the operator–*trp*-repressor complex. In such cases the long-range interactions are provided by protein contacts, allowing the detection of longer range structural features, such as bends and twists of the double helix.

Details of NMR studies of oligonucleotide structures, of their complexes with a variety of drug molecules and of the methods developed for this purpose are given in several articles elsewhere in this Encyclopedia. A critical evaluation of the applicability of NMR methods to solution structure of nucleic acids, published in 1991 by Wemmer,[46] should be read by anyone concerned with the significance of published oligonucleotide structures derived from NMR data. In no other field of biological applications of NMR has the disregard for the principles and pitfalls of NMR structure determination outlined in the preceding section produced as much questionable, and outright erroneous, published information. A dramatic claim for the existence of highly bent, twisted and otherwise distorted, nearly doughnut-shaped DNA segments had already been published in 1988.[47] A re-examination of the method of analysis used in these studies brings to light the danger of overinterpreting the precision of distance constraints by calibrations that do not take either spin diffusion or internal motions into account and using a global optimization procedure with a set of only local constraints. Structures calculated by such oversimplified procedures are not likely to be correct. The extent to which the use of NMR methods for studies of nucleic acid structures is meaningful has not changed since it was succinctly summarized by Wemmer: 'Aspects of secondary structure and the general positioning of bases can be determined readily from NMR data. Highly quantitative structure analyses must be viewed as quite questionable at this time.'

2.3 Solution Structures of Noncovalent Complexes

The solution structure of noncovalent complexes (in particular DNA–protein and small ligand–protein complexes) can also be defined by the procedures described above. The only difference is that docking constraints (e.g. NOEs between the ligand and the protein or between two macromolecules) have to be used in addition to the usual set of constraints defining the geometry of each of the components. The docking constraints play a crucial role in defining both the topology of the complex and the structural changes that occur upon complex formation. For DNA–protein complexes, relatively few docking constraints will define the geometry and, where applicable, the symmetry of the complex, and identify the regions of contact. Many such constraints are required to define the fine structure of the interface and the structural changes resulting from complex formation. In the case of the operator–*trp*-repressor complex already mentioned as the largest NMR structure to have been determined so far, a considerable distortion of both the DNA and the protein structure occurs upon binding in the presence of tryptophan, so that simple docking of the independently determined operator and repressor structures using only experimental docking constraints gives only an approximate structure, although its symmetry is correct. A complete de novo structure determination was necessary in this case to account for all of the data in detail. The resulting structure is shown in Figure 11.[16]

Two considerations are of importance when viewing reported ligand–protein structures. First, several of the structures that are found in the literature are based on model building only—i.e. on rigid body docking of independently determined ligand and protein structures (in the case of DNA based on a standard B-DNA model).[48] Such structures must be regarded as hypothetical and must be distinguished from structures obtained by a bona fide complete structure determination, to which, as the *trp*-system example shows, they are by no means equivalent. Second, discrepancies between NMR structures and crystal structures of the same complex must be examined with care, as they may provide important information. In the case of the *trp*-repressor–operator complex, direct hydrogen bonding contacts between the DNA and the protein are compatible with all observed NMR constraints. In the crystal structures of the same complex, several protein–DNA contacts are mediated by water molecules, a rather unusual

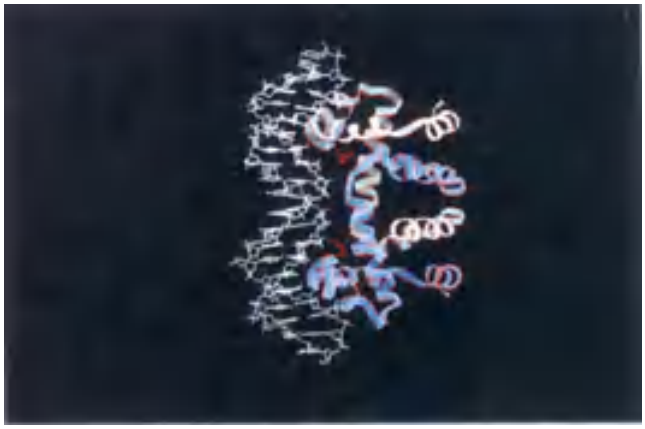

Figure 11 Solution structure of the *trp*-repressor–ODNA complex. The view shows the repressor backbone with DNA at full atomic representation. (Reproduced from H. Zhang, D. Zhao, M. Revington, W. Lee, X. Jia, C. Arrowsmith and O. Jardetzky, *J. Mol. Biol.*, 1994, **238**, 592)

feature even among protein–DNA complexes determined by X-ray diffraction. For the study of noncovalent complexes, NMR may prove to be the better method. In several reported cases it is apparent that flexible protein segments are involved in the interaction with DNA,[49] and flexible peptides are found at protein binding sites.[50,51] The flexibility of such structures means that they are particularly vulnerable to the action of external forces, and specifically those that are responsible for crystallization. Whereas distortion of tightly packed covalent protein structures upon crystallization is generally regarded as minimal, this is not necessarily the case when the much weaker noncovalent complexes are examined. One should therefore expect to encounter artifacts resulting from crystallization which would not occur in the solution structure. Only a minor distortion of specific contacts is required to allow water molecules in the crystallized complex where they would not normally occur in solution, creating the potentially erroneous impression that they play a functional role.

3 MACROMOLECULAR DYNAMICS

NMR spectra are sensitive to molecular motions over a wide range of frequencies. The timescales on which each of the principal measurable NMR parameters—chemical shifts, line intensities, coupling constants and relaxation rate constants (including linewidths and NOEs), and proton exchange rates —provide dynamic information are summarized in Figure 12.[52] The total range spans from picoseconds to hours, days and weeks, making NMR a uniquely useful method for the study of dynamic processes in molecules (as in the case of structure) at atomic resolution. Although other spectroscopic methods allow the study of dynamic processes at selected points in a protein structure, focusing on a single atom or a group of atoms, no other method allows the *simultaneous* observation of dynamic phenomena in different parts of the molecule at atomic resolution. Application of high resolution NMR to the study of proteins has led to the discovery of several types of dynamic phenomena in protein molecules, most of which are as yet not fully understood. We can distinguish at least five categories of such phenomena: (1) variation of fast (i.e. nanosecond) motional frequencies along the polypeptide backbone; (2) enhanced conformational flexibility of longer backbone segments on different timescales (nanoseconds to seconds); (3) 'breathing' of folded protein made evident by the free rotation of aromatic amino acid side chains in the tightly packed core of many proteins or by rapid exchange of backbone NH protons with the solvent (micromillisecond); (4) conformational equilibria involving entire domains (usually on a millisecond to second timescale); and (5) dynamic states of partially folded structures observed under denaturing conditions. Variations of motional (rotational) frequencies along an amino acid side chain on the protein surface might be considered as a sixth category, but they are relatively well understood and of interest for the understanding of protein function only in the special cases when the motion becomes hindered by interactions.

3.1 Protein Dynamics

3.1.1 Fast Motional Frequencies along the Backbone

The possibility of resolving and assigning individual resonances for most atomic groups in the protein has brought with it the possibility of mapping the motional frequencies, which are reflected in relaxation parameters, for each individual group. Generally, a combination of relaxation parameters—T_1, T_2 and $T_{1\rho}$, and for ^{13}C and ^{15}N atoms with covalently bonded protons, also the NOE—has to be used to define the motions of interest and their frequencies. A most exact analysis of the motions along the peptide backbone allows the direct calculation of individual spectral density functions for individual interatomic vectors from experimental data without recourse to any (always arbitrary) model for their analysis. This type of analysis does not directly define a physical picture of the motions—a motional model giving a correct prediction of the spectral density functions is required for this purpose. However, *variations* in motional frequencies and amplitudes along the backbone can be mapped, although it should be said that they are also evident from the raw relaxation data themselves, independently of any method of analysis. The experimental results reported so far reflect two types of situation: (a) relatively rigid proteins, e.g. the IIA domain of glucose permease,[53] for which the variation in the magnitude of measured relaxation parameters along the polypeptide backbone is minimal; and (b) proteins containing segments of varying flexibility, e.g. staphylococcal nuclease, eglinC, gal4, calmodulin[54] and others. Larger amplitude motions are frequently observed in loops and at hinges between compact domains. In some cases these motions may involve the entire loop, leading to a poor definition of the NMR structure, whilst in others they are limited to one or a few residues at each end of the loop, the remainder of the loop appearing well structured. In other cases large-amplitude motions affect a group of residues within a unit of secondary structure, as in the case of interleukin or staphylococcal nuclease. There is as yet no clearly recognizable pattern to the distribution of amplitudes and frequencies of these fast motions, and it is not yet clear whether they play any role in protein function or are irrelevant byproducts of protein architecture.

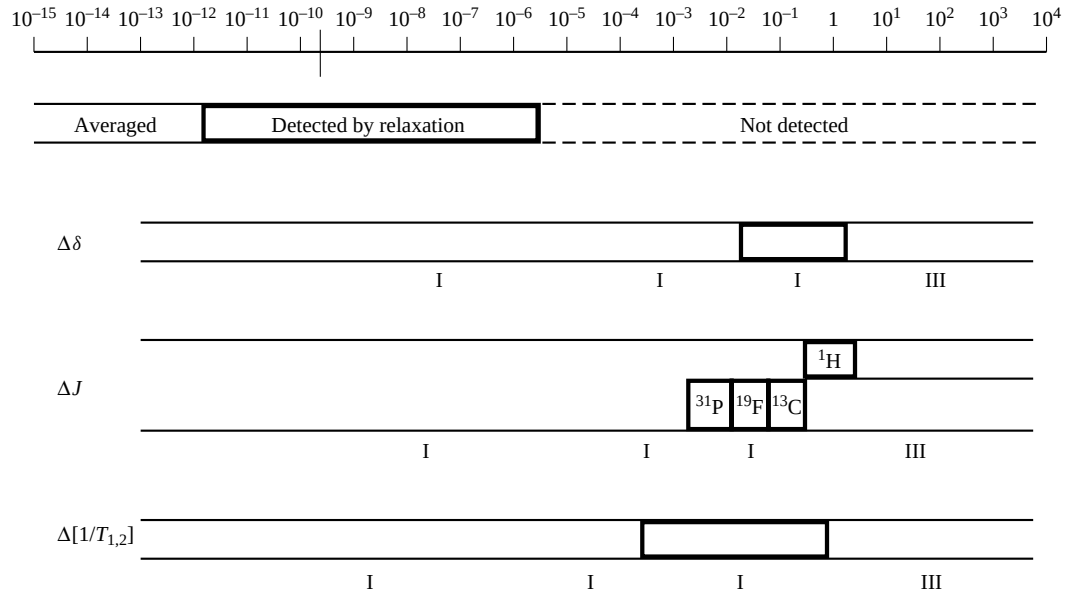

Figure 12 Timescales in seconds defined by NMR parameters. (I) Region of fast exchange; (II) region of intermediate exchange; (III) region of slow exchange. (Reproduced from O. Jardetzky and G. C. K. Roberts, 'NMR in Molecular Biology', Academic Press, New York, 1981)

The interpretation of the observed spectral density functions in terms of motional parameters, i.e. amplitudes and frequencies, depends of course on the construction of an appropriate model. Such models are necessarily complex and are only now beginning to emerge. The models used initially—anisotropic rigid body rotation, fast rigid rotor on a slower rigid rotor, wobbling on a cone[55,56]—were too simplistic to account for more than a few data points. Model-free approaches, which have enjoyed some popularity, can generate detailed motional maps, but fail to provide a complete insight into their nature. The original model-free approach of King and Jardetzky[57] can account for the observed motional frequencies, but not for the detailed amplitude characteristics of the motion. The model-free approach of Lipari and Szabo[58] actually represents a very restrictive model, equivalent to rigid body rotation with one degree of internal motional freedom or a two-term expansion of the King–Jardetzky formalism. Not surprisingly, it fails to account for the more detailed motional maps now obtainable experimentally,[59] just as any other of the oversimplified models. In the experimental maps, one can frequently see regions affected by slower motions of some kind, largely reflected in anomalous values of T_2. No fully satisfactory treatment of such slow motions has as yet been developed, although it has been suggested that they represent concerted motions, such as solitons.[60] Molecular dynamics simulations have shown promise in accounting for fast rotations in protein side chains.[42] Their great attraction is that they allow an independent, rigorous, a priori calculation of spectral density functions, which can then be compared with those obtained from experiments. In principle, molecular dynamics can provide a complete explanation of all dynamic processes observed in proteins, including the slower (micro- to millisecond) motions. Unfortunately for the nanosecond and slower motions observed along the backbone, rigorous molecular dynamics simulations are not yet practical. A complete and correct description of the patterns of the motions observed along the polypeptide chain remains a subject for future research, as does the evaluation of their functional significance.

3.1.2 Conformational Flexibility

Conformational flexibility of a longer contiguous segment of the peptide backbone may occur on any timescale and can be reflected in a different set of NMR parameters in different cases. Many examples of flexible segments varying in length from 7 to 25 or even more amino acid residues are now known. Some occur at the *N*- and *C*-terminals of peptide chains and some in their interior. The earliest discoveries of flexible segments—those of the RNA-binding site in Tobacco Mosaic Virus (TMV),[61] the DNA-binding domain of the *lac*-repressor,[62] histones,[63] and the S1 domain of myosin[64]—were based on the finding of anomalously narrow lines (long T_2) reflecting free rotation on a nanosecond timescale. In the crystal structure of TMV the corresponding segment was found to be disordered. In the more recent examples—the DNA-binding domains of the *trp*-repressor[65] and antennapedia homeodomain,[66] and the B-chain of insulin analogs[67]—fast motions do not play a prominent role, and the most striking finding is the absence of NOEs needed to define the structure of the segment. This finding is usually accompanied by the finding of unusually rapid exchange rates for the peptide backbone protons. Structure calculations on molecules containing such segments lead to the conclusion that the segments are disordered in solution. However, the apparent disorder may reflect averaging between two or more well-defined conformations. In the absence of line narrowing and other anomalies in the relaxation parameters, the conclusion must be drawn that the conformational averaging occurs on timescales longer than nanoseconds. In favorable cases, where the segment undergoes transitions between a closed and an open form of a secondary structure (e.g. a helix-coil transition), the rates of conformational averaging can be estimated from rates of backbone proton exchange. A very detailed study

of conformational flexibility in the DNA-binding domain of the *trp*-repressor has led to the conclusion that the interplay of dynamic processes in peptide segments can be quite complicated. It is thus necessary to distinguish between *true flexibility*, or *true disorder*, and *apparent flexibility*, or *apparent disorder*. In the case of true flexibility one will find 'random coil' behavior by all NMR criteria—rapid averaging of chemical shifts and coupling constants, rapid proton exchange and rapid motions reflected in narrow lines, as well as disappearance of NOEs and other cross peaks in multidimensional spectra. These are findings typical of the N- and C-terminal peptide segments in several proteins. On the other hand, in cases of apparent disorder or flexibility the findings tend to be contradictory, as they are in the case of the *trp*-repressor. The DNA binding segment appears disordered if one relies on the observations of sequential NOEs, backbone proton exchange rates and backbone ^{1}H T_1 measurements. At the same time, it appears ordered from the ^{15}N relaxation profile and from the finding of α-CH shifts typical of α-helical structures. The findings can be reconciled if one infers that the segments are largely helical on a nanosecond timescale, but the helices are unstable on longer (in this case millisecond) timescales, and the closed state (corresponding to the formation of a hydrogen bond) at all sites exists less than 100% of the time. One is thus dealing not with a continuum of conformational states, which defines true flexibility, but rather with a structure that is unstable and hence 'flexible' only on a much longer timescale. A similar phenomenon is known to occur in the ready unfolding of the *lac*-repressor DNA-binding domain. In this case sufficient NOEs were found initially to define a helical structure, but the structure was shown to be unstable under a variety of ambient conditions.[68]

The quantitative analysis of the apparent disorder cases requires a wide range of NMR measurements and can be rather complicated. Selective attention to only some of the NMR parameters (e.g. only the set of observable NOEs, which has become common practice in NMR structure determination) will confuse true and apparent disorder and lead to erroneous conclusions, as will the uncritical application of commonly used theoretical treatments [e.g., those for backbone proton exchange, which are based on simplified assumptions of relatively stable secondary structures (see ***Hydrogen Exchange and Macromolecular Dynamics***), and do not apply in the general case]. The paradigm for the analysis of the general case was first worked out for the *trp*-repressor and is briefly summarized here because of its wide applicability. The picture of the repressor helix–turn–helix DNA-binding domain that has emerged from this analysis is as follows: the region consists of two helices which retain their overall helical shape at all times, but with hydrogen bonds opening, one at a time, on a millisecond time scale.

Three types of experiment are necessary to calculate the exchange rates (or lifetimes) between the different states in this type of situation. First, the classical hydrogen–deuterium exchange experiments can identify hydrogen bonds that are stable on timescales from minutes to years. Second, proton T_1 relaxation, with and without solvent presaturation, will identify those hydrogen bonds undergoing an exchange on a millisecond to second timescale. Third, the pH dependence of the T_1 will allow calculation of opening and closing rates, since the intrinsic exchange rate is known to be pH dependent and can be independently evaluated from the amino

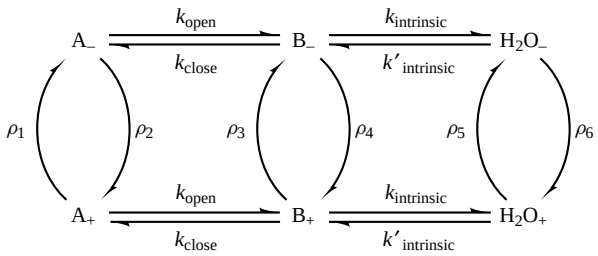

Figure 13 The generalized Linderstrøm–Lang model

acid sequence (see ***Hydrogen Exchange and Macromolecular Dynamics***).

The simplest model that can account for the observation is the generalized Linderstrøm–Lang model, which is free of all of the usual assumptions about the relative magnitudes of helix opening, helix closing and intrinsic exchange rates[69,70] (Figure 13). The magnetization transfer equations describing this model without arbitrary simplification are the generalized McConnell equations:

$$\left.\begin{aligned}
\frac{dM_A}{dt} &= -R_{1A}(M_A - M_A^{EQ}) - k_{open}M_A + k_{close}M_B \\
\frac{dM_B}{dt} &= -R_{1B}(M_B - M_B^{EQ}) + k_{open}M_A - k_{close}M_B \\
&\quad - k_{intr}M_B + k'_{intr}M_{H_2O} \\
\frac{dM_{H_2O}}{dt} &= -R_{1H_2O}(M_{H_2O} - M_{H_2O}^{EQ}) - k'_{intr}M_{H_2O} + k_{intr}M_B
\end{aligned}\right\} \quad (15)$$

whose solution is:

$$\begin{aligned}
M_A &= C_1 e^{\lambda_1 t} + C_2 e^{\lambda_2 t} + C_3 \\
M_B &= D_1 e^{\lambda_1 t} + D_2 e^{\lambda_2 t} + D_3
\end{aligned} \quad (16)$$

The symbols are defined in the Appendix at the end of this article.

The solution of these equations predicts pH independent single exponential behavior for the NHs of slowly exchanging (stable) hydrogen bonds, and pH dependent double exponential behavior for hydrogen bonds exchanging on a timescale comparable to the intrinsic relaxation rate, T_1 (milliseconds to seconds).[71,72]

In the study of the pH dependence of relaxation in the *trp*-repressor, the observation was made that, even though the data could be accounted for by this model, the conclusions drawn about the percentage helicity and opening and closing of helices were contradicted by other experimental findings. The contradictions are summarized in Table 2.

To account for all the data simultaneously, one either has to assume that the 'open' state in the Linderstrøm-Lang model is not completely open, characterized by $k_{intrinsic}$ slower than the rate observed in a free peptide, or alternatively, invoke a three-state model allowing for the observed slow exchange between

Table 2 Contradictory Evidence on the Percentage Helicity and Opening and Closing of Helices

Helix–Coil Transition	Process Monitored by T_1
$\geq$90% helicity (δ, ^{15}N)	20–40% 'helicity'
$k_{ex} > 100$ Hz ($\Delta\delta$, temperature dependent)	$0.4 < k_{ex} < 4$ Hz

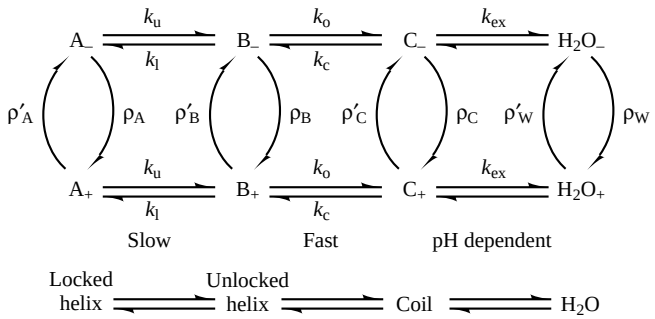

Figure 14 The three-state model

'locked' and 'unlocked' states of the DNA-binding helices, and a rapid helix–coil equilibrium (Figure 14). The equations for this model, too complex to be reproduced here, reduce to the form of equations (15) and (16) if the helix–coil equilibrium is rapid. The physical meaning of the observed rates is, however, in either case different than that originally envisioned. This underscores the importance of comparing different types of NMR and other data if one is to arrive at a correct description of solution structures and their dynamics.

The functional significance of segmental flexibility—either true or apparent—may well be to facilitate conformational adjustments on binding to ligands. It is probably no accident that segmental flexibility appears prevalent in the binding domains of DNA (and RNA) binding proteins. Especially in the case of repressors, such as the *trp*-repressor, which are known to interact with more than one DNA sequence, such conformational flexibility could be necessary to make the optimal contacts in each case, using the same amino acid sequence and the same secondary structure. Similarly, in the case of insulin, flexibility of residues 20–30 in the B chain could facilitate conformational adjustments upon receptor binding. A very interesting example of flexibility associated with the ability of a segment to assume a helical conformation in the crystal and a β-turn conformation in solution has been described for chicken egg-white cystatin.[73] The function of this segment is as yet unknown, and much remains to be learned about protein function from the NMR study of similar phenomena in other proteins.

3.1.3 'Breathing' Motions

Breathing motions first became apparent in the spectra of selectively deuterated staphylococcal nuclease, which showed that the tyrosines in the interior of the molecule had motionally averaged spectral lines.[74] This phenomenon was extensively studied on several proteins in the 1970s, and the rates for the 180° flip were estimated to lie between 102 and 104 s^{-1}. A temperature dependent transition from the 'frozen' configuration at low temperatures to the freely rotating state at room temperature was described for ferrocytochrome *C*.[75] In the case of parvalbumin, low amplitude librations of phenylalanine rings in the core on a nanosecond timescale, detectable by ^{13}C relaxation, could be shown to precede the relatively rare 180° flips on a microsecond timescale, evident from chemical shift averaging.[76] Rotation of rings in the interior of the protein has been and always needs to be considered in the interpretation of NOEs used for a protein structure determination.[18] The relationships of such 'breathing' motions to backbone motions and segmental flexibility have not yet been sufficiently studied, but it may be expected that they will emerge from comparisons of the relative timescales, directions, and amplitudes. Ideally, the relationship should be given by molecular dynamics calculations, but molecular dynamics simulations on the required micromillisecond timescales are impractical at present.

3.1.4 Conformational Transitions

Conformational transitions usually manifest themselves as changes of local structure. The ease of detecting and describing them depends on the lifetimes of the conformational states involved. If the exchange between the states is slow on the chemical shift timescale, i.e. the lifetimes of the states are long compared to the inverse of the chemical shift difference between the peaks representing the two states, the states can be observed and described separately by standard structure determination methods. Into this category fall the conformational readjustments occurring in Ca^{2+} binding proteins upon addition of Ca^{2+}, which have been studied extensively and are described elsewhere in this Encyclopedia, and many others. If the exchange rate is of the same order as the frequency difference of chemical shifts between the two states, the transition is often observable as a selective line broadening. The early NMR detection of conformational equilibria, even in simple enzymes such as pancreatic ribonuclease A,[77] was based on this phenomenon. As the exchange rate becomes more rapid on the chemical shift timescale, the individual conformational states can no longer be resolved. In the intermediate exchange range it is possible to infer from the data that an exchange process is occurring, but not the nature of the conformers or their number. In the rapid exchange case, even the existence of the exchange process itself is not directly detectable. This leads to the well-known problem that a structure determination on a system undergoing rapid averaging between two or more distinct conformations leads to a structure that has no physical meaning.[52,78] Attempts to resolve this dilemma by modeling the individual conformers and calculating the pattern of NMR parameters that would correspond to a dynamic average of the multiple states have been published.[79] A residual of uncertainty as to the adequacy of the dynamic model invoked will always remain for structures determined on systems undergoing conformational averaging. In formulating and testing such a dynamic model, it is therefore advisable to invoke a wide range of NMR experiments and test the interpretation of results for internal consistency.

3.1.5 Dynamic States of Partially Folded Structures and the Problem of Protein Folding

These topics are an active area of current research, and NMR approaches to this problem are discussed in detail elsewhere in this Encyclopedia. Suffice it to say here that studies of this type—conducted on objects known to be unstable—are especially vulnerable to the problems of conformational averaging discussed above. At the same time, it must be pointed out that even NMR 'structures' of intermediates which have no physical existence ('apparent structures') may be useful as indicators of the trends of changes occurring in

the structure as it folds or unfolds, respectively, and thus point to the deciphering of the folding pathway. An interesting recent example has been provided by the work of Dobson and coworkers[80] on the folding pathway for the assembly of hen egg-white lysozyme. The pathway appears to proceed from: (1) the formation of α-helices; to (2) the formation of two-helix bundles; to (3) the addition of a β-structure to form a 'molten globule' that topologically resembles the final structure, but is not well defined in detailed contacts and must undergo a rearrangement to yield, (4) the fully folded lysozyme.[73] A caveat emerging from this study is that alternative pathways are also compatible with all of the available NMR data. This reflects the ambiguity of the NMR data, but may also reflect the actual existence of multiple folding pathways. In a case of this kind, extensive correlation of the NMR findings with findings obtained by other physical methods is essential for the resolution of ambiguities.

3.1.6 Implications of Internal Motions and Flexibility for Structure Determination by NMR

The most serious problem to be considered when deriving solution structures of proteins from NMR data is that of conformational averaging, as discussed above. The problem is ubiquitous, and the burden of proof that the reported structure is rigid as calculated, remains on the investigator. For small compact globular proteins the problem is minimal. Averaging in a single potential well around a single set of coordinates is, for all practical purposes, indistinguishable from the case of a rigid structure, and corrections for this type of averaging have been proposed.[42] Short disordered regions are easily detected by the absence of NOEs, as in the case of insulin. The problem is much more serious for larger proteins, where averaging between ordered local structures may occur, as in the case of the *trp*-repressor. In such cases a detailed study of the dynamics becomes necessary, before the proposed structure can be given full credence. As has been pointed out already, many years ago,[23,78] to derive correctly a protein solution structure from NMR data, it is necessary to understand the dynamics of the protein in detail, and vice versa. Simple NMR structure determination is limited to simple objects. For most proteins, the study of structure and dynamics must, of necessity, go hand in hand.

3.2 Nucleic Acid Dynamics

Two types of rapid motion are known to occur in nucleic acid structures: (1) puckering of the phosphate backbone, reflected in the rapid averaging of ^{31}P chemical shifts so that typically, with few exceptions, only a single phosphate NMR signal is observed in both short oligonucleotide double helices and long (300–600 base pair) stretches of DNA; and (2) puckering of the sugar rings (deoxyribose in DNA and ribose in RNA, respectively), usually described as an exchange between a 2′-*endo* and a 3′-*endo* conformation.[81] Since the exchange rate is rapid on both the chemical shift and the coupling constant timescales (so that only time-averaged parameters are observed and individual states can not be resolved), it remains possible, but unprovable, that the exchange involves more than two states. Both of these motions clearly reflect thermal fluctuations. If they have any functional significance, it is to reflect the inherent flexibility of nucleic acid strands, necessary for the unwinding of double-stranded structures in the processes of replication, transcription and translation. It has been proposed that these motions may be accompanied by changes in helical twist.[82] On the other hand, wobbling of bases in double-stranded structures is rarely of sufficient amplitude to be reflected in NMR parameters, except at the fraying ends of oligonucleotide sequences.[83] Motions within the DNA double strand can be modulated and damped by the binding of intercalating agents. For purposes of structure calculations, short double-helical oligonucleotide strands can be treated as if they were rigid, since all of the described motions result only in averaging about a single energy minimum, i.e. within a single potential well. As yet, insufficient NMR data on the structure and dynamics of RNA are available to judge whether the more complex RNA structures found in crystallographic studies also undergo more complex and functionally significant motions. The existence of such motions can for the present only be inferred from the diversity of binding and catalytic interactions within the RNA family, observed in biological experiments. Conformational flexibility is a prerequisite for such diversity. Specific examples of nucleic acid dynamics are discussed elsewhere in this Encyclopedia (see ***Nucleic Acids: Spectra, Structures, and Dynamics***).

4 MOLECULAR INTERACTIONS

Molecular interactions of small ligands with macromolecules were among the first biological problems to be successfully studied by NMR. As early as 1961 a relaxation method for the determination of the groups involved in ligand–protein interactions had been developed in the author's laboratory.[84,85] With the methods then available, it was possible to infer which part of the flexible ligand—e.g. the phenyl ring of penicillin, rather than the penicillanic acid moiety—was bound to the protein. Interesting observations on different modes of binding in the sulfonamide family could be made, distinguishing binding by the sulfonamide ring from binding of an aromatic substituent to the same protein.[86] Later, it became possible to infer structures of inhibitor binding sites from a combination of NMR observations of ligand and protein side chains, as in the cases of pancreatic ribonuclease[87] and staphylococcal nuclease.[88] The binding of a transition state analog to lysozyme was also the subject of one of the early studies.[89] With modern technology it is possible to obtain detailed structures of binding sites, even for proteins that are for the time being too large to be amenable to a complete structure determination. A classic example is the detailed study of the binding of substrates and cofactors to dihydrofolate reductase, carried out by Roberts and coworkers.[90] In these studies it was found, long before a complete structure determination, that the cofactors NAD and NADH bound in different orientations, and, in a corresponding study of the dynamics, that the bound heterocyclic rings were able to undergo 180° flips in the bound state. A similar detailed study of the anti-TEMPO hapten antibody Fab fragment binding site by McConnell and coworkers[91] revealed that hapten binding caused a conformational change involving the displacement of a tyrosine side chain near the binding site to accommodate the hapten moiety. A detailed NMR structure of the Fab

fragment is not yet available. A complete structure of the tryptophan binding site in the *trp*-repressor was obtained in the course of the structure determination. It must be said, however, that the precision with which noncovalent structures can be defined from NMR data still leaves something to be desired, although the general configuration of the complex can be clearly outlined and the possibilities of forming different contacts evaluated. In dynamic NMR studies of ligand–protein interactions, the lifetimes of the bound and free states and the binding constants can be estimated. For typical small molecule ligands, the dwelling time on a protein falls in the millisecond range.

NMR studies of binding sites are particularly attractive when a comparison of the binding modes of different ligands (e.g., in a series of analogs) are needed, because of the relative speed and efficiency with which comparisons can be made. For ligands binding in a similar manner, the spectral changes (e.g., in the observed NOE pattern) from one compound to the next will be minor, and similarity of binding can be inferred from the similarity of the spectra without a complete reanalysis of the spectra in each case. Only when the binding patterns are different will the spectral changes be marked and require a de novo interpretation. A further advantage of NMR studies in this context is that comparative kinetic information on the exchange rates between the bound and free states is readily obtainable.

5 PROTEIN FUNCTION

Studies of protein function made possible by NMR fall into several categories. Very few detailed studies of this kind have as yet been carried out, but the possibilities have been clearly recognized.

The function of enzymes can be studied at several levels. Rates of enzymatic catalysis can be followed by observing the disappearance of substrates and appearance of products in (real) time. Structures of enzyme–inhibitor, enzyme–substrate or enzyme–transition-state analog complexes can be determined and examined for clues concerning the involvement of different groups at the binding site in the process. The first successful example of such a study was that of pancreatic ribonuclease A,[77,87] leading to a proposed mechanism that has since been confirmed by several kinetic and structural methods. Conformational changes and conformational equilibria involved in allosteric regulation can be defined, as described above. The obvious advantage of NMR over X-ray diffraction in this context is that the enzyme can be studied in its natural environment in solution, and that the dynamic processes involved can in many cases (though not always) be observed directly rather than being inferred from the initial and final states that can be crystallized.

The function of regulatory proteins, in which points of contact between the protein and DNA can be altered by a small molecule ligand, can be examined in much the same way as the function of allosteric enzymes. The study of the operator–*trp*-repressor complex, which forms in the presence of tryptophan and dissociates in its absence, can serve as the prototype for all studies of this type. This system is not only, as already noted, the largest molecular entity determined by NMR, but also the only complete allosteric regulatory complex analyzed by NMR methods in detail. All other NMR studies of protein–DNA interactions that have been reported involve binary complexes between the two macromolecules, with the regulatory function and ligand binding sites having been lost in the preparation of DNA-binding domains small enough to be easily studied by NMR. Structural studies of the complete system, including the ternary ligand–protein–DNA complex revealed a first conformational change on corepressor tryptophan binding and a further conformational change on the formation of the ternary complex with operator DNA. Dynamic studies revealed a stabilization of the DNA binding region by the binding of tryptophan and a further stabilization upon the formation of the ternary complex. The actual process is therefore more complex than the simple model commonly used for regulatory proteins—a single ligand induced conformational transition which aligns the DNA binding sites for better docking. It is to be expected that further, as yet unanticipated, variants of regulation by structural change will be uncovered in the course of studies on other systems.

Proteins involved in signal transduction and information transfer are also thought to function by undergoing structural transitions and, therefore, can be studied by the same techniques as those applied to the *trp*-repressor system, as can transport proteins functioning by an allosteric mechanism.

6 CONCLUSIONS

In summary, it can be said that the biological-NMR literature to date has laid all the necessary foundations for the study of protein structure, dynamics, interactions and function, devising and testing the required techniques and prototype experimental protocols on selected prototype systems. To a lesser extent, this can also be said of nucleic acids. Some technical development still remains to be done, in particular testing combinations of techniques to solve specific problems. The full range of potential applications remains in the future.

7 APPENDIX: DEFINITION OF SYMBOLS USED IN EQUATION (16)

$$\lambda_1 = \frac{-\frac{1}{T_{1A}} - k_{open} - \frac{1}{T_{1B}} - k_{close} - k_{intrinsic} + \sqrt{\left(\frac{1}{T_{1A}} + k_{open} - \frac{1}{T_{1B}} - k_{close} - k_{intrinsic}\right)^2 + 4k_{close}k_{open}}}{2}$$

$$\lambda_2 = \frac{-\frac{1}{T_{1A}} - k_{open} - \frac{1}{T_{1B}} - k_{close} - k_{intrinsic} - \sqrt{\left(\frac{1}{T_{1A}} + k_{open} - \frac{1}{T_{1B}} - k_{close} - k_{intrinsic}\right)^2 + 4k_{close}k_{open}}}{2}$$

$$C_1 = \left(\lambda_1 + \frac{1}{T_{1B}} + k_{close} + k_{intrinsic}\right)\left\{\frac{(M_A^i - C_3)\left(\lambda_2 + \frac{1}{T_{1A}} + k_{open}\right) - k_{close}(M_B^i - D_3)}{\left(\lambda_2 + \frac{1}{T_{1A}} + k_{open}\right)\left(\lambda_1 + \frac{1}{T_{1B}} + k_{close} + k_{intrinsic}\right) - k_{open}k_{close}}\right\}$$

$$C_2 = k_{open}\left\{\frac{(M_B^i - D_3)\left(\lambda_1 + \frac{1}{T_{1B}} + k_{close} + k_{intrinsic}\right) - k_{open}(M_A^i - C_3)}{\left(\lambda_z + \frac{1}{T_A} + k_{open}\right)\left(\lambda_1 + \frac{1}{T_{1B}} + k_{close} + k_{intrinsic}\right) - k_{open}k_{close}}\right\}$$

$$D_1 = k_{close}\left\{\frac{(M_A^i - C_3)\left(\lambda_2 + \frac{1}{T_{1A}} + k_{open}\right) - k_{close}(M_B^i - D_3)}{\left(\lambda_2 + \frac{1}{T_{1A}} + k_{open}\right)\left(\lambda_1 + \frac{1}{T_{1B}} + k_{close} + k_{intrinsic}\right) - k_{open}k_{close}}\right\}$$

$$D_2 = \left(\lambda_2 + \frac{1}{T_{1A}} + k_{open}\right)\left\{\frac{(M_B^i - D_3)\left(\lambda_1 + \frac{1}{T_{1B}} + k_{close} + k_{intrinsic}\right) - k_{open}(M_A^i - C_3)}{\left(\lambda_2 + \frac{1}{T_{1A}} + k_{open}\right)\left(\lambda_1 + \frac{1}{T_{1B}} + k_{close} + k_{intrinsic}\right) - k_{open}k_{close}}\right\}$$

$$C_3 = M_A^{EQ} + \frac{f k_{close}}{\left(\frac{1}{T_{1A}} + k_{open}\right)\left(\frac{1}{T_{1B}} + k_{close} + k_{intrinsic}\right) - k_{open}k_{close}}$$

$$D_3 = M_B^{EQ} + \frac{f\left(\frac{1}{T_{1A}} + k_{open}\right)}{\left(\frac{1}{T_{1A}} + k_{open}\right)\left(\frac{1}{T_{1B}} + k_{close} + k_{intrinsic}\right) - k_{open}k_{close}}$$

For presaturation experiments: $f = -k_{intrinsic}\boldsymbol{M}_B^{EQ}$. For no-presaturation experiments: $f = 0$.

8 REFERENCES

1. M. Saunders, A. Wishnia, and J. G. Kirkwood, *J. Am. Chem. Soc.*, 1957, **79**, 3289.
2. G. M. Clore and A. M. Gronenborn, *Prog. NMR Spectrosc.*, 1991, **23**, 43.
3. C. H. Arrowsmith, L. Treat-Clemons, L. Szilágyi, R. Pachter, and O. Jardetzky, *Makromol. Chem., Macromol. Symp.*, 1990, **34**, 33.
4. J. Czaplicki, C. Arrowsmith, and O. Jardetzky, *J. Biomol. NMR*, 1991, **1**, 349.
5. M. Takeda and O. Jardetzky, *J. Chem. Phys.*, 1957, **26**, 1346; see also O. Jardetzky and C. D. Jardetzky, *J. Am. Chem. Soc.*, 1957, **79**, 5322.
6. O. Jardetzky, *Adv. Chem. Phys.*, 1964, **7**, 499.
7. W. A. Gibbons, D. Crepaux, J. Delayre, J.-J. Dunand, G. Hajdukovic, and H. R. Wyssbrod, in *Peptides: Chemistry, Structure and Biology*, eds. R. Walter and J. Meienhofer, Ann Arbor, New York, 1976, pp. 127–137.
8. C. H. Arrowsmith, R. Pachter, R. B. Altman, S. B. Iyer, and O. Jardetzky, *Biochemistry*, 1990, **29**, 6332.
9. M. Ikura, L. E. Kay, and A. Bax, *Biochemistry*, 1990, **29**, 4659.
10. G. T. Montelione and G. Wagner, *J. Magn. Reson.*, 1990, **87**, 183.
11. R. Powers, D. S. Garrett, C. J. March, E. A. Frieden, A. M. Gronenborn, and G. M. Clore, *Biochemistry*, 1992, **31**, 4334.
12. M. Ikura, G. M. Clore, A. M. Gronenborn, G. Zhu, C. B. Klee, and A. Bax, *Science*, 1992, **256**, 632.
13. R. Powers, G. M. Clore, A. Bax, D. S. Garrett, S. J. Stahl, P. T. Wingfield, and A. M. Gronenborn, *J. Mol. Biol.*, 1991, **221**, 1081.
14. W. J. Fairbrother, J. Cavanaugh, H. J. Dyson, A. G. Palmer, S. L. Sutrina, J. Reizer, M. H. Saier, Jr, and P. E. Wright, *Biochemistry*, 1991, **30**, 6896.
15. R. Powers, D. S. Garrett, C. J. March, E. A. Frieden, A. M. Gronenborn, and G. M. Clore, *Science*, 1992, **256**, 1673.
16. H. Zhang, D. Zhao, M. Revington, W. Lee, X. Jia, C. Arrowsmith, and O. Jardetzky, *J. Mol. Biol.*, 1994, **238**, 592.
17. D. M. LeMaster, *Prog. NMR Spectrosc.*, 1994, **26**, 371.
18. O. Jardetzky and A. N. Lane, in *Physics of NMR Spectroscopy in Biology and Medicine*, ed. B. Maraviglia, Italian Physical Society/North-Holland Physics, Amsterdam, 1988, pp. 267–301.
19. J. D. Forman-Kay, G. M. Clore, P. T. Wingfield, and A. M. Gronenborn, *Biochemistry*, 1991, **30**, 2685.
20. K. Kato, C. Matsunaga, T. Igarashi, H.-H. Kim, A. Odaka, I. Shimada, and Y. Arata, *Biochemistry*, 1991, **30**, 270.
21. D. Zhao and O. Jardetzky, *J. Mol. Biol.*, 1994, **239**, 601.
22. M. Karplus, *J. Chem. Phys.*, 1959, **30**, 11.
23. O. Jardetzky, in *Progress in Bioorganic Chemistry and Molecular Biology. Proceedings of the International Conference on the Frontiers of Bio-organic Chemistry and Molecular Biology, Moscow-Alma Ata*, ed. Yu. A. Ovchinnikov, Elsevier Science, Amsterdam, 1984, pp. 55–63.
24. T. F. Havel, G. M. Crippen, and I. D. Kuntz, *Biopolymers*, 1979, **18**, 73.
25. T. A. Holak, J. H. Prestegard, and J. D. Forman, *Biochemistry*, 1987, **26**, 4652.
26. R. B. Altman and O. Jardetzky, *J. Biochem.*, 1986, **100**, 1403.
27. I. D. Kuntz, J. F. Thomason, and C. M. Oshiro, *Methods Enzymol.*, 1989, **177**, 159.
28. G. M. Crippen, *Distance Geometry and Molecular Conformation*, Wiley, Chichester, 1988.
29. E. Madelung, *Die Mathematischen Hilfsmittel des Physikers*, Dover, New York, 1943.

30. J. C. Hoch and A. S. Stern, *J. Biomol. NMR*, 1992, **2**, 535.
31. R. B. Altman, R. Pachter, E. A. Carrara, and O. Jardetzky, *QCPE Bull.*, 1990, **10**(4), Program 596.
32. P. Koehl, J.-F. Lefèvre, and O. Jardetzky, *J. Mol. Biol.*, 1992, **223**, 299.
33. C. Arrowsmith, R. Pachter, R. Altman, and O. Jardetzky, *Eur. J. Biochem.*, 1991, **202**, 53.
34. B. R. Brooks, R. E. Bruccoleri, B. D. Olafson, D. J. States, S. Swaminathan, and M. Karplus, *J. Comput. Chem.*, 1983, **4**, 187.
35. A. T. Brünger, *X-PLOR Software Manual Version 2.1*, Yale University, New Haven, CT, 1990.
36. A. T. Brünger and M. Karplus, *Acc. Chem. Res.*, 1991, **24**, 54, (and references therein).
37. D. Zhao and O. Jardetzky, *J. Phys. Chem.*, 1993, **97**, 3007.
38. J. W. Keepers and T. L. James, *J. Magn. Reson.*, 1984, **57**, 404.
39. S. Macura and R. R. Ernst, *Mol. Phys.*, 1980, **41**, 95.
40. M. Nilges, J. Habazettl, A. T. Brünger, and T. A. Holak, *J. Mol. Biol.*, 1991, **219**, 499.
41. P. Yip and D. A. Case, *J. Magn. Reson.*, 1989, **83**, 643.
42. A. E. Torda, R. M. Scheek, and W. F. van Gunsteren, *Chem. Phys. Lett.*, 1989, **157**, 289.
43. G. M. Clore and A. M. Gronenborn, *J. Magn. Reson.*, 1989, **84**, 398.
44. Y. Liu, D. Zhao, R. Altman, and O. Jardetzky, *J. Biomol. NMR*, 1992, **2**, 373.
45. G. M. Clore, M. A. Robien, and A. M. Gronenborn, *J. Mol. Biol.*, 1993, **231**, 82.
46. D. E. Wemmer, *Curr. Opin. Struct. Biol.*, 1991, **1**, 452.
47. A. S. Benight, J. M. Schurr, P. F. Flynn, B. R. Reid, and D. E. Wemmer, *J. Mol. Biol.*, 1988, **200**, 377.
48. T. Hard, E. Kellenbach, R. Boelens, B. A. Maler, K. Dahlman, L. P. Freedman, J. Carlstedt-Duke, K. R. Yamamoto, J.-A. Gustafson, and R. Kaptein, *Science*, 1991, **249**, 157.
49. O. Jardetzky and J.-F. Lefèvre, *FEBS Lett.*, 1994, **338**, 246.
50. H.-C. Guo, T. S. Jardetzky, T. P. J. Garrett, W. S. Lane, J. L. Strominger, and D. C. Wiley, *Nature*, 1992, **360**, 364.
51. T. S. Jardetzky, J. C. Gorga, R. Busch, J. Rothbard, J. L. Strominger, and D. C. Wiley, *EMBO J.*, 1990, **9**, 1797.
52. O. Jardetzky and G. C. K. Roberts, *NMR in Molecular Biology*, Academic Press, New York, 1981, Chap. 4
53. M. J. Stone, W. J. Fairbrother, A. G. Palmer, III, J. Reizer, M. H. Saier, Jr., and P. E. Wright, *Biochemistry*, 1992, **31**, 4394.
54. G. Barbato, M. Ikura, L. E. Kay, R. W. Pastor, and A. Bax, *Biochemistry*, 1992, **31**, 5269.
55. O. W. Howarth, *J. Chem. Soc., Faraday Trans. II*, 1978, **74**, 1031.
56. O. W. Howarth, *J. Chem. Soc., Faraday Trans. II*, 1979, **75**, 863.
57. R. King and O. Jardetzky, *Chem. Phys. Lett.*, 1978, **55**, 15.
58. G. Lipari and A. Szabo, *J. Am. Chem. Soc.*, 1982, **104**, 4546.
59. J. W. Peng and G. Wagner, *J. Magn. Res.*, 1992, **98**, 308.
60. O. Jardetzky and R. King, in *Mobility & Function in Proteins & Nucleic Acids (Ciba Foundation Symposium 93)*, Pitman, London, 1982, p. 291.
61. O. Jardetzky, K. Akasaka, D. Vogel, S. Morris, and K. C. Holmes, *Nature*, 1978, **273**, 564.
62. N. Wade-Jardetzky, R. P. Bray, W. W. Conover, O. Jardetzky, N. Geisler, and K. Weber, *J. Mol. Biol.*, 1979, **128**, 259.
63. E. M. Bradbury and H. W. E. Rattle, *Eur. J. Biochem.*, 1972, **27**, 270.
64. S. Highsmith and O. Jardetzky, in *Mobility & Function in Proteins & Nucleic Acids (Ciba Foundation Symposium 93)*, Pitman, London, 1982, pp. 156–168.
65. C. H. Arrowsmith, J. Carey, L. Treat-Clemons, and O. Jardetzky, *Biochemistry*, 1989, **28**, 3875.
66. Y. Q. Qian, G. Otting, K. Furukubo-Tokunaga, M. Affolter, W. J. Gehring, and K. Wüthrich, *Proc. Natl. Acad. Sci. U.S.A.*, 1992, **89**, 10738.
67. Q. X. Hua, S. E. Shoelson, and M. A. Weiss, *Biochemistry*, 1992, **31**, 1 1940.
68. D. Wemmer, A. A. Ribeiro, R. P. Bray, N. G. Wade-Jardetzky, and O. Jardetzky, *Biochemistry*, 1981, **20**, 829.
69. A. Hvidt and S. O. Nielsen, *Adv. Protein Chem.*, 1966, **21**, 287.
70. S. Spera, M. Ikura, and A. Bax, *J. Biomol. NMR*, 1991, **1**, 155.
71. Z. Zheng, M. R. Gryk, M. D. Finucane, and O. Jardetzky, *J. Magn. Res., Ser. B*, 1995, **108**, in press.
72. M. R. Gryk, M. D. Finucane, Z. Zheng, and O. Jardetzky, *J. Mol. Biol.*, 1995, **246**, 618.
73. E. A. Auerswald, G. Genenger, R. Mentele, S. Lenzen, I. Assfalg-Machleidt, L. Mitschang, H. Oschkinat, and H. Fritz, *Eur. J. Biochem.*, 1991, **200**, 131.
74. O. Jardetzky, in *Molecular Properties of Drug Receptors*, eds. R. Porter and M. O'Connor, J. & A. Churchill, London, 1970, pp. 113–132.
75. I. D. Campbell and C. M. Dobson, *Methods Biochem. Anal.*, 1979, **25**, 1.
76. D. J. Nelson, S. J. Opella, and O. Jardetzky, *Biochemistry*, 1976, **15**, 5552.
77. D. H. Meadows, O. Jardetzky, R. M. Epand, H. H. Ruterjans, and H. A. Scheraga, *Proc. Natl. Acad. Sci. U.S.A.*, 1968, **60**, 766.
78. O. Jardetzky, *Biochim. Biophys. Acta*, 1980, **621**, 227.
79. Y. Kim and J. H. Prestegard, *Biochemistry*, 1989, **28**, 8792.
80. S. E. Radford, C. M. Dobson, and P. A. Evans, *Nature*, 1992, **358**, 302.
81. O. Jardetzky and G. C. K. Roberts, *NMR in Molecular Biology*, Academic Press, New York, 1981, Chap. 6
82. M. E. Hogan and O. Jardetzky, *Proc. Natl. Acad. Sci. U.S.A.*, 1979, **76**, 6341.
83. J.-F. Leféyre, A. N. Lane, and O. Jardetzky, *Biochemistry*, 1987, **26**, 5076.
84. O. Jardetzky and J. J. Fischer, in *Proceedings of the 4th International Conference on Medical Electronics New York, 1961*, p. 46.
85. O. Jardetzky, J. J. Fischer, and P. Pappas, *Biochem. Pharmacol.*, 1961, **8**, 387.
86. O. Jardetzky and N. G. Wade-Jardetzky, *Mol. Pharmacol.*, 1965, **1**, 214.
87. D. H. Meadows, G. C. K. Roberts, and O. Jardetzky, *J. Mol. Biol.*, 1969, **45**, 491.
88. J. L. Markley and O. Jardetzky, *J. Mol. Biol.*, 1970, **50**, 223.
89. S. L. Patt, J. H. Baldo, K. Boekelheide, G. Weisz, and B. D. Sykes, *Can. J. Biochem.*, 1978, **56**, 624.
90. G. C. K. Roberts, in *Protein Structure and Engineering*, ed. O. Jardetzky, Plenum, New York, 1989, pp. 209–220, and references therein.
91. P. P. Theriault, D. J. Leahy, M. Levitt, H. M. McConnell, and G. S. Rule, *J. Mol. Biol.*, 1991, **221**, 257.

Biographical Sketches

Oleg Jardetzky. *b* 1929. B.A., 1950, Chemistry & Biology, Macalester College, St. Paul MN, M.S., 1953, Physiological Chemistry, M.D., 1954, Medicine, Ph.D., 1956, Physiology & Physical Chemistry, University of Minnesota, St. Paul, MN. National Research Council Fellow, Department of Chemistry, CalTech, 1956–57; Associate in Pharmacology, 1957–59, Assistant Professor of Pharmacology, Harvard Medical School, 1959–66; Director, Department of Biophysics & Pharmacology, Merck, Sharp & Dohme, 1966–68; Executive Director of Basic Medical Science, Merck Institute for Therapeutic Research, 1968–69; Professor of Pharmacology, 1969–present, Director, Stanford Magnetic Resonance Laboratory, Stanford University, 1975–present. Approx. 230 publications. Current research interests: structure dynamics and function of proteins involved in regulatory processes; the mechanism of action of *trp*-repressor; use of high-resolution NMR spectroscopy and other physical methods to define mechanisms of conformational transition and protein folding.

Biological Macromolecules: Structure Determination in Solution

Kurt Wüthrich

Eidgenössische Technische Hochschule Zürich, Switzerland

1	Introduction	1
2	Survey of the Method	2
3	Sample Preparation for NMR Structure Determinations	2
4	NMR Spectroscopy with Biological Macromolecules	2
5	Resonance Assignments	3
6	Identification of Regular Polypeptide Secondary Structures in Proteins	5
7	Structure Calculation from NMR Data	6
8	Conclusion	7
9	Related Articles	7
10	References	7

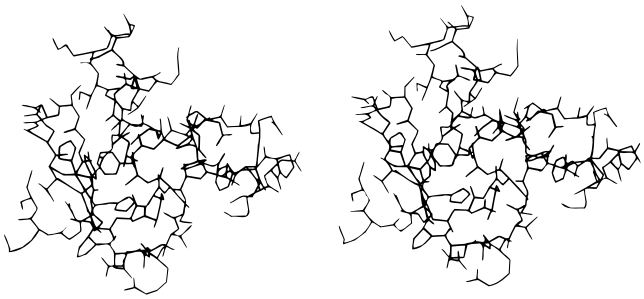

Figure 1 Stereo view of the three-dimensional NMR solution structure of the protein bull seminal proteinase inhibitor IIA (BUSI IIA), determined in 1984. All bonds connecting heavy atoms are shown for the entire polypeptide chain of 57 residues. (The drawing was prepared using the atom coordinates from Williamson et al.[4])

1 INTRODUCTION

Atomic resolution structure determination of biological macromolecules dates back to the 1950s, when the first amino acid sequence determination was achieved with insulin[1] and the first 3D protein structures were obtained by X-ray diffraction in single crystals of myoglobin[2] and hemoglobin.[3] Nearly three decades later, in 1984, the first NMR structure determination of a globular protein in solution was completed (Figure 1),[4] using a strategy that was described explicitly 2 years earlier.[5,6] Structure determination by NMR is thus a recent addition to the arsenal of experimental techniques available in structural biology. However, compared with the slow growth of protein crystallography in the 1960s, where only one additional structure determination was completed within 8 years after the initial success with myoglobin and hemoglobin, there were numerous practical applications of the NMR structure determination method for proteins and nucleic acids soon after 1985. During the 3 year period 1990–1992, 121 new NMR structures were published[7–9] (for comparison, 405 new X-ray crystal structures were published during the same period[7–9]), and the pace is still accelerating. As a result, the field has evolved rapidly, and in addition to academic institutions the modern biotechnology industry has become heavily involved in biomolecular NMR structure determination.

The introduction of NMR as a second method for macromolecular structure determination is of fundamental interest because NMR can provide data that are in many ways complementary to those obtained from X-ray crystallography. Combined use of the two techniques thus promises, in particular, to widen our view of protein molecules for a better grasp of the relationships between structure and function, and thus to provide a more refined platform for rational, structure-based drug design, and more generally engineering of proteins with improved or entirely novel functions. These intimate links between structural biology and protein biotechnology have greatly influenced the rapid evolution of NMR structure determination.

The complementarity of the structural information obtained from diffraction techniques or from NMR results from the fact that the timescales of the two types of measurements are widely different[10,11] and that, in contrast to the need for single crystals in diffraction studies, the NMR measurements use proteins or nucleic acids in solution or in other noncrystalline states. The most obvious consequence is that NMR can be applied to proteins for which no single crystals are available, thus yielding new structures that cannot be solved by any other method. Conversely, the solution NMR method has so far been applied successfully only to relatively small proteins or nucleic acid fragments with molecular weights up to about 20 000. In the future this size limit may possibly be increased twofold, but X-ray diffraction will foreseeably remain the method of choice for the determination of large structures (perhaps supplemented by solid state NMR in the not too distant future). To provide a balanced view of the potentialities of solution NMR it should be added that present biochemical technology can open ways for NMR investigations of larger systems. For example, individual, biologically functional domains excised by enzymatic or chemical cleavage from large proteins, or expressed separately as recombinant proteins, may be accessible for NMR structure determination. Or, in a more general vein, conclusions from systematic comparisons of small proteins in crystals and in solution may be projected to larger molecules for which only a crystal structure is available. Comparisons of corresponding structures in single crystals and in noncrystalline states are therefore highly relevant, all the more since the solution conditions for NMR studies can often be chosen so as to coincide closely with the natural, physiological environment of the protein.[10]

Having staked out potentialities and areas of applications for macromolecular NMR structure determination in solution, the remainder of this article is focused on ‘how to do it’. As numerous other contributions in this Encyclopedia relate to this theme, the attempted goal is to provide a framework that can accommodate the different, presently used technical approaches. Also, for simplicity of the presentation the discussion will be mainly focused on proteins, with some reference to work with deoxyribonucleic acids (DNA) and ribonucleic acids (RNA).

2 SURVEY OF THE METHOD

Figure 2 presents an outline of the course of an NMR structure determination.[10] Individual steps are the sample preparation, the NMR measurements, the crucial problem of obtaining assignments of the NMR lines to individual atoms in the polymer chain, and the collection and structural interpretation of NMR conformational constraints. These individual steps will be further discussed in the following sections.

In present practice[10,12] the sequence of steps taken during a structure determination corresponds largely to the flow diagram of Figure 2. Thereby, as is indicated by the arrows in Figure 2, one goes through repeated cycles of collection of conformational constraints and structure calculation, and even some sequence-specific resonance assignments may be reassessed during the structure calculation. In principle, however, the entire spectral analysis from peak picking to resonance assignments to the final structure determination is largely self-contained, and might conceivably at some future stage be handled as a single, computer-supported process.

It is a special feature of protein structure determination by NMR that the secondary polypeptide structure, including the connections between individual segments of regular secondary structure, may be known early on from the data used for obtaining the resonance assignments, actually before the structure calculation is even started.[13–15] This contrasts with the situation in X-ray crystallography, where regular secondary structures are usually identified only at later stages of a project, and it opens interesting possibilities for the support of X-ray crystal structure determinations on the basis of solution NMR data.[16]

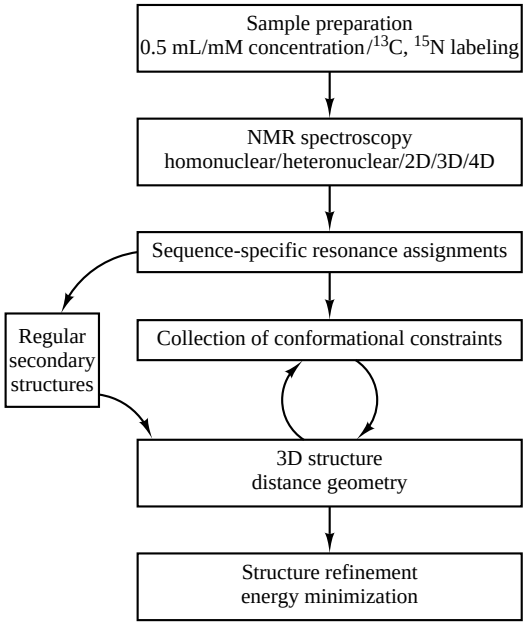

Figure 2 Diagram outlining the course of a macromolecular structure determination by NMR in solution (see text)

3 SAMPLE PREPARATION FOR NMR STRUCTURE DETERMINATIONS

Let us assume that we start work with a highly purified, homogeneous preparation of the molecule to be studied. For proteins, such samples may either be isolated from natural sources, obtained by recombinant techniques or, for smaller polypeptides, prepared by chemical synthesis. For nucleic acids, complete structure determinations have so far been achieved only with synthetic fragments. The compound is dissolved in 0.5 mL of water, and the ionic strength, pH, and temperature may be adjusted so as to ensure near-physiological conditions (for proteins it is advantageous to work in the slightly acidic pH range from 3 to 5[10]). The concentration should be about 1 mM, ideally 2–5 mM, so that, for example, 5–25 mg of a protein with a molecular weight of 10 000 should be available for a structure determination. Although this concentration is high relative to that of most proteins in their physiological milieu, it is not far from the total protein concentration in typical body fluids. For molecular sizes above approximately 10 000, quite often also for smaller sizes, the NMR study will have to include the preparation of compounds enriched with ^{15}N and/or ^{13}C. Uniformly isotope-labeled recombinant proteins are obtained with commonly available techniques; nonetheless, preparation of a suitable protein sample is often the bottleneck in a project. For RNA, labeling techniques have been introduced only recently, and they are still used only by a few groups. For DNA, labeling techniques are still in the process of being worked out.

Clearly, being able to work with solutions is a great asset of the NMR method. Not only can we work in near-physiological milieus, but we also get around the preparation of suitable crystals, which has been a bottleneck for so many promising X-ray structural studies. However, working with solutions also has its inherent potential difficulties. Most of all, many biological macromolecules tend to self-aggregate at the concentrations needed for NMR spectroscopy, which has slowed down many projects in our laboratory; sometimes in such situations, biochemical studies can lead to a protein analog with suitable solution behavior. Furthermore, practical difficulties may arise with the combined analysis of successive experiments, because it is nontrivial to achieve identical solution conditions in different NMR samples of the same compound.

4 NMR SPECTROSCOPY WITH BIOLOGICAL MACROMOLECULES

Two basic notions govern the selection of spectroscopic techniques used for macromolecular structure determinations. Firstly, the information needed for 3D structure determination comes almost entirely from ^{1}H–^{1}H NOEs,[5,10] with other experimentally accessible parameters serving primarily to support rapid convergence of the structure calculations and, mostly in molecular regions with a scarcity of NOE distance constraints, contributing to the refinement of the final structure. Secondly, a twofold spectral resolution problem needs to be solved: hundreds or even thousands of resonance lines in the ^{1}H NMR spectrum of a biological macromolecule must be observed as separate peaks, and selective

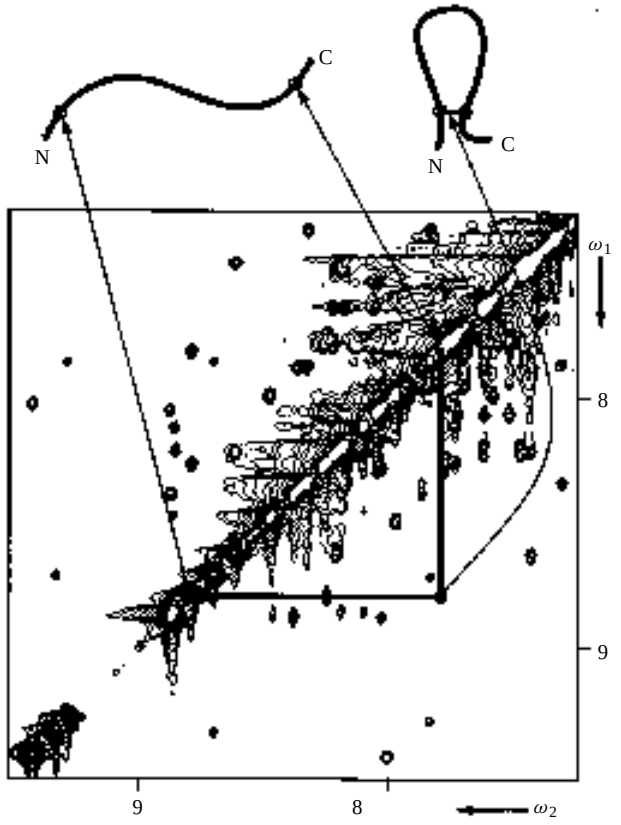

Figure 3 Protein structure determination and $^1H-^1H$ NOEs. The region ($\omega_1 = \omega_2 = 7.2-9.4$ ppm) of a 2D [^1H,^1H]-NOESY spectrum of the *Antennapedia* homeodomain is shown, together with a line representing a polypeptide chain, where the N- and C-terminal chain ends are identified. Two proton positions are identified by circles, and straight arrows connect the corresponding diagonal peaks in the NOESY spectrum with these protons. The presence of the NOESY cross peak that correlates the two assigned diagonal peaks shows that these two protons are separated by a distance of less than about 0.4 nm, and therefore the observation of this NOE imposes a circular structure on the polypeptide chain

correlations between pairs of spins (or groups of equivalent spins) need to be established in crowded spectral regions where, for example, selective irradiation of individual resonance lines in 1D experiments would be a major technical challenge. Although the foundations of the NMR structure determination method were laid and initial polypeptide structure determinations obtained using 1D NMR experiments[6] (see also ***Wüthrich, Kurt: NMR Structures of Biological Macromolecules***), these demands are in practice met by multidimensional NMR.

As an illustration of the spectroscopic work to be done, Figure 3 visualizes part of the scheme of Figure 2 for the case of a protein structure determination. In a [^1H,^1H]-NOESY spectrum each cross peak establishes a correlation between two diagonal peaks, as indicated in Figure 3 by a horizontal and a vertical line, and tells us that the protons corresponding to the two correlated diagonal peaks are separated only by a short distance, say less than 0.4 nm. This information is used in the following way. First, sequence-specific resonance assignments must be obtained, i.e. for all protons in the polypeptide chain the corresponding diagonal peak positions must be identified. This is indicated in Figure 3 by the straight arrows linking two proton positions in the polypeptide with their diagonal peaks in the NOESY spectrum. With the availability of the resonance assignments, each NOESY cross peak now shows that two protons in known locations along the polypeptide chain are separated by a short distance in the 3D protein structure. Since the overall length of an extended polypeptide chain with 100 amino acid residues is about 35 nm, the NOEs may impose stringent constraints on the polypeptide conformation. In Figure 3 this is schematically indicated by the formation of a circular structure. Typically, the NOESY spectra of proteins contain hundreds of cross peaks, indicating that the 3D fold of the polypeptide chain involves a large number of circular structures of the type shown in Figure 3. With increasing size of the molecule studied and concomitant increase of the number of NMR peaks, it becomes more and more difficult to resolve and assign individual resonances in homonuclear 2D NMR spectra. In heteronuclear 3D or 4D spectra recorded with recombinant proteins that are uniformly labeled with ^{15}N and/or ^{13}C, the peaks are spread out in a third and possibly fourth dimension along the ^{15}N and ^{13}C chemical shift axes.[17] For example, in the 3D ^{15}N-correlated [^1H,^1H]-NOESY spectrum of Figure 4 the NMR peaks have been further spread out along a third frequency axis, which corresponds to the NMR frequencies of the ^{15}N spins in the ^{15}N-labeled protein. As a result, the same number of NMR peaks as would be observed in a 2D [^1H,^1H]-NOESY spectrum (see Figure 3) are distributed among multiple $^1H-^1H$ planes, typically 64 or 128. The ensuing further improved separation of the peaks in the individual planes is indispensable for work with larger proteins. To a more limited extent, improved peak separation for unlabeled proteins from natural sources can be obtained with homonuclear 3D ^1H NMR experiments.[18,19]

5 RESONANCE ASSIGNMENTS

Proteins contain multiple units of chemically identical amino acid residues, and nucleic acids contain multiple identical nucleotides in different sequence positions. Although different types of amino acids or nucleotides can be distinguished from their NMR spin systems, multiple copies of the same monomeric unit in different sequence locations have identical spin systems. Therefore, obtaining sequence-specific assignments for biopolymers is intrinsically nontrivial. For proteins the problem was solved with the sequential assignment strategy:[13,20,21] segments of two or several sequentially adjoining amino acid residues are identified by NMR experiments, and by comparison with the chemically determined amino acid sequence attributed to unique positions in the polypeptide chain. Two fundamentally different approaches for obtaining sequential assignments are outlined in Figure 5 and Figure 6, and are briefly explained in the following discussion.

Assignments using sequential NOEs (Figure 5) can be obtained for proteins with natural isotope distribution. The $^1H-^1H$ connectivities which identify the different amino acid types are established via scalar spin–spin couplings, using COSY, TOCSY, and multiple quantum spectroscopy. Relations between protons in sequentially neighboring amino acid residues i and $i + 1$ are established by NOEs manifesting close approach between α-CH_i and NH_{i+1} ($d_{\alpha N}$), NH_i and NH_{i+1} (d_{NN}), and β-CH_i and NH_{i+1} ($d_{\beta N}$). For Xxx-Pro,

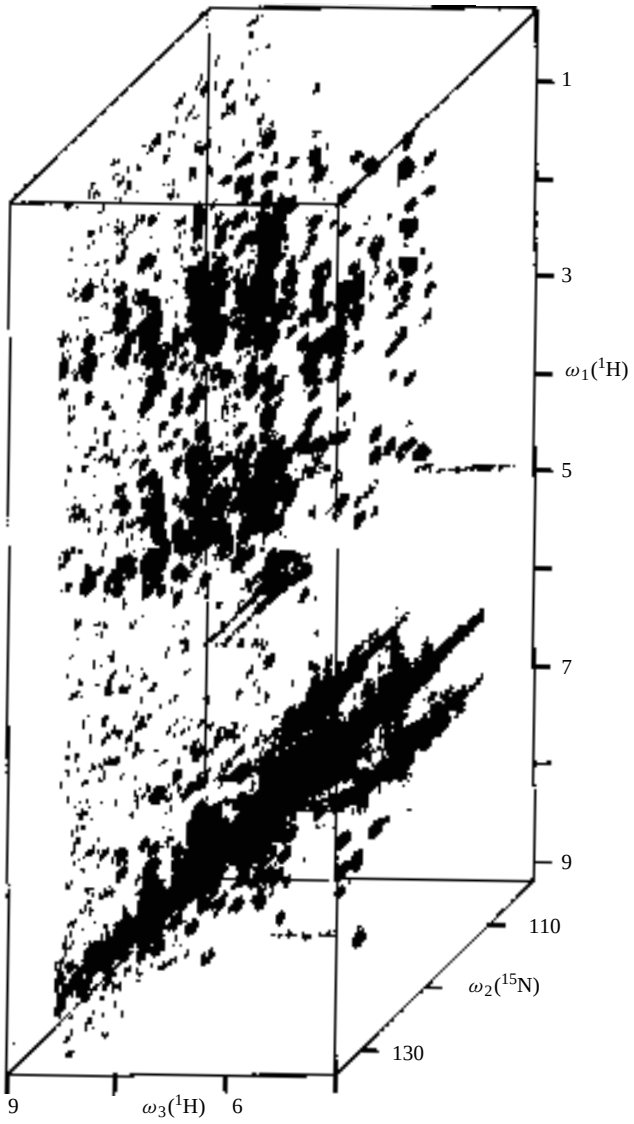

Figure 4 3D ^{15}N-correlated [^{1}H,^{1}H]-NOESY spectrum of the N-terminal domain comprising residues 1–76 of the protein P22 c2 repressor. The protein was uniformly labeled with ^{15}N to the extent of 95%. (Reproduced by permission from K. Wüthrich, *J. Biol. Chem.*, 1990, **265**, 22059)

corresponding connectivities are observed to δ-CH_2 of Pro in the place of the amide proton. In Figure 5, for example, observation of a NOESY cross peak corresponding to $d_{\alpha\delta}$ tells us that the protein studied contains the dipeptide segment Val-Pro. This dipeptide is then matched against the independently known amino acid sequence. If the latter contains Val-Pro only once, the assignment problem is solved. Otherwise, to distinguish between multiple Val-Pro sites, tri- or tetrapeptide segments including Val-Pro must be identified by NMR and matched against the amino acid sequence. Since in globular proteins with up to about 200 amino acid residues the probability is small that identical tri- or tetrapeptide segments occur more than once, the procedure is in principle generally applicable,[10] and for small proteins it can rely entirely on homonuclear ^{1}H NMR experiments. Limitations arise when a substantial proportion of the H-α and amide proton chemical

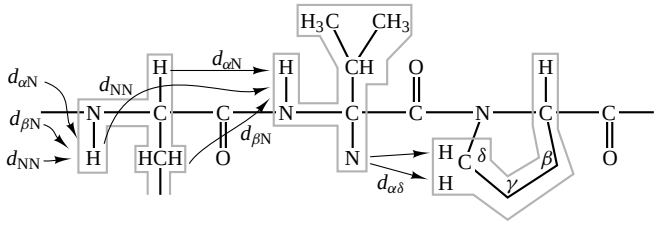

Figure 5 Segment of a polypeptide chain with arrows indicating the sequential NOE connectivities with amino acids, $d_{\alpha N}$, d_{NN}, and $d_{\beta N}$, and with *trans*-proline, $d_{\alpha\delta}$ ($d_{N\delta}$ and $d_{\beta\delta}$ not shown). Stippled lines outline the individual amino acid ^{1}H spin systems, which can be identified via homonuclear ^{1}H–^{1}H scalar couplings. (Reproduced by permission of Walter de Gruyter from K. Wüthrich, P. Güntert, and K. D. Berndt, in 'Innovations in Proteases and their Inhibitors', ed. F. X. Avilés, Walter de Gruyter, Berlin, 1993)

shifts are degenerate. Improved peak separation can then be obtained with homonuclear 3D NMR,[18,19] or with 3D or 4D heteronuclear-resolved [^{1}H,^{1}H]-NOESY using uniformly isotope-labeled protein (see Figure 4).

Sequential assignments can alternatively be obtained entirely via heteronuclear scalar couplings (Figure 6). Although this approach had already been applied in 1979 by the group of the late Vladimir Bystrov, who thus obtained assignments for the polypeptide hormone apamin using the unlabeled peptide and multiple irradiation 1D NMR,[22] it became a practical technique only a decade later with the availability of recombinant isotope-labeled proteins. Today, an impressive array of 3D and 4D triple resonance NMR experiments are available for the identification of intraresidual and sequential multiatom fragments in uniformly ^{13}C,^{15}N doubly labeled polypeptide chains (Figure 6),[17] which can provide the desired sequential assignments.

A general recipe on what to use in different projects is difficult to provide. Sequential NOEs studied with homonuclear ^{1}H NMR provide an efficient approach for most proteins with up to about 80 residues, and proteins with up to 130 residues ($M_r \sim 15\,000$) have thus been assigned. Using the additional spectral resolution obtained with uniform ^{15}N labeling (see Figure 4), assignments based on sequential NOEs have been achieved for proteins with 150–200 residues. The largest proteins assigned using ^{13}C,^{15}N double labeling and

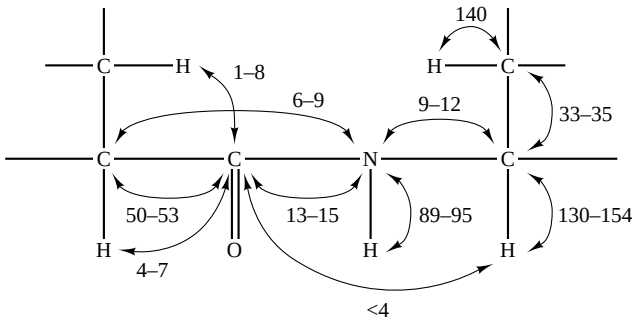

Figure 6 Segment of a polypeptide chain with indication of the scalar spin–spin couplings that provide the basis for obtaining sequential assignments by triple-resonance experiments with uniformly ^{13}C,^{15}N doubly labeled proteins. The arrows and numbers indicate typical values, in hertz, of one-bond and multiple-bond heteronuclear coupling constants $J(^{13}C,^1H)$, $J(^{15}N,^1H)$, $J(^{13}C,^{13}C)$, and $J(^{15}N,^{13}C)$

triple-resonance experiments to correlate groups of atoms via the spin–spin couplings of (Figure 6) are in the range 250–300 residues. Two limiting situations are that sequential NOEs (see Figure 5) are at present the only practical way for studies of unlabeled proteins from natural sources, and that double labeling is a must for work with proteins of M_r 20 000. Otherwise, the selection of the approach may be largely influenced by the expertise and instrumentation available in the laboratory pursuing the investigation. As a rule of thumb: in any given situation, restraint in the use of isotope labeling goes along with less extensive requirements for instrument time and more exacting demands on highly qualified scientists involved in the spectral analysis. It must also be added that obtaining sequence-specific assignments for the entire polypeptide backbone does not necessarily mean that a satisfactory level of side-chain assignments can be achieved with the same approach. As was pointed out early on by the groups of Matsune Kainosho and John Markley,[23] uniform ^{13}C labeling may be indispensable for obtaining complete side-chain assignments even in relatively small proteins. Finally, it should be added that isotope labeling offers additional possibilities beyond support of a structure determination, such as relaxation studies relating to molecular dynamics, which may also play a role in making decisions on the strategy to be followed with a given system.

For nucleic acids, assignment procedures were largely patterned after those used for proteins. In contrast to the situation with polypeptide chains, assignments using intranucleotide, sequential and interstrand ^{1}H–^{1}H NOEs are necessarily based on the assumption of a particular conformation type for the compound studied.[10] For B-type DNA this approach, which was implemented primarily by the groups of Robert Kaptein, David Kearns, and Brian Reid, is highly efficient for duplexes with up to about 20 base pairs. A conformation-independent approach is also available, which uses heteronuclear scalar ^{1}H–^{31}P couplings to establish sequential assignments.[24] In unlabeled compounds these assignments cannot readily be extended to include the resonances of the bases, which limits their usefulness.[10] With suitably ^{15}N- and ^{13}C-labeled compounds, base–backbone connections can be established via heteronuclear scalar couplings, which may in the future enable complete assignments for oligonucleotide segments with non-regular conformations.

6 IDENTIFICATION OF REGULAR POLYPEPTIDE SECONDARY STRUCTURES IN PROTEINS

As was mentioned in section 2, regular secondary structures can be identified at an early stage of a protein structure determination by NMR. This is based on the following. The sequential NOEs (see Figure 5) are dependent on the local backbone conformation and thus indicative of regular secondary structure elements.[13] Corresponding information on the local backbone conformation comes from $^3J_{\mathrm{HN}\alpha}$ coupling constants.[15] Furthermore, when identifying sequential NOEs, all NOEs between amide protons, H-α and H-β need to be analyzed, which includes medium-range NOEs that are unique for helices and tight turns.[14] This information is usually collected in a presentation of the type shown in Figure 7, where patterns of successive small $^3J_{\mathrm{HN}\alpha}$ coupling constants and strong d_{NN} NOEs combined with the presence of

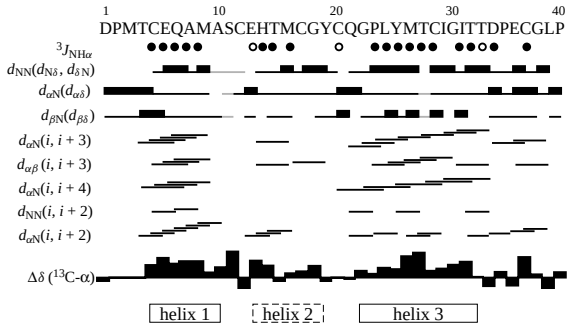

Figure 7 Standard presentation of the data used to identify regular secondary structures in proteins. The 40-residue pheromone E*r*-2 is used as an illustration. Below the amino acid sequence, open and solid circles identify residues with $^3J_{\mathrm{HN}\alpha} > 8.0$ Hz, and $^3J_{\mathrm{HN}\alpha} < 6.0$ Hz, respectively. For the sequential NOE connectivities $d_{\alpha\mathrm{N}}$, d_{NN}, and $d_{\beta\mathrm{N}}$ ($d_{\mathrm{N}\delta}$, $d_{\alpha\delta}$, and $d_{\beta\delta}$ for Xxx-Pro dipeptides, $d_{\delta\mathrm{N}}$ for Pro-Xxx), thick and thin bars indicate strong and weak NOE intensities (hatched bars indicate connectivities that were observed only at 30°C, whereas all the other data were measured at 10°C). Observed medium-range NOEs, such as $d_{\alpha\mathrm{N}}(i, i+3)$, are indicated by lines connecting the two residues that are related by the NOE. At the bottom of the figure, ^{13}C-α chemical shifts relative to the random coil values, $\Delta\delta$(^{13}C-α), are plotted, where positive values are shifts to higher frequency and the largest shift is about 5.8 ppm. High-frequency shifts of the size observed here are indicative of helical secondary structure.[25] The sequence locations of three helices are identified at the bottom. (Reproduced by permission from M. Ottiger, T. Szyperski, P. Luginbühl, C. Ortenzi, P. Luporini, R. A. Bradshaw, and K. Wüthrich, *Protein Sci.*, 1994, **3**, 1515)

medium-range NOEs provide a reliable identification of helical secondary structure.[14] Using additional long-range $d_{\alpha\alpha}(i, j)$ NOE connectivities and amide proton exchange data, β-sheet structures can similarly be identified.[10] Recently, ^{13}C-α chemical shifts have been added as yet another indicator of regular secondary structure,[25] as is illustrated at the bottom of Figure 7.

Secondary structure determination is not a necessary step in a protein structure determination (see Figure 2), since the conformational constraints of Figure 7 are in any case part of the input for the structure calculation. However, it is a useful asset in several different ways. Firstly and most importantly, it may be a valuable result in itself in situations where a structure determination cannot immediately be completed. This is typical for projects where uniform or residue-selective ^{15}N labeling enables complete sequence-specific polypeptide backbone assignments via sequential NOEs (see Figure 5), but the extent of the side-chain assignments in the absence of ^{13}C labeling is insufficient as a basis for a complete structure determination. Secondly, since the covalent connections between regular secondary structure elements can be unambiguously determined, NMR secondary structure determination has been helpful in tracing low-resolution electron density maps for the determination of the corresponding X-ray crystal structure.[16] Thirdly, the NMR structure determination itself may be supported in cases where NOE distance constraints are scarce during the early cycles of the structure calculation. By inclusion of supplementary dihedral angle constraints that enforce more precise formation of the regular secondary structures, convergence of the initial calculations may be improved, which in turn provides the basis for further collection of NOE distance constraints (Figure 2).

7 STRUCTURE CALCULATION FROM NMR DATA

Although complete relaxation matrix treatments of the relationships between NOEs and molecular structure have been implemented by several different groups, including ourselves,[26] the use of the initial-rate approximation for the NOE build-up is still representative for presently performed NMR structure calculations.[10] The input data have the format of allowed distance ranges, which circumvents intrinsic difficulties that might arise from attempts at quantitative distance measurements. The lower limit is usually taken to correspond to the sum of two hydrogen atomic radii, i.e. 0.2 nm. For short-range connectivities between protons separated by not more than three single bonds in the chemical structure, that is, intraresidual and sequential distances,[10] the NOE intensities are translated into corresponding upper bounds, typically in steps of 0.25, 0.30, and 0.40 nm. For longer-range connectivities, a predetermined upper limit, usually 0.40 or 0.50 nm., depending on the protein and the experimental conditions used, is applied. Unless stereospecific assignments were obtained, in particular for the β-methylene groups in amino acid side chains and the isopropyl groups of valine and leucine, correction factors for the use of pseudoatoms must be added to the upper limits on distances to prochiral groups of protons.[27] The resulting allowed distance ranges may then be as large as from 0.20 to about 1.0 nm. Supplementary conformational constraints, for example, from spin–spin coupling constants, are represented in the input by similar allowed ranges, which account for the limited accuracy of the measurements. In computer-supported collection of the input data, the stepwise classifications may be replaced by a smoothed fit of upper distance bounds versus NOE intensity. Furthermore, this calibration may be updated in successive cycles of the structure calculation (see Figure 2).

Distance geometry algorithms can be used to obtain the Cartesian coordinates of spatial molecular structures that are consistent with a predetermined set of intramolecular, interatomic distances.[28] To this end, such algorithms identify the conformations shown in equation (1),

$$\{r_i = (x_i, y_i, z_i); \quad i = 1, 2, \ldots, N\} \tag{1}$$

which are consistent with inequality (2),

$$L_{ij} \leq |r_i - r_j| \leq U_{ij} \tag{2}$$

where L_{ij} and U_{ij} are lower and upper bounds, respectively, on the Euclidian distance $|r_i - r_j|$ between the points r_i and r_j, and N the number of points (or atoms) in the system studied. The problem described by inequality (2) may alternatively be expressed in the form of an error function, which can then be minimized. In the process of this conversion of distance information into Cartesian coordinates, one inevitably encounters the problem of local minima.[29] Metric matrix methods[30] and variable target functions in dihedral angle space[31,32] have been implemented in the search for protein conformations obeying inequality (2), and the energy functions in molecular dynamics programs have been supplemented with terms representing the constraints expressed by inequality (2).[33,34] Overall, corresponding results are obtained with these different computational approaches, although details may be subject to further analysis.

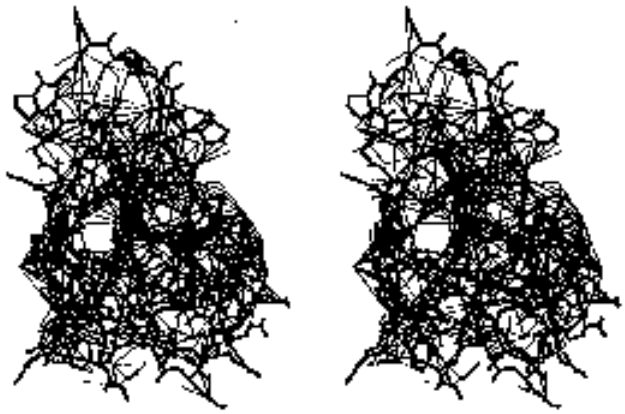

Figure 8 Illustration of an input of NOE upper distance constraints used for a high-quality NMR structure determination. The bold lines afford a stereo view of an all-heavy-atom representation of a 57-residue protein, Toxin K. Each of the 809 upper distance constraints used in the calculation of the structure is shown by a thin line connecting the two protons (or pseudoatoms) involved in the constraint. (Reproduced by permission of Walter de Gruyter from K. Wüthrich, P. Güntert, and K. D. Berndt, in 'Innovations in Proteases and their Inhibitors', ed. F. X. Avilés, Walter de Gruyter, Berlin, 1993)

Model calculations at the time of the first structure determination (see Figure 1) had shown that the quality of an NMR structure determination depends critically on the density of NOE distance constraints, while the procedure is remarkably robust with regard to low precision of the individual distance constraints.[35] Multiple rounds of data collection and structure calculation (see Figure 2) are usually needed to obtain the desired, high-density input (Figure 8), since many NOEs can be unambiguously assigned only by reference to an approximate molecular structure.[36]

The result of a single distance geometry calculation (see Figure 1) represents one molecular geometry that is compatible with the NMR experiments, but it cannot tell whether this solution is unique. Thus the calculation is repeated with different starting conditions. For each calculation, convergence is judged by the residual constraint violations, and all satisfactory solutions are included in a group of conformers representing the structure of the protein. The final result of a structure determination is then commonly presented as a superposition of a group of conformers for pairwise minimum root mean square deviation (RMSD) relative to a predetermined conformer. Figure 9 shows a superposition of the polypeptide backbone in 19 conformers of the *Antennapedia* homeodomain that were selected to represent the solution structure.[37] The precision of the structure determination, as reflected by the dispersion among this group of conformers, varies along the polypeptide chain. From residues 9 to 58, all conformers are similar, have nearly the same overall dimensions, and contain the same secondary structure, showing that this part of the structure is well defined by the NMR data. In contrast, both chain ends are (dynamically) disordered, as is manifested by the large dispersion among the 19 conformers. Large variations are typically observed also in the precision of the structure determination of the amino acid side chains, with well defined interior side chains representing the protein core and flexibly

Figure 9 Stereo view of the polypeptide backbone of 19 energy-refined conformers selected to represent the NMR solution structure of the *Antennapedia* homeodomain. Conformers 2–19 were superimposed for pairwise minimum RMSD of the backbone atoms N, C-α, and C′ of residues 7–59 with conformer 1. N and C identify the start and the end of the polypeptide chain, which comprises 68 residues. (Reproduced by permission from M. Billeter, Y. Q. Qian, G. Otting, M. Müller, W. J. Gehring, and K. Wüthrich, *J. Mol. Biol.*, 1990, **214**, 183)

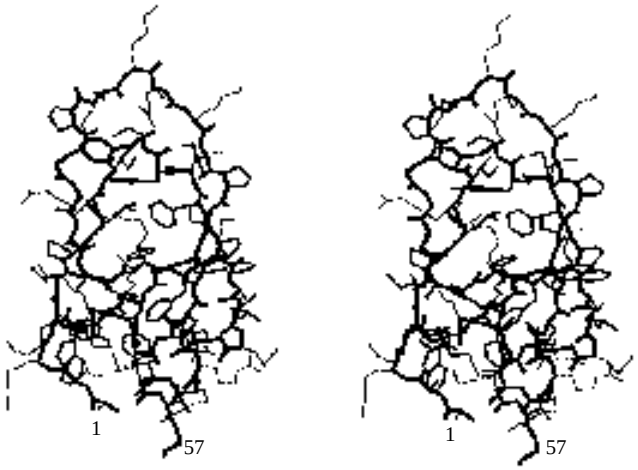

Figure 10 Stereo view of the all-heavy-atom representation of an NMR conformer of Toxin K after energy refinement. The backbone atoms N, C-α, C′, and O′ are connected by thick lines, best-defined side-chains are drawn with lines of medium thickness, and other, flexibly disordered side chains are drawn with thin lines. The locations of the first (1) and last (57) residues are identified. (Reproduced by permission of Walter de Gruyter from K. Wüthrich, P. Güntert, and K. D. Berndt, in 'Innovations in Proteases and their Inhibitors', ed. F. X. Avilés, Walter de Gruyter, Berlin, 1993)

disordered side chains located predominantly near the protein surface (Figure 10).

The individual conformers obtained as the solutions of distance geometry calculations generally contain some close interatomic contacts and correspondingly high conformational energies. These can be removed in a separate final refinement step (see Figure 2). Alternatively, in typical molecular dynamics calculations the energy minimization may be performed in concert with the fit to the distance constraints.

Structure determination with nucleic acids is pursued along similar lines as described here for proteins. As a general guide to an evaluation of the results obtained, one can assume that global folds, for example the formation of duplexes, triplexes, quadruplexes, or loops, can be well defined by NMR data. On the other hand, because of the short range and the low precision of individual NOE distance measurements, information on details in a given nucleic acid structure type, for example bending of DNA duplexes or nonregular base stacking, may be more difficult to characterize.

8 CONCLUSION

NMR with biological macromolecules in solution has for many years been a lively field, as is amply demonstrated by numerous articles in this Encyclopedia. There are reasons to believe that this will continue to be so also in the foreseeable future, although the main interest may shift somewhat more from methods' development to the investigation of structural biology problems. Indications that a certain degree of maturity has been attained can be found in the fact that more and more commercial software for computer support of the most laborious steps in the scheme of Figure 2 is becoming available, with the promise that scientists in this field will spend more and more time on the beach while their NMR spectra are transformed into 3D structures.

9 RELATED ARTICLES

Wüthrich, Kurt: NMR Structures of Biological Macromolecules; Biological Macromolecules; Biological Macromolecules: NMR Parameters; Distance Geometry; Half-Filter Experiments: Proton–Carbon-13; Pancreatic Trypsin Inhibitor; Peptide and Protein Secondary Structural Elements; Peptides and Polypeptides; Radiofrequency Pulses: Response of Nuclear Spins; Time-of-Flight Method of MRA.

10 REFERENCES

1. F. Sänger and E. O. P. Thompson, *Biochem. J.*, 1953, **53**, 366.
2. J. C. Kendrew, *Science*, 1963, **139**, 1259.
3. M. F. Perutz, *Science*, 1963, **140**, 863.
4. M. P. Williamson, T. F. Havel, and K. Wüthrich, *J. Mol. Biol.*, 1985, **182**, 295.
5. K. Wüthrich, G. Wider, G. Wagner, and W. Braun, *J. Mol. Biol.*, 1982, **155**, 311.
6. K. Wüthrich, *Acc. Chem. Res.*, 1989, **22**, 36.
7. W. A. Hendrickson and K. Wüthrich (ed.), *Macromolecular Structures 1991*, Current Biology, London, 1991.
8. W. A. Hendrickson and K. Wüthrich (ed.), *Macromolecular Structures 1992*, Current Biology, London, 1992.
9. W. A. Hendrickson and K. Wüthrich (ed.), *Macromolecular Structures 1993*, Current Biology, London, 1993.
10. K. Wüthrich, *NMR of Proteins and Nucleic Acids*, Wiley, New York, 1986.
11. T. L. Blundell and L. N. Johnson, *Protein Crystallography*, Academic Press, New York, 1976.
12. K. Wüthrich, *Science* 1989, **243**, 45.
13. M. Billeter, W. Braun, and K. Wüthrich, *J. Mol. Biol.*, 1982, **155**, 321.
14. K. Wüthrich, M. Billeter, and W. Braun, *J. Mol. Biol.*, 1984, **180**, 715.
15. A. Pardi, M. Billeter, and K. Wüthrich, *J. Mol. Biol.*, 1984, **180**, 741.

16. J. Kallen, C. Spitzfaden, M. G. M. Zurini, G. Wider, H. Widmer, K. Wüthrich, and M. D. Walkinshaw, *Nature*, 1991, **353**, 276.
17. A. Bax and S. Grzesiek, *Acc. Chem. Res.* 1993, **26**, 131.
18. T. A. Holak, J. Habazettl, H. Oschkinat, and J. Otlewski, *J. Am. Chem. Soc.*, 1991, **113**, 3196.
19. G. W. Vuister, R. Boelens, A. Padilla, G. J. Kleywegt, and R. Kaptein, *Biochemistry*, 1990, **29**, 1829.
20. A. Dubs, G. Wagner, and K. Wüthrich, *Biochim. Biophys. Acta*, 1979, **577**, 177.
21. G. Wagner and K. Wüthrich, *J. Mol. Biol.*, 1982, **155**, 347.
22. V. V. Okhanov, V. A. Afanas'ev, and V. F. Bystrov, *J. Magn. Reson.*, 1980, **40**, 191.
23. W. M. Westler, M. Kainosho, H. Nagao, N. Tomonaga, and J. L. Markley, *J. Am. Chem. Soc.*, 1988, **110**, 4093.
24. A. Pardi, R. Walker, H. Rapoport, G. Wider, and K. Wüthrich, *J. Am. Chem. Soc.*, 1983, **105**, 1652.
25. S. Spera and A. Bax, *J. Am. Chem. Soc.*, 1991, **113**, 5490.
26. J. E. Mertz, P. Güntert, K. Wüthrich, and W. Braun, *J. Biomol. NMR*, 1991, **1**, 257.
27. K. Wüthrich, M. Billeter, and W. Braun, *J. Mol. Biol.*, 1983, **169**, 949.
28. T. F. Havel, I. D. Kuntz, G. M. Crippen, *Bull. Math. Biol.*, 1983, **45**, 665.
29. G. Némethy and H. A. Scheraga, *Q. Rev. Biophys.*, 1977, **10**, 239.
30. T. F. Havel and K. Wüthrich, *Bull. Math. Biol.* 1984, **46**, 673.
31. W. Braun and N. Gō, *J. Mol. Biol.*, 1985, **186**, 611.
32. P. Güntert, W. Braun, and K. Wüthrich, *J. Mol. Biol.*, 1991, **217**, 517.
33. R. Kaptein, E. R. P. Zuiderweg, R. M. Scheek, S. R. Boelens, and W. F. van Gunsteren, *J. Mol. Biol.*, 1985, **182**, 179.
34. A. T. Brünger, G. M. Clore, A. M. Gronenborn, and M. Karplus, *Proc. Natl. Acad. Sci. USA*, 1986, **83**, 3801.
35. T. F. Havel and K. Wüthrich, *J. Mol. Biol.*, 1985, **182**, 281.
36. P. Güntert, K. D. Berndt, and K. Wüthrich, *J. Biomol. NMR*, 1993, **3**, 601.
37. M. Billeter, Y. Q. Qian, G. Otting, M. Müller, W. J. Gehring, and K. Wüthrich, *J. Mol. Biol.*, 1990, **214**, 183.

Acknowledgments

Our own research covered in this article was generously supported by the ETH Zürich, the Schweizerischer Nationalfonds, the Kommission zur Förderung der wissenschaftlichen Forschung and Bruker-Spectrospin AG. I wish to thank Mr. R. Marani for the careful processing of the manuscript.

Biographical Sketches

Kurt Wüthrich. *b* 1938. Licentiat, 1962, Physics, Mathematics, Chemistry, University of Bern, Eidgenössisches Sportlehrerdiplom, 1964, University of Basel, Ph.D., 1964, Inorganic Chemistry (supervisor Professor S. Fallab), University of Basel. Postdoctoral work at University of Basel (supervisor Professor S. Fallab), University of California, Berkeley (Professor R. E. Connick), Bell Telephone Laboratories, Murray Hill, USA (supervisor Dr. R.G. Shulman). Since 1969 at ETH Zürich, currently Professor of Biophysics and Head of the Institute of Molecular Biology and Biophysics. Approx. 500 publications. Research specialties: NMR structure determination of biological macromolecules, drug design, and protein engineering.

Cadmium-113 NMR: A Surrogate Probe for Zinc and Calcium in Proteins

Kate McAteer, Andrew S. Lipton and Paul D. Ellis
Battelle, Pacific Northwest Laboratories, Richland, WA, USA

1	Introduction	1
2	Solution State Cadmium-113 NMR Studies	1
3	Solid State Studies	3
4	Summary	6
5	Related articles	6
6	References	6

1 INTRODUCTION

The overall objective of our research program in this area is to develop NMR methods to a point where they can be used to study the metal sites in diamagnetic metalloproteins. The metals of initial interest have been zinc and calcium. In the past several years we have developed and utilized Cd(II) via ^{113}Cd NMR spectroscopy as a 'spin spy' to study the Zn(II) and Ca(II) sites in metalloproteins. The reasoning behind this strategy is the fact that Zn(II) and Ca(II) have such poor spectroscopic properties since Zn(II) and Ca(II) do not have unpaired electrons and hence one cannot perform an ESR experiment. Likewise, Zn(II) and Ca(II) have closed d-electron configurations, and as a result UV–visible spectrophotometry does not provide any clearly definable transitions that could be utilized to monitor the status of ligation.

The nuclear spin of ^{67}Zn is $\frac{5}{2}$ and that of ^{43}Ca is $\frac{7}{2}$ and as such they both have prohibitively broad lines in the solution NMR spectrum. Consequently, a viable alternative is to employ a surrogate probe as a means of studying these metals in this important class of biological systems. Such a strategy demands that a great deal of care be exercised in the selection of the probe. In the case of Zn(II), Cd(II) is a natural selection. This is based on parallel chemistry and size considerations. In every case studied to date, the surrogate strategy has worked, i.e. it has provided results which are consistent with the known chemistry of the system of interest. This article outlines our efforts in support of the objective described above. Although other work is mentioned, we have made no effort for this to be a comprehensive review of ^{113}Cd NMR spectroscopy.

2 SOLUTION STATE CADMIUM-113 NMR STUDIES

The metal center of many metalloproteins plays an active role in biological function so it is important to obtain as much structural information as we can about this site. Solution state ^{113}Cd NMR spectroscopy of metalloproteins is an informative technique for studying such systems in an environment that closely resembles that of their native state. The large chemical shift range of approximately 900 ppm of the cadmium nucleus when the metal is coordinated to the mixtures of oxygen, sulfur, and nitrogen atoms found in proteins affords a probe that can provide not only structural information but can help develop a better understanding of enzymatic mechanisms. The chemical shifts observed for cadmium-substituted metalloproteins are qualitatively consistent with the general trends found in nonbiological model systems.

An excellent review of ^{113}Cd NMR spectroscopy of small inorganic and organometallic cadmium complexes was published by Ellis in 1983.[1] The most shielding ligand is oxygen, the most deshielding is sulfur. For example, a metalloprotein whose metal center is coordinated through the sulfur atoms of thiolate groups alone will give rise to a ^{113}Cd NMR spectrum with resonances in the 600–700 ppm range, whereas signals from a Cd(II) ion that is coordinated exclusively via the oxygen atoms of carbonyl ligands will be observed between 0 and −125 ppm. The chemical shifts of those that contain a combination of nitrogen and oxygen ligands will be found in the 0–300 ppm range. Figure 1 illustrates the chemical shift ranges of a number of Cd-substituted metalloproteins and Cd complexes.

Since the technique was first published as an effective metallobioprobe of the zinc-containing proteins carbonic anhydrase and alkaline phosphatase by Armitage et al. in 1976,[2] ^{113}Cd NMR has been used to examine the metal center(s) of more than 20 different metalloproteins. In almost every case enzyme activity has been fully or partially retained. For a detailed description of ^{113}Cd NMR spectroscopic data on these systems, the reader is referred to a review published

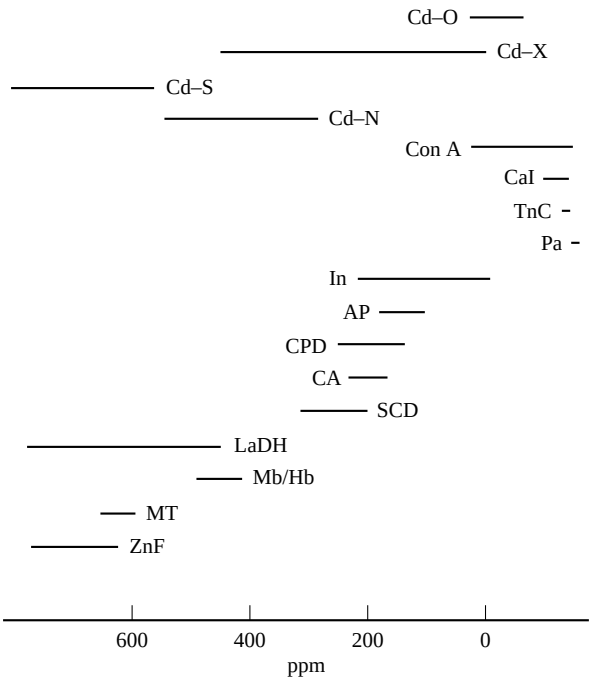

Figure 1 Chemical shift ranges for Cd-substituted metalloproteins and Cd complexes. Abbreviations: Con A, concanavalin A; Cal, calmodulin; TnC, skeletal troponin C; Pa, parvalbumin; In, insulin; AP, alkaline phosphatase; CPD, carboxypeptidase; CA, carbonic anhydrase; SOD, superoxide dismutase; Mb, myoglobin; Hb, hemoglobin; LADH, liver alcohol dehydrogenase; MT, metallothionein, ZnF, zinc fingers

by Summers in 1988.[3] A more recent approach taken in the study of metalloproteins involving ^{113}Cd NMR spectroscopy is the use of ^{1}H–^{113}Cd couplings observed in 2D NMR spectra to investigate metal–ligand connectivities.[4–6] The technique has been particularly helpful in the elucidation of the number and type of coordinating ligands at metal centers in 'zinc fingers'.[7–9] A recent review by Coleman describes the experimental techniques used and the results obtained in greater detail.[10] Here we have limited our discussion to our work on the calcium-binding proteins skeletal troponin C and concanavalin A, and to metallothionein. In addition, we will show that ^{113}Cd NMR is a suitable probe for a different type of biological system, namely the heme proteins.

2.1 Metallothionein

The only naturally-occurring protein known to bind cadmium is metallothionein (MT) and it was one of the earlier metalloproteins to be studied by solution state ^{113}Cd NMR.[11,12] This protein was ideally suited for these purposes because of its small size (M_r ca. 6800) and more importantly because of the large number of metals that can be found in the native protein. Metallothioneins typically contain 6–9 equiv. of metals, the more common ones being zinc, cadmium, mercury, and copper. Earlier samples usually contained an inhomogeneous mixture of metals which made analysis of the ^{113}Cd NMR spectrum difficult, but the chemical shifts observed in the 550–700 ppm range indicated bridging of Cd(II) ions by cysteine thiolate groups.

The preparation of a pure Cd_7-MT led to a greater understanding of the individual metal binding sites in the protein and their relationship to one another, because the ^{113}Cd chemical shift is sensitive to the small differences in the coordination environment of each of the seven sites. In addition, the spin–spin couplings observed between Cd(II) ions located at adjacent sites in the protein were used to determine that rabbit liver MT contained two separate metal clusters, one containing four metals, the other containing three. This information was unavailable prior to ^{113}Cd NMR studies because of difficulties encountered in trying to obtain a detailed X-ray crystal structure.

2.2 Skeletal Troponin C

Ellis and co-workers observed four resonances in the ^{113}Cd NMR solution state spectrum of skeletal troponin C (TnC), two of which are sharp signals and two are broad and undetectable at high fields.[1] These broad resonances are observable at lower temperatures. Research involving Ca(II) and Cd(II) titrations and equilibrium binding studies led to the assignment of the resonances to two classes of metal-binding sites. In the protein there exist two 'high-affinity' or structural binding sites and two 'low-affinity' or regulatory binding sites. The binding of Ca(II) to these regulatory sites is responsible for controlling muscle contraction.

The temperature dependence of the ^{113}Cd NMR spectrum is shown in Figure 2. At room temperature the two structural sites give rise to resonances at −107.8 and −112.7 ppm with respect to a 0.1 M solution of $Cd(ClO_4)_2$. Lowering the temperature alters the chemical exchange dynamics, resulting

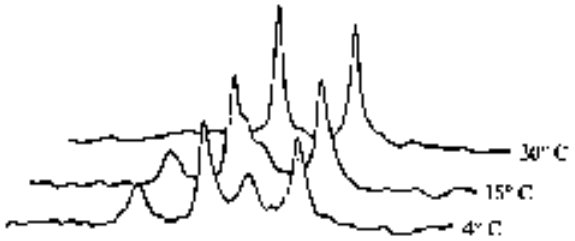

Figure 2 ^{113}Cd NMR spectra of TnC at the temperatures indicated. (Reproduced by permission of the American Association for the Advancement of Science from P. D. Ellis, *Science* 1983, **221**, 1141)

in a four-line spectrum. The two new resonances at −103.1 and −109.8 ppm arise from Cd(II) bound to the regulatory sites. These chemical shift values indicate an oxygen coordination environment for each bound metal ion. However, it is the temperature dependence of the chemical shifts that is most interesting as this can be used to investigate how changes in protein conformation can be related to the occupancy of the metal sites.

2.3 Concanavalin A

Concanavalin A (Con A) is a multisubunit protein involved in carbohydrate binding. Each subunt contains two metal-binding sites; the S1 site in the native protein binds Mn(II) and the S2 site binds Ca(II). An extensive ^{113}Cd NMR study of this protein was carried out in our group and it was discovered that the protein can exist in two forms, locked or unlocked.[13] The former gives three ^{113}Cd signals whereas the locked form has only one. It is thought that in the latter the metals are exchanging rapidly between free and bound states making the observation of bound ^{113}Cd resonances difficult.

Three resonances are observed in the ^{113}Cd NMR spectrum of the locked form at 68, 46 and −125 ppm. The signal at 68 ppm was attributed to free cadmium and it is the signal observed in the unlocked species. The others at 46 and −125 ppm were assigned to Mn and Ca sites, respectively, by simply carrying out competitive binding studies with the metals in question. Additional solution state ^{113}Cd NMR work has shown that other metals have high affinities for both the S1 and S2 site. As Figure 3 illustrates, Pb(II) displaces bound Cd(II) ions causing the ^{113}Cd resonances in the NMR spectrum to decrease in intensity and finally disappear when displacement is complete.

2.4 Heme Proteins

Cadmium-113 NMR spectroscopy has become a valuable technique for studying the role(s) of the metal(s) in predominantly calcium- and zinc-containing metalloenzymes. We will now show some data that indicate its effectiveness as a probe for a different type of biological system, namely the prosthetic group in heme-containing proteins. The function of each of these proteins is centered at the metal site in the porphyrin part of the molecule, hence ^{113}Cd NMR should be an ideal probe of these sites. In initial studies carried out in our group the model complexes used to mimic the heme site in these proteins

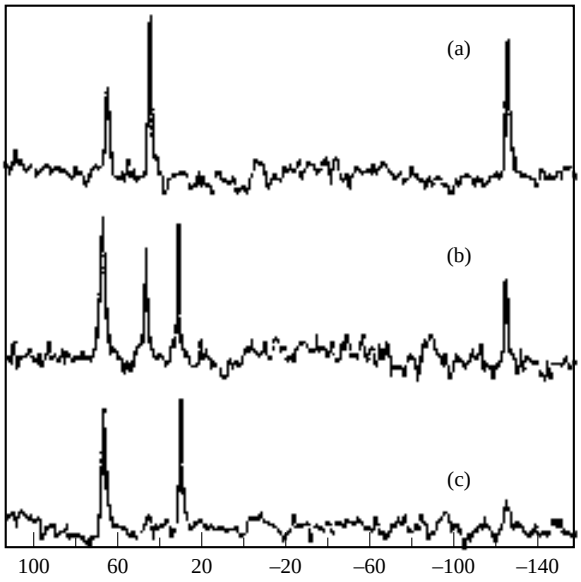

Figure 3 (a) ^{113}Cd NMR spectra of Cd:Cd Con A for reference. The resonances are at 68, 46, and −125 ppm. (b) The same sample after addition of 1.0 equiv. of Pb(II). (c) The same sample as (a) but with 2.0 equiv. of Pb(II) added. The resonances are at 68 and 32 ppm. (Reproduced by permission of the American Chemical Society from A. R. Palmer, D. B. Bailey, W. D. Behnke, A. D. Cardin, P. P. Yang, and P. D. Ellis, *Biochemistry*, 1980, **19**, 5063)

were cadmium-substituted porphyrins.[14,15] Solid state methods which were employed to overcome difficulties encountered in solution state work will not be discussed here as they are reviewed in Section 3.

A single resonance at 411 ppm was observed in the solution state spectrum of ^{113}Cd protoporphyrin IX dimethyl ester (^{113}Cd-PPIXDME) at 20 °C. A chemical exchange process was revealed by lowering the temperature from 20 °C to −60 °C. At −60 °C two resonances are observed, one at 405 ppm, the other at 374 ppm. These results indicate that there are two distinct magnetic sites at the Cd(II) ion, one existing via chelation to the four nitrogens of the porphyrin's pyrrole rings, the other being a five-coordinate species in which the metal ion is axially coordinated intermolecularly to an adjacent carbonyl oxygen of a propionic ester side chain. In the solution state spectrum of ^{113}Cd-PPIX in 70:30 pyridine/aqueous KOH at 20 °C, a single resonance is observed at 435 ppm whose chemical shift is also dependent on temperature. However in this case the fifth axial ligand is clearly pyridine which coordinates through a nitrogen atom.

Kennedy and Ellis first examined cadmium-substituted myoglobin (Cd-Mb) by solution state ^{113}Cd NMR in 1989.[15] As in the case of the porphyrins they observed a single resonance in the NMR spectrum whose linewidth is independent of temperature, but whose chemical shift is temperature-dependent with greater shielding at higher temperatures. Cd-Mb appears to be undergoing fast chemical exchange between four-coordinate Cd-PPIX and five-coordinate Cd-PPIX axially coordinated to the proximal histidine of the globin chain.

Present work is being carried out on cadmium-substituted hemoglobin (Cd-Hb). We expect to observe a two-line spectrum for the fully substituted molecule, i.e. Cd_4-Hb where Cd(II) has replaced iron in all four heme sites. One line may arise from Cd(II) in a four-coordinate species where Cd-PPIX is noncovalently bound in the heme pocket, and the second may arise from a five-coordinate species in which the proximal histidine donates a fifth axial ligand to the metal center.

The question arises whether or not each of these resonances can be assigned to a specific chain in hemoglobin or are they the result of the quaternary effect in the molecule? We hope to answer this question by first preparing a hybrid hemoglobin in which we will substitute only the α-chains with Cd(II) and reconstitute them with native β-chains. The ^{113}Cd NMR spectrum of such a molecule would only reflect what is happening at the metal center in the α-chain. Further experiments will involve the preparation of a series of mixed-metal hemoglobins in which we hope to exploit the sensitivity of ^{113}Cd NMR to axial bonding changes by observing the change in the chemical shift tensor when various ligands bind to the metal sites. This will involve both solution- and solid-state studies. By comparing future ^{113}Cd NMR results with the vast amount of information already available on hemoglobin, we hope to show the validity of ^{113}Cd NMR as an effective probe for the prosthetic groups present in heme proteins.

3 SOLID STATE STUDIES

A complication in the spectral analysis of solution state ^{113}Cd NMR data has been dynamical effects such as exchange averaging of the chemical shifts. There have been occasions when these processes have even prevented the observation of a resonance.[2,11,16] Another obstacle to the interpretation of the solution state spectra is a dependence of the isotropic chemical shift on temperature, concentration, and solvent effects. One apparent answer to the problem of solution dynamics is to use supercooling to slow down the chemical exchange.[17] However, this method does not resolve the other problems described previously. An alternative to the supercooled aqueous solutions is to exploit solid state NMR methods, and it is these techniques that we will focus upon here.

One advantage of using solid state NMR over solution state NMR is the extra information that can be provided. Instead of a single isotropic resonance, now all the principal elements of the chemical shift tensor are accessible. These data can be obtained by simulating a static powder spectrum and/or an analysis of MAS sideband patterns.[18,19] Utilizing single crystal experiments, one obtains the relative orientations of the chemical shielding tensor relative to a molecular fixed coordinate system. This benefit of going to solid state NMR is exemplified in the case of cadmium-substituted porphyrin systems.[14,15,20–22]

3.1 Heme Proteins

An example was the study of *meso*-tetraphenylporphyrin (TPP) and its pyridine adduct by Jakobsen et al.[14,20] The first problem encountered in this investigation was that no signal in the liquid phase could be obtained from the 'unliganded' Cd-TPP. However, a ^{113}Cd spectrum of the material in the solid state could be obtained. The static powder spectrum of free 'unliganded' Cd-TPP is contrasted with that of the

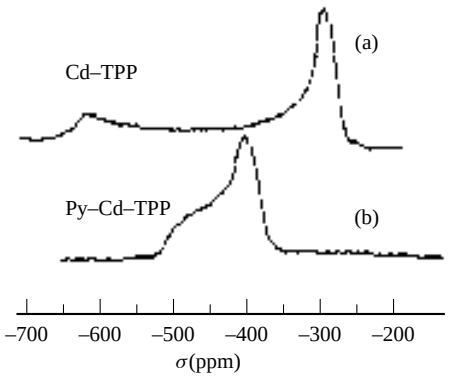

Figure 4 Cross polarization (CP), solid state ^{113}Cd NMR powder spectra of (a) 'free' Cd-TPP and (b) the pyridine-^{15}N adduct of Cd-TPP. The shielding constant (σ) scale is positive to larger shieldings and is referenced to a sample of solid $Cd(ClO_4)\cdot 6H_2O$. (Reproduced by permission of the American Chemical Society from H. J. Jakobsen, P. D. Ellis, R. R. Inners, and C. F. Jensen, *J. Am. Chem. Soc.*, 1982, **104**, 7442)

pyridine-adducted metalloporphyrin in Figure 4. The chemical shift anisotropy (CSA) of the Py–Cd-TPP is less than a third of the CSA for the free Cd-TPP, which was attributed to the axial ligand pulling the metal out of the plane of the porphyrin. If the pyridine had been bound to the cadmium without disturbing the existing structure, one would expect little change in the unique tensor element, not the 124 ppm change observed. Note that the tensor elements in the pyridine adduct move in opposite directions. Such a pattern will cause problems in the interpretation of the isotropic chemical shifts.

A logical extension of this work with metalloporphyrins came from Kennedy and Ellis in their investigation of Cd(II)-substituted heme and myoglobin.[15] In that study they measured the effects of solvent and temperature on the ^{113}Cd chemical shift. The cadmium protoporphyrin IX dimethyl ester (PPIXDME) has a similar coordination of TPP and therefore a similar chemical shift tensor. Binding a pyridine axially to the Cd-PPIXDME in an attempt to mimic the histidine binding of myoglobin (Mb) shifts the ^{113}Cd resonance approximately 43 ppm in solution and not at all in the solid state. Again the tensor elements move in opposite directions. Further, from the data depicted in Figure 5, one can see that the Cd-Mb CSA has an opposite sign to that of the model, Cd-PPIXDME–Py. In considering only the isotropic shifts, one would be led to the incorrect assumption that the binding of the metal is similar in these two coordination centers. By utilizing the tensor parameters extracted from the static powder lineshapes, Kennedy and Ellis postulated that the change in CSA was in fact a measure of the strength of the axial ligand, pulling the metal further out of the plane of the heme.

An important point needs to be made with regard to these observations. Namely, the isotropic chemical shift of a metal center may be difficult to interpret because of this phenomenon of shielding tensor elements moving in opposite directions. Because of this potential problem, the solid state and liquid state methods become complementary. This situation is not unique to ^{113}Cd NMR and should be applicable to any 'heavy metal' nuclide.

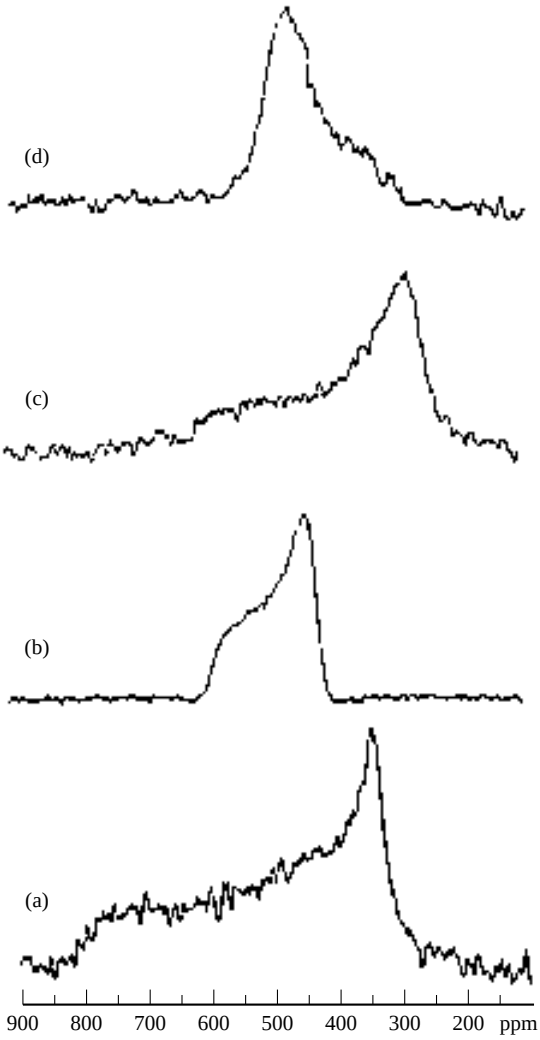

Figure 5 Cross polarization, solid state, static powder 66.5 MHz ^{113}Cd NMR spectra of (a) Cd-PPIXDME (16 914 transients), 0.013 s acquisition time, 7.0 ms contact time, 3.0 s recycle delay, (b) Cd-PPIXDME–Py (9308 transients), 0.003 s acquisition time, 5.0 ms contact time, 4.0 s recycle delay, (c) Cd-PPIX (11 479 transients), 80 μs acquisition time, 5.0 ms contact time, 8.0 s recycle delay, and (d) lyophylized Cd-Mb (45 313 transients), 0.026 s acquisition time, 4.0 ms contact time, 6.0 s recycle delay. (Reproduced by permission of the American Chemical Society from M. A. Kennedy and P. D. Ellis, *J. Am. Chem. Soc.*, 1989, **111**, 3195)

3.2 Other Proteins

Some other proteins studied by solid state ^{113}Cd NMR are substituted skeletal troponin C (STnC),[23] parvalbumin from carp muscle,[24] concanavalin A (Con A),[24] and carboxypeptidase A (CPA).[25] Marchetti et al.[24] demonstrated that lyophilized proteins have considerably disordered metal-binding sites. After rehydration, the resulting protein spectra exhibit significant line narrowing and a substantial improvement in signal-to-noise ratio. A large body of work on ^{113}Cd(II)-CPA has been done by Rivera and Ellis,[25] studying the protein with[25b] and without inhibitors.[25a] Among the complexes (inhibitors and/or substrates) investigated were 1-benzylsuccinate, glycyl-1-tyrosine, the phosphoramidite ZGP, and polypeptide potato tuber inhibitor. One major difficulty in

obtaining CP MAS spectra is that high speed spinning for an extended period tends to spin out the water, dehydrating the sample. As with the parvalbumin, the dehydration causes disordering of the cadmium resonance, and following rehydration the local structure about the metal is restored.

3.3 Cadmium Oxo Model Compounds

In order to correlate the chemical shift information with the protein structure, several model compounds were investigated. There are a vast number of solid state NMR investigations of cadmium oxo compounds in the literature.[26] The coordination number of cadmium in these compounds varies from six to eight, while the isotropic chemical shifts range from 150 to −100 ppm. However, the solid state data on the powders of the cadmium oxo compounds were difficult to interpret in terms of structure. In order to gain a better understanding the relationship between cadmium coordination geometry and/or number and isotropic chemical shift was to undertake a detailed study of selected cadmium oxo compounds via single crystal NMR methods.[27]

3.3.1 Single Crystal Studies

Using single crystal NMR methods, the shielding interactions are placed in the crystal axis system. The compounds surveyed ranged from the all-oxygen environments of $Cd(NO_3)_2{\cdot}4H_2O$, $3CdSO_4{\cdot}8H_2O$, $CdCa(OAc)_4{\cdot}6H_2O$, $Cd(C_4H_2O_4){\cdot}2H_2O$, $Cd(HCO_2)_4{\cdot}4H_2O$, and $Cd(OAc)_2{\cdot}2H_2O$[28] to various mixed donor atom combinations of oxygen, nitrogen, sulfur, and chlorine.[29] The tensor elements of the complexes containing exclusively oxygen donor atoms are compared graphically in Figure 6. Following these investigations four correlations between tensor elements and structure have been recognized:

1. Tensor elements of like magnitude have similar orthogonal environments.
2. The most deshielded element is aligned nearly orthogonal to planes containing water.
3. If water oxygens are not present in the coordination sphere, the least shielded element is oriented to maximize the shortest Cd−O shielding contributions.
4. The most shielded tensor element is nearly perpendicular to the longest Cd−O bond.

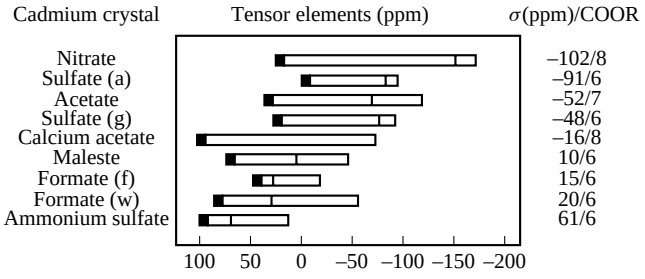

Figure 6 Summary of the ^{113}Cd shielding tensors for cadmium oxo compounds determined by single crystal experiments. Vertical bars represent the position of individual elements relative to σ_{iso} for solid $Cd(ClO_4)_2$. The deshielded element of each tensor is designated by either a cross-hatch or a solid bar. Solid bars represent elements with intramolecular shielding contributions dominated by water oxygens. Cross-hatched elements indicate predominant short-bond shielding contributions. Sulfate suffixes correspond to cadmium in general and special positions. (Reproduced by permission of the American Chemical Society from R. S. Honkonen, and P. D. Ellis, *J. Am. Chem. Soc.*, 1984, **106**, 5488)

These empirical rules have been extended by other groups to additional model compounds,[26e,30] some with mixed atom donors to cadmium, such as cadmium−sulfur or cadmium−selenium coordination systems by Santos et al.[31] and others.[32] In each case, the applicable paradigms have proven to be generalized to these other ligand systems.

3.4 Mixed Donor Atom Combinations

Barrie et al.[30] explored some nitrogen and oxygen mixed coordination to cadmium using bisglycinatocadmium(II) monohydrate and bis-L-alaninatocadmium(II) trihydrate. Both of these compounds are nearly octahedral with N_2O_4 coordination about the cadmium. The solid state spectra of these compounds exhibit fine structure due to a dipolar coupling between ^{113}Cd and ^{14}N, which Barrie has utilized to determine the number of nitrogen atoms coupled to the cadmium. As in the case of ligated Cd(II) in PPIXDME and myoglobin,[15] the ^{113}Cd isotropic chemical shifts of bisglycinatocadmium(II) monohydrate and bis-L-alaninatocadmium(II) trihydrate determined by Barrie and co-workers[30] are identical, yet the principal components of the shielding tensor are very different. This again illustrates the power of multiphase NMR investigations with so-called 'heavy' nuclides such as ^{113}Cd, as the sensitivity of the shielding tensor to changes in geometry (internuclear distances and orientations within the crystallite) shows.

3.4.1 Poly(pyrazolyl)borates

To confirm that compounds with donor atoms other than oxygen follow the patterns laid out by the cadmium oxo study, an extensive series of models using nitrogen donor atoms is being undertaken. The family of ligands being utilized are the poly(pyrazolyl)borates, whose chemistry with cadmium is only now being fully explored. Other model compounds such as cadmium diimidazole diacetate, which has been the only model employed in the interpretation of ^{113}Cd-substituted carboxypeptidase-A (CPA), tend to polymerize.[33] This polymerization generates a significantly different structure from that of the CPA, making the interpretation of the ^{113}Cd shielding tensor data of CPA difficult. The bulky nature of the pyrazolylborates makes them ideally suited to generate monomeric complexes with nitrogen donor atoms. A few studies using pyrazolylborates as models for histidine coordination to copper have already appeared in the literature.[34]

The basic structure of the poly(pyrazolyl)borate ligands coordinated to cadmium is depicted in Figure 7. These ligands are extremely versatile because the number of donor atoms can be varied in going from the dihydrobis-, hydrotris-, to tetrakis(pyrazolyl)borate. By altering the poly(pyrazolyl)borate ligand, one can control the core atoms to range from N_4 to N_6 and several mixed-ligand donor atom combinations (i.e., N_5, N_3S_2, N_3O_2, N_3H_2, N_3C, and N_3H).[35]

The initial solid state NMR study of these complexes with four- and six-coordinate nitrogen donors allowed a comparison with porphyrin coordination and a correlation between ligand

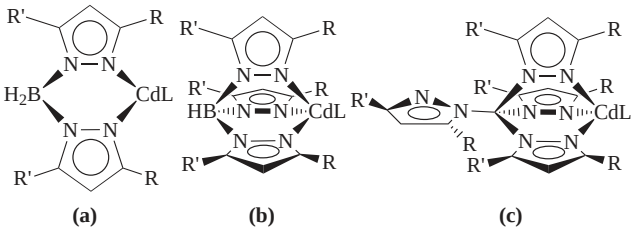

Figure 7 General structures of some poly(pyrazolyl)borate ligands bound to a cadmium; (a) dihydrobis(pyrazolyl)borate, (b) hydrotris(pyrazolyl)borate, and (c) tetrakis(pyrazolyl)borate. The R groups are in the 3-position and the R′ groups are in the 5-position of the pyrazolyl rings, where R and/or R′ can be H, Me, *t*-Bu, or Ph. (Reproduced by permission of the American Chemical Society from A. S. Lipton, S. S. Mason, D. L. Reger, and P. D. Ellis, *J. Am. Chem. Soc.*, in press)

geometry and the shielding tensor.[36] To facilitate interpretation of protein data, a further expanded basis set of model compounds is needed. Toward this end, several five-coordinate complexes with mixed donor atoms were also studied,[37] as well as some four-coordinate alkyl derivatives.[38] The principal components of the shielding tensors derived for a sampling of these complexes are presented in Figure 8. Other interesting complexes generated with pyrazolylborate chemistry were a cadmium hydride and the first reported cadmium–cadmium bond.[35c]

The poly(pyrazolyl)borate ligands are indeed well suited for studying cadmium coordination chemistry and chemical shielding effects. Minor changes, such as methylation of the pyrazolyl rings of the ligand, can lead to large variations in the elements of the shielding tensor, while leaving differences in the isotropic shifts relatively small. These minor changes in similar ligands can be utilized to tailor the model compounds to approximate more closely the metal environment of a protein.

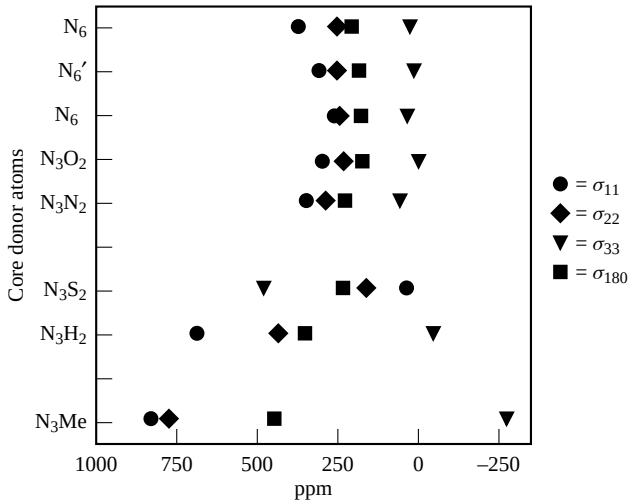

Figure 8 Sampling of the ^{113}Cd shielding tensors derived from the CP MAS spectra of several poly(pyrazolyl)borate cadmium complexes. The core donor atoms given are the atoms bound to the metal center. The chemical formulas of the compounds, from top to bottom, are as follows: $[B(pz)_4]_2Cd$, $[B(3\text{-}Mepz)]_2Cd$, $[HB(3,5\text{-}Me_2pz)_3]_2Cd$, $Cd[HB(3\text{-}Phpz)_3]^tBu\text{-}acac$, $[HB(3,5\text{-}Me_2pz)_3Cd[H_2B(pz)_2][HB(3,5\text{-}Me_2pz)_3Cd[S_2CN(Et)_2][HB(3,5\text{-}Me_2pz)_3]CdBH_4$, and $[HB(3,5\text{-}Me_2pz)_3]CdMe$ (where pz = pyrazolyl). The chemical shifts are referenced to an external sample of a 0.1 M solution of $Cd(ClO_4)_2$

4 SUMMARY

To date the surrogate probe strategy has worked well. However, great care has to be exercised at all times. We are currently pursuing the ab initio calculation of ^{113}Cd chemical shifts.[39] Our data base of shielding tensor data should provide excellent benchmarks for a comparison between theory and experiment. Such calculations should provide unambiguous correlations between chemical shielding and structure. Such relationships are essential to further our understanding of the role of metals in metalloproteins.

5 RELATED ARTICLES

Calcium-Binding Proteins; Calmodulin; Carbonic Anhydrase; Chemical Shifts in Biochemical Systems; Hemoglobin; Myoglobin

6 REFERENCES

1. P. D. Ellis, in *The Multinuclear Approach to NMR Spectroscopy*, eds. J. B. Lambert and F. G. Siegel, Riedel, Boston, MA, 1983, Chap. 22
2. I. M. Armitage, R. T. Pajer, A. J. M. Schoot Uiterkamp, J. F. Chlebowski, and J. E. Coleman, *J. Am. Chem. Soc.*, 1976, **98**, 5710.
3. M. F. Summers, *Coord. Chem. Rev.*, 1988, **86**, 43.
4. M. H. Frey, G. Wagner, M. Vasak, O. W. Sorenson, D. Neuhaus, E. Worgotter, J. H. R. Kagi, R. R. Ernst, and K. Wuthrich, *J. Am. Chem. Soc.*, 1985, **107**, 6847.
5. P. R. Blake, J. B. Park. M. W. W. Adams, and M. F. Summers, *J. Am. Chem. Soc.*, 1992, **114**, 4931.
6. O. Zerbe, D. L. Poutney, W. von Philipsborn, and M. Vasak, *J. Am. Chem. Soc.*, 1994, **116**, 377.
7. T. L. South, B. Kim, and M. F. Summers, *J. Am. Chem. Soc.*, 1989, **111**, 395.
8. D. P. Giedroc, B. A. Johnson, I. M. Armitage, and J. E. Coleman, *Biochemistry*, 1989, **28**, 2410.
9. K. H. Gardner, T. Pan, S. Narula, E. Rivera, and J. E. Coleman, *Biochemistry*, 1991, **30**, 11292.
10. J. E. Coleman, in *Methods in Enzymology*, eds J. F. Riordan and B. L. Vallee, Academic Press, San Diego, CA, 1993, Vol. 227, Chap. 2
11. I. M. Armitage, A. J. M. Schoot Uiterkamp, J. F. Chlebowski, and J. E. Coleman, *J. Magn. Reson.*, 1978, **29**, 375.
12. J. L. Sudmeier, S. J. Bell, M. C. Storm, and M. F. Dunn, *Science*, 1981, **212**, 560.
13. A. R. Palmer, D. B. Bailey, W. D. Behnke, A. D. Cardin, P. P. Yang, and P. D. Ellis, *Biochemistry*, 1980, **19**, 5063.
14. H. J. Jakobsen, P. D. Ellis, R. R. Inners, and C. F. Jensen, *J. Am. Chem. Soc.*, 1982, **104**, 7442.
15. M. A. Kennedy and P. D. Ellis, *J. Am. Chem. Soc.*, 1989, **111**, 3195.
16. P. D. Ellis, P. Strang, and J. D. Potter, *J. Biol. Chem.*, 1984, **259**, 10 348.

17. (a) M. J. B. Ackerman, and J. J. H. Ackerman, *J. Phys. Chem.*, 1980, **84**, 3151; (b) H. J. Jakobsen, and P. D. Ellis, *J. Phys. Chem*, 1981, **85**, 3367.
18. U. Haeberlen, *High Resolution NMR in Solids Selective Averaging*, 2nd edn., Springer-Verlag, Berlin, 1976.
19. (a) M. M. Maricq and J. S. Waugh, *J. Chem. Phys.*, 1979, **70**, 3300; (b) J. Herzfeld and A. E. Berger, *J. Chem. Phys.*, 1980, **73**, 6021; (c) J. M. Koons, E. Hughes, and P. D. Ellis, *Anal. Chem. Acta.*, 1993, **283**, 1045.
20. P. D. Ellis, R. R. Inners, and H. J. Jakobsen, *J. Phys. Chem.*, 1982, **86**, 1506.
21. P. S. Marchetti, S. Bank, T. W. Bell, M. A. Kennedy, and P. D. Ellis, *J. Am. Chem. Soc.*, 1989, **111**, 2063.
22. M. A. Kennedy, J. L. Sessler, T. Murai, and P. D. Ellis, *Inorg. Chem.*, 1990, **29**, 1050.
23. (a) P. D. Ellis, *Science*, 1983, **221**, 1141; (b) R. R. Inners, F. D. Doty, A. R. Garber, and P. D. Ellis, *J. Magn. Reson.*, 1981, **45**, 503.
24. P. S. Marchetti, P. D. Ellis, and R. G. Bryant, *J. Am. Chem. Soc.*, 1985, **107**, 8191.
25. (a) E. Rivera, M. A. Kennedy, and P. D. Ellis, *Adv. Magn. Reson.*, 1989, **13**, 257; (b) E. Rivera, *Ph.D. Dissertation*, University of South Carolina, 1990, Chap. 4
26. (a) J. J. H. Ackerman, T. V. Orr, V. J. Bartuska, and G. E. Maciel, *J. Am. Chem. Soc.*, 1979, **101**, 341; (b) P. G. Mennitt, M. P. Shatlock, V. J. Bartuska, and G. E. Maciel, *J. Phys. Chem.*, 1981, **85**, 2087; (c) P. D. Murphy, and B. C. Gerstein, *J. Am. Chem. Soc.*, 1981, **103**, 3282; (d) P. D. Murphy, W. C. Stevens, T. T. P. Cheung, S. Lacelle, and B. C. Gerstein, *J. Am. Chem. Soc.*, 1981, **103**, 4400; (e) V. W. Miner and J. H. Prestegard, *J. Am. Chem. Soc.*, 1985, **107**, 2177.
27. (a) M. A. Kennedy, and P. D. Ellis, *Con. Magn. Reson.*, 1989, **1**, 35; (b) M. A. Kennedy, and P. D. Ellis, *Con. Magn. Reson.*, 1989, **1**, 109.
28. (a) R. S. Honkonen, F. D. Doty, and P. D. Ellis, *J. Am. Chem. Soc.*, 1983, **105**, 4163; (b) R. S. Honkonen, and P. D. Ellis, *J. Am. Chem. Soc.*, 1984, **106**, 5488.
29. (a) R. S. Honkonen, P. S. Marchetti, and P. D. Ellis, *J. Am. Chem. Soc.*, 1986, **108**, 912; (b) P. S. Marchetti, R. S. Honkonen, and P. D. Ellis, *J. Magn. Reson.*, 1987, **71**, 294; (c) M. A. Kennedy and P. D. Ellis, *Inorg. Chem.*, 1990, **29**, 541; (d) M. A. Kennedy, P. D. Ellis, and H. J. Jakobsen, *Inorg. Chem.*, 1990, **29**, 550; (e) E. Rivera, and P. D. Ellis, *Inorg. Chem.*, 1992, **31**, 2096.
30. P. J. Barrie, A. Gyani, M. Motevalli, and P. O'Brien, *Inorg. Chem.*, 1993, **32**, 3862.
31. (a) R. A. Santos, E. S. Gruff, S. A. Koch, and G. S. Harbison, *J. Am. Chem. Soc.*, 1990, **112**, 9257; (b) R. A. Santos, E. S. Gruff, S. A. Koch, and G. S. Harbison, *J. Am. Chem. Soc.*, 1991, **113**, 469; (c) R. A. Santos, *Ph.D. Dissertation*, 1992, State University of New York at Stony Brook, Chap. 5 (d) R. Subramanian, N. Govindaswamy, R. A. Santos, S. A. Koch, and G. S. Harbison, *J. Am. Chem. Soc.* submitted for publication.
32. J. Sola, P. González-Duarte, J. Sanz, I. Casals, T. Alsina, I. Sobrados, A. Alvarez-Larena, J. F. Piniella, and X. Solans, *J. Am. Chem. Soc.*, 1993, **115**, 10 018.
33. E. Rivera, M. A. Kennedy, R. D. Adams, and P. D. Ellis, *J. Am. Chem. Soc.*, 1990, **112**, 1400.
34. (a) C. S. Arcus, J. L. Wilkinson, C. Mealli, T. J. Marks, and J. A. Ibers, *J. Am. Chem. Soc.*, 1974, **96**, 7564; (b) J. S. Thompson, J. L. Zitzmann, T. J. Marks, and J. A. Ibers, *Inorg. Chim. Acta*, 1980, **46**, L101.
35. (a) D. L. Reger, S. S. Mason, A. L. Rheingold, and R. L. Ostrander, *Inorg. Chem.*, 1993, **32**, 5216; (b) D. L. Reger, S. S. Mason, J. Takats, X. W. Zhang, A. L. Rheingold, and B. S. Haggerty, *Inorg. Chem.*, 1993, **32**, 4345; (c) D. L. Reger, S. S. Mason, and A. L. Rheingold, *J. Am. Chem. Soc.*, 1993, **115**, 10 406; (d) D. L. Reger and S. S. Mason, *Organometallics*, 1993, **12**, 2600.
36. A. S. Lipton, S. S. Mason, D. L. Reger, and P. D. Ellis, *J. Am. Chem. Soc.* 1994, **116**, 10182.
37. A. S. Lipton, S. S. Mason, S. M. Myers, D. L. Roger, and P. D. Ellis, submitted for publication.
38. A. S. Lipton, S. S. Mason, S. M. Myers, D. L. Roger, and P. D. Ellis, in preparation.
39. (a) P. D. Ellis, J. D. Odom, A. S. Lipton, and J. M. Gulick, *J. Am. Chem. Soc.*, 1993, **115**, 755; (b) P. D. Ellis, J. D. Odom, A. S. Lipton, Q. Chen, and J. M. Gulick, in *Nuclear Magnetic Shieldings and Molecular Structure*, ed. J. A. Tossell, Kluwer, Dordrecht, The Netherlands, 1993, Vol. 386, p. 539; (c) Q. Chen, Ph.D. Dissertation, University of South Carolina, 1994; (d) K. McAteer, A. S. Lipton, M. A. Kennedy, and P. D. Ellis, submitted for publication.

Acknowledgments

During his years at USC (where most of this research was carried out), P.D.E. enjoyed the support of many of his colleagues, faculty, postdoctorals, and graduate students, and wishes to thank them for their support through the years. Further, this work could not have been accomplished without the financial support of the National Science Foundation and the National Institutes of Health. For their support P.D.E. is grateful. The authors would also like to acknowledge additional support from Battelle Pacific Northwest Laboratories.

Biographical Sketches

Kate McAteer. *b* 1968. B.Sc., 1990, University of Ulster, Northern Ireland, UK. Graduate student, University of South Carolina, 1990–93. Currently continuing graduate research under the direction of P. D. Ellis at Batelle Pacific Northwest Laboratories. Research interests: ^{113}Cd NMR of Cd-substituted hemoglobins, ultrahigh field NMR studies of DNA oligomers.

Andrew S. Lipton. *b* 1965. B.S., 1987, Ph.D., 1993, Chemistry, University of South Carolina. Spent approximately two years as a laboratory technician for George C. Levy and Philip N. Borer at Syracuse University before undertaking Ph.D. research under the guidance of Paul D. Ellis. Current research interests: solid state NMR of cadmium model complexes and quadrupolar nuclides.

Paul D. Ellis. *b* 1944. B.S., 1966, Ph.D., 1970, Chemistry, University of California at Davis. Assistant, associate, and George H. Bunch, Sr. Professor of Chemistry, University of South Carolina, 1970–93; Associate Director, Macromolecular Structure and Dynamics Group, Battelle Pacific Northwest Laboratories, 1993–present. Approx. 150 publications. Current research interests: heterogeneous catalysis, structural biology.

Calcium-Binding Proteins

Sture Forsén, Sara Linse, Mikael Akke and Johan Kördel
Lund University, Sweden

1 Introduction 1
2 Solution Structures of CABPs in the Presence and Absence of Ca^{2+} 2
3 Dynamic Properties of CABPs 3
4 Chemical Exchange Rates and Metal Ion Binding Constants 4
5 Direct Observation of $^{43}Ca^{2+}$ Signals from Ca^{2+} Bound to CABPs 5
6 ^{111}Cd, ^{113}Cd, and Other Substitution Probes 5
7 Studies of ^{25}Mg, ^{23}Na, and ^{39}K interacting with CABPs 6
8 Related Articles 6
9 References 7

1 INTRODUCTION

Although the occurrence of calcium in mammalian bone, sea shells, and other mineralized tissue was established shortly after the discovery of calcium as an element, the fundamental role of Ca^{2+} ions as regulators in a wide variety of cellular processes was perceived only recently. Today several hundred calcium-binding proteins [CABPs] have been identified in biological tissue,[1] but details of their biological function is known only for a minor fraction. Merely a handful have so far been subjected to extensive NMR studies. Before we embark on a survey of these studies and what type of information they have yielded, we will attempt very briefly to highlight some basic properties of CABPs and their biological distribution.

In eukaryotic cells, a large number of activities are governed by the intracellular concentration of Ca^{2+} ions. In a resting cell, the free Ca^{2+} concentration is ca. 100–200 nM. In contrast, the extracellular concentration is of the order of a few mM.[2] As a result of some hormonal stimulation at the outer cell surface, the intracellular Ca^{2+} concentration is rapidly (ms timescale) increased by a factor of 10^3–10^4. This increased level may be the result of influx from the extracellular milieu but more likely from intracellular Ca^{2+} stores, for example the sarcoplasmic or endoplasmic reticulum. Present in eukaryotic cells are also a number of specific regulatory CABPs, often with several putative Ca^{2+} binding sites with an affinity for Ca^{2+} such that in a resting cell these sites will be largely unoccupied ($K_a \simeq 10^5$–$10^6\ M^{-1}$). At the increased Ca^{2+} level they will, however, be nearly fully occupied. In response to Ca^{2+}-binding, these proteins may undergo conformational changes, for example exposure of hydrophobic surfaces, that cause them to form complexes with, and influence the biological activity of, various enzymes. Among the most well known and studied regulatory CABPs of this type are calmodulin [CaM; M_r = 16 700] and troponin C [TnC; M_r = 18 000]. The former is a highly conserved protein found in all eukaryotic cells, while the latter is observed in muscle cells in a complex with two other proteins, troponin I (TnI) and troponin T.

The Ca^{2+}-binding sites in CaM and TnC consist of a structural motif called the EF-hand, which consists of α-helix–'loop'–α-helix. The central 12-residue sequence contains the calcium coordinating residues, is highly conserved, and comprises a loop and short segments of the flanking α-helices. The EF-hand motif was first identified[3] in the crystal structure of a CABP with high Ca^{2+} affinity called parvalbumin [PV; M_r = 12 000]. EF-hands occur in pairs in CaM, TnC, and a large number of other CABPs, and cooperative Ca^{2+} binding has been established in many cases. Some 20 subfamilies of EF-hand proteins have been described.[4] One of these, the S-100 subfamily, contains a variant hand with two extra amino acids in the loop. Members appear in widely different cell types and include the vitamin D_3-induced proteins calbindin D_{9k} [CB-9; M_r = 8700], the cystic fibrosis antigens MRP-8 and MRP-14, and the proteins that gave the name to the subfamily, S-100a and S-100b.[5,6] The biological function of the S-100 proteins is far from established and subject to intense studies. Among the many CABPs in the central nervous system, the three EF-hand proteins calbindin D_{28k} (CB-28), calretinin, and PV are particularly striking in their abundance and in the specificity of their distribution in different cell types.[7,8]

Important non-EF-hand intracellular CABPs include the annexins, which interact with phospholipid membranes and are presumed to promote membrane fusion,[9] and the highly acidic proteins calsequestrin and calreticulin that serve as weakly chelating 'buffers' for Ca^{2+} ions in the Ca^{2+}-rich organelles SR and ER, respectively.[10]

If we now look at the extracellular milieu, we find new roles for Ca^{2+}. Several proteolytic enzymes of the serine protease type, e.g. trypsin, elastase, etc., have a moderately strong Ca^{2+}-binding site ($K_a \simeq 10^3$–$10^4\ M^{-1}$)[11] that is occupied under the prevailing Ca^{2+} concentration. The Ca^{2+} ion is here coordinated with ligands from different parts of the protein.[12] It is not part of the active site but appears to have a general stabilizing role. The Ca^{2+} ion is however part of the active site in another enzyme, phospholipase A_2 (PPASE),[13] where it plays a role in the mechanism of the catalyzed reaction.[14]

Blood coagulation—so essential to human survival—is a carefully regulated cascade of molecular events involving many proteins and dependent on the presence of Ca^{2+} ions.[15] Several of these proteins are built up of many domains, some of which contain the amino acids γ-carboxyglutamic acid (Gla) and β-hydroxylated aspartic acid (Hya) or asparagine (Hyn).

Bone is a remarkable composite of inorganic (calcium hydroxyapatite) and organic constituents.[16] A number of Gla containing CABPs in the organic matrix have been described: osteocalcin [M_r = 5 300], the matrix Gla protein [$M_r \simeq$ 10 000], the acid glycoproteins osteonectin [apparent M_r = 32 000], and thrombospondin [M_r = 150 000 per monomer].[17]

Although the intracellular Ca^{2+} levels in some prokaryotic microorganisms such as *E. coli* appear to be strictly regulated,[18] little is presently known about their CABPs. At the time of writing, only one prokaryotic protein with a proper EF-hand has been described: calerythrin from *S. erythraea* [M_r = 20 000].[19,20] Interestingly, however, the D-galactose-binding protein in the periplasmic space of *E. coli* is found to have a Ca^{2+} site in which the ligand arrangement is virtually identical

to that of an EF-hand, although the ligands are presented by amino acids from different parts of the protein.[21] It is clear that Ca^{2+} ions are also important for the structural integrity of many prokaryotic proteins, in some cases acting merely as a stabilizing entity, but in other cases required for enzymatic activity as in staphylococcal nuclease (NASE).

NMR studies of CABPs have been concerned with a wide variety of problems: solution structures and dynamics, interactions with other molecules and ions, binding affinities and chemical exchange rates, as well as the detailed nature of the cooperativity of Ca^{2+} binding observed for many proteins. The large amount of work performed on CaM is covered in a separate chapter in this Encyclopedia (***Calmodulin***) and will only be mentioned in passing here.

2 SOLUTION STRUCTURES OF CABPs IN THE PRESENCE AND ABSENCE OF Ca^{2+}

In early NMR studies, structural information was mainly obtained from a limited set of the available NMR observables. For example, the chemical shift displacement of ^1H NMR resonances upon binding of metal ions to CB-9 provided some insight into the metal ion induced conformational changes.[22,23] The replacement of Ca^{2+} with Yb^{3+} to induce paramagnetic shifts for ^1H resonances from residues in the vicinity of the ion-binding sites enabled Sykes and co-workers to infer very minor differences in the structure of different PVs.[24,25] Substitution of Gd^{3+} for Ca^{2+} can provide distance information based on the paramagnetic relaxation line broadening of protein ^1H resonances; this strategy was applied to a 13-residue synthetic peptide comprising site III of TnC in conjunction with comparisons with crystal structures.[26] Photo-CIDNP experiments have been employed in order to study the environment around individual residues in different forms of PV[27] and different states of CB-9.[23]

The next level of structure information, short of a full three-dimensional structure determination, is provided by studies that involve careful analyses of a large number of NMR parameters, in particular NOEs, enabling characterization of the secondary structure elements and the overall fold of the protein. In this fashion, the solution structure of Ca^{2+}-loaded PV has been described.[28] Comparative studies of CB-9 in several different states have been presented at this level of detail,[29–32] providing information on the structural and dynamical changes that occur upon binding of ions, and insights into the molecular basis for cooperative Ca^{2+} binding. The Edmonton groups have in a series of studies assessed the solution conformations of synthetic polypeptides comprising individual binding sites, as well as hetero- or homodimers of the C-terminal EF-hand domains of TnC.[33–35]

Three-dimensional solution structures have been reported for several CABPs, in some cases for both the Ca^{2+}-free and Ca^{2+}-bound states. A medium-resolution structure has been presented for native, porcine $(Ca^{2+})_2$–CB-9,[36] showing a very close similarity to the crystal structure of the bovine protein. High-resolution solution structures of three different states of bovine CB-9 [$(Ca^{2+})_2$, $(Cd^{2+})_1$, and apo] have been determined,[37–39] allowing comparisons with the crystal structure as well as between the different solution structures. These studies thus provide detailed information on the structural changes that occur upon ion binding. A remaining problem with NMR-derived structures of EF-hand proteins is that the loop regions—which may be of central interest to the researcher—are among the least well defined parts of the protein because of their exposed location in the structure and consequent lower number of NOE contacts with the rest of the protein. However, the attainable precision of the ion-binding loops is high enough that the differences between the loop conformations of standard and pseudo-EF-hands can readily be distinguished, as further demonstrated for the solution structures of two CB-9 mutants with modified calcium-binding sites.[40] It is possible that future structural studies that utilize heteronuclear coupling constants to a larger extent may alleviate this inherent problem, and improve the definition of the loop structures; alternatively, constraints between the calcium ions and the protein that have been inferred from crystal structures can be included in the calculations. The latter strategy was used in the structure determination of a homodimer of the fourth EF-hand domain of TnC,[41] yielding rather well defined ion-binding loops. Three-dimensional structures have also been calculated for the homodimers of synthetic EF-hands comprising site III in TnC.[42] Other EF-hand proteins for which high-resolution NMR structures will soon appear include recoverin, which is a Ca^{2+} sensor in vision,[43] and calcineurin B, which has four EF-hands and is highly homologous to CaM,[44] and a fragment comprising the two N-terminal EF-hands in CB-28.[45]

The interactions between regulatory CABPs and their targets is a subject of much interest. The NMR-derived structure of a CaM–peptide complex is discussed in the ***Calmodulin*** article. An application of transferred NOEs enabled the structure determination of a synthetic inhibitory peptide from troponin I (TnI) complexed to skeletal muscle TnC, showing that the peptide binds to a hydrophobic surface on TnC that becomes exposed upon binding of calcium.[46]

Turning to CABPs outside of the EF-hand family, high-resolution structural studies have been described for the EGF-like domains of coagulation factor IX in the Ca^{2+}-free state[47] and factor X in both the Ca^{2+}-free and Ca^{2+}-loaded states.[48,49] Direct structural identification of the Ca^{2+} site was thus achieved for the EGF-like domain of factor X. In distinct contrast to the EF-hand proteins, here the Ca^{2+} site is located in a cleft between structural elements (a two-stranded β-sheet and the extended N-terminal segment of the domain) that have a large number of NOE contacts, resulting in a quite well-defined calcium-binding site in these solution structures (see Figure 1).[49] Another interesting structural study is that of the acyl carrier protein—a small protein with two sites, each capable of binding Mg^{2+} or Ca^{2+}. In this case the solution structure was first determined in the presence of Ca^{2+} ions using ^1H NMR.[50] The location of the divalent cation sites was then determined using relaxation perturbed 2D NMR spectroscopy on a protein with the paramagnetic Mn^{2+} ion as a substitute for Ca^{2+}, an experiment that yields ion–proton distances in the range 3.0–9.0 Å.[51] The solution structure of NASE (149 residues) has been determined in the presence of Ca^{2+} and an inhibitor using ^1H, ^{13}C, and ^{15}N NMR,[52] and structural consequences of Ca^{2+} and inhibitor binding were inferred from chemical shift comparisons between the bound and free forms of the protein.[53] The solution structure of a 173 residue CABP of the soil bacterium *M. xanthus*, named protein S, has recently been solved using multidimensional

Figure 1 Stereo drawing of the calcium-binding site of the N-terminal EGF module in factor X, as determined by ^{1}H NMR. Side chains that are unambiguously identified as calcium ligands are shown in gold with the calcium coordinating oxygens in red, and a potential ligand is drawn in pale green with the oxygens in brown. Reprinted from Selander-Sunnerhagen et al. with permission of the American Society for Biochemistry and Molecular Biology, Inc.

heteronuclear MR spectroscopy on a ^{13}C- and ^{15}N-labeled sample.[54,55] A recent low-resolution structure of a 32 residue fragment from annexin I bound to micelles[56] shows promise for further studies of membrane-bound CABPs.

3 DYNAMIC PROPERTIES OF CABPs

A large body of work shows a marked difference in thermodynamic stability between the calcium-saturated and calcium-free forms of CABPs.[57,58] An interpretation of this could be that in the presence of Ca^{2+} the protein largely prefers one conformation, while in the absence of Ca^{2+} the protein samples a larger volume of the conformational space. NMR spectroscopy has been used to address these questions by studying the dynamical properties of CABPs. Two principal techniques have been used covering the motional timescales of ps–ns (heteronuclear relaxation measurements) and ms and longer (amide proton exchange studies), respectively. At the time of writing, CB-9 is the CABP for which the dynamics on these two timescales has been most extensively studied for several different ion ligation states. In addition, other parameters such as aromatic ring flip rates[30] and chemical shift differences between side chain methylene protons for calcium-ligating residues[59] have been reported to show that the apo form of this protein has a higher internal mobility than the calcium-loaded state. These studies will therefore be covered in some detail in the following.

Amide proton exchange rates have been measured for three forms of CB-9; apo, $(Cd^{2+})_1$, and $(Ca^{2+})_2$.[31,60,61] Both direct $^{1}H \rightarrow {}^{2}H$ exchange of slowly exchanging amide protons and indirect proton exchange via saturation transfer from water to rapidly exchanging amide protons were studied. The addition of Ca^{2+} or Cd^{2+} was found to retard the exchange of many amides over the whole protein indicating a reduction in the molecular flexibility. These marked changes in dynamical properties of CB-9 stand in stark contrast to the minute structural changes upon ligation of calcium. The hydrogen exchange rates also show that the reduction in flexibility is largest for the first binding step. This observation implies a larger positive contribution to the free energy of the system in binding of the first ion than the second, partly explaining the positive cooperativity observed in the binding of calcium ions to CB-9.[31] A remark is in place here. Positive cooperativity implies that the free energy change associated with binding a calcium ion to a site is more negative if the other site is already occupied. The free energy change is thus less negative, or more positive, if the other site is empty. Grzesiek and Bax have recently presented a rapid and sensitive 2D NMR approach for measuring exchange rates and NOEs with water for rapidly exchanging amide protons. They have applied their technique to calcineurin B for which they have found that, in analogy with CaM, the long α-helix is not rigid in solution.[62]

The first ^{15}N-relaxation study involving the majority of the backbone amide nitrogens was presented for NASE in the presence of Ca^{2+} and inhibitor.[63] This study involved measurements of ^{15}N spin–lattice (R_2) relaxation rates as well as $\{^{1}H\}$-^{15}N NOEs. These data were analyzed using a model-free formalism incorporating the overall rotational correlation time, a generalized order parameter (S^2), and an effective internal correlation time for each amide group. The NASE study suggests that there is no correlation between the rapid small amplitude motions and location of secondary structure elements in this enzyme. Inconsistency in the analysis of some of the NASE data led to the development of an extended model-free formalism in which two distinct internal motions are incorporated.[64] Carbon-13, R_1, R_2 and $\{^{1}H\}$-^{13}C NOEs have been measured for leucine methyl groups in NASE using a labeled preparation of the protein. In these studies significant changes in the R values were observed for methyl groups close to the ligand-binding site upon addition of inhibitor.[65] Nitrogen-15 relaxation rate measurements have also been made for three states of CB-9: apo, $(Cd^{2+})_1$, and $(Ca^{2+})_2$.[66,67] In the $(Cd^{2+})_1$ and $(Ca^{2+})_2$ states the helices and calcium-binding loops have very similar order parameters ($S^2 \simeq 0.8$) indicating similar amplitudes of motion. However, the linker region joining the two EF-hands shows a substantially higher flexibility in all three forms of the protein. This study identifies the origin of the low structural definition in this linker region as structural disorder while the reason for the structural uncertainty in the calcium-binding loops of the ion-loaded states is a byproduct of methodological shortcomings rather than a dynamical phenomenon,[66] (see Figure 2). It was also found that the two binding loops respond differently to metal-ion ligation. The N-terminal ion-binding loop (the pseudo EF-hand) does not change its high frequency (10^{9}–10^{12} s^{-1}) fluctuations upon ligation, while residues G57–E60 in the C-terminal binding loop have significantly lower order parameters in the apo state than in the metal-bound states.[67] These results show that dynamical processes on the ps–ns timescale also contribute entropically to the cooperative phenomenon of calcium-binding for the pathway in which the first ion binds to the C-terminal site.

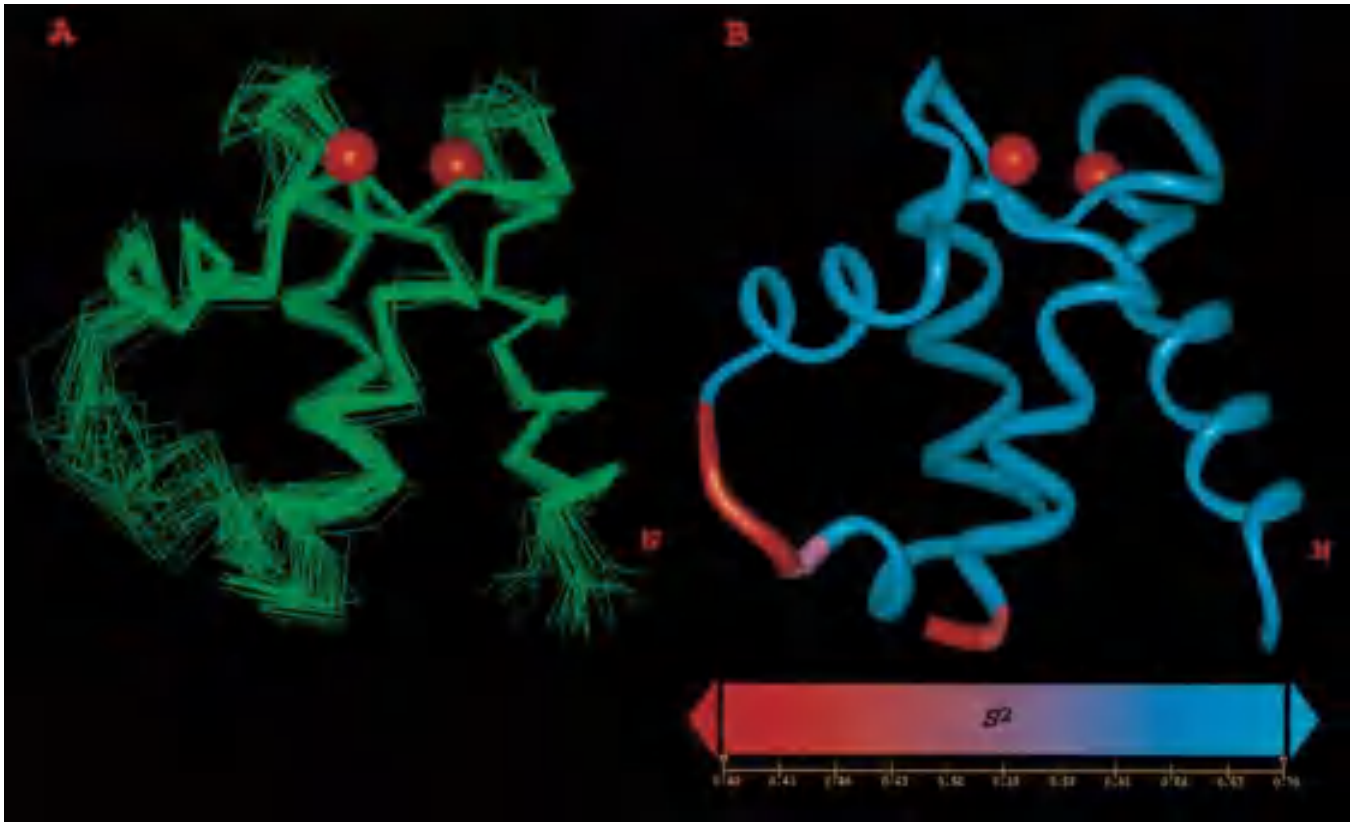

Figure 2 (Opposite) Comparison of structural definition (a) and dynamical properties on the ps–ns timescale (b) for calcium-loaded CB-9 in solution.[66] In (a) the α-carbon trace is shown for 33 structures that are overlayed using backbone atoms. The termini, calcium-binding loop regions, and linker region show structural dispersion. In (b) the ^{15}N order parameter, S^2, has been mapped in color onto the average structure. Red represents flexible regions and blue represents more rigid regions. Only the linker region and the C-terminus show enhanced flexibility on the ps–ns timescale

Of considerable interest also are the studies of amide proton exchange and ^{15}N NMR relaxation in CaM as well as CaM complexed with peptides from the CaM binding site on the myosin light chain kinase as covered in the article by Ikura (***Calmodulin***).

4 CHEMICAL EXCHANGE RATES AND METAL ION BINDING CONSTANTS

Chemical exchange rates and Ca^{2+}-binding constants can be determined by NMR in a straightforward manner when their values fall in certain ranges. Calcium ion dissociation rates can be deduced from lineshape analysis as a function of temperature or amount of added metal ion. The accessible range normally covers from 50 to 10^4 s^{-1}. Measurements of equilibrium binding constants can be achieved by stepwise additions of metal ion to the apo protein followed by recording the NMR spectra at each step. The range of binding constants that can be covered is given by the protein concentrations that are possible to use, since both the bound and free ion have to constitute a distinguishable fraction of the total ion concentration, at least at some points in the titration. Protein concentrations above 1–10 mM often cause aggregation, whereas the signal-to-noise ratio of the NMR spectrum might be unreasonably low at concentrations below 30–100 μM, even for proton NMR. The binding constant range that can be covered with NMR therefore seldom exceeds $1–10^6$ M^{-1}.

The assessment of the binding constant involves computer fitting to a spectral parameter as a function of total ion concentration. The spectral parameter of choice is one that can be obtained with good precision throughout the titration and is significantly different in the apo and metal ion bound states. In the case of slow exchange, one usually follows the intensity of a signal that either increases or decreases throughout the titration, whereas in the case of fast exchange it is common to follow the chemical shift of a resonance which is shifted as a consequence of ion binding. When metal ion NMR is used, the parameter of choice is often the signal linewidth which, in the case of fast exchange, decreases during the course of titration. The observed value of the spectral parameter, X, at each titration step, is given by

$$X = (p \cdot X_{\mathrm{Ca}} + [1 - p] \cdot X_{\mathrm{apo}}) \cdot F \qquad (1)$$

where X_{Ca} and X_{apo} are the parameter values in the calcium-bound and -free states, respectively, and p is the fraction of protein that has bound calcium. The quantity p is given by the total calcium concentration, total protein concentration, and the equilibrium binding (association) constant K_{a}. When the observed parameter is affected by dilution as a consequence of ion additions (as for signal intensities), F is the initial volume divided by the volume at the particular titration step. Otherwise

(as for chemical shifts and linewidths), $F = 1$ throughout the titration.

Excellent examples of this kind of treatment are given in studies of calcium binding to the EGF-like domain in the blood clotting factor X,[68] peptide analogs of EF-hand calcium-binding sites,[69,70] PPASE,[71] as well as to CB-9 mutants in which the affinity for one of the two sites is markedly reduced.[72] In those cases where the protein contains additional sites with affinities within two orders of magnitude from that of the site of interest, the accuracy of the deduced binding constant is much increased if the additional site(s) are taken into account.[73,74] A large number of NMR studies have been devoted to determination of Ca^{2+} affinities of CABPs and the references cited herein constitute just a subset.

In cases where many sites have similar affinities, NMR studies offer the unique possibility of distinguishing ion binding at separate sites and thus provide a measure of the relative affinities of those sites, even in those cases where the absolute affinities are too high to be measured by NMR. Such approaches have been used to study cation exchange at separate sites in PV[75] and oncomodulin.[76] Combined data from Ca^{2+} titrations monitored by ^1H NMR and competition with a chromophoric chelator have made it possible to assess quantitatively the free energy of interaction between binding events at the two sites in CB-9 wild-type as well as charge-substitution mutants.[77] Calcium ion titrations as followed by ^1H NMR are also very useful in assessing which sites are affected by certain mutations, as in CaM.[78] The calcium-binding process of CaM has in fact been more extensively studied than that of any other protein, although, or maybe because, the presence of as many as four calcium sites precludes straightforward extraction of conclusive results. A breakthrough in the studies of CaM has been the use of tryptic fragments, which comprise the two globular (two-site) domains. Comparable experiments on both these fragments and intact CaM has made it possible to identify which domain contains the strong and weak calcium sites, respectively,[79] and to assign Ca^{2+} off-rates to separate sites.[80] Similar studies on the structurally homologous protein TnC also include the effect of added Mg^{2+} on Ca^{2+}-exchange rates.[81] A more complete picture of Ca^{2+}-binding studies of CaM is given by Ikura (***Calmodulin***).

5 DIRECT OBSERVATION OF $^{43}Ca^{2+}$ SIGNALS FROM Ca^{2+} BOUND TO CABPs

An alternative way of using NMR in the study of the interactions between a protein and a metal ion is to observe directly the NMR resonance(s) for an NMR-active isotope of the metal ion and how the binding to the protein will perturb different NMR parameters. The only naturally occurring calcium isotope amenable for NMR studies is ^{43}Ca ($I = \frac{7}{2}$; $eQ = -0.05 \times 10^{-28}\,m^2$). Its natural abundance is only 0.145% and it has a magnetogyric ratio such that the NMR frequency is 33.5 MHz at $B_0 = 11.7$ T. Most, if not all, biological applications of ^{43}Ca NMR have been made with isotope-enriched samples—usually 40–60%. Although ^{43}Ca is a quadrupolar nucleus, its quadrupolar moment is relatively small and under conditions such that the effective electric field gradient at the nucleus is modest, its relaxation rate is low. In dilute aqueous solutions of calcium salts it is of the order of $1\,s^{-1}$,[82] while in binding sites of near octahedral symmetry in moderately large proteins the transverse relaxation rate is observed to be of the order of 10^3–$10^4\ s^{-1}$ (cf. further below). While in the case of rapid isotropic motion, the transverse and longitudinal relaxation rates of a spin $I = \frac{7}{2}$ nucleus are equal and follow a single exponential, the situation becomes more complex in the case of slow isotropic motion—a situation that might prevail in a protein-binding site. Here the relaxation is no longer exponential, but the weighted sum of four exponentials. In addition, the NMR signals may be affected by a phenomenon called second-order dynamic frequency shifts. Thanks to efforts by Bull, Halle, Hubbard, Wennerström, Werbelow, Westlund, and others the theoretical framework, and its practical implications in biological applications, is now well advanced.[83–88] For a comprehensive outline, see Forsén et al.[89]

Early applications of ^{43}Ca NMR to the study of CABPs were concerned with systems in which the Ca^{2+} ions were in stoichiometric excess and in fast chemical exchange between 'free' and protein-bound states. Through the combined use of isotope-enriched samples, high magnetic fields, specially designed probes and FT NMR using pulse sequences intended to minimize probe ringing at low NMR frequencies, around 1980 it also became possible to observe ^{43}Ca NMR signals from ions firmly bound to millimolar concentrations of CABPs.[90,91] The signal-to-noise ratio was sufficiently high to permit measurements of the longitudinal relaxation rates ($R_1 \simeq 10^3\ s^{-1}$). But more important was the fact that the temperature dependence of the ^{43}Ca NMR lineshape in many systems was quite considerable and allowed rather precise determinations of chemical exchange rates of the Ca^{2+} ions under equilibrium conditions.[92] The chemical shift of $^{43}Ca^{2+}$ ions bound to EF-hand sites is found to be about 10 ppm to high-frequency of the shift of 'free' Ca^{2+} ions, meaning that the NMR signal from Ca^{2+} ions in stoichiometric excess will show up as a separate, usually very narrow, resonance. In non-EF-hand proteins the free and bound signals may overlap, but it has been found that anionic lanthanide shift reagents, e.g. $Dy(PPP)_2$,[7] may displace the free signal away from the position of the bound ion(s).[93]

In summary, ^{43}Ca NMR can be profitably used in the study of CABPs to obtain information about binding constants in the range 1–$10^4\,M^{-1}$, rates of exchange of Ca^{2+} ions in the range $k_{off} \simeq 10$–$5000\,s^{-1}$, pK_a values of groups responsible for Ca^{2+} binding, and the competition of other cations or small molecules for the Ca^{2+} site(s) or the influence of these on dynamic parameters. An overview of the methodology and performed studies was recently given.[94] The ^{43}Ca NMR spectra in Figure 3 are taken from a publication which describes the combined use of ^{43}Ca NMR, ^{113}Cd NMR (cf. below), and stopped flow to assess structural and dynamic properties of the calcium-binding site in bovine serine proteases and their zymogens.[11]

6 ^{111}Cd, ^{113}Cd, AND OTHER SUBSTITUTION PROBES

Cadmium has two isotopes that are amendable to NMR studies—^{111}Cd and ^{113}Cd, of which the latter has been

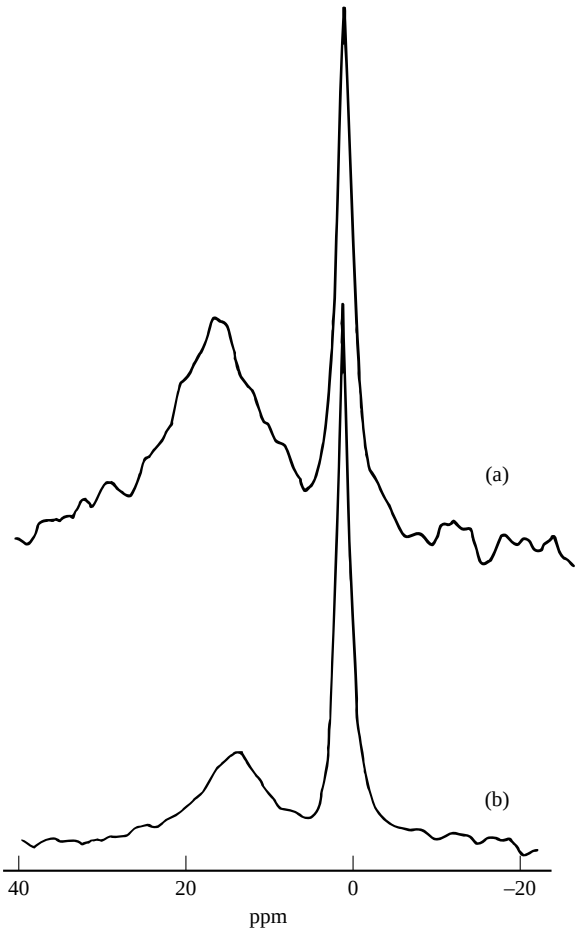

Figure 3 ^{43}Ca NMR spectra at 24.34 MHz of (a) 2 mM tosyltrypsin and 2.5 mM $^{43}Ca^{2+}$ and (b) 1 mM tosyltrypsinogen and 1.3 mM $^{43}Ca^{2+}$. In both spectra the sharp signal at 0 ppm corresponds to free $^{43}Ca^{2+}$ ions and the broad signal to protein-bound $^{43}Ca^{2+}$. A 30 Hz line-broadening function was used to enhance the signal to noise ratio. Redrawn after Chiancone et al.[11] with permission of Academic Press Inc. (London) Ltd

extensively used as a Ca^{2+}-substitution probe in NMR investigations of CABPs. (See ***Cadmium-113 NMR: A Surrogate Probe for Zinc and Calcium in Proteins***.) Since both ^{111}Cd and ^{113}Cd are a spin-$\frac{1}{2}$ nuclei, they give much sharper NMR resonances than the quadrupolar ^{43}Ca nucleus. The chemical shift range for $^{113}Cd^{2+}$ bound to proteins covers about 1000 ppm and the chemical shift is highly sensitive to the number, nature, and disposition of the metal-coordinating ligands. In addition, the ionic radius of Cd^{2+} is similar to that of Ca^{2+}, and the site preferences are often the same for the two ions. An exception to this rule is CB-9 in which the two sites bind calcium with similar affinity, whereas cadmium is bound first at the C-terminal site.[95] Therefore, ^{113}Cd NMR provides a parameter indicative of the extent of site–site interaction; the chemical shift displacement of the $^{113}Cd^{2+}$ ion bound to the C-terminal site as a consequence of cadmium entering the N-terminal site.[95] Mutational studies have shown that there is a high correlation between the value of the chemical shift displacement and the free energy of interaction between the sites.[77,96] For this particular protein, ^{113}Cd NMR has been extensively used in the assessment of structural perturbations caused by mutations in and around the calcium sites.[97,98] Studies of this and several other EF-hand proteins, e.g. CaM,[99] skeletal[81,100] and cardiac[101] muscle TnC, as well as PV,[102,103] show that the chemical shifts of $^{113}Cd^{2+}$ ions bound to normal EF-hand sites fall in a rather narrow range (−85 to −115 ppm), in contrast to $^{113}Cd^{2+}$ bound to the pseudo-EF-hand in CB-9 which resonates at −155 ppm. Cadmium-113 NMR has been used also in the study of the interaction of CaM with hydrophobic drugs[79,105] and amphiphatic peptides.[106] The latter study showed that both globular domains of CaM participate in peptide binding, in agreement with ^{1}H NMR studies and structure determination (see ***Calmodulin***).

Overviews of ^{113}Cd NMR studies of CABPs are given in two recent reviews of metal-ion NMR.[89,106] Another substitution probe for Ca^{2+} is yttrium, which has 100% natural abundance as the NMR-active isotope ^{89}Y. Yttrium −89 NMR studies of Y^{3+} ions bound to the two calcium sites in PV have been reported.[107]

7 STUDIES OF ^{25}Mg, ^{23}Na, AND ^{39}K INTERACTING WITH CABPs

The biological environment of CABPs often contains high levels of Mg^{2+}, Na^{+}, and/or K^{+}. The interaction of these metal ions with CABPs, as well as their influence on the calcium binding process, is therefore of considerable importance. The quadrupolar isotopes ^{25}Mg, ^{23}Na, and ^{39}K can be observed directly by NMR, and the spectral properties and analysis are analogous to that of ^{43}Ca (cf. above and Forsén et al.). Tsai et al. used ^{25}Mg NMR in a thorough analysis of the Mg^{2+}-binding properties of the four EF-hand sites in CaM, and provide a comprehensive outline of the methodology.[108] Magnesium-25 NMR has also been used to assess the Mg^{2+}-binding properties of many other CABPs, for example prothrombin fragment 1,[109] PV,[110] and β-casein.[111] The Na^{+}-binding properties of TnC and its tryptic fragments, in relation to calcium binding, have been studied by ^{23}Na NMR.[112] Combination of ^{39}K NMR, for determining the K^{+} affinity for CB-9, and 2D ^{1}H NMR to assess chemical shift perturbations caused by K^{+} binding, has shown that K^{+} associates weakly on the surface of this protein without causing structural changes.[77]

8 RELATED ARTICLES

Biological Macromolecules: Structure Determination in Solution; Biological Macromolecules: NMR Parameters; Biological Systems: Spin-3/2 Nuclei; Calmodulin; Protein Dynamics from NMR Relaxation; Cadmium-113 NMR: A Surrogate Probe for Zinc and Calcium in Proteins; Relaxation Theory for Quadrupolar Nuclei; Structures of Larger Proteins, Protein-Ligand, and Protein-DNA Complexes by Multi-Dimensional Heteronuclear NMR

9 REFERENCES

1. S. Nakayama and R. H. Kretsinger, *J. Mol. Evol.*, 1993, **36**, 458.
2. S. Forsén and J. Kördel, in I. Bertini, H. B. Gray, S. Lippard and J. Valentine, eds, *Bioorganic Chemistry*, University Science Books, Mill Valley, CA, 1993, Chap. 3
3. R. H. Kretsinger and C. W. Nockolds, *J. Biol. Chem.*, 1973, **248**, 3313.
4. S. Nakayama, N. D. Moncrief, and R. H. Kretsinger, *J. Mol. Evol.*, 1992, **34**, 416.
5. C. W. Heizmann, *Gener. Physiol. Biophys.*, 1992, **11**, 411.
6. D. C. Hilt and D. Kligman, in C. W. Herzmann, ed., *Novel Calcium Binding Proteins. Fundamentals and Clinical Implications*, Springer, Heidelberg, 1991, pp. 65–103.
7. K. G. Baimbridge, M. R. Celio, and J. H. Rogers, *Trends Neurosci.*, 1992, **15**, 303.
8. C. Andressen, I. Blümcke, and M. R. Celio, *Cell Tissue Res.* 1993, **271**, 181.
9. S. E. Moss, *The Annexins, a Novel Class of Calcium Binding Proteins*, Portland Press, London, 1992.
10. R. E. Milner, K. S. Famulski, and M. Michalak, *Mol. Cell. Biochem.*, 1992, **112**, 1.
11. E. Chiancone, T. Drakenberg, O. Teleman, and S. Forsén, *J. Mol. Biol.*, 1985, **185**, 201.
12. W. Bode and P. Schwager, *J. Mol. Biol.*, 1975, **98**, 693.
13. B. W. Dijkstra, R. Renetseder, K. H. Kalk, W. G. J. Hol, and J. Drenth, *J. Mol. Biol.*, 1983, **168**, 163.
14. D. L. Scott, S. P. White, Z. Otwinowski, W. Yuan, M. H. Gelb, and P. B. Sigler, *Science* 1990, **250**, 1541.
15. E. W. Davie, K. Fujikawa, and W. Kisiel, *Biochemistry*, 1991, **30**, 10363.
16. *Connect. Tissue Res.*, 1991, **21** (the whole volume is dedicated to bone biochemistry).
17. P. G. Robey, *Endocrinol. Metab. Clin. N. Am.*, 1991, **18**, 859.
18. M. R. Knight, A. K. Campbell, S. M. Smith, and A. J. Trewavas, *FEBS Lett.*, 1991, **282**, 405.
19. P. F. Leadley., G. Roberts, and J. E. Walker, *FEBS Lett.*, 1984, **178**, 157.
20. N. Bylsma, T. Drakenberg, I. Andersson, P. F. Leadley, and S. Forsén, *FEBS Lett.*, 1992, **299**, 44.
21. N. K. Vyas, M. N. Vyas, and F. A. Quiocho, *Science*, 1988, **242**, 1290.
22. D. C. Dalgarno, B. A. Levine, R. J. P. Williams, C. S. Fullmer, and R. H. Wasserman, *Eur. J. Biochem.*, 1983, **137**, 523.
23. J. G. Schelling, B. D. Sykes, J. D. J. O'Neil, and T. Hofmann, *Biochemistry*, 1983, **22**, 2649.
24. L. Lee and B. D. Sykes, *Biochemistry*, 1983, **22**, 4366.
25. L. Lee, D. C. Corson, and B. D. Sykes, *Biophys. J.*, 1985, **47**, 139.
26. J. Gariepy, L. E. Kay, I. D. Kuntz, B. D. Sykes, and R. S. Hodges, *Biochemistry* 1985, **24**, 544.
27. T. C. Williams, D. C. Corson, W. D. McCubbin, F. Oikawa, C. M. Kay, and B. D. Sykes, *Biochemistry*, 1986, **25**, 1826.
28. A. Padilla, A. Cavé, and J. Parello, *J. Mol. Biol.*, 1988, **204**, 995.
29. J. Kördel, S. Forsén, and W. J. Chazin, *Biochemistry* 1989, **28**, 7065.
30. N. J. Skelton, J. Kördel, S. Forsén, and W. J. Chazin, *J. Mol. Biol.*, 1990, **213**, 593.
31. M. Akke, S. Forsén, and W. J. Chazin, *J. Mol. Biol.*, 1991, **220**, 173.
32. G. Carlström and W. J. Chazin, *J. Mol. Biol.*, 1993, **231**, 415.
33. B. J. Marsden, R. S. Hodges, and B. D. Sykes, *Biochemistry*, 1989, **28**, 8839.
34. G. S. Shaw, R. S. Hodges, and B. D. Sykes, *Science*, 1990, **249**, 280.
35. G. S. Shaw, W. A. Findlay, P. D. Semchuk, R. S. Hodges, and B. D. Sykes, *J. Am. Chem. Soc.*, 1992, **114**, 6258.
36. M. Akke, T. Drakenberg, and W. J. Chazin, *Biochemistry*, 1992, **31**, 1011.
37. J. Kördel, N. J. Skelton, M. Akke, and W. J. Chazin, *J. Mol. Biol.*, 1993, **231**, 711.
38. M. Akke, S. Forsén, and W. J. Chazin, unpublished.
39. N. J. Skelton, J. Kördel, M. Akke, S. Forsén, and W. J. Chazin, 1994, *Nature Struct. Biol.*, 1994, **1**, 239.
40. C. Johansson, M. Ullner, and T. Drakenberg, *Biochemistry*, 1993, **32**, 8429.
41. L. E. Kay, J. D. Forman-Kay, W. D. McCubbin, and C. M. Kay, *Biochemistry*, 1991, **30**, 4323.
42. G. S. Shaw, R. S. Hodges, and B. D. Sykes, *Biochemistry*, 1992, **31**, 9572.
43. J. B. Ames, T. Parumb, T. Tandea, M. Ikura, and L. Stryer, *J. Biol. Chem.*, 1995, **270**, 4526.
44. J. Anglister, S. Grzesiek, A. C. Wang, H. Ren, C. B. Klee, and A. Bax, *Biochemistry*, 1993, **33**, 3540.
45. A. M. Labhardt, W. Klaus, S. Grzesiek, and W. Hunziker, *J. Cell. Biochem.*, 1993, **17 C**, 307a.
46. A. P. Campbell and B. D. Sykes, *J. Mol. Biol.*, 1991, **222**, 405.
47. M. Baron, D. G. Norman, T. S. Harvey, P. A. Handford, M. Mayhew, A.G.D. Tse, G. G. Brownlee, and I. D. Campbell, *Protein Sci.*, 1992, **1**, 81.
48. M. Ullner, M. Selander, E. Persson, J. Stenflo, T. Drakenberg, and O. Teleman, *Biochemistry*, 1992, **31**, 5974.
49. M. Selander-Sunnerhagen, M. Ullner, E. Persson, O. Teleman, J. Stenflo, and T. Drakenberg, *J. Biol. Chem.*, 1992, **267**, 19 642.
50. T. A. Holak, S. K. Kearsley, Y. Kim, and J. H. Prestegard, *Biochemistry*, 1988, **27**, 6135.
51. A. F. Frederick, L. E. Kay, and J. H. Prestegard, *FEBS Lett.*, 1988, **238**, 43.
52. D. A. Torchia, S. W. Sparks, and A. Bax, *Biochemistry*, 1989, **28**, 5509.
53. J. Wang, A. P. Hinck, S. N. Loh, D. M. LeMaster, and J. L. Markley, *Biochemistry*, 1992, **31**, 921.
54. S. Bagby, T. S. Harvey, S. G. Eagle, S. Inouye, and M. Ikura, *Structure*, 1994, **2**, 107.
55. S. Bagby, T. S. Harvey, S. G. Eagle, S. Inouye, and M. Ikura, *Proc. Natl. Acad. Sci. USA*, 1994, in press.
56. F. Macquire, F. Baleux, T. Huynh-Dinh, D. Roughe, J.-M. Neuman, and A. Sanson, *Biochemistry*, 1993, **32**, 7244.
57. H. Brzeska, S. V. Venyaminov, Z. Grabarek, and W. Drabikowski, *FEBS Lett.*, 1983, **153**, 169.
58. B. Wendt, T. Hofmann, S. R. Martin, P. Bayley, P. Brodin, T. Grundström, E. Thulin, S. Linse, and S. Forsén, *Eur. J. Biochem.*, 1988, **175**, 439.
59. J. Kördel, Ph.D. Thesis, Lund, Sweden, 1991.
60. S. Linse, O. Teleman, and T. Drakenberg, *Biochemistry*, 1990, **29**, 5925.
61. N. J. Skelton, J. Kördel, M. Akke, and W. J. Chazin, *J. Mol. Biol.*, 1992, **227**, 1100.
62. S. Grzesiek and A. Bax, *J. Biomol. NMR*, 1993, **3**, 627.
63. L. E. Kay, D. A. Torchia, and A. Bax, *Biochemistry*, 1989, **28**, 8972.

64. G. M. Clore, A. Szabo, A. Bax, L. E. Kay, P. C. Driscoll, and A. M. Gronenborn, *J. Am. Chem. Soc.*, 1990, **112**, 4989.
65. L. K. Nicholson, L. E. Kay, D. M. Baldisseri, and J. Arango, *Biochemistry*, 1992, **31**, 5253.
66. J. Kördel, N. J. Skelton, M. Akke, A. G. Palmer III, and W. J. Chazin, *Biochemistry*, 1992, **31**, 4856.
67. M. Akke, N. J. Skelton, J. Kördel, A. G. Palmer III, and W. J. Chazin, *Biochemistry*, 1993, **32**, 9832.
68. E. Persson, M. Selander. S. Linse, T. Drakenberg, A.-K. Öhlin, and J. Stenflo, *J. Biol. Chem.*, 1989, **264**, 16897.
69. G. S. Shaw, R. S. Hodges, and B. D. Sykes, *Biochemistry*, 1991, **30**, 8339.
70. G. S. Shaw, L. F. Golden, R. S. Hodges, and B. D. Sykes, *J. Am. Chem. Soc.*, 1991, **113**, 5557.
71. T. Andersson, T. Drakenberg, S. Forsén, T. Wieloch, and M. Lindström, *FEBS Lett.*, 1981, **123**, 115.
72. C. Johansson, P. Brodin, T. Grundström, E. Thulin, S. Forsén, and T. Drakenberg, *Eur. J. Biochem.* 1990, **187**, 455.
73. B. J. Marsden, R. S. Hodges, and B. D. Sykes, *Biochemistry*, 1988, **27**, 4198.
74. C. Valcarce, M. Selander-Sunnerhagen, A.-M. Taemlitz, T. Drakenberg, I. Björk, and J. Stenflo, *J. Biol. Chem.*, 1993, **268**, 26673.
75. Y. Blancuzzi, A. Padilla, J. Parello, and A. Cavé, *Biochemistry*, 1993, **32**, 1302.
76. T. C. Williams, D. C. Corson, B. D. Sykes, and J. P. MacManus, *J. Biol. Chem.*, 1987, **262**, 6248.
77. S. Linse, C. Johansson, P. Brodin, T. Grundström, T. Drakenberg, and S. Forsén, *Biochemistry*, 1991, **30**, 154.
78. M. A. Starovasnik, D.-R. Su, K. Beckingham, and R. E. Klevit, *Protein Sci.*, 1992, **1**, 245.
79. E. Thulin, A. Andersson, T. Drakenberg, S. Forsén, and H. J. Vogel, *Biochemistry*, 1984, **23**, 1862.
80. A. Teleman, T. Drakenberg, and S. Forsén, *Biochim. Biophys. Acta.*, 1986, **873**, 204.
81. T. Drakenberg, S. Forsén, E. Thulin, and H. J. Vogel, *J. Biol. Chem.*, 1987, **262**, 672.
82. S. Forsén and B. Lindman, *Methods Biochem. Anal.*, 1981, **27**, 289.
83. P. S. Hubbard, *J. Magn. Reson.*, 1970, **53**, 985.
84. T. E. Bull, *J. Magn. Reson.*, 1972, **8**, 344.
85. L. G. Werbelow and A. G. Marshall, *J. Magn. Reson.*, 1981, **43**, 443.
86. B. Halle and H. Wennerström, *J. Magn. Reson.*, 1981, **44**, 89.
87. L. G. Werbelow and G. Pouzard, *J. Phys. Chem.*, 1981, **85**, 3887.
88. P. O. Westlund and H. Wennerström, *J. Magn. Reson.*, 1982, **50**, 451.
89. S. Forsén, T. Drakenberg, and H. Wennerström, *Q. Rev. Biophys.*, 1987, **19**, 83.
90. T. Andersson, T. Drakenberg, S. Forsén, E. Thulin and M. Swärd, *J. Am. Chem. Soc.*, 1982, **104**, 576.
91. S. Forsén, T. Andersson, T. Drakenberg, E. Thulin, and M. Svärd, *Fed. Proc., Fed. Am. Soc. Exp. Biol.*, 1982, **41**, 2981.
92. T. Drakenberg, S. Forsén, and H. Lilja, *J. Magn. Reson.*, 1983, **53**, 412.
93. H. J. Vogel, T. Andersson, W. Braulin, T. Drakenberg, and S. Forsén, *Biochem. Biophys. Res. Commun.*, 1984, **122**, 1350.
94. S. Forsén, C. Johansson, and S. Linse, *Methods Enymol.*, 1994, **227**, 107.
95. H. J. Vogel, T. Drakenberg, and S. Forsén, *Biochemistry*, 1985, **24**, 3870.
96. S. Linse, N. Bylsma, E. Thulin, S. Forsén, A. Svensson, I. Zaitseva, V. Zaitsev, and V. Marek, to be published.
97. P. Brodin, C. Johansson, S. Forsén, T. Drakenberg, and T. Grundström, *J. Biol. Chem.* 1990, **265**, 11125.
98. C. Johansson, P. Brodin, T. Grundström, S. Forsén, and T. Drakenberg, *Eur. J. Biochem.*, 1991, **202**, 1283.
99. A. Andersson, S. Forsén, E. Thulin, and J. J. Vogel, *Biochemistry*, 1983, **22**, 2309.
100. S. Forsén, E. Thulin, and H. Lilja, *FEBS Lett.*, 1979, **104**, 123.
101. O. Teleman, T. Drakenberg, S. Forsén, and E. Thulin, *Eur. J. Biochem.*, 1983, **134**, 453.
102. T. Drakenberg, B. Lindman, A. Cavé, and J. Parello, *FEBS Lett.*, 1978, **92**, 346.
103. C. Zhang and D. J. Nelson, *J. Alloys Compd.*, 1992, **180**, 349.
104. S. Forsén, E. Thulin, T. Drakenberg, J. Krebs, and K. Seamon, *FEBS Lett.*, 1980, **117**, 189.
105. S. Linse, T. Drakenberg, and S. Forsén, *FEBS Lett.*, 1986, **199**, 28.
106. C. Johansson and T. Drakenberg, *Annu. Rep. NMR Spectrosc.*, 1989, **22**, 1.
107. R. C. Holz and W. D. Horrocks, Jr., *J. Magn. Reson.*, 1990, **89**, 627.
108. M.-D. Tsai, T. Drakenberg, E. Thulin, and S. Forsén, *Biochemistry*, 1987, **26**, 3635.
109. H. C. Marsh, P. Robertson, Jr., M. E. Scott, K. A. Koehler, and R. G. Hiskey, *J. Biol. Chem.*, 1979, **254**, 10268.
110. A. Cave, J. Parello, T. Drakenberg, E. Thulin, and B. Lindman, *FEBS Lett.*, 1979, **100**, 148.
111. N. M. Wahlgren, P. Dejmek, and T. Drakenberg, *J. Dairy Res.*, 1993, **60**, 65.
112. A. Delville, J. Grandjean, P. Laszlo, C. Gerday, Z. Grabarek, and W. Drabikowski, *Eur. J. Biochem.*, 1980, **105**, 289.

Biographical Sketches

Sture Forsén. *b* 1932. M.S., 1956, Stockholm, Ph.D., 1962, Stockholm. Professor in Physical Chemistry, 1964–67, Stockholm; Professor in Physical Chemistry, Lund, 1966–present. Approx. 270 publications. Research interests include structure, dynamics, and function of proteins, and the role of calcium in biological systems.

Sara Linse. *b* 1962. M.S., 1985 Lund and Stanford, Ph.D., 1993, Lund. Introduced to NMR by S. Forsén. Approx. 30 publications. Research interests include protein biophysics, especially molecular basis of calcium binding affinity and cooperativity.

Mikael Akke. *b* 1961. M.S., 1987, Lund, Ph.D., 1993, Lund. Introduced to NMR by S. Forsén and W. J. Chazin. Approx. 15 publications. Research interests include structure and dynamics of macromolecules in relation to stability and function.

Johan Kördel. *b* 1962. M.S., 1986, Lund, Ph.D., 1991, Lund. Introduced to NMR by S. Forsén. Approx. 30 publications. Research interests include structural and dynamic properties of protein complexes.

Calmodulin

Mitsuhiko Ikura

University of Toronto, Canada

1	Introduction	1
2	Interactions with Metal Ions and Drugs	2
3	Calcium–Calmodulin Complex	4
4	Calcium–Calmodulin–Peptide Ternary Complexes	4
5	Related Articles	6
6	References	6

1 INTRODUCTION

Calmodulin (CaM) was discovered as an activator of cyclic nucleotide phosphodiesterase in brain by Cheung[1] and by Kakiuchi and Yamazaki[2] in 1970. Since then, it has became clear that CaM is a ubiquitous intracellular calcium receptor present in eukaryotic cells and that its structure has been highly conserved during evolution.[3] The amino acid and gene sequences of CaM from various species have been determined.[4–6] Figure 1 shows the amino acid sequence of bovine brain CaM.[4] The molecular weight of CaM is ca. 16 700. The amino terminal is acetylated and lysine-115 is trimethylated at the ϵ position. CaM consists of four repeated sequences of about 35 amino acid residues, each of which forms a helix–loop–helix Ca^{2+}-binding motif of the EF-hand type, first discovered in parvalbumin by Kretsinger and co-workers.[7] The biophysical properties of CaM have been extensively studied (for reviews, see Cohen and Klee[5]). CaM is an acidic (pI = 4.3) and heat stable protein which binds four Ca^{2+} ions. The four Ca^{2+}-binding motifs can be classified into the high affinity sites III and IV in the C-terminal region ($K_d \approx 10^{-6}$ M) and the low affinity sites I and II in the N-terminal region ($K_d \approx 10^{-5}$ M).[8]

A number of enzymes and proteins have been reported to date to be stimulated by CaM.[4] These include myosin light chain kinase (MLCK), CaM kinase II, phosphorylase kinase, calcineurin, myristoylated alanine-rich C kinase substrate (MARCKS), and many others (for reviews, see Cohen and Klee[5] and Crivici and Ikura[6]). Thus, CaM plays a role as a multifunctional activator or regulator in various Ca^{2+}-dependent cellular processes. CaM-binding regions in many target enzymes and proteins have been mapped. These regions are generally small (14–27 amino acid residues) and rich in basic and hydrophobic residues. Most of the CaM-binding sequences identified so far appear to have a propensity for helix formation. A number of naturally occurring peptides are also known to bind CaM in a Ca^{2+}-dependent manner.[9] These peptides include insect venom peptides such as mastoparans and melittin, and certain hormones and opioids such as ACTH, VIP, glucagon, and substance P. In addition, phenothiazines and other hydrophobic drugs including trifluroperazine (TFP), chlorpromazine, and W-7, bind CaM and inhibit the CaM-mediated activation of enzymes.[10] Proteolytic fragments and synthetic peptides comprising the CaM-binding regions of target proteins, as well as the insect and hormone peptides and the hydrophobic drugs, have been extensively used to study the structural and biochemical properties of the interaction of CaM with targets.

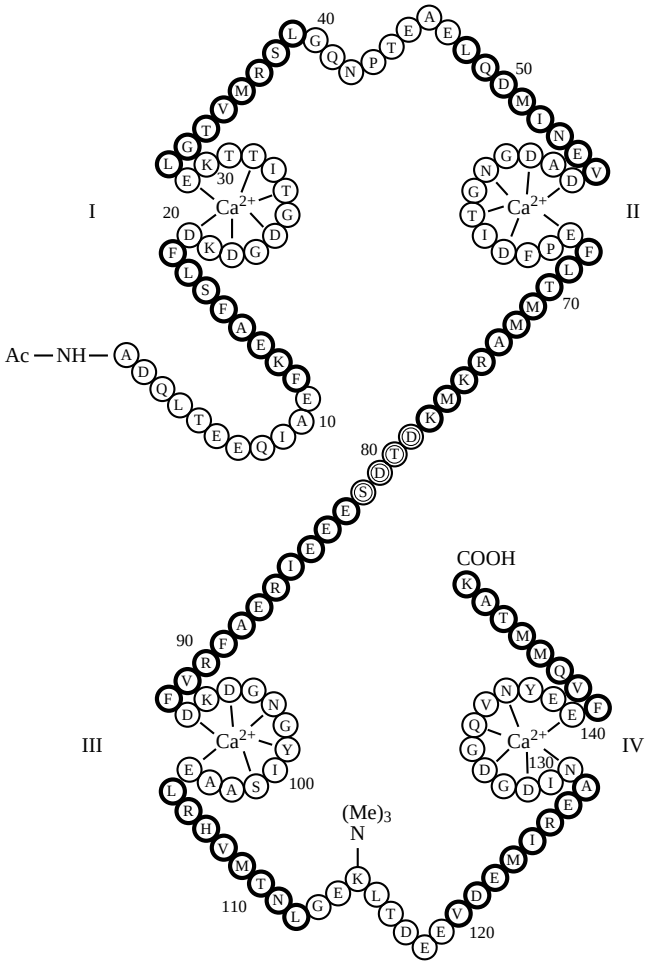

Figure 1 The amino acid sequence of bovine brain calmodulin[4] [Courtesy of C. B. Klee]

The crystal structures of Ca^{2+}-loaded CaM were reported by Babu et al.[11] in 1985 and by Kretsinger et al.[12] in 1986. The structures have an unusual dumbbell shape [Figure 2(a)] in which the N- and C-terminal globular domains are connected by a long α-helix. The length of the molecule is about 65 Å, with each lobe having approximate dimensions of 25 × 20 × 20 Å.[3] Each domain possesses a hydrophobic patch, which is considered to be responsible for target binding. Similar structural features were found in the crystal structure of a homologous Ca^{2+}-binding protein, skeletal muscle troponin C[13] (see ***Calcium-Binding Proteins*** and ***Muscle Proteins***). In 1992, an NMR structure of CaM complexed with a 26-residue CaM-binding peptide derived from skeletal muscle MLCK was determined[14] [Figure 2(b)]. Subsequently, a crystal structure of CaM complexed with a smooth muscle MLCK peptide was also solved at 2.4 Å. More recently, a crystal structure of CaM complexed with a CaM kinase II peptide has been reported.[16]

Detailed mechanisms by which CaM regulates the activity of target enzymes and proteins are still not yet fully understood even for a single case. Nevertheless, NMR spectroscopy has contributed tremendously to our understanding of the structural basis of the action of CaM in the context of interactions with

Ca^{2+}, and peptides and drugs. In the following discussion NMR studies on CaM reported during the period of 1979–93 will be summarized.

2 INTERACTIONS WITH METAL IONS AND DRUGS

The first 250- and 360-MHz ^{1}H NMR spectra of bovine brain CaM were reported by Seamon[17,18] in 1979 and 1980, who demonstrated that dramatic Ca^{2+}-dependent spectral changes could be monitored by ^{1}H NMR. Aromatic proton resonances of Tyr-99, His-107, and Tyr-138, and a unique trimethyl group of ϵ-trimethylated Lys-115 were identified. Klevit et al.[19] and Krebs and Carafoli[20] studied the interaction of bovine brain CaM with TFP using ^{1}H NMR. Shimizu et al.[21,22] used ^{19}F NMR to study the interactions of porcine brain and *Tetraphymena pyriformis* CaM with TFP. All these studies indicate that one CaM molecule binds two TFP molecules.

More detailed assignments for aromatic ring and methyl protons in scallop testis CaM were reported by Ikura et al.[23] in 1983. Using those resonance assignments, Ca^{2+}-induced conformational changes have been examined.[24] Figure 3 illustrates Ca^{2+}-induced changes in the aromatic region of the ^{1}H NMR spectra. The results show that many resonances C-terminal domain (Phe-99, His-107, trimethyl Lys-115, and Tyr-138) are shifted in an early stage of Ca^{2+} titration (0–2 mol Ca^{2+} per mol of CaM), thus concluding that the C-terminal domain contains the high affinity sites for Ca^{2+}. Forsén and co-workers independently reached the same conclusion from ^{43}Ca and ^{113}Cd NMR studies[25,26] using two tryptic fragments

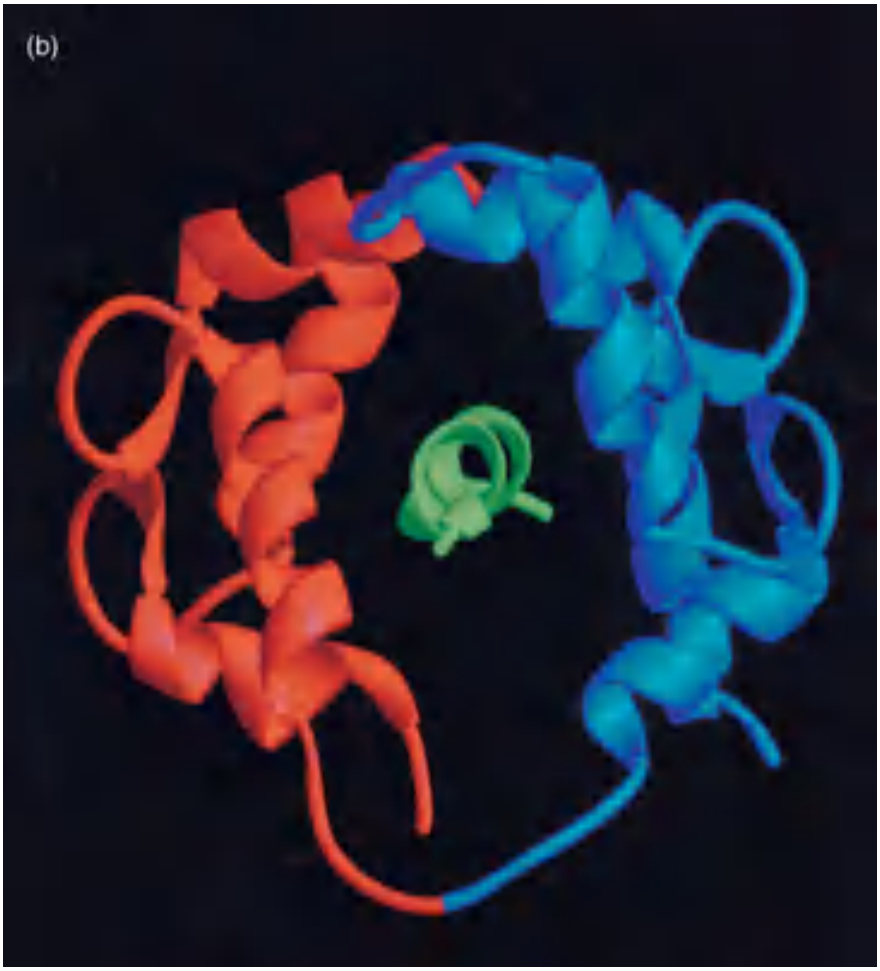

Figure 2 Ribbon diagram representations of (a) Ca^{2+}–CaM[11] and (b) the Ca^{2+}–CaM–M13 complex[14] as generated by the program ribbons. The CaM N-terminal domain is shown in blue and the C-terminal domain in red. In Figure 2(b), the structure is viewed parallel to the M13 peptide helix axis

of CaM (TR_1C, fragment 1–75; TR_2C, fragment 78–148). These half-fragments were found to be extremely useful for NMR studies of CaM. In 1984, ^1H NMR studies on the half-fragments were reported by three groups[27–30] almost at the same time. Two uniquely low-frequency shifted ring proton resonances at 6.46 and 6.50 ppm of apo-CaM were assigned to phenylalanines in the N-terminal domain. All these studies provided further evidence for the order of Ca^{2+} binding to four sites in CaM. Together with ^{43}Ca and ^{113}Cd NMR[25,26] and other biophysical studies,[4,5,8] it became clear that the two tryptic half-fragments retain the conformations which they assume in whole CaM. The property was shown for both the Ca^{2+}-free and Ca^{2+}-bound forms.

Because of the complexity of the ^1H NMR spectra of whole CaM, several groups used the tryptic half-fragments to elucidate the structural details of CaM. In 1984, Aulabaugh et al.[31] applied 2D ^1H NMR at 600 MHz to fragment TR_2C in the absence of Ca^{2+} and obtained assignments for many side-chain proton resonances to particular amino acid types. In 1985, Ikura et al.[32] applied 2D ^1H NMR techniques to the TR_2C fragment both in the presence and the absence of Ca^{2+}, and obtained about 30% backbone and side-chain proton assignments in each state using the sequential assignment procedure proposed by Wüthrich and co-workers (see ***Biological Macromolecules: Structure Determination in Solution*** and ***Structures of Larger Proteins, Protein-Ligand, and Protein-DNA Complexes by Multi-Dimensional Heteronuclear NMR***). Extremely high-frequency shifted amide proton resonances (10.0–11.0 ppm) were assigned to the glycine residues at the fifth position of the Ca^{2+}-binding loops. These uniquely shifted glycine amide resonances were further characterized using both TR_1C and TR_2C fragments.[33] Such large shifts of the amide protons of this conserved glycine residues in EF-hand Ca^{2+}-binding loops were also found in troponin C[34] and calbindin[35] (see ***Calcium-Binding Proteins***), suggesting that this feature is universal among the members of the EF-hand superfamily. Hoffman and Klevit[36] reported 2D ^1H NMR analysis of the Ca^{2+}-free TR_1C fragment in the absence of Ca^{2+}, indicating hydrophobic contacts between Phe-16 and Val-35 which are absent in the Ca^{2+}-bound form of the crystal structure.[11,12] More recently, Finn et al.[37] obtained the complete backbone ^1H resonance assignments of the Ca^{2+}-free TRC fragment, indicating that the Ca^{2+}-free state retains the helix–loop–helix secondary structure similar to that observed in the Ca^{2+}-bound form.[11,12,38]

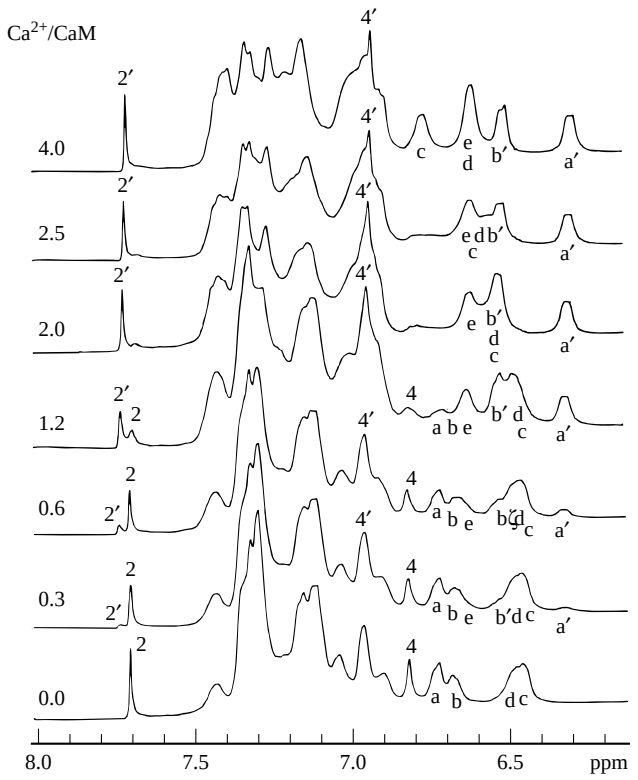

Figure 3 The aromatic region of the 400 MHz ^{1}H NMR spectra of scallop testis calmodulin at various Ca^{2+} concentrations. (Reproduced by permission of the American Chemical Society from Ikura et al.[24])

Several different NMR techniques were used to study the kinetics of Ca^{2+} binding to CaM and its fragments. Calcium-43 and ^{113}Cd NMR studies[25,26] indicate that the resonances from metal ions bound to sites III and IV show much slower exchange on the NMR timescale than those from metal ions bound to sites I and II. ^{1}H NMR saturation transfer and spectral simulation methods were employed to obtain the exchange rate constants and activation parameters between Ca^{2+}-free and Ca^{2+}-bound forms of two half-fragments.[39] Two distinct rate constants of $3-10\,s^{-1}$ and $300-500\,s^{-1}$ were found at 22 °C for the C-terminal and the N-terminal fragments, respectively. All these results confirm the identification of sites III and IV as being the high affinity sites.

Starovasnik et al[40] studied the Ca^{2+} binding and structural properties of CaM from the yeast *Saccharomyces cerevisiae* using flow dialysis and ^{1}H NMR. The amino acid sequence of yeast CaM is 60% identical to that of vertebrate CaM, whereas all known vertebrate CaM sequences are totally identical. The results indicate that, unlike vertebrate CaM, yeast CaM binds only three Ca^{2+} ions and that all three sites exhibit slow-exchange behavior upon Ca^{2+} binding. Thermal denaturation properties of yeast CaM as well as of its half-fragments were also studied. Starovasnik et al.[41] studied a series of four site-directed mutants using the same techniques, demonstrating interactions between the Ca^{2+}-binding sites in CaM.

Vogel and co-workers have extensively studied lysine residues in CaM using ^{1}H and ^{13}C NMR. The pK_a values of *N*-dimethylated lysine residues were obtained both in apo and Ca^{2+}-bound forms, as well as in a complex with a 22-residue peptide comprising the CaM-binding region of skeletal muscle MLCK.[42,43] Zhang et al.[44] applied ^{14}N NMR to ϵ-trimethyl Lys-115 in both vertebrate and yeast CaMs. The ϵ-trimethyl group of this posttranslated lysine gives rise to a sharp ^{14}N NMR resonance because of its unique tetrahedral symmetry. Selenium-77 NMR was used to study the microenvironments of the nine methionine residues in CaM, all of which were biosynthetically substituted with selenomethionine.[45]

3 CALCIUM–CALMODULIN COMPLEX

During the period 1989–93, CaM was extensively used by Bax's group at the NIH to develop multidimensional heteronuclear MR methods (see ***Multidimensional Spectroscopy: Concepts***, and ***Three- and Four-Dimensional Heteronuclear Magnetic Resonance***). This methodology requires isotope enrichment of proteins with ^{15}N and ^{13}C. Uniformly ^{15}N- and ^{13}C-labeled CaM was obtained using an *E. coli* expression system.[46] Figure 4 shows a ^{1}H–^{15}N heteronuclear single quantum coherence (HSQC) spectrum of Ca^{2+}-loaded recombinant CaM labeled uniformly with ^{15}N, illustrating that a high-quality ^{1}H–^{15}N shift correlation spectrum can be obtained at 1 mM protein concentration. Ikura et al.[38,47] reported complete backbone and side-chain ^{1}H, ^{13}C, and ^{15}N assignments of Ca^{2+}-loaded recombinant *Drosophila* CaM using a series of triple- and double-resonance 3D and 4D experiments. The secondary structure in solution was then characterized using NOE, $^3J_{NH\alpha}$ coupling constants, and ^{13}C chemical shift data.[38] These results confirm the crystal structure[11,12] in that both the N- and C-terminal globular domains assume a pair of the EF-hand type helix–loop–helix motifs. However, the central helix portion (residues 65–92), found in the crystal structure, appears to contain a nonhelical region at residues 78–81 in solution. Nitrogen-15 relaxation studies reported by Barbato et al.[48] further indicate that this nonhelical portion has considerable flexibility, consistent with other studies using solution techniques such as small angle X-ray or neutron scattering.[49] The ^{15}N relaxation studies[48] (see ***Protein Dynamics from NMR Relaxation***) provide additional interesting insights into the structure and dynamics of Ca^{2+}–CaM. The rotational correlation times obtained for the N- and C-terminal domain (7.1 ns and 6.3 ns, respectively) do not reflect the overall motion of a 16.7 kDa protein, but rather correspond to that of a smaller protein (ca. 12 kDa). Further, the correlation times for the individual amide bond vectors vary to a much lesser degree than predicted by hydrodynamic calculations for rigid dumbbell models. These results indicate that the two domains move independently in solution.

4 CALCIUM–CALMODULIN–PEPTIDE TERNARY COMPLEXES

In 1985, Klevit et al.[50] using ^{1}H NMR studied the interaction of CaM with a 26-residue synthetic peptide (known as M13) comprising the CaM-binding domain of skeletal muscle myosin light chain kinase. These data indicate that both the N- and C-terminal domains must participate in the interaction with the M13 peptide. The ^{113}Cd NMR studies of mastoparan binding to Cd_4CaM have shown that both the N- and C-terminal domains undergo conformational

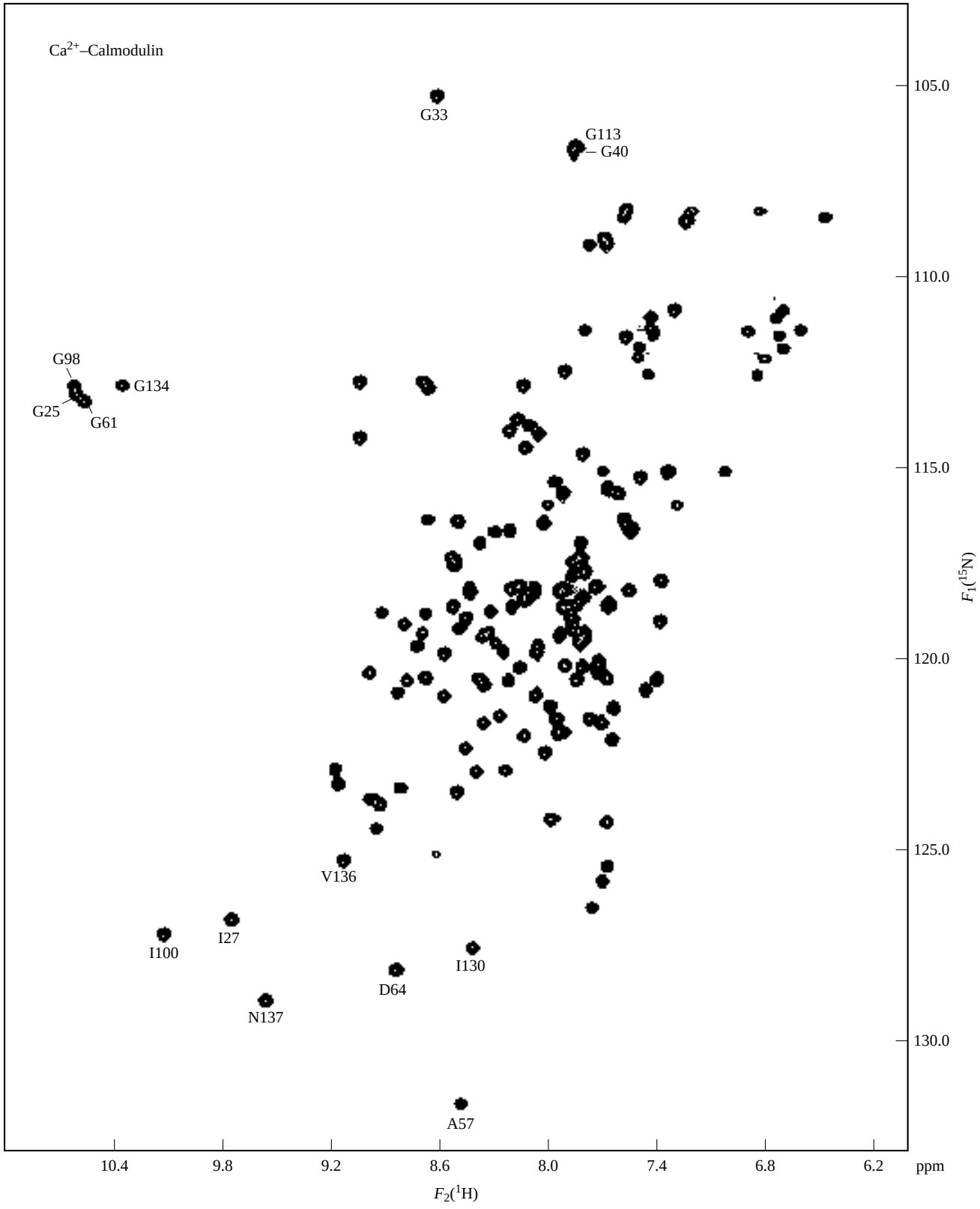

Figure 4 The 500 MHz $^{1}H-^{15}N$ HSQC shift correlation spectrum of *Xenopus laevis* calmodulin. The spectrum was recorded using a pulse sequence combined with the pulse field gradient technique described by Kay et al.[66] The full backbone amide assignment of *Xenopus* calmodulin is available from the author

changes upon binding of the peptide (see ***Calcium-Binding Proteins***). Seeholzer et al.[51] also used ^{1}H NMR to study the interaction of melittin with [^{1}H]- and [^{2}H]-CaM, suggesting that melittin assumes an α-helical conformation upon binding CaM, consistent with earlier conclusions based on circular dichroism spectra. Yazawa et al.,[52] using the ^{1}H NMR signal of His-107, showed that in the presence of M13 the Ca^{2+}-dependent conformational change becomes completely cooperative between the N- and C-terminal domains. Ikura et al.[53] studied the Cd^{2+} dependence of the interactions of CaM with M13 and mastoparan using ^{113}Cd NMR, supporting the notion of the higher cooperativity of metal binding in the presence of these peptides. Ohki et al.[54,55] studied the interaction of mastoparan with CaM under various solution conditions using ^{1}H NMR. It was shown that the N-terminal domain may interact with a second mastoparan molecule with a lower affinity, and that Mg^{2+} reduces the cooperative Ca^{2+} binding to CaM in the presence of mastoparan.

In 1991, Ikura et al.[56] completed ^{1}H, ^{13}C, and ^{15}N backbone assignments of Ca^{2+}–CaM complexed with M13 by using multidimensional heteronuclear MR methods. Proton assignments of M13 in the complex were also obtained using ^{15}N/^{13}C-filtered techniques[57] (see ***Half-Filter Experiments: Proton–Carbon-13***). Based on these assignments, the three-dimensional NMR structure of the Ca^{2+}–CaM–M13 ternary complex was determined.[14] Figure 2(b) shows a schematic ribbon model of the restrained minimized mean structure. A striking difference in conformation can be seen as compared with the crystal structure of Ca^{2+}–CaM[11] [Figure 2(a)]. The N- and C-terminal domains of CaM (residues 6–73 and 83–146) remain essentially unchanged upon complexation. The long central helix, (residues 65–93), however, which connects the two domains in the crystal structure of Ca^{2+}–CaM [Figure 4(a)], is disrupted into two helices connected by a long flexible loop (residues 74–82), thereby enabling the two domains to clamp residues 3–21 of the bound peptide which adopt a helical conformation. Key residues of the peptide are Trp-4 and Phe-17, which serve to anchor the N- and C-terminal halves of the peptide to the C- and N-terminal domains of CaM, respectively. This characteristic structure of Ca^{2+}–CaM complexed with the M13 peptide was confirmed by a crystallographic study on Ca^{2+}–CaM complexed with a similar peptide derived from smooth muscle MLCK.[15] Based on the knowledge of the structural features of these Ca^{2+}–CaM–peptide complexes, Prumb et al.[58] produced a hybrid CaM–peptide molecule and characterized the structural and Ca^{2+}-binding properties using ^{1}H–^{15}N HSQC and flow dialysis experiments.

Roth et al.[59,60] revealed the secondary structure of a 19-residue smooth muscle MLCK peptide and CaM in their complex using heteronuclear multidimensional NMR techniques. Most of the backbone amide nitrogen nuclei in the MLCK peptide were labeled with ^{15}N, which allowed the characterization of the α-helix structure of the peptide. Precheur et al.[61] also used a similar labeling technique on a 17-residue model peptide proposed by DeGrado et al.,[62] and showed a stable α-helical structure in the N-terminal 11 residues of the complex. Zhang et al.,[63,64] using 2D ^{1}H NMR, studied three synthetic CaM binding peptides which are derived from skeletal muscle MLCK, rat cerebellar nitric oxide synthase, and smooth muscle caldesmon. The MLCK[63] and caldesmon[64] peptides were found to assume an α-helical conformation in an aqueous trifluoroethanol mixture (75%/25%) The nitric oxide synthase peptide[66] also adopts an α-helical structure in aqueous solution at pH 5.5 and 5 °C.

In summary, CaM has provided an excellent example of the power of the high-resolution multinuclear magnetic resonance approach. Various NMR studies have provided valuable information on the structural and physical properties of CaM as a Ca^{2+}-sensitive molecular switch in cells. Yet, further studies have to come in order to elucidate secrets involved in multitarget recognition of this amazing molecule.

5 RELATED ARTICLES

Biological Macromolecules; Biological Macromolecules: NMR Parameters; Calcium-Binding Proteins; Half-Filter Experiments: Proton–Carbon-13; Multidimensional Spectroscopy: Concepts; Muscle Proteins; Protein Dynamics from NMR Relaxation; Structures of Larger Proteins, Protein-Ligand, and Protein-DNA Complexes by Multi-Dimensional Heteronuclear NMR; Three- and Four-Dimensional Heteronuclear Magnetic Resonance

6 REFERENCES

1. W. Y. Cheung, *Biochem. Biophys. Res. Commun.*, 1970, **38**, 533.
2. S. Kakiuchi and R. Yamazaki, *Biochem. Biophys. Res. Commun.*, 1970, **41**, 1104.
3. A. R. Means, J. S. Tash, and J. G. Chafouleas, *Physiol. Rev.*, 1982, **62**, 1.
4. D. M. Watterson, F. Sharief, and T. Vanaman, *J. Biol. Chem.*, 1980, **255**, 962.
5. P. Cohen and C. B. Klee (eds.), *Calmodulin*, Elsevier, Amsterdam, 1988.
6. A. Crivici and M. Ikura, *Annu. Rev. Biophys. Biomol. Struct.*, 1995, **24**, 85.
7. P. C. Moews and R. H. Kretsinger, *J. Mol. Biol.*, 1975, **91**, 201; *Cell Calcium*, 1992, **13**, 353.
8. O. Minowa and K. Yagi, *J. Biochem. (Tokyo)*, 1984, **96**, 1175.
9. S. R. Anderson and D. A. Malencik, in *Calcium and Cell Function*, Academic Press, New York, 1986, Vol. 6, pp. 1–42.
10. H. Hidaka, T. Yamaki, T. Totsuka, and M. Asano, *Mol. Pharmacol.*, 1979, **15**, 49.
11. Y. S. Babu, J. S. Sack, T. J. Greenhough, C. E. Bugg, A. R. Means, and W. J. Cook, *Nature (London)*, 1985, **315**, 37.
12. R. H. Kretsinger, S. E. Rudnick, and L. J. Weissman, *J. Inorg. Biochem.*, 1986, **28**, 289.
13. O. Herzberg and M. N. G. James, *Nature (London)*, 1985, **313**, 653.
14. M. Ikura, G. M. Clore, A. M. Gronenborn, G. Zhu, C. B. Klee, and A. Bax, *Science*, 1992, **256**, 632.
15. W. E. Meador, A. R. Means, and F. A. Quiocho, *Science*, 1992, **257**, 1251.
16. W. E. Meador, A. R. Means, and F. A. Quiocho, *Nature*, **262**, 1718.
17. K. B. Seamon, *Biochem. Biophys. Res. Commun.*, 1979, **86**, 1256.
18. K. B. Seamon, *Biochemistry*, 1980, **19**, 207.
19. R. E. Klevit, B. A. Levine, and R. J. P. Williams, *FEBS Lett.*, 1981, **123**, 25.
20. J. Krebs and E. Carafoli, *Eur. J. Biochem*, 1982, **124**, 619.

21. T. Shimizu and M Hatano, *FEBS Lett.*, 1983, **160**, 182.
22. T. Shimizu, M. Hatano, S. Nagao, and Y. Nozawa, *Biochem. Biophys. Res.* Commun., 1982, **106**, 1112.
23. M. Ikura, T. Hiraoki, K. Hikichi, T. Mikuni, M. Yazawa, and K. Yagi, *Biochemistry*, 1983, **22**, 2568.
24. M. Ikura, T. Hiraoki, K. Hikichi, T. Mikuni, M. Yazawa, and K. Yagi, *Biochemistry*, 1983, **22**, 2573.
25. S. Forsén A. Andersson, T. Drakenberg, O. Teleman, E. Thulin, and H. J. Vogel, *Calcium-Binding Proteins* Elsevier, Amsterdam, 1983, p.# 121.
26. A. Andersson, S. Forsén, E. Thulin, and H. J. Vogel, *Biochemistry*, 1983, **22**, 2309.
27. E. Thulin, A. Andersson, T. Drakenberg, S. Forsen, and H. J. Vogel, *Biochemistry*, 1984, **23**, 1862.
28. M. Ikura, T. Hiraoki, K. Hikichi, O. Minowa, H. Yamaguchi, M. Yazawa, and K. Yagi, *Biochemistry*, 1984, **23**, 3124.
29. D. C. Dalgarno, B. A. Levine, R. J. P. Williams, C. S. Fullmer, and R. H. Wasserman, *Eur. J. Biochem.*, 1983, **137**, 523.
30. R. E. Klevit, D. C. Dalgarno, B. A. Levine, and R. J. P. Williams, *Eur. J. Biochem.*, 1984, **139**, 109.
31. A. Aulabaugh, W. P. Niemczura, T. L. Blundell, and W. A. Gibbons, *Eur. J. Biochem.*, 1984, **143**, 409.
32. M. Ikura, O. Minowa, and K. Hikichi, *Biochemistry*, 1985, **24**, 4264.
33. M. Ikura, O. Minowa, M. Yazawa, K. Yagi, and K. Hikichi, *FEBS Lett.*, 1987, **219**, 17.
34. S. Tsuda, K. Ogura, Y. Hasegawa, K. Yagi, and K. Hikichi, *Biochemistry*, 1990, **29**, 4951.
35. J. Kördel, S. Forsén, T. Drakenberg, and W. J. Chazin, *Biochemistry*, 1990, **29**, 4400.
36. R. Hoffman and R. E. Klevit, in *Techniques in Protein Chemistry II*, Academic Press, New York, 1991, p. 383.
37. B. E. Finn, T. Drakenberg, and S. Forsén, *FEBS Lett.*, 1994, **336**, 368.
38. M. Ikura, S. Spera, G. Barbato, L. E. Kay, M. Krinks, and A. Bax, *Biochemistry*, 1991, **30**, 9216.
39. M. Ikura, *Biochem. Biophys. Acta*, 1986, **872**, 195.
40. M. A. Starovasnik, T. N. Davis, and R. E. Klevit, *Biochemistry*, 1993, **32**, 3261.
41. M. A. Starovasnik, D.-R. Su, K. Beckingham, and R. E. Klevit, *Protein Sci.*, 1992, **1**, 245.
42. M. E. Huque and H. J. Vogel, *J. Protein Chem.*, 1993, **12**, 693.
43. M. Zhang and H. J. Vogel, *J. Biol. Chem.*, 1993, **268**, 22420.
44. M. Zhang, M. E. Huque, and H. Vogel, *J. Biol. Chem.*, 1994, **269**, 5099.
45. M. Zhang and H. J. Vogel, *J. Mol. Biol.*, submitted for publication.
46. M. Ikura, D. Marion, L. E. Kay, H. Shih, M. Krinks, C. B. Klee, and A. Bax, *Biochem. Pharmacol.*, 1990, **40**, 153.
47. M. Ikura, L. E. Kay, and A. Bax, *Biochemistry*, 1990, **29**, 4659.
48. G. Barbato, M. Ikura, L. E. Kay, R. W. Pastor, and A. Bax, *Biochemistry*, 1992, **31**, 5269.
49. T. Trewhella, *Cell Calcium*, 1992, **13**, 377, and references cited therein.
50. R. E. Klevit, D. K. Blumenthal, D. E. Wemmer, and E. G. Krebs, *Biochemistry*, 1985, **24**, 8152.
51. S. H. Seeholzer, M. Cohn, J. A. Putkey, A. R. Means, and H. L. Crespi, *Proc. Natl. Acad. Sci. USA*, 1986, **83**, 3634.
52. M. Yazawa, M. Ikura, K. Hikichi, L. Ying. and K. Yagi, *J. Biol. Chem.*, 1987, **262**, 10 951.
53. M. Ikura, N. Hasegawa, S. Aimoto, M. Yazawa, and K. Yagi, and K. Hikichi, *Biochem. Biophys. Res. Commun.*, 1989, **161**, 1233.
54. S. Ohki, M. Yazawa, K. Yagi, and K. Hikichi, *J. Biochem.*, 1991, **110**, 737.
55. S. Ohki, U. Iwamoto, S. Aimoto, M. Yazawa, and K. Hikichi, *J. Biol. Chem.*, 1993, **268**, 12 388.
56. M. Ikura, L. E. Kay, M. Krinks, and A. Bax, *Biochemistry*, 1991, **30**, 5498.
57. M. Ikura and A. Bax. *J. Am. Chem. Soc.*, 1992, **114**, 2433.
58. T. Prumb, P. Yau, T. S. Harvey, and M. Ikura, *Protein Eng.*, 1994, **7**, 109.
59. S. M. Roth, D. M. Schneider, L. A. Strobel, M. F. A. van Berkum, A. R. Means, and A. J. Wand, *Biochemistry*, 1991, **30**, 10 078.
60. S. M. Roth, D. M. Schneider, L. A. Strobel, M. F. A. van Berkum, A. R. Means, and A. J. Wand, *Biochemistry*, 1992, **31**, 1443.
61. B. Precheur, H. Munier, J. Mispelter, O. Barzu, and C. T. Craescu, *Biochemistry*, 1992, **31**, 229.
62. W. F. DeGrado, F. G. Prendergast, H. R. Wolfe, Jr., and J. A. Cox, *J. Cell. Biochem.*, 1985, **29**, 83.
63. M. Zhang, T. Yuan, and H. J. Vogel, *Protein Sci.*, 1993, **2**, 1931.
64. M. Zhang and H. J. Vogel, *Biochemistry*, 1994, **33**, 1163.
65. M. Zhang and H. J. Vogel, *J. Biol. Chem.*, 1994, **269**, 981.
66. L. E. Kay, P. Keifer, and T. Saarinen, *J. Am. Chem. Soc.*, 1992, **114**, 10 663.

Biographical Sketches

Mitsuhiko Ikura. *b* 1956. B.S., 1979, Ph.D., 1986, Hokkaido University, Japan, where he was introduced to NMR by Kunio Hikichi. Postdoctoral work with Ad Bax at National Institutes of Health, USA, 1988–91. Senior scientist, Ontario Cancer Institute University of Toronto, Canada, 1991–present. Approx. 80 publications. Current research specialty: structural biology of calcium binding proteins and other biological macromolecules.

Carbohydrates and Glycoconjugates

Herman van Halbeek
The University of Georgia, Athens, GA, USA

1	Introduction	1
2	Carbohydrates and Glycoconjugates: Structure and Function	1
3	The Past: Primary Structure	3
4	The Present: Solution Conformation and Dynamics	9
5	The Future: Glycoconjugates in (Inter-)Action at the Membrane Surface	23
6	Conclusions	26
7	Related Articles	26
8	Abbreviations	26
9	References	26

1 INTRODUCTION

The expansion of glycobiology into the realm of the structure–function relationships of carbohydrates is strongly dependent upon advances in technology. Unquestionably, nuclear magnetic resonance (NMR) spectroscopy has made the most significant impact on structural studies of oligosaccharides and glycoconjugates. While researchers in the past (1960–84) concerned themselves in the first place with the study of primary carbohydrate structures, NMR spectroscopy has recently (1985–94) reached a level of sophistication which allows the conformational analysis of oligosaccharides, glycopeptides, and glycolipids in solution. This article briefly summarizes the early days of carbohydrate NMR, reviews the application of current NMR spectroscopic techniques to the structural and conformational characterization of oligosaccharides from glycoproteins and glycolipids, and ends with a discussion of some questions about carbohydrate structure, dynamics, and function that can be addressed by NMR in the near future.

2 CARBOHYDRATES AND GLYCOCONJUGATES: STRUCTURE AND FUNCTION

The carbohydrate moieties of glycoconjugates, i.e., glycoproteins and glycolipids, generally have complex structures featuring highly varied chemical functionalities. These oligosaccharide chains, varying in size from two to 20 or more residues, are composed of neutral monosaccharides such as d-mannose (Man) and d-galactose (Gal), amino sugars such as *N*-acetyl-d-glucosamine (GlcNAc) and *N*-acetyl-d-galactosamine (GalNAc), the C-6-deoxy sugar l-fucose (Fuc), and the nine-carbon-atom acidic sugars of the sialic acid family of which *N*-acetylneuraminic acid (Neu5Ac) is the most commonly found representative (for structures, see Figure 1). In glycoproteins, these oligosaccharide chains are covalently attached to the side chains of specific amino acids such as Asn, Ser, and Thr. Glycoproteins are anchored to the outer surface of the cell's plasma membrane by either a transmembrane peptide fragment or by a phosphatidyl-inositol anchoring lipid. Complex carbohydrate chains similar to those of glycoproteins may also be found attached to lipids similarly inserted in the plasma membrane where they present the hydrophilic carbohydrate chain to the extracellular environment (Figure 1).

Because of their structural diversity, glycoconjugate oligosaccharides are potentially rich sources of biological information. Although the precise function of the carbohydrate chains of glycoproteins and glycolipids is not fully understood, it has been proposed that they are informational macromolecules with signals encoded in their structure that are crucial to the biological functions of the cells carrying them.[1] As this information apparently relates to intercellular communication and control of cellular growth and differentiation, it is possible that complex carbohydrates play an important role in such important processes as developmental biology and tumor metastasis. Areas of focus in current glycobiology research include the importance of oligosaccharides to immune mechanisms, the association of certain structural changes with diseases such as malignant cancer growth and rheumatoid arthritis, and the potential for the development of novel therapeutic strategies [recombinant glycoproteins such as erythropoietin and tissue plasminogen activator are already in widespread clinical use for the treatment of anemia and myocardial infarction, respectively, while the glycolipid 'ganglioside G_{M1}' (Figure 1) is administered to alleviate the symptoms of cholera].

From a structure–function point of view, the 20th century has come full circle: Landsteiner's discovery, around 1900, of the ABH blood group antigens inspired structural studies that culminated in the identification of the antigens as tri- and tetrasaccharide epitopes at the nonreducing termini of the glycoprotein and glycolipid carbohydrate chains found on the cell surface of erythrocytes and many other mammalian tissues (Figure 1). Landsteiner's pioneering work sparked investigations into the involvement of carbohydrates in immune protection and in graft versus host reactions in blood transfusions and other organ transplants. The presence of sialic acid on erythrocyte surfaces proved to be a necessary requirement for their infection by the influenza virus. Malignant tumor cells were found to exhibit certain tumor-associated antigens (TAA), carbohydrate sequences not found on membrane glycoproteins and glycolipids of normal cells. TAA-like epitopes were discovered on cell surfaces in the early stages of embryonic development (hence, they are known as onco-fetal antigens).[2–4] Around 1990, the discovery and identification of sialylated Lewis blood group carbohydrates (sLe^a and sLe^x, Figure 1) as ligands for selectins (cell adhesion molecules)[5,6] added the latest exciting chapter to the involvement of oligosaccharides in an important biological process, in this case endothelial leukocyte adhesion being the key to inflammation.

From the beginning it was understood that an insight into the biological and physicochemical functions of complex carbohydrates at the molecular level would require a precise knowledge of the primary and secondary structures of these often highly branched polymers with their intriguing blend of segmental rigidity and flexibility. The complete structural characterization of complex carbohydrates involves

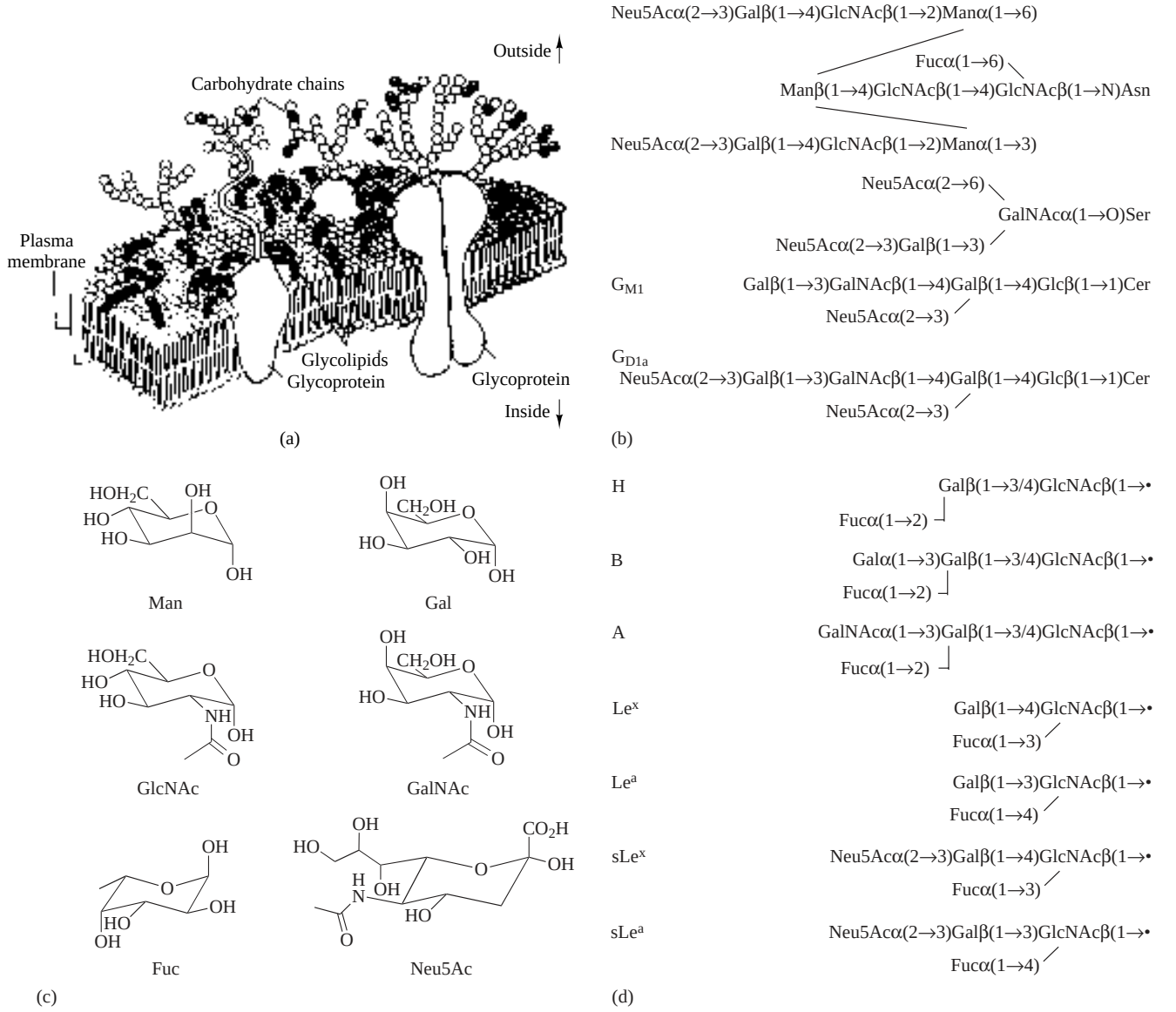

Figure 1 (a) Schematic representation of a cell's plasma membrane with an emphasis on the glycoprotein and glycolipid carbohydrate chains, the cell's communication organelles. (b) Primary structures of some commonly found glycoprotein and glycolipid carbohydrate chains. Represented from top to bottom: a diantennary *N*-type glycoprotein oligosaccharide, an *O*-type glycoprotein tetrasaccharide, and the monosialo and disialo gangliosides G_{M1} and G_{D1a} (Asn = l-asparagine; Ser = l-serine; Cer = ceramide, the generic name for an *N*-acylated sphingosine). (c) Structures of typical constituent monosaccharides of glycoprotein and glycolipid oligosaccharide chains (Man, Gal, GlcNAc, GalNAc, Fuc, and Neu5Ac, drawn in the α-configuration of their thermodynamically most stable pyranose ring forms). (d) Structures of selected blood group and differentiation antigens

determining (i) the type, number, and primary sequence of the constituting glycosyl residues, including the occurrence of branch points and the location of appended noncarbohydrate groups and (ii) their three-dimensional (3D) conformation(s) and dynamics in solution. Although determining the complete structure of a carbohydrate usually requires the application of a combination of chemical, enzymatic, and spectrometric methods,[7,8] NMR spectroscopy has emerged as the single most powerful technique for the accomplishment of this task. The nuclei of predominant interest in NMR studies of carbohydrates are ^{1}H and ^{13}C. The natural allocation of hydrogen and carbon atoms in carbohydrate molecules lends itself to the revelation of their complete primary structure through ^{1}H and ^{13}C NMR analysis. Whereas the primary structural characterization of carbohydrates relies on a combination of techniques, only one of which is NMR spectroscopy, solution conformation analysis is almost entirely the domain of NMR spectroscopy. X-ray structures of glycoconjugates are not commonly available (and if they are, carbohydrates are usually not well-defined), and molecular modeling of carbohydrates, although a hotly contested area of research, is still in its infancy and, therefore, of little help to the experimentalist to date.

The purpose of this review is to put NMR of carbohydrates and glycoconjugates in its historical perspective; not surprisingly, a chronological account shows a remarkable parallel with primary and three-dimensional structure analysis. It should be noted that NMR of carbohydrates covers a much

broader area than solution-state ^{1}H and ^{13}C NMR of monosaccharides, oligosaccharides, and glycoconjugates. Polysaccharides are the topic of the article by Bush (***Polysaccharides and Complex Oligosaccharides***), and ^{2}H NMR of glycolipids is covered in Jarrell's article (***Glycolipids***). Here we will cover neither the application of solid state NMR to carbohydrates nor touch upon ^{31}P NMR of sugar phosphates, ^{15}N NMR of amino sugars, ^{17}O NMR of carbohydrates, and NMR of X-nuclei (^{11}B, ^{119}Sn, etc.) in carbohydrate adducts (see, for example, Bush[9]). We will further limit the discussion in this article largely to pyranose ring systems. For the discussion of furanose rings and their flexibility, the reader is referred to articles by Altona (***Vicinal Coupling Constants and Conformation of Biomolecules***), Hilbers (***Nucleic Acids: Spectra, Structures, and Dynamics***), and others covering NMR of nucleic acids. Furthermore, the molecules (peptides/proteins, lipids) that serve as appended groups of carbohydrates in glycoconjugates are discussed elsewhere throughout this Encyclopedia.

3 THE PAST: PRIMARY STRUCTURE

The initial discovery of the potential value of NMR spectroscopy for carbohydrate structural and conformational analysis is described by Lemieux in his book entitled 'Explorations with Sugars: How Sweet It Was'.[10] We quote:

> In spite of the difficulties and shortcomings of the NMR technique [in 1955], it became evident that acetylated sugars, because of large differences in chemical shifts, were very interesting substances with which to explore the possible use of ^{1}H NMR spectroscopy in organic chemistry. It soon became apparent that an equatorially oriented hydrogen generally gave rise to a signal at a lower field compared with that of a chemically similar but axial hydrogen.[11] This discovery was very encouraging. However, the big excitement came when [...] significant improvements in resolution were made. Examination of the spectra of [...] cyclohexanol acetates firmly established that the spin–spin coupling constants for vicinal hydrogens in antiperiplanar orientation were two to three times larger than those for vicinal hydrogens in a synclinal relationship.[12] [...] The discovery provided the long-sought definitive basis for the assessment of the preferred conformations of the sugar acetates in solution. [...] The spectra of *trans*,*trans*- and *cis*,*trans*-di-*O*-methylcyclohexanol acetate, shown in Figure 2, represent the first application of NMR for the establishment of the relative configurations of chiral centers in organic compounds. Thus, the experimental foundation was laid for the Karplus relationship[13] between the vicinal coupling constant and the torsion angle and for the use of the time-averaged coupling constants to estimate conformer populations.

The stereochemistry of a particular monosaccharide provides its signature in the ^{1}H NMR spectrum; the ^{1}H signals of most monosaccharides can readily be assigned to the appropriate (aliphatic) protons by making use of the observed chemical shifts and splitting patterns. Thus, the foundation for the identification of carbohydrates by ^{1}H NMR spectroscopy had been laid.

Section 3.1 below elaborates on the empirical rules that emerged from the inspection of ^{1}H and ^{13}C NMR spectra of monosaccharides and simple oligosaccharides of known primary structure. Sections 3.2 and 3.3 below summarize 1D ^{1}H NMR spectroscopy as a fingerprinting method for

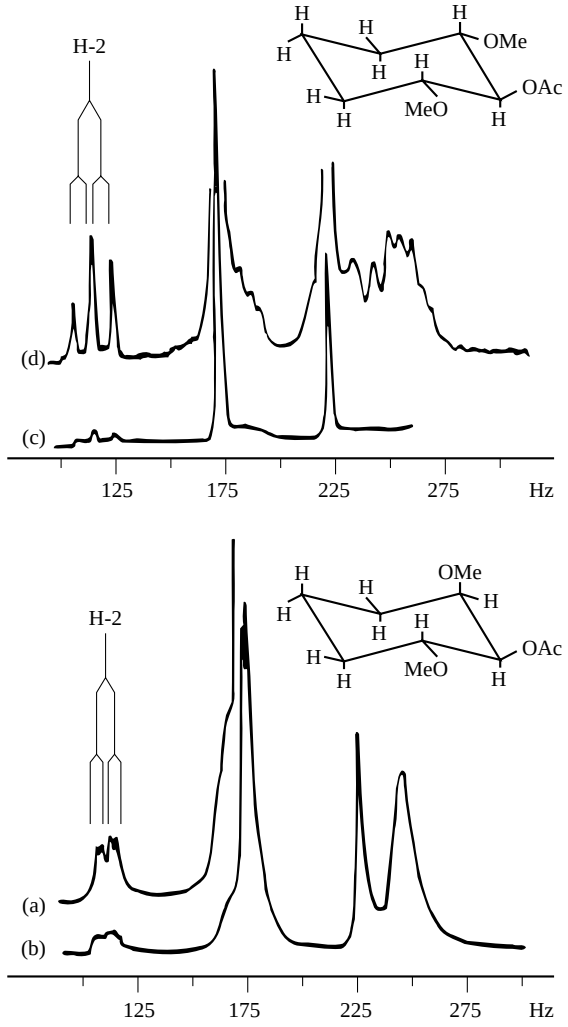

Figure 2 The first application of ^{1}H NMR spectroscopy, at 40 MHz, for the determination of stereochemical configuration (adapted from Lemieux et al.;[14] spectra reproduced with permission from the American Chemical Society). For the *cis*,*trans* isomer, ^{3}J(H-1,H-2) = 3 Hz and ^{3}J(H-2,H-3) = 7 Hz (traces a and b); for the *trans*,*trans* isomer, ^{3}J(H-1,H-2) = ^{3}J(H-2,H-3) = 7 Hz (traces c and d)

the characterization of the primary structure of glycoprotein and glycolipid oligosaccharide chains, respectively, and the usefulness of an empirical concept that emerged during the 1980s for the interpretation of the ^{1}H NMR spectrum of a glycoprotein or glycolipid carbohydrate in terms of its primary structure is outlined. Ongoing efforts aimed at computer-assisted carbohydrate NMR spectral 'interpretation' are mentioned as well. Finally, Section 3.4 takes the concepts developed in previous sections to the level of de novo primary structural elucidation of glycoconjugate carbohydrates by 1D and 2D ^{1}H and ^{13}C NMR spectroscopy.

3.1 Monosaccharides and Simple Oligosaccharides

As their generic name implies, carbohydrate molecules contain numerous carbon and hydrogen nuclei. It follows that the magnetically active nuclei in carbohydrates that are of practical interest to NMR spectroscopists are those of ^{1}H

and ^{13}C atoms. For example, each hexosyl residue [such as the galactosyl residue in Figure 3(a)] has six carbon atoms, seven hydrogens that are involved in CH linkages, and four hydrogens in OH groups. Each of these nuclei in a glycosyl residue has its own characteristic environment and, thus, its own chemical shift. For primary structural characterization of a carbohydrate by ^1H NMR spectroscopy, the observation of the aliphatic protons suffices. Observation of hydrogens in OH groups would unnecessarily complicate spectra aimed at primary structural characterization. Therefore, the carbohydrate sample is typically dissolved in D_2O (no chemical derivatization is necessary), effectively removing any OH signals from the spectrum. Chemical shifts are referenced to the methyl signal of DSS (sodium 4,4-dimethyl-4-silapentane-1-sulfonate). The ^1H NMR spectrum of an oligosaccharide is essentially a superposition of the spectra of the individual glycosyl residues which are slightly modified because of their linkages to each other. For example, the ^1H NMR spectra of typical glycoprotein Ser-linked tri- and tetrasaccharides are shown in Figures 3(b) and 3(c).[15] The subspectrum of the β-galactosyl residue is recognizable in the spectra of both the linear trisaccharide and the branched tetrasaccharide. Furthermore, Figure 3(c) clearly illustrates the difference in the NMR appearance of an $\alpha(2\rightarrow3)$- versus an $\alpha(2\rightarrow6)$-linked sialic acid.

The following empirical 'rules' have emerged to guide the interpretation of ^1H NMR spectra of simple carbohydrates:

1. The nonanomeric ring-skeleton protons in a glycosyl residue have very similar electron densities and, thus, chemical shifts; all of their signals appear between 3 and 4 ppm (Figures 3 and 4). In the spectrum of an oligosaccharide, the signals of the nonanomeric protons partially overlap; they constitute a broad envelope of signals in the middle of the spectrum having little fine structure and, therefore, almost no readily accessible structural information. However, anomeric protons (H-1) show signals at significantly higher chemical shifts due to their neighboring glycosidic and ring oxygens. Anomeric proton doublets are typically found between δ 4.3–5.6 ppm.

2. A proton in an equatorial position at a certain carbon atom in a pyranose ring has a chemical shift ~0.5 ppm higher than the corresponding axial proton attached to the same carbon. Therefore, for d-residues involved in α-glycosidic linkages (H-1 equatorial), δ(H-1) ~ 4.9–5.6 ppm, while for β-anomeric linkages (H-1 axial), δ(H-1) ~ 4.3–4.7 ppm. For carbohydrates in D_2O at ambient temperature, these positions correspond to the near left and right of the HDO signal (at δ ~ 4.80), respectively. Further illustrating this rule, the equatorial Man H-2 signals are typically found ~0.5 ppm further to the left than the axial GlcNAc or Gal H-2 signals (Figure 4). Also, Gal H-4 protons resonate ~0.5 ppm further to the left than GlcNAc H-4 protons (compare Figure 3).

3. Each anomeric proton, by virtue of its ^3J(H,H) scalar coupling to H-2, resonates as a doublet. The magnitude of the coupling constant reflects the relative orientation of neighboring protons. The coupling constant ^3J(H-1,H-2) for two neighboring protons (H-1 and H-2, separated from each other by three covalent bonds) that are both in axial orientation is 7–8 Hz (i.e., relatively large), while coupling constants ^3J(H-1,H-2) between two neighboring protons, one of which is axial and the other equatorial, or between two equatorial protons, are 3–4 Hz (relatively small). Thus, the anomeric configuration of a glycosyl residue can be inferred both from

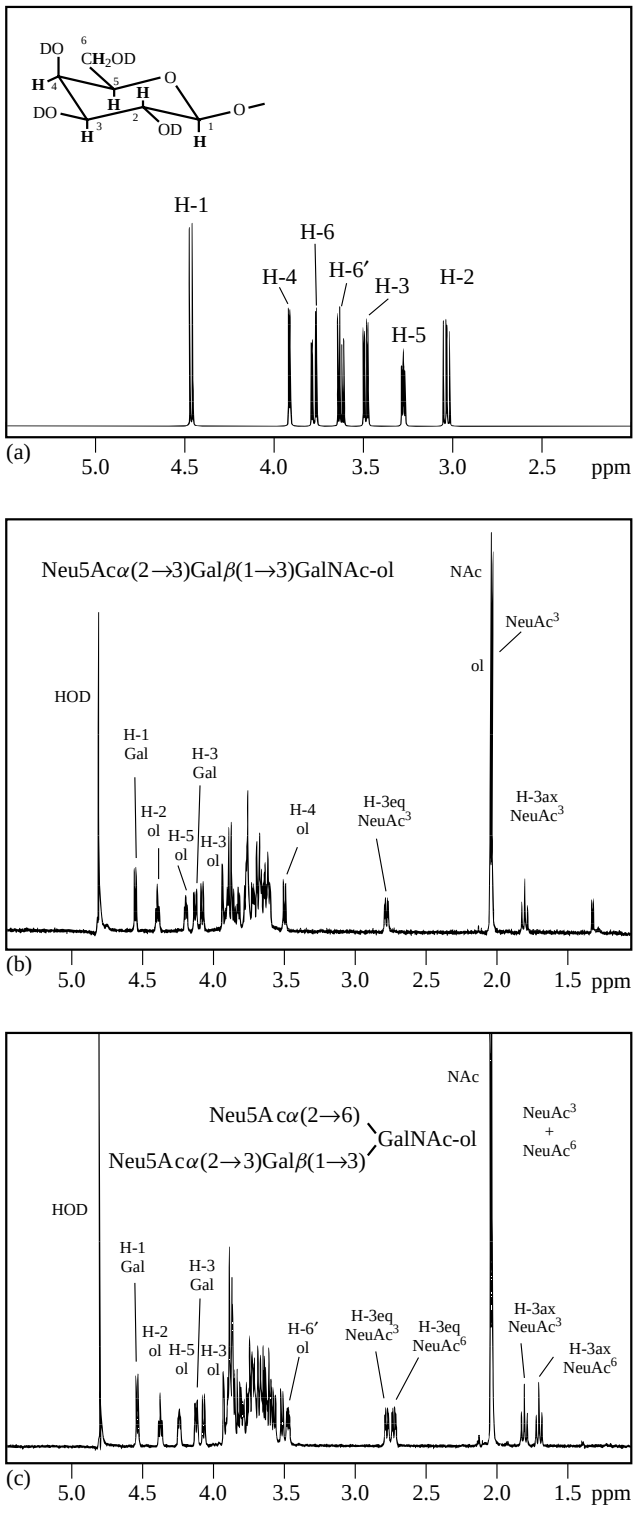

Figure 3 (a) The computer-simulated ^1H NMR spectrum of a β-linked galactopyranosyl residue in D_2O. (b) The 600 MHz ^1H NMR spectrum (D_2O, pD = 6, 23 °C) of a linear *O*-type trisaccharide-alditol (70 μg) obtained from a glycoprotein via reductive alkalinolysis.[15] (c) The 600 MHz ^1H NMR spectrum (D_2O, pD = 6, 23 °C) of an *O*-type tetrasaccharide-alditol (75 μg) released from a glycoprotein via reductive alkalinolysis.[15] Superscripts in $NeuAc^3$ and $NeuAc^6$ refer to the position of the linkage in which these residues are involved

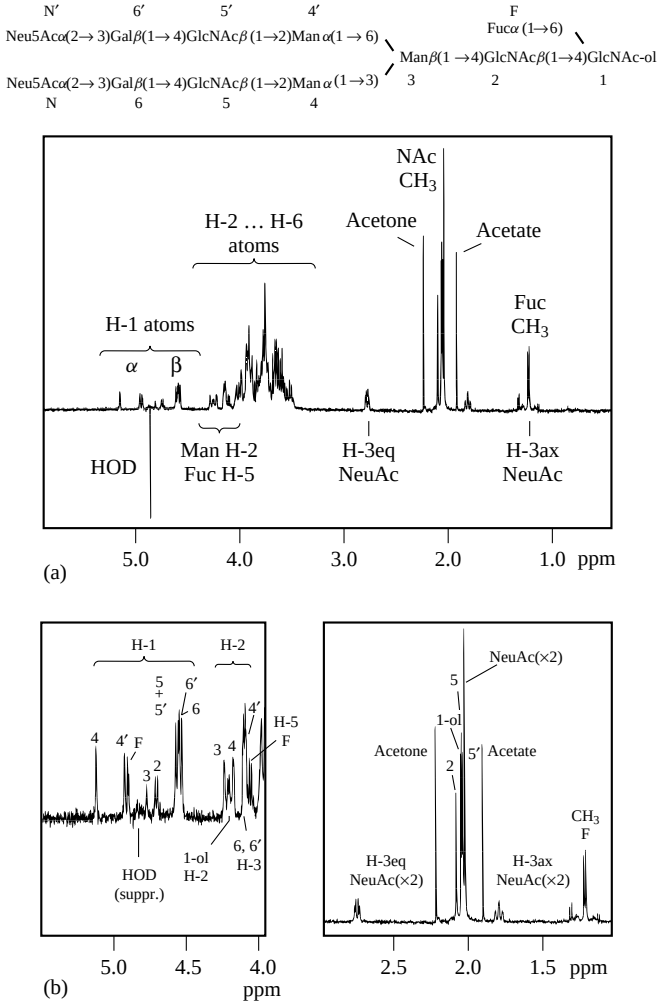

Figure 4 (a) The 500 MHz ^{1}H NMR spectrum (D_2O, pD = 6, 21 °C) of a typical diantennary *N*-type oligosaccharide side chain of a glycoprotein (250 μg, examined as oligosaccharide-alditol, obtained by *N*-glycanase digestion of the glycoprotein and subsequent chemical reduction). The residual HOD signal was suppressed by low-power presaturation. (b) Structural-reporter-group regions of spectrum (a). The numbers in the spectra refer to the corresponding glycosyl residues in the structure

the chemical shift and the coupling constant of its anomeric-proton signal in the ^{1}H NMR spectrum.

4. When a glycosyl residue has either an additional glycosyl residue or a noncarbohydrate group attached at a certain carbon position, the signal of the proton attached to this carbon tends to shift ~0.2–0.5 ppm to the left in the spectrum. Therefore, signals of nonanomeric protons that are attached to linkage sites usually appear just outside the envelope resonance of skeleton protons ($3.9 < \delta < 4.4$) (Figure 4); they become individually observable 'structural-reporter' signals (Section 3.2). Thus, if the nonanomeric proton signals that emerge in the region between δ 3.9 and 4.4 ppm can be assigned, linkage positions can be deduced from a ^{1}H NMR spectrum.

These rules are the result of the extrapolation and rationalization of numerous NMR data obtained on mono- and disaccharides of known primary structure. Noteworthy review articles on general applications of NMR to carbohydrates, developing interalia the above concepts, have appeared[2,16,17] including one recently.[18] Additionally, the scientific literature includes extensive ^{1}H databases of chemical shifts for mono- and small oligosaccharides.[19,20]

The first reports on ^{13}C NMR spectroscopy of carbohydrates appeared in the late 1960s.[21,22] It was found that the ring ^{13}C methine signals of pyranosyl residues are typically observed between 65 and 110 ppm downfield from DSS. Anomeric carbons usually resonate between 90 and 110 ppm. The magnitude of the one-bond ^1J(C-1,H-1) coupling for the anomeric carbon atoms reflects the configuration at the anomeric center. As a rule of thumb, ^1J(C-1,H-1) ~ 170 Hz indicates the α-anomeric configuration, whereas ^1J(C-1,H-1) ~ 160 Hz indicates the β-anomeric configuration. The exocyclic methylene signals of monosaccharides (in CH_2OH groups) are observed at ~60–70 ppm [unless the glycosyl residue is involved in a (1→6) linkage]. Extensive ^{13}C databases for mono- and simple oligosaccharides are found in the literature.[23–28] Glycosylation shifts ($\Delta\delta$ ~10 ppm for ^{13}C at the site of substitution, $\Delta\delta$ −1 to −2 ppm for the adjacent ^{13}C atoms) are more reproducible in ^{13}C NMR than in ^{1}H NMR of carbohydrates. Computer-assisted interpretation of NMR spectra of carbohydrates in terms of primary sequence based solely on ^{13}C chemical shifts[29–31] preceded that of ^{1}H NMR spectra.[32–34]

3.2 Complex Oligosaccharides Related to Glycoproteins

The carbohydrate side chains of glycoproteins are amenable to high-resolution ^{1}H NMR spectroscopy either as glycopeptides or as free oligosaccharides. These can be obtained from the glycoprotein by enzymatic or chemical procedures.[7,8] A typical example of a ^{1}H NMR spectrum of a glycoprotein-derived *N*-type oligosaccharide is shown in Figure 4(a). In the early 1970s, when the complete interpretation of ^{1}H NMR spectra of carbohydrates of this size seemed impossible, the spectrum of an oligosaccharide was regarded by the glycobiologist primarily as a fingerprint, a readily obtainable 'identity card' of a carbohydrate. A mere comparison of the ^{1}H NMR spectra of compounds (without detailed interpretation) was used to demonstrate whether they were identical and/or pure substances. Thus, at first, a 1D ^{1}H NMR study appeared valuable for the primary structure determination of glycoprotein carbohydrates only if the oligosaccharide had been characterized previously by ^{1}H NMR in conjunction with chemical and other spectrometric methods.

However, in the late 1970s the first successful attempts were made to interpret the ^{1}H NMR spectra of glycoprotein oligosaccharides, even when the spectra did not match exactly any of the spectra in existing databases. Using the *structural-reporter-group concept*,[15,35,36] the spectra were interpreted in terms of (partial elements of) carbohydrate primary structure, including anomeric configurations and positions of glycosidic linkages. The crux of this concept is that it appeared sufficient to inspect only certain regions in the spectrum [see Figure 4(b)] in order to ascertain the primary structure of the glycoprotein carbohydrate from its NMR spectrum. Perceived by some in the field as 'mystical' or 'voodoo NMR', the structural-reporter-group concept is merely an extrapolation of the empirical rules listed in Section 3.1 to larger oligosaccharides. The concept ignores the crowded region in the center of the spectrum (between 3–4 ppm, see

Figure 4); only the positions and patterns of those signals that are more or less individually observable are examined. Particularly useful structural-reporter groups are (i) the anomeric (H-1) protons, (ii) the protons attached to the carbon atoms in the direct vicinity of a linkage position, (iii) the protons attached to deoxy carbon atoms and (iv) methyl protons, e.g., in *N*-acetyl groups. The structural-reporter-group regions of the spectrum in Figure 4(a) are expanded in Figure 4(b). For the interpretation of a ^{1}H NMR spectrum such as depicted in Figure 4, structural-reporter-group signals are cataloged by chemical shift and coupling constants; these values are then compared with literature data on similar oligosaccharides and/or glycopeptides. A highly refined set of empirical rules was developed to rationalize the effects of structural elongations, as typically found in glycoprotein oligosaccharides, on structural-reporter-group chemical shifts. For example, the structural-reporter-group concept developed rules to identify the degree of branching as well as the type of linkage and branch location of sialic acid and fucosyl residues.[15,35,36] Several glycoprotein carbohydrate structural-reporter-group ^{1}H chemical shift databases are currently available for *N*-type glycopeptides and oligosaccharides[36–38] and *O*-type oligosaccharide-alditols[39] in D_2O; other noteworthy databases are also available.[40–43] The structural-reporter-group approach continues to enjoy considerable popularity as a method for the primary structural characterization of glycoprotein and glycolipid (for gangliosides, see Section 3.3) carbohydrates by NMR spectroscopy.

An important advantage of NMR spectroscopy over other techniques used for structural analysis of carbohydrates is its nondestructive nature. Oligosaccharide and glycopeptide samples, after NMR analysis, can be recovered unimpaired and used for other analyses, biological activity tests, etc. Glycoprotein oligosaccharides with 15–20 constituent glycosyl residues have been successfully characterized by 500 MHz one-dimensional (1D) ^{1}H NMR spectroscopy. Also, mixtures of components with closely related structures have been analyzed successfully. The most important limitation of NMR spectroscopy lies in its relatively low level of sensitivity. At least 10 nmol of pure carbohydrate is required to record an NMR spectrum and, even at 600 MHz, heterogeneity occurring in low abundance in the sample may escape attention. NMR spectroscopy, by its very nature, may also fail to detect the presence of nonmagnetically active nuclei, e.g. the occurrence of sulfate esters, in the carbohydrate.

Until now, the most laborious part of the NMR structural analysis of carbohydrates has been spectral interpretation. Partial or even complete primary structure determination is possible from the structural-reporter-group regions of a 1D ^{1}H NMR spectrum only if structurally closely related compounds have been previously characterized by ^{1}H NMR spectroscopy. The multitude of extremely refined rules resulting from the structural-reporter-group inspection of spectra makes interpretation of spectra of novel compounds a tedious effort. Even the basically simple process of retrieving previously recorded spectra and comparing them with a newly recorded spectrum becomes a considerable task, given the exponential growth of the amount of ^{1}H NMR data collected on glycoprotein and glycolipid oligosaccharides from 1980 to 1994. Assistance from computers to facilitate this aspect of the method is being sought along two different lines. The use of a computer search algorithm to compare a list of structural-reporter-group chemical shifts with those in a database appears rather straightforward. Indeed, several such computer programs have been written to assist the interpretation of glycoprotein oligosaccharide ^{1}H NMR spectra.[33,34,44] A more elegant and much faster method involves the use of the entire spectrum (including the 3–4 ppm envelope region with its high information density) for pattern recognition by artificial intelligence techniques. The NMR spectrum, already available in digital format, need not be reduced to a list of chemical shifts, as is commonly done for human interpretation. Artificial neural networks (ANN) have been successfully applied for pattern recognition of NMR spectra.[45,46] Recently, this work has been extended to include the 500 MHz ^{1}H NMR spectra of glycoprotein carbohydrates.[47] In the foreseeable future, NMR spectral databases will be linked to the complex carbohydrate structure database (CCSD),[48] and the neural network search algorithms will be incorporated into CarbBank. This approach will not only render much of the previously necessary laborious supporting structural analysis work superfluous for oligosaccharides already in the database, it will also allow the interpretation of spectra by the rules resulting from the structural-reporter-group concept, thus 'automating' empirical NMR spectral interpretation.

An unexpected but welcome development in the application of the ANN technology for the analysis of ^{1}H NMR spectra lies in the potential increase in sensitivity of the method by two or three orders of magnitude. For a spectrum of a given oligosaccharide with fairly good signal-to-noise ratio (S/N) already in the database (i.e., when a neural network has been trained to recognize this spectrum in terms of the associated carbohydrate structure), the oligosaccharide can be recognized again from its ^{1}H NMR spectrum with a 100 to 1000-fold less S/N than the original spectrum (such as would be obtainable for subnanomole amounts of carbohydrate).[47] In the very near future, the ANN technology will make NMR competitive in terms of sensitivity with any other technique in the primary structural determination of carbohydrates related to glycoproteins and glycolipids.

In principle, ^{13}C NMR spectra can also be used for the fingerprinting of glycoprotein carbohydrates.[49] The ^{13}C spectra, recorded under ^{1}H decoupling conditions, consist exclusively of singlets. Further favored by the large chemical shift dispersion ($\Delta\delta \sim 100$ ppm), ^{13}C NMR spectra [even for intact glycoproteins (Section 5.1)] are often characterized by high resolution. Attempts were made to develop ^{13}C chemical shift databases for glycoprotein carbohydrate chains,[50] and to derive rules for the interpretation of spectra of novel compounds based on those of observed larger or smaller related structures. However, these efforts met with little success because of the higher demands on amounts of material needed for recording spectra and the much greater ease with which the same goal of primary structure characterization was achievable by ^{1}H NMR spectroscopy.

3.3 Complex Oligosaccharides Related to Glycolipids

The ^{1}H NMR spectroscopy principles and methodology discussed in the previous section are not only valid for glycoprotein-related carbohydrates. They apply equally well to glycolipids[51,52] and glycosyl phosphatidyl-inositol (GPI)

anchors,[53] polysaccharides,[24] and proteoglycans.[54] Here we will limit the discussion to glycolipids. Unlike glycoproteins, glycolipids are amenable to high-resolution ^{1}H NMR analysis in their native state; however, they cannot be investigated in aqueous solution. Solvents such as DMSO and DMF have been successfully applied, and volumes of data that are valuable for primary structural analysis have been collected over the years. Examples of ^{1}H NMR databases of glycolipids in DMSO are given elsewhere.[51,55–59]

To take advantage of the massive amount of NMR data on glycoprotein-related oligosaccharides in water, the removal of the lipid by enzymatic (endoglycoceramidase) or chemical (ozonolysis) procedures is currently employed as a standard technique for allowing the glycolipid oligosaccharides to be examined under the same circumstances as glycoprotein/glycopeptide carbohydrates and free oligosaccharides [see, for example, Figure 5(b) versus Figure 5(a)].[60]

3.4 De Novo Sequencing of Glycoconjugate Carbohydrates

Although useful for the primary structural analysis of carbohydrates within the closely knit framework of structures presented abundantly by Nature for glycoprotein and glycolipid oligosaccharides, collections of chemical shifts contribute little to our understanding of NMR. However, as of the early 1980s, NMR spectroscopy provides the tools necessary to determine any novel carbohydrate structure de novo, without significant help from other techniques.

When the 1D ^{1}H spectrum does not resemble that of a known oligosaccharide structure, a combination of multiple pulse ^{1}H NMR spectroscopic techniques, primarily two-dimensional (2D) COSY, TOCSY, and NOESY or ROESY, may be applied for the de novo sequencing of the carbohydrate[9,55,58] provided that 20–50 nmol of pure substance (2–5-times the amount of sample mentioned for the 1D analysis) is available for the analysis. The TOCSY technique permits subspectral editing of the ^{1}H spectrum for each constituting glycosyl residue[61,62] and, consequently, the virtually complete assignment of all of the multiplet patterns in the ^{1}H NMR spectrum (including those in the envelope region between 3–4 ppm). Subsequently, depending on the size of the oligosaccharide and the magnetic field strength of the spectrometer used, NOESY or ROESY spectra enable the inference of the glycosyl-residue sequence, including the positions of glycosidic linkages, based on the detection of through-space connectivities.[63]

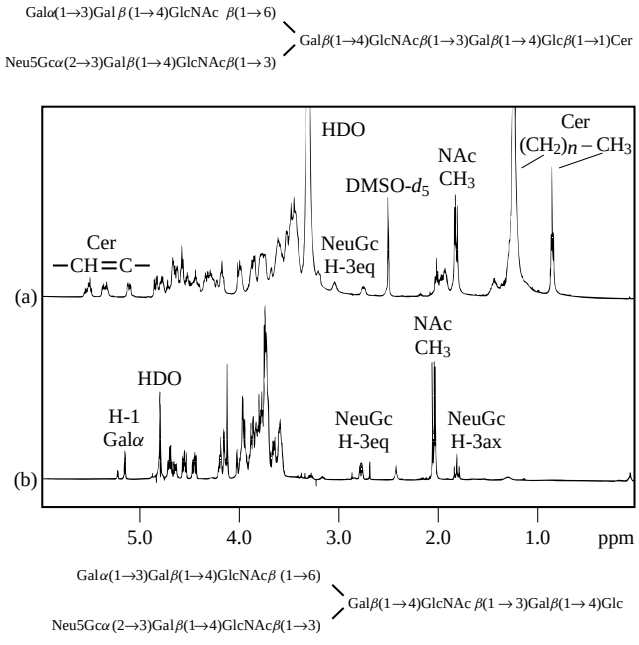

Figure 5 (a) The 500 MHz ^{1}H NMR spectrum (DMSO-d_6/D_2O, 98:2, v/v; 27 °C) of an intact ganglioside. (b) The 500 MHz ^{1}H NMR spectrum (D_2O, pD = 6, 23 °C) of the oligosaccharide released from the ganglioside by endoglycoceramidase digestion[60]

Examples of the application of this general strategy are manifold.[18,64–68] Because of its importance, we will briefly illustrate the strategy for a novel tetrasaccharide found *O*-linked to Ser_{61} in Factor IX, a serum glycoprotein involved in the human blood clotting cascade.[69,70] Figure 6(a) shows the 1D ^{1}H NMR spectrum of a glycopeptide (20 nmol) obtained from human Factor IX consisting of four glycosyl residues and nine amino acids. At the start of the NMR studies, the peptide sequence was known to be Leu_{57}–Asn–Gly–Gly–Ser–Cys*–Lys–Asp–Asp_{65} (where Cys* indicates an *S*-carboxymethylated Cys residue). Also, it was known that the carbohydrate portion of the glycopeptide contained Gal, GlcNAc, Fuc, and Neu5Ac in equimolar ratios. In order to decipher the primary sequence of the tetrasaccharide, to pinpoint the side chain of Ser_{61} as the site of glycosylation in the peptide, and to elucidate which of the four sugar residues was involved in the linkage to Ser_{61}, the complete assignment of the ^{1}H NMR spectrum of the glycopeptide was required. However, not only did the presence of the nonapeptide obscure many of the saccharide ^{1}H signals, it was not even possible (unlike for many other glycopeptide NMR spectra) to assign any signals in the 1D spectrum of the Factor IX glycopeptide simply by inspection. Neither the usually well-resolved structural-reporter-group signals of sugar anomeric and deoxy protons nor the amino acid H-α protons were recognizable off-hand. However, 2D correlated spectroscopy (in particular, COSY and TOCSY) was successfully applied for the identification of the spin systems of the individual sugar and amino acid residues. Figure 6(b) shows the relevant portion of the TOCSY spectrum. The resulting connectivity patterns in the COSY and TOCSY spectra were assigned to sugar and amino acid residue types based on their comparison with literature data for the individual spin systems. Subspectra for the sugar residues were traced starting from their H-1 signals (found between 4.4 and 5.5 ppm) or, in the case of Neu5Ac, from the H-3ax and H-3eq protons (expected around 1.8 and 2.7 ppm, respectively; see Figure 3). The H-1,H-2 connectivities for Gal, GlcNAc, and Fuc were particularly clear in the COSY spectrum. The TOCSY subspectra through H-1 included (in addition to the H-2 signals) the Fuc H-3, Gal H-3 and H-4, and GlcNAc H-3, H-4, H-5, and H-6/6′ [Figure 6(b)].

Once the chemical shifts of 80% of the sugar protons had been established, the structural-reporter-group concept (Section 3.2) enabled the assignment of the linkage configurations and partial sequence of the four residues. The combination of chemical shifts for Neu5Ac H-3ax and H-3eq

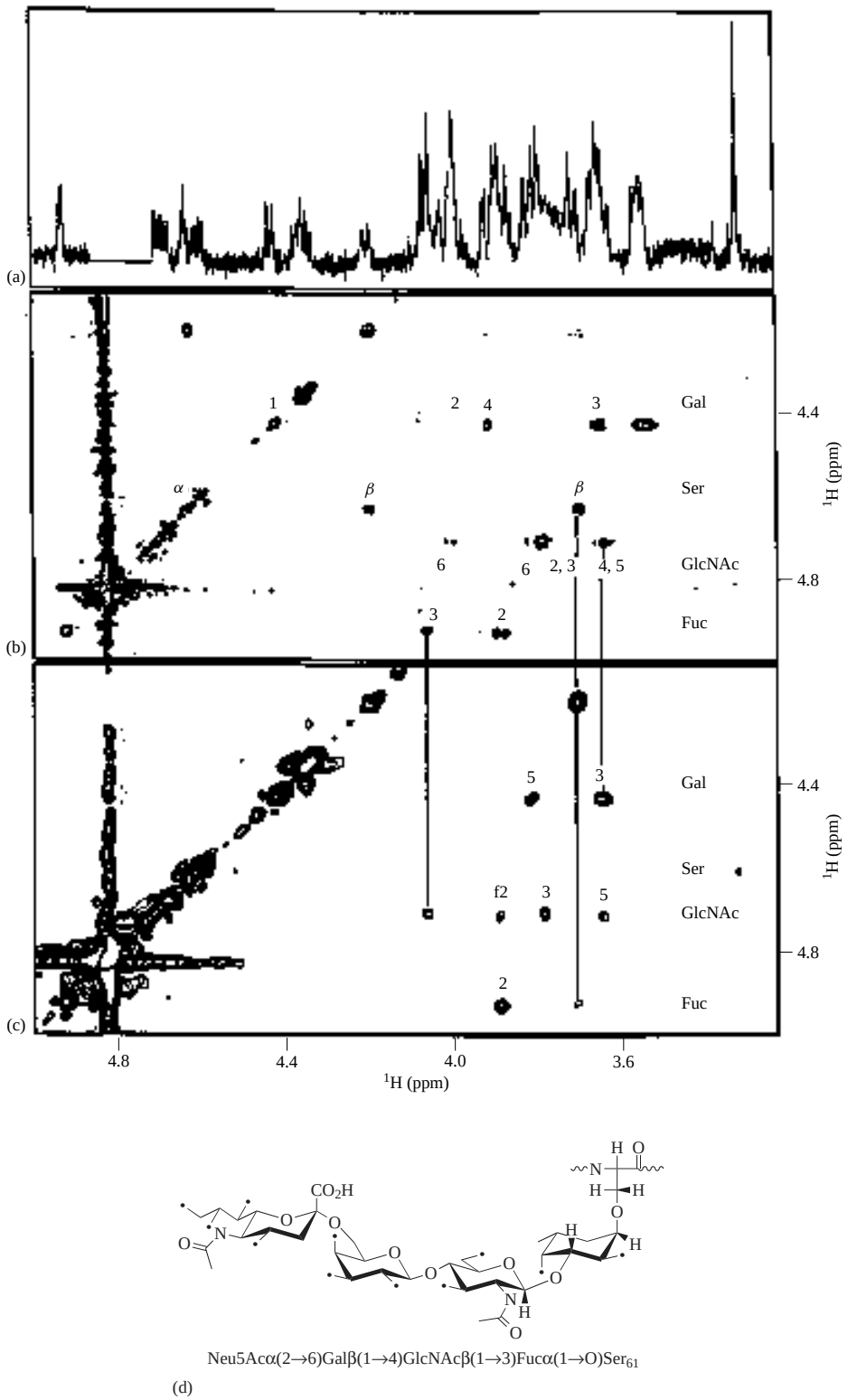

Figure 6 (a) The 600 MHz 1D ^{1}H NMR spectrum (D_2O, pD = 7.2, 23 °C) of the Factor IX glyco-nonapeptide (~20 nmol).[69] (b) Regions of the 2D ^{1}H TOCSY (mixing time 108 ms) and (c) ROESY (mixing time 200 ms) spectra of Factor IX glyco-nonapeptide. The sequence of the structural entities Galβ(1→4)GlcNAc, GlcNAcβ(1→3)Fuc, and Fucα(1→O)Ser is indicated by the vertical lines that connect ROESY and TOCSY cross peaks. The numbers in the spectra refer to the protons in the respective glycosyl residues. (d) Schematic structure of the tetrasaccharide Neu5Acα(2→6)Galβ(1→4)GlcNAcβ(1→3)Fuc α-linked to Ser$_{61}$ of human Factor IX. The • —— symbolizes an OH group. Sugar ring H atoms are not shown, with the exception of the GlcNAc H-1, Fuc H-3, Fuc H-1, and Ser H-β protons in order to illustrate their spatial arrangement relevant to the observed NOE effects

at 1.72 and 2.67 ppm, known to be sensitive to the linkage in which the residue is involved and the type of sugar to which it is attached, indicated that the Neu5Ac residue was $\alpha(2\rightarrow6)$-linked to the Gal residue (compare Figure 3). Furthermore, the Gal H-1 chemical shift of 4.43 ppm and its coupling ^3J(H-1,H-2) of 7.8 Hz were characteristic of its involvement in a $\beta(1\rightarrow4)$ linkage to GlcNAc in a sialyl-*N*-acetyllactosamine moiety. Likewise, the positions and coupling constants for the Fuc [4.92 ppm; ^3J(H-1,H-2) = 4.2 Hz] and GlcNAc H-1 [4.71 ppm; ^3J(H-1,H-2) = 8.0 Hz] signals indicated the involvement of these residues in α- and β-glycosidic linkages, respectively. At this point, it was evident from the NMR data that the tetrasaccharide consisted of a terminal Neu5Ac$\alpha(2\rightarrow6)$Gal$\beta(1\rightarrow4)$GlcNAc$\beta(1\rightarrow\bullet)$ moiety and an α-linked Fuc residue.

To complete the structural analysis of the tetrasaccharide, 2D NOE experiments were performed in order to gather information about the distance between pairs of protons and, thus, sequence information. A ROESY spectrum of the glycopeptide provided a number of transglycosidic NOEs [Figure 6(c)]. Among them were a NOE between GlcNAc H-1 and the proton resonating at 4.06 ppm assigned to Fuc H-3 by TOCSY, and a NOE between Fuc H-1 and a proton at 3.72 ppm, i.e., one of the β-protons on Ser_{61}. The aforementioned interresidue NOE effects [between the protons highlighted in the schematic structure in Figure 6(d)] pointed to GlcNAc(1 $\rightarrow$ 3)Fuc and Fuc(1 $\rightarrow$ O)Ser linkages, respectively. Thus, NMR spectroscopy allowed the unambiguous establishment of the linearity of the tetrasaccharide's structure. Fuc was found present in this tetrasaccharide as an internal residue, providing the 'bridge' between GlcNAc in the sialyl-*N*-acetyllactosamine moiety and Ser in the peptide. The NMR data are therefore compatible with the structure Neu5Ac$\alpha(2 \rightarrow 6)$Gal$\beta(1 \rightarrow 4)$GlcNAc$\beta(1 \rightarrow 3)$Fuc$\alpha(1 \rightarrow$ O)Ser_{61}.

The methodology described here is generally applicable for the complete primary structure analysis of carbohydrates as free oligosaccharides and as constituents of glycoconjugates; anomeric configurations and positions of all glycosidic linkages and, indeed, full sequences can be unraveled. The only potential problem is that ^{1}H/^{1}H transglycosidic NOEs are not always the largest magnitude interresidue NOEs. The resulting ambiguity in the definition of the linkage position, however, can be solved by ^{1}H-detected ^{13}C,^{1}H multiple-bond correlation (HMBC) spectroscopy.[71] Detailed applications of this technique for glycoprotein oligosaccharides have been described.[72] Briefly, when ^{13}C and ^{1}H NMR spectroscopy are used together, NMR demonstrates its real power in the de novo delineation of carbohydrate structures from first principles. Heteronuclear ^{13}C,^{1}H correlation NMR techniques are the most informative NMR experiments for carbohydrate primary structures.[72,73] The sensitivity limitations for these types of experiments were overcome by the introduction of the ^{1}H-detected versions of many ^{13}C,^{1}H correlated spectroscopies. The HMQC experiment, providing a one-bond ^{13}C,^{1}H correlation map, is generally sufficient to assign unambiguously all resonances in the ^{13}C NMR spectrum, provided that the entire ^{1}H spectrum is assigned by the COSY/TOCSY approach. The tracing of long-range transglycosidic ^3J(C,H) values from the HMBC spectrum completes the primary structural analysis by unambiguously providing the linkage positions and the sequence of the glycosyl residues in the complex carbohydrate. Heteronuclear correlation experiments also allow the location of appended noncarbohydrate groups (such as acetates[74] and phosphates[75]) in oligosaccharides. For further examples, see the article by Bush (***Polysaccharides and Complex Oligosaccharides***) in this Encyclopedia.

At the present time, the NMR methodology for nondestructively deciphering any unknown carbohydrate primary structure is available. Isolating and purifying carbohydrates in amounts sufficient to perform these analyses is currently the bottleneck to their structural characterization.

4 THE PRESENT: SOLUTION CONFORMATION AND DYNAMICS

Due to the competition of more sensitive procedures, NMR spectroscopy may not always be the method of choice for the de novo determination of oligosaccharide primary structures. However, NMR spectroscopy easily outperforms any other available method of structural analysis when molecular conformation and motional characteristics are the focus of attention, and it yields the most complete picture of oligosaccharide structure and dynamic behavior in solution. A knowledge of conformation and dynamics is essential to understanding how oligosaccharides mediate biological recognition on cell surfaces. The NMR parameters holding the key information regarding oligosaccharide conformation and flexibility include scalar and dipolar couplings, relaxation times, and chemical exchange rates. Section 4.1 discusses how these parameters can be related to internuclear distance and torsion angle information and, therefore, to pyranose ring pucker, ensembles of rotamers around bonds that allow for certain flexibility, glycosidic linkage conformation, hydrogen bonding, and rotational correlation times for molecular tumbling and internal motions. Section 4.2 highlights some of the multipulse NMR spectroscopic techniques currently used to gather the constraints required to define the conformation and dynamics of an oligosaccharide in aqueous solution. Noteworthy review articles dealing with the application of multipulse *n*D NMR for carbohydrate conformational analysis are available.[9,18,55,58,59,64,66,72,76–78] Most of the NMR methodology reviewed in this section will be concerned with selective excitation experiments[79,80] which, for carbohydrates, are extremely useful in the retrieval of any desired information from NMR spectra. Upon critical evaluation of this information, it becomes clear that all oligosaccharides are, to a greater or lesser extent, flexible. The number of conformers adopted by small oligosaccharides is, however, not infinitely large; even oligosaccharides that include a $(1\rightarrow6)$ linkage fluctuate between a relatively small number of rather well-defined conformations. As an example, the process of deriving an ensemble of conformations from a sufficiently large set of NMR constraints is illustrated for sialyl-$\alpha(2\rightarrow$b)lactose. This discussion will be followed immediately by the description of NMR experiments which are capable of revealing internal motion in an oligosaccharide for which, at first glance, all measured NMR constraints seem to favor a rigid-body model. For example, we demonstrate that sucrose, the disaccharide that for years has been the paradigm of carbohydrate rigidity in solution, more than likely experiences fast internal motion around its glycosidic bond. Finally, Sections 4.3 and 4.4 will summarize the current knowledge on glycoprotein and glycolipid carbohydrate conformations and dynamics.

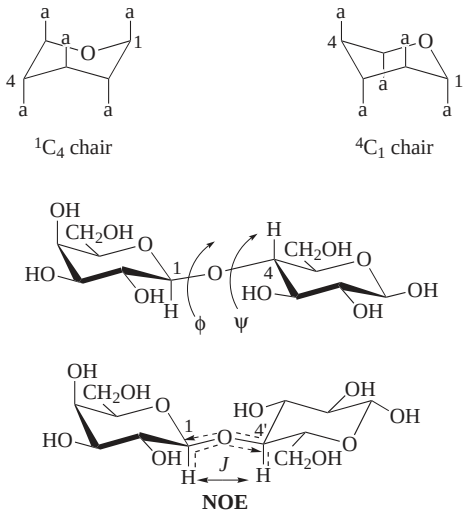

Figure 7 (a) Definition of the chair conformations of d-hexopyranose rings (a = axial substituent). For most monosaccharides, the $^1C_4$ and $^4C_1$ chairs are energetically favored over any boat conformers. For example, Man and Gal typically adopt the $^4C_1$ chair conformation, while Fuc and Neu5Ac adopt the $^1C_4$ chair (called the $^2C_5$ chair for Neu5Ac) [see Figure 1(c)]. (b) Definition of the torsion angles ϕ and ψ around a typical glycosidic linkage [in this case, the (1→4) linkage in lactose]: ϕ = H-1−C-1−O-1−C-4′ and ψ = C-1−O-1−C-4′−H-4′. In conjunction with ^3J(H-1,C-4′) and ^3J(C-1,H-4′) the NOE between H-1 and H-4′ across the glycosidic bond is used for linkage conformation analysis

4.1 Three-Dimensional Carbohydrate Structure

Once an oligosaccharide's primary sequence has been elucidated, its 3D structural characterization is typically approached in the following steps: (i) the ring conformation for each of the constituent glycosyl residues is defined [see Figure 7(a)]; (ii) the intraresidue conformation is completed by attempting to define, relative to the ring, the conformation(s) of any pendant (CH_2OH and OH) groups; (iii) the conformations of each of the glycosidic linkages in the oligosaccharide are characterized [see Figure 7(b)]; and (iv) additional distance constraints which could be indicative of hydrogen bonding or other types of interaction between residues, both adjacent and nonadjacent in the primary structure, are sought. Oligosaccharide conformations are ultimately defined in terms of the relative (Cartesian or spherical) coordinates of the atoms in 3D space; these coordinates are obtained via the measurement of internuclear distances and torsion angles around bonds. The pioneering work of Solomon[81] and Karplus[13,82] has demonstrated the possibility of probing the geometry of molecules in solution via NMR by measurements of NOE effects and scalar couplings, respectively. NOE effects are dependent on internuclear distance, while scalar couplings between nuclei separated by three chemical bonds (^3J) depend on the dihedral angle between two planes containing those nuclei. The advent of multidimensional and multinuclear spectroscopy enabled the measurement of a large number of homo- and heteronuclear NOE contacts and vicinal coupling constants, including those from extremely overlapped oligosaccharide NMR spectra. If a sufficient number of constraints can be obtained from NMR, the 3D structure(s) of the carbohydrate can be computed.[66,76,83] Carbohydrate NMR has reached a level of sophistication at which the number of detectable constraints is sometimes large enough to be incompatible with a single rigid conformer, prompting the consideration of ensemble average models. Help is then sought from molecular modeling (potential energy calculations) to provide candidate low-energy structures that may contribute to the ensemble average. Sometimes, rather deceptively, all measured constraints seem to favor one rigid conformation for the oligosaccharide in question. In these cases, it is particularly important to remember to take into consideration that J and NOE values are intrinsically motionally averaged. Perhaps more often, modeling of carbohydrates is hampered by the existence of very few detectable NOE contacts. Unfortunately, the number of detectable structural constraints usually proves insufficient to unambiguously define the carbohydrate's conformation. The latter phenomenon is most often attributed to more pronounced conformational flexibility.[58] As soon as carbohydrate NMR spectroscopists became aware of the dynamic nature of oligosaccharides, they attempted to measure NMR parameters which could be used to characterize internal motions more quantitatively. Internal motion in biomolecules can be detected and quantified by NMR spectroscopy if it occurs relatively slowly or relatively quickly compared with the overall motion of the molecule.[84] NMR parameters that can be related to internal dynamics include the temperature and magnetic-field-strength dependences of relaxation times (T_1 and $T_{1\rho}$) and cross-relaxation rates (homo- and heteronuclear NOEs).[85]

4.1.1 Conformation

For the determination of pyranoid ring conformations, a complete set of vicinal ^3J(H,H) couplings for the spin system suffices due to the relative rigidity of this type of ring structure. One or more intraresidue $^1H/^1H$ NOEs may be useful in refining the pyranose ring pucker. Conformations of pendant groups require the measurement of all pertinent vicinal J(H,H) scalar couplings [for example, ^3J(H-5,H-6) and ^3J(H-5,H-6′) for CH_2OH in hexopyranoses; ^3J(HOCH) couplings for OH groups]. Additionally, $^1H/^1H$ NOEs and heteronuclear scalar couplings may be measured. For the conversion of ^3J(H,H′) scalar couplings into torsion angles, carbohydrate spectroscopists use the Karplus equation as parameterized by Haasnoot et al. to account for substitution and electronegativity effects along the H−C−C′−H′ pathway[86,87] [see also Altona (***Vicinal Coupling Constants and Conformation of Biomolecules***) in this Encyclopedia]:

$$^3J(\mathrm{H,H'}) = 13.22\cos^2\theta - 0.99\cos\theta + \sum_i \Delta\chi_i[0.87 - 2.46\cos^2(\xi_i\theta)] \qquad (1)$$

where θ is the H−C−C′−H′ torsion angle, and $\Delta\chi_i$ are the Huggins electronegativities of substituent i relative to that of H. The value of ξ_i is either +1 or −1, depending on the orientation of the substituents.[86] As for the pendant groups, the conformation of the hydroxymethyl group in hexopyranoses is predominantly determined by the rotation around the C-5−C-6 bond described by the dihedral angle ω_H (Figure 8). As was reviewed by Bock and Duus,[88] information about the

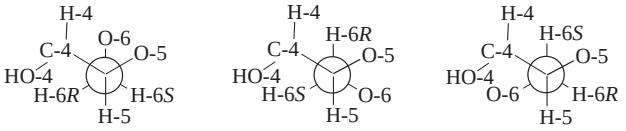

Figure 8 Definition of the three staggered conformations for the hydroxymethyl group in d-glucopyranose. For NMR spectroscopy, ω_H is defined as the dihedral angle H-5–C-5–C-6–O-6. (In crystallography, ω is commonly defined as O-5–C-5–C-6–O-6; hence, the subscript H in ω_H when using H-5 as the reference atom.) The three staggered conformers are described as *gg*, *gt*, and *tg* (*g* = *gauche*, *t* = *trans*; the first letter in the pair refers to the O-6 position relative to O-5, the second to the orientation of O-6 with respect to C-4). Thus, *gg*, *gt*, and *tg* correspond to ω_H = 180°, 60°, and −60°, respectively

conformational preferences of the hydroxymethyl group can be obtained via NMR using ^3J(H-5,H-6*R*) and ^3J(H-5,H-6*S*) provided that the stereospecific assignment of the H-6 atoms is either known or can be achieved via NMR:[89]

$$^3J(\text{H-5, H-6}R) = 13.22\cos^2\theta - 0.99\cos\theta - 6.4\cos^2(25.87-\theta) - 0.96\cos^2(7.96+\theta) + 2.61 \quad (2a)$$

$$^3J(\text{H-5, H-6S}) = 13.22\cos^2\theta - 0.99\cos\theta - 3.2\cos^2(25.87-\theta) - 3.2\cos^2(25.87+\theta) - 0.96\cos^2(7.96+\theta) + 2.61 \quad (2b)$$

If one assumes that the three low-energy staggered rotamers (ω_H = 60°, −60°, and 180°) (Figure 8) are the exclusive contributors to the average conformer, the measured values $[^3J(\text{H-5,H-6}R)]_{exp}$ and $[^3J(\text{H-5,H-6}S)]_{exp}$ are analyzed as linear combinations of the calculated values of these couplings for the pure *gg*, *gt*, and *tg* rotamers; the coefficients p_{gg}, p_{gt}, and p_{tg} in these equations are interpreted as relative populations, i.e., the mole fractions in which the respective staggered rotamers contribute to the time-averaged conformation as measured by NMR:

$$J_{exp} = p_{gg}\cdot J_{gg} + p_{gt}\cdot J_{gt} + p_{tg}\cdot J_{tg} \quad (3a,b)$$

(where J_{exp} is ^3J(H-5, H-6*R*) or ^3J(H-5, H-6*S*)

$$p_{gg} + p_{gt} + p_{tg} = 1 \quad (3c)$$

However, if constraints other than the two ^3J(H-5,H-6) homonuclear couplings are available, it is not necessary to make the aforementioned assumption. More advanced methods applied to the analysis of the rotamer population around the C-5–C-6 bond use the conformational entropy (S) associated with an ensemble; S can be calculated as:

$$S = -R\sum_i p_i \ln p_i \quad (4)$$

where the sum is over all the conformations, p_i is the probability of the ith conformation occurring in the ensemble, and R is the gas constant. Given the number of measurable NMR constraints, computerized methods attempt to maximize the conformational entropy.[90,91]

Linkage conformations cannot be defined by ^nJ(H,H′) measurements; their analysis requires the measurement of interglycosidic NOEs and ROEs (both ^{1}H/^{1}H NOE and ROE, and ^{13}C/^{1}H NOE, if possible), in combination with transglycosidic ^3J(C,H) couplings. Distances are typically calculated as $r_{ij} = (igma_{ref}/\sigma_{ij})^{\frac{1}{6}} r_{ref}$, where σ_{ref} and r_{ref} are the cross-relaxation rate and the distance, respectively, of a pair of reference protons within the rigid pyranose ring system. Glycosidic bond angles are calculated from ^3J(C,H) values according to the Karplus equation as parameterized by Tvaroska et al.[92] (see also Mulloy et al.[93]) based on seminal work by Perlin and co-workers:[94]

$$^3J(\text{C, H}) = 5.7\cos^2\theta - 0.6\cos\theta + 0.5 \quad (5)$$

where θ is the H–C–O–C torsion angle. In addition, ^1J(C,H) values may be used to assist in the determination of bond conformations.[95,96] If carbohydrates can be obtained uniformly or selectively ^{13}C isotopically-enriched,[97] long-range ^{13}C,^{1}H couplings become easier to measure. In addition, ^1J(C,C), ^2J(C,C), and ^3J(C,C) become detectable as conformational constraints. However, notwithstanding the advances that are being made in combining chemical and enzymatic syntheses, procedures to obtain uniformly ^{13}C isotopically-enriched ('labeled') carbohydrates, particularly glycoconjugate side chains, are by no means straightforward.

4.1.2 Hydrogen Bonding

Hydroxyl resonances in the ^{1}H NMR spectra of oligosaccharides in aprotic solvents such as DMSO have long been used as structural probes. However, as most biologists are primarily interested in carbohydrate conformations in aqueous solutions, only glycolipid NMR researchers have put any significant effort into investigating these signals in DMSO (Section 3.3). Although hydroxyl proton resonances in aqueous solutions of sugars were first observed over 14 years ago,[98] the utility of these protons in the conformational analysis of carbohydrates has been demonstrated only recently.[99–103] Hydroxyl resonances potentially provide a wealth of structural information in the form of chemical shifts, J couplings, NOEs, exchange rates, and isotope shifts. However, this information is accessible only if the intermolecular exchange of OH protons with H_2O in the aqueous solvent can be slowed sufficiently. At room temperature, hydroxyl protons in aqueous solutions of carbohydrates engage in fast chemical exchange with water. Several researchers have applied mixed solvents (water/acetone and water/methanol) to study OH groups at low temperatures (−5 °C to −10 °C) (see, e.g., Poppe and Van Halbeek).[99] Recently, ^{1}H NMR studies of hydroxyl groups in dilute solutions of mono- and disaccharides in pure H_2O under supercooled (−15 °C to −20 °C) conditions have been reported.[101] The chemical exchange effects under these conditions are reduced to such an extent that separate signals can be observed for each hydroxyl site; thus, all hydroxyl proton resonances can be assigned on the basis of scalar connectivities to nonlabile aliphatic protons. The scalar ^3J(HOCH) couplings can be analyzed[103] by equations (1) and (3)[3,4]3, in conjunction with more advanced statistical methods. The linewidths,

temperature-shift coefficients, and coupling constants of OH protons are valuable hydration and hydrogen-bonding probes in NMR studies. H/D isotope effects of hydroxyl protons on ^{13}C resonances may be used to obtain additional evidence of the involvement of OH groups in intra- or interresidue hydrogen bonds.104 Protruding farther from the glycosyl ring systems, OH protons may additionally serve as long-range sensor conformational probes which can be interrogated by NOESY and ROESY experiments of the carbohydrate in aqueous solution.[99,105,106]

4.1.3 Dynamics

NOEs and ROEs (or, more strictly speaking, the cross-relaxation rates $\sigma^{\parallel}$ and $\sigma^{\perp}$), as well as scalar coupling constants, are time-averaged parameters when the interconversion of conformers is fast on the NMR timescale.[107] However, interpretation of the measured NMR constraints in terms of the existence of several conformers and their interconversion rates is not easily accomplished. An extensive use of molecular modeling is usually required.[66,76,83,107,108] The experimental approach to the problem of flexibility involves the measurement of different relaxation rates (^{13}C and ^{1}H T_1 and $T_{1\rho}$, as well as $^{1}H/^{1}H$ and $^{13}C/^{1}H$ NOE) at a number of different frequencies (ω) in order to sample the spectral density $J(n\omega)$:[109–112]

$$J(n\omega) = \left(\frac{2}{5}\right) \cdot \frac{\tau_c}{1 + (n\omega\tau_c)^2} \tag{6}$$

where n = 0, 1, or 2, and τ_c, the rotational correlation time, is directly related to relaxation times T_1 and $T_{1\rho}$ (see, for example, Wagner and others).[112–115] The laboratory and rotating frame homonuclear cross-relaxation rates, $\sigma^{\parallel}$ and $\sigma^{\perp}$, respectively, are expressed by equations (7a) and (7b):

$$\sigma^{\parallel} = K[6J(2\omega) - J(0)] \tag{7a}$$

$$\sigma^{\perp} = K[3J(\omega) + 2J(0)] \tag{7b}$$

where $K = 0.1\ \Sigma_1 \gamma^4 h^2/4\pi^2 r_{kl}^6$, γ is the ^{1}H gyromagnetic ratio, h is Planck's constant, r is the internuclear distance between nuclei k and l, and the summation index runs over all interactions.[113,114,116] Similar expressions for $^{13}C/^{1}H$ cross-relaxation rates have been documented.[112]

Spectral density is most conveniently interpreted at the molecular level by the model-free approach of Lipari and Szabo[117,118] in which the types of molecular motion of an oligosaccharide are distinguished by their different timescales. The total motion of the molecule is separated into the tumbling of the entire molecule (with rotation correlation time τ_o) modulated by more rapid internal (segmental) motion with characteristic correlation time (τ_i) and amplitude expressed by an order parameter (S^2):

$$J(n\omega) = S^2 \left(\frac{2}{5}\right) \cdot \frac{\tau_o}{1 + (n\omega\tau_o)^2} + (\langle r^{-6} \rangle - S^2) \left(\frac{2}{5}\right) \cdot \frac{\tau}{1 + (n\omega\tau)^2} \tag{8a}$$

where n = 0, 1, or 2, $S^2 = \sum_{m=-2}^{m=2} |\langle (5/4\pi)^{-1/2} Y_{2m}(\Omega)/r^3 \rangle|^2$, $Y_{2m}(\Omega)$ are spherical harmonics functions with r and Ω corresponding to the distance and polar angle of a given proton pair in the molecular frame; $\langle \ldots \rangle$ denotes ensemble average; and $\tau^{-1} = \tau_o{}^{-1} + \tau_i{}^{-1}$. A slightly more simplified expression for $J(n\omega)$ may be used when taking only fluctuations due to molecular reorientation, but not internuclear separation, into account (Section 5.2); S^2 becomes distance independent, and equation (8a) becomes equation (8b):

$$J(n\omega) = S^2 \left(\frac{2}{5}\right) \cdot \frac{\tau_o}{1 + (n\omega\tau_o)^2} + (1 - S^2) \left(\frac{2}{5}\right) \cdot \frac{\tau}{1 + (n\omega\tau)^2} \tag{8b}$$

Either way, the generalized order parameter is a measure of the spatial restriction of the internal reorientation ($S^2 = 1$ in the absence of internal motion; $S^2 = 0$ in the presence of complete, isotropic reorientation).

Often applicable to oligosaccharides, this model predicts that, if there is significant relaxation through internal motion in the saccharide, the ratio of the NOEs (and the T_1 values) at different field strengths should differ for those protons relaxing with neighboring protons within fixed distances (i.e., neighbors on the same pyranose ring) versus those relaxing with neighbors at fluctuating distances (i.e., across the glycosidic linkage). The separation of the motions into distinct regimes is crucial to the success of this method. For internal motions to contribute significantly to the relaxation, their time scale must be fast compared with that of the overall tumbling (i.e., $\tau_o \sim 0.1$ ns for a disaccharide). Thus the internal dynamics (segmental motions) of carbohydrate molecules in solution can be assessed by NMR spectroscopy if the rearrangements occur much faster (or much slower) than the overall molecular tumbling. Physical models for the temperature dependences of τ_o, τ_i, and NOEs are in existence as well, but they are less successful in reproducing the dynamic behavior of oligosaccharides.

4.2 Di- and Trisaccharides

Analyses of the solution conformation and dynamics of carbohydrates encompass the following steps: (i) the complete assignment of ^{1}H and ^{13}C NMR spectra of the carbohydrate, (ii) the measurement of NOEs and vicinal couplings in order to establish spatial (distance and/or torsion angle) constraints between atoms, (iii) the measurement of ^{1}H and ^{13}C relaxation parameters (T_1, $T_{1\rho}$, homo- and heteronuclear NOEs) as a function of temperature and field strength, and (iv) the evaluation of experimental data with the use of computational strategies, including statistical methods, potential energy calculations, and molecular dynamics (MD) or Monte Carlo (MC) simulations (as well as comparison with crystal structures, if available). With the application of at least two of the aforementioned steps, a large number of di- and trisaccharides have been examined, including sucrose (see below), maltose [Glcα(1→4)Glc],[119] cellobiose [Glcβ(1→4)Glc],[120] lactose [Galβ(1→4)Glc],[97,121] melibiose [Galα(1→6)Glc],[122] gentiobiose [Glcβ(1→6)Glc] (see below), xylobiose [Xylβ(1→4)Xyl],[123] mannobioses [Manα(1→3)Man and Manα(1→2)Man],[108,124] chitobiose [GlcNAcβ(1→4)GlcNAc], and chitotriose. For an overview of

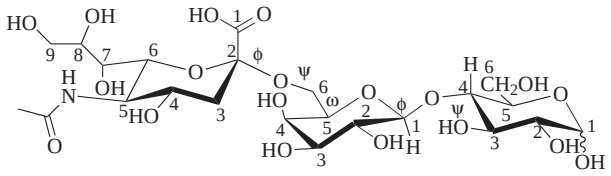

Figure 9 Schematic structure of sialyl-$\alpha(2\rightarrow6)$-lactose. The numbering of the carbon atoms and their substituents is indicated. The torsion angles ϕ and ψ around the $(1\rightarrow4)$ glycosidic bond are defined as in Figure 7(b): ϕ(H-1′–C-1′–O-1′–C-4) and ψ(C-1′–O-1′–C-4–H-4). The angles ϕ and ψ around the $(2\rightarrow6)$ glycosidic linkage are defined as ϕ(C-1′–C-2′–O-2′–C-6) and ψ(C-2′–O-2′–C-6–C-5), while ω is (O-5–C-5–C-6–O-2′); the definition of ϕ differs from that given in the legend to Figure 7(b) due to the absence of an anomeric proton in Neu5Ac. The conformation of the $(1\rightarrow4)$ linkage was studied by measuring ^3J(H-1′,C-4) and ^3J(C-1′,H-4) (compare Figure 14), as well as interglycosidic NOEs. Angle ϕ for the $(2\rightarrow6)$ linkage was studied by ^{1}H/^{1}H ROE and ^{13}C/^{1}H NOE experiments, while ψ for the $(2\rightarrow6)$ linkage was deduced from ^3J(C-2′,H-6*R*) and ^3J(C-2′,H-6*S*) measurements (Table 2). For ω around the $(2\rightarrow6)$ linkage, the Gal ^3J(H-5,H-6*R*) and ^3J(H-5,H-6*S*) were measured (Figure 13 and Table 1).[106] The Neu5Ac glycerol side-chain conformation was defined by the ^3J(H-6,H-7), ^3J(H-7,H-8), ^3J(H-8,H-9) and ^3J(H-8,H-9′) couplings (for the latter two, see Figure 12) in conjunction with the existence of a hydrogen bond between O-8 and the C–O bond of the C-1 carboxyl group[106]

di- and trisaccharide structures determined by X-ray crystallography, NMR spectroscopy and/or theoretical computations, the reader is referred elsewhere.[77,125–128] Because of the importance of sialyl oligosaccharides in the biology of glycoproteins and glycolipids, an illustration is provided of the typical procedures involved in the NMR conformational analysis of a trisaccharide similar to the terminal entity found on various glycoprotein and ganglioside oligosaccharides, namely, sialyl-$\alpha(2\rightarrow6)$-lactose [Neu5Ac$\alpha(2\rightarrow6)$Gal$\beta(1\rightarrow4)$Glc].[106] Comparisons are drawn with the conformations of Neu5Ac$\alpha(2\rightarrow3)$Gal[129] and sialyl-$\alpha(2\rightarrow3)$-lactose.[130] A schematic drawing of the structure of sialyl-$\alpha(2\rightarrow6)$-lactose is shown in Figure 9, and definitions of torsion angles ϕ, ψ, ω, and other pertinent parameters are included in the legend to that figure.

4.2.1 ^{1}H and ^{13}C Spectral Assignments

Attractive alternatives to the 2D COSY and TOCSY techniques currently used for the complete assignment of the ^{1}H NMR spectrum of an oligosaccharide (Section 3.4) are their 1D selective analogs.[79,131] Despite the overlap of ~85% of the aliphatic proton resonances within approximately 1 ppm in a typical carbohydrate spectrum, the resonances of the structural-reporter groups, including those of the anomeric protons, are separated and accessible for selective excitation, providing suitable entries for transfer of magnetization through scalar couplings to other protons in the spin system of a glycosyl residue. In fact, carbohydrates are often cited in the magnetic resonance literature as being used as toy systems for new selective excitation sequences (see Kupce and Freeman,[132] for example). To reveal the entire spin system, i.e., trace the scalar connectivity from H-1 through H-6 for a hexosyl residue, two methods are currently being applied; (i) multistep correlated (relayed COSY) experiments[133,134] in which magnetization is transferred in successive steps from the selectively excited resonance, and (ii) isotropic mixing (TOCSY) pulse sequences[62,135] that distribute selectively excited magnetization in a more uniform manner among coupled spins. Magnetization transfer in TOCSY experiments is more efficient than in relayed COSY experiments, which suffer from larger losses of magnetization due to T_2 relaxation; also, TOCSY signals occur as in-phase multiplets. The major obstacles to tracing glycosyl spin systems are small coupling constants (e.g., those between H-1 and H-2 in mannosyl, H-4 and H-5 in galactosyl, and H-6 and H-7 in Neu5Ac residues). In order to overcome these 'bottlenecks' in TOCSY experiments, researchers have applied a number of different schemes which rely on multiple selective excitation, e.g. double-TOCSY[136] or double-DANTE TOCSY[137] or relayed TOCSY[138] (where isotropic mixing is followed by a COSY step). Parenthetically, it should be mentioned that extensions of ^{1}H 1D and 2D techniques to 3D and 4D NMR techniques have been described for carbohydrates;[139,140] however, full-blown 3D and 4D data acquisition is time-consuming and rarely necessary to solve a carbohydrate structural problem. (Multi-)selective 1D and 2D analogs of 3D and 4D NMR experiments[80,141] are far more efficient methods of obtaining the desired information from a carbohydrate ^{1}H NMR spectrum. For example, the 2D selective analog of the 3D TOCSY–COSY experiment and the 3D selective analog of the 4D TOCSY–TOCSY–COSY experiment have been applied for tracing scalar connectivities in GlcNAc residues for medium-sized oligosaccharides.[140,142] Pulse sequences which are successfully utilized for isotropic mixing include: MLEV-17,[62] WALTZ-16,[143] DIPSI-2,[144] clean-CITY,[145] and mixing sequences proposed by Glaser and Drobny.[146] Selective excitation is accomplished by DANTE pulse trains[147] or any one of a variety of shaped pulses.[79,80,148]

Once the ^{1}H NMR spectrum of an oligosaccharide has been assigned, the assignment of the protonated ^{13}C resonances on the basis of one-bond ^{13}C,^{1}H correlation spectroscopy (e.g., HMQC) is relatively straightforward (Section 3.4). Nonprotonated ^{13}C signals can be assigned by an HMBC experiment. These ^{1}H-detected (or 'inverse-detected') schemes[149] allow the acquisition of correlation spectra for submillimolar amounts of carbohydrate sample within a few hours of data acquisition. Employing the combination of TOCSY and HMQC/HMBC spectroscopy, the ^{1}H and ^{13}C spectra of sialyl-$\alpha(2\rightarrow6)$-lactose in D_2O have been fully assigned.[106]

4.2.2 Distance and Torsion Angle Constraints

4.2.2.1 Ring Conformation. The establishment of pyranose ring pucker involves the accurate measurement of homonuclear vicinal scalar couplings; this is best accomplished with the use of ^{1}H selective excitation experiments such as 1D TOCSY [Figure 10(a)]. The signals in 1D TOCSY spectra are obtained in pure absorption if the admixture of antiphase dispersive lines is averaged out by stepwise incrementation of the isotropic mixing time[135] or by incorporation of a *z* filter.[62] The values of the ^3J(H,H′) couplings acquired for sialyl-$\alpha(2\rightarrow6)$-lactose[106] show each of the ring systems in the trisaccharide to be in its typical pyranose chair conformation, i.e., $^4C_1$ for Glc and Gal, $^2C_5$ for Neu5Ac [compare Figures 1(c) and 7, and Sabesan et al.].[158]

4.2.2.2 Exocyclic Groups. In order to evaluate rotamer populations around the C-5–C-6 bond in hexopyranoses, the

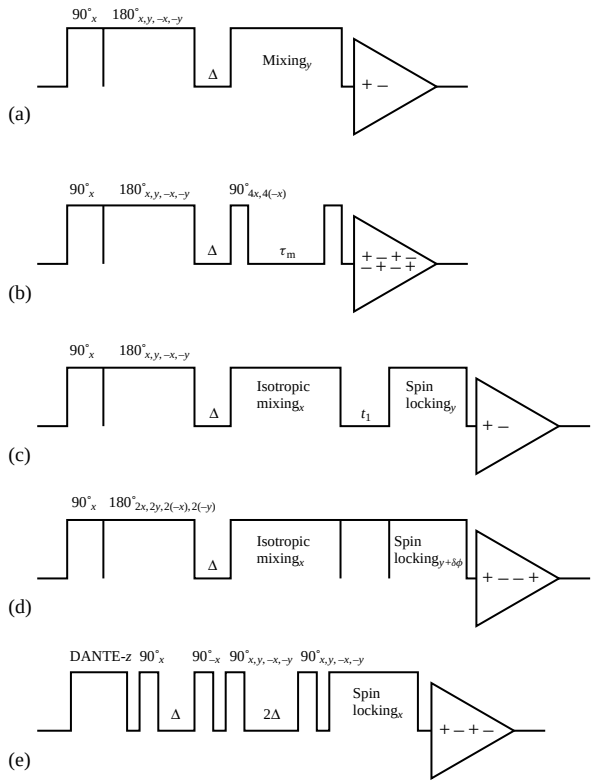

Figure 10 Pulse sequences commonly used for ^{1}H selective excitation experiments on carbohydrates. Selective excitation uses either a composite 90° pulse[150] consisting of two consecutive DANTE pulse trains,[147] traces (a)–(d) or a DANTE-*z* sequence[151] consisting of two interleaved pulse trains with different phase properties, trace (e). In all cases, $\Delta \sim 0.63t_{90}$, where t_{90} is the duration of the selective 90° pulse. The basic phase cyclings, as listed, may be extended following CYCLOPS and EXORCYCLE procedures.[152] (a) 1D TOCSY or 1D ROESY experiment. Isotropic mixing is performed with[146] composite pulses R = (290°_x,330°_{-x},290°_x) arranged into the supercycle (R*RR*R RR*RR* *RRR*R *RR*RR, 180°_y) analogous to the MLEV-17 sequence;[153] italicized letters indicate phase inversion of the element. The mixing time is flanked by two short (~2 ms) trim pulses. For mixing in the ROESY experiment, a train of short (~20°) pulses is used.[154] (b) 1D NOESY experiment. (c) Selective 3D TOCSY–ROESY experiment.[150,155] (d) Double selective 3D TOCSY–ROESY experiment. The selective α pulse, when achieved with a DANTE pulse train,[156] can have any tilt angle in the range of 60° to 180°. The phase increment $\delta\phi$, associated with the change of offset during a finite time interval, is determined experimentally. (e) 1D experiments in H_2O solution utilizing 1–1 echo water suppression.[157] The DANTE-*z* pulse train can be used either for spin inversion or presaturation. The delay Δ determines the width of the excitation profile; typical values of Δ tailored for carbohydrate NMR spectra are 200–400 μs. A short (~2 ms) spin lock pulse may serve to purge the dispersive part of the residual water signal. The experiments are typically performed in the difference mode, with pertinent shift of carrier frequencies, using a single power level of excitation (typically $t_{90} \sim 60$ μs)

protons in the exocyclic CH_2OH group must be assigned stereospecifically. Since the methylene protons, together with ring proton H-5, form a mutually coupled three-spin system, they can be recognized with, for example, a 2D triple quantum filtered COSY[76] or triple quantum correlated spectroscopy experiment.[64,78,159,160] Proton multiplets from exocyclic groups are more readily retrievable from selective 1D TOCSY spectra or, alternatively, from 1D COSY spectra recorded with a chemical-shift-selective filter.[161,162] If the pertinent coupling constants cannot be accurately measured from such ^{1}H spectra, either due to extreme spectral overlap or second-order effects, then the goal can be attained with inverse ^{13}C,^{1}H correlation experiments in which the proton multiplets are more likely to occur separately due to the larger chemical shift dispersion in the ^{13}C spectrum. Usually, the method of choice is the modified over-Bodenhausen experiment[163] as depicted in Figure 11(a); this selective 1D heteronuclear single quantum coherence (HSQC) experiment gives pure absorptive ^{1}H lineshapes. An additional advantage of this pulse sequence lies in the ease with which it can be applied selectively; this is accomplished by either replacing the first ^{13}C 180° pulse with its selective analog[169] or by performing t_1 incrementation in analogy to a chemical-shift-selective filter (by jittering of delay, δ).[161,166] Application of this method to sialyl-α(2→6)-lactose yields well separated, first-order H-9*R* and H-9*S* multiplets for the Neu5Ac side chain (Figure 12).

The stereospecific assignment of the exocyclic methylene protons is particularly critical when analyzing the conformation of a (1→6) linkage between two glycosyl residues [for example, the linkage between Neu5Ac and Gal in sialyl-α(2→6)-lactose (Figure 9)]. When the stereospecifically mono-C-6 (or mono-C-9, if Neu5Ac is concerned) deuterated analogs of the oligosaccharide are available, the assignment of H-6*R* (H-9*R*) and H-6*S* (H-9*S*) is readily accomplished. However, the stereospecific chemical synthesis of a mono-C-6-deuterated analog of a mono- or disaccharide is usually a rather laborious procedure. Fortunately, NMR spectroscopy can, for some oligosaccharides, assign the C-6 methylene protons stereospecifically without the aid of deuteration. To accomplish this, one needs to be able to measure the pertinent vicinal ^3J(H-5,H-6) and ^3J(H-5,H-6′) coupling constants in conjunction with either the H-4/H-6,6′ NOE effects[78] or the ^3J(C-4,H-6) and ^3J(C-4,H-6′) scalar couplings.[89,170] The measurement of heteronuclear coupling constants will be discussed later in this section. As to the stereospecific assignment of H-6*R* and H-6*S* based on 'NOE-labeling', valuable spectral information can be obtained from selective analogs of 3D NOE-labeling experiments in many cases.[80,150,171] Figure 13 shows a selective 3D TOCSY–ROESY spectrum obtained for sialyl-α(2→6)-lactose with the pulse sequence shown in Figure 10(d). The NOE connectivities originating from Gal H-4 appear well-resolved. The values of the Gal ^3J(H-5,H-6) coupling constants (Table 1), along with the observation of NOE between Gal H-4 and only one of the H-6 protons (Figure 13), enabled the stereospecific assignment of Gal H-6*R* and Gal H-6*S*.[106] Subsequent analysis of the vicinal ^3J(H-5,H-6*R*) and ^3J(H-5,H-6*S*) coupling constants using equations (3a)–(3c) provided the rotamer populations around ω for sialyl-α(2→6)-lactose (Table 1). This interpretation was refined by the application of the maximum entropy method.[90] The availability of a relatively large set of structural constraints is required for this approach [for example, the values of the Gal ^3J(H-5,H-6*R*′), ^3J(H-5,H-6*S*′), ^3J(C-4,H-6*R*) and ^3J(C-4,H-6*S*) scalar couplings and the H-5/H-6*R*, H-5/H-6*S*, H-4/H-6*R*, and H-4/H-6*S* NOEs were used in the analysis of the rotameric distribution; see Table 2]. When applied to gentiobiose [Glcβ(1→6)Glc] to characterize the conformational flexibility around the C-5–C-6 bond which is part of the disaccharide's glycosidic linkage,

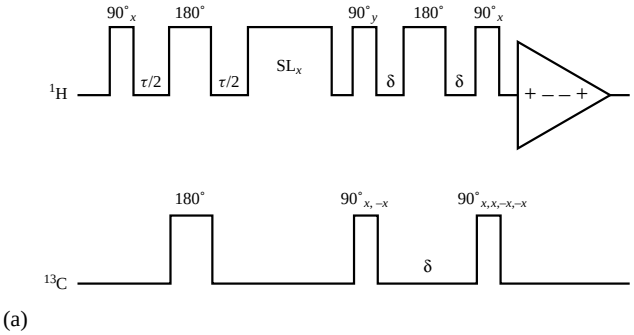

(a)

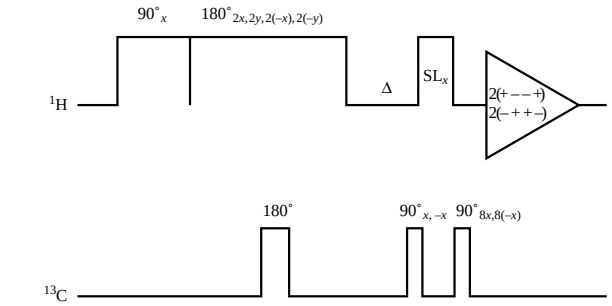

(b)

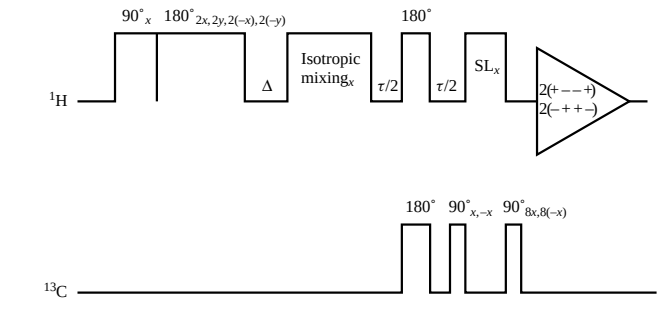

(c)

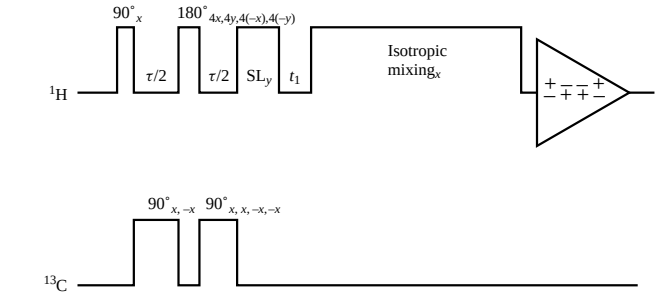

(d)

Figure 11 Pulse sequences for measuring long-range nJ(C,H) (n = 2, 3, 4, . . .) with ^{1}H detection. SL denotes spin lock; the other symbols are as defined in Figure 10. (a) Modified HSQC experiment.[163–165] The pulse marked with is either selective or nonselective. The delay δ is either systematically or stochastically incremented[166] to obtain selectivity in the carbon domain. The delay τ is taken long enough for the evolution due to heteronuclear long-range couplings to become manifest. The resulting proton multiplets are in antiphase with respect to one- or multibond ^{13}C,^{1}H couplings and in-phase with respect to homonuclear couplings. (b) Modified HSQC and (c) relay TOCSY–HSQC experiments[167] tailored for measuring interglycosidic ^{3}J(C,H) in oligosaccharides. (d) ^{13}C-selective 2D analog of a 3D exclusive-type ^{13}C,^{1}H correlation experiment.[168] The ^{13}C 90° pulses are 1–2 ms long; $\tau \sim [2^{1}J(\mathrm{C,H})]^{-1}$

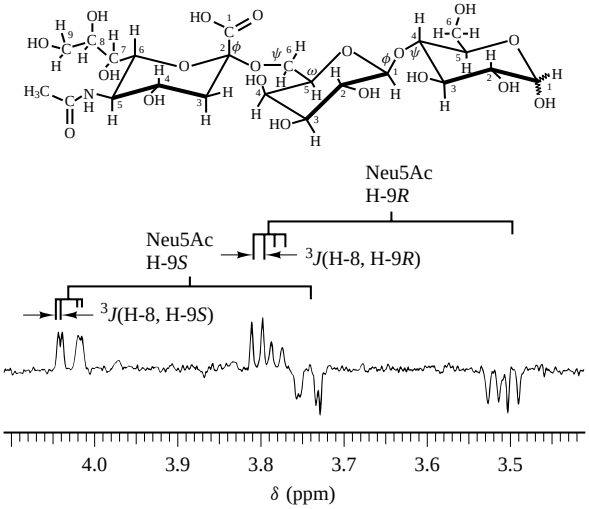

Figure 12 Editing ^{1}H multiplets according to their ^{13}C chemical shift. Spectrum of sialyl-$\alpha(2\rightarrow6)$-lactose in D_2O solution obtained with the pulse sequence shown in Figure 11(a); τ is set to 3 ms. The Neu5Ac C-9 frequency was selected by randomly jittering the delay δ. In the ^{1}H spectrum of the ^{12}C-9 isotopomer, H-8–H-9*S*–H-9*R* constitute a second-order ABX spin system; no value for the homonuclear coupling ^{3}J(H-8,H-9*S*) can be derived from that spectrum (reproduced with permission from Escom Science Publishers)[106]

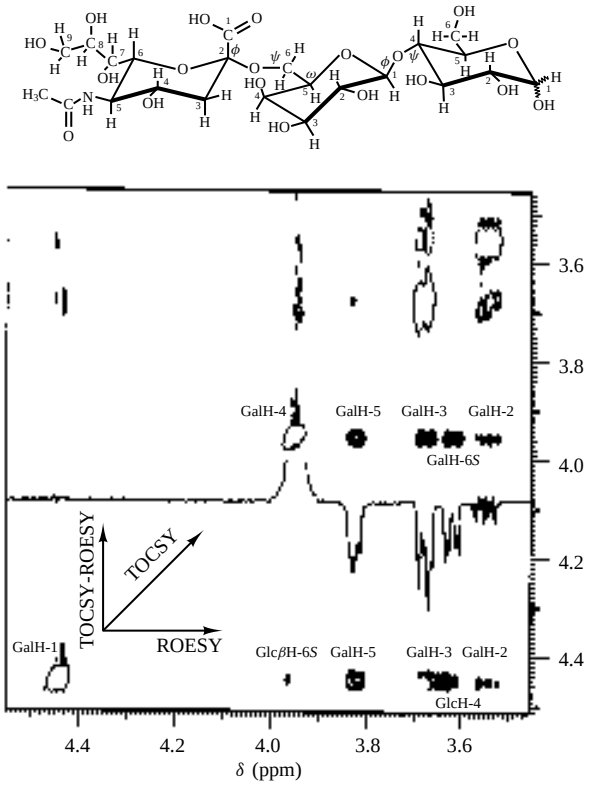

Figure 13 Selective 3D TOCSY–ROESY spectrum of sialyl-$\alpha(2\rightarrow6)$-lactose in D_2O solution (~30 mM) obtained with the pulse sequence shown in Figure 10(c) at 500 MHz and ambient temperature. The Gal H-1 proton was selectively excited (for 60 ms), followed by 77 ms of TOCSY and 140 ms of ROESY mixing. The digital resolution in the resulting 2D spectrum is 0.73 Hz pt^{-1} and 4.3 Hz pt^{-1} in the ω_2 and ω_1 dimensions, respectively; the total acquisition time was less than 5 h (reproduced with permission from Escom Science Publishers)[106]

the maximum entropy method yields results that differ significantly from the results of traditional rotameric distribution calculations employing force-field-based analysis of the ^{3}J(H-5,H-6) couplings by a Karplus-type equation;[90] however, for sialyl-$\alpha(2\rightarrow6)$-lactose that difference was insignificant.

4.2.2.3 Linkage Conformations from ^{3}J(C,H). Long-range heteronuclear scalar couplings [^{3}J(C,H)] through the glycosidic bonds (H–C–O–C′ and C–O–C′–H′) [Figure 7(b)] provide spatial constraints for the torsion angles ϕ and ψ, respectively, around the glycosidic linkages. Most of the NMR pulse sequences developed for the sensitive and accurate measurement of ^{3}J(C,H) values for carbohydrates are based on the ^{1}H-detected HSQC experiment.[163,164] The experiments can be conducted in true 2D or selective 2D mode by selective excitation and/or chemical-shift filtering of the protons and/or carbons of interest[167,169,172] (Figure 11). If the proton of interest is not accessible for selective excitation, the anomeric proton of the relevant monosaccharide is excited first, and the magnetization is transferred to the desired proton by a TOCSY step preceding the HSQC experiment [Figures 11(c) and 14].[167] With the aid of these methods, the pertinent ^{3}J(Glc C-4, Gal H-1) and ^{3}J(Glc H-4, Gal C-1) couplings in sialyl-$\alpha(2\rightarrow6)$-lactose were determined to be 4.2 and 5.1 Hz, respectively (Table 2).

As a valuable alternative to HSQC, a double INEPT type polarization transfer step may be used in the ^{1}H-detected measurement of long-range ^{13}C,^{1}H couplings; examples of such ^{1}H- and ^{13}C-selective, ^{1}H-detected 2D and pseudo 2D experiments have been reported.[173] Selective and nonselective measurements of interglycosidic ^{3}J(C,H) are greatly facilitated by the incorporation of ^{13}C labels at the positions involved in glycosidic linkages, as was demonstrated for sucrose.[174]

The elusive long-range heteronuclear scalar coupling parameters are also present in 2D ^{13}C-filtered ^{1}H,^{1}H correlation spectra, e.g., TOCSY[175] and NOESY/ROESY spectra,[176] which exhibit an exclusive type cross-peak structure. In these spectra, the long-range coupling constants are measured in the ω_2 dimension as a displacement of the proton multiplets that are resolved in the ω_1 dimension by the (large) ^{1}J(C,H) coupling. One-dimensional versions of this experiment have been applied to carbohydrates[89,177] to measure, for example, the ^{3}J(C-4,H-6*R*) and ^{3}J(C-4,H-6*S*) scalar couplings in glucose and galactose residues. Alternatively, a ^{13}C-filtered ROESY experiment has been introduced to measure ^{3}J(C,H) coupling constants through the glycosidic bonds of a cyclic glucan.[178]

Table 1 Rotamer Distribution around Gal C-5–C-6 in Sialyl-$\alpha(2\rightarrow6)$-Lactose

Coupling constant	4 °C	21 °C	77 °C
^{3}J(H-5,H-6*R*)	8.5 ± 0.2	8.3 ± 0.2	7.8 ± 0.2
^{3}J(H-5,H-6*S*)	3.7 ± 0.2	3.8 ± 0.2	4.2 ± 0.2
Population[a]	4 °C	21 °C	77 °C
p_{gg}	0.18 ± 0.03	0.20 ± 0.03	0.22 ± 0.02
p_{gt}	0.74 ± 0.03	0.71 ± 0.03	0.64 ± 0.02
p_{tg}	0.08 ± 0.03	0.08 ± 0.03	0.14 ± 0.02

[a]Calculated from the vicinal coupling constants ^{3}J(H-5,H-6*R*) and ^{3}J(H-5,H-6*S*) using equations (3a)–(3c). See Figure 8 for explanation of *gg*, *gt*, *tg* notation.

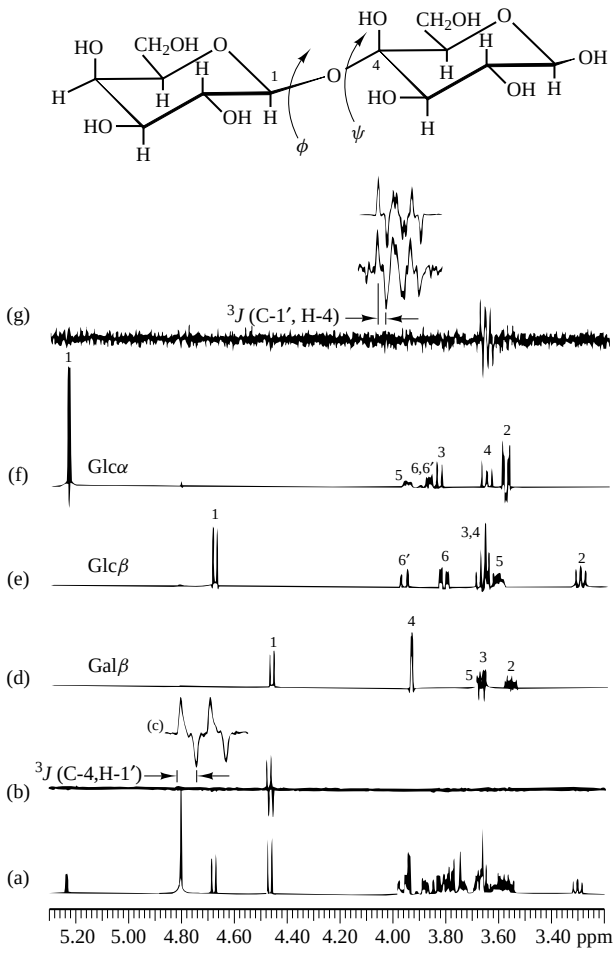

Figure 14 The measurement of heteronuclear long-range coupling constants across a glycosidic linkage illustrated for lactose in D_2O (50 mg mL^{-1}). (a) Reference spectrum. (b) Spectrum obtained with the pulse sequence shown in Figure 11(b). A ^1H composite pulse of 60 ms was applied selectively at Gal H-1, while the Glc ^{13}C-4 selective pulse was 2 ms long. (c) The heteronuclear coupling ^3J(C-4,H-1′) causes the antiphase pattern of the observed Gal H-1 multiplet. It is evident from the 1D TOCSY traces (d), (e), and (f) that ^3J(C-1′,H-4) cannot be obtained via the experiment shown in Figure 11(b) (note the overlap of Glc H-4 with Gal H-3); therefore, a relay TOCSY–HSQC experiment [Figure 11(c)] in which magnetization was selectively transferred from Glcα H-1 to H-4 was necessary (trace g). The duration of the entire pulse sequence in Figure 11(c) was close to 200 ms; 5500 scans were accumulated. (h) The heteronuclear coupling ^3J(C-1′,H-4) is read from the antiphase structure of the observed Glcα H-4 multiplet, computer-simulated in trace (i). The values ^3J(C-4,H-1′) and ^3J(C-1′,H-4) are 4.0 and 5.1 Hz, respectively (reproduced with permission from Academic Press)[167]

These methods, successfully applied to oligosaccharides with a natural abundance of ^{13}C, show their greatest potential in the measurement of long-range heteronuclear scalar couplings in ^{13}C isotopically-enriched carbohydrates (cf. Montelione et al.).[179] The pulse sequence in Figure 11(d) presents the selective version of 3D experiments originally designed for measurements of heteronuclear couplings in isotopically-enriched proteins.[179,180] The long-range carbon–proton coupling constants are measured independently of the linewidth from the exclusive-type scalar couplings correlation patterns,[168,179,180] as demonstrated (Figure 15) for glucose, 99% ^{13}C-labeled at C-1. Furthermore, the direction of the multiplet displacements allows the determination of the signs of the relevant coupling constants (cf. Serianni and Podlasek).[181]

Table 2 Average Distances and Vicinal Coupling Constants for Sialyl-$\alpha(2\rightarrow6)$-Lactose in Aqueous Solution[106]

Atom pair	$\langle r_{app}\rangle$ (Å)[a] or J_{exp} (Hz)[b]	$\langle r_{sim}\rangle$ or J^c_{sim} Family I[d]	Family II[d]
Neu5Ac/Gal			
H-3_{ax}/H-6*R*	3.3	4.35	2.35
H-3_{ax}/H-6*S*	3.3	4.63	2.53
H-3_{ax}/H-4	>5	6.34	4.78
H-3_{eq}/H-6*R*	5	4.54	3.37
H-3_{eq}/H-6*S*	4	4.33	3.84
H-3_{eq}/H-5	5	5.15	4.62
H-3_{eq}/H-4	>5	6.53	5.62
OH-8/H-6*R*	3.5	3.58	6.56
OH-8/H-6*S*	>4	5.07	5.67
O-7/Glc O-3	3[e]	3.43	5.64
C-2/H-6*R*	2.6	2.56	2.79
C-2/H-6*S*	>2.6	2.90	2.67
^3J(C-2,H-6*S*)	1.8	1.22	3.42
^3J(C-2,H-6*R*)	2.8	3.95	3.01
Gal/Gal			
^3J(H-5,H-6*R*)	8.5[f]	9.25	6.46
^3J(H-5,H-6*S*)	3.7[f]	3.97	4.17
^3J(C-4,H-6*R*)	2.9	2.48	2.39
^3J(C-4,H-6*S*)	1.8	1.75	3.07
H-4/H-6*R*	3.3	3.02	2.88
H-4/H-6*S*	2.6	2.65	2.75
Gal/Glc			
H-1/H-4	2.5	2.39	2.48
H-1/H-6*S*	3.5	2.72	2.69
H-6*R*/OH-3	3.5	4.17	4.39
^3J(H-1,C-4)	4.2[g]	2.58	2.08
^3J(C-1,H-4)	5.1[g]	5.07	5.22
H-6*R*/O-3	[h]	4.28	4.43
H-6*S*/O-3	[h]	5.09	5.01

[a]The distances r_{app} were evaluated with the formula $r_{ij} = r_{kl}(I_{kl}/I_{ij})^{\frac{1}{6}}$, in which I_{ij} and I_{kl} are the integrated signal intensities; I_{kl} corresponds to a reference interaction. For ROESY spectra, the intensities were scaled by the offset dependent factors $(\sin\theta_i \cdot \sin\theta_j)^{-2}$, in which $\theta_i = \arctan(\omega_i/\langle\gamma B_1\rangle)$; ω_i represents the offset from the carrier frequency and $\langle\gamma B_1\rangle$ the effective field strength in Hz. The precision of the distances is estimated to be $\sim 0.1r$.

[b]The precisions of the J_{exp} values are ±0.2 Hz, except those of ^3J(C-1,H-4) (±0.4 Hz) and ^3J(C-4,H-6*R*) and ^3J(C-4,H-6*S*) (±0.2 Hz).

[c]MMC simulated distances[106] were calculated according to the formula $\langle r^{-3}\rangle^{-\frac{1}{3}}$. The $\langle r_{sim}\rangle$ and J_{sim} values were scaled to 27 °C.

[d]Family I corresponds to the MMC simulation that started with ϕ of the (2→6)-linkage being set to −60°; for family II, the pertinent angle was set to 180°.

[e]This distance reflects the occurrence of a hydrogen bond between Neu5Ac OH-7 and Glc O-3.

[f]See Table 1.

[g]Compare with Figure 14.

[h]An anomerization effect ($\Delta\delta_{\alpha-\beta}$) was observed for Gal H-6*R*, but not for Gal H-6*S*, indicating that the former proton is closer to the Glc reducing end, i.e. near O-3 of the Glc residue; see Figure 16.

4.2.2.4 Linkage Conformations from Interresidue $^1H/^1H$ NOE. Early in the history of carbohydrate NMR, conformational studies of small and medium-sized oligosaccharides in solution were based on steady-state NOE measurements.[113]

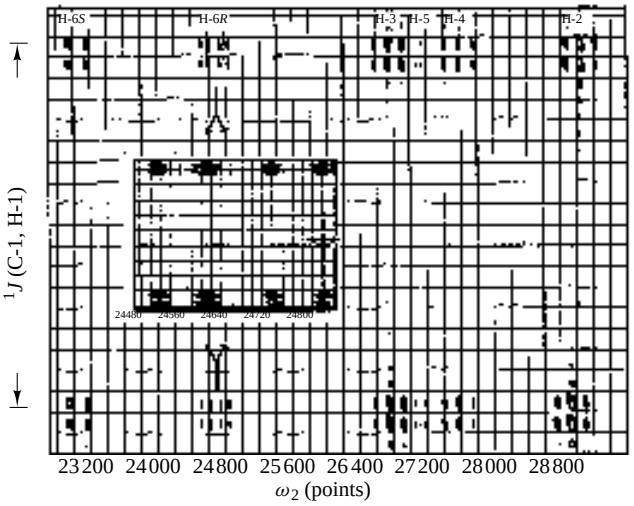

Figure 15 The measurement of heteronuclear coupling constants nJ(C-1,H) within glucose, ^{13}C-labeled at C-1, utilizing the pulse sequence shown in Figure 11(d). The heteronuclear couplings are read from the chemical shift difference between corresponding upper and lower multiplets. The digital resolution in the ω_2 domain is 0.055 Hz pt^{-1}, allowing the ^4J(C-1,H-6*R*) and ^4J(C-1,H-6*S*) couplings to be determined as 0.2 ± 0.05 and 0.4 ± 0.1 Hz, respectively

The major disadvantage of this approach lies in the fact that weak, direct interactions are frequently obscured by indirect effects and, thus, escape observation. More recent studies are based on measurements of cross-relaxation rates between two nuclei. Values for these parameters can be obtained either from multiselective relaxation time measurements[115] or analyses of 1D transient or 2D NOESY spectra.[114] The cross-relaxation rates are extracted from NOESY experiments on the basis of the two-spin approximation[182] or by 'full relaxation matrix analysis'.[183] The latter method has proven to be the most reliable in conformational analyses of carbohydrates.[66] Selective 1D NOESY experiments can give accurate (within 3%) estimations for cross-relaxation rates in small and medium-sized oligosaccharides, even at long mixing times. Moreover, selective spectra are free from zero quantum interferences which particularly obscure analysis of 2D NOESY spectra at short mixing times. Another crucial issue in quantitatively analyzing NOE data lies in their avoidance of contamination by indirect magnetization transfers. Undesired three-spin effects can be eliminated by (multi-)selective irradiation of potential mediators of spin diffusion during the NOESY mixing time.[184]

In order to overcome the problem of trying to detect vanishingly small NOE effects for tri- and tetrasaccharides at ~400–500 MHz, a novel technique for measuring cross-relaxation rates in the rotating frame was proposed. After its first application to a tetrasaccharide,[63] the technique's name was changed from CAMELSPIN to ROESY[185] spectroscopy and steadily gained the confidence of NMR spectroscopists as being an invaluable addition to the assortment of techniques used for the conformational analysis of molecules of all sizes. A major problem in the quantitative analysis of ROESY spectra are Hartmann–Hahn effects which occur in coupled spin systems.[154,186] These effects can, however, be minimized experimentally by a judicious choice of the carrier frequency.[154] An important feature of ROESY spectra is that NOE and chemical-exchange-mediated magnetization transfers can be readily distinguished.[187,188] Sialyl-$\alpha(2\rightarrow6)$-lactose, when investigated at 500 MHz and ambient temperature, is characterized by laboratory frame ^{1}H/^{1}H NOEs close to zero. Therefore, most of the distance constraints listed for the trisaccharide in Table 2 were obtained via 1D selective ROESY experiments.[106]

4.2.2.5 Hydrogen Bonding. The detection of intramolecular hydrogen bonds requires the observation of chemical shifts, linewidths, temperature shift coefficients, NOEs, and, if possible, ^3J(HOCH) couplings and exchange rates of assigned OH signals. In order to use OH protons as conformational probes for oligosaccharides, special techniques for water suppression must be utilized.[157,189–191] Additionally, isotope effects on ^{13}C chemical shifts examined in H_2O/D_2O (1:1, v/v) may be interpreted in terms of hydrogen bonding.[104]

If chemical exchange rates are of the same order of magnitude as the vicinal coupling constants, the assignment of hydroxyl protons on the basis of scalar correlation spectroscopy will not be possible. In these cases, assignments can be based on spatial proximities to the ring protons gained from steady-state NOE spectra [see Figure 10(c) for the pulse sequence]. This procedure requires, however, a good deal of caution, as spin diffusion and NOE enhancements mediated by chemical exchange could lead to erroneous assignments. In mixed solvents at temperatures well below 0 °C, chemical exchange is often retarded to an extent that transient NOE techniques can be utilized. As may be expected, even at low temperatures, the ^3J(HOCH) couplings for mono- and disaccharides obtained are found to be indicative of rotational averaging of the 'dangling' hydroxyl groups in most cases.[103] However, NOESY experiments performed on supercooled di- and trisaccharides strongly suggest that the majority of the intramolecular hydrogen bonds inferred from their crystal structures persist in solution.[101]

Most of the OH signals of sialyl-$\alpha(2\rightarrow6)$-lactose, investigated in mixed solvent systems at temperatures as low as −12 °C and in H_2O/D_2O at 1 °C, were assigned by 1D steady-state NOE experiments. Based on their linewidths and temperature shift coefficients (in conjunction with isotope shift effects observed in the ^{13}C spectra of the trisaccharide in H_2O/D_2O), three OH groups were found to be involved in intramolecular hydrogen bonds. First, Neu5Ac OH-8 is involved in an intraresidue hydrogen bond to the C-1 carboxyl group;[99] secondly, the hydrogen bond between Glc OH-3 and Gal O-5 is reminiscent of that found in lactose,[101] both in solution and in the crystal structure. Finally, the hydrogen bond observed between Neu5Ac OH-7 and Glc O-3 is an example of a long-range structural constraint of great value in the construction of the preferred conformation of sialyl-$\alpha(2\rightarrow6)$-lactose in aqueous solution. Modeling of the trisaccharide was based on 25 interresidue NMR constraints (Table 2). Analysis by MMC simulations[106,192] has shown that sialyl-$\alpha(2\rightarrow6)$-lactose occurs predominantly in two families of conformers that differ in the ϕ angle around the (2→6)-linkage (−60° versus 180°). The average structure of the predominant (>80%) family of conformers is depicted in Figure 16; it is the family stabilized by the three intramolecular hydrogen bonds.

4.2.3 Dynamics

The 3D structure of the disaccharide sucrose [Fru$\beta(2\leftrightarrow1)$ αGlc] (Figure 17), particularly the conformation of its glycosidic linkage, has been the subject of numerous investigations.

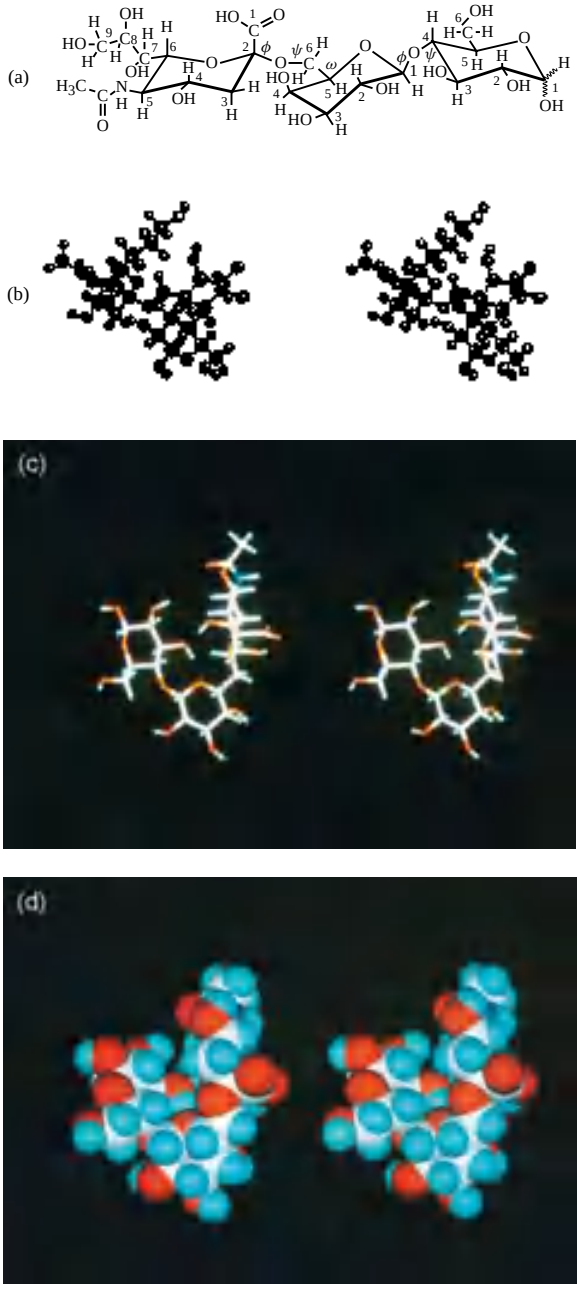

Figure 16 Stereo plots [ball-and-stick (b), Dreiding models (c), CPK models (d)] of the predominant conformer ('family I', Table 2) of sialyl-$\alpha(2\rightarrow6)$-lactose (a) in aqueous solution as derived from NMR data.[106] The Neu5Ac O-7:::H:::Glc O-3 and Glc O-3:::H:::Gal O-5 hydrogen bonds are clearly visible

Data obtained on sucrose in the crystalline[193,194] and solution states[93,174,195] have led to uncertainties concerning the degree of rigidity of the linkage conformation in solution, thus posing the question whether it is the same as in the crystal structure. A great deal of effort was spent examining intramolecular hydrogen bonding[196,197] and its effect, if any, on the overall conformation of sucrose in solution. McCain and Markley[198] were the first to measure ^{13}C T_1 relaxation times on sucrose as a function of the magnetic field strength. They realized the importance of knowing the timescale of internal motion when modeling carbohydrate conformations. As discussed in Section 4.1.3, this information can, in principle, be gained from nuclear relaxation rate measurements, preferably at different field strengths and different temperatures. The number of such studies performed on carbohydrates is remarkably small, and a model rigid on the timescale of molecular reorientation is often assumed on the basis of ^{13}C T_1 relaxation times. Accordingly, McCain and Markley's careful ^{13}C T_1 measurements for sucrose revealed very fast and small amplitude torsional and vibrational motions[198–200] and different mobility of exocyclic groups;[200] however, the glycosidic linkage was judged to be rigid on the basis of this type of measurements, and similar in conformation to that observed in the crystalline state. Presenting a quantitative analysis of the field strength dependence of $^1H/^1H$ NOE data, Poppe and Van Halbeek[105] questioned the rigidity of the sucrose glycosidic bond in solution and explained the reasons why this type of flexibility was not revealed by McCain and Markley's data. The evidence is briefly reviewed below.

Seeking to reveal as large a set of interresidue distance constraints as possible and to shed light on the existence of any hydrogen bonds in sucrose in aqueous solution, sucrose was investigated at low temperatures in aqueous solutions with the purpose of including the OH signals in the analyses. All of the sucrose OH signals were indeed observed in 1–1 echo experiments [Figure 17(a)], and had lines sufficiently narrow to be assigned by 2D and selective 1D TOCSY experiments. To measure interresidue distance constraints, 1D ROESY [Figure 10(a)] and multiselective TOCSY–ROESY [Figure 10(d)] experiments were performed; these experiments benefited from the excellent water suppression by an inhomogeneous, transverse $\boldsymbol{B}_1$ field [see Figure 17(b–f)]. The concept of selective 3D TOCSY–NOESY and TOCSY–ROESY spectroscopy [as mentioned for the assignment of the Gal H-6 protons in sialyl-$\alpha(2\rightarrow6)$-lactose, Figure 13] was extended to include multiple selective excitations. In an analogous manner to a 1D NOE experiment, these experiments allowed the measurement of NOEs between H-5 g and its spatial neighbors, in addition to NOEs between H-1 g and its neighbors ('g' denotes the glucose, 'f' the fructose moiety in sucrose). An example of a double selective pseudo 3D TOCSY–ROESY spectrum of sucrose is shown in Figure 17(c). Selective excitation of the H-4 g resonance was followed by a TOCSY step, a second selective pulse applied to the H-5 g resonance, and finally a ROESY step. Thus, NOE connectivities originating from H-5 g, which could not have been excited in a single selective experiment, were successfully measured. Special care was taken to ensure that NOEs were free of spin diffusion artifacts before converting them into distances. The standard 1D NOESY spectrum of sucrose after selective excitation of the H-1 g resonance [Figure 18(a)] revealed NOE enhancements to H-11′f, H-66′f, H-4f, H-5f, and H-3f. To determine the amount of the H-1 g/H-3f NOE due to direct magnetization transfer, H-11′f, H-4f, and H-5f were selectively and simultaneously spin locked during the mixing time of a second experiment [Figure 18(b)], thereby cutting off all possible indirect magnetization transfer pathways from H-1 g to H-3f. The results of the quantitative NOE measurements are compiled in Table 3. Interestingly, all NOE connectivities (and the lone exchange interaction, see below) found for sucrose in water solution

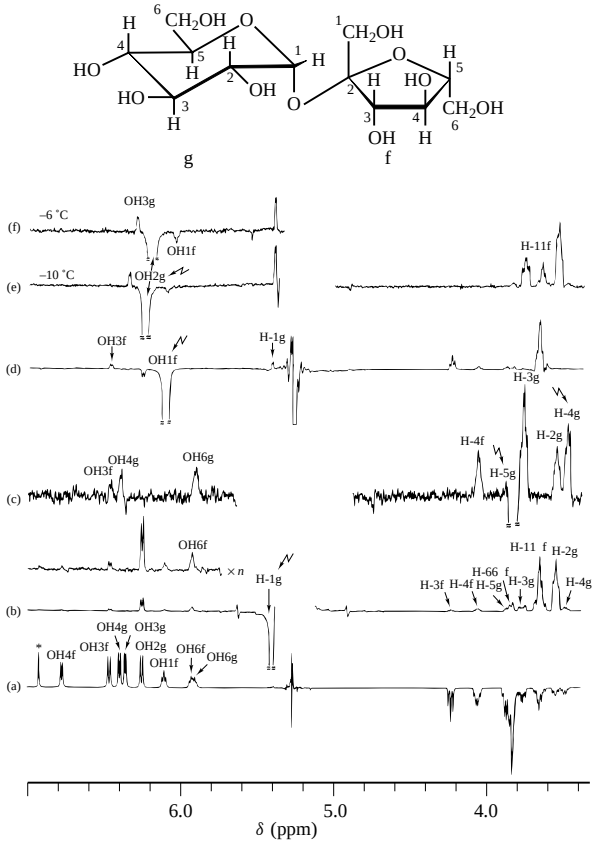

Figure 17 500 MHz ^{1}H NMR spectra of sucrose [Fruβ(2 1)αGlc; g = Glc, f = Fru] (5 mg in 0.5 ml of $H_2O/(CH_3)_2CO$, 6:1, v/v) obtained at $-10\,^{\circ}C$ (except trace f). (a) Spectrum obtained with a 1–1 echo pulse sequence. (b) 1D ROESY spectrum (320 scans) obtained with the pulse sequence shown in Figure 10(a); selective excitation of the H-1 g resonance was followed by a 200 ms spin lock pulse train. (c) Double-selective 3D TOCSY–ROESY spectrum obtained with the pulse sequence shown in Figure 10(d). Selective irradiation of H-4 g was followed by 30 ms of isotropic mixing, the selective irradiation of H-5 g, and a 200 ms spin lock pulse train; 640 scans were accumulated. (d, e) 1D ROESY spectra (320 scans) with selective irradiation of OH-1f and OH-2 g, respectively. (f) 1D ROESY spectrum, recorded at $-6\,^{\circ}C$, with selective irradiation of OH-2 g. A comparison of traces (e) and (f) reveals an OH-2 g/OH-1f chemical exchange interaction, suggesting the existence of an O-1f:::H:::O-2 g hydrogen bond in solution under the applied conditions[105]

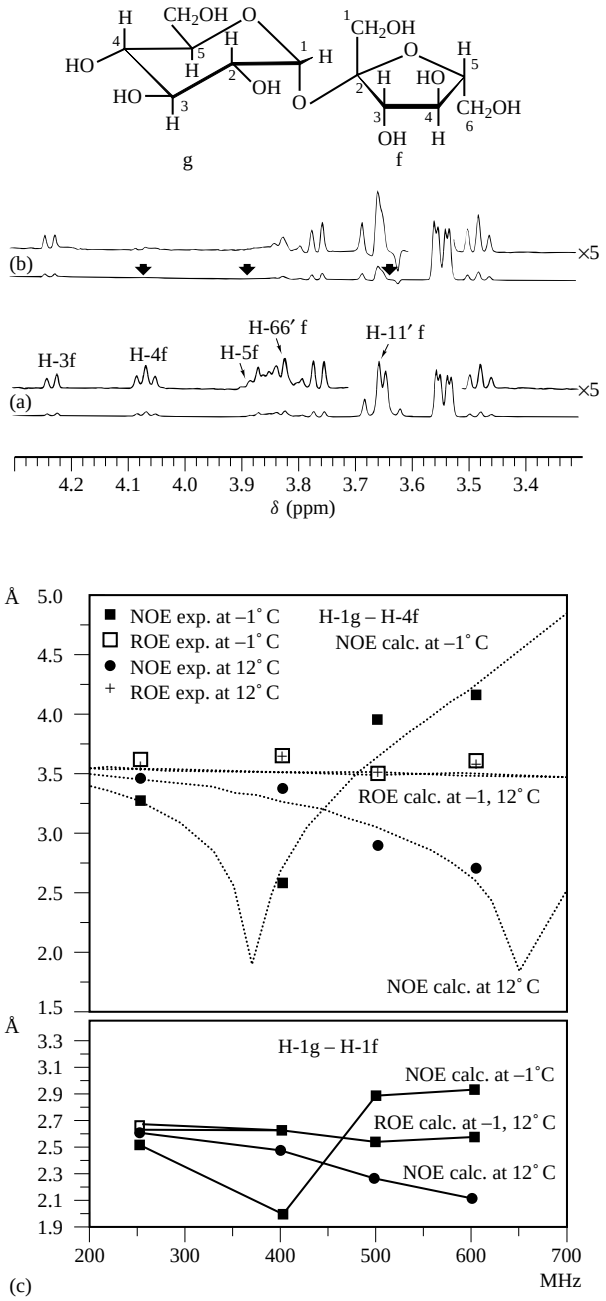

Figure 18 (a) 1D NOESY spectrum (500 MHz; τ_{mix} = 0.4 s) of sucrose [Fruβ(2 1)αGlc; g = Glc, f = Fru] in a $D_2O/(CH_3)_2CO$ (6:1, v/v solution) at $-5\,^{\circ}C$. The interresidue NOE enhancements of fructose ring protons obtained after selective excitation of Glc H-1 are indicated [see the pulse sequence in Figure 10(b)]. (b) Identical to (a), with the addition of the triple-selective spin locking of H-4f, H-5f, and H-11′f (marked with arrows) during the mixing time using a triple-DANTE pulse train. As all possible indirect magnetization transfer pathways from spin H-1 g to spin H-3f are cut off in experiment (b), the measured H-1 g/H-3f NOE enhancement is solely the result of direct dipolar interaction between these two spins. (c) Distances $r_{H-1\,g-H-4f}$ and $r_{H-1\,g-H-1f}$ as determined from 1D NOESY and 1D ROESY measurements on sucrose in H_2O solution at two different temperatures ($-1\,^{\circ}C$ and $12\,^{\circ}C$) and four magnetic field strengths (250, 400, 500, and 600 MHz). Theoretical values for $r_{H-1\,g-H-4f}$ (dotted lines) were predicted from a model described by Poppe and Van Halbeek,[105] assuming rapid interconversion of three different rotameric conformations around the glycosidic linkage

can be explained in terms of a single conformation, which is virtually identical to that in its crystal structure.

However, when measuring specific $^1H/^1H$ cross-relaxation rates as a function of magnetic field strength and temperature, large conformational changes occurring much faster than the overall motion were revealed around the glycosidic bond.[105] Selective excitation at the H-1 g resonance was followed by the detection of NOEs at H-11′f, H-4f, and several protons in the glucopyranose ring. The NOEs between protons on different rings proved to be field-strength-dependent, while this did not seem to be the case for NOEs between protons in the glucopyranose ring [Figure 18(c)]. This observation is interpreted as evidence for the occurrence of rearrangements around the glycosidic bond between the glucosyl and fructosyl residue which are much faster than the tumbling time of the molecule in solution ($\tau_o \sim 0.2$ ns). This type of internal motion is transparent

Table 3 $^{1}H/^{1}H$ Distances for Sucrose in Aqueous Solution Derived from Interglycosidic NOE Contacts[105]

Proton pair[a]	Distance[b] (Å)
H-1g/H-1f	2.6[c]
H-1g/H-3f	4.6
H-1g/ H-4f	3.5[c]
H-1g/H-6f	4.0
H-5g/H-4f	3.0
H-1g/OH-1f	3.6
H-1g/OH-6f	3.4
H-1g/OH-3f	4.0
H-5g/OH-3f	3.8
OH-2g/H-1f	3.2

[a]Data for aliphatic protons were acquired at 27 °C, data for hydroxyl protons at −10 °C; 'g' denotes the glucosyl, 'f' the fructosyl ring.

[b]Distances were calculated using the formula $r_{ij} = (\sigma_{\mathrm{ref}}/\sigma_{ij})^{\frac{1}{6}} r_{\mathrm{ref}}$ in which σ_{ref} and r_{ref} represent the cross-relaxation rate of and the distance between a reference pair of protons. Intraglucosyl distances H-1g/H-2g (2.4 Å), H-1g/H-3g (3.7 Å), and H-1g/H-4g (4.0 Å) were used as references. The precision of the distances r_{ij} is estimated to be $0.1r$.

[c]See Figure 18(c).

to relaxation parameters, including ^{13}C T_1, if it occurs on the timescale of overall molecular tumbling; this seems to be the case for sucrose at ambient temperature. Thus, the accurate measurement of ^{1}H cross-relaxation rates ($\sigma_{\mathrm{H,H}}$) has the following advantages over traditional ^{13}C T_1 measurements: (i) a higher spectral sensitivity; (ii) an increased ability to detect internuclear fluctuations; (iii) a dependence on spectral density at zero frequency and, therefore, sensitivity to slow motions, and (iv) the greater diversity of geometric orientations of the H−H vectors in a rigid pyranose ring, as compared with the parallel orientation of most of the C−H vectors, allowing more efficient sampling of spectral densities.

Additionally, the observation of chemical exchange between OH-1f and OH-2 g [Figures 17 (e) and (f)] provides reasonable evidence for the existence of an OH-1f:::O-2 g hydrogen bond in solution under the applied conditions. In summary, it appears that intramolecular hydrogen bonding in sucrose is concentration-dependent; the existence of hydrogen bonds OH-1f:::O-2 g, OH-3f:::O-2 g, and OH-6f:::O-5 g at higher concentrations has been postulated, based interalia on ^{13}C isotope effects.[196] The existence of the first two hydrogen bonds at high concentration in solution implies flexibility and fast interconversion between two conformers around the glycosidic linkage in solution (in the crystal only OH-1f:::O-2 g and OH-6f:::O-5 g are observed).

Once fast internal motion in sucrose was detected by measuring a number of interglycosidic NOEs as a function of magnetic field strength and temperature of the solution,[105] similar observations were reported for other di- and trisaccharides.[201–204] It is now widely accepted that small oligosaccharides are flexible molecules, experiencing intramolecular rearrangements that are fast compared with the overall tumbling of the molecules.

4.3 Glycoprotein Oligosaccharides

Although, during the past decade, NMR spectroscopy has become sophisticated enough to handle conformational analysis of glycoprotein-related oligosaccharides and glycopeptides in solution, few of these oligosaccharides have yet been examined as rigorously as the di- and trisaccharides mentioned in Section 4.2. In hindsight, the relatively slow pace in which oligosaccharide conformational analysis has developed is primarily due to glycobiologists' expectations concerning the models for glycoprotein carbohydrates; they expected a single, rigid 3D shape for an oligosaccharide of any given primary structure. This school of thought was based on pioneering investigations of the ABH and Lewis blood group determinants [for primary structures see Figure 1(d)]. However, as it turned out later, these branched tri- and tetrasaccharide epitopes happened to be far more rigid than most small oligosaccharides, leading to the misguided concept of carbohydrate 3D structural rigidity and the resultant overconfidence that modeling of any carbohydrate could be handled by the HSEA approach (hard-sphere representation of nonbonded interactions dominated by the *exo*-anomeric effect). Most glycoprotein oligosaccharides are flexible to some degree and are continually experiencing dynamic fluctuations in structure. Their flexibility is important because it may allow them to fit into the binding sites of carbohydrate-binding proteins (lectins, antibodies, receptors) (Section 5.3). In chronological order, we will summarize the work on blood group oligosaccharides which are known to occur in the peripheral portions of glycoprotein and ganglioside carbohydrate chains, followed by more typical *N*-type and *O*-type glycoprotein carbohydrate structures (Figure 1).

4.3.1 Peripheral Epitopes

The conformations of blood group oligosaccharides were first investigated by Lemieux et al.,[205] who reported ^{1}H and ^{13}C NMR assignments for trisaccharide fragments of the oligosaccharides denoted A, B, H, Le^x, and Le^y in Figure 1(d). Qualitative NOE data, along with primitive conformational energy calculations, were thought to indicate single conformations for each of these oligosaccharides. The influence of hydrogen bonding and other electrostatic effects was proposed to be unimportant; the rigid conformations were thought to be mainly determined by steric or nonbonded interactions and by torsional potentials.[206]

With the advent of more sophisticated NMR techniques, as well as a less naive approach to oligosaccharide modeling, Bush and co-workers set out to apply much more rigorous tests to these proposals in the late 1980s. This group of investigators acquired large collections of carefully measured NOE data on blood group and related oligosaccharides in various solvents at a number of sample temperatures.[207–215] Full relaxation matrix analysis of those data, along with MD simulations, revealed that the blood group epitopes found on glycoproteins and glycolipids assume relatively rigid conformations. The latest results obtained by Bush and co-workers on the Le^x trisaccharide and sialyl-Le^x tetrasaccharide[208,216] indicate that the Le^x portions of the molecules are rigid, but the Neu5Acα(2→3)-linkage shows transitions between two predominant conformational states [experimentally defined by ROE and ^{3}J(C,H) values]. Other investigators[217,218] concur with these findings on the issue of the rigidity of the Le^x portion of the molecule [i.e., the conformation can be described by one set of ϕ,ψ-values for the Fucα(1→3)GlcNAc and Galβ(1→4)GlcNAc linkages each] and support a model featuring fast exchange between two different conformations

of the Neu5Acα(2→3)Gal-linkage. The dynamics of fucosyl-α(1→2)-lactose and related oligosaccharides are currently being reinvestigated along the lines discussed in Section 4.2[203,204]

4.3.2 N- and O-Type Glycoprotein Oligosaccharides

The NOE-based conformational analysis of *N*-type glycoprotein oligosaccharides began simultaneously and independently in Toronto[219–222] and Oxford.[223] The conformations of the various linkages in the diantennary *N*-acetyllactosamine-type oligosaccharide [Figure 1(b)] and its high-mannose analogs were evaluated and, at first, judged to be fairly rigid with the exception of the α(1→6)-linkage. In 1987, however, both the Toronto[224–226] and the Oxford[227–229] groups realized that they had proposed 'virtual conformations' for the *N*-type core structures up to that point. When carefully scrutinized, the increased amount of NOE constraints available at that time appeared to be inconsistent with one conformation per linkage and prompted a reevaluation of the concept of carbohydrate structure rigidity. The ensemble representation was introduced for the oligosaccharides, as NMR observables calculated as ensemble averages gave better agreement with experimental values than those derived from single structures. Since then, MD simulations and NOE measurements at different field strengths have been helping each other over a number of 'barriers' to the further understanding of glycoprotein carbohydrate dynamics. Both the Oxford and the Toronto groups have recently resorted to small di-, tri- and tetrasaccharide building elements of the *N*-type oligosaccharides in order to assess carefully their dynamic behavior, while simultaneously attempting to improve the molecular modeling methods for carbohydrates.[76,107,108,201,230–234] Currently, detailed NMR studies on larger *N*-type oligosaccharides covalently linked to proteins are being conducted as well (Section 5.1). Impartial review articles[18,66,83,235] keep the glycobiology community abreast of continuing developments in this area of research.

Additional insight into the conformation of the core pentasaccharide $Man_3GlcNAc_2$ in an *N*-type glycopeptide was provided by a study of a hen ovomucoid glycodecapeptide.[236] TOCSY and NOESY experiments on the glycopeptide in H_2O, supported by ^3J(N,H) data, provided evidence that the C-2–N-2 bond in Asn-linked GlcNAc is rigid; however, this rigidity could not be attributed to any intramolecular hydrogen bond. Although these and other sophisticated tricks of the NMR trade are just beginning to be applied to larger oligosaccharides and glycopeptides, we now have a reasonable picture of the conformation and flexibility of *N*-type oligosaccharides of the high-mannose and the *N*-acetyllactosamine type. Similar investigations of *O*-type Ser/Thr-linked oligosaccharides[78,237,238] and small sialyl oligosaccharides (Section 4.2) are currently being conducted. Given the similarities of the backbone and peripheral structural elements of *N*-type and *O*-type oligosaccharides, the results should be applicable to both classes of glycoprotein carbohydrates.

4.4 Glycolipids and Glycolipid-Related Oligosaccharides

Oligosaccharides released from gangliosides and other glycolipids (by endoglycoceramidase digestion or ozonolysis) are amenable to, and have been investigated by, the same NMR techniques as mentioned for glycoprotein oligosaccharides (Section 4.3). For example, the 1D TOCSY subspectra of the Gal and Neu5Ac residues in the G_{D1a} oligosaccharide (Figure 19) serve to illustrate that, despite the abundance of small couplings, magnetization can be propagated over the entire spin system of each residue allowing the complete assignment of these spectra. The conformations of the oligosaccharide portions of gangliosides such as G_{M1}, G_{M2}, G_{D1a} (for primary structures, see Figure 1), and GPI anchors[239,240] have been studied in aqueous environments by $^1H/^1H$ NOESY methods in combination with molecular modeling.[241,242] Frequently, the results obtained on the free oligosaccharides have been compared to those obtained by examinations of the intact glycolipids in DMSO solutions and other aprotic solvents.[51,55–57,64,187,188,243–247] In particular, the study of peripheral blood group elements which are so abundant on glycolipids features prominently in this work; not unexpectedly (see Section 4.3.1), the conformations of these epitopes are independent of the solvent. Although the results of these studies in DMSO are interesting from a basic science point of view, we will not review their details because of their relative lack of biological significance. Instead, we will turn to micellar systems formed by glycolipids in aqueous solutions (Section 5.2), emulating the cell's plasma membrane, and compare the carbohydrate's structures under those circumstances to the structures of the free glycolipid oligosaccharides in water.

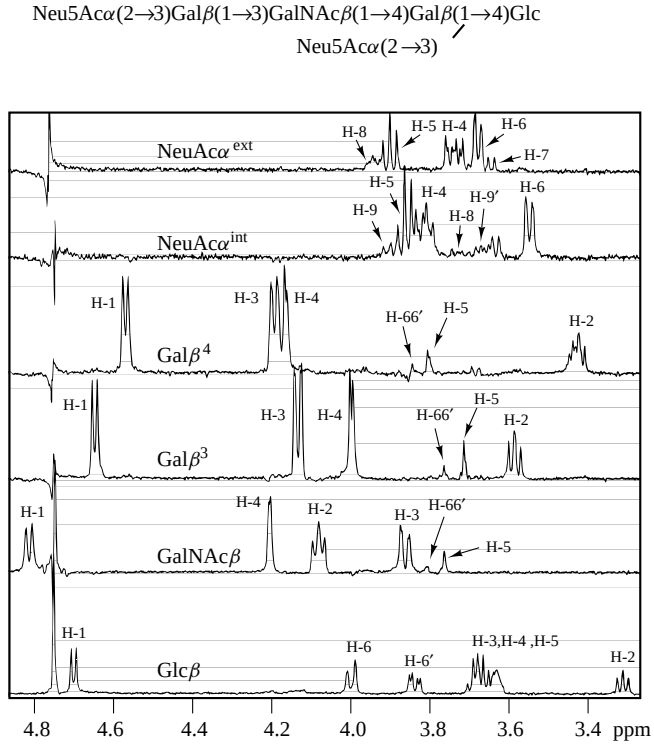

Figure 19 Subspectral editing of the ^1H NMR spectrum (600 MHz) of the G_{D1a} oligosaccharide in D_2O [16 mg mL^{-1}] by 1D TOCSY [see the pulse sequence in Figure 10(a)]. The H-1 signals of the hexosyl residues and the H-3ax signals of the Neu5Ac residues, respectively, were selectively excited. Superscripts in Gal^3 and Gal^4 refer to the position of the linkage in which these residues are involved (ext = external; int = internal). The constant isotropic mixing time was 370 ms; 160 scans were accumulated per spectrum

Due to the relative ease with which they can be ^{13}C-enriched, glycolipids have recently inspired the development of several new NMR spectroscopic techniques. Heteronuclear 3D NMR experiments, employing ^{13}C chemical shift editing of homonuclear correlation spectra, are an effective means of reducing spectral overlap for larger carbohydrates, particularly when ^{13}C-enriched carbohydrates are available for investigation.[235,248] Complete ^{1}H assignments for uniformly ^{13}C-labeled carbohydrates have been obtained with the use of HCCH–COSY and HCCH–TOCSY experiments.[249] By employing the ^{13}C,^{13}C coupling pathway [^{1}J(C,C) $\sim$ 40 Hz] for magnetization transfer, these techniques overcome the T_2 relaxation [^{3}J(H,H) $\ll$ linewidth] problems observed in ^{3}J(H,H)-mediated ^{1}H,^{1}H COSY and TOCSY spectra of glycoconjugates of high molecular weights and yield well-resolved spectra for polysaccharides and glycolipids. The 2D constant evolution time HCCH–COSY and HCCH–TOCSY experiments are particularly useful for the study of carbohydrates due to the relatively constant value of ^{1}J(C,C) couplings around the carbohydrate ring (36–45 Hz) which facilitates optimization of the fixed delay for ^{13}C,^{13}C magnetization transfer. The resulting ^{13}C,^{13}C decoupling simplifies the analysis of the ^{1}H spectra as traces in the 2D plots. Alternatively, ^{1}H-detected ^{13}C,^{13}C COSY experiments may be performed for complete ^{1}H and ^{13}C assignments of ^{13}C-enriched oligosaccharides (as was illustrated for the uniformly ^{13}C-labeled carbohydrate headgroup in a sulfolipid[250]). The sensitivity and resolution of the ^{1}H-detected 3D ^{13}C COSY experiments can be considerably improved by the implementation of pulsed field gradients, as demonstrated for a digalactosyl diacylglyceride which was biosynthetically uniformly ^{13}C-enriched to $\sim$15%.[251]

5 THE FUTURE: GLYCOCONJUGATES IN (INTER-)ACTION AT THE MEMBRANE SURFACE

The molecular behavior of an oligosaccharide chain isolated from a glycoprotein or glycolipid differs considerably from the behavior of the chain when bound to a protein or lipid. For example, the molecular motion of a freely tumbling oligosaccharide will be substantially different from that of the same oligosaccharide anchored to a protein backbone and/or in a lipid bilayer. It is quite conceivable that both molecular conformation and internal dynamics are affected upon the covalent binding of an oligosaccharide to a protein. Thus, appropriate caution must be exercised when extrapolating NMR-derived results concerning conformation and dynamics of isolated oligosaccharides to similar structures linked to proteins or lipids. NMR efforts are now underway to examine the conformation and dynamics of oligosaccharides as covalent parts of larger molecular weight glycoconjugates, both intact glycoproteins (Section 5.1) and glycolipids dispersed in lipid bilayers (Section 5.2). Also, the study of noncovalent carbohydrate–protein interactions via NMR methods is producing its first encouraging results (Section 5.3).

5.1 Glycoproteins

It has been known for quite some time[252] that the ^{13}C NMR spectra of intact glycoproteins in solution display signals arising from the oligosaccharide component that are considerably sharper than those arising from the polypeptide backbone. This observation suggests that the oligosaccharides of at least some intact glycoproteins possess motional characteristics other than those conferred on them by the tumbling of the protein; in other words, local (segmental) motion is experienced by the oligosaccharide chain. In 1982, Goux et al.[253] reported on ovalbumin in which nonreducing Gal was enriched in ^{13}C. Off-resonance rotating frame relaxation data showed that the carbohydrate had a 40–80 ps motion superimposed on the slow overall tumbling ($\tau_o \sim 25$ ns) of the protein.

Several NMR studies are currently being designed to elucidate the conformational effects of covalently linked carbohydrates on peptides in glycoproteins and vice versa. The glycoprotein ribonuclease B (RNase B) has most often served as the 'guinea pig'. The consensus with regard to this glycoprotein and several others seems to be that oligosaccharide and peptide do not mutually affect each other's conformation; instead, the oligosaccharide causes a decrease in the peptide's conformational mobility near the glycosylation site and vice versa. Thus, mutual effects have been observed on the local dynamics of peptide and oligosaccharide rather than on their conformation per se. For example, NMR measurements of amide H/D exchange rates on RNase A and B revealed that glycosylation of the protein leads to the protection of amide proton resonances from solvent exchange for a large number of amino acid residues in the vicinity of the glycosylation site and in more remote locations.[254,255] The detailed influence of a high-mannose oligosaccharide on the enzyme's properties was also explored with a combination of MD simulations of the carbohydrate, employing a novel force field parameterization for glycoproteins (GLYCAM-93), and structural model building based on the 2.5 Å X-ray crystal structure of the enzyme;[256] the results are currently awaiting NMR experimental verification.

Studies[108,231] focusing on the local dynamics of the $Man_5GlcNAc_2$ carbohydrate chain in RNase B took advantage of the protein's presence; the protein is, in essence, a large mass which, relative to the timescale of the internal motions, tethers the reducing end of the glycan. This causes the relaxation parameters to become much more sensitive to differential motion along the glycan chain. In addition, the overall motion of the glycoprotein can be considered to be isotropic, considerably simplifying data analysis. The order parameter S^2 was measured for reorientation of the C-1–H-1 vector of each glycosyl residue. As computed from ^{13}C T_1 values, S^2 was found to be $\sim$0.5 for internal residues and $\sim$0.1 for terminal residues (most distal to the protein). The rate of internal motion was found to be an order of magnitude higher for the distal than for the proximal residues. These data strongly support the existence of significant torsional oscillations about glycosidic bonds in high-mannose oligosaccharides.

However, there is at least one well-characterized glycoprotein in which carbohydrate and protein conformation do affect each other considerably: the F_c fragment of immunoglobulin G (IgG) containing an *N*-linked carbohydrate chain at Asn_{297} in the hinge region. There is compelling evidence, both from X-ray structural data and molecular modeling,[77,257] that the (1→6)-arm of the diantennary oligosaccharide interacts with Phe_{243}, Pro_{244}, and Thr_{260} residues of the protein. These interactions result not only in the loss of the flexibility associated with the (1→6)-arm, but also in a conformation of the

diantenna very different from that of the free oligosaccharide in solution. Recently, the F_c fragment in which ^{13}C-labeled Gal had been biosynthetically incorporated in terminal position of both arms of the diantenna in a similar way to the aforementioned studies on ovalbumin, was probed by ^1H-detected $^{13}C,^1H$ NMR. The two Gal residues were distinctly different in their NMR parameters (chemical shifts, linewidth), providing evidence for the strong interaction in solution of one arm of the diantenna with the peptide backbone.

5.2 Dynamics of Membrane-Bound Carbohydrates

Due to their amphipathic nature, isolated glycolipids aggregate in aqueous solution to form micelles. With their long overall rotational correlation times, these systems lend themselves to high-resolution NMR studies and are the most revealing probes currently used for the study of internal motions in lipid-linked oligosaccharides. Poppe and coworkers have studied the conformation and dynamics of the carbohydrate headgroups of a number of glycolipids inserted in deuterated dodecylphosphocholine (DPC) micelles in D_2O and/or H_2O, including globoside,[129,187] Forssman antigen,[162] and the gangliosides G_{M4},[258] G_{M3} and Neu4Ac5Gc-G_{M3},[259] G_{M1},[188] and G_{D1a}.[260] The researchers typically measured interglycosidic $^1H/^1H$ NOEs and used these to build tentative 3D structures of the oligosaccharide using a distance mapping procedure.[188] Figure 20 shows 1D NOESY spectra for one of the galactose residues in the G_{D1a} ganglioside/micelle system in D_2O solution. Selective spin locking during the mixing time, obtained with a double-DANTE pulse sequence,[261] allowed the calculation of, for example, the intraring Gal H-1–H-4 distance based upon a spin-diffusion-free NOE effect.

Figure 21 shows that G_{D1a} in a micellar membrane in H_2O is singularly suited for high-resolution NMR studies, particularly those focusing on its OH signals at low temperature, without the use of organic solvents. It appeared[260] that the observed NOEs could not be explained by the occurrence of the G_{D1a} oligosaccharide in a single conformation such as the reasonably rigid structures proposed for the G_{D1a}-free oligosaccharide[242] in D_2O and glycolipid[245] in DMSO on the basis of ^{13}C T_1 data. At least two families of carbohydrate conformers, differing in the relative orientation of the Neu5Acα(2→3)Galβ(1→3) external disaccharide arm, must exist in this model membrane system to account for the NOE constraints. The internal dynamics of the oligosaccharide were probed by ^1H detection of the ^{13}C relaxation parameters (T_1, $T_{1\rho}$, and heteronuclear NOEs) of the micellar system at ^{13}C natural abundance. The internal reorientations were found to occur with a rotation correlation time of 0.35 ns. The slow tumbling of the micelle ($M_r \sim 8$ kDa) provided the distinct timescale (τ_o = 2.8 ns), facilitating the discovery of the faster internal motion of two flexible glycosidic linkages in the carbohydrate headgroup.[260]

Applications of these methods to larger complex oligosaccharides, as well as to those tethered to proteins or lipid membranes, will continue to provide valuable evidence with which to address the question of internal motions on a timescale of the reciprocal of the NMR frequency range used in the experiment (0.1–1 ns). Motions on a slower timescale, which would not be detectable by ^{13}C T_1 experiments, can be studied with rotating frame relaxation data ($T_{1\rho}$). With control of the spin locking field strength, the latter parameter can reveal motions on the μs timescale.

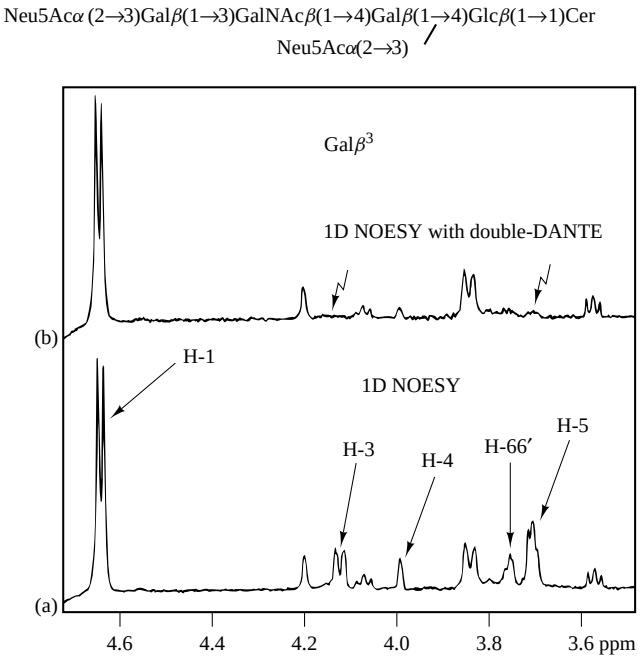

Figure 20 1D NOESY spectra (600 MHz, 25 °C) of G_{D1a}/DPC-d_{38} micelles in D_2O solution. Mixing time 0.4 s. (a) Selective irradiation of Gal^3 H-1. The labels indicate intraresidue NOEs that are significantly compromised by spin diffusion. (b) Selective irradiation of Gal^3 H-1 with double-selective spin locking of Gal^3 H-3 and H-5 during the mixing time. The resulting H-1/H-4 NOE intensity is devoid of indirect magnetization transfers

Alternative approaches to unmasking the conformation and dynamics of glycolipids embedded in model membranes include the study of the angular dependence of NOE in oriented systems of G_{M3} ganglioside with partially ^{13}C-labeled sialic acid[262] at the surface of magnetically oriented membranes. Dipolar interactions measured between $^{13}C,^{13}C$ and $^{13}C,^1H$ pairs located in the ^{13}C-labeled sialic acid moiety of G_{M3} are interpreted as indications that the G_{M3} structure is well extended from the membrane surface. In fact, membrane-bound G_{M3} was shown to bind wheat germ agglutinin (WGA), leading to the conclusion that the dominant G_{M3} structure at the membrane surface is favored for binding by the lectin. These and other aspects of NMR studies of glycolipids at model membrane surfaces are covered in detail by Jarrell (***Glycolipids***) in this Encyclopedia.

5.3 Carbohydrate–Protein Interactions

The general argument made in Section 2 for the role of complex carbohydrates as informational macromolecules implies that there must be a mechanism for decoding the information which is stored in their structures. Apparently, this decoding depends on a group of multivalent carbohydrate-binding proteins known as (se)lectins. Lectins are widely distributed in animal tissues (albeit in small quantities) and bind simultaneously to at least two carbohydrate determinants (epitopes). Some lectins are membrane-bound, others are soluble; both are thought to function by facilitating communication between

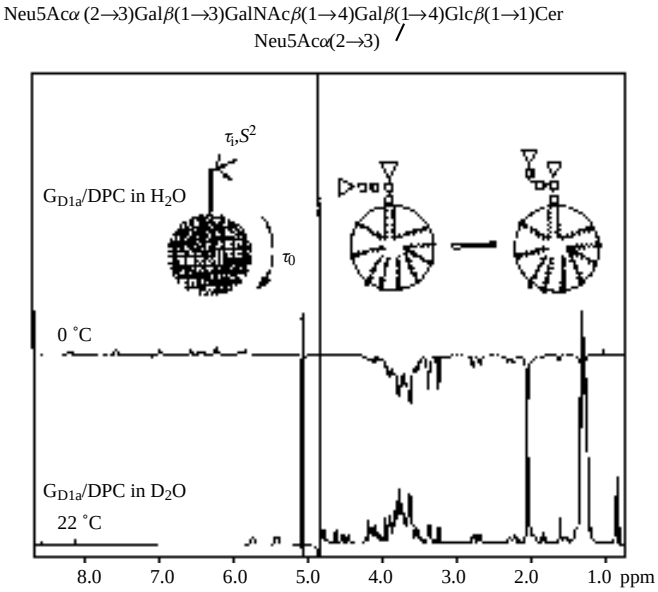

Figure 21 ^{1}H NMR spectra of G_{D1a}/DPC-d_{38} micelles in aqueous solutions; (bottom trace) spectrum in D_2O at 22 °C; (top trace) spectrum in 90% H_2O/10% D_2O at 0 °C, obtained with the 1–1 echo water suppression technique. The experimental data obtained on the micellar G_{D1a} system are compatible with the existence of two conformations of the external Neu5Ac–Gal portion of the oligosaccharide relative to the core tetrasaccharide anchored into the micelle. Interconversion between the two conformers is fast (τ_i = 0.35 ns; S^2 = 0.55 for the external disaccharide unit) relative to the overall tumbling of the micellar system ($M_r \sim 8$ kDa; τ_o = 2.8 ns; S^2 = 1)[260]

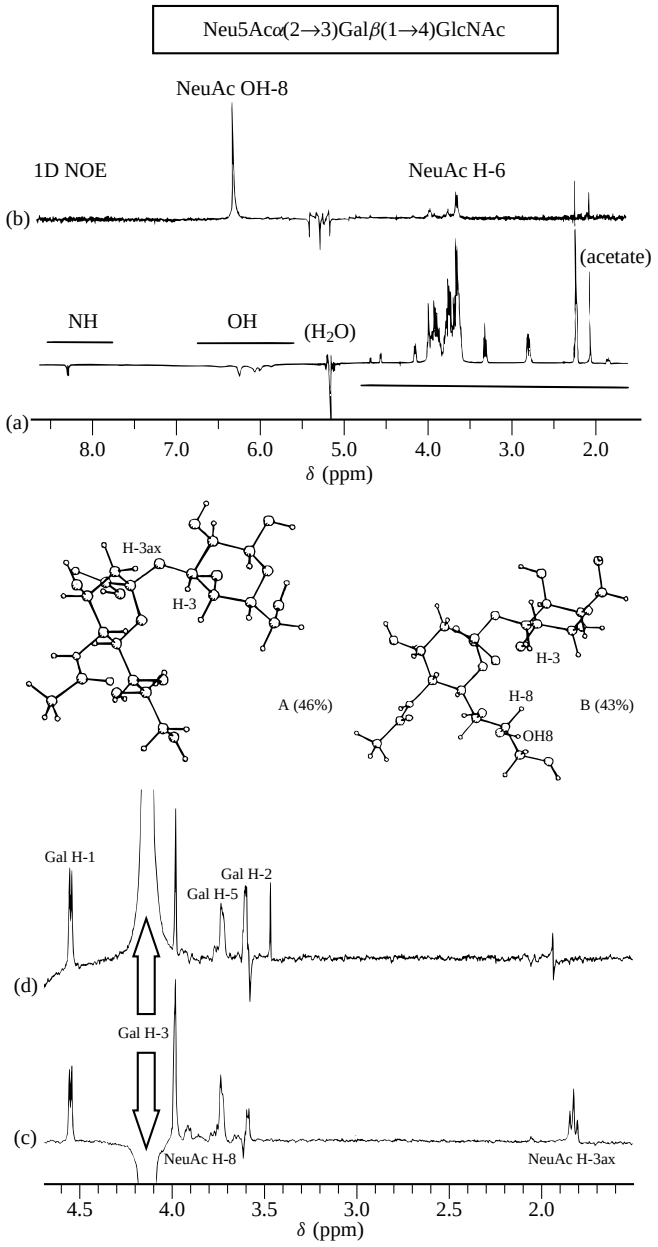

Figure 22 (a) The 500 MHz ^{1}H NMR spectrum of sialyl-α(2→3)-lactose [5 mM in H_2O/$(CD_3)_2CO$, 8:1, v/v] obtained at −12 °C with the 1–1 echo water suppression technique. Among the OH signals, the Neu5Ac OH-8 signal is characterized by the smallest exchange contribution to the linewidth and the smallest temperature variation of chemical shift (~0.001 ppm °C^{-1}). (b) 1D pre-steady-state NOE difference spectrum obtained subsequent to presaturation of OH-8 under the conditions described in (a); a strong NOE contact to Neu5Ac H-6 is observed. (c) 1D clean-ROESY[272] spectrum of sialyl-α(2→3)-lactose (5 mM in D_2O, 25 °C, 600 MHz). (d) 1D transferred NOESY spectrum of sialyl-α(2→3)-lactose in complex with wheat germ agglutinin (4 mM trisaccharide; 0.08 mM WGA; pD = 7, D_2O, 25 °C, 600 MHz). Note the absence of an NOE between GalH-3 and Neu5Ac H-3ax in trace (d) while Neu5Ac H-8 experiences a NOE, suggesting that the conformation of sialyl-α(2→3)-lactose that binds to WGA is the less populated[129] conformation free in solution (conformation B; middle right)

cells by linking them together. Antibodies are another class of soluble proteins involved in biological interactions with carbohydrates.

NMR spectroscopy is beginning to emerge as an experimental approach to the study of carbohydrate–protein interactions. Although limited by the size (molecular weight) and solubility of the protein, NMR spectroscopy is particularly useful for detailed studies of protein–carbohydrate interactions in solution when the complex has a molecular weight less than 35 kDa; under favorable circumstances, NMR can provide information about larger molecular weight systems as well. In general, if detailed information about conformation is sought, it is preferable that the ligand or the protein be ^{15}N, ^{13}C and ^{13}C,^{15}N doubly labeled in order to provide a sufficient amount of structural constraints. For the larger M_r protein–carbohydrate complexes this is a necessity; for the smaller M_r complexes it is highly desirable (cf. Otting[263]).

NMR spectroscopic studies on the interactions between proteins and carbohydrates have focused on several systems, including the lectins wheat germ agglutinin[264,265], concanavalin A, *Sambucus nigra* agglutinin, *Ricinus communis* B,[122] and *Aleuria aurantia* agglutinin[266] with their respective ligands, and several monoclonal antibodies with their oligosaccharide antigenic counterparts.[267–269] The typically weak carbohydrate–protein binding and intermediate-to-fast exchange between the free and the bound ligand permit transferred NOE (TrNOE) studies[108,263,270,271] and lineshape analysis. The aim of a TrNOE experiment is to measure *negative*

NOEs on easily detectable free or averaged carbohydrate resonances following the irradiation of other carbohydrate resonances in order to obtain conformational information on the *bound* ligand. The true advantage of studying TrNOEs is that the effect is not restricted by the M_r value of the complex; instead, it continues to be favorable as the protein size increases. The TrNOE experiment is one of the few experiments capable of yielding information on the conformation of bound ligands in complex with large-size proteins. In general, the amount of information gained about the system will not be as large as from ^{13}C-labeled systems in the tight-binding/slow-exchange regime, and extreme care must be given to the analysis of the NOE-derived distances. For exchange rates $>100\,s^{-1}$, one can analyze the data with relative ease; for rates between $10-100\ s^{-1}$, the use of an extended relaxation matrix is necessary, as was demonstrated for the analysis of the binding of β-methylmelibiose to ricin B.[122] The lectin preferentially selects one of the two conformations that melibiose adopts when free in solution. Similarly, WGA preferentially binds one of the two major conformations that sialyl-$\alpha(2\rightarrow3)$-lactose adopts around the Neu5Ac−Gal linkage when free in solution. A preliminary TrNOE study of WGA isolectin 1 in complex with sialyl-$\alpha(2\rightarrow3)$-lactose (Figure 22) suggests that conformation B is the one which preferentially binds to the lectin, in accordance with the crystal structure of the complex of WGA isolectin 1 with sialyl-$\alpha(2\rightarrow3)$-lactose.[273] More detailed studies are in progress to confirm this hypothesis. The studies follow the protocol of a recent NMR and X-ray study of the complex of a monoclonal antibody with a branched trisaccharide epitope.[269] For this complex, Bundle and co-workers measured NOE build-up rates from TrNOE experiments which show that the trisaccharide undergoes a protein-induced conformational shift around a specific glycosidic linkage when bound in solution. Distance constraints derived from the TrNOE studies are consistent with two bound trisaccharide conformations, one of which correlates with the ligand conformation in the crystalline trisaccharide−antibody complex.

6 CONCLUSIONS

Since its first application to monosaccharide derivatives in the late 1950s, NMR spectroscopy has greatly contributed to our current knowledge of the structures and functions of complex carbohydrates. The importance of oligosaccharides in their own right and as the 'business ends' of glycoconjugates are becoming increasingly appreciated, and the role that NMR has played in this accomplishment cannot easily be overestimated. First of all, NMR spectroscopy provides a powerful nondestructive means with which to characterize the primary structures of carbohydrates and has, therefore, become an integral part of the current methodology of protein glycosylation site mapping. Moreover, the vast potential of NMR to unravel 3D carbohydrate structures and dynamics, as well as to study carbohydrate−protein interactions, is just beginning to penetrate into the collective mind of the glycobiology community. At the same time, NMR spectroscopists long preoccupied with the study of protein−peptide and protein−nucleic acid interactions are beginning to see the merits of investigating protein−carbohydrate interactions. Biological data point to a pivotal function for glycoproteins in the control of growth and differentiation in the complex cell organization of eukaryotic systems. In fact, some complex oligosaccharides are implicated as onco-fetal antigens. Thus, the biological function of the complex carbohydrate chains of glycoproteins and glycolipids in animals is perhaps one of the most interesting unanswered fundamental questions in modern biochemistry. Unmasking carbohydrate structure−function relationships has been marked as the next frontier in molecular biology; the glycobiology community now finds itself turning to NMR spectroscopy to provide the instrumental means with which to enter this 'promised land'.

7 RELATED ARTICLES

Glycolipids; Nucleic Acids: Spectra, Structures, and Dynamics; Polysaccharides and Complex Oligosaccharides; Protein Structures: Relaxation Matrix Refinement; Vicinal Coupling Constants and Conformation of Biomolecules.

8 ABBREVIATIONS

The abbreviations used for monosaccharides, blood group determinants, and gangliosides are defined in the legend to Figure 1. Other abbreviations are: ANN, artificial neural network; CCSD, complex carbohydrate structure database; DANTE, delays alternated with nutations for tailored excitation; DIPSI, decoupling in the presence of scalar interaction; DPC, dodecylphosphocholine; DSS, 4,4-dimethyl-4-silapentane-1-sulfonate; GPI, glycosyl phosphatidyl-inositol; HMBC, heteronuclear multiple-bond connectivity; HMQC, heteronuclear multiple quantum coherence; HSEA, hard-sphere *exo*-anomeric; HSQC, heteronuclear single quantum coherence; Le^a, Lewis a; (M)MC, (Metropolis) Monte Carlo; MD, molecular dynamics; MLEV, pulse sequence first proposed by Malcolm Levitt; *n*D, *n*-dimensional (where n = 1, 2, 3, or 4); sLe^x, sialyl-Lewis x; TAA, tumor-associated antigens; TrNOE, transferred NOE; UGA, The University of Georgia; WGA, wheat germ agglutinin.

9 REFERENCES

1. A. Varki, *Glycobiology*, 1993, **3**, 97.
2. R. C. Hughes, *Glycoproteins*, Chapman and Hall, London, 1983.
3. M. Fukuda (ed.), *Cell Surface Carbohydrates and Cell Development*, CRC Press, Boca Raton, FL, 1992.
4. N. Sharon and H. Lis, *Lectins*, Chapman and Hall, London, 1989.
5. R. P. McEver, *Thromb. Haemost.*, 1991, **65**, 223.
6. L. A. Lasky, *Science*, 1992, **258**, 964.
7. W. J. Lennarz and G. W. Hart (eds.), *Methods in Enzymology*, Academic Press, San Diego, 1994, Vol. 230.
8. E. F. Hounsell (ed.), *Methods in Molecular Biology*, Humana Press, Totowa, NJ, 1993, Vol. 14.
9. C. A. Bush, *Bull. Magn. Reson.*, 1988, **10**, 73.
10. R. U. Lemieux, *Explorations with Sugars: How Sweet It Was*, American Chemical Society, Washington, DC, 1990.

11. R. U. Lemieux, R. K. Kullnig, H. J. Bernstein, and W. G. Schneider, *J. Am. Chem. Soc.*, 1957, **79**, 1005.
12. R. U. Lemieux, R. K. Kullnig, H. J. Bernstein, and W. G. Schneider, *J. Am. Chem. Soc.*, 1958, **80**, 6098.
13. M. Karplus, *J. Chem. Phys.*, 1959, **30**, 11.
14. R. U. Lemieux, R. K. Kullnig, and R. Y. Moir, *J. Am. Chem. Soc.*, 1958, **80**, 2237.
15. H. van Halbeek, *Methods Enzymol.*, 1994, **230**, 132.
16. G. Kotowycz and R. U. Lemieux, *Chem. Rev.*, 1973, **73**, 669.
17. A. S. Perlin and B. Casu, in *The Polysaccharides*, ed. G. O. Aspinall, Academic Press, New York, 1982, Vol. I, p. 133.
18. A. S. Serianni, in *Glycoconjugates: Composition, Structure, and Function*, eds. H. J. Allen and E. C. Kisailus, Marcel Dekker, New York, 1992, p. 71.
19. K. Bock and H. Thøgersen, *Annu. Rep. NMR Spectrosc.*, 1982, **13**, 1.
20. A. S. Shashkov, N. E. Nifant'ev, V. Y. Amochaeva, and N. K. Kochetkov, *Magn. Reson. Chem.*, 1993, **31**, 599.
21. F. J. Weighert, M. Jautelat, and J. D. Roberts, *Proc. Natl. Acad. Sci. USA*, 1968, **60**, 1152.
22. A. S. Perlin and B. Casu, *Tetrahedron Lett.*, **1969**, 2921.
23. K. Bock and C. Pedersen, *Adv. Carbohydr. Chem. Biochem.*, 1983, **41**, 27.
24. K. Bock, C. Pedersen, and H. Pedersen, *Adv. Carbohydr. Chem. Biochem.*, 1984, **42**, 193.
25. J. H. Bradbury and G. A. Jenkins, *Carbohydr. Res.*, 1984, **126**, 125.
26. G. Strecker, S. Fièvre, J.-M. Wieruszeski, J.-C. Michalski, and J. Montreuil, *Carbohydr. Res.*, 1992, **226**, 1.
27. J.-M. Wieruszeski, J.-C. Michalski, J. Montreuil, and G. Strecker, *Glycoconjugate J.*, 1990, **7**, 13.
28. G. Strecker, J.-M. Wieruszeski, J.-C. Michalski, and J. Montreuil, *Glycoconjugate J.*, 1989, **6**, 271.
29. K. Hermansson, P.-E. Jansson, L. Kenne, G. Widmalm, and F. Lindh, *Carbohydr. Res.*, 1992, **235**, 69.
30. P.-E. Jansson, L. Kenne, and G. Widmalm, *Carbohydr. Res.*, 1989, **188**, 169.
31. P.-E. Jansson, L. Kenne, and G. Widmalm, *Anal. Biochem.*, 1991, **199**, 11.
32. E. F. Hounsell, D. J. Wright, A. S. R. Donald, and J. Feeney, *Biochem. J.*, 1984, **223**, 129.
33. D. S. M. Bot, P. Cleij, H. A. van 't Klooster, H. van Halbeek, G. A. Veldink, and J. F. G. Vliegenthart, *J. Chemometrics*, 1988, **2**, 11.
34. J. A. van Kuik, K. Hård, and J. F. G. Vliegenthart, *Carbohydr. Res.*, 1992, **235**, 53.
35. H. van Halbeek, in *Methods in Molecular Biology*, eds. C. Jones, B. Mulloy, and A. H. Thomas, Humana Press, Totowa, NJ, 1993, Vol. 17, p. 115.
36. J. F. G. Vliegenthart, L. Dorland, and H. van Halbeek, *Adv. Carbohydr. Chem. Biochem.*, 1983, **41**, 209.
37. J. P. Carver and A. A. Grey, *Biochemistry*, 1981, **20**, 6607.
38. I. Brockhausen, A. A. Grey, H. Pang, H. Schachter, and J. P. Carver, *Glycoconjugate J.*, 1988, **5**, 419.
39. J. P. Kamerling and J. F. G. Vliegenthart, in *Biological Magnetic Resonance*, eds. L. J. Berliner and J. Reuben, Plenum Press, New York, 1992, Vol. 10, p. 1.
40. J. F. G. Vliegenthart, L. Dorland, H. van Halbeek, and J. Haverkamp, in *Sialic Acids: Chemistry, Metabolism and Function*, ed. R. Schauer, Springer, Vienna/New York, 1982, p. 127.
41. J. F. G. Vliegenthart, H. van Halbeek, and L. Dorland, *Pure Appl. Chem.*, 1981, **53**, 45.
42. G. Grönberg, P. Lipniunas, T. Lundgren, K. Erlansson, F. Lindh, and B. Nilsson, *Carbohydr. Res.*, 1989, **191**, 261.
43. H. van Halbeek, *Biochem. Soc. Trans.*, 1984, **12**, 601.
44. E. F. Hounsell and D. J. Wright, *Carbohydr. Res.*, 1990, **205**, 19.
45. J. U. Thomsen and B. Meyer, *J. Magn. Reson.*, 1989, **84**, 212.
46. B. Meyer, T. Hansen, D. Nute, P. Albersheim, A. Darvill, W. York, and J. Sellers, *Science*, 1991, **251**, 542.
47. J. P. Radomski, H. van Halbeek, and B. Meyer, *Nature Struct. Biol.*, 1994, **1**, 217.
48. S. Doubet, K. Bock, D. Smith, A. Darvill, and P. Albersheim, *Trends Biochem. Sci.*, 1989, **14**, 475.
49. D. A. Cumming, C. Hellerqvist, and O. Touster, *Carbohydr. Res.*, 1988, **179**, 369.
50. A. Allerhand and E. Berman, *J. Am. Chem. Soc.*, 1984, **106**, 2400.
51. R. K. Yu, T. A. W. Koerner, Jr., J. N. Scarsdale, and J. H. Prestegard, *Chem. Phys. Lipids*, 1986, **42**, 27.
52. F. Inagaki, *Magn. Reson. Chem.*, 1992, **30**, S125.
53. S. W. Homans, M. A. J. Ferguson, R. A. Dwek, T. W. Rademacher, R. Anand, and A. F. Williams, *Nature (London)*, 1988, **333**, 269.
54. A. S. Perlin, in *NMR Applications in Biopolymers*, eds. J. W. Finley, S. Schmidt, and A. S. Serianni, Plenum Press, New York, 1990, p. 7.
55. T. A. W. Koerner, Jr., J. H. Prestegard, and R. K. Yu, *Methods Enzymol.*, 1987, **138**, 38.
56. T. A. W. Koerner, Jr., J. H. Prestegard, P. C. Demou, and R. K. Yu, *Biochemistry*, 1983, **22**, 2676.
57. T. A. W. Koerner, Jr., J. H. Prestegard, P. C. Demou, and R. K. Yu, *Biochemistry*, 1983, **22**, 2687.
58. J. Dabrowski, *Methods Enzymol.*, 1989, **179**, 122.
59. J. Dabrowski, in *Methods in Stereochemical Analysis*, eds. W. R. Croasmun and R. M. K. Carlson, VCH, New York, 1987, Vol. 9, p. 349.
60. S. Dasgupta, E. L. Hogan, J. Glushka, and H. van Halbeek, *Arch. Biochem. Biophys.*, 1994, **310**, 373.
61. S. W. Homans, R. A. Dwek, J. Boyd, N. Soffe, and T. W. Rademacher, *Proc. Natl. Acad. Sci. USA*, 1987, **84**, 1202.
62. S. Subramanian and A. Bax, *J. Magn. Reson.*, 1987, **71**, 325.
63. A. A. Bothner-By, R. L. Stephens, J.-M. Lee, C. D. Warren, and R. W. Jeanloz, *J. Am. Chem. Soc.*, 1984, **106**, 811.
64. J. Dabrowski, in *Methods in Stereochemical Analysis*, 2nd edn., eds. W. R. Croasmun and R. M. K. Carlson, VCH, New York, 1994, Vol. 9, p. 741.
65. S. W. Homans, in *NMR of Macromolecules. A Practical Approach*, ed. G. C. K. Roberts, Oxford University Press, New York, 1993, p. 289.
66. C. A. Bush and P. Cagas, in *Advances in Biophysical Chemistry*, ed. C. A. Bush, JAI Press, Greenwich, Ct, 1992, Vol. 2, p. 149.
67. F. Inagaki, S. Tate, H. Kubo, and M. Hoshi, *J. Biochem. (Tokyo)*, 1992, **112**, 286.
68. F. J. Cassels and H. van Halbeek, *Methods Enzymol.*, 1995, **253**, 69.
69. R. J. Harris, H. van Halbeek, J. Glushka, L. J. Basa, V. T. Ling, K. J. Smith, and M. W. Spellman, *Biochemistry*, 1993, **32**, 6539.
70. R. J. Harris, L. J. Basa, V. T. Ling, M. W. Spellman, K. J. Smith, J. Glushka, R. W. Carlson, and H. van Halbeek, in *Techniques in Protein Chemistry V*, ed. J. W. Crabb, Academic Press, New York, 1994, p. 71.

71. A. Bax and M. F. Summers, *J. Am. Chem. Soc.*, 1986, **108**, 2093.
72. H. van Halbeek, in *Frontiers of NMR in Molecular Biology (UCLA Symposia Series*, Vol. 109), eds. D. Live, I. M. Armitage, and D. Patel, Alan R. Liss Inc., New York, 1990, p. 195.
73. C. Abeygunawardana and C. A. Bush, in *Advances in Biophysical Chemistry*, ed. C. A. Bush, JAI Press, Greenwich, CT, 1993, Vol. 3, p. 199.
74. D. A. Powell, W. S. York, H. van Halbeek, J. T. Etse, A. I. Gray, and P. G. Waterman, *Can. J. Chem.*, 1990, **68**, 1044.
75. J. Glushka, F. J. Cassels, R. W. Carlson, and H. van Halbeek, *Biochemistry*, 1992, **31**, 10 741.
76. S. W. Homans, *Prog. NMR Spectrosc.*, 1990, **22**, 55.
77. B. Meyer, *Top. Curr. Chem.*, 1990, **154**, 141.
78. H. van Halbeek and L. Poppe, *Magn. Reson. Chem.*, 1992, **30**, S74.
79. R. Freeman, *Chem. Rev.*, 1991, **91**, 1397.
80. H. Kessler, S. Mronga, and G. Gemmecker, *Magn. Reson. Chem.*, 1991, **29**, 527.
81. I. Solomon, *Phys. Rev.*, 1955, **99**, 559.
82. M. Karplus, *J. Am. Chem. Soc.*, 1963, **85**, 2870.
83. C. A. Bush, *Curr. Opin. Struct. Biol.*, 1992, **2**, 655.
84. J. McConnell, *The Theory of Nuclear Magnetic Relaxation in Liquids*, Cambridge University Press, Cambridge, UK, 1987.
85. J. H. Prestegard and Y. M. Kim, in *Computational Aspects of the Study of Biological Macromolecules by Nuclear Magnetic Resonance Spectroscopy*, eds. J. C. Hoch, F. M. Poulsen, and C. Redfield, Plenum Press, New York, 1991, p. 269.
86. C. A. G. Haasnoot, F. A. A. M. De Leeuw, and C. Altona, *Tetrahedron*, 1980, **36**, 2783.
87. L. A. Donders, F. A. A. M. De Leeuw, and C. Altona, *Magn. Reson. Chem.*, 1989, **27**, 556.
88. K. Bock and J. Ø. Duus, *J. Carbohydr. Chem.*, 1994, **13**, 513.
89. L. Poppe, S. Sheng, and H. van Halbeek, *Magn. Reson. Chem.*, 1994, **32**, 97.
90. L. Poppe, *J. Am. Chem. Soc.*, 1993, **115**, 8421.
91. Z. Dzakula, W. M. Westler, A. S. Edison, and J. L. Markley, *J. Am. Chem. Soc.*, 1992, **114**, 6195.
92. I. Tvaroska, M. Hricovíni, and E. Petráková, *Carbohydr. Res.*, 1989, **189**, 359.
93. B. Mulloy, T. A. Frenkiel, and D. B. Davies, *Carbohydr. Res.*, 1988, **184**, 39.
94. J. A. Schwarcz and A. S. Perlin, *Can. J. Chem.*, 1972, **50**, 3667.
95. M. Hricovíni and I. Tvaroska, *Magn. Reson. Chem.*, 1990, **28**, 862.
96. S. Uhrínová, D. Uhrín, T. Liptaj, J. Bella, and J. Hirsch, *Magn. Reson. Chem.*, 1991, **29**, 912.
97. R. Barker and A. S. Serianni, *Acc. Chem. Res.*, 1986, **19**, 307.
98. M. C. R. Symons, J. A. Benbow, and J. M. Harvey, *Carbohydr. Res.*, 1980, **83**, 9.
99. L. Poppe and H. van Halbeek, *J. Am. Chem. Soc.*, 1991, **113**, 363.
100. B. R. Leeflang and J. F. G. Vliegenthart, *J. Magn. Reson.*, 1990, **89**, 615.
101. L. Poppe and H. van Halbeek, *Nature Struct. Biol.*, 1994, **1**, 215.
102. J. Dabrowski and L. Poppe, *J. Am. Chem. Soc.*, 1989, **111**, 1510.
103. B. Adams and L. E. Lerner, *Magn. Reson. Chem.*, 1994, **32**, 225.
104. J. C. Christofides and D. B. Davies, *J. Am. Chem. Soc.*, 1983, **105**, 5099.
105. L. Poppe and H. van Halbeek, *J. Am. Chem. Soc.*, 1992, **114**, 1092.
106. L. Poppe, R. Stuike-Prill, B. Meyer, and H. van Halbeek, *J. Biomol. NMR*, 1992, **2**, 109.
107. J. P. Carver, *Curr. Opin. Struct. Biol.*, 1991, **1**, 716.
108. S. W. Homans, *Glycobiology*, 1993, **3**, 551.
109. S. Bagley, H. Kovacs, J. Kowalewski, and G. Widmalm, *Magn. Reson. Chem.*, 1992, **30**, 733.
110. P. J. Hajduk, D. A. Horita, and L. E. Lerner, *J. Am. Chem. Soc.*, 1993, **115**, 9196.
111. J. Kowalewski and G. Widmalm, *J. Phys. Chem.*, 1994, **98**, 28.
112. G. Wagner, *Curr. Opin. Struct. Biol.*, 1993, **3**, 748.
113. J. H. Noggle and R. E. Schirmer, *The Nuclear Overhauser Effect*, Academic Press, New York, 1971.
114. D. Neuhaus and M. P. Williamson, *The Nuclear Overhauser Effect in Structural and Conformational Analysis*, VCH, New York, 1989.
115. P. Dais and A. S. Perlin, *Adv. Carbohydr. Chem. Biochem.*, 1987, **45**, 125.
116. T. E. Bull, *Prog. NMR Spectrosc.*, 1992, **24**, 377.
117. G. Lipari and A. Szabo, *J. Am. Chem. Soc.*, 1982, **104**, 4546.
118. G. Lipari and A. Szabo, *J. Am. Chem. Soc.*, 1982, **104**, 4559.
119. A. S. Shashkov, G. M. Lipkind, and N. K. Kochetkov, *Carbohydr. Res.*, 1986, **147**, 175.
120. L. M. J. Kroon-Batenburg, J. Kroon, B. R. Leeflang, and J. F. G. Vliegenthart, *Carbohydr. Res.*, 1993, **245**, 21.
121. M. L. Hayes, A. S. Serianni, and R. Barker, *Carbohydr. Res.*, 1982, **100**, 87.
122. V. L. Bevilacqua, Y. Kim, and J. H. Prestegard, *Biochemistry*, 1992, **31**, 9339.
123. A. J. Duben, M. Hricovíni, and I. Tvaroska, *Carbohydr. Res.*, 1993, **247**, 71.
124. S. W. Homans and T. Rutherford, *Biochem. Soc. Trans.*, 1993, **21**, 449.
125. G. M. Lipkind, A. S. Shashkov, S. S. Mamyan, and N. K. Kochetkov, *Carbohydr. Res.*, 1988, **181**, 1.
126. A. D. French and J. W. Brady (eds.), *No. 43 of ACS Symp. Ser. 43*, Am. Chem. Soc., Washington, DC, 1990.
127. A. Imberty, S. Gerber, V. Tran, and S. Pérez, *Glycoconjugate J.*, 1990, **7**, 27.
128. A. Imberty, M.-M. Delage, Y. Bourne, C. Cambillau, and S. Pérez, *Glycoconjugate J.*, 1991, **8**, 456.
129. L. Poppe, J. Dabrowski, C.-W. von der Lieth, K. Koike, and T. Ogawa, *Eur. J. Biochem.*, 1990, **189**, 313.
130. C. Mukhopadhyay and C. A. Bush, *Biopolymers*, 1994, **34**, 11.
131. H. Kessler, M. Gehrke, and C. Griesinger, *Angew. Chem., Int. Ed. Engl.*, 1988, **27**, 490.
132. E. Kupce and R. Freeman, *J. Magn. Reson.*, 1992, **100**, 208.
133. P. Berthault, F. Djedaini, and B. Perly, *J. Magn. Reson.*, 1991, **91**, 102.
134. G. Batta and K. E. Kövér, *Tetrahedron*, 1991, **47**, 3535.
135. L. Braunschweiler and R. R. Ernst, *J. Magn. Reson.*, 1983, **53**, 521.
136. R. Bazzo, C. J. Edge, R. A. Dwek, and T. W. Rademacher, *J. Magn. Reson.*, 1990, **86**, 199.
137. L. Poppe and H. van Halbeek, *Magn. Reson. Chem.*, 1991, **29**, 355.
138. F. Inagaki, I. Shimada, D. Kohda, A. Suzuki, and A. Bax, *J. Magn. Reson.*, 1989, **81**, 186.

139. G. W. Vuister, P. De Waard, R. Boelens, J. F. G. Vliegenthart, and R. Kaptein, *J. Am. Chem. Soc.*, 1989, **111**, 772.
140. T. J. Rutherford and S. W. Homans, *Glycobiology*, 1992, **2**, 293.
141. D. Uhrín, J.-R. Brisson, and D. R. Bundle, *J. Biomol. NMR*, 1993, **3**, 367.
142. S. W. Homans, *J. Magn. Reson.* 1990, **90**, 557.
143. A. Bax, *Isr. J. Chem.*, 1988, **28**, 309.
144. S. P. Rucker and A. J. Shaka, *Mol. Phys.*, 1989, **68**, 509.
145. J. Briand and R. R. Ernst, *Chem. Phys. Lett.*, 1991, **185**, 276.
146. S. J. Glaser and G. P. Drobny, *Adv. Magn. Reson.*, 1990, **14**, 35.
147. G. A. Morris and R. Freeman, *J. Magn. Reson.*, 1978, **29**, 433.
148. E. Gaggelli and G. Valensin, *Concepts Magn. Reson.*, 1993, **5**, 19.
149. L. Lerner and A. Bax, *Carbohydr. Res.*, 1987, **166**, 35.
150. V. Sklenár and J. Feigon, *J. Am. Chem. Soc.*, 1990, **112**, 5644.
151. D. Boudot, D. Canet, J. Brondeau, and J. C. Boubel, *J. Magn. Reson.*, 1989, **83**, 428.
152. G. Bodenhausen, R. Freeman, and D. L. Turner, *J. Magn. Reson.*, 1977, **27**, 511.
153. A. Bax and D. G. Davis, *J. Magn. Reson.*, 1985, **63**, 207.
154. A. Bax, *J. Magn. Reson.*, 1988, **77**, 134.
155. L. Poppe and H. van Halbeek, *J. Magn. Reson.*, 1992, **96**, 185.
156. X.-L. Wu, P. Xu, and R. Freeman, *J. Magn. Reson.*, 1989, **83**, 404.
157. V. Sklenár and A. Bax, *J. Magn. Reson.*, 1987, **74**, 469.
158. S. Sabesan, K. Bock, and J. C. Paulson, *Carbohydr. Res.*, 1991, **218**, 27.
159. P. J. Hore, R. M. Scheek, and R. Kaptein, *J. Magn. Reson.*, 1983, **52**, 339.
160. S. Brownstein and J. Bornais, *J. Magn. Reson.*, 1990, **86**, 247.
161. L. D. Hall and T. J. Norwood, *J. Magn. Reson.*, 1988, **76**, 548.
162. L. Poppe, J. Dabrowski, and C.-W. von der Lieth, *Biochem. Biophys. Res. Commun.*, 1991, **174**, 1169.
163. G. Otting and K. Wüthrich, *J. Magn. Reson.*, 1988, **76**, 569.
164. G. Bodenhausen and D. J. Ruben, *Chem. Phys. Lett.*, 1980, **69**, 185.
165. L. Poppe and H. van Halbeek, *J. Magn. Reson.*, 1991, **92**, 636.
166. M.-A. Delsuc, E. Guittet, and J.-Y. Lallemand, *Magn. Reson. Chem.*, 1985, **23**, 213.
167. L. Poppe and H. van Halbeek, *J. Magn. Reson.*, 1991, **93**, 214.
168. A. S. Edison, W. M. Westler, and J. L. Markley, *J. Magn. Reson.*, 1991, **92**, 434.
169. L. Poppe and H. van Halbeek, *Magn. Reson. Chem.*, 1991, **29**, 848.
170. C. Morat, F. R. Taravel, and M. R. Vignon, *Magn. Reson. Chem.*, 1988, **26**, 264.
171. R. Brüschweiler, J. C. Madsen, C. Griesinger, O. W. Sørensen, and R. R. Ernst, *J. Magn. Reson.*, 1987, **73**, 380.
172. D. Uhrín, A. Mele, J. Boyd, M. R. Wormald, and R. A. Dwek, *J. Magn. Reson.*, 1992, **97**, 411.
173. D. Uhrín, A. Mele, K. E. Kövér, J. Boyd, and R. A. Dwek, *J. Magn. Reson., Ser. A*, 1994, **108**, 160.
174. J. M. Duker and A. S. Serianni, *Carbohydr. Res.*, 1993, **249**, 281.
175. U. Wollborn and D. Leibfritz, *J. Magn. Reson.*, 1992, **98**, 142.
176. G. Otting and K. Wüthrich, *Q. Rev. Biophys.*, 1990, **23**, 39.
177. J.-M. Nuzillard and J.-M. Bernassau, *J. Magn. Reson., Ser. B*, 1994, **103**, 284.
178. L. Poppe, W. S. York, and H. van Halbeek, *J. Biomol. NMR*, 1993, **3**, 81.
179. G. T. Montelione, M. E. Winkler, P. Rauenbuehler, and G. Wagner, *J. Magn. Reson.*, 1989, **82**, 198.
180. G. Wider, D. Neri, G. Otting, and K. Wüthrich, *J. Magn. Reson.*, 1989, **85**, 426.
181. A. S. Serianni and C. A. Podlasek, *Carbohydr. Res.*, 1994, **259**, 277.
182. G. M. Clore and A. M. Gronenborn, *J. Magn. Reson.*, 1985, **61**, 158.
183. B. A. Borgias, M. Gochin, D. J. Kerwood, and T. L. James, *Prog. NMR Spectrosc.*, 1990, **22**, 83.
184. W. Massefski, Jr.and A. G. Redfield, *J. Magn. Reson.*, 1988, **78**, 150.
185. D. G. Davis and A. Bax, *J. Magn. Reson.*, 1985, **64**, 533.
186. A. A. Bothner-By and R. Shukla, *J. Magn. Reson.*, 1988, **77**, 524.
187. L. Poppe, C.-W. von der Lieth, and J. Dabrowski, *J. Am. Chem. Soc.*, 1990, **112**, 7762.
188. D. Acquotti, L. Poppe, J. Dabrowski, C.-W. von der Lieth, S. Sonnino, and G. Tettamanti, *J. Am. Chem. Soc.*, 1990, **112**, 7772.
189. V. Sklenár, R. Tschudin, and A. Bax, *J. Magn. Reson.*, 1987, **75**, 352.
190. V. Sklenár and A. Bax, *J. Magn. Reson.*, 1987, **75**, 378.
191. M. Guéron, P. Plateau, and M. Decorps, *Prog. NMR Spectrosc.*, 1991, **23**, 135.
192. T. Peters, B. Meyer, R. Stuike-Prill, R. Somorjai, and J.-R. Brisson, *Carbohydr. Res.*, 1993, **238**, 49.
193. V. H. Tran and J. W. Brady, *Biopolymers*, 1990, **29**, 961.
194. V. H. Tran and J. W. Brady, *Biopolymers*, 1990, **29**, 977.
195. C. Hervé du Penhoat, A. Imberty, N. Roques, V. Michon, J. Mentech, G. Descotes, and S. Pérez, *J. Am. Chem. Soc.*, 1991, **113**, 3720.
196. D. B. Davies and J. C. Christofides, *Carbohydr. Res.*, 1987, **163**, 269.
197. B. Adams and L. Lerner, *J. Am. Chem. Soc.*, 1992, **114**, 4827.
198. D. C. McCain and J. L. Markley, *Carbohydr. Res.*, 1986, **152**, 73.
199. D. C. McCain and J. L. Markley, *J. Am. Chem. Soc.*, 1986, **108**, 4259.
200. D. C. McCain and J. L. Markley, *J. Magn. Reson.*, 1987, **73**, 244.
201. M. Hricovíni, R. N. Shah, and J. P. Carver, *Biochemistry*, 1992, **31**, 10 018.
202. I. Braccini, V. Michon, C. Hervé du Penhoat, A. Imberty, and S. Pérez, *Int. J. Biol. Macromol.*, 1993, **15**, 52.
203. A. Ejchart, J. Dabrowski, and C.-W. von der Lieth, *Magn. Reson. Chem.*, 1992, **30**, S105.
204. A. Ejchart and J. Dabrowski, *Magn. Reson. Chem.*, 1992, **30**, S115.
205. R. U. Lemieux, K. Bock, L. T. J. Delbaere, S. Koto, and V. S. R. Rao, *Can. J. Chem.*, 1980, **58**, 631.
206. H. Thøgersen, R. U. Lemieux, K. Bock, and B. Meyer, *Can. J. Chem.*, 1982, **60**, 44.
207. P. Cagas and C. A. Bush, *Biopolymers*, 1992, **32**, 277.
208. K. E. Miller, C. Mukhopadhyay, P. Cagas, and C. A. Bush, *Biochemistry*, 1992, **31**, 6703.
209. C. Mukhopadhyay and C. A. Bush, *Biopolymers*, 1991, **31**, 1737.
210. P. Cagas and C. A. Bush, *Biopolymers*, 1990, **30**, 1123.
211. Z.-Y. Yan and C. A. Bush, *Biopolymers*, 1990, **29**, 799.

212. B. N. N. Rao and C. A. Bush, *Carbohydr. Res.*, 1988, **180**, 111.
213. Z.-Y. Yan, B. N. N. Rao, and C. A. Bush, *J. Am. Chem. Soc.*, 1987, **109**, 7663.
214. C. A. Bush, Z.-Y. Yan, and B. N. N. Rao, *J. Am. Chem. Soc.*, 1986, **108**, 6168.
215. B. N. N. Rao, V. K. Dua, and C. A. Bush, *Biopolymers*, 1985, **24**, 2207.
216. C. Mukhopadhyay, K. E. Miller, and C. A. Bush, *Biopolymers*, 1994, **34**, 21.
217. T. J. Rutherford, D. G. Spackman, P. J. Simpson, and S. W. Homans, *Glycobiology*, 1994, **4**, 59.
218. H. Kogelberg and T. J. Rutherford, *Glycobiology*, 1994, **4**, 49.
219. J.-R. Brisson and J. P. Carver, *J. Biol. Chem.*, 1983, **258**, 1431.
220. J.-R. Brisson and J. P. Carver, *Biochemistry*, 1983, **22**, 3671.
221. J.-R. Brisson and J. P. Carver, *Biochemistry*, 1983, **22**, 3680.
222. J. P. Carver and J.-R. Brisson, in *Biology of Carbohydrates*, eds. V. Ginsburg and P. W. Robbins, Wiley, New York, 1984, Vol. 2, p. 289.
223. S. W. Homans, R. A. Dwek, D. L. Fernandes, and T. W. Rademacher, *FEBS Lett.*, 1983, **164**, 231.
224. D. A. Cumming, R. N. Shah, J. J. Krepinsky, A. A. Grey, and J. P. Carver, *Biochemistry*, 1987, **26**, 6655.
225. D. A. Cumming and J. P. Carver, *Biochemistry*, 1987, **26**, 6664.
226. D. A. Cumming and J. P. Carver, *Biochemistry*, 1987, **26**, 6676.
227. S. W. Homans, R. A. Dwek, and T. W. Rademacher, *Biochemistry*, 1987, **26**, 6553.
228. S. W. Homans, R. A. Dwek, and T. W. Rademacher, *Biochemistry*, 1987, **26**, 6571.
229. S. W. Homans, A. Pastore, R. A. Dwek, and T. W. Rademacher, *Biochemistry*, 1987, **26**, 6649.
230. S. W. Homans, *Biochemistry*, 1990, **29**, 9110.
231. T. J. Rutherford, J. Partridge, C. T. Weller, and S. W. Homans, *Biochemistry*, 1993, **32**, 12 715.
232. J. P. Carver, D. Mandel, S. W. Michnick, A. Imberty, and J. W. Brady, *ACS Symp. Ser., No. 430*, Am. Chem. Soc., Washington, DC, 1990, p. 266.
233. J. P. Carver, *Pure Appl. Chem.*, 1993, **65**, 763.
234. A. Imberty, S. Pérez, M. Hricovíni, R. N. Shah, and J. P. Carver, *Int. J. Biol. Macromol.*, 1993, **15**, 17.
235. H. van Halbeek, *Curr. Opin. Struct. Biol.*, 1994, **4**, 697.
236. J. T. Davis, S. Hirani, C. Bartlett, and B. R. Reid, *J. Biol. Chem.*, 1994, **269**, 3331.
237. A. Pollex-Krüger, B. Meyer, R. Stuike-Prill, V. Sinnwell, K. L. Matta, and I. Brockhausen, *Glycoconjugate J.*, 1993, **10**, 365.
238. D. V. Renouf and E. F. Hounsell, *Int. J. Biol. Macromol.*, 1993, **15**, 37.
239. S. W. Homans, C. J. Edge, M. A. J. Ferguson, R. A. Dwek, and T. W. Rademacher, *Biochemistry*, 1989, **28**, 2881.
240. S. W. Homans, A. Mehlert, and S. J. Turco, *Biochemistry*, 1992, **31**, 654.
241. S. Sabesan, K. Bock, and R. U. Lemieux, *Can. J. Chem.*, 1984, **62**, 1034.
242. S. Sabesan, J. Ø. Duus, T. Fukunaga, K. Bock, and S. Ludvigsen, *J. Am. Chem. Soc.*, 1991, **113**, 3236.
243. J. Dabrowski, P. Hanfland, and H. Egge, *Biochemistry*, 1980, **19**, 5652.
244. T. A. W. Koerner, Jr., J. N. Scarsdale, J. H. Prestegard, and R. K. Yu, *J. Carbohydr. Chem.*, 1984, **3**, 565.
245. J. N. Scarsdale, J. H. Prestegard, and R. K. Yu, *Biochemistry*, 1990, **29**, 9843.
246. S. B. Levery, *Glycoconjugate J.*, 1991, **8**, 484.
247. S. B. Levery, E. H. Holmes, D. D. Harris, and S. I. Hakomori, *Biochemistry*, 1992, **31**, 1069.
248. C. Griesinger, H. Schwalbe, J. Schleucher, and M. Sattler, in *Two-Dimensional NMR Spectroscopy. Applications for Chemists and Biochemists*, 2nd edn., eds. W. R. Croasmun and R. M. K. Carlson, VCH, New York, 1994, p. 457.
249. L. Yu, R. Goldman, P. Sullivan, G. F. Walker, and S. W. Fesik, *J. Biomol. NMR*, 1993, **3**, 429.
250. Y. Q. Gosser, K. P. Howard, and J. H. Prestegard, *J. Magn. Reson., Ser. B*, 1993, **101**, 126.
251. J. Chung, J. R. Tolman, K. P. Howard, and J. H. Prestegard, *J. Magn. Reson., Ser. B*, 1993, **102**, 137.
252. K. Dill, E. Berman, and A. A. Pavia, *Adv. Carbohydr. Chem. Biochem.*, 1985, **43**, 1.
253. W. J. Goux, C. Perry, and T. L. James, *J. Biol. Chem.*, 1982, **257**, 1829.
254. H. C. Joao and R. A. Dwek, *Eur. J. Biochem.*, 1993, **218**, 239.
255. P. M. Rudd, H. C. Joao, E. Coghill, P. Fiten, M. R. Saunders, G. Opdenakker, and R. A. Dwek, *Biochemistry*, 1994, **33**, 17.
256. R. J. Woods, C. J. Edge, and R. A. Dwek, *Nature, Struct. Biol.*, 1995, **1**, 499.
257. R. Stuike-Prill and B. Meyer, *Eur. J. Biochem.*, 1990, **194**, 903.
258. L. Poppe, J. Dabrowski, C.-W. von der Lieth, M. Numata, and T. Ogawa, *Eur. J. Biochem.*, 1989, **180**, 337.
259. H.-C. Siebert, G. Reuter, R. Schauer, C.-W. von der Lieth, and J. Dabrowski, *Biochemistry*, 1992, **31**, 6962.
260. L. Poppe, H. van Halbeek, D. Acquotti, and S. Sonnino, *Biophys. J.*, 1994, **66**, 1642.
261. H. Geen, X.-L. Wu, P. Xu, J. Friedrich, and R. Freeman, *J. Magn. Reson.*, 1989, **81**, 646.
262. Y. Aubin, Y. Ito, J. C. Paulson, and J. H. Prestegard, *Biochemistry*, 1993, **32**, 13 405.
263. G. Otting, *Curr. Opin. Struct. Biol.*, 1993, **3**, 760.
264. K. A. Kronis and J. P. Carver, *Biochemistry*, 1982, **21**, 3050.
265. K. A. Kronis and J. P. Carver, *Biochemistry*, 1985, **24**, 826.
266. T. Weimar and T. Peters, *Angew. Chem., Int. Ed. Engl.*, 1994, **33**, 88.
267. C. P. J. Glaudemans, L. Lerner, G. D. Daves, Jr., P. Kovác, R. Venable, and A. Bax, *Biochemistry*, 1990, **29**, 10 906.
268. B. Bechtel, A. J. Wand, K. Wróblewski, H. Koprowski, and J. Thurin, *J. Biol. Chem.*, 1990, **265**, 2028.
269. D. R. Bundle, H. Baumann, J.-R. Brisson, S. M. Gagné, A. Zdanov, and M. Cygler, *Biochemistry*, 1994, **33**, 5183.
270. A. P. Campbell and B. D. Sykes, *Annu. Rev. Biophys. Biomol. Struct.*, 1993, **22**, 99.
271. B. D. Sykes, *Curr. Opin. Biotechnol.*, 1993, **4**, 392.
272. T.-L. Hwang and A. J. Shaka, *J. Am. Chem. Soc.*, 1992, **114**, 3157.
273. C. S. Wright, *J. Mol. Biol.*, 1990, **215**, 635.

Acknowledgments

Research in the author's laboratory is supported by National Institutes of Health Grants P41-RR-05351, R01-AI-29751, and R01-AI-32899. The author thanks Drs. Leszek Poppe, John Glushka, and Shuqun Sheng for fruitful collaborations and stimulating discussions enjoyed over the course of many years, and Ms. Traci Swanson for editing the manuscript.

Biographical Sketch

Herman van Halbeek. *b* 1953. B.Sc., 1978, Ph.D., 1982, Bioorganic Chemistry, University of Utrecht, The Netherlands. Introduced to NMR by Robert Kaptein and Cornelis A. G. Haasnoot at the National NMR Facilities in Groningen and Nijmegen, The Netherlands. Postdoctoral fellow of the Dutch Cancer Foundation (Koningin Wilhelmina Fonds), 1982–85. Member of the Faculty in the Complex Carbohydrate Research Center at the University of Georgia (UGA), 1985–present. Currently Professor of Biochemistry and Chemistry at UGA. Approx. 185 publications. Research specialty: solution state NMR and its application to problems in glycobiology.

Carbon & Nitrogen Chemical Shifts of Solid State Enzymes

Ann McDermott and Zhengtian Gu

Columbia University, New York City, NY, USA

1	Introduction	1
2	Chemical Shifts: Overview and Referencing	1
3	Linewidths and General Considerations for Sample Preparation	2
4	Covalent Adducts at the Active Site	3
5	Conformational Analysis and Protein Structure	6
6	Ionization and Hydrogen Bonding	7
7	Conclusions	9
8	Related Articles	9
9	References	9

1 INTRODUCTION

Solid state NMR (SSNMR) is now established as a common method for answering questions about active-site chemistry in proteins. The technique has usually been applied to study insoluble proteins such as membrane proteins and structural proteins. In some cases chemical intermediates trapped at low temperatures have been studied. Recently there have been extraordinary advances in the development of SSNMR dipolar methods that are applicable to biological solids (reviewed elsewhere in this Encyclopedia). However, the majority of mechanistic problems solved with solid state NMR to date have relied on measurements of chemical shifts. In these studies, carbon, nitrogen or phosphorus spectra are measured using excitation by cross polarization from protons, and line-narrowing methods such as magic angle spinning and proton decoupling (CP MAS).[1,2] Chemical shift measurements in proteins have usually been interpreted by comparison with the spectra of characterized 'model' compounds.

The anisotropy, or distribution of chemical shift values as a function of the spatial orientation of the sample in the magnetic field, can be measured in the solid state and is compactly summarized in the form of three values for three principal directions, δ_{11}, δ_{22}, and δ_{33}. These three values of the chemical shift anisotropy (CSA) are usually measured by simulation of the magic angle spinning spectra taken at low spinning speeds.[3,4] For some of the protein work described here, the full CSA was reported but in the majority of cases only isotropic values were reported [which is equivalent to the centerband value: $\delta_{\rm iso} \equiv \frac{1}{3}(\delta_{11} + \delta_{22} + \delta_{33})$]. There are a few important cases in which the chemical shift anisotropy tensor measured in the solid state gives more dramatic and unmistakable chemical trends than solution state measurements, especially for studies of ionization and hydrogen bonding, and we will highlight this point in the review.

In this review we attempt to emphasize examples of the kinds of problems that have been solved by solid state NMR, and consequently the examples are organized by the general types of chemical topics rather than by aspects of the NMR methods, for example detection of covalent modification, conformational strain, or nonbonded interactions.

2 CHEMICAL SHIFTS: OVERVIEW AND REFERENCING

The typical range of ^{13}C and ^{15}N isotropic shifts and CSA values for most functional groups commonly found in proteins is indicated pictorially in Figure 1. A database of chemical shifts for characterized solids has been recently compiled,[5] and this review includes anisotropic tensor values for a broad variety of chemical classes and nuclei. For the case of ^{13}C chemical shift anisotropy, there is an excellent older review

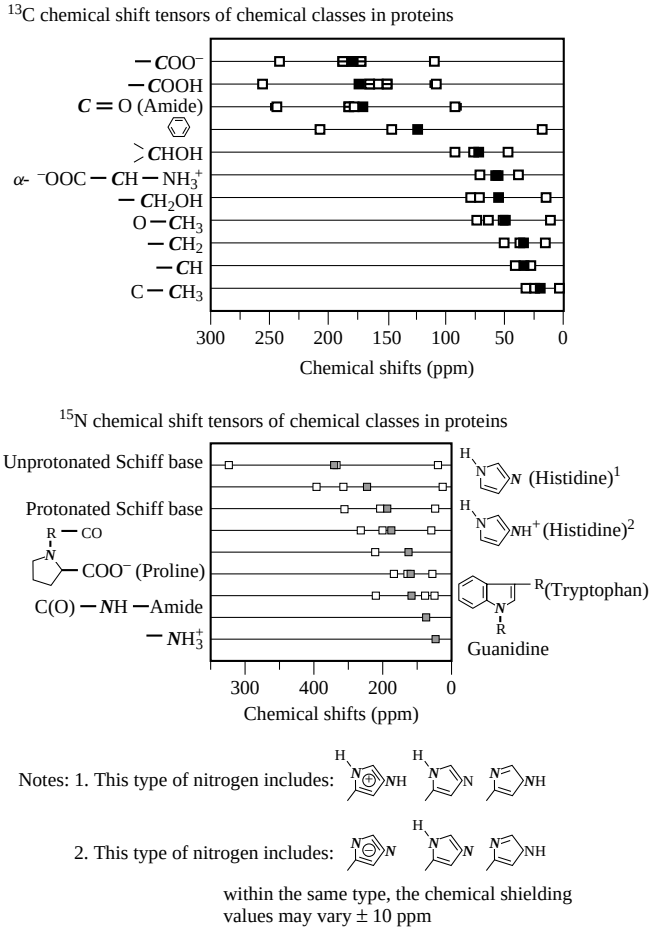

Figure 1 Typical ^{13}C and ^{15}N chemical shift tensors of interesting chemical classes typically found in proteins. Open squares represent CSA elements δ_{11}, δ_{22}, and δ_{33}, from left to right, respectively, and closed squares represent the isotropic chemical shift, $\delta_{\rm iso}$. The square around δ_{22} of the carbonyl group indicates the variation of that tensor element, which is caused by hydrogen bonding. A description of the spatial orientation of the CSA tensor for several carbons can be found in Veemun;[6] for amides, see also Ando et al.[74] and Asakawa et al.;[75] for carboxy groups, Gu and McDermott[67] describe chemical trends and orientations. For the ^{15}N NMR of amides, Oas et al.[66] describe the orientations

of the typical values for various chemical classes and their associated spatial directions.[6]

In Figure 1, a general trend in increased anisotropy with increased deshielding is apparent, reflecting the spatial anisotropy of the low-lying molecular orbitals that induce large paramagnetic effects. When the CSA is less than ca. 2 kHz the anisotropic values are difficult to measure and are not reported, such as the case for ^{15}N measurements of amines and many proton CSA measurements. We have throughout followed the nomenclature that $\delta_{11} > \delta_{22} > \delta_{33}$ in ppm where δ_{11} is the deshielded or higher frequency (downfield) element and $\delta_{\rm iso} = \frac{1}{3}(\delta_{11} + \delta_{22} + \delta_{33})$. In many references alternative nomenclature is used. For example the labels δ_{xx}, δ_{yy}, and δ_{zz} are defined by the criterion $|\delta_{zz} - \delta_{\rm iso}| > |\delta_{xx} - \delta_{\rm iso}| > |\delta_{yy} - \delta_{\rm iso}|$. The CSA is often described in terms of width and rhombicity. Commonly, δ, $\delta(\sigma)$, or the Hebrew letter Beth (ב), refer to the spectral width defined as $\delta_{zz} - \delta_{\rm iso}$, and the rhombicity or anisotropy, η, is defined as $(\delta_{yy} - \delta_{xx})/(\delta_{zz} - \delta_{\rm iso})$. A less common nomenclature utilizes μ as a measure of the spectral width and ρ as a measure of rhombicity:

$$\mu = 2\Pi\gamma H_0(\delta_{11} - \delta_{33})/\nu_{\rm r} \quad \text{and}$$
$$\rho = (\delta_{33} + \delta_{11} - 2\delta_{22})/(\delta_{33} - \delta_{11}) \qquad (1)$$

where γ is the gyromagnetic ratio, H_0 is the applied magnetic field and $\nu_{\rm r}$ is the MAS spinning speed. When a uniaxial approximation is acceptable (as is frequently used in solution T_1 studies) $\Delta\sigma$ refers to the width defined as $\delta_{zz} - \frac{1}{2}(\delta_{xx} + \delta_{yy})$ and η is assumed to be zero.

Carbon spectra are generally referenced to tetramethylsilane (TMS) at 0 ppm; in practice the larger and more shielded of the two carbon peaks (the methylene peak) of adamantane is used experimentally and set to 38.6 ppm relative to TMS. Nitrogen spectra can be referenced to any of a number of compounds and in the absence of consistent literature adherence to the IUPAC standard (neat nitromethane), it is worthwhile to compare the various standards that are commonly used. Protein data in solution are usually referenced to liquid ammonia at -50°C as 0 ppm. In this article we will report all shifts on this scale, correcting from the references if necessary.

In Table 1 we list many of the common ^{15}N references collected from several sources.[5,7,8] [Note that several groups have used 1 M HNO_3 solution but reversed the normal direction of the scale, i.e. they indicate more shielded nitrogens with larger (positive) shift values.] Phosphorus-31 NMR spectra are referenced to 85% H_3PO_4.

A recent article reports the ^{13}C chemical shift anisotropies of solid amino acids.[9] It is of note that the practice of assigning the resonances on the basis of a comparison of the isotropic shifts measured in the solid state with the solution values has led to some errors: in particular the methyl assignments are generally ambiguous and there are clear errors in the γ-carbon of aspartic acid, the C-1 for Asn and Gln, as well as the terminal amides for both. Examination of all three tensor elements and comparison with previously determined tensors is usually a more reliable method for assignments if the group is known to be essentially static. When this is ambiguous, then a more definitive assignment is possible by selective labeling or more sophisticated editing and 2D methods.

Table 1 Nitrogen Chemical Shift References of Standard Compounds

Chemical shift standard	Chemical shift (ppm)
Liquid ammonia ($-50\,^\circ$C)	0
Liquid ammonia (25 °C)	−3.37
Amine of NH_4NO_3(aq.)	18.23 (1–10 M)
Amine of NH_4NO_3 (saturated, 25 °C)	17.31
NH_4Cl (1 M in 2 M HCl solution)	18.5
NH_4Cl (2.9 M in 1 M HCl solution)	21.56
NH_4Cl (1 M in 10 M HCl solution	26.94
NH_4Cl (saturated solution, 5.6 M)	23.97
NH_4Cl (solid)	38.5
1 M HNO_3	372.4
Nitromethane in $CDCl_3$ [1:1, 0.03 M $Cr(acac)_3$]	376.23
Nitromethane (neat)	376.86

3 LINEWIDTHS AND GENERAL CONSIDERATIONS FOR SAMPLE PREPARATION

In general, solid state NMR measurements require specific introduction of a rare isotope, usually ^{15}N or ^{13}C, and this can at times present a practical limitation since the preparation of the appropriately labeled compounds can be an arduous task, especially because of the limited number of appropriately labeled starting materials that are commercially available in an inexpensive form. For this reason, the application of solid state methods is usually limited to situations of special interest, or where other methods have encountered some limitations. The label is most often introduced to an active site ligand or chemical modification agent, or by specific labeling of amino acids introduced into a protein in an overexpression system. The availability of appropriate model compounds can also be a limitation when the proposed chemistry at the enzyme active site is unusual and involves unstable compounds. So in at least two regards the recent progress in SSNMR has been directly dependent upon chemical synthetic efforts. For adequate sensitivity, in the case of CP MAS measurements it is necessary to have more than 0.1 μmol of spins and preferably 1 μmol when possible. One important exception is the spectroscopy of 'high-gamma' nuclei such as ^{19}F, where the detection of 10 nmol is possible.

Since the molecular weight range is often discussed as a criterion for selecting solution versus solid state methods, we will attempt to identify some cases of interest regarding detection of signals from large proteins in the solution state. It is particularly notable that studies of high molecular weight proteins (280 kDa) in viscous solvents at low temperatures have given nice linewidths by solution NMR (vide infra),[34] so that when a protein is rather soluble it is worthwhile making a deliberate choice between solution and solid state methods. It is also noteworthy that several groups have characterized the NMR spectra of insoluble proteins, such as fragments of intrinsic membrane proteins, using solution NMR in organic solvents.[76,77]

Carbon or nitrogen linewidths measured with CP MAS ($\sim$1 ppm) are typically much greater than in solution ($\leq$0.2 ppm), and so many of the conformational effects that are reliably correlated with chemical shift in solution might be subtle in the solid state. Linewidths for solid state small molecules are usually strongly dependent upon both the crystallinity of the sample and on instrumental parameters such as the strength

and frequency of the proton decoupling or the adjustment of the magic angle. The linewidths of enzyme-bound species can depend very strongly upon details of the solid state enzyme preparation. Often lyophilized samples have rather broad lines, and it has been reported in one case that the rate of freezing is important in determining the linewidth and in another that the degree of hydration is very important.[10a,b]

Preparation of frozen solutions has also had varied success; for this approach it is often necessary to lower the temperature well below 0°C to obtain a true solid in which cross polarization and other standard solid state techniques are successful. The internal mobility of the sample can have the effect of interfering with cross polarization or with line-narrowing methods. As a result, when motion on the μs to ms timescale is present, signals can be weak or disappear entirely.[7,8] Simple hydrated pellets of membrane proteins normally give acceptable linewidths if the labeled ligand is in a well-defined binding pocket. These samples can sometimes be measured at room temperature, for example, if the sample consists of large fragments of intact membrane, but if their correlation times are too rapid, such as the case when excess detergent used in purification is present, then low temperatures must be used. Good quality spectra have been taken of microcrystals of enzymes. In many cases precipitants that preserve enzyme activity can be found, and enzymatic activity is normal even in the presence of precipitants such as polyethylene glycols.

4 COVALENT ADDUCTS AT THE ACTIVE SITE

Chemical shift analysis in the solid state often gives rather direct indication of covalent modification. Some of the exciting applications of this method involve active-site chemistry, either in the catalytic cycle or in mimics of the catalytic cycle. In rare situations actual kinetic intermediates can be detected by time-resolved low-temperature methods and solution NMR methods,[11,12] and the same cases are likely candidates for stopped-flow and rapid freeze techniques with solid state NMR spectroscopy.[13] An intermediate will build up to a large steady-state population in the special case that the rate for conversion from intermediate to product is slow in comparison with the rate at which it is generated. Such a situation is actually rather rare, since typically the intermediate is unstable and reactive when compared with the Michaelis complex. The lifetime must also be slow compared with the instrumental detection time and practical rates of sample manipulations (several ms). However, in special cases the intermediates are long-lived and detection is possible, such as the hemiketal formed on shikimate synthetase (discussed below).

The formation of a covalent (but unstable) intermediate in chemical catalysis is quite common and inhibitors are often fashioned on the principle of forming an analogous but more stable bond. These inhibited complexes can help delineate the scope of the chemistry of the active site, and normally they are considerably easier to detect than the intermediates of catalysis. Establishing these structures for the covalent adducts has often been of significance to pharmaceutical design efforts and has been difficult by other methods. The goal of the studies enumerated here has usually been to prove that inhibition *definitely* proceeds by a mechanism that is analogous to the *proposed* catalytic pathway. Numerous examples of inhibition reactions at the active sites of enzymes have been studied by CP MAS. Although this kind of work has few general lessons, it is of impressive scope at this point in time.

A related class of applications of solid state NMR for the study of active-site compounds is the detection of bound-state products. While it is rare that either the Michaelis complex or a true intermediate can be kinetically trapped, it is quite common that the bound-state product can; such complexes are commonly studied by crystallography. A relatively early example of the application of SSNMR to mechanistic enzymology was the in situ detection of a cleaved glycyl tyrosine at the active site of carboxypeptidase A.[14]

4.1 Trapped Hemiketal Intermediates: Shikimate Synthetase and Mimics for Protease Intermediates

In the case of shikimate synthetase (EPSP synthetase, Scheme 1), it has been possible to detect a tetrahedral intermediate formed by attack of shikimate-3-phosphate (S3P) on phosphoenolpyruvate (PEP) along the kinetic pathway by both low temperature solution NMR in a cryosolvent (10% glycerol at 6°C) and solid state NMR methods.[15–17] A recent SSNMR study of EPSP synthetase also delineated the structure of the S3P–glycophosphate inhibitor of this enzyme.[18] Both the solution and the solid state linewidths were quite broad, but the solution linewidth was significantly narrower than that of the solid state and the sensitivity appeared to be better. Here the chemical shift of the tetrahedral carbon in the hemiketal intermediate was found at ca. 100 ppm as expected, while the substrate alkene was found at ca. 160 ppm, so they could be distinguished easily simply using the isotropic shift. A comprehensive and practical perspective on the future of low temperature solid state NMR of proteins has recently been published.[13]

During the catalysis of an amide or ester hydrolysis reactions, a tetrahedral hemiketal intermediate is formed by attack of an enzyme serine or cysteine side chain or a bound water molecule on substrate carbonyl. This type of reaction has been extensively studied via inhibitors. Stable intermediate mimic compounds are made by the principle of proximity: the pseudoscicile carbonyl is localized near the attacking serine by some other covalent attachment, such as some of

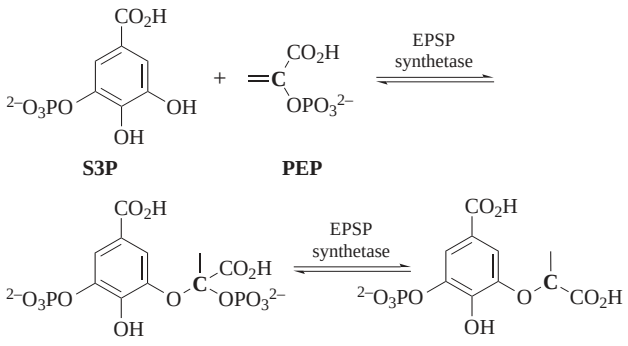

	δ_{iso} (ppm)
[2-^{13}C] PEP of [E-I] complex	104
[2-^{13}C] PEP of EPSP	151

Scheme 1

the covalent irreversible inhibitors of serine proteases used in preparative biochemistry, for example tosylphenylalanyl chloromethyl ketone (TPCK). Other inhibitors are based on the idea of replacing the reactive carbonyl with a more reactive aldehyde group: in the case of proteases, this means that the Pl′ sites (and more distant sites on the C terminus of the substrate) are vacant. For these examples detection of the hemiketal mimic of the intermediate is straightforward using ^{13}C CP MAS or the carbonyl ^{13}C-labeled inhibitor, since the carbonyls resonate at 170–200 ppm and the hemiketal near 100 ppm (Scheme 2). Solid state carbon NMR of these trapped hemiketal complexes has facilitated confirmation of an intact protease active site in a variety of organic solvents in a detailed and quantitative fashion, despite the poorly defined amorphous nature of the sample.[18]

To produce a stable mimic of the hemiketal species, the carbonyl group has been replaced by a phosphate group, resulting in phosphoramidate and phosphinate transition state analog compounds for proteases. Phosphorus NMR of a phosphoramidate inhibitor of thermolysin (Scheme 3) shows a major perturbation of the ^{31}P CSA values upon binding to the enzyme, particularly in the case of benzoxycarbonyl Phe–phosphoramidate–Leu–Ala (ZF^{p}LA) which has a 60 pM binding constant.[19] Such massive changes are indicative of a change in geometry and bonding character, presumably because of tight coordination of the phosphate with the zinc cofactor. A thorough discussion of the trends in CSA for phosphates has been published[20] but such an analysis for phosphinates or phosphoramidates, particularly including the effects of metal chelation, is lacking.

In the study of thermolysin it was also established that there is no major perturbation to the nitrogen environment and that the P–N bond length was essentially unaffected by binding. These results imply that binding-induced perturbations on the phosphoramidate moiety mainly involve complexation of Zn by the oxygens, which was not clear from crystallography.

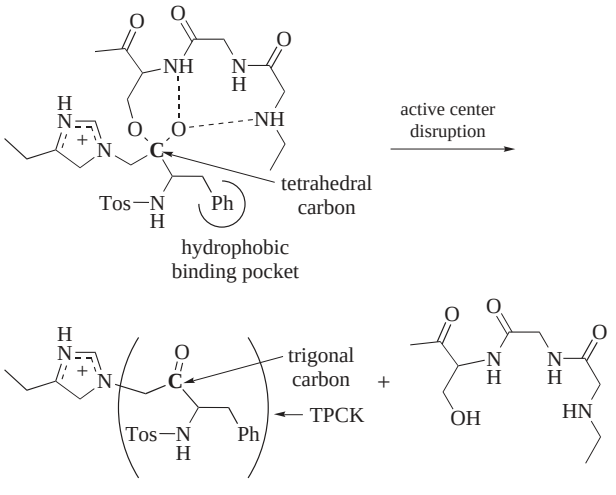

	δ_{iso} (ppm)
carbonyl (trigonal carbon)	205
unprotected hemiketal center	103
protonated hemiketal center (tetrahedral carbon)	99

Scheme 2

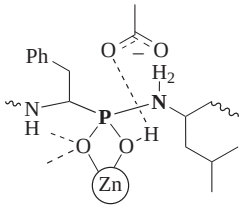

	^{15}N-δ_{iso}	^{31}P-δ_{iso}	^{31}P-δ_{11}	^{31}P-δ_{22}	^{31}P-δ_{33} (ppm)
free ZF^{p}LA	50.7	17.9	94	13	–53
E-ZF^{p}LA	54.8	36.7	91	43	–23
free ZG^{p}LA	56.5	23.6	100	10	–39
E-ZG^{p}LA	58.5	28.1	95	21	–31

ZG^{p}LA: carbobenzoxy-Gly^{P}-L-leucyl-L-alanine
ZG^{p}LA: carbobenzoxy-Phe^{P}-L-leucyl-L-alanine

Scheme 3

4.2 Amide Bond Formation and Cross-Linking

Another classic reaction type involving a tetrahedral transition state is provided by the amide bond-formation reactions. These often begin by phosphorylation of a carboxylic acid to form a good leaving group, followed by attack at the carbon by a neutral amine to form the tetrahedral complex. A phosphinate mimic of such an intermediate is a slow-binding inhibitor of the enzyme, D-Ala–D-Ala ligase (Scheme 4). Demonstration of the phosphorylation of this inhibitor at the active site by solid state NMR was accomplished using both homonuclear dipolar methods and chemical shift analysis;[21] the values of the ^{31}P chemical shift anisotropy of the phosphinate changed dramatically upon binding indicating a covalent modification of the phosphinate to a phosphophosphinate (see Scheme 4). These results confirmed the analogy with proposed active-site chemistry of the substrate and explained the need for ATP. The poor stability of the phosphophosphinate species precluded detection by chemical methods, so an in situ probe was required.

Similar studies concerning inhibitors of glutamine synthetase are in progress (unpublished). The phosphorus NMR spectrum of the bound-state inhibitor was difficult to detect in the solution state, mainly because of the poor solubility of this membrane-associated enzyme. Moreover, in solution NMR spectra nonspecifically adhered phosphates gave rise to large and sharp signals. The signals due to these phosphates were weak and broad in the solid state spectrum. These differences in relative intensity are probably due to the relative mobility and strengths and specificity of binding constants, and they produce an accidental but very useful editing of the solid state spectrum.

Transglutaminases catalyze cross-linking of glutamine and lysine side chains for a variety of important structural proteins. Their mechanism involves a critical thioester–acyl enzyme intermediate (Scheme 5) and their inhibition has been of

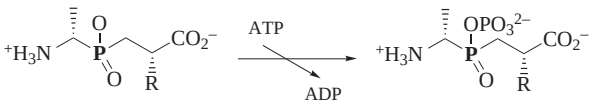

	δ_{iso}	δ_{11}	δ_{22}	δ_{33} (ppm)
Reactant	36	110	25	–27
Product	53	105	89	–35

Scheme 4

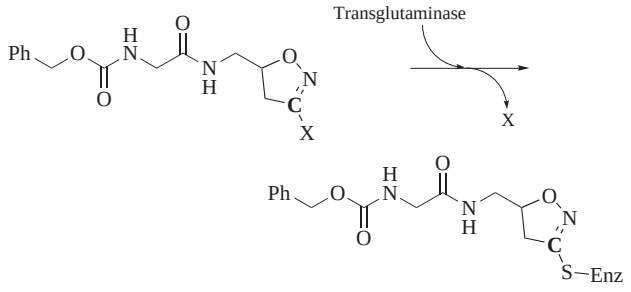

Model compounds	δ_{iso} (ppm)
X = Br	137
X = Cl	149
X = SEt	156
Actual enzyme–inhibitor	156

Scheme 5

general medical interest. Recently, solid state NMR was used to prove that halodihydroisoxazole inhibitors also form covalent imino thioether complexes at the active site.[22] In this project the signal from the ^{13}C-labeled inhibitor was not detected by solution NMR methods when the inhibitor was bound to the 76.6 kDa enzyme, but the signal was readily detected by SSNMR. Tensorial information was not reported.

A combination of selective labeling, CP MAS, and sophisticated $^{1}H-^{15}N-^{13}C$ double cross polarization filtered solid state NMR approaches has allowed the in situ determination of chemical cross-links in a variety of structural, exoskeletal, and peptidoglycan structures. In the case of bacterial peptidoglycan structures the extent of cross-linking was determined.[23–25] In the case of insect cuticle,[26,27] unambiguous chemical shift and dipolar evidence was presented for an unusual cross-linked structure with direct catechol–histidyl bonds (Scheme 6). Such a structure is also likely to occur for the Black Coral skeleton.[28] Studies of the adhesive plaques from mussels indicate that the cross-linking in the protein glue does not involve lysine.[29] In these examples, in situ detection is of particular importance. Analogous methods have also been used to account quantitatively for small molecule bacterial metabolism.[30,31]

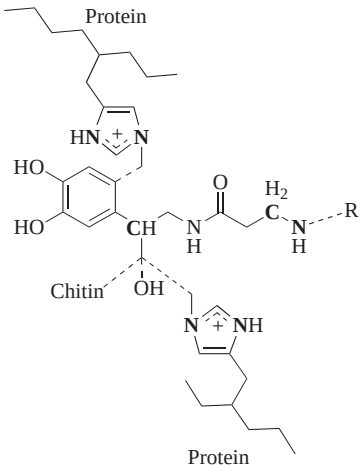

Scheme 6

4.3 Other Mechanism Based Inhibitors: Schiff Base, etc

For several proteins, Schiff base or imine linkage at the enzyme active site has been confirmed based on chemical shifts, and the ionization state of the nitrogen has also been measured. In two cases the limited stability and insolubility of the enzymes made SSNMR an attractive approach. The usual tensor values for Schiff bases are quite distinct as compared with the amines from which they would usually be formed.

In the pyridoxylphosphate (PLP)-dependent reaction of alanine racemase (Scheme 7), transaldimination of the resting state PLP–lysine imine to form the alanine(substrate)–PLP imine has been proposed. Alanine phosphonate is a slow-dissociating inhibitor of alanine racemase. Solid state NMR data indicate that this compound forms a protonated imine with PLP at the active site, thus confirming that inhibition proceeds by the same mechanism as has been proposed for catalysis.[32]

In bacteriorhodopsin the Schiff base linkage between the retinal and a lysine side chain has been demonstrated by ^{15}N tensor analysis,[33] and it is known now to be protonated in all states studied with the exception of the 'M' photointermediate (Scheme 9). The effects of the counterion on the chemical shift appear in the middle and deshielded only tensor elements (δ_{22} and δ_{11}) in a fairly systematic fashion, indicating that tensorial information will be useful for assigning the causes of changes in shift for this case.[4]

It is worth noting for comparison that the active-site chemistry and Schiff base formation of an enzyme of molecular weight 280 000 has been studied using ^{15}N and ^{13}C solution NMR with direct detection methods at elevated temperature (37°C), employing samples which were not only isotopically enriched but also had directly attached protons substituted with deuterium.[34] Some of the reported linewidths were less than 1 ppm. In this study it was established that porphinobilogin synthetase, which catalyzes the first common step of tetrapyrrole synthesis, proceeds via a Schiff base between C-4 of 5-aminolevulinic acid (ALA) and an active site lysine. Solution NMR of the 4-C labeled ALA indicated formation of a Schiff base with *E* stereochemistry following enzyme modification by methanethiosulfanate, but in the holoenzyme it appeared at a shift characteristic of a deprotonated amine. Determination of the protonation state of the Schiff base was am-biguous, presumably because of rapid proton-transfer reactions.

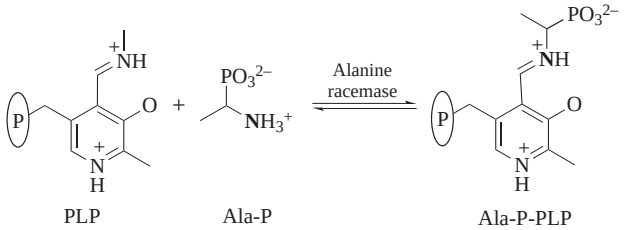

	δ_{iso}	δ_{11}	δ_{22}	δ_{33} (ppm)
Ala-P, pH 7.5	40.3			
Ala-P, pH 13.5	33.8			
Ala-P-PLP aldimine, pH 13.5	325.4	638	333	6
Ala-P-PLP aldimine, pH 7.5	192.4	345	204	31
Ala-P-alanine racemase complex, pH 7.5	188.4	344	188	33

Scheme 7

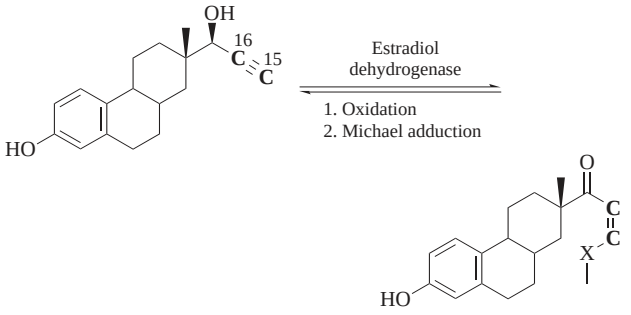

	DANTE irradiation*	δ_{iso} (ppm)
Ketone–enzyme	148.6	1 50, 117
Ketone–enzyme	156.5	157, 86
Cysteine mimic (X = S)	148.6	149.1, 115.5
Lysine mimic (X = NH)	156.5	153.2, 85.4

* The species of interest was selectively detected, despite a crowded spectrum, by selective (DANTE) irradiation of C-15 wherby C-16 and C-15 were correlated.

Scheme 8

An unusual example of a mechanism-based active-site inhibitor is the 14,15-secoestra-1,3,5(10)-triene-15-yne-3,17β-diol, a highly modified steroid inhibitor of estradiol dehydrogenase (Scheme 8). Oxidation of the hydroxy group at the 17-position to the corresponding ketone results in the formation of an yne-one. A subsequent Michael addition involving its yne-one fragment and nucleophiles in the enzyme active site (both lysine and cysteine) was demonstrated in situ by CP MAS.[35]

5 CONFORMATIONAL ANALYSIS AND PROTEIN STRUCTURE

Another classic application of chemical shift analysis in solid proteins has been in situ detection of constrained conformations, such as changes in a dihedral angle accompanied by alteration of the partial double bond character or steric congestion. For such studies the anisotropic shift information is usually more definitive because a perturbation often appears specifically in one tensor element, and this observation will help in establishing its origin.

5.1 Retinal

Some of the earliest biological applications in conformational analysis of enzyme active sites by CSA resulted in the determination of the conformation of retinal in the resting states of bacteriorhodopsin (BR) and rhodopsin (Scheme 9). Many of these conclusions have subsequently been arduously confirmed by rotational resonance distance measurements and dynamics measurements. The so-called gamma *gauche* effect was used extensively to determine conformation in the polyene chain: in ^{13}C NMR this effect refers to the observation of a 5–10 ppm additional shielding due to steric crowding for the carbons in a polyene directly flanking a *cis* double bond.[36,37] Oddly, the specific tensor element that exhibits this effect seems to depend on the particular example, but for typical polyenes the effect is normally seen in the most shielded element (δ_{33}, which is normal to the polyene plane[37]). Measuring the full CSA values could be useful in the diagnosis of the origin of a gamma *gauche* effect. Application of CSA analysis to retinals led to the conclusion that bR is 6-*s*-*trans* in all states in the photocycle, while rhodopsin is 6-*s*-*cis*. Compounds which are 6-*s*-*cis* show shielded values for the 5-carbon relative to the corresponding 6-*s*-*trans* isomers (here the change appears in the *least* shielded element). A similar effect is expected for the *Z* (*syn*) versus *E* (*anti*) nitriles and Schiff bases (here it apparently affects the *middle* tensor element of the flanking carbons). This effect was also used to predict that the dark adapted bR555 is 13-*cis* C–N *syn*, light-adapted bR568 is 13-*trans* C–N *anti*, and the M and N photointermediates are 13-*cis* C–N *anti.* These studies and parallel studies of rhodopsin have been reviewed recently[38] (see also ***Bacteriorhodopsin and Rhodopsin***). Similarly, observation of the isotropic shift of the 14-^{13}C-labeled spheroidene carotinoid in the photosynthetic reaction center (RC) from purple nonsulfur bacteria has been used to conclude that the conformation is 15,15′-*Z* in the protein.[39]

5.2 Amide Conformation by CSA Values

Several surveys of the correlation between carbon or nitrogen shift and protein backbone conformation have been reported, encompassing solution[40–42] and solid state NMR data[43–47] (see also ***Solid Biopolymers***). The most clear correlations utilize the carbon shift of the α-carbon or the carbonyl carbon, which are both $\sim$5 ppm more deshielded for the α-helix (56 and 175 ppm typical values, respectively) than for the β-sheet (52 and 170 ppm typical values, respectively). The reverse trend appears to be true for the β-carbon (26 ppm for the α-helix and 30 ppm for the β-sheet) and the proton of the NH (ca. 8.1 ppm for the helix and 8.5 for the sheet). The α and β shifts are also dependent upon the type of amino acid side chain. Some correlations between side chain conformation and carbon chemical shift have also been observed for the aromatic side chains.[48]

The situation for ^{15}N shifts for the amide backbone is more complicated. Hydrogen bonding, backbone and side chain conformation, and local electrostatic field all contribute to give a range of approximately 30 ppm. Although the dispersion is quite good, no clear-cut trends with any one structural parameter are observed.[40] The chemical shifts in solution and solid state for staphylococcal nuclease have been compared; assignments made with solution NMR methods often apply to solid state samples as well.[49] This lends further support to the notion that the shifts are relating specific information about the folded form of the protein and this observation will be useful in planning further studies of proteins.

5.3 Amide Conformation by Static Oriented Samples

A novel application of chemical shift anisotropy to obtain structures of proteins involves the measurement of partially ordered and static samples as a function of sample orientation in the applied field.[50–52] This approach has allowed the structural characterization of coat proteins from filamentous bacteriophage, a particle of 16 MDa molecular weight.

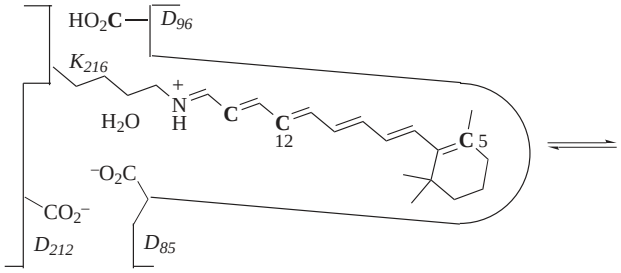

bR568
(light adapted)

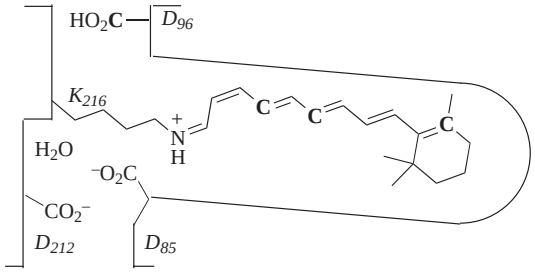

bR555
(dark adapted)

	^{13}C retinal	δ_{iso}	δ_{11}	δ_{22}	δ_{33} (ppm)
5-^{13}C	6-*s*-*trans*-R	136	237	143	27
	6-*s*-*cis*-R	129	217	141	28
	6-*s*-*cis*-S	126	202	143	33
	bR555	144.8	237	170	28
	bR568	144.8	237	170	28
	M	139.8			
	N	139.4	232	161	26
12-^{13}C	bR555	124.2	206	132	35
	bR568	134.3	210	135	58
	M	126.4			
	N	124.4			
14-^{13}C	bR555	110.5	179	107	45
	bR568	122.0	182	134	50
	M	125.7			
	N	115.2			

R = retinoic acid; S = Schiff base

[ε-^{15}N] Lys-labeled bR	δ_{iso}	δ_{11}	δ_{22}	δ_{33} (ppm)
bR555 (13-*cis*)	174.6	284	202	37
bR568 (all -*trans*)	167.5	284	181	38
M	319.2			
N	174.6			

4-^{13}C-aspartates	δ_{iso}	δ_{11}	δ_{22}	δ_{33} (ppm)
Asp212	176.0	235	185	110
Asp85	173.0	230	180	105
Asp96	171.3	245	150	120

Scheme 9

Application of similar methods to gramicidin has resulted in a molecularly detailed three-dimensional structure of the protein in the hydrated lipid bilayer.[53]

5.4 Mobility Probed by CSA Studies

The partial averaging of chemical shift anisotropy in static samples, in conjunction with relaxation measurements, has been used to determine the internal mobilities and dynamics of several structural proteins in the solid state on the ms to ns timescale.[54–56] CSA values are often used for analyses of ns timescale internal motions via T_1 values in solution NMR. Frequently the 'uniaxial' approximation is made, i.e. $\eta = 0$ or $\delta_{xx} = \delta_{yy}$. Figure 1 illustrates that this is a good approximation for the ^{13}C tensor of some alcohols, where the unique axis is most shielded and is along the C–O bond, or for some methyl groups where it is along the C–C bond, or for some aromatic carbons where it is orthogonal to the plane. However, this approximation is poor for many cases such as the backbone carbons of a protein and nitrogens in cyclic compounds. Orientations are described elsewhere in the text for the amides and carboxy groups.

6 IONIZATION AND HYDROGEN BONDING

Identifying the ionization states of the amino acid side chains is fundamental to an understanding of the energetics of protein folding. Electrostatic interactions in proteins are also dominant interactions for analyzing enzyme mechanisms. NMR is a proven method for determining ionization state and hydrogen bonding environment, and we will discuss particular aspects of solid state measurements in the following.

It is useful first to summarize the functional groups of interest and their typical behavior. The 'permanently' ionized arginine side chains are rarely found in protein interiors and normally are engaged in ion pairing on the surface of the enzyme or in the active site; the 'sometimes' ionized histidyl, aspartic, glutamic, and lysine side chains can be found in the protein interior, and often participate in important interactions at the active site. The ionization states of these four side chains can sometimes be inferred from the structural context, for example by X-ray crystallography, but this approach is prone to error in lower resolution structures. Although spectroscopic characterization could give an unambiguous determination of both the ionization state and the hydrogen-bonding strengths for carboxyl as well as imidazole side chains, it has been undertaken in few cases.

The NMR spectra of the residues that have commonly been observed to change ionization state (His, Asp, Glu) have been studied systematically in the solid state and it is clear that more information is available from the complete tensor analysis than from the isotropic values alone. SSNMR might also be useful for the study of residues which are normally capable of forming moderate strength hydrogen bonds but rarely change ionization state stably (alcohols, amides, amine, arginine); fewer model compound studies have been done for these cases.

6.1 Nitrogen-15 Studies of Histidine

There have been several studies of the ^{15}N tensors of histidine. The values are very much affected by the ionization state of the imidazole ring. The nitrogen with attached proton exhibit isotropic shifts of 160–200 ppm and a breadth ($\delta_{33}-\delta_{11}$) of ca. 200 ppm. The more deshielded values correspond to stronger hydrogen bonding. The nitrogen with attached proton shows an isotropic shift of 235–250 ppm and a breadth of ca. 380 ppm and here stronger hydrogen bonding

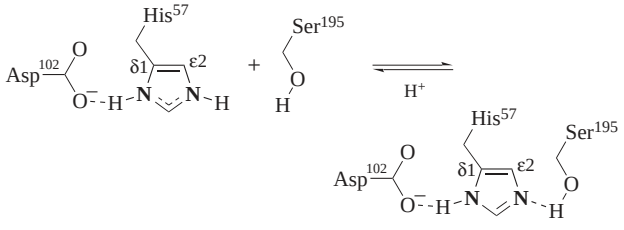

Model study	δ_{iso} (ppm)	
	No hydrogen bond	With hydrogen bond
NH	162	172
N	244	234
+NH	171	181
α-Lytic protease	Nδ1	Nε2
pH < 7.0	179.6	167.2
pH = 10.4	175.2	234.9

NH: NH within a neutral imidazole ring
N: N within a neutral imidazole ring
+NH: NH within a protonated imidazole ring

Scheme 10

leads to shielded values.[57–59] In the solution state, near neutral pH values, the proton transfer reactions of histidine are very fast, the ionizable ^{1}H resonances are undetectable, and the ^{15}N spectrum can be a weighted average of various tautomers and ionization states. The solid state spectrum with full tensor information could, in principle, indicate more clearly the predominant species present, whenever a chemically meaningful solid state preparation can be prepared. It is noteworthy, however, that in certain cases the solution ^{15}N NMR of histidine did give an unambiguous indication of the average ionization state in an enzyme (including specification of the tautomer and hydrogen-bond strength) and this approach has been used in several enzyme mechanistic studies.[59,60]

Nitrogen-15 CP MAS analysis has been applied to the active-site histidine in α-lytic protease (Scheme 10). These studies brought into focus the results of diffraction and solution NMR studies and cleared up a long-standing confusion concerning the interpretation of the hydrogen-bonding network at the active site of the serine proteases.[61] The crystallographic conditions apparently substantially affected the pK_a value of the active-site histidine and as a result the organization of the hydrogen-bond network was artifactual. In particular, in the absence of crystallization, the enzyme would be active at pH 7, the active-site His would be neutral, and would engage in hydrogen-bond formation with serine and aspartic acid. However, in some studies the addition of salts for precipitation raised the pK_a value of the histidine so that it was ionized at pH 7 and consequently the hydrogen bond with serine was artifactually broken. It is known from other studies (unpublished) that some common crystallization salts inhibit a variety of enzymes, despite the fact that under the same conditions the general fold of the protein is intact. Measurements of ^{15}N shifts of active-site histidine have also been used to probe the patency of serine protease active sites in organic solvents;[62] in certain solvents the enzyme was inactive but native-like active sites were indicated by NMR. Unfortunately, anisotropies were not reported for the protein studies.

6.2 Nitrogen-15 Studies of Amine, Amide, and Guanidine

The ^{15}N chemical shift anisotropy of protonated amines is quite narrow.[57] The protonated guanidino group ^{15}N NMR has been studied both in model compounds and in the arginines of bacteriorhodopsin. The chemical shift anisotropy for the ϵ and δ-nitrogen of the guanidino group is also quite narrow, so that anisotropy was effectively undetected at low spinning speeds. Interestingly, counterion effects are observed on the δ-nitrogen but not on the ϵ-, both for the model systems and the proteins. The chemical trends in the δ-shift are currently under analysis.[63]

Amide ^{15}N shift anisotropy has been extensively studied. Tensors are generally quite broad with isotropic values at ca. 118 ppm and widths of 200 ppm. The tensor elements have been shown to shift further to high frequency with increasing hydrogen-bonding strength (particularly the δ_{33} tensor element).[64,65] Careful determinations of both the values of the tensor elements and their spatial directions have been reported for several amides, and variation in the values but not the directions were observed[66] with the most shielded element being near the C–N bond (offset by 9°) and the middle element out of the amide plane. It is noteworthy that, in general, the tensors are not strictly uniaxial, which may be important for the study of dynamics in proteins via the measurement of nitrogen relaxation.

6.3 Carbon-13 Studies of Carboxy Groups

Carbon-13 CSA is a good probe of the environment of the carboxy group and is readily interpreted. The protonated state of the carboxyl group in aspartic and glutamic acids in solid state amino acids and proteins can easily be determined from the δ_{11} values of the carbon chemical shift tensors which are below 250 ppm for deprotonated and above 250 ppm for protonated groups as indicated schematically in Figure 1.[67] The δ_{22} element for both protonated and deprotonated forms varies strongly as a result of hydrogen bonding and correlates with established measures of hydrogen bonding, namely the IR stretching frequencies of the carbonyl and the asymmetric stretching frequency for the protonated and deprotonated carboxy groups, respectively, and O···H hydrogen-bonding distances from the carbonyl of protonated acids to the nearest proton donor.

There is a fixed geometry for the protonated acids and a variable and complicated geometry for hydrogen-bond interactions in deprotonated carboxylates. Correspondingly, the correlations between NMR, IR, and diffraction data seem more convincing for the protonated acids. In contrast to the CSA, the average or isotropic chemical shift for the carbon in carboxy groups is rather insensitive to ionization state and hydrogen bonding. Therefore, measurements of the tensor values in the solid state for the carboxy group can be much more informative than solution measurements. These trends have subsequently been explained by ab initio methods.

SSNMR ^{13}C measurements have been used to delineate the protonation state of the transition-state analog inhibitor of triose phosphate isomerase (TIM), phosphoglycolic acid (PGA)[68] (Scheme 11). The carboxy group is deprotonated when bound to TIM and is involved in a strong hydrogen bond, which established that it is a mimic of the catalytic

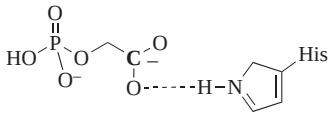

PGA

	δ_{iso}	δ_{11}	δ_{22}	δ_{33}	(ppm)
Glycolic acid	177	264	158	108	
PGA–TIM complex	178	241	177	115	

Scheme 11

intermediate in which charge develops on the carbonyl of the substrate dihydroxyacetone phosphate, and is stabilized by nearby histidine and lysine residues.

The aspartic acid residues in bacteriorhodopsin have been labeled and the CSA measured for the carboxy side chains. These spectra gave an unambiguous ionization state for several of the active-site residues.[69,70] Some of the carboxy groups also show evidence of motional averaging of the CSA, so for determination of the ionization and hydrogen-bonding strengths, corrections for the motional averaging must be made. Asp-85, -96, and -212 are necessary amino acids for proton pumping activity. Asp-85 and -212 are known to be on the cytosolic side of the membrane (the proton 'sink'). Based on these CSA values, both are clearly deprotonated, and Asp-85 is engaged in a relatively strong hydrogen bond. Asp-85 is perturbed by the light-induced conversion from bR555 to bR568, although it appears to remain deprotonated. These observations would support a model in which it is in a hydrogen-bonding or counterion interaction with the Schiff base. Asp-96, which is on the extracellular side (the 'source' for protons) is evidently protonated in dark and light-adapted bR based upon these CSA studies, and the values imply a rather weak hydrogen-bonding environment, perhaps a hydrophobic pocket. The intermediates of the photocycle, M and N, have been proposed to have Asp-85 protonated[70] and Asp-96 deprotonated, respectively, but further investigations of these points by low-temperature SSNMR are necessary.

6.4 Carbon-13 Studies of Tyrosine and Amides

The ^{13}C chemical shift anisotropies of the hydroxylated ring carbon of tyrosine and phenol-containing organic solids have been studied (e.g. 4-^{13}C-tyrosine). The corresponding anions are readily identified on the basis of deshielded δ_{22} values: the neutral, protonated forms are in the range 151–170 while the anions are 180–205. Both δ_{11} and δ_{33} appeared to be less sensitive to environment, with values of 57–73 and 233–258, respectively.[71] There was some indication that δ_{22} is also sensitive to hydrogen bonding but this effect was not systematically studied. Applications to the study of bacteriorhodopsin showed that although the tyrosinate is detectable under very basic conditions (when the protein is presumably unfolded), under normal conditions, even for catalytic intermediates, there is no evidence for tyrosinate formation.[71,72] In these studies there was difficulty in resolving several tyrosines in one protein. Similarly, the 4-^{13}C-tyrosine in the reaction centers of purple nonsulfur bacteria were detected, but the signals had to be deconvoluted by lineshape analysis due to poor resolution.[73] For the interpretations of the chemical shift spreads in both proteins, additional database work would probably be helpful.

Systematic trends in the ^{13}C CSA of amides as a function of the amino acid, the hydrogen-bonding environment, and the backbone geometry have been reviewed elsewhere.[74,75] The effect of hydrogen bonding on the carbon shift is to cause a deshielding effect on the middle tensor element, quite similar to the effect observed for protonated carboxylic acids.

7 CONCLUSIONS

Solid state NMR heteroatom chemical shift measurements of selectively-labeled proteins have had an important role in several problems in protein structure and active-site chemistry. For these kinds of studies, solid state NMR has advantages over solution state NMR when the protein is not very soluble under the conditions of interest, or when direct comparison with crystallography is desired; however, when the enzyme is very large (above 100 kDa) and rather soluble, the comparison of sensitivity between solid state and solution state NMR methods is unclear. In several important cases the analysis of the tensor in the solid state provides more information than the isotropic value alone: this analysis could allow the assignment of the physical origin of an environmentally-induced shift.

There have been many strong applications of chemical shift analysis for conformation or structure studies of solid proteins in the past two decades. For example, shift measurements including analysis of anisotropy were the first definitive tool for determining the conformation of retinal in the retinal-binding proteins bacteriorhodopsin and rhodopsin. The shifts of oriented, static samples have been used in structure determination for phage-coat proteins and intrinsic membrane proteins such as gramicidin. The partial averaging of the anisotropy has been used to probe mobility in a variety of proteins, mainly structural proteins such as collagen. Changes in isotropic shifts have been used to determine the extent and type of cross-linking in peptidoglycan, cuticle, and exoskeletal proteins.

Solid state shift measurements have been used extensively to probe active-site chemistry in enzymes as enumerated in detail in this review. The covalent modifications are usually apparent from the values of the isotropic shifts alone and several examples are illustrated in the Schemes. The studies of nonbonded interactions at the enzyme active site by heteroatom shift tensors are discussed, especially hydrogen bonding and ionization state changes of imidazole and carboxy groups viewed by ^{15}N and ^{13}C shifts, respectively. For these two functional groups a CSA database for chemical interpretation has been partly assembled and demonstrates the utility of full tensor analysis, while for other functional groups the database is still small.

8 RELATED ARTICLES

Bacteriorhodopsin and Rhodopsin; Biological Macromolecules; Biological Macromolecules: NMR Parameters; Chemical Shift Tensor Measurement in Solids; Nitrogen NMR; Proton Chemical Shift Measurements in Biological Solids; Solid Biopolymers.

9 REFERENCES

1. A. Pines, A. Gibby, and J. Waugh, *J. Chem. Phys.*, 1973, **59**, 569.
2. S. O. Smith and R. G. Griffin, *Annu. Rev. Phys. Chem.*, 1988, **39**, 511.
3. J. Herzfeld and A. E. Berger, *J. Chem. Phys.*, 1980, **73**, 6021.
4. H. de Groot, G. Harbison, J. Herzfeld, and R. G. Griffin, *Biochemistry*, 1989, **28**, 3346.
5. T. M. Duncan, *A Compilation of Chemical Shift Anisotropies*, Farragut Press, Chicago, IL, 1990.
6. W. S. Veeman, *Prog. NMR Spectrosc.*, 1984, **16**, 193.
7. P. R. Srinivasan and R. L. Lichter, *J. Magn. Reson.*, 1977, **28**, 227.
8. M. Witanowski, L. Stefraniak, S. Symanski, and H. Januszewski, *J. Magn. Reson.*, 1977, **28**, 217.
9. C. Ye, R. Fu, J. Hu, and S. Ding, *Magn. Reson. Chem.*, 1993, **31**, 699.
10. A. M. Christensen and J. Schaefer, *Biochemistry*, 1993, **32**, 2868; S. Kennedy and R. Bryant, *Biopolymers*, 1990, **29**, 1801, and references contained therein.
11. J. P. G. Malthouse, *Prog. NMR Spectrosc.*, 1986, **18**, 1.
12. K. Anderson and K. Johnson, *Chem. Rev.*, 1990, **90**, 1131.
13. A. E. Derome and S. Bowden, *Chem. Rev.*, 1991, **91**, 1307.
14. B. Mackenzie, P. Fagerness, and I. Scott, *J. Chem. Soc., Chem. Commun.*, **1985**, 635.
15. K. S. Anderson, R. D. Sammons, G. C. Leo, J. A. Sikorski, A. J. Benesi, and K. A. Johnson, *Biochemistry*, 1990, **29**, 1460.
16. J. Evans, R. J. Appleyard, and W. A. Shuttleworth, *J. Am. Chem. Soc.*, 1993, **115**, 1588.
17. P. N. Barlow, R. J. Appleyard, B. J. O. Wilson, and J. N. S. Evans, *Biochemistry*, 1989, **28**, 7985.
18. P. Burke, R. G. Griffin, and A. M. Klibanov, *J. Biol. Chem.*, 1992, **267**, 20 057.
19. V. Copie, A. Kolbert, D. Drewry, P. Bartlett, T. Oas, and R. G. Griffin, *Biochemistry*, 1990, **29**, 9176.
20. S. Un and M. P. Klein, *J. Am. Chem. Soc.*, 1989, **111**, 5119.
21. A. McDermott, F. Creuzet, R. G. Griffin, L. Zawadzke, Q. Ye, and C. Walsh, *Biochemistry*, 1990, **29**, 5767.
22. M. Auger, A. McDermott, V. Robinson, A. Castelhano, R. Billedeau, R. D. Pliura, A. Krantz, and R. G. Griffin, *Biochemistry*, 1993, **32**, 3930.
23. Y. Pan, N. Shenouda, E. Wilson, and J. Schaefer, *J. Biol. Chem.*, 1993, **268**, 18 692.
24. T. Forrest, G. Wilson, Y. Pan, and J. Schaefer, *J. Biol. Chem.*, 1991, **266**, 24 485.
25. G. Jacob, J. Schaefer, and G. Wilson, *J. Biol. Chem.*, 1983, **258**, 10 824.
26. A. Christensen, J. Schaefer, K. Kramer, T. Morgan, and T. Hopkins, *J. Am. Chem. Soc.*, 1991, **113**, 6799.
27. J. Schaefer, K. J. Kramer, J. R. Garbow, G. S. Jacob, E. O. Stejskal, T. L. Hopkins, and R. D. Speirs, *Science*, 1987, **235**, 1200.
28. S. M. Holl, J. Schaefer, W. M. Goldberg, K. J. Kramer, T. D. Morgan, and T. L. Hopkins, *Arch. Biochem. Biophys.*, 1992, **292**, 107.
29. S. M. Holl, D. Hansen, J. H. Waite, and J. Schaefer, *Arch. Biochem. Biophys.*, 1993, **302**, 255.
30. G. Jacob, J. Schaefer, and G. E. Wilson, *J. Biol. Chem.*, 1985, **260**, 2777.
31. L. McDowell, E. Cohen, and J. Schaefer, *J. Biol. Chem.*, 1993, **268**, 20 768.
32. V. Copie, W. S. Faraci, C. T. Walsh, and R. G. Griffin, *Biochemistry*, 1988, **27**, 4966.
33. G. Harbison, J. Herzfeld, and R. G. Griffin, *Biochemistry*, 1983, **22**, 1.
34. E. Jaffe, G. Markham, and J. Rajagopalan, *Biochemistry*, 1990, **29**, 8345.
35. R. Auchus, D. Covey, V. Bork, and J. Schaefer, *J. Biol. Chem.*, 1988, **263**, 11 640.
36. S. O. Smith, I. Palings, V. Copie, D. P. Raleigh, J. Courtin, J. A. Pardoen, J. Lugtenburg, R. A. Mathies, and R. G. Griffin, *Biochemistry*, 1987, **26**, 1606; G. S. Harbison, S. O. Smith, J. A. Pardoen, P. Mulder, J. Lugtenburg, J. Herzfeld, R. Mathies, and R. G. Griffin, *Biochemistry*, 1984, **23**, 2662.
37. M. Mehring, T. Weber, W. Muller, and G. Wegner, *Solid State Commun.*, 1982, **45**, 1079; T. Terao, S. Maeda, T. Yamabe, K. Akagi, and H. Shirakawa, *Chem. Phys. Lett.*, 1984, **103**, 347; G. Harbison, P. Mulder, H. Pardoen, J. Lugtenburg, J. Herzfeld, and R. Griffin, *J. Am. Chem. Soc.*, 1985, **110**, 7221.
38. L. Zheng and J. Herzfeld, *J. Bioenerg. Biomembr.*, 1992, **24**, 139.
39. R. Gebhardt, K. van def Hoef, C. Violette, H. de Groot, H. Frank, and J. Lugtenburg, *Pure. Appl. Chem.*, 1991, **63**, 115.
40. A. C. de Dios, J. G. Pearson, and E. Oldfield, *Science*, 1993, **260**, 1491.
41. S. Spera and A. Bax, *J. Am. Chem. Soc.*, 1991, **113**, 5490.
42. D. S. Wishart, B. D. Sykes, and F. M. Richards, *J. Mol. Biol.*, 1991, **222**, 311.
43. A. Shoji, T. Ozaki, H. Saito, R. Tabeta, and I. Ando, *Macromolecules*, 1984, **17**, 1472.
44. H. R. Kricheldorf and D. Muller, *Macromolecules*, 1983, **16**, 615.
45. I. Ando, H. Saito, R. Tabeta, A. Shoji, and T. Ozaki, *Macromolecules*, 1984, **17**, 457.
46. I. Ando, T. Yamanobe, and T. Asakura, *Prog. NMR Spectrosc.*, 1990, **22**, 349.
47. H. Saito, R. Tabeta, A. Shoji, T. Ojaki, and I. Ando, *Macromolecules*, 1983, **16**, 1050.
48. H. Miyamoto, T. Komoto, H. Kurosu, I. Ando, T. Ozaki, and A. Shoji, *J. Mol. Struct.*, 1990, **220**, 251.
49. H. B. Cole and D. A. Torchia, *Chem. Phys.*, 1991, **158**, 271; H. B. Cole, S. W. Sparks, and D. Torchia, *Proc. Natl. Acad. Sci. USA*, 1988, **85**, 6362.
50. T. Cross and S. Opella, *J. Am. Chem. Soc.*, 1983, **105**, 306.
51. S. Opella, P. Stewart, and K. Valentine, *Q. Rev. Biophys.*, 1987, **19**, 7.
52. S. Opella and P. Stewart, *Methods Enzymol.*, 1989, **176**, 242.
53. R. R. Kethcham, W. Hu, and T. A. Cross, *Science*, 1993, **261**, 1475.
54. L. W. Jelinsky and D. A. Torchia, *J. Mol. Biol.*, 1980, **138**, 255.
55. S. K. Sarkar, Y. Hiyama, C. H. Niu, P. E. Young, J. T. Gerig, and D. A. Torchia, *Biochemistry*, 1987, **26**, 6793; J. W. Mack, D. A. Torchia, and P. Steinert, *Biochemistry*, 1988, **27**, 5418.
56. J. Garbow, G. S. Jacob, E. O. Stejskal, and J. Schaefer, *Biochemistry*, 1989, **28**, 1362.
57. G. Harbison, J. Herzfeld, and R. G. Griffin, *J. Am. Chem. Soc.*, 1981, **103**, 4752.
58. M. Munowitz, W. Bachovchin, J. Herzfeld, C. Dobson, and R. G. Griffin, *J. Am. Chem. Soc.*, 1982, **104**, 1192.
59. W. Bachovchin, *Biochemistry*, 1986, **25**, 7751.
60. P. Lodi and J. Knowles, *Biochemistry*, 1991, **30**, 6948.
61. S. O. Smith, S. Farr-Jones, R. G. Griffin, and W. Bachovchin, *Science*, 1989, **244**, 961.

62. P. Burke, S. Smith, W. Bachovchin, and A. Klibanov, *J. Am. Chem. Soc.*, 1989, **111**, 8290.
63. K. V. Lakshmi, A. McDermott, J. Herzfeld, and R. G. Griffin, unpublished results.
64. S. Kuroki, N. Asakawa, S. Ando, I. Ando, A. Shoji, and T. Ozaki, *J. Mol. Struct.*, 1991, **245**, 69.
65. S. Kuroki, S. Ando, I. Ando, A. Shoji, and T. Ozaki, and G. Webb, *J. Mol. Struct.*, 1990, **240**, 19.
66. T. Oas, C. Hartzell, F. Dahlquist, and G. Drobney, *J. Am. Chem. Soc.*, 1987, **109**, 5962.
67. Z. Gu and A. McDermott, *J. Am. Chem. Soc.*, 1993, **115**, 4282; *ibid.*, in press.
68. Y. Tomita, E. O'Connor, and A. McDermott, *J. Am. Chem. Soc.*, 1994, in press.
69. G. Metz, F. Siebert, and M. Englehard, *Biochemistry*, 1992, **31**, 455.
70. M. Englehard, F. Hess, D. Emeis, G. Metz, W. Kreutz, and F. Siebert, *Biochemistry*, 1989, **28**, 3967; G. Metz, F. Siebert, and M. Englehardt, *FEBS Lett.*, 1992, **303**, 237.
71. J. Herzfeld, S. Das Gupta, M. Farrar, G. Harbison, A. McDermott, S. Pelletier, D. P. Raleigh, S. O. Smith, C. Winkel, J. Lugtenburg, and R. G. Griffin, *Biochemistry*, 1990, **29**, 5567.
72. A. McDermott, L. Thompson, C. Winkel, M. Farrar, S. Pelletier, J. Lugtenburg, J. Herzfeld, and R. G. Griffin, *Biochemistry*, 1991, **30**, 8366.
73. M. Fisher, H. de Groot, J. Raap, C. Winkel, A. Hoff, and J. Lugtenburg, *Biochemistry*, 1992, **31**, 11 038.
74. S. Ando, I. Ando, A. Shoji, and T. Ozaki, *J. Am. Chem. Soc.*, 1988, **110**, 3380.
75. N. Asakawa, S. Kuroki, H. Kurosu, I. Ando, A. Shoji, and T. Ozaki, *J. Am. Chem. Soc.*, 1992, **114**, 3261; N. Asakawa, H. Kurosu, I. Ando, A. Shoji, and T. Ozaki, *J. Mol. Struct.*, 1994, **317**, 119.

Biographical Sketches

Ann McDermott. *b* 1960. B.Sc., 1981, Harvey Mudd College, Ph.D., 1987, University of California, Berkeley, with Professor Ken Sauer and Dr. Melvin Klein. Postdoctoral Research, MIT, 1988–90, and Francis Bitter National Magnet Laboratory, with Professor Robert Griffin; Postdoctoral research, Université Catholique de Louvain, Institute for Clinical Pathology, 1990–91; Assistant Professor of Chemistry, Columbia University, 1991–1995; Associate Professor of Chemistry and Biology, 1995–present.

Zhengtian Gu. *b* 1971. B.Sc., 1991, University of Science and Technology of China, M.A., 1992, Columbia University. More than 10 publications on biophysical chemistry and solid state chemistry.

Carbonic Anhydrase

Sven Lindskog and Bengt-Harald Jonsson

Umeå University, Sweden

1	Introduction	1
2	NMR Studies of the Active Center	1
3	Water Proton Relaxation in Metal-Substituted Carbonic Anhydrases	2
4	NMR Studies of Inhibitor Binding	2
5	NMR Studies of Substrate Binding and Interconversion	3
6	Future Prospects	3
7	References	4

1 INTRODUCTION

Carbonic anhydrase is a zinc-containing enzyme catalyzing the reversible hydration of carbon dioxide as well as the hydrolysis of certain esters and the hydration of aldehydes.[1] Mammals have seven carbonic anhydrase genes encoding different isozyme forms. The cytosolic isozymes, I, II, and III ($M_r \approx 29\,000$) have been studied in particular detail. They are stable, highly soluble, monomeric proteins which are readily purified in large quantities. These properties have contributed to make carbonic anhydrase an excellent 'beginner's enzyme' for spectroscopists wishing to apply their methods to biochemical systems. The catalytic and inhibitor-binding properties of Co(II)-substituted carbonic anhydrase are very similar to those of the native Zn(II)–enzyme. Therefore, the Co(II)–enzyme has been frequently used as a functional model in spectroscopic studies.

To our knowledge, the first NMR study of carbonic anhydrase was published in 1969 and involved measurements of ^{35}Cl linewidths to illustrate the interaction between inhibiting chloride ions and the zinc center.[2] Since then well over 100 papers have appeared describing a variety of NMR investigations of this enzyme system. The major findings are summarized here in a biochemist's rather than an NMR spectroscopist's perspective. We apologize to all those whose papers are not cited because of the limited space allotted to us.

2 NMR STUDIES OF THE ACTIVE CENTER

The active center of carbonic anhydrase is located in a 15 Å deep cavity which is about 15 Å wide at the entrance. The zinc ion is near the bottom of the cavity and firmly bound to three imidazole groups from His-94, His-96, and His-119 in a tetrahedral geometry with H_2O or OH^- as the fourth ligand. Isozyme I from most species has three additional active-site histidines, His-64, His-67, and His-200, whereas isozyme II has only one, His-64.[1]

To test if one of these histidines corresponds to the catalytic group with pK_a ca. 7, postulated from kinetic results to control CO_2 hydration as well as ester hydrolysis,[1] Campbell et al.[3] recorded ^1H NMR spectra of human isozymes I and II (previously called B and C, respectively) at various pH values in ^2H_2O solutions. They could identify resonances from the Cϵ1 protons of all solvent-exposed histidine residues including the three metal ligands. Resonances from active-site residues were discriminated from those from surface residues by their sensitivity to inhibitors, and individual assignments of most active-site resonances could be made. The results showed that the only active-site resonances reflecting the behavior of the catalytic group were those from some of the ligands. It was concluded that the catalytic group is not a titratable histidine but must be tightly associated with the metal center. The current model involves the zinc-bound H_2O ionizing to OH^-, but an alternative hypothesis with a ligand imidazole ionizing to an imidazolate anion had also been proposed on the basis of similar NMR results.[4]

This hypothesis was tested by Campbell et al.[3] who observed exchangeable NH proton resonances located between 12 and 15 ppm. In human isozyme II, five of these were sensitive to inhibitors and to pH changes near pH 7 where the activity-linked group titrates. They could be observed over the whole pH range between 5.5 and 9.6. Three of these resonances were assigned to the ligand imidazoles. It was concluded that the imidazolate model is unlikely, since it requires a rapidly exchanging NH proton which would be unobservable under the conditions of these measurements.

Bertini et al.[5] detected a number of paramagnetically shifted resonances in the ^1H NMR spectra of Co(II) substituted carbonic anhydrase. They could assign pH-sensitive resonances in the 50–65 ppm range to the NH protons of the ligand imidazoles. Their results confirmed that the imidazolate model for the catalytic group can be ruled out.

The degree of resolution of paramagnetically shifted resonances from the Co(II)–enzyme seems to depend on the coordination geometry of the metal ion. When the high spin Co(II) ion is tetrahedral, as in uninhibited isozyme II or in the NCO^- adduct, electronic correlation times are relatively long ($\tau_e > 10^{-11}$ s) and many resonances are broadened beyond detection. In the presence of certain anionic inhibitors, such as SCN^-, ClO_4^-, and NO_3^-, the Co(II) ion is presumably pentacoordinated with characteristically short τ_e values in the range $(3–6) \times 10^{-12}$ s.[6] In these cases, a multitude of shifted resonances has been observed. In an extensive study of the ClO_4^- and NO_3^- adducts of bovine Co(II)–isozyme II using 1D NOE as well as 2D ^1H NMR, Banci et al.[7] assigned several resonances to specific active-site protons. Such data might be particularly useful in future structural studies of site-specific mutants.

The close link between the metal ion and catalytic properties has been further illustrated in NMR studies of ^{113}Cd-substituted enzyme.[8,9] For example, Jonsson et al.[8] found that the chemical shift of the ^{113}Cd resonance from human isozyme II varied continuously from 229 ppm at low pH to 275 ppm at high pH, indicating a rapid exchange between a low pH form and a high pH form (presumably a metal-bound H_2O ionizing to OH^-). The estimated pK_a of 9.2 agrees reasonably well with that determined from the pH-dependence of the esterase activity. The binding of HCO_3^- resulted in a shift to 216 ppm. In the presence of the powerful inhibitor $^{13}CN^-$, a doublet centered at 354 ppm with a $^{113}Cd–^{13}C$ spin

coupling constant of 1040 Hz provided evidence of a direct metal–cyanide interaction.

Human carbonic anhydrase I is partially inactivated by bromo- or iodoacetate.[1] The reaction specifically occurs at Nϵ2 of His-200 resulting in an *N*-carboxymethyl derivative. Khalifah et al.[10] recorded the ^{13}C NMR spectrum of [1-^{13}C]carboxymethyl human isozyme I as a function of pH detecting two ionizations with pK_a values of 6.0 and 9.0. These and subsequent data[11] indicated that the carboxy group of the carboxymethyl moiety coordinates to the metal ion in the intermediate pH range, while it dissociates from the metal ion as the imidazole ring becomes protonated around pH 6. The pK_a of 9 probably reflects the displacement of the carboxy group by OH^-.

3 WATER PROTON RELAXATION IN METAL-SUBSTITUTED CARBONIC ANHYDRASES

An early NMR study by Fabry et al.[12] seemed to upset the notion that the catalytic group of carbonic anhydrase is an H_2O molecule, coordinated as a fourth ligand of the tetrahedral metal ion, and ionizing to OH^- with pK_a near 7.[1] These authors measured the relaxation rates (T_1^{-1}) of water protons as functions of pH and Larmor frequency in the presence of Co(II)-substituted carbonic anhydrase. The paramagnetic contribution to the relaxation rate increased with pH along a titration curve with a pK_a value similar to that estimated from activity measurements. The data were compatible with the presence of one rapidly exchanging, metal-bound H_2O molecule at high pH, while it was suggested that there is no coordinated H_2O or, possibly, a slowly exchanging H_2O at low pH. Seemingly, the dilemma caused by these results has later been resolved. Thus, Koenig et al.[13] have proposed a mechanism for the rapid exchange of a proton from Co(II)-bound OH^- involving an unstable, pentacoordinated exchange intermediate with an additional water molecule in the coordination sphere. The low relaxation rate at low pH can be explained by the presence of inhibiting anions (such as sulfate) displacing metal-bound water and/or by the presence of a significant fraction of a low pH form with a shorter electronic correlation time such as in a pentacoordinated complex with two metal-bound water molecules.[6,13]

Water proton relaxation has also been measured with other metal-substituted carbonic anhydrases to explore the properties of the metal-ion binding site.[1] In one of the most thorough studies, Kushnir and Navon[14] measured T_1 and T_2 for both ^{1}H and ^{2}H in the presence of the Mn(II)–enzyme in a mixed $^1H_2O/^2H_2O$ solvent. They derived a hydration number of 1 and estimated an exchange lifetime for the Mn(II)-bound water of 75 ns.[14]

4 NMR STUDIES OF INHIBITOR BINDING

Inhibitors of the catalytic activities of carbonic anhydrase bind to the metal ion or in its close vicinity.[1,15] There are three major classes of inhibitors, inorganic and organic anions, sulfonamides, and a variety of neutral, organic compounds. Representatives of all three classes have been studied by NMR.

Carbonic anhydrase very effectively relaxes the quadrupolar ^{35}Cl nucleus in Cl^- ions.[2] This suggests a direct Zn^{2+}–Cl^- interaction in the enzyme. From the temperature-dependence of the $^{35}Cl^-$ line broadening, Ward and Cull[16] concluded that the chloride ions are in slow exchange and estimated a residence time of about 1 μs for the interaction with human isozyme I.

Cyanide is one of the most potent anionic inhibitors of carbonic anhydrase.[1] The observed ^{113}Cd–^{13}C spin coupling of 1040 Hz in the cyanide complex of ^{113}Cd-substituted enzyme is clear evidence of a direct metal–inhibitor bond.[8] The chemical shift position at ca. 76 ppm of $^{13}CN^-$ bound to native Zn(II)–enzyme has been taken to imply metal coordination.[17] In view of these and other spectroscopic results,[1] it was quite unexpected that the crystal structure of the cyanide complex with native human isozyme II showed that CN^- does not displace the zinc-bound H_2O molecule but is located in the vicinity of the metal ion at a distance of 3.4 Å.[15] The significance of this result has been challenged by Bertini et al.[18] who compared ^{13}C linewidths from $^{13}C^{15}N^-$ in the presence of bovine isozyme II containing ^{67}Zn ($I = \frac{5}{2}$) and ^{64}Zn (I = 0), respectively. They obtained considerably broader lines with ^{67}Zn than with ^{64}Zn and interpreted these results in terms of a direct zinc–cyanide coordination. However, the largest effects were observed at high temperatures (50–60°C) where the enzyme is not fully stable. In our opinion, the possibility that the observed effects are related to interactions of $^{13}C^{15}N^-$ with a denatured state of the enzyme should not be ignored.

In crystals of human isozyme II, NCO^- binds like CN^-.[15] In the Co(II)–enzyme, however, large paramagnetic effects on T_1 for bound $N^{13}CO^-$ suggest cobalt–cyanate coordination.[18] Possibly, different binding modes are energetically favored by the Co(II)– and Zn(II)–enzymes, or there are two energetically similar binding modes for some anionic inhibitors such as NCO^-, and one of them predominates under the experimental conditions used in the crystal structure studies and another under the conditions used in spectroscopic studies.

The interaction between carbonic anhydrase and acetate ion has been the subject of several NMR studies. Lanir and Navon[19] found evidence for two acetate-binding sites in ^{1}H NMR studies of the bovine Zn(II)– and Mn(II)–enzymes. Only one of these sites is linked to the inhibition of the catalytic activity, but both appeared to be rather close to the metal ion. The crystal structure of the acetate complex of human isozyme II reveals only the inhibitory site, and the location of the other site remains unknown. In the crystal structure, the carboxy group of acetate has a similar location as the NCO^- ion (see above) and does not displace the metal-bound water molecule.[15] However, one of the carboxy oxygen atoms is a weak Zn(II) ligand (Zn–O distance, 2.4 Å) in a distorted, trigonal bipyramid with His-96 and acetate in the axial positions. Bertini et al.[20] have arrived at similar structures for the acetate and formate complexes of bovine Co(II)–isozyme II. From the ^{13}C relaxation rates of carboxyl-labeled inhibitors, they concluded that the anions are coordinated to the Co(II) ion. The relaxation rates of paramagnetically shifted ligand protons in the 200 MHz ^{1}H NMR spectra of these adducts suggested a pentacoordinated metal ion. Finally, ^{1}H NOE measurements connected the formate and acetate protons with resonances that could

tentatively be assigned to the active-site residues, Val-143 and Val-207, in 2D ^{1}H NMR experiments.

While Bertini et al.[20] sought structural information, Taylor et al.[21] could calculate residence times in the μs range for the formate, mono-, di-, and trifluoroacetate adducts of human Co(II)–isozyme II from ^{1}H and ^{19}F linewidth measurements under conditions where slow exchange prevailed.

Aromatic sulfonamides are potent inhibitors of carbonic anhydrase. They bind to the metal ion as anions, RSO_2NH^-, displacing the coordinated water molecule.[1,15] NMR evidence for this comes from the observation that the proton-coupled ^{15}N resonance of benzenesulfonamide bound to human isozyme I is a doublet.[22] While X-ray crystallography cannot differentiate between O and N atoms, NMR has provided proof of nitrogen coordination. Thus, Evelhoch et al.[23] found a ^{113}Cd–^{15}N coupling constant of 190–210 Hz in the ^{113}Cd NMR spectra of complexes between sulfon[^{15}N]amides and human ^{113}Cd–isozymes I and II. In a similar study using ^{111}Cd, Blackburn et al.[24] found a ^{111}Cd–^{15}N coupling constant of 176 Hz for 4-fluorobenzenesulfon[^{15}N]amide bound to bovine ^{111}Cd–isozyme II. For 4-fluoro-*N*-hydroxybenzenesulfon[^{15}N]amide, A coupling constant of 249 Hz was observed.

Sulfonamides dissociate very slowly from the active site of carbonic anhydrase. Gerig and Moses[25] calculated a dissociation rate constant of 0.02 s^{-1} for the complex between pentafluorobenzenesulfonamide and human isozyme II from results of ^{19}F saturation transfer experiments. Their results also suggested that ring rotation is appreciably faster with a rate constant of 4 s^{-1}.[25]

Imidazole inhibits human isozyme I by binding near the metal ion without displacing the coordinated water molecule.[1] This binding mode is compatible with the observation that the resonance assigned to the Cϵ1 proton of the ligand His-94 undergoes a substantial ring current shift to lower frequency upon imidazole binding.[3] The paramagnetic effects of Co(II)–carbonic anhydrase on proton relaxation rates in imidazole, 1,2,3-triazole, 1,2,4-triazole, and tetrazole have been taken to imply coordination to the metal ion.[26] In the case of 1,2,4-triazole this has been confirmed by crystallographic results on the complex with human isozyme II.[15]

5 NMR STUDIES OF SUBSTRATE BINDING AND INTERCONVERSION

Carbonic anhydrase is a very efficient catalyst of the reversible hydration of CO_2. The most active form, isozyme II, can turn over 10^6 substrate molecules per second at 25°C.[1,27] Simonsson et al.[28] estimated $^{13}CO_2$–$H^{13}CO_3^-$ exchange rates from line broadenings in the slow exchange region and found that the maximal rate of catalyzed exchange is the same in ^1H_2O and ^2H_2O, and is independent of added buffers in contrast to the maximal rate of turnover measured by conventional steady state kinetic techniques. This combination of kinetic data obtained at chemical equilibrium and in the steady state, respectively, has been of critical importance for the understanding of the catalytic mechanism of the enzyme.[27]

Considerable efforts have been made to determine how the substrates, CO_2 and HCO_3^-, interact with the active center. NMR has been an important tool in this work in which the paramagnetic effects of the Co(II)–, Cu(II)–, or Mn(II)–enzymes on the relaxation rates of $^{13}CO_2$ and $H^{13}CO_3^-$ have been measured. In summary, these measurements have shown that HCO_3^- is most probably coordinated to the metal ion while the binding of CO_2 is very weak.

Thus, Williams and Henkens[29] measured T_1 values and linewidths for the $^{13}CO_2$ and $H^{13}CO_3^-$ resonances in the presence of the catalytically active human Co(II)–isozyme I. From the T_1 values for HCO_3^- (rapid exchange), a Co(II)–^{13}C distance of 3.2 Å was calculated, while the paramagnetic contribution to T_2 (slow exchange) gave a HCO_3^- residence time of 44 μs for this low-activity form of carbonic anhydrase.

Bertini et al.[30] used the catalytically inactive Cu(II)–enzyme to study the interaction with $^{13}CO_2$ and $H^{13}CO_3^-$ at high CO_2 pressures. From the results of T_1 measurements, the authors concluded that CO_2 binds very weakly to a site near the metal ion. The HCO_3^- ion exchanges slowly with the Cu(II)–enzyme and residence times of 2.3 ms and 0.2 ms were estimated for human isozyme I and bovine isozyme II, respectively.

Substrate interactions with human Mn(II)–isozyme I have been studied by ^{13}C NMR. This enzyme has some catalytic activity and Led and Neesgaard[31] used magnetization transfer techniques to estimate a maximal exchange rate constant of 400 s^{-1} which is about 100-times smaller than the value for native isozyme I.[28] A variety of additional parameters were calculated from results of extensive relaxation rate measurements, including an Mn(II)–^{13}C distance of 2.7 Å for the HCO_3^- complex.

Rather few studies have been published on the aldehyde hydration activity of carbonic anhydrase. However, Chesnovsky and Navon[32] used ^{1}H saturation transfer to measure chemical exchange between the hydrated and unhydrated forms of acetaldehyde catalyzed by bovine isozyme II. A careful analysis of the observed linewidths indicated that acetaldehyde also binds to sites distinct from the active site.

6 FUTURE PROSPECTS

In the past, NMR has given valuable contributions to our understanding of the catalytic mechanism of carbonic anhydrase and its interactions with various ligands. About 80% of the NMR papers on this enzyme were published between 1971 and 1985, and other techniques have dominated the recent carbonic anhydrase literature. However, since the human isozymes I, II, and III have been expressed in a bacterial system, which permits general or selective labeling with suitable isotopes, we expect that this 'beginner's enzyme' and site-specific mutants thereof will be used in future multidimensional NMR studies despite its relatively large molecular mass of about 29 kDa.[33,34]

Carbonic anhydrase has become a popular model for studies of protein folding, and has been shown to fold into its native structure via a molten globule intermediate. Assignment of peptide NH hydrogens in 3D NMR spectra of ^{15}N-labeled enzyme will form the basis for deuterium-exchange experiments which can give detailed structural information on the molten globule and other intermediate states.

7 REFERENCES

1. S. Lindskog, in *Zinc Enzymes*, ed. T. G. Spiro, Wiley-Interscience, New York, 1983, p. 77
2. R. L. Ward, *Biochemistry*, 1969, **8**, 1879.
3. I. D. Campbell, S. Lindskog, and A. I. White, *J. Mol. Biol.*, 1974, **90**, 469; *J. Mol. Biol.*, 1975, **98**, 597; *Biochim. Biophys. Acta*, 1977, **484**, 443.
4. J. M. Pesando, *Biochemistry*, 1975, **14**, 681; R. K. Gupta and J. M. Pesando, *J. Biol. Chem.*, 1975, **250**, 2630.
5. I. Bertini, G. Canti, C. Luchinat, and F. Mani, *J. Am. Chem. Soc.*, 1981, **103**, 7784.
6. I. Bertini, G. Canti, and C. Luchinat, *Inorg. Chim. Acta*, 1981, **56**, 99.
7. L. Banci, L. B. Dugad, G. N. La Mar, K. A. Keating, C. Luchinat, and R. Pierattelli, *Biophys. J.*, 1992, **63**, 530.
8. N. B.-H. Jonsson, L. A. E. Tibell, J. L. Evelhoch, S. J. Bell, and J. L. Sudmeier, *Proc. Natl. Acad. Sci. USA*, 1980, **77**, 3269.
9. A. J. M. Schoot Uiterkamp, I. M. Armitage, and J. E. Coleman, *J. Biol. Chem.*, 1980, **255**, 3911.
10. R. G. Khalifah, D. J. Strader, S. H. Bryant, and S. M. Gibson, *Biochemistry*, 1977, **16**, 2241.
11. P. K. Jeffers, W. McI. Sutherland, and R. G. Khalifah, *Biochemistry*, 1978, **17**, 1305.
12. M. E. Fabry, S. H. Koenig, and W. E. Schillinger, *J. Biol. Chem.*, 1970, **245**, 4256.
13. S. E. Koenig, R. D. Brown, III, I. Bertini, and C. Luchinat, *Biophys. J.*, 1983, **41**, 179.
14. T. Kushnir and G. Navon, *J. Magn. Reson.*, 1984, **56**, 373.
15. A. Liljas, K. Håkansson, B. H. Jonsson, and Y. Xue, *Eur. J. Biochem.*, 1994, **219**, 1.
16. R. L. Ward and M. D. Cull, *Arch. Biochem. Biophys.*, 1972, **150**, 436.
17. J. Feeney, A. S. V. Burgen, and E. Grell, *Eur. J. Biochem.*, 1973, **34**, 107.
18. I. Bertini, C. Luchinat, R. Pierattelli, and A. J. Vila, *Inorg. Chem.*, 1992, **31**, 3975.
19. A. Lanir and G. Navon, *Biochim. Biophys. Acta*, 1974, **341**, 65; *Biochim. Biophys. Acta*, 1974, **341**, 75.
20. I. Bertini, C. Luchinat, R. Pierattelli, and A. J. Vila, *Eur. J. Biochem.*, 1992, **208**, 607.
21. P. W. Taylor, J. Feeney, and A. S. V. Burgen, *Biochemistry*, 1971, **10**, 3866.
22. K. Kanamori and J. D. Roberts, *Biochemistry*, 1983, **22**, 2658.
23. J. L. Evelhoch, D. F. Bocian, and J. L. Sudmeier, *Biochemistry*, 1981, **20**, 4951.
24. G. M. Blackburn, B. E. Mann, B. F. Taylor, and A. F. Worrall, *Eur. J. Biochem.*, 1985, **153**, 553.
25. J. T. Gerig and J. M. Moses, *J. Chem. Soc., Chem. Commun.*, **1987**, 482.
26. G. Alberti, I. Bertini, C. Luchinat, and A. Scozzafava, *Biochim. Biophys. Acta*, 1981, **668**, 16.
27. D. N. Silverman and S. Lindskog, *Acc. Chem. Res.*, 1988, **21**, 30.
28. I. Simonsson, B.-H. Jonsson, and S. Lindskog, *Eur. J. Biochem.*, 1979, **93**, 409; *Eur. J. Biochem.*, 1982, **129**, 165.
29. T. J. Williams and R. W. Henkens, *Biochemistry*, 1985, **24**, 2459.
30. I. Bertini, C. Luchinat, R. Monnanni, S. Roelens, and J. M. Moratal, *J. Am. Chem. Soc.*, 1987, **109**, 7855.
31. J. J. Led and E. Neesgaard, *Biochemistry*, 1987, **26**, 183.
32. D. Chesnovsky and G. Navon, *Biochemistry*, 1980, **19**, 1866.
33. B. T. Farmer, Jr, R. A. Venters, L. D. Spicer, M. G. Wittekind, and L. Müller, *J. Biomol. NMR*, 1992, **2**, 195.
34. I. Bertini, B.-H. Jonsson, C. Luchinat, R. Pierattelli, and A. J. Vila, *J. Magn. Reson. Ser. B*, 1994, **104**, 230.

Biographical Sketches

Sven Lindskog. *b* 1934. Fil.Mag., 1956, Fil.Lic., 1960, Uppsala University, Fil.Dr., 1968, University of Göteborg (supervisor Bo G. Malmström). Docent at the University of Göteborg, 1968–77. Introduced to NMR by Ian D. Campbell, Oxford University in 1972. Professor of Biochemistry, Umeå University, 1977–present. Approx. 90 publications. Current research specialty: structure–function relationships in carbonic anhydrase and mercuric reductase.

Bengt-Harald Jonsson. *b* 1949. Fil.Kand., 1973, Fil.Dr., 1979, University of Göteborg. Postdoctoral work with James L. Sudmeier at University of California, Riverside, 1979–80. Research fellow at Umeå University, 1980–87, and senior lecturer there since 1987. Approx. 50 publications. Current research specialty: mechanism of protein folding.

Cell Suspensions

Dieter Leibfritz and Rolf Altenburger
Universität Bremen, Bremen, Germany

1	Introduction	1
2	Methodology	1
3	Applications	4
4	Conclusions and Perspectives	9
5	Related Articles	9
6	References	9

1 INTRODUCTION

In this review cell suspensions can be unicellular organisms or isolated cultured cell lines of mammalian or plant tissues. In connection with cellular NMR studies, both terms 'in vivo' and 'in vitro' are in use. This semantic differentiation may be misleading, because most isolated mammalian cells represent an in vitro system, whereas blood cells, many plant cells, and microorganisms represent true in vivo systems. For simplification, the term in vivo will be used if viable intact cells are considered. True in vitro systems are perfused subcellular compartments like isolated mitochondria and chloroplasts or cellular extracts.

In vivo NMR spectra from intact human organs or animal models are obtained within several minutes to half an hour. Because of the intrinsically large volume needed for a good signal-to-noise ratio, the signals obtained do not originate from a homogeneous cell population. The selected tissue normally consists of metabolically different cell types. In order to assign metabolites to individual cell types, isolated cell cultures are preferred although they are missing the specific intercellular communication as in the case of neurons and glia cells. This constraint limits the significance of uniform cellular models with respect to the actual situation in vivo. On the other hand, uniform cell populations allow control over biochemical and physiological parameters that are not independently accessible in intact organisms or perfused organs. Studies of cells give access to elementary metabolism such as biochemical pathways, variations of biochemical pathways in different cell types, principles of cellular homeostasis, intra-/extracellular transport phenomena, etc. The NMR technique is able to monitor the metabolism of complex biological systems noninvasively. No prior separation of individual compounds is necessary. Even dedicated multipulse techniques are applicable to the in situ identification of metabolites. These aspects alleviate the intrinsic disadvantage of NMR, namely its low sensitivity.

This review will deal primarily with biochemical topics of cellular NMR spectroscopy to exemplify the potential of this method rather than to evaluate the advantages of individual NMR sensitive nuclei, which are primarily ^{1}H, ^{13}C, ^{15}N, ^{19}F, ^{23}Na, and ^{31}P in this context. Several reviews have described various aspects of cellular NMR spectroscopy in great detail.[1–6]

2 METHODOLOGY

The inherently low sensitivity of NMR spectroscopy demands 10^7-10^{10} cells per mL (corresponding to 1–100 mg mL^{-1} w/w) within the receiver coil. Cells with a very small volume like prokaryotic cells may require an order of magnitude more cells depending upon the field strength used. In general, prokaryotic cells and unicellular eukaryotic plant cells,[6] but also blood cells[7,8] and, in particular, a large variety of human and other mammalian tumor cell lines,[9–12] proliferate fast enough or are available in sufficiently large quantities to meet this requirement.

In order to get the full benefit of in vivo studies the cell samples have to be kept under viable conditions, and the interpretation of the spectra has to be based on reliable assignment techniques and on the quantitation of metabolite concentrations.

2.1 Cellular Extracts

A simple but time-consuming way to follow cellular metabolism is to extract parallel grown cell batches at different times. The cells will always be kept under optimum growth conditions and control of nutrient supply in the incubator. This procedure corresponds to the well-known invasive biochemical techniques like radiotracer methods. Studying extracts gains the benefits from the high-resolution conditions such as narrow linewidths, resolved coupling constants, better signal-to-noise ratio, and unlimited spectral acquisition time (i.e. metabolic concentration of a few μmol are detectable compared with $\geq$0.5 mmol concentration in vivo), applicability of multipulse and/or multidimensional techniques,[13] and the avoidance of unfavorable nuclear Overhauser effects (NOE) in heteronuclear experiments[14] (see Figure 1). Pulse label experiments with ^{15}N labeled precursor molecules may suffer from a nulling NOE in vivo if plant cells with high amounts of paramagnetic ions are recorded.

Proton NMR spectra from living cells are difficult to accumulate, because they are kept in an aqueous medium and need water suppression procedures (see Section 2.2). This is circumvented when studying cell extracts, as they are lyophilized and taken up in D_2O before recording.

Standard extraction techniques use perchloric acid (PCA) to obtain the water-soluble, low molecular weight metabolites.[15] Cells are quickly rinsed before harvest with isotonic buffer to remove unwanted compounds from the nutrient medium or exported metabolites by the cells. Thereafter, the cells are immediately frozen with liquid nitrogen, extracted with cold PCA (1 mmol L^{-1}), neutralized, centrifuged, and lyophilized. By this means enzymatic reactions are stopped abruptly and further degradation of metabolites prevented. Dry frozen extracts can be stored for some weeks. Similar recipes use alcohol or alcohol/HCl mixtures.[16] Lipophilic components can be extracted with methanol/chloroform solutions from the residual pellet after centrifugation.[17] Again the extraction should be done quickly and the isolated lipids kept cold. Lipid extracts reflect cell specific variations in the phospholipid composition of different cell types.[18] Also lipophilic drugs, which are retained within the cellular membranes, reappear in the lipophilic extract.

Signal intensities obtained from extracts sometimes do not correlate with those from cells in vivo. Some metabolites

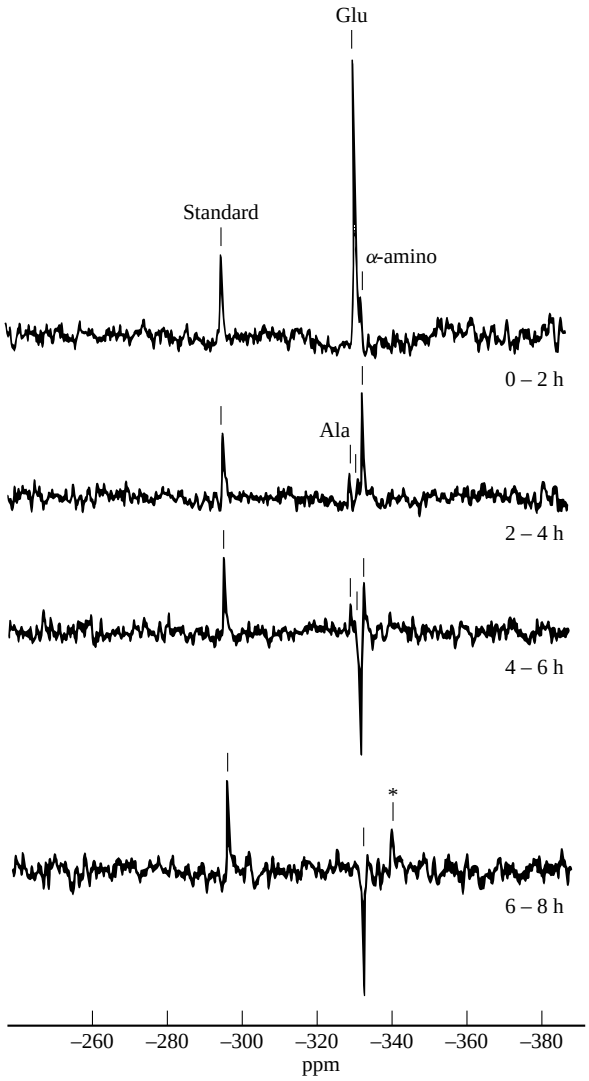

Figure 1 Time course of in situ ^{15}N labeling in the green alga *Chlorella fusca* using a 20 mmol L^{-1} glutamate pulse. The sample was illuminated and bubbled with 95% N_2/5% CO_2. Signals assigned to α-amino groups of amino acids, alanine, glutamate, and γ-amino butyric acid (GABA), δ-ornithine, ϵ-lysine, or polyamine were detected. The external reference standard was urea. The signal from the α-NH_3 of glutamate was positive in the beginning, i.e. showed a NOE, underwent zero transition, and became negative

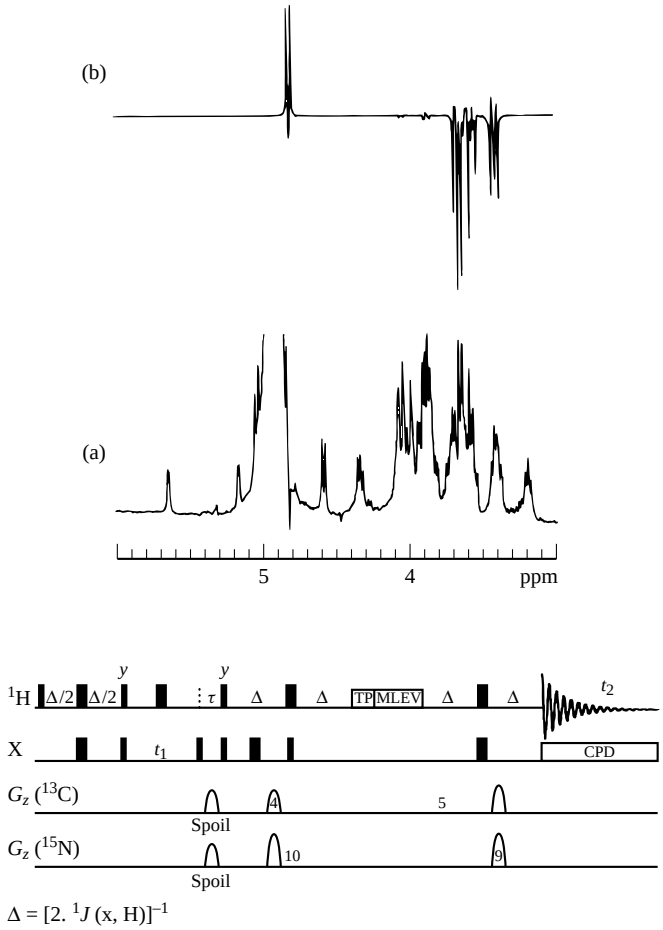

Figure 2 Pulse sequence for a gradient selected (gs) 2D HSQC TOCSY experiment with long range editing (e.g. Willker et al.[24]) Spectrum (a) shows the 1D proton spectrum of a cell medium from C6 glioma cells fed with ^{13}C-labeled glucose. Spectrum (b) depicts the row for 1-^{13}C-β-D-glucose from the gs HSQC TOCSY spectrum. The H-1 signal is positive, the other protons have negative signal intensity

seen in extracts may be partly or completely invisible in vivo because they are immobilized and/or associated with macromolecules. Lower intensity in extract spectra may be due to losses during extraction by enzyme reactions, chemical degradation, or instability against acids.[19]

The peak assignment of extract spectra can be done in different ways: simply by comparison with chemical shift reference lists (^{1}H,[20] ^{13}C,[21] ^{31}P[22]), by spiking the extract solution with the authentical reference compound, by pH titration, by complexation with metal ions, or by de novo assignment of a metabolite within the extract solution by NMR[13] or by enzymatic transformation.[23] A very efficient way of an in situ assignment is gradient selected inverse multiquantum coherence (MQC) spectroscopy.[24] Figure 2 gives an example where magnetization is transferred frequency-selectively from proton to C-1 of β-D-glucose and back to the proton domain followed by a TOCSY transfer revealing the complete spectrum of β-glucose. By this means it is possible to identify one individual compound in a complex mixture without interference from others.

Numerous publications have appeared on cell extracts in the past 15 years. These are beyond the scope of this short survey, but many are covered in excellent reviews.[1–6] Cell extracts are still the method of choice for sensitive and anchorage-dependent primary cells or cells with demanding growth conditions like brain cells, i.e. neurons, astrocytes, and oligodendrocytes.[25–27] Figure 3 compares the ^{1}H NMR spectra of primary rat neurons and astrocytes. Neurons exclusively exhibit *N*-acetylaspartate in NMR-detectable amounts as a neuron specific marker molecule, whereas astrocytes contain myo-inositol as a cell specific marker.

2.2 Cell Suspensions

The simplest way to comply with the constraint of a high density of viable cells within the receiver coil of an NMR probe is to use cell suspensions in the NMR tube. In

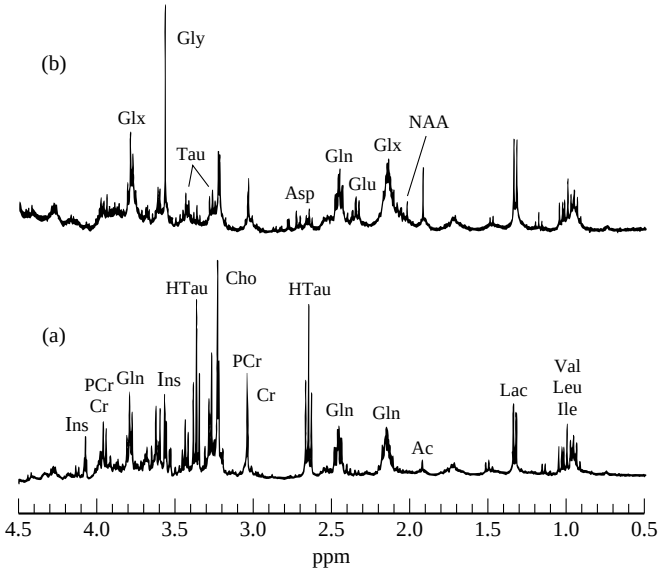

Figure 3 ^{1}H NMR spectra of (a) primary glia cells and (b) primary neurons from rat. Abbreviations are for valine (Val), leucine (Leu), lactate (Lac), alanine (Ala), acetate (Ac), *N*-acetylaspartate (NAA), glutamate (Glu), glutamine (Gln), glutamate/glutamine (Glx), aspartate (Asp), creatine/phosphocreatine (Cr/PCr), choline-containing metabolites (Cho), taurine (Tau), hypotaurine (HTau), glycine (Gly), and myo-inositol (Ins), isoleucine (Ilc)

order to maintain the sample under physiological conditions during the measurement, it is necessary to provide a sufficient nutrient and oxygen supply, to remove waste products, to control extracellular pH and sample temperature, to prevent cell sedimentation, and to provide adequate illumination in the case of photoautotrophic cells. It is not possible to meet all these requirements for cell suspensions, at least not for long time periods. Nevertheless, photoautotrophic plant cells can be kept viable in NMR tubes for many hours.

Sedimentation is prevented if the cells are bubbled with air, oxygen, carbogen (95% O_2/5% CO_2), nitrogen, or argon. This defines at the same time the oxidative state of the cell system and buffers the medium if gas mixtures with carbon dioxide are used. As gas bubbles spoil the $\boldsymbol{B}_0$ homogeneity within the sensitive volume, the gas flow has to be triggered by the spectrometer to allow time-shared data acquisition and bubbling.[28,29] If bubbling is not satisfactory, an airlift system driving the medium around above the transmitter coil is an alternative approach.[30–32] Foaming, which occurs at high gas flow rates, also has to be avoided.[32] Alternatively, a mechanical stirrer has been used to prevent sedimentation.[33,34]

To keep the cells in a defined kinetic state the sample temperature has to be controlled. This is particularly important if proton decoupling and illumination are used simultaneously. Hence, temperature is monitored by a thermocouple or thermometer placed above the coil within the tube. Alternatively, the temperature can be measured by NMR with ethylene glycol.[35] The temperature is normally maintained at 37 °C for mammalian cells or ambient temperature for others; it may be advantageous to lower the temperature to 4 °C to slow down the chemical kinetics and to extend the viability of densely packed cell suspensions.

A severe shortcoming of cell suspensions is the lack of a continuous nutrient supply and the removal of waste products.

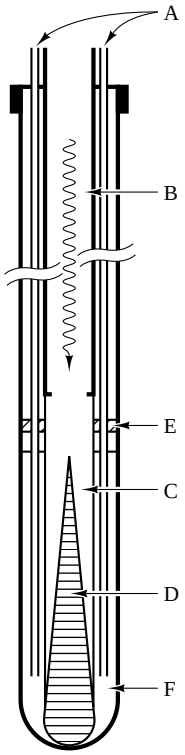

Figure 4 Illumination and aeration system mounted in an NMR tube. (A) Gas inlet tubes; (B) optical cable; (C) glass tube containing D_2O standard, (D) a Teflon cone for light reflection; (E) star-shaped centering device; and (F) cell suspension. The loss of sensitive volume due to the illumination tube amounts to 25% of the sample volume. (Reproduced by permission of Academic Press from Callies et al.[40])

Large cells can be locked between two perforated Teflon discs, while the medium circulates with low pressure.[36] In a similar manner, a nylon mesh filter may surround the cell suspension.[37]

Photosynthetic studies by in vivo NMR spectroscopy require an apparatus to illuminate the cell suspension within the spectrometer. The illumination has to yield a high enough light intensity and be homogeneously distributed within the sample. Usually the light energy of a powerful light bulb is transferred with a light pipe to the cell suspension.[38–40] Bubbling with gas prevents shading of parts of the cell population and the radiation damage caused by high light intensities. IR components are filtered between the light source and the light pipe. An efficient light distribution is achieved (Figure 4) if the end of the light pipe is connected to a conical piece of Teflon to scatter the light.[40] This arrangement induces no further line broadening. The yield for photosynthesis in situ in the NMR spectrometer reaches about 50% of that attained for the same number of cells under standard culture conditions.

A particular concern of proton NMR of cells is the intense extra- and intracellular water signal, which has to be suppressed. Different strategies have been used to overcome this problem,[41,42] i.e. only the frequency region of interest is excited, while the water is left out, or the water magnetization is zeroed (saturated) before data acquisition starts, or multiple quantum filter (MQF) techniques are used, or the water contribution is removed by numerical methods.

2.2.1 Cell Organelles

To trace back individual parts of the cellular metabolism, isolated cell organelles have been examined by NMR. The first study[43] on isolated mitochondria and later publications[44,45] used suspensions of mitochondria. Immediately after preparation they are suspended with medium and transferred to the NMR instrument. Oxygen or carbogen is bubbled through the sample. Viability is controlled in a parallel bath with an oxygen electrode. The high mitochondrial protein concentration was suspected to make part of ATP and Pi invisible.[43] However, extra- and intramitochondrial ATP can be discriminated by chelating extramitochondrial ATP with additional magnesium.[44] Detailed information on mitochondrial tricarboxylic acid (TCA) cycle reactions may be obtained by ^{13}C NMR.[45] Chloroplasts obtained from spinach leaves have also been used in NMR investigations.[46] Immediately utilized after preparation, they showed, however, little more than a Pi resonance. Studies with chromatophore preparations from photoautotrophic bacteria have been more successful; here not only measurements of pH shifts, but also rates of photophosphorylation could be determined.[47] Vacuoles have been isolated and used for ^{31}P NMR studies on cellular pH regulation.[48]

2.2.2 Perfused Microorganisms

Because of their small size, up to 10^{11} cells per mL are necessary to obtain acceptable spectra. Cell suspensions are used for short data acquisitions as described in Section 2.2, whereas the entrapment techniques are applied for longer periods. In addition, special flow systems have been designed where the suspension is recirculated.

2.3 Perfused Cells

The problem of maintaining the viability of a dense cell population for a longer period of time (hours and days) has been solved in several ways based on the principle of immobilizing or entrapping cells to allow sufficient perfusion in the NMR tube. As these techniques have been reviewed elsewhere (see ***Cells and Cell Systems MRS***), they are only listed here for completeness.[2,4,5] Cells are grown on microcarrier beads,[49,50] entrapped in a gel matrix of agarose,[51] or in a basement membrane gel named Matrigel,[2,4] or in alginate gel beads.[52] Various subtle techniques use semipermeable hollow fibers to separate cells from flowing medium[53] (see also ***Bioreactors and Perfusion***). Another approach uses Nylon mesh to support cells.[54] Advantages and disadvantages of the various methods have been reviewed previously.[4]

3 APPLICATIONS

3.1 General

Historically, in vivo NMR began with studies of red blood cells[55,56]—a cell type widely available and of only modest experimental demands. Later on Shulman and coworkers started to exploit the biochemical potential of NMR in anaerobic cells (bacteria,[57] yeast[58]) and aerobic mammalian cells (liver cells,[59] tumor cells[60]). This had a strong impact on the use of NMR as a noninvasive biochemical tool to monitor the cellular metabolism with or without arbitrarily set constraints. In the following, only a few selected topics will briefly mentioned. Further applications are compiled in recent reviews.[1–6,61]

3.1.1 pH Measurement

As the intracellular pH is tightly regulated (pH homoeostasis), deviations from the normal value may be induced to study mechanisms of pH regulation.[62] Different Pi signals indicate subcellular compartments with different pH, i.e. cytosol, vacuoles,[48] chloroplasts,[63] and chromatophores.[47]

3.1.2 Enzymatic Rates In Vivo

NMR is one of the exceptional techniques for measuring enzyme kinetics noninvasively. Two distinct types of techniques are used depending upon the rate constants. Slow reactions ($k \leq 1\,\mathrm{min}^{-1}$) are measured by recording the peak areas as a function of time, i.e. the time course of glycolysis.[64] Faster reactions ($k \approx 1\,\mathrm{s}^{-1}$) require spin exchange techniques[65–68] (i.e. saturation transfer, inversion transfer, 2D chemical exchange spectroscopy (ECSY), ACCORDION spectroscopy). By this means, rate constants and unidirectional fluxes through enzymes have been determined. In general this approach is able to differentiate between two sites (or multisites) of a molecule or molecular fragment. Hence, the technique is also suited to measure membrane transport phenomena provided the chemical shift differs in different sites.[65]

3.2 Mammalian Cells

3.2.1 Energy Metabolism

A domain of ^{31}P NMR is the depiction of the energetic status of cells.[3,5,69] Steady-state concentrations of energy-rich phosphates and/or their ratios are used as an indicator of cell viability. However, the energy charge of cells is very well buffered provided the oxygen and nutrient supply is sufficient. Therefore, in contrast to intact organisms, the energy status will only change after dramatic interference. In this respect the energy status is, amongst other indicators, also used to indicate the toxicity of drugs.

3.2.2 Metabolic Pathways

One of the most intriguing features of NMR is the possibility of monitoring the steady state and dynamics of metabolism. The high abundance isotopes (^{1}H, ^{31}P) are suited to characterize the steady state, whereas low abundance isotopes (^{13}C, ^{15}N) give access to dynamic aspects of steady state metabolism. Two major components of cell metabolism, cytosolic glycolysis and the TCA cycle, have been followed in a pioneering study on hepatocytes.[70,71] This demonstrates the advantage of NMR using stable isotopes with direct molecular information compared with radioisotopes without immediate molecular information.

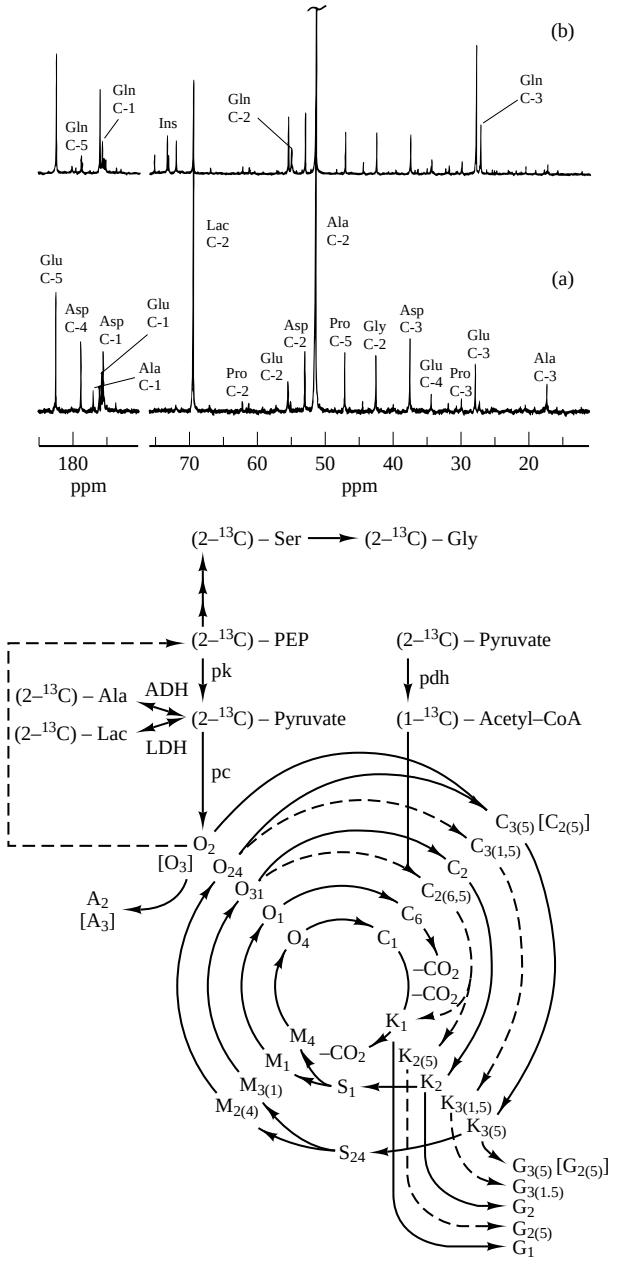

Figure 5 ^{13}C NMR spectra of cell extracts from (a) F98 glioma and (b) N1E-115 neuroblastoma obtained after an incubation period of 3 h with 2-^{13}C-pyruvate. Abbreviations as in Figure 3. The pathways depicted relate to the fate of the ^{13}C label after influx into the TCA cycle via pyruvate dehydrogenase (pdh) or pyruvate carboxylase (pc). Abbreviations are citrate (C), α-ketoglutarate (K), glutamate (G), succinate (S), malate (M), oxaloacetate (O), lactate (Lac), alanine (Ala), phosphoenol pyruvate (PEP), serine (Ser), glycine (Gly). Index number indicates the label position via pc activity or in brackets via pdh activity. (Reproduced by permission of S. Karger AG, Basel from Brand et al.[74])

Whereas hepatocytes are the almost exclusive cell type in liver, other organs consist of morphologically and metabolically different cells. NMR studies on isolated uniform cell populations are an ideal means to characterize their individual contributions to the integral metabolism of an organ. Various kidney cells are functionally and metabolically different, i.e. proximal tubule cells are capable of gluconeogenesis while medulla cells are not.[72] A similar, but even more complex, situation is faced in the brain, where neurons, astrocytes, and oligodendrocytes differ metabolically reflecting their individual duties[25–27,73,74] (see Figure 5). It should be noted that during maturation[74] or in the presence of systemic pathologies (e.g. diabetes)[75] enzymatic fluxes may change. Figure 5 describes the different TCA cycle activities in neurons and glia cells.

Phosphorus-31 NMR revealed novel metabolites of carbohydrate metabolism (sorbitol 3-phosphate, fructose 3-phosphate) in the mammalian lens and erythrocytes.[76,77] Another expanding field of ^{31}P NMR is phospholipid metabolism[78,79] which is affected in cells with abnormal proliferation,[2] but also involved in volume regulation.

3.2.3 Redox Status of Cells

Redox homeostasis may have the highest priority within the hierarchy of intracellular homeostasis, although it might be impossible to monitor all parts of this system simultaneously by NMR. The reconstitution of $NAD^+/NADP^+$ can be concluded from the lactate/pyruvate and β-hydroxybutyrate/acetoacetate ratio,[80] but in other cases the dihydroxyacetone phosphate/glycerol 3-phosphate equilibrium is involved as well.[81,82] Another approach uses labeled nicotinamide to measure $NAD(P)^+/NAD(P)H$ ratios directly.[83] A further part of the redox system, glutathione, can be monitored by ^{1}H NMR.[84]

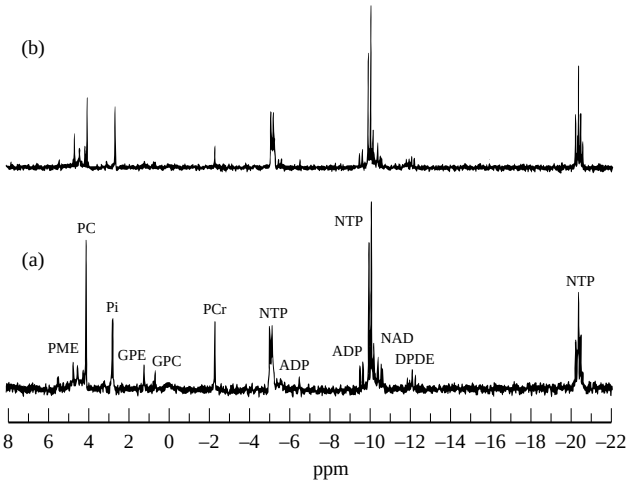

Figure 6 ^{31}P NMR spectra from (a) F98 glioma cells kept in isotonic Dulbecco's modified Eagle medium (DMEM) medium and (b) for 2 h in a hypotonic DMEM (220 mosmol). Abbreviations are nucleotide triphosphate (NTP), adenosine diphosphate (ADP), phosphocreatine (PCr), diphosphate diester (DPDE), glycerophosphocholine (GPC), glycerophosphoethanolamine (GPE), inorganic phosphate (Pi), phosphocholine (PC), and phosphomonoester (PME). GPE, GPC are no longer present under hypotonic conditions and PC is reduced

3.2.4 Osmoregulation and Cell Volume

Cell swelling is a histopathological concomitant of many pathologies like ischemia, spreading depression, even barbiturate anesthesia, etc. NMR spectroscopy of cells provides experimental tools for various problems: efflux or influx of

ions and organic osmolytes upon osmotic stress (see Figure 6) and following regulatory volume decrease or increase; determination of cell volume; differentiation between extra- and intracellular substances.

Cells will swell (shrink) if they are exposed to a hypo-(hyper-)osmolar medium. Short-term and long-term regulation may be followed invasively by quantitative analysis of extracts,[85] or noninvasively on perfused cells.[86] In the latter case, it is necessary to differentiate between extra- and intracellular localization of metabolites. This is achieved if a spin in a particular metabolite has different properties inside and outside the cell.[4] This may be a different chemical shift because of different pH,[86] the presence of shift reagents,[87] different relaxation times, or different diffusion constants.[4] The latter is more generally applicable in vivo and for each nucleus. The use of pulsed gradient spin echoes by Stejskal and Tanner[88] makes it possible to distinguish between fast diffusing extracellular metabolites and slow diffusing intracellular ones. By this means it is possible to measure intra- and extracellular diffusion constants, the relative change of cell volume, intra- and extracellular low molecular weight metabolites and their exchange.[87]

The cell volume is determined from the equilibrium distribution of indicator compounds given to the cell sample in a defined concentration. Reporter nuclei are phosphorus,[90] fluorine,[91,92] or sodium.[46,93]

The same approach is chosen to measure the amount of extra- and intracellular sodium, where paramagnetic shift reagents induce a chemical shift change in the extracellular compartment.[94] Correspondingly, potassium ratios are accessible if potassium is partially substituted by rubidium.[95] Extracellular sodium may be filtered by a multiple quantum filter.[96] However, even better suppression is accomplished by a triple quantum filter in the presence of paramagnetic lanthanide shift reagents.[97]

Intracellular calcium is chelated by 5-fluoro BAPTA and recorded by ^{19}F NMR.[98] Intracellular magnesium can be assessed either from the exchange-averaged chemical shift of β-ATP (equilibrium between Mg–ATP and ATP)[99] or again by complexation with a fluorinated chelator.[98]

3.2.5 *Tumor Cells*

NMR studies on tumor cell lines make up the majority of published papers on cell suspensions and perfused cells.[4,5,9–12,100] These cells proliferate fast enough to the required biomass and they are an accepted model for the metabolism of primary cells[101] in substrate utilization, metabolic pathways, pH, energy status, membrane permeability, etc. Besides the similarity with normal cells, tumor cells are an excellent model for testing the cytotoxicity of cytostatic drugs and their pharmacological effects,[102,103] biotransformation of drugs,[104–107] metabolic differences between normal and drug-resistant cells,[108] hyperthermia,[109] and radiotherapy.[11]

Tumor cells have also been used to test the hypothesis that a small cytosolic alkaline shift initiates mitogenic stimulation.[110,111]

3.2.6 *Erythrocytes*

Red blood cells are well suited for NMR because of their anaerobic metabolism.[7,8,112,113] Their intrinsic paramagnetic susceptibility favors techniques for studying exchange and transport reactions,[65] cell volume, volume regulation,[93,94] and water transport.[114]

3.3 Plant Cells

For the purpose of this review, NMR applications are considered using isolated organelles, protoplasts, cell suspension cultures, unicellular organisms, and, whenever suitable, even tissue cultures and organ fragments of photoautotrophic organisms. There are several recent reviews related to NMR studies that cover aspects of plant cellular metabolism[3,6,115–117] (see also ***Plant Physiology***).

3.3.1 *Energy Metabolism*

Aspects of photosynthesis have been addressed using NMR techniques. Applying ^{31}P NMR, the light-dependent alkalinization of the cell cytoplasm has been repeatedly reported.[44,118–122] There is, however, a persisting debate as to whether a fraction of detectable Pi in eukaryotic cells might stem from the chloroplast.[63,121,123–125] NMR work on isolated chloroplasts reveals a strong Pi resonance as almost the only signal from this organelle in vitro.[46,126] Studies on chromatophore preparations also succeeded in quantifying adenylates with a temporal resolution of 2–3 min.[47]

The energetic status of photoautotrophs is usually investigated with intact cells.[38,118,125–128] The partial NMR invisibility of adenylates,[129] however, does not interfere with a rather consistent picture derivable from time-resolved quantifications of the adenylate energy charge and the phosphorylation potential[130,131] (Figure 7).

Access to autotrophic CO_2 fixation and reductive carbon metabolism has been gained by analyzing ^{13}C scrambling patterns subsequent to carbonate or succinate tracer feeding in sycamore cell suspensions[132] and in a thermophilic archebacterium, respectively.[133]

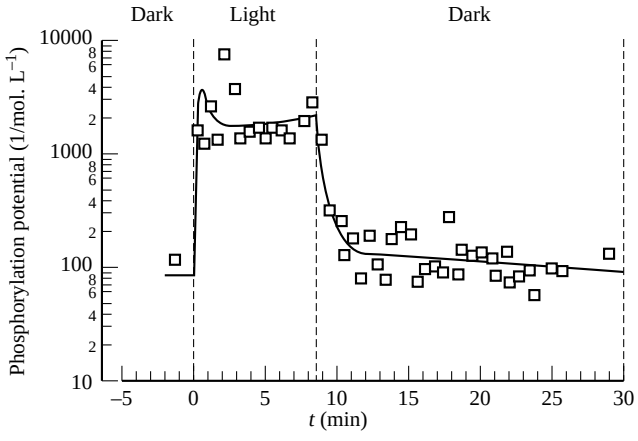

Figure 7 Phosphorylation potential during a transient from dark-to-light metabolism and vice versa in the cyanobacterium *Synechococcus leopoliensis*. The time resolution was achieved by the block-averaging technique on the basis of single ^{31}P spectra resulting from 1300 transients. (Reproduced from Maretzek[131])

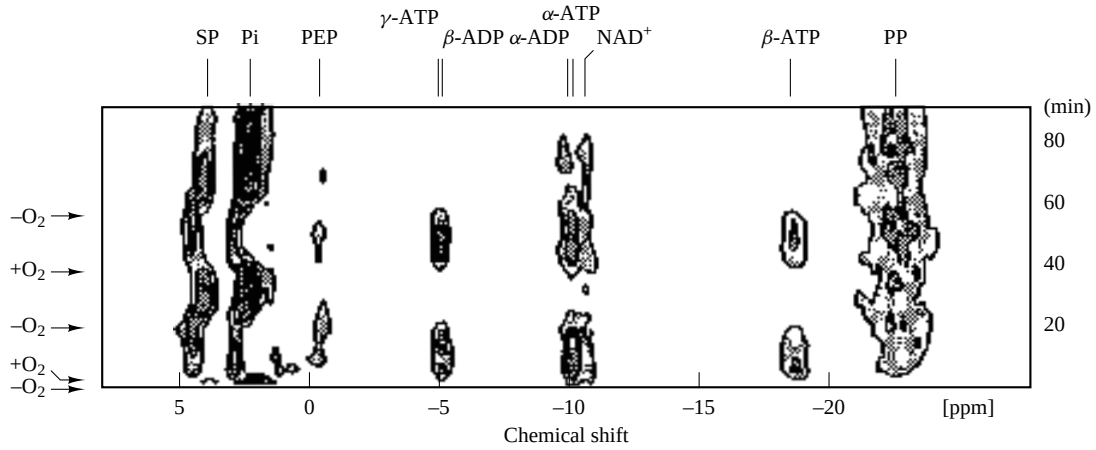

Figure 8 Contour plot from ^{31}P spectra from a *Chlorella fusca* suspension during transition from anaerobic to aerobic conditions and vice versa in the dark. The contour plot was generated on the basis of spectra resulting from 200 transients equivalent to 100 s (Offermann et al.[216])

Energy metabolism during dark respiration has been studied using ^{31}P NMR with algae[29] and plant cell suspension cultures (Figure 8).

3.3.2 Nutrient Metabolism

Nitrogen uptake and intracellular distribution have been examined in a marine macroalga[135] as well as in several higher plant tissues[136–138] using ^{14}N NMR signal intensities and lineshape analysis.

Routes of nitrogen incorporation into organic compounds have been discussed on the basis of ^{15}N labeling patterns analyzed in extracts,[139] protoplasts,[140] and in intact cells with the additional application of specific enzyme inhibitors.[141,142] ^{15}N pulse labeling experiments within the NMR tube using tissue cultures[137] and cell suspensions,[143] as well as actively photosynthesizing algae and cyanobacteria,[14,142,144,145] have elucidated the function of glutamate dehydrogenase in different species and thereby contributed to the understanding of primary ammonium assimilation in plants.

Ammonium assimilation has also been intensively studied in fungi, bacteria, and archebacteria, and even N_2 fixation has been subject to ^{15}N NMR analysis (see Walter et al.[6]).

Specific aspects of amino acid metabolism have been studied with ^{13}C NMR on suspension cultures.[146,147] Cross polarization with magic angle spinning (CP MAS and DCP MAS) ^{15}N NMR has been applied to analyze the nitrogen utilization for protein synthesis in tissue cultures.[148,149]

Phosphorus uptake and distribution between the vacuole and the cytoplasm have been studied in great detail utilizing pH-sensitive ^{31}P resonances. Among the systems studied are isolated vacuoles,[48,150] cell suspension cultures,[36,151–153] and algae.[135,154] NMR data on Pi compartmentation is already used to calibrate other soluble distribution data.[155]

Questions on the intracellular localization and function of polyphosphates occurring in lower plants have been addressed using ^{31}P NMR.[124,154,156–159] Surprisingly, saturation transfer techniques which are well suited for studying the specific enzyme kinetics of phosphate metabolism[66,160] have not yet received much attention in investigations on plant cell suspensions.[63]

3.3.3 Homeostasis and Stress Physiology

Maintaining a regulated internal milieu against variable external conditions is a major task of cells. From the various indicators used to study this physiological effort, NMR work has mainly contributed to the understanding of pH regulation and osmoregulation. Monitoring of cytoplasmic pH is almost routinely performed using pH-sensitive resonances, usually the chemical shift of Pi. Vacuolar pH may also be determined on the basis of Pi,[48,150] though ^{13}C resonances would be more suitable like the C-1 of malate,[161] the C-3 of glycerol 3-phosphate,[162] or the CH_2-linked carboxyl groups (C-1 + C-5) of citric acid[163] as this compartment typically shows pH values around 5.5. In any case it should be kept in mind that changes in pH can be recorded more accurately than absolute values which rely heavily on the quality of calibration data.[3,160]

The effect of the external pH regime on the cytoplasmic pH maintenance has been investigated for cell suspension cultures[37,134,163] and unicellular algae.[164–168] Cytoplasmic pH is almost independent of external pH over a range from pH 5.5–8.0. This might, however, be extremely costly in terms of cellular energy requirements.[168] Dependence of the energetic state of cells on the cytoplasmic pH has been reported for various plant cells in response to anaerobiosis,[29,120,167–170] as well as for light–dark transitions.[118,119,121,165,166,170]

Detailed ^{31}P NMR work has been carried out to investigate the trans-tonoplast pH gradient and thus the connection between short-term and long-term regulation of cytoplasmic and vacuolar pH.[48,150,163,171]

Temperature changes,[166] as well as elicitor treatment[172] or pulses of ammonium,[14,173] have been reported to cause pH shifts in cells within the physiological range.

The effect of salt stress on cytoplasmic pH has been described.[174–176] Osmoregulation, however, has mainly been addressed by characterizing the type and quantities of low molecular weight organic compounds like glycerol in their function as osmoregulatory solutes. Carbon-13 NMR applied to halotolerant unicelluar algae[174–179] and cyanobacteria[180–183] have been employed in this research.

Sodium-23 NMR spectroscopy[184] was applied to estimate intracellular sodium content at different external salinity.

Naturally occurring unfavorable conditions have been examined using NMR methods. Relaxation times of water protons were determined to estimate the effects of chilling injury to cultured green cells of lavender.[185] Intracellular free amino acids were observed with ^{15}N NMR to follow the effect of cellular regreening after a period of nitrogen starvation.[186] Polyphosphate hydrolysis has been studied during the regreening after nitrogen starvation in *Chlorella fusca*[187] and in response to alkaline stress in *Dunaliella salina*.[159] The cascade of events following sucrose deprivation in sycamore cell suspension cultures has been studied in great detail applying ^{31}P and ^{13}C spectroscopy.[36,188]

3.3.4 Drug Action

Modes of action of the photosystem-II inhibitors diuron and cyanobacterin, a new natural herbicide, have been compared in a cyanobacterium using ^{31}P NMR.[127] The differences in the response indicated cyanobacterin effect on photosynthetic electron transport through an action on the proton pumping mechanism. The metabolic degradation of glyphosate, an amino acid biosynthesis inhibitor, by *Pseudomonas* sp. has been revealed using ^{13}C CP MAS methodology.[189] In vivo accumulation of shikimate after glyphosate application could be demonstrated in sycamore cell suspensions.[190] The difference in susceptibility to glufosinate exposure between a cyanobacterium and a green alga could be explained in terms of an alternative pathway of ammonium assimilation in the green alga as described by ^{15}N NMR.[191]

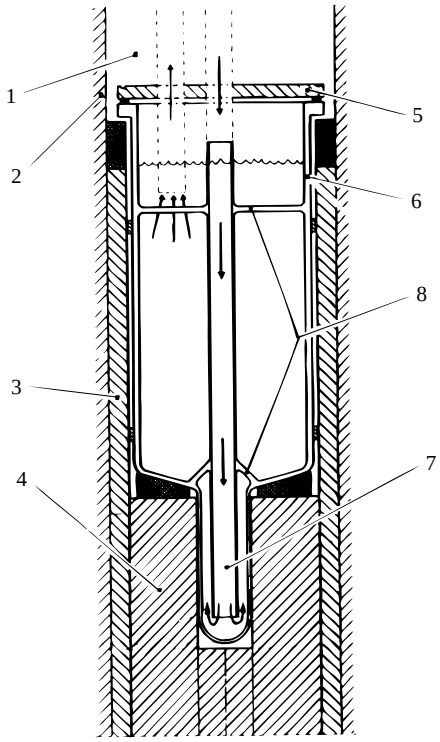

Figure 9 Continuous-flow NMR bioreactor (375 mL content). Arrows indicate flow direction caused by a centrifugal pump: 1, magnet bore (89 mm); 2, magnet inner wall; 3, shim coil section without spinner turbine; 4, rf coil section; 5, bioreactor lid; 6, prepolarizing chamber; 7, 10-mm tube; 8, glass support for tube. (Reproduced by permission of Academic Press from de Graaf et al.[192])

3.4 Microorganisms

Microorganisms, in particular bacteria and fungi, are available in a large variety of different strains obtained either by natural selection or more recently by genetic engineering. Their metabolites are natural resources of biomolecules either with natural structure or tailored molecular properties for pharmaceutical or synthetic purposes. NMR spectra of microorganisms have been recorded from cell suspensions, perfused cells, or with specially designed continuous flow bioreactors[192–196] (Figure 9) (see also ***Bioreactors and Perfusion***). A few reviews on yeast[64,192] and microorganisms in general[198,199] have been published.

Because of the dense biomass typically used in bioreactors, it may be necessary to slow down metabolic activity by lowering the temperature to 20–25 °C. Viability is controlled by ^{31}P NMR. It should be noted that microorganisms have relatively large subcellular compartments (vacuoles, microbody) with a different pH compared with the cytosol.[198] Visible polyphosphate is located in vacuoles, exchanges Pi with the cytosol and is also used for energy storage.[200] Intracellular pH is also an indicator of cell division, fermentation, chemiosmotic hypothesis, and germination.[64,197] Another intriguing property of NMR is its capability to reveal futile cycles in biochemical reactions (e.g. through phosphoenolpyruvatecarboxykinase and pyruvate dehydrogenase).[98] Futile cycles are difficult to identify by radioisotope labeling.

Besides normal substrate utilization,[64,197,198] stable isotope labeling studies have been used to follow-up the biosynthesis of porphyrins,[201] of actinomycin D and its amino acid precursors,[202] of erythritol,[203] the involvement of cyclic 2,3-diphosphoglycerate in gluconeogenesis in a thermoautotrophic methanobacterium,[204] conversion of succinate to 4-hydroxybutyrate,[205] and biosynthesis of polyols.[206]

Time-dependent labeling experiments have been used to measure quantitative fluxes in aerobic and anaerobic glycolysis,[197] glycolytic control during the Pasteur effect,[197] maintenance of redox homeostasis by equal fluxes through glycolysis, and pyruvate synthase during acetate utilization by *C. vinosum*.[207] ATPase mutants in *E. coli* strains have been characterized by NMR.[64]

Heat shock treatment of yeast leads to pH disorders[208] and in a similar manner so does cold shock.[209] Labeled acetate was used to follow-up the failure to initiate sporulation in a mutant of yeast.[210] Osmotic stress is answered by the synthesis of glycerol to lower the osmotic pressure, causing a transient ATP decrease during this adjustment.[211] By ^{23}Na NMR it is possible to separate intracellular free sodium from cell-bound sodium.[212] The energy metabolism of yeast recovers incompletely if active dry yeast is rehydrated at 0 °C compared with 40 °C.[213] Glucose degradation in *Zymomonas mobilis* is prevented by ethanol concentrations higher than 10% because phosphoglyceratemutase and enolase are inhibited.[214] In the same organism, membrane transport and fermentation of various carbohydrates have been studied.[215]

4 CONCLUSIONS AND PERSPECTIVES

NMR spectroscopy is now an accepted biochemical tool for noninvasively studying cellular metabolism and transport. Studies on the most different cells with respect to their types and physiological demands may be carried out. Improvements in NMR hardware and the refinement of cell immobilization and/or perfusion techniques have made it possible to record metabolite concentrations of 100 μmolar with a time resolution of several seconds. An increase in field strength and improved probe design promise further enhancement in sensitivity and/or time resolution. The potential of a dozen different NMR active isotopes, the use of inverse detection, and gradient selection techniques will undoubtedly stimulate many new experiments in the future. The almost free choice to set any biological constraints, the use of transgenic cells or natural mutants, and the possibility of manipulating intercellular interactions of uniform and heterogenous cell populations open many new fields of metabolic and physiological studies. Basic biochemistry and the evaluation of the biotechnological productivity of microorganisms will require NMR methods. Cellular models are important test objects for the genesis and understanding of pathologies.

Finally, it is important that the low sensitivity of NMR spectroscopy is compensated by its nonspecificity in detecting cellular metabolites. The presence of unexpected or new compounds is easily recognized, and their chemical class can be estimated from their chemical shifts.

5 RELATED ARTICLES

Animal Methods in MRS; Biological Systems: Spin-3/2 Nuclei; Bioreactors and Perfusion; Biosynthesis and Metabolic Pathways: Carbon-13 and Nitrogen-15 NMR; Cation Movements Across Cell Walls of Intact Tissues using MRS; Cells and Cell Systems MRS; Enzymatic Transformations: Isotope Probes; Enzyme-Catalyzed Exchange: Magnetization Transfer Measurements; Plant Physiology; Plants, Seeds, Roots, and Soils as Applications of Magnetic Resonance Microscopy; Tissue and Cell Extracts MRS; Tissue NMR Ex Vivo.

6 REFERENCES

1. R. J. Gupta (ed.), *NMR Spectroscopy of Cells and Organisms*, CRC Press, Boca Raton, FL, 1987, Vols. I and II.
2. J. S. Cohen, R. C. Lyon, and P. F. Daly, *Methods Enzymol.*, 1989, **177B**, 435.
3. P. Lundberg, E. Harmsen, C. Ho, and H. J. Vogel, *Anal. Biochem.*, 1990, **191**, 193.
4. O. Kaplan, P. C. M. van Zijl, and J. S. Cohen, *NMR Basic Principles and Progress*, 1992, **28**.
5. B. S. Szwergold, *Annu. Rev. Physiol.*, 1992, **54**, 775.
6. L. Walter, R. Callies, and R. Altenburger, in *Magnetic Resonance in Biology and Medicine*, eds. J. D. de Certaines, W. M. M. J. Bovée, and F. Podo, Pergamon Press, Oxford, UK, 1992, p. 573.
7. P. W. Kuchel, H. A. Berthon, W. A. Bubb, L. M. McIntyre, N. K. Nygh, and D. R. Thorburn, *Biomed. Biochim. Acta*, 1990, **49**, 105.
8. O. Kaplan and J. S. Cohen, *J. Biol. Chem.*, 1991, **266**, 3688.
9. J. D. de Certaines, V. A. Larsen, F. Podo, G. Carpinelli, O. Briot, and O. Hendriksen, *NMR Biomed.*, 1993, **6**, 345.
10. P. F. Daly, R. C. Lyon, R. C. Faustino, and J. S. Cohen, *J. Biol. Chem.*, 1987, **262**, 14 875.
11. C. E. Ng, K. A. McGovern, J. P. Wehrle, and J. D. Glickson, *Magn. Reson. Med.*, 1992, **27**, 296.
12. F. Desmoulin, J. P. Galons, P. Canioni, J. Marvaldi, and P. Cozzone, *Cancer Res.*, 1986, **46**, 3768.
13. D. Stryjewsky and D. Leibfritz, *Phys. Medica*, 1992, **8** (Suppl. 1), 15.
14. R. Altenburger, S. Abarzua, R. Callies, L. H. Grimme, A. Meyer, and D. Leibfritz, *Arch. Microbiol.*, 1991, **156**, 471.
15. M. Barany and T. Glonek, *Methods Enzymol.*, 1982, **85**, 624.
16. B. Munch-Petersen, G. Tyrsted, and B. Dupont, *Exp. Cell Res.*, 1973, **79**, 249.
17. E. B. Bligh and W. J. Dyer, *Can. J. Biochem. Physiol.*, 1959, **37**, 911.
18. H. T. Edzes, T. Teerlink, M. S. van der Knaap, and J. Valk, *Magn. Reson. Med.*, 1992, **26**, 46.
19. N. Askenazy, T. Kushnir, N. Askenasy, and G. Navon, *NMR Biomed.*, 1990, **3**, 220.
20. D. Y. Sze and O. Jardetzky, *Biochim. Biophys. Acta*, 1990, **1054**, 181, 198.
21. M. Barany, C. Arus, and Y.-C. Chang, *Magn. Reson. Med.*, 1985, **2**, 289.
22. P.-M. L. Robitaille, P. A. Robitaille, G. G. Brown, Jr., and G. G. Brown, *J. Mag. Reson.*, 1991, **92**, 73.
23. B. S. Choi and M. F. Roberts, *Biochim. Biophys. Acta*, 1987, **928**, 259.
24. W. Willker, D. Leibfritz, R. Kerssebaum, and W. Bermel, *Magn. Reson. Chem.*, 1993, **31**, 287.
25. U. Sonnewald, S. B. Petersen, J. Krane, N. Westegaard, and A. Schousboe, *Magn. Reson. Med.*, 1992, **23**, 166.
26. J. Urenjak, S. R. Williams, D. G. Gadian, and M. Noble, *J. Neurosci.*, 1993, **13**, 981.
27. A. Brand, J. Engelmann, and D. Leibfritz, *Biochimie*, 1992, **74**, 941.
28. S. Ogawa, R. G. Shulman, P. Glynn, T. Yamane, and G. Navon, *Biochim. Biophys. Acta*, 1978, **502**, 45.
29. J. Sianoudis, A. C. Küsel, T. Naujokat, W. Offermann, A. Mayer, L. H. Grimme, and D. Leibfritz, *Eur. Biophys. J.*, 1985, **13**, 89.
30. K. Ugurbil, H. Rottenberg, P. Glynn, and R. G. Shulman, *Biochemistry*, 1982, **21**, 1068.
31. H. Santos and D. L. Turner, *J. Magn. Reson.*, 1986, **68**, 345.
32. G. G. Fox, R. G. Ratcliffe, and T. W. E. Southon, *J. Magn. Reson.*, 1989, **82**, 360.
33. K. Nicolay, R. Kaptein, K. J. Hellingwerf, and W. N. Konings, *Eur. J. Biochem.*, 1981, **116**, 191.
34. R. S. Balaban, D. G. Gadian, G. K. Radda, and G. G. Wong, *Anal. Biochem.*, 1981, **116**, 450.
35. W. A. Bubb, K. Kirk, and P. W. Kuchel, *J. Magn. Reson.*, 1988, **77**, 363.
36. C. Roby, J.-B. Martin, R. Bligny, and R. Douce, *J. Biol. Chem.*, 1987, **262**, 5000.
37. G. G. Fox and R. G. Ratcliffe, *Plant Physiol.*, 1990, **93**, 512.
38. J. C. Waterton, I. G. Bridges, and M. P. Irving, *Biochim. Biophys. Acta*, 1983, **763**, 315.
39. F. Mitsumori and O. Ito, *J. Magn. Reson.*, 1984, **60**, 106.
40. R. Callies, R. Altenburger, A. Mayer, L. H. Grimme, and D. Leibfritz, *J. Magn. Reson.*, 1990, **90**, 561.

41. D. Leibfritz, in *Magnetic Resonance Spectroscopy in Biology and Medicine*, ed. J. D. Certaines, W. M. M. J. Bovée, and F. Podo, Pergamon Press, Oxford, UK, 1992, p. 150.
42. P. C. M. van Zijl and C. T. Moonen, in *NMR Basic Principles and Progress*, Springer Verlag, Berlin, 1992, Vol. 26, p. 67.
43. S. Ogawa and T. M. Lee, *Biochemistry*, 1982, **21**, 4467.
44. S. M. Hutson, D. Berkich, G. D. Williams, K. F. LaNoue, and R. W. Briggs, *Biochemistry*, 1989, **28**, 4325.
45. W. Offermann, E. Fiedler, C. Helmle-Kolb, W. Hofer, H. Kugel, T. Reese, W. Werk, and D. Leibfritz, *Magn. Reson. Chem.*, 1992, **30**, 347.
46. C. Foyer, D. Walker, C. Spencer, and B. Mann, *Biochem. J.*, 1982, **202**, 429.
47. M. Ohta, T. Nozawa, M. Hatano, H. Hayashi, M. Tasumi, and K. Shimada, *Biochim. Biophys. Acta*, 1989, **1011**, 33.
48. Y. Mathieu, J. Guern, A. Kurkdjian, P. Manigault, J. Manigault, T. Zielinska, B. Gillet, J. C. Beloeil, and J.-Y. Lallemand, *Plant Physiol.*, 1989, **89**, 19.
49. K. Ugurbil, D. C. Guernsey, T. R. Brown, P. Glynn, N. Tobkes, and I. S. Edelman, *Proc. Natl. Acad. Sci. USA*, 1981, **78**, 4843.
50. M. Neeman and H. Degani, *Cancer Res.*, 1989, **49**, 589.
51. D. L. Foxall and J. S. Cohen, *J. Magn. Reson.*, 1983, **52**, 346.
52. K. S. Narayan, E. A. Moress, J. C. Chatham, and P. B. Parker, *NMR Biomed.*, 1990, **3**, 23.
53. R. J. Gilles, P. G. Scherer, N. Raghunand, L. S. Okerlund, R. Martinez-Zaguilan, L. Hesteberg, and B. F. Dale, *Magn. Reson. Med.*, 1991, **18**, 181.
54. M. Neeman, E. Rushkin, A. Kadouri, and H. Degani, *Magn. Reson. Med.*, 1988, **7**, 236.
55. N. A. Matwiyoff and T. E. Needham, *Biochem. Biophys. Res. Commun.*, 1972, **49**, 1158.
56. R. B. Moon and J. H. Richards, *J. Biol. Chem.*, 1973, **248**, 7276.
57. G. Navon, S. Ogawa, R. G. Shulman, and T. Yamane, *Proc. Natl. Acad. Sci. USA*, 1977, **74**, 87.
58. J. A. den Hollander, T. R. Brown, K. Ugurbil, and R. G. Shulman, *Proc. Natl. Acad. Sci. USA*, 1979, **76**, 6096.
59. S. M. Cohen and R. G. Shulman, *Philos. Trans. R. Soc. London, Ser. B.*, 1980, **289**, 407.
60. G. Navon, R. Navon, R. G. Shulman, and T. Yamane, *Proc. Natl. Acad. Sci. USA*, 1978, **75**, 489.
61. F. Seguin, A. Le Pape, and S. R. Williams, in *Magnetic Resonance Spectroscopy in Biology and Medicine*, ed. J. D. Certaines, W. M. M. J. Bovée and F. Podo, Pergamon Press, Oxford, UK, 1992, p. 479.
62. A. W. H. Jans, K. Amsler, B. Griewel, and R. K. H. Kinne, *Biochim. Biophys. Acta*, 1987, **927**, 203.
63. S. Hentrich, M. Hebeler, L. H. Grimme, D. Leibfritz, and A. Mayer, *Eur. Biophys. J.*, 1993, **22**, 31.
64. K. Ugurbil, R. G. Shulman, and T. R. Brown, in *Biological Applications of Magnetic Resonance*, ed. R. G. Shulman, Academic Press, New York, 1979, p. 537.
65. P. W. Kuchel, *NMR Biomed.*, 1990, **3**, 102.
66. K. M. Brindle and I. D. Campbell, *Q. Rev. Biophys.*, 1987, **19**, 159.
67. J. R. Alger and R. G. Shulman, *Q. Rev. Biophys.*, 1984, **17**, 83.
68. E. Le Rumeur, in *Magnetic Resonance Spectroscopy in Biology and Medicine*, ed. J. D. Certaines, W. M. M. J. Bovée and F. Podo, Pergamon Press, Oxford, UK, 1992, p. 169.
69. B. Chance, *NMR Biomed.*, 1989, **2**, 179.
70. S. M. Cohen, P. Glynn, and R. G. Shulman, *Proc. Natl. Acad. Sci. USA*, 1981, **78**, 60.
71. S. M. Cohen, in *NMR Spectroscopy of Cells and Organisms*, ed. R. J. Gupta, CRC Press, Boca Raton, FL, 1987, Vol. I, p. 31.
72. A. W. H. Jans and D. Leibfritz, *NMR Biomed.*, 1989, **1**, 171.
73. U. Sonnnewald, N. Westergard, S. B. Petersen, G. Unsgard, and A. Schousboe, *J. Neurochem.*, 1993, **61**, 1179.
74. A. Brand, C. Richter-Landsberg, and D. Leibfritz, *Develop. Neurosci.*, in the press.
75. A. W. H. Jans and R. Willem, *Biochem. J.*, 1989, **263**, 231.
76. A. Petersen, B. S. Szwergold, F. Kappler, M. Weingarten, and T. R. Brown, *J. Biol. Chem.*, 1990, **265**, 17 424.
77. B. S. Szwergold, F. Kappler, and T. R. Brown, *Science*, 1990, **247**, 451.
78. P. F. Daly, R. C. Lyon, P. J. Faustino, and J. S. Cohen, *J. Biol. Chem.*, 1987, **262**, 14 875.
79. A. C. Kuesel, G. Grashew, W. E. Hull, W. Lorenz, and H. W. Thielmann, *NMR Biomed.*, 1987, **3**, 78.
80. T. Jue, Y. Chung, and R. G. Shulman, *J. Magn. Reson.*, 1987, **76**, 178.
81. O. Ben-Yoseph, R. S. Badar-Goffer, P. G. Morris, and H. S. Bachelard, *Biochem. J.*, 1993, **291**, 915.
82. U. Flogel, W. Willker, and D. Leibfritz, *NMR Biomed.*, 1994, **7**, 157.
83. C. J. Unkefer and R. E. London, *J. Biol. Chem.*, 1989, **259**, 2311.
84. F. F. Brown, I. D. Campbell, W. P. Kuchel, and D. L. Robenstein, *FEBS Lett.*, 1977, **82**, 12.
85. Y. H. H. Lien, J. L. Shapiro, and L. Chan, *J. Clin. Invest.*, 1990, **85**, 1427; *ibid.*, 1991, **88**, 303.
86. Y. H. H. Lien, H. Z. Zhou, C. Job, J. A. Barry, and R. J. Gillies, *Biochimie*, 1992, **74**, 931.
87. G. A. Smith, R. T. Hesketh, J. C. Metcalfe, J. Feeney, and P. G. Morris, *Proc. Natl. Acad. Sci. USA*, 1983, **80**, 7178.
88. J. E. Tanner and E. O. Stejskal, *J. Chem. Phys.*, 1965, **42**, 288; *ibid.*, 1968, **49**, 1768.
89. P. C. M. van Zijl, C. T. Moonen, P. J. Faustino, O. Kaplan, J. Pekar, and J. S. Cohen, *Proc. Natl. Acad. Sci. USA*, 1991, **88**, 3228.
90. J. E. Raftos, K. Kirk, and P. W. Kuchel, *Biophys. Biochim. Acta*, 1988, **968**, 160.
91. R. E. London and S. A. Gabel, *Biochemistry*, 1989, **28**, 2378.
92. A. S.-L. Xu, J. Potts, and P. W. Kuchel, *Magn. Reson. Med.*, 1991, **18**, 193.
93. A. Mancuso, E. J. Fernandez, H. W. Blanch, and D. S. Clark, *Biotechnology*, 1990, **8**, 1282.
94. R. K. Gupta (ed.), *NMR Spectroscopy of Cells and Organisms*, CRC Press, Boca Raton, FL, 1987, Vol. II, p. 1.
95. I. Kieselhorst and U. Pilatus, *Soc. Magn. Reson. Med.*, 1992, 3532.
96. J. Pekar, P. F. Renshaw, and J. S. Leigh, Jr, *J. Magn. Reson.*, 1987, **72**, 159.
97. G. Navon, *Soc. Magn. Reson. Med.*, 1992, 843.
98. H. L. Kirschenlohr, J. C. Metcalfe, P. G. Morris, G. C. Rodrigo, and G. A. Smith, *Proc. Natl. Acad. Sci. USA*, 1988, **85**, 9017.
99. R. K. Gupta and P. Gupta, in *NMR Spectroscopy of Cells and Organisms*, ed. R. K. Gupta, CRC Press, Boca Raton, FL, Vol. II, p. 33.
100. C. E. Mountford, W. B. Mackinnon, E. J. Delikatny, and P. Russell, in *Magnetic Resonance Spectroscopy in Biology and Medicine*, eds. J. D. Certaines, W. M. M. J. Bovée, and F. Podo, Pergamon Press, Oxford, UK, 1992, p. 507.
101. K. Shankar-Narayan, E. A. Moress, J. C. Chatham, and P. B. Barker, *NMR Biomed.*, 1990 **3**, 23.

102. M. Neeman and H. Degani, *Cancer Res.*, 1989, **49**, 589.
103. V. L. Boyd, J. D. Robbins, W. Egan, and S. M. Ludeman, *J. Biol. Chem.*, 1986, **29**, 1206.
104. O. Kaplan and J. S. Cohen, *Trends Pharmacol. Sci.*, 1990, **11**, 398.
105. J. D. Bell, D. G. Gadian, and N. Preece, *Eur. J. Drug. Metab. Pharmacokinet.*, 1990, **15**, 127.
106. H. M. Sonawat, D. Leibfritz, J. Engel, and P. Hilgard, *Biochim. Biophys. Acta*, 1990, **1052**, 36.
107. M. C. Malet-Martino and R. Martino, in *Magnetic Resonance Spectroscopy in Biology and Medicine*, eds. J. D. Certaines, W. M. M. J. Bovée, and F. Podo, Pergamon Press, Oxford, UK, 1992, p. 493.
108. O. Kaplan, G. Navon, R. C. Lyon, P. J. Faustino, E. J. Straka, and J. S. Cohen, *Cancer Res.*, 1990, **50**, 544.
109. N. Suzuki, I. L. Kwee, L. B. Tamas, and T. Nakada, *Magn. Reson. Med.*, 1991, **19**, 422.
110. B. S. Szwergold, T. R. Brown, and J. J. Freed, *J. Cell Physiol.*, 1989, **138**, 227.
111. M. Bental and C. Deutsch, *Magn. Reson. Med.*, 1993, **29**, 317; *Soc. Magn. Reson. Med.*, 1993, 1164.
112. S. T. Oxley, R. Portemus, K. M. Brindle, J. Boyd, and I. D. Campbell, *Biophys. Biochim. Acta*, 1984, **805**, 19.
113. P. W. Kuchel, B. E. Chapman, Z. H. Endre, G. F. King, D. R. Thorburn, and M. J. York, *Biomed. Biochim. Acta*, 1984, **43**, 6.
114. C. Gasparovic and N. A. Matwiyoff, *Magn. Reson. Med.*, 1992, **26**, 274.
115. R. Bligny, C. Roby, and R. Douce, in *Nuclear Magnetic Resonance in Agriculture*, eds. P. E. Pfeffer and W. V. Gerasimowicz, CRC Press, Boca Raton, FL, 1989, p. 71.
116. R. G. Ratcliffe and J. K. M. Roberts, *Magn. Reson. Med. Biol.*, 1990, **4**, 77.
117. H. J. Vogel and P. Lundberg, in *NMR Applications in Biopolymers*, ed. J. Finley, Plenum Press, New York, 1990, p. 329.
118. T. Kallas and F. W. Dahlquist, *Biochemistry* 1981, **20**, 5900.
119. T. Mimura and Y. Kirino, *Plant Cell Physiol.*, 1984, **25**, 813.
120. I. Enami, H. Akutsu, and Y. Kyogoku, *Plant Cell Physiol.*, 1986, **27**, 1351.
121. J. Sianoudis, A. C. Kusel, A. Mayer, L. H. Grimme, and D. Leibfritz, *Arch. Microbiol.*, 1987, **147**, 25.
122. Y. Tominaga, K. Kuchitsu, M. Katsuhara, M. Tazawa, and S. Miyachi, *Plant Cell Physiol.*, 1991, **32**, 261.
123. F. Mitsumori and O. Ito, *FEBS Lett.*, 1984, **174**, 248.
124. J. Sianoudis, A. Mayer, and D. Leibfritz, *Org. Magn. Reson.*, 1984, **22**, 364.
125. J. Sianoudis, T. Naujoks, A. Mayer, D. Leibfritz, and L. H. Grimme, in *Magnetic Resonance in Biology and Medicine*, eds. G. Govil, C. L. Khetrapal, and A. Savan, McGraw-Hill, New York, 1985, p. 429.
126. R. Bligny, P. Gardestrom, C. Roby, and R. Douce, *J. Biol. Chem.*, 1990, **265**, 1319.
127. W. J. Thoma and F. K. Gleason, *Biochemistry*, 1987, **26**, 2510.
128. L. Packer, S. Spath, R. Bligny, J.-B. Martin, and C. Roby, *Methods Enzymol.*, 1988, **167**, 667.
129. M. A. Hooks, R. A. Clark, R. H. Nieman, and J. K. M. Roberts, *Plant Physiol.*, 1989, **89**, 963.
130. Y. Yazaki, N. Asukagawa, Y. Ishikawa, E. Ohta, and M. Sakata, *Plant Cell Physiol.*, 1988, **29**, 919.
131. A. F. Maratzek, Ph.D. Thesis, Universität Bremen, 1992.
132. E. Gout, R. Bligny, N. Pascal, and R. Douce, *J. Biol. Chem.*, 1993, **268**, 3986.
133. S. Schäefer, M. Götz, W. Eisenreich, A. Bacher, and G. Fuchs, *Eur. J. Biochem.*, 1989, **184**, 151.
134. V. Wray, O. Schiel, J. Berlin, and L. Witte, *Arch. Biochem. Biophys.*, 1985, **236**, 731.
135. P. Lundberg, R. G. Weich, P. Jensén, and H. J. Vogel, *Plant Physiol.*, 1989, **89**, 1380.
136. P. S. Belton, R. B. Lee, and R. G. Ratcliffe, *J. Exp. Bot.*, 1985, **36**, 190.
137. T. A. Thorpe, K. Bagh, A. J. Cutler, D. I. Dunstan, D. D. McIntyre, and H. J. Vogel, *Plant Physiol.*, 1989, **91**, 193.
138. R. B. Lee and R. G. Ratcliffe, *Planta*, 1991 **183**, 359.
139. F. Martin and M. Ben Driss, in *Fundamental, Ecological and Agricultural Aspects of Nitrogen Metabolism in Higher Plants*, eds. H. Lambers, J. J. Neeteson, and I. Stulen, Martinus Nijhoff Publishers, Dordrecht/Boston/Lancaster, 1986, p. 191.
140. M. Neeman, D. Aviv, H. Degani, and E. Galun, *Plant Physiol.*, 1985, **77**, 374.
141. E. B.-I. Monselise, D. Kost, D. Porath, and M. Tal, *New Phytol.*, 1987, **107**, 341.
142. R. Callies, R. Altenburger, S. Abarzua, A. Mayer, L. H. Grimme, and D. Leibfritz, *Plant Physiol.*, 1992, **100**, 1584.
143. S. A. Robinson, A. P. Slade, G. G. Fox, R. Philips, R. G. Radcliffe, and G. R. Stewart, *Plant Physiol.*, 1991, **95**, 509.
144. L. Walter, R. Altenburger, R. Callies, L. H. Grimme, D. Leibfritz, and A. Mayer, *Isotopenpraxis*, 1992, **28**, 73.
145. S. Abarzua, R. Altenburger, R. Callies, L. H. Grimme, A. Mayer, D. Leibfritz, and U. Schiewer, *Physiol. Plantarum*, 1993, **89**, 659.
146. D. J. Ashworth and I. J. Mettler, *Biochemistry*, 1984, **23**, 2252.
147. J. W. Heyser, M. J. Chacon, and R. S. Warren, *J. Plant Physiol.*, 1989, **135**, 459.
148. T. A. Skokut, J. E. Varner, J. Schaefer, E. O. Stejskal, and R. A. McKay, *Plant Physiol.*, 1982, **69**, 308.
149. T. A. Skokut, J. Manchester, and J. Schaefer, *Plant Physiol.*, 1985, **79**, 579.
150. J. Guern, Y. Mathieu, A. Kurkdjian, P. Manigault, J. Manigault, B. Gillet, J. C. Beloeil, and J.-Y. Lallemand, *Plant Physiol.*, 1989, **89**, 27.
151. P. Brodelius and H. J. Vogel, *J. Biol. Chem.*, 1985, **260**, 3556.
152. F. Rébeilé, R. Bligny, J.-B. Martin, and R. Douce, *Biochem. J.*, 1985, **226**, 679.
153. K. Sakano, Y. Yazaki, and T. Mimura, *Plant Physiol.*, 1992, **99**, 672.
154. A. Elgavish, G. A. Elgavich, M. Halmann, T. Berman, and I. Shomer, *FEBS Lett.*, 1980, **117**, 137.
155. J. Preisser, H. Sprügel, and E. Komor, *Planta*, 1992, **186**, 203.
156. J. Sianoudis, A. C. Kuesel, A. Mayer, L. H. Grimme, and D. Leibfritz, *Arch. Microbiol.*, 1986, **144**, 48.
157. H. Kugel. A. Mayer, G. O. Kirst, and D. Leibfritz, *Eur. Biophys. J.*, 1987, **14**, 461.
158. A. C. Kuesel, J. Sianoudis, D. Leibfritz, L. H. Grimme, and A. Mayer, *Arch. Microbiol.*, 1989, **152**, 167.
159. U. Pick and M. Weiss, *Plant Physiol.*, 1991, **97**, 1234.
160. P. G. Morris, *Annu. Rep. NMR. Spectrosc.*, 1988, **20**, 1.
161. M. A. Stidham, D. E. Moreland, and J. N. Siedow, *Plant Physiol.*, 1983, **73**, 517.
162. V. P. Chacko and R. G. Weiss, *Am. J. Physiol.*, 1993, **264**, C755.
163. E. Gout, R. Bligny, and R. Douce, *J. Biol. Chem.*, 1992, **267**, 13 903.
164. H. Kugel, A. Mayer, G. O. Kirst, and D. Leibfritz, *Eur. Biophys. J.*, 1987, **14**, 461.

165. H. Gimmler, H. Kugel, D. Leibfritz, and A. Mayer, *Physiol. Plant.*, 1988, **74**, 521.
166. M. Ginzburg, R. G. Ratcliffe, and T. E. Southon, *Biochim. Biophys. Acta*, 1988, **969**, 225.
167. A. C. Küsel, J. Sianoudis, D. Leibfritz, L. H. Grimme, and A. Mayer, *Arch. Microbiol.*, 1990, **153**, 254.
168. H. Kugel, A. Mayer, G. O. Kirst, and D. Leibfritz, *Biochim. Biophys. Acta*, 1990, **1054**, 33.
169. G. Ben-Hayyim and G. Navon, *J. Exp. Bot.*, 1985, **36**, 1877.
170. H. Gimmler, U. Weis, C. Weiss, H. Kugel, and B. Treffny, *New Phytol.*, 1989, **113**, 175.
171. M. A. Horn, R. P. Meadows, I. Apostol, C. R. Jones, D. G. Gorenstein, P. F. Heinstein, and P. S. Low, *Plant Physiol.*, 1992, **98**, 680.
172. I. Ojalvo, J. S. Rokem, G. Navon, and I. Goldberg, *Plant Physiol.*, 1987, **85**, 716.
173. M. Ohmori, T. Oh-hama, K. Furihata, and S. Miyachi, *Plant Cell Physiol.*, 1986, **27**, 563.
174. K. Kuchitsu, M. Katsuhara, and S. Miyachi, *Plant Cell Physiol.*, 1989, **30**, 407.
175. M. Katsuhara, K. Kuchitsu, T. Takeshige, and M. Tazawa, *Plant Physiol.*, 1989, **90**, 1102.
176. M. Bental, U. Pick, M. Avron, and H. Degani, *Eur. J. Biochem.*, 1990, **188**, 111.
177. H. Degani, I. Sussman, G. A. Peschek, and M. Avron, *Biochim. Biophys. Acta*, 1985, **846**, 313.
178. M. Oren-Shamir, M. Avron, and H. Degani, *FEBS Lett.*, 1988, **233**, 124.
179. M. Bental, M. Oren-Shamir, M. Avron, and H. Degani, *Plant Physiol.*, 1988, **87**, 320.
180. R. S. Norton, M. A. McKay, and L. J. Borowitzka, *Biochem. J.*, 1982, **202**, 699.
181. E. Tel-Or, S. Spath, L. Packer, and R. J. Mehlhorn, *Plant Physiol.*, 1986, **82**, 646.
182. L. Packer, S. Spath, J.-B. Martin, C. Roby, and R. Bligny, *Arch. Biochem. Biophys.*, 1987, **256**, 354.
183. R. H. Reed, *Methods Enzymol.*, 1988, **167**, 528.
184. M. Bental, H. Degani, and M. Avron, *Plant Physiol.*, 1988, **87**, 813.
185. H. Morikawa, H. Fukao, E. Suzuki, N. Nagashima, and Y. Yamada, *Agric. Biol. Chem.*, 1988, **52**, 2085.
186. A. C. Kuesel, W. Kuhn, J. Sianoudis, L. H. Grimme, D. Leibfritz, and A. Mayer, *Arch. Microbiol.*, 1989, **151**, 434.
187. A. C. Kuesel, J. Sianoudis, D. Leibfritz, L. H. Grimme, and A. Mayer, *Arch. Microbiol.*, 1989, **152**, 158.
188. P. Genix, R. Bligny, J.-B. Martin, and R. Douce, *Plant Physiol.*, 1990, **94**, 717.
189. G. S. Jacob, J. Schaefer, E. O. Stejskal, and R. A. McKay, *J. Biol. Chem.*, 1985, **260**, 5899.
190. E. Gout, R. Bligny, P. Genix, M. Tissut, and R. Douce, *Biochimie*, 1992, **74**, 875.
191. R. Altenburger, R. Callies, L. H. Grimme, A. Mayer, and D. Leibfritz, in preparation.
192. A. A. de Graaf, R. M. Wittig, U. Probst, J. Stohhaecker, S. M. Schoberth, and H. Sahm, *J. Magn. Reson.*, 1992, **98**, 654.
193. H. W. Kramer and J. E. Bailey, *Biotechnol. Bioeng.*, 1991, **37**, 205.
194. A. J. Meehan, C. J. Eskey, A. P. Koretsky, and M. U. Domach, *Biotechnol. Bioeng.*, 1992, **40**, 1359.
195. C. A. Braisco, S. F. Karel, and C. R. Robertson, *Biotechnol. Bioeng.*, 1990, **36**, 887.
196. R. Chen and J. E. Bailey, *Biotechnol. Bioeng.*, 1993, **42**, 215.
197. S. L. Campbell-Burk and R. G. Shulman, *Annu. Rev. Microbiol.*, 1987, **41**, 595.
198. K. Nicolay, *DECHEMA-Monogr.*, 1987, **105**, 97.
199. K. Nicolay, *Trends Food Sci. Technol.*, 1992, **3**, 225.
200. K. Nicolay, W. A. Scheffers, P. M. Bruinenberg, and R. Kaptein, *Arch. Microbiol.*, 1982, **133**, 82.
201. G. Burton, P. M. Jordan, N. E. MacKenzie, P. E. Fagerness, and A. I. Scott, *Biochem. J.*, 1983, **194**, 627.
202. L. Inbar and A. Lapidot, *J. Bacteriol.*, 1991, **173**, 7790.
203. M. Veiga de Cunha, P. Firme, S. M. V. Romao, and H. Santos, *Appl. Environ. Microbiol.*, 1992, **58**, 2271.
204. A. Gorkovenko and M. F. Roberts, *J. Bacteriol.*, 1993, **175**, 4087.
205. R. A. Wolff, G. W. Urben, S. M. O'Herrin, and W. R. Kenealy, *Appl. Environ. Microbiol.*, 1993, **59**, 1876.
206. C. Dijkema, H. C. M. Koster, and J. Visser, *Proc. Natl. Acad. Sci. USA*, 1985, **82**, 1583.
207. K. Nicolay, H. van Gemerden, K. J. Hellingwarf, K. N. Konings, and R. Kaptein, *J. Bacteriol.*, 1983, **155**, 634.
208. G. Weitzel, U. Pilatus, and L. Rensing, *Exp. Cell Res.*, 1987, **170**, 64.
209. S. C. Kaul, K. Obuchi, and Y. Komatsu, *Cell. Mol. Biol.*, 1992, **38**, 135.
210. J. R. Dickinson and M. J. E. Hewlins, *J. Gen. Microbiol.*, 1991, **137**, 1033.
211. P. J. van Zijl, S. G. Kilian, and B. A. Prior, *Appl. Microbiol. Biotechenol.*, 1993, **39**, 235.
212. H. Gilboa, H. Kogul, S. Chalamish, R. Regev, Y. Avi-Dor, and N. J. Russell, *J. Bacteriol.*, 1991, **173**, 7021.
213. A. Peña, S. Uribe, M. Clemente, and N. Sánchez, *Arch. Microbiol.*, 1992, **158**, 75.
214. J. Strohhaecker, A. A. de Graaf, S. M. Schoberth, R. M. Wittig, and H. Sahm, *Arch. Microbiol.*, 1993, **159**, 484.
215. S. M. Schoberth and A. A. de Graaf. *Anal. Biochem.*, 1993, **210**, 123.
216. W. Offermann, W. Kuhn, S. Soboll, T. Ishikawa, and D. Leibfritz, *Magn. Reson. Med.*, 1987, **4**, 507.

Biographical Sketches

D. Leibfritz. *b* 1944. Ph.D., 1970, University of Tübingen (with H. Kessler). Postdoctoral research fellow at CalTech (with J. D. Roberts) 1970–72; Habilitation, 1976, University of Frankfurt; Full Professor, University of Bremen, 1977–present. Approx. 150 publications. Research interests include metabolism of brain, tumor, and plant cells; fast MRI and in vivo spectroscopy; high-resolution NMR pulse techniques for structure determination.

R. Altenburger. *b* 1958. Ph.D., 1991, University of Bremen. Postdoctoral research work (with L. H. Grimme), 1991–93. 18 publications. Research topics include plant physiology and drug action, aquatic toxicology.

DNA Triplexes, Quadruplexes, and Aptamers

Juli Feigon

University of California, Los Angeles, CA, USA

1	Introduction	1
2	DNA Triplexes	1
3	DNA Quadruplexes	3
4	DNA Aptamers	5
5	Related Articles	5
6	References	5

1 INTRODUCTION

The first folded nucleic acid structure to be studied by NMR was tRNA. In the classic paper by Kearns et al.[1] the first observation of resonance signals from hydrogen bonded imino protons from the base pairs of the tRNA was reported. It was immediately obvious that the spread in chemical shifts of these resonances contained information on the three-dimensional structure of the tRNA. Nearly 25 years later, NMR studies of nucleic acids have finally progressed to the point where complete three-dimensional structures of folded nucleic acids, although still only of molecular weights less than half that of tRNA, can be determined from NMR data. These more recent studies have predominantly been of DNA oligonucleotides, primarily because until recently NMR quantities of RNA oligonucleotides were largely unavailable.

Three major developments have contributed to the study of DNA structure by NMR: (1) the advent of higher field magnets for NMR spectroscopy, (2) the development of multidimensional NMR techniques for the study of macromolecules, and (3) the development of methods for the efficient chemical synthesis of DNA oligonucleotides. The applications of multidimensional NMR to the study of nucleic acids have lagged somewhat behind proteins. For duplex DNA, one problem has been that the three-dimensional structure of B-DNA was already known at the resolution that most protein structures could be determined by NMR. Fine details of the structure of the DNA, i.e. base tilt, twist, etc., present a challenging problem for NMR studies because of the lack of sufficient proton NOEs to define these details unambiguously. Recently, several different types of folded DNA structures have been studied by multidimensional proton NMR spectroscopy. These folded DNA structures are of special interest both for their biological relevance and from the spectroscopic point of view, since the tertiary structure provides extra constraints for the three-dimensional structure determination. In this article, the use of modern NMR techniques in the structure determination of DNA triplexes, quadruplexes, and aptamers is reviewed.

2 DNA TRIPLEXES

Application of modern NMR techniques to the study of DNA triplexes began with a report in *Nature* in 1989 on NMR studies of DNA triplexes formed by d(GAGAGAGA) and d(TCTCTCTC).[2] At low pH values and in the presence of excess pyrimidine strand, imino and amino proton resonances corresponding to C·G·C and T·A·T base triplets (Figure 1 were observed. These and other triplexes were further described in subsequent publications from several groups. These studies showed conclusively that DNA triplexes with the expected Hoogsteen base pairing of the second pyrimidine strand in the major groove of the Watson–Crick paired duplex were formed. However, it was difficult to characterize these triplexes further because other conformations such as duplex, single strand, and self-complex of the purine strand were also present. In 1990, an NMR study on a single strand of DNA that was designed to fold to form an intramolecular triplex was reported.[3] Figure 2 shows the one-dimensional ^{1}H spectra of the exchangeable imino and cytosine amino proton resonances of this oligonucleotide as a function of pH. Since Hoogsteen pairing of the cytosine residues in the second pyrimidine strand requires protonation at N-3, the triplex structure is favored at low pH. Imino resonances corresponding to six base triplets and one G·C base pair are seen at pH 5, indicating triplex formation. The characteristically high-frequency (low-field) shifted amino resonances from the protonated Cs are also present. The triplex form predominates up to pH 6.5. At pH 7.0 there are about equal amounts of the intramolecular triplex and the partial duplex. Above pH 7.0, the partial duplex predominates. Assignments of the resonances were obtained by analysis of two-dimensional NOESY spectra of the molecule in H_2O. The intramolecular triplex model system has since

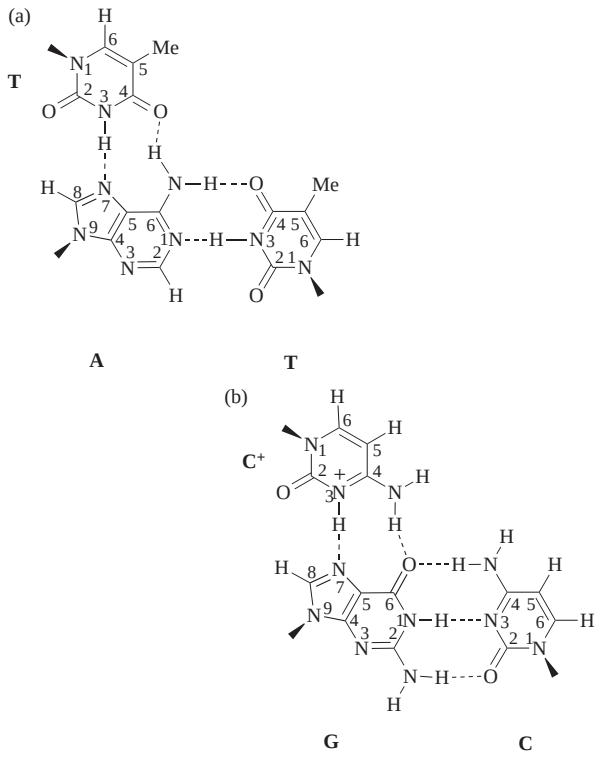

Figure 1 Hydrogen bonding of base triplets (a) T·A·T and (b) (C·G·C)

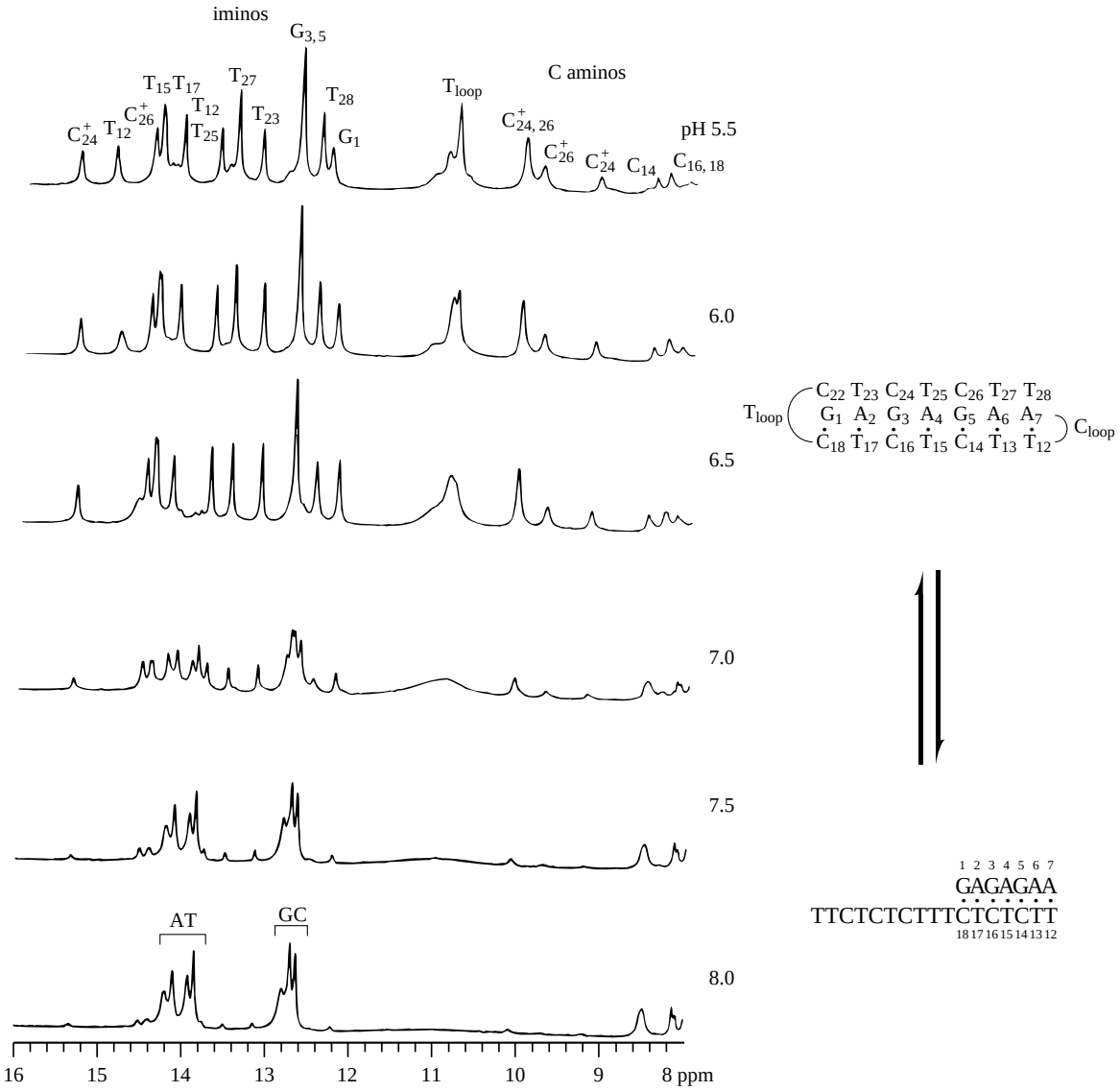

Figure 2 One-dimensional proton NMR spectra of the imino and C amino proton resonances of d(GAGAGAACCCCTTCTCTCTTTCTCTCTT) as a function of pH (left). Illustration of the equilibrium between the folded triplex structure and the partial duplex (right). (Adapted from Sklenář and Feigon [3])

been used to characterize a number of triplexes containing other triplets.[4–9]

Two different classes of triplex have been identified: (1) the pyrimidine motif, in which the third strand is pyrimidines, and binds parallel to the purine strand, forming T·A·T and C·G·C triplexes, and (2) the purine motif, in which the third strand is primarily purines, and binds antiparallel to the Watson–Crick paired purine strand, forming G·G·C and A·A·T or T·A·T triplets. The pyrimidine motif is the best characterized. The base–H-1′ region of a NOESY spectrum of a 32-base pyrimidine triplex is shown in Figure 3 to illustrate some of the ^{1}H spectral characteristics of triplexes.[4] Three sets of base–deoxyribose H-1′ sequential connectivities are observed, corresponding to the three strands of the triplex. These sequential connectivites are consistent with a regular right-handed helical structure. The intramolecular triplex also showed unambiguously that the second pyrimidine strands binds parallel to the purine strand via Hoogsteen base pairing in the major groove of the DNA. Previous structural information of DNA triplexes was derived from fiber diffraction work on poly(dT·dA·dT).[10] From this work, it was concluded that DNA triplexes were A-DNA-like with C-3′-*endo* sugar puckers. However, analysis of COSY cross-peak patterns of the H-1′–H-2′/ H-2″ resonances (Figure 4) of the intramolecular triplex indicated that the majority of the deoxyribose conformations are in the C-2′-*endo* range characteristic of B-DNA.[11] Thus, from the NMR data it was concluded that the DNA triplexes were more similar to B-DNA than A-DNA in structure. Intramolecular triplexes have also been used to investigate a number of different mismatch or noncanonical triplets within the pyrimidine motif. In general, the base-pairing scheme was deduced from analysis of the NMR spectra of the exchangeable imino and amino resonances. Further details on the structures were obtained from analysis of the D_2O spectra, and several model structures based on NMR data have been reported.[4,8,9]

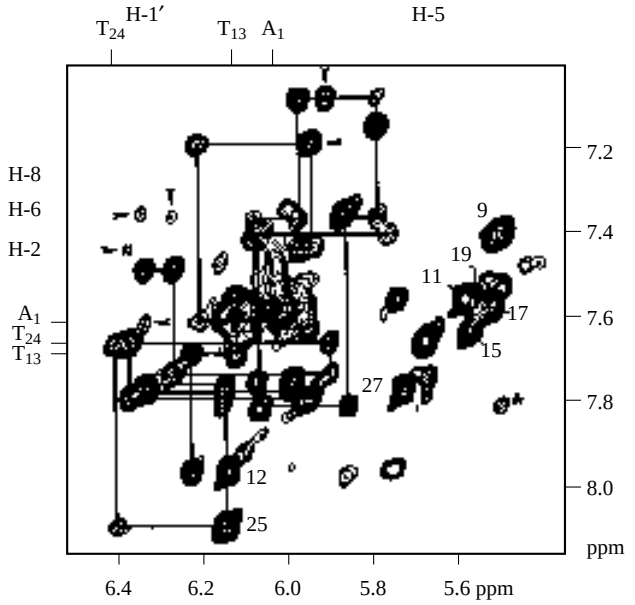

Figure 3 Portion of NOESY spectrum showing the base–H-1′ cross peaks of the intramolecular triplex formed from d(AGAGAGAA**CCCC**TTCTCTCT**TTT**TCTCTCT). Bases forming the loops are in bold. The sequential connectivities along each of the three strands of the triplex are indicated by solid lines. (Adapted from Macaya et al [4])

Purine motif triplexes have been less well studied. This is partially because the conditions for formation of these triplexes are less well established. The base pairing and strand orientation for intramolecular purine motif triplexes were established by the NMR studies of Radhakrishnan and Patel.[9] In the presence of Li^+ counterions, intramolecular triplexes containing G·G·C and T·A·T or G·G·C and A·A·T triplets were formed.

3 DNA QUADRUPLEXES

It was established over 30 years that guanosine and its derivatives can hydrogen bond in a tetrameric arrangement to form guanine quartets (Figure 5) (reviewed by Guschlbauer et al.[12]). This hydrogen bonding also seems to be related to the fact that guanosine mono- and oligonucleotides easily form viscous gels in the presence of monovalent cations. This propensity for aggregation in guanine-rich oligonucleotides has limited the structural characterization of guanine-rich DNAs by NMR. Early NMR work on guanosine 5′-phosphate and guanine oligomers investigated the role of specific cations in self-assembly of these gels. These studies provided evidence for formation of tetrameric structures.

The current interest in DNA quadruplexes arose from observations that a variety of DNA oligonucleotides composed of biologically relevant guanine-rich sequences seemed to form some unusual structures in vitro. Guanine-rich sequences are found in immunoglobulin switch regions, telomeres, the dimerization domain of the HIV-1 genome, and other sites in eukaryotic genomes. In several cases, it was proposed that these unusual structures might be quadruplex structures. Much of the recent work on guanine-rich DNAs has focused

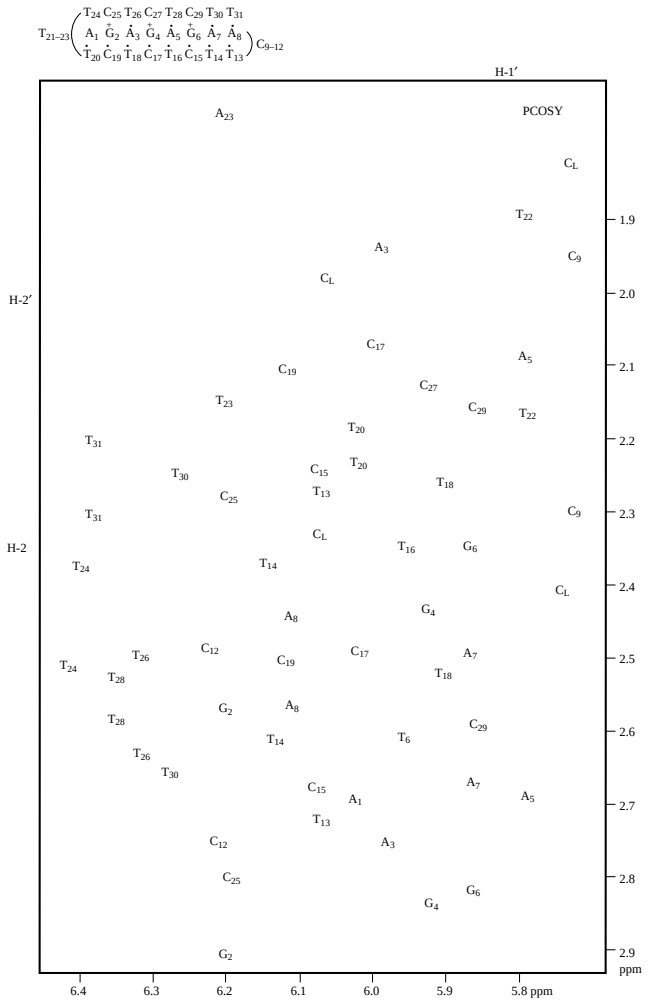

Figure 4 Portion of P.COSY spectrum of the intramolecular triplex formed from d(AGAGAGAA**CCCC**TTCTCTCT**TTT**TCTCTCT) showing the H-1′–H-2′ and H-1′–H-2′′ cross peaks. (Adapted from Macaya et al.[4])

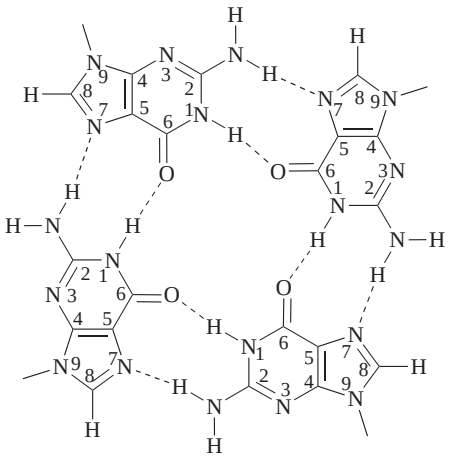

Figure 5 Structure of a guanine quartet

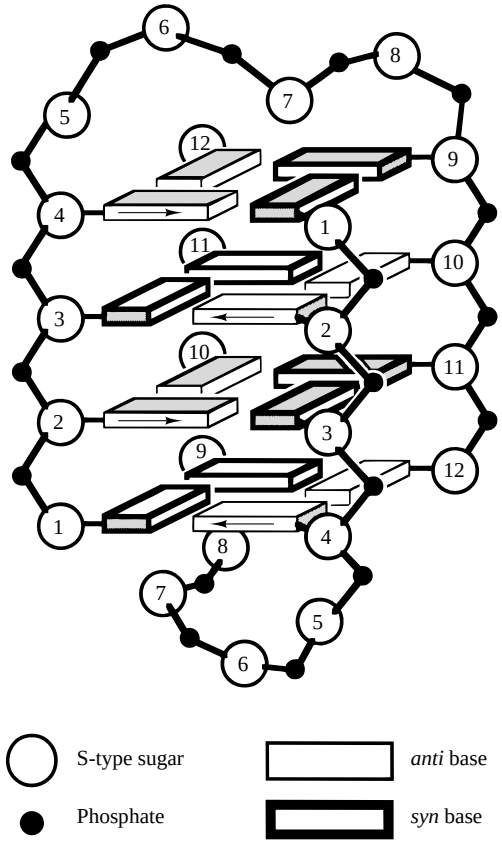

Figure 6 Schematic of the quadruplex structure of Oxy-1.5. (Adapted from J. Feigon, F. W. Smith, R. Macaya, and P. Schultze, 'DNA Quadruplexes: From Telomeres to Aptamers', ed. R. H. Sarma and M. H. Sarma, Adenine Press, Schenectady, NY, 1993, p. 127)

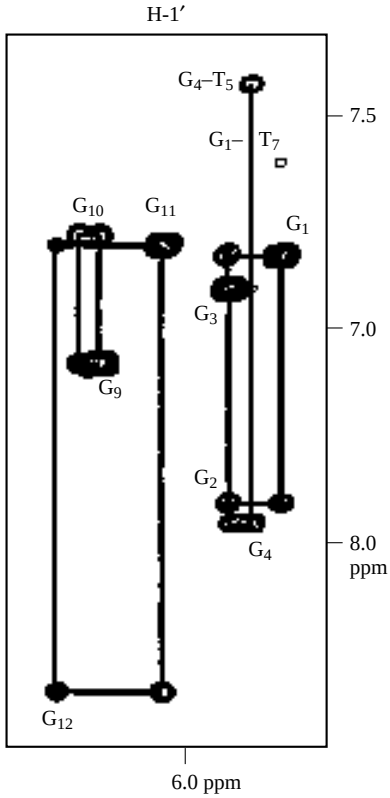

Figure 7 Portion of NOESY spectrum of Oxy-1.5 showing the cross peaks between the base and H-1′ proton resonances. Connectivities between pairs of *syn* and *anti* guanines are indicated by solid lines. (Adapted from F. W. Smith and J. Feigon, *Biochemistry*, 1993, **32**, 8682)

on the structures of DNA oligonucleotides which contain the telomere repeat sequence of various organisms. The first NMR evidence that such oligonucleotides formed an unusual structure was an investigation of oligonucleotides containing the *Tetrahymena* repeat $d(T_2G_4)$.[13] No assignments were made, but the authors were able to determine that some of the guanine nucleotides were *syn* on the basis of two-dimensional ^{1}H NMR spectra. NMR studies of $d(G_2T_4CG_2)$ and $d(G_2T_5G_2)$ indicated that the guanines were 5′-*syn*–*anti*-3′, but the molecularity of the structures formed was not established.[14,15] In 1992, Smith and Feigon[16] reported NMR studies of two DNA oligonucleotides containing the telomere repeat sequence $d(T_4G_4)$ from *Oxytricha nova*, $d(G_4T_4G_4)$ (Oxy-1.5) and $d(G_4T_4G_4T_4G_4T_4G_4)$ (Oxy-3.5). The oligonucleotides form a symmetrical dimeric (Figure 6) and a unimolecular quadruplex, respectively. Both structures have four guanine quartets formed from nucleotides that alternate *syn* and *anti* along each guanine tract. A model structure of Oxy-1.5 was refined with NOE constraints. This structure was subsequently refined from metric matrix distance geometry derived starting structures. A surprising feature of the solution structure is that the thymines looped diagonally across the end quartets, rather than across an edge. A concurrently published crystal structure of Oxy-1.5 had the thymines looping across a wide groove at each end of the quadruplex.[17] The different solution and crystal structures have been a source of some controversy. The solution structure has since been confirmed by several different methods, and it seems unlikely that it is in error. Another diagonally looped structure has recently been reported for the human telomere repeat oligonucleotide $d[AG_3(T_2AG_3)_3]$.[18] This unimolecular quadruplex has two edge loops at one end of the quadruplex and a diagonal loop at the other end, similar to Oxy-3.5.

Fold-back DNA quadruplexes have several unique ^{1}H NMR spectral features. Each guanine residue involved in quartet formation gives rise to a hydrogen-bonded imino proton resonance. These protons exchange with water unusually slowly and often can be observed long after the sample has been transferred to D_2O. The guanine quartet structure can be identified by a series of NOE cross peaks in NOESY spectra in H_2O between guanine imino, amino, and H-8 protons. Another unusual feature arises from the presence of *syn* nucleotides. This gives rise to a completely different pattern of NOE cross peaks between the base H-8/6 and deoxyribose H-1′ than seen for B-DNA, as illustrated for Oxy-1.5 in Figure 7. Since standard sequential assignments are not possible due to a break in connectivities between 5′ *anti* and 3′ *syn* nucleotides, alternative approaches must be used in making assignments. One useful method is the use of derivatives containing inosine in place of guanine. This allows unambiguous identification of

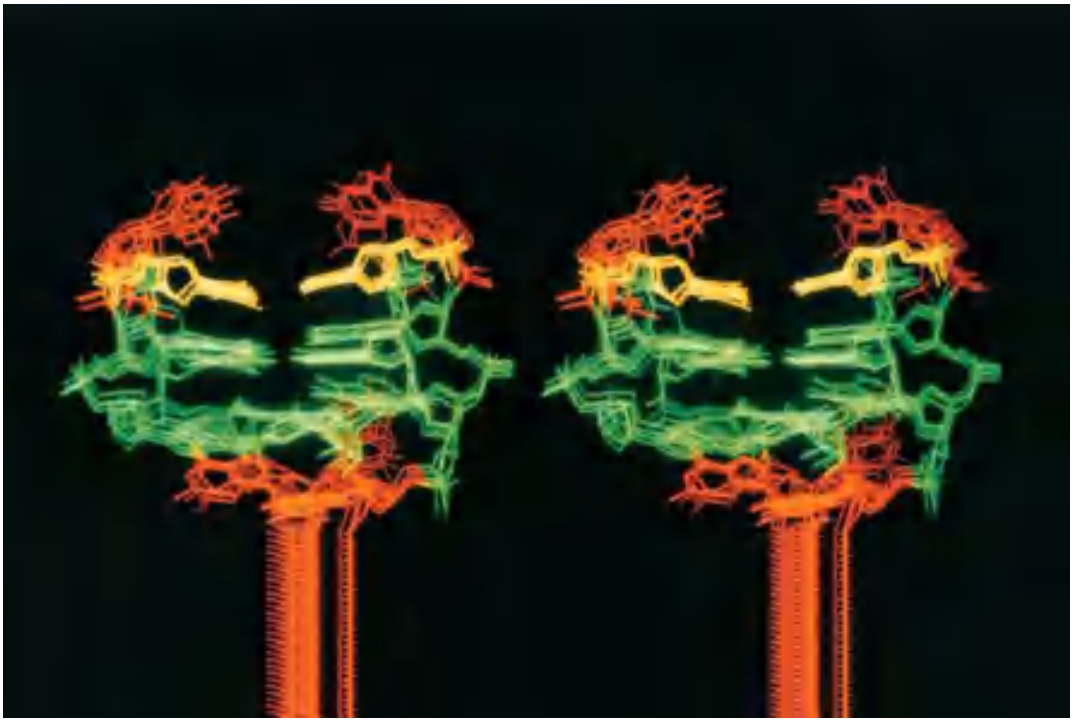

Figure 8 Three-dimensional structure of the thrombin-binding aptamer. A view into the wide groove is shown. The two guanine quartets are colored green, the conserved thymines that form a T·T base pair are colored yellow, and the non-conserved thymines (top) T-G-T loop (bottom) are colored red. The eight best (lowest energy) calculated structures are shown superimposed. (Adapted from Schultze et al.[26])

the inosine H-2 resonance, which replaces the guanine amino resonance.

A number of tetrameric quadruplexes have also been solved by NMR. These include quadruplexes formed by $d(T_2AG_3)$, $d(T_2G_4)$,[19] $d(TG_4T)$,[20] and $r(UG_4U)$.[21] These tetrameric quadruplexes have four parallel strands with all *anti* guanine nucleotides.

4 DNA APTAMERS

'Aptamer' is a name coined for DNA or RNA oligonucleotides which have been selected for binding to a specific target molecule from a large pool of oligonucleotides containing a region of random nucleotide sequence.[22] The isolation process involves repeated cycles of selection for, and enrichment of, oligonucleotides with an affinity to a specific target, followed by amplification of these sequences using the polymerase chain reaction (PCR). Oligonucleotides with the selected characteristics, i.e. binding to a specific molecule, are finally identified through cloning and sequencing. The potential of these methods for the development of oligonucleotide-based therapeutics has excited much interest in the pharmaceutical industry.

Aptamers present a special challenge both for NMR and from the nucleic acid structural point of view, since new folding motifs may appear from the in vitro selection. To date, the structure of only one (DNA) aptamer has been solved. DNA oligonucleotides were selected for the ability to bind to and inhibit thrombin, an essential protein in the blood-clotting cascade.[23] The particular thrombin-binding aptamer which has been studied by NMR has the sequence d(GGTTGGTGTGGTTGG). The overall fold of the molecule was determined independently by Wang et al.[24] and Macaya and co-workers[25,26] using two-dimensional ^{1}H methods. The thrombin-binding aptamer forms a unimolecular quadruplex containing two guanine quartets. These are connected by two T-T loops across the narrow groves at one end and a T-G-T loop across a wide groove at the other end of the mini-quadruple helix (Figure 8). The thrombin aptamer structure has been refined from metrix matrix distance geometry-generated starting structures using restrained molecular dynamics and direct NOE refinement.

5 RELATED ARTICLES

DNA: A-, B-, and Z-; DNA–Cation Interactions: Quadrupolar Studies; Nucleic Acid Flexibility and Dynamics: Deuterium NMR; Nucleic Acid Structures in Solution: Sequence Dependence; Nucleic Acids: Base Stacking and Base Pairing Interactions; Nucleic Acids: Chemical Shifts; Nucleic Acids: Phosphorus-31 NMR; Nucleic Acids: Spectra, Structures, and Dynamics; Ribosomal RNA; RNA Structure and Function: Modified Nucleosides.

6 REFERENCES

1. D. R. Kearns, D. J. Patel, and R. G. Shulman, *Nature (London)*, 1971, **229**, 338.
2. P. Rajagopal and J. Feigon, *Nature (London)*, 1989, **339**, 637.
3. V. Sklenář and J. Feigon, *Nature (London)*, 1990, **345**, 836.
4. R. F. Macaya, E. Wang, P. Schultze, V. Sklenář, and J. Feigon, *J. Mol. Biol.*, 1992, **225**, 755.

5. E. Wang, S. Malek, and J. Feigon, *Biochemistry*, 1992, **31**, 4838.
6. R. F. Macaya, D. E. Gilbert, S. Malek, J. S. Sinsheimer, and J. Feigon, *Science*, 1991, **254**, 270.
7. I. Radhakrishnan, X. Gao, C. de los Santos, D. Live, and D. J. Patel, *Biochemistry*, 1991, **30**, 9022.
8. I. Radhakrishnan and D. J. Patel, *Structure*, 1994, **2**, 17.
9. I. Radhakrishnan and D. J. Patel, *Structure*, 1993, **1**, 135.
10. S. Arnott and E. Selsing, *J. Mol. Biol.*, 1974, **88**, 509.
11. R. F. Macaya, P. Schultze, and J. Feigon, *J. Am. Chem. Soc.*, 1992, **114**, 781.
12. W. Guschlbauer, J.-F. Chantot, and D. Thiele, *J. Biomol. Struct. Dyn*., 1990, **8**, 491.
13. E. Henderson, C. C. Hardin, S. K. Walk, I. Tinoco Jr., and E. H. Blackburn, *Cell*, 1987, **51**, 899.
14. Y. Wang, R. Jin, B. Gaffney, R. A. Jones, and K. J. Breslauer, *Nucleic Acids Res*., 1991, **19**, 4619.
15. Y. Wang, C. de los Santos, X. Gao, K. Greene, D. Live, and D. J. Patel, *J. Mol. Biol*., 1991, **222**, 819.
16. F. W. Smith and J. Feigon, *Nature (London)*, 1992, **356**, 164.
17. C. Kang, X. Zhang, R. Ratliff, R. Moyzis, and A. Rich, *Nature (London)*, 1992, **356**, 126.
18. Y. Wang and D. J. Patel, *Structure*, 1993, **1**, 263.
19. Y. Wang and D. J. Patel, *Biochemistry*, 1992, **31**, 8112.
20. F. Aboul-ela, A. I. H. Murchie, and D. M. J. Lilley, *Nature (London)*, 1992, **360**, 280.
21. C. Cheong and P. B. Moore, *Biochemistry*, 1992, **31 8406**.
22. J. W. Szostak, *TIBS*, 1992, **17**, 89.
23. L. C. Bock, L. C. Griffin, J. A. Latham, E. H. Vermaas, and J. J. Toole, *Nature (London)*, 1992, **355**, 564.
24. K. Y. Wang, S. McCurdy, R. G. Shea, S. Swaminathan, and P. H. Bolton, *Biochemistry*, 1993, **32**, 1899.
25. R. F. Macaya, P. Schultze, F. W. Smith, J. A. Roe, and J. Feigon, *Proc. Natl. Acad. Sci. USA*, 1993, **90**, 3745.
26. P. Schultze, R. F. Macaya, and J. Feigon, *J. Mol. Biol*., 1994, **235**, 1532.

Biographical Sketch

Juli Feigon. *b* 1954. B.A. Occidental College, 1976; Ph.D., University of California, San Diego, 1982. Introduced to NMR by D. R. Kearns. Postdoctoral work at Massachusetts Institute of Technology, 1982–85 (with Alexander Rich). Professor of Chemistry and Biochemistry at University of California, Los Angeles, 1985–present. Approx. 50 publications. Research interest: nucleic acid structure and interactions with proteins and drugs, multidimensional, multinuclear MR spectroscopy for the study of macromolecular structure.

DNA: A-, B-, and Z-

David E. Wemmer
University of California, Berkeley, USA

1 Introduction 1
2 Basic Features of NMR Spectra of DNA 1
3 Assignments of DNA Spectra 2
4 Couplings and Conformation 4
5 Motion and Hydration 6
6 Summary 6
7 Related Articles 6
8 References 6

1 INTRODUCTION

There has been a long history of studying DNA with NMR techniques, most focusing on the proton and phosphorus resonances. In the earliest days, as with all biopolymers, resonance assignments were very difficult to establish, and only qualitative correlations with other types of data could be developed. However, with the development of higher field and two-dimensional spectroscopy came the ability to assign resonances rigorously and make more detailed studies of structure. Here studies of three forms of DNA, A, B, and Z, are described, with some historical perspective.

The original descriptors of 'A' and 'B' DNA came from fiber X-ray diffraction studies in which it was noted that the diffraction pattern changed in certain characteristic ways upon changes in hydration (controlled through relative humidity of the surroundings of the fiber) and salt.[1] At moderate levels of salt, the ordered pattern which formed first with increasing hydration (at least 4 water molecules per nucleotide for a double-helical form) was called the A-form, which converted spontaneously to B-form at higher hydration (about 20 water molecules per nucleotide when hydration is complete). These patterns formed for natural DNA and, with relatively little variation, for essentially all double stranded, complementary (G with C, and A with T) synthetic polymer DNAs. Of course such fiber diffraction data played a critical role in the development of the correct hydrogen bonded, duplex structure of DNA proposed by Watson and Crick.[2] Both of these forms correspond to right-handed helices, with slightly different repeats and local structure. Fairly detailed models were developed from the fiber data, eventually extended with single crystal data. The A- and B-forms differ in position of base pairs with respect to the helix axis, the tilt of the base pairs, and in the sugar conformation.

Later a new structure was found in single crystals grown of alternating $(C\text{-}G)_3$ sequences, in which the helix was left-handed and the repeating unit was a C-G repeat rather than a single nucleotide. This form was termed Z-DNA.[3] In addition to the change in handedness of the helix, there were also a number of other differences in local conformation relative to the A- and B-forms. A number of different experiments,[4] including NMR and circular dichroism, indicated that this form was also found in solution at very high salt concentrations or with addition of salt and alcohol, although these data were insufficient to characterize the form of the DNA unambiguously before the crystal structure was solved. Drawings of models for eight base pair sequences of the B-, A-, and Z-forms of DNA are shown in Figure 1. This highlights the fact that there are dramatic differences in overall helix morphology, in spite of the fact that the base pairing is the same in each case.

Although diffraction data provided information about fibers, and later single crystals of oligomers, an important question which remained was how well these crystalline forms represented what was present in solution. With quite a number of short oligomers (6 to 10 residues in length), crystal structures indicated that the DNA was in the A-conformation. Circular dichroism and qualitative NMR studies, however, seemed to indicate that the same oligomers were in the B-form in solution. An interesting case is a section of DNA recognized by the transcription factor TFIIIA. Since TFIIIA binds to both DNA and RNA, it was speculated (supported by some digestion and methylation experiments) that the DNA was A-form, at least when recognized.[5] Further support came from the fact that a nine base pair sequence containing this site crystallized in the A-form.[6] However, solution NMR experiments demonstrated clearly that this sequence is the unexceptional B-form DNA in solution.[7] It now appears that different parts of TFIIIA recognize DNA and RNA.

A major contribution of NMR has been to provide a method through which detailed characterization of the solution structure of DNA can be achieved. The solution conditions can be adjusted reasonably to approximate the conditions which the DNA experiences in vivo and hence may be better for understanding functions and interactions of the DNA than conditions used for crystallization. There are features of DNA which make structure determination more difficult than for typical globular proteins[8] (see ***Nucleic Acid Structures in Solution: Sequence Dependence***). However when care is used (see ***Relaxation Matrix Refinement of Nucleic Acids***), important structural information (especially about local structure) may be obtained.

2 BASIC FEATURES OF NMR SPECTRA OF DNA

The structures of the Watson–Crick base pairs of the four common natural nucleotides are shown in Figure 2. The protons can be logically grouped as those attached to nitrogen (exchangeable, disappearing rapidly in D_2O as solvent) and those attached to carbon (nonexchangeable), which are conveniently well dispersed in terms of their chemical shifts (see ***Nucleic Acids: Chemical Shifts***). The imino protons of G and T are convenient markers of hydrogen bonding since they occur one per base pair, and are strongly shifted to high frequency, typically being found in the 12–14 ppm range. If these protons are exposed to solvent water the exchange rate is sufficient to broaden them significantly (see ***Nucleic Acids: Base Stacking and Base Pairing Interactions***). However, when hydrogen bonded, the rate is dramatically slowed and the protons can be seen as sharp resonances, as in the high frequency (downfield) part of Figure 3. The amino protons of C, G, and A resonate in the 6.5–9 ppm range, overlapping the H-8 and H-6 aromatic protons of the bases. The A and G resonances are frequently very broad due to rotational

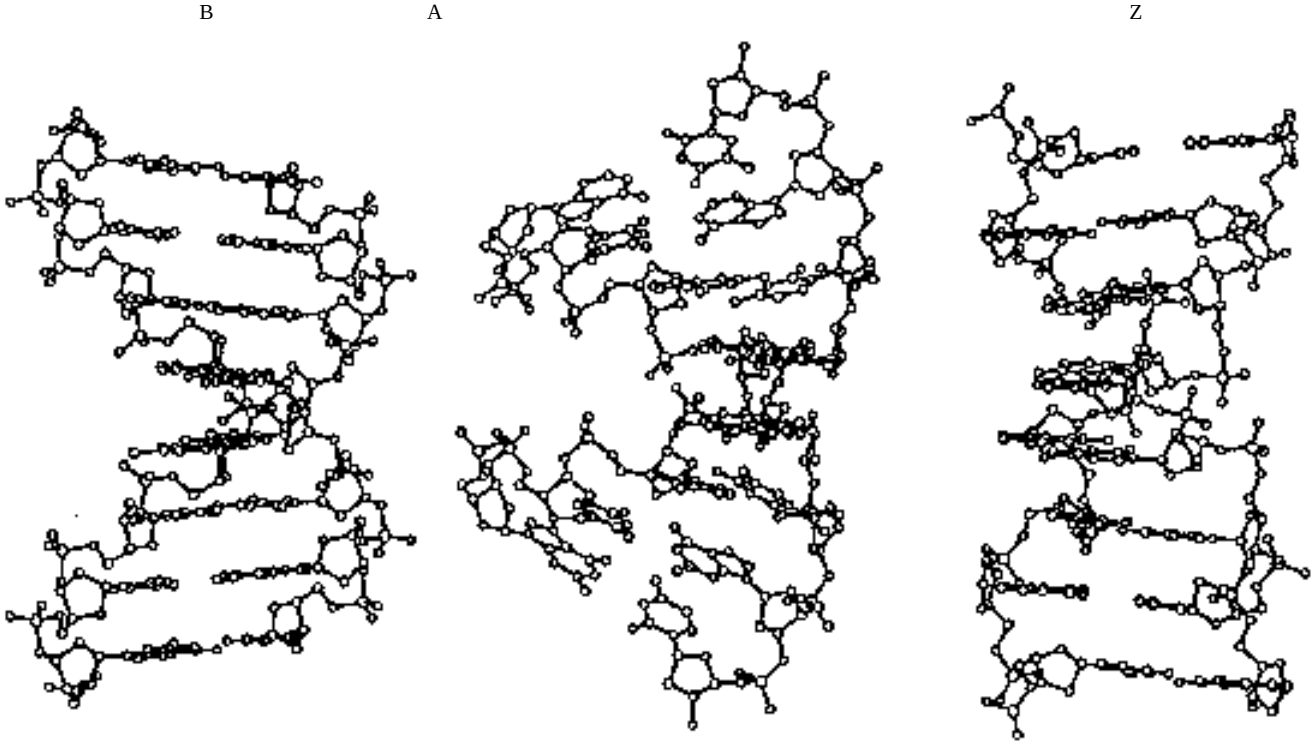

Figure 1 Eight base pair segments of the B-, A-, and Z-forms of DNA. Although the base pairing is the same in each, there are differences in stacking, backbone conformation and handedness of the helix (A- and B-forms right-handed, Z-form left-handed). Only the heavy atoms (C, N, O, and P) are shown

exchange between the hydrogen bonded and exposed positions. The peaks associated with the cytosine amino protons are slightly broadened, but not as greatly as those of A and G. The anomeric sugar protons, H-1′, and cytosine H-5 aromatic proton resonances overlap in the 5.5–6.5 ppm region. Sugar H-3′ resonances fall near the water resonance (4.5–5.2 ppm), with the H-4′, H-5′, and H-5″ resonances slightly further to low frequency (upfield) extending to about 4 ppm. The H-2′ and H-2″ resonances fall furthest to low frequency of the sugar resonances, at 1.8–3 ppm. At the low frequency end of the spectrum, the thymine methyl protons are found, in the 1.5–2 ppm region. Each of these regions is easy to identify in the spectrum shown in Figure 3.

3 ASSIGNMENTS OF DNA SPECTRA

The key to full interpretation of DNA solution structures is having complete resonance assignments. This can be done with different approaches, one based upon combining information from $^{1}H-^{1}H$ and $^{1}H-^{31}P$ couplings in COSY and HETCOR type experiments, and the other based upon ^{1}H COSY and NOESY data. The general ideas for these sequential assignment approaches were first developed for proteins,[9] but were extended to DNA by several workers at about the same time. In the coupling approach,[10] groups of coupled spins within each sugar are identified from the COSY (or TOCSY) data (up to seven if all can be resolved, numbered with respect to the attached carbon atom 1′ through 5′ as in Figure 1). Neighboring sugars are identified by the fact that their sugar protons (H-3′, H-4′, or H-5′,5″) are coupled to the same phosphate's ^{31}P resonance, identified in the HETCOR spectrum (see ***Nucleic Acids: Phosphorus-31 NMR***). Although this is a very good approach in principle,

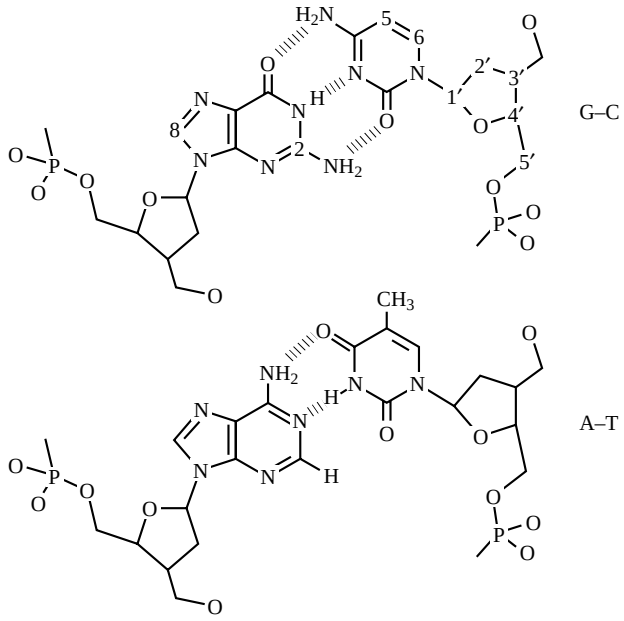

Figure 2 The structures of Watson–Crick base pairs, showing the numbering of some of the atoms indicated for reference to the text. Purines G and A are to the left, the pyrimidines C and T to the right. Hydrogen bonds are indicated by the dashed lines

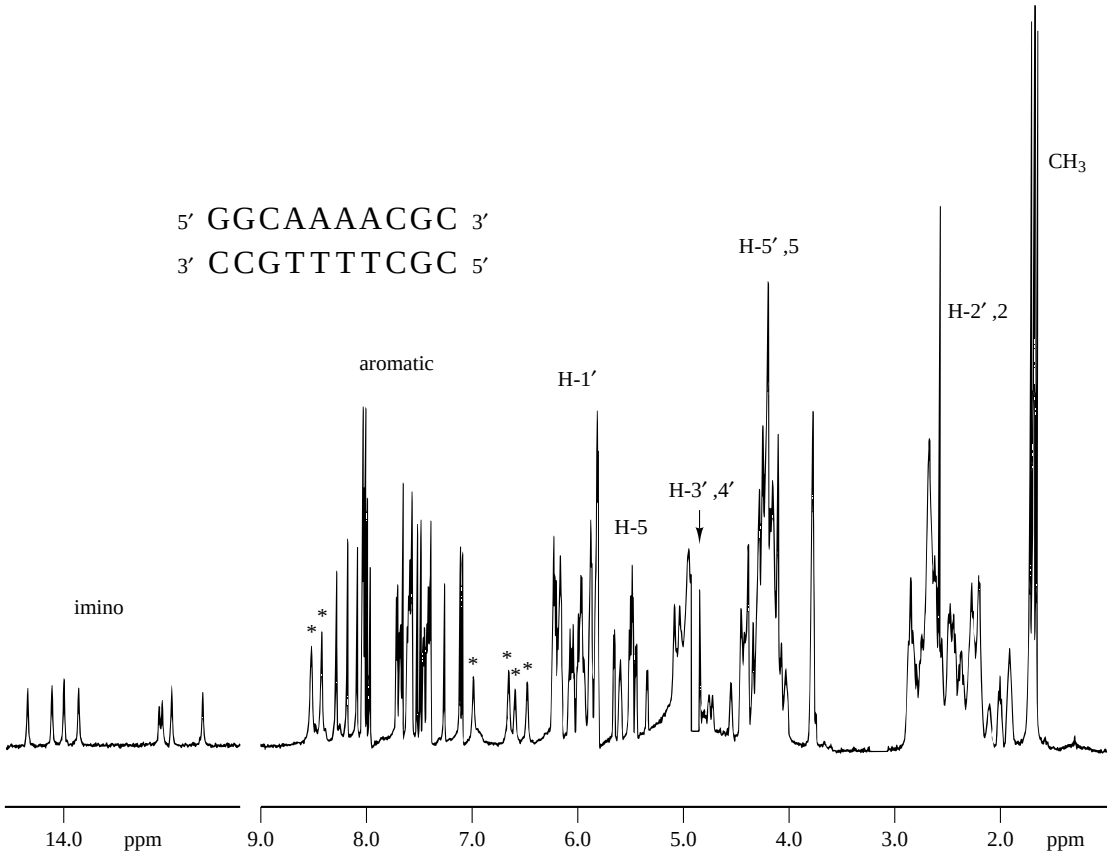

Figure 3 The one-dimensional ^{1}H NMR spectrum of the DNA oligomer CGCAAAAGGC:CGGTTTTGCG. The spectrum was acquired in H_2O solution with presaturation of the solvent water resonance. Protons resonating in various regions of the spectrum are indicated. *The amino resonances of cytosines

with no assumptions required about the structure, there are several technical problems: the heteronuclear couplings are rather small, and hence cross peaks become weak as the molecular weight increases; the couplings to the phosphate occur to the sugar H-3′ on one side, and the sugar H-4′, H-5′, and H-5″ on the other side, all of which occur in rather crowded regions; and, finally, the phosphate resonances are often also rather poorly dispersed in chemical shift. This last problem can be avoided by just using the ^{31}P to relay the proton couplings; however, crowding in the spectrum of the sugar protons is still a significant problem.

In the second approach,[11] the COSY (or TOCSY) data again serve to identify coupled groups of protons. In addition to those within the sugars, the H-5–H-6 pairing for each cytosine base, and the H-6–CH_3 pairing for each thymine can be seen. Guanine and adenine each give rise to singlets for the H-8 (G and A) and H-2 (A) resonances. NOESY cross peaks then provide information about the proximity of protons, and hence about which bases are neighbors in the sequence. It is a fortunate fact that most nucleic acid structures (and certainly the A-, B-, and Z-forms) are stabilized by base stacking. Hence the residues which are in closest proximity are neighbors in the primary sequence.

In the A- and B-forms the stacking is regular (about the same at each base step), and hence a regular pattern of cross peaks is seen in the NOESY spectrum. A section of a B-form helix is shown in Figure 4, in which lines are drawn from each aromatic proton to both its own sugar H-1′ and H-2′,2″, and also to the neighboring H-1′ and H-2′,2″. The distances are all within the range which gives rise to NOESY peaks (about 0.4 nm). Spin diffusion pathways contribute to the intensities of some of the peaks, but this does not confuse the assignments.

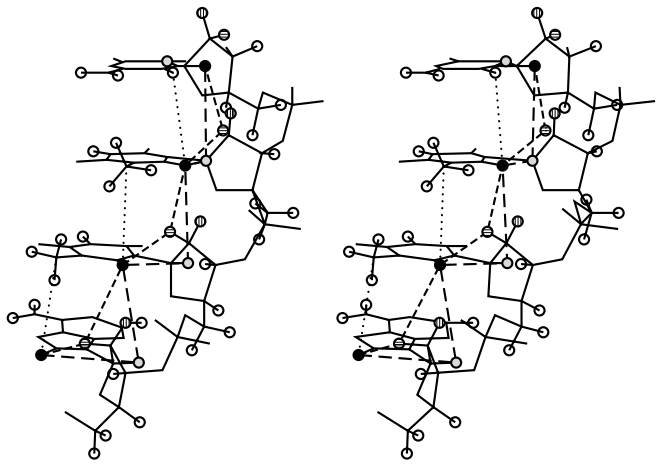

Figure 4 A four base segment of one strand of a B-DNA duplex is shown as a stereo pair (sequence 5′-ATTC-3′ running bottom to top). The connectivities which can be seen in different regions of the spectrum are indicated by dotted and dashed lines. Aromatic hydrogens are solid black, H-1 protons are gray and others connected by lines are H-2′, H-2″ protons. All hydrogens are indicated by circles

For steps with pyrimidines (C and T) there is an additional connectivity from the H-5 or CH_3 to the preceding aromatic proton, which is useful for verifying connectivities.

The expansions of these two NOESY regions are shown for a DNA duplex with 11 base pairs in Figure 5. The DNA sequence is not self-complementary, and hence each strand leads to a separate set of connectivities. Any degeneracies in resonances are resolved by identifying the type of base (T, C, or purine) from the COSY data, and knowing that the final assignments have to include all resonances and follow the known primary sequence of the DNA.

The patterns of the NOEs which are seen during the assignment in fact confirm that the DNA is in a right-handed helix. When the intensities of the NOEs within the sugars are analyzed, their patterns can be used to determine the sugar conformation as well (though this is often more easily done with couplings, as described below). Observation of both types of pattern for a particular DNA is a strong indication that the DNA is in a B-type conformation. The assignment process and qualitative NOE analysis are fairly simple for DNAs of up to about 20 base pairs (40 nucleotides). In fact, almost all duplex DNAs examined in water solution have been found to be in the B-form. For larger DNAs, more extensive coupling information from double quantum spectra is needed, but with the collection of many data sets it has even been possible to assign a 64 nucleotide Holiday junction,[12] comprising four DNA duplexes joined into a cross. This corresponds to a molecular weight of about 21 kDa.

There have been few studies of A-form DNA in solution.[13] This is primarily because dehydration is required (such as can be accomplished by addition of ethanol to the solution), but then the solubility of the DNA is very low. There are indications that polyvalent cations can also drive the B $\rightarrow$ A transition under conditions where NMR is practical.[14] In RNA the extra 2′-OH relative to DNA changes the conformational preference to the A-form under normal conditions. The pattern which would be expected for A-form DNA is actually rather similar to B-form, since both are right-handed helices, with base stacking. However, there are some differences in distances, making the sequential connectivities through H-1′ weaker. But, by using moderately long mixing times spin diffusion strengthens these, and the assignment pathways can be followed very much as in the B-form.

The patterns of the NOEs for Z-form DNA are quite different from those of the A- and B-forms due to the dinucleotide repeat, and the different stacking of the bases.[15] One dramatic difference is that the relative orientation of the sugar and purine bases [G residues in the classical $(C\text{-}G)_n$ sequences which take on the (*Z*) conformation] are *syn* rather than *anti*, as occurs in B-DNA. This reduces the H-1′–H-8 distance from about 0.37 nm (*anti*) to 0.24 nm (*syn*), giving much stronger and thus very characteristic H-8–H-1′ NOESY peaks. In steps from G to C there are a number of aromatic proton to sugar distances which are short enough to give rise to NOESY peaks, but in C to G steps the only protons which are close are the sugar H-4′, H-5′, and H-5″ protons. Since these occur in very crowded regions of the spectrum, they are not very useful for sequential assignments.

In an early study of $(m^5C\text{-}G)_3$, in which the methyl group on cytosine makes the transition occur at lower salt or added alcohol, advantage was taken of the ability to control the equilibrium.[14] A sample was titrated with methanol until about equal amounts of the B- (assigned with the sequential method described above) and Z-forms were present. Although the kinetics of this transition are slow, it was possible to use a very long mixing time in the NOESY experiment (1.4 s) to detect exchange cross peaks between the two conformers. Since the B-form was assigned, the assignments of the Z-form aromatic protons were then determined directly. The sugar resonances were then assigned primarily using intraresidue NOEs. It is interesting to note that the conformation of the phosphates in Z-DNA also alternate, which gives rise to a grouping in the ^{31}P chemical shift of the GpC versus CpG type phosphates.

The same principles were applied to a DNA oligomer *CG*CGAT*CG*CG, where *C is Br^5-C, which like the methyl modification facilitates the transition.[16] This sequence violates the alternating C-G (and even purine–pyrimidine) which favors Z-DNA formation, yet with addition of 3 M NaCl in 33% methanol clear changes in the spectrum were seen. It was found that a *Z* type conformation was found, with all of the Cs and the A in the *anti* conformation, but the Gs and the T were *syn*. The phosphates appear much as expected for an 'ordinary' Z-form oligomer. A similar phosphate pattern was also seen for longer polymers of $d(A\text{-}m^5C)\cdot d(G\text{-}T)$ at 5.4 M salt and 65°C, again indicating a *Z* type conformation.[17]

4 COUPLINGS AND CONFORMATION

Although the overall helical character of DNA is not strongly dependent on the local conformation at each nucleotide, there are correlations of local conformation with overall structure which makes identifiers of local conformation valuable. One of the most commonly used is the conformation of the sugar. The five-membered deoxyribose ring occurring in each residue of a DNA can take on many different conformations,[1] often called puckers. However, each of these has one or two atoms out of the plane of the ring (*endo* or *exo*, depending upon whether it is on the side from which the base and C-5′ protrude or the opposite side). The conformation of the sugar then really only has two free parameters: which atom(s) are out of the plane, and by how far. If the sugar ring is considered as a circle, then the atom lying out of the plane can also be described through an angle, known as the 'pseudorotation angle.' The distance the atom(s) are out of the plane is called the 'pucker amplitude'. Sugars with puckers near the top of the circle are also referred to as north, while those near the bottom are south.

B-Form DNAs typically have sugars near the C-2′ *endo* (south) conformation. Of course as the conformation of the sugar changes, so do the dihedral angles between protons and hence the coupling constants. Therefore, couplings provide a sensitive probe of the sugar conformation (see ***Vicinal Coupling Constants and Conformation of Biomolecules***), which can be determined from a number of variations of the COSY experiment.[18] The general pattern of which cross peaks are seen can often be a good qualitative indicator, requiring no detailed analysis. In the C-2′ *endo* conformation the coupling of H-1′ to both H-2′ and H-2″ is large enough to give a clear cross peak. However, the H-3′ coupling to H-2′ is very small, while H-3′ to H-2″ is moderate. Therefore, only the H-3′ to H-2″ cross peak is seen. Since the H-1′, H-2′, and H-2″ resonances are usually well resolved, this pattern of peaks can be identified fairly easily.

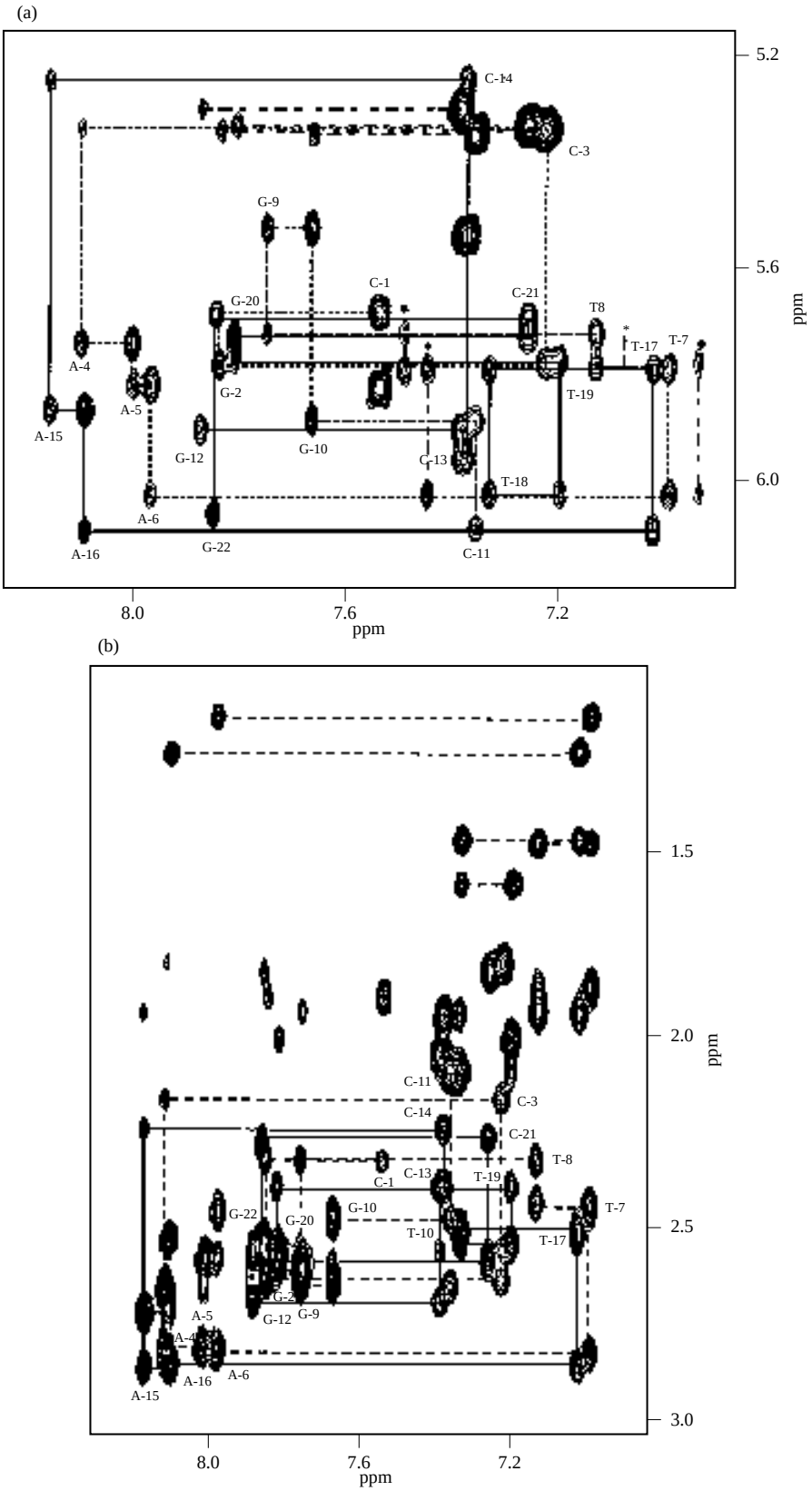

Figure 5 (a) The aromatic to H-1′ cross peak region of a NOESY spectrum of the DNA oligomer CGCAAATTGGC:GCCAATTTGCG. The spectrum was recorded in D_2O solution with a mixing time of 200 ms. (—, - - - -) The tracing of assignments along the two strands are shown with solid and dashed lines. The peaks which are intraresidue are labeled with the identity of the residue; sequential peaks are not labeled. The unconnected horizontal lines indicate connectivities involving the cytosine H-5 atoms. *Peaks and unconnected vertical lines involve the adenosine H-2 aromatic and H-1′ atoms from both strands. These are not used for assignments, and are typically seen only in A-rich sequences. (b) The aromatic to H-2′,H-2″ region of the same NOESY spectrum as in (a). The sequential connectivities are again indicated by solid and dashed lines. The intraresidue aromatic H-2″ peaks are labeled. The unconnected horizontal lines at the top are connectivities involving the thymine methyl protons

In the A-form conformation the typical sugar pucker is C-3′ *endo* (north). In this case the H-1′ to H-2′ coupling is very small, and the H-1′ to H-2″ coupling is moderate, so that only the latter cross peak is seen. On the other hand, the H-3′ couplings to both H-2′ and H-2″ are large enough to give clear cross peaks, again making a qualitative determination of the sugar conformation easy.

In Z-DNA there is an alternation of sugar conformation, with the G residues C-3′ *endo* and the C residues C-2′ *endo*. Of course, with residues assigned by NOEs it is possible to recognize this alternating conformation feature as another marker of Z-DNA.

5 MOTION AND HYDRATION

Solid state NMR has also played a role in understanding DNA structure and dynamics (for methods see ***Protein Dynamics from Solid State NMR***). As noted above, in solid samples the interconversion between A- and B-DNA can be controlled by hydration. Studies of the ^{31}P chemical shift anisotropy lineshape, and relaxation time have provided information about the range of motions of the phosphate in different forms of DNA.[19] It was found that narrowing occurred gradually with increasing hydration, with plateaus seen in the regions corresponding to A- and B-DNA. However, as hydration increased, there was a continuous increase in the amplitude of motion of the phosphate. Later, the same features were examined using selectively deuterated bases[20] and sugars,[21] with the quadrupole coupling tensor as the probe. Again, increasing hydration increased the amplitude of motion, although to a lesser extent than was seen for the phosphate. Ordered DNAs, such as fibers, can also be used for studies of hydration.[22]

Studies of hydration in solution have also been carried out, the first one being reported in 1954.[23] The broadening of the water resonance by DNA indicated interaction between them. Much later, site specific interactions were detected by using NOE data, with which more tightly bound water could be distinguished from loose surface water.[24] More studies of different sequences will certainly follow.

6 SUMMARY

More details on many aspects of structural and dynamic studies of DNA are given in other chapters of this Encyclopedia, as indicated at various points above. In this section the basics of DNA conformation have been described, together with the information about how resonances are assigned and what markers of conformational features exist in the NMR data. Local conformational features may be determined fairly directly; however, more global features are determined by complex combinations of different types of data. Because of the indirect nature of the structure analysis, and the fact that only local distances are determined from NOE data, one must be careful and critical about global features of the structures. In spite of the difficulties, NMR has been very useful in understanding solution structures of DNAs and the implications that the structures have for biological activity.

7 RELATED ARTICLES

Nucleic Acid Structures in Solution: Sequence Dependence; Nucleic Acids: Base Stacking and Base Pairing Interactions; Nucleic Acids: Chemical Shifts; Nucleic Acids: Phosphorus-31 NMR; Protein Dynamics from Solid State NMR; Relaxation Matrix Refinement of Nucleic Acids; Vicinal Coupling Constants and Conformation of Biomolecules.

8 REFERENCES

1. W. Saenger, *Principles of Nucleic Acid Structure*, Springer, New York, 1983.
2. J. D. Watson and F. H. C. Crick, *Nature*, 1953, **171**, 737.
3. A. H.-J. Wang, G. J. Quigley, F. J. Kolpak, J. L. Crawford, J. H. van Boom, G. van der Marel, and A. Rich, *Nature*, 1979, **282**, 680.
4. D. J. Patel, L. L. Canuel, and F. M. Pohl, *Proc. Natl. Acad. Sci. USA*, 1979, **76**, 2508; F. M. Pohl and T. M. Jovin, *J. Mol. Biol.*, 1972, **67**, 375; F. M. Pohl, *Nature*, 1976, **260**, 365.
5. D. Rhodes and A. Klug, *Cell*, 1986, **46**, 123.
6. M. McCall, T. Brown, W. N. Hunter, and O. Kennard, *Nature*, 1986, **322**, 661.
7. F. Aboul-ela, G. Varani, G. T. Walker, and I. Tinoco, Jr, *Nucleic Acid. Res.*, 1988, **16**, 3559.
8. D. E. Wemmer, *Curr. Opin. Struct. Biol.*, 1991, **1**, 452, and references therein.
9. K. Wüthrich, *NMR of Proteins and Nucleic Acids*, Wiley, New York, 1986.
10. A. Pardi, R. Walker, H. Rapoport, G. Wider, and K. Wüthrich, *J. Am. Chem. Soc.*, 1983, **105**, 1652; D. Marion and G. Lancelot, *Biochem. Biophys. Res. Commun.*, 1984, **124**, 774.
11. R. M. Scheek, N. Russo, R. Boelens, R. Kaptein, and J. H. van Boom, *J. Am. Chem. Soc.*, 1983, **105**, 2914; J. Feigon, W. Leupin, W. A. Denny, and D. R. Kearns, *Biochemistry*, 1983, **22**, 5943; D. R. Hare, D. E. Wemmer, S.-H. Chou, G. Drobny, and B. R. Reid, *J. Mol. Biol.*, 1983, **171**, 319.
12. S.-M. Chen, F. Heffron, W. Leupin, and W. J. Chazin, *Biochemistry*, 1991, **30**, 766.
13. J. Kypr, V. Sklenář, and M. Volíč-Ková, *Biopolymers*, 1986, **25**, 1803.
14. Q. Xu, R. K. Shoemaker, and W. H. Braunlin, *Biophys. J.*, 1993, **65**, 1039.
15. J. Feigon, A. H.-J. Wang, G. A. van der Marel, J. H. van Boom, and A. Rich, *Nucleic Acid. Res.*, 1984, **12**, 1243.
16. J. Feigon, A. H.-J. Wang, G. A. van der Marel, J. H. van Boom, and A. Rich, *Science*, 1985, **230**, 82.
17. L. P. McIntosh, I. Grieger, F. Eckstein, D. A. Zarling, J. H. van de Sande, and T. M. Jovin, *Nature*, 1983, **304**, 83.
18. H. Widmer and K. Wüthrich, *J. Magn. Reson.*, 1987, **74**, 316.
19. M. T. Mai, D. E. Wemmer, and O. Jardetzky, *J. Am. Chem. Soc.*, 1983, **105**, 7149.
20. A. Kintanar, W.-C. Huang, D. C. Schindele, D. E. Wemmer, and G. Drobny, *Biochemistry*, 1989, **28**, 282.
21. T. M. Alam, J. Orban, and G. P. Drobny, *Biochemistry*, 1991, **30**, 9229.
22. R. Brandes, A. Rupprecht, and D. R. Kearns, *Biophys. J.*, 1989, **56**, 683.
23. B. Jacobson, W. A. Anderson, and J. T. Arnold, *Nature*, 1954, **173**, 772.

24. M. G. Kubinec and D. E. Wemmer, *J. Am. Chem. Soc*., 1992, **114**, 8739; E. Liepinsh, G. Otting, and K. Wüthrich, *Nucleic Acid. Res.*, 1992, **20**, 6549.

Biographical Sketch

David E. Wemmer. *b* 1951. B.S., University of California at Davis, 1973; Ph.D., University of California at Berkeley, 1979. Introduced to NMR by G. N. LaMar and A. Pines. Faculty in Chemistry, University of California at Berkeley 1985–present. Approx. 100 publications. Research interests include understanding structure–function relationships in biological molecules, and applications of NMR in biomolecular structure studies.

DNA–Cation Interactions: Quadrupolar Studies

Veronica M. Stein, Laura A. Wright, Charles F. Anderson and M. Thomas Record, Jr

University of Wisconsin Madison, USA

1 Introduction 1
2 The Composition Dependence of Quadrupolar Relaxation Rates 3
3 Survey of Experimental Results on Cation–DNA Interactions 5
4 Additional Methods of Studying Cation–DNA Interactions 8

1 INTRODUCTION

The thermodynamic and molecular properties of polyelectrolytes in solution depend strongly on the amount of added salt. In particular, the conformational transitions and binding interactions of nucleic acids in aqueous solution exhibit pronounced dependences on salt concentration, which result from Coulombic interactions between electrolyte ions and the phosphate charges on the nucleic acid (for early but comprehensive reviews see Manning[1] and Record et al.[2]). Information about ion–nucleic acid interactions is therefore a crucial component of any quantitative description of the conformational transitions of nucleic acids and of their interactions with other biopolymers. On the molecular level, the measurement of NMR relaxation rates for the quadrupolar nuclei of alkali and alkaline earth ions has emerged as a useful experimental method for studying the equilibrium and dynamic aspects of cations interacting with DNA. Several reviews are available.[3–6] The present article is focused primarily on the use of NMR relaxation rates of quadrupolar nuclei to investigate the extent of association of one or more types of cation with DNA in solutions dilute enough to be isotropic.

Fundamentals of the NMR relaxation processes of quadrupolar ions, the physical variables, and the types of information that can be gained by measuring them, are reviewed in the remainder of this section. In the second section we discuss the two state model, which provides a basis for analyzing the concentration dependence of relaxation rates in order to investigate the distribution(s) of cations surrounding DNA. Experimental studies using the NMR relaxation rates of quadrupolar nuclei to investigate cation–DNA interactions are reviewed in the third section, and the fourth summarizes some less common NMR approaches and alternatives to NMR as a means of probing various aspects of cation–DNA interactions.

1.1 Fundamentals of the Quadrupolar Relaxation Process

All the inorganic (K^+, Na^+, Mg^{2+}, and Ca^{2+}) and organic (polyamines) cations present at significant concentrations in vivo, as well as all other alkali and alkaline earth metal ions and quaternary ammonium ions, have isotopes with nuclear spins (I) greater than $\frac{1}{2}$. Specifically, $I = 1$ for ^{14}N, $\frac{3}{2}$ for ^{23}Na and ^{39}K, $\frac{5}{2}$ for ^{25}Mg, and $\frac{7}{2}$ for ^{43}Ca. The nuclei of these cations have quadrupole moments which dominate the relaxation of the nuclear magnetic dipole by coupling with the fluctuating electric field gradients (EFGs) produced by diffusional motions in the local environment. In aqueous solution the quadrupolar relaxation of monatomic ions such as ^{23}Na is due to intermolecular field gradients caused by surrounding ions and water dipoles, in contrast to the (generally much stronger) intramolecular field gradient experienced by a quadrupolar nucleus involved in covalent bonding (such as ^{14}N in CN^-).

In dilute solutions of biopolymers, the NMR relaxation processes of quadrupolar cations are in the 'extreme narrowing' limit when $\omega_0\tau_c \ll 1$, where ω_0 is the nuclear Larmor frequency and τ_c is the (mean) correlation time for the fluctuations of the EFG at the nucleus. Under conditions of extreme narrowing (at low enough magnetic fields and/or high enough temperature) the longitudinal and transverse NMR relaxation processes both decay as single exponential functions of time with the same rate constant:[7]

$$R_1 = R_2 = \frac{3}{40}\left[\frac{(2I+3)}{I^2(2I-1)}\right]\left[1+\frac{\eta^2}{3}\right]\chi^2\tau_c \qquad (1)$$

where R_1 and R_2 are the longitudinal and transverse relaxation rates, respectively; I is the nuclear spin quantum number; χ is the quadrupole coupling constant, which is the product of ($\langle eq \rangle$), the mean square average local EFG and (eQ), the nuclear quadrupole moment; and η is the asymmetry parameter, which is generally zero for nuclei that experience intermolecular field gradients in isotropic environments. In the limit of extreme narrowing, for any type of quadrupolar nucleus the NMR relaxation process (longitudinal or transverse) is a single exponential with a rate constant that does not depend on ω_0. The Fourier-transformed NMR lineshape is a single Lorentzian with a linewidth at half height $\Delta\nu_{\frac{1}{2}}$ (in hertz), from which the transverse relaxation rate constant can be determined directly with the expression $R_2 = \pi\Delta\nu_{\frac{1}{2}}$.

When $\omega_0\tau_c$ is not negligible in comparison to unity, the transverse and longitudinal relaxation processes are no longer equivalent, and the functional forms of their time dependences depend critically on the magnitude of I, as well as that of $\omega_0\tau_c$. Outside the limit of extreme narrowing, the dependence of R_1 and of R_2 on χ^2 and τ_c becomes more complicated than in equation (1), and in some situations explicit analytic expressions for the relaxation processes cannot be given. When $\omega_0\tau_c$ is much greater than unity, the quadrupolar relaxation is in the slow motion regime, where various manifestations of quadrupolar splitting may be observed.[8] At sufficiently high concentrations (high fields and/or low temperatures), slow motion effects may be manifested by quadrupolar nuclei in solutions of nucleic acids. Some studies of these effects are considered in Section 3.4, but the rest of this article is concerned with NMR relaxation subject to the condition of 'motional narrowing' (that is, outside the 'slow motion' limit).

Outside the limit of extreme narrowing for nuclei with spin $I = 1$ (e.g. ^{14}N) both the transverse and the longitudinal relaxation process are single exponential functions with different characteristic time constants at all field strengths.[7] For nuclei with spin $I = \frac{3}{2}$ (e.g. ^{23}Na or ^{39}K), an analogous

situation exists only up to $\omega_0\tau_c \approx 1.5$,[9] beyond which the transverse and (at least in principle) the longitudinal relaxation process become biexponential, each with two distinct rate constants. For this case the general relaxation equation may be found in Hubbard's original article.[7] The Fourier transformation of this biexponential transverse relaxation process yields a spectrum in the frequency domain that consists of two Lorentzians whose peaks coincide or are separated by a (generally) small dynamic shift. The linewidth at halfheight of this bi-Lorentzian spectrum bears no simple relationship to either of the two relaxation rate constants. Evaluation of these can be accomplished only by deconvoluting the full lineshape. For nuclei with $I > \frac{3}{2}$ the time dependence of the magnetization cannot be expressed in a closed form outside the extreme narrowing limit.[7] However, as shown by Westlund and Wennerström,[10] analytic expressions for the Fourier-transformed spectrum in the frequency domain can be derived for nuclei with $I > \frac{3}{2}$. A recent example of the use of these equations to analyze the lineshape of ^{25}Mg in DNA solutions has been reported by Wright and Lerner.[11]

When the NMR relaxation processes of quadrupolar nuclei are outside the limit of extreme narrowing at a given composition and temperature, a study of the dependence of the relaxation processes on magnetic field strength can in favorable cases permit separate evaluation of the factors χ^2 and τ_c that comprise R_1 and R_2. Such an analysis is generally based on an assumed form of the correlation function that describes the modulation of the local EFG by various kinds of diffusional molecular motions. Often the quadrupolar correlation function is taken to be a single exponential, the simplest form that may be physically realistic. However, in the case of DNA solutions, Leyte and co-workers[12] have definitively shown that the quadrupolar correlation function is biexponential, consisting of a linear superposition of contributions from a 'slow' process (outside the limit of extreme narrowing at typical field strengths) and a 'fast' process that may be due primarily to interactions with water dipoles.

Correlation times and quadrupolar coupling constants can be evaluated by various methods in addition to determining the field dependence of relaxation rate(s). For nuclei having $I = 1$, or $I = \frac{3}{2}$ provided $\omega_0\tau_c < 1.5$, separate determinations of R_1 and R_2 at one field strength may suffice to evaluate τ_c if the correlation function is a single exponential. Recently, more sophisticated methods have been developed to detect multiple quantum transitions that contain information about the spectral densities from which the form(s) of the correlation function(s) can be investigated.[13,14]

1.2 Overview of the Relaxation Characteristics of Quadrupolar Nuclei

The ease with which quadrupolar lineshapes and relaxation rates can be measured for cations in solutions containing polyions depends primarily on the natural abundance of the NMR active isotope and on its gyromagnetic ratio γ. One of the most common intracellular cations is K^+. Although the NMR nucleus ^{39}K ($I = \frac{3}{2}$) has a substantial natural abundance (93.1%), its small magnetogyric ratio makes it relatively difficult to detect accurately. At magnetic field strengths presently available, however, ^{39}K can be studied accurately at concentration levels as low as 1 mM, which has enabled some direct observations of intracellular ^{39}K.[15] In most intracellular environments, Na^+ is present at much lower concentration than K^+, but since ^{23}Na ($I = \frac{3}{2}$) has 100% natural abundance and its gyromagnetic ratio is more than five times larger than that of ^{39}K, it is more readily detectable at a given concentration. Other quadrupolar cations found in vivo, such as ^{25}Mg ($I = \frac{5}{2}$) and ^{43}Ca ($I = \frac{7}{2}$), have both low natural isotopic abundances (10% and 0.145%, respectively) and low magnetogyric ratios. (For ^{43}Ca the exceptionally small quadrupole moment further complicates accurate measurements of its NMR relaxation rates.)

Quantitative as well as qualitative information on cation–DNA interactions has been obtained by analyzing the dependence of cation relaxation rates on cation concentration, DNA phosphate concentration, temperature, and magnetic field strength. Since ^{23}Na is the most 'sensitive' (in the NMR context) of the quadrupolar nuclei typically found in vivo, it has been the most extensively investigated. ^{23}Na is used either as a direct probe of sodium–DNA interactions, or in competition experiments, as an indirect probe of the interactions of other monovalent and oligovalent cations (including Mg^{2+}, Ca^{2+}, and polyamines) with DNA.[12,16–35]

Under most conditions for quadrupolar nuclei other than ^{23}Na there are serious difficulties arising from low NMR sensitivity and/or complications associated with describing the relaxation processes. Increasing the field strength tends to alleviate problems of low NMR sensitivity, but if the field strength is high enough to take the relaxation out of the extreme narrowing limit, considerable complexity in the relaxation process can result for nuclei having $I > \frac{3}{2}$. Nevertheless, the following quadrupolar nuclei have been used as informative NMR probes: the alkali metal nuclei ^{39}K, ^{87}Rb, ^{133}Cs, and ^{7}Li;[30,31,36–38] the alkaline earth nuclei ^{43}Ca and ^{25}Mg;[11,21, 39–44] ^{59}Co in $Co(NH_3)_6^{3+}$;[20,21,45,75] and ^{14}N in polyamines.[28,29]

Figure 1 summarizes results of competitive titrations of NaDNA ([P] = 15 mM; $[Na^+]/[P]$ = 1.6) with salts of various

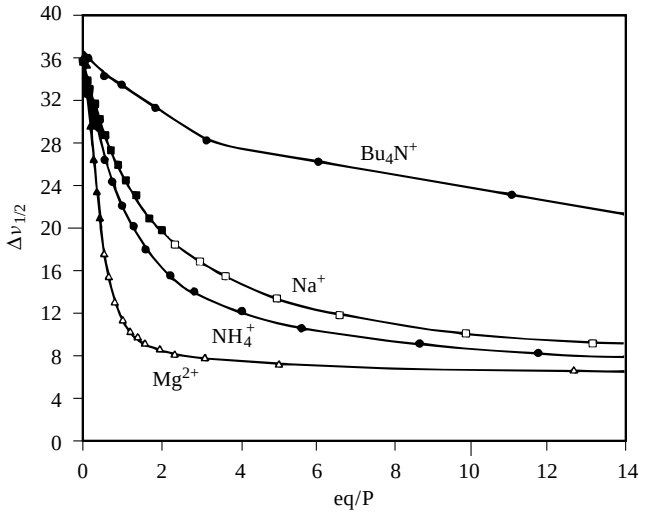

Figure 1 Representative plots of ^{23}Na NMR linewidths ($\Delta\nu_{\frac{1}{2}}$) in calf thymus NaDNA solutions (0.015 M in DNA phosphate) as a function of the ratio of equivalents of added salt to DNA phosphate (eq/P). (Reproduced with permission of the National Academy of Sciences, USA, from Bleam et al.[17])

cations.[17] In this study (at relatively low magnetic field) the lineshapes are in each case single Lorentzians, implying the 'extreme narrowing' limit. Therefore, transverse relaxation rates, R_2 can be obtained directly from measurements of linewidths at half height ($\Delta\nu_{\frac{1}{2}}$). The initial ^{23}Na linewidth (36 Hz for $\Delta\nu_{\frac{1}{2}}$, or 113 s^{-1} for the transverse relaxation rate) is significantly enhanced compared with the linewidth of Na^+ in aqueous NaCl solution without DNA (approximately 6 Hz or 18 s^{-1}). As additional cations (either Na^+ or competitive cations) are added to the NaDNA solution, the observed ^{23}Na linewidth decreases and eventually approaches the linewidth of Na^+ in a NaCl solution. Quantitative information regarding cation–DNA interactions is obtainable from analysis of these titrations of NaDNA with Na^+ and other cations. In particular, the noncompetitive Na^+ titration indicates that the extent of accumulation of Na^+ in the vicinity of DNA is relatively insensitive to NaCl concentration. The competitive titrations indicate that the order of cation affinities for DNA is $Mg^{2+} > NH_4^+ > Na^+ > Bu_4N^+$. The extent of Na^+ accumulation and the relative affinities of other cations have been quantified on the basis of model assumptions, as described in the following section.

2 THE COMPOSITION DEPENDENCE OF QUADRUPOLAR RELAXATION RATES

2.1 Fundamentals of the Two State Model for Quadrupolar NMR Relaxation Rates

In systems where two or more magnetically distinguishable states are accessible to nuclei whose rate(s) of exchange among these states greatly exceed(s) their NMR relaxation rates in any state, the observable NMR relaxation rate is the population-weighted average of the relaxation rates characteristic of the individual states. Although there can be complicating effects for quadrupolar nuclei due to the interplay of dynamic frequency shifts with the exchange and relaxation rates,[10] a decrease in relaxation rates with increasing temperature often suffices to demonstrate that quadrupolar nuclei are in fast exchange on the NMR timescale. The NMR relaxation process may begin to manifest effects of 'slow exchange', especially for cations of charge higher than one and in solvents other than pure water. In the (rare) situations where the NMR relaxation is governed entirely by slow exchange, the observed NMR relaxation rate constant is related simply to the kinetic rate constant for the exchange process. With a few exceptions,[11,39] in this article we consider only systems where the effects of slow exchange (if any) can be neglected for the purpose of analyzing the concentration dependence of NMR relaxation rates.

From the standpoint of describing the NMR relaxation of rapidly exchanging cations in a nucleic acid solution, they can be classified as either 'bound' or 'free' by their proximity to a molecule of nucleic acid. The 'free' state consists of those ions that are far enough removed from the vicinity of any DNA molecule that their relaxation rates are not significantly perturbed by the presence of DNA in solution. Generally, R_F^M is equated to the relaxation rate observed in an aqueous solution containing no polyelectrolyte. The term 'bound', defined empirically by the effects of DNA on the quadrupolar relaxation rates (χ and/or τ_c) of nearby nuclei, does not necessarily imply a specifically localized long-lived complex with any particular site on DNA. The two state model has been used to analyze relaxation data for many types of cation in DNA solutions (^{23}Na, ^{39}K, ^{87}Rb, ^{133}Cs, and ^{14}N in hexamethonium and ^{43}Ca).[16,18,20,21,26,29,32,36,37]

For nuclei undergoing rapid exchange between these 'bound' and 'free' states, the observed relaxation rate can be described as a population-weighted average of the relaxation rates in the two states:

$$R_{obs}^M = p_F^M R_F^M + p_B^M R_B^M \tag{2}$$

where R_{obs}^M denotes the observed transverse (R_2) or longitudinal (R_1) relaxation rate of the cationic nucleus M; R_B^M is the (average) relaxation rate characteristic of the fraction of the total population of M^{x+} ions that are in the 'bound' state (p_B^M); and R_F^M characterizes the fraction of nuclei in the 'free' state (p_F^M). Equation (2) can be rewritten to emphasize the dependence of R_{obs}^M on the extent of binding of the ion bearing the nucleus whose relaxation rate is being observed:

$$R_{obs}^M = R_F^M + p_B^M(R_B^M - R_F^M) \tag{3}$$

It proves convenient to express p_B^M as $[P]r_M/z[M^{x+}]$, where r_M is the fraction of the DNA phosphates that are, in effect, neutralized by the complement of M that are bound by the NMR criterion. Introducing this definition into equation (3) yields:

$$R_{obs}^M = R_F^M + r_M(R_B^M - R_F^M)\frac{[P]}{x[M^{x+}]} \tag{4}$$

The effects of proximity to the surface of DNA on the relaxation of individual cationic nuclei may be manifested as an enhancement of their coupling constant(s) and/or their correlation time(s). In general, the bound relaxation R_B may be an average over a diverse set of environments that are, in principle, magnetically distinguishable. However, R_B often appears to be invariant to changes in the composition of the solution. Thus, in this situation consideration of a single (average) bound state suffices, and detailed information about the distribution of nuclei among the various bound states that differ magnetically cannot be elicited from the composition dependence of quadrupolar NMR relaxation rates. In fact, an unequivocal separation of even the single averaged quantity R_B from composition variables is rarely possible. Moreover, there is as yet no completely reliable a priori theoretical means of predicting absolute values of R_B under typical conditions of interest, though progress toward this important goal continues to be made.[46] Despite the limitations imposed at present by these experimental and theoretical considerations, much has been learned from studies of the composition dependences of quadrupolar NMR relaxation rates. Studies of this type are the primary concern of this article.

2.2 Noncompetitive Titrations

In solutions containing only one type of counterion M^{x+}, titrations of DNA with M^{x+} yield plots of R_{obs}^{M} versus $[P]/z[M^{x+}]$ that, within uncertainty limits, are linear with an extrapolated y intercept equal to the free relaxation rate R_F^M. The product $r_M(R_B^M - R_F^M)$ must therefore be constant. Insufficient information is available from any noncompetitive titration to determine the individual parameters r_M and R_B^M. These parameters must either remain individually constant, or vary in a compensatory manner, as $[P]/z[M^{x+}]$ changes. The latter alternative is made less likely by the observation of linear noncompetitive titration plots for a variety of cationic nuclei (including both univalent and divalent ions) in DNA solutions.[12,16,18,19,27,32,36,37] The physical factors that could impart a concentration dependence to r and R_B are interrelated, and for univalent ions some degree of compensation may be expected on theoretical grounds.[47,48]

2.3 Competitive Titrations

Competitive titrations can be analyzed, on the basis of some additional assumptions, in order to separate the terms r_M and R_B from the product $r_M(R_B^M - R_F^M)$ which can be evaluated from a noncompetitive titration. In DNA solutions containing more than one type of cation, the ion exchange process can be analyzed using the two state model by introduction of two additional composition-independent parameters: an ion-exchange affinity coefficient D_m, and a stoichiometric coefficient n.[16,17,29] The dimensionless ion-exchange parameter D_m is defined as:

$$D_m = (p_B^L)(p_F^M)^n/(p_F^L)(p_B^M)^n \quad (5)$$

where p_B^L is the fraction of competitive ions (L^{z+}) that are in the 'bound' state, and $p_F^L = 1 - p_B^L$. In comparing two different competitors, the one having the larger value of D_m as defined by equation (5) has the larger affinity (relative to M) for DNA. By assumption, the stoichiometric coefficient, n in equation (5) also characterizes the cumulative displacement of M^{x+} by L^{z+}; this is expressed as:

$$n = (r_M^o[P] - [M^{x+}]_B)/[L^{z+}]_B \quad (6)$$

The larger the value of n, the more effective is L^{z+} in displacing M^{x+} from DNA. To prevent depleting the total amount of positive charge due to small mobile ions near DNA, n must be less than or equal to $[z/x]$. Provided that the binding of the competitive ion does not cause any significant long range alterations in the charge density of the nucleic acid, this upper bound is plausible.

According to the two state model for the competitive titration, the observed relaxation rate can be expressed by combining equations (2) and (6):

$$R_{obs}^M = R_F^M + (r_M^o - np_B^L[L^{z+}]/[P])(R_B^M - R_F^M)\frac{[P]}{[M^{x+}]} \quad (7)$$

where $p_B^L = [L^{z+}]_B/[L^{z+}]$ is implicitly defined in equation (5),[18] and $r_M{}^o$ is the extent of association of M^{x+} (usually Na^+) in the absence of L^{z+}. The superscript 'o' designates the initial state before the addition of another type of cation.

In analyzing a complete titration curve according to the equations specified above, a constraint can be placed on the number of parameters by fitting the initial linear region, which in most cases ranges over $0 < [L^{z+}]/[P] < 0.1$. The quotient r_M^o/n can be determined as the ratio of the slope to the intercept of the initial linear portion of the titration curve (if initially $p_B^L = 1$). Then, r_M^o can be calculated assuming $n = z$, which is the maximum number of M^{x+} that can be displaced by the competitive cation M^{+1}, without depleting the number of positive charges in the vicinity of the polyion.

2.4 Physical Interpretation of the Bound State

Although the two state model stipulates that each observable NMR relaxation rate is a population-weighted average of 'bound' and 'free' states, no particular physical interpretation of these states is implied by the model. Both polyelectrolyte theory and mass action models of ligand–DNA binding have been used to interpret the 'bound' and 'free' states.

The mass action model describes the exchange of cations between occupied and unoccupied 'sites' on the polyion as an equilibrium:

$$M_F + S_F \quad MS \quad (8)$$

where $[M_F]$ and $[S_F]$ are the concentrations of the 'free' ions and available 'sites', respectively, and [MS] is the concentration of occupied 'sites' ('bound' ions). The equilibrium quotient pertaining to equation (8) is defined as:

$$K_{eq} = \frac{[MS]}{[M_F][S_F]} \quad (9)$$

The mass action equation [equation (9)], in conjunction with the two state model has been solved either by estimating [MS] at each point of a titration and using an iterative procedure to solve for K_{eq} or by taking the limit of $[S_T] \ll [M_T]$ to simplify the solution for K_{eq}.[30,49]

Other analytical approaches used to describe the 'bound' and 'free' states are given by two theories applicable to cylindrical polyelectrolytes: Manning's counterion condensation (CC) model, and the Poisson–Boltzmann (PB) equation. Both of these theoretical approaches specify a dimensionless parameter to define the average axial charge density:

$$\xi = e^2/\epsilon kTb \quad (10)$$

where ϵ is the dielectric constant of pure solvent, b is the average axial distance between phosphate groups, e is the electronic charge, k is the Boltzmann constant, and T is the absolute temperature.

Manning's counterion condensation theory, applied to a polyion with $\xi > 1$, predicts that the concentration of ions within a well-defined annular volume surrounding the polyion is high and only weakly variable with salt concentration.[50] Specifically, for a DNA solution containing only univalent cations, the extent of condensation binding per phosphate is predicted to be $1 - \xi^{-1}$ (0.76 for helical NaDNA in H_2O at 25°C). The concentration of 'territorially bound' counterions

in the condensation layer is predicted to be independent of changes in the bulk salt concentration up to about 0.1 M. For bulk electrolyte concentrations above 0.1 M, the local surface concentration increases as the bulk salt concentration increases up to about 1 M, where they approach each other.

PB theory assumes that the local ion gradients surrounding a cylindrically symmetric highly charged polyion can be described as a continuous function given by a Boltzmann factor in the mean electrostatic potential energy (see for example, Fuoss et al.[51]). According to solutions of the cylindrical PB equation, a high (>2 M) local concentration of cations exists at the surface of double-helical DNA, and decreases radially to the bulk electrolyte concentration. The volume of solution surrounding DNA does not completely exclude co-ions (as in the CC model), but their local concentration is predicted to be much lower than in the bulk solution. PB theory predicts that the concentration of cations at the surface of the DNA polyanion is buffered against changes in the bulk electrolyte concentration, but that the local concentrations of both cations and anions increase significantly with increasing electrolyte concentration in the typical experimental range.[52]

Both CC and PB theories are based on the same model of the polyelectrolyte solution, but incorporate different assumptions and approximations. Monte Carlo (MC) simulations provide a means of testing the various model assumptions.[52–55] For a simple 'primitive' model, which represents the DNA as a rigid uniformly charged impenetrable cylinder and the cations as hard spheres, MC simulations have been used to calculate the radial distribution functions of small ions.[52–55] For monatomic ions with hydrated radii in the usual (∼0.3 nm) range, MC simulations yield ion distributions which agree with the corresponding predictions of PB theory.

The relative affinities of the univalent cations for DNA that have been quantified by means of ^{23}Na NMR[17] have been accounted for theoretically by means of MC simulations.[55] For divalent alkaline earth ions, interactions with DNA in addition to the Coulombic interactions described by the primitive model appear necessary to account for the initial region of a competitive titration curve, but for some methylated polyamines the agreement with theoretical prediction is satisfactory.[27] Neither PB calculations nor MC simulations based on the standard primitive model are capable of accounting for the remarkable constancy of r that has been inferred from ^{23}Na NMR measurements (and is a central feature of the CC theory). A more complete discussion of the implications of quadrupolar NMR measurements for theoretical descriptions of counterion radial distributions surrounding DNA has been given in a recent review.[56]

3 SURVEY OF EXPERIMENTAL RESULTS ON CATION–DNA INTERACTIONS

3.1 Noncompetitive Titrations

3.1.1 Nucleic Acids Titrated with Na^+

Since ^{23}Na is the most accurately detectable of the quadrupolar cationic nuclei, it has been the probe chosen in the majority of quadrupolar NMR studies. The earliest investigation of the interactions of Na^+ with nucleic acids was performed by James and Noggle,[49] who studied counterion–yeast tRNA interactions and observed a linear relationship [as expected by rearrangement of equation (4)] between $(R_{obs}^{Na} - R_F^{Na})^{-1}$ and $[Na^+]$, until aggregation of the RNA occurred.[49] Reuben et al.[30] performed ^{23}Na relaxation experiments using sonicated salmon testes DNA, and observed a linear relationship between the observed relaxation rate and $[Na^+]_B/[Na^+]$. $[Na^+]_B$ was estimated for each point of the noncompetitive titration.[30] Both studies used the mass action model to determine equilibrium binding constants and 'bound' relaxation rates ($R_B{}^{Na}$). For Na–DNA ([P] = 26.2 mM), the equilibrium binding constant (K_{eq}) was determined to be 91 M^{-1}; for Na–RNA (10–2.46 mg ml^{-1} RNA) equilibrium constants ranged from 195 to 457 M^{-1}. The two state model [equation (4)] was used to calculate the 'bound' relaxation rates: for DNA, R_B^{Na} was approximately 170 s^{-1}; for RNA, R_B^{Na} ranged from 202 to 227 s^{-1}. With these values of R_B^{Na} and the corresponding reported values of K_{eq}, [P], $[Na^+]$, and r_{Na} in equation (4) can be evaluated. Values of r_{Na} calculated in this way from the study of Reuben et al.[30] lie in the range 0.91–0.96, close to total neutralization of the DNA phosphates. This value is significantly higher than that predicted by Manning's CC model[50] and still higher than the range of values that have been predicted by solving the PB equation or MC simulations.[53] For tRNA the data of James and Noggle[44] yield values of r_{Na} in the range 0.74–0.98 for the experimental range of salt concentrations (50–500 mM).

Titrations of polymeric (sonicated) NaDNA with NaCl have been performed at several different field strengths, temperatures, and initial ratios of Na^+ to DNA phosphate.[12,16–18,20,21,23–25,29,32] In these studies, $R_{1,obs}^{Na}$ (or $R_{2,obs}^{Na}$) was plotted against [P]/$[Na^+]$ (the ratio of the total DNA phosphate concentration to the total sodium ion concentration) and analyzed by the two state model (equation (4)).

Table 1 presents values of the parameters of the noncompetitive two state model obtained from plots of observed R_1 and R_2 versus [P]/$[Na^+]$ for a variety of polymeric samples of native DNA (sonicated calf thymus, *Micrococcus lysodeikticus*, *Clostridium perfringens*, and phage T7). These noncompetitive titrations of NaDNA with ^{23}Na include all published data (in the indicated temperature range)[17,25,27,29] and unpublished work from the authors' laboratory.[32] Because the relaxation rate is dependent on temperature, the data in Table 1 represent only those data obtained in the temperature range 23–27°C. No explicit temperature corrections were applied. In papers where the authors did not report a number for the slope $[(r_{Na}(R_B - R_F)]$ or intercept (R_F), it was extracted for the table by analyzing the reported data. Values of R_B were estimated using a value for r_{Na} of 0.6, as was estimated in competitive titrations of NaDNA with Mg^{2+} and $Co(NH_3)_6{}^{3+}$.[19,27,28]

Examination of the slopes and intercepts in Table 1 indicates the following generalizations.

1. R_F typically is within the uncertainty of the relaxation rate of Na^+ in the absence of DNA (18.0 ± 1 s^{-1}) at 25°C.[57] Thus, it is reasonable to use the relaxation rate of Na^+ in aqueous solution containing only NaCl as an estimate of the relaxation rate in the 'free' state. The values for R_F are also field independent, so that the relaxation of nuclei in the 'free' state must be in the 'extreme narrowing' limit.
2. The slope, $r_{Na}(R_B - R_F)$ decreases with increasing field strength. Since R_F and r_{Na} (the fraction of phosphates neutralized by Na^+) are both independent of field strength,

Table 1 Summary of Results from NaDNA Titration with Na^+

DNA[a]	T(°C)	ω_{Na}(MHz)	$R_F(s^{-1})(s^{-1})$	$r_{Na}(R_b - R_f)$	$R_B(s^{-1})$	Relaxation rate	References
CT	25 (±1)	26.45	18.5 (±1)	154 (±2)	275 (±3)	R_2	Bleam et al.[17]
T7	25 (±1)	26.45	18.8 (±1)	162 (±2)	289 (±3)	R_2	Bleam et al.[17]
CT	27.0 (±?)	66.128	19.0 (±1)	78 (±4)	149 (±7)	R_1	Hald and Jacobsen[25]
CT	24.0 (±0.5)	95.263	18.9 (±0.2)	67.8 (±0.6)	132 (±1)	R_1	Padmanabhan[27]
CT	24.0 (±0.5)	95.263	18.4 (±0.3)	56.5 (±0.7)	113 (±1)	R_1	Stein[32]
ML	24.0 (±0.5)	95.263	18.7 (±0.4)	66.7 (±1.0)	130 (±2)	R_1	Stein[32]
CP	24.0 (±0.5)	95.263	17.7 (±0.4)	56.0 (±1.2)	111 (±2)	R_1	Stein[32]
CT	27.0 (±?)	66.128	19.0 (±1.5)	94 (±5)	176 (±8)	R_{2s}	Hald and Jacobsen[25]
CT	24.0 (±0.5)	95.263	19.3 (±0.4)	61 (±4)	121 (±7)	R_{2s}	Padmanabhan et al.[29]
CT	24.0 (±0.5)	95.263	19.3 (±0.7)	82.8 (±1.7)	157 (±3)	R_{2s}	Padmanabhan[27]
CT	24.0 (±0.5)	95.263	17.9 (±1)	76.0 (±2.6)	145 (±4)	R_{2s}	Stein[32]
ML	24.0 (±0.5)	95.263	18.6 (±0.5)	76.9 (±1.1)	147 (±2)	R_{2s}	Stein[32]
CP	24.0 (±0.5)	95.263	18.9 (±0.7)	70.2 (±2.2)	136 (±4)	R_{2s}	Stein[32]
CT	27.0 (±?)	66.128	19.0 (±1.5)	180 (±6)	319 (±10)	R_{2f}	Hald and Jacobsen,[25]
CT	24.0 (±0.5)	95.263	19.3 (±0.4)	129 (±4)	234 (±7)	R_{2f}	Padmanabhan et al.[29]
CT	24.0 (±0.5)	95.263	22.2 (±1.2)	149 (±3)	271 (±5)	R_{2f}	Padmanabhan[27]
CT	24.0 (±0.5)	95.263	22.7 (±2.2)	105 (±6)	198 (±10)	R_{2f}	Stein[32]
ML	24.0 (±0.5)	95.263	19.6 (±0.6)	113 (±2)	208 (±3)	R_{2f}	Stein[32]
CP	24.0 (±0.5)	95.263	17.6 (±1.4)	145 (±4)	259 (±7)	R_{2f}	Stein[32]

[a]CT, Calf thymus: ML, *Micrococcus lysodeikticus;* CP, *Clostridium perfringens*; T7, phage T7.

the relaxation of nuclei in the 'bound' state must be outside of the extreme narrowing limit.

3. A comparison of values reported for $r_{Na}(R_B - R_F)$ or R_B at a single field strength (Table 1) indicates little consistency for either parameter. In addition to the range of temperatures (23–27°C), this variability may be due to the variety in sample conditions (i.e. buffered versus unbuffered) used in previous investigations.
4. As discussed previously, linearity is observed when R_{obs}^{Na} is plotted as a function of [P]/[Na^+], which indicates that either r_{Na} $(R_B - R_F)$ is constant or that the two individual parameters, r_{Na} and R_B are variable but effectively compensate each other. Although the simplest inference is that $r_{Na}(R_B - R_F)$ is constant,[16,18,25,29] direct compensation of r_{Na} and R_B has not been disproved and may be indicated theoretically under some conditions.[46,47]

3.1.2 MDNA Titrated with M^{x+} (Cations other than Na^+)

Several noncompetitive DNA–cation titration studies have been performed using NMR nuclei other than ^{23}Na; ^{39}K with KDNA,[36] ^{87}Rb with RbDNA,[30] and ^{14}N with HexDNA (Hex^{2+} is a divalent methylated polyamine [hexamethonium, $(CH_3)_3N^+–(CH_2)_4–N^+(CH_3)_3$]).[29] These studies reached conclusions analogous to those reported for ^{23}Na NMR relaxation studies with Na–DNA: the observed relaxation rate is a linear function of the concentration ratio [P]/[M^{x+}].

3.2 Competitive Titrations

3.2.1 MDNA Titration with L^{z+} Monitored by ^{23}Na NMR

In addition to Na–DNA titrations with NaCl, various organic (NH_4^+, polyamines, and tetraethyl- or tetrabutylammonium), alkali metal (Cs^+, Li^+ and K^+), alkaline earth (Mg^{2+} and Ca^{2+}), and the inorganic cationic complex $Co(NH_3)_6^{3+}$ have been used in competitive titrations with NaDNA. From these titrations, Anderson et al.[16] and Bleam et al.[17] have shown that the relative affinities of univalent cations for DNA are $NH_4^+ > Cs^+ > K^+ > Li^+ > Na^+ > Et_4N^+ > Bu_4N^+$. In general, univalent ions have a smaller affinity for DNA than do the divalent cations (Mg^{2+}, Ca^{2+} or polyamines). Within the group of divalent cations, the alkaline earth metal ions, in general, have greater affinities for DNA than do polyamines.[6,36] Divalent Mg^{2+} and putrescine(2+) have lower affinities for DNA than do the trivalent spermidine(3+) and cobalt hexamine, $Co(NH_3)_6^{3+}$.[36] As in the case of the divalent cations, the affinity of the spherical inorganic trivalent cation $Co(NH_3)_6^{3+}$ is higher than that of the elongated, low-charge-density spermidine(3+).

3.2.2 DNA Titrations Monitored by NMR of Multivalent Ions

Reimarrson et al.[42] demonstrated the feasibility of studying the interactions of Mg^{2+} and Ca^{2+} with DNA by measuring the ^{25}Mg and ^{43}Ca NMR linewidths, even though both nuclei have unfavorable NMR characteristics (low natural abundance and sensitivity). This initial study was done at very low magnetic field strength and (of necessity) high concentrations of ^{25}Mg and ^{43}Ca counterions. For both ^{25}Mg and ^{43}Ca, the temperature dependence of the linewidths was judged inconsistent with nuclei in fast exchange.

NMR studies following the initial work of Reimarrson et al.[42] have yielded complicated and somewhat contradictory results. Competitive titration studies by Rose et al.[43,44] implied that titration of MgDNA with mono- or divalent counterions (Na^+, Ca^{2+}, Zn^{2+}, Ni^{2+}, and Hg^{2+}) did not result in the displacement of all of the 'bound' Mg^{2+} ions, as inferred by the inability to reduce the ^{25}Mg linewidth to 2.5 Hz, its value in the absence of DNA. This result was interpreted as evidence

for at least two different types of 'bound' population. However, more recently, Braunlin and co-workers[20,21] have performed competitive titrations with Ca^{2+} and MgDNA at smaller ratios of $[Mg^{2+}]/[P]$ than those investigated by Rose et al.[44] The more recent titrations gave no evidence for a 'bound' ^{25}Mg population that could not be displaced by excess Ca^{2+}.

The possibility that various cations may have specific interactions with nucleic acids has been investigated for DNA of differing GC content. In these studies ^{23}Na,[26,45] ^{59}Co in $Co(NH_3)_6^{3+}$,[58,59] and ^{43}Ca[45] relaxation rates, and ^{59}Co and ^{43}Ca chemical shifts,[45,58] were measured in titration studies of *Micrococcus lysodeikticus* (72% GC), *Escherichia coli* (41% GC), calf thymus (39% GC), *Clostridium perfringens* (31% GC), and oligonucleotides varying in GC content.[59] No discernible dependence on GC content was observed in the ^{23}Na studies, a finding which is in agreement with the long-standing inference that (at least under typical experimental conditions in vitro) there is no NMR evidence for the existence of site binding of Na^+ to native DNA.[16] Use of the mass action model to describe the accumulation of sodium ions in the vicinity of DNA must therefore be considered a parameterization. By contrast, in the studies utilizing ^{59}Co and ^{43}Ca, large differences in both chemical shifts and relaxation rates were measured as a function of GC content. Thus, these higher valent cations exhibit some degree of specificity in their interactions with DNA.

3.3 Other NMR Studies of Interactions of Divalent Ions with DNA

Rose et al.[43,44] performed temperature dependent studies on the ^{25}Mg linewidth, which yielded results similar to the initial observations of Reimarrson et al.[42] The ^{25}Mg linewidths exhibited a gradual increase with increasing temperature, which is inconsistent with fast exchange between two sites. This study was also first to report a non-Lorentzian lineshape for ^{25}Mg in a Mg–DNA system, which was hypothesized to result from a residual first-order nuclear quadrupole interaction.

Berggren et al.[39] carried out the first quantitative analysis of the temperature dependence of the linewidths and longitudinal relaxation rates for ^{25}Mg in Mg–DNA systems. In this study the authors fitted the temperature dependences to an isotropic two-site discrete exchange model based on that developed by Westlund and Wennerström.[10] This model, which can be used to describe quadrupolar systems undergoing (not necessarily rapid) exchange between two classes of sites, also takes into account the dynamic frequency shifts between each of the three transitions for a spin-$\frac{5}{2}$ nucleus. With this model, Berggren et al.[39] could not fit quantitatively the temperature dependences of both the linewidths and the longitudinal relaxation rates using a single set of parameters, although the qualitative trends in both data sets at higher temperatures could be reproduced. On the basis of qualitative trends, Berggren et al.[39] concluded that the Mg–DNA system could be modeled as a two state system in which the exchange rate between 'bound' and 'free' populations was of the order of milliseconds.

Wright and Lerner[11] performed a frequency-dependence study of ^{25}Mg linewidths in Mg–DNA systems in which the Westlund and Wennerström[10] isotropic two state exchange model was used to fit the field dependence of the lineshapes. The results of this study demonstrated that this model could not reproduce the experimental field dependence of the lineshapes. More complicated models, including, for example, nonisotropic relaxation in the bound state, multiple correlation times for the bound state and/or multiple bound populations, must therefore be required to describe the composition dependence of ^{25}Mg in solutions of Mg–DNA. This study was also the first to report a co-ion dependence for the ^{25}Mg relaxation rates in DNA solution. Specifically, the temperature dependence of the linewidth varies with the nature of the co-ion (SO_4^{2-}, Cl^-, and ClO_4^-) (the last measured by Berggren et al.)[39] The co-ion dependence demonstrates that exchange rates, relaxation rates, or other parameters determined in a particular Mg^{2+}–co-ion–DNA system cannot necessarily be generalized to Mg–DNA interactions in solutions containing other types of co-ion.

3.4 NMR Studies of Ion–DNA Interactions in Concentrated Solution

The preceding sections have dealt with the use of quadrupolar NMR relaxation to study interactions of cations with DNA in dilute solution (1–30 mM). More recently, quadrupolar NMR has also been applied to concentrated solutions ($\geq$450 mg ml^{-1}).[14,33,34] Strzelecka and Rill[33,34] reported ^{23}Na NMR relaxation experiments on concentrated 147 base pair DNA samples from nucleosome core particles at several sodium ion concentrations (0.01, 0.1, and 1 M) and Groot et al.[14] used chicken erythrocyte nucleosome core DNA. The observed R_1 increases as the DNA concentration is increased (10–290 mg ml^{-1} DNA), whereas R_1 decreases as the temperature increases (20–60°C). As the DNA concentration is increased, the solution changes phase from isotropic to anisotropic, and the slope of the R_1 versus $[P]/[Na^+]$ plot becomes steeper. The authors propose that the abrupt increase in the slope is due to an increase in the number of counterions in the vicinity of DNA and an increase in the average electric field gradient experienced by the 'bound' ions. Increasing the DNA concentration and the temperature affects the distance between the DNA and the cholesteric pitch (i.e. as the DNA concentration increases the distance between DNA molecules decreases).

Several authors have showed the feasibility of ^7Li and ^{133}Cs NMR on oriented DNA fibers.[13,31,60–62] Some of these ^7Li and ^{133}Cs NMR investigations of oriented DNA fibers involved the use of multiple quantum coherence experiments, which provide information about the dynamics of the cation.[61,62] In addition, two-dimensional experiments (two-dimensional quadrupole echo and two-dimensional spin echo) were used to measure homogenous linewidths, which can be evaluated in terms of fast and slow motional correlation times for the ions in the presence of DNA.

Schultz et al.[31] used both single pulse and double quantum filtered pulse sequences to determine the quadrupolar splitting for macroscopically oriented fibers of NaDNA, LiDNA, and CsDNA. In a highly concentrated DNA solution, the ^{23}Na signal is split into three peaks due to nonzero molecular motion of the anisotropic system. The dependence of quadrupolar splitting on temperature and extent of hydration (controlled by

relative humidity) for ^{23}Na, ^{133}Cs, and ^{7}Li has been studied in order to elucidate changes in the counterion distributions and binding of Na^+, Cs^+, and Li^+ with Na–DNA. Using the temperature dependence of the quadrupolar splitting at different relative humidities, the authors found that a three site model (consisting of free ions and specifically and nonspecifically 'bound' ions) was more consistent with their data than a two site model. In the context of the three site model, Li^+ binds less specifically to DNA than does Na^+ or Cs^+. For both Na–DNA and Li–DNA, the quadrupolar splitting increases with decreasing concentration of salt (Na^+ or Li^+).

4 ADDITIONAL METHODS OF STUDYING CATION–DNA INTERACTIONS

The focus of this review has been on the applications of quadrupolar NMR relaxation measurements to investigate cation–DNA interactions in dilute solutions, where motional narrowing governs the form of the quadrupolar relaxation processes, and in concentrated solutions. The dilute solution studies represent the earliest, and the largest, body of work in this general field. The concentrated solution studies represent a rapidly growing area, which may be of direct relevance to cation–nucleic acid interactions in vivo.

Several other kinds of NMR spectroscopic measurements have also been utilized in studies of cation–DNA interactions. Pulsed field gradient spin diffusion methods have been used to measure the translational diffusion of cations in cation–DNA systems.[63,64] Applications of these methods will continue to increase as pulsed field gradient technology becomes more readily accessible. The more traditional proton NMR methods are finding increasing popularity as a means of characterizing cation–DNA interactions. For example, the structural effects of cation type and/or concentration on the ^{1}H spectroscopic characteristics of specific sequence oligonucleotides have been determined in order to correlate changes in ^{1}H chemical shifts and coupling constants with the B to A transition of a GC-rich octamer induced by $^{59}Co(NH_3)_6^{3+}$.[65] Spectroscopic measurements on ^{1}H, ^{13}C, and ^{31}P have been used in a similar study to investigate the specific interaction of Zn^{2+} with the N-7 position on guanine nucleotides in the self-complementary oligonucleotide d(ATGGGTACCCAT).[66]

In addition to NMR, thermodynamic and spectroscopic methods have been used to characterize the interactions of cations with DNA. Thermodynamic data have been obtained from Donnan equilibrium and solvent activity measurements, which yield, respectively, preferential interaction coefficients[67–70] and osmotic coefficients[71] characterizing the thermodynamic consequences of electrolyte–polyelectrolyte interactions. Calorimetry and ultraviolet spectrophotometry have been applied to investigate the effect of salt concentration on the thermal stability of DNA; these data have been interpreted in terms of the difference between preferential interactions of electrolyte ions with native and denatured states.[72] Methods other than NMR that have been used to obtain detailed molecular information regarding aspects of the cation radial distribution include small angle neutron scattering[73] and fluorescence.[74]

5 REFERENCES

1. G. S. Manning, *Q. Rev. Biophys.*, 1978, **11**, 179.
2. M. T. Record, Jr, C. F. Anderson, and T. M. Lohman, *Q. Rev. Biophys.*, 1978, **11**, 103.
3. W. H. Braunlin, T. Drakenberg, and S. Forsén, *Curr. Topics Bioenerg.*, 1985, **14**, 97.
4. S. Forsén, T. Drakenberg, and H. Wennerström, *Q. Rev. Biophys.*, 1987, **19**, 83.
5. S. Forsén and B. Lindman, *Methods Biochem. Anal.*, 1981, **27**, 289.
6. S. Padmanabhan, M. Paulsen, C. F. Anderson, and M. T. Record, Jr, in *Monovalent Cations in Biological Systems*, ed. C. A. Pasternak, CRC, Boca Raton, FL, 1990, pp. 321–338.
7. P. S. Hubbard, *J. Chem. Phys.*, 1970, **53**, 985.
8. W. D. Rooney, T. M. Barbara, and C. S. Springer, Jr, *J. Am. Chem. Soc.*, 1988, **110**, 674.
9. B. Halle and H. Wennerström, *J. Magn. Reson.*, 1981, **44**, 89.
10. P.-O. Westlund and H. Wennerström, *J. Magn. Reson.*, 1982, **40**, 451.
11. L. A. Wright and L. E. Lerner, *Biopolymers*, 1994, **34**, 691.
12. L. van Dijk, M. L. H. Gruwel, W. Jesse, J. de Bleijser, and J. C. Leyte, *Biopolymers*, 1987, **26**, 261.
13. L. Einarsson, L. Nordenskiöld, A. Rupprecht, I. Furó, and T. C. Wong, *J. Magn. Reson.* 1991, **93**, 34.
14. L. C. A. Groot, J. R. C. vander Maarel, and J. C. Leyte, *J. Phys. Chem.*, 1994, **98**, 2699.
15. B. Richey, S. Cayley, M. Mossing, C. Kolka, C. F. Anderson, T. C. Farrar, and M. T. Record, Jr, *J. Biol. Chem.*, 1987, **15**, 7157.
16. C. F. Anderson, M. T. Record, Jr, and P. A. Hart, *Biophys. Chem.*, 1978, **7**, 301.
17. M. L. Bleam, C. F. Anderson, and M. T. Record, Jr, *Proc. Natl. Acad. Sci. USA.*, 1980, **6**, 3085.
18. M. L. Bleam, C. F. Anderson, and M. T. Record, Jr, *Biochemistry* 1983, **22**, 5418.
19. W. H. Braunlin, C. F. Anderson, and M. T. Record, Jr, *Biopolymers*, 1986, **25**, 205.
20. W. H. Braunlin, C. F. Anderson, and M. T. Record, Jr, *Biochemistry*, 1987, **26**, 7724.
21. W. H. Braunlin, T. Drakenberg, and L. Nordenskiöld, *Biopolymers*, 1987, **6**, 1047.
22. D. R. Burton, S. Forsén, and P. Reimarsson, *Nucleic Acid. Res.*, 1981, **9**, 1219.
23. M. Casu, A. Lai, C. Meloni, and G. Saba, *Chem. Phys. Lett.*, 1987, **137**, 533.
24. A. Delville, P. Laszlo, and R. Schyns, *Biophys. Chem.*, 1986, **24**, 121.
25. M. Hald and J. P. Jacobsen, *Chem. Phys.*, 1992, **159**, 257.
26. L. Nordenskiöld, D. K. Chang, C. F. Anderson, and M. T. Record, Jr, *Biochemistry*, 1984, **23**, 4309.
27. S. Padmanabhan, Ph.D. Thesis, University of Wisconsin, Madison, 1988.
28. S. Padmanabhan, V. M. Brushaber, C. F. Anderson, and M. T. Record, Jr, *Biochemistry*, 1991, **30**, 7550.
29. S. Padmanabhan, B. Richey, C. F. Anderson, and M. T. Record Jr, *Biochemistry*, 1988, **27**, 4367.
30. J. Reuben, M. Shporer, and E. J. Gabbay, *Proc. Natl. Acad. Sci. USA.*, 1975, **72**, 245.
31. J. Schultz, L. Nordenskiöld, and A. Rupprecht, *Biopolymers*, 1992, **32**, 1631.
32. V. M. Stein, Ph.D. Thesis, University of Wisconsin, Madison, 1994.

33. T. E. Strzelecka and R. L. Rill, *Biopolymers*, 1990, **30**, 803.
34. T. E. Strzelecka and R. L. Rill, *J. Phys. Chem.*, 1992, **96**, 7796.
35. D. Vasilescu and G. Mallet, *Biopolymers*, 1985, **24**, 1845.
36. W. H. Braunlin and L. Nordenskiöld, *Eur. J. Biochem.*, 1984, **142**, 133.
37. D. K. Chang, Ph.D. Thesis, University of Wisconsin, Madison, 1984.
38. L. Einarsson, P.-O. Eriksson, L. Nordenskiöld, and A. Rupprecht, *J. Phys. Chem.*, 1990, **94**, 2696.
39. E. Berggren, L. Nordenskiöld, and W. H. Braunlin, *Biopolymers*, 1992, **32**, 1339.
40. W. H. Braunlin, L. Nordenskiöld, and T. Drakenberg, *Biopolymers*, 1989, **28**, 1339.
41. W. H. Braunlin, L. Nordenskiöld, and T. Drakenberg, *Biopolymers*, 1991, **31**, 1343.
42. P. Reimarrson, J. Parello, T. Darkenberg, H. Gustavsson, and B. Lindman, *FEBS Lett.*, 1979, **108**, 439.
43. D. M. Rose, M. L. Bleam, M. T. Record, Jr, and R. G. Bryant, *Proc. Natl. Acad. Sci. USA*, 1980, **77**, 6289.
44. D. M. Rose, C. F. Polnasek, and R. G. Bryant, *Biopolymers*, 1982, **21**, 653.
45. W. H. Braunlin and Q. Xu, *Biopolymers*, 1992, **32**, 1703.
46. S.-W. W. Chen and P. J. Rossky, *J. Phys. Chem.*, 1993, **97**, 10803.
47. R. J. Bacquet and P. J. Rossky, *J. Phys. Chem.*, 1984, **88**, 2660.
48. R. J. Bacquet and P. J. Rossky, *J. Phys. Chem.*, 1988, **92**, 3604.
49. T. L. James and J. H. Noggle, *Proc. Natl. Acad. Sci. USA.*, 1969, **62**, 644.
50. G. S. Manning, *Biophys. Chem.*, 1977, **7**, 95.
51. R. M. Fuoss, A. Katchalsky, and S. Lifson, *Proc. Natl. Acad. Sci. USA*, 1951, **37**, 579.
52. P. Mills, C. F. Anderson, and M. T. Record, Jr, *J. Phys. Chem.*, 1986, **90**, 6541.
53. P. Mills, C. F. Anderson, and M. T. Record, Jr, *J. Phys. Chem.*, 1985, **89**, 3984.
54. C. S. Murthy, R. Bacquet, and P. J. Rossky, *J. Phys. Chem.*, 1985, **89**, 701.
55. M. D. Paulsen, C. F. Anderson, and M. T. Record, Jr, *Biopolymers*, 1988, **27**, 1249.
56. C. F. Anderson and M. T. Record, Jr, *Ann. Rev. Biophys. Biophys. Chem.*, 1990, **19**, 423.
57. M. Eisenstadt and H. L. Friedman, *J. Chem. Phys.*, 1967, **46**, 2182.
58. W. H. Braunlin, T. Drakenberg, and L. Nordenskiöld, *J. Biomol. Struct. Dynam.*, 1992, **10**, 333.
59. Q. W. Xu, H. Deng, and W. H. Braunlin, *Biochemistry*, 1993, **48**, 13130.
60. H. T. Edzes, A. Rupprecht, and H. J. C. Berendsen, *Biochem. Biophys. Res. Commun.*, 1972, **46**, 790.
61. L. Einarsson, J. Kowalewski, L. Nordenskiöld, and A. Rupprecht, *J. Magn. Reson.*, 1989, **85**, 228.
62. J. Kowalewski, L. Einarsson, L. Nordenskiöld, and A. Rupprecht, *J. Magn. Reson.*, 1988, **76**, 337.
63. B. Andreasson, L. Nordenskiöld, W. H. Braulin, J. Schultz, and P. Stilbs, *Biochemistry*, 1993, **32**, 961.
64. R. L. Haner and T. Schleich, *Methods. Enzymol.*, 1989, **176**, 418.
65. Q. W. Xu, S. R. B. Jampani, and W. H. Braunlin, *Biochemistry*, 1993, **48**, 11754.
66. J. Xin, G. Zon and L. G. Marzilli, *Inorg. Chem.*, 1991, **30**, 228.
67. L. M. Gross and U. P. Strauss, in *Chemical Physics of Ionic Solutions*, ed. B. E. Conway and R. G. Barradas, Wiley, New York, pp. 361–389.
68. C. F. Anderson and M. T. Record, Jr, *Biophys. Chem.*, 1980, **11**, 353.
69. C. F. Anderson and M. T. Record, Jr, *Ann. Rev. Phys. Chem.*, 1982, **33**, 191.
70. C. F. Anderson and M. T. Record, Jr, in *Structure and Dynamics: Nucleic Acids and Proteins*, ed. E. Clementi and R. H. Sarma, Adenine, New York, 1993, p. 301.
71. M. W. Capp, J. P. Bond, C. F. Anderson, and M. T. Record, Jr, 1995, in preparation.
72. J. P. Bond, C. F. Anderson, and M. T. Record, Jr, *Biophys. J.*, 1994, **67**, 1.
73. S. L. Chang, S. H. Chen, R. L. Riu, and J. S. Lin, *J. Phys. Chem.*, 1990, **94**, 8025.
74. T. G. Wensel, C. F. Meares, V. Vlachy, and J. B. Matthew, *Proc. Natl. Acad. Sci. USA.*, 1986, **83**, 3267.
75. Q. W. Xu, R. K. Shoemaker, and W. H. Braunlin, *Biophys. J.*, 1993, **65**, 1039.

Acknowledgments

We thank Harry Guttman and S. Padmanabhan for discussions of aspects of this review, Sheila Aiello for preparation of the manuscript, and NIH GM34351 (MTR) for financial support.

Biographical Sketches

Charles F. Anderson. Ph.D. (equilibrium and kinetic properties of inorganic systems with the NMR of quadrupolar nuclei) with Prof. H. Taube, Stanford University and Los Alamos Scientific Laboratory. Postdoctoral associate at the State University of New York, Stony Brook with Prof. H. Friedman (developing various aspects of the relaxation rate theory for quadrupolar nuclei outside extreme narrowing). University of Wisconsin-Madison (initially applying the NMR of ^{23}Na and similar nuclei to biological systems in collaboration with Prof. M. T. Record), presently Senior Scientist researching NMR and related areas.

M. Thomas Record, Jr. Ph.D., 1967 (Biophysical Chemistry), University of California, San Diego. Supervisor: Bruno Zimm. NSF Postdoctoral Fellow in Biochemistry with R. L. Baldwin and A. Dale Kaiser, Stanford University. 1970–present, University of Wisconsin-Madison, presently John D. Ferry Professor of Chemistry and Biochemistry. Research concerns: the thermodynamics and kinetics of nucleic acid interactions in vitro and in vivo.

Veronica Stein. Ph.D., University of Wisconsin-Madison. Supervisor: Prof. M. Thomas Record. Presently, assistant professor, Peoria Community College, Illinois.

Laura A. Wright. Ph.D., University of Wisconsin-Madison. Supervisor: Prof. Laura E. Lerner. Postdoctoral associate, University of Wisconsin-Madison and subsequently University of California at San Francisco. Presently Staff Scientist with Prof. Judith Burstyn, University of Wisconsin-Madison.

Drug–Nucleic Acid Interactions

W. David Wilson
Georgia State University, Atlanta, GA, USA

1	Introduction	1
2	Reversible DNA Complexes: Intercalators	2
3	Reversible DNA Complexes: Minor-Groove Interactions	5
4	Covalent DNA Complexes	8
5	Overview	9
6	Related Articles	9
7	References	9

1 INTRODUCTION

Initial analysis of drug complexes with double-helical DNA molecules by hydrodynamic methods indicated that there are two primary binding modes by which drugs interact noncovalently with nucleic acid duplexes: intercalation and minor-groove complexes.[1,2] Groove-binding molecules can slide into the concave structure represented by the groove, and the compounds typically cause relatively minor structural changes in the double helix. For intercalation to occur, however, a pair of adjacent base pairs must move apart to create a space that is filled by an aromatic system of the intercalator. Because of these structural changes, intercalators cause an increase in the viscosity of linear DNA solutions and an unwinding of closed-circular supercoiled DNA when they bind to the double helix, whereas groove-binding molecules do not cause unwinding of superhelical DNA or increases in the viscosity of linear DNA solutions.[1] It should be noted that intercalators can have substituents with significant interactions in the DNA major and/or minor grooves.

Although the initial studies described above clearly defined the binding modes for a large number of drugs, they provided very limited specific information about the structure of drug–nucleic acid complexes. It was clear with the development of commercial Fourier transform NMR instruments in the early 1970s that NMR could provide valuable new information on intercalation and groove complexes, but the difficulty was to obtain nucleic acid samples appropriate for NMR analysis. Natural DNA under native conditions exists as a double-stranded helix of high molecular weight and limited internal motion. NMR spectra of this molecule and its complexes in solution are too broad to provide useful information.[3] Natural RNA, even though single stranded, exists under physiological conditions as highly structured species with extensive sections of intramolecular duplex, and generally gives complex NMR spectra with overlapping signals that are difficult to interpret.[4] Two initial techniques were developed to obtain NMR information on nucleic acids and their drug complexes: (1) use of synthetic dinucleotides that could potentially form minihelical intercalation complexes, and (2) use of sonicated natural DNA or synthetic polymers to obtain lower molecular weight duplexes that could bind both intercalators and groove-binding drugs and still give experimentally useful linewidths in NMR spectra.[5]

The studies with dinucleotides were initiated by Chan and co-workers[6] as part of their research on the interaction of the intercalator ethidium bromide (Figure 1) with single-stranded nucleic acids. These were followed by a very thorough series of NMR studies by Krugh and co-workers[7] on dinucleotides that could form miniduplexes with intercalators. The work with sonicated DNA provided sequences that were long enough to form complexes with groove-binding drugs as well as intercalators. The hydrodynamic studies described above had been able to group compounds as intercalators or groove binders, but the NMR results showed that more complex, sequence-dependent, binding behavior can occur.[5]

NMR studies showed that classical intercalators, such as ethidium bromide (see Section 2), which contain fused aromatic ring systems, fill the cavity created when two base pairs separate by a distance of 0.34 nm.[5,7] Groove-binding agents, such as netropsin (see Section 3), contain a series of small, unfused aromatic systems that have torsional mobility to match the twist of the DNA minor groove.[1,2] Both types of compounds are organic cations that typically have heterocyclic aromatic systems as part of their structure. The effects of nucleic acids on the chemical shifts of intercalators and groove-binding agents are strikingly different.[5] Nuclei in intercalators experience significant upfield shifts on complex formation primarily due to the shielding effects generated by the aromatic ring currents of the stacked base pairs in duplex structures. The effects on nuclei in the grooves of the double helix are smaller and can be either shielding or deshielding, depending on the location with respect to the base pair edges and other factors that influence chemical shifts.

The development of economical techniques and instruments for the large-scale preparation and purification of nucleic acid oligomers in the late 1970s provided the next major step in the analysis of nucleic acid–drug complexes. Oligonucleotides from the hexamer to dodecamer size were found to form specific double-helical structures with linewidths that were sufficiently narrow to allow high-resolution structural analysis by NMR methods. An explosion of information on the structural and dynamic properties of nucleic acids and their complexes has resulted from the continued developments in NMR and oligomer preparation technologies.

Two major problems can arise in quantitative NMR analysis of nucleic acid–drug complexes. Many of the drugs of interest are organic cations with significant hydrophobic character. These features can give strong complexes with nucleic acids, but they can also cause precipitation and aggregation. A second major problem is the potential for the drugs to form more than one complex with a nucleic acid sequence. This can lead to very complex spectra and/or averaging of NMR results for the different species, depending on the exchange rates among the bound species.[5] At some exchange rates there can also be a significant decrease in the NOE intensities used for quantitative structural analysis of the complexes. Some of these problems are prevented in the study of covalent complexes. The difficulties with dynamics in the analysis of drug–nucleic acid complexes also exist in the study of these complexes by all solution methods, whether they are recognized or not. Even in the presence of multiple binding modes with dynamics, however, NMR methods can still

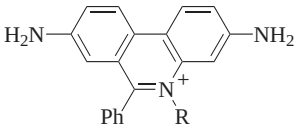

Propidium: R = $(CH_2)_3N(Et)_2Me$
Ethidium: R = Et

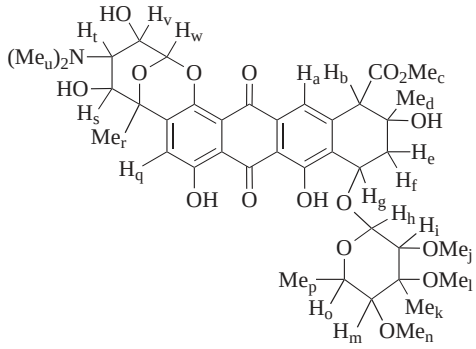

Nogalamycin

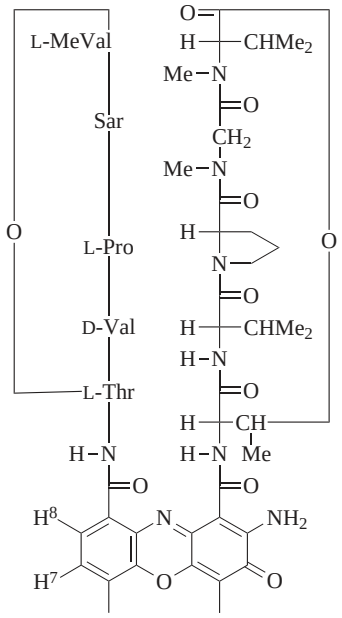

Actinomycin D

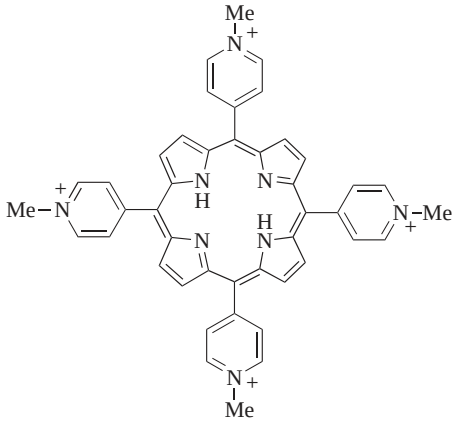

TMpyP(4)

Figure 1 Structures of some intercalators that have been investigated by NMR methods

provide qualitative information on complexes that in many cases can be combined with molecular modeling methods to define a limiting set of structures for the complex.

NMR results for drug–nucleic acid complexes to be presented will be grouped into categories for noncovalent intercalation and groove-binding agents with a separate category for covalent adducts. One feature of nucleic acid–drug complexes that was not anticipated from other solution or X-ray studies was the binding of drugs to nucleic acids as dimers. Such dimer complexes have been observed by NMR methods for the intercalator actinomycin,[8,9] for the AT-specific minor-groove agent distamycin,[10,11] and for the GC-specific minor-groove agent chromomycin.[12–14] Such dimer complexes provide significant information about cooperativity in nucleic acid interactions, and have provided new ideas for drug design.

2 REVERSIBLE DNA COMPLEXES: INTERCALATORS

There are 10 dinucleotide intercalation sites in antiparallel RNA and DNA duplexes.[1,2] To create an intercalation site, torsional angle changes occur in the backbone chain to separate the stacked base pairs and unwind the helix, and these changes typically cause downfield shifts in ^{31}P NMR spectra.[15] The ring current effects of the base pairs are typically smaller than for the intercalated ring, and most base pair aromatic and imino proton signals at the intercalation site shift to low frequency (upfield) on formation of an intercalation complex. The aromatic proton signals of the intercalator also typically shift to low frequency on transfer from the solvent environment to the base-stacked intercalation complex.[5] Of the compounds shown to bind to DNA by intercalation, very few have significant binding selectivity for one of the 10 dinucleotide intercalation sites, and the multiple site interactions can complicate NMR studies of their complexes.

Sonicated DNA polymers such as poly[d(G-C)$_2$] and poly[d(A-T)$_2$] have single imino proton signals which are shifted upfield by simple intercalators such as ethidium and acridine derivatives.[16] A number of solution studies indicate that binding of simple intercalators saturates at one intercalator per two base pairs, the neighbor exclusion principle. On addition of ethidium to the above polymers, none of the original imino signal remains at saturation, and a single sharp signal for the bound species is obtained; these results indicate that simple intercalators bind at alternating sites on the polymer.[16] If the intercalators clustered into regions on the polymer with other regions relatively free of intercalation, some free GC imino signal would remain, and the bound signal would be more complex.

Oligomers[17] provide higher-resolution NMR spectra, but yield the same basic conclusions as with the polymers. Phosphorus-31 signals for the oligomers fall in the −4.2 to −4.7 ppm range (relative to trimethyl phosphate), and on addition of simple intercalators to saturation move to high frequency in a manner characteristic of intercalation. These results provide strong support for a general intercalation model with the fused intercalation ring system maximally stacked over the DNA base pairs at the binding site. Barton and coworkers[18] have designed a number of metallo-intercalators, and have conducted NMR studies on Δ-Rh(phen)$_2$phi^{3+}

(phen = phenanthroline; phi = phenanthrene quinone diimide) with the duplex sequence d(GTCGAC). Chemical shift and NOE results indicate that the phi system intercalates with some preference at the C-G step with the phenanthroline rings in the DNA major groove. These and other biophysical studies have resulted in a proposal that such metallo-intercalators can be used to distinguish nucleic acid conformations through a combination of intercalation and nucleic acid shape-specific recognition by the metal ligands in the nucleic acid grooves.[18]

Significant intercalation specificity has been observed in studies of DNA complexes of some cationic porphyrins which have a variety of biological activities[19,20] (Figure 1). Addition of TMpyP(4) to sonicated poly[d(G-C)$_2$][20] resulted in a high-frequency ^{31}P signal at -0.9 ppm relative to the normal polymer ^{31}P signal at -4.2 ppm. The high-frequency signal clearly identifies the binding mode as intercalation, and is the largest shift observed for an intercalator complex. TMpyP(4) complexes with oligomers containing 5′-CG-3′ intercalation sites have the characteristic porphyrin ^{31}P NMR downfield peak at ~ -1.0 ppm; however, complexes with oligomers containing either 5′-GC-3′ or 5′-GG-3′ sites but no CG do not have the high frequency signal.[20] Addition of TMpyP(4) to the GC polymer oligomers with CG sites resulted in the appearance of new low-frequency peaks in the imino proton spectra, while oligomers without CG sites did not give the low-frequency imino signals. Surprisingly large imino proton shifts were obtained for protons adjacent to the bases at the CG-binding site. For imino protons that lie at different distances above the porphyrin ring, as expected for an intercalation complex, the imino protons would be at approximately 0.34, 0.68, and 1.02 nm above the porphyrin center for each base pair step away from the bound compound. From these distances, low-frequency shifts of $\sim$4, $\sim$1.2, and $\sim$0.4 ppm, respectively, are predicted for the imino signals from the ring current–chemical shift map for tetraphenylporphyrin,[21] and the observed shifts are in agreement with the predicted values. In porphyrin–oligomer complexes, very complicated sets of overlapping signals, with different exchange kinetics, are observed in the nonexchangeable proton NMR spectral region, and this system illustrates some of the problems that can arise to prevent detailed structural studies of DNA complexes by NMR methods.

Actinomycin D (ActD), a peptide intercalator (Figure 1) with anticancer and antibiotic activities, is unusual in that it is a neutral molecule which binds strongly to DNA with GC base pair specificity.[1] ActD is generally more well behaved in NMR experiments than the intercalators discussed above, and it was one of the first molecules studied in NMR experiments with dinucleotides and oligonucleotides.[7] To obtain more detailed information on cooperativity in drug–DNA interactions, ActD complexes with oligonucleotides that contain multiple GC sites have been examined by NMR spectroscopy.[8,9]

Titration of d(ATGCGCAT) with ActD to a ratio of one ActD molecule per duplex results in a complex imino proton spectrum that no longer has two-fold symmetry. The benzenoid side of the phenoxazone ring of ActD (Figure 1) has a significantly larger ring current than the quinoid side,[22] and the observed sets of signals can be explained by the two possible orientations of bound ActD in slow exchange. Increasing the ratio of ActD/duplex to 2:1 results in the disappearance of the 1:1 imino signals, and a significant simplification of the spectrum. At the ratio of 2.0, single signals are seen

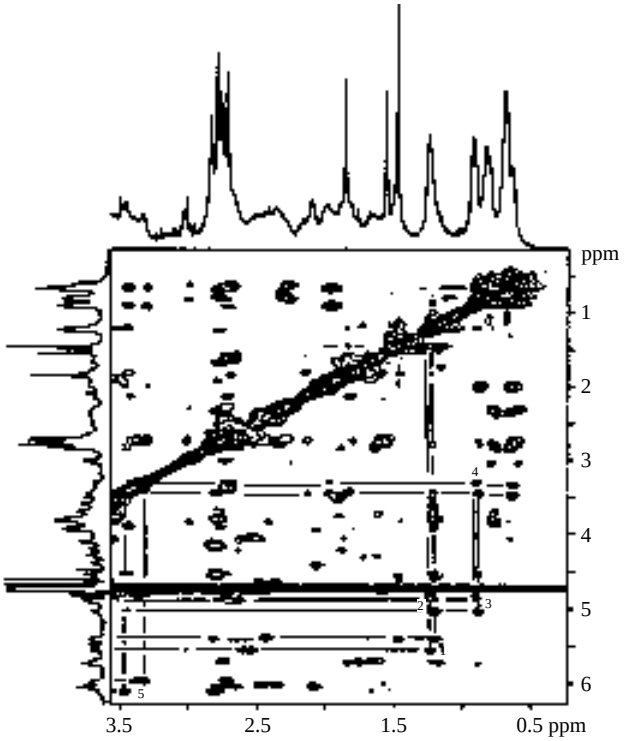

G H-1′ $\rightarrow$ Thr-γ $\rightarrow$ Thr-β $\rightarrow$ D-Val-β $\rightarrow$ D-Val-γ $\rightarrow$ Pro-α
1 2 3 4 5

Figure 2 A portion of the NOESY spectrum (250 ms mixing time) of the 2:1 ActD complex with the duplex from d(ATGCGCAT). Connectivities within each peptide chain are shown along with the guanine H-1′ to Thr-γ cross peak

for the phosphate groups at the intercalation site, and they are shifted significantly downfield.[8,9] The nonexchangeable proton spectrum of the 1:1 ActD complex is also quite complex; however, the spectrum of the 2:1 complex shows a spectral simplification and return to C_2 symmetry, as with the imino and ^{31}P spectra.[23]

COSY and NOESY (Figure 2) 2D NMR spectra have provided information for assignment of most proton signals, and for a model of ActD in the dimer complex.[9] A guanine H-8 resonance at 7.51 ppm and a cytosine H-6 resonance at 7.15 ppm both have NOEs to the ActD H-8 and H-7 signals, showing them to be close to the benzenoid side of the phenoxazone ring of ActD and to be adjacent bases. By a process of elimination, the other guanine H-8 resonance at 7.57 ppm and the cytosine H-6 resonance at 6.59 ppm are close to the quinoid side of the phenoxazone ring and adjacent to each other. A NOE from the thymine H-6 resonance at 6.91 ppm assigns this resonance to the 5′-ATGC end of the oligomer since only the G_3 H-8 of the two guanine residues present can have a NOE to a thymine H-6 signal. Since the guanine H-8 signal at 7.57 ppm is quinoid-G_3, the following order is established: 5′-d($A_1T_2G_3$-quinoid-C_4G_5-benzenoid-$C_6A_7T_8$)-3′. Assignments of the ActD peptide proton resonances and peptide–DNA cross peaks provide the critical information for orientation of the two ActD molecules in the 2:1 complex (Figure 2).

In the 2:1 complex of ActD with d(ATGCGCAT) at least one type of proton in each amino acid could be identified as

belonging to either the benzenoid or quinoid peptides, and, therefore, the two cyclic peptide chains in the 2:1 complex must be in different conformations (Figure 2). Thus, both the oligomer and the antibiotic undergo conformational changes to form the tightly packed 2:1 complex. There is good stacking of the ActD phenoxazone ring with the GC base pairs at the 5′-GC-3′ intercalation site, and the amide NH and CO on both peptides of ActD at each GC site are positioned to form hydrogen bonds with the guanine N-3 and amino groups in the minor groove to account for the binding specificity of the intercalator. The N–CH_3 group of *N*-methylVal points into the helix and makes close contact with the A_7 H-2, to give strong NOE cross peaks. Binding of the two ActD molecules in close proximity on the double helix could not be predicted from other studies of ActD complexes, and suggests that drugs of very high specificity and binding strength could be prepared by covalent linking of two ActD molecules.

A shift from the C-2′ *endo* to C-3′ *endo* sugar conformation, as a result of ActD binding, is suggested by NOESY and COSY results for T_2, C_4, and C_6. These sugar conformational changes can cause a substantial widening of the minor groove, and provide a possible answer to the question of how the four large peptide rings of the ActD 2:1 complex can fit into the narrow minor groove of B-form DNA. Such drug-induced conformational changes demonstrate the inherent flexibility of DNA and its ability to respond to ligand interactions. This type of conformational change may be a common feature of binding of compounds with bulky groups that must fit into the minor groove. Previous ideas, based on the dimensions of the DNA grooves from the B-form structure, concerning the size of the molecules that could fit the major or minor groove, must be reconsidered.

Simple intercalators and even the more complex ActD bind to intercalation sites with the long axis of their aromatic systems approximately parallel to the long axes of the base pairs at the intercalation site. X-ray and other studies of a number of anthracycline drugs, however, indicate that these compounds bind in a bayonet fashion, with their long axis approximately perpendicular to the long axes of the base pairs.[24,25] Nogalamycin (Figure 1) is an example of naturally occurring anthracyclines which have significant antibiotic and antitumor activity, and its DNA complexes have been extensively studies by NMR methods.

Searle et al.[26] obtained 2D NMR spectra on the 2:1 complex formed between nogalamycin and the oligomer d(GCATGC), while Zhang and Patel[27] obtained spectra for the complex with d(AGCATGCT). Nogalamycin intercalates at each of the two CA/TG steps and, although three possible complexes are possible, only a single symmetrical complex is observed. The NMR results support a threading intercalation mode with the two sugar moieties residing in opposite grooves—the bicyclic amino sugar occupying the major groove and the nogalose lying in the minor groove. The conformation with sugar residues in opposite grooves is also consistent with the slow association and dissociation kinetics, in that the base pairs at the binding site must temporarily open to allow one of the bulky sugars to slide through during the intercalation reaction. NOE results indicate that the amino and nogalose sugars are directed towards the ends of the duplex. Molecular dynamics calculations constrained by NOE distances were used by Zhang and Patel[27] to generate a structure for the complex. In the energy-minimized conformation the bicyclic amino sugar is in close proximity to the floor of the major groove with its two hydroxyl groups positioned to form hydrogen bonds with N-7 and O-6 of G_6. Additional hydrogen bonding between the nogalose and the G_2 and G_6 amino groups in the minor groove is predicted by the model.

Wang and co-workers examined the 2:1 complex formed between nogalamycin and the hexamer $d(CGTACG)_2$ by NMR and related hexamers by X-ray crystallography.[25,28] They found that the nogalose and bicyclic amino sugars are in the minor and major grooves, respectively, with the intercalation site characterized by a wedge shape with significant buckling of the base pairs. Nogalamycin intercalates at the two terminal CG sites in the $d(CGTACG)_2$ hexamer with the nogalose and bicyclic amino sugars directed toward the center of the oligomer.[25] This is in contrast to earlier studies[26,27] which found the nogalose and bicyclic amino sugars directed toward the ends of the oligomer. To investigate the molecular basis for these differences, Patel and co-workers[29] conducted NMR studies on duplexes, $d(G_1C_2G_3T_4)\cdot d(A_5C_6G_7C_8)$ and d(GCAT)·d(ATGC). The latter oligomer forms complexes similar to those observed earlier by Zhang and Patel,[27] whereas the d(GCGT) duplex binds nogalamycin in two different complexes of almost equal amounts. In both complexes, nogalamycin is intercalated at the CG sequence with the bicyclic and nogalose sugars in the major and minor grooves, respectively, as in the previous complexes. In one complex the intercalated ring is stacked on the C_6-G_7 bases with the sugars directed at the $G_1\cdot C_8$ terminus, while in the other complex the ring is stacked with the C_2-G_3 bases with the sugars pointed to the $T_4\cdot A_5$ terminus.[29] The first complex is similar to that observed by Zhang and Patel,[27] whereas the second complex is more similar to that observed by Wang and co-workers.[28] All of the results are consistent if a nogalamycin has binding specificity for the 3′ side of C.[29] In this model, nogalamycin binds at the 3′ side of a cytosine residue and wraps around the G·C base pair. Formation of specific hydrogen bonds can establish the observed specificity and orientation of the drug.[29]

Intercalation of compounds containing two or more intercalating rings with DNA has been of interest due to their enhanced potential as anticancer drugs.[1,2] An initial idea in the development of bis-intercalators was that the antitumor activity of intercalating drugs could be correlated with their DNA binding affinity and dissociation rate, and these features could be enhanced by incorporating more than one intercalator into the same molecular system. The anticancer bis-intercalator ditercalinium (Figure 3) has been extensively investigated with NMR methods by Rogues and co-workers.[30] Bis-intercalation with d(CGCG) is confirmed by ^{1}H NMR and ^{31}P NMR, and the neighbor exclusion effect is evidenced by the observed NOE cross peak between the G_2 H-1′ and the C_3 H-6, and the lack of connectivities from C_1 to G_2 and from C_3 to G_4 in the d(CGCG) complex. NOEs between ditercalinium aromatic protons and the DNA base protons provide clear evidence for orientation of the aromatic groups of ditercalinium, and require location of the linker chain of the bis-intercalator in the DNA major groove.

Zimmerman and co-workers[31] have prepared a series of macrocyclic bisacridines (SDM in Figure 3) to determine if such compounds can bind to DNA. NOESY and COSY spectra of the SDM complex with the tetramer d(CGCG) show that the aromatic proton resonances of SDM are shifted upfield upon complex conformation, and that the chemical shift differences

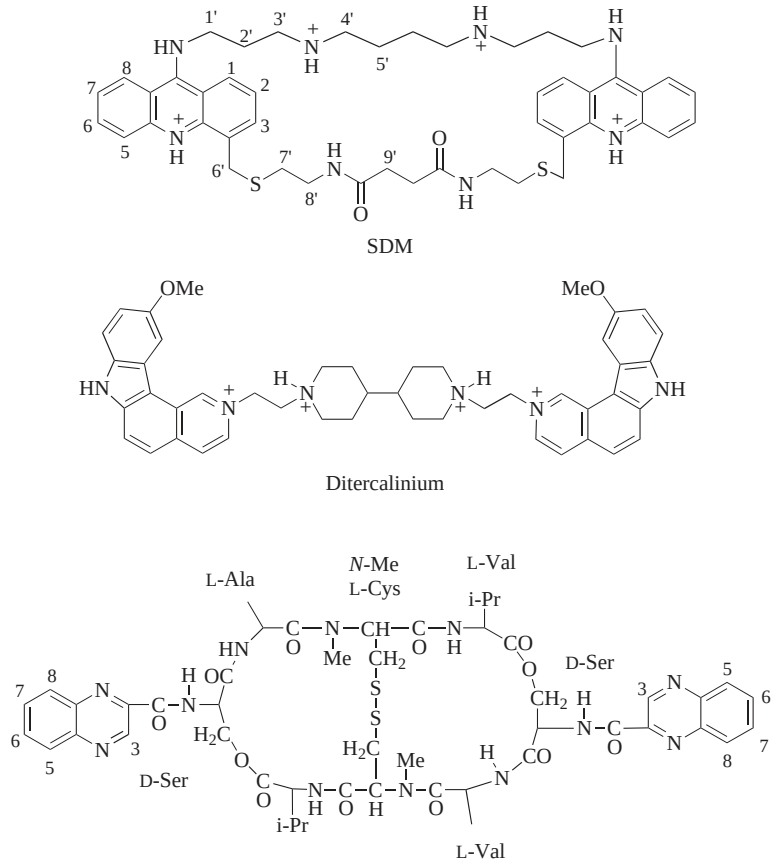

Figure 3 Structures of some natural and synthetic bis-intercalators that have been investigated by NMR methods

between the free and bound states are relatively uniform for all aromatic signals.[32] The strongest intermolecular NOE cross peaks are observed between the SDM 2, 3, and 6 resonances and C_1 2′/2″ resonances, with less intense cross peaks from SDM 3 to C_3 1′ and SDM 2 to G_2 2″. Significant SDM intramolecular cross peaks are seen between the bisamide side chain and acridines. The NMR evidence is most consistent with a model in which the side chains are in opposite grooves and the acridine rings are both fully intercalated with their long axes approximately parallel to the long axes of the base pairs. Observed cross peaks between the SDM 3 and C_3 1′ NOE protons support a model in which the spermine and bisamide side chains are in the major and minor grooves, respectively. Three pieces of evidence—the lack of full extension for the bisamide linker, the apparent SDM 2 to G_2 2″ cross peak, and the apparent SDM-binding site size of three base pairs—all suggest a model in which SDM bis-intercalates in violation of the neighbor exclusion principle.[32] As with ditercalinium, SDM results illustrate the important structural information that can be obtained on complex and nonideal systems by 2D NMR methods.

Very high DNA sequence recognition is found with bis-intercalators of the quinoxaline antitumor, antibiotic family such as TANDEM (Figure 3). Echinomycin is specific for NCGN sequences while TANDEM binds to sequences centered around TA.[13,33,34] These compounds give well-behaved DNA complexes, and NMR analyses of their complexes with short oligomers have been conducted by Feigon,[33] Patel,[34] and their co-workers. Results for CysMeTANDEM (Figure 3) complexes with the self-complementary duplex, d(GATATC), are typical of this group and illustrate their sequence recognition mechanism.[33] Distance and angle constraints for the complex were derived from NOESY and COSY data sets, while initial structures were obtained from distance geometry, and were refined with the NMR-derived constraints. The two aromatic rings bis-intercalate at the AT sequence steps, and the cyclic peptide is in the minor groove at the TA sequence. Specific hydrogen bonds between the Ala NH and adenine N-3 groups at the TA step along with specific van der Waals interactions account for much of the AT specificity of TANDEM derivatives.[33] Similar interactions at CG sequences account for the specificity of echinomycin-type bis-intercalators, although complex peptide and groove interactions, which are still not completely understood, are apparently required for the high observed level of specificity.[13,33,34] NMR results for these peptide-linked bis-intercalators provide a striking example of DNA sequence recognition differences that occurs as a result of relatively small changes in the peptide systems.

3 REVERSIBLE DNA COMPLEXES: MINOR-GROOVE INTERACTIONS

There are a number of antibiotics and synthetic drugs (Figure 4) that have been shown to bind with base pair

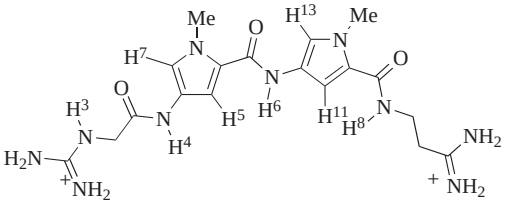

Netropsin

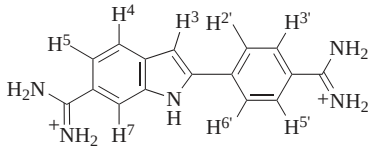

DAPI

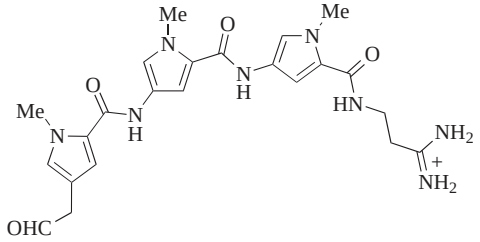

Distamycin

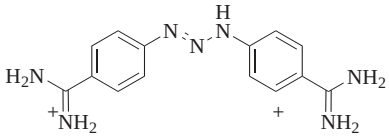

Berenil

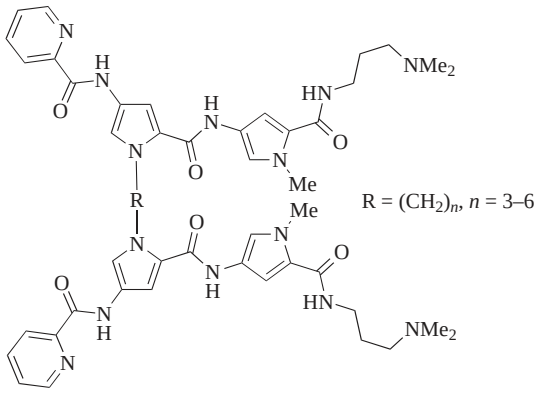

Peptide dimer

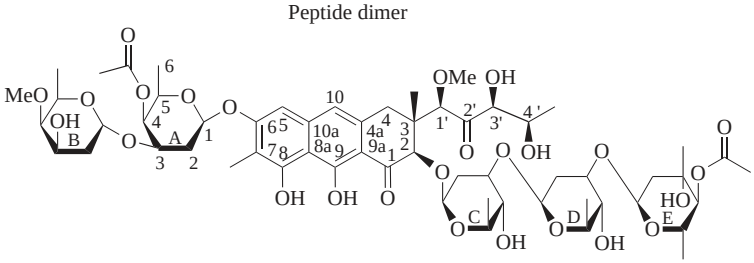

Chromomycin

Figure 4 Structures of some natural and synthetic minor-groove binding drugs that have been investigated by NMR methods

specificity in the minor groove of DNA.[1,2] Compounds such as netropsin form hydrogen bonds with groups on the floor of the minor groove, and the 0.34 nm thickness of the conjugated system of the drugs allows formation of good van der Waals contacts with the walls of the narrow minor groove in AT-rich sequences.[1,2] The amino group of guanine generally prevents such molecules from sliding deeply into the minor groove at GC sites, and the minor groove is generally wider with a less negative electronic potential in sequences with GC base pairs. Wemmer, Dervan, and co-workers[10,11,35] have shown, however, that dimers of distamycin and analogs can bind in the minor groove of GC-containing DNA sequences. Chromomycin binds exclusively in the minor groove at GC sites as a magnesium ion-linked dimer.[12–14] DAPI (Figure 4) has extremely interesting sequence-dependent interactions with DNA.[36–38] NMR and other biophysical studies indicate that DAPI binds strongly in the minor groove in AT sequences, but intercalates in GC sequences. The compounds in Figure 4, thus, have very different interactions with DNA, and an analysis of NMR results for some of their complexes is presented here.

Pelton and Wemmer[10] used NMR distance constraints in molecular mechanics calculations for distamycin–d(CGCGA ATTCGCG), and derived a structure with distamycin in the minor groove at AATT. The amidinium group is in the center of the groove, and there are several hydrogen bonds, generally somewhat long, between the amidine N-H and the adenine N-3 and thymine O-2 atoms at the floor of the minor groove. A very interesting stacking of deoxyribose O-1′ atoms over each of

the three pyrrole rings of distamycin, which may be a common feature in nucleic acid groove complexes, was observed.

Analyses of distamycin complexes with oligomers that have longer AT sequences were surprising.[11] With the sequence d(CGCAAATTGGC) and its complementary chain (referred to as A_3T_2), NMR evidence suggested that four possible single distamycin-binding sites, each with four consecutive AT base pairs, were populated at low ratios of distamycin. As the ratio was increased, however, a new set of peaks appeared and, at a 2:1 ratio, these new peaks were the only ones present. These observations, and the fact that two sets of distamycin NMR signals are present, indicated that two distamycin molecules bind in different orientations at the 2:1 ratio. Intermolecular NOESY peaks indicate that the bound drugs are oriented in opposite directions, with their positive charges pointing to the ends of the duplex. In the 2:1 model the binding of two adjacent distamycins in the AT-rich minor groove must cause a significant widening of the groove to accommodate the two bound drugs.[11] Since the minor groove in AT sequences is normally quite narrow, this involves a significant conformational change.

Wemmer, Dervan, and co-workers have extended the dimer analysis by preparation and NMR analysis of a methylene bridge-linked series of distamycin analogs (Figure 4).[35] Binding of the dimers and monomer unit were investigated by NMR titrations with the DNA sequence d(GCATGACTCGG) and its complementary strand. The monomer bound as a cooperative dimer in the 5′-TGACT-3′ site to give a unique peptide–DNA complex. The covalent dimers all formed 1:1 complexes with the same site, suggesting that very similar complexes were formed with the cooperative and covalent dimers. The linker length had little effect on the complexes with this system. 2D NMR studies indicated that both the 2:1 monomer and 1:1 dimer complexes bound in an antiparallel manner, with the aromatic rings of one ligand overlapping the amide bonds of the other unit, as observed for the distamycin dimer.[35] In all complexes one peptide unit spans the TGAC sequence while the other contacts the AGTC sequence on the opposite strand. Such an orientation allows the two pyridine systems of the dimer to form hydrogen bonds with the 2-amino groups of the guanine residues at the floor of the minor groove, and can account for the sequence recognition for these linked systems. NMR studies played the key role in the discovery and characterization of these dimer systems, which present exciting new possibilities for drug development.[10,11,35]

Chromomycin (CRA, Figure 4) belongs to the aureolic acid group of antitumor antibiotics that exert their biological effects through complex formation with DNA.[1] All compounds of this group have pronounced GC base pair binding specificity, and require a divalent cation such as Mg^{2+} for strong DNA binding. Gao and Patel[12,13] observed complex ^{31}P chemical shift changes on addition of CRA to the sequence d($T_1T_2G_3G_4C_5C_6A_7A_8$): signals for the T_2-G_3 and G_3-G_4 phosphate groups moved to high frequency, and signals for the G_4-C_5, C_6-A_7, and C_5-C_6 phosphates moved significantly to low frequency in the CRA complex. These results are highly suggestive of groove binding, and they demonstrate that CRA–DNA interactions are unusually complex. A single new signal for each imino proton is observed from low ratios of CRA to 2:1 CRA/oligomer, and at a 1:1 ratio bound and free signal areas are approximately equal. These results indicate that two CRA molecules bind per oligomer in a unique 1 Mg^{2+}:2CRA:1 duplex complex that maintains the C_2 symmetry present in self-complementary oligomers.[12–14]

2D NMR results establish both the minor-groove binding mode of CRA and the orientation of the CRA sugar rings in the bound dimer.[12–14] The E-sugar of CRA (Figure 4), for example, has several NOE cross peaks with the A_7 protons in the sequence d(TTGGCCAA), indicating that the E-sugar makes close contact with the 3′ end of the strands of the duplex. The chromophore methyl group protons have a weak NOE with the G_3 amino protons in the sequence, and this contact orients the hydrophilic face of the CRA aromatic systems into the minor groove in the bound dimer. Spectral changes in some deoxyribose residues that are characteristic of a shift from the C-2′ to a C-3′ *endo*-type conformation suggest that a transition to a more A-like conformation, with a wider and more shallow minor groove is occurring in the complex. Gao and Patel[12,13] found that the dimer of CRA could be docked into a sterically acceptable complex with an A-form DNA conformation, and that such a complex satisfied the proton–proton distances predicted from the NOE results. Hydrogen bonds from the CRA phenolic group to guanine stabilize the complex, and could account for the GC binding specificity of CRA. The DNA sequence recognition motif of CRA is, thus, quite different from that of the AT-specific minor-groove agents which bind in the narrow minor groove in B-form DNA at AT-rich sequences.

DAPI and berenil (Figure 4) are aromatic diamidines with the charges, molecular shape, and array of N–H hydrogen bond donating groups on one face of the molecule that are characteristic of AT-specific, minor-groove interactions.[1,2] NMR results with DAPI–poly[d(A-T)$_2$][36] and berenil–d(CGCGAATTCGCG)[39] complexes are similar to those obtained with netropsin, and support an AT-specific, minor-groove interaction for the diamidines. The size and planarity of the aromatic system of DAPI, however, suggested that in GC sequences, where minor-groove binding is inhibited, DAPI could bind by intercalation.[36–38] This concept of sequence-dependent binding modes is difficult to detect with most biophysical techniques, but it was confirmed with comparative NMR studies of DAPI–DNA complexes. Addition of poly[d(G-C)$_2$] causes dramatic upfield shifts of the DAPI aromatic protons, as expected for intercalation.[37] The relative shifts of the protons on the indole ring are particularly informative (Figure 5). In the GC complex the H-3 and H-4 atoms, near the center of the molecule, shift significantly farther to low frequency then H-5, which is at the edge of the molecular long axes. This is exactly the shift pattern expected for intercalation of the DAPI molecule with its long axis approximately parallel to the long axes of the base pairs at the intercalation site. The protons H-3, H-4, and H-5 all shift slightly to high frequency in the complex with poly[d(A-T)$_2$].[36] The high-frequency shift of H-7 in the AT complex is larger than for the other protons of DAPI, and this finding agrees with the proposed minor-groove binding model for DAPI with the indole H-7 and the NH group facing into the edges of the AT base pairs in the minor groove. The deshielding effects of the base pair ring currents are maximized at their edges and H-7, thus, experiences the largest deshielding shift in the AT–DAPI complex.[36]

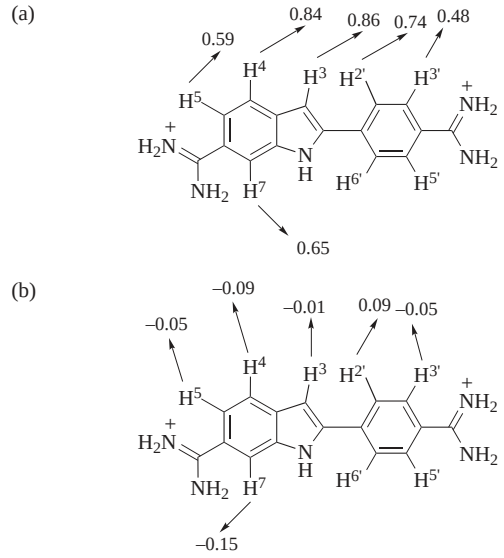

Figure 5 A schematic of the observed proton NMR chemical shift changes that occur when DAPI binds to (a) GC and to (b) AT sites in DNA

Other NMR results also support the sequence-dependent binding modes of DAPI. The imino proton on poly[d(A-T)$_2$] becomes deshielded and the imino proton of poly[d(G-C)$_2$] shielded on the addition of DAPI. The ^{31}P signals of the AT polymer shift to low frequency, and those of the GC polymer to high frequency, as expected, respectively, for groove and intercalation binding modes. The inescapable conclusion is that DAPI binds by intercalation at GC and mixed AT/GC sites, and in a minor-groove complex at AT sequences. Recent NMR studies with RNA complexes of DAPI provide information about the influence of helix type on binding mode. In RNA sequences containing only AU base pairs, NMR studies indicate that DAPI binds by intercalation, not by complex formation in the minor groove as with AT sequences in DNA.[38] Since the minor groove conformations of A-form RNA and B-form DNA are very different, but intercalation sites in DNA and RNA can be quite similar, intercalation of DAPI with RNA AU sequences fits quite well with current knowledge of nucleic acid conformation and its influence on binding mode.[38] NMR studies have been essential in establishing the sequence and helix-type dependence of the DAPI-binding mode, and show that the binding mode with the lowest free energy is determined by factors such as the nucleic acid sequence and conformation as well as by the shape and substituents of the ligand.

4 COVALENT DNA COMPLEXES

A number of covalent drug–DNA adducts have been investigated with NMR methods. Covalent adducts have been found as intercalated as well as both major- and minor-groove species. The major-groove complexes are best represented by the widely used anticancer metallo-drug *cis*-Pt(NH$_3$)$_2$Cl$_2$ (*cis*-diamminedichloroplatinum, *cis*-DDP) and related derivatives. Marzilli and co-workers[40,41] have shown with NMR that the reaction of *cis*-DDP with DNA can cause dramatic structural changes in the duplex. Hurley and co-workers have conducted

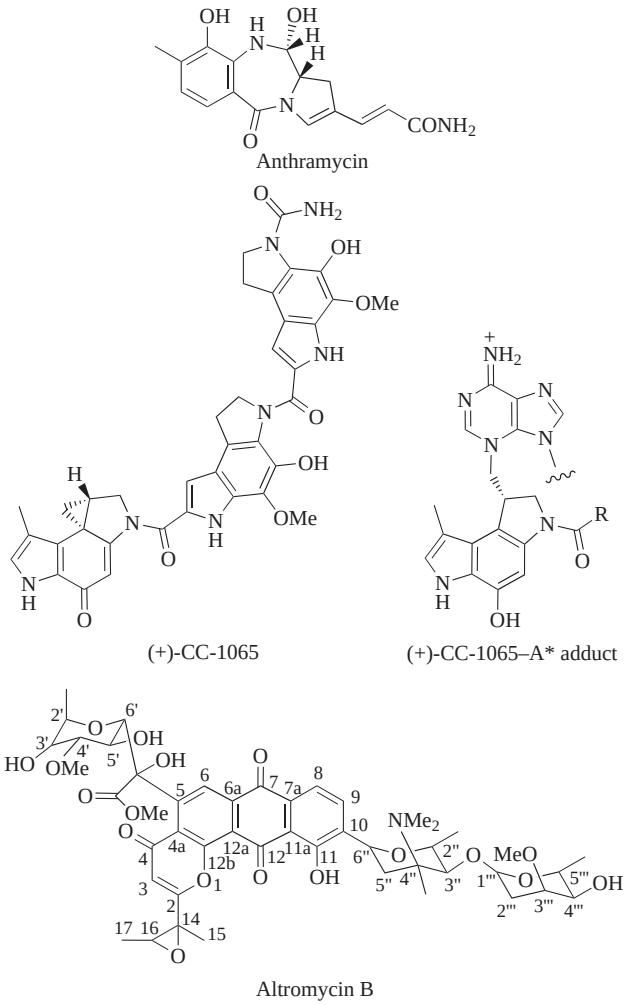

Figure 6 Structures of some anticancer drugs that bind covalently to DNA and have been investigated by NMR methods. A portion of the covalent adduct of CC-1065 with N-3 of A is also shown

detailed NMR studies of covalent organic compounds that react in the minor groove at guanine residues, such as anthramycin,[42] or at adenine residues, such as CC-1065,[43] or which intercalate, such as altromycin B[44] (Figure 6).

The adducts formed between *cis*-DDP and N-7 of guanine are the principal products formed on reaction with DNA, the likely in vivo target of the drug.[40,41] A major product involves reaction at intrastrand adjacent guanine N-7 atoms, and this adduct can cause severe distortion of the DNA duplex. The difficulty with NMR studies of such distorted DNA complexes is that key NOE cross peaks can be lost, and standard sequential ^{1}H assignment procedures may not be possible. In such cases, ^{13}C NMR methods can provide useful assistance for ^{1}H assignments, and can give valuable structural information. The model system d(T$_1$G$_2$G$_3$T$_4$)–Pt(en), where en = ethylenediamine, which has N-7 of both guanines reacted with platinum, has been studied by a variety of NMR methods.[41] Heteronuclear scalar connectivities assisted in the assignment of the complex, and ^{13}C NMR chemical shift changes were used to identify the platinum cross-linking sites. The C-3′ signal of G$_2$ was shielded by 6.6 ppm on reaction of the tetramer with the platinum drug, and such shifts are characteristic of a sugar conformational change from C-2′ *endo*

to C-3′ *endo*. The ^{13}C spectrum of the platinum–oligomer does not change significantly with temperature while the spectrum of the free oligomer shows significant changes with temperature. These comparisons indicate that the platinum reaction of DNA induces large conformational changes, and that the resulting conformations are quite stable to temperature changes.[41]

Results with CC-1065 illustrate a number of interesting features of covalent complexes of organic drugs with DNA, and demonstrate the use of NMR methods to define the molecular basis of sequence selectivity and induced conformational changes in DNA.[43,45] The drug reacts preferentially at two consensus DNA sequences: 5′-PuNTTA* and 5′-AAAAA* (where A* indicates the modified base, see Figure 6). The reactive cyclopropane ring alkylates N-3 of adenine when CC-1065 binds to the above sequences. NMR studies have shown that in the product the major form of the reacted adenine is as the cationic doubly protonated amino form (Figure 6), and that a water molecule organized in the noncovalent initial complex is part of a catalytic mechanism for the reaction of CC-1065 with DNA.[43,45] The structured water molecule has been detected by proton NMR analysis of the covalent product in ^{17}O-enriched water. Selective broadening of the phenolic hydrogen in the reactive-A subunit (see Figure 5) in ^{17}O-enriched water suggests that a structured water bridges the phenolic group and a phosphate oxygen on the strand of DNA that is not reacted with CC-1065. A $\sim$2 ppm deshielding of the phenolic proton on the A relative to the B and C subunits in the complex supports this model. The ordered water apparently plays a role in activation of CC-1065 for covalent linkage to N-3 of A after the drug binds in the minor groove.[45]

The ^{17}O results also suggest that a structured water is necessary to bridge the amino group of the reacted adenine and its complementary thymine.[45] Bending of DNA and propeller twist of base pairs near the site of reaction may require the additional water in the major groove to bridge the reacted base pair. Ordered water, as demonstrated by NMR methods with CC-1065, may play a role in other nucleic acid reactions, recognition mechanisms, and structure stabilizations. NMR results have also demonstrated that the bend in the DNA helix induced by reaction with CC-1065 is similar to the natural bend caused by repeating adenine tracts.[43,45] The results suggest that deformability of DNA sequences may be an additional significant contributor to the sequence selectivity in reaction of CC-1065. Covalent drugs, thus, initially bind to DNA with the same sequence recognition mechanisms as noncovalent drugs, but in their reaction with DNA other factors, such as catalytic activation and sequence deformability, can play a major additional role in refining sequence recognition.[43,45]

5 OVERVIEW

In the relatively short period of overlap of modern high-field FT NMR and oligomer synthesis capabilities, a wealth of new and, in many cases surprising, results have appeared for drug–nucleic acid complexes. Some of the unexpected and very interesting results that have been presented in this article include: the dimer-binding modes of distamycin, chromomycin and actinomycin; the AT minor-groove and GC intercalation modes for some unfused aromatic cations such as DAPI; a structured water involved in catalysis of the CC-1065 reaction with N-3 of adenine in the minor groove; and a variety of findings on the molecular basis of binding specificity and complex dynamics. Detailed understanding of these important features of nucleic acid complexes has only been possible through high-resolution NMR studies. As NMR and oligomer synthesis capabilities continue to advance, it is certain that more interesting, unexpected, and important new results for drug–nucleic acid complexes lie in our future.

6 RELATED ARTICLES

DNA: A-, B-, and Z-; DNA–Cation Interactions: Quadrupolar Studies; DNA Triplexes, Quadruplexes, and Aptamers; Nucleic Acid Structures in Solution: Sequence Dependence; Nucleic Acids: Base Stacking and Base Pairing Interactions; Nucleic Acids: Chemical Shifts; Nucleic Acids: Phosphorus-31 NMR; Nucleic Acids: Spectra, Structures, and Dynamics; RNA Structure and Function: Modified Nucleosides.

7 REFERENCES

1. M. Waring, in *The Molecular Basis of Antibiotic Action*, 2nd edn., ed. E. F. Gale, E. Cundiffe, P. E. Reynolds, M. H. Richmond, and M. J. Waring, Wiley, London, 1981, p. 274
2. W. D. Wilson, in *Nucleic Acids in Chemistry and Biology*, ed. G. M Blackburn and M. J. Gait, IRL Press, Oxford, 1990, Chap. 8
3. C. C. McDonald, W. D. Phillips, and S. Penman, *Science*, 1969, **144**, 1234.
4. G. Varani and I. Tinoco, Jr., *Quart. Rev. Biophys.*, 1990, **24**, 479.
5. W. D. Wilson, Y. Li, and J. M. Veal, in *Advances in DNA Sequence Specific Agents*, ed. L. H. Hurley, JAI Press, Greenwich, 1992, Vol. 1, p. 89.
6. G. P. Kreishman, S. I. Chan, and W. Bauer, *J. Mol. Biol.*, 1971, **61**, 45.
7. T. R. Krugh and M. E. Nuss, in *Biological Applications of Magnetic Resonance*, ed. R. G. Schulman, Academic Press, New York, 1979, Chap. 3
8. E. V. Scott, R. L. Jones, D. L. Banville, G. Zon, L. G. Marzilli, and W. D. Wilson, *Biochemistry*, 1988, **27**, 915.
9. E. V. Scott, G. Zon, L. G. Marzilli, and W. D. Wilson, *Biochemistry*, 1988, **27**, 7940.
10. J. G. Pelton and D. E. Wemmer, *Biochemistry*, 1988, **27**, 8088.
11. J. G. Pelton and D. E. Wemmer, *Proc. Natl. Acad. Sci. USA*, 1989, **86**, 5723.
12. X. Gao and D. J. Patel, *Biochemistry*, 1989, **28**, 751.
13. X. Gao and D. J. Patel, *Quart. Rev. Biophys.*, 1989, **22**, 93.
14. D. L. Banville, M. Keniry, M. Kam, and R. H. Shafer, *Biochemistry*, 1990, **29**, 6521.
15. D. G. Gorenstein, in *Phosphorous-31 NMR*, ed. D. G. Gorenstein, Academic Press, Orlando, 1984, p. 7.
16. S. Chandrasekaran, C. R. Krishnamoorthy, R. L. Jones, J. C. Smith, and W. D. Wilson, *Biochem. Biophys. Res. Commun.*, 1984, **122**, 804.
17. W. D. Wilson, R. L. Jones, G. Zon, D. L. Banville, and L. G. Marzilli, *Biopolymers*, 1986, **25**, 1997.
18. S. S. David and J. K. Barton, *J. Am. Chem. Soc.*, 1993, **115**, 2984.
19. R. J. Fiel, *J. Biomol. Struct. Dyn.*, 1989, **6**, 1259.
20. L. G. Marzilli, D. L. Banville, G. Zon, and W. D. Wilson, *J. Am. Chem. Soc.*, 1986, **108**, 4188.

21. R. J. Abraham, G. R. Bedford, D. McNeillie, and B. Wright, *Org. Magn. Reson.*, 1980, **14**, 418.
22. C. Giessner-Prettre and B. Pullman, *C.R. Acad. Sci., Paris, Ser. D*, 1976, **283**, 675.
23. W. D. Wilson, R. L. Jones, G. Zon, E. V. Scott, D. L. Banville, and L. G. Marzilli, *J. Am. Chem. Soc.*, 1986, **108**, 7113.
24. J. W. Lown (ed.), *Anthracycline and Anthracenedione-Based Anticancer Agents*, Elsevier, Amsterdam, 1988.
25. Y.-G. Gao. Y.-C. Liaw, H. Robinson, and A. H.-J. Wang, *Biochemistry*, 1990, **29**, 10307.
26. M. S. Searle, J. G. Hall, W. A. Denny, and L. P. G. Wakelin, *Biochemistry*, 1988, **27**, 4340.
27. X. Zhang and D. S. Patel, *Biochemistry*, 1990, **29**, 9451.
28. H. Robinson, Y.-C. Liaw, G. A. van der Marel, J. H. van Boom, and A. H.-J. Wang, *Nucleic Acids Res.*, 1990, **18**, 4851.
29. L. P. A. van Houte, C. J. van Garderen, and D. J. Patel, *Biochemistry*, 1993, **32**, 1667.
30. M. Delepierre, J. Igolen, and B. P. Rogues, *Biopolymers*, 1988, **27**, 957.
31. S. C. Zimmerman, C. R. Lamberson, M. Cory, and T. A. Fairly, *J. Am. Chem. Soc.*, 1989, **111**, 6805.
32. J. M. Veal, Y. Li, S. C. Zimmerman, C. R. Lamberson, M. Cory, G. Zon, and W. D. Wilson, *Biochemistry*, 1990, **29**, 10918.
33. K. J. Addess, J. S. Sinsheimer, and J. Feigon, *Biochemistry*, 1993, **32**, 2498.
34. X. Gao and D. J. Patel, *Biochemistry*, 1988, **27**, 1744.
35. T. J. Dwyer, B. H. Geierstanger, M. Mrksich, P. B. Dervan, and D. E. Wemmer, *J. Am. Chem. Soc.*, 1993, **115**, 9900.
36. W. D. Wilson, F. A. Tanious, H. J. Barton, R. L. Jones, K. Fox, R. L. Wydra, and L. Strekowski, *Biochemistry*, 1990, **29**, 8452.
37. W. D. Wilson, F. A. Tanious, H. J. Barton, L. Strekowski, D. W. Boykin, and R. L. Jones, *J. Am. Chem. Soc.*, 1989, **111**, 5008.
38. F. A. Tanious, J. M. Veal, H. Buczak, L. S. Ratmeyer, and W. D. Wilson, *Biochemistry*, 1992, **31**, 3103.
39. A. N. Lane, T. C. Jenkins, T. Brown, and S. Neidle, *Biochemistry*, 1991, **30**, 1372.
40. L. G. Marzilli, S. Mukundan, Jr., Y. Xu, G. Zon, A. Bergman, P. Yohannes, and M. D. Reily, in *Platinum and Other Metal Coordination Compounds in Cancer Chemotherapy*, ed. S. B. Howell, Plenum Press, New York, 1991, p. 101.
41. S. Mukundan, Jr., Y. Xu, G. Zon, and L. G. Marzilli, *J. Am. Chem. Soc.*, 1991, **113**, 3021.
42. J. A. Mountzouris and L. H. Hurley, in *Advances in DNA Sequence Specific Agents*, ed. L. H. Hurley, JAI Press, Greenwich, 1992, Vol. 1, p. 263.
43. D. Sun, C. H. Lin, and L. H. Hurley, *Biochemistry*, 1993, **32**, 4487.
44. D. Sun, M. Hansen, J. J. Clement, and L. H. Hurley, *Biochemistry*, 1993, **32**, 8068.
45. C. H. Lin, J. M. Beale, and L. H. Hurley, *Biochemistry*, 1991, **30**, 3597.

Biographical Sketch

David Wilson. *b* 1944. B.S., University of North Carolina, 1966, Ph.D., Purdue, 1970. Began NMR studies on DNA–drug and DNA–peptide complexes in 1974 with Professor Edmond Gabbay at the University of Florida. Faculty in Chemistry at Georgia State University 1971–present. Approx. 150 publications. Research interests: biophysical analysis of nucleic acid structure and interactions with particular emphasis on the use of NMR information in conjunction with molecular modeling to understand drug action and to design new nucleic acid-interactive drugs.

Half-Filter Experiments: Proton–Carbon-13

Gottfried Otting

Karolinska Institute, Stockholm, Sweden

1	Introduction	1
2	Half-Filter Elements	1
3	Implementation of Half-Filters in Pulse Sequences	2
4	Double Half-Filter	3
5	Half-Filters and Multidimensional NMR	3
6	Related Article	3
7	References	3

1 INTRODUCTION

Proton–carbon-13 half-filters divide a ^{1}H NMR spectrum into two subspectra, where one contains the signals from protons bound to ^{13}C and the other the signals of the protons bound to ^{12}C. Half-filters can be applied quite generally to heteronuclear two-spin systems where both nuclei carry a spin-$\frac{1}{2}$ and are coupled to each other. Apart from ^{1}H–^{13}C half-filters, ^{1}H–^{15}N half-filters are of the greatest use with biological samples. Originally, half-filters were used in combination with selective labeling of the biomolecules at defined positions with ^{13}C or ^{15}N to obtain a considerably simplified subspectrum of the ^{13}C or ^{15}N 'labeled' protons.[1,2] The name 'half-filter' was chosen because any one of these filter elements acts exclusively in one dimension of a 2D NMR experiment without selecting amongst the resonances in the other frequency dimension. This property is also the main difference to the so-called *X* filters, which select the cross peaks between protons coupled to the same heteronuclear spin *X*.[3] Further related filters have been developed for special applications that select the protons coupled to more than one heteronuclear spin.[4] With the availability of more powerful computers and larger disks, uniform ^{13}C and ^{15}N labeling has become increasingly popular, because the development of a ^{1}H–^{1}H 2D NMR spectrum into a third and fourth dimension by the heteronuclear chemical shifts often provides sufficient resolution to assign a large number of ^{1}H–^{1}H cross peaks with a single isotope enriched sample. In the context of uniform isotope enrichment, half-filters have a particular interest in studies of protein–ligand complexes, where the protein partner is uniformly enriched with ^{13}C or ^{15}N while the ligand is not.[5] In this situation, a ^{1}H–^{13}C half-filter is able to select the cross peaks with the ^{12}C bound protons of the ligand whereas a higher-dimensional experiment using the ^{13}C chemical shift in an additional dimension would suppress the signals of the ^{12}C bound protons. The combination of two half-filter elements in the experiment results in a so-called double half-filter, which allows the selective observation of the ^{1}H–^{1}H cross peaks between the unlabeled ligand protons in the complex, while the cross peaks with the labeled protein are directed into different subspectra. Clearly, the spectral editing can be extended further by combining a ^{1}H–^{13}C half-filter with a ^{1}H–^{15}N half-filter or an *X* filter, and one could in principle also imagine half-filters between two nonproton spins, e.g. ^{3}H and ^{13}C. In biological applications, the proton spins are of most interest because of their high natural abundance and sensitivity, and because of the structural information contained in ^{1}H–^{1}H NOEs. In the following discussion, ^{1}H–^{13}C and ^{1}H–^{15}N half-filters will be referred to as ^{13}C half-filters and ^{15}N half-filters, respectively. The present article uses ^{13}C half-filters as examples to discuss the principles of half-filters and presents illustrative applications.

2 HALF-FILTER ELEMENTS

There are two different half-filter elements which can be used in a pulse sequence. The half-filter element of Figure 1(a) refocuses the one-bond $^1J(^{13}\mathrm{C}, ^1\mathrm{H})$ coupling so that ^{13}C broadband decoupling can be used throughout the rest of the pulse sequence. The half-filter element of Figure 1(b) is shorter, but results in heteronuclear antiphase magnetization which precludes heteronuclear decoupling unless the filter is used only to select for ^{12}C bound protons. The delay τ is set to $1/[2^1J(^{13}\mathrm{C}, ^1\mathrm{H})]$. Two data sets are recorded which differ only by the phase ϕ of the editing 90°(^{13}C) pulse (Figure 1).

The functioning of a half-filter is most easily understood in terms of a product operator description[6] for the spins of an isolated ^{1}H–^{13}C group and of a ^{1}H–^{12}C group. Because of the 180°(^{1}H) pulse in the center of the filter elements, the chemical shift evolution of the protons is refocused so that only the evolution under the heteronuclear coupling needs to be considered. Starting from in-phase proton magnetization along the *x* axis, H_x, the heteronuclear coupling leads to antiphase magnetization, $2H_yC_z$, at the end of the delay τ for the ^{1}H–^{13}C group. The following two 90°(^{13}C) pulses are either of the same or the opposite phase, resulting in, respectively, an effective 180°(^{13}C) pulse which inverts the sign of the magnetization $2H_yC_z$, or a 0°(^{13}C) rotation which has no further effect on the magnetization. The magnetization of the ^{12}C bound proton is in no instance affected by the pulses applied at the ^{13}C frequency. Therefore, subtraction of the data recorded with and without the effective 180°(^{13}C) pulse selects the magnetization of the ^{1}H–^{13}C group and cancels the response from the ^{1}H–^{12}C group, whereas summation of the data selects the proton signal from the ^{1}H–^{12}C group and suppresses the signal of the ^{1}H–^{13}C group.

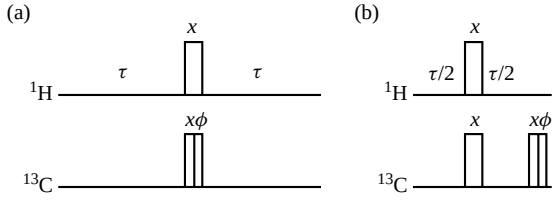

Figure 1 Carbon-13 half-filter elements. In this and the following figures, narrow and wider rectangles denote 90° and 180° pulses, respectively. The delay τ is optimally set to $1/[2^1J(^{13}\mathrm{C}, ^1\mathrm{H})]$. In recording an experiment with a half-filter, two data sets are recorded with the phase ϕ of the second 90°(^{13}C) pulse (the 'editing pulse') set to $+x$ for one data set and $-x$ for the other. (a) Half-filter element with refocusing. (b) half-filter element without refocusing

The description of the half-filter technique in terms of isolated H–C groups also holds to a good approximation for the more complicated spin systems encountered in biomolecules, because the one-bond coupling $^1J(^{13}C, ^1H)$ is much larger than any scalar coupling between protons. Moreover, the one-bond coupling constant is nearly the same for all $^1H-^{13}C$ groups, so that the delay τ can be set rather accurately to $1/[2^1J(^{13}C, ^1H)]$. If $\tau \neq 1/[2^1J(^{13}C, ^1H)]$, some of the signal intensity from the ^{13}C bound protons will appear in the sum spectrum instead of in the difference spectrum ('crosstalk').[4] In principle, the half-filter technique neither generates nor suppresses any of the cross peaks present in the unedited experiment. Losses in effective peak intensities have to be expected only from the relaxation during the short filter delay, any spread among the different one-bond $^1H-^{13}C$ coupling constants, and pulse imperfections. Loss of signal due to off-resonance effects of the ^{13}C pulses can be reduced by inserting a refocusing $180°(^{13}C)$ pulse between the two $90°(^{13}C)$ pulses of the ^{13}C half-filter.[7]

3 IMPLEMENTATION OF HALF-FILTERS IN PULSE SEQUENCES

Half-filters can be used with any of the evolution periods in a multidimensional NMR experiment or with the detection period. The names $^{13}C(\omega_1)$ half-filter, $^{13}C(\omega_2)$ half-filter, etc., can be used to emphasize the fact that the half-filter will be effective only in the respective frequency dimensions. Figure 2(a) and (b) illustrate how the half-filter element of Figure 1(a) can be implemented in a NOESY pulse sequence as a $^{13}C(\omega_2)$ half-filter and a $^{13}C(\omega_1)$ half-filter, respectively. This filter element can be used with ^{13}C decoupling, which is achieved by a $180°(^{13}C)$ pulse in the middle of the t_1 evolution period and broadband decoupling during the detection period, or broadband decoupling during both t_1 and t_2.

Figure 3 shows an example of a NOESY spectrum with a $^{15}N(\omega_2)$ half-filter recorded with the pulse sequence of Figure 2(b).[2] The compound is a peptide where the residues Gly10, Ala17, and Gly20 were selectively labeled with ^{15}N. Figure 3(a) shows the conventional NOESY spectrum with heteronuclear broadband decoupling but without a half-filter. The amide proton resonances of the three ^{15}N-labeled residues are around 8 ppm, where they overlap with the signals from other amide protons. The two subspectra obtained with the $^{15}N(\omega_2)$ half-filter are shown in Figure 3(b) and (c). Figure 3(b) was obtained as the difference between the two data sets recorded with different phases of the editing $90°(^{15}N)$ pulse. It contains exclusively those diagonal and cross peaks which involve the resonances of the three isotope-labeled amide protons in the ω_2 frequency dimension. Figure 3(c) is the sum spectrum which contains all other peaks from the unfiltered NOESY spectrum of Figure 3(a).

Figure 2(c) shows an example of the filter element of Figure 1(b) implemented in a TOCSY pulse sequence. The half-filter has been supplemented by a spin lock pulse which is applied with the same phase as the first $90°(^1H)$ pulse. Its effect is to purge the magnetization of the ^{12}C bound protons and to retain only the magnetization of the ^{13}C bound protons so that only the difference spectrum contains meaningful information. The purpose of the purge pulse is to suppress

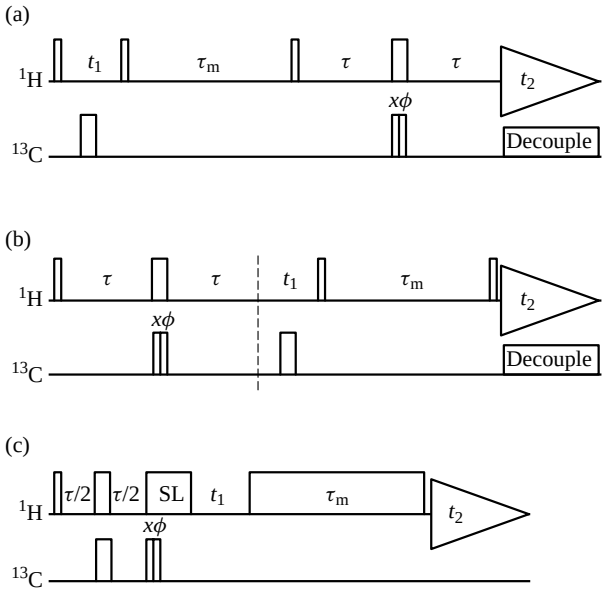

Figure 2 2D NMR experiments with ^{13}C half-filters. (a) NOESY with $^{13}C(\omega_2)$ half-filter. (b) NOESY with $^{13}C(\omega_1)$ half-filter. (c) TOCSY with the $^{13}C(\omega_1)$ half-filter element of Figure 1(b) supplemented by a spin lock purge pulse SL of about 1–2 ms duration. The TOCSY mixing sequence during τ_m is denoted by a long bar. For appropriate phase cycles see Otting and Wüthrich[4]

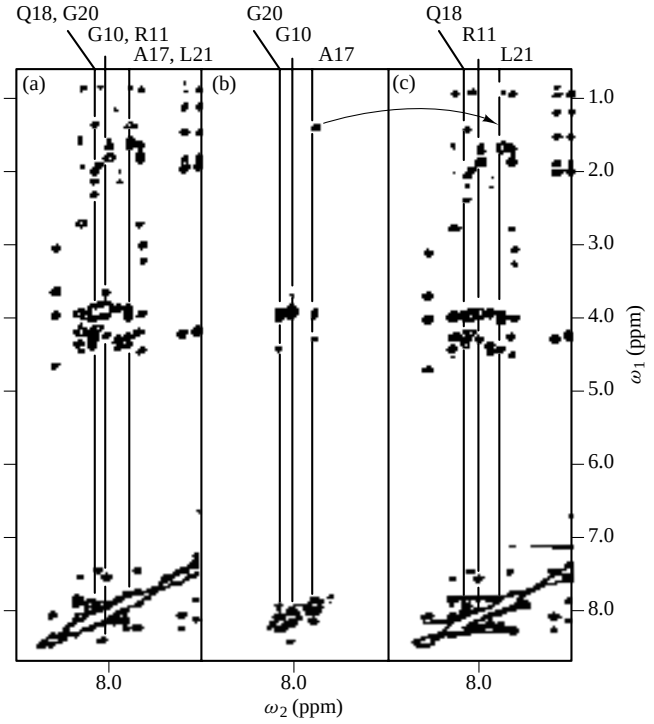

Figure 3 NOESY spectra of the fragment 7–23 from the atrial natriuretic factor in sodium dodecyl sulfate micelles. Nitrogen-15 decoupling in ω_1 and ω_2 was used in all experiments. (a) Conventional NOESY spectrum. (b), (c) Difference and sum spectrum of the NOESY experiment with a $^{15}N(\omega_2)$ half-filter. The half-filter delay τ was set to 5.38 ms. At the top the amide proton chemical shifts are indicated for selected amino acid residues. The residues G10, A17, and G20 were selectively labeled with ^{15}N. (Reproduced by permission of Academic Press from Fesik et al.[2])

the signals from the $^1H-^{12}C$ groups sufficiently to obtain an artifact-free subspectrum of the protons bound to ^{13}C at natural abundance. This pulse sequence has been used to observe the cross peaks between ^{13}C bound protons and ^{12}C bound protons in BPTI (bovine pancreatic trypsin inhibitor) (see ***Pancreatic Trypsin Inhibitor***) at natural isotope abundance.[4] Since no pulses are applied at the ^{13}C frequency after the half-filter element [Figure 2(c)], each cross peak has an ECOSY-type appearance[8] with two major multiplet components, where the relative displacements in the ω_1 and ω_2 dimensions represent, respectively, the large $^1J(^{13}C, ^1H)$ coupling constant, and the long range heteronuclear coupling constants between the protons detected along ω_2 and the ^{13}C spin of the CH groups detected along ω_1. The technique enables the measurement of heteronuclear coupling constants which are smaller than the linewidth of the signal.[9]

4 DOUBLE HALF-FILTER

Two half-filter elements may be used with different evolution or detection periods in the same experiment, resulting in a double half-filter.[4] Figure 4(a) shows an example of a NOESY pulse sequence with a $^{13}C(\omega_1, \omega_2)$ double half-filter. The combination of the $^{13}C(\omega_1)$ half-filter with the $^{13}C(\omega_2)$ half-filter leads to the presence of two $90°(^{13}C)$ editing pulses. Each editing pulse is applied either with the same or the opposite phase relative to the phase of the preceding $90°(^{13}C)$ pulse of the respective half-filter element. The four data sets recorded with the four possible combinations of phase settings of the editing pulses can be combined into four different subspectra which select or reject ^{13}C bound protons along ω_1 or ω_2.

Figure 5 presents as an illustration the four different subspectra of a homeodomain–DNA complex recorded with the pulse sequence of Figure 4(a).[10,11] The protein was uniformly enriched with ^{13}C, while the DNA was unlabeled. The four different subspectra contain the following NOESY peaks: (a) diagonal peaks and cross peaks between ^{13}C bound protons in ω_1 and ω_2 that correspond to the intramolecular NOEs of the ^{13}C-labeled protein; (b) diagonal peaks and cross peaks between ^{12}C bound protons in ω_1 and ω_2 that correspond to the intramolecular NOEs between the protons of the DNA; (c) cross peaks between ^{12}C bound protons in ω_1 and ^{12}C bound protons in ω_2 that correspond to intermolecular NOEs between the DNA and the protein; and (d) cross peaks between ^{13}C bound protons in ω_1 and ^{12}C bound protons in ω_2. The last subspectrum corresponds to the subspectrum of Figure 5(b) with mutually exchanged frequency axes.

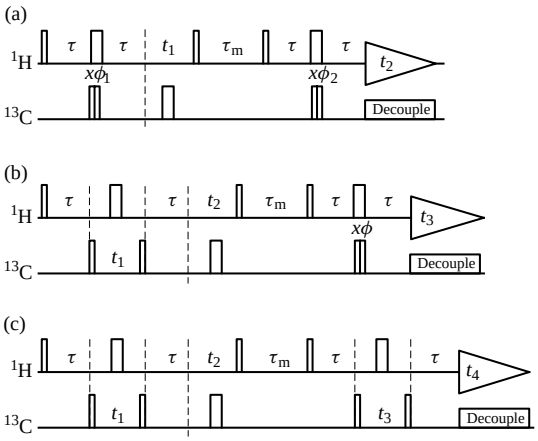

Figure 4 Pulse sequences of (a) 2D NOESY with a $^{13}C(\omega_1, \omega_2)$ double half-filter, (b) 3D HMQC–NOESY with a $^{13}C(\omega_3)$ half-filter, (c) 4D HMQC–NOESY–HMQC experiment. For appropriate phase cycles see Otting and Wüthrich[4] and Clore and Gronenborn[16]

Variants of the double half-filter include the use of ^{13}C and ^{15}N half-filters in different dimensions of the same experiment,[7] or the simultaneous application of ^{13}C and ^{15}N half-filters in a time-shared fashion.[12]

5 HALF-FILTERS AND MULTIDIMENSIONAL NMR

In principle, any experiment containing a ^{13}C half-filter element can be expanded into a new experiment with the chemical shifts of the ^{13}C nuclei in a further dimension. As a drawback, the signals from the ^{12}C bound protons cannot follow the expansion into the new dimension and are usually eliminated by the phase cycling. Half-filters are therefore the most attractive alternative when the signals of ^{12}C bound protons need to be selectively observed without losing the corresponding cross peaks with the ^{13}C bound protons. If the information on the ^{13}C bound protons can be dispensed with, a specifically optimized ^{13}C reject filter may be more efficient in selecting the resonances of the ^{12}C bound protons.[13–15]

It is instructive to compare the different NOESY experiments which would give the maximum resolution for the $^1H-^1H$ NOEs in a protein–ligand complex in which the protein is uniformly enriched with ^{13}C and the ligand unlabeled. The 4D HMQC–NOESY–HMQC experiment [Figure 4(c)] would resolve the intramolecular NOEs of the protein by frequency labeling each proton chemical shift with the chemical shift of the directly bonded ^{13}C spin in another dimension.[16] Comparison of the pulse sequences of Figure 4(a) and (c) shows that the sequence of the 4D HMQC–NOESY–HMQC experiment can be derived from the sequence of the 2D NOESY with a $^{13}C(\omega_1, \omega_2)$ double half-filter simply by insertion of an incrementable evolution period between the two $90°(^{13}C)$ pulses of each of the half-filter elements. Expanding only one of the ^{13}C half-filters into a HMQC element leads to the 3D HMQC–NOESY experiment with a $^{13}C(\omega_3)$ half-filter of Figure 4(b) or to the equivalent 3D NOESY–HMQC experiment with a $^{13}C(\omega_1)$ half-filter (sequence not shown). The latter two experiments enable the selective observation of intermolecular NOEs between ^{13}C and ^{12}C bound protons at the resolution of a 3D NMR experiment while at the same time the cross peaks between ^{13}C bound protons are directed into another 3D subspectrum.

6 RELATED ARTICLES

Pancreatic Trypsin Inhibitor.

7 REFERENCES

1. G. Otting, H. Senn, G. Wagner, and K. Wüthrich, *J. Magn. Reson.*, 1986, **70**, 500.

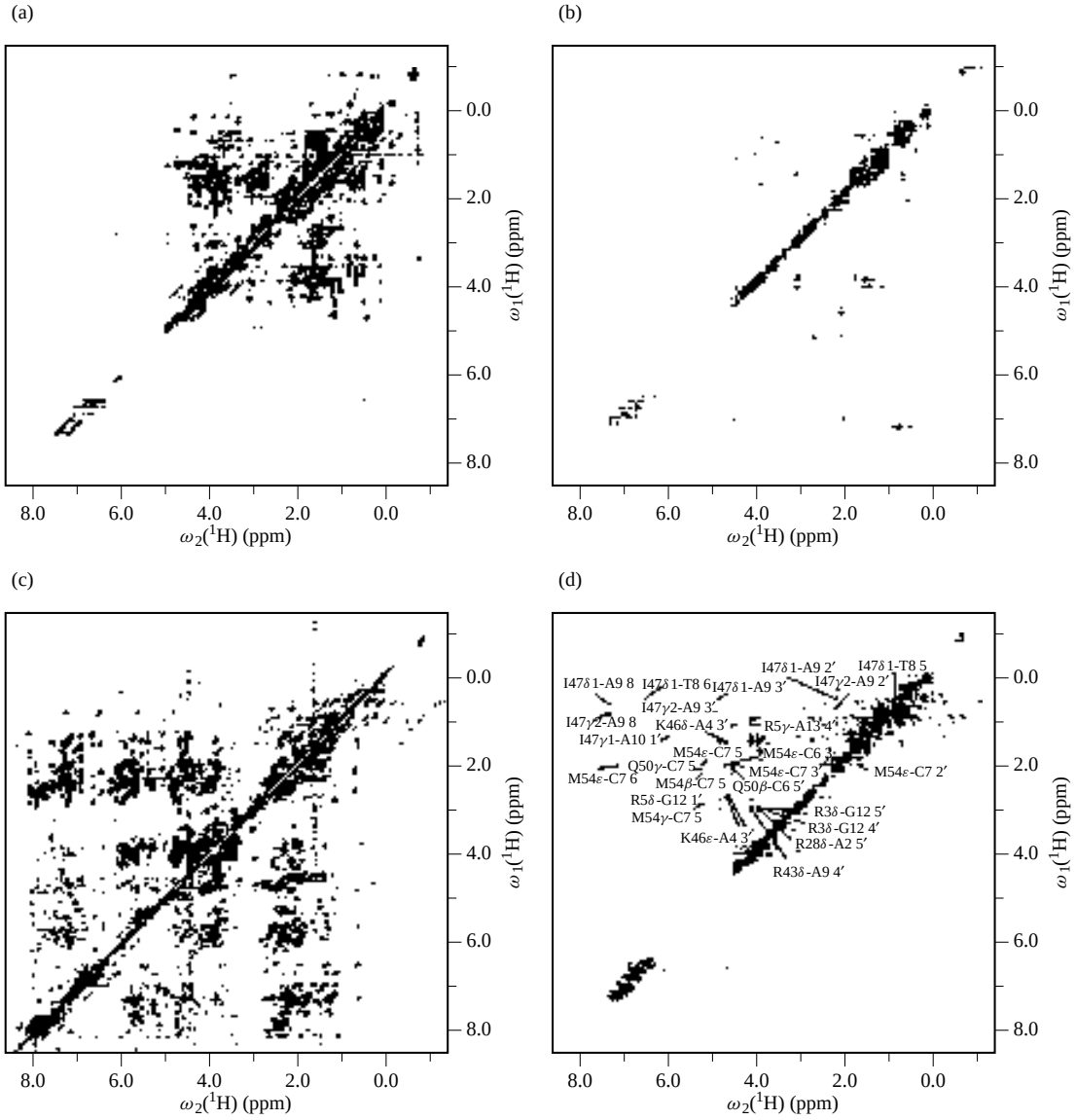

Figure 5 NOESY experiment with a $^{13}C(\omega_1, \omega_2)$ double half-filter recorded with a 2.3 mM solution of uniformly ^{13}C-labeled *Antp*(C39 S) homeodomain and an unlabeled 14 base pair DNA duplex at 36°C, pH 6.0, using a mixing time of 60 ms. (a) Subspectrum with ^{13}C bound protons selected in both dimensions. (b) Subspectrum with ^{13}C bound protons rejected in both dimensions. (c) Subspectrum with ^{13}C bound protons rejected in ω_1 and selected in ω_2. (d) Subspectrum with ^{13}C bound protons selected in ω_1 and rejected in ω_2. (Reproduced by permission of Academic Press from Qian et al.[10] and Billeter et al.[11])

2. S. W. Fesik, R. T. Gampe, Jr., and T. W. Rockway, *J. Magn. Reson.*, 1987, **74**, 366.
3. E. Wörgötter, G. Wagner, and K. Wüthrich, *J. Am. Chem. Soc.*, 1986, **108**, 6162.
4. G. Otting and K. Wüthrich, *Quart. Rev. Biophys.*, 1990, **23**, 39.
5. B. J. Stockman and J. L. Markley, *Curr. Opin. Struct. Biol.*, 1992, **2**, 52.
6. O. W. Sørensen, G. W. Eich, M. H. Levitt, G. Bodenhausen, and R. R. Ernst, *Prog. Nucl. Magn. Reson. Spectrosc.*, 1983, **16**, 163.
7. O. Zerbe, J. H. Welsh, J. A. Robinson, and W. von Philipsborn, *J. Magn. Reson.*, 1992, **100**, 329.
8. C. Griesinger, O. W. Sørensen, and R. R. Ernst, *J. Chem. Phys.*, 1986, **85**, 6837.
9. G. T. Montelione, M. E. Winkler, P. Rauenbuehler, and G. Wagner, *J. Magn. Reson.*, 1989, **82**, 198.
10. Y. Q. Qian, G. Otting, M. Billeter, M. Müller, W. J. Gehring, and K. Wüthrich, *J. Mol. Biol.*, 1993, **234**, 1070.
11. M. Billeter, Y. Q. Qian, G. Otting, M. Müller, W. J. Gehring, and K. Wüthrich, *J. Mol. Biol.*, 1993, **234**, 1084.
12. M. Burgering, R. Boelens, and R. Kaptein, *J. Biomol. NMR*, 1993, **3**, 709.
13. G. Gemmecker, E. T. Olejniczak, and S. W. Fesik, *J. Magn. Reson.*, 1992, **96**, 199.
14. M. Ikura and A. Bax, *J. Am. Chem. Soc.*, 1992, **114**, 2433.
15. A. Bax, S. Grzesiek, A. M. Gronenborn, and G. M. Clore, *J. Magn. Reson. A*, 1994, **106**, 269.
16. G. M. Clore and A. M. Gronenborn, *Prog. Nucl. Magn. Reson. Spectrosc.*, 1991, **23**, 43.

Biographical Sketch

Gottfried Otting. *b* 1958. Diploma in Chemistry, Freiburg, Germany, 1984; Ph.D. (supervisor Kurt Wüthrich), ETH-Zürich, Switzerland, 1987; Professor of Molecular Biophysics, Karolinska Institute, 1992–present. Approx. 80 publications. Research interests: biomedical applications of NMR including structure determinations of proteins and protein–ligand complexes, isotope labeling and spectral editing techniques, studies of protein dynamics.

Haptens and Antibodies

Raymond A. Dwek
The University of Oxford, Oxford, UK

1	Introduction	1
2	The DNP Binding IgA (λ_2) Mouse Protein—M315	2
3	The Phosphorylcholine Binding IgA M603	4
4	The Sugar Binding IgA Mouse Myelomas U61 and E109	4
5	Conclusions and Future Studies	5
6	References	6

1 INTRODUCTION

Antibodies form the basis of the body's defence against infection. The central importance of antibodies to biology is expressed in the functional versatility of the antibody molecule and realized through its unique structure (Figure 1). Thus, the organization of the antibody molecule into domains allows recognition of a virtually unlimited range of antigens by the variable part of the structure, whereas the constant part mediates a small number of effector systems related to antigen elimination and/or immobilization. In this article we will confine the discussion to our work on defining the structural basis for the initial recognition of antigens by antibodies. X-ray data have confirmed the idea that antibody combining site involves a cleft or groove constructed from both the heavy and light chain (Figure 1). The amino acids in the site vary for different antibodies, and are thus termed hypervariable.

1.1 Antibody Specificity

One of the central problems in immunochemistry is the structural basis of antibody specificity; how does such a high diversity in molecular recognition reside in what seems to be a family of proteins closely related in their chemical structure? The pioneering X-ray analysis of Fab′ fragments of homogenous myeloma proteins led to the elucidation of the three-dimensional structure of the binding site of two antibodies: the human protein New, which bound vitamin K, and the mouse protein McPC 603, which bound phosphorylcholine.[1,2] From these studies it was clear that the residues forming the sites that are complementary to the antigen are contributed by the hypervariable regions[3] (three segments of 5–10 residues each, in both light and heavy chains) and that replacements of amino acid residues in these segments will generate binding sites with new specificities. Such replacement will not disturb the 'immunoglobulin fold' of the variable domains, which remains similar in all antibodies. Thus on a background of a common three-dimensional structure a vast number of specificities can be generated. This diversity in recognition is the essence of the immune system, and therefore a comparative analysis of combining sites is required in order to provide the details of molecular recognition by antibodies. In this respect, it was also important to develop new methodologies by which the structure of the antibody site could be analyzed in solution and yield information comparable with that obtained from crystal studies.

1.2 NMR Approach to Studying Binding Sites

Our approach to studying combining sites mainly involved using high-resolution NMR together with crystallographic data,[4–6] and our general scheme is shown in Figure 2. When refined crystal structures are available, the NMR data can usually be interpreted directly on the basis of that structure. The contribution of NMR in such cases is then mainly to measure binding constants and to probe the role of ionizable groups (thermodynamic measurement) to give information on pairwise interactions [which allow the precise positioning of nuclei (< 0.05 nm)] and to give information on motional dynamics of nuclei on individual amino acid residues. Where X-ray structural data are not available, NMR can still be used to give a 'fingerprint' of the site, and while this is useful in comparing different antibody sites, it is essentially a qualitative approach.

1.2.1 The Immunoglobulin Fold

Immunoglobulin molecules possess a unique structural fold—the immunoglobulin fold—which suggests that it is possible to predict structures of combining sites. This would then offer a starting point for the interpretation of NMR studies. This predictive method follows from X-ray work, which has established that the structure of immunoglobulin domains is very similar and that the basis for this similarity is the conservation of a framework structure, i.e. the immunoglobulin fold.[7–11] Similarity is particularly marked when equivalent domains are compared. Thus, it is possible to predict the structure of an immunoglobulin domain by aligning its amino acid sequence with that of an equivalent domain of a known structure.[11,12] A binding site can be generated by building the conserved framework (the immunoglobulin fold) and attaching to it the (hypervariable) sequences of amino acids which form the antigen binding site. The resulting model may then be tested against NMR and the physicochemical data, and modified accordingly.[6] If validated, such a procedure provides an important complementary approach to crystallographic studies and is of particular use for immunoglobulins which cannot be crystallized or for which high resolution X-ray data cannot be collected. When combined with site-directed mutageneses the NMR approach allows the importance of individual amino acid residues in binding to be assessed.

1.2.2 Three Different Types of Binding Sites

The main test case of the spectroscopic and combined model building approach to studying antibody combining sites is clearly the DNP (2,4-dinitrophenyl) binding IgA (immunoglobulin A) myeloma M315, which is probably the myeloma protein most studied by physical techniques and for which preliminary crystal data are now available.[13,14] There is broad agreement with the NMR model. This suggests that

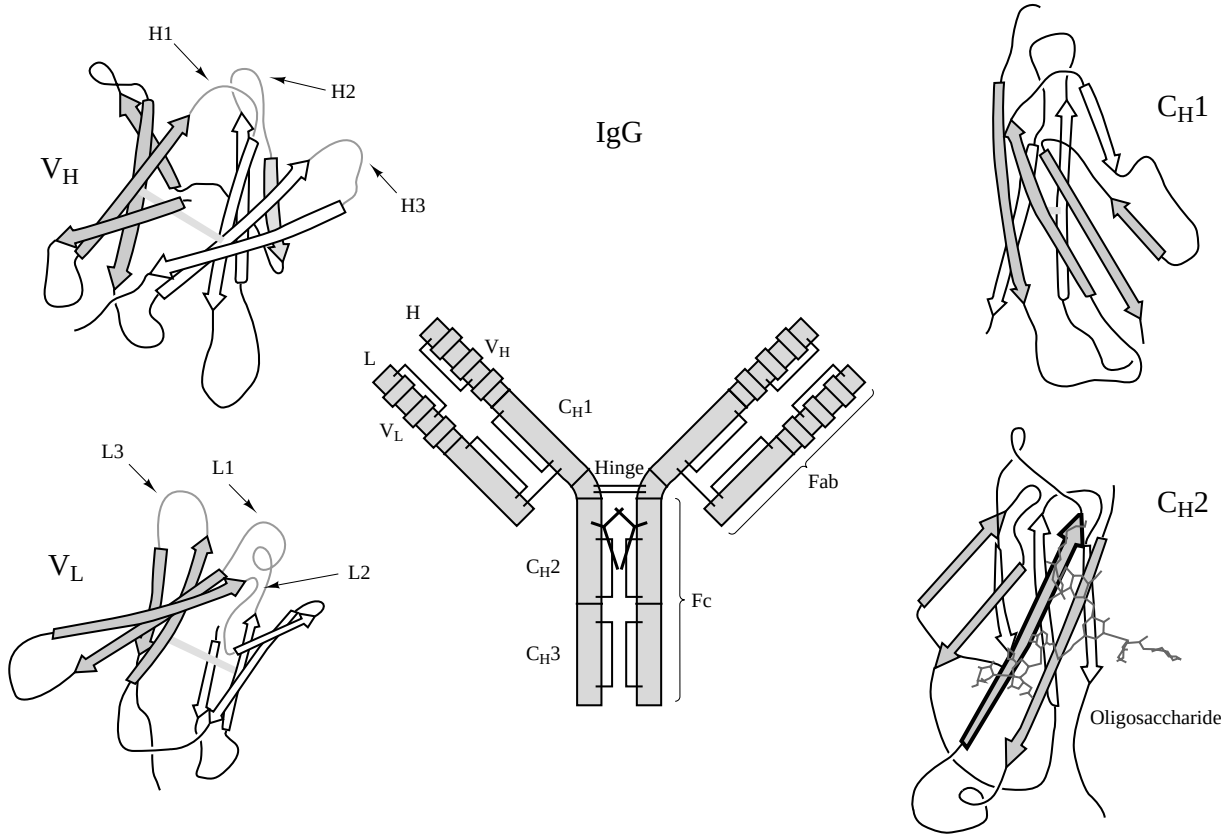

Figure 1 Basic antibody structure showing the constant (C) and variable domains (V) of the heavy (H) and light (L) chains. In a given class the amino acids in the constant regions do not differ greatly with different specificities in contrast to those on the variable region. Those amino acid residues actually contributing to the site within the (V) regions are termed hypervariable. There are three such regions for each chain (H1, H2, H3 and L1, L2, L3). Immunoglobulin G (IgG)

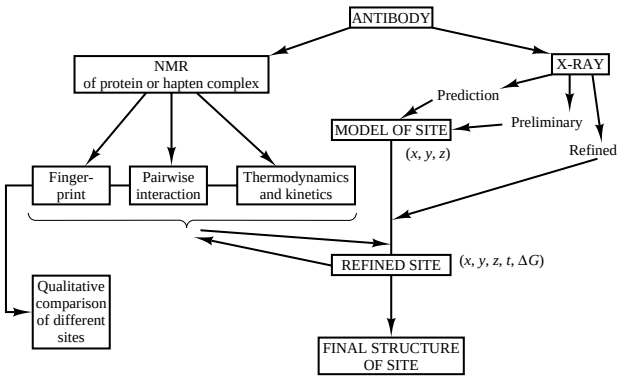

Figure 2 NMR approaches to antibody binding sites and prediction of hapten sites

the approach outlined here may provide a general method for studying any antibody combining site.

The majority of our work involved studying the resonance of the ligand (or hapten) when bound in the antibody combining site. However, in many cases, the use of the ^{1}H NMR difference spectra obtained with the addition of the ligand proved surprisingly successful. Such NMR difference spectra have been analyzed and shown to contain resonances from those relatively few nuclei of the amino acids in and near the combining site. This provides an NMR 'subspectrum' of the antibody site which can be used in comparative studies. For example,[15] Figure 3 shows the poorly resolved aromatic region of the Fab fragments (molecular mass 50 000 Da) of the sugar binding antibody U61: the addition of inulotriose perturbs very few resonances, with the area in the difference spectrum corresponding to approximately 20 protons. Figure 4 compares the aromatic region difference spectra for inulotriose binding to E109 and U61, and indicates that these antibodies have very similar binding sites (see Section 3).

In this article we summarize the main conclusions of our work on three main types of binding sites. These are the DNP binding M315, for which a structure has been predicted, the phosphorylcholine binding M603 for which X-ray data are available, and the sugar (inulotriose) binding E109 and U61 for which only qualitative conclusions are made.

2 THE DNP BINDING IgA (λ_2) MOUSE PROTEIN—M315

The binding site is shown in Figure 5, with DNP-glycine in the site. The main results from our studies on this myeloma are listed below, and the techniques used in each case are shown in parentheses. Further details can be found in the appropriate references.

1. The combining site has a depth of 1.1–2 nm and lateral dimensions of 0.08 × 1.1 nm. The entrance to the site is

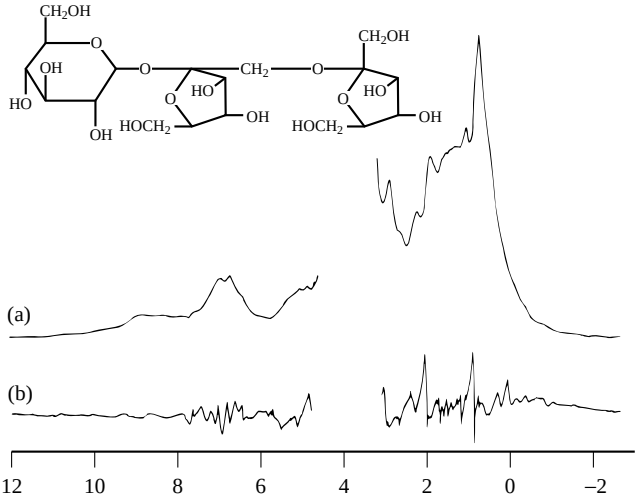

Figure 3 (a) Proton NMR spectrum at 270 MHz of the Fab (1.5 mM) of U61 and (b) the difference spectrum (×2) after addition of 1:1 inulotriose (Glc_p1-1 $fruc_f$ 2-1 $fruc_f$, p = pyranose, f = furanose ring) (pH^+ = 7.08 and T = 303 K)

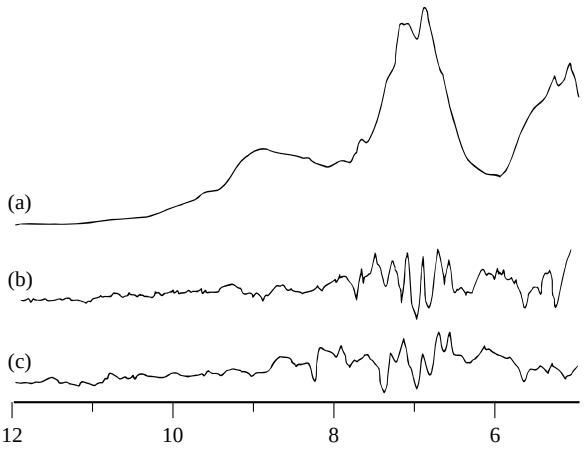

Figure 4 Proton NMR aromatic region at 270 MHz of Fab of (a) U61, (b) U61 difference spectrum (×2) with inulotriose, and (c) E109 difference spectrum with lotriose

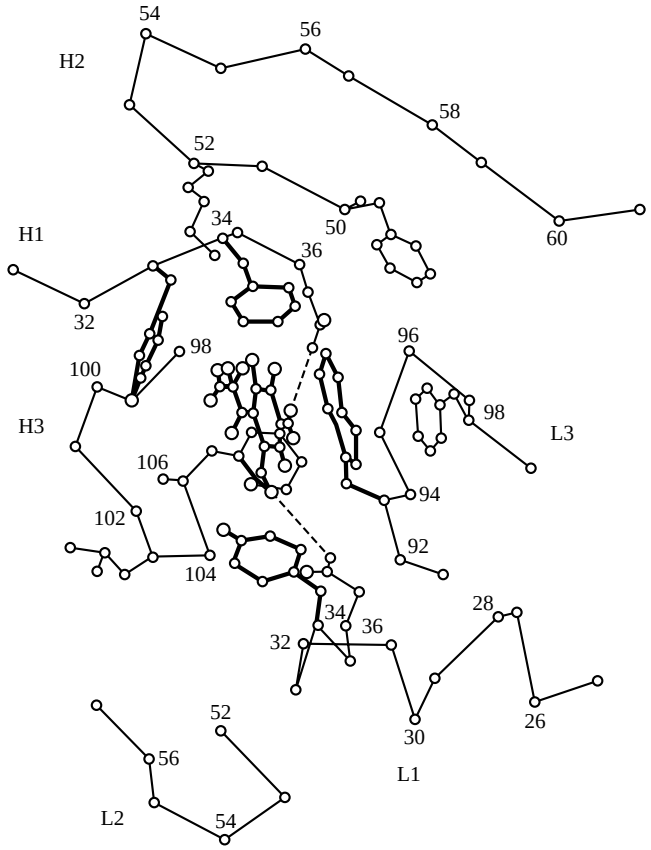

Figure 5 Postulated refined structure of the binding site of M315, with DNP-glycine. Note the key residues $Trp93_L$, $Phe34_H$, and $Tyr33_H$, and the possible polar contacts between $Asn36_L$, $Asn36_H$, and the two nitro groups of the hapten

symmetric with respect to the plane of the DNP ring. The DNP ring is rigidly held as judged from the ESR timescale, ~ 1 ns. (ESR mobility mapping.)[16]

2. $Arg95_L$ and His102 (not shown in diagram) are located at the entrance to the site. (ESR mobility mapping. ^{31}P NMR, pK_a mapping, ^1H NMR difference spectroscopy.)[17]
3. The DNP binding site is highly aromatic, the hapten being contained in an aromatic box of amino acid residues assigned to $Trp93_L$, $Phe34_H$, $Tyr34_L$, and $Tyr33_H$. (Proton NMR spectroscopy, ring current calculations, model building, ultraviolet absorption, and in vivo deuteration.)[18,19]
4. $Tyr34_L$ and $Tyr33_H$ interact with suitable side chains of the DNP ligands. In DNP-glycine, $Tyr33_H$ is in van der Waals contact with the CH_2 group. (Proton NMR spectroscopy, chemical modifications of individual chains and formation of recombinant antibody molecules, pK_a mapping.)[20,21]
5. The major interactions of the haptens are with the light chain. The environments of these contact amino residues around the DNP ring are not perturbed by substitution of a V_H domain by a V_L domain. [Preparation of light chain variable region dimers $(V_L)_2$. Proton NMR difference spectroscopy.][22]
6. The free energy of interaction of the DNP ring with $Trp93_L$ is -14.6 kJ mol^{-1}. (Proton NMR.)[23]
7. The nitro groups of these haptens are involved in specific interactions with the protein (possibly $Asn36_H$ and $Asn36_L$). The strength of these are 4–8 kJ mol^{-1}. (Laser Raman spectroscopy on ^{15}N enriched haptens, ^{15}N NMR, ^1H NMR difference spectroscopy, substitution of nitro groups by chlorine, model building, chemical modification.)[24,25]
8. The combining site has a broad range of specificity for aromatic compounds—there is no evidence for multiple binding sites. (Fluorescence, ^1H NMR difference spectroscopy.)[13,15,26]
9. There is very little structural change on hapten binding. However, there are resonances arising from residues in or near the combining site that may be exchange broadened. The timescale for the exchange when combined with the interpretation from T jump experiments would suggest that conformational changes are localized in the binding sites. (Proton NMR difference spectroscopy.)[27]
10. The combining site is identical in the IgA, Fab, and Fv fragments. (Proton NMR difference spectroscopy.)[28]

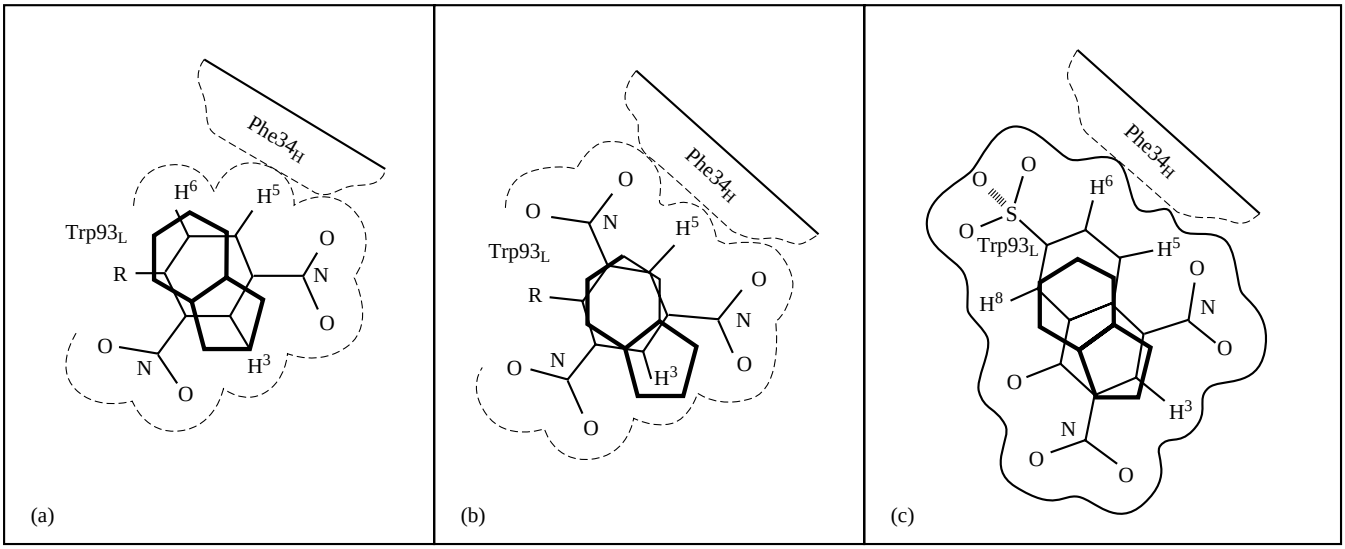

Figure 6 Side view of the arrangement of $Trp93_L$ and $Phe34_H$ in the combining site of M315 for (a) DNP-aspartate (b) TNP-glycine, and (c) dinitronapthol-7-sulfonate. These haptens are representative of the range of haptens that bind to M315. All bind in the site with only minimal adjustments in the positions of the proteins side chains

11. By using the concept of framework invariance in immunoglobulins, a model of the combining site of M315 was generated using the X-ray coordinates of the immunoglobulin fold and the sequence of M315.[11] Figure 5 shows the refinement of this model[28] using the NMR and other physical data. In this way, residues forming the binding site were thus assigned.
12. In this model, haptens of different size and shape may be accommodated in the site, in a way which is compatible with the experimental data and require only minimal adjustments in the position of the protein side chains. Figure 6 gives the arrangements of $Phe34_H$ and $Trp93_L$ for DNP-aspartate, TNP (2,4,6-trinitrophenyl)-glycine, and dinitronapthol-7-sulfonate, which are representative of the entire range of haptens studied.

We also concluded that the specificity is essentially a shape problem with the additional possibility of hydrogen bonding to the two nitro groups. The major binding energy appears to come from desolvation of the aromatic hapten. This would account for the broad range of aromatic binding specificity.

The very detailed studies involved here were necessary in attempting to establish the general method and to make as rigorous as possible the NMR interpretations. This also entailed work on model systems, in particular lysozyme, to check the basis of the ring current calculations used in structure analysis. New ring current calibrations for tryptophan residues were obtained,[23] and their use will be of general importance in the NMR studies of proteins.

Although the detailed X-ray model of the binding site is not yet available, it is of interest to note the following from the D.Phil. thesis of Bannock:[14]

> It can be concluded that the current X-ray model of the site is completely consistent with the biophysical data, and confirms the validity of the assumption about the spatial distribution of the hypervariable loops on the basis of which the NMR site was constructed. This result means that it is entirely feasible to combine the two sources of information in a semi-predictive approach to the modelling of antibody combining sites.

3 THE PHOSPHORYLCHOLINE BINDING IgA M603

The refined X-ray structure is shown in Figure 7. Our NMR studies were confined to the Fab fragment, and our intention was to investigate the various subsites. Thus, we used ^{31}P NMR studies on the two phosphorus nuclei of the phosphonium analog ($Me_3P^+CH_2CH_2OPO_3^{2-}$) of phosphorylcholine to monitor the charged subsites and the ^1H NMR to position the aromatic rings in the choline subsite.[27] Our results were as follows:

1. The pK_a of the phosphate groups are decreased by 0.5 units on binding to M603. This is consistent with the phosphate group being hydrogen bonded to $Tyr33_H$ and $Arg95_L$, as suggested from the X-ray structure (Figure 6). The decrease in pK_a also implies that the binding energies for the mono- and dianion are similar.
2. The P^+Me_3 moiety probes the electrostatic interactions in the choline subsite. Titration of the ^{31}P chemical shift of the phosphonium phosphorus reflects a group on the protein which has a pK_a value <5—which from the refined X-ray structure of the site is assigned to $Asp97_L$.
3. The choline subsite is monitored using ^1H NMR difference spectra, which indicate that the subsite is highly aromatic. This is as expected from the crystal structure, which places $Trp107_H$ and $Tyr100_L$ in this subsite. The ring current interactions from these rings can account for the ^1H NMR chemical shift data on choline.

All the NMR results are consistent with the major interactions between hapten and antibody as suggested on the basis of the crystal structure. This therefore provides an important control for the NMR method.

Finally, we note that our binding studies and those of other workers again indicate that the specificity is mainly a 'shape problem' and that, as expected, the binding energy, has a significant electrostatic contribution in this class of antibodies.

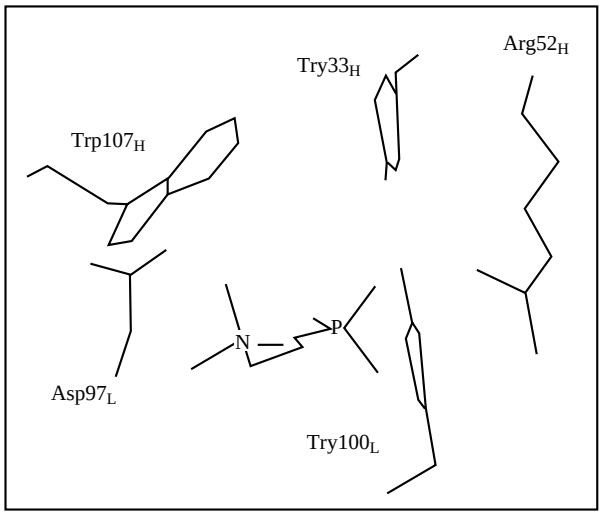

Figure 7 Hapten contact residues in M603 (kindly supplied by Dr. D. Davies) on the coordinates from the refinement at 0.27 nm together with a 0.31 nm difference Fourier map from the phosphorylcholine complex. The numbering system is that of Davies, and differs somewhat from the immunologists' numbering system

4 THE SUGAR BINDING IgA MOUSE MYELOMAS U61 AND E109

Saccharides form a widely distributed and very important class of naturally occurring antigens.[15] Little structural data were available on E109 and U61 and at the time when the experiments were carried out, even the sequences were not complete. However, several general conclusions emerged from the NMR studies (the techniques used are given in parentheses):

1. There was little structural change in the protein on binding inulotriose to E109 and U61 (^{1}H NMR difference spectra—see Figures 3 and 4).
2. The binding sites were highly aromatic (^{1}H NMR difference spectra).
3. The combining sites of E109 and U61 were almost identical (Figure 4) (^{1}H NMR difference spectra).
4. The sugars may be internally hydrogen bonded (^{13}C NMR).
5. The combining site appears to be composed of distinct subsites (binding studies).

Three distinct interactions expect to contribute to the thermodynamics of association of neutral oligosaccharides with antibody combining sites: hydrophobic, hydrogen bonding, and van der Waals. We suggest the importance of aromatic residues in the combining sites for D-sugars arises, in part, from the sugars adopting a ^4C_1D conformation, in which there is a planar hydrophobic face. This can interact with the planar rings of the aromatic residues to form favorable hydrophobic contacts (Figure 8). Support for the concept that sugars can form hydrophobic interactions with aromatic amino acids can be found from the X-ray crystallographic studies on the Fc fragment of IgG and from similar work on the lysozyme–sugar complex. Sugars in aqueous solution will be extensively hydrogen bonded with the solvent. The simple transference of these hydrogen bonds with solvent to an array within a combining site which is itself extensively hydrated would not be expected to contribute significantly to the energetics of association. However, an important contribution may be envisaged if the hydrogen bonds of the complex were formed in an environment of low dielectric constant such as may well arise in a combining site comprised predominantly of nonpolar amino acids. The third factor, van der Waals interaction, is difficult to estimate for sugars at the present time.

A basic difference between sugar and nonsugar binding proteins is the concept of distinct subsites in the former. The shape and topology of these subsites will determine the specificity for a particular sequence of sugars. An individual subsite which may be aromatic might not distinguish between sugars and other hydrophobic (e.g. aromatic) ligands which have the correct shape. The specificity of sugar binding proteins such as those studied here will therefore arise from the presence of several subsites (shown by the increasing strength of binding of the tetra- and trisaccharides compared with that of the monosaccharide). This was also true in lysozyme, where, for instance, trisaccharides bind three orders of magnitude more strongly than the monosaccharides. These subsites, therefore, favor carbohydrate antigens which are frequently polymeric and discriminate against smaller, hydrophobic ligands, which bind to an individual subsite but with relatively low affinity.

5 CONCLUSIONS AND FUTURE STUDIES

Antibody specificity for haptens is essentially a 'shape' problem involving the three-dimensional complementarity between the haptens and the amino acid residues in the combining sites. The combining site comprises a cleft or groove constructed from two distinct chains. Different antigens alter their position within the combining site to maximize noncovalent interactions. If the antigen has the correct shape it will fit into the site, but the actual binding energy depends on the extent of complementarity that can be obtained.

X-ray crystallographic studies have confirmed the idea that the structural mechanism used to generate the diversity of antigen binding sites is a conserved framework, the immunoglobulin fold, to which the hypervariable sequences which form the antigen binding site are attached. It is now considered feasible to construct models of immunoglobulin combining sites for which no X-ray studies exist, on the basis of their presumed homology with known structures. Further aspects of antibody specificity may then be investigated by use of these models, which can be tested and refined by NMR. In NMR the resolution of pairwise interactions is often better than 0.05 nm, and frequently at this resolution details of specificity are required. This means that NMR studies can also complement X-ray studies on combining sites.

Current studies involve the binding specificities of antibodies for protein molecules. For instance, how much of the surface of an antibody molecule or of the protein antigen is involved in binding to an antigenic site on the protein? Also, proteins, in contrast to small haptens or ligands, can have multiple antigenic binding sites. This means that the total immune response to even a small protein may involve multiple specificities. A study of the molecular basis of antibody recognition of a protein must be approached in terms of specific binding sites. The method of choice is to use monoclonal antibodies that can be sequenced and structurally studied.

The development therefore by Milstein and colleagues of the cell fusion technique for producing monoclonal antibodies

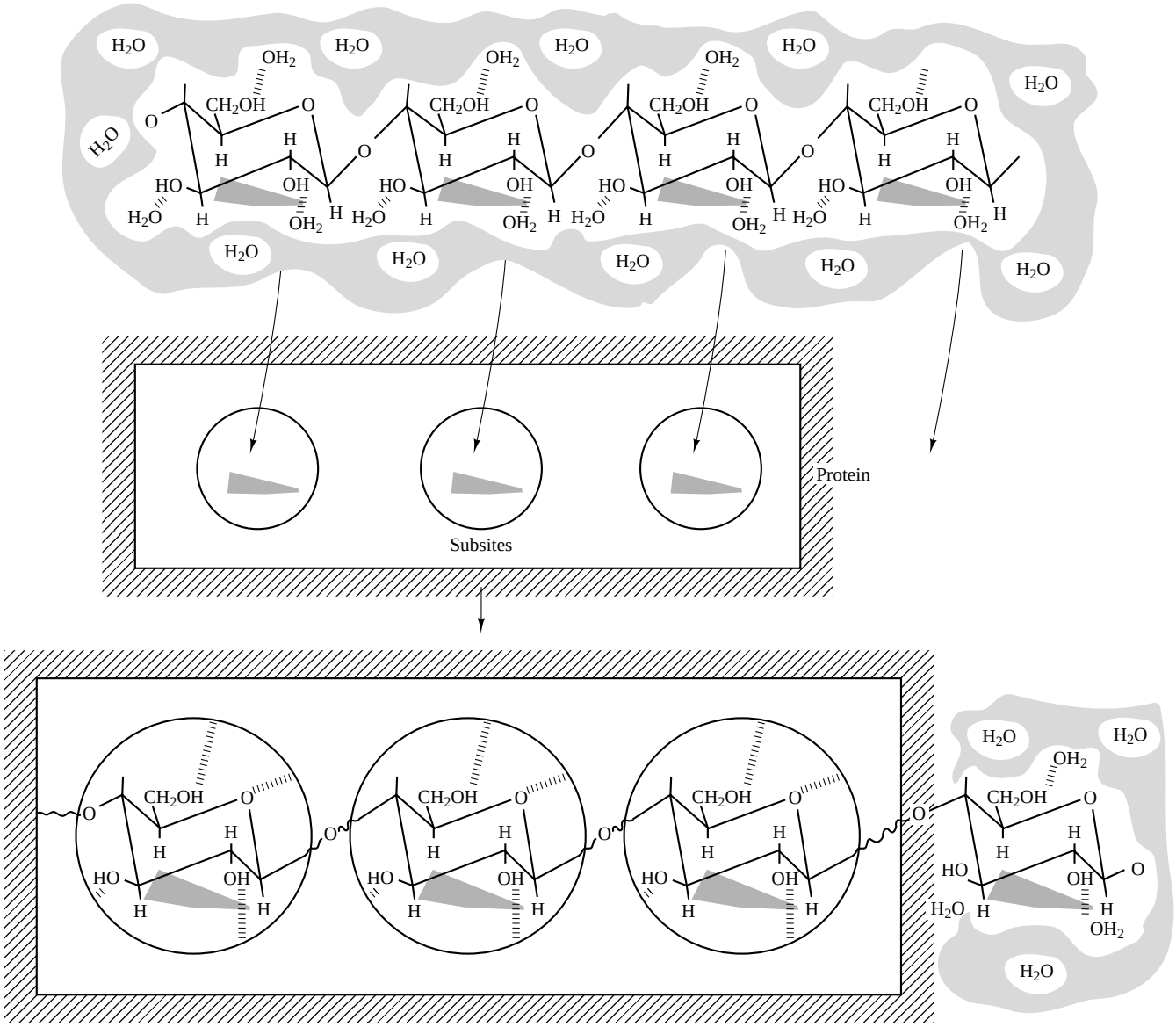

Figure 8 Diagrammatic representation of the hydrophobic face of sugars in the ^4C_1D conformation. This hydrophobic face can interact with planar hydrophobic residues in the site. Sugar binding proteins usually have distinct subsites

of defined specificity and class still has immense potential for the study of antibody specificity and function and for providing diagnostic therapeutic tools for medicine. The ability to sequence rapidly at the DNA level, and the possibility of structure prediction and testing (or even filtering) by NMR with other physical methods will be complementary techniques for studying the functional aspects of not only the molecular basis for immune recognition but also of any class of receptors to which antibodies can be raised.

6 REFERENCES

1. L. M. Amzel, R. J. Poljak, F. Saul, J. M. Varga, and F. F. Richards, *Proc. Natl. Acad. Sci. USA*, 1974, **71**, 1427.
2. D. M. Segal, E. A. Padlan, G. H. Cohen, S. Rudikoff, M. Potter, and D. R. Davies, *Proc. Natl. Acad. Sci. USA*, 1974, **71**, 4298.
3. T. T. Wu and E. A. Kabat, *J. Exp. Med.*, 1974, **132**, 211.
4. S. K. Dower and R. A. Dwek, in *Magnetic Resonance in Biology*, ed. R. Shulman, Academic Press, London 1979, p. 271.
5. S. K. Dower and R. A. Dwek, *Int. J. Biol. Macromol. 1*, **1979**, 119.
6. R. A. Dwek, S. Wain-Hobson, S. Dower, P. Gettins, B. Sutton, S. J. Perkins, and D. Givol, *Nature*, 1977, **266**, 31.
7. D. R. Davies, E. A. Padlan, and D. M. Segal, *Ann. Rev. Biochem.*, 1975, **44**, 639.
8. D. R. Davies, E. A. Padlan, and D. M. Segal, *Cont. Topics Mol. Immunol.*, 1975, **4**, 127.
9. A. B. Edmundson, K. R. Ely, E. E. Abola, M. Schiffer, and N. Panagiotopoulos, *Biochemistry*, 1975, **14**, 3953.
10. O. Epp, E. E. Lattman, M. Schiffer, R. Huber, and W. Palm, *Biochemistry*, 1975, **14**, 4943.
11. E. A. Padlan, D. R. Davies, I. Pecht, D. Givol, and C. E. Wright, *Cold Spring Harbour Symp. Quant. Biol.*, 1976, **41**, 627.
12. R. J. Poljak, L. M. Amzel, H. P. Avey, B. L. Chen, R. P. Phizackerley, and F. Saul, *Proc. Natl. Acad. Sci. USA*, 1973, **70**,

3305; R. J. Poljak, L. M. Amzel, H. P. Avey, B. L. Chen, R. P. Phizackerly, and F. Saul, *Proc. Natl. Acad. Sci. USA*, 1974, **71**, 3440.

13. R. Aschaffenburg, D. C. Phillips, D. R. Rose, B. J. Sutton, S. K. Dower, and R. A. Dwek, *J. Biochem.*, 1979, **181**, 497.
14. S. A. Bannock, *D. Phil Thesis, Oxford University*, 1985.
15. P. Gettins, J. Boyd, C. P. J. Glaudemans, M. Potter, and R. A. Dwek, *Biochemistry*, 1981, **20**, 7463.
16. B. J. Sutton, P. Gettins, D. Givol, D. Marsh, S. Wain-Hobson, K. J. William, and R. A. Dwek, *J. Biochem.*, 1977, **165**, 177.
17. S. Wain-Hobson, S. K. Dower, P. Gettins, D. Givol, A. C. McLaughlin, I. Pecht, C. A. Sunderland, and R. A. Dwek, *J. Biochem.*, 1977, **165**, 227.
18. S. K. Dower, S. Wain-Hobson, P. Gettins, D. Givol, W. R. C. Jackson, S. J. Perkins, C. A. Sunderland, B. J. Sutton, C. E. Wright, and R. A. Dwek, *J. Biochem.*, 1977, **165**, 207.
19. P. Gettins and R. A. Dwek, *FEBS Lett.*, 1981, **124**, 248.
20. M. Gavish, Y. Ben-Neriah, R. Zakut, D. Givol, R. A. Dwek, and W.R.C. Jackson, *Mol. Immunol.*, 1979, **16**, 957.
21. R. J. Leatherbarrow, W. R. C. Jackson, and R. A. Dwek, *Biochemistry*, 1982, **21**, 5124.
22. W. R. C. Jackson, R. J. Leatherbarrow, M. Gavish, D. Givol, and R. A. Dwek, *Biochemistry*, 1981, **20**, 2339.
23. W. R. C. Jackson and R. A. Dwek, *Mol. Immunol.*, 1981, **18**, 499.
24. P. Gettins, D. Givol, and R. A. Dwek, *J. Biochem.*, 1978, **173**, 713.
25. P. Gettins, R. A. Dwek, and R. N. Perutz, *J. Biochem.*, 1981, **197**, 119.
26. S. Wain-Hobson, *D. Phil Thesis. Oxford University*, 1977.
27. P. Gettins, M. Potter, R. J. Leatherbarrow, and R. A. Dwek, *Biochemistry*, 1982, **21**, 4927.
28. A. T. Morris, D. Givol, and R. A. Dwek, *Immunology*, 1978, **115**, 519.

Acknowledgments

The decision to study antibodies by NMR was inspired by the late Professor R. R. Porter, the Nobel Laureate, who was Head of the Department of Biochemistry during the time of this work. To him and to all my colleagues who worked with me on the project, I owe an immense debt of gratitude. Likewise, I feel a debt of gratitude to my colleagues in Oxford who in the early years from 1970 onward helped pioneer the use of NMR in biology. Amongst those were Rex Richards, David Phillips, George Radda, Iain Campbell, and Bob Williams.

Biographical Sketch

Raymond A. Dwek. *b* 1941. MSc., 1963 (Manchester), D.Phil. 1966 (Oxford), M.A., D.Sc., 1985 (Oxford). C.Chem. F.R.S.C. Research at Manchester University 1963–4, Oxford University 1964–9. Departmental demonstrator, University of Oxford, 1969–74. University lecturer, and Professor of Glycobiology and Director of the Glycobiology Institute, 1976–present. Approx. 400 publications. Research specialties; effector functions of the antibody molecule and study of attached carbohydrates.

Homonuclear Three-Dimensional NMR of Biomolecules

Rolf Boelens and Robert Kaptein

Utrecht University, Utrecht, The Netherlands

1	Introduction	1
2	Why Higher Dimensions?	1
3	Classification of Multidimensional NMR Experiments	2
4	The Design of Multidimensional Homonuclear Experiments	2
5	Selective and Nonselective Homonuclear 3D NMR	3
6	Principles of Homonuclear 3D Spectroscopy	3
7	Practical Aspects	5
8	Applications	7
9	Prospects for 3D NMR Spectroscopy	12
10	Related Articles	13
11	References	13

1 INTRODUCTION

High-resolution NMR can be used for determining structures of small biomolecules in solution.[1] Such studies are based upon the measurement of interactions between protons. The NOE, the origin of which is dipolar cross relaxation between protons, is especially crucial since it can be used to determine distances between closely spaced protons. The other proton–proton interaction is the J coupling, which is used to identify spin systems during the resonance assignment stage but which can also give information on torsion angles and, in this way, leads to more accurate structures. For small biomolecules these proton–proton interactions are most conveniently measured by 2D NMR techniques.[2] Thus, the J coupling manifests itself as cross peaks in COSY and TOCSY (or 2D HOHAHA) spectra and the NOE as cross peaks in NOESY (or 2D NOE) spectra.

Except for some favorable cases, however, 2D NMR studies have been limited to small biomolecules with molecular masses of less than 12 kDa. Several problems arise with larger molecules. Both the number of proton resonances and the resonance linewidth increase with size. This leads to overlap of resonances, which prohibits the unambiguous assignment of 2D cross peaks to specific proton pairs. The spectral resolution can be increased by adding a third[3–8] or even a fourth frequency domain.[9,10] In this way, overlapping protons can be characterized with the additional frequency of an associated nucleus that will help in establishing the interpretation of cross peaks. An extra complication is, however, that due to the increase in linewidth for large biomolecules, it becomes more difficult to observe small proton–proton J couplings and that magnetization transfer in 3D spectra based on such J couplings becomes weak. This disadvantage may be overcome in homonuclear 3D NOESY–NOESY spectroscopy,[11] but the complexity of the 3D NOESY–NOESY spectra can be high and their sensitivity low. More recently, a number of heteronuclear 3D experiments have been developed, such as 3D NOESY–HMQC, 3D TOCSY–HQMC[12–15] and 3D triple resonance techniques for (^{13}C, ^{15}N) doubly labeled molecules.[16,17]

These heteronuclear techniques overcome the aforementioned problems, because they rely on strong heteronuclear J coupling constants and because the magnetization transfer is unique in many cases. The sensitivity of heteronuclear 3D and 4D experiments can be high and the spectral complexity low, and there is no doubt that for large biomolecules such methods are preferable to the homonuclear ones. However, the heteronuclear techniques have one clear disadvantage. They require that the biomolecular material is enriched in ^{13}C, ^{15}N or both isotopes, which is problematic if the material can only be obtained in low yields or if the biomolecule cannot be isolated from cell cultures. This applies to a large group of very interesting biomolecules, including glycoproteins, oligosaccharides, and oligonucleotides.

Several reviews on multidimensional NMR techniques have appeared, and a thorough account of various theoretical and practical aspects of 3D NMR has been given by Griesinger et al.[18] Triple resonance techniques for studies on (^{13}C, ^{15}N) doubly labeled proteins have been reviewed thoroughly by Clore and Gronenborn[19] and by Bax and Grzesiek.[20] A recent survey was provided by Oschkinat et al.[21] Our main focus will be homonuclear 3D NMR of biomolecules (see ***Three- and Four-Dimensional Heteronuclear Magnetic Resonance*** and ***Three-Dimensional HMQC-NOESY, NOESY-HMQC, and NOESY-HSQC***).

2 WHY HIGHER DIMENSIONS?

Most interactions in NMR spectroscopy are pairwise by nature. In principle, two frequency domains and, thus, 2D NMR should suffice to establish such pair interactions between magnetic nuclei.[22] Certainly for large biomolecules, however, there is a high chance of overlap for resonances of different nuclei. In that case 2D relayed experiments have been proposed, where the magnetization is transferred from the second overlapping nucleus to a third one via an additional mixing step.[23,24] Both homonuclear and heteronuclear coherence transfer steps can be used to resolve ambiguous NOEs in a new frequency domain.[25–28] For small biomolecules the comparison of resonances in the direct domain of the original 2D experiment and the indirect domain of the 2D relay experiment is in many cases sufficient to resolve most ambiguities.[29] However, for large molecules it is likely that a new overlap exists in this indirect domain. This overlap may then be resolved by a simultaneous registration of the direct and the relayed frequencies. In this way a 3D spectrum is created where overlap for the receiving nuclei can be resolved (Figure 1). If overlap exists for the originating nuclei, the magnetization in their domain may also be relayed. Modulation at both the direct and the relayed frequencies for the originating and the receiving nuclei would lead to a 4D spectrum. Higher dimensionality is probably not practical.[20,22]

In multidimensional NMR one can distinguish between the interactions of interest and those that are suitable for relaying the information to other frequency domains. The structure

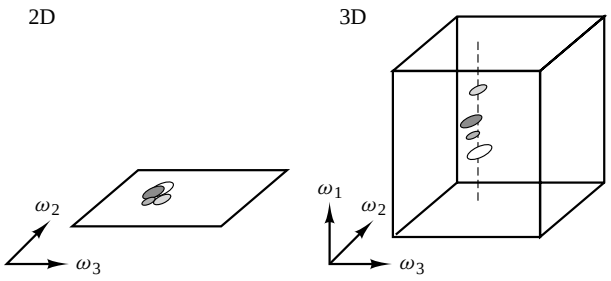

Figure 1 Illustration of the increase in resolution due to the increase in dimensionality. In the 2D spectrum four cross peaks overlap. By correlation with a third resonance frequency each cross peak achieves a different position along a line in the 3D spectrum, thus resolving the overlap problem

determination of biomolecules is mainly based on the interpretation of proton–proton NOEs, while for the prerequisite assignment of proton resonances considerable use is made of J coupling data. Therefore, it is of great importance to establish the absence and presence of these interactions unambiguously. Optimally, the frequencies connected by the relayed transfer are not linearly correlated, the relayed nuclei involved are abundant, the transfer will be very efficient introducing only low signal losses, all proton resonances can be relayed, and the relay interaction can be interpreted uniquely. In practice this is not the case, but the requirements are best met by combinations of various heteronuclear 3D and 4D experiments on (^{13}C, ^{15}N) doubly labeled compounds. When isotope labeling is not possible, however, homonuclear 3D methods may be preferable, but the analysis of the resulting spectra can be complex. A large part of this review will summarize methods for analyzing such homonuclear spectra.

3 CLASSIFICATION OF MULTIDIMENSIONAL NMR EXPERIMENTS

Over the years many pulse sequences have been proposed to establish homonuclear and heteronuclear interactions between pairs of nuclei.[2] Of course, all these pair transfers can be used as building blocks of multidimensional NMR experiments. The interactions in high-resolution ^{1}H NMR can have a coherent or an incoherent nature. Incoherent sources for interaction are kinetic exchange and dipolar cross relaxation, while the homonuclear and heteronuclear J couplings have a coherent nature. Two types of 2D experiments can be discriminated by which these processes can be measured: the large COSY family for identifying J interactions within spin systems[2,30] and the 2D exchange or NOE category for the analysis of kinetic equilibria,[31] NOESY,[32,33] and ROESY[34,35] effects. Most 2D experiments involve magnetization transfer due to a single type of interaction and thus will fall in one of these two categories. Most 3D experiments (but also relayed 2D experiments) should then belong to combinations of these two. The basic categories for double transfer will be J–J, J–NOE, NOE–J, and NOE–NOE. Of these, the J–NOE and NOE–J type experiments will contain the same information and can be brought into one category. It is obvious that one can classify 3D COSY–COSY,[5,6] 3D COSY–NOESY,[6] 3D NOESY–TOCSY experiments,[7,8] or 3D NOESY–ROESY in one of these groups. Of course, with 4D spectroscopy, or better triple transfer techniques, eight (but only six unique) classes can then already be defined, and for quadruple transfer experiments even 16. In general it can be anticipated that the J–J and J–J–J type experiments should be useful for assignment purposes, while triple transfer J–NOE–J type experiments can be helpful for identifying NOEs.

It is clear that by combination of the 'building blocks' used in 2D spectroscopy a countless number of different types of experiments can be constructed.

4 THE DESIGN OF MULTIDIMENSIONAL HOMONUCLEAR EXPERIMENTS

Each multidimensional experiment will start with a preparation period. Generally, this is a delay to bring the spin system to Boltzmann equilibrium followed by a 90° rf pulse. This will be followed by one or more evolution periods and a detection period, all separated by magnetization transfer steps similar to those in two-dimensional NMR. The experiments can be designed by the appropiate combination of two 2D NMR pulse schemes. A 3D NMR experiment can be regarded as the combination of two 2D experiments, in which the detection period of the first experiment has been replaced by the evolution, mixing, and detection periods of the second.[5] For example, a NOESY and TOCSY experiment can combine to form a 3D NOESY–TOCSY experiment.[7,8] As shown in Figure 2, the FID in the time domain t_3 is then recorded as a function of two variable times t_1 and t_2, which are independently incremented. After Fourier transformation in the three dimensions a 3D NMR spectrum is obtained with three independent frequency axes. A cross peak in the 3D spectrum arises when magnetization of one proton is transferred during the first (NOE) mixing period to a second proton and then during the second (TOCSY or HOHAHA) mixing period to a third one. Figure 3 shows a number of 3D pulse schemes and their division into preparation, evolution, and mixing periods, but basically the same principles apply to all experiments.

In 3D experiments using TOCSY, NOESY, and ROESY mixing periods the magnetization is transferred not to one but to a number of other spins. Therefore, the J or NOE interactions can be observed at a number of 3D cross

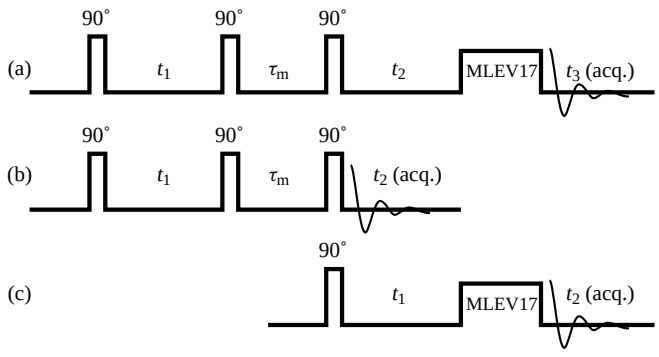

Figure 2 (a) Pulse sequence for a 3D NOESY–TOCSY experiment, constructed from (b) a 2D NOE experiment, and (c) a TOCSY experiment with a MLEV-17 mixing sequence

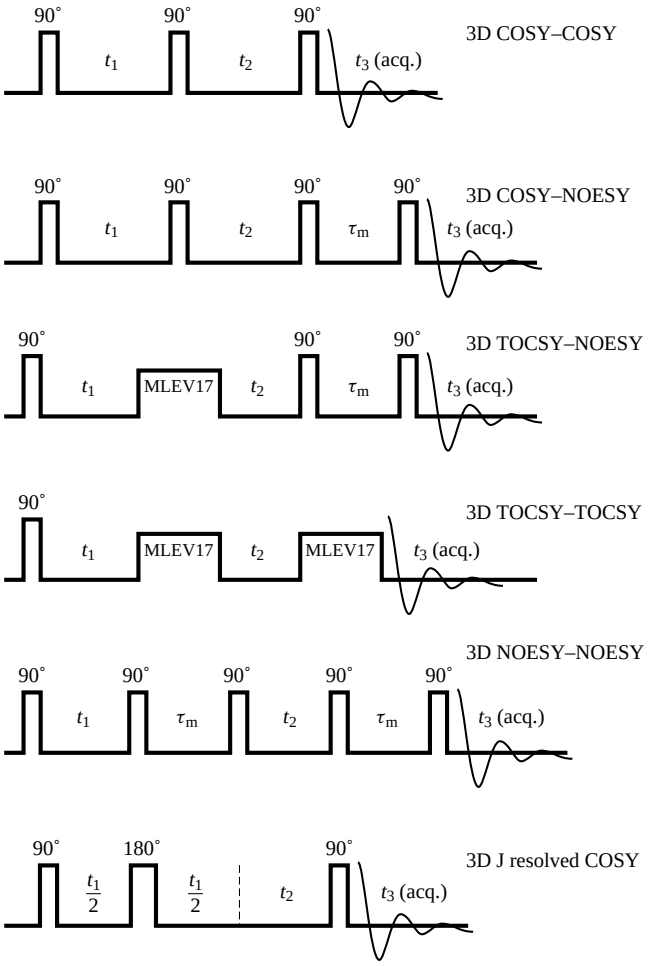

Figure 3 Pulse sequences for homonuclear 3D experiments

peaks. A coincidental overlap at one 3D cross peak can then be overcome by another nonoverlapping one. However, the disadvantages of such an approach are an increase in complexity of the 3D spectra and a reduction of signal intensity by dilution. 3D spectra which use COSY-like relays, where magnetization is transferred to one other nucleus only, lead to spectra which are much more amenable for analysis. However, for protons the ^3J(H, H) coupling, which forms the basis for the COSY magnetization transfer, is relatively weak, and the necessary development of antiphase magnetization during the evolution and acquisition periods can take a long time compared with the T_2 relaxation time. This makes 3D experiments involving a proton–proton COSY transfer insensitive for biomolecules with a short T_2, and the long sampling of the t_1 or t_2 evolution periods may create excessively long recording times. The favorable J magnetization transfer induced by the HOHAHA effect is much more suitable for homonuclear 3D experiments of biomolecules. For large (>20 kDa) biomolecules the HOHAHA transfer can also become weak. In order to avoid complex analysis the selectivity of a relayed HOHAHA or a relayed NOE transfer may be optimized by choosing a relatively short mixing time. Other suitable building blocks for homonuclear 3D experiments of biomolecules are NOESY (or EXSY) and ROESY mixing periods.

5 SELECTIVE AND NONSELECTIVE HOMONUCLEAR 3D NMR

Since both the t_1 and t_2 domains of a 3D experiment (see Figure 2) have to be incremented independently, a large number of FIDs are recorded in order to obtain a sufficiently high resolution for these two domains. In principle, this could lead to long measuring times and to practical problems in handling large data sets.

Reduction of measuring time, the amount of collected data or a need for high digitization in a selected spectral area may require that the frequency sampling in the t_1 and t_2 domains is limited by means of using semiselective rf pulses which excite only a small portion of the NMR spectrum.[5–7] In this way one zooms in, as it were, onto a part of the complete 3D spectrum. Most of the early examples of homonuclear 3D experiments were semiselective: the semiselective COSY–COSY,[5,6] the semiselective NOESY–COSY,[6] and the semiselective NOESY–TOCSY.[7,36,37] The 3D J-resolved experiments[3,4] fall in a slightly different category, since they do not correlate chemical shifts across all mixing periods, but here also the recording time is relatively short. As in 2D J-resolved spectroscopy the aim of such experiments is the separation of chemical shifts and scalar (or dipolar) interactions, which may require a very different digitization.

In the nonselective 3D NMR experiments,[8] only hard pulses are used for the t_1 and t_2 domain, which allows for a complete sampling of all frequencies in the three dimensions. Although prolonged measuring times can be anticipated, some gain is obtained through the relative simplicity of the rf pulse sequences which makes short phase cycling schemes possible. In fact, most of the nonselective homonuclear 3D NMR experiments can be carried out within 2–5 days.

In terms of analysis, however, the semiselective and nonselective 3D NMR techniques are similar.

6 PRINCIPLES OF HOMONUCLEAR 3D SPECTROSCOPY

The 3D NOESY–TOCSY spectrum recorded with the pulse scheme of Figure 2 and obtained after 3D Fourier transformation of the FIDs can be schematically presented as a cube with three frequency axes, f_1, f_2, and f_3. In a 3D spectrum obtained in this way, a body diagonal ($f_1 = f_2 = f_3$) can be identified, which contains magnetization that was not transferred during any of the mixing periods. Additionally, intensity accumulates on the three cross-diagonal planes, which is shown in Figure 4. In the case of the 3D NOESY–TOCSY experiment, the plane $f_2 = f_3$ (NOE plane) contains magnetization transferred only during the first (NOE) mixing period, whereas the plane $f_1 = f_2$ (TOCSY or HOHAHA plane) contains magnetization transferred during the second (HOHAHA) mixing period. Finally, the plane $f_1 = f_3$ (back-transfer plane) contains magnetization that was transferred during the first (NOE) mixing period from proton a to proton b and then back to proton a during the second (HOHAHA) mixing period. For the analysis of 3D NMR spectra, cross sections perpendicular to one of the frequency axes can be used. Figure 5 shows an f_1–f_2 plane (which is perpendicular to the f_3 axis). The three diagonal planes of

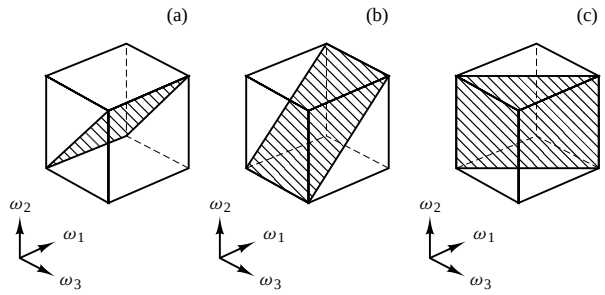

Figure 4 Cross-diagonal planes in a 3D NOESY–TOCSY spectrum: (a) NOE plane, (b) HOHAHA or TOCSY plane, and (c) back-transfer plane

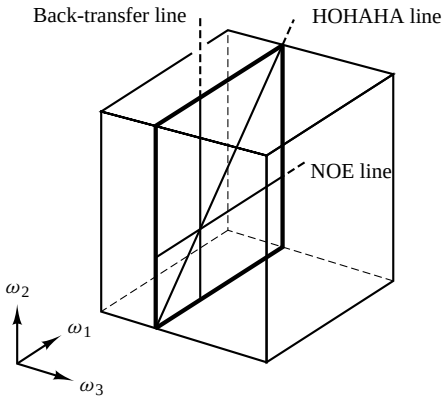

Figure 5 Schematic representation of an f_1–f_2 plane, perpendicular to the f_3 axis. The NOE, HOHAHA and back-transfer lines constitute the intersection with the three planes indicated in Figure 4

Figure 4 intersect this plane at the three lines indicated as NOE (or N), HOHAHA (or H) and back-transfer (or B) lines. These lines all share one point on the body diagonal of the spectrum.

Cross peaks that are present on the NOE and HOHAHA lines in the cross section taken at $f_3 = f_a$ represent single step magnetization transfer (by NOE and HOHAHA, respectively) to a proton a. Hence, the 3D NOESY–TOCSY spectrum contains the information that is present in traditional 2D NOESY and TOCSY spectra as a subset. All cross peaks outside the NOE and HOHAHA planes are due to double magnetization transfer. The double magnetization transfer that gives rise to peaks in the back-transfer plane is unique for homonuclear 3D experiments, since both mixing periods cover the same spectral frequencies. The closest 2D analogues of 3D NOESY–TOCSY experiments are relayed NOESY experiments[25,26] 2D TOCSY–NOESY,[27] and 2D ROESY–TOCSY and TOCSY–ROESY.[29] The information content of such spectra is present in the 3D spectrum as a projection onto the f_1–f_3 groundplane. However, since the cross peaks are labeled by three different frequencies, fewer ambiguities will arise in a 3D spectrum.

Figure 6 shows the nonselective 3D NOESY–TOCSY spectrum of a 109 residue protein, parvalbumin, in ^1H_2O. The spectrum contains a large number of cross peaks. Most of the intensity accumulates on the body diagonal and the NOE

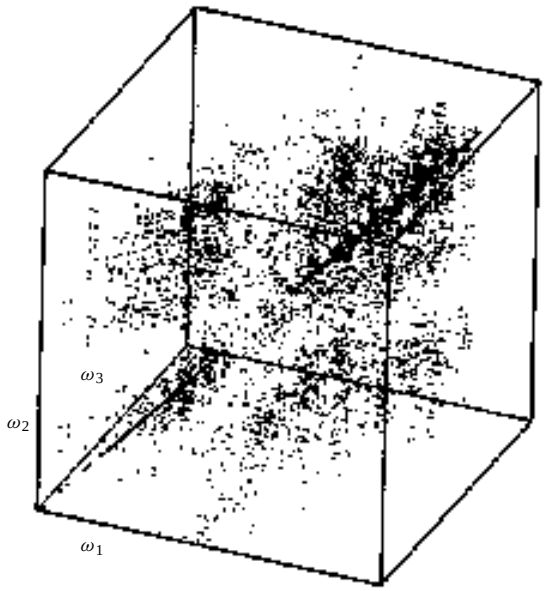

Figure 6 3D NOESY–TOCSY spectrum of a 109-residue protein in ^1H_2O. The spectrum shows local intensity maxima for most cross peaks. The data set was recorded in 171 h at 500 MHz using an eight-scan phase cycle, as described by Vuister et al.[8] The NOE mixing time was 150 ms and the HOHAHA mixing time was 47 ms. The data were processed to a resolution of 256 × 256 × 256. The sample contained 8.7 mM pike parvalbumin at pH = 4.1, 315 K, 10% D_2O.[8] (Reproduced by permission from Vuister et al.[8])

and HOHAHA planes. Less intensity accumulates on the back-transfer plane, because the associated magnetization must have gone through a double transfer. Intensities at positions ($f_1 \neq f_2 \neq f_3$), i.e. not on the three diagonal planes, correspond to magnetization which was transferred during both mixing periods. Figure 7 shows a contour plot of the NOE plane of the same 3D spectrum. This plot is very similar to a contour plot of the NOESY spectrum of this protein and indicates the need to increase the resolution for proteins of this size by using a third domain. Similarly, the HOHAHA plane resembles a TOCSY spectrum.

The analysis of 3D spectra can be accomplished in planes perpendicular to any axis of the 3D spectrum. In Figure 8(a) the flow of magnetization is sketched as observed in an f_1–f_2 plane of a 3D NOESY–TOCSY experiment. A cross peak at (f_a, f_b, f_c) indicates that magnetization started on a nucleus with frequency f_a was transferred by NOE to a nucleus with frequency f_b and was then transferred by isotropic mixing to a nucleus at f_c on the diagonal. Figure 8(b) shows the same flow in an f_2–f_3 plane, but now the magnetization originates from the diagonal. Finally Figure 8(c) shows this flow in an f_1–f_3 plane. The flow in a TOCSY–NOESY spectrum goes in the opposite direction, and the same planes can be constructed for the equivalent cross peak (f_c, f_b, f_a). Figure 8(d), 8(e) and 8(f) show the equivalence of the f_2–f_3, f_1–f_2, and f_1–f_3 planes of a 3D TOCSY–NOESY spectrum with that of the f_1–f_2, f_2–f_3, and f_3–f_1 planes of a 3D NOESY–TOCSY spectrum, respectively. Only the flow, as indicated by the arrows, is inverted, while the appearance of the spectrum is the same.

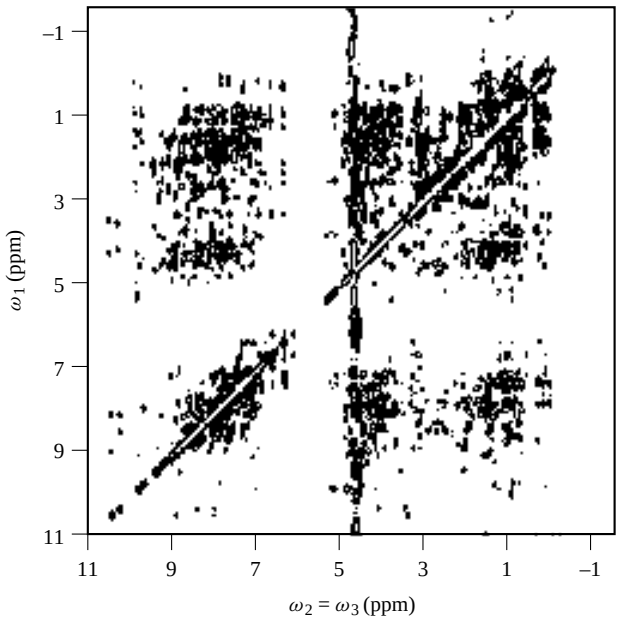

Figure 7 NOE plane of a 3D NOESY–TOCSY spectrum of the 109-residue protein of Figure 6. (Reproduced by permission from Vuister et al.[8])

The cross peaks in 3D spectra reflect connectivities between the spins. To describe the connectivities the C notation can be used: $C[M_1, M_2]_{abc}$ (i, j, k) or shorthand C_{abc} (i, j, k) means that magnetization of proton a in residue i is interacting via mixing step M_1 with proton b of residue i and next via mixing step M_2 to proton c of residue k. Thus, 3D NOESY–TOCSY and 3D TOCSY–NOESY spectra contain the same connectivity information: a $C[NOE, J]_{abc}$ (i, j, j) pathway is equivalent to a $C[J, NOE]_{cba}$ (j, j, i) pathway. Both represent the same combination of interactions. Experimentally, however, differences in t_1 and t_2 noise and in domain resolution make it quite different, whether a $C_{NN\alpha}$ $(i + 1, i, i)$ connectivity is observed in an f_1–f_2 plane at f_3 of the α proton (such as in 3D NOESY–TOCSY) or at f_3 of the NH proton (as in 3D TOCSY–NOESY).

7 PRACTICAL ASPECTS

7.1 Sensitivity

For 3D spectra a better signal-to-noise ratio is required than that of the 2D analogs, since the aim of 3D experiments is the observation of weak double magnetization transfers. Therefore, 3D techniques should only be applied in case of overlap in optimally recorded 2D spectra.

The sensitivity of a 3D experiment is determined by the efficiency of magnetization transfer in the mixing periods, by T_2 relaxation during the evolution and acquisition periods, and the method of selecting the evolved magnetization. As in 2D spectroscopy most mixing periods select only the x or y component of the magnetization from the previous evolution period, and by phase cycling the other term is removed. This leads to the loss of half of the magnetization and half of the noise power. Therefore, as pointed out by Bax and Grzesiek,[20] each addition of dimensionality may lead to a signal-to-noise reduction by 1/ 2. This loss in the signal-to-noise ratio can, however, be avoided by retaining both orthogonal magnetization components across the mixing periods (see Cavanagh and Rance[38] for a review). This method has been applied to 3D NOESY–TOCSY.[39] A drawback may be, however, an increase in experiment time due to additional phase cycling in order to obtain phase-sensitive spectra.

In 3D spectrocopy the signal accumulates independently in all domains. By minimizing the length of the evolution periods, loss of sensitivity due to T_2 relaxation can be avoided. The length of the evolution periods should be only so long that overlap of cross peaks is avoided, or as required for the further analysis of the 3D spectra. Since there is a lower chance of overlap in 3D than in 2D spectra the evolution periods can clearly be shorter in 3D spectra. With the crowded spectra of biomolecules, however, it is difficult to predict which resolution is finally needed until the analysis is completed. As a guideline it is noted that sampling with the evolution periods beyond $0.9T_2$ is only to increase resolution, while sampling below $0.9T_2$ will add signal to the multidimensional cross peaks. The sensitivity of the NOE and HOHAHA planes of an optimally recorded 3D NOESY–TOCSY spectrum will be similar to that of the two 2D counterparts recorded together in the same total time. However, the aim of a 3D experiment is clearly the observation of double magnetization transfer, and the corresponding cross peaks will be much weaker.

For good sensitivity of multidimensional experiments it is extremely important to optimize the transfer efficiencies of the mixing periods. For TOCSY, various improvements have been published, compensating relaxation by 'clean' TOCSY pulse sequences[40] or increasing sensitivity by orthogonal magnetization transfer, as discussed above. For ROESY, potential J transfer should be minimized.[35] For NOESY no fundamental optimizations are possible, but accurate and homogeneous 90° rf pulses will enhance the transfer. In all cases the transfer efficiencies may be optimized by adapting the length of the mixing period. Since the cross-peak intensity in 3D spectroscopy is proportional to the product of the constituent 2D transfer efficiencies, an optimal 2D mixing time will also be the optimum for three dimensions.

Another important factor for sensitivity is the number of rf pulses in combination with pulse imperfections, i.e. inaccurate flip angles or B_1 inhomogeneities. Generally, phase cycles of 2D and 3D experiments are set up so that only coherences are selected which pass the sequence assuming ideal 90° and 180° pulses and that coherences created by the imperfections are suppressed. Since most homonuclear 3D sequences contain only a few rf pulses or a self-compensated isotropic mixing period, only a small amount of magnetization is lost in this way.

However, in many cases the actual sensitivity is less favorable due to t_1 and t_2 noise caused by instrument instabilities. Such instabilities are present in 2D spectroscopy as well, but the 3D technique may sample additional instabilities due to the length of the experiment and the wish to minimize recording time. On some NMR instruments undefined delays may be introduced between the FIDs. A constant steady state magnetization may be maintained by a buffered acquisition method or by steady state pulses.

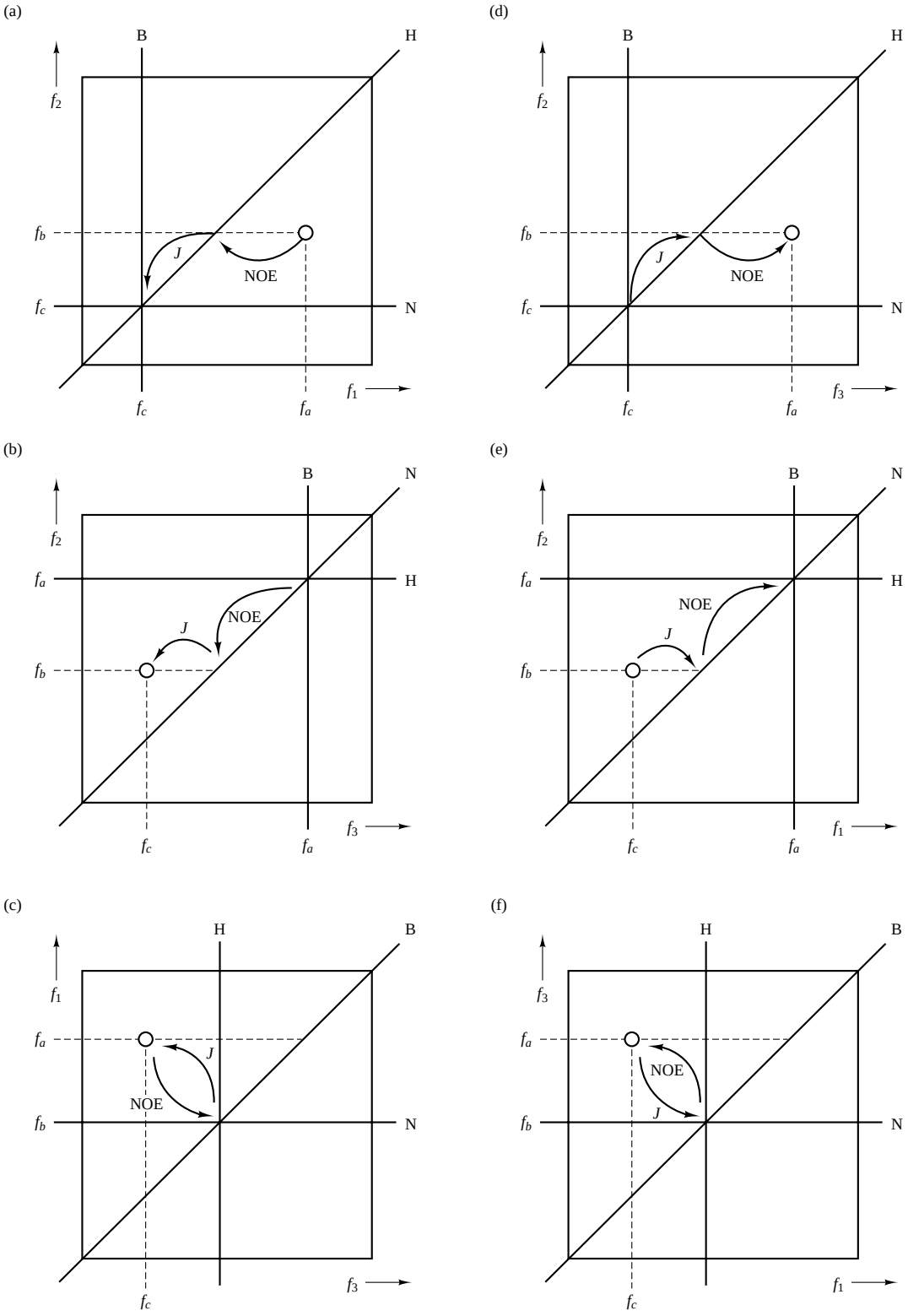

Figure 8 Flow of magnetization for a cross peak (f_a, f_b, f_c) in a 3D NOESY–TOCSY spectrum and the equivalent cross peak (f_c, f_b, f_a) in a 3D TOCSY–NOESY spectrum. (a)–(c) The f_1–f_2, f_2–f_3, and the f_1–f_3 planes of a 3D NOESY–TOCSY spectrum. (d)–(f) The f_2–f_3, f_1–f_2, and the f_1–f_3 planes of a 3D TOCSY–NOESY spectrum. The lines indicated by N, H, and B are the cross-diagonal NOE, HOHAHA (or TOCSY), and back-transfer lines, respectively. Only the flow of magnetization in the two spectra reverses; the appearance of both spectra is the same

Fluctuations in the extent of sample heating due to the pulse sequence are more difficult to avoid.

7.2 Phase Cycling and Recording Time

Both phase cycling or field gradients can be used for selecting the coherence transfer pathway in 3D experiments. Since the gradients do the selection in single experiments, use of gradients is preferable for 3D spectroscopy. Thus, the NOE effect can be selected by a single gradient pulse in the NOE mixing period.[31] However, the number of phase cycling steps can also be minimized in 3D spectroscopy. For large biomolecules the phase cycling to select NOE mixing can be short, since most undesirable coherences have decayed at the end of the NOE mixing time. Suppression of single quantum coherences is normally sufficient and can be accomplished by two phase steps. The HOHAHA mixing requires no selection of coherence level at all, if a 'clean' MLEV sequence is used.[40] Axial peaks due to T_1 relaxation can be suppressed by inversion of the first 90° rf pulse, which will double the phase cycle. Inaccurate 90° or 180° rf pulses may lead, however, to an axial plane at the f_1–f_3 ground plane of a 3D spectrum, which can be removed by inverting all pulses before the t_2 period. In order to separate positive and negative frequencies in the t_1 and t_2 domains, either a time proportional phase increment (TPPI) or a States–TPPI sampling scheme should be used, which will put potential axial peaks at the sides of the 3D cube. Homonuclear 3D spectroscopy with minimal phase cycling has been demonstrated for 3D NOESY–NOESY[41] and for 3D TOCSY–NOESY.[42] In practice, 3D TOCSY–TOCSY and gradient enhanced 3D TOCSY–NOESY with axial peak suppression in t_1 will have a minimal two-step phase cycle inverting only the very first rf pulse. Without gradients the minimal phase cycling for 3D TOCSY–NOESY becomes four and for 3D NOESY–NOESY already eight, while inclusion of axial plane correction brings this to eight and 16, respectively.

NMR receiver imperfections may require additional phase cycling in order to remove dc bias and quad-image artifacts, but they can be mixed into the phase cycle for coherence selection. Thus, depending on the level of artifact suppression needed, phase cycles of 1–6 scans can be used. Typically, 128–256 independent t_1 and t_2 increments are used to sample the corresponding domains, with an acquisition size of 512–1024 words. In order to reduce measuring time, the relaxation delay between each scan is set to a value close to the T_1 relaxation time of the biomolecule, which results in some saturation. In this fashion, the repetition rate per scan is about 1 s, and a typical 160 × 256 × 1024 3D TOCSY–NOESY experiment takes between 46 h for a four-scan and 182 h for a 16-scan version and will create 42 Mwords of data.

7.3 Processing

The heavily truncated interferograms in the t_1 and t_2 periods of 3D datasets are in principle not suitable for frequency analysis by fast Fourier transforms. Apodization functions such as the Hamming or Kaiser windows vastly decrease the amount of 'ripple' (cf. Ernst et al.[2]). A better approach is frequency analysis by parametric methods based on linear prediction[43–45] and by the maximum entropy or Bayesian methods,[46] but these methods can be computationally expensive. A more modest but practical approach is the extension of the experimental data set by linear prediction, followed by window multiplication and a fast Fourier transform.[47] Phasing parameters for the evolution periods can either be calculated from initial delay values and rf pulse widths[48] or estimated by visual inspection of the data. After the Fourier transform the 3D spectrum can be baseline corrected in all domains by a variety of methods.[49,50] Offsets and baseline distortions in the f_1 and f_2 domains can, however, already be minimized by data sampling techniques.[51,52]

For the manual analysis of 3D spectra, contour plots can be produced for all cross sections that contain cross peaks. This approach may be sufficient for settling overlap in crowded 2D spectra. Since bookkeeping of all peaks in a 3D spectrum can be cumbersome, analysis with a workstation is to be preferred. Programs have been developed that can assist the manual analysis of such spectra.[53–56] A step further is the automatic or semiautomatic analysis of patterns of correlated cross peaks, e.g. for assigning 3D proton spectra.[54,57,58] The input of such programs may require further processing of the spectra, e.g. searches of local maxima and peak boundaries, peak decomposition, and determination of intensities.

8 APPLICATIONS

8.1 3D *J*-Resolved Spectroscopy

The 3D *J*-resolved experiment can be visualized as a 2D *J*-resolved experiment in which the acquisition period has been replaced by the evolution period, mixing period, and acquisition period of a second 2D experiment. Both COSY[3,4,59] and NOESY[60] have been suggested for this second experiment. Such 3D *J*-resolved spectra can become useful when overlap interferes with the analysis of multiplet patterns in a 2D *J*-resolved spectrum. A drawback of *J*-resolved spectroscopy for measuring *J* couplings as compared with ECOSY techniques[61] is that the multiplet pattern is not simplified, but remains at full complexity. This explains the limited application of the method for high-resolution studies of biomolecules. Related 3D experiments in solid state NMR for separating chemical shift and dipolar interactions have found more extensive use.[62,63] The 3D *J*-resolved method demonstrated, however, the feasibility of 3D NMR and started the development of a large number of other 3D techniques.

8.2 3D TOCSY–NOESY and 3D NOESY–TOCSY Spectroscopy

For most biomolecular studies both the *J* coupling and the NOE interaction must be measured. Such interactions can be obtained by separate NOESY and COSY or TOCSY experiments, but it is logical to combine both into one 3D experiment in which one mixing period contains the NOE effect and the other the *J* coupling. Two types of homonuclear experiments can be envisaged: 3D NOE–*J* and 3D *J*–NOE. The first implementation was shown by Griesinger et al.[6] in a semiselective 3D NOESY–COSY experiment. However, for larger biomolecules the *J* effect is transferred much more efficiently by a HOHAHA mixing period, as was demonstrated

by Oschkinat et al.[7] in a semiselective 3D NOESY–TOCSY experiment of a 46-residue protein. Shortly after, it was shown that complete nonselective 3D NOESY–TOCSY experiments of proteins can also be executed in a reasonable time.[8] Later improvements used 'clean' MLEV sequences[37,64,65] and orthogonal isotropic mixing[39] to enhance the amount of transferred magnetization.

8.3 Observation of Sequential NOEs in Proteins

The combined observation of J couplings and NOE interactions in 3D NOESY–TOCSY spectra makes it possible to assign the proton resonances in the protein spectrum by a similar sequential assignment strategy as developed by Wüthrich and his co-workers[1] for 2D spectra. In the 2D approach, the spin systems of the protons belonging to one amino acid residue are identified by exhaustively analyzing the through-bond proton–proton connectivities in COSY and TOCSY spectra. The sequentially neighboring amino acid spin systems are then identified by observation of the sequential d_{NN}, $d_{\alpha N}$ and $d_{\beta N}$ connectivities in 2D NOE spectra. Starting at a unique spin system or by matching unique di- and tripeptide sequences on the complete protein sequence, the spin systems can be assigned to specific amino acids. In a simplified view, the spin system analysis can be reduced to observing αN connectivities between the J-coupled α and NH protons of each amino acid residue, while the sequential assignment is based (among others) on αN connectivities between neighbors. In 3D NOESY–TOCSY and 3D TOCSY–NOESY experiments, we can measure both types of connectivity simultaneously in one $C[NOE,J]_{N\alpha N}(i + 1, i, i)$ connectivity. In fact, two types of NαN connectivities exist: sequential $C_{N\alpha N}(i + 1, i, i)$ and intraresidue $C_{N\alpha N}(i, i, i)$ connectivities. Both connectivities can be observed in the scheme shown in Figure 9. The intraresidue $C_{N\alpha N}(i, i, i)$ connectivity of residue i will be found on the back-transfer line of an f_1–f_2 plane, whereas the sequential $C_{N\alpha N}(i + 1, i, i)$ connectivity to residue $(i - 1)$ will be found on a line parallel to the NOE line through the intraresidue $C_{N\alpha N}(i, i, i)$ connectivity. This then defines the NH f_3 frequency for the next f_1–f_2 plane, where we can repeat the search for both connectivities. An example of such a sequential assignment is given in Figure 10 for the 3D NOESY–TOCSY spectrum of pike parvalbumin from Asp92 to Ile97.

Complete descriptions of the sequential assignment strategy using 3D NOESY–TOCSY or 3D TOCSY–NOESY spectra were given by Vuister et al.[66] and by Oschkinat et al.[67] A full analysis of all possible 3D sequential connectivities in proteins was given, and estimates of the relative intensities of cross peaks corresponding to such connectivities for α-helical and β-sheet conformations, as summarized in Table 1 (for α- and N-protons only). Thus, by searching the 3D spectrum for such connectivities it is possible to analyze the secondary structure of the protein.

The method has been applied to the 109 amino acid residue protein parvalbumin. Most of the sequential backbone cross peaks of this protein were observed[68] in a single 3D TOCSY–NOESY spectrum of parvalbumin. The assignment based on these 3D data corresponds completely with a previous one using extensive 2D data. Even some novel NOEs, hidden due to overlap in the 2D spectra of parvalbumin,

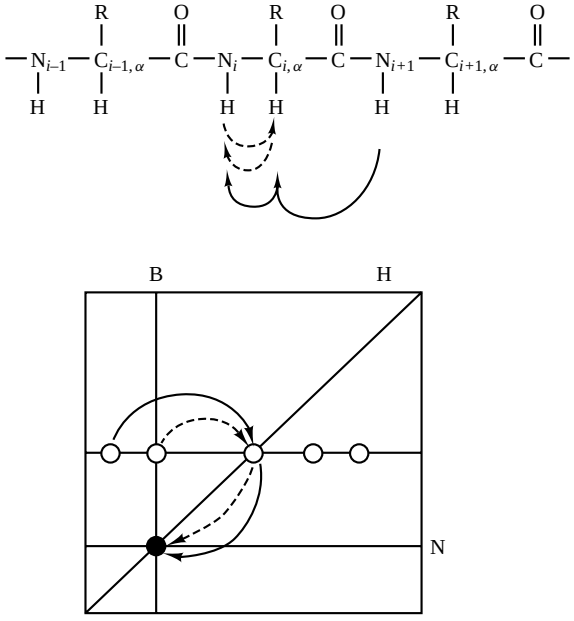

Figure 9 Sequential and intraresidue $C_{N\alpha N}$ connectivities in an f_1–f_2 plane of a 3D NOESY–TOCSY spectrum. The lines indicated by N, H, and B are the cross diagonal NOE, HOHAHA (or TOCSY), and back-transfer lines, respectively. The two dotted arrows starting at a back-transfer cross peak indicate the intraresidue $C_{N\alpha N}(i, i, i)$ connectivity, where the first arrow represents the NOE transfer from N to α and the second one the J transfer from α back to N. The two solid arrows show the interresidue $C_{N\alpha N}(i + 1, i, i)$ connectivity

could be identified. Similar results have been obtained for α-purothionin,[37] bovine pancreas trypsin inhibitor (BPTI),[67] the 113-residue protein aponeocarzinostatin,[69] a 90-residue phospholipid transfer protein,[70] a 137-residue flavodoxin,[65] the 128-residue blue copper protein azurin,[71] the 153-residue interleukin-4,[21] and the monomeric 143-residue heme protein leghemoglobin.[72] In most cases the analysis of the homonuclear 3D data led to additions or corrections in previously established assignments. The assignment for one residue was corrected for α-purothionin. Parvalbumin was shown to contain one amino acid residue more than expected on the basis of the amino acid sequence. For flavodoxin, 15 additional residues were identified from the 3D spectra. For neocarzinostatin it was possible to correct inconsistent assignments from three previous publications.

It is clear that the combination of NOE transfer and isotropic mixing in one 3D experiment is very useful in sequential assignment procedures of protein NMR spectra. Since the information is contained in one data set, these procedures may be better suited for automation than methods which rely on matching two different NOESY and TOCSY spectra. Furthermore, the increased resolution and the presence of the two-step connectivities will reduce overlap in spectra of larger biomolecules. Semiautomated approaches for analyzing 3D NOESY–TOCSY spectra of proteins have been demonstrated by Oschkinat et al.[57,58] and Kleywegt et al.[54] In this latter procedure, sets of J-coupled resonances are obtained from a peak list of the 3D spectrum. These sets are then ranked as possible spin systems using chemical shift rules and the sets are ordered using sequential 3D connectivities. By matching long stretches of such sequentially linked spin systems versus

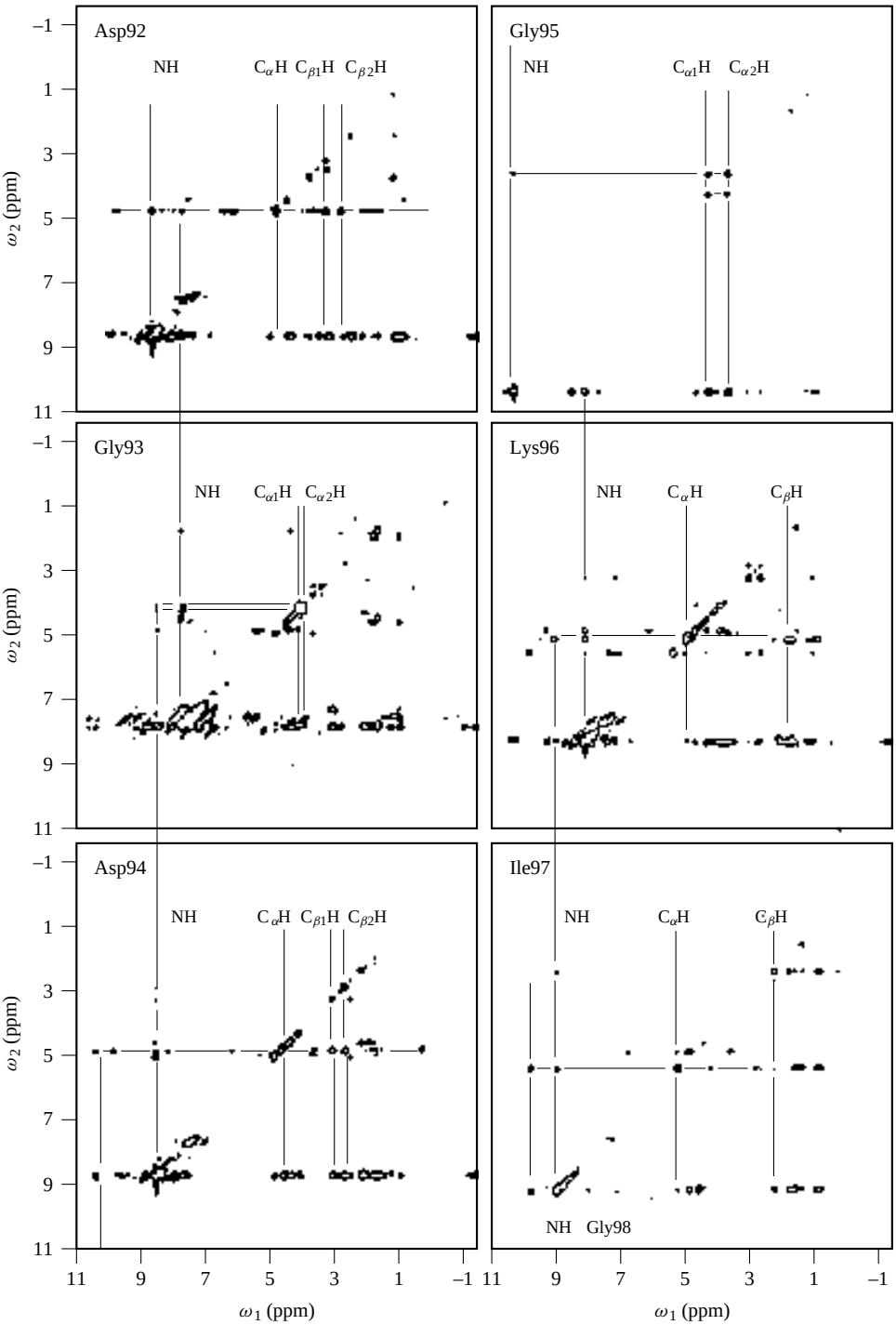

Figure 10 Sequential walk through f_1–f_2 planes in the NH region of the 3D NOESY–TOCSY spectrum of parvalbumin for f_3 frequencies of NH(Asp92) to NH(Ile97), taken from Vuister et al.[8] The spin system is indicated by vertical lines for each plane. The NOEs with the C-α atom can be found on the horizontal line parallel to the NOE line at the C-α resonance frequency. A back-transfer peak, $C_{N\alpha N}(i, i, i)$, is found at the crossing with the vertical NH line. The other cross peaks on this horizontal line in the NH region represent potential sequential cross peaks $C_{N\alpha N}(i + 1, i, i)$. The vertical line connecting to the next f_1–f_2 plane defines the NH frequency of the neighboring residue. The number of choices for sequential connectivities is significantly reduced compared with that observed in 2D spectra. Note that at Gly95 the sequential $C_{N\alpha N}(i + 1, i, i)$ connectivity is lacking, but that in this case use has been made of the single-step d_{NN} connectivity on the NOE line. (Reproduced by permission from Vuister et al.[8])

Table 1 Sequential Connectivities in 2D and 3D NMR[a]

	α-helix	β-sheet
2D NOE or NOE plane		
$d_{\alpha N}$	w	s
d_{NN}	m	a
3D NOESY–TOCSY		
$d_{\alpha N}$ $C_{N\alpha N}(i+1,i,i)$	a–w	s
$C_{\alpha N\alpha}(i-1,i,i)$	a–w	s
d_{NN} $C_{NN\alpha}(i+1,i,i)$	m	a–w
$C_{NN\alpha}(i-1,i,i)$	m	a–w

[a]Cross peak intensities: s, strong; m, medium; w, weak or a, absent. The estimates for the intensities in the 2D NOE spectra are taken from Wüthrich,[1] those for the 3D NOESY–TOCSY spectra are calculated as described by Vuister et al.[66]

the amino acid sequence it is possible to assign almost all residues of parvalbumin.[54]

In a semiautomatic procedure the analysis of 3D spectra can take place in f_1–f_2, f_2–f_3, or f_1–f_3 planes: the relationships among the cross peaks in different planes are established by the rules within the program. In an interactive analysis, especially on paper, patterns are more easily recognized in a single plot. The analysis of 3D TOCSY–NOESY and 3D NOESY–TOCSY spectra in f_1–f_3 planes has been found to be convenient, since the pattern of HOHAHA related cross peaks and the NOE relationship of this pattern with other resonances can be observed in one plane. Such planes are useful for identifying amino acid spin systems and a sequential assignment strategy mainly using f_1–f_3 planes has been outlined.[42,65]

Of course, it is not necessary to use just one 3D TOCSY–NOESY spectrum for assigning the resonances. A pragmatic approach uses 2D TOCSY and NOESY spectra for identifying the interactions between nonoverlapping resonances, whereas ambiguities are sorted out using the 3D spectra. Such procedures have been used for neocarzinostatin,[69] leghemoglobin,[72] procolipase,[73] the DNA binding domains of LexA repressor,[74] and the transcription elongation factor TFIIS.[75] Also for interleukin-4[21] and for azurin,[71] 3D TOCSY–NOESY and 3D NOESY–(^{15}N, ^{1}H)–HMQC were used together to resolve ambiguities in the assignments.

8.4 Identification of Spin Systems using 3D TOCSY–TOCSY Spectroscopy

An essential step for the sequential analysis of protein NMR spectra is the identification of spin systems. It has been demonstrated that 3D TOCSY–TOCSY spectroscopy can be of great help for deciphering spin systems.[76] The analysis of a 3D TOCSY–TOCSY spectrum is more straightforward than that of a 3D TOCSY–NOESY spectrum, since each 3D cross peak already defines three frequencies of the spin system. Similarly as in 3D TOCSY–NOESY spectra, it is relatively easy to recognize in the f_1–f_3 planes the 3D cross peaks belonging to one spin system, even in the case of overlap at the f_2 frequency. Oschkinat et al.[58] have proposed a strategy for automated assignment of proteins, where the spin systems would be identified using a 3D TOCSY–TOCSY spectrum and the sequential connectivities between the spin systems are obtained from a 3D TOCSY–NOESY spectrum. 3D TOCSY–TOCSY spectra can be very useful in those cases where strong overlap prohibits the analysis of spin systems but where efficient HOHAHA transfer is still present.

8.5 Analysis of 3D NOESY–NOESY Spectra

For larger proteins it becomes more difficult to establish the proton–proton J coupling via COSY and HOHAHA transfer steps. A 3D technique, where both mixing periods are due to cross relaxation, is in principle not limited by molecular weight. Suitable mixing periods are NOE or ROE. Thus, 3D NOESY–NOESY spectroscopy was proposed, where a NOE is now relayed by NOE to another nucleus.[11] However, since the relay can be to any neighboring nucleus, the analysis of 3D NOESY–NOESY spectra can be complex. Furthermore, since in general the NOE is weak and the relay can be to several other nuclei, a relatively low sensitivity for the 3D NOESY–NOESY could be expected. Nevertheless, 3D NOESY–NOESY spectra of good quality have been presented.[41,77–79] For proteins it has been demonstrated that the amide protons show connectivity patterns very similar to 3D NOESY–TOCSY spectra.[77] A statistical analysis of expected connectivities in 3D NOESY–NOESY spectra for 28 crystal protein structures shows that patterns of highly correlated cross peaks exist, suggesting that assignments for proteins could be based largely on NOE data.[80] A very complete analysis of sequential and medium range connectivities has been made for the 3D NOESY–NOESY spectrum of parvalbumin.[41,78] For the 109-residue parvalbumin the HOHAHA transfer is generally more efficient than the NOE transfer, thus the number of sequential and medium range connectivities in the 3D NOESY–NOESY spectrum is slightly less than that of a 3D TOCSY–NOESY spectrum. For proteins with a less efficient HOHAHA transfer, however, 3D NOESY–NOESY may perform better.

8.6 Structural Studies of Proteins

Stretches of sequential and medium range 3D connectivities can be used as indicators for α-helical, β-sheet, or turn-like structures. Thus, for the proteins parvalbumin[68] and aponeocarzinostatin[69] it was demonstrated that most of the secondary structure assignments found in 2D NOE spectra can be obtained from a 3D TOCSY–NOESY spectrum, but with fewer ambiguities. The secondary structures of a phospholipid transfer protein[70] and of leghemoglobin[72] are based on a combination of homonuclear 2D and 3D data. For ferrocytochrome c_{553} several crucial long range NOEs could be established from 3D TOCSY–NOESY spectra.[81] Similarly, many NOE restraints used for the structure determinations of procolipase[73] and the DNA binding domain of LexA repressor[74] were obtained with help from 3D TOCSY–NOESY data.

Long-range NOEs can also be observed by 3D NOESY–NOESY. Thus, 3D NOESY–NOESY data resolved crucial long range connectivities for the structure determination of the DNA binding domain of LexA repressor.[74] The analysis of 3D NOESY–NOESY spectra is complex, since a large number of cross peaks can be expected and the magnetization transfer is not limited to spin systems. The analysis improves by

comparing patterns of 3D cross peaks. For example, if for spin B a characteristic pattern of cross peaks {(A, B, P), (A, B, Q), and (A, B, R)} has been observed, the 3D NOESY–NOESY spectrum can be searched systematically for the patterns {(C, B, P), (C, B, Q), and (C, B, R)} and {(P, B, C), (Q, B, C), and (R, B, C)}. If the pattern at the row defined by (f_1, f_2) = (A, B) was observed virtually without overlap, this search is effectively a convolution of the 3D spectrum with this row. Visually, this pattern can be easily recognized in an f_1–f_3 plane. Next, one has to analyze the pattern at (f_1, f_2) = (B, C) in order to establish the nature of nucleus C. In this way the pattern of relayed intensities, which was unfavorable for an optimal signal-to-noise ratio of the 3D spectrum, turns out to be beneficial for pattern recognition. Once the 3D cross peaks have all been assigned, the intensities of the 3D cross peaks can be converted into constraints for structure refinement.

8.7 Distance Constraints from 3D Data

For structure refinement it is important to obtain as many distance constraints as possible.[1] For this, 3D spectra can be very useful, since they may resolve many ambiguities in the spectral interpretation of NOE data, and therefore lead to more restraints.[82] It is, however, also possible to use the 3D spectra directly for obtaining distance constraints. The 3D cross-peak intensity is proportional to the product of the two transfer efficiencies of the two mixing periods of a 3D experiment:

$$I_{ijk} \propto T_{ij} T_{jk} \tag{1}$$

Several approaches have been described for interpreting the 3D intensity. The ratio of the intensity of the cross peak C(A,B,C) of a 3D TOCSY–NOESY, or a 3D NOESY–NOESY spectrum and the intensity of the cross-diagonal cross peak C(A,B,B) defines the transfer efficiency T_{bc}:

$$I\{\mathrm{C(A,B,C)}\}/I\{\mathrm{C(A,B,B)}\} = T_{bc}/(1 - T_{bc}) \tag{2}$$

From this NOE transfer efficiency, T_{bc} distances can be obtained in a similar way as from regular 2D data. The relationship between NOE transfer efficiency and cross relaxation rates is

$$\mathbf{T} = \exp(-\tau_{\mathrm{m}}\mathbf{R}) \tag{3}$$

where **T** and **R** are the NOE transfer and cross-relaxation matrices, respectively, and τ_{m} the NOE mixing period. Generally, transfer efficiencies are compared with those of protons at known distances and the approximate relationship

$$T_{bc}/T_{de} = (r_{de}/r_{bc})^6 \tag{4}$$

is used. In the case of overlap at the cross-diagonal planes it is still possible to obtain the ratio of the cross peaks C(A,B,C) and C(A,B,F) which defines the ratio T_{bc}/T_{bf} and thus the ratio of the distances r_{bc}/r_{bf}.[83] If the distance r_{bf} is known, the distance r_{bc} can be derived.

A more quantitative approach uses the cross-peak intensities of a 3D NOESY–NOESY spectrum. The relationship between NOE and distance is only an approximate one, due to spin diffusion at longer NOE mixing times. Approximating this multiple-step NOE transfer to second order, the NOE intensity is equal to

$$T_{ij} = -R_{ij}\tau_{\mathrm{m}} + \sum R_{ik}R_{kj}\tau_{\mathrm{m}}^2 \ldots \tag{5}$$

The second term in equation (5) describes spin diffusion via other spins. The intensity of a cross peak in a 3D NOESY–NOESY spectrum is to a first approximation equal to

$$T_{ikj} = R_{ik}R_{kj}\tau_{\mathrm{m}}^2 \ldots \tag{6}$$

Thus the cross peaks in a 3D NOESY–NOESY spectrum define the contributions of the several spin diffusion paths via other nuclei.[11] Therefore the 3D NOESY–NOESY intensities can be used to obtain more accurate cross-relaxation rates between proton pairs, as has been shown by Kessler et al.[84] and Habazettl et al.[85]

The 3D NOESY–NOESY intensities can also be used as direct constraints for a structure refinement. This requires the calculation of the gradients of the 3D intensities with respect to the coordinates of the protons in a molecule. The gradient of a 3D NOESY–NOESY peak with a net transfer T_{ijk} can be written[86] as the sum of two terms containing the separate gradients of T_{ij} and T_{jk}:

$$\nabla T_{ijk} = T_{ij}\nabla T_{jk} + \nabla T_{ij} T_{jk} \tag{7}$$

The transfer efficiencies T_{ij} and T_{jk} can be obtained from relaxation matrix methods (cf. Bonvin et al.[87]), while the derivatives of the 2D efficiencies can be solved exactly[88] or be approximated.[89] equation (7) has been used to obtain 3D NOE restraining potentials for use in restrained molecular dynamics calculations:[86,90,91]

$$V_{\mathrm{3D\,NOE}} \sim \sum_{ijk} (T_{ijk} - T_{ijk}^{\mathrm{obs}})^2 \tag{8}$$

where T_{ijk} and $T_{ijk}{}^{\mathrm{obs}}$ are the calculated and observed transfer efficiencies, respectively. The minimization of the 3D NOE potential requires the calculation of $\nabla V_{\mathrm{3DNOE}}$. This can be accomplished by combining equations (7) and (8) as

$$\nabla V_{\mathrm{3D\,NOE}} \sim \sum_{ijk} 2(T_{ijk} - T_{ijk}^{\mathrm{obs}})(T_{ij} \cdot \nabla T_{jk} + \nabla T_{ij} \cdot T_{jk}) \tag{9}$$

It has been shown that the use of the 3D cross-peak intensities can lead to a better definition of the structures of proteins than the use of only 2D NOE data.

8.8 Protein Hydration Studies

Cross peaks in a NOESY spectrum at a line corresponding to the f_1 frequency of water can identify protons with a close proximity to water.[92] The overlap of proton signals on this line can be removed by transferring the magnetization in a second magnetization transfer step to a third nucleus. Thus, Otting et al.[93] have demonstrated the use of 3D NOESY–TOCSY and 3D ROESY–TOCSY for studies of protein hydration,

whereas Holak et al.[94] have used 3D NOESY–NOESY. In contrast to 2D methods, where the NOEs with water protons are all observed on a single frequency axis, the f_2–f_3 planes of 3D spectra at the f_1 frequency of water reveal the protons interacting with water via cross peaks in a two-dimensional map. This reduces overlap and helps to assign the protons involved. The comparison of the sign and intensities of the cross peaks in the f_2–f_3 planes of the 3D NOESY–TOCSY and 3D ROESY–TOCSY spectra distinguishes NOE and exchange effects.

8.9 Homonuclear 3D NMR of Oligosaccharides

The small chemical shift dispersion of the sugar-skeleton protons of oligosaccharides poses a major problem for structural studies. It is often still possible to obtain assignments on the basis of 2D HOHAHA experiments by exploiting the chemical shift dispersion of the anomeric protons. However, the unique identification of NOEs involving protons in the bulk region between 3 and 4 ppm is very difficult. The resolution in the bulk region can be increased by the application of 3D NOESY–TOCSY techniques, which relay the magnetization from the bulk protons to the anomeric signals.[83,95]

An example is given in Figure 11, which shows the f_1–f_2 plane at the f_3 frequency of the Man-4 H-2 anomeric signal of a biantennary asparagine-linked oligosaccharide at 4.19 ppm. An interesting 3D cross peak is observed at the f_1 frequency of Man-3 H-2, which shows the presence of an NOE between Man-4 H-5 and Man-3 H-2. The existence of this NOE was the subject of considerable discussion in the literature, although it was settled later by deuteration studies (see Vuister et al.[95] for a discussion). This NOE effect is found directly in the 3D NOESY–TOCSY spectrum.

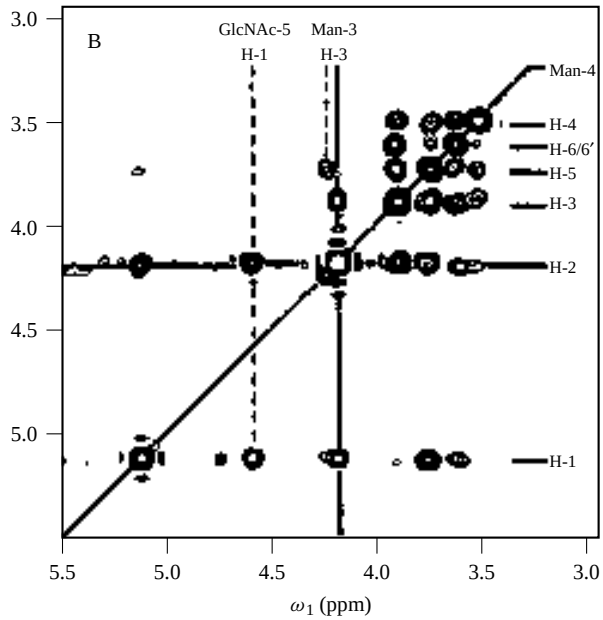

Figure 11 f_1–f_2 plane of the 3D NOESY–TOCSY spectrum of 20 mM biantennary oligosaccharide in D_2O at 304 K and pH = 7. The cross section shown is at the f_3 resonance position of Man-4 H-2 (4.19 ppm). The 144 × 144 × 1024 data set was recorded at 500 MHz in 63 h using eight scans. The NOE mixing time was 350 ms and the HOHAHA mixing time 94 ms. The spectrum was processed to a resolution of 256 × 256 × 512. (Adapted by permission from Vuister et al.[95])

8.10 Homonuclear 3D NMR of DNA and RNA Fragments

For the sequential assignment of DNA and RNA fragments it is necessary to correlate the NOEs of the aromatic protons of the nucleic acid bases with their own sugar protons and those of their neighbor. 3D TOCSY–NOESY spectra can be used for this purpose.[96,97] It turns out that even the very crowded 4′,5′,5″ region of DNA fragments now becomes accessible for analysis. Thus, 3D TOCSY–NOESY was used for a 15-residue DNA hairpin,[96] and 3D NOESY–TOCSY for a 31-residue pyrimidine–purine–pyrimidine DNA triplex.[97] Homonuclear 3D methods are very useful for RNA fragments, where considerable overlap exists for most sugar protons. Thus, most proton assignments can be obtained from a single 3D TOCSY–NOESY spectrum, as demonstrated for a 12-mer RNA duplex.[98]

Structural studies of DNA fragments can use 3D NOESY–TOCSY methods for resolving ambiguities in the assignment of cross peaks in 2D NOE spectra. Such methods have been applied for the analysis of the NOEs of a 12-mer DNA duplex containing a GG mismatch[99] and for analysis of a modified 12-mer DNA duplex.[100] In both cases the 3D spectra clarified unusual NOEs, with important consequences for the geometry.

For larger DNA and RNA fragments the HOHAHA transfer could turn out to be inefficient. In this situation 3D NOESY–NOESY is an alternative, since it is not based on a possibly weak homonuclear J coupling, and cross relaxation becomes increasingly efficient at higher molecular weights. It has been demonstrated that 3D NOESY–NOESY spectra of good quality can be recorded for a 22-mer duplex.[11] Similarly, 3D NOESY–NOESY has been applied to a 40-base three-stranded DNA junction,[101] where it allowed the completion of the proton assignments and confirmed the unusual geometry at the junction, and to a hybrid DNA–RNA dodecamer duplex,[102] where it resolved superimposed cross peaks of the RNA strand.

9 PROSPECTS FOR 3D NMR SPECTROSCOPY

The NOE effect and the J coupling can be combined in three different ways in homonuclear 3D NMR experiments. 3D experiments with a simple magnetization transfer such as in 3D COSY–COSY are most amenable for analysis. However, the linewidth of larger biomolecules is of a similar magnitude to the ^3J(H, H) coupling, which leads to weak 3D cross-peak intensities. Magnetization transfer by HOHAHA is less sensitive to line broadening, and is therefore preferable for most applications. Thus, spin systems of biomolecules with molecular masses below 20 kDa can be analyzed using 3D TOCSY–TOCSY and 3D NOESY–TOCSY spectra. Furthermore, these latter spectra turn out to be useful in assigning resonances and analyzing the secondary and even the tertiary structure of proteins. For biomolecules of greater mass than 20 kDa or with a large linewidth, mixing periods based on J(H, H) couplings may not be efficient. In this case 3D NOESY–NOESY or 3D ROESY–ROESY experiments can

be used for resolving the overlap of cross peaks in NOESY and ROESY spectra.

The analysis of many multidimensional NMR spectra may benefit from the development of programs which allow the graphical and interactive bookkeeping of the spectra on workstations. This is particularly true for the homonuclear 3D spectra of biomolecules, where the large number of interactions and the fact that the relay is to many other nuclei often leads to many cross peaks. Since the analysis of such spectra can be complex, a practical approach where the 3D spectra assist the analysis of 2D TOCSY and NOESY spectra seems to be the most fruitful. A further improvement for all multidimensional techniques is the application of field gradient methods using shielded gradient coils. This may allow a reduction in the phase cycling for coherence selection and artifact suppression, so that spectra can be obtained with a significant higher resolution per domain. This is particularly important for the automated analysis of multidimensional spectra, where a large tolerance in the coordinates of a cross peak due to low resolution may result in a large number of possible assignments.

Another class of 3D NMR experiments, not discussed in detail in the present overview, is formed by the heteronuclear 3D NMR experiments, such as 3D TOCSY–HMQC and 3D NOESY–HMQC. These methods also use a third dimension to increase the resolution. Compared with the homonuclear proton methods they have the advantage of an efficient J transfer due to the large $^{15}N-^{1}H$ and $^{13}C-^{1}H$ coupling constants. For sufficient sensitivity, it is generally necessary to obtain isotopically enriched biological material. For doubly (^{13}C, ^{15}N) labeled proteins and ^{13}C labeled oligonucleotides straightforward and powerful methods have been developed both for assigning resonances and for structural studies (see Clore and Gronenborn[19] and Oschkinat et al.[21] for reviews). In many cases, however, labeling may be impossible to realize, and then homonuclear 3D methods are still possible. In other cases only ^{15}N labeling may feasible. It is then possible to record 3D TOCSY–NOESY–(^{15}N, ^{1}H)–HSQC spectra[103,104] or 4D TOCSY–NOESY–(^{15}N, ^{1}H)–HSQC spectra[105] to resolve ambiguities in 3D NOESY–(^{15}N, ^{1}H)–HSQC spectra. It turns out that the analysis of such spectra is very similar to that of the homonuclear 3D TOCSY–NOESY spectra.

During the past few years many homonuclear and heteronuclear 3D NMR experiments have been developed. These methods can complement each other and should be explored to their limits for studying larger and more complex biomolecular systems.

10 RELATED ARTICLES

Three-Dimensional HMQC-NOESY, NOESY-HMQC, and NOESY-HSQC; Three- and Four-Dimensional Heteronuclear Magnetic Resonance; Multidimensional Spectroscopy: Concepts; Protein Hydration; Relayed Coherence Transfer Experiments.

11 REFERENCES

1. K. Wüthrich, *NMR of Proteins and Nucleic Acids*, Wiley, New York, 1986.
2. R. R. Ernst, G. Bodenhausen, and A. Wokaun, *Principles of Nuclear Magnetic Resonance in One and Two Dimensions*, Clarendon Press, Oxford, 1987.
3. H. D. Plant, T. H. Mareci, M. D. Cockman, and W. S. Brey, *27th Experimental NMR Conference, Baltimore, Maryland, April 13–17, 1986*.
4. G. W. Vuister and R. Boelens, *J. Magn. Reson.*, 1987, **73**, 328.
5. C. Griesinger, O. W. Sørensen, and R. R. Ernst, *J. Magn. Reson.*, 1987, **73**, 574.
6. C. Griesinger, O. W. Sørensen, and R. R. Ernst, *J. Am. Chem. Soc.*, 1987, **109**, 7227.
7. H. Oschkinat, C. Griesinger, P. J. Kraulis, O. W. Sørensen, R. R. Ernst, A. M. Gronenborn, and G. M. Clore, *Nature*, 1988, **332**, 374.
8. G. W. Vuister, R. Boelens, and R. Kaptein, *J. Magn. Reson.*, 1988, **80**, 176.
9. L. E. Kay, G. M. Clore, A. Bax, and A. M. Gronenborn, *Science*, 1990, **249**, 411.
10. G. M. Clore, L. E. Kay, A. Bax, and A. M. Gronenborn, *Biochemistry*, 1991, **30**, 12.
11. R. Boelens, G. W. Vuister, T. M. G. Koning, and R. Kaptein, *J. Am. Chem. Soc.*, 1989, **111**, 8525.
12. S. W. Fesik and E. R. P. Zuiderweg, *J. Magn. Reson.*, 1988, **78**, 588.
13. E. R. P. Zuiderweg and S. W. Fesik, *Biochemistry*, 1989, **28**, 2387.
14. D. Marion, L. E. Kay, S. W. Sparks, D. A. Torchia, and A. Bax, *J. Am. Chem. Soc.*, 1989, **111**, 1515.
15. D. Marion, P. C. Driscoll, L. E. Kay, P. T. Wingfield, A. Bax, A. M. Gronenborn, and G. M. Clore, *Biochemistry*, 1989, **28**, 6150.
16. G. T. Montelione and G. Wagner, *J. Magn. Reson.*, 1990, **87**, 183.
17. M. Ikura, L. E. Kay, and A. Bax, *Biochemistry*, 1990, **29**, 4659.
18. C. Griesinger, O. W. Sørensen, and R. R. Ernst, *J. Magn. Reson.*, 1989, **84**, 14.
19. G. M. Clore and A. M. Gronenborn, *Prog. Nucl. Magn. Reson. Spectrosc.*, 1991, **23**, 43.
20. A. Bax and S. Grzesiek, *Acc. Chem. Res.*, 1993, **26**, 131.
21. H. Oschkinat, T. Müller, and T. Dieckmann, *Angew. Chem., Int. Ed. Engl.*, 1994, **33**, 277.
22. O. W. Sørensen, *J. Magn. Reson.*, 1990, **89**, 210.
23. G. W. Eich, G. Bodenhausen, and R. R. Ernst, *J. Am. Chem. Soc.*, 1982, **104**, 3731.
24. P. H. Bolton and G. Bodenhausen, *Chem. Phys. Lett.*, 1982, **89**, 139.
25. G. Wagner, *J. Magn. Reson.*, 1984, **57**, 497.
26. F. J. M. Van der Ven, C. A. G. Haasnoot, and C. W. Hilbers, *J. Magn. Reson.*, 1985, **61**, 181.
27. H. Kessler, G. Gemmecker, and S. Steuernagel, *Angew. Chem., Int. Ed. Engl.*, 1988, **100**, 600.
28. P. De Waard, R. Boelens, G. W. Vuister, and J. F. G. Vliegenthart, *J. Am. Chem. Soc.*, 1990, **112**, 3232.
29. H. Kessler, G. Gemmecker, and B. Haase, *J. Magn. Reson.*, 1988, **77**, 401.
30. W. P. Aue, E. Bartholdi, and R. R. Ernst, *J. Chem. Phys.*, 1976, **64**, 2229.
31. J. Jeener, B. H. Meier, P. Bachmann, and R. R. Ernst, *J. Chem. Phys.*, 1979, **71**, 4546.
32. S. Macura and R. R. Ernst, *Mol. Phys.*, 1980, **41**, 95.
33. A. Kumar, G. Wagner, R. R. Ernst, and K. Wüthrich, *J. Am. Chem. Soc.*, 1981, **103**, 3654.

34. A. A. Bothner-By, R. L. Stephens, J. Lee, C. D. Warren, and R. W. Jeanloz, *J. Am. Chem. Soc.*, 1984, **106**, 811.
35. A. Bax and D. G. Davies, *J. Magn. Reson.*, 1985, **65**, 355.
36. H. Oschkinat, C. Cieslar, A. M. Gronenborn, and G. M. Clore, *J. Magn. Reson.*, 1989, **81**, 212.
37. H. Oschkinat, C. Cieslar, T. A. Holak, G. M. Clore, and A. M. Gronenborn, *J. Magn. Reson.*, 1989, **83**, 450.
38. J. Cavanagh and M. Rance, *Prog. Nucl. Magn. Reson. Spectrosc.*, 1993, **27**, 1.
39. F. Ni, *J. Magn. Reson.*, 1992, **100**, 391.
40. C. Griesinger, G. Otting, K. Wüthrich, and R. R. Ernst, *J. Am. Chem. Soc.*, 1988, **110**, 7870.
41. R. Boelens, C. Griesinger, L. E. Kay, D. Marion, and E. R. P. Zuiderweg, *Nato ASI Ser., Ser. A*, 1991, **A225**, 127.
42. J.-P. Simorre and D. Marion, *J. Magn. Reson.*, 1991, **94**, 426.
43. H. Barkhuizen, R. deBeer, W. M. M. J. Bovee, and D. van Ormondt, *J. Magn. Reson.*, 1985, **61**, 465.
44. H. Gesmar, J. J. Led, and F. Abildgaard, *Prog. Nucl. Magn. Reson. Spectrosc.*, 1990, **22**, 255.
45. G. Zhu and A. Bax, *J. Magn. Reson.*, 1990, **90**, 405.
46. M. Robin, M.-A. Delsuc, E. Guitet, and J.-Y. Lallemand, *J. Magn. Reson.*, 1991, **92**, 645.
47. E. T. Olejniczak and H. L. Eaton, *J. Magn. Reson.*, 1990, **87**, 628.
48. D. Marion and A. Bax, *J. Magn. Reson.*, 1989, **83**, 205.
49. R. Saffrich, W. Beneicke, K.-P. Neidig, and H. R. Kalbitzer, *J. Magn. Reson. B*, 1993, **101**, 304.
50. L. Mitschang, C. Cieslar, T. A. Holak, and H. Oschkinat, *J. Magn. Reson.*, 1991, **92**, 208.
51. G. Otting, H. Widmer, G. Wagner, and K. Wüthrich, *J. Magn. Reson.*, 1986, **66**, 187.
52. D. Marion and A. Bax, *J. Magn. Reson.*, 1988, **79**, 352.
53. P. J. Kraulis, *J. Magn. Reson.*, 1989, **84**, 627.
54. G. J. Kleywegt, G. W. Vuister, A. Padilla, R. M. A. Knegtel, R. Boelens, and R. Kaptein, *J. Magn. Reson.*, 1993, **102**, 166.
55. M. Kjaer, K. V. Andersen, S. Ludvigsen, H. Shen, P. Windekinde, B. Sørensen, and F. M. Poulson, *Nato ASI Ser., Ser. A*, 1991, **A225**, 291.
56. K.-P. Neidig, R. Saffrich, M. Lorenz, and H. R. Kalbitzer, *J. Magn. Reson.*, 1990, **89**, 543.
57. C. Cieslar, T. A. Holak, and H. Oschkinat, *J. Magn. Reson.*, 1990, **87**, 400.
58. H. Oschkinat, T. A. Holak, and C. Cieslar, *Biopolymers*, 1991, **31**, 699.
59. R. E. Hoffman and D. B. Davies, *J. Magn. Reson.*, 1988, **80**, 337.
60. P. A. Mirau, S. A. Heffner, and F. A. Bovey, *J. Magn. Reson.*, 1990, **89**, 572.
61. C. Griesinger, O. W. Sørensen, and R. R. Ernst, *J. Chem. Phys.*, 1986, **85**, 6387.
62. Y. Yang, A. Hagemeyer, K. Zemke, and H. W. Spiess, *J. Chem. Phys.*, 1990, **93**, 7740.
63. B. S. Arun Kumar and S. J. Opella, *J. Magn. Reson.*, 1993, **101**, 333.
64. G. W. Vuister, Ph.D. Thesis, Utrecht University, 1990.
65. S. S. Wijmenga and C. P. M. van Mierlo, *Eur. J. Biochem.*, 1991, **195**, 807.
66. G. W. Vuister, R. Boelens, A. Padilla, G. J. Kleywegt, and R. Kaptein, *Biochemistry*, 1990, **29**, 1829.
67. H. Oschkinat, C. Cieslar, and C. Griesinger, *J. Magn. Reson.*, 1990, **86**, 453.
68. A. Padilla, G. W. Vuister, R. Boelens, G. J. Kleywegt, A. Cavé, J. Parello, and R. Kaptein, *J. Am. Chem. Soc.*, 1990, **112**, 5024.
69. X. Gao and W. Burkhart, *Biochemistry*, 1991, **30**, 7730.
70. J.-P. Simorre, A. Caille, D. Marion, D. Marion, and M. Ptak, *Biochemistry*, 1991, **30**, 11 600.
71. M. van de Kamp, G. W. Canters, S. S. Wijmenga, A. Lommen, C. W. Hilbers, H. Nar, A. Messerschmidt, and R. Huber, *Biochemistry*, 1992, **31**, 10 194.
72. D. Morikis, C. A. Lepre, and P. E. Wright, *Eur. J. Biochem.*, 1994, **219**, 611.
73. J. N. Breg, L. Sarda, P. J. Cozzone, R. Boelens, and R. Kaptein, *Biochemistry*, 1994, in press.
74. R. Fogh, G. Ottleben, H. Rüterjans, M. Schnarr, R. Boelens, and R. Kaptein, *EMBO J.*, 1994, **13**, 3936.
75. X. Qian, S. N. Gozani, H. S. Yoon, C. J. Jeon, K. Agarwal, and M. A. Weiss, *Biochemistry*, 1993, **32**, 9944.
76. C. Cieslar, T. A. Holak, and H. Oschkinat, *J. Magn. Reson.*, 1990, **87**, 184.
77. J. N. Breg, R. Boelens, G. W. Vuister, and R. Kaptein, *J. Magn. Reson.*, 1990, **87**, 646.
78. A. Padilla, *Cahiers IMABIO CNRS (Paris)*, 1992, **3**, 19.
79. A. Ross, J. Freund, C. Cieslar, H. Oschkinat, M. Schleicher, and T. A. Holak, *J. Magn. Reson.*, 1991, **95**, 567.
80. G. W. Vuister, R. Boelens, A. Padilla, and R. Kaptein, *J. Biomol. NMR*, 1991, **1**, 421.
81. D. Marion and F. Guerlesquin, *Biochemistry*, 1992, **31**, 8171.
82. T. A. Holak, J. Habazettl, H. Oschkinat, and J. Otlewski, *J. Am. Chem. Soc.*, 1991, **113**, 3196.
83. P. de Waard, B. R. Leeflang, J. F. G. Vliegenthart, R. Boelens, G. W. Vuister, and R. Kaptein, *J. Biomol. NMR*, 1992, **2**, 211.
84. H. Kessler, S. Seip, and J. Saulitis, *J. Biomol. NMR*, 1991, **1**, 83.
85. J. Habazettl, A. Ross, H. Oschkinat, and T. A. Holak, *J. Magn. Reson.*, 1992, **97**, 511.
86. A. M. J. J. Bonvin, R. Boelens, and R. Kaptein, *J. Magn. Reson.*, 1991, **95**, 626.
87. A. M. J. J. Bonvin, R. Boelens, and R. Kaptein, in *Computer Simulation of Biomolecular Systems*, eds. W. F. van Gunsteren, P. K. Weiner, and A. J. Wilkinson, Escom, Leiden, 1993, Vol. 2, p. 403.
88. P. Yip and D. A. Case, *J. Magn. Reson.*, 1989, **83**, 643.
89. A. M. J. J. Bonvin, R. Boelens, and R. Kaptein, *J. Biol. NMR*, 1991, **1**, 305.
90. J. Habazettl, M. Schleicher, J. Otlewski, and T. A. Holak, *J. Mol. Biol.*, 1992, **228**, 156.
91. R. Bernstein, A. Ross, C. Cieslar, and T. A. Holak, *J. Magn. Reson.*, 1993, **101**, 185.
92. G. Otting and K. Wüthrich, *J. Am. Chem. Soc.*, 1989, **111**, 1871.
93. G. Otting, E. Liepinsh, B. T. Farmer II, and K. Wüthrich, *J. Biomol. NMR*, 1991, **1**, 209.
94. T. A. Holak, R. Witscheck, and A. Ross, *J. Magn. Reson.*, 1992, **97**, 632.
95. G. W. Vuister, P. de Waard, R. Boelens, J. F. G. Vliegenthart, and R. Kaptein, *J. Am. Chem. Soc.*, 1989, **111**, 772.
96. M. M. W. Mooren, C. W. Hilbers, G. A. van der Marel, J. H. van Boom, and S. S. Wijmenga, *J. Magn. Reson.*, 1991, **94**, 101.
97. I. Radhakrishnan, D. J. Patel, and X. Gao, *Biochemistry*, 1992, **31**, 2514.

98. S. S. Wijmenga, H. A. Heus, B. Werten, G. A. van der Marel, J. H. van Boom, and C. W. Hilbers, *J. Magn. Reson.*, 1994, **103**, 134.
99. M. E. Piotto and D. G. Gorenstein, *J. Am. Chem. Soc*., 1991, **113**, 1438.
100. X. Gao and P. W. Jeffs, *J. Biomol. NMR*, 1994, **4**, 17.
101. M. A. Rosen and D. J. Patel, *Biochemistry*, 1993, **32**, 6563.
102. X. Gao and P. W. Jeffs, *J. Biomol. NMR*, 1994, **4**, 367.
103. L. Mueller, S. Campbell-Burk, and P. Domaille, *J. Magn. Reson.*, 1992, **96**, 408.
104. S. Boentges, J. M. Schmidt, T. Levante, and R. R. Ernst, *15th International Conference on Magnetic Resonance in Biological Systems, Jeruzalem, Israel, August 1992*.
105. R. Boelens, *Cahiers IMABIO CNRS (Paris)*, 1992, **3**, 33.

Biographical Sketches

Rolf Boelens. *b* 1951. M.S., 1977, University of Groningen, Ph.D., 1984, University of Amsterdam. Postdoctoral associate with R. Kaptein, Groningen. Associate professor at Utrecht University, 1987–present. Over 130 publications. Research specialties: NMR method development, structure determination of biomolecules by NMR and studies on protein–DNA interaction.

Robert Kaptein. *b* 1941. M.S., 1965, Ph.D., Leiden, 1971; postdoctoral fellow with Ray Freeman, Varian 1971–1972; Shell Research Laboratory, Amsterdam, 1972–1975; Groningen University, 1975–1987; Utrecht University, Professor of Chemistry 1987–present. Research interests: biomolecular structure determination, NMR methodology, protein–DNA interactions.

Lipoproteins

Joel D. Morrisett
Baylor College of Medicine, Houston, TX, USA

and

James A. Hamilton
Boston University School of Medicine, Boston, MA, USA

1	Introduction	1
2	Isolated Native Lipoproteins	1
3	Lipoproteins in Plasma	4
4	Modified Lipoproteins	6
5	Model and Recombined Lipoproteins	6
6	Peptide Fragments of Apolipoproteins	7
7	Conclusion	8
8	Related Articles	8
9	References	8

1 INTRODUCTION

Plasma lipoproteins are multimolecular complexes composed of varying proportions of protein, phospholipid, cholesterol, cholesteryl ester, and triglyceride.[1] The three major classes of plasma lipoproteins are the very low density lipoproteins (VLDL), low density lipoproteins (LDL), and high density lipoproteins (HDL). The VLDL transport endogenously synthesized triglyceride from the liver to peripheral tissues, where they undergo lipolysis to provide free fatty acids (FFA) required for energy metabolism, and membrane biosynthesis. Progressive lipolysis of VLDL triglycerides produces a cascade of remnant particles ultimately leading to the formation of LDL. LDL particles, although poor in triglyceride, are rich in cholesteryl ester, which is delivered to various peripheral cells by predominantly receptor mediated uptake. Plasma concentrations of LDL are directly correlated with coronary artery disease. HDL are relatively protein rich lipoproteins that take up excess cholesterol from the surface of peripheral cells and transport it to the liver where it is either reutilized or catabolized and excreted. The plasma concentration of HDL is inversely correlated with coronary artery disease. Other normally less abundant lipoproteins such as chylomicrons, Lp[a], β-VLDL, and IDL represent variants of the above described major classes. The central role played by lipoproteins in lipid metabolism and several disease states have elicited their intensive study by many investigators using numerous techniques. NMR has been especially effective in elucidating the structure and monitoring the metabolism of lipoproteins because they contain an abundance of naturally occurring, magnetically active nuclei (^{31}P, ^{1}H, and ^{13}C), and because of the sensitivity of NMR to the diverse chemical and physical environments in which these nuclei occur.

Since the last comprehensive review on NMR of lipoproteins,[2] technical advances have included higher field magnets, faster computational hardware, and improved data processing software. These developments have made possible increasingly sophisticated applications of NMR to the study of lipoproteins, not only in their purified form but also in whole plasma, resulting in intensive interest in the use of NMR spectroscopy for medical diagnosis. This article provides a concise summary of some of these more recent applications, as well as a survey of NMR studies of native, modified, and model lipoproteins.

2 ISOLATED NATIVE LIPOPROTEINS

Phosphorus-31 NMR spectra of plasma lipoproteins are quite simple, since the ^{31}P nucleus is present almost exclusively in the phosphate group of phospholipids. The first reported ^{31}P spectra of HDL showed two narrow resonances which quantitatively reflected the major phospholipid species of HDL, phosphatidylcholine (PC) and sphingomyelin.[3,4] Their chemical shifts are consistent with location of the phospholipid polar groups at the aqueous interface; the narrow lines indicate that the phosphate groups have homogeneous environments and rapid molecular motions. Quantification of the intensity of the ^{31}P NMR resonances of LDL suggests that a small fraction of phospholipids interact with the protein (apoB-100), similar to the interaction of boundary membrane lipids with membrane proteins.[5] The effects of several paramagnetic reagents on the ^{31}P resonances in spectra of HDL and LDL have been studied. Although all studies showed at least 50% diminution of the intensity of these resonances by paramagnetic reagents, consistent with the phosphoryl groups being at the aqueous interface, different reagents had quantitatively different effects.[4,6,7] Use of the paramagnetic ion Pr^{3+} demonstrated a phospholipid bilayer structure in the abnormal lipoprotein LP-X, which is present in the plasma of patients with obstructive liver disease and lecithin–cholesterol acyltransferase deficiency.[8] Lateral diffusion of phospholipids in various lipoproteins has been estimated from the viscosity dependence of ^{31}P linewidths; LDL phospholipids exhibit a large increase in diffusion rate over the temperature range of the phase transition of cholesteryl esters in the hydrophobic core.[9] The phospholipids of lipoproteins can be quantified accurately according to headgroup species by detergent solubilization.[10] An interesting application to lipoprotein metabolism is the use of ^{31}P NMR to monitor phospholipase A_2 hydrolysis of HDLs.[11] The time-dependent intensity changes for resonances reflecting PC and lyso-PC accurately describe the reaction rate, and the constancy of the linewidths suggests that there are no major changes in the interfacial structure. In general, ^{31}P NMR has seen limited application in studies of lipoprotein structure and dynamics since the spectra provide information about only one region of one lipid type present in lipoproteins.

The use of ^{13}C NMR spectroscopy to study plasma lipoproteins was not feasible before the development of Fourier transform NMR and large probes accommodating 15 and 20 mm sample tubes in order to overcome the inherently low sensitivity and abundance of the ^{13}C nucleus. The main advantage of ^{13}C, compared with ^{1}H, NMR for the study of lipoproteins was demonstrated in the earliest published spectra;[12,13] ^{13}C spectra even at low field (1.4 T, Figure 1) are better resolved and contain more accessible information than ^{1}H spectra at much higher field. Improved resolution,

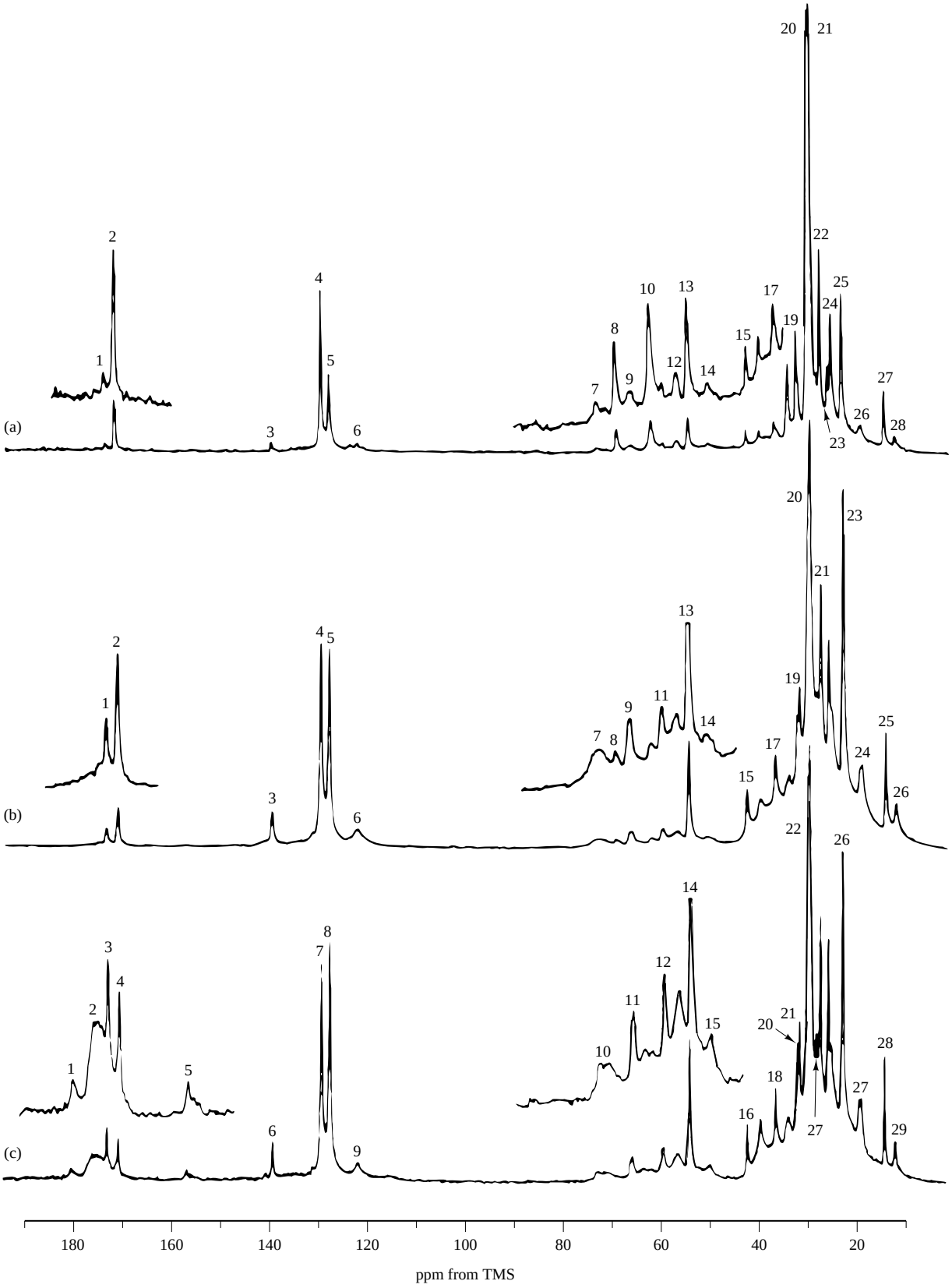

Figure 1 Natural abundance ^{13}C Fourier transform NMR spectra (15.2 MHz) of human plasma lipoproteins at 36 °C recorded with ^{1}H decoupling in 20 mm sample tubes. Conditions: 250 ppm spectral width, 4096 time domain points, 0.555 s recycle time. The insets were printed with a 4 × vertical expansion. Digital broadening of 0.3 Hz (full spectra) and 2.4 Hz (insets) was used to improve the signal-to-noise ratio. Peak numbers are the same as those shown in parentheses in Table 1. (a) VLDL, 37 mg mL^{-1}, pH 7.5 after 165 254 accumulations (25 h); (b) LDL, 110 mg mL^{-1}, pH 7.5, after 65 536 accumulations (10 h); (c) HDL, 70 mg mL^{-1}, pH 8.6, after 65 536 accumulations (10 h). (Reproduced by permission of American Society of Biological Chemists from Hamilton et al.[13])

Table 1 Chemical Shifts and Assignments of ^{13}C Resonances of Human Serum Lipoproteins[a]

Assignment	Chemical shift (ppm) VLDL	LDL	HDL
Glu carboxyl			181.0 (1)
Protein carbonyl			175 (2)
Carbonyl	173.7 (1)	173.6 (1)	173.6 (3)
Carbonyl	171.7 (2)	171.2 (2)	171.3 (4)
Arg C-6			157.2 (5)
Tyr C-6			[b]
Cholesterol C-5	139.8 (3)	139.8 (3)	139.8 (6)
$-\mathbf{C}H=\mathbf{C}H-CH_2-CH_2$	129.7 (4)	129.7 (4)	129.7 (7)
$-CH=\mathbf{C}H-CH_2-\mathbf{C}H=CH-$	128.1 (5)	128.0 (5)	128.0 (8)
Cholesterol C-6	122.2 (6)	122.3 (6)	122.3 (9)
Cholesterol C-3	73.2 (7)	72.4 (7)	72.4 (10)
Glycerol CH	69.1 (8)	69.0 (8)	[c]
Choline CH_2N	66.2 (9)	66.1 (9)	66.1 (11)
Glycerol CH_2	62.0 (10)	61.9 (10)	[c]
Choline CH_2O	59.6 (11)	59.6 (11)	59.6 (12)
Cholesterol C-14, C-17	56.6 (12)	56.6 (12)	56.8 (13)
Choline $(CH_3)_3N$	54.3 (13)	54.2 (13)	54.2 (14)
Cholesterol C-9	50.2 (14)	50.2 (14)	50.2 (15)
Cholesterol C-13	42.4 (15)	42.4 (15)	42.4 (15)
Cholesterol C-24[d]	39.7 (16)	39.6 (16)	39.7 (17)
Cholesterol C-10	36.6 (17)	36.6 (17)	36.6 (18)
$-CH_2-\boldsymbol{C}H_2-CO-$	33.8 (18)	33.7 (18)	34.0 (19)
$CH_3-CH_2-\boldsymbol{C}H_2-CH_2-$	32.1 (19)	32.1[e]	32.1 (20)
	31.7[e]	31.6 (19)	31.6 (21)
Fatty acyl $(CH_2)_n$	29.9 (20)		29.9[e]
	29.5 (21)	29.5 (20)	29.5 (22)
Cholesterol C-25	[f]	[f]	28.1 (23)
$-CH_2-\boldsymbol{C}H_2-CH=CH-$	27.3 (22)	27.3 (21)	27.3 (24)
$-CH=CH-\boldsymbol{C}H_2-CH=CH-$	25.7 (23)	25.7 (22)	25.7 (25)
$-\boldsymbol{C}H_2-CH_2-CO-$	24.9 (24)	25.0[e]	25.1[e]
$CH_3-\boldsymbol{C}H_2-CH_2-$	22.8 (25)	22.7 (23)	22.8 (26)
Cholesterol C-26, C-27		19.2[e]	19.3[e]
Cholesterol C-19, C-21	19.1 (26)	18.9 (24)	18.9 (27)
$\boldsymbol{C}H_3-CH_2-$	14.1 (27)	14.1 (25)	14.1 (28)
Cholesterol C-18	12.0 (28)	11.9 (26)	12.0 (29)

[a]Chemical shifts are in ppm with increasing frequency from tetramethylsilane. The terminal methyl group of fatty acyl chains at 14.1 ppm was used as an internal reference. Numbers in parentheses after chemical shifts are the peak designations in the spectra of VLDL [see Figure 1(a)], LDL [see Figure 1(b)], and HDL [see Figure 1(c)]. Unless otherwise noted, the assignments refer to the fatty acyl chain. ***C*** indicates the specifically assigned type of carbon. Chemical shifts accurate to ± 0.2 ppm (Hamilton et al.13).
[b]Shoulders down frequency from peak 5 in Figure 1(c).
[c]Could not be identified unambiguously.
[d]May also contain ϵ-carbon of lysine and β-carbon of leucine in HDL spectrum.
[e]Shoulder in Figure 1.
[f]Barely discernible at about 28 ppm.

together with the absence of spin couplings, make assignments (Table 1) easier and more reliable. Peaks representing the major lipids of each lipoprotein class were detected (Table 1). The ^{13}C spectra of HDL and LDL (Figure 1) showed greater differences than the corresponding ^{1}H spectra.[2] Notably, minor contributions of protein signals were seen in the spectrum of HDL. Comparative HDL studies at 1.4,[13] 4.7,[14] and 9.4[15] T show a significant difference in resolution between spectra acquired at the two lower fields, and a more modest difference at the two higher fields. In ^{13}C NMR spectra at >4.7 T, at least one well resolved single carbon resonance for each lipid type is observed. Higher magnetic fields and instrument improvements have led to greatly increased sensitivity so that large sample volumes and extremely long accumulation times are no longer required to obtain high quality ^{13}C spectra of lipoproteins.

Carbon-13 NMR studies have led to a more detailed description of the molecular motions, structure, and organization of the lipids in lipoproteins than perhaps any other single technique. The narrow widths of lipid resonances that dominate the spectrum, together with the measured spin–lattice relaxation times (T_1), indicate a liquid-like state for most lipoprotein lipids.[12,13] Generally, resonances of corresponding carbons on different acyl chains within the same lipid molecule (e.g. PC and triglyceride) are not distinguishable by chemical shift; hence T_1 (as well as linewidth and NOE) measurements represent an average of potentially different values. However, ^{13}C NMR is fully capable of distinguishing between esterified and

unesterified cholesterol because of significant differences in the chemical shift for C-3, C-4, C-5, and C-6 steroid ring carbons. The resolved cholesteryl ester C-6 resonance can be used as a probe of steroid ring motions; T_1, linewidth, and NOE values for this carbon show that steroid ring motions are in the nanosecond range, indicative of a viscous environment for this lipid type in lipoproteins.[12,13] In the spectrum of HDL, the observed narrow cholesterol resonances (C-5 and C-6) represent only about one-third of the total cholesterol; this pool of cholesterol is considered most likely to be in the liquid core.[14–16] The second, more motionally restricted pool of cholesterol was suggested to be in the surface based on studies using exogenously added cholesterol enriched at C-4.[17]

Carbon-13 NMR spectroscopy has helped to define the emulsion structure of lipoproteins, particularly the structural organization of the neutral lipid core. Observation of single carbon signals from the steroid ring of cholesteryl esters has permitted direct detection of the cholesteryl ester phase transition in LDL.[18] ^{13}C NMR has shown that the transition reflects a liquid phase to ordered phase change; however, this ordered phase does not closely resemble the smectic phase of isolated cholesteryl esters, as suggested by X-ray diffraction studies. Carbon-13 resonances from phospholipid carbons located at the aqueous interface (i.e. choline and carbonyl carbons) are only slightly affected by temperature changes, indicating an essentially separate uncoupled 'core' phase. An important extension of the above investigation was the detection of lipid signals in intact (excised) human arterial tissue containing atherosclerotic plaques.[18] Spectra of plaques reflected lipid deposits rather than membrane constituents, and a liquid–ordered phase transition of cholesteryl esters was observed below body temperature. The spectra of plaque had a striking overall resemblance to the spectra of thermally disrupted LDLs. A similar approach was used to correlate the structural organization of cholesteryl esters in rabbit lipoproteins and aortic atherosclerotic lesions.[19] Temperature dependent ^{13}C spectra revealed a cholesteryl ester phase transition above physiological temperature in lesions and in lipoproteins (LDLs and cholesteryl ester-rich VLDL) from these cholesterol-fed rabbits. The cholesteryl ester phase transitions in cholesteryl ester-rich VLDL from cholesterol-fed rabbits was studied in detail by ^{13}C NMR.[20] Accompanying data from spin labeled cholesteryl esters and phospholipids showed that neither of these spin-labeled lipids detected the core transition, but the acyl chain order of phospholipids was greater in cholesteryl ester-rich VLDL than in normal VLDL. The structural organization and molecular motions of cholesteryl esters in HDL have also been studied in detail.[14] Temperature dependent spectra showed no evidence of a core transition, and the molecular motions of cholesteryl esters were well modeled by a cholesteryl ester–triglyceride mixture.

As with other types of NMR, ^{13}C NMR has limitations in applications to lipoproteins. Some of these limitations are the inability to detect minor components or to discriminate resonances arising from corresponding carbons on different acyl chains, problems that can be overcome by ^{13}C enrichment (see below). ^{13}C NMR spectra of native lipoproteins reveal very little about the protein moieties, primarily because of the much greater linewidths of most of the protein signals and much higher molar concentration of lipids.[12,13] Consequently, few details of lipid–protein interactions in lipoproteins have been elucidated by ^{13}C NMR to date, except in the case of albumin reconstituted with ^{13}C-enriched fatty acids and a few model lipoprotein systems described below.

The first application of NMR spectroscopy to lipoproteins utilized ^{1}H NMR, because of the high NMR sensitivity, abundance, and wide distribution of protons. Considering the vast number of chemically different protons in the lipids and proteins of plasma lipoproteins, the ^{1}H spectra are remarkably simple. The first published spectra (at 60 MHz) showed very few peaks, and these were attributed to the lipid components based on comparison of spectra of intact lipoproteins with those of sonically dispersed lipids.[21] Early ^{1}H spectra at a higher field (220 MHz) showed additional resonances, some of which were thought to represent protein but which could not be unambiguously assigned.[22] More recently, all resonances of ^{1}H spectra of lipoproteins have been attributed to lipids,[2] consistent with heteronuclear (^{13}C, ^{1}H) 2D NMR spectral assignments.[23]

In practice, the large amount of information contained in the ^{1}H spectrum is of limited accessibility. The poor resolution of ^{1}H NMR lipoprotein spectra complicates not only assignments but interpretation of linewidth and spin–lattice relaxation data. Except for lipoproteins that contain a predominance of one lipid type (e.g. chylomicrons and VLDL containing triglyceride; LP-X containing unesterified cholesterol), ^{1}H spectra consist mainly of overlapping resonances for different lipid types. The splitting of peaks by scalar coupling also makes quantitative interpretation of ^{1}H linewidths difficult; splittings are observed clearly only in the narrow triglyceride resonances of chylomicrons and VLDL, and are obscured by line broadening in spectra of LDL and HDL. Interpretation of ^{1}H T_1 values is complicated by the contribution of both intra- and intermolecular contributions to ^{1}H relaxation processes.[24]

In spite of inherent limitations, ^{1}H NMR spectroscopy has helped to define general features of the structural organization of plasma lipoproteins. The earliest studies suggested that lipid–lipid interactions were dominant and that most of the lipids were in a liquid state.[21] The sensitivity of the choline methyl resonance to shift reagents has been used to demonstrate that this moiety is present at the aqueous interface.[25,26] In LDL and HDL, the existence of a hydrophobic core which can undergo thermal changes was shown by temperature dependent peak intensity changes. In LDL, a discrete phase transition can be attributed to a liquid to ordered phase change of cholesteryl esters by comparison with spectral changes of pure cholesteryl esters, although specific resonances for cholesteryl esters are not seen in the ^{1}H spectrum of intact LDL.[24] Spectra of VLDL and chylomicrons are dominated by the constituent triglycerides, and the liquid to solid phase transition of triglycerides can be monitored readily.[27,28]

^{1}H is the most sensitive NMR nucleus (except for ^{3}H), giving ^{1}H NMR spectroscopy an important versatility. Numerous spectra can be acquired as a function of a given variable, and high quality spectra can be obtained in a short time with <1 mg lipid mL^{-1}. The higher sensitivity of ^{1}H NMR has led to its application in studies of whole plasma (see below).

3 LIPOPROTEINS IN PLASMA

Proton spectra of plasma reflect its multiple lipid components with different molecular structures and mobilities. Quantitative

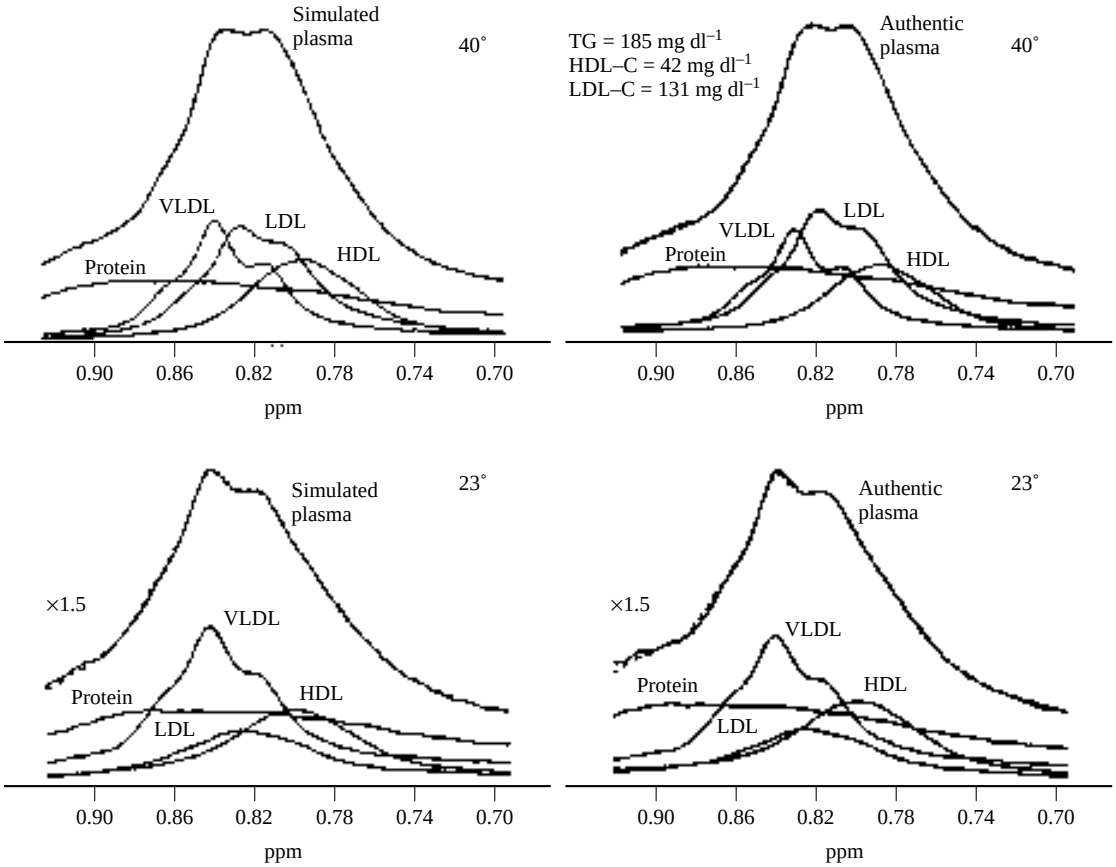

Figure 2 Results of methyl resonance lineshape analysis of ^{1}H spectra obtained at 23 and 40 °C for a simulated plasma sample of known lipoprotein composition (left) and an authentic plasma sample (right). Beneath the experimental (solid line) and calculated (dashed line) plasma spectra are shown the derived amplitudes of the four component spectra used for the fit. The 23 °C spectra are plotted with 50% increased vertical scaling compared with the 40 °C spectra. The authentic plasma sample contained 1.85 g (2.09 mmol) of triglyceride, 0.42 g (1.09 mmol) of HDL cholesterol, and 1.31 g (3.39 mmol) of LDL cholesterol per liter. (Reproduced by permission of American Association of Clinical Chemists from Otvos et al.[29])

measurements of linewidths and intensities are also complicated by extensive resonance overlap and temperature dependent spectral effects. The lower frequency (0–2.0 ppm) region of the ^{1}H spectrum of plasma is dominated by lipoprotein lipids which give rise to envelopes of methylene (~1.2 ppm) and methyl (~0.8 ppm) resonances. Because of the small but significant differences in the average chemical shifts for the CH_2 and CH_3 envelopes in the different lipoprotein classes,[29] the shapes of these envelopes in the plasma spectrum are controlled by the relative abundance of the different lipoprotein classes. Otvos et al.[29] have developed a method for quantifying the concentrations of chylomicrons, VLDL, LDL, and HDL in whole plasma based on spectral deconvolution of the CH_3 envelope (Figure 2). The effects of temperature (15–45 °C) on lineshapes and intensities were analyzed quantitatively. The rapid, accurate measurement of these lipoprotein classes has immediate application for the diagnosis of specific types of hyperlipoproteinemia such as hyperchylomicronemia (type 1), hypercholesterolemia (type 2), and hyper-α-lipoproteinemia.

Analysis of the methylene envelope (~1.2 ppm) may sometimes be compromised by the presence of other nonlipid species such as ethanol (1.2 ppm), lactate (1.34 ppm), and β-hydroxybutyrate (1.21 ppm).[30] Experimental conditions which might affect the lineshape, chemical shift, or amplitude of these two spectral envelopes include sample storage temperature and spectral acquisition conditions (water suppression technique, sample temperature, and magnetic field inhomogeneity).[31]

Fossel and associates,[32] using the average width of the methyl and methylene resonances of proton spectra, measured values for plasma from normal control subjects (39.5 ± 1.6 Hz) that were significantly greater than those for patients with untreated cancer (29.9 ± 2.5 Hz). This study led to the conclusion that proton NMR spectroscopy of plasma is potentially valuable for the detection of cancer and monitoring its therapy. The possibility of using a noninvasive method to detect cancer attracted much attention to NMR spectroscopy in general, and to spectroscopy of lipoproteins in particular. However, it was soon pointed out that there are several important caveats and significant limitations to using this method for cancer detection.[33] Dietary variations as well as numerous abnormal nonmalignant conditions can lead to alterations in the amounts and composition of different lipoproteins, which, as indicated above, make different contributions to the composite shape of the CH_2 and CH_3 envelopes. For example, nonfasted subjects or those with fasting hypertriglyceridemia can be expected to have elevated levels of triglyceride-rich lipoproteins whose acyl chains have high segmental flexibility and relatively narrow

spectral lines.[27,28] Indeed, individuals with triglyceride levels above 110 mg dL^{-1} will have average CH_2 and CH_3 resonance linewidths that may be interpreted erroneously to indicate cancer if the suggested threshold of 33 Hz is used.[34] Since fasting plasma triglyceride levels of less than 190 mg dL^{-1} are generally considered normal, such positive results could represent a substantial proportion of normal healthy subjects. A number of studies have been performed to determine the value of the ^1H NMR spectrum of plasma for the accurate diagnosis of metastatic disease.[35–39] Some of these studies have found a significant difference between the means of the average linewidths of normal subjects and untreated cancer patients. However, most of the reported studies have also found considerable overlap in the groups classified with or without disease. The extent of this overlap has been the center of considerable controversy since the original report by Fossel et al.[32] In a typical study, the degree of overlap corresponded to 74% sensitivity and 59% specificity, results which do not allow use of this methodology to diagnose malignant disease accurately.[31]

Proton NMR spectroscopy has also been evaluated for its utility in diagnosing other disease states or metabolic conditions. The methyl and methylene linewidths alone, as well as their average, are strongly inversely correlated with triglyceride-rich lipoprotein levels in both the fasting and postprandial states.[40,41] In a study of subjects with liver disease (hepatocarcinoma or liver cirrhosis), the average linewidth of the methyl envelope (41.3 Hz) was significantly different from that of normal controls (29.6 Hz); however, the methylene envelope did not have this diagnostic potential.[42] In a study of more than 400 plasma samples from 46 patients who had undergone heart transplantation, the methyl/methylene envelope average linewidth was significantly lower for patients without rejection than those with (positive and negative predictive values of 90 and 91%, respectively).[43] Similar approaches have been used in the study of malaria[44] and for monitoring chemotherapy.[45]

4 MODIFIED LIPOPROTEINS

LDL undergo a number of interactions that can potentially alter local lipid dynamics and/or tumbling of the entire particle. LDL particle tumbling rates can be greatly reduced by increasing the viscosity of the medium, by forming an LDL gel by ultracentrifugation, or by precipitation with heparin. The ^{31}P NMR spectra of LDL gels have broad, powder-like lineshapes with the sign and magnitude of the anisotropy characteristic of the bilayer mesophase. This resonance narrows over the same temperature range as the core cholesterol ester liquid crystalline to liquid phase transition (5–45 °C), suggesting interactions between the surface and core in such gel samples. The ^{31}P lineshapes of LDL–heparin insoluble complexes are also powder-like, but are broader than native LDL gels. Phosphorus-31 lineshape simulations suggest that insoluble complex formation slows phospholipid lateral diffusion in the LDL monolayer and alters the orientation and/or order of the headgroup.[46] Even soluble complexes of LDL formed by interaction with heparin (HEP) or chondroitin sulfate (CS) exhibit substantial increases in ^{31}P linewidth with increasing HEP/LDL or CS/LDL ratio, a phenomenon related to the Stokes radius of the resulting complex.[47] The binding of lipopolysaccharide (LPS) to LDL gives ^{31}P spectra that suggest the motions of phospholipid polar headgroups are more restricted in the complex than in LDL alone;[48] however, the paramagnetic shift reagent, Pr^{3+}, has the same effect on the LDL/LPS complex as it does on LDL alone, suggesting equivalent steric accessibility of phospholipid headgroups in both systems.[49]

The oxidation of lipids and lipoproteins has taken on increased significance since the recent demonstration that increasing oxidation of LDL leads to decreasing uptake by the LDL cell surface receptor and increasing uptake by the scavenger receptor on macrophages; extensive intracellular cholesterol accumulation, foam cell formation, and atherosclerosis are the natural sequelae. Tumor necrosis factor (TNF-α) has been implicated in the oxidation of polyunsaturated fatty acids in the plasma of normal mice. When mice were injected with TNF-α, the intensity of the polyolefinic fatty acyl carbon resonance (~128 ppm) diminished significantly compared with the mono-olefinic resonance (~130 ppm).[50] Human LDL have been oxidized to different stages in vitro and ^1H, ^{13}C, and ^{31}P NMR have demonstrated changes in (a) mobilities of lipids, (b) lipid–protein interactions, (c) the abundance of conjugated and oxodienes, (d) polyunsaturated/monounsaturated fatty acid ratio, and (e) lyso-PC abundance.[51] Similarly, in vitro oxidation of human HDL with Cu^{2+} studied by ^1H and ^{31}P NMR demonstrated almost complete loss of polyunsaturated moieties, the appearance of fatty acid epoxide systems, and the formation of oxidized cholesterol derivatives.[52]

Natural abundance ^{13}C NMR spectra of lipoproteins yield little if any information about the protein moieties. One strategy for overcoming this limitation is to couple ^{13}C-enriched reporter groups covalently to the apolipoprotein(s). A mild and minimally perturbing method for placing a reporter group on proteins involves the reductive dimethylation of lysine ϵ-amino groups. The resulting dimethyllysine (DML) moieties have pK_a values very similar to their unlabeled counterparts. This approach has been used to tag about 65% of the lysine residues of the major protein of LDL, apoB-100. The ^{13}C spectrum of DML–LDL contains two new resonances (42.8 and 43.2 ppm) with different pK_a values (8.9, 10.5), suggesting two different types of microenvironments for the labeled lysines.[53] Methylation of LDL containing familial defective apoB-100 (Arg500 → Gln) results in a decreased abundance of DML residues with a pK_a of 8.9, demonstrating a remarkable sensitivity of this technique to the conformation of an extremely large (513 kDa) protein.[53] Methylation of apoE in canine HDL also results in two new resonances in the ^{13}C spectrum of this modified lipoprotein. The two pools of DML titrate with pK_a values of 10.4 and 9.3. In contrast, eight different DML peaks (42.5–44.5 ppm) with pK_a values ranging from 7.8 to 10.5 are observed for apoE in discoidal complexes with dimyristoyl-PC (DMPC).[54]

5 MODEL AND RECOMBINED LIPOPROTEINS

Model systems have been devised to probe features of lipid structural organization not readily observed in spectroscopic studies of intact lipoproteins. For example, the general organization of lipoproteins consists of a polar shell containing primarily surface-active lipids (e.g. phospholipids and cholesterol), and a core containing mainly weakly polar lipids (e.g.

cholesteryl esters and triglycerides). However, this structure does not readily explain the capacity of water-soluble lipid transfer proteins and lipolytic enzymes to interact with lipids localized predominantly in the core. The possibility that small amounts of weakly polar lipids might be present in the surface of lipoproteins has been investigated with model systems comprised of phospholipid bilayers and small proportions of ^{13}C-carbonyl labeled cholesteryl esters or triglycerides. Carbon-13 NMR studies of these systems revealed a low but finite solubility (2–3%) of each of these lipids in the phospholipid bilayer.[55–58] Triglycerides and cholesteryl esters do not strongly compete for the interface and are expected to partition into the lipoprotein interface in proportion to their concentration in the core.[59] Unesterified cholesterol diminishes but does not prohibit the incorporation of triglycerides and cholesterol esters into phospholipid bilayers.[60] Weakly polar lipids in the surface monolayer of lipoproteins can be recognized by lipolytic enzymes and by cholesteryl ester transfer protein, which exchanges cholesteryl esters and triglycerides between lipoproteins. Similarly, microemulsions containing phospholipids and cholesteryl esters or triglycerides in proportions similar to their abundance in lipoproteins have been used to investigate surface–core interactions.[61]

Another use of model systems has been to study properties of minor lipid constituents such as fatty acids, whose NMR signals at natural abundance are too weak to detect. In this case, isotopic enrichment permits detection of the minor component. For example, fatty acids with ^{13}C enrichment of the carboxyl carbon have been used to monitor the ionization behavior of fatty acids and partitioning between the surface and core of lipoproteins. The apparent pK_a of oleic acid is different in HDL, LDL, and VLDL, decreasing with decreasing particle size.[62] The apparent pK_a of oleic acid in VLDL and chylomicrons is similar to that in protein-free triglyceride rich emulsions.[63]

Albumin transports lipids (primarily fatty acids) in blood and can be considered a lipoprotein.[64] In contrast to other plasma lipoproteins, the noncovalent complexes of fatty acids with albumin are comprised of only a few lipid molecules per protein molecule, and NMR signals of the fatty acid are detectable only with ^{13}C enrichment. Individual fatty acids with ^{13}C enrichment in a specific carbon can be added to fatty acid-free albumin for NMR studies. The spectrum of albumin complexed with a ^{13}C-carboxyl enriched long chain fatty acid such as oleic acid shows multiple fatty acid carboxyl resonances reflecting heterogeneous binding sites on albumin.[65] ^{13}C-carboxyl enriched fatty acids have been used to study lipid–protein interactions as a function of mole ratio of fatty acid, pH, fatty acid chain length, and temperature.[66–69] Three high affinity sites for long chain fatty acids have been localized on bovine serum albumin by ^{13}C NMR studies of binding to proteolytic fragments.[70] Fatty acids ^{13}C enriched at positions C-3′ and C-14′ have allowed probing molecular motions of fatty acids while occupying specific binding sites.[71] Fatty acid–albumin complexes represent a unique case in which lipid–protein interactions are defined in detail by NMR spectroscopy.[68] In contrast, the proteins in other native and model lipoproteins interact with many lipid molecules, making the study of detailed lipid–protein interactions by NMR much more difficult.

The effect of apoA-I on the structure and dynamics of the lipids in a DMPC/ApoA-I (100:1 mole ratio) complex has been studied above, at, and below the thermal transition of the complex (27 °C).[72] The ^{13}C resonance arising from the C-3′ of the fatty acyl chains is a doublet, split by approximately 0.2 ppm, suggesting that the C-3′ atoms occupy two magnetically inequivalent sites. Temperature dependent changes in chemical shifts and T_1 values reveal dynamic and conformational changes characteristic of gel to liquid crystalline phase transitions observed in pure phospholipid systems. For the DMPC/Apo-I complex at 37 °C, the fatty acyl C-4′–C-11′ methylene envelope and the C-7′ and C-13′ resonances occur at significantly higher frequencies than those of the corresponding envelope and resonances for the DMPC vesicle. These results suggest that the apoprotein rigidifies the acyl chains by increasing their number of *trans* conformers.[72] The conformation of apoA-I in complexes containing 1-palmitoyl-2-oleoyl-PC (POPC) and cholesteryl oleate (CO) has been investigated in NMR studies of apoA-I ^{13}C methylated on its lysine side chains (DML). The observation of multiple resolved resonances at pH 10 with pK_a values ranging from 8.3 to 10.5 suggests that apoA-I assumes different conformations on differently sized discoidal particles. For two spherical populations, the titration behavior of these DML residues is essentially the same in the small and large spherical particles, indicating that apoA-I conformation is similar in these two populations.[73]

ApoC-I contains a single methionine residue at position 38 that resides in a putative amphipathic helical segment that extends from Glu33 to Leu53. The involvement of the sequence around Met38 in phospholipid binding was evaluated by selective enrichment of the thiomethyl group with $^{13}CH_3I$.[74] The linewidth and spin–lattice relaxation time changes observed for the thiomethyl resonance of ^{13}C-enriched apoC-I suggests that Met38 resides in a region of the apoprotein that undergoes significant secondary and/or tertiary structural change upon unfolding in guanidine hydrochloride and upon refolding with phospholipid.

6 PEPTIDE FRAGMENTS OF APOLIPOPROTEINS

For NMR studies, several difficulties are encountered in studying lipid-free apolipoproteins such as their limited solubility and/or tendency toward extensive aggregation. Sometimes these difficulties can be overcome by using shorter synthetic peptide fragments. For example, 18-residue peptides of altered sequence have been used to model the 22-residue segments of apoA-I that readily form amphipathic helices in the lipid associated state.[75] The relative importance of the cationic side chains of lysine or the anionic side chain of glutamic acid were evaluated in terms of their effect on phospholipid structure and dynamics. Both the ‘cationic interface’ and ‘anionic interface’ peptides strongly disrupt phospholipid bilayer structure, as indicated by narrower ^{1}H and ^{31}P NMR resonances for the peptide–DMPC complexes than for DMPC bilayer vesicles. Motional properties of the polar headgroup suggest no strong interactions between the zwitterionic phospholipid headgroups and the side chains of polar amino acids of either peptide. Human apoC-II is a 79-amino acid apoprotein that reversibly binds to VLDL and HDL, and activates lipoprotein lipase, an enzyme that hydrolyzes primarily triglycerides. Lycksell and co-workers[76] have studied a 30-residue fragment, apoC-II (50–79), which

retains the capacity to activate lipoprotein lipase. Standard NOESY, COSY, and TOCSY experiments in water with hexafluoroisopropanol at 600 MHz were used to demonstrate the formation of a stable α helix from Ile66 to Gly77, and suggested the possibility of another α-helical turn between Lys55 and Ala59.

7 CONCLUSION

The remarkable versatility of NMR will likely stimulate continued studies of plasma lipoproteins as native particles in whole plasma or in the isolated state, as particles with specially modified moieties, and as model systems. The potential of high field multidimensional NMR is just beginning to be used to elucidate the structure of apolipoproteins which, to date, have been extremely difficult to study in biologically relevant systems. The use of perdeuterated lipids, and peptides covalently coupled to various lipid moieties affords additional advantages that should make it feasible to study the structure of apoproteins in at least quasi-native states.

8 RELATED ARTICLES

Lipid Polymorphism; Liquid Crystalline Samples: Carbon-13 NMR; Membrane Proteins; Membranes: Carbon-13 NMR; Membranes: Phosphorus-31 NMR; Peptide and Protein Secondary Structural Elements; Polysaccharides and Complex Oligosaccharides; Sonicated Membrane Vesicles; Synthetic Peptides.

9 REFERENCES

1. A. M. Gotto Jr., H. J. Pownall, and R. J. Havel, *Meth. Enzymol.*, 1986, **128**, 3.
2. J. A. Hamilton and J. D. Morrisett, *Meth. Enzymol.*, 1986, **128**, 472.
3. T. Glonek, T. O. Henderson, A. W. Kruski, and A. M. Scanu, *Biochim. Biophys. Acta*, 1974, **348**, 155.
4. G. Assmann, E. A. Sokoloski, and H. B. Brewer Jr., *Proc. Natl. Acad. Sci. USA*, 1974, **71**, 549.
5. P. L. Yeagle, R. G. Langdon, and R. B. Martin, *Biochemistry*, 1977, **16**, 3487.
6. T. O. Henderson, A. W. Kruski, L. G. Davis, T. Glonek, and A. M. Scanu, *Biochemistry*, 1975, **14**, 1915.
7. P. L. Yeagle, R. B. Martin, L. Pottenger, and R. G. Langdon, *Biochemistry*, 1978, **17**, 2707.
8. J. R. Brainard, E. H. Cordes, A. M. Gotto Jr., J. R. Patsch, and J. D. Morrisett, *Biochemistry*, 1980, **19**, 4273.
9. D. B. Fenske, R. S. Chana, Y. I. Parmer, W. D. Treleaven, and R. J. Cushley, *Biochemistry*, 1990, **29**, 3973.
10. J. Bradamante, E. Barchiesi, L. Barenghi, and F. Zoppi, *Analyt. Biochem.*, 1990, **1185**, 299.
11. E. B. Brasure, T. O. Henderson, T. Glonek, N. M. Pattnaik, and A. M. Scanu, *Biochemistry*, 1978, **17**, 3934.
12. J. A. Hamilton, C. Talkowski, E. Williams, E. M. Avila, A. Allerhand, E. H. Cordes, and G. Camejo, *Science*, 1973, **180**, 193.
13. J. A. Hamilton, C. Talkowski, R. F. Childers, E. Williams, A. Allerhand, and E. H. Cordes, *J. Biol. Chem.*, 1974, **249**, 4872.
14. J. A. Hamilton and E. H. Cordes, *J. Biol. Chem.*, 1978, **253**, 5193.
15. H. Hauser and G. M. Kostner, *Biochim. Biophys. Acta*, 1979, **573**, 375.
16. E. M. Avila, J. A. Hamilton, J. A. K. Harmony, A. Allerhand, and E. H. Cordes, *J. Biol. Chem.*, 1978, **253**, 3983.
17. S. Lund-Katz and M. C. Phillips, *Biochemistry*, 1984, **23**, 1130.
18. J. A. Hamilton, E. H. Cordes, and C. J. Glueck, *J. Biol. Chem.*, 1979, **254**, 5435.
19. P. A. Kroon, D. M. Quinn, and E. H. Cordes, *Biochemistry*, 1982, **21**, 2745.
20. J. D. Morrisett, J. W. Gaubatz, A. P. Tarver, J. K. Allen, H. J. Pownall, P. Laggner, and J. A. Hamilton, *Biochemistry*, 1984, **23**, 5343.
21. J. M. Steim, O. J. Edner, and F. G. Bargoto, *Science*, 1968, **162**, 909.
22. D. Chapman, R. B. Leslie, R. Hirz, and A. M. Scanu, *Biochim. Biophys. Acta*, 1969, **176**, 524.
23. S. Coffin, M. Limm, and D. Cowburn, *J. Magn. Reson.*, 1984, **59**, 268.
24. P. A. Kroon, M. Kainosho, and S. I. Chan, *Biochim. Biophys. Acta*, 1976, **433**, 282.
25. E. G. Finer, R. Henry, R. B. Leslie, and R. N. Robertson, *Biochim. Biophys. Acta*, 1975, **380**, 320.
26. H. Hauser, in *The Lipoprotein Molecule*. *NATO Advanced Study Institutes Series*, ed. H. Peeters, Plenum Press, New York, 1978.
27. J. A. Hamilton, D. M. Small, and J. S. Parks, *J. Biol. Chem.*, 1983, **258**, 1172.
28. S. Bennett-Clark, D. Atkinson, J. A. Hamilton, T. Forte, B. Russell, E. B. Feldman, and D. M. Small, *J. Lipid Res.*, 1982, **23**, 28.
29. J. D. Otvos, E. J. Jeyarajah, and D. W. Bennett, *Clin. Chem.*, 1991, **37**, 377.
30. J. L. Bock, *Clin. Chem.*, 1982, **28**, 1873.
31. S. D. Buchthal, M. A. Hardy, and T. R. Brown, *Am. J. Med.*, 1988, **85**, 528.
32. E. T. Fossel, J. M. Carr, and J. McDonagh, *N. Engl. J. Med.*, 1986, **315**, 1369.
33. D. M. Small and J. A. Hamilton, *N. Engl. J. Med.*, 1987, **316**, 1412.
34. M. P. Mims, J. D. Morrisett, C. A. Mattioli, and A. M. Gotto Jr., *N. Engl. J. Med.*, 1989, **320**, 1452.
35. L. Holmberg, U. Jakobsson, A. Berglund, and H. O. Adami, *Br. J. Cancer*, 1993, **68**, 389.
36. T. Engan, J. Krane, O. Klepp, and S. Kvinnsland, *N. Engl. J. Med.*, 1990, **322**, 949.
37. F. E. Herring, P. S. Phillips, H. Pritchard, H. Silver, and K. P. Whittal, *Magn. Reson. Med.*, 1990, **16**, 35.
38. P. Okunieff, A. Zietman, J. Kahn, S. Singer, L. J. Neuringer, R. A. Levine, and F. E. Evans, *N. Engl. J. Med.*, 1990, **322**, 953.
39. R. L. Scher, M. E. Ropka, D. A. Neal, S. Berr, T. Trouard, B. Deutsch, R. W. Cantrell, and P. A. Levine, *Otolarynogol. Head Neck Surg.*, 1990, **102**, 34.
40. P. Wilding, M. B. Senior, T. Inubushi, and M. L. Ludwick, *Clin. Chem.*, 1988, **34**, 505.
41. R. B. Verdery, D. F. Benham, I. McLennan, M. J. Busby, J. P. Wehrle, and J. D. Glickson, *Biochim. Biophys. Acta*, 1989, **1006**, 287.
42. S. Ono, F. Moriyasu, T. Tamada, T. Kawasaki, Y. Yamashita, T. Kimura, K. Kajimura, H. Someda, N. Hamato, and M. Okuma, *Jpn. J. Gastroenterol*, 1990, **87**, 2623.

43. M. Eugene, L. LeMoyec, J. Di-Certaines, M. Desruennes, E. Le Rumeur, J. B. Fraysse, and C. Cabrol, *Magn. Reson. Med.*, 1991, **18**, 93.
44. M. Nishina, E. Hori, K. Matsushita, M. Takahashi, K. Kato, and A. Ohsaka, *Physiol. Chem. Phys. Med. NMR*, 1988, **20**, 269.
45. S. J. Borners-Price and P. J. Sadler, *J. Inorg. Biochem.*, 1987, **31**, 267.
46. D. B. Fenske and R. J. Cushley, *Chem. Phys. Lipids*, 1990, **54**, 9.
47. D. B. Fenske and R. J. Cushley, *Chem. Phys. Lipids*, 1988, **49**, 15.
48. A. V. Victorov, N. V. Medvedeva, E. M. Gladkaya, A. D. Morozkin, E. A. Podrez, V. A. Kosykh, and V. A. Yurkiv, *Biochim. Biophys. Acta*, 1989, **984**, 119.
49. A. V. Victorov, E. M. Gladkaia, and V. A. Iurkiv, *Biokhimiia*, 1989, **54**, 549.
50. J. McDonagh, E. T. Fossel, R. L. Kradin, S. M. Dubinett, M. Laposata, and Y. A. Hallaq, *Blood*, 1992, **80**, 3217.
51. L. Barenghi, S. Bradamante, G. A. Giudici, and L. Vergani, *Free Radicals Res. Commun.*, 1990, **8**, 175.
52. S. Bradamante, L. Barenghi, G. A. Giudici, and C. Vergani, *Free Radicals Biol. Med.*, 1992, **12**, 193.
53. S. Lund-Katz, T. L. Innerarity, K. S. Arnold, L. K. Curtiss, and M. C. Phillips. *J. Biol. Chem.*, 1991, **266**, 2701.
54. S. Lund-Katz, K. H. Weisgraber, R. W. Mahley, and M. C. Phillips, *J. Biol. Chem.*, 1993, **268**, 23 008.
55. J. A. Hamilton and D. M. Small, *Proc. Natl. Acad. Sci. USA*, 1981, **78**, 6878.
56. J. A. Hamilton and D. M. Small, *J. Biol. Chem.*, 1982, **257**, 7318.
57. J. A. Hamilton, *Biochemistry*, 1989, **28**, 2514.
58. J. A. Hamilton, D. A. Fujito, and C. F. Hammer, *Biochemistry*, 1991, **30**, 2894.
59. J. A. Hamilton, K. W. Miller, and D. M. Small, *J. Biol. Chem.*, 1983, **258**, 12 821.
60. P. J. R. Spooner, J. A. Hamilton, D. L. Gantz, and D. M. Small, *Biochim. Biophys. Acta*, 1986, **860**, 345.
61. M. P. Mims, J. R. Guyton, and J. D. Morrisett, *Biochemistry*, 1986, **25**, 474.
62. J. A. Hamilton, in *Carbon-13 NMR Spectroscopy of Biological Systems*, ed. N. Beckmann, Academic Press, London, 1995, pp. 117–155
63. P. J. R. Spooner, S. Bennett Clark, D. L. Gantz, J. A. Hamilton, and D. M. Small, *J. Biol. Chem.*, 1988, **263**, 1444.
64. A. A. Spector, *Biochemistry and Biology of Plasma Lipoproteins*, Dekker, New York, 1986, p. 247.
65. J. S. Parks, D. P. Cistola, D. M. Small, and J. A. Hamilton, *J. Biol. Chem.*, 1983, **258**, 9262.
66. D. P. Cistola, D. M. Small, and J. A. Hamilton, *J. Biol. Chem.*, 1987, **262**, 10 971.
67. D. P. Cistola, D. M. Small, and J. A. Hamilton, *J. Biol. Chem.*, 1987, **262**, 10 980.
68. J. A. Hamilton, *News Physiolog. Sci.*, 1992, **7**, 264.
69. M. A. Kenyon and J. A. Hamilton, *J. Lipid Res.*, 1994, **35**, 458.
70. J. A. Hamilton, S. Era, and R. G. Reed, *Proc. Natl. Acad. Sci. USA*, 1991, **88**, 2051.
71. J. A. Hamilton, D. P. Cistola, J. D. Morrisett, J. T. Sparrow, and D. M. Small, *Proc. Natl. Acad. Sci. USA*, 1984, **81**, 3718.
72. J. R. Brainard, R. D. Knapp, J. D. Morrisett, and H. J. Pownall, *J. Biol. Chem.*, 1984, **259**, 10 340.
73. D. L. Sparks, M. C. Phillips, and S. Lund-Katz, *J. Biol. Chem.*, 1992, **267**, 25 830.
74. T.-C. Chen, R. D. Knapp, M. F. Rohde, J. R. Brainard, A. M. Gotto, Jr., J. T. Sparrow, and J. D. Morrisett, *Biochemistry*, 1980, **19**, 5140.
75. R. M. Epand, W. K. Surewicz, D. W. Hughes, H. Mantsch, J. P. Segrest, T. M. Allen, and G. M. Anantharamaiah, *J. Biol. Chem.*, 1989, **264**, 4628.
76. P.-O. Lycksell, A. Öhman, G. Bengtsson-Olivecrona, L. B-Å. Johansson, S. S. Wijmenga, D. Wernic, and A. Gräslund, *Eur. J. Biochem.*, 1992, **205**, 223.

Biographical Sketches

The editorial assistance of Evanson Joseph is gratefully acknowledged. Some of the research described herein has been supported in part by grants from the United States Public Health Service (HL-27341 and HL-32971 to JDM; HL-26335 and HL-41904 to JAH).

Biographical Sketches

Joel D. Morrisett. *b* 1942. B. S., 1964, Chemistry, Davidson College. Ph.D., 1969, Chemistry, University of North Carolina–Chapel Hill. Postdoctoral research, Stanford, 1970. Assistant professor, associate professor, and Professor of Medicine and Biochemistry, Baylor College of Medicine, 1971–present. Research interests include use of magnetic resonance methods for elucidating the structure and function of lipids, lipoproteins, and lipid-metabolizing enzymes.

James A. Hamilton. *b* 1947. B.S., 1969, Ph.D., 1974, Chemistry, Indiana University. Faculty in Biophysics and Director of NMR Laboratory, Biophysics Department, Boston University School of Medicine, 1978–present. Research specialties: high-resolution ^{13}C NMR applications to lipid structure and function, and lipid–protein interactions; solid state ^{13}C and ^{31}P MAS NMR applications to lipid and membrane structure; multidimensional NMR of lipid-binding proteins.

Liquid Crystalline Samples: Application to Macromolecular Structure Determination

Ad Bax, James J. Chou, and Benjamin E. Ramirez

Laboratory of Chemical Physics, National Institute of Diabetes, and Digestive and Kidney Diseases, National Institutes of Health, Bethesda, MD, USA

1	Introduction	1
2	Theoretical Considerations	1
3	Measurement of Dipolar Couplings	3
4	Alignment Media for Macromolecules	6
5	Relation between Alignment and Shape	9
6	Structure Validation	10
7	Concluding Remarks	11
8	Related Articles in Volumes 1–8	11
9	References	11

1 INTRODUCTION

NMR spectra of small molecules dissolved in organic liquid crystalline media permit measurement of large numbers of intramolecular dipolar couplings that carry very precise information on molecular structure.[1,2] However, for molecules with more than half a dozen protons, the strong degree of solute alignment obtained in such media typically results in a vast number of large, non-first-order splittings that make these spectra difficult to analyze. On the other hand, very weak alignment, caused by a molecule's own magnetic susceptibility anisotropy, also gives rise to measurable dipolar couplings.[3,4] However, typically only the largest couplings are detectable and manifest themselves as small, field-dependent changes in the corresponding J splittings. The advantages of such ultra-weak alignment are that the NMR spectrum retains its regular high-resolution simplicity and that, owing to the extremely weak magnetic forces involved, it does not perturb the structure of the molecule.

Tolman et al.[5] demonstrated that small dipolar couplings, on the order of a few hertz, could be measured for the backbone amides in paramagnetic myoglobin, and that these data correlate well with values expected on the basis of its crystal structure. Tjandra et al. subsequently measured a substantial number of very small ^{15}N–^{1}H and ^{13}C$^{\alpha}$–^{1}H$^{\alpha}$ dipolar couplings in a diamagnetic protein-DNA complex and demonstrated that incorporation of these data as restraints in the structure calculation yields a remarkable improvement in both local and global geometry.[6] In particular, by defining the relative orientation of structural elements in a macromolecule with few interconnecting NOEs, these dipolar restraints solve a long-standing problem.

General applicability of the weak alignment approach greatly increased when the suitability of very dilute liquid crystalline media for this purpose was discovered.[7–14] The macromolecules are dispersed in the aqueous phase that separates the highly ordered liquid crystalline particles, which have a spacing much larger than the diameter of the molecule under study. Despite the typically rather large macroscopic viscosity of such samples, the ordered particles are spaced by essentially pure water, and usually no adverse effect on rotational diffusion is therefore observed.[7] However, exceptions to this rule can occur in cases where alignment is dominated by attractive electrostatic interactions between the nematogen and the solute.[15] As discussed in Section 4.6, an alternate way for inducing weak alignment relies on axially compressed or stretched polyacrylamide gels. From a theoretical perspective, alignment in gels and in dilute lyotropic liquid crystalline suspensions are very similar.

The ability to tune the degree of macromolecular alignment over more than an order of magnitude, usually in the range from 3×10^{-4} to 3×10^{-3}, makes it possible to measure a whole plethora of short-range dipolar interactions, including those between directly bonded ^{1}H–^{13}C, ^{1}H–^{15}N, ^{13}C–^{13}C and ^{13}C–^{15}N pairs, and also between spatially proximate nonbonded ^{1}H–^{1}H, ^{1}H–^{13}C and ^{1}H–^{15}N spin pairs.[8,16–18] The measurement and application of dipolar couplings and CSA effects in weakly oriented macromolecules has already proven to be extremely useful in biomolecular structural studies. Several reviews have appeared on various aspects of this work,[19–22] and further developments in this area of research are occurring at a very rapid pace. Even at present, a comprehensive review of this area would fill hundreds of pages, and is therefore well beyond the scope of this article. Instead, the relation between this work and conventional liquid crystal NMR will be highlighted, as well as illustrating some of the advantageous features of the weak ordering approach.

2 THEORETICAL CONSIDERATIONS

Although standard theory described for liquid crystals elsewhere in this encyclopedia is directly applicable to the case of very weakly ordered macromolecules, the early applications of the weak ordering technology derive from the magnetic-susceptibility induced alignment. As a result, the terminology differs somewhat and will be briefly reviewed below.

2.1 Dipolar Couplings in Aligned Macromolecules

The relation between the internuclear vector and the dipolar coupling between two spins, A and B can be found in numerous textbooks. For the purpose of deriving the resonance frequencies (i.e., dipolar splittings) only the z component of the local field of one nuclear dipole at the position of the second nucleus is relevant (secular approximation):

$$H_{dd} = D_{\max}^{AB} \langle I_{Az} I_{Bz} (3\cos^2 \zeta - 1) \rangle \qquad (1a)$$

where the $\langle\rangle$ brackets refer to the time or ensemble average, which are equivalent for isotropic and liquid crystalline

solutions, ζ is the angle between the $A - B$ internuclear vector and the magnetic field, and

$$D^{AB}_{\max} = \frac{-\mu_o(H/2\pi)\gamma_A\gamma_B}{(4\pi^2 r^3_{AB})} \tag{1b}$$

is the static dipolar coupling in SI units (21.7 kHz for H–N pairs, assuming an internuclear distance $r_{NH} = 1.04$ Å. The constant, $-\mu_o$, is the magnetic permittivity of vacuum, h is Planck's constant, γ_X is the magnetogyric ratio of spin X, and r_{AB} is the distance between nuclei A and B. The residual dipolar splitting between spins A and B equals

$$D^{AB} = D^{AB}_{\max}\langle P_2(\cos\zeta)\rangle \tag{1c}$$

with $P_2(x) = (3x^2 - 1)/2$. Note that some texts differ in the definition of the dipolar coupling, D_{AB}, by a factor two.

If the molecule is rigid, the orientation of the internuclear vector, r_{AB}, in an arbitrary molecular coordinate system can be described by the angles α_x, α_y, and α_z between the vector and the x, y, and z axis of the coordinate system. The $P_2(\cos\zeta)$ term can be expressed as

$$\langle P_2(\cos\zeta)\rangle = \sum_{i,j=\{x,y,z\}} S_{ij}\cos\alpha_i\cos\alpha_j \tag{2}$$

where S is a traceless symmetric 3×3 matrix, commonly referred to as the Saupe matrix, the Saupe order matrix, or simply the order matrix.

If the structure of the molecule is known, i.e., $\cos\alpha_i$ factors in equation (2) are known, the five independent elements of S generally can be solved provided that dipolar couplings for at least five internuclear vectors are available. However, if any pair of internuclear vectors is parallel, and for other special cases such as a set that includes three mutually orthogonal interactions, more measured couplings are required. For macromolecules, many more dipolar couplings are frequently measured, and S is overdetermined. The Saupe matrix elements are then best determined using singular value decomposition.[23]

The order matrix is real and symmetric, and it therefore is always possible to define a molecular axis system where S becomes diagonal. In a number of applications it can be advantageous to work in this principal axis frame, where D^{AB} now can be expressed in terms of the polar coordinates of the $A-B$ internuclear vector:

$$D^{AB}(\theta,\phi) = \frac{3}{2}D^{AB}_{\max}[\cos^2\theta A_{zz} + \sin^2\theta\cos^2\phi A_{xx} + \sin^2\theta\sin^2\phi A_{yy}] \tag{3a}$$

where A is the diagonalized alignment tensor, with $|A_{zz}| > |A_{yy}| > |A_{xx}|$. This frequently is rewritten as

$$D^{AB}(\theta,\phi) = D^{AB}_{\max}\left[P_2(\cos\theta)A_a + \frac{3}{4}A_r\sin^2\theta\cos 2\phi\right] \tag{3b}$$

where $A_a = 3A_{zz}/2$ is the axial component of the alignment tensor, and $A_r = (A_{xx} - A_{yy})$ is referred to as its rhombic component.

Note that the maximum value for A_a equals one when the z axis of the principal alignment tensor is fully aligned with the static field. In practice, the dilute liquid crystal work discussed in this article concerns A_a values on the order of 10^{-3}. Equation (3b) is sometimes rewritten as

$$D^{AB}(\theta,\phi) = D^{AB}_a\left[(3\cos^2\theta - 1) + \frac{3}{2}R\sin^2\theta\cos 2\phi\right] \tag{3c}$$

where $D^{AB}_a = 1/2A_aD^{AB}_{\max}$ is referred to as the magnitude of the dipolar coupling tensor, frequently normalized to the N–H dipolar interaction, and $R = A_r/A_a$ is the rhombicity. Note that $0 \le R \le 2/3$.

2.2 Estimate for Alignment Tensor in Case of Unknown Structure

When working with a molecule of unknown structure, the above-described singular value decomposition approach for determining the order matrix is not applicable. However, as briefly discussed below, a reasonable estimate for the principal components of the alignment tensor can be obtained from the range and distribution of observed dipolar couplings.

First, it is convenient to normalize all observed one-bond and two-bond dipolar couplings to, for example, the N–H dipolar coupling, by multiplying the observed $P - Q$ dipolar coupling by $(\gamma_N\gamma_H r^3_{PQ})/(\gamma_P\gamma_Q r^3_{NH})$. Empirically determined optimum scaling factors are listed in Table 1. In the absence of measurement error in the dipolar couplings, the bond vector with the largest absolute value for the normalized dipolar coupling provides a lower limit for $2D^{NH}_a$ in equation (3c). Similarly, an estimate for the rhombicity R in equation (3c) can be obtained from the dipolar coupling value, D_{opposite}, with the other extreme value (negative for $D^{NH}_a > 0$; positive for $D^{NH}_a < 0$). The value of R itself, defined in this manner, is always positive and follows from $D_{\text{opposite}} = -D^{NH}_a\,[1 + 3/2R]$, or

$$R = -\frac{2}{3}\left[1 + \left(\frac{D_{\text{opposite}}}{D^{NH}_a}\right)\right] \tag{4}$$

This approach only uses the extreme values of the distribution of observed dipolar couplings. A more robust approach plots the histogram of the entire ensemble of normalized dipolar couplings.[24] Figure 1 shows an example of such histograms for the two globular domains of Ca^{2+}-ligated calmodulin. The histograms have been compiled from nearly complete sets of ${}^1D_{NH}$, ${}^1D_{C\alpha H\alpha}$, ${}^1D_{C'N}$, ${}^2D_{C'H\alpha}$ and ${}^1D_{C'C\alpha}$ couplings, recorded in a medium of filamentous phage *Pf1*.

Table 1 Magnitude of dipolar couplings relative to ${}^1D_{NH}$

	NMR[a]	X-ray[b]
${}^1D_{C\alpha H\alpha}$	2.08	2.02
${}^1D_{C\alpha C'}$	0.198	0.198
${}^1D_{C'N}$	0.120	0.121
${}^2D_{C'HN}$	0.300	0.319
${}^1D_{CH3}$	0.628	0.628

[a]Values that result in the lowest energy NMR structure of ubiquitin and yield best fit to ${}^{13}C'$ CSA.[74]
[b]Optimized by fitting experimental couplings to the ubiquitin X-ray structure.[16]

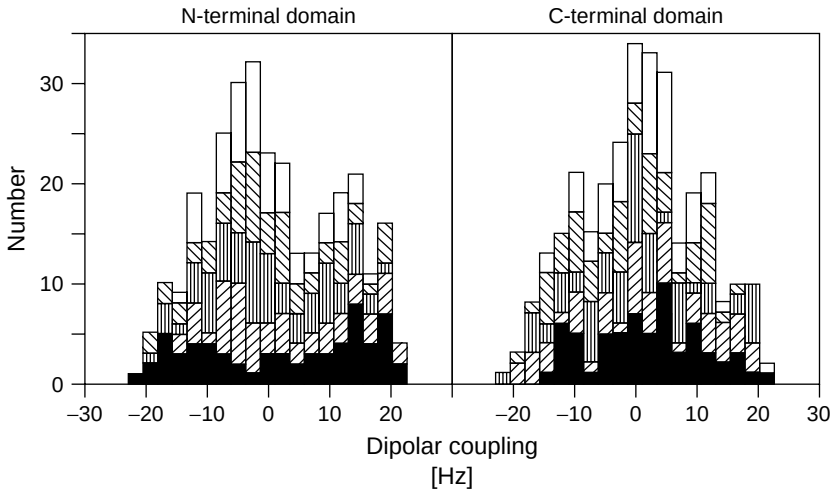

Figure 1 Histogram of normalized dipolar couplings measured in the N- and C-terminal domains of Ca^{2+}-ligated calmodulin, dissolved in a liquid crystalline medium containing 15 mg Pf1/ml and 10 mM KCl. Dipolar couplings are normalized relative to the one-bond ^{15}N–^{1}H interaction. SVD fits to the crystal structure and the use of a freely floating alignment tensor during structure calculation[77] both yield $D_a^{NH} = 11.0$ Hz; $R = 0.38$ and $D_a^{NH} = 10.1$ Hz; $R = 0.66$ for the N- and C-terminal domains, respectively. Note that even while the two histograms cover the same width, they have considerably different asymmetries (rhombicity, R). A dearth of bond vectors parallel to the z-axis of the alignment tensor causes the absence of dipolar couplings >22 Hz for the N-terminal domain. Different types of dipolar couplings are shaded separately in the histograms: $^{1}D_{NH}$ – solid; $^{1}D_{C\alpha H\alpha}$ – shaded (///); $^{1}D_{C'N}$ – shaded (\\\); $^{1}D_{C'C\alpha}$ – shaded (|||); $^{2}D_{C'H\alpha}$ – blank

It can be shown that for a uniform distribution of bond vectors, such a histogram will resemble the solid state powder pattern observed for chemical shift anisotropy.[25] In the present case, the singularities in the powder pattern correspond to D_{zz}^{NH}, D_{xx}^{NH} and D_{yy}^{NH}, with the condition that $D_{zz}^{NH} + D_{xx}^{NH} + D_{yy}^{NH} = 0$. The relation between the powder pattern singularities D_{zz}^{NH}, D_{xx}^{NH}, D_{yy}^{NH} and the parameters D_a^{NH} and R is given by:[24]

$$D_{zz}^{NH} = 2D_a^{NH} \tag{5a}$$

$$D_{yy}^{NH} = -D_a^{NH}(1 + 1.5R) \tag{5b}$$

$$D_{xx}^{NH} = -D_a^{NH}(1 - 1.5R) \tag{5c}$$

If outliers appear to be present in the histogram, it is worth while checking the origin of these extreme dipolar couplings. They may correspond to $^{1}D_{C'N}$, $^{2}D_{C'H\alpha}$ or $^{1}D_{C'C\alpha}$ couplings derived from weak or partially overlapping correlations, and critical visual inspection of the raw data may be needed before including them.

3 MEASUREMENT OF DIPOLAR COUPLINGS

To date, measurement of dipolar couplings has focused primarily on one-bond interactions, which as a result of their known internuclear distance, are readily interpreted in terms of orientation. Also, they are generally the easiest to measure. Two-bond interactions also have the benefit of a fixed internuclear distance, but owing to their larger separation, they can be more difficult to measure at the same level of relative accuracy. New analysis schemes promise to make measurement of ^{1}H–^{1}H dipolar couplings more straightforward, and they may also become popular as structural restraints. Except for geminal ^{1}H–^{1}H interactions and pairs of protons in structural elements of fixed geometry, the interproton distance is an additional parameter influencing the dipolar coupling. This therefore results in a less direct relation between the value of the coupling and the orientation of the corresponding vector. However, structure calculation programs such as CNS[26] can readily deal with this additional complexity.[27]

So far, most measurements of dipolar couplings have focused on the one-bond and two-bond couplings along the polypeptide backbone in proteins (Figure 2), but dipolar couplings within and between sidechains are becoming increasingly used. Below, some of the most widely used techniques for measuring the various types of couplings are briefly discussed, with particular emphasis on ^{15}N–^{13}C labeled proteins. With the exception of couplings between protons separated by more than three bonds, where the J coupling is usually negligible, the coupling observed in the liquid crystalline phase represents the sum of the scalar and dipolar contributions. Considerable variation in the scalar couplings frequently exists,

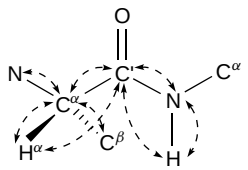

Figure 2 Protein backbone fragment, with dipolar interactions that can readily be measured marked by dashed lines. Although $D_{NC\alpha}$ can be measured experimentally, its relative accuracy tends to be lower, and for *trans*-peptide bonds its normalized value is very similar to that of $^{1}D_{C'C\alpha}$ of the preceding residue. $^{1}D_{C\alpha C\beta}$ is most useful in perdeuterated proteins, where no value for $^{1}D_{C\alpha H\alpha}$ can be measured and where the slow transverse relaxation of the deuterated $^{13}C^{\alpha}$ permits its accurate measurement

making it necessary to measure the couplings both in the isotropic and aligned environment.

Two conceptually different approaches can be used for measurement of J or dipolar splittings. First, the splitting can be measured directly from a two- or three-dimensional spectrum recorded in the absence of decoupling of the interaction of interest. Frequently, an E.COSY,[28] S^3E,[29] or IPAP version[30] of the multi-dimensional experiment is used in order to reduce overlap. Second, in a so-called quantitative-J correlation experiment,[31] the size of the splitting can be derived from the intensity of a given resonance relative to that of a reference.

3.1 Accuracy of Measured Splitting

For splittings measured from relative peak displacements in the multi-dimensional NMR spectrum, the accuracy of a peak position is directly proportional to its signal-to-noise ratio, and inversely related to its line width. Although the accuracy also depends on the method used for peak position determination and on the digital resolution, a reasonable approximation for the root-mean-square uncertainty, ΔJ, in a measured splitting for a well resolved, undistorted, pure phase or pure antiphase doublet is given by:

$$\Delta J = \frac{LW}{SN} \tag{6}$$

where LW is the line width at half height (in the dimension where the splitting is being measured), and SN is the signal-to-noise ratio. Note that equation (6) provides a lower limit for the true accuracy of the measurement, because other distortions such as partial overlap or imperfect phasing can contribute to the error in a reproducible manner.

3.2 Measurement of $^1J_{HN}$

One-bond $^1D_{NH}$ dipolar coupling were the first ones to be measured in a weakly oriented protein, simply by recording a ^1H–^{15}N HSQC spectrum without the regular ^1H 180° decoupling pulse applied at the midpoint of the t_1 evolution period. Transverse relaxation is considerably slower in the ^{15}N dimension compared to the ^1H dimension, and measurement in the indirect ^{15}N dimension is therefore preferred over measurement in the ^1H dimension. However, the spectral crowding doubles when HSQC spectra are recorded without decoupling, typically resulting in an unacceptable degree of resonance overlap.

A conceptually very simple method for measuring $^1J_{NH}$ separates the F_1-coupled HSQC into two separate subspectra, containing only the upfield or downfield components of the F_1 ^{15}N–{^1H} doublets. This is done by interleaving two experiments: one where the F_1 ^{15}N–{^1H} doublets are in phase, and one where they are exactly antiphase. The sum of the antiphase and the in-phase spectra yields a spectrum containing only the downfield components, whereas the difference yields the upfield components (Figure 3). This approach is referred to as IPAP (for in-phase and anti-phase)[32] and is easily extended to higher dimensionality experiments.

A small region of the two-dimensional ^1H–^{15}N IPAP-HSQC spectrum of calmodulin is shown in Figure 3. Isotropic ^1H–^{15}N J splittings are ca. 93 Hz, and the large deviations

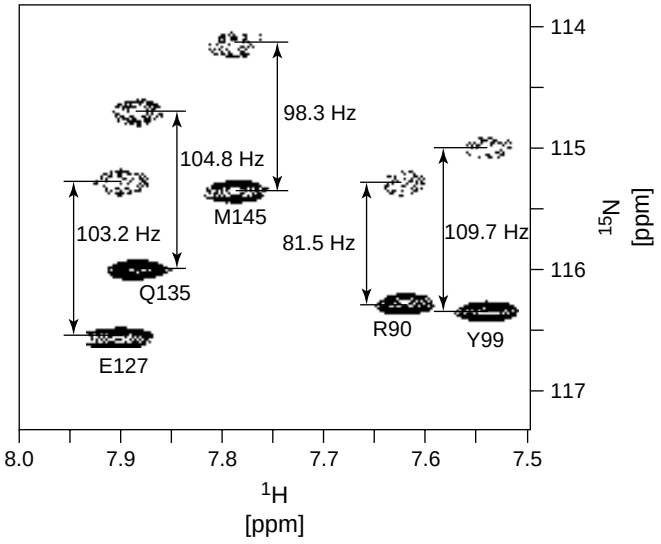

Figure 3 Small region of the IPAP ^{15}N–^1H HSQC spectrum of Ca^{2+}-ligated calmodulin in *Pf1* medium. The solid and dashed contours correspond to the downfield and upfield ^{15}N–{^1H} doublet components, which are separated into two two-dimensional subspectra. These subspectra are superimposed in this plot for visual simplicity, as none of the resonances overlap one another in the displayed region of the spectrum. The size of the splittings are marked in the figure and correspond to $|^1J_{NH} + {}^1D_{NH}|$

from this value correspond to the dipolar contributions to these splittings. So, both the sign and the magnitude of the dipolar coupling are obtained from such spectra.

3.3 Measurement of $^1J_{C'C\alpha}$

Due to the longer internuclear distance, and the lower product of the gyromagnetic ratios involved, the $^1D_{C'C\alpha}$ coupling is inherently five times smaller than the one-bond ^1H–^{15}N coupling (Table 1). In order to obtain meaningful information, it therefore is necessary to measure this coupling at high accuracy. There are two ways to measure $^1J_{C'C\alpha}$: observation of the C^α or of the C' resonance in the absence of decoupling the non-observed spin. For protonated proteins at moderate field strengths ($\leq$14 T), the $C'T_2$ is invariably much longer than the $C^\alpha T_2$, favoring detection of C' for most accurate measurement of $^1J_{C'C\alpha}$. For perdeuterated proteins, detection of $^{13}C^\alpha$ in the presence of ^2H and $^{13}C^\beta$ decoupling yields narrower ^{13}C resonances, particularly at higher fields.

Usually, the most accurate method for measurement of $^1J_{C'C\alpha}$ is to simply record a 3D HNCO spectrum where the C^α pulse, normally applied at the midpoint of the $^{13}C'$ evolution period, is omitted.[33] The HNCO experiment yields among the best resolved triple resonance spectra and the two-fold increase in the number of resonances relative to the $^{13}C^\alpha$-decoupled spectrum is generally not much of a problem. The $^{13}C'$ transverse relaxation rate is dominated by its chemical shift anisotropy, and $^{13}C'$ line widths at 600 MHz are about 30% larger than at 500 MHz ^1H frequency. It is therefore preferable to measure the $^1J_{C'C\alpha}$ splitting at a relatively low magnetic field strength.

3.4 Measurement of $^1J_{C'N}$ and $^2J_{C'HN}$

Dipolar couplings across the peptide bond between $^{15}N_i$ and $^{13}C'_{i-1}$ are inherently 8.3 times weaker than $^1D_{NH}$ (Table 1). Therefore, accuracy of their measurement is critical for making optimal use of these small couplings in structure determination. Owing to the favorable relaxation properties of ^{15}N, especially when selecting the downfield ^{15}N–{^1H} doublet component, the $^1J_{C'N}$ coupling is detected through the ^{15}N and not the $^{13}C'$ nucleus. The simplest method just records a two-dimensional HSQC on the $^{13}C/^{15}N$ doubly labeled protein, and inserts a $^{13}C^\alpha$ but not a $^{13}C'$ 180° decoupling pulse at the mid-point of ^{15}N evolution.[34] The resulting doublet in the ^{15}N dimension corresponds to $^1J_{C'N}$. Interestingly, the detected amide proton is also coupled to $^{13}C'$ (which has not changed its spin state during or after ^{15}N evolution). Therefore, the two doublet components are also displaced relative to one another by the $^2J_{C'HN}$ coupling in the $^1H^N$ dimension. Although normally this splitting would be very difficult to resolve because the $^1H^N$ line width is typically much larger than the $^2J_{C'HN}$ coupling, the E.COSY principle[28] effectively separates the two $^1H^N$–{$^{13}C'$} doublet components (Figure 4).

An interesting alternative approach, based on the principle of quantitative J correlation, derives $^1J_{C'N}$ from the relative intensities of two interleaved 3D TROSY-HNCO spectra.[35] In one experiment (reference spectrum) the pulse scheme uses optimal one-bond ^{15}N–{$^{13}C'$} dephasing of 33 ms, whereas in the second experiment (attenuated spectrum) the dephasing delay is set near the null condition (66 ms). Any deviation from $^1J_{C'N} + {}^1D_{C'N} = (66\,\text{ms})^{-1}$ results in non-zero intensity in the second spectrum. The relative intensities of these two spectra then give a very precise measure for $^1J_{C'N}$, and permit

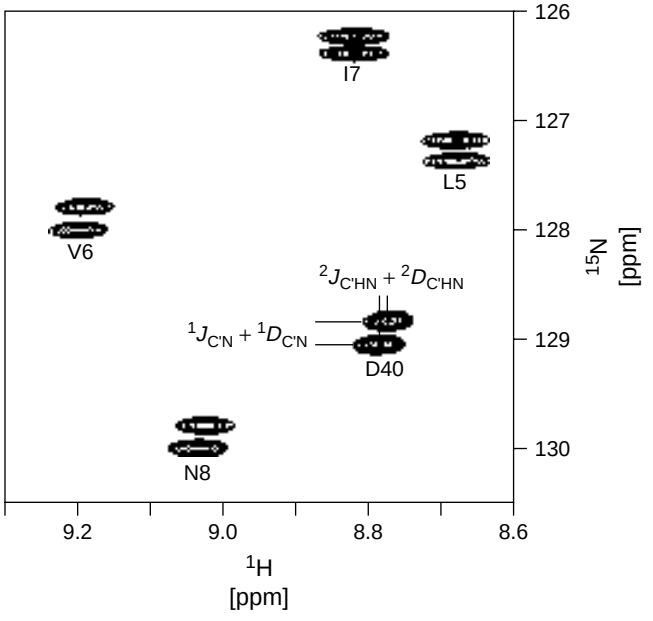

Figure 4 Small region of the ^{15}N–^1H HSQC spectrum of the first immunoglobulin binding domain of protein G, recorded in the absence of $^{13}C'$ decoupling in *Pf1* liquid crystal (11 mg ml^{-1}). The vertical and horizontal displacements within each doublet correspond to $|^1J_{C'N} + {}^1D_{C'N}|$ and $|^2J_{C'HN} + {}^2D_{C'HN}|$, respectively. Doublets are labeled by their one-letter residue type and number

$^1D_{C'N}$ to be derived at an accuracy that is a fraction of a hertz, provided the signal to noise in the reference spectrum exceeds 20 : 1.

3.5 Measurement of $^1J_{C\alpha H\alpha}$ and $^1J_{C\alpha C\beta}$

Although, in principle, $^1J_{C\alpha H\alpha}$ can be measured from a ^1H–^{13}C two-dimensional correlation spectrum, recorded in the absence of heteronuclear decoupling in either the F_1 or F_2 dimension, the increase in spectral crowding frequently leads to unacceptable overlap for all but the smallest proteins. In practice, therefore, $^1J_{C\alpha H\alpha}$ is most commonly measured either from a series of J_{CH}-modulated HSQC spectra, simultaneous to measurement of sidechain J_{CH} couplings (see below), or from a H^α-coupled HN(CO)CA or (HA)CA(CO)NH spectrum. This latter experiment makes it easy to decouple the $^1J_{C\alpha C\beta}$ coupling by using a constant-time C^α evolution period, and is therefore preferred when dealing with small or medium-size proteins. Its pulse sequence is identical to a scheme previously used for measuring relaxation interference between the $^{13}C^\alpha$ CSA tensor and the $^{13}C^\alpha - {}^1H^\alpha$ dipolar interaction,[36] but now it is the splitting itself rather than the difference in doublet intensities that is the focus of the measurement.

In perdeuterated proteins, $^1J_{C\alpha H\alpha}$ is inaccessible, but the long $^{13}C^\alpha$ transverse relaxation time permits measurement of $^1J_{C\alpha C\beta}$ from a regular HNCA experiment, recorded in the presence of ^2H decoupling during $^{13}C^\alpha$ evolution.[37]

3.6 Measurement of Sidechain $^1J_{CH}$ Couplings

To date, most attention has focused on measurement of backbone-related dipolar couplings. Nevertheless, dipolar couplings also are starting to become used for studying sidechain conformations. However, a significant fraction of the sidechains may be subject to rotameric averaging, which reduces the dipolar coupling relative to a static, single conformation. If the smaller dipolar coupling is imposed during structure calculation as if it were rigid, this can result in distorted sidechain conformations with high energy. A way around this is to impose the observed dipolar coupling as a lower bound for the true dipolar coupling.[38] An even better way would be to evaluate for each site separately what the degree of sidechain mobility is by conducting the requisite relaxation experiments.

For small and medium-size proteins, an accurate way for extracting both backbone $^1J_{C\alpha H\alpha}$ and sidechain $^1J_{CH}$ couplings is the recording of a set of CT-HSQC spectra, in which the ^1H 180° decoupling pulse is systematically shifted. The intensity modulation pattern observed in the fully decoupled CT-HSQC spectrum then provides an accurate measure for $^1J_{CH}$. For methylene groups, the modulation frequency corresponds to the sum of the two $^1J_{CH}$ couplings. Methyl group intensities are modulated by $^1J_{CH}$ and by $3 \times {}^1J_{CH}$, with amplitudes of the modulation having a ratio of approximately 1 : 3. As a result of the rapid three-fold rotation about the three-fold symmetry axis of the methyl group, the $^1D_{CH}$ dipolar coupling is scaled down by -0.31 relative to its static value.[39] Figure 5 compares the $^1D_{CH}$ and $^1D_{CC}$ dipolar couplings for methyl groups in ubiquitin. The tight correlation seen in this figure testifies to the precision at which these dipolar couplings can be measured. As suggested by this figure, for structure calculation

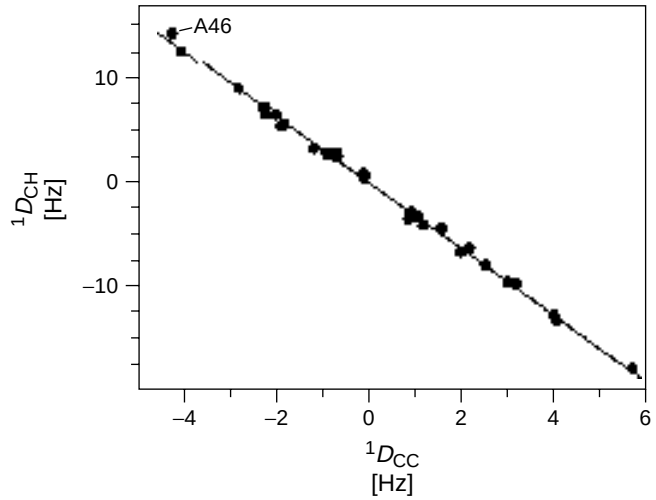

Figure 5 Plot of $^1D_{CH}$ versus $^1D_{CC}$ residual dipolar couplings of methyl groups in the protein ubiquitin, dissolved in a liquid crystalline medium containing 5% (w/v) bicelles. The solid line represents the best fit of the data by linear regression, with a slope of -3.17 ± 0.03. The outlier, labeled A46, corresponds to an alanine residue with a positive ϕ angle, for which there is a steric clash between the methyl group and a backbone carbonyl oxygen. (Reprinted, with permission, from Ottiger et al.[39])

purposes the methyl group $^1D_{CH}$ value may be converted into $^1D_{CC}$, thereby restraining the C–C(H_3) orientation.

For larger proteins, the lower sensitivity and increased spectral overlap in a CT-HSQC spectrum frequently result in a relatively small fraction of residues for which the $^1J_{CH}$ coupling can be measured. As an alternative, spectra recorded with CCH-COSY or HCCH-COSY, without decoupling in the detected dimension may be used for measurement of J_{CH}. An additional benefit of this approach is that for the case of non-equivalent methylene protons, both J_{CH} couplings can be measured separately. In favorable cases, the ^{1}H–^{1}H multiplet structure in such spectra also permits measurement of $^2J_{HH}$.[40]

3.7 Measurement of ^{1}H–^{1}H Couplings

The history of measuring ^{1}H–^{1}H J couplings is particularly rich and has been reviewed in numerous places. The E.COSY approach, applied in either a homo- or heteronuclear manner has proven particularly useful in this respect.[28] However, few of these methods are suitable for measurement of ^{1}H–^{1}H dipolar couplings. When oriented, ^{1}H–^{1}H multiplet structure tends to become very complex as a result of the multitude of coupling partners any given proton experiences. Fortunately, in heteronuclear type E.COSY spectra this does not pose a serious problem, and the utility of triple resonance experiments for measurement of both the sign and magnitude of intraresidue and sequential $J_{H\alpha HN}$ couplings has been demonstrated in oriented media.[41] Nevertheless, with some exceptions,[42,43] such experiments tend to be less suitable for measurement of dipolar couplings that are spatially proximate but far apart in the covalent bond network. Alternatively, the popular HNHA experiment can be used for measuring ^{1}H–^{1}H dipolar couplings that involve an amide proton.[6,44] In this experiment, the magnitude of $|J_{HH} + D_{HH}|$ is derived from the diagonal to cross peak intensity ratio. So, except for the intraresidue H^N–H^α interaction, where there also is a significant scalar contribution to the interaction, the sign of D_{HH} is not available from this experiment.

4 ALIGNMENT MEDIA FOR MACROMOLECULES

A prerequisite for studying macromolecules in a liquid crystalline phase is that the order imposed on the macromolecule is very small, typically less than 0.002. The order of the liquid crystal particles themselves is invariably much higher, in the 0.5–0.85 range. Clearly, for achieving such a weak solute alignment in the strongly oriented liquid crystalline medium, interaction between the macromolecule and the liquid crystal must be very weak. The medium must also be aqueous, such that the proteins or nucleic acids remain in their natural environment. An efficient way to satisfy these conditions is the use of a very dilute ($\leq$10% (w/v)) lyotropic nematic liquid crystalline suspension, where the nematogenic unit itself is a large particle. In a liquid crystalline phase, the weak steric and electrostatic interactions between liquid crystal particles cause their cooperative alignment. There is a lower limit for the nematogen concentration, c_n, required to form a stable liquid crystalline phase. If the sample is diluted below this threshold, it separates into an isotropic phase with concentration c_i and a nematic phase, with the c_n being 5–20% higher than c_i. The aspect ratio of the nematogenic particle is a critical determinant for the lowest concentration at which liquid crystalline ordering occurs. The time needed for formation of a homogeneous liquid crystalline phase strongly depends on the nematogen concentration, and can be very long for concentrated samples, but also for samples that are close to the threshold concentration, where separation between microscopic aligned and isotropic domains takes place.

All liquid crystalline media that have proven to be useful for weak ordering of proteins and nucleic acids consist of large (>1000 Å), water-soluble particles, with relatively low surface charge densities ($\leq 0.5\, e\, nm^{-2}$). The interaction between the liquid crystal particles results in increased macroscopic viscosity relative to pure water. However, rotational diffusion of the macromolecule itself is virtually unchanged, unless it has a weak affinity for the liquid crystal particle. In the latter case, the degree of order typically is much too large and therefore is of little practical interest. For all lyotropic liquid crystals discussed below, the degree of order imposed on the solute can be adjusted by changing the concentration of the liquid crystal itself over the range where it yields an ordered phase. There is not yet a single, ideal liquid crystal. For example, phospholipases without inhibitors cannot be studied in bicelles as they break down the phospholipids; active proteases can destroy phage-based liquid crystals; other proteins may stick to phospholipids, or the surface charge distribution of the liquid crystal may cause too strong an electrostatic interaction with the solute. Also, liquid crystals require some degree of surface charge to keep their order and may fail to remain liquid crystalline at high salt concentrations. Below, several of the most widely used systems are briefly discussed.

4.1 Bicelles

Bicelles were the first liquid crystalline medium used for weak alignment of proteins and DNA.[7,8] These are planar

bilayered particles that usually consist of regular saturated phospholipids. Most commonly, a mixture of dimyristoyl phosphatidyl choline (DMPC) and dihexanoyl phosphatidyl choline (DHPC) is used. DMPC makes up the bilayer, which constitutes the plane of the bicelle, and the DHPC detergent protects the long DMPC alkyl chains at the rims of the bilayer from exposure to solvent. Bicellar liquid crystals were originally developed by Prestegard, Sanders and co-workers for the purpose of studying lipophilic molecules, anchored in these highly ordered membranes.[45,46] The DMPC/DHPC combination was found to be particularly robust. When raising the temperature above 25 °C, the system switches from isotropic to a nematic liquid crystalline phase.[47] This temperature corresponds to the melting temperature of DMPC, i.e., the temperature at which the saturated alkane chains of DMPC melt from a crystalline or gel state, in which the alkane chains are all *trans*, to a flexible, liquid crystalline phase. Near this transition temperature, the sample has high macroscopic viscosity and tends to be slightly opaque. Below 25 °C the solution remains clear and unordered and both small angle neutron scattering and NMR diffusion experiments indicate the bicelles to be disk-shaped bilayers in this unordered phase.[48,49]

The phase diagram of the DMPC/DHPC mixture is very complex and depends on a large number of variables, including the absolute concentration, the molar ratio [DMPC]/[DHPC] = q, temperature, ionic strength, and on the presence of charged amphiphilic molecules such as sodium dodecyl sulfate (SDS) or cetyl trimethylammonium bromide (CTAB). Bicelles were long believed to remain disk-shaped above the DMPC melting temperature, with a diameter determined by q. However, the diameters predicted by such a model are incompatible with the very dilute concentrations (down to $\leq$2% (v/v)) at which the sample remains liquid crystalline. Recent tracer diffusion obstruction and neutron scattering data indicate the liquid crystalline phase to consist of highly porous bilayers, presumably with the detergent covering the rims of the pores.[49,50]

Intrinsically, DMPC/DHPC bicelles can form a liquid crystalline phase over the temperature range of 25–45 °C. However, near the lower end of this range (25–30 °C), dilute samples tend to be unstable and they frequently separate into an aligned and an isotropic phase. This can be prevented by addition of a small molar fraction (typically 1–3%, relative to DMPC) of charged amphiphiles, such as CTAB (positive) or SDS (negative).[51] Alternatively, charged phospholipids such as dimyristoyl phosphatidylserine (negative), or dimyristoyl trimethylammonium propane (positive) can be used. Charging the bicelles in this manner helps prevent phase separation and widens the part of the phase diagram over which the liquid crystalline phase remains stable. The electrostatic potential repels and attracts oppositely charged groups on the solute, and generally causes a change in both the orientation and magnitude of the alignment tensor. This can be a highly beneficial side effect, as it permits measurement of dipolar couplings under multiple orientations of the protein (Figure 6).[52] Usually, this change in orientation is approximately linear with charge. So, if more than two different samples are prepared in this manner, they simply yield alignment tensors that are linear combinations of one another.[53]

Regular phospholipids are subject to acid- and base-catalyzed hydrolysis of the carboxyester linkage between the alkyl chain and the glycerol backbone. The rate of hydrolysis is minimal at pH 6.5, but rapidly increases once the pH differs by more than one unit from this value.[54] Use of ether lipids, where the carboxyester bond is replaced by an ether linker can prevent this hydrolysis and such samples can be stable over a very wide range of pH[55,56] for periods of several years.

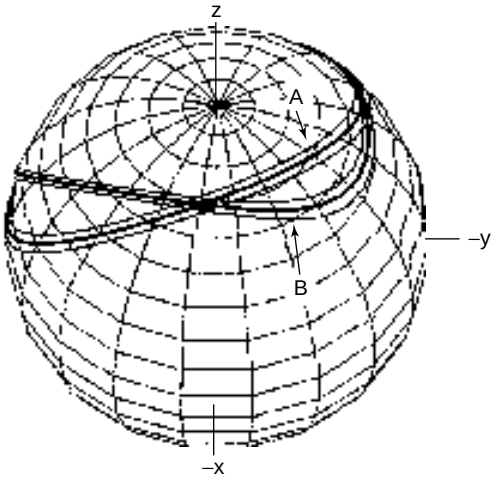

Figure 6 Orientations of the Gln[40] N–H vector in ubiquitin compatible with the ^{15}N–^{1}H one bond dipolar coupling measured in undoped bicelles (band A) and in positively charged bicelles (band B). Orientations are given in the coordinate frame of the X-ray structure of this protein. Heavy lines correspond to the measured dipolar couplings; thinner lines correspond to orientations if D_{NH} is increased or decreased by 1 Hz. The solid dot marks the orientation of the N–H vector when the protons are model-built into the crystal structure, assuming H^N is located on the line bisecting the C′–N–C$^\alpha$ angle. (Adapted, with permission, from Ramirez and Bax[52])

The temperature range over which the bicelles are liquid crystalline can be extended either by introducing a small fraction of mono-unsaturated DMPC, which lowers the melting temperature of the alkane chain,[54] or by using shorter alkane chains. Use of shorter alkane chain phospholipids, such as dilauroyl PC (12-C chains)[57] or ditridecanoyl PC (13-C chains)[55] lowers the transition temperature by about 12 and 6 °C, respectively, and increases the upper temperature limit as well. However, the macroscopic viscosity of these solutions below the transition temperature tends to be much higher than for DMPC/DHPC bicelles, such that preparation of the sample can be more cumbersome, particularly when using a microcell.

4.2 Filamentous Phage

Use of a liquid crystalline solution consisting of filamentous phages for aligning macromolecules was introduced in 1998.[9,10,58] Clore et al. used a medium based on the filamentous phage fd, and also demonstrated the potential of tobacco mosaic virus (TMV). The Pardi group demonstrated the utility of the phage *Pf1*, which is similar to *fd*, but which at a contour length of ca. 2 μm is nearly twice as long. Both phages have a diameter of 6.5 nm, and are quite rigid, with a persistence length of ca. 1 μm. As a result of the high aspect ratios of these particles, solutions can remain liquid crystalline down to very low concentrations, as low as a

few $mg\,ml^{-1}$. Although it was suggested that liquid crystallinity is independent of ionic strength, we find this to be true only at higher phage concentrations,[15] whereas at lower concentrations ($\sim 13\,mg\,ml^{-1}$ for *Pf1*) the degree of alignment becomes sensitive to ionic strength, and at very high salt concentrations the samples become isotropic. In contrast to *fd*, *Pf1* solutions tend to remain homogeneous when their concentration is lowered below the nematic threshold concentration, c_n. However, below this threshold, the degree of both phage and solute alignment becomes a function of the magnetic field strength, characteristic of a so-called paranematic phase.[15]

The negative surface charge (ca. $0.5\,e\,nm^{-2}$) is necessary to maintain a uniform suspension of these large particles. When lowering the pH below 6, partial protonation of the glutamate and aspartyl sidechains of the phage coat protein reduces the net charge of the virus particle and the phage precipitates. However, *fd* has been shown to be soluble and liquid crystalline when the pH is reduced further, to ca. 3.[59]

As highlighted by Clore et al. for an immunoglobulin-binding domain of Streptococcal protein G, the alignment tensor in the phage medium can be very different from that in the bicelle medium.[10] This is advantageous as it permits measurement of dipolar couplings relative to two independent axis systems, thereby resolving much of the degeneracy that occurs in interpreting a dipolar coupling in terms of two orientational variables, θ and ϕ in equation (3c). The phage particles are aligned with their long axis parallel to the magnetic field. Therefore, if the alignment of solute macromolecules were caused exclusively by steric interaction, the alignment tensor would be very similar to that in the bicelle medium. In practice, the alignment tensors in phage and bicelle media tend to be quite different as there usually are relatively strong electrostatic interactions between the phage and the solute (see also Section 5).

4.3 Alkyl-poly(ethylene glycol) Based Media

A lyotropic liquid crystal consisting of a mixture of alkyl-poly(ethylene glycol) and hexanol is another very useful medium for protein and nucleic acid alignment.[14] Alkyl-poly(ethylene glycol) type compounds generally do not tend to bind to proteins, making this an attractive medium for a wide range of biological systems. In contrast to bicelles, the liquid crystal is not subject to hydrolysis and it can remain stable for years, provided the concentration of hexanol does not decrease as a result of slow evaporation. The medium remains liquid crystalline over a wide pH range and a considerable temperature range of 10–40 °C, which is tunable by varying the type of alkyl-poly(ethylene glycol) and the chain length of the alcohol.[14]

The different alkyl-poly(ethylene glycol) compounds are referred to as C*m*E*n*, where *m* is the number of carbons in the alkyl group, and *n* is the number of ethylene glycol units. Typically, a hexanol to $C_{12}E_5$ molar ratio of 0.96 (5 wt.% $C_{12}E_5$ in H_2O) is used yielding a particularly stable liquid crystal that is easy to prepare, but the medium is relatively tolerant to changes in the absolute and relative concentrations. $C_{12}E_5$ is commercially available at low cost. In many cases, the sample can simply be recovered from the liquid crystal by extensive dialysis.

4.4 Other Liquid Crystals

Ternary mixtures of cetylpyridinium chloride (CPCl) or bromide (CPBr), hexanol, and NaCl or NaBr in water can form stable liquid crystalline phases over a wide range of conditions. Prosser et al.[11] demonstrated that the CPCl version yielded alignment for the protein ubiquitin, and Barrientos et al.[12] described the use of the CPBr based medium. Remarkable differences were found between the CPBr and CPCl based liquid crystals, with CPBr being more suitable for low ionic strength measurements (10–40 mM NaBr) and the CPCl system requiring higher salt concentrations (200–500 mM NaCl).[12]

Dilute suspensions of natural cellulose fibers, derived either from wood pulp or from filter paper by careful sulfuric acid hydrolysis, also can form a liquid crystalline phase suitable for macromolecular ordering.[60] Although negatively charged, the net surface charge density is lower than for filamentous phage, making it a useful complement to the other media, mentioned above. However, the lower surface charge and the smaller aspect ratio relative to filamentous phage result in a higher minimal threshold concentration for liquid crystal formation.

A suspension of purple membrane (PM) fragments has also been shown suitable for inducing a weak degree of macromolecular order.[53,61] These fragments consist primarily (75% (w/w)) of bacteriorhodopsin, an integral membrane protein with seven transmembrane helices. The PM fragments have an average diameter of about 1 μm. This is sufficiently large that the total magnetic susceptibility anisotropy of such a particle causes it to align nearly 100% when placed in a strong magnetic field ($\geq$11 T), with the membrane plane orthogonal to the direction of the magnetic field.[62] So, in contrast to the bicelle, phage and CPBr systems, PM does not need to form a liquid crystalline phase for obtaining alignment.

The strong net negative surface charge of PM causes very weak transient binding of solute proteins that carry clusters of positively charged groups on their surfaces, and thereby can result in net alignment.[53,61] The electrostatic interactions are typically weak enough not to distort the structure of globular proteins. However, as is the case with all liquid crystal studies in this chapter, when studying flexible regions in a protein, care must be taken when interpreting the dipolar coupling data as the protein only transiently interacts with the liquid crystal. Interaction with the nematogen may be favored when the flexible region temporarily adopts a given shape, whereas other, non-binding conformations of the flexible region may not be sampled.

4.5 Polyacrylamide Gel

In order to prevent sedimentation, suspensions of large particles such as phages, bicelles, and cellulose require a repelling interaction, i.e., a net surface charge. These local electrostatic fields generally result in stronger solute alignment, which then may become too strong for facile dipolar coupling measurement. In other cases, solutes may cause the liquid crystal particles to aggregate and precipitate. For example, no stable liquid crystal has yet been described that is suitable for detergent-solubilized proteins. So, although the above mentioned liquid crystalline systems will cover the majority of systems of interest, there remain exceptions.

Recently, a very useful alternative method for inducing weak alignment has been developed that is known as strain-induced alignment in a gel (SAG).[63,64] This method relies on anisotropically compressed polyacrylamide gel, which forms an extremely stable and inert aqueous matrix for solute proteins, and even permits their study under partially or fully denaturing conditions.[65] The gels may either be compressed or stretched in the axial direction,[64] with stretching generally yielding stronger alignment.[66] The robustness of such a medium makes it particularly useful for challenging applications such as detergent-solubilized systems.[66] The solutes may either be diffused into the gel, or they may be included in the medium before polymerization of the hydrogel is induced.

Compression of the gel can simply be achieved by first casting it in a narrow diameter (3–3.5 mm) cylinder. Then, after soaking in the solute of interest, it is transferred to a regular 4.2-mm inner diameter (ID) NMR sample tube, followed by axial compression by a susceptibility-matched plunger. Stretching can be achieved by radial compression, using a funnel-like device to squeeze a larger diameter gel (5–7 mm) into a regular 4.2-mm ID NMR sample tube.[66] Polyacrylamide gels appear to yield the most widely applicable method for inducing weak macromolecular alignment as the system is very inert and stable. Their principal disadvantage is a potential decrease in rotational diffusion rate of the solute, resulting in line broadening.[64,67] This latter effect can be minimized by using gel concentrations as low as possible ($\leq$5%) combined with high degrees of stretching, and by using low cross-linking ratios ($\leq$1 : 40).

4.6 Use of Multiple Alignment Media

As discussed in Section 5, solute alignment is defined by both steric and electrostatic interaction. So, by using nearly neutral liquid crystals, such as bicelles or the alkyl poly(ethylene-glycol) medium, and a charged medium such as phage or the cetyl-pyridinium based phase, a single molecule can be studied using two or more independent alignment tensors. As illustrated in Figure 6, this removes much of the degeneracy in the relation between dipolar coupling and internuclear vector orientation.[52] A dipolar coupling measured in a given medium defines the internuclear vector to be on one of two oppositely oriented cones. The alignment tensor in a second medium will generally be oriented differently relative to the molecular frame and a dipolar coupling defines the same vector to be situated on a different cone. The true internuclear vector orientation then must be located on one of the intersections between the two sets of cones (Figure 6). In the general case of a non-axially symmetric (rhombic) alignment tensor there are up to eight intersections. If a third, independent alignment tensor can be obtained, this degeneracy may be reduced to two-fold. The true orientation and its inverse can never be distinguished from measurements on a single dipolar interaction, and two-fold degeneracy is therefore the best that can be achieved for a single vector.

Besides changing the liquid crystal medium, the alignment tensor may also be altered by subtly changing the protein. For example, when the pH is altered such that the surface charge distribution becomes different, this will affect the alignment tensor in the charged liquid crystalline media. Similarly, if protein preparations are available with and without a His-tag tail, their alignment tensors will generally be different, although not necessarily by a large amount. Also, for a protein with a His-tag, a relatively small change in pH from 6 to 7.5 can significantly alter the alignment tensor.

If one-bond dipolar couplings are measured for a set of non-collinear interactions in a fragment of known secondary structure, such as an α-helix, there are four different ways to orient the fragment relative to the alignment tensor. Dipolar couplings measured in a second, independent medium, can lift this degeneracy, defining its orientation uniquely.[68]

5 RELATION BETWEEN ALIGNMENT AND SHAPE

Tjandra et al. demonstrated that in a bicelle medium the principal axes of the molecular alignment tensor closely coincide with those of the rotational diffusion tensor.[8,69] This shows that in this nearly neutral medium, alignment is defined by the solute's shape. As mentioned above, the alignment tensor can be modified by adding a net charge to the bicelles, by doping them with either CTAB (+) or SDS (−). This demonstrates that electrostatic interactions also play a role. In fact, for an oriented medium of strongly negatively charged, rod-shaped viral particles, or oriented PM fragments, electrostatic interactions usually dominate alignment of solute proteins.

A simple steric model has been proposed that quantitatively describes the relation between the solute's shape and its alignment in the type of lyotropic liquid crystals described in this article.[70] So far, it has only been demonstrated for the case of (nearly) neutral particles, such as bicelles, but preliminary results indicate that the method can be extended to account for the effect of charge.

In the so-called steric-obstruction model, the solute sample can be simulated as a collection of randomly oriented, uniformly distributed molecules, from which the fraction that sterically clashes with the ordered array of liquid crystal particles is removed. For example, for a lamellar phase such as bicelles or $C_{12}E_5$, a larger fraction of molecules oriented orthogonal to the bilayer will be obstructed than molecules parallel to the surface, resulting in net ordering of the remaining, non-obstructed molecules. For each non-obstructed molecule a Saupe order matrix is calculated, using equation (2). Averaging of the Saupe matrices for all non-obstructed proteins than yields the sterically predicted alignment tensor.[70] In an extension of this method that accounts also for the effect of electrostatics, different weighting factors are given to each of the non-obstructed solute molecules, depending on the Boltzmann factor calculated when taking the electrostatic potential into account (M. Zweckstetter, unpublished results).

Figure 7 shows the correlation between the ^{15}N–^{1}H dipolar couplings measured for the Ig binding domain of Streptococcal protein G, and that predicted from its 1.0 Å crystal structure, using an alignment tensor that is not best-fitted to the data, but calculated on the basis of its shape.[69] When ignoring electrostatics, the predicted alignment tensors for bicelle and phage media are very similar. However, the experimentally observed dipolar couplings in the two media are very different and, as expected, good agreement is only observed for the bicelle medium (Figure 7). When electrostatic terms are included in the calculations for the phage medium, the

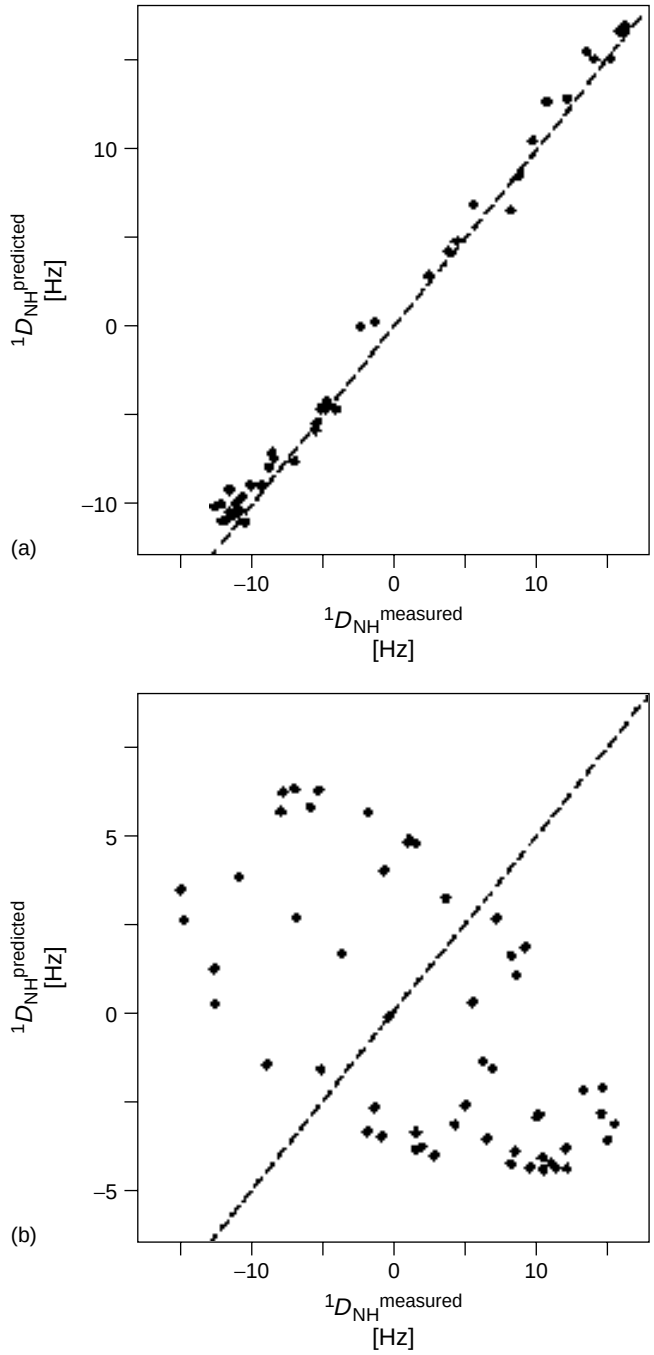

Figure 7 Correlations between experimental $^1D_{NH}$ values and values calculated from the shape-predicted alignment tensor of the third immunoglobulin binding domain of protein G in (a) 5% (w/v) bicelle medium, and (b) 28 mg ml^{-1} *fd* medium. Dashed lines correspond to $y = x$. The poor correlation in (b) indicates that in phage medium the protein alignment is dominated by electrostatic interactions, which are ignored in the alignment tensor prediction, and not by steric interaction. (Adapted, with permission, from Zweckstetter and Bax[15])

agreement becomes nearly as good as for the neutral bicelle medium. Note that in contrast to the results of an SVD fit, the data shown in Figure 7 do not include any adjustable parameters. So, the alignment tensor orientation and magnitude are calculated on the basis of the protein's shape, and subsequently dipolar couplings are predicted on the basis of the orientation of the internuclear vector relative to this alignment tensor.

6 STRUCTURE VALIDATION

One particularly attractive feature of dipolar couplings is that they can be used in a very direct manner to evaluate the accuracy of any given structure: the more accurate the structure, the better the agreement is between experimental dipolar couplings and this structure. In order to evaluate this agreement, one first needs to determine the alignment tensor or Saupe matrix. As mentioned earlier, there are two conceptually different ways to do this. One can either predict the alignment on the basis of the molecule's shape and charge distribution, or one can determine the Saupe matrix elements of equation (2) simply by singular value decomposition. There are five independent elements in the Saupe matrix. If the number of experimentally measured independent (i.e., non-collinear) dipolar interactions is much larger than five, the SVD approach is preferred as it eliminates the effect of errors in the shape-predicted alignment tensor. Clearly, for effective validation it is necessary that the number of observables (dipolar couplings) is much larger than the number of variables in the SVD fit. If this condition is not met, corrections can be made for the significance of the correlation in terms of F statistics. For proteins, typically the number of observed dipolar couplings is much larger than five, and the goodness of the fit provides a direct measure for the accuracy of the structure.

Figure 8 shows a typical example of the correlation between measured dipolar couplings and those predicted by two structures of the C-terminal domain of Ca^{2+}-calmodulin (after best fitting the Saupe matrix to the experimental couplings). The first correlation (Figure 8a) is calculated by using the 1.0-Å X-ray crystal structure of Paramecium tetraurelia calmodulin to fit the data measured for the highly homologous mammalian protein. It yields a Pearson's correlation coefficient, R^P, of 0.95. The second structure was calculated on the basis of N–H, C′–N, H^α–C^α and C′–C^α dipolar couplings, and the H^α–C′ couplings are best-fit to this structure. Clearly, the NMR structure ($R^P = 0.98$) predicts the experimental H^α–C′ couplings better than the X-ray structure, which is related to a slight rearrangement of relative helix orientations in solution relative to the crystalline state.[71]

When accurate experimental dipolar couplings are available, it is always advantageous to incorporate them into the structure calculation process. However, once this is done, they no longer are useful for validation purposes. A way around this is to compare the observed and predicted changes in chemical shift between isotropic and aligned samples for a type of nucleus with a well-defined chemical shift anisotropy. The first application of this idea was for the change in ^{15}N chemical shift with field strength in a small protein-DNA complex,[72] caused by the anisotropy of the magnetic susceptibility of this complex. Although the changes were minute ($\leq$5 ppb), a clear improvement in the correlation was observed upon incorporation of dipolar couplings in the structure calculation process. Subsequently, comparison of much larger ^{13}C′ chemical shift changes between a protein in isotropic and aligned bicellar medium also showed an excellent correlation with structure.[73]

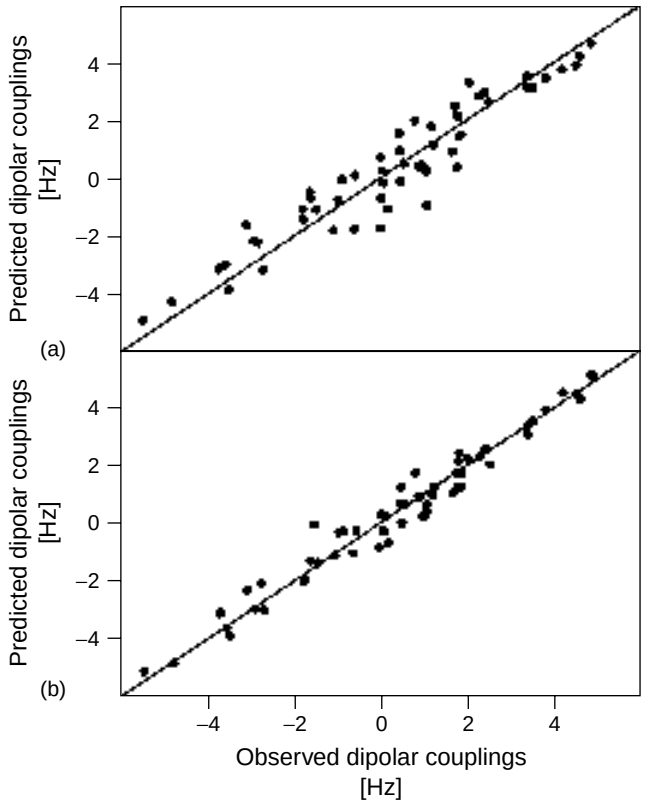

Figure 8 Correlation between measured, normalized $^2D_{C'H\alpha}$ dipolar couplings and those predicted by the 1.0-Å X-ray crystal structure (a), and by the NMR structures of the C-terminal domain of Ca^{2+}-calmodulin, calculated without $^2D_{C'H\alpha}$ couplings (b). The slightly better fit to the NMR structure is caused by a small rearrangement of the relative helix orientations in solution relative to those observed in the crystalline state of this protein[71]

7 CONCLUDING REMARKS

The introduction of methods for generating tunable, very weak alignment of macromolecules makes it possible to measure the one-bond and other short range dipolar couplings with a remarkable degree of accuracy. Even while the splittings are reduced by about three orders of magnitude relative to their static values, the narrow line widths and relatively high signal-to-noise ratio attainable in high resolution NMR more than compensate for the low degree of order. For example, one-bond ^{15}N–^{1}H dipolar couplings typically can be measured with an accuracy of ca. 0.1 Hz, whereas their range covers up to 50 Hz. Even for the intrinsically much smaller interactions, such as the one-bond ^{15}N–$^{13}C'$ dipolar coupling, the error typically is smaller by up to two orders of magnitude relative to the range of couplings observed. Similarly, chemical shift effects can be measured at a relative accuracy that rivals that attainable in solid state NMR, but the problem of resonance overlap is much less severe because isotropic shifts in solution are more effective at dispersing NMR spectra. Experimental correlations between $^{13}C'$, ^{15}N, and $^{1}H^{N}$ CSA tensors and secondary structure in proteins could be clearly established from such data.[74]

Dipolar couplings are not very sensitive to small amplitude oscillations about an average orientation. Conversely, relatively small discrepancies between observed and predicted magnitudes of dipolar couplings require rather large amplitude angular fluctuations if this discrepancy is entirely attributed to dynamic effects.[75,76] Nevertheless, because averaging of the observed dipolar interactions is sensitive to motions that cover the entire time scale from milliseconds to femtoseconds, it can potentially provide a powerful complement for the study of dynamic processes.

Measurement of tensorial interactions in macromolecules is a new and rapidly expanding area in structural biology. It offers numerous new opportunities, including rapid determination of backbone folds, rapid structure determination, refinement of conventional NMR structures, and the study of relative orientations of components in multi-molecular complexes. It is likely that a further marriage between conventional solid-state NMR techniques and the weak alignment approach may expand these areas even further.

8 RELATED ARTICLES IN VOLUMES 1–8

Biological Macromolecules: Structure Determination in Solution, Volume 2; Liquid Crystals: General Considerations, Volume 4; Liquid Crystals: Mixed Magnetic Susceptibility Solvents, Volume 4; Two-Dimensional NMR of Molecules Oriented in Liquid Crystalline Phases, Volume 8.

9 REFERENCES

1. A. Saupe and G. Englert, *Phys. Rev. Lett.*, 1963, **11**, 462–464.
2. J. W. Emsley in 'Encyclopedia of NMR', eds D. M. Grant and R. K. Harris, Wiley: Chichester, 1996, Vol. 4, pp 2788–2799.
3. E. W. Bastiaan, C. Maclean, P. C. M. vanZijl, and A. A. Bothner-By, *Annu. Rep. NMR Spectrosc.*, 1987, **19**, 35–77.
4. A. A. Bothner-By, in 'Encyclopedia of NMR', eds D. M. Grant and R. K. Harris, Wiley: Chichester, 1996, Vol. 5, pp 2932–2938.
5. J. R. Tolman, J. M. Flanagan, M. A. Kennedy, and J. H. Prestegard, *Proc. Natl. Acad. Sci. USA*, 1995, **92**, 9279–9283.
6. N. Tjandra, J. G. Omichinski, A. M. Gronenborn, G. M. Clore, and A. Bax, *Nature Struct. Biol.*, 1997, **4**, 732–738.
7. A. Bax and N. Tjandra, *J. Biomol. NMR*, 1997, **10**, 289–292.
8. N. Tjandra and A. Bax, *Science*, 1997, **278**, 1111–1114.
9. M. R. Hansen, L. Mueller, and A. Pardi, *Nature Struct. Biol.*, 1998, **5**, 1065–1074.
10. G. M. Clore, M. R. Starich, and A. M. Gronenborn, *J. Am. Chem. Soc.*, 1998, **120**, 10 571–10 572.
11. R. S. Prosser, J. A. Losonczi, and I. V. Shiyanovskaya, *J. Am. Chem. Soc.*, 1998, **120**, 11 010–11 011.
12. L. G. Barrientos, C. Dolan, and A. M. Gronenborn, *J. Biomol. NMR*, 2000, **16**, 329–337.
13. K. Fleming, D. Gray, S. Prasannan, and S. Matthews, *J. Am. Chem. Soc.*, 2000, **122**, 5224–5225.
14. M. Ruckert and G. Otting, *J. Am. Chem. Soc.*, 2000, **122**, 7793–7797.
15. M. Zweckstetter and A. Bax, *J. Biomol. NMR*, 2001, **20**, 365–377.
16. M. Ottiger and A. Bax, *J. Am. Chem. Soc.*, 1998, **120**, 12 334–12 341.
17. D. W. Yang, R. A. Venters, G. A. Mueller, W. Y. Choy, and L. E. Kay, *J. Biomol. NMR*, 1999, **14**, 333–343.
18. P. Permi, P. R. Rosevear, and A. Annila, *J. Biomol. NMR*, 2000, **17**, 43–54.
19. J. H. Prestegard, *Nature Struct. Biol.*, 1998, **5**, 517–522.
20. N. Tjandra, *Struct. Fold. Des.*, 1999, **7**, R205–R211.

21. A. Bax, G. Kontaxis, and N. Tjandra, *Methods Enzymol.*, 2001, **339**, 127–174.
22. E. Brunner, *Concepts Magn. Reson.*, 2001, **13**, 238–259.
23. J. A. Losonczi, M. Andrec, M. W. F. Fischer, and J. H. Prestegard, *J. Magn. Reson.*, 1999, **138**, 334–342.
24. G. M. Clore, A. M. Gronenborn, and A. Bax, *J. Magn. Reson.*, 1998, **133**, 216–221.
25. D. M. Grant, in 'Encyclopedia of NMR', eds D. M. Grant and R. K. Harris, Wiley: Chichester, 1996, Vol. 2, pp 1298–1321.
26. A. T. Brunger, P. D. Adams, G. M. Clore, W. L. DeLano, P. Gros, R. W. Grosse-Kunstleve, J. S. Jiang, J. Kuszewski, M. Nilges, N. S. Pannu, R. J. Read, L. M. Rice, T. Simonson, and G. L. Warren, *Acta Crystallogr. Sec. D-Biol. Crystallogr.*, 1998, **54**, 905–921.
27. N. Tjandra, J. Marquardt, and G. M. Clore, *J. Magn. Reson.*, 2000, **142**, 393–396.
28. C. Griesinger, O. W. Sørensen, and R. R. Ernst, *J. Magn. Reson.*, 1987, **75**, 474–492.
29. A. Meissner, J. O. Duus, and O. W. Sorensen, *J. Biomol. NMR*, 1997, **10**, 89–94.
30. M. Ottiger, F. Delaglio, and A. Bax, *J. Magn. Reson.*, 1998, **131**, 373–378.
31. A. Bax, G. W. Vuister, S. Grzesiek, F. Delaglio, A. C. Wang, R. Tschudin, and G. Zhu, *Methods Enzymol.*, 1994, **239**, 79–105.
32. M. Ottiger, F. Delaglio, and A. Bax, *J. Magn. Reson.*, 1998, **131**, 373–378.
33. S. Grzesiek and A. Bax, *J. Magn. Reson.*, 1992, **96**, 432–440.
34. F. Delaglio, D. A. Torchia, and A. Bax, *J. Biomol. NMR*, 1991, **1**, 439–446.
35. J. J. Chou and A. Bax, *J. Biomol. NMR*, 2000, **18**, 101–105.
36. N. Tjandra and A. Bax, *J. Am. Chem. Soc.*, 1997, **119**, 9576–9577.
37. J. Evenas, A. Mittermaier, D. W. Yang, and L. E. Kay, *J. Am. Chem. Soc.*, 2001, **123**, 2858–2864.
38. M. Ottiger, F. Delaglio, J. L. Marquardt, N. Tjandra, and A. Bax, *J. Magn. Reson.*, 1998, **134**, 365–369.
39. M. Ottiger and A. Bax, *J. Am. Chem. Soc.*, 1999, **121**, 4690–4695.
40. E. T. Olejniczak, R. P. Meadows, H. Wang, M. L. Cai, D. G. Nettesheim, and S. W. Fesik, *J. Am. Chem. Soc.*, 1999, **121**, 9249–9250.
41. M. L. Cai, H. Wang, E. T. Olejniczak, R. P. Meadows, A. H. Gunasekera, N. Xu, and S. W. Fesik, *J. Magn. Reson.*, 1999, **139**, 451–453.
42. G. Otting, M. Ruckert, M. H. Levitt, and A. Moshref, *J. Biomol. NMR*, 2000, **16**, 343–346.
43. W. Peti and C. Griesinger, *J. Am. Chem. Soc.*, 2000, **122**, 3975–3976.
44. G. W. Vuister and A. Bax, *J. Am. Chem. Soc.*, 1993, **115**, 7772–7777.
45. C. R. Sanders and J. H. Prestegard, *Biophys. J.*, 1990, **58**, 447–460.
46. C. R. Sanders and J. H. Prestegard, *J. Am. Chem. Soc.*, 1991, **113**, 1987–1996.
47. C. R. Sanders and J. P. Schwonek, *Biochemistry*, 1992, **31**, 8898–8905.
48. P. A. Luchette, T. N. Vetman, R. S. Prosser, R. E. W. Hancock, M. P. Nieh, C. J. Glinka, S. Krueger, and J. Katsaras, *Biochim. Biophys. Acta–Biomembranes*, 2001, **1513**, 83–94.
49. S. Gaemers and A. Bax, *J. Am. Chem. Soc.*, 2001, in press.
50. M. P. Nieh, C. J. Glinka, S. Krueger, R. S. Prosser, and J. Katsaras, *Langmuir*, 2001, **17**, 2629–2638.
51. J. A. Losonczi and J. H. Prestegard, *J. Biomol. NMR*, 1998, **12**, 447–451.
52. B. E. Ramirez and A. Bax, *J. Am. Chem. Soc.*, 1998, **120**, 9106–9107.
53. J. Sass, F. Cordier, A. Hoffmann, A. Cousin, J. G. Omichinski, H. Lowen, and S. Grzesiek, *J. Am. Chem. Soc.*, 1999, **121**, 2047–2055.
54. M. Ottiger and A. Bax, *J. Biomol. NMR*, 1998, **12**, 361–372.
55. M. Ottiger and A. Bax, *J. Biomol. NMR*, 1999, **13**, 187–191.
56. S. Cavagnero, H. J. Dyson, and P. E. Wright, *J. Biomol. NMR*, 1999, **13**, 387–391.
57. H. Wang, M. Eberstadt, E. T. Olejniczak, R. P. Meadows, and S. W. Fesik, *J. Biomol. NMR*, 1998, **12**, 443–446.
58. M. R. Hansen, M. Rance, and A. Pardi, *J. Am. Chem. Soc.*, 1998, **120**, 11 210–11 211.
59. L. G. Barrientos, J. M. Louis, and A. M. Gronenborn, *J. Magn. Reson.*, 2001, **149**, 154–158.
60. K. Fleming, D. Gray, S. Prasannan, and S. Matthews, *J. Am. Chem. Soc.*, 2000, **122**, 5224–5225.
61. B. W. Koenig, J. S. Hu, M. Ottiger, S. Bose, R. W. Hendler, and A. Bax, *J. Am. Chem. Soc.*, 1999, **121**, 1385–1386.
62. B. A. Lewis, C. Rosenblatt, R. G. Griffin, J. Courtemanche, and J. Herzfeld, *Biophys. J.*, 1985, **47**, 143–150.
63. R. Tycko, F. J. Blanco, and Y. Ishii, *J. Am. Chem. Soc.*, 2000, **122**, 9340–9341.
64. H. J. Sass, G. Musco, S. J. Stahl, P. T. Wingfield, and S. Grzesiek, *J. Biomol. NMR*, 2000, **18**, 303–309.
65. D. Shortle and M. S. Ackerman, *Science*, 2001, **293**, 487–489.
66. J. J. Chou, S. Gaemers, B. Howder, J. M. Louis, and A. Bax, *J. Biomol. NMR*, 2001, **21**, 377–382.
67. Y. Ishii, M. A. Markus, and R. Tycko, *J. Biomol. NMR*, 2001, **21**, 141–151.
68. H. M. Al-Hashimi, H. Valafar, M. Terrell, E. R. Zartler, M. K. Eidsness, and J. H. Prestegard, *J. Magn. Reson.*, 2000, **143**, 402–406.
69. E. de Alba, J. L. Baber, and N. Tjandra, *J. Am. Chem. Soc.*, 1999, **121**, 4282–4283.
70. M. Zweckstetter and A. Bax, *J. Am. Chem. Soc.*, 2000, **122**, 3791–3792.
71. J. J. Chou, S. Li, C. B. Klee, and A. Bax, *Nature Struct. Biol.*, 2001, **8**, 990–997.
72. M. Ottiger, N. Tjandra, and A. Bax, *J. Am. Chem. Soc.*, 1997, **119**, 9825–9830.
73. G. Cornilescu, J. L. Marquardt, M. Ottiger, and A. Bax, *J. Am. Chem. Soc.*, 1998, **120**, 6836–6837.
74. G. Cornilescu and A. Bax, *J. Am. Chem. Soc.*, 2000, **122**, 10 143–10 154.
75. J. R. Tolman, J. M. Flanagan, M. A. Kennedy, and J. H. Prestegard, *Nature Struct. Biol.*, 1997, **4**, 292–297.
76. J. Meiler, J. J. Prompers, W. Peti, C. Griesinger, and R. Bruschweiler, *J. Am. Chem. Soc.*, 2001, **123**, 6098–6107.
77. S. Moltke and S. Grzesiek, *J. Biomol. NMR*, 1999, **15**, 77–82.

Biographical Sketch

Ad Bax, *b* 1956. Ph.D. 1981 Applied Physics, Delft University of Technology, The Netherlands. Research associate, Colorado State University, 1982–83; National Institutes of Health, Visiting Scientist, NMR Section, Laboratory of Chemical Physics, NIDDK, 1983–88. National Institutes of Health, Chief, Biophysical NMR Spectroscopy Section, 1988-present. Approx. 300 publications. Current research interests: NMR and its applications in chemistry, biology and medicine.

Membrane Lipids of *Acholeplasma laidlawii*

Ronald N. McElhaney and Ruthven N. A. H. Lewis
University of Alberta, Edmonton, AB, Canada

1 Introduction 1
2 ^{2}H NMR Studies of the A. laidlawii Membrane Lipids 1
3 ^{19}F NMR Spectroscopy of Membrane Lipids 4
4 Related Articles 5
5 References 5

1 INTRODUCTION

The mycoplasmas are a diverse group of prokaryotic microorganisms that lack a cell wall. Since the mycoplasmas are genetically and morphologically the simplest organisms capable of autonomous replication, they provide useful models for the study of a number of problems in molecular and cellular biology. Mycoplasmas are particularly valuable for studies of the structure and function of cell membranes. Being nonphotosynthetic prokaryotes, as well as lacking a cell wall or outer membrane, mycoplasma cells possess only a single membrane, the limiting or plasma membrane. This membrane contains essentially all the cellular lipid, and, because these cells are small, a substantial fraction of the total cellular protein is membrane protein. Because of the absence of a cell wall, substantial quantities of highly pure membranes can usually be easily prepared by gentle osmotic lysis followed by differential centrifugation, a practical advantage not offered by other prokaryotic microorganisms.[1–3]

Another useful property of mycoplasmas is the ability to induce dramatic yet controlled variations in the fatty acid composition of their membrane lipids. Thus, relatively large quantities of a number of exogenous saturated, unsaturated, branched-chain, or alicyclic fatty acids can be biosynthetically incorporated into the membrane phospho- and glycolipids of these organisms. In cases in which de novo fatty acid biosynthesis is either inhibited or absent, fatty acid-homogeneous membranes (membranes whose glycerolipids contain only a single species of fatty acyl chain) can sometimes be produced. Moreover, by growing mycoplasmas in the presence or absence of various quantities of cholesterol or other sterols, the amount of these compounds present in the membrane can be dramatically altered. The ability to manipulate membrane lipid fatty acid composition and cholesterol content, and thus to alter the phase state and fluidity of the membrane lipid bilayer, makes these organisms ideal for studying the roles of lipids in biological membranes.[1–3]

The unique advantages of mycoplasmas for membrane studies, especially for studies of membrane lipid organization and dynamics, have induced a large number of investigators to study these microorganisms using a wide variety of physical techniques. For this reason, we probably know more about the physical properties of lipids in mycoplasma membranes in general, and in the *Acholeplasma laidlawii* membrane in particular, than in any other biological membrane.[1–3] In this review we will briefly summarize the results of ^{2}H and ^{19}F NMR spectroscopic studies of the organization of the hydrocarbon chains of the lipids of the *A. laidlawii* membrane as determined by the chemical composition of the lipid bilayer and by the presence of membrane proteins.

2 ^{2}H NMR STUDIES OF THE A. lAIDLAWII MEMBRANE LIPIDS

The technique of ^{2}H NMR spectroscopy has proven to be of great value in studies of lipid conformation, orientational order, and dynamics in lipid bilayers and natural membranes.[4–9] This technique has been widely used to study lipid hydrocarbon chain orientational order and dynamics in model and biological membranes, particularly in the membrane of *A. laidlawii*. In addition to being relatively nonperturbing, the deuterium nucleus, having a low natural abundance, can be selectively placed at various positions in the fatty acyl chain. Furthermore, the electric quadrupole moment of deuterium allows a direct measurement of the molecular order parameter of the lipid hydrocarbon chain, a measure of the time-averaged orientation relative to the bilayer normal, from the observed quadrupole splittings. Direct measurements of the rates of motion (relaxation times) of the hydrocarbon chains of the *A. laidlawii* membrane lipids, the other component of fluidity, have not yet been made by ^{2}H NMR. However, such determinations have been made for lipid model membranes and for the membranes of another mycoplasma (see below). The only significant disadvantage of deuterium is its low sensitivity, which until recently required the presence of relatively high probe levels (typically 50 mol% or more) in the membrane of interest.

2.1 Effect of Lipid Fatty Acid Structure

Oldfield et al. were the first to apply ^{2}H NMR to the *A. laidlawii* membrane.[10] These workers selectively labeled the entire membrane lipid hydrocarbon chain by growing this organism in the presence of exogenous, fully deuterated lauric or palmitic acids. The ^{2}H NMR spectra obtained from isolated membranes, recorded at the growth temperature of 37 °C, consist of a broad, unstructured envelope of numerous overlapping resonances. Nevertheless, the spectral shape observed is qualitatively that expected from the simultaneous presence of both lamellar gel and liquid crystalline lipid phases, in agreement with previous calorimetric and X-ray diffraction studies for *A. laidlawii* membranes enriched with saturated fatty acids.

Stockton et al. pioneered the use of specifically deuterated fatty acids in NMR studies of biological membranes.[11] *A. laidlawii* membranes were highly enriched by the biosynthetic incorporation of exogenous palmitic acid labeled only at the terminal methyl group with deuterium, and ^{2}H NMR spectra were recorded at a variety of temperatures. Although instrumental limitations precluded direct observation of the broad gel-phase signal present at lower temperatures, the intensity of the liquid crystalline spectra, which first appear at 20 °C, increases with increasing temperature from 20 to 44 °C. At 37 °C, about half the lipid appears to exist in the

fluid state. Above 44 °C, the orientation order decreases fairly rapidly with increasing temperature.

Stockton et al. later extended the above study to include palmitic acid probes labeled at a variety of positions from C-2 through C-16 of the hydrocarbon chain.[12] In this study, both the gel and liquid crystalline spectra could be observed directly and the phase boundaries assigned in the previous study could thus be confirmed. In addition, the orientational order parameter profile for lipid existing just above the upper boundary of the lipid phase transition could be determined. It was found that a plot of order parameter versus the position of the deuteron in the chain reveals a 'plateau' region of roughly constant order extending from C-2 through C-10, after which the order parameter declines progressively more rapidly toward the methyl terminus, just as observed with model membranes composed of dipalmitoylphosphatidylcholine (DPPC) above their phase transition temperature.[4–9] Using the fully deuterated palmitic acid probe, it was also shown that the effect of cholesterol on the liquid crystalline membrane lipids is to increase orientational order, particularly in the plateau region.

The spectrum of membranes enriched with 2,2-dideuteropalmitate differed from all other probes tested in revealing an unusual lineshape which appeared to consist of three overlapping powder doublets, whereas all other positions produced single doublet signals. These authors suggested that these multiple signals, which are also observed in C-2-labeled synthetic phospholipid liquid crystalline bilayers systems, could be due to differences in the initial conformation of the two acyl chains, to differences in the polar lipid headgroups, or to the presence of membrane protein. This first suggestion has since been confirmed by ^{2}H NMR and by X-ray and neutron diffraction studies of model membranes, which have revealed that the fatty acyl chain at the 1-position of the glycerol backbone projects directly downward toward the bilayer core, while the chain esterified at position 2 begins nearly parallel to the bilayer plane before binding to become perpendicular to the bilayer plane at the C-2 position of the hydrocarbon chain.[6–8] Three signals are observed because the C-2 chain may exist in one of two forms within the generally preferred conformation, the orientational orders of these two forms being significantly different. Subsequent studies by Rance et al. demonstrated that the conformations of the membrane lipids in the region of the C-2 position are qualitatively similar for all the various lipid classes and that the presence of membrane protein has little if any effect on these conformations.[13]

The properties of the gel and liquid crystalline lipid domains of the *A. laidlawii* membrane were subsequently studied in more detail by Smith et al.[14] Membranes enriched with 13,13-dideuteropalmitic acid at 45 °C, just above the calorimetrically determined upper phase transition boundary, exhibit an almost perfect powder pattern, characteristic of fluid lipid bilayers with only a single quadrupole splitting, just as in the case of the total membrane lipids dispersed in water. Thus the presence of the membrane protein does not perturb the average orientational order of the lipid hydrocarbon chains and the lipid molecules must be exchanging rapidly on the NMR timescale between the bulk and protein boundary lipid domains. These results contrast with those obtained by electron spin resonance (ESR) spectroscopy using nitroxide fatty acid probes, where the presence of membrane protein appears to immobilize and disorder the lipid hydrocarbon chains and where the exchange between bulk and boundary lipid domains is slow on the ESR timescale.[15] Within the calorimetrically determined phase transition boundaries, separate gel and liquid crystalline spectral components coexist, indicating that the lipids of these domains are in slow exchange ($<10^5$ times s^{-1}). At the lower boundary of the phase transition, the gel state spectrum indicates a distribution of order parameters, the average being about one-half of the theoretical maximum for totally immobilized chains in the all-*trans* extended conformation. As the temperature is lowered still further, the observed quadrupole splitting eventually approaches its theoretical maximum, but only at temperatures well below the phase transition lower boundary. These authors suggested that the membrane lipid hydrocarbon chains exist in the all-*trans* extended conformation as they enter the gel state but continue to undergo rapid rotational motion about their long axes, this rotational motion being slowly decreased with further decreases in temperature. This interpretation has been challenged by Pink and Zuckerman, who have presented theoretical and reviewed experimental data indicating that transitions between different chain rotational conformational states, through the formation of *gauche* bonds, do occur in gel-state lipids, although on a rapid timescale compared with the ^{2}H NMR timescale.[16] However, the early Raman spectroscopic studies of model membranes on which this argument is based, and which indicate substantial numbers of *gauche* conformers in the gel, are not correct, and recent Fourier transform infrared spectroscopic studies indicate that few if any *gauche* conformers are present below the phase transition temperature.[17,18] Thus the original ^{2}H NMR interpretations appear to be correct.

Generally similar results were reported for a ^{2}H NMR study of *A. laidlawii* membranes highly enriched ($\geq$90 mol%) in myristic acid by Jarrell et al., except that the length of the plateau region of the order parameter profile appeared to be shortened somewhat compared with membranes enriched in palmitic acid.[19] In addition, although the average order parameters of liquid crystalline hydrocarbon chains were the same in intact membranes as in an aqueous dispersion of membrane lipids, an increase in *linewidth* of about 20% was detected in the membrane, indicating that the presence of membrane proteins increases the heterogeneity of order distribution without affecting its average value. Furthermore, in the gel state a small fraction of lipid hydrocarbon chains in the membrane (but not in the lipid–water dispersion) remain disordered near their methyl terminal region, even at very low temperatures, indicating a small membrane-protein disordering effect. Finally, the gel state of membranes highly enriched in myristic acid was found to be more highly ordered than previously observed for membranes less highly enriched in myristic acid, suggesting that fatty acid heterogeneity may affect lipid gel state organization more than the presence of protein.

Rance et al. have also investigated the orientational order of *A. laidlawii* membranes enriched in unsaturated instead of saturated fatty acids, utilizing biosynthetically incorporated, specifically deuterated, oleic acid.[20] The orientational order of the oleoyl chain was determined at a variety of temperatures from −50 to +41 °C. Above 10–15 °C, a single, sharp quadrupolar powder pattern was observed for all C^2H_2 segments except the C-9 and C-10 positions (and of course the C-2 segment). The C-9–C-10 spectra appear to consist of two overlapping powder patterns of equal integrated

intensity, indicating motional inequivalence of the C-9 and C-10 deuterons. This could only occur if the *cis*-double bond is not parallel to the bilayer normal, but instead it is slightly tilted. Below 10−15 °C, a second, broader spectral component, due to gel-phase lipid, begins to appear and grow at the expense of the liquid crystal component as the temperature is reduced. These spectra indicate that the center of the solid−fluid phase transition is about −12 °C, in good agreement with differential scanning calorimetry (DSC) studies. As noted in previous ^{2}H NMR studies, some relatively rapid hydrocarbon chain rotation, at least in the terminal half of the chain, persists down to −30 to −35 °C, well below the lower boundary of the calorimetrically detectable phase transition, and this was again ascribed to a disordering effect of the membrane protein.

A plot of orientation order parameter versus oleoyl chain position revealed a profile parameter somewhat different from that previously observed with palmitate-enriched *A. laidlawii* membranes. Instead of a plateau region extending from C-2 to C-10, the oleate-enriched membranes exhibit a shortened plateau region extending only to about C-7, followed by a 'dip' in the profile with a local minimum at C-10, after which the order parameters again increase before falling off toward the methyl terminus of the oleoyl chain. Although this profile would appear to indicate a markedly decreased order in the center of the oleoyl chain compared with palmitate, in fact this behavior is due largely to the geometry of the double bond and its tilted alignment with respect to the bilayer normal. Actually, the fluctuations about the average orientation of this segment of the oleoyl chain appear to be rather similar to the corresponding region of the palmitoyl chain if compared at the same reduced temperature (i.e., at the same temperature relative to the phase transition temperature). The major effect of the presence of the double bond then seems to be to cause a local organizational perturbation in its immediate vicinity, which, although not profound, is sufficiently strong to cause the formation of predominantly fluid rather than predominantly gel-state lipid at physiological temperatures.[20]

The temperature dependence of the order parameters of the various C^2H_2 segments of the oleoyl chains was also determined in the study summarized above. The temperature dependence in the liquid crystalline state was approximately linear, with order decreasing with increasing temperature. In absolute terms, the change in order parameter with temperature was greatest in the plateau region (here C-2−C-6 or C-7) and smallest at the methyl end of the hydrocarbon chain. The opposite was true, however, if the change in order parameter with temperature was expressed as a percentage change in the quadrupolar splittings observed. Similar findings were also made for *A. laidlawii* membranes highly enriched in fully perdeuterated palmitic acid.[21]

Monck et al. have recently employed ^{2}H NMR spectroscopy to determine the orientational order parameter profiles of *A. laidlawii* membranes containing equimolar amounts of perdeuterated palmitic acid and an unsaturated fatty acid.[22] These workers showed that at the optimal growth temperature of this organism of 37 °C, the chain-averaged order parameter values decreased in the order perdeuterated palmitic acid plus elaidic > oleic > linoleic acid, as expected from the increasing potency of a single *trans*, a single *cis*, or two *cis*-double bonds in lowering the phase transition temperature of the *A. laidlawii* membrane lipids. The chain-averaged order parameter value also decreases as the perdeuterated palmitic acid/oleic acid ratio of the membrane lipids decreases. Again, order parameter profiles are essentially identical in intact membranes and in bilayers prepared from the total membrane lipids, demonstrating the absence of an effect of membrane proteins on average hydrocarbon chain orientational order. It was found that only a certain range of membrane lipid hydrocarbon chain orientational order is compatible with optimal membrane function and cell growth.

Jarrell et al. studied the orientational order and dynamics of *A. laidlawii* membranes enriched with a cyclopropyl-containing fatty acid by ^{2}H NMR.[23] Specifically, dihydrosterculic acid (*cis*-9,10-methyleneoctadecanoic acid), specifically deuterated at several positions along the chain, was biosynthetically incorporated into the membrane lipids of this organism. The transition from the gel to the liquid crystalline phase was determined to occur from −15 to 0 °C, a range somewhat narrower than, but with a midpoint similar to, that found for membranes enriched with oleic acid. The acyl chains of dihydrosterculic acid-containing membranes are less mobile in the gel and in the liquid crystalline state than those of oleic acid-containing membranes. Above 0 °C, the lipids are in the liquid crystalline phase and give rise to powder spectra characteristic of axially symmetric motion. The overall ordering is greater everywhere than that of oleoyl chains and features a maximum at the cyclopropyl moiety, in contrast to the plateau found with saturated chains. Detailed analysis of the data for the cyclopropane ring indicates that the C-9−C-10 bond is inclined at 89° relative to the director of motional averaging, in sharp contrast to the 3° estimated for oleic acid in the same membranes. These authors suggest that the replacement of a *cis*-double bond by a *cis*-cyclopropane ring in the lipid fatty acyl chains of eubacterial membranes gives rise to a less fluid lipid bilayer with generally similar but not identical physical properties.

It should be noted that in all of the ^{2}H NMR studies reviewed thus far, the *A. laidlawii* membranes highly enriched in palmitic acid residues behave in all respects quite similarly to DPPC model membranes, whereas the *A. laidlawii* membranes enriched in palmitate and oleate are very similar in behavior to bilayers of 1-palmitoyl-2-oleoylphosphatidylcholine. This finding supports the suitability of simple phospholipid bilayer membranes as reasonable models for more complex biological membranes, at least as far as hydrocarbon chain orientation and dynamics are concerned. Moreover, Kang et al. showed that the ^{2}H NMR spectra of freshly isolated or lyophilized membranes (enriched with specifically deuterated myristic or palmitic acids) and aqueous dispersions of the total membrane lipids are identical.[24] Together, these findings emphasize that the presence of membrane proteins has only a small effect on the average organization of membrane lipid fatty acyl chains, at least on the NMR timescale.

2.2 Effect of Lipid Bilayer Cholesterol Content

The effect of the presence of cholesterol on the orientational order of palmitate-enriched, oleate-enriched, and dihydrosterculate-enriched *A. laidlawii* membranes has been studied in some detail by Rance et al., Davis et al., and Jarrell et al., respectively.[20,21,23] In fully perdeuterated palmitate-containing membranes, the incorporation of relatively large amounts of cholesterol (39 mol%) essentially

abolishes a discreet gel-to-liquid-crystalline phase transition, as detected by both ^{2}H NMR and DSC. Between 20 and 45 °C, the normal boundaries of the lipid phase transition in palmitate-enriched membranes not containing cholesterol, the cholesterol-enriched membranes exhibit an order parameter profile qualitatively similar to that normally observed for the liquid crystalline phase in the absence of cholesterol. However, the cholesterol-containing membranes have a higher average order and an extended plateau region. In absolute terms, the increase in order is greatest in the plateau region and smallest at the methyl end of the chains, although the reverse is true if the increase in order is expressed in percentage terms. Below 20 °C, the ^{2}H NMR spectra of cholesterol-enriched membranes are multicomponent, suggestive of complex motional and/or phase behavior. In oleate-enriched and dihydrosterculate-enriched *A. laidlawii* membranes, the order parameters of the various segments of the oleoyl or dihydrosterculoyl chain increase more or less linearly with cholesterol concentration from 0 to 27 mol%. The effect of cholesterol on the liquid crystalline order parameter profile is quite similar to that just described for palmitate-enriched membranes. Interestingly, the temperature dependence of the ^{2}H NMR spectra, and the NMR-determined phase transition position and width characteristic of oleic acid-enriched and dihydrosterculic acid-enriched membranes lacking cholesterol, are very little affected by the presence of up to 27 mol% cholesterol. This is in contrast with the ^{2}H NMR and calorimetrically reported behavior of palmitate-enriched membranes, and with the behavior of cholesterol in DPPC model membranes as determined by DSC and other techniques, where similar amounts of cholesterol significantly broaden the gel-to-liquid-crystalline phase transition and may also alter the phase transition midpoint temperature.[26]

Huang et al. recently employed ^{2}H NMR spectroscopy to study the effect of cholesterol and lanosterol on the orientational order and dynamics of the lipid hydrocarbon chains of another mycoplasma, the *Mycoplasma capricolum* membrane.[27] As reported previously for *A. laidlawii*, the incorporation of increasing quantities of cholesterol increases the order of the lipid hydrocarbon chain at the optimal growth temperature of 37 °C and abolishes the formation of gel-state lipid at lower temperatures. As well, the presence of high levels of cholesterol abolishes the temperature dependence of the spin lattice (T_1) and the transverse (T_{2e}) relaxation times. In contrast, the incorporation of comparable amounts of lanosterol is much less effective in this regard. The average order and T_1 values of the hydrocarbon chains in isolated membranes and total membrane-lipid dispersions are comparable at a given temperature and cholesterol level, indicating that the presence of membrane protein has little effect on the average orientation or on the rates of the fast motions of the lipid hydrocarbon chains. In contrast, the T_{2e} values of the isolated membranes are much smaller than those of the total membrane-lipid dispersions, indicating that the presence of membrane proteins introduces a slow motion of the various phospholipid molecules which is not present in their absence. Markedly reduced T_{2e} values are also observed upon the addition of integral transmembrane proteins to model lipid bilayer membranes.[8] The growth rates of *M. capricolum* cells are positively correlated with the relatively more ordered and less dynamic state of the membrane-lipid hydrocarbon chains induced by the incorporation of increasing quantities of cholesterol.

Monck et al. have recently presented DSC and ^{2}H NMR spectroscopic evidence for the existence of two pools of cholesterol in the *A. laidlawii* membrane.[28] Membranes from cells grown in the presence of large amounts of exogenous cholesterol contain as much as 40 mol% cholesterol according to chemical determinations. However, the ^{2}H NMR-determined order parameter profiles and the DSC-determined thermotropic phase behavior indicate that cholesterol is present at significantly lower levels (10–15 mol%) *in the lipid bilayer* of this membrane. A further incorporation of cholesterol into the *A. laidlawii* membrane lipid bilayer was found to occur when cells or isolated membranes were exposed to high temperature. Deuterium NMR spectra of membrane preparations containing deuterium-labeled cholesterol indicate that most of the cholesterol present in the nonbilayer pool exists in a solid form. However, the exact nature and location of this second pool of membrane-associated cholesterol remains to be determined.

2.3 Effect of Lipid Polar Headgroup Structure

Eriksson et al. recently studied the hydrocarbon chain orientational order and dynamics of the major glucoglycerolipids of the *A. laidlawii* A membrane using ^{2}H NMR spectroscopy and biosynthetically incorporated perdeuterated palmitic acid.[29] The hydrocarbon chains of monoglucosyl diacylglycerol (MGDG) in lipid–water dispersions were found to exhibit a higher degree of orientational order than those of the diglucosyl diacylglycerol (DGDG) but the MGDG chains appeared to undergo a larger amplitude of slow reorientational motion than the DGDG chains, due perhaps to an increased rate of bilayer fluctuation or lateral diffusion over a curved bilayer surface. Interestingly, similar results have been reported for aqueous dispersions of synthetic phosphatidylethanolamines (PEs) and phosphatidylcholines (PCs), with the former exhibiting the larger degree of hydrocarbon chain order and slow-motion fluctuation. Since both MGDG and PEs are membrane lipids with relatively small, poorly hydrated, but strongly interacting, polar headgroups, that tend to form nonlamellar phases at higher temperatures, these authors suggest the relatively high orientational order of the MGDG hydrocarbon chains and their greater amplitude of collective motions may be related to the tendency of this lipid to induce curvature and instability into the liquid crystalline bilayer phase, due to its inverted cone shape. However, Monck et al. showed that phosphatidylglycerol, which is a bilayer-forming lipid, has a comparable order parameter profile to MGDG of similar fatty acid composition, suggesting that lipid shape may not be the only relevant variable.[22] Wieslander et al. had previously used ^{2}H NMR (and ^{1}H NMR) spectroscopy to show that MGDG (or mixtures of MGDG and DGDG), isolated from *A. laidlawii* membranes enriched in oleic acid, can form reversed cubic as well as reversed hexagonal phases when dispersed in water.[30]

3 ^{19}F NMR SPECTROSCOPY OF MEMBRANE LIPIDS

The technique of ^{19}F NMR spectroscopy has recently been applied to the *A. laidlawii* membranes by McDonough

et al.[31] and Macdonald et al.[32] In these studies small amounts of palmitic acid probes containing a single fluorine atom at various positions along the hydrocarbon chain were biosynthetically incorporated into the membrane lipids. The much greater sensitivity of the ^{19}F compared with the ^{2}H nucleus in the NMR experiment allows usable information to be collected with only small incorporations of probe (5–10 mol%), thus allowing the study of membranes that are very highly enriched in a variety of other exogenous fatty acids. This technique also avoids the laborious and expensive synthesis of a complete series of specifically deuterated fatty acids for each exogenous fatty acid to be studied, which had been necessary in previous ^{2}H NMR studies. Other potential advantages include the ability to determine order parameters in the gel state and to study the rates of motion of various segments of the hydrocarbon chains via relaxation measurements. Physical, biochemical, and biological evidence was presented that the biosynthetic incorporation of this monofluoropalmitic acid does not greatly perturb the structure or function of the *A. laidlawii* membrane.

The orientational order parameter profiles of *A. laidlawii* membranes highly enriched in pentadecanoic, methyl isopalmitic, methyl anteisopalmitic and palmitelaidic acids were studied by ^{19}F NMR as a function of temperature in the liquid crystalline state.[32] In this series of fatty acids, which have nearly the same effective chain lengths, the effect of the presence of a methyl group substitution or of a *trans*-double bond on chain order could be determined. At all temperatures the *n*-saturated and methyl-branched fatty acid-enriched membranes exhibit the typical plateau profile already described for palmitic acid-containing membranes, whereas the palmitelaidic acid-enriched membranes show a progressive decrease in order on going from near to the carbonyl function toward the methyl terminus, without a clear-cut plateau region. At the growth temperature of 37 °C the chain-average order parameter values decrease in the order pentadecanoic > isopalmitic > anteisopalmitic > palmitelaidic acid-enriched membranes, which is also the order of decreasing phase transition temperatures as determined by DSC. Thus, at a constant absolute temperature (37 °C), the introduction of a methyl isobranch, a methyl anteisobranch or of a *trans*-double bond into an *n*-saturated fatty acyl chain results in progressively more disorder of the liquid crystalline bilayer hydrocarbon core. Interestingly, however, if the chain-average order parameters are compared at comparable reduced temperatures (i.e., at similar temperatures relative to their phase transition temperatures), then the results are exactly opposite to those obtained at 37 °C.

Experimental and theoretical results indicate that the rotation of the membrane lipid hydrocarbon chains in the gel state remains sufficiently rapid to allow for complete motional averaging and thus axially symmetric spectra on the ^{19}F NMR but not the ^{2}H NMR timescale.[33] This permits a detailed determination of the orientational order of the C–F bond in fluoropalmitic acid-labeled gel-state lipid in model and biological membranes, which is not possible with ^{2}H NMR. Macdonald et al. thus determined the orientational order parameter profiles of *A. laidlawii* membranes highly enriched in a number of linear, saturated, methyl iso- and anteiso-branched, and *cis*- and *trans*-monounsaturated and cyclopropyl fatty acids.[34–38] The effect of the position of the *cis*- or *trans*-double bond within the membrane lipid hydrocarbon chain on gel-state order was determined as well.[35,36] These workers found that at temperatures below the phase transition temperature, all types of hydrocarbon chains are relatively highly ordered, but that there are much larger differences between the chain-average order of different classes of fatty acids in the gel and in the liquid crystalline state. At comparable reduced temperatures in the gel state, order parameter values decrease in the order pentadecanoic > isopalmitic > palmitelaidic > anteisopalmitic > palmitoleic acid. This decreasing sequence of orientational order correlates well with the decreasing phase transition temperatures of the membrane lipids determined by DSC. Thus, membrane lipids whose hydrocarbon chains can pack in the most highly ordered array exhibit the most stable, highest-melting gel states. However, the membrane lipids with the highest phase transition temperatures form the least ordered liquid crystalline states once melting occurs. This is probably because at the higher temperatures necessary to induce melting of the more stable gel phases, the increased thermal energy possessed by the fluid hydrocarbon chains produces higher rates of motion and lower orientational order than is the case for membranes having lower phase transition temperatures. Although the detailed chemical structure of the fatty acyl group also has an effect on chain order, the lipid phase transition is the prime determinant of this parameter. For a more detailed summary of ^{19}F NMR studies of the relationship between fatty acyl chain structure, orientational order, and lipid phase state in *A. laidlawii* membranes, the reader is referred to reviews by Macdonald et al.[34,39]

Macdonald et al. also compared the orientational order parameter profiles and the chain average order values for intact *A. laidlawii cells*, isolated membranes, and total membrane-lipid dispersions having the same lipid polar headgroup and fatty acid compositions.[32] They found that all three systems behave identically within the experimental error of their determinations. Thus the presence of cytoplasmic or membrane protein does not appear significantly to perturb membrane-lipid hydrocarbon chain organization in either the gel or the liquid crystalline states, a result in agreement with the ^{2}H NMR studies reviewed earlier.

4 RELATED ARTICLES

Bilayer Membranes: Deuterium and Carbon-13 NMR; Bilayer Membranes: Proton and Fluorine-19 NMR; Glycolipids; Lipid Polymorphism; Membranes: Carbon-13 NMR; Membranes: Deuterium NMR; Membranes: Phosphorus-31 NMR; Molecular Motions: T_1 Frequency Dispersion in Biological Systems; Sonicated Membrane Vesicles.

5 REFERENCES

1. R. N. McElhaney, *Biochim. Biophys. Acta*, 1984, **779**, 1.
2. R. N. McElhaney, *Crit. Rev. Microbiol.*, 1989, **17**, 1.
3. R. N. McElhaney, in *Subcellular Biochemistry*, ed. S. Rottem and I. Kahane, Plenum, New York, 1993, Vol. 20, Chap. 3
4. J. Seelig, *Q. Rev. Biophys.*, 1977, **10**, 353.
5. J. Seelig and A. Seelig, *Q. Rev. Biophys.*, 1980, **13**, 19.
6. J. A. Davis, *Biochim. Biophys. Acta*, 1983, **737**, 117.
7. I. C. P. Smith, and H. C. Jarrell, *Acc. Chem. Res.*, 1983, **16**, 266.

8. M. Bloom and I. C. P. Smith, in *Progress in Protein–Lipid Interaction*, eds. A. Watts and J. J. H. H. M. dePont, Elsevier, Amsterdam, 1985, Vol. 1, Chap. 2
9. J. Seelig and P. M. Macdonald, *Acc. Chem. Res.*, 1987, **20**, 221.
10. E. Oldfield, D. Chapman, and W. Derbyshire, *Chem. Phys. Lipids*, 1972, **9**, 69.
11. G. W. Stockton, K. G. Johnson, K. W. Butler, C. F. Polnaszek, R. Cyr, and I. C. P. Smith, *Biochim. Biophys. Acta*, 1975, **401**, 535.
12. G. W. Stockton, K. G. Johnson, K. W. Butler, A. P. Tulloch, Y. Boulanger, I. C. P. Smith, J. H. Davis, and M. Bloom, *Nature (London)*, 1977, **269**, 267.
13. M. Rance, I. C. P. Smith, and H. C. Jarrell, *Chem. Phys. Lipids*, 1983, **32**, 57.
14. I. C. P. Smith, K. W. Butler, A. P. Tulloch, J. H. Davis, and M. Bloom, *FEBS Lett.*, 1979, **100**, 57.
15. D. Marsh, in *Progress in Protein–Lipid Interactions*, eds. A. Watts and J. J. H. H. M. dePont, Elsevier, Amsterdam, 1985, Vol. 1, Chap. 4
16. D. A. Pink and M. J. Zuckerman, *FEBS Lett.*, 1980, **109**, 5.
17. R. Mendelsohn, M. A. Davies, J. W. Brauner, H. F. Schuster, and R. A. Dluhy, *Biochemistry*, 1989, **28**, 8934.
18. H. L. Casal and R. N. McElhaney, *Biochemistry*, 1990, **29**, 5423.
19. H. C. Jarrell, K. W. Butler, A. Byrd, R. Deslauriers, I. Ekiel, and I. C. P. Smith, *Biochim. Biophys. Acta*, 1984, **688**, 622.
20. M. Rance, K. R., Jeffrey, A. P. Tulloch, K. W. Butler, and I. C. P. Smith, *Biochim. Biophys. Acta*, 1980, **600**, 245.
21. J. H. Davis, M. Bloom, K. W. Butler, and I. C. P. Smith, *Biochim. Biophys. Acta*, 1980, **597**, 477.
22. M. A. Monck, M. Bloom, M. Lafleur, R. N. A. H. Lewis, R. N. McElhaney, and P. R. Cullis, *Biochemistry*, 1992, **31**, 10037.
23. H. C. Jarrell, A. P. Tulloch, and I. C. P. Smith, *Biochemistry*, 1983, **22**, 5611.
24. S.-Y. Kang, R. A. Kinsey, S. Rajan, H. S. Gutowsky, M. G. Gabridge, and E. Oldfield, *J. Biol. Chem.*, 1981, **256**, 1155.
25. M. Rance, K. R. Jeffrey, A. P. Tulloch, K. W. Butler, and I. C. P. Smith, *Biochim. Biophys. Acta*, 1982, **688**, 191.
26. R. N. McElhaney, *Chem. Phys. Lipids*, 1982, **30**, 229.
27. T. Huang, A. J. DeSiervo, and Q.-X. Yang, *Biophys. J.*, 1991, **59**, 691.
28. M. A. Monck, M. Bloom, M. Lafleur, R. N. A. H. Lewis, R. N. McElhaney, and P. R. Cullis, *Biochemistry*, 1993, **32**, 3081.
29. P.-O. Eriksson, L. Rilfors, A. Wieslander, A. Lundberg, and G. Lindblom, *Biochemistry*, 1991, **30**, 4916.
30. A. Wieslander, L. Rilfors, L. B.-A. Johansson, and G. Lindblom, *Biochemistry*, 1981, **20**, 730.
31. B. McDonough, P. M. Macdonald, B. D. Sykes, and R. N. McElhaney, *Biochemistry*, 1983, **22**, 5097.
32. P. M. Macdonald, B. McDonough, B. D. Sykes, and R. N. McElhaney, *Biochemistry*, 1983, **22**, 5103.
33. P. M. Macdonald, B. D. Sykes, and R. N. McElhaney, *Biochemistry*, 1984, **23**, 4496.
34. P. M. Macdonald, B. D. Sykes, and R. N. McElhaney, *Isr. J. Med. Sci.*, 1984, **20**, 803.
35. P. M. Macdonald, B. D. Sykes, R. N. McElhaney, and F. D. Gunstone, *Biochemistry*, 1985, **24**, 177.
36. P. M. Macdonald, B. D. Sykes, and R. N. McElhaney, *Biochemistry*, 1985, **24**, 2237.
37. P. M. Macdonald, B. D. Sykes, and R. N. McElhaney, *Biochemistry*, 1985, **24**, 2412.
38. P. M. Macdonald, B. D. Sykes, and R. N. McElhaney, *Biochemistry*, 1985, **24**, 4651.
39. P. M. Macdonald, B. D. Sykes, and R. N. McElhaney, *Can. J. Biochem. Cell Biol.*, 1984, **62**, 1134.

Biographical Sketches

Ronald N. McElhaney. *b* 1942. B.S., 1964, Washington and Jefferson College; Ph.D., 1969, University of Connecticut; postdoctoral fellowship, State University of Utrecht, The Netherlands (Prof. Dr. L. L. M. van Deenen), 1969. Faculty, Department of Biochemistry, University of Alberta, 1970–present. Approx. 150 publications. Research interests include the structure and function of biological membranes, especially the *Acholeplasma laidlawii* membrane, lipid thermotropic phase behavior, lipid organization and dynamics in lamellar and nonlamellar phases, and lipid/cholesterol and lipid/protein interactions.

Ruthven N. A. H. Lewis. *b* 1949. B.S., 1975, Ph.D., 1978, Durham University (UK); MRC postdoctoral fellow (Dr. R. N. McElhaney), 1979–1982. Research Associate, Department of Biochemistry, University of Alberta, 1982–present. Approx. 60 publications. Research interests include the structure and function of biological membranes, especially the *Acholeplasma laidlawii* membrane, lipid thermotropic phase behavior, lipid organization and dynamics in lamellar and nonlamellar phases, and lipid/cholesterol and lipid/protein interactions.

Membrane Proteins

Stanley J. Opella and Francesca M. Marassi
University of Pennsylvania, Philadelphia, PA, USA

1	Introduction	1
2	Early NMR Studies of Membranes	1
3	Applications to Membrane Proteins in Micelles	2
4	Solid state NMR Spectroscopy of Membrane Proteins in Lipid Bilayers	3
5	NMR Studies of the Membrane Bound Form of Filamentous Bacteriophage Coat Protein	6
6	Prospects for NMR Studies of Membrane Proteins	8
7	Related Articles	8
8	References	8

1 INTRODUCTION

Membrane proteins are responsible for many important biological functions, including some that are unique, such as those of receptors and ion channels, as well as some that overlap with those of soluble proteins, such as enzymes. Even though more than half of all proteins are associated with membranes, and there are many additional reasons to be interested in their structural biology, only a few high-resolution structural studies of membrane proteins have been reported.[1–4] This is largely because samples of membrane proteins are problematic for the most commonly used methods of structural biology. Proteins complexed with lipids are difficult to crystallize in forms suitable for X-ray diffraction and conventional multidimensional solution NMR methods are hampered by their slow overall reorientation rates. However, in spite of its limitations, NMR spectroscopy has played an important role in the characterization of membrane proteins and, more importantly, it has the potential to play a dominant role in future studies. The development of high-resolution solid state NMR methods gives NMR spectroscopy sufficient versatility to determine the structures and describe the dynamics of proteins in bilayer samples. Further development of the instrumentation and methods for multidimensional solution NMR spectroscopy will also improve its effectiveness in studies of membrane proteins in micelle samples.

The key to NMR studies of membrane proteins is sample preparation.[5] Figure 1 illustrates the molecular arrangements in phospholipid bilayers and detergent micelles, the two well-characterized model membrane systems used in a wide variety of biophysical investigations including NMR spectroscopy. Each micelle, of detergents most commonly used in NMR studies, contains approximately 50–60 single chain lipid molecules and a single polypeptide. In contrast, lipid bilayers are very large supramolecular structures with many phospholipid and polypeptide molecules in extended two-dimensional arrays. Proteins in micelles reorient relatively slowly, although rapidly enough to be suitable for most heteronuclear multidimensional solution NMR experiments in high-field spectrometers, while those in bilayers are immobile on the relevant

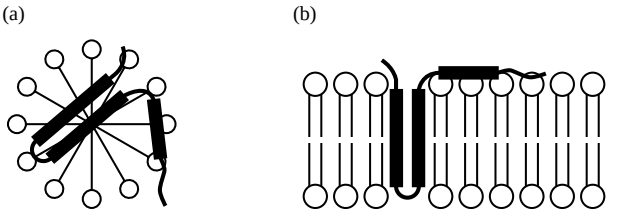

Figure 1 Schematic drawings of a protein in membrane environments: (a) detergent micelle; (b) phospholipid bilayer

NMR timescales, enabling them to be treated spectroscopically as solids. Therefore, the most important advantage of utilizing these two different types of model membrane is that they permit the use of both high-resolution solid state NMR and multidimensional solution NMR methods with membrane proteins. The results from these two essentially independent spectroscopic approaches can be combined to describe structural features of membrane proteins that are otherwise inaccessible to any single method of structure determination. Solid state NMR spectroscopy of oriented and unoriented bilayer samples and multidimensional solution NMR spectroscopy of micelle samples are most effective when the proteins are suitably labeled with stable isotopes and the samples are carefully prepared. The dynamics of backbone and side-chain sites can be described over a wide range of timescales through the analysis of nuclear spin relaxation in both micelle and bilayer samples, and motionally averaged powder pattern lineshapes in bilayer samples.[6] Local protein motions have a dramatic effect on many spectral parameters; therefore mobile residues in loop and terminal segments can be readily identified in both types of sample.[7,8]

2 EARLY NMR STUDIES OF MEMBRANES

NMR spectroscopy was applied to proteins within a decade of its initial demonstration. The first NMR spectrum of a protein reported in 1957 was that of a small globular protein, ribonuclease, in aqueous solution.[9] This spectrum, despite its low sensitivity and limited resolution, encouraged additional development by demonstrating the basic feasibility of NMR spectroscopy for the study of proteins in aqueous solution. However, the development and application of NMR spectroscopy has been conspicuously focused on soluble proteins that do not aggregate and reorient rapidly in solution. Technical advances, especially high-field magnets and small, fast computers, and methodological advances, especially multidimensional experiments utilizing pulsed irradiation at several rf frequencies, led to the development and implementation of approaches to structure determination of globular proteins in solution by the mid-1980s.[10,11]

The immediate application of NMR to the study of membrane proteins was precluded by the difficulty of identifying resonances that could be attributed to the relatively small amounts of protein in spectra dominated by resonances from the highly abundant lipids and by the broad lines and hence, poor sensitivity and resolution obtained from proteins bound to native membranes, or multilamellar liposomes or sonicated vesicles in reconstituted systems. For these reasons the majority of the early NMR studies of membrane systems was

devoted to dynamics and organization of the lipids in bilayers, and to some extent the influence of proteins and peptides on the properties of the lipids. Nevertheless, the results of NMR experiments, especially in combination with those from contemporary ESR experiments, strongly influenced the understanding of biological membranes as dynamic entities. The NMR studies gave a picture of protein–lipid interaction where the proteins generally have a disordering effect on the membrane lipids; there is little evidence of selectivity in the interaction between proteins and lipids, with the exception of some charged species; and there is a fast exchange between protein-associated and bulk lipid, on the NMR timescale. There are a number of thorough review articles on these subjects.[12,13]

A substantial amount of the early research on membranes was devoted to conformational studies of small membrane active polypeptide antibiotics and their interactions with phospholipids. Certain such peptides are known to induce cation permeation across cells and artificial membranes, and to form lipid soluble complexes. Early NMR studies of peptides such as alamethicin and gramicidin[14,15] set the stage for later detailed investigations of peptide ion channels and their interaction with membranes.

The initial studies of native and reconstituted membranes demonstrated that high-resolution NMR spectra suitable for detailed structural analysis of membrane proteins could not be readily obtained.[16] Sonicated vesicle samples have the advantage of being bilayers, albeit highly curved, and sealed chambers suitable for transport studies. Although spectra obtained from lipids in sonicated vesicles are considerably narrower than those in multilamellar bilayers, the overall correlation time (approximately 10^{-6} s) of the vesicles is extremely inconvenient. This means that any resonances from protein, or other molecular constituents immobilized within the vesicle are very broad because of efficient relaxation.[17] These resonances do not respond to solid state NMR procedures because their breadth is due to relaxation rather than powder pattern characteristics. Therefore there have been very few ^{1}H or ^{13}C NMR studies of proteins in vesicles. However, some results have been obtained with ^{19}F-labeled proteins, since the number of resonances is greatly reduced and there is no interference from lipid resonances. For example, the motional properties of the M13 major coat protein, fluorinated at its two tyrosyl residues, have been examined in this manner.[18,19] The filamentous bacteriophage coat proteins have turned out to be very valuable model systems for many types of NMR study of membrane proteins.

In 1968, Kamat and Chapman[20] showed that the resolution and sensitivity of ^{1}H NMR spectra could be substantially improved by solubilizing native membranes in lysolipid or detergent micelles. Around 1979, the first high-resolution NMR studies of membrane associated peptides in small perdeuterated micelles were reported.[21,22] The relatively well-resolved spectra, and the observation of homonuclear NOEs in well-behaved and stable samples set the stage for many fruitful multidimensional solution NMR studies of membrane associated peptides and proteins.

3 APPLICATIONS TO MEMBRANE PROTEINS IN MICELLES

Multidimensional solution NMR methods can be applied to peptides and proteins in micelles because the reorientation of the protein–micelle complex in solution is rapid enough to average the spectral parameters from the various nuclear spin interactions to their isotropic values. This enables the indirect effects of their fluctuations, as monitored by relaxation phenomena, to describe local dynamics as well as provide spatial information in the form of relative proximities. However, the methods of solution NMR spectroscopy are somewhat limited, at least compared with what can be done with well-behaved globular proteins in solution, by the broad linewidths and efficient spin diffusion that accompany the relatively slow reorientation of protein–micelle complexes in solution. These limitations can be minimized with careful sample preparation, especially through specific, selective, and uniform isotopic labeling of the protein, and through careful preparation of the micelles by ensuring sufficient detergent and salt concentrations to form uniform, small micelles.[23] Some membrane proteins are soluble in organic solvents or mixed aqueous solvents without lipids, and these preparations have been used in NMR studies. While well-resolved protein resonances can be observed in many cases, there is always considerable concern about the status of the protein in these solvents, especially in the popular trifluoroethanol because of its helix forming propensity. However, as the methods for studying proteins in micelles improve, there is less need to rely on solubilizing membrane proteins in organic solvents.

Protein structure determination by multidimensional NMR spectroscopy is straightforward for relatively small globular proteins in solution, especially when uniformly ^{15}N and ^{13}C labeled samples are available. There are several basic steps in protein structure determination, as widely utilized with globular proteins in aqueous solution, including: the resolution and assignment of backbone and side-chain resonances based on through-bond and through-space interactions observed in multidimensional NMR spectra; the measurement of many homonuclear ^{1}H–^{1}H NOEs among the assigned resonances, supplementing these short range distances with other structural constraints including spin–spin coupling constants; the interpretation of all structural constraints in terms of secondary structure; and the generation of a family of three-dimensional protein structures using distance geometry, molecular dynamics, and other calculations.

Melittin has been studied extensively by NMR spectroscopy after its initial use as an example to show the feasibility of micelle samples.[24,25] This 26-residue peptide disrupts membranes. Solution NMR studies of melittin in detergent micelles show that the amino terminal and carboxyl terminal regions are α-helical and separated by a kink. The NMR data from melittin have been subjected to considerable refinement, and provide a model for other amphipathic helical peptides that interact with membranes. The bombolitins are another class of peptides isolated from the venom of bees, whose functions include the lysis of erythrocytes and liposomes. The structures of bombolitin I and III have been investigated by ^{1}H NMR both in sodium dodecyl sulfate (SDS) micelles and in aqueous solution.[26] In micelles the presence of strong NH(i)–NH(i + 1) NOEs over the full range of the molecules is indicative of helical structures. In water, bombolitin I lacks any observable secondary structure, while bombolitin III adopts a highly helical structure which is believed to arise from extensive peptide aggregation.

Membrane modifying channel-forming peptides of fungal origin, that are rich in hydrophobic amino acids including α-aminoisobutyric acid (Aib), have been the focus of many NMR investigations. Alamethicin is a 20 amino acid peptide known to induce voltage gated conductance in bilayers. This peptide has been studied extensively by solution NMR, both in organic solvents and, more definitively, in SDS micelles.[27] Interproton distances obtained from the NOE data suggest a structure for alamethicin where the amino terminus is predominantly α-helical while the carboxyl terminus is less regular and more flexible.

δ-Hemolysin is another 26 residue peptide that interacts with membranes. NMR studies of the peptide in micelles indicate that it forms an extended helix.[28] Typical of many membrane bound amphipathic helical peptides, δ-hemolysin gives a quite well-resolved one-dimensional ^{1}H NMR spectrum, with some limitations in the two-dimensional spectrum, resulting from the broad resonance linewidths and efficient spin diffusion. The 32 residue polypeptide hormone calcitonin was characterized in SDS micelles and found to have an amphipathic helix running into the amino terminal disulfide bridged loop.[29]

The major functional channels in membranes, such as the nicotinic acetylcholine receptor and cation channels, are large oligomeric proteins. Structural studies of these proteins are limited by their overall size and the difficulty in crystallizing them. A promising approach to their analysis is to synthesize and study peptide sequences corresponding to segments of the proteins. We have studied the peptide M2 selected from the δ subunit of the torpedo acetylcholine receptor, because homology and model studies suggest that this sequence-specific motif is responsible for specific functions in the channel activity of the receptor and the 23 residue M2 δ peptide forms channels by self-association when added to membranes. Solution NMR experiments demonstrate that there is substantial helical secondary structure in the M2 δ peptide in micelles.[30]

Many membrane interactive peptides have antibiotic activities. Cecropin A, a 37 residue peptide found in *Hyalophora cecropia* and other insects, is part of their defense mechanism against bacteria. NMR studies show that this peptide is essentially a random coil in aqueous solution. This peptide has also been studied in hexafluoroisopropyl alcohol solutions by NMR spectroscopy.[31,32] Interproton distance restraints determined by nuclear Overhauser enhancement measurements and distance restraints hydrogen bonds were used as a basis for three-dimensional structure determination by simulated annealing. The resulting converged structures indicate that there are two α-helical regions extending from residues 5–21 and 24–37. Magainins are a family of 21–26 residue peptides that protect frogs from infections, even after severe injury, with a broad spectrum of antibacterial and antifungal activities. These peptides interact strongly with bacterial and model membranes. Their antibiotic activity appears to be associated with the disruption of the electrochemical ionic gradient across cell membranes. Multidimensional solution NMR spectra, as shown in Figure 2, indicate that magainins are unstructured in aqueous solution, but completely α-helical in detergent micelles[33] and trifluoroethanol/water solutions.[34]

Adenosine 5′-triphosphate (ATP) synthase consists of two main components; the water soluble complex F_1, and the membrane-bound complex F_0. The latter, in turn, consists of three subunits (a, b and c), all of which are needed

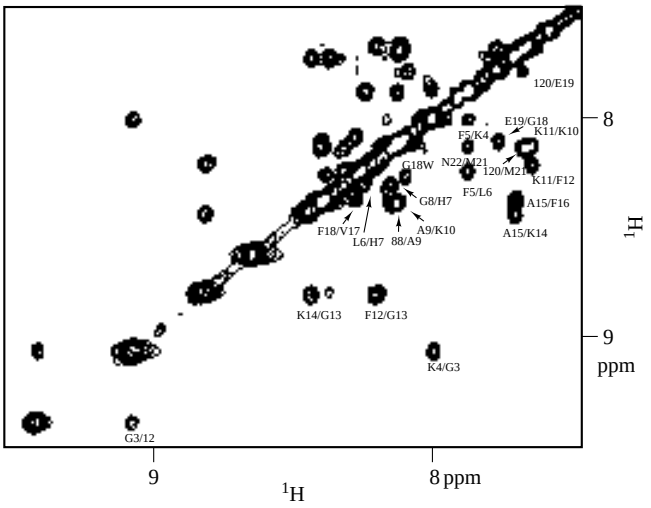

Figure 2 Amide region of two-dimensional ^{1}H/^{1}H NOE spectrum of magainin-2 in micelles

for the maintenance of proton pumping. Subunit c is the smallest (79 amino acids) and most abundant subunit. The structure of subunit c dissolved in mixed organic solvents has been investigated by multidimensional solution NMR spectroscopy. The secondary structure was determined from a combination of homonuclear NOE connectivities, and coupling constant measurements. The protein consists of two long and predominantly helical segments separated by a mobile, unstructured, eight residue stretch. The amino and carboxyl termini are close together, such that the molecule is folded in a hairpin arrangement.[35–37]

Bacteriorhodopsin, the principal component of the outer membrane of *Halobacterium halobium*, where it serves as a light-driven proton pump, is one of the most intensively studied membrane proteins. It consists of 248 amino acids and its structure is dominated by seven transmembrane hydrophobic helices. The protein binds a retinal chromophore to absorb light and translocate protons across the membrane. Solution NMR spectroscopy has been useful in characterizing the structure of bacteriorhodopsin. Fragments corresponding to several of the transmembrane helical sections have been obtained by proteolytic cleavage or peptide synthesis, and have been studied in both organic solvents and detergent micelles. For example, the 34–65 fragment peptide, corresponding to the membrane spanning segment B, was investigated in SDS micelles where it was found to adopt a right-handed helix from residues 41 to 62 with a kink at residue 50, and a disordered amino terminus from residues 34 to 40.[38] The longer 163–231 fragment peptide, corresponding to the transmembrane segments F and G, was also investigated in a similar fashion and found to contain extensive regions of right-handed helix and a flexible amino terminus.[39]

4 SOLID STATE NMR SPECTROSCOPY OF MEMBRANE PROTEINS IN LIPID BILAYERS

Polypeptides that are strongly associated with phospholipids are well suited for solid state NMR spectroscopy,[30,40,41] because their structured regions are essentially completely

immobilized on the timescales defined by the spectral ranges (10^3-10^6 Hz) of the chemical shift, dipolar, and quadrupolar spin-interactions of the nuclei present in proteins. This immobilization preserves the anisotropic characteristics of the nuclear spin interactions averaged out by the rapid isotropic reorientation that occurs in solution, including proteins in micelles. Since it is possible to prepare both oriented and unoriented samples of proteins in fully hydrated phospholipid bilayers, many different parameters can be resolved and measured from single line and powder pattern spectra.

In solid state NMR spectroscopy rf irradiation supplemented by mechanical sample spinning or orientation replace molecular motions as line-narrowing mechanisms. Not only do solid state NMR methods give spectra with high-resolution and sensitivity, they also enable measurements of distance and orientational parameters. There are two complementary methods for protein structure determination by solid state NMR spectroscopy. In one approach, orientational constraints for bonds and chemical groups are derived from spectral parameters observed in samples of peptides and proteins embedded in lipid bilayers oriented between glass plates.[42] In the other approach, unoriented or powder samples examined in the presence of magic angle sample spinning employ procedures to preserve the dipolar couplings so they can be used for distance measurements.[43,44]

Very favorable spectroscopic properties are associated with uniaxially oriented samples where the axis of molecular orientation lies parallel to the direction of the applied magnetic field.[45] Spectra from these samples consist of single line resonances (or multiplets) rather than powder patterns from each isotopically labeled site. Since the observed resonance frequencies (or splittings) are directly related to the orientations of individual atoms or bonds relative to the axis defined by the direction of the applied magnetic field, spectroscopic measurements on oriented samples provide the basis for protein structure determination. The nuclear spin interactions provide spectral parameters that vary as a function of the angle between a bond (or a chemical group) and the direction of the applied magnetic field.

High-resolution structures can be determined with two or more spectroscopic measurements for each structural element, such as a peptide plane or indole ring, since each orientation can be related to a common axis defined by the direction of macroscopic molecular orientation and the applied magnetic field.[46] The orientational constraints together with the established covalent geometry of the molecule are sufficient to define the complete three-dimensional structure. Limited but worthwhile orientational information can be derived from single spectroscopic measurements on oriented samples.[42] Once the secondary structure of a polypeptide segment is established, for example from multidimensional solution NMR experiments on samples in micelles, a single spectral parameter is often sufficient to establish the orientation of a helix relative to the plane of the bilayer, which is especially valuable in studies of membrane proteins where helices are often the dominant secondary structural feature.

The structure of a protein can be determined from the measurement of many short-range distances. Distances can be measured quantitatively between pairs of nuclei with solid state NMR experiments. Magic angle sample spinning enables high resolution spectra to be obtained from unoriented samples; however, since the spinning averages out both the unwanted broadening from the chemical shift anisotropy as well as the dipolar couplings essential for the measurements, it is necessary to cancel out selectively the effects of the spinning on the dipolar interactions. Different experimental approaches are used depending on whether homo- or heteronuclear dipole–dipole couplings are the source of distance information. This application of solid state NMR spectroscopy is rapidly increasing in popularity for structural studies of a variety of biopolymers, including peptides and proteins in lipid bilayers.[47]

It is possible to arrange for heteronuclear dipole–dipole interactions to be present at locations throughout polypeptides by isotopic labeling, enabling distance measurements between specific sites of interest. Rotational echo double-resonance (REDOR) NMR spectroscopy is a general method for measuring internuclear distances between two different nuclei that utilizes rf pulses at the resonance frequency for one of the types of coupled spins to interfere with the averaging of the dipole–dipole interactions.[43] Rotational resonance spectroscopy is also used with magic angle sample spinning to measure weak dipole–dipole couplings,[44] although, unlike REDOR, it is a homonuclear method measuring distances between the same kind of nuclei. The method depends on special effects that occur when the spinning frequency is an integral multiple of the chemical shift difference between the two labeled sites.

Helical peptides are of interest in studies of membrane proteins because they serve as independent structural or functional entities of monomers, oligomers, or domains of larger proteins associated with membranes. Helical peptides, whether hydrophobic or amphipathic, have been found to adopt either transmembrane or in-plane orientations in bilayers, and solid state NMR experiments on oriented samples are adept at differentiating between these two situations. Once the secondary structure is established as helical, then a single solid state NMR measurement is generally sufficient to determine the orientation of the helix in the bilayer. Both qualitative and quantitative analyses of the orientational parameters have given consistent results in determining transmembrane and in-plane orientations of helices. The ^{15}N chemical shift for labeled amide sites is particularly useful for distinguishing between transmembrane and in-plane orientations of helices because of the convenient orientation of the chemical shift tensor in the molecular frame.[42] A conformation with the N–H bond approximately parallel to the field, which occurs for a transmembrane helix in oriented bilayers, has a ^{15}N chemical shift with a frequency near $\sigma_{\parallel}$, while a conformation with the N–H bond approximately perpendicular to the field, which occurs for an in-plane helix in oriented bilayers, has a ^{15}N chemical shift with a frequency near $\sigma_{\perp}$. These frequencies are separated by the full breadth of the chemical shift anisotropy powder pattern illustrated with the spectra in Figure 3. For example, the spectrum in Figure 3(c) is from a single ^{15}N labeled amide site in a 23 residue peptide with the sequence corresponding to the M2 helical segment of the δ subunit of the acetylcholine receptor, which has been shown to be helical.[30] The M2 peptide is shown to have a transmembrane orientation (Figure 4) because its ^{15}N resonance frequency is near the low frequency (high field) ($\sigma_{\parallel}$) edge of the powder pattern. This orientation is consistent with the model for its functioning as a channel by oligomerization within the bilayers.

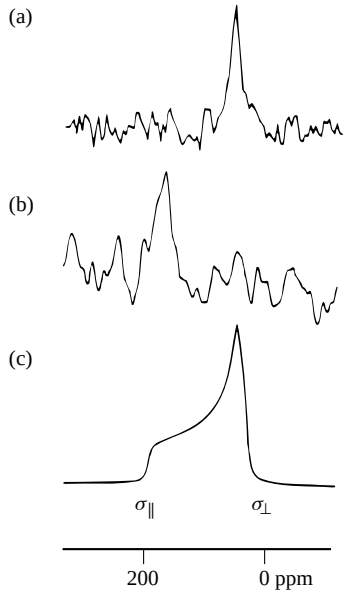

Figure 3 (a,b) Experimental solid state ^{15}N NMR spectra of 23 residue amphipathic peptides in oriented bilayers. (a) [^{15}N]Ala-labeled magainin-2. (b) [^{15}N]Ala-12-labeled M2 δ peptide. (c) Simulation of the powder pattern for an immobile ^{15}N amide site

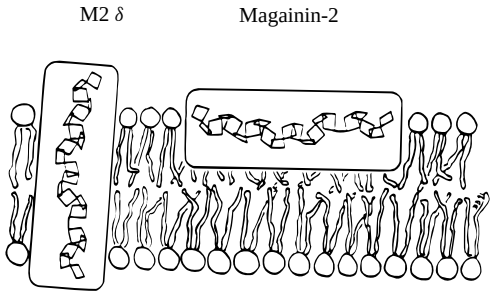

Figure 4 Schematic drawing of in-plane (magainin-2) and transmembrane (M2 δ) orientations of 23-residue amphipathic helical peptides in lipid bilayers. The helical backbones are represented by their 22 peptide bond planes, whereas the white boxes indicate the extending side chains

Contrast the position of the ^{15}N resonance from the M2 transmembrane peptide in Figure 3(b) to that from the magainin-2 peptide in Figure 3(a), which has a ^{15}N resonance frequency near the high frequency ($\sigma_{\perp}$) edge of the powder pattern. This large 170 ppm difference in resonance frequencies is due solely to the difference in orientations of the peptides in the bilayer. Magainin antibiotic peptides from frog skin have been investigated by solid state NMR spectroscopy in lipid bilayers. Their secondary structure has been demonstrated to be a helical by a variety of methods, including solid state NMR spectroscopy.[48] Spectra, such as that shown in Figure 3(b), from many labeled sites indicate that these peptides are oriented through their entire length in the plane of the bilayers, as shown in Figure 4. In other experiments the heteronuclear dipole–dipole splittings associated with the labeled sites have been measured, providing a second spectral parameter for each site. This enabled the structural determination of four contiguous residues of magainin-2 based only on solid state NMR experiments of oriented samples. The α-helical secondary structure is in complete agreement with that determined by a variety of other methods, including multidimensional solution NMR spectroscopy in micelles. However, solid state NMR spectroscopy of oriented bilayer samples is unique in being able to determine the in-plane orientation of the helix in the bilayer.

Rotational resonance spectroscopy has been used to measure the distances between ^{13}C labeled sites in peptides with sequences corresponding to the transmembrane domain of glycophorin A protein in lipid bilayers.[49] These measurements indicate a helical geometry throughout the peptide, with some evidence of unraveling of the helix near the membrane surface. Measurements have also been made of the distances between sites on the lipids and on the peptides, indicating the feasibility for using these methods to characterize fundamental peptide–membrane interactions.[50]

Gramicidin A is a linear polypeptide of 15 amino acid residues having alternating D and L stereochemistry. As an amino terminus to amino terminus dimer, gramicidin forms a monovalent cation selective channel across lipid bilayers and natural membranes. The channel conformation is a β-strand that forms a helix with 6.3 residues per turn. Solid state NMR spectra of oriented samples provide very high resolution constraints, making it possible to define each peptide plane orientation with respect to the magnetic field. By combining data from adjacent planes and the tetrahedral geometry of the C-α atom, the $\Phi\Psi$ torsion angles can be determined.[51] Considerable effort has been devoted to a characterization of the gramicidin side-chain conformation and dynamics,[52,53] in particular to the four indole groups per monomer.[54,55] The orientation for each indole ring with respect to the channel axis and bilayer normal has been determined. This information contributes to models for the roles of indoles in channel conductance. REDOR has been used to measure the dipolar coupling between the Gly-2 ^{13}C-1 carbon and Ala-3 [^{15}N]amide nitrogen atom in a sample of gramicidin where the peptide was in lipid bilayers.[56] This effective coupling was used to determine the orientation of this bond with respect to the bilayer normal. A significant feature of these measurements is that they give the magnitude and sign of the dipolar coupling, enabling the angle to be reduced to a single value and its supplement. This information about the Gly-2-Ala-3 ^{13}C–^{15}N peptide bond angle was consistent with the data obtained from orientational constraints, showing that gramicidin is a right-handed, single-stranded β-helical dimer in lipid bilayers.

Bacteriorhodopsin has been used in the development of many methods, including solid state NMR spectroscopy,[57] for probing the structures of membrane proteins. The configuration of the single molecule of retinal bound to bacteriorhodopsin and involved in its mechanism of action is the key to understanding its chemical mechanism. Watts and co-workers have labeled both ring[58] and individual methyl groups[59] along the retinal moiety with ^{2}H. From oriented preparations and the resulting orientational constraints a detailed picture of the bound chromophore conformation has been established. These results add to the large number of prior studies of the retinal with rotational resonance methods. Rotational resonance methods have also been used to measure distances between sites on the retinal chromophore and protein residues.[60] By utilizing the ^{13}C-labeled retinals and ^{13}C-ϵ lysine labeled bacteriorhodopsin, it was possible to take advantage of the

unique chemical shift of the C-ϵ atom of the lysine involved in the Schiff base.

5 NMR STUDIES OF THE MEMBRANE BOUND FORM OF FILAMENTOUS BACTERIOPHAGE COAT PROTEIN

The membrane bound filamentous bacteriophage coat protein is a small, but typical membrane protein with both amphipathic and hydrophobic helices. It has been the subject of extensive NMR studies in both micelle and bilayer samples and provides an excellent system to illustrate what can be done by combining results from both of these methods. fd is a filamentous bacteriophage that infects *Escherichia coli* and has approximately 2700 copies of a 50 residue major coat protein surrounding its DNA. The viral coat protein is synthesized with an amino terminal signal sequence which directs it to the bacterial inner membrane before being removed by cleavage with leader peptidase. The coat protein becomes the most abundant membrane in infected cells, and then subunits assemble to form the outer coat of the virus particles as they are extruded through the membrane.

fd coat protein in micelles was the first protein shown to have such heterogeneous backbone dynamics that resonances from mobile residues could be clearly distinguished from the rigid residues on the basis of multiple relaxation parameters. Initially, about eight of the backbone C-α resonances were observed to have much narrower linewidths, longer T_1 values, and larger heteronuclear NOEs than the rest of the C-α resonances in natural abundance ^{13}C NMR spectra of fd coat protein in SDS micelles.[61] The presence of mobile amide backbone sites near the amino and carboxyl termini in the membrane bound form of fd coat protein was also shown with ^{15}N-labeled samples in micelles by the observation of large negative heteronuclear ^{1}H/^{15}N NOEs and in bilayers with the observation of narrow isotropic resonance intensity in ^{15}N solid state NMR spectra.[8] The observation of narrow ^{13}C resonance linewidths for some carbonyl sites confirmed that the coat protein had mobile backbone sites in micelle samples.[62] Additional evidence for mobile residues comes from labeled side-chain sites with the observation of isotropic resonance intensity in ^{2}H solid state NMR spectra of samples in bilayers[63] and with the analysis of the relaxation properties of $^{13}CH_3$ labeled alanine residues.[64]

Additional evidence concerning protein backbone dynamics comes from the kinetics of hydrogen exchange at amide sites; however, these data are more difficult to interpret directly in terms of protein structure and fluctuations. There are substantial qualitative differences in the exchange rates of amides in different parts of the protein.[61,65] The exchange rates of individual amide sites throughout the protein have been measured;[66] the finding was that residues 28 and 45 undergo very slow exchange, while residues 7 and 20 exchange more rapidly, although not nearly as fast as for unstructured solvent exposed sites.

The determination of the secondary structure of fd coat protein in SDS micelles utilizes multidimensional NMR spectroscopy.[66–68] The majority of the sequential assignments of the amide resonances were made using homonuclear ^{1}H NOE data from two- and three-dimensional NOE/HMQC

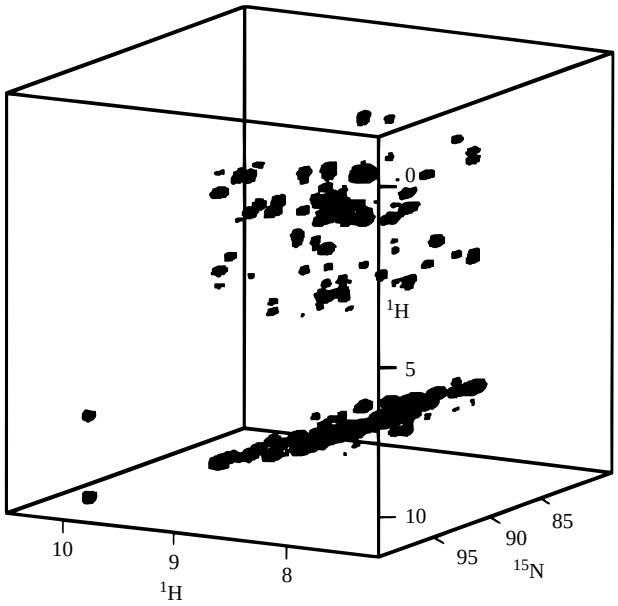

Figure 5 Three-dimensional (^{1}H/^{15}N HMQC/^{1}H/^{1}H NOE) solution spectrum of uniformly ^{15}N labeled fd coat protein in SDS micelles in solution

experiments as shown in Figure 5, supplemented with information from TOCSY/HMQC experiments, and spectra of selectively ^{15}N-labeled samples.[67] All the NOE data are consistent with extensive helical secondary structure in the protein; in particular, NOEs are observed between NH–NH(i, i + 1), NH–C-αH(i, i + 1), NH–C-βH(i, i + 1), NH–C-αH(i, i + 3), and NH–C-αH(i, i + 4) for many residues determined to have helical secondary structure. The ^{1}H/^{1}H strips in Figure 6 at ^{15}N chemical shifts corresponding to S13, L14, and Q15 show the presence of NOEs between resonances from hydrogen atoms on adjacent amide nitrogens, and α- and β-carbon atoms; these residues are part of an amphipathic helix that lies in the plane of the lipid bilayer. K40, L41, and F42 also exhibit these characteristic NOEs and are a part of

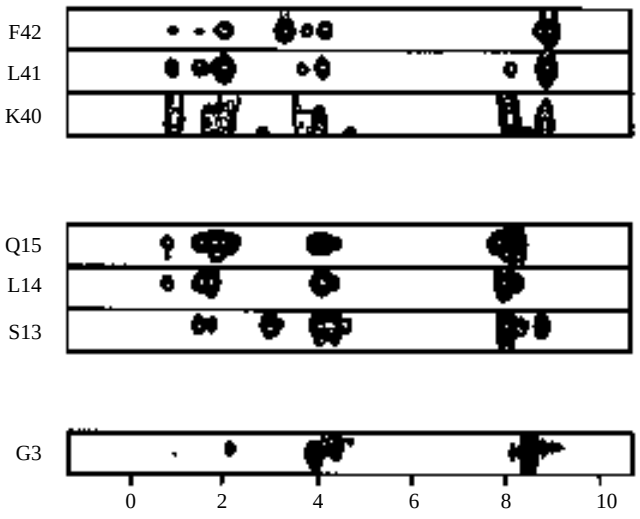

Figure 6 Strips taken from the three-dimensional spectrum shown in Figure 5

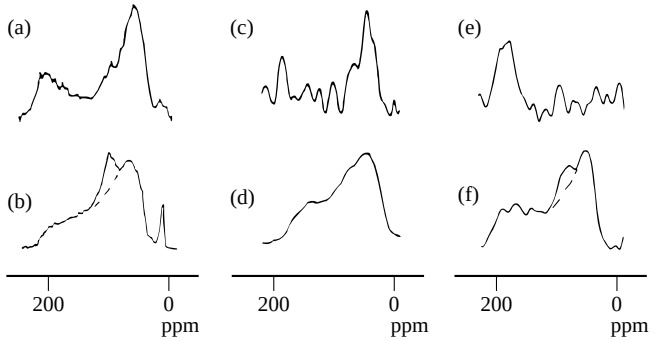

Figure 7 Solid state ^{15}N NMR spectra of uniformly and selectively ^{15}N-labeled fd coat protein in phospholipid bilayer samples. (a) Uniformly ^{15}N-labeled fd coat protein in bilayers oriented between glass plates. (b) Uniformly ^{15}N-labeled fd coat protein in unoriented bilayers. (c) Selectively [^{15}N]leucine-labeled fd coat protein in bilayers oriented between glass plates. (d) Selectively [^{15}N]leucine-labeled fd coat protein in unoriented bilayers. (e) Selectively [^{15}N]tyrosine-labeled fd coat protein in bilayers oriented between glass plates. (f) Selectively [^{15}N]tyrosine-labeled fd coat protein in unoriented bilayers

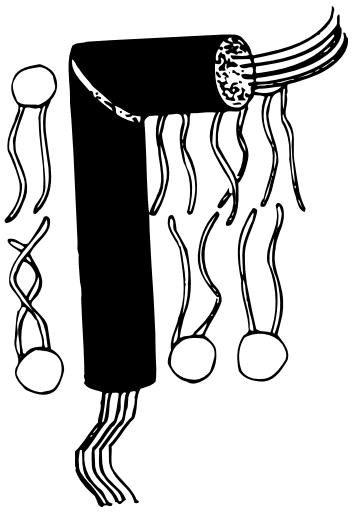

Figure 8 Model of the membrane-bound form of fd coat protein. The amphipathic helix is parallel to the plane of the bilayer, the hydrophobic helix spans the membrane, and the terminal residues and bend are mobile

the hydrophobic transmembrane helix. The numerous NOEs observed for residues 13−15 and 40−42 are between NH−C-αH(i, i + 3) and NH−C-αH(i, i + 4) sites, and strongly support the presence of helical secondary structure for these residues. The absence of NOEs for residues 1−5 at the amino terminus of the coat protein indicates that these residues do not participate in stable secondary structure, and the strip from the NOE/HMQC experiment (corresponding to G3 in Figure 8 below) has no NOEs to any other residue. Residues 1−5 are highly mobile, as seen in relaxation data of the coat protein in micelle samples.[8]

The ^{15}N chemical shift powder patterns from unoriented samples of uniformly [Figure 7(b)] and selectively ^{15}N-labeled fd coat protein in lipid bilayers [Figure 7(d)] establish that the membrane bound form of the protein has both mobile and rigid backbone sites. The amide groups of both L14 and L41 are immobile in membrane bilayers because the powder pattern spectrum in Figure 7(d) shows little evidence of motional averaging. However, the spectrum in Figure 7(b) from the uniformly ^{15}N-labeled sample has substantial isotropic intensity from the mobile amino and carboxyl terminal residues.

^{15}N solid state NMR spectra of selectively [^{15}N]leucine-labeled coat proteins in unoriented phospholipid bilayers and in oriented phospholipid bilayers are shown in Figure 7(d) and (c), respectively. The comparison of these spectra shows the effect of sample orientation; the two ^{15}N resonances go from a broad, characteristically shaped powder pattern to narrow, single lines with frequencies determined by the orientation of the peptide planes with respect to the direction of the magnetic field. Comparison of the spectra in Figure 7(a) and (b) also shows the effect of sample orientation, although at lower resolution because of multiple overlapping resonances in the uniformly ^{15}N-labeled samples. However, the resonance bands occur at the positions expected for transmembrane and in-plane helices. Since the secondary structure for the two leucine residues is established as helix by the NOE data in Figure 6, the resonance frequency of each nitrogen site can be used to establish the orientations of the helices relative to the plane of the bilayer. The spectrum of [^{15}N]leucine-labeled coat protein in oriented bilayers [Figure 7(c)] has one line with a resonance frequency near $\sigma_{\parallel}$ and a second line with a resonance frequency near $\sigma_{\perp}$, indicating that the hydrophobic helix spans the bilayer because the N−H bond of one of the leucine residues is parallel to the direction of orientation and that the amphipathic helix is in the plane of the bilayer because the N−H bond of the other leucine residue is perpendicular to the direction of orientation.

Figure 8 summarizes the results of the NMR experiments.[67] The structure and dynamics of the membrane bound form of fd coat protein were determined by combining results from solid state NMR experiments of the coat protein in bilayers with solution NMR results of the coat protein in micelles. The secondary structure of the protein is almost entirely helical, based on the observation of NOEs among all amide resonances from adjacent residues 7−50 and the NOEs between hydrogen atoms on the nitrogen amide and the α-carbon atoms three and four residues away. The orientation of the helical segments were determined by solid state NMR experiments that showed residues in the amphipathic helix lying parallel to the plane of the bilayer and residues in the hydrophobic helix spanning the bilayer. Tyr-21 is located between the two helices; it is structured on short timescales but shows evidence of mobility on the slower solid state NMR timescale, as shown in Figure 7(f). The presence of strong NH−NH(i, i + 1) and NH−C-αH(i, i + 2) NOEs, and the mobility of Y21 on slow timescales suggest that it participates in a turn that connects the two helical regions. Residues 1−5 at the amino terminus of the protein are highly mobile based on a variety of relaxation data in micelle samples and motional averaging of lineshapes in bilayer samples. Residues at the carboxyl terminus are also mobile in both bilayer and micelle samples; however, the observation of homonuclear NOEs indicates that helical secondary structure extends through to the carboxyl terminal on some timescales.

The features of the model of the membrane bound form of fd coat protein are similar to those found for the membrane bound form of Pf1 coat protein,[69] in spite of the absence of sequence homology between these proteins. The structure and dynamics

of the membrane bound forms of both fd and Pf1 coat proteins were characterized by combining the results of solution and solid state NMR spectroscopies. Both proteins consist of helical secondary structure intermixed with mobile termini and loop regions. The helical regions in fd and Pf1 coat protein consist of two segments, with hydrophobic residues forming a transmembrane helix and amphipathic residues forming a helix parallel to the bilayer plane. The two proteins differ most in the extent of mobility of the segment connecting the two helices. The connecting loop residues in Pf1 are highly mobile on both slow (10^{-4} s) and fast (10^{-9} s) timescales with an absence of homonuclear ^{1}H NOE cross peaks involving the amide resonances for these residues. In contrast, fd coat protein has homonuclear NOE cross peaks throughout the sequence, including the residues involved in the turn connecting the two helices; there is evidence of limited motional averaging for Tyr-21.

6 PROSPECTS FOR NMR STUDIES OF MEMBRANE PROTEINS

Structural studies devoted to membrane proteins seek to determine their three-dimensional structure and dynamics, with the ultimate aim of integrating these properties into models for their mechanism of action within the natural environment of the biological membrane. Since the structure and function of membrane proteins are intimately related to their hydrophobic membrane environment, serious investigations of these species must, at some stage, focus on the entire supramolecular assembly. NMR spectroscopy has proved itself to be a well suited and sufficiently versatile technique for this purpose, with the micelle and the bilayer samples providing excellent supramolecular model systems for multidimensional NMR solution and solid state NMR studies, respectively. Thus, considering the already large impact of NMR spectroscopy in the membrane protein field, there is good reason to be optimistic that, as the sample preparation and spectroscopic methods are improved, NMR spectroscopy will become generally applicable to the study of membrane proteins.

The development of multidimensional solution NMR spectroscopy of membrane proteins in micelles will be similar to that for larger globular proteins, since the limiting factor, the rotational correlation time, is the same in both cases. The solid state NMR methods that utilize uniaxially oriented samples or implement magic angle sample spinning to achieve resolution, provide measurements of angles and distances between bonds and chemical groups which can be interpreted in terms of structures. The former method has the added advantage of providing details about the orientation of the protein structural elements with respect to the plane of the lipid bilayer. Thus, by using macroscopically and uniaxially oriented membrane samples it becomes possible to distinguish between the case where the protein is membrane spanning and that where the protein associates only superficially with the membrane, or, yet again, where the protein interacts with the bilayer in a wedge-like manner. This is important for understanding the functions of membrane proteins, since they interact asymmetrically with the membrane, imparting different properties to its inner and outer leaflets. The situation is a very different from the more or less isotropic environment of the cell cytoplasm and periplasm occupied by globular proteins. As a result, NMR spectroscopy has the potential of opening up an entire area of structural biology by providing an added dimension for membrane protein studies.

7 RELATED ARTICLES

Bacteriorhodopsin and Rhodopsin; Bilayer Membranes: Deuterium and Carbon-13 NMR; Bilayer Membranes: Proton and Fluorine-19 NMR; Gramicidin Channels: Orientational Constraints for Defining High-Resolution Structures; Membranes: Carbon-13 NMR; Membranes: Phosphorus-31 NMR; Protein Dynamics from Solid State NMR; Structures of Larger Proteins, Protein-Ligand, and Protein-DNA Complexes by Multi-Dimensional Heteronuclear NMR.

8 REFERENCES

1. J. Deisenhofer, O. Epp, K. Miki, R. Huber, and H. Michel, *Nature*, 1985, **318**, 618.
2. D. Rees, H. Komiga, T. Yeates, J. Allen, and G. Feher, *Ann. Rev. Biochem.*, 1989, **58**, 607.
3. R. Henderson, J. Baldwin, T. Cesko, F. Zemlin, E. Beckmann, and K. Downing, *J. Mol. Biol.*, 1990, **213**, 899.
4. M. Weiss, U. Abele, J. Weckesser, W. Welte, E. Schiltz, and G. Schulz, *Science*, 1991, **254**, 1627.
5. S. J. Opella, Y. Kim, and P. McDonnell, *Methods Enzymol.*, 1994, **239**, 536.
6. S. J. Opella, *Methods Enzymol.*, 1985, **131**, 327.
7. M. A. Keniry, H. S. Gutowsky, and E. Oldfield, *Nature*, 1984, **307**, 383.
8. M. J. Bogusky, G. C. Leo, and S. J. Opella, *Proteins: Structure, Function, Genet.*, 1988, **4**, 123.
9. M. Saunders, A. Wishnia, and J. G. Kirkwood, *J. Am. Chem. Soc.*, 1957, **79**, 3289.
10. G. Clore and A. Gronenborn, *CRC Crit. Rev. Biochem. Mol. Biol.*, 1989, **24**, 479.
11. K. Wüthrich, *NMR of Proteins and Nucleic Acids*, Wiley, New York, 1986.
12. A. Watts, in *Phospholipids Handbook*, ed G. Cevc, Dekker, New York, 1993, p. 687.
13. J. H. Davis, *Chem. Phys. Lipids*, 1986, **40**, 223.
14. H. Hauser, E. G. Finer, and D. Chapman, *J. Mol. Biol.*, 1970, **53**, 419.
15. D. W. Urry, *Proc. Natl. Acad. Sci. USA*, 1971, **68**, 672.
16. D. Chapman, V. B. Kamat, J. Degier, and S. A. Penkett, *Nature*, 1967, **213**, 74.
17. S. I. Chan, M. P. Sheetz, C. H. A. Seiter, G. W. Feigenson, M. C. Hsu, A. Lau, and A. Yan, *Ann. NY Acad. Sci.*, 1973, **222**, 499.
18. D. S. Hagen, J. H. Weiner, and B. D. Sykes, *Biochemistry*, 1978, **17**, 3860.
19. M. L. Wilson and F. W. Dahlquist, *Biochemistry*, 1985, **24**, 1920.
20. V. B. Kamat and D. Chapman, *Biochim. Biophys. Acta*, 1968, **163**, 411.
21. L. R. Brown, *Biochim. Biophys. Acta*, 1979, **557**, 135.
22. J. Lauterwein, Ch. Boesch, L. R. Brown, and K. Wüthrich, *Biochim. Biophys. Acta*, 1979, **163**, 411.

23. P. A. McDonnell and S. J. Opella, *J. Magn. Reson. B*, 1993, **102**, 120.
24. C. E. Dempsey, R. Bazzo, T. S. Harvey, I. Syperek, G. Boheim, and I. D. Campbell, *FEBS Lett.*, 1991, **281**, 240.
25. T. Ikura, N. Go, and F. Inagaki, *Proteins*, 1991, **9**, 81.
26. E. Bairaktari, D. F. Mierke, S. Mammi, and E. Peggion, *Biochemistry*, 1990, **29**, 10 090.
27. J. C. Franklin, J. F. Ellena, S. Jayasinghe, L. P. Kelsh, and D. S. Cafiso, *Biochemistry*, 1994, **33**, 4036.
28. K. H. Lee, J. E. Fitton, and K. Wüthrich, *Biochim. Biophys. Acta*, 1987, **911**, 144.
29. A. Motta, A. Pastore, N. A. Goud, and M. A. C. Morelli, *Biochemistry*, 1991, **30**, 10 444.
30. S. J. Opella, J. Gesell, and B. Bechinger, in *The Amphipathic Helix*, ed. R. Epand, CRC Press, Boca Raton, 1993, pp. 87–106.
31. T. Holak, A. Engstrom, P. Kraulis, G. Lindeberg, H. Bennich, T. Jones, A. Gronenborn, and G. M. Clore, *Biochemistry*, 1988, **27**, 7620.
32. D. Sipos, M. Andersson, and A. Ehrenberg, *Eur. J. Biochem.*, 1992, **209**, 163.
33. J. Gesell, M. Zasloff, and S. J. Opella, unpublished results.
34. D. Marion, M. Zasloff, and A. Bax, *FEBS Lett.*, 1989, **227**, 21.
35. M. F. Moody, P. T. Jones, J. A. Carver, J. Boyd, and I. D. Campbell, *J. Mol. Biol.*, 1987, **193**, 759.
36. T. J. Norwood, D. A. Crawford, M. E. Steventon, P. C. Driscoll, and I. D. Campbell, *Biochemistry*, 1992, **31**, 6285.
37. M. E. Girvin and R. H. Fillingame, *Biochemistry*, 1993, **32**, 12 167.
38. K. V. Pervushin, A. S. Arseniev, A. T. Kozhich, and V. T. Ivanov, *J. Biomol. NMR*, 1991, **1**, 313.
39. I. L. Barsukov, G. V. Abdulaeva, A. S. Arseniev, and V. F. Bystrov, *Eur. J. Biochem.*, 1990, **192**, 321.
40. S. J. Opella, and P. A. McDonnell, in *NMR of Proteins*, ed. A. M. Gronenborn and G. M. Clore, MacMillan, 1993, pp. 159–189.
41. S. J. Opella, in *Membrane Protein Structure: Experimental Approaches*, ed. S. H. White, Oxford, 1994, in press.
42. B. Bechinger, Y. Kim, L. E. Chirlian, J. Gesell, J.-M. Neumann, M. Montal, J. Tomich, M. Zasloff, and S. J. Opella, *Biomol. NMR*, 1991, **1**, 167.
43. T. Gullion and J. Schaefer, *J. Magn. Reson.*, 1989, **81**, 196.
44. D. P. Raleigh, M. H. Levitt, and R. G. Griffin, *Chem. Phys. Lett.*, 1988, **146**, 71.
45. S. J. Opella, and J. S. Waugh, *J. Chem. Phys.*, 1977, **66**, 4919.
46. S. J. Opella, P. L. Stewart, and K. G. Valentine, *Q. Rev. Biophys.*, 1987, **19**, 7.
47. S. O. Smith, *Curr. Opinion Struct. Biol.*, 1993, **3**, 755.
48. B. Bechinger, M. Zasloff, and S. J. Opella, *Protein Sci.*, 1993, **2**, 2077.
49. S. O. Smith, R. Jonas, M. Braiman, and B. J. Bormann, *Biochemistry*, 1994, **33**, 6334.
50. S. O. Smith, J. Hamilton, A. Salmon, and B. J. Bormann, *Biochemistry*, 1994, **33**, 6327.
51. R. R. Ketchem, W. Hu, and T. A. Cross, *Science*, 1993, **261**, 1457.
52. J. A. Killian, M. J. Taylor, and R. E. Koeppe II, *Biochemistry*, 1992, **31**, 11 283.
53. K.-C. Lee and T. A. Cross, *Biophys. J.*, 1994, **66**, 1380.
54. W. Hu, K.-C. Lee, and T. A. Cross, *Biochemistry*, 1993, **32**, 7035.
55. R. R. Koeppe II, J. A. Killian, and D. V. Greathouse, *Biophys. J.*, 1994, **66**, 14.
56. A. W. Hing and J. Schaefer, *Biochemistry*, 1993, **32**, 7593.
57. S. O. Smith and R. G. Griffin, *Ann. Rev. Phys. Chem.*, 1968, **39**, 511.
58. A. S. Ulrich, M. P. Heyn, and A. S. Watts, *Biochemistry*, 1992, **31**, 10 390.
59. A. S. Ulrich, A. Watts, I. Wallat, and M. P. Heyn, *Biochemistry*, 1994, **33**, 5370.
60. L. K. Thompson, A. E. McDermott, J. Raap, C. M. Van der Wielen, J. Lugtenburg, J. Herzfeld, and R. G. Griffin, *Biochemistry*, 1992, **31**, 7931.
61. T. A. Cross and S. J. Opella, *Biochem. Biophys. Res. Commun.*, 1980, **92**, 478.
62. G. D. Henry, J. H. Weiner, and B. D. Sykes, *Biochemistry*, 1987, **26**, 3619.
63. G. C. Leo, L. A. Colnago, K. G. Valentine, and S. J. Opella, *Biochemistry*, 1987, **26**, 854.
64. G. D. Henry, J. H. Weiner, and B. D. Sykes, *Biochemistry*, 1986, **25**, 590.
65. J. D. J. O'Neil and B. D. Sykes, *Biochemistry*, 1988, **27**, 2753.
66. G. D. Henry and B. D. Sykes, *Biochem. Cell. Biol.*, 1990, **68**, 318.
67. P. A. McDonnell, K. Shon, Y. Kim, and S. J. Opella, *J. Mol. Biol.*, 1993, **233**, 447.
68. F. J. M. van de Ven, J. W. M. van Os, J. M. A. Aelen, S. S. Wymenga, M. L. Remerowski, R. N. H. Konings, and C. W. Hilbers, *Biochemistry*, 1993, **32**, 8322.
69. K. Shon, Y. Kim, L. A. Colnago, and S. J. Opella, *Science*, 1991, **252**, 1303.

Biographical Sketches

Stanley J. Opella. *b* 1947. B.S., 1969, chemistry, University of Kentucky (undergraduate research with S. L. Smith); Ph.D., 1974 chemistry, Stanford University, (with O. Jardetzky and H. McConnell). Postdoctoral fellow, 1975–76, M.I.T. (with J. S. Waugh). Professor of Chemistry, University of Pennsylvania, 1976–present. Approx. 125 publications. Research interests: development and application of NMR spectroscopy for the study of proteins, especially protein structure determination by solid state NMR spectroscopy.

Francesca M. Marassi. *b* 1963. B.Sc., 1987, chemistry (undergraduate research with J. C. Rucklidge), M.Sc., 1989, chemistry (with M. Thompson), Ph.D., 1993, chemistry, (with P. M. Macdonald), University of Toronto, Natural Sciences and Engineering Research Council postdoctoral fellow, University of Pennsylvania, 1993–present. Approx. 8 publications. Research interests: structural investigation of membrane proteins, and protein–lipid interactions by means of solid state NMR spectroscopy.

Metallothioneins

Ian M. Armitage
University of Minnesota, Minneapolis, MN, USA

and

Lazaros T. Kakalis
Yale University School of Medicine, New Haven, CT, USA

and

James D. Otvos
North Carolina State University, Raleigh, NC, USA

1 Introduction 1
2 Cadmium-113 NMR 1
3 NMR Studies of Metallothioneins 4
4 Solution Structure of Metallothioneins 5
5 Related Articles 6
6 References 6

1 INTRODUCTION

Metallothioneins (MTs) are a unique group of low molecular weight, cysteine-rich proteins that bind both essential (e.g. copper and zinc) and nonessential (e.g. cadmium and mercury) metals.[1] Since their discovery in 1957 in equine kidney cortex, MTs have been identified from a variety of mammals, birds, fish, invertebrates, plants, eukaryotic microorganisms, and some prokaryotes. The widespread occurrence of MTs in nature suggests that they serve an important biological function, although their exact role has yet to be defined. Since MT gene transcription is inducible by the same heavy metals that are subsequently found bound to the protein, MTs are thought to act as heavy metal detoxifying agents by sequestering such toxic metals as cadmium, mercury, and a variety of other heavy metal ions under conditions of stressful metal overloads. It is also likely that MTs participate in essential zinc and copper metabolism or homeostasis, perhaps serving in a storage or transport capacity. Various aspects of the MT chemistry, biochemistry, molecular biology, physiology, and toxicology have been reviewed.[2,3]

Metallothioneins are subdivided into three classes: class I comprises MTs of mammalian and other origin with related primary structure, class II includes MTs unrelated to the mammalian forms, and class III consists of atypical polypeptides with γ-glutamylcysteine residues (Figure 1). Of the 61 amino acid residues in mammalian MTs, there are 20 cysteines that serve as ligands to the 7 g-atoms mol^{-1} of divalent metal ion bound by the protein. In addition, MTs contain several serines and lysines in highly conserved positions in the sequence, whereas aromatic residues and His are completely absent.

These highly unusual compositional features of MTs consisting of multiple metals bound presumably exclusively to cysteine sulfhydryl groups plagued early attempts using spectrophotometric and complexometric titration data to characterize the tertiary structure of these proteins. On the basis of these studies, the prevailing model until the late 1970s consisted of multiple, separate metal-binding sites as depicted schematically in Figure 2. These very features, coupled with the fact that this was the first, and until this day the only, naturally occurring cadmium-containing protein, attracted our interest to this protein in our early efforts to establish the usefulness of ^{113}Cd NMR methods to probe the structure of the ^{113}Cd-substituted metal-binding site(s) in a variety of metalloproteins.[4] Fortunately, both our intuition and the spin physics of the spin-$\frac{1}{2}$ $^{113}Cd^{2+}$ ion cooperated, and with this technique we were able to resolve each of the individual metal-binding sites in this protein, which laid the foundation for studies that ultimately led to the elucidation of this protein's three-dimensional (3D) structure (see below).

2 CADMIUM-113 NMR

Numerous investigators have employed ^{113}Cd NMR in studying the properties of a variety of metalloproteins and biological events in which the native Zn^{2+}, Ca^{2+}, Mg^{2+}, Mn^{2+}, Cu^{2+}, or Cd^{2+} ions were replaced by $^{113}Cd^{2+}$.[4–7] Some of the chemical and magnetic properties of the $^{113}Cd^{2+}$ ion to which this approach owes its success are the following:

1. The coordination of Cd^{2+} is quite similar to that of Zn^{2+} and Ca^{2+}, and Cd^{2+} and Ca^{2+} have similar ionic radii of 0.97 and 0.99 Å, respectively.
2. Cd^{2+} has been substituted for the native Zn^{2+} in a variety of metalloenzymes and deoxyribonucleic acid (DNA)-binding proteins. In the former, catalytic efficiency and specificity are frequently altered but usually not abolished, whereas in the latter, DNA binding is retained.
3. Cadmium-113 chemical shifts are extremely sensitive to the nature, number, and geometric arrangement of the ligands within the coordination sphere. This sensitivity is reflected in the chemical shift range of almost 900 ppm observed for the resonances from $^{113}Cd^{2+}$-substituted metalloproteins. This property is useful not only in helping to identify the ligands at a particular metal-binding site, but also because it virtually guarantees the resolution of individual ^{113}Cd resonances in systems containing multiple metal ions as is the case in MTs.

2.1 Sensitivity

There are two naturally occurring, diamagnetic, spin-$\frac{1}{2}$ cadmium isotopes, ^{113}Cd and ^{111}Cd, which are present at 12.3% and 12.7% natural abundance, respectively. Despite the fact that the two isotopes have virtually identical NMR properties, ^{113}Cd has been used almost exclusively for biological NMR studies. The inherent sensitivity of the ^{113}Cd nucleus is about 1% that of ^{1}H and 70% that of ^{13}C. At natural abundance levels, the sensitivity of ^{113}Cd is 7.6 times that of ^{13}C which is still insufficient for most biological Cd NMR studies. Instead, 96% isotopically enriched ^{113}Cd is employed, affording an 8-fold enhancement in sensitivity. Reasonable spectra may be obtained from approximately 2 mL of a 1 mM sample of a Cd-substituted metalloprotein in 5–10 h of data accumulation at intermediate/high fields.

	20	40	60
Class I			
Human (MT-2)	M D P N C S C A A G D S C T C A G S C K C K E C K C T S C K K S C C S C C P V G C A K C A Q G C I C K G A S D K C S C C A		
Chicken	M D P Q D C T C A A G D S C S C A G S C K C K N C R C R S C R K S C C S C C P A G C N N C A K G C V C K E P A S S K C S C C H		
Trout (MT-b)	M D P C E C S K T G S C N C G G S C K C S N C A C T S C K K S C C P C C P S D C S K C A S G C V C K G K T C D T S C C Q		
Crab (MT-2)	P D P C C N D K C D C K E G E C K T G C K C T S C R C P P C E Q C S S G C K C A N K E D C R K T C S K P C S C C P		
N. crassa	G D C G C S G A S S C N C G S G C S C S N C G S K		
Class II			
Sea urchin (MT_a)	M P D V K C V C C T E G K E C A C F G Q D C C V T G E C C K D G T C C G I C T N A A C K C A N G C K C G S G C S C T E G N C A C		
Yeast	Q N E G H E C Q C Q C G S C K N N E Q C Q K S C S C P T G C N S D D K C P C G N K S E E T K K S C C S G K		
Wheat germ (E_C protein)	G C N D K C G C A V P C P G G T G C R C T S A R S G A A A G E H T T C G C G E H C G G N P C A C G G E G T P S G C A N		
Cyanobacterium	T S T T L V K C A C E P C L C N V D P S K A I D R N G L Y Y C C E A C A D G H T G G S K G C G H T G C N C		

Figure 1 Amino acid sequences of representative MTs. Open positions denote deletions introduced for optimal alignment of class I MTs; numeration refers to the sequence determined for human MT-2

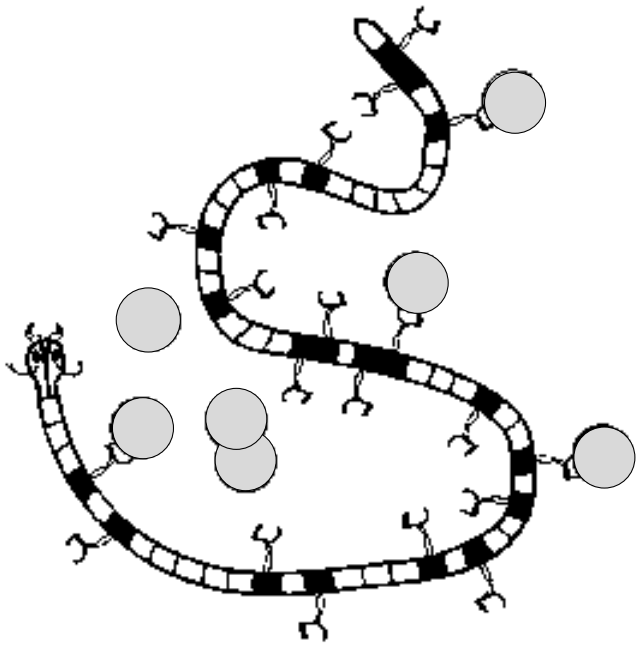

Figure 2 Model for mammalian MT consisting of separate metal-binding sites that was adapted from a drawing by Ab Tulp (in Y. Kojima and J. H. R. Kägi, *Trends Biol. Sci*, 1978, 90). The darkened residues represent cysteine

2.2 Chemical Shifts

Studies of Cd^{2+} complexes in aqueous solutions show a consistent correlation between the chemical shift and the identity of the ligands to the metal ion. Oxygen ligands provide the greatest shielding, nitrogen and halide ligands are relatively deshielding, and sulfur ligands are the most deshielding.[4–7] Ideally, one would like to be able to interpret ^{113}Cd chemical shifts for proteins in terms of the identity, number, and geometric arrangement of the ligands at the binding site. Unfortunately, two obstacles have so far restricted the establishment of such a detailed structure–chemical shift correlation. The first problem stems from the facile chemical exchange that usually exists between hydrated cadmium complexes in aqueous solution. The consequence of this is that the solution ^{113}Cd chemical shift of a cadmium compound of known structure will not necessarily be indicative of that complex alone, but will instead be a weighted average of the chemical shifts of multiple species in rapid equilibrium. This difficulty may be overcome either by bringing the labile inorganic system into the slow exchange regime by the use of supercooled aqueous solutions, or by recording the chemical shifts of solid cadmium complexes using cross polarization magic angle spinning techniques.[5,8] To date, an insufficient number of structurally defined cadmium compounds has been examined by these methods to provide the necessary data base for a detailed ^{113}Cd chemical shift–structure correlation. The second, and more serious, difficulty is a lack of suitable model compounds to mimic the distorted coordination geometries and outer-sphere interactions that are found at the metal-binding sites of most biological macromolecules. From the limited data that are presently available, differences in coordination number and geometry and outer-sphere effects seem to exert significant influences on chemical shift, with higher coordination number complexes being more shielded.[5]

Thus, although we have not yet achieved the desired level of quantification, the existing qualitative structure–chemical shift correlation is sufficiently well established to permit its use for tentative assignments of metal ligand types in biological systems. In every case in which ^{113}Cd chemical shift determinations have been made in proteins whose binding sites had previously been characterized by X-ray diffraction, good correspondence has been found between the observed shift and that expected on the basis of the protein–metal ligands. This is demonstrated in Figure 3, which shows a compilation of the solution ^{113}Cd chemical shifts of many $^{113}Cd^{2+}$-substituted metalloproteins reported to date with characterized metal-binding sites(s). Resonances from cadmium bound to sites consisting exclusively of oxygen ligands are invariably found in the region of 0 to −125 ppm, those from sites containing a combination of oxygen and nitrogen ligands appear between 0 and 300 ppm, and resonances from sites containing two or more thiolate sulfur ligands are found in the highest frequency (most downfield) region between 450 and 750 ppm.

2.3 Coupling Constants

The observation of scalar coupling in the ^{113}Cd NMR resonances in biological macromolecules can provide unequivocal information about the nature of the ligands and their mode of binding. Table 1 shows the range of coupling constant values reported for nuclei of biological interest. In the case of the MTs, the observation of ^{113}Cd–^{113}Cd two-bond couplings was instrumental in the elucidation of the two-cluster structure arrangement (see below). Similarly, identification of the heteronuclear three-bond couplings between each ^{113}Cd ion and the β protons of their cysteine ligands was indispensable in the determination of the solution tertiary structure of MT by two-dimensional (2D) NMR methods.[9] Exploitation of the Karplus-type dependence of these couplings on the Hβ–Cβ–S–Cd dihedral angle is expected to provide an even

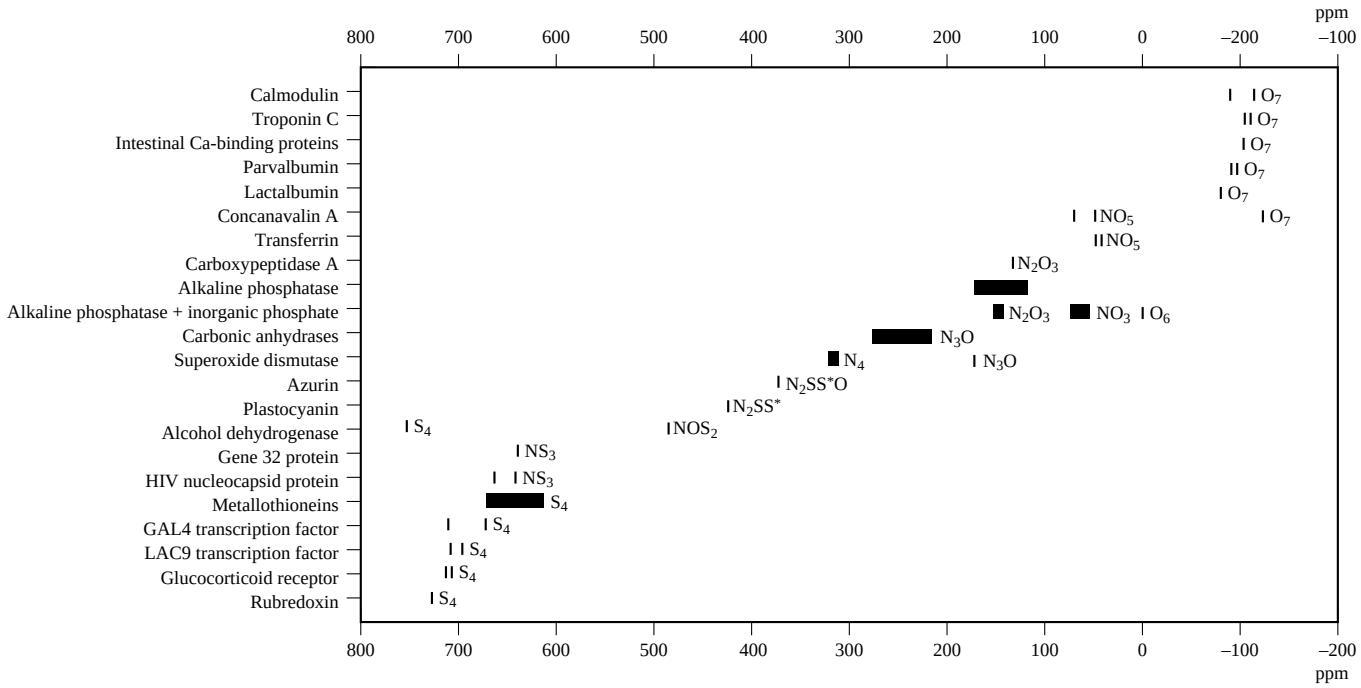

Figure 3 Observed ^{113}Cd chemical shifts for ^{113}Cd-substituted metalloproteins. All shifts are reported relative to external 0.1 M $Cd(ClO_4)_2$. A bar indicates that a range of values have been observed for the same site under a variety of conditions or, in the case of mammalian MT, the distribution of the seven ^{113}Cd signals from the two metal clusters. The identity and number of metal ligands is also indicated. S and S* denote cysteine and methionine sulfur ligation, respectively. The ^{113}Cd NMR data are from Armitage and Otvos,[4] Summers,[6] Coleman[7] (and references cited therein), and Kiang et al., *Magn. Reson. Chem.*, 1993, **31**, 5110 (transferrin). The crystallographically determined metal coordinations are from Babu et al., *J. Mol. Biol.*, 1988, **204**, 191 (calmodulin), Acharya et al., *J. Mol. Biol.*, 1991, **221**, 571 (lactalbumin), Rees et al., *J. Mol. Biol.*, 1983, **268**, 367 (carboxypeptidase), Kim and Wyckoff, *J. Mol. Biol.*, 1991, **218**, 449 (alkaline phosphatase), Håkansson et al., *J. Mol. Biol.*, 1992, **227**, 1192 (carbonic anhydrase), Tainer et al., *J. Mol. Biol.* 1982, **160**, 181 (superoxide dismutase), Baker, *J. Mol. Biol.*, 1988, **203**, 1071 (azurin), Guss and Freeman, *J. Mol. Biol.*, 1983, **169**, 521 (plastocyanin), Eklund et al., *J. Mol. Biol.*, 1976, **102**, 27 (alcohol dehydrogenase), Frey et al., *J. Mol. Biol.*, 1987, **197**, 525 (rubredoxin), Satyshur et al., *J. Biol. Chem.*, 1988, **263**, 1628 (troponin), Szebenyi and Moffat, *J. Biol. Chem.*, 1986, **261**, 8761 (intestinal Ca-binding protein), Becker et al., *J. Biol. Chem.*, 1975, **250**, 1513 (concanavalin), Kumar et al., *Biochemistry*, 1990, **29**, 1404 (parvalbumin), Bailey et al., *Biochemistry*, 1988, **27**, 5804 (transferrin), Marmorstein et al., *Nature (London)*, 1992, **356**, 408 (GAL4), Luisi et al., *Nature (London)*, 1991, **352**, 497 (glucocorticoid receptor)

Table 1 Scalar Coupling Constants of ^{113}Cd with Nuclei of Biological Interest for Model Compounds and Metalloproteins in Aqueous Solution5, 6, 7, 10

Coupling	^1J (Hz)	^2J (Hz)	^3J (Hz)
^{113}Cd–^{1}H	–	50–53	0.5–80
^{113}Cd–^{13}C	498–1060	3–19	5–45
^{113}Cd–^{15}N	140–210	–	–
^{113}Cd–^{31}P	1200–1710	2–30	–
^{113}Cd–^{113}Cd	–	29–48	–

more accurate definition of the metal-binding site arrangements in future MT structure determinations by NMR.[10] It is also noteworthy that, in addition to structural information, the observation of ^{113}Cd scalar coupling in MT and other metalloproteins is indicative of slow exchange of the metal(s) at the binding sites ($k_{off} \leq 10^2\ s^{-1}$).

2.4 Relaxation Properties

The spin relaxation properties of ^{113}Cd in a given system are of interest for at least two reasons. The first is a purely practical one: a working knowledge of the spin–lattice relaxation time T_1 and the nuclear Overhauser enhancement (NOE) is essential for determining the most efficient conditions for data collection. The second reason is more fundamental: by analyzing the relaxation data in terms of appropriate theoretical models one can derive valuable information concerning motional dynamics at the metal-binding site. Unfortunately, owing to the lack of the detailed characterization of the contributions to ^{113}Cd relaxation in macromolecular systems, this potential source of information remains largely unexploited.

The important relaxation mechanisms operative for the ^{113}Cd nucleus in metalloproteins are chemical shift anisotropy (CSA) and ^{113}Cd–^{1}H dipole–dipole (DD) interactions.[4,5,7] At magnetic fields above about 6 T, CSA is usually dominant but resonance broadening has not been as severe as to impair detection (Figure 4). Dipole–dipole relaxation is relatively inefficient since the protons on typical metal ligands are usually $\geq$3.5 Å distant, with exchangeable protons in the first hydration sphere, if present, being somewhat closer ($\approx$2.9 Å). Therefore, if only DD relaxation were operative, ^{113}Cd T_1 values of metalloproteins would be excessively long. Measured ^{113}Cd T_1 values of metalloproteins range from 0.1 to 10 s,[7,11] with those of MT being about 0.5 s at 4.7 T or about 0.1 s at 11.7 T.

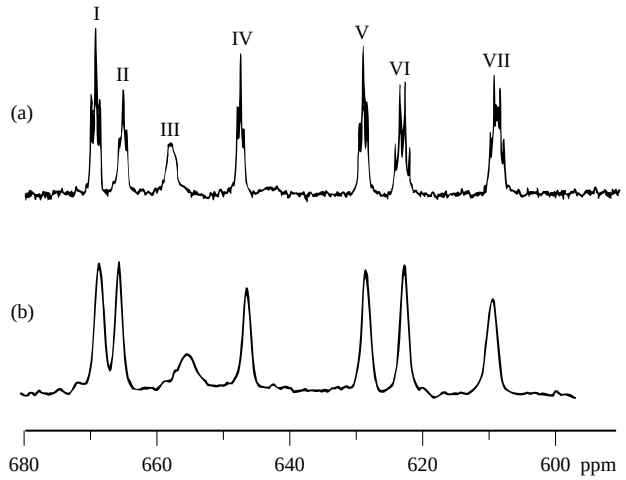

Figure 4 Proton-decoupled ^{113}Cd NMR spectra at 55 MHz (a) and 110 MHz (b) of reconstituted rabbit [$^{113}Cd_7$]–MT-2. The ^{113}Cd–^{113}Cd splittings seen in the 55 MHz spectrum are obscured at 110 MHz by the increased linewidth due to more efficient CSA relaxation

The relative contributions of CSA and DD may be estimated from solid state ^{113}Cd spectra[8] that yield the CSA $\Delta\sigma$, and from ^{113}Cd{^{1}H} NOE measurements,[4,5] respectively, with prior knowledge or assumption(s) about correlation time(s), number of relaxing protons, and Cd–H distances. The very limited CSA data on calcium-binding proteins suggest $\Delta\sigma$ values in the 90–140 ppm range, and generally asymmetric metal-binding sites.[6,8]

Because of the negative magnetogyric ratio of ^{113}Cd, proton decoupling can in many circumstances cause a complete disappearance of Cd signal intensity owing to the induction of a NOE close to -1.[4,5] Such has been observed for mammalian MT at 2.1 T.[4] For this reason, plus the fact that ^{113}Cd–^{1}H splittings are often of smaller magnitude than the natural or exchange-broadened linewidths of the ^{113}Cd resonances, proton decoupling is rarely employed in ^{113}Cd NMR studies of metalloproteins.

2.5 Chemical Exchange

The observation of ^{113}Cd NMR resonances is frequently compromised in biological systems by the presence of chemical exchange broadening. The problem stems from the great sensitivity of ^{113}Cd chemical shifts to even minor fluctuations in the inner- or outer-sphere coordination environment. Processes that modulate the environments of protein-bound metal ions often occur at rates that are too fast to influence the NMR signals of the protein proper, but fall into the intermediate exchange regime of ^{113}Cd.

Dissociation of Cd^{2+} from most proteins would be accompanied by a chemical shift change of at least 100 ppm. Thus, only relatively large off-rates (10^4 s^{-1} or higher) would be expected to lead to significant exchange broadening of a protein-bound metal ion. The only sites likely to fall into this category are the low-affinity sites of calcium-binding proteins. A more important source of exchange modulation is that created by competition of solvent and counterion molecules for any 'open' metal coordination sites not occupied by protein ligands. Solvent exchange rates are known to be quite rapid and can easily fall within the range that can create intermediate exchange ^{113}Cd broadening. Less is known about the rates of exchange of ligands contributed by the protein or dynamic changes in the metal coordination environment brought about by protein conformational changes. Both of these processes, however, are considered likely to be capable of inducing significant exchange broadening. In the event that an expected ^{113}Cd resonance remains undetectable within the limits of the conventional experimental parameters, including variations of pH, temperature, and ionic conditions, alternative methods such as the use of supercooled microemulsions or solid state NMR should be considered.[5,8] The latter approach has been used to confirm that the solution state ^{113}Cd chemical shifts of rabbit MT are not influenced by ligand exchange rates.[5]

3 NMR STUDIES OF METALLOTHIONEINS

That the seven divalent metal ions in mammalian MTs are coordinated exclusively by the thiolate sulfurs of the protein's 20 cysteine residues was originally inferred by the invariant amino acid sequence positions of the cysteines plus the absence of any disulfide bonds. Cadmium-113 NMR was capable of resolving all seven resonances (Figure 4) and provided the first direct proof that the metals reside in polynuclear clusters, as evidenced by the observed spin–spin splittings that arose from the two-bond ^{113}Cd–^{113}Cd scalar coupling.[12] In agreement with other spectroscopic results, the observed range of ^{113}Cd chemical shifts (about 600–670 ppm) supported the proposal that all metals adopt tetrahedral-like coordination to four thiolate ligands. To reconcile the stoichiometry of about three cysteines (Cys) per metal ion with tetrahedral coordination, a metal–thiolate cluster arrangement was proposed in which there is sharing of some thiolate ligands by two adjacent metal ions, and is consistent with the observed ^{113}Cd–^{113}Cd coupling.

In mammalian and crab MTs, the metals reside in two distinct clusters.[4] Homonuclear ^{113}Cd decoupling studies on mammalian MTs readily allowed the separation of the resonances into two linkage groups, Cd_4Cys_{11}, or cluster α, and Cd_3Cys_9 or cluster β (Figure 5). This arrangement was subsequently confirmed by ^{113}Cd COSY spectroscopy[13] (Figure 6) and independently verified by limited enzymatic proteolysis.[5] The ^{113}Cd NMR spectrum of the isolated $Cys_{11}Cd_4$ C-terminal domain showed four resonances with chemical shifts corresponding to the four resonances of the 4-metal cluster in the intact protein. Similar homonuclear

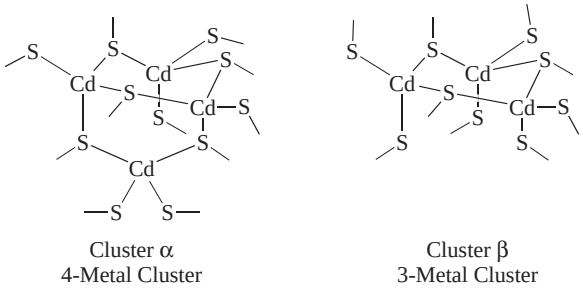

Figure 5 Structures of the 4-metal and 3-metal clusters existing in MTs

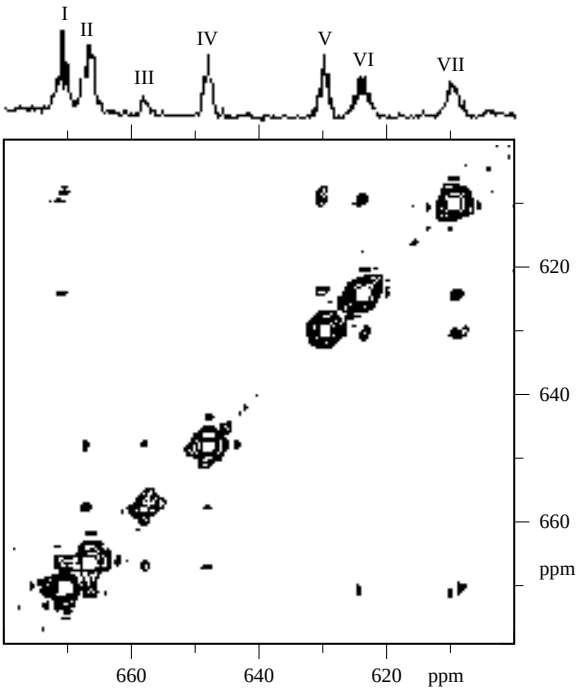

Figure 6 Cadmium-113 chemical shift correlation (COSY) spectrum of rabbit liver [$^{113}Cd_7$]–MT-2. The data are consistent with the arrangement of the ^{113}Cd resonances in two separate clusters: I, V, VI, VII and II, III, IV

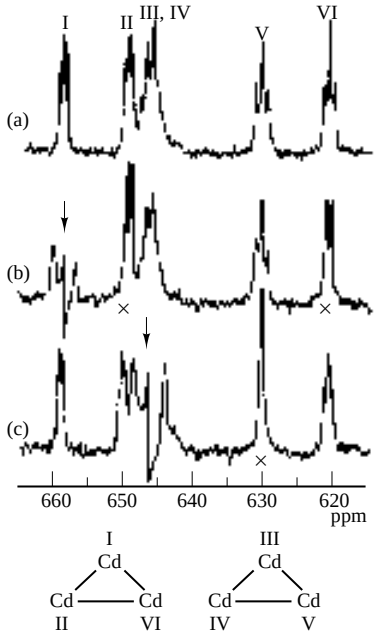

Figure 7 (a) Cadmium-113 NMR spectrum at 44.4 MHz of native crab [$^{113}Cd_6$]–MT-1. (b) and (c), same as (a) but with homonuclear decoupling pulses applied at the frequencies indicated by the arrows. This results in the collapse of the multiplet structure of coupled ^{113}Cd resonances marked with X, i.e., II and VI while decoupling I and V while decoupling the overlapping III and IV resonances

decoupling studies for the crab $^{113}Cd_6$–MT revealed that the six metals are arranged in two 3-metal clusters (Figure 7).[5]

Despite binding very tightly, the metals in mammalian MTs participate in surprisingly facile ligand exchange reactions that induce rapid intermolecular metal transfer between β-domain 3-metal cluster sites.[14] This dynamic aspect of MT structure was deduced from ^{113}Cd NMR saturation transfer studies that showed that the lifetime of a Cd^{2+} ion in a 3-metal cluster site is only about 1 s. By demonstrating that saturation transfer occurs between different MT isoforms, it was inferred that metal ions continually move from the β-domain of one MT molecule to that of another via a series of metal–ligand exchange reactions.[14] The dynamics predicted by this model, involving many individual metal–thiolate bond making and bond breaking events, is what is believed to be responsible for the chemical exchange broadening of resonance III in Figure 4 as well as the temperature-dependent modulation of the widths of the other β-domain signals.[14]

4 SOLUTION STRUCTURE OF METALLOTHIONEINS

Contrary to what one might expect from molecular size considerations alone, the solution tertiary structure of MTs could not be determined solely from standard, homonuclear, 2D ^1H NMR methods.[9] The reason is twofold. There is considerable degeneracy in the amino acid composition and the tertiary protein fold is practically devoid of regular elements of secondary structure. The latter is reflected in the relatively small number of ^1H–^1H NOE distance constraints that results from the presence of the metal clusters in the place of the core of hydrophobic amino acid residues of a typical globular protein.

In the case of ^{113}Cd MTs, additional constraints corresponding to the metal–protein coordination bonds were generated from ^1H–^{113}Cd HMQC experiments[15–17] that relate each ^{113}Cd resonance to the C-βH_2 protons of the coordinating Cys residues. Such information combined with the sequential ^1H NMR assignments unequivocally established the topology of the Cd–thiolate clusters and their position with respect to the MT primary structure (Figure 8). Similarly, the isomorphic replacement of the Cu(I) in yeast copper–MT by the spin-$\frac{1}{2}$ ^{109}Ag(I) ion allowed individual ^{109}Ag resonances to be correlated with their associated Cys ligands (Figure 9). These data indicated the presence of a single Ag_7Cys_{10} cluster with mixed metal-coordination number.[18,19]

Heteronuclear correlation experiments are usefully complemented by heteronuclear-filtered ^1H NMR spectra that contain

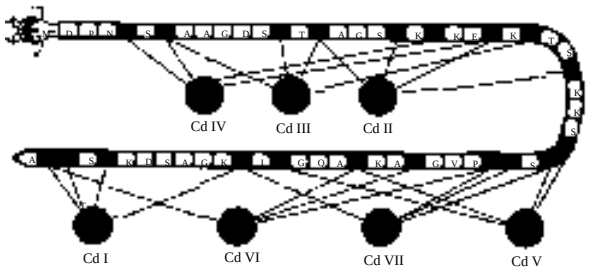

Figure 8 Cadmium–cysteine connectivities of human MT-2 established by 2D ^1H–^{113}Cd HMQC NMR spectroscopy. The metals are numbered according to their increasing ^{113}Cd NMR chemical shifts. The darkened residues represent cysteine

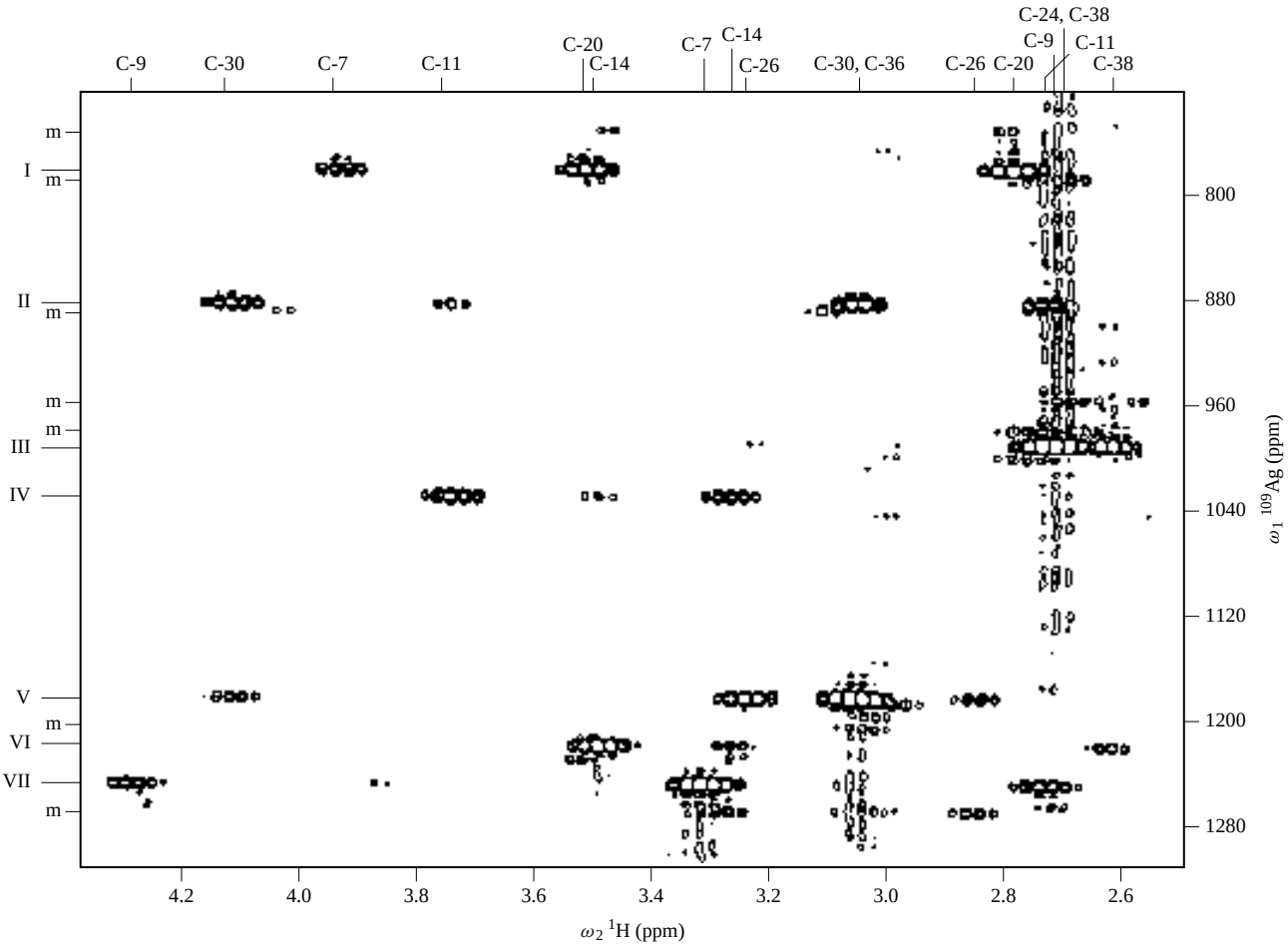

Figure 9 Heteronuclear ^{1}H–^{109}Ag multiple quantum coherence transfer spectrum of yeast Ag–MT acquired *antiphase*. The seven ^{109}Ag resonances are labeled by Roman numerals according to their increasing chemical shifts. The positions of seven low-intensity ^{109}Ag resonances are indicated by the letter m. The assignments of various cross peaks along ω_2 to specific H^{β} of cysteine obtained from sequential assignment methods are indicated on the top of the diagram

resonances only from the X-coupled protons. Such experiments permit a straightforward measurement of ^{113}Cd–^{1}H coupling constants and a direct distinction to be made between bridging and terminal Cys ligands in the MT metal clusters.[20]

The knowledge of the metal cluster geometries and metal–Cys connectivities, together with the experimentally determined ^{1}H–^{1}H distance constraints and the dihedral angle constraints from the measured coupling constants allowed the elucidation of the 3D solution structure of rabbit, rat, human, crab, and yeast MTs.[21–25] In all mammalian MTs, despite some amino acid substitutions, the polypeptide wraps around the metal–thiolate clusters in a closely similar way (Figure 10) and there is conservation of local structural features. As a result of the absence of interdomain constraints, their relative orientation cannot be obtained from NMR, only from the X-ray crystal structure of rat MT, which showed identical molecular architecture with the solution structure.[26]

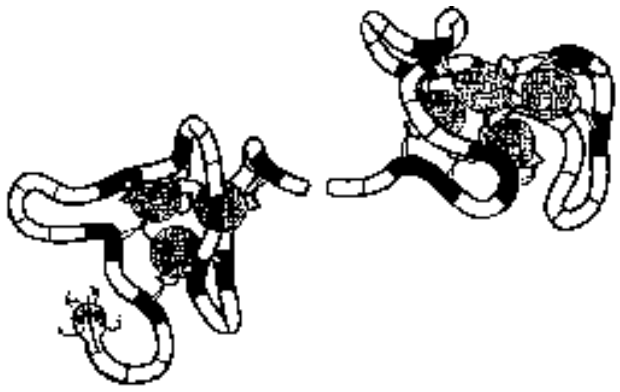

Figure 10 The 3D solution structure of the β-domain (left) and α-domain (right) of human [Cd_7]–MT-2. The coordinates are from Messerle et al.,[23] files 1MHU and 2MHU, in Brookhaven Protein Data Bank

5 RELATED ARTICLES

Cadmium-113 NMR: A Surrogate Probe for Zinc and Calcium in Proteins; Chemical Exchange Effects on Spectra.

6 REFERENCES

1. J. H. R. Kägi and A. Schäffer, *Biochemistry*, 1988, **27**, 8509.

2. K. T. Suzuki, N. Imura, and M. Kimura (eds.), *Metallothionein III; Biological Roles and Medical Implications*, Birkhäuser, Basel, 1993.
3. J. F. Riordan and B. L. Vallee (eds.), *Methods Enzymol.*, 1991, **205**.
4. I. M. Armitage and J. D. Otvos, *Biol. Magn. Reson.* 1982, **4**, 79, and references cited therein.
5. I. M. Armitage and Y. Boulanger, in *NMR of Newly Accessible Nuclei*, ed. P. Laszlo, Academic Press, New York, 1983, Vol. 2, pp. 337–365, and references cited therein.
6. M. F. Summers, *Coord. Chem. Rev.*, 1988, **86**, 43, and references cited therein.
7. J. E. Coleman, *Methods Enzymol.*, 1993, **227**, 16, and references cited therein.
8. P. S. Marchetti, P. D. Ellis, and R. G. Bryant, *J. Am. Chem. Soc.*, 1985, **107**, 8191.
9. K. Wüthrich, *Methods Enzymol.*, 1991, **205**, 502, and references cited therein.
10. O. Zerbe, D. L. Pountney, W. Philipsborn, and M. Vašák, *J. Am. Chem. Soc.*, 1994, **116**, 377.
11. J. Kördel, C. Johansson, and T. Drakenberg, *J. Magn. Reson.*, 1992, **100**, 581.
12. J. D. Otvos and I. M. Armitage, *Proc. Natl. Acad. Sci. U.S.A.*, 1980, **77**, 7094.
13. J. D. Otvos, H. R. Engeseth, and S. Wehrli, *Biochemistry*, 1985, **24**, 6735.
14. J. D. Otvos, X. Liu, H. Li, G. Shen, and M. Basti, in *Metallothionein III*, eds. K. T. Suzuki, N. Imura, and M. Kimura, Birkhäuser, Basel, 1993, pp. 57–74.
15. D. Live, I. M. Armitage, D. C. Dalgarno, and D. Cowburn, *J. Am. Chem. Soc.*, 1985, **107**, 1775.
16. J. D. Otvos, H. R. Engeseth, and S. Wehrli, *J. Magn. Reson.*, 1985, **61**, 579.
17. M. H. Frey, G. Wagner, M. Vašák, O. W. Sørensen, D. Neuhaus, E. Wörgötter, J. H. R. Kägi, R. R. Ernst, and K. Wüthrich, *J. Am. Chem. Soc.*, 1985, **107**, 6847.
18. S. S. Narula, R. K. Mehra, D. R. Winge, and I. M. Armitage, *J. Am. Chem. Soc.*, 1991, **113**, 9354.
19. S. S. Narula, D. R. Winge, and I. M. Armitage, *Biochemistry*, 1993, **32**, 6773.
20. E. Wörgötter, G. Wagner, M. Vašák, J. H. R. Kägi, and K. Wüthrich, *J. Am. Chem. Soc.*, 1988, **110**, 2388.
21. A. Arseniev, P. Schultze, E. Wörgötter, W. Braun, G. Wagner, M. Vašák, J. H. R. Kägi, and K. Wüthrich, *J. Mol. Biol.*, 1988, **201**, 637.
22. P. Schultze, E. Wörgötter, W. Braun, G. Wagner, M. Vašák, J. H. R. Kägi, and K. Wüthrich, *J. Mol. Biol.*, 1988, **203**, 251.
23. B. A. Messerle, A. Schäffer, M. Vašák, J. H. R. Kägi, and K. Wüthrich, *J. Mol. Biol.*, 1990, **214**, 765.
24. S. S. Narula, M. Brouwer, and I. M. Armitage, *Biochemistry*, 1995, submitted.
25. C. W. Peterson, S. S. Narula, and I. M. Armitage, *FEBS Lett.*, 1995, submitted.
26. W. Braun, M. Vasák, A. H. Robbins, C. D. Stout, G. Wagner, J. H. R. Kägi, and K. Wüthrich, *Proc. Natl. Acad. Sci. U.S.A.*, 1992, **89**, 10 124.

Biographical Sketches

Ian M. Armitage. *b* 1947. B.Sc. 1968, Chemistry Bishops University. Ph.D., 1972, Physical Organic Chemistry, University of British Columbia (with Prof. L. D. Hall). Postdoctoral Fellow (1973–74) California Institute of Technology (with Prof. J. D. Roberts). Assistant/Associate Professor, Physical Sciences and Molecular Biophysics and Biochemistry, Yale University School of Medicine, 1974–83. Professor Adjunct of Research, Molecular Biophysics and Biochemistry, and Diagnostic Radiology, Yale University School of Medicine, 1983–1991. Professor Adjunct of Research, Pharmacology and Diagnostic Radiology, Yale University School of Medicine, 1991–95. Professor, Biochemistry, University of Minnesota, 1995–present. Over 100 publications. Research interests: structure/function studies of metalloproteins and proteins of the immune system using various NMR approaches.

Lazaros T. Kakalis. *b* 1958. Diploma, 1981, Chemistry, Aristotelion University, Greece. M.S., 1984, Food Chemistry/Biochemistry, Cornell University, USA, Ph.D., 1988, Food Chemistry, University of Illinois, USA. Research Chemist at US Dept. Agriculture, Philadelphia, 1988–89. Postdoctoral Associate in Pharmacology, Yale University, 1992–present. Approx. 11 publications. Research interests: applications of NMR in protein structure/function and the study of intermolecular interactions.

James D. Otvos. *b* 1947. B.A., 1969, Chemistry, Ph.D., 1976, Comparative Biochemistry, University of California-Berkeley. Postdoctoral work at Yale University (with Ian M. Armitage). Assistant/Associate Professor of Chemistry, University of Wisconsin-Milwaukee, 1980–90. Professor of Biochemistry, North Carolina State University, 1990–present. Approx. 60 publications. Research interests: NMR applied to metalloproteins, clinical analytical uses of NMR.

Molecular Motions: T_1 Frequency Dispersion in Biological Systems

Rainer Kimmich
Universität Ulm, Germany

1	Introduction	1
2	Fluctuations in Proteins	1
3	Fluctuations in Lipid Bilayers	2
4	Deuteron T_1 Frequency Dispersion of Protein Solutions in D_2O	2
5	Critical Water Contents	4
6	Proton T_1 Frequency Dispersion of Tissue	5
7	$T_{1\rho}$ Frequency Dispersion Imaging	5
8	Related Articles	6
9	References	6

1 INTRODUCTION

The information provided by the frequency dependence ('dispersion') of spin–lattice relaxation times (or rates) in the laboratory frame T_1 (T_1^{-1}), or in the rotating frame $T_{1\rho}$ ($T_{1\rho}^{-1}$), is the type and the timescale of molecular motion. Studies of this sort are mainly based on the field cycling [or NMR dispersion (NMRD)] technique[1,2] often supplemented by rf pulse experiments in stationary magnetic fields. Molecular dynamics can be specified on this basis in great detail, although chemical shift distributions normally cannot be resolved.

The essence of the field cycling principle is to generate nonequilibrium spin populations by switching the magnetic field to a variable relaxation field, the flux density of which is normally lower than that of the polarization field. The relaxation curve of the magnetization is then probed point by point by switching to a fixed detection field, where the magnetization is read out in the form of a FID or a spin echo. A prerequisite of the technique is that relaxation during the switching intervals is minor. The maximum frequency is determined by technical restrictions, whereas the lower frequency limit is given by the local fields within the sample or by incompletely compensated external fields such as the Earth field. Operational order-of-magnitude ranges of the frequency are $10^3 < \nu < 10^8$ Hz for protons and $10^2 < \nu < 10^7$ Hz for deuterons.

Molecular motions cause fluctuations of the spin interactions; these are normally the dipolar interaction among the spin-bearing particles or the coupling of quadrupole nuclei to electric field gradients. The fluctuating interactions induce spin transitions, making the ensemble relax towards equilibrium. The spin–lattice relaxation rate $1/T_1$ in *homogeneous systems* is given by intensity functions (or spectral densities) $I(\omega)$ at the transition frequencies ω of the spin system.[3] These functions are proportional to the FTs of the time autocorrelation functions of spherical harmonics of order 2, $G(t)$. The fluctuations of quadrupolar interactions and the low-frequency part of fluctuations of dipolar interactions are normally dominated by intramolecular contributions. The T_1 frequency dispersion thus probes the correlation function (or the corresponding intensity function) of molecular reorientations and, in certain circumstances, translations.

Systems of biological origin tend to be *heterogeneous* in the sense that the investigated nuclei occur in different environments with different molecular dynamics and spin interactions. It is then a matter of exchange rates whether spin–lattice relaxation is determined by average intensity functions ('fast exchange' relative to relaxation times) so that monoexponential relaxation decays arise, or whether multiexponential distributions occur.[4] In the context of water relaxation in biological systems, the two-site fast exchange model turned out to be very successful. Note, however, that the term 'exchange' refers to material transport as well as to (immaterial) spin diffusion or magnetization transfer.[12,13]

The element usually detected in T_1 frequency dispersion experiments is hydrogen, via proton or deuteron resonance. (In exceptional cases, ^{31}P relaxation studies might also be feasible.[5]) Other nuclear species can be probed indirectly via cross relaxation if their relaxation rates are fast enough to act in combination with proton spin diffusion as relaxation sinks. This can be expected in particular with quadrupole nuclei. The cross relaxation then manifests itself as 'quadrupole dips' at the resonance crossing frequencies,[6] as demonstrated in Figure 1 for polyalanine protons cross relaxed by the amide ^{14}N relaxation sinks.

The T_1 frequency dispersion may be influenced further by electron paramagnetic constituents such as, for example, molecular oxygen,[8] paramagnetic ions,[9,10] or heme groups.[7,11] Relaxation mechanisms of this sort, however, are not considered in this article.

T_1 frequency dispersion studies have been performed with many different (diamagnetic) systems of biological origin, including: dissolved,[12,14] wet,[15] or dry[16] proteins; DNA;[6] lipid bilayers;[17,18] tissue;[15] eye lenses;[19] and small animals in vivo.[20]

The dominant constituents of biological systems are biopolymers (or oligomers) and water. The water component (including all exchangeable hydrogen atoms of the biopolymers) can be conveniently prepared in deuterated form so that separate studies of the dynamics in the two components can be performed. Figure 2 shows the T_1 frequency dispersions of water deuterons and of nonexchangeable biopolymer protons measured in a solution of bovine serum albumin (BSA) in D_2O as a typical system.[21] The entirely different nature of the fluctuations within the two constituents is obvious.

2 FLUCTUATIONS IN PROTEINS

Molecular motions of proteins can comprise main chain ('backbone') fluctuations, side-group motions and tumbling of the whole macromolecule. The latter can easily be identified by considering the concentration dependence of the reorientation rates (see below). Side-group motions, such as restricted rotational diffusion and ring flips, are a matter of the local structure and chemical composition. Proteins, for instance, therefore tend to be characterized by a broad distribution of the side-group correlation times.

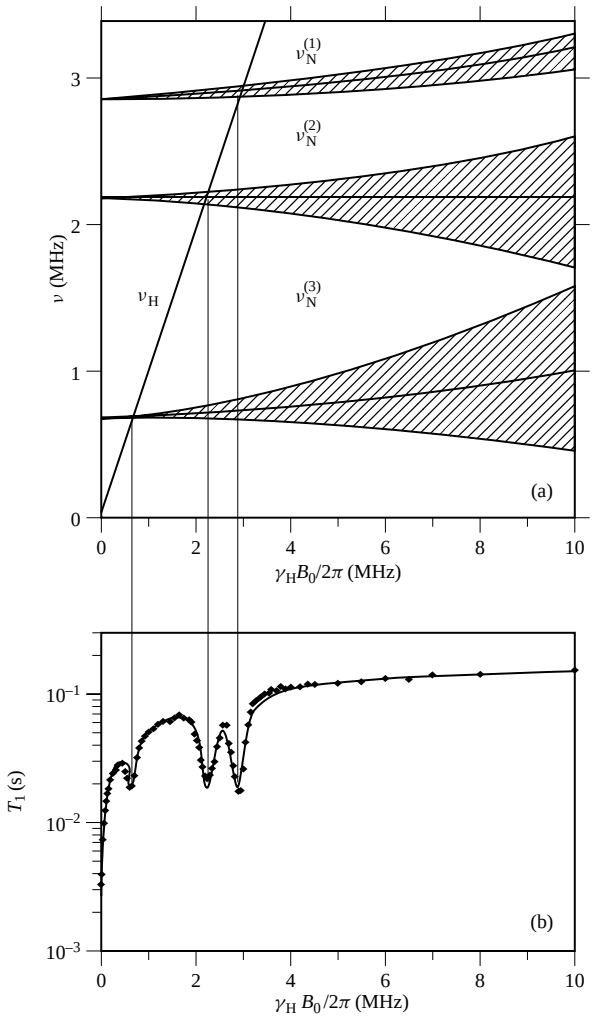

Figure 1 (a) Field dependence of the ^{1}H and ^{14}N resonance frequencies of amide groups. The hatched areas indicate the range covered in a powdery sample. The solid lines within these areas represent the powder averages. The magnetic flux density $\boldsymbol{B}_0$ is expressed in units of the proton Larmor frequency. (b) T_1 frequency dispersion of poly-L-alanine at $-1\,^\circ$C. The three ^{14}N–^{1}H quadrupole dips at the resonance crossings are obvious. (Reproduced by permission of Academic Press from R. Kimmich, F. Winter, W. Nusser, and K.-H. Spohn, *J. Magn. Reson.*, 1986, **68**, 263)

Backbone fluctuations in proteins and polypeptides, on the other hand, appear to be governed by homogeneous modes leading to an apparently universal T_1 dispersion behavior at low frequencies where side-group motions are of minor importance. The frequency dependence in the absence of molecular tumbling can be described over a wide range by the power law[6] $T_1 \propto \nu^{0.74\pm0.06}$, which can be explained by one-dimensional multiple trapping diffusion of defects locally dilating the structure.[16] The corresponding correlation function is given by the error function ('erf') expression:

$$G_{\mathrm{mtd}}(t) = a_1 \left\{ \mathrm{erf}\left(\frac{b^2}{2\langle\xi^2\rangle}\right)^{1/2} - \left(\frac{2\langle\xi^2\rangle}{\pi b^2}\right)^{1/2} \times \left[1 - \exp\left(-\frac{b^2}{2\langle\xi^2\rangle}\right)\right]\right\} + a_2 \qquad (1)$$

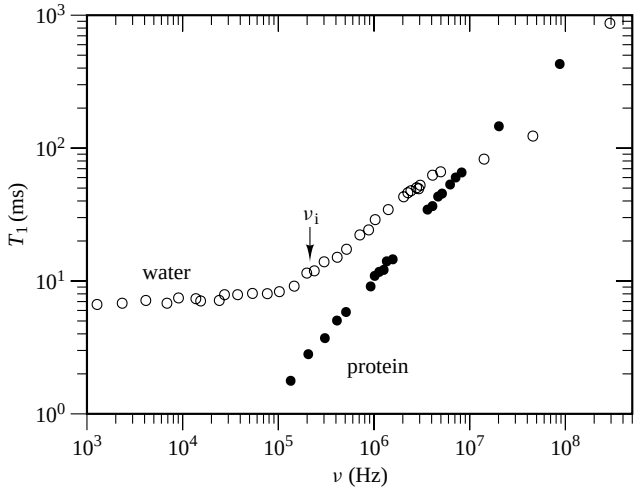

Figure 2 Frequency dependence of the proton (•) and deuteron (○) spin–lattice relaxation times of a D_2O solution of bovine serum albumin (35 wt.%) at 291 K. The data in the vicinity of the ^{14}N–^{1}H quadrupole dips are omitted. The different T_1 frequency dispersions indicate different fluctuation processes dominant for water (including exchangeable hydrogen atoms) and for the protein molecules. (Reproduced by permission of the American Chemical Society from W. Nusser and R. Kimmich, *J. Phys. Chem.*, 1990, **94**, 5637)

where $a_2 = 1 - a_1$ represents the residual correlation at long times, b represents the extension of the defect, and $\langle\xi^2\rangle \propto t^{\frac{1}{2}}$ represents the (anomalous) mean-square displacement of the defects in a time interval t.

3 FLUCTUATIONS IN LIPID BILAYERS

Lipid bilayers form another system whose dynamics are governed by dynamic modes. In experiments with partially deuterated samples, one can distinguish between the alkyl chain and the headgroup part of the bilayers. In the gel phase, one-dimensional restricted diffusion of defects (chain orientation conserving rotational isomers) permits the perfect description of the T_1 frequency dispersion of the alkyl chains.[17] The corresponding intensity function for defect diffusion is characterized by the limits

$$I_{\mathrm{dd}}(\omega) = \begin{cases} \frac{2}{3}(\tau_b^{1/2}\tau_d^{1/2} - \tau_b) & \text{for } \omega\tau_d \ll 1 \\ \frac{\tau_d\tau_b^{1/2} - 2\tau_b\tau_d^{1/2}}{(\tau_d^{1/2} - \tau_b^{1/2})^2}\omega^{-1/2} & \text{for } \omega\tau_b \ll 1 \ll \omega\tau_d \\ \frac{\tau_d^{1/2}}{\tau_d^{1/2}\tau_b^{1/2} - \tau_b}\omega^{-3/2} & \text{for } \omega\tau_b \gg 1 \end{cases} \qquad (2)$$

where τ_d is the mean diffusion time across the bilayer (from headgroup to headgroup) and τ_b is the mean diffusion time over a length equal to the width of the defect.

In the liquid crystalline phase, collective modes ('director fluctuations') tend to dominate at low frequencies.[18] The behavior is, however, much more complex because other mechanisms such as rotational isomerism, chain rotations, and diffusion along the curved shape of the bilayer are superimposed.

4 DEUTERON T_1 FREQUENCY DISPERSION OF PROTEIN SOLUTIONS IN D_2O

The proton signals observed in tissue, diluted aqueous biopolymer solutions, and diluted aqueous lipid bilayer dispersions tend to be dominated by water. In such systems, the polar surfaces of the macromolecular constituents are covered by hydration shells; however, these shells form only a minor fraction of the total water. Nevertheless, a strong enhancement of the spin–lattice relaxation of water occurs as first observed in protein solutions.[22]

Also at a rather early stage, it was found by means of NMR spectroscopy that water molecules in the hydration shell are oriented relative to the biopolymer surface[23,24] and congeal far below the freezing point of bulk water.[25] Nonfreezing water actually may be an operational definition of hydration water, the fraction of which can be quantitatively determined in this way.

Another striking finding is that translational diffusion within the hydration shells is relatively fast. Even in frozen protein solutions not far below 0 °C, where diffusion is restricted to thin (about a monolayer thick) films of liquid water on the surface of the macromolecules, the diffusion coefficient is merely reduced by one order of magnitude relative to liquid bulk water.[26] On the other hand, orientation correlation times up to six orders of magnitude longer than those in bulk water must be concluded from T_1 frequency dispersion experiments.[15]

The T_1 frequency dispersion of the water phases in protein/D_2O solutions was measured selectively using deuteron resonance.[15] In the frame of the two-site fast exchange model, the effective water spin–lattice relaxation rate is given by:

$$\frac{1}{T_1} \approx \frac{1 - p_h}{T_1^f} + \frac{p_h}{T_1^h} \tag{3}$$

where T_1^f and T_1^h are the spin–lattice relaxation times in the 'free' (i.e. bulk) and 'hydration' water phases, respectively, and p_h is the fraction of hydration water.

The description of the T_1 frequency dispersion of hydration water is principally based on four competitive mechanisms:

1. Tumbling of the macromolecule including its hydration shell (correlation time τ_t).
2. Restricted rotational diffusion of water molecules about axes perpendicular to the local surface (correlation time τ_r).
3. Exchange between free and hydration water (correlation time = residence time in the hydration shell $\tau_\perp$).
4. Reorientations mediated by translational displacements (RMTDs) along the more or less rugged and curved surface of the macromolecule: water molecules diffuse along the surface and, as a consequence, alter their orientations which are defined by the local surface structure. The longest correlation of this mechanism is designated by $\tau_\parallel$.

Using the orientational structure factor formalism,[27] the RMTD correlation function was derived as:

$$G_{RMTD}(t) = \frac{1}{2(k_u - k_l)}\sqrt{\frac{\pi}{Dt}}[\mathrm{erf}(\sqrt{Dt}k_u) - \mathrm{erf}(\sqrt{Dt}k_l)] \tag{4}$$

where k_u and k_l are the upper and lower cut-off wavenumbers of the equipartition distribution assumed for the surface structure. D is the average translational water diffusion coefficient in the hydration shell. The lower cut-off wavenumber is connected with a cut-off correlation time:

$$\tau_\parallel = (Dk_l^2)^{-1} \tag{5}$$

revealing itself as the 'inflection point' $2\pi\nu_i\tau_\parallel \approx 1$ in the absence of molecular tumbling (see Figure 3). Equation (4) produces the square root frequency dependence typical for water relaxation in aqueous protein solutions at intermediate frequencies.

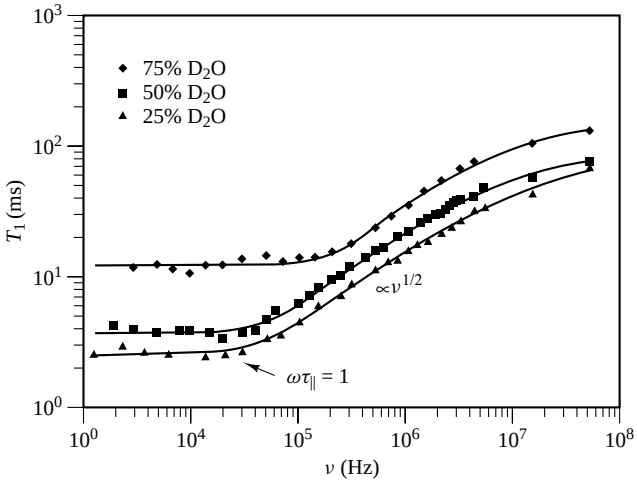

Figure 3 Deuteron T_1 frequency dispersion of D_2O solutions of bovine serum albumin at 291 K. The solid lines were calculated using the RMTD formalism taking into account protein tumbling [equation (8)] and restricted rotational diffusion of the water molecules (high-frequency regime). Note that the T_1 frequency dispersions at a water content of 25 wt.% (no free water) and 50 wt.% (with free water) are qualitatively the same, apart from differences in the absolute values of the relaxation times. In these cases, the low-frequency dispersion is dominated by RMTD. At 75 wt.%, the inflection point is shifted to higher frequencies due to the competitive action of protein tumbling. (Reproduced by permission of Elsevier from R. Kimmich, W. Nusser, and T. Gneiting, *Colloids Surf.*, 1990, **45**, 283)

Restricted rotational diffusion, exchange with free water and macromolecular tumbling can be represented by exponential correlation function. Restricted rotational diffusion is only important for the high-frequency dispersion, whereas the exchange mechanism is normally too slow (relative to the other contributions) to affect the reorientation behavior. What remains as a mechanism effective in the low-frequency regime is macromolecular tumbling and RMTD.

On the basis of this scheme, the deuteron T_1 frequency dispersion of D_2O in aqueous protein solutions can be described perfectly.[15] Inserting the water diffusion coefficient experimentally determined with the NMR field gradient technique, a length scale can be estimated from the RMTD correlation time $\tau_\parallel$ [equation (5)] revealing itself via the inflection point in the absence of macromolecular tumbling. The result is half the protein circumference, as required by RMTD.[27] In other words, the mean diffusion time around half the circumference of the protein molecule is calculated, on the basis of the experimental diffusion coefficient and the known short and long axes of the protein, to be of the order of 10^{-6} s, which is in perfect agreement with the inflection point measured in the absence of macromolecular tumbling.

The RMTD mechanism accounts very well for the weak temperature dependence of spin–lattice relaxation. Transient irrotational binding of a small percentage of the hydration water at certain sites, as suggested in several studies,[22,28] would require binding energies twice as high as the apparent activation energies estimated from the experimental T_1 data. With RMTD, long correlation times are due to the geometry of the system rather than to high binding energies at certain sites. Furthermore, transient irrotational binding would result in slopes of the T_1 frequency dispersion at intermediate frequencies which are four times as high as found experimentally.

Another question is the origin of the long residence times of water molecules in the hydration shells. This, of course, is no problem, in principle, if free water is absent or frozen. Adding more and more water to a protein sample which initially has saturated hydration shells but no free water, does not change the qualitative behavior of relaxation or diffusion.[15,26] With the exception of the onset of macromolecular tumbling (described below), there is no evidence for new relaxation mechanisms of hydration water due to the presence of free water.

The relaxation scheme outlined above can also be applied to a certain degree to systems modeling hydrated globular proteins. Water adsorbed on agglomerates of fine particles of silica of a similar diameter again shows a T_1 frequency dispersion reflecting the surface structure.[30]

While the surfaces of fine particles of silica are expected to be smooth and chemically homogeneous, those of proteins are extremely heterogeneous with respect to polarity and hydrogen binding ability. On such surfaces water diffusion is more likely to resemble a hopping process among the preferential binding sites or areas. Translational displacements may then be governed by waiting time and step-length distributions.[31] Nevertheless, in timescales that are long compared with typical waiting times, i.e. in the fast-jump limit, an effective diffusion coefficient can be defined. This also includes exchange processes in the sense that molecules (or hydrogen atoms) leave and reenter the hydration shell to and from other environments such as free water or sites within the protein. In this case, the surface is probed only selectively by a set of discrete binding sites. Correspondingly, the spin–lattice relaxation then originates from reorientation jumps.

From the experimental point of view, the fast jump/exchange limit reveals itself by giving monoexponential attenuation curves in diffusion as well as in spin–lattice relaxation experiments. This is what one normally observes, to a reasonably good approximation.[26] In this case, effective diffusion coefficients D_{eff} and effective spin–lattice relaxation times $T_{1,\text{eff}}$ can be evaluated.

The microphases (or molecular environments) can be characterized by weights p_i, diffusion coefficients D_i, and spin–lattice relaxation times $T_{1,i}$. The following exchange formulas are then valid:

$$D_{\text{eff}} = \sum_i p_i D_i \tag{6}$$

$$\frac{1}{T_{1,\text{eff}}} = \sum_i \frac{p_i}{T_{1,i}} \tag{7}$$

where $\Sigma_i\, p_i = 1$.

D_{eff} tends to be governed by environments with high molecular mobility, whereas $1/T_{1,\text{eff}}$ is dominated by the slowly reorienting molecules, that sit for relatively long periods on sites with certain orientations. Thus, high effective diffusion coefficients, long orientation correlation times, and low thermal activation energies do not contradict each other a priori.

If distributions of microphases exist, the continuous-diffusion treatment must be regarded as an approximate description of phenomena that tend to be discrete in reality. RMTD in this case probes only those sites of the surface at which spin–lattice relaxation effectively takes place (irrespective of the exchange pathways that the molecules or atoms follow in between). In principle, the applicability of the concept comprises continuous and step-by-step, surface-bound and multiphase diffusion, as long as the experiments provide *effective* diffusion coefficients and spin–lattice relaxation times.

5 CRITICAL WATER CONTENTS

In the limit of low frequencies, the T_1 frequency dispersion of water in protein solutions terminates at a certain 'inflection frequency' ν_i in a plateau (see Figure 2 and Figure 3). As an indication of the competitive nature of RMTD and macromolecular tumbling, this quantity depends strongly on the water content c_w (Figure 4).[29]

Tumbling can only take place if the water content exceeds the saturation concentration c_s defined by the saturation of

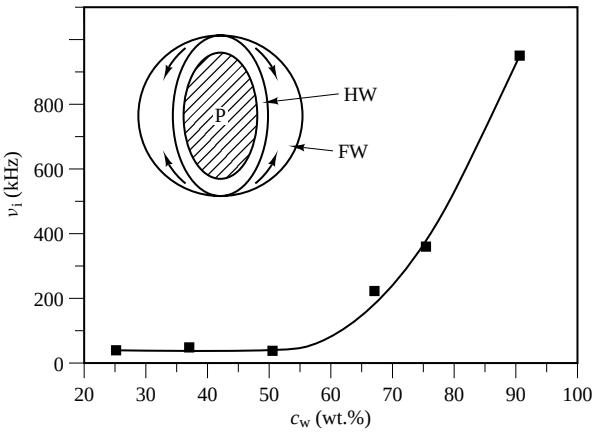

Figure 4 Inflection frequency of the deuteron T_1 dispersion of BSA/D_2O solutions at 291 K versus water content. This dependence can be described by the 'free-water volume' model of macromolecular tumbling illustrated in the upper left-hand corner of the diagram. A protein molecule (P) including hydration water (HW) can only tumble if sufficient free water (FW) is available. The minimum free-water volume corresponds to the circumscribing sphere. Below a critical water content $c_0 \approx 65$ wt.%, macromolecular tumbling is slower than the RMTD process of water on the surface, so that the inflection frequency is governed by RMTD. Above c_0, tumbling becomes faster than this limit. The inflection frequency is then determined by the tumbling rate of the macromolecules. The experimental data were evaluated directly from the T_1 dispersion curves, the solid line was calculated on the basis of the formalism described in the text. (Reproduced by permission of Hüthig & Wepf from R. Kimmich, *Makromol. Chem., Macromol. Symp.*, 1990, **34**, 237)

the hydration shells. In this case 'free water' is present so that, with a certain probability, a macromolecule is surrounded by enough free water for rotational jumps. The 'free-water volume' formalism[15] leads to a macromolecular tumbling correlation time:

$$\tau_t = \tau_t^0 \exp\left[\gamma^*(r-1)\frac{1-c_w+c_s}{c_w-c_s}\right] \quad (c_w \rangle c_s) \qquad (8)$$

where $\tau_t^0 = \eta(v_p + v_s)/(k_B T)$ is the Stokes–Einstein expression for tumbling of a particle with volume $v_p + v_s$ (bare protein plus the saturated hydration shell) in a solvent with viscosity η; $0.5 < \gamma^* < 1$ is a numerical constant; and r is the ratio of the volumes of the circumscribing sphere and the hydrated protein molecule itself approximated by an ellipsoid (see Figure 4). The critical water content c_0 at which macromolecular tumbling becomes competitive to the correlation time $\tau_\parallel$ corresponding to the lower cut-off wavenumber k_1 of the RMTD process, is then defined by the condition $\tau_\parallel = \tau_t$. From this, one finds that

$$c_0 = c_s + \frac{\tilde{\gamma}}{1+\tilde{\gamma}} \qquad (9)$$

where $\tilde{\gamma} = (r-1)\gamma * / \ln(\tau_\parallel/\tau_t^0)$. For aqueous bovine serum albumin (BSA) solutions, $c_s \approx 30$ wt.% and $c_0 \approx 65$ wt.%, that is $\tilde{\gamma} \approx 0.5$.

6 PROTON T_1 FREQUENCY DISPERSION OF TISSUE

Although water is normally the most abundant compound in tissue, and therefore provides the dominant contribution to hydrogen signals recorded in relaxation experiments, the behavior observed in tissue is determined by the interaction and the cross relaxation with the macromolecular constituents. The description must therefore refer to fluctuations in the water phases as well as in the macromolecules. Assuming fast exchange between all components, it is possible to reproduce the experimental T_1 frequency dispersion of tissue by considering the combined action of RMTD in the hydration shells, tumbling and backbone fluctuations of the proteins, restricted rotational diffusion of hydration water molecules, and (with regard to the quadrupole dip frequency region) $^{14}N^1H$ cross relaxation. Figure 5 shows two representative data sets.[15]

Treatments of this sort are crucial for our understanding of the basic mechanisms contributing to relaxation in tissue. For the practical characterization of tissue, it may be more useful to describe the T_1 frequency dispersion by empirical intensity functions or just qualitatively. The T_1 frequency dispersion of a number of different tissues have been characterized in this way, showing significant differences.[32–34]

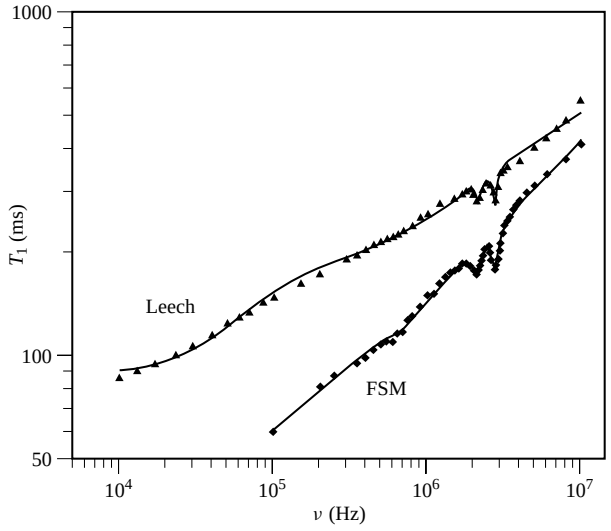

Figure 5 Proton T_1 frequency dispersion of a leech (in vivo) and freshly excised frog sartorius muscle (FSM) in the relaxed state in vitro. The solid lines were calculated on the basis of macromolecular tumbling, RMTD, restricted rotational diffusion of hydration water, protein backbone fluctuations and terms representing the $^{14}N-^1H$ cross relaxation quadrupole dips. (Reproduced by permission of Elsevier from R. Kimmich, W. Nusser, and T. Gneiting, *Colloid. Surf.*, 1990, **45**, 283)

7 $T_{1\rho}$ FREQUENCY DISPERSION IMAGING

The molecular motions revealing themselves in the T_1 frequency dispersion are substantial for image contrasts in

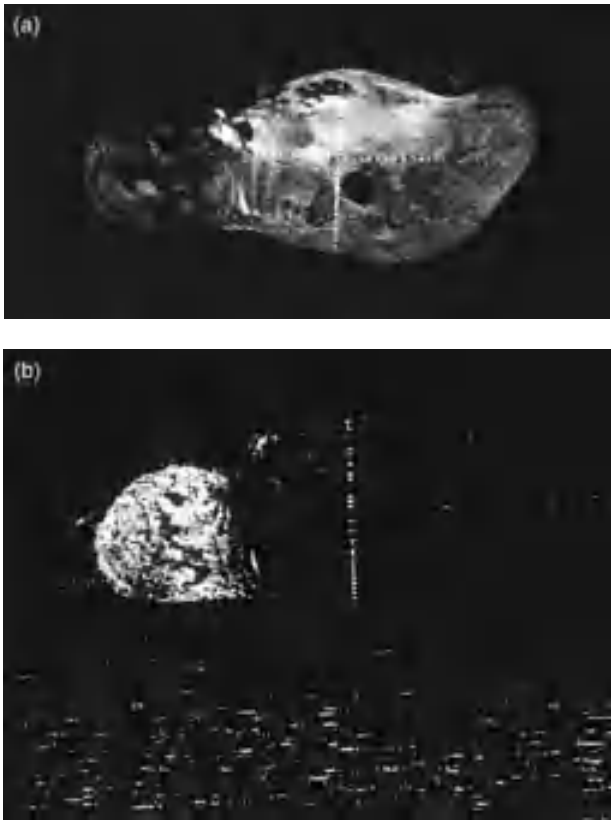

Figure 6 Cross-sectional NMR images of a mouse with an implanted tumor (left). (a) Conventional two-dimensional spin echo FT image. (b) Rotating frame dispersion image (RODI) rendering the $T_{1\rho}$ frequency dispersion as gray scale contrasts. The tumorous tissue (left) can be clearly distinguished from muscle tissue (right). (Reproduced by permission of Academic Press from E. Rommel and R. Kimmich, *Magn. Reson. Med.*, 1989, **12**, 390)

NMR tomography. At conventional magnetic flux densities, the relaxation contrasts originate from relative fast motions and represent the relaxation rates rather than the T_1 frequency dispersion. Using on- and off-resonance variants of spin–lattice relaxation in the rotating frame, an imaging sequence was proposed that gives directly the spatial distribution of the $T_{1\rho}$ frequency dispersion,[35,36] which is indicative for slow motions, macromolecular tumbling, and RMTD.

Figure 6 shows images of a tumorous mouse recorded with this rotating frame dispersion imaging (RODI) technique and conventional tomography for comparison. Striking differences are obvious. RODI provides strong contrast of the tumorous tissue, whereas muscle tissue is suppressed. In the conventional spin echo FT image, on the other hand, both sorts of tissue are rendered with equivalent intensity. Thus biomedical applications of the low-frequency dispersion of spin–lattice relaxation suggest themselves.

8 RELATED ARTICLES

Dynamics of Water in Biological Systems: Inferences from Relaxometry; Field Cycling Experiments; Protein Hydration; Relaxation Theory: Density Matrix Formulation; Relaxometry of Tissue; Rotating Frame Spin–Lattice Relaxation Off-Resonance; Slow and Ultraslow Motions in Biology; Whole Body Studies Involving Spin-Lattice Relaxation in the Rotating Frame.

9 REFERENCES

1. R. Kimmich, *Bull. Magn. Reson.*, 1980, **1**, 195.
2. F. Noack, *Prog. NMR Spectrosc.*, 1986, **18**, 171.
3. A. Abragam, *The Principles of Nuclear Magnetism*, Clarendon, Oxford, 1961.
4. J. R. Zimmerman and W. E. Brittin, *J. Phys. Chem.*, 1957, **61**, 1328.
5. G. Schauer, W. Nusser, M. Blanz, and R. Kimmich, *J. Phys. E: Sci. Instrum.*, 1987, **20**, 43.
6. R. Kimmich, F. Winter, W. Nusser, and K.-H. Spohn, *J. Magn. Reson.*, 1986, **68**, 263.
7. R. Kimmich, *Z. Naturforsch., Teil b*, 1971, **26**, 1168.
8. R. Kimmich and A. Peters, *Chem. Phys. Lipids*, 1975, **14**, 350.
9. S. H. Koenig and W. E. Schillinger, *J. Biol. Chem.*, 1969, **244**, 6520.
10. S. D. Kennedy and R. G. Bryant, *Biophys. J.*, 1986, **50**, 669.
11. S. H. Koenig, R. D. Brown III, and T. R. Lindstrom, *Biophys. J.*, 1981, **34**, 397.
12. R. Kimmich and F. Noack, *Z. Naturforsch., Teil a*, 1970, **25**, 1680.
13. H. T. Edzes and E. T. Samulski, *J. Magn. Reson.*, 1978, **31**, 207.
14. S. H. Koenig and W. E. Schillinger, *J. Biol. Chem.*, 1969, **244**, 3283.
15. R. Kimmich, W. Nusser, and T. Gneiting, *Colloid. Surf.*, 1990, **45**, 283.
16. W. Nusser, R. Kimmich, and F. Winter, *J. Phys. Chem.*, 1988, **92**, 6808.
17. R. Kimmich, G. Schnur, and A. Scheuermann, *Chem. Phys. Lipids*, 1983, **32**, 271.
18. E. Rommel, F. Noack, P. Meier, and G. Kothe, *J. Phys. Chem.*, 1988, **92**, 2981.
19. S. H. Koenig, R. D. Brown III, A. K. Kenworthy, A. D. Magid, and R. Ugolini, *Biophys. J.*, 1993, **64**, 1178.
20. R. Kimmich, W. Nusser, and F. Winter, *Phys. Med. Biol.*, 1984, **29**, 593.
21. W. Nusser and R. Kimmich, *J. Phys. Chem.*, 1990, **94**, 5637.
22. O. K. Daszkiewicz, J. W. Hennel, and B. Lubas, *Nature*, 1963, **200**, 1006.
23. H. J. C. Berendsen, *J. Chem. Phys.*, 1962, **36**, 3297.
24. C. Migchelson and H. J. C. Berendsen, *J. Chem. Phys.*, 1973, **59**, 296.
25. I. D. Kuntz and W. Kauzmann, *Adv. Protein Chem.*, 1974, **28**, 239.
26. R. Kimmich, F. Klammler, V. D. Skirda, I. A. Serebrennikova, A. I. Maklakov, and N. Fatkullin, *Appl. Magn. Reson.*, 1993, **4**, 425.
27. R. Kimmich and H. W. Weber, *Phys. Rev. B*, 1993, **47**, 11 788.
28. S. H. Koenig, R. D. Brown III, and R. Ugolini, *Magn. Reson. Med.*, 1993, **29**, 77.
29. R. Kimmich, *Makromol. Chem., Macromol. Symp.*, 1990, **34**, 237.
30. S. Stapf, R. Kimmich, and J. Niess, *J. Appl. Phys.*, 1994, **75**, 529.
31. J. Noolandi, *Phys. Rev. B*, 1977, **16**, 4474.
32. G. Held, F. Noack, V. Pollak, and B. Melton, *Z. Naturforsch., Teil c*, 1973, **28**, 59.
33. S. H. Koenig, R. D. Brown III, D. Adams, D. Emerson, and D. G. Harrison, *Inv. Radiol.*, 1984, **19**, 76.
34. H. W. Fischer, Y. van Haverbeke, P. A. Rinck, I. Schmitz-Feuerhake, and R. N. Muller, *Magn. Reson. Med.*, 1989, **9**, 315.
35. E. Rommel and R. Kimmich, *Magn. Reson. Med.*, 1989, **12**, 390.
36. E. Rommel, R. Kimmich, H. Körperich, C. Kunze, and K. Gersonde, *Magn. Reson. Med.*, 1992, **24**, 149.

Biographical Sketch

Rainer Kimmich. *b* 1941. Dipl.-Phys., (Technical) Universities of Munich and Stuttgart, 1967; Dr. rer. nat., University of Stuttgart, 1971. Introduced to NMR by F. Noack; Priv.-Doz., Ulm, 1975. Professor of Physics at the University of Ulm 1976–present. Approx. 170 publications. Research specialties: NMR field cycling relaxation spectroscopy, NMR field gradient diffusion studies, NMR microscopy and localized spectroscopy in liquid and solid systems, porous media, polymers, and biological systems.

Muscle Proteins

Carolyn M. Slupsky and Brian D. Sykes

University of Alberta, Edmonton, Alberta, Canada

1	Introduction	1
2	Thick Filament Proteins	1
3	Thin Filament Proteins	3
4	Other Proteins of the Muscle	8
5	Future Work in Muscle Research by NMR	9
6	Related Articles	10
7	References	10

1 INTRODUCTION

Muscle tissue is important in the body for producing motion, pumping the heart, and operating the viscera and blood vessels. These muscles can be classified into three categories: skeletal, cardiac, and smooth. Skeletal and cardiac muscles are very similar in protein content, but differ in their mechanism of excitation–contraction coupling.[1] Smooth muscles, on the other hand, are different, and because they are more difficult to work with experimentally, are not as well understood. The events leading to muscle contraction involve a complex set of proteins, all acting together. In this article we concentrate on the most well studied skeletal and cardiac muscle proteins.

Skeletal and cardiac muscles are composed of a large number of multinucleated cells. Muscle cells are composed of fibers surrounded by an electrically excitable membrane called the sarcolemma. The fibers consist of myofibrils which are bundles of several hundred protein filaments in parallel.[2] Of particular importance is the presence of a network of tubules surrounding the myofibrils called the sarcoplasmic reticulum (SR). The SR is an intracellular store of calcium ions and contains proteins which are involved in the release and uptake of calcium. The myofibrils consist of what are called thick and thin filaments due to the way that they look under a microscope.[2] The thick filament is composed of myosin and its associated light chains, whereas the thin filament is composed of actin, tropomyosin, and the troponin complex (troponin I (TnI), troponin T (TnT), and troponin C (TnC).

Muscle contraction in skeletal muscle starts by the transmission of an impulse through a motor nerve. This gives rise to action potentials which are conducted down the transverse tubules.[1] Depolarization of the transverse tubule membrane results in release of calcium into the sarcoplasm. In the resting state of muscle, the interaction of actin with myosin is inhibited by tropomyosin and the troponin complex. When calcium is released by the SR, TnC binds calcium which then confers a conformational change throughout the troponin complex and tropomyosin and releases the inhibition of the interaction of actin with myosin. The myosin ATPase then hydrolyzes adenosin as in adenosine triphosphate (ATP), resulting in shortening of the muscle (sliding of the filaments past one another), or contraction.

For muscle contraction to occur, there must be a very tight association and communication between the proteins. For this reason and the fact that the proteins actually involved in the muscle contraction are very large, NMR of muscle proteins is a difficult task. Novel techniques have been developed in order to study these proteins, and most of these techniques are discussed in this article. The discussion in this article is restricted to the proteins of the thick and thin filaments and a few of the other proteins of the muscle system. Ion binding using ^{113}Cd NMR, ^{43}Ca NMR, and ^{23}Na NMR are not discussed here, as this is covered elsewhere in the Encyclopedia.

One final protein of note is parvalbumin. Parvalbumin is a protein present in the sarcoplasm and has been described as a calcium carrier between the myofibril and the SR, behaving as a soluble relaxing factor.[3] Being soluble, smaller than, and homologous to the calcium binding protein TnC, it has been studied quite extensively by NMR.

2 THICK FILAMENT PROTEINS

Myosin is the major protein in the thick filament [Figure 1(a)]. The complex (MW 520 kDa) consists of two (220 kDa) heavy chains and four light chains that are between 15 and 22 kDa in size.[4] Each heavy chain forms a globular head, which contains an actin binding site and a nucleotide binding (ATPase active) site. Each chain also contains a long C-terminal α-helical tail which combines with another heavy chain to form the coiled-coil thick filament backbone. Myosin can be cleaved proteolytically by trypsin[5] into light meromyosin (the C-terminal coiled-coil portion of myosin) and heavy meromyosin (the N-terminal portion of myosin containing the two globular heads and a portion of the coiled-coil structure). Further digestion of heavy meromyosin (HMM) by papain results in two globular heads with their associated light chains (S1) and the coiled-coil hinge region (S2)[5] [Figure 1(b)].

The crystal structure of myosin S1 has been determined to 0.28 nm resolution[4] and is found to be 45% α-helical. The nucleotide binding pocket is formed from several different α-helical and loop regions of the molecule. Of particular interest is an α-helical region which lies under the binding site. This contains the two highly reactive sulfhydryl groups SH_1 and SH_2 (cysteine-707 and cysteine-697), which have been labeled and studied in many chemical and spectroscopic studies. These cysteines lie in small clefts that face toward the solvent on opposite sides of the molecule. The actin binding site appears to be on the opposite side of the S1 head to the nucleotide binding site.[4] Associated with the globular S1 head are the essential and regulatory light chains. The essential light chain interacts with the C-terminal long helical end of S1, which presumably joins up to the α-helical coiled-coil backbone [Figure 1(a)]. This light chain appears to have conformational flexibility in the crystal structure.[4] The regulatory light chain interacts with the region further to the C-terminal end of S1.[4] Both the essential and regulatory light chains share sequence similarity and structural homology to calmodulin and TnC, although only one divalent cation binding site is still functional.

There have been many NMR studies of intact myosin,[6–11] the light chains,[12–20] the nucleotide binding site,[21–32] the actin binding site,[7,13,18,19,33,34] the S2 region,[35] and light meromyosin (LMM).[36]

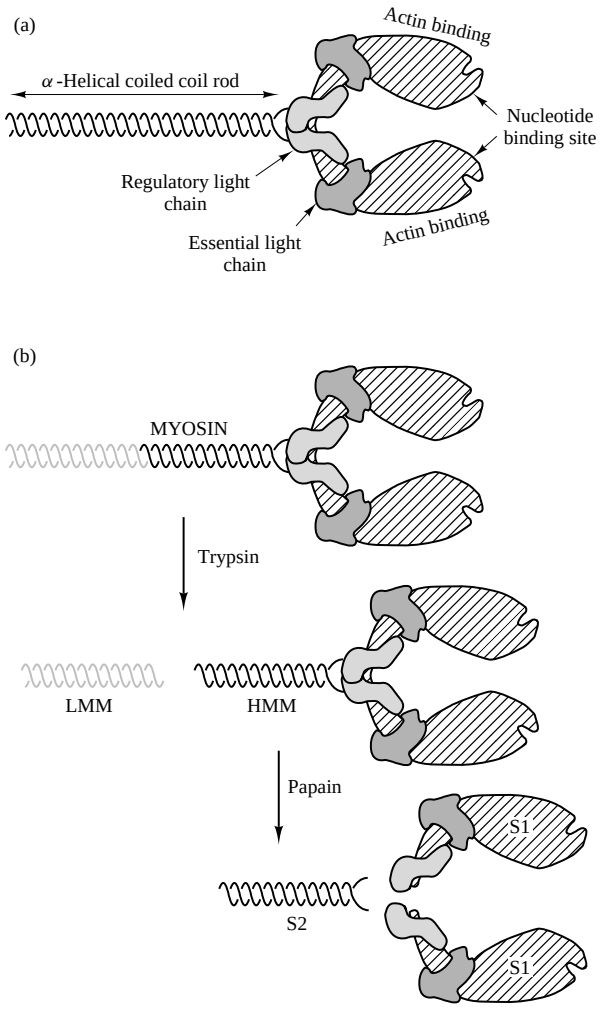

Figure 1 (a) Schematic diagram of the myosin molecule. Shown in green are the two heavy chains which form globular heads at their N-terminus (containing the actin binding site and the nucleotide binding site), and wind around one another at their C-terminus to form an α-helical coiled coil. Shown in red and yellow are the essential and regulatory light chains, respectively. (b) Cleavage products of myosin. Myosin may be enzymatically cleaved with trypsin to form two cleavage products: LMM (light meromyosin) and HMM (heavy meromyosin) containing the globular heads, their associated light chains and a portion of the coiled-coil tail of myosin. HMM may be further cleaved by papain into S2 (coiled-coil hinge region) and S1 (myosin globular heads with its associated light chains)

2.1 Myosin

One of the first NMR studies on skeletal myosin used 360 MHz ^{1}H NMR to compare spectra of myosin, HMM, S1, and LMM.[7] The results were quite striking in that myosin, HMM, and S1 all exhibited sharp resonance lines due to a high mobility of some amino acids. Careful ^{1}H NMR spin echo studies on gizzard myosin also illustrated mobility arising predominantly from the myosin S1 units.[10] This increased mobility was also observed in ^{1}H spectra of skinned muscle fibers[11] and ^{13}C NMR spectra of S1.[9] ATP binding,[7] surface-directed paramagnetic probes,[8] or solvent viscosity[8] had no effect on these sharp, mobile resonances. One proposal was that the mobility arose from a disordered interior;[7,8] however, it was shown that this mobility arose from at least one of the light chains.[13,17] Indeed, the crystal structure[4] supports the latter hypothesis.

2.1.1 Nucleotide Binding Site

There have been two types of study to monitor the mobility of the bound nucleotide in the ATPase site. One of these studies monitored mobility of the γ-phosphate of ATP,[21] while the other study monitored the mobility of the adenine ring.[27] To monitor the γ-phosphate mobility, ^{31}P NMR was employed to study the time-course of ^{18}O exchange between [^{18}O]Pi and H_2O catalyzed by S1 in the presence of MgADP.[21] All the [^{18}O]Pi that bound to S1 underwent complete exchange and was released as [$^{16}O_4$]Pi, indicating that this phosphate interconverted rapidly between M**ADP · Pi and M* · ATP + H_2O. Using 2-fluoro-ADP bound to S1,[27] a rotational correlation time close to myosin S1 itself was observed for the ^{19}F resonance, indicating a relatively constrained adenine ring.

Recently, two new reagents have been found to trap ADP in the nucleotide binding site of S1 and to inhibit the ATPase activity of S1. These reagents are aluminum fluoride and beryllium fluoride.[31,32] These tetrahedral fluoroaluminate and fluoroberyllate anions act as phosphate analogs binding to the position normally occupied by the γ-phosphate of ATP. Neither the myosin–ADP–fluoroaluminate nor the myosin–ADP–fluoroberyllate complex could bind to actin.[32] When fluoroberyllate bound to S1, it bound as one of four complexes, depending on how much it was hydroxylated.

The response of S1 or HMM to nucleotide binding was monitored by labeling S1[26] or HMM[28] with *N*-(4-trifluoromethylphenyl)iodoacetamide. The SH_1 group was preferentially modified in each case. S1 was found to exist in two discrete states under a wide variety of conditions.[26] Furthermore, these states could exist in the absence of nucleotide, and one of the states was identical with the state induced by binding Mg · ADP or magnesium:adenosine 5′-β,γ-imidotriphosphate to the active site.[26] HMM was found to behave almost identically to S1, except for a hysteresis-like effect in which the ^{19}F NMR chemical shift depended on the temperature at which the previous experiment had been performed.[28] These data indicated a coupling of the globular region with a second region forming a distinctly different cooperative unit than the one present in the S1 monomer alone.[28]

2.1.2 Actin Binding Site

The study of myosin binding to actin has revealed two binding sites on myosin. The first site belongs to the essential light chain's [S1(A1)] N-terminal 41-residue segment,[18,19,33] and the second site is close to the SH_1 group on S1.[37]

As actin was titrated into S1, the narrow ^{1}H NMR resonances (see above) in the aliphatic region reduced and disappeared as the actin/myosin ratio was increased to more than 1:1.[7,13,18,19,33] Nucleotide binding to this complex restored the sharp, mobile resonance lines by dissociation of the acto–S1 complex. It was found that there was an interaction between the N-terminal 41-residue segment of S1(A1) and, in particular, the *N*-trimethyl group of S1(A1) (see below) and actin.[18,19,33] Covalently labeling cysteine-374 of actin (near the C-terminus) with a spin label and

monitoring the signal arising from the *N*-trimethyl protons revealed a broadening upon actin binding, indicating that these protons are close (within 1.5 nm) to the C-terminus of actin.[19] The N-terminal region of S1(A1) was also found to alter the thermodynamic characteristics of the regulated acto–S1 interaction, thus operating as a functional linkage in the thin filament based regulatory mechanism.[18] LC2 (see below) did not display binding to actin.[18]

The two accessible cysteine groups of S1 (SH_1 and SH_2), modified by (trifluoromethyl)mercuric bromide, illustrated significant broadening in the ^{19}F spectrum of SH_1, while broadening of SH_2 occurred to a lesser extent upon binding of actin.[38] The binding site of S1 for actin was therefore inferred to be closer to SH_1 than SH_2.

2.1.3 S2

S2 is the portion of HMM that connects S1 to LMM. It has been thought that this region of myosin contains a hinge, which aids in the power stroke of myosin. Stewart and Roberts[35] have used NMR to see if a flexible region associated with a hinge could be identified. They were able to observe some sharp resonances (probably due to side-chain mobility), but not enough to suggest a major flexible region.

2.1.4 LMM

Kalbitzer et al.[36] studied the C-terminal portion of LMM (262 amino acids) by ^1H NMR and determined that these molecules assemble to form an α-helical coiled-coil structure as is found in myosin. The last 12 C-terminal residues of one polypeptide chain and the last nine C-terminal residues of the other chain are very mobile. This unfolded character probably aids in the assembly into thick filaments.

2.2 Essential Light Chain

The essential or alkali light chain has two isoforms referred to as A1 (MW 25 kDa) and A2 (MW 17 kDa). These isoforms have an identical 141 residue C-terminus and are homologous over the preceding eight residues. A1 differs from A2 in that it possesses a 41 residue N-terminal tail rich in proline, alanine, and lysine residues. Difference ^1H NMR spectra of S1(A1) and S1(A2) reveal resonances arising from lysine, alanine, and proline,[13,17] which arise from the additional 41 amino acids found at the N-terminus of A1. In particular, there is an intense resonance in the spectrum at 3.23 ppm attributed to an N-terminal *N*-trimethyl blocking group.[14] Isolation of residues 1 to 37 of A1 revealed that the proline residues were primarily in the *trans* configuration, consistent with an elongated structure.[18] Furthermore, this conformation was found to be present in intact S1, suggesting that this segment may undergo lateral and rotational diffusion independent of the rest of the complex. The *N*-trimethyl group of the essential light chain was found to be less than 1.5 nm away from an SH_1 spin label on the heavy chain.[19]

2.3 Regulatory Light Chain

The regulatory 5,5′-dithiobis-2-nitrobenzoic acid light chain LC2 is thought to play a role in modulating the actomyosin interaction during long-term stimulation of muscle.[16] LC2 may be phosphorylated at serine-14 or -15. ^{31}P NMR of phosphorylated LC2 attached to whole myosin revealed a linewidth of 40 Hz, indicating significant internal mobility of the phosphate of LC2. When the light chains were purified, a linewidth of 10 Hz was obtained.[12,20] This light chain also contains *N*-trimethyl protons, but the lines of these are broader than for LC1, indicating less mobility.[15] The segmental mobility of the N-terminal region of the LC2 light chain is independent of the rest of the molecule due to the relatively narrow linewidths when attached to whole myosin. ^{19}F NMR on S1, labeled with *N*-4-(trifluoromethyl)phenyliodoacetamide or *N*-3,5-di(trifluoromethyl)phenyliodoacetamide at SH_1, complexed with LC2 has revealed that LC2 does not interact anywhere near SH_1 nor does it alter the energetics of the structural transition.[16] It was also shown that papain-digested S1 in the presence of LC2 was able to bind a near stoichiometric amount of calcium with high affinity (LC2 was able to bind calcium).[16]

3 THIN FILAMENT PROTEINS

3.1 Actin

Actin is the major structural component of the thin filament of muscle.[6] Actin interacts with tropomyosin and troponin in a calcium mediated manner to control muscle contraction. The interaction of actin with myosin mediates the force development in muscle (Figure 2).

In the absence of salt, actin exists as a globular protein known as G-actin. It changes upon the addition of salt into a highly asymmetrical fibrous polymer known as F-actin. Each actin monomer has 375 residues, five of which are sulfhydryl residues (residues 10, 217, 257, 285, and 374). The crystal structure of G-actin complexed with DNase I has recently been determined to 0.28 nm resolution with ATP bound and

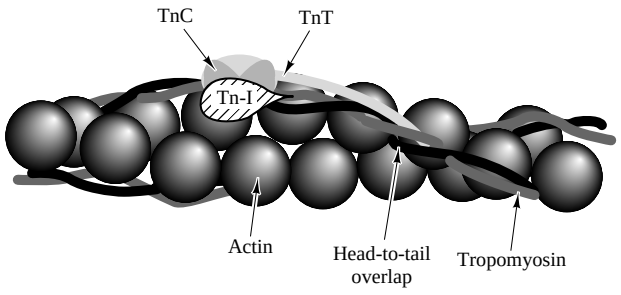

Figure 2 Schematic diagram of the thin filament. The actin filament is composed of two strands of polymerized actin monomers. Tropomyosin, polymerized in a head-to-tail manner, lies in the grooves of the actin filament, one tropomyosin monomer spanning seven actin monomers. The troponin complex interacts with both actin and tropomyosin, the troponin T (TnT) component overlapping tropomyosin in its C-terminal region including the head-to-tail overlap. Troponin I (TnI) binds to TnC and actin and is the inhibitory component, and troponin C (TnC) is the calcium binding component responsible for the calcium sensitivity of the complex. (Reproduced by permission of The American Society for Biochemistry & Molecular Biology from D. H. Heeley, D. Golosinska, and L. B. Smillie, *J. Biol. Chem.*, 1987, **262**, 9971)

0.3 nm resolution with ADP bound.[39] The actin structure has two domains, with the nucleotide and calcium ion bound in the cleft between the two domains.

One of the first published ^{1}H NMR spectra of actin used 50 μM actin in D_2O at a field strength of 400 MHz.[40] The spectra indicated that a number of residues in G-actin were rotationally constrained. The study of actin at low concentrations in the presence and absence of KCl, as well as a chemically modified form at higher concentrations, illustrated no observable difference of actin before it polymerized.[41]

Three of the easily accessible cysteine residues of G-actin (cysteine-10, -284, and -374) were modified with 3-bromo-1,1,1-trifluoropropanone[38,42] or 4-perfluoro-*t*-butylphenyliodoacetamide,[43] or (trifluoromethyl)mercuric bromide.[38] Only cysteine-374 broadened upon polymerization, indicating that this cysteine is near the site of polymerization.[38,42,43] The structure of ATP bound to G-actin was unaltered upon cysteine labeling as ^{31}P NMR studies of the three phosphates of ATP detected no appreciable changes to the structure of actin after reaction.[42] Furthermore, the protein could polymerize easily, indicating that the cysteine residues were not essential for polymerization.[42]

3.1.1 Nucleotide and Ion Binding

The ^{31}P NMR spectra of ATP-bound G-actin revealed a slow exchange of ATP on the NMR timescale.[44] Nitration of G-actin with tetranitromethane to form an unpolymerizable derivative did not affect ATP binding.[45] The rotational correlation times for the γ, α, and β phosphates of bound ATP were determined to be 41, 40, and 44 ns, respectively. Since the theoretical tumbling time for G-actin was determined to be 36 ns, the correlation times of the phosphates indicate that the ATP molecule is tightly bound to G-actin and that there is no appreciable rapid internal mobility.[45,46] An electrophilic group was found to interact with the nonbridging oxygen atoms of the phosphate groups in ATP, increasing the electronegativity of those oxygen atoms.[45]

^{31}P NMR was used to determine that the high-affinity metal binding site and the ATP binding site are close together (less than 1.0 nm).[47] By binding Mn^{2+} to the Ca^{2+} binding site, the NMR resonances of the bound ATP in the complex were too broad to be detected due to the paramagnetic behavior of Mn^{2+}. The crystal structure[39] confirms that the binding of calcium to G-actin involves the phosphate groups of ATP.

Actin can bind either calcium or magnesium in the muscle cell. The conformation of actin changed when calcium was substituted for magnesium in the high affinity cation binding site.[48] Mg^{2+}/Ca^{2+} exchange in the primary cation site resulted in a six-fold increase in the ATP off rate, indicating that the conformational change, when magnesium binds, can be related to ATP hydrolysis.[42]

3.1.2 Interaction of Actin with Myosin and other Proteins of the Thin Filament

There have been several studies on the interaction between actin and myosin. Upon alkylation of cysteine-10 with 3-bromo-1,1,1-trifluoropropanone, it was shown that the ^{19}F NMR spectrum was broadened when actin was incubated with myosin S1.[38] Labeling of lysine-61 of actin with pentafluorophenylisothiocyanate (PFPITC), revealed no change in the ^{19}F spectrum when actin was polymerized, but when PFPITC was replaced by a fluorescein-5-isothiocyanate (FITC) label, actin polymerization was prevented, probably due to the fact that FITC is much larger than PFPITC.[37] Since lysine-61 was not buried when actin was polymerized, and since lysine-61 could still be modified by PFPITC when actin was polymerized, lysine-61 must be close to the site of polymerization of actin monomers.[37] Binding of tropomyosin to actin broadened the linewidth of the label attached to lysine-61 beyond detection.[37] Addition of troponin to this mixture did not alter the broadening of the lysine-61 line.[37] The binding of S1 to actin resulted in a complete broadening of the lysine-61 line.[37] It was concluded, then, that lysine-61 is near all three binding sites (S1 binding site, tropomyosin binding site and the site of interaction between actin monomers), but furthest away from the site of actin monomer interaction. These results support the view that myosin and tropomyosin compete for the same site on actin,[37] and that tropomyosin and myosin bind to F-actin in the groove formed by packing of the actin monomers in the long pitch of the helices.

Another way to study the interaction of proteins is to use synthetic peptides which encompass a binding site. Two such studies have been done using NMR on actin 1–28.[49,50] It was shown that actin 1–28 binds to S1 and increases the ATPase activity by 150%.[49] The maximal activity occurred at a peptide/HMM ratio of 0.5:1, suggesting that one peptide binds to one head of the myosin dimer, and therefore there must be cooperative interactions occurring between the two heads. Actin 1–28 binds troponin in the absence of calcium but not in the presence of calcium, indicating that the interaction between actin and TnI is sensitive to the calcium dependent changes in TnC.[49] It was also shown that TnI 104–115 successfully competes with TnI for actin 1–28. Using the transferred NOE experiment, the authors were able to determine that there is a change from an extended structure to a helix-like conformation between residues 1 and 7 of actin 1–28 when troponin is bound.[49]

3.2 Tropomyosin

Tropomyosin is of central importance in the regulation of contraction. Tropomyosin serves to propagate conformational changes which start in the troponin complex with the actomyosin ATPase. Tropomyosin is composed of two polypeptide chains, each 284 amino acids long. There are two species in skeletal and cardiac muscle, α and β. Tropomyosin is in an α-helical coiled-coil conformation except for the ends, the chains being parallel and in register (Figure 2). The ends of tropomyosin overlap with one another by 8 to 11 residues in a head-to-tail fashion. Tropomyosin lies along the grooves of the double helix of F–actin with one molecule spanning seven actin monomers. There are two sets of seven zones that bind to actin. One tropomyosin molecule interacts with one troponin molecule. There have been several studies done involving tropomyosin using NMR, mainly to describe the dynamics of tropomyosin.

Early ^{1}H NMR work on tropomyosin, which involved observing tyrosine resonances,[51] revealed that the coiled-coil structure of tropomyosin near neutral pH is a flexible, open structure in the monomeric and polymerized forms. A histidine titration[52,53] revealed that histidine-153 has multiple

resonances, suggesting the existence of intermediates in the thermal unfolding of the tropomyosin coiled-coil and that the C-terminus is less stable than the rest of the molecule. The splitting of histidine derives from conformational differences in the local structure about the histidine residues which produce the different pK_a values.[53] In addition, it was shown that the two histidine residues (153 and 273), which are quite far apart on the coiled-coil (separated by 18 nm), have significant cooperativity in their pH titrations only in polymerized tropomyosin.[54] This cooperativity must derive from a common conformational transition. These data were confirmed using amide hydrogen exchange rates on smooth and cardiac tropomyosins.[55]

One phosphorylation site of tropomyosin exists at the penultimate serine-283 residue, but only a small fraction of tropomyosin molecules are phosphorylated.[56] It was found that this phosphorylated serine could form salt linkages with lysines-6 and -12 to stabilize the head-to-tail overlap. It was shown that this residue is exposed to the solvent and can undergo protonation or deprotonation in the polymerized and unpolymerized state. Furthermore, the linewidth of the phosphorylated residue would suggest considerable flexibility in the monomer and polymer.[56] When tropomyosin was digested with carboxypeptidase, and the spectra of digested and undigested tropomyosin compared, there was a reduction in the narrow resonances corresponding to mobile residues at the C-terminus.[57] This mobility may be involved in reforming the coiled-coil structure once the tropomyosin polymerizes, since the heptapeptide repeats of the hydrophobic residues are intact in this region.

3.2.1 Interaction of Tropomyosin with Troponin

When polymerized tropomyosin was complexed with troponin, very little of the aromatic envelope of troponin was broadened.[58] This suggests a relatively flexible troponin complex when complexed with tropomyosin. Troponin binds to tropomyosin through the component of the troponin complex known as troponin T (TnT) which increases the head-to-tail polymerization of tropomyosin. In particular, the cyanogen bromide fragment CB1 (1–151) of TnT was able to invoke the same head-to-tail polymerization of tropomyosin observed with whole TnT.[59] Furthermore, studies have shown that CB1 binds close to the C-terminal end of tropomyosin and induces formation of a ternary complex with N- and C-terminal fragments of tropomyosin under conditions in which no interaction between these fragments could be detected.[59] Using a method similar to that previously described for measuring tropomyosin dynamics, namely observing histidine resonances, Brisson et al.[59] were able to show directly, by observing changes in the pH titration profile of histidine-153 of tropomyosin upon CB1 binding, that CB1 binds close to the C-terminal end of tropomyosin.

3.3 TnT

Troponin T is the largest, and least well studied (by NMR methods), component of the troponin complex which attaches the complex to tropomyosin. TnT has two phosphorylation sites, one at the N-terminal serine hydroxyl, and one at serine-194 in the C-terminal cyanogen bromide fragment CN4.[60] The ^{31}P NMR spectrum of the N-terminal resonance revealed a narrow resonance which titrated in pH identically to free phosphoserine, indicating that the phosphorylation site is highly mobile.[61] The same result was obtained with CB1[61] and when TnT was bound to the rest of the troponin complex or nonpolymerizable tropomyosin or tropomyosin fragments.[61,62] The role of phosphorylation in muscle seems to be correlated to the change in calcium sensitivity of the actomyosin ATPase.

3.4 TnI

TnI is a member of the troponin complex and is the inhibitory component of the ATPase activity of actomyosin. The calcium-dependent interaction between TnC and TnI is one of the key processes in the regulation of contraction in skeletal muscle. Residues 1–21 and 96–116 of TnI interact with TnC. The peptide 105–115 of TnI comprises the minimum sequence necessary for inhibition of the actomyosin ATPase activity. Experiments on binding troponin, tropomyosin, or actin to myosin S1(A1) have shown that the acto–S1(A1) interaction involving the N-terminal segment of A1 is calcium sensitive, and the presence of TnI alone markedly inhibits this interaction.[63]

In cardiac muscle, phosphorylation of TnI occurs upon β-andrenergic stimulation, which is correlated to the change in calcium sensitivity of the actomyosin ATPase.[60] Bovine cardiac TnI phosphorylates at positions 23 and 24, the chemical shifts of which are altered by binding magnesium.[60]

Structural studies on whole TnI have not been accomplished so far due to the size of TnI (21 kD). In order to study the interaction of TnI and TnC, the synthetic peptide 104–115 (TnIp), which is the minimum sequence necessary for the inhibition of the actomyosin ATPase activity, was synthesized and bound to TnC, and the stoichiometry and structure of this fragment was determined.[64,65] It was found that TnIp bound to TnC with a stoichiometry of binding ratio of 1:1.[64] Using the transferred NOE experiment, the structure of the synthetic inhibitory peptide was determined when bound to TnC.[65] The structure revealed an amphiphilic helix distorted around the two central proline residues, bringing together the hydrophobic residues to form a hydrophobic pocket. The hydrophilic, basic residues extend from the opposite face of the peptide[64,65] (Figure 3). The interaction of this peptide with TnC is discussed in the following section.

3.5 TnC

Troponin C (TnC) is the calcium-binding, regulatory protein of the troponin complex. TnC is an 18 kD protein utilizing four EF hand, helix–loop–helix motifs for binding calcium. Each calcium ion is bound by seven oxygen ligands, resulting in a pentagonal bipyramidal coordination geometry. The structure of two-calcium TnC has been solved to 0.2 nm resolution,[66,67] revealing that TnC has two globular domains separated by a helical linker. Each domain contains two ion binding sites, the C-domain sites being the high-affinity calcium/magnesium binding sites with $K_{Ca} = 2 \times 10^7\ M^{-1}$ or $K_{Mg} = 2 \times 10^3\ M^{-1}$, and the N-domain sites being the low affinity calcium specific binding sites with a $K_{Ca} = 3 \times 10^5\ M^{-1}$.

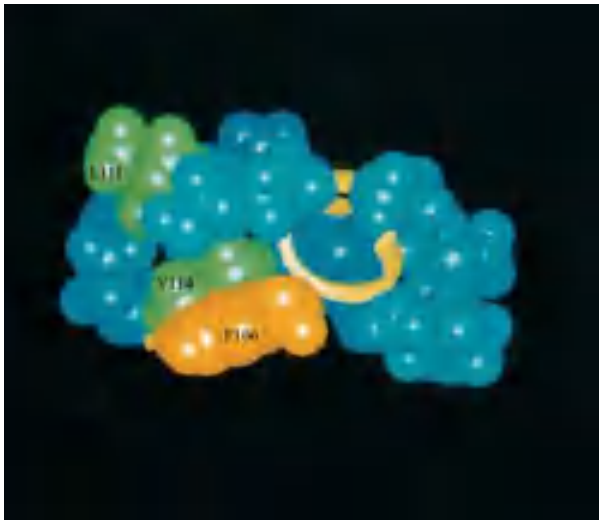

Figure 3 Structure of the TnI peptide (104–115)[65] representing the minimum sequence necessary for the inhibition of the actomyosin ATPase activity. When bound to TnC, this peptide reveals a structure with an amphiphilic α-helix distorted around two central proline residues bringing together hydrophobic residues to form a hydrophobic pocket. Shown in yellow is the phenylalanine-106 residue; green indicates the hydrophobic leucine-111 and valine-114 residues. Shown in blue are the hydrophilic lysine and arginine residues which extend away from the hydrophobic pocket. The backbone is represented by the yellow solid ribbon

TnC is one of the proteins most studied by NMR. Indeed, its small size and homologous calcium binding sites have allowed numerous studies on whole TnC, fragments involving calcium binding, and the interaction between TnC and TnI or TnC and other drugs. Most of the work on TnC by NMR has been motivated by a need to understand the mechanism of the calcium switch that leads to the release of inhibition by TnI of the actomyosin interaction. In this portion of this article, we omit those studies involving other metals such as sodium, cadmium, and potassium binding to TnC, and concentrate on the calcium and magnesium binding, structural studies, and the interaction of TnC with other members of the troponin complex.

^{1}H NMR studies of TnC were first done by Seamon et al.[68] and Levine et al.[69] in 1977. ^{1}H NMR studies revealed that calcium induces a large folding of the backbone of the high affinity sites.[68,69] Calcium binding to the low affinity sites did not alter the backbone of these sites significantly, but changed the hydrophobic interactions.[69] A comparison of magnesium and calcium binding to the C-domain demonstrated differences in the degree of backbone folding of this domain and altered interactions between hydrophobic residues when magnesium was bound.[68,70] This led to the proposal that the important physiological sites were the N-terminal calcium specific sites and that the C-terminal sites are always filled with either calcium or magnesium. In 1988, Tsuda and coworkers,[71,72] using high-resolution ^{1}H NMR techniques, also studied magnesium binding to TnC. They demonstrated that all calcium binding sites in the N- and C-domains bound calcium and magnesium, but magnesium binding to the N-domain did not induce a conformational change in the hydrophobic region.[72] This was illustrated by resonances in both domains being influenced by magnesium binding. Studies of TnC from different sources such as rabbit and pike revealed very similar properties.[73]

Cardiac TnC (cTnC) has also been studied by NMR. This protein is quite different from skeletal TnC (sTnC) in the N-domain, where site I has lost the ability to bind calcium due to amino acid insertions and substitutions. Hincke et al.[74] observed spectral changes of cTnC that were similar in nature to changes of sTnC when calcium was bound. Another study[75] revealed that the structure of cTnC was extremely stable, as calcium addition could produce native-like features in 6 M urea. Later studies on cTnC involved high-resolution two-dimensional NMR.[76–78] Mutation of one of the residues in site III of whole cTnC, designed to prevent calcium binding to that site, resulted in a greater instability of the C-domain relative to a mutant at site IV.[79] A study of one-dimensional double quantum filtered COSY, and NOESY spectra illustrated that the tertiary fold of the C-domain of the site IV mutant, but not the site III mutant, was similar to wild type cTnC.[79] Calcium binding to site III was shown to be more crucial than calcium binding to site IV in stabilizing and folding the C-terminal domain of TnC[79] (see below, Shaw et al.[80–83] and Kay et al.[84]). Other studies[77,78] on cTnC where aspartic acid-65 was replaced by alanine revealed that calcium binding to the N-domain was inhibited (the changes associated with formation of a β-sheet in the N-domain upon calcium binding were not observed) without significantly altering the solution conformation of the N-domain.[77] This mutant could not trigger muscle contraction.[77] These results illustrate the importance of aspartic acid-65 in maintaining the calcium binding site (see also Marsden et al.[85]).

3.5.1 Fragments and Domains of TnC

There have been several studies on proteolytic or chemically cleaved and synthesized fragments of TnC. A CB9 fragment of 52 residues comprising the calcium binding site III of TnC (84–135),[86,87] along with CB8 (46–77)[87] and TH2 (121–159),[87] were studied. CB8 was observed to have some secondary structure in the apo peptide while CB9 and TH2 exhibited very little secondary structure.[87] Calcium binding led to the spectral changes of CB9 and TH2, consistent with an increased restriction of backbone mobility and the adoption of a more compact form.[86,87] CB9 was also shown to have a TnI interacting region. CB8 was unfolded and unperturbed upon calcium addition, indicating that other interactions may be responsible for its stabilization.[87]

Studies on the C-terminal domain of TnC (TR2 C 89–159 and TR2E 101–159) have illustrated that there is a strong cooperativity in calcium binding to the C-domain.[88] As with native TnC, the difference between magnesium and calcium binding is a difference in backbone torsion angles and ring-plane orientations as a result of altered interhelical packing.[88] Removal of the N-terminal segment of TR2C to form TR2E resulted in perturbations of the hydrophobic region and reduced calcium affinity.[88] It was also shown that the affinity of the C-terminal binding site for calcium was reduced by cleavage of the linkage between the two calcium binding sites.[88]

The use of synthetic peptides for the NMR study of TnC has gained widespread use. Gariépy et al.[89] synthesized several SCIII peptides of differing helical lengths. From the reduced calcium affinities of these peptides, they were able to show that

the N- and C-terminal helical regions stabilize the cation in the binding loop. Furthermore, the importance of metal charge and radius on the metal binding affinity was illustrated.[129] Other studies involved determining the essential residues comprising the calcium binding sites.[85,90] Study of the calcium binding EF hands from many sources revealed that the invariant residues in the calcium binding loop are: aspartic acid-1 ($+x$), aspartic acid/asparagine-3 ($+y$), glycine-6, isoleucine-8, and glutamic acid-12 ($-z$).[85] It was shown that the helices surrounding the calcium binding loop account for 50% of the calcium binding affinity, while the interaction of the sites provides 43%.[85]

The first NMR structure of TnC fragments was determined in 1990 by Shaw et al.[80] (Figure 4). A helix–loop–helix calcium binding peptide was synthesized which was unstructured without calcium but, upon calcium binding, formed a homodimer similar in tertiary structure to the C-domain of TnC (as determined by X-ray crystallography). The dimer exhibited an approximate two-fold rotational symmetry, with hydrophobic residues and a three-residue β-sheet at the interface of the two sites stabilizing the protein domain.[80,83] When this dimer was mutated[81] to include calcium ligands from site II, the K_d of calcium decreased slightly, but when all the residues in the calcium binding sites were mutated to site II residues the K_d decreased even further. These results suggest that differences in the coordinating ligands between sites II and III have very little effect on calcium affinity, and noncoordinating residues in site II are responsible for the low affinity of site II as compared to the high affinity of site III.

Kay et al.[84] also determined the structure of the 39 amino acid proteolytic fragment of rabbit skeletal TnC containing the fourth calcium binding site (TH2). Without calcium, TH2 adopts a random coil conformation. The dissociation constant of calcium for this heterodimer was found to be 1 M, indicating that a calcium/peptide ratio of 20:1 was needed to induce dimer formation. Even though the calcium affinity was low, the structure of this homodimer was similar to the site III homodimer and the C-terminal domain of TnC.

When an equimolar mixture of 34-residue peptides representing SCIII and SCIV were mixed in the apo form, a ^{1}H NMR spectrum typical of a random coil conformation was observed.[82] When calcium was added, however, a heterodimer resulted (which showed a ^{1}H NMR spectrum substantially different from either the apo or homodimer spectra) with a calcium affinity greater than that of the homodimer. The spectrum of the heterodimer was very similar to the spectrum of TR2C, indicating the heterodimer to be a good model of the C-domain of TnC.

Findlay and Sykes[91] and Findlay et al.[92] studied the apo TR1C structure of skeletal TnC (Figure 5). TR1C comprises helices A to D in the N-domain. They observed that the secondary structure of the two-calcium binding sites in the N-domain are different, as was observed in the crystal structure. The structures and orientation of helices A, B, and D and the β-sheet region are well defined and agree closely with that region in the X-ray structure. Helix C was determined to be well defined, but its orientation to the other helices was not. This questionable orientation was clarified in the apo-N-domain structure reported by Gagné et al.[93]

3.5.2 Interaction of TnC with TnI

One of the first studies on delineating the interaction between TnC and TnI involved placing a paramagnetic spin label on cysteine-98 of rabbit skeletal TnC and studying the interaction of the TnC peptide CN4 (96–116) with a CN5 (1–21) peptide of TnI.[94] An interaction between these two peptides as well as between CN5 and whole TnC was observed.[94] Back-titration with EGTA resulted in a loss of the paramagnetic broadening of CN5 with no alteration of the signals of CN4, indicating a calcium sensitivity of CN5 binding to TnC.[94]

TnI binding to TR2C[88] was shown to alter the relative dispositions of several methyl groups with respect to the

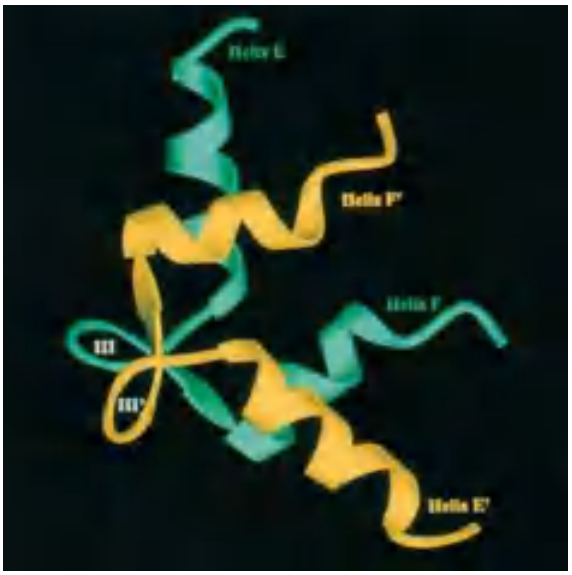

Figure 4 Structure of the SCIII homodimer.[80,81] Two peptides representing the helix–loop–helix calcium binding site III of TnC can adopt a fold similar to the crystal structure C-domain where residues 112, 113, and 114 of one peptide form an antiparallel β-sheet with the same residues on another peptide. The two monomers are represented in yellow and green; their approximate two-fold rotational symmetry is evident

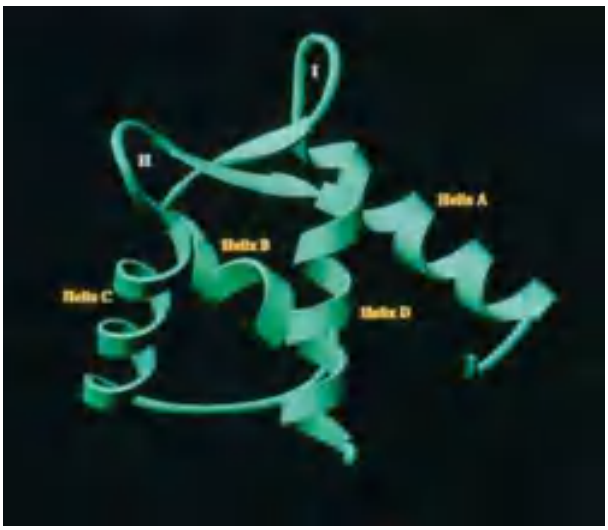

Figure 5 Structure of apo TR1 C (residues 12 to 87 of turkey skeletal TnC).[91,92] The size and orientation of helices A–D as well as the β-sheet region of this average structure are similar to the crystal structure

aromatic rings, while retaining the overall structural features of the tertiary fold of TnC, and reduce the off rate of calcium in the complex.

A TnI peptide (TnIp), corresponding to the region of TnI representing the minimum sequence necessary for the inhibition of actomyosin ATPase activity (TnI(104–115)–NH_2), was synthesized.[95] A perturbation of the aliphatic, aromatic, and charged residues upon interaction of TnIp with TnC was observed.[95] Slupsky et al.[96] studied TnIp when it was complexed with TnC and with a site III/site IV heterodimer representing the C-domain of TnC. Similar changes in the C-terminal aromatic envelope, in both TnC and the heterodimer were observed, suggesting that the heterodimer is a good model for the C-terminal domain of TnC and illustrating that three relatively unstructured peptides can bind an ion and fold to mimic a larger system. Slupsky and Sykes[97] subsequently formulated a model for the binding of this TnI peptide to the C-terminal domain of TnC based on the NMR structure of calmodulin binding of the MLCK peptide (Figure 6). Tsuda et al.[98] also studied the CN4 fragment of TnI (96–116) binding to Ca_4TnC, and observed a change in chemical shift of C-terminal as well as N-terminal residues. This peptide was able to increase the transition temperature of the N-domain, and thus was thought to interact with both domains. When this peptide was added to Mg_4TnC, however, only C-terminal residues were perturbed.[98]

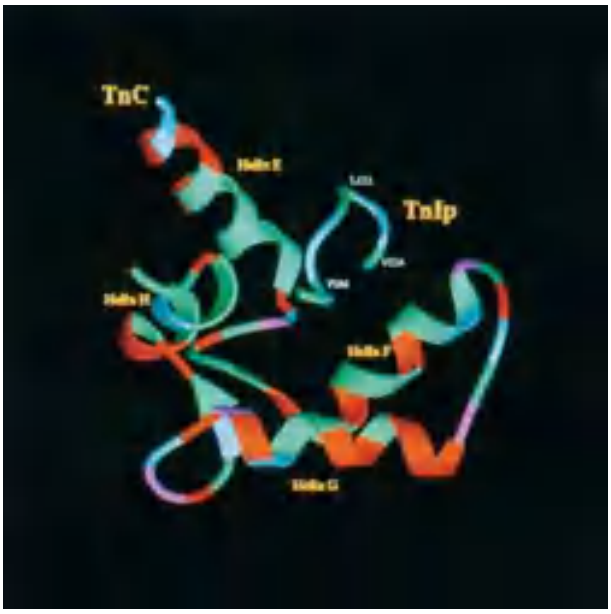

Figure 6 Ribbon model of the interaction between the C-domain of TnC and TnI(104–115) (TnIp). (Green) Hydrophobic residues; (red/acidic pink/purple) polar residues; (blue) basic residues. The TnIp hydrophobic residues face in toward the hydrophobic pocket of the C-terminal domain of TnC. The TnIp/TnC complex model was obtained by overlaying TnIp and TnC onto the CaM–MLCK peptide structure[128] to obtain a minimum root-mean-square deviation (rmsd). The relative orientation of TnIp in the complex was subsequently optimized under energy criteria using a combined Monte Carlo/energy minimization approach. Comparison of the backbone atoms of the calmodulin/MLCK complex (203, 204, 205, 206 of MLCK and 98, 99, 100, 101 of CaM) with the TnC/TnIp complex (105, 106, 107, 108 of TnIp and 111, 112, 113, 114 of TnC) produced a rmsd of 1.45

3.5.3 Interaction of TnC with Drugs

MacLachlan et al.[99] and Reid et al.[100] studied the binding of drugs to TnC. Bepridil binding to cTnC was able to alter resonances of the N-domain and reduce the rate of calcium release from the low affinity site only.[99] Binding of calmidazolium to skeletal TnC was found[100] to induce changes to both domains. The binding stoichiometry of both bepridil and calmidazolium to TnC was found to be 1:1.

Tsuda and Hikichi[101] studied mastoparan binding to rabbit skeletal TnC in its apo, calcium saturated, and half saturated forms. Titration of apo TnC with mastoparan revealed mastoparan interacting with the N-domain. Titration of Ca_4TnC with mastoparan revealed an interaction of mastoparan with the C-terminal domain. Titration of Ca_2TnC with mastoparan revealed an interaction with both the N- and C-domains of TnC. In each TnC state, mastoparan broadened resonances in the hydrophobic cluster. The N-domain stability increased when one molar equivalent of mastoparan was bound to Ca_2TnC or Ca_4TnC, suggesting a mastoparan-induced interaction between the N- and C-domains of TnC. The downfield shifted $C^{\alpha}H$ resonances were moved upfield upon mastoparan binding, indicating an increased distance between the two strands of the β-sheet. The affinity of mastoparan for the C-domain of TnC was stronger than that for the N-domain.[101]

4 OTHER PROTEINS OF THE MUSCLE

4.1 Calsequestrin

Only one paper has appeared describing NMR studies of this member of the SR.[102] Calsequestrin is a highly acidic protein of molecular weight 44 kDa, and can bind up to 50 calcium molecules per molecule of protein with a binding constant of 1 mM. The function of calsequestrin is to act as a calcium buffer, effectively to lower the free calcium concentration within the SR. In the absence of calcium, calsequestrin appeared to be largely in the random coil form. Calcium binding to calsequestrin caused an increase in α-helix content to 35% and a broadening and loss of intensity in the aromatic and aliphatic regions of the spectrum by about 70%.[102] The decrease in intensity could be due to a compaction of the molecule, as determined in hydrodynamic studies where the protein was largely extended in the absence of calcium, but more compact in the presence of calcium.

4.2 Dystrophin

Dystrophin is a recently discovered multidomain (MW 427 kDa) protein, the lack of which is associated with muscular dystrophies.[103] Dystrophin is rod-like in shape and has been found associated with the membrane of the muscle cell. Since ion permeability is increased in dystrophic muscle cells, dystrophin must function in muscle membrane structure.[103] The N-terminal sequence of dystrophin is homologous to α-actinin, and thus there have been two recent studies employing NMR to determine the interaction between dystrophin and actin.[103,104] Synthetic peptides corresponding to regions of the dystrophin molecule that may interact with F-actin

were studied. Peptides comprising residues 1–32 and 10–32 interacted with actin.[103,104] Furthermore, it was shown that the peptide 10–32 did not compete with TnI for binding to actin, nor did it have an effect on the inhibition of the magnesium-activated ATPase of actomyosin by TnI. Another peptide, 3429–3220, did not interact with F-actin at all.[103,104] Thus it was concluded that the region represented by residues 10–32 of dystrophin interacts with actin.

4.3 Parvalbumin

Parvalbumin is a protein found in the cytosol of muscle cells and is thought to act as a one-way calcium messenger, being particularly important in cold-blooded animals such as fish and amphibians. The crystallographic structure of parvalbumin[105] indicates that each of its two calcium binding domains has the EF hand structure. It is of interest to note that all calcium binding proteins give similar assigned NMR fingerprints for each pair of two hands, indicating that the hands are similar.[106] Parvalbumins are of low molecular weight (approximately 12 kDa), and are characterized by a high calcium ion affinity (approximately $10^8\ M^{-1}$). The polypeptide chain is arranged in six helical fragments (A–F) whose spatial organization reveals a core of hydrophobic residues, much like TnC. Comparison of the amino acid sequences from different species indicates the presence of two distinct phylogenetic lineages termed α (pI 5.0) and β (pI 4.1).[107]

Parvalbumin has been studied using ^{13}C NMR[108–111] and ^{19}F NMR[112,113] with a fluorine label attached to the cysteine-18 residue. ^{13}C NMR revealed significant internal motional freedom of the phenylalanine residues in the calcium-loaded parvalbumin.[110] ^{19}F NMR of labeled parvalbumin revealed a change from exposure to solvent in the calcium free state to buried in the calcium saturated state,[113] resulting from changes in the relative disposition of the helices upon calcium binding. This was also shown using ^1H NMR[114] for several parvalbumins.

Removal of calcium ions from parvalbumin leads to a structure similar to that obtained by chemical or thermal denaturations shown by ^1H NMR.[115] The calcium binding affinity of parvalbumin was determined to be dependent on the tertiary structure.[116] The tertiary structure was found to vary reversibly between a compact $PaCa_2$ structure and a more expanded Pa(0) structure.[116] Observation of amide proton exchange rates of residues located in calcium-loaded parvalbumin revealed that residues in the A–B helices exchanged faster than residues in the C–D and E–F helices for $PaCa_2$.[117] This difference did not exist for $PaMg_2$, where faster exchange rates were observed over all of the sequence.[117] The NOE networks were conserved between the calcium and magnesium loaded forms of parvalbumin, indicating that the structures of the two are very similar. Other studies involving rat apo and metal-bound α-parvalbumin also showed similar structures upon binding of different ions.[118] The thermal stability was shown to decrease upon complexation with ions other than calcium.[118]

The binding of other metal ions to parvalbumin and possible differences of ion binding in the different isoforms of parvalbumin was studied by Lee and Sykes[119] and Lee et al.[120] Their approach involved determining the orientation and principal elements of the magnetic susceptibility tensor of the protein bound Yb^{3+} ion. This resulted in agreement between a calculated spectrum based on the X-ray structure of parvalbumin and an observed spectrum, demonstrating the utility of NMR in determining subtle differences in structure upon ion binding. Other studies of the metal ion binding site involved using NOE build-up curves to determine differences in the spin diffusion of residues in the calcium binding loop and relating this to slight calcium binding differences between parvalbumins.[121]

The three-dimensional structure of pike pI 5.0 parvalbumin (a member of the α series) has been determined using two-dimensional NMR techniques and DISGEO (distance geometry).[122,123] The overall shape of this parvalbumin is a compact organization of polypeptide chains with six helical domains labeled A–F, all helices (except D) being in a regular α-helix. The six helices displayed the characteristic spatial organization of parvalbumin, with A and B in an antiparallel arrangement, and C and D and E and F in a perpendicular arrangement, the CD and EF helices coming in close contact to form a short antiparallel β-sheet at the level of residues 57, 58, and 59, and 96, 97 and 98. The structure of α-parvalbumin was shown to be similar to the crystal structure[105] of the β-parvalbumins in the folding of its polypeptide chain, the difference being that α-parvalbumin has one extra residue at the C-terminal end of the F helix.[122] It turns out that this lengthening of the helix is a general feature of α-parvalbumins, resulting in an enhanced conformational stability due to this C-terminal region coming in close contact with the B helix. Indeed, a NOE was observed between the C-terminal alanine 109 of the F helix and lysine 27 of the B helix.[122] It was also shown[124] that the protonation/deprotonation of histidine 25 and histidine 106 causes a conformational change in the B helix/F helix region.

With the advent of homonuclear three-dimensional techniques such as the three-dimensional HOHAHA NOE experiment,[125,126] better structures of parvalbumin will be determined due to less resonance overlap and better resolution of NOE data.

5 FUTURE WORK IN MUSCLE RESEARCH BY NMR

NMR has always been an extremely useful tool in the field of muscle research. It has helped, and will continue to help, in defining the interaction sites between actin monomers, actin and myosin, actin and tropomyosin, tropomyosin and troponin, as well as interactions within the troponin complex. NMR has also been useful in determining the kinetics of transitions and binding constants. With the advent of the new three- and four-dimensional NMR techniques, as well as techniques of protein enrichment with ^{15}N, ^{13}C, and ^2H isotopes, structural studies of muscle proteins are now possible. The muscle proteins accessible using these techniques include TnC, TnI, the essential and regulatory light chains, as well as actin (TnT may be too difficult due to its low solubility). Peptides representing regions of interaction between these proteins may also be used to probe interaction sites. Indeed, our group has nearly completed the solution structure of calcium-loaded TnC,[130,131] and the apo and calcium loaded N-domain of TnC,[93,127] and is currently investigating the interaction of domains of TnC with fragments of TnI.

6 RELATED ARTICLES

Cadmium-113 NMR: A Surrogate Probe for Zinc and Calcium in Proteins; Calcium-Binding Proteins; Calmodulin.

7 REFERENCES

1. W. A. Catterall, *Cell*, 1991, **64**, 871.
2. G. H. Pollack, *Muscles and Molecules*, Ebner, Seattle, WA, 1990.
3. J. C. Rüegg, *Calcium in Muscle Activation*, Springer, Berlin, 1986.
4. I. Rayment, W. R. Rypniewski, K. Schmidt-Bäse, R. Smith, D. R. Tomchick, M. M. Benning, D. A. Winkelmann, G. Wesenberg, and H. M. Holden, *Science*, 1993, **261**, 50.
5. L. Stryer, *Biochemistry*, W. H. Freeman, San Francisco, CA, 1981.
6. A. Riberio, J. Parello, and O. Jardetzky, *Prog. Biophys. Mol. Biol.*, 1984, **43**, 95.
7. S. Highsmith, K. Akasaka, M. Konrad, R. Goody, K. Holmes, N. Wade-Jardetzky, and O. Jardetzky, *Biochemistry*, 1979, **18**, 4238.
8. S. Highsmith and O. Jardetzky, *Biochemistry*, 1981, **20**, 780.
9. T. M. Eads and L. Mandelkern, *J. Biol. Chem.*, 1984, **259**, 10689.
10. L. E. Sommerville, G. D. Henry, B. D. Sykes, and D. J. Hartshorne, *Biochemistry*, 1990, **29**, 10855.
11. H. R. Kalbitzer, M. Schrumpf, and J. Wray, *FEBS Lett.*, 1992, **298**, 226.
12. B. Koppitz, K. Feldmann, and L. M. G. Heilmeyer, Jr., *FEBS Lett.*, 1980, **117**, 199.
13. H. P. Prince, H. R. Trayer, G. D. Henry, I. P. Trayer, D. C. Dalgarno, B. A. Levine, P. D. Cary, and C. Turner, *Eur. J. Biochem.*, 1981, **121**, 213.
14. G. D. Henry, D. C. Dalgarno, G. Marcus, M. Scott, B. A. Levine, and I. P. Trayer, *FEBS Lett.*, 1982, **144**, 11.
15. M. Roux-Fromy, and R. Cardinaud, *FEBS Lett.*, 1984, **172**, 198.
16. U. Tollemar, K. Cunningham, and J. W. Shriver, *Biochim. Biophys. Acta*, 1986, **873**, 243.
17. H. R. Trayer, H. P. Prince, G. D. Henry, and I. P. Trayer, *Biochem. Soc. Trans.*, 1980, **8**, 650.
18. D. G. Bhandari, B. A. Levine, I. P. Trayer, and M. E. Yeadon, *Eur. J. Biochem.*, 1986, **160**, 349.
19. I. P. Trayer, H. R. Trayer, and B. A. Levine, *Eur. J. Biochem.*, 1987, **164**, 259.
20. B. A. Levine, H. S. Griffiths, V. B. Patchell, and S. V. Perry, *Biochem. J.*, 1988, **254**, 277.
21. M. R. Webb, G. G. McDonald, and D. R. Trentham, *J. Biol. Chem.*, 1978, **253**, 2908.
22. P. Rösch, R. S. Goody, H. R. Kalbitzer, and H. Zimmerman, *Arch. Biochem. Biophys.*, 1981, **211**, 622.
23. J. W. Shriver, and B. D. Sykes, *Biochemistry*, 1981, **20**, 6357.
24. J. W. Shriver and B. D. Sykes, *Biochemistry*, 1981, **20**, 2004.
25. B. D. Sykes, *Can. J. Biochem. Cell. Biol.*, 1983, **61**, 155.
26. J. W. Shriver and B. D. Sykes, *Biochemistry*, 1982, **21**, 3022.
27. J. H. Baldo, P. E. Hansen, J. W. Shriver, and B. D. Sykes, *Can. J. Biochem. Cell Biol.*, 1983, **61**, 115.
28. L. E. Kay, J. M. Pascone, B. D. Sykes, and J. W. Shriver, *J. Biol. Chem.*, 1987, **262**, 1984.
29. M. Tanokura, and S. Ebashi, *J. Biochem.*, 1993, **113**, 19.
30. F. André, M. Garrigos, and J. M. Neumann, *Bull. Magn. Reson.*, 1989, **11**, 389.
31. G. D. Henry, S. Maruta, M. Ikebe, and B. D. Sykes, *Biochemistry*, 1993, **32**, 10451.
32. S. Maruta, G. D. Henry, B. D. Sykes, and M. Ikebe, *J. Biol. Chem.*, 1993, **268**, 7093.
33. D. C. Dalgarno, H. P. Prince, B. A. Levine, and I. P. Trayer, *Biochim. Biophys. Acta*, 1982, **707**, 81.
34. B. A. Levine, A. J. G. Moir, A. L. Goodearl, and I. P. Trayer, *Biochem. Soc. Trans.*, 1991, **19**, 423.
35. M. Stewart and G. C. K. Roberts, *FEBS Lett.*, 1982, **146**, 293.
36. H. R. Kalbitzer, K. Maeda, A. Rösch, Y. Maéda, M. Geyer, W. Beneicke, K. P. Neidig, and A. Wittinghofer, *Biochemistry*, 1991, **30**, 8083.
37. J. A. Barden and L. Phillips, *Biochemistry*, 1990, **29**, 1348.
38. J. A. Barden, L. Phillips, B. A. Cornell, and C. G. dos Remedios, *Biochemistry*, 1989, **28**, 5895.
39. W. Kabsch, H. G. Mannherz, D. Suck, E. F. Pai, and K. C. Holmes, *Nature*, 1990, **347**, 37.
40. P. D. Burns and L. D. Burtnick, *Biochem. Int.*, 1981, **3**, 233.
41. J. A. Barden, C. C. Wu, and C. G. dos Remedios, *Biochim. Biophys. Acta*, 1983, **748**, 230.
42. M. Brauer and B. D. Sykes, *Biochemistry*, 1986, **25**, 2187.
43. H. R. Kalbitzer, G. Rohr, E. Nowak, R. S. Goody, W. Kuhn, and H. Zimmermann, *NMR in Biomedicine*, 1992, **5**, 347.
44. M. Brauer and B. D. Sykes, *Biochemistry*, 1981, **20**, 2060.
45. M. Brauer and B. D. Sykes, *Biochemistry*, 1981, **20**, 6767.
46. P. J. Cozzone, D. F. Nelson, and O. Jardetzky, *Biochem. Biophys. Res. Commun.*, 1974, **60**, 341.
47. M. Brauer, and B. D. Sykes, *Biochemistry*, 1982, **21**, 5934.
48. J. A. Barden and C. G. dos Remedios, *Eur. J. Biochem.*, 1985, **146**, 5.
49. J. E. Van Eyk, F. D. Sönnichsen, B. D. Sykes, and R. S. Hodges, *Peptides as Probes in Muscle Research*, Springer, Berlin, 1991, p. 15.
50. F. D. Sönnichsen, J. E. Van Eyk, R. S. Hodges, and B. D. Sykes, *Biochemistry*, 1992, **31**, 8790.
51. B. F. P. Edwards and B. D. Sykes, in *NMR in Biology*, ed. R. A. Dwek, I. D. Campbell, and R. E. Richards, Academic, London, 1977, p. 157.
52. B. F. P. Edwards and B. D. Sykes, *Biochemistry*, 1978, **17**, 684.
53. B. F. P. Edwards and B. D. Sykes, *Biochemistry*, 1980, **19**, 2577.
54. B. F. P. Edwards and B. D. Sykes, *Biochemistry*, 1981, **20**, 4193.
55. C. Sanders, B. D. Sykes, and L. B. Smillie, *Biochemistry*, 1988, **27**, 7000.
56. H. J. Vogel and W. A. Bridger, *Can. J. Biochem., Cell Biol.*, 1983, **61**, 363.
57. M. Stewart and G. C. K. Roberts, *J. Mol. Biol.*, 1983, **166**, 219.
58. B. F. P. Edwards, L. Lee, and B. D. Sykes, in *Biomolecular Structure and Function*, ed. P. F. Agris, Academic, New York, 1978, p. 275.
59. J.-R. Brisson, K. Golosinska, L. B. Smillie, and B. D. Sykes, *Biochemistry*, 1986, **25**, 4548.
60. K. Swiderek, K. Jaquet, H. E. Meyer, C. Schächtele, F. Hofmann, and L. M. G. Heilmeyer, Jr., *Eur. J. Biochem.*, 1990, **190**, 575.
61. M. Brauer and B. D. Sykes, *Methods Enzymol.*, 1984, **107**, 36.

62. J. E. Sperling, K. Feldmann, H. Meyer, U. Jahnke, and L. M. G. Heilmeyer, Jr., *Eur. J. Biochem.*, 1979, **101**, 581.
63. R. J. A. Grand, G. Henry, A. Moir, S. V. Perry, I. Trayer, D. C. Dalgarno, B. A. Levine, and S. B. Parker, in *Calcium Binding Proteins*, ed. B. de Bernard, G. L. Sottocasa, G. Sandri, E. Carafoli, A. N. Taylor, T. C. Vanaman, and R. J. P. Williams, Elsevier, Amsterdam, 1983, p. 379.
64. A. P. Campbell, P. J. Cachia, and B. D. Sykes, *Biochem. Cell Biol.*, 1991, **69**, 674.
65. A. P. Campbell, and B. D. Sykes, *J. Mol. Biol.*, 1991, **222**, 405.
66. K. A. Satyshur, S. T. Rao, D. Pyzalska, W. Drendel, M. Greaser, and M. Sundaralingam, *J. Biol. Chem.*, 1988, **263**, 1628.
67. O. Herzberg and M. N. G. James, *J. Mol. Biol.*, 1988, **203**, 761.
68. K. B. Seamon, D. J. Hartshorne, and A. A. Bothner-By, *Biochemistry*, 1977, **16**, 4039.
69. B. A. Levine, D. Mercola, D. Coffman, and J. M. Thronton, *J. Mol. Biol.*, 1977, **115**, 743.
70. B. A. Levine, J. M. Thornton, R. Fernandes, C. M. Kelly, and D. Mercola, *Biochim. Biophys. Acta*, 1978, **535**, 11.
71. S. Tsuda, Y. Hasegawa, M. Yoshida, K. Yagi, and K. Hikichi, *Biochemistry*, 1988, **27**, 4120.
72. S. Tsuda, K. Ogura, Y. Hasegawa, K. Yagi, and K. Hikichi, *Biochemistry*, 1990, **29**, 4951.
73. W. D. McCubbin, K. Oikawa, B. D. Sykes, and C. M. Kay, *Biochemistry*, 1982, **21**, 5948.
74. M. T. Hincke, B. D. Sykes, and C. M. Kay, *Biochemistry*, 1981, **20**, 3286.
75. M. T. Hincke, B. D. Sykes, and C. M. Kay, *Biochemistry*, 1981, **20**, 4185.
76. L. K. MacLachlan, D. G. Reid, and N. Carter, *J. Biol. Chem.*, 1990, **265**, 9754.
77. G. A. Krudy, R. M. M. Brito, J. A. Putkey, and P. R. Rosevear, *Biochemistry*, 1992, **31**, 1595.
78. R. M. M. Brito, J. A. Putkey, N. C. J. Strynadka, M. N. G. James, and P. R. Rosevear, *Biochemistry*, 1991, **30**, 10236.
79. R. M. M. Brito, G. A. Krudy, J. C. Negele, J. A. Putkey, and P. R. Rosevear, *J. Biol. Chem.*, 1993, **268**, 20966.
80. G. S. Shaw, R. S. Hodges, and B. D. Sykes, *Science*, 1990, **249**, 280.
81. G. S. Shaw, R. S. Hodges, and B. D. Sykes, *Biochemistry*, 1991, **30**, 8339.
82. G. S. Shaw, W. A. Findlay, P. D. Semchuk, R. S. Hodges, and B. D. Sykes, *J. Am. Chem. Soc.*, 1992, **114**, 6258.
83. G. S. Shaw, R. S. Hodges, and B. D. Sykes, *Biochemistry*, 1992, **31**, 9572.
84. L. E. Kay, J. D. Forman-Kay, W. D. McCubbin, and C. M. Kay, *Biochemistry*, 1991, **30**, 4323.
85. B. J. Marsden, G. S. Shaw, and B. D. Sykes, *Biochem. Cell Biol.*, 1990, **68**, 587.
86. E. R. Birnbaum and B. D. Sykes, *Biochemistry*, 1978, **17**, 4965.
87. P. C. Leavis, J. S. Evans, and B. A. Levine, *J. Inorg. Biochem.*, 1982, **16**, 257.
88. W. Drabikowski, D. C. Dalgarno, B. A. Levine, J. Gergely, Z. Grabarek, and P. C. Leavis, *Eur. J. Biochem.*, 1985, **151**, 17.
89. J. Gariépy, B. D. Sykes, R. E. Reid, and R. S. Hodges, *Biochemistry*, 1982, **21**, 1506.
90. P. Kanellis, J. Yang, H. C. Cheung, and R. E. Lenkinski, *Arch. Biochem. Biophys.*, 1983, **220**, 530.
91. W. A. Findlay and B. D. Sykes, *Biochemistry*, 1993, **32**, 3461.
92. W. A. Findlay, F. D. Sönnichsen, and B. D. Sykes, *J. Biol. Chem.*, 1994, **269**, 6773.
93. S. M. Gagné, S. Tsuda, M. X. Li, M. Chandre, L. B. Smillie, and B. D. Sykes, *Protein Sci.*, 1994, **3**, 1961.
94. D. C. Dalgarno, R. J. A. Grand, B. A. Levine, A. J. G. Moir, G. M. M. Scott, and S. V. Perry, *FEBS Lett.*, 1982, **150**, 54.
95. P. J. Cachia, B. D. Sykes, and R. S. Hodges, *Biochemistry*, 1983, **22**, 4145.
96. C. M. Slupsky, G. S. Shaw, A. P. Campbell, and B. D. Sykes, *Protein Sci.*, 1992, **1**, 1595.
97. C. M. Slupsky and B. D. Sykes, unpublished results.
98. S. Tsuda, S. Aimoto, and K. Hikichi, *J. Biochem.*, 1992, **112**, 665.
99. L. K. MacLachlan, D. G. Reid, R. C. Mitchell, C. J. Salter, and S. J. Smith, *J. Biol. Chem.*, 1990, **265**, 9764.
100. D. G. Reid, L. K. MacLachlan, K. Gajjar, M. Voyle, R. J. King, and P. J. England, *J. Biol. Chem.*, 1990, **265**, 9744.
101. S. Tsuda and K. Hikichi, *Biochim. Biophys. Acta*, 1992, **1121**, 213.
102. B.-M. B. Aaron, K. Oikawa, R. A. F. Reithmeier, and B. D. Sykes, *J. Biol. Chem.*, 1984, **259**, 11876.
103. S. V. Perry, B. A. Levine, A. J. G. Moir, and V. B. Patchell, *Peptide Probes in Muscle Research*, Springer, Berlin, 1991, p. 161.
104. B. A. Levine, A. J. G. Moir, V. B. Patchell, and S. V. Perry, *FEBS Lett.*, 1990, **263**, 159.
105. R. H. Kretsinger and C. E. Nockolds, *J. Biol. Chem.*, 1973, **248**, 3313.
106. D. C. Dalgarno, B. A. Levine, and R. J. P. Williams, *Biosci. Rep.*, 1983, **3**, 443.
107. A. Cavé, A. Saint-Yves, J. Parello, M. Swärd, E. Thulin, and B. Lindman, *Mol. Cell Biochem.*, 1982, **44**, 161.
108. S. J. Opella, D. J. Nelson, and O. Jardetzky, *J. Am. Chem. Soc.*, 1974, **96**, 7157.
109. D. J. Nelson, S. J. Opella, and O. Jardetzky, *Biochemistry*, 1976, **15**, 5552.
110. D. J. Nelson, S. J. Opella, W. C. Hutton, and M. A. Wells, in *Biomolecular Structure and Function*, ed. P. F. Agris, Academic, New York, 1978, p. 393.
111. C. Zhang, H. Speno, C. Clairmont, and D. J. Nelson, *J. Inorg. Biochem.*, 1990, **40**, 59.
112. D. J. Nelson, *Inorg. Chim. Acta*, 1978, **27**, L71.
113. K. Bose and A. A. Bothner-By, *Biochemistry*, 1983, **22**, 1342.
114. A. Cavé, C. M. Dobson, J. Parello, and R. J. P. Williams, *FEBS Lett.*, 1976, **65**, 190.
115. J. Parello, A. Cavé, P. Puigdomenech, C. Maury, J.-R. Capony, and J.-P. Pechère, *Biochimie*, 1974, **56**, 61.
116. A. Cavé, M. Pages, P. Porin, and C. M. Dobson, *Biochimie*, 1979, **61**, 607.
117. C. Baldellon, A. Padilla, and A. Cavé, *Biochimie*, 1992, **74**, 837.
118. T. C. Williams, D. C. Corson, K. Oikawa, W. D. McCubbin, C. M. Kay, and B. D. Sykes, *Biochemistry*, 1986, **25**, 1835.
119. L. Lee, and B. D. Sykes, *Biochemistry*, 1983, **22**, 4366.
120. L. Lee, D. C. Corson, and B. D. Sykes, *Biophys. J.*, 1985, **47**, 139.
121. T. C. Williams and B. D. Sykes, in *Calcium-binding Proteins in Health and Disease*, Norman et al., Academic, San Diego, CA, 1987, p. 427.
122. A. Padilla, A. Cavé, and J. Parello, *J. Mol. Biol.*, 1988, **204**, 995.
123. A. Padilla, A. Cavé, and J. Parello, *J. Mol. Biol.*, 1989, **208**, 723.
124. T. C. Williams, D. C. Corson, W. D. McCubbin, K. Oikawa, C. M. Kay, and B. D. Sykes, *Biochemistry*, 1986, **25**, 1826.

125. A. Padilla, G. W. Vuister, R. Boelens, G. J. Kleywegt, A. Cavé, J. Parello, and R. Kaptein, *J. Am. Chem. Soc.*, 1990, **112**, 5024.
126. G. W. Vuister, R. Boelens, A. Padilla, G. J. Kleywegt, and R. Kaptein, *Biochemistry*, 1990, **29**, 1829.
127. S. M. Gagné, S. Tsuda, M. X. Li, L. B. Smillie, and B. D. Sykes, *Nature Struct. Biol.*, 1995, in press.
128. M. Ikura, G. M. Clore, A. M. Gronenborn, G. Zhu, C. B. Klee, and A. Bax, *Science*, 1992, **256**, 632.
129. J. Gariépy, L. E. Kay, I. D. Kuntz, B. D. Sykes, and R. S. Hodges, *Biochemistry*, 1985, **24**, 544.
130. C. M. Slupsky, F. C. Reimach, L. B. Smillie, and B. D. Sykes, *Protein Sci.*, 1995, **4**, 1279.
131. C. M. Slupsky and B. D. Sykes, *Biochemistry*, 1995, in press.

Acknowledgments

The authors gratefully acknowledge Perry d'Obrenan for his help with the myosin and actin schematics. The authors would also like to acknowledge Dr Frank Sönnichsen and Mr Stéphane Gagné for helpful advice in preparation of Figures 3 to 6, and Dr Larry Calhoun for his critical reading of the manuscript.

Biographical Sketches

Carolyn M. Slupsky. *b* 1966. B.Sc., Biochemistry, 1988; Ph.D., 1995 University of Alberta, Canada. Introduced to NMR in 1987 by Dr Sykes, University of Alberta. University of British Columbia, 1995–present. Approx. 8 publications. Research specialties: muscle research, troponin C, structure determination of larger proteins.

Brian D. Sykes. *b* 1943. B.Sc., 1965, Ph.D., 1969, Chemistry, Stanford University, USA. Assistant to Associate Professor of Chemistry, Harvard University, 1969–75; Associate to Full Professor of Biochemistry, University of Alberta, 1975–present. Approximately 250 publications. Research specialty: solution structures of biological macromolecules, especially muscle and calcium binding proteins.

Nucleic Acid Structures in Solution: Sequence Dependence

Thomas L. James

University of California, San Francisco, CA, USA

1	Introduction	1
2	Structure Determination	1
3	Criteria to Assess the Quality of NMR-Derived Structures	6
4	Complications from Conformational Flexibility	8
5	Conclusions	11
6	Related Articles	11
7	References	11

1 INTRODUCTION

Crucial biological processes central to the molecular biology of animals and plants entail interactions of proteins and other nucleic acids with double helical deoxyribonucleic acid (DNA). These interactions can involve recognition of subtle structural variations in the DNA double helix that are sequence-dependent. Furthermore, these structural details may also direct mutagen or drug recognition. A detailed understanding of these processes requires the determination of biologically relevant structures. With subtle sequence-dependent structural features, a meaningful structure for a double helix may compel a high-precision structure. Analysis of X-ray diffraction from oligonucleotides in single crystals has demonstrated a significant sequence-dependent heterogeneity of DNA structure. However, single crystal X-ray diffraction has serious problems. Perhaps the most readily acknowledged problem has been that crystallizing DNA fragments does not generally leave them in the B form, i.e., the form in which they are nearly always found in solution. Even in those cases where the B form is obtained for a crystal, there is concern about the influence of crystal packing forces on the DNA structure. In a couple of different cases now, crystallization of a B DNA duplex into two different crystalline types has had a substantial impact upon many local structure parameters.

Nuclear magnetic resonance has recently provided an option. The methodology for determination of structures with sufficient resolution via NMR has not been easily achieved, but the ability to determine an accurate, high-precision structure of nearly any DNA double helix of length less than 15 base pairs (bp) is now possible if sufficient care and effort are expended. Before resorting to the relatively troublesome task of 'determining a structure', however, we should acknowledge that some insight into toxicologic, pharmacologic, or biological function can often be derived from NMR spectral data without resorting to real structure determination.[1,2] For example, it can be quite useful to discover what part of a DNA is interacting with a ligand moiety. This can be learned from a relatively small amount of experimental data, e.g., from just a few NOE contacts. One can even model a chemically reasonable structure from these small amounts of data; but this does not constitute structure determination.

The structure of any molecule can be determined with a sufficient number of structural restraints, e.g., internuclear distances and bond torsion angles, in conjunction with holonomic constraints of bond lengths, bond angles, and steric limitations. Nuclear magnetic resonance, in conjunction with appropriate computational algorithms, has become the method of choice for determination of high-precision solution structures. Multidimensional NMR has the capability of yielding interproton distances and bond torsion angles as experimental structural restraints.[3–6] These experimental structural restraints are used with algorithms, such as distance geometry (DG) and restrained molecular dynamics (rMD), which search conformational space to define all structures consistent with the experimental restraints. If these resulting structures are closely related and there is confidence that pertinent parts of conformational space have not been neglected, it is concluded that the structure has been determined. It is preferable that the array of structures generated by the search algorithms be large enough to map out the conformational space, which will accommodate all available experimental data.

Our ability to determine solution structures of a DNA duplex by NMR is limited by the quantity, quality, and distribution of distance and torsion angle restraints that can be extracted from the NMR data. The problem is exacerbated by degeneracy in secondary structure, lack of tertiary structure, and monotony of monomers. Further complications may ensue from limited conformational flexibility. In spite of these obstacles, high-precision structures can be determined. Higher 'resolution' can be achieved with more structural restraints and with more accurate structural restraints. Techniques used to establish these restraints and to assess structure are constantly improving.

In the following discussion, I will discuss the current state-of-the-art in the methodology to determine high-resolution NMR structures, with a particular emphasis on DNA duplexes. This discussion will include suggestions on particular methodology to be employed, a mention of some pitfalls and complications, and how to assess the structures determined.

2 STRUCTURE DETERMINATION

There has never been a consensus on the exact methodology to use for determining molecular structure via NMR; basically, however, NMR data must be acquired that permit assignment of resonances and which can be (semi)quantitatively related to the local structure. A search of conformational space must be made in an attempt to satisfy simultaneously all geometric requirements imposed by the holonomic constraints of atom connectivities, bond lengths and bond angles (and, in the case of rMD, energetics), as well as all the experimental NMR structural data. The procedure should reveal what structures are compatible with the available data. It is intuitively clear that more structural data will generally lead to a more closely related family of compatible structures, i.e., to a better defined or higher 'resolution' structure.

Unlike proteins, where assignment of resonances is often the bottleneck in structure determination, making proton

resonance assignments in a DNA duplex is fairly quick and straightforward.[2] All structures determined to date have utilized structural restraints from NOE cross peaks. Some structures have also utilized torsion angle restraints from the oligonucleotide backbone or sugar ring. However, the manner of determining distance and torsion angle restraints and the use of these data in structure determination has varied with time and from laboratory to laboratory. As the quality of the structure derived depends on the structural restraints and the structure refinement algorithms, some description of these topics follows.

2.1 Distance Restraints

The intensities of the cross peaks in a two-dimensional (2D) NOE spectrum are related to the distances between protons, which are in close spatial proximity (<5–6 Å) in a structure and can be used to estimate those distances. In principle, we might anticipate that accurate cross-peak intensities would be desired in order to obtain accurate distances. However, obtaining intensities accurately reflecting the interproton distance generally requires that (a) the pulse repetition time (*TR*) of the experiment be long compared with the longest proton T_1 value, i.e., for relaxation to be nearly complete, (b) contributions to the cross peaks from multiple quantum coherences must be minimal, (c) good, flat base planes in the well-digitized spectra must be produced to enable good integration, and (d) peak overlap must be minimal (or very reliable deconvolution software must be available). Note that these requirements are not extreme. For example, if we arbitrarily find an error of 5% in measurement of the interproton distance *r* acceptable, we could tolerate an error in cross peak intensity of about 35%. (This assumes only the first order relationship that cross-peak intensity $\propto r^{-6}$, see below.) Other NMR laboratories typically use a *TR* of $\leq$2 s, which would alone decrease intensities for typical DNA duplexes by 25–50% for most cross peaks, and by up to 90% for those entailing adenine H-2 protons. I point out that our laboratory has always used a *TR* of 8–12 s.

The effect of cross relaxation between two neighboring protons during the mixing time period τ_m of the 2D NOE experiment is to transfer magnetization between them. The efficiency of this transfer depends on the distance between the two protons and upon the rate of molecular motion. With transfer of magnetization, the cross-peak intensities in the spectrum will be modified. Consequently, the cross-peak intensities have structural information, i.e., distances, embedded in them. In interesting molecules, the two protons giving rise to a particular cross peak are not the only protons in the molecule. Rather, they belong to an array of all protons in the molecular structure which, in principle, experience dipole–dipole interactions with all the others. So cross relaxation between the two protons is part of a coupled relaxation network. There are different methods of analyzing 2D NOE spectra to obtain internuclear distances. The commonly employed two-spin or isolated spin pair approximation (ISPA) can be used:

$$r_{ij} = r_{\text{ref}} \left(\frac{a_{\text{ref}}}{a_{ij}} \right)^{1/6} \tag{1}$$

where r_{ij} is the interproton distance to be estimated and a_{ij} is the corresponding 2D NOE cross-peak intensity, while r_{ref} and a_{ref} are, respectively, a known interproton distance and its cross-peak intensity. This equation derives from truncation after the linear term of the Taylor series expansion of the complete rate expression accounting for all proton dipole–dipole interactions:[7]

$$\mathbf{a}(\tau_m) = e^{-\mathbf{R}\tau_m} \approx \mathbf{1} - \mathbf{R}\tau_m + \tfrac{1}{2}\mathbf{R}^2\tau_m^2 - \cdots + \frac{(-1)^n}{n!}\mathbf{R}^n\tau_m^n + \cdots \tag{2}$$

where **a** is the matrix of 2D NOE intensities, **R** is the matrix describing the complete dipole–dipole relaxation network, and τ_m is the mixing time for the experiment. The truncation is valid in the limit of short mixing time τ_m. The elements of the relaxation matrix **R** depend on spin-state transition probabilities, written below as zero-, single-, and double-quantum transition probabilities W_m^{ij}, as follows:

$$R_{ii} = 2(n_i - 1)(W_1^{ii} + W_2^{ii}) + \sum_{j \neq i} n_j (W_0^{ij} + 2W_1^{ij} + W_2^{ij}) + R_{1i} \tag{3a}$$

$$R_{ij} = n_i (W_2^{ij} - W_0^{ij}) \tag{3b}$$

Here n_i is the number of equivalent spins in a group such as a methyl rotor. For a rigid molecule undergoing isotropic random reorientation with correlation time τ_c, the following equations for transition probabilities hold:

$$W_0^{ij} = \frac{q\tau_c}{r_{ij}^6} \quad W_1^{ij} = 1.5\frac{q\tau_c}{r_{ij}^6}\frac{1}{1+(\omega\tau_c)^2}$$
$$W_2^{ij} = 6\frac{q\tau_c}{r_{ij}^6}\frac{1}{1+4(\omega\tau_c)^2} \tag{4}$$

where ω is the Larmor frequency of the protons, $q = 0.1\gamma^4\hbar^2$ and γ is the proton gyromagnetic ratio. The term R_{1i} represents external sources of relaxation such as paramagnetic impurities. Spectral densities more complicated than simple isotropic tumbling can be readily accommodated.[8,9] Truncation of the series expansion of equation (2) to the first term linear in **R** is valid if τ_m is sufficiently short, which is equivalent to assuming that each cross-peak intensity depends only on the cross-relaxation rate between the two pertaining protons, i.e., ISPA. ISPA can lead to sizable systematic as well as random distance errors due to the multispin effects commonly called 'spin diffusion'.[8,10–12] The general method of assessing the impact of spin diffusion has been to obtain 2D NOE buildup curves, i.e., cross-peak intensities as a function of mixing time. Spin diffusion is usually considered to be negligible if the buildup is initially linear, i.e., in the short mixing time limit. This assumption, however, is not good at mixing times commonly employed.[10,13] For example, for mixing times generally accepted as being sufficiently short (i.e., 50–100 ms) and not including internal motions, ISPA can result in systematic errors of 45–80% in distances over 3.5 Å, a range which is quite important in defining molecular structure. Limiting analysis to 2D NOE spectra with short mixing times

also yields cross peaks with a lower signal-to-noise ratio and is inconsistent with our wish to eliminate spectral contributions from zero quantum coherence.

2.1.1 Complete Relaxation Matrix Analysis

Complete relaxation matrix analysis of proton homonuclear 2D NOE spectra enables many accurate interproton distances to be calculated by accounting for all dipole–dipole interactions, thereby obviating 'spin diffusion' effects.[8,12] For this we utilize linear algebra and the simplifications that arise from working with the characteristic eigenvalues and eigenvectors of a matrix.[8] The rate matrix **R** can be represented by a product of matrices:

$$\mathbf{R} = \boldsymbol{\chi}\boldsymbol{\lambda}\boldsymbol{\chi}^{\mathrm{T}} \tag{5}$$

where $\boldsymbol{\chi}$ is the unitary matrix of orthonormal eigenvectors ($\boldsymbol{\chi}^{-1} = \boldsymbol{\chi}^{\mathrm{T}}$), and $\boldsymbol{\lambda}$ is the diagonal matrix of eigenvalues. Since $\boldsymbol{\lambda}$ is diagonal,

$$\mathbf{a} = \boldsymbol{\chi}\, \mathrm{e}^{-\lambda\tau_{\mathrm{m}}}\boldsymbol{\chi}^{-1} \tag{6}$$

We have developed the program CORMA (for COmplete Relaxation Matrix Analysis) for calculating NOE cross-peak intensities from either interproton distances or atomic coordinates.[8,10] Such calculation of 2D NOE peak intensities (intensity matrix **a**) from a model structure is often called 'back calculation'.

Instead of simply comparing model structures, we prefer to determine a structure, so we need structural restraints. The most efficient techniques for calculating accurate distances entail an iterative approach.[10,14–16] The MARDIGRAS algorithm permits the determination of a large number of accurate distance restraints and aids in individually setting bounds for those distances. It may be apparent from the above equations that we should be able to calculate distances directly from intensities, i.e., the reverse of the CORMA calculation outlined above. The matrix of experimental intensities at time τ_{m}, however, will generally be incomplete for biopolymers due to experimental limitations such as resolution (i.e., peak overlap) and (realistic) signal-to-noise ratio. As a consequence, the corresponding relaxation matrix does not represent the spatial arrangement of protons leading to the intensities: A direct back calculation of **R** will therefore fail to yield accurate, unbiased distances.[10,11] The incomplete experimental intensity matrix can be augmented with intensities calculated for a model structure to form a hybrid intensity matrix.[14–16] In an iterative fashion, the relaxation rate matrix is made internally self-consistent. As a consequence, distances emanating from the self-consistent relaxation rate matrix will not be biased. An important aspect of the MARDIGRAS algorithm is that all intensities are used to obtain all distances simultaneously, i.e., the entire cross-relaxation network is employed; this is in distinct contrast to the old paradigm of a one-to-one mapping of intensities and distances.

Recent improvements in MARDIGRAS account for the presence of explicit molecular motions[9] or molecular motions implied by order parameters[17] and incorporate effects of exchange with bulk water in the case of exchangeable protons.[18] Due to exchange of imino and amino protons of nucleic acid duplexes with bulk water, the intensity of 2D NOE cross peaks involving these exchangeable protons can be strongly altered (see below). Without taking such exchange into account, calculation of distances to exchangeable protons is risky. However, the additional structural information from using such distances is extremely valuable.

Any method used for calculating interproton distances from NOE data requires an estimate of the correlation time. In general, an isotropic correlation time is assumed for the overall tumbling of the DNA duplex; this assumption is reasonable up to a length of approx. 14 base pairs. Calculations using a cylindrical model have demonstrated that errors in interproton distances, which are dependent on interproton vector orientation, can result as the length-to-diameter ratio of the DNA 'cylinder' increases.[19] We have incorporated the capability of utilizing overall anisotropic tumbling motions in MARDIGRAS calculations.[17] For a trisdecamer (13 bp), the hydrated length-to-radius ratio can be calculated to be about 2.2, based on a hydrated diameter of 20.5 ± 1.0 Å found for a couple of oligonucleotide duplexes,[20] and a rise per base pair of 3.4 to 3.5 Å. This cylindrical ratio of 2.2 corresponds to a ratio of 2.4 in the ratio of long-axis versus short-axis tumbling.[20,21] (The ratio is even smaller if one uses a value for the hydrated radius of 24–25 Å which is obtained from classical DNA hydrodynamics studies.) A ratio of 2.4 in the tumbling rate of a cylinder, compared with isotropic tumbling, has a negligible effect (<3%) on the values of distances calculated with either the MARDIGRAS algorithm or with other distance calculation procedures.[19,22] Consequently, overall molecular tumbling can be considered to be effectively isotropic and well-approximated by a single correlation time. The correlation time of the duplex can be estimated from experimentally measured T_1 and T_2 relaxation times for individual resolved protons.[23]

2.1.2 Distance Restraint Bounds

To search conformational space to find structures consistent with our experimental data, we need an estimate of the accuracy of our distance restraints. In particular, they are needed for setting bounds in distance geometry or flat-well size in rMD calculations. Most structural studies have utilized ISPA to estimate interproton distances, but estimates of the error, reflected by the upper and lower bounds assigned, vary widely throughout the literature. Tighter distance bounds (smaller error bars) lead to a higher resolution structure. But distance bounds made tighter than warranted by experimental accuracy mislead to a highly defined (small atomic root-mean-square deviation, RMSD) but incorrect structure.[24] So we wish bounds to be as tight as possible but not so tight that the real distance can lie outside the bounds.

More accurate distances available via MARDIGRAS minimize the possibility of an estimated distance lying outside the bounds. MARDIGRAS can also aid our choice of bounds, set individually for each proton pair.

1. The 'error bar' for the distance between two nuclei can be estimated from the fit of the corresponding element of the converged MARDIGRAS intensity matrix with the experimental cross-peak intensity, using as a minimum the error dictated by the experimental noise level.[16]
2. We have found MARDIGRAS to be surprisingly robust, generating a largely correct set of distances independent

of the starting model used in the iterative process.[15,16] However, there are some distance variations with starting structure; this variation can also aid our choice of bounds.

3. Distances are determined from a single 2D NOE spectrum using MARDIGRAS, rather than using buildup curves constructed from a set of spectra at several mixing times. It is still desirable to obtain spectra at a few different mixing times. Depending on the internuclear distance and proton environment, different mixing times will be optimum for different proton pairs. This enables distances determined independently from spectra acquired at different mixing times to be compared. Of course, the range of distance values measured from different spectra for any given proton pair can aid in the choice of bounds.
4. MARDIGRAS calculates bounds for distances to protons undergoing motional or overlap averaging, i.e., methyl, methylene, and aromatic protons.[9] As a consequence of iteration, MARDIGRAS converges to an internally consistent, relaxation rate matrix (and equivalently, a 2D NOE intensity matrix) in good agreement with experimental spectra. Distances are calculated from the individual cross-relaxation rates. Distances entailing protons averaged by motion or spectral overlap may be in serious error if the averaging is ignored. The cross-relaxation rates in these cases will depend on orientation as well as distance. MARDIGRAS does a second level of iteration, varying the orientation and distances of all dipole-dipole interactions to find the best fit.[9] Most importantly, however, MARDIGRAS lists the distances corresponding to the worst-case geometries, enabling upper and lower bounds to be set for distances involving protons averaged by either overlap or internal motions.
5. Chemical exchange can alter cross-peak intensities,[25–27] leading to inaccurate distances. Cross peaks entailing exchangeable protons in biopolymers (e.g., imino, amino, amide) depend on the exchange rate with bulk water. Exchange effects are included in the MARDIGRAS algorithm, with exchange involving bulk water emphasized.[18] To be significant, exchange rates with water must be >1 s^{-1}. Ignoring these effects will lead to overestimated distances. If the exchange rate is not known, it may still be possible to estimate an upper limit to the exchange rate: Use of this upper limit to exchange in the calculation can lead to a lower distance bound estimate.[18,28,29] In recent work, we measured imino proton exchange rates using the method of Adams and Lerner,[30] so the exchange rate values can be incorporated into MARDIGRAS calculations yielding more accurate distances involving imino protons.[31]

2.2 Torsion Angle Restraints

Bond torsion angles can be determined using Karplus correlations with vicinal coupling constants, which can be derived from various correlation spectroscopic techniques, e.g., ECOSY, PCOSY and double quantum filtered COSY (2QF-COSY).[32–34] In principle, these should enable us to determine pucker conformation in deoxyribose rings. Broad lines have prevented direct analysis of all coupling constants in DNA oligomers greater than about 8 bp in length. Consequently, most laboratories determine only those that can be readily measured, or determine sums of coupling constants, e.g., ΣH-2′, the sum of all coupling constants involving the H-2′ proton of a deoxyribose ring. We have found that limiting analysis to these can leave ambiguities, but fitting of experimental cross peaks to cross peaks simulated using the SPHINX/LINSHA program package[35] enables extraction of vicinal coupling constants and, subsequently, torsion angle restraints.[36–38] A comparison of simulated and experimental 2QF-COSY cross peaks for couple of deoxyribose rings in a trisdecamer duplex is shown in Figure 1. The torsion angles for the deoxyribose rings are determined using a parameterization of the relationship between torsion angles and coupling constants.[2,39,40] The major difficulty with this approach is in establishing the correct linewidth to be employed.[31,37] However, the choice of linewidth can usually be constrained such that limits (bounds) on torsion angles describing sugar pucker can be made. An improvement in procedure was recently described: the 2QF-COSY simulations were augmented by extraction of explicit vicinal coupling constants between H-1′ and the H-2′/H-2″ protons from ECOSY cross peaks.[31]

In studies of about 10 DNA duplexes, examining all scalar coupling-based cross peaks, we find that a single conformer will rarely account for all measured coupling constants, but reasonable fits are obtained with a two-state model representing a rapid interconversion between S- and N-type sugar puckers.[41] Unrestrained molecular dynamics calculations in our laboratory and elsewhere suggest that more than two sugar pucker states may exist, and recent molecular dynamics calculations using exponentially weighted, time-averaged restraints also indicate that sugar puckers other than standard N- and S-states are significantly populated for some nucleotides in a sequence.[42,43] To employ the simplest model to account for the data, in recent years we have utilized the two-state model. The pseudorotational phase angles of the major S- and minor N-conformers (P_S and P_N, respectively), as well as the relative populations and amplitudes of these conformers are typically derived. For nonterminal nucleotides, we generally find that the S conformer dominates, being populated 75–95% of the time; there are a few exceptions.

2.3 Structure Refinement from Restraints

With a sufficiently large number of well-distributed structural restraints, we can proceed to generate a structure.[44] Ideally, we should try to determine all structures that will satisfy the experimental structural restraints, so that the accessible conformational space can be mapped out. In some sense, this gives us a fuzzy picture of the structure. With more restraints, more accurate restraints, and tighter (but not unreasonable) bounds, the structural picture becomes sharper. Methods entailing systematic searches of conformational space have been advocated, but they are computationally too expensive at present for biopolymers. So a guided search of conformational space is preferred at present. While it is possible simultaneously to refine restraints and structure iteratively, we advocate separating the restraint determination step and the structure generation step. This should diminish any possibility of being trapped in a local energy minimum in the vicinity of early iteration structures which are trying to satisfy inaccurate restraints. Also, individual assessment of the bounds for each structural restraint can be determined and then used in the structure refinement procedure.

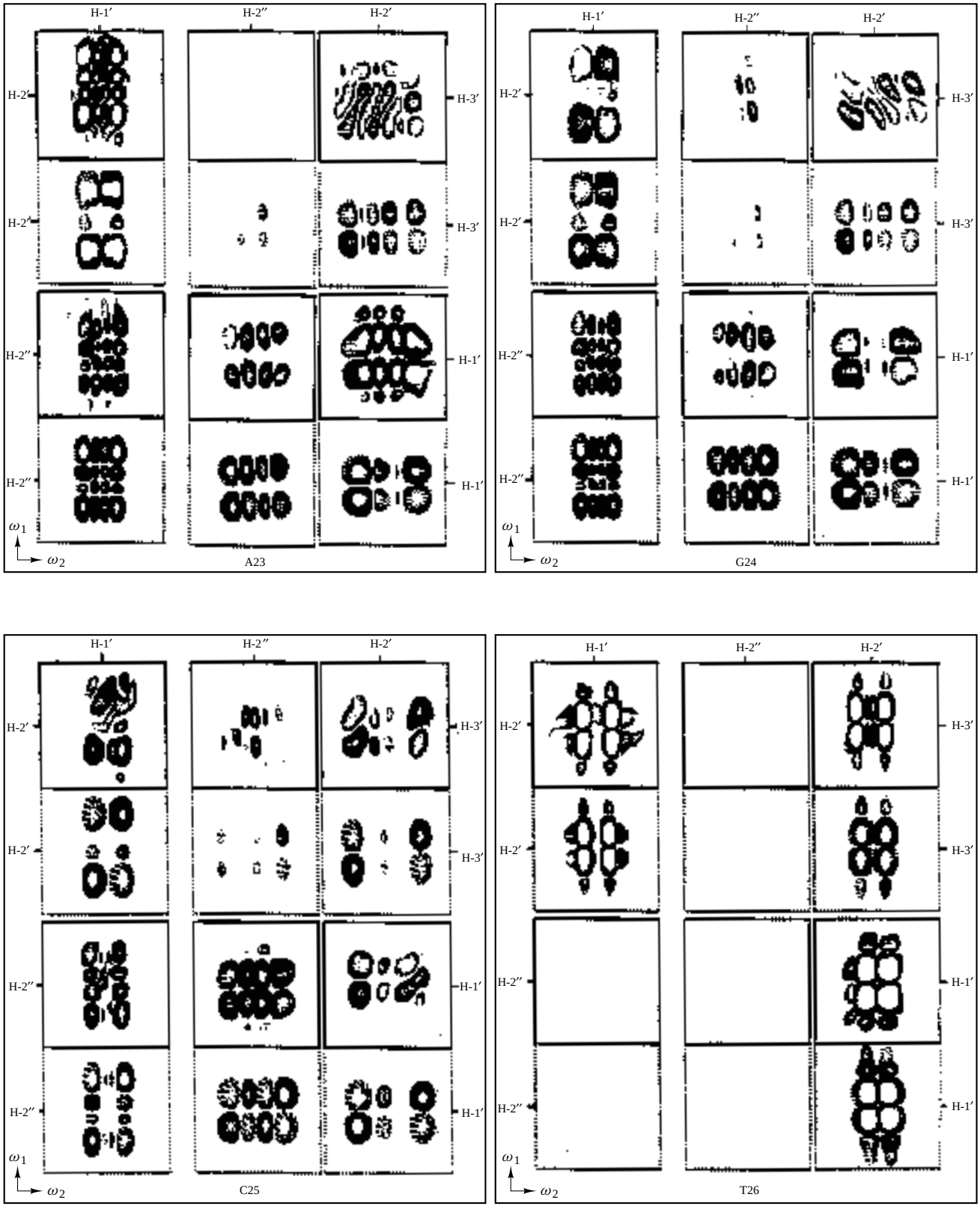

Figure 1 Comparison of experimental (solid boxes) and simulated (broken boxes) double quantum filtered COSY cross peaks for some representative deoxyribose rings in d(AGCTTGCCTTGAG) · d(CTCAAGGCAAGCT). Negative components are shaded for experimental peaks and dashed for simulated peaks. Note that the experimental cross peaks displayed in some cases also exhibit partial cross peaks from other nearby or overlapping cross peaks

Distance geometry and restrained molecular dynamics (also called simulated annealing) calculations are commonly used for structure generation and refinement. Both entail two key facets: (a) a search of conformational space to yield a structure consistent with all restraints, and (b) optimization of any resulting structure. Although distance geometry has been employed, there is an apparent consensus among practitioners that for DNA duplex structure determination we should attempt to reconcile experimental structural restraints with energetic considerations, generally via restrained molecular dynamics simulations. Molecular dynamics simulations have been reviewed recently.[45,46] It should be understood that an rMD simulation is not the same as a molecular dynamics (MD) simulation, which is generally concerned with following the molecular motions of a molecule over the femtosecond to nanosecond timescale. Rather, rMD uses the mathematics of MD to search conformational space. The kinetic energy in an MD simulation allows energy barriers of approximate amplitude kT to be crossed in a search for the global energetic minimum, which maintains a balance between maintenance of the 'classical' energy terms and the experimental restraints. In rMD, the potential energy is modified to incorporate experimental NMR restraints:

$$V_{\text{total}} = V_{\text{bond}} + V_{\text{angle}} + V_{\text{dihedral}} + V_{\text{van der Waals}} + V_{\text{coulomb}} + V_{\text{H bond}} + V_{\text{NOE}} + V_{J\ \text{coupling}} \quad (7)$$

The first five terms monitor the classical potential energy of the molecule. There may or may not be an explicit term used to maintain hydrogen bonds. The final two terms serve as penalty functions, monitoring the NOE-derived distance restraints and scalar coupling-derived torsion angle restraints, respectively. Some studies have not incorporated torsion angle restraints, but all have utilized distance restraints. Different functional forms have been employed for these penalty functions; we employ a flat-well potential with quadratic boundaries beyond the experimental upper and lower distance bounds:

$$V_{\text{NOE}} = \sum_{\text{all NOEs}} \begin{cases} k_2(r - r_1)^2 & \text{when } r < r_1 \\ 0 & \text{when } r_1 \le r \le r_u \\ k_3(r - r_u)^2 & \text{when } r_u < r \\ 4k_2(r - r_u) & \text{when } r \rangle r_u + 2.0 \end{cases} \quad (8)$$

where the lower (r_1) and the upper (r_u) bounds can be derived from MARDIGRAS (see above) to define the size of the flat-well width individually for each proton pair. Similarly, $V_{J\text{coupling}}$ can be defined. We currently use AMBER 4.1 for rMD simulations.[47]

Whereas force constants to be used for the conventional energy terms are rather well established, such has not been the case for the experimental restraint energy terms. We have consequently examined the effects of changing the force constant for the restraint energy terms in some detail for four different DNA duplexes. While the apparently optimum value varies somewhat for the different duplexes, as long as the force constant is in the range 10–40 kcal mol^{-1} Å^{-2} for simulations near 300 K, the exact value chosen is not a strong influence. On the basis of our experience, I would recommend that a value of 20 kcal mol^{-1} Å^{-2} be utilized in the absence of an evaluation for any particular duplex. The force constant for torsion angle restraint violations should be 3–4 times larger than that for distance restraint violations. Of course, in a simulated annealing protocol, where the temperature is raised, the force constants should be commensurately increased.

For rMD simulations, starting structures should be chosen in different regions of conformational space, e.g., A-DNA, B-DNA and possibly some other model structure. In addition, different random initial trajectories should be used for each starting structure. Newton's equations of motion are solved with the forces resulting from taking the derivative of the potential expressed in equation (7). In a successful simulation, a global energy minimum is achieved. Indeed, the same global minimum should be reached with all the different initial structures and different initial trajectories. In reality, the structures resulting from different simulations will not be identical, but they should be similar, i.e., with small atomic RMSD between the individual structures little bigger than atomic displacements from librational motions (approx. 0.5 Å): generally <1.0 Å is considered adequate. While structures resulting from the different trajectories are typically averaged and a 'final' structure reported, the envelope of individual structures, which appears as a 'fuzzy' structure, is perhaps a better representation. An example is shown in Figure 2.

There are methods other than DG and rMD for generating structures from NMR data, but there are few cases where different structure refinement methods have been independently applied to the same data set and the resulting structures compared. A Monte Carlo search in torsion angle space has been developed and results reported for one DNA octamer duplex.[48] Use of generalized helical parameters, rather than Cartesian coordinates, to define DNA conformation, increases efficiency by decreasing the number of parameters by an order of magnitude. Using an idealized geometry for the aromatic rings eliminates the small distortions sometimes observed with structures emanating from rMD due to the force field, permitting some distortion of bond angles and lengths in a compromise to fit the experimental restraints. Various different, simulated, annealing protocols were employed: The Metropolis Monte Carlo algorithm was used to generate the Boltzmann distribution of DNA structures at a series of different (increasing then decreasing) temperatures in each case. Convergence of final structures via restrained Monte Carlo (rMC) calculations is easily achieved from A-DNA and B-DNA (atomic RMSD <0.3 Å for all rMC simulations) without use of torsion angle restraints. For rMD, it is difficult (but sometimes possible) to achieve convergence to a global minimum starting from A-DNA without torsion angle restraints. The structures resulting from rMC and rMD are in agreement (RMSD <0.5 Å for all structures generated) despite the different force fields used and despite the fact that rMD utilized deoxyribose torsion angle restraints. The structures generated with rMC and rMD were both in reasonable accord with experimental 2D NOE peak intensities and with experimental scalar coupling data from 2QF-COSY spectra. Agreement with the scalar coupling data is particularly satisfying because those data were used in the rMD refinement but not the rMC refinement.

3 CRITERIA TO ASSESS THE QUALITY OF NMR-DERIVED STRUCTURES

It is common practice to cite the atomic RMSD (or variance) for a set of structures resulting from DG or rMD:

Figure 2 Ten superimposed structures of [d(AGCTTGCCTTGAG) · d(CTCAAGGCAAGCT)], a completely conserved sequence from the 3′-long terminal repeat of the HIV-1 genome. The structures are from 10 rMD simulations, each of 30-ps duration, five using A-DNA and five using B-DNA as starting structure, but each with a different initial trajectory. Convergence to an atomic RMSD of approx. 0.9 Å is achieved, compared with RMSD approx. 6.5 Å between the two different starting models, A-DNA and B-DNA. A total of 267 distance restraints (approx. 10 per nucleotide) and 130 torsion angle restrains (five per nucleotide) were employed

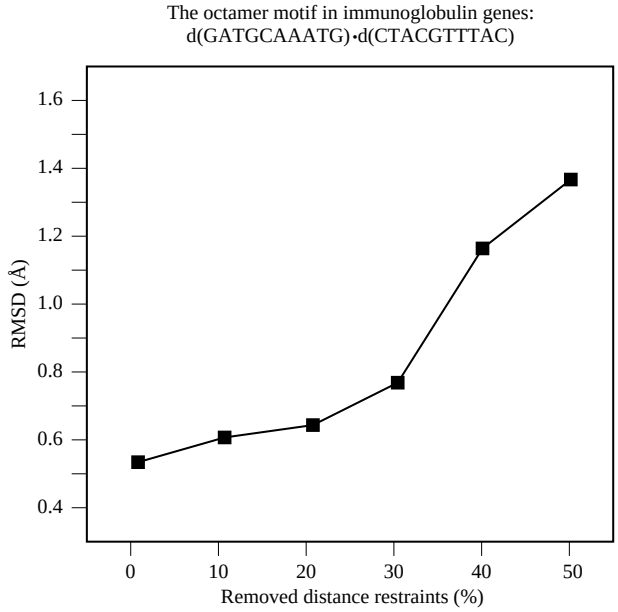

Figure 3 Influence of the fraction of experimental distance restraints utilized in rMD refinement on the structure of [d(GATGCAAATG) · d(CTACGTTTAC)]. The atomic rms difference between several structures refined against full and against partial data sets is shown as a function of the fraction of experimentally determined distance restrains randomly deleted from the restraints' list. The starting structure was energy-minimized B-DNA; the RMSD with none of the distances removed reflects the difference between independently refined structures using different initial velocities in the rMD procedure

the lower the value, the better. Sometimes the RMSD is interpreted as an indicator of the accuracy of a structure, or at least the precision of a structure. It should be kept in mind, however, that it is really only a convenient means of assessing the extent to which the structures generated have converged, although it is useful in a semiquantitative sense, as the atomic RMSD is related to the 'resolution' of the structure derived. For example, the structure of the trisdecamer duplex shown in Figure 2 is relatively well restrained by the experimental structural restraints (approx. 10 distance restraints and five torsion angle restraints per nucleotide[28]) but the spectral resolution of some DNA duplexes studied in our laboratory have permitted more restraints to be determined leading to structures with lower atomic RMSD values. For [d(GATGCAAATG) · d(CTACGTTTAC)], the inner eight base pairs of which comprise the octamer motif found in promoter and enhancer regions of immunoglobulin genes and are recognized by the POU domain of certain transcription factors, approx. 20 distance restraints and five torsion angle restraints per nucleotide were obtained.[29] Several rMD simulations resulted in a well-defined structure. With so many restraints available, it was possible to investigate the effect on the derived structure of randomly eliminating some of the distance restraints. As seen in Figure 3, randomly reducing the distance restraints to an average of $\geq$12 per residue has little effect on the final structure derived. As reflected in the atomic RMSD, however, fewer than about 12 distance restraints per residue apparently results in a less defined DNA structure. It should be noted though that with only 50% of the restraints, the experimental restraints still largely determine the structure; there is a difference of more than 5 Å RMSD between energy-minimized A- and B-DNA structures.

One should be cautious about comparing RMSD values from one study with another. In fact, one should be careful about trying to push the value too low. It is possible to make the RMSD smaller by various means, e.g., by using larger force constants for the restraint violation terms in rMD simulations, by inadequate sampling in DG calculations, and by choosing very tight restraint bounds. While we want the restraint bounds to be tight to improve resolution, restraint bounds made tighter than the experimental accuracy will result in a better RMSD and also lead to inaccuracies in the structure.[24]

While it provides some insight, the atomic RMSD is definitely not a measure of accuracy and is only a modest descriptor of precision. Other criteria can be cited, however. For example, we can compare the final structure, or interim structures, with the experimental NMR data. In X-ray crystallography, an evaluation of the fit of a derived structure with the original electron densities via a residual index (*R* factor) is requisite for any published structure. Yet such a comparison of the derived structure with the original data is rarely done for NMR

structures. However, we can quantitatively compare calculated 2D NOE spectral intensities for any proposed molecular structure with the experimental intensities. We could use a residual index analogous to the crystallographic R factors:

$$R_1 = \frac{\sum_i |a_o^i - a_c^i|}{\sum_i (a_o^i)} \tag{9}$$

R_1 gives equal weighting to all deviations between observed and calculated intensities a_o and a_c, so stronger peaks (from shorter distances, i.e., <2.5 Å) will generally dominate. Consequently, we prefer a sixth-root residual index which scales roughly with atomic distances:[12,24,49]

$$R_1^x = \frac{\sum_i |a_o^{1/6}(i) - a_c^{1/6}(i)|}{\sum_i a_o^{1/6}(i)} \tag{10}$$

R_1^x permits longer interactions, e.g., approx. 4 Å, to have a role in the calculated R factor. Longer distance restraints are most important in structure determination, so it would be good to have their input into assessing structure quality. It has been pointed out that R factors are, in principle, dependent on the sign of the errors between the model structure's intensities and the experimental data, so a quality factor (Q_1) was proposed.[50] We have subsequently incorporated this idea into the MARDIGRAS program which now reports the following Q factors in addition to R factors:

$$Q_1 = \frac{\sum_i |a_o^i - a_c^i|}{\sum_i (a_o^i) + \sum_i (a_c^i)} \quad Q_2 = \left[\frac{\sum_i (a_o^i - a_c^i)^2}{\sum_i (a_o^i)^2 + \sum_i (a_c^i)^2} \right]^{1/2} \tag{11}$$

$$Q_1^x = \frac{\sum_i |a_o^{1/6}(i) - a_c^{1/6}(i)|}{\sum_i a_o^{1/6}(i) + \sum_i a_c^{1/6}(i)}$$

$$Q_2^x = \left\{ \frac{\sum_i [a_o^{1/6}(i) - a_c^{1/6}(i)]^2}{\sum_i [a_o^{1/6}(i)]^2 + \sum_i [a_c^{1/6}(i)]^2} \right\}^{1/2} \tag{12}$$

Unlike X-ray crystallography, it is possible to define a subset of NOE cross peaks and calculate an R or Q factor pertaining to some particular aspect of the structure, e.g., interresidue vs. intraresidue, or one selected region of the molecule. Analysis is capable of indicating regions of good (or bad) fit between any model structure and the true solution structure.

In principle, we might wish to generate a structure with the lowest R factor possible. However, we should be prudent in our efforts to push an R factor to its lowest value. R factors are also of limited value when assessing the accuracy of a refined model. A small restraint set can be easily overfit to a low R value, although the structure is only poorly defined by the data. Other complications arise from the nonrandom nature of errors in experimental intensities and our limited knowledge of molecular motions. Although the exact nature of the molecular motions is not a strong determinant in the calculations of the 2D NOE intensities, motions can still influence the intensities.[8] Therefore, lack of knowledge about internal motions will render the calculation of some intensities for the model structure inexact. However, using the approximation that all methyl motions are fast and all aromatic ring flips are slow compared with the overall molecular tumbling rate in proteins, enables a quite reasonable approximation of the intensities and, consequently, a reasonable calculation of R or Q factors.[9]

Recently, a free R factor, R_1^{free}, has been proposed as a reliable and unbiased indicator for assessing X-ray crystal structures and NMR structures.[51] In the case of NMR, R_1^{free} measures the fit of a model structure's NOE intensities to a randomly selected set of experimental NOE intensities that are not used in structure refinement: approx. 10% of the total are in the test set, the other 90% are used in structure refinement. This avoids any model bias in calculating the R value. It is to be expected that R_1^{free} will be larger than R_1, since the test data were not used in structure generation. However, discounting noise in the data, if the test data are consistent with the structure determined, R_1^{free} should not be too much larger. The exact amount considered acceptable probably awaits more experience with real data. It might be pointed out that R_1^{free} is 50–100% larger than R_1 for the few proteins examined so far, and we found it to be 60% larger in one DNA decamer duplex. Note the total range of the X-ray R factor (with a maximum value of 0.83) is much more limited than an NMR R factor (with a maximum value of ∞).

Consistency of the final structure with scalar-coupling-based multidimensional NMR spectra may be assessed as well. For example, the RMSD between experimental and theoretical coupling constants can be calculated according to $J_{rms} = (1/N)\sqrt{\sum (J_{exp} - J_{theor})^2}$. The summation is over N, which constitutes all or any subset of the coupling constants.[48] Of course, this assumes that a well-parameterized Karplus relationship has been established between the dihedral angles and three-bond coupling constants.[2]

There are other criteria that depend on the method of refinement. A residual distance violation is the difference between a particular interproton distance in a structure and the closest of either the upper or lower bound. An evaluation of the structures resulting from distance geometry in terms of the violations (typically weighted according to σ^4) is standard practice. For structures resulting from rMD or rMC refinement, the restraints' violation energies ($V_{NOE} + V_{Jcoupling}$) should be low, and the total of the other terms should not be too much greater than in the absence of the experimental restraints.

Naturally, any structure we generate should be consistent with any other experimental data available on the oligomer in solution. In principle, we can compare our structure with any available crystal structure. However, in the case of a DNA duplex, it is highly unlikely that a good diffracting crystal in anything other than A form, i.e., not comparable to a solution structure, can be obtained. We must even be careful about any B form crystal structure due to the influence of crystal packing forces (see above).

4 COMPLICATIONS FROM CONFORMATIONAL FLEXIBILITY

A serious attempt to determine structure in solution with high precision must be cognizant of the possibility of multiple conformers and molecular motions. First, we need to consider the effect of molecular motion on our ability to determine an accurate time-averaged structure: i.e., will internal motions lead to systematically biased

distances and distorted structures. Second, we would like to impose molecular motion information on the time-averaged structure and thus obtain a dynamic picture of the DNA fragment. Librational motions are typically on the picosecond timescale and could entail interatomic distance fluctuations of up to 0.5 Å. These will not have serious effects on our structure determination. More difficult problems are posed by conformational fluctuations, which may occur on any timescale depending on the size of the energy barrier between the different conformers. Of course, with high barriers, conformational fluctuations are slow compared with chemical shift differences and separate resonances will be observed indicating the existence of different conformers. More deleterious are fast conformational fluctuations which average resonances.

If they are not recognized, internal motions can lead to systematically biased distances and distorted structures. Complicating the situation, the manner in which distances are averaged depends on the rate of exchange between conformers. The averaging in any case is not a simple geometric average of distances in the different conformers. Rather, when the internal motion is faster than the overall correlation time, e.g., with methyl rotation, the measured distance is subject to $\langle r^{-3}\rangle$ averaging, i.e., the apparent distance between a nucleus i and the set of motionally averaged nuclei j (e.g., the methyl protons) is generally slightly weighted toward the shorter of the distances if the internal motion is not isotropic,[8] but the apparent distance is identically equal to the distance between nucleus i and the geometric mean position of nuclei j that are undergoing isotropic jumps.[52] There is some evidence to suggest that sugar repuckering motions may occur in this time range and would thus be subject to $\langle r^{-3}\rangle$ averaging. However, if jumps between the individual conformers are slow compared with the reciprocal of the overall correlation time but fast compared with the relaxation time, the apparent distance is subject to $\langle r^{-6}\rangle$ averaging over individual proton positions; so, the apparent distance may be strongly distorted from the geometric average position. The occurrence of this situation might be expected for aromatic ring flips and maybe some methylene motions in proteins, but there is no evidence to date for motions in this time regime for DNA oligomers. As already noted, we have incorporated some motional information into our structure approach, such that the distortion of the *time-averaged* structure should be minimized. MARDIGRAS already accounts for methyl rotation and averaging of protein aromatic ring and methylene protons for determination of both best fit distances and bounds. Other conformational fluctuations can be explicitly specified by use of an order parameter at present.

Torsion angle restraints and scalar coupling follow a Karplus relationship, so they too are not geometrically averaged by conformational fluctuations. Even with perfect data, with such nongeometric averaging, the individual distance and torsion angle restraints will be internally inconsistent. In addition, any particular structural restraint which is averaged by conformational jumps is likely to have an averaged value that is not physically, i.e. energetically, reasonable. Of course, in practice, we have a compromise of the experimental restraints with maintenance of reasonable energies in the classical potential energy terms. So, if we are studying a molecule that does have a solution structure and only limited conformational fluctuations, we can obtain a reasonable time-averaged structure.

There have been few detailed relaxation studies of DNA oligomers. However, with the advent of isotopic labeling (laborious as it is for DNA), from relaxation studies we can expect more information about the spectral densities associated with molecular motions in the near future. Relaxation data are well-suited to inform us about frequencies of motions and are modestly adapted to inform us about amplitudes of motions. However, they do not reveal the exact type of motion. We have been trying to develop a framework in which we can examine structure and relaxation data in a molecular context.

In spite of the increased accuracy of interproton distances afforded by MARDIGRAS analysis, we find certain discrepancies in distances, which can most readily be ascribed to limited conformational flexibility (internal motions). For example, for the octamer d(GTATAATG) · d(CATATTAC), the final structure resulting from rMD manifested some nonplanarity of some bases. This did contribute to an improvement in apparent agreement with the experimental data.[48] (Note that rMD does permit some distortion of bond lengths, bond angles, and torsion angles, with the energetic price paid in the classical potential energy terms compensated by a lowering of the experimental restraint violation energy. In contrast, the rMC method we employ dictates idealized base geometries.) Perhaps the most distorted base is A5. The experimental restraints, H-8A5–H-8A6 (2.69–2.99 Å) and H-2A5–H-2A6 (3.16–3.39 Å), cannot be satisfied simultaneously by any single conformation. As noted already, the rMC structures calculated for the octamer are essentially the same as the rMD structures (<0.5 Å RMSD). In rMC structures with idealized base geometries, the above two distances are 3.61–3.64 and 3.98–3.99 Å, respectively; but they are reduced to 3.52 and 3.75 Å in the final rMD structure. The latter values result from compromise between repulsive van der Waals forces and pseudoenergy forces from experimental restraints causing some distortion of A5.

We had previously found from $T_{1\rho}$ measurements that H-2A5 is involved in some dynamic process.[53] If there are some conformational fluctuations in this region causing changes in the relative orientations of the A5 and A6 bases, as illustrated in Figure 4, the H-8A5–H-8A6 and H-2A5–H-2A6 distances would fluctuate leading to an average value being determined. With averaging due to conformational fluctuations, the distance determined will likely be shorter than the geometric mean (see above). So measured distances for both H-8A5–H-8A6 and H-2A5–H-2A6 could be too short to be mutually consistent.

The H-6/H-8–H-2′/H-2″ and H-6/H-8–H-3′ intraresidue distances are often internally inconsistent. The 2D NOE

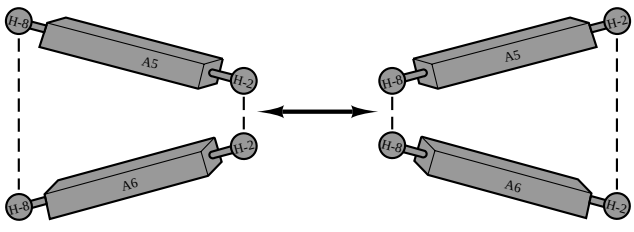

Figure 4 Schematic of bases A5 and A6 of the base pair step AZ5-A6:T11-T12 of d(GTATAATG) · d(CATATTAC), exaggerating the effect of conformational flexibility on the H-8A5-8A6 and H-2A5-H-2A6 distances, which are shown by broken lines

intensities corresponding to H-6/H-8–H-2′/H-2″ distances are usually satisfied by all refined structures. Significant H-6/H-8–H-2′/H-2″ interactions imply that the deoxyribose conformation spends a large part of the time in an S-type conformation, i.e., with pseudorotation angle P_S in the range 120–210°. However, H-6/H-8–H-3′ intraresidue distances are typically slightly larger in refined rMD and rMC structures than would be implied by experimental cross peak intensities. This apparent inconsistency may be due to repuckering motions in the sugar ring. Such a repuckering is implied by our experimental scalar coupling data, where it is rarely possible to interpret the results in terms of a single sugar conformer (see above).

Since conformational fluctuations may influence the value of distance restraints extracted from 2D NOE spectra, an alternative distance penalty function has been proposed for use with restrained MD calculations.[46] The distance between any two protons and the associated penalty function is monitored as a running average with exponential weighting to emphasize more recent steps during an rMD simulation. This permits a broader search of conformational space in an rMD simulation, as the calculation does not demand that the measured value of the distance be satisfied exactly at every single step of the simulation. A theoretical study suggested that this may be a valuable approach.[54] We have explored the use of MD with weighted time-averaged restraints (MD-tar) and found it can resolve some of the dynamics-related shortcomings of rMD and provide insight into the mechanics of DNA molecular motion.[42,43] For d(GTATAATG) · d(CATATTAC), it was found that MD-tar, using only experimental distance restraints, generates an ensemble of structures that, as an ensemble, fit both the experimental 2D NOE data and the scalar coupling data better than the best structure obtained via traditional rMD methods.

With an ensemble of structures resulting from such an analysis, it is most appropriate to examine the structural parameters of the ensemble as a distribution of values. While we have calculated a large number of backbone torsion angles and helical parameters for the ensemble of 400 structures, only a representative three pseudorotation angle distributions are displayed in Figure 5. For A13, the distribution is similar to that of rMD, i.e., there is mostly only a single S conformer. For T14, a significant minor N conformer is also apparent in

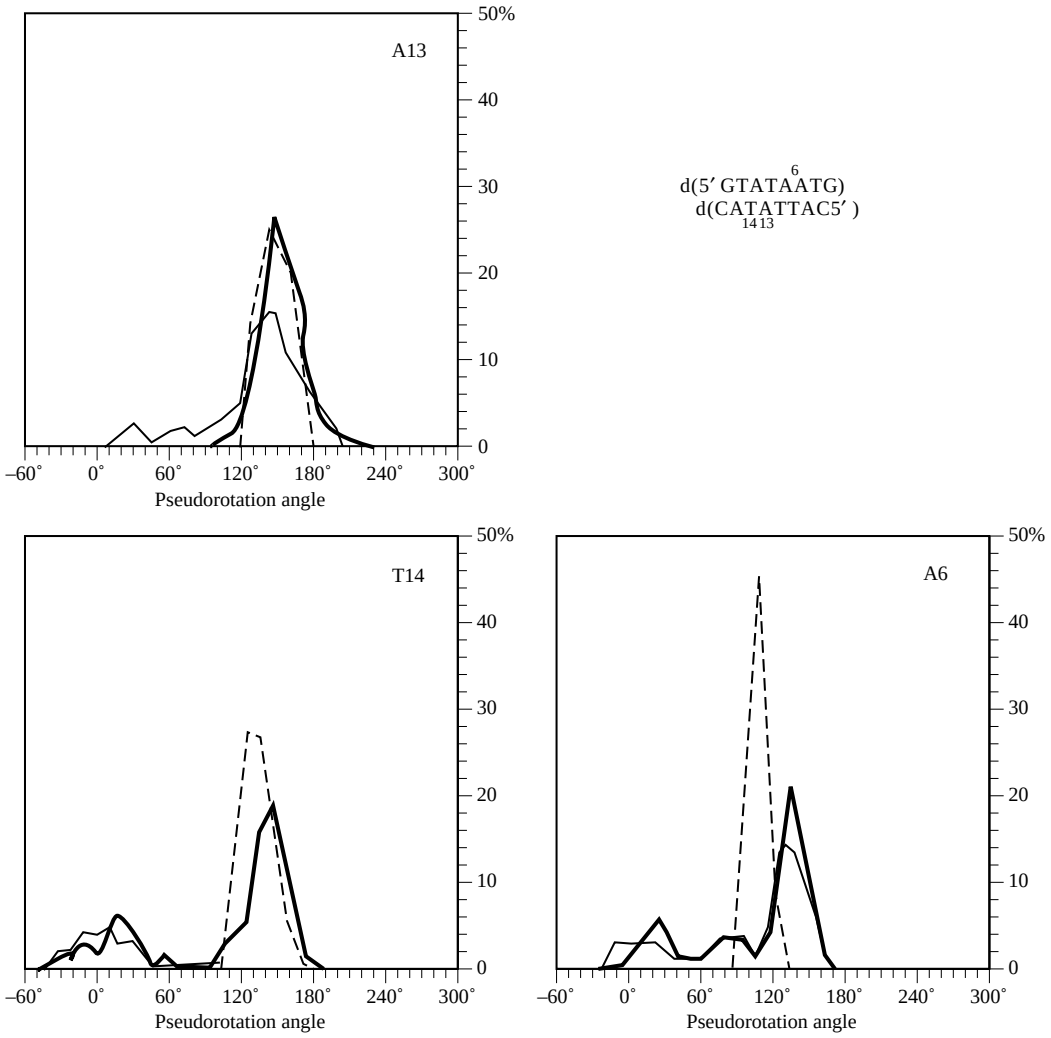

Figure 5 Distribution of deoxyribose pseudorotation angles for three representative nucleotides in d(GTATAATG) · d(CATATTAC). Each distribution is composed of 400 values, calculated for the ensemble of 400 structures chosen every 0.25 ps during the last 100 ps of an MD-tar simulation: standard rMD with explicit solvent (- - - -), MD-tar in vacuo (——), and MD-tar with explicit solvent (———)

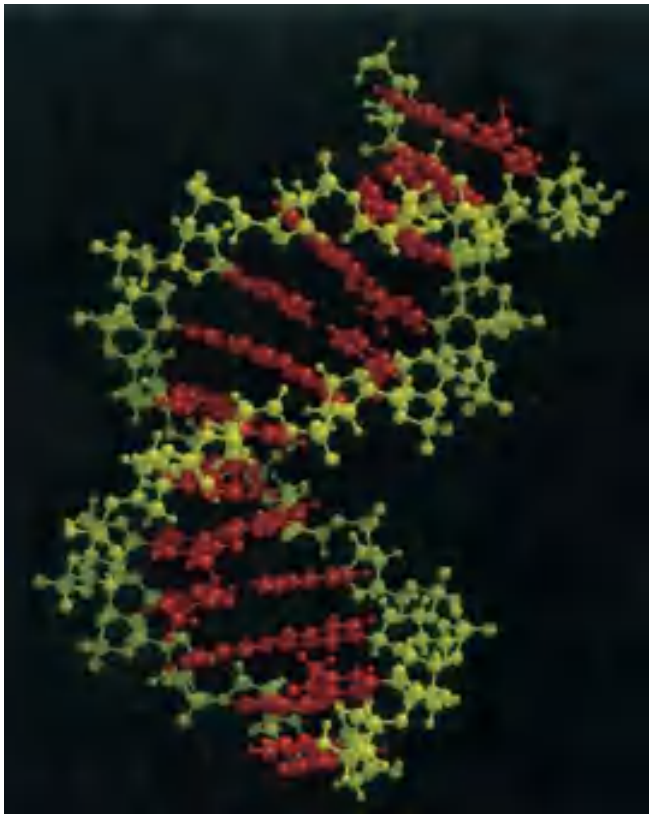

Figure 6 The final refined structure of d(AGCTTGCCTTGAG) · d(CTCAAGGCAAGCT) obtained from rMD calculations

the MD-tar distribution, which is unlike the single S conformer resulting from standard rMD refinement. This is in accord with the two-state deoxyribose repuckering model often used to explain the scalar coupling constant data (see section 2.2), i.e., a major conformer nearly C-2′-*endo* and a minor conformer nearly C-3′-*endo*. However, the sugar rings of some residues manifest a distribution similar to that of A6, in which a minor S conformer, approximately O-4′-*endo*, is evident. In all the standard rMD refinements we have carried out, only a single conformer is obtained. As noted already, this is in conflict with our scalar coupling data, which indicate that in most residues at least one minor conformer must also exist. Clearly, the MD-tar results are in better agreement with these experimental results. We also found that the *R* factor calculated for the ensemble was in better accord with our experimental 2D NOE results than any single structure we had determined using rMD.

It was noted above that the H-8A5–H-8A6 and H-2A5–H-2A6 distances and the H-6/H-8–H-2′/H-2″ and H-6/H-8–H-3′ intraresidue distances are inconsistent. Both sets of distances were better satisfied on a time-average basis in MD-tar simulations of the octamer due to repuckering of the sugar rings.

5 CONCLUSIONS

In summary, it is now possible to determine the time-averaged structure of a DNA duplex with fairly high precision and apparent accuracy, and it is possible to assess the quality of the structure. To do so, however, requires a large number of accurate structural restraints well distributed in the molecule (especially distances) and a careful refinement of the structure using those restraints. Soon it may be possible to learn of some generalities in sequence-dependent structural features. Even with the few DNA duplexes for which we have determined high-precision structures, it is possible to discern a few tentative generalities. For example, the average helical twist in the structures of the three DNA duplexes mentioned in this article is 34.6°, in remarkable agreement with independent solution state data on DNA, and the value for DNA in crystals is 36°.[55] The duplex d(AGCTTGCCTTGAG) · d(CTCAAGGCAAGCT), whose structure is shown in Figure 6, has two CTTG moieties and [d(GATGCAAATG) · d(CTACGTTTAC)] has one TG step. At all three TG steps, local structural variations work together to create bending into the major groove of the duplex. Although there are a few other suggestive structural generalities, more structural information is required.

Although we can now obtain good time-averaged structures, we are clearly at a stage when it is time to examine the dynamic aspects of structure. Conformational averaging, of course, complicates any determination of NMR-derived solution structures. However, the sensitivity of NMR to dynamic processes is ultimately an advantage rather than a shortcoming, because it can be used to study the conformational flexibility of DNA.

6 RELATED ARTICLES

DNA: A-, B-, and Z-; Nucleic Acid Flexibility and Dynamics: Deuterium NMR; Nucleic Acids: Base Stacking and Base Pairing Interactions; Nucleic Acids: Chemical Shifts; Nucleic Acids: Phosphorus-31 NMR; Nucleic Acids: Spectra, Structures, and Dynamics; Relaxation Matrix Refinement of Nucleic Acids; Vicinal Coupling Constants and Conformation of Biomolecules.

7 REFERENCES

1. J. Feigon, V. Sklenár, E. Wang, D. E. Gilbert, R. F. Macaya, and P. Schultze, *Methods Enzymol.*, 1992, **211**, 235.
2. S. S. Wijmenga, M. M. W. Mooren and C. W. Hilbers, in *NMR of Macromolecules*, ed. G. C. K. Roberts, IRL Press, Oxford, 1993, pp. 217–288.
3. T. L. James and V. J. Basus, *Annu. Rev. Phys. Chem.*, 1991, **42**, 501.
4. G. Wagner, S. G. Hyberts, and T. F. Havel, *Annu. Rev. Biophys. Biomol. Struct.*, 1992, **21**, 167.
5. N. J. Oppenheimer and T. L. James (eds), *Methods Enzymol.*, 1989, **176**.
6. T. L. James and N. J. Oppenheimer (eds), *Methods Enzymol.*, 1994, **239**.
7. S. Macura and R. R. Ernst, *Mol. Phys.*, 1980, **41**, 95.
8. J. W. Keepers and T. L. James, *J. Magn. Reson.*, 1984, **57**, 404.
9. H. Liu, P. D. Thomas, and T. L. James, *J. Magn. Reson.*, 1992, **98**, 163.
10. B. A. Borgias and T. L. James, *J. Magn. Reson.*, 1988, **79**, 493.
11. C. B. Post, R. P. Meadows, and D. G. Gorenstein, *J. Am. Chem. Soc.*, 1990, **112**, 6796.

12. T. L. James, *Curr. Opin. Struct. Biol.*, 1991, **1**, 1042.
13. B. A. Borgias, M. Gochin, D. J. Kerwood, and T. L. James, *Prog. Nucl. Magn. Reson. Spectrosc.*, 1990, **22**, 83.
14. R. Boelens, T. M. G. Koning, G. A. van der Marel, J. H. van Boom, and R. Kaptein, *J. Magn. Reson.*, 1989, **82**, 290.
15. B. A. Borgias and T. L. James, *Methods Enzymol.*, 1989, **176**, 169.
16. B. A. Borgias and T. L. James, *J. Magn. Reson.*, 1990, **87**, 475.
17. A. Kumar, T. L. James, and G. C. Levy, *Isr. J. Chem.*, 1992, **32**, 257.
18. H. Liu, A. Kumar, K. Weisz, U. Schmitz, K. D. Bishop, and T. L. James, *J. Am. Chem. Soc.*, 1993, **115**, 1590.
19. J. M. Withka, S. Swaminathan, and P. H. Bolton, *J. Magn. Reson.*, 1990, **89**, 386.
20. W. Eimer, J. R. Williamson, S. G. Boxer, and R. Pecora, *Biochemistry*, 1990, **29**, 799.
21. M. M. Tirado, C. Lopez Martinez, and J. García de la Torre, *J. Chem. Phys.*, 1984, **81**, 2047.
22. A. C. Wang, S.-G. Kim, P. F. Flynn, E. Sletten, and B. R. Reid, *J. Magn. Reson.*, 1992, **100**, 358.
23. E.-I. Suzuki, N. Pattabiraman, G. Zon, and T. L. James, *Biochemistry*, 1986, **25**, 6854.
24. P. D. Thomas, V. J. Basus, and T. L. James, *Proc. Natl. Acad. Sci. U.S.A.*, 1991, **88**, 1237.
25. J. Jeener, B. H. Meier, P. Bachmann, and R. R. Ernst, *J. Chem. Phys.*, 1979, **71**, 4546.
26. S. B. Landy and B. D. Nageswara Rao, *J. Magn. Reson.*, 1989, **81**, 371.
27. B. Choe, G. W. Cook, and N. Rama Krishna, *J. Magn. Reson.*, 1991, **94**, 387.
28. A. Mujeeb, S. M. Kerwin, G. L. Kenyon, and T. L. James, *Biochemistry*, 1993, **32**, 13 419.
29. K. Weisz, R. H. Shafer, W. Egan, and T. L. James, *Biochemistry*, 1994, **33**, 354.
30. B. Adams and L. Lerner, *J. Magn. Reson.*, 1992, **96**, 604.
31. K. D. Bishop, F. J. H. Blocker, W. Egan, and T. L. James, *Biochemistry*, 1994, **33**, 427.
32. U. Piantini, O. W. Sørensen, and R. R. Ernst, *J. Am. Chem. Soc.*, 1982, **104**, 6800.
33. D. Marion and A. Bax, *J. Magn. Reson.*, 1988, **80**, 528.
34. C. Griesinger, O. W. Sørensen, and R. R. Ernst, *J. Am. Chem. Soc.*, 1985, **107**, 6394.
35. H. Widmer and K. Wüthrich, *J. Magn. Reson.*, 1987, **74**, 316.
36. B. Celda, H. Widmer, W. Leupin, W. J. Chazin, W. A. Denny, and K. Wüthrich, *Biochemistry*, 1989, **28**, 1462.
37. U. Schmitz, G. Zon, and T. L. James, *Biochemistry*, 1990, **29**, 2357.
38. R. Stolarski, W. Egan, and T. L. James, *Biochemistry*, 1992, **31**, 7027.
39. L. J. Rinkel and C. Altona, *J. Biomol. Struct. Dyn.*, 1987, **4**, 621.
40. K. Weisz, R. H. Shafer, W. Egan, and T. L. James, *Biochemistry*, 1992, **31**, 7477.
41. C. Altona and M. Sundaralingam, *J. Am. Chem. Soc.*, 1972, **94**, 8205.
42. U. Schmitz, A. Kumar, and T. L. James, *J. Am. Chem. Soc.*, 1992, **114**, 10 654.
43. U. Schmitz, N. B. Ulyanov, A. Kumar, and T. L. James, *J. Mol. Biol.*, 1993, **234**, 373.
44. T. L. James, *Curr. Opin. Struct. Biol.*, 1994, **4**, 275.
45. A. T. Brünger and M. Karplus, *Acc. Chem. Res.*, 1991, **24**, 54.
46. W. F. van Gunsteren, *Curr. Opin. Struct. Biol.*, 1993, **3**, 277.
47. D. A. Pearlman, D. A. Case, J. Caldwell, G. L. Seibel, U. C. Singh, P. K. Weiner, and P. A. Kollman, *AMBER 4.0 (UCSF)*, University of California, San Francisco, 1991.
48. N. B. Ulyanov, U. Schmitz, and T. L. James, *J. Biomol. NMR*, 1993, **3**, 547.
49. D. J. Kerwood, G. Zon, and T. L. James, *Eur. J. Biochem.*, 1991, **197**, 583.
50. J. M. Withka, J. Srinivasan, and P. H. Bolton, *J. Magn. Reson.*, 1992, **98**, 611.
51. A. Brünger and M. Nilges, *Q. Rev. Biophys.*, 1993, **26**, 49.
52. D. M. LeMaster, L. E. Kay, A. T. Brünger, and J. H. Prestegard, *FEBS Lett.*, 1988, **236**, 71.
53. U. Schmitz, I. Sethson, W. M. Egan, and T. L. James, *J. Mol. Biol.*, 1992, **227**, 510.
54. D. A. Pearlman and P. A. Kollman, *J. Mol. Biol.*, 1991, **220**, 457.
55. N. B. Ulyanov and T. L. James, *Appl. Magn. Reson.*, 1994, **7**, 21.

Acknowledgments

I wish to express grateful appreciation to my co-workers who have carried out the research from our laboratory, some of whom have contributed materially by providing Figures used here. The research described in this article from our laboratory was supported by National Institutes of Health grants GM39247, GM41639, and RR01695. Some of the computations were carried out at the Pittsburgh Supercomputing Center (supported by grant number 1 P41 RR06009 from the NIH National Center for Research Resources). For visualizing the structures, I also acknowledge our use of the University of California, San Francisco, Computer Graphics Laboratory (supported by NIH Grant RR01081).

Biographical Sketch

Thomas L. James. *b* 1944. B.S., 1965, Chemistry, University of New Mexico, Ph.D., 1969, Chemistry, University of Wisconsin, Madison, with Joseph H. Noggle. Postdoctoral work, 1971–73, Biophysics, at University of Pennsylvania with Mildred Cohn. Faculty at University of California, San Francisco, 1973–present. Currently, Professor of Chemistry, Pharmaceutical Chemistry and Radiology. Approx. 270 publications. Current research interests: biochemical and biological applications of NMR.

Nucleic Acids: Base Stacking and Base Pairing Interactions

Martin P. Schweizer
Departments of Medicinal Chemistry and Radiology, University of Utah, Salt Lake City, Utah, USA

1	Introduction	1
2	Self-Association of Bases	1
3	Summary	3
4	Related Articles	4
5	References	4

1 INTRODUCTION

Contemporary evaluation of the mounds of experimental data and theoretical work on the subject of nucleic acid structure, stability, recognition, and function concludes, not surprisingly, that stacking and pairing interactions of constituent nitrogenous bases constitute the greatest influence. Hence, issues such as polymorphism, curvature, and deformation at the polymer level may be best addressed via consideration of base composition and sequence. It is the steric, van der Waals, and electrostatic interactions of these units that primarily determine polymer properties.[1,2]

More than three decades ago, with far less information and experience, similar conclusions were drawn by many working on nucleic acid structure, particularly dwelling upon helix–coil transformations wrought by heat and organic solvents.[3–7] Studies on the tendencies of the bases and corresponding nucleosides to associate in aqueous media[8–10] led to the postulate that these nucleic acid constituents mingled primarily via vertical stacking interactions of the bases rather than by hydrogen bonding mechanisms.

It is the intent of the present contribution to describe how proton NMR studies on these nucleic acid units definitively demonstrate vertical stacking combinations involving the bases themselves, and within higher ordered structures. Whereas these modes of association predominate in aqueous media, hydrogen-bonding-type interactions are shown by NMR to occur in denaturing solvents which prevent stacking and coincidentally denature nucleic acid helices, again demonstrating the importance of stacking in the structure and stability of these biopolymers.

Although we will trace the thread of import involving base interactions among higher ordered species, contributions by Hilbers, James, Cowburn, etc., are more focused upon aspects of structure, conformation, and dynamics at these levels of complexity (see ***Nucleic Acids: Spectra, Structures, and Dynamics***; ***Nucleic Acid Structures in Solution: Sequence Dependence***, and ***Nucleic Acids: Chemical Shifts***, respectively).

2 SELF-ASSOCIATION OF BASES

2.1 Stacking Interactions

The suggestion that the mode of association for nucleic acid bases was different from the known hydrogen bonding motif of compounds such as urea was based upon their considerably disparate osmotic properties[8–10] and influences upon lowering the thermal denaturation transition temperature, T_m, of DNA.[11] Inasmuch as purine and its 6-methyl derivative had association constants of 2.1 and 6.7 *m* and corresponding standard free energies −8.8 and −4686.1 J, the values for urea were 0.04 *m* and +4979 J. Moreover, urea was only 10% as efficient in lowering T_m for the thermal denaturation of DNA as purine. Consequently, in the light of the sensitivity of chemical shifts to shielding environments, ^{1}H NMR measurements of purine and 6-methylpurine versus concentration in water were conducted, and attempts made to elucidate the nature of their interactions.[12]

Presented in Figures 1 and 2 are the chemical shifts of nonexchangeable purine and 6-methylpurine protons in aqueous solution over the concentration range 0.05–1.0 *m*. Despite the somewhat primitive techniques available 30 years ago, namely, resonance frequency determined via superposition of audio sidebands from suitable references (in this case external chloroform and acetonitrile for aromatic and methyl protons, respectively), these proton peak positions, corrected for bulk susceptibility, are estimated to be accurate to ±1 Hz at 56.4 MHz (1.33 T). The magnitudes of these concentration-induced low-frequency changes over the range 0.0 (extrapolated) to 1.0 *m* vary from about 0.5 ppm for H-8 of both bases to 0.6–0.8 ppm for protons on the pyrimidine rings, with larger effects seen for 6-methylpurine. The greater shift changes for the latter are consistent with the greater association tendencies measured by vapor pressure osmometry. Movement of the resonance position to lower frequency with increasing concentration is a consequence of diamagnetic ring current moments exerting shielding upon protons of neighboring associating bases arrayed in partial overlapping stacks

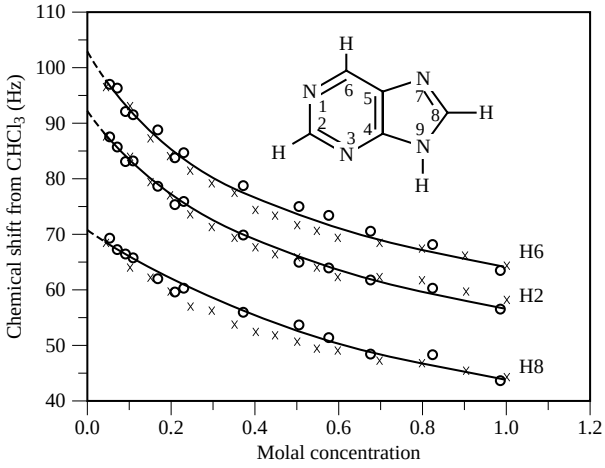

Figure 1 Concentration dependence of the ^{1}H chemical shifts for purine in aqueous solution at 25 °C (corrected for bulk susceptibility); shifts measured from external chloroform reference: (○) experimental values; (×) calculated values from overall average model

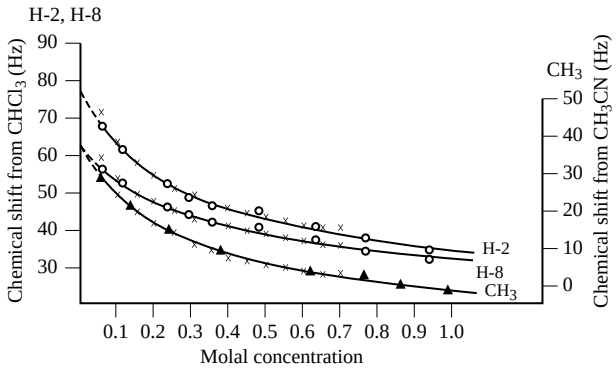

Figure 2 Concentration dependence of the ^{1}H chemical shifts for 6-methylpurine in aqueous solution at 25 °C (corrected for bulk susceptibility): (○) experimental values for H-2, H-8 proton shifts measured from external chloroform reference (left-hand coordinates); (▲) experimental values for methyl protons, shifts measured from external acetonitrile reference (right-hand coordinates); (×) calculated values from overall average model

(Figure 3). This interpretation is solidified via computation of expected shifts (xs in Figures 1 and 2) based upon the osmotic data and consideration of noticeable contributions from dimer and higher ordered arrays in fast 'making and breaking' exchange with monomer bases.[13]

The fact that attachment of an apolar methyl group increased the association, whereas increased temperature, solvents such as dimethyl sulfoxide (DMSO) and dimethylformamide, and generation of positive charges on the purine ring all obliterated the shift changes, led one to conclude at the time that the bases are complexing via some general descriptor such as 'hydrophobic' forces. Nowadays, in the light of more refined theoretical approaches,[1] it may be appreciated that

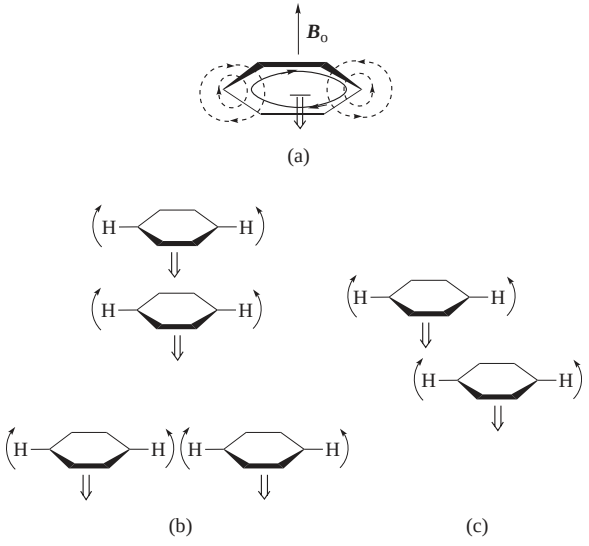

Figure 3 (a) Ring current-induced diamagnetic moment in aromatic ring system. (b) Total overlap and inplane interactional models with indication of positive reinforcement of peripheral-induced paramagnetic moments, thus shifts to higher frequency with such arrangements. (c) Partial vertical overlapping arrangement illustrating diamagnetic effects of one ring upon protons of neighboring ring, thus shifts to lower frequency

electrostatic interactions between stacking heteroaromatic bases involve fixed partial atomic charges and asymmetric σ and π electron distributions, as well as van der Waals steric considerations. Hydrophobic effects, e.g., the clustering of apolar solutes such as these bases, whilst maximizing solvent–water intermolecular hydrogen bonding networks are indeed also important, but are in balance with the aforementioned electrostatic attractive forces. For instance, whereas partial base overlap tends to maximize $\sigma-\pi$ attraction (and this orientation is consistent with the concentration-induced upfield proton shifts), hydrophobic considerations would tend to drive the bases into complete overlap.

2.2 Base–Base Stacking Interactions in Nucleosides and Nucleotides

Further insight into the specific characteristics of the interactions of nucleic acid bases in more sophisticated structures was garnered via ^{1}H NMR studies of purine associating with pyrimidine nucleosides,[14] purine nucleoside associations,[10] and the interactions of mononucleotides with one another.[13,15,16] The distillation of these studies revealed that the primary site(s) for the interactions in these systems were the bases. For instance, the diamagnetic effects accruing to purine base ring currents fell off with distance from the base as one traversed the carbohydrate moieties from the site of aglycone attachment to the exocyclic 5′-protons. Moreover, the greatest concentration-dependent upfield shifts were noted for the more highly base-methylated purine nucleotides. Finally, it was noted that the coulombic repulsion of the anionic phosphates diminished the concentration-dependent diamagnetic behavior in the mononucleotides.

2.3 Base–Base Stacking in Oligonucleotides

Although intimate discussion of structure and conformation in oligonucleotides and polymers is beyond the scope of this communication, it is instructive to highlight the influence of base stacking in some selected species containing sugar–phosphate backbones. Adenylyl(3′–5′)-adenosine (ApA) has been studied by a number of workers.[17–22] The upshot of all these NMR investigations is that the adenine–adenine intramolecular base–base stacking in aqueous media is very strong, persisting even at 90 °C,[19,20] but is obliterated in denaturing DMSO milieu. As a consequence of this strong propensity toward maintenance of base–base overlap, ribose ring puckering shifts to 3′-*endo* from the 2′-*endo* form favored in the mononucleotides, the glycosidic torsion angle moves toward zero degrees (more stringent *anti* conformation), and there is less flexibility in rotational conformers at other sites along the sugar–phosphate backbone.[22]

Proton NMR studies of various diribonucleoside monophosphates with all combinations of purine and pyrimidine bases[21,23,24] have revealed sequence-dependent base-stacking interactions and backbone conformations. While details of these molecular properties may be found elsewhere in this Encyclopedia, it is worth noting that if one uses backbone torsional angle criteria as a means of judging the extent of base–base interaction, one can derive the relative strengths of these associations as pyrimidine (pyr)–purine (pu) < pyr–pyr

< pu−pu < pu−pyr.[23,24] However, using diamagnetic ring current induced 'dimerization' chemical shift changes,[21] one would order the ascending strengths of base interactions as pyr−pyr < pyr−pu < pu−pu < pu−pyr. The latter ranking is based upon the predominant *anti*,*anti* glycosidic conformation plus right-handed helical sense of the backbone.

2.4 Base Stacking as the Predominant Influence in Nucleic Acid Structure

There appear to be two current views on the relative importance of base stacking versus sugar−phosphate backbone flexibility and conformational preference in the overall three-dimensional structures of oligonucleotides and nucleic acids. (1) Maximizing the strong base−base stacking interactions drives the conformational properties of the backbone. (2) The reverse, i.e., base stacking, happens as a consequence of the backbones being in one or more suitable arrangements. Based upon the foregoing discussions of monomer association tendencies, involving strong electrostatic, dispersion, and van der Waals forces accompanying base−base contact plus the need to minimize disruption of solvent−water structure, one might opt for choice (1). As a matter of fact, current thought emphasizes the preeminent influence of base stacking and the nature of base-paired dimer 'steps' in determination of nucleic acid preferred overall structure.[1,2] It is the contention in these two cited works that the 'B' to 'A' transition as well as the existence of the ubiquitous Z-DNA are all dependent upon the sequence of base-stacked pairs, which may interact in two or more 'stable' arrangements, thus providing energy wells for the overall conformational characteristics.

2.5 Thermodynamics of Base Stacking

Thermodynamic considerations reinforce the NMR data demonstrating the strong base stacking association. For instance, Tinoco et al.[25] summarize the results of several optical studies giving the enthalpy of adenine−adenine stacking in ApA as -20 to $-41.8\,\mathrm{kJ\ mol^{-1}}$. In fact, from the temperature dependence of the NMR spectrum of the cyclophosphate derivative of ApA, ApA > , which yielded equilibrium constants for the exchange between stacked and unstacked forms, Hruska and Danyluk[17] derive a base stacking enthalpy of $-34.3\,\mathrm{kJ\ mol^{-1}}$. These findings point out the considerable stabilizing influence of base stacking in nucleic acid structures.

2.6 What About Base Pairing?

It is universally known that recognition and genetic information transfer in nucleic acid interactions involves specific base pairing. The demonstration of these specific hydrogen bonding interactions involving imino and amino protons using NMR in aqueous media, as described elsewhere in this Encyclopedia, is also well known. It is difficult to observe these specific base pairing hydrogen bonding interactions for aqueous solutions of oligonucleotides smaller than pentamers (other than at high concentrations and/or low temperatures) because the negative enthalpy change for such pairing is probably no more than some hundred J $\mathrm{mol^{-1}}$, thus lifetimes for the hydrogen bonded states are short and exchange with solvent is rapid. Moreover, when one does observe base pairing between small oligomers at high concentrations and low temperatures, trimeric species form.[25]

2.7 Monomer Base Pairing in Organic Solvents

At approximately the same point in history that NMR techniques were being used to demonstrate base stacking in aqueous solution, they were being similarly employed to illustrate base pairing in aprotic solvents such as chloroform and DMSO, solvents in which, particularly the latter, stacking interactions are nil and nucleic acid structure denatured. Katz and Penman,[26] and Shoup et al.[27] showed via large specific downfield shifts at 60 MHz (1.41 T) that complementary Watson−Crick (WC) hydrogen bonded complexes formed between guanine and cytosine derivatives in DMSO. In this strong hydrogen bond accepting solvent, acidic imino protons of guanine shifted 1−2 ppm to higher frequency and guanine and cytosine amino proton shifts shifted 0.5−1 ppm, depending upon the mole ratios of donor and acceptor molecules. These shifts were much larger than those found for self-association of the interactants and no low-frequency shifts for carbon-bound protons with concentration increase were noted, reinforcing the statements made earlier that DMSO obliterates base stacking.

Adenine and thymine (or uracil) hydrogen bonding interactions were quite weak in DMSO, but in chloroform, offering less competition for hydrogen bond acceptance, Katz and Penman found large high-frequency shifts in mixtures of 9-ethyladenine and 1-cyclohexyluracil, the magnitude again reflecting the relative acidities, e.g., about 3 ppm for uracil N-3 imino and 0.7 ppm for adenine amino protons. No non-WC pairs were in evidence. These results in chloroform complemented the infrared studies of Hamlin et al.,[28] and Pitha et al.,[29] who showed that the WC pairing led to specific hydrogen bond stretching bands.

In a higher field (2.35 T) study with chemical shifts accurate to ± 0.1 Hz, Newmark and Cantor[30] demonstrated that guanosine does form hydrogen bonded dimers in DMSO, most likely similar to the arrangements found in the gel state in aqueous solution [Figure 4(a)]. Shifts to higher frequency were of the order of 0.08 to 0.020 ppm with a formation constant of $0.18\ \mathrm{l\,mol^{-1}}$ at 32 °C. As Newmark and Cantor note, dimers form in DMSO, but large aggregates, e.g. gels, form in water,[30] implying large base stacking free energies in the aqueous environment.

This guanosine self-interaction pales in comparison with the guanosine−cytidine base pairing [Figure 4(b)] as noted above, where one finds as did Katz and Penman, that guanosine amino and imino protons shift to higher frequency by 0.5 and 1.5 ppm, respectively, while cytidine amino groups move 0.4 ppm to higher frequency. Newmark and Cantor calculate a formation constant of $3.7\ \mathrm{l\ mol^{-1}}$ and an enthalpy change of $-25\,\mathrm{kJ\ mol^{-1}}$ for this complementary WC pairing interaction (from van't Hoff plots of the logarithm of the dimer formation constant vs. reciprocal temperature).

3 SUMMARY

Three decades ago ^{1}H NMR investigations revealed that simple nitrogenous bases self-associated in aqueous media

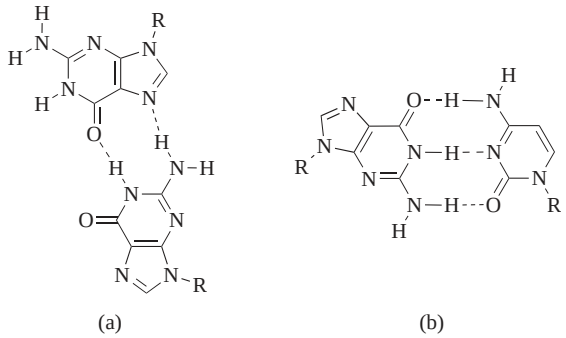

(a) (b)

Figure 4 (a) Hydrogen bonding scheme for guanosine dimer formation in DMSO. (b) Watson–Crick complementary hydrogen bonding between guanosine and cytidine in DMSO

via vertical stacking with partial ring overlap. These strong solute–solute interactions, on the order of -20 to $-41.8\,\text{kJ mol}^{-1}$, are believed to have electrostatic and dispersive origins by virtue of asymmetric π and σ electron distributions as well as hydrophobic contributions from solvent water. Evidence from ^{1}H NMR of base stacking persists with higher structural order, in nucleosides and nucleotides, oligonucleotides, and nucleic acid polymers. Stacking of bases is thus a major contributor to nucleic acid structural integrity and in fact may govern overall polynucleotide configurational states.

Complementary WC base pairing in aprotic solvents was also observed by ^{1}H NMR over 30 years ago. These interactions, now readily monitored directly at high field, although contributing less to structure than stacking, are the crux of information transfer.

4 RELATED ARTICLES

Biological Macromolecules: Structure Determination in Solution; Biological Macromolecules; Biological Macromolecules: NMR Parameters; DNA: A-, B-, and Z-; Homonuclear Three-Dimensional NMR of Biomolecules; Hydrogen Bonding; Nucleic Acid Structures in Solution: Sequence Dependence; Nucleic Acids: Chemical Shifts; Nucleic Acids: Phosphorus-31 NMR; Nucleic Acids: Spectra, Structures, and Dynamics.

5 REFERENCES

1. C. A. Hunter, *J. Mol. Biol.*, 1993, **230**, 1025.
2. C. R. Calladine and H. R. Drew, *J. Mol. Biol.*, 1984, **178**, 773.
3. H. DeVoe and I. Tinoco, Jr., *J. Mol. Biol.*, 1962, **4**, 500.
4. T. T. Herskovits, *Arch. Biochem. Biophys.*, 1962, **97**, 474.
5. T. T. Herskovits, S. J. Singer, and E. P. Geiduschek, *Arch. Biochem. Biophys.*, 1961, **94**, 99.
6. G. K. Helmkamp and P. O. P. Ts'o, *J. Am. Chem. Soc.*, 1961, **83**, 138.
7. S. Hanlon, *Biochem. Biophys. Res. Commun.*, 1966, **23**, 861.
8. (a) P. O. P. Ts'o, I. S. Melvin, and A. C. Olsen, *J. Am. Chem. Soc.*, 1963, **85**, 1289. (b) P. O. P. Ts'o, in *Basic Principles in Nucleic Acid Chemistry*, ed. P. O. P. Ts'o, Academic Press, New York, 1974, Vol. 1, Chap. 6
9. P. O. P. Ts'o and S. I. Chan, *J. Am. Chem. Soc.*, 1964, **86**, 4176.
10. A. D. Broom, M. P. Schweizer, and P. O. P. Ts'o, *J. Am. Chem. Soc.*, 1967, **89**, 3612.
11. P. O. P. Ts'o, G. K. Helmkamp, and C. Sander, *Proc. Natl. Acad. Sci. U.S.A.*, 1962, **48**, 686.
12. S. I. Chan, M. P. Schweizer, P. O. P. Ts'o, and G. K. Helmkamp, *J. Am. Chem. Soc.*, 1964, **86**, 4182.
13. O. Jardetzky, *Biopolym. Symp.*, 1964, No. **1**, 501.
14. M. P. Schweizer, S. I. Chan, and P. O. P. Ts'o, *J. Am. Chem. Soc.*, 1965, **87**, 5241.
15. M. P. Schweizer, A. D. Broom, P. O. P. Ts'o, and D. P. Hollis, *J. Am. Chem. Soc.*, 1968, **90**, 1042.
16. S. S. Danyluk and F. E. Hruska, *Biochemistry*, 1968, **7**, 1038.
17. F. E. Hruska and S. S. Danyluk, *Biochim. Biophys. Acta*, 1968, **157**, 238.
18. F. E. Hruska and S. S. Danyluk, *J. Am. Chem. Soc.*, 1968, **90**, 3266.
19. R. C. Davis and I. Tinoco, Jr., *Biopolymers*, 1968, **6**, 223.
20. S. I. Chan and J. H. Nelson, *J. Am. Chem. Soc.*, 1969, **91**, 168.
21. P. O. P. T'so, N. S. Kondo, M. P. Schweizer, and D. P. Hollis, *Biochemistry*, 1969, **8**, 997.
22. N. S. Kondo and S. S. Danyluk, *Biochemistry*, 1976, **15**, 756.
23. C.-H. Lee, F. S. Ezra, N. S. Kondo, R. H. Sarma, and S. S. Danyluk, *Biochemistry*, 1976, **15**, 3627.
24. F. S. Ezra, C.-H. Lee, N. S. Kondo, S. S. Danyluk, and R. H. Sarma, *Biochemistry*, 1977, **16**, 756.
25. I. Tinoco, Jr., R. C. Davis, and S. R. Jaskunas, in *Molecular Associations in Biology*, ed. B. Pullman, Academic Press, New York, 1968, p. 77.
26. L. Katz and S. Penman, *J. Mol. Biol.*, 1966, **15**, 220.
27. R. R. Shoup, H. T. Miles, and E. D. Becker, *Biochem. Biophys. Res. Commun.*, 1966, **23**, 194.
28. R. M. Hamlin, Jr., R. C. Lord, and A. Rich, *Science*, 1965, **148**, 1734.
29. J. Pitha, R. N. Jones, and P. Pithova, *Can. J. Chem.*, 1966, **44**, 1045.
30. R. A. Newmark and C. R. Cantor, *J. Am. Chem. Soc.*, 1968, **90**, 5010.

Biographical Sketch

Martin P. Schweizer. *b* 1935. B.A. 1960, M.A., 1963, Ph.D., 1968, Physical Biochemistry The Johns Hopkins University (P .O. P. Ts'o, supervisor). Postdoctoral, Roswell Park Cancer Institute, Buffalo. Biophysical Chemistry, ICN Nucleic Acid Research Institute, 1968–74. Biophysics Program Director, National Science Foundation, 1974–8. Associate then full Professor, Medicinal Chemistry, 1978–present. Research Professor, Radiology, University of Utah, 1993–present. Approx. 60 papers. Current research focus: clinically relevant MR spectroscopy and imaging.

Nucleic Acids: Phosphorus-31 NMR

David G. Gorenstein

Purdue University, Department of Chemistry, West Lafayette, IN, USA

1 Introduction 1
2 Assignment of the ^{31}P NMR Spectra of Oligonucleotides 1
3 ^{1}H–^{31}P and ^{13}C–^{31}P Coupling Constants 1
4 ^{31}P NMR of Polynucleic Acids 3
5 Sequence-Specific Variation in ^{31}P Chemical Shifts and Coupling Constants of Duplex Oligonucleotides 3
6 Related Articles 5
7 References 5

1 INTRODUCTION

It would have been difficult to imagine in the early development of NMR that ^{31}P NMR, with such relatively low sensitivity, could ever be used for understanding the detailed structure and dynamics of macromolecules such as deoxyribonucleic acid (DNA). With the tremendous increase in sensitivity in modern FT NMR spectrometers, biological applications of ^{31}P NMR spectroscopy grew dramatically during the 1970s and 1980s and has continued to grow into the 1990s, as briefly described in Volume 1 of this series.[1] A number of monographs[2–5] entirely devoted to ^{31}P NMR, covering theory and applications to organophosphorus, and biological and medical aspects of the field have been published. A number of review articles on ^{31}P NMR of nucleic acids and nucleic acid complexes[6–11] have also appeared.

Until recently ^{31}P NMR studies of nucleic acids were restricted to partial identification of signals for polymeric nucleic acids and oligodeoxyribonucleotide sequences of less than six base pairs in length.[2] However, synthetic schemes have now been developed where defined deoxy- (and more recently ribo-, and backbone modified-) oligonucleotides can be routinely produced in multimilligram quantities. The concomitant development of sequence-specific two-dimensional (2D) ^{1}H/^{1}H and ^{1}H/^{31}P NMR assignment methodologies[12–21] has made the assignment of the ^{31}P NMR spectrum of modest size oligonucleotides (8–14 base pairs) possible.

Traditionally the phosphate ester moiety is often overlooked and viewed as a passive element of nucleic acid structure. Base pairing and other nucleic acid base-oriented structural features have been assumed to control nucleic acid structure and conformation. More recently (and as discussed in this chapter) we have begun to appreciate the important role played by the phosphate ester in defining the structure and dynamics of nucleic acids as well as nucleic acid–drug or –protein complexes.

Phosphorus-31 chemical shifts and ^{1}H–^{31}P coupling constants of nucleic acids can provide valuable information on the conformation of the phosphodiester backbone.[11,22–25] It is now widely appreciated that significant local conformational heterogeneity exists in the global as well as the local structures of nucleic acids.[26–29] The internucleotide linkage is defined by six torsional angles from one phosphate atom to the next along the DNA backbone. Theoretical studies have shown that the conformation of two of the six torsional angles (α: O-3′–P–O-5′–C-5′ and ζ: C-3′–O-3′–P–O-5′) appear to be most important in determining ^{31}P chemical shifts.[22,25,30] Molecular dynamics calculations,[31] X-ray diffraction,[32] and 2D NMR[33–35] spectroscopy have also shown that the phosphate ester conformation is the most variable and dynamic part of nucleic acid structure.

2 ASSIGNMENT OF THE ^{31}P NMR SPECTRA OF OLIGONUCLEOTIDES

Prior to the development of multidimensional NMR methods for the sequence-specific assignment of the ^{31}P spectra of nucleic acids, ^{17}O-labeling provided the only unambiguous assignment methodology.[19,36–40] However, the site-specific labeling of the monesterified phosphoryl oxygens of the backbone with ^{17}O or ^{17}O/^{18}O suffers by being expensive and time consuming. Multidimensional ^{31}P–^{1}H NMR spectroscopy[20,39,41,42] has provided a convenient, inexpensive alternative for the assignment of ^{31}P chemical shifts in moderately sized oligonucleotides. Conventional 2D ^{31}P–^{1}H heteronuclear correlation (HETCOR) NMR spectroscopy has been applied with limited success to short oligonucleotides.[20,38] For oligonucleotides longer than 4 or 5 nucleotide residues the simple heteronuclear correlation measurements suffer from poor sensitivity as well as poor resolution in both the ^{1}H and ^{31}P dimensions. The poor sensitivity is largely due to the fact that the ^{1}H–^{31}P scalar coupling constants are about the same size or smaller than the ^{1}H–^{1}H coupling constants. Sensitivity is substantially improved by using a heteronuclear version of the 'constant time' coherence transfer technique, referred to as COLOC (COrrelation spectroscopy via LOng range Coupling), originally proposed for ^{13}C–^{1}H correlations,[43] and implemented in a Pure Absorption phase Constant time pulse sequence (PAC) to emphasize ^{1}H–^{31}P correlations in oligonucleotides.[39]

Besides the ^{31}P–^{1}H long-range constant time HETCOR,[39,44] 2D heteronuclear *J* cross-polarization heteroTOCSY,[45–49] 2D heteronuclear TOCSY-NOESY,[50] 2D TOCSY/^{1}H–^{31}P INEPT,[45,51] and other indirect detection (^{1}H detection) HETCOR experiments,[42,52,53] have been successfully used to assign ^{31}P signals in 6–14 base pair (bp) duplex DNA and ribonucleic acid (RNA). A very nice 3D heteroTOCSY-NOESY experiment[54] has recently been developed that promises increased spectral dispersion by adding a third frequency dimension. This may prove to be extremely valuable for ribooligonucleotides where very little ^{1}H spectral dispersion in the sugar protons is unfortunately observed.[50]

3 ^{1}H–^{31}P AND ^{13}C–^{31}P COUPLING CONSTANTS

In order to understand the structural factors contributing to the variation in ^{31}P chemical shifts of nucleic acids, it has proven to be critical to be able to measure the

backbone torsional angles. Fortunately the three-bond $J(^{31}P,H\text{-}3')$ coupling constants in oligonucleotide duplexes can often be readily determined from the selective 2D J-resolved spectrum.[55] In nearly all duplex oligonucleotides a very interesting pattern of monotonically decreasing coupling constants for the signals to higher field is observed[30,55–59] and strongly supports a correlation between ^{31}P chemical shifts and $J(^{31}P,H\text{-}3')$ coupling constants.

The observed three-bond coupling constants can be analyzed with a proton–phosphorus Karplus relationship to measure the H-3′–C-3′–O–P torsional angle θ from which the C-4′–C-3′–O–P torsional angle ϵ ($= -\theta - 120^\circ$) may be calculated.[60] As shown by Dickerson and Drew[26,27] there is a strong correlation ($R = -0.92$) between torsional angles C-4′–C-3′–O-3′–P (ϵ) and C-3′–O-3′–P–O-5′ (ζ) in the crystal structures of various duplexes. Thus both torsional angles ϵ and ζ can often be calculated from the measured P–H-3′ coupling constant.

A plot of observed ^{31}P chemical shifts and $J(^{31}P,H\text{-}3')$ coupling constants is shown Figure 1.[57] In addition the Karplus relationship is plotted.[60] The Karplus relationship provides for four different torsional angle solutions for each value of the same coupling constant. Although all four values are shown in Figure 1, the limb that includes ϵ values between 0 and -270° is sterically inaccessible in nucleic acids.[28] Generally it is assumed that the coupling constants, which can vary only between 1 and 11 Hz, all correspond to ϵ torsional angles on a single limb nearest the crystallographically observed average for nucleic acids[28] ($\epsilon = -169 \pm 25^\circ$). This need not always be true, especially since phosphate ester conformations corresponding to either of the other two solutions are observed crystallographically.[28] However, as shown in Figure 1, nearly all of the phosphates for normal Watson–Crick duplexes fall along only a single limb of the Karplus curve. Exceptions include several phosphates adjacent to some guanine–adenine (GA) mismatch duplexes.[61,62] In addition, it is quite interesting that the measured ^{31}P chemical shifts and coupling constants for the two phosphates at the site of a tetramer duplex actinomycin D–drug complex do not fit on the main limb of the Karplus curve, although the values do fit nicely on the other two solutions of the curve (Figure 1). Indeed crystal structures[28] of related intercalator duplex complexes confirm that the phosphates are often constrained to conformations that best correspond to the other solutions. These intercalator drug–duplex complexes quite generally show large high-frequency (downfield) shifts of the ^{31}P signals.[23,63,64]

It is important to emphasize that ^{31}P chemical shifts are dependent on factors other than torsional angles alone.[22,65–69] Under normal physiological solution conditions, the intrinsic torsional effects appear largely to dominate ^{31}P chemical shifts of phosphate esters. Thus, for 'normal' B-DNA geometries, there is an excellent correlation (-0.81; Figure 1) between the phosphate resonances and the observed torsional angle, whereas phosphates that are greatly distorted in their geometry must be more carefully analyzed.[30] Importantly, knowledge of both the ^{31}P chemical shift and the $J(^{31}P,H\text{-}3')$ coupling constant can be very helpful in the proper interpretation of phosphate ester conformation.

Analysis of natural abundance 2D $^{13}C-^{1}H$ HMQC and HSQC spectra also allows the measurement of additional $^{31}P-^{1}H$ and $^{31}P-^{13}C$ coupling constants.[70] This should in the future provide further verification of the conformational dependence on ^{31}P chemical shifts.

Roongta et al.[57] have analyzed the variation in the ^{31}P chemical shifts and $J(^{31}P,H\text{-}3')$ values (Figure 1) in terms of fractional populations of the two thermodynamically stable, B-DNA backbone conformational states, B_I and B_{II}. In the normally favored B_I state $\epsilon = t$ (*trans*, 180°) and $\zeta = g^-$ (*gauche*, -60°), whereas in the B_{II} state $\epsilon = g^-$ and

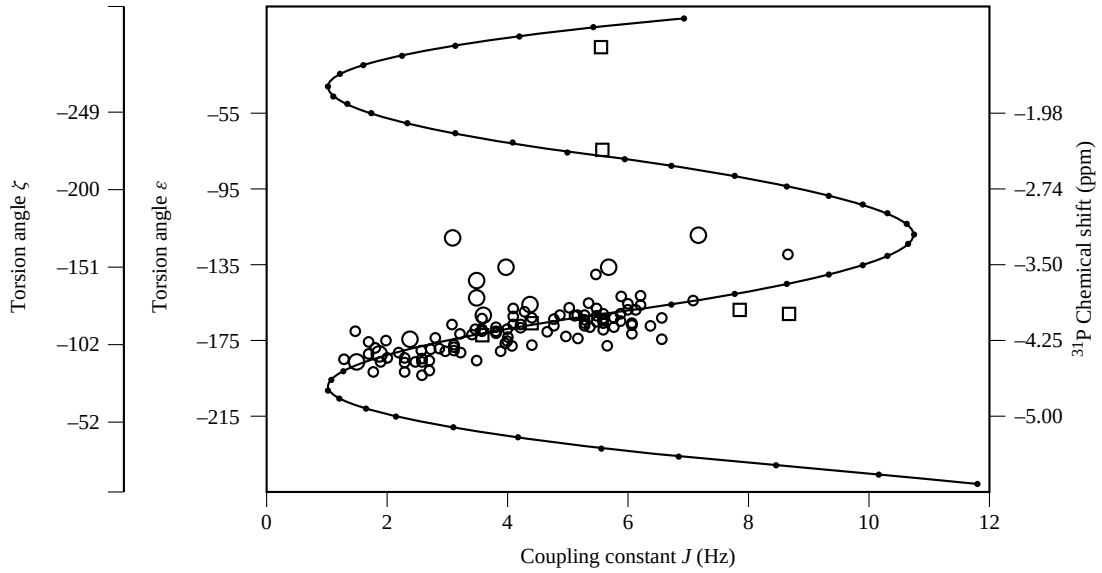

Figure 1 Plot of ^{31}P chemical shifts for the oligonucleotide sequences previously studied in our laboratory[30,57,107] (○) and the actinomycin-D-bound $d(CGCG)_2$ tetramer complex[108] (□) with their measured $J(^{31}P,H\text{-}3')$ coupling contants (the ○ data points correspond to phosphates in a tandem GA-mismatch decamer duplex,[62] which shows unusual, slowly exchanging signals). Also shown are the theoretical ϵ and ζ torsion angles (solid curve) as a function of coupling constant derived from the Karplus relationship (ϵ) and the relationship $\zeta = -317 - 1.23\epsilon$. Phosphorus-31 chemical shifts are reported relative to trimethyl phosphate. Reproduced by permission of the American Chemical Society from Nikonowicz and Gorenstein[62]

$\zeta = t$. Actually in the crystal structure data, the average ϵ torsional angle value for the B_I state is -190° and for the B_{II} state is -105°.[26,27] These ϵ values approximate the maximum possible range of $J(^{31}P,H\text{-}3')$ coupling constants [for $\epsilon = -105^\circ$, $J(^{31}P,H\text{-}3') = 10.0$ Hz and for $\epsilon = -190^\circ$, $J(^{31}P,H\text{-}3') = 1.3$ Hz]. In addition in this torsional angle range, the Karplus curve is nearly a single-valued function (actually it is only single valued in the range of $\epsilon \approx -200$ to -120°; between -105 and -120° the coupling constant is in the range of 10.0–10.8 Hz.). The measured coupling constant then represents the weighted average of the coupling constants in the two states. The ^{31}P chemical shift and $J(^{31}P,H\text{-}3')$ coupling constant of a phosphate in a purely B_I conformational state is estimated to be about -4.6 ppm and 1.3 Hz, respectively. Similarly the ^{31}P chemical shift and $J(^{31}P,H\text{-}3')$ coupling constants of a phosphate in a purely B_{II} conformational state should be about -3.0 ppm and 10 Hz, respectively. The ^{31}P chemical shift difference between the B_I and B_{II} conformational states is thus estimated to be 1.6 ppm. Earlier chemical shift calculations[71–73] and later empirical studies indicated that a phosphate diester in a B_I conformation should have a ^{31}P chemical shift 1.5 ppm upfield from a phosphate diester in the B_{II} conformations.[7,64] It is thus extremely gratifying that the experimentally observed results fully support the original hypothesis.

The dispersion in the ^{31}P chemical shifts of regular oligonucleotides is thus likely to be attributable to different ratios of populations of the B_I and B_{II} states for each phosphate in the sequence. Assuming that only the staggered rotamers define stable conformations, the phosphate is assumed to make rapid jumps between the two states. Alternatively the phosphate could be considered to be constrained to a single, intermediate P–O ester conformation. This latter explanation appears to be ruled out by restrained molecular dynamics simulations[31] that clearly show that these intermediate conformational states are only transiently populated as the phosphate makes rapid jumps between the B_I and B_{II} states (see Section 5). Thus the measured coupling constant appears generally to reflect the populations of these two possible conformational states.

4 ^{31}P NMR OF POLYNUCLEIC ACIDS

Phosphorus-31 NMR may usefully be applied to the study of polynucleic acids as well.[6] As described above, the range of ^{31}P chemical shifts for individual phosphates in duplex fragments is generally <0.9 ppm. It is not surprising therefore that individually resolved signals are not observed for longer (>100 bp) nucleic acid fragments, for which much broader lines are expected. In favorable circumstances, however, separate signals may be resolved.

Thus sonicated poly(A)·poly(U) (U = uridine) ^{31}P spectra show two equal intensity signals separated by about 0.4 ppm (-1.2 and -1.6 ppm relative to 85% H_3PO_4).[74] Joseph and Bolton[40] showed by ^{17}O labeling of the phosphates that the two main ^{31}P signals are associated with phosphates in alternating conformations along the duplex poly(A)·poly(U) rather than the phosphates in the two different strands.

One of the earliest, most direct indications that ^{31}P chemical shifts were dependent on phosphate ester conformations comes from the study of poly d(GC) duplex (C = cytidine) and shorter oligomeric GC and related base duplexes. In high salt, the ^{31}P spectra of these alternating duplexes (including an RNA duplex) shows two signals of equal area with a chemical shift difference of 1.4–2.0 ppm.[75–79] The crystal structures of this high-salt left-handed Z-DNA conformation show an alternation along the sugar phosphate backbone (α, ζ) of either B_I-like (g^+, g^+ for CpG; p = phosphate) and B_{II} type (g^+,t or g^-,t for GpC) phosphates.[80–82] Skelenar and Bax[83] have nicely used the 2D heteronuclear indirect detection experiment to assign the downfield shifted signal to the B_{II} type of phosphates.

5 SEQUENCE-SPECIFIC VARIATION IN ^{31}P CHEMICAL SHIFTS AND COUPLING CONSTANTS OF DUPLEX OLIGONUCLEOTIDES

As pointed out by Ott and Eckstein[84] and Schroeder et al.[14,19] variations in local, sequence-specific, and induced environmental distortions in the duplex geometry appear to be responsible for the variations in ^{31}P chemical shifts. Earlier attempts in my laboratory and that of Eckstein utilized a set of simple 'Calladine Rules' to predict local helical structure. Thus Dickerson and co-workers[85] had shown that the helical distortions observed in the crystal structure of $d(GCGCAATTGGC)_2$ (d = deoxy; T = thymine) could be quantitatively predicted through a series of simple 'Calladine rule' sum function relationships.[86] Based upon the ^{31}P assignments of over a dozen oligonucleotides, we were able to establish a modest correlation between ^{31}P chemical shifts and the helical twist sum function for a number of the oligonucleotides.[14,19,30,87]

However, it is now clear that the failure to observe significant correlation between ^{31}P chemical shifts of all phosphates in duplex oligonucleotides and the sequence-specific local helical structural 'rules', as derived from X-ray crystal structures, simply reflects the failure of the rules themselves to predict accurately the solution state sequence-specific local, helical, structural variations.[7,31,88–93] Further, recent NMR studies have suggested that the duplex conformation in solution may not be identical to the static picture provided by X-ray diffraction in the crystal state,[42,94] as one might expect.

5.1 Origin of Sequence-Specific Variations

Analysis of the X-ray crystal structures[26–28] and NOESY distance-refined structures[95] of B-form oligodeoxyribonucleotides has shown that torsional angles α, β and γ on the 5′-side of the sugar are largely constrained to values $g^-(-60^\circ)$, $t(180^\circ)$, $g(+60^\circ)$, whereas significant variations are observed on the 3′-side of the deoxyribose phosphate backbone. The greatest variation in backbone torsional angles is observed for ζ (P–O-3′), followed by ϵ (C-3′–O-3′), and then δ (C-4′–C-3′). It is important to note that many of these torsional angle variations are correlated as in the B_I/B_{II} states.[26–28,30]

It is largely this variation in δ, ϵ, and ζ that allows the sugar phosphate backbone to 'stretch' or 'contract' to allow for sequence-specific variations in the local base-pair geometry of B-DNA. Thus the possible basis for the correlation between base sequence and ^{31}P chemical shifts in both nucleic acids can be analyzed in terms of sugar phosphate

backbone distortions.[30] This backbone linkage provides a connection between ^{31}P spectral changes and variations in local helical parameters such as rise, twist, and roll. Indeed a correlation exists between the $J(^{31}\text{P,H-3}')$ coupling constant and calculated intersugar distances derived from the NOESY distance-restrained molecular dynamics (MD) refined structure for a decamer.[31] Thus, a lengthening of the tether requires an increase in the population of the B_{II} conformation and shifts the ^{31}P signal to higher frequency.

5.2 Correlation of Local Helical Geometry with Backbone Conformation

X-ray, NMR, and computational methods now all agree that there are major backbone conformation changes introduced as a result of sequence-specific, local helical variations. Various molecular modeling studies[30,96] have shown that B_{II} phosphates are associated with high values of helix twist[30] and large negative values of helix roll.[58,96] High twist and low positive roll perturb the phosphate ester backbone and decrease base stacking interactions in TpA relative to ApT.[58,97] Similar effects are noted for the Py-Pu (Py = pyrimidine, Pu = purine) sequence CpG vs. Pu-Py sequence GpC.[58,97,98] When both B_{II} phosphates are opposite each other in a duplex step, as the phosphates turn toward the minor groove, they force the base pairs to be displaced into the major groove by up to 2 Å.[96] This results in some loss of stacking energy. With a large negative roll, the effect is to produce a kink toward the minor groove in the DNA at this juncture, producing a significant local bend in the duplex. Indeed in several instances of a GA mismatch, a very high twist value is found at a base step with either phosphates always in a B_{II} conformation[99] or phosphates predominantly in the B_{II} conformation.[62]

High-frequency phosphate signals generally appear to be associated with Py-Pu base steps[30,57,58,96,100] that have high helical twist. High twist produces an increase in the length of the sugar phosphate tether, also lowering the relative energy difference (and energy barrier?) between the two phosphate states. This produces a more flexible phosphate site in which transitions can occur more readily and in higher frequency, as appears to be observed in the MD simulations. CpG steps generally show high-frequency signals with large 3-bond coupling constants, whereas ApT steps show low-frequency signals with small 3-bond coupling constants.

5.3 Conformation and Dynamics of the Phosphate Ester Backbone

As described above ^{31}P chemical shifts and $^{1}\text{H}-^{31}\text{P}$ coupling constants clearly indicate sequence-specific variations in the backbone conformation. Unfortunately, $^{1}\text{H}/^{1}\text{H}$ 2D nuclear Overhauser effect spectra (NOESY) give no direct information on the phosphate ester conformation and NOESY distance-constrained structures have been suggested to be effectively disordered in this part of the structure.[95] The solution structural refinements of a $d(CGCTTAAGCG)_2$ decamer duplex, tandem GA mismatch decamer, and several tetradecamers[101–103] by a hybrid relaxation matrix/NOESY distance-restrained MD methodology (MORASS)[7,94,104–106] provided important indicators that full analysis of DNA structure requires a complete picture of the internal dynamics.

The NMR restrained MD trajectory (time course) of the variations in the six backbone torsional angles, $\alpha-\zeta$ of the internucleotide linkage in various duplexes, have indicated that most of these torsional angles show relatively small amplitude fluctuations about the average B-DNA values for the 45 picosecond restrained MD calculation. As noted above in B-DNA the ϵ and ζ torsional angles show the largest variability, and indeed calculations demonstrate that large amplitude fluctuations occur for these two torsional angles.[26,27] These torsional angle changes reflect a transition from the low-energy B_I conformation to the higher energy B_{II} conformation. These transitions were short lived and relaxed back to the low-energy conformation. Other internucleotide phosphates show similar transitions, although the fraction of B_I/B_{II} states varies for each phosphate. These calculations also provided strong support for the coupled 'elbow' conformational transition between the B_I and B_{II} conformations and the strong correlation between the ϵ and ζ torsion angles observed in the X-ray crystal structures of B-DNA.[26,27]

As shown in Figure 2 the NOESY distance-restrained MD calculations for the tandem GA-mismatch $d(CCAAGATTGG)_2$ are able to reproduce the observed variation in the ϵ torsional angles for the decamer as calculated from the experimental $J(^{31}\text{P,H-3}')$ coupling constants.[62] (The ϵ torsional angles also rather accurately parallel the variation in ^{31}P chemical shifts.) The ϵ torsional angles were calculated by averaging over 160 ps dynamics of the 2D NOESY restrained MD refinement. It is clear that a remarkably strong correlation exists between the pattern of the variation of the torsional angles derived from the restrained MD calculations and the experimentally measured coupling constants (the fit is poorer to an alternate conformation that is in slow chemical exchange; • in Figure 2). Similar correlations between the averaged torsional angles from restrained MD refinement of the $d(CGCTTAAGCG)_2$ base-paired B-DNA decamer have also been demonstrated.[31]

It is important to note that the ϵ torsional angles in Figure 2 derived from the restrained MD calculations represent time averages during which large amplitude fluctuations are

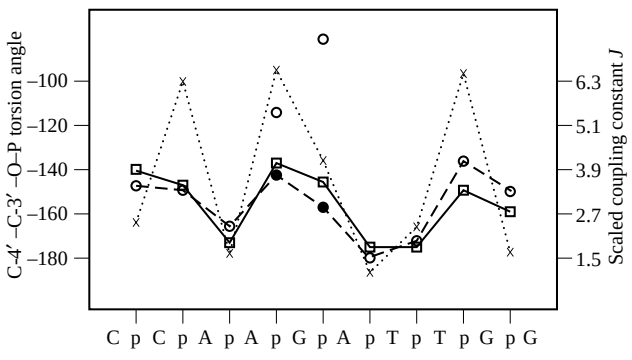

Figure 2 Plot of the ϵ torsion angle from the crystal structure (×) and final solution structure (□) vs. phosphate position along the 5′–3′ strand for duplex decamer $d(CCAAGATTGG)_2$. The experimental $J(^{31}\text{P,H-3}')$ coupling constant (○, •) vs. phosphate position is also shown. The $J(^{31}\text{P,H-3}')$ coupling constant vs. sequence plot has been scaled to reflect the ϵ torsion angle variations. Reproduced by permission of the American Chemical Society from Nikonowicz and Gorenstein[62]

observed on the picosecond timescale. The time course of the restrained MD calculated fluctuations about the six sugar phosphate torsional angles in the GA-mismatch decamer show relatively small amplitude fluctuations about the average B-DNA values except for the ϵ and ζ torsional angles. These torsional angle changes again generally reflect a transition from the low-energy B_I conformation to the higher energy B_{II} conformation.

Figure 2 also demonstrates that the variation in the backbone conformation in the crystal state follows the same pattern of variation in the measured coupling constants and the averaged torsional angles derived from the restrained MD refinement. In the crystal state, most of the phosphates appear frozen in either pure B_I or pure B_{II} conformations. At any single snapshot of the restrained MD calculations, some phosphates are also frozen in pure B_I or pure B_{II} conformations. However analysis of the ϵ torsional angle in any single snapshot during the MD trajectory leads to an incorrect value for the ϵ torsional angles as measured by the $J(^{31}\text{P,H-3}')$ coupling constants. It is only the time average of the torsional angles that correctly describes the pattern of $J(^{31}\text{P,H-3}')$ coupling constants. (In another tandem, GA-mismatch duplex conformational constraints on the backbone are sufficiently strong so as to keep two of the phosphates locked in a B_{II} state; and the ^{31}P chemical shifts of these phosphates are shifted to higher frequency as expected.[99]) These results and those described in the previous section provide strong support for our hypothesis that *dynamic* variations in the backbone torsional angles are largely responsible for ^{31}P chemical shift variations in duplex oligonucleotides.

6 RELATED ARTICLES

DNA: A-, B-, and Z-; Drug–Nucleic Acid Interactions; Nucleic Acid Structures in Solution: Sequence Dependence; Nucleic Acids: Base Stacking and Base Pairing Interactions; Nucleic Acids: Spectra, Structures, and Dynamics.

7 REFERENCES

1. D. G. Gorenstein, in *Encyclopedia of Nuclear Magnetic Resonance*, eds. D. M. Grant and R. K. Harris, Wiley, New York, 1995.
2. D. G. Gorenstein, in *Phosphorus-31 NMR: Principles and Applications*, ed. D. G. Gorenstein, Academic Press, Orlando, FL, 1984.
3. L. D. Quin and J. G. Verkade, *Phosphorus-31 NMR Spectroscopy in Stereochemical Analysis*, VCH, Deerfield Beach, FL, 1987.
4. C. T. Burt, *Phosphorus NMR in Biology*, CRC Press, Boca Raton, FL, 1987.
5. L. D. Quin and J. G. Verkade, *Phosphorus-31 NMR Spectral Properties in Compound Characterization and Structural Analysis*, VCH, New York, 1994.
6. C. W. Chen and J. S. Cohen, in *Phosphorus-31: NMR Principles and Applications*, ed. D. G. Gorenstein, Academic Press, Orlando, FL, 1984, p. 233.
7. D. G. Gorenstein, R. P. Meadows, J. T. Metz, E. P. Nikonowicz, and C. B. Post, in *Advances in Biophysical Chemistry*, ed. C. A. Bush, JAI Press, Greenwich, CT, 1990, p. 47.
8. M.-D. Tsai, *Phosphorus-31 NMR: Principles and Applications*, ed. D. Gorenstein, Academic Press, Orlando, FL, 1984, p. 175.
9. P. A. Hart, in *Phosphorus-31 NMR: Principles and Applications*, ed. D. G. Gorenstein, Academic Press, Orlando, FL, 1984, p. 317.
10. T. L. James, in *Phosphorus-31 NMR: Principles and Applications*, ed. D. G. Gorenstein Academic Press, Orlando, FL, 1984, p. 349.
11. D. G. Gorenstein, in *DNA Structures, Methods in Enzymology*, eds. D. M. Lilley and J. E. Dahlberg, Academic Press, Orlando, FL, 1992, 211, p. 254.
12. J. Feigon, W. Leupin, W. A. Denny, and D. R. Kearns, *Biochemistry*, 1983, **22**, 5943.
13. D. R. Hare, D. E. Wemmer, S. H.- Chou, G. Drobny, and B. R. Reid, *J. Mol. Biol.*, 1983, **171**, 319.
14. S. A. Schroeder, J. M. Fu, C. R. Jones, and D. G. Gorenstein, *Biochemistry*, 1987, **26**, 3812.
15. D. R. Kearns, *Crit. Rev. Biochem.*, 1984, **15**, 237.
16. D. Frechet, D. M. Cheng, L. S. Kan, and P. O. P. Ts'o, *Biochemistry*, 1983, **22**, 5194.
17. M. A. Broido, G. Zon, and T. L. James, *Biochem. Biophys. Res. Commun.*, 1984, **119**, 663.
18. R. M. Scheek, R. Boelens, N. Russo, J. H. van Boom, and R. Kaptein, *Biochemistry*, 1984, **23**, 1371.
19. D. G. Gorenstein, S. A. Schroeder, M. Miyasaki, J. M. Fu, V. Roongta, P. Abau, J. T. Metz, and C. R. Jones, *Bull. Magn. Reson.*, 1986, **8**, 137.
20. A. Pardi, R. Walker, H. Rappoport, G. Wieder, and K. Wüthrich, *J. Am. Chem. Soc.*, 1983, **105**, 1652.
21. K. Lai, D. O. Shah, E. Derose, and D. G. Gorenstein, *Biochem. Biophys. Res. Commun.*, 1984, **121**, 1021.
22. D. G. Gorenstein, in *Phosphorus-31 NMR: Principles and Applications*, ed. D. G. Gorenstein, Academic Press, Orlando, 1984, p. 7.
23. D. G. Gorenstein, *Annu. Rev. Biophys. Bioeng.*, 1981, **10**, 355.
24. D. G. Gorenstein, J. B. Findlay, R. K. Momii, B. A. Luxon, and D. Kar, *Biochemistry*, 1976. **15**, 3796.
25. D. G. Gorenstein, *Chem. Rev.*, 1987, **87**, 1047.
26. R. E. Dickerson, *J. Mol. Biol.*, 1983, **166**, 419.
27. R. E. Dickerson and H. R. Drew, *J. Mol. Biol.*, 1981, **149**, 761.
28. W. Saenger, *Principles of Nucleic Acid Structure*, Springer, New York, 1984.
29. O. Kennard and W. N. Hunter, *Angew Chem., Int. Ed. Engl.*, 1991, **30**, 1254.
30. D. G. Gorenstein, S. A. Schroeder, J. M. Fu, J. T. Metz, V. Roongta, and C. R. Jones, *Biochemistry*, 1988, **27**, 7223.
31. R. Powers, C. R. Jones, and D. G. Gorenstein, *J. Biomol. Struct. Dyn.*, 1990, **8**, 253.
32. M. Sundaralingam, *Biopolymers*, 1969, **7**, 821.
33. R. Powers and D. G. Gorenstein, *Biochemistry*, 1990, **29**, 9994.
34. E. P. Nikonowicz, R. P. Meadows, P. Fagan, and D. G. Gorenstein, *Biochemistry*, 1991, **30**, 1323.
35. P. Wisniowski, C. Karslake, M. E. Piotto, B. Spangler, A. C. Moulin, E. P. Nikonowicz, K. Kaluarachchi, and D. G. Gorenstein, in *Structure & Function*, eds. R. H. Sarma and M. H. Sarma, Adenine Press, Schenectady, NY, 1992, p. 17.
36. M. Petersheim, S. Mehdi, and J. A. Gerlt, *J. Am. Chem. Soc.*, 1984, **106**, 439.
37. B. A. Connolly and F. Eckstein, *Biochemistry*, 1984, **23**, 5523.
38. D. O. Shah, K. Lai, and D. G. Gorenstein, *J. Am. Chem. Soc.*, 1984, **106**, 4302.

39. J. M. Fu, S. A. Schroeder, C. R. Jones, R. Santini, and D. G. Gorenstein, *J. Magn. Reson.*, 1988, **77**, 577.
40. A. P. Joseph and P. H. Bolton, *J. Am. Chem. Soc.*, 1984, **106**, 437.
41. D. M. Cheng, L.-S. Kan, P. S. Miller, E. E. Leutzinger, and P. O. P. Ts'o, *Biopolymers*, 1982, **21**, 697.
42. V. Sklenár, H. Miyashiro, G. Zon, H. T. Miles, and A. Bax, *FEBS Lett.*, 1986, **208**, 94.
43. H. Kessler, C. Griesinger, J. Zarbock, and H. R. Loosli, *J. Magn. Reson.*, 1984, **57**, 331.
44. C. R. Jones, S. A. Schroeder, and D. G. Gorenstein, *J. Magn. Reson.*, 1988, **80**, 370.
45. M. G. Zagorski and D. G. Norman, *J. Magn. Reson.*, 1989, **83**, 167.
46. D. W. Bearden and L. R. Brown, *Chem. Phys. Lett.*, 1989, **163**, 432.
47. G. A. Morris and A. Gibbs, *J. Magn. Reson.*, 1991, **91**, 444.
48. D. Y. Artemov, *J. Magn. Reson.*, 1991, **91**, 405.
49. G. W. Kellogg, *J. Magn. Reson.*, 1992, **98**, 176.
50. G. W. Kellogg, A. A. Szewczak, and P. B. Moore, *J. Am. Chem. Soc.*, 1992, **114**, 2727.
51. H. Hiroaki and S. Uesugi, *FEBS Lett.*, 1989, **244**, 43.
52. D. Williamson and A. Bax, *J. Magn. Reson.*, 1988, **76**, 174.
53. K. V. R. Chary, V. K. Rastogi, and G. Govil, *J. Magn. Reson.*, 1993, **102B**, 81.
54. G. W. Kellogg and B. I. Schweitzer, *J. Biomol. NMR*, 1993, **3**, 577.
55. V. Sklenár and A. Bax, *J. Am. Chem. Soc.*, 1987, **109**, 7525.
56. E. Ragg, R. Mondelli, A. Garbesi, F. P. Colonna, C. Battistini, and S. Vioglio, *Magn. Reson. Chem.*, 1989, **27**, 640.
57. V. A. Roongta, C. R. Jones, and D. G. Gorenstein, *Biochemistry*, 1990, **29**, 5245.
58. S. Elantri, P. Bittoun, O. Mauffret, M. Monnot, O. Convert, E. Lescot, and S. Fermandjian, *Biochemistry*, 1993, **32**, 7079.
59. Y. L. Lyubchenko, L. S. Shlyakhtenko, E. Appella, and R. E. Harrington, *Biochemistry*, 1993, **32**, 4121.
60. P. P. Lankhorst, C. A. G. Haasnoot, C. Erkelens, and C. Altona, *J. Biomol. Struct. Dyn.*, 1984, **1**, 1387.
61. S.-H. Chou, J.-W. Cheng, and B. R. Reid, *J. Mol. Biol.*, 1992, **228**, 138.
62. E. P. Nikonowicz and D. G. Gorenstein, *Biochemistry*, 1990, **29**, 8845.
63. D. J. Patel, *Biochemistry*, 1974, **13**, 2388.
64. D. G. Gorenstein and E. M. Goldfield in *Phosphorus-31 NMR: Principles and Applications*, ed. D. G. Gorenstein, Academic Press, Orlando, FL, 1984, p. 299.
65. E. J. Corey, M. A. Tius, and J. Das, *J. Am. Chem. Soc.*, 1980, **102**, 7612.
66. A. J. R. Costello, T. Glonek, and J. R. Van Wazer, *J. Inorg. Chem. Soc.*, 1976, **15**, 972.
67. D. G. Gorenstein, *J. Am. Chem. Soc.*, 1975, **97**, 898.
68. D. G. Gorenstein, *Methods Enzymol.*, 1989, **177**, 295.
69. S. Un and M. P. Klein, *J. Am. Chem. Soc.*, 1989, **111**, 5119.
70. P. Schmieder, J. H. Ippel, H. Van der Elst, G. A. van der Marel, J. H. van Boom, C. Altona, and H. Kessler, *Nucleic Acids Res.*, 1992, **20**, 4747.
71. D. G. Gorenstein and D. Kar, *Biochem. Biophys. Res. Commun.*, 1975, **65**, 1073.
72. F. R. Prado, C. Geissner-Prettre, B. Pullman, and J. P. Daudey, *J. Am. Chem. Soc.*, 1979, **101**, 1737.
73. C. Giessner-Pettre, B. Pullman, F. R. Prado, D. M. Cheng, V. Iuorno, and P. O. P. Ts'o, *Biopolymers*, 1984, **23**, 377.
74. J. L. Alderfer and G. L. Hazel, *J. Am. Chem. Soc.*, 1981, **103**, 5925.
75. C. W. Chen, J. S. Cohen, and M. Behe, *Biochemistry*, 1983, **22**, 2136.
76. D. J. Patel, L. L. Canuel, and F. M. Pohl, *Proc. Natl. Acad. Sci. U.S.A.*, 1979, **76**, 2508.
77. J. S. Cohen, J. B. Wooten, and C. L. Chatterjee, *Biochemistry*, 1981, **20**, 3049.
78. K. Hall, P. Cruz, I. Tinoco, Jr., T. M. Jovin, and J. H. van de Sande, *Nature (London)*, 1984, **311**, 584.
79. D. G. Gorenstein, B. A. Luxon, E. M. Goldfield, K. Lai, and D. Vegeais, *Biochemistry*, 1982, **21**, 580.
80. A. Rich, A. Nordheim, and A. H.-J. Wang, *Annu. Rev. Biochem.*, 1984, **53**, 791.
81. H. Drew, T. Takano, S. Tanaka, K. Itakura, and R. E. Dickerson, *Nature (London)*, 1980, **286**, 567.
82. R. G. Brennan, E. Westhof, and M. Sundaralingam, *J. Biomol. Struct. Dyn.*, 1986, **3**, 649.
83. V. Sklenár and A. Bax, *J. Am. Chem. Soc.*, 1987, **109**, 2221.
84. J. Ott and F. Eckstein, *Biochemistry*, 1985, **24**, 2530.
85. A. V. Fratini, M. L. Kopka, H. R. Drew, and R. E. Dickerson, *J. Biol. Chem.*, 1982, **257**, 14686.
86. C. R. Calladine, *J. Mol. Biol.*, 1982, **161**, 343.
87. D. G. Gorenstein and K. Lai, *Biochemistry*, 1989, **28**, 2804.
88. G. G. Privé, U. Heinemann, S. Chandrasegaran, L. S. Kan, M. L. Kopka, and R. E. Dickerson, *Science*, 1987, **238**, 498.
89. J. D. Baleja, R. T. Pon, and B. D. Sykes, *Biochemistry*, 1990, **29**, 4828.
90. M. Nilges, G. M. Clore, A. M. Gronenborn, N. Piel, and L. W. McLaughlin, *Biochemistry*, 1987, **26**, 3734.
91. R. Powers, R. K. Olsen, and D. G. Gorenstein, *J. Biomol. Struct. Dyn.*, 1989, **7**, 515.
92. J. F. Lefevre, A. N. Lane, and O. Jardetzky, *Biochemistry*, 1987, **26**, 5076.
93. U. Heinemann and C. Alings, *J. Mol. Biol.*, 1989, **210**, 369.
94. E. P. Nikonowicz, R. P. Meadows, and D. G. Gorenstein, *Biochemistry*, 1990, **29**, 4193.
95. F. J. M. van de Ven and C. W. Hilbers, *Eur. J. Biochem.*, 1988, **178**, 1.
96. B. Hartmann, D. Piazzola, and R. Lavery, *Nucleic Acids Res.*, 1993, **21**, 561.
97. K. Grzeskowiak, K. Yanagi, G. G. Privé, and R. E. Dickerson, *J. Biol. Chem.*, 1991, **266**, 8861.
98. O. Mauffret, B. Hartmann, O. Convert, R. Lavery, and S. Fermandjian, *J. Mol. Biol.*, 1992, **227**, 852.
99. S.-H. Chou, J.-W. Cheng, O. Y. Fedoroff, V. P. Chuprina, and B. R. Reid, *J. Am. Chem. Soc.*, 1992, **114**, 3114.
100. S. A. Schroeder, V. Roongta, J. M. Fu, C. R. Jones, and D. G. Gorenstein, *Biochemistry*, 1989, **28**, 8292.
101. C. B. Post, R. P. Meadows, and D. G. Gorenstein, *J. Am. Chem. Soc.*, 1990, **112**, 6796.
102. E. P. Nikonowicz, R. Meadows, and D. G. Gorenstein, *Bull. Magn. Reson.*, 1989, **11**, 226.
103. D. G. Gorenstein, *Organophosphorus Chemistry*, Marcel Dekker, New York, 1993.
104. R. Boelens, T. M. G. Koning, and R. Kaptein, *J. Mol. Struct.*, 1988, **173**, 299.
105. R. Boelens, T. M. G. Koning, G. A. van der Marel, J. H. van Boom, and R. Kaptein, *J. Magn. Reson.*, 1989, **82**, 290.

106. B. A. Borgias and T. L. James, *J. Magn. Reson.*, 1990, **87**, 475.
107. E. P. Nikonowicz, V. Roongta, C. R. Jones, and D. G. Gorenstein, *Biochemistry*, 1989, **28**, 8714.
108. M. Delepierre, C. Van Heijenoort, J. Igolen, J. Pothier, M. Le Bret, and B. P. Roques, *J. Biomol. Struct. Dyn.*, 1989, **7**, 557.

Acknowledgments

Supported by NIH (AI27744), the Purdue University Biochemical Magnetic Resonance Laboratory, which is supported by the NSF-designated Biological Facilities Center on Biomolecular NMR, Structure and Design at Purdue (grants BBS 8614177 and DIR-9000360 from the Division Biological Instrumentation), and the NIH-designated AIDS Research Center at Purdue (AI727713). The contributions of Indrasiri Kumaralal, Edward Nikonowicz, Vikram A. Roongta, Robert Powers, Claude R. Jones, Josepha Fu, Stephen A. Schroeder, James T. Metz, and Robert Powers are much appreciated.

Biographical Sketch

David G. Gorenstein. *b* 1945. B.S., 1966, Ph. D., 1969, Chemistry, Harvard University, USA (with Frank Westheimer). Assistant, associate, and full professor, University of Illinois at Chicago, USA. Professor of Chemistry and Director of Purdue Magnetic Resonance Laboratory, Purdue University, USA (1985–94). Currently Professor of Human Biological Chemistry and Genetics and Director of the Sealey Center for Structural Biology, University of Texas Medical Branch, USA. Senior Fulbright Fellow, Oxford University (1977–8), Oxford, UK and Guggenheim Fellow at University of California at San Francisco, USA (1986). Approx. 160 publications. Current research specialty: NMR, structure and dynamics of biological macromolecules.

Nucleic Acids: Spectra, Structures, and Dynamics

Cornelis W. Hilbers and Sybren S. Wijmenga
University of Nijmegen, Nijmegen, The Netherlands

1	Introduction	1
2	Nomenclature	1
3	Structural Parameters	1
4	Spectral Interpretation	6
5	Structure Determination	10
6	Hairpin Structures	10
7	Dynamics	11
8	Related Articles	13
9	References	13

1 INTRODUCTION

NMR spectroscopy has come a long way since its inception. Initially used to study the (relaxation) properties of nuclear spins, the discovery of the chemical shift established it as one of the essential analytical techniques in chemical research laboratories. More recently it has developed into the most powerful technique for the determination of (bio)molecular structure in solution and has thereby made its way into the field of structural biology. This is one of the fascinating developments of this spectroscopy, never anticipated at the time of its conception.

In X-ray diffraction, traditionally used to determine the three-dimensional structure of biomacromolecules at atomic resolution, the wavelength of the electromagnetic radiation needed to obtain well-resolved diffraction patterns is of the order of the interatomic distances in the molecule, i.e. of the order of angstroms. The situation is quite different for NMR spectroscopy, where the wavelength is of the order of meters. Here, the required structural information has to be deduced from suitable spectral parameters, i.e. the intensity of the resonance lines, which corresponds to the number of nuclei in a particular chemical group, the splittings of the individual resonance lines from which torsion angles may be derived, and the relaxation properties leading to the nuclear Overhauser effect from which the short range distances (<5 Å) in the molecule can be calculated.

The complicated spectra of biomacromolecules with their strongly overlapping resonances do not lend themselves to easy abstraction of spectral parameters needed for structure determination, and ingenious methods have been devised to achieve this goal, revolutionizing the field of NMR. Although most of these developments have been initiated in protein studies, this is also reflected in present-day nucleic acid NMR. Part of the progress was connected with the possibility of performing heteronuclear NMR of uniformly ^{13}C- and ^{15}N-enriched proteins. Preparation of uniformly isotope-enriched ribonucleic acid (RNA) has now also come within reach and has led to a situation that, in principle, a complete interpretation of the spectra of these molecules can be obtained.

Here we will outline the methods by which such an interpretation can be achieved and how the results are translated into structure. Subsequently, some hairpin structures and their loop folding will be discussed as examples. Aspects of internal mobility in nucleic acids are considered in the last part of this article.

2 NOMENCLATURE

A discussion of the spectral interpretation and structure determination of nucleic acids requires a definition of the parameters describing the geometry of the molecules, i.e. for our particular purpose an atom-numbering scheme and a definition of the torsion angles. The numbering scheme for the furanose ring and the five common bases in deoxyribonucleic acid (DNA) and RNA, as well as the definition of the sugar–phosphate backbone torsion angles, of the torsion angles of the sugar ring, and of the glycosidic torsion angle are presented in Figure 1 (see for their definition also Table 1). The values of the torsion angles are defined via the so-called Newman projections. Examples of such projections with the corresponding sign convention for the staggered conformations, *gauche*-minus (g^-), *gauche*-plus (g^+), and *trans* (t) are given in Figure 2. A more extensive treatment of this material can be found in Saenger.[1] The furanose ring is most conveniently described in terms of the phase angle of pseudorotation, P, and the puckering amplitude, Φ_m (see below).

3 STRUCTURAL PARAMETERS

A typical aspect of NMR spectroscopy is that only local or short range structural information can be obtained. Thus, distances derived from NOE measurements are generally ≤ 5 Å and only individual torsion angles can be derived from J couplings between protons, between protons and so-called heteronuclei (^{13}C, ^{15}N, ^{31}P), and between heteronuclei (^{13}C, ^{15}N,

Table 1 Definition of Torsion Angles

	Atom sequence defining torsion angle
Sugar–phosphate backbone torsion angle	
α	O-3′–P–O-5′–C-5′
β	P–O-5′–C-5′–C-4′
γ	O-5′–C-5′–C-4′–C-3′
δ	C-5′–C-4′–C-3′–O-3′
ϵ	C-4′–C-3′–O-3′–P
ζ	C-3′–O-3′–P–O-5′
χ(Pyrimidine)	O-4′–C-1′–N-1–C-2
χ(Purine)	O-4′–C-1′–N-9–C-4
Endocyclic sugar torsion angle	
ν_0	C-4′–O-4′–C-1′–C-2′
ν_1	O-4′–C-1′–C-2′–C-3′
ν_2	C-1′–C-2′–C-3′–C-4′
ν_3	C-2′–C-3′–C-4′–O-4′
ν_4	C-3′–C-4′–O-4′–C-1′

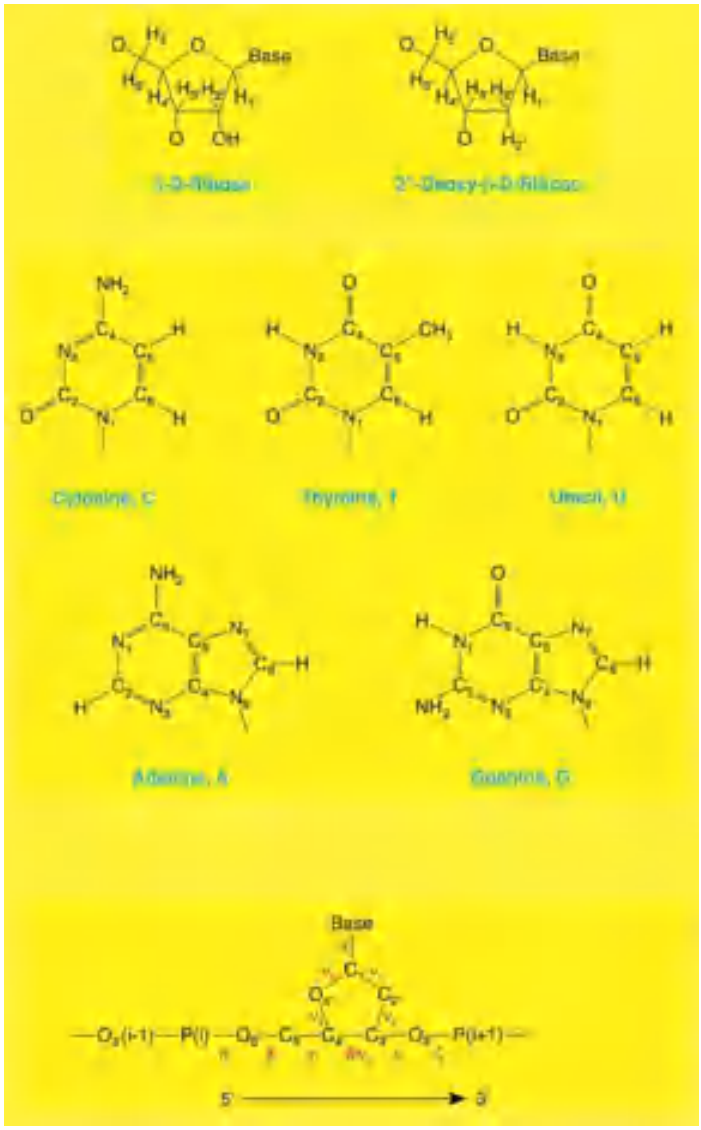

Figure 1 Structures and standard atom numbering of the β-D-riboses and the five common bases (pyrimidines: C, T, and U; purines: G and A) in DNA and RNA according to the IUPAC/IUB guidelines (*Eur. J. Biochem.*, 1983, **131**, 9). Notice that the atoms in the sugar moieties are primed in contrast with the atoms in the bases. Note that the C, H numberings are only depicted as subscripts *within* the Figure, e.g. C_6 in Figure $\equiv$ C-6 in text. The numbering of the primed and double primed hydrogen atoms attached to C-5′ is obtained by looking along the main chain: proceeding in the counterclockwise direction the atoms attached to C-5′ are C-4′, H-5′ and H-5″ (see Figure 2, upper right). The lower part of the Figure provides a definition of the torsion angles in the sugar–phosphate backbone: α, β, γ, δ, ϵ, and ζ, the glycosidic torsion angle χ, and the endocyclic torsion angles ν_0–ν_4 in the sugar ring

^{31}P). Moreover, the short-range distances are solely derived from the NOE measurements between protons. To derive a structure, the available NMR data have to be complemented by incorporating so-called holonomic constraints such as bond angles and bond lengths.

Short-range distances characteristic of typical conformations are ubiquitous in nucleic acid structures, i.e. in mononucleotide conformations as well as in the secondary structural elements, the double helices. Therefore systematic studies of short-range ^{1}H–^{1}H distances in these structural elements have been made to serve as a basis for NMR conformational studies of nucleic acids.[2,3] The typical short-range distances are important for spectral interpretation as well, and have been used extensively for this purpose; examples are presented below.

Similar remarks can be made with respect to the torsion angles and their corresponding J couplings. Quite reliable Karplus equations are available to relate the torsion angles to J couplings (see below). Furthermore, methods that rely on coherence transfer, thus on the value of J couplings, become increasingly important for spectral interpretation. Therefore, an overview of important coupling constants is presented in Figures 3 and 4. The ranges introduced for the three-bond coupling constants are related to their dependence on the value of the corresponding torsion angle. In view of the importance for spectral interpretation and structure determination this is discussed more extensively in the following sections. We note that of the backbone torsion angles α, β, γ, δ, ϵ and ζ, the torsion angles α and ζ cannot be determined via J coupling analysis.

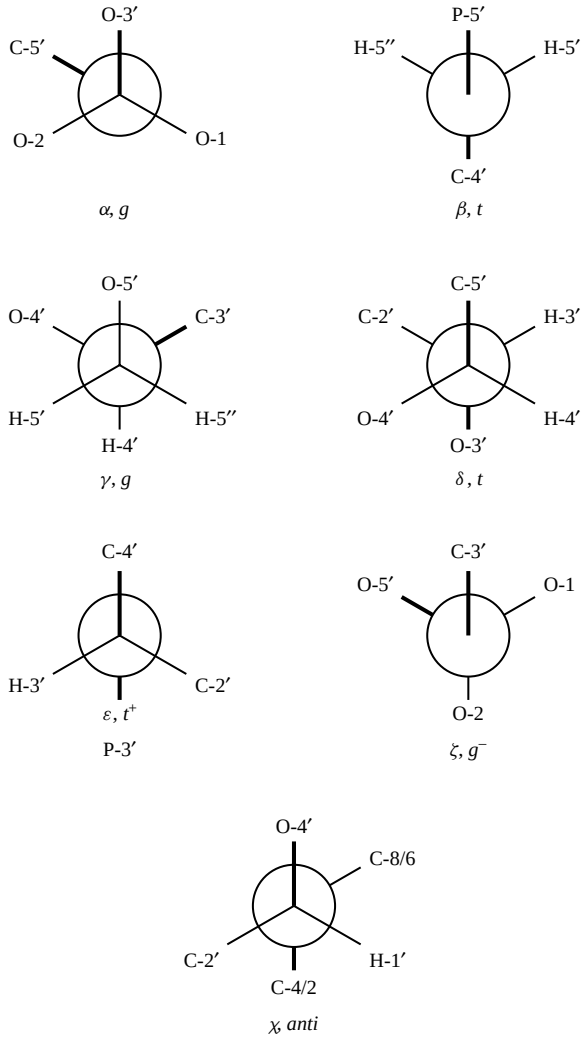

Figure 2 Newman projections of the torsion angles α, β, γ, δ, ϵ, and ζ shown in the staggered conformations *gauche*-minus (g^-), *gauche*-plus (g^+), and *trans* (t). The sign convention of the angles is as follows: a positive torsion angle is obtained after a clockwise turn (about the central bond perpendicular to the paper) of the bond to the back (thick line) from the eclipsed position with bond (thick line) in the front to its present position. The glycosidic torsion angle χ is called *anti* when $\chi = 180 \pm 90^\circ$ and *syn* when $\chi = 0 \pm 90^\circ$

3.1 The Furanose Ring

The structural characterization of this moiety has attracted considerable attention, partly because of its intrinsic interest as a subject of conformational analysis, partly because its conformation is thought to be representative of the more global nucleic acid structure, e.g. compare A- and B-type helices where the sugar conformation is C-3′-*endo* vs. C-2′-*endo* respectively.

The most popular description of the furanose conformation makes use of the concept of pseudorotation which was introduced by Pitzer and collaborators[4] to describe the conformation of cyclopentane. The application of this model to furanose rings was introduced by Altona and Sundaralingam.[5] In this approach the 5-membered ring is characterized by two parameters, the phase angle of pseudorotation, P, and the pucker amplitude, Φ_m. For equilateral 5-membered rings the relationship between their endocyclic torsion angles and the pseudorotational parameters is simply given by:[5]

$$\nu_j = \Phi_m \cos[P + 144(j - 2)] \quad (1)$$

where j varies from 0 to 4 and ν_j is the j^{th} torsion angle. For the nonequilateral, heterocyclic furanose ring with unequal bond distances and angles this equation has been adapted as follows:[3]

$$\Phi_{1'2'} = 121.4 + 1.03\Phi_m \cos(P - 144) \quad (2a)$$

$$\Phi_{1'2''} = 0.9 + 1.02\Phi_m \cos(P - 144) \quad (2b)$$

$$\Phi_{2'3'} = 2.4 + 1.06\Phi_m \cos(P) \quad (2c)$$

$$\Phi_{2''3'} = 122.9 + 1.06\Phi_m \cos(P) \quad (2d)$$

$$\Phi_{3'4'} = -124.0 + 1.09\Phi_m \cos(P + 144) \quad (2e)$$

The Φ_{ij} terms are the torsion angles defined by the protons of the sugar ring. With this parameterization a satisfactory description can be provided of the furanose conformation. Values of P around the C-2′-*endo* conformation, the so-called S conformation, amount to $140-180^\circ$, and values of P around the C-3′-*endo* conformation, the so-called N conformation, amount to $0-40^\circ$.

An exact description of 5-membered ring conformations, which accounts for changes in bond distances and angles when the pseudorotation cycle of the furanose is traversed, has been given recently.[6,7] The impact and importance of this more complete approach on and for NMR-derived structures has not yet been explored.

3.2 Torsion Angle β

The J couplings defining β are summarized in Table 2. Examination of Figure 3 shows that $^3J\{\text{P}(n),\text{C-4}'(n)\}$ may vary between 1 and 11 Hz. Low values ($\approx$ 1 Hz) of $^3J\{\text{P}(n),\text{C-4}'(n)\}$ are only obtained when β is in the g^+ or g^- domain. These are energetically unfavorable rotamers. Commonly, β resides in the *trans* domain and the coupling constant is then found between 7 and 11 Hz. Interestingly, when β is in the g^- or g^+ range $^3J\{\text{P}(n),\text{H-5}'(n)\}$ or $^3J\{\text{P}(n),\text{H-5}''(n)\}$ becomes quite large, i.e. approaches 23 Hz (see Figure 3). On the other hand, when β is in the *trans* domain these coupling constants are rather small but, for standard A- and B-helices, still sufficiently different to be useful as structural diagnostic tools (see below). Finally, it is mentioned that the four-bond coupling, $^4J\{\text{P}(n),\text{H-4}'(n)\}$, depends on the conformation of the sequence P–O–C-5′–C-4′–H-4′. When it takes on a W shape, i.e. a planar geometry, the coupling constant may approach a value of 3 Hz; for this to happen β needs to be in the *trans* and γ in the g^+ domain.

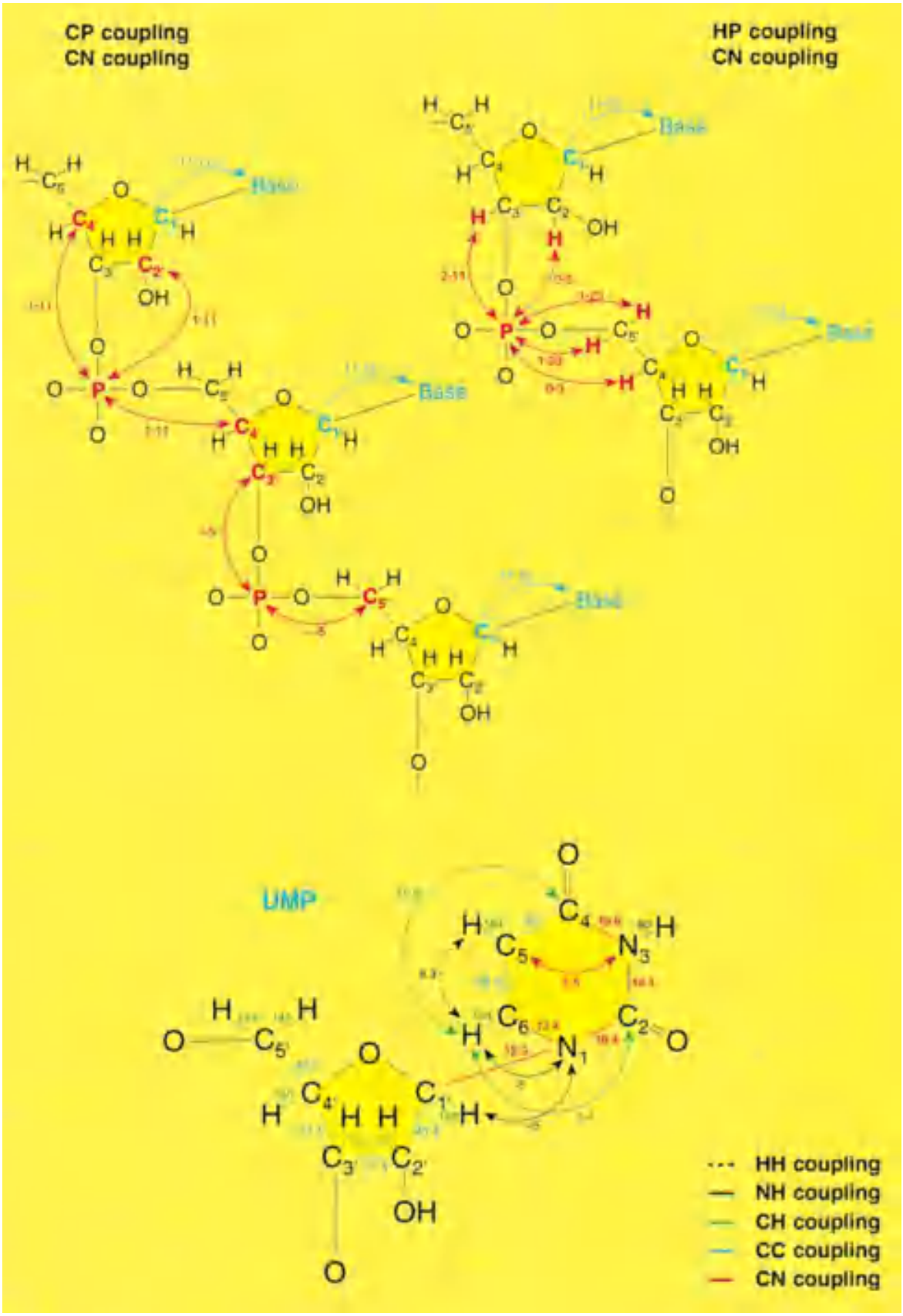

Figure 3 *J* coupling constants between different nuclei in the sugar–phosphate backbone, in the sugar moiety, and in the uridine base, which serve as a basis for coherence transfer experiments. *J* couplings for which a range of values is indicated depend on the torsion angle. In the lower figure (UMP) the *J* couplings are taken from the literature[29] and checked where possible and revied when necessary based on NMR measurements on a ^{13}C and ^{15}N enriched UMP mononucleotide. UMP = uridine 5′-phosphate. Note that the C numberings are only depicted as subscripts *within* the Figure, e.g. C_6 in Figure ≡ C-6 in text

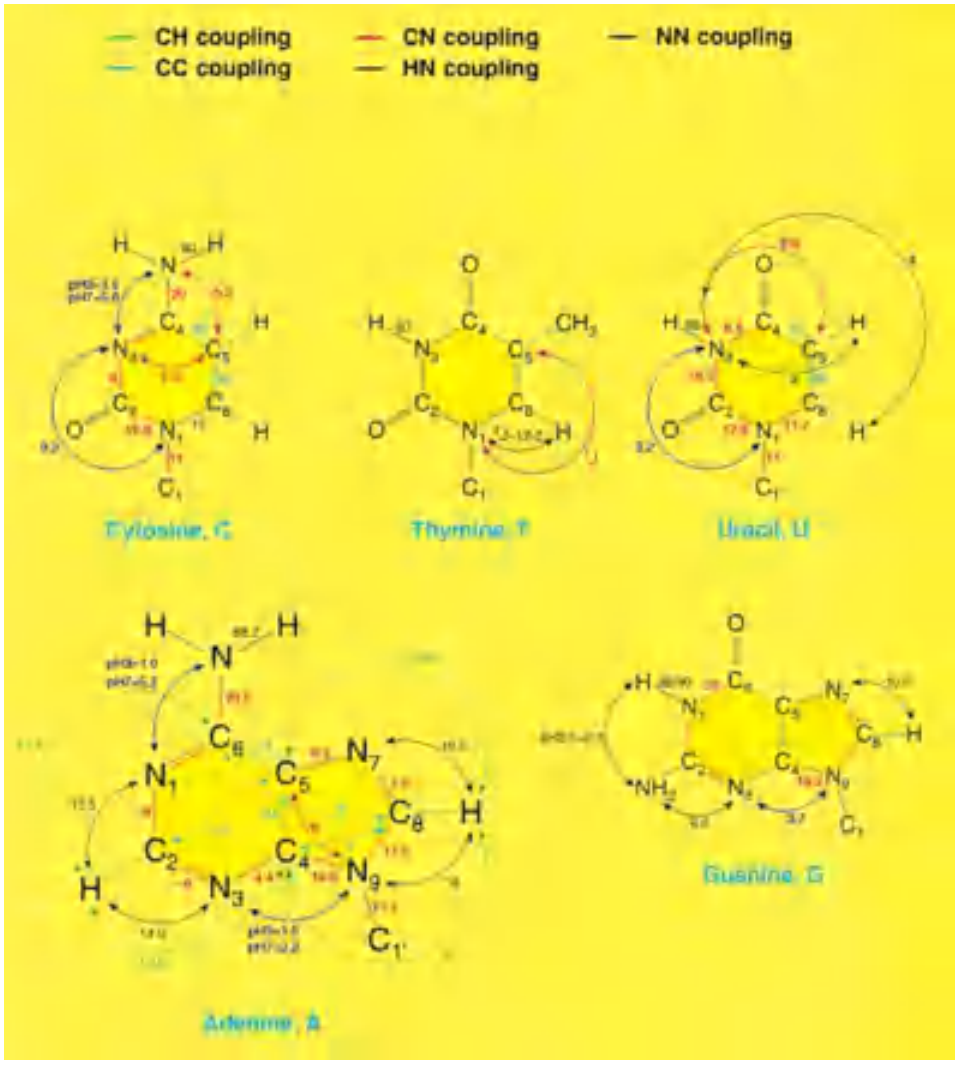

Figure 4 J coupling constants found in the different bases. The J couplings in uracil and adenine have been checked and revised when necessary, based on NMR measurements on ^{13}C and ^{15}N enriched UMP and AMP mononucleotides, respectively. Those coupling constants that depend on pH are indicated for two different pH values. Note that the C numberings are only depicted as subscripts *within* the Figure, e.g. C_6 in Figure ≡ C-6 in text

Table 2 J Couplings Between Nuclei, Monitoring Backbone Torsion Angles

Torsion angle	J coupled nuclei			
α	–	–	–	–
β	C-4′P-5	H-5′P-5	H-5″P-5	–
γ	H-4′H-5′	H-4′H-5″	C-3′H-5′	C-3′H-5″
δ	H-3′H-4′	C-5′H-3′	C-5′C-2′	–
ϵ	H-3′P-3	C-4′P-3	C-2′P-3	–
ζ	–	–	–	–
χ				

3.3 Torsion Angle γ

This torsion angle can be monitored by $^3J\{\text{H-4}'(n),\text{H-5}'(n)\}$, $^3J\{\text{H-4}'(n),\text{H-5}''(n)\}$, $^3J\{\text{C-3}'(n),\text{H-5}'(n)\}$ and $^3J\{\text{C-3}'(n),\text{H-5}''(n)\}$ (see Table 2). Determination of the value of γ is only possible when a stereospecific assignment of the H-5′ and H-5″ resonances can be achieved. It is mentioned in passing that the two-bond couplings $^2J\{\text{H-4}'(n),\text{C-5}'(n)\}$, $^2J\{\text{C-4}'(n),\text{H-5}'(n)\}$, and $^2J\{\text{C-4}'(n),\text{H-5}''(n)\}$ also depend on γ and can aid in the identification of the H-5′ and H-5″ resonances. Both topics are discussed in Section 4.4 dealing with sterospecific assignments.

3.4 Torsion Angle δ

This torsion angle is determined by the conformation of the furanose ring, i.e. by the angle of pseudorotation and the pucker amplitude. Once these have been established δ can be deduced.[3]

3.5 Torsion Angle ϵ

The J couplings that monitor this torsion angle are collected in Table 2. $^3J\{\text{H-3}'(n),\text{P}(n+1)\}$ is not particularly informative for an analysis of ϵ. The two rotamers about

epsilon usually considered are ϵ^t and ϵ^- and these are more or less symmetrically positioned with respect to the H-3′–C-3′–O-3′–P angle, rendering this J coupling less suitable for a distinction between the two conformations. Similar to the situation encountered for β, the coupling constant $^3J\{P(n+1),C\text{-}4'(n)\}$ may increase from 1 to 11 Hz when ϵ decreases from 300° to 180°, i.e. ϵ changes from ϵ^- to ϵ^t. It is important to observe that, simultaneously, $^3J\{P(n+1),C\text{-}2'(n)\}$ decreases from 11 to 1 Hz. A change from ϵ^- to ϵ^t is also monitored by the four-bond coupling $^4J\{P(n+1),H\text{-}2'(n)\}$. When the sequence H-2′–C-2′–C-3′–O-3′–P adopts a W shape, which is only possible when ϵ is in the g^- domain and the sugar adopts an S pucker, the coupling constant approaches 3 Hz.

4 SPECTRAL INTERPRETATION

4.1 The NOE-Based Approach

Originally, systematic studies of the spectra of ‘larger’ nucleic acid molecules were focused on the imino proton resonances, e.g. of double helical DNA fragments and transfer RNA (tRNA) molecules. Successful interpretation of these spectra was initially achieved via the use of one-dimensional NOE difference spectra and only later on the basis of two-dimensional (2D) NOE experiments.

With the advent of 2D spectroscopy, new sequential assignment procedures were devised on the basis of intra- and interresidue NOE connectivities between the sugar and base protons. This approach (crucially) depends on the assumption that the sugar–phosphate backbone conformation of the molecule under study closely resembles that found in A- and B-type double helices. In these configurations the distances between the H-1′, H-2′, and H-2″ on the one hand, and H-6/H-8 on the other, are all smaller than 5 Å, i.e. for the distances within a nucleotide and for the distances between the ring H-6/H-8 protons and the sugar protons of the 5′-neighboring nucleotide (see Figure 5). Use of these connectivities may lead to sequential assignment as indicated in Figure 6 for the pathway H-8(n) → H-1′(n) → H-6($n+1$) → H-1′($n+1$) → H-8($n+2$) → H-1′($n+2$).

All sequential connectivities are steered along the individual H-6/H-8 base protons. Thus, the occurrence of overlap requires additional experiments or the trying out of alternative pathways until a selfconsistent solution is obtained. Overlap may also occur for the sugar proton resonances, but then the combined use of sequential pathways running along the H-1′ or the H-2′/H-2″ resonances may help to alleviate the problem. This approach works less well for RNA molecules where the H-2″ proton is replaced by a hydroxyl group as a result of which the H-2′ resonances shift to high frequency (downfield) and overlap with the other sugar proton resonances, except for the H-1′ resonances. Still, most of the successful structure determinations carried out so far for nucleic acid molecules with molecular masses of up to approximately 7200 Da have followed this approach. Examples are discussed below.

4.2 Assignment Through Coherence Transfer

As mentioned the NOE-based assignment procedure depends on the structure of the single strand considered and is not guaranteed to work for unusual conformations. Therefore experiments based on coherence transfer methods have been developed that provide complementary and structurally independent information.

In nucleic acid structures several continuous networks of vicinal J couplings can be distinguished that can be used in coherence transfer experiments and may aid in the assignment and identification of individual mononucleotides and in sequential assignment. Ideally, one would like to link these networks in such a way that a complete interpretation of the spectrum could be achieved solely through the use of coherence transfer experiments. Sometimes this is very cumbersome, e.g. the J coupling between the sugar H-1′ proton and the H-6/H-8 protons is so small (≈0.3 Hz) that only in idealized cases can their signals be correlated through coherence transfer.[8] Then one has to rely on the NOE-based approach outlined above (see, however, assignments in isotope-enriched RNAs in Section 4.3).

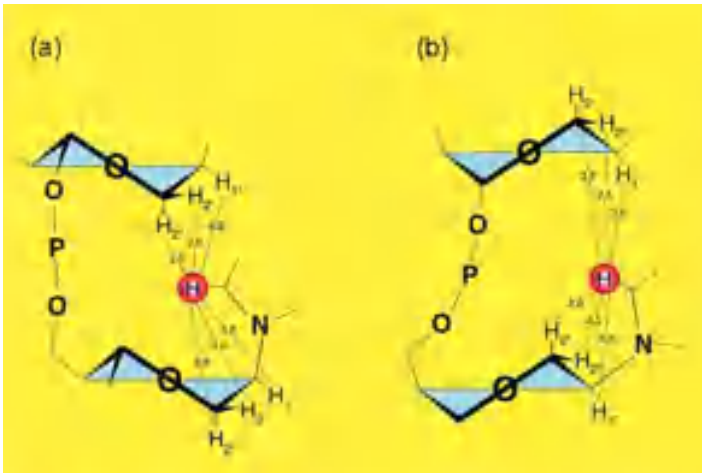

Figure 5 Distances between the H-6 or H-8 ring protons of a base and the H-1′, H-2′, and H-2″ protons of its own sugar and of the sugar of the 5′-neighboring nucleotide for A type (a) and B type (b) helices. Note that H numberings are denoted as subscripts only *within* the Figure, e.g. $H_{1'} \equiv$ H-1′

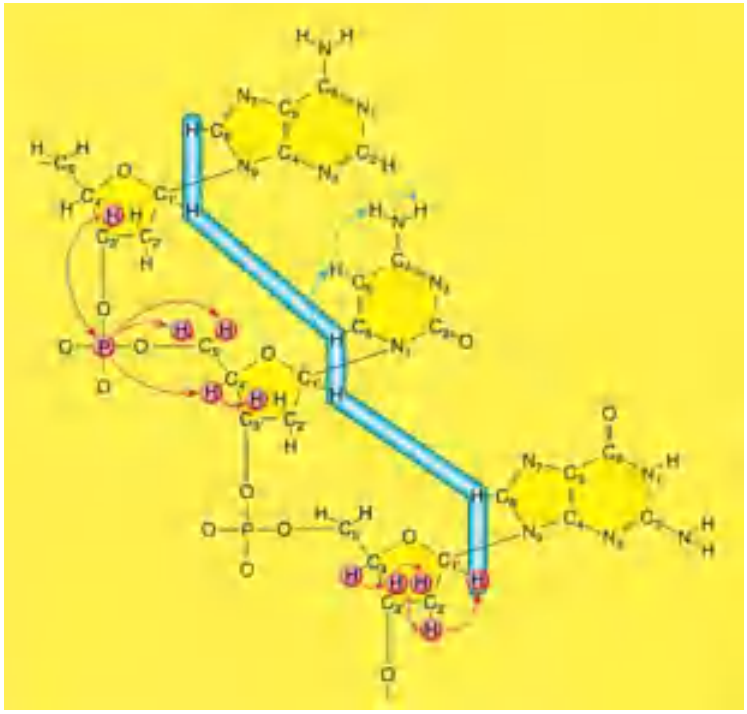

Figure 6 Different pathways used in assignment procedures of nucleic acid spectra. The NOE pathway formed by the base ring protons and the H-1′ sugar protons is indicated in blue. The coherence transfer pathways between sugar protons and phosphorus atoms in the sugar–phosphate backbone and between the protons within the sugar moiety are indicated by red arrows. Note that the C numberings are only depicted as subscripts *within* the Figure, e.g. C_6 in Figure ≡ C-6 in text

Given that the connection between the base and sugar protons has been established, the sequential assignment can be continued by employing the following chain of ^{1}H–^{1}H spin–spin couplings:

$$\left.\begin{matrix} {}^3J(1',2') \\ {}^3J(1',2'') \end{matrix}\right\} \rightarrow {}^3J(2',3') \rightarrow {}^3J(3',4') \rightarrow \left\{\begin{matrix} {}^3J(4',5') \\ {}^3J(4',5'') \end{matrix}\right.$$

in the sugar ring (Figure 6). This network of spin–spin couplings can be used in COSY and TOCSY experiments to assign the sugar ring protons of individual mononucleotides. Through the identification of the H-1′ or H-2′/H-2″ resonances in the sequential assignment described above, the sugar resonances may be attributed to a particular nucleotide in the sequence. In this approach the interpretation can in most cases be extended to involve the H-4′ resonances. Assignment of the H-5′/H-5″ protons has been much more limited since the spectral region containing the H-4′, H-5′, and H-5″ resonances is so crowded. The resulting overlap is worsened by the often small chemical shift differences between the H-4′, H-5′, and H-5″ resonances, which places the cross peaks close to the diagonal. Interesting exceptions have been found in the strongly folded regions in hairpin loop molecules.[9] Obviously, the problem becomes worse for larger molecules. It can, however, be (appreciably) reduced by application of homonuclear three-dimensional experiments, e.g. TOCSY–NOESY experiments have been conducted where it was possible to assign the resonances in the very crowded H-4′, H-5′, H-5″ spectral region by shifting the information to the better-resolved H-1′, H-3′, and H-2′/H-2″ region.[3, 27, 28]

Subsequently, the network of coupled spins of the sugar ring can be connected to the resonances of the backbone nuclei by making use of the following chain of J couplings (see Figure 3):

$${}^3J\{\text{H-3}'(n), \text{P}(n+1)\} \rightarrow \begin{matrix} {}^3J\{\text{P}(n+1), \text{H5}'(n+1)\} \\ {}^3J\{\text{P}(n+1), \text{H-5}''(n+1)\} \\ {}^4J\{\text{P}(n+1), \text{H-4}'(n+1)\} \end{matrix}$$

which have been used in ^{31}P–^{1}H hetero-double-quantum-filtered (DQF)–COSY experiments. The values of the J couplings and thus the intensity of the cross peaks depend on the backbone conformation. For the standard B-DNA backbone conformation ${}^3J\{\text{P}(n+1),\text{H-5}'(n+1)\} \approx 1$ Hz, and ${}^3J\{\text{P}(n+1),\text{H-5}''(n+1)\} \approx 7$ Hz. Hence, the P(n + 1)–H-5′(n + 1) connectivity generally is weak, but the P(n + 1)–H-5″(n + 1) connectivity is clearly visible in a ^{31}P–^{1}H hetero-DQF–COSY spectrum. For the standard A-RNA conformation ${}^3J\{\text{P}(n+1),\text{H-5}'(n+1)\}$ as well as ${}^3J\{\text{P}(n+1),\text{H-5}''(n+1)\} \approx 2.5$ Hz giving rise to weak cross peaks. Yet, ^{31}P–^{1}H hetero-DQF–COSY spectra have been used to study RNA molecules.[10] The four-bond coupling constant ${}^4J\{\text{P}(n+1),\text{H-4}'(n+1)\}$ achieves its maximum (≈ 3 Hz) when the atoms P–O-5′–C-5′–C-4′–H-4′ lie in the same plane and form a W shaped conformation (see above). This situation is approached in the standard B-DNA but not in the A-RNA backbone conformation. To our knowledge connectivities between H-4′(n) and P(n + 1) have not been observed, the reason being that the backbone atom sequence H-4′–C-4′–C-3′–O-3′–P does not form the mentioned W shape required to generate a sufficiently large four-bond J coupling. This would require that

the torsion angle ϵ falls in the g^+ domain, which is forbidden on steric grounds.

Strong overlap of the phosphate, on the one hand, and the sugar H-4′ on the other hand, and H-5′/H-5″ resonances have limited the application of the described approach to 'smaller' molecules. However, recently, improved probe technology has allowed the use of hetero-TOCSY experiments or variants thereof,[11] and the aforementioned limitation has been overcome to a significant extent by being able to correlate ^{31}P resonances with the better resolved sugar resonances, e.g. the H-1′ or H-3′ resonances, in analogy with the homonuclear TOCSY–NOESY experiments (see above). This approach has been successfully demonstrated for the double helix formed by the so-called Dickerson dodecamer, d(CGCGAATTCGCG) (d = deoxy, A = adenosine, C = cytidine, G = guanosine, T = ribosylthymine). The H-3′ sugar resonances are quite well resolved and on the basis of H-3′(n) → P(n + 1) → H-3′(n + 1) sequential connectivies, ^{31}P assignments could be established without prior knowledge of ^{1}H resonance assignments.[11] A drawback of most ^{1}H, ^{31}P correlation methods is their limited sensitivity, which is a consequence of the large number of possible transfer routes. This leads to destructive interference during the transfer and 'dilutes' the amount of coherence giving rise to detectable signal.

4.3 Sequential Assignment of Isotope-Enriched RNAs

NMR structural studies of proteins have benefitted enormously from the use of uniformly ^{13}C and ^{15}N isotope-enriched material. In combination with newly developed pulse sequences, which specifically take advantage of these heteronuclei (see ***Structures of Larger Proteins, Protein-Ligand, and Protein-DNA Complexes by Multi-Dimensional Heteronuclear NMR*** and ***Three- and Four-Dimensional Heteronuclear Magnetic Resonance***), it has been possible to assign completely the spectrum of polypeptides, even for proteins with a chain length of 270 amino acids.

Recently, methods for isotope enrichment of RNA have also become available and the production of well-defined, uniformly enriched fragments is now feasible on a more or less routine basis.[12] Hopefully, in the near future, this will also be feasible for DNA molecules. In analogy with the developments in ^{1}H NMR, suitable pulse sequences have been or are being developed to broaden the basis for the interpretation of nucleic acid spectra, in particular those of larger molecules.

4.3.1 The NOE-Based Approach

The approach is very similar to what has been discussed earlier for nonenriched nucleic acids. The difference lies in the possibility of achieving more resolution by using ^{13}C-edited NOESY spectra, which can be obtained from NOESY–HMQC or HMQC–NOESY experiments (see ***Three-Dimensional HMQC-NOESY, NOESY-HMQC, and NOESY-HSQC***). Similarly, for imino and amino resonances ^{15}N-edited NOESY spectra can be acquired with increased resolution.[13]

4.3.2 Coherence Transfer

For ^{13}C and ^{15}N isotope-enriched RNA a complete spectral interpretation can basically be obtained solely through the use of coherence transfer pathways. These have been sketched in Figure 3 in the form of a network of J couplings in the sugar phosphate backbone and in the sugar ring, and a combination of J couplings connecting the sugar ring to the bases. To a large extent these coherence pathways are complementary to those in nonenriched RNA, but the presence of the isotopes allows the development of more powerful methods for spectral interpretation, in analogy with ^{1}H NMR. Thus, uniform ^{13}C enrichment of RNA allows for an extension of the sequential assignment of the backbone resonances discussed above by involving the ^{13}C spins.

This has been demonstrated in a three-dimensional so-called HCP experiment.[14] In this experiment ^{1}H coherence is transferred into ^{13}C coherence using the direct $^1J(^{13}\text{C},^1\text{H})$ coupling. Subsequently, ^{13}C coherence is transferred into ^{31}P coherence and then, via the reverse route, this coherence is transferred back into ^{1}H coherence. In the HCP experiment, therefore, the following correlation can be found: C-4′(n) → P-3′(n + 1) → H-4′(n), C-4′(n) → P-5′(n) → H-4′(n), C-5′(n) → P-5′(n) → H-5′/H-5″(n), C-3′(n) → P-3′(n + 1) → H-3′(n). This allows a sequential walk along the backbone using the C-4′(n) → P(n + 1) → C-4′(n + 1) correlations (see Figure 7). In the process assignments are also obtained for the C-3′ and C-5′ resonances, alongside those for the H-3′, H-4′ and H-5′/H-5″ resonances. In case the torsion angle ϵ is shifted to the g^- domain, the pathway C-4′(n) → P(n + 1) becomes blocked. Then concomitantly the pathway C-2′(n) → P(n + 1) becomes available and can be used as a detour in the sequential assignment procedure (Figure 3).

In the next step the backbone resonances can be connected to the sugar ring resonances through so-called H–C–C–H experiments in which coherence is transferred along the indicated pathway. The power of this approach has been demonstrated by Nikonowicz and Pardi using INEPT transfer.[13] A more sensitive approach is provided through CCH TOCSY experiments in which the transfer step from C → H is achieved via cross polarization instead of INEPT.[14]

Correlation between signals of the sugar ring and the base by means of coherence transfer, which as mentioned in the preceding section is difficult to achieve for nonenriched material, can be conveniently established for doubly labeled ^{13}C- and ^{15}N-enriched material in a three-dimensional so-called HCN experiment. Use is made of the coupling pathway

$$J(\text{H-1}', \text{C-1}') \Rightarrow \begin{cases} (\text{C-1}',\ \text{N-9}) \Leftrightarrow J(\text{N-9},\ \text{C-8}) \\ \Rightarrow J(\text{C-8},\ \text{H-8})\ \text{(for purines)} \\ J(\text{C-1}',\ \text{N-1}) \Leftrightarrow J(\text{N-1},\ \text{C-6}) \\ \Rightarrow J(\text{C-6},\ \text{H-6})\ \text{(for pyrimidines)} \end{cases}$$

Successful experiments have been performed on a 30-mer RNA molecule which contains the binding site for the Rev protein encoded by Human Immunodeficiency Virus.[15] The intranucleotide H-1′–H-6/H-8 connectivities obtained in this experiment allow for a distinction of intra- and internucleotide H-1′–H-6/H-8 NOE cross peaks in NOESY experiments.

The J couplings between the spins in the bases form a complicated network (see Figures 3 and 4). In some cases they are large enough to allow the assignment of the signals of the rest of the nuclei in the ring. For example in cytidine

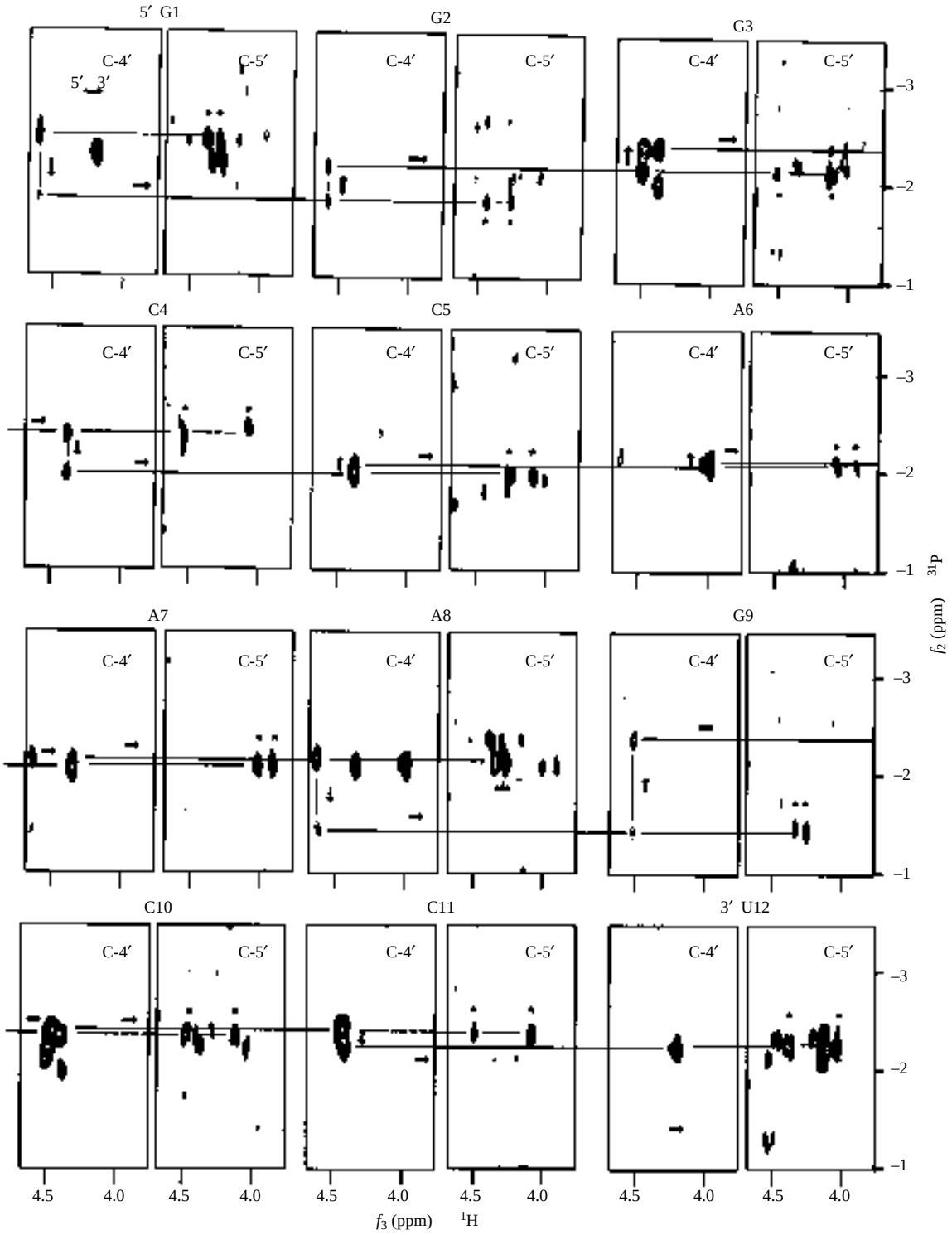

Figure 7 Cross sections through the three-dimensional HCP spectrum at the positions of the C-4′ and C-5′ resonances of the individual nucleotides of the hairpin formed by r(GGGCC-AAAGCCU) (r = ribose). The C-4′ planes show the sequential walk through the sugar–phosphate backbone from the first residue G1 (at the 5′-end) to the final residue U12 (at the 3′-end) as indicated by the arrows and the drawn lines. The two cross peaks marked by asterisks in the C-5′(*i*) planes indicate the H-5′/H-5″ resonance positions of residue *i*; the dotted line connects these H-5′/H-5″ cross peaks with the P-5′ cross peak in the C-4′(*i*) plane

and uridine the ^{13}C resonances of C-4, C-5, and C-6 are easily identified in this manner (Figure 4).

4.4 Stereospecific Assignment

Important for structure determination is the stereospecific assignment of resonances. In nucleic acids this concerns H-5′/H-5″ and, only in DNA, also the H-2′/H-2″ resonances. The latter pair generally does not present too many problems. In the absence of spin diffusion the H-1′–H-2″ NOE cross peak is always more intense than the H-1′–H-2′ cross peak, independent of the sugar pucker. The values of J(H-1′,H-2′) and J(H-1′,H-2″) vary with the sugar conformation. In the N state J(H-1′,H-2′) $\leq$ 1 Hz and much smaller than J(H-1′,H-2″). For the S conformation, however, J(H-1′,H-2′) > J(H-1′,H-2″).[3,5]

The stereospecific assignment of the H-5′/H-5″ resonances is, however, more involved. For regular double-helical structures H-5″ resonates to low frequency of H-5′.[3] For more irregular structures this need not be the case. Then by a combination of J(H-4′,H-5′/H-5″) couplings and Overhauser effects between H-3′ and H-5′/H-5″ and between H-4′ and H-5′/H-5″ the relative positions of these signals can be established.[8,9] In this approach the stereospecific assignment is intimately related to the determination of the value of the torsion angle γ.

Introduction of ^{13}C enrichment offers an elegant and perhaps more reliable approach to the problem. It has been recognized that the two-bond couplings ^2J(C,H) in the system H–C–^{13}C–X, where X is an electronegative atom, depend on the torsion angle θ defined by the mutual orientation of H and X. Thus, for ethanol it was found that ^2J(C,H) is negative for $0^\circ \leq \theta < 90^\circ$ and positive for $90^\circ < \theta \leq 180^\circ$, with maximum absolute values at 0° and 180°. Adopting these results for the torsion angle defined by O-5′–C-5′–C-4′–H-4′, the relative signs of the coupling constants J(C-4′,H-5′), J(C-4′,H-5″), and J(C-5′,H-4′) can be measured, and the stagger of γ as well as the stereospecific assignment become directly available.[16] It is noted in passing that this approach can also be used to establish the pucker of the sugar ring.

5 STRUCTURE DETERMINATION

After the development of multidimensional NMR techniques and the invention of reliable resonance assignment procedures, a burst of activities ensued in investigations of nucleic acid structure. By the end of 1988 a great number of different species including canonical double helices, double helices with mismatches, with bulges, and with chemically modified bases, and double helices complexed to drugs, had been studied extensively. Mostly, these studies were conducted on a more qualitative level of interpretation of the spectral parameters. Subsequently, methods permitting a more quantitative handling of the spectral data became available leading to improved structure determination.

The distribution of protons in nucleic acids that can be used for structure determination is rather unevenly divided. The sugar moiety is most blessed with protons but their value for a conformational analysis of the ring is strongly limited.[17] In fact J couplings play a major role in the derivation of its structure.[5,17] In the bases, there is a relative paucity of protons, which often renders a determination of their orientation with respect to their surroundings more difficult. Definition of a reliable structure therefore necessitates the deduction of accurate proton distances from available NOEs, and a range of different programs that account for spin diffusion (IRMA, MARDIGRAS, NO2DI, MORASS)[3] have been developed to achieve this purpose (see ***Nucleic Acid Structures in Solution: Sequence Dependence***). Additionally, J coupling information remains to be required for a proper structure elucidation, especially for the sugar ring, and also for the sugar–phosphate backbone. For instance, the J couplings J(H-1′,H-2′), J(H-2″,H-3′), and J(H-3′,H-4′) are good monitors of the sugar conformation.[3] Reliable Karplus equations, summarized in Table 3, are available to relate J couplings to torsion angles for the deduction of the sugar ring structure, and also for the determination of the sugar–phosphate backbone.

Applications of these methods have led to more quantitative structural NMR studies. Here we describe some results obtained for hairpin molecules and show that insights into rules of folding emerge on the basis of such studies. Elsewhere in this Encyclopedia other nucleic acid structures are considered (***DNA Triplexes, Quadruplexes, and Aptamers*** and ***Nucleic Acid Structures in Solution: Sequence Dependence***).

6 HAIRPIN STRUCTURES

Hairpins have received a great deal of attention in NMR structural studies. Most of the investigated molecules exhibit a reasonably well-defined structure, but this may have more to do with the particular choice of the systems used in these NMR studies than with a general phenomenon of hairpin loops always being structured.

The choice of RNA hairpins in these investigations was very much dictated by the results of phylogenetic comparisons of ribosomal and of messenger RNA, which showed a strong preference for the occurrence of 4-membered loops with distinct, conserved sequences. Interestingly, many of these conserved sequences, e.g. -UUCG- (U = uridine), -UACG-, and -GAAA-, were found to render the hairpins unusually stable.[18] In DNA studies the choice was guided by the discovery of unexpectedly stable ‘minihairpins’,[19–21] by theoretical considerations that 4-membered loops would be most stable, and that stability would be increased by the formation of a base pair between the first and the last base of the loop.[9,22]

A number of hairpins have now been subjected to quantitative structural studies. Here we consider two examples, one hairpin formed by the sequence d($A_1T_2C_3C_4T_5A_6$-$T_7T_8T_9A_{10}$-$T_{11}A_{12}G_{13}G_{14}A_{15}T_{16}$) the other by d($A_1T_2C_3C_4$ T_5A_6-$G_7T_8T_9A_{10}$-$T_{11}A_{12}G_{13}G_{14}A_{15}T_{16}$), which are typical of the 4-membered hairpins studied to date. In both cases the three-dimensional structure was obtained on the basis of available NMR distance and torsion angle constraints and on a multiconformational analysis approach (the -TTTA- hairpin) or a variable target function and a molecular dynamics approach (the -GTTA- hairpin) followed in both cases by unconstrained energy minimization. In the process the results were checked by back calculation of the NOESY spectrum. The structures of these hairpins are presented in Figure 8. In both hairpins, the loops exhibit a compact folding pattern. The first and the last base form noncanonical base pairs, in the -TTTA- loop a

Table 3 Karplus Equations for Relationships Between Torsion Angles, Φ (deg), and J Couplings (Hz)[a]

$$^3J(^1\mathrm{H}, ^1\mathrm{H}) = 13.7\cos^2\Phi - 0.73\cos\Phi - \sum \Delta\chi_i[0.56 - 2.47\cos^2(\xi_i\Phi + 16.9|\Delta\chi_i|)] + \Delta J \quad (3a)$$

$$^3J(^1H\ \mathrm{CO}^{31}P) = 15.3\cos^2\Phi - 6.2\cos\Phi + 1.5 \quad (3b)$$

$$^3J(^{13}C\mathrm{CO}^{31}P) = 8.0\cos^2\Phi - 3.4\cos\Phi + 0.5 \quad (3c)$$

The meanings of the symbols in **1** are as follows:

$\Delta\chi_i = \Delta\chi_{i,\alpha} - 0.14\sum\Delta\chi_{ij,\beta}$

$\Delta\chi_{i,\alpha}$, $\Delta\chi_{ij,\beta}$: Huggins electronegativity difference between α or β substituents and H, with $\Delta\chi_{i,\alpha}$, $\Delta\chi_{ij,\beta}$ = 1.3(O), 0.4(C), 0.85(N), −0.05(P).

ξ_i: relative orientation factor of substituents. In the Newman projection of H-a, S-1α, S-3α−C-1−C-2, S-2α, S-4α, H-b: S-1α has a positive position, ξ_i = +1, if H-a−C-1−S-$i\alpha$ = 120°, a negative position, ξ_i = −1, if angle = −120°.

ΔJ: $-2.0\cos(P - 234)$ for $144^\circ < P < 324^\circ$ for J(H-1′,H-2″)

$-0.5\cos(P - 288)$ for $198^\circ < P < 360^\circ$ and $0^\circ < P < 18^\circ$ for J(H-2′,H-3″).

In all other cases ΔJ = 0.0

[a]The constants in **1** are average values. For more accurate numbers the reader is referred to the literature.[3,23]

T.A Hoogsteen pair and in the -GTTA-loop a G.A pair of the form indicated in Figure 8. The disposition of the second base is characteristic of two classes of 4-membered hairpin loops so far encountered, i.e. in the -TTTA- loop this base is turned into the minor groove and in the -GTTA- loop stacks upon the first base. After the third residue the sugar−phosphate backbone exhibits a sharp turn essentially changing its direction by 180°. Finally, as mentioned, the base of the fourth residue turns into the loop to form a base pair with the first. These features are common to a number of well-defined hairpins.[24] Depending on the sequence of the 4-membered loop, a base pair is formed between the first and the last base of the loop. A cytidine in the 5′- and a guanine in the 3′-terminal position of the loop form a normal Watson−Crick CG base pair. Other combinations of terminal bases turn out to form noncanonical base pairs. Given complementary bases, base pair formation is facile for a pyrimidine at the 5′- and a purine at the 3′-end of the loop, but not the other way around. A purine in the 5′- and a pyrimidine in the 3′-position hinders, but does not strictly forbid, the formation of a base pair. However, destabilization of the hairpin is observed with respect to its counterpart, i.e. with respect to the hairpin with a pyrimidine at the 5′- and a purine at the 3′-end of the loop.

For the 4-membered loops two different folding classes emerge. They are exemplified by the two hairpin structures described above. In one class the second loop residue is turned into the minor groove and in the other the first three bases continue to stack on the stem although the position of the third base is often less well-defined.

In a hairpin the two chains of the stem which run in opposite directions are connected by the loop in which the change of directionality of the phosphate backbone is located. It turns out that in most cases the course of the backbone is altered abruptly by one sharp turn between two nucleotides. For DNA hairpins this turn is found between the third and the fourth base (nucleotide) in the loop, even in the aforementioned two different classes of loop folding. In the sharp turn the torsion angle γ has always been found in the *trans* domain while its neighbor β remains in the normal *trans* domain or changes to the g^+ domain, but only for about 50% of the time. For RNA the situation is as yet less well-defined. For the two examples available the sharp turn occurs between either the first and the second or the third and the fourth residue.[24]

7 DYNAMICS

There is overwhelming evidence for the occurrence of conformational heterogeneity and internal mobility of nucleic acids. Developments up to 1989 have been reviewed.[17] The perhaps most simple example is the rotation of the methyl groups in thymines. Its influence on the dipole−dipole relaxation and thus on the intensity of nuclear Overhauser effects has been analyzed extensively. It is important to make a distinction between situations in which methyl rotation is fast and in which it is slow with respect to the molecular tumbling. In the first case, averaging of the distance of the methyl protons to some other neighboring proton shows up as $\langle 1/r^3\rangle^2$, and in the latter case as $\langle 1/r^6\rangle$ in the spectral density function.

In particular, double-helical DNA fragments have been subjected to NMR relaxation studies, and here use has been made of ^{1}H nuclei, and also the relaxation properties of ^{2}H, ^{13}C, and ^{31}P have been studied. In general a rigid rod model turns out to be inadequate to account for the observed relaxation rates. Phosphorus-31 investigations of DNA fragments of 150−500 base pairs long reveal motions of the phosphate groups taking place on the nanosecond timescale. Carbon-13 relaxation studies have indicated that the (deoxy)ribose units exhibit an enhanced mobility relative to the bases, but it seems that some base motions such as propeller twisting and tilting have little effect on ^{13}C relaxation.

As mentioned, the determination of the sugar conformation is most reliably performed via a J coupling analysis. Very often, however, it is not possible to obtain a set of coupling constants that is consistent with one particular sugar conformation. This observation has been interpreted to arise from the coexistence of two conformations in the

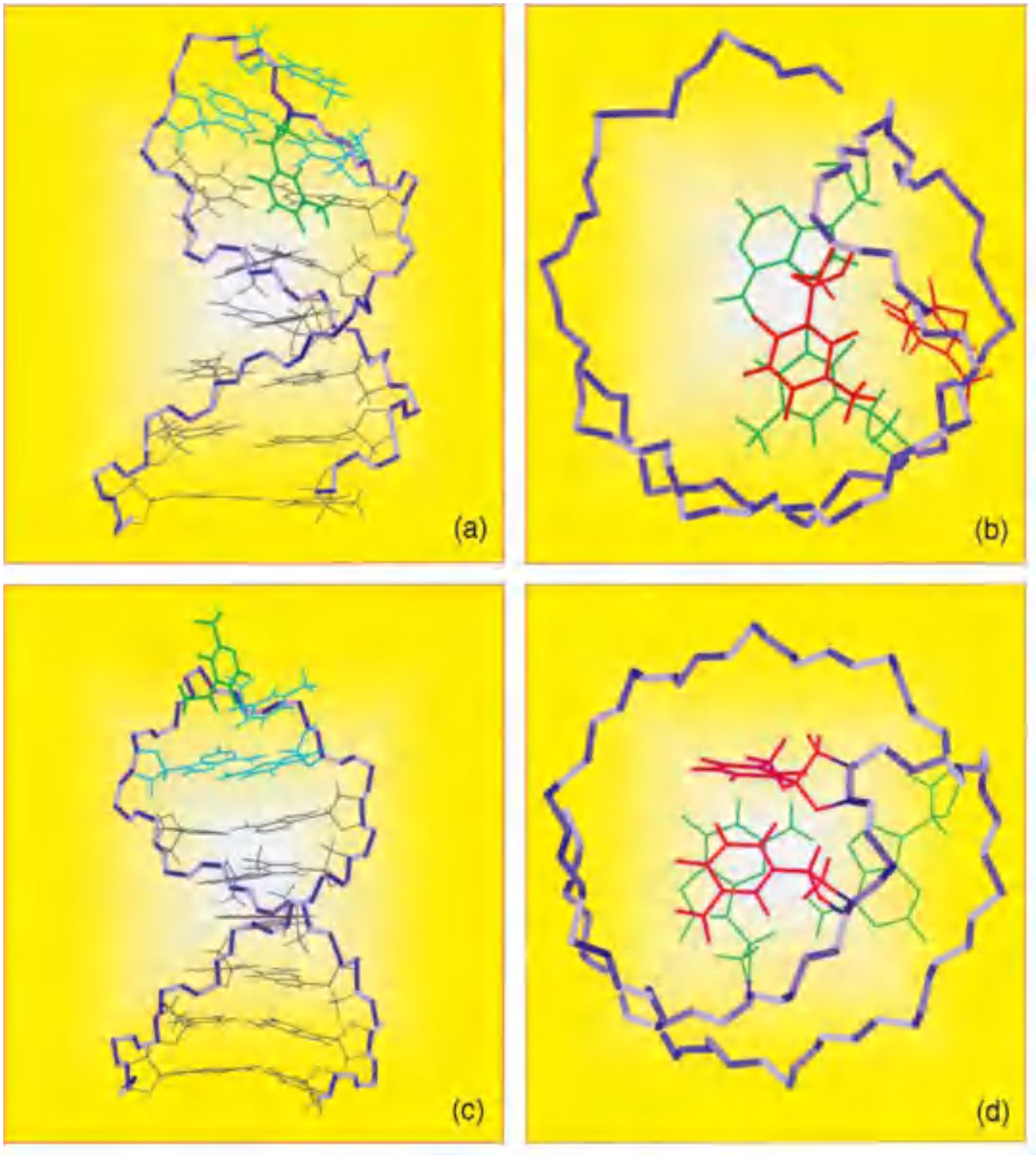

Figure 8 Structural models of the hairpins formed by d(ATCCTA-TTTA-TAGGAT) and d(ATCCTA-GTTA-TAGGAT). (a) A view of the hairpin with the -TTTA- loop in which the helix axis is in the plane of the Figure. The green base is part of the second loop residue which folds into the minor groove. The Hoogsteen T.A base pair (see text) and the third loop residue are indicated in blue. An alternative view is given in (b) where the structure is viewed along the helix axis. The Hoogsteen T.A base pair is indicated in green. The manner in which the third thymidine in the loop stacks upon this base pair is indicated. (c) The structure of the hairpin with the -GTTA- loop, viewed perpendicular to the helix axis. In this molecule the second loop residue (in blue) stacks upon the G.A base pair (in blue). (d) The molecule viewed along the helix axis; it is clear that the second residue (in red) stacks upon the guanine base of the G.A base pair (in green)

aforementioned N- and S-domains (see Section 3.1), which are in rapid equilibrium with one another. The observed J couplings then are the weighted average of the J couplings in the N- and S-conformations:

$$J_{obs} = f_N J_N + f_S J_S \quad (3)$$

where J_{obs} stands for the observed coupling constant, J_N and J_S for the coupling constants in the N- and S-conformation, respectively, and f_N and f_S are the fraction of the N- and S-conformers, respectively. So far no exhaustive studies have been conducted of the percentages of the occurrence of N- and S-conformations as a function of sequence and structure. However, it has been found that sugar rings in B-DNA duplexes seldom display 100% S type conformational purity. Purine residues approach this situation more closely than pyrimidine residues, i.e. on average one finds that the fraction of S conformers $f_S \approx 90\%$, whereas for pyrimidines $f_S \approx 78\%$.[23]

Considerable attention has been devoted to imino proton relaxation. At low temperatures and low pH the relaxation is dominated by dipolar interactions, whereas at higher temperatures exchange of the imino protons becomes increasingly important. The dipolar relaxation studied in B type and Z type helices indicates bending of the double helix and out-of-plane motion of the bases. This is also suggested by ^2H relaxation data of G($^2H_8$) deuterated calf-thymus DNA. The data can, however, also be explained by a 'jumping in a cone' model. This exemplifies a more general aspect of NMR relaxation studies: relaxation data can often be accounted for by different models.

For a quantitative measure of local motion a 'model-free description' has been developed but in this approach only the timescale, orientation, and amplitude of the motion can be determined.

The exchange observed for the imino protons at higher temperatures provides insight into the lifetimes of the base pairs; this subject has been reviewed recently.[25] There is a strong consensus of opinion that the transfer of imino protons in the base pair to water is mediated through an open state. Thus, to relate the lifetime of the base pair to the relaxation properties of the imino protons (at least) a three-site exchange problem has to be considered. However, addition of a suitable catalyst often enhances the imino proton exchange rate and it can be shown that for high (infinite) catalyst concentration the transfer rate is a direct measure of the base pair lifetime. Based on this approach Guéron and collaborators[25] found in a series of 20 B-DNA duplexes that, at 15 °C, the lifetime of A·T base pairs is in the range of 0.7–7 ms and that of G·C pairs in the range of 5–50 ms. This may change in molecules with particular sequences, in drug-DNA complexes or in more complicated molecules. Thus, in Z-DNA the base pair lifetimes are 2 orders of magnitude longer than in B-DNA. The observation that in A·T tracts containing DNA the lifetime of A·T pairs may be significantly longer than in normal B-DNA is of considerable interest. The tRNA molecule is an example where the base pair lifetime may vary between milliseconds and minutes. Studies of d(TCCCCC) and related deoxycytidine-rich sequences conducted at low pH showed that these molecules form remarkable structures consisting of two parallel-stranded duplexes with $C{\cdot}C^+$ base pairs that form tetrads through interdigitation.[26] In the tetraplex the two duplexes are in an antiparallel orientation. The intercalation sites generated at every base pair in each duplex allow alternate stacking of the $C{\cdot}C^+$ base pairs from the duplexes. Base pair lifetimes of this complex are comparable to the longest lifetimes observed in tRNA. It is also interesting to mention that the imino proton in the $C{\cdot}C^+$ base pair switches between the two bases at a rate larger than 80 000 s^{-1}.

Attempts have been made to establish and describe the physical motion of the base pair opening event, and to find out whether the disruption of base pairs takes place independently, i.e. as an independent fluctation of the equilibrium structure, or coupled to bending or twisting motions of the DNA helix. An interesting pathway in which a base rotates toward the major groove around an axis that is parallel to the helix axis and intersects the sugar moiety, has been proposed by Ramstein and Lavery.[25] This proposal, as well as suggestions in which base pair opening is a feature of long-range fluctuations of the double helix, await experimental verification.

8 RELATED ARTICLES

Biosynthesis and Metabolic Pathways: Carbon-13 and Nitrogen-15 NMR; Biosynthesis and Metabolic Pathways: Deuterium NMR; NOESY; Nucleic Acid Flexibility and Dynamics: Deuterium NMR; Nucleic Acid Structures in Solution: Sequence Dependence; Nucleic Acids: Base Stacking and Base Pairing Interactions; Nucleic Acids: Chemical Shifts; Nucleic Acids: Phosphorus-31 NMR; Protein Dynamics from NMR Relaxation; Protein Dynamics from Solid State NMR; Protein Hydration; Protein Structures: Relaxation Matrix Refinement; Proteins and Protein Fragments: Folding; Structures of Larger Proteins, Protein-Ligand, and Protein-DNA Complexes by Multi-Dimensional Heteronuclear NMR; Three-Dimensional HMQC-NOESY, NOESY-HMQC, and NOESY-HSQC; Three- and Four-Dimensional Heteronuclear Magnetic Resonance.

9 REFERENCES

1. W. Saenger, *Principles of Nucleic Acid Structure*, Springer, New York, 1984.
2. K. Wüthrich, *NMR of Proteins and Nucleic Acids*, Wiley, New York, 1986.
3. S. S. Wijmenga, M. M. W. Mooren, and C. W. Hilbers in *NMR of Macromolecules. A Practical Approach*, ed. G. C. K. Roberts, Oxford University Press, Oxford, 1993, Chap. 8
4. J. E. Kilpatrick, K. S. Pitzer, and R. Spitzer, *J. Am. Chem. Soc.*, 1947, **69**, 2483.
5. C. Altona, *Recl. Trav. Chim. Pays-Bas*, 1982, **101**, 413.
6. C. J. Marzec and L. A. Day, *J. Biomol. Struct. Dyn.*, 1993, **10**, 1091.
7. C. J. Marzec and L. A. Day, *J. Biomol. Struct. Dyn.*, 1993, **10**, 1125.
8. P. Gundhi, K. V. R. Chary, and R. V. Hosur, *FEBS Lett.*, 1985, **191**, 92.
9. M. J. J. Blommers, F. J. M. van de Ven, G. A. van de Marel, J. H. van Boom, and C. W. Hilbers, *Eur. J. Biochem.*, 1991, **201**, 33.
10. G. Varani, C. Cheong, and I. Tinoco, Jr., *Biochemistry*, 1991, **30**, 3280.

11. G. W. Kellogg and B. I. Schweitzer, *J. Biomol. NMR*, 1993, **3**, 577.
12. J. F. Milligan, D. R. Groebe, G. W. Witherell, and O. C. Uhlenbeck, *Nucleic Acids Res.*, 1987, **15**, 8783.
13. E. P. Nikonowicz and A. Pardi, *J. Mol. Biol.*, 1993, **232**, 1141.
14. H. A. Heus, S. S. Wijmenga, F. J. M. van de Ven, and C. W. Hilbers, *J. Am. Chem. Soc.*, 1994, **116**, 4983.
15. V. Sklenár, R. D. Peterson, M. R. Rejante, and J. Feigon, *J. Biomol. NMR*, 1993, **3**, 721.
16. J. V. Hines, G. Varani, S. M. Landry, and I. Tinoco, Jr., *J. Am. Chem. Soc.*, 1993, **115**, 11002.
17. F. J. M. van de Ven and C. W. Hilbers, *Eur. J. Biochem.*, 1988, **178**, 1.
18. V. P. Antao, S. Y. Lai, and I. Tinoco, Jr., *Nucleic Acids Res.*, 1991, **19**, 5901.
19. L. P. M. Orbons, G. A. van der Marel, J. H. van Boom, and C. Altona, *Nucleic Acids Res.*, 1986, **14**, 4187.
20. G. Gupta, M. H. Sarma, R. H. Sarma, R. Bald, U. Engelke, S. L. Oei, R. Gessner, and V. A. Erdmann, *Biochemistry*, 1987, **26**, 7715.
21. I. Hiroa, Y. Nishimura, T. Naraoka, K. Watanabe, Y. Arata, and K.-I. Miura, *Nucleic Acids Res.*, 1989, **17**, 2223.
22. C. A. G. Haasnoot, M. J. J. Blommers, and C. W. Hilbers, in *Structure, Dynamics and Function of Biomolecules*, eds. A. Ehrenberg, R. Rigler, A. Graslund, and L. Nilsson, *Springer Series in Biophysics*, Berlin, 1987, Vol. 1, p. 212.
23. J. van Wijk, B. D. Huckriede, J. H. Ippel, and C. Altona, *Methods Enzymol.*, 1992, **211**, 286.
24. C. W. Hilbers, H. A. Heus, M. J. P. van Dongen, and S. S. Wijmenga, in *Nucleic Acids and Molecular Biology*, eds. F. Eckstein and D. M. J. Lilley, Springer, Berlin, 1994, 8, 56.
25. M. Guéron and J.-L. Leroy, in *Nucleic Acids and Molecular Biology*, eds. F. Eckstein and D. M. J. Lilley, Springer, Berlin, 1992, Vol. 6, p. 1.
26. K. Gehring, J.-L. Leroy, and M. Guéron, *Nature (London)*, 1993, **363**, 561.
27. M. M. W. Mooren, C. W. Hilbers, and S. S. Wijmenga, *J. Magn. Reson.*, 1991, **94**, 101.
28. S. S. Wijmenga, H. A. Heus, B. A. Werten, van der Marel, J. H. van Boom, and C. W. Hilbers, *J. Magn. Reson.*, 1994, **103**, 134.
29. G. J. Martin, M. L. Martin, and J. P. Gouesnard, in *NMR Basic Principles and Progress*, eds. P. Diehl, E. Fluck, and R. Kosfeld, Springer, Berlin, 1981, Vol. 18, p. 1.

Biographical Sketches

Cornelis W. Hilbers. *b* 1937. 'Doctoraal' degree (= M.A.), 1970; Ph.D., 1971, Physical Chemistry, Vrije Universiteit, Amsterdam. Introduced to NMR by Prof. C. MacLean (Amsterdam) and Prof. R. G. Shulman (Yale, New Haven). Presently Professor at the Department of Biophysical Chemistry, University of Nijmegen, The Netherlands; Director of the Nijmegen SON Research Center (NSR Center). Approx. 170 publications. Research interests: high-resolution NMR of nucleic acids and proteins.

Sybren S. Wijmenga. *b* 1953. 'Doctoraal' degree (= M.A.), 1978, Chemical Physics (X-ray diffraction), University of Groningen; Ph.D., 1984, Physical Chemistry, (with Professor M. Mandel), University of Leiden, The Netherlands. At N.I.H.–N.I.D.D.K. Chemical Physics Laboratory, Bethesda, MD, 1984–87 (with Dr. E. Charney). Presently Supervisor at the SON National HF-NMR Facility, University of Nijmegen, The Netherlands. Approx. 40 publications. Research interests: high-resolution NMR of nucleic acids and proteins.

Oxygen-18 in Biological NMR

John M. Risley
University of North Carolina at Charlotte, NC, USA

1	Introduction	1
2	Properties of the ^{18}O Isotope Shifts in NMR	1
3	Studies Utilizing ^{18}O Isotope Shifts in ^{13}C, ^{15}N, and ^{31}P NMR	2
4	Related Articles	5
5	References	5

1 INTRODUCTION

Isotopic substitution is the smallest perturbation that may be introduced into a molecule without changing the chemical properties of a molecule. This property of isotopic substitution is of particular importance in biological studies where small structural differences in molecules can dramatically alter the biological effects. One isotope that is extremely useful in biological NMR studies involving oxygen is ^{18}O. Oxygen-18 is an NMR-inactive isotope. As a result, the effect of ^{18}O on NMR-active nuclei is classified as an intrinsic secondary isotope effect because ^{18}O isotopic substitution changes the shielding of other nuclei in the molecule. Therefore, the NMR signals of chemically identical nuclei for ^{16}O and ^{18}O isotopomers will have different chemical shifts. In general, the chemical shifts of nuclei in ^{18}O isotopomers will be at a lower frequency than the ^{16}O isotopomers, and thus the heavier isotope shields the nuclei. The natural abundances of the oxygen isotopes are 99.76% ^{16}O, 0.04% ^{17}O, and 0.20% ^{18}O. Therefore, the magnitudes of this secondary isotope effect are often measured relative to the ^{16}O isotopomers by calculating the differences between the chemical shifts of the two isotopomers, and are called ('upfield') '^{18}O isotope shifts' (or 'isotope-induced shifts', or 'isotope effects'). A chemical shift for ^{18}O isotopomers at lower frequency would imply that these 'upfield' ^{18}O isotope shifts have negative values. However, both negative and positive values have been used for the isotope shifts. Therefore, unless otherwise indicated, it should be assumed that the ^{18}O isotope shifts are to lower frequency regardless of the convention utilized in a specific paper to calculate the isotope shift. Because the magnitude of the ^{18}O isotope shifts are field dependent, they are properly reported in chemical shift terms (ppm) and not hertz.

^{18}O isotope shifts have been reported for 14 NMR nuclei: ^{1}H, ^{13}C, ^{15}N, ^{17}O, ^{29}Si, ^{31}P, ^{51}V, ^{53}Cr, ^{55}Mn, ^{93}Nb, ^{95}Mo, ^{99}Tc, ^{129}Xe, and ^{195}Pt.[1] The first ^{18}O isotope shift was reported in 1970 in ^{1}H NMR. It was not until later that ^{18}O isotope shifts for other nuclei were reported: ^{55}Mn in 1976, ^{95}Mo in 1977, ^{31}P in 1978, ^{13}C in 1979, and the remainder in 1981–87. Therefore, the intrinsic secondary isotope effect of ^{18}O in NMR spectroscopy is a fairly recently known phenomenon, but it has made a significant contribution in biological NMR. The ^{18}O isotope shifts that have been of greatest importance in biological NMR are in ^{13}C NMR, ^{15}N NMR, and ^{31}P NMR; each of these is discussed here following a brief description of the general properties of the ^{18}O isotope shifts.

2 PROPERTIES OF THE ^{18}O ISOTOPE SHIFTS IN NMR

There are a number of general properties for the different ^{18}O isotope shifts in NMR. The magnitudes of the isotope shifts are small relative to the chemical shift range for the NMR nuclide. In general, the ^{18}O isotope shifts are less than 1 ppm, and are more conveniently referred to in parts per billion (ppb; 1 ppb = 0.001 ppm). The smallest isotope shift that has been reported is 0.93 ppb in ^{13}C NMR in dimethylmaleic anhydride, and the largest isotope shift is 100_0 ppb (per ^{18}O) in ^{195}Pt NMR for tetraaquaplatinum(II). The one-bond and long-range (two or more bonds) chemical shifts for all the ^{18}O isotopomers are at a lower frequency (upfield), except for two long-range effects reported in ^{13}C NMR over three bonds in 2,6-dimethyl-4-pyrone[2] and over four bonds in artemisinin[3] where shifts to higher frequency (downfield) were observed. The magnitude of an ^{18}O isotope shift is highly dependent on the structure of the functional group; this is most clearly seen in the ^{18}O isotope shifts in ^{13}C NMR, ^{15}N NMR, and ^{31}P NMR, where studies of the relationship between the structure of the functional groups and the isotope shifts have been most complete.[1,4] The magnitudes of ^{18}O isotope shifts are additive over one bond and long range, and, in general, are temperature independent and sometimes exhibit a small solvent dependence. Oxyanions, for example phosphate and carboxylates, show a significant pH dependence for the ^{18}O isotope shifts that reaches a maximum near the pK_a of the acid. Finally, symmetrical molecules such as succinic acid, pyrophosphate, and dimethylglyoxime can have their chemical shift equivalence removed by asymmetrical ^{18}O isotopic substitution; this can result in the transformation of a simple NMR spectrum into a very strongly coupled AB pattern when the magnitude of the ^{18}O isotope shift is small relative to the magnitude of the scalar coupling constant.

Because the natural abundance of ^{18}O is very small (0.20%), observation of ^{18}O isotope shifts at natural abundance on NMR-active nuclei have been reported only under ultrahigh resolution conditions in a few rare instances. Highly enriched $^{18}O_2$ and $H_2{}^{18}O$ (up to approximately 99 atom % ^{18}O) are commercially available, as well as other highly enriched ^{18}O compounds. Generally, these compounds are used to synthesize ^{18}O-labeled compounds of NMR-active nuclei at natural abundance or using molecules enriched in the NMR nuclei. Basic outlines of experimental procedures to follow in studies utilizing the ^{18}O isotope shifts in ^{13}C NMR and ^{15}N NMR[5] and in ^{31}P NMR[6] have been described. A very important property of the ^{18}O isotopomers is that the spin–lattice relaxation time (T_1) is not changed.

Some of these properties are illustrated in Figures 1 and 2. One-bond, long-range, and the additivity of the ^{18}O isotope shifts are illustrated in Figure 1 at natural abundance ^{13}C NMR in the six ^{16}O and ^{18}O isotopomers of dimethylmaleic anhydride [Figure 1(c)].[7] The ^{13}C NMR signals for the alkenic carbon atoms [Figure 1(a)] and the carbonyl carbon atoms

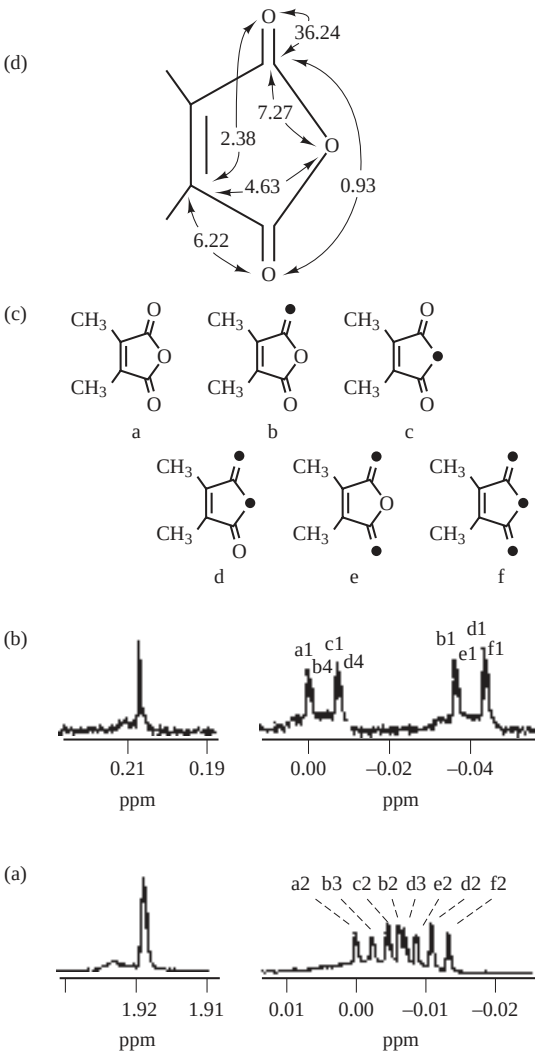

Figure 1 The natural abundance ^{13}C NMR spectrum of 53% ^{18}O-labeled dimethylmaleic anhydride shows one-bond and long-range ^{18}O isotope shifts of (a) the alkenic carbon region and (b) the carbonyl carbon region. The six ^{16}O, ^{18}O isotopomers are given in (c), where ^{18}O is denoted by solid circles. The peak assignments are indicated by a letter for the isotopomer and a number for the carbon atom in that molecule. Symmetrical isotopomers (a, c, e, and f) have only one signal in each region, while asymmetrical isotopomers (b and d) have two signals in each region. The signals for the alkenic carbon (carbon atoms 2 and 3) and for the carbonyl carbon (carbon atoms 1 and 4) of the ^{16}O isotopomer (species a) are assigned a value of 0 ppm; the signals to the left in (a) and (b) are the C-1 of citraconic anhydride and the quaternary carbon of benzyl alcohol, respectively, added as internal standards to preclude the possibility of fine splittings arising from magnetic field inhomogeneities. The values for the ^{18}O isotope shifts observed in the spectrum are given in ppb in (d) as positive numbers for upfield shifts. (Reprinted by permission of the American Chemical Society from T. L. Mega and R. L. Van Etten, *J. Am. Chem. Soc.*, 1993, **115**, 12 056)

[Figure 1(b)] clearly show individual NMR signals for each of the isotopic species. The magnitudes of each of the ^{18}O isotope shifts are summarized in Figure 1(d). The ^{15}N NMR spectrum of [^{15}N,^{18}O]dimethylglyoxime shown in Figure 2 illustrates that asymmetrical ^{18}O isotopic substitution removes the chemical shift equivalence in a symmetrical molecule and

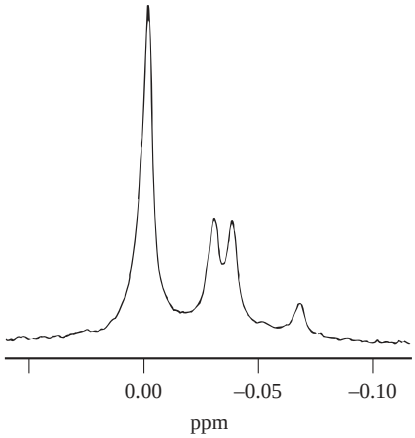

Figure 2 The ^{15}N NMR spectrum of dimethylglyoxime (95% ^{15}N, 27% ^{18}O) shows signals for the $(^{15}N^{16}O)_2$ isotopomer at 0.0 ppm and for the $(^{15}N^{18}O)_2$ isotopomer at −0.067 ppm (a low frequency shift). The asymmetrical ($^{15}N^{16}O$, $^{15}N^{18}O$) isotopomer reduces the degeneracy of the magnetically equivalent nuclei to yield an AB spectrum, which is centered at −0.0335 ppm. Only the central doublet of the AB quartet is observed; the outer resonances are 1.4% of the central doublet, and therefore are buried in the baseline. The three-bond $^{15}N-^{15}N$ geminal coupling constant of 5.7 Hz was calculated from the spectrum. (Reprinted by permission of the American Chemical Society from G. Rajendran, R. E. Santini, and R. L. Van Etten, *J. Am. Chem. Soc.*, 1987, **109**, 4357)

produces an AB spectrum, from which a three-bond coupling constant may be calculated.[8]

3 STUDIES UTILIZING ^{18}O ISOTOPE SHIFTS IN ^{13}C, ^{15}N, AND ^{31}P NMR

The intrinsic secondary ^{18}O isotope effects in ^{13}C NMR and ^{31}P NMR have been used widely and successfully in a broad range of studies, and have generally proven their values as primary experimental techniques. The intrinsic secondary ^{18}O isotope effect in ^{15}N NMR has not been used as extensively. There are advantages that the ^{18}O isotope shift technique has over other techniques. Analysis of a reaction mixture by NMR is direct, requiring only that the relevant NMR signals be resolved; little or no sample manipulation, such as derivatization, is generally required. Because of the dependence of the ^{18}O isotope shifts on the structures of the functional groups, positional information may be obtained directly and simultaneously at different sites in a molecule, which is important in some studies to remove ambiguities regarding the position of an oxygen atom. In numerous studies nearly continuous acquisition of kinetic data may be obtained, with a possibility of answering simultaneously more than one experimental question. For some studies, the ^{18}O isotope shifts in NMR are virtually the only technique available due to experimental restrictions imposed by other techniques that make them very difficult to use. In other studies, the ^{18}O isotope shifts in NMR may be considered to be a complementary technique to other techniques, but the particularly simple design and interpretation of the results make the use of ^{18}O isotope shifts in NMR the technique of choice. A disadvantage of ^{18}O isotope shifts in NMR is

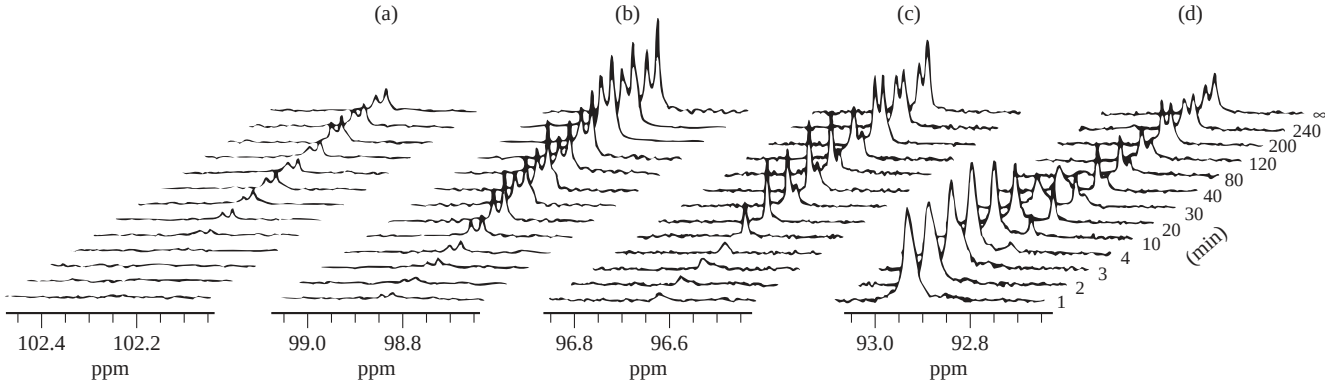

Figure 3 The hydrolysis of sucrose in 60% [^{18}O]water at pH 2.9 and 80°C was followed as a function of time using natural abundance ^{13}C NMR. The NMR signals correspond to the anomeric carbons of (a) β-D-fructofuranose, (b) β-D-fructopyranose, (c) β-D-glucopyranose, and (d) sucrose glucosyl C-1 and α-D-glucopyranose. As the hydrolysis of sucrose proceeds, the intensity of the sucrose glucosyl C-1 anomeric carbon signal decreases, while the intensities of the anomeric carbon atoms of the products increase; the pseudo-first-order rate constant for the reaction is 4×10^{-4} s^{-1}. The point of bond cleavage at the fructosyl–(bridge)oxygen bond is observed directly from the ^{18}O isotope shifts: the isotopic composition of the fructose anomers is the same as the solvent upon hydrolysis, while the glucose anomers undergo an oxygen exchange reaction until their isotopic compositions are the same as the solvent. (Reprinted by permission of the American Chemical Society from T. L. Mega and R. L. Van Etten, *J. Am. Chem. Soc.*, 1988, **110**, 6372)

that a significant amount of material may be required for analysis, whereas other techniques require much less material. Nevertheless, studies utilizing ^{18}O isotope shifts have been of major importance in biological NMR.

Any reaction involving carbon–oxygen bonds is potentially amenable to analysis utilizing the ^{18}O isotope shift in ^{13}C NMR. Biological molecules contain many carbon–oxygen bonds, and these bonds are very important sites of reactions. Therefore, it is not unexpected that the ^{18}O isotope shift in ^{13}C NMR has been widespread in biological NMR. These reactions are studied at natural abundance ^{13}C (1.1%), or using ^{13}C-enriched (up to 99 atom %) molecules. A particular experiment will indicate whether the ^{18}O isotopomer(s) should be synthesized, or whether the ^{18}O should be introduced exogenously as $^{18}O_2$, $H_2{}^{18}O$, etc.; both designs are used. The studies can be broadly classified as mechanistic studies and biosynthetic studies. Mechanistic studies include the reactions of enzymes and the reactions of biological molecules in the absence of enzymes. Among the mechanistic studies are oxygen exchange reactions, points of bond cleavage, oxidation reactions, rearrangement reactions, and the source of oxygen in reactions.[1] These studies have provided important information on the reactivity of carbon–oxygen bonds in solution, the bioenergetics and kinetics of reactions under different experimental conditions, the solution (equilibrium) structure of biological molecules, and mechanistic information on enzyme-catalyzed reactions. Figures 3 and 4 illustrate the information available in mechanistic studies. Figure 3 shows the hydrolysis of sucrose in $H_2{}^{18}O$ at natural abundance ^{13}C NMR.[9] This is a reaction where the point of bond cleavage at the glucosyl–(bridge)oxygen or at the fructosyl–(bridge)oxygen had remained unresolved, despite intense scrutiny with experimental evidence supporting both proposals. The reaction in Figure 3 shows that the acid-catalyzed reaction proceeds by fructosyl–(bridge)oxygen bond fission, but simultaneously the rates of sucrose hydrolysis and of oxygen exchange reactions of the products could be determined; this long-standing problem was resolved quite elegantly. Figure 4 shows the rat liver microsomal

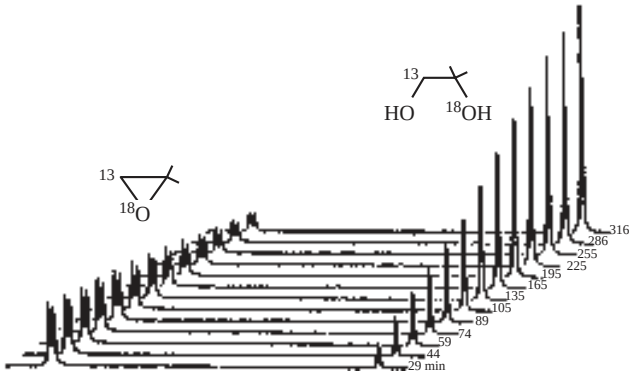

Figure 4 Homogeneous rat liver microsomal epoxide hydratase (EC 3.3.2.3) catalyzes the hydrolysis of 2,2-dimethyl[3-^{13}C,^{18}O]oxirane at the primary carbon–oxygen bond with a pseudo-first-order rate constant of 9.98×10^{-5} s^{-1} at 35°C. An isotope shift of −0.031 ppm is observed for the primary carbon atom in the ^{13}C-enriched oxirane that is not observed in the ^{13}C-enriched 2-methylpropane-1,2-diol hydrolysis product. (Reprinted by permission of the American Chemical Society from J. M. Risley, F. Kuo, and R. L. Van Etten, *J. Am. Chem. Soc.*, 1983, **105**, 1647)

epoxide hydratase-catalyzed hydrolysis of 2,2-dimethyl[3-^{13}C, ^{18}O]oxirane.[10] From this reaction it is possible simultaneously to determine that the enzyme catalyzes the hydrolysis of the sterically favored primary carbon–oxygen bond and the rate at which the reaction occurs; by contrast, the acid-catalyzed hydrolysis reaction occurs with fission of the tertiary carbon–oxygen bond.

A significant application of the ^{18}O isotope shift in ^{13}C NMR has been the elucidation of the source/origin of oxygen atoms in biosynthetic studies of natural products.[1] The ^{18}O isotope shift in ^{13}C NMR is a nondestructive technique that permits direct, semiquantitative localization of the ^{18}O label even in highly oxygenated natural products; this technique was a valuable improvement to ascertain the position of the ^{18}O label(s) that had often required circuitous approaches to

resolve. The source of the oxygen in the biosynthesis of natural products may be from ^{18}O-labeled small molecule precursors (such as acetate, propionate, etc.), from $^{18}O_2$, or from $H_2{}^{18}O$. These experiments may be performed at natural abundance ^{13}C or using ^{13}C-enriched molecules. Therefore, there are a number of different approaches to these studies, and, in general, a variety of approaches are taken that involve each of these, which includes the synthesis of ^{13}C-enriched, ^{18}O-labeled precursors. From the labeling pattern obtained for each source of oxygen in a natural product, it is often possible to propose a mechanism (or reduce the number of possible mechanisms) for the synthesis of the natural product. Figure 5 illustrates the use of the ^{18}O isotope shift in ^{13}C NMR to determine the incorporation of oxygen from $^{18}O_2$ into streptonigrin biosynthesis.[11] The natural abundance ^{13}C NMR spectrum shows eight isotope shifts from the incorporation of $^{18}O_2$ at five sites. These results supported an oxidative β-carboline cleavage mechanism in the biosynthesis of streptonigrin rather than other proposed mechanisms.

Any reaction involving nitrogen–oxygen bonds is potentially amenable to analysis utilizing the ^{18}O isotope shift in ^{15}N NMR. However, biological molecules contain few nitrogen–oxygen bonds (compared with carbon–oxygen bonds and phosphorus–oxygen bonds), and therefore the ^{18}O isotope shift in ^{15}N NMR has not been used extensively.[1] Because the natural abundance of ^{15}N (0.37%) is very low, ^{15}N-enriched compounds have been used in these studies. All studies have been investigations into the source/origin of oxygen in biosynthetic studies: the oxidation of ammonia to nitrite by *Nitrosomonas europaea* utilizes one oxygen atom from $^{18}O_2$ and the second oxygen atom from $H_2{}^{18}O$; Nitrobacter agilis utilizes $H_2{}^{18}O$ to oxidize nitrite to nitrate; the oxygen atoms in 3-nitropropanoic acid synthesized by *Penicillium atrovenetum* are from $^{18}O_2$; and the oxygen atoms in the nitro group of dioxapyrrolomycin produced by *Streptomyces fumanus* are from nitrate.

Any reaction involving phosphorus–oxygen bonds is potentially amenable to analysis utilizing the ^{18}O isotope shift in ^{31}P NMR. Biological molecules contain many phosphorus–oxygen bonds, and by far the most important are phosphate bonds. Thus, the primary focus of studies utilizing the ^{18}O isotope shift in ^{31}P NMR has been on the phosphate bonds in various molecules. In general, the ^{18}O label is incorporated into the phosphate molecule for analysis by

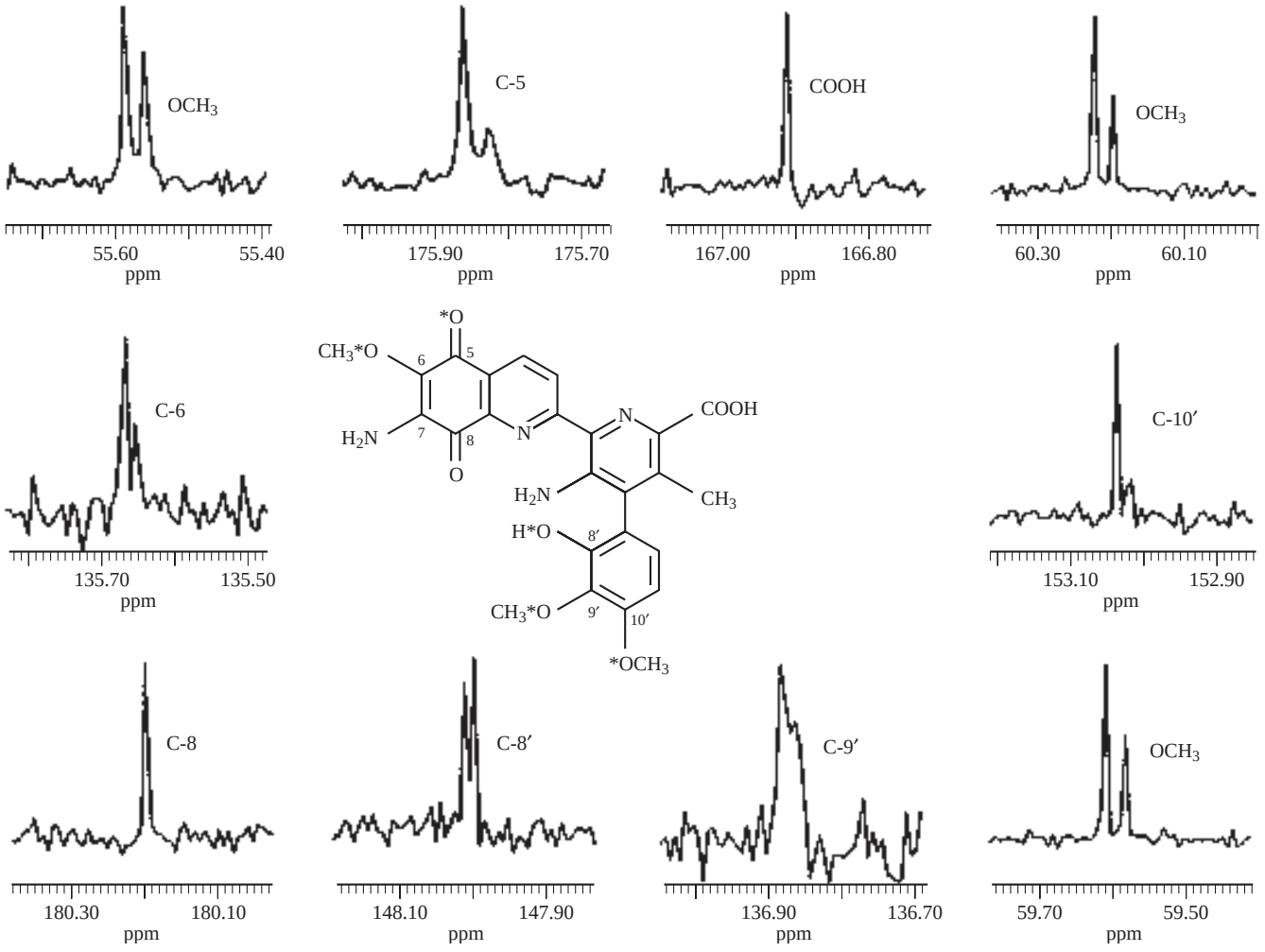

Figure 5 Natural abundance ^{13}C NMR was used to ascertain the incorporation of $^{18}O_2$ in the biosynthesis of streptonigrin by *Streptomyces flocculus*. The oxygen atoms in streptonigrin derived from O_2 are indicated by an asterisk from the isotope shifts of the specific NMR signals. (Reprinted by permission of the American Chemical Society from W. R. Erickson and S. J. Gould, *J. Am. Chem. Soc.*, 1985, **107**, 5831)

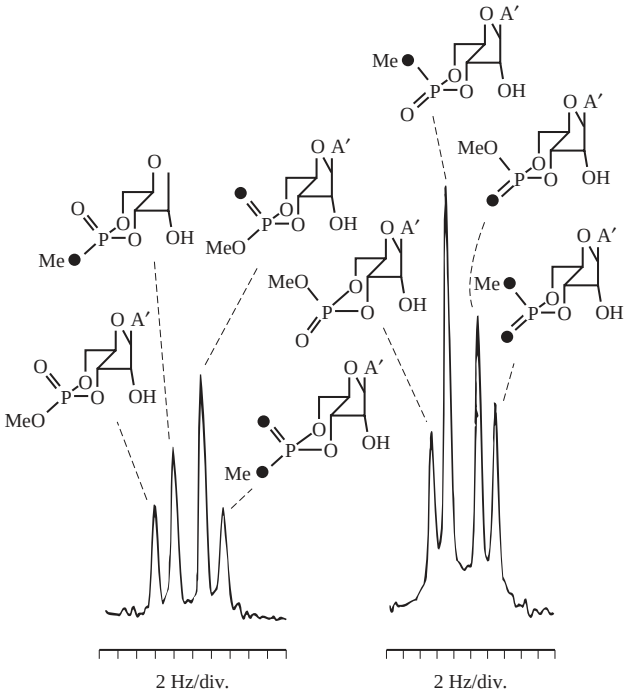

Figure 6 The stereochemical course of isoleucyl-tRNA synthetase-catalyzed activation of isoleucine by ATP was elucidated from the isotopomers of the diastereoisomeric triesters of 3′,5′-cAMP (shown at the top; (•) ^{18}O). The ^{31}P NMR spectrum for the equatorial triester is shown on the left and the axial triester is shown on the right. The important ^{31}P NMR signals are the two middle signals for the mono-^{18}O-isotopomer of each diastereoisomer. The ratios of [$^{16}O_{ax}$, $^{18}O_{eq}$] and [$^{18}O_{ax}$, $^{16}O_{eq}$] indicated a stereochemical mechanism involving inversion of configuration at the P-α atom. (Reprinted by permission of the American Chemical Society from G. Lowe, B. S. Sproat, G. Tansley, and P. M. Collis, *Biochemistry*, 1983, **22**, 1229)

^{31}P NMR (^{31}P is 100% natural abundance), although the use of exogenous $H_2{}^{18}O$ is possible in some studies. The studies can be generally classified as oxygen exchange reactions, positional isotope exchange, bond cleavage reactions, and stereochemistry studies. These studies have provided important mechanistic information, in particular, for enzyme-catalyzed reactions. Oxygen exchange reactions in inorganic phosphate proceed sequentially with exchange of one oxygen atom per event, or with multiple exchange of more than one oxygen per event. Positional isotope exchange occurs in a reversible reaction that involves rotational symmetry of a chemical group where the position of an isotope is exchanged by rotation within a substrate; among these reactions are the reversible γ-PO_3 transfer in ATP reactions by different enzymes. The sites of phosphorus–oxygen bond fission have been ascertained in bond cleavage reaction studies. The stereochemical course of phosphate transfer can occur with retention of configuration or with inversion of configuration. These reactions require the synthesis of a chiral substrate, such as a [^{16}O,^{17}O,^{18}O]phospho or [^{18}O]phosphothio substrate. Analysis of the stereochemical course of these reactions involves the stereospecific cyclization of a chiral phosphate monoester of a chiral diol into a cyclic phosphate diester, esterification of the diester to give diastereoisomeric cyclic phosphate triesters, and determining the ratios of the [$^{16}O_{ax}$,$^{18}O_{eq}$] and [$^{18}O_{ax}$,$^{16}O_{eq}$] axial and equatorial triesters. Figure 6 shows the ^{31}P NMR spectrum for the stereochemical course of isoleucyl-tRNA synthetase-catalyzed activation of [$^{18}O_2$]isoleucine by adenosine 5′-[(*R*)-α-^{17}O]triphosphate.[12] Analysis of the diastereoisomeric triesters of the isolated [^{16}O,^{17}O,^{18}O]AMP showed inversion of configuration at the α phosphorus atom, which supported a direct in-line displacement of pyrophosphate from P-α of ATP by isoleucine rather than a double-displacement mechanism involving an adenylyl–enzyme intermediate.

4 RELATED ARTICLES

Biosynthesis and Metabolic Pathways: Carbon-13 and Nitrogen-15 NMR; Biosynthesis and Metabolic Pathways: Deuterium NMR; Carbon-13 Studies of Deuterium Labeled Compounds; Enzymatic Transformations: Isotope Probes; Isotope Effects in Carbocation Chemistry; Isotope Effects on Chemical Shifts and Coupling Constants; Natural Products.

5 REFERENCES

1. J. M. Risley and R. L. Van Etten, *NMR Basic Principles Prog.*, 1990, **22**, 81.
2. W. Arias and J. M. Risley, *J. Org. Chem.*, 1991, **56**, 3741.
3. N. Acton and R. J. Roth, *J. Org. Chem.*, 1992, **57**, 3610.
4. F. M. Raushel and J. J. Villafranca, *CRC Crit. Rev. Biochem.*, 1988, **23**, 1.
5. J. M. Risley and R. L. Van Etten, *Methods Enzymol.*, 1989, **177**, 376.
6. J. J. Villafranca, *Methods Enzymol.*, 1989, **177**, 390.
7. T. L. Mega and R. L. Van Etten, *J. Am. Chem. Soc.*, 1993, **115**, 12 056.
8. G. Rajendran, R. E. Santini, and R. L. Van Etten, *J. Am. Chem. Soc.*, 1987, **109**, 4357.
9. T. L. Mega and R. L. Van Etten, *J. Am. Chem. Soc.*, 1988, **110**, 6372.
10. J. M. Risley, F. Kuo, and R. L. Van Etten, *J. Am. Chem. Soc.*, 1983, **105**, 1647.
11. W. R. Erickson and S. J. Gould, *J. Am. Chem. Soc.*, 1985, **107**, 5831.
12. G. Lowe, B. S. Sproat, G. Tansley, and P. M. Cullis, *Biochemistry*, 1983, **22**, 1229.

Biographical Sketch

John M. Risley. *b* 1952. B.S., Ball State University, 1976; Ph.D., Purdue University, 1980. Postdoctoral, research scientist, and visiting assistant professor, Purdue University. Faculty in Chemistry, University of North Carolina at Charlotte, 1988–present. Introduced to NMR in undergraduate research and continued at Purdue University with the first report of the ^{18}O isotope shifts in ^{13}C and ^{15}N NMR. Approx. 30 publications. Research interests: ^{18}O isotope shift ^{13}C NMR and study of lysosomal enzymes.

Pancreatic Trypsin Inhibitor

Kurt Wüthrich

Eidgenössische Technische Hochschule Zürich, Switzerland

1	Introduction	1
2	Growing up with BPTI	2
3	Survey of Key NMR Experiments with BPTI	2
4	BPTI and NMR Spectroscopy with Proteins	3
5	BPTI and Resonance Assignments in Proteins	3
6	BPTI and Protein Structure Determination by NMR	4
7	BPTI and Amide Proton Exchange	4
8	BPTI and Internal Mobility in Proteins	5
9	BPTI and Protein Folding	5
10	Concluding Remarks	6
11	Related Article	7
12	References	7

1 INTRODUCTION

> The basic pancreatic trypsin inhibitor (BPTI) from bovine pancreas[1] has a molecular weight of 6500 and consists of 58 amino acid residues. The amino acid sequence and the molecular conformation in single crystals[2] are known, and it has been found that the solution conformation of BPTI is unusually stable towards denaturing agents and heat. Some time ago we briefly discussed proton NMR data which revealed yet another rather unexpected structural feature of BPTI, i.e. very slow exchange of some of the amide protons.[3] This paper presents new data on the denaturation of BPTI and the proton exchange in solutions of BPTI in D_2O. An obvious goal of the investigations of BPTI is to understand in more detail the mode of action of this inhibitor. In addition, since BPTI is by its small size amenable to detailed studies by different techniques, work on this molecule could on a more general basis be particularly valuable for the further development of the investigations of molecular conformations in proteins. In view of the temperature stability of BPTI, some of the data on this protein might conceivably even be relevant for the investigation of conformational features in proteins from thermophilic organisms.

This quotation represents the introduction of the first paper from my laboratory that was devoted entirely to BPTI.[4] We started work on this protein in 1972, and at the time no one could have guessed that I would some day be asked to write an article on BPTI for the *Encyclopedia of Nuclear Magnetic Resonance*. However, the prediction made lightheartedly in 1973, that work with BPTI might be 'particularly valuable' for the future development of research on protein structures, turned out to have been, if anything, an understatement. In the meantime my laboratory has published more than 70 papers on experiments with BPTI and 15 papers on work with chemical modifications and homologs of BPTI, and by now the output of NMR papers on BPTI by other groups exceeds these numbers by far. Outside of the NMR field, BPTI was one of the first proteins, in 1975, for which a refined high-resolution X-ray crystal structure became available,[5] which in turn made BPTI a preferred object for theoretical studies on protein structure and dynamics.[6] At that time BPTI was also already used for studies on protein folding.[7] In 1982, BPTI was the first protein for which the ^1H NMR spectrum was completely assigned,[8] which contributed greatly to making it a focal point for research on amide proton exchange in proteins.[9] More recently, numerous projects on protein-folding studies and amide proton exchange measurements with BPTI relied heavily on the use of NMR for characterization of molecular structures and for kinetic measurements. For the sake of completeness it should also be added that a vast body of literature on the biochemistry and physiology of BPTI provides the platform for the physicochemical and structural investigations.

Figure 1 presents a ribbon drawing of the polypeptide backbone fold in BPTI, and a stereo view of the complete NMR solution structure[10] is shown in Figure 2. The polypeptide backbone forms a 3_{10}-helix from residues 3 to 7, a β-hairpin of residues 18–35, a one-residue third antiparallel β-strand of residue 44, and an α-helix of residues 47–56. There are three disulfide bonds linking the cysteinyl residues 5–55, 14–38, and 30–51. The molecule contains four phenylalanyl residues in positions 4, 22, 23, and 45, and the four tyrosyl residues 10, 21, 23, and 35 as the only aromatic side chains. The arrangement of the polypeptide backbone and the interior side chains (green and blue in Figure 2) is nearly identical in crystals[5] and in solution.[10] The conformation of the protein surface (red in

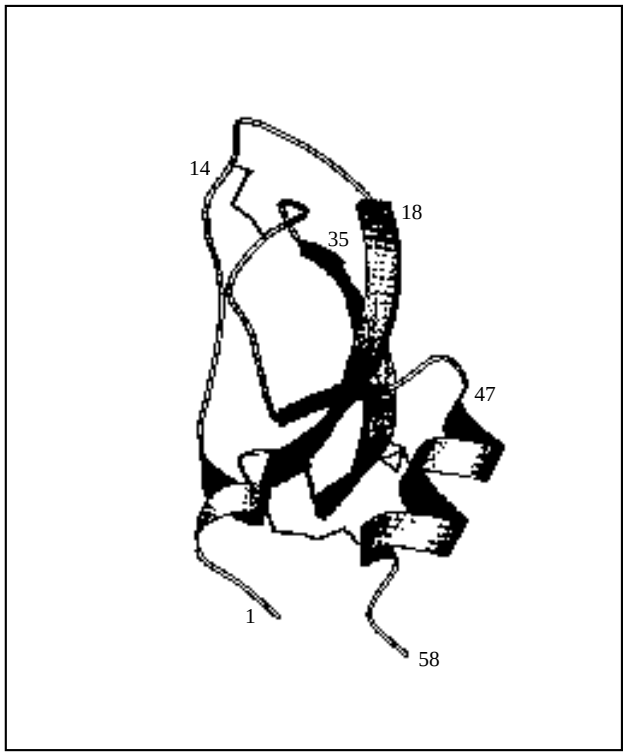

Figure 1 Ribbon drawing of the three-dimensional NMR solution structure of BPTI.[10] The three disulfide bonds 5–55, 14–38, and 30–51 are displayed as solid lines tracing the covalently linked side chains. For easy reference some residue positions have been identified. (Drawing prepared using the atom coordinates from Berndt et al.[10])

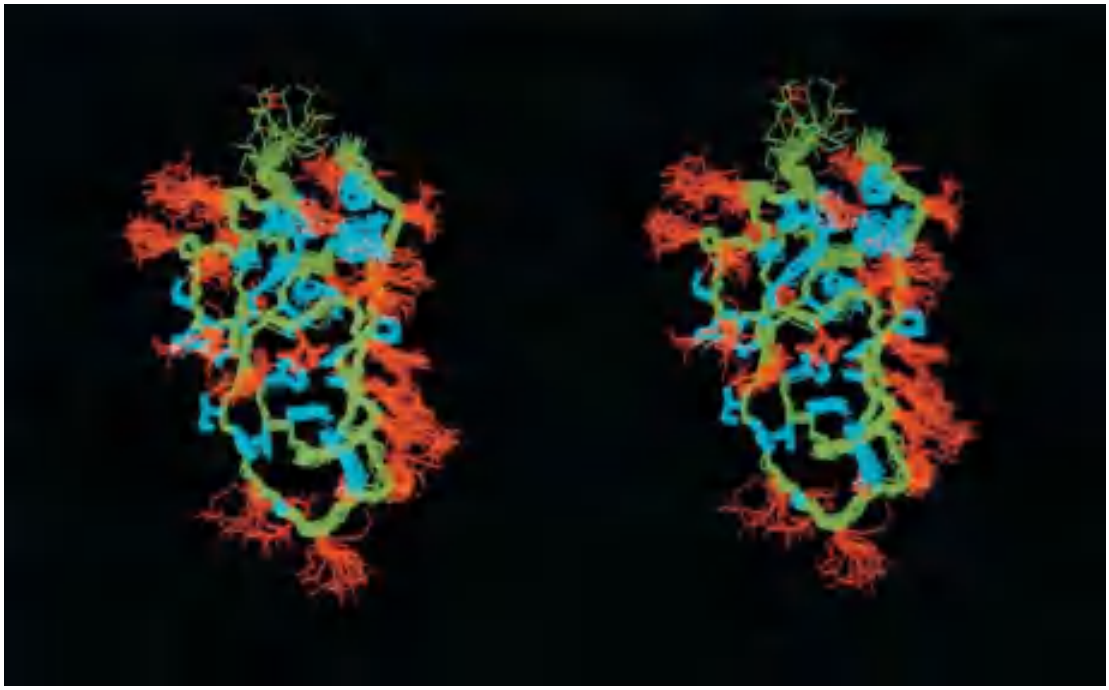

Figure 2 Stereo view of the NMR solution structure of BPTI represented as a superposition of 20 conformers. All heavy atoms are displayed. Color code: green, polypeptide backbone; blue, core side chains; red, surface side chains. A close fit among the 20 conformers indicates regions of the molecule where the structure is well defined, whereas a large dispersion implicates the presence of (dynamically) disordered structure. (Drawing prepared using the atom coordinates from Berndt et al.[10])

Figure 2) and the surface hydration[11] in solution are highly dynamic and different from the X-ray structure because of crystal lattice effects. The globular structure of BPTI is stable over the pH range 2–10 at ambient temperature, and over the temperature range 1–90 °C at neutral pH. Physicochemical studies of the folded protein can thus be performed with extensive variation of the experimental conditions.

2 GROWING UP WITH BPTI

Considering the long years of our involvement with BPTI, it is inevitable that this account has a personal note. There is only one other protein that influenced the activities of my group in a comparable way, i.e. cytochrome *c* (see ***Wüthrich, Kurt: NMR Structures of Biological Macromolecules***). However, it was with BPTI that we were introduced to protein structures and the physical chemistry of proteins. When dealing with cytochrome *c* our interest was focused on the one hand on NMR experimentation, and on the other hand on the heme group and its immediate surroundings. For example, all our theoretical work connected with cytochrome *c* and other hemoproteins related to ligand field treatments of the electronic states of the heme iron. With BPTI we became motivated to understand protein structure at a more general level, and through frequent contacts with Robert Huber's group in Munich we also learned about protein crystallography. In particular, during the first 3 years of our NMR work, when we mostly tried to rationalize NMR spectral properties on the basis of the BPTI crystal structure, Deisenhofer and Steigemann[5] refined the original BPTI structure at 0.15 nm resolution, and we got access to the improvements from the original molecular model[2] to the final refined structure in several steps. At that time, the X-ray data were visualized by physical molecular models, and the coordinates were obtained by measuring interatomic distances in these models. I remember a day when local structural features contained in a preliminary set of atom coordinates provided by the Munich group completely upset some calculations in my laboratory. A trip to Munich then revealed that there had been an impact on the BPTI model by an unidentified object (probably a broomstick in the hands of the cleaning personnel) before the atom coordinates were measured. Unimportant as this story is in perspective, it was the kind of experience we needed to develop a realistic view of experimental protein structure determination.

As happens so often with timely research projects, we were not alone in 1973 in starting publishing NMR work with BPTI. Brian Sykes and his co-workers reported studies of the amide protons and the tyrosyl rings,[12] and pursued the investigations of the tyrosyls with the use of chemical modification.[13] We thus had an opportunity to practice functioning under the pressure of direct competition. Starting around 1975, more and more theoretical work appeared that related directly to our experimental data,[6] which gave us good motivation to get more thoroughly educated in this area.

3 SURVEY OF KEY NMR EXPERIMENTS WITH BPTI

In Table 1 I have identified 19 key events which have been directly associated with BPTI during the period from the initial NMR experiments with BPTI in 1972[3,4,12] until the completion of the first NMR structure determination of a protein in

Table 1 Key NMR Experiments with BPTI, 1973–84

Year	Experiment/Observation	Ref.
1973	^{1}H NMR of individual amide protons	4, 12
1974	Ring flips of Phe and Tyr	14
1975	Theory of ring flips	6, 15
1976	Sine-bell for digital filtering	16
1977	Homonuclear 2D *J*-resolved NMR	17
1978	Quantitative NMR studies of amide proton exchange	18–20
1978	Dynamic model for globular proteins	18
1978	Sequential assignments using 1D NMR	21
1979	Mechanisms for amide proton exchange in BPTI	22, 23
1979	SECSY	24
1979	NOESY	25
1980	2D ^{1}H NMR with proteins in H_2O solution	26
1980	Sequential assignments using 2D NMR	27, 28
1981	NOE build-up measured with 2D NOESY	29
1981	Complete ^{1}H NMR assignment of a protein	8
1981	Amide proton exchange in the EX_1 regime	30, 31
1981	NH trap experiment for detection of early folding events	30, 32
1983	Phase sensitive 2QF-COSY	33
1984	Structure calculation from NMR data using the program DISGEO	34

1984.[35] These were either developments of new NMR experiments, important steps toward protein structure determination from NMR data, or NMR observations relating to novel features of protein conformation, and they will be discussed in more detail in the following sections. The selection is based on general considerations of the follow-up activities as reflected, for example, in the citation record, but also on my memory of the impact from these events on our subsequent projects. Table 1 contains mostly references to our own work, since besides several papers on amide proton exchange, mostly by Clare Woodward's group,[19, 22] only seven NMR studies with BPTI were published by others up to 1984. These are four papers by Brian Sykes's group,[12] of which three are on nitrotyrosyl derivatives of BPTI,[13] two are on refolding of heat-denatured, modified BPTI,[36] and a theoretical paper is on chemical shift averaging.[37] In addition, by 1984 BPTI was more and more widely used as a standard to check instrument performance.

In recent years in my laboratory, BPTI has lost its pivotal role of the 'heroic era' up to 1984, but elsewhere applications of NMR techniques became more and more widespread in projects on the folding, stability, and dynamics of BPTI (see Section 10 below).

4 BPTI AND NMR SPECTROSCOPY WITH PROTEINS

In the 1970s my group worked mainly with hemoproteins, oligopeptides, and BPTI (see ***Wüthrich, Kurt: NMR Structures of Biological Macromolecules***). Among the proteins studied, BPTI was the most robust (see above), and it could be dissolved in water at concentrations up to 20 mM. It is not surprising, therefore, that it was used for most of the NMR technique developments in my laboratory. The first such entry in Table 1 is the sine-bell,[16] which was of particular practical importance during all those years when absolute value presentations of the 2D NMR spectra were used.[8, 17, 24–29] It continues to be widely applied, and is a fitting tribute to the beautiful spectroscopy performed by the late Antonio DeMarco during his all too short life span.

The remaining technique entries refer to early 2D NMR experiments. 2D *J*-resolved spectroscopy had previously been developed in Richard Ernst's laboratory, but the BPTI paper in 1977[17] presents not only the first 2D NMR spectrum of a protein, but also the first 2D spectra recorded with a data size that made the technique useful for practical applications beyond observation of the classical test compounds, such as CH_3I or CH_3CH_2OH. SECSY[24] was designed as an alternative to the previously described COSY scheme to overcome limitations imposed by the then available computer capacities. For several years, until phase sensitive 2D NMR became available as a daily routine,[38, 39] the concept of delayed aquisition used in SECSY was widely propagated also by the instrument manufacturers. From our 1D experiments with BPTI[21] (see also the following section) and cytochrome *c*[40, 41] it was clear in 1978 that NOEs would be the key parameter for studies of macromolecular structures. The first 2D NOESY spectrum on record[25] was obtained with BPTI by Anil Kumar in my laboratory during the Christmas recess of 1979. Funding for this project was obtained through a grant application submitted jointly with Richard Ernst in 1978, which requested support for developing improved NOE measurements, including 2D NOESY. Within weeks after the first successful NOESY experiment we recorded homonuclear 2D NMR spectra in H_2O solutions of proteins.[26] This was an important step ahead, which enabled the extension of the NMR assignments in the protein core, where the amide protons exchange sufficiently slowly to be observed in D_2O, to the molecular surface. Although the preirradiation used to suppress the solvent line lacks the sophistication of other solvent suppression schemes, it turned out to be exactly what was needed for complete protein structure determinations by NMR. A further fundamentally important advance was to repeat the earlier 1D NMR measurements of NOE build-up curves for BPTI using 2D NOESY.[29] BPTI was also used in the first application of a two quantum filter for further improvement of the high-resolution phase sensitive COSY spectra of proteins[33] which we had obtained with the earlier implementation of time proportional phase incrementation (TPPI) by Dominique Marion.[38]

5 BPTI AND RESONANCE ASSIGNMENTS IN PROTEINS

In 1975, initial resonance assignments in BPTI were obtained for the aromatic region by Brian Sykes's group using chemical derivation of the tyrosyl rings[13] and in my laboratory using spectroscopic techniques.[42] In the following years we tried just about any available approach to add assignments for other amino acid side chains in BPTI,[43] but the decisive breakthrough that opened the way to NMR structure determination of proteins[44, 45] came in 1978 with the successful 'sequential NOE walk' by Andreas Dubs and Gerhard Wagner for obtaining sequential assignments of the

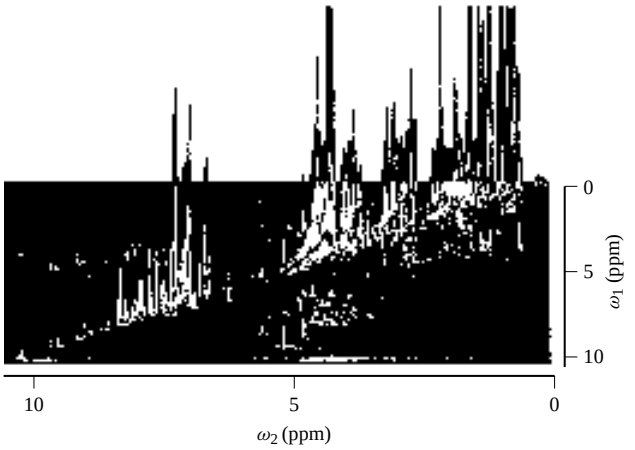

Figure 3 Stacked-plot representation of a symmetrized, absolute-value 500 MHz ^{1}H COSY spectrum of a 0.02 M solution of BPTI in a mixed solvent of 90% H_2O and 10% D_2O, pH = 4.6. T = 80°C. The spectrum was recorded in ~24 h. The digital resolution is 5.3 Hz/point. Due to the symmetrization the residual perturbations from the water suppression appear as a band of weak peaks parallel to the diagonal. (Reproduced with permission from G. Wagner and K. Wüthrich, *J. Mol. Biol.*, 1982, **155**, 347)

β-sheet in BPTI (see Figure 1).[21] This approach was based on detailed inspection of the BPTI crystal structure (see the following section) and on NMR techniques used previously in our laboratory for a similar sequential walk around the heme group in hemoproteins.[40] Once the aforementioned 2D NMR experiments were available, the assignments could be extended to other regions of BPTI,[27,28] and when we obtained a 500 MHz spectrometer in 1981 the complete polypeptide chain in BPTI was assigned.[8] Figure 3 shows a COSY spectrum from the assignment paper,[8] illustrating Gerhard Wagner's mastery of the art of NMR spectroscopy with proteins. Over the years this figure has appeared more than 10 times on the cover of books and journals, and a decade after its original publication I was quite surprised to find it also on the EENC poster.

6 BPTI AND PROTEIN STRUCTURE DETERMINATION BY NMR

From joint inspection of NMR data and the high-resolution X-ray crystal structure of BPTI, which was started in a systematic way by Andreas Dubs and Gerhard Wagner in connection with the initial sequential assignment,[21] we obtained important insights which resulted in a theoretical basis for the sequential resonance assignment technique[46] and a pattern recognition approach for the identification of secondary structures in proteins.[47,48] The crucial BPTI contribution to structure calculation from NMR data, however, was the paper with Timothy Havel listed as the last entry in Table 1.[34] Using the program DISGEO and simulated input data sets of NOE upper-distance constraints derived from the BPTI crystal structure, this paper demonstrated that complete protein structures at atomic resolution could indeed be obtained from experimental NMR data, and by extensive controlled variation of the simulated input it could also be shown that the method would be robust with respect to incomplete collection of input data as well as low precision of the individual NOE distance measurements.

Considering the extent to which our activities in the early 1980s were focused on BPTI, the questions must arise why even in 1987 only a low-resolution NMR structure had been published,[49] and why a complete high-quality structure determination was achieved only in 1992.[50] An initial BPTI structure calculation from NMR data had indeed already been performed in 1982 by Werner Braun and Gerhard Wagner (unpublished). The software used was an implementation of a metric matrix distance geometry algorithm that had the capacity of handling all-atom structures of oligopeptides with up to about 10 amino acid residues, which had been used successfully for a structure determination of the nonglobular polypeptide hormone glucagon.[51,52] For the calculations with BPTI a simplified presentation of the polypeptide chain had to be adopted, with each amino acid residue described by two spheres representing the backbone and the side chain, respectively. The fit of the resulting structure with the X-ray crystal structure[5] was not significantly better than that of model calculations done at the same time by others without use of experimental data. I accepted this outcome as a clear-cut documentation that protein structure calculations from NMR data have to be performed with the complete covalent polypeptide structure to represent properly both the van der Waals constraints and the chirality of the individual residues. We also realized, from comparison with other proteins as well as with simulated input data from the BPTI crystal structure, that we were not obtaining a good quality input of conformational NMR constraints for BPTI. Eventually it turned out that the generally available BPTI preparations contain about 10% of closely related BPTI analogs. Although this did not interfere either with the use of BPTI for the development of NMR techniques or with the resonance assignments, it made the collection of an extensive set of NOE distance constraints as input for a structure determination difficult, since the assignments of many NOESY cross peaks remained ambiguous. Furthermore, work with a recombinant isotope-labeled mutant BPTI also confirmed earlier observations by Gerhard Wagner that some resonance lines were not observed because of conformational exchange, which was now traced to a dynamic equilibrium between the two different chiral forms of the disulfide bridge 14–38 (see Figure 1).[53] Based on this information and with the use of a homogeneous protein sample, a high-quality structure determination was finally obtained in 1992.[50]

7 BPTI AND AMIDE PROTON EXCHANGE

Figure 4 shows the first BPTI spectrum published by my laboratory in 1973[3,4] (comparison with Figure 3 affords a good illustration of the progress made during the following decade), and the high-frequency region illustrates part of an early amide proton exchange measurement. The protein was dissolved in D_2O, and the replacement of individual amide protons by deuterons was followed by measurement of the decrease of the intensities of the corresponding resonance lines with time. In Figure 4, the loss of intensity between the two spectra recorded within 10 min and 170 h after sample preparation, respectively, is readily apparent. This was one of the few experiments with proteins that could be done well in 1973 (see ***Wüthrich, Kurt:***

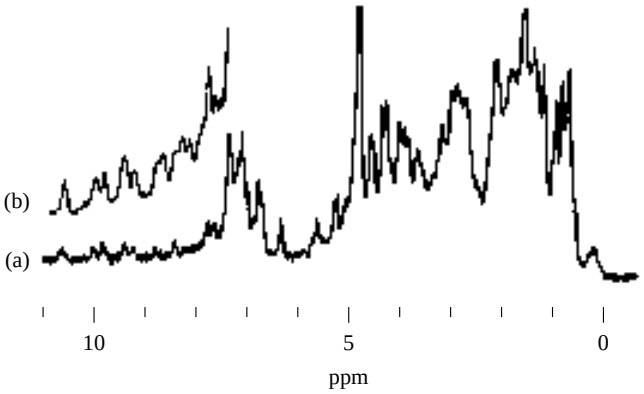

Figure 4 Proton NMR spectrum at 220 MHz of a 0.01 M solution of BPTI in D_2O, pD = 7.7, T = 20°C. Two spectra were recorded 170 h (a) and 10 min (b) after the preparation of the solution. (Reproduced with permission from A. Masson and K. Wüthrich, *FEBS Lett.*, 1973, **31**, 114)

NMR Structures of Biological Macromolecules), and so we started to collect exchange data with BPTI under a wide variety of conditions of pH, temperature, and ionic strength, and subsequently also with homologs and chemical modifications of BPTI.

Amide proton exchange measurement has been a classical approach in protein chemistry long before any such studies were started with BPTI, dating back to the days of the Linderstrøm–Lang laboratory in Copenhagen.[54] The NMR measurements with BPTI added a new element in that the exchange from individual sites in the protein could be followed, whereas earlier techniques yielded information only on the percentage of the ensemble of all amide protons that had exchanged after a certain time span.[54] The new potentialities of NMR were soon recognized by those specializing in the field of amide proton exchange,[55] and in particular Clare Woodward and her group[19,22] started to perform NMR exchange measurements with BPTI under a wide range of conditions. The follow-up to the NMR studies on amide proton exchange listed in Table 1[18–20] continues to the present, and the mechanisms for amide proton exchange in BPTI proposed in 1979[22,23] provide a much discussed background.

The next advance came with the individual assignments of amide proton NMR lines,[21] so that exchange rates could be attributed to unique sites in the BPTI crystal structure.[20,23] This step was completed in 1982, when a map of all individual exchange rates in BPTI was obtained.[56] The last entry on this topic in Table 1[30,31] covers experiments by Heinrich Roder in which experimental conditions were identified where the exchange in a chemically modified BPTI derivative proceeds via a so-called EX_1 process, so that the exchange rates are directly related to the frequencies of protein structure fluctuations.[54] This paper shows that EX_1 processes for amide proton exchange in proteins can be obtained only under extreme conditions which are not normally used for exchange measurements. Therefore, nearly all available exchange data are governed by EX_2 processes, where the exchange rates are not directly related to the frequencies of internal motions in the protein structure but rather to the acid/base-catalyzed reaction at the amide group modulated by conformational equilibria in the protein.[23]

8 BPTI AND INTERNAL MOBILITY IN PROTEINS

In the X-ray crystal structure of BPTI the aromatic rings of phenylalanine and tyrosine are among the side chains with the smallest temperature factors.[5] For each ring the relative values of the B-factors increase toward the periphery, so that the largest positional uncertainty is indicated for the C-4 position on the symmetry axis through the $C\beta-C\gamma$ bond. The observation of ring-flipping motions on the millisecond to microsecond timescale (Figure 5)[14] was therefore a genuine surprise, since it appeared to be incompatible with the crystal structure. Theoretical studies performed in a collaboration of my group with Robert Huber's laboratory,[15] and independently by Martin Karplus's group[6] then showed that the crystallographic B-factors sample multiple rotation states about the $C\alpha-C\beta$ bond, whereas the ring flips about the $C\beta-C\gamma$ bond seen by NMR are very rapid 180° rotations connecting two indistinguishable equilibrium orientations of the ring. The B-factors do not manifest these rotational motions because the populations of all nonequilibrium rotational states about the $C\beta-C\gamma$ bond are vanishingly small. The ring flip phenomenon, which turned out to be a general feature of globular proteins, thus showed that there are low-frequency internal motions in protein molecules, which have activation energies of 60–100 kJ mol^{-1} and amplitudes of $\gtrsim$0.1 nm, and involve concerted displacements of numerous groups of atoms. Ring flips have since been the subject of a long series of theoretical and experimental investigations.

Working with a series of chemical modifications of BPTI and homologous proteins, we observed in 1978[18] that amide proton exchange rates measured under conditions of EX_2 exchange are correlated with the thermal stability of the protein, i.e. corresponding protons would exchange more rapidly in the less stable proteins. In contrast, the ring flip rates, which are directly related to the frequencies of internal protein structure fluctuations, were found to be insensitive to protein stability as long as the 3D structure was preserved at the conditions of the experiment.

BPTI continues to be a source of observations on dynamic features which turn out to be common to globular proteins at large. Most important, it was with BPTI that we succeeded in 1989 in observing individual molecules of hydration water by NMR,[57] to demonstrate that internal hydration water molecules exchange with the bulk solvent on a millisecond timescale or faster,[58] and to distinguish qualitatively between interior hydration sites and surface hydration,[11] which provides a rationale for the generally observed dynamic surface disorder in NMR solution structures of globular proteins (see Figure 2). Another novel dynamic feature identified recently in BPTI is the aforementioned slow interconversion between two conformation states of the disulfide bond 14–38,[53] which was also clearly manifested in ^{15}N $T_{1\rho}$ measurements.[59]

9 BPTI AND PROTEIN FOLDING

One of the 1981 entries in Table 1 is the amide proton trap experiment for studies of early events in protein refolding, which was performed as part of Heinrich Roder's Ph.D. thesis in 1981.[30,32] This experiment and refined forms thereof became very popular in the late 1980s, and it is now one of

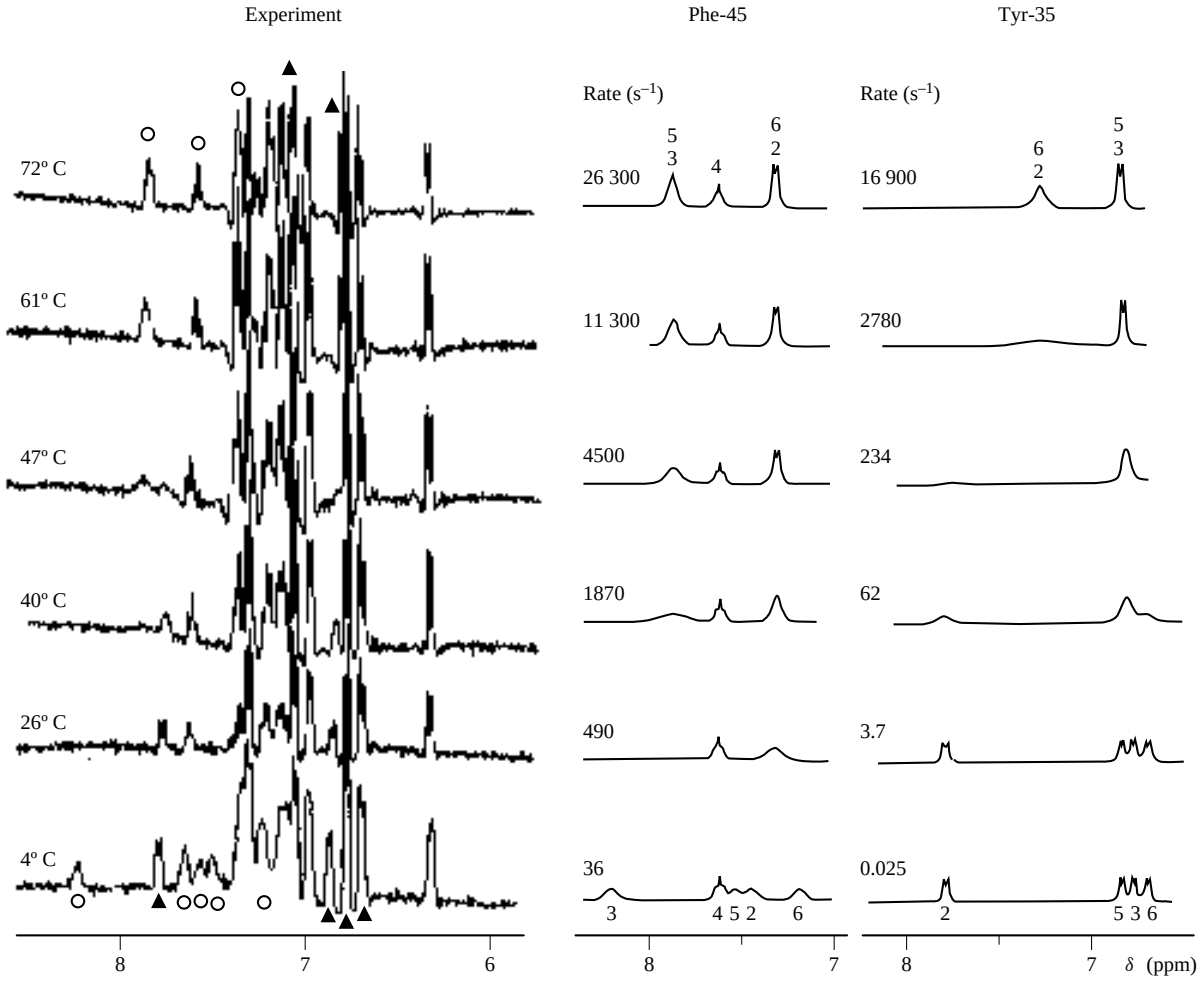

Figure 5 1D 360 MHz ^{1}H NMR spectra at variable temperature of a 0.01 M solution of BPTI in D_2O, pD = 7.8. The region from 6.0 to 8.5 ppm is shown. The resonances of the aromatic rings of Phe-45 (○) and Tyr-35 (▲) were simulated in the center and on the right, respectively, using the ring flip frequencies indicated with the individual spectra. The resonance assignments in the simulated spectra refer to the standard numeration for the aromatic rings of phenylalanine and tyrosine. (Reproduced by permission of Wiley from K. Wüthrich, 'NMR of Proteins and Nucleic Acids', 1986)

the standard techniques in laboratories working on the protein-folding problem.

As mentioned in the introduction, BPTI has long played an important role in the area of protein folding,[7] and early attempts to use NMR experiments for folding studies have already been cited.[32,36] More recently, NMR has been used extensively for structural characterization of BPTI folding intermediates containing only part of the native disulfide bonds (see Figure 1), mainly in the laboratories of Thomas Creighton[60] and Peter Kim.[61]

10 CONCLUDING REMARKS

BPTI has been a focal point for my research group from 1973 until about 1984, when our main activities shifted away from method development toward applications of NMR for protein structure determination in a variety of different systems. This article covers mainly the period of our intense involvement with this protein. Around 1985 we undoubtedly had a feeling of saturation with BPTI, which was also nurtured by referee comments on 'yet another paper on BPTI'. Things were rather quiet for several years after 1985, but in the late 1980s research with BPTI picked up momentum again, triggered primarily by the production of recombinant mutants of BPTI and the possibility of labeling the recombinant proteins with isotopes. Although crystal structures of at least 10 BPTI mutants have been described during the last few years, most of the structural work is done using NMR in connection with folding studies.[60,61] These were recently very much in the limelight due to a widely publicized controversy between Thomas Creighton and Peter Kim on certain aspects of the BPTI refolding pathway. Listening to a presentation by Clare Woodward at the 1994 Annual Meeting of the US Biophysical Society I also learned that the correlation between thermal stability of the folded protein and amide proton exchange rates[18,23] is being further investigated with the use of recombinant BPTI mutants. Overall, considering the advanced techniques now available for protein preparation and NMR investigations, we can look forward to many more years of excitement in research with BPTI.

11 RELATED ARTICLES

Biological Macromolecules: Structure Determination in Solution.

12 REFERENCES

1. M. Kunitz and J. H. Northrop, *J. Gen. Physiol.*, 1936, **19**, 991.
2. R. Huber, D. Kukla, A. Rühmann, and W. Steigemann, *Cold Spring Harbor Symp. Quant. Biol.*, 1971, **36**, 141.
3. K. Wüthrich, *Naturwissenschaften*, 1973, **60**, 221.
4. A. Masson and K. Wüthrich, *FEBS Lett.*, 1973, **31**, 114.
5. J. Deisenhofer and W. Steigemann, *Acta Crystallogr.*, 1975, **B31**, 238.
6. B. R. Gelin and M. Karplus, *Proc. Natl. Acad. Sci. USA*, 1975, **72**, 2002.
7. T. E. Creighton, *J. Mol. Biol.*, 1974, **87**, 579.
8. G. Wagner and K. Wüthrich, *J. Mol. Biol.*, 1982, **155**, 347.
9. G. Wagner, *Q. Rev. Biophys.*, 1983, **16**, 1.
10. K. D. Berndt, P. Güntert, L. P. M. Orbons, and K. Wüthrich, *J. Mol. Biol.*, 1992, **227**, 757.
11. G. Otting, E. Liepinsh, and K. Wüthrich, *Science*, 1991, **254**, 974.
12. S. Karplus, G. H. Snyder, and B. D. Sykes, *Biochemistry*, 1973, **12**, 1323.
13. G. H. Snyder, R. Rowan III, S. Karplus, and B. D. Sykes, *Biochemistry*, 1975, **14**, 3765.
14. K. Wüthrich and G. Wagner, *FEBS Lett.*, 1975, **50**, 265.
15. R. Hetzel, K. Wüthrich, J. Deisenhofer, and R. Huber, *Biophys. Struct. Mech.*, 1976, **2**, 159.
16. A. DeMarco and K. Wüthrich, *J. Magn. Reson.*, 1976, **24**, 201.
17. K. Nagayama, K. Wüthrich, P. Bachmann, and R. R. Ernst, *Biochem. Biophys. Res. Commun.* 1977, **78**, 99.
18. G. Wagner and K. Wüthrich, *Nature*, 1978, **275**, 247.
19. B. D. Hilton and C. K. Woodward, *Biochemistry*, 1978, **17**, 3325.
20. R. Richarz, P. Sehr, G. Wagner, and K. Wüthrich, *J. Mol. Biol.*, 1979, **130**, 19.
21. A. Dubs, G. Wagner, and K. Wüthrich, *Biochim. Biophys. Acta*, 1979, **577**, 177.
22. B. D. Hilton and C. K. Woodward, *Biochemistry*, 1979, **18**, 5834.
23. G. Wagner and K. Wüthrich, *J. Mol. Biol.*, 1979, **134**, 75.
24. K. Nagayama, K. Wüthrich, and R. R. Ernst, *Biochem. Biophys. Res. Commun.*, 1979, **90**, 305.
25. Anil Kumar, R. R. Ernst, and K. Wüthrich, *Biochem. Biophys. Res. Commun.*, 1980, **95**, 1.
26. Anil Kumar, G. Wagner, R. R. Ernst, and K. Wüthrich, *Biochem. Biophys. Res. Commun.*, 1980, **96**, 1156.
27. K. Nagayama and K. Wüthrich, *Eur. J. Biochem.*, 1981, **114**, 365.
28. G. Wagner, Anil Kumar, and K. Wüthrich, *Eur. J. Biochem.*, 1981, **114**, 375.
29. Anil Kumar, G. Wagner, R. R. Ernst, and K. Wüthrich, *J. Am. Chem. Soc.*, 1987, **103**, 3654.
30. H. Roder, Ph.D. Thesis 6932, Eidgenössische Technische Hochschule, Zürich, 1981.
31. H. Roder, G. Wagner, and K. Wüthrich, *Biochemistry*, 1985, **24**, 7396.
32. H. Roder and K. Wüthrich, *Proteins*, 1986, **1**, 34.
33. M. Rance, O. W. Sørensen, G. Bodenhausen, G. Wagner, R. R. Ernst, and K. Wüthrich, *Biochem. Biophys. Res. Commun.*, 1983, **117**, 479.
34. T. F. Havel and K. Wüthrich, *J. Mol. Biol.*, 1985, **182**, 281.
35. M. P. Williamson, T. F. Havel, and K. Wüthrich, *J. Mol. Biol.*, 1985, **182**, 295.
36. D. J. States, C. M. Dobson, M. Karplus, and T. E. Creighton, *J. Mol. Biol.*, 1984, **174**, 411.
37. J. C. Hoch, C. M. Dobson, and M. Karplus, *Biochemistry*, 1982, **21**, 1118.
38. D. Marion and K. Wüthrich, *Biochem. Biophys. Res. Commun.*, 1983, **113**, 967.
39. D. J. States, R. A. Haberkorn, and D. J. Ruben, *J. Magn. Reson.*, 1982, **48**, 286.
40. R. M. Keller and K. Wüthrich, *Biochim. Biophys. Acta*, 1978, **533**, 195.
41. S. L. Gordon and K. Wüthrich, *J. Am. Chem. Soc.*, 1978, **100**, 7094.
42. G. Wagner, A. DeMarco, and K. Wüthrich, *J. Magn. Reson.*, 1975, **20**, 565.
43. K. Wüthrich, G. Wagner, R. Richarz, and S. J. Perkins, *Biochemistry*, 1978, **17**, 2253.
44. K. Wüthrich, G. Wider, G. Wagner, and W. Braun, *J. Mol. Biol.*, 1982, **155**, 311.
45. K. Wüthrich, *NMR of Proteins and Nucleic Acids*, Wiley, New York, 1986.
46. M. Billeter, W. Braun, and K. Wüthrich, *J. Mol. Biol.*, 1982, **155**, 321.
47. K. Wüthrich, M. Billeter, and W. Braun, *J. Mol. Biol.*, 1984, **180**, 715.
48. A. Pardi, M. Billeter, and K. Wüthrich, *J. Mol. Biol.*, 1984, **180**, 741.
49. G. Wagner, W. Braun, T. F. Havel, T. Schaumann, N. Gō, and K. Wüthrich, *J. Mol. Biol.*, 1987, **196**, 611.
50. K. D. Berndt, P. Güntert, L. P. M. Orbons, and K. Wüthrich, *J. Mol. Biol.*, 1992, **227**, 757.
51. W. Braun, C. Bösch, L. R. Brown, N. Gō, and K. Wüthrich, *Biochim. Biophys. Acta*, 1981, **667**, 377.
52. W. Braun, G. Wider, K. H. Lee, and K. Wüthrich, *J. Mol. Biol.*, 1983, **169**, 921.
53. G. Otting, E. Liepinsh, and K. Wüthrich, *Biochemistry*, 1993, **32**, 3571.
54. A. Hvidt and S. O. Nielsen, *Adv. Protein Chem.*, 1966, **21**, 287.
55. S. W. Englander and N. R. Kallenbach, *Q. Rev. Biophys.*, 1984, **16**, 521.
56. G. Wagner and K. Wüthrich, *J. Mol. Biol.*, 1982, **160**, 343.
57. G. Otting and K. Wüthrich, *J. Am. Chem. Soc.*, 1989, **111**, 1871.
58. G. Otting, E. Liepinsh, and K. Wüthrich, *J. Am. Chem. Soc.*, 1991, **113**, 4363.
59. T. Szyperski, P. Luginbühl, G. Otting, P. Güntert, and K. Wüthrich, *J. Biomol. NMR*, 1993, **3**, 151.
60. C. P. M. van Mierlo, J. Kemmink, D. Neuhaus, N. J. Darby, and T. E. Creighton, *J. Mol. Biol.*, 1994, **235**, 1044.
61. J. P. Staley and P. S. Kim, *Proc. Natl. Acad. Sci. USA*, 1992, **89**, 1519.

Acknowledgments

Our own research covered in this article was generously supported by the ETH Zürich, the Schweizerischer Nationalfonds, the Kommission zur Förderung der wissenschaftlichen Forschung and Bruker-Spectrospin AG. I would like to thank Bayer AG for providing us with

a generous supply of BPTI (Trasylol) during more than two decades, and Mr. R. Marani for the careful processing of the manuscript.

Biographical Sketch

Kurt Wüthrich. *b* 1938. Licentiat, 1964, Physics, Mathematics, Chemistry, University of Bern, Eidgeñssisches Sportlehrerdiplom, 1964, Ph.D., 1964, Inorganic Chemistry (Prof. S. Fallab), University of Basel. Stein and Moore Award, 1989; Horwitz prize, 1991; Prix Jeantet, 1993. Postdoctoral work, University of Basel (Prof. S. Fallab), University of California, Berkeley (Prof. R. E. Connick), Bell Telephone Laboratories, Murray Hill, USA (Supervisor Dr. R. G. Shulman). Professor of Biophysics and Head of the Institute of Molecular Biology and Biophysics, ETH Zürich, 1969–present. Approx. 500 publications. Research specialties: NMR structure determination of biological macromolecules, drug design, and protein engineering.

Peptide and Protein Secondary Structural Elements

Josep Rizo and Lila M. Gierasch

University of Texas Southwestern Medical Center, Dallas, TX, USA

1	Introduction	1
2	β-Turns	2
3	α-Helices	3
4	β-Sheets	6
5	Related Articles	9
6	References	9

1 INTRODUCTION

Peptides and proteins carry out an immense variety of biological functions. In order to perform these roles, the polypeptide molecules adopt well-defined three-dimensional structures. Despite the fact that the number of possible combinations of backbone torsion angles for a given polypeptide chain is essentially infinite, a large percentage of the residues in a protein are usually found in standard elements of secondary structure such as β-turns, α-helices, and β-sheets. Thus, determination of the secondary structure of a protein is a major step towards elucidating its global tertiary fold. The same elements of secondary structure are also found commonly in the bioactive conformations of naturally occurring peptides, and identification of such elements is crucial if bioactive conformations are to be defined.

NMR spectroscopy is the most powerful technique for analyzing in detail the secondary structure of peptides and proteins in solution. Pioneering work by Wüthrich and coworkers[1,2] showed that elements of secondary structure in polypeptides could be easily identified from observed NOE patterns, since each type of secondary structure is characterized by a different set of short interproton distances. This is illustrated in Figure 1, where the most common types of secondary structure (type I and II β-turns, α-helix, and antiparallel and parallel β-sheet) are represented, and the most characteristic, close interproton interactions for each type of structure are indicated by arrows. The relevant interproton distances and standard backbone torsion angles are listed in Table 1. In addition to NOE patterns, other NMR parameters such as coupling constants, chemical shifts, amide temperature coefficients, and amide H/D exchange rates, can also be used to define the secondary structure of polypeptides.

In this article we illustrate how information obtained by NMR spectroscopy techniques in solution can be used to analyze the presence of β-turns, α-helices, and β-sheets in peptides and proteins, and we discuss particular facets associated with the identification of each type of secondary structure. Examples from both the peptide and the protein NMR literature will be used. Although the principles involved in the conformational analysis of peptides and proteins by NMR are the same, some differences exist in the methodology used, both because of diversity in the goals pursued and because of general distinctions in structural and dynamic characteristics.

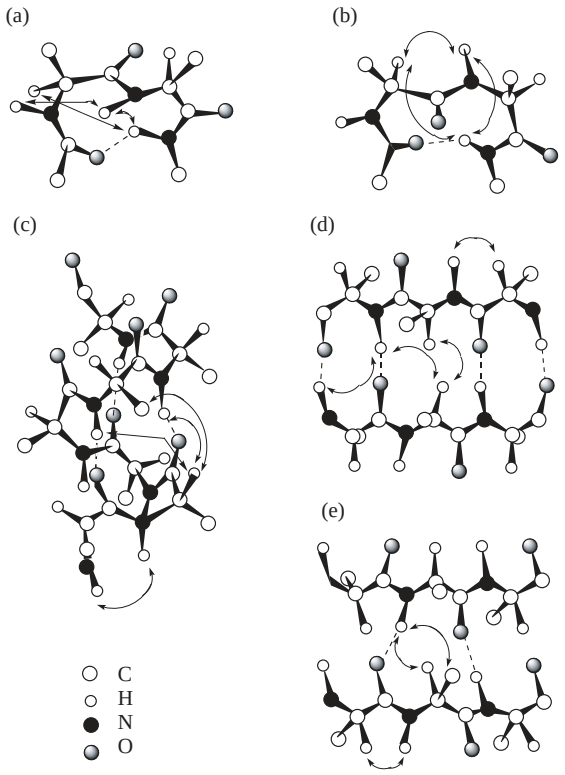

Figure 1 Characteristic short interproton distances in β-turns, α-helices, and β-sheets. Dashed lines indicate hydrogen bonds and curved arrows indicate the characteristic interproton distances (only one example of each interaction is indicated). The values of the interproton distances are shown in Table 1. The following types of secondary structure and corresponding interproton distances are shown: (a) type I β-turn, $d_{NN}(i + 1,i + 2)$, $d_{NN}(i + 2,i + 3)$, $d_{\alpha N}(i + 1,i + 3)$; (b) type II β-turn, $d_{\alpha N}(i + 1,i + 2)$, $d_{NN}(i + 2,i + 3)$, $d_{\alpha N}(i + 1,i + 3)$; (c) α-helix, $d_{NN}(i,i + 1)$, $d_{\alpha N}(i,i + 3)$, $d_{\alpha\beta}(i,i + 3)$, $d_{\alpha N}(i,i + 4)$; (d) antiparallel β-sheet, $d_{\alpha N}(i,i + 1)$, $d_{\alpha\alpha}(i,j)$, $d_{\alpha N}(i,j)$, $d_{NN}(i,j)$; (e) parallel β-sheet, $d_{\alpha N}(i,i + 1)$, $d_{\alpha N}(i,j)$, $d_{NN}(i,j)$

Naturally occurring peptides are usually unstructured in solution and only adopt a specific conformation(s) when they perform their function, for instance upon interaction with a receptor. Direct observation of the bioactive conformation is usually hindered because most receptors are membrane bound proteins. Thus, much of the research on conformational analysis of biologically active peptides has concentrated on analogs incorporating constraints that limit their conformational degrees of freedom and favor adoption of their bioactive conformations.[3] A large body of work on peptide conformation has also been directed to peptides as models of protein substructures,[3] with the goal of understanding the preferences of individual amino acid residues for different types of secondary structure. The model peptides often contain constraints and are designed with specific amino acid sequences to favor a particular type of structure. Analysis of peptides is often performed in the presence of organic solvents such as deuterated 2,2,2-trifluoroethanol (TFE), which induce the formation of secondary structure. Even with the aid of constraints and

Table 1 Characteristic Short Interproton Distances (nm) and Standard Backbone Torsion Angles in β-Turns, α-Helices and β-Sheets[a]

	Type I β-turn			Type II β-turn		α-Helix	Antiparallel β-sheet	Parallel β-sheet
Torsion angles (deg.)								
ϕ	−60	−90	−60		80	−57	−139	−119
ψ	−30	0	120		0	−47	135	113
Interproton distances (nm)								
$d_{\alpha N}(i,i+1)$	0.35	3.2	0.21	0.32	0.32	0.35	0.21	0.21
$d_{\alpha N}(i,i+2)$	0.36		0.32			0.45		
$d_{\alpha N}(i,i+3)$	0.32–0.44			0.38–0.48		0.35		
$d_{\alpha N}(i,i+4)$						0.41		
$d_{NN}(i,i+1)$	0.26	0.24	0.46		0.25	0.27	0.44	0.43
$d_{NN}(i,i+2)$	0.39		0.42			0.42		
$d_{\beta N}(i,i+1)$	0.29–0.43	0.36–0.46	0.36–0.46		0.36–0.46	0.25–0.40	0.32–0.44	0.37–0.46
$d_{\alpha\beta}(i,i+3)$						0.26–0.44		
$d_{\alpha\alpha}(i,j)$							0.23	0.47
$d_{\alpha N}(i,j)$							0.31	0.30
$d_{NN}(i,j)$							0.33	0.39

[a]The interproton distances where measured on model alanine-based peptides using the program INSIGHT (Biosym Technologies Inc.). The most characteristic NOE interactions are indicated in 1 by curved arrows. In the α-helix and β-sheet, residue i corresponds to an arbitrary residue in the sequence. In the β-sheet, residue j corresponds to a residue apposed to residue i in a contiguous strand. The four residues in a β-turn are numbered i to $i+3$. Torsion angles correspond to residues $i+1$ (left) and $i+2$ (right). The $d(i,i+1)$ distances indicated refer to $d(i+1,i+2)$ (left) and $d(i+2,i+3)$ (right), while $d(i,i+2)$ refers to $d(i+1,i+3)$

structure-inducing solvents, it is paramount to consider the possibility of conformational averaging in any study of peptide conformation. Conformational analysis of peptides is also hindered by the fact that most protons are in the periphery of the molecule and thus only a small number of NOEs per residue can be measured. However, measurement of interproton distances can usually be accomplished with higher accuracy for peptides than for proteins, due to higher simplicity of the spectra, longer relaxation times, and less spin diffusion.

Proteins usually have well-defined structures, and conformational averaging occurs only in flexible turns or loops. Although the measurement of accurate interproton distances is hindered by spin diffusion, the existence of a large number of NOE interactions per residue facilitates the determination of high resolution structures. The emphasis in protein structure determination[2,4,5] is generally on analyzing native structures with the highest detail possible, understanding interactions with ligands, and determining conformational changes associated with the execution of their biological roles. However, there is increasing interest in the analysis of denatured states of proteins,[6] which are important to protein folding and have higher flexibility than the native states.

2 β-TURNS

β-Turns are sites where the polypeptide chain reverses its overall direction, allowing proteins to adopt a globular shape (for a review see Rose et al.[7]). Because of their surface location and because they facilitate side-chain exposure, β-turns provide ideal sites for molecular recognition. Thus, β-turns also occur very often in the bioactive conformations of naturally occurring peptides. β-Turns comprise four amino acid residues (usually numbered i to $i+3$), and the different types of β-turn are distinguished by the backbone torsion angles of the central residues ($i+1$ and $i+2$). Type I and II β-turns (see Figure 1 and Table 1) are the ones most commonly found in proteins.[8] Their mirror images, type I′ and II′ β-turns, are less common and have a tendency to appear in β-hairpins.

The interproton distances characteristic of type I and type II β-turns are similar, with the exception of those between the amide proton of residue $i+2$ and the H-α and HN protons of residue $i+1$ (Table 1). The NMR parameter that is most characteristic of β-turns is the strong NOE between the amide protons of residues $i+2$ and $i+3$. Type II β-turns are easily identified because of the absence of other d_{NN} NOEs and the presence of a strong $d_{\alpha N}(i+1,i+2)$ interaction. In contrast, in type I β-turns the $d_{\alpha N}(i+1,i+2)$ NOE is weak, and there is usually a $d_{NN}(i+1,i+2)$ NOE. Thus, the sequential NOE patterns associated with type I β-turns are similar to those of an α-helix. Type I β-turns can be distinguished from α-helices because of the presence of a $d_{\alpha N}(i+1,i+3)$ NOE (also characteristic of type II β-turns) and the absence of a repetitive pattern of d_{NN}, $d(i,i+3)$, and $d(i,i+4)$ interactions. In both type I and type II β-turns the amide protons of the corner residues ($i+1$ and $i+2$) are exposed to the solvent, while the amide proton of residue $i+3$ is usually hydrogen bonded with the carbonyl group of residue i; thus, the latter amide proton usually has decreased H/D exchange rate and its chemical shift has a low temperature coefficient.

Although the formation of stable secondary structure in linear peptides is unusual, several cases of linear peptides adopting substantial populations of β-turn conformations have been described. Particularly interesting is the finding of a significant population of a β-turn conformation in the first four residues of the pentapeptide Tyr-Pro-Tyr-Asp-Val,[9] corresponding to the immunodominant region of a larger peptide derived from influenza virus hemaglutinin. The turn conformation was mainly deduced from the presence of $d_{NN}(3,4)$ and $d_{\alpha N}(2,4)$ NOEs, and from the low temperature

coefficient of the Asp^4 HN. The temperature coefficient of Asp^4 HN in a series of analogous peptides, where Tyr^3 was replaced by other residues, was used as a measure of the β-turn populations in the peptides, and these populations correlated with β-turn probabilities calculated from protein crystal structures.

NMR studies on the propensities of amino acid residues to occur in different positions of β-turns have been more commonly performed using constrained peptide models,[3,7,10] in particular cyclic peptides. These studies have shown, for instance, that proline residues have a high tendency to occur in the $i + 1$ position of both type I and type II β-turns, and that glycine has a preference for the $i + 2$ position of type II β-turns and for the $i + 1$ position of type II′ β-turns, in good correlation with the preferences observed in proteins. The positions preferred by Gly residues are characterized by torsion angles corresponding to regions of the Ramachandran map that are energetically unfavorable for L-amino acids, but not for D-amino acids. Indeed, replacement of Gly residues by D-amino acids stabilizes the turn conformations, and L-Xaa-D-Yaa and D-Xaa-L-Yaa dyads have a high tendency to be in the corner positions of type II and type II′ β-turns, respectively. Observations such as the above have been used in peptide analog design to stabilize turn conformations hypothesized to be important for biological activity in naturally occurring peptides. An example is gonadotropin releasing hormone (GnRH), whose bioactive conformation was proposed to contain a type II′ β-turn around the residues Gly^6-Leu^7. A series of highly potent, constrained GnRH antagonists containing a covalent bridge between residues 4 and 10, and D-amino acids in position 6, was designed. Analysis by NMR of one of these compounds[11] showed that it adopts the predicted type II′ β-turn conformation, as evidenced by the observation of a very low temperature coefficient for the amide proton of residue 8, and of the following interproton distances: $d_{\alpha N}(6,7) = 0.22$ nm, $d_{\alpha N}(7,8) = 0.31$ nm, and $d_{NN}(7,8) = 0.25$ nm (note that in this case the interproton distances corresponding to a type II′ β-turn are the same as in a type II β-turn, described in Table 1). This example also illustrates the high accuracy that can be achieved in the measurement of interproton distances for small peptides.

NMR studies of cyclic pentapeptides have provided a good example of conformational averaging between a discrete number of conformations involving β-turns.[12] NMR data obtained for cyclo(Gly-Pro-D-Ala-Gly-Asn), cyclo(D-Ala-Pro-Asn-Gly-Pro), and cyclo(Gly-Pro-Ala-D-Phe-Pro) showed that the three peptides adopt β-turn conformations with Pro^2 in position $i + 1$. Buildup curves of the NOEs between Pro^2 H-α and the HN in position 3 for the three peptides, obtained from one-dimensional NOE difference spectra, are shown in Figure 2. The distance measured for the Pro-D-Ala peptide (0.20 nm) is consistent with the presence of a type II β-turn, which is favored by the LD sequence. However, the distances observed for the Pro-Asn and Pro-Ala peptides were 0.245 and 0.29 nm, respectively, which are intermediate between those expected for type I (0.35 nm) and type II (0.21 nm) β-turns (Table 1). Other measured interproton distances and molecular dynamics simulations supported the conclusion that these two peptides exist in an equilibrium between type I and type II β-turn conformations (fast on the NMR timescale), rather than adopting an intermediate conformation between the two types of turn. From the interproton distances it was calculated that the population of type II β-turn conformations in the Pro-Asn and Pro-Ala peptides is about 35% and 10%, respectively, which correlates very well with the observed frequency of occurrence of Asn and Ala in the $i + 2$ position of protein type II β-turns.[8] Equilibrium between type I and type II β-turns in peptides has also been observed by circular dichroism.[13]

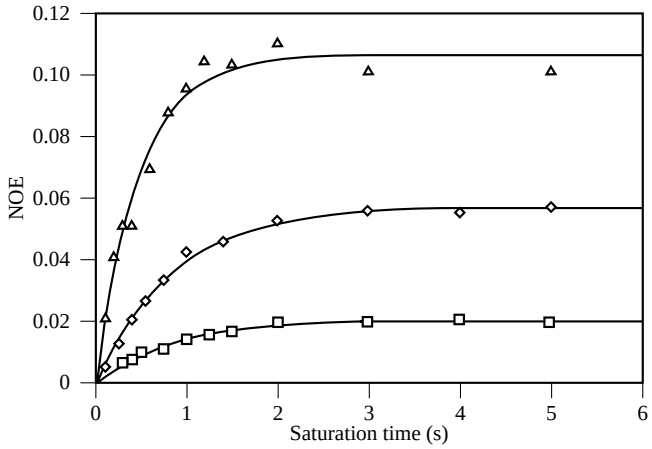

Figure 2 NOE buildup curves obtained from the integrated intensities of Pro^2 H-α resonances, after saturation of the HN signal of residue 3, in one-dimensional NOE difference spectra of: (△) cyclo(Gly-Pro-D-Ala-Gly-Asn), (◇) cyclo(D-Ala-Pro-Asn-Gly-Pro), and (□) cyclo(Gly-Pro-Ala-D-Phe-Pro). (Reproduced by permission of John Wiley & Sons, Inc., from S. J. Stradley, J. Rizo, M. D. Bruch, A. N. Stroup, and L. M. Gierasch, *Biopolymers*, 1990, **29**, 263)

The parameters used to recognize β-turns in proteins are in principle analogous to those used for peptides. Identification of β-turns at the ends of β-sheet strands is straightforward because they represent a clear interruption of the regular pattern of NOEs characteristic of β-sheets. However, it is difficult to distinguish type I β-turns at either the N- or the C-terminus of helices, in particular 3_{10} helices, because of the similarity between the NOE patterns associated with both types of secondary structure and the difficulty in measuring accurate interproton distances in proteins. The latter reason, and the lack of a repetitive pattern of NOEs characteristic of β-turns, also hinder the location of β-turns in segments of the polypeptide chain with nonregular secondary structure. Thus, many of the β-turns in proteins cannot be located unambiguously until determination of the tertiary structure with a complete set of short-, medium-, and long-range interproton distances.[1] The type of turn can usually be distinguished from the intensity of the $d_{\alpha N}(i + 1,i + 2)$ NOE, the presence or absence of a $d_{NN}(i + 1,i + 2)$ interaction, and sometimes from tertiary interactions involving the amide proton in position $i + 2$. However, the possibility of interconversion between different turn conformations is hard to assess because of the difficulty in measuring accurate interproton distances.

3 α-HELICES

The α-helix is the most abundant element of secondary structure in proteins, and the structures of some proteins such as those in the globin family comprise only α-helices

and loops. α-Helices are formed by an array of consecutive residues with backbone torsion angles around the standard values indicated in Table 1. Since formation of α-helices requires a minimum number of residues and their stability increases with their length, α-helices are less common than β-turns in the bioactive conformations of short, naturally occurring peptides. However, α-helix formation is a common determinant of biological activity in longer peptides such as growth-hormone releasing factor.

The most characteristic feature to identify the presence of an α-helix by NMR spectroscopy is the presence of a pattern of consecutive, medium-to-strong $d_{\mathrm{NN}}(i,i+1)$ NOE connectivities, accompanied by numerous $d_{\alpha\beta}(i,i+3)$, $d_{\alpha\mathrm{N}}(i,i+3)$, and $d_{\alpha\mathrm{N}}(i,i+4)$ interactions (Table 1). Some $d_{\mathrm{NN}}(i,i+2)$ NOEs may also be observed, and $d_{\beta\mathrm{N}}(i,i+1)$ NOEs are usually stronger than in β-sheet or in random conformations. The less usual 3_{10} helices, which are characterized by similar interproton distances to those of an α-helix, can be distinguished by the regular presence of $d_{\alpha\mathrm{N}}(i,i+2)$ NOEs and the absence of $d_{\alpha\mathrm{N}}(i,i+4)$ interactions.[14] α-Helices are also characterized by small $^3J_{\mathrm{HN}\alpha}$ coupling constants. Although the expected value of $^3J_{\mathrm{HN}\alpha}$ is 3.9 Hz for the standard α-helix geometry,[2] it is unusual to observe such low values for α-helical peptides and, even in regions that have high populations of α-helical conformation, $^3J_{\mathrm{HN}\alpha}$ coupling constants of about 5–6 Hz are usually found. This observation probably reflects the intrinsic flexibility of the polypeptide chain in the absence of the tertiary interactions that stabilize protein structures. Since the large linewidths associated with protein resonances hinder the accurate measurement of small coupling constants, $^3J_{\mathrm{HN}\alpha}$ in proteins are usually classified as 'large' ($\geq$7 Hz) or 'small' ($\leq$6 Hz), and α-helices are distinguished by a string of consecutive 'small' $^3J_{\mathrm{HN}\alpha}$ coupling constants. Another characteristic of α-helices is that all their amide protons, except those at the N-terminus, participate in CO(i)/HN(i + 4) hydrogen bonds, which results in decreased H/D exchange rates.

Although peptide and protein chemical shifts have traditionally been difficult to understand in theoretical terms, unequivocal correlations between certain chemical shifts and secondary structure are now well established. Such correlations are based on the differences between the observed chemical shifts and random coil chemical shifts; the differences are known as 'secondary shifts' or 'conformational shifts'. Perhaps the best established correlation is the low-frequency (upfield) conformational shifts of H-α protons in α-helical conformations (on average 0.39 ppm) and the high-frequency shifts for H-α protons in β-sheets (on average 0.37 ppm).[15] A chemical shift index for assigning secondary structure in proteins, based on such shifts, has been described by Wishart et al.[16] In α-helices, amide protons also experience a low-frequency conformational shift,[15] while the ^{13}C-α resonances are shifted to high frequency.[17] Correlations involving H-β and ^{13}C-β chemical shifts have also been noted, but are less clear-cut. In general, ^{13}C conformational shifts are more reliable indicators of secondary structure than proton conformational shifts because they are less likely to be affected by other factors such as ring-current shifts from aromatic residues. Although the backbone ^{15}N conformational shifts correlate with those of their directly bonded amide protons, it is more difficult to establish correlations based on backbone ^{15}N chemical shifts because the random coil values are affected by both the side chain of the same residue and by that of the preceding residue; thus 400 rather than 20 random coil chemical shifts need to be defined. In addition to complementing NOE data in the determination of native three-dimensional structures of proteins by NMR, conformational shifts provide a useful tool for characterizing secondary structure in non-native states of proteins, for which resonance overlap may hinder the obtention of critical NOE data. In peptides, H-α chemical shifts can be used to estimate the relative populations of α-helical conformation at each residue[18] (see below). Other parameters that have been used to obtain such estimates include the intensities of $d_{\alpha\beta}(i,i+3)$ NOEs,[19] ratios between $d_{\mathrm{NN}}(i,i+1)$ and $d_{\alpha\mathrm{N}}(i,i+1)$ NOE intensities,[20] and $^3J_{\mathrm{HN}\alpha}$ coupling constants.[20]

A large number of conformational studies on linear peptides have analyzed the factors that determine α-helix formation and the intrinsic propensities of individual amino acid residues to adopt the α-helical conformation. Structure-inducing solvents such as TFE are often used in these studies to increase the tendency of the peptides to form α-helical conformation. While circular dichroism has been most widely used to evaluate overall helix content in these studies, NMR spectroscopy is the technique of choice for determining the location of the helix and obtaining residue-specific information. An example of these studies is an analysis of the conformations of isolated wild type (WT) and mutant outer membrane protein A (OmpA) signal peptides in membrane mimetic environments, performed to compare the propensities of these peptides to adopt an α-helical conformation with their in vivo ability to mediate protein secretion.[18] Figure 3 gives a summary of the $^3J_{\mathrm{HN}\alpha}$ coupling constants and conformationally relevant NOEs observed for the WT OmpA signal peptide in TFE-d_3/water 1 : 1 (v/v) at 25 °C. These data show that the peptide forms an α-helical conformation throughout most of the sequence, from Lys^3 to Ala^{21}. The conformational shifts of H-α protons observed for this peptide (Figure 4) agree with this conclusion and show that the helix is somewhat interrupted in the middle of the sequence (near Gly^{14}), which was confirmed by measurement of H/D exchange rates (not shown). Comparison of the conformational shifts of the mutant peptides with those of the WT peptide (Figure 4) provided a sensitive method for detecting differences among the family

Figure 3 Summary of NOE and ^3J(H,N-α) data defining the α-helical conformation of the isolated wild type OmpA peptide in TFE-d_3/water 1 : 1 (v/v). For the sequential NH(i)/NH(i + 1) interactions, the height of the boxes reflects the NOE intensity. Boxes and solid lines indicate NOEs that could be identified; question marks and dashed lines indicate NOEs whose presence could not be assessed due to resonance overlap. (Reproduced by permission of the American Chemical Society from J. Rizo, F. J. Blanco, B. Kobe, M. D. Bruch, and L. M. Gierasch, *Biochemistry*, 1993, **32**, 4881)

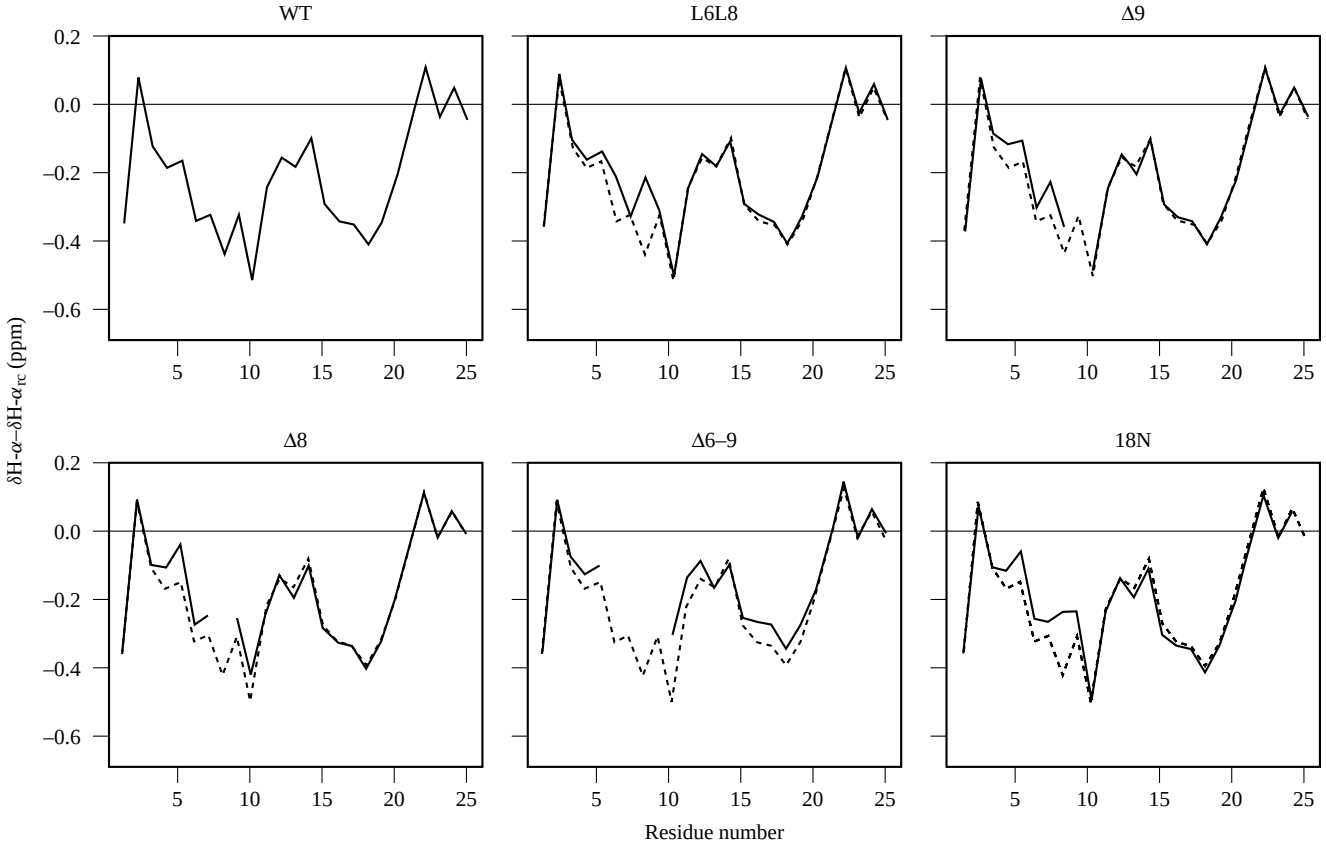

Figure 4 Conformational shift maps for wild type and five mutant OmpA peptides in TFE-d_3/water 1 : 1 (v/v) (solid lines). The wild type sequence is shown in Figure 3. The L6L8 mutant contains Ile^6 > Leu and Ile^8 > Leu mutations, and the I8 N peptide contains an Ile^8 > Asn mutation. The Δ8, Δ9, and Δ6–9 mutants contain deletions at residues Ile^8, Ala^9, and Ile^6-Ala^7-Ile^8-Ala^9, respectively. In the maps for the mutant peptides, the profiles are compared with the wild type profile (dashed lines). (Reproduced by permission of the American Chemical Society from J. Rizo, F. J. Blanco, B. Kobe, M. D. Bruch, and L. M. Gierasch, *Biochemistry*, 1993, **32**, 4881)

of peptides in the populations of α-helix at different residues. Indeed, overall helical contents calculated from the average conformational shifts agreed very well with helical contents calculated from circular dichroism data. The same set of OmpA peptides was also analyzed by NMR in deuterated sodium dodecyl sulfate micelles, revealing a clear correlation between the α-helical contents of the peptides in the micelles and their in vivo activity.[18] In addition, comparison with the data obtained in TFE-d_3/water showed that the correlation was due to a combination of hydrophobic and electrostatic interactions of the peptides with the micelles.

An increasing number of short peptides have been shown to adopt an α-helical structure in aqueous solutions, without the help of organic solvents. Most notable are peptides with sequences corresponding to segments of protein chains that adopt an α-helical conformation in the native structure of the proteins. A classical example is the C-peptide of ribonuclease A (the N-terminal 13-residue segment produced by cleavage with cyanogen bromide). Analysis of this peptide and its analogs by circular dichroism provided ample evidence for the formation of α-helical structure in aqueous solution at low temperatures. An NMR analysis of an analog of the C-peptide in aqueous solution at 3 °C was carried out to determine local conformational effects of α-helix stabilizing interactions in the peptide. A high population of an α-helical conformation extending throughout most of the sequence was observed, but the α-helix was distorted at the N-terminus to accommodate a salt bridge between the side chains of residues 2 and 10.[21] The distortion was evidenced by a number of NOEs that are not characteristic of an α-helix. Strikingly, the same salt bridge and a similar distortion of the helix is observed in the X-ray structure of ribonuclease A. In another study of the tendency of isolated segments of proteins to adopt native secondary structure, a peptide corresponding to the H-helix of myoglobin was analyzed by NMR in aqueous solution.[19] The peptide was shown to adopt an α-helical conformation that is most stable in the middle of the sequence and frayes at both termini. The H-helix is present in a molten globule state of apomyoglobin, and is one of the first elements of secondary structure formed in the folding pathway of the protein, as evidenced by H/D exchange pulse labeling experiments monitored by NMR.[22] These and other studies have shown that certain α-helices present in the native structures of proteins can be formed as independent folding units, and thus could act as initiators of protein folding.

The α-helical regions of proteins are characterized by small dispersion of chemical shifts, and severe overlap usually hinders the sequential resonance assignment. Use of heteronuclear three-dimensional NMR experiments[23] such as $^1H-^{15}N$ three-dimensional TOCSY–HMQC (heteronuclear multiple quantum coherence) and three-dimensional NOESY–HMQC can greatly alleviate this problem. Indeed, if there is no simultaneous degeneracy of amide ^1H and ^{15}N chemical shifts, the

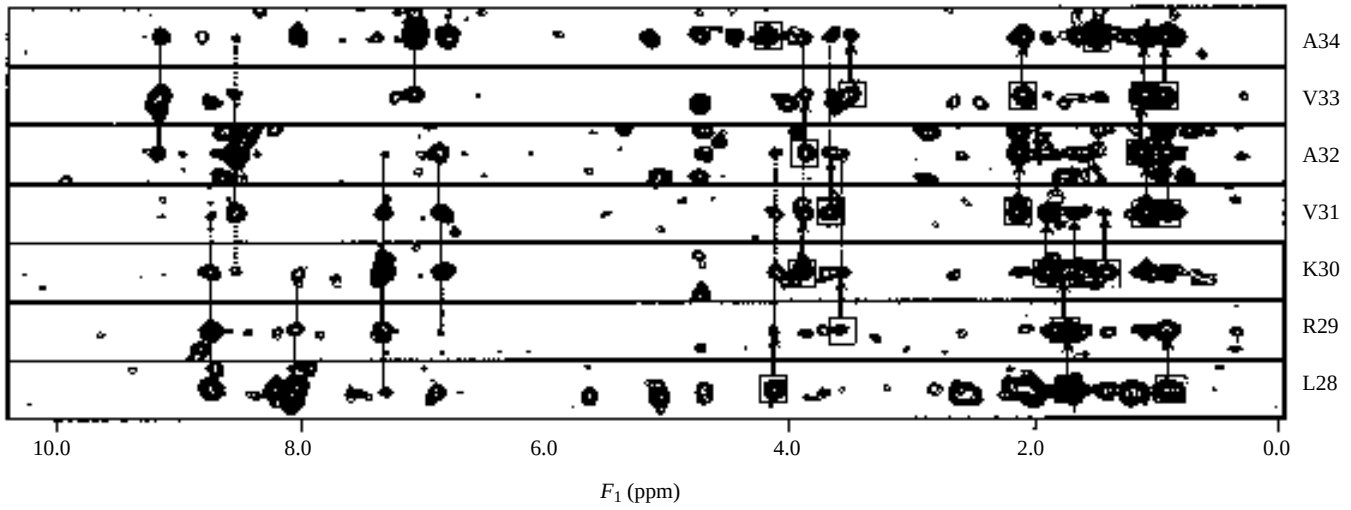

Figure 5 Assignment of the second helix of CRABP illustrated with (ω_1,ω_3) strips from a ^{1}H–^{15}N three-dimensional NOESY–HMQC spectrum, taken at ω_2 values corresponding to the ^{15}N chemical shift of the amide nitrogen of each residue. Boxes indicate intraresidue NOEs, arrows point to sequential NOEs involving H-α or side-chain protons, and solid lines indicate $d_{NN}(i,i + 1)$ connectivities. Dashed lines indicate $d_{NN}(i,i + 2)$, $d_{\alpha N}(i,i + 3)$, and $d_{\alpha N}(i,i + 4)$ NOEs

characteristic NOE patterns associated with the α-helical conformation make it straightforward to sequentially assign α-helical regions from the sets of NOEs observed for each amide proton. This point is illustrated in Figure 5, where selected strips of a ^{1}H–^{15}N three-dimensional NOESY–HMQC spectrum of cellular retinoic acid binding protein (CRABP),[24] corresponding to part of one of the two α-helices of this protein, are shown. The sequential assignment can be easily performed from the $d_{NN}(i,i + 1)$ connectivities alone. Numerous sequential and $d_{\alpha N}(i,i + 3/4)$ NOEs provide additional information for resolving possible ambiguities in the interpretation of the $d_{NN}(i,i + 1)$ interactions. A feature which also facilitates the assignments is the fact that, because any two consecutive amide protons in a helix are close to each other, there is usually a good number of protons that are simultaneously close to both amide protons; thus, consecutive amide protons generally have many NOEs in common (sometimes more than 10).

For proteins with molecular weight above 10 kDa and containing mostly α-helical conformation, severe resonance overlap may hinder the sequential assignment even using ^{1}H–^{15}N three-dimensional TOCSY–HMQC and NOESY–HMQC data. These problems can be overcome using a series of triple resonance experiments on uniformly ^{15}N- and ^{13}C-labeled protein samples, which provide two and sometimes three different pathways to the sequential assignments.[25] The power of these experiments was demonstrated in the analysis of the mostly α-helical protein calmodulin (16.7 kDa)[25,26] and of its complex with a 26-residue peptide derived from skeletal muscle myosin light chain kinase.[27] Calmodulin is a Ca^{2+} binding protein that regulates the activity of a large number of proteins. The structure of calmodulin contains two domains, with two helix–loop–helix 'EF-hand' Ca^{2+} binding domains each, that are connected by a long central helix. While the central helix appears to be continuous in the crystal structure of calmodulin, NMR analysis showed that four residues in the middle of the helix were actually quite unstructured and flexible in solution,[26] allowing the N- and C-terminal domains to tumble independently.[28] Solution of the structure of the complex with the 26-residue peptide showed that the peptide binds in an α-helical conformation, and that the central helix of calmodulin unravels further upon peptide binding, thus (using the words of the authors) 'enabling the two domains to come together to grip the peptide rather like two hands capturing a rope'.[27] The structure of the complex also explained how calmodulin is able to bind a variety of polypeptide chains.

4 β-SHEETS

β-Sheets constitute the second most abundant type of regular secondary structure found in proteins. In contrast to turns and helices, β-sheets are not usually formed by a single segment of a polypeptide chain, but rather by at least two segments aligned in a parallel or antiparallel arrangement so that the amide groups of one segment form hydrogen bonds with the amide groups of the other segment (Figure 1). In addition, β-sheets are stabilized by nonbonding interactions between the side chains of the two strands. Thus, in the case of β-sheets, the formation of secondary structure is coupled to the establishment of tertiary interactions. Consequently, β-sheets are unusual in the conformations of monomeric peptides in solution, and β-sheet formation in peptides is most often concomitant with aggregation. However, interaction with a receptor can stabilize β-structure, and short β-hairpins, where two peptide segments connected by a β-turn form an antiparallel β-sheet, have been proposed to be present in the bioactive conformations of some naturally occurring peptides, e.g. GnRH.[11]

The torsion angles characteristic of both parallel and antiparallel β-sheets (Table 1) correspond to extended conformations of the polypeptide chain and the associated patterns of sequential NOEs are similar to those of random coils: $d_{\alpha N}(i,i + 1)$ NOEs are strong, $d_{NN}(i,i + 1)$ NOEs are very weak or absent, and $d_{\beta N}(i,i + 1)$ NOEs are usually weaker than in α-helices. No $d(i,i + 2)$, $d(i,i + 3)$, or $d(i,i + 4)$ interactions are usually observed in β-sheets. However, interstrand NOEs (Table 1)

can help distinguish β-sheets from nonspecific extended conformations. Among these interactions, medium-to-strong $d_{\alpha\alpha}$ NOEs are the hallmark of antiparallel β-sheet structure, while other interstrand NOEs in either parallel or antiparallel β-sheets are usually weak. The identities of the interstrand NOEs provide unequivocal evidence of the relative orientation of the strands, and thus distinction between parallel and antiparallel β-sheets is straightforward from such NOEs. β-Sheets are also characterized by large ($\geq$8.0 Hz) $^3J_{\mathrm{HN}\alpha}$ coupling constants. Most amide protons in β-sheets have decreased amide H/D exchange rates due to hydrogen bonding, except at the edges where alternate amide protons are exposed to the solvent. High frequency conformational shifts are observed in general for H-α and HN protons in β-sheets,[15] while ^{13}C-α resonances are usually shifted to low frequency.[17]

The structural factors that influence the adoption of β-sheet structure are less well understood than those determining α-helix formation, due in part to the fact that peptides with a propensity to form β-structure usually have also a high tendency to aggregate. Nevertheless, an example of a short linear peptide adopting a substantial population of a β-hairpin conformation in solution has been reported recently.[29] This peptide, with sequence YQNPDGSQA, was designed as an analog of the segment 15–23 of tendamistat (YQSWRYSQA), which forms a β-hairpin in the native protein; the four residues NPDG were introduced to optimize the probability of β-turn formation. Analysis by NMR showed that the peptide YQNPDGSQA exists in equilibrium among multiple conformations in solution, but a significant population of a β-hairpin structure was demonstrated by the observation of several interstrand NOEs, including a Gln^2 H-α/Gln^8 H-α interaction. A control nonapeptide including the NPDG sequence did not adopt the β-hairpin conformation, indicating that the residues flanking the β-turn play a role in stabilization of the β-hairpin. Other examples of monomeric peptides forming β-sheets have involved the use of covalent constraints. A good example of peptide β-hairpins stabilized by cyclization has been provided by a series of peptides derived from the flap of human renin, a β-hairpin loop that corresponds to a strongly antigenic region of the protein.[30] The peptides contained eight or twelve residues from the sequence of the flap and two cysteines, one at each termini, forming a disulfide bond. NMR analysis of the peptides showed several interstrand NOE interactions characteristic of the proposed β-hairpin structure. The two cyclic peptides were recognized by human renin antibodies, while their linear analogs did not bind to the antibodies. Disulfide bonds have also been used in the design of constrained peptide models for β-sheets, and continuing progress is being made in the improvement of such models, as well as in the design of β-sheet nucleating templates (see Rizo and Gierasch[3]). These molecules will be very useful tools for studying the rules that determine β-sheet formation in polypeptides.

The NMR spectra of proteins containing mostly β-structure generally have good dispersion of chemical shifts, which facilitates their sequential assignment. It is typical to observe abundant H-α resonances above 5 ppm and amide proton signals between 9 and 10 ppm. The large dispersion of chemical shifts arises in part from diversity in the backbone torsion angles, since the β-structure corresponds to the widest region of energetically favorable conformations in the Ramachandran map; thus, larger deviations from standard geometries are observed in β-sheets than in α-helices. Selected strips corresponding to a ^{1}H–^{15}N three-dimensional NOESY–HMQC spectrum of CRABP, a 136-residue protein with two five-stranded antiparallel β-sheets and a helix–turn–helix motif,[24] are shown in Figure 6. The strips illustrate the assignment of the C-terminal β-strand (residues 128–136) which, in the tertiary structure of the protein, is contiguous to the segments 7–14 and 117–123. The sequential assignment is based primarily on the strong $d_{\alpha\mathrm{N}}(i,i+1)$ NOEs, and the observation of some sequential connectivities involving side chains provides checks for

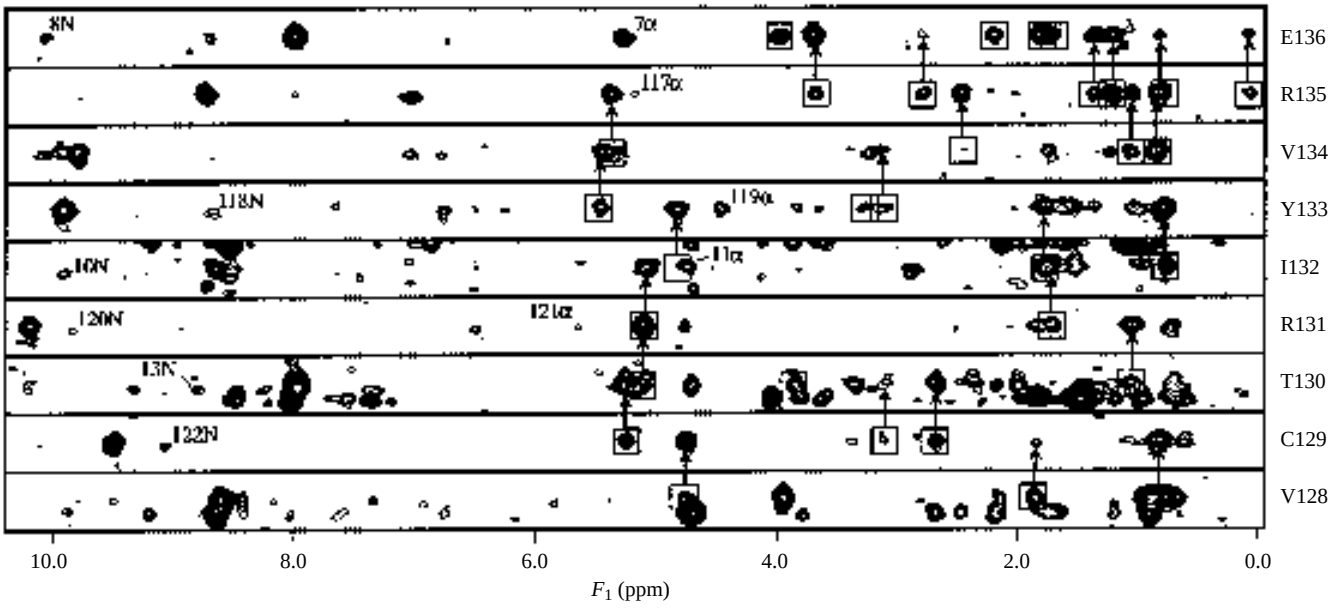

Figure 6 Assignment of the C-terminal β-strand of CRABP illustrated with (ω_1,ω_3) strips from a ^{1}H–^{15}N three-dimensional NOESY–HMQC spectrum, taken at ω_2 values corresponding to the ^{15}N chemical shift of the amide nitrogen of each residue. Boxes indicate intraresidue NOEs and arrows point to sequential NOEs involving H-α or side-chain protons. Long range NOEs corresponding to interstrand interactions have been labeled

the assignments. However, consecutive amide protons in β-sheets have, in general, many fewer NOEs in common than in α-helices, and thus it is more difficult to ensure the correctness of the sequential assignment when there is degeneracy in the H-α chemical shifts. For proteins the size of CRABP and larger, such degeneracy is common, despite the good chemical shift dispersion, and the difficulty in the assignment is further compounded by the lack of residue type information for many amide protons, due to the absence of many relayed connectivities between amide and side-chain protons in $^{1}H-^{15}N$ three-dimensional TOCSY–HMQC data. NMR analysis of selectively ^{15}N-labeled protein samples can be of great help in circumventing these problems,[24] or, alternatively, the assignment can be performed using the triple resonance experiments cited above, which are not based on NOE interactions and can be applied independently of the type of secondary structure.[25]

Once the sequential assignments of a β-sheet protein have been obtained, the observation of numerous interstrand NOEs (see Figure 6) offers additional checks for the assignments. As mentioned above, the strongest of these interactions in antiparallel β-sheets are $d_{\alpha\alpha}$ NOEs, which do not appear in the $^{1}H-^{15}N$ three-dimensional NOESY–HMQC data but can be easily identified in two-dimensional NOESY spectra obtained in D_2O. As an example, Figure 7 shows the α/α region of a NOESY spectrum of the mostly β-sheet protein interleukin 1β.[31] The $d_{\alpha\alpha}$ cross peaks are usually well resolved because of the almost complete absence of other types of interaction in this region of the NOESY data, and because of the small likelihood that a pair of interacting H-α protons in a β-sheet has both H-α chemical shifts identical to another H-α/H-α interacting pair. The interstrand NOEs yield critical information on the relative positions and orientations of the β-strands in the three-dimensional structure of the protein. Indeed, due to the large number of tertiary interactions involving exclusively backbone protons, assignment of the backbone resonances and of the secondary structure elements in predominantly β-sheet proteins can often yield a rather good model for the overall folding of the protein. This situation is in contrast with α-helical proteins, where tertiary packing of different polypeptide chain segments involves more side-chain/side-chain contacts and fewer backbone/backbone

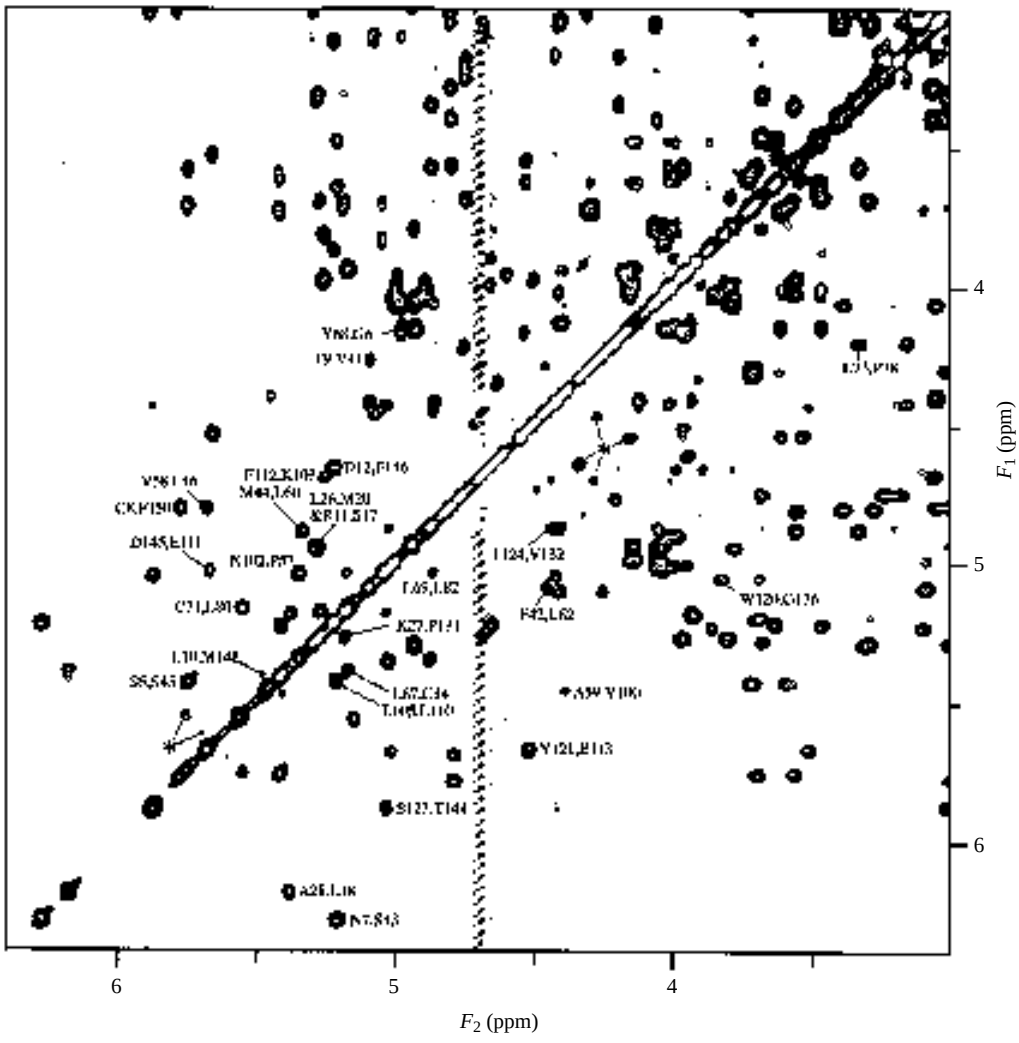

Figure 7 Expansion corresponding to the H-α/H-α region of a NOESY spectrum of interleukin 1β in D_2O. Labeled cross peaks correspond to $d_{\alpha\alpha}(i,j)$ NOEs. (Reproduced by permission of the American Chemical Society from P. C. Driscoll, A. M. Gronenborn, P. T. Wingfield, and G. M. Clore, *Biochemistry*, 1990, **29**, 4668)

interactions. On the other hand, the larger number of short range NOEs observed in α-helical proteins enable a more facile definition of the local chain conformation. As a consequence of the smaller number of short-range interactions and larger deviations of the torsion angles from standard values, good definition of the local conformation in β-sheet proteins cannot be achieved until determination of the complete three-dimensional structure. Interestingly, these NMR observations may reflect fundamental differences between the mechanisms of folding of mostly α-helical and mostly β-sheet proteins.

5 RELATED ARTICLES

Amino Acids, Peptides and Proteins: Chemical Shifts; Biological Macromolecules: Structure Determination in Solution; Calmodulin; Chemical Shifts in Biochemical Systems; Peptide Hormones; Peptides and Polypeptides; Proteins and Protein Fragments: Folding; Structures of Larger Proteins, Protein-Ligand, and Protein-DNA Complexes by Multi-Dimensional Heteronuclear NMR; Synthetic Peptides; Three-Dimensional HMQC-NOESY, NOESY-HMQC, and NOESY-HSQC; Vicinal Coupling Constants and Conformation of Biomolecules.

6 REFERENCES

1. K. Wüthrich, M. Billeter, and W. Braun, *J. Mol. Biol.*, 1984, **180**, 715.
2. K. Wüthrich, *NMR of Proteins and Nucleic Acids*, Wiley, New York, 1986.
3. J. Rizo and L. M. Gierasch, *Annu. Rev. Biochem.*, 1992, **61**, 387.
4. A. Bax, *Annu. Rev. Biochem.*, 1989, **58**, 223.
5. G. M. Clore and A. M. Gronenborn, *CRC Crit. Rev. Biochem. Mol. Biol.*, 1989, **24**, 479.
6. K. Wüthrich, *Curr. Opin. Struct. Biol.*, 1994, **4**, 93.
7. G. D. Rose, L. M. Gierasch, and J. A. Smith, *Adv. Protein Chem.*, 1985, **37**, 1.
8. C. M. Wilmot and J. M. Thornton, *J. Mol. Biol.*, 1988, **203**, 221.
9. H. J. Dyson, M. Rance, R. A. Houghten, R. A. Lerner, and P. E. Wright, *J. Mol. Biol.*, 1988, **201**, 161.
10. J. Rizo, M. M. Dhingra, and L. M. Gierasch, in *Molecular Conformation and Biological Interactions*, ed. P. Balaram and S. Ramaseshan, Indian Academy of Sciences, Bangalore, 1991, p. 469.
11. J. Rizo, S. C. Koerber, R. J. Bienstock, J. Rivier, A. T. Hagler, and L. M. Gierasch, *J. Am. Chem. Soc.*, 1992, **114**, 2852.
12. S. J. Stradley, J. Rizo, M. D. Bruch, A. N. Stroup, and L. M. Gierasch, *Biopolymers*, 1990, **29**, 263.
13. A. Perczel, M. Hollósi, P. Sándor, and G. D. Fasman, *Int. J. Peptide Protein Res.*, 1993, **41**, 223.
14. G. Wagner, D. Neuhaus, E. Wörgötter, M. Vašák, J. H. R. Kägi, and K. Wüthrich, *J. Mol. Biol.*, 1986, **187**, 131.
15. D. S. Wishart, B. D. Sykes, and F. M. Richards, *J. Mol. Biol.*, 1991, **222**, 311.
16. D. S. Wishart, B. D. Sykes, and F. M. Richards, *Biochemistry*, 1992, **31**, 1647.
17. S. Spera and A. Bax, *J. Am. Chem. Soc.*, 1991, **113**, 5490.
18. J. Rizo, F. J. Blanco, B. Kobe, M. D. Bruch, and L. M. Gierasch, *Biochemistry*, 1993, **32**, 4881.
19. J. P. Waltho, V. A. Feher, G. Merutka, H. J. Dyson, and P. E. Wright, *Biochemistry*, 1993, **32**, 6337.
20. E. K. Bradley, J. F. Thomason, F. E. Cohen, P. A. Kosen, and I. D. Kuntz, *J. Mol. Biol.*, 1990, **215**, 607.
21. J. J. Osterhout, Jr., R. L. Baldwin, E. J. York, J. M. Stewart, H. J. Dyson, and P. E. Wright, *Biochemistry*, 1989, **28**, 7059.
22. P. A. Jennings and P. E. Wright, *Science*, 1993, **262**, 892.
23. G. M. Clore and A. M. Gronenborn, *Annu. Rev. Biophys. Biophys. Chem.*, 1991, **20**, 29.
24. J. Rizo, Z.-P. Liu, and L. M. Gierasch, *J. Biomol. NMR*, 1994, **4**, 741.
25. M. Ikura, L. E. Kay, and A. Bax, *Biochemistry*, 1990, **29**, 4659.
26. M. Ikura, S. Spera, G. Barbato, L. E. Kay, M. Krinks, and A. Bax, *Biochemistry*, 1991, **30**, 9216.
27. M. Ikura, G. M. Clore, A. M. Gronenborn, G. Zhu, C. B. Lee, and A. Bax, *Science*, 1992, **256**, 632.
28. G. Barbato, M. Ikura, L. E. Kay, R. W. Pastor, and A. Bax, *Biochemistry*, 1992, **31**, 5269.
29. F. J. Blanco, M. A. Jiménez, J. Herranz, M. Rico, J. Santoro, and J. L. Nieto, *J. Am. Chem. Soc.*, 1993, **115**, 5887.
30. J.-A. Fehrentz, A. Heitz, R. Seyer, P. Fulcrand, R. Devilliers, B. Castro, F. Heitz, and C. Carelli, *Biochemistry*, 1988, **27**, 4071.
31. P. C. Driscoll, A. M. Gronenborn, P. T. Wingfield, and G. M. Clore, *Biochemistry*, 1990, **29**, 4668.

Biographical Sketches

Josep Rizo. *b* 1959. B.S. (chemistry), 1981; B.S. (physics), 1988; Ph.D. (chemistry), 1988, University of Barcelona, Spain. Introduced to NMR by Ernest Giralt and Miquel Pons. Postdoctoral fellow (with Lila M. Gierasch) and currently Assistant Professor at the University of Texas Southwestern Medical Center at Dallas, Texas. Approx. 30 publications. Research interests: conformational analysis of peptides and proteins to correlate structure and function; protein folding.

Lila M. Gierasch. *b* 1948. A.B. (chemistry), 1970, Mount Holyoke College; Ph.D. (biophysics), Harvard University. Introduced to NMR by Elkan Blout and Brian Sykes. Faculty appointments at Amherst College, University of Delaware, the University of Texas Southwestern Medical Center, and currently Head of the Department of Chemistry, University of Massachusetts. President of the Biophysical Society. Approx. 140 publications. Current research interests: the conformations of peptides and proteins; and protein folding, both in vitro and in vivo.

Peptide Hormones

Victor J. Hruby

University of Arizona, Tucson, AZ, USA

1	Introduction	1
2	Structure: Biological Considerations	1
3	General Strategy for Conformational Analysis of Peptides Using NMR	1
4	Conformational Analysis: Relation to Biological Activity and Selected Examples	3
5	Future Perspectives	4
6	Related Articles	5
7	References	5

1 INTRODUCTION

Peptide hormones and neurotransmitters[1] are chemical messengers found throughout the animal kingdom that are critical for intercellular communication, for integration of responses to outside stimuli, for maintenance of homeostasis, and for control and development of life. In animals they control, modulate, or stimulate such diverse biological functions as growth, pigmentation, learning, digestion, cardiovascular function, kidney function, pain, glucose production, metabolic rates, and many others. Hence, efforts to understand the relationships of their structures to biological activities have been of great interest to scientists and medical doctors since they have great potential for the control and cure of many diseases.

Historically, a peptide hormone was defined as a polypeptide produced in one cell type, released from that cell in response to a stimulus, and biologically active at some other cell. The cells involved could be far apart (e.g. oxytocin—found in the pituitary gland and having its effect at the uterus), or close together (e.g. somatostatin—found in cells in the pancreas adjacent to glucagon and insulin containing cells). In all cases, however, their biological function is initiated by interactions with receptors found in the plasma membrane. Recently, many of these receptors have been isolated and their structures determined by cloning.

Though some peptide hormones are proteins with over 100 to several hundred residues (e.g. growth hormone, luteinizing hormone, etc.), most are small peptides (3–60 residues). They are formed by the processing of larger precursor proteins that generally are not biologically active (presumably because the recognition site on the hormone is partially or completely inaccessible for interaction with its receptor). Usually the peptide hormone or neurotransmitter is found in secretory granules where it is stored pending a signal to release it.

The fact that most peptide hormones are small peptides has presented difficulties in determining their conformation in solution and their conformational structure–biological activity relationships. NMR studies have demonstrated multiple conformational properties for many of these compounds. This has stimulated efforts to develop approaches to stabilizing or restricting these conformations that are compatible with potent biological activity so that NMR could be used to help determine the 'bioactive' conformation.

In this article we discuss how specific aspects of NMR methodology can be used in conjunction with biological and other biophysical considerations for conformational analysis of peptide hormones and its relation to biological activity, and then provide a few examples from the literature. There is no opportunity in the space allotted to be comprehensive (in 1973 a comprehensive review[2] had over 700 references). We apologize to the many contributors whose work is not discussed here.

2 STRUCTURE: BIOLOGICAL CONSIDERATIONS

Since most peptide hormones are small, linear polypeptides, they tend to have multiple conformations in solution, and these conformations generally interconvert rapidly on the NMR timescale. Hence NMR analysis may lead to the erroneous result of an 'average' conformation that may not reflect any specific conformation. This problem was recognized at an early stage using NMR and other biophysical methods,[2] and led several laboratories to develop approaches to overcome it.

One approach that has been taken is to lower the temperature to $-80\,^{\circ}C$ or lower in cytoprotective solvents. However, many peptides still appear to have multiple conformations and it has been difficult to determine a single conformation. In cases where conformational insights have been obtained, it generally has not been clear whether they are of biological significance.

The more general approach has been that of conformational constraints.[3–7] In this approach specific conformational constraints involving unusual amino acid residues, cyclization, or other structural perturbations are introduced and their effects on biological activity examined. If the design has been consistent with the structural, conformational and dynamic requirements of the receptor, biological potency can be maintained or even enhanced. Alternatively, the properties may be inconsistent for interaction with the receptor and the biological potency will be greatly reduced. In either case, if the conformation is sufficiently rigid, NMR and other biophysical studies can be performed that can provide unique insights into peptide conformation–biological activity relationships. The most useful situation is when structurally closely related, conformationally restricted, peptides with greatly diverse biological potency can be examined and compared to provide insight, and in some cases a pharmacophore model. Some general methods of conformational constraint are given in Table 1 (a few excellent reviews and overviews are indicated[3–7]). In addition, the use of very large peptide and nonpeptide libraries (see e.g. Houghton et al.[8] and Lam et al.[9]) can provide another general method of obtaining a lead structure.

In all cases it is generally necessary to utilize more than one biological assay. Many (most) peptide hormones have multiple biological effects (in terms of the receptor, multiple receptor types, and subtypes). Hence if insights into the conformational structure requirements for selectivity and specificity are to be obtained, multiple assays are needed. Indeed, since it often has been found that conformational constraints provide peptide analogs with enhanced selectivity, much information can be lost unless multiple assays are utilized.

Table 1 Methods of Conformational Constraint That Have Proven Useful for Peptide Conformation Activity Studies

Local Constraints	Global Constraints
N^{α}-Alkyl or Aryl	Disulfide ring
C^{α}-Alkyl or Aryl	Sulfide, lactam, lactone or macrocyclic ring
C^{β}-Alkyl, Aryl, OH, etc. (χ constraint)	N- to C-terminal cyclic
β,β-Dialkyl cysteine	Side chain to N- or C-terminal cyclic
D-Amino acids	Side chain to backbone cyclic
Reverse turn mimetic or mimic	Backbone to backbone cyclic

Table 2 NMR Criteria for Establishing Conformational Homogeneity

1.	Large differences in chemical shifts and coupling constants of similar amino acids in the peptide
2.	Significant chemical shift differences for diastereotopic protons or groups
3.	Large differences in chemical shifts and temperature dependencies
4.	Large deviations in the coupling constants from the mean value of about 7.5 Hz
5.	Linearity of temperature dependence of NH chemical shift and/or no dependence of NH proton chemical shifts
6.	No change in chemical shifts or coupling constants with concentration
7.	Independence of spectral parameters with solvent change

3 GENERAL STRATEGY FOR CONFORMATIONAL ANALYSIS OF PEPTIDES USING NMR

Despite the caveats given above, it often is useful to use NMR to examine short linear peptides of biological significance for proof of structure, evidence for *cis–trans* isomerism, examination of conformational flexibility, and determination of anisotropic effects or unusual NOEs that provide insights into an overall conformation which may be useful for design of constraints. In addition, using labeled (^{2}H, ^{13}C, ^{19}F, etc.) peptides it is possible to obtain insights into peptide hormone–receptor/acceptor interactions using NMR techniques. Such studies will not be discussed here for lack of space, but useful reviews are available.[10,11] A major emphasis here is to outline those approaches where conformational constraints have been sufficient to lead to a peptide or peptide mimetic with a preferred conformation. It will be recognized that the conformation of the backbone will be most easily obtained, whereas, unless some local constraint has been introduced, side-chain conformation determination will still be difficult.

Criteria that are generally applied from NMR as evidence of conformational homogeneity are listed in Table 2 (see also Kessler[3]). Not one of these criteria is in itself conclusive, nor do all have to be satisfied without exception. Rather, when all the criteria are met, with explainable deviations, generally one can conclude that the peptide has a strong conformational preference.

With the above caveats in mind, a general strategy for conformational analysis can be outlined (Table 3). First, all nuclei observed (^{1}H, ^{13}C, etc.) must be correctly assigned. In general, one begins by obtaining a high-resolution one-dimensional ^{1}H NMR spectrum using the highest field possible. Since most amino acids are chiral, β and further removed protons generally are prochiral. Thus, spectra often rapidly become quite complex. The closer one can approach first-order spectra, the more accurate NMR parameters can be obtained. The general spectral characteristics for each amino acid residue are well established,[12,13] and in many cases assignments can be made by recognition of subspectra associated with particular residues. In favorable cases accurate coupling constants also can be obtained. In most cases one needs to turn to two-dimensional NMR techniques. A large, increasing number of techniques are available to obtain a variety of information. Space does not permit a detailed discussion of how to proceed, but a general outline follows.

When strong proton overlap occurs, double quantum (DQ) COSY experiments, relayed H–H COSY, and TOCSY experiments are recommended. Occasionally, indirect methods of detection are needed (H–C COSY, etc.). For assignment of carbon or nitrogen signals, H–X COSY experiments are utilized. Particularly important in some cases is the assignment of the carboxyl carbon atoms. Since they have no attached proton, ^{1}H-α, ^{13}C′ coupling is needed.

Once all the subspectra have been assigned, it is necessary to obtain the complete sequence of the peptide. For this purpose, interactions across the peptide bond are needed. Essentially two approaches are possible: homonuclear (e.g. $C_{\alpha}{}^{i}H - N_{\alpha}{}^{i+1}H$, four bond, difficult) or heteronuclear (e.g. $C_{\alpha}{}^{i}H - N_{\alpha}{}^{i+1}H$, three bond, possible) through-bond coupling. In all cases success depends on the presence of unique amino residues, or unambiguous starting points to ensure that the correct sequence assignments are made. In any case, proton–proton coupling across amide bonds is only of limited use, whereas heteronuclear coupling [for example to assigned carboxyl (C′) carbons] is more reliable for obtaining sequence information.

Experience has shown that often it is necessary to utilize alternative through-space connectivities. In this case, sequential neighboring amino acid ^{1}H spin systems are identified by the use of through-space NOE connectivities. Most commonly these involve $C_{\alpha}{}^{i}H - N_{\alpha}{}^{i+1}H$ and/or $N_{\alpha}{}^{i}H - N_{\alpha}{}^{i+1}H$ connectivities, though in some cases $C_{\beta}{}^{i}H - N_{\alpha}{}^{i+1}H$ connectivities can be observed. Generally the chemical shift information does not provide direct conformational information (however, see e.g. Jiao et al.[14]).

Conformational analysis depends on utilizing NMR spectral parameters that are directly dependent on spatial arrangements. In addition, temperature dependence of peptide amide protons and chemical shift effects as a result of anisotropy can be very useful.

Table 3 General Strategy for Obtaining NMR Parameters Needed for Peptide Conformational Analysis

Evidence	NMR Methods
Complete assignments	One-dimensional ^{1}H, ^{13}C high-resolution spectra; ^{1}H–^{1}H COSY; ^{1}H–^{13}C COSY; TOCSY; NOESY, ROESY; HMQC; Heteronuclear inverse detection; etc.
Accurate determination of chemical shifts	As above; *cis–trans* X*AA*-Pro-^{13}C-β and -γ
Accurate determination of coupling constants	One-dimensional NMR; phase-sensitive H–H COSY and 2QF COSY; spectral simulation; *z* filtered heteronuclear HMQC–TOCSY; etc.
Quantitative determination of NOEs	Phase-sensitive NOESY; one-dimensional difference; ROESY

Once all the NMR parameters have been obtained, several possible conformations may satisfy most of the NMR parameters. To obtain the most reliable conformation, molecular dynamics (MD) simulations generally are required. Both homo- and heteronuclear coupling constant constraints and NOE distance constraints are needed to derive a conformation that will satisfy all the NMR parameters.[15,16] Conformations consistent with X-ray data for crystalline peptides and with NMR data have been obtained in a few cases.

4 CONFORMATIONAL ANALYSIS: RELATION TO BIOLOGICAL ACTIVITY AND SELECTED EXAMPLES

4.1 Oxytocin

Oxytocin (OT; H-Cys-Tyr-Ile-Gln-Asn-Cys-Pro-Leu-Gly-Nh_2), has a special place in peptide hormone chemistry, since it was the first peptide to be isolated and its structure proven by total synthesis. For this work Vincent du Vigneaud received the Nobel Prize in Chemistry in 1955. Since then, OT has played a pivotal role in the development of strategies for determining hormone structure-activity relationships.[17] It was the first peptide hormone for which a conformation in solution (dimethyl sulfoxide; DMSO) was proposed based primarily on NMR studies,[18] and for which a complete analysis of the NMR in aqueous solution was provided.[19] Based on the NMR results and known structure–activity relationships, Walter[20] proposed the 'cooperative model' for oxytocin activity at the uterine receptor. Based on ^{1}H NMR studies of a conformationally constrained antagonist, [1-penicillamine]oxytocin ([Pen^1]OT; Pen, β,β-dimethylcysteine)[22] and other antagonist analogs, Hruby and co-workers proposed a conformational and dynamic model that distinguished antagonists from agonists[17c,21] and led to the suggestion that oxytocin agonists and antagonists have different conformational structure–biological activity relationships.[17c,22]

Subsequently, an X-ray crystal structure of the highly potent agonist, desamino-oxytocin ([β-Mpa^1]OT; β-Mpa, β-mercaptopropionic acid) was determined.[23] Two conformations were found in the unit cell with opposite disulfide chiralities. A β-turn in the ring involving the Tyr-Ile-Gln-Asn sequence proposed from NMR was found in both structures.

More recently, NMR studies using the transfer NOE and extensive constrained molecular dynamics and molecular mechanics calculations, have led to the determination of the conformation of oxytocin bound to its carrier protein in neurosecretory granules, neurophysin I.[24] A much different conformation from that of deamino-oxytocin in the crystal or solution state was observed (Figure 1).

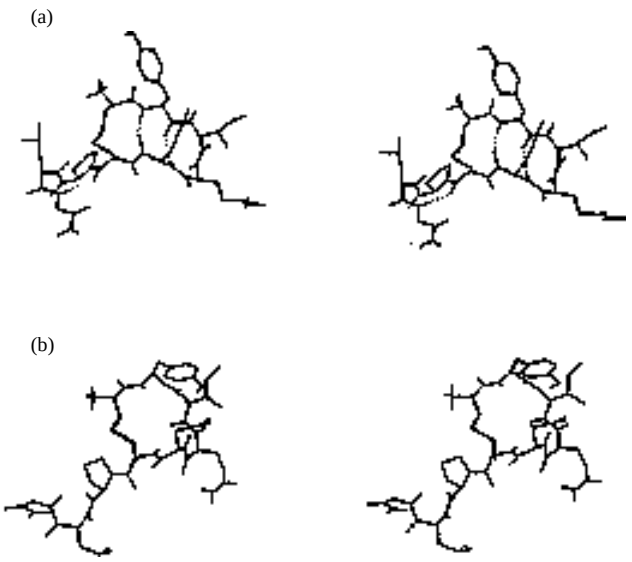

Figure 1 Stereoviews of the crystal structure of (a) deamino-oxytocin and (b) the NMR conformation of oxytocin bound to neurophysin I

Very recently, using two-dimensional NMR methods in conjunction with extensive molecular dynamics simulations and molecular mechanics calculations,[25] the conformation of the highly potent bicyclic oxytocin antagonist analog [β-Mpa^1, Glu^4, Cys^6, Lys^8]OT[26] was determined, which included a β-turn in the 20-membered disulfide bridge involving the Cys-Tyr-Ile-Glu sequence and a *cis* Cys^6-Pro^7 peptide bond. This quite rigid bicyclic conformation provides a different topographic presentation of the Tyr^2 (and other) side-chain groups, and an excellent model for a bioactive conformation for OT antagonists.

4.2 Somatostatin

The cyclic peptide H-Ala-Gly-Cys-Lys-Asn-Phe-Phe-Trp-Lys-Thr-Phe-Thr-Ser-Cys-OH, which has a variety of proposed biological activities (including inhibition of the release

of growth hormone from the pituitary, and insulin and glucagon from the pancreas), serves as an excellent example of the use of conformational thinking in conjunction with NMR for peptide design. The suggestion by Veber and coworkers of a β-turn about the Phe-Trp-Lys-Thr sequence was supported by structure–activity studies and NMR,[27] and led through a series of cyclic peptides of increasingly reduced ring size to the cyclic hexapeptides c(Pro-Phe-D-Trp-Lys-Thr-Phe) and c(N-MeAla-Phe-D-Trp-Lys-Thr-Phe),[28] which were found to be highly potent. Subsequently, extensive NMR studies on these compounds by Kessler et al.[29] and by Veber[30] have provided direct evidence that a type II′ β-turn about the D-Trp-Lys residues was a low energy structure, and topographical features important to biological activity have subsequently been investigated by NMR.[31] In a very interesting study, Kessler et al.[32] made retro-analogs of the cyclic hexapeptide series which had cytoprotection activity in the inhibition of cholate uptake in isolated hepatocyctes, and greatly reduced or completed suppressed somatostatin-like activity.

Highly potent and selective disulfide-containing analogs of somatostatin have been prepared such as D-Phe-Cys-Phe-D-Trp-Lys-Thr-Cys-Thr-(ol) (SMS 201-995) which is a superpotent somatostatin analog[33] and also has some opioid-like activities. Conformational analysis using NMR indicated that these compounds retained the β-turn conformation about the Phe-D-Trp-Lys-Thr sequence with a γ-turn also possible.[34] Utilizing this β-turn template it was possible to design cyclic analogs with high potency and selectivity for μ opioid receptors such as D-Phe-Cys-Tyr-D-Trp-Lys-Thr-Pen-Thr-Nh_2[35] (CTP) and greatly reduced (1000 fold) somatostatin-like activity. The use of topographical constraints in χ space (χ_1 and χ_2 constraints) in conjunction with the β-turn structure, and careful conformational analysis using NMR[36,37] led to a detailed understanding of the conformational and topographical properties of D-Tic-Cys-Tyr-D-Trp-Arg-Thr-Pen-Thr-NH_2 (Tic, 1,2,3,4-tetrahydroisoquinoline-3-carboxylate) which has no somatostatin-like activity and is highly μ opioid selective. This suggests that there should be considerable similarities, but some differences, in μ opioid receptors and somatostatin receptors. Recently, both these receptor types have been cloned, and the somatostatin and μ opioid receptors have extensive sequence homology. Interestingly, some of these constrained peptides also have considerable agonist potency at δ opioid receptors. It is fascinating that a single ligand can be agonist at one receptor type and an antagonist at other.

4.3 Opioid Peptides

Since the discovery of [Leucine^5]- and [Methionine^5]-enkephalin (H-Tyr-Gly-Gly-Phe-Leu-OH and H-Tyr-Gly-Gly-Phe-Met-OH, respectively) in the mid-1970s, much has been done to examine the possible conformations of these and other endogenous peptides such as the dynorphins [e.g. dynorphin A (1–11), (Tyr-Gly-Gly-Phe-Leu-Arg-Arg-Ile-Arg-Pro-Lys-OH), the dermorphins (H-Tyr-D-Ala-Phe-Gly-Tyr-Pro-Ser-NH_2), the deltorphins (e.g. deltorphin I, H-Tyr-D-Ala-Phe-Asp-Val-Val-Gly-NH_2) and dermenkephalin (H-Tyr-D-Met-Phe-His-Leu-Met-Asp-NH_2)]. Though early NMR studies were made,[38] no general consensus developed regarding their conformation in solution or their bioactive conformation.[39] Furthermore, it became increasingly evident that several types of opioid receptor (δ, μ, and κ) were present in animals, and thus it was necessary to examine the bioactive conformations of these compounds for the different requirements of each opioid receptor type. This led to the design of conformationally constrained cyclic analogs some of which were highly potent opioid receptor selective cyclic compounds,[40] including: H-D-Pen-Gly-Phe-D-Pen-OH (DPDPE) (δ selective); H-Tyr-D-Cys-Phe-D-Pen-LH (JOM-13) (δ selective); H-Tyr-D-Orn-Atc-Glu-NH_2 (μ selective); H-Tyr-D-Pen-Phe-Asp-Pen-Val-Gly-NH_2 (δ selective); and H-Tyr-Gly-Gly-Phe-Cys-Arg-Arg-Ile-Arg-Pro-Cys-NH_2 (κ selective). Extensive NMR and related studies have been made on these and related compounds. From these studies a consensus is emerging regarding likely conformations for these compounds,[41–44] and predictions regarding likely bioactive conformations. The use of χ_1 and χ_2 constrained aromatic amino acid derivatives with preferred side-chain conformations provides, in conjunction with NMR, further insights regarding the topographical requirements for agonists and antagonists.[45–48]

4.4 Others

Numerous other NMR studies have been made on many peptide hormones and neurotransmitters, including insulin, glucagon, luteinizing hormone releasing hormone, α-melanotropin, endothelin, vasopressin, substance P, and other tachykinins, cholecystokinin, angiotensin, bradykinin, etc., and these have led to new insights into the conformational and dynamic properties of these compounds and their analogues.

5 FUTURE PERSPECTIVES

Investigations of peptide hormones by NMR have a very bright future due to the coincidence of rapid developments in several areas. First, the rapid expansion of NMR technology in terms of sensitivity, dispersion, and control of nuclear spin state. Many of the peptide hormones and neurotransmitters have ‘simple’ structures but they interact with complex receptor systems which include the membrane bound receptor and associated proteins such as G proteins, and currently most are being cloned and expressed. Though it still is not possible to express these in quantities sufficient for NMR and X-ray crystallography studies, this is changing rapidly. There are rapid advances being made in the design and synthesis of the peptide hormones themselves, and of analogs constrained in ϕ,ψ space and in χ space, including advances in synthetic methodology related to asymmetric synthesis. The ability specifically to design in isotopes, reporter moieties, and other ‘structures’ of interest for use by the NMR spectroscopist will greatly aid in continued rapid development.

Finally, all these advances are being enhanced and catalyzed by the rapid developments of computer software which greatly aid not only in the analysis of NMR data but also in computer assisted design of peptide and peptidomimetic ligands and in strategies for these syntheses. The power of NMR to help analyze these systems will play an increasingly powerful role in developing an understanding of these very important molecules.

6 RELATED ARTICLES

Amino Acids, Peptides and Proteins: Chemical Shifts; Biological Macromolecules: Structure Determination in Solution; Distance Geometry; Proton Chemical Shift Measurements in Biological Solids; Peptide and Protein Secondary Structural Elements; Peptides and Polypeptides; Synthetic Peptides.

7 REFERENCES

1. Peptide neurotransmitters are found in the central or peripheral nervous system, and have been thought of as separate from hormones. However, recent experience has demonstrated time and again that peptide hormones first discovered in peripheral tissues also are found in the central nervous system, and vice versa.
2. V. J. Hruby, in *Chemistry and Biochemistry of Amino Acids, Peptides and Proteins*, ed. B. Weinstein, Dekker, New York, 1974, Vol. 3, pp. 1–188.
3. For an early review see: H. Kessler, *Angew. Chem., Int. Ed. Engl.*, 1982, **21**, 512.
4. For an early review, see: V. J. Hruby, *Life Sci.*, 1982, **31**, 189.
5. C. Toniolo, *Int. J. Peptide Protein Res.*, 1990, **35**, 287.
6. V. J. Hruby, F. Al-Obeidi, and W. M. Kazmierski, *Biochem. J.*, 1990, **268**, 249.
7. J. Rizo and L. M. Gierasch, *Annu. Rev. Biochem.*, 1992, **61**, 387.
8. R. A. Houghton, C. Pinilla, S. E. Blondelle, J. R. Appel, C. T. Dooley, and J. H. Cuervo, *Nature*, 1991, **354**, 84.
9. K. S. Lam, S. E. Samon, E. M. Hersh, V. J. Hruby, W. M. Kazmierski and R. J. Knapp, *Nature*, 1991, **354**, 82.
10. (a) M. Blumenstein, in *The Peptides: Analysis, Synthesis, Biology*, ed. V. J. Hruby, Academic, New York, 1985, Vol. 7, p. 355 and references therein; (b) D. H. Live, D. Cowburn, and E. Breslow, *Biochemistry*, 1987, **26**, 6415.
11. S. W. Fesik, *J. Biomol. NMR*, 1993, **3**, 261.
12. K. Wüthrich, *^{1}NMR of Proteins and Nucleic Acids*, Wiley, New York, 1986.
13. H. Kessler, W. Bermel, A. Müller, and K.-H. Pook, in *The Peptides: Analysis, Synthesis, Biology*, ed. V. J. Hruby, Academic, New York, 1985, Vol. 7, p. 437.
14. D. Jiao, M. Barfield, and V. J. Hruby, *J. Am. Chem. Soc.*, 1993, **115**, 10 883.
15. D. F. Mierke and H. Kessler, *Biopolymers*, 1992, **32**, 1277.
16. G. V. Nikiforovich, O. Prakash, C. A. Gehrig, and V. J. Hruby, *J. Am. Chem. Soc.*, 1993, **115**, 3399.
17. (a) C. W. Smith (ed.), *The Peptides: Analysis, Synthesis, Biology*, Academic, New York, 1987, Vol. 8; (b) K. Jost, M. Lebl, and F. Brtnik, *Handbook of Neurohypophyseal Hormone Analogs*, CRC, Boca Raton, FL, 1987 Vols 1 and 2; (c) V. J. Hruby, in *Topics in Molecular Pharmacology*, ed. A. S. V. Burgen and G. C. K. Roberts, Elsevier/North Holland, Amsterdam, 1981, p. 99.
18. D. W. Urry and R. Walter, *Proc. Natl. Acad. Sci. USA*, 1971, **68**, 956.
19. A. I. R. Brewster and V. J. Hruby, *Proc. Natl. Acad. Sci. USA*, 1973, **70**, 3806.
20. R. Walter, *Fed. Proc. Am. Soc. Exp. Biol.*, 1977, **36**, 1872.
21. J.-P. Meraldi, V. J. Hruby, and A. I. R. Brewster, *Proc. Natl. Acad. Sci. USA*, 1977, **74**, 1373.
22. V. J. Hruby, *Trends Pharm. Sci.*, 1987, **8**, 336.
23. S. P. Wood, I. J. Tickle, A. M. Treharne, J. E. Pitts, Y. Mascarenhas, J. Y. Li, J. Husain, S. Cooper, T. L. Blundell, V. J. Hruby, H. R. Wyssbrod, A. Buku, and A. J. Fishman, *Science*, 1986, **232**, 633.
24. G. Lippens, K. Hallenga, D. VanBelle, S. J. Wodak, N. R. Nirmala, P. Hill, K. C. Russell, D. D. Smith, and V. J. Hruby, *Biochemistry*, 1993, **32**, 9423.
25. M. Shenderovich, K. Kövér, N. Collins, S. Wilke, and V. J. Hruby, *J. Am. Chem. Soc.*, submitted.
26. P. S. Hill, D. D. Smith, J. Slaninova, and V. J. Hruby, *J. Am. Chem. Soc.*, 1990, **112**, 3110.
27. B. H. Arison, R. Hirschmann, W. S. Paleveda, S. F. Brady, and D. F. Veber, *Biochem. Biophys. Res. Commun.*, 1981, **100**, 1148.
28. R. M. Freidinger and D. F. Veber, in *Conformationally Directed Drug Design*, ed. J. A. Vida and M. Gordon, American Chemical Society, Washington, DC, No. 251, p. 169.
29. H. Kessler, M. Bernd, H. Kogler, J. Zarbock, O. W. Sørensen, G. Bodenhausen, and R. R. Ernst, *J. Am. Chem. Soc.*, 1983, **105**, 6944.
30. D. F. Veber, in *Peptides: Chemistry and Biology*, ed. J. A. Smith and J. E. Rivier, ESCOM Science Publications, Leiden, 1992, p. 3.
31. Z. Huang, X.-B. He, K. Raynor, M. Tallent, T. Reisine, and M. Goodman, *J. Am. Chem. Soc.*, 1992, **114**, 9390, and references therein.
32. H. Kessler, M. Klein, and K. Wagner, *Int. J. Pept. Protein Res.*, 1988, **31**, 481.
33. R. Maurer, B. H. Gaehwiler, A. H. Buescher, R. C. Hill, and D. Roemer, *Proc. Natl. Acad. Sci. USA*, 1982, **79**, 4815.
34. C. Wyants, G. VanBinst, and H. R. Loosli, *Int. J. Pept. Protein Res.*, 1985, **25**, 608.
35. J. T. Pelton, K. Gulya, V. J. Hruby, S. P. Duckles, and H. I. Yamamura, *Proc. Natl. Acad. Sci. USA*, 1985, **82**, 236.
36. W. Kazmierski and V. J. Hruby, *Tetrahedron*, 1988, **44**, 697.
37. W. M. Kazmierski, H. I. Yamamura, and V. J. Hruby, *J. Am. Chem. Soc.*, 1991, **113**, 2275.
38. (a) B. P. Roques, C. Garbay-Jaureguiberry, R. Oberlin, M. Anteunis, and A. K. Lala, *Nature*, 1976, **262**, 778; (b) C. R. Jones, W. A. Gibbons, and V. Garsky, *Nature*, 1976, **262**, 779; (c) H. F. Bleich, J. D. Cutnell, A. R. Day, R. J. Freer, J. A. Glasel, and J. F. McKelvy, *Proc. Natl. Acad. Sci. USA*, 1976, **73**, 2589.
39. P. W. Schiller, in *The Peptides: Analysis, Synthesis, Biology*, ed. S. Udenfriend and J. Meienhofer, Academic, New York, 1984, Vol. 6, pp. 220–268.
40. (a) V. J. Hruby and C. A. Gehrig, *Med. Res. Rev.*, 1989, **9**, 343; (b) P. W. Schiller, *Prog. Med. Chem.*, 1991, **28**, 301.
41. V. J. Hruby, L.-F. Kao, B. M. Pettitt, and M. Karplus, *J. Am. Chem. Soc.*, 1988, **110**, 3351.
42. H. I. Mosberg, K. Sobczyk-Kojiro, P. Subramanian, G. M. Crippen, K. Ramalingam, and R. W. Woodard, *J. Am. Chem. Soc.*, 1990, **112**, 822.
43. D. F. Mierke, P. W. Schiller, and M. Goodman, *Biopolymers*, 1990, **29**, 943.
44. G. V. Nikiforovich, O. Prakash, C. A. Gehrig, and V. J. Hruby, *J. Am. Chem. Soc.*, 1993, **115**, 3399.
45. V. J. Hruby, G. Toth, C. A. Gehrig, L.-F. Kao, R. Knapp, G. K. Liu, H. I. Yamamura, T. H. Kramer, P. Davis, and T. F. Burks, *J. Med. Chem.*, 1991, **34**, 1823.
46. P. W. Schiller, G. Weltrowska, T. M.-D. Nguyen, C. Lemieux, N. N. Chung, B.-J. Marsdin, and B. C. Wilkes, *J. Med. Chem.*, 1991, **34**, 3125.
47. V. J. Hruby, G. Toth, O. Prakash, P. Davis, and T. F. Burks in *Peptides 1988*, ed. G. Jung and E. Bayer, Gruyter, Berlin, 1989, p. 616.
48. T. Yamazaki, O. E. Said-Nejad, P. W. Schiller, and M. Goodman, *Biopolymers*, 1991, **31**, 877.

Biographical Sketch

Victor J. Hruby. *b* 1938. B.S., 1960, M.S. (with A. W. Johnson), 1962, University of North Dakota; Ph.D. (with A. T. Blomquist), Cornell University 1965. Learned NMR while graduate student at Cornell. Faculty, Chemistry (Biochemistry, Arizona Research Laboratories), University of Arizona, 1968–present. Approx. 550 publications, including editor of *The Peptides: Analysis, Synthesis, Biology*, Vol. 7, *Conformation in Biology and Drug Design*. Research interests: peptide hormone and neurotransmitter structure/function; relation of conformation and dynamics to bioactivity; asymmetric synthesis; amino acid, peptide, and protein synthesis; bioorganic chemistry; host–guest chemistry; NMR and conformational analysis; peptidomimetics; drug design; peptide and other organic libraries; and peptide and protein receptors.

Peptides and Polypeptides

Horst Kessler and Wolfgang Schmitt

Technical University, Munich, Germany

1	Introduction	1
2	Assignment of Resonances	1
3	NMR Parameters for the Determination of the Spatial Structure	4
4	*cis–trans* Isomerization	6
5	Diastereotopic Assignment	6
6	Structure Calculation	6
7	Conformational Flexibility	8
8	Conclusion	9
9	Related Articles	9
10	References	9

1 INTRODUCTION

Peptides are responsible for a wide range of biological functions. They can act, for example, as hormones, neurotransmitters, or inhibitors. The three-dimensional structure of bioactive peptides defines their specific function. Hence, structure determination of active compounds and analogs is the basis for peptide-derived rational drug design. In addition, the analysis of the conformational space of linear peptides and protein fragments becomes increasingly interesting as a model to understand the pathways of protein folding.

In general, peptides are flexible molecules adopting many conformations that interconvert rapidly on the NMR timescale. In particular, linear peptides up to about 15 residues do not normally show a defined secondary structure. Such peptides often exhibit only a slight preference for some parts of their conformational space,[1] which may not coincide with the bioactive conformation when bound to its receptor. They usually adopt their 'active conformation' via an induced fit toward the receptor or by interaction with a hydrophobic environment, namely membranes. Larger polypeptides containing more than about 20 amino acids often already form secondary or tertiary structural elements (like α-helices or β-bends) that are defined by the primary structure, i.e., the peptide sequence. Some rules for the preference of distinct amino acids to form secondary structures have been applied to protein structure prediction (Chou–Fasman[2,3]). In β-turn structures the $i + 1$ position is often occupied by proline, *N*-alkylated or D-amino acids.[1] In proline or *N*-alkylated amino acid containing peptides an equilibrium between the *cis* and *trans* isomers at the peptide bond is often found. In some cases the *cis* isomer is populated up to 50%. However, it is not yet possible to predict unequivocally protein structures from their primary sequences.

A second factor for the stabilization of a particular conformation is the environment, namely the solvent. Trifluoroethanol (TFE) or mixtures of TFE and water are found to stabilize α-helices.[4,5] Cryomixtures such as dimethyl sulfoxide (DMSO) and water (80:20) allow the measurement of NMR spectra in a solvent of similar polarity to water, but at a lower temperature to slow down conformational exchange.[6–8] Also methanol can be used successfully for low-temperature measurements.[9,10] Peptides in sodium dodecyl sulfate (SDS) micelles often show a preferred conformation,[11] whereas in isotropic solvents such as water or DMSO a random coil structure is observed.[12] For structure–activity studies the best method to reduce the flexibility is cyclization.[13] Due to steric strain and the reduced number of degrees of freedom small cyclic peptides often prefer only a single backbone conformation. If this leads to high biological activity the structure thus obtained is assumed to be close to the bioactive conformation, especially when the conformation is not changed in different solvents. Incorporation of D-amino acids, proline, or turn mimetics into such small cyclopeptides can be used for a screening of the conformational space.[14]

For the determination of peptide structures by NMR spectroscopy it is also necessary to be aware of the dynamics and the influence of the environment on the conformational equilibrium. An example of the influence on conformation induced by the environment is cyclosporin A, a cyclic undecapeptide that has been studied in several different solvents [chloroform-*d* ($CDCl_3$),[15–17] benzene,[15–17] tetrahydrofuran (THF),[18] CD_3OD[19]], with the addition of lithium salts,[20] and in the crystal state,[17] as well as when bound to its natural receptor cyclophilin.[21,22]

A large number of NMR pulse sequences exist which have been the subject of many reviews.[23,24] Here we concentrate on those that are essential for the assignment and the extraction of conformationally relevant parameters in peptides.[25–27] The modular structure of peptide spectra, resulting in separate spin systems for each amino acid, facilitates structural analysis, but the more or less free rotations about bonds to the α-carbons (about angles ϕ, ψ, and χ_1) as well as the side chains, make the determination of their three-dimensional (3D) structures problematic. To analyze such flexible compounds one has to get as many experimental restraints as possible. Apart from NOE or rotating frame Overhauser enhancement (ROE) effects, homo- and heteronuclear coupling constants and temperature coefficients of the H_N protons are the most important. NOE or ROE intensities should be quantitatively converted into distances. The classification as strong, medium, and weak, often used for proteins, is not sufficient for peptides. Conformational averaging is different for NOEs, for *J* coupling constants and for molecular geometry over a trajectory of a molecular dynamic (MD) calculation.[28]

Compared with proteins the surface-to-core ratio of (small) peptides is much larger. This not only leads to the high sensitivity of peptide conformations to environmental effects (see above) but also leads to a reduced number of NOE/ROE data. For a reliable analysis of peptide conformations and dynamics, this has to be taken into account by providing enough carefully assigned (including stereochemical assignments) and quantitatively well-determined data. Nonagreement of NOE or *J* coupling derived structures can be used to identify conformational heterogeneity.

2 ASSIGNMENT OF RESONANCES

The first step of spatial structure determination is the assignment of all resonances.[29] Correct assignment provides the proof of the constitution (connectivity) of the peptide. The structures (constitutions) of many naturally occurring

peptides have been established by NMR. For this purpose a complete assignment of all resonances (including, for example, diastereotopic β-protons) is not required. However, for the determination of the 3D structures full assignment is a must.

The experiments to be chosen depend on the complexity of the structure, the amount of compound available, spectrometer equipment, and available measuring time. Complete assignment is normally achieved by using only a few experiments. COSY and TOCSY lead to the assignment of the spin systems, whereas NOESY or ROESY experiments give sequential connectivities. In some cases, for example, similar spin systems or larger sequences, more sophisticated heteronuclear two-dimensional (2D) or even 3D techniques have to be used. Generally the scheme in the following sections is applied for the assignment (see also Table 1).

2.1 Identification of the Nature of the Amino Acid

2.1.1 Classification According to Their Spin System

The spin systems of each amino acid (HN–H-α–H-β ...) can be determined using the direct proton correlation obtained by a double quantum filtered (DQF)–COSY experiment[30–32] [see Figure 1(a)]. Some of the naturally occurring amino acids have a unique spin system which can be directly identified. When long aliphatic chains are involved [e.g. lysine (Lys) or proline (Pro)] it might be difficult to obtain the complete proton connectivity. A TOCSY spectrum[33–36] [see Figure 1(b)] with a long mixing time (60–80 ms) resulting in a magnetization transfer from the HN proton along the whole spin system usually yields the required information. In strongly overlapping cases editing of the proton spectra via the attached carbons will remove most of the problems. This can be done with a heteronuclear multiple quantum coherence (HMQC) experiment[37–39] [see Figure 1(c)] which leads to direct H,C correlations, or is very efficient via an HMQC experiment with TOCSY transfer (HMQC–TOCSY)[40] [see Figure 1(d)]. Both experiments use a BIRD pulse[41] to suppress protons bound to ^{12}C.[42,43] They have longer relaxation times than those bound to ^{13}C. Their suppression allows a higher repetition rate.

The resonance assignment using both ^{1}H and ^{13}C is particularly recommended when several similar spin systems occur or proton shifts have a low dispersion, as is probable in linear flexible peptides. Carbon-13 resonances are spread over a larger spectral range than protons. Generally, in HMQC–TOCSY spectra all proton spin systems are well separated and can easily be identified. When even higher resolution of the ^{13}C resonances is required, folding in this dimension is applied.[44] Another possibility of achieving higher resolution is via pulse sequences for selection and editing of multiplicities, such as HQQC[45] to select $^{13}CH_3$ groups [see Figure 1(e)] or DEPT–HMQC[46,47] [see Figure 1(f)], which results in extremely well-separated spectra.

2.1.2 Connecting Apparently Isolated Spin Systems in Side Chains

Several amino acids have very similar AMXY patterns for their HN, H-α, H-β, and H-β' protons. A full identification of the amino acid requires establishing the connectivity to the rest of the side chain. For example, aromatic amino acids such as phenylalanine (Phe), tyrosine (Tyr), tryptophan (Trp) and histidine (His) can be identified in many cases and distinguished from the very similar AMXY spin system of cysteine via long-range couplings between the β-protons and aromatic protons. It is more efficient to connect these spin systems via heteronuclear long range coupling (HMBC)[48] [see Figure 1(g)] using the quaternary carbon as a spy looking into both spin systems. Apparently isolated proton spin systems can also be connected via NOE effects [ROESY, see Figure 1(h), or NOESY, see Figure 1(i)]. Caution is required because proximity in space does not always correspond to proximity

Table 1 Overview of the Best Experiments for the Signal Assignment of Peptides

Purpose	Experiment	
	First choice	Second choice
Identification of amino acids		
establishing proton spin systems	TOCSY	COSY
connecting isolated proton spin systems in the side chains	HMBC	NOESY
		ROESY
proof of α ... ω connectivity, remove overlap	HMQC–TOCSY	
Sequential assignment		
using heteronuclear long-range coupling	HMBCS	
using NOE effects		NOESY
		ROESY
Full assignment		
(a) stereospecific assignment using only coupling constants [^3J(H,H), ^3J(C,H), ^3J(N,H)]	PECOSY	
	HMBC	
	HETLOC	
using homonuclear coupling constants and NOE[a]	PECOSY	NOESY
		ROESY
(b) Full side-chain assignment		
aromatic protons	HMBC	NOESY
		ROESY
methyl groups	HQQC-TOCSY	

[a]Does not lead in all cases to unambiguous assignment. However it is sufficient for restricted systems such as proline.

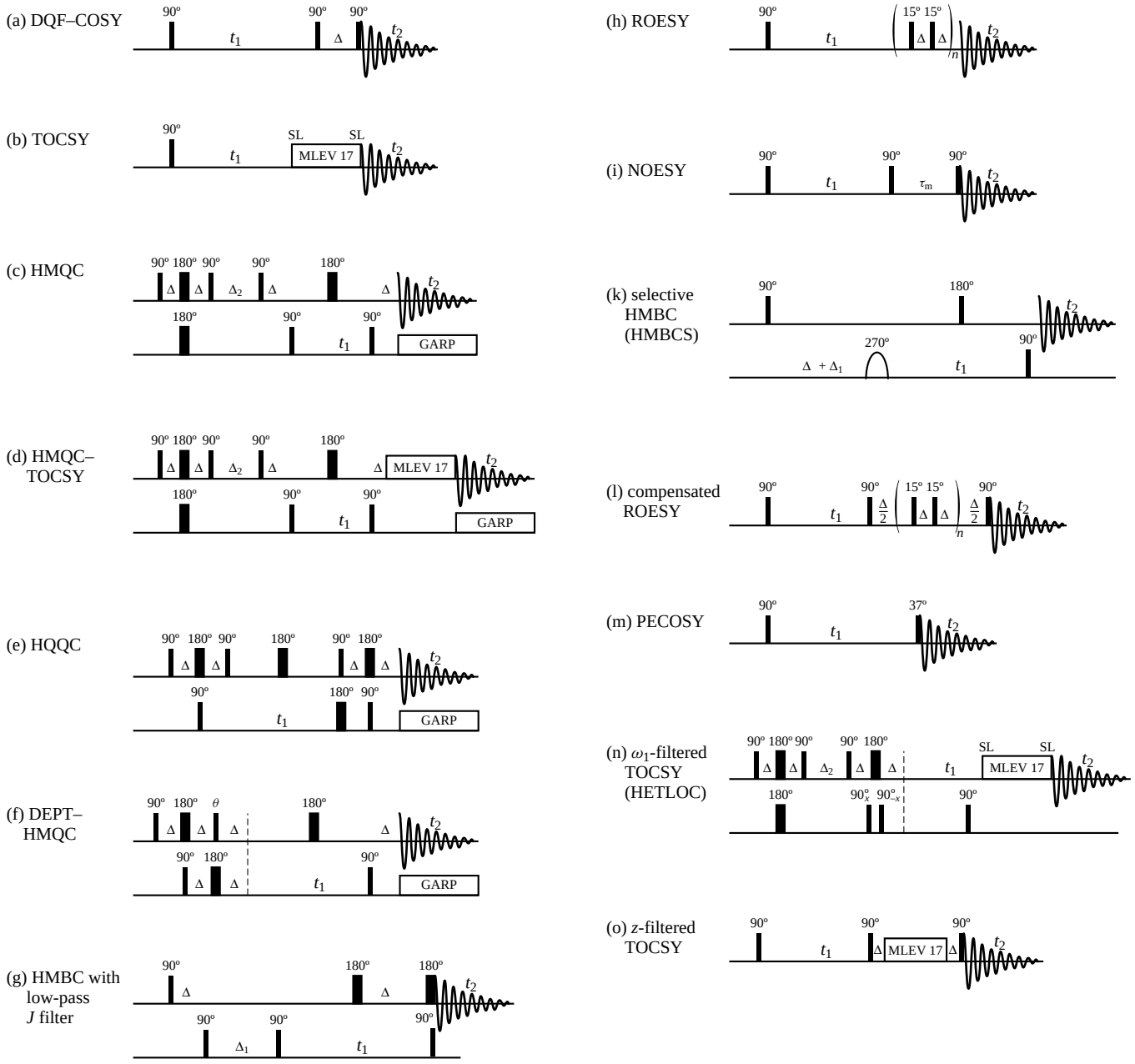

Figure 1 Pulse sequences of all NMR experiments in this article

according to chemical bonds. Hence, if possible, through-bond connectivity provided by coupling constants is preferred.

Trp and His can also be distinguished from Phe and Tyr by the typical low-frequency shifts of their β-carbon.[49]

2.1.3 Identification via Sequencing

Another way of identifying the spin system of amino acids is the comparison of the known primary sequence with the information obtained from spectral sequencing as described in the following section (see also Figure 2). However, sequencing of proteins[29] or peptides in micellar solution may require more sophisticated techniques involving ^{15}N and/or ^{13}C labeling[50,51] to circumvent problems of overlap and faster relaxation (broad signals).

2.2 Sequential Assignment

Sequential assignment is necessary if not all of the spin systems can be assigned unequivocally or if some amino acids occur several times in the peptide sequence. It simultaneously provides proof of the correct assignment of the spin systems. NOESY[52] and ROESY[53–55] experiments both contain sequential information. Dipolar relaxation results in cross peaks from the HN proton of one residue to its own α-proton and to the α-proton of the preceding residue. Using this information the sequence can be obtained in almost all cases. Exceptions only occur when distinct secondary or tertiary structural elements lead to additional long-range HNH-α NOEs. An unambiguous method is the use of HMBC spectra. Long-range coupling leads to signals from the carbonyl of one

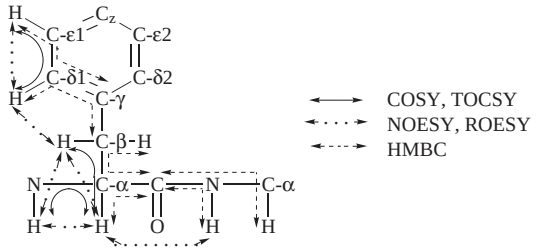

Figure 2 Scheme of information for the assignment of resonances resulting from different experiments

residue to the α- and/or β-protons of its own spin system and to the HN, and often also to the α-proton of the following residue. As carbonyl carbons resonate in a small spectral range, selective excitation of the carbonyl carbons via a 270° Gaussian selective pulse is recommended to reduce the spectral range in the ^{13}C dimension and improve its resolution[56] [HMBCS, see Figure 1(k)].

3 NMR PARAMETERS FOR THE DETERMINATION OF THE SPATIAL STRUCTURE

3.1 Distance Restraints

Distance restraints can be obtained via dipolar relaxation experiments using NOE.[57,58] The NOE (and the cross-relaxation rate σ) depend on the Larmor frequency and the correlation time of the molecule:

$$\sigma \sim \omega\tau_c \tag{1}$$

Due to their long correlation times, large molecules like proteins exhibit NOEs of −100%, which give rise to intensive positive cross peaks (with respect to the diagonal) in NOESY spectra. For small peptides the NOE is positive (maximum: 50%) but often close to zero (depending on the field strength, the viscosity of the solution, and the molecular size). Only weak NOE cross peaks can be detected. Sometimes positive and negative cross peaks appear in the same spectrum when internal mobility differs in different parts of the molecule. In these cases it is convenient to use the ROE for the determination of proton−proton distances. The ROE is always positive and can therefore be observed even with a cross relaxation σ close to zero ($\tau_c^{-1} \approx \omega$). If the nature of the solvent allows, lowering the temperature to shift the molecular tumbling in the direction of the slow motion limit of NMR spectroscopy ($\tau_c^{-1} \ll \omega$) is also recommended. Low-temperature NOESY spectra have been successfully applied to lipophilic peptides such as antamanide[59,60] and cyclosporin,[16] and yielded a dramatically improved data set.

For the conversion of the integral values of the observed cross peaks into distances, the isolated two-spin approximation is commonly used. The cross-peak intensities in the initial buildup regime are proportional to the referring distances according to

$$I_1/I_2 = r_1^{-6}/r_2^{-6} \tag{2}$$

The calibration of the distances is achieved by the use of a known distance, e.g., the cross-peak intensity of geminal protons which refers to a distance of 178 pm. Another approach starts with a calibration guess and, after performing a restrained MD calculation, recalibration is done to achieve better agreement between all restraints and calculated distances. This optimal fit is iteratively obtained.

It is important to mention that spin diffusion occurs for long mixing times, especially in the slow motion limit, and distributes the magnetization in the worst case equally over the whole spin system, eliminating the linearity between intensity and distance. A compromise has to be found: the mixing time has to be long enough to observe intense cross peaks but short enough for the system still to be in the linear buildup region of the NOE. Proton−proton distances of small peptides can normally be obtained with mixing times in the range of 100−250 ms. For the determination of buildup curves a number of NOESY or ROESY spectra with different mixing times have to be recorded. Aggregating peptides or peptides in highly viscous solvents have to be treated similarly to large proteins. Spin diffusion can be taken into account by solving the relaxation matrix.[61] A practical approach is the use of the iterative relaxation matrix approach (IRMA)[62–64] or MARDIGRAS.[65] For example the lithium complex of cyclosporin A is already aggregated and IRMA was necessary to obtain reliable distances. On the other hand, pure cyclosporin A in $CDCl_3$ or THF solution can be investigated even at low temperatures without taking spin diffusion into account.

Intensities of ROESY cross peaks depend on the frequency offset of the spin locking field. This has to be taken into account in the form of an offset correction.[66,67]

$$A(\gamma B_1) = A \sin^2 \theta_k \sin^2 \theta_l \tag{3}$$

$$A_{comp}(\gamma B_1) = A \sin \theta_k \sin \theta_l \tag{4}$$

Equation (3) describes the modulation in a normal ROESY spectrum, with $\theta_{k,l} = \tan^{-1}(\gamma B_1/\Omega_{k,l})$ and $\Omega_{k,l}$ as the offset of the spins k and l from the transmitter frequency, whereas equation (4) is the analogous expression for a compensated ROESY spectrum[67] [see Figure 1(l)].

3.2 Measurement of Coupling Constants

Vicinal coupling constants contain supplementary information about the conformation of peptides. They are related to the corresponding dihedral angles via the Karplus equation:[68,69]

$$^3J = A \cos^2 \Theta + B \cos \Theta + C \tag{5}$$

Parameters are available for a variety of possible homo- and heteronuclear coupling constants in peptides[70,71] (see Table 2). There are four coupling constants that describe the same dihedral angle ϕ, namely the homonuclear coupling ^3J(HN,H-α) and the heteronuclear couplings ^3J(C-β,NH), ^3J(CO,NH) and ^3J[CO($i-1$),H-αi].[72] Heteronuclear coupling constants are now easy to obtain even in natural abundance (see below). The χ_1 angle can be described by the

Table 2 *A*, *B* and *C* Parameters for the Karplus Curves of Homonuclear and Heteronuclear Coupling Constants[a]

Dihedral angle	Coupling constant	*A*	*B*	*C*
ϕ	^3J(HN,H-α)	9.4	−1.1	0.4
	^3J(HN,H-α)	6.7	−1.3	1.5[b]
	^3J(CO,NH)	5.8	−2.7	0.1
	^3J(C-β,NH)	4.5	−1.5	−0.2
	^3J[CO-i,H-$\alpha(i+1)$]	9.0	−4.4	−0.8
χ_1	^3J(H-α,H-β)	9.5	−1.6	1.9
	^3J(CO,H-β)	6.1	−2.7	1.0

[a]Bystrov.[70]
[b]Ludvigsen et al.[71]

homonuclear coupling ^3J(H-α, H-β) and the heteronuclear coupling constants ^3J(CO,H-β), ^3J(N,H-β) and ^3J(C-γ,H-α).

Constraints for the ψ angle are much more difficult to obtain. Possible vicinal couplings defining the range of this dihedral angle have to contain the peptide nitrogen. The vicinal coupling constants ^3J[N(i + 1),C-βi] and ^3J[N(i + 1),H-αi] can only be obtained for ^{15}N-enriched samples and their range of values is too small to determine the related dihedral angle precisely. Another method of determining restraints for the ψ angle is the use of the one-bond coupling constant ^1J(C-α,H-α).[73] The value of this coupling constant depends on the orientation of both, the ϕ and the ψ angle. The appropriate Karplus curve is:[74]

$$^1J(\text{C-}\alpha, \text{H-}\alpha) = A + B\cos^2(\phi + \delta) + C\cos^2(\psi + \delta) \quad (6)$$

Parameters for this equation have been determined (A = 138.4, B = 13.7, C = −5.2). A slightly different equation has also been derived, but this function is almost identical to the one given here.[75] The disadvantage of using ^1J(C-α,H-α) is the relatively small dependence on ψ, as can be seen from the coefficient C, which is about three times smaller than B. But if the ϕ angle is well determined the ψ angle restriction according to equation (6) can be used as a conformational restraint (see below).

The values for the ^3J(HN,N-α) coupling constants can often be obtained from the HN doublets of the one-dimensional ^{1}H spectrum recorded with 32K or 64K data points resolution. In cases of small shift dispersion of the HN protons, often occurring when the peptide is very flexible, they have to be extracted from DQF−COSY- or PECOSY spectra [see Figure 1(m)]. Directly reading the coupling constant from the splitting in the antiphase cross peak leads to an overestimated value, due to cancellation in the overlapping region and subsequent shifts of the maxima of the antiphase pattern. The method of Kim and Prestegard[76] uses a trace of the HN−H-α cross peak phased to the pure absorption mode and to the pure dispersion mode resulting in two splitting values ν_a and ν_d respectively (see Figure 3), from which the exact value of the coupling constant can be calculated according to equation (7).

$$J^6 - \nu_d^2 J^4 + (-\tfrac{9}{4}\nu_a^4 + \tfrac{3}{2}\nu_a^2\nu_d^2 + \tfrac{3}{4}\nu_d^4)J^2 + \tfrac{81}{64}\nu_a^6 - \tfrac{9}{16}\nu_a^4\nu_d^2 - \tfrac{21}{32}\nu_a^2\nu_d^4 - \tfrac{1}{16}\nu_d^6 + \frac{\nu_d^8}{64\nu_a^2} = 0 \quad (7)$$

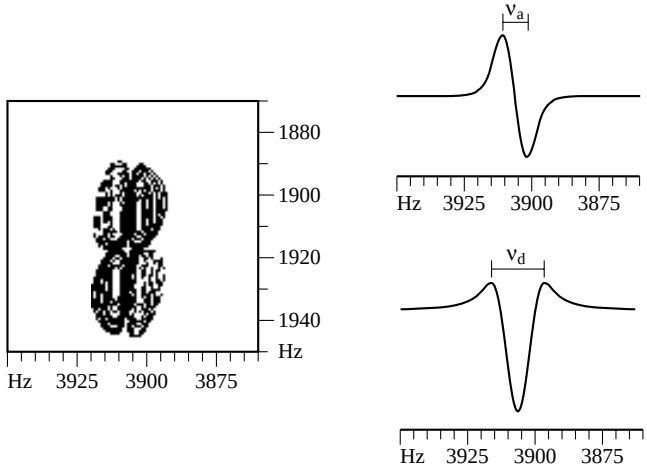

Figure 3 Determination of the HN−H-α coupling constant from a COSY spectrum cross peak

The ^3J(H-α,H-β) coupling constants can be measured from the related α,β cross-peak patterns of COSY experiments using the DISCO procedure[77,78] or by ECOSY,[79] resulting in simpler cross-peak patterns. A simple alternative to the original ECOSY is PECOSY,[80] where the second 90° pulse of the normal COSY sequence is replaced by a smaller flip angle (normally a 20−40°) pulse. Transitions connected directly in the term scheme are strongly suppressed. The dispersive diagonal signals are subtracted via a separate reference spectrum. The ECOSY cross peak between two spins A and B contains the coupling to the third spin (the so-called passive coupling) by an inphase shift of the submultiplet from which the passive coupling constant can be read (see Figure 4). The reader is referred to the literature for further information.[24]

The determination of the heteronuclear coupling constants requires much more effort. The ^3J(HN,C-β) and ^3J(N,H-β) coupling constants can be measured with the ω_1-filtered TOCSY (HETLOC)[81,82] [see Figure 1(n)]. Similar to that mentioned above for the HMQC, a BIRD pulse is used to suppress the proton signals bound to ^{12}C. The resulting cross peaks also show an ECOSY type pattern. The signals are separated in the F_1 dimension by the large ^1J heteronuclear coupling constant [^1J(C,H) = 140 Hz for aliphatic carbons or ^1J(N,H) = 92 Hz] so that the small vicinal coupling constant can be measured in F_2. With this method coupling constants even smaller than the linewidth can be obtained.

Heteronuclear coupling constants to heteronuclei that do not have a proton attached can be obtained by a method introduced by Titman et al.[83] and Titman and Keeler.[84] This procedure is a combination of a slightly modified HMBC [Figure 1(g)] and a homonuclear reference spectrum. If the signals are overlapped in the one-dimensional reference spectrum a z-filtered TOCSY[83,84] [see Figure 1(o)] can be used instead. The heteronuclear HMBC cross peak, e.g. between a CO carbon and a β-proton, in the F_2 dimension contains all homonuclear couplings of the proton and is additionally modulated by the desired heteronuclear long-range coupling, whereas a corresponding signal of the homonuclear reference spectrum contains only the homonuclear coupling constants. The reference signal is multiplied by the additional modulating term containing a trial heteronuclear coupling constant. The

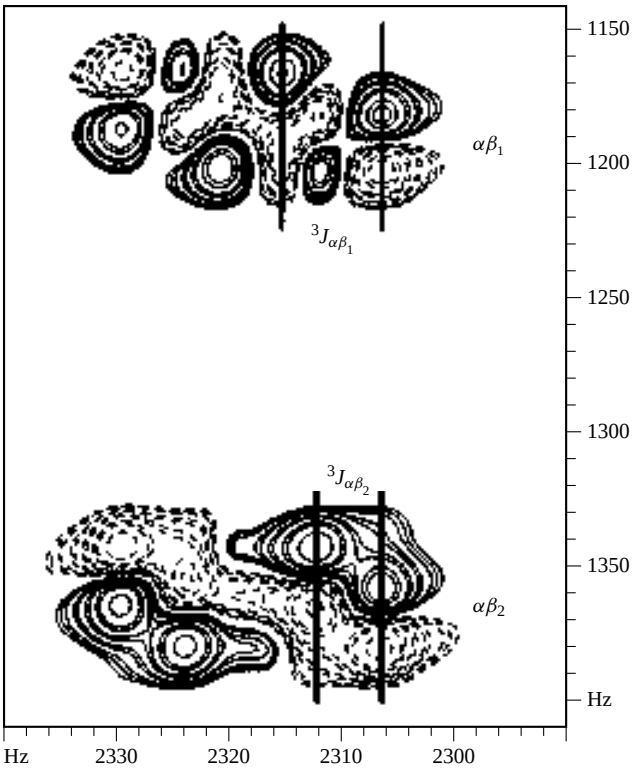

Figure 4 Determination of the ^3J(H-α,H-β) coupling constants from an α,β cross peak of a PECOSY spectrum

shape of this calculated signal is then compared with that of the actually measured HMBC cross peak. With an iterative procedure, varying the value of the heteronuclear coupling constant, the calculated signal can be fitted to the experimental one.

Values for the one-bond ^1J(C-α,H-α) coupling constants can be measured by simply recording an HMQC experiment without decoupling during acquisition.

3.3 Temperature Coefficients

The chemical shift values of HN protons change with the temperature depending on their orientation to the solvent. One-dimensional spectra at different temperatures (300–330 K) with a stepwidth of 5 K are usually recorded to study this effect. In cases where the amide region is too crowded it is more convenient to use 2D correlation spectra (e.g. TOCSY, COSY). A temperature gradient larger than -3×10^{-3} ppm K^{-1} in DMSO indicates shielding from the solvent which often (but not always!) indicates involvement in internal hydrogen bonds.[85,86] Also exchange rates of HN protons with deuterium (adding D_2O) can be used for the same purpose; fast exchange then indicates solvent exposure.

4 *cis–trans* ISOMERIZATION

Peptides containing proline or *N*-alkylated amino acids often exhibit *cis–trans* isomerization about the unknown (Xaa)–Pro peptide bond. At room temperature, exchange between these conformations is normally slow on the NMR timescale (rates of 0.01–1 s^{-1}) and a double signal set can be identified. The relative population is strongly dependent on the primary structure,[3] on the solvent, on the temperature, and often also on the concentration. The *cis–trans* isomerism can be proven by coalescence at higher temperatures or by exchange cross peaks in NOESY or ROESY spectra in the slow exchange regime.[23] ROESY spectra are more suitable for this purpose due to the different signs of ROE and exchange peaks. The NOE/ROE cross peak between the two α protons of the *cis* rotamer can be applied for the assignment of *cis* and *trans* conformers. A strong NOE between the Pro δ protons and the H-α of the preceding residue is indicative of the *trans* isomer.

Peptide bonds not involving *N*-alkylated amino acids strongly prefer the *trans* rotamer. A few exceptions have been found including even relatively unconstrained hexapeptides.[87–89]

5 DIASTEREOTOPIC ASSIGNMENT

A reliable conformational analysis requires assignment of the diastereotopic protons, e.g., the two β-protons of Phe, etc. Without this assignment pseudoatoms for these methylene groups have to be used for structure calculations. In this case, a correction term of 0.9 Å has to be added to the upper distance limit. The resulting range of restraints can become so large that there is essentially no remaining restriction.

The assignment of the diastereotopic β-protons in peptides is based on the (reasonable) assumption of only the staggered rotamers of the side-chain dihedral angle χ_1 being populated.[90,91] The two homonuclear couplings ^3J(H-α,H-β) and ^3J(H-α,H-β') directly yield the amount of the rotamer $P_{III}(\chi_1 = +60^\circ)$ assuming a *gauche* ($\pm sc$) coupling constant of 2.6 Hz and a *trans* (*ap*) coupling of 13.6 Hz. The difference between ^3J(H-α,H-β) and ^3J(H-α,H-β') indicates the ratio of P_I ($\chi_1 = -60^\circ$) and P_{II} ($\chi_1 = 180^\circ$). With P_{II} dominating, a relatively large coupling of the carbonyl carbon to the β^{proR}-proton is observed, whereas for P_I the amide nitrogen atom shows a large coupling to the β^{proS}-proton. The combination of homonuclear and heteronuclear coupling constants is a reliable technique for the assignment of β-protons without stereoselective deuteration (see Table 3).

Often also NOEs can be combined with homonuclear coupling constants.[92–94] This is the preferred way when the amount of peptide is small but this procedure depends also on the conformation of adjacent bonds and hence may fail.

For the assignment of the β-protons in proline it is normally sufficient to use the H-α–H-β NOEs because the ring structure of proline avoids ambiguities. The shortest distance is always the NOE between the α- and the β^{proS}-proton. The γ- and δ-protons of proline can be assigned in many cases using their NOEs to the β- and α-protons.

6 STRUCTURE CALCULATION

The conformation of a peptide is obtained by using the experimental restraints (NOE-derived distances and *J*-derived bond angles). In the first approximation it is assumed that only one predominant (backbone) conformation exists. If

Table 3 Homonuclear and Heteronuclear Coupling Constants and NOE Values for the Diastereopic Assignment of β-Protons. (−) Denotes a Small Value of the Coupling Constant and (++) a Large One

	Rotamer P_I	Rotamer P_{II}	Rotamer P_{III}
	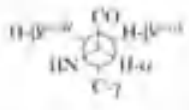	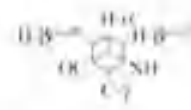	
χ_1 (deg)	−60	180	+60
$^3J(H_\alpha,H_\beta^{pro-R})$ (Hz)	13.6	2.6	2.6
$^3J(H_\alpha,H_\beta^{pro-S})$ (Hz)	2.6	13.6	2.6
$^3J(CO,H_\beta^{pro-R})$ (Hz)	−	++	
$^3J(CO,H_\beta^{pro-S})$ (Hz)	−	−	++
$d(HN,H_\beta^{pro-R})$ (pm)	260–380	250–380	370–480
$d(HN,H_\beta^{pro-S})$ (pm)	370–480	250–380	260–380
$d(H_\alpha,H_\beta^{pro-R})$ (pm)	310	255	250
$d(H_\alpha,H_\beta^{pro-S})$ (pm)	255	310	250

all experimental data are fulfilled and the final structure is energetically reasonable (according to the force field) one has obtained 'a structural model'. It has still to be proven whether there are alternative models which would also fulfil the data. This is especially critical if only few data are available. Often in the literature there are structures repesented that are based on a very limited data set which are impossible to prove or disprove.

If there is no agreement with calculated and experimental parameters and a data set of high quality is available, one has to assume conformational averaging. In particular, when NOEs and J coupling constants are used, conformational averaging is easier to detect, because both 'parameter-average' differently. A structural average (e.g. over an MD trajectory) is different from an NOE- or a J-average because they are not linearly dependent on each other.[28,95]

Averaged conformations may be analyzed by time-dependent NOE or J restraints,[96–98] by distance geometry calculations, or by ensemble calculations.[99]

The procedure for calculation is described in more detail in ***Synthetic Peptides***. However a short outline of the procedure is given here.

6.1 Starting Structure

The easiest way is to build a starting structure manually. It is recommended that the starting point should be far from what is expected and a short high-temperature simulated annealing protocol should then be performed.

To avoid bias, distance geometry calculations can be applied to produce typically 50–100 structures that are refined in four-dimensional and 3D space using the measured distances and J restraints. Recently the use of an additional restraint potential for amide protons involved in hydrogen bonding has been introduced.[100] The structures with the lowest total and the lowest restraint energy are then analyzed. If all structures converge to a single conformation then this one is used as a starting structure in a subsequent simulation including the solvent.

The latter method using distance geometry is preferable to the MD calculations with many different starting structures, because it is less time consuming and a better conformational sampling is provided. For underdetermined systems, where too few experimental data are available, distance-geometry (DG) calculations will not converge to a single conformation. In these cases MD simulations using a full force field can be applied, but a very careful interpretation is needed because the 'structure' depends on the calculated energy, i.e. the force field.

6.2 Restraints

It is now standard to use NOE-derived distances as lower and upper bound restraints. To increase the quality of the determined structures J coupling constants must also be considered as restraints for structure determination, not only (as often can be found) to check the results of an NOE-based calculation.

For a specific J coupling constant up to four solutions exist. Hence, when using J coupling constants as restraints the full Karplus curve has to be programmed to allow the molecule to get all four solutions in an MD run.[101] The energy penalty function is analogous to that commonly used for NOEs

$$E_J = \sum k(J_{\text{theo}} - J_{\text{exp}})^2 \tag{8}$$

where J_{theo} = theroretical J value according to the actual dihedral angle in the trajectory, J_{exp} = experimental J value, and k is a type of force constant to adjust the restraint. By this procedure several different coupling constants can also be used to describe a single bond angle,[102,103] which results in a reduced number of possible minima (see Figure 5).

6.3 Solvents

The relatively large surface-to-core ratio of small compounds such as peptides leads to a strong dependence of their conformation on the surrounding solvent. Experimental restraints can be used to mimic solvent effects; however it is still very problematic to perform calculations without explicit solvent. To reduce artifacts from charged groups a scaling down of

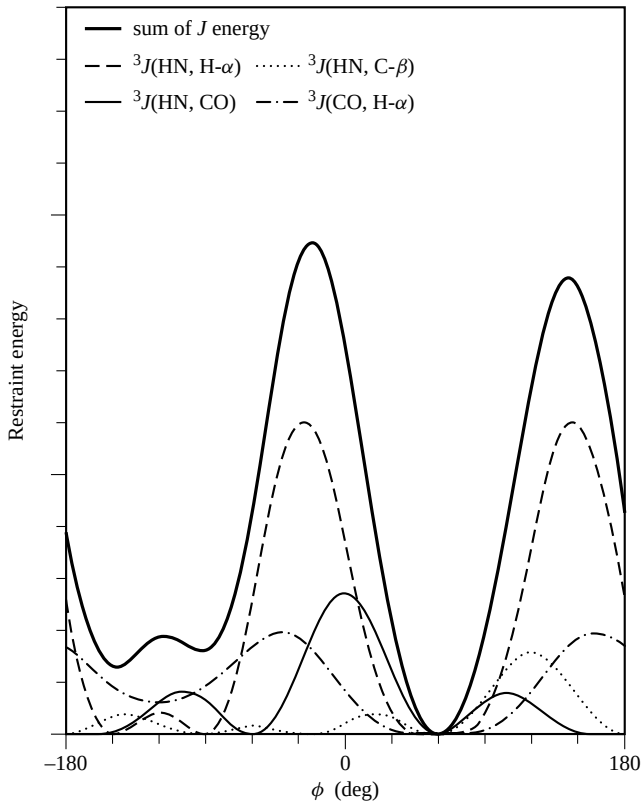

Figure 5 Potential energy of the coupling constant penalty term for coupling constants fitting a ϕ angle of +60°

charges of HN protons according to the measured temperature dependence[104] or a higher pK have also been used. However we have shown that only explicit solvents yield reasonable results.[105,106] There are force fields available for H_2O, CCl_4, $CDCl_3$, DMSO, CH_3CN, CH_3OH, CF_3CH_2OH, and the calculation should be done close to the experimental conditions. The starting structure is placed in a box of solvent molecules and equilibrated. A MD simulation using NOEs and J coupling constants of about 100–150 ps is calculated. It is recommended to use another 30–150 ps of free dynamics (without any experimental restraints) in the solvent to check if the structure is stable and reasonable.

When the NMR measurements have been performed in SDS or DMPC a two-phase box[107] can be used. It contains a mixture of CCl_4 and water, mimicking an anisotropic membrane surrounding. A good example for the application of this system is the bradykinin antagonist HOE 140.[12] NMR measurements in isotropic solvents like water or DMSO showed that this molecule is highly flexible (random coil). Applying a combined approach of NMR measurements in SDS micelles and MD simulations in this two-phase box, the conformation and its orientation at the phase interface could be determined.

6.4 Flexibility and Exchange

The above-mentioned simulation techniques result only in structures that fulfill all measured data if the considered molecule strongly populates one single conformation under the conditions of the measurement. In the case of nonagreement (see above) or other good reasons to assume conformational averaging due to multiple conformations in fast equilibrium, other approaches have to be applied. There exists no method to date that can handle more than just a few rapidly interconverting conformations. The treatment of systems with just a few conformers can be performed with MD calculations using time-dependent NOEs and J coupling constants as restraints.[96–98] This method takes into account that the measured values may be averaged for different conformations which interconvert rapidly on the NMR timescale. Recently a second approach for the determination of peptide structures for molecules with more than one conformation has been introduced. Distance geometry calculations with an ensemble of low-energy structures using the ensemble averages for the distance- and dihedral-restraint penalty functions result in a few different families of conformations.[99,108]

7 CONFORMATIONAL FLEXIBILITY

Conformational averaging can be identified via the analysis of NOE/ROE data and J coupling constants. Values for the homonuclear ^3J(HN, H-α) or ^3J(H-α, H-β) coupling constants of about 7 Hz indicate fast averaging of the ϕ and the χ_1 angles respectively. The appearance of rigid secondary structure elements like β-turns or α-helices is accompanied by a characteristic pattern of HN–HN and HN–H-α NOEs. Together with the values of related coupling constants the type of the turns (βI, βII, ...)[109] or helices can be determined. The occurrence of all sequential and intraresidual HN–H-α NOEs and the absence of medium- or long-range NOEs is generally an indicator of a random coil conformation.

Proof of the flexibility of a molecule under the experimental conditions can be obtained via the analysis of relaxation data. A full analysis is not necessary for small, linear peptides. It is sufficient to determine the ^{13}C T_1 relaxation times using the fast inversion–recovery experiment.[110] The determined T_1 relaxation parameters depend on the correlation time τ_c of the CH_n groups.[58] This relationship is not unequivocal; two possible solutions can be obtained. For small peptides the shorter τ_c of the two values is normally the true one, but a comparison of the measurements at different field strengths results in a single solution (see Figure 6). A comparison of the determined T_1 values for the α-carbons leading to correlation times of around 0.5 ns for peptides[111] hints at a uniform mobility for the whole peptide. If the T_1 relaxation times differ some domains are considered to be more flexible than others. The dynamics of side-chain motions can also be detected in this way, as has been shown for the dynamics of Pro side chains in antamanide examined via the T_1 relaxation times of the C-γ protons.[112,113]

If there are hints for conformational flexibility as normally occurs in small, linear peptides there are several possibilities of influencing the equilibrium or the exchange rates. The easiest method is just to perform the NMR experiments at lower temperature to slow down the correlation times of the molecule and thereby the exchange rate between the conformers. If the temperature is low enough possible interconverting conformations may show discrete sets of signals. But so far restricted rotations about ϕ,ψ angles in noncyclic peptides have never been observed. Suitable solvents are CD_3OD, TFE, $CDCl_3$, or cryomixtures like DMSO/H_2O (80:20). At a

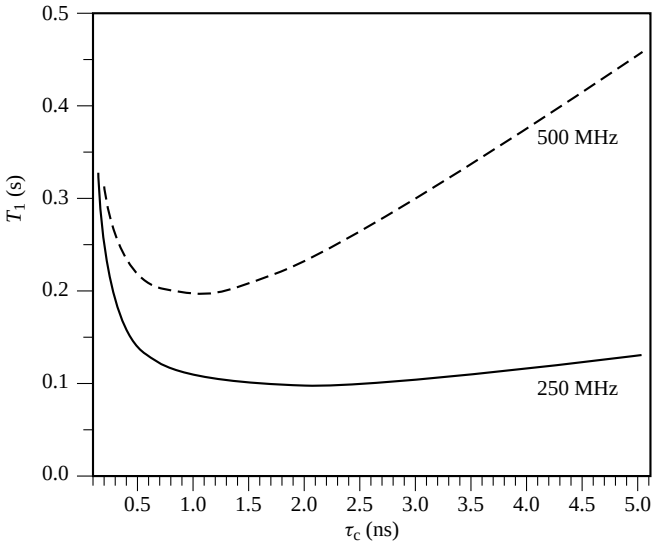

Figure 6 Plot of the T_1 relaxation time versus the correlation time τ_c for different field strengths: 250 MHz, solid line; 500 MHz, broken line

temperature of 243 K the latter solvent is isodielectric with water at 295 K,[6] but leads to increased NOEs[7] due to the lower viscosity. Sometimes simply a change from one solvent to another will shift the equilibrium observed for *cis–trans* conformers about peptide bonds because of the different polarity or specific solvation effects. Recently a distinct flip of the whole peptide bond about adjacent bonds (ϕ,ψ), a process which is often found in cyclic peptides,[114–116] was induced in the cyclic peptide hymenistatin when changing the solvent from $CDCl_3$ to DMSO. A different solvation of the amide bond in the two conformations can explain this difference.[117] Cyclosporin A, for example, exists in chloroform in a single conformation,[15–17] whereas in CD_3OD four distinct sets of signals can be detected.[19] A rather drastic change occurs in the measurement in anisotropic, membrane-mimicking solvents (SDS, DMPC), which represents a more realistic environment for peptides naturally occurring in membrane surroundings.

8 CONCLUSION

The high flexibility, the high surface-to-core ratio, the relatively small number of restraints, and the strong polar nature of peptides, all make reliable peptide conformational analysis still a difficult task, which requires spectra of good quality, a set of designed pulse sequences, careful extraction of parameters, and critical and competent calculational procedures; otherwise 'structures' remain 'pictures' of fictitious character.

9 RELATED ARTICLES

COSY Two-Dimensional Experiments; Coupling Constants Determined by ECOSY; Distance Geometry; Heteronuclear Shift Correlation Spectroscopy; Homonuclear Three-Dimensional NMR of Biomolecules; Multidimensional Spectroscopy: Concepts; Peptide Hormones; Peptide and Protein Secondary Structural Elements.

10 REFERENCES

1. P. Y. Chou and G. D. Fasman, *Biochemistry*, 1974, **13**, 222.
2. G. D. Fasman, *Prediction of Protein Structure and the Principles of Protein Conformation*, Plenum Press, New York, 1989.
3. H. J. Dyson, M. Rance, R. A. Houghten, R. A. Lerner, and P. E. Wright, *J. Mol. Biol.*, 1988, **201**, 161.
4. J. W. Nelson and N. R. Kallenbach, *Biochemistry*, 1989, **28**, 5256.
5. R. W. Storrs, D. Truckses, and D. E. Wemmer, *Biopolymers*, 1992, **32**, 1695.
6. A. Motta, D. Picone, T. Tancredi, and P. A. Temussi, *J. Magn. Reson.*, 1987, **75**, 364.
7. S. W. Fesik and E. T. Olejniczak, *Magn. Reson. Chem.*, 1987, **25**, 1046.
8. P. A. Temussi, D. Picone, G. Saviano, P. Amodeo, A. Motta, T. Tancredi, S. Salvadori, and R. Tomatis, *Biopolymers*, 1992, **32**, 367.
9. J. W. Bean, K. D. Kopple, and C. E. Peishoff, *Peptides 1992*, eds. C. H. Schneider and A. N. Eberle, ESCOM Science Publishers, Leiden, 1993.
10. K. D. Kopple, P. W. Baures, J. W. Bean, C. A. D'Ambrosio, J. L. Hughes, C. E. Peishoff, and D. S. Eggleston, *J. Am. Chem. Soc.*, 1992, **114**, 9615.
11. K. H. Lee, J. E. Fitton, and K. Wüthrich, *Biochim. Biophys. Acta*, 1987, **911**, 144.
12. W. Guba, R. Haessner, G. Breitpohl, S. Henke, J. Knolle, V. Santagada, and H. Kessler, *J. Am. Chem. Soc.*, 1994, **116**, 7532.
13. H. Kessler, *Angew. Chem., Int. Ed. Engl.*, 1982, **21**, 512.
14. M. Gurrath, G. Müller, H. Kessler, M. Aumailly, and R. Timpl, *Eur. J. Biochem.*, 1992, **210**, 911.
15. H. Kessler, H. R. Loosli, and H. Oschkinat, *Helv. Chim. Acta*, 1985, **68**, 661.
16. H. Kessler, M. Köck, T. Wein, and M. Gehrke, *Helv. Chim. Acta*, 1990, **73**, 1818.
17. H.-R. Loosli, H. Kessler, H. Oschkinat, H.-P. Weber, T. J. Petcher, and A. Widmer, *Helv. Chim. Acta*, 1985, **68**, 682.
18. H. Kessler, M. Gehrke, J. Lautz, M. Köck, D. Seebach, and A. Thaler, *Biochem. Pharmacol.*, 1990, **40**, 169.
19. S. Y. Ko and C. Dalvit, *Int. J. Pept. Protein Res.*, 1992, **40**, 380.
20. M. Köck, H. Kessler, D. Seebach, and A. Thaler, *J. Am. Chem. Soc.*, 1992, **114**, 2676.
21. C. Weber, G. Eider, B. von Freyberg, R. Traber, W. Braun, H. Widmer, and K. Wüthrich, *Biochemistry*, 1991, **30**, 6563.
22. S. W. Fesik, R. T. Gampe, Jr., H. L. Eaton, G. Gemmecker, E. T. Olejniczak, P. Neri, T. F. Holzman, D. A. Eagan, R. Edalji, R. Simmer, R. Helfrich, J. Hochlowski, and M. Jackson, *Biochemistry*, 1991, **30**, 6574.
23. R. R. Ernst, G. Bodenhausen, and A. Wokaun, *Principles of Nuclear Magnetic Resonance in One and Two Dimensions*, Clarendon, Oxford, 1991.
24. H. Kessler, M. Gehrke, and C. Griesinger, *Angew. Chem., Int. Ed. Engl.*, 1988, **27**, 490.
25. H. Kessler and S. Seip, in *Two-Dimensional NMR Spectroscopy; Applications for Chemists and Biochemists*, eds. W. R. Croasmun and M. K. Carlson, VCH, New York, 1994.
26. H. Kessler, W. Bermel, A. Müller, and K.-H. Pook, in *The Peptides; Analysis, Synthesis, Biology*, eds. S. Udenfried and J. Meienhofer, Academic Press, New York, 1985, Vol. 7, pp. 437–473.
27. H. Kessler, G. Gemmecker, A. Haupt, J. Lautz, and M. Will, in *NMR Spectroscopy and Drug Research*, eds. J. W. Jaroszewski,

K. Schaumburg, and H. Kofod, Munksgaard, Copenhagen, 1988, pp. 138–152.
28. O. Jardetzky, *Biochim. Biophys. Acta*, 1980, **621**, 227.
29. K. Wüthrich, *NMR of Proteins and Nucleic Acids*, Wiley, New York, 1986.
30. W. P. Aue, E. Bartholdi, and R. R. Ernst, *J. Chem. Phys.*, 1976, **64**, 2229.
31. U. Piantini, O. W. Sørensen, and R. R. Ernst, *J. Am. Chem. Soc.*, 1982, **104**, 6800.
32. M. Rance, O. W. Sørensen, G. Bodenhausen, G. Wagner, R. R. Ernst, and K. Wüthrich, *Biochem. Biophys. Res. Commun.*, 1983, **117**, 479.
33. L. Braunschweiler and R. R. Ernst, *J. Magn. Reson.*, 1983, **53**, 521.
34. A. Bax, R. A. Byrd, and A. Aszalos, *J. Am. Chem. Soc.*, 1984, **106**, 7632.
35. A. Bax and D. G. Davis, *J. Magn. Reson.*, 1985, **65**, 355.
36. C. Griesinger, G. Otting, K. Wüthrich, and R. R. Ernst, *J. Am. Chem. Soc.*, 1988, **110**, 7870.
37. L. Müller, *J. Am. Chem. Soc.*, 1979, **101**, 4481.
38. M. R. Bendall, D. T. Pegg, and D. M. Dodrell, *J. Magn. Reson.*, 1983, **52**, 81.
39. A. Bax, R. H. Griffey, and B. L. Hawkins, *J. Magn. Reson.*, 1983, **55**, 301.
40. A. L. Lerner and A. Bax, *J. Magn. Reson.*, 1986, **69**, 375.
41. J. R. Garbow, D. P. Weitekamp, and A. Pines, *Chem. Phys. Lett.*, 1982, **93**, 504.
42. A. Bax and S. Subramanian, *J. Magn. Reson.*, 1986, **67**, 565.
43. R. A. Byrd, M. F. Summers, G. Zon, C. Spellmeyer Fouts, and L. G. Marzilli, *J. Am. Chem. Soc.*, 1986, **108**, 504.
44. P. Schmieder, S. Zimmer, and H. Kessler, *Magn. Reson. Chem.*, 1991, **29**, 375.
45. H. Kessler, P. Schmieder, M. Köck, and M. Reggelin, *J. Magn. Reson.*, 1991, **91**, 375.
46. H. Kessler, P. Schmieder, and M. Kurz, *J. Magn. Reson.*, 1989, **85**, 400.
47. H. Kessler and P. Schmieder, *Biopolymers*, 1991, **31**, 621.
48. A. Bax and M. F. Summers, *J. Am. Chem. Soc.*, 1986, **108**, 2093.
49. K. Wüthrich, *NMR in Biological Research: Peptides and Proteins*, Elsevier, New York, 1976.
50. G. Wagner, *Prog. Nucl. Magn. Reson. Spectrosc.*, 1990, **22**, 101.
51. H. Oschkinat, T. Müller, and T. Dieckmann, *Angew. Chem., Int. Ed. Engl.*, 1994, **33**, 277.
52. J. Jeener, B. H. Meier, P. Bachmann, and R. R. Ernst, *J. Chem. Phys.*, 1979, **71**, 4546.
53. A. A. Bothner-By, R. L. Stephens, J. Lee, C. D. Warren, and R. W. Jeanloz, *J. Am. Chem. Soc.*, 1984, **106**, 811.
54. A. Bax and D. G. Davis, *J. Magn. Reson.*, 1985, **63**, 207.
55. H. Kessler, C. Griesinger, R. Kerssebaum, K. Wagner, and R. R. Ernst, *J. Am. Chem. Soc.*, 1987, **109**, 607.
56. H. Kessler, P. Schmieder, M. Köck, and M. Kurz, *J. Magn. Reson.*, 1990, **88**, 615.
57. J. H. Noggle and E. E. Schirmer, *The Nuclear Overhauser Effect, Chemical Applications*, Academic Press, New York, 1971.
58. D. Neuhaus and M. Williamson, *The Nuclear Overhauser Effect in Structural and Conformational Analysis*, VCH, Weinheim, 1989.
59. H. Kessler, A. Müller, and K.-H. Pook, *Justus Liebigs Ann. Chem.*, 1989, 903.
60. H. Kessler, J. W. Bats, J. Lautz, and A. Müller, *Justus Liebigs Ann. Chem.*, 1989, 913.
61. B. A. Borgias, M. Gochin, D. J. Kerwood, and T. L. James, *Prog. Nucl. Magn. Reson. Spectrosc.*, 1990, **22**, 83.
62. R. Boelens, T. M. G. Koning, and R. Kaptein, *J. Mol. Struct.*, 1988, **173**, 299.
63. R. Boelens, T. M. G. Koning, G. A. van der Marel, J. H. van Boom, and R. Kaptein, *J. Magn. Reson.*, 1989, **82**, 290.
64. R. Boelens, T. M. G. Koning, and R. Kaptein, *J. Magn. Reson.*, 1990, **90**, 111.
65. B. A. Borgias and T. L. James, *J. Magn. Reson.*, 1990, **87**, 475.
66. A. Bax, *J. Magn. Reson.*, 1988, **77**, 134.
67. C. Griesinger and R. R. Ernst, *J. Magn. Reson.*, 1987, **75**, 261.
68. M. Karplus, *J. Chem. Phys.*, 1959, **30**, 11.
69. M. Karplus, *J. Am. Chem. Soc.*, 1963, **85**, 2870.
70. V. F. Bystrov, *Prog. Nucl. Magn. Reson. Spectrosc.*, 1976, **10**, 41.
71. S. Ludvigsen, K. V. Andersen, and F. M. Poulsen, *J. Mol. Biol.*, 1991, **217**, 731.
72. P. Schmieder and H. Kessler, *Biopolymers*, 1992, **32**, 435.
73. D. F. Mierke, S. Golic Grdadolnik, and H. Kessler, *J. Am. Chem. Soc.*, 1992, **114**, 8283.
74. H. Egli and W. von Philipsborn, *Helv. Chim. Acta*, 1981, **64**, 976.
75. G. W. Vuister, F. Delaglio, and A. Bax, *J. Am. Chem. Soc.*, 1992, **114**, 9674.
76. Y. Kim and J. H. Prestegard, *J. Magn. Reson.*, 1989, **84**, 9.
77. H. Kessler, A. Müller, and H. Oschkinat, *Magn. Reson. Chem*, 1985, **23**, 844.
78. H. Kessler, C. Griesinger, and H. Oschkinat, *J. Am. Chem. Soc.*, 1985, **109**, 6927.
79. C. Griesinger, O. W. Sørensen, and R. R. Ernst, *J. Am. Chem. Soc.*, 1985, **107**, 6394.
80. L. Mueller, *J. Magn. Reson.*, 1987, **72**, 191.
81. M. Kurz, P. Schmieder, and H. Kessler, *Angew. Chem., Int. Ed. Engl.*, 1991, **30**, 1329.
82. U. Wollborn and D. Leibfritz, *J. Magn. Reson.*, 1992, **98**, 142.
83. J. J. Titman, D. Neuhaus, and J. Keeler, *J. Magn. Reson.*, 1989, **85**, 111.
84. J. J. Titman and J. Keeler, *J. Magn. Reson.*, 1990, **89**, 640.
85. M. Llinás and M. P. Klein, *J. Am. Chem. Soc.*, 1975, **97**, 4731.
86. Y. A. Bara, A. Friedrich, H. Kessler, and M. Molter, *Chem. Ber.*, 1978, **111**, 1045.
87. D. F. Mierke, T. Yamazaki, O. E. Said-Nejad, E. R. Felder, and M. Goodman, *J. Am. Chem. Soc.*, 1989, **111**, 6847.
88. E. Bairaktari, D. F. Mierke, S. Mammi, and E. Peggion, *J. Am. Chem. Soc.*, 1990, **112**, 5383.
89. H. Kessler, U. Anders, and M. Schudok, *J. Am. Chem. Soc.*, 1990, **112**, 5908.
90. K. G. R. Pachler, *Spectrochim. Acta*, 1963, **19**, 2085.
91. K. G. R. Pachler, *Spectrochim. Acta*, 1964, **20**, 581.
92. G. Wagner, W. Braun, T. F. Havel, T. Schaumann, N. Go, and K. Wüthrich, *J. Mol. Biol.*, 1987, **196**, 611.
93. S. G. Hyberts, W. Märki, and G. Wagner, *Eur. J. Biochem.*, 1987, **164**, 625.
94. A. S. Arsenviev, P. Schultze, E. Wörgötter, W. Braun, G. Wagner, M. Vasák, J. H. R. Kägi, and K. Wüthrich, *J. Mol. Biol.*, 1988, **201**, 637.
95. D. F. Mierke, T. Huber, and H. Kessler, *J. Comput. Aided Mol. Des.*, 1994, **8**, 29.
96. A. E. Torda, R. M. Scheek, and W. F. van Gunsteren, *Chem. Phys. Lett.*, 1989, **157**, 289.

97. A. E. Torda, R. M. Sheek, and W. F. van Gunsteren, *J. Mol. Biol.*, 1990, **214**, 223.
98. A. E. Torda, R. M. Brunne, T. Huber, H. Kessler, and W. F. van Gunsteren, *J. Biomol. NMR*, 1993, **3**, 55.
99. D. F. Mierke, M. Kurz, and H. Kessler, *J. Am. Chem. Soc.*, 1994, **116**, 1042.
100. D. F. Mierke, A. Geyer, and H. Kessler, *Int. J. Pept. Protein Res.*, 1994, **44**, 325.
101. D. F. Mierke and H. Kessler, *Biopolymers*, 1993, **33**, 1003.
102. D. F. Mierke and H. Kessler, *Biopolymers*, 1992, **32**, 1277.
103. M. Eberstadt, D. F. Mierke, M. Köck, and H. Kessler, *Helv. Chim. Acta*, 1992, **75**, 2583.
104. H. Kessler, U. Anders, and M. Schudok, *J. Am. Chem. Soc.*, 1990, **112**, 5908.
105. M. Kurz, D. F. Mierke, and H. Kessler, *Angew. Chem., Int. Ed. Engl.*, 1992, **31**, 210.
106. H. Kessler, S. Mronga, G. Müller, L. Moroder, and R. Huber, *Biopolymers*, 1991, **31**, 1189.
107. W. Guba and H. Kessler, *J. Phys. Chem.*, 1994, **98**, 23.
108. D. F. Mierke, R. M. Scheek, and H. Kessler, *Biopolymers*, 1994, **34**, 559.
109. G. D. Rose, L. M. Gierasch, and J. A. Smith, *Adv. Protein Chem.*, 1985, **37**, 1.
110. D. Canet, G. C. Levy, and I. R. Peat, *J. Magn. Reson.*, 1975, **18**, 199.
111. H. Kessler, J. W. Bats, C. Griesinger, S. Koll, M. Will, and K. Wagner, *J. Am. Chem. Soc.*, 1988, **110**, 1033.
112. Z. I. Mádi, C. Griesinger, and R. R. Ernst, *J. Am. Chem. Soc.*, 1990, **112**, 2908.
113. J. M. Schmidt, R. Brüschweiler, R. R. Ernst, R. L. Dunbrock, Jr., D. Joseph, and M. Karplus, *J. Am. Chem. Soc.*, 1993, **115**, 8747.
114. H. Kessler, C. Griesinger, J. Lautz, A. Müller, W. F. van Gunsteren, and H. J. C. Berendsen, *J. Am. Chem. Soc.*, 1988, **110**, 3393.
115. R. M. Brunne, W. F. van Gunsteren, R. Brüschweiler, and R. R. Ernst, *J. Am. Chem. Soc.*, 1993, **115**, 4764.
116. K. D. Kopple, J. W. Blan, K. A. Bhandary, J. Briand, C. A. D'Ambrosio, and C. E. Peishoff, *Biopolymers*, 1993, **33**, 1093.
117. R. K. Konat, D. F. Mierke, H. Kessler, B. Kutscher, M. Bernd, and R. Voegeli, *Helv. Chim. Acta*, 1993, **76**, 1649.

Biographical Sketches

Horst Kessler. *b* 1940. Ph.D. 1966, chemistry, Leipzig and Tübingen. Habilitation, 1969, Tübingen. Full Professor of Organic Chemistry, J. W. Goethe University, Frankfurt/Main, 1971–1989. Technical University of Munich, 1989–present. Approx. 325 publications. Foundation and first Chairman of the Fachgruppe Magnetic Resonance Spectroscopy of the German Chemical Society. Research specialties: design of bioactive peptides based on conformation, development and application of new multidimensional NMR techniques, chemical synthesis of peptidomimetics, DG and MD calculations including more experimental parameters and with explicit solvents.

Wolfgang Schmitt. *b* 1966. Studied chemistry in Munich, presently working on Ph.D. thesis. Research specialties: NMR spectroscopy of bioactive peptides and peptidomimetics, DG and MD calculations.

Polysaccharides and Complex Oligosaccharides

C. Allen Bush

University of Maryland, Baltimore County, Baltimore, MD, USA

1	Introduction	1
2	Covalent Structure Determination	1
3	Conformation and Dynamics	3
4	Related Articles	5
5	References	5

1 INTRODUCTION

Complex oligosaccharides and polysaccharides are composed of a wide variety of different monosaccharides in different linkages. They are not involved as energy sources in metabolism but should be considered rather as 'informational macromolecules' encoding information which is generally important in intercellular communication. The information which they store is decoded by interaction with specific binding proteins known as lectins.[1] The cell surface oligosaccharides of membrane glycoproteins and glycolipids have been implicated in such important biological functions as inflammation[2] and cellular differentiation.[3] The cell surface polysaccharides of bacteria, including lipopolysaccharides, capsular polysaccharides, and other cell wall polysaccharides are implicated in bacterial adhesion and coaggregation.[4,5] Two different aspects of the structure are important to an understanding of the biology of these interactions. First, one must determine the covalent chemical structure of complex oligosaccharides and polysaccharides including the absolute configuration of the constituent monosaccharides. Secondly, one must also determine their three-dimensional folding and their conformation. If they do not adopt a single conformation but rather exist in multiple conformations which exchange, then one must also determine the dynamics of the conformational exchange. This knowledge will make a major contribution to our understanding the interactions of complex oligosaccharides with lectins. High-resolution NMR spectroscopy has been important in all three facets of the structure of complex oligosaccharides and polysaccharides.

2 COVALENT STRUCTURE DETERMINATION

Determination of the covalent structure of a complex oligosaccharide or polysaccharide is not so simple as determination of a peptide sequence or of a nucleotide sequence. With the possibility of two sugar ring forms (furanoside or pyranoside) and of two anomeric forms (α and β) as well as multiple linkage positions, much more detailed information is required for a description of the structure of a complex oligosaccharide which often includes branching. At present there is no single established method for structure determination and many different methods involving enzymatic digestion, chemical degradation, and methylation analysis are used for various problems. The catalog of available *endo*- and *exo*-glycosidases is inadequate and the outcome of chemical reactions involving sugars is notoriously unpredictable. These facts contribute to the attractiveness of instrumental methods such as mass spectrometry and NMR spectroscopy which require minimal chemistry.

2.1 Proton NMR Spectroscopy

The first major contribution of high-resolution ^{1}H NMR spectroscopy to this problem was the structural reporter group method which became useful with the introduction of high-field superconducting spectrometers operating at 360 MHz. An oligosaccharide or polysaccharide in the quantity range of 100 nmol to 1 μmol is dissolved in D_2O and a ^{1}H spectrum is recorded with chemical shifts referred to DSS.[6,7] In this method, which was first used in glycopeptides and was later extended to glycolipids in DMSO solution, certain well-resolved resonances can often be recognized in one-dimensional spectra. For example the anomeric region at ca. 4.4–5.4 ppm usually contains resonances of anomeric protons most of which are isolated (see ***Carbohydrates and Glycoconjugates***). Accurately measured values of the chemical shift can be combined with the multiplet splitting to characterize the oligosaccharide or polysaccharide. Other structural reporter resonances which contribute to the fingerprint include methyl doublets near 1.3–1.5 ppm typical of 6-deoxyhexoses and methyl singlets around 2.0 ppm characteristic of *N*- or *O*-acetyl methyl groups. Methylene resonances of 3-deoxy sugars can be found between 1.8 and 2.3 ppm. But many overlapping resonances of the methine protons between 3.5 and 4.0 ppm are unresolved and contribute minimal information. The chemical shifts and multiplet structures of the isolated structural reporter resonances can be used to characterize the oligosaccharide or polysaccharide, since no two distinct structures have ever been found to have the same NMR spectrum.

Although the structural reporter method has been used primarily for *N*-linked glycopeptides and glycolipids, it can be used on any oligosaccharide or polysaccharide for which a reference library of closely related structures is available (see ***Carbohydrates and Glycoconjugates***). The method has also been used extensively for the oligosaccharide alditols isolated from the alkaline borohydride degradation of mucin glycoproteins.[8–10] In polysaccharides with a repeating subunit, only the structural reporter resonances of the repeat unit are observed and the spectrum resembles that of an oligosaccharide without a reducing terminal. The method works well in any system of closely related bacterial polysaccharides.[11] Although the structural reporter method has been generally associated with ^{1}H NMR spectroscopy, a very similar approach has been used in the ^{13}C NMR of bacterial polysaccharides as will be described below. The structural reporter method for ^{1}H spectra is fast (~30 min) requiring less spectrometer time than other NMR methods and is comparatively sensitive yielding at least some information on samples as small as 20–100 nmol.

A complete assignment of all the proton signals is more difficult, but it provides much more information

on the structure of a polysaccharide for which there are no available spectra for closely similar compounds. A complete assignment of the ^{1}H spectrum can in principle be established by spin correlation since each sugar ring forms a chain of scalar coupled spins. While correlation by scalar coupling was originally done by spin decoupling, usually by difference methods, two-dimensional methods such as COSY are generally preferred for modern instrumentation. The experiment is usually performed in a phase-sensitive mode with a double quantum filter.[11,12] Spin correlation is started at the anomeric proton resonance or at some other structural reporter resonance such as a methyl doublet of a 6-deoxyhexose. Correlation through the entire spin system by COSY can be augmented by 2D HOHAHA or TOCSY which is especially valuable for resonances which are close in chemical shift, giving rise to COSY cross peaks close to the diagonal.[13] From these 2D COSY and TOCSY spectra, one can extract the homonuclear coupling constants which are very useful in assigning the stereochemistry of the sugar pyranoside residue. Two vicinally coupled protons which are axial make a dihedral angle of 180° implying a large coupling constant which is observed in practice to range from 7–11 Hz, whereas any coupling involving equatorial protons exhibits a small *gauche* coupling constant ranging in practice from 0.5–3 Hz (see ***Vicinal Coupling Constants and Conformation of Biomolecules***). Hence these data reveal whether substituents are axial or equatorial, providing the anomeric configuration of the glycosidic linkage as well as the identity of the sugar residue. The identities of the monosaccharides are then to be confirmed by carbohydrate analysis by a method such as HPLC.

Two common difficulties arise which may prevent the above scheme from providing a successful assignment of the ^{1}H spectrum. The first problem is strong coupling which is all too common in the crowded 3.4–4.4 ppm region of the carbohydrate spectrum. It arises when the chemical shifts of two resonances which are coupled are separated by an amount which is not large compared with the coupling constant. Homonuclear two-dimensional TOCSY or HOHAHA spectroscopy can be used to obtain cross peaks which are well removed from the diagonal in many cases. But if the difference in chemical shift is less than twice the coupling constant, the multiplet shape cannot be extracted interfering with the assignment of stereochemistry by homonuclear coupling, ^3J(H,H). In this case, heteronuclear NMR methods involving ^{13}C resolution are required, as will be discussed below. A second problem in spin correlation about the ring arises for very small values of ^3J(H,H) associated with some *gauche* protons.

NOESY correlations can often be used to correlate such *gauche* protons since they are close in space. A hybrid homonuclear method combining TOCSY with ROESY or NOESY may be useful in such cases and long-range heteronuclear coupling correlation can also be useful as will be described below (see ***Carbohydrates and Glycoconjugates***).

Although the scheme outlined above for spin correlation can be used to assign all proton resonances in a ring and to identify the sugar residues and their anomeric configuration, it does not provide the sequence of residues or their linkage and branching. For this purpose, homonuclear spin correlation is not informative and correlation through space by NOESY can be employed. The anomeric proton of one residue is often close to the aglycone proton directly across the glycosidic linkage, giving rise to NOESY cross peaks which identify the linkage.[13,14] Unfortunately this proximity depends on the conformation of the glycosidic linkage and many exceptions are observed in which a large NOE is seen between the anomeric proton resonance and that of the proton adjacent to the linkage position. This situation arises most often when the adjacent proton is equatorial.[11,13] Although the NOESY data can be useful for the assignment of oligosaccharide sequences, the information on the linkage position is not definitive unless the conformation is known, which is usually not the case for a completely new polysaccharide of unknown structure. Thus the linkage position must be confirmed by some other type of data, such as methylation analysis or long-range heteronuclear correlation to be described below.

Observation of NOESY in oligosaccharides and polysaccharides is complicated by difficulties arising from a dependence on the rotational correlation time. NOE is positive for small molecules and negative for larger ones such as proteins and DNA duplexes.[15] (See ***Nuclear Overhauser Effect***.) For intermediate sized molecules having a rotational correlation time τ_c approximately equal to the reciprocal of the spectrometer frequency ω, the NOE disappears altogether. This is approximately the case for a tetrasaccharide at 500 MHz. One solution to this problem is to change the viscosity of the solution, and thus the τ_c, by changing the sample probe temperature[16] or the viscosity of the solvent by the addition of a viscous cosolvent such as DMSO.[17,18] If it is not desirable to alter the solvent conditions, one can resort to NOE in the rotating frame for which NOEs are positive for all rotational correlation times (see ***ROESY*** and ***Carbohydrates and Glycoconjugates***.) One difficulty with this experiment, which is known as ROESY, is that one must be careful to account for magnetization transfer by the HOHAHA mechanism which leads to cross peaks of the opposite sign and which may cancel ROESY peaks.

The observation of a NOE in polysaccharides is usually straightforward since it is commonly large and negative. Wide variations in flexibility are observed among polysaccharides depending strongly on the linkages. Thus wide variations of linewidth are observed, but generally the NOE is negative.[11] The dynamics of the internal motion in polysaccharides is a complex topic which will be addressed below.

2.2 Carbon-13 NMR Spectroscopy

The ^{13}C spectra of carbohydrates generally show much better chemical shift dispersion than do the ^{1}H spectra. In D_2O solution referenced to DSS, the anomeric signals are dispersed between 95 and 110 ppm and methyl carbon resonances are observed at 15–25 ppm. Since the signals corresponding to the methine carbon atoms of the sugar ring are spread over a much wider spectral region (between 55 and 85 ppm) than are the corresponding signals in the ^{1}H spectrum, there is only a moderate amount of overlap of the signals even at the low fields typical of iron core magnet NMR spectrometers (20–25 MHz carbon ^{13}C frequency). With the introduction of Fourier transform ^{13}C spectroscopy in the 1970s, the spectra of many carbohydrates were recorded, revealing both the promise and some of the difficulties with this type of spectroscopy. A major problem arises from the low sensitivity associated with the direct observation of ^{13}C in natural abundance, especially

with low magnetic field strength spectrometers. Although the requirement for sample sizes of 20–50 μmol severely limited applications to oligosaccharides from eukaryotic glycopeptides and glycolipids, bacterial polysaccharides are often available in such quantities and spectra were reported for a number of bacterial polysaccharides such as the *O*-antigen chains of lipopolysaccharides (LPS), capsular polysaccharides, and other bacterial cell wall polysaccharides.[19–21] A second problem with these early studies of ^{13}C NMR spectra of carbohydrates was the lack of a simple method for the rigorous assignment of ^{13}C signals analogous to the ^3J(H,H) correlation method described above for the assignment of ^{1}H spectra. In the absence of a correlation method, the only data upon which to base resonance assignments were ^{13}C chemical shifts and extensive sets of rules for 'glycosylation shifts' were developed.[22,23] Recently more sophisticated computer-based schemes for this type of correlation have been developed for complex oligosaccharides.[24–26] Although the large chemical shift dispersion of ^{13}C spectra leads to well-resolved spectra, the large effects complicate any rational scheme for assignment based on regular differences in chemical shifts. This situation has led to many revisions of the spectral assignments of the ^{13}C spectra of complex carbohydrates as more rigorous correlation-based methods for assignment were introduced. These methods include specific ^{13}C incorporation by chemical synthesis,[27] DEPT methods which count the protons bonded to a particular carbon atom,[28] or comparison of chemical shifts in D_2O and H_2O solution (DIS).[29] In spite of the difficulties in obtaining reliable ^{13}C resonance assignments in these early ^{13}C studies, the data proved to be immensely useful in studies of bacterial polysaccharide structure.[19,20]

Major advances in ^{13}C NMR spectroscopy of polysaccharides have resulted from the more common use of correlation methods which follow chemical bonds. Rigorous assignment of the ^{13}C spectrum can be derived from the ^{1}H assignment by one-bond C–H coupling correlation. While such a correlation is not very practical for ^{13}C detection in macromolecules, the recent introduction of inverse detection or ^{1}H-detected ^{13}C spectroscopy has greatly increased the utility of this approach. Not only is the sensitivity of ^{1}H-detected ^{13}C spectra greatly improved, but it also gives the ^{1}H spectrum the higher resolution of the detected dimension where it is most needed. In a convenient implementation called HMQC[30] the rather crowded ^{1}H spectrum is resolved in the F_1 dimension by the excellent dispersion of the ^{13}C dimension. This spreads out the resonances that would otherwise overlap in the ^{1}H spectrum and also provides a scheme for the assignment of the ^{13}C resonances once a rigorous assignment of the ^{1}H spectrum is derived from homonuclear spin correlation as described above.[31] Another advantage of HMQC arises in the case of strongly coupled ^{1}H resonances, which are often resolved by the difference in ^{13}C chemical shift. The large value of ^1J(C,H) (~140 Hz) removes the strong coupling for natural abundance samples in which there is only one ^{13}C atom in the average sugar ring.[11] In the absence of strong coupling, the correct homonuclear multiplet shape can be deduced as required for the assignment of the stereochemistry of the pyranoside ring and identification of the sugar. With hybrid methods such as coupled HMQC–COSY, one can assign the correct multiplet shape and chemical shift even in cases for which the ^{1}H resonances exactly overlap.[32] The combination of ^{1}H homonuclear correlation and ^{1}H-detected ^{13}C correlation enables a complete assignment of both spectra for complex carbohydrates which are available in quantities of about 1 μmol. This is reasonable for bacterial polysaccharides, but may not be suitable for glycopeptides or glycolipids from eukaryotes which are often not available in such large quantities.

Another important extension of these heteronuclear methods is long-range correlation of ^{1}H with ^{13}C over two and three bonds by the method popularly known as HMBC.[33] The pulse sequence is similar to that used for HMQC but it involves longer delays to allow antiphase magnetization to develop over the smaller coupling. In this experiment, there is a reduction in sensitivity due to the long delays (30–50 ms) which are required and if T_2 is not much longer than the delays, substantial signal is lost. Particularly for polysaccharide samples with wide lines, this experiment is less sensitive than HMQC and can require as much as 10 μmol of sample depending on the linewidth. HMBC spectra provide valuable confirmation of ^{1}H and ^{13}C resonance assignments through correlation within the sugar ring, and also complete assignments for cases in which vicinal homonuclear coupling constants are too small to provide correlation.[11] But the main function of HMBC spectra is correlation across the glycosidic linkage.[31] This allows assignment of the glycosidic linkage in a rigorous way which follows the chemical bonds. This method has found a number of recent applications for determining glycosidic linkages in bacterial polysaccharides.[11] In favorable cases, this information can take the place of data from methylation analysis and a complete structure of a polysaccharide can be determined essentially by NMR methods with very little ancillary data.

3 CONFORMATION AND DYNAMICS

The question of the three-dimensional conformation of complex oligosaccharides and polysaccharides is distinct from the primary or covalent structure. A truly detailed understanding of the conformation and dynamics requires contributions from a number of techniques, but at the present time data from NMR spectroscopy have made the most significant contributions to the solution of this problem. Computer molecular modeling is generally essential to the satisfactory interpretation of the experimental NMR data.[34] It seems likely that contributions from other experimental biophysical methods such as X-ray crystallography and fluorescence spectroscopy can be expected to increase as the importance of oligosaccharide–lectin interactions becomes more apparent.[35]

An early contribution of NMR data to oligosaccharide conformation was the homonuclear ^3J(H,H) values which are especially useful for determining the puckering of the pyranoside rings of sugars. Since the six-membered pyranoside rings generally assume defined chairs, their ^3J(H,H) values are either large (7–11 Hz) for coupling between axial protons or small (0–3 Hz) for coupling involving equatorial protons, as is described above in connection with the assignment of ring stereochemistry. For furanosides, the pucker is much more complicated, with the five-membered rings adopting envelope conformations in rapid exchange. Measurements of ^3J(H,H) for furanosides have been useful in determining the relative contributions from the various envelope conformations which are important in DNA and RNA conformation.[36]

(See ***Vicinal Coupling Constants and Conformation of Biomolecules***.) A combination of empirical and ab initio calculations has been used to model the furanoside rings and to fit the ^3J(H,H) data to the model.

For oligosaccharides composed of relatively rigid pyranoside rings, the glycosidic dihedral angles describe the conformation and dynamics of the polysaccharide.[37] Homonuclear coupling data are uninformative regarding the relative conformation of the rings with respect to each other and much more information on oligosaccharide and polysaccharide conformation has been derived from ^{1}H NOE data which report on distances through space.[15] (See ***Nuclear Overhauser Effect***.) The strategy is similar to that used in the determination of protein structure in solution by NMR methods which relies heavily on computer modeling methods for an interpretation of the NMR data (See ***Structures of Larger Proteins, Protein-Ligand, and Protein-DNA Complexes by Multi-Dimensional Heteronuclear NMR***). The earliest studies of oligosaccharide conformation were performed on chemically synthesized models of blood group oligosaccharides in which steady-state NOEs were interpreted qualitatively.[38] Models were built with a simple empirical energy function and the NOE data were interpreted qualitatively to confirm these models. This method has also been used in bacterial polysaccharides.[39,40]

A more quantitative method for incorporating the NOE data into molecular modeling schemes follows methods often used in the interpretation of NMR data of proteins in which experimental distance constraints are derived from the NOE data. The distance constraints, which are most commonly derived from the 'isolated spin pair approximation', are treated as pseudo energy terms in the modeling to force a conformation which is consistent with the experimental NOE data (see ***Structures of Larger Proteins, Protein-Ligand, and Protein-DNA Complexes by Multi-Dimensional Heteronuclear NMR***). Choe et al.[41] have used NOE constraints to study the core oligosaccharide of the glycosamino glycans and Scarsdale et al.[42] have described an application to gangliosides. Homans and Forster[43] have also outlined a detailed method for restrained molecular dynamics for oligosaccharides.

A slightly different approach to the quantitative evaluation of NOE data for modeling of oligosaccharides is spin matrix analysis. In this method a molecular model is built and interactions among all the ^{1}H spins are treated to include three spin effects and spin diffusion (see ***Protein Structures: Relaxation Matrix Refinement***). The model is then adjusted to determine whether any conformation can be found for which all the simulated NOE data agree with experiment. This method was first introduced by Brisson and Carver[44] for steady-state NOE in glycopeptides. The matrix method for oligosaccharides was later extended to transient two-dimensional NOESY data which are technically more convenient.[45] The spin matrix method has been adapted to include quantitative interpretation of rotating frame or ROESY data.[46]

An inherent problem with both methods outlined above for the quantitative interpretation of NOE data for oligosaccharides is that they ignore internal motion. The matrix method begins with the assumption of a simple isotropically rotating rigid model and the restrained molecular modeling methods are generally assumed to converge to a single conformation. Careful analysis of the results of either method can be used to test for consistency of a single rigid model with the experimental data, but it is difficult to incorporate internal motion into a quantitative NOESY calculation. The question of the flexibility of complex oligosaccharides is important and remains somewhat controversial.[47,48] Certainly, the relatively narrow lines observed in NMR spectra of polysaccharides (2–15 Hz) having molecular weights as high as 100 kDa suggest that there must be some type of flexibility. One possible interpretation is that certain types of oligosaccharides, such as the blood group epitopes, do assume relatively rigid conformations, while other sugar linkages are flexible, providing structural 'hinges'.[34,48]

One approach to the interpretation of NOE in the presence of internal motion is to assume that the molecular modeling results are correct, assign statistical weights to the minimum energy conformations, and then calculate average NOE. Under the assumption that the rate of conformational exchange is fast compared with T_1 but slow compared with the overall τ_c of the oligosaccharide, one may average the values of the spin matrix elements and then solve the problem.[45,48] Unfortunately it is not known whether this assumption about the kinetics of conformational exchange is correct.

The uncertainty about the details of the conformational dynamics of polysaccharides suggests that additional types of experimental information are needed. The interpretation of NOESY data for a system with internal motion can be quite complex since motion can modulate not only the orientation of ^{1}H–^{1}H vectors but also the distances between protons. It has been recognized for many years that heteronuclear coupling ^3J(C,H) values could be used to correlate with dihedral angles (see ***Vicinal Coupling Constants and Conformation of Biomolecules***). Interpretation of coupling data such as ^3J(C,H) in an oligosaccharide with internal motion is much simpler than NOE since the motion is almost certainly fast compared with the timescale of the interaction (ms). But it has proven to be technically very difficult to measure these coupling constants for macromolecules with ^{13}C in natural abundance. Data were first reported from 1D ^{13}C spectra and ^{1}H spectra of oligosaccharides synthesized with specific ^{13}C enrichment.[27] More recently, long-range heteronuclear coupling constants have been measured in natural abundance by ^{13}C-detected ^{1}H spin echo methods.[49] But the low sensitivity of ^{13}C-detected methods presents a serious limitation and this method requires a resolved ^{1}H spectrum which is a rarity in complex carbohydrates. The improved sensitivity of ^{1}H detection, which has been described above for long-range ^{13}C–^{1}H correlation, provides a method for encoding values of ^3J(C,H).[50] Several one-dimensional versions of ^{1}H-detected ^3J(C,H) have been demonstrated in disaccharides and trisaccharides by Poppe and van Halbeek.[51] In spite of the improved sensitivity, cancellation of the antiphase components of heteronuclear doublets hampers accurate measurements for macromolecules. When the linewidths are comparable to the values of the coupling constants (1–8 Hz), the latter cannot be accurately measured due to antiphase cancellation. In the ECOSY method of Montelione et al.,[52] large one-bond coupling to resolve the long-range coupling removes the problem of overlap making it possible to measure accurately coupling constants much smaller than the linewidth.[53] (See ***Coupling Constants Determined by ECOSY***.) This approach has been used in carbohydrates in natural abundance with ^{13}C selective filters,[54] and in polysaccharides with uniform ^{13}C enrichment.[55]

The question of internal motion in complex polysaccharides can also be addressed by spin relaxation methods in which $J(\omega)$, the spectral density, is sampled at a number of different frequencies to measure the different types of motion which contribute to nuclear relaxation. Measurements of different relaxation rates, T_1, T_2, $T_{1\rho}$, and NOE of ^{15}N or ^{13}C can be combined in order to provide this information.

4 RELATED ARTICLES

Carbohydrates and Glycoconjugates; Coupling Constants Determined by ECOSY; Glycolipids; NOESY; Nuclear Overhauser Effect; Polysaccharide Solid State NMR; ROESY; Structures of Larger Proteins, Protein-Ligand, and Protein-DNA Complexes by Multi-Dimensional Heteronuclear NMR; Vicinal Coupling Constants and Conformation of Biomolecules.

5 REFERENCES

1. K. Drickamer, *J. Biol. Chem.*, 1988, **263**, 9557.
2. A. Varki, *Curr. Opin. Cell Biol.*, 1992, **4**, 257.
3. T. Feizi, *Curr. Opin. Struct. Biol.*, 1991, **1**, 766.
4. I. Ofek and R. J. Doyle, *Bacterial Adhesion to Cells and Tissues*, Chapman & Hall, New York, 1993.
5. P. E. Kolenbrander, N. Ganeshkumar, F. J. Cassels, and C. V. Hughes, *FASEB J.*, 1993, **7**, 406.
6. J. F. G. Vliegenthart, H. van Halbeek, and L. Dorland, *Pure Appl. Chem.*, 1981, **53**, 45.
7. J. F. G. Vliegenthart, L. Dorland, and H. van Halbeek, *Adv. Carbohydr. Chem. Biochem.*, 1983, **41**, 209.
8. A. Klein, C. Carnoy, G. Lambin, P. Roussel, J. A. van Kuik, P. de Waard, and J. F. G. Vliegenthart, *Eur. J. Biochem.*, 1991, **198**, 151.
9. J. A. van Kuik, P. de Waard, J. F. G. Vliegenthart, A. Klein, C. Carnoy, G. Lambin, and P. Roussel, *Eur. J. Biochem.*, 1991, **198**, 169.
10. G. Strecker, J. M. Wieruszeski, O. Cuvillier, J. C. Michalski, and J. Montreuil, *Biochimie*, 1992, **74**, 39.
11. C. Abeygunawardana and C. A. Bush, *Adv. Biophys. Chem.*, 1993, **3**, 199.
12. J. Dabrowski, *Methods Enzymol.*, 1989, **179**, 122.
13. C. A. Bush, *Bull. Magn. Reson.*, 1988, **10**, 73.
14. T. A. W. Koerner, Jr., J. H. Prestegard, P. C. Demou, and R. K. Yu, *Biochemistry*, 1983, **22**, 2687.
15. D. Neuhaus and M. Williamson, *The Nuclear Overhauser Effect in Structural and Conformational Analysis*, VCH Publishers, New Yorka, 1989.
16. B. N. N. Rao, V. K. Dua, and C. A. Bush, *Biopolymers*, 1985, **24**, 2207.
17. H. Kovacs, S. Bagley, and J. Kowalewski, *J. Magn. Reson.*, 1989, **85**, 530.
18. P. Cagas and C. A. Bush, *Biopolymers*, 1992, **32**, 277.
19. P. A. J. Gorin, *Adv. Carbohydr. Chem. Biochem.*, 1981, **38**, 113.
20. H. J. Jennings, *Adv. Carbohydr. Chem. Biochem.*, 1983, **41**, 155.
21. P. K. Agrawal, *Phytochemistry*, 1992, **31**, 3307.
22. A. Allerhand and E. Berman, *J. Am. Chem. Soc.*, 1984, **106**, 2400.
23. A. Allerhand and E. Berman, *J. Am. Chem. Soc.*, 1984, **106**, 2412.
24. P. E. Jansson, L. Kenne, and G. Widmalm, *J. Chem. Inf. Comput. Sci.*, 1991, **31**, 508.
25. P. E. Jansson, L. Kenne, and G. Widmalm, *Anal. Biochem.*, 1991, **199**, 11.
26. G. M. Lipkind, A. S. Shashkov, N. E. Nifantev, and N. K. Kochetkov, *Carbohydr. Res.*, 1992, **237**, 11.
27. R. Barker and A. S. Serianni, *Acc. Chem. Res.*, 1986, **19**, 307.
28. D. M. Doddrell, D. T. Pegg, and M. R. Bendall, *J. Magn. Reson.*, 1982, **48**, 323.
29. P. E. Pfeffer, K. M. Valentine, and F. W. Parrish, *J. Am. Chem. Soc.*, 1979, **101**, 1265.
30. A. Bax, R. H. Griffey, and B. L. Hawkins, *J. Magn. Reson.*, 1983, **55**, 301.
31. R. A. Byrd, W. Egan, M. F. Summers, and A. Bax, *Carbohydr. Res.*, 1987, **166**, 47.
32. C. Abeygunawardana, C. A. Bush, and J. O. Cisar, *Biochemistry*, 1991, **30**, 8568.
33. A. Bax and M. F. Summers, *J. Am. Chem. Soc.*, 1986, **108**, 2093.
34. C. A. Bush, *Curr. Opin. Struct. Biol.*, 1992, **2**, 655.
35. K. G. Rice, P. Wu, L. Brand, and Y. C. Lee, *Curr. Opin. Struct. Biol.*, 1993, **3**, 669.
36. J. Raap, J. H. Van Boom, H. C. Van Lieshout, and C. A. G. Haasnoot, *J. Am. Chem. Soc.*, 1988, **110**, 2736.
37. J. W. Brady, *Adv. Biophys. Chem.*, 1990, **1**, 155.
38. T. H. Thogersen, R. U. Lemieux, K. Bock, and B. Meyer, *Can. J. Chem.*, 1982, **60**, 44.
39. T. Peters, J.-R. Brisson, and D. R. Bundle, *Can. J. Chem.*, 1990, **68**, 979.
40. K. Bock, H. Lönn, and T. Peters, *Carbohydr. Res.*, 1990, **198**, 375.
41. B.-Y. Choe, G. C. Ekborg, L. Rodén, S. C. Harvey, and N. R. Krishna, *J. Am. Chem. Soc.*, 1991, **113**, 3743.
42. J. N. Scarsdale, P. Ram, J. H. Prestegard, and R. K. Yu, *J. Comput. Chem.*, 1988, **9**, 133.
43. S. W. Homans and M. Forster, *Glycobiology*, 1992, **2**, 143.
44. J. R. Brisson and J. P. Carver, *Biochemistry*, 1983, **22**, 1362.
45. C. A. Bush, *Methods Enzymol.*, 1994, **240**, 446.
46. R. Bazzo, C. J. Edge, M. R. Wormald, T. W. Rademacher, and R. A. Dweck, *Chem. Phys. Lett.*, 1990, **174**, 313.
47. J. P. Carver, *Curr. Opin. Struct. Biol.*, 1991, **1**, 716.
48. C. A. Bush and P. Cagas, *Adv. Biophys. Chem.*, 1992, **2**, 149.
49. C. Morat, F. R. Taravel, and M. R. Vignon, *Magn. Reson. Chem.*, 1988, **26**, 264.
50. T. J. Norwood, J. Boyd, N. Soffe, and I. D. Campbell, *J. Am. Chem. Soc.*, 1990, **112**, 9638.
51. L. Poppe and H. van Halbeek, *J. Magn. Reson.*, 1991, **93**, 214.
52. G. T. Montelione, M. E. Winkler, P. Rauenbuehler, and G. Wagner, *J. Magn. Reson.*, 1989, **82**, 198.
53. C. Biamonte, C. B. Rios, B. A. Lyons, and G. T. Montelione, *Adv. Biophys. Chem.*, 1994, **4**, in press.
54. L. Poppe, W. S. York, and H. van Halbeek, *J. Biomol. NMR*, 1993, **3**, 81.
55. R. Gitti, G. Lond, and C. A. Bush, *Biopolymers*, 1994, **34**, 1327.

Acknowledgments

Research supported by NIH Grant GM 31449.

Biographical Sketch

C. Allen Bush. *b* 1938. B.A., 1961, Cornell University, Ph.D., 1965, University of California, Berkeley. Faculty, Illinois Institute of Technology, 1968–89. Currently Professor of Biochemistry, University of Maryland, Baltimore County. Approx. 100 publications. Research interests: structural chemistry of complex carbohydrates by NMR, computer modeling, circular dichroism and HPLC.

Protein Hydration

Gottfried Otting

Karolinska Institute, Stockholm, Sweden

1	Introduction	1
2	NMR Experiments	1
3	Experimental Results	2
4	Theoretical Models	3
5	Comparison with X-Ray Diffraction Studies of Single Crystals	4
6	Related Articles	5
7	References	5

1 INTRODUCTION

The present article describes the results from studies of protein hydration by way of nuclear Overhauser effects (NOEs) observed between the water signal and the proton resonances of the protein (see also ***Dynamics of Water in Biological Systems: Inferences from Relaxometry***). Intermolecular NOEs between peptides and hydration water were already reported in the 1970s.[1] However, their sensitivity with respect to on the dynamics of protein hydration was only realized almost 20 years later.[2]

The NOE provides a mechanism for magnetization transfer that arises from the dipole−dipole interaction between the nuclear magnetic moments of spins that are close in space. The strength of the interaction decays rapidly with increasing internuclear separation, so that, in practice, sizeable NOEs are observable only between protons that are closer than about 5 Å. The short-range nature of the NOE interaction thus ensures that of all the water in the solution, only hydration water from the first shell of hydration around a protein is detected by the NOE experiment.

In principle, NOEs observed between the protons of hydration water molecules and protein protons provide distance constraints that can be used to complement a protein structure with the coordinates of hydration water molecules (see ***Biological Macromolecules: Structure Determination in Solution***; ***Distance Geometry***, and ***Structures of Larger Proteins, Protein-Ligand, and Protein-DNA Complexes by Multi-Dimensional Heteronuclear NMR***).[3,4] In practice, this task is complicated by the fact that only a single signal is observed for all water protons in the ^{1}H NMR spectrum of an aqueous protein solution. The degeneracy of the proton chemical shifts of water molecules in hydration sites and water in the bulk of the solution is a consequence of the rapid chemical exchange of water molecules (or at least their protons) between these two different chemical environments with rates beyond about $1000\,s^{-1}$.[5] Therefore, the distinction between different hydration water molecules requires the accurate knowledge of the three-dimensional (3D) structure of the protein, which makes it possible to assess the number of water molecules required to explain all the experimentally observed water−protein NOEs. Furthermore, the three-dimensional structure is also needed to distinguish NOEs with hydration water from NOEs with labile protein protons, which appear at the chemical shift of the water resonance because of rapid exchange with the water.

Water−protein NOEs have been found to occur with positive and negative signs. A negative water−protein cross peak is observed in NOESY experiments, when the motional reorientation of the vector connecting a water proton with a protein proton occurs in a time span shorter than the angular Larmor frequency. The present article discusses why this motional reorientation is best interpreted in terms of a diffusion model where positive and negative signs of the NOESY cross peaks indicate that the residence times of the hydration waters are, respectively, longer or shorter than about 0.5 ns with respect to the protons of the protein. Negative cross peaks are usually observed for hydration water on protein surfaces, whereas water molecules in interior protein cavities give rise to positive cross peaks with the protein protons.

Overall, NMR studies of protein hydration identify the hydrated protein protons and convey information on the lifetime of hydration. In contrast, X-ray diffraction studies of proteins in single crystals detect water molecules by their statistical probability of being at defined positions and are far less sensitive to their residence times.

2 NMR EXPERIMENTS

The water signal in the ^{1}H NMR spectrum of an aqueous protein solution is typically about 10 000 times more intense than the individual proton signals of the protein. This dynamic range exceeds by far what modern NMR spectrometers can sensibly handle and calls for some method of water suppression.

Saturation of the water signal by selective irradiation is the most frequently used technique of water suppression in homonuclear NMR experiments. Water suppression by selective preirradiation is also commonly used with the two-dimensional NOESY experiment, which is the standard experiment for the detection and assignment of NOEs in proteins (see ***Biological Macromolecules: Structure Determination in Solution***, ***Structures of Larger Proteins, Protein-Ligand, and Protein-DNA Complexes by Multi-Dimensional Heteronuclear NMR***, and ***Water Signal Suppression in NMR of Biomolecules***). However, no cross peaks can be detected between the resonances of the water and the protein in this experiment, since the presaturation of the water signal eliminates the water magnetization before it can be transferred to the protein resonances via NOE during the mixing period. The result is an excitation profile that is uniform along the ω_2 dimension, but contains a bleached region along the ω_1 frequency axis at the frequency of the water signal [Figure 1(a)]. In principle, cross peaks between protein resonances in ω_1 and the water resonance in ω_2 are still present in this experiment, but they are obscured by the strong band of t_1 noise from the residual water signal.

Intermolecular water−protein cross peaks are reliably detected in two-dimensional NOESY experiments using an excitation profile that is uniform along the ω_1 dimension and zero at the water frequency along the ω_2 frequency axis [Figure 1(b)]. Such an excitation profile is obtained if the water signal is suppressed only before the detection period t_2, but not before the evolution period t_1. In this experiment, the water magnetization is fully excited, transferred to protein spins during the

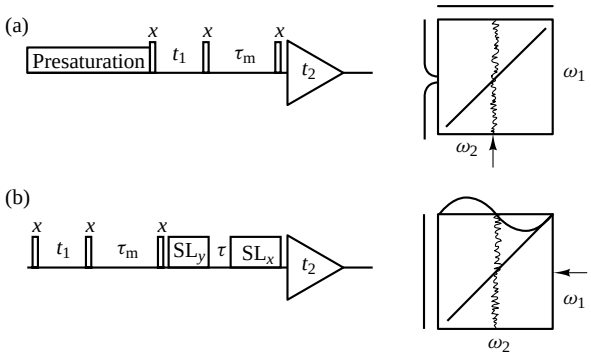

Figure 1 Pulse sequences for the detection of water–protein NOEs. The resulting excitation profiles are plotted alongside the schematic two-dimensional spectra. The position of the diagonal is indicated by a straight line, a wavy line indicates the band of t_1 noise from the incompletely suppressed water signal, and arrows identify the cross-sections containing the water–protein cross peaks. The phases indicated with the pulses are for a single transient of the phase cycle only. (a) NOESY sequence with suppression of the water signal by selective presaturation. The water–protein cross peaks at the ω_2 frequency of the water resonance are obscured by the t_1 noise of the residual water signal, and there are no cross peaks at the ω_1 frequency of the water resonance. (b) NOESY sequence with spin lock (SL) pulses for water suppression. Water–protein NOEs are observed in the cross-section at the ω_1 frequency of the water resonance

mixing time τ_m, and destroyed immediately before the detection of the FID. The tricky part in the experiment is the water suppression between the mixing time τ_m and the detection period, which needs to be achieved in as short a time period as possible to minimize the relaxation of the magnetization before detection. Different water suppression techniques have been devised in this context, which, unlike saturation of the water signal by selective irradiation, achieve water suppression within a few milliseconds (see ***Water Signal Suppression in NMR of Biomolecules***).

Figure 1(b) presents as an example a pulse sequence where the water magnetization is suppressed by two short spin lock pulses before data acquisition.[6] The phase of the first spin lock pulse is shifted by 90° with respect to the phases of the preceding 90° pulse and the following spin lock pulse. The spin lock pulses have the property of defocusing any magnetization vertical to the spin lock axis, but retaining magnetization of the same phase as the spin lock axis. With the phases indicated in Figure 1(b), the first spin lock pulse selects the desired y magnetization generated by the previous $90_x°$ pulse. During the following short delay τ, the proton magnetizations precess toward the x axis with a speed depending on their frequency difference Ω with respect to the carrier frequency. The subsequent spin lock pulse selects the x magnetization and defocuses the y magnetization. The resulting excitation profile is given by $\sin(\Omega\tau)$. With the carrier frequency at the frequency of the water resonance, the null of the excitation profile is at the water frequency [Figure 1(b)].

Spin lock pulses and other water suppression schemes have similarly been used in further experiments designed for the detection of water–protein NOEs. These include ROESY,[7] homonuclear 3D NOESY–TOCSY and 3D ROESY–TOCSY,[6] and heteronuclear 3D NMR experiments.[8–10] Of these, the ROESY experiment presents valuable information on the water–protein interaction that is complementary to the NOESY experiment. First, the ROESY experiment enables one to distinguish NOE interactions from chemical exchange peaks that arise from a direct proton transfer between the water and the protein.[7,11] For short mixing times, NOE peaks and chemical exchange peaks are always of opposite sign in ROESY. Second, NOEs may still be observable in ROESY, when the motional fluctuation of the internuclear interaction is in a time regime, where the cross-relaxation rate changes its sign in NOESY.[11] The 3D experiments are designed to help with the resonance assignment of complicated protein NMR spectra.

3 EXPERIMENTAL RESULTS

Figure 2 shows an example of a NOESY spectrum recorded for the observation of water–protein NOEs with an aqueous solution of basic pancreatic trypsin inhibitor (BPTI), a small protein containing 58 amino acid residues (see also ***Pancreatic Trypsin Inhibitor***). The water–protein cross peaks are aligned along the ω_2 frequency axis at the ω_1 chemical shift of the water signal (arrow in Figure 2). From the corresponding ROESY experiment some of the cross peaks were identified as chemical exchange peaks of labile protein protons, like the amino protons of lysyl residues or the hydroxyl protons of tyrosyl residues. Furthermore, the 3D structure of BPTI and the set of NOEs observed with the hydroxyl protons of BPTI under different conditions suggest that a few additional cross peaks arise predominantly from the less interesting magnetization transfer pathway, where chemical exchange of water protons with labile hydroxyl protons of the protein is followed by intramolecular NOEs with nonlabile protein protons.[12] Yet, most of the cross peaks represent NOEs with protons that are close to four hydration water molecules trapped in the interior of the protein. All protein protons in the vicinity of these interior water molecules show NOEs with the water signal in the spectrum of Figure 2.

The NOEs between surface hydration water and BPTI are not visible in Figure 2, since these NOEs are very weak and they overlap with the exchange peaks and the NOEs with the interior hydration water molecules. NOEs with surface hydration water are more easily observed in NOESY and ROESY experiments with small peptides, which have fewer resonances and no interior water. Figure 3 shows the cross-sections taken at the ω_1 chemical shift of the water resonance in NOESY and ROESY experiments on the nonapeptide oxytocin. Almost the entire one-dimensional spectrum [Figure 3(a)] is represented by the water–peptide NOEs in these cross-sections, i.e. all protons are in contact with the solvent. The few positive cross peaks in the NOESY cross-section have chemical exchange contributions like the broad signal at 8.35 ppm, which comes from the amino protons of Cys-1. All negative cross peaks in the NOESY cross-section reflect direct intermolecular NOEs with hydration water. They are also present in the ROESY cross-section. The cross peaks between water and oxytocin are the only negative cross peaks of the NOESY spectrum, which was recorded at 6 °C to ensure that all intramolecular NOESY cross peaks of oxytocin are positive. The water–oxytocin cross peaks become positive only at temperatures well below 0 °C (with acetone added to prevent freezing).[13] The negative sign of the NOESY cross peaks with the hydration water is clear

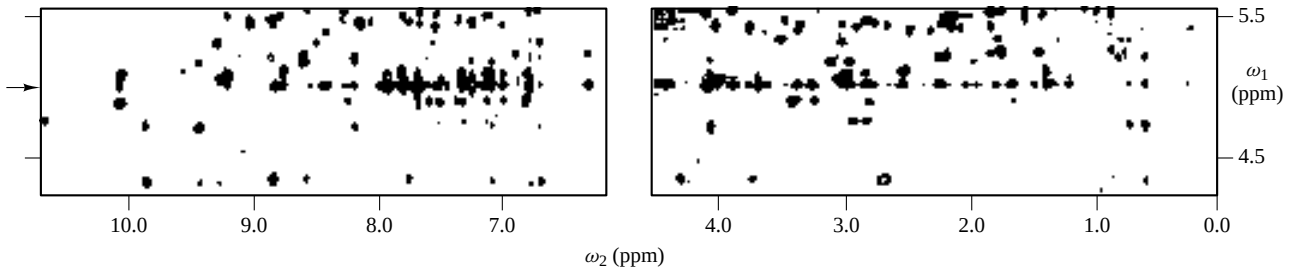

Figure 2 Spectral regions of a NOESY spectrum recorded at 4 °C with a 20 mM solution of BPTI in 90% H_2O/10% D_2O, pH 3.5. The arrow on the left indicates the frequency of the water signal with the intermolecular water–protein cross peaks along the ω_2 frequency axis. (Reproduced by permission of the American Chemical Society from Otting et al.[5])

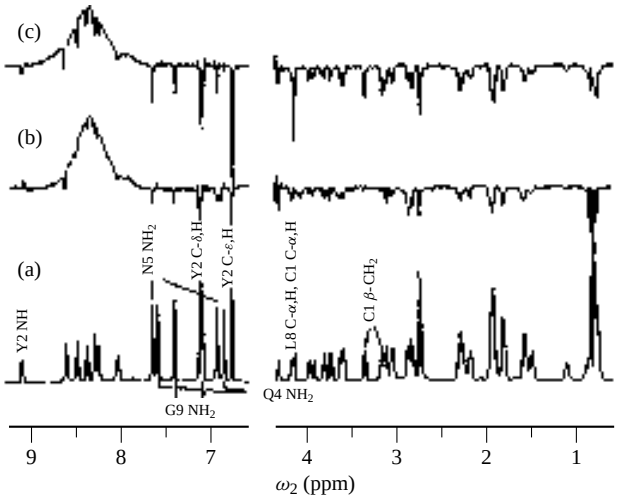

Figure 3 (a) One-dimensional NMR spectrum recorded at 6 °C with a 50 mM solution of oxytocin in 90% H_2O/10% D_2O, pH 3.5. (b) and (c) Cross-sections through, respectively, NOESY and ROESY spectra along ω_2 at the ω_1 frequency of the water line. Both spectra were recorded with 30 ms mixing time and the pulse sequence of Figure 1(b). The low-frequency half of the spectrum was inverted to revert the sign change in the excitation profile [Figure 1(b)]. (Reproduced by permission of the American Association for the Advancement of Science from Otting et al.[2])

evidence for an increased modulation of the vectors connecting oxytocin protons with the protons of the hydration water. Model calculations show that the modulation must act on the subnanosecond timescale and is difficult to explain other than by the diffusion of the water molecules relative to the peptide.

4 THEORETICAL MODELS

In the limit of very short mixing times, the ratios of the cross-peak intensities over the diagonal peak intensities in, respectively, NOESY and ROESY, reflect directly the cross-relaxation rates σ^{NOE} and σ^{ROE}. Thereby, positive σ values lead to negative cross peaks and vice versa. The cross-relaxation rates σ^{NOE} and σ^{ROE} in NOESY and ROESY depend on the spectral density function $J(\omega)$:[11]

$$\sigma^{NOE} = 6J(2\omega_0) - J(0) \quad (1)$$

$$\sigma^{ROE} = 3J(\omega_0) + 2J(0) \quad (2)$$

where ω_0 is the Larmor frequency of the protons. Equation (2) shows that σ^{ROE} is always positive because the spectral densities $J(\omega)$ are positive for all frequencies. In contrast, the sign of σ^{NOE} depends on the relative weight of $J(2\omega)$ and $J(0)$ [equation (1)]. The calculation of the spectral densities depends on the model used to describe the modulation of the dipole–dipole interaction.

Figure 4 shows three different models for which the spectral densities can be calculated from analytical formulas. In all three models the protein is approximated by a sphere undergoing free rotational diffusion, and the water–protein interaction is described as a two-spin interaction between a protein proton and a water proton. In model (a), a water molecule is rigidly bound to the protein surface,[14] whereas in model (b) the water molecule is undergoing local motions in its hydration site, including rotations and a wobbling motion of an assumed hydrogen bond to the protein ('wobbling in a

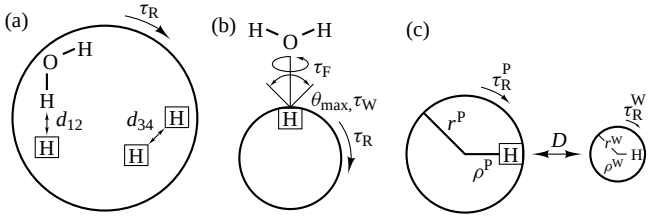

Figure 4 Three models for the calculation of dipole–dipole cross-relaxation rates σ^{NOE} and σ^{ROE} between water protons and protein protons. (a) Isotropic rotational diffusion of a rigid sphere. The hydration water molecules are considered to be part of the sphere representing the protein. Squares represent polypeptide protons. The vector d_{12} connects a polypeptide proton with a hydration water proton, and d_{34} connects two polypeptide protons. τ_R is the correlation time for the overall rotation of the sphere. (b) Wobbling in a cone model. The residence time of the water molecules in the hydration sites is assumed to be long compared with the rotational correlation time τ_R of the sphere, which represents the hydrated protein, but the water rotates with a correlation time τ_F around a hydrogen bond to the protein, and this rotation axis is free to wobble with a correlation time τ_W within a cone with an opening angle $\theta_{max} = \pm 45°$. (c) Random, independent translation and rotation of the protein and the water molecule. The two molecules are represented by spheres of radius r^P and r^W, respectively, with the proton spin displaced from the center by ρ^P and ρ^W. The translational diffusion coefficient D characterizes the relative translational motions of the two molecules. The two spheres reorientate isotropically with correlation times τP/R and τW/R, respectively. (Reproduced by permission of the American Association for the Advancement of Science from Otting et al.[2])

cone').[15,16] In model (c), the water molecules are represented as spheres of smaller radius than the protein; both protein and water undergo free rotational and translational diffusion.[17]

The NOESY and ROESY cross relaxation rates calculated for the three different models of Figure 4 are compared in Figure 5. Model (a) describes the intramolecular cross relaxation between two polypeptide protons. At a Larmor frequency of 600 MHz, positive σ^{NOE} values are predicted for molecules with rotational correlation times τ_R shorter than about 300 ps. The rotational correlation times of oxytocin and BPTI at 5 °C were estimated from ^{13}C relaxation measurements to be 2 and 8 ns, respectively,[2] which is in line with the observation of negative σ^{NOE} values for the intraprotein NOEs in the NOESY spectra. The different sign of the σ^{NOE} values for water–protein NOEs cannot be explained by model (a), which assumes that the water–protein interaction can be described by the same parameters as the intramolecular NOEs in the protein.

The cross-relaxation rates in model (b) depend on the rotational correlation time of the protein and two further correlation times characterizing the wobbling in a cone motion

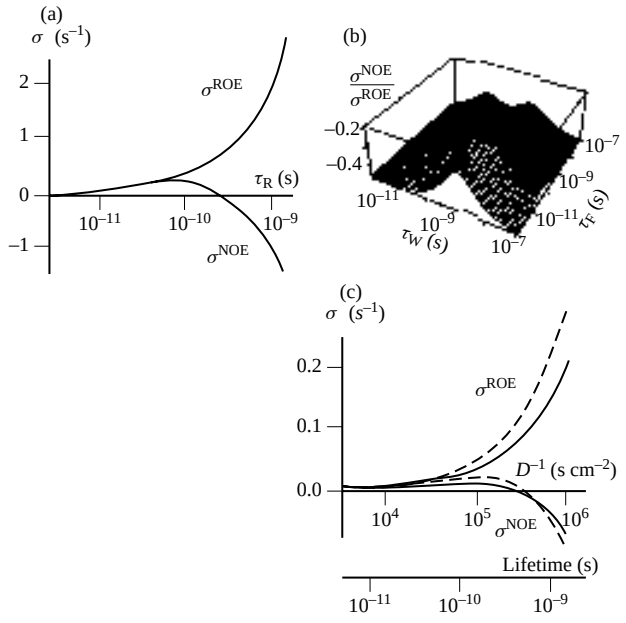

Figure 5 Cross-relaxation rates σ^{NOE} and σ^{ROE} for a pair of proton spins calculated for the three models of Figure 4. (a) Model of Figure 4(a) with a ^1H–^1H distance of 2.0 Å; ^1H frequency 600 MHz. (b) wobbling in a cone model [Figure 4(b)]. H–O distance = 2.0 Å, $—\theta_{max}—$ = 45°, τ_R = 2 ns, ^1H frequency = 600 MHz. For τ_R = 8 ns, the maximum value of $\sigma^{NOE}/\sigma^{ROE}$ over the complete range of the (τ_W,τ_F)-plane would be about −0.4. (c) Diffusion model [Figure 4(c)] with r^W = 2.0 Å, ρ^W = 1.0 Å, and $\tau W/R$ = 4 ps. The solid curve was calculated with r^P = 12.0 Å, ρ^P = 11.0 Å, ^1H frequency = 500 MHz, and $\tau P/R$ = 8 ns to simulate the intermolecular water proton-protein ^1H cross relaxation in BPTI at 4 °C. The broken curve was calculated with r^P = 4.0 Å, ρ^P = 3.0 Å, ^1H frequency = 600 MHz, and τ_R = 2 ns to approximate the situation for oxytocin at 6 °C (Figure 3). At the bottom the inverse of the translational diffusion coefficient, $1/D$, was converted into the corresponding lifetimes of the hydration water molecules with the relation $\tau = x^2/D$ setting $\sqrt{x^2} = 4$ Å. (x^2 is the average square of displacement of a water molecule by diffusion.) (Reproduced by permission of the American Association for the Advancement of Science from Otting et al.[2])

of the hydration water molecule. It turns out that for wobbling motions within a cone of ±45° opening angle, the ratio of $\sigma^{NOE}/\sigma^{ROE}$ is negative for all values of the correlation times τ_F and τ_W, which describe the frequency of the motions [Figure 5(b)]. This model would predict positive σ^{NOE} values only for significantly larger opening angles of the wobbling cone. However, this would displace the water molecule by more than its own diameter, so that a new water molecule is likely to fill the empty space left behind completing a chemical exchange reaction.

The diffusion model [Figure 4(c)] is the only model that describes the experimental data in a plausible way. The intermolecular cross-relaxation rates depend primarily on the diffusion coefficient. Positive σ^{NOE} values are predicted for diffusion coefficients larger than 3×10^{-10} m^2 s^{-1}, which is only about four times less than the self-diffusion coefficient of water at 5 °C. To obtain an impression of the short lifetime of protein hydration, it is instructive to convert the diffusion coefficient into a residence time of the hydration water near the protein using the Einstein–Smoluchowski relationship [caption of Figure 5(c)]. With the assumption that a water molecule has left its hydration site once it has diffused by more than 4 Å, the sign of the NOE changes for residence times shorter than about 0.5 ns. This time span is much shorter than the lifetime of a water molecule with respect to proton exchange,[18] so that positive σ^{NOE} values must arise from the exchange of entire water molecules rather than proton dissociation.

Even the most sophisticated analytical model is a coarse approximation of the real situation. An improved calculation would have to take into account that the protein surface is not smooth, the amino acid side chains are flexible, and the water molecules are subject to orientating forces due to hydrogen bonding. In principle, the appropriate spectral densities could be calculated from a molecular dynamics simulation, except that the simulation would have to cover much longer times than what is computationally affordable today. A preliminary analysis has been based on a molecular dynamics calculation, where BPTI was simulated for over 1 ns in a water bath at 4 °C.[19] In this simulation, the residence time of a bulk water molecule within the hydration shell of another bulk water molecule was found to be approximately four times shorter than the residence time of water near, e.g., backbone carbonyl groups, and no water molecule stayed for longer than 200 ps in the hydration shell of a given surface atom of BPTI.

5 COMPARISON WITH X-RAY DIFFRACTION STUDIES OF SINGLE CRYSTALS

Three-dimensional NOESY–TOCSY experiments recorded with BPTI showed, with a single exception, positive or vanishing cross-relaxation rates between the water protons and the protons on the protein surface, which indicates hydration lifetimes in the subnanosecond time range. Large positive cross-relaxation rates were exclusively observed with the four interior water molecules in BPTI.

The comparison of the intermolecular water–protein NOEs observed in BPTI with the hydration water molecules observed by X-ray crystallography provides an instructive example of a different view on protein hydration resulting from these two

methods.[2] The X-ray structures of three different crystal forms of BPTI have been determined at high resolution.[20–22] All show the four interior water molecules completely shielded from access by the bulk water. The number and position of surface hydration water molecules varies between the different crystal structures, and only six out of about 60 X-ray-observable water molecules were found to have conserved hydrogen-bonding partners. There is no evidence from the NMR data that any of these conserved surface hydration water molecules are bound with lifetimes longer than 0.5 ns. The apparent discrepancies are explained by the fact that water is detected by X-ray diffraction, when the electron densities of the water molecules fall in the time average into the same place, irrespective of the actual residence times at the hydration sites. In contrast, the NOE is most sensitive to the residence times of the hydration water and thus is a good indicator of the intimacy of the protein–water contacts.

In special cases, longer residence times have been observed also for hydration water molecules that are accessible to bulk water. The best example is that of the well-ordered water molecules belonging to the 'spin of hydration' in the minor groove of DNA duplexes (see also ***Nucleic Acids: Spectra, Structures, and Dynamics***). It is thought that the spine of hydration, which was first discovered by X-ray crystallography, is important for stabilizing the B-DNA conformation.[23] Strong, negative cross-relaxation rates were observed in the NOESY experiments between these hydration water molecules and the closest protons of the DNA, which shows that they must be bound for longer than 1 ns.[24,25]

6 RELATED ARTICLES

Biological Macromolecules: Structure Determination in Solution; Distance Geometry; Dynamics of Water in Biological Systems: Inferences from Relaxometry; Nucleic Acids: Spectra, Structures, and Dynamics; Pancreatic Trypsin Inhibitor; Structures of Larger Proteins, Protein-Ligand, and Protein-DNA Complexes by Multi-Dimensional Heteronuclear NMR; Water Signal Suppression in NMR of Biomolecules.

7 REFERENCES

1. T. P. Pitner, J. D. Glickson, J. Dadok, and G. R. Marshall, *Nature (London)*, 1974, **250**, 582.
2. G. Otting, E. Liepinsh, and K. Wüthrich, *Science*, 1991, **254**, 974.
3. J. D. Forman-Kay, A. M. Gronenborn, P. T. Wingfield, and G. M. Clore, *J. Mol. Biol.*, 1991, **220**, 209.
4. R. X. Xu, R. P. Meadows, and S. W. Fesik, *Biochemistry*, 1993, **32**, 2473.
5. G. Otting, E. Liepinsh, and K. Wüthrich, *J. Am. Chem. Soc.*, 1991, **113**, 4363.
6. G. Otting, E. Liepinsh, B. T. Farmer II, and K. Wüthrich, *J. Biomol. NMR*, 1991, **1**, 209.
7. G. Otting and K. Wüthrich, *J. Am. Chem. Soc.*, 1989, **111**, 1871.
8. B. A. Messerle, G. Wider, G. Otting, C. Weber, and K. Wüthrich, *J. Magn. Reson.*, 1989, **85**, 608.
9. G. M. Clore, A. Bax, P. T. Wingfield, and A. M. Gronenborn, *Biochemistry*, 1989, **29**, 5671.
10. Y.Q. Qian, G. Otting, and K. Wüthrich, *J. Am. Chem. Soc.*, 1993, **115**, 1189.
11. A. A. Bothner-By, R. L. Stephens, J. Lee, C. D. Warren, and R. W. Jeanloz, *J. Am. Chem. Soc.*, 1985, **106**, 811.
12. E. Liepinsh, G. Otting, and K. Wüthrich, *J. Biomol. NMR*, 1992, **2**, 447.
13. G. Otting, E. Liepinsh, and K. Wüthrich, *J. Am. Chem. Soc.*, 1992, **114**, 7093.
14. A. Abragam, *Principles of Nuclear Magnetism*, Oxford University Press, London, 1961, Chap. 8
15. R. Richarz, K. Nagayama, and K. Wüthrich, *Biochemistry*, 1980, **19**, 5189.
16. T. Fujiwara and K. Nagayama, *J. Chem. Phys.*, 1985, **83**, 3110.
17. Y. Ayant, E. Belorizky, P. Fries, and J. Rosset, *J. Phys. (Paris)*, 1977, **38**, 325.
18. S. Meiboom, *J. Chem. Phys.*, 1961, **34**, 375.
19. R. M. Brunne, E. Liepinsh, G. Otting, K. Wüthrich, and W. F. van Gunsteren, *J. Mol. Biol.*, 1993, **231**, 1040.
20. J. Deisenhofer and W. Steigemann, *Acta Crystallogr., Sect. B*, 1975, **31**, 238.
21. A. Wlodawer, J. Walter, R. Huber, and L. Sjölin, *J. Mol. Biol.*, 1984, **180**, 301.
22. A. Wlodawer, J. Nachman, G. L. Gilliland, W. Gallagher, and C. Woodward, *J. Mol. Biol.*, 1987, **198**, 469.
23. R. E. Dickerson, *Sci. Am.*, 1983, **249**, 94.
24. M. G. Kubinec and D. E. Wemmer, *J. Am. Chem. Soc.*, 1992, **114**, 8739.
25. E. Liepinsh, G. Otting, and K. Wüthrich, *Nucleic Acids Res.*, 1992, **20**, 6549.

Biographical Sketch

Gottfried Otting. *b* 1958. Diploma in Chemistry, Freiburg, Germany, 1984; Ph.D. (supervisor Kurt Wüthrich), ETH-Zürich, Switzerland, 1987; Professor of Molecular Biophysics, Karolinska Institute, 1992–present. Approx. 80 publications. Research interests: biomedical applications of NMR including structure determinations of proteins and protein–ligand complexes, isotope labeling and spectral editing techniques, studies of protein dynamics.

Protein Modules

Iain D. Campbell

University of Oxford, Oxford, UK

1 Introduction 1
2 Module Structure Determination 1
3 NMR and Protein Modules 2
4 A Specific Example – Fibronectin 4
5 The Future 5
6 References 5

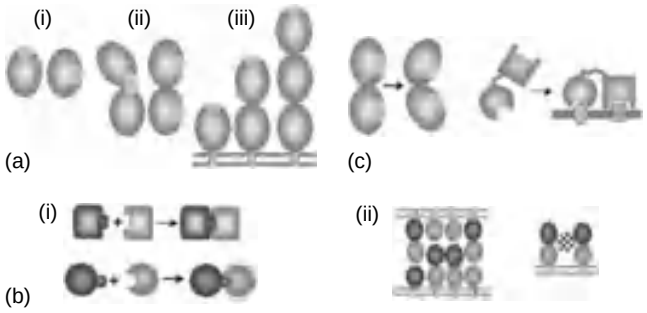

Figure 1 Some advantages of modular proteins. (a) Binding surfaces can be **presented:** (i) on different places on the same scaffold; (ii) on two or more modules to give extra variation; (iii) in different positions. (b) Various structures can be **assembled:** (i) with different covalent connections, including rigid end-to-end joins, flexible end-to-end joins or 'adapter' connections where the N- and C-termini are close together; (ii) complex non-covalent assemblies can be formed – examples include assembly at the T-cell surface, growth factor receptor complexes and the extracellular matrix. (c) Enzyme or receptor activity can be **regulated** by a module rearrangement

1 INTRODUCTION

I will begin with a few definitions. A **domain** is a compact structural unit in a protein; the amino-acid sequence need not be contiguous. **Modules** are a subset of domains that are contiguous in sequence and repeatedly used as 'building blocks' in functionally diverse proteins; they have identifiable amino-acid patterns that can be described by a 'consensus' sequence. A **repeat** is a modular unit that does not occur as a single copy – several repeats are needed to form a super-structure.

In the early 1970s, X-ray crystallography had been used to determine the 3D structures of relatively few proteins, yet it was already becoming apparent that they contained recurring domains.[1] In the 1980s, when sequence databases were beginning to expand, analysis of amino-acid sequences, revealed that many proteins were constructed in a modular fashion.[2–8] By the 1990s, the idea of modular proteins was well established and hunting for new modules in the expanding sequence databases, by means of an identified consensus sequence, became a popular pastime. Efforts to classify modules and to evaluate their structure and function were also undertaken.[9–12] Today, extensive databases of modules, identified by multiple sequence alignments and other data, have been created.[13] These module databases are continuously being updated and annotated to incorporate new information gleaned from the expanding sequence and structural databases.

The number of protein modules is finite (∼3000). They range in size from about 30 to 500 amino-acids. Since modules occur in most of the proteins in the various genomes, information about their structure and potential functions can have an impact on a wide range of fields. The diversity and spread of modular proteins is illustrated by a recent analysis of the entire *C. elegans* genome, in terms of extracellular modular proteins.[14]

Modules represent convenient and stable protein folds that have been found and retained during the evolution of biological systems. Once such a suitable structure, or scaffold, has been found, it can be used repeatedly in a variety of ways; some of which are shown schematically in Figure 1. One of the main uses of modules seems to be to provide a binding surface to facilitate interactions between different macromolecules. The structural scaffold is the stable evolutionary entity; other features, such as the nature of the binding surface and the ways in which the modules are assembled, can evolve and change relatively rapidly to provide a range of functions. New modules can be inserted readily in a protein, because intron–exon boundaries, especially those in extracellular proteins, often correspond to module boundaries.[7] Thus modules are sometimes inserted in a macromolecule as spacers, to present a binding function in the right position. Modular proteins also seem to be convenient for constructing larger assemblies. Examples include the formation of growth factor/receptor complexes that generate intracellular signals; another is the assembly of various receptors at the surface of T-cells, to form part of the immune response;[15,16] further examples of modular assemblies include complexes involved in blood clotting and intracellular signalling. Flexible connections seem to be useful in assembling these modular arrays. Some connections between modules are thus found to be relatively rigid while, in other cases, the interface is highly flexible. Another role of intermodule flexibility is to allow a module rearrangement to provide regulatory 'on/off' control.

In this article I will briefly outline studies of module structure and function, largely from a personal viewpoint, but applications of nuclear magnetic resonance (NMR) to modular proteins will also be placed in a wider context. I will concentrate mainly on proteins found in the extracellular matrix, a heterogeneous assembly of proteins, proteoglycans and oligosaccharides that forms outside cells to perform a variety of essential functions.

2 MODULE STRUCTURE DETERMINATION

I first became involved in NMR studies of proteins in the early 1970s, when I collaborated with several Oxford colleagues to study a variety of enzymes.[17–19] After an excursion into studies of cell suspensions,[20,21] I returned to protein studies in the mid-1980s after it had been shown, mainly by Wüthrich, that solution-state structures of small

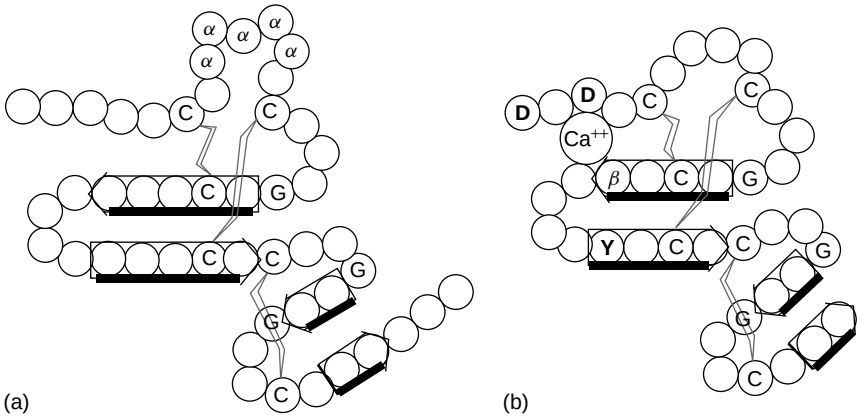

Figure 2 Representation of the structure of (a) epidermal growth factor (EGF), as determined by NMR. Cysteine (C) and glycine (G) residues that are conserved in EGF modules are indicated. Also shown are disulphide bonds (grey lines), β-sheets (large arrows) and helical regions (α). (b) is a schematic view of the structure of an EGF module that is found in a wide range of proteins; the observation of conserved amino-acids aspartate (D), tyrosine (Y) and a β-hydroxyaspartate (β), shown in bold lettering, predicts the presence of a calcium binding site

proteins could be solved ab initio. My first involvement with a protein module arose from collaboration with Brian Sheard, an ex co-worker in Rex Richards' lab. Brian was by then working at ICI Pharmaceuticals, and he persuaded me to try to solve the structure of epidermal growth factor (EGF). With Rob Cooke, Tony Wilkinson and others we published the structure in 1987.[22] Our primary concern was to explain the role of EGF as an essential growth factor in terms of its structure. Although the general importance of protein modularity was not then widely realised, we did appreciate that the EGF fold occurred in other contexts. Almost as an aside in that paper, we drew attention to probable structural features of EGF homologues, including a calcium-binding site, that had been identified in several blood-clotting proteins (see Figure 2). EGF as a module is even more interesting than EGF as a growth factor, since it occurs in so many, essential extracellular proteins.[23] That initial paper led to a long line of experiments on EGF modules that are still going on in this lab – now mostly being done by Kristy Downing (see e.g., Refs.[23,24])

After that first, somewhat serendipitous, foray into module research, we decided to attempt a more systematic approach. Our next venture depended heavily on a brave graduate student, Martin Baron. We thought we should try to express a module of unknown structure and we decided to try to study a type I module from human fibronectin. This was a high-risk project. We had no assay for correctness of fold and essentially no experience of protein expression. However, Martin exploited expertise on yeast expression available in the Kingsman lab in Oxford and managed not only to produce a folded module but also to determine its structure.[25] Using a similar approach, he later went on to solve the structure of the RGD-containing type 3 module from fibronectin (^{10}F3) with Alison Main.[26] These early successes led to great interest and a supply of other protein modules from a number of collaborating labs. As a result we solved, in the next few years, several other module structures. These included the CP module,[27] found in a number of complement proteins, and the SH2[28] and SH3[29] modules found in intracellular kinases. Paul Driscoll also solved the structure of the first domain of the T-cell receptor, CD2; surprisingly the fact that this was an Ig module[30] was still controversial at that time. Some of the extracellular modules structures solved in this lab are shown in Figure 3. They include ones that are predominantly helical and others that are exclusively β-sheet. The primary common feature they have is that they are used repeatedly by biological systems in different biological contexts.

The contributions of many other research groups to module structure determination must be acknowledged. Many of these structures have been solved using NMR but X-ray crystallography has been increasingly successful especially, recently, with larger modules (>200 amino-acids). Rather than catalogue these achievements here, the reader is referred to well-annotated, module databases.[13] For example, in the SMART database, on 22nd April 2001, 530 modules are listed; about half of the 185 listed as 'extracellular' have known structure.

3 NMR AND PROTEIN MODULES

The study of modules and modular proteins embraces virtually the whole of modern molecular biology. What particular contributions can high-resolution solution-state NMR make? An obvious advantage of the method is that structures can be solved in solution, without recourse to crystals and heavy atom derivatives. However, as proteins get larger they seem to be easier to crystallise. The technology of X-ray crystallography has also improved dramatically over the last decade, with 3rd generation synchrotrons, cryo-cooling, CCD detectors and sophisticated data analysis packages becoming more readily available to a wide range of users. These advances, together with the fact that many of the more readily available, smaller protein structures have now been solved, have somewhat reduced the relative impact of NMR as a structural tool, since the early 1990s.

This does not mean that NMR plays an insignificant role. NMR technology has also improved in the last decade; 900 MHz spectra and cooled probes are now with us, yielding resolution and sensitivity beyond the dreams of a scientist beginning NMR in the 1970s. Devices such as isotope labelling, including deuteration, TROSY,[31] increased tumbling rates,[32] together with a range of multi-dimensional experiments can further enhance the available resolution. One

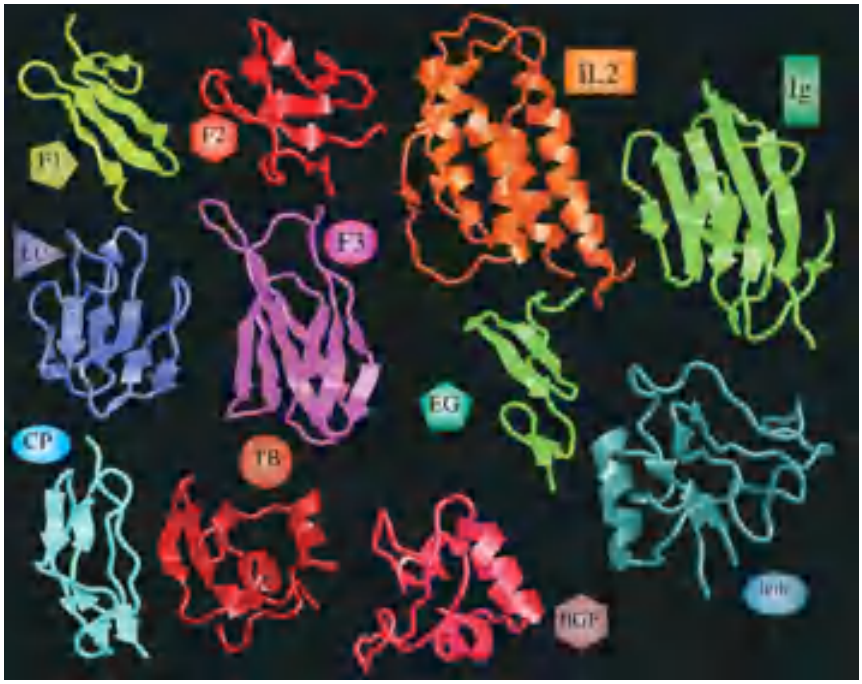

Figure 3 Some of the extracellular module structures determined in this laboratory in the last 12 years. More information can be obtained at *http://www.ocms.ox.ac.uk/idc/structures*. The symbols, nomenclature and colouring scheme of the modules is that used by the SMART database (*http://smart.embl-heidelberg.de/*; see also – *http://www.bork.embl-heidelberg.de/Modules/01-nomenclature.gif*)

problem with the NMR structure-determination methods that were developed in the 1980s, is that they depend on short-range distance information – mainly nuclear Overhauser effect (NOEs). New experiments to obtain longer-range information are now available, including use of long-range scalar coupling[33] and motional anisotropy that can be detected by analysis either of residual dipolar couplings (RDCs), introduced by partial alignment of the protein studied,[34] or of T_1/T_2 ratios of ^{15}N-labelled amide resonances.[35] Long-range information is particularly valuable when dealing with modular proteins.

A major advantage of NMR, compared to crystallography, is that it can deal with proteins that are very flexible, with no well-defined fold. It can also study weak ligand interactions and, perhaps most importantly, define relative motion in a system. Relative module motion can be very important for module assembly and regulation of function (Figure 1). While a crystal structure determination requires two modules to have a relatively fixed orientation, NMR can deal with various types of connection between modules. Some of the different ways that modules can be connected are shown schematically in Figure 4. The effect the different kinds of connection have on various NMR parameters is also summarised there. Intimate contact between modules leads to relatively large induced chemical shifts, many intermodule ^{1}H–^{1}H NOEs and motional anisotropy that is greater than that observed for a single module. As the intermodule motion increases and contacts diminish, the detectable NMR effects are reduced.

In recent years we have concentrated more on how combinations of modules are assembled and how modules interact with their biological ligands than on structure determination per se. This forms part of an overall 'dissect and rebuild' strategy that we have applied for the last decade.[9] This strategy will now be illustrated, with reference to studies on a protein that we have studied for a number of years.[36] Features where NMR has particular advantages over other methods, such as studies of ligand binding, module assembly and module dynamics, will be emphasised.

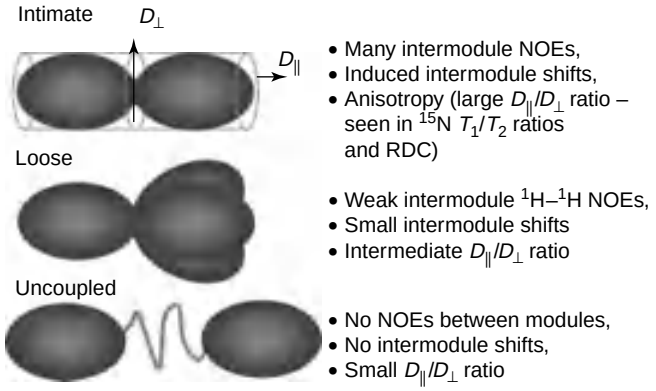

Figure 4 Three different kinds of module connection that can exist in an assembly of modules. The different observed NMR parameters arising in the three situations are indicated on the right. If the modules have an intimate and rigid connection, then many ^{1}H–^{1}H NOEs will be seen between modules. On addition of the second module, large induced chemical shifts and a significant increase in motional anisotropy will be introduced in the system. In the figure, $D_\parallel$ and $D_\perp$ represent axes of an axially symmetric diffusion tensor. Motional anisotropy can be measured by analysing T_1/T_2 ratios of ^{15}N amide resonances or by residual dipolar couplings (RDC) introduced by partial alignment of the system – e.g., by bicelles. In the completely uncoupled case, no NOEs or chemical shifts or will be induced upon covalent addition of a second module and there will be no increase in anisotropy. The 'loose' coupling case gives intermediate effects

4 A SPECIFIC EXAMPLE – FIBRONECTIN

Fibronectin is a large glycosylated protein found both in the extracellular matrix and in plasma.[37] It is a disulphide-linked dimer of two chains, each made up almost entirely of just three module types – type I (F1), type II (F2) and type III (F3). Fibronectin is involved in embryogenesis, wound healing and cell development. A measure of its importance is given by the fact that gene knockout is lethal at the embryo stage.[38] Some of the different functional regions of this molecule have been determined previously. For example the N-terminal F1 modules (^{1}F1–^{5}F1) bind fibrin and bacteria; the ^{6}F1.^{1}F2.^{2}F2.^{7}F1 region binds collagen, a major component of the extracellular matrix, and the ^{9}F3.^{10}F3 region binds to cell surface adhesion molecules called integrins; the ^{13}F3.^{14}F3 region binds heparin. The modular structure and binding functions of fibronectin are illustrated in Figure 5; note that the nomenclature ^{1}F1 means the first type 1 module.

One of many interesting features of fibronectin is that it is more active in binding to integrins when it is in the extracellular matrix, than when it is in plasma. Various hydrodynamic and other studies have suggested that this is because it is in a compact 'pretzel' form in plasma and an extended form in the matrix (see Ref.[39] and references therein). An ability to change shape like this requires considerable intermodule flexibility.

Consider first the N-terminal region, made up of the first five F1 modules. This region binds the clotting protein, fibrin, and several pathogenic bacteria, including *Staphylococcus aureus* and *Streptococcus pyogenes*. Studies of the ^{1}F1.^{2}F1 pair showed no intermodule connections[40] while the ^{4}F1.^{5}F1 pair has been shown, using normal structure determination methods and relaxation anisotropy, to have a well-defined interface and an extended structure.[41] The bacterial binding proteins seem to start off as unfolded chains, but, in the complex, they zip up along the β-strands of the F1 modules.[42,43] A good way of detecting these peptide/F1 interactions is to monitor chemical shifts induced in Heteronuclear Single Quantum Coherence (HSQC) spectra of ^{15}N labelled protein. NMR is also good at detecting changes in motional anisotropy when the peptide binds. The ^{4}F1.^{5}F1 pair retains a similar, relatively large, anisotropy before and after a bacterial peptide binds across the two modules. In contrast, the ^{1}F1.^{2}F1 pair starts off with an anisotropy expected for a single module and stiffens up to give a much higher anisotropy when a similar peptide binds across the two modules (Werner, J. et al., unpublished data).

The collagen-binding region of fibronectin has been shown to involve the region containing the ^{6}F1.^{1}F2.^{2}F2.^{7}F1 stretch of modules. We have dissected this region extensively to explore its structure and function. The work includes studies of the ^{7}F1, ^{1}F2 and ^{2}F2 modules on their own, the ^{6}F1.^{1}F2 pair[44] and the ^{6}F1.^{1}F2.^{2}F2 triple.[45] Interestingly the non-contiguous ^{6}F1 and ^{2}F2 modules come together to interact strongly in the triple. This interaction is readily detected, both by the observation of large shifts induced when the extra module is added, and by many NOEs detected across the interface. The ability of the triple to bind collagen also increases markedly compared to single and double modules.[45] Extensive studies of the ^{6}F1.^{1}F2[46] and ^{1}F2.^{2}F2[47] pairs have been carried out to define the relative motion of these modules in solution. The ^{6}F1.^{1}F2 pair is relatively well defined and its structure can be refined using RDC and relaxation anisotropy data.[46] In contrast, the ^{1}F2.^{2}F2 pair is completely 'uncoupled' and the addition of one module to the other induces no shifts and no increase in motional anisotropy.[47]

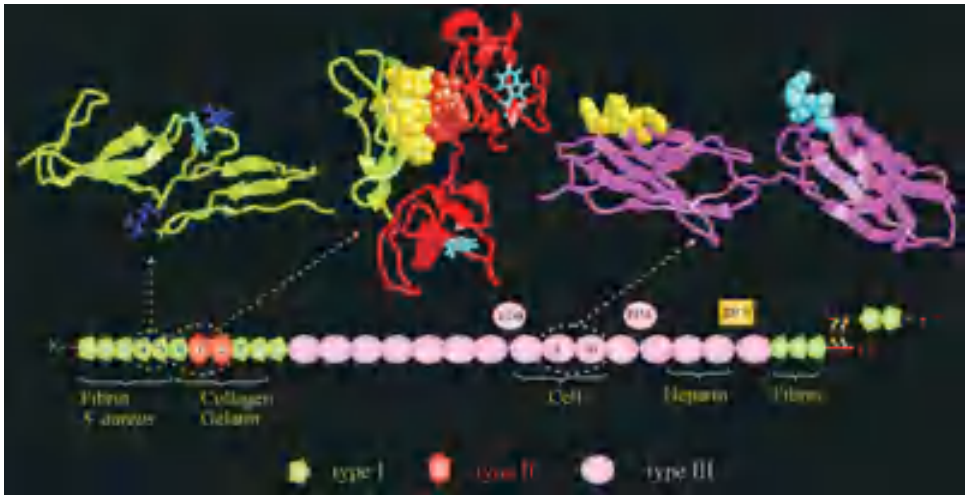

Figure 5 The modular structure of fibronectin. This large extracellular matrix protein is a dimer of two chains, largely constructed from F1 (type I), F2 (type II) and F3 (type III) modules. Some functional regions are indicated – e.g., the N-terminal F1 modules bind fibrin. Some extra modules, such as EDA, EDB and IIICS are sometimes spliced into the molecule. Several single modules, as well as various combinations of modules, have been studied in this laboratory.[36] The F1 modules in the ^{4}F1.^{5}F1 pair are tightly associated[41] and strong NOEs are seen across the module interface – for example between a tryptophan (cyan) and an arginine (blue). In a triplet of modules from the collagen-binding region,[45] the non-contiguous ^{6}F1 and ^{2}F2 modules make a tight interface with each other (residues in contact are shown in yellow and orange respectively). The two collagen-binding regions on the ^{2}F2 modules, marked by a tryptophan (cyan), point away from each other. In the cell-binding region, ^{9}F3.^{10}F3 are known to be very important; ^{10}F3 contains an RGD loop (cyan) that interacts with integrins. Additional binding affinity can arise from a site (yellow) on ^{9}F3; NMR investigations of this module pair, derived from human[49,50] and mouse[51] fibronectin, have shown that the RGD loop is flexible and that the modules have a considerable degree of intermodule flexibility

The region of fibronectin that is mainly responsible for binding to cell surfaces via integrins is ^{9}F3.^{10}F3. Particularly important is ^{10}F3 that has a loop between β-strands containing the residues Arg.Gly.Asp (RGD). We determined the structure of ^{10}F3 and showed that the RGD loop was flexible in solution.[26] For some integrins, such as $\alpha_5\beta_1$, an additional 'synergy' site on ^{9}F3 is also needed before complete binding and biological activity of fibronectin is realised. There is a crystal structure of the ^{7}F3–^{10}F3 region that has clear electron density for the RGD loop, indicating that it is rigid in the crystal.[48] The relative orientation of ^{9}F3 with respect to ^{10}F3 is also well defined in the crystal, although they have a distinctly different relative orientation compared to other F3 pairs and the buried surface area between modules is relatively small. NMR studies of the ^{9}F3.^{10}F3 pairs from human[49,50] and mouse[51] fibronectin showed that the RGD loop remains relatively flexible in solution and that the modules have a significant degree of intermodule flexibility. This is a good example of the complementary nature of NMR and X-ray crystal studies.

For structural studies of a large flexible molecule like fibronectin, a 'dissect and rebuild' strategy is going to be essential. While crystallography has been successful in defining the structure of stretches of F3 domains,[48,52] NMR has also made significant contributions. In the case of the ^{9}F3.^{10}F3 cell-binding region, NMR complemented X-ray studies by showing that the F3 modules can have significantly more flexibility than shown in the crystals. Only NMR structures are available for fibronectin F1 and F2 modules; NMR studies of several pairs (^{1}F1.^{2}F1, ^{4}F1.^{5}F1, ^{6}F1.^{1}F2 and ^{1}F2.^{2}F2) have revealed several different kinds of connection with different flexibility. NMR is also a very powerful tool in defining how fibronectin interacts with its various biological ligands by following induced chemical shifts and by analysing motional anisotropy. It is worth noting that NMR can also be applied to many other large modular proteins like fibronectin; an example is fibrillin, that is associated with the genetic disease the Marfan syndrome.[24]

5 THE FUTURE

Protein module research has made great strides in the last decade. In the new millennium, modules appear to be ideal targets for a co-ordinated program in 'Structural Genomics' that aims to determine representative structures of the protein folds found in biological systems. It seems likely that the structure of at least one representative module from all module classes found in biology will have been solved within the next decade. This knowledge will allow features of proteins in all genomes to be modelled reasonably accurately. What will remain unknown, in many cases, is how the modules are used by biology to perform their function in a complex and dynamic macromolecular assembly. In other words much will remain to be done in 'Functional Genomics', that aims to define the biological role of all the genomic products. This will require investigations of how modules are joined together in a modular protein, the extent of intermodule flexibility and the nature of their various interactions. It seems likely that NMR will continue to make a very significant contribution to this area of research in the foreseeable future.

Significant technical advances are also likely to continue in NMR, as they have done over the last 55 years. As mentioned above, higher fields, long-range structural restraints and other techniques promise to facilitate NMR structure determination. Advances are also likely in other areas. Chemical shifts are the most precise probes of subtle structural changes, yet they are hard to interpret in a quantitative way. Ab initio density functional theory calculations of chemical shielding of small molecular systems are now feasible because of the availability of the Gaussian suite of computational chemistry programs. This is likely to enhance our understanding and hence the power of NMR methods in the future. The most difficult part of a programme to investigate modules, however, is the production of large amounts of pure, folded, well-behaved, isotopically labelled protein. Current worldwide efforts to produce proteins on a large scale for structural studies will have a large impact in this area. An ability to splice in a labelled module[53] among a series of unlabelled ones will also greatly enhance and extend the size of module assemblies that can be studied.

6 REFERENCES

1. S. T. Rao and M. G. Rossmann, *J. Mol. Biol.*, 1973, **76**, 241.
2. L. Banyai, A. Varadi, and L. Patthy, *FEBS Lett.*, 1983, **163**, 37.
3. R. F. Doolittle, D. F. Feng, and M. S. Johnson, *Nature*, 1984, **307**, 558.
4. T. E. Petersen, H. C. Thogersen, K. Skorstengaard, K. Vibe-Pedersen, P. Sahl, L. Sottrup-Jensen, and S. Magnusson, *Proc. Natl. Acad. Sci. USA*, 1983, **80**, 137.
5. T. Yamamoto, C. G. Davis, M. S. Brown, W. J. Schneider, M. L. Casey, J. L. Goldstein, and D. W. Russell, *Cell*, 1984, **39**, 27.
6. L. Patthy, *Cell*, 1985, **41**, 657.
7. L. Patthy, *FEBS Lett.*, 1987, **214**, 1.
8. A. F. Williams and A. N. Barclay, *Annu. Rev. Immunol.*, 1988, **6**, 381.
9. M. Baron, D. G. Norman, and I. D. Campbell, *Trends Biochem. Sci.*, 1991, **16**, 13.
10. R. F. Doolittle, *Annu. Rev. Biochem.*, 1995, **64**, 287.
11. P. Bork, A. K. Downing, B. Kieffer, and I. D. Campbell, *Q. Rev. Biophys.*, 1996, **29**, 119.
12. P. Bork, J. Schultz, and C. P. Ponting, *Trends Biochem. Sci.*, **22**, 1997, 296.
13. http://smart.embl-heidelberg.de/ and http://www.sanger.ac.uk/Software/Pfam/
14. H. Hutter, B. E. Vogel, J. D. Plenefisch, C. R. Norris, R. B. Proenca, J. Spieth, C. Guo, S. Mastwal, X. Zhu, J. Scheel, and E. M. Hedgecock, *Science*, 2000, **287**, 989.
15. I. D. Campbell, *Immunol. Rev.*, 1998, **163**, 11.
16. M. F. Krummel, M. D. Sjaastad, C. Wulfing, and M. M. Davis, *Science*, 2000, **289**, 1349.
17. A. Bennick, I. D. Campbell, R. A. Dwek, N. C. Price, G. K. Radda, and A. G. Salmon, *Nature*, 1972, **234**, 1.
18. I. D. Campbell, C. M. Dobson, and R. J. P. Williams, *Proc. R. Soc. Lond. B*, 1975, **189**, 503.
19. C. A. Browne, I. D. Campbell, P. A. Kiener, D. C. Phillips, S. G. Waley, and I. A. Wilson, *J. Mol. Biol.*, 1976, **100**, 319.
20. F. F. Brown and I. D. Campbell, *Phil. Trans. R. Soc. B*, 1980, **289**, 395.
21. K. M. Brindle and I. D. Campbell, *Q. Rev. Biophys.*, 1987, **19**, 159.
22. R. M. Cooke, A. J. Wilkinson, M. Baron, A. Pastore, M. J. Tappin, I. D. Campbell, H. Gregory, and B. Sheard, *Nature*, 1987, **327**, 339.
23. I. D. Campbell and P. Bork, *Curr. Opin. Struct. Biol.*, 1993, **3**, 385.
24. I. D. Campbell and A. K. Downing, *Nature Struct. Biol.*, 1998, **5**, 496.

25. M. Baron, D. Norman, A. Willis, and I. D. Campbell, *Nature*, 1990, **345**, 643.
26. A. L. Main, T. S. Harvey, M. Baron, J. Boyd, and I. D. Campbell, *Cell*, 1992, **71**, 671.
27. D. G. Norman, P. N. Barlow, M. Baron, A. J. Day, R. B. Sim, and I. D. Campbell, *J. Mol. Biol.*, 1991, **219**, 717.
28. G. W. Booker, A. L. Breeze, A. K. Downing, G. Panayotou, I. Gout, M. D. Waterfield, and I. D. Campbell, *Nature*, 1992, **358**, 684.
29. G. W. Booker, I. Gout, A. K. Downing, P. C. Driscoll, J. Boyd, M. D. Waterfield, and I. D. Campbell, *Cell*, 1993, **73**, 813.
30. P. C. Driscoll, J. G. Cyster, I. D. Campbell, and A. F. Williams, *Nature*, 1991, **353**, 762.
31. R. Riek, K. Pervushin, and K. Wüthrich, *Trends Biochem. Sci.*, 2000, **25**, 462.
32. A. J. Wand, M. R. Ehrhardt, and P. F. Flynn, *Proc. Natl. Acad Sci. USA*, 1998, **95**, 15 299.
33. A. J. Dingley and S. Grzesiek, *J. Am. Chem. Soc.*, 1998, **120**, 8293.
34. N. Tjandra, J. G. Omichinski, A. M. Gronenborn, G. M. Clore, and A. Bax, *Nature Struct. Biol.*, 1997, **4**, 732.
35. N. Tjandra, D. S. Garrett, A. M. Gronenborn, A. Bax, and G. M. Clore, *Nature Struct. Biol.*, 1997, **4**, 443.
36. J. R. Potts and I. D. Campbell, *Matrix Biol.*, 1996, **15**, 313.
37. R. O. Hynes, 'Fibronectins', Springer-Verlag: New York, 1990.
38. E. L. George, H. S. Baldwin, and R. O. Hynes, *Blood*, 1997, **90**, 3073.
39. R. O. Hynes, *Proc. Natl. Acad. Sci. USA*, 1999, **96**, 2588.
40. J. R. Potts, J. R. Bright, D. Bolton, A. R. Pickford, and I. D. Campbell, *Biochemistry*, 1999, **38**, 8304.
41. I. Q. H. Phan, J. Boyd, and I. D. Campbell, *J. Biomol. NMR*, 1996, **8**, 369.
42. C. M. Penkett, C. M. Dobson, L. J. Smith, J. R. Bright, A. R. Pickford, I. D. Campbell, and J. R. Potts, *Biochemistry*, 2000, **39**, 2887.
43. U. Schwarz-Linek, M. J. Plevin, A. R. Pickford, M. Höök, I. D. Campbell, and J. R. Potts, *FEBS Lett.*, 2001, **497**, 137.
44. A. A. Bocquier, J. R. Potts, A. R. Pickford, and I. D. Campbell, *Structure*, 1999, **7**, 1451.
45. A. R. Pickford, S. P. Smith, D. Staunton, J. Boyd, and I. D. Campbell, *EMBO J.*, 2001, **20**, 1519.
46. Y. Hashimoto, S. P. Smith, A. R. Pickford, A. A. Bocquier, I. D. Campbell, and J. M. Werner, *J. Biomol. NMR*, 2000, **17**, 203.
47. S. P. Smith, Y. Hashimoto, A. R. Pickford, I. D. Campbell, and J. M. Werner, *Biochemistry*, 2000, **39**, 8374.
48. D. J. Leahy, I. Aukhil, and H. P. Erickson, *Cell*, 1996, **84**, 155.
49. C. Spitzfaden, R. P. Grant, H. J. Mardon, and I. D. Campbell, *J. Mol. Biol.*, 1997, **265**, 565.
50. R. P. Grant, C. Spitzfaden, H. Altroff, I. D. Campbell, and H. J. Mardon, *J. Biol. Chem.*, 1997, **272**, 6159.
51. V. Copié, Y. Tomita, S. K. Akiyama, S. Aota, K. M. Yamada, R. M. Venable, R. W. Pastor, S. Krueger, and D. A. Torchia, *J. Mol. Biol.*, 1998, **277**, 663.
52. A. Sharma, J. A. Askari, M. J. Humphries, E. Y. Jones, and D. I. Stuart, *EMBO J.*, 1999, **18**, 146.
53. R. Xu, B. Ayers, D. Cowburn, and T. W. Muir, *Proc. Natl. Acad. Sci. USA*, 1999, **96**, 388.

Acknowledgements

I gratefully acknowledge the contributions of many excellent co-workers over the last three decades. In recent times I also acknowledge the support of the Wellcome Trust and the Oxford Centre for Molecular Sciences that is funded by BBSRC, MRC and EPSRC.

Biographical Sketch

Iain D Campbell, *b* 1941, B.Sc. (1963) Ph.D. (1967) in Physics at St. Andrews University. First involved with NMR on joining Rex Richards as a post-doctoral fellow in 1967, at the Physical Chemistry Laboratory, University of Oxford. Managed Oxford Enzyme Group NMR facilities in 1970s. Faculty member, Department of Biochemistry, University of Oxford, since 1976. Fellow of St. John's College since 1987. Professor of Structural Biology since 1992. Elected member of EMBO in 1990 and FRS in 1995. Approx. 230 publications. Current research interests: structure and function of modular proteins in cell adhesion and signalling.

Proteins and Protein Fragments: Folding

H. Jane Dyson and Peter E. Wright
The Scripps Research Institute, La Jolla, CA, USA

1	Introduction	1
2	Folding Pathways of Proteins by NMR	1
3	NMR of Denatured Proteins	4
4	NMR of Protein Folding Intermediates and Partially Folded Structures	4
5	NMR of Peptide Fragments of Proteins	5
6	Future Prospects	8
7	Related Articles	8
8	References	8

1 INTRODUCTION

There is currently a great deal of interest in the mechanism of protein folding, and a number of theoretical and experimental approaches to the problem have been developed in the past few years. Advances in hardware and software have made NMR an exceptionally important technique for studies of protein folding; it has been used to obtain novel insights into the folding process. The development of quench-flow hydrogen exchange methods[1] has opened up a new window into folding events that occur on the millisecond to second timescale. Using known resonance assignments for the folded form of the protein, it has been possible to obtain assignments and structural information on unfolded forms[2] and folding intermediates.[3] Insights into the earliest steps of the folding process have been provided by NMR studies of peptide fragments of proteins.[4] These and other studies on the protein folding process will be briefly reviewed in this article; limitations of space prevent an exhaustive review.

2 FOLDING PATHWAYS OF PROTEINS BY NMR

2.1 Slow Folding Events and Equilibrium Studies

Since the timescale of the NMR experiment is slow compared with classic optical spectroscopic methods for measuring kinetics, the use of NMR to monitor protein folding processes directly is not usually possible. Folding can be observed by NMR, and rate information can be extracted from the measurements. For example, an upper limit of the rate of the slow unfolding of trp repressor in urea was estimated to be $50\,s^{-1}$ from the observation of separate signals in 4 M urea corresponding to the native and unfolded states.[5] Attempts have been made to detect intermediates by NMR spectroscopy at equilibrium in the folding–unfolding reaction,[1,6] and NMR has been used to demonstrate independent unfolding of the domains of urokinase.[7] In general these methods give information only on the slowest steps of protein folding.

A variety of NMR techniques has been used to study one of the well-known slow processes in protein folding, the *cis–trans* isomerization of prolines. A number of studies have utilized magnetization transfer NMR, which, under favorable conditions, can also be used to obtain information on the kinetics of protein folding itself.[8] The magnetization transfer technique has been used for staphylococcal nuclease to demonstrate the presence of two native states that differ in the isomerization state of Pro-117[9,10] and to study the folding and interconversion of these two forms.[10] A peptide model of the site of isomerization did not show any evidence of *cis* isomeric forms in aqueous solution, an indication that they are probably absent in the fully unfolded form of staphylococcal nuclease.[11] Differences in rates of isomerization of prolines in the presence of isomerases have been studied by dynamic NMR spectroscopy.[12]

2.2 NMR Hydrogen Exchange Pulse Labeling

An important advance in the understanding of the structural basis of protein folding came with the realization that a combination of quenched-flow methods, hydrogen–deuterium exchange and NMR could give detailed site-specific information about the folding process (see Roder[1] and Englander and Mayne[13] for reviews). The method was suggested by Roder and Wüthrich[14] as an extension of the $^1H-^3H$ exchange methods developed by Baldwin and co-workers,[15,16] and its power was demonstrated in 1988 with the simultaneous publication of two folding studies, one on ribonuclease A[17] and one on cytochrome *c*.[18] Since then, a number of proteins have been studied by the hydrogen exchange pulse-labeling method, and representative examples will be discussed below.

The method aims to label intermediates in the folding pathway in such a way that they can be studied at leisure by NMR once folding is complete. There are many advantages of working with native folded proteins, including greater stability to aggregation at NMR concentrations, better dispersion of resonances in the NMR spectra, and usually more readily available resonance assignments. The pulse labeling technique requires the use of a sophisticated temperature-controlled syringe system, obtainable from several commercial sources. For folding studies, a 5-syringe unit is used, as shown in Figure 1. Mixing is performed in mixing chambers fed by computer-controlled drive syringes. For a typical refolding experiment, the protein can be pulse-labeled either with ^1H_2O from a ^2H_2O buffer[17–19] or with ^2H_2O from a ^1H_2O buffer.[20] Denatured protein (S1) is rapidly diluted with refolding buffer (S2) and allowed to refold for variable times determined by the length of the delay line DL-1. The lower limit of the refolding time is determined by the mixing characteristics of the quenched-flow apparatus and is usually 4–6 ms or more. The partially refolded protein is pulse-labeled (S3, M2) for about 50 ms (DL-2) under conditions where the intrinsic peptide hydrogen exchange time constant is about 1 ms.[21] The amide protons in unstructured parts of the protein are exchanged during the pulse, but the protons that are involved in hydrogen-bonded secondary structure (and which are slowly exchanging in the native protein; see below) are protected from exchange. The labeling pulse is quenched (S4, M3) by lowering the pH to conditions where amide proton exchange is slow, and the folding process allowed to proceed to completion

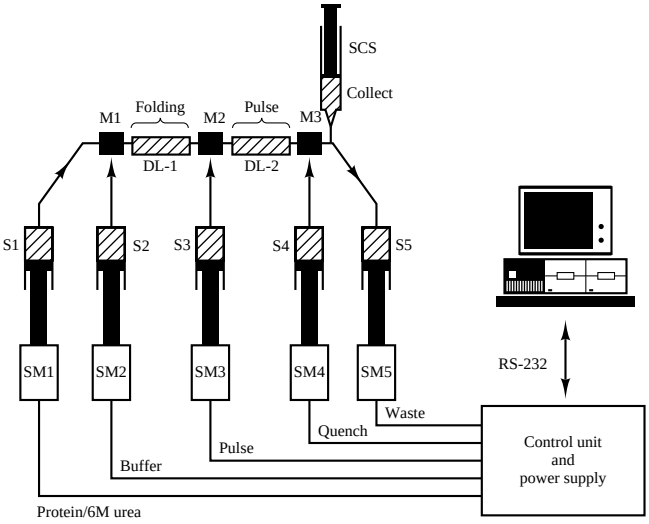

Figure 1 Schematic diagram showing the arrangement of syringes, mixing chambers, and delay lines in the Bio-Logic QFM-5 quench-flow apparatus, one of several commercially available systems. M1–M3, mixers; DL-1, DL-2, delay lines; S1–S4, drive syringes; S5, waste collection syringe; SCS, sample collection syringe, SM1–SM5, stepping motors. (Adapted by Dr P. A. Jennings from the manual for the Bio-Logic quench-flow apparatus with permission)

in the sample collection syringe. A schematic picture of the stages in the quench-flow pulse-labeling experiment with the denatured protein in ^1H_2O and the labeling pulse in ^2H_2O is shown in Figure 2.

Quench-flow hydrogen exchange studies of the folding of a number of proteins have now been reported. It is interesting to note that there has so far been little similarity revealed in these studies between the folding mechanisms of proteins in different structural families. For ribonuclease A (disulfide bonds intact),[17,19] one early folding intermediate is formed rapidly and contains all of the slowly exchanging amide protons in the β-sheet. These protons are only marginally protected early in the folding pathway, but become more protected at later stages, an indication that subsequent events stabilize the formation of the sheet. There are only a few

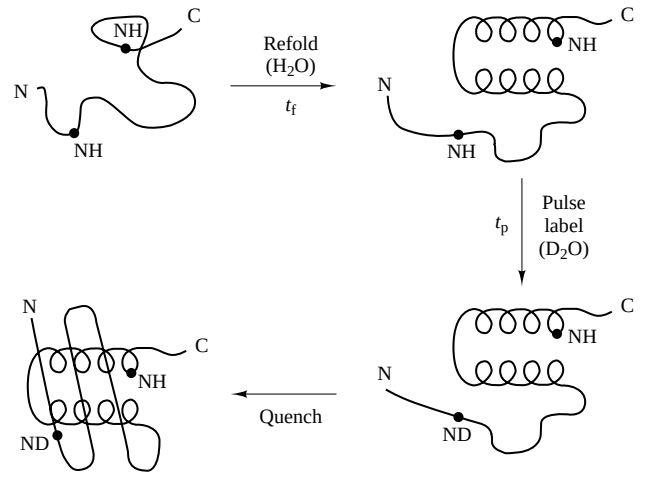

Figure 2 Schematic diagram showing the state of the protein at various stages in the mixing and labeling process

probes (i.e. only a few slowly exchanging amide protons in the native folded state) in the three helices, so information is scanty in these regions. An analysis of the results in terms of a sequential model for folding showed that the intermediate contains the majority of the β-sheet secondary structure of ribonuclease A, but is not fully populated when first formed.[19]

The structure of cytochrome *c* is quite different from that of ribonuclease A, and consists largely of helix, with little or no β-sheet. Unlike ribonuclease A, there are a large number of amide proton probes in the helices, so this molecule provides a good system for study of the folding of a helical protein.[18] Several amide protons in the N- and C-terminal helices are apparently protected within the 4 ms dead time of the quench-flow apparatus, an indication that folding is initiated very rapidly in these regions of the protein, probably by rapid formation of helical secondary structure, followed by or perhaps concomitant with stabilization of the initial folded form by docking of the two helices. This behavior is apparently different from that of the α/β protein ribonuclease A, although it is difficult to determine whether the helices are in fact formed early in the latter protein, due to the lack of probes in the helices. A two-peptide model of the cytochrome *c* folding intermediate showed enhanced helicity by NMR when the two component peptides were combined,[22] indicating that interactions between marginally stable elements of secondary structure are important in forming tertiary subdomains (intermediates) in the folding of the intact protein.

The folding pathways of ribonuclease A and cytochrome *c* appear to be rather simple, consistent with the small size of the proteins and their compact single-domain structure. Lysozyme shows more complex folding behavior, giving evidence of multiple pathways associated with two folding domains.[23,24] NMR experiments based on competition between hydrogen exchange and the refolding process[23] showed that the rapid and slow refolding populations of lysozyme correspond to the helical and sheet regions of the molecule respectively, an indication that the two domains fold independently. In addition, different populations of molecules fold by kinetically distinct, parallel pathways, some of which may involve reorganization of incorrectly folded structure.[24]

Parallel folding pathways have also been invoked to explain the results obtained for the folding of ribonuclease T_1,[25] which folds much more slowly than most other proteins studied by the quench-flow hydrogen exchange method. Two intermediates were postulated on the kinetic folding pathway of ribonuclease T_1, a native-like intermediate and a molten globule.[25] Molten globule intermediates have been suggested for many of the protein folding pathways studied so far, although the definition of what constitutes a molten globule sometimes appears to vary with the protein studied. Intermediates of this kind were postulated for T4 lysozyme,[26] ubiquitin,[27] and barnase,[28] with the interesting similarity in these cases that both α-helices and β-sheets containing stable backbone hydrogen bonds were formed in the earliest folding events (within a few milliseconds). In contrast, refolding of the all-β-sheet protein interleukin-1β leads to rapid formation (within 25 ms) of an intermediate contining 90% of the β-sheet secondary structure but without stable hydrogen bonds.[29] Formation of stable, hydrogen-bonded secondary structure begins only after $\sim$1 s. Another all-β-sheet protein, plastocyanin, displays

similar behavior: a folding intermediate containing unstable β-sheet structure is formed, which provides only slight protection of backbone amide protons from exchange.[30] Isomerization of a key proline residue, Pro-16, to the *cis* form allows correct packing of the incipient, fluxional β-sheets to form stable, hydrogen-bonded secondary structure during the final, slow, folding step.

While the evidence that molten globule intermediates of many types participate in the folding pathways of a number of proteins is persuasive, in none of the systems described so far was the intermediate demonstrated to participate in the actual kinetic folding pathway of the protein. In one well-studied system, that of apomyoglobin, the intermediate observed in equilibrium experiments has been shown to be identical to that observed by the quench-flow NMR hydrogen exchange method. Further, the intermediate was shown to be on the kinetic pathway of folding, the first demonstration of such a phenomenon.

Myoglobin and apomyoglobin (without the heme prosthetic group) have been studied extensively both by theoretical and experimental techniques. Circular dichroism (CD) spectroscopic measurements as a function of pH[31] indicated that a stable intermediate species exists at pH ~4. The structure of this species has been characterized by amide exchange trapping[32] (see later), which showed that a region of the protein is folded in the intermediate, while the rest of the protein is flexible or unfolded. The folded region consists of the two C-terminal helices, termed the G- and H-helices, which form a helical hairpin structure in the fully folded myoglobin and also probably in apomyoglobin,[33,34] together with the N-terminal helix, termed the A-helix. These regions are shown mapped onto the structure of native myoglobin in Figure 3. The question as to whether this intermediate is formed during the folding of apomyoglobin was addressed by Jennings and Wright.[20] Using both hydrogen exchange pulse labeling and stopped-flow CD measurements they showed that an intermediate was formed in less than 5 ms, where amide proton probes were fully protected in the A-, G-, and H-helical regions of the protein and a part of the B-helix. Slower folding steps saw the protection of the remainder of the B-helix, the C- and E-helices and the CD connecting loop. These regions are precisely the same as those previously identified as being folded in the equilibrium intermediate observed at pH ~4. There is clearly a close structural similarity between the earliest detectable kinetic intermediate and the intermediate observed under equilibrium conditions,[32] providing strong evidence that this molten globule intermediate participates in the kinetic folding pathway.

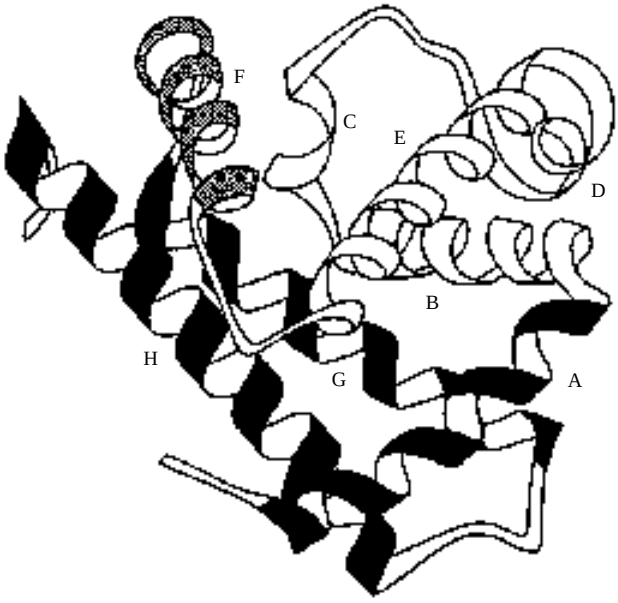

Figure 3 Location of the structured regions found in the kinetic intermediate of apomyoglobin, mapped onto the X-ray structure[106] of the native protein (the heme group is omitted from the diagram for the sake of clarity). Helices B–E are unshaded and are proposed to be predominantly unfolded in the intermediate. The F-helix is unshaded to denote the absence of amide proton probes and structural information. The A-, G-, and H-helices are darkly shaded, and are proposed to be folded into a native-like structure in the intermediate. (Reproduced by permission from Hughson et al.[32])

2.3 NMR Amide Exchange Trapping

The NMR quench-flow pulse-labeling method has a problem, particularly severe for smaller proteins: only a subset of the NH protons can be studied. Only those amide protons that are resistant to exchange into ^2H_2O in the native protein during the experiment can be used as probes during the kinetic folding studies. In addition, most of the probe amide protons are usually present in regular secondary structure: if these are all protected in a folding intermediate, then there is little information to be gained on the sequence of folding events, and it is unclear whether the amide protons are protected in native-like secondary structure in the intermediate. A partial solution to this problem is available in the form of the amide exchange trapping experiment.[35,36] In this experiment, both the locations and the hydrogen exchange rates (protection factors) of the protected amide protons are measured. A comparison of the protection factors for the intermediate and for the native state of the protein can then be used to determine whether the hydrogen-bonded secondary structure in the intermediate is native-like. As mentioned above, this method was used to show that the low pH intermediate of apomyoglobin contained native-like secondary structure.[32] An extensive study of cytochrome *c* using this technique was made by Englander and co-workers,[37,38] who concluded that native-like secondary structure was formed in the cytochrome *c* folding intermediates (termed submolecular folding units) that are formed at low pH in high salt.

The partially folded state of α-lactalbumin (termed the A-state or molten globule state) is also formed at low pH and has been characterized by NMR pH-jump refolding studies[39] and by amide exchange trapping.[40] A specific element of residual secondary structure present in the A-state of α-lactalbumin[39] is thought to be native-like, and to consist of two helices, with a region of highly compact (though not necessarily native-like) hydrophobic packing between them. The highly protected nature of this hydrophobic region is shown by the high degree of protection of an indole NH from a Trp residue in the A-state. The method has been applied to proteins denatured by alcohols, monellin in ethanol or trifluoroethanol,[41] and lysozyme in trifluoroethanol.[42] The characteristic feature of these alcohol-denatured states appears to be a higher content of helical secondary structure than the native state. The amide exchange trapping experiment demonstrated that, in the case

of monellin, a specific part of the molecule had apparently changed from β-sheet secondary structure in the native protein to α-helix.[41] By contrast, the protected amides found in the experiments on alcohol-denatured lysozyme were present in regions that were helical in the native folded state, and little protection was found for the sheet and loop regions of the protein. For lysozyme, the side chains were found to be averaged.[42]

3 NMR OF DENATURED PROTEINS

The study of the denatured states of proteins is difficult, for several reasons. The denatured state of a protein is prone to aggregation, especially at NMR concentrations, the solution conditions under which denatured proteins are studied are often not ideal for NMR, and the spectra themselves are often highly overlapped, consistent with the generally random nature of the polypeptide chain. However, contrary to earlier assumptions, the denatured state may not be 'simply' a random coil, but may contain residual structure, as has been found for some peptides (see later). Direct measurement of amide proton exchange rates in heat-denatured ribonuclease A showed no difference from that expected for a disordered peptide, though some anomalies in the pH dependence were pointed out.[43] This was despite the observation of residual signal in the CD spectrum, which could be eliminated by the addition of denaturing agents. The authors concluded that no stable hydrogen-bonded secondary structure was present in thermally denatured ribonuclease A.

The ribonuclease experiments were performed as a high-temperature variant of the original quench-flow experiment,[17] which, as explained above, makes the actual NMR measurements on the native state after reconstitution. Direct measurements of the resonances of the denatured state and their assignment by exchange correlation have also been made for ribonuclease A.[44] Exchange correlation has also been used for lysozyme to demonstrate the presence of hydrophobic clusters in the thermally denatured protein.[45] An interesting new application of the photochemically induced dynamic nuclear polarization (CIDNP) technique has also been used for lysozyme to confirm the presence of hydrophobic interactions involving some of the Trp residues buried in the native state of the protein.[46] In these experiments, the lysozyme denatured by dimethyl sulfoxide appeared to have more random behavior than that denatured by urea or high temperatures, a further indication that hydrophobic interactions are involved.

While NMR is potentially a powerful method for direct characterization of residual structure and dynamics of unfolded proteins, applications have been rather limited to date because of the difficulty of assigning the poorly dispersed spectrum of the unfolded state. In one approach, resonance assignments in a urea-unfolded fragment of 434 repressor were made using chemical exchange to transfer assignments from the folded to the unfolded species.[47,48] From NOE measurements on the 434 repressor fragments in 7 M urea, specific hydrophobic interactions were identified and the local structure of the polypeptide chain in this vicinity was calculated.[49] The residual structure in the urea-denatured protein is similar to the corresponding region in the structure of the native protein, prompting the hypothesis that the formation of this hydrophobic cluster could serve as an initiation site for the folding of the repressor.

More recently, heteronuclear multidimensional NMR methods have been applied to obtain ^{1}H, ^{13}C, and ^{15}N resonance assignments for uniformly labeled FK506 binding protein unfolded in 6.3 M urea or 2 M guanidine hydrochloride.[50] Although the protein displayed extensive conformational averaging, local regions of secondary structure could be identified. These methods should be generally applicable for NMR structural studies of unfolded or partly folded proteins, and have now been applied to a denatured 131-residue fragment of staphylococcal nuclease.[51]

4 NMR OF PROTEIN FOLDING INTERMEDIATES AND PARTIALLY FOLDED STRUCTURES

For most proteins, the intermediates formed during the folding process are populated only transiently, so that under normal circumstances they cannot be directly studied by NMR. Experiments such as quench-flow hydrogen exchange and amide proton trapping are generally the preferred methods to give information on these states. In some proteins, under certain conditions, folding intermediates can be directly observed. Ingenious experimental design, such as the continuous recycled-flow method,[52] have been used to circumvent the problems of the short lifetimes of intermediates.

Partly folded forms of several proteins have been studied by NMR. Of these, the most extensive studies have been on ubiquitin, α-lactalbumin, and bovine pancreatic trypsin inhibitor (BPTI). The A-state of ubiquitin is present at pH $\sim$2 in 60% methanol/40% water at 298 K, and three separate studies of the same state of the protein[53–55] reach broadly similar conclusions that nevertheless differ considerably in detail (an illustration of the difficulties inherent in these types of measurements). Harding et al.[53] used two-dimensional (2D) ^{1}H NMR spectroscopy to assign slowly exchanging amide proton resonances in the A-state, concluding that there was no gross structural reorganization from the native state of the protein but that the A-state contained a subset of the secondary structure found in the native state, including the first two strands of the 5-strand β-sheet, part of the third strand, and a partially structured α-helix packed on the hydrophobic side of the sheet. No evidence was found for the turns and 3_{10} helical structure present in the native state of the protein.

Pan and Briggs[54] made an extensive study of the protection factors of amide protons in the A-state of ubiquitin. They too found a structure with native-like secondary structure, but concluded that almost all of the native secondary structure persists in the intermediate, apparently destabilized by several kilojoules per mole compared with the native form of the protein. Differences in the method of sample preparation were thought to account for the differences in the results between the two studies. In a third study, this time using heteronuclear three-dimensional methods, Stockman et al.[55] were able to assign unambiguously more than 90% of the resonances of the A-state in 60% methanol, and to resolve a number of NOEs that define the limits of secondary structure. These results indicate that, contrary to the conclusions of the two previous studies, only the first two β-strands are present in the A-state, and suggest that the C-terminus, rather than being part of the β-sheet as in the native protein, becomes helical in the presence of methanol, an interesting parallel to the behavior of monellin.[41]

The ^{1}H NMR spectrum of the A-state of α-lactalbumin formed at acid pH differs substantially from those of both the native and denatured states.[39] Chemical shift dispersion in the A-state is limited, indicating that long-range tertiary structure present in the native state is absent in the intermediate.[56] No evidence for native-like hydrophobic clustering is observed, but interresidue NOEs indicate that a new aromatic cluster, consisting of residues at positions 103, 104, and 107 in the polypeptide chain, is present. The identity of this structure as a local interaction is confirmed by the observation of similar NOEs in a short peptide containing these residues.[56] These residues form part of a helix in the native form of the protein, and the stabilization of helices by (i, i + 1, i + 4) hydrophobic interactions has previously been noted.[57,58] It is possible that this sequence behaves in the A-state of α-lactalbumin like the nascent helix observed in peptide fragments of proteins[58] (see later), as a precursor to the formation of helical structures in the folded protein.

The most intensely studied protein, in terms of folding, is probably BPTI. Recently, a number of studies using NMR to probe the structure of the folding intermediates containing only one or two of the three disulfides of the native protein have been performed, using mutant proteins where various Cys residues have been replaced by Ser[59–61] or Ala.[62] The intermediates generally show many of the characteristics of the folded form of BPTI, although a Cys-Ser mutant containing only the 30–51 disulfide appears from NMR studies to be largely unfolded at the N-terminus.[60] However, the secondary structure that forms the core of the molecule is already formed and stabilized by hydrogen bonds even in the presence of only one disulfide bond.[59,61] A disulfide-bridged peptide mimic of the helix/sheet secondary structure of BPTI was also shown to be folded.[63] It thus appears that much of the folding process of BPTI is achieved before the first disulfide is even formed, and the intermediates modeled by the mutant proteins are sufficiently stable to be studied at length by NMR.

Another long-lived folding intermediate that has been studied by NMR is the partially folded form of subtilisin BPN′, which cannot form the native, fully folded protein in the absence of a 77-amino acid pro-sequence.[64] The intermediate possesses secondary structure, but tertiary structure only in small regions, including the location of a high-affinity calcium-binding site. The authors conclude that the function of the pro-sequence is to lower the energy of the transition state between the intermediate and the fully folded molecule.

5 NMR OF PEPTIDE FRAGMENTS OF PROTEINS

The power of NMR methods in the study of protein folding is emphasized by the quantity and variety of research reported to date, and the continuing development of new techniques, as briefly described above. NMR is able to describe folding intermediates and processes in a site-specific manner that cannot be rivaled by any other technique, but is limited at present to a timescale of milliseconds or longer. For most proteins, a number of steps in the folding process are already complete in 5 ms; for apomyoglobin, for example, the first intermediate is already fully formed in this time.[20] The earliest events in the folding process (Figure 4) are thus not amenable to direct study by NMR spectroscopy on the whole protein. An approach to characterize the probable initiation events in protein folding has been proposed[65,66] in which the protein is dissected into peptide fragments, and NMR methods are used to identify elements of secondary structure or hydrophobic clustering in aqueous solution. The majority of linear peptides are unstructured in aqueous solution, that is, they are present as a conformational ensemble containing conformers with widely different structures. For some peptides it is possible to observe a conformational preference for a folded form. However, it should be stressed firmly that, in the absence of covalent conformational constraints, all linear peptides must be considered to consist of conformational ensembles in solution. Even cyclic peptides are flexible, and their NMR spectra show signs of conformational averaging.

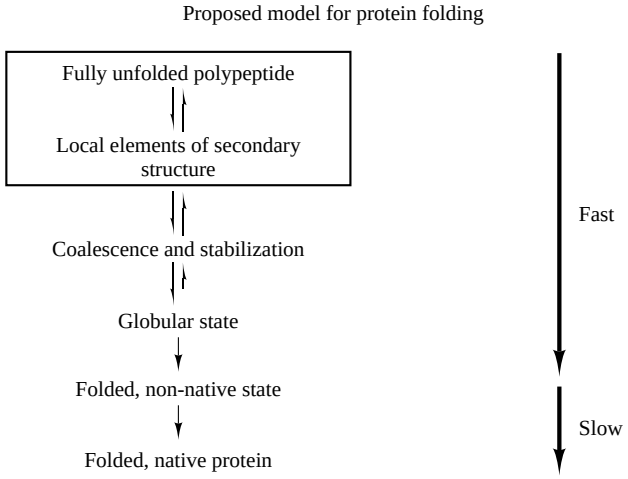

Figure 4 Schematic diagram of the folding process

The S-peptide of ribonuclease A was the first peptide for which a conformational preference for a folded helical form was observed, by CD spectroscopy, in aqueous solution.[67] One-dimensional NMR was later used to demonstrate the formation and dissolution of secondary structure in the S-peptide[68] and in three-residue peptides from other regions of ribonuclease A.[69] Turn-like conformations were inferred from the latter data, consistent with the hypothesis that the formation of β-turns is important in the initiation of folding of ribonuclease A. A conformational preference for a well-defined turn was found using 2D NMR methods in a nine-residue peptide derived from influenza virus hemagglutinin.[70] Since then, many studies of peptide fragments of protein have been reported, a selection of which will be summarized below. Several reviews have recently appeared on this subject, including a summary of the techniques used for identifying structured states in the conformational ensemble.[71] The connection between the NMR observation of structured conformers in peptide fragments of proteins and the initiation of protein folding was initially suggested in 1988:[65] since that time evidence has accumulated that peptides can be used as models for the initiation of protein folding, and some surprising behavior relevant to the folding process has also been seen.

5.1 Turn Conformations Observed in Peptides by NMR

Turn conformations are logical sites for initiation of protein folding. While much is known of the sequence

preferences of turn conformations in folded proteins from a consideration of X-ray structures,[72] the incidence of turns in unfolded proteins and by implication in peptides was unknown. Following the original discovery of the turn conformation in the hemagglutinin peptide,[70] an extensive study of the sequence preferences of turns was made in several series of five-residue peptides.[73] The original turn conformation was present in the sequence Tyr-Pro-Tyr-Asp-Val with a *trans* configuration of the Tyr–Pro peptide bond; by varying the amino acid residues at each position of the turn, while keeping the other residues constant, a profile of the ideal turn-forming sequence in a peptide or unfolded protein was obtained. The best residue for turn formation at position 3 is glycine (Gly), and at position 4 is Asp.[73] If these two residues are kept constant and position 1 of the turn is varied, the residue that most favors turn formation is Ala.[74] The best residue at position 2 is the original Pro, but, perhaps surprisingly, peptides in the series Ala-X-Gly-Asp-Val, with X other than Pro, also contain substantial turn populations,[74] an indication that the Pro residue is not essential at position 2 as long as the other three residues are favorable for turn formation.

We thus conclude that, for peptides in solution, the optimal sequence for turn formation is Ala-Pro-Gly-Asp. While many of the examples of this and similar sequences do form turns in protein structures, this is not always the case. This is an illustration of the difference between the relatively fixed conformation in the folded protein, where many factors including long-range tertiary interactions can influence the local backbone conformation, and the flexible conformation in the linear peptide, where unfolded states are always accessible and the observation is of a conformational preference only. A corollary of this is that the conformational preferences observed in peptides or unfolded proteins need not necessarily be present as a structure in the final folded protein, even if the preference observed in the peptide is indeed a site of initiation of protein folding. The initial events probably involve the restriction of conformational space by the reversible formation of structures such as turns. Since this process is rapid and reversible, the initial turn conformation could be eliminated from the final structure by subsequent folding events that make other conformations more energetically favorable for this particular sequence. Nevertheless, a correlation has been observed between the values obtained for the turn propensity in peptides and the empirical sequence preferences obtained from protein structures,[73] an important link between the behavior of peptides in solution and structure in proteins (Figure 5).

The population of the turn conformation in Tyr-Pro-Gly-Asp-Val containing the *trans* form of the the Tyr–Pro peptide bond was estimated to be approximately 50%, and it showed behavior more consistent with turn type II than type I.[73] By contrast, the *cis* form of several peptides with sequences such as Ser-Tyr-Pro-Tyr-Asp-Val showed evidence of an exceptionally high population of a different turn conformation, identified as type VI, in the four-residue sequence Ser-Tyr-Pro-Tyr.[73] A sequence dependence of this turn conformation showed that it was highly favored when there were aromatic residues on either side of the *cis* Pro, and when Asp was present at position 5, following the turn.[75] Since the population of the folded conformation was so high (>70% of the *cis* peptide), and since its structure did not obviously correspond to any well-known secondary structure, a three-dimensional

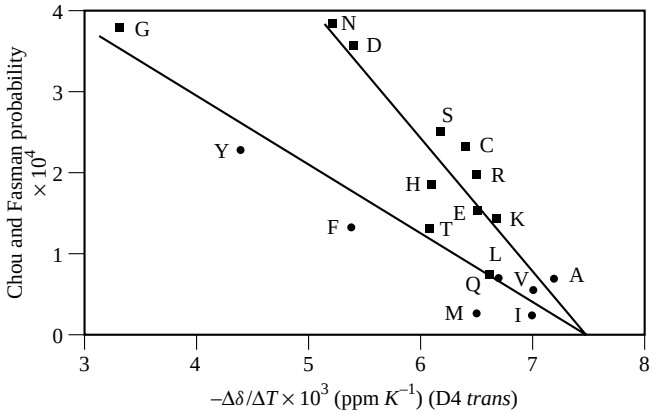

Figure 5 Probability of the occurrence of a turn conformation in a particular sequence in a folded protein[72] plotted against the temperature coefficient observed for the amide proton at position 4 in the series of peptides Tyr-Pro-X-Asp-Vol, where X is any amino acid residue. The letters are the single-letter codes for the amino acids at position 3. (Adapted with permission from Dyson et al.[73])

structure of the folded form of one of the peptides, Ser-Tyr-Pro-Phe-Asp-Val, was calculated.[76] It was essential to exclude NOE contributions from the unstructured states of the peptide from the constraint list for structure calculation. The structure reveals a specific stacking interaction between the two aromatic rings and the Pro ring, which explains not only the stability of this conformation in solution, but also several unusual features of the NMR spectrum, including the low-frequency shifted resonances of the *cis* Pro. The stability and high population of the structure is attested to by the results of an NOE/ROE study of the hydration of Ser-Tyr-Pro-Phe-Asp-Val,[77] which shows that the Pro ring protons with the furthest low-frequency shifted resonances are differentially protected from solvent, consistent with their presence in a highly populated structure where they are closely stacked onto the adjacent aromatic rings.

Specific turn conformations in proteins and other polypeptides have been modeled by studying peptides in solution. In particular, it was found using NOE experiments that the internalization sequence of the low-density lipoprotein receptor adopts a turn conformation in solution,[78] an important piece of information both for understanding of surface recognition and export and for molecular design. A result relevant to the problem of protein folding in vivo was the discovery that the sequence that is altered in temperature-sensitive mutants of the P22 phage tailspike protein, which had been shown to be deficient in the folding of the protein at the restrictive temperature,[79] contains a conformational preference for a turn in a peptide corresponding to the wild-type sequence, but not in the corresponding peptide with the mutant sequence.[80] These results provide convincing support for the importance of turn formation in the initiation of folding of proteins.

5.2 Helices and Nascent Helices

A conformational preference for helix in a peptide is easier to detect by CD spectroscopy than is a preference for a turn conformation, though this is possible if the peptide is sufficiently short.[73] Helices are indicated by NMR through

observation of medium range NOEs and small ^3J(H,N-α) coupling constants,[81] and peptides that contain helices according to the CD spectrum have also been shown to do so by NMR.[82,83] The site-specific information obtained from the NMR experiment allows the determination of the location and, to a certain extent, the local population of the helix: in most cases it appears that the helix is most populated in the center of the peptide, and frayed toward the ends. Even in the most highly helical peptides, however, unfolded forms are present in solution.[82,83]

NMR is a more sensitive technique for the detection of helix-like forms than CD; for detection of helix by CD, it must be quite regular.[84] An interesting structure detected by NMR in linear peptides is the so-called nascent helix,[58] which is characterized by $d_{NN}(i, i + 1)$ NOEs, intermediate-to-small ^3J(H,N-α) values, intermediate-to-low amide-proton temperature coefficients, and the presence of a number of $d_{\alpha N}(i, i + 2)$ NOEs, which are normally associated with turns.[71] The nascent helical peptide can readily be induced to form ordered helix by the addition of solvents such as trifluoroethanol (TFE). These results are interpreted in terms of a molecular model in which folding (and unfolding) of helices proceeds by way of turn-like intermediates. Indeed, such structures are populated in molecular dynamics simulations of the unfolding of helical peptides (reviewed by Brooks and Case[85]).

5.3 Immunogenic Peptides

Peptides can be used as immunogens to elicit antibodies that will in many cases recognize the cognate sequence in the folded protein.[86] These peptides quite often display conformational preferences for folded conformations in solution.[87] NMR studies of short peptides have also been used as a convenient way to model the conformations of immunogenic peptides, in systems where the protein immunogens are inaccessible to structure determination, for example, in protein antigens from *Herpes simplex*,[88] *Plasmodium falciparum*,[89] and HIV.[90–92] While no direct structural information can or should be inferred from the conformational preferences seen in these peptides, they can at least give a guide to the design of possible better immunogens.

5.4 Proteins in Pieces and Pieces of Proteins

In an attempt to delineate protein folding initiation sites for different protein structural motifs, several proteins have been examined by dissecting their sequences into a series of peptide fragments and examining the fragments by NMR in aqueous solution. The protein sequences studied include myohemerythrin, a four-helix bundle protein,[58,93] plastocyanin, a β-sandwich protein,[94] myoglobin,[95–99] ubiquitin,[100] BPTI,[101] and barnase.[102,103] The studies on myohemerythrin and plastocyanin each involved a series of overlapping peptides spanning the entire sequence of the protein. It was found that the peptides derived both from the helical segments of myohemerythrin and the interhelix loops have a marked preference toward secondary structure formation in solution, including turn, helix, and nascent helix conformational preferences. By contrast, the peptides from plastocyanin showed very little evidence for structured forms in solution, except for one turn conformation and a hydrophobic cluster (see below). The results suggest that these two protein structural motifs may require different propensities for formation of local elements of secondary structure to initiate folding, and that there is a prepartitioning of conformational space, dictated by the protein sequence, that is different for the helical and β-sandwich motifs. These results are in agreement with the general trends shown by the folding of proteins of different classes in quench-flow hydrogen exchange experiments (see Section 2.2).

A number of fragments of the myoglobin sequence in the region of the G- and H-helices (see Figure 3) were studied[97–99] in an attempt to determine which parts of the early intermediate formed in the folding pathway of apomyoglobin (see Section 2.2) were formed first and could therefore be termed the folding initiation sites. The peptides derived from the G- and H-helix portions of the protein exhibited different propensities to fold into helix in solution: the H-helix peptide showed significant helix formation in water solution both by NMR and CD spectroscopy, while the G-helix was not helical in water solution but became strongly helical in TFE solution.[97] The peptide derived from the sequence between the helices contained a significant population of β-turn, which persisted in fragments of varying lengths[98] and under a variety of solution conditions. This sequence provides a good candidate for the folding initiation site in the G–H region of apomyoglobin. A 51-residue peptide was synthesized to mimic the G–H helical hairpin in apomyoglobin[99] and to test whether the helical hairpin portion of the A–G–H intermediate could exist in isolation. The peptide was designed to be monomeric, as it was known that the H-helix peptide, for example, would aggregate to produce four-helix bundle-like structures.[97] The 51-residue peptide showed almost identical behavior to that of the isolated component peptides: no additional helix was formed, for example, that could have been interpreted as evidence for the formation of the helical hairpin structure. These studies therefore indicated that the formation of the A–G–H molten globule intermediate in the folding of apomyoglobin probably does not involve prior formation of an isolated G–H helical hairpin structure, but rather that the developing structure in the intermediate, initiated by the formation of the G–H turn and the helical structure in the H-helix, is stabilized by tertiary interactions involving the A-helix.

A comparison was made of the secondary structure preferences of two fragments corresponding to different lengths of the N-terminal sequence of ubiquitin and the A-state of ubiquitin in methanol.[100] Although the peptides were unstructured in water solution, the NMR spectra of the three systems showed a number of similarities in methanol solution. The chemical shifts were similar between the shortest peptide, corresponding to residues 1–21 of the protein (the site of a β-hairpin in the native and A-states of the protein), and the analogous regions of the 35-residue peptide (containing the sequence of the β-hairpin and a helix) and the A-state. These results suggest that there are stronger intrinsic structural preferences in the N-terminal half of ubiquitin, which is apparently folded to a greater extent in the A-state than the C-terminal part of the molecule.

Peptide fragments of barnase have been studied by NMR.[102,103] In an NMR study of a single barnase fragment,[102] the authors conclude by extrapolation from TFE data not shown in the paper that the peptide is helical in water, although

none of the usual determinants of either helix or nascent helix were present in the water spectra shown in the paper. Structures were calculated for several barnase fragments[103] on the basis of the observation of $d_{NN}(i, i + 1)$ NOEs alone. No attempt was made in this work to quantitate the population of the folded form, so the significance of the calculated structures is highly questionable. This work, and several similar papers that have now been published, illustrate the difficulty and questionable validity of structure calculations for short, linear peptides in the absence of a thorough understanding of the nature of the peptide conformational ensemble.

5.5 Effect on the Peptide Conformational Ensemble of Receptor/Protein Binding

Peptides interact with larger molecules in many systems, and it appears that a binding interaction with a receptor or protein can cause the conformational ensemble of the peptide to be restricted to the point where it can be said to have a single conformation, at least along part of its length. Binding to the receptor has traditionally been thought to mediate the induced-fit conformation of peptide hormones, which are generally unstructured in solution unless conformationally restricted, and the transferred NOE observed in certain systems where the dissociation rate of the peptide is favorable has been used to infer the bound structure. In systems where the dissociation rate is too slow for the transferred NOE to be observed, a number of NMR experiments have been used to determine the conformation of the bound peptide ligand. For example, NMR methods have been used to investigate the conformation of a peptide, part of the myohemerythrin C-helix (see Section 5.4) bound to an antibody fragment. The peptide, labeled site-specifically with ^{15}N and ^{13}C, was bound to the Fab fragment ($M_r \sim 56\ 000$) of an antibody, which had been raised to the C-helix peptide and which also recognized the native folded myohemerythrin protein. The conformation of the bound peptide was investigated by inverse-detected NMR methods.[104] The peptide conformation appears to be helical when bound to the antibody, although it forms only a nascent helix when free in solution. It is encouraging that NMR experiments can be used to gain important information on biological systems as large as Fab–peptide complexes. In another approach, exemplified by the structure determination of a calmodulin–target-peptide complex,[105] isotope-edited multidimensional NMR methods have been applied to a system consisting of ^{13}C,^{15}N-labeled protein and unlabeled peptide. High-resolution structures were obtained for both the protein and the bound peptide, which was found to fold into a helix upon binding to calmodulin.

6 FUTURE PROSPECTS

Major advances in understanding the molecular mechanisms by which proteins fold into their correct tertiary structures have come from applications of NMR technology to the protein folding problem. With its ability to identify the structures populated in the conformational ensemble of peptide fragments of proteins in aqueous solution under conditions that favor folding, NMR has provided new insights into the probable events occurring at the earliest stages of the initiation of protein folding. Applications to further proteins and to more complex peptide models of early folding species are to be expected. Relatively new multidimensional NMR experiments now allow complete resonance assignments to be made for unfolded proteins under a variety of denaturing conditions. Such experiments hold exceptional promise for identification of residual structure in denatured proteins and will allow detailed structural characterization of the initial states in the folding process. Application of quenched-flow hydrogen exchange pulse labeling to further protein classes is likely to contribute significantly to our understanding of millisecond timescale folding events, and may ultimately result in a generalized model of the slower steps in the protein folding pathway. Finally, heteronuclear multidimensional NMR studies of stabilized molten globule intermediates are now possible for some proteins and promise to provide important new insights into the three-dimensional structure and dynamics of these states. There can be little doubt that NMR will continue to play a fundamental role in unravelling the protein folding puzzle.

7 RELATED ARTICLES

Amino Acids, Peptides and Proteins: Chemical Shifts; Hydrogen Exchange and Macromolecular Dynamics; Peptide and Protein Secondary Structural Elements; Peptides and Polypeptides; Protein Hydration.

8 REFERENCES

1. H. Roder, *Methods Enzymol.*, 1989, **176**, 446.
2. K. Wüthrich, *Curr. Opin. Struct. Biol.*, 1994, **4**, 93.
3. R. L. Baldwin, *Curr. Opin. Struct. Biol.*, 1993, **3**, 84.
4. H. J. Dyson and P. E. Wright, *Curr. Opin. Struct. Biol.*, 1993, **3**, 60.
5. A. N. Lane and O. Jardetzky, *Eur. J. Biochem.*, 1987, **164**, 389.
6. K. Wüthrich, H. Roder, and G. Wagner, in *Protein Folding*, ed. R. Jaenicke, Elsevier/North-Holland Biomedical Press, Amsterdam, 1980, p. 549.
7. M. J. Bogusky, C. M. Dobson, and R. A. G. Smith, *Biochemistry*, 1989, **28**, 6728.
8. C. M. Dobson and P. A. Evans, *Biochemistry*, 1984, **23**, 4267.
9. R. O. Fox, P. A. Evans, and C. M. Dobson, *Nature (London)*, 1986, **320**, 192.
10. P. A. Evans, R. A. Kautz, R. O. Fox, and C. M. Dobson, *Biochemistry*, 1989, **28**, 362.
11. D. P. Raleigh, P. A. Evans, M. Pitkeathly, and C. M. Dobson, *J. Mol. Biol.*, 1992, **228**, 338.
12. D. Hübner, T. Drakenberg, S. Forsén, and G. Fischer, *FEBS Lett.*, 1991, **284**, 79.
13. S. W. Englander and L. Mayne, *Annu. Rev. Biophys. Biomol. Struct.*, 1992, **21**, 243.
14. H. Roder and K. Wüthrich, *Proteins*, 1986, **1**, 34.
15. F. X. Schmid and R. L. Baldwin, *J. Mol. Biol.*, 1979, **135**, 199.
16. P. S. Kim and R. L. Baldwin, *Biochemistry*, 1980, **19**, 6124.
17. J. B. Udgaonkar and R. L. Baldwin, *Nature (London)*, 1988, **335**, 694.
18. H. Roder, G. A. Elöve, and S. W. Englander, *Nature (London)*, 1988, **335**, 700.

19. J. B. Udgaonkar and R. L. Baldwin, *Proc. Natl. Acad. Sci. USA*, 1990, **87**, 8197.
20. P. A. Jennings and P. E. Wright, *Science*, 1993, **262**, 892.
21. R. S. Molday, S. W. Englander, and R. G. Kallen, *Biochemistry*, 1972, **11**, 150.
22. L. C. Wu, P. B. Laub, G. A. Elöve, J. Carey, and H. Roder, *Biochemistry*, 1993, **32**, 10271.
23. A. Miranker, S. E. Radford, M. Karplus, and C. M. Dobson, *Nature (London)*, 1991, **349**, 633.
24. S. E. Radford, C. M. Dobson, and P. A. Evans, *Nature (London)*, 1992, **358**, 302.
25. L. S. Mullins, C. N. Pace, and F. M. Raushel, *Biochemistry*, 1993, **32**, 6152.
26. D. N. Brems, *Biochemistry*, 1988, **27**, 4541.
27. M. S. Briggs and H. Roder, *Proc. Natl. Acad. Sci. USA*, 1992, **89**, 2017.
28. M. Bycroft, A. Matouschek, J. T. Kellis, Jr., L. Serrano, and A. R. Fersht, *Nature (London)*, 1990, **346**, 488.
29. P. Varley, A. M. Gronenborn, H. Christensen, P. T. Wingfield, R. H. Pain, and G. M. Clore, *Science*, 1993, **260**, 1110.
30. S. Koide, H. J. Dyson, and P. E. Wright, *Biochemistry*, 1993, **32**, 12299.
31. Y. V. Griko, P. L. Privalov, S. Y. Venyaminov, and V. P. Kutyshenko, *J. Mol. Biol.*, 1988, **202**, 127.
32. F. M. Hughson, P. E. Wright, and R. L. Baldwin, *Science*, 1990, **249**, 1544.
33. M. J. Cocco, Y. H. Kao, A. T. Phillips, and J. T. J. Lecomte, *Biochemistry*, 1992, **31**, 6481.
34. M. J. Cocco and J. T. J. Lecomte, *Biochemistry*, 1990, **29**, 11067.
35. D. Loftus, G. O. Gbenle, P. S. Kim, and R. L. Baldwin, *Biochemistry*, 1986, **25**, 1428.
36. R. L. Baldwin and H. Roder, *Curr. Biol.*, 1991, **1**, 218.
37. M.-F. Jeng and S. W. Englander, *J. Mol. Biol.*, 1991, **221**, 1045.
38. M.-F. Jeng, S. W. Englander, G. A. Elöve, A. J. Wand, and H. Roder, *Biochemistry*, 1990, **29**, 10433.
39. J. Baum, C. M. Dobson, P. A. Evans, and C. Hanley, *Biochemistry*, 1989, **28**, 7.
40. C.-L. Chyan, C. Wormald, C. M. Dobson, P. A. Evans, and J. Baum, *Biochemistry*, 1993, **32**, 5681.
41. P. Fan, C. Bracken, and J. Baum, *Biochemistry*, 1993, **32**, 1573.
42. M. Buck, S. E. Radford, and C. M. Dobson, *Biochemistry*, 1993, **32**, 669.
43. A. D. Robertson and R. L. Baldwin, *Biochemistry*, 1991, **30**, 9907.
44. K. Akasaka, A. Naito, and M. Imanari, *J. Am. Chem. Soc.*, 1991, **113**, 4688.
45. P. A. Evans, K. D. Topping, D. N. Woolfson, and C. M. Dobson, *Proteins*, 1991, **9**, 248.
46. R. W. Broadhurst, C. M. Dobson, P. J. Hore, S. E. Radford, and M. L. Rees, *Biochemistry*, 1991, **30**, 405.
47. D. Neri, G. Wider, and K. Wüthrich, *FEBS Lett.*, 1992, **303**, 129.
48. D. Neri, G. Wider, and K. Wüthrich, *Proc. Natl. Acad. Sci. USA*, 1992, **89**, 4397.
49. D. Neri, M. Billeter, G. Wider, and K. Wüthrich, *Science*, 1992, **257**, 1559.
50. T. M. Logan, Y. Thériault, and S. W. Fesik, *J. Mol. Biol.*, 1994, **236**, 637.
51. A. T. Alexandrescu, C. Abeygunawardana, and D. Shortle, *Biochemistry*, 1994, **33**, 1063.
52. M. Adler and H. A. Scheraga, *Biochemistry*, 1988, **27**, 2471.
53. M. M. Harding, D. H. Williams, and D. N. Woolfson, *Biochemistry*, 1991, **30**, 3120.
54. Y. Pan and M. S. Briggs, *Biochemistry*, 1992, **31**, 11405.
55. B. J. Stockman, A. Euvrard, and T. A. Scahill, *J. Biomol. NMR*, 1993, **3**, 285.
56. A. T. Alexandrescu, P. A. Evans, M. Pitkeathly, J. Baum, and C. M. Dobson, *Biochemistry*, 1993, **32**, 1707.
57. V. I. Lim, in *Protein Folding*, ed. R. Jaenicke, Elsevier/North-Holland Biomedical Press, Amsterdam, 1980, p. 149.
58. H. J. Dyson, M. Rance, R. A. Houghten, P. E. Wright, and R. A. Lerner, *J. Mol. Biol.*, 1988, **201**, 201.
59. C. P. M. van Mierlo, N. J. Darby, J. Keeler, D. Neuhaus, and T. E. Creighton, *J. Mol. Biol.*, 1993, **229**, 1125.
60. C. P. M. van Mierlo, N. J. Darby, D. Neuhaus, and T. E. Creighton, *J. Mol. Biol.*, 1991, **222**, 353.
61. C. P. M. van Mierlo, N. J. Darby, D. Neuhaus, and T. E. Creighton, *J. Mol. Biol.*, 1991, **222**, 373.
62. J. P. Staley and P. S. Kim, *Proc. Natl. Acad. Sci. USA*, 1992, **89**, 1519.
63. T. G. Oas and P. S. Kim, *Nature (London)*, 1988, **336**, 42.
64. J. Eder, M. Rheinnecker, and A. R. Fersht, *Biochemistry*, 1993, **32**, 18.
65. P. E. Wright, H. J. Dyson, and R. A. Lerner, *Biochemistry*, 1988, **27**, 7167.
66. J. M. Beals, E. Haas, S. Krausz, and H. A. Scheraga, *Biochemistry*, 1991, **30**, 7680.
67. J. E. Brown and W. A. Klee, *Biochemistry*, 1971, **10**, 470.
68. P. S. Kim and R. L. Baldwin, *Nature (London)*, 1984, **307**, 329.
69. G. T. Montelione, E. Arnold, Y. C. Meinwald, E. R. Stimson, J. B. Denton, S.-G. Huang, J. Clardy, and H. A. Scheraga, *J. Am. Chem. Soc.*, 1984, **106**, 7946.
70. H. J. Dyson, K. J. Cross, R. A. Houghten, I. A. Wilson, P. E. Wright, and R. A. Lerner, *Nature (London)*, 1985, **318**, 480.
71. H. J. Dyson and P. E. Wright, *Annu. Rev. Biophys. Biophys. Chem.*, 1991, **20**, 519.
72. P. Y. Chou and G. D. Fasman, *J. Mol. Biol.*, 1977, **115**, 135.
73. H. J. Dyson, M. Rance, R. A. Houghten, R. A. Lerner, and P. E. Wright, *J. Mol. Biol.*, 1988, **201**, 161.
74. H. J. Dyson, L. Bolinger, V. A. Feher, J. J. Osterhout, Jr., and P. E. Wright, unpublished observations.
75. J. Yao, V. A. Feher, B. F. Espejo, M. T. Reymond, P. E. Wright, and H. J. Dyson, *J. Mol. Biol.*, 1994, **243**, 736.
76. J. Yao, H. J. Dyson, and P. E. Wright, *J. Mol. Biol.*, 1994, **116**, 754.
77. J. Yao, R. Brüschweiler, H. J. Dyson, and P. E. Wright, *J. Am. Chem. Soc.*, 1994, **116**, 12 051.
78. A. Bansal and L. M. Gierasch, *Cell*, 1991, **67**, 1195.
79. M. H. Yu and J. King, *J. Biol. Chem.*, 1988, **263**, 1424.
80. A. N. Stroup and L. M. Gierasch, *Biochemistry*, 1990, **29**, 9765.
81. K. Wüthrich, M. Billeter, and W. Braun, *J. Mol. Biol.*, 1984, **180**, 715.
82. J. J. Osterhout, Jr., R. L. Baldwin, E. J. York, J. M. Stewart, H. J. Dyson, and P. E. Wright, *Biochemistry*, 1989, **28**, 7059.
83. G. Merutka, D. Morikis, R. Brüschweiler, and P. E. Wright, *Biochemistry*, 1993, **32**, 13089.
84. M. C. Manning, M. Illangasekare, and R. W. Woody, *Biophys. Chem.*, 1988, **31**, 77.
85. C. L. Brooks III and D. A. Case, *Chem. Rev.*, 1993, **93**, 2487.

86. R. A. Lerner, *Nature (London)*, 1982, **299**, 592.
87. H. J. Dyson, R. A. Lerner, and P. E. Wright, *Annu. Rev. Biophys. Biophys. Chem.*, 1988, **17**, 305.
88. M. P. Williamson, M. J. Hall, and B. K. Handa, *Eur. J. Biochem.*, 1986, **158**, 527.
89. H. J. Dyson, A. C. Satterthwait, R. A. Lerner, and P. E. Wright, *Biochemistry*, 1990, **29**, 7828.
90. M. B. A. Oldstone, A. Tishon, H. Lewicki, H. J. Dyson, V. A. Feher, N. Assa-Munt, and P. E. Wright, *J. Virol.*, 1991, **65**, 1727.
91. K. Chandrasekhar, A. T. Profy, and H. J. Dyson, *Biochemistry*, 1991, **30**, 9187.
92. H. J. Dyson, E. Norrby, K. Hoey, D. E. Parks, R. A. Lerner, and P. E. Wright, *Biochemistry*, 1992, **31**, 1458.
93. H. J. Dyson, G. Merutka, J. P. Waltho, R. A. Lerner, and P. E. Wright, *J. Mol. Biol.*, 1992, **226**, 795.
94. H. J. Dyson, J. R. Sayre, G. Merutka, H.-C. Shin, R. A. Lerner, and P. E. Wright, *J. Mol. Biol.*, 1992, **226**, 819.
95. J. P. Waltho, V. A. Feher, and P. E. Wright, in *Current Research in Protein Chemistry*, ed. J. J. Villafranca, Academic Press, New York, 1990, p. 283.
96. J. P. Waltho, V. A. Feher, R. A. Lerner, and P. E. Wright, *FEBS Lett.*, 1989, **250**, 400.
97. J. P. Waltho, V. A. Feher, G. Merutka, H. J. Dyson, and P. E. Wright, *Biochemistry*, 1993, **32**, 6337.
98. H.-C. Shin, G. Merutka, J. P. Waltho, P. E. Wright, and H. J. Dyson, *Biochemistry*, 1993, **32**, 6348.
99. H.-C. Shin, G. Merutka, J. P. Waltho, L. L. Tennant, H. J. Dyson, and P. E. Wright, *Biochemistry*, 1993, **32**, 6356.
100. J. P. L. Cox, P. A. Evans, L. C. Packman, D. H. Williams, and D. N. Woolfson, *J. Mol. Biol.*, 1993, **234**, 483.
101. J. Kemmink and T. E. Creighton, *J. Mol. Biol.*, 1993, **234**, 861.
102. J. Sancho, J. L. Neira, and A. R. Fersht, *J. Mol. Biol.*, 1992, **224**, 749.
103. T. Ikura, N. Go, D. Kohda, F. Inagaki, H. Yanagawa, M. Kawabata, S. Kawabata, S. Iwanaga, T. Noguti, and M. Go, *Proteins*, 1993, **16**, 341.
104. P. Tsang, M. Rance, T. M. Fieser, J. M. Ostresh, R. A. Houghten, R. A. Lerner, and P. E. Wright, *Biochemistry*, 1992, **31**, 3862.
105. M. Ikura, G. M. Clore, A. M. Gronenborn, G. Zhu, C. B. Klee, and A. Bax, *Science*, 1992, **256**, 632.
106. J. Kuriyan, S. Wilz, M. Karplus, and G. A. Petsko, *J. Mol. Biol.*, 1986, **192**, 133.

Acknowledgments

We thank Dr Patricia Jennings for helpful discussions and for allowing us to use her version of Figure 1. This work was supported by grants GM-38794 (HJD, PEW) and DK 34909 (PEW) from the National Institutes of Health.

Biographical Sketches

H. Jane Dyson. *b* 1951. B.Sc. 1973; Ph.D., 1977, Sydney. Postdoctoral work, MIT, 1977–78; Chemistry Faculty, University of New South Wales, 1979–1984. NMR work at Scripps Clinic in 1984 in collaboration with Peter Wright. Faculty at Scripps 1984–present. Approx. 60 publications. Research interests: conformation of short peptides, protein folding and structure–function studies of proteins including thioredoxin.

Peter E. Wright. *b* 1947. B.Sc., 1968; M.Sc., 1969; Ph.D., 1972, Auckland. Postdoctoral work, Oxford, 1972–1976 with R. J. P. Williams in protein NMR; Inorganic Chemistry Faculty, University of Sydney, 1976–1984. Faculty at Scripps 1984–present. Currently Chairman, Department of Molecular Biology, Cecil and Ida Green Chair in Biomedical Research. Approx. 200 publications. Research interests: applications of NMR to peptide conformation, protein folding, solution structure and dynamics of proteins, and DNA–protein interactions.

Ribosomal RNA

Peter B. Moore

Yale University, New Haven, CT, USA

1	Introduction	1
2	What Can rRNA Spectroscopy Contribute?	1
3	5S rRNA	1
4	Colicin Fragment	2
5	Synthetic Fragments from the Large rRNAs	2
6	Other rRNA Studies	4
7	Related Articles	4
8	References	4

1 INTRODUCTION

The enzymes responsible for the messenger RNA-directed synthesis of proteins are the ribonucleoprotein particles called ribosomes. They range in molecular weight from around 2.5×10^6 to 4.5×10^6, depending on species. Their interspecific variations notwithstanding, all ribosomes have similar structures and work the same way.[1]

There are single copies of each of three RNA molecules in bacterial ribosomes: 23S rRNA ($M_r \sim 10^6$), 16S rRNA ($M_r \sim 0.5 \times 10^6$), and 5S rRNA ($M_r \sim 40\,000$). Mammalian cytoplasmic ribosomes contain four RNAs: 28S rRNA ($M_r \sim 1.6 \times 10^6$), 18S rRNA ($M_r \sim 0.6 \times 10^6$), 5.8S rRNA ($M_r \sim 52\,000$), and 5S rRNA ($M_r \sim 40\,000$). These RNAs are involved in every aspect of ribosome function; interest has never been higher. Nevertheless, remarkably little is known about rRNA conformation at atomic resolution.

2 WHAT CAN rRNA SPECTROSCOPY CONTRIBUTE?

Ribosomal RNAs (rRNAs) are too big to be characterized fully by NMR; even the smallest rRNA, 5S rRNA, is far larger than the largest biological macromolecule whose conformation has been determined so far. Nevertheless, rRNA spectroscopy is not a fool's errand.

Ribosomal RNAs, like all other single-stranded RNAs, satisfy the hydrogen-bonding propensities of their bases by forming hairpin-like structures called stem/loops, many of which have molecular weights below 10 000, and include sequences whose hydrogen-bonding patterns are difficult to diagnose by other means. In addition, many retain their native conformations in isolation, and some bind ribosomal proteins or have other interesting properties. Small RNAs like these are appropriate for spectroscopic investigation.

The parts of large RNAs that fold up into stem/loops or other, more complicated motifs can be identified by comparing the sequences of homologues from many species.[2] The analysis is based on the proposition that RNAs which perform identical functions must have identical structures despite sequence difference. Experience shows that the secondary structure models that result are accurate. Thus sequences within large RNAs that might yield to the spectroscopist can be identified in advance.

Some rRNA fragments can be obtained in useful amounts by limited nuclease digestion, but the divide-and-conquer approach to rRNA conformation has come into its own only recently as methods for RNA synthesis have become available.[3,4] Before that, only two rRNAs were studied: 5S rRNA[5] and a 16S rRNA sequence called colicin fragment.

3 5S rRNA

The function of 5S rRNA is unknown, but because of its small size and ready availability it has received a lot of attention over the years.[6]

3.1 Counting Imino Protons

The modern era of nucleic acid spectroscopy began in 1971 with the discovery that the imino protons of hydrogen-bonded guanines (Gs) and uracils (Us) resonate between 10 and 15 ppm.[7,8] The imino protons of exposed Gs and Us exchange too fast to be detected under physiological conditions, and even when they are involved in base pairing, their resonances can only be observed in water, which creates difficulties (see ***Water Signal Suppression in NMR of Biomolecules***). Nevertheless, this discovery suggested that nucleic acid secondary structures might some day be determined spectroscopically, which they can.

The goals of the first imino proton investigations were to determine the total numbers of base pairs in RNAs by integrating their downfield spectra, and to use the generic difference in imino proton chemical shifts of AUs and GCs to separate that total into its AU and GC contributions.

5S rRNA was one of the first RNAs analyzed this way. The first downfield integration results were reported for 5S rRNA in 1972, and there have been numerous reports since.[9–16] A consensus emerged that there are about 35 base pairs in native 5S rRNAs, irrespective of species, but the estimates were never accurate enough to be decisive because 5S imino spectra are poorly resolved, and poorly resolved spectra are hard to integrate.

Resolution of the 5S imino proton spectrum into its AU and GC parts on the basis of chemical shift proved even more problematic, both because of chemical shift range overlap and because 5S rRNAs include non-Watson–Crick base pairs with unusual imino proton chemical shifts. Resolution was achieved only recently using 5S rRNA samples labeled with ^{15}N at UN3 positions. UN3 resonances were distinguished from GN1 resonances by editing, and five GUs, five AUs, and two unclassifiable, U-containing base pairs were identified in *E. coli* 5S rRNA.[17]

3.2 Imino Proton Assignments

About 1978, it was discovered that the NOEs produced by the cross relaxation of imino protons in adjacent base pairs of nucleic acid helices can be detected.[18–22] Furthermore, it was found that the imino proton resonances of AU pairs have NOE signatures that distinguish them from the imino proton

resonances of GC or GU pairs. This meant that imino proton spectra can be assigned sequentially. The first 5S rRNA imino proton assignments appeared shortly thereafter.

The most thoroughly investigated 5S-related RNA in this regard is a fragment obtained from *E. coli* 5S rRNA by limited RNAse A digestion which includes the 3′ half of the molecule.[23] It behaves like a domain of the intact molecule.[14] It binds one of the ribosomal proteins that interacts with 5S rRNA, and the spectral perturbations that result are the same as those observed when the same protein binds to intact 5S rRNA.[24] The high-frequency (downfield) spectrum of this fragment was completely assigned using the native fragment, mutant variants, and ^{15}N-labeled samples.[25–31] A nuclease-resistant fragment from the 5′ half of 5S rRNA (*E. coli*) was also isolated, and its high-frequency spectrum was assigned in part.[32]

The data confirmed the 5S model obtained phylogenetically, but at the same time demonstrated how poorly the molecule's unpaired loops are understood.[33] In addition, they did not support the class of 5S models that calls for tertiary base-pairing interactions between 5S stem/loops. Recently, imino proton NOEs have been cited as evidence in favor of such a model in the case of a plant 5S rRNA,[34] but since no resonances were assigned no conclusion can be drawn.

Instead of concentrating on a single 5S rRNA, Marshall's group studied the imino proton spectra of 5S rRNAs and 5S rRNA fragments from several different species. The existence of the terminal helix of *Bacillus subtilis* 5S rRNA[35] and of yeast 5S rRNA was confirmed,[36] and many of the imino proton resonances in the 5′ arm of wheat germ 5S rRNA were assigned.[37,38] Studies of fragments of *T. utilis* 5S rRNA resulted in assignments for its 3′ half,[39] and assignments are also available for imino protons in the 5′ half of 5S rRNA of *B. megaterium*.[40,41]

3.3 Other Observations

Unlike tRNAs, 5S rRNAs include no imino protons that exchange so slowly that solvent exchange can be followed in real time by NMR.[42,43] The exchange rates of 5S imino protons are reduced significantly when ribosomal proteins bind, however.[43] This does not mean that 5S rRNA is 'floppy', however. 5S correlation times have been measured using 5-fluorouracil-labeled samples. Most Us in 5S rRNA have correlation times greater than 10 ns, which is roughly the rotational correlation time 5S rRNA would have if it were a rigid sphere.[44,45]

It is also true that 5S rRNA is not as contorted as tRNA. As judged by ^{31}P chemical shift, the number of phosphate groups in unusual conformations is much smaller in 5S rRNA than it is in tRNA.[13,46,47]

3.4 Backbone Assignments and Structural Models

The sequential assignment methodology based on multidimensional NMR, which revolutionized protein spectroscopy in the early 1980s (see ***Biological Macromolecules: Structure Determination in Solution***), did not begin having an impact on rRNA spectroscopy until the end of the decade. Marshall's group did one of the first sequential assignment studies in connection with their analysis of conformational ambiguity in a wheat germ 5S fragment that runs from C26 to G51.[40,48,49] A structural model was not produced, however.

A three-dimensional model did result, however, from the study of a 22-residue fragment from *E. coli* 5S rRNA that includes the molecule's terminal helix, helix I.[50] Helix I is an A-type RNA helix, as expected, but there is a considerable conformational variation from one base pair to the next which seems to be due to purine–purine base stacking; the biggest excursion occurs at the GU at the top of the helix. 'Distortions' of this kind account for the tendency of GU imino protons to give NOEs to the imino protons of base pairs on the 3′ side of the G, but not to those on the 5′ side.

About the same time, Tinoco's group examined two synthetic oligonucleotides whose sequences were based on that of loop E from *Xenopus laevis* 5S rRNA (U72–C78, G97–A102). Following a study of a mutant sequence, whose conformation turned out to be grossly abnormal,[51,52] the wild type sequence was examined.[53] There is no reason to talk about the model that emerged here because the loop E motif—quite remarkably—also appears in the sarcin/ricin loop, which is discussed below.

4 COLICIN FRAGMENT

Colicin E3 is a bactericidal protein that inactivates ribosomes by cleaving 16S rRNA 49 bases in from its 3′ end. The fragment released—colicin fragment—includes a nine base pair stem which is capped with a GGAA loop. The first G in the loop is methylated at the N2 position, and both As are dimethylated at N6. Ribosomes in which the As are unmethylated are resistant to kasugamycin, an antibiotic that inhibits initiation.[54]

The existence of the nine base pair stem in colicin fragment has been proven spectroscopically and its imino proton spectrum assigned.[55] Removal of the methyl groups from As in the loop perturbs the base pairs at the top of the stem somewhat.[56] The effect of methylation has also been examined in *B. stearothermophilus*. Three forms of its colicin fragment were studied: the normal (methylated) form, the kasugamycin-resistant (only the G methylated) form, and a synthetic form, which is totally unmethylated. Methylation has only a small effect on the high-frequency spectra of these molecules, but it does affect stem/loop stability; the fewer the number of methyl groups on the loop, the more stable the stem.[56]

Colicin fragment samples have been prepared carrying ^{13}C-labeled methyl groups.[57] Carbon-13 data show that the methylated exocyclic nitrogen of free *N*-6-dimethyladenosine rotates so rapidly that its methyl groups are magnetically equivalent, but when it is part of the colicin loop the rotation is hindered enough to make its methyl groups distinguishable.

The imino proton and nonexchangeable proton spectra of complexes between colicin fragment and initiation factor IF-3 have also been examined.[58] There are clear indications that a specific complex forms, but it has not been characterized further.

5 SYNTHETIC FRAGMENTS FROM THE LARGE rRNAs

Structures have been obtained recently for synthetic rRNA fragments containing two types of tetraloops (four base loops)

and the sarcin/ricin loop. The tetraloops characterized—the UNCG type and the GNRA type—are the ones most common in rRNAs.[59] ['N' means any base and 'R' means purine.] Helical stems terminated by UNCG tetraloops are unusually stable.[60] All 23S-like rRNAs include a sarcin/ricin loop which plays a critical role in the elongation phase of protein synthesis.

5.1 rRNA Tetraloops

In the late 1980s, Tinoco's group determined the conformation of a synthetic stem/loop that is terminated with a UUCG tetraloop.[61,62] The oligonucleotide's proton spectrum was almost completely assigned, and a conformational model resulted from the analysis of its NOEs and coupling constants. The key to the structure is a reverse-wobble base pair (UO2−GN3, UN3−GO2) between the 5′ U of the loop and its 3′ G. The distance between the phosphates of the two strands is so reduced by that pairing that it can be spanned by two C2′-*endo* residues. Additional stabilization is provided by a hydrogen bond involving the amino group of the tetraloop C with an oxygen of the phosphate group between the two Us, and by base stacking.

The elegant economy of means evident in UNCG tetraloops is also manifest in GNRA tetraloops. Two such tetraloops have been examined: GCAA and GAAA.[63] They are essentially the same. The reverse-wobble GUs in UNCG tetraloops are replaced by (AN6−GN3, AN7−GN2) GA pairs. Like reverse-wobble GUs, these AG pairs close the stem to the point that the remaining gap can be spanned by two C2′-*endo* residues. Additional stability is provided by a hydrogen bond between the amino group of the G and an oxygen that is part of the phosphate joining the (last) two As. All of the bases in the GAAA tetraloop stack neatly on their neighbors. The C residue in the GCAA version of the loop appears not to stack. The loop at the top of the structure shown in Figure 1 is a GNRA tetraloop.

The destabilizing effect of methylation on the colicin fragment stem/loop mentioned earlier is easy to rationalize. The colicin loop, GGAA, is a GNRA tetraloop. Dimethylation of N6 of the final A should prevent the formation of that loop's

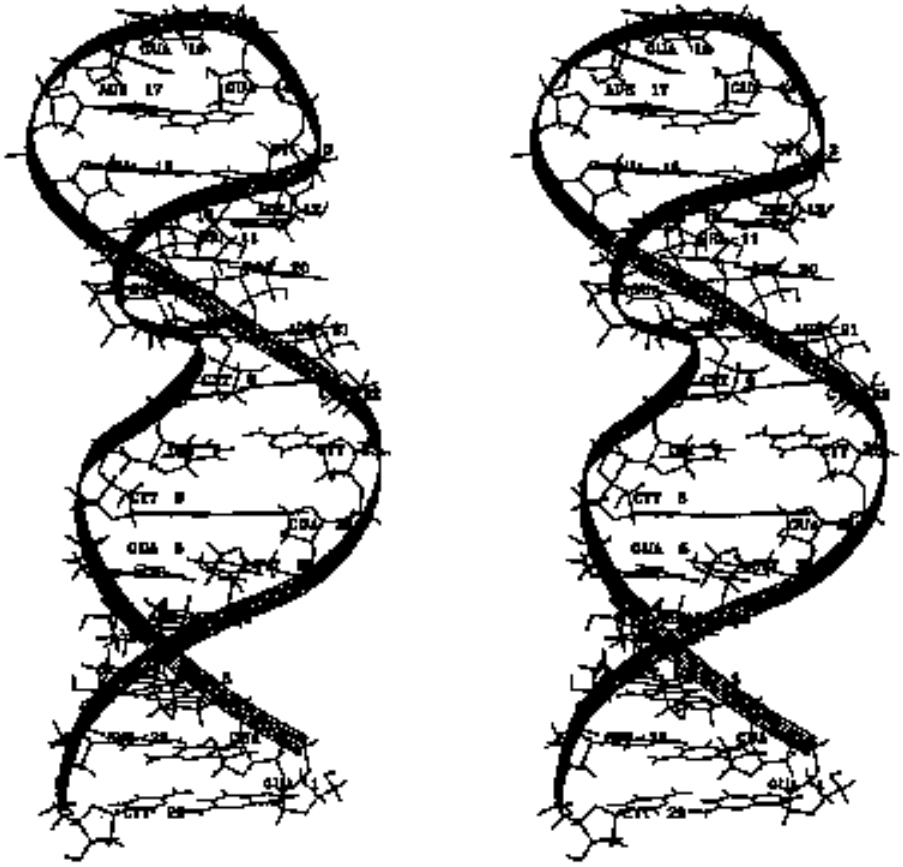

Figure 1 A stereo drawing of the sarcin/ricin loop. The mammalian form of the sarcin/ricin loop is shown in the conformation determined for it by NMR.[67] (Drawing donated by Dr. A. Szewczak, Yale University)

critical GA, which should destabilize it. Methylation at the N-2 position of the G in the GA pair should also be damaging, but less so since one of the two possible rotamers places the methyl in an innocuous position.

5.2 The Sarcin/Ricin Loop

The sarcin/ricin loop is the most recent addition to the list of fully characterized rRNA fragments. All 23S-like rRNAs have a loop that includes a 12-base sequence that is the longest invariant sequence in rRNAs. It is attacked by two protein toxins, α-sarcin and ricin, which kill eukaryotic cells by cleaving covalent bonds in the invariant sequence. These cleavages inhibit the interaction of ribosomes with elongation factors during protein synthesis, which is lethal for the cells in question.[64]

A 29-nucleotide sequence, that includes the entire sarcin/ricin loop in its mammalian form, has been analyzed. All its ^{31}P and nearly all its ^{1}H resonances were assigned, and a model built based on NOEs and coupling constants (Figure 1).[65] The top of the loop, where it is attacked by toxins, is a GNRA tetraloop motif as already indicated. Immediately below that, the sarcin/ricin loop contains a loop E motif. Thus this structure embodies the rRNA spectroscopist's fondest hope, that it will be possible to produce accurate models for the conformations of large RNAs by assembling them from small pieces whose conformations are already understood.

Working from top to bottom in Figure 1, the loop E motif begins with a conventional GC base pair (C13–G18) below which is a GA pair (A12N7–G19N2, A12N6–G19N3), and then a reversed-Hoogsteen AU (A20N6–U11O2, A20N7–U11N3). This juxtaposition positions G10 so that it can extend across the major groove; it is a bulged base. The backbone distortions that result are resolved by a severe kink on the 5′ side of the loop, which is stabilized by a symmetric AA pair (A9–A21). Two pyrimidine–pyrimidine pairs follow before Watson–Crick pairing resumes. The bulged G and the bases that surround it are in the same conformation as the bases in loop E in eukaryotic 55 RNA.

6 OTHER rRNA STUDIES

The downfield spectrum of 5.8S rRNA has been examined, and some of its resonances assigned.[66] The relaxation properties of ^{31}P resonances in intact ribosomes and ribosomes partially degraded with RNAse A have been measured. There is reason to believe that rRNA phosphate groups are less mobile in intact ribosomes than they are in free RNA.[67]

7 RELATED ARTICLES

Biological Macromolecules: Structure Determination in Solution; Biological Macromolecules; Biological Macromolecules: NMR Parameters; Nucleic Acid Structures in Solution: Sequence Dependence; Nucleic Acids: Base Stacking and Base Pairing Interactions; Nucleic Acids: Chemical Shifts; Nucleic Acids: Phosphorus-31 NMR; Nucleic Acids: Spectra, Structures, and Dynamics; RNA Structure and Function: Modified Nucleosides.

8 REFERENCES

1. W. E. Hill, A. Dahlberg, R. A. Garrett, P. B. Moore, D. Schlessinger, and J. R. Warner (eds.), *The Ribosome. Structure Function, and Evolution*, American Society for Microbiology, Washington, DC, 1990.
2. See R. R. Gutell, H. F. Noller, and C. R. Woese, *EMBO J.*, 1986, **5**, 1111.
3. J. F. Milligan, D. R. Groebe, G. W. Witherell, and O. C. Uhlenbeck, *Nucleic Acids Res.*, 1987, **15**, 8783.
4. See S.-H. Chou, P. Flynn, and B. Reid, *Biochemistry*, 1989, **28**, 2422.
5. See A. G. Marshall and J. Wu, *Biol. Magn. Rescon.*, 1989, **9**, 55.
6. See P. B. Moore, in *Ribosomal RNA: Structure, Evolution, Processing, and Function in Protein Synthesis*, eds. R. A. Zimmermann and A. E. Dahlberg, CRC Press, Boca Raton, FL, in press.
7. D. R. Kearns, D. Patel, and R. G. Shulman, *Nature (London)*, 1971, **229**, 338.
8. D. R. Kearns, D. Patel, R. G. Shulman, and T. Yamane, *J. Mol. Biol.*, 1971, **61**, 265.
9. Y. P. Wong, D. R. Kearns, B. R. Reid, and R. G. Shulman, *J. Mol. Biol.*, 1972, **72**, 741.
10. D. R. Kearns and Y. P. Wong, *J. Mol. Biol.*, 1974, **87**, 755.
11. G. A. Luoma, P. D. Burns, R. E. Bruce, and A. G. Marshall, *Biochemistry*, 1980, **19**, 5456.
12. P. D. Burns, G. A. Luoma, and A. G. Marshall, *Biochem. Biophys. Res. Commun.*, 1980, **96**, 805.
13. P. J. M. Salemink, H. A. Raué, A. Heerschap, R. J. Planta, and C. W. Hilbers, *Biochemistry*, 1981, **20**, 265.
14. M. J. Kime and P. B. Moore, *FEBS Lett.*, 1983, **153**, 199.
15. L. H. Chang and A. G. Marshall, *Biopolymers*, 1986, **25**, 1299.
16. S. J. Li and A. G. Marshall, *Biochemistry*, 1986, **25**, 3673.
17. D. R. Davis, Z. Yamaizumi, S. Nishimura, and C. D. Poulter, *Biochemistry*, 1989, **28**, 4105.
18. P. D. Johnston and A. G. Redfield, *Nucleic Acids Res.*, 1978, **4**, 3599.
19. P. D. Johnston and A. G. Redfield, *Biochemistry*, 1981, **20**, 1147.
20. S. Roy and A. G. Redfield, *Biochemistry*, 1983, **22**, 1386.
21. S. Roy and A. G. Redfield, *Nucleic Acids Res.*, 1981, **9**, 7073.
22. V. Sánchez, A. G. Redfield, P. D. Johnston, and J. Tropp, *Proc. Natl. Acad. Sci. USA*, 1980, **77**, 5659.
23. S. Douthwaite, R. A. Garrett, R. Wagner, and J. Feunteun, *Nucleic Acids Res.*, 1979, **6**, 2453.
24. M. J. Kime and P. B. Moore, *Biochemistry*, 1983, **22**, 2622.
25. M. J. Kime and P. B. Moore, *Biochemistry*, 1983, **22**, 2615.
26. M. J. Kime, D. T. Gewirth, and P. B. Moore, *Biochemistry*, 1984, **23**, 3559.
27. M. J. Kime, *FEBS Lett.*, 1984, **175**, 259.
28. M. J. Kime, *FEBS Lett.*, 1984, **173**, 342.
29. D. T. Gewirth, S. R. Abo, N. B. Leontis, and P. B. Moore, *Biochemistry*, 1987, **26**, 5213.
30. D. T. Gewirth and P. B. Moore, *Biochemistry*, 1987, **26**, 5657.
31. P. Zhang and P. B. Moore, *Biochemistry*, 1989, **28**, 4607.
32. N. B. Leontis and P. B. Moore, *Biochemistry*, 1986, **25**, 3916.
33. See C. Brunel, P. Romby, E. Westhof, C. Ehresmann, and B. Ehresmann, *J. Mol. Biol.*, 1991, **221**, 293.
34. M. Z. Barciszewska, H.-W. Huang, A. G. Marshall, V. A. Erdmann, and J. Barciszewska, *J. Biol. Chem.*, 1992, **267**, 16 692.
35. L. H. Chang and A. G. Marshall, *Biochemistry*, 1986, **25**, 3056.

36. K. M. Lee and A. G. Marshall, *Biochemistry*, 1987, **26**, 5534.
37. S. J. Li and A. G. Marshall, *Biochemistry*, 1986, **25**, 3673.
38. S. J. Li, J. Wu, and A. G. Marshall, *Biochemistry*, 1987, **26**, 1578.
39. S. M. Chen and A. G. Marshall, *Biochemistry*, 1986, **25**, 5117.
40. J. H. Kim and A. G. Marshall, *Biochemistry*, 1990, **29**, 632.
41. J. H. Kim and A. G. Marshall, *Biochem. Biophys. Res. Commun.*, 1990, **169**, 1068.
42. J.-L. LeRoy, D. Broseta, and M. Guéron, *J. Mol. Biol.*, 1985, **184**, 165.
43. N. B. Leontis and P. B. Moore, *Biochemistry*, 1986, **25**, 3916.
44. A. G. Marshall and J. L. Smith, *J. Am Chem. Soc.*, 1977, **99**, 635.
45. A. G. Marshall and J. L. Smith, *Biochemistry*, 1980, **19**, 5955.
46. P. Zhang, P. Popieniek, and P. B. Moore, *Nucleic Acids Res.*, 1989, **17**, 8645.
47. D. G. Gorenstein, *Phosphorus-31 NMR. Principles and Applications*, Academic Press, New York, 1984.
48. J. Wu and A. G. Marshall, *Biochemistry*, 1990, **29**, 1722.
49. J. Wu and A. G. Marshall, *Biochemistry*, 1990, **29**, 1730.
50. S. A. White, M. Nilges, A. Huang, A. T. Brunger, and P. B. Moore, *Biochemistry*, 1992, **31**, 1610.
51. G. Varani, B. Wimberly, and I. Tinoco, Jr., *Biochemistry*, 1989, **28**, 7760.
52. See I. Leal de Stevenson, P. Romby, F. Baudin, C. Brunel, E. Westhof, C. Ehresmann, B. Ehresmann, and P. J. Romaniuk, *J. Mol. Biol.*, 1991, **219**, 243.
53. B. Wimberly, G. Varani, and I. Tinoco, Jr., *Biochemistry*, 1993, **32**, 1078.
54. P. H. van Knippenberg, in *Structure, Function, and Genetics of Ribosomes*, eds. B. Hardesty and G. Kramer, Springer Verlag, New York, 1986, p. 412.
55. H. A. Heus, A. van Kimmenade, P. H. van Knippenberg, C. A. G. Haasnoot, S. H. de Bruin, and C. W. Hilbers, *J. Mol. Biol.*, 1983, **170**, 939.
56. H. A. Heus, L. J. Formenoy, and P. H. van Knippenberg, *Eur. J. Biochem.*, 1990, **188**, 275.
57. R. van Charldorp, J. J. Verhoeven, and P. H. van Knippenberg, *Nucleic Acids Res.*, 1982, **10**, 4237.
58. E. Wickstrom, H. A. Heus, C. A. G. Haasnoot, and P. H. van Knippenberg, *Biochemistry*, 1986, **25**, 2770.
59. C. R. Woese, S. Winker, and R. R. Gutell, *Proc. Natl. Acad. Sci. USA*, 1990, **87**, 8467.
60. C. Tuerk, P. Gauss, C. Thermes, D. R. Groebe, M. Gayle, N. Guild, G. Stormo, Y. d'Aubenton-Carata, O. C. Uhlenbeck, I. Tinoco, Jr., E. N. Brody, and L. Gold, *Proc. Natl. Acad. Sci. USA*, 1988, **85**, 1364.
61. C. Cheong, G. Varani, and I. Tinoco, Jr., *Nature (London)*, 1990, **346**, 680.
62. G. Varani, C. Cheong, and I. Tinoco, Jr., *Biochemistry*, 1991, **30**, 3280.
63. H. A. Heus and A. Pardi, *Science*, 1991, **253**, 191.
64. Y. Endo and I. G. Wool, *J. Biol. Chem.*, 1982, **257**, 9054.
65. A. A. Szewczak, P. B. Moore, Y.-L. Chan, and I. G. Wool, *Proc. Natl. Acad. Sci. USA*, 1993, **90**, 9581.
66. K. M. Lee and A. G. Marshall, *Biochemistry*, 1986, **25**, 8245.
67. P. H. Bolton, G. Clawson, V. J. Basus, and T. L. James, *Biochemistry*, 1982, **21**, 6073.

Biographical Sketch

Peter B. Moore. *b*. 1939. B.S., 1961, biophysics, Yale, Ph.D., 1966, Harvard. Postdoctoral research at Institut de Biologie Moleculaire, University of Geneva (Switzerland), 1966–67, and at MRC Laboratory of Molecular Biology, Cambridge (UK), 1967–69. Introduced to NMR by R. J. P. Williams, University of Oxford (UK) while a Guggenheim Fellow, 1979–80. Approximately 120 publications. Research interests: biophysical chemistry, with emphasis on the analysis of the structures and functions of the RNAs and proteins involved in protein synthesis.

RNA Structure and Function: Modified Nucleosides

Paul F. Agris

North Carolina State University, Raleigh, NC, USA

1	Introduction: History	1
2	Approaches to Modified Nucleoside Heteronuclear Magnetic Resonance and Dynamics	1
3	Monomers to RNA Domains: NMR Solution Conditions, Importance, and Difficulties	3
4	Homonuclear 1D and 2D NMR of Modified Nucleoside-Containing Domains	4
5	The Future of Modified Nucleoside NMR	5
6	Related Articles	6
7	References	6

1 INTRODUCTION: HISTORY

RNA, in general, and transfer RNA (tRNA) in particular, have played important historical roles in the development of NMR techniques for the study of both RNA and DNA structure/function relationships. However, the small numbers of crystal structures of tRNAs, yeast $tRNA^{Phe}$ being the first,[1] and tRNAs with their cognate aminoacyl–tRNA synthetases, remain the largest, completely resolved nucleic acid structures. Each tRNA is composed of some 76 nucleosides connected by phosphodiester bonds and, thus, is of a molecular weight approximating 26 000 Da (Figure 1). In addition, as many as 25% of the nucleosides are enzymatically modified after the molecule has been biosynthesized, a process designated posttranscriptional modification.[2] The tRNA is folded into a 'cloverleaf' secondary structure (Figure 1) held together by some 24 Watson–Crick hydrogen bonds between complementary bases (A·U and G·C). An 'L-shaped' tertiary structure is maintained by some six additional, and noncanonical, H-bonds and includes four internal sites where metal ions (Mg^{2+}) bind tightly (Figure 1). Therefore, the complete determination of a tRNA's three-dimensional structure in solution becomes a formidable task requiring innovative NMR methods.

Soon after publication of the crystallographic structure of yeast $tRNA^{Phe}$ (Figure 1),[1] identification of the 'low field', H_2O-exchangeable, imino proton resonances that arose from the secondary and tertiary structure hydrogen bonding within native tRNAs became an obviously important NMR approach to understanding the solution structure of tRNA and other nucleic acids.[3] The first ^1H NMR spectra of tRNA were published in 1971.[4] In that paper, the highest frequency proton resonances of a tRNA spectrum, 10–15 ppm, were identified as those from the H-bonded imino protons, one from each of the secondary and tertiary structure H bonds. Because the modified nucleosides tend to reside in the loops of the clover leaf structure, some of the most interesting of the H bonds are those in which the minor, or modified bases participate in creating tertiary structure interactions and chemistry, including metal ion binding sites, important to tRNA function. The methods to identify unambiguously the secondary and tertiary imino base paired protons in tRNA required the development of new technologies that were completed a decade later. Now the well-established techniques of two-dimensional homonuclear NOE, NOESY, and the ^{15}N-edited NOESY in H_2O are used regularly for both RNA and DNA analyses.[5] Carbon-bound, proton resonances from the base ring carbons provide additional information about tRNA conformation.[6] Carbon-bound protons of modifications are useful in the unambigous identification of the nucleoside residue of which they are a part. Of particular interest are the assignments of individual signals from the carbon-bound protons of each ribose moiety, which would lead to identification of each nucleoside's spin system, sugar pucker and glycosidic (base to ribose) bond angle when combined with information on the individual bases and their modifications. The rotation around the 3′–4′ and 4′–5′ bonds of each ribose are part of the tRNA's (or for that matter all nucleic acids') backbone, and thus knowledge of sugar pucker (from scalar couplings) leads to the resolution of backbone torsion angles. (See ***Vicinal Coupling Constants and Conformation of Biomolecules***.) This information plus identification of individual ^{31}P resonances and J(H,P) couplings, for the 3′- and 5′-associated phosphates (see ***Nucleic Acids: Phosphorus-31 NMR***), has the potential for characterizing the tRNA backbone. Because of their involvement in unique tertiary structure interactions, the identification of the various modified nucleoside spin systems is particularly important.[2,3] However, the complete signal assignment of a tRNA molecule has yet to be accomplished.

The first heteronuclear experiment, that of natural abundance ^{13}C, was accomplished in 1972.[7] In general, ^{13}C spectra for complex molecules tend to be more resolved than ^1H spectra. These spectra also provide valuable information for the determination of molecular dynamics. However, the major drawback to natural abundance ^{13}C spectroscopy is that some of the most interesting resonances, that of the modified nucleosides, are the weakest. The great advantage of heteronuclear enrichment of specific atoms and nucleosides for signal assignments, and for the analysis of structure and dynamics, was realized early with the 1975 report of a ^{13}C enrichment, in vivo, of all methyl group modifications of *E. coli* tRNAs.[8]

2 APPROACHES TO MODIFIED NUCLEOSIDE HETERONUCLEAR MAGNETIC RESONANCE AND DYNAMICS

Site specific, natural, structure/function NMR probes of tRNA that neither disrupt structure nor function but occur at multiple locations are essential because of tRNA's size and the size of the nucleic acids and proteins with which it interacts.[9] Methyl and methylene ^{13}C-enrichment is applicable to the vast majority of the 80+ known modifications. In addition, ^{13}C-enrichment of modified base ring carbons, such as the 2-positions of adenosine for methyl-2-adenosine (m^2A) and methylthio-2-adenosine (ms^2A), and thio-2-uridine (s^2U), offer additional information by having distinctly different chemical

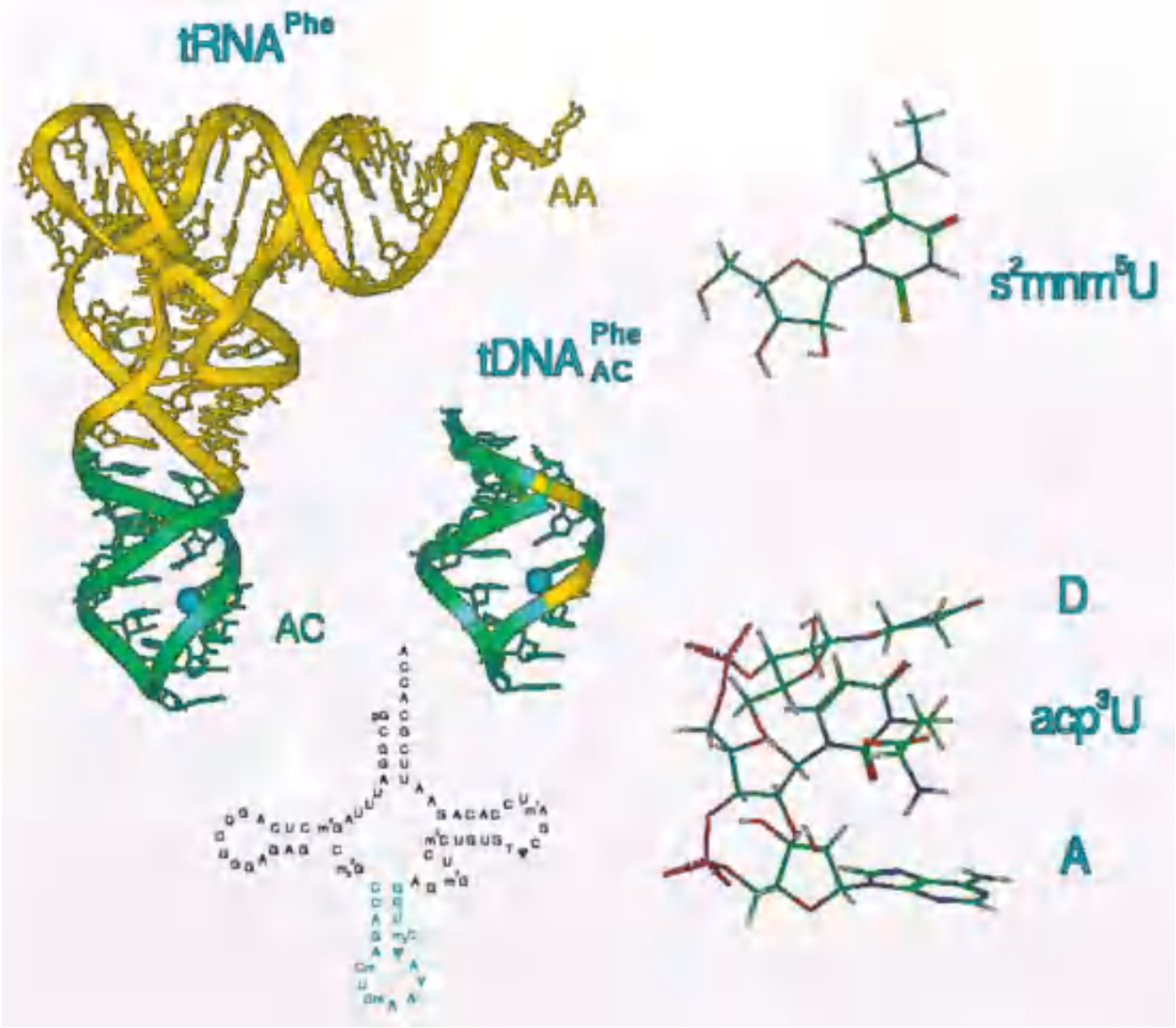

Figure 1 Structures of a modified mononucleoside and modified nucleoside-containing trimer, heptadecamer and yeast $tRNA^{Phe}$. The structure of yeast $tRNA^{Phe}$, derived from X-ray crystallography,[1] is shown with the backbone as a ribbon. The amino acid accepting, 3′-terminus is designated AA; the anticodon stem and loop in green is designated AC. There are four tight metal ion binding sites, but only the one occurring in the anticodon is shown because of its relevance to the studies described here. Below this structure is its nucleoside sequence drawn in the 'cloverleaf' depiction of the secondary structure base pairings. A heptadecamer DNA analog of the $tRNA^{Phe}$ anticodon stem and loop is also drawn with the green ribbon backbone. The mononucleoside is the anticodon wobble position nucleoside s^2mnm^5U; the trimer, Dp–acp^3Up–A, occurs in the D loops of tRNAs for Asn and Val

shifts from that of the unmodified nucleosides, A and U. Peak widths for the $^{13}C_2$s for folded tRNA were determined largely by chemical shift nonequivalence.[10] Measurements of T_2 for the specifically enriched carbons in tRNA suggested that the intrinsic linewidths were between 2–4 Hz for the C-2 of the pyrimidines, whereas adenine with a directly bonded proton exhibited a 40 Hz linewidth. Consideration of dipolar relaxation and chemical shift anisotropy (CSA) led to a calculated rotational correlation time of $1.6 \pm 0.4 \times 10^{-8}$ s for the adenosines.

Carbon-13 enrichment of methyl groups led to the first resolution of single carbon resonances in a nucleic acid and proved that methyl probes were sensitive to changes in local structure, a requisite criterion for ^{13}C NMR of tRNA to be a useful tool.[11,12] For instance, multiple peaks for the ^{13}C-enriched methyl groups of T_{54} (methyl-5-U) in *E. coli* $tRNA^{Phe}$ and $tRNA^{Tyr}$ and ribose 2′-O-methylated G_{17} of $tRNA^{Tyr}$ indicated multiple structural forms that coalesced in the presence of Mg^{2+}, whereas tRNAs specific for Cys and Ser existed in only one major conformation throughout their structures, even in the absence of Mg^{2+}.[13] Proton NMR spectra of the $^{13}CH_3$-enriched tRNAs exhibited the expected resonance splittings with J(C,H) values of 130–145 Hz for all the methyl resonances. Values of spin–lattice relaxation times, NOEs, and linewidths for the $^{13}CH_3$ carbons in the presence of Mg^{2+} were utilized for determining rotational reorientation correlation times. The different tRNAs had

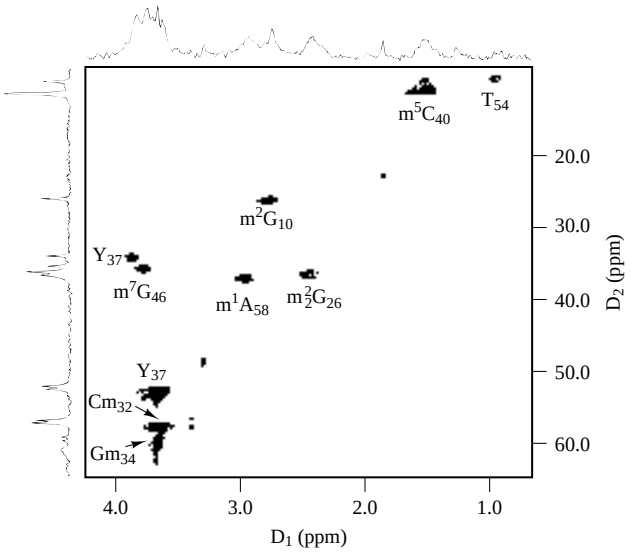

Figure 2 ^{1}H-detected, ^{1}H–^{13}C HMQC of $^{13}CH_3$-enriched native yeast tRNA^{Phe}. Data were acquired on a 500 MHz GE-Omega spectrometer at 25 °C in phase-sensitive mode; 1024 complex points were used in the ^{1}H dimension and 256 blocks were collected. Data were processed using Felix (D. Hare Software) with a line broadening of 2 Hz in the ^{1}H dimension and a Kaiser window function in the ^{13}C dimension. Data were zero filled in the F_1 dimension to 512 complex points

significantly different (by factors of two) apparent overall rotational correlation times (τ_R). Since the molecules are approximately the same in molecular weight, τ_R probably reflects true differences in the motional capabilities of large sections of the different tRNAs. Internal correlation times for the methyl groups on axis (τ_i) varied between 0.4–1.6 ps for the methyl of T, and between 0.8–2.0 ps for the methyl of methylthio-2-isopentenyl-6-adenosine (ms^2i^6A) of four different tRNAs. Enough differences in spectra, relaxation rates, NOEs, and calculated τ_R and τ_i values of the tRNAs were found to conclude that specific differences in structure and dynamics were probed by each of the modified nucleosides.[13]

Yeast tRNA (Figure 1), having many more modified nucleosides than *E. coli* tRNAs and having methyl groups located in various positions throughout the structure, provides a considerable advantage to probing tRNA structure, chemistry, and dynamics with $^{13}CH_3$-enrichment.[14,15] Twelve resolved, prominent and readily assigned $^{13}CH_3$-enriched resonances are seen in the ^{13}C spectrum of purified yeast tRNA^{Phe} (Figure 2). The methyl resonances have a wide chemical shift dispersion between 10 and 60 ppm (Figure 2). Half of the signals are from modified nucleosides of the anticodon domain of the molecule (Figure 1). The assignments of methyl and methylene peaks in tRNA ^{1}H NMR spectra have relied on thermal melting studies where resonances are followed from high temperature (unfolded) to low temperature (folded). This method breaks down when peaks undergo slow chemical exchange dynamics, disappearing from one position and reappearing at another.[16] In addition, the high temperature and extended acquisition times can lead to the degradation of the molecule and to the formation of unnatural, but stable, intermediate tertiary structures. The introduction of $^{13}CH_3$-enrichment permits an alternative method to signal assignments based on scalar coupling of ^{13}C and ^{1}H and resulted in the first application of carbon–proton correlation spectroscopy to a native nucleic acid, yeast, and *E. coli* tRNA^{Phe}.[15] By associating the specifically $^{13}CH_3$-enrichment to the ^{1}Hs, via a heteronuclear ^{1}H-detected multiple quantum coherence (HMQC) experiment, complete assignments can be made readily even in the presence of a H_2O ('jump and return') or residual H_2O signal (with suppression by presaturation) that would normally conceal the ^{1}H signals of some of the modifications (Figure 2).

Comparison of carbon-methyl chemical shifts of the *N*-methylated, $^{13}CH_3$-enriched m^1A_{58} and m^7G_{46} in yeast tRNA^{Phe} with that of the mononucleosides m^1A and m^7G under various conditions provided a means by which the chemical character of these nucleosides could be explored within the native tRNA structure.[15] The methyl group carbon chemical shifts of the two nucleosides in the tRNA were indicative of fully protonated and positively charged chemical species. The modified nucleosides were protonated through tertiary structure H bonding, resulting in two full positive charges within the native tRNA. Interaction of the tRNA with other macromolecules could break these specific H bonds, removing the charges, and thus, prepare tRNA for the next step in translation.

Yeast tRNA^{Phe} $^{13}CH_3$ groups have been used as probes of internal dynamics at specific locations.[17] Values of ^{13}C T_1 and NOE are determined at various magnetic field strengths and used to extract generalized order parameters (S^2) and effective correlation times (τ_e) for the internal motion of the C–H internuclear vectors. For all methyl groups, S^2 compared favorably with the value of 0.111 predicted for a rapidly spinning methyl group rigidly mounted on a spherical macromolecule. However, values of τ_e, 4–16 ps, were generally shorter than that measured for the methyls of amino acids in proteins! Somewhat surprising was the fact that the methyl esters at the end of a long methionine-derived side chain attached to the tricyclic nucleoside wyosine (Y_{37}), a hypermodification of G_{37} 3′-adjacent to the anticodon (Figure 1), had order parameters (S^2), only 25% less than that of a methyl directly bonded to the same base ring structure. The side chain may have stabilizing interactions within the anticodon domain of the tRNA. If motion of the methyl group axis were described as random diffusion within a cone, the values of the order parameter S^2_{ax} corresponded to cone semiangles of 11° to 37°.[17] This model-free approach to the analyses of the $^{13}CH_3$ data indicated that the anticodon domain was the most highly motion-restricted portion of tRNA, a conclusion since confirmed by other NMR techniques and other methods.[17]

In ^{13}C spectra of tRNA^{Phe} taken at 75.5 MHz with proton decoupling gated off during acquisition, unequal linewidths are observed for individual transitions in the CH_3 quartets. The most important mechanism contributing to this differential line broadening is probably interference between the dipolar and CSA relaxation mechanisms.[17] The differential line broadening is not the same for every methyl group. The mathematical formalism of this phenomenon can serve as an additional means by which the motional parameters of tRNA may be calculated and compared with that derived from T_1 and NOE measurements.

3 MONOMERS TO RNA DOMAINS: NMR SOLUTION CONDITIONS, IMPORTANCE, AND DIFFICULTIES

The NMR investigations of modified nucleoside contributions to the chemistry, structure, and dynamics of the complete tRNA molecule, as summarized above, although instructive and informative, reveal limited information because of the large size of the molecule. However, one approach that is worth reiterating is the comparison of modified nucleoside conformation derived from the NMR of an RNA oligomer with data from the individual modified mononucleoside taken under identical solution and temperature conditions, as with the analyses of m^1A and m^7G. The contributions of the modified nucleosides to the RNA can be determined by NMR, along with the effects of the polymerization on the nucleoside conformation and chemistry. Of particular interest are the modified uridines; thio-2-methylaminomethyl-5-uridine (s^2mnm^5U) is depicted in Figure 1. The s^2Us with various 5-position derivatizations occur at the anticodon 'wobble' position 34 in tRNAs for Glu, Gln, and Lys. Proton and carbon NMR analyses of the s^2U derivatives showed that the thio-substituted carbonyl restricts the nucleoside conformation and dynamics of the mononucleoside, no matter the character of the 5-position derivative. The highly restricted conformation is retained in dimers and affects the torsion angles of the 3′-phosphodiester bond investigated through $^1H-^{31}P$ and $^{13}C-^{31}P$ correlation spectroscopy.[18] Because the restrained s^2U conformation restricts these tRNAs to binding codons ending in A, i.e. no 'wobble', a modified wobble hypothesis has been presented.[19]

One of the most common of the modified uridines is the hydrophobic dihydrouridine, D, which occurs in loop I of almost all tRNAs, sometimes adjacent to the hydrophilic 3-[3-(*S*)-amino-3-carboxypropyl]uridine, acp^3U, in the sequence Dp−acp^3Up−A (Figure 1).[20] NMR of this trimer illustrates how the perceived complexity of its proton spectrum can be approached successfully with heteronuclear and homonuclear two-dimensional spectroscopy. Signal assignments of the modified and unmodified nucleoside ribose protons, especially the 5′ and 5″ protons, within RNA oligomers can be difficult because of tRNA size and the size of the nucleic acids and proteins with which it interacts. However, the $^1H-^{13}C$ HMQC of Dp−acp^3Up−A depicted in Figure 3 illustrates the relative ease with which these assignments can be made. With oligomers of the size of Dp−acp^3Up−A, there can be a difference in the time-dependence of the NOE for the trimer in aqueous solvent versus DMSO. The correlation time of Dp−acp^3Up−A in D_2O was such that $\omega\tau_c \approx 1$, so that NOEs tended toward zero. The cross relaxation rate in DMSO was about 20-fold that in D_2O. Therefore, to aid in the determination of NOE cross peaks in D_2O, a ROESY experiment is preferred (Figure 4). The NOE observed from the ^{1}H-6 proton to the ribose ring can be used as a marker to decide whether the predominant conformation is *syn* or *anti*. Thus, when the dipolar correlation from H-6 to H-2′ is stronger than that from H-6−H-1′, the *anti* conformation is indicated. When the relative intensity of the correlations is reversed, the *syn* conformation is indicated. Both cross peaks were observed, indicating the presence of both *syn* and *anti* conformations, but with *anti* dominating. The solution conditions of these studies have to be strictly controlled because many modified nucleosides, such as acp^3U and s^2mnm^5U, bind metal ions. For example, when part of an oligomer or RNA domain acp^3U will bind metal ions, Mg^{2+} in particular, this changes the chemical shifts and scalar couplings, and alters the conformation of the oligomer (unpublished results).

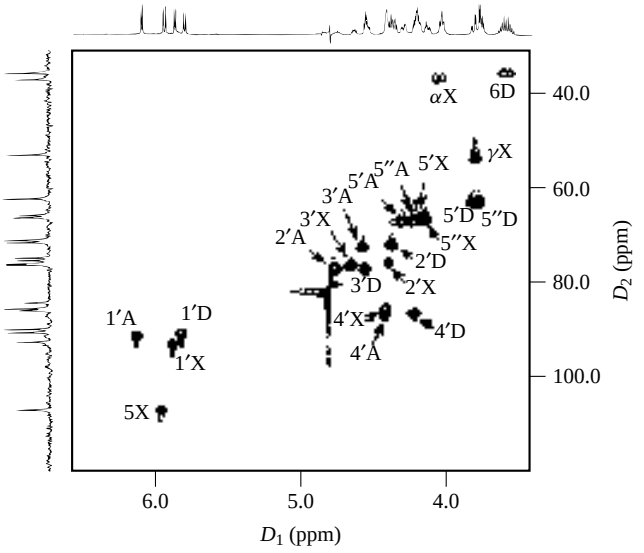

Figure 3 ^{1}H-detected, $^1H-^{13}C$ HMQC of Dp−acp^3Up−A. Data were acquired and processed as explained in the legend to Figure 2

Although modified nucleoside-containing small oligomers have some of the properties of their sequences within tRNA, they are not functionally recognized domains of the tRNA molecule. One approach to understanding the contributions of single modifications is the NMR spectral comparison of fully modified tRNA species with that derived from a bacterial or yeast mutant strain lacking a particular nucleoside modification enzyme.[21] This approach is limited by the small number of mutant strains. In order to arrive at a complete structural determination of functional domains of tRNA, and for that matter other RNAs and DNA that contain modified nucleosides, we developed synthetic methods to complement the NMR approach. The anticodon stem/loop domain of yeast $tRNA^{Phe}$, $tRNA^{Phe}_{AC}$ (Figure 1), being a physically separate entity of the crystal structure,[1] highly modified with five modified nucleosides out of 17, of moderate size at 5400 Da, and functionally recognized by both yeast phenylalanyl−tRNA synthetase and the ribosome, met all the criteria of a domain. The synthesis of this molecule with one to four modified nucleosides was achieved in good yield by the now standard automated chemical synthesis of RNA from 2′-*O*-silyl-*t*-butyl-5′-*O*-dimethyltritylnucleoside-3′-phosphoramidites. Some of the modified nucleosides required additional protection (unpublished results).

4 HOMONUCLEAR 1D AND 2D NMR OF MODIFIED NUCLEOSIDE-CONTAINING DOMAINS

The $tRNA^{Phe}_{AC}$ structure modified with a $d(m^5C_{14})$ at the position analogous to m^5C_{40} of native $tRNA^{Phe}$, has been investigated by ^{1}H NMR.[22] The high-frequency portion of the spectrum, that included the H_2O-exchangeable, base

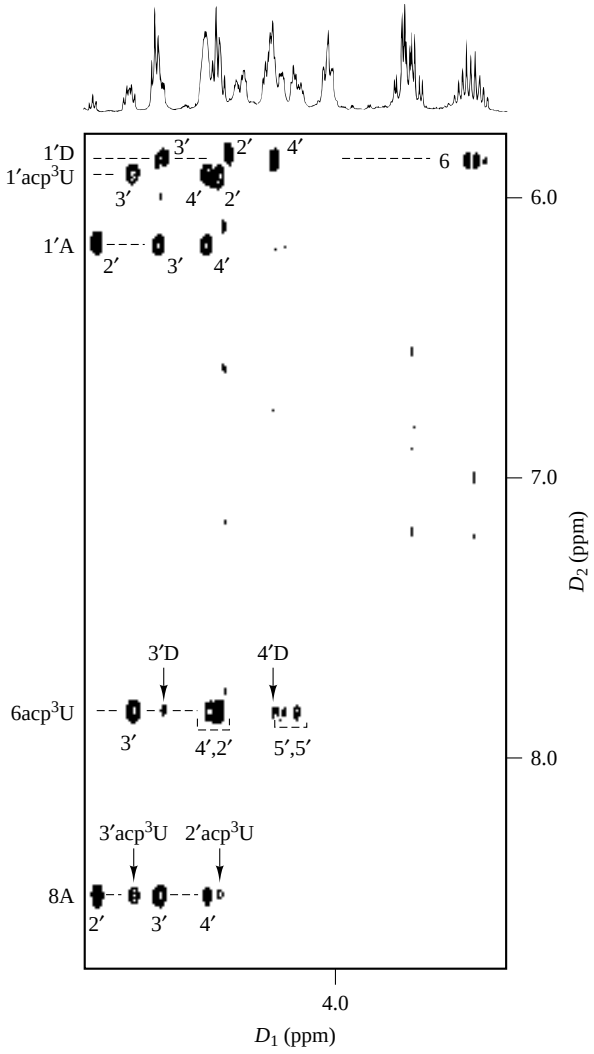

Figure 4 ROESY of Dp−acp^{3}Up−A. Data were acquired on a 500 MHz GE-Omega spectrometer at 20 °C in phase-sensitive mode with 1024 complex points and a 300 ms mixing time. Data from 256 blocks were processed with Felix with a 15° phase-shifted sine-bell window function in both dimensions and were zero filled in the F_1 dimension to 1024 complex points. The cross-peak annotations within the figure denote NOEs between the proton signal on the F_2, first, to that on the F_1, second

paired imino proton signals, was assigned by NOE difference spectroscopy. The results clearly indicated that, in the presence of Mg^{2+}, the molecule had a double stranded stem of five base pairs and two additional base pairs across what was a seven-membered loop in the unmodified $tRNA^{Phe}_{AC}$.[22] Methylation of cytidine in the yeast $tRNA^{Phe}_{AC}$ enables the molecule to form more than one conformation through a process regulated by Mg^{2+} concentration. Thus, the simplest of the posttranscriptional modifications of tRNA, a methylation, is involved in a somewhat distant, internal-site Mg^{2+} binding and stabilization of the tRNA structure, especially that of the anticodon stem and loop. However, with the introduction of a second modification, m^1G the precursor to Y, at the site of Y_{37}, one of the two cross loop, canonical base pairs was broken and a more open loop resulted. Nonexchangeable proton signals are determined by double quantum filtered COSY (DQF−COSY), HOHAHA and NOESY. (A detailed description of the NMR techniques directed at determination of tRNA anticodon structure, dynamics and function is available.[23])

In order to evaluate the importance of the RNA 2′-OH to RNA structure relative to modifications, we have synthesized and analyzed modified nucleoside-containing DNA analogs of the $tRNA^{Phe}$ anticodon stem and loop. The NOESY (Figure 5), DQF−COSY, and HOHAHA spectra of the DNA 17mer have provided sufficient information to begin modeling the structure with distance and torsion angle constraints (Figure 1). Almost all of the molecule's nucleosides have the B-form DNA 2′-*endo* conformation obtained from the ribose scalar couplings, with the exception of those around the Mg^{2+} binding site at the bottom of the stem. Aromatic to ribose NOEs showed that all nucleoside glycosidic bonds are *anti* with the one possible exception of the bulged A_{12} in the loop before the 3′-side of the stem. Similar to the $tRNA^{Phe}_{AC}$, the DNA analog has a 3′-stack easily recognized by following the trace of NOEs from the anticodon to the 3′-terminal nucleoside (Figure 5).

5 THE FUTURE OF MODIFIED NUCLEOSIDE NMR

The contributions of the naturally occurring modified nucleosides to the chemistry, structure, and function of RNAs and DNA cannot be ignored. As demonstrated here, even the simplest of modified nucleosides, the methylated and thio-substituted, can dramatically affect the chemistry and structure in ways that are detected and analyzed by NMR. Therefore, why not use modified nucleosides as site-specific NMR probes of structure and function? Modified nucleosides create sites of positive (quaternary nitrogens) and negative (carboxylic acid derivatives) charges that can be assessed by ^{13}C and ^{15}N NMR. Metal ion binding sites are created indirectly through a modified nucleoside alteration in backbone, m^5C, and directly by providing ligands, acp^3U, which can be detected by chemical shift and scalar coupling changes during metal ion titrations. The metal ion ligands would conceivably be detected by changes in chemical shift and linewidth during paramagnetic ion replacements. Modified nucleosides produce restricted local motion (through higher conformational energy barriers) that are determined by heteronuclear NMR. The selected hydrogen bonding produced by modified nucleosides (by restricting nucleoside conformation, and by negating either Watson−Crick or noncanonical base pairing) is detected with analysis of the H_2O-exchangeable imino proton region of the spectrum of modified RNA in comparison to that of the unmodified RNA.

At present there are only two synthetic pathways to the production of site-specific, modified nucleoside-containing RNA in quantities for NMR: isolation and purification of in vivo synthesized species, or automated chemical synthesis. In vitro T7 transcription, though capable of yielding large amounts of RNA for NMR, neither produces site-selectively modified, nor site-selective stable isotope enrichment of the RNA. The in vivo production is effective for obtaining the fully modified, native RNA with ^{13}C and ^{15}N labeling via precursors of the modifications. Unfortunately, most modified RNA species of interest are only a few percent of the total RNA. Overproduction from a cloned gene usually leads to a completely unmodified, or multiple isomers of partially modified RNA.

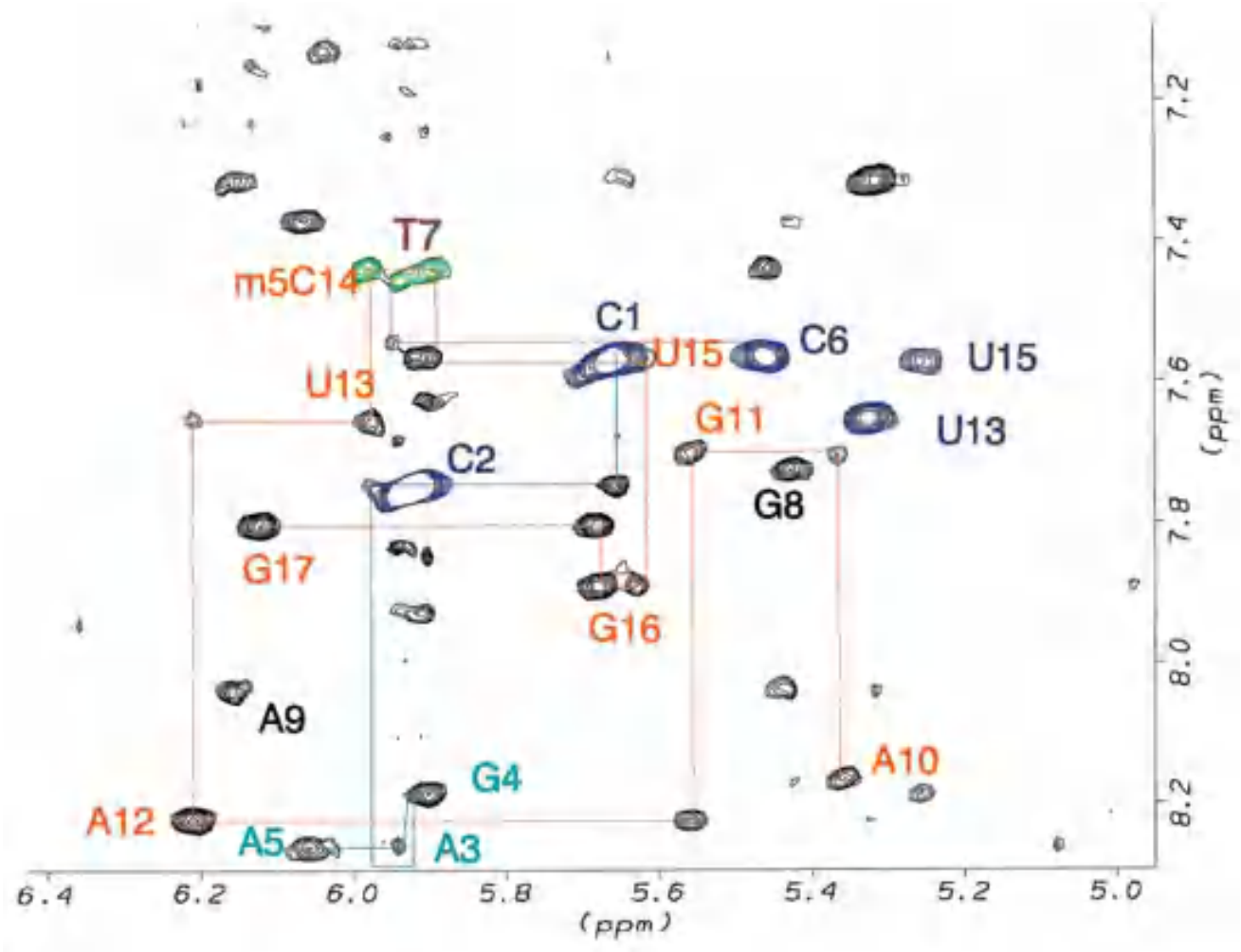

Figure 5 NOESY of the m^5C-containing anticodon stem loop domain of $tDNA^{Phe}$. The anticodon stem loop-analog domain of yeast $tRNA^{Phe}$ was synthesized with $d(m^5C)$ at the location analogous to m^5C in the tRNA.[22] Data were acquired on a 500 MHz GE-Omega spectrometer in the phase-sensitive mode at 10 °C with a mixing time of 200 ms; 256 blocks were collected. Data were processed under the same conditions as Figure 4

Automated chemical synthesis has the advantage of a controlled approach to the synthesis of NMR quantities and to the introduction of one or more modified nucleosides, native or nonnative, at the natural residues or other positions. It also has the potential for the introduction of any modified nucleosides, ribo- or deoxyribo-, at any position in the nucleic acid, thus providing an avenue to chimeric RNA/DNA oligomers. Finally, through the chemical synthesis of isotope-enriched bases and sugars of modified and unmodified nucleoside phosphoramidites, heteronuclear two-dimensional and isotope-edited multidimensional NMR approaches to modified nucleoside contributions to nucleic acid chemistry, structure, and dynamics will be attained.

6 RELATED ARTICLES

Nucleic Acid Structures in Solution: Sequence Dependence; Nucleic Acids: Base Stacking and Base Pairing Interactions; Nucleic Acids: Chemical Shifts; Nucleic Acids: Spectra, Structures, and Dynamics; Relaxation Matrix Refinement of Nucleic Acids; Ribosomal RNA.

7 REFERENCES

1. S. H. Kim, G. J. Quigley, F. L. Suddath, A. McPherson, D. Sneden, J. J. Kim, J. Weinzierl, and A. Rich, *Science*, 1972, **179**, 285.
2. C. W. Gehrke, J. A. Desgres, K. O. Gerhardt, P. F. Agris, G. Keith, H. Sierzputowska-Gracz, M. S. Tempesta, and K. C. Kuo, in *Chromatography and Modification of Nucleosides*, eds. C. W. Gehrke and K. C. Kuo, Elsevier, Amsterdam, 1990, p. 159.
3. P. H. Bolton and D. R. Kearns, *Biol. Magn. Reson.*, 1978, **1**, 91.
4. D. R. Kearns, D. J. Patel, and R. G. Shulman, *Nature (London)*, 1971, **229**, 338.
5. R. H. Griffey and A. G. Redfield, *Q. Rev. Biophys.*, 1987, **19**, 51.
6. R. V. Kastrup and P. G. Schmidt, *Biochemistry*, 1975, **14**, 3612.
7. R. A. Komoroski and A. Allerhand, *Proc. Natl. Acad. Sci. USA*, 1972, **69**, 1804.
8. P. F. Agris, F. G. Fujiwara, C. F. Schmidt, and R. N. Loeppky, *Nucleic Acids Res.*, 1975, **2**, 1503.
9. J. G. Tompson and P. F. Agris, *Nucleic Acids Res.*, 1979, **7**, 765.
10. P. G. Schmidt, J. G. Tompson, and P. F. Agris, *Nucleic Acids Res.*, 1980, **8**, 643.
11. P. F. Agris and P. G. Schmidt, *Nucleic Acids Res.*, 1980, **8**, 2085.

12. J. G. Tompson, F. Hayashi, J. V. Paukstelis, R. N. Loeppky, and P. F. Agris, *Biochemistry*, 1979, **18**, 2079.
13. R. A. Kooper, P. G. Schmidt, and P. F. Agris, *Biochemistry*, 1983, **22**, 1396.
14. C. Smith, P. G. Schmidt, J. Petsch, and P. F. Agris, *Biochemistry*, 1985, **24**, 1434.
15. P. F. Agris, H. Sierzputowska-Gracz, and C. Smith, *Biochemistry*, 1986, **25**, 5126.
16. G. T. Robillard, C. E. Tarr, F. Vosman, and B. R. Reid, *Biochemistry*, 1977, **16**, 5261.
17. P. G. Schmidt, H. Sierzputowska-Gracz, and P. F. Agris, *Biochemistry*, 1987, **26**, 8529.
18. W. S. Smith, H. Sierzputowska-Gracz, E. Sochacka, A. Malkiewicz, and P. F. Agris, *J. Am. Chem. Soc.*, 1992, **114**, 7989.
19. P. F. Agris, *Biochimie*, 1991, **73**, 1345.
20. W. S. Smith, B. Nawrot, A. Malkiewicz, and P. F. Agris, *Nucleosides Nucleotides*, 1992, **11**, 1683.
21. D. R. Davis and C. D. Poulter, *Biochemistry*, 1991, **30**, 4223.
22. Y. Chen, H. Sierzputowska-Gracz, R. Guenther, K. Everett, and P. F. Agris, *Biochemistry*, 1993, **32**, 10 249.
23. P. F. Agris and S. C. Brown, *Methods Enzymol.*, 1995, **261**, 270.

Acknowledgments

The author acknowledges the contributions of his associates, Mufeed Basti, Keith Everett, Richard Guenther, Andrzej Malkiewicz, Barbara Nawrot, Hanna Sierzputowska-Gracz, Elzbieta Sochacka, and John Stuart, and the support of the National Science Foundation and the National Institutes of Health.

Biographical Sketch

Paul F. Agris. *b* 1944. B.S., 1966, chemistry and biology, Bucknell, Ph.D., 1971, biochemistry, Massachusetts Institute of Technology. Introduced to modern NMR by Iain Campbell (Oxford) and Paul G. Schmidt (at Oklahoma Medical Research Fndn.). Assistant, associate and professor, University of Missouri, 1973–87; Head of Biochemistry, North Carolina State University, 1988–93; presently Professor of Biochemistry, NCSU. Approximately 100 publications. Research interests: NMR determination of structure/function relations of modified nucleosides in nucleic acids.

Saccharide-Protein Interactions

J. H. Prestegard, N. U. Jain, and S. B. Levery

University of Georgia, Athens, GA USA

1 Introduction 1
2 Transferred NOE Studies 3
3 Residual Dipolar Coupling Studies 4
4 References 7

1 INTRODUCTION

Carbohydrates, and in particular carbohydrates bound to proteins, present a formidable challenge in structural characterization of biologically important systems. Nuclear Magnetic Resonance has played, and will continue to play, a pivotal role in meeting this challenge. We hope to briefly review this role in what follows, but the reasons behind the importance of NMR in these applications offers equally interesting insight into the experiments used and how these experiments will evolve in the future. We hope to offer some of this insight as well.

Aside from their importance in the biosynthesis and degradation of polysaccharides and glycoconjugates, protein–carbohydrate interactions play key roles in intracellular targeting and trafficking of glycoproteins, and in modulating communication of cells with each other and with their environment.[1,2] Biochemical and physiological processes mediated by these interactions include control of glycoprotein folding and clearance from circulation, selective adhesion and aggregation of specific cell types, developmentally regulated guidance of cell migration and organization, chemotaxis, signaling by hormones and transcription factors, immune and autoimmune responses, sperm-egg recognition, and maintenance of central and peripheral nerve cell myelination.[1–9] Add to this the myriad of pathogens that use similar interactions in the course of invading their hosts, and one begins to gain an appreciation for the potential importance of understanding the structural basis for protein–carbohydrate interactions. We cannot review many examples here, but the interaction of selectins with cell surface oligosaccharides can serve to illustrate the process.[10–12] Selectins are proteins found on the surface of endothelial cells, leukocytes, and platelets. Endothelial selectins are expressed in response to injury and initiate recruitment of leucocytes to these sites by interacting with oligosaccharides attached to glycoproteins on the surface of leucocytes to slow their passage to a point of "rolling" along the injured surface. Other selectins serve to extend this interaction to the point where leucocytes invade the injured tissue. This is normally a desirable process, but one that also goes awry in events such as rheumatoid arthritis and reperfusion injury following stroke or other ischemic episodes. Development of drugs that can combat these undesirable events is one activity that benefits from a structural understanding of the interactions of proteins with carbohydrates. There are other examples, many of which are detailed in a collection of articles in a recent issue of the journal *Science*.[13]

The reason that structural characterization of carbohydrate–protein interactions is challenging begins with structural diversity of carbohydrates themselves. Building blocks (or residues) that dominate the N-linked oligosaccharides of glycoproteins are approximately 6 in number. This is only slightly larger than the number of nucleotide building blocks that encode genetic information in DNA. However, unlike the linear nucleic acid polymers (or peptide polymers), carbohydrate oligomers can be branched, and linkages can be made through four different residue hydroxyls with two possible forms at the anomeric center (alpha and beta). Given this additional variability one reaches an astounding 48,384 different possible primary structures for just trisaccharides. Of course, not all of these are produced biosynthetically, but we have also not counted O-linked oligosaccharides of proteins, the oligosaccharides of glycolipids, or the oligosaccharides in carbohydrate polymers such as heparin, plant cell walls, and outer membranes of gram negative bacteria. Add to this the fact that glycoproteins are estimated to constitute approximately half of all proteins, and one begins to appreciate the magnitude of the analytical challenge. Examples of oligosaccharides taken from parts of N-linked glycosides are given in Figure 1.

The reason that NMR has proven so useful in characterizing primary structures of molecules such as those described above is that it requires only the presence of magnetically active nuclei; carbohydrates have abundant ^{1}H and ^{13}C sites. Carbohydrates are also devoid of other types of convenient spectroscopic markers. NMR has also provided a convenient source of conformational information. Except for 1–6 linkages, common glycosidic linkages between sugar residues have two torsional variables, ϕ and φ, much like the linkages between peptide residues in proteins. As can be seen in Figure 1(b), close approach of proton pairs across the glycosidic linkage can allow the detection of NOEs that provide both information on the linkage site and a distance constraint on the glycosidic torsion angles. More recently measurement of three bond scalar couplings between the anomeric proton and the transglycosidic carbon or transglycosidic proton and anomeric carbon have allowed a more robust method of identification of linkage position and torsional constraint.[14] A number of reviews presenting approaches to the determination of oligosaccharide structure in solution exist.[15,16]

Despite the promise of contributions that NMR can make, there are also some challenges. Carbohydrates are not very diverse in terms of functional groups, being composed primarily of hydroxylated methines. This leads to a concentration of resonances from most non-exchangeable hydrogens 3–5 ppms downfield of the TMS resonance. The availability of high field NMR spectrometers and multidimensional heteronuclear editing methods has helped immensely in dealing with the resulting resolution problem. Flexibility about the glycosidic bonds poses another problem. Except in the cases of sterically crowded linkages, measurements that relate to conformational preferences really reflect an average over a distribution of conformers. Combining measurements that average with different weighting of conformational states, such as the NOE and three

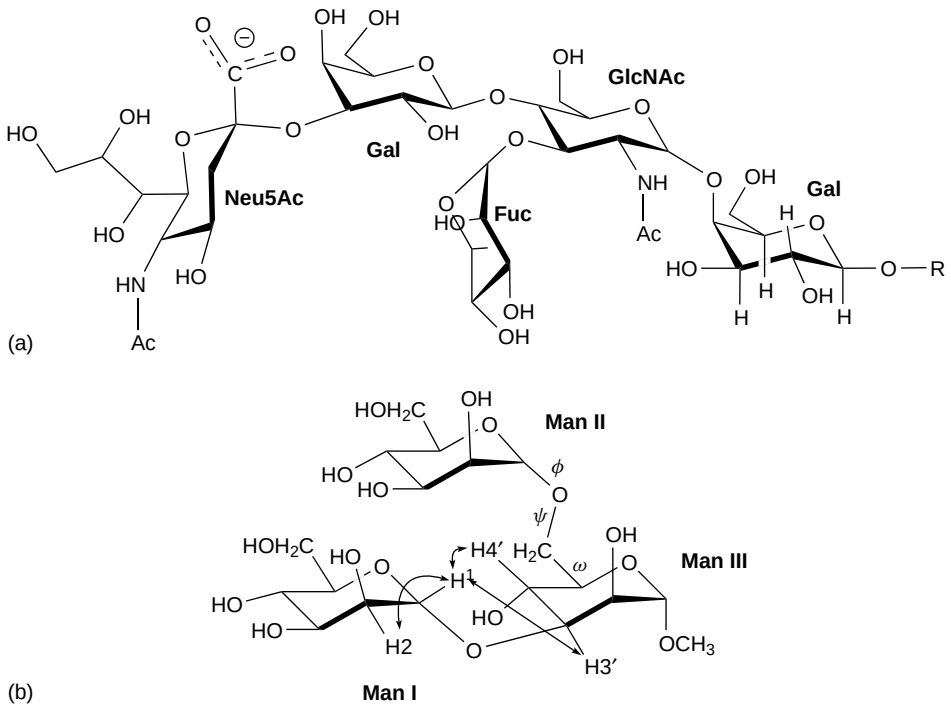

Figure 1 Schematic representation of two N-linked glycosides (a) Sialyl Lewis-X terminated and (b) a trimannoside with the individual pyranose units as labeled in the figure. Some of the intra and inter residue NOEs observed in the trimannoside structure and relevant to the text are depicted in the figure. The glycosidic torsional angles are denoted by ϕ, ψ and ω

bond scalar couplings, as well as analyzing spin relaxation measurements, have offered insight into the nature of these averages.

The issue of an oligosaccharide's conformation, as it exists in a protein binding site, offers a challenge of its own. Many of the proteins that bind oligosaccharides are large, and with NMR line widths scaling up with effective molecular weight, direct observation of tightly bound oligosaccharide ligands is difficult. In a few cases difficulties have been surmounted through the use of isotope enrichment. ^{13}C enriched oligosaccharides have become available through both synthetic routes[17–19] and the use of oligosaccharides produced by bacteria as capsular polysaccharides.[20,21] However, by far the most common solution is to collect spectra on oligosaccharides that exchange rapidly between bound and free states and in the process average narrow line widths of the free state with the broad line widths of the bound state to achieve an acceptable compromise. Fortunately, many oligosaccharide binding proteins exhibit rather weak binding from the point of view of isolated sites and exchange tends to be rapid ($>100\,s^{-1}$); they achieve the high effective binding affinities needed for many biological actions by cooperating in multimeric aggregates.

Scalar coupling information averages with equal weights between bound and free states, resulting in an average coupling that contains too little information about the bound state to be useful. However, NOEs average with a weighting roughly proportional to the molecular weights of the free and complexed forms. This arises because the cross relaxation leading to NOEs has an efficiency that, for large systems, scales up in proportion to molecular weight. For a 80 kDa protein binding an 800 Da oligosaccharide this means that the bound state NOE will dominate by a factor of ten even if the free oligosaccharide is in ten fold excess. Domination can be even greater than this as the product of correlation time for the free molecule, and the Larmor frequency at which the spectrometer operates, approaches one. NOEs pass through zero as they change from positive to negative in going from the small molecule to the large molecule limit for spin relaxation. This very desirable property has obviously led to a large number of applications of what is referred to as a transferred NOE or TRNOE. This is one aspect that we will review in some detail below.

While transferred NOEs have been very valuable in providing information on the internal geometry of a bound ligand, they seldom provide information about placement of the ligand on the protein surface. There are some auxiliary experiments that help place ligands. These range from chemical shift perturbation of crosspeaks in HSQC spectra of the protein itself,[22–24] to perturbation of the intensities of those cross peaks by spin labeled analogs of ligands.[25–27] In a recent study of human acidic fibroblast growth factor the chemical shift perturbation approach was used to study its interaction with a heparin-derived hexasaccharide.[28] Upon titration of the protein with the hexasaccharide, monitored by 2-D ^{1}H–^{15}N HSQC spectra recorded after each addition, appreciable chemical shift changes of selected peptide H^N, N, C′, and C^α resonances were taken as evidence of a binding interaction. The localization of these perturbations in specific regions implied that the protein underwent no significant overall conformational changes upon formation of the complex. It is worth noting that the magnitude of a given perturbation doesn't necessarily correlate with the strength of the interaction at the associated residue, but it is reasonable to expect that significant chemical shift changes will map residues in or near the contact region with the ligand. Using a similar approach, the carbohydrate binding site of a

family IIb xylan-binding domain was mapped to one face of the protein by titration with a xylohexaose.[29]

We do not intend to review these applications in further detail, but focus instead on another recent approach that gives both information on internal oligosaccharide geometry and geometry relative to the protein surface. This approach relies on residual dipolar couplings – a parameter that contributes to the splitting of resonances much like a scalar coupling, but one that can only be measured when the molecule of interest is partially oriented in the magnetic field. These parameters again average between free and bound states, and one might expect bound contributions to be too small to be of use in an averaging system. However, the level of order for protein complex and free oligosaccharide need not be the same. If the protein can be induced to order more strongly, properties of the bound form can be detected even in the presence of excess free ligand.

2 TRANSFERRED NOE STUDIES

Transferred NOE studies of oligosaccharides bound to proteins have been reviewed recently.[30–32] We outline only the basic principles and a few examples here. The structural information obtained from a transferred NOE experiment is in principle the same as that obtained from a normal NOE.[33,34] Experiments can be conducted in one, two, or three dimensional form. In all cases one will find a segment that begins with a perturbation of the equilibrium magnetization associated with one spin (periodic if multidimensional, inversion or saturation if one dimensional). This is followed by a delay during which magnetization is transferred to nearby spins by dipole-dipole cross relaxation. The spins are nearly always protons because of the high magnetic moment and enhanced efficiency of interaction for these spins. The efficiency of the transfer process depends on the cross relaxation rate, which in turn depends on the inverse of the interproton distance as given by this equation for a pair of interacting protons that tumble isotropically with correlation time, τ_c, in a magnetic field giving a frequency, ω_0:

$$\sigma_{ij} = \left(\left(\frac{\mu_0}{8\pi^2}\right)h\gamma_i\gamma_j\right)^2 (r^{-6})\left(\frac{(3\tau_c/5)}{(1+4\omega_0^2\tau_c^2)} - \left(\frac{\tau_c}{10}\right)\right) \quad (1)$$

For short delays the transfer is linear with time and the relative intensities (I_{ij}, I_{ik}) of cross peaks (or difference spectrum peaks for a one dimensional spectrum), obey the relation, $I_{ij}/I_{ik} = (r_{ik}/r_{ij})^6$, where r_{ij} and r_{ik} are the distances between a spin pair at an unknown distance and a spin pair at a known distance respectively. For oligosaccharides an intra residue pair of protons such as the H1–H2 pair highlighted in Figure 1 often provide a reference distance, and trans-glycosidic pairs such as H1–H4′ are at distances that can provide useful constraints on glycosidic torsional angles.

The transferred NOE differs in that there is an equilibrium between bound and free states. The cross relaxation rates will be different in these states both because of the correlation times for tumbling of the molecules (τ_c) differ and the inter proton distances differ (if the conformation in the bound state differs from that in the free state). If exchange is rapid compared to cross relaxation the observed effect will be the weighted average:

$$\sigma_{ij}^{\text{eff}} = P_{\text{free}}\sigma_{ij}^{\text{free}} + P_{\text{bound}}\sigma_{ij}^{\text{bound}} \quad (2)$$

Looking at the correlation time dependence of equation (1), it is clear that it is easy to make $\sigma_{ij}^{\text{bound}}$ dominate by binding the ligand to a sufficiently large protein (τ_c increases linearly with molecular weight).

Verifying that one is approximately in this limit is easy. Again looking at equation (1), one sees that the sign of the cross relaxation rate changes as $\omega_0\tau_c$ approaches 1. It is positive for small molecules and leads to intensity enhancement over the equilibrium value; it is negative for large molecules and leads to intensity reductions. Figure 2 shows an example with a simple trisaccharide, methyl 3,6-di-O-(α-D-mannopyranosyl)-(α-D-mannopyranoside), free and bound to mannose binding protein (MBP).[35] The anomeric proton resonance from the $\alpha(1-3)$ linked mannose (Man I in Figure 1b) is being inverted. For the free trimannoside, resonances from the nearby intra ring H2 resonance and the H4′ resonance of the linked residue are selectively enhanced. For the bound trimannoside, the same resonances, plus a resonance from the H3′ trans-glycosidic proton show decreases in intensity.

Quantitative analysis of intensities in terms of distances is actually a little more complex for a transferred NOE. Complexities are illustrated in Figure 3. Rates of exchange

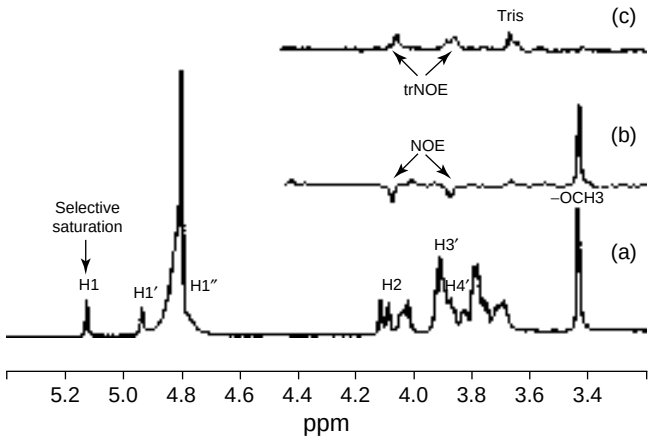

Figure 2 (a) ^{1}H NMR spectrum of trimannoside (2 mM, 90% D_2O) recorded at 800 MHz. The NOE difference spectrum (298 K) recorded for (b) free trimannoside (2 mM, 100% D_2O, 298 K) and (c) trimannoside bound to Mannose binding protein (0.1 mM, 25 mM Tris-Cl, pH 7.8, 90% D_2O). The NOE difference spectra in (b) and (c) show the result of selective saturation of the H1 anomeric proton of Man I (Figure 1b). In the free state, intra and inter residue positive NOEs are observed for H2 and H4′ only. However, in the bound state, the NOEs undergo a change in sign with negative transfer NOEs observed for H2, H3′ and H4′ protons. The NOE difference spectra were recorded using a saturation transfer scheme, where the H1 anomeric proton was selectively saturated for a long period of time (2 s), followed by a 90° observe pulse to detect the saturation transfer on other protons. A control scan was interleaved in the pulse sequence for the difference spectrum, where the saturation was applied to a region where no resonances are present. The total acquisition time for each difference spectrum was approximately 1 hour and refer to protons from Man III and Man II respectively, while 'Tris' refers to the resonance observed from the Tris-Cl buffer solution in the sample

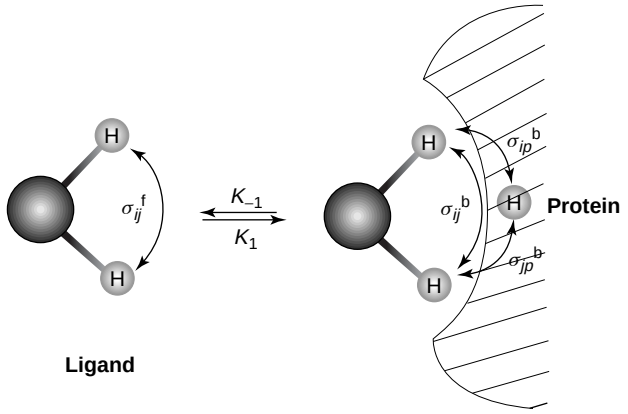

Figure 3 Effects of spin diffusion on cross-relaxation rates of protons in close vicinity to each other. K_1 and K_{-1} are the exchange rates for protons on and off the protein. The σ's represent the cross-relaxation rates for individual protons under the influence of other protons in close vicinity

on and off the protein can complicate cross relaxation rates by accentuating spin diffusion effects (three spin effects). Spin diffusion would be a serious concern if the Man II anomeric proton had been inverted and intensity changes in both H6a and H6b resonances of the Man III ring had been seen. The geminal pair, H6a and H6b, are very close (2 Å) and successive transfer from H1 to H6a to H6b is likely to be as efficient as a direct transfer from H1 to H6b. Contributions from the indirect path are normally minimized by shortening the transfer time. But, if the exchange rate is slow, one can reach the point where the time on the protein governs indirect transfer and not the transfer time allowed in the pulse sequence. One solution is to explicitly include exchange and undertake a complete relaxation matrix simulation of transfers.[36,37] The later presumes that one knows the geometric relationship of all protons that can be involved. This is feasible if they are all on the ligand, but protein protons can also enter as shown in Figure 3. In many cases positions and identities of these protons is not known. Another approach is to collect both transferred NOESY and transferred ROESY experiments.[38] ROESY, or the rotating frame analog of the NOESY experiment, has the effect of reducing the effective frequency (ω_0) to the point where cross relaxation is positive for even a large complex. Step wise transfers now give alternate signs for cross peaks, positive for the direct transfer from a saturated or inverted peak, negative for second transfer from the enhanced peak. The difference in sign can identify problem peaks. Quantitatively removing the effects when both direct and indirect pathways contribute can be more of a problem. More recently an approach termed Quite-NOESY has been devised.[39] This uses pair wise inversion of peaks in selected spectral regions to eliminate unwanted effects of protein peaks. Because of the distinct regions in which carbohydrate resonances lie in comparison to resonances from protein sidechains, this is often possible in protein–carbohydrate interaction studies.

With the refinements in TRNOE techniques there have been some significant applications to protein-saccharide systems.[18,40,41] Some of these were reviewed specifically for carbohydrate–protein interactions a few years ago,[31,42] there are also examples contained in more recent general reviews of protein–ligand interaction studies.[30] One of the more interesting examples is that of oligosaccharide binding to E-selectin or chimeric constructs containing the oligosaccharide binding domain of that protein; this is one of the biologically interesting systems mentioned in our introduction. This system has been the subject of at least five independent studies, many reporting significantly different conformations for the bound sialyl Lewis-X (sLe^x) oligosaccharide (Figure 1) (more than 30 degree deviations in some torsional angles).[18,43–46] The most recent study used the enhanced resolution of a 3D experiment on ^{13}C enriched ligand and complete relaxation matrix analysis of the data in an attempt to resolve the differences.[18] There are significant additional NOEs observed in the heteronuclear experiment that lead to an improved definition of the conformation. Even the most recent study, however, was not able to take account of possible three spin effects from protein protons. The bound ligand, nevertheless, appears to be in a low energy conformation, suggesting that no severe distortions from indirect NOEs exist.

Another recent application to E-selectin takes advantage of transferred NOEs in a different way. This application uses the transferred NOE as a method for screening a library of potential drug lead compounds for those that bind to E-selectin in a selective fashion.[47] Oligosaccharides and their mimics when near 1000 Da have either small negative or small positive NOEs when alone in solution. As illustrated above for the trimannoside of N-linked oligosaccharides, these turn to strong negative NOEs when bound to a large protein. 2D NOE spectra of a mixture of potential ligands are, therefore, dominated by peaks from compounds that bind to a protein. The authors screened a mixture of 11 compounds that mimic sLe^x. The resulting spectrum was consistent with structural features of only two compounds in the library. Further comparison to NOE spectra for these two led to the identification of the selectively bound compound. While this does not push the structural determination aspects of the transferred NOE the application clearly makes use of one of its unique properties in a way that is of significant use to the pharmaceutical industry.

3 RESIDUAL DIPOLAR COUPLING STUDIES

The same dipolar interaction that gives rise to the NOE actually contains both angle and distance dependent terms. This can be seen in equation (3) written for the interaction in frequency units for a pair of spin 1/2 nuclei (i, j) separated by distance r along a vector at angle θ relative to the magnetic field. Both terms are in principle useful sources of structural information.

$$D_{ij}^{\text{res}} = -\left(\frac{\mu_0}{4\pi}\right)\frac{\gamma_i\gamma_j h}{2\pi^2 r_{ij}^3}\frac{\langle 3\cos^2\theta - 1\rangle}{2} \qquad (3)$$

In the NOE, the angle dependent part is responsible for modulation of the interaction as a protein tumbles in solution and is essential for making the distance dependence of NOEs measurable as a spin relaxation phenomenon. However, it normally makes no direct contribution to spin state energy differences that might be efficiently measured through variations in resonance positions. This is because the angular term

rigorously averages to zero over the time course of molecular tumbling in isotropic solutions.

If the angular term did not average to zero, the interaction between a pair of distinguishable spin 1/2 nuclei would lead to a splitting of each resonance of magnitude D_{ij}^{res}. This would appear much like a scalar coupling, and in fact, the contribution would simply add to the scalar contribution to splitting when both contributions were present. In the case of directly bonded pairs of spin 1/2 nuclei (^{1}H–^{15}N, ^{1}H–^{13}C, etc.), where the internuclear distances are known, the residual dipolar contribution to splitting would become a simple function of internuclear vector orientation and a rich source of structural data.

Direct measurement of residual dipolar couplings from resonance splittings, thus, depends on restoring some level of directional order to molecules as they tumble in solution. To maintain high resolution we would want the level of order to be small because large levels would produce large residual interactions and strong coupling among spins much as we see in solids NMR. Restoring small levels of order has a lot of precedence in the liquid crystal field[48] and in work with paramagnetic molecules that simply orient in the presence of high magnetic fields.[49] Recently there has been a revival of interest in working with partially ordered molecules of biological interest using aqueous liquid crystal media including bicelles,[50–52] phage,[53,54] cellulose microcrystals,[55] cetylpyridinium chloride/hexanol/brine,[56] and mechanically distorted polyacrylamide gels.[57,58]

Inducing small levels of order, as opposed to perfect order, adds a complication in that the level and anisotropy of order for the whole molecule become variables in addition to the orientation of an interaction vector of interest. These additional variables are conveniently included in equation (3) as follows:

$$D_{ij}^{\text{res}} = -\left(\frac{\mu_0}{4\pi}\right)\frac{\gamma_i\gamma_j h}{2\pi^2 r_{ij}^3}\sum_{kl} S_{kl}\cos(\alpha_k)\cos(\alpha_l) \qquad (4)$$

Here the angular term has been expressed in terms of elements of an order tensor (S_{ij}), and direction cosines relating the internuclear vector to a principal order frame ($\cos(\alpha_k)$).[59] Despite the apparent complexity of the equation, it has only five independent parameters; these can alternately be described in terms of three Euler angles relating the orientation of a molecular fragment to a principle alignment frame and principal and rhombic alignment parameters.[52] If a sufficient number of independent measurements of dipolar couplings can be made within a semi-rigid fragment, the five parameters can be calculated directly and complete structures assembled from orientations of fragments relative to a common alignment frame. When fewer data are available the measurements can be used as constraints in more general structure search protocols.

Part of the appeal of residual dipolar couplings measurements is the efficiency with which these data can be acquired. Measurement of ^{13}C–^{1}H dipolar couplings of directly bonded pairs in a sugar ring can be based on simple modifications of an HSQC experiment. Modifications can be as simple as removing the normal 180° pulse used for refocusing proton scalar coupling during the indirect detection period. When this is done, the single cross peak for each pair turns into a doublet with a splitting at the sum of one bond scalar and dipolar contributions. The resulting spectrum is illustrated in Figure 4 for the trimannoside core found in all N-linked glycosides. These data were taken at natural abundance on a 20 mM sample with approximately a 6 hour acquisition. With new cryogenic probes

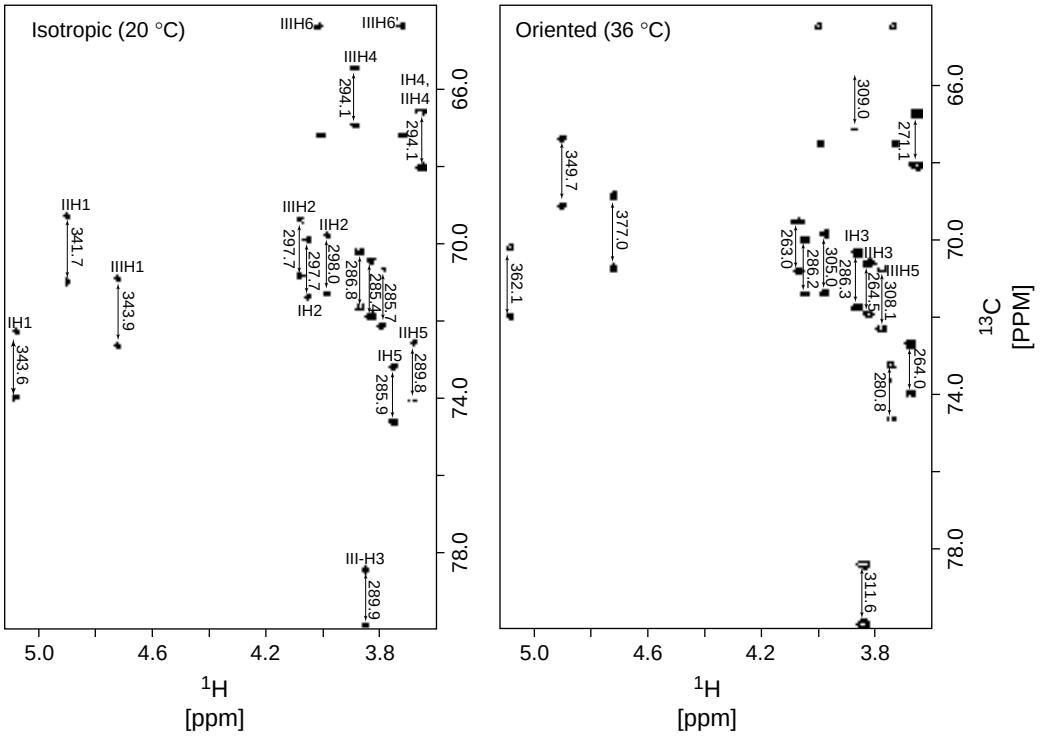

Figure 4 Constant-time, coupling enhanced HSQC (CT-CE-HSQC) spectra of trimannoside in dilute bicelle media at 20 and 36 °C. The measured ^{1}H–^{13}C couplings for trimannoside are as shown in the figure. Residual dipolar couplings correspond to the differences in measured couplings in the two spectra (derived from Ref.[68])

promising to increase sensitivity of NMR spectrometers by a factor of three or four, work with 2–3 mM samples should be feasible in 24 hour acquisitions. The dipolar part is usually extracted by acquiring spectra under both isotropic and oriented conditions. This can be simply done using bicelle systems in which isotropic and ordered states can be produced by changing from lower temperature to higher temperature (e.g., from 25 to 35 °C). At 25° only scalar couplings contribute, and splittings are all of similar magnitude. At 35° the bicelles, which are simply discoidal pieces of lipid bilayer, order with normals perpendicular to the magnetic field. Occasional collisions of the oligosaccharide with the ordered surfaces impart a small degree of order; the dipolar contributions to couplings between ^{1}H and ^{13}C nuclei fail to average to zero, and splittings increase or decrease depending on the angles that a particular internuclear vector makes with the axes of the order frame. There are of course a number of more sophisticated pulse sequences that allow measurement of $^{1}H-^{13}C$ couplings from either intensity variation or frequency variation of cross peaks.[51,60,61] Also, experiments that allow measurement of $^{1}H-^{1}H$ interactions have been devised.[56,62] The use of several different kinds of coupling allows sufficient interaction vectors to be measured within single sugar rings.

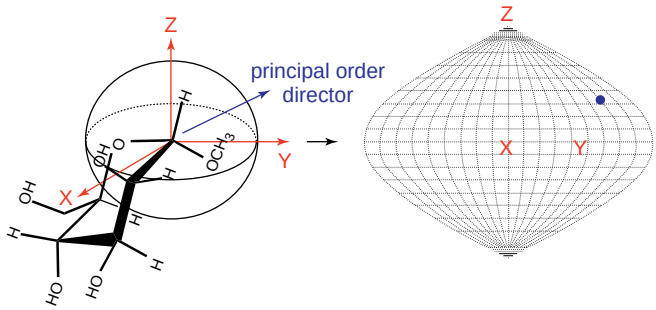

The Z axis is perpendicular to the O-C1-C2 plane and the Y axis is along O-C1 bond.

$X = \lambda \cos\phi$, $Y = \phi$

where ϕ is the latitude and λ is the longitude

Figure 5 Illustration of structure determination for a simple oligosaccharide using the order tensor approach. The direction of highest order is represented by a director in the initial molecular frame denoted by X, Y and Z axes (derived from Ref.[68])

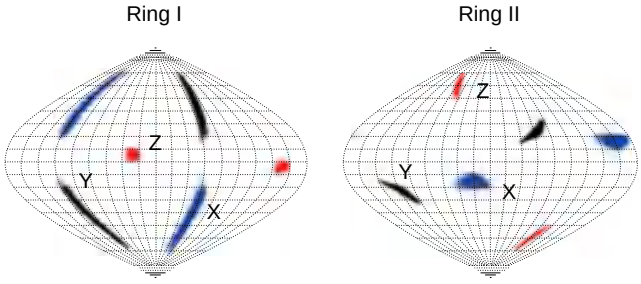

Figure 6 Sauson-Flamsteed projections of two rings of trimannoside depicting the orientations of the alignment tensor principal axis system in the initial molecular frame (derived from Ref.[68])

One structure determination approach is illustrated in Figure 5 for a simple oligosaccharide. Pyranose rings are considered to be semi-rigid fragments and a canonical fragment frame is defined using the C1, O5, and C2 atoms. Measured couplings are used to define both order parameters and directions of alignment frame axes relative to the fragment frame. These axis directions are often depicted as points on a globe called a Sauson-Flamsteed projection as shown for the z axis in Figure 5. Normally x and y axis directions are depicted as well. Figure 6 shows the projections for two rings of the trimanoside core of common N-linked glycosides discussed previously. Note that axis directions come in pairs offset by 180 degrees. This insensitivity to inversion is a fundamental limitation of the measurements and normally leads to a four fold degeneracy in choice of fragment orientation. For sugar residues directly connected by short glycosidic bonds covalent geometry restrictions often lift this degeneracy as well as fixing translational degrees of freedom. The use of multiple alignment media can also lift this degeneracy. Figure 7 shows the derived structure.

Incidentally, the third ring of the trimannoside cannot be aligned so easily. Its principal order parameters depart significantly from those of the other two, a clear indication that internal motions exist and that the entire molecule cannot be considered a single rigid structure. There are now several other examples of structure determination of oligosaccharides using primarily residual dipolar coupling data.[56,63] Some of these studies have also highlighted the detection and characterization of internal motions in oligosaccharides.[64]

Using residual dipolar coupling to deduce the geometry of protein bound oligosaccharides is still in its infancy. As

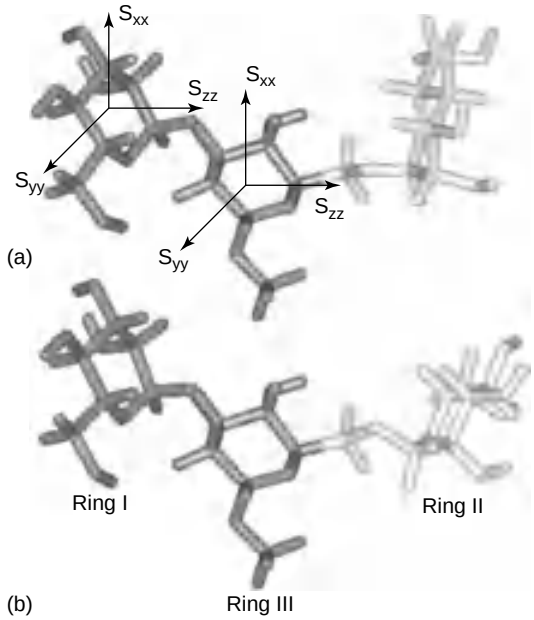

Figure 7 (a) The average structure of trimannoside ring I and ring III assembled by aligning the order tensor principal axis determined from bicelle media. Superimposed on ring I and ring III are coordinate frames representing the order tensor principal axis determined separately for each ring. (b) The average structure of trimannoside ring I and ring III assembled by aligning the order tensor principal axis determined from phage media. The structure is oriented to show the similarity of conformations about the α (1,3) linkage

suggested above the key to the widespread use of these measurements would be an alignment medium that strongly oriented the protein and weakly oriented the free oligosaccharide. Such an ideal medium has not yet been found, but even moderate preference for protein alignment combined with known binding constants have allowed deconvolution of residual dipolar couplings coming from the bound state. The necessity of working with higher protein to ligand ratios than required in transfer NOE experiments has restricted measurements to ^{13}C enriched oligosaccharides and measurements of one bond ^{13}C–^{1}H couplings. Nevertheless some interesting examples have appeared. In one the binding of the trisaccharide, Galα1-4Galβ1-4Glc to the B subunit of an *E. coli* toxin was examined. The relative orientation of the two Gal residues could be determined and was found to agree with a conformation determined via transferred NOE methods.[65] Significantly, the authors point out that the data are free from protein mediated effects in transferred NOE experiments and can be made with significantly lower amounts of material. In a second application to the same trisaccharide, which happens to constitute the oligosaccharide from the glycolipid receptor of verotoxin-1 B subunit, data were used to distinguish among conformations found for different sites occupied in the crystal structure of the oligosaccharide verotoxin complex.[66] The derived data fit the conformation seen in site two. In this case transferred NOE data had been inadequate to distinguish between two previously proposed oligosaccharide conformations for this site.

In a third application the binding of a simple methyl glycoside, α-methyl mannose, to mannose binding protein was studied.[67] This study was different in that the target was determination of relative orientation of protein and a single sugar ring rather than relative orientations of multiple rings. In general one would have to use a structure for the protein and ^{15}N–^{1}H dipolar coupling from the protein to derive the orientation of the protein. In the case studied this step could be eliminated because of the existence of a three fold rotational symmetry axis in the trimeric protein. The placement of the ligand in the binding site was found to be energetically allowed, but significantly different from that observed in a crystal structure of a homologous complex.

Although preliminary in nature and small in number, these examples of applications to protein-oligosaccharide complexes are promising. The advantages in not having to observe large numbers of inter-residue NOEs to constrain conformation, and the avoidance of complications due to spin diffusion are very significant. Improvements in sensitivity coming from cryogenic probes should allow increased use of molecules at natural abundance, and improvements in media allowing amplification of bound oligosaccharide data should allow greater use of ^{1}H–^{1}H couplings in the future.

4 REFERENCES

1. A. Varki, *Glycobiology*, 1993, **3**, 97–130.
2. A. Helenius and M. Aebi, *Science*, 2001, **291**, 2364–2369.
3. T. Feizi, *Glycoconjugate J.*, 2000, **17**, 553–565.
4. C. R. Bertozzi and L. L. Kiessling, *Science*, 2001, **291**, 2357–2364.
5. J. B. Lowe, *Cell*, 2001, **104**, 809–812.
6. L. L. Kiessling, J. E. Gestwicki, and L. E. Strong, *Curr. Opin. Chem. Biol.*, 2000, **4**, 696–703.
7. K. J. Mengerink and V. D. Vacquier, *Glycobiology*, 2001, **11**, 37R–43R.
8. P. M. Rudd, T. Elliott, P. Cresswell, I. A. Wilson, and R. A. Dwek, *Science*, 2001, **291**, 2370–2376.
9. K. A. Sheikh, J. Sun, Y. J. Liu, H. Kawai, T. O. Crawford, R. L. Proia, J. W. Griffin, and R. L. Schnaar, *Proc. Natl. Acad. Sci. USA*, 1999, **96**, 7532–7537.
10. C. R. Bertozzi, *Chem. Biol.*, 1995, **2**, 703–708.
11. A. Leppanen, S. P. White, J. Helin, R. P. McEver, and R. D. Cummings, *J. Biol. Chem.*, 2000, **275**, 39 569–39 578.
12. W. I. Weis, *Structure*, 1994, **2**, 147–150.
13. J. Alper, *Science*, 2001, **291**, 2338–2343.
14. C. A. Bush, *Glycobiology*, 1999, **9**, 185.
15. D. Acquotti and S. Sonnino, *Methods Enzymol.*, 2000, **312**, 247–272.
16. J. O. Duus, C. H. Gotfredsen, and K. Bock, *Chem. Rev.*, 2000, **100**, 4589.
17. D. H. Live, L. J. Williams, S. D. Kuduk, J. B. Schwarz, P. W. Glunz, X. T. Chen, D. Sames, R. A. Kumar, and S. J. Danishefsky, *Proc. Natl. Acad. Sci. USA*, 1999, **96**, 3489–3493.
18. R. Harris, G. R. Kiddle, R. A. Field, M. J. Milton, B. Ernst, J. L. Magnani, and S. W. Homans, *J. Am. Chem. Soc.*, 1999, **121**, 2546–2551.
19. Y. Aubin, Y. Ito, J. C. Paulson, and J. H. Prestegard, *Biochemistry*, 1993, **32**, 13 405–13 413.
20. M. Martin-Pastor and C. A. Bush, *Biophys. J.*, 1999, **76**, A247–A247.
21. S. Q. Sheng and R. Cherniak, *Carbohydrate Res.*, 1997, **301**, 33–40.
22. B. J. Stockman, *Prog. Nucl. Magn. Reson. Spectrosc.*, 1998, **33**, 109–151.
23. J. L. Weaver and J. H. Prestegard, *Biochemistry*, 1998, **37**, 116–128.
24. P. J. Hajduk, R. P. Meadows, and S. W. Fesik, *Q. Rev. Biophys.*, 1999, **32**, 211–240.
25. P. A. Kosen, *Methods Enzymol.*, 1989, **177**, 86–121.
26. J. Kormos, P. E. Johnson, E. Brun, P. Tomme, L. P. McIntosh, C. A. Haynes, and D. G. Kilburn, *Biochemistry*, 2000, **39**, 8844–8852.
27. N. U. Jain, A. Venot, K. Umemoto, H. Leffler, and J. H. Prestegard, *Protein Sci.*, 2001, **10**, 2393–2400.
28. K. Ogura, K. Nagata, H. Hatanaka, H. Habuchi, K. Kimata, S. Tate, M. W. Ravera, M. Jaye, J. Schlessinger, and F. Inagaki, *J. Biomol. NMR*, 1999, **13**, 11–24.
29. P. J. Simpson, D. N. Bolam, A. Cooper, A. Ciruela, G. P. Hazlewood, H. J. Gilbert, and M. P. Williamson, *Structure Folding Design*, 1999, **7**, 853–864.
30. G. C. K. Roberts, *Drug Discovery Today*, 2000, **5**, 230–240.
31. J. Jimenez-Barbero, J. L. Asensio, F. J. Canada, and A. Poveda, *Curr. Opin. Struct. Biol.*, 1999, **9**, 549–555.
32. A. Poveda and J. Jimenez-Barbero, *Chem. Soc. Rev.*, 1998, **27**, 133–143.
33. F. Ni, *Prog. Nucl. Magn. Reson. Spectrosc.*, 1994, **26**, 517–606.
34. L. Y. Lian, I. L. Barsukov, M. J. Sutcliffe, K. H. Sze, and G. C. K. Roberts, *Methods Enzymol.*, 1994, **239**, 657–700.
35. W. I. Weis, *Structure*, 1994, **2**, 1227–1240.
36. V. L. Bevilacqua, Y. M. Kim, and J. H. Prestegard, *Biochemistry*, 1992, **31**, 9339–9349.
37. E. Z. Eisenmesser, A. P. R. Zabell, and C. B. Post, *J. Biomol. NMR*, 2000, **17**, 17–32.
38. J. Fejzo, W. M. Westler, S. Macura, and J. L. Markley, *J. Am. Chem. Soc.*, 1990, **112**, 2574–2577.
39. S. J. F. Vincent, C. Zwahlen, C. B. Post, J. W. Burgner, and G. Bodenhausen, *Proc. Natl. Acad. Sci. USA*, 1997, **94**, 4383–4388.
40. F. Casset, A. Imberty, S. Perez, M. E. Etzler, H. Paulsen, and T. Peters, *Eur. J. Biochem.*, 1997, **244**, 242–250.
41. M. Rinnbauer, E. Mikros, and T. Peters, *J. Carbohydrate Chem.*, 1998, **17**, 217–230.

42. A. Poveda and J. Jimenez-Barbero, *Chem. Soc. Rev.*, 1998, **27**, 133–143.
43. R. M. Cooke, R. S. Hale, S. G. Lister, G. Shah, and M. P. Weir, *Biochemistry*, 1994, **33**, 10 591–10 596.
44. K. Scheffler, B. Ernst, A. Katopodis, J. L. Magnani, W. T. Wang, R. Weisemann, and T. Peters, *Angew. Chem.-Int. Edn. Engl.*, 1995, **34**, 1841–1844.
45. K. Scheffler, J.-R. Brisson, R. Weisemann, J. L. Magnani, W. T. Wong, B. Ernst, and T. Peters, *J. Biomol. NMR*, 1997, **9**, 423–436.
46. L. Poppe, G. S. Brown, J. S. Philo, P. V. Nikrad, and B. H. Shah, *J. Am. Chem. Soc.*, 1997, **119**, 1727–1736.
47. D. Henrichsen, B. Ernst, J. L. Magnani, W. T. Wang, B. Meyer, and T. Peters, *Angew. Chem.-Int. Edn.*, 1999, **38**, 98–102.
48. J. N. Emsley and J. C. Lindon, 'NMR Spectroscopy Using Liquid Crystal Solvents', Pergamon Press: Oxford, 1995.
49. E. W. Bastiaan, C. Maclean, P. C. M. Van Zijl, and A. A. Bothner-By, *Annu. Rep. NMR Spectrosc.*, 1987, **19**, 35–77.
50. C. R. Sanders, B. J. Hare, K. P. Howard, and J. H. Prestegard, *Prog. Nucl. Magn. Reson.*, 1994, **26**, 421–444.
51. M. Ottigerand and A. Bax, *J. Biomol. NMR*, 1998, **12**, 361–372.
52. N. Tjandra and A. Bax, *Science*, 1997, **278**, 1111–1114.
53. G. M. Clore, A. M. Starich, and A. M. Gronenborn, *J. Am. Chem. Soc.*, 1998, **120**, 10 571–10 572.
54. M. R. Hansen, L. Mueller, and A. Pardi, *Nature Struct. Biol.*, 1998, **5**, 1065–1074.
55. K. Fleming, D. Gray, S. Prasannan, and S. Matthews, *J. Am. Chem. Soc.*, 2000, **122**, 5224–5225.
56. M. Martin-Pastor and C. A. Bush, *J. Biomol. NMR*, 2001, **19**, 125–139.
57. R. Tycko, F. J. Blanco, and Y. Ishii, *J. Am. Chem. Soc.*, 2000, **122**, 9340–9341.
58. H. J. Sass, G. Musco, S. J. Stahl, P. T. Wingfield, and S. Grzesiek, *J. Biomol. NMR*, 2000, **18**, 303–309.
59. J. H. Prestegard, H. M. Al-Hashimi, and J. R. Tolman, *Q. Rev. Biophys.*, 2001, **33**, 371–424.
60. J. R. Tolman and J. H. Prestegard, *J. Magn. Reson.*, 1996, **112**, 245–252.
61. J. R. Tolman and J. H. Prestegard, *J. Magn. Reson., Series B*, 1996, **112**, 269–274.
62. F. Tian, P. J. Bolon, and J. H. Prestegard, *J. Am. Chem. Soc.*, 1999, **121**, 7712–7713.
63. C. Landersjo, C. Hoog, A. Maliniak, and G. Widmalm, *J. Phys. Chem. B*, 2000, **104**, 5618–5624.
64. H. Neubauer, J. Meiler, W. Peti, and C. Griesinger, *Helv. Chim. Acta*, 2001, **84**, 243–258.
65. H. Shimizu, A. Donohue-Rolfe, and S. W. Homans, *J. Am. Chem. Soc.*, 1999, **121**, 5815–5816.
66. G. S. Thompson, H. Shimizu, S. W. Homans, and A. Donohue-Rolfe, *Biochemistry*, 2000, **39**, 13 153–13 156.
67. P. J. Bolon, H. M. Al-Hashimi, and J. H. Prestegard, *J. Mol. Biol.*, 1999, **293**, 107–115.
68. F. Tian, H. M. Al-Hashimi, J. L. Craighead, and J. H. Prestegard, *J. Am. Chem. Soc.*, 2001, **123**, 485–492.

Acknowledgements

This work was supported by a grant from the National Institutes of Health, GM33225.

Biographical Sketches

James Prestegard received his B.S. in chemistry in 1966 from the University of Minnesota and his Ph.D. in chemistry from the California Institute of Technology in 1971. Prior to joining the CCRC in January 1998, Dr. Prestegard spent 27 years in the Chemistry Department at Yale University where he held positions of assistant professor, associate professor, and professor. In addition to his normal professorial duties, he now directs the regional NMR facilities at the University of Georgia. Dr. Prestegard serves on the editorial boards of several journals, including the *Journal of Magnetic Resonance* and the *Journal of Biomolecular NMR*, and is a frequent member of advisory and review panels.

Nitin U. Jain, *b* 1973. M.S., 1995, Ph.D., 1999, Brandeis. First involved with NMR on joining Brandeis University in 1995, where he worked on the NMR of paramagnetic proteins and was involved in developing strategies for the assignment of heteronuclear resonances in the paramagnetic region of ferredoxins in particular. Approx. 6 papers and 1 patent in NMR related aspects. Research interests: NMR studies of protein-carbohydrate interactions using residual dipolar couplings.

Steven B. Levery received his B.A. (1971) and M.S. (1975) in chemistry from Northeastern University, and his Ph.D. (1993) in chemistry from the University of Washington. He spent 15 years in the laboratories of Dr. Sen-itiroh Hakomori, initially as a research technologist and supervisor in glycoconjugate structural analysis at the Fred Hutchinson Cancer Research Center, Seattle, WA (1980–1987); and later as a staff scientist and head of the laboratory for Analytical & Structural Biochemistry at the Biomembrane Institute, Seattle, WA (1987–1995). He is currently an Associate Research Scientist in the University of Georgia Complex Carbohydrate Research Center (CCRC) and Department of Biochemistry and Molecular Biology; he is also Technical Director of the NIH Resource for Biomedical Complex Carbohydrates located at the CCRC.

SH2 Domain Structures

David Cowburn and Michael Overduin

The Rockefeller University, New York, NY, USA

1	Introduction	1
2	Solution Structure of the Abl SH2 Domain	1
3	General Topology	1
4	Structural and Sequential Alignment of Related Sequences	1
5	Comparison with Other Determined SH2 Domain Structures	2
6	Ligand Binding for Abl SH2	3
7	Modularity of the SH2 Domain	4
8	Mutagenic Data Explained by the Structure	4
9	Conclusions	5
10	Related Articles	5
11	References	5

1 INTRODUCTION

Signals induced by a variety of polypeptide growth hormones are transduced from cell surface receptors through pathways of interacting cytoplasmic proteins. Many of these intracellular signal transducing proteins, notably the non-receptor protein kinases, contain Src homology 2 (SH2) regions,[1] which have a strong binding affinity for target protein sequences that contain a phosphorylated tyrosine residue. Many receptors have tyrosine kinase domains that are directly activated by ligand binding and which autophosphorylate themselves, creating binding sites for proteins with SH2 regions.

The c-*abl* gene product is a nonreceptor tyrosine kinase that, when mutagenically activated in a variety of ways, can induce neoplastic transformation of pre-B cells and fibroblasts. An intact SH2 region is required for the transformation by activated c-Abl. The oncogenic activity of the Abl oncoprotein appears to depend on the ability of the SH2 to bind phosphotyrosine, since a series of conservative point mutations in the highly-conserved FLVRESES motif of the SH2 region coordinately impaired both binding to tyrosine-phosphorylated proteins and transforming activity.[2] It was suggested from these studies that the Arg and two Ser residues of the FLVRESES motif were involved in phosphotyrosine binding.

2 SOLUTION STRUCTURE OF THE Abl SH2 DOMAIN

The solution structure of the SH2 of Abl has been determined and consists of a compact α/β domain with a phosphotyrosine ligand-binding site on a face distal from the termini. Assignments of nearly all ^{1}H and ^{15}N resonances of the SH2 domain have been obtained from homonuclear and heteronuclear NMR experiments.[3] The tertiary structure has been calculated using 1754 interproton distance constraints, 33 pairs of hydrogen bond constraints and 79 pairs of ϕ angle constraints and is well defined with regular secondary structure the two β-sheets and two α-helices.[4]

A family of solution structures determined from NMR constraints reveals that the SH2 domain of Abl contains two antiparallel β-sheets and two α-helices folded together in an apparently novel fashion (Figure 1).[4] The arrangement of secondary structural elements ('supersecondary structure') determined by NMR[3] was used to trace the backbone elements through the electron density of the Src SH2, leading to a high-resolution crystal structure for two low-affinity peptide complexes.[5]

Protein structure determination by NMR provides information about secondary structural elements at an early stage, so this cooperation with X-ray structure determination may be expected to be repeated. Comparison of NMR and X-ray determined structures is obviously of significance in identifying crystal packing effects, and variations of structure associated with solution conditions. Additionally, early levels of structural detail from NMR provide the information needed for a structural biological analysis—the general topology of the protein, surface features likely to provide binding sites, improved alignment of the family of sequences related to the target sequence, modularity of the structure, and explanation of previous mutagenesis experiments.

3 GENERAL TOPOLOGY

The central architectural feature of Abl SH2 is a large antiparallel β-sheet that consists of the three strands; βB(32−38), βC(44−51), and βD(54−60) (Figures 1 and 2). Based on mutagenesis data discussed later, it appears that the putative phosphotyrosyl binding site is formed by conserved residues in this sheet and in a short amphipathic α-helix, αA(17−25), that runs along the central strand. Arg-18 emerges from underneath the helix to lie over the aromatic ring of His-57 on βD (see Figure 1). Arg-36, an absolutely conserved residue in the FLVR sequence, projects toward Arg-18 from βB. A conserved positively charged residue represented by Arg-59 in the Abl SH2 domain is located on βD across from Arg-36. All three arginine side chains are solvent exposed and structurally unconstrained at their termini. Crystallographic studies definitively establish this area as the site of phosphotyrosine binding in phosphotyrosyl peptides.[5−7]

4 STRUCTURAL AND SEQUENTIAL ALIGNMENT OF RELATED SEQUENCES

A group of SH2 domains[3] are aligned with the Abl sequence on the basis of conserved secondary structure in Figure 2. Particular emphasis has been placed on the preservation of glycine and proline residues at turns and to the retention of the amphiphilic character of β-strands and α helices. Deletions and insertions are placed in loop-and-turn regions. Considerable conservation of amino acid identity or at least hydrophobicity allow all the elements of secondary structure including the six β-strands, two mini-β-strands, and two α helices to be aligned relatively easily by visual inspection. The hydrophobic face of the αA-helix spanning Ser-17−Leu-25 in Abl contains conserved leucine and alanine residues. Likewise,

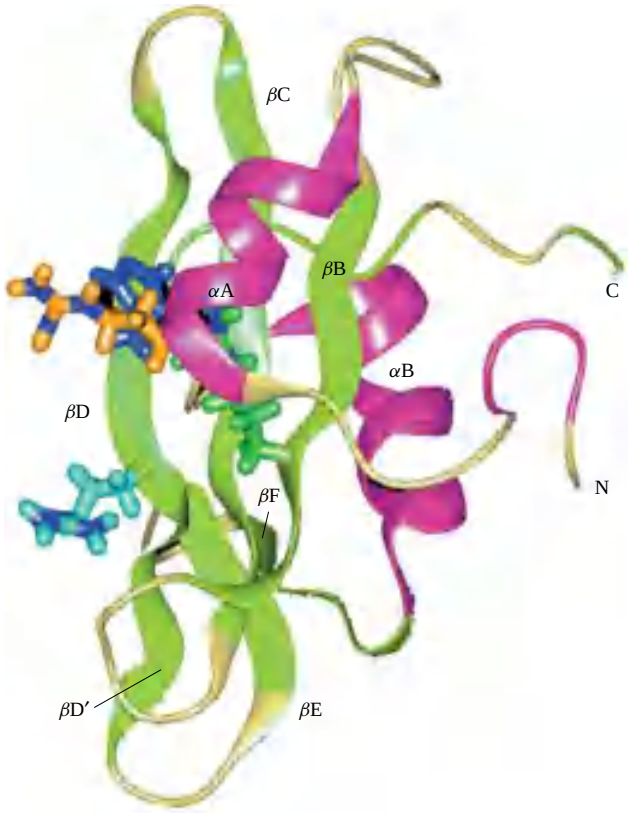

Figure 1 Schematic ribbon drawing of the Abl SH2 domain. Strands are shown in light green (βB, C, D, D′, E, F). Helices are colored red. The N- and C-termini are indicated. Three arginyl residues implicated in the binding site are shown as full side chains; the positions of atoms beyond the β atoms is arbitrary. These are Arg-36 (light green), in the FLVR sequence (see text), Arg-18 at the end of the first helix (yellow), and Arg-59 (light blue). The side chain of His-57, close to Arg-18, is also shown in dark blue

the hydrophobic face of αB consisting of residues Leu-79, Leu-82, Val-83, His-83, and His-86 in Abl is conserved.

The length of the αA–βB loop is highly conserved. An exception is the N-terminal SH2 of PLC-γ1 where a five-residue insertion including two glycines and two oppositely charged residues is inserted to form a flexible and exposed loop. Also highly conserved is an aliphatic residue in the third position of the loop. This hydrophobic residue is represented by Val-15 in the Abl SH2 and is in a position to interdigitate with the conserved leucine of the FLVR sequence. Such an interdigitation could not be confirmed with NOEs due to the lack of a complete Leu-34 spin system assignment. However, only the C-terminal p85α SH2 does not have an aliphatic at this position in βB. In addition, the C-terminal p85α SH2 is the only SH2 without an aromatic residue immediately following the absolutely conserved tryptophan. This pattern suggests a structural interaction between these two spatially proximal residue positions (on βB and the mini-β-strand, βA) that can take the form of either a polar–polar (as in p85α) or aromatic–aliphatic stabilizing interaction.

The large β-sheet is the most highly conserved region. No glycines are found in any of the SH2 sequences here, indicating that the curvature of the sheet is maintained. However, a proline is found in the sixth position of βB in the SH2 of D-Srcl and the N-terminal SH2 of PTP1C. This proline would alter the inflection of the phosphate binding loop.

Two classes of junction between βC and βD are evident in Figure 2. Most SH2 domains are similar to the Abl sequence with a tight turn formed at Glu-52–Gly-53. The sequence alignment with other SH2 sequences shown in Figure 2 reveals that although the consensus sequence for such a type II turn is Xxx–Gly–(Ser/Thr)–Xxx, in SH2 domains the second position of this turn is usually occupied by a charged or polar residue while the third position of this four residue turn is typically a glycine. In contrast, SH2 domains from the *src* family have a hydrophilic insertion here while maintaining a Gly at the last turn position. Such an insertion does not disrupt the pairing of conserved residues, it merely extends the loop. The larger size of this turn in Src suggests the name 'Src family insertion point'. Those SH2s that contain such an insertion invariably include an aromatic at the first position of the turn and invariably have a simultaneously inserted leucine immediately following αA. As these positions on the two loops are near each other, a stabilizing hydrophobic interaction could occur between them.

The point of juncture between the two β-sheets is conserved except in the cases of Crk and the N-terminal SH2 domains of PLC-γ1 and PLC-γ2. Due to the amino acid sequence heterogeneity in the βD′ strand, it is difficult to predict whether the insertions in these three SH2s would contribute to D′E or E–F loops. In the case of the Crk SH2, the insertion consists of 17 residues consisting primarily of alanines, arginines, glycines, and prolines. The glycine in the D′E loop is highly conserved and suggests the conservation of a β-bulge here.

The conservation of the final turn of the αB-helix is relatively poor. For example, positively charged dipeptides could serve to disrupt the third turn of this helix in the C-terminal GAP, Hck, Nck, and PTP-1C SH2 domains, and may impact the shape of the hydrophobic pocket found to provide specific interactions with bound peptides in the crystal structures of Src and Lck SH2s. An extended sequence with considerable heterogeneity in both length and amino acid composition follows αB. In the cases of SH2 domains of the p85α, Nck, Vav, Fps/Fer, and PTP1C types, sufficient sequence is inserted to allow the formation of a two stranded antiparallel β-sheet as has been found in the case of the N-terminal p85α SH2.[8]

5 COMPARISON WITH OTHER DETERMINED SH2 DOMAIN STRUCTURES

Two other SH2 domain structures were reported at the same time as the Abl SH2 domain structure. The crystal structure of the Src SH2[5] and the solution structure of the N-terminal p85 PI 3-K[8] do not differ in their folds from each other or the Abl SH2 structure. Two minor differences result from small insertions. Five additional residues are found between the βB and βC-strands in the Src SH2 and result in the formation of a hydrophobic loop which is disordered in the crystal structure. Insertion of several residues after the helix αB of the p85α SH2 introduces a second strand which pairs with a second strand similar to the extended segment that runs through the core of the Abl SH2.

A difference between the number of β-strands in the solution and crystal structures was originally reported as being

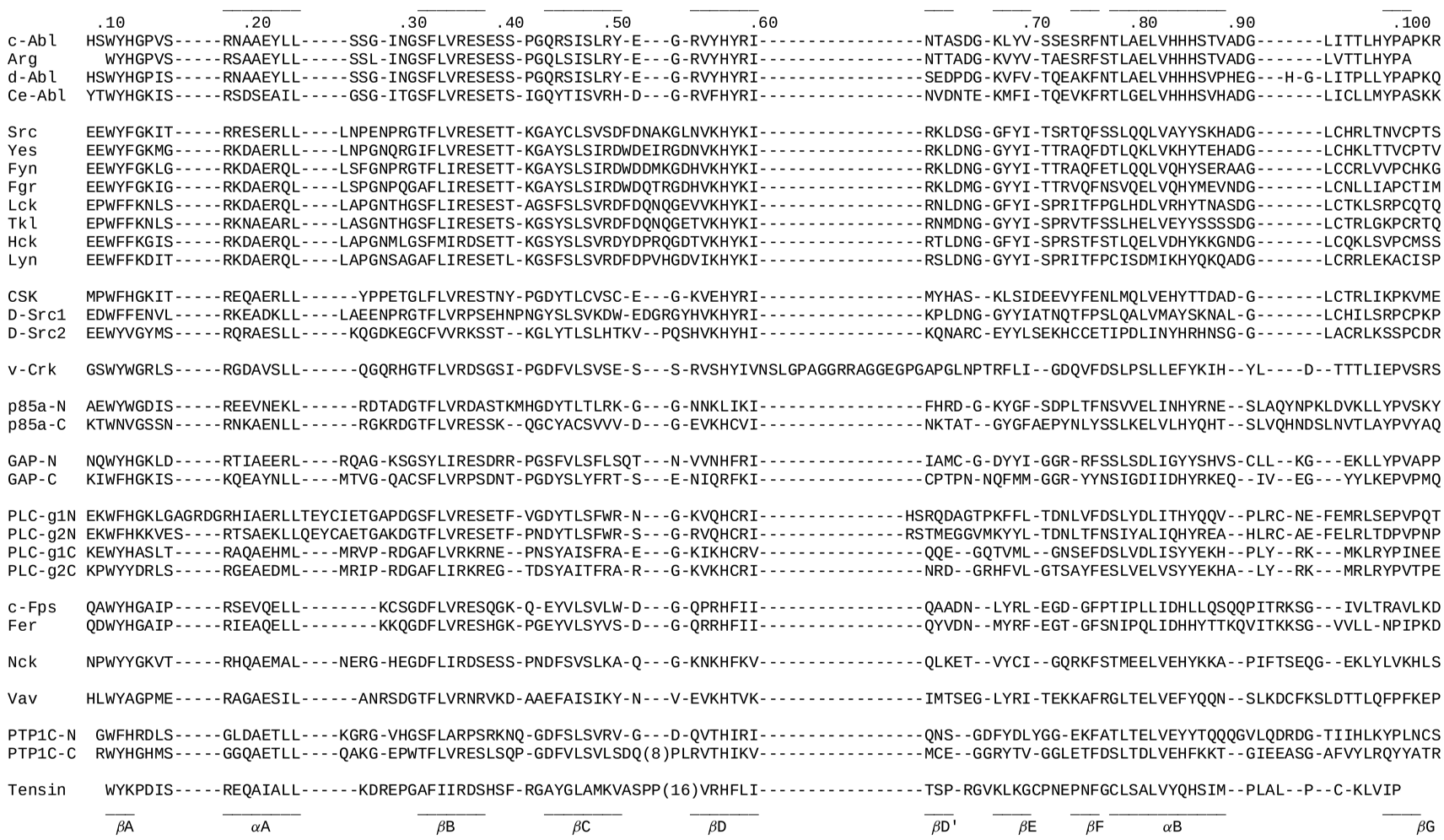

Figure 2 Alignment of SH2 sequences with that of Abl based on the derived secondary structure of Abl. Most sequences were previously tabulated.[1] Amino acid residues are numbered relative to the c-Abl SH2 sequence. The naming of the segments follows previous suggestions[6]

due to the addition of two mini-β-strands which pair with the βB-strand of the crystal structure. The NOE spectra of the Abl SH2 have been reinvestigated to determine if two such mini-β-strands are present and if they align with the βB-strand in a parallel fashion. A conserved parallel alignment is found for the two mini-β-strands. However, the weak $d_{\alpha\alpha}$(12, 36) NOE and $d_{\alpha\alpha}$(32, 99) NOEs indicate that the two mini-β-strands do not have standard pairing interactions with βB. The majority of stabilizing interaction juxtaposing the elements originate from buried aromatic groups rather than conventional interstrand forces such as hydrogen bonds.

Structural comparisons to the peptide-bound form of the Src SH2[5] reveal differences in the conformation of the phosphate binding loop. In the case of the Src SH2, this loop is more inflected and is hydrogen bonded to the bound phosphate, while in the Abl SH2 this loop is more disordered and less inflected. The relative orientation of the helices and sheets are essentially identical.

There is, however, ample evidence that there are significant variations in some SH2 structures in other gene products. For example, the SH2 in STAT91 is likely to be significantly different in the C-terminal portion of its structure from the SH2s mentioned here, on the basis of alignment, and its probable role in forming a dimer on phosphorylation in a intermolecular self-recognition complex.[9]

6 LIGAND BINDING FOR Abl SH2

Previous mutational studies have established the significance of the 'FLVRESES' site for phosphotyrosine binding.[2] The disruption of binding by conservative mutations of the Arg-36, Ser-38, and Ser-40 residues in this motif can be seen to be consistent with their exposed positions on the βI-strand and phosphate binding loop. In the Abl SH2 domain structure, the side chains of all three residues are exposed with the serine residues projecting from the side of the five-residue βB–βC loop that is inflected toward Arg-36. Other studies have found that mutation of the conserved Arg-18 and His-57 residues perturb the function of SH2 domains.[10–12] In the Abl SH2 domain structure, the aromatic ring of His-57 contacts the side chain of Arg-18 while the side chain of Arg-36 is nestled between αA and βC, and in some structures is oriented towards the His-57 ring. The spatially proximal side chain of Arg-59 is also in a position to contribute to the binding of the phosphotyrosine. The buffer specific chemical shifts of the amide resonances of Glu-39 and Ser-41 in the phosphate binding loop described earlier also provide experimental evidence for the role of the loop in phosphate coordination.[13] The specific interactions of this phosphotyrosine ligand binding mechanism can be seen in the peptide-Src SH2 complex crystal structure.[5] The high degree of conservation of Arg-18, Arg-36, and His-57, and the preference for a positive charge at residue 59, suggest that this basic cluster constitutes a common phosphotyrosine binding site within the SH2 domain family.

The two loops tethering αA to the rest of the domain appear to be flexible, with conserved glycyl residues found at either end. Within the SH2 domain family the exposed residues of the central βC-strand maintain a preference for small polar residues, providing a 'slick' surface that could allow αA to shift transiently from its alignment along βC. A helix-containing 'trough' on the surface of the major β-sheet is formed by Val-55 on βD and Leu-34 on βB. The exposed side chains of Ala-20 and Leu-24 on the helix could then roll from their exposed positions toward conserved Leu-34 on βB during the insertion of a phosphotyrosine group. Furthermore, the lack of slowly exchanging amides in all but the last residue of the αA-helix suggests that the beginning of the helix which points into the binding site is conformationally flexible.

The crystal structures of Src[7] and Lck[6] complexed with specifically bound peptides containing the pYEEI (pY = phosphotyrosyl residue) sequence reveal a number of intermolecular polar and hydrophobic interactions. These interactions presumably determine the peptide specificities of the Src class of SH2s. The Abl SH2 binds with highest affinity to pYENP sequences,[14] implying that contacts to the pY + 2 and + 3 positions should provide discrimination between the specificity of the Abl and Src-type SH2s. No direct contacts are made to the pY + 2 Glu in either SH2 crystal structure, although two water-mediated hydrogen bonds are made to Ile and Arg of Src SH2 that are equivalent to Val-70 and Asn-61, respectively, in the Abl SH2. The Arg–Asn-61 substitution in the SH2s may result in the Glu–Asn specificity switch at the pY + 2 positions. Thus, electrostatic interactions appear to constitute a specific determinant for the pY + 2 position of the peptide.

A hydrophobic pocket engulfs the pY + 3 position of the Src SH2 and Lck specific complexes. This hydrophobic pocket is formed from the βE–βF loop and the loop following αB. Of the Src and Lck SH2 residues that contact the pY + 3 position, only three differ in the Abl SH2 but do not differ between Lck and Src. Equivalent positions in the Abl SH2 sequence to these residues are Val-70, Glu-73, and His-86, and correspond to an Ile, Arg, and Tyr, respectively, in the Src/Lck sequences. The interaction provided by the $C\gamma H_3$ group of the Ile could be mimicked by Abl's Val-70. The Arg side chain lies over the rim of Lck's hydrophobic pocket to contact the pY + 4 backbone carbonyl group. In the Abl SH2, the Glu at this position could fold over the pocket but would not be expected to interact in an analogous electrostatic manner with the residue at position pY + 4.

The last residue capable of directly determining peptidic specificity is the buried aromatic provided by αB. This residue is highly conserved and is represented by a Tyr and a His in the SH2s of all members of the Src and Abl families, respectively. In the case of the Src SH2, the *meta* position of the Tyr is 4.4 Å from the $C^{\delta}H_3$ of the peptide's Ile at position pY + 3. Abl SH2's His-86 would not make a comparable contact to a Pro at this peptidic position since the Pro would not be expected to insert as deeply into the core. However, subtle differences in the core architecture could allow the Abl SH2 domain to make specific interactions to the pY + 3 proline.

7 MODULARITY OF THE SH2 DOMAIN

The residues between Trp-11 and Leu-97 appear to be absolutely necessary to form the tightly packed structure of the Abl SH2 domain. Both residues contribute to the hydrophobic core and are absolutely conserved. The tryptophan side chain is very bulky, and it acts as an essential anchor by holding the first mini-β-strand against the βB-strand. Similarly, the bulky leucine side chain acts to anchor the sequence immediately

prior to the second mini-β strand (G) in the hydrophobic core. Turns near both the C- and N-terminal regions direct the two termini in a parallel fashion away from the body of the domain. This orientation would allow the SH2 domain to be rooted by its termini on the surface of a larger protein while leaving its putative ligand-binding region exposed to solvent.

8 MUTAGENIC DATA EXPLAINED BY THE STRUCTURE

A large number of mutations of SH2 domains have been generated by several groups to explain SH2 behavior. The effects of these mutations can now be reinterpreted in the light of the conserved tertiary structure. In particular, mutations that appear to disrupt the binding of the phosphotyrosine or the adjacent ligand sequence and would disrupt the tertiary structure were generated. For example, the apparent destabilization caused by mutation of the Phe of c-Src's FLVR sequence to a Pro[15] can be seen to result from the major perturbation it would cause in the twist of the major β-sheet.

A number of mutations of the c-Src SH2 result in increased kinase and/or transforming activity but are not as transforming as v-Src,[12] presumably by disrupting the intramolecular autoinhibitory association between the Src's C-terminal, phosphorylated Tyr-527 residue with its adjacent SH2 domain. In particular, point mutations of the absolutely conserved, N-terminal Trp to an Arg, of the conserved Arg in αA involved in ligand recognition to a Ser, or of the Gly immediately preceding βB to a Leu in c-Src all appear to deactivate the SH2. The Arg–Ser mutant would remove a point of coordination of the bound phosphotyrosine and would lead to a direct loss of SH2 binding function. The Trp–Arg mutation would introduce a buried charge and would be destabilizing. The Gly–Leu mutation introduces an exposed aliphatic that could be destabilizing or complicate the folding of the domain, or else it could deactivate the SH2 by lowering an essential conformational flexibility of the attached αA-helix.

Mutation of the Ser at the fifth position of the βC strand to a Glu slightly reduced kinase and transforming activity of Src,[16] presumably by altering the packing of the αA-helix against the β-sheet and thus compromising the phosphotyrosine binding interactions. Replacement of the Glu at the fifth position of the αA-helix to an Ala, Asp, or Lys residue all reduce the kinase and catalytic activity of Fps in a similar fashion.[1] Substitution of the conserved and exposed Tyr in the N-terminal mini-β-strand with a Ser–Arg–Asp tripeptide dramatically reduced the transforming activity of Fps,[17] presumably by deactivating the SH2 by altering the structure of the phosphate binding site. Also not surprising is the negligible effect[16] of replacing the exposed second Arg of the αA of Src SH2 with a Leu since this Arg plays no identified role in phosphopeptide recognition.

A few mutants relevant to peptide binding specificity determinants have also been reported. Most significantly, the Arg-205 $\rightarrow$ Leu mutation would be predicted to change Src's specificity for the pY + 2 peptide position, since this residue makes specific contacts to the peptide in the SH2-peptide complex.[7] In fact, no change in the transforming or kinase activity of this Y527F-derived Src mutant was found,[16] indicating that the specificity of the SH2s was not discernibly affected. Mutation of the conserved Val in the buried portion of central turn of αB to a Glu would be expected to disrupt core packing and the hydrophobic pocket that contacts the pY + 3 position of the peptide.[7] A small gain of function of this Y527F Src mutant, however, was reported[16] indicating that the transforming role of Src can be independent of the ability of its SH2 to bind peptide specifically.

9 CONCLUSIONS

The modular design of the SH2 domain allows it to be easily inserted into protein sequences without gross structural changes and permits the formation of multidomain assemblages with interactive signalling functions. The novel fold of this structure was elucidated independently for Abl and the simultaneously reported and topologically identical SH2 domains of the p85α[8] and Src[5] proteins. The Src SH2 crystal structures were determined using the secondary and supersecondary structure information from the Abl SH2 to trace several disordered loops connecting the resolved β-strands and α-helices, and to determine β strand directions. Those crystal structures provided a defined view of the ligation of phosphotyrosine and how this is discriminated from other phosphorylated products. This is the first reported use of supersecondary NMR information to trace a crystal structure of a protein with a novel fold, and demonstrates the emerging power of NMR as a structural biology tool. NMR structural information at many levels provides a rich source of interpretation of the results from complementary biological techniques.

10 RELATED ARTICLES

Biological Macromolecules: Structure Determination in Solution; Biological Macromolecules; Biological Macromolecules: NMR Parameters; Calcium-Binding Proteins; Nuclear Overhauser Effect; Nucleic Acid Structures in Solution: Sequence Dependence; Protein Hydration; Protein Structures: Relaxation Matrix Refinement; Proteins and Protein Fragments: Folding; Structures of Larger Proteins, Protein-Ligand, and Protein-DNA Complexes by Multi-Dimensional Heteronuclear NMR.

11 REFERENCES

1. C. A. Koch, D. Anderson, M. F. Moran, C. Ellis, and T. Pawson, *Science*, 1991, **252**, 668.
2. B. J. Mayer, P. K. Jackson, and D. Baltimore, *Proc. Natl Acad. Sci. USA*, 1991, **88**, 627.
3. M. Overduin, B. J. Mayer, C. B. Rios, D. Baltimore, and D. Cowburn, *Proc. Natl Acad. Sci. USA*, 1992, **89**, 11 673.
4. M. Overduin, C. B. Rios, B. J. Mayer, D. Baltimore, and D. Cowburn, *Cell*, 1992, **70**, 697.
5. G. Waksman, D. Kominos, S. C. Robertson, N. Pant, D. Baltimore, R. B. Birge, D. Cowburn, H. Hanafusa, B. J. Mayer, M. Overduin, M. D. Resh, C. B. Rios, L. Silverman, and J. Kuriyan, *Nature (London)*, 1992, **358**, 646.

6. M. J. Eck, S. E. Shoelson, and S. C. Harrison, *Nature (London)*, 1993, **362**, 87.
7. G. Waksman, S. E. Shoelson, N. Pant, D. Cowburn, and J. Kuriyan, *Cell*, 1993, **72**, 779.
8. G. W. Booker, A. L. Breeze, A. K. Downing, G. Panayotou, I. Gout, M. D. Waterfield, and I. D. Campbell, *Nature (London)*, 1992, **358**, 684.
9. K. Shuai, C. M. Horvath, L. H. T. Huang, S. Qureeshi, D. Cowburn, and J. E. Darnell, Jr., *Cell*, 1994, **76**, 821.
10. H. Hirai and H. E. Varmus, *Mol. Cell. Biol.*, 1990, **10**, 1307.
11. M. Matsuda, B. J. Mayer, and H. Hanafusa, *Mol. Cell. Biol.*, 1991, **11**, 1607.
12. M. C. O'Brien, Y. Fukui, and H. Hanafusa, *Mol. Cell. Biol.*, 1990, **10**, 2855.
13. M. Overduin, Ph.D. Thesis, Rockefeller University, 1993.
14. Z. Songyang, S. E. Shoelson, M. Chaudhuri, G. Gish, T. Pawson, W. G. Haser, F. King, T. Roberts, S. Ratnofsky, R. J. Lechleider, B. G. Neel, R. B. Birge, J. E. Fajardo, M. M. Chou, H. Hanafusa, B. Schaffhausen, and L. C. Cantley, *Cell*, 1993, **72**, 767.
15. H. Hirai and H. E. Varmus, *Genes Dev.*, 1990, **4**, 2342.
16. H. Hirai and H. E. Varmus, *Proc. Natl Acad. Sci. USA*, 1990, **87**, 8592.
17. K. A. Johnson and J. C. Stone, *J. Virol.*, 1990, **64**, 3337.

Biographical Sketches

David Cowburn. *b* 1945. B.Sc., 1965, University of Manchester Institute of Science and Technology; Ph.D., 1970, London University; D.Sc., 1980, London University. Fascinated during Ph.D. by the potential for NMR as a structural tool in biochemistry. Faculty of Rockefeller University, 1973–present. Approx. 100 publications. Research interests include structure–function relationships in biological chemistry, development of magnetic resonance techniques in biomedical research, determination of molecular conformation by spectroscopic techniques, particularly magnetic resonance and applications of these to understanding molecular mechanism of control of genetic expression, and of intracellular signal transduction.

Michael Overduin. *b* 1967. B.S., 1988, Ph.D., 1993, The Rockefeller University, USA. Postdoctoral fellow at the University of Toronto (with Mitsu Ikura) 1993–1995. Faculty, University of Colorado School of Medicine, 1995–present. Approx. 15 publications. Research specialty: elucidation of the structure and function of protein domains involved in signal transduction.

Sonicated Membrane Vesicles

Wen-guey Wu

National Tsing Hua University, Hsinchu, Taiwan

1	Introduction	1
2	Monolayer Packing Asymmetry in Bilayers with Curvature	1
3	Structure and Dynamics of Phosphatidylcholine in Vesicles	3
4	Other Lipid Systems	6
5	Related Articles	6
6	References	6

1 INTRODUCTION

Current understanding of the structure and dynamics of lipids in membranes is, to a large extent, promoted by the availability of various membrane model systems. Sonicated membrane vesicles, or small unilamellar vesicles first characterized and prepared by Huang in 1969, have been utilized extensively in NMR studies because of the high-resolution features in their spectra. A reflection on how the original idea was conceived to prepare a homogeneous fraction of a sonicated membrane vesicle is given by C. Huang.[1] Much structural and dynamic information of membrane lipids was thus inferred before the advent of solid state NMR spectroscopy suitable for unsonicated membrane studies. Therefore, solution NMR studies of sonicated membrane vesicles may be considered to have played a pioneering role for the solid state NMR investigation of planar membranes.

The interest in studying sonicated membrane vesicles, however, extends beyond a simple model membrane system for NMR studies. There is a growing interest in how curvature of the lipid/water interface affects packing of the lipid acyl chains.[2,3] It has been suggested that the curved membrane surface may be important in affecting protein–lipid interactions. The discussions and endeavors for settling the controversial issue in the interpretation of fatty acyl chain order derived from NMR studies of small vesicles in comparison to planar membranes has also attracted many ingenious NMR approaches. Progress in the application of NMR lineshape analysis to studies of the molecular ordering and conformations of membrane lipids and in the interpretation of nuclear spin relaxation experiments has been made possible partially because of these efforts.

One of the important criteria for the quantitative interpretation of the NMR spectra of sonicated membrane vesicles, unfortunately often neglected, is the homogeneity of the spin systems used for experiments.

First, simple sonication of aqueous dispersions of phospholipids does not produce the homogeneous preparation of vesicles. In fact, the vesicles produced by extensive ultrasonication are extremely heterogeneous if they are not further purified carefully by gel filtration or ultracentrifugation. From the practical standpoint of model membrane preparation, gel filtration chromatography is highly suitable for the fractionation of phospholipid vesicles after phospholipids have been subjected to prolonged ultrasonic irradiation in buffered aqueous solution under an N_2 atmosphere. Although ultracentrifugation can, in some cases, yield a similar homogeneous preparation, it should be borne in mind that the centrifugation conditions for vesicles with different lipid composition are different, and thus subject to variation depending on the preparation. (Many drawbacks of the gel filtration technique listed by Barenholz et al.[4] can be avoided by using the new gel filtration medium.)

Secondly, severe surface curvature in small unilamellar vesicles imposes structural and dynamic differences on the lipid measurements of the inner and outer monolayers of small vesicles; the two halves of the bilayer have different radii of curvature both in sign and magnitude. Therefore, even if a homogeneous vesicle system is used, the obtained NMR signals, if not distinguished between the inner and outer monolayers, would still contain intrinsic heterogeneous factors. In this respect, the ^{1}H NMR spectra observed at low frequency or the ^{2}H NMR spectra obtained from synthetic lipids should be considered as superimpositions of two spin systems in sonicated membrane vesicles.

In order to illustrate how NMR studies can lead to useful information about the molecular order and packing arrangement of phospholipid in vesicles, we first consider sonicated phosphatidylcholine vesicles. The single-component phosphatidylcholine vesicle system has been well characterized by many physical techniques, including ^{1}H NMR, ^{2}H NMR, ^{13}C NMR, ^{19}F NMR and ^{31}P NMR. The results of these studies not only provide information concerning the monolayer packing asymmetry of phosphatidylcholine in highly curved vesicles (Section 2), but also shed light on the membrane structure and dynamics (Section 3). Finally, we consider how the NMR studies of other lipid vesicle systems could add an additional dimension in future membrane studies (Section 4).

2 MONOLAYER PACKING ASYMMETRY IN BILAYERS WITH CURVATURE

Sonicated membrane vesicles have been widely used as a model system for magnetic studies, not only because of the suitability of their homogeneous preparations for solution NMR investigations, but also due to the availability of a large number of physical properties. Herein, we illustrate how these physical properties, with the help of the information provided by NMR measurement, could lead to additional understanding of the membrane bilayer structure at molecular level.

2.1 Combined Hydrodynamic and NMR Measurements

From a series of hydrodynamic studies,[5] sonicated egg phosphatidylcholine vesicles were shown to be spherical with unhydrated vesicle radius (R_c) of 99 Å and molecular weight (M) of 1.88×10^6 Da. Since the partial specific volume (v), or the average volume per lipid molecule, has been determined to be 0.9848 mL g^{-1}, one can thus impose a simple geometric constraint on the vesicles as follows:

$$M = \{768\ \text{Da}(n_o + n_i)\} = N(\tfrac{3}{4}\pi(R_c^3 - R_a^3)\}/v \qquad (1)$$

where 768 Da is the average molecular mass of an egg phosphatidylcholine molecule, N is Avogadro's number, R_a is the radius of the water cavity trapped inside the vesicle, and $(n_o + n_i)$ is the summation of the number of molecules in the outer monolayer, n_o, and in the inner monolayer, n_i, of the spherical vesicle. Assuming that the average volume per lipid molecule is the same for the phosphatidylcholine molecules in the two monolayers of the vesicle, i.e., $v_o = v_i$, one can obtain the other geometric constraints as

$$n_o/n_i = (R_c^3 - R_b^3)/(R_b^3 - R_a^3) \quad (2)$$

$$v_o = \tfrac{4}{3}\pi(R_c^3 - R_b^3)/n_o \quad (3)$$

$$v_i = \tfrac{4}{3}\pi(R_b^3 - R_a^3)/n_i \quad (4)$$

where v_o and v_i are the volume available to each lipid molecule within the outer monolayer and the inner monolayer, respectively, and R_b is the radius at the acyl chain interface between the two lipid monolayers. One can therefore solve all the geometric radial parameters (Figure 1) if the value of n_o/n_i, the ratio of the number of molecules in the outer monolayer to that in the inner monolayer, can be measured.

Paramagnetic ions such as europium (Eu^{3+}), when applied exogenously to the sonicated membrane vesicles, shift the NMR signals of the accessible lipid molecules.[6] Since the membrane bilayer is impermeable to most ions and the osmotic effect of small vesicles is negligible, the amount of lipid molecules located either in the inner or the outer monolayer can be determined by simply measuring their respective NMR signal intensity. After considering the change of the signal intensity caused by the relaxation effect of the shift reagent introduced, the molecular ratio of the two halves of sonicated egg phosphatidylcholine vesicle bilayers has been spectrally determined to be about 2.1. Similar results can also be obtained by employing various lanthanide ions in ^{1}H, ^{13}C, and ^{31}P NMR studies to determine the phospholipid asymmetry in vesicle bilayers.[5]

The packing parameters for the sonicated egg phosphatidylcholine vesicles have been calculated on the basis of NMR values of n_o/n_i and equations (1) and (2). The results are illustrated in Figure 1. It can be seen that the average area per molecule for lipids in the *outer monolayer* is less at the center (46 Å^2) of the bilayer than it is at the surface (74 Å^2), whereas for lipids in the *inner monolayer* the average area per molecule is greater at the bilayer center (97 Å^2) than at the surface (61 Å^2). In addition, the average chain length (L) for the lipid in the outer monolayer (21 Å) is longer than that in the inner monolayer (16 Å). These packing asymmetries are caused by the higher degree of surface curvature of the inner monolayer relative to the outer monolayer in a small vesicle with a radius of approximately 100 Å. Similar conclusions have also been drawn for dipalmitoyl phosphatidylcholine vesicles.

The monolayer packing asymmetry in the highly curved bilayer, though simple and clear, needs to be considered seriously if the membrane structure and dynamics are to be inferred from NMR data obtained from sonicated membrane vesicles.

2.2 Comparison with Phospholipid Packings of Hexagonal Phases

From the geometric point of view, the phospholipid packing of the inner monolayer of sonicated membrane vesicles is similar to that of the inverted hexagonal H_{II} phase, whereas the packing of the outer monolayer is similar to that of hexagonal H_I phase. Since the segmental order parameters in the acyl chain of both hexagonal H_I and H_{II} phases have been measured by solid state ^{2}H NMR and compared to those of lamellar phase,[3] it is instructive to make a comparison between the packing constraints of the hexagonal H_I/H_{II} phases and the

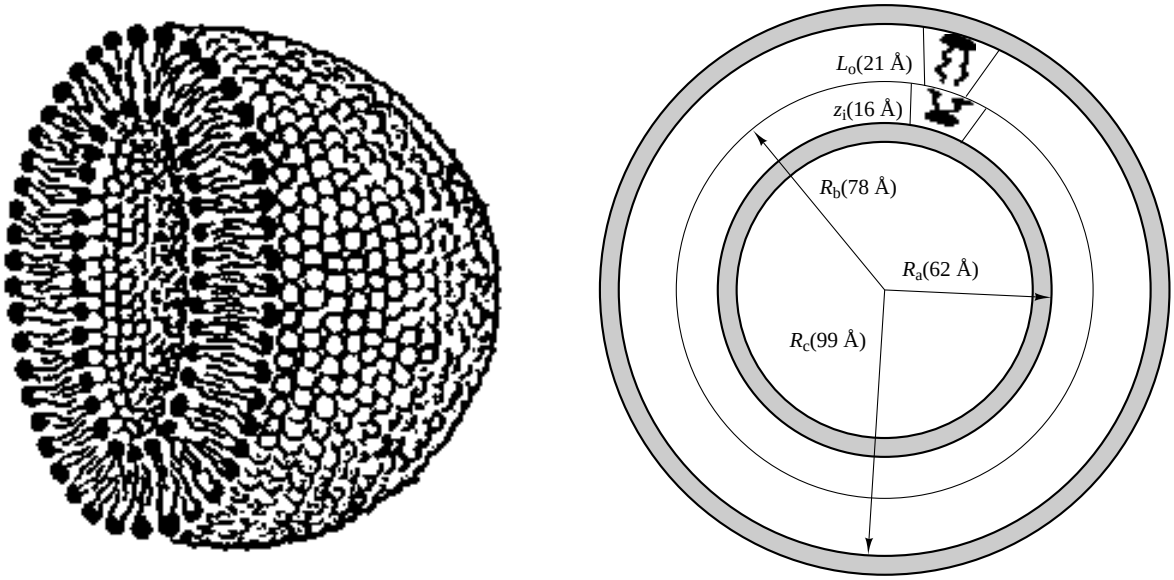

Figure 1 Cross section of vesicle bilayer defining the three radial parameters R_a, R_b, and R_c used in the lipid packing analysis. The two shaded areas represent hydration layers of sonicated egg phosphatidylcholine vesicles. The distances L_o and L_i represent the monolayer thickness of the phospholipid located in the outer and inner halves of the vesicles, respectively. The average area/molecule is shown schematically as the section occupied by the lipid molecules, the values for which are described in the text

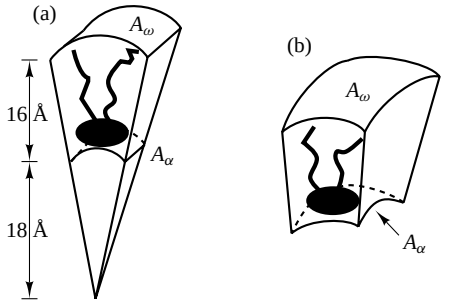

Figure 2 Geometric comparison between the phospholipids located in the inverted hexagonal H_{II} phase (a) and the inner monolayer of sonicated membrane vesicles (b). The radial parameters shown for the inverted hexagonal H_{II} phase are subject to variation with an estimated deviation of 2 Å.[3] The values for the cross-sectional areas at the lipid/water interface, A_α, and at the end of the acyl chain, A_ω, for the inner monolayer of vesicle can be found in the text and Figure 1. The values of A_ω/A_α, and thus the geometric packing constraints, for the two systems are found to be similar

outer/inner monolayers based on their aggregate geometry. The main difference between these two lipid systems is that the curvature of the H_I/H_{II} phases distributes on a cylindrical surface, whereas the curvature of the outer/inner monolayers distributes on a spherical surface.

As depicted in Figure 2, quantitative comparison can be made for the packing constraint between the inner monolayer of sonicated membrane vesicles and the reverse hexagonal H_{II} phase. By using the surface area values obtained in Figure 1, the ratio of the cross-sectional areas at the end of the acyl chains, A_ω, and at the lipid/water interface, A_α, for the inner monolayer of vesicles can be found to be about 1.6. With the available radial parameters of the reverse hexagonal H_{II} phase, similar A_ω/A_α values ranging from 1.7–2.0 are obtained. This simple geometrical calculation, though crude because of the uncertainty in defining the headgroup region, illustrate that packing constraints for the two monolayers of the sonicated membrane vesicles can be similar to those of hexagonal phases although sonicated membrane vesicles have a larger radius of curvature. It is important to note that the surface area ratio for the cylindrical structure depends only on the first order of the radius. To a first approximation, one can estimate the effect of sonication on the molecular order of fatty acyl chains in the two monolayers by using the values determined from the hexagonal H_I/H_{II} phases. It will become clear that the NMR data obtained from sonicated membrane vesicles are indeed consistent with the above notion.

3 STRUCTURE AND DYNAMICS OF PHOSPHATIDYLCHOLINE IN VESICLES

Due to the asymmetric packing arrangement, the curvature affects the polar headgroup and fatty acyl chain regions of the phosphatidylcholine in vesicles differently. Therefore, our discussion in this section will be divided into two parts, keeping in mind that each region of the phospholipid molecule may be located either at the inner monolayer or at the outer monolayer.

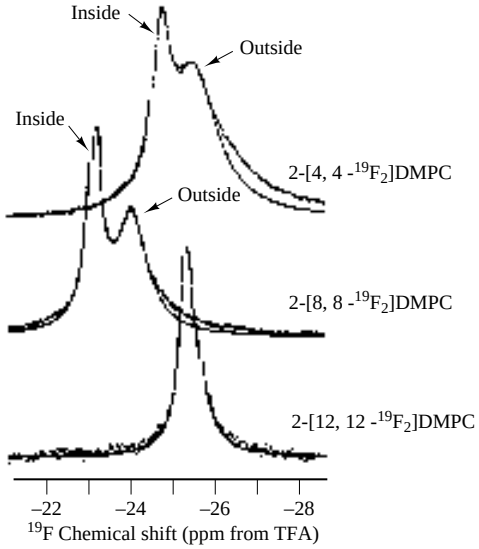

Figure 3 ^{19}F NMR spectra of ^{19}F-labeled phosphatidylcholine in sonicated membrane vesicles at 282.4 MHz and 29 °C. The assignments for the resonances from molecules located at the inner and outer monolayers of vesicles are shown for ^{19}F-labeled phospholipid at the 4- and 8-positions. The linewidths obtained from the inner and outer monolayers differ approximately by a factor of 2

3.1 Fatty Acyl Chain Region

The simplest physical model to account for the NMR results obtained for the fatty acyl chain region was initiated by Chan and co-workers and developed further by many others.[2,7] Basically, there are at least four motions of phospholipids in sonicated membrane vesicles: (i) chain reorientation (wobbling); (ii) chain isomerization (*trans–gauche* isomerization); (iii) lateral diffusion; and (iv) vesicle tumbling. Although different research groups may emphasize different parts of the motions or even introduce new types of motion,[7] these four types of motion provide an adequate foundation for the treatment of NMR data obtained from sonicated membrane vesicles. (A collection of the references on the controversial issue of fatty acyl chain packing has been given by Fenske and Cullis.[8])

In order to illustrate how the monolayer packing asymmetry and the aforementioned four types of motion can be considered in the NMR studies of sonicated membrane vesicles, we discuss results obtained from phosphatidylcholine vesicles labeled with a $C^{19}F_2$ group in the 4-, 8-, or 12-positions of the 2-acyl chain.[9]

^{19}F NMR spectra of sonicated unilamellar vesicles differ dramatically from those of lamellae. Instead of axially symmetric powder spectra, two overlapping Lorentzian resonances with different linewidths are observed (Figure 3). By applying a suitable shift reagent, it can be shown that the two signals originate from labeled phospholipids located at the inner and outer monolayers of the vesicles. Since both ^{19}F chemical shift anisotropy (CSA) and homonuclear dipolar interaction (DD) are averaged to zero on a timescale of 10^{-5}–10^{-6} s, the narrow lines may simply result from averaging of the powder spectra by the isotropic tumbling of the spherical vesicles.[10,11]

To relate the ^{19}F NMR spectra of vesicles and of multilamellar dispersions, we define a correlation time, τ_v, describing the tumbling of the entire vesicle in the solution and diffusion of the lipids around the surface of the vesicle

with correlation times, τ_r and τ_d:

$$\tau_v^{-1} = \tau_r^{-1} + \tau_d^{-1} \quad (5)$$

If the Stokes–Einstein results apply to the vesicle, an assumption validated by hydrodynamic measurements, the defined correlation times for the lipid located in the two monolayers can be rewritten as follows:

$$\tau_{o,i}^{-1} = kT/8\pi R_o^3\eta + D/R_{o,i}^2 \quad (6)$$

where R_o is the outer vesicle radius, R_i is the inner vesicle radius, η the solvent viscosity, and D the lateral diffusion coefficient of the lipid molecules. The values of R_o and R_i can be taken from those of R_c and R_a, respectively, except that a hydration layer of approximately 6 Å should be included. By substituting appropriate values of η (1 cP) and D (10^{-8} cm^2 s^{-1}), the effective correlation time, τ_o, for the outer monolayer is about 10^{-6} s at room temperature. Note that the deduced correlation time depends on the cube of the radius. However, it depends linearly on the rate of lipid lateral diffusion. The second term in the right-hand side of Equation (6) will only slightly decrease the deduced correlation time and therefore the measured linewidth by about 10–20%, depending on whether the lipid is located in the outer or inner monolayer.[10]

The effective correlation time can also be calculated from the experimental ^{19}F NMR linewidth of the vesicles, assuming that other contributions to the linewidth from T_1 and DD (less than 10%) can be neglected, as follows:

$$\Delta\nu_{1/2}(\text{CSA}) = 1/(\pi T_2) = (16\pi/45)(\Delta\nu_{\text{CSA}})^2\tau_v \quad (7)$$

Using the CSA value obtained from the multilamellar liposomes[12] and taking the F-labeled phospholipid at the 8-position as an example, the effective correlation time for the lipid located in the outer monolayer has been calculated to be 4×10^{-7} s. This is about a factor of two smaller than the value estimated from the tumbling motion of sonicated membrane vesicles. Considering the approximation used in the calculation, the agreement between the experimental result and the theoretical prediction is, indeed, remarkable.

A further reduction of the linewidth for the ^{19}F NMR signal obtained from the F-labeled phospholipid located at the inner monolayer is detected as shown in Figure 3. Depending on the labeled position and the temperature, the reduction factor as compared to the outer monolayer ranges from two to three. A similar degree of reduction for the ^{1}H NMR linewidth obtained from the phospholipid fatty acyl chain in the inner monolayer has also been observed at 500 MHz.[13] This could be due to the smaller radius of the inner monolayer, resulting in more effective modulation of the linewidth by phospholipid lateral diffusion,[7] and also to the asymmetric packing of phospholipid in the inner monolayer, resulting in the reduced order parameter profile.[2] The order parameter for the inverse hexagonal H_{II} phase of perdeuterated phosphatidylethanolamine at the 8-labeled position, for instance, is found to be reduced by approximately 30% to 50% as compared to that of the lamellar phase.[3] Since the linewidth depends on the square of the order parameter, one would expect a reduction by a factor of two for the linewidth of the inner monolayer as compared with that of the outer monolayer.

It has been well established from the temperature and frequency dependence of T_1 measurements by ^{1}H, ^{2}H, and ^{13}C NMR in lipid bilayers that two or more characteristic correlation times must exist for the fatty acyl chain motion.[2] For simplicity, one can assume that the observed T_1^{-1} is the sum of two independent contributions:

$$T_1^{-1} = T_{1f}^{-1} + T_{1s}^{-1} \quad (8)$$

where T_{1f}^{-1} indicates the contribution from relatively fast motion and T_{1s}^{-1} is the contribution from slower motion. Much effort has been made to characterize the motional modes responsible for the observed temperature and frequency dependence of T_1^{-1}.

It is generally agreed that the fast internal *trans–gauche* isomerization dynamics in the phospholipid acyl chain dominate the temperature dependence of T_1^{-1}. Assuming the applicability of an isotropic model for the chain isomerization, in the short correlation time range (i.e., $\omega_o\tau_c \ll 1$), the short correlation times are found to be about 10^{-10} s.

Studies of the frequency dependence of T_1^{-1} have allowed the characterization of slow motions in sonicated membrane vesicles. By analyzing the T_1^{-1} dispersion of ^{2}H NMR relaxation data, it has been suggested that restricted chain reorientation, or the wobbling motion of the phosphatidylcholine molecules, is responsible for the frequency dependence in the range of 10–100 MHz. The vesicle T_1^{-1} dispersion of ^{2}H NMR relaxation data below 10 MHz is, however, due to vesicle tumbling and lipid lateral diffusion.[7] Therefore, chain reorientation, lipid lateral diffusion, and vesicle tumbling are three major types of motion responsible for slow motions in sonicated membrane vesicles.

In the following, we address the question as to which part of the motion, slow or fast, is perturbed by the curvature of the sonicated membrane vesicles.

The value of $T_{1\rho}$, but not of T_1, has been found to be different for ^{19}F NMR resonances obtained from ^{19}F-labeled phospholipids located in the inside and outside monolayers of sonicated membrane vesicles.[9] When $T_{1\rho}$ is measured in the presence of an off-resonance magnetic field, the motions sensitive to the effective field at low frequency, rather than stationary field at high frequency, are monitored. The result indicates that slow motions are responsible for the perturbed packing of fatty acyl chain located in the inner monolayer of vesicles. Since the fast motion (10^{-10} s) has been attributed primarily to *trans–gauche* isomerization of the lipid acyl chain, sonication apparently has not substantially changed the isomerization motion along the fatty acyl chain.

The effective correlation time determined by ^{19}F off-resonance $T_{1\rho}$ measurement is approximately 10^{-7} s, almost an order of magnitude lower than the effective correlation time estimated from the vesicle tumbling motion. A motion with similar correlation time has also been detected by studying the spin relaxation of ^{1}H-coupled ^{13}C spectra of fatty acids in sonicated membrane vesicles.[14] Since restricted chain reorientation has been suggested to dominate the corresponding T_1^{-1} frequency dependence, it is tempting to suggest that the effect of sonication on the dynamics of phospholipid in vesicles is to increase the amplitude of chain reorientation on this timescale.

3.2 Polar Headgroup Region

The surface area of molecules in the outer monolayer is larger than that in the inner monolayer. The surface area

of the inner monolayer is similar to the surface area of a planar bilayer in the liquid crystalline state, while the surface area of the outer monolayer is somewhat expanded by curvature (Figure 1). A simple geometrical consideration would show that the average lipid–lipid distances in the headgroup region are stretched almost 1 Å further apart in the outer monolayer. Such an expansion would unquestionably influence the electrostatic interactions of the headgroup in the outer monolayer and therefore the conformation of the polar headgroup. Three examples cited here illustrate how temperature and vesicle size can differently affect the inner and outer monolayers in the phosphocholine headgroup region.

The organization of the zwitterionic phosphocholine headgroup has been studied by $^{31}P\{^1H\}$ NOE and ^{31}P NMR T_1 relaxation of sonicated membrane vesicles.[15] Phosphatidylcholine headgroup packing has been found to consist of the positively charged quaternary amines of each lipid associating with the negatively charged phosphates of adjacent neighbors. In other words, the charged pair of the phosphocholine lies approximately along the plane of bilayer surface. Quantitative analysis of the NOE has suggested that the distance between intermolecular charged pairs is less than 3 Å. It should be pointed out that the monolayer packing asymmetry in sonicated membrane vesicles was not considered in these studies.

Phosphorus-31 NMR signals of the inner and outer monolayer in sonicated membrane vesicles can be studied by applying shift reagents.[16] Temperature-dependent ^{31}P NMR T_1 studies have shown the existence of a distinct minimum relaxation time constant for the two monolayers. They have also revealed a very complicated picture, which suggests the need to reconsider the quantitative analysis of NOE. Nevertheless, ^{31}P NMR temperature-dependent studies of T_1 show that the position of the T_1 minimum for the inner monolayer was 9 °C higher than that of the outer monolayer, indicating a higher level of motional restriction for the inner monolayer.

The ^1H NMR signals of sonicated membrane vesicles at a magnetic field of 7 T or higher show easily distinguishable resonances due to the phosphatidylcholine polar headgroup moiety $-N(CH_3)_3$ located in the two monolayers (Figure 4).[17] Local magnetic effects due to headgroup organization are the important determinant of the difference in the NMR chemical shift between the inner and outer monolayer of vesicles. A difference in headgroup organization may be a result of a variation in the intermolecular electrostatic interactions of the zwitterionic headgroup.[18]

The two resolvable signals of the phosphocholine provide a simple tool for the investigation of the structure and dynamics of the polar headgroup in the two monolayers of sonicated membrane vesicles. In the following discussion we show how this phenomenon can be explained by the monolayer packing asymmetry for the polar headgroup region.

Figure 4 shows the choline *N*-methyl portion, $-N(CH_3)_3$, of the ^1H NMR spectra of sonicated distearoyl phosphatidylcholine vesicles at various temperatures. The chemical shift difference between the inner and outer choline *N*-methyl resonances increases abruptly as the temperature is lowered to the phospholipid phase transition temperature of 50 °C. Careful analysis of the spectra has revealed that the changes result mainly from the low-frequency) shift of the inner monolayer resonance.[17] Therefore, at the phase transition, there is a change in the organization of the inner monolayer headgroup which does not occur for the outer monolayer headgroup.

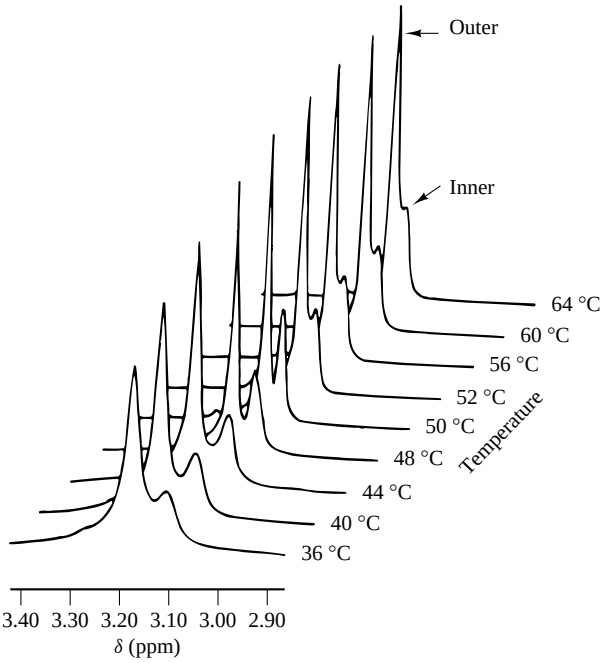

Figure 4 Choline *N*-methyl portion of the 360 MHz ^1H NMR spectrum of sonicated membrane vesicles at various temperatures (°C), Resonances due to molecules on the inner and outer monolayers of the vesicles are indicated by arrows. (Reproduced by permission of Elsevier Science Publishers from K. E. Eigenberg and S. I. Chan *Biochim. Biophys. Acta*, 1980, **599**, 330)

In the liquid crystalline state, the conformation of the inner monolayer headgroups remains unperturbed by curvature since the inner headgroup area remains roughly the same as in a planar membrane. However, in the gel state, its organization is expected to change due to the reduced surface area, and thus the altered electrostatic interactions, at temperatures below the lipid phase transition. This effect is reflected in the abrupt change of the inner monolayer ^1H NMR chemical shift of $-N(CH_3)_3$. The corresponding outer monolayer signal remains similar, presumably because the packing of the headgroup in the outer monolayer is still expanded by the outwardly curved surface in small vesicles.

The experiments discussed so far provide a consistent picture to explain the available data regarding the packing arrangements of both the polar headgroup and fatty acyl chain regions of sonicated membrane vesicles. Because of the opposite packing constraints in the headgroup and fatty acyl chain region, one observes a reduced molecular order, or a perturbed packing, for the polar headgroup located in the outer monolayer and for the fatty acyl chain located in the inner monolayer. In the following discussion we provide another example to suggest that, analogous to the study of the fatty acyl chain region, the perturbed packing of the phosphatidylcholine headgroup in the outer monolayer can also be monitored by studying the linewidths of its NMR signal.

Sonication of the cholesterol/phospholipid dispersions produces small unilamellar vesicles with radii slightly different from single component phosphatidylcholine vesicles. Followed by gel filtration, a homogeneous population of vesicles with diameters ranging from 220 Å to 320 Å can be prepared for NMR investigation.[19]

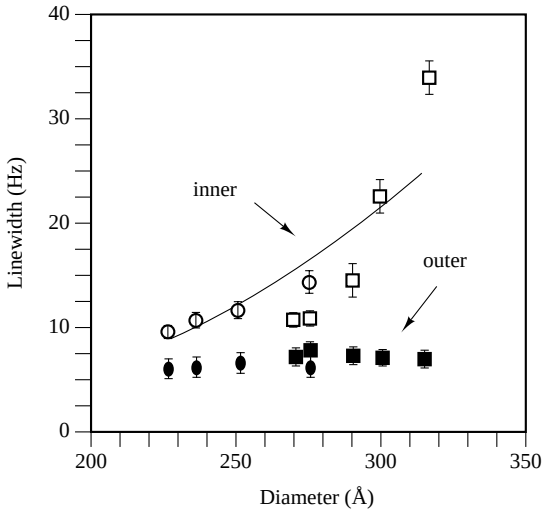

Figure 5 Dependence of the ^{1}H NMR linewidths of *N*-methyl protons as a function of vesicle radius. The vesicles with designated radii were prepared by sonication of cholesterol/egg phosphatidylcholine (squares) and cholesterol/lyso phosphatidylcholine (circles) dispersions at known compositions. The linewidths obtained from phospholipid in the inner monolayer can be empirically fitted by the cube of the radius of the vesicles. The open and solid symbols represent the linewidth estimated from the NMR signals of the inner and outer monolayers, respectively

Figure 5 shows the ^{1}H NMR linewidth obtained from the *N*-methyl proton located in the inner and outer monolayers of sonicated cholesterol/phospholipid vesicles as a function of vesicle size. The ^{1}H NMR linewidth of the inner monolayer increased almost threefold when the diameter of the vesicles increased from 220 Å to 320 Å. According to Equation (7), the linewidth depends roughly on the cube of the vesicle radius. Increasing the vesicle size by 50% would increase the NMR linewidth by a factor of three. Therefore, the variation of the ^{1}H NMR linewidth of the choline *N*-methyl proton in the inner monolayer can be explained by considering the change in vesicle size. Qualitatively similar effects have been observed by ^{31}P NMR studies of the polar headgroup in larger vesicles.[20]

The ^{1}H NMR linewidths obtained from *N*-methyl protons located in the outer monolayers of sonicated vesicles are several-fold smaller than those obtained from the inner monolayers. In addition, they remain relatively constant in the vesicle preparations studied. This indicates that additional motion is present for the phosphocholine headgroup of the lipid molecules located in the outer monolayers. This must be due to the perturbed packing of polar headgroup in the outer monolayers because more effective modulation of the linewidth by phospholipid lateral diffusion can only occur in the inner monolayers.

In conclusion, the linewidth of the *N*-methyl group appears to be a function of the vesicle radius and is also dependent on whether the molecules sit in the inner or outer monolayer. Based on this observation, it is impossible to obtain the same order parameter for the phospholipid molecule in the small vesicles and in the planar bilayer if analysis of the NMR linewidth is undertaken by considering only one NMR signal which actually contains both sharp and broad components. It also explains why the detected NMR linewidth of the fatty acyl chain in small vesicles was markedly smaller than that estimated from the second moment of the planar bilayer and, at the same time, modulated by the solvent viscosity.[2,11]

4 OTHER LIPID SYSTEMS

Our discussion on the structure and dynamics of sonicated membrane vesicles has mainly concentrated on phosphatidylcholine molecules. Biological membranes actually contain many lipid molecules such as cholesterol, phosphatidylethanolamine, phosphatidylserine, sphingomyelin, cerebrosides, etc. With the advent of solid state NMR spectroscopy, especially broadline ^{2}H NMR and magic angle spinning ^{13}C NMR, most of the structural and dynamic information concerning various types of lipid molecules are now obtained from unsonicated lipid membranes. We are therefore left with the question whether the sonicated membrane vesicle can still provide a useful model membrane system for NMR studies of other lipid molecules.[21]

Although we have discussed the polar headgroup and fatty acyl chain regions quite extensively, little has been said about the effect of curvature on the pivotal interfacial region of the lipid molecule. One attractive approach might be studies of exchangeable protons of sphingolipids in sonicated membrane vesicles.[22] By studying the exchange rate of amide protons in several sphingomyelin-containing sonicated membrane vesicles as a function of pH, the existence of intermolecular hydrogen bonding at the interfacial region has been inferred.

The kinetics of proton exchange for phosphatidylethanolamine in sonicated mixed membrane vesicles has also been studied.[23] This may provide information on the mechanism responsible for proton transport in and to membrane surfaces. It will be interesting to ascertain whether curvature significantly changes the kinetics of these processes.

Finally, there is a great deal of interest in the asymmetric distribution of lipids in both model and biological membranes. With the availability of lipid transfer proteins, small unilamellar vesicles with synthetic lipid molecules in designated monolayers can be prepared. Sonicated membrane vesicles will no doubt continue to be useful in future NMR studies of membrane structure and dynamics.

5 RELATED ARTICLES

Bilayer Membranes: Deuterium and Carbon-13 NMR; Bilayer Membranes: Proton and Fluorine-19 NMR; Lipid Polymorphism; Membrane Lipids of Acholeplasma laidlawii; Membranes: Carbon-13 NMR; Membranes: Phosphorus-31 NMR.

6 REFERENCES

1. C. Huang, in *Contemporary Classics in the Life Sciences*, ed. J. T. Barrett, ISI Press, Philadelphia, Vol.2, p. 38
2. D. F. Bocian and S. I. Chan, *Annu. Rev. Phys. Chem.*, 1978, **29**, 307.
3. R. L. Thurmond, G. Lindblom, and M. F. Brown, *Biochemistry*, 1993, **32**, 5394.

4. Y. Barenholz, D. Gibbes, B. J. Litman, J. Gol, T. E. Thompson, and F. D. Carlson, *Biochemistry*, 1977, **16**, 2806.
5. J. T. Mason and C. Huang, *Ann. N.Y. Acad. Sci.*, 1978, **308**, 29.
6. L. D. Bergelson, in *Methods in Membrane Biology*, ed. E. D. Korn, Plenum Press, New York/London, 1978, Vol.9, p. 275.
7. B. Halle, *J. Phys. Chem.*, 1991, **95**, 6724.
8. D. B. Fenske and P. R. Cullis, *Biophys. J.*, 1993, **64**, 1482.
9. W. Wu, S. R. Dowd, V. Simplaceanu, Z-Y Peng, and C. Ho, *Biochemistry*, 1985, **24**, 7153.
10. G. W. Stockton, C. F. Polnaszek, A. P. Tulloch, F. Hasan, and I. C. P. Smith, *Biochemistry*, 1976, **15**, 954.
11. M. Bloom, E. E. Burnell, A. L. MacKay, C. P. Nichol, M. I. Valic, and G. Weeks, *Biochemistry*, 1978, **17**, 5750.
12. Z-Y Peng, V. Simplaceanu, I. J. Lowe, and C. Ho, *Biophys. J.*, 1988, **54**, 81.
13. J. R. Schuh, U. Banerjee, L. Muller, and S. I. Chan, *Biochim. Biophys. Acta*, 1982, **687**, 219.
14. M. M. Fuson and J. H. Prestegard, *J. Am. Chem. Soc.*, 1983, **105**, 168.
15. P. Yeagle, in *Phosphorus NMR in Biology*, ed. C. T. Burt, CRC Press, Boca Raton, FL, 1987, Chap. 5
16. J. S. Tauskela and M. Thompson, *Biochim. Biophys. Acta*, 1992, **1104**, 137.
17. K. E. Eigenberg and S. I. Chan, *Biochim. Biophys. Acta*, 1980, **599**, 330.
18. J. Seelig, P. M. Macdonald, and P. G. Scherer, *Biochemistry*, 1987, **26**, 7535.
19. W. Wu, S.-W. Leu, C.-H. Hsieh, and L.-M. Chi, *Chem. Phys. Lipids*, 1991, **58**, 241.
20. E. E. Burnell, P. R. Cullis, and B. De Kruijff, *Biochim. Biophys. Acta*, 1980, **603**, 63.
21. E. Oldfield, J. L. Bowers, and J. Forbes, *Biochemistry*, 1987, **26**, 6919.
22. W. Wu, *Z. Phys. Chem., Neue Folge*, 1987, **153**, S87.
23. E. K. Ralph, Y. Lange, and A. G. Redfield, *Biophys. J.*, 1985, **48**, 1053.

Acknowledgments

This work was supported in part by the National Science Council under grant NSC 85-2113-M-007-035 Y.

Biographical Sketch

Wen-guey Wu. *b* 1954. B.S., 1976, Tsing Hua University, Ph.D., 1983, University of Virginia. Introduced to lipid physical chemistry by C. Huang. Postdoctoral NMR work at Mellon Institute, Pittsburgh (with C. Ho). Faculty in the Department of Life Sciences, National Tsing Hua University, 1985–present. Approx. 40 publications. Research interests include snake venoms, and the application of NMR to study the structure and dynamics of model and biological membranes.

Structures of Larger Proteins, Protein–Ligand, and Protein–DNA Complexes by Multidimensional Heteronuclear NMR

G. Marius Clore and Angela M. Gronenborn
National Institutes of Health, Bethesda, MD, USA

1 Introduction 1
2 General Strategy for the Determination of Three-dimensional Structures of Larger Proteins and Protein Complexes by NMR 1
3 Application of Three- and Four-dimensional NMR to Structure Determination of Larger Proteins: the Structure of Interleukin-1β 5
4 Combining Experimental Information from Crystal and Solution Studies: Joint X-ray and NMR Refinement 7
5 Structure Determination of Protein–Peptide and Protein–DNA Complexes 9
6 Concluding Remarks 18
7 Related Articles 19
8 References 19

1 INTRODUCTION

The last few years have seen a quantum jump in both the accuracy of the determination and in the size of protein structures that can be determined by NMR.[1] Thus it is now possible to determine the structures of proteins in the 15–25 kDa range at a resolution comparable to 0.2 nm resolution for crystal structures.[2] This advance is attributable to the development of three- and four-dimensional heteronuclear NMR techniques which circumvent problems associated with chemical shift overlap and degeneracy, on the one hand, and large linewidths on the other.[1,3–5] In this article, we summarize some of these developments and illustrate their application to the structure determination of interleukin-1β (IL-1β),[6] a complex of calmodulin with a target peptide,[7] and a complex of the DNA binding domain of the transcription factor GATA-1 with its cognate DNA target site.[8]

2 GENERAL STRATEGY FOR THE DETERMINATION OF THREE-DIMENSIONAL STRUCTURES OF LARGER PROTEINS AND PROTEIN COMPLEXES BY NMR

The main source of geometric information used in protein structure determination lies in the nuclear Overhauser effect (NOE) which can be used to identify protons separated by less than 0.5 nm.[9] This distance limit arises from the fact that the NOE is proportional to the inverse sixth power of the distance between the protons. Hence the NOE intensity falls off very rapidly with increasing distance between proton pairs. Despite the short range nature of the observed interactions, the short approximate interproton distance restraints derived from the NOE measurements can be highly conformationally restrictive, particularly when they involve residues that are far apart in the sequence but close together in space.

The power of NMR over other spectroscopic techniques results from the fact that every proton gives rise to an individual resonance in the spectrum which can be resolved by higher (i.e. two, three and four) dimensional techniques. Bearing this in mind, the principles of structure determination by NMR can be summarized very simply by the scheme depicted in Figure 1. The first step is to obtain sequential resonance assignments using a combination of through-bond and through-space correlations; the second step is to obtain stereospecific assignments at chiral centers and torsion angle restraints using three-bond scalar couplings combined with intraresidue and sequential interresidue NOE data; the third step is to identify through-space connectivities between protons separated by less than 0.5 nm and, finally, the fourth step involves calculating three-dimensional structures on the basis of the amassed interproton distance and torsion angle restraints using one or more of a number of algorithms[10–12] such as distance geometry and/or simulated annealing. It is not essential to assign all the NOEs initially. Indeed, many may be ambiguous and several possibilities may exist for their assignments. However, once a low-resolution structure has been calculated from a subset of the NOE data which can be interpreted unambiguously, it is then possible to employ iterative methods to resolve the vast majority of ambiguities. Consider, for example, an NOE cross peak which could be attributable to a through-space interaction between either protons A and B or between protons A and C. Once a low-resolution structure is available it is usually possible to discriminate between these two possibilities. Thus, if protons A and C are significantly greater than 0.5 nm apart while protons A and B are less than 0.5 nm apart, it is clear that the cross peak must arise from an NOE between protons A and B.

The quality of an NMR protein structure determination increases as the number of restraints increase.[1,4,13–15] This progression in coordinate precision is illustrated in Figure 2 which shows four generations of structures, ranging from the first generation which simply provides a picture of the polypeptide fold with little detail, to the fourth generation which is broadly equivalent to a 0.2 nm resolution X-ray structure.

2.1 Sequential Resonance Assignment

Conventional sequential resonance assignment relies on two-dimensional homonuclear $^1H-^1H$ correlation experiments to identify amino acid spin systems coupled with two-dimensional $^1H-^1H$ NOE experiments to identify sequential connectivities along the backbone of the type $C^\alpha H(i)$–$NH(i + 1, 2, 3, 4)$, $NH(i)$–$NH(i \pm 2)$ and $C^\alpha H(i)$–$C^\beta H(i + 3)$.[16,17] This methodology has been successfully applied to proteins of less than 100 residues. For larger proteins, the

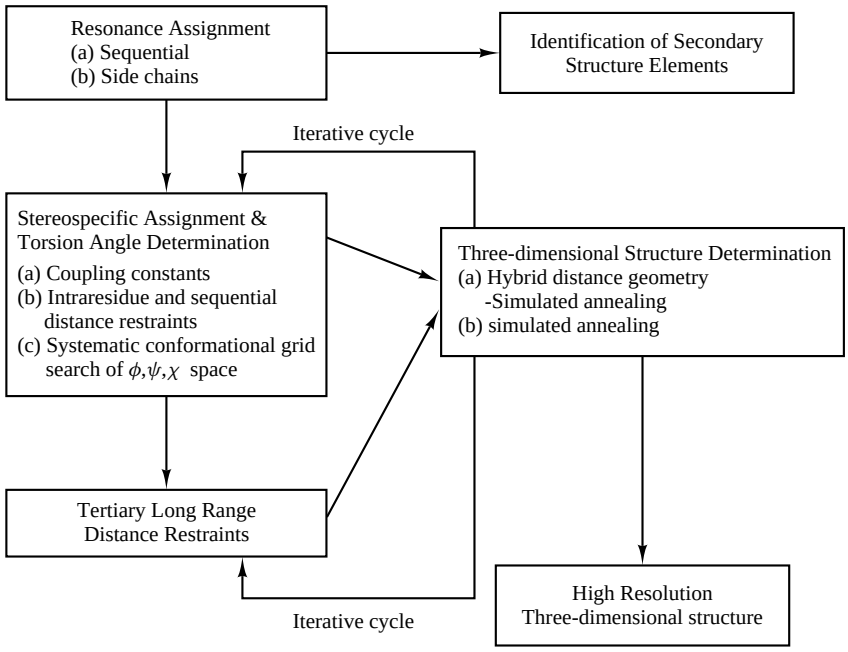

Figure 1 Summary of the general strategy employed to solve three-dimensional structures of macromolecules by NMR. (Adapted from G. M. Clore and A. M. Gronenborn, *Science*, 1991, **252**, 1390)

spectral complexity is such that two-dimensional experiments no longer suffice, and it is essential to increase the spectral resolution by increasing the dimensionality of the spectra.[18] In some cases it is still possible to apply the same strategy by making use of three-dimensional heteronuclear (^{15}N or ^{13}C) edited experiments to increase the spectral resolution, as illustrated in Figure 3.[19–22] In many cases, however, numerous ambiguities still remain and it is advisable to adopt a sequential assignment strategy based solely on well defined heteronuclear scalar couplings.[3,5,23–25] The double and triple resonance experiments that we currently use, and the correlations that they demonstrate, are summarized in Table 1. With the advent of pulse field gradients to eliminate undesired coherence transfer pathways,[26] it is now possible to employ only two-step phase cycles without any loss in sensitivity (other than that due to the reduction in measurement time) such that each three-dimensional experiment can be recorded in as little as 7 h. In most cases, however, signal-to-noise ratio requirements necessitate 1–3 days of measuring time, depending on the experiment.

2.2 Stereospecific Assignments and Torsion Angle Restraints

It is often possible to obtain stereospecific assignments of β-methylene protons on the basis of a qualitative interpretation of the homonuclear $^3J(\alpha,\beta)$ coupling constants and the intraresidue NOE data involving the NH, C$^\alpha$H and C$^\beta$H protons.[27,28] A more rigorous approach, which also permits one to obtain ϕ, ψ, and χ_1 restraints, involves the application of a conformational grid search of ϕ,ψ,χ_1 space on the basis of the homonuclear ^3J(N-α,H) and $^3J(\alpha,\beta)$ coupling constants (which are related to ϕ and χ_1, respectively), and the intraresidue and sequential ($i \pm 1$) interresidue NOEs involving the NH, C$^\alpha$H and C$^\beta$H protons.[29,30] This information can be supplemented by the measurement of heteronuclear ^3J(N,H-β) and ^3J(CO,H-β) couplings which are also related to χ_1.[31] Stereospecific assignment of valine methyl groups can be made on the basis of ^3J(C-γ,CO) and ^3J(N,C-γ) couplings,[31] as well as on the basis of the pattern of intraresidue NOEs involving the NH, C$^\alpha$H and C$^\gamma$H protons.[32] Finally, stereospecific assignments of leucine methyl groups can be made on the basis of heteronuclear ^3J(C-δ,C-α) and ^3J(C-δ,H-β) couplings[31] in combination with the pattern of intraresidue NOEs, provided that the stereospecific assignment of the β-methylene protons and the χ_1 rotamer have been previously determined.[33]

2.3 Assignment of Through-space Proton–Proton Interactions within a Protein

While the panoply of three-dimensional heteronuclear experiments is sufficient for the purposes of spectral assignment, yet further increases in resolution are required for the reliable identification of NOE through space interactions. This can be achieved by extending the dimensionality still further to four dimensions.[34] This is illustrated in Figure 4. Consider a simple two-dimensional spectrum demonstrating 11 cross peaks from aliphatic resonances to a single NH resonance position. In the two-dimensional spectrum it is impossible to ascertain whether this involves one NH proton or many. Extending the spectrum to three dimensions by separating the NOE interactions according to the ^{15}N chemical shift of the nitrogen attached to each amide proton reveals that there are three NH protons involved. The identity of the originating aliphatic protons, however, is only specified by their proton chemical shifts. Yet the extent of spectral overlap in the aliphatic region of the spectrum vastly exceeds that in the amide region. This can be resolved by adding a further dimension in which each plane of the three-dimensional spectrum now constitutes a cube in the

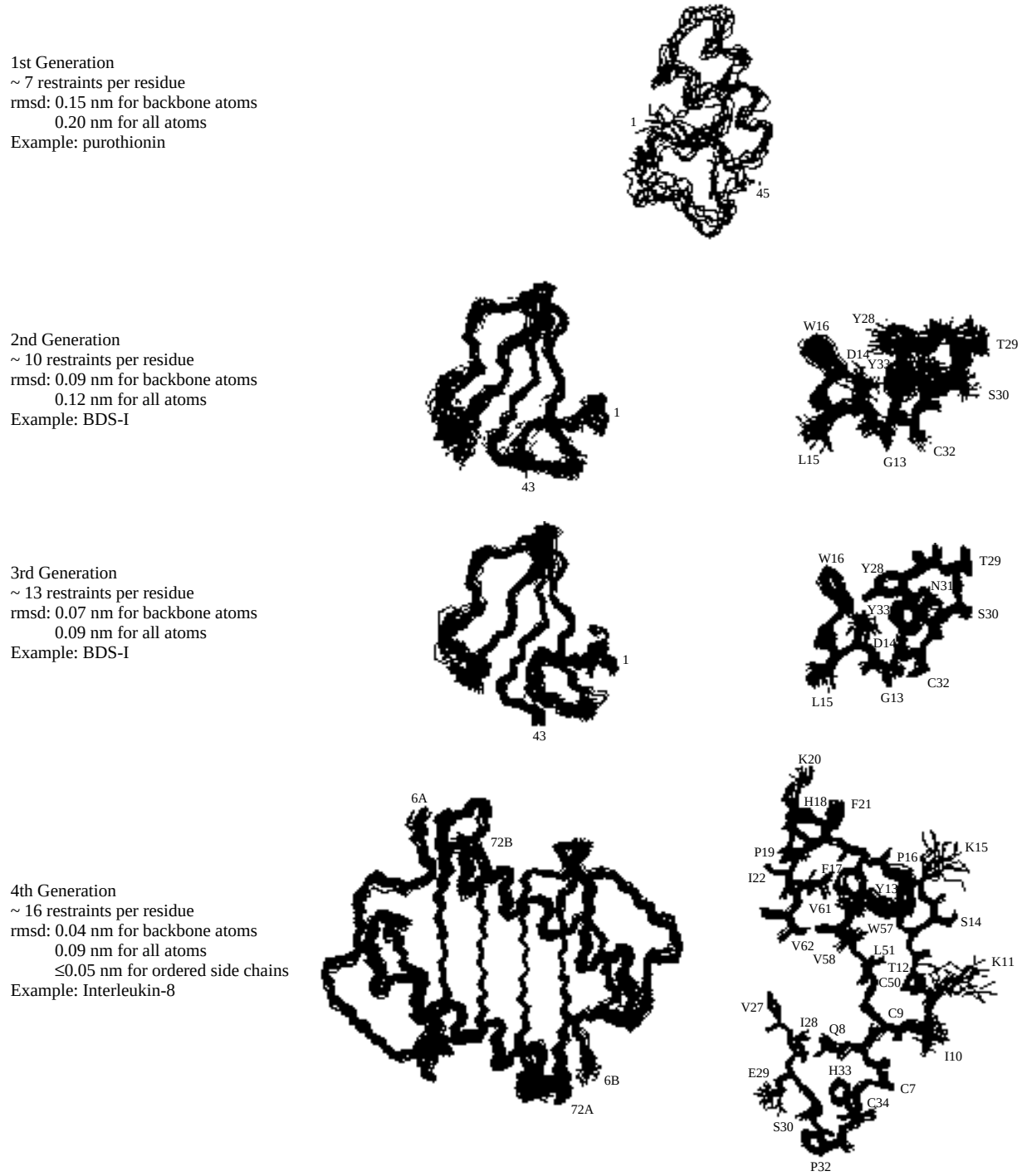

Figure 2 Illustration of the progressive improvement in the precision and accuracy of NMR structure determinations with increasing number of experimental restraints. All the structures have been calculated using the hybrid distance geometry, simulated annealing method, and in each case the NOE derived interproton distance restraints have been grouped into the three broad ranges: 0.18–0.27, 0.18–0.33, and 0.18–0.5 nm, corresponding to strong, medium and weak NOEs, respectively. (Adapted from G. M. Clore and A. M. Gronenborn, *Science*, 1991, **252**, 1390)

four-dimensional spectrum edited by the ^{13}C shift of the carbon atom attached to each aliphatic proton. In this manner, each $^{1}H-^{1}H$ NOE interaction is specified by four chemical shift coordinates, the two protons giving rise to the NOE and the heavy atoms to which they are attached. The resolving power of four-dimensional heteronuclear-edited NOE spectroscopy is illustrated in Figure 5.

Because the number of NOE interactions present in each two-dimensional plane of a four-dimensional $^{13}C/^{15}N$ or $^{13}C/^{13}C$ edited NOESY spectrum is so small, the inherent resolution in a four-dimensional spectrum is extremely high, despite the low level of digitization. Indeed, spectra with equivalent resolution can be recorded at magnetic field strengths considerably lower than 600 MHz, although this

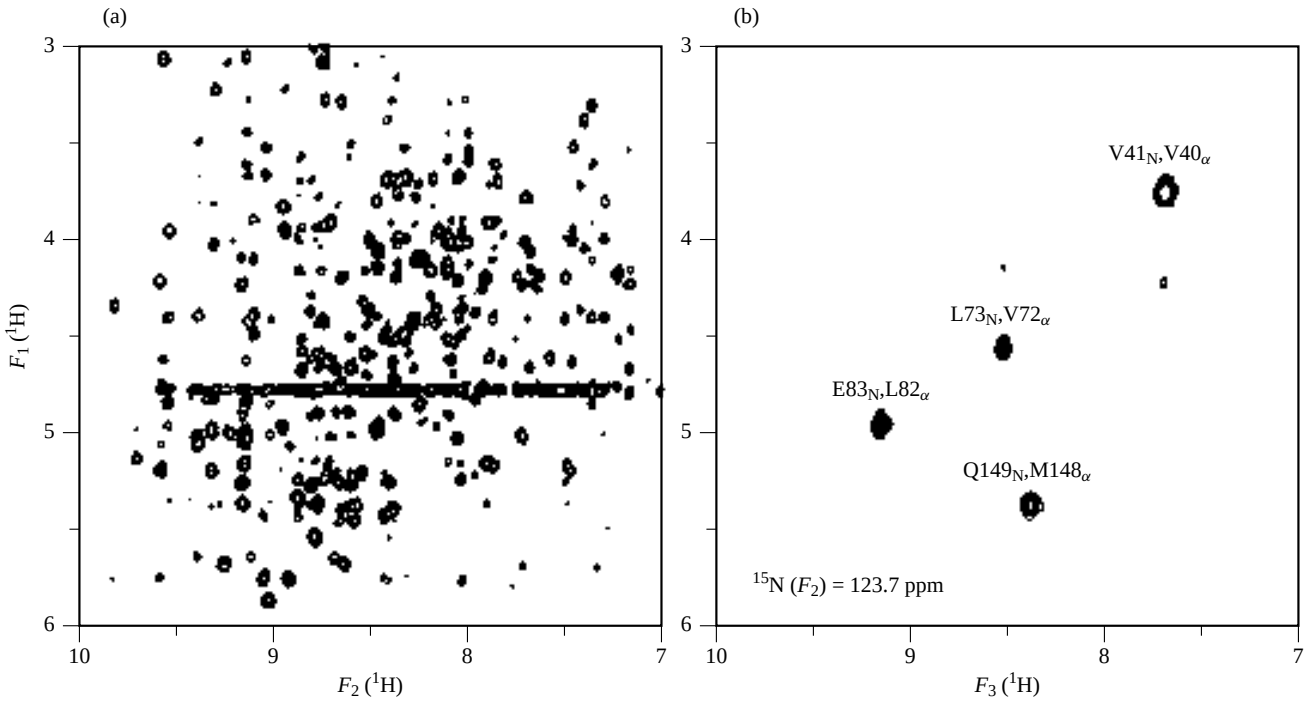

Figure 3 Comparison of the NH–C$^\alpha$H/C$^\beta$H region of a two-dimensional ^{15}N-edited NOESY spectrum (a) with that of a single plane taken from the three-dimensional ^{15}N-edited NOESY spectrum of interleukin-1β (b), illustrating the increase in spectral resolution afforded by increasing the dimensionality from two to three. (Adapted from D. Marion, P. C. Driscoll, L. E. Kay, P. T. Wingfield, A. Bax, A. M. Gronenborn, and G. M. Clore, *Biochemistry*, 1989, **28**, 6150)

Table 1 Summary of Correlations Observed in the Three-dimensional Double and Triple Resonance Experiments used for Sequential and Side-Chain Assignments in our Laboratory

Experiment	Correlation	J Coupling[a]
^{15}N edited HOHAHA	C$^\alpha$H(i)–^{15}N(i)–NH(i)	^3J(N-α,H)
	C$^\beta$H(i)–^{15}N(i)–NH(i)	^3J(N-α,H) and ^3J(α,β)
HNHA	C$^\alpha$H(i)–^{15}N(i)–NH(i)	^3J(N,H)
H(CA)NH	C$^\alpha$H(i)–^{15}N(i)–NH(i)	^1J(N,C-α)
	C$^\alpha$H($i-1$)–^{15}N(i)–NH(i)	^2J(N,C-α)
HNCA	^{13}C$^\alpha$(i)–^{15}N(i)–NH(i)	^1J(N,C-α)
	^{13}C$^\alpha$($i-1$)–^{15}N(i)–NH(i)	^2J(N,C-α)
HN(CO)CA	^{13}C$^\alpha$($i-1$)–^{15}N(i)–NH(i)	^1J(N,CO) and ^1J(C-α,CO)
HNCO	^{13}CO($i-1$)–^{15}N(i)–NH(i)	^1J(N,CO)
HCACO	C$^\alpha$H(i)–^{13}C$^\alpha$(i)–^{13}CO(i)	^{1}J(C-α,CO)
HCA(CO)N	C$^\alpha$H(i)–^{13}C$^\alpha$(i)–^{15}N($i+1$)	^1J(C-α,CO) and ^1J(N,CO)
CBCA(CO)NH	^{13}C$^\beta$($i-1$)/^{13}C$^\alpha$($i-1$)–^{15}N(i)–NH(i)	^1J(C-α,CO), ^1J(N,CO) and ^1J(C,C)
CBCANH	^{13}C$^\beta$(i)/^{13}C$^\alpha$(i)–^{15}N(i)–NH(i)	^1J(N,C-α) and ^1J(C,C)
	^{13}C$^\beta$($i-1$)/^{13}C$^\alpha$($i-1$)–^{15}N(i)–NH(i)	^2J(N,C-α) and ^1J(C,C)
HBHA(CO)NH	C$^\beta$H($i-1$)/C$^\alpha$H($i-1$)–^{15}N(i)–NH(i)	^1J(C-α,CO), ^1J(N,CO) and ^1J(C,C)
HBHANH	C$^\beta$H(i)/C$^\alpha$H(i)–^{15}N(i)–NH(i)	^1J(N,C-α) and ^1J(C,C)
	C$^\beta$H($i-1$)/C$^\alpha$H($i-1$)–^{15}N(i)–NH(i)	^2J(N,C-α) and ^1J(C,C)
C(CO)NH	^{13}C^j($i-1$)–^{15}N(i)–NH(i)	^1J(C-α,CO), ^1J(N,CO) and ^1J(C,C)
H(CCO)NH	H^j($i-1$)–^{15}N(i)–NH(i)	^1J(C-α,CO), ^1J(N,CO) and ^1J(C,C)
HCCH-COSY	H^j–^{13}C^j–^{13}C$^{j\pm1}$–H$^{j\pm1}$	^1J(C,C)
HCCH-TOCSY	H^j–^{13}C^j ... ^{13}C$^{j\pm n}$–H$^{j\pm n}$	^1J(C,C)

[a]In addition to the couplings indicated, all the experiments make use of the ^1J(C,H) ($\approx$140 Hz) and/or ^1J(N,H) ($\approx$ 95 Hz) couplings. The values of the couplings employed are as follows: ^3J(N-α,H) $\approx$ 3–10 Hz, ^1J(C,C) $\approx$ 35 Hz, ^1J(C-α,CO) $\approx$ 55 Hz, ^1J(N,CO) $\approx$ 15 Hz, ^1J(N,C-α) $\approx$ 11 Hz, ^2J(N,C-α) $\approx$ 7 Hz.

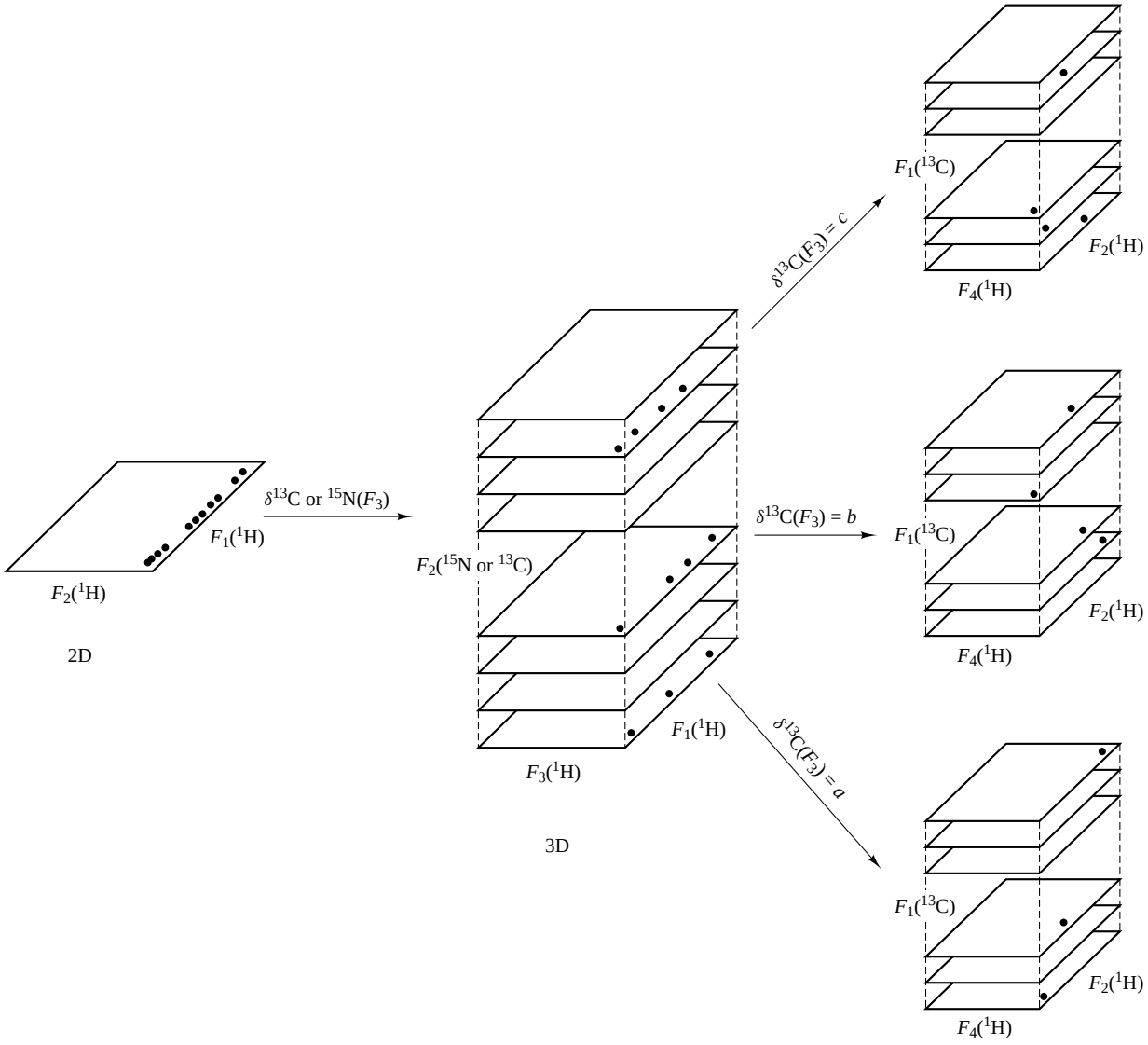

Figure 4 Schematic illustration of the progression and relationship between two-, three-, and four-dimensional heteronuclear-edited NMR spectroscopy. (Adapted from G. M. Clore and A. M. Gronenborn, *Science*, 1991, **252**, 1390)

would obviously lead to a reduction in sensitivity. Furthermore, it can be calculated that four-dimensional spectra with virtual lack of resonance overlap and good sensitivity can be obtained on proteins with as many as 400 residues. Thus, once complete ^{1}H, ^{15}N, and ^{13}C assignments are obtained, analysis of four-dimensional ^{15}N/^{13}C and ^{13}C/^{13}C edited NOE spectra[34–37] should permit the automated assignment of almost all NOE interactions.

3 APPLICATION OF THREE- AND FOUR-DIMENSIONAL NMR TO STRUCTURE DETERMINATION OF LARGER PROTEINS: THE STRUCTURE OF INTERLEUKIN-1β

While the potential of heteronuclear three- and four-dimensional NMR methods in resolving problems associated with both extensive resonance overlap and large linewidths is obvious, how does this new approach fare in practice? In this regard it should be borne in mind that resonance assignments are only a means to an end, and the true test of multidimensional NMR lies in examining its success in solving the problem which it was originally designed to tackle, namely the determination of high-resolution three-dimensional structures of larger proteins in solution.

The first successful demonstration of these new methods was the determination of the high-resolution solution structure of interleukin-1β (IL-1β), a cytokine of 153 residues and molecular weight 17.4 kDa, which plays a key role in the immune and inflammatory responses.[6] At the time IL-1β was 50% larger, in terms of the number of residues, than the previously largest protein structures solved by NMR, namely human[38] and *Escherichia coli*[39] thioredoxin which have 105 and 108 residues, respectively. Moreover, IL-1β still represents one of the most highly refined and precise structures for proteins of this size solved by NMR.

Despite extensive analysis of two-dimensional spectra obtained at different pH values and temperatures, as well as

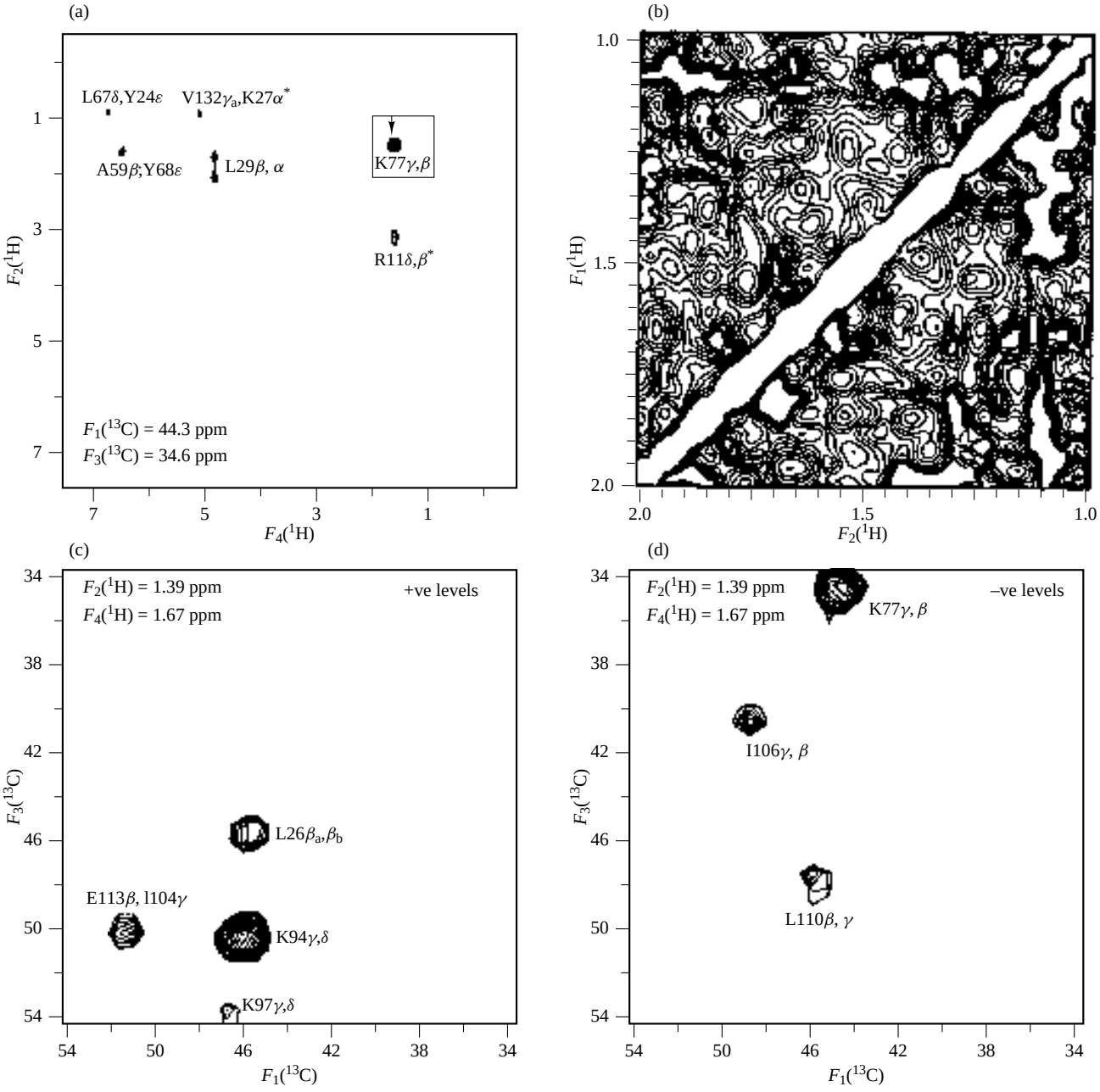

Figure 5 Example of the increase in spectral resolution afforded by four-dimensional $^{13}C/^{13}C$-edited NOE spectroscopy, illustrated with IL-1β. (a) $^{1}H(F_2)-^{1}H(F_4)$ plane of the four-dimensional spectrum at $\delta^{13}C(F_1)$ = 44.3 ppm and $\delta^{13}C(F_3)$ = 34.6 ppm; the region between 1 and 2 ppm is boxed in and the arrow indicates the position of the Lys77 $C^{\gamma}H-C^{\beta}H$ NOE cross peak. (b) Two-dimensional $^{1}H-^{1}H$ NOE spectrum between 1 and 2 ppm; the X marks the chemical shift position of the Lys77 $C^{\gamma}H-C^{\beta}H$ NOE cross peak seen in (a). (c, d) Positive and negative contours in the $^{13}C(F_1)-^{13}C(F_3)$ plane of the four-dimensional spectrum at the ^{1}H chemical shift coordinates $\delta^{1}H(F_2)$ = 1.39 ppm and $\delta^{1}H(F_4)$ = 1.67 ppm corresponding to the Lys77 $C^{\gamma}H-C^{\beta}H$ NOE cross peak seen in (a) and the X mark shown in (b). Because extensive folding is employed, the ^{13}C chemical shifts are given by $x \pm n$SW, where x is the ppm value listed in the figure, n is an integer, and SW is the spectral width (20.71 ppm). Peaks folded an even number of times are of opposite sign to those folded an odd number of times. All the peaks in (a) are positive, except for the two indicated by an asterisk which are negative. (Adapted from G. M. Clore and A. M. Gronenborn, *Science*, 1991, **252**, 1390)

examination of two-dimensional spectra of mutant proteins, it did not prove feasible to obtain unambiguous ^{1}H assignment for more than about 30% of the residues of interleukin-1β.[22] Thus, any further progress could only be made by resorting to higher dimensionality heteronuclear NMR. The initial step involved the complete assignment of the ^{1}H, ^{15}N, and ^{13}C resonances of the backbone and side chains using many of the double and triple resonance three-dimensional experiments listed in Table 1.[22,40,41] In the second step, backbone and side-chain torsion angle restraints, as well as stereospecific assignments for β-methylene protons, were obtained by means of a three-dimensional systematic grid search of ϕ,ψ,χ_1 space.[30] In the third step, approximate interproton distance restraints between nonadjacent residues

were derived from analysis of three- and four-dimensional heteronuclear-edited NOE spectra. Analysis of the three-dimensional heteronuclear-edited NOE spectra alone was sufficient to derive a low-resolution structure on the basis of a small number of NOEs involving solely NH, $C^{\alpha}H$ and $C^{\beta}H$ protons.[42] However, further progress using three-dimensional NMR was severely hindered by the numerous ambiguities still present in these spectra, in particular for NOEs arising from the large number of aliphatic protons. Thus, the four-dimensional heteronuclear-edited NOE spectra proved to be absolutely essential for the successful completion of this task. In addition, the proximity of backbone NH protons to bound structural water molecules was ascertained from a three-dimensional ^{15}N-separated ROESY spectrum which permits one to distinguish specific protein–water NOE interactions from chemical exchange with bulk solvent.[43] In this regard it should be emphasized that all the NOE data were interpreted in as conservative a manner as possible, and were simply classified into three distance ranges: 0.18–0.27, 0.18–0.33, and 0.18–0.50 nm, corresponding to strong, medium, and weak intensity NOEs, respectively.

With an initial set of experimental restraints in hand, three-dimensional structure calculations were initiated using the hybrid distance geometry–dynamical simulated annealing method.[44] A key aspect of the overall strategy lies in the use of an iterative approach whereby the experimental data are reexamined in the light of the initial set of calculated structures in order to resolve ambiguities in NOE assignments, to obtain more stereospecific assignments (e.g. the α-methylene protons of glycine and the methyl groups of valine and leucine) and torsion angle restraints, and to assign backbone hydrogen bonds associated with slowly exchanging NH protons as well as with bound water molecules. The iterative cycle comes to an end when all the experimental data have been interpreted.

The final experimental data set for IL-1β comprised a total of 3146 approximate and loose experimental restraints made up of 2780 distance and 366 torsion angle restraints.[6] This represents an average of about 21 experimental restraints per residue. If one takes into account that interresidue NOEs affect two residues, while intraresidue NOE and torsion angle restraints only affect individual residues, the average number of restraints influencing the conformation of each residue is approximately 33. Superpositions of the backbone atoms and selected side chains for 32 independently calculated structures are shown in Figures 6(b) and 6(d). All 32 structures satisfy the experimental restraints within their specified errors, display very small deviations from idealized covalent geometry, and have good nonbonded contacts. It can be seen that both the backbone and ordered side chains are exceptionally well defined. Indeed, the atomic root-mean-square (rms) distribution about the mean coordinate positions is 0.04 nm for the backbone atoms, 0.08 nm for all atoms, and 0.05 nm for side chains with $\leq$40% of their surface (relative to that in a tripeptide Gly-X-Gly) accessible to solvent.[6]

The structure of IL-1β itself resembles a tetrahedron and displays three-fold internal pseudosymmetry. There are 12 β-strands arranged in an exclusively antiparallel β-structure, and six of the strands form a β-barrel [seen in the front of Figure 6(a)] which is closed off at the back of the molecule by the other six strands. Each repeating topological unit is composed of 5 strands arranged in an antiparallel manner with respect to each other, and one of these units is shown in Figure 6(c). Water molecules occupy very similar positions in all three topological units, as well as at the the interface of the three units, and are involved in bridging backbone hydrogen bonds. Thus, in the case of the topological unit shown in Figure 6(c), the water molecule labeled W5 accepts a hydrogen bond from the NH of Phe112 in strand IX and donates two hydrogen bonds to the backbone carbonyls of Ile122 in strand X and Thr144 in strand XII. The packing of some internal residues with respect to one another, as well as the excellent definition of internal side chains, is illustrated in Figure 6(d). Because of the high resolution of the IL-1β structure it was possible to analyze in detail side-chain–side-chain interactions involved in stabilizing the structure. In addition, examination of the structure in the light of mutational data permitted us to propose the presence of three distinct sites involved in the binding of IL-1β to its cell surface receptor.[6]

4 COMBINING EXPERIMENTAL INFORMATION FROM CRYSTAL AND SOLUTION STUDIES: JOINT X-RAY AND NMR REFINEMENT

It is clear from the preceding discussion that NMR is a valid method, alongside X-ray crystallography, for determining high-resolution structures of small to medium sized proteins of less than about 35 kDa. IL-1β offers an ideal system for comparing the results of NMR and X-ray crystallography as, in addition to the solution structure, there are three independently solved X-ray structures at 0.2 nm resolution of the same crystal form.[45–47] The backbone atomic rms difference between the NMR and the X-ray structures is about 0.1 nm, with the largest differences being confined to some of the loops and turns connecting the β-strands.[2] Interestingly, however, the atomic rms distribution of the 32 calculated solution structures about their mean coordinate positions (about 0.04 nm for the backbone atoms, about 0.08 nm for all atoms, and about 0.05 nm for all atoms of internal residues) is approximately the same as the atomic rms differences between the three X-ray structures, indicating that the positional errors in the atomic coordinates determined by the two methods are similar.[2] Upon initial inspection, the X-ray structures appear to be incompatible with the NMR data, as manifested by a relatively large number of NOE and torsion angle violations and, conversely, the NMR structure fits the X-ray data poorly with an R factor of 40–50%. Because of the very different nature of the two methods, it is not immediately apparent that these discrepancies reflect genuine differences between the solution and X-ray structures or whether they reflect differences in the computational procedures employed. To analyze this in more detail we have developed a new method of structure determination in which the NMR and X-ray data are combined and used simultaneously in the structure refinement.[48] Using this approach we have shown that a model can readily be generated from a joint NMR/X-ray refinement which is compatible with the data from both techniques. Thus, there are only minimal violations of the NMR restraints (NOEs and torsion angles), the value of the crystallographic R factor is comparable to, if not better than, that derived from refinement against the crystallographic data alone, and the deviations from idealized covalent geometry are small. In addition, the R free[49] for the model refined with the NMR and

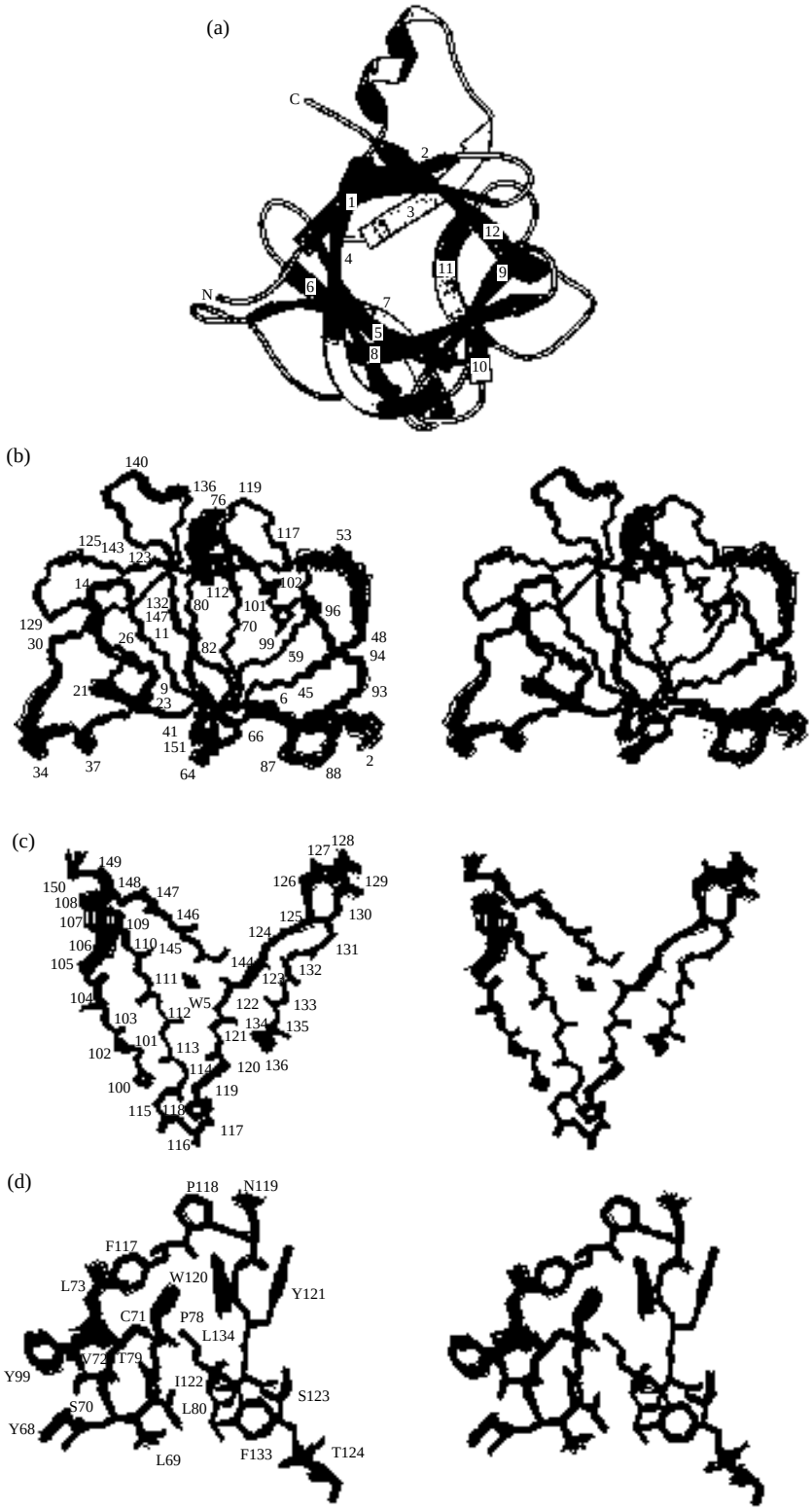

Figure 6 Solution structure of IL-1β determined by three- and four-dimensional heteronuclear NMR spectroscopy. (a) Ribbon diagram of the polypeptide fold. (b) Superposition of the backbone (N, C^{α}, and C) atoms of 32 simulated annealing structures calculated from the experimental NMR data. (c) Superposition of the backbone (N, C^{α}, C, and O) atoms of one of the three repeating topological units, illustrating the position of tightly bound water at the interface of the three central strands of the unit. (d) Superposition of all atoms (excluding protons) for selected side chains. The diagram in (a) was made using the program MOLSCRIPT.[102] The coordinates are from Clore et al.[6] (PDB accession code 6I1B). (Adapted from G. M. Clore, P. T. Wingfield, and A. M. Gronenborn, *Biochemistry*, 1991, **30**, 2315)

X-ray restraints is smaller than that of the model obtained by conventional crystallographic refinement, indicating that the crystallographic phases obtained by the joint NMR/X-ray refinement are more accurate. Moreover, the few NMR observations that are still violated by the model serve as an indicator for genuine differences between the crystal and solution structures.

The implications of the joint NMR/X-ray refinement method to structural biology are of considerable significance. In particular, the full potential and future use of the method will be for structure determinations of multidomain proteins, for which only low-resolution X-ray data for the entire protein are available but for which detailed structural information may be obtained by NMR on the individual domains. Using the joint X-ray/NMR refinement approach in such cases will open the way to the study of proteins which may otherwise never be structurally accessible by either of the two methods alone.

5 STRUCTURE DETERMINATION OF PROTEIN–PEPTIDE AND PROTEIN–DNA COMPLEXES

Provided the ligand (e.g. a peptide, an oligonucleotide, or a drug) presents a relatively simple spectrum that can be assigned by two-dimensional methods, the most convenient strategy for dealing with protein–ligand complexes involves one in which the protein is labeled with ^{15}N and ^{13}C and the ligand is unlabeled (i.e. at natural isotopic abundance).[50] It is then possible to use a combination of heteronuclear filtering and editing to design experiments in which correlations involving only protein resonances, only ligand resonances, or only through-space interactions between ligand and protein are observed. These experiments are summarized in Table 2 and were first applied successfully to a complex of calmodulin with a target peptide from skeletal muscle myosin light chain kinase,[7] and subsequently to the specific complex of the DNA binding domain of the transcription factor GATA-1 with its cognate DNA target site.[8]

5.1 The Structure of the Calmodulin–Target Peptide Complex

Calmodulin (CaM) is a ubiquitous Ca^{2+} binding protein of 148 residues which is involved in a wide range of cellular Ca^{2+}-dependent signaling pathways, thereby regulating the activity of a large number of proteins.[51] The crystal structure of Ca^{2+}-CaM was solved a number of years ago.[52] It is a dumb-bell shaped molecule with an overall length of about 6.5 nm and consisting of two globular domains, each of which contains two Ca^{2+} binding sites of the helix–loop–helix type, connected by a long, solvent exposed, rigid central helix some eight turns in length (residues 66–92). In solution, on the other hand, $^{1}H-^{15}N$ NMR relaxation measurements have demonstrated unambiguously that the central helix is disrupted near its midpoint, with residues 78–81 adopting an essentially unstructured 'random coil' conformation which is so flexible that the N- and C-terminal domains of Ca^{2+}-CaM effectively tumble independently of each other.[58] Thus, in solution, the so-called 'central helix' is not a helix at all but is a 'flexible tether' the purpose of which is to keep the two domains in close proximity for binding to their target.

In order to understand the way in which Ca^{2+}-CaM recognizes its target sites, we set out to solve, in collaboration with Ad Bax, the solution structure of a complex of Ca^{2+}-CaM with a 26 residue peptide (known as M13) comprising residues 577–602 of the calmodulin binding domain of skeletal muscle myosin light chain kinase. The solution structure was determined on the basis of 1995 experimental NMR restraints including 133 interproton distance restraints between the peptide and the protein. The N-terminus (residues 1–5) and C-terminus (residues 147–148) of CaM, the tether connecting the two domains of CaM (residues 74–82), and the N-terminus (residues 1–2) and C-terminus (residues 22–26) of M13 were ill-defined by the NMR data and appear to be disordered in solution. The atomic rms distribution about the mean coordinate positions for the rest of the structure (i.e. residues 6–73 and 83–146 of CaM, and residues 3–21 of M13) is 0.1 nm for the backbone atoms and 0.14 nm for all atoms. Thus this structure represents a second generation

Table 2 Summary of Heteronuclear-filtered and -edited NOE Experiments used to Study Protein–Ligand Complexes Comprising a Uniformly $^{15}N/^{13}C$ Labeled Protein and an Unlabeled Ligand

Type of contact	Connectivity
A Intramolecular protein contacts	
4D $^{13}C/^{13}C$-edited NOE in D_2O	$H(j)-^{13}C(j)\text{---}H(i)-^{13}C(i)$
4D $^{15}N/^{13}C$-edited NOE in H_2O	$H(j)-^{15}N(j)\text{---}H(i)-^{13}C(i)$
3D $^{15}N/^{15}N$-edited NOE in H_2O	$H(j)-^{15}N(j)\text{---}H(i)-^{15}N(i)$
B Intramolecular ligand contacts	
2D $^{12}C,^{14}N(F_1)/^{12}C,^{14}N(F_2)$ filtered NOE in H_2O[a]	$H(j)-^{12}C(j)\text{---}H(i)-^{12}C(i)$
	$H(j)-^{14}N(j)\text{---}H(i)-^{12}C(i)$
	$H(j)-^{12}C(j)\text{---}H(i)-^{14}N(i)$
	$H(j)-^{14}N(j)\text{---}H(i)-^{14}N(i)$
2D $^{12}C(F_1)/^{12}C(F_2)$ filtered NOE in D_2O[a]	$H(j)-^{12}C(j)\text{---}H(i)-^{12}C(i)$
C Intramolecular protein–ligand contacts	
3D ^{15}N-edited $(F_1)/^{14}N,^{12}C(F_3)$ filtered NOE in H_2O	$H(j)-^{15}N(j)\text{---}H(i)-^{12}C(i)$
	$H(j)-^{15}N(j)\text{---}H(i)-^{14}N(i)$
3D ^{13}C-edited $(F_1)/^{12}C(F_3)$ filtered NOE in D_2O	$H(j)-^{13}C(j)\text{---}H(i)-^{12}C(i)$

[a]Similar heteronuclear filtered two-dimensional correlation and Hartmann–Hahn spectra can also be recorded to assign the spin systems of the ligand.

structure in the classification of Clore and Gronenborn.[1] A stereoview showing a best fit superposition of the 24 calculated structures is shown in Figure 7(a).

The major conformational change in Ca^{2+}-CaM that occurs upon binding M13 involves an extension of the flexible tether (residues 78–81) in the middle of the 'central' helix of the solution structure of free Ca^{2+}-CaM to a long flexible loop extending from residues 74–81, flanked by two helices (residues 65–73 and 83–93), thereby enabling the two domains to come together, gripping the peptide rather like two hands capturing a rope. The hydrophobic channel formed by the two domains is complementary in shape to that of the peptide helix. This is clearly illustrated by the schematic ribbon drawings shown in Figures 7(b) and 7(c) which also serve to highlight the approximate two-fold pseudosymmetry of the complex. Thus, whereas the two domains of CaM are arranged in an approximately orthogonal manner to each other in the crystal structure of Ca^{2+}-CaM,[52] in the Ca^{2+}-CaM–M13 complex they are almost symmetrically related by a 180° rotation about a two-fold axis. A large conformational change also occurs in the M13 peptide upon complexation from a random coil state to a well defined helical conformation. Indeed, the helix involves all the residues (3–21) of M13 that interact with CaM, while the N-terminus (residues 1–2) and C-terminus (residues 22–26) of the peptide which do not interact with CaM, remain disordered.

Upon complexation there is a decrease in the accessible surface area of CaM and M13 of 18.48 and 14.77 nm^2, respectively, which corresponds to a decrease in the calculated solvation free energy of folding[53] of 18 and 20 kcal mol^{-1} (75–83 kJ mol^{-1}), respectively. This large decrease in solvation free energy would account for the very tight binding ($K_{ass} \approx 10^9\ M^{-1}$) of M13 to calmodulin. In addition, the accessible surface area of the portion of M13 (residues 3–21) in direct contact with CaM in the complex is only 4.94 nm^2 compared with an accessible surface of area 31.23 nm^2 for a random coil and 22.50 nm^2 for a helix. Thus, over 80% of the surface of the peptide in contact with CaM is buried.

In the view shown in Figure 7(b), the roof of the channel is formed by helices II (residues 29–38) and VI (residues 102–111) of the N- and C-terminal domains, respectively, which run antiparallel to each other; and the floor is formed by the flexible loop (residues 74–82) connecting the two domains and by helix VIII (residues 138–146) of the C-terminal domain. The front of the channel in Figure 7(b) and the left wall of the channel in Figure 7(c) are formed by helices I (residues 7–19) and IV (residues 65–73) and the mini-antiparallel β-sheet comprising residues 26–28 and 62–64, all from the N-terminal domain; the back of the channel in Figure 7(b) and the right wall of the channel in Figure 7(c) are formed by helices V (residues 83–93) and VIII (residues 138–146) and the miniantiparallel β-sheet comprising residues 99–101 and 135–137, all from the C-terminal domain. The two domains of CaM are staggered with a small degree of overlap such that the hydrophobic face of the N-terminal domain mainly contacts the C-terminal half of the M13 peptide, while the C-terminal domain principally interacts with the N-terminal half of M13 (Figure 7(b)).

The overall Ca^{2+}-CaM–M13 complex has a compact globular shape approximating to an ellipsoid with dimensions 4.7 × 3.2 × 3.0 nm. The helical M13 peptide passes through the center of the ellipsoid at an angle of about 45° to its long axis. By way of contrast, the approximate dimensions of the Ca^{2+}-CaM X-ray structure are 6.5 × 3.0 × 3.0 nm.[52] In addition, the calculated radius of gyration for Ca^{2+}-CaM–M13 is about 1.7 nm which is completely consistent with the decrease in the radius of gyration from about 2.1 to about 1.6 nm observed by both small angle X-ray and neutron scattering upon complexation of Ca^{2+}-CaM with M13.[54]

The Ca^{2+}-CaM–M13 complex is stabilized by numerous hydrophobic interactions which are summarized in Figure 8. Particularly striking are the interactions of Trp4 and Phe17 of the peptide which serve to anchor the N- and C-terminal halves of M13 to the C-terminal and N-terminal hydrophobic patches of CaM, respectively [Figure 7(c)]. These interactions also involve a large number of methionine residues which are unusually abundant in CaM, in particular four methionine residues in the C-terminal domain (Met109, Met124, Met144, and Met145) and three methionine residues in the N-terminal domain (Met36, Met51, and Met71). As methionine is an unbranched hydrophobic residue extending over four heavy atoms (C-β, C-γ, S-δ, and C-ϵ), the abundance of methionine residues can generate a hydrophobic surface the detailed topology of which is readily adjusted by minor changes in side-chain conformation, thereby providing a mechanism to accommodate and recognize different bound peptides.[55]

In addition to hydrophobic interactions, there are a number of possible electrostatic interactions that can be deduced from the calculated NMR structures. Putative interactions exist between the Arg and Lys residues of M13 and the Glu residues of CaM, and these are also included in Figure 8. Glu11 and Glu14 in helix I are within 0.5 nm of Lys5 and Lys6 of M13; Glu83, Glu84, and Glu87 in helix V of CaM are close to Lys19, Arg16, and Lys18, respectively, of M13; and Glu127 in helix VII of CaM is close to Arg3 of M13.

The solution structure of the Ca^{2+}-CaM–M13 complex explains a number of interesting observations. Studies of backbone amide exchange behavior have shown that upon complexation with M13, the amide exchange rates of residues 75–79 are substantially increased.[56] Prior NMR studies on Ca^{2+}-CaM indicated that the long central helix is already disrupted near its middle (from Asp78 to Ser81) in solution[57] and that large variations in the orientation of one domain relative to the other occur randomly with time.[58] The further disruption of the central helix upon complexation seen in the structure of the complex is manifested by the increased amide exchange rates, and supports the view of the central helix serving as a flexible linker between the two domains. Similarly, the structure of the complex explains the finding that as many as four residues can be deleted from the middle of the central helix without dramatically altering the stability or shape of the Ca^{2+}-CaM–M13 complex,[59,60] as the long flexible loop connecting the two domains can readily be shortened without causing any alteration in the structure (see Figure 7). The observation from photoaffinity labeling studies that the two domains of CaM interact simultaneously with opposite ends of the peptide such that residue 4 of the peptide (numbering for M13) can be cross-linked to Met124 or Met144 of the C-terminal domain and that residue 13 of the peptide can be cross linked to Met71 of the N-terminal domain,[61] is readily explained by the structural finding that the N-terminal half of the peptide interacts predominantly with the C-terminal domain, while the C-terminal half of the peptide interacts predominantly with the N-terminal domain (Figures 7 and 8).

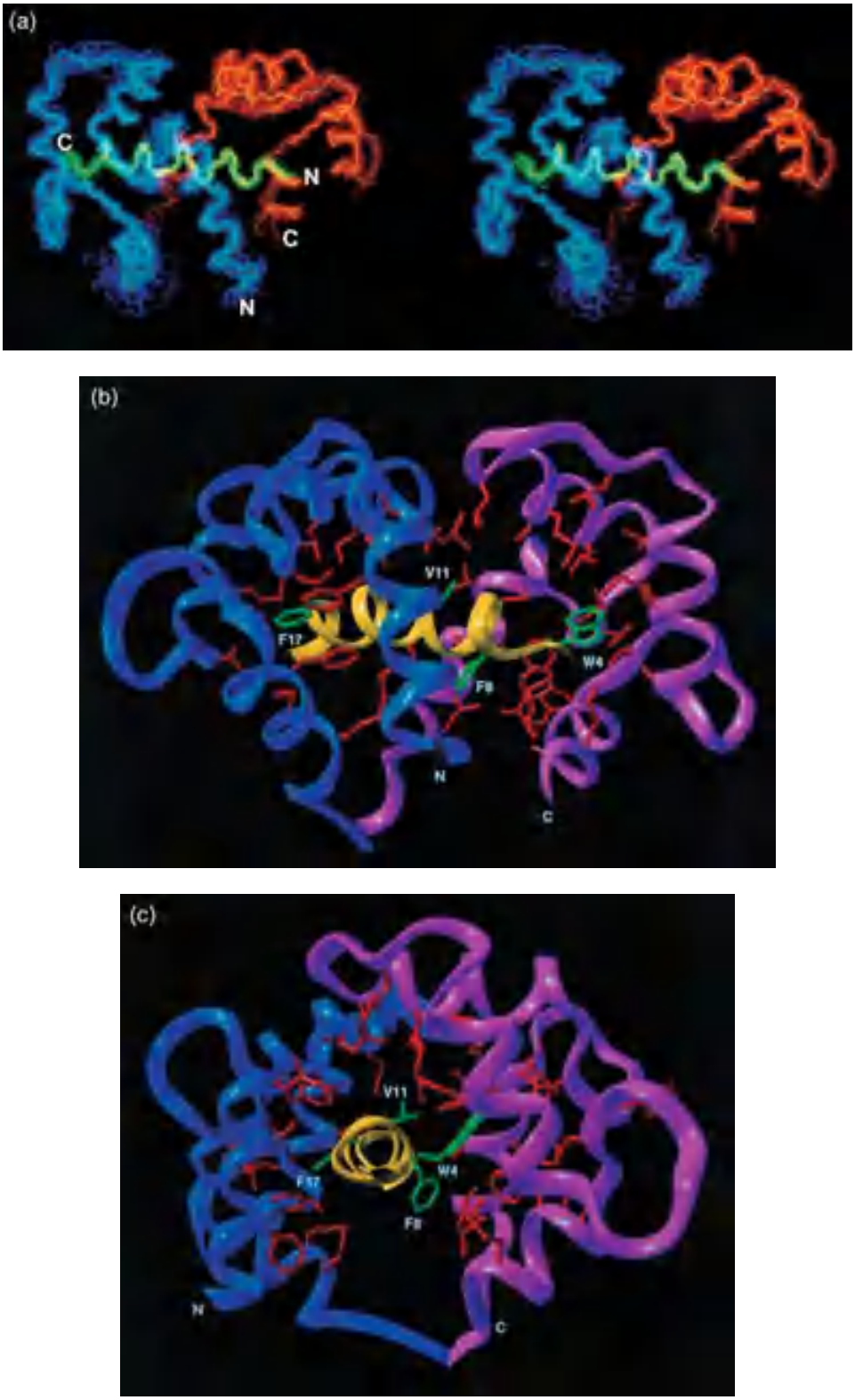

Figure 7 Solution structure of the Ca^{2+}–CaM–M13 peptide complex determined by three- and four-dimensional heteronuclear NMR spectroscopy. (a) Superposition of the backbone (N, C^{α}, and C) atoms of 24 simulated annealing structures calculated from the experimental NMR data; the N- and C-terminal domains of calmodulin are shown in blue and red, respectively, and the M13 peptide is in green; the restrained regularized average structure is highlighted. (b, c) Two orthogonal views of a schematic ribbon drawing representation of the structure with the N- and C-terminal domains of CaM in blue and purple, respectively, the M13 peptide in yellow, the hydrophobic side chains of the protein in red, and Trp4, Phe8, Va111, and Phe17 side chains of the peptide in green. The diagrams in (b) and (c) were generated using the program VISP.[103] The coordinates are from Ikura et al.[7] (PDB accession code 1BBM). (Adapted from M. Ikura, G. M. Clore, A. M. Gronenborn, G. Zhu, C. B. Klee, and A. Bax, *Science*, 1992, **256**, 632)

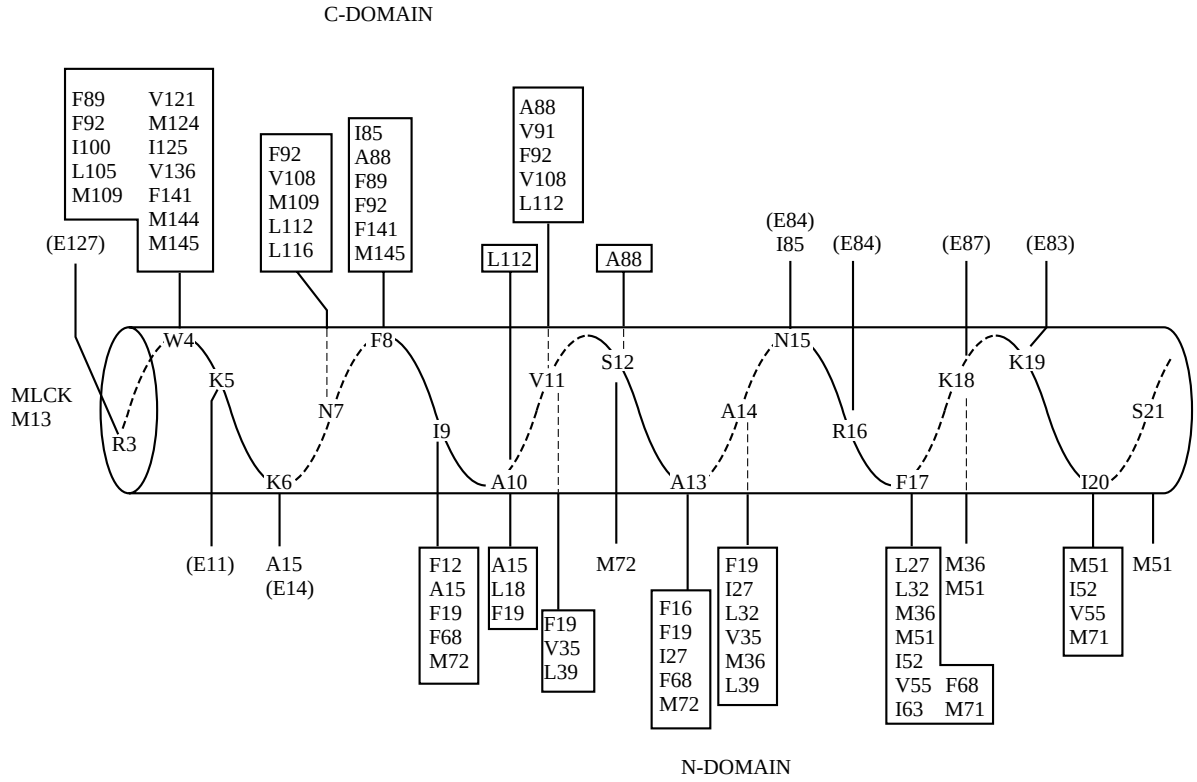

Figure 8 Summary of residue pairs for which intermolecular NOEs between CaM and M13 are observed. CaM residues involved in hydrophobic interactions are boxed. Also included are potential electrostatic interactions between negatively charged Glu residues of CaM (shown in parentheses) and positively charged Lys and Arg residues of M13. (Adapted from M. Ikura, G. M. Clore, A. M. Gronenborn, G. Zhu, C. B. Klee, and A. Bax, *Science*, 1992, **256**, 632)

The observation that at least 17 residues of the M13 peptide from either skeletal muscle or smooth muscle are necessary for high affinity binding[62,63] is readily explained by the intimate interactions of the C-terminal hydrophobic residue (i.e. Phe17) with the N-terminal domain of CaM by which the peptide is anchored. Finally, the structure accounts for experiments in which cross-linking of residues 3 and 146 of CaM, mutated to Cys, has no effect on the activation of myosin light chain kinase, even if the central helix is cleaved proteolytically at Lys77 by trypsin.[64] Thus, while the atoms of the residues 3 and 146 are 3.7 nm apart in the X-ray structure of Ca^{2+}-CaM, they are only about 2.0 nm apart in the solution structure of the Ca^{2+}-CaM–M13 complex, which is close enough to permit cross-linking to occur.

A large body of experimental data shows that CaM binds to numerous proteins whose binding domains exhibit a propensity for α-helix formation.[51] A comparison of these sequences reveals little homology. Nevertheless, many of the very tightly binding peptides ($K_{ass} \geq 5 \times 10^7\ M^{-1}$) have the common property of containing either aromatic residues or long-chain hydrophobic residues (Leu, Ile, or Val) separated by 12 residues, as summarized in Figure 9. In the case of M13, these two residues are Trp4 and Phe17 which are exclusively in contact with the C- and N-terminal domains, respectively,

		1							5							10							15							20							25			
SK-MLCK	M13							K	R	R	W	K	K	N	F	I	A	V	S	A	A	N	R	F	K	K	I	S	S	S	G	A	L	M			
SM-MLCK	M13							R	R	K	W	Q	K	T	G	H	A	V	R	A	I	G	R	L	S	S	S											
Ca pump	C24W							Q	I	L	W	F	R	G	L	N	R	I	Q	T	Q	I	R	V	V	N	A	F	R	S	S							
	C20W	L	R	R	G	Q	I	L	W	F	R	G	L	N	R	I	Q	T	Q	I	K																		
Calspermin					A	R	R	K	L	K	A	A	V	K	A	V	V	A	S	S	R	L	G	S															
Calcineurin				A	R	K	E	V	I	R	W	K	I	R	A	I	G	K	M	A	R	V	S	F	V	L													
Mastaporan									I	N	L	K	A	L	A	A	L	A	K	K	I	L																	
Mastaporan	X								I	N	W	K	G	I	A	A	M	A	K	K	L	L																	
Mellitin				G	I	G	A	V	L	K	V	L	T	T	G	L	P	A	L	I	S	W	I	K	R	K	R	Q	Q									
Interacting domain of CaM									C				C			C						N																
																N																							

Figure 9 Alignment of tightly binding ($K_{ass} \geq 5 \times 10^7\ M^{-1}$) CaM binding sequences based on the structural role of Trp4 and Phe17 in anchoring the M13 peptide to the C- and N-terminal domains, respectively, of CaM. (Adapted from M. Ikura, G. M. Clore, A. M. Gronenborn, G. Zhu, C. B. Klee, and A. Bax, *Science*, 1992, **256**, 632)

of CaM, (Figure 7 and Figure 8). Given that these two residues are involved in more hydrophobic interactions with CaM than any other residues of the peptide (see Figure 8), it seems likely that this feature of the sequence can be used to align the CaM binding sequences listed in Figure 9, thereby permitting one to predict their interaction with CaM. It is clear from this alignment that the pattern of hydrophobic and hydrophilic residues is, in general, comparable for the various peptides, suggesting that the mode of binding and the structure of the corresponding complexes with Ca^{2+}-CaM are also likely to be similar. For example, there is, in general, conservation of hydrophobic residues at the positions equivalent to Phe8 which interacts with the C-terminal domain and Val11 which interacts with both domains (see Figures 7 and 8). In addition, there are no acidic residues present which would result in unfavorable electrostatic interactions with the negatively charged Glu residues on the surface of CaM (see Figure 7). The minimum length of peptide required for high affinity binding to Ca^{2+}-CaM is defined by the 14 residue mastaporans which comprise the two hydrophobic residues at the N- and C-termini (Figure 9) and have approximately the same equilibrium association constant ($K_{ass} \approx 1-3 \times 10^9\ M^{-1}$) as M13.[65] This structural alignment also predicts that a peptide stopping just short of the second hydrophobic residue of the pair (i.e. the residue equivalent to Phe17) would only bind to the C-terminal domain and that the resulting complex would therefore retain the dumb-bell shape of Ca^{2+}-CaM. This is exactly what has been observed by small angle X-ray scattering using two synthetic peptides, C24 W and C20 W (Figure 9), comprising different portions of the CaM binding domain of the plasma membrane Ca^{2+} pump.[66] The complex with the C24 W peptide which corresponds to residues 1–24 of M13 and contains a Trp at position 4 and a Val at position 17, has a globular shape similar to that of Ca^{2+}-CaM–M13. The complex with the C20 W peptide, on the other hand, which corresponds to residues −4 to 16 of M13 and therefore lacks the C-terminal hydrophobic residue of the pair, retains the dumb-bell shape of Ca^{2+}-CaM, suggesting that the peptide only binds to the C-terminal domain.

Thus the solution structure of the complex of Ca^{2+}-CaM with M13 reveals an unusual binding mode in which the target peptide is sequestrated into a hydrophobic channel formed by the two domains of CaM with interactions involving 19 residues of the target peptide (i.e. residues 3–21 of M13). In addition, a key requirement appears to be the presence of two long-chain hydrophobic or aromatic residues separated by 12 residues in order to anchor the peptide to the two domains of CaM (Figure 7). By analogy, the rope (i.e. the CaM binding domain of the target) has to be long enough and have two knots at each end for the two hands (i.e. domains) of CaM to grip it. This particular mode of binding is therefore only likely to occur if the CaM binding site is located either at an easily accessible C- or N-terminus or in a long exposed surface loop of the target protein. An example of the former is myosin light chain kinase and of the latter is calcineurin, and, in accordance with their location, the CaM binding sites are susceptible to proteolysis.[63,67] Clearly, other types of complex between Ca^{2+}-CaM and its target proteins are possible, given the inherent flexibility of the central helix. For example, in the case of the γ-subunit of phosphorylase kinase, it appears that there are two discontinuous CaM binding sites which are capable of binding to Ca^{2+}-CaM simultaneously,[68] and binding of a peptide derived from one of these sites causes elongation rather than contraction of Ca^{2+}-CaM,[69] indicating that the complex is of a quite different structural nature. Similarly, in the case of cyclic nucleotide phosphodiesterase[70] and CaM kinase II,[71] the CaM binding sequences do not have the same spacing of hydrophobic residues seen in M13 and the other sequences listed in Figure 13 (see below) and, in addition, CaM kinase II is not susceptible to proteolysis in the absence of phosphorylation,[72] suggesting that the mode of binding is different again. Thus, in all likelihood, the complexes of Ca^{2+}-CaM with target peptides from skeletal and smooth muscle myosin light chain kinase represent one of a range of Ca^{2+}-CaM binding modes achieving CaM–target protein interactions in an efficient and elegant manner.

5.2 The Structure of the Specific Complex of the Transcription Factor GATA-1 with DNA

The erythroid specific transcription factor GATA-1 is responsible for the regulation of transcription of erythroid-expressed genes and is an essential component required for the generation of the erythroid lineage.[73] GATA-1 binds specifically as a monomer to the asymmetric consensus target sequence (T/A)GATA(A/G) found in the *cis*-regulatory elements of all globin genes and most other erythroid specific genes that have been examined.[74] GATA-1 was the first member of a family of proteins, which now includes regulatory proteins expressed in other cell lineages, characterized by their recognition of the GATA DNA sequence and by the presence of two metal binding regions of the form Cys-X-X-Cys-$(X)_{17}$-Cys-X-X-Cys separated by 29 residues. Mutation and deletion studies on GATA-1 have indicated that the N-terminal metal binding region is not required for specific DNA binding,[75] and studies with synthetic peptides have demonstrated conclusively that a 59 residue fragment (residues 158–216 of chicken GATA-1) comprising the C-terminal metal binding region complexed to zinc and 28 residues C-terminal to the last Cys constitutes the minimal unit required for specific binding ($K_{ass} \approx 1.2 \times 10^8\ M^{-1}$).[76] In order to understand the mechanism of specific DNA recognition by GATA-1 we set out to solve the solution structure of the specific complex of a 66 residue fragment (residues 158–223) comprising the DNA binding domain of chicken GATA-1 (cGATA-1) with a 16 base pair oligonucleotide containing the target sequence AGATAA, by means of multidimensional heteronuclear filtered and separated NMR spectroscopy.[8]

The structure calculations were based on a total of 1772 experimental NMR restraints, including 117 intermolecular interproton distance restraints between the protein and the DNA. A stereoview of a best-fit superposition of 30 calculated structures (residues 2–59 of the protein and base pairs 6 to 13 of the DNA) is shown in Figure 10. The N-terminus (residue 1) and C-terminus (residues 60–66) of the protein are disordered. Base pairs 6 to 13 of the DNA are in contact with the cGATA-1 DNA binding domain and are well defined both locally and globally. The orientation, however, of the first five and last three base pairs of the DNA, which are not in contact with the protein, is poorly defined with respect to the core of the complex, although the conformation of each of these bases at a local level is reasonably well defined. This is due to the fact that, in addition to their approximate

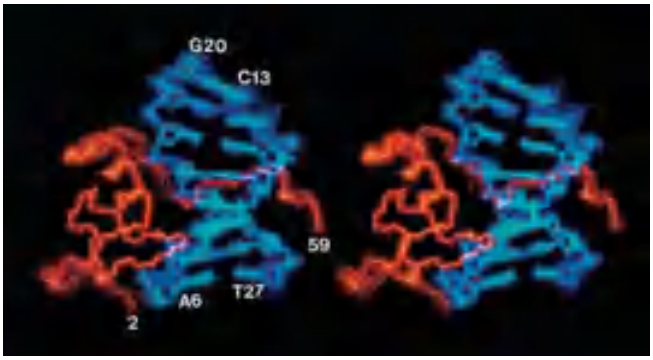

Figure 10 Stereoview showing a superposition of the 30 simulated annealing structures of the specific complex of the DNA binding domain of cGATA-1 with DNA calculated on the basis of the experimental NMR data derived from three- and four-dimensional heteronuclear NMR spectroscopy. The backbone (N, C^{α}, and C) atoms of cGATA-1 are shown in red and all the non-hydrogen atoms of the DNA in blue. The restrained regularized mean structure of the complex is highlighted. The coordinates are from Omichinski et al.[8] (PDB accession code 1GAT). (Adapted from J. G. Omichinski, G. M. Clore, O. Schaad, G. Felsenfeld, C. Trainor, E. Appella, S. J. Stahl, and A. M. Gronenborn, *Science*, 1993, **261**, 438)

nature, the interproton distance restraints within the DNA are solely sequential. Hence, they are inadequate to ascertain the relative orientation of base pairs separated by more than 5–6 steps with any great degree of precision and accuracy. The global conformation of the central eight base pairs, on the other hand, is determined not only by the restraints within the DNA, but more importantly by the large number of intermolecular interproton distance restraints between the protein and DNA. The atomic rms distribution of the 30 SA structures about the mean coordinate positions for the complex proper (i.e. residues 2–59 of the protein and base pairs 6–13 of the DNA) is 0.070 $\pm$ 0.013 and 0.113 $\pm$ 0.008 nm for protein backbone plus DNA and all protein atoms plus DNA, respectively.

The protein can be divided into two modules: the protein core which consists of residues 2–51 and contains the zinc coordination site, and an extended C-terminal tail (residues 52–59).

A schematic ribbon drawing of the core is presented in Figure 11(a). The core starts out with a turn (residues 2–5), followed by two short irregular antiparallel β-sheets, a helix (residues 28–38) and a long loop (residues 39–51) which includes a helical turn (residues 44–47), as well as an Ω like loop (residues 47–51). β-strands 1 (residues 5–7) and 2 (residues 11–14) form the first β-sheet, while β-strands 3 (residues 18–21) and 4 (residues 24–27) form the second β-sheet.

Part of the core of the cGATA-1 DNA binding domain is structurally similar to that of the N-terminal zinc containing module of the DNA binding domain of the glucocorticoid receptor.[77] Thus the C^{α} atoms of 30 residues of these two proteins can be superimposed with an rms difference of only 0.14 nm Figure 11(b). Apart from the four Cys residues that coordinate the zinc atom, only 1 residue (Lys36 in the cGATA-1 DNA binding domain and Lys465 in the glucocorticoid receptor) is conserved between the two proteins. The structural similarity extends from the N-terminus up to the end of the helix (residues 3–39 of the cGATA-1 DNA binding domain and residues 436 to 468 of the glucocorticoid receptor), and the Zn–Sγ geometry, as well as the side-chain conformations of the four coordinating cysteines, are identical. The loop between strands β2 and β3 has three deletions, and the turn between strands β3 and β4 has one deletion in the glucocorticoid receptor with respect to cGATA-1. The topology and polypeptide trace following the carboxyl end of the helix, however, are entirely different in the two proteins. Thus, in the DNA binding domain of the glucocorticoid receptor there is a second compact zinc containing module (residues 470–514) made up of two strands and two helices, while in the cGATA-1 DNA binding domain there is a long loop (residues 38–51) and extended strand (residues 52–59).

The overall topology and structural organization of the complex is shown in Figures 12(a) and 12(b). The conformation of the oligonucleotide is of B type. The helix and the loop connecting strands β2 and β3 (which is located directly beneath the helix) are located in the major groove, while the C-terminal tail wraps around the DNA and lies in the minor groove, directly opposite the helix. The overall appearance is analogous to that of a right hand holding a rope, with the rope representing the DNA, the palm and fingers of the hand the core of the protein, and the thumb the C-terminal tail. It is this pincer-like configuration of the protein that causes a small 10° kink in the DNA. The long axis of the helix lies at an angle of about 40° to the base planes of the DNA [Figure 12(a)], while the C-terminal tail is approximately parallel to the base planes [Figure 12(b)].

Views of side-chain contacts with the DNA in the major and minor grooves are shown in Figures 12(c) and 12(d), respectively, while a schematic representation of all the contacts is provided in Figure 13. The cGATA-1 DNA binding domain makes specific contacts with eight bases, seven in the major groove (A6, G7, A8, T25, A24, T23, and T22) and one in the minor groove (T9). All the base contacts in the major groove involve the helix and the loop connecting β-strands 2 and 3. In contrast to other DNA binding proteins, the majority of base contacts involve hydrophobic interactions. Thus, Leu17 interacts with A6, G7, and T25; Thr16 with A24 and T25; Leu33 with A24 and T23; and Leu37 with T23 and T22. This accounts for the predominance of thymidines in the DNA target site. Indeed, there are only three hydrogen-bonding interactions: namely, between the side chain of Asn29 and the N-6 atoms of A24 and A8 in the major groove, and between the $N\zeta H_3^+$ of Lys57 and the O-2 atom of T9 in the minor groove. In this regard, it is interesting to note that there is a reduction of 11.27 nm^2 in the surface accessible area of the cGATA-1 DNA binding domain in the presence of DNA (corresponding to a 20% decrease in the accessible surface), and a decrease in the calculated solvation free energy of folding[53] of 13 kcal mol^{-1} (54 kJ mol^{-1}). This latter effect can clearly make a sizable contribution to the specific binding constant ($K_{ass} \approx 1.2 \times 10^8\ M^{-1}$).

The remaining contacts involve the sugar–phosphate backbone, the majority of which are located on the second strand (that is G20 to T27). Salt bridges and/or hydrogen bonds with the phosphates of G7, A24, and T22 are made by Arg19, Arg47, and His38, respectively, in the major groove, and with the phosphates of C13, T25, C26 and T27 by Arg54, Thr53, Arg56, and Ser59, respectively, in the minor groove. The interactions of Arg54, and Arg56 above and below the polypeptide chain span the full length of the target site and are probably responsible for the bending of the DNA in the direction of the

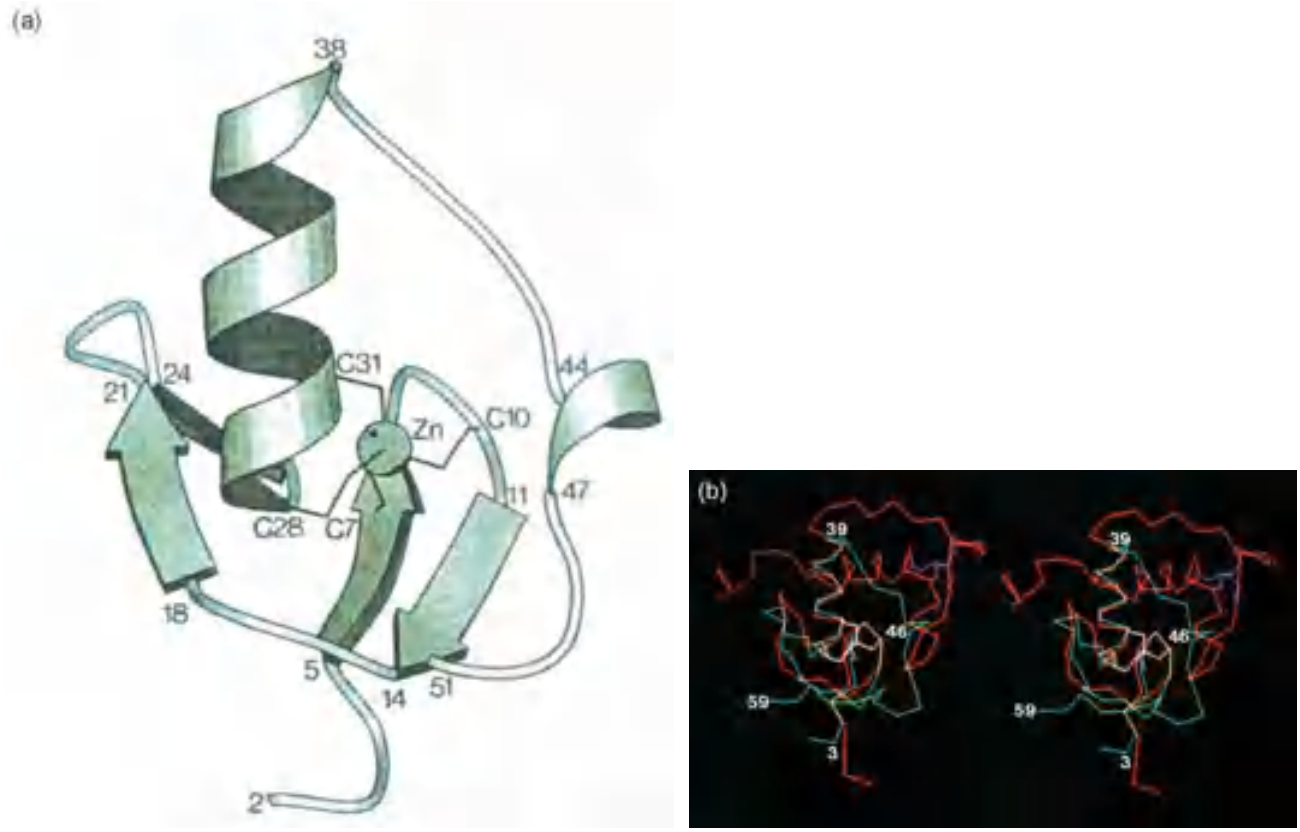

Figure 11 (a) Schematic ribbon drawing of the core of the cGATA-1 DNA binding domain. (b) Superposition of the C^{α} atoms of the cGATA-1 (green) and glucocorticoid receptor (red) DNA binding domains. The zinc and coordinating cysteines are shown in yellow for cGATA-1 and in purple for the glucocorticoid receptor; the residues are labeled according to the numbering in cGATA-1. The alignment of cGATA-1 with the glucocorticoid receptor is as follows: residues 3–13, 18–21, 25–39, and 46 of cGATA-1 are superimposed on residues 436–446, 448–451, 454–468, and 490, respectively, of the glucocorticoid receptor with a C^{α} atomic rms of 0.14 nm. The diagram in (a) was made using the program MOLSCRIPT.[102] The coordinates of the glucocorticoid receptor DNA binding domain shown in (b) are taken from Luisi et al.[79] The cGATA-1 coordinates are from Omichinski et al.[8] (PDB accession code 1GAT). (Adapted from J. G. Omichinski, G. M. Clore, O. Schaad, G. Felsenfeld, C. Trainor, E. Appella, S.J. Stahl, and A. M. Gronenborn, *Science*, 1993, **261**, 438)

minor groove. Likewise, all the sugar contacts involve the second strand. In the major groove they are hydrophobic in nature, and involve contacts between the sugars of T22, T23 and A24 with Tyr34, Leu33 and Ala30, and Ile51 and Thr16, respectively. In the minor groove, hydrophobic sugar DNA–protein interactions are made by C-13 with the aliphatic portion of the side chain of Arg54, T23 and T24 with Gln52, T25 and C26 with the aliphatic portion of the side chain of Arg 56, and C26 with Ser59. In addition, there is a hydrogen bond between the side-chain amide of Gln52 and the sugar O-3′ atom of T23.

The mode of specific DNA binding protein that is revealed in this structure is distinct from that observed for the other three classes of zinc containing DNA binding domains whose structures have previously been solved.[77–82] Features specific to the complex with the DNA binding domain of cGATA-1 include: the relatively small size of the DNA target site (eight base pairs of which only a contiguous stretch of six is involved in specific contacts); the monomeric nature of the complex in which only a single zinc binding module is required for specific binding; the predominance of hydrophobic interactions involved in specific base contacts in the major groove; the presence of a basic C-terminal tail which interacts with the DNA in the minor groove and constitutes a key component of specificity; and, finally, the pincer-like nature of the complex in which the core and tail subdomains are opposed and surround the DNA just like a hand gripping a rope. The structure of the cGATA-1 DNA binding domain reveals a modular design. The fold of residues 3–39 is similar to that of the N-terminal zinc binding module of the DNA binding domain of the glucocorticoid receptor, although, with the exception of the four Cys residues that coordinate zinc, there is no significant sequence identity between these regions of the two proteins. Residues 40–66 are part of a separate structural motif. In this regard it is interesting to note that, in addition to both zinc binding modules being encoded on separate exons in the cGATA-1 gene (exons 4 and 5), the next intron/exon boundary lies between amino acids 39 and 40 (current numbering scheme) of the DNA binding domain, thereby separating the C-terminal zinc binding domain from the basic tail[83].

5.3 Hydration of the Specific Complex of the Transcription Factor GATA-1 with DNA

A number of recent high resolution crystal structures of protein–DNA complexes have suggested that bound water may play an important role in the recognition process in the

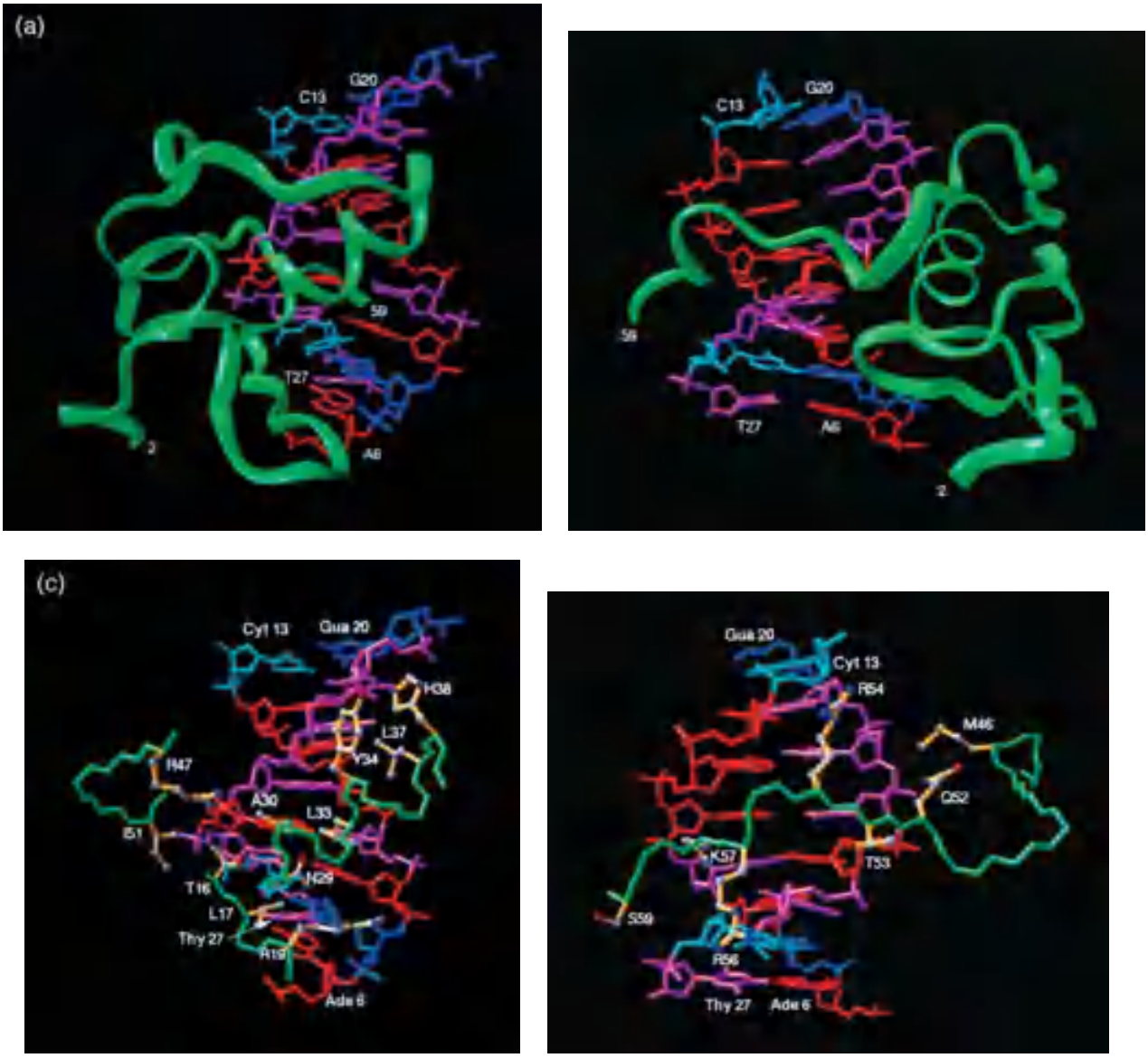

Figure 12 (a, b) Schematic ribbon drawings illustrating the interactions of cGATA-1 with DNA. (c, d) Side-chain interactions between cGATA-1 and the DNA in the major and minor grooves, respectively. The protein backbone is shown in green and the protein side chains in yellow; the color code for the DNA bases is as follows: red for A, lilac for T, dark blue for G, and light blue for C. The diagrams were made using the program VISP.[103] The coordinates of the cGATA-1–DNA complex are from Omichinski et al.[8] (PDB accession code 1GAT). (Adapted from J. G. Omichinski, G. M. Clore, O. Schaad, G. Felsenfeld, C. Trainor, E. Appella, S. J. Stahl, and A. M. Gronenborn, *Science*, 1993, **261**, 438)

form of indirect read-out in which the bound water molecules serve to bridge hydrogen bonds between functional groups on the protein and the DNA bases.[84–86] In addition, a bound water molecule has been detected at the interface of the complex between the *Antp*(C39 S) homeodomain and a 14-base pair duplex in solution using NMR spectroscopy.[87] In contrast to other protein–DNA complexes, in which the majority of specific interactions involve hydrogen bonds between the protein and the DNA bases, the structure of the specific complex of GATA-1 with DNA, as indicated in the previous section, suggests that hydrophobic effects constitute a large proportion of the specific binding energy.[8] This would predict that water of hydration would be excluded from the interface between GATA-1 and the DNA bases in the major groove, but would be present at the interface between GATA-1 and the sugar–phosphate backbone, as well as at the solvent exposed surface of the protein. To test this hypothesis we carried out selective two-dimensional H_2O NOE and H_2O rotating frame Overhauser effect (ROE) $^1H-^{15}N$ and $^1H-^{13}C$ heteronuclear single quantum correlation experiments[88] to detect through space (<0.4 nm) contacts between bound water and protons of the protein, thereby identifying the location of bound water molecules in the specific complex of chicken GATA-1 with DNA.[89]

A number of water molecules could be detected between the protein and the phosphate backbone, as well as at the solvent exposed surface of the protein. However, no water molecules could be observed at the interface of the protein with the bases of the DNA. With only one exception, the bound water molecules have a residency time greater than 200–300 ps. On

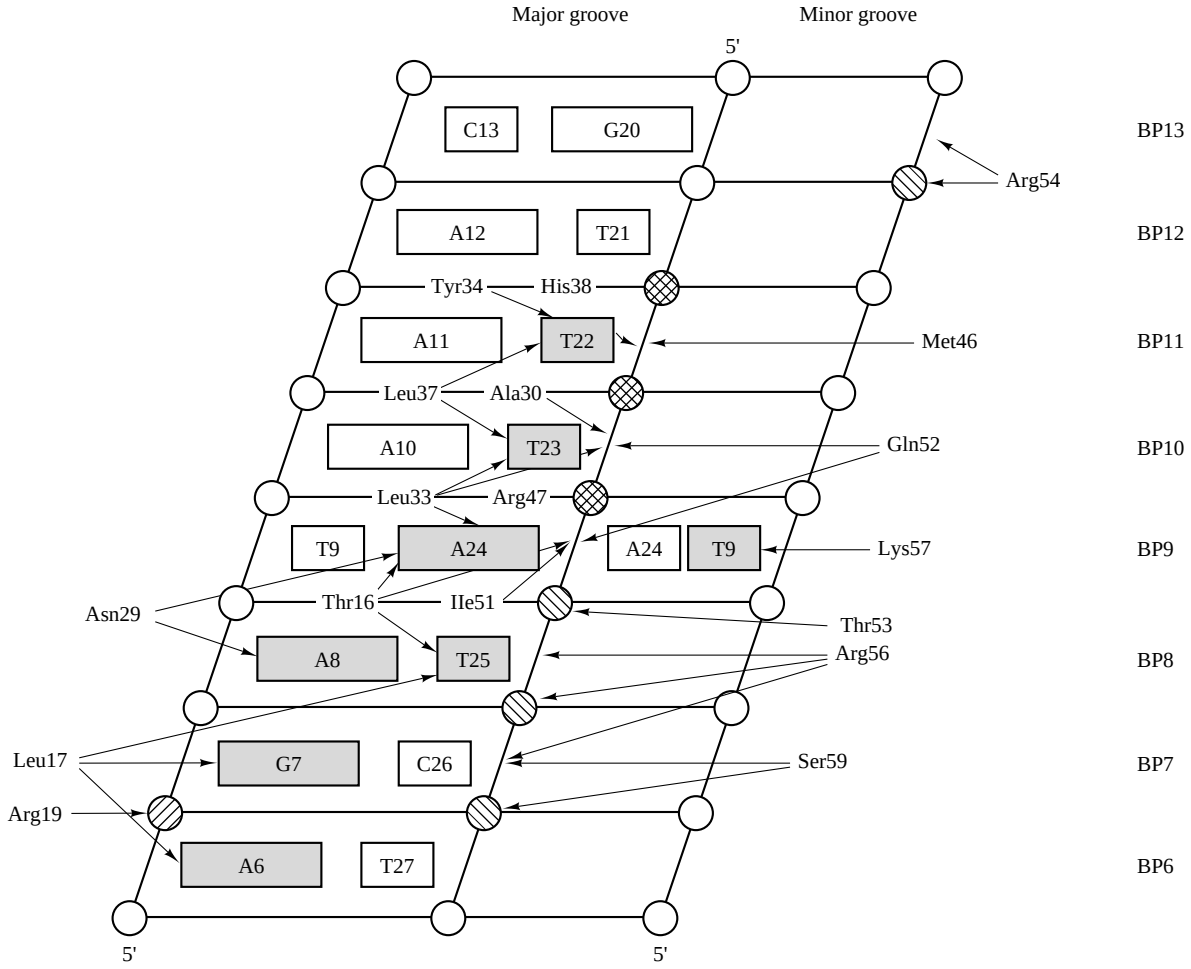

Figure 13 Schematic diagram summarizing the contacts between cGATA-1 and DNA. The DNA is represented as a cylindrical projection. Bases interacting with the protein are shaded; phosphates are represented as circles; cicles with hatches directed towards the right and left indicate sites of interaction with sugar or phosphate or both in the major and minor grooves, respectively. (Adapted from J. G. Omichinski, G. M. Clore, O. Schaad, G. Felsenfeld, C. Trainor, E. Appella, S. J. Stahl, and A. M. Gronenborn, *Science*, 1993, **261**, 438)

the basis of the structure of the complex of GATA-1 with DNA,[8] we were able to identify unambiguously 17 methyl protons and 3 backbone NH protons in close proximity to bound water.[89] The location of the protein residues near bound water are indicated in the structure of the complex of GATA-1 with DNA shown in Figure 14.

An approximate estimate of the residency times of these bound water molecules can be obtained from the sign of the NOE.[9,90] If a water molecule is bound to a macromolecule with a correlation time in the spin diffusion limit (i.e. greater than about 2 ns), the NOE between water and a protein proton will be zero for a residency time of about 300 ps, while for residency times smaller and longer than 300 ps the NOE will be positive and negative, respectively. In contrast, the ROE remains positive for all residency and correlation times. The NH protons of Ala30, Tyr34, and Tyr35 and the methyl goups of Ala3, Ala30, Met46, and Ile51 (γ_m and δ_m) exhibited negative NOEs to water, indicating a residency time greater than about 500 ps. The methyl protons of Met23 exhibited a positive NOE to water, indicative of a residency time of 100–300 ps. For the remaining surface methyl protons, the NOEs (at a mixing time of 60 ms) to water were too weak to observe and only ROEs were seen, indicating residency times in the range 200–500 ps.

All methyl groups that are exposed to solvent are associated with bound water molecules. These include Ala3, Val6 (γ_1 and γ_2), Leu17 (δ_2 only), Met23, Val40 (γ_1 and γ_2), Leu44 (δ_1 and δ_2), and Val58 (γ_1 and γ_2). Bound water molecules in contact with exposed hydrophobic surfaces are rarely seen in protein crystal structures as the water molecules are only well ordered (high occupancy and low thermal factor) if the protein donates anchor points in suitable hydrogen-bonding positions.[91] In the absence of hydrogen bonding, low occupancies and high thermal *B* factors render such water molecules unobservable.[91] Indeed, there is only one crystallographic example where water surrounding an exposed hydrophobic group has been seen in the absence of hydrogen bonding, namely the water pentagons surrounding Leu18 in the 0.088 nm resolution crystal structure of crambin.[92] In contrast to the crystallographic case, bound water can be readily detected by NMR over a very wide range of residency times (with a lower limit of 50–100 ps) and is not eliminated by rapid independent rotation of a water pentagon around a rotating methyl group. Moreover, the NMR experiment is not dependent on uniform ordering insofar as the bound water could be in somewhat different positions

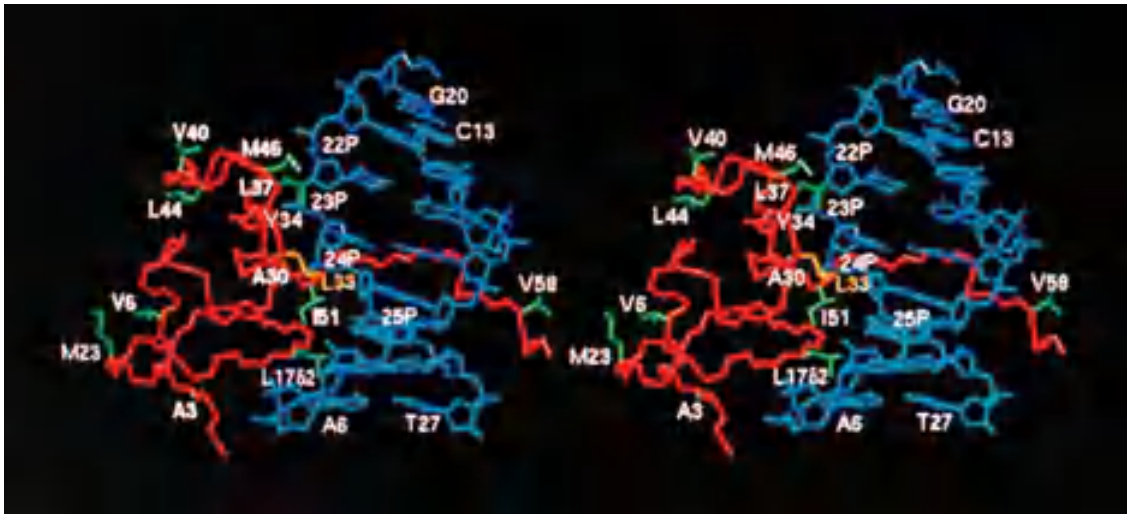

Figure 14 Stereoview of the solution structure of the specific complex of GATA-1 and DNA, illustrating the location of groups in close proximity to bound water. The DNA is displayed in blue, the protein backbone in red, and the side chains in close proximity to bound water detected in the H_2O ROE/NOE HSQC (heteronuclear single quantum correlation) experiments in green. The side chain of Leu33 which interacts directly with the bases of the DNA in the major groove and is not close to bound water is shown in orange. In the case of Leu17, only the surface exposed $C^{\delta 2}H_3$ methyl group gives rise to a ROE with bound water; the $C^{\delta 1}H_3$ methyl group which interacts directly with the DNA bases is not close to bound water. The model is taken from the solution NMR structure given by Omichinski et al.[8] (PDB accession number 1GAT) and was generated using the program VISP.[103] (Adapted from G. M. Clore, A. Bax, J. G. Omichinski, and A. M. Gronenborn, *Structure*, 1994, **2**, 89)

in different molecules. In the X-ray diffraction experiment, on the other hand, bound water could only be detected if it occupied the same position in different protein molecules; that is to say there has to be uniform ordering of the bound water throughout the protein molecules of the crystal. Consequently, rapid rotation of a water pentagon about a methyl group, in the absence of discrete hopping, would result in smearing of the electron density beyond the limit of detectability.

The ubiquitous presence of bound water molecules close to exposed hydrophobic groups observed by NMR is completely consistent with the thermodynamic results of Privalov and Makhatadze,[93,94] who showed that the hydration of methyl groups is associated with a large negative entropy ($-40.3\,J\,mol^{-1}\,K^{-1}$), a negative enthalpy ($-8.28\,kJ\,mol^{-1}$) and only a small positive Gibbs free energy ($3.72\,kJ\,mol^{-1}$). Indeed, the entropy of hydration of methyl groups is comparable to that of polar groups (-41 to $-50\,J\,mol^{-1}\,K^{-1}$), indicating that their ordering power for water is comparable.

All methyl groups that are in close proximity to the phosphodiester backbone but do not interact with the bases are also associated with bound water molecules. In these cases, it is clear that the water is stabilized by hydrogen bonding interactions with either the phosphate group or the O-5′ and O-3′ oxygen atoms. Interestingly, similarly located water molecules have also been observed in crystal structures of DNA–protein complexes.[95,96] The results on the specific complex of GATA-1 with DNA indicate the presence of a cluster of water molecules in the vicinity of the sugar–phosphate backbone of T22, T23, A24, and T25. It is important to note, however, that these interactions do not confer specificity. In the minor groove there is a bound water molecule(s) between the $C^{\epsilon}H_3$ of Met46, the sugar of T22 and the phosphate of T23. In the major groove, four clusters of bound water molecules are observed: namely between the $C^{\delta 2}H_3$ methyl group of Leu37 and the sugar and phosphate of T22; between the $C^{\delta 1}H_3$ of Leu37, the backbone NH protons of Tyr34 and Ty35, and the phosphate of T23; between the methyl group of Ala30, the NH proton of Ala30, and the phosphate of A24; and finally between the $C^{\gamma}H_3$ and $C^{\delta}H_3$ methyl groups of Ile51, the sugar of A24 and the phosphate of T25. In all likelihood, the water molecule(s) associated with the NH protons Tyr34 and Tyr35, and with the NH proton of Ala30, participate in bridging hydrogen bonds between the relevant amide group of the protein and the sugar–phosphate backbone of the DNA.

In contrast to the above methyl groups, no NOEs or ROEs to water were observed for either of the two Leu33 methyl groups or the $C^{\delta 1}H_3$ methyl group of Leu17, all of which are involved in hydrophobic interactions with the bases.[8] This indicates that water is excluded from the interface between the protein and the DNA bases in the major groove. In addition, complementary conventional two-dimensional $^1H-^1H$ NOE experiments with ^{12}C filtering failed to detect any bound water close to the thymine methyl groups of the DNA, providing further evidence for the exclusion of water at the interface of the protein and the DNA bases. The absence of water at the interface between the protein and the DNA bases in the major groove lends further credence to the importance of hydrophobic interactions in stabilizing the specific interaction between chicken GATA-1 and DNA, and indicates that hydrophobic interactions can play an important role in protein–DNA recognition and specificity.

6 CONCLUDING REMARKS

From the examples presented in this article it should be clear that the recent development of a whole range of highly sensitive multidimensional heteronuclear edited and filtered NMR experiments has revolutionized the field of protein structure determination by NMR. Proteins and protein–ligand complexes in the 15–25 kDa range are now amenable to detailed

structure analysis in solution. Moreover, the potential of the current methods can probably be extended to systems even up to 40 kDa, providing that they are very well behaved from an NMR perspective. Nevertheless, despite these advances, it should always be borne in mind that there are a number of key requirements that have to be satisfied to permit a successful structure determination of larger proteins and protein complexes by NMR. The protein in hand must be soluble and should not aggregate up to concentrations of about 1 mM, it must be stable at room temperature or slightly higher for many weeks, it should not exhibit significant conformational heterogeneity that could result in extensive line broadening, and finally it must be amenable to uniform ^{15}N and ^{13}C labeling. At the present time there are only a few examples in the literature of proteins in the 15–25 kDa range that have been solved by means of multidimensional heteronuclear NMR spectroscopy. In addition to the three examples presented here, only the structures of interleukin-4,[33,97,98] glucose permease IIA,[99] the complex of cyclophilin with cyclosporin,[100] and the *Antennapedia* homeodomain–DNA complex[101] have been published. It is hoped that over the next few years, the widespread use of these multidimensional heteronuclear experiments coupled with semiautomated assignment procedures will result in many more NMR structures of such larger proteins and protein–ligand complexes.

7 RELATED ARTICLES

Distance Geometry; DNA: A-, B-, and Z-; Peptide and Protein Secondary Structural Elements; Peptides and Polypeptides; Protein Dynamics from NMR Relaxation; Protein Hydration; Protein Structures: Relaxation Matrix Refinement.

8 REFERENCES

1. G. M. Clore and A. M. Gronenborn, *Science*, 1991, **252**, 1390.
2. G. M. Clore and A. M. Gronenborn, *J. Mol. Biol.*, 1991, **221**, 47
3. G. M. Clore and A. M. Gronenborn, *Prog. Nucl. Magn. Reson. Spectrosc.*, 1991, **23**, 43.
4. G. M. Clore and A. M. Gronenborn, *Annu. Rev. Biophys. Biophys. Chem.*, 1991, **20**, 29.
5. A. Bax and S. Grzesiek, *Acc. Chem. Res.*, 1993, **26**, 131.
6. G. M. Clore, P. T. Wingfield, and A. M. Gronenborn, *Biochemistry*, 1991, **30**, 2315.
7. M. Ikura, G. M. Clore, A. M. Gronenborn, G. Zhu, C. B. Klee, and A. Bax, *Science*, 1992, **256**, 632.
8. J. G. Omichinski, G. M. Clore, O. Schaad, G. Felsenfeld, C. Trainor, E. Appella, S. J. Stahl, and A. M. Gronenborn, *Science*, 1993, **261**, 438.
9. R. R. Ernst, G. Bodenhausen, and A. Wokaun, *Principles of Nuclear Magnetic Resonance in One and Two Dimensions*, Clarendon, Oxford, 1987.
10. T. F. Havel, I. D. Kuntz, and G. M. Crippen, *Bull. Math. Biol.*, 1983, **45**, 665.
11. W. Braun, *Q. Rev. Biophys.*, 1987, **19**, 115.
12. G. M. Clore and A. M. Gronenborn, *CRC Crit. Rev. Biochem. Mol. Biol.*, 1989, **24**, 479.
13. T. F. Havel and K. Wüthrich, *J. Mol. Biol.*, 1985, **182**, 281.
14. T. F. Havel, *Prog. Biophys. Mol. Biol.*, 1991, **56**, 43.
15. G. M. Clore, M. A. Robien, and A. M. Gronenborn, *J. Mol. Biol.*, 1993, **231**, 82.
16. G. M. Clore and A. M. Gronenborn, *Protein Eng.*, 1987, **1**, 275.
17. K. Wüthrich, *NMR of Proteins and Nucleic Acids*, Wiley, New York, 1986.
18. H. Oschkinat, C. Griesinger, P. J. Kraulis, O. W. Sørensen, R. R. Ernst, A. M. Gronenborn, and G. M. Clore, *Nature*, 1998, **332**, 374.
19. D. Marion, P. C. Driscoll, L. E. Kay, P. T. Wingfield, A. Bax, A. M. Gronenborn, and G. M. Clore, *Biochemistry*, 1989, **28**, 6150.
20. S. W. Fesik and E. R. P. Zuiderweg, *J. Magn. Reson.*, 1988, **78**, 588.
21. S. W. Fesik and E. R. P. Zuiderweg, *Q. Rev. Biophys.*, 1990, **23**, 97.
22. P. C. Driscoll, G. M. Clore, D. Marion, P. T. Wingfield, and A. M. Gronenborn, *Biochemistry*, 1990, **29**, 3542.
23. G. T. Montelione and G. Wagner, *J. Am. Chem. Soc.*, 1989, **111**, 5474
24. G. T. Montelione and G. Wagner, *J. Magn. Reson.*, 1990, **87**, 183.
25. M. Ikura, L. E. Kay, and A. Bax, *Biochemistry*, 1990, **29**, 4659.
26. A. Bax and S. S. Pochapsky, *J. Magn. Reson.*, 1992, **99**, 638.
27. G. Wagner, W. Braun, T. F. Havel, T. Schaumann, N. Go, and K. Wüthrich, *J. Mol. Biol.*, 1987, **196**, 611.
28. S. G. Hyberts, W. Märki, and G. Wagner, *Eur. J. Biochem.*, 1987, **164**, 625.
29. P. Güntert, W. Braun, M. Billeter, and K. Wüthrich, *J. Am. Chem. Soc.*, 1989, **111**, 3997.
30. M. Nilges, G. M. Clore, and A. M. Gronenborn, *Biopolymers*, 1990, **29**, 813.
31. A. Bax, G. W. Vuister, S. Grzesiek, F. Delaglio, A. C. Wang, R. Tschudin, and G. Zhu, *Methods Enzymol.*, 1994, **239**, 79.
32. E. R. P. Zuiderweg, R. Boelens, and R. Kaptein, *Biopolymers*, 1985, **24**, 601.
33. R. Powers, D. S. Garrett, C. J. March, E. A. Frieden, A. M. Gronenborn, and G. M. Clore, *Biochemistry*, 1993, **32**, 6744.
34. L. E. Kay, G. M. Clore, A. Bax, and A. M. Gronenborn, *Science*, 1990, **249**, 411.
35. G. M. Clore, L. E. Kay, A. Bax, and A. M. Gronenborn, *Biochemistry*, **30**, 1991, 12.
36. E. R. P. Zuiderweg, A. M. Petros, S. W. Fesik, and E. T. Olejniczak, *J. Am. Chem. Soc.*, 1991, **113**, 370.
37. G. W. Vuister, G. M. Clore, A. M. Gronenborn, R. Powers, D. S. Garrett, R. Tschudin, and A. Bax, *J. Magn. Reson., Ser. B*, 1993, **101**, 210.
38. J. D. Forman-Kay, G. M. Clore, P. T. Wingfield, and A. M. Gronenborn, *Biochemistry*, 1991, **30**, 2685.
39. H. J. Dyson, G. P. Gippert, D. A. Case, A. Holmgren, and P. E. Wright, *Biochemistry*, 1990, **29**, 4129.
40. P. C. Driscoll, A. M. Gronenborn, P. T. Wingfield, and G. M. Clore, *Biochemistry*, 1990, **29**, 4668.
41. G. M. Clore, A. Bax, P. C. Driscoll, P. T. Wingfield, and A. M. Gronenborn, *Biochemistry*, 1990, **29**, 8172.
42. G. M. Clore, P. C. Driscoll, P. T. Wingfield, and A. M. Gronenborn, *J. Mol. Biol.*, 1990, **214**, 811.
43. G. M. Clore, A. Bax, P. T. Wingfield, and A. M. Gronenborn, *Biochemistry*, 1990, **29**, 5671.
44. M. Nilges, G. M. Clore, and A. M. Gronenborn, *FEBS Lett.*, 1988, **229**, 317.

45. B. C. Finzel, L. L. Clancy, D. R. Holland, S. W. Muchmore, K. D. Watenpaugh, and H. M. Einspahr, *J. Mol. Biol.*, 1989, **209**, 779.
46. J. P. Priestle, H. P. Schär, and M. G. Grütter, *Proc. Natl. Acad. Sci. USA*, 1989, **86**, 9667.
47. B. Veerapandian, G. L. Gilliland, R. Raag, A. L. Svensson, Y. Masui, Y. Hirai, and T. L. Poulos, *Protein Struct. Function Genet.*, 1991, **12**, 10.
48. B. Shaanan, A. M. Gronenborn, G. H. Cohen, G. L. Gilliland, B. Veerapandian, D. R. Davies, and G. M. Clore, *Science*, 1992, **257**, 961.
49. A. T. Brünger, *Nature*, 1992, **355**, 472.
50. M. Ikura and A. Bax, *J. Am. Chem. Soc.*, 1992, **114**, 2433.
51. P. Cohen and C. B. Klee, *Molecular Aspects of Cellular Regulation*, Elsevier, New York, 1988, Vol. 5.
52. Y. S. Babu, J. S. Sack, T. J. Greenhough, C. E. Bugg, A. R. Means, and W. J. Cook, *Nature*, 1985, **315**, 37.
53. D. Eisenberg and A. D. McLachlan, *Nature*, 1986, **319**, 199.
54. D. B. Heidorn, P. A. Seeger, S. E. Rokop, D. K. Blumenthal, A. R. Means, H. Crespi, and J. Trewhella, *Biochemistry*, 1989, **28**, 6757.
55. K. T. O'Neil and W. F. DeGrado, *Trends Biochem.* 1990, **15**, 59.
56. S. Spera, M. Ikura, and A. Bax, *J. Biomol. NMR*, 1991, **1**, 155.
57. M. Ikura, L. E. Kay, M. Krinks, and A. Bax, *Biochemistry*, 1991, **30**, 5498.
58. G. Barbato, M. Ikura, L. E. Kay, R. W. Pastor, and A. Bax, *Biochemistry*, 1992, **31**, 5269.
59. A. Persechini, D. K. Blumenthal, H. W. Jarrett, C. B. Klee, D. O. Hardy, and R. H. Kretsinger, *J. Biol. Chem.*, 1989, **264**, 8052.
60. M. Kataoka, J. F. Head, A. Persechini, H. Kretsinger, and D. M. Engelman, *Biochemistry*, 1991, **30**, 1188.
61. K. T. O'Neil, S. Erickson-Viitanen, and W. F. DeGrado, *J. Biol. Chem.*, 1989, **264**, 14 571.
62. T. J. Lukas, W. H. Burgess, F. G. Prendergast, W. Lau, and D. M. Watterson, *Biochemistry*, 1986, **25**, 1458.
63. D. K. Blumenthal and E. G. Krebs, *Methods Enzymol.*, 1987, **139**, 115.
64. A. Persechini and R. H. Kretsinger, *J. Biol. Chem.*, 1988, **263**, 12175.
65. J. A. Cox, M. Comte, J. E. Fitton, and W. F. DeGrado, *J. Biol. Chem.*, 1985, **260**, 2527.
66. M. Kataoka, J. F. Head, T. Vorherr, J. Krebs, and E. Carafoli, *Biochemistry*, 1991, **30**, 6247.
67. D. Guerini and C. B. Klee, *Adv. Protein Phosphatases*, 1991, **6**, 391.
68. M. Dasgupta, T. Honeycutt, and D. K. Blumenthal, *J. Biol. Chem.*, 1989, **264**, 17 156.
69. J. Trewhella, D. K. Blumenthal, S. E. Rokup, and P. A. Seeger, *Biochemistry*, 1990, **29**, 9316.
70. H. Charbonneau, S. Kumar, J. P. Novack, D. K. Blumenthal, P. R. Griffin, J. Shabanowitz, D. F. Hunt, J. A. Beavo, and K. A. Walsh, *Biochemistry*, 1991, **30**, 7931.
71. M. K. Bennett and M. B. Kennedy, *Proc. Natl. Acad. Sci. USA*, 1987, **84**, 1794.
72. A. P. Kwiatkowski and M. M. King, *Biochemistry*, 1989, **28**, 5380.
73. S. H. Orkin, *Blood*, 1992, **80**, 575.
74. T. Evans, and G. Felsenfeld, *Cell*, 1989, **58**, 877.
75. D. I. K. Markin and S. H. Orkin, *Genes Dev.*, 1986, **4**, 1886.
76. J. G. Omichinski, C. Trainor, T. Evans, A. M. Gronenborn, G. M. Clore, and G. Felsenfeld, *Proc. Natl. Acad. Sci. USA*, 1993, **90**, 1676.
77. B. F. Luisi, W. X. Xu, Z. Otwinowski, L. P. Freedman, K. R. Yamamoto, and P. B. Sigler, *Nature*, 1991, **352**, 497.
78. N. P. Pavletich and C. O. Pabo, *Science*, 1991, **252**, 809.
79. N. P. Pavletich and C. O. Pabo, *Science*, 1993, **261**, 1701.
80. R. Mamorstein, M. Carey, M. Ptashne, and S. C. Harrison, *Nature*, 1992, **356**, 408.
81. J. W. R. Schwabe, L. Chapman, J. T. Finch, and D. Rhodes, *Cell*, 1993, **75**, 567.
82. L. Fairall, J. W. R. Schwabe, L. Chapman, J. T. Finch, and D. Rhodes, *Nature*, 1993, **366**, 483.
83. R. Hannon, T. Evans, G. Felsenfeld, and H. Gould, *Proc. Natl. Acad. Sci. USA*, 1991, **88**, 3004.
84. Z. Otwinowski, R. W. Schevitz, R.-G. Zhang, C. I. Lawson, A. Joachimiak, E. Q. Mamorstein, B. F. Luisi, and P. B. Sigler, *Nature*, 1988, **335**, 321.
85. C. L. Lawson and J. Carey, *Nature*, 1993, **366**, 178.
86. K. L. Clark, E. D. Halay, E. Lai, and S. K. Burley, *Nature*, 1993, **364**, 412.
87. Y. Q. Qian, G. Otting, and K. Wüthrich, *J. Am. Chem. Soc.*, 1993, **115**, 1189.
88. S. Grzesiek and A. Bax, *J. Biomol. NMR.*, 1993, **3**, 627.
89. G. M. Clore, A. Bax, J. G. Omichinski, and A. M. Gronenborn, *Structure*, 1994, **2**, 89.
90. G. Otting, E. Liepinsh, and K. Wüthrich, *Science*, 1991, **254**, 974.
91. G. A. Jeffrey and W. Saenger, *Hydrogen Bonding in Biological Structures*, Springer, Berlin, 1991.
92. M. M. Teeter, *Proc. Natl. Acad. Sci. USA*, 1984, **81**, 6014.
93. G. I. Makhatadze and P. L. Privalov, *J. Mol. Biol.*, 1993, **232**, 639.
94. P. I. Privalov and G. I. Makhatadze, *J. Mol. Biol.*, 1993, **232**, 660.
95. A. K. Aggarwal, D. W. Rodgers, M. Drottar, M. Ptashne, and S. C. Harrison, *Science*, 1998, **242**, 899.
96. R. S. Hegde, S. R. Grossman, L. A. Laimins, and P. B. Sigler, *Nature*, 1992, **359**, 505.
97. R. Powers, D. S. Garrett, C. J. March, E. A. Frieden, A. M. Gronenborn, and G. M. Clore, *Science*, 1992, **256**, 1673.
98. L. J. Smith, C. Redfield, J. Boyd, G. M. P. Lawrence, R. G. Edwards, R. A. G. Smith, and C. M. Dobson, *J. Mol. Biol.*, 1992, **224**, 899.
99. W. J. Fairbrother, G. P. Gippert, J. Reizer, M. J. Saier, Jr., and P. E. Wright, *FEBS Lett.*, 1992, **296**, 148.
100. Y. Théuriault, T. M. Logan, R. Meadows, L. Yu, E. T. Olejniczak, T. F. Holzman, R. L. Simmer, and S. W. Fesik, *Nature*, 1993, **361**, 88.
101. M. Billeter, Y. Q. Qian, G. Otting, M. Müller, W. Gehring, and K. Wüthrich, *J. Mol. Biol.*, 1993, **234**, 1084.
102. P. J. Kraulis, *J. Appl. Crystallogr.*, 1991, **24**, 946.
103. E. de Castro and S. Edelstein, *VISP 1.0 User's Guide*, University of Geneva, 1992.

Acknowledgments

We thank our many colleagues, past and present, who have contributed to the work carried out in our laboratory. Above all, we thank Ad Bax with whom we have shared numerous stimulating discussions, fruitful experiments, and a continuous and most enjoyable collaboration in the best of scientific spirits. This work was supported in part by

the AIDS Targeted Anti-Viral Program of the Office of the Director of the National Institutes of Health. This article is adapted from two reviews: *Protein Science*, 1994, **3**, 372, and *Progress in Biophysical and Molecular Biology*, 1994, **62**, 153..

Biographical Sketches

G. Marius Clore. *b* 1955. B.Sc. University College London, 1976; M.D., University College Hospital Medical School, London, 1979; Ph.D., National Institute for Medical Research, London, 1982. Scientific staff, National Institute for Medical Research, London, 1980–1984; Joint Head, Biological NMR Group, Max-Planck Institute for Biochemistry, Martinsried, West Germany 1984–1988; Chief, Section of Protein NMR, Laboratory of Chemical Physics, National Institutes of Health 1988 – present. Approx. 260 publications, and with A. M. Gronenborn the book 'NMR of Proteins'. Research interests include biological NMR spectroscopy and structural biology.

Angela M. Gronenborn. *b* 1950. Dipl. Chem., 1975; Ph.D., 1978, University of Cologne; Scientific staff, National Institute for Medical Research, London, 1979–1984; Joint Head, Biological NMR Group, Max-Planck Institute for Biochemistry, Martinsried, West Germany 1984–1988; Chief, Section of Structural Biology, Laboratory of Chemical Physics, National Institutes of Health, 1988 – present. Approx. 250 publications, and with G. M. Clore the book 'NMR of Proteins'. Research interests include biological NMR spectroscopy and structural biology.

Synthetic Peptides

Murray Goodman
University of California, San Diego, La Jolla, CA, USA
and
Dale F. Mierke
Clark University, Worcester, MA, USA

1 Introduction 1
2 Conformation of Peptides 1
3 Synthetic Methods 1
4 Computer Simulations 2
5 NMR Investigations of Synthetic Peptides 3
6 Related Articles 8
7 References 8

1 INTRODUCTION

Over many years we have been involved with the synthesis and characterization of peptides as biologically active agents. The goal of this research has been to develop structure and biological function relationships. The structure–activity relationships are then used in the rational design of new molecules with greater activity, enhanced duration of action, and/or increased selectivity. The number of peptides with interesting biological activity has been rising rapidly. These peptides possess a wide range of biological activities acting as antibiotics, enzyme inhibitors, taste ligands, hormones, immunosuppressants, neurotransmitters, and neuromodulators.

We have undertaken a multifaceted program including synthesis and spectroscopic characterization, with NMR the most important, coupled with various computational techniques. In this article we shall focus our attention on the use of NMR in the conformational analysis of synthetic peptides. However, it is important to note the significant roles of the other components of our approach within this field of study. In no way is this article intended to be an all-inclusive review of the examination of synthetic peptides by NMR, an undertaking which would all too soon be out of date and would require a complete volume on its own. In contrast, we will concentrate on a few important points within the field, using examples mainly taken from our own research.

2 CONFORMATION OF PEPTIDES

The inherent flexibility of peptides remains one of the biggest obstacles in their conformational study. Before one can hope to understand the relationship between structure and activity, the molecule under study must have predominant conformations. Usually, a linear peptide in solution has too many degrees of freedom, and can adopt an overwhelmingly large number of conformations. Because of their small size, synthetic peptides do not possess a hydrophobic core, which helps stabilize many of the secondary elements, α-helices or β-sheets, often found in proteins. As a result, the surface area of a peptide is extremely large. This greatly increases the influence of the environment or solvent on the conformation of a peptide, as well as on its dynamics and molecular motions.

To reduce the number of accessible conformations and to induce preferred conformations, molecular constraints are introduced by synthetic chemists. The challenge is to introduce constraints into the molecule, while at the same time maintaining the favorable biological properties. We therefore begin with a brief overview of the most important tools in the synthetic peptide chemists' arsenal to prepare constrained molecules. We then address some of the specific concerns in the computational refinement of peptide structures using NMR data. Finally, we discuss important aspects of the NMR investigation of synthetic peptides.

3 SYNTHETIC METHODS

Cyclized structures represent the most important approach to introduce conformational constraints. Cyclization can most obviously be achieved by the formation of a covalent bond between the N-amino terminal and C-carboxyl terminal moieties of the peptide. In many cases, including somatostatin and thymopoietin, such structures have led to active analogs while reducing the number of possible conformations. However, in many cases this approach destroys biological activity.

Another route to cyclic structures involves side-chain bonding. The side chain of the amino terminus of lysine (Lys) or carboxyl terminus of glutamic acid (Glu) and aspartic acid, can be covalently connected to each other or to either the N or C backbone termini.[1] The formation of a lactam bridge greatly reduces the number of conformations. The number of methylene groups within the side-chain linkers can be reduced by using ornithine, α,γ-diaminobutyric acid, or α,β-diaminopropionic acid in place of the Lys.

Side-chain cyclization can also be accomplished by using the disulfide bond of cysteine (Cys). This method has been incorporated in a number of important peptide-producing systems. To reduce the flexibility even further penicillamine (β,β-dimethylated-cysteine) can be used in place of Cys.

A new approach in cyclization has recently been reported in which the nitrogen atom of a backbone amide is alkylated and terminated with an acid or amino group.[2] This reacting group can then be connected to one of the termini (backbone–C-terminal cyclization, or backbone–N-terminal cyclization) or to another linker extending from the backbone of another residue within the sequence.

The naturally occurring proline (Pro) residue can be considered as a constraining residue. The five-membered ring greatly reduces the possible conformations about the ϕ-dihedral angle. However, Pro also often introduces complications into the NMR spectra because of *cis*/*trans* isomerization. This can complicate the spectra of small peptides. The opioid morphiceptin, Tyr-Pro-Phe-Pro-NH_2 (where Tyr = tyrosine, Phe = phenylalanine) shows a complex NMR spectrum. *cis*/*trans* isomerization can arise between the Tyr-Pro and Phe-Pro residues. All four different possible configurational isomers (*trans*–*trans*, *cis*–*trans*, *trans*–*cis*, and *cis*–*cis*) were observed in the ^{1}H and ^{13}C spectra.[3] To simplify the spectra, the Pro was substituted by a peptidomimetic residue,

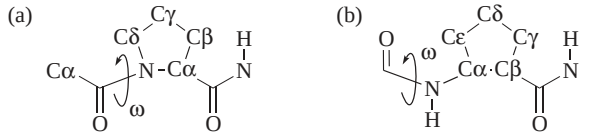

Figure 1 Structural formulae of (a) Pro and (b) 2-aminocyclopentanoic acid. The dihedral angle about the peptide bond, ω, is indicated

2-aminocyclopentanoic acid, which maintains a similar conformational constraint of Pro while not allowing for the *cis*/*trans* isomerization.[4] The amide group in the mimetic residue is a secondary amine which removes the possibility of *cis*/*trans* isomerization (Figure 1).

The control of the orientation of side chains has recently become a major focus of research interest. The approach usually involves the attachment of additional groups to the beta positions of the side chains. One or both of the beta protons can be replaced with methyl groups or a covalent linkage between the backbone and the side chain introduced to maintain preferred orientations.

4 COMPUTER SIMULATIONS

There are some specific concerns in the computational refinement of peptide structures from NMR data. There are far fewer NOEs than typically found for proteins on an NOE per residue basis. However, because of the better resolution of the cross peaks from NOESY spectra, the distances deduced for peptides can be considered to be more accurate. This comes from the fact that the intensity of the cross peaks can be integrated which must be contrasted with the grouping of NOEs into strong, medium, and weak categories, the method used in the NMR examination of larger biomolecules. The intensities are then converted into a range of distances using the cross-peak intensity of a reference pair of protons of known distance (isolated two-spin approximation). This method assumes that each proton−proton vector has the same correlation time, an assumption which, from molecular dynamics simulations, introduces about a 10% error.[5] Therefore the upper and lower distance restraints should be adjusted by plus and minus 10%, respectively. Often in addition to the cross peaks, the diagonal peaks can be integrated and the ratio of the intensities can be used to generate distances.[6] In a recent examination of a small synthetic molecule, both of these approaches were compared and found to produce very similar distances.[7]

Although the calculation of the distances may be rather straightforward with peptides, it is important that flexibility is always kept in mind. In the presence of conformational averaging, fast on the NMR timescale, the measured NOEs represent an average structure that may not exist in solution or even be physically possible. The distances generated from the NOEs are weighted as a function of the inverse sixth power of the different conformations so that small distances contribute heavily to the average. Although this is true for all systems studied by NMR, it is especially problematic for peptides because of their inherent flexibility.

Computational procedures which utilize average experimental restraints, rather than instantaneous restraints, have been developed for situations of conformational averaging. The method can be simply illustrated by the following penalty function:

$$\text{Penalty} = \tfrac{1}{2}K(\text{experimental} - \langle\text{calculated}\rangle)^2 \quad (1)$$

where K is a force constant to weight the significance of the penalty with respect to the other terms used in the refinement calculation. The value of the observable (i.e. NOE, coupling constant, chemical shift) is averaged, denoted by the angle brackets, before it is compared with the experimentally measured value. If the average value is removed from the experimental value the penalty function is applied.

One method used in molecular dynamics simulations calculates the observable over a specific time period before application of the restraint.[8] If the average value calculated over this time span is removed from the experimental value, the penalty function is applied. This method of time-dependent restraints was first used for NOEs and has recently been applied to coupling constant restraints.[9]

Another approach to applying experimental restraints for systems undergoing conformational averaging uses an ensemble of structures.[10] The ensemble approach utilizes a large number of structures, an ensemble, rather than the single structure used in standard refinement calculations. For NOEs, the average distance is calculated from the ensemble, properly weighted to the inverse sixth power, and if removed from the experimental value, the penalty function applied to the ensemble. The ensemble method has recently been modified to include coupling constant restraints.[11]

Of course, both the time-dependent and the ensemble procedures should produce the same answer. In practice, small differences have been noted, but these can be attributed to the different methods of calculation employed.[12] Nevertheless, it is clear that since the experimental observables (i.e NOEs, coupling constants) are average quantities, the restraints must also be applied as such in the refinement calculations.

One important aspect in the computational refinement of the structure of synthetic peptides derives from their small size which allows for a more thorough and systematic conformational search. Procedures for systematic searching have been shown to be quite useful. Although all of the possible conformations cannot usually be examined, many approximate methods can be used. As an example, for each low-energy backbone conformation found, all of the possible side-chain orientations are examined. With the approximation that the side chains adopt only the three staggered rotamers, -60°, 180°, and 60°, the number of conformations to examine becomes quite manageable.[13] Distance geometry methods can be employed to study many different starting structures. Although distance geometry has historically been used for systems with a large number of loosely defined restraints, some new methods, namely random metrization,[14] have been introduced which should help in the examination of peptides, where the number of NOEs is limited.

One last point in the refinement of peptide structures is consideration of the environment (i.e. inclusion of the solvent explicitly or a computational method to mimic the solvent). The large surface area of the peptide means that solvent plays a significant role in conformational preferences and molecular dynamics. It is therefore important that the environment be simulated during the calculations. In recent years, progress in this area has been reported. Many of the

organic solvents commonly used in the NMR investigations of synthetic peptides are available for computer simulations.[15,16]

5 NMR INVESTIGATIONS OF SYNTHETIC PEPTIDES

The NMR examination of synthetic peptides is quite unique, when compared with other biomolecules. There are many problems which are not present in the study of proteins or nucleic acids. The typical size of the molecules renders the NOESY experiment, which provides the most conformationally relevant information, very inefficient. In addition, the lack of secondary structure and therefore inherent flexibility of peptides, which we have touched upon above, alters the general approach of the NMR investigation.

5.1 ROESY Experiments

The most important development in the NMR field for the study of the structure of peptides has to be the idea of the NOE within the rotating frame, first called CAMELSPIN,[17] now more commonly referred to as ROESY.[18] Most synthetic peptides have a motional correlation time, τ_c, which at the high fields standardly used today (400–600 MHz), produces the condition of $\omega\tau_c = 1$ (where ω is the Larmor frequency), a condition in which the intensity of the NOE approaches zero. In simple terms, the buildup of the NOE is governed by the cross-relaxation rate which depends on the spectral density (a measure of the molecular motions that the molecule is undergoing) consisting of both positive and negative terms. At $\omega\tau_c = 1$ these two terms are equal and the cross-relaxation rate is approximately zero. In contrast, under the spin lock conditions used in the ROESY experiment, the terms for the cross-relaxation rate are all positive. Therefore the intensity of the dipole–dipole coupling is always positive, varying from a theoretical intensity of 38% to 67% (Figure 2).[17]

This rather simple experiment had a great effect on the NMR study of peptides. Before the ROESY experiments, the only hope of observing an NOE was to change the conditions of the experiment either to slow down or speed up the molecular tumbling (i.e. to increase or decrease τ_c). Variation of temperature was sometimes successful, but often limited by the freezing or boiling points of the solvent. More viscous solvents were often employed. The addition of dimethyl sulfone to dimethyl sulfoxide greatly increased the viscosity, allowing for the measurement of NOEs. Other methods include using the greatly reduced eutectic point of an equal mixture of water and dimethyl sulfoxide ($-70\,^{\circ}$C) to observe NOEs.[19] This mixture has the advantage that the dielectric constant is identical to that of water at 25 °C.

The illustration of the ROESY experiment eliminated the need for these methods. The dipole–dipole couplings, often called ROEs, could now be measured for small synthetic peptides without any modification of the solution. The temperature and solvent was chosen to enhance resolution and not for the development of distance restraints.

Another important advantage of the ROESY experiment with regard to the study of peptide structure is the unambiguous identification of cross peaks arising from chemical exchange. In this experiment, the cross peaks from the dipole–dipole coupling will be positive while those from the exchange of conformation will be of the opposite sign. This is important for the large number of peptides containing prolines, which can undergo exchange between a *cis* and *trans* configuration about the amide bond.

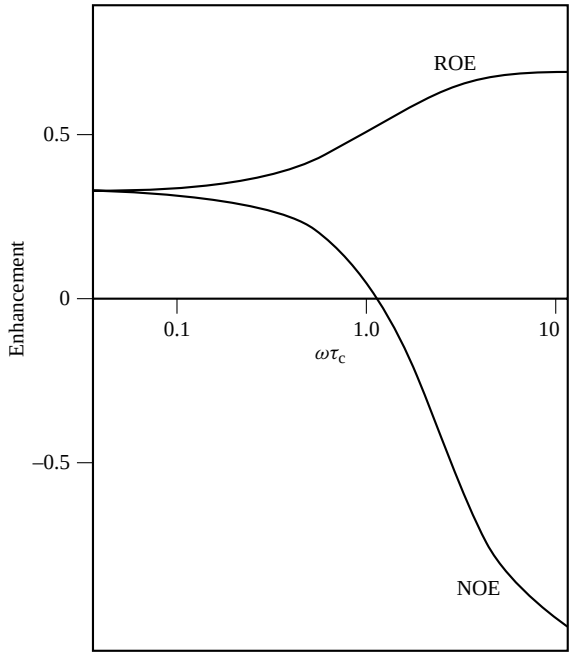

Figure 2 The theoretical enhancement of NOEs and ROEs as a function of correlation time. A field strength of 500 MHz has been utilized

A complexity from the ROESY experiment is the appearance of cross peaks from scalar spin–spin couplings, which arise through Hartmann–Hahn matching, a condition that occurs when the two spins are experiencing equally effective spin lock fields. In the homonuclear case, this occurs when the spins have equal offsets from the spin locking field. Hartmann–Hahn matching is used to great advantage in the TOCSY (total correlation spectroscopy) experiment by which magnetization can be transferred through long spin–spin coupled systems: up to ^5J(H,H) and ^6J(H,H) are commonly observed for peptides. However, the Hartmann–Hahn or TOCSY peaks can greatly complicate the interpretation of ROESY spectra. To overcome this it is necessary to ensure the condition of unequal precession frequencies of the two spins. This can be accomplished through the use of a spin locking field comprised of pulses with very small flip angles[20] or which is very weak and off resonance.[21] For synthetic peptides, placing the source of the spin locking field just downfield of the H-α region, will ensure that the resonances involved in the amide HN–H-α and H-α–side-chain (H-β, H-γ) correlations will have unequal precession frequencies. With the spin locking field located just to low frequency of the aromatic region, a second experiment is run, to minimize the occurrence of TOCSY peaks for amide HN–side-chain correlations.

If the ROESY interactions are to be used to develop internuclear distances, it is important that the field strength or resonance offset are varied and the cross-peak intensities examined carefully. A method has been described to remove the field dependence from the cross-peak intensity, commonly referred to as compensated ROESY.[22] In addition, the

dependence of the cross-peak intensity on mixing time build-up rates, should be examined. This is important since ROESY is more susceptible to spin diffusion than the NOESY experiment.

5.2 Chemical Shift

There has been considerable utilization of chemical shifts in the examination of proteins. Long stretches of α-helices or β-sheets can be readily identified by chemical shift. The utility of chemical shifts to identify secondary structural elements is greatly increased when all of the chemical shifts of the peptide backbone are examined, including the α-protons, α- and β-carbon atoms and, to a lesser extent, the nitrogen atom and proton of the amide.

For peptides, the utilization of chemical shifts for conformational information is not clear-cut. The lack of long stretches of secondary structure seems to be the major complication. One abnormal chemical shift caused by the close proximity of one side chain will not be significant in a long stretch of α-helix; the general trend of chemical shifts can still be identified. In a peptide, the differentiation of the trend from the abnormal chemical shift is not possible. In addition, the greater surface area of peptides increases the effect of solvent on chemical shifts.

Chemical shifts are used in the study of the structure of synthetic peptides for the unambiguous identification of *cis*/*trans* isomerization about the amide bonds of Pro. The difference in the chemical shifts of the β- and γ-carbon atoms of the Pro can be used to identify the configuration about the amide bond. Large differences (8–10 ppm) are indicative of *cis* amide bonds, while small differences (4–6 ppm) indicate *trans* configurations.

5.3 Chemical Exchange

We have discussed the necessity of introducing constraints into peptides to allow for meaningful conformational analysis. Constraints are important if the conformations are to be useful in the development of structure–activity relationships. However, a consequence of peptide constraints, particularly for cyclic molecules, can be the introduction of different conformational isomers of significantly high energy not normally observed.

During our investigation of a series of 14-membered cyclic enkephalin analogs, additional sets of resonances were observed in the proton spectra.[23] From ROESY spectra, the additional sets of signals could be assigned to different configurational isomers; chemical exchange cross peaks were observed for the additional sets of resonances. From a careful inspection of the ROEs, the additional isomers could be assigned as arising from structures with *cis* peptide bonds. These peptides do not contain Pro or any other N-substituted amino acids and therefore *cis* peptide bonds were indeed unexpected. In fact, for one of the peptides examined, the major component contained a *cis* peptide bond; the all-*trans* isomer accounted for only 28% (two other structures with *cis* peptide bonds accounted for 51% and 21%, respectively) (Figure 3).[23]

The rate of interconversion between the different isomers is fast on the NMR timescale. Chemical exchange peaks

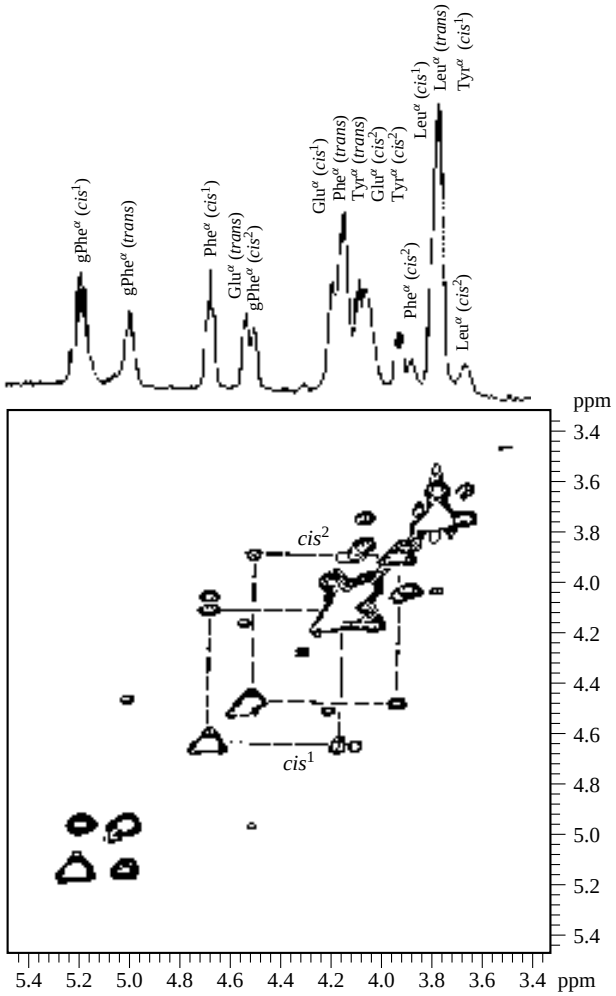

Figure 3 Expansion of a two-dimensional ROESY spectrum illustrating chemical exchange between configurational isomers containing *cis* and *trans* amide bonds of the cyclic enkephalin analog, Tyr-c[-D-Glu-Phe-gPhe-D-retroLeu-] obtained in dimethyl sulfoxide at 40 °C with a mixing time of 300 ms. The NOEs (negative intensity) indicating the *cis* amide bonds have been labeled cis^1 and cis^2. The remaining cross peaks, positive intensity as is the diagonal, indicate chemical exchange between the different isomers

were observed in ROESY spectra with mixing times as small as 200 ms. The actual exchange rate can be calculated from the integration of the exchange peaks as a function of the mixing time from ROESY experiments. If resonances from one proton of both the *cis* and *trans* isomer are well separated, the measurement of the rate can be much more quickly determined with a one-dimensional saturation transfer experiment described many years ago by Forsén and Hoffman.[25] For the enkephalin analogs, the rates were measured for the conversion of both *cis* to *trans*, and *trans* to *cis*. The simple ratio of these rates should agree with the integrated intensity of the two configurational isomers. Measurement of the rate of chemical exchange at different temperatures then allowed for the calculation of the free energy of the transition. For the specific enkephalins values of 72–76 kJ mol^{-1} were obtained. It is interesting to note that similar values were obtained for the *cis*/*trans* isomerization about the peptide bond of Pro containing linear peptides.[26]

Since our original report of these unusual *cis* peptide bonds, many other groups have reported similar occurrences in cyclic peptides.[27] It is therefore important to keep the possibility of slow conversion between the different configurational isomers in mind when studying cyclic peptides. The observation of a *cis* peptide bond in a linear heptadecapeptide when associated with detergent micelles has also been reported.[28]

5.4 Hydrogen Bonds

The presence of *intra*molecular hydrogen bonds is important for the determination of conformation. There are a number of methods to probe for the presence of hydrogen bonds. It was one of the earliest parameters used in the conformational examination of peptides, mainly because of the ease of the measurement. However, the interpretation and application of the data as a conformational restraint are not straightforward.

Amide protons involved in hydrogen bonds exchange with the solvent at a much slower rate than amide protons exposed to solvent. This simple fact can be used to probe the presence of intramolecular hydrogen bonds. A deuterated, protic solvent can be added and the intensity of the amide protons monitored as a function of time. Those amide protons exposed to solvent quickly disappear while those involved in hydrogen bonds remain for extended periods of time depending on the temperature, pH, and stability of the hydrogen bond.

Another method to probe for hydrogen bonds involves the change of the chemical shift of the amide protons with temperature. The method depends on the increase of molecular motion of the solvent with temperature. Those amide protons which are exposed and forming hydrogen bonds to the solvent are strongly affected by the change in temperature, since the increased molecular motion reduces the length of time that the hydrogen bond is present. Since the bonding to the solvent is present for shorter periods, the amide proton is less deshielded and there is a significant low frequency (upfield) shift. In contrast, the amide protons involved in *intra*molecular hydrogen bonds are much less affected by temperature change, and therefore the change in chemical shift is small.

The usefulness of temperature coefficients varies with solvent. The method works well for solvents that form strong bonds with the amides, particularly for those that can only act as donors (e.g. dimethyl sulfoxide). Temperature coefficients that are smaller than -2.0×10^{-3} ppm deg^{-1} are assumed to be involved in an *intra*molecular hydrogen bond, while values greater than -4.0×10^{-3} ppm deg^{-1} are thought to be solvent exposed.

For solvents that do not interact with the amide protons, temperature coefficients become more difficult to interpret. This is particularly true for chloroform. Although the trends are the same as those observed for dimethyl sulfoxide, the differences are much smaller because of the lack of strong interaction with the amide proton. The interpretation of temperature coefficients of peptides in aqueous solutions is difficult since water can act both as a donor and an acceptor for *inter*molecular hydrogen bonds. The difficulties in explaining temperature coefficients in water lie between that of dimethyl sulfoxide and chloroform. One of the most thorough examinations of temperature coefficients in many different solvents remains the work of Llinás and Klein.[29] The authors studied two cyclic hexapeptides in trifluoroacetic acid, trifluoroethanol, chloroform, dimethyl sulfoxide, water, dimethylformamide, and pyridine solvents with a wide distribution of dielectric constants, pK_as and abilities to act as hydrogen bond donors or acceptors.

It is important to realize that there are other reasons in addition to involvement in hydrogen bonds that could limit the exposure of an amide proton to the solvent. The amide proton may be buried within the peptide or shielded from the solvent by side chains. Neither of the methods mentioned above can differentiate between simple solvent shielding and hydrogen bonds.

The use of hydrogen bonds to develop conformational preference is also problematic. Only the donor, the amide proton of the hydrogen bond, can be experimentally identified. The acceptor of the hydrogen bond cannot be determined (although some studies to correlate the chemical shift of the carbonyl with the involvement in hydrogen bonds have been attempted). Therefore, the information that a particular amide proton is involved in a hydrogen bond can only be used as a secondary check: conformations of a peptide are developed using other experimental restraints (i.e. NOEs) and then the structures are examined. Those structures with amide protons that have low temperature coefficients involved in hydrogen bonds are selected. The experimental data are not used to generate conformations (i.e. conformational restraint).

Some attempts to use the presence of hydrogen bonds in calculations of conformations have appeared. An approach used in molecular dynamics simulations alters the partial charges assigned to the amide proton and nitrogen atom according to their temperature coefficients, decreasing the charge with larger temperature coefficients.[30] Therefore, those amide protons more likely to be involved in intramolecular hydrogen bonds (low temperature coefficients) will have higher partial charges and greater attraction to carbonyls from the Coulombic term in the force field.

Another approach utilizes the hydrogen-bonding information during a second refinement stage. During the first calculation only NOEs are used. From this initial structure the carbonyls which form hydrogen bonds to the amides that are experimentally determined to be involved in hydrogen bonds are found. Distance restraints between the amide and carbonyl are then included and the refinement repeated. Recently this approach has come under some criticism, since the structures produced are far better than justified from the experimental data.[31] The hydrogen-bond restraints are too conformationally restrictive. It is important to note that with the requirement of planar peptide bonds, one hydrogen-bond restraint affects not only the two residues directly involved but also the residue preceding the donor and after the acceptor (Figure 4).

5.5 Solvent Studies

The large surface areas of peptides greatly increase the effect that solvent has on conformation. It is therefore imperative that the solvent be taken into consideration in the development of conformational preferences. Probably the best example of the large effect of solvent is cyclosporin A, a cyclic undecapeptide immunosuppressant, which has been examined in a number of different solvents. In chloroform, there is only one set of resonances, while in dimethyl sulfoxide there are seven different configurational isomers (arising from *cis* and

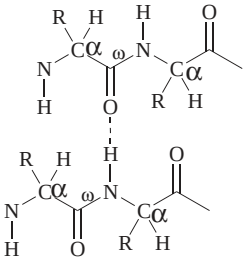

Figure 4 Illustration of the large effect of one hydrogen-bond restraint on peptide conformation. The planarity of the peptide bond, dihedral angle ω, produces a large effect on the preceding residue of the donor NH (bottom) and the residue following the acceptor carbonyl group (top)

trans isomerization about the many *N*-methylated residues in cyclosporin A). It is interesting to note that the conformation of cyclosporin A while bound to cyclophilin, the cytoplasmic receptor of cyclosporin A, contains only *trans* amide bonds.

Solvent titrations are often employed to investigate the effect of solvent on conformation. Titrations are advantageous since the assignments need only be made once; the resonances can usually be followed during the titration. It is important to consider the possibility of high, local concentrations of solvent during the titration. For example, for a peptide in a chloroform solution, the addition of a small amount of dimethyl sulfoxide has a large effect on the NMR observables (chemical shifts, NOE pattern); during the remainder of the titration only small changes are observed. The peptide is for all practical purposes completely solvated with dimethyl sulfoxide after the initial small addition.

We have examined many small cyclic peptides in dimethyl sulfoxide and carried out titrations with water. This provides a facile method to probe the conformations of a peptide in an aqueous environment when the peptide is not highly soluble in water (up to the concentrations required for NMR). For these constrained systems, only minor conformational changes are observed; most of the structural differences involve the hydrogen-bonding patterns of the peptide backbone.[32–34] The different hydrogen bonds come about since water can act as both acceptor and donor, while dimethyl sulfoxide can only act as a donor. However, it is important to stress that these peptide systems are cyclic and constrained with 12 to 14-membered ring systems. If sufficient conformational constraint has been built into the molecule, only minor differences are expected with a change of solvent.

A minor difference was recently observed in the examination of a cyclic octapeptide [-Pro-Pro-Tyr-Val-Pro-Leu-Ile-Ile-], where Val = valine, Leu = leucine, Ile = isoleucine. The peptide was studied in dimethyl sulfoxide and chloroform by NMR and extensive molecular dynamics simulations carried out in the same solvents as used in the NMR studies.[35] The overall conformations of the peptide in the two solvents were very similar. A difference was observed for the orientation of an amide bond in the middle of a β-turn; in chloroform the carbonyl group projected into the solvent, while in dimethyl sulfoxide there was a 180° rotation of the peptide bond and the amide proton projected into the solvent (i.e. in chloroform a βI-type turn, in dimethyl sulfoxide a βII-type turn). The computer simulations clearly indicate the basis for this change; there are atom-specific interactions between chloroform and the carbonyl group, while dimethyl sulfoxide only forms *inter* molecular hydrogen bonds to the amide proton. The solvent stabilizes the different conformations through interactions with the central amide group of the β-turn.

5.6 Coupling Constants as Conformational Restraints

As discussed above, there are a smaller number of NOEs for synthetic peptides than are commonly observed for large biomolecules. To overcome this fact, the use of coupling constants as conformational constraints has recently been reported. The addition of coupling constants as experimental restraints, in addition to NOEs, has greatly improved the structures obtained for small peptides.

Coupling constants provide conformational information about the dihedral angles subtended by the coupled atoms. The equation most often used, developed by Karplus from simple valence bond electron calculations many years ago,[36]

$$^3J = A\cos^2(\theta) + B\cos(\theta) + C \qquad (2)$$

relates the coupling constant to the dihedral angle (θ) subtended by the coupled atoms. However, the application of this equation to develop conformational information is not straightforward.

The early uses of this equation were limited. Similar to the application of temperature coefficients, after the development of a conformation from NOEs, the dihedral angles were used to calculate the coupling constants and the agreement with the experimental values examined. The agreement was almost always found to be good, mainly because of the large range of values that are produced by the Karplus equation. Since only the absolute value of the dihedral angle is important, two answers are produced for every θ, which in addition to the quadratic nature of the equation, produces four answers (depending on the A, B, and C coefficients and the measured coupling constant). If a reasonable error of 20° is added to each of these answers, it quickly becomes possible to obtain a wide range of acceptable dihedral angles. The agreement between the experimental and calculated coupling constants is therefore not surprising.

To address the wide range of allowed values, the measurement of additional coupling constants about the same dihedral angle has been undertaken. Recently a large number of new methods have appeared to measure heteronuclear couplings for samples in natural abundance.[37,38] Using this approach, only the dihedral angles that are in agreement with all of the couplings are retained. This usually allows some of the solutions to the Karplus equation to be eliminated. However, the coupling constants are still being employed as a secondary measure of the fit of the experimental observables with a structure; the coupling constant data are not employed to produce the conformation (i.e. conformational restraint).

The application of dihedral angle restraints was one of the first uses of coupling constants in calculations. For large or small coupling constants, a range of allowed dihedral angles was chosen and a penalty function applied. For the most commonly measured coupling constant, ^3J(HN,H-α), a value larger than 8.5 Hz indicated a small range centered at −120°; for couplings smaller than 6.0 Hz, the range of values was increased to −160° to −40°.

A more direct application of coupling constants in structural refinement calculations was introduced by Kim and Prestegard.[39] The penalty function proposed is similar to that utilized for NOE distance restraints;

$$V_J = \tfrac{1}{2} K_J (J_{\text{exp}} - J_{\text{theo}})^2 \quad (3)$$

where J_{exp} is the experimental coupling constant, K_J is a force constant to weight each coupling individually, and J_{theo} is the theoretical coupling calculated using the Karplus equation. The difference between the experimental and theoretical values is minimized during the refinement calculation. This approach allows all of the coupling constants to be utilized in the refinement calculations without any approximations of the ranges of dihedral angles that are appropriate.[40] An illustrative penalty function is shown in Figure 5.

There are numerous homonuclear and heteronuclear coupling constants that can be measured for the ϕ and χ_1 dihedral angles [e.g. ^3J(HN,H-α), ^3J(HN,C-β), ^3J(C′,H-α) and ^3J(C,H-β) ^3J(N,H-β), ^3J(H-α,H-β)]. For the other backbone dihedral angle, ψ, there are a limited number of three-bond couplings that can be measured. Those that can be measured, e.g. ^3J(N,H-α), are very small and therefore have a large associated error. It was with this in mind that we developed the possibility of using one-bond coupling constants as conformational constraints. It was illustrated many years ago by Egli and von Philipsborn[41] that the one-bond coupling between the α-proton and α-carbon atom depends both on the ϕ and ψ dihedral angles, as shown below,

$$^1J(\text{C-}\alpha, \text{H-}\alpha) = 14.0\cos^2(\phi + 30^\circ) - 5.2\cos^2(\Psi - 30^\circ) + 136.2 \quad (4)$$

We have used this relationship to develop conformations with the sole use of coupling constants that are similar to those calculated with NOEs.[42] This method has the advantage of the great ease with which the one-bond coupling can be measured [i.e. the acquisition of a heteronuclear multiple quantum coherence (HMQC) experiment without decoupling of the carbon resonances]. There are limitations to the use of the one-bond coupling, including the large number of minima produced for one coupling constant which is magnified when experimental error is taken into account.

In addition to the conformational information obtained from coupling constants, dynamics can also be probed. This is particularly important for fast conformational averaging taking place on the NMR timescale, a situation addressed in the computer refinement section above. With the measurement of both NOEs and coupling constants, the presence of fast conformational exchange can be unambiguously identified.

Coupling constants and NOEs depend on different structural factors; the dihedral angle subtended by the coupled atoms and the internuclear distance between the dipole-coupled atoms, respectively. These quantities average differently in the presence of conformational exchange. The NOEs average as the sixth inverse power of the distance between the dipoles (i.e. R^{-6}), while the coupling constant averages as the cosine series of the subtended dihedral angle θ (i.e. $\cos^2\theta$ and $\cos\theta$). The average structures consistent with the NOEs are not the same as those consistent with the coupling constants.[43] The application of the two restraints therefore provides a method of identifying fast conformational averaging on the NMR timescale.

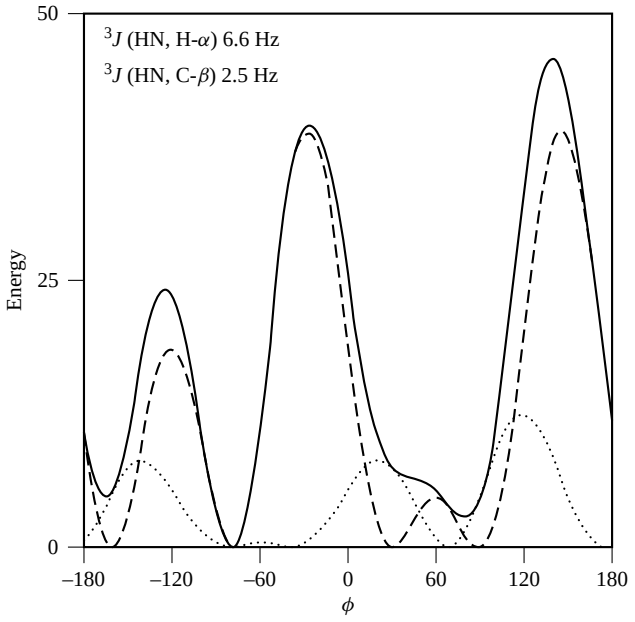

Figure 5 Example of the penalty function used for coupling constant restraints. The penalty 'energy' is illustrated for two coupling constants about the ϕ dihedral angle: ^3J(HN,H-α) (broken line) and ^3J(HN-Cβ) (dotted line). The sum of the two couplings is shown as the solid line

5.7 Determination of Configuration

Many of the synthetic modifications discussed above produce at least two possible configurations with peptidomimetic residues incorporated. In most cases the two can be separated using HPLC or other methods. The task becomes the unambiguous assignment of the correct configuration to the isolated molecules. The most straightforward method is to measure as many experimental restraints as possible for the isomers and simply fit the restraints to both possible choices. This approach worked in the examination of the Pro mimetic, 2-aminocyclopentanoic acid, which was noted above.[4] The synthetic routes can be configurationally controlled to produce only the *cis* or only the *trans* isomer. However, there are two possibilities for the *cis* (*R*,*S* and *S*,*R*) and the *trans* (*S*,*S* and *R*,*R*) isomers. Each of the isomers were separated and biologically assayed. Since there was a wide variation in the biological activities, it was important to determine the configuration of the centers of the 2-aminocyclopentanoic acid residues; the configurations have a great impact on the topological arrangement of the residues before and after them in the peptide sequence. From the distance restraints developed from the NOEs measured for each isomer, the assignment of the relative chirality was obtained. The assignment is illustrated in Figure 6. The lowest energy structures found from the molecular dynamics simulations are shown. Three key NOEs, which allow for the differentiation between the two isomers are also shown in the Figure.

The problem with this approach is that the number of possibilities increases as a function of 2^N, where N is the number of unknown chiral centers. It is also important that the region of interest be high in proton density, so that there are many experimental restraints involving the questionable chiral centers. The method proposed above will often fail when the chiral center of interest has no proton directly attached.

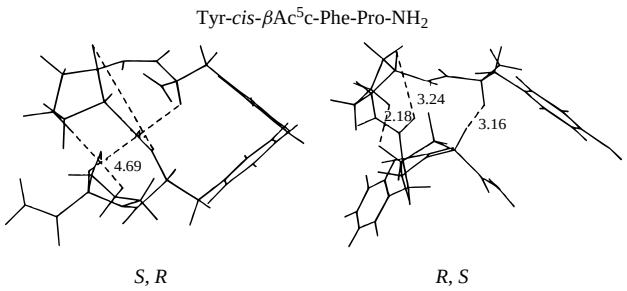

Figure 6 Illustration of the three NOEs that allowed the assignment of the chirality of the 2-aminocyclopentanoic acid residue (βAc^{5}c). The NOEs are fulfilled by the *R*,*S* analog, not by the *S*,*R* analog. The NOEs are: Tyr H-α–Pro H-α, βAc^{5}c H-α–Phe HN, and βAc^{5}c H-β–Pro H-δ

The resolution of the peptide conformation is greatly enhanced when the protons of side-chain methylene groups can be stereospecifically assigned. Without these assignments, distances calculated for these protons must be adjusted to allow for both possibilities, the pro-*R* and pro-*S* protons. This is accomplished by adding a distance correction, often 0.9 Å, to the upper distance restraint.[44,45] This seemingly small addition has a significant effect on the conformations produced from the refinement calculations. The more loosely defined distances allow for many more possible conformations. The same is true for the diastereotopic methyl groups of the amino acids Leu and Val. The upper limit distance restraints for a methyl group not diastereotopically assigned should be increased by over 1.5 Å. The conformational information of such a NOE is therefore greatly reduced by the lack of diastereotopic assignments.

There are a number of methods of making diastereotopic assignments. The least ambiguous method involves the measurement of coupling constants. For β-methylene protons, the homonuclear ^3J(H-α,H-β) and heteronuclear ^3J(C′,H-β) coupling constants usually provide for the unambiguous assignment. It is often the case that only an estimate of the size of the heteronuclear coupling is sufficient. For the assignment of the methyl groups, heteronuclear ^3J(C,H) coupling constants can be measured with the ω1-filtered TOCSY experiment.[46] In this experiment, the proton magnetization is filtered, selecting only the protons coupled to the heteronuclei (i.e. ^{13}C), before the TOCSY sequence which mixes the magnetization of all protons. This produces a standard TOCSY spectrum with the cross peaks split in the F_1 dimension by ^1J(C,H) (140 Hz) and in the F_2 dimension by the long-range coupling constant, ^3J(C,H). This experiment is ideal for the assignment of the side-chain methyl groups of Leu and Val, since it is quite sensitive when the heteronuclei, here the carbon, have three protons. The measurement of ^3J(C-γ,H-α) for Val and ^3J(C-δ,H-β) for Leu, along with the homonuclear couplings, usually allow for the unambiguous diastereotopic assignment of the methyl groups of these residues.

For peptides where the measurement of coupling constants is not possible, there is a very powerful method often used in the examination of proteins. It involves the use of floating chiralities.[47] During the computational refinement the methylene protons or methyl groups can switch stereospecific positions driven solely from the distance restraints of the NOEs. For proteins, where the number of NOEs is large, the method is extremely useful. For peptides, the sole use of NOEs usually is not sufficient to allow for an unambiguous assignment. We have found that the addition of coupling constant restraints, in addition to the NOEs, greatly increases the efficiency of the floating chirality procedure.[48] The low-frequency and high-frequency proton signals are arbitrarily assigned to pro-*R* or pro-*S* for both the NOE and coupling constant restraints. Then during the simulation the chiralities are allowed to change positions, i.e. float. One note of caution must be made with the use of floating chiralities; the method will produce an answer (i.e. one proton will be pro-*R*, the other pro-*S*), no matter what the extent of the experimental restraints is. The number of restraints gives little insight into the confidence of the assignment. Also important is the nature of the restraints, a few restraints from different angles or orientations will be of more use than a larger number of NOEs from one direction. The method that we employ to examine the confidence in the diastereotopic assignment is a graphical representation of the NOEs for each of the chiral centers.

6 RELATED ARTICLES

Amino Acids, Peptides and Proteins: Chemical Shifts; Peptide Hormones; Vicinal Coupling Constants and Conformation of Biomolecules.

7 REFERENCES

1. C. M. Deber, V. Madison, and E. R. Blout, *Acc. Chem. Res.*, 1976, **9**, 106.
2. C. Gilon, D. Halle, M. Chorev, Z. Selinger, and G. Byk, *Biopolymers*, 1991, **31**, 745.
3. M. Goodman and D. F. Mierke, *J. Am. Chem. Soc.*, 1989, **111**, 3489.
4. D. F. Mierke, G. Nöbner, P. W. Schiller, and M. Goodman, *Int. J. Peptide Protein Res.*, 1990, **35**, 35.
5. E. T. Olejniczak, C. M. Dobson, M. Karplus, and R. M. Levy, *J. Am. Chem. Soc.*, 1984, **106**, 1923.
6. G. Esposito and A. Pastore, *J. Magn. Reson.*, 1988, **76**, 331.
7. M. Reggelin, H. Hoffmann, M. Köck, and D. F. Mierke, *J. Am. Chem. Soc.*, 1992, **114**, 3272.
8. A. E. Torda, R. M. Scheek, and W. F. van Gunsteren, *Chem. Phys. Lett.*, 1989, **157**, 289.
9. A. E. Torda, R. M. Brunne, T. Huber, H. Kessler, and W. F. van Gunsteren, *J. Biomol. NMR*, 1993, **3**, 55.
10. J. Kemmink, C. P. M. van Mierlo, R. M. Scheek, and T. E. Creighton, *J. Mol. Biol.*, 1993, **230**, 312.
11. D. F. Mierke, R. M. Scheek, and H. Kessler, *Biopolymers*, 1994, **34**, 559.
12. D. F. Mierke, T. Huber, and H. Kessler *J. Comput. Aided Mol. Des.*, 1994, **8**, 29.
13. T. Yamazaki, S. Ro, M. Goodman, N. N. Chung, and P. W. Schiller *J. Med. Chem.*, 1993, **36**, 708.
14. T. F. Havel, *Prog. Biophys. Mol. Biol.*, 1991, **56**, 43.
15. D. F. Mierke and H. Kessler, *J. Am. Chem. Soc.*, 1991, **113**, 9466.
16. W. L. Jorgenson, J. M. Briggs, and M. L. Contreras, *J. Phys. Chem.*, 1990, **94**, 1683.
17. A. A. Bothner-By, R. L. Stephens, J. Lee, C. D. Warren, and R. W. Jeanloz, *J. Am. Chem. Soc.*, 1984, **106**, 811.

18. A. Bax and D. G. Davis, *J. Magn. Reson.*, 1985, **63**, 207.
19. A. Motta, Dr Picone, T. Tancredi, and P. A. Temussi, *J. Magn. Reson.*, 1987, **75**, 364.
20. H. Kessler, C. Griesinger, R. Kerssebaum, K. Wagner, and R. R. Ernst, *J. Am. Chem. Soc.*, 1987, **109**, 607.
21. A. Bax, *J. Magn. Reson.*, 1988, **77**, 134.
22. C. Griesinger and R. R. Ernst, *J. Magn. Reson.*, 1987, **75**, 261.
23. D. F. Mierke, T. Yamazaki, O. E. Said-Nejad, E. Felder, and M. Goodman, *J. Am. Chem. Soc.*, 1989, **111**, 6847.
24. T. Yamazaki, D. F. Mierke, O. E. Said-Nejad, E. Felder, and M. Goodman, *Int. J. Peptide Protein Res.*, 1992, **39**, 161.
25. S. Forsén and R. A. Hoffman, *J. Chem. Phys.*, 1963, **39**, 2892.
26. C. Grathwohl and K. Wüthrich, *Biopolymers*, 1981, **20**, 2623.
27. H. Kessler, U. Anders, and M. Schudok, *J. Am. Chem. Soc.*, 1990, **112**, 5908.
28. E. Bairaktari, D. F. Mierke, S. Mammi, and E. Peggion, *J. Am. Chem. Soc.*, 1990, **112**, 5383.
29. M. Llinás and M. P. Klein, *J. Am. Chem. Soc.*, 1975, **97**, 4731.
30. H. Kessler, J. W. Bats, C. Griesinger, S. Koll, M. Will, and K. Wagner, *J. Am. Chem. Soc.*, 1988, **110**, 1033.
31. T. F. Havel, in *Proteins: Structure, Dynamics and Design*, eds. V. Rengugopalakrishnan, P. R. Carey, I. C. P. Smith, S. G. Huand, and A. C. Storer, ESCOM, Leiden, 1991, pp. 110–115.
32. N. J. Mammi and M. Goodman, *Biochemistry*, 1986, **25**, 7607.
33. N. J. Mammi, M. Hassan, and M. Goodman, *J. Am. Chem. Soc.*, 1985, **107**, 4008.
34. D. F. Mierke, P. W. Schiller, and M. Goodman, *Biopolymers*, 1990, **29**, 943.
35. R. Konat, D. F. Mierke, H. Kessler, B. Kutscher, M. Bernd, and R. Voegeli, *Helv. Chim. Acta*, 1993, **76**, 1649.
36. M. Karplus, *J. Am. Chem. Soc.*, 1963, **85**, 2870.
37. P. Schmieder, M. Kurz, and H. Kessler, *J. Biomol. NMR*, 1991, **1**, 403.
38. G. T. Montelione, S. D. Emerson, and B. A. Lyons, *Biopolymers*, 1992, **32**, 327.
39. Y. Kim and J. T. Prestegard, *Proteins Struct. Funct. Genet.*, 1990, **8**, 377.
40. D. F. Mierke and H. Kessler, *Biopolymers*, 1992, **32**, 1277.
41. H. Egli and W. von Philipsborn, *Helv. Chim. Acta*, 1981, **64**, 976.
42. D. F. Mierke, S. Golic-Grdadolnik, and H. Kessler, *J. Am. Chem. Soc.*, 1992, **114**, 8283.
43. D. F. Mierke, M. Kurz, and H. Kessler, *J. Am. Chem. Soc.*, 1994, **116**, 1042.
44. K. Wüthrich, M. Billeter, and W. Braun, *J. Mol. Biol.*, 1983, **169**, 949.
45. J. de Vlieg, R. Boelens, R. M. Scheek, R. Kaptein, and W. F. van Gunsteren, *Isr. J. Chem.*, 1986, **27**, 181.
46. P. Schmieder and H. Kessler, *Biopolymers*, 1992, **32**, 435.
47. P. L. Weber, R. Morrison, and D. Hare, *J. Mol. Biol.*, 1988, **204**, 483.
48. S. Golic-Gradadolnik, D. F. Mierke, G. Bye, I. Zeltser, C. Gilon and H. Kessler, *J. Med. Chem.*, 1994, **37**, 2145.

Biographical Sketches

Murray Goodman, *b* 1949. B.S., Brooklyn College, Ph.D., 1953, University of California, Berkeley, Postdoctoral Fellow, Massachusetts Institute of Technology and Cambridge University, UK. Professor, Polytechnic Institute of Brooklyn, 1956–69. Professor, University of California, San Diego, 1970–present. Approx. 350 publications. Current research specialty: design of bioactive molecules, synthesis of peptides and peptidomimetics, and spectroscopic characterization of novel biomolecular systems.

Dale F. Mierke, B.S., 1984, University of California, Irvine; Ph.D., 1988, University of California, San Diego. Research fellow Biopolymer Research Institute, Padova, Italy, 1989. Fulbright Scholar, Technical University Munich, Germany (with Horst Kessler) 1990–93. Approx. 60 publications. Current research specialty: high-resolution NMR investigation of the molecular association of peptides and proteins, computational techniques in the development of conformation of polypeptides.

Thioredoxin and Glutaredoxin

H. Jane Dyson

The Scripps Research Institute, La Jolla, CA, USA

1	Introduction	1
2	NMR of *Escherichia coli* Thioredoxin	1
3	NMR of Human Thioredoxin	3
4	NMR of *Escherichia coli* Glutaredoxin	4
5	Related Articles	6
6	References	6

1 INTRODUCTION

Thioredoxins and glutaredoxins are ubiquitous small proteins involved in redox reactions in cells and viruses, including ribonucleotide reduction, sulfate metabolism, and both oxidative and reductive thiol−disulfide reactions with proteins.[1,2] Recent work implicates thioredoxin in cellular redox control mechanisms and also in mammalian virus systems, with possible applications in therapeutics.[3] The active sites of thioredoxin and glutaredoxin are similar, consisting of two cysteine (Cys) residues which are separated by two other residues and which are present as a disulfide in the oxidized protein and as a dithiol in the reduced protein. The active-site sequence in thioredoxin is -Cys-Gly-Pro-Cys- (where Gly = glycinexs, Pro = proline) and in glutaredoxin is -Cys-Pro-Tyr-Cys- (where Tyr = tyrosine).[2]

NMR spectra of *Escherichia coli* thioredoxin were reported as early as 1976,[4] but extensive NMR studies on these proteins were not made until the advent of high-field spectrometers in the 1980s. The NMR spectrum of a protein gives information on the three-dimensional (3D) structure (see ***Structures of Larger Proteins, Protein-Ligand, and Protein-DNA Complexes by Multi-Dimensional Heteronuclear NMR***). Structure determination has provided a major impetus in the study of thioredoxins and glutaredoxins by NMR, since, with the exception of the well-known X-ray crystal structure of the oxidized form of *E. coli* thioredoxin,[5] X-ray crystallography could not be used to derive structures because crystals were not formed. Oxidized *E. coli* thioredoxin was crystallized in the presence of Cu^{2+};[6] crystals of reduced *E. coli* thioredoxin have not been found under the same conditions due to the redox reaction between the copper ions and the protein dithiol. Its 3D structure has therefore been solved by NMR spectroscopy,[7] and a recent high-resolution structure determination by NMR for both oxidized and reduced *E. coli* thioredoxin[8] has allowed direct comparison of the two forms of the protein under identical conditions.

The structure of reduced human thioredoxin cloned from T-lymphocytes and overexpressed in *E. coli* has also been solved by NMR,[9] and the structures of both oxidized and reduced forms of a mutant protein have recently been published.[10] Although the glutaredoxin from T4 bacteriophage has been crystallized and its structure determined by X-ray crystallography,[11] *E. coli* glutaredoxin has not been crystallized; the structures of both oxidized and reduced glutaredoxin have recently been determined by NMR.[12,13]

The NMR spectrum of a protein also gives a great deal of useful site-specific information, and can be used to probe enzyme mechanism and function and ligand binding. A number of such studies have been performed for thioredoxins and glutaredoxins and are summarized in this article, together with work on the structures of these proteins.

2 NMR OF ESCHERICHIA COLI THIOREDOXIN

2.1 Solution Conditions for NMR

The stability and small size of *E. coli* thioredoxin (108 amino acids, M_r 11 700) make it a suitable candidate for NMR spectroscopy. Both the oxidized and reduced forms are soluble to approximately 4 mM at pH 5.7 in 100 mM phosphate buffer[4,14] and to 5−8 mM in 150 mM NaCl/20 mM phosphate, pH 5.7.[15] Dithiothreitol (DTT)-free reduced thioredoxin is prepared from the oxidized form of the protein by the addition of DTT and subsequent passage of the solution through a short column of Sephadex G25 equilibrated under argon.[16] The NMR spectrum is well dispersed with narrow resonance lines under these conditions. At pH values below 5.5 broadening of resonances in the NMR spectrum is observed, indicating the onset of aggregation, which occurs as the pI ($\sim$ 4) is approached.[4] The NMR spectrum as a whole is unaffected by pH changes up to pH 10, indicating that the structure of the protein is largely unaffected by pH in this range.[17] Certain resonances shift with pH due to the titrations of the N-terminal amine, the single histidine residue, and a buried aspartate near the active site in both oxidized and reduced thioredoxins, and by the titrations of the two thiol groups in reduced thioredoxin.[17]

2.2 Resonance Assignments and Structure Determination

A number of methods have been used for resonance assignment of *E. coli* thioredoxin. Pioneering studies in the use of isotope labeling were performed with oxidized thioredoxin, including the development of random fractional deuteration as a means of spectrum simulation and stereospecific assignment,[15,18,19] and specific labeling of amino acids as a means of sequential resonance assignment.[20,21] Backbone and C-β,H ^{1}H resonance assignments of the oxidized form of *E. coli* thioredoxin were largely completed using these methods combined with conventional ^{1}H two-dimensional (2D) spectroscopy.[15] Proton-only 2D NMR was used to obtain complete ^{1}H assignments for both oxidized and reduced *E. coli* thioredoxin,[16] and these assignments were used as a basis for the calculation of the solution structure of reduced *E. coli* thioredoxin using distance and dihedral angle restraints from ^{1}H 2D NOESY and COSY spectra.[7] The NMR spectra of reduced and oxidized *E. coli* thioredoxin are very similar, differing only in the region of the active site,[14,16] and the NMR solution structure of reduced thioredoxin is virtually identical to the X-ray crystal structure of oxidized thioredoxin.[5] Even

in the active site region where the NMR spectra of the two forms are different, the backbone conformations of the two forms of the protein are superimposable, and there are only the most subtle differences in the disposition of the side chains in this region. A total of 853 interresidue and 391 intraresidue distance constraints and 43 dihedral angle constraints were used in the calculation of the structure using the program DISGEO, and the resulting structures were refined with molecular dynamics (AMBER), for a final average rms deviation from the average structure of 0.564 for backbone heavy atoms of residues 3–108.[7]

The NMR solution structure of reduced *E. coli* thioredoxin represents probably one of the largest that has been calculated using ^{1}H 2D methods alone. Resonance overlap and the resulting ambiguities in estimates of internuclear distance lower the number of available distance and dihedral angle restraints, and hence the potential resolution of the structure. The additional resolution provided by the use of protein uniformly labeled with ^{13}C and ^{15}N[22,23] allows the addition of a significantly greater number of restraints to the calculation, resulting in a higher resolution structure. High-resolution structures have recently been calculated, using the program DIANA followed by refinement with molecular dynamics (AMBER), for both oxidized and reduced *E. coli* thioredoxin[8] using 2846 (reduced) and 2710 (oxidized) NOE distance restraints from 3D ^{13}C and ^{15}N heteronuclear NOESY spectra and 131 (reduced) and 136 (oxidized) dihedral angle restraints obtained from coupling constants. Final backbone average rms deviations from the average structure of 0.29 Å and 0.35 Å were obtained for the well-defined residues (4–107) of 30 reduced and oxidized thioredoxin structures respectively.[8] A superposition of 20 of each of the calculated structures is shown in Figure 1.

2.3 Nitrogen-15 Relaxation and Polypeptide Backbone Dynamics

The backbone and tryptophan side-chain dynamics of oxidized and reduced thioredoxin have been estimated using uniformly ^{15}N-labeled protein,[24] and show a number of regions, especially in turns and loops, where backbone flexibility is high compared with that of the polypeptide present in ordered secondary structure. The rather low proportion of flexible regions in thioredoxin is consistent with the exceptionally high thermal stability of this protein in either oxidation state.[25] The active site loop is also apparently flexible, but measurements are hampered because the sequence contains Gly and Pro, for which the ^{15}N relaxation parameters are not measurable. Differences in the flexibility of loops adjacent to the active site occur between the oxidized and reduced forms of the protein (see Section 2.5).

2.4 pH-Dependence of the Mechanism of Thioredoxin Dithiol–Disulfide Exchange

The mechanism of reduction by thioredoxin is thought to proceed via nucleophilic attack by a thiolate anion belonging to Cys-32, with formation of a mixed disulfide.[26] Control of the pH in the active site region is therefore likely to be crucial to the reaction. The pK_a for deprotonation of Cys-32 was shown in chemical modification studies to be considerably lowered from normal, to a value of about 6.7,[26] consistent with its postulated role as primary nucleophile. However, the mechanism is apparently quite complex, as shown by an NMR study of reduced and oxidized thioredoxin as a function of pH between 5.7 and 10.[17] pK_a values of 7.1 and 8.4 were obtained

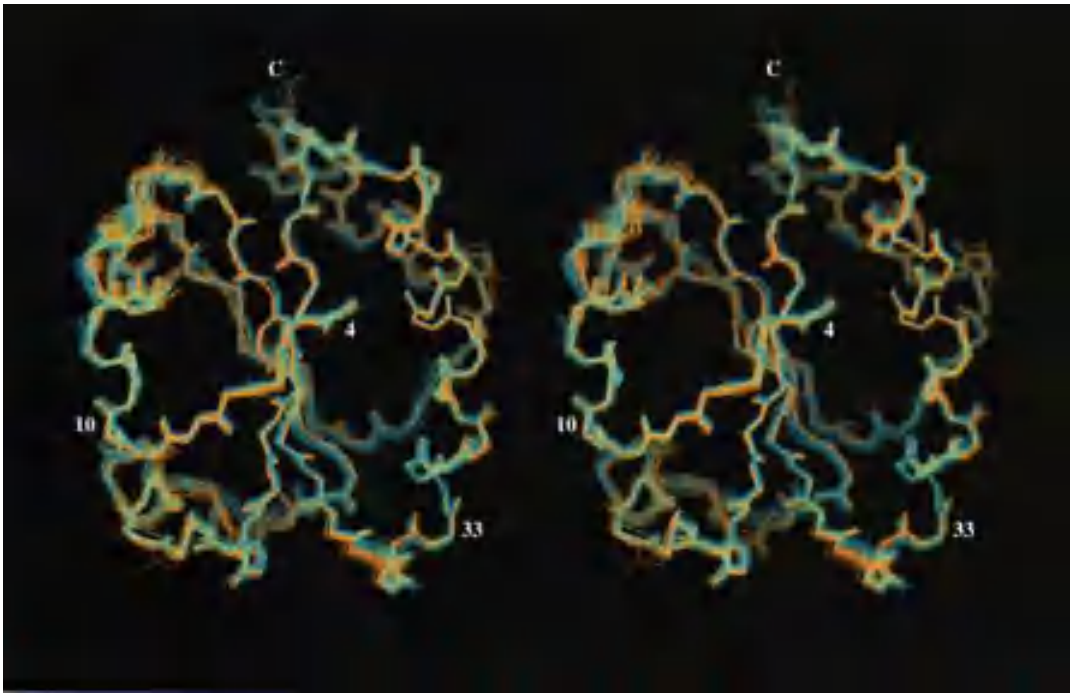

Figure 1 Stereo view showing the best-fit superposition for residues 4–107 of 20 NMR solution structures of reduced *E. coli* thioredoxin (yellow) and oxidized thioredoxin (blue) obtained using the distance geometry program DIANA followed by molecular dynamics refinement with AMBER. The active site (residues 32–35) is at the bottom right of the structure. (Reproduced by permission from Jeng et al.[8])

for two groups titrating in the active site region of reduced thioredoxin, consistent with the values previously obtained for the two active site thiols.[26] However, a third group also titrates in the active site region, giving a pK_a of 7.5 in oxidized thioredoxin and ∼7.1 in reduced thioredoxin. Mutant studies by NMR[27] and other methods[28,29] indicate that this titrating group is most likely the buried carboxyl group of aspartic acid (Asp)-26, which is thus revealed as an important factor in the pH control of the mechanism of *E. coli* thioredoxin.

2.5 Structural and Functional Differences between Oxidized and Reduced Thioredoxin

There are a number of functional differences between oxidized and reduced thioredoxin that are not due entirely to the presence or absence of thiol groups. Reduced thioredoxin is required for the assembly of filamentous bacteriophages[30,31] and is an essential subunit of the DNA polymerase induced by T7 phage.[32] Oxidized thioredoxin does not function in these systems. Mutants where one or both Cys residues are replaced with serine (Ser) or alanine (Ala) are partially functional,[31,33] suggesting some structural or conformational difference between the two forms that can be differentiated in the phage systems. The extremely small structural differences between the two forms of thioredoxin is illustrated in Figure 1. Indeed, the only significant difference appears to be a slight change in the backbone configuration at the active site due to the change in position of the reduced sulfur of Cys-32,[8] as shown in Figure 2. In the absence of a strongly marked change in the structure, the difference may lie in the relative mobility of the polypeptide chain in the vicinity of the active site. Backbone dynamics of both oxidized and reduced thioredoxin were studied using ^{15}N relaxation[24] and revealed a significant difference in the local flexibility of several of the loops that abut the active site. In particular, the sequence that precedes the highly conserved *cis*-Pro at position 76 is more flexible in reduced thioredoxin, suggesting that certain structural states may be kinetically accessible to reduced thioredoxin but not to the oxidized form due to the constraint imposed by the disulfide bond. This interpretation is borne out by a comparison of the rates of amide proton hydrogen exchange in the two forms of the protein,[34] which indicate a significantly greater protection in the active site region in oxidized thioredoxin, consistent with lower flexibility of the polypeptide chain. If one or more of these low-energy states was required for thioredoxin function in the filamentous and T7 phage systems, then reduced thioredoxin would be functional and the oxidized form would not. A recent NMR study of a double Cys-to-Ser mutant of *E. coli* thioredoxin[27] revealed that its behavior most closely resembled reduced rather than oxidized thioredoxin, consistent with these ideas and with previous functional studies of mutants.[31]

3 NMR OF HUMAN THIOREDOXIN

3.1 Solution Conditions for NMR

The thioredoxin cloned from human T-lymphocytes (105 amino acids) is approximately 25% homologous with the *E. coli* protein, mainly in the active site region.[35] Reduced human thioredoxin is soluble to at least 2 mM and solutions prepared

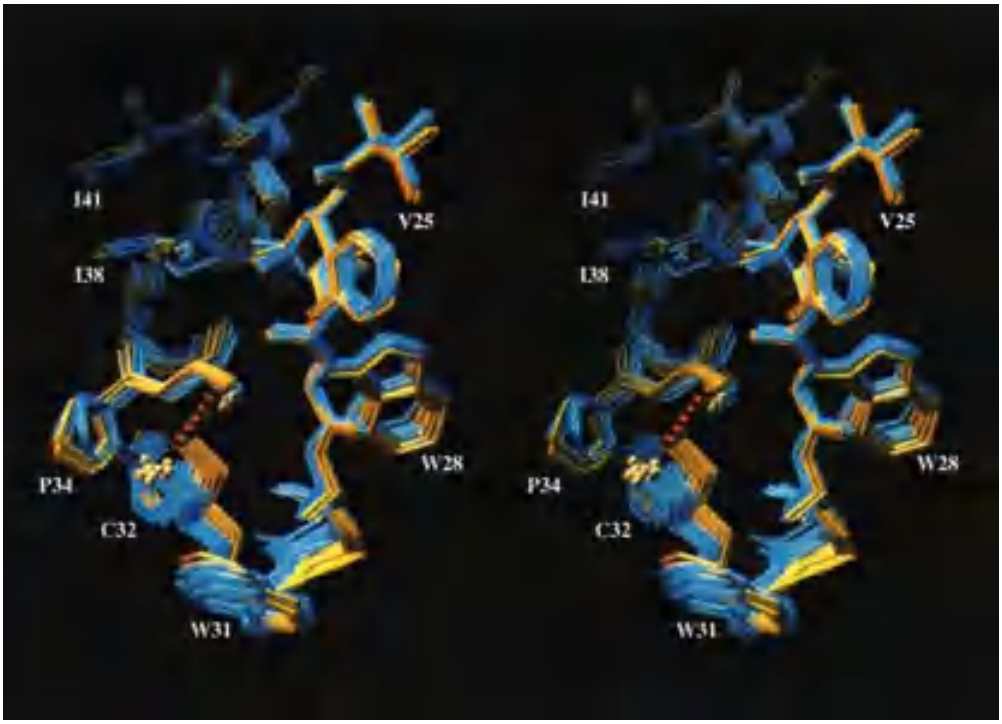

Figure 2 Stereo superposition (on the backbone of the entire molecule, residues 4–107, as in Figure 1) of the active site, including selected side chains, for 20 structures each of reduced (yellow) and oxidized (blue) thioredoxin. The disulfide bond is indicated by the hatched red and black bars, and the positions of the Cys sulfur atoms in reduced thioredoxin are shown by yellow spheres. (Reproduced by permission from Jeng et al.[8])

in 100–150 mM phosphate buffer containing 0.2 mM DTT under argon appear to be stable at pH 7.0 or 5.5 for at least 2 months, over a temperature range of 4–50 °C.[36] Solubility is reduced at pH values below 5.6.[37] Only the reduced form of unmodified human thioredoxin has so far been studied by NMR, because of the presence of three Cys residues in addition to the two in the active site. The presence of these additional thiol groups causes problems with aggregation of the protein upon oxidation. The recombinant human thioredoxin isolated from an *E. coli* expression system is heterogeneous at the N-terminus, with about 30% of the protein containing an extra methionine residue,[36] although the N-terminal methionine is processed more efficiently during bacterial growth in minimal media.[38] A triple Cys-to-Ala mutant of human thioredoxin has been constructed to allow NMR studies of both oxidation states of human thioredoxin.[39]

3.2 Resonance Assignments and Structure Determination

The ^{1}H resonances of reduced human thioredoxin were initially assigned and a description of the secondary structure was obtained using ^{1}H 2D methods.[36] Extensive ^{15}N assignments and coupling constant measurements have been made for reduced human thioredoxin,[38] and a high-resolution structure has been calculated.[9] A family of NMR solution structures of reduced human thioredoxin (Figure 3) were calculated using a hybrid distance geometry–simulated annealing method[9] with 1294 interresidue and 689 intraresidue distance restraints obtained from NOESY and ^{15}N heteronuclear multiple quantum coherence (HMQC)–NOESY experiments and 241 torsion angle restraints obtained from coupling constants. Proton and ^{15}N resonance assignments have also been made for the reduced form of a triple mutant of human thioredoxin, in which the three Cys residues other than those in the active site have been mutated to Ala residues,[39] and structures have been calculated for the oxidized and reduced forms of this mutant[10] using 2571 distance restraints, 273 torsion angle restraints, and 89 ^{3}J(HN-α) coupling constant restraints for the reduced form, and 2649 distance restraints, 278 torsion angle restraints, and 91 ^{3}J(HN-α) coupling constant restraints for the oxidized form. The backbone atomic rms deviations from the mean structure were 0.19 Å and 0.18 Å respectively for 40 structures of reduced and oxidized mutant thioredoxin.[10] The structure consists of a 5-stranded twisted β-sheet surrounded by four α-helices and the overall structure is similar to those of *E. coli* thioredoxins.[5,7] The major differences between the thioredoxins from these two different sources is in helices α_1 and α_3, which are longer and more regular in human thioredoxin. The active site conformations are all very similar, as would be expected from the high degree of sequence homology in this region.

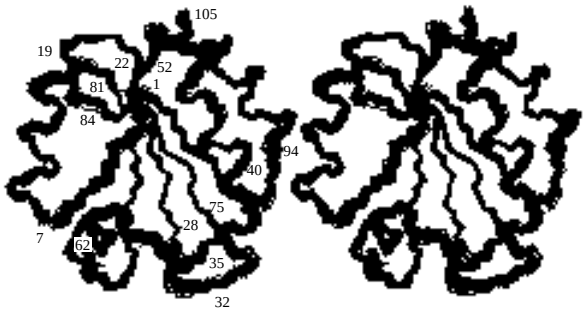

Figure 3 Stereo view (approximately the same view as Figure 1) showing the best-fit superpositions of the backbone (N, C-α, and C) atoms of 33 NMR solution structures of reduced human thioredoxin obtained by a distance geometry–simulated annealing method. (Reproduced by permission from Forman-Kay et al.9)

3.3 Bound Water Molecules in the Structure of Human Thioredoxin

The positions of relatively tightly bound water molecules in the structure of reduced human thioredoxin have been determined using 3D ^{1}H–^{15}N ROESY–HMQC spectroscopy.[40] A number of backbone amide protons are in close proximity to a total of four best-fit bound water molecules in structures recalculated to include them. Two of the water molecules could be located in fairly tight families, one in the β-bulge between strands 4 and 5 of the β-sheet and one associated with the C-terminal ends of the α_2 and α_4 helices. Of the other two water molecules, one occupies two positions near the loop between α_1 and β_2 and the other occupies two positions close to the N-terminus of α_2, near the active site. Several of the positions found for the bound water molecules in the solution structure of reduced human thioredoxin[40] are similar to those found in the X-ray crystal structure of oxidized *E. coli* thioredoxin.[5]

3.4 Electrostatics and Redox Function in Human Thioredoxin

An extensive study of the pH-dependent behavior of reduced human thioredoxin was made using ^{1}H and ^{15}N NMR spectroscopy.[37] Inclusion of measurements on solutions of pH lower than 5.6 allowed determination of the pK_a values of aspartate and glutamate side chains, although many of the titration curves exhibit complex behavior due to the effects of interacting titrating groups. Unlike *E. coli* thioredoxin,[17] no clear-cut effect of the titration of the buried carboxyl side chain of Asp-26 was observed, and the pK_a of the thiol of Cys-32 was measured to be 6.3, lower than the value for *E. coli* thioredoxin. The anomalously low pK_a for the Cys-32 thiol was attributed[37] to an interaction of the S-γ atom of Cys-32 with the amide group of Cys-35 seen in the solution structure of reduced human thioredoxin.[9]

4 NMR OF *ESCHERICHIA COLI* GLUTAREDOXIN

4.1 Solution Conditions for NMR

E. coli glutaredoxin (85 residues, M_r ~10 000) is a heat-stable acidic protein which reacts with glutathione and is responsible for mediating many glutathione-dependent redox functions in the cell. There is very little sequence homology between *E. coli* glutaredoxin and thioredoxin, although both contain an active site disulfide/dithiol group. The solution conditions required for NMR studies of glutaredoxin are less than optimal for structure determination.[41] Oxidized

glutaredoxin is insoluble at pH values below 5.5 and the NMR spectrum shows evidence of aggregation at pH 6.0. The protein appears to be stable and monomeric at pH 7.0 and 28 °C, at a concentration of 2.5 mM in 50 mM phosphate buffer. Reduced glutaredoxin is prepared from the oxidized form of the protein at 4 °C by the addition of DTT followed by buffer exchange in an ultrafiltration cell.[12] Final solution conditions were 3 mM protein in 50 mM phosphate, pH 7.0, 28 °C.

4.2 Resonance Assignments and Structure Determination

Nearly complete resonance assignments have been made for oxidized[41] and reduced[12] *E. coli* glutaredoxin, using mainly ^{1}H 2D methods, with the addition of 3D ^{15}N NOESY spectra for the resolution of ambiguities in NOE assignments and for measurement of ^{3}J(HN-α) coupling constants. Initial NMR spectra showed some heterogeneity, as glutaredoxin is apparently susceptible to proteolysis; this problem was overcome by the use of protease inhibitors.[41] Additional heterogeneity in the NMR spectra of oxidized glutaredoxin was also due to the presence of about 10% of a form elongated at the N-terminus or to conformational isomerism.[41] No conformational heterogeneity was reported for reduced glutaredoxin.[12] Three-dimensional structures were calculated for both forms of glutaredoxin using the program DIANA followed by simulated annealing. For oxidized glutaredoxin, 563 interresidue and 219 intraresidue distance constraints and 74 dihedral angle constraints were used.[13] For reduced glutaredoxin, 402 interresidue and 221 intraresidue distance constraints and 191 dihedral angle constraints were used.[12] The structure of glutaredoxin, shown in Figure 4, consists of a 4-stranded β-sheet and three helices, and is very similar in both oxidized and reduced forms of the protein.[13] Exchange rates of slowly exchanging amide protons are similar, indicating similar hydrogen-bonding patterns, but

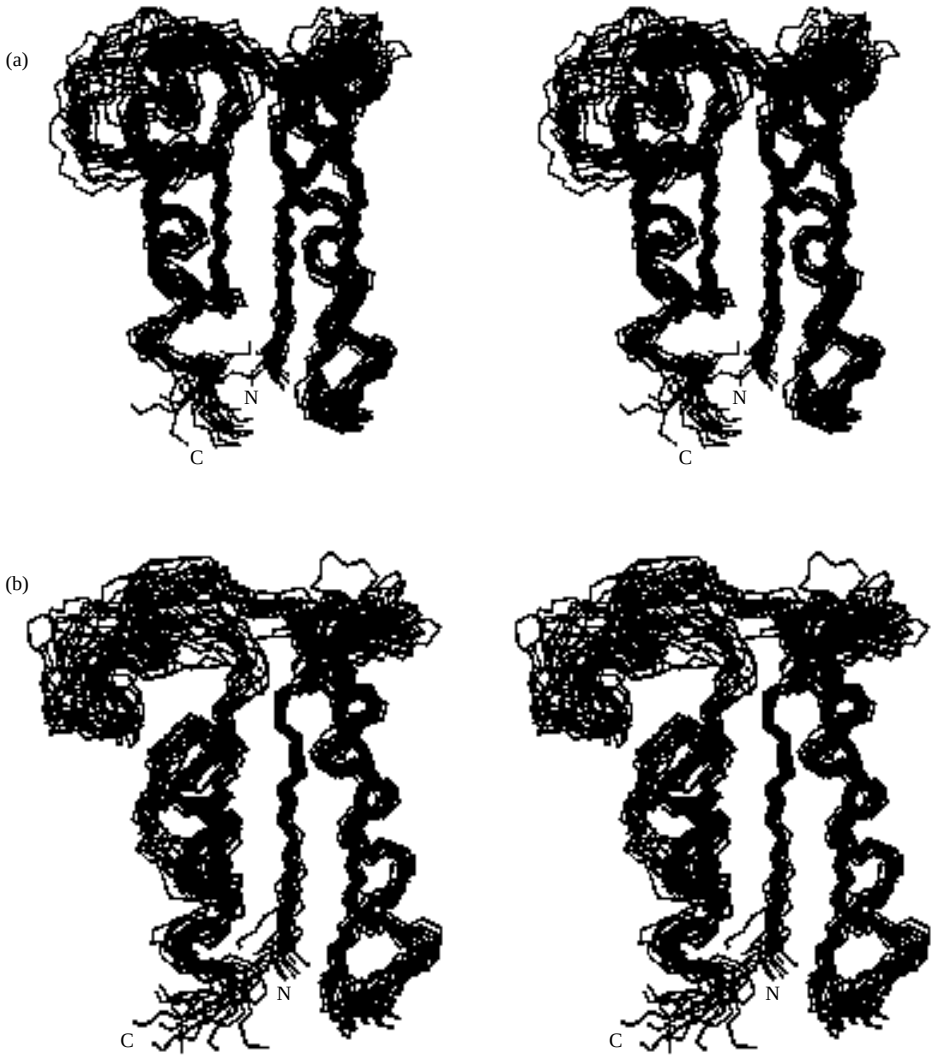

Figure 4 Stereo views of the 20 conformers used to represent the solution structure of (a) reduced and (b) oxidized *E. coli* glutaredoxin obtained using the program DIANA followed by simulated annealing. The complete polypeptide backbone from residues 1 to 85 is shown. The conformers 2–20 were superimposed with conformer 1 (which has the smallest residual violations) for pairwise minimal rms deviation of the backbone atoms N, C-α, and C′ of residues 1–8, 13–43, and 60–83. The active site (residues 11–14) is at the top right of the structure. (Reproduced by permission from (a) Sodano et al.[12] and (b) Xia et al.[13])

differences in local dynamics are evident near the active site and the C-terminal α-helix.[13] A comparison of Figures 1–4 shows that, despite the low sequence homology between glutaredoxin and thioredoxin, the overall folds of thioredoxin and glutaredoxin are quite similar.

4.3 Structure of a Mixed Disulfide Complex of Glutathione and Glutaredoxin

As for thioredoxin, the mechanism of thiol–disulfide exchange of glutaredoxin was thought to proceed via a mixed disulfide intermediate between one of the active site thiols and a molecule of glutathione.[42] In order to probe the structure of such an intermediate, a mutant glutaredoxin was prepared with one of the active site cysteines, Cys-14, substituted by Ser. The physiological substrate, glutathione, could then be bound to the remaining cysteine, Cys-11, forming a mixed disulfide which ought to have the same structure as that of the wild-type, but which is stable since reaction of the second thiol (now a Ser) with a second molecule of glutathione and release of the oxidized glutathione dimer is not possible. The C14 $\rightarrow$ S glutaredoxin mutant and the mixed disulfide complex with glutathione have been prepared and characterized by NMR,[42] and the structure of the complex has recently been reported.[43] Nitrogen-15 NMR studies[42] confirmed that the glutathione molecule is attached via a disulfide bond to Cys-11, and the structure shows that it lies along a shallow cleft in the protein that includes a number of hydrophobic residues.[43]

5 RELATED ARTICLES

Amino Acids, Peptides and Proteins: Chemical Shifts; Biological Macromolecules: Structure Determination in Solution; Enzymatic Transformations: Isotope Probes; Motional Effects on Protein Structure: Acyl Carriers; Peptides and Polypeptides; Protein Dynamics from NMR Relaxation; Protein Hydration; Structures of Larger Proteins, Protein-Ligand, and Protein-DNA Complexes by Multi-Dimensional Heteronuclear NMR; Three- and Four-Dimensional Heteronuclear Magnetic Resonance.

6 REFERENCES

1. A. Holmgren, *Annu. Rev. Biochem.*, 1985, **54**, 237.
2. A. Holmgren, *J. Biol. Chem.*, 1989, **264**, 13 963.
3. J. Yodoi and T. Tursz, *Adv. Cancer Res.*, 1991, **57**, 381.
4. A. Holmgren and G. Roberts, *FEBS Lett.*, 1976, **71**, 261.
5. S. K. Katti, D. M. LeMaster, and H. Eklund, *J. Mol. Biol.*, 1990, **212**, 167.
6. A. Holmgren and B.-O. Söderberg, *J. Mol. Biol.*, 1970, **54**, 387.
7. H. J. Dyson, G. P. Gippert, D. A. Case, A. Holmgren, and P. E. Wright, *Biochemistry*, 1990, **29**, 4129.
8. M.-F. Jeng, A. P. Campbell, T. Begley, A. Holmgren, D. A. Case, P. E. Wright, and H. J. Dyson, *Structure*, 1994, **2**, 853.
9. J. D. Forman-Kay, G. M. Clore, P. T. Wingfield, and A. M. Gronenborn, *Biochemistry*, 1991, **30**, 2685.
10. J. Qin, G. M. Clore, and A. M. Gronenborn, *Structure*, 1994, **2**, 503.
11. B.-O. Söderberg, B.-M. Sjöberg, U. Sonnerstam, and C.-I. Brändén, *Proc. Natl. Acad. Sci. U.S.A.*, 1978, **75**, 5827.
12. P. Sodano, T.-H. Xia, J. H. Bushweller, O. Björnborg, A. Holmgren, M. Billeter, and K. Wüthrich, *J. Mol. Biol.*, 1991, **221**, 1311.
13. T.-H. Xia, J. H. Bushweller, P. Sodano, M. Billeter, O. Björnberg, A. Holmgren, and K. Wüthrich, *Protein Sci.*, 1992, **1**, 310.
14. H. J. Dyson, A. Holmgren, and P. E. Wright, *FEBS Lett.*, 1988, **228**, 254.
15. D. M. LeMaster and F. M. Richards, *Biochemistry*, 1988, **27**, 142.
16. H. J. Dyson, A. Holmgren, and P. E. Wright, *Biochemistry*, 1989, **28**, 7074.
17. H. J. Dyson, L. L. Tennant, and A. Holmgren, *Biochemistry*, 1991, **30**, 4262.
18. D. M. LeMaster, *FEBS Lett.*, 1987, **223**, 191.
19. D. M. LeMaster, *FEBS Lett.*, 1988, **233**, 326.
20. D. M. LeMaster and F. M. Richards, *Biochemistry*, 1985, **24**, 7263.
21. D. M. LeMaster and F. M. Richards, in *Thioredoxin and Glutaredoxin Systems: Structure and Function*, eds. A. Holmgren, C.-I. Brändén, H. Jörnvall, and B.-M. Sjöberg, Raven Press, New York, 1986, p. 67.
22. K. Chandrasekhar, G. Krause, A. Holmgren, and H. J. Dyson, *FEBS Lett.*, 1991, **284**, 178.
23. K. Chandrasekhar, A. P. Campbell, M.-F. Jeng, A. Holmgren, and H. J. Dyson, *J. Biomol. NMR*, 1994, **4**, 411.
24. M. J. Stone, K. Chandrasekhar, A. Holmgren, P. E. Wright, and H. J. Dyson, *Biochemistry*, 1993, **32**, 426.
25. T. Hiraoki, S. B. Brown, K. J. Stevenson, and H. J. Vogel, *Biochemistry*, 1988, **27**, 5000.
26. G. B. Kallis and A. Holmgren, *J. Biol. Chem.*, 1980, **255**, 10 261.
27. H. J. Dyson, M.-F. Jeng, P. Model, and A. Holmgren, *FEBS Lett.*, 1994, **339**, 11.
28. K. Langsetmo, J. A. Fuchs, and C. Woodward, *Biochemistry*, 1991, **30**, 7603.
29. K. Langsetmo, J. A. Fuchs, C. Woodward, and K. A. Sharp, *Biochemistry*, 1991, **30**, 7609.
30. M. Russel and P. Model, *Proc. Natl. Acad. Sci. U.S.A.*, 1985, **82**, 29.
31. M. Russel and P. Model, *J. Biol. Chem.*, 1986, **261**, 14 997.
32. S. Adler and P. Modrich, *J. Biol. Chem.*, 1983, **258**, 6956.
33. H. E. Huber, M. Russel, P. Model, and C. C. Richardson, *J. Biol. Chem.*, 1986, **261**, 15 006.
34. M.-F. Jeng and H. J. Dyson, *Biochemistry*, 1995, **34**, 10 101.
35. H. Eklund, F. K. Gleason, and A. Holmgren, *Proteins*, 1991, **11**, 13.
36. J. D. Forman-Kay, G. M. Clore, P. C. Driscoll, P. Wingfield, F. M. Richards, and A. M. Gronenborn, *Biochemistry*, 1989, **28**, 7088.
37. J. D. Forman-Kay, G. M. Clore, and A. M. Gronenborn, *Biochemistry*, 1992, **31**, 3442.
38. J. D. Forman-Kay, A. M. Gronenborn, L. E. Kay, P. T. Wingfield, and G. M. Clore, *Biochemistry*, 1990, **29**, 1566.
39. J. D. Forman-Kay, G. M. Clore, S. J. Stahl, and A. M. Gronenborn, *J. Biomol. NMR*, 1992, **2**, 431.
40. J. D. Forman-Kay, A. M. Gronenborn, P. T. Wingfield, and G. M. Clore, *J. Mol. Biol.*, 1991, **220**, 209.
41. P. Sodano, K. V. R. Chary, O. Björnberg, A. Holmgren, B. Kren, J. A. Fuchs, and K. Wüthrich, *Eur. J. Biochem.*, 1991, **200**, 369.
42. J. H. Bushweller, F. Åslund, K. Wüthrich, and A. Holmgren, *Biochemistry*, 1992, **31**, 9288.

43. J. H. Bushweller, M. Billeter, A. Holmgren, and K. Wüthrich, *J. Mol. Biol.*, 1994, **235**, 1585.

Acknowledgments

I wish to acknowledge Dr Peter Wright for helpful discussions and a critical reading of the manuscript and Dr Mei-Fen Jeng for preparing Figures 1 and 2. This work was supported by grant GM43238 from the National Institutes of Health.

Biographical Sketch

H. Jane Dyson. *b* 1951. B.Sc.(hons), 1973; Ph.D. 1977, Sydney. Postdoctoral in Biology, MIT, 1977–78, Chemistry faculty, University of New South Wales, 1979–1984. NMR work begun in earnest at Scripps Clinic in 1984 in collaboration with Peter Wright; faculty at Scripps 1984–present. Approx. 50 publications. Research interests in the conformation of short peptides and in structure–function studies of proteins including thioredoxin.

Transverse Relaxation-optimized NMR Spectroscopy with Biomacromolecular Structures in Solution

Kurt Wüthrich and Gerhard Wider
Institut für Molekularbiologie und Biophysik, Eidgenössische Technische Hochschule Zürich, Zürich, Switzerland

1	Introduction	1
2	The Foundations of Transverse Relaxation-optimized Spectroscopy (TROSY)	1
3	TROSY in NMR Experiments with Biological Macromolecules	4
4	New Stable Isotope Labeling Strategies for TROSY NMR with Large Structures	8
5	Combining TROSY with Cross Correlated Relaxation-induced Polarization Transfer for Studies of Very Large Structures	8
6	Conclusions and Outlook	8
7	Related Article in this Volume	9
8	Related Articles in Volumes 1–8	9
9	References	9

1 INTRODUCTION

NMR spectroscopy with biological macromolecules has been limited to relatively small structures, with molecular weights up to about 50 kDa, and the size distribution of the approximately 2500 NMR deposits in the Protein Data Bank peaks near a molecular weight of 10 kDa.[1] In spite of this limitation, NMR is one of the principal experimental techniques in structural biology.[2,3] Nonetheless, the availability of solution NMR techniques for studies of larger structures is of keen interest, in particular for applications in the newly emerging field of structural and functional genomics.[4] With the presently described principles of transverse relaxation-optimized spectroscopy (TROSY) the size limit for molecular structures that are amenable to high resolution NMR studies in solution has been extended severalfold.[5–7] TROSY-based NMR experiments are particularly well suited for applications with proteins and nucleic acids,[8] which are a main focus also in the present article.

2 THE FOUNDATIONS OF TRANSVERSE RELAXATION-OPTIMIZED SPECTROSCOPY (TROSY)

At the high magnetic fields typically used for studies of proteins and nucleic acids, chemical shift anisotropy (CSA) of ^{1}H, ^{15}N and ^{13}C nuclei can be a significant source of transverse relaxation, in addition to the omnipresent relaxation due to dipole–dipole coupling. As a consequence the individual multiplet components in heteronuclear two-spin systems, such as ^{15}N–^{1}H in amide groups and aromatic ^{13}C–^{1}H moieties, may have different transverse relaxation times (Figure 1), and in large structures studied at high magnetic fields these individual relaxation rates are actually largely different.[7] Heteronuclear decoupling, which is routinely applied in conventional NMR spectroscopy,[9] will then lead to a deteriorated averaged signal due to the mixing of the different relaxation rates. In TROSY-type experiments the multiplet structures (Figures 1 and 2) are not decoupled, and only the narrowest, most slowly relaxing line of each multiplet is retained.[10]

2.1 Theory

For a system of two scalar-coupled spin 1/2, I and S, a straightforward description of TROSY can be obtained with the use of single-transition, zero-quantum and double-quantum basis operators.[7] In this basis the individual transverse relaxation rates of all six coherences in a coupled two-spin system

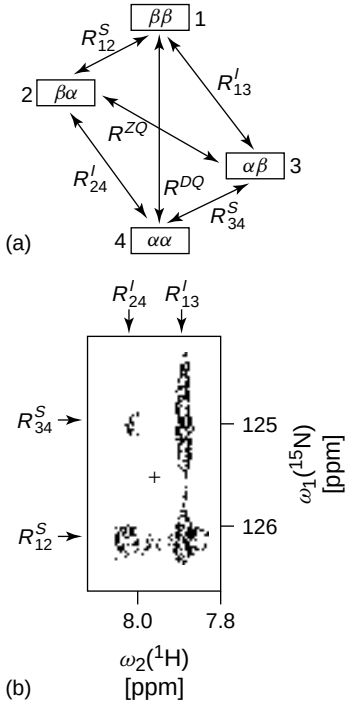

Figure 1 (a) Diagram of the energy levels 1–4 of a system of two scalar-coupled spins 1/2, I and S, with indication of the transverse relaxation rates, R, of the individual transitions. The abbreviations ZQ and DQ stand for zero-quantum and double-quantum transitions. (b) Cross-peak of a backbone amide moiety from a two-dimensional [^{15}N,^{1}H]-HSQC spectrum of uniformly ^{2}H,^{13}C,^{15}N-labeled 7,8-dihydroneopterin aldolase (DHNA) from *Staphylococcus aureus* measured without ^{1}H and ^{15}N decoupling. DHNA is a homo-octameric protein of molecular weight 110 kDa.[44] The NMR sample contained 0.4 mM DHNA octamer, solvent 90% H_2O/10% D_2O, pH = 6.5, T = 20 °C, ^{1}H frequency = 750 MHz. The relaxation rates that are effective for the individual multiplet components are indicated at the top and on the left. The cross marks the center of the multiplet, i.e., the position of the single-component cross peak in a ^{1}H and ^{15}N broadband decoupled spectrum

(Figure 1) can readily be expressed. Taking only dipole–dipole coupling and CSA relaxation into account, the differential equation (1) describes the time evolution of the system in the slow tumbling limit, where we retain only terms with the spectral density at zero frequency, $J(0)$:

$$\frac{d}{dt}\begin{bmatrix}\langle I_{13}^{\pm}\rangle\\ \langle I_{24}^{\pm}\rangle\\ \langle S_{12}^{\pm}\rangle\\ \langle S_{34}^{\pm}\rangle\\ \langle DQ^{\pm}\rangle\\ \langle ZQ^{\pm}\rangle\end{bmatrix} = -\begin{bmatrix}\pm i\omega_{13}^{I}+R_{13}^{I} & & & & & \\ & \pm i\omega_{24}^{I}+R_{24}^{I} & & 0 & & \\ & & \pm i\omega_{12}^{S}+R_{12}^{S} & & & \\ & & & \pm i\omega_{34}^{S}+R_{34}^{S} & & \\ & 0 & & & \pm i\omega_{14}^{DQ}+R_{14}^{DQ} & \\ & & & & & \pm i\omega_{23}^{ZQ}+R_{23}^{ZQ}\end{bmatrix}\cdot\begin{bmatrix}\langle I_{13}^{\pm}\rangle\\ \langle I_{24}^{\pm}\rangle\\ \langle S_{12}^{\pm}\rangle\\ \langle S_{34}^{\pm}\rangle\\ \langle DQ^{\pm}\rangle\\ \langle ZQ^{\pm}\rangle\end{bmatrix} \quad (1)$$

ω_{ik} are the frequencies of individual transitions in the *IS* spin system, and R_{ik} are the associated transverse relaxation rates (Figure 1). DQ stands for double-quantum transition, and ZQ for zero-quantum transition. With the assumption that the CSA tensor is axially symmetric, the relaxation rates R_{ik} are

$$R_{13}^{I} = (p^2 + 2f_I p\delta_I + \delta_I^2)\cdot 4J(0) \quad (2a)$$

$$R_{24}^{I} = (p^2 - 2f_I p\delta_I + \delta_I^2)\cdot 4J(0) \quad (2b)$$

$$R_{12}^{S} = (p^2 + 2f_S p\delta_S + \delta_S^2)\cdot 4J(0) \quad (2c)$$

$$R_{34}^{S} = (p^2 - 2f_S p\delta_S + \delta_S^2)\cdot 4J(0) \quad (2d)$$

$$R^{DQ} = (\delta_I^2 + 2f_c\delta_I\delta_S + \delta_S^2)\cdot 4J(0) \quad (2e)$$

$$R^{ZQ} = (\delta_I^2 - 2f_c\delta_I\delta_S + \delta_S^2)\cdot 4J(0) \quad (2f)$$

In equation (2), p is the dipolar interaction energy,

$$p = \frac{u_0 h\gamma_1\gamma_s}{16\pi^2\sqrt{2}r_{IS}^3} \quad (3)$$

δ_s the ^{15}N-chemical shift anisotropy interaction,

$$\delta_S = \frac{\gamma_S B_o \Delta\sigma_S}{3\sqrt{2}} \quad (4)$$

and δ_I the ^{1}H-chemical shift anisotropy interaction,

$$\delta_I = \frac{\gamma_I B_o \Delta\sigma_I}{3\sqrt{2}} \quad (5)$$

The factor f_i accounts for the angular dependence of cross correlated relaxation effects, with

$$f_i = \frac{3\cos^2\Theta_i - 1}{2} \quad (6)$$

For dipole–dipole coupling/CSA cross correlation, Θ_i is the angle between the principal axis of the axially symmetric CSA tensor and the chemical bond linking the spins I and S (in equation (6), $i = S$ or I; see equation (2)). For CSA/CSA cross correlation, Θ_i is the angle between the two CSA tensor principal axes (in equation (6), $i = c$; see equation (2)). For isotropically tumbling spherical structures the spectral density function at zero frequency is given by

$$J(0) = \frac{2\tau_c}{5} \quad (7)$$

where τ_c is the rotational correlation time of the molecule.

Equation (2) shows that for non-vanishing CSA values the single-quantum transitions, which represent the two fine structure components of the I and S doublets, have different relaxation rates. Since p is field-independent and the CSA interaction increases in proportion to the field strength, there is a 'magic field' for one of the doublet components where its relaxation rate will be near zero, whereas the other component deteriorates due to rapid relaxation. For ^{15}N in peptide ^{15}N–^{1}H groups one approaches this situation at the highest presently available ^{1}H frequencies of 900 MHz, and for the amide proton a minimal transverse relaxation rate is expected near 1000 MHz.[5,7] For the zero-quantum and double-quantum transitions a different mechanism is responsible for the different relaxation rates of the individual fine structure components, i.e., cross correlation between the CSAs of the I and S spins [equations (2e) and (2f)]. This effect has been exploited for relaxation optimization in the three-dimensional NOESY-[^{1}H,^{15}N,^{1}H]-ZQ-TROSY experiment.[11]

For the practice of TROSY-NMR, one should keep in mind that some leakage is anticipated even for the 'magic field condition' of complete quenching of the transverse relaxation for an isolated two-spin system. Most important, relaxation of the spins in ^{15}N–^{1}H moieties by dipole–dipole coupling with 'remote' protons, i.e., all protons outside of the ^{15}N–^{1}H group, is the same for conventional NMR and for TROSY. This effect is minimized in uniformly deuterated proteins, where remote couplings are limited to other amide protons. For ^{15}N–^{1}H groups the relative contributions from remote dipolar couplings to the overall transverse relaxation rates of the two spins are widely different. ^{15}N relaxation is dominated by the CSA of ^{15}N and the dipole–dipole interactions with the directly attached proton even in protonated proteins, but $^{1}H^{N}$ transverse relaxation is significantly enhanced by dipole–dipole interactions with remote protons, H_k, at distances r_k from the amide proton, as given by

$$R_L = \sum_{k=1}^{n} 5p_k^2 \cdot J(0) \quad (8)$$

with

$$p_k = \frac{u_0 h\gamma_H^2}{16\pi^2\sqrt{2}r_k^3} \quad (9)$$

The overall relaxation rates for the individual multiplet components are obtained by addition of R_L (equation (8)) to one of the rates given in equations (2a), (2b), (2e) or (2f).[7] In addition to remote dipolar couplings, deviations of the CSA tensors from axial symmetry and variable spatial orientations of the CSA tensors relative to the molecular structure may prevent the ideal 'magic field condition' for a given two-spin moiety, and cause the individual ^{15}N–^{1}H groups in a protein to get closest to the 'magic field condition' at slightly different polarizing magnetic fields B_o.

2.2 Experimental Implementation of TROSY

Essential features of successful TROSY implementations are that the multiplet fine structure of the *IS* moieties is not decoupled, and that the desired slowly relaxing component, i.e., the one with the relaxation rates R_{13}^{I} and R_{12}^{S} [see Figure 1 and equation (2); note in equation (2) that for $I = {}^{1}$H and $S = {}^{15}$N, p is a negative value], can be selectively detected with high sensitivity. A simple scheme for the application

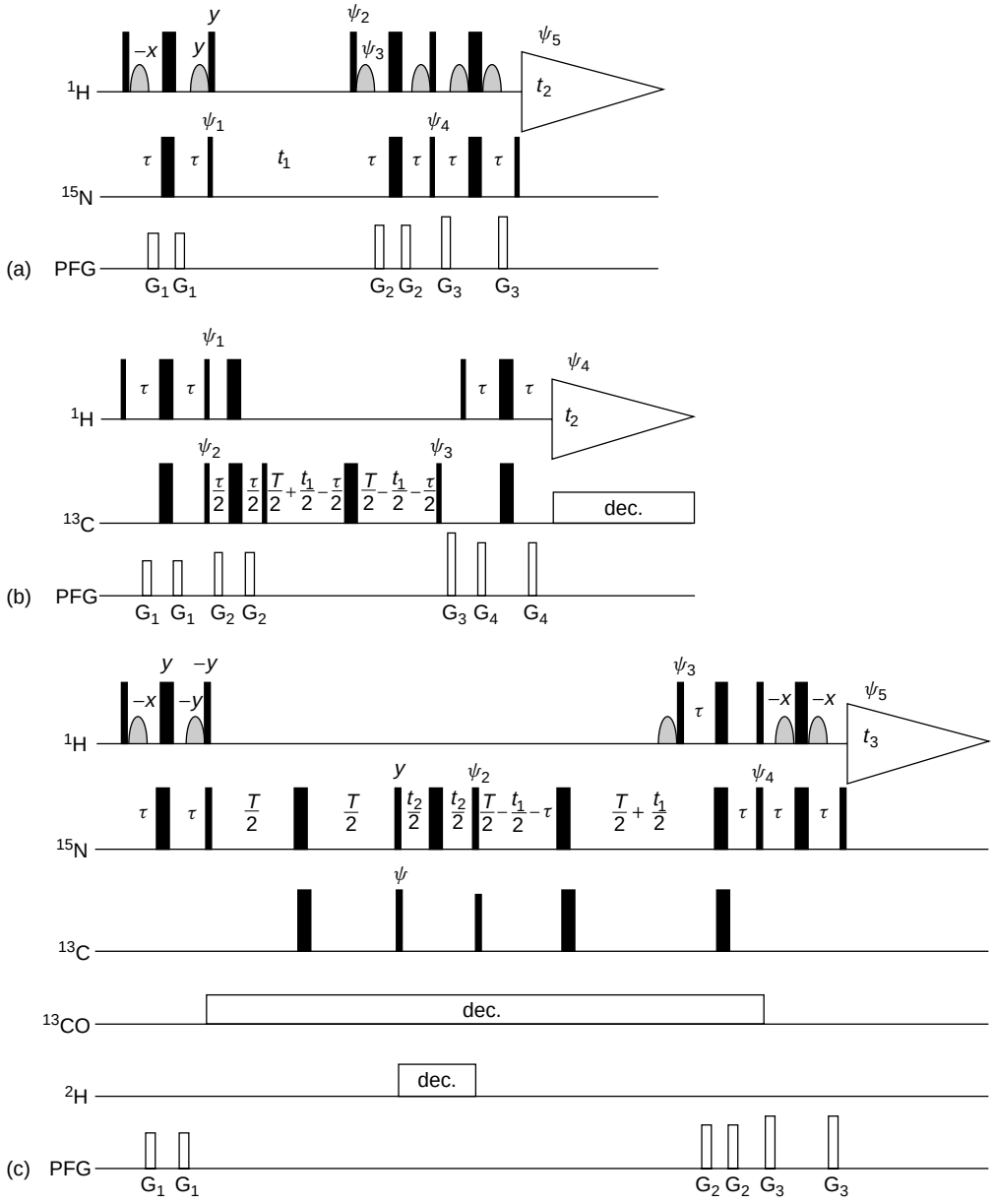

Figure 2 Experimental schemes for three TROSY-type NMR experiments: (a) [^{15}N,^{1}H]-TROSY correlation experiment; (b) ct-[^{13}C,^{1}H]-TROSY correlation experiment; (c) [^{15}N,^{1}H]-TROSY-HNCA triple resonance experiment. On the lines marked ^{1}H,^{13}C and ^{15}N, narrow and wide bars stand for non-selective 90° and 180° radio-frequency pulses, respectively. In (a) and (c), water saturation is minimized by keeping the water magnetization along the $+z$-axis during the entire experiment, using the water-selective 90° rf-pulses indicated by curved shapes on the line ^{1}H.[9] The phases of the pulses are set to x unless indicated otherwise above the pulse. In (a) and (c), the ^{15}N evolution period is marked t_1, in (b) the ^{13}C evolution period is t_1, in (c) the ^{13}C evolution period is t_2, and in all experiments the ^{1}H detection period is represented by a triangle. The line marked PFG indicates the pulsed magnetic field gradients applied along the z-axis. On the lines ^{13}C in (b), and ^{13}CO and ^{2}H in (c), the horizontal bars marked 'dec.' indicate periods of broadband decoupling. In (a), the time period τ is set to 2.7 ms; the phases for the pulses are $\psi_1 = \{y, -x\}$, $\psi_2 = \{-y\}$, $\psi_3 = \{y\}$, $\psi_4 = \{-y\}$, ψ_5(receiver) $= \{y, -x\}$, and a complex interferogram is obtained by recording a second FID for each t_1 delay, with $\psi_1 = \{y, x\}$, $\psi_2 = \{y\}$, $\psi_3 = \{-y\}$, $\psi_4 = \{y\}$. In (b), $\tau = 1.6$ ms, $T = 17.6$ ms; the phases for the pulses are $\psi_1 = \{-y\}$, $\psi_2 = \{\pi/4, 5\pi/4\}$, $\psi_3 = \{x, -x, -x, -x\}$, $\psi_4 = \{x, -x, -x, x\}$. A phase-sensitive spectrum in the t_1 dimension is obtained as described in Ref.[12] In (c), $\tau = 2.7$ ms, $T = 22$ ms; the phases for the pulses are $\psi_1 = \{x, x, -x, -x\}$, $\psi_2 = \{y, -y, -x, x\}$, $\psi_3 = \{y\}$; $\psi_4 = \{y\}$, $\psi_5 = \{y, -y, -x, x, -y, y, x, -x\}$. A phase-sensitive spectrum in the indirect dimensions is obtained as described in Ref.[45]

of the TROSY principle is the single-quantum ^{15}N–^{1}H correlation experiment (Figure 2a). For brevity we refer to this experiment as two-dimensional [^{15}N,^{1}H]-TROSY.[12] There is no heteronuclear decoupling in the scheme of Figure 2(a), so that the transitions with different relaxation rates (Figure 1) are not mixed. The phase cycling, the pulsed field gradients and the additional pulse on ^{15}N immediately before acquisition ensure that only the most slow relaxing transition in a ^{15}N–^{1}H moiety is retained. The effects on the appearance of the spectrum are illustrated in Figure 3.[10] In the conventional two-dimensional [^{15}N,^{1}H]-COSY experiment,[13] decoupling of ^{15}N and ^{1}H during the evolution and detection periods, respectively, leads to

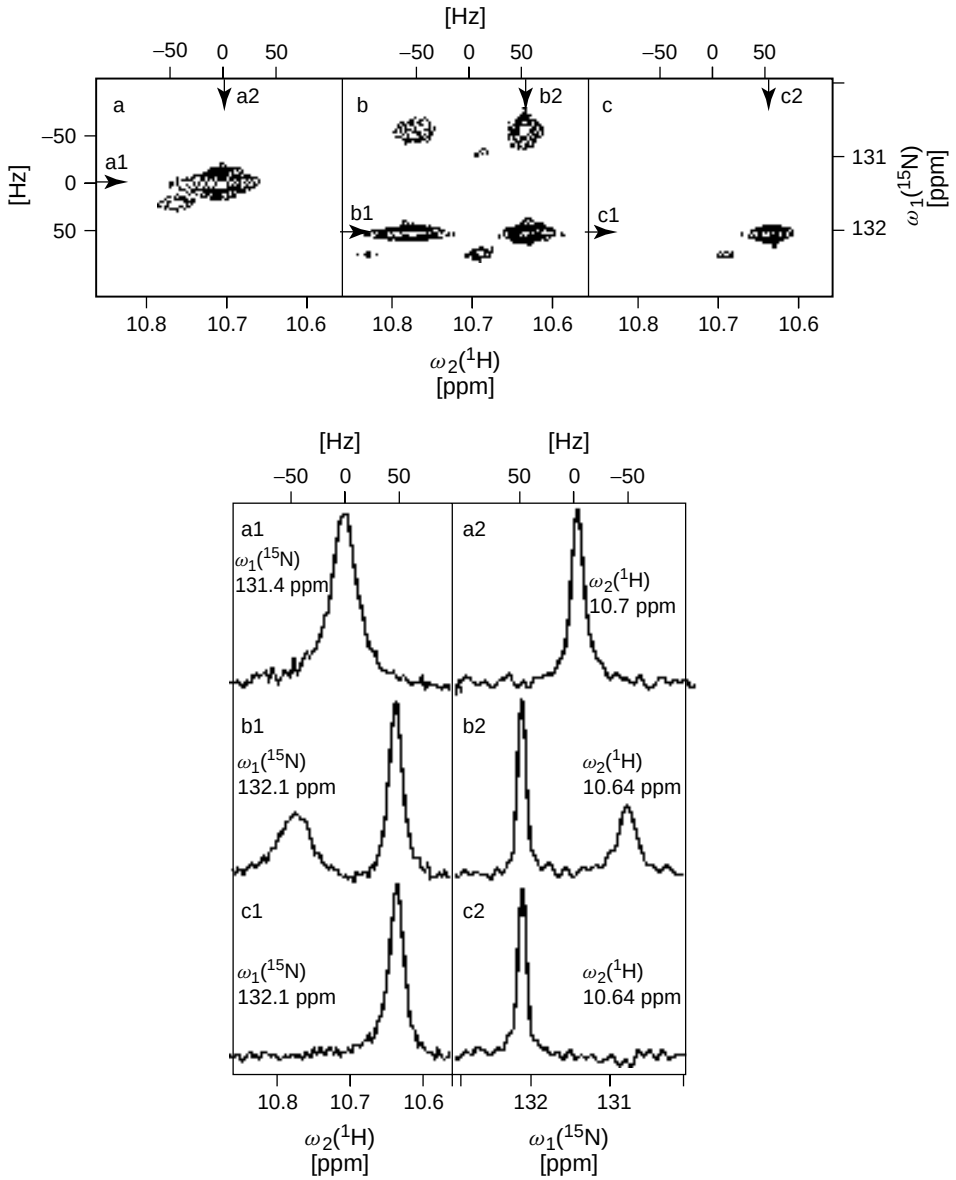

Figure 3 Contour plots and cross sections of a backbone amide $^{15}N-^{1}H$ correlation cross peak (see also Figure 1) obtained from three different types of $^{15}N-^{1}H$ correlation experiments. The data was recorded with the uniformly ^{15}N-labeled protein *fushi tarazu* homeodomain in an 18 kDa complex with unlabeled DNA, solvent 95% H_2O/5% D_2O, $T = 4\,^{\circ}C$, pH = 6.0, ^{1}H frequency = 750 MHz. (a) Conventional broad-band-decoupled [^{15}N,^{1}H]-COSY spectrum. (b) Same as (a) without decoupling during the evolution and detection periods. (c) [^{15}N,^{1}H]-TROSY recorded with the scheme of Figure 2(a). The arrows in the contour plots indicate the positions of the cross sections displayed in the bottom panels. The figure visualizes why corresponding peaks in COSY and TROSY spectra are displaced by $0.5\,^{1}J_{IS}$ (ca. 45 Hz for $^{15}N-^{1}H$) along both frequency axes. (Adapted from Ref.[10])

observation of a single correlation peak per $^{15}N-^{1}H$ moiety (Figure 3a). If the same spectrum is recorded without decoupling, a four-line fine structure is observed where the individual components have largely different linewidths (Figure 3b). Only the narrowest one of these four lines is observed in [^{15}N,^{1}H]-TROSY (Figure 3c).

The anticipated sensitivity loss due to retaining only one of the four multiplet components in [^{15}N,^{1}H]-TROSY can be largely made up by the use of new polarization transfer elements. In the scheme of Figure 2(a), the ST2-PT element is used before data acquisition, which retains 50% rather than only 25% of the original proton polarization.[12] Furthermore, in the absence of decoupling the steady-state heteronuclear magnetization can be used in addition to the proton polarization.[12,14] Overall, when working with structure sizes above 20 kDa, a superior ratio of peak height to noise is thus typically achieved with TROSY when compared with the corresponding conventional experiments (see Section 3).

3 TROSY IN NMR EXPERIMENTS WITH BIOLOGICAL MACROMOLECULES

3.1 TROSY in $^{15}N-^{1}H$ Correlation Experiments

The Figure 4(a) shows a two-dimensional [^{15}N,^{1}H]-TROSY spectrum measured with the experimental scheme

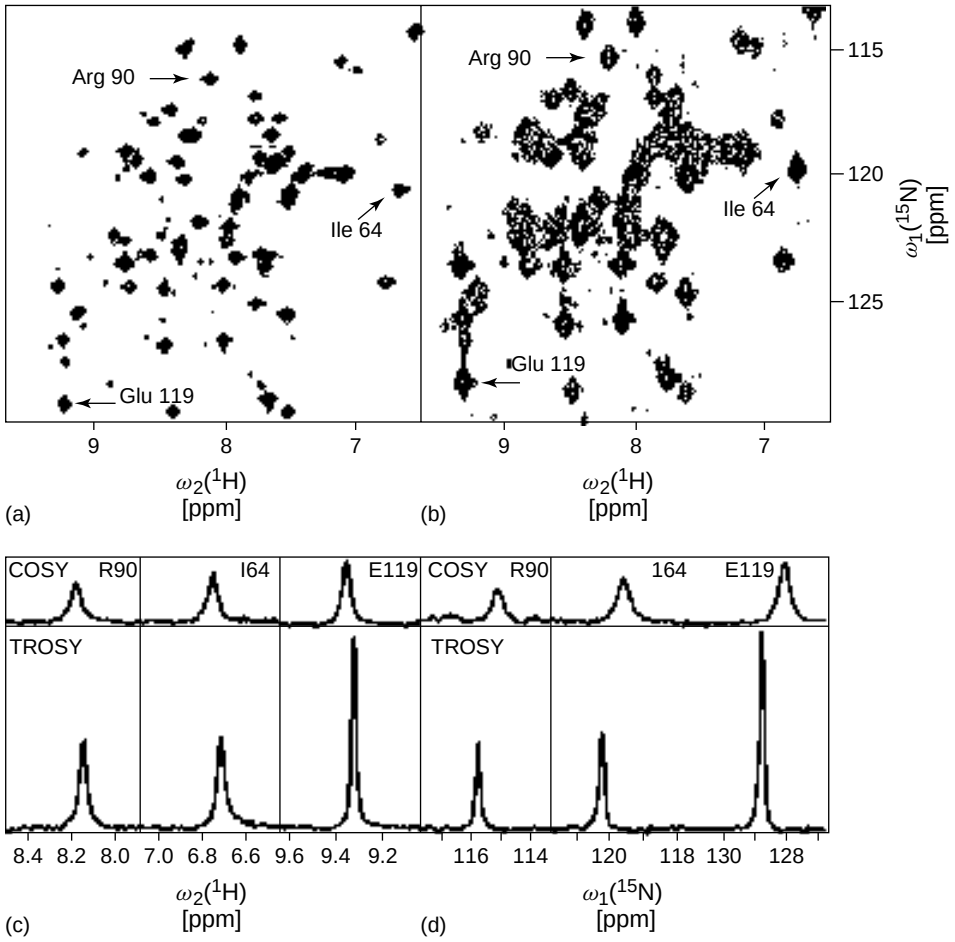

Figure 4 Comparison of conventional and TROSY-type $^{15}N-^{1}H$ correlation spectra recorded with the 110 kDa protein DHNA (same sample as in Figure 1). (a) Contour plot of [^{15}N,^{1}H]-TROSY; (b) Contour plot of single-quantum [^{15}N,^{1}H]-COSY; (c) and (d) Cross sections along $\omega_2(^1H)$ and $\omega_1(^{15}N)$, respectively, through the three peaks identified in the contour plots with an arrow, the amino acid symbol and the sequence position. In the cross sections one readily observes that corresponding peaks in [^{15}N,^{1}H]-COSY and [^{15}N,^{1}H]-TROSY spectra are displaced along both frequency axes by about 45 Hz (see Figure 3)

of Figure 2(a) for the 110 kDa homo-octameric protein DHNA (see legend to Figure 1). The gain in spectral resolution is readily apparent from comparison with the corresponding conventional two-dimensional [^{15}N,^{1}H]-COSY experiment (Figure 4b). Two-dimensional [^{15}N,^{1}H]-TROSY experiments can provide a 'fingerprint' for proteins in severalfold larger structures than with conventional NMR.[15] The $^{15}N-^{1}H$ fingerprint is highly sensitive to changes in the protein environment and thus presents a many-parameter NMR probe for studies of intermolecular interactions. For example, chemical shift mapping of the amide groups is used in SAR by NMR (SAR stands for 'structure-activity relationship'),[16] which is a screening method for high-affinity ligands of macromolecular receptors. With the use of two-dimensional [^{15}N,^{1}H]-TROSY this approach will now be applicable for much bigger receptor molecules, with molecular weights of the order of 100 kDa. Similarly, comparison of the fingerprints of individual proteins in the free state and incorporated in supramolecular structures enables the mapping of intermolecular contacts with these proteins in the higher-order structures.[17] The introduction of the TROSY technique thus opens a wide range of new applications for solution NMR, in particular also in the newly emerging field of functional genomics.

3.2 TROSY in $^{13}C-^{1}H$ Correlation Experiments

The TROSY principle is not limited to $^{15}N-^{1}H$ groups, but may be effective in a variety of multi-spin systems with cross correlated relaxation effects. As an illustration, we present here a constant-time $^{13}C-^{1}H$ correlation experiment with aromatic rings of a protein, which can also be applied with ring $^{13}C-^{1}H$ moieties of DNA and RNA. The spectrum of Figure 5 was obtained with the experiment of Figure 2(b). Since the aromatic protons have very small CSA, TROSY is used only in the ^{13}C dimension and the experiment includes decoupling during acquisition. In this constant-time experiment, TROSY does not affect the line shape but improves the sensitivity.[14] Figure 5 shows that a four- to ten-fold signal enhancement was achieved for individual resonances of the aromatic rings in an experiment with a protein of molecular weight 16 kDa, and similar signal enhancements have been obtained for RNA and DNA molecules.[18,19] For aromatic

$^{13}C-^{1}H$ groups the 'magic field' is approached near a ^{1}H frequency of 600 MHz, and applications of [^{13}C, ^{1}H]-TROSY are of interest for ^{13}C-labeled proteins and nucleic acids of all sizes.

3.3 TROSY for Observation of Scalar Couplings Across Hydrogen Bonds

Hydrogen bonds are key elements for the architecture of three-dimensional structures of proteins and nucleic acids as well as for intermolecular recognition. Their presence in biological macromolecules is usually only indirectly inferred from experimental data.[20] The improved spectral resolution achieved with TROSY now enables observation of scalar couplings across hydrogen bonds in nucleic acids as well as in proteins.[21–24] As an illustration, Figure 6 shows a [^{15}N,^{1}H]-TROSY correlation experiment recorded with high resolution along the $\omega_1(^{15}N)$ dimension for the determination of scalar couplings across hydrogen bonds in Watson-Crick base pairs. Such data can be obtained using transverse relaxation optimization during a long ^{15}N evolution period, thereby accepting low sensitivity in order to achieve high resolution along the 'indirect' heavy-atom frequency axis. The $^{h2}J_{NN}$ couplings seen in Figure 6 are in the range 3–7 Hz; for smaller couplings across hydrogen bonds, more refined observation schemes are available.[24]

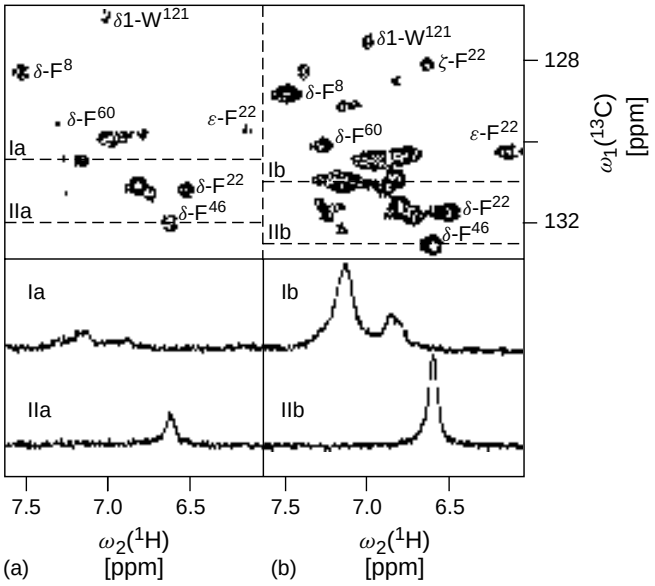

Figure 5 Comparison of two different $^{1}H-^{13}C$ correlation experiments recorded with the uniformly ^{13}C-labeled 16 kDa protein cyclophilin A. In the NMR sample the protein concentration was 1 mM, solvent D_2O, pD = 6.5, $T = 10\,^{\circ}C$, ^{1}H frequency 750 MHz. The spectral region shown contains aromatic resonances. (a) Two-dimensional ct-[^{13}C,^{1}H]-COSY; (b) Two-dimensional ct-[^{13}C,^{1}H]-TROSY, recorded using the pulse scheme of Figure 2(b). Corresponding peak positions in the spectra (a) and (b) differ by about 80 Hz along $\omega_1(^{13}C)$, as indicated by the horizontal broken lines, which also identify the locations of the cross sections along ω_2 that are shown in the bottom panels. The assignments of selected cross-peaks are indicated. (Adapted from Ref.[14])

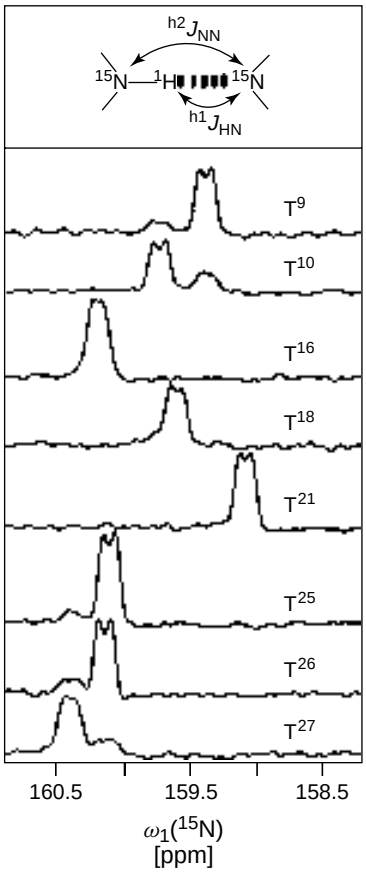

Figure 6 NMR observation of scalar $^{15}N-^{15}N$ couplings across hydrogen bonds in DNA. The definitions of the scalar couplings $^{h2}J_{NN}$ and $^{h1}J_{HN}$ in Watson-Crick base pairs are shown at the top. Cross sections were taken along the $\omega_1(^{15}N)$ dimension through the individual cross peaks of the thymine imino $^{15}N-^{1}H$ moieties in a [^{15}N,^{1}H]-TROSY spectrum of a uniformly ^{13}C,^{15}N-labeled 14-base pair DNA duplex. The splitting of the resonance lines manifests scalar couplings $^{h2}J_{NN}$ of about 6 Hz across the Watson-Crick hydrogen bonds. The nucleotides are numbered in the 5′-to-3′ direction for both strands. (Adapted from Ref.[22])

3.4 TROSY in Triple Resonance Experiments for NMR Assignments in Large Structures

The assignment of the chemical shifts to individual nuclei is indispensable as a basis for detailed studies of either molecular structure or intermolecular interactions, and most of the information contained in NMR spectra can only be extracted and exploited on the basis of individual resonance assignments.[15] Once high-quality spectra became available with TROSY, it was therefore of keen interest to develop NMR techniques that can provide resonance assignments for large proteins. Both, assignment by sequential NOEs with ^{2}H,^{15}N- or ^{15}N-labeled proteins and by triple resonance experiments with ^{2}H,^{13}C,^{15}N- or ^{13}C,^{15}N-labeled proteins appear to be amenable to this task,[9,15,25] but most of the work so far was done on the adaptation of triple resonance experiments for assignments in large molecules. In these experiments magnetization is transferred between $^{1}H^{N}$,^{15}N and ^{13}C. Without the use of TROSY they have been routinely applied with structures of size 15 to about 30 kDa.

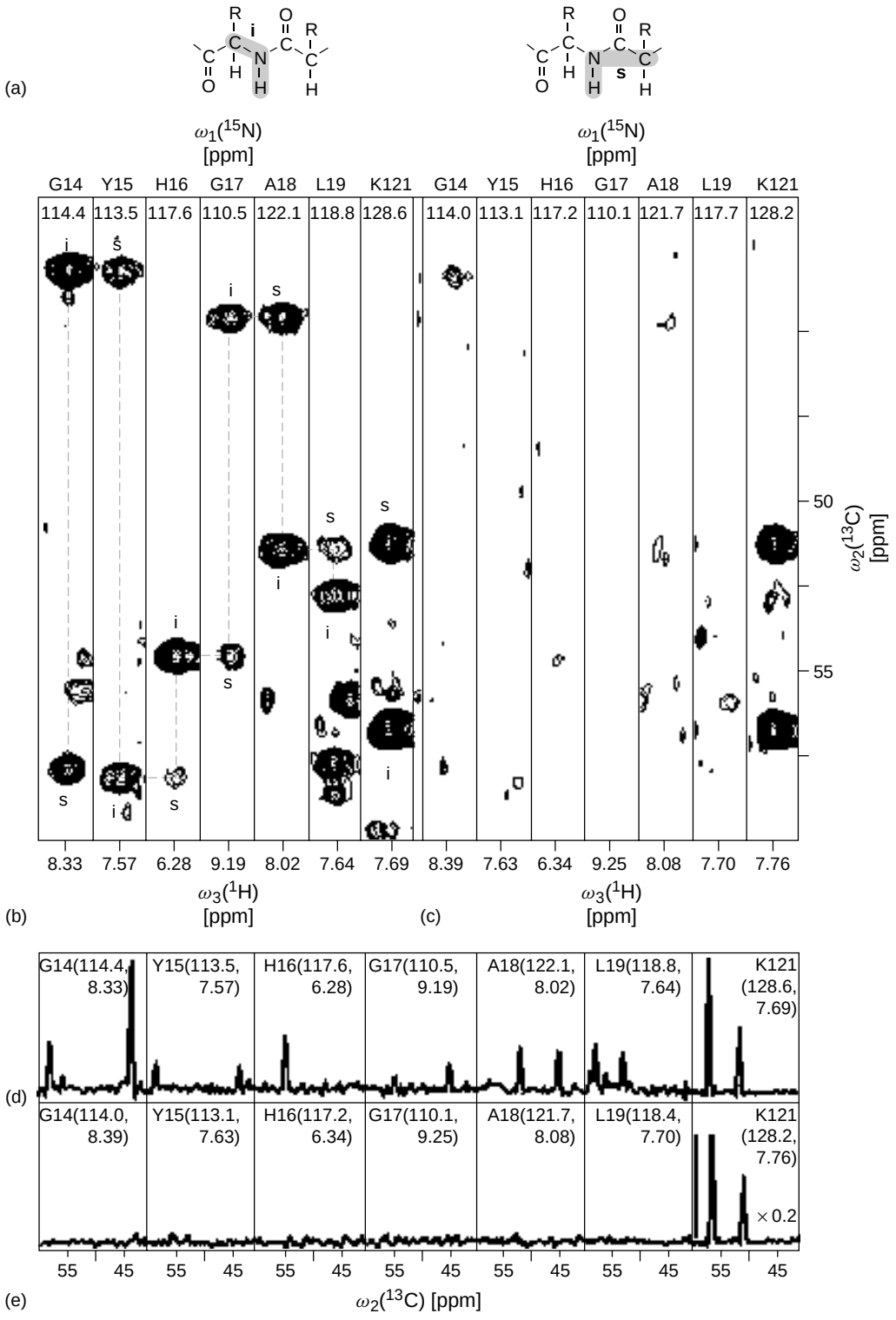

Figure 7 Impact of TROSY on the sequential resonance assignment of the polypeptide backbone in the 110 kDa protein DHNA (same sample as in Figure 1) using the HNCA triple resonance experiment of Figure 2(c). (a) The HNCA experiment correlates the ^1H and ^{15}N chemical shifts of a given amide $^{15}N-^1H$ group with the $^{13}C^{\alpha}$ chemical shifts of the same residue, i, and the preceding residue, s, as indicated here by gray shading of the intraresidual and sequential transfer pathways. (b) and (d) Three-dimensional [^{15}N,^1H]-TROSY-HNCA spectrum.[46] (c) and (e) Conventional three-dimensional HNCA spectrum. (b) and (c) show strips taken along the $\omega_2(^{13}C)$ dimension at the ^1H and ^{15}N resonance frequencies of the residue indicated at the top of the strip. The width of the strips along the ^1H-dimension is 130 Hz. (d) and (e) are one-dimensional cross sections along the $\omega_2(^{13}C)$ axis through the peaks in these strips. The dotted line in (b) indicates the sequential assignment pathway for the polypeptide segment 14–19, where the intraresidual and sequential cross peaks are identified with 'i' and 's', respectively (see (a)). The highly flexible C-terminal Lys 121 is the only residue that was observed in both spectra, and it is added here as an internal reference for this experiment (see text). (Adapted from Ref.[28])

In triple-resonance experiments with large proteins the implementation of TROSY prevents fast transverse relaxation of ^{15}N during the extended time periods with transverse ^{15}N magnetization that are needed for polarization transfers and ^{15}N evolution, and reduces the transverse ^{1}H relaxation rate during the acquisition of the amide proton signal.[26] This is illustrated here with the HNCA experiment. The magnetization transfer pathway is indicated in Figure 7(a), and an experimental scheme is shown in Figure 2(c). Since the triple resonance experiments of interest usually contain a 'constant-time evolution period' for ^{15}N,[9,27] implementation of TROSY does not affect the ^{15}N line shape but yields important gains in sensitivity, which are dependent on the size of the molecule studied. The use of TROSY in triple resonance experiments has enabled backbone assignments for proteins in large structures, such as the 110 kDa $^{2}H,^{13}C,^{15}N$-labeled octameric protein DHNA.[28] For this structure, TROSY yielded 20- to 50-fold signal enhancements for individual residues in the structured segments of the polypeptide chain, and only the highly flexible C-terminal residue Lys 121 gave comparable results with and without TROSY (Figure 7).

With TROSY-type triple resonance experiments, sequential assignments can now routinely be obtained for proteins in structures with molecular weights of 100 000 and beyond. On top of this 'basic TROSY effect' the modified triple resonance experiments can be further optimized, for example, for improved spectral resolution through the use of ^{13}C constant-time evolution,[29] or for further optimization of the sensitivity with the introduction of one of a variety of sensitivity enhancement schemes, which have in part also been used for [$^{15}N,^{1}H$]-TROSY and [$^{13}C,^{1}H$]-TROSY.[7]

4 NEW STABLE ISOTOPE LABELING STRATEGIES FOR TROSY NMR WITH LARGE STRUCTURES

With TROSY enabling the recording of high-quality solution NMR spectra of large structures, one can anticipate being faced with highly complex NMR spectra. Actually, many large systems give spectra of manageable complexity. Examples are uniformly labeled oligomeric proteins with high internal symmetry, and isotope-labeled proteins in complexes with unlabeled nucleic acids or unlabeled lipids and detergents. In contrast, uniformly labeled proteins without internal symmetry show increasing complexity of the NMR spectrum with increasing size. As a response to this challenge there are now already new biochemical approaches available for reducing the spectral complexity to a manageable level even for large proteins, using segmental isotope labeling.[30–33]

Segmental isotope labeling for protein NMR has been achieved using either transplicing or chemical ligation to assemble proteins from two or more independently generated polypeptide fragments, which are separately produced in bacteria and can thus be obtained with and without isotope labeling. The solution structure of the labeled domain can then be studied by NMR without interference from NMR lines originating from the other domains. By repetition of the NMR experiments using different protein preparations with isotope labeling of different individual domains, the intact protein can become accessible for detailed studies by TROSY-NMR, although it would, because of its large size produce overcrowded NMR spectra if uniform isotope labeling were used.

5 COMBINING TROSY WITH CROSS CORRELATED RELAXATION-INDUCED POLARIZATION TRANSFER FOR STUDIES OF VERY LARGE STRUCTURES

In the common heteronuclear NMR experiments, magnetization is transferred between the different types of nuclei via scalar spin–spin couplings, using INEPT transfers.[9,34] With TROSY being applied only during the evolution and detection periods (Figure 2), rapid transverse relaxation during the INEPT transfers becomes a limiting factor for structures with molecular weights above approximately 100–150 kDa. Cross correlated relaxation-enhanced polarization transfer (CRINEPT) overcomes this limitation by combining INEPT with cross-correlated relaxation-induced polarization transfer (CRIPT).[35,36] The transfer efficiency of CRIPT increases proportional to the size of the molecule, so that it becomes a highly efficient transfer mechanism for structure sizes above 200 kDa in aqueous solution. Compared to combining INEPT with the use of TROSY during the evolution and acquisition periods (Figure 2), substitution of INEPT by CRINEPT can thus yield a further significant gain in sensitivity when studying very large structures. In addition to the improved transfer efficiency, the combination of TROSY and CRINEPT results in an experiment with transverse relaxation optimization throughout the entire pulse sequence. In practice, CRINEPT has so far mainly been used in $^{15}N-^{1}H$-correlation experiments,[8] and high quality fingerprints have been recorded for structures with molecular weights up to 900 kDa.

6 CONCLUSIONS AND OUTLOOK

The most immediate applications of the potentialities of TROSY and CRINEPT are based on observing fingerprints of proteins in $^{15}N-^{1}H$-correlation spectra recorded for structures with mass up to 100 kDa and beyond (Figure 4), for which sequence-specific NMR assignments can be obtained (Figure 7). Practical use for studies of intermolecular interactions in supramolecular assemblies has been described,[17,37] and the way is open for acquiring structure–activity relationship data with large receptor molecules.[38] TROSY-based NOESY experiments for the collection of structural constraints should enable three-dimensional solution structure determination of proteins larger than 50 kDa,[11,39,40] if segmental labeling is also applied. An exciting immediate prospect are structure determination and further physical-chemical and functional characterization of small membrane proteins reconstituted in water-soluble detergent or lipid micelles, which may then have overall molecular weights of the order 100 kDa.[41–43] Further exploration of the potentialities of TROSY and CRINEPT will be supported by future refinement of isotope labeling techniques for proteins and nucleic acids, the use of spectrometers operating at 900 MHz and beyond, and other advances in NMR techniques.[5]

7 RELATED ARTICLE IN THIS VOLUME

Relaxation Effects Involving Cross Correlation in Biomolecules.

8 RELATED ARTICLES IN VOLUMES 1–8

Relaxation: An Introduction, Volume 6; Relaxation Mechanisms: Magnetization Modes, Volume 6; Relaxation of Coupled Spins from Rotational Diffusion, Volume 6; Relaxation Processes: Cross Correlation & Interference Terms, Volume 6; Relaxation Processes in Coupled-Spin Systems, Volume 6; Relaxation of Transverse Magnetization for Coupled Spins, Volume 6; Relaxation Theory: Density Matrix Formulation, Volume 6; Selective Relaxation Techniques in Biological NMR, Volume 7.

9 REFERENCES

1. P. Güntert, *Q. Rev. Biophys.*, 1998, **31**, 145.
2. K. Wüthrich, *Acta Cryst. D*, 1995, **51**, 249.
3. G. Wider, *BioTechniques*, 2000, **29**, 1278.
4. T. Smith ed, Structural Genomics, *Nature Struct. Biol.*, 2000, **7**, 927.
5. K. Wüthrich, *Nature Struct. Biol.*, 1998, **5**, 492.
6. G. Wider and K. Wüthrich, *Curr. Opin. Struct. Biol.*, 1999, **9**, 594.
7. K. Pervushin, *Q. Rev. Biophys.*, 2000, **33**, 161.
8. R. Riek, K. Pervushin, and K. Wüthrich, *Trends Biochem. Sci.*, 2000, **25**, 462.
9. G. Wider, *Prog. NMR Spectrosc.*, 1998, **32**, 193.
10. K. Pervushin, R. Riek, G. Wider, and K. Wüthrich, *Proc. Natl. Acad. Sci. USA*, 1997, **94**, 12 366.
11. K. Pervushin, G. Wider, R. Riek, and K. Wüthrich, *Proc. Natl. Acad. Sci. USA*, 1999, **96**, 9607.
12. K. Pervushin, G. Wider, and K. Wüthrich, *J. Biomol. NMR*, 1998, **12**, 345.
13. G. Bodenhausen and D. J. Ruben, *Chem. Phys. Lett.*, 1980, **69**, 185.
14. K. Pervushin, R. Riek, G. Wider, and K. Wüthrich, *J. Am. Chem. Soc.*, 1998, **120**, 6394.
15. K. Wüthrich, 'NMR of Proteins and Nucleic Acids', Wiley: New York, 1986.
16. S. B. Shuker, P. J. Hajduk, R. P. Meadows, and S. W. Fesik, *Science*, 1996, **274**, 1531.
17. M. Pellecchia, P. Sebbel, U. Hermanns, K. Wüthrich, and R. Glockshuber, *Nature Struct. Biol.*, 1999, **6**, 336.
18. B. Brutscher, J. Boisbouvier, A. Pardi, D. Marion, and J. P. Simorre, *J. Am. Chem. Soc.*, 1998, **120**, 11 845.
19. R. Fiala, J. Czernek, and V. Sklenár, *J. Biomol. NMR*, 2000, **16**, 291.
20. G. A. Jeffrey and W. Saenger, 'Hydrogen Bonding in Biological Structures', Springer: Berlin, 1991.
21. A. J. Dingley and S. Grzesiek, *J. Am. Chem. Soc.*, 1998, **120**, 8293.
22. K. Pervushin, A. Ono, C. Fernandéz, T. Szyperski, M. Kainosho, and K. Wüthrich, *Proc. Natl. Acad. Sci. USA*, 1998, **95**, 14 147.
23. F. Cordier and S. Grzesiek, *J. Am. Chem. Soc.*, 1999, **121**, 1601.
24. Y. X. Wang, J. Jacob, F. Cordier, P. Wingfield, S. J. Stahl, S. Lee-Huang, D. Torchia, S. Grzesiek, and A. Bax, *J. Biomol. NMR*, 1999, **14**, 181.
25. L. E. Kay and K. H. Gardner, *Curr. Opin. Struct. Biol.*, 1997, **7**, 722.
26. M. Salzmann, G. Wider, K. Pervushin, H. Senn, and K. Wüthrich, *J. Am. Chem. Soc.*, 1999, **121**, 844.
27. A. Bax and S. Grzesiek, *Acc. Chem. Res.*, 1993, **26**, 131.
28. M. Salzmann, K. Pervushin, G. Wider, H. Senn, and K. Wüthrich, *J. Am. Chem. Soc.*, 2000, **122**, 7543.
29. M. Salzmann, K. Pervushin, G. Wider, H. Senn, and K. Wüthrich, *J. Biomol. NMR*, 1999, **14**, 85.
30. T. Yamazaki, T. Otomo, N. Oda, K. Kyogoku, K. Uegaki, N. Ito, Y. Ishino, and H. Nakamura, *J. Am. Chem. Soc.*, 1998, **120**, 5591.
31. T. W. Muir, D. Sondhi, and P. A. Cole, *Proc. Natl. Acad. Sci. USA*, 1998, **95**, 6705.
32. T. Otomo, K. Teruya, K. Uegaki, T. Yamazaki, and Y. Kyogoku, *J. Biol. NMR*, 1999, **14**, 105.
33. R. Xu, B. Ayers, D. Cowburn, and T. W. Muir, *Proc. Natl. Acad. Sci. USA*, 1999, **96**, 388.
34. G. A. Morris and R. Freeman, *J. Am. Chem. Soc.*, 1979, **101**, 760.
35. R. Riek, G. Wider, K. Pervushin, and K. Wüthrich, *Proc. Natl. Acad. Sci. USA*, 1999, **96**, 4918.
36. M. Goldman, *J. Magn. Reson.*, 1984, **60**, 437.
37. H. Takahashi, T. Nakanishi, K. Kami, Y. Arata, and I. Shimada, *Nature Struct. Biol.*, 2000, **7**, 220.
38. M. Pellecchia, D. S. Sim, and K. Wüthrich, *Nature Rev. Drug Disc.*, 2002, **4**, 211.
39. G. Zhu, X. M. Kong, and K. H. Sze, *J. Biomol. NMR*, 1999, **13**, 77.
40. A. Meissner and O. W. Sørensen, *J. Magn. Reson.*, 2000, **142**, 195.
41. C. Fernandéz, K. Adeishvili, and K. Wüthrich, *Proc. Natl. Acad. Sci. USA*, 2001, **98**, 2358.
42. C. Fernandéz, C. Hilty, S. Bonjour, K. Adeishvili, K. Pervushin, and K. Wüthrich, *FEBS Lett.*, 2001, **504**, 173.
43. A. Arora, F. Abildgaard, J. H. Bushweller, and L. Tamm, *Nature Struct. Biol.*, 2001, **8**, 334.
44. C. Hennig, A. Arcy, I. Hampele, M. G. P. Page, C. Oefner, and G. E. Dale, *Nature Struct. Biol.*, 1998, **5**, 357.
45. M. Salzmann, G. Wider, K. Pervushin, and K. Wüthrich, *J. Biomol. NMR*, 1999, **15**, 181.
46. M. Salzmann, K. Pervushin, G. Wider, H. Senn, and K. Wüthrich, *Proc. Natl. Acad. Sci. USA*, 1998, **95**, 13 585.

Acknowledgements

Financial support was obtained from the Schweizerischer Nationalfonds (Project 31.49047.96).

Biographical Sketches

Kurt Wüthrich, *b* 1938. Licentiat, 1962, Physics, Mathematics, Chemistry, University of Bern. Eidgenössisches Sportlehrerdiplom, 1964, University of Basel. PhD, 1964, Inorganic Chemistry (Prof. S. Fallab), University of Basel. Postdoctoral work University of Basel (Prof. S. Fallab), University of California, Berkeley, CA (Prof. R.E. Connick), Bell Telephone Laboratories, Murray Hill, NJ (Dr. R.G. Shulman). Since 1969 at ETH Zurich, currently Professor of Biophysics. Since 2001 Cecil H. and Ida M. Green Visiting Professor of Structural Biology, The Scripps Research Institute, La Jolla, CA. 3 monographs and 600 publications. Research specialities: NMR structure determination of biological macromolecules, structural biology, structural genomics.

Gerhard Wider, *b* 1952. Diploma, 1978, Physics, ETH Zürich. PhD, 1982, natural sciences (Prof. K. Wüthrich), ETH Zürich. NMR application and development, BRUKER Switzerland 1982–84. General Manager, BRUKER Australia 1984–86, NMR Product Manager, BRUKER Switzerland 1987–88. Since 1988 ETH Zurich. Habilitation, 1998, Biophysics. 90 publications. Research interests: NMR with biological macromolecules. Technical aspects of NMR spectroscopy.

Biosynthesis and Metabolic Pathways: Carbon-13 and Nitrogen-15 NMR

Ursula Mocek
Panlabs, Bothell, WA, USA

Heinz G. Floss
University of Washington, Seattle, WA, USA

1	Introduction	1
2	Labeling with ^{13}C	1
3	Labeling with ^{15}N	4
4	References	5

1 INTRODUCTION

The use of precursors labeled with stable isotopes, especially ^{13}C and ^{15}N, in biosynthetic feeding experiments with subsequent analysis of the biosynthesized compounds by high-field NMR spectroscopy has become one of the most powerful tools for studying natural product biosynthesis. The NMR method provides information about the location or distribution of the isotope in the metabolite and, by analysis of homonuclear or heteronuclear coupling patterns, can reveal information about metabolic pathways or the nature of bond-forming reactions.

An important prerequisite for the use of NMR in biosynthesis studies is the unequivocal assignment of all proton, carbon, and nitrogen resonances in the target molecule. After recording ^{1}H and broadband proton-decoupled ^{13}C NMR spectra, the most common 2D NMR techniques employed are: COSY[1] (to determine all proton–proton correlations); DEPT[2] (to determine the multiplicity of carbon atoms or nitrogen atoms); HETCOR[3] and HMQC[4] (to determine which protons are attached to specific carbons or nitrogens); COLOC[5] and HMBC[6] (to determine long-range couplings to assign quaternary carbons or nitrogens and correlations between different partial structures which are essential to assemble the molecule). The advent of inverse detection techniques such as HMQC and HMBC has greatly facilitated the assignment of ^{15}N resonances.

2 LABELING WITH ^{13}C

2.1 Singly Labeled Precursors

Carbon-13 NMR spectroscopy was first reported in the 1950s and applied to biosynthetic studies almost two decades later. In the early days, ^{1}H NMR was used to detect the $^{1}H–^{13}C$ coupling due to the isotopically enriched carbon nuclei, a method which usually did not give information about quaternary carbons and was therefore limited in its application. The disadvantages of ^{13}C NMR, low natural abundance (1.1%) and a small magnetogyric ratio ($\gamma = 6.72 \times 10^{7}$), resulting in low sensitivity (^{13}C resonances are about 6000 times less sensitive than ^{1}H resonances), were overcome by advances in instrumentation, especially the development of the pulse Fourier transform technique, which increased the sensitivity dramatically.[7]

Feeding a precursor with a single ^{13}C label allows the fate of the labeled atom to be traced through a metabolic sequence. In the ^{13}C NMR spectrum of the product, the enrichment is indicated by an increased intensity of the signal(s) corresponding to the atom or atoms that arise from the labeled atom of the precursor. Comparing integrals of singlets with integrals of multiplets which result with and without decoupling, respectively, is not a precise method. To allow a fairly accurate assessment of the incorporation, the ^{13}C NMR spectra of the unlabeled material and the biosynthesized product are normally acquired in the proton-decoupled, inverse-gated mode in order to obtain the decoupled signals without the NOE. Integration of the enriched signals in comparison to other signals in the spectrum and to the signal of the nonlabeled material correlates to the percentage of incorporation of the precursor into the product. Enrichments should be at least 0.5% ^{13}C above natural abundance to be unequivocally detectable. In cases of very high incorporation, the natural abundance signal will be small compared with the enriched signal, and for quantification purposes the rate of incorporation will be determined more precisely by integration of the ^{13}C satellites in the ^{1}H NMR spectrum. If the precursor is incorporated into multiple sites of the metabolite, either a carbon which does not derive from this precursor has to be chosen as a reference carbon or it is necessary to introduce an unlabeled carbon by derivatization.

The literature is replete with studies using this approach of feeding precursors carrying single ^{13}C labels. Particularly numerous are studies on the biosynthesis of various polyketide-derived natural products, as exemplified by the dimeric benzoisochromanquinone, actinorhodin (Figure 1).[8] In this case, the labeling experiment also established the point of dimerization: the two carbon atoms 10 and 10′, which appear as quaternary carbons, not the methine carbons 9 and 9′, are derived from the methyl group of acetate.

In some experiments with whole cells, a precursor may not be incorporated due to its inability to penetrate the cell membrane. This is often the case with carboxylic acids, such as malonic acid or shikimic acid. Sometimes the problem can be overcome by feeding a derivative which can be cleaved inside the cell, e.g. diethyl malonate instead of the free acid.

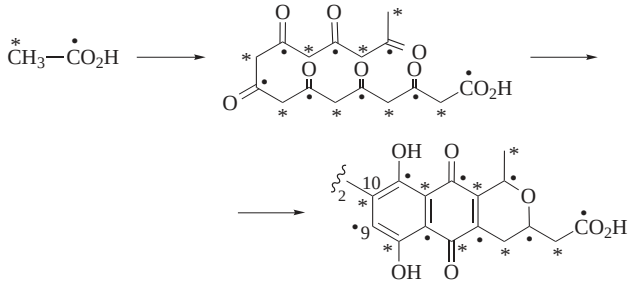

Figure 1 Biosynthesis of actinorhodin

In other cases where a precursor does not penetrate to the site of synthesis, evidence for its involvement may be attained indirectly. An example is the biosynthesis of the antibiotic asukamycin,[9] where ^{13}C-labeled shikimic acid gave only very poor incorporation. However, feeding a more general precursor such as [U-$^{13}C_3$]glycerol resulted in the expected shikimate-type labeling pattern for the isolated asukamycin. The ^{13}C NMR spectrum showed the presence of two doubly coupled spin systems (C-7′/C-8′/C-9′, C-11′/C-12′/C-13′) and a single, enriched, noncoupled signal for C-10′, indicating that all seven carbon atoms of this moiety derive directly from shikimate, not via aromatic amino acids. In other instances of impermeability of cell membranes to specific precursors, e.g. phosphate esters, information may only become available from in vivo studies with cell-free systems or purified enzymes where the precursor will always be able to reach the site of synthesis. Many studies in carbohydrate metabolism fall into this category. For example, the definitive proof for a rearrangement of ribulose 5-phosphate into a tetrulose 4-phosphate in riboflavin biosynthesis[10] required the use of various ^{13}C-labeled ribulose 5-phosphates in a cell-free system from the riboflavin producer *Candida guilliermondii*.

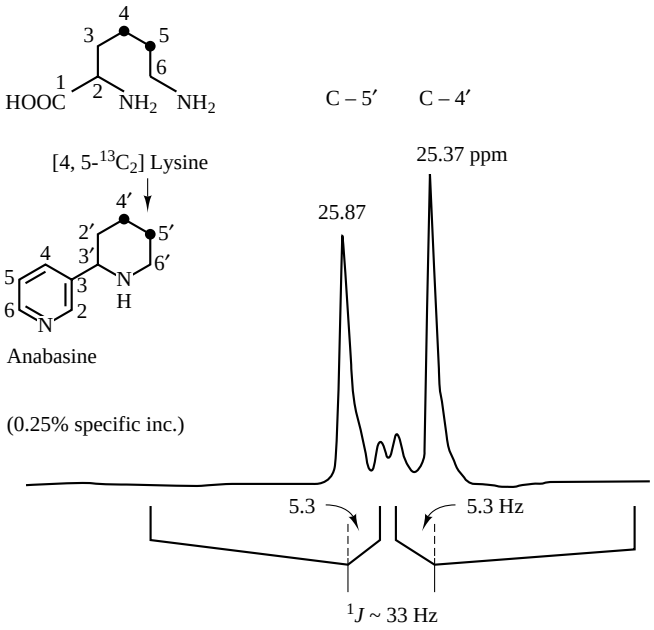

Figure 2 Detail of the ^{13}C NMR spectrum of anabasine derived from [4,5-$^{13}C_2$]lysine at the enriched C-4′ and C-5′ positions

2.2 Multiply ^{13}C-Labeled Precursors

In contrast to experiments with singly labeled precursors where the fate of atoms is explored, in the case of multiply labeled precursors the fate of bonds can be followed through a metabolic reaction sequence. If the doubly labeled precursor in which the ^{13}C atoms are adjacent is incorporated intact, the ^{13}C NMR signal of each labeled carbon atom is split into a doublet due to coupling to the neighboring ^{13}C atom. Since one-bond carbon–carbon couplings are much larger (−20 to 200 Hz) than two- or three-bond couplings (0–16 Hz), adjacent labeled carbon atoms are easy to detect in the ^{13}C NMR spectra. The administered precursor is diluted with unlabeled material which is either formed in the biological system from unlabeled nutrients or is added externally together with the labeled sample. If the bond between the two enriched carbons is broken during the metabolic conversion, the stable isotope at each terminus will be diluted with a large amount of ^{12}C. Thus the probability of reconnecting two ^{13}C nuclei in the same molecule again becomes very low. If the coupling is retained in the product, the two nuclei must have originated from the same molecule, therefore suggesting that the bond between them has never been broken.

A major advantage of this approach is the increase of detection sensitivity in cases of low incorporation, a common problem in higher plants. The reason is that intact incorporation of the precursor now gives rise to new signals, the coupled satellites, rather than a small increase in existing natural abundance signals. This was neatly demonstrated in the biosynthesis of the alkaloid anabasine from [4,5-$^{13}C_2$]lysine in *Nicotiana glauca* (Figure 2).[11] The resulting anabasine showed the presence of contiguous ^{13}C atoms at C-4′ and C-5′. The coupled carbons have very similar chemical shifts (δ 25.87 and 25.37) and therefore only the inner satellites [J(C-4′,C-5′) = 33 Hz] could be observed. The specific incorporation was calculated from the intensities of these inner satellites as 0.25%.

The bond-labeling approach is used extensively to evaluate the mode of incorporation of precursors into more complex products, for example the way a polyketide chain folds to cyclize into a polycyclic aromatic system. The pioneering study demonstrating the utility of this approach was carried out by Seto and co-workers,[12] and followed the incorporation of [1,2-^{13}C]acetate into the polyketide mollisin, a metabolite of *Mollisia caesia*. The intact incorporation of six pairs of carbons from acetate allowed the authors to derive a pathway other than the two which were originally proposed. A limitation in the application of this methodology to more complex precursors is the labor and cost involved in the synthesis of the requisite labeled compounds, if they are not commercially available. Bond labeling is also widely used in combinations of ^{13}C with other nuclei to probe for intact incorporation of ^{13}C–^{18}O or ^{13}C–^{2}H bonds (i.e. for retention of these heteroatoms on the carbon framework), but detailed discussions of this topic would go beyond the scope of this article.

Multiple labeling can also be used to probe for the occurrence of rearrangement reactions in which new carbon–carbon connectivities are established, and whether such reactions are intra- or intermolecular. A rearrangement of tryptophan was postulated to account for the formation of an unusual indolic acid moiety in the biosynthesis of the thiopeptide antibiotic nosiheptide (Figure 3).[13] In the proposed reaction the carboxyl group of tryptophan would be connected to C-2 of the indole ring, while the α-carbon and the amino group of the tryptophan side chain are removed and the methylene carbon is converted into a methyl group. This was probed by preparing and feeding [*carboxyl,indole*-2-$^{13}C_2$]tryptophan. The ^{13}C NMR spectrum of the resulting nosiheptide showed a one-bond coupling of 75.5 Hz between the Ind–CO and Ind–C-2 resonances, proving that this unusual rearrangement of tryptophan does take place and that it is a strictly intramolecular process.

Figure 3 Formation of the indolic acid moiety of nosiheptide from tryptophan

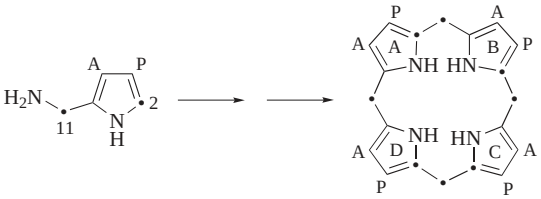

Figure 4 Incorporation of [2,11-$^{13}C_2$]porphobilinogen into uroporphyrinogen-III

A classic example of multiple labeling, in this case in nonadjacent positions, to probe for a rearrangement reaction can be found in porphyrin biosynthesis. [2,11-$^{13}C_2$]Porphobilinogen (one part labeled and four parts unlabeled material to ensure dilution) was converted with an enzyme preparation into uroporphyrinogen-III.[14] The ^{13}C NMR spectrum revealed the unique labeling and coupling pattern shown in Figure 4, proving that the enzyme assembles four intact units of porphobilinogen, but inverts one of these units to generate the type III substitution pattern.

Uniformly ^{13}C-labeled precursors such as glucose or glycerol are useful for mapping unknown metabolic pathways. Detailed analysis of the resulting $^{13}C-^{13}C$ coupling patterns can reveal which major metabolic pathways provide the various components of the product molecule. The complexity of these coupling patterns necessitated the development of techniques such as ^{13}C COSY and double quantum coherence NMR (e.g. 2D INADEQUATE). The ^{13}C COSY technique was employed in a biosynthetic study of the *Klebsiella* K3 serotype polysaccharide using [U-$^{13}C_6$]glucose as a precursor.[15] Due to the appearance of additional multiplets within the cross peaks, ^{13}C COSY spectra are quite different from ^{1}H COSY spectra. The observed cross peaks are a combination of superimposed responses from molecules with different patterns of ^{13}C labeling. These additional peak components are attributable to substrate catabolism which results in ^{13}C loss at various sites. It was shown that the major biosynthetic pathway for polysaccharide formation proceeds via intact incorporation of the hexose unit into the polysaccharide and that 30% of the glucose substrate is catabolized prior to incorporation into the polysaccharide, almost exclusively via the phosphogluconate pathway.

In the case of the antibiotic reductiomycin[16] the question was whether one part of the molecule was derived from a shikimate pathway. The broadband decoupled ^{13}C NMR spectrum of the antibiotic labeled from [U-$^{13}C_3$]glycerol indicated extensive enrichment and coupling throughout the molecule. A doubly coupled assembly of three carbon atoms (C-3″/C-4′/C-5′) indicated intact incorporation of a glycerol unit. However, the C-4′ signal displayed an eight line pattern

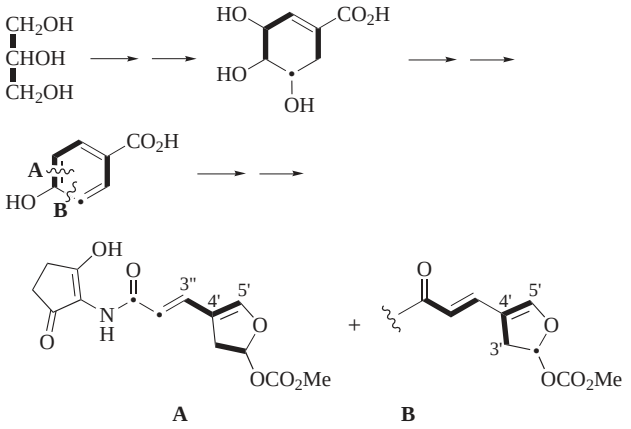

Figure 5 Labeling and $^{13}C-^{13}C$ coupling pattern in the dihydrofuranylacrylic acid moiety of reductiomycin from [U-$^{13}C_3$]glycerol

instead of the expected four lines, implying the presence of another coupled two- or three-bond system involving C-3′. A 2D INADEQUATE experiment clearly revealed that C-3′ was coupled to both C-2′ and C-4′ with a coincident coupling of 41 Hz. In the contour projection, C-4′ again showed an eight-line pattern, which would be expected for a superimposition of two arrays of three coupled carbons. The two possible arrangements of an intact three-carbon unit involving C-3′ and C-4′ were distinguished by spectral simulation with the Bruker PANIC program that calculated an excellent match for the superimposition of a C-3″/C-4′/C-5′ and C-3′/C-4′/C-5′ coupling pattern (Figure 5), pointing to formation from shikimate via a symmetrical intermediate.

Use of [U-$^{13}C_3$]glycerol (or [U-$^{13}C_3$]glucose) as a biosynthetic probe can result in very complex coupling patterns due to intact incorporation with coupling of all three involved carbon signals, intact incorporation of two of the three glycerol carbons or of only one of the labeled carbons. This scenario with doubly and singly coupled patterns will create difficulties in data interpretation, especially in larger molecules. A 2D INADEQUATE experiment identifying the doubly coupled species will not separate them from singly coupled patterns. By using a triple quantum version of a 2D INADEQUATE experiment,[17] it is possible to observe selectively doubly coupled species in the presence of singly coupled species and determine their molecular connectivities. This was demonstrated in the biosynthesis of acarbose, an inhibitor of α-glucosidases. A strong signal indicated the presence of a contiguous array of three ^{13}C nuclei representing C-6, C-1, and C-2 of the valienamine moiety.

Inverse detection of ^{13}C multiple quantum coherence in biosynthetic studies[18] was demonstrated for the first time in the biosynthesis of cycloheptanecarboxylic acid from [U-$^{13}C_6$]glucose in *Bacillus cycloheptanicus*. Cycloheptanecarboxylic acid serves as the starter unit to which five acetate units are added in the formation of ω-cycloheptyl fatty acids. Double and triple quantum INADEQUATE experiments were unsuccessful due to low sample concentrations. Glucose labels, as expected, the 10 chain carbons and also the cycloheptane ring with intact two- and four-carbon units. The four-carbon unit appears to be derived from a three- and a one-carbon unit of glucose (i.e., erythrose) and has a C_2 axis of symmetry. The coupling pattern pointed to an aromatic amino acid,

phenylalanine, as the proximate precursor. This inverse technique provides higher sensitivity because it uses fewer pulses and is therefore less susceptible to instrumental imperfections.

3 LABELING WITH ^{15}N

3.1 Direct Detection

Until recently, ^{15}N NMR was limited in its applications due to the low natural abundance of ^{15}N (0.37%). Its sensitivity is 0.2% compared with ^{1}H NMR and it requires longer relaxation times than ^{13}C NMR. Its negative magnetogyric ratio causes negative NOE and can consequently decrease or null out signals. Therefore, ^{15}N NMR spectra are usually acquired in the inverse-gated mode, which consumes more instrument time. Additionally, the ^{15}N chemical shifts are often very solvent-dependent. Nevertheless, there are numerous examples where direct detection of ^{15}N has been applied in biosynthetic studies of secondary metabolites[19] and in biological systems.[20]

Nitrogen-15 NMR spectroscopy has been used to study the conversion of L-lysine to D-lysine by *Neurospora crassa*.[21] Analysis by mass spectrometry had shown that the ^{15}N label from L-[2-^{15}N]lysine was lost, whereas the ^{15}N label from L-[6-^{15}N]lysine had been retained. The ^{15}N NMR spectrum of D-lysine from the latter experiment revealed that the label wasattached to C-2, suggesting that L-pipecolic acid is an intermediate in the conversion (Figure 6).

In a recent study, the origin of specific nitrogens in the highly modified peptide antibiotic nosiheptide (Figure 7) was investigated by ^{15}N NMR.[22] Assignment of the ^{15}N signals to the 13 nitrogens in the molecule was accomplished by HMQC[4] and HMBC[6] techniques. Comparative analysis of samples enriched by feeding $^{15}NH_4Cl$, [^{15}N]glycine, and [^{15}N]glycine plus unlabeled serine revealed that the carboxy-terminal amide nitrogen in the antibiotic is derived specifically from another molecule of serine, whose carbon skeleton is removed in the process.

3.2 Indirect Detection of ^{15}N

Indirect detection of ^{15}N by ^{13}C NMR spectroscopy relies on the observation of carbon signals coupled to ^{15}N. Generally, one-, two-, and three-bond couplings are observed. Due to the negative magnetogyric ratio, the ^{3}J and most of the ^{1}J values are negative. In contrast to $^{13}C-^{1}H$ coupling constants, the $^{13}C-^{15}N$ two-bond coupling can be larger than the one-bond coupling.[23] The coupling constants vary depending on the structure and are difficult to predict. Tables with numerous examples are given in the literature.[23]

Various precursors containing ^{13}C and ^{15}N adjacent to each other, for example, [2-^{13}C,^{15}N]amino acids, have been incorporated into different metabolites with the $^{13}C-^{15}N$ bond intact. In the biosynthesis of the potent anticancer agent streptonigrin,[24] it was shown that tryptophan is the precursor of the phenylpicolinic acid moiety (Figure 8). The first step is presumably the conversion to a β-carboline undergoing hydroxylation and ring cleavage. The site of ring cleavage was determined by feeding [2-^{13}C,1-^{15}N]tryptophan to *Streptomyces flocculus* and analyzing the ^{13}C NMR spectrum of the isolated streptonigrin. The spin-coupled doublet flanking the C-5 natural abundance singlet clearly proved that the original indole nitrogen had been retained and that an unprecedented bond cleavage had occurred. Another interesting example is the formation of the isonitrile function in the biosynthesis of hapalindole A,[25] the major isonitrile in the terrestrial cyanophyte *Hapalosiphon fontinalis*. In the natural abundance ^{13}C NMR spectrum of hapalindole A, the isonitrile carbon signal is split into a broad triplet [J(^{13}C,^{14}N) = 4 Hz]. The ^{13}C NMR spectrum of the material resulting

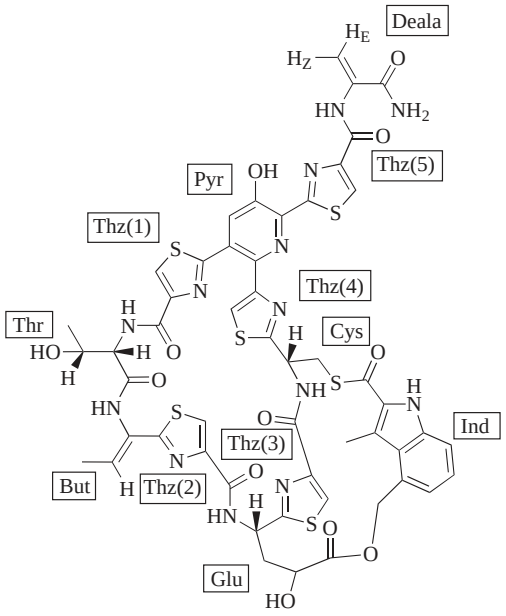

Figure 7 Structure of nosiheptide

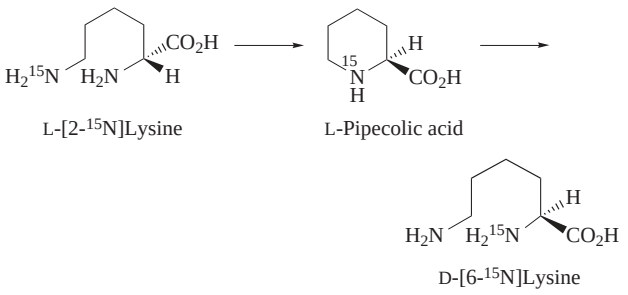

Figure 6 Interconversion of L- and D-lysine via L-pipecolic acid

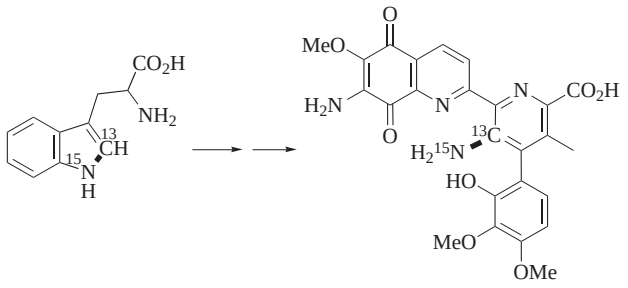

Figure 8 Biosynthesis of streptonigrin from [2-^{13}C,1-^{15}N]tryptophan

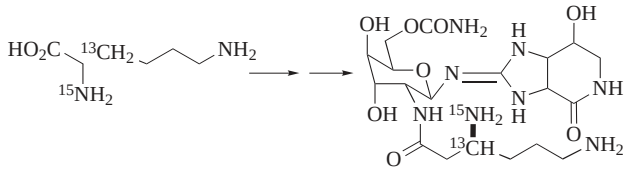

Figure 9 1,2 migration of an amino group of lysine in the biosynthesis of streptothricin F

from feeding [2-^{13}C,^{15}N]glycine showed a 100% enhancement of the isonitrile carbon signal at δ 157.9 (1% incorporation) and a sharp doublet [J(^{13}C,^{15}N) = 6 Hz] superimposed onto the broad triplet. Therefore, the C-2–N assembly of glycine is incorporated intact into the isonitrile group, without significant loss of ^{15}N label due to transamination of the glycine prior to isonitrile formation.

As with multiple ^{13}C labeling, precursors carrying ^{13}C and ^{15}N in nonadjacent positions can be used to probe the nature of rearrangement reaction, by looking for the formation of a ^{13}C–^{15}N bond in the product. An example for a 1,2 migration of a ^{15}N label is found in the biosynthesis of streptothricin F.[26] [3-^{13}C,^{15}N]Lysine was fed to *Streptomyces* L-1689-23; the ^{13}C NMR spectrum of the resulting antibiotic exhibited a doublet [J(CN) = 3.4 Hz] for C-16, proving that the original α-amino nitrogen had been retained but that it had migrated to C-3 in an intramolecular process (Figure 9).

4 REFERENCES

1. A. Bax and R. Freeman, *J. Magn. Reson.*, 1981, **44**, 542.
2. D. M. Doddrell, D. T. Pegg, and M. R. Bendall, *J. Magn. Reson.*, 1982, **48**, 323.
3. G. Bodenhausen and R. Freeman, *J. Am. Chem. Soc.*, 1978, **100**, 320.
4. A. Bax and S. Subramanian, *J. Magn. Reson.*, 1986, **67**, 565.
5. H. Kessler, C. Griesinger, J. Zarbock, and H. R. Loosli, *J. Magn. Reson.*, 1984, **57**, 331.
6. A. Bax and M. F. Summers, *J. Am. Chem. Soc.*, 1986, **108**, 2093.
7. R. R. Ernst and W. A. Anderson, *Rev. Sci. Instrum.*, 1966, **37**, 93.
8. C. P. Gorst-Allman, B. A. M. Rudd, C.-j. Chang, and H. G. Floss, *J. Org. Chem.*, 1981, **46**, 455.
9. R. Thiericke, A. Zeeck, A. Nakagawa, S. Omura, R. E. Herrold, S. T. S. Wu, J. M. Beale, and H. G. Floss, *J. Am. Chem. Soc.*, 1990, **112**, 3979.
10. P. Nielsen, G. Neuberger, I. Fujii, D. H. Bown, P. J. Keller, H. G. Floss, and A. Bacher, *J. Biol. Chem.*, 1986, **261**, 3661.
11. E. Leete, *J. Nat. Prod.*, 1982, **45**, 197.
12. H. Seto, L. W. Cary, and M. Tanabe, *J. Chem. Soc. Chem. Commun.*, **1973**, 867.
13. D. R. Houck, L.-C. Chen, P. J. Keller, J. M. Beale, and H. G. Floss, *J. Am. Chem. Soc.*, 1988, **110**, 5800.
14. A. R. Battersby, E. Hunt, and E. McDonald, *J. Chem. Soc., Chem. Commun.*, **1973**, 442.
15. D. N. M. Jones and J. K. M. Sanders, *J. Am. Chem. Soc.*, 1989, **111**, 5132.
16. H. Cho, J. M. Beale, C. Graff, U. Mocek, A. Nakagawa, S. Omura, and H. G. Floss, *J. Am. Chem. Soc.*, 1993, **115**, 12296.
17. J. M. Beale, C. E. Cottrell, P. J. Keller, and H. G. Floss *J. Magn. Reson.*, 1987, **72**, 574.
18. T. K. Pratum and B. S. Moore, *J. Magn. Reson., Series B*, 1993, **102**, 91.
19. M. Witanowski, L. Stefaniak, and G. A. Webb, *Annu. Rep. NMR Spectrosc.*, **1992**, 25.
20. K. Kanamori and J. D. Roberts, *Acc. Chem. Res.*, 1983, **16**, 35.
21. N. Fangmeier and E. Leistner, *J. Biol. Chem.*, 1980, **255**, 10205.
22. U. Mocek, A. R. Knaggs, R. Tsuchiya, T. Nguyen, J. M. Beale, and H. G. Floss, *J. Am. Chem. Soc.*, 1993, **115**, 7557.
23. G. C. Levy and R. L. Lichter, *Nitrogen-15 Nuclear Magnetic Resonance Spectroscopy*, Wiley, New York, 1979.
24. S. J. Gould, C. C. Chang, D. S. Darling, J. D. Roberts, and M. Squillacote, *J. Am. Chem. Soc.*, 1980, **102**, 1707.
25. V. Bornemann, G. M. L. Patterson, and R. E. Moore, *J. Am. Chem. Soc.*, 1988, **110**, 2339.
26. S. J. Gould and T. K. Thiruvengadam, *J. Am. Chem. Soc.*, 1981, **103**, 6752.

Biographical Sketches

Ursula Mocek. *b* 1956. B.S., 1978, M.S., 1982, Ph.D., 1985, University of Bonn, Germany. Postdoctoral work at The Ohio State University, Columbus (with Heinz G. Floss). Research Faculty, 1988–1993, University of Washington, Seattle. Currently Project Manager, Panlabs, Inc. Research specialty: biosynthetic studies of natural products, biological NMR.

Heinz G. Floss. *b* 1934. B.S., 1956, M.S., 1959, Technical University Berlin, Germany, Ph.D., in Organic Chemistry (1961) Technical University Munich, Germany. Postdoctoral work at UC Davis with Eric E. Conn in Biochemistry (1964–1965). Faculty, Department of Medicinal Chemistry and Pharmacognosy, Purdue University, 1966–1982 (Department Head 1968–1969, 1974–1979), Department of Chemistry, The Ohio State University, 1982–1987 (Department Chair 1982–1986), Department of Chemistry, University of Washington, Seattle, 1988 to present. Research interests: biosynthesis of natural products, stereochemistry of enzyme reactions.

Biosynthesis and Metabolic Pathways: Deuterium NMR

James Staunton and Helen C. Hailes
University of Cambridge, UK

1	Introduction	1
2	Mechanistic Studies	1
3	Precursor–Product Relationships	3
4	Conclusions	3
5	Related Articles	4
6	References	4

1 INTRODUCTION

Many investigations of biosynthetic pathways rely on tracing the fate of one or more particular hydrogen atoms in a precursor when it is transformed into the final metabolite.[1] The approach is especially useful when investigating alternative pathways where one necessarily involves loss of a key hydrogen atom whereas the other allows its retention. More generally, labeling with a hydrogen isotope can also be used to demonstrate the incorporation of complete structural fragments of a precursor as long as the isotope is attached via a bond which is unlikely to be broken in the course of the proposed biosynthetic transformations.

Both isotopes of hydrogen, deuterium and tritium, have been used in this way, but deuterium has proved to be by far the more popular choice. The isotope can be detected in the final metabolite directly by mass spectrometry or ^{2}H NMR or indirectly by the diminution of a proton signal in the ^{1}H NMR spectrum. The most effective method is unquestionably direct observation of the isotope by ^{2}H NMR.

Deuterium is a quadrupole nucleus with spin 1. As a consequence of the low magnetogyric ratio (0.154), deuterium resonates at 61 MHz in a magnetic field of 9.4 T compared with 400 MHz for ^{1}H. The chemical shift values observed in ^{2}H NMR spectra are closely similar to those of the equivalent protons, although the scale (in hertz) is only 15% that of the ^{1}H NMR spectra. Coupling constants $J(^2\text{H},^1\text{H})$ also approximate to one-sixth the value of $J(^1\text{H},^1\text{H})$. The close correspondence of ^{1}H and ^{2}H NMR spectra is invaluable for biosynthetic studies, because assignments made using ^{1}H NMR techniques on unlabeled material can be extrapolated into the ^{2}H NMR spectrum.

The relaxation behavior of deuterium is dominated by a quadrupolar mechanism and this results in extensive line broadening. This effect combined with the limited dispersion means that ^{2}H NMR spectra are characterized by spectral crowding and poor resolution. Relaxation times are short, however, which, combined with the absence of a NOE effect, minimizes the possibility of partial saturation. This factor insures that the extent of enrichment in a partially deuterated molecule may be determined accurately by integration. Other advantages of using ^{2}H NMR in biosynthetic study are firstly, that the isotope is an inexpensive tracer which, unlike tritium, is nonradioactive and does not require special handling; and, secondly, that the low natural abundance (0.016% compared with 1.1% for ^{13}C) enables the incorporation of deuterium-labeled precursors to be positively identified (by a doubling in peak height over natural abundance) even after 6600-fold dilution of the precursor in the metabolic pool.

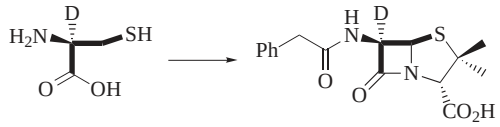

(1) **(2)**

Scheme 1

2 MECHANISTIC STUDIES

In a pioneering study in which L-[1-^{2}H]cystine (**1**) was fed to the mold *Penicillium chrysogenum* it was shown by ^{2}H NMR that all of the isotopic label incorporated was present at C-6 of the derived penicillin G (**2**).[2] An α,β-dehydrocysteine residue could thus be discounted as an intermediate in the biosynthetic transformations which lead from (**1**) to (**2**). This work provides a striking demonstration of the mechanistic use of deuterium labeling in that the positive incorporation rules out obligatory loss of the isotopic label at one of the steps in the biosynthetic pathway.

Another early study provided detailed mechanistic and stereochemical insights into the processes of griseofulvin (**3**) biosynthesis.[3] The metabolite is biosynthesized by the head-to-tail linkage of seven acetate units, as indicated in Scheme 2. Following incorporation of CD_3CO_2H, four of the seven methyl derived sites, (3, 3′, 5′, and 7) gave rise to signals in the ^{2}H NMR spectrom (the rest had been stripped of their hydrogen atoms). Significantly, only one of the two hydrogen atoms at C-5′ was labeled (the α-position) showing that the second hydrogen atom was not derived from the CD_3 group of the precursor. The ^{2}H NMR spectrum also showed weak signals from two O−Me groups, indicating that some of the deuterium of the acetate precursor had ‘leaked’ through incidental pathways of primary metabolism to enter the *O*-methyl groups. This study demonstrates a key advantage of

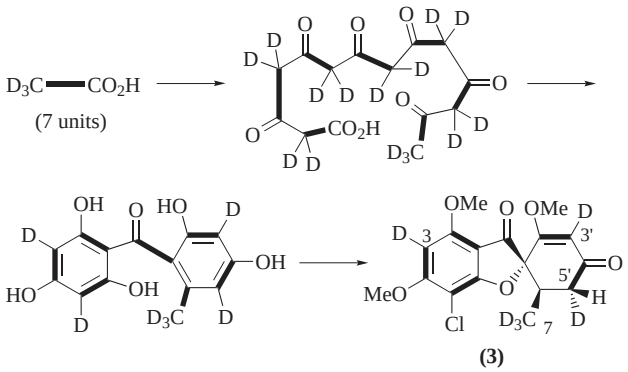

(3)

Scheme 2

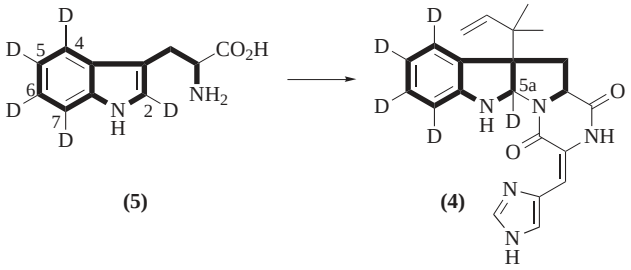

(5) **(4)**

Scheme 3

^{2}H NMR over mass spectrometry as an analytical technique in biosynthetic studies. ^{2}H NMR not only shows that deuterium is present in a nondestructive way, it also gives information as to how the isotope is distributed over the different labeled sites in the molecule. The observation of deuterium in the *O*-methyl groups emphasizes the need for caution in interpreting the results of deuterium isotopic incorporation studies. In a more recent example of a mechanistic study it was shown that H-5a of roquefortine (**4**) is derived from H-2 of tryptophan (**5**) (Scheme 3).[4] The precursor was administered in multiply-labeled form with deuterium at all four sites in the carbocyclic ring as well as at the key site H-2 (the extra four deuterium atoms serve as an internal standard). An enriched M + 5 ion in the mass spectrum of the resulting metabolite established that all five deuterium atoms were retained. The ^{2}H NMR spectrum showed five enriched signals corresponding to the presence of deuterium at the indicated sites. The signal for deuterium at position 5a was well resolved even in the ^{2}H NMR spectrum, so the incorporation of deuterium at that site was established unambiguously. It is worth noting here that an earlier investigation using ^{1}H NMR to detect incorporation of ^{2}H at C-5a had failed to establish this point.

^{2}H NMR has also been used as an analytical tool for investigating biosynthetic pathways in plants, where dilution of the isotopic label is usually a more serious problem than in microorganisms. In one of many successful applications of the technique, the labeling patterns in (−)-anagurine (**7**) derived biosynthetically from (*R*)- and (*S*)-[1-^{2}H]cadaverines, (**5**) and (**6**) respectively, were established (Scheme 4).[5] A point of interest in this investigation was the danger of incorrectly assigning the enriched peaks in the metabolite because of the variability in the chemical shift depending on sample conditions. This was overcome by running the ^{1}H NMR spectrum as a control on each sample analysed by means of ^{2}H NMR.

In the same investigation the patterns of incorporation of (**5**) and (**6**) into the related alkaloid (+)-sparteine (**8**) were also established by using ^{2}H NMR. The close correspondence of the labeling patterns for (**7**) and (**8**) produced in these experiments (with the notable exception of C-6) supports the idea that (**7**) might be derived biosynthetically via (**8**). If so, the piperidone ring of (**7**) is likely to derive from ring D of (**8**). However, the epimerization at C-6 in this overall conversion without loss of deuterium presents a puzzling problem.

In an earlier study, the incorporation of (**5**) and (**6**) into (**9**), the enantiomer of (**8**), was also investigated by using ^{2}H NMR.[6] Once again the complete labeling pattern could be assigned. Comparison of (**8**) and (**9**) reveals that rings A and D have the same stereochemical labeling pattern, but that the

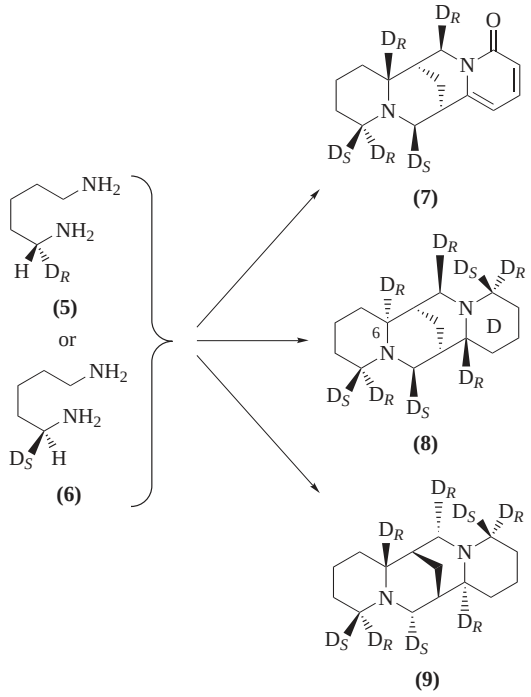

Scheme 4

labels associated with the two central rings are opposite in configuration at equivalent sites. These results demonstrate the power of ^{2}H NMR spectroscopy for elucidating the stereochemistry as well as the sites of deuterium incorporation. Further examples of elegant mechanistic studies can be found in related studies of lupinine biosynthesis.[7]

The literature is rich in examples of the use of ^{2}H NMR to study mechanistic aspects of the biosynthesis of terpenes. Two examples are presented here, both of which were pioneering studies which excited great interest by demonstrating the power of this approach.

When the deuterated mevalonate (**10**) was incorporated into the microbial terpene ovalicin (**11**), five deuterium atoms were detected by ^{2}H NMR.[8] The observed labeling pattern considerably narrowed the range of possible biosynthetic pathways.

In a subsequent study, chirally labeled mevalonates (**12**) and (**13**) were incorporated into the fungal terpene rosenonolactone (**14**) (Scheme 6).[9] The ^{2}H NMR spectrum revealed that the two hydrogen atoms of the vinyl group in (**14**) are specifically derived from those at C-4 of mevalonate with the pro-(*R*) and pro-(*S*) hydrogen atoms destined to become (*Z*) and (*E*) hydrogen atoms, respectively. This evidence allowed

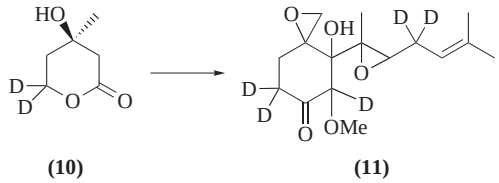

(10) **(11)**

Scheme 5

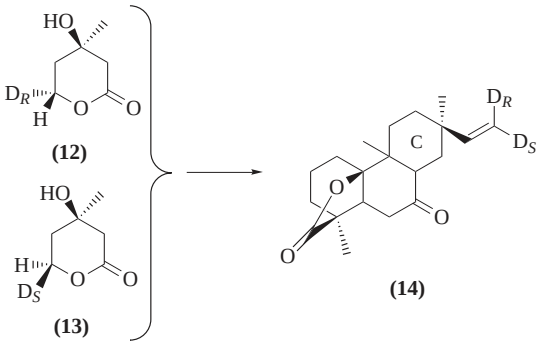

Scheme 6

deductions to be made concerning the stereochemistry of the cyclization process in which ring C of the natural product is formed.

3 PRECURSOR–PRODUCT RELATIONSHIPS

The incorporation of advanced precursors has also been studied by ^{2}H NMR spectroscopy. In many such cases the aim is to use the ^{2}H label to trace the structure of the administered precursor as a whole, rather than probe the mechanism or stereochemistry of reactions involving hydrogen atoms at particular sites. There is then a greater choice of site of labeling, which is often dictated by the ease of synthesis of the precursor or the ease and reliability of determining the site of labeling in the product. As far as the latter point is concerned, signals arising from predicted sites of incorporation should be well resolved in the ^{2}H NMR spectrum.

In a recent example of this type of experiment the advanced precursor (**15**) was synthesized specifically labeled by deuterium (Scheme 7).[10] Its specific incorporation into colletodiol (**16**) was established by ^{2}H NMR of the metabolite which showed a single enriched peak corresponding to the expected position C-4. No other deuterium-enriched peaks were observed, showing that biodegradation of the labeled precursor to produce other acceptable labeled precursors had not occurred to a significant extent. The site of label in this study was dictated mainly by synthetic considerations.

A second example involved a study of the biosynthesis of the ionophore antibiotic tetronasin (**18**) (Scheme 8).[11] Here the precursor (**17**) was labeled in separate experiments by deuterium at two alternative methyl groups as indicated. The acyl group (C-10) destined to be incorporated was derivatized

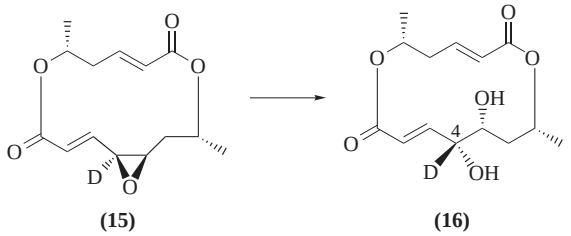

Scheme 7

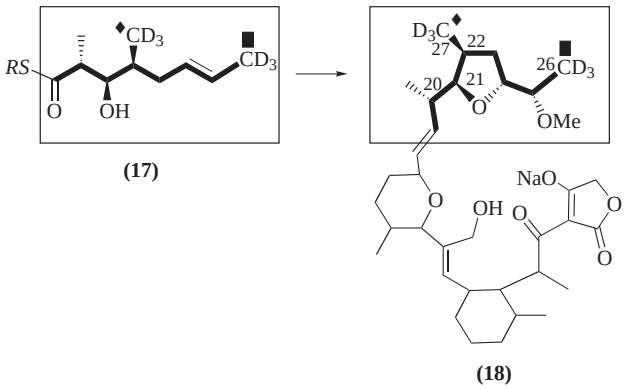

Scheme 8

as a thioester to aid incorporation. The acyl chain of (**17**) is readily degraded by the organism to produce smaller labeled building blocks (CD_3 labeled acetate or propionate) acceptable to the biosynthetic pathway. Initially, degradation was the dominant fate of the precursor, and this resulted in the production of metabolite multiply labeled at many sites, a situation which was readily detected by ^{2}H NMR. Subsequently, conditions were found under which specific incorporation of the intact C-10 acyl residue occurred to give specifically labeled metabolite. The two labeled forms of (**17**) were fed in separate experiments to produce differently labeled forms of metabolite. From the positions of the ^{2}H NMR signals in the spectra of the metabolite it was evident that the two labeled methyl groups were specifically incorporated at the predicted sites confirming intact incorporation of the acyl residue. The choice of site of labeling in this study was dictated partly by NMR considerations (the signal for the CD_3 groups at C-26 and C-27 are completely resolved), but once again synthetic considerations were important. It will be apparent that the configurations at C-20, C-21, and C-22 of (**18**) match those of the equivalent sites of the precursor. Other labeled diastereoisomers of (**17**) were tested, but none resulted in a specific incorporation, showing that the stereochemistry of the precursor is retained.

4 CONCLUSIONS

The examples presented in this account represent but a small fraction of the successful applications of ^{2}H NMR in biosynthetic studies. Even when the efficiency of incorporation is very low, satisfactory spectra on the resulting labeled metabolite can be acquired by extending the acquisition time. Good resolution is vital, as is sensitivity. The advent of higher powered instruments has helped in both respects and ^{2}H NMR spectroscopy is now one of the main techniques of biosynthetic study. As molecules increase in size, however, lines become relatively broader, and it has been reported that the technique was unsuitable on this account in a study of corrin biosynthesis.[12] It is advisable to check this point by running the natural abundance ^{2}H NMR spectrum of the metabolite, before embarking on extended incorporation studies with labeled compounds.

5 RELATED ARTICLES

Bilayer Membranes: Deuterium and Carbon-13 NMR; Biosynthesis and Metabolic Pathways: Carbon-13 and Nitrogen-15 NMR; Carbon-13 Studies of Deuterium Labeled Compounds; Isotope Effects on Chemical Shifts and Coupling Constants; Nucleic Acid Flexibility and Dynamics: Deuterium NMR; Membranes: Deuterium NMR; Oxygen-18 in Biological NMR

6 REFERENCES

1. For general biosynthesis reviews which include the use of ^{2}H NMR, see: (a) M. J. Garson and J. Staunton, *Chem. Soc. Rev.*, 1979, **8**, 539; (b) T. J. Simpson, *Chem. Soc. Rev.*, 1987, **16**, 123; (c) T. J. Simpson, *Modern Methods of Plant Analysis*, eds. H. F. Linskens and J. F. Jackson, Springer-Verlag, Berlin, 1986, Vol. 2, p. 1; (d) C. Abell, *Modern Methods of Plant Analysis*, eds. H. F. Linskens and J. F. Jackson, Springer-Verlag, Berlin, 1986, Vol. 2, p. 60
2. B. W. Bycroft, C. M. Wels, K. Corbett, and D. A. Lowe, *J. Chem. Soc., Chem. Commun.*, **1975**, 123.
3. Y. Sato, T. Oda, and H. Saitô, *Tetrahedron Lett.*, **1976**, 2695.
4. B. Bhat, D. M. Harrison, and H. M. Lamont, *J. Chem. Soc., Chem. Commun.*, **1990**, 1518.
5. A. M. Brown, D. S. Rycroft, and D. J. Robins, *J. Chem. Soc. Perkin Trans. 1*, **1991**, 2353.
6. A. M. Fraser and D. J. Robins, *J. Chem. Soc. Perkin Trans. 1*, **1987**, 105.
7. W. M. Golebiewski and I. D. Spenser, *Can. J. Chem.*, 1985, **63**, 2707.
8. D. E. Cane and S. L. Buchwald, *J. Am. Chem. Soc.*, 1977, **99**, 6132.
9. D. E. Cane and P. P. N. Murthy, *J. Am. Chem. Soc.*, 1977, **99**, 8327.
10. J. A. O'Neill, T. J. Simpson, and C. L. Willis, *J. Chem. Soc., Chem. Commun.*, **1993**, 738.
11. H. C. Hailes, S. Handa, P. F. Leadlay, I. C. Lennon, S. V. Ley, and J. Staunton, *Tetrahedron Lett.*, 1994, **35**, 311.
12. A. R. Battersby, C. Edington, C. J. R. Fookes, and J. H. Hook, *J. Chem. Soc., Chem. Commun.*, **1982**, 181.

Biographical Sketches

J. Staunton. *b* 1935. B.Sc., 1956, Ph.D., 1959, Liverpool. Postdoctoral (with C. Djerassi), Stanford University, 1959–61. Lecturer at Liverpool University, 1962–69. Appointed lecturer at Cambridge University 1969; current post, Reader. Publications cover many aspects of bioorganic chemistry, including organic synthesis, NMR and MS methodology, elucidation of biosynthetic pathways, structure and function of biocatalytic proteins.

H. C. Hailes. *b* 1965. B.A., 1987, Ph.D., 1991, Cambridge. Postdoctoral at Imperial College, London, 1992–1994. Appointed lecturer at University College London 1994. Research interests include total synthesis of natural products, elucidation of biosynthetic pathways, new synthetic methods.

Biological Macromolecules: NMR Parameters

Oleg Jardetzky and Tais H. Schmitt
Stanford University, CA, USA

1	Introduction	1
2	NMR Parameters	1
3	Averaging of NMR Parameters—Fast Exchange	9
4	Related Articles	11
5	References	11

1 INTRODUCTION

The parameters measurable in NMR spectra—chemical shifts, coupling constants, relaxation times and the nuclear Overhauser effect (NOE)—reflect faithfully, though in ways that are not always easy to decipher, the electric and magnetic forces acting in the environment of the observed nucleus, and hence the structure and dynamics of this environment. In the words of John Wertz, author of the first review of chemical applications of NMR in 1955: 'Atomic nuclei act as spies sending out radio signals reporting on the properties of their environment.'[1] If the nucleus is part of only a single atom or a simple small molecule, a simple and rigorous physical theory will account for the magnitude of each of the parameters measured. As the complexity of the system—in essence the number of neighbors in close proximity—increases, so does the number of contributions that are reflected in each parameter. The theory, though still applicable in principle, loses its rigor. It is not possible to measure each of the contributions individually, but only their sum. Nor is it possible to compute the interactions between all neighbors precisely, because of their large number. For systems as large and complex as biological macromolecules, the interpretation of NMR parameters in terms of their structure and dynamics rests on qualitative—at best, semiquantitative—arguments. The fact that it is nevertheless possible to extract an enormous amount of structural and dynamic information from the NMR spectra of macromolecules reflects the wealth of empirical findings obtained over the past 40 years. These have shown that certain structural and dynamic features of a macromolecule exert a very pronounced effect on the NMR parameters of nuclei embedded in it that can be interpreted, even if not measured exactly. To cite but a few examples, chemical shifts are known to change as a peptide segment forms a helix, coupling constants change if the rotation of a backbone or side chain is restricted, and relaxation parameters reflect distances to nearby nuclei. The theoretician, faced with the hopeless task of disentangling the sum of dozens of components whose individual magnitudes cannot be measured, has thus been helped by the experimentalist. As the number of empirical correlations multiplies, an increasingly precise interpretation of NMR parameters in terms of macromolecular structure and dynamics becomes possible.

The purpose of this article is to summarize the information content of NMR parameters as measured on macromolecules. The text of this section is a condensation and update of the more extensive treatment given in Chapters I, II and IV of Jardetzky and Roberts, 'NMR in Molecular Biology'.[2] To be found elsewhere in this work are the elementary theory of the parameters and details of empirical correlations that have been established. Suffice it to say here that: the mechanism of the chemical shift arises from the polarization of the electron cloud around each nucleus by the external magnetic field of the spectrometer. This causes the electron cloud to generate an opposing magnetic field, thus 'shielding' the nucleus. The magnitude of the chemical shift depends on the density and symmetry of the electronic charge surrounding the nucleus. This in turn depends in the first instance on the distribution of chemical bonds in the molecule, and in the second on the polarization of the electron charges comprising the bonds by surrounding electric and magnetic fields originating both in the molecule and in the surrounding solvent. The physical principle of spin–spin coupling is fundamentally the same, except that the polarizing field in this case arises from a neighboring magnetic nucleus connected to the observed nucleus by the electron cloud of one or more chemical bonds. Since the external field depends on the experimenter, whereas the field of a neighboring nucleus does not, one will find that the chemical shift depends on the imposed external field, i.e. on the spectrometer frequency, but spin–spin coupling does not. On the other hand, spin–spin coupling will depend on the orientation of the polarizing nuclei with respect to the external field—splitting the observed line into two or more components that correspond to different orientations in the external field.

The most important physical mechanism of relaxation in macromolecules is direct through-space magnetic coupling between two nuclear magnets. In this case, better quantitative interpretation is possible than in the case of chemical shifts, coupling constants and of relaxation parameters dominated by chemical shift anisotropy or quadrupolar coupling. This is due to the fact that the theory of pure magnetic coupling between permanent nuclear magnets is simpler than it is for coupling that involves polarizable electronic structures.

2 NMR PARAMETERS

2.1 Chemical Shift

The range of chemical shifts observed in biological macromolecules is roughly the same as that observed for small molecules. The experimentally found ranges for nuclei of biological interest are shown in Figure 1. The chemical shift between two resonance lines is directly proportional to the observing spectrometer frequency. To correct for this known dependence, shifts, δ, are generally given in parts per million (ppm) relative to a spectral line chosen as a standard and calculated from the formula:

$$\delta = \frac{\nu - \nu_0}{\nu_0} \times 10^6 \qquad (1)$$

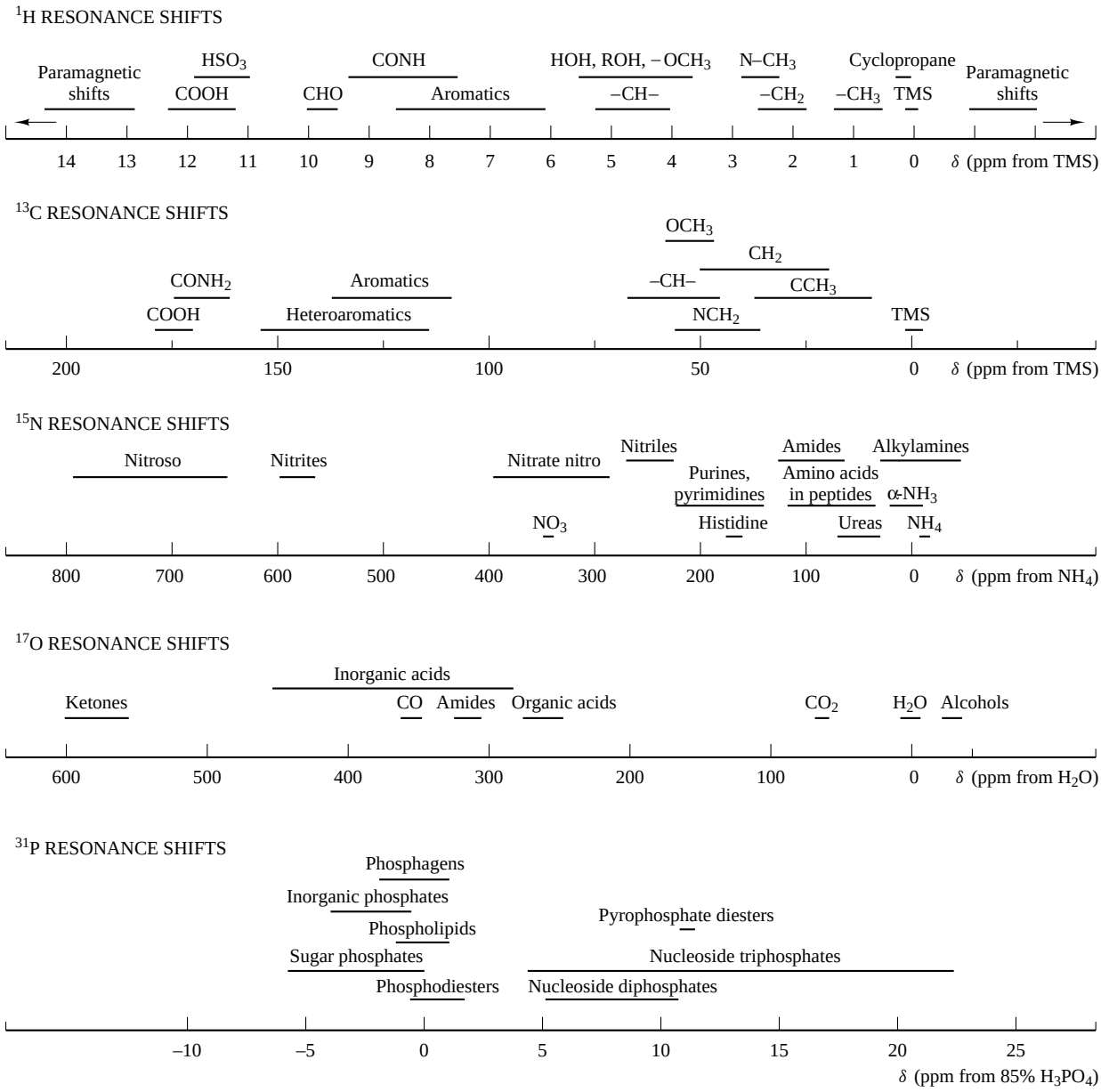

Figure 1 Ranges of chemical shifts for ^{1}H, ^{13}C, ^{15}N, ^{17}O and ^{31}P. (From Jardetzky and Roberts[2])

where ν and ν_0 are the frequencies of the shifted and the standard reference spectral lines, respectively; ν_0 is effectively the spectrometer frequency. Normalization to the observing frequency makes it possible to compare directly shifts observed at different frequencies and to evaluate the shift as a characteristic of the molecule, independent of the conditions of observation.

The foregoing definition of δ applies only to the averaged chemical shift observable in solution. Within the molecular framework, the chemical shift cannot be described by a single number, because the distribution of electrons around each nucleus is not spherically symmetric (except for isolated atoms), and the magnitude of the shift will depend on the orientation of the molecule with respect to the external magnetic field. This is clearly demonstrable by NMR experiments on molecules oriented in the solid state. In general, the chemical shift must be represented by a second-order tensor (nine numbers), but it is usually sufficient to describe it as a first-order tensor:

$$|\delta| = \begin{vmatrix} \delta_{xx} & \delta_{xy} & \delta_{xz} \\ \delta_{yx} & \delta_{yy} & \delta_{yz} \\ \delta_{zx} & \delta_{zy} & \delta_{zz} \end{vmatrix} \qquad (2)$$

where δ is the shielding constant. Only in the case of completely isotropic tumbling does one observe the single value averaged to spherical symmetry by isotropic molecular motion. When interpreting shifts on biological macromolecules it is therefore very important to ascertain the adequacy of averaging for each system under study. Some macromolecules—especially the rod-like nucleic acids—may

orient in the external magnetic field, in which case the component of the chemical shift tensor aligned with the observing radiofrequency field will largely be seen.

Examination of Figure 1 reveals the well-established general pattern of ^{1}H and ^{13}C chemical shifts. Taking amino acids as examples, methyl proton resonances appear at lowest frequency (0.8–1.6 ppm), followed by methylene protons (1.1–4.1 ppm), α-CH protons (3.0–4.5 ppm), and aromatic protons (6.9–8.8 ppm). A similar pattern can be seen for ^{13}C: methyl carbon atoms (10–30 ppm), methylene (30–60 ppm), and α-carbon atoms (50–70 ppm) resonating at progressively higher frequency, followed by aromatic carbon atoms (120–140 ppm), the guanidino carbon atom of arginine (150 ppm), and carboxyl carbon atoms (160–180 ppm). Within each of these broad categories, the effects of substituent electronegativity on the chemical shifts can be clearly discerned. For example, the hydroxyl substituent in serine shifts both the ^{13}C and ^{1}H resonances of the β-CH group to higher frequency. In threonine and alanine the methyl proton resonances are shifted to significantly higher frequency of those of valine, leucine, and isoleucine due to the electronegative substituents on C-β and C-α, respectively, while in lysine and arginine the methylene group attached to nitrogen in the side chain also has its ^{1}H and ^{13}C resonances shifted to higher frequency.

A useful distinction can be made between the *intrinsic* chemical shift, which depends only on the properties of the covalent molecular structure surrounding the nucleus, and the *extrinsic* or environmental chemical shift, comprising contributions arising from surroundings that are not part of the immediate covalent structure. The distinction is clear-cut for small molecules, where the electronic structure of the molecule determines the former and properties of the solvent determine the latter. In macromolecules the distinction is slightly blurred, since environments within a folded structure are generated by neighbors whose covalent connection to the observed nucleus is through a long chain of bonds. The distinction nevertheless remains useful, especially for purposes of calculation, since it distinguishes between effects that are transmitted through the intervening chemical bonds from those transmitted through space. The structural chemical shifts observed in folded proteins are for the most part extrinsic. Three kinds of structural chemical shift have been empirically shown to be of diagnostic value in structural studies of biological macromolecules: (1) the stacking shifts, (2) the secondary structure shifts, and (3) tertiary folding shifts. Stacking shifts are observed when groups are placed in the vicinity of aromatic rings—typically two nucleic acid bases or two phenylalanine rings stacked in parallel, or a methyl group placed in the structure above a tryptophan ring. The highly anisotropic aromatic or heterocyclic rings generate strong, anisotropic magnetic fields when placed into an external field. Generally, nuclei placed in the plane of the ring experience a high frequency shift, whereas those placed above or below the plane of the ring experience a low frequency shift. These shifts can be quite large (up to 3–4 ppm) and the stacking shift is the main reflection of helical structure in nucleic acids. Typical secondary structure shifts in proteins have first been observed for the α-CH groups of amino acids and are smaller (on average, +0.4 ppm to low frequency for α-helices and −0.3 ppm to high frequency for β-strands).[3] Tertiary structure shifts generally (including stacking shifts for proteins) reflect the environment created by the folding of a protein chain and vary in the range 0.2–4 ppm. Their magnitude and direction depend on a variety of factors—all of which reflect proximity in space of charges, polar groups, hydrophobic groups, double bonds, etc.

The systematic analysis of chemical shifts in proteins and nucleic acids, especially of the structural shifts, is a difficult and incompletely solved theoretical problem. At the same time, the existence of structural shifts and a qualitative understanding of their nature is the basis for all structural and dynamic studies of proteins and nucleic acids by NMR. If structural shifts did not exist, chemically equivalent amino acid residues in a protein could not be distinguished, assignment of separate spectral lines to residues in different parts of the structure would not be possible, and neither would be the determination of three-dimensional structures and detailed studies of their behavior.

The fact that the spectrum of a folded protein depends on the nature of the folding was first conclusively demonstrated in the years 1964–1968 by comparisons of the spectra of native and denatured proteins, as well as of helical and random coil amino acid homopolymers.[4–6] The equivalent modern experiment illustrating this fundamental finding is shown in Figure 2. The magnitudes of the different kinds of structural shifts empirically established in our original experiments at that time[6] have recently been confirmed by analysis of much more extensive experimental material that has since become available.

Both theoretical calculations[7] and statistical analysis[8–10] have shown that the C-α proton chemical shift of an amino acid residue in peptides and proteins is shifted to low frequency (lower chemical shift values) in α-helices and to high frequency (higher chemical shift values) in β-strands in comparison to those in the random-coil structure. The degree of overlap of values is remarkably small, making the examination of the C-α proton chemical shifts an easy method for a preliminary qualitative check for the presence of secondary structure elements. Also, similarities among

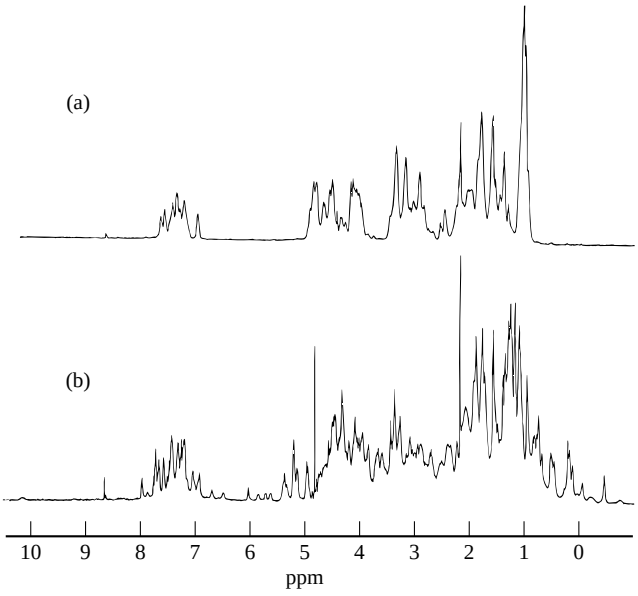

Figure 2 500 MHz ^{1}H NMR spectra of hen lysozyme in D_2O. (a) Thermally denatured (85 °C) protein; (b) native (40 °C) protein

homologous proteins have been used to help the assignment of the spectra or to interpret the shift.

Similar trends have been observed for amide proton chemical shifts,[9,10] and an opposite trend for side chain proton chemical shift values, i.e. α-helices induce a shift to higher frequency while β-strand conformations induce a low-frequency shift. However, the degree of overlap of values displayed by these two groups of protons limits the degree of conformational information extractable from chemical shifts. On the other hand, the shifts of amide protons are very sensitive to hydrogen bonding[10,11] and this observation could constitute a practical application. Since the strength of hydrogen bonds is related to distance, amide chemical shift data could be used to determine intramolecular distances, providing oxygen to proton distances as additional restraints. This kind of information could greatly improve the quality and accuracy of protein structures determined by NMR spectroscopy. However, much work on this regard is clearly needed before this method can reach its full potential.

Other relationships between proton chemical shifts and protein conformation have been observed, such as a correlation between proton amide chemical shifts and helix dipole effects, as well as a relationship between C-α proton chemical shifts and main-chain flexibility or backbone dihedral angles.[10] These observations are worthy of further investigation.

The improvement of isotopic substitution strategies and the development of new methodologies of heteronuclear two- and three-dimensional NMR provided a larger number of peptides and proteins with nearly complete ^{13}C and ^{15}N sequential assignments, making possible the analysis of the dependence of the chemical shifts of these nuclei on secondary structure. The examination of the ^{13}C-α, ^{13}C-β and amide ^{15}N chemical shifts also revealed a dependence on the secondary structure;[7,12] however, the trends are less clear than in the case of C-α and amide protons, due to the small data base available up to now.

Although the chemical shift value carries information about folded structures, it rarely by itself provides sufficient quantitative information to draw unequivocal structural conclusions. The reason for this is that the individual determinants of chemical shifts are in general known only qualitatively. The principal determinants are summarized in Table 1. The early work developed by Lamb, Ramsey, Pople, and Buckingham for quantitative calculations, discussed elsewhere,[2] has for many years provided rough guidelines in the face of a lack of suitable physical data with which accurately to define the parameters needed in the calculations. The observed chemical shift for any nucleus in a biological macromolecule must be analyzed as a structure-dependent sum of several individual contributions—including the empirically identified structural shifts. The individual components of the sum can be identified, as in the equation:

$$\delta_{\text{obs}} = \delta_{\text{electrostatic}} + \delta_{\text{dipolar}} + \delta_{\text{induced dipolar}} + \delta_{\text{solvent}} + \delta_{\text{double bonds}} + \delta_{\text{ring current}} \quad (3)$$

These components are not truly independent and additive, however, but the magnitude of each depends on that of several others because each term contains the polarization of each contributing atom, and that, in turn, has a strong dependence on the polarization of every atom in the vicinity.

Until very recently it has not been possible to calculate chemical shifts in proteins. Although theoretical models have been available for many years, the lack of assigned signals in proteins with well-characterized three-dimensional structures, precluded the test of the models and the derivation of parameters suitable for proteins. However, two-dimensional and three-dimensional NMR techniques have yielded a number of protein assignments, providing the experimental data to test the models. It has been shown that chemical shifts can be calculated using the existing models, to a reasonable degree of accuracy.[13,14]

The best understood conformation-dependent contribution to chemical shifts is the ring-current contributions associated with conjugated groups. For protein side-chain protons, the ring current theoretical forms reasonably explain large structural shifts, with linear correlations between calculated and observed shifts in the range of 0.7–0.8 and root-mean-square (rms) errors of 0.2–0.4 ppm.[15–17] The correlation is poorer for C-α and amide protons of the backbone,[15–17] suggesting that additional mechanisms contribute for structural chemical shifts in these cases. Additional contributions that might operate as well are magnetic anisotropy of the peptide group and electrostatic and hydrogen-bonding effects. In fact, it has been shown that the introduction of magnetic anisotropy and electric field contributions, in addition to ring-current contributions, significantly improve the correlation between observed and calculated chemical shifts for C-α protons to the range of 0.8–0.9, with rms errors of 0.18–0.3.[13,14] The correlation between chemical shifts and secondary structures tends to improve as the factors determining the extent of the shift are better understood. An additional factor that has to be taken into account is that proteins are mobile in solution, therefore, the observed shift value might result in a conformational average.

In recent years, with the increasing application of high-speed computation to solve many-body problems numerically, progress in the precision of quantum calculations and a better definition of interatomic potentials through the experience with molecular dynamics, more quantitative approaches to the calculation of chemical shifts have aroused renewed interest. One promising approach is for ab initio calculation of chemical shifts in proteins, discussed elsewhere in this volume (see ***Chemical Shifts in Biochemical Systems***). It should be noted, however, that a quantitative calculation

Table 1 Principal Determinants of Chemical Shifts[a]

Electric effects (exerted by electric fields which polarize electrons surrounding the observed nucleus and change their induced magnetization):
1. Nearby charges (e.g. H^+, Na^+, NH_3^+, Mg^{2+}, Cl^-, PO_4^{2-}
2. Nearby permanent dipoles (HOH, $-NH_2$, C=O, polar groups generally)
3. Nearby induced dipoles, especially if observed nucleus is part of a polar group (all structures are polarizable)

Magnetic effects (magnetic fields of neighboring structures):
1. Double and triple bonds, (e.g. CH=CH, C(O)=O, HNC=O
2. Ring currents of aromatic and heterocyclic rings
3. Species containing unpaired electrons (ions and free radicals)

[a]The two types of effect are separable only by order of magnitude. Magnetic fields of neighboring structures are also subject to polarization effects by nearby electric fields. Electron currents surrounding the observed nucleus are subject to change by neighboring magnetic fields.

of all chemical shifts, including especially the structural shifts, requires prior knowledge of the structure. The distance dependence of chemical shift contributions from surrounding fields of the type listed in Table 1 is inextricably linked with the magnitude of the induced electronic dipoles. As already noted, these in turn reflect the highly distance-dependent mutual polarization of all surrounding atoms, introducing the need to consider higher order interaction terms, and making a simple determination of any single distance for all practical purposes impossible. Qualitatively, proximity can often be inferred from dramatic changes in chemical shifts, and this has been shown to be useful in the study of molecular complexes of macromolecules with small ligands. A very rough topology of the complex can, in fact, be defined on that basis.[18] Beyond that, geometric information not available from chemical shifts is needed to make a quantitative calculation. It may be expected, nevertheless, that as the accuracy of chemical shift calculations for a known protein or nucleic acid geometry improves, the calculated chemical shifts will be able to serve as a double-check on the correctness of the structure and a guideline for its refinement.

2.2 Coupling Constants

Coupling constants arise from the interactions between neighboring atomic nuclei mediated by the intervening chemical bond (or bonds). The electron cloud of the intervening bond is polarized by the mutual orientation of two (or more) neighboring nuclei. Since nuclei assume only a discrete number of orientations in an external magnetic field, the resonance position of each nucleus will undergo a discrete set of changes resulting from this additional polarization. In the simplest case of two nuclei of spin 1/2, each of the two spectral lines will be split into a doublet, corresponding to an orientation of the neighbor against the external field. Groups of two or more identical nuclei will produce more complex patterns, as shown in Figure 3. The frequency separation between two peaks of a multiplet is a measure of the coupling constant, J.

Coupling constants in the spectra of biological macromolecules are of great practical importance for several reasons. First, the characteristic coupling patterns within the side chains of amino acid residues serve to identify the spectra of specific amino acids and establish a 'first stage' assignment of the spectrum of amino acid type. Second, scalar coupling, especially that involving the (larger) heteronuclear coupling constants, can be useful for tracing covalent connectivities along the polypeptide chain, thus aiding in the sequential (residue specific, 'second stage') assignment of the spectrum (see ***Biological Macromolecules***). Third, coupling constants across three covalent bonds can provide information on the magnitude of the intervening dihedral angle, thus aiding in the definition of both the peptide chain and side-chain conformations.

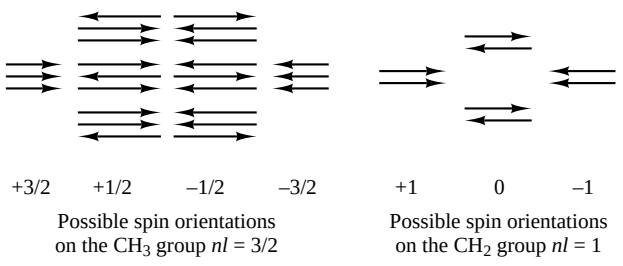

Figure 3 Possible spin orientations for ^1H in an ethyl group. (From Jardetzky and Roberts[2])

Table 2 Typical Ranges of Scalar Coupling Constants

		Hz
$^1H-^1H$		
Geminal	$^1H-C-^1H$	−12 to −15
Vicinal	$^1H-C-C-^1H$	2–14
		7 (free-rotation average)
	$^1H-C=C-^1H$	10 (*cis*)
		17 (*trans*)
	$^1H-C\equiv C-^1H$	∼2
	$^1H-N-C-^1H$	1–10
Long-range		0.5–3
$^1H-^{13}C$		
Single bond	$^1H-^{13}C$ (sp^3)	110–130
Long-range	$^1H-C-^{13}C$	∼5
	$^1H-C=^{13}C$	∼2 (ethylene)
$^1H-^{15}N$		
Single bond	$^1H-^{15}N$	61 (ammonia)
	$^1H-^{15}N$	89–95 (peptides)
Long-range	$^1H-C-^{15}N$	15–23 (peptides)
$^1H-^{17}O$		
Single bond	$^1H-^{17}O$	70
Long-range	$^1H-C-^{17}O$	8–10
$^1H-^{31}P$	$^1H-^{31}P$	170–230 (trivalent ^{31}P)
		700–900 (pentavalent ^{31}P)
	$^1H-O-^{31}P$	15–25
	$^1H-C-O-^{31}P$	2–20
$^{31}P-^{31}P$	$^{31}P-O-^{31}P$	10–30 (pentavalent ^{31}P)
$^1H-^{19}F$	$^1H-C-^{19}F$	40–50
	$^1H-C-C-^{19}F$	5–20
$^1H-^2H$	$^1H-C-^2H$	∼ −2
	$^2H-C-^2H$	∼ 0.3

Typical ranges of coupling constants between neighboring nuclei observable in biological structures are given in Table 2. The use of coupling patterns in conjunction with the known chemical shift pattern, to identify amino acid side chains in a two-dimensional COSY spectrum is shown in Figure 4.[19] The ease of distinguishing between most, though not all of the amino acids in a complex spectrum is readily apparent. It is worth noting that the patterns and the values of the coupling constants observed reflect free rotation around most of the side chain bonds. This free rotation is observable in amino acids, peptides and proteins. One important exception is the rotation about the α-CH$-\beta$-CH_2 bond in larger peptides and proteins, where the rotation is often hindered, so that separate coupling constants $\alpha-\beta$ and $\alpha-\beta'$ can be resolved. The exception is important, inasmuch as it makes it possible to derive geometric information from the two coupling constants, as discussed below. Geometric information cannot be obtained from coupling constants averaged by rotation around a single bond.

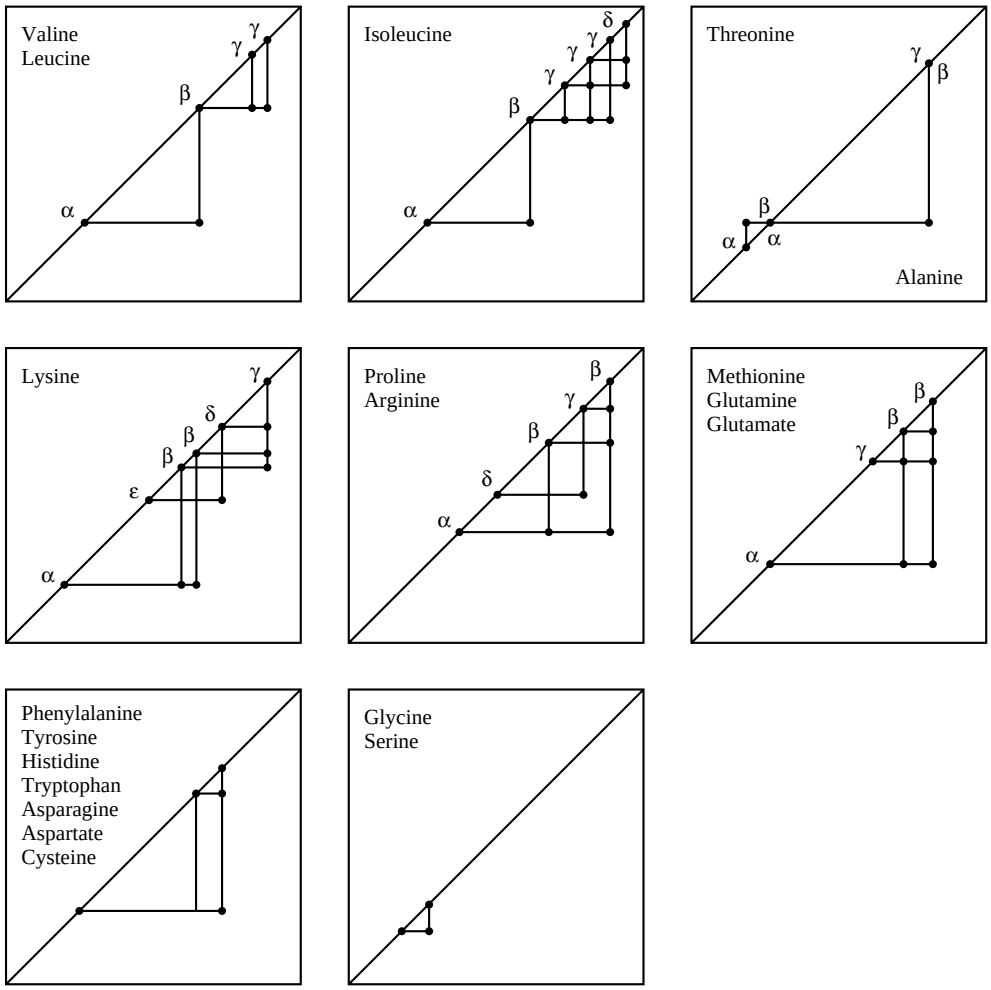

Figure 4 Diagram of the COSY spin–spin connectivities pattern for the 20 common amino acids. (From Lichtarge[19])

The use of homo- and heteronuclear coupling constants for the sequential assignment of protein spectra is discussed elsewhere in this Encyclopedia. Of considerable general importance is the fact that the possibility of using coupling constants for this, as for all other purposes, is limited by the ability to resolve them. In contrast to chemical shifts, coupling results in relatively small line separations, which are independent of the external field and hence cannot be improved by the use of higher frequency spectrometers. The resolution of coupling constants is therefore primarily sensitive to linewidths, and these in turn to the molecular weight of the macromolecule. The use of proton coupling constants for sequential assignment is generally limited to proteins <10 kDa, since most of the relevant NH–α-CH constants are of the order of 3–5 Hz. The corresponding use of heteronuclear coupling constants on normal (fully protonated) proteins appears limited to structures <30 kDa, since the limiting constant across the peptide bond (between the CO(i) and NH($i-1$)) is of the order of 8–15 Hz. It becomes unobservable at higher molecular weights. The possibility of extending the use of coupling constants to structural studies on larger macromolecules by using extensively deuterated analogs to reduce line broadening has been suggested and demonstrated in the case of the *trp*-repressor–DNA complex (37 kDa), the largest structure thus far solved by NMR. The ultimate molecular weight limit for the use of coupling constants still remains to be established.

Coupling constants are an important and frequently used, but not foolproof, source of geometric information on biological macromolecules. As in the case of chemical shifts, the theoretical calculation of coupling constants has met with only limited success, since it depends on detailed knowledge of electron distributions, which is missing in most cases. The relative contributions of σ-and π-electrons to the magnitude of J in different systems, evaluated by the equations developed by Ramsey[20] and McConnell,[21] are to be understood as rough, rather than accurate, estimates. Nevertheless, some useful relationships between coupling constants and structural parameters have a semitheoretical basis.

Of greatest interest in biochemistry is the relationship between the magnitude of the coupling constants across three bonds (vicinal coupling constants) and the dihedral angle θ about the central bonds (see Figure 5). It was originally derived for coupling in the ^{1}H–C–C–^{1}H fragment by the theoretical calculations of Karplus[22] and can be approximated in the form:

$$J = A + B\cos\theta + C\cos^2\theta \qquad (4)$$

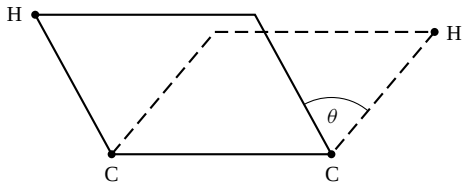

Figure 5 Dihedral angle, θ formed by the H–C–C and C–C–H planes. (From Jardetzky and Roberts[2])

where A, B, and C are coefficients that depend upon the electronegativity of the surrounding atoms. The values of A and C, originally calculated from theory (B was taken as zero), have generally been superseded by semiempirical values calibrated on specific groups of compounds. In some forms of the Karplus relation an electronegativity correction is explicitly introduced, while in others it is reflected in the magnitude of coefficients A, B, and C.

The Karplus relationship [equation (4)] suggests that it might be possible to determine conformations about any single bond that lies between two bonds connecting to atoms observable by NMR. 'Karplus relations' have been developed for ^{1}HNC^{1}H, ^{31}POC^{1}H, and many other molecular fragments. The form of the dependence of J on θ is shown in Figure 6.[23–26] Two points are generally relevant to all relations of this type and should always be borne in mind:

1. The relationship between coupling constant and dihedral angle [equation (4)] is valid for a rigid molecular fragment. In flexible molecules the averaging of J and θ follows different rules since the dependence of J on θ is not linear. Therefore, the proper average θ cannot be calculated from the observed average J. If this is not taken into account, wrong conclusions about the structure will be drawn.[27]
2. The relationship is a truncated cosine expansion and as such an approximation; its inherent precision is not very great, particularly since the coefficients are semiempirical. It characterizes the general trend of the angular dependence of the coupling constant, but the limits of the precision with which an angle can be estimated from equation (4) are unknown, even for a rigid molecular fragment.

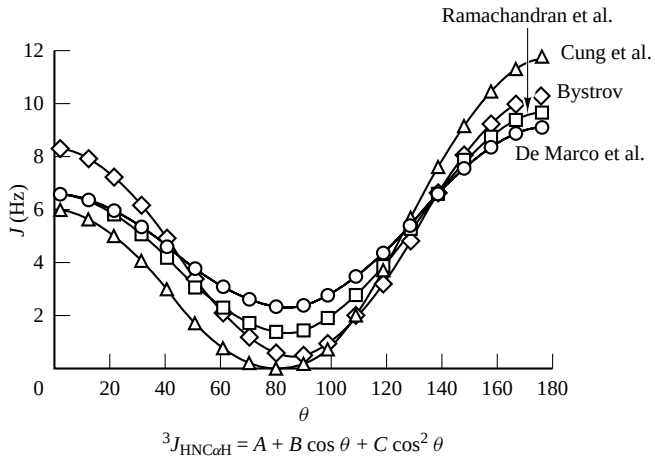

Figure 6 The Karplus curve: the coupling constant, J, as a function of the dihedral angle, θ, for amide compounds.[23–26] (From Lichtarge[19])

Karplus-type curves have been calibrated for heteronuclear constants across the peptide bond, especially by Bystrov.[25] Calibrations of this type are now frequently being used for the purpose of defining protein structures. However, the error bars on all calibrations of the Karplus relationship are rather large, so that very precise statements about the values of the dihedral angles derived from them are likely to involve an overinterpretation of the data. In contrast, the broad general features of a molecular conformation derived from Karplus curves are likely to be valid, if one is dealing with a segment with restricted rotation or, in the case of flexible molecules, if averaging has been properly taken into account.

2.3 Relaxation Parameters

The relaxation parameters—respectively, spin–lattice relaxation time (T_1), spin–spin relaxation time (T_2), spin–lattice relaxation time in a rotating coordinate system ($T_{1\rho}$), and nuclear Overhauser effect (NOE)—were first used for structural studies on biological macromolecules as early as 1961[28] and have retained a prominent role in modern studies of macromolecular structure and dynamics. Their importance derives from the fact that they reflect a relatively simple relationship between the experimentally observed quantities and internuclear distances. Unlike the chemical shifts and coupling constants, which depend on polarizable electron clouds and their highly variable induced magnetic fields, relaxation parameters depend on the interaction between permanent dipoles.

Information on protein dynamics can be extracted from values of the relaxation times T_1 and T_2. Regions affected by fast or slow motions, conformational flexibility, disordered regions, helix–coil transitions, 'breathing' motions and dynamic states of partially folded structures can be identified by anomalous values of the relaxation times.

The most detailed information comes from the NOE, the magnitudes of which can be used to determine constraints in proton–proton distances, and, in turn, to generate three-dimensional structures. The basic two-dimensional NOE experiment is obtained from a three pulse sequence:[29] (delay time $-90^\circ - t_1 - 90^\circ - \tau_m - 90^\circ - t_2)_n$, where τ_m is the mixing time. Double Fourier transformation with respect to times t_1 and t_2 result in the two-dimensional NOE spectrum containing the cross peaks, whose intensities are proportional to the inverse of the sixth power of the distance, r, between the protons, and to the correlation time (τ_c) :

$$\text{NOE} \propto \left\langle \frac{1}{r^6} \right\rangle f(\tau_c) \qquad (5)$$

The main complications in the relationship between the measured relaxation parameter and the molecular structural parameter—the internuclear distance—is the simultaneous dependence of relaxation on the rates of molecular motion, which are subjected to some variation. Other factors complicating the relationship between relaxation and molecular parameters may be the operation of relaxation mechanisms other than dipole–dipole interaction, such as chemical shift anisotropy, scalar or quadrupolar coupling and exchange. If there is no reason to believe that such mechanisms play a non-negligible role, their contribution must be quantitatively evaluated.

Table 3 Relaxation Mechanisms

Observed total relaxation rate $(1/T_1)_i$:

$$(1/T_1)_i = (1/T_1)_{\rho i} + (1/T_1)_{Di} + (1/T_1)_{\sigma i} + (1/T_1)_{pi}$$

$$(1/T_1)_\rho = \hbar^2\gamma_p^2\left(\frac{3}{2}\gamma_p^2\sum_j r_{ij}^{-6}\tau_{\rho ij} + \gamma_f^2\sum_f {*}r_{if}^{-6}\tau_{\rho if}\right)$$

$$(1/T_1)_D = \hbar^2\gamma_p^2\left(\frac{3}{2}\gamma^2\sum_k r_{ik}^{-6}\tau_{Dijk} + \gamma_e^2\sum_e {*}r_{ie}^{-6}\tau_{Die}\right)$$

$$(1/T_1)_\sigma = \frac{2}{15}\gamma_p^2 H_z^2(\Delta\sigma)^2\tau_\rho$$

$$(1/T_1)_\rho = \left(\frac{3\gamma_p^2\mu_{eff}^2}{r_{is}^3}\right)N_s\tau_{Dis}$$

For nuclei with a quadrupole moment, an additional term applies:

$$(1/T_1)_Q = \frac{3}{8}\hbar^2(eQ)^2(eq)^2\tau_c$$

$(1/T_1)_{\rho i}$ is the relaxation rate resulting from interaction with nuclei in the same molecule (intramolecular or rotational relaxation).
$(1/T_1)_{Di}$ is the rate resulting from interaction with nuclei in other molecules (intermolecular or transitional relaxation).
$(1/T_1)_{\sigma i}$ (shielding anisotropy term) is the rate resulting from interaction with magnetic fields generated by shielding anisotropy.
$(1/T_1)_{pi}$ (paramagnetic term) is the rate resulting from interactions with the magnetic moments of unpaired electrons.
γ_p, γ_{fj} and γ_e, respectively, the gyromagnetic ratios of nuclei of the same and of a different chemical species as nucleus i; r_{ij}, r_{if}, r_{ik} and r_{ie}, the internuclear distances; r_{is}, the distance between nucleus i and an impartial electron.
τ_ρ, the correlation time for rotational diffusion; τ_D, the correlation time for translational diffusion for pairs of particles ij, ik, etc.
Correlation times for intramolecular and intermolecular movements of a rigid molecule are expressed in terms of the diffusion coefficient of the molecule containing the relaxing nucleus:

$$(\tau_c)_{intra} = \frac{2a^2}{9D} \quad \text{and} \quad (\tau_c)_{inter} = \frac{r^2}{12D}$$

where a is the radius of the molecule, r is the average intermolecular distance, and D is the diffusion coefficient. D is given by the Stokes–Einstein relationship:

$$D = \frac{kT}{6\pi\eta a}$$

where k is the Boltzmann constant, T is the absolute temperature, η is the viscosity, and a is the molecular radius.

The basic theory of relaxation parameters is discussed elsewhere in this work. The different relaxation mechanisms and their dependence on molecular parameters are summarized in Table 3.

Unfortunately, a set of rigorous criteria for distinguishing between the different relaxation mechanisms does not exist, except for the ideal case of a rigid structure with a single resonance line and a single dominant relaxation mechanism. Field or frequency dependence of the relaxation rates can provide useful guidelines, since for a rigid structure relaxation rates will decrease with increasing field if the mechanism is dipolar or quadrupolar, and increase proportionately to the square of the field if the mechanism is chemical shift anisotropy. Either an increase or a decrease with increasing field may be observed for a scalar mechanism. However, for flexible systems, and wherever several mechanisms operate simultaneously, these simple relationships may be obscured. Heterogeneity of chemical shifts and relaxation rates, unobservable at lower field, may also make quantitative comparisons difficult. Information or intuition to the NMR measurement will often be required to make a decision.

Even in the case of pure dipolar relaxation, intuition and judgment are required to decide which form of the relaxation equations for the calculation of the experimental relaxation parameters actually applies to a given situation. For the simple case of two isolated spins on a rigid body, the dipolar component of the relaxation equations can be written in the form:

$$\frac{1}{T_1} = \frac{9}{8}\frac{\gamma^4\hbar^2}{r^6}\{J(\omega) + J(2\omega)\}$$

$$\frac{1}{T_2} = \frac{9}{32}\frac{\gamma^4\hbar^2}{r^6}\{J(0) + 10J(\omega) + J(2\omega)\} \qquad (6a)$$

$$\text{NOE} = 1 + \frac{\{6J(\omega_H + \omega_C) - J(\omega_H - \omega_C)\}}{\{J(\omega_H - \omega_C) + 3J(\omega_C) + 6J(\omega_H + \omega_C)\}}$$

where the spectral density function, $J(\omega)$, is given by a single Lorentzian term:

$$J(\omega) = \frac{\lambda}{\omega_0^2 + \lambda^2} \qquad (6b)$$

Strictly speaking, this simple formulation never applies to biological macromolecules, and when it applies, represents a drastic oversimplification. The oversimplification can be useful to get a rough impression of the structural parameters reflected in the relaxation parameters, but it is a mistake to treat it as a source of accurate and precise information.

In macromolecules, two complicating factors have to be taken into account. The first one is that any observed nucleus interacts not with one, but generally with several of its neighbors, and each of these, in turn with each of the others. Multiple interactions can be taken into account by generalized Bloch equations:

$$\frac{dM_i}{dt} = -\rho_i[M_i - M_i(0)] - \Sigma\sigma_{ij}[M_j - M_j(0)];\ i \neq j \quad (7)$$

which can also include different spectral density functions for different pairs of nuclei. The equation describes multiple pathways—or diffusion—of magnetization transfer within a system of spins, replacing magnetization exchange between two spins. This has become known as ‘spin diffusion’, borrowing the term with a slightly altered meaning from solid state physics. The importance of spin diffusion stems from the

fact that the intensity of magnetization observed at any given time—and hence the magnitude of the calculated relaxation parameters—may be more or less than the magnitude predicted from the simple relationship in equation (6). A wrong estimate of the distance would be obtained without a correction for spin diffusion. In structure determination, the generalized Bloch equations are now commonly used for the back-calculation of spectra to verify and refine an approximate starting structure derived from equation (6). Structural information is thus derived not from a single relaxation parameter for each nucleus, but from the sum total of the interactions determining the pattern of relaxation. The multispin relaxation effects can be fully accounted for if one manages to measure the complete density matrix $\mathbf{V}_{t_m}$. The relaxation matrix can then be obtained from:

$$\mathbf{R} = -\ln\left(\frac{\mathbf{V}_{t_m}}{\mathbf{V}_0}\right)\left(\frac{1}{t_m}\right) \tag{8}$$

where $\mathbf{V}_0$ represents the intensities of the diagonal peaks at $t_m = 0$ (corresponding to the one-dimensional spectrum) and $\mathbf{R}$ is the relaxation matrix. The proton distances can be derived from the corresponding off-diagonal elements of the relaxation matrix $\mathbf{R}$. The measurement of all the intensities, including diagonal peaks, is an unattainable goal in real cases. Consequently, several iterative approaches have been developed to cope with incomplete intensity information. All the approaches are designed to minimize the deviation between measured and calculated intensities. They can be divided into two classes. The first class utilizes the self-consistency of the relaxation matrix, modifying the matrix until there is agreement between calculated and measured intensities. The most popular program of this class is called MARDIGRAS.[30] In the second class, a comparison between the theoretical and experimental intensities is used to define how close the structure is to the experimental data, while refining the structure, with the help of distance geometry of molecular dynamic methods. The algorithm IRMA was developed under this approach.[31]

The second complicating factor that has to be taken into account is that when multiple internal motions occur, as they do in biological macromolecules, the explicit form of the density function, $J(\omega)$, can be quite complicated, and different for different pairs of nuclei. The calculation of a specific density function for each pair of nuclei requires a specific motional model. As discussed elsewhere in this Encyclopedia (see ***Biological Macromolecules***), the formulation of accurate models for internal motions occurring in biological macromolecules is still in its infancy. Until the problems of such motions are better understood, we are limited to crude, and rarely accurate, approximations.

3 AVERAGING OF NMR PARAMETERS—FAST EXCHANGE

Many molecular processes have rates much more rapid than the rates reflected in NMR spectra ($10-10^4$ s^{-1}, not counting relaxation phenomena). Rotational diffusion occurs at rates of 10^6-10^{12} s^{-1}. Rotations about single bonds may have frequencies in the microwave and infrared region (rates of $10^{10}-10^{13}$ s^{-1}). Diffusional collisions have typical frequencies of 10^7-10^9 s^{-1} and even the 'slow' conformational changes in macromolecules detected by various spectroscopic methods can occur at rates of 10^4-10^6 s^{-1}. It is therefore to be expected that observed NMR parameters will often be averaged by molecular motions. While the interpretation of NMR data for the slow and intermediate exchange cases is relatively straightforward, for the rapid exchange case it is not. The observation of an average is not immediately informative. To extract the desired information from the measurement of average properties—or at least to understand the limits of the information that can be derived from such measurements—the nature of the averaging must be understood. This problem has been largely neglected in the NMR literature and as a consequence many untenable conclusions, especially concerning the conformations of flexible molecules, have been reported.

The core of the problem is that no direct indication can be obtained from an averaged spectrum, either concerning the number of molecular species or states contributing to the average, or concerning the characteristics of their individual spectra. In some cases it may be possible to set a lower limit to the number of species involved. In most cases, however, the spectrum must be interpreted in terms of a hypothetical model of the equilibria involved, and if this model does not correspond to the real situation, the structural parameters derived from the analysis will not have the anticipated meaning.

The problems of averaging can be best understood in the context of conformational analysis, although exactly the same principles apply to the study of the fast exchange processes, such as occur in molecular interactions. Consider the two potential energy diagrams shown in Figure 7. Figure 7(a) corresponds to a single conformation, permitting oscillation about a single distance or angle, or more generally, to a rigid body held together by vibrating bonds. We will call averaging about a single minimum *averaging of the first kind*. Isotropic averaging, as in rotational diffusion, may be regarded as a limiting case of this type, the potential energy curve being flat for all possible orientations. Figure 7(b) corresponds to the averaging of well-defined conformations, each corresponding to a well-defined energy minimum; for example, averaging of the rotamers about a single bond or averaging of the T and R states in the Monod–Wyman–Changeux model of conformational transitions in proteins. We will refer to this as *averaging of the second kind*.

Now suppose that the NMR data obtained for a given system are interpreted in terms of a model involving one single, fixed conformation. It can easily be seen that the geometric parameters derived from the data, and the structures deduced from them, have a physical meaning only if the real situation corresponds to Figure 7(a), the single minimum. This is the only case in which a single preponderant value of r or θ exists, and the measured average NMR parameter will reflect it. Even in this case some caution is necessary, since this is strictly true only if the averaging is symmetric. If the energy well (Figure 7) is asymmetric, as it often is for interatomic distances, $\langle r\rangle_{\mathrm{av}}$ or $\langle\theta\rangle_{\mathrm{av}}$ may differ somewhat from the r and θ corresponding to the energy minimum. However, if the minimum is relatively sharp, the error may be small and might be neglected. In that case the structure behaves for purposes of computation as if it were rigid, except for the vibrations.

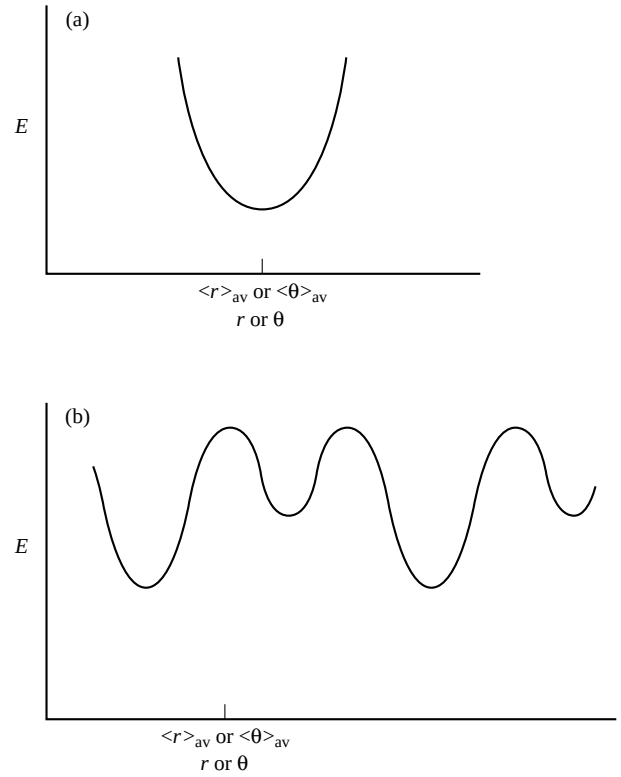

Figure 7 Potential energy diagrams illustrating (a) motional averaging about a single energy minimum, (b) motional averaging of different conformers. Each minimum corresponds to an actual conformer. Distance $\langle r\rangle_{av}$ or angle $\langle\theta\rangle_{av}$ corresponds to a value calculated from an averaged NMR parameter. (From Jardetzky and Roberts[2])

All relationships between NMR and structural parameters will hold as a first approximation.

However, none of these relationships will hold if the real situation corresponds to Figure 7(b), i.e. if the averaging is of the second kind. It is often stated in the literature that analyzing the NMR data in terms of a 'single conformation' model, the conformation one obtains is the 'average' conformation. In fact, this is not the case, as shown by the following argument.[27] The physical averaging of distances and angles by exchange between, say, two states A and B will be linear,

$$\bar{r} = \alpha r_A + (1-\alpha) r_B \tag{9}$$

where α denotes the fractional population of A. Similarly, the NMR parameters characteristic of the two states will average linearly, e.g.

$$\langle 1/T_1\rangle_{av} = \alpha/T_{1A} + (1-\alpha)/T_{1B} \tag{10}$$

However, since the NMR parameters have a nonlinear dependence on distances and angles, their average will reflect a nonlinear average of the latter. For example, $\langle 1/T_1\rangle_{av}$ will yield $\langle r^6\rangle_{av}$. It can easily be shown that this is not the same as the $\bar{r}$ of equation (9). Thus from equation (10)

:

$$\frac{J^*(\omega)}{\langle r\rangle_{av}^6} = \frac{\alpha J_A(\omega)}{r_A^6} + \frac{(1-\alpha) J_B(\omega)}{r_B^6} \tag{11}$$

where $J^*(\omega)$ is the spectral density function assumed in the calculation, and $J_A(\omega)$ and $J_B(\omega)$ the true (unknown) spectral density functions for species A and B. Even assuming $J^*(\omega) = J_A(\omega) = J_B(\omega)$:

$$\langle r\rangle_{av} = \frac{r_A r_B}{[\alpha r_B^6 + (1-\alpha) r_A^6]^{1/6}} \tag{12}$$

and clearly $\langle r\rangle_{av} \neq \bar{r}$. Similarly, it can readily be shown that coupling constants (from the Karplus equation) and chemical shifts yield conformational parameters that are not simply related to the conformations A and B or to their linear average. *The conformation calculated from the averaged NMR parameters will therefore not correspond to the average of the conformations assumed by the molecule*.

There is a further fundamental problem in the interpretation of $\langle r\rangle_{av}$, $\bar{r}$, or other 'average' conformational parameters. A basic assumption implicit in the equations for rapid averaging of the second kind, i.e. between several energy minima, is that the time spent in transit between states is negligible in comparison with the lifetime of each state. The lifetimes of individual states also define a timescale. The 'states' defined by $\langle r\rangle_{av}$, $\langle\theta\rangle_{av}$, $\bar{r}$ and $\bar{\theta}$ have an infinitesimal lifetime in this or any longer timescale. Thus, in situations where averaging of the second kind occurs, the 'average structures' calculated by applying any of the equations discussed earlier to the analysis of any measured averaged NMR parameter are fictitious; on the timescale of the real states assumed by the molecular structure, they do not exist. For a more complete discussion of the relationships between 'apparent' and 'true' geometric parameters in cases involving motional averaging, the reader is referred to Chap. IV of 'NMR in Molecular Biology' by Jardetzky and Roberts.[2]

The general relationships defining the 'average' structural parameters $\langle r\rangle_{av}$ and $\langle\theta\rangle_{av}$ derived from averaged NMR parameters, J and $1/T_{1,2}$, in terms of the individual values of r and θ for exchange between N energy minima are given in Table 4.

A meaningful analysis of NMR data in terms of structural parameters in the case of rapid averaging is therefore possible only if the correct model is used in the analysis of the data. NMR data generally do not provide criteria for the choice of a model, with few exceptions. Although some models can be disproved by NMR data alone, it can never be proved that the model being used does correspond to the real situation.

The interpretation of individual NMR parameters in terms of the structure, dynamics and function of biological macromolecules is thus seen to be less than straightforward. If it is nevertheless possible to draw very significant conclusions about macromolecular structure and dynamics, it is because these conclusions rest on the interpretation of the pattern of parameters observed for a macromolecule in its entirety rather than on the interpretation of any single parameter. The uncertainty inherent in the interpretation of a single parameter can be minimized by checks of consistency with the interpretation of other parameters. Averaging is a perennial problem that needs more attention than it has received, with the result that some of the published macromolecular structures remain open to doubt. In very few cases has a detailed analysis of the effects of averaging by molecular motions on different timescales been carried out, the most thorough being the case of the *trp*-repressor from *Escherichia coli*, in which

Table 4 Relationships of 'Average' Structural Parameters Derived from Averaged NMR Parameters to the Real Parameters for N Energy Minima

1. The distance $\langle r \rangle_{\text{av}}$ derived from averaged relaxation parameters

$$\langle r \rangle_{\text{av}} \equiv \langle r^{-6} \rangle^{1/6} = \frac{\prod_i^N r_i}{\left(\sum_i^N \prod_j^{N-1} \alpha_i r_{j \neq 1}^6 \right)^{1/6}}$$

2. The dihedral angle $(\theta)_{\text{av}}$ derived from averaged coupling constants

$$\langle \theta \rangle_{\text{av}} = \arccos \left\{ \frac{-B \pm \left[B^2 - 4C \sum_i^N \alpha_i (A + B \cos\theta_i + C \cos^2 \theta_i) \right]^{1/2}}{2C} \right\}$$

$$\langle \theta \rangle_{\text{av}} \neq \overline{\theta} = \sum_i^N \alpha_i \overline{\theta}_i$$

the DNA binding, helix–turn–helix domain shows an instability on a millisecond timescale.[32] In general, it is to be expected that such an analysis will be necessary for most larger proteins and protein–nucleic acid structures. Macromolecules can only be completely understood in terms of a specific structural–dynamic model that correctly and completely accounts for thesum total of NMR parameters that can be measured in its spectra.

4 RELATED ARTICLES

Biological Macromolecules; Chemical Shifts in Biochemical Systems

5 REFERENCES

1. J. E. Wertz, *Chem. Rev.*, 1955, **55**, 829.
2. O. Jardetzky and G. C. K. Roberts, *NMR in Molecular Biology*, Academic Press, New York, 1981.
3. J. L. Markley, D. H. Meadows, and O. Jardetzky, *J. Mol. Biol.*, 1967, **27**, 25.
4. O. Jardetzky, *Proceedings of the International Conference on Magnetic Resonance*, The Chemical Society of Japan, Tokyo, Japan, 1965, N-3-14, 1.
5. C. C. McDonald and W. D. Phillips, *J. Am. Chem. Soc.*, 1967, **89**, 6332.
6. J. S. Cohen and O. Jardetzky, *Proc. Natl. Acad. Sci. USA*, 1968, **60**, 92.
7. N. J. Clayden and R. J. P. Williams, *J. Magn. Reson.*, 1982, **49**, 393.
8. L. Szilà'gyi and O. Jardetzky, *J. Magn. Reson.*, 1989, **83**, 441.
9. A. Pastore and V. Saudek, *J. Magn. Reson.*, 1990, **90**, 165.
10. D. S. Wishard, B. D. Sykes, and F. M. Richards, *J. Mol. Biol.*, 1991, **222**, 311.
11. N. E. Zhou, B.-Y. Zhu, B. D. Sykes, and R. S. Hodges, *J. Am. Chem. Soc.*, 1992, **114**, 4320.
12. S. Spera and A. Bax, *J. Am. Chem. Soc.*, 1991, **113**, 5490.
13. K. Ösapay and D. A. Case, *J. Am. Chem. Soc.*, 1991, **113**, 9436.
14. M. P. Williamson and T. Asakura, *J. Magn. Reson., Ser. B*, 1993, **101**, 63.
15. S. J. Perkins and R. A. Dwek, *Biochemistry*, 1980, **19**, 245.
16. C. Redfield, J. C. Hoch, and C. M. Dobson, *FEBS Lett.*, 1983, **159**, 132.
17. G. P. Gippert, P. F. Yip, P. E. Wright, and D. A. Case, *Biochem. Pharmacol.*, 1990, **40**, 15.
18. O. Jardetzky, in *Molecular Properties of Drug Receptors (Ciba Foundation Symposium)*, eds. R. Porter and M. O'Connor, J. & A. Churchill, London, 1970, p. 113; see also Jardetzky and Roberts,[2] Chap. IX.
19. O. Lichtarge, *Structure Determination of Proteins in Solution by NMR*, Ph.D. Thesis, Program in Biophysics, Stanford University, CA, 1986.
20. N. F. Ramsey, *Phys. Rev., Ser. 2*, 1953, **91**, 303.
21. H. M. McConnell, *J. Chem. Phys.*, 1956, **24**, 764.
22. M. Karplus, *J. Chem. Phys.*, 1959, **30**, 11.
23. G. N. Ramachandran, R. Chandrasekharan, and K. D. Kopple, *Biopolymers*, 1971, **10**, 2113.
24. M. T. Cung, M. Marroud, and J. Neel, *Macromolecules*, 1974, **7**, 606.
25. V. F. Bystrov, *Prog. NMR Spectrosc.*, 1976, **10**, 41.
26. A. De Marco, M. Llinás, and K. Wüthrich, *Biopolymers*, 1978, **17**, 637.
27. O. Jardetzky, *Biochim. Biophys. Acta*, 1980, **621**, 227.
28. O. Jardetzky and J. J. Fischer, in *Proceedings of the 4th International Conference on Medical Electronics, New York, 1961*, p. 46.
29. A. Kumar, R. R. Ernst, and K. Wüthrich, *Biochem. Biophys. Res. Commun.*, 1980, **95**, 1.
30. B. A. Borgias and T. L. James, *J. Magn. Reson.*, 1990, **87**, 475.
31. R. Boelens, T. M. G. Konig, and R. Kaptein, *J. Mol. Struct.*, 1988, **173**, 299.
32. D. Zhao, C. H. Arrowsmith, X. Jia, and O. Jardetzky, *J. Mol. Biol.*, 1993, **229**, 735.

Biographical Sketches

Oleg Jardetzky. *b* 1929. B.A., 1950, Chemistry & Biology, Macalester College, St. Paul MN, M.S., 1953, Physiological Chemistry, M.D., 1954, Medicine, Ph.D., 1956, Physiology & Physical Chemistry, University of Minnesota, St. Paul, MN. National Research Council Fellow, Department of Chemistry, CalTech, 1956–57; Associate in Pharmacology, 1957–59, Assistant Professor of Pharmacology, Harvard Medical School, 1959–66; Director, Department of Biophysics & Pharmacology, Merck, Sharp & Dohme, 1966–68; Executive Director of Basic Medical Science, Merck Institute for Therapeutic Research, 1968–69; Professor of Pharmacology, 1969–present, Director, Stanford Magnetic Resonance Laboratory, Stanford University, 1975–present. Approx. 230 publications. Current research interests: structure dynamics and function of proteins involved in regulatory processes; the mechanism of action of *trp*-repressor; use of high-resolution NMR spectroscopy and other physical methods to define mechanisms of conformational transition and protein folding.

Tais Helena Schmitt. *b.* 1963. Pharmacy Degree, 1986, University of Sao Paulo, Brazil. Ph.D. (Hon.), 1994, Chemistry Institute, University of Sao Paulo, Brazil. Apprentice pharmacist, Faculty of Pharmaceutical Sciences, University of Sao Paulo, 1985–86. Research assistant to Dr Shirley Schreier, Department of Biochemistry, Chemistry Institute, University of Sao Paulo, 1987–94. Federal International Exchange Research Fellow, National Biomedical ESR Center, Medical College of Wisconsin, Milwaukee, WI, (advisor: Dr James Hyde), 1991–92. Postdoctoral Research Fellow, Stanford Magnetic Resonance Laboratories, Stanford University (recipient of 2+ year Fellowship from the state of Sao Paulo), 1994–present.

Chemical Shifts in Biochemical Systems

Angel C. de Dios and Eric Oldfield

University of Illinois, Urbana-Champaign, IL, USA

1	Introduction	1
2	Empirical Shift–Structure Correlations in Proteins	1
3	The Ab Initio Approach to Protein Shielding	2
4	Nucleic Acids	5
5	Carbohydrates	6
6	Structure from Shielding: Prediction, Refinement, and Validation	6
7	Conclusions	6
8	Related Articles	6
9	References	6

1 INTRODUCTION

The purpose of this article is to outline briefly recent progress in understanding chemical shifts in biochemical systems–proteins, nucleic acids, carbohydrates, and lipids. The chemical shift is probably the most sensitive spectroscopic probe of local structure and environment, but until quite recently it has been quite refractory to detailed analysis, at least in macromolecules. In small molecules, this sensitivity manifests itself in isotope shifts, temperature dependence, gas-to-liquid shifts, and solvent shifts. In macromolecules, sensitivity is manifested as chemical shift nonequivalencies. The NMR chemical shift in biological systems contains a wealth of encoded structural information, and in order to decode this information it is first necessary to be able to predict chemical shifts from known structures.

From a theoretical standpoint, insights gained in studying chemical shifts in biological systems should also greatly help in testing, modifying, and improving present theories of the chemical shift. For example, proteins provide a unique test case for investigating the dependencies of the chemical shift on factors such as torsion angles, hydrogen bonding, and electrostatics. In sharp contrast, gas phase studies of small molecules would not be capable of yielding the torsional dependencies of the chemical shift. This is because variable-temperature measurements, in which the torsional effects would be visible, also include significant contributions from centrifugal distortion, and, in addition, a change in one torsion angle may significantly change the overall shape of a small molecule, and consequently the way it interacts with its environment. Proteins, on the other hand, do not require variable-temperature studies, since sites which differ only in torsion angles are already present. Hence, the ability to interpret and reproduce chemical shift nonequivalencies in biological systems should not only be useful for structure elucidation, but is also of fundamental importance for the evaluation, development, and design of methods for chemical shift computation in general.

Chemical shift nonequivalencies due to folding have been known in proteins for more than two decades. McDonald and Phillips[1] first observed that several residues in hen egg white lysozyme could be resolved in ^{1}H NMR, and this was then followed by Allerhand et al. who observed a ∼6 ppm range for the ^{13}C chemical shift of C-γ of the six tryptophan residues in hen egg white lysozyme.[2] Although such chemical shift inequivalencies have made multidimensional NMR studies of proteins possible,[3,4] understanding of the origins of such chemical shift nonequivalencies remained a very major challenge until recently, when a first-principles reproduction of the NMR spectra of the heavier nuclei (^{13}C, ^{15}N, and ^{19}F) in proteins was demonstrated to be feasible.[5] Here, we trace the development of NMR chemical shift interpretations in biological systems, starting from the discovery of empirical correlations between shift and structure in proteins, up to the present ab initio interpretation of protein, nucleic acid, and carbohydrate chemical shifts, and the derivation of structure from shielding.

2 EMPIRICAL SHIFT–STRUCTURE CORRELATIONS IN PROTEINS

The earliest attempts at unraveling the relationship be-tween secondary structure and chemical shifts were focused on H-α.[6–8] Due to the small chemical shift range and the sensitivity of ^{1}H shielding to not only electrostatic effects but also magnetic factors, such as ring currents and the anisotropy of the diamagnetic susceptibility of peptide groups, only general trends were found between structure and shielding.[9,10] In contrast to ^{1}H NMR, the heavier nuclei exhibit a much wider chemical shift range, rendering such magnetic effects of minor importance. Hence, ^{13}C and ^{15}N nuclei offer more promise, and considerable efforts were made in interpreting these shifts as soon as they became available.

In early work, Kricheldorf et al.[11] and Saito et al.[12] showed that ^{13}C chemical shifts in peptides were mainly influenced by the torsion angles ϕ and ψ. Theoretical attempts involving a semiempirical finite perturbation–incomplete neglect of differential overlap (FPT–INDO) method aimed at reproducing these observations were somewhat successful in demonstrating the nonequivalency between helical and sheet residues,[13] but the calculated differences were much smaller than the range observed experimentally. With an increasing number of assigned C-α and C-β resonances in various proteins—bovine pancreatic trypsin inhibitor (BPTI), calmodulin, interleukin-1β and staphylococcal nuclease—Spera and Bax introduced the first empirical ϕ, ψ chemical shift surface for C-α and C-β using known X-ray data,[14] shown in Figures 1(a) and (b). Figure 1(c) shows histograms of the secondary shift distribution in α-helical and β-sheet residues. From the presently available database of ^{13}C chemical shifts it is clear that C-α resonances of helical sites are deshielded compared with those residues which occur in sheet regions. The opposite trend is evident for C-β, where helical sites are more shielded.[14] Such empirical observations have found use in the chemical shift index,[15] which permits prediction of helical and sheet structure, based on C-α C-β, C^{o}, and H-α shifts.

Considerable attention was also given early on to ^{15}N shifts in proteins.[16,17] However, the problem of whether or

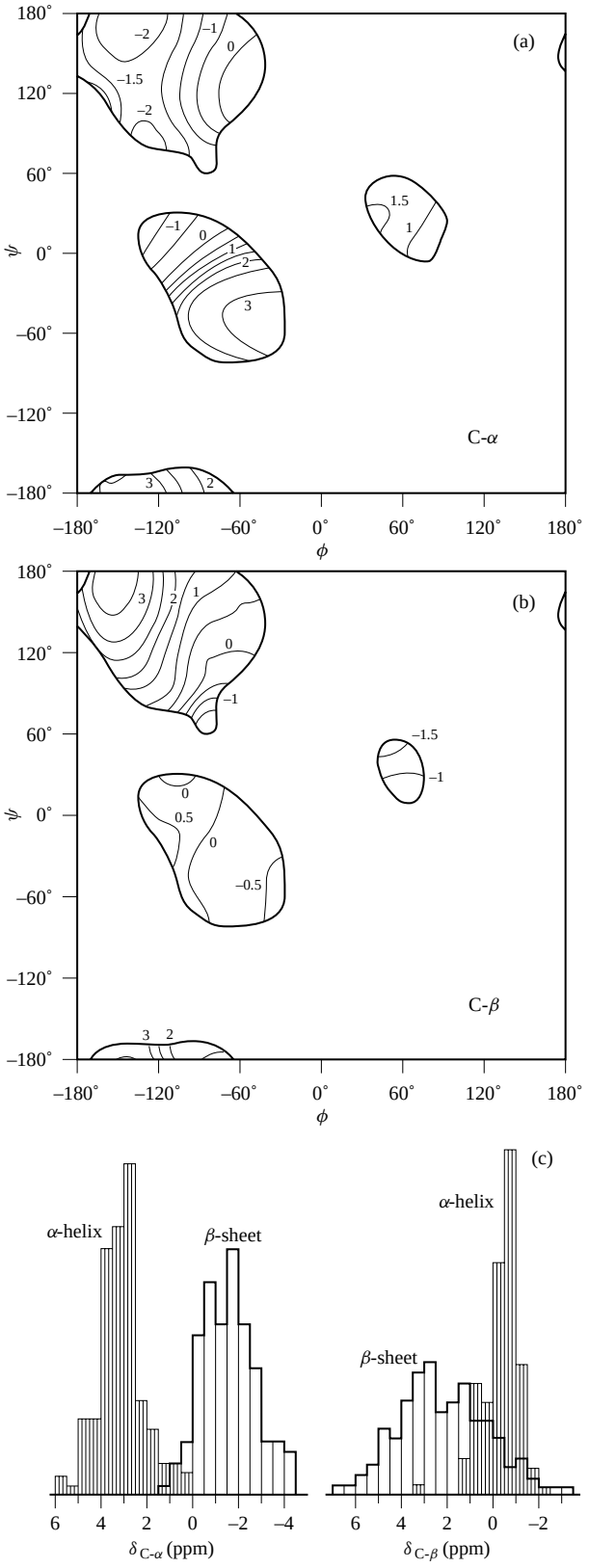

Figure 1 Secondary chemical shift surfaces $\Delta\delta(\phi,\psi)$ and secondary chemical shift histograms for C-α and C-β sites in proteins. (a) Empirical secondary chemical shift surface for C-α nuclei in proteins; (b) as in part (a) but for C-β; (c) histogram showing the distribution of observed secondary shifts for C-α and C-β. (Reproduced by permission of the American Chemical Society from S. Spera and A. Bax, *J. Am. Chem. Soc.*, 1991, **113**, 5490)

not ^{15}N chemical shifts can provide information regarding local structure remained unanswered. Glushka et al. then noticed a correlation between ^{15}N chemical shifts and the torsion angle ψ_{i-1} for residues in sheet regions in BPTI and apamin, but no other structural or 'interaction' features were found.[18] More recently, using a much larger database (consisting of 14 proteins and 1477 ^{15}N chemical shifts), Le and Oldfield[19] found a better empirical correlation between the peptide ^{15}N chemical shift and the torsion angles ϕ_i and ψ_{i-1}, indicating that there is indeed a significant relationship between ^{15}N chemical shifts and secondary structure. The larger number of points permitted study of individual amino acid shift surfaces. Figures 2(a)–(c) show the agreement obtained between experimentally obtained ^{15}N chemical shifts and those derived from the empirically fitted individual shift surfaces, for aspartic acid, lysine, and valine. The presence of an intrinsic relationship between ^{15}N chemical shifts and secondary structure becomes evident from these studies. However, it can also be inferred that there are other factors, such as electrostatic interactions, side-chain conformation, and hydrogen bonding, which all potentially influence ^{15}N shielding. The side chain of valine, for example, introduces an additional angle χ^1, which can modify the ^{15}N chemical shift behavior, since the presence of a substituent at the β-carbon site introduces a γ-*gauche* effect, as noted earlier by Tonelli.[20] In order to take this into account, a much larger database would be needed in order to create separate shift surfaces for each of the three common χ^1 conformers. Empirical database approaches are thus useful in indicating trends, but it would clearly be desirable to be able to predict shifts accurately using first principles or ab initio approaches. For example, the ^{15}N-valine χ^1-torsional problem is one which can easily be solved if the torsional dependencies can be derived from first principles. As demonstrated recently, this is now possible.[15] In addition, sensitivity to side-chain conformation is not exclusive to ^{15}N, since ^{13}C shifts for C-α and C-β sites are also expected to exhibit a χ^1 dependence. This, however, would be difficult to see with only a small database of assigned ^{13}C shifts. Ab initio methods therefore clearly have an advantage over empirical approaches since chemical shift surfaces for individual amino acids, as well as for various χ^1 conformers, can in principle be evaluated.

With the rapidly growing database of ^{1}H chemical shifts,[21] there has been renewed interest in using ^{1}H NMR in protein structure studies.[22–27] These studies have taken advantage of the availability of large numbers of ^{1}H chemical shifts to relate chemical shifts to structure. In addition to the correlation found between secondary structure and the chemical shifts of H-α and H-N, the large amount of spectroscopic information available has also permitted a breakdown of ^{1}H shielding into electrostatic and peptide magnetic anisotropy effects. Thus, the coefficients needed in order to evaluate electrostatic contributions from nearby polar groups, as well as the anisotropy effects arising from peptide bonds, have been derived empirically. The complexity and number of factors that affect ^{1}H chemical shifts, however, make a direct chemical shift to structure route very difficult, although structure refinement using H-α shifts has promise.[30]

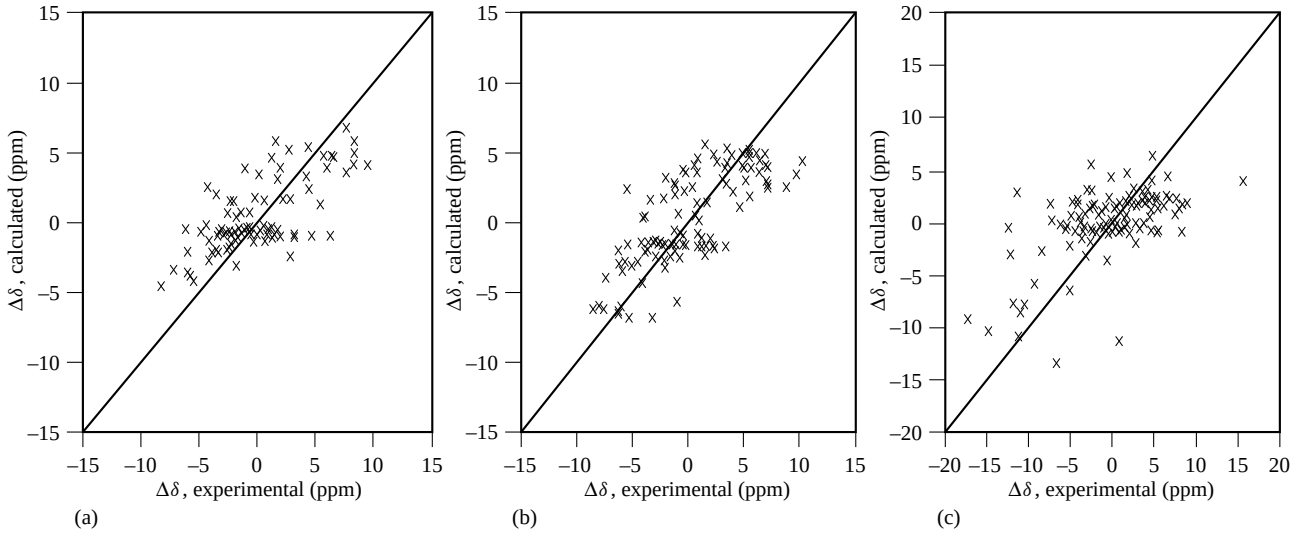

Figure 2 Correlation between experimental secondary ^{15}N chemical shifts and those computed from empirically fitted individual secondary chemical shift surfaces. (a) Aspartic acid; (b) lysine, and (c) valine. (Reproduced by permission of ESCOM Science Publishers BV from H. Le and E. Oldfield, *J. Biomol. NMR*, 1994, **4**, 341)

3 THE AB INITIO APPROACH TO PROTEIN SHIELDING

Although empirical and semiempirical approaches for ^{1}H NMR are useful for analyzing secondary structures, these approaches are more limited for the heavier nuclei. The reason for this is that long range magnetic anisotropy effects will be very small for ^{13}C and ^{15}N, due to the large ^{13}C and ^{15}N shift ranges (~8–30 ppm). Moreover, C-α and C-β, being both sp^3-hybridized carbons, are not expected to have their chemical shift greatly influenced by electrostatic factors. Thus, in order successfully to predict and interpret the chemical shift of heavy nuclei in proteins, it is desirable to apply ab initio methods. These, in general, successfully predict shielding for such heavy elements—at least for ^{13}C, ^{15}N, and ^{19}F. The system, however, consists of so many atoms that a computation which includes the whole protein would be prohibitive, even with supercomputers. Fortunately, however, since the chemical shift is inherently a localized property, it is wrong to suppose that the effects of all atoms in a protein need to be incorporated into the computation. One approach is to separate the total shielding, σ_t, into three parts[31]

$$\sigma_t = \sigma_s + \sigma_l + \sigma_0 \quad (1)$$

where σ_s refers to the short-range contribution, σ_l corresponds to long range electrostatic effects, and σ_0 contains the magnetic effects. Although orthogonality may not be achieved, such a partitioning of the various chemical shift contributions helps develop computational strategies for solving each contribution.

The short range contribution can be further divided into several categories: local structure, repulsive interactions, and strong hydrogen bonding. Local structure includes the dependencies of the chemical shift on bond lengths, bond angles, and torsion angles. For the long range electrostatic contributions, several methods can now be used. One can either incorporate the charge field at the self-consistent field (SCF) level,[32] or use the multipole shielding polarizability (MSP) approach.[33] Lastly, σ_0 can be calculated by a variety of classical methods, basically as discussed above for ^{1}H NMR. This contribution is, however, still within the error limits of present ab initio methods for calculating σ_s and σ_l, although it can still be expected to help somewhat with shift predictions. For further discussions on intra- and intermolecular factors which influence shielding, several recent reviews are available.[34,35]

Hence, for a protein, atoms belonging to the residue which contains the nucleus of interest can be regarded as contributing to σ_s, while the rest of the protein contributes to σ_l. This partitioning greatly reduces the size of the fragment on which full ab initio calculations need to be performed. When combined with recent improvements in hardware (such as powerful workstations) and a method which avoids gauge errors in calculating the shielding property [the gauge-including atomic orbital (GIAO) method],[36] together with the application of new algorithms to improve code efficiency,[37] the ab initio reproduction of chemical shifts in proteins is now at hand.

In recent work,[5] it was shown that a small molecular fragment, *N*-formyl-L-alanine amide, interacting with formamide molecules (used to represent hydrogen bond partners) and point charges (representing the rest of the protein) successfully reproduced the experimentally observed ^{13}C chemical shifts for the 12 alanine C-α and C-β sites in the protein staphylococcal nuclease, as shown in Figure 3. The ability to predict the chemical shift opens up a new avenue for protein structure elucidation, especially if the factors which lead to such nonequivalencies can be identified. The partitioning of the shielding as described above greatly facilitated this quest.[5,38] As expected, C-α and C-β chemical shift nonequivalencies were found to be dominated by the local structure, or short-range factors, σ_s.[36] In addition, based upon an examination of the dependencies of C-α and C-β shielding on bond lengths, bond angles, and torsion angles, it was established that torsion angles clearly dominate the experimentally observed trends. In particular, it was also noted that the chemical shifts at these

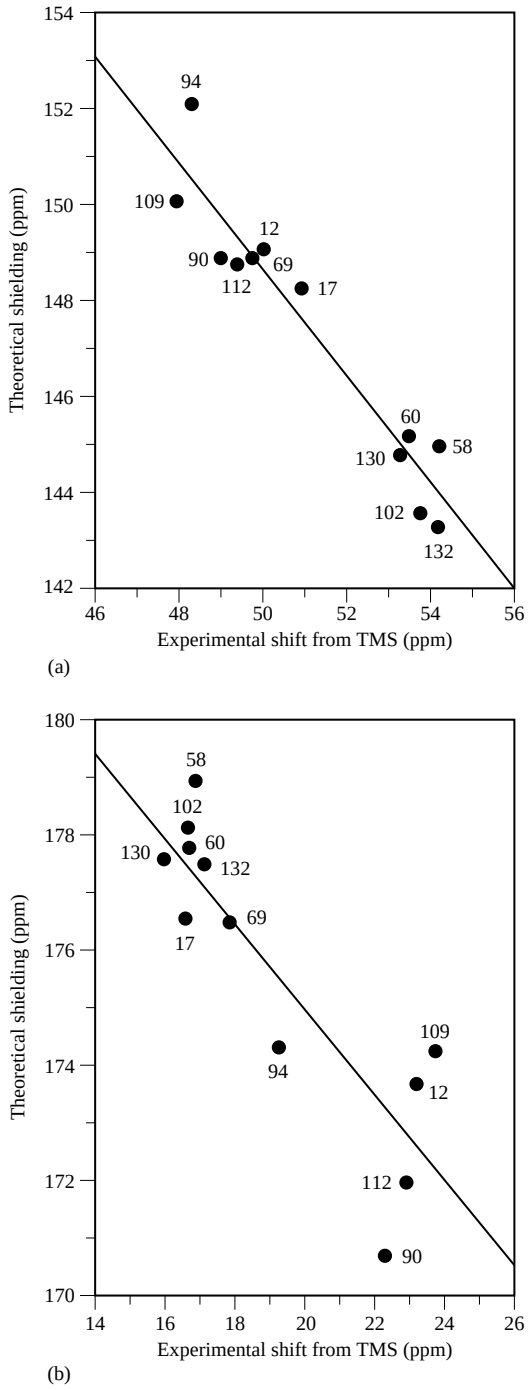

Figure 3 Comparison between calculated ^{13}C NMR shieldings and experimental chemical shifts for alanine residues in staphylococcal nuclease. (a) C-α, (b) C-β. (Reproduced by permission of the American Association for the Advancement of Science from A. C. de Dios, J. G. Pearson, and E. Oldfield, *Science*, 1993, **260**, 1491)

sites were extremely sensitive to bond lengths. In fact, the variations in bond lengths of the same type of residue seen in a single-crystal X-ray structure were shown to lead to a chemical shift range as large as the experimentally measured range, but the predicted shifts were wholly uncorrelated with experiment.[39] Residues of the same type in a protein therefore have bond lengths that are much more similar to each other than X-ray structures would suggest. Nevertheless, from these same studies, ϕ- and ψ-angles were found to be highly correlated with C-α and C-β shifts. Shielding surfaces have therefore been constructed using a model fragment, *N*-formyl-L-alanine amide, in order to map out the effects of ϕ and ψ on C-α and C-β shieldings.[38] With this surface serving as a look-up table, and knowledge of ϕ and ψ, ^{13}C shieldings (or chemical shifts) for any alanine site in a protein can readily be obtained—at least in the absence of large-amplitude motions.

Nitrogen-15 shieldings are expected to be more difficult to predict, since well-defined ϕ and ψ correlations have not been observed, and hydrogen bonding and electrostatic effects could also be important. Recent work,[5] however, has shown that ^{15}N chemical shifts in proteins can now be predicted using the GIAO method, with explicit hydrogen bond partners, and point charges representing the rest of the protein. Figure 4 shows results for valine residues in staphylococcal nuclease.[5] The results in Figure 4(a) were obtained by using a molecular fragment; formyl-L-alanyl-L-valine amide. In Figure 4(b), hydrogen bond partners were explicitly included (as formamide molecules), while Figure 4(c) includes the rest of the protein, represented as point charges. Although the dominance of torsion angles found in ^{13}C chemical shifts is less dramatic with ^{15}N, the generally good accord between calculated and observed values when long range factors are included indicates that ^{15}N NMR is a potentially powerful technique for structure validation. Its sensitivity to long range interactions extends the structural information that can be obtained beyond the local torsion angles, thus complementing ^{13}C NMR.

Although not naturally occurring in most proteins, ^{19}F is a particularly sensitive probe of electrostatic field effects in proteins. Its incorporation, for example, into tryptophan residues of *Escherichia coli* galactose-binding protein (GBP)[40] and hen egg white lysozyme[41] has generated information on how long range factors, such as van der Waals and electrostatic interactions, influence the chemical shift. Using point charges, GIAO has been shown[5] to reproduce satisfactorily the observed ^{19}F NMR spectrum of 5-F-Trp-labeled GBP, except for solvent-exposed sites. With prior knowledge of how shielding is affected by a uniform electric field, field gradient, and field hypergradient (the MSP approach), dynamic averaging becomes tractable,[5] and even shielding at sites that are highly mobile and solvent exposed can be satisfactorily reproduced.[39]

Overall, ^{13}C chemical shifts show great promise in structure elucidation, as noted above for alanine. Successful prediction of ^{13}C chemical shifts has also been shown for glycine and valine residues.[39] Here, the dominance of ϕ and ψ is similarly evident. The correlation between calculated and experimental shieldings for glycine sites is less satisfactory than with alanine and valine, possibly due to glycine mobility. On the other hand, the presence of the side chain in valine introduces an additional angle that can influence both C-α and C-β shieldings. Taking advantage of this additional dependency, crystal-to-solution structural differences became apparent upon close examination of the C-α and C-β shifts of valine residues in calmodulin.[42] Corroborated by coupling constant information, this work demonstrated that five out of the seven valine residues assume a side-chain conformation different from that seen by X-ray crystallography.

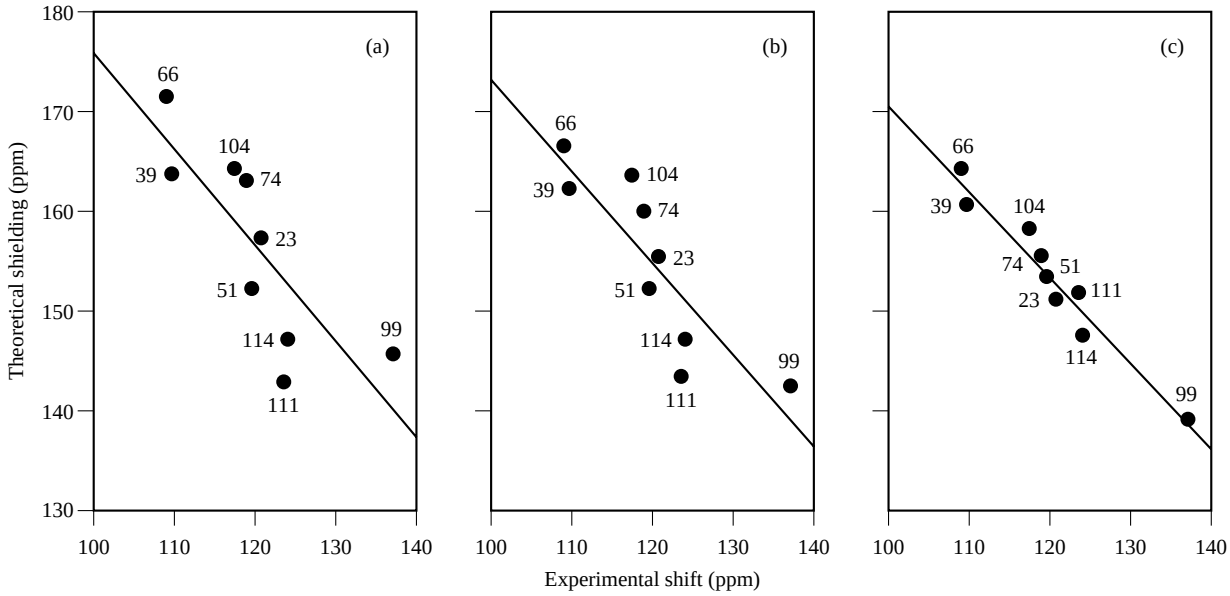

Figure 4 Calculated ^{15}N chemical shieldings versus experimental shifts for the valine sites in staphylococcal nuclease. (a) Using isolated valine fragments; (b) as in part (a) but with inclusion of a hydrogen bond partner; (c) as in part (b) but with incorporation of point charges to represent the rest of the protein. (Reproduced by permission of the American Association for the Advancement of Science from A. C. de Dios, J. G. Pearson, and E. Oldfield, *Science*, 1993, **260**, 1491)

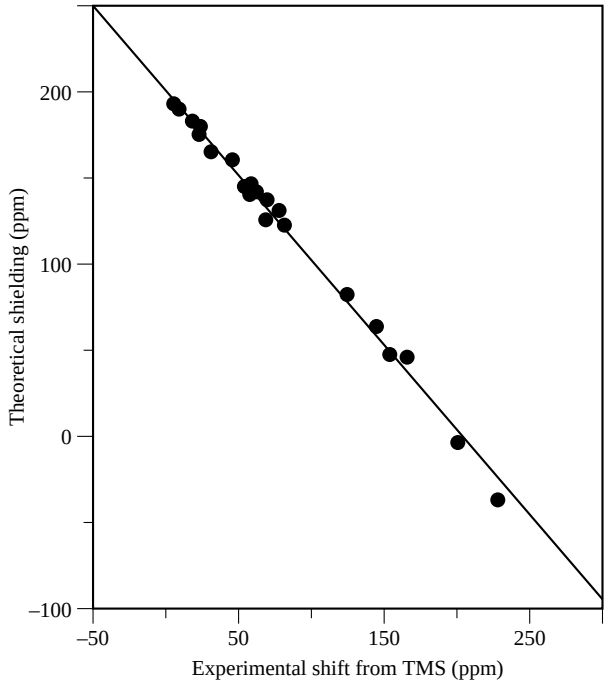

Figure 5 Experimental and theoretical ^{13}C shielding tensor elements for L-threonine in the icosahedral representation. Reprinted with permission from A. C. De Dios et al., *J. Am. Chem. Soc.*, **116**, 5307. Copyright 1994 American Chemical Society

Finally, we briefly consider shielding as a tensor quantity. Here, all elements and their directions need to be evaluated—six parameters versus one isotropic shift, representing a serious challenge for theory. For amino acid crystals, the charge field perturbation gauge including atomic orbital (CFP–GIAO) method gives excellent agreement with experiment.[43] Figure 5 shows a comparison between calculated and experimental shielding components for the ^{13}C nuclei in L-threonine[43] in the icosahedral representation[44] of the shielding tensor. The results shown here clearly illustrate the adequacy of present theoretical methods of predicting chemical shieldings, even in complex (zwitterionic, polar amino acid) systems.

4 NUCLEIC ACIDS

The usefulness of chemical shifts in studying biological systems is naturally not restricted to proteins. Chemical shifts of nucleic acids should similarly encode a wealth of information regarding structure, protonation sites, hydrogen bonding, and electrostatic field effects. The shielding caused by magnetic anisotropy effects on ^{1}H NMR spectra has already been studied using semiempirical methods,[45] and more recently ab initio methods have been used to study the pyrimidine base cytosine.[46] However, these early results were obtained using only a split valence set, insufficiently saturated with basis functions. A more recent study using a larger basis was performed by Schindler[47] using the individual gauge for localized molecular orbitals (IGLO) method.[48] The shielding tensors, as well as the magnetic susceptibilities, were calculated for cytosine, thymine, and uracil, as well as adenine and guanine. The calculated values compared favorably with experiment, but in general the computation of shielding tensors in nucleic acid bases is difficult because definite molecular structures that correspond to the systems on which the NMR measurements were taken are usually not available. In particular, the relative amounts of tautomers depend strongly on the solvent and pH, and the ^{15}N chemical shifts were found to be very sensitive to such environmental effects. Nevertheless, using ab initio optimized structures, it was shown that the calculated ^{15}N shielding trends caused by

protonation could indicate which species dominate in solution. However, the lack of a supportive trend from ^{13}C shieldings did not permit a more precise determination of the dominant tautomer.

5 CARBOHYDRATES

With the importance of carbohydrates in lipid and (glyco)protein structure, as well as in, for example, substrate/inhibitor binding (e.g. in lysozyme), and the occurrence of carbohydrates in metabolism, cell surface antigens, etc., it is surprising that so little work has been reported on ^{13}C and ^{17}O NMR shielding, at the ab initio level. An exception to this is the pioneering work of Grant et al.[49] on ^{13}C shieldings in methyl α-D-glycopyranoside and sucrose. Grant et al. showed that a root mean square deviation (rmsd) of $\sim$3 ppm between theory and experiment (the rmsd from the straight line connecting shift and shielding) with R^2 $\sim$0.97 and a slope of -0.99 (methyl glucoside), could be obtained at the 6-31G level, permitting a convincing reassignment of some earlier chemical shift assignments.

6 STRUCTURE FROM SHIELDING: PREDICTION, REFINEMENT, AND VALIDATION

The ability to predict the NMR spectra of biologically important molecules via ab initio methods heralds a new era in the use of the easiest NMR parameter to measure, the isotropic chemical shift. For proteins, the intimate relationship found between the torsion angles ϕ and ψ and the ^{13}C chemical shifts of C-α and C-β sites strongly suggests that it should be possible to derive structural information from chemical shifts in ways not founded on empirical relationships, size of database, or on X-ray structures. One such method of extracting torsion angles from spectroscopic parameters has recently been proposed.[48] Referred to simply as the 'Z-surface method', it begins with the assumption that a given spectroscopic parameter, P, can be represented as a function of a torsion angle α

$$P = f(\alpha) \tag{2}$$

and the probability that a given value P_i corresponds to a value of α can be cast as in

$$Z_i = \exp[-(P_i - f(\alpha))^2 / W] \tag{3}$$

W is a search width of typically about 1 ppm, and takes into account uncertainties in theoretical and experimental results, e.g. basis deficiencies, referencing errors, etc. Equation (3), of course, assumes a knowledge of $f(\alpha)$, which can be obtained via ab initio methods or from experiment. A plot of Z_i over possible values of α constitutes a probability surface for the angle α. Since the chemical shifts of C-α and C-β are both functions of torsion angles ϕ and ψ, a map of the whole Ramachandran space that shows which pair of ϕ- and ψ-angles closely agree with the observed chemical shifts can be easily constructed. For alanine residues in a variety of proteins, using this approach and the theoretical shielding surfaces for C-α and C-β, plus an experimental surface for H-α, yields values for ϕ and ψ that have only $\sim$10° rmsd values from the X-ray values.[50]

Although ^{15}N chemical shifts are more susceptible to environmental effects, and ^{19}F shift inequivalencies are largely due to electrostatic interactions, this sensitivity of the ^{19}F and ^{15}N shieldings to electrostatic interactions can be utilized in testing present force fields, molecular dynamics programs, and electrostatic field calculations.[51] Moreover, ^{15}N being sensitive to factors other than local structure, it can complement ^{13}C NMR in validating the overall structure of a protein.

7 CONCLUSIONS

Chemical shifts have been reported in biochemical systems for about 30 years. However, only very recently has it been possible to solve the chemical shift problem, and successfully predict chemical shifts in macromolecules, such as proteins.[5] Since chemical shifts can now be intimately related to structure, and vice versa, it seems likely that many new applications to structure prediction, refinement, and validation will stem from these developments. Until recently, it was thought by many to be impossible to predict protein chemical shifts. However, the continuing revolution in computer/disk price/performance ratios now enables study of much larger fragments than heretofore possible. In the future, we believe that many such applications of 'biochemical shifts' and quantum chemistry will contribute greatly to our studies of lipid, protein, nucleic acid, and carbohydrate structure.

8 RELATED ARTICLES

Shielding Calculations: LORG and SOLO Approaches; Chemical Shift Scales on an Absolute Basis; Chemical Shift Tensor Measurement in Solids; Chemical Shift Tensors in Single Crystals; Shielding Calculations: IGLO Method; Shielding Calculations: Perturbation Methods; Shielding: Overview of Theoretical Methods; Shielding in Small Molecules; Shielding Tensor Calculations; Shielding Theory: GIAO Method.

9 REFERENCES

1. C. C. McDonald and W. D. Phillips, *J. Am. Chem. Soc.*, 1969, **91**, 1513.
2. A. Allerhand, R. F. Childers, and E. Oldfield, *Biochemistry*, 1973, **12**, 1335.
3. A. Bax, M. Ikura, L. E. Kay, D. A. Torchia, R. Tschudin, *J. Magn. Reson.*, 1991, **86**, 304.
4. G. M. Clore and A. M. Gronenborn, *Prog. Nucl. Magn. Reson. Spectros.*, 1991, **23**, 43.
5. A. C. de Dios, J. G. Pearson, and E. Oldfield, *Science*, 1993, **260**, 1491.
6. J. L. Markley, D. H. Meadows, and O. Jardetzky, *J. Mol. Biol.*, 1967, **27**, 25.
7. H. Sternlicht and D. Wilson, *Biochemistry*, 1967, **6**, 2881.
8. H. L. Tigelaar and W. H. Flygare, *J. Am. Chem. Soc.*, 1972, **94**, 343.

9. N. J. Clayden and R. J. P. Williams, *J. Magn. Reson.*, 1982, **49**, 383.
10. A. Pardi, G. Wagner, and K. Wuthrich, *Eur. J. Biochem.*, 1983, **137**, 445.
11. H. R. Kricheldorf, W. E. Hull, and D. Muller, *Macromolecules*, 1985, **18**, 2135.
12. H. Saito, R. Tabeta, A. Shoji, T. Ozaki, I. Ando, and T. Asakura, in *Magnetic Resonance in Biology and Medicine*, ed G. Govil, C. L. Khetrapal, A. Saran, Tata McGraw-Hill, New Delhi, 1985, pp. 195–215.
13. I. Ando, H. Saito, R. Tabeta, A. Shoji, and T. Ozaki, *Macromolecules*, 1984, **17**, 457.
14. S. Spera and A. Bax, *J. Am. Chem. Soc.*, 1991, **113**, 5490.
15. D. S. Wishart and B. D. Sykes, *J. Biomol. NMR*, 1994, **4**, 171.
16. G. C. Levy and R. L. Lichter, in *Nitrogen-15 NMR spectroscopy*, Wiley-Interscience, New York, 1979.
17. M. Witanowski, L. Stefaniak, G. A. Webb, *Annu. Rev. NMR Spectrosc.*, 1986, **18**, 65.
18. J. Glushka and D. Cowburn, *J. Am. Chem. Soc.*, 1987, **109**, 7879.
19. H. Le and E. Oldfield, *J. Biomol. NMR*, 1994, **4**, 341.
20. A. E. Tonelli, *J. Am. Chem. Soc.*, 1980, **102**, 7635.
21. B. R. Seavey, E. A. Farr, W. M. Westler, and J. L. Markley, *J. Biomol. NMR*, 1991, 217.
22. M. A. Jiménez, J. L. Nieto, J. Herranz, M. Rico, and J. Santoro, *FEBS Lett.*, 1987, **221**, 320.
23. L. Szilágyi and O. Jardetzky, *J. Magn. Reson.*, 1989, **83**, 441.
24. M. P. Williamson, *Biopolymers*, 1990, **29**, 1423.
25. A. Pastore and V. Saudek, *J. Magn. Reson.*, 1990, **90**, 165.
26. D. S. Wishart, B. D. Sykes, and F. M. Richards, *J. Mol. Biol.*, 1991, **222**, 311.
27. I. D. Kuntz, P. A. Kosen, and E. C. Craig, *J. Am. Chem. Soc.*, 1991, **113**, 1406.
28. K. Ösapay and D. A. Case, *J. Am. Chem. Soc.*, 1991, **113**, 9436.
29. M. P. Williamson and T. Asakura, *FEBS Lett.*, 1992, **302**, 185.
30. K. Ösapay and D. A. Case, *NATO Adv. Study Inst.*, ed. J. A. Tossel, Kluwer, Dordrecht, 1993, 572; D. A. Case and P. E. Wright, in *NMR of Proteins*, ed. G. M. Clore, and A. M. Gronenborn, Macmillan, New York, 1993, pp. 53–91.
31. A. C. de Dios and E. Oldfield, *Chem. Phys. Lett.*, 1993, **205**, 108.
32. A. D. Buckingham and K. P. Lawley, *Mol. Phys.*, 1960, **3**, 219.
33. J. D. Augspurger, C. E. Dykstra, and E. Oldfield, *J. Am. Chem. Soc.*, 1991, **113**, 2447.
34. C. J. Jameson and A. C. de Dios, in *Nuclear Magnetic Shieldings and Molecular Structure*, ed. J. A. Tossell, Kluwer, Dordrecht, 1993, pp. 95–116.
35. A. C. de Dios and C. J. Jameson, *Annu. Rep. NMR Spectrosc.*, 1994, **29**, 1.
36. R. Ditchfield, *J. Chem. Phys.*, 1972, **56**, 5688.
37. K. Wolinski, J. F. Hinton, and P. Pulay, *J. Am. Chem. Soc.*, 1990, **112**, 8251.
38. A. C. de Dios, J. G. Pearson, and E. Oldfield, *J. Am. Chem. Soc.*, 1993, **115**, 9768.
39. D. D. Laws, A. C. de Dios, and E. Oldfield, *J. Biomol. NMR*, 1993, **3**, 607.
40. L. A. Luck and J. J. Falke, *Biochemistry*, 1991, **30**, 4248.
41. C. Lian, H. Le, B. Montez, J. Patterson, S. Harrell, D. D. Laws, I. Matsumura, J. G. Pearson, and E. Oldfield, *Biochemistry*, 1994, **33**, 5238.
42. A. C. de Dios and E. Oldfield, *J. Am. Chem. Soc.*, 1994, **116**, 5307.
43. A. C. de Dios, D. D. Laws, and E. Oldfield, *J. Am. Chem. Soc.*, 1994, **116**, 7784.
44. D. W. Alderman, M. H. Sherwood, and D. M. Grant, *J. Magn. Reson.* 1993, **101**, 188.
45. C. Giessner-Prettre and B. Pullman, *Biochem. Biophys. Res. Commun.*, 1976, **70**, 578.
46. F. R. Prado and C. Giessner-Prettre, *J. Magn. Reson.*, 1982, **47**, 103.
47. M. Schindler, *J. Am. Chem. Soc.*, 1988, **110**, 6623.
48. M. Schindler and W. Kutzelnigg, *J. Chem. Phys.*, 1982, **76**, 1919.
49. D. M. Grant, J. C. Facelli, D. W. Alderman, and M. H. Sherwood, in *Nuclear Magnetic Shieldings and Molecular Structure*, ed. J. A. Tossell, Kluwer, Dordrecht, 1993, pp. 367–384.
50. H. Le, J. G. Pearson, A. C. de Dios, and E. Oldfield, *J. Am. Chem. Soc.*, 1995, **117**, 3800.
51. J. G. Pearson, E. Oldfield, F. S. Lee, and A. Warshel, *J. Am. Chem. Soc.*, 1993, **115**, 6851.

Acknowledgments

Work supported by NIH grant HL-19481.

Biographical Sketches

Angel C. de Dios. *b* 1965. B.S., 1985, Ateneo de Manila University, Philippines, Ph.D., 1992 (supervisor Cynthia Jameson), University of Illinois at Chicago, USA. Postdoctoral work at University of Illinois at Urbana-Champaign, USA (with Eric Oldfield). Postdoctoral research associate, University of Illinois at Urbana-Champaign, 1992–present. Approx. 20 publications. Research specialities: intra- and intermolecular effects on chemical shifts, gas phase NMR spectroscopy.

Eric Oldfield. *b* 1948. B.Sc., 1969, University of Bristol, Ph.D., 1972 (supervisor Dennis Chapman), University of Sheffield, D.Sc., 1982, University of Bristol, UK. Postdoctoral work at Indiana University, Bloomington (with Adam Allerhand) and Massachusetts Institute of Technology, Cambridge (with John S. Waugh). Professor, University of Illinois at Urbana-Champaign, 1975–present. Approx. 170 publications. Research specialties: inorganic and biochemical applications, especially proteins, membranes, and heterogeneous catalysts.

Nucleic Acids: Chemical Shifts

David Cowburn

The Rockefeller University, New York, NY, USA

1	Introduction	1
2	DNA Oligomers	1
3	^{13}C and ^{15}N Shifts	1
4	Temperature Dependence of ^{13}C Shifts	2
5	Issues with RNA	3
6	^{15}N Sites as Structural Indicators	3
7	Conclusions	3
8	Related Articles	3
9	References	3

1 INTRODUCTION

This article concentrates on chemical shifts in nucleic acids as indicators of conformation. Shifts of ^{1}H, ^{13}C, and ^{15}N are reviewed. A complete treatment of ^{31}P shifts is given elsewhere by Gorenstein (see ***Nucleic Acids: Phosphorus-31 NMR***), as is the characterization of unusual bases by Agris (see ***RNA Structure and Function: Modified Nucleosides***). The nomenclature used is that of Saenger.[1] In this short article, it is not possible to review the whole subject, so emphasis is placed on areas of major impact, without attempt to be comprehensive or to apply historical credit.

Nucleic acid structures in solution continue to be a major research topic, because of both general chemical interest and the burgeoning industry of understanding the detailed interactions of nucleic acids in biological processes. Two examples of special interest are how proteins and nucleic acids recognize each other and whether there are general rules, and how some ribonucleic acids (RNAs) achieve catalytic activities. The use of chemical shifts continues to be of importance because the structures of many nucleic acids are dynamic and polymorphic. Shift analysis can attempt to achieve the simple objective of defining whether there is predominantly a single structure (or small family) to be analyzed, and can, in favorable cases, achieve the more complex objective of a reasonable level of secondary structural information. To address the more complex biological areas, higher molecular weight complexes require study, since the structures of the nucleic acid components alone rarely provide any clear perspective on the mode of binding and interaction, as vividly illustrated in the dramatic twisting of the deoxyribonucleic acid (DNA) strands in complexes with Transcriptional Binding Protein (TBP)[2] a result entirely unanticipated from solution studies of the DNA oligomers alone. Higher molecular weight complexes, often with proteins or other nonnucleic acid components, have extensively overlapped spectra, so the additional dispersion from the use of heteronuclei and multidimensional NMR becomes imperative.

2 DNA OLIGOMERS

The naming of atom positions in the bases and in deoxyribose are shown in Figure 1, which also illustrates the base pairing expected in the Watson–Crick form. In this form, imino and amino hydrogens have reduced rates of exchange with solvent hydrogen, and so the appearance of these normally exchangeable hydrogens in the spectrum is diagnostic of base pairing. The observation of well-resolved imino resonances of comparable width and intensity to nonexchangeable hydrogen resonances then provides definitive evidence for a single well-defined structure. Successful structural investigations appear to rely heavily on this characteristic to find conditions of temperature, pH, cations, etc., favorable to the determination.

Standard procedures exist for assignment of most exchangeable[3,4] and nonexchangeable hydrogens.[5–8] The shifts of nonexchangeable hydrogens in B type DNA have been thoroughly analyzed in over 600 nucleotides. The shifts of H-2′, H2″, H3′, H4′ and H6/H8 are dominated by the identity of the attached base. Cytidine (C) H-5 and thymine (T) CH_3 are influenced by the adjacent 5′ base, while H-1′ is influenced by the adjacent 3′ base. The averaged values and their distribution profiles are for oligonucleotides observed under fairly wide solution conditions and temperatures, so highly precise reference values are probably best obtained by using those from a closely related sequence under similar solution and temperature conditions.[5]

Shifts outside the normal ranges can be used as preliminary identification of sites of binding or modification. For example, the shifts of base and sugar H-1′ in a modified duplex with benzopyrene diol epoxide have been used as supporting evidence for the stacking of the benzopyrene ring directly over the sugar of one base in the minor groove.[9] In closely analogous sequences, similarities of many shifts of the unchanged residues can then be used to infer similarity of structure. For example, the base and 2′,2″ shift of an A_3 bulge (A = adenosine) from a duplex are virtually identical to those in an AIA bulge (I = inosine), when the I substitution is used to separate otherwise isochronous A H8 signals for the purposes of sequential assignment by COSY and NOESY.[10]

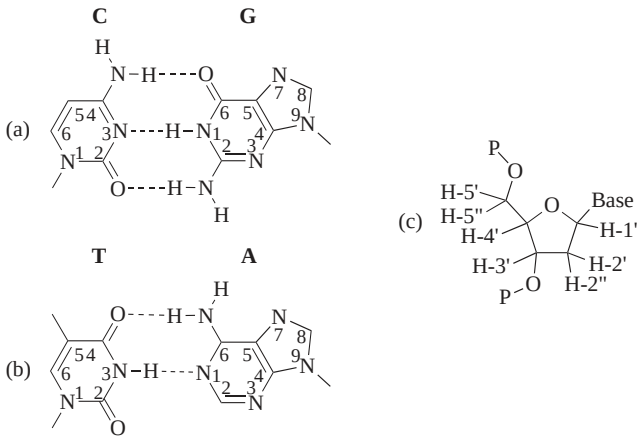

Figure 1 Scheme of Watson–Crick base pairing in deoxynucleotides for (a) cytosine and guanine, and (b) thymine, and adenine. (c) Nomenclature for the deoxyribose ring

3 ^{13}C AND ^{15}N SHIFTS

The extension of these uses of shifts of hydrogens to other nuclei was a natural development, impeded by the difficulties of synthetic incorporation of stable isotope labels, and/or by low NMR sensitivity. Incorporation of labels still remains very expensive, and for DNA the precursor deoxynucleotides present difficulties. Labeling of RNA has become practical and efficient for designed sequences,[11,12] and transfer RNAs have been biosynthetically labeled for assignment purposes for many years. Indirect detection methods, and their elaboration into methods for connectivity determination using multidimensional NMR,[13] have similarly alleviated sensitivity issues. Indirect detection methods have made it practical to observe ^{13}C and ^{15}N shifts without enrichment, and these have provided, complementarily to earlier studies with short oligonucleotides,[14] an adequate base for assignment and interpretation for DNA oligomers.[15–17] For example, for ^{13}C shifts, purine C-2 resonances are sufficiently separated from purine C-8 and pyrimidine C-6 resonances, that the overlap in the hydrogen spectra of the appropriate H2, H8, and H6 resonances can be partially resolved by inspection. Similarly, H1′ and pyrimidine H5 can be type assigned by two-dimensional (2D) separation of the C-1′ and C5 resonances, and H3′, H4′, H5′, and H5″ are separable also. Purine C-8 can be discriminated from pyrimidine C6 by the C8s larger $^{1}J(^{13}\mathrm{C},^{1}\mathrm{H})$ value in coupled spectra. For ^{15}N parameters, in the critical imino area, pyrimidine N3 and purine N1 are separated by about 10 ppm, permitting considerable additional resolution of the imino hydrogens in a $^{15}\mathrm{N}/^{1}\mathrm{H}$ 2D map. These experiments are still relatively little used, despite their clear and rich information content.[18–20]

4 TEMPERATURE DEPENDENCE OF ^{13}C SHIFTS

The profiles of chemical shifts with temperature have received considerable attention, especially those for hydrogen. This approach provides a potential avenue to understanding the contributions of individual components to the melting phenomena, in contrast to the bulk properties observed by ultraviolet absorption or circular dichroism. The interpretation of the changes of shifts observed has not proved to be entirely simple, and increasingly elaborate models have been used.[21] Variable temperature studies using ^{13}C have been more limited. This is in spite of the potential for using relaxation dynamics, or the effects of pseudorotation of the ribose ring on shifts.[22] Detailed temperature profiles of a small number of oligomers are available for base[16] and sugar[22] carbons. These provide a highly detailed grounding from which to consider the origin of shifts in oligonucleotides.

The observations for bases may be summarized as follows. A range of shifts of about 3 ppm for each class of carbon in the low-temperature duplex narrows to <1 ppm range at high temperature. Residues at the termini show smaller transitions than others. The slopes of $\mathrm{d}\delta/\mathrm{d}T$ are mixed (positive, negative, around zero), with most showing the largest change at around the melting temperature, but with clear evidence for one or more 'pretransitions' below that temperature, especially at carbons at guanosine G2, G6, and T4. There is essentially no obvious neighboring dependence for each pair of base types.

Detailed quantum mechanical calculations of the shifts for bases[23,24] and sugars[25] are available. Naturally, the match of experiment and theory will be limited by neglect of conformation averaging, of solvation, and by the limited orbital sets used. For bases, the melting effects have been summarized[16] as arising from changes in hydrogen bonding, both that to a partner base and that to solvent, from base stacking effects, and from steric compression. Hydrogen bond related changes occur on those carbons adjacent to a nitrogen or carbonyl participating in hydrogen bonding. Since those sites may be involved in hydrogen bonding with other bases, or with solvent water, changes are then the summation of multiple effects depending on the relative strengths of the different hydrogen bonds involved. The expectation is then that substantial negative $\mathrm{d}\delta/\mathrm{d}T$ values should be seen for C2 and 6 in G, and 4 in T, with lesser effects at 2, 5, and 6 in A, and 2, 4, 5, and 6 in C. Base stacking effects are similarly complex in effect, and it may be concluded that a geometric effect similar to a ring current shift would be expected to produce a positive $\mathrm{d}\delta/\mathrm{d}T$ going from a stacked to a single-stranded form. It seems unlikely that steric compression effects could play a major role in shifts in such duplexes, where there are considerable degrees of backbone freedom.[1] The most reasonable hypothesis concerning the temperature dependence of base shifts then centers on the cooperative transition of melting changing simultaneously the oppositely signed contributions of geometric stacking and of hydrogen bonding. The individual changes then reflect the different roles of each carbon with respect to the geometry of the stacking, or the adjacency to a hydrogen bonding site. A plausible hypothesis for the premelting changes is that there is apparent weakening of the hydrogen bonding prior to the principal transition.

In the case of deoxyribose sugars,[22] the temperature dependence of carbon shifts might be expected to shed light on the much discussed issue of pseudorotation in the sugar ring. Early work[26] suggested that fitting the observed vicinal coupling constants in deoxyribosides needed at least a two-state model, incorporating the 'N' (North), 3′-*endo*, or 'S' (South), 2′-*endo* conformers of the ring.[1] This is now generally,[27] though not universally,[28,29] accepted for oligonucleotide analysis also, with the caveat that other sugar puckers may be significantly populated, but cannot be easily experimentally analyzed, so Occam's razor reduces us to using the simplest model.[27] This and other issues[30,31] continue to point out possible limitations of high-precision attempts to determine DNA oligomer using single conformer models. Sugar ^{13}C shifts might be a useful additional characteristic of ring pucker, and this has been established for some RNA oligonucleotides,[20,32] in a relatively straightforward way. Detailed studies of DNA oligomers do not support this kind of analysis, and deviations of shifts with respect to temperature show quite different patterns.[22] A general explanation is that indeed multiple ring conformers do exist, and that the deoxyribose and ribose rings naturally have different sets of conformers. The general magnitude of the alteration of shift with melting is, however, quite small (about 1–2 ppm), so it is very difficult to make a complete differentiation of shift effects arising solely through ring conformation, from those arising from ring current (magnetic anisotropy) and other more distant effects. In general, the conclusion that these melting curves require a more complex explanation than an S–N conversion

alone is fully justified, and more detailed studies of the effects of sequence seem appropriate.

5 ISSUES WITH RNA

Spectral assignment in RNA had previously been difficult, because of the overlap of sugar hydrogens in the 4–5 ppm region. Resolution by multidimensional heteronuclear shift correlation with ^{13}C provides a straightforward additional dispersion, with C-5′, C-3′, C-2′, C-4′, and C-1′ being ordered in increasing shift in relatively well-separated groups.[33] It remains to be seen, in the large structural variations of bulges, internal loop, duplexes, and hairpins, whether these simple classifications will suffice. The success of a multidimensional, triple resonance approach using $^{13}C/^{15}N$ dual-labeled duplex dodecamer,[34] bodes well for complete assignment of significantly larger RNAs. This approach similarly depends on the large ^{13}C dispersion to separate out sugar hydrogens.

Using the characteristic imino hydrogen region, several laboratories made remarkable progress in assigning larger RNAs, especially transfer RNAs and 5S RNA. Additional information from ^{15}N shifts has also been widely used, mainly for group-specific assignments.

6 ^{15}N SITES AS STRUCTURAL INDICATORS

It will be readily apparent by inspection of Figure 1, that nitrogens are potentially reporters at the sites of the major interactions of the bases. They participate in the Watson–Crick hydrogen bonding (C,3,4; G,1,2; T,3; and A,1,6), serving as donor in all cases, and recipient at C3 and A1. The major groove of a double helix is also lined with the amino groups of A and C, and the nitrogen at position 7 in purines A and G, while the purine position 3 is exposed in the minor groove. The known perturbations of shifts on hydrogen bonding, for donor or recipient, then provide a specific window into the major recognition elements of the bases. This simple reporting may be invaluable in larger complexes where full determination of structure is presently impractical. Some existing studies include the investigation of Hoogsteen hydrogen bonding in triple helices[19] and guanine tetrads,[35] investigations of the effects of *O*-methylation,[36,37] and studies of netropsin/duplex complexes.[17,38]

DNA triplexes can be readily formed by appropriate sequences in which a purine-rich tract makes Watson–Crick contacts with a pyrimidine-rich strand, and then a subsequent pyrimidine-rich strand make predominantly Hoogsteen pairing to the central purine-rich portion, and the Watson–Crick pairing is readily apparent in the shifts of G1 and T3 nitrogens.[19] In guanine-rich tetrads, the shift variation between duplex, tetrad, and single strand forms for the N-7 of G in two sequences was found to be rather small, and while hydration effects and hydrogen bonding may be usefully investigated in lower molecular weight complexes,[35] the prospects for use in larger complexes are not clear.

Several oligomers containing [1′-^{15}N]- and [2-^{15}N]-O^6-methyl-2′-deoxyguanosine have been studied, confirming expected base pairings in mismatches against C and T. These studies elegantly illustrate the positional specificity available from NMR studies for base–base hydrogen bonding and for the pH and temperature dependence of such bonding. For the O^6MeGT pair, there is direct hydrogen bonding at N-2 but not N-1, with N-1 probably fully solvated.[36] In contrast, the O^6MeGC pair has a very complex, pH-dependent, wobble pairing.[37] The low-frequency melting shift of the [1-^{15}N]O^6MeGC resonance (3 ppm) is similar to that for other hydrogen bond acceptors, whereas the high-frequency shift of [2-^{15}N]O^6MeGC (8 ppm) is not similarly matched. This is in line with expected differences in hydrogen bond strength: the apparent high-frequency shift of an O^6MeG $^{15}N2$ as an sp^3 hydrogen bond donor to an sp^2 nitrogen acceptor is significantly greater than that associated with NH_2–O interaction.

The structures of netropsin/DNA oligomer complexes have been extensively studied by X-ray and NMR methods. Nitrogen-15 studies are fully consistent with the general view that netropsin displaces water of hydration from the minor groove, without significant perturbation of the duplex structure. Shifts from positions 3 in A,[38] 1 in G, and 3 in T[17] are all indicative of modulated hydrogen bonding on complexation at the expected positions. The suggestion[17] that larger perturbations of 3 in T result from the alterations of the adjacent carbonyl's hydrogen bonding indicates a possible sensor of the critical pyrimidine 2-position in the minor groove, but requires further experimental support.

7 CONCLUSIONS

The major motivation for continuing interest in this area is the need for better tools to study macromolecular interactions involving larger pieces of nucleic acids than are currently normally studied. Shifts on formation of DNA–protein complexes have been reported for several cases.[39–41] In general, these shifts are interpretable using the same rationales, interrelation, major or minor groove binding, disruption of pairing and/or stacking, and possible displacement of water, and it may be expected that their extension with ^{13}C and ^{15}N labeled nucleic acid components would be invaluable. Continuing efforts in rationalizing the observed shift effects then also remain a priority.

8 RELATED ARTICLES

Nucleic Acid Flexibility and Dynamics: Deuterium NMR; Nucleic Acid Structures in Solution: Sequence Dependence; Nucleic Acids: Base Stacking and Base Pairing Interactions; Nucleic Acids: Phosphorus-31 NMR; Nucleic Acids: Spectra, Structures, and Dynamics.

9 REFERENCES

1. W. Saenger, *Principles of Nucleic Acid Structure*, Springer, New York, 1983.
2. J. L. Kim, D. B. Nikolov, and S. K. Burley, *Nature (London)*, 1993, **365**, 520.
3. D. J. Patel, L. Shapiro, and D. Hare, *Q. Rev. Biophys.*, 1987, **20**, 35.

4. J. Feigon, V. Sklenár, E. Wang, D. E. Gilbert, R. F. Macaya, and P. Schultze, *Methods Enzymol.*, 1992, **211**, 235.
5. F. J. M. v. d. Ven, and C. W. Hilbers, *Nucleic Acids Res.*, 1988, **16**, 5713.
6. S. H. Chou, D. R. Hare, D. E. Wemmer, and B. R. Reid, *Biochemistry*, 1983, **22**, 3037.
7. A. Kintanar, R. E. Klevit, and B. R. Reid, *Nucleic Acids Res.*, 1987, **15**, 5845.
8. K. Wüthrich, *NMR of Proteins and Nucleic Acids*, Wiley, New York, 1986.
9. C. de los Santos, M. Cosman, B. E. Hingerty, V. Ibanez, L. A. Margulis, N. E. Geacintov, S. Broyde, and D. J. Patel, *Biochemistry*, 1992, **31**, 5245.
10. I. Radhakrishnan, C. de los Santos, and D. J. Patel, *J. Mol. Biol.*, 1993, **234**, 188.
11. E. P. Nikonowicz, A. Sirr, P. Legault, F. M. Jucker, L. M. Baer, and A. Pardi, *Nucleic Acids Res.*, 1992, **20**, 4507.
12. R. T. Batey, M. Inada, E. Kujawinski, J. D. Puglisi, and J. R. Williamson, *Nucleic Acids Res.*, 1992, **20**, 4515.
13. G. M. Clore and A. Gronenborn, *Science*, 1991, **252**, 1390.
14. P. P. Lankhorst, C. A. Haasnoot, C. Erkelens, H. P. Westerink, G. A. van der Marel, J. H. van Boom, and C. Altona, *Nucleic Acids Res.*, 1985, **13**, 927.
15. W. Leupin, G. Wagner, W. A. Denny, and K. Wüthrich, *Nucleic Acids Res.*, 1987, **15**, 267.
16. S. R. La Plante, E. A. Boudreau, N. Zanatta, G. C. Levy, P. N. Borer, J. Ashcroft, and D. Cowburn, *Biochemistry*, 1988, **27**, 7902.
17. J. Ashcroft, D. H. Live, D. J. Patel, and D. Cowburn, *Biopolymers*, 1991, **31**, 45.
18. D. H. Live, I. Radhakrishnan, V. Misra, and D. J. Patel, *J. Am. Chem. Soc.*, 1991, **113**, 4687.
19. I. Radhakrishnan, X. Gao, C. de los Santos, D. Live, and D. J. Patel, *Biochemistry*, 1991, **30**, 9022.
20. G. Varani and I. Tinoco, *J. Am. Chem. Soc.*, 1991, **113**, 9349.
21. J. M. L. Pieters, J. R. Mellema, H. van den Elst, G. A. van der Marel, J. H. van Boom, and C. Altona, *Biopolymers*, 1989, **28**, 717.
22. S. R. LaPlante, N. Zannatta, A. Hakkinen, A. H.-J. Wang, and P. N. Borer, *Biochemistry*, 1994, **33**, 2430.
23. C. Giesner-Prettre, *J. Biomol. Struct. Dyn.*, 1984, **2**, 233.
24. C. Giessner-Prettre, *J. Biomol. Struct. Dyn.*, 1986, **4**, 99.
25. C. Giessner-Prettre, *J. Biomol. Struct. Dyn.*, 1985, **3**, 145.
26. C. Altona and M. Sundaralingam, *J. Am. Chem. Soc.*, 1972, **94**, 8205.
27. K. D. Bishop, F. J. H. Blocker, W. Egan, and T. L. James, *Biochemistry*, 1994, **33**, 427.
28. J. T. Davis, S. Hirani, C. Bartlett, and B. R. Reid, *J. Biol. Chem.*, 1994, **269**, 3331.
29. S. G. Kim and B. R. Reid, *Biochemistry*, 1992, **31**, 12103.
30. W. J. Metzler, C. Wang, D. B. Kitchen, R. M. Levy, and A. Pardi, *J. Mol. Biol.*, 1990, **214**, 711.
31. F. J. M. van de Ven and C. W. Hilbers, *Eur. J. Biochem.*, 1988, **178**, 1.
32. P. P. Lankhorst, C. Erkelens, C. A. G. Haasnoot, and C. Altona, *Nucleic Acids Res.*, 1983, **11**, 7215.
33. G. Varani and I. Tinoco, Jr., *Q. Rev. Biophys.*, 1991, **24**, 479.
34. E. P. Nikonowicz and A. Pardi, *J. Mol. Biol.*, 1993, **232**, 1141.
35. B. L. Gaffney, C. Wang, and R. A. Jones, *J. Am. Chem. Soc.*, 1992, **114**, 4047.
36. B. Goswami, B. L. Gaffney, and R. A. Jones, *J. Am. Chem. Soc.*, 1993, **115**, 3832.
37. B. L. Gaffney, B. Goswami, and R. A. Jones, *J. Am. Chem. Soc.*, 1993, **115**, 12607.
38. Y. S. Rhee, C. Wang, B. L. Gaffney, and R. A. Jones, *J. Am. Chem. Soc.*, 1993, **115**, 8742.
39. G. Otting, Y. Q. Qian, M. Billeter, M. Muller, M. Affolter, W. J. Gehring, and K. Wüthrich, *EMBO J.*, 1990, **9**, 3085.
40. M. Shirakawa, H. Matsuo, Y. Serikawa, N. Suzuki, and Y. Kyogoku, in *Molecular Structure and Life: Molecular Recognition of Nucleic Acids*, eds. Y. Kyogoku and Y. Nishimura, Japan Science Society Press, Tokyo, 1992.
41. R. M. J. N. Lamerichs, R. Boelens, G. A. van der Marel, J. H. van Boom, R. Kaptein, F. Buck, B. Fera, and H. Rüterjans, *Biochemistry*, 1989, **28**, 2985.

Biographical Sketch

David Cowburn. *b* 1945. B.Sc., 1965, University of Manchester Institute of Science and Technology; Ph.D., 1970, London University; D.Sc., 1980, London University. Fascinated during Ph.D. by the potential for NMR as a structural tool in biochemistry. Faculty of Rockefeller University, 1973–present. Approx. 100 publications. Research interests include structure–function relationships in biological chemistry, development of magnetic resonance techniques in biomedical research, determination of molecular conformation by spectroscopic techniques, particularly magnetic resonance and applications of these to understanding molecular mechanism of control of genetic expression, and of intracellular signal transduction.

Oxygen-17 NMR: Applications in Biochemistry

John G. Pearson and Eric Oldfield

University of Illinois at Urbana-Champaign, IL, USA

1	Introduction	1
2	^{17}O NMR Parameters	1
3	Biophosphates	1
4	Amino Acids and Polypeptides	2
5	CO and O^2 in Hemoproteins	2
6	Summary and Prospects	2
7	Related Article	2
8	References	2

1 INTRODUCTION

^{17}O is the least utilized of the NMR active nuclei commonly found in biological systems. While oxygen atoms play an important role in the hydrogen bonding, electrostatics, and hydration of biomolecules, the very low natural abundance (0.037%) and quadrupolar nature ($I = \frac{5}{2}$) of ^{17}O nuclei have hindered the development of ^{17}O NMR as compared with ^{1}H, ^{13}C, ^{15}N, and ^{31}P NMR in biological systems. Over the last decade, however, the availability of both ^{17}O enriched materials and ever higher field FT NMR spectrometers have led to the utilization of ^{17}O nuclei as probes of biomolecular structure and function, some 40 years after the nucleus was first observed.[1]

It is the intention of this article to review the characteristic parameters governing the use of ^{17}O NMR in, and how the behavior of ^{17}O nuclear spin magnetization has been applied to, biological systems. The effects of ^{17}O quadrupolar relaxation on ^{31}P magnetization are also important, but are beyond the scope of this review.

2 ^{17}O NMR PARAMETERS

The detailed quantum chemical description of sites in biologically relevant molecules is, in general, extremely complex. The task is greatly simplified in NMR by modeling nuclear spin interactions as independent of the rest of the system, with time-dependent interactions between spins and the bulk (or lattice) being termed 'relaxation'. This, and other considerations, allows for the simplification of the ^{17}O NMR of biomolecules to the study of ^{17}O chemical shielding, ^{17}O relaxation (resulting from couplings between the nuclear quadrupole and its local environment), and ^{17}O quadrupole couplings.

The chemical shielding of a nucleus is a function of the electronic structure near the nucleus. ^{17}O nuclei are particularly sensitive to differences in chemical environment; for example, the two distinct oxygen sites in ozone are separated by 566 ppm.[2] Differences in chemical shift between sites in a molecule can be used to determine molecular structures, as well as to study dynamical processes in these structures, such as conformational changes, substrate binding, and hydrogen bonding. The ^{17}O chemical shift is commonly referenced to $H_2{}^{17}O$ in biological NMR studies.

All nuclei with $I > \frac{1}{2}$ have a nuclear quadrupole moment eQ. The interaction of eQ with an electric field gradient eq is quite strong, typically dominating the NMR spectrum of a quadrupolar nucleus. For most biomolecules, the interaction between the eQ of ^{17}O and eq is modulated by rotational motion, either molecular tumbling or internal rotations, making it an efficient relaxation mechanism. In the extreme narrowing limit (very fast motions on the NMR timescale), the nuclear quadrupole relaxation rate essentially determines the resonance linewidth L which can be expressed as

$$L \approx (12\pi/125)(1 + \eta^2/3)\chi^2\tau_r \qquad (1)$$

where $\chi = e^2qQ/h$ is the nuclear quadrupole coupling constant, η is the asymmetry parameter of the electric field gradient tensor, and τ_r is the rotational correlation time.[3] ^{17}O linewidths are therefore proportional to the square of the electric field gradient at the nucleus, and are generally inversely proportional to the molecular correlation time. This limits the applicability of ^{17}O NMR either to relatively small molecules or to sites in molecules where χ is much less than typically found for ^{17}O nuclei (about 10 MHz, see Kintzinger[4]). Within this limitation, ^{17}O relaxation can be used to measure differences in χ and τ_r for either two sites in the same molecule, or the same site under different conditions. For slow molecular motions ($\tau_r \gg 1/\nu_L$) relaxation is a weighted sum of three exponentials, resulting in deviations from Lorentzian lineshapes, and such effects have been observed experimentally for C^{17}O bound to heme proteins, where χ values are very small (about 1–2 MHz).[5]

3 BIOPHOSPHATES

Biophosphates are involved in many biological processes, such as energy transport and utilization, information storage and retrieval, and membrane structure and transport. Examples of such compounds are adenosine diphosphate (ADP), adenosine triphosphate (ATP), DNA, RNA, and phospholipids.

Tsai et al.[6] have demonstrated that bridging and phosphoryl ^{17}O resonances in biophosphates can be assigned from their relative linewidths, due to differences in χ between the various sites. Linewidths are all relatively broad, and several groups have demonstrated improved spectral resolution upon sample heating,[7–11] which decreases τ_r and thereby the ^{17}O linewidths, allowing for more accurate determination of ^{17}O chemical shifts and spin–spin coupling constants, $J(^{31}P, ^{17}O)$. Gerothanassis and Sheppard[11] also demonstrated the utility of using ^{17}O depleted water to minimize the background $H_2{}^{17}O$ solvent peak, which in aqueous samples frequently overwhelms the resonance from even an ^{17}O enriched sample.

The pH dependence of the ^{17}O chemical shift has been determined for phosphoryl oxygen atoms in several phosphates, including adenosine monophosphate (AMP), ADP, and

ATP,[9,10] demonstrating the effect of protonation upon the phosphoryl ^{17}O chemical shift.

The binding of several diamagnetic ions to ATP has been studied using ^{17}O relaxation rates.[12,13] The phosphoryl ^{17}O linewidth increases markedly upon ion binding, indicating the coordination sites for Mg(II), Co(III), Sc(III), La(III), and Lu(III) in $M \cdot ATP_n$ complexes.

The hydrogen bonding of uridine derivatives has been studied using ^{17}O NMR.[14] Equilibrium constants and interaction enthalpies of water–uridine hydrogen bond complexes were determined by observing changes in ^{17}O chemical shift as a function of water concentration, in acetonitrile.

^{17}O spectra of hemiacetal and aldehydic abasic sites in DNA of importance in DNA damage and repair have been studied,[15] demonstrating the ability to observe approximately 10 μM aldehyde signals in the presence of approximately 20 M solvent ^{17}O.

4 AMINO ACIDS AND POLYPEPTIDES

The tertiary structures of polypeptides and proteins in aqueous solution are strongly influenced by hydrogen bonding, both within the solute molecule and with the solvent, and ^{17}O NMR has been used to gain insights into these interactions.

The effects of proton exchange between peptide termini and water on ^{17}O chemical shifts have been used to probe the electronic structures of amino acids,[11,16] dipeptides,[17,18] and peptide carboxamides.[19] The ^{17}O chemical shift has also been used to monitor the presence of hydrogen bonding in peptide models,[20] dipeptides,[18] peptide carboxamide,[19] acylprolines (model β- and γ-turns),[21–23] and small polypeptides.[24]

The hydration and aggregation of peptides has been studied using ^{17}O relaxation measurements. ^{17}O linewidths of amino acids,[16,25] dipeptides,[18] peptide carboxamides,[19] and small polypeptides[24] have been determined in various solvents, locating hydration sites at carboxylate and carbonyl oxygen atoms, in addition to providing a method of monitoring peptide aggregation. In addition, a ^{17}O relaxation study of ATP binding to adenylate kinase[26] has been reported, demonstrating the feasibility of studying enzyme–substrate interactions via ^{17}O NMR, providing the ligand is not rigidly held.

^{17}O chemical shifts have also been found to be torsion-angle dependent in aryl carboxylic esters, acids, and amides,[27] and ^{17}O NMR promises to be a powerful technique for elucidating the structures of membrane peptides and proteins, using oriented samples.

5 CO AND O_2 IN HEMOPROTEINS

The nature of Fe–O_2 and Fe–CO bonding in heme proteins and model compounds has been studied using ^{17}O NMR. ^{17}O resonance frequencies and linewidths have been measured for O_2 bound to Vaska's compound,[28] O_2 bound to picket-fence and basket-handle porphyrin model compounds,[29–31] CO bound to peroxidases,[32] as well as other hemoproteins,[5,33] and O_2 bound to hemoproteins in the solid state.[31] Results were found to be in general agreement with Pauling's ideas of end-on bonding, with additional electrostatic field effects being proposed to take into account the chemical shift variation seen from protein to protein.[34] In Fe–O_2 systems, the chemical shift difference between the two oxygen nuclei has been found to be about 600 ppm,[29–31] comparable to that found in ozone, consistent with previous analogies between FeO_2 bonding and that found in O_3.

6 SUMMARY AND PROSPECTS

Given the central importance of oxygen in biochemical systems (lipids, proteins, nucleic acids and carbohydrates), there have been remarkably few studies of ^{17}O NMR chemical shifts, and even fewer studies aimed at detailed, quantum chemical analyses of chemical shifts and quadrupolar couplings. ^{17}O NMR in biochemistry is therefore still in its infancy. However, with the advent of 750 MHz spectrometers, the current development of 900–1000 MHz machines, as well as recent development in quantum chemical applications to macromolecules,[35] ^{17}O NMR can be expected to benefit enormously over the next few years. Thus, ^{17}O chemical shifts and quadrupole couplings can be exploited to analyze, for example, lipid headgroup and backbone orientations in membranes, sterol orientations and interactions, peptide/protein structures in condensed phases, carbohydrate conformations and interactions, as well as small DNA structures. For ^{17}O, only relatively low resolution magnets are required, thus the sensitivity gains possible with very high-field operation can be readily exploited. Indeed, most ^{17}O NMR studies of biochemical systems reported to date could have been obtained at about 1 ppm resolution only. With recent improvements in computer price/performance ratios, and much more efficient algorithms, theoretical analyses of ^{17}O shifts and χ values are also to be expected. Thus, ^{17}O NMR in biochemistry undoubtedly has an extremely bright future.

7 RELATED ARTICLES

Oxygen-17 NMR.

8 REFERENCES

1. F. Alder and F. C. Yu, *Phys. Rev.*, 1951, **81**, 1067.
2. I. J. Solomon, J. N. Keith, A. J. Kacmarek, and J. K. Raney, *J. Am. Chem. Soc.*, 1968, **90**, 5408.
3. A. Abragam, *The Principles of Nuclear Magnetism*, ed W. C. Marshall and D. H. Williamson, Oxford University, Oxford, 1961, pp. 297–305.
4. J.-P. Kintzinger and H. Marsmann, in *NMR Basic Principles and Progress*, ed. P. Diehl, E. Fluck, and R. Kosfeld, Springer, Berlin, 1981, Vol. 17, pp. 1–64.
5. H. C. Lee and E. Oldfield, *J. Am. Chem. Soc.*, 1989, **111**, 1584.
6. M.-D. Tsai, S. L. Huang, J. F. Kozlowski, and C. C. Chang, *Biochemistry*, 1980, **19**, 3531.
7. C. Rodger, N. Sheppard, H. C. E. McFarlane, and W. McFarlane, in *NMR and the Periodic Table*, ed. R. K. Harris and B. E. Mann, Academic, London, 1978, Chap. 12A.
8. H. M. Schwartz, M. MacCoss, and S. S. Danyluk, *Tetrahedron Lett.*, 1980, **21**, 3837.

9. J. A. Coderre, S. Mehdi, P. C. Demou, R. Weber, D. D. Traficante, and J. A. Gerlt, *J. Am. Chem. Soc.*, 1981, **103**, 1870.
10. J. A. Gerlt, P. C. Demou, and S. Mehdi, *J. Am. Chem. Soc.*, 1982, **104**, 2848.
11. I. P. Gerothanassis and N. Sheppard, *J. Magn. Res.*, 1982, **46**, 423; I. P. Gerothanassis, R. Hunston, and J. Lauterwein, *Helv. Chim. Acta*, 1982, **65**, 1764.
12. S. L. Huang and M.-D. Tsai, *Biochemistry*, 1982, **21**, 951.
13. Y.-J. Shyy, T.-C. Tsai, and M.-D. Tsai, *J. Am. Chem. Soc.*, 1985, **107**, 3478.
14. H. M. Schwartz, M. MacCoss, and S. S. Danyluk, *J. Am. Chem. Soc.*, 1983, **105**, 5901.
15. J. A. Wilde, P. H. Bolton, A. Mazumder, M. Manoharan, and J. A. Gerlt, *J. Am. Chem. Soc.*, 1989, **111**, 1894.
16. B. Valentine, T. St. Amour, R. Walter, and D. Fiat, *J. Magn. Reson.*, 1980, **38**, 413.
17. C. S. Irving and A. Lapidot, *J. Chem. Soc., Chem. Commun.*, 1976, 43.
18. B. Valentine, A. Steinschneider, D. Dhawan, M. I. Burgar, T. St. Amour, and D. Fiat, *Int. J. Peptide Protein Res.*, 1985, **25**, 56.
19. A. Steinschneider and D. Fiat, *Int. J. Peptide Protein Res.*, 1984, **23**, 591.
20. A. Steinschneider, M. I. Burgar, A. Buku, and D. Fiat, *Int. J. Peptide Protein Res.*, 1981, **18**, 324.
21. J. Lauterwein, I. P. Gerothanassis, and R. N. Hunston, *J. Chem. Soc., Chem. Commun.*, 1984, 367.
22. R. N. Hunston, I. P. Gerothanassis, and J. Lauterwein, *J. Am. Chem. Soc.*, 1985, **107**, 2654.
23. N. Birlirakis, I. P. Gerothanassis, C. Sakarellos, and M. Marraud, *J. Chem. Soc., Chem. Commun.*, 1989, 1122.
24. C. Sakarellos, I. P. Gerothanassis, N. Birlirakis, T. Karayannis, and M. Sakarellos-Daitsiotis, *Biopolymers*, 1989, **28**, 15.
25. J. Lauterwein, I. P. Gerothanassis, R. N. Hunston, and M. Schumacher, *J. Phys. Chem.*, 1991, **95**, 3804.
26. D. A. Wisner, C. A. Steginsky, Y.-J. Shyy, and M.-D. Tsai, *J. Am. Chem. Soc.*, 1985, **107**, 2814.
27. A. L. Baumstark, P. Balakrishnan, M. Dotrong, C. J. McCloskey, M. G. Oakley, and D. W. Boykin, *J. Am. Chem. Soc.*, 1987, **109**, 1059.
28. H. C. Lee and E. Oldfield, *J. Magn. Reson.*, 1986, **69**, 367.
29. I. P. Gerothanassis and M. Momenteau, *J. Am. Chem. Soc.*, 1987, **109**, 6944.
30. I. P. Gerothanassis, M. Momenteau, and B. Loock, *J. Am. Chem. Soc.*, 1989, **111**, 7006.
31. E. Oldfield, H. C. Lee, C. Coretsopoulos, F. Adebodun, K. D. Park, S. Yang, J. Chung, and B. Phillips, *J. Am. Chem. Soc.*, 1991, **113**, 8680.
32. H. C. Lee, K. Cummings, K. Hall, L. P. Hager, and E. Oldfield, *J. Biol. Chem.*, 1988, **263**, 16118.
33. K. D. Park, K. Guo, F. Adebodun, M. L. Chiu, S. G. Sligar, and E. Oldfield, *Biochemistry*, 1991, **30**, 2333.
34. J. D. Augspurger, C. E. Dykstra, and E. Oldfield, *J. Am. Chem. Soc.*, 1991, **113**, 2447.
35. A. C. de Dios, J. G. Pearson, and E. Oldfield, *Science*, 1993, **260**, 1491.

Acknowledgments

This work was supported by the United States Public Health Service (Grant HL-19481). J. G. P. was a USPHS Postdoctoral Fellow (grant GM-14545).

Biographical Sketches

John G. Pearson. *b* 1963. B.S., University of California at Santa Barbara; 1986; Ph.D., (Supervisor Alexander Pines), University of California at Berkeley, USA, 1991. Successively, postdoctoral work (with Eric Oldfield), postdoctoral research fellow, University of Illinois at Urbana–Champaign, 1991–present. Approx. 20 publications. Research specialties: protein chemical shifts and multiple quantum NMR.

Eric Oldfield. *b* 1948. B.Sc., 1969, University of Bristol, Ph.D., 1972 (supervisor Dennis Chapman), University of Sheffield, D.Sc., 1982, University of Bristol, UK. Postdoctoral work at Indiana University, Bloomington (with Adam Allerhand) and Massachusetts Institute of Technology, Cambridge (with John S. Waugh). Professor, University of Illinois at Urbana-Champaign, 1975–present. Approx. 200 publications. Research specialties: inorganic and biochemical applications, especially proteins, membranes, and heterogeneous catalysts.

Vicinal Coupling Constants and Conformation of Biomolecules

Cornelis Altona

Leiden University, Leiden, The Netherlands

1	Introduction	1
2	Vicinal Proton–Proton Coupling Constants ^3J(H,C,C,H)	1
3	Vicinal Coupling Constants Involving Heteroatoms	6
4	Selected Applications of ^3J in the Field of Biomolecules	8
5	Caveats	13
6	Related Articles	13
7	References	13

1 INTRODUCTION

The discovery[1] that the vicinal (three-bond) proton–proton coupling constant, ^3J(H,H), varies smoothly with the associated H–C–C–H torsion angle ϕ(HH) in ethane had a profound impact on the acceptance of NMR as an indispensable tool in stereochemistry and conformational analysis. The well-known Karplus equation,[1,2] also called the cosine-square rule [equation (1)], was derived from valence bond calculations on the unperturbed ethane molecule.

$$^3J(\mathrm{H,H}) = C_0 + C_1\cos(\phi_{\mathrm{HH}}) + C_2\cos(2\phi_{\mathrm{HH}}) \quad (1a)$$

The Fourier series embodied in equation (1) is more often written as:

$$^3J(\mathrm{H,H}) = A\cos^2(\phi_{\mathrm{HH}}) + B\cos(\phi_{\mathrm{HH}}) + C \quad (1b)$$

Of course, simple relationships exist between C_0, C_1, C_2 and A, B, C, respectively: $C_0 = 0.5A + C$, $C_1 = B$, $C_2 = 0.5A$. Karplus[2] predicted that ^3J(H,H) depends on various other molecular parameters, such as the electronegativity of the substituents, bond lengths, and bond angles. In the same paper[2] he issued a caveat against the indiscriminate application of his equation and the theoretically derived parameters [coefficients in equation (1)] to 'estimate torsion angles to an accuracy of one or two degrees'.

The general shape of the Karplus curve, large ^3J at $\phi = 0^\circ$ (eclipsed, sp) and at or near $\phi = 180^\circ$ (*trans*, *anti* or *ap*), and decreasing to a minimum value ($^3J \approx 0$ Hz) near $\phi = 90^\circ$, in the course of time was shown to be applicable to many molecular fragments, including ^3J(H,H) with heteroatoms in the coupling path and also ^3J(X,H) and ^3J(X,Y) with X,Y NMR-active heteronuclei like ^{13}C, ^{15}N, and ^{31}P, for example ^3J(H,C,O,H), ^3J(H,N,C,H), ^3J(N,C,C,H), ^3J(C,C,C,H), ^3J(H,C,O,P), ^3J(C,C,O,P). Several of these more exotic vicinal couplings are useful in the conformational analysis of bio-molecules such as peptides, proteins, nucleic acids, and polysaccharides.

In suitable cases direct (^1J) and geminal (^2J) coupling constants provide additional structural information, albeit of a more qualitative nature. Long-range couplings (^nJ, $n > 3$) are often highly useful, especially ^4J couplings (planar W path). However, the present contribution focuses entirely on vicinal (^3J) couplings.

The coupling constant ^3J(H,C,C,H) with C saturated carbon is by far the best investigated and will be treated in depth in the present article. A selection of more simple Karplus equations involving heteroatoms will be presented and briefly discussed. Familiarity with the basic tenets and methods of conformational analysis is assumed. The multitude of techniques that are currently available to measure the coupling constants of interest remain outside the scope of the present contribution (see Section 7 for related articles). Clearly, the approaches that are found useful in the conformational analysis of biomolecules are applicable to many other molecular fragments in organic chemistry. The article concludes with some applications in the field of (poly)peptides and nucleic acids, and caveats are issued. The reader is advised to consult the selection of references given for further details and for references therein.

2 VICINAL PROTON–PROTON COUPLING CONSTANTS ^3J(H,C,C,H)

2.1 General Background

In the late 1950s experiments already showed[3] that the *time-averaged* ^3J(H,H) [equation (2)] in monosubstituted ethanes CH_3CH_2X decreases more or less linearly with increasing electronegativity of the substituent X.

$$\langle ^3J(\mathrm{H,H})\rangle = [J(60) + J(180) + J(300)]/3 \quad (2)$$

Studies carried out in the early 1960s[4,5] confirmed these findings. Perhaps unfortunately, the (erroneous) notion that ^3J(H,H) in all situations decreases with increasing electronegativity became firmly lodged in the minds of NMR spectroscopists. A second, also erroneous, assumption was generally accepted and that is the linear additivity of (relative) electronegativities $\Delta\chi_1 = \chi_i - \chi_{\mathrm{H}}$. In other words, the general validity of equation (3) was accepted without question, although proper analysis of the experimental data on monosubstituted ethanes and 2-substituted propanes, already available in the early 1960s, could have shown differently.

$$^3J(\mathrm{H,H}) = \mathrm{f}(\phi) + a\Sigma_i\Delta\chi_i \quad (3a)$$

or alternatively:

$$^3J(\mathrm{H,H}) = \mathrm{f}(\phi)[1 - a(\Sigma_i\Delta\chi_i)/\mathrm{f}(\phi)] \quad (3b)$$

where f(ϕ) denotes a Karplus function of ϕ_{HH}; a/f(ϕ) is usually written as k.

In the case of coupling to the fast-rotating methyl protons, for example in substituted ethanes and 2-substituted propanes [equation (2)], the ϕ-dependent terms in equation (1a) vanish and f(ϕ) reduces to the 'constant' C_0. The following comparison is obtained (Hz):

$$CH_3CH_2X:^3\ C_0 = 7.5,\ a = -0.4$$

$$CH_3CH_2X:^4\ C_0 = 7.9,\ a = -0.7$$

$$CH_3CHXCH_3:^3\ C_0 = 7.0,\ a = -0.55$$

$$\text{Combined}:^5\ C_0 = 7.7,\ a = -0.80$$

In the remainder of this article the slope (a) will be denoted C_{01}. The 'goodness of fit' of these least-squares regressions (± 0.3 Hz) is disappointing, moreover, several workers[4,5] noted a breakdown of linearity in cases where X and Y in CH_3CHXY represent highly electronegative substituents like fluorine or oxygen. It should be noted that the measured coupling to methyl cannot yield the electronegativity dependence of the 'constants' C_1 and C_2 in equation (1); it was simply assumed that these dependences were all equal.

In 1965 Booth[6] noted that an electronegative substituent located on the C–C fragment constituting the coupling path and in antiparallel (*ap*) position relative to one of the two coupling *gauche* (*sc*) protons causes an 'extra' diminution of their mutual coupling constant (Booth's rule). In hindsight it is easy to see that this observation implies a breakdown of the symmetry inherent to a Fourier series with cosine terms only, e.g., equation (1a), but it was not so interpreted at the time. On the contrary, one might say, and for a long time the Durette–Horton equation[7] [equation (4)], was popular in the field.

$$^3J(\mathrm{H,H}) = [C_0 + C_1\cos(\phi) + C_2\cos(2\phi)](1 - k\sum_1^4 \Delta\chi_i) \qquad (4)$$

Equation (4) is simply a combination of equations (1a) and (3b), rewritten here in terms of cosine Fourier coefficients C; ϕ denotes the torsion angle between the coupling nuclei indicated in parentheses on the left-hand side of equation (4), $\Delta\chi_i$ are relative electronegativities of substituents according to either the Pauling[8] or the Huggins[9] scale.

Unfortunately, equation (4) embodies at least four questionable or even erroneous assumptions:

1. The orientation of any electronegative substituent with respect to the coupling protons is unimportant (in negation of Booth's rule).
2. Coefficients C_0, C_1, C_2 have the same electronegativity dependence.
3. Substituent effects are linearly additive.
4. The standard atomic electronegativity scales[8,9] can be applied to polyvalent substituents, regardless of the remaining atoms or groups attached.

At this point it should be mentioned that many workers in the field of stereochemistry in a way circumvented assumptions 2, 3, and 4 by the calibration of Karplus parameters for given classes of molecules of interest with the aid of model compounds with known or estimated torsion angles. Even today this approach often remains the only sensible course of action available in the case of couplings to heteronuclei, e.g., ^3J(C,H), ^3J(N,H), ^3J(P,H), ^3J(P,C), vide infra. More refined approaches are now possible in the case of ^3J(H,H) in sp^3–sp^3 H–C–C–H fragments.

2.2 Substituent-Induced Asymmetry in the Karplus Curve

The first systematic investigation into the orientational effects of substituents on ^3J(H,H) was carried out by Abraham and Gatti[10] with the aid of a series of 1,2-disubstituted ethanes CH_2X–CH_2Y. Their results are summarized in Figure 1.

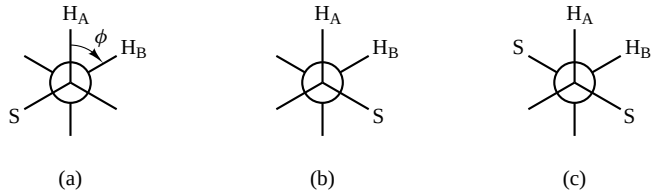

Figure 1 Newman projections along the central bond of a H_A–C–C–H_B fragment, H_A and H_B are mutually coupled. (a) Situation pertaining to Booth's rule (strong decrease of ^3J(H,H) for an electronegative substituent S); (b) situation pertaining to Abraham's rule [weak increase of ^3J(H,H)]; (c) situation where Abraham's rule applies twice. This configuration occurs, for example, in cyclohexanes with H_A, H_B diequatorial and the S substituents diaxial

For most practical purposes one needs to distinguish three different situations:

(a) *Gauche* (*sc*) protons, J_g, with X in an *anti* orientation X_t: J_g decreases strongly with increasing electronegativity of X (Booth's rule);
(b) *Gauche* (*sc*) protons, J_g, and a substituent X in a *gauche* orientation with respect to its vicinal coupling proton, X_g: J_g increases with increasing electronegativity of X (Abraham's rule);
(c) *Anti* or *trans* (*ap*) protons, J_t, with X necessarily in a *gauche* position (not shown in Figure 1): J_t decreases with increasing electronegativity of X.

For X = oxygen in conformationally rigid pyranose sugars, a statistical analysis[11] of a large set of couplings indicated the following changes of ^3J from X = H: situation (a) -1.8 Hz; (b) $+0.5$ Hz; (c) -1.45 Hz. This example clearly illustrates the fact that *gauche* (*sc*) couplings do not obey the simple cosinesquare rule. The various effects are additive to a good approximation, 24 additivity constants (eight different substituent types) gave an rms error of only 0.29 Hz for a test set consisting of 305 couplings.

Extended Hückel molecular orbital theory (EHT) calculations of ^3J(H,H), carried out by Pachler[12,13] on CH_3CH_2X(X = H, CH_3, NH_2, OH, F), CH_3CHF_2, and CH_2FCH_2F, indicated that an X substituent (or the C–X bond) induces an asymmetry in the Karplus curve. More refined EHT calculations[14,15] confirmed this important finding and showed[15] that mutual interaction between substituents cannot be neglected. Pachler[12,13] described the calculated influence of the X substituent in terms of the summation of two effects: (1) an attenuation of the Fourier coefficients, i.e., as in equation (4) but with different k values for C_0, C_1, and C_2; (2) a phase shift, assumed to be proportional to the electronegativity of the substituent (Figure 2).

A phase shift can be formulated in several ways, for example by the introduction of sine terms.[12,13] This leads to equation (5).

$$^3J(\mathrm{H,H}) = C_0 + C_1\cos(\phi) + C_2\cos(2\phi) + S_1\sin(\phi) + S_2\sin(2\phi) \qquad (5a)$$

with

$$C_m = C_{m0} + C_{m1}\Sigma_i\Delta\chi_i \quad \text{and} \quad S_m = S_{m1}\Sigma_i s_i\Delta\chi_i \qquad (5b)$$

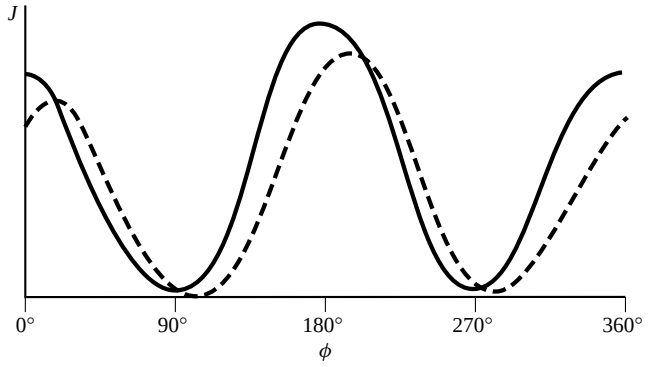

Figure 2 The calculated coupling constants (EHT method[14]) for ethane (solid line) and fluoroethane (dashed line) as a function of the HH torsion angle ϕ; the positive direction of ϕ is defined according to IUPAC,[17] the F atom occupies the S_1 substituent position shown in Figure 3 (sign factor s_i = +1). (Reproduced with permission from Elsevier Science Ltd., Kidlington, UK, from K. G. R. Pachler, *Tetrahedron*, 1971, **27**, 187)

In equation (5) the original Pachler equation[12,13] is recast into a general Fourier expression.[15] Moreover, the use of a separate and cumbersome proton-substituent torsion angle $\cdot\Phi_{HX}$[12,13] is avoided by the introduction of the 'sign' factor s_i for each substituent S_i, s_i is +1 or −1 according to the definition by Haasnoot et al.[16] (see Figure 3). (In this paper, as well as in others,[15] the sign factor S_i was denoted ξ_i.)

It is important to keep in mind that the sign factors s_i of the substituents S_1 and S_2 (*not* to be confused with the Fourier coefficients S_1 and S_2) depend exclusively upon their stereochemical position with respect to their 'own' geminal coupling proton H_A. The following recipe applies: choose a Newman projection along the coupling path in such a manner that the chosen coupling proton H_A is located on the front side (Figure 3): S_1 is found at 120° and S_2 at −120° (positive angle defined as clockwise). Repeat the procedure with H_B up front, S_3 is at 120° and S_4 at −120°. The sign factors (s_i = +1 for substituents S_1 and S_3, s_i = −1 for S_2 and S_4) are thus uniquely defined and are *independent* of the actual value of the torsion angle ϕ_{AB}. It goes without saying that in the case of a CH_2 group ($CH_{A1}H_{A2}$) one has to take care to select the proper H_A (interchange of H_{A1} and H_{A2} means a change of sign factor for the remaining substituent). Equation (6) simplifies the computer programming:

$$\Sigma_i s_i \Delta\chi_i = \Delta\chi_1 - \Delta\chi_2 + \Delta\chi_3 - \Delta\chi_4 \qquad (6)$$

It is easily appreciated that the sine terms vanish in all cases where equivalent substituents (same $\Delta\chi_i$) occupy a +1 and a −1 position at the same time, for example in $-CH_2-CHX_2$ and the +, − coupling in the $-CHX-CH_2X$ molecular fragment. The above sign factor definition is associated with the definition of the positive direction of ϕ_{AB} according to IUPAC rules:[17] positive when H_B rotates clockwise away from H_A, with the H_A,H_B eclipsed position taken as zero angle. Since the sine terms change sign at ϕ_{AB} = 0° a change of substituent position from +1 to −1 can be depicted as a mirroring of the ΔJ curve (Figure 4). Equation (5) is invariant under electronegativity scale changes,[15] aside from changes in the values of the coefficients C_m and S_m. It is a valid procedure to choose the relative electronegativity of hydrogen as zero and to fix $\Delta\chi$ of one other substituent. For practical reasons, a value λ_{OR} = 1.40 was selected, vide infra.

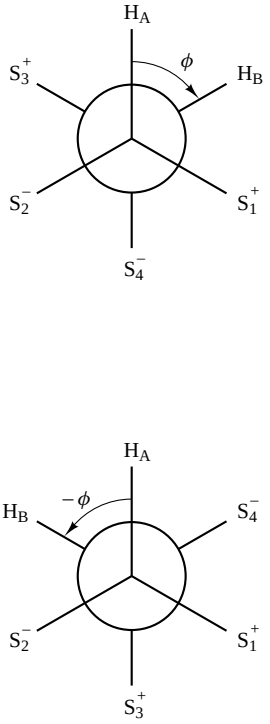

Figure 3 Definition of substituents with positive (S_1 and S_3) and negative (S_2 and S_4) sign factors s_i. Note that with each coupling nucleus in an sp^3–sp^3 fragment two geminal substituents with opposite sign factors are associated. The result of rotation of H_B with respect to H_A in the $-\phi$ direction is mathematically equivalent to the result of a $+\phi$ rotation with concomittant interchange of S_1 and S_2. (Reproduced with permission of Elsevier Science Ltd., Kidlington, UK, from C. A. G. Haasnoot, F. A. A. M. de Leeuw, and C. Altona, *Tetrahedron*, 1980, **36**, 2783)

Haasnoot et al.[16] also sought to describe the generalized Karplus equation by superimposing a phase shift upon the symmetrical ethane curve [equation (7) and Figure 4].

$$^3J(\mathrm{H,H}) = P_1\cos^2(\phi) + P_2\cos(\phi) + P_3 + \Sigma_i \Delta\chi_i[P_4 + P_5\cos^2(s_i(\phi) + P_6 \mid \Delta\chi_i \mid)] \qquad (7)$$

Comparison with equation (5) shows that C_{11} and S_{11} have been set to zero, and that in the cos(2ϕ) and sin(2ϕ) terms

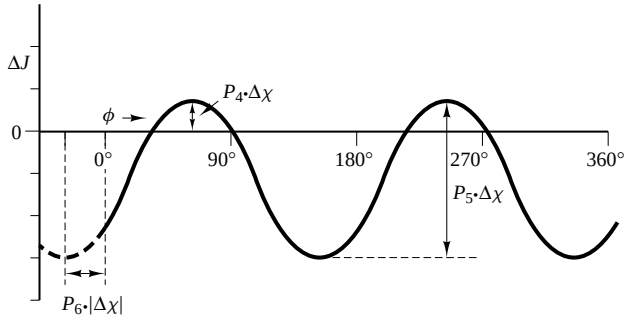

Figure 4 The calculated difference curve $\Delta J = J(CH_3CH_2S) - J(CH_3CH_3)$ for a substituent S with a positive sign factor, showing the rationale behind the phase-shift parameters P_4, P_5, and P_6 in the Haasnoot equation (7)[16]

both a constraint (through a common parameter P_5) and a nonlinear $\Delta\chi_i$ dependence have been introduced. The invariance property (vide supra) does not hold for equation (7). The parameters P_1–P_6 were empirically determined with the aid of a test set containing 315 couplings and corresponding ϕ_{HH} values.[16] Each substituent was assigned a $\Delta\chi_i$ value according to Huggins,[9] but empirically modified to account for the moderation of the electronegativity of the α substituent by attached atoms or groups (β substituents), other than hydrogen. A least-squares regression (J_{calc} versus J_{obs}) showed an rms error of 0.48 Hz and a correlation coefficient R of 0.992, in contrast to a similar regression using three parameters only, equation 1(a) (rms = 1.20 Hz, R = 0.947).[16]

2.3 Group Electronegativities and Nonadditivity Effects

Analysis[15] of the results of a systematic series of calculations of ^3J(H,H) in a variety of mono-, di-, tri-, and tetrasubstituted ethanes by means of the EHT method (1404 J values) suggested that: (a) the use of standard relative electronegativities $\Delta\chi_i$ should perhaps be abandoned in favor of 'best values' of substituent constants λ_i derived from the data set at hand; (b) the nonadditivity effect (interaction between substituents) can be well described by the introduction of cross terms involving products $\Delta\chi_i\Delta\chi_j$ or $\lambda_i\lambda_j$. Díez et al.[18] allowed the coefficients of equation (5b) to be quadratically dependent upon λ. It was shown that only certain combinations of cross terms can survive in such an expansion because of symmetry. Neglecting interactions between more than two substituents, one obtains equation (8), which is in fact an extension of equation (5).

$$C_m = C_{m0} + C_{m1}\Sigma_i\lambda_i + C_{m11}\Sigma_i\lambda_i^2 + C_{m12}(\lambda_1\lambda_2 + \lambda_3\lambda_4) + C_{m13}(\lambda_1\lambda_3 + \lambda_2\lambda_4) + C_{m14}(\lambda_1\lambda_4 + \lambda_2\lambda_3) \quad (8a)$$

$$S_m = S_{m1}\Sigma_i s_i\lambda_i + S_{m11}\Sigma_i s_i\lambda_i^2 + S_{m13}(\lambda_1\lambda_3 + \lambda_2\lambda_4) \quad (8b)$$

How can we determine the 'substituent constants' or 'group electronegativities' λ_i (which may contain other factors beside electronegativity)? Which of the cross terms in equation (8) are important and which can be neglected safely? In an attempt to answer these questions a combined empirical and theoretical approach was taken.

First, a large body of accurate (±0.02 Hz) coupling data from mono- and 1,1-disubstituted ethanes was measured and analyzed.[19] Because of torsional averaging, one isolates the 'constant' C_0 in equation (8a), m = 0. Excluding the self-quadratic term C_{011} from consideration,[15] we obtain equation (9).

$$\langle^3J(\mathrm{H,\ H})\rangle = C_{00} + C_{01}(\lambda_1 + \lambda_2) + C_{012}(\lambda_1\lambda_2) \quad (9)$$

Not only were the coefficients C_{00}, C_{01}, and C_{012} optimized, but also the λ_i values. As explained above, parameter redundancies were removed by fixing the λ values of two different substituents present in the set: λ_H = 0.00 and λ_{OR} = 1.40 (measurements in solvent $CDCl_3$). The 'best' least-squares regression[19] yielded equation (10):

$$\langle^3J(\mathrm{H,\ H})\rangle = 7.836 - 0.594(\lambda_1 + \lambda_2) - 0.423(\lambda_1 \cdot \lambda_2) \quad (10)$$

and in addition 50 λ_i values[19] from 84 couplings; rms deviation = 0.018 Hz, maximum deviation = 0.06 Hz. A similar regression with the use of Huggins's relative electronegativities yielded a 10-times larger rms deviation;[19] however, this regression also underlined the importance of the $\lambda_1\lambda_2$ cross term, at least for coupling to methyl protons.

Table 1 Substituent Parameters λ_i (Relative Group Electronegativities) Deduced from $\langle^3J\rangle$ of Various Mono- and 1,1-Disubstituted Ethanes in $CDCl_3$ and in D_2O, Equation (10). More Detailed Data are Given Elsewhere.[19,20,24] R Signifies Carbon, Usually Alkyl; Z Signifies any Substituent, Except Hydrogen and Halogens.[19] Fixed Points are Indicated by an Asterisk; 90% Confidence Limits (×100) are Shown in Parentheses. Note That Several Values Are Not Applicable to Mono-Substituted Ethanes[19,20]

Group	$\lambda_i(CDCl_3)$	$\lambda_i(D_2O)$
H	0.00*	0.00
CN	0.33(3)	0.33(3)
COOH	0.39(3)	0.33(3)
COO^-	–	0.41(4)
$COOR/CONH_2$	0.42(2)	–
Ph	0.45(4)	–
C(=O)R	0.50(3)	0.50
$C(Me)_3$	0.48	–
CHMeZ[a]	0.62	–
CH_2Z[b]	0.72	–
CH_3	0.80	–
SH	0.75(3)	0.75(3)
I	0.63(4)	–
Br	0.80(3)	–
Cl	0.94(3)	0.94(3)
F	1.37(5)	–
NRC(=O)R (*S-cis*)	0.52(4)	0.52(4)
9-Purines	0.56(2)	0.56(2)
1-Pyrimidines	0.56(2)	0.56(2)
NHC(=O)R	0.85(3)	0.81(3)
NH_3^+	–	0.82(4)
NR_2	1.12(5)	1.00(5)
NHR	1.15(5)	1.02(5)
NH_2	1.19(4)	1.09(4)
NO_2	0.77(3)	0.77(3)
OC(=O)R	1.16(3)	1.16(3)
OSO_2OR	1.19(9)	–
OPO_2OR	–	1.25(4)
$OPO(OR)_2$	1.29(4)	1.25(4)
OH	1.33(4)	1.25(4)
OR	1.40*	1.26(4)
OAr	1.42(5)	1.34(5)

[a] λ_i range 0.60–0.62; for Z = halogen: Cl 0.85, Br 0.92, I 1.02.
[b] λ_i range 0.65–0.78; for Z = halogen: F 0.65, Cl 0.82, Br 0.92, I 0.99.

Equation (10) proved to be highly useful for determining λ_i values of substituents not present in the original data set. Recently, special attention[20] was paid to solvent effects, in particular to the influence of the solvent D_2O in cases where the α substituent carries at least one nonconjugated lone pair of electrons that can readily act as a hydrogen bond acceptor. The vicinal coupling constants (and thus λ values) measured in common organic solvents (like acetone-d_6, CD_3CN, and DMSO) hardly differ from those established in $CDCl_3$. Table 1 presents a selection of λ_i values of substituents that are of particular value in the analysis of couplings measured in biomolecules.

Second, the least-squares analysis of the set of 1404 J values indicated[15] that only two more cross terms (besides C_{012}) are probably important for use in equation (8a): C_{214} and either S_{211} or S_{213}.

Table 2 Final rms Deviations Obtained for ^3J(H,H) with the Aid of the 299 J Test Set in the Various Approximations[a]

Approximations	rms($\Delta\chi_i$)[b] (Hz)	rms(λ_i)[c] (Hz)	N[d]
1. Karplus[e]	1.18	1.18	3
2. Karplus (linear)[f]	0.73	0.70	5
3. Pachler[g]	0.38	0.39	6
4. Haasnoot[h]	0.37	0.36	6
5. Díez–Donders[i]	0.38	0.33	6
6. Díez–Donders[j]	0.37	0.32	8
7. Díez–Donders[k]	0.36	0.31	7

[a]The C_{11} coefficient in equation (5b) was set to zero in all parameter optimizations. It is strongly correlated to some other coefficients.
[b]With the use of Huggins's relative electronegativity scale[9] without β substituent correction.[16]
[c]With the use of experimental 'group electronegativity' values λ_i.[19,20]
[d]Number of optimized parameters.
[e]Equation (1a).
[f]Equation (5), C coefficients only.
[g]Equation (5), S_2 added (the rms error does not change when C_{11} and S_{11} are also added).
[h]Equation (7), the coefficients (based on λ_i) are shown in equation (11).
[i]Equation (8): C_{00}, C_{01}, C_{10}, C_{20}, C_{21}, S_{211} used, the coefficients (based on λ_i) are shown in equation (12).
[j]Equation (8): C_{00}, C_{01}, C_{012}, C_{10}, C_{20}, C_{21}, C_{214}, S_{211} used.
[k]Equation (8), as in footnote [??], but C_{01} fixed on the 'ethane' value, and C_3 added (C_3 = 0.1 taken as the fixed value); the coefficients (based on λ_i) are shown in equation (13).

2.4 Parameter Optimizations

In order to test the ideas developed in the previous sections, an empirical approach was again taken. The original data set (315 J set)[16] was first reduced to 299 J values (299 J set) by the deletion of norbornane- and norbornene-like structures [equations (5) and (7) do not contain correction terms for through-space effects,[21] nor for deviations of CCH bond angles from the tetrahedral value, see Section 5]. Group electronegativities λ_i were selected for the various substituents present in the data set. The corresponding torsion angles were recalculated with the aid of the MM2-85 force field.[22]

A series of least-squares parameter optimizations were carried out (see Table 2). It is of interest to watch the successive improvement, as judged by the drop in rms deviation, as we start (entry 1) from the original three-parameter Karplus equation [equation (1a)], and successively add (entry 2) an electronegativity dependence of the C_0 and C_2 coefficients, add (entry 3) the sine terms of the modified Pachler equation [equation (5)], use (entry 4) the Haasnoot approximation [equation (7)], and finally the Díez–Donders equation [equation (8)], the latter in three forms: (1) (entry 5), all cross terms zero, except the S_{211} $\sum_u S_i$ $\lambda_i{}^2$; (2) (entry 6) as (1) but C_{012} ($\lambda_1\lambda_2$ + $\lambda_3\lambda_4$) and C_{214} ($\lambda_1\lambda_4$ + $\lambda_2\lambda_3$) cos(2ϕ) added; (3) (entry 7) as (2) plus a small threefold term C_3 cos(3ϕ) added. In the latter parameter optimization, the C_{01} parameter was kept fixed on the value obtained from the 'ethane set' [equation (10)]; C_3 was fixed at −0.10, a value close to that suggested by ab initio calculations.[23]

The current parameters are shown in equations (11)–(13), with reference to the entries in Table 2.

Entry 4, Haasnoot:

$$^3J(\mathrm{H,H}) = 14.64\cos^2(\phi) - 0.78\cos(\phi) + 0.58 + \Sigma_i\lambda_i[0.34 - 2.31\cos^2(s_i(\phi) + 18.40|\lambda_i|)] \quad (11)$$

Entry 5, Díez–Donders:

$$^3J(\mathrm{H,H}) = (7.82 - 0.79\Sigma_i\lambda_i) - 0.78\cos(\phi) + (6.54 - 0.64\Sigma_i\lambda_i)\cos(2\phi) + (0.70\Sigma_i s_i\lambda_i^2)\sin(2\phi) \quad (12)$$

Entry 7, Díez–Donders:

$$^3J(\mathrm{H,H}) = [7.41 - 0.59\Sigma_i\lambda_i - 0.27\Sigma_i(\lambda_1\lambda_2 + \lambda_3\lambda_4)] - 0.85\cos(\phi) + [6.84 - 0.87\Sigma_i\lambda_i + 0.29(\lambda_1\lambda_4 + \lambda_2\lambda_3)]\cos(2\phi) - 0.10\cos(3\phi) + (0.71\Sigma_i s_i\lambda_i^2)\sin(2\phi) \quad (13)$$

The coefficients of equation (13) differ from previous ones[24] mainly because a constraint is now laid upon the cos(3ϕ) coefficient, vide supra.

2.5 Summary of Results

1. In previous work the unsatisfactory rms deviation (0.48 Hz) obtained with the use of equation (7) and the full 315 J calibration set, prompted Haasnoot et al.[16] to propose a division of the set into three parts. In other words, separate parameters were presented for ethane-like fragments which contained two, three, and four substituents, i.e. for CH_2-CH_2, $CH-CH_2$, and $CH-CH$ moieties, respectively. In contrast, all of the parameter optimizations reported in Table 2 were carried out on the full 299 J test set and it was found that a single optimization suffices to reach an acceptable rms deviation (0.37 Hz). Presumably, the improved agreement between J_{obs} and J_{calc} is at least, in part, the result of an improvement in calculated ϕ_{HH} values in the present calibration set.
2. The extended five-parameter Karplus equation [terms up to cos(2ϕ) and linear electronegativity dependence of the Fourier coefficients C_0 and C_2] gives a 'best' rms deviation of only 0.70 Hz. Introduction of the asymmetry effect induced by a substituent diminishes the rms error in a dramatic way to less than 0.4 Hz. Systematic theoretical and experimental investigations into the effect of asymmetry on other types of vicinal couplings: ^3J(C,H), ^3J(N,H), ^3J(P,H), ^3J(P,C), unfortunately appear to be lacking, but see Section 3.2.
3. The Pachler Fourier series equation, equation (5), postulates a linear electronegativity dependence of the asymmetric part, expressed as $S_{21}\sum_i s_i\Delta\chi_i$ sin(2ϕ) or in the present work also as $S_{21}\sum S_i\lambda_i$ sin(2ϕ). The Haasnoot[16] formulation, equation (7), implicitly contains $\Delta\chi_i{}^2$ cos(2ϕ) and $\Delta\chi_i{}^2$ sin(2ϕ) terms. The Díez–Donders equation, equation (8), explicitly uses an $S_{211}\sum_i S_i\lambda_i{}^2$ sin(2ϕ) term. This term alone, in combination with the use of empirical group electronegativities λ_i, is responsible for a substantial decrease in the rms deviation compared with the linear Fourier: 0.33 Hz versus 0.39 Hz, compare entries 5 and 3 in Table 2.

4. The introduction of two more cross terms (C_{012} and C_{214}) in the Díez–Donders formulation is only slightly effective, compare entries 5 and 6. This result comes as a surprise in view of the importance of the C_{012} term in the ethane/2-propane series [equation (10)].
5. The use of a Pauling/Huggins-type electronegativity scale appears perfectly justified up to a certain level of approximation.

3 VICINAL COUPLING CONSTANTS INVOLVING HETEROATOMS

3.1 General Background

Measurement of heteronuclear coupling constants is an essential factor in the conformational analysis of biomolecules.[25–28] Over the past three decades much effort has been invested into the delineation of Karplus-type relations for couplings involving one or more heteronuclei, either as coupling partner or contained in the coupling path. Unfortunately, there exists no firmly established quantitative correlation between ^3J(H,C,C,H) and corresponding couplings to heteronuclei [^3J(X,C,C,H), X = ^{13}C, ^{15}N, ^{31}P], nor simple rules that predict the behavior of a vicinal coupling when a carbon atom in the coupling path is replaced by a heteroatom. In short, for each different combination of nuclei and coupling path, a Karplus-type equation must be parameterized from scratch, preferably on the basis of a large number of experimental couplings (calibration points). Semiempirical calculationsn of vicinal couplings cannot predict ^3J with an accuracy desired by NMR spectroscopists, but such calculations, especially when carried out for a series of related molecular fragments,[25] may reveal details that would otherwise not be considered.

Thus far, the proposed parameterizations, resulting in a set of Karplus coefficients, rarely appear to have gone beyond the level of the three-parameter equation (1b). The problem of substituent effects on the A, B, and C coefficients is usually circumvented by the use of model compounds that contain the same (or at least similar) substituents as the compounds that one is interested in. The torsion angles necessary for such a parameterization are either estimated from molecular models, calculated by means of force-field methods, or taken from X-ray studies. Thus, one may hope to work effectively on the level of the five-parameter Karplus expression. It should be remembered that in the case of ^3J(H,C,C,H) this level yields an rms deviation of 0.7 Hz (299 experimental calibration points); inclusion of an asymmetry term causes the rms deviation to drop to less than 0.4 Hz, vide supra.

A selection of coefficients for use in equation (1b) that are currently used in structural and conformational studies of proteins (Table 3) and nucleic acids (Table 4) is presented here. Some parameterizations have been carried out solely on the basis of semiempirical MO calculations in various approximations and these should perhaps be taken only as a rough guide. The coefficients for ^3J(C,C,C,H) in Table 3 were determined from measurements[33] in norbornanes and are not necessarily representative for this coupling in open-chain compounds.

The most important asset that these coefficients presently offer is *not* their overall reliability (statistically tested in a small minority of cases) but the opportunities that are provided to remove ambiguities. For example, a single coupling constant ^3J(H,H), measured along a given bond in an open-chain molecule, in the general case (single conformer assumed) corresponds to any one out of four torsion angles ϕ_{HH}. The situation is even more complex in the case of a conformational mixture. Modern NMR techniques allow us to measure accurately one or more ^3J(X,H) and sometimes ^3J(X,Y) along the same bond. The various Karplus curves are phase-shifted with respect to one another, because the X and/or Y nuclei are shifted by $\pm 120^\circ$ (sp^3) or 180° (sp^2). Thus, comparison of the various couplings often solves an assignment problem, always acute when dealing with diaster-eotopic nuclei, and/or may result in the selection of only one conformation that fits all the data.[38] Other applications are discussed in Section 4.

3.2 Vicinal Carbon–Proton Couplings ^3J(C,C,C,H)

This particular coupling constant appears to have resisted[39] all attempts to formulate satisfyingly simple and general trigonometric relationships similar to those developed for ^3J(H,C,C,H). Although early MO calculations[40] on ^3J(C,H) in substituted propanes already indicated that these couplings indeed obey a Karplus-type equation, in practice severe complications arose and progress remains slow. The present situation concerning ^3J(C,H), Figure 5, can be summarized as follows:

(a) The ratio ^3J(C,H)/^3J(H,H) in molecular fragments where C replaces a corresponding H varies from 0.50 to 0.85 (mean 0.61 $\pm$ 0.065).[27] Thus, this ratio cannot be used with confidence to scale ^3J(H,H) couplings or Karplus coefficients to fit ^3J(C,H) data.

(b) The influence of electronegative substituents on rotationally averaged $\langle ^3J(C,H)\rangle$ in t-butyl derivatives correlates well with ^3J(H,H), with the former slightly more sensitive to the electronegativity effect.[41] More recently, an analysis of ^3J(C,H) in carbohydrates[42] suggested that oxygen (and carbon) substituents require a different set of coefficients [including the sin(2ϕ) term] when moved from the β position to the γ position with respect to the coupling carbon nucleus, Figure 5. This implies that the minimum number of Karplus coefficients could be twice as large compared with the six that suffice to describe ^3J(H,H).

(c) When the coupling ^{13}C nucleus itself carries one or more substituents besides hydrogen, matters are even more complicated. It has long been known that the nature of the X substituent has a profound influence on the magnitude of the rotationally averaged ^3J(C,H) in $(CH_3)_3{}^{13}CX$ compounds.[43] Other factors besides electronegativity appear to be operative here. Moreover, MO calculations of ^3J(C,H) in 1-fluoropropane[40] (Figure 5,

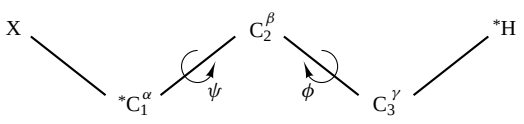

Figure 5 Torsion angles ϕ and ψ and atomic numbering for ^3J(C,C,C,H). The coupling nuclei are marked with an asterisk

Table 3 Selection of Coefficients (Hz) for Use in the Standard $\cos^2$ Karplus Equation [Equation (1b)] for Couplings Relevant to Amino Acids and Polypeptides; $^3J_{ap}$, $^3J_{sc}$ and the Rotationally Averaged Value $\langle ^3J \rangle$ are Also Given. In the Column Remarks MO Stands for Semiempirical Calculations; (Exp(N) Denotes Experimental Calibration on N Data Points. See Figures 6 and 7 for Atom Numbering and Definition of Torsion Angles. In Many Amino Acids X = C^γ

Main torsion angle	^3J monitored	A	B	C	$^3J_{ap}$	$^3J_{sc}$	$\langle ^3J \rangle$	Remarks
ϕ	$HNC^\alpha H^\alpha$	6.7	−1.3	1.5	9.5	2.5	4.8	Exp(112)[29]
		6.4	−1.4	1.9	9.7	2.8	5.1	Exp(37)[30]
		9.4	−1.1	0.4	10.9	2.2	5.1	Exp(22)[25]
ϕ	$HNC^\alpha C^\beta$	4.7	−1.5	−0.2	6.0	0.2	2.1	MO *trans*-amides[25]
ϕ	$HNC^\alpha C'$	5.7	−2.7	0.1	8.5	0.2	3.0	MO *trans*-amides[25]
ϕ	$C'NC^\alpha H^\alpha$	9.0	−4.4	−0.8	12.6	−0.8	3.7	Exp(3) tentative[25]
		4.5	−1.3	−1.2	4.6	−0.7	1.1	MO *trans*-amides[25]
		4.0	−1.8	0.8	6.6	0.9	2.8	Exp(12) *cis*-amides[31]
ϕ	$C'NC^\alpha C\beta$	1.8	−0.2	0.5	2.5	0.9	1.4	Exp(17) *cis*-amides[31]
		1.3	−0.6	−0.1	1.8	−0.1	0.5	MO *trans*-amides[25]
ϕ	$C'NC^\alpha C'$	1.4	−0.8	−0.3	1.9	−0.4	0.4	MO *trans*-amides[25]
χ	$H^\alpha C^\alpha C^\beta H^\beta$	see equation (12) and Table 5						Exp(299)
$\chi_1\chi_2$	$H^\alpha C^\alpha C^\beta C^\gamma$	10.2	−1.3	0.2	11.7	2.1	5.3	Exp(6) ornithines[32]
χ	$C'C^\alpha C^\beta H^\beta$	7.7	−0.9	0.0	8.6	1.5	3.9	Exp(10) norbornanes[33]
		–	–	–	10.0	1.0	4.0	Exp[a, 34]
		–	–	–	11.9	0.4	4.2	Exp[a, 34]
χ	$NC^\alpha C^\beta H^\beta$	–	–	–	−5.4	−1.7	−2.9	Exp[a, 36]
χ	$C'C^\alpha C^\beta C^\gamma$	1.4	−0.8	−0.3	1.9	−0.4	0.4	MO *trans*-amides[25]
ψ	$H^\alpha C^\alpha C'N$	−5.1	2.2	0.9	−6.4	0.7	−1.7	MO diamide[25]
		−5.3	2.2	0.9	−6.6	0.7	−1.7	MO N–Me acetamide[37]

[a]Assumption made that populations about χ follow from ^3J(H,C,C,H): $^3J_{ap}$ = 13.6 Hz, $^3J_{sc}$ = 2.6 Hz.

Table 4 Selection of Coefficients (Hz) for Use in the Standard $\cos^2$ Karplus Equation [Equation (1b)] for Couplings Relevant to Nucleic Acids. In the Column Remarks Exp(N) Denotes Experimental Calibration on N Data Points. See Figures [8, 10, 11] for Atom Numbering and Definition of Torsion Angles

Main torsion angle	^3J monitored	A	B	C	$^3J_{ap}$	$^3J_{sc}$	$\langle ^3J \rangle$	Remarks
χ	C(=C)NCH	6.2	−2.4	0.1	8.7	0.5	3.2	Exp(5)[47]
χ	C(=O)NCH	5.0	−2.1	0.1	7.2	0.3	2.6	Exp(4)[47]
β,ϵ	HCOP	15.3	−6.1	1.6	23.0	2.4	9.3	Exp(7)[45]
β,ϵ	CCOP	6.9	−3.4	0.7	11.0	0.7	4.1	Exp(10)[45]
γ Sugar	HCCH	see equation (12) and Table 7						Exp(299)

X = F) predicted that this coupling is substantially larger when ψ_{FC} is set at 180° than when it is set at 60°. In a recent MO study[44] on a series of 1-substituted propanes (Figure 5, X = H, CH_3, NH_2, OH, and F) both ϕ and ψ were varied from 0° to 360° in 30° steps. The rotation of ψ indeed appears to have a profound effect on ^3J(C,H). For example, for ϕ_{CH} = 180° the calculated ^3J(C,H)(X = F) varies from 8.0 Hz (ψ_{FC} = 0°) to 12.0 Hz (ψ_{FC} = 150°). These predictions were experimentally verified by measurements on *cis*- and *trans*-4-*t*-butylcyclohexanols, where the effect is even larger than predicted for X = OH.[44] In the same paper[44] the set of 340 calculated $^{13}C-H$ couplings was fitted (rms = 0.27 Hz) with the aid of a nine-coefficient Karplus-type expression. A 15-coefficient approximation was used to fit 39 experimental ^3J(C,H) values of cycloalkanols and pyranose sugars (rms = 0.30 Hz).[42]

In summary, much work has to be done before ^3J(C,H) can be used to calculate torsion angles. In the meantime, it appears safe to apply the general rule: $^3J_{ap} \gg {}^3J_{sc}$.

3.3 Vicinal Proton–Proton Couplings ^3J(H,N,C,H)

This coupling, usually denoted $^3J_{HN\alpha}$, deserves some attention because it can be measured with precision in proteins and affords important information concerning the

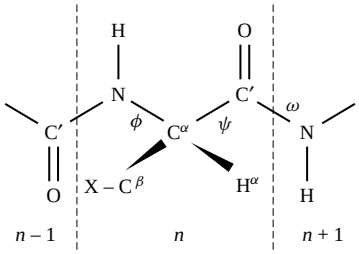

Figure 6 Schematic representation of the main-chain torsion angles ϕ, ψ, and ω in polypeptides and proteins. The χ_1 angle is defined as the torsion angle N–C^{α}–C^{β}–X; in many amino acids X = C^{γ}

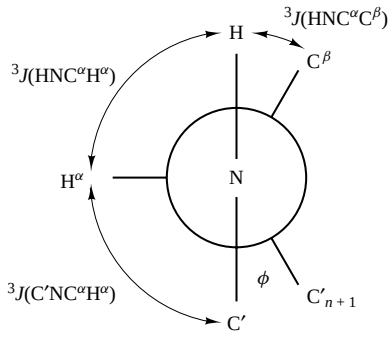

Figure 7 Newman projection along the N–C^{α} bond of a peptide backbone showing three important vicinal coupling constants that supply information about the ϕ torsion angle

local backbone geometry along the ϕ angle (Figures 6 and 7). It should be noted here that in protein chemistry the torsion angle between coupling nuclei is denoted as θ; for θ_{HNCH} one uses the relationship $\theta = \phi - 60^{\circ}$ (Figure 7).

Independent calibrations in terms of A, B, and C [equation (1b)], were carried out by Pardi et al.[30] (37 data points, rms = 0.87 Hz) and by Ludvigsen et al.[29] (112 data points, rms = 1.01 Hz), Table 3, on the basis of known X-ray structures. Inspection of the plots given suggests that corrections for differences in electronegativity of the various side chains might improve the rms deviation, especially for θ_{HNCH} near 180° and near 0°. The Karplus coefficients proposed by Bystrov[25] predict $J(180) = 10.9$ Hz and $J(0) = 8.7$ Hz, the latter value is probably too large by about 1.5–2.0 Hz.

3.4 Vicinal ^{1}H and ^{13}C Couplings to ^{31}P in Phosphate Diesters

The vicinal couplings ^{3}J(P,O,C,H) and ^{3}J(P,O,C,C), taken in combination, yield important conformational information concerning two backbone torsion angles in nucleic acids: β (angle PO5′C5′C4′) and ϵ (angle C4′C3′O3′P), (Figure 8). The Karplus coefficients that describe the angular dependence of ^{3}J(P,H) and ^{3}J(P,C) are relatively large. This fact contributed to the success of a different approach taken in the parameterization,[45] necessitated by the knowledge that phosphates (and sulfates) often display 'nonclassical' torsion angles, i.e. large deviations from 'classical' 180° and 60° angles. Moreover, it is desirable to avoid the use of crystallographic information which in individual cases can

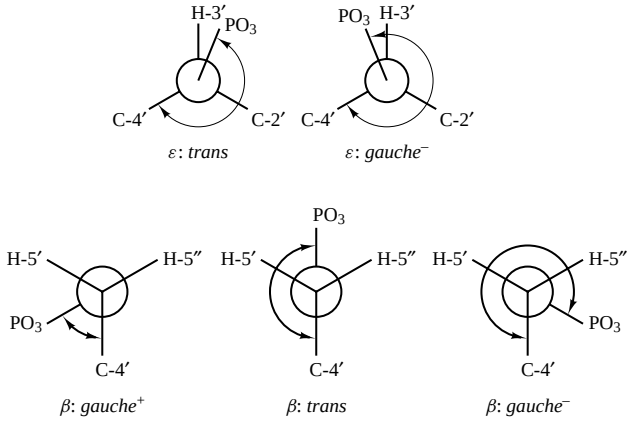

Figure 8 Newman projections along the main-chain torsion angle ϵ and β in nucleic acids. The negative charge on the phosphate group is omitted. These angles are monitored by ^{3}J(P,O,C,H) and ^{3}J(P,O,C,C). (Reproduced by permission of Adenine Press from P. P. Lankhorst, C. A. G. Haasnoot, C. Erkelens, and C. Altona, *J. Biomol. Struct. Dyn*., 1984, **1**, 1387)

be biased by crystal-packing effects. Instead, the unknown backbone angle (ϵ) can be determined simultaneously with the Karplus coefficients, provided that several different couplings along the same central bond are available and that conformational purity along this bond can be attained. In the case discussed here, six Karplus coefficients and four torsion angles were determined from 17 experimental couplings in RNA compounds (rms = 0.2 Hz). As it turned out, the *mean* NMR value of ϵ_{ap} in the RNA molecules in the stacked form (219°) corresponded well with the *mean* of crystallographic determinations in similar RNAs (218°). The same Karplus coefficients (Table 4) are transferable to DNA molecules.[46]

4 SELECTED APPLICATIONS OF ^{3}J IN THE FIELD OF BIOMOLECULES

4.1 General Remarks

For more than a decade the conformational situation ('structure') of biopolymers, such as proteins and nucleic acids, was judged from characteristic NOEs. More recently, interatomic distances or NOEs were introduced as constraints in MD (molecular dynamics calculations) trajectories. However, without additional information, it is very difficult to judge whether or not conformational homogeneity exists along each chemical bond of interest. This is especially true in cases where a given conformer predominates; minor forms may then escape detection altogether. Contradictory NOEs certainly point to the simultaneous existence of various rotamers, but these are not easily quantified from NOE information. With the advent of more powerful NMR spectrometers and techniques, investigators are becoming more and more aware that homo- and heteronuclear coupling constants offer a rich source of the additional information that is required.

An important recent application[48,49] of the Karplus coefficients involves the introduction of coupling constant restraints into molecular dynamics calculations. Defining $\Delta J = J_{\mathrm{obs}} -$

J_{calc}, one adds a penalty function in the form of a pseudoenergy term $\frac{1}{2}k_i \Delta J_i^2$ to the force field for each conformational constraint along given torsion angles, in addition to the usual distance constraints obtained from NOEs. One of the advantages of this approach, when applied to multiple couplings along a chosen bond, is that conformational equilibria, which occur on a short timescale, can be handled with more confidence. Of course, the k_i 'force constants' should be weighed according to the reliability of J_{obs} and J_{calc}, but to date such information on J_{calc} is limited to a few types of vicinal couplings, see Sections 3.2–3.5. It was also proposed to incorporate time-averaged J values[50] as constraints; this idea was succesfully tested on a cyclic peptide, antamanide ($^3J_{HN\alpha}$). Extension to multiple couplings about certain bonds undoubtedly will follow soon.

4.2 Amino Acids, Peptides, and Proteins

4.2.1 Main Chain Torsion Angles in Polypeptides and Proteins

The main chain in an amino acid sequence is characterized by three sequential torsion angles: ϕ, ψ, ω (Table 3 and Figure 6). For several reasons most attention was and still is focused on ϕ. This particular angle is correlated with the local shape of the sequence (α-helix, β-sheet, and various turns). In principle, ϕ can be monitored by the use of six different coupling constants (Table 3). Of these, $^3J(H,N,C^\alpha, H^\alpha)$ is the easiest one to measure, even in large proteins, followed by $^3J(H,N,C^\alpha, C^\beta)$.[38] Coupling to carbonyl carbon requires more effort and is difficult to obtain when the coupling is small. Nevertheless, a qualitative insight into the magnitude of two more ϕ couplings can be gained, at least in small cyclic peptides, from natural abundance NMR spectra; $^3J(C^\alpha, C',N,H)$ and $^3J(C',N,C^\alpha,H^\alpha)$.[38,51] Now that $^{13}C^{15}N$ isotopically-enriched proteins are becoming available, 3D and 4D NMR techniques offer new possibilities for measuring previously 'unmeasurable' couplings in large proteins, e.g., $^3J(H,N,C^\alpha,C')$.[52] The ψ angle remains elusive. For $^3J(H^\alpha,C^\alpha,C',N)$ and $^3J(C^\beta,C^\alpha,C',N)$ very little reference material is available at present. A similar remark applies to $^3J(C^\alpha,C',N,H)$, which coupling monitors the ω angle. In rigid domains, both ψ and ω can be determined from NOEs, however.

4.2.2 Side-Chain Conformations of Amino Acid Residues

The heteronuclear $^3J(C',C^\alpha,C^\beta,H^\beta)$ and $^3J(N,C^\alpha,C^\beta,H^\beta)$ couplings along with the two homonuclear $^3J(H^\alpha,C^\alpha,C^\beta,H^\beta)$ couplings allow the unambiguous diastereotopic assignment of the two β-methylene protons of the side chain of amino acid residues.[51,53] Given the correct assignment of H^β(pro-*R*) and H^β(pro-*S*) (Figure 9), the conformational populations of the equilibrating three rotameric species can be calculated from the two $^3J(H^\alpha,C^\alpha,C^\beta,H^\beta)$ couplings when the limiting values ($^3J_{ap}$ and $^3J_{sc}$) are known. The Pachler[54] values $^3J_{ap}$ = 13.6 Hz and $^3J_{sc}$ = 2.6 Hz are still widely used in the literature, although Abraham et al.[55] in 1977 already pointed out that differentiation according to the electronegativity of the side chain as well as the inclusion of substituent orientation was called for. In that work[55] a simple additivity scheme of substituent constants for the prediction of $^3J_{sc}$ was proposed. For example, for X = carbon, the two $^3J_{sc}$ values predicted were 3.4 Hz and 4.2 Hz, for X = oxygen, values of 2.2 Hz and 4.9 Hz were proposed. A more refined, but similar, approach is now possible through the use of equations (11), (12) or (13) in conjunction with the experimental group electronegativities λ_i. It appears best to distinguish three different groups of side chains A through C according to the respective λ_i values given in Table 1.

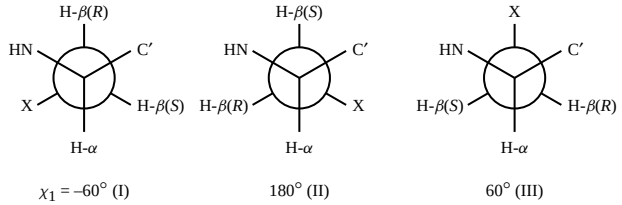

Figure 9 Newman projections of the three staggered χ_1 side-chain conformations in an amino acid with two H-β protons. The three rotamers are designated I, II, and III for $\chi_1 = -60°$, 180°, and 60°, respectively. For the sake of clarity pro-*R* and pro-*S* are abbreviated as *R* and *S*, respectively

A: λ_i = 0.42 (Asn, Asp, His, Phe, Trp, Tyr)
B: λ_i = 0.60–0.75 (Arg, Cys, Gln, Glu, Leu, Lys, Met)
C: λ_i = 1.25(Ser in D_2O),λ_i = 1.33 (Ser in $CDCl_3$)

The predicted $H^\alpha H^\beta$ limiting coupling constants for each of the three rotamers along χ_i in peptides and proteins (idealized staggered geometry assumed), differentiated according to the electronegativity of the side chain, are shown in Table 5. The nature of the solvent plays a role only in the cases of free amino acids and N-terminal residues, because $\lambda(NH_2) > \lambda(NH_3^+)$ (Table 1).

Some examples of $H^\alpha H^\beta$ coupling constants and rotamer populations are displayed in Table 6. For purposes of comparison, the populations calculated with standard values[54] are also given. The differences between the new and the old population values are usually $\leq$ 7%, except for Ser ($\leq$10%). It is concluded that the trends recorded in the literature thus far remain valid. For future work requiring high precision, the new values are recommended. It is noted in passing that application of equations (11), (12), or (13) allows us to predict safely couplings pertaining to any deviation from ideal staggered geometries. A good example of nonstaggered situations occurs in proline residues. An analysis of the 10 coupling constants of proline and of 12 model compounds[59] with the aid of the Haasnoot equation [equation (7)][16] in conjunction with the pseudorotation model for five-membered rings[60] showed that the unsubstituted proline ring occurs in a practically 1:1 conformational equilibrium between N-type and S-type forms (see Section 4.3.1 for a discussion of N- and S-conformers). Recently, Karplus and co-workers[61] successfully used the Haasnoot equation [equation (7)] to probe the motional characterisitics of the four proline residues in the cyclic decapeptide antamanide on a picosecond time scale.

4.3 Nucleic Acids

The structural properties and current nomenclature rules[17] of nucleic acid conformations have been treated by Wüthrich[28] and by Saenger.[62] The conformational analysis of oligonucleotides with the aid of coupling constants has been reviewed by Altona,[63] backbone torsion angles are shown in Figures 8, 10, and 12.

Table 5 Predicted Limiting $H^{\alpha}H^{\beta}$ Coupling Constants (Hz) [Equation (13)] for Each of the Three Rotamers Along $C^{\alpha}C^{\beta}$ in Peptides and Proteins. Idealized Staggered Models Assumed. Three Classes of Amino Acid Residues A–C (See Text) are Differentiated According to the Group Electronegativity λ_i of the Side-Chain Substituent X, Figure 9. Because $\lambda(NH_2) > \lambda(NH_3^+) \approx \lambda$[NHC(=O)R] (Table 1) N-Terminal Residues are Further Differentiated According to Solvent Conditions

	I(χ^-)		II(χ^t)		III(χ^+)	
ϕ_{HH}	pro-*R* 180°	pro-*S* −60°	pro-*R* 60°	pro-*S* 180°	pro-*R* −60°	pro-*S* 60°
D_2O (neutral or acidic: all residues) or nonaqueous solutions (except N-terminals)						
A	12.9	3.1	3.7	12.9	3.0	3.5
B	12.6	3.2	3.8	12.6	2.8	3.3
C	11.7	3.7	4.4	11.8	1.9	2.4
D_2O (basic) or nonaqueous solution: amino acids and N-terminal residues						
A	12.4	2.7	4.0	12.5	2.5	3.7
B	12.1	2.8	4.0	12.2	2.4	3.6
C	11.2	3.3	4.6	11.5	1.5	2.6

Table 6 Examples of $H^{\alpha}H^{\beta}$ Coupling Constants and χ Rotamer Populations in L-Amino Acids and Proteins.[a] The Appropriate Limiting Couplings are Given in Table 5. In Parentheses are the Populations Calculated with J_{ap} = 13.6 Hz and J_{sc} = 2.6 Hz[54]

		$^3J_{exp}$(Hz)		Rotamer populations (%)		
Residue	pH or solvent	$\alpha\beta$(pro-*R*)	$\alpha\beta$(pro-*S*)	I	II	III
Phe[56]	9.8	8.4	4.9	57(53)	20(21)	23(26)
Phe[56]	2.2	8.3	4.5	53(52)	13(17)	34(31)
AcPSer[57]	8.0	5.6	3.3	37(27)	4(6)	59(67)
AcSer[57]	7.5	6.2	3.8	42(32)	9(11)	49(57)
Cyclosporin A[58] MeLeu[4]	$CDCl_3$	12.0	4.5	91(85)	12(17)	−3(−2)
Cyclosporin A[58] MeLeu[6]	$CDCl_3$	6.0	10.5	24(31)	77(72)	−1(−3)
Cyclohexapeptide[58] Phe[7]	DMSO	4.5	9.0	11(17)	59(58)	30(25)
Cyclohexapeptide[58] Trp[8]	DMSO	10.9	4.2	79(75)	11(15)	10(10)
Cyclohexapeptide[58] Phe[11]	DMSO	11.5	3.1	86(80)	2(5)	12(15)

[a]The rotamer populations are computed from three equations with three unknowns using standard matrix methods; for the sake of clarity pro-*R* and pro-*S* are abbreviated as *R* and *S*, respectively:

$$J_{obs(R)} = p_I\, J_{I(R)} + p_{II}\, J_{II(R)} + p_{III}\, J_{III(R)}$$

$$J_{obs(S)} = p_I\, J_{I(S)} + p_{II}\, J_{II(S)} + p_{III}\, J_{III(S)}$$

$$p_I + p_{II} + p_{III} = 1$$

The computation is simpler when it is assumed that all J_{sc} values are equal.[54]

4.3.1 The Furanose Ring

The flexible five-membered sugar ring plays a pivotal role in nucleic acid structure and dynamic behavior. Structural differences between A-, B-, and Z-type duplexes are intimately correlated with specific conformational ranges of individual sugars. Within the B-DNA family each sugar responds to its surroundings (e.g., the base-stacking pattern) by an appropriate adaptation of its geometry. Careful analysis of sets of ^3J(H,H) values reveals intimate details on the 'atomic level' that cannot be obtained from NOEs.[64,65] Various reviews are available[24,63–65] and only a brief outline of the coupling constant approach is sketched here.

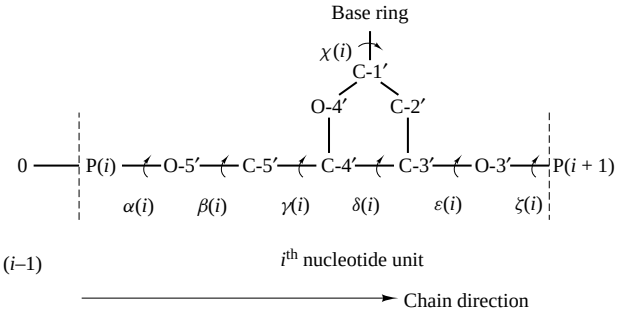

Figure 10 Conformational notation of the torsion angles of the backbone and χ of the base in nucleic acids[17]

Two distinct D-ribose conformations (better: conformational ranges) occur in nucleic acids, N-type (North, roughly C-3′-*endo*) and S-type (South, roughly C-2′-*endo*), Figure 11, which occur in fast equilibrium unless the stereochemical requirements of the helix impose restraints. For example, an RNA double helix consists of an N–N–N sequence of sugars, Z DNA of an S–N–S–N alternation. In B DNA the duplex structure allows the sugars some mobility to flip from S to N and vice versa. Pyrimidine sequences are relatively more mobile (78 ± 13% S) than are purine sequences (90 ± 7% S).[24] One always measures time-averaged couplings and shifts under 'fast-exchange' conditions. Nevertheless, it remains possible to extract quantitative information on geometry and conformational population from the couplings thanks to the fact that the five endocyclic torsion angles υ_i are mutually dependent via the two-parameter equation (14).

$$\upsilon_j = \phi_m \cos\{P + 0.8\pi(j-2)\},\ j = 0-4 \qquad (14)$$

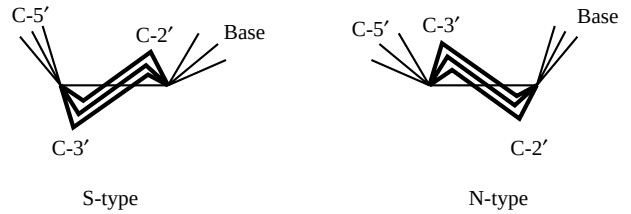

Figure 11 Schematic composite representation of the furanose conformations in nucleic acids: S-type (C-2′-*endo*/C-3′-*exo*) (left) and N-type (C-2′-*exo*/C-3′-*endo*) (right). (Reproduced by permission of Academic Press from J. van Wijk, B. D. Huckriede, J. H. Ippel, and C. Altona, *Methods Enzymol*., 1992, **211**, 286)

in which ϕ_m represents the amplitude of pucker and P the phase angle of pseudorotation.[60] The torsion angles are numbered clockwise, starting with υ_0(C4′–O4′–C1′–C2′). In D-sugars, N-type conformers are characterized by a positive sign of υ_3, S-type forms by a negative sign of υ_3. The (exocyclic) proton–proton torsion angles ϕ_{HH} are related to the υ_j-values via the pseudorotation parameters ϕ_m and P [equation (15)]:[66]

$$\phi_{HH} = a + b\phi_m \cos(P + \text{phase shift}) \tag{15}$$

where, in the idealized approximation, $b = 1$ and $a = 0^\circ$ for *cis* protons and $\pm 120^\circ$ for *trans* protons. Empirically established values for the parameters a and b in equation (15) for deoxyribose, ribose, arabinose, lyxose, and xylose are available.[66,67] Equations (14) and (15) and the extended Karplus equation [equation (13)] are employed in the iterative least-squares program PSEUROT.[68] Given a complete set of experimental proton–proton couplings $J(1',2')$, $J(2',3')$, and $J(3',4')$ for riboses and, in addition, $J(1',2'')$ and $J(2'',3')$ for deoxyriboses, the program minimizes the functional $R = \sum(J_{exp} - J_{calc})^2$ and yields the pseudorotation parameters of the two stable furanose conformers and the mole fractions. The accuracy of the procedure is greatly enhanced when the conformational equilibrium displays a strong shift with temperature. Version 4.0 of the PSEUROT program is in the public domain (*Quantum Chemistry Program Exchange No. 463*, Indiana State University, 1983); this version employs equation (7) and the original coefficients.[16] Later versions (PC, IBM compatible) 5.4 and 6.0 (see text) are available under licence from the author. Note that the PSEUROT programs are designed to yield the conformational characteristics of any saturated five-membered ring, provided that the appropriate vicinal ^{1}H–^{1}H couplings are input.

In NMR practice it is not always feasible to carry out the laborious spectral simulations that are required to obtain the individual coupling constants. Often, the sums of couplings to given protons are easily available, however, and these contain much the same information.[24,69] In the case of DNA we define:

$$\Sigma 1' = J(1',2') + J(1',2'') \tag{16a}$$

$$\Sigma 2' = J(1',2') + J(2',3') + J(2',2'') \tag{16b}$$

$$\Sigma 2'' = J(1',2'') + J(2'',3') + J(2',2'') \tag{16c}$$

$$\Sigma 3'\{^{31}\text{P}\} = J(2',3') + J(2'',3') + J(3',4) \tag{16d}$$

The $\sum 2'$ and $\sum 2''$ terms include the absolute value of $^2J(2',2'')$ (approximately 14 Hz in deoxyribofuranose). A graphical method, based on the theory employed in PSEUROT, successfully utilizes graphs of $\sum J$ versus P and $\sum J$ versus populations to solve the conformational problems.[24,69] Recently, the graphical procedure was automated in program PSEUROT, Version 6.0.[68]

4.3.2 Orientation of the Nucleic Acid Base

The glycosyl torsion angle χ (not shown) defines the orientation of the base with respect to the sugar ring.[62] Two major orientations are known: *anti* and *syn*. In the more common *anti* form, the C-8-H-8 and C-6-H-6 vectors of the purine and the pyrimidine bases point roughly in the direction of the C-1′–O-4′ bond and are antiparallel to the C-1′–H-1′ bond. From pyrimidine model compounds the Karplus coefficients for ^3J(C-6,N-1,C-1′,H-1′) and ^3J(C-2,N-1,C-1′,H-1′) were determined[47] (Table 4) and from these values one predicts the following (very approximate) characteristics:

$$anti\text{base}: {}^3J(\text{C}-6, \text{H}-1') \approx 9\text{Hz}, {}^3J(\text{C}-2, \text{H}-1') \approx 3\text{Hz}$$

$$syn\text{base}: {}^3J(\text{C}-6, \text{H}-1') \approx 4\text{Hz}, {}^3J(\text{C}-2, \text{H}-1') \approx 7\text{Hz}$$

In a regular B-DNA structure with *anti* bases, the angle χ is well defined ($\pm 10^\circ$) from three NOE contacts: H-6/H-8–H-2′, H-6/H-8–H-2″, H-6/H-8–H-3′, but in exceptional cases where the base enjoys more conformational freedom measurement of ^3J(C,H) may well supply valuable additional information.

4.3.3 Backbone Conformations of RNA and DNA

The six torsion angles along the nucleic acid backbone are denoted α–ζ, starting with P–O-5′ as the central bond for α, Figure 10. NMR spectroscopy provides no direct grip upon the important phosphate diester torsions ζ and α; these are usually determined from NOE-constrained MD trajectories. The remaining backbone angles β, γ, δ, and $\in$ are monitored by various vicinal coupling constants. Because X-ray crystallography[62] has made it clear that important deviations from pure staggered geometries (180°, 60°) in double-helical structures commonly occur, it is the task of the NMR spectroscopist to deduce at the same time values for the backbone angles as well as conformational populations. This is possible in principle because Nature has conveniently provided a sufficient number of coupling nuclei along the backbone that can be put into use.

It is often helpful to study the behavior of sums of couplings versus rotation about a given torsion angle. As an aid to the discussion, Table 7 has been prepared. The Karplus coefficients used to calculate the ^3J(P,H) and ^3J(P,C) values in Table 7 are taken from Table 4.

Torsion angle β (P–O5′–C5′–C4′), Figure 8. In 5′-mononucleotides of RNA and DNA, the $\beta^t(ap)$ rotamer is invariably preferred (>70%). In stacked oligonucleotides, the β^t angle is confined to a small range of values (176 ± 4°). Under the additional assumption that in unstacked ('melted') states an equilibrium exists between two or three rotamers (β^t, 175°; β^+, 60°; β^-, 300°), a sum rule is easily derived [equation (17)]:

$$p(\beta^t) = (25.4 - \Sigma')/20.5 \tag{17}$$

where p stands for the fractional population and $\sum' = J(5',\text{P}) + J(5'',\text{P})$. Stereospecific assignments of H-5′ and H-5″ are not

Table 7 Backbone Angles β, γ, and ϵ(°) of Nucleic Acids in the Most Populated Ranges and Corresponding Calculated Vicinal Coupling Constants (Hz) (See Text)

β^t	170	175	180	185	190
J(P,H − 5′)	4.0	3.1	2.4	1.8	1.3
J(P,H − 5″)	1.3	1.8	2.4	3.1	4.0
$\sum'$	5.3	4.9	4.8	4.9	5.3
J(P,C − 4′)	10.7	10.9	11.0	10.9	10.7
β^+	50	55	60	65	70
J(P,H − 5′)	1.3	1.8	2.4	3.1	4.0
J(P,H − 5″)	22.5	22.9	23.0	22.9	22.5
$\sum'$	23.8	24.7	25.4	26.0	26.5
J(P,C − 4′)	1.4	1.0	0.7	0.5	0.3
β^-	−50	−55	−60	−65	−70
J(P,H − 5′)	22.5	22.9	23.0	22.9	22.5
J(P,H − 5″)	1.3	1.8	2.4	3.1	4.0
$\sum'$	23.8	24.7	25.4	26.0	26.5
J(P,C − 4′)	1.4	1.0	0.7	0.5	0.3
γ^+	45	50	55	60	65
J(H − 4′,H − 5′)	1.1	1.5	2.0	2.5	3.2
J(H − 4′,H − 5″)	2.9	2.2	1.6	1.2	0.8
$\sum$	4.0	3.7	3.6	3.7	4.0
γ^t	165	170	175	180	185
J(H − 4′,H − 5′)	5.1	4.5	3.6	3.0	2.4
J(H − 4′,H − 5″)	11.0	11.0	10.9	10.6	10.2
$\sum$	16.1	15.5	14.5	13.6	12.6
γ^-	−80	−75	−70	−65	−60
J(H − 4′,H − 5′)	9.5	10.1	10.5	10.8	10.9
J(H − 4′,H − 5″)	1.9	2.4	3.1	3.8	4.6
$\sum$	11.4	12.5	13.6	14.6	15.4
ϵ^t	180	190	200	210	220
J(P,H − 3′)	2.4	4.0	5.9	7.8	9.4
J(P,C − 2′)	0.7	0.3	0.3	0.7	1.5
J(P,C − 4′)	11.0	10.7	10.0	8.8	7.4
ϵ^-	−105	−100	−95	−90	−85
J(P,H − 3′)	10.0	9.9	8.6	7.8	6.9
J(P,C − 2′)	6.6	7.4	8.1	8.8	9.5
J(P,C − 4′)	2.0	1.5	1.1	0.7	0.5

necessary at this stage. Unfortunately, we have no information concerning the true values of the β^+ and β^- angles, but it can be verified that nonclassical β_{sc} rotamers (e.g. β_{sc}, ±90°) would introduce less than 2% error in the $p(\beta^t)$ value calculated from equation (17). The C-4′,P coupling can be used as an independent check on the β^t population [equation (18)]:

$$p(\beta^t) = [^3J(\text{C-4}', \text{P}) - 0.7]/10.2 \tag{18}$$

Assuming that the H-5′ and H-5″ resonances are assigned stereospecifically from NOEs, approximate values of the minor populations $p\beta^+$ and $p\beta^-$ are derived from J(5′,P) and J(5″,P). Preference for β^+ was found to occur locally in a minihairpin loop.[70]

Torsion angle γ(O5′–C5′–C4′–C3′), Figure 12. Nucleosides and mononucleotides in the solid state display a preference for γ^+ (76%), followed by γ^t (18%) and γ^-(6%). This rotamer distribution in the crystalline state is mirrored by the distribution found in aqueous solution at ambient temperatures. Crystallographic data reveal trends toward nonclassical angles: γ^+, 53°; γ^t, 180°; γ^-, 290°. The right-handed helix requires a pure γ^+ rotamer; upon melting, conformational mobility is regained. The population γ^+ again follows from a sum rule

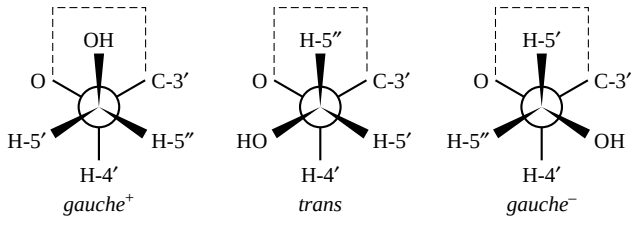

Figure 12 Newman projections of the three γ rotamers in nucleosides. In nucleotides the OH group is replaced by an O–PO_3^- group

[equation (19)]:

$$p(\gamma^+) = (13.6 - \Sigma)/10.0 \tag{19}$$

where $\sum = J_{4'5'} + J_{4'5''}$. A pure or almost pure γ^t form is adopted by dG residues in Z DNA[62] and at the 5′–3′ loop stem junction in small hairpin loops in DNA, i.e. at the position of the local sharp turn of the backbone.[70] Such a turn is revealed by a large (>9 Hz) value of $^3J_{4'5''}$.

Torsion angle δ (C5′–C4′–C3′–O3′): This torsion angle is directly related to the pseudorotation parameters P and ϕ_m of

the D-(deoxy)ribose sugar by equation (20).[63]

$$\delta = 120.6 + 1.1\phi_m \cos(P + 145.2) \quad (20)$$

Torsion angle ϵ (C4′–C3′–O3′–P), Figure 8. The study of the conformational behavior of this backbone angle is virtually impossible without the aid of vicinal $^{13}C-^{13}P$ couplings because only a single ^3J(P,H) value is measured for each residue. The ϵ^+ rotamer is sterically 'forbidden'[63] and need not be considered. The two allowed conformational ranges, ϵ^t and ϵ^-, are more or less symmetrically disposed with respect to H-3′ and, without further information, ^3J(P,H) can give few clues concerning the ϵ^t/ϵ^- rotamer population distribution. It is known, however, that ^3J(P,H-3′) of single-stranded RNA oligomers increases with increasing population of stacked (single-helical) conformer to a maximum of about 9 Hz, whereas ^3J(P,H-3′) in similar DNA compounds decreases to a minimum of about 4 Hz when fully stacked. This difference in behavior was quantitatively interpreted with the aid of ^{13}C NMR data.[45,46,71] It turned out that there exists a strong correlation between the conformation of the sugar ring and the ϵ^t angle. In RNA the stacked state strongly biases the sugar towards the N-type form [$\epsilon^t{}_N$ = 219°; ^3J(P,C-4′) ≈ 8 Hz; ^3J(P,H-3′) ≈ 9 Hz], whereas in DNA the sugar mainly occupies the S-type range [$\epsilon^t{}_S$ = 192°; ^3J(P,C-4′) ≈ 10.7 Hz; ^3J(P,H-3′) ≈ 4.5 Hz]. The $\epsilon^-{}_N$ combination appeared 'forbidden', whereas $\epsilon^-{}_S$ = 266°, corresponding with ^3J(P,C-2′) ≈ 8.3 Hz, remains allowed. The latter combination must be considered important, because X-ray crystallography has shown that it occurs in various residues throughout the double helix (BII form). We expect that the BII form will be studied in solution as soon as ^{13}C-enriched synthetic DNAs become available. Finally, it should be mentioned that $\epsilon^t{}_N$ in DNA (212°) is smaller than $\epsilon^t{}_N$ in RNA (219°).[71]

5 CAVEATS

The original optimism that arose among stereochemists when Karplus's first paper[1] on ^3J(H,H) in ethane appeared in 1959 soon gave way to grave scepticism in the course of the 1960s.[2] Nevertheless, the Karplus-type relationships are by now firmly rooted in stereochemical thinking. Perhaps unfortunately, not all the known ramifications are widely appreciated. Moreover, even in the situation of the best-known coupling, ^3J(H,C,C,H) along sp^3-sp^3 C–C bonds, some influences that affect couplings have not been taken into consideration in the present contribution. At least three of these (perhaps not unrelated) influences are known, but as yet not understood to the extent that quantitative corrections to calculated couplings can be brought into play: (a) the β effect, the orientation of a β substituent appears to affect ^3J(H,C,C,H), an increase of about 0.5 Hz is noted for $^3J_{ap}$ when a C–O bond occurs in the *ap* position with respect to one of the coupling protons;[11] (b) the through-space (Barfield) transmission effect,[72,73] first noted in norbornane-like structures but not necessarily limited to highly strained compounds; (c) bond angle deformations, semiempirical calculations[2,74] predict that vicinal couplings depend significantly on the bond angles HCC′ and CC′H′ of the HCC′H′ fragment. The effect would be maximal for $^3J_{ap}$ and $^3J_{sp}$. At this point a dilemma arises. Assuming that reliable empirical corrections for influences (a)–(c) can be established, it would be necessary to introduce much detailed structural information concerning the molecular fragment under study into play before a measured coupling can be interpreted quantitatively in terms of the same structure. Undoubtedly, in the future this will be done for selected fragments which are of vital interest to researchers. However, we may also expect that for times to come present-day knowledge will suffice to solve stereochemical problems routinely along the lines pioneered by Karplus in 1959.[1]

6 RELATED ARTICLES

Amino Acids, Peptides and Proteins: Chemical Shifts; Biological Macromolecules: Structure Determination in Solution; Biological Macromolecules: NMR Parameters; Carbohydrates and Glycoconjugates; Coupling Constants Determined by ECOSY; Coupling Through Space in Organic Chemistry; DNA: A-, B-, and Z-; DNA Triplexes, Quadruplexes, and Aptamers; Half-Filter Experiments: Proton–Carbon-13; Homonuclear Three-Dimensional NMR of Biomolecules; Indirect Coupling: Semiempirical Calculations; Nucleic Acid Structures in Solution: Sequence Dependence; Nucleic Acids: Phosphorus-31 NMR; Nucleic Acids: Spectra, Structures, and Dynamics; Quantitative Measurements; Structures of Larger Proteins, Protein-Ligand, and Protein-DNA Complexes by Multi-Dimensional Heteronuclear NMR; Three-Dimensional HMQC-NOESY, NOESY-HMQC, and NOESY-HSQC; Three- and Four-Dimensional Heteronuclear Magnetic Resonance; Two-Dimensional J-Resolved Spectroscopy; Vicinal ^1H, ^1H Coupling Constants in Cyclic π-Systems.

7 REFERENCES

1. M. Karplus, *J. Chem. Phys.*, 1959, **30**, 11.
2. M. Karplus, *J. Am. Chem. Soc.*, 1963, **85**, 2870.
3. R. E. Glick and A. A. Bothner-By, *J. Chem. Phys.*, 1956, **25**, 362.
4. C. N. Banwell and N. Sheppard, *Discuss. Faraday Soc.*, 1962, **34**, 115.
5. R. J. Abraham and K. G. R. Pachler, *Mol. Phys.*, 1964, **7**, 165.
6. H. Booth, *Tetrahedron Lett.*, 1965, 411.
7. P. L. Durette and D. Horton, *Org. Magn. Reson.*, 1971, **3**, 417.
8. L. Pauling, *The Nature of the Chemical Bond*, 3rd edn., Cornell University Press, Ithaca, NY, 1960.
9. M. L. Huggins, *J. Am. Chem. Soc.*, 1953, **75**, 4123.
10. R. J. Abraham and G. Gatti, *J. Chem. Soc. B*, 1969, 961.
11. C. Altona and C. A. G. Haasnoot, *Org. Magn. Reson.*, 1980, **13**, 417.
12. K. G. R. Pachler, *Tetrahedron*, 1971, **27**, 187.
13. K. G. R. Pachler, *J. Chem. Soc. Perkin Trans. 2*, 1972, 1935.
14. F. A. A. M. de Leeuw, C. A. G. Haasnoot, and C. Altona, *J. Am. Chem. Soc.*, 1984, **106**, 2299.
15. L. A. Donders, F. A. A. M. de Leeuw, and C. Altona, *Magn. Reson. Chem.*, 1989, **27**, 556.
16. C. A. G. Haasnoot, F. A. A. M. de Leeuw, and C. Altona, *Tetrahedron*, 1980, **36**, 2783.

17. IUPAC Tentative Rules for the Nomenclature of Organic Chemistry, *J. Org. Chem.*, 1970, **35**, 2849; for nucleic acids, see JCBN Recommendations, *Eur. J. Biochem.*, 1983, **131**, 9; *J. Biol. Chem.*, 1986, **261**, 13.
18. E. Díez, J. San-Fabián, J. Guilleme, C. Altona, and L. A. Donders, *Mol. Phys.*, 1989, **68**, 49.
19. C. Altona, J. H. Ippel, A. J. A. Westra Hoekzema, C. Erkelens, M. Groesbeek, and L. A. Donders, *Magn. Reson. Chem.*, 1989, **27**, 564.
20. C. Altona, R. Francke, R. de Haan, J. H. Ippel, G. J. Daalmans, and J. van Wijk, *Magn. Reson. Chem.*, 1994, **32**, 670.
21. F. A. A. M. de Leeuw, A. A. van Beuzekom, and C. Altona, *J. Comp. Chem.*, 1983, **4**, 438.
22. N. L. Allinger, *Quantum Chemistry Program Exchange MMP(85)*, Indiana State University, 1985.
23. J. San-Fabián, J. Guilleme, E. Díez, P. Lazzeretti, M. Malagoli, and R. Zanasi, *Chem. Phys. Lett.*, 1993, **206**, 253.
24. J. van Wijk, B. D. Huckriede, J. H. Ippel, and C. Altona, *Methods Enzymol.*, 1992, **211**, 286.
25. V. F. Bystrov, *Prog. Nucl. Magn. Reson. Spectrosc.*, 1976, **10**, 41.
26. P. E. Hansen, *Prog. Nucl. Magn. Reson. Spectrosc.*, 1981, **14**, 175.
27. J. L. Marshall, *Carbon–Carbon and Carbon–Proton NMR Couplings*, Verlag Chemie Int., Deerfield Beach, FL, 1983.
28. K. Wüthrich, *NMR of Proteins and Nucleic Acids*, Wiley, New York, 1986.
29. S. Ludvigsen, K. V. Anderson, and F. M. Poulsen, *J. Mol. Biol.*, 1991, **217**, 731.
30. A. Pardi, M. Billeter, and K. Wüthrich, *J. Mol. Biol.*, 1985, **180**, 741.
31. L.-F. Kao and M. Barfield, *J. Am. Chem. Soc.*, 1985, **107**, 2323.
32. A. de Marco and M. Llinas, *Biochemistry*, 1979, **18**, 3847.
33. R. Aydin, J. P. Loux, and H. Günther, *Angew. Chem., Int. Ed. Engl.*, 1982, **21**, 449.
34. M. C. Reddy, B. P. Nagy Reddy, K. R. Sridharan, and J. Ramakrishna, *Org. Magn. Reson.*, 1984, **22**, 464.
35. P. E. Hansen, J. Feeney, and G. C. K. Roberts, *J. Magn. Reson.*, 1975, **17**, 249.
36. D. Cowburn, D. H. Live, A. J. Fishman, and W. C. Agosta, *J. Am. Chem. Soc.*, 1983, **105**, 7435.
37. M. Barfield and H. L. Gearhart, *Mol. Phys.*, 1974, **27**, 899.
38. P. Schmieder and H. Kessler, *Biopolymers*, 1992, **32**, 435.
39. F. H. Cano, C. Foces-Foces, J. Jiménez-Barbero, A. Alemany, M. Bernabé, and M. Martin-Lomas, *J. Am. Chem. Soc.*, 1987, **52**, 3367.
40. R. Wasylishen and T. Schaefer, *Can. J. Chem.*, 1973, **51**, 961.
41. T. P. Forrest and S. Sukumar, *Can. J. Chem.*, 1977, **55**, 3686.
42. A. A. van Beuzekom, *Thesis*, Leiden University, 1989.
43. G. J. Karabatsos and C. E. Orzech, Jr., *J. Am. Chem. Soc.*, 1965, **87**, 560.
44. A. A. van Beuzekom, F. A. A. M. de Leeuw, and C. Altona, *Magn. Reson. Chem.*, 1990, **28**, 68.
45. P. P. Lankhorst, C. A. G. Haasnoot, C. Erkelens, and C. Altona, *J. Biomol. Struct. Dyn.*, 1984, **1**, 1387.
46. P. P. Lankhorst, C. A. G. Haasnoot, C. Erkelens, H. P. Westerink, G. A. van der Marel, J. H. van Boom, and C. Altona, *Nucleic Acids Res.*, 1985, **13**, 927.
47. D. B. Davies, P. Rajani, M. MacCoss, and S. Danyluk, *Magn. Reson. Chem.*, 1985, **23**, 72.
48. Y. Kim and J. H. Prestegard, *Proteins*, 1990, **8**, 377.
49. D. F. Mierke and H. Kessler, *Biopolymers*, 1993, **33**, 1003.
50. A. E. Torda, R. M. Brunne, T. Huber, H. Kessler, and W. F. van Gunsteren, *J. Biomol. NMR*, 1993, **3**, 55.
51. M. Eberstadt, D. F. Mierke, M. Köck, and H. Kessler, *Helv. Chim. Acta*, 1992, **75**, 2583.
52. G. W. Vuister and A. Bax, *J. Magn. Reson.*, 1992, **98**, 428.
53. P. Schmieder, M. Kurz, and H. Kessler, *J. Biolmol. NMR*, 1991, **1**, 403.
54. K. G. R. Pachler, *Spectrochim. Acta*, 1964, **20**, 581.
55. R. J. Abraham, P. Loftus, and W. A. Thomas, *Tetrahedron*, 1977, **33**, 1227.
56. J. Feeney, *J. Magn. Reson.*, 1976, **21**, 473.
57. L. Pogliani, D. Ziessow, and C. H. Krüger, *Tetrahedron*, 1979, **35**, 2867.
58. H. Kessler, C. Griesinger, and K. Wagner, *J. Am. Chem. Soc.*, 1987, **109**, 6927.
59. C. A. G. Haasnoot, F. A. A. M. de Leeuw, H. P. M. de Leeuw, and C. Altona, *Biopolymers*, 1981, **20**, 1211.
60. C. Altona and M. Sundaralingam, *J. Am. Chem. Soc.*, 1972, **94**, 8205.
61. J. M. Schmidt, R. Brüschweiler, R. R. Ernst, R. L. Dunbrack, Jr., D. Joseph, and M. Karplus, *J. Am. Chem. Soc.*, 1993, **125**, 8747.
62. W. Saenger, *Principles of Nucleic Acid Structure*, Springer, New York, 1984.
63. C. Altona, *Recl. Trav. Chim. Pays-Bas*, 1982, **101**, 413.
64. C. Altona, in *Theoretical Biochemistry and Molecular Biophysics*, ed. D. L. Beveridge and R. Lavery, Adenine Press, New York, 1990, p. 1.
65. F. J. M. van de Ven and C. W. Hilbers, *Eur. J. Biochem.*, 1988, **178**, 1.
66. C. A. G. Haasnoot, F. A. A. M. de Leeuw, H. P. M. de Leeuw, and C. Altona, *Org. Magn. Reson.*, 1981, **15**, 43.
67. F. A. A. M. de Leeuw and C. Altona, *J. Chem. Soc., Perkin Trans. 2*, 1982, 375.
68. F. A. A. M. de Leeuw and C. Altona, *J. Comp. Chem.*, 1983, **4**, 428.
69. L. J. Rinkel and C. Altona, *J. Biomol. Struct. Dyn.*, 1987, **4**, 621.
70. J. M. L. Pieters, E. de Vroom, G. A. van der Marel, J. H. van Boom, Th. M. G. Koning, R. Kaptein, and C. Altona, *Biochemistry*, 1990, **29**, 788.
71. P. P. Lankhorst, C. A. G. Haasnoot, C. Erkelens, and C. Altona, *Nucleic Acids Res.*, 1984, **12**, 5419.
72. M. Barfield, *J. Am. Chem. Soc.*, 1980, **102**, 1.
73. F. A. A. M. de Leeuw, A. A. van Beuzekom, and C. Altona, *J. Comp. Chem.*, 1983, **4**, 438.
74. M. Barfield and W. B. Smith, *J. Am. Chem. Soc.*, 1992, **114**, 1574.

Biographical Sketch

Cornelis Altona. *b* 1931. Ph.D., 1964, Leiden University. Introduced to NMR by E. Havinga and L. J. Oosterhoff. Visiting lecturer, Case Western University, 1967–69. Faculty of Chemistry, Leiden University, 1964—present. Approximately 185 publications. Research interests include: stereoelectronic effects (anomeric effect, *gauche* effect); conformational analysis (of five-membered rings in particular); generalized Karplus-type equations for vicinal spin—spin coupling constants; conformation, structure and dynamics of oligonucleotides (DNA, RNA) in aqueous solution, including hairpin loops and four-way junctions; force-field calculations and charge distributions; application of ab initio methods.

Protein Structures: Relaxation Matrix Refinement

Alexandre M. J. J. Bonvin, Rolf Boelens and Robert Kaptein

Utrecht University, Utrecht, The Netherlands

1	Introduction	1
2	The Nuclear Overhauser Effect	1
3	Structure Calculations	5
4	Quality of the Structures	7
5	Application: The ARC Repressor	7
6	Conclusion	9
7	Related Articles	9
8	References	9

1 INTRODUCTION

In the last decade, NMR spectroscopy has become an important alternative to X-ray crystallography for the structural studies of molecules of biological interest. The principal advantage of NMR is that it allows the study of biomolecules in solution, thus closer to their real physiological environment. The method is limited, however, to biomolecules of relatively small size due to limitations in spectral resolution and line-broadening effects. The upper limit is presently situated around molecular weights of 30 kDa. Knowledge of three-dimensional (3D) structures might lead, for example, to a better understanding of structure–function relationships or recognition processes. For this purpose, accurate structures are required and, as we shall see, the use of so-called relaxation matrix approaches provides a means of improving the accuracy of the method.

The process of structure determination based on NMR data can be divided into four stages:

1. assignments of the proton resonances,
2. determination of structural constraints from NOE and J coupling data,
3. generation of structures,
4. refinement of these structures.

The first and laborious task of assigning proton resonances is still the main bottleneck of the structure determination, but progress is being made in this area by the development of new multidimensional NMR techniques [3D and four-dimensional (4D)][1–6] and the use of labeled samples (^{15}N, ^{13}C). Computational approaches are also being developed toward an automatic assignment of the NMR spectra (see ***Analysis of Spectra: Automatic Methods***). We will not treat this aspect of the problem here, but concentrate on the last three stages involving the determination of structural constraints (distances, dihedral angles) and the generation and refinement of the structures.

Structure determination by NMR is based primarily on the nuclear Overhauser effect (NOE)[7] (see ***Nuclear Overhauser Effect***). Its origin is dipolar cross relaxation between protons, which is a function of distances and molecular motions. Because of the approximate r^{-6} dependence of the NOEs on the interproton distances, these can only be measured between protons relatively close in space ($<$ about 0.5 nm). NOEs are generally transformed into distance constraints which are then used, together with dihedral angle constraints obtained from J coupling data, for the generation of structures using Distance Geometry (DG)[8] (see ***Distance Geometry***) or Simulated Annealing (SA) techniques.[9,10] These structures are then usually refined with a combination of restrained Energy Minimization and Molecular Dynamics (MD) simulations.[11] Genetic algorithms[12] and heuristic methods based on Kalman filter techniques[13] can also be used for this purpose. Several approaches have been proposed for the interpretation of NOEs in terms of distances. The simplest one classifies the NOEs into strong, medium, and weak peaks and attributes corresponding distance ranges to these three categories. However, more accurate distances can be obtained from relaxation matrix calculations, which take into account all indirect magnetization transfers ('spin diffusion').[14–23] A more direct method for refinement was proposed by Yip and Case,[24] in which NOE intensities are directly used as structural constraints, thus avoiding the transformation into distances. In this method, the structures are directly refined against experimental NMR data by comparison of theoretical and experimental NOE intensities.

In addition to NOEs and J couplings, chemical shifts can also provide structural information on biomolecules. Recent developments that permit the prediction of ^{1}H, ^{13}C, ^{15}N, and ^{19}F chemical shifts should open new avenues to the structure refinement of proteins[25–29] (see ***Amino Acids, Peptides and Proteins: Chemical Shifts***; ***Chemical Shifts in Biochemical Systems***).

In this review, we will first discuss the underlying theory of the NOE, including a description of intramolecular motions. The use of NOEs as structural constraints, indirectly by conversion into distances or directly by comparison of experimental and theoretical intensities, will be presented together with the most common methods used to generate and refine structures. This will be illustrated with results from our laboratory for the structure determination and refinement of the Arc repressor of phage P22, a dimeric DNA-binding protein (2×53 residues).

2 THE NUCLEAR OVERHAUSER EFFECT

2.1 Relaxation Matrix Theory

Multispin relaxation in a biomolecule in solution can be approximately described by the generalized Bloch equations. The evolution of the longitudinal magnetization components in a system of N spins is governed by a set of coupled differential equations of the form[30]

$$\frac{\mathrm{d}}{\mathrm{d}t}\Delta \boldsymbol{M}(t) = -\mathbf{R}\Delta \boldsymbol{M}(t) \qquad (1)$$

where the vector $\Delta \boldsymbol{M}(t)$ comprises the deviations from thermal equilibrium for all spins i

$$\Delta M(t)_i = [M_z(t) - M_0]_i \qquad (2)$$

and **R** is the relaxation matrix. It comprises contributions from cross relaxation and from external relaxation. For a system of dipolar-coupled spins, neglecting cross correlation, **R** has the dimension of the number of spins N in the systems. Since the dipolar interaction is a function of time, the relaxation rates are intimately connected with the molecular motion. The elements of **R** can be expressed as[7,30]

$$R_{ii} = \rho_{ii} = K \sum_{j \neq i} [J_{ij}^0(0) + 3J_{ij}^1(\omega_0) + 6J_{ij}^2(2\omega_0)] + R_{\text{leak}}$$

$$R_{ij} = \sigma_{ij} = K[-J_{ij}^0(0) + 6J_{ij}^2(2\omega_0)] \tag{3}$$

where ω_0 is the Larmor frequency and $K = (2\pi/5)\gamma^4\hbar^2$; ρ_{ii} is the auto relaxation rate, with R_{leak} as an additional term to account for all nondipolar relaxation mechanisms, and σ_{ij} is the cross-relaxation rate between spins i and j. ${J_{ij}}^m(\omega)$ denotes the spectral densities at multiple values of the spin Larmor frequency [$(m \times \omega_0)$ with $m = 0, 1, 2$]. Cross relaxation is normally measured by observing intensity changes upon saturation or inversion of spins. Two-dimensional (2D) NMR techniques have been developed to investigate the resulting NOEs[31] (see ***Nuclear Overhauser Effect***; ***NOESY***). The integrated intensities I_{ij} in a 2D NOE spectrum recorded with mixing time τ_m, are given by the matrix equation[31]

$$\mathbf{I}(\tau_m) = \exp(-\mathbf{R}\tau_m)\boldsymbol{M}(0) = \mathbf{A}\boldsymbol{M}(0) \tag{4}$$

which is the formal solution of the differential equation (1) where $\boldsymbol{M}(0)$ specifies the starting conditions. This defines the exponential matrix of normalized NOE intensities **A**,

$$\mathbf{A} = \exp(-\mathbf{R}\tau_m) \tag{5}$$

that will be referred to as 'the NOE matrix'.

The spectral densities ${J_{ij}}^m(\omega)$ in the definitions of the relaxation rates ρ_{ii} and σ_{ij} are cosine Fourier transforms

$$J_{ij}^m(\omega) = \int_0^\infty C_{ij}^m(t)\cos(\omega t)\,\mathrm{d}t \tag{6}$$

where the $C(t)$ are correlation functions describing the time evolution of the dipolar interaction. Assuming that the molecule is a rigid body moving isotropically in solution, the correlation functions in equation (6) can be described by a simple exponential of the form $\exp(-t/\tau_c)$, τ_c being the correlation time for the overall rotation of the molecule. With this simple definition, the spectral density ${J_{ij}}^m(\omega)$ becomes

$$J_{ij}^m(\omega) = \frac{1}{4\pi r_{ij}^6}\left[\frac{\tau_c}{1+(\omega\tau_c)^2}\right] \tag{7}$$

If the assumption of a rigid body is not valid, which is usually the case for biomolecules, the description of $C(t)$ by a simple exponential is no longer correct. The correlation function should then be defined in a more general form as

$$C_{ij}^m(t) = \left\langle \frac{Y_{2m}[\Phi_{ij}^{\text{lab}}(t_0+t)]Y_{2m}^*[\Phi_{ij}^{\text{lab}}(t_0)]}{r_{ij}^3(t_0+t)r_{ij}^3(t_0)} \right\rangle \tag{8}$$

Here the angular brackets indicate a time average over t_0 (which is equivalent to an ensemble average); Y_{2m} are the second-order spherical harmonics and r and Φ^{lab} denote the length and polar angles of the interproton vector in the laboratory frame of coordinates. The form of the spectral density functions ${J_{ij}}^m(\omega)$ could be obtained experimentally from relaxation measurements. The feasibility of this approach has been recently demonstrated by Peng and Wagner[32,33] who mapped the spectral densities of N–H vectors using heteronuclear relaxation experiments. In theory, this function can also be computed from a long MD trajectory. With present-day computational facilities $C(t)$ can only be computed with sufficient statistical accuracy for t values of the order of 0.1–1.0 ns. Fortunately, for many interproton vectors $C(t)$ is observed to reach a plateau value after a few ps, indicating that fast picosecond motions are well separated from slower processes.[34,35]

Following the approach developed by Lipari and Szabo,[36,37] a 'model-free' description of $C(t)$ can be set up in terms of two characteristic times, τ_p, the time in which $C(t)$ decays to the initial plateau value due to the fast internal motions, and τ_c, the correlation time for the overall rotation of the molecule. Assuming isotropic tumbling, and transforming to molecule fixed coordinates Φ^{mol} one has[34]

$$C_{ij}^m(t) = \frac{\exp(-t/\tau_c)}{4\pi} C_{ij}^{\text{int}}(t) \tag{9}$$

where the internal motion correlation functions $C^{\text{int}}(t)$ are defined as

$$C_{ij}^{\text{int}}(t) = \frac{4\pi}{5}\sum_{n=-2}^{2}\left\langle \frac{Y_{2n}[\Phi_{ij}^{\text{mol}}(t_0+t)]Y_{2n}^*[\Phi_{ij}^{\text{mol}}(t_0)]}{r_{ij}^3(t_0+t)r_{ij}^3(t_0)} \right\rangle \tag{10}$$

According to the addition theorem ${C_{ij}}^{\text{int}}(0) = \langle {r_{ij}}^{-6}\rangle$. The plateau value of the correlation function, ${C_{ij}}^{\text{int}}(t)$, can thus be defined quite generally as ${S_{ij}}^2\langle {r_{ij}}^{-6}\rangle$, where ${S_{ij}}^2$ is a generalized order parameter. It has a value between 0 and 1, and can be calculated from an MD trajectory by using equation (10) and estimating the plateau value for each interproton vector. Within this simplified model the functions ${C_{ij}}^{\text{int}}(t)$ can be written as

$$C_{ij}^{\text{int}}(t) = \left\langle \frac{1}{r_{ij}^6} \right\rangle [S_{ij}^2 + (1 - S_{ij}^2)\exp(-t/\tau_p)] \tag{11}$$

where the initial decay has been written as an exponential. Combining equations (6) and (8)–(11), one arrives at[34,35]

$$J_{ij}^m(\omega) = \frac{1}{4\pi}\left\langle \frac{1}{r_{ij}^6} \right\rangle \left[\frac{S_{ij}^2\tau_c}{1+(\omega\tau_c)^2} + \frac{(1-S_{ij}^2)\tau_{cp}}{1+(\omega\tau_{cp})^2} \right] \tag{12}$$

with ${\tau_{cp}}^{-1} = {\tau_c}^{-1} + {\tau_p}^{-1}$. Assuming that $\tau_p \ll \tau_c$, the second term in equation (12), related to the initial decay, vanishes and ${J_{ij}}^m(\omega)$ becomes

$$J_{ij}^m(\omega) = \frac{1}{4\pi}\left\langle \frac{1}{r_{ij}^6} \right\rangle \frac{S_{ij}^2\tau_c}{1+(\omega\tau_c)^2} \tag{13}$$

Besides the effects of fast local motions, other dynamic processes like, for example, methyl group rotation and aromatic ring flips can affect the relaxation behavior of

biomolecules. Their inclusion in the calculation of the theoretical NOE intensities has been described in detail by Koning et al.[38]

2.2 Computational Aspects

Basically two methods are available for the computation of theoretical NOE intensities. These have been reviewed by Forster.[39] The first involves finding the eigenvectors and eigenvalues of the real symmetrical matrix **R** by standard matrix techniques:[14]

$$\Lambda = \mathbf{X}^{-1}\mathbf{R}\mathbf{X} \tag{14}$$

Combining this expression with equation (5) leads to

$$\mathbf{A} = \exp(-\mathbf{R}\tau_m) = \mathbf{X}\exp(-\Lambda\tau_m)\mathbf{X}^{-1} \tag{15}$$

The matrix diagonalization scales as N^3, where N is the dimension of the matrix **R**, and can become extremely time-consuming when N increases. The calculations can be speeded up by making use of the sparseness of the relaxation matrix; due to the r^{-6} dependence on the distances of the cross-relaxation rates, only a few elements of **R** are significantly larger than zero. Thus, it is possible to apply a spherical cutoff around each proton pair defining a subset of NOEs with only the neighbors. In this way, for each peak, a small eigenvalue problem can then be solved. The second approach[40] for the calculation of theoretical intensities is based on a numerical integration of the differential equations [equation (1)] describing the time dependence of the NOE intensities. Several integration schemes exist (Taylor series integration, Euler algorithm, various Runge–Kutta methods) and their accuracy and performance have been addressed by Forster.[39] A choice between the various methods has to be made depending on the dimension of the system and on the purpose of the NOE calculation; for example, numerical integration is no longer suitable if eigenvalues and/or eigenvectors are required (e.g. for the analytical NOE gradient; see Section 2.4).

2.3 From NOEs to Distances

2.3.1 Two-Spin Approximation

Proton–proton distance constraints are most conveniently derived from cross-peak intensities in 2D NOE spectra taken at various short mixing times. The initial buildup rate of these peaks is proportional to the cross-relaxation rates σ_{ij} between protons i and j.[41] Therefore, these cross-relaxation rates can be measured either from a single 2D NOE spectrum taken with a sufficiently short mixing time or, more accurately, from a buildup series recorded with various mixing times.[41–43] For a large molecule, assuming isotropical tumbling and no internal motions, the $J_{ij}^0(0)$ term in equation (3) dominates the cross-relaxation rate σ_{ij} which becomes simply related to the distance r_{ij} and the correlation time τ_c:

$$\sigma_{ij} \propto -\tau_c r_{ij}^{-6} \tag{16}$$

Therefore, with a known calibration distance r_{cal}, the proton–proton distances follow from the relationship

$$r_{ij} = r_{cal}(\sigma_{cal}/\sigma_{ij})^{1/6} \tag{17}$$

In practice equations (16) and (17) are only approximately valid. There are two main problems associated with accurate determination of proton–proton distances. The first is that proteins are not rigid bodies, and intramolecular mobility leads to nonlinear averaging of distances and to different effective correlation times for the different interproton vectors in the molecule. The second is that of indirect magnetization transfer or 'spin diffusion'.[44] In reality the NOE cross peaks are the result of multispin relaxation and only in the limit of extremely short mixing times (where the signal-to-noise ratio is poor) is the two-spin approximation of equation (16) valid. For these reasons, a common approach is that of translating the NOE intensities into distance ranges (e.g. 0.2–0.3, 0.2–0.4, 0.2–0.5 nm for strong, medium, and weak NOEs, respectively) rather than attempting to obtain precise distances.[45]

It has become possible to circumvent the spin diffusion problem by the use of relaxation matrix calculations, which take into account all indirect magnetization transfers. These methods will be developed in the next section.

2.3.2 Relaxation Matrix Approaches

When a model for the structure and dynamics of a molecule is available, the NOEs can be calculated from the spectral densities as shown above [see equations (3), (5), (14), and (15)]. The opposite route from experimental NOEs to relaxation parameters is also possible. The relaxation matrix **R** can be obtained after diagonalization of the NOE matrix **A**.[15]

$$\mathbf{X}^{-1}\mathbf{A}\mathbf{X} = \mathbf{D} = \exp(-\Lambda\tau_m) \tag{18}$$

$$\mathbf{R} = -\mathbf{X}\left(\frac{\ln \mathbf{D}}{\tau_m}\right)\mathbf{X}^{-1} \tag{19}$$

Thus, theoretically the matrix **R** can be obtained directly from 2D NOE experiments taken at suitably chosen mixing times. In practice, this is not possible for large molecules, since the experimental NOE matrix is incompletely known due to overlap and missing assignments. Hybrid matrix methods have been proposed to circumvent this problem, in which the experimental data are supplemented by theoretical NOEs calculated from a model structure as implemented in IRMA,[16,17] MARDIGRAS,[18] MORASS,[46] FIRM,[22] and CROSREL.[23] An overview of the Iterative Relaxation Matrix Approach (IRMA) is given in Figure 1.

The starting point for the calculations can be a single structure or an ensemble of structures, the relaxation matrix being built from the distances of the corresponding contributions averaged as $\langle r^{-6}\rangle$ in the latter case. A theoretical NOE matrix is then computed using standard matrix techniques [cf. equation (14) and equation (15)] and combined with the experimental data. The resulting matrix can then be transformed back to a corrected relaxation matrix from which new distances are calculated. These distances are used to generate an improved model. The whole process is repeated until convergence is obtained. In other implementations (MARDIGRAS, MORASS, FIRM), the theoretical information is progressively introduced in the hybrid matrix and the back-calculated corrected relaxation matrix is directly used to calculate new NOE

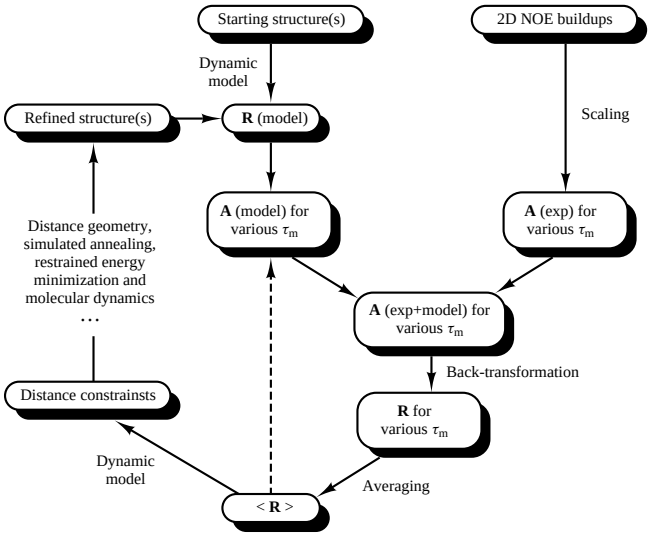

Figure 1 Overview of the IRMA scheme. [The broken line indicates the possible direct use of the back-calculated relaxation matrix for the computation of new theoretical NOEs for a progressive mixing of theoretical and experimental NOE data as found in other implementations (see text)]

matrices (broken line path in Figure 1). Only after a few cycles are distances calculated and used to generate new structures. To increase the accuracy, the calculations can be performed for a series of mixing times; upper and lower bound margins can then be related to the precision with which the elements of $\langle \mathbf{R} \rangle$ can be calculated, i.e. their variation with the mixing time. It has been shown that distances obtained from these relaxation matrix procedures result in an increased accuracy of the structures.[47,48]

Similar procedures have been developed that do not rely on a starting model.[19–21] We have shown, however, that the choice of the model structure in IRMA has little effect on the calculated distances:[48] for crambin, a 46 amino acid protein, distances obtained from a linear chain of crambin and from the well-refined crystal structure only differ on average by 0.015 nm, with a maximum deviation of 0.065 nm for long-range contact in a β-sheet. In general, however, relaxation matrix calculations will usually start from low-resolution model structures that have been obtained at previous structure determination stages from qualitative distance restraints.

2.4 Direct Use of NOEs as Structural Constraints

2.4.1 2D NOE Intensities

Yip and Case[24] proposed a method for structure refinement based on a direct comparison of experimental and theoretical NOE intensities, avoiding the conversion to distance constraints. The experimental NOE intensities are directly introduced as constraints in a refinement procedure using a penalty function of the form:

$$V_{\mathrm{NOE}} = \sum w_{ij}[(f A_{ij}^{\mathrm{theo}})^x - (A_{ij}^{\mathrm{exp}})^x]^y \qquad (20)$$

where $A_{ij}{}^{\mathrm{exp}}$ and $A_{ij}{}^{\mathrm{theo}}$ represent the experimental and theoretical NOE intensities between protons i and j, respectively, f is a scaling factor, and w_{ij} a weighting function. Often a quadratic potential is used ($y = 2$), directly with the NOE intensities ($x = 1$)[24,49–51] or with their sixth-root ($x = \frac{1}{6}$)[52] or inverse sixth-root ($x = -\frac{1}{6}$),[53] the last two definitions being closer to a standard distance-based potential. To account for the fact that NMR experimental data are collected as time- and ensemble-averaged quantities, the theoretical intensities in equation (20) can be replaced by their time- or ensemble-averages denoted as $\overline{A_{ij}^{\mathrm{theo}}}$ in a similar way as for distances[54,55] and J coupling restraints.[56] The averaged intensities, and no longer those calculated from a single static structure, are now required to satisfy the experimental constraints.[57]

2.4.1.1 Calculation of the NOE Forces. Calculation of the NOE forces requires the calculation of the gradient of the NOE potential function of equation (20) and therefore the calculation of the gradient of the NOE intensities ∇A^{theo}. An analytical solution of this gradient has been proposed by Yip and Case,[24] which has since been implemented also by others:[51,52,58]

$$\begin{aligned} \nabla_\mu A_{ij}^{\mathrm{theo}} &= \sum_{rstu} X_{ir} X_{rs}^{-1} (\nabla_\mu R)_{st} X_{tu} X_{uj}^{-1} f_{ru} \\ f_{ru} &= \frac{\exp(-\Lambda_r \tau_{\mathrm{m}}) - \exp(-\Lambda_u \tau_{\mathrm{m}})}{(\Lambda_r - \Lambda_u)} \quad (r \neq u) \\ f_{rr} &= -\tau_{\mathrm{m}} \exp(-\Lambda_r \tau_{\mathrm{m}}) \end{aligned} \qquad (21)$$

Another approach is based on a numerical evaluation of ∇A^{theo}.[49,59] Both methods are time consuming. An approximation for the calculation of ∇A^{theo} can be based on the first two terms of the power series of the exponential of equation (5)[50]

$$\mathbf{A} = \exp(-\tau_{\mathrm{m}}\mathbf{R}) = 1 - \tau_{\mathrm{m}}\mathbf{R} + \frac{1}{2}\tau_{\mathrm{m}}^2\mathbf{R}^2 \cdots \qquad (22)$$

and the gradient becomes

$$\nabla A_{ij} = \nabla(1 - \tau_{\mathrm{m}}\mathbf{R})_{ij} = -\tau_{\mathrm{m}} \nabla R_{ij} \qquad (23)$$

With this simple approximation, the NOE forces F_{NOE} can be computed rapidly, each NOE peak only giving rise to forces on the corresponding protons. The computational costs are considerably reduced in comparison with those for an analytical evaluation of the gradient, the time consuming part becoming the computation of the theoretical NOE intensities. The entire procedure scales as an N^3 problem if a diagonalization method is used for calculating the NOEs. This can be reduced by the use of a spherical cutoff around each proton pair ij defining an experimental NOE peak. With this approximation the spin diffusion contributions of all neighbors within two spheres around the two protons defining an NOE peak are taken into account. For each NOE a small relaxation matrix is calculated.

Recently, new methods have been proposed for an efficient and exact calculation of the NOE gradient[60,61] that should allow a further speed-up of the computations. Particularly promising is the method proposed by Yip[61] based on an integral expression of the NOE gradient using standard perturbation expansion techniques as in quantum mechanics.

The derivative of A_{ij} with respect to the relaxation matrix element R_{kl} is defined as:

$$\frac{\partial A_{ij}}{\partial R_{kl}} = \lim_{h \to 0} \frac{A(\mathbf{R} + \mathbf{D})_{ij} - A(\mathbf{R})_{ij}}{h} \tag{24}$$

where $A(\mathbf{R} + \mathbf{D}) = \exp[-(\mathbf{R} + \mathbf{D})\tau_m]$ and $\mathbf{D}$ is a perturbation of $\mathbf{R}$ whose only nonvanishing component is h. By using standard quantum-mechanics perturbation expansion techniques one can identify the NOE matrix $\mathbf{A}$ as the evolution operator, the relaxation rate matrix $\mathbf{R}$ as the Hamiltonian, and τ_m as the imaginary time i. $A(\mathbf{R} + \mathbf{D})_{ij}$ can then be approximated to first-order in h as

$$A(\mathbf{R} + \mathbf{D})_{ij} = A(\mathbf{R})_{ij} - h \int_0^{\tau_m} \exp[-\mathbf{R}(\tau_m - s)]_{ik} \exp(-\mathbf{R}s)_{lj}\, ds \tag{25}$$

Substituting this expression in equation (23) gives the derivative of the NOE with respect to R_{kl}:

$$\frac{\partial A_{ij}}{\partial R_{kl}} = -\int_0^{\tau_m} \exp[-\mathbf{R}(\tau_m - s)]_{ik} \exp(-\mathbf{R}s)_{lj}\, ds \tag{26}$$

The integral in equation (26) can be computed efficiently with numerical integration techniques. In addition, since no eigenvectors of $\mathbf{R}$ are required as for the expression in equation (21) any technique that allows a fast and accurate evaluation of the NOE intensities can be used in place of the diagonalization method. The derivative in equation (26) has been shown to be equivalent to the analytical expression proposed by Yip and Case[24] [equation (21)] and, from preliminary results, appears to be significantly faster than the expression in equation (21).[61]

2.4.2 3D NOE–NOE Intensities

For larger molecules considerable overlap can exist in 2D spectra. This overlap can be overcome by spreading the peaks in a third dimension and new multidimensional NMR techniques were therefore developed.[1–6] A similar procedure as with the refinement of NOE data from one-dimensional and 2D spectra can be followed for the treatment of NOE intensities from 3D spectra.

The intensities of cross peaks in a 3D spectrum are proportional to the transfer efficiencies of the two mixing periods of the experiment. The net transfer can be described in general as:

$$T_{ijk}^{3D} = T_{ij}(1) T_{jk}(2) \tag{27}$$

where $T_{ij}(1)$ and $T_{jk}(2)$ describe the magnetization transfer efficiencies for each separate mixing period and correspond to NOE transfer, exchange, or J transfer. The use of cross-peak intensities in a structure refinement procedure requires calculation of the gradients of these 3D intensities with respect to the coordinates of the protons in a molecule. The gradient of a 3D peak can be written as the sum of two terms containing the separate gradients of $T_{ij}(1)$ and $T_{jk}(2)$:

$$\nabla T_{ijk}^{3D} = T_{jk}(2) \nabla T_{ij}(1) + T_{ij}(1) \nabla T_{jk}(2) \tag{28}$$

These equations can be generalized for even higher dimensional experiments. Thus, given a valid model for the calculation of the magnetization transfer efficiencies and their derivatives, 3D peaks can be used as constraints in a direct refinement procedure.

In particular, 3D NOE–NOE spectra appear to be suitable for this purpose. This latter technique was developed for the direct observation of indirect NOE magnetization transfer ('spin diffusion') as occurs in larger biomolecules.[62] Kessler et al.[63] and Habazettl et al.[64] described the quantitative use of 3D NOE–NOE cross peaks for obtaining distance constraints, which are used by DG or restrained MD computations. It is also possible to use the intensities of such 3D spectra as direct constraints for structure refinement.[65] In a 3D NOE–NOE spectrum the 3D cross-peak intensities $A_{ijk}{}^{3D}$ can be calculated from their separate 2D NOE transfer efficiencies. The computation of the 3D NOE–NOE intensity $A_{ijk}{}^{3D}$ then amounts to the multiplication of the calculated 2D contributions A_{ij} and A_{jk}. A similar NOE restraining potential function can be defined as for the direct refinement with 2D NOE data.[65] The same approximations as for 2D data can be used for the computation of the 3D NOE–NOE forces.

The feasibility of direct NOE refinement with 3D NOE–NOE data was demonstrated by Bonvin et al.[65] for a small peptide with synthetic 3D data using a simple approximation for the derivative of the NOE intensity based on the first two terms of the expansion of the exponential function [equation (23)].[65] A similar approach has been developed since by Habazettl et al.[66] and applied to the structure refinement of a few proteins [*Cucurbita maxima* trypsin inhibitor I (CMTI-I), hisactophilin, mucous protease inhibitor (MPI)].[66,67] The main problem with the application of the method lies in the assignment of cross peaks of a 3D NOE–NOE spectrum. The huge amount of data contained in a 3D experiment requires an efficient program for automatic assignment and peak-picking before a refinement based on 3D NOE–NOE intensities can be undertaken.

3 STRUCTURE CALCULATIONS

3.1 Distance Geometry (DG)

The metric matrix DG algorithm[68,69] was known well before structure determination by NMR became possible.[70,71] This method does not rely on a starting conformation, is free from operator bias in this respect, and is therefore very attractive for structure determination. The DG procedure amounts to the following. First, upper and lower bound matrices $\mathbf{U}$ and $\mathbf{L}$ are set up for all atom–atom distances of the molecule. Some of the elements u_{ij} and l_{ij} follow from standard bond lengths and bond angles of the covalent structure and from experimentally found distance ranges from NOEs and J coupling constants. A bound smoothing procedure using triangle inequalities extends the constraints to all elements of $\mathbf{U}$ and $\mathbf{L}$. This procedure can even be extended to satisfy tetrangle inequalities as for example implemented in the DG-II package[8] (see ***Distance Geometry***). Then, a distance matrix $\mathbf{D}$ is set up with distances chosen randomly between upper and lower bounds, $l_{ij} \leq d_{ij} \leq u_{ij}$. The elements of $\mathbf{D}$ can be chosen in such a way that they not only lie between their respective upper and lower

bounds, but also themselves obey the triangle inequalities; this latter technique is known as *random metrization*. The so-called 'embedding' algorithm then finds the best 3D structure consistent with the distances d_{ij}. This structure must be optimized with an error function consisting of chirality and distance constraints. This forces the amino acid side chains to adopt the correct chirality and the distances to satisfy the upper and lower bound criteria, although usually the DG structures still contain a number of violations of the distance bounds. By repetition of the DG calculations with randomly chosen distance matrices **D**, families of structures can be obtained that allow one to judge how uniquely the structure is determined by the constraints.

Another method, also termed distance geometry, but using a quite different mathematical procedure, was suggested by Braun and Gō.[72] Here, the biomolecular conformation is calculated by minimizing a distance constraint error function. Special features of the method are that dihedral angles are used as independent variables rather than Cartesian coordinates and that it uses a variable target function, first satisfying local constraints (between amino acids nearby in the polypeptide chain) and later including long-range constraints. This approach avoids becoming trapped in a local minimum of the target function. Usually one starts with various initial conformations obtained by taking random values for the dihedral angles. This method, which has been implemented since in various programs, e.g. DISMAN[72] and more recently DIANA,[73] has rather similar efficiency and convergence properties as the metric matrix distance-geometry algorithm.

3.2 Simulated Annealing (SA)

Although the DG methods do not need starting structures and are therefore not subject to operator bias, this does not mean that they sample the allowed conformational space (consistent with the bounds) in a truly random fashion. Simplified MD calculations with only geometric constraints were developed to increase the sampling of the DG methods. These are termed, in general, simulated annealing (SA) procedures. Although these can be directly used to generate structures starting from random coordinates, they are most commonly combined with DG calculations, the starting structures for the SA stage being obtained by DG embedding. Simulated annealing involves raising the temperature of the system followed by slow cooling in order to overcome local minima and locate the region of the global minimum of the target function V_{tot} (cf. Nilges et al.)[9]. This is achieved by solving Newton's equations of motion

$$m_i \ddot{\boldsymbol{r}}_i = \boldsymbol{F}_i \tag{29}$$

with the forces given by

$$\boldsymbol{F}_i = -\partial V_{\text{tot}}/\partial \boldsymbol{r}_i \tag{30}$$

The potential V_{tot} usually contains the following terms:

$$V_{\text{tot}} = V_{\text{covalent}} + V_{\text{repel}} + V_{\text{disre}} + V_{\text{dihre}} + V_{\text{NOE}} \tag{31}$$

V_{covalent} is a potential to maintain correct bond lengths, angles, planes and chirality, V_{repel} is a simple repulsion term to prevent unduly close nonbonded contact, V_{disre} and V_{dihre} represent the experimental NOE distance and dihedral angle constraints, respectively, and V_{NOE} is an extra term for direct comparison of theoretical and experimental NOE intensities as defined in equation (20). Usually the NOE distance constraints are represented by a flat well potential of the form

$$V_{\text{disre}} = \begin{cases} \frac{1}{2}K_{\text{disre}}(d_{ij} - l_{ij})^2 & 0 \le d_{ij} \le l_{ij} \\ 0 & l_{ij} \le d_{ij} \le u_{ij} \\ \frac{1}{2}K_{\text{disre}}(d_{ij} - u_{ij})^2 & u_{ij} \le d_{ij} \end{cases} \tag{32}$$

where l_{ij} and u_{ij} are the value of lower and upper limits of the target distances, respectively. Other forms that contains a linear part at long distances are also used[74] to avoid too large energies, which may give computational problems. A similar definition as in equation (32) can be used for dihedral angle constraints, but other forms have also been proposed such as:[75]

$$V_{\text{dihre}} = K_{\text{dihre}}[1 - \cos(\phi - \phi_0)] \tag{33}$$

where ϕ_0 represents the dihedral angle value obtained from J coupling data. The various terms in equation (31) have variable force constants, which can be progressively increased during the annealing.

The combination of DG, for generating starting structures with an approximate folding by embedding a subset of atoms, and SA calculations, provides a powerful and efficient tool for the structure determination of biomolecules.[9,76] This hybrid method should be particularly useful for solving the structure of large proteins for which computational costs may become a limiting factor.

3.3 Restrained Molecular Dynamics and Energy Minimization (RMD, REM)

The quality of biomolecular structures based on geometric constraints can be improved by taking energy considerations into account. For instance, in DG structures amino acid side chains often adopt eclipsed conformations. Also, hydrogen bonds and salt bridges may not be formed unless they are specifically introduced as constraints. In RMD refinement structures are optimized simultaneously with respect to a potential energy function and a set of experimental restraints. Of course the success of this method now depends to a large extent on the quality of the force field used. It is therefore important to realize the limitations and approximate nature of this force field, especially when the calculations do not include solvent molecules.

In RMD calculations, equation (29) and equation (30) are integrated with the potential function given by

$$\begin{aligned} V_{\text{tot}} = {} & V_{\text{bond}} + V_{\text{angle}} + V_{\text{torsion}} + V_{\text{vdW}} \\ & + V_{\text{Coulomb}} + V_{\text{disre}} + V_{\text{dihre}} + V_{\text{NOE}} \end{aligned} \tag{34}$$

The first two terms tend to keep bond lengths and angles at their equilibrium values. V_{torsion} is a sinusoidal potential describing rotations about bonds; for V_{vdW} (the van der Waals interaction) usually a Lennard–Jones potential is taken, and V_{Coulomb} describes the electrostatic interactions. The three last

terms, similar to those in equation (31), distinguish RMD from more conventional MD simulations.

An RMD simulation is usually preceded and followed by REM using steepest descent or conjugated gradient methods to bring the energy down to an acceptable level. Using the same potential energy function as RMD [equation (34)] REM usually induces only small changes in the structures by driving them to the closest minimum and is not able to take them out of this. By contrast, RMD is able to overcome barriers of the order of kT because of the kinetic energy in the system and therefore has a much larger radius of convergence. The RMD method works as an efficient minimizer, since excess potential energy, converted to kinetic energy, is drained off by coupling the system to a thermal bath of constant temperature. Sampling of the conformational space consistent with the experimental constraints can be increased by using high-temperature simulations[77] or potential energy annealing conformational search methods (PEACS)[78] in which the potential energy is coupled to a reference energy bath whose energy level is progressively decreased over the run, or by introducing a fourth dimension[79] as recently implemented in GROMOS (4D MD),[80] which, by increasing the number of degrees of freedom in the system, allows one to circumvent energy barriers present in the 3D potential energy hypersurface.

Further extensions of the method, especially useful for highly mobile structures, include time-averaging[54] or ensemble-averaging[55] of the experimental restraints. In these methods, V_{disre} is calculated from time- or ensemble-averaged distances instead of instantaneous ones. Forces are thus applied on the corresponding protons only if the *averaged* distance violates the restraint. These methods allow a larger conformational freedom consistent with the NOE restraints. The use of time-averaged restraints has recently been described for direct structure refinement with J coupling[56] and NOE[57] data.

4 QUALITY OF THE STRUCTURES

Important factors for assessing the quality of the NMR structures usually obtained with a combination of the above described methods are the number and distribution of the NOE and dihedral angle constraints and the number of stereospecific assignments. Several other criteria have also to be considered, but these will all depend, to some extent, on the factors mentioned above. The precision of the structure is generally given by the average root mean squared deviations (rmsd) (pairwise or from the average coordinates). These are usually calculated for the backbone and all atoms, respectively, and sometimes on a substructure. The rmsd as a function of the residue sequence can also be useful for identifying less well-defined regions in a structure. Another useful parameter to assess the precision of solution structures is the angular order parameter proposed by Hyberts et al.[81]

$$S_{\phi}^{\text{angle}} = \frac{1}{N_{\text{struc}}}\left[\left(\sum \cos\phi\right)^2 + \left(\sum \sin\phi\right)^2\right]^{1/2} \quad (35)$$

It has the advantage that, contrary to rmsd, it does not require the superimposition of the structures. Angular order parameters (S^{angle}) are generally given as a function of the residue sequence for backbone ϕ, ψ and side-chain χ_1 dihedral angles. S^{angle} values of 0.9 and 0.8, for example, indicate very well-defined dihedral angles with fluctuations of $\pm 24^\circ$ and $\pm 40^\circ$, respectively. We have to keep in mind, however, that the rmsd etc and angular order parameters give an indication of the precision of the structure, but are not a direct indication of its accuracy. Structures with very low rmsd can still be wrong! To judge the quality, we have to take several other criteria into account: the stereochemical quality (e.g. via ϕ, ψ Ramachandran plots), the deviations from the idealized covalent geometry, the conformational energy, residual restraints violations, the presence of hydrogen bonds, and a good packing of the structures; these are criteria commonly used for this purpose. Studies of the stereochemical quality of crystal and NMR protein structures have resulted in useful criteria to assess the quality of these structures.[82,83] These criteria, among which are the percentage of residues in the favorable area of the Ramachandran plot and the χ_1 dihedral angles- and hydrogen-bond energy standard deviations, can be easily checked with the program PROCHECK,[82] which allows a fast and simple evaluation of the stereochemical quality of a protein structure. Another criterion to assess the quality of the structures obtained from NMR data is directly to compare calculated and experimental NOEs. The fit can be described by a residual index or R factor in a similar manner as in X-ray crystallography. Several R factor definitions have been proposed[47,84,85] and can all be represented by a general equation of the form:

$$R = \frac{\sum_i w_i |N_i^{\text{theo}} - N_i^{\text{exp}}|}{\sum_i w_i |N_i^{\text{ref}}|} \quad (36)$$

where $N_i = A_i$ or $N_i = (A_i)^{\frac{1}{6}}$ with, in the denominator, N_i^{ref} defined as $N_i^{\text{ref}} = N_i^{\text{exp}}$ or $N_i^{\text{ref}} = \frac{1}{2}(N_i^{\text{exp}} + N_i^{\text{theo}})$, w_i are weighting factors that can be chosen equal to the mixing times, since NOEs measured at longer mixing times are expected to have a better signal-to-noise ratio. The simplest one, with $N_i = A_i$ and $N_i^{\text{ref}} = N_i^{\text{exp}}$, is similar to the X-ray definition.[84] For NMR, however, other functions may be more appropriate since we are dealing principally with two problems. First, the range of NOE intensities is quite extended (by more than a factor of 1000) and R might be dominated by strong peaks, corresponding to short distances in the structures which are expected to be less important for determining the 3D structure. A sixth-root residual index, $R^{\frac{1}{6}}$, where $N_i = (A_i)^{\frac{1}{6}}$, allows for a more even contribution of weak and strong NOEs in the R factor.[47,84] The second problem inherent to the R factor comes from the approximate r^{-6} dependence of the NOEs. Because of this extreme distance dependence, the R factor function is asymmetric, the error increasing strongly when the distances are shorter than the target distances. Normalizing the errors by the sum of both experimental and theoretical NOE intensities, $N_i^{\text{ref}} = \frac{1}{2}(N_i^{\text{exp}} + N_i^{\text{theo}})$, should avoid this problem.[85] To give a better picture of the quality of the structures, a distinction can be made between intra- and interresidue peaks and the R factors can be calculated as a function of the residue sequence, which allows one to recognize problem regions in the structures.

5 APPLICATION: THE ARC REPRESSOR

The structure refinement process using relaxation matrix calculations can be best illustrated using a specific example: the Arc repressor. The solution structure of the Arc repressor of *Salmonella* bacteriophage P22, a dimeric sequence-specific DNA-binding protein,[86] has been determined from 2D NMR data using an 'ensemble' IRMA followed by direct NOE refinement with DINOSAUR.[87]

An 824 NOE buildup series in H_2O and D_2O and 130 additional qualitative distance constraints were collected for Arc. This resulted in a set of 954 constraints consisting of 350 intraresidue, 215 sequential, 181 medium range, and 208 long-range constraints; 144 of the total set correspond to intermonomer constraints. Twenty-four hydrogen bonds were also explicitly defined. The constraints were duplicated to account for the dimeric nature of Arc giving a total set of 2004 constraints (NOEs + hydrogen bonds). Of the set of 954 constraints per monomer, 824 NOEs with good quality buildup curves were used in the IRMA and DINOSAUR calculations, the others being introduced as qualitative constraints. From the stereospecific assignment procedure, which resulted in the assignment of 16 β-methylene diastereotopic proton pairs (40%) and of the methyl groups of four valine residues, constraints could be imposed on 21 χ_1 dihedral angles.

In the initial stage, a set of 51 structures was generated with DG and further refined with a combination of REM and RMD using the GROMOS force field[88] in a parallel refinement protocol. Distance constraints were obtained from the set of 854 NOE buildups via relaxation matrix calculations from the ensemble of structures, except for the initial cycle in which a structure obtained by Breg et al.[89] was chosen as the model. Methyl group rotation, aromatic ring flips, and internal mobility effects (via order parameters obtained from a free MD run in water) were included in these calculations. Convergence was obtained after three IRMA cycles. The best 16 structures were finally refined with direct NOE constraints following a slow-cooling SA protocol from 600 to 1 K in 1.5 ps followed by REM.[88] In this final refinement stage, theoretical NOE intensities were directly compared with the experimental data using a simple quadratic restraining potential [$x = 1$, $y = 2$ in equation (20)] with, as weighting factor, an experimental error defined as $w_{ij} = (N + \varepsilon A_{ij}^{\exp})^{-2}$.[50] N corresponds to a noise level and ϵ to a relative error on the experimental intensities. The forces were derived using the simple two-spin approximation for the gradient of the NOE function [equation (23)]. Dynamic assignment was applied to the peaks involving unassigned diastereotopic groups.

A view of the backbone of the 16 best Arc structures at various stages during the refinement (DG/SA, IRMA 1st, 2nd, and 3rd cycles, and DINOSAUR) is presented in Figure 2, which clearly shows the improvement of the structures. The precision of the well-defined region of Arc (residues 8–48) including the β-sheet and the two α-helices increases during the IRMA refinement as confirmed by the rmsd (from the average) shown in Figure 3(a). The rmsd for the backbone atoms decreases from 1.0 Å for the DG/SA structures to 0.50 Å for the structures obtained after the third IRMA cycle. This value increases slightly to 0.55 Å after the direct NOE refinement indicating that the use of direct NOE constraints might introduce more variability in the structures (due to spin diffusion effects there are more ways to fulfill a NOE constraint than a distance constraint). The R factors ($Q^{\frac{1}{6}}$ definition),[87] however, show a substantial decrease during the DINOSAUR refinement step as can be seen from Figure 3(b). The final structures satisfy the NMR constraints with no significant deviations from dihedral angle restraints obtained from J coupling data and very low R factors, indicating a very good agreement with the experimental NOE data.

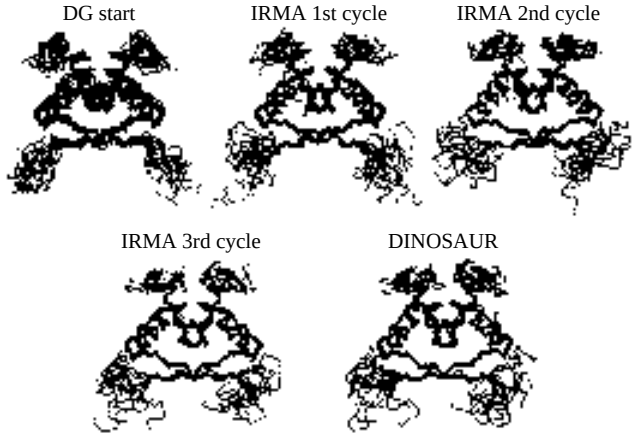

Figure 2 View of the Arc repressor structures during the refinement with NMR constraints. The structures corresponding to the 16 best final conformations are shown directly after the DG/SA calculations in the first IRMA cycle, after each IRMA cycle, and after direct NOE refinement with DINOSAUR. The structures were superimposed on C-α,C,N atoms of the well-defined region of Arc (residues 8–48 of each monomer)

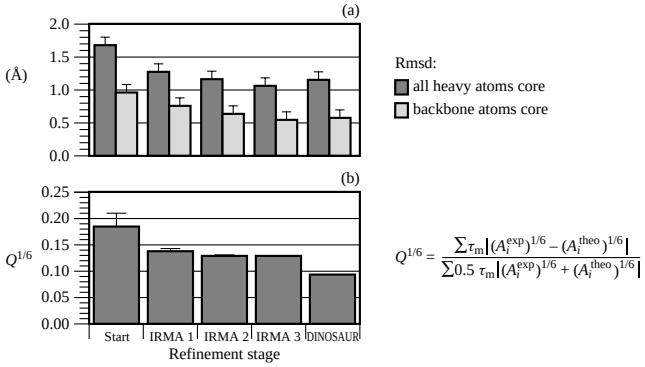

Figure 3 (a) All heavy atom and backbone atom rmsd from the average for the well-defined region of the Arc repressor (residues 8–48 of each monomer) calculated for an ensemble of 16 structures as a function of the refinement. The structures were superimposed on backbone atoms of the well-defined core. (b) R factors ($Q^{\frac{1}{6}}$ definition) of the Arc structures as a function of the refinement

The distribution of the experimental constraints as a function of the residue sequence is plotted in Figure 4, together with the precision (rmsd on C-α and all heavy atoms), the backbone angular order parameters [equation (35)] and the $Q^{\frac{1}{6}}$ factors. A correlation can be noticed between the number of constraints and the precision per residue, but no such relationship can be found for the $Q^{\frac{1}{6}}$ factors which all represent low values (~0.05) (for comparison, the $Q^{\frac{1}{6}}$ factors for a linear chain of Arc have values of around 0.55). Regions of high variability are found in the N- and C-terminal parts for which few

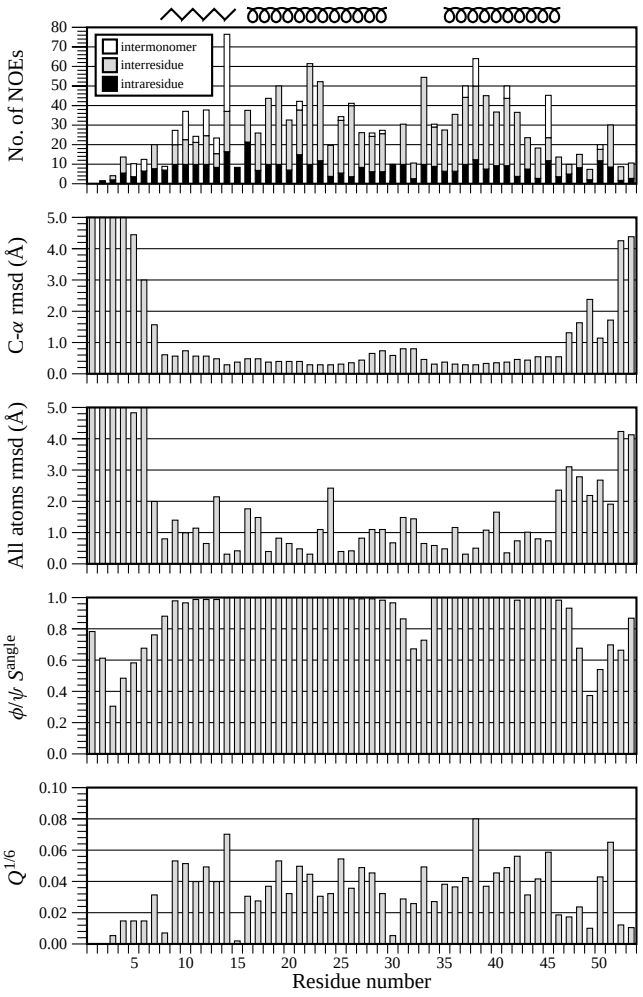

Figure 4 Number of constraints, rmsd (from the average) on C-α atoms and on all heavy atoms [the structures were superimposed on C-α,C,N atoms of the well-defined region of Arc (residues 8–48 of each monomer)], backbone angular order parameters (averages from ϕ and ψ angular order parameters) [equation (35)], and $Q^{\frac{1}{6}}$ factors as a function of the residue sequence for the final Arc structures. Secondary structure elements in Arc are indicated. (The rmsd of the first four residues are off-scale and have values of up to 10 Å)

constraints are available. The structures, which have been deposited in the Brookhaven Protein Data Bank (entry 1ARR), have good stereochemical qualities and present an extensive pattern of hydrogen bonds and a good packing with a very well defined core.

6 CONCLUSION

The use of relaxation matrix calculations for the refinement of protein structures from NMR, as illustrated here for the Arc repressor, should result in a more accurate representation of the solution structure of a biomolecule. In addition, such methods also offer a tool to identify errors or overinterpretation in distance constraints and assess the quality of the NMR structures by a direct comparison of theoretical and experimental data. They should however not be used as single criteria for accuracy, but should be used together with others, such as the stereochemical quality of the structure. An adequate description of motional effects like internal mobility (e.g. via order parameters, fast methyl group rotation, and aromatic ring flips) or conformational heterogeneity, allows a dynamic description of the structure in solution. A treatment of the experimental NMR data as time- and/or ensemble-averaged restraints should even lead us further toward a more realistic description of solution structures. Additional work is however required in this direction since the motional model is the most controversial point in the use of relaxation matrix calculations. The new developments both in software and hardware should extend the range of such computations to proteins of increasing size and allow the use of more detailed motional models for a better description of solution structure.

7 RELATED ARTICLES

Amino Acids, Peptides and Proteins: Chemical Shifts; Analysis of Spectra: Automatic Methods; Chemical Shifts in Biochemical Systems; Distance Geometry; NOESY; Nuclear Overhauser Effect.

8 REFERENCES

1. C. Griesinger, O. W. Sørensen, and R. R. Ernst, *J. Magn. Reson.*, 1989, **84**, 14.
2. L. E. Kay, D. Marion, and A. Bax, *J. Magn. Reson.*, 1989, **84**, 72.
3. S. W. Fesik and E. R. P. Zuiderweg, *Q. Rev. Biophys.*, 1990, **23**, 97.
4. R. Boelens, C. Griesinger, L. E. Kay, D. Marion, and E. R. P. Zuiderweg, in *Computational Aspects of the Study of Biological Macromolecules by Nuclear Magnetic Resonance Spectroscopy*, ed. J. C. Hoch et al., Plenum, New York, 1991, pp. 127–150.
5. G. M. Clore and A. M. Gronenborn, *Prog. NMR Spectrosc.*, 1991, **23**, 43.
6. A. Bax and C. Grzesiek, *Acc. Chem. Res.*, 1993, **26**, 131.
7. D. Neuhaus and M. Williamson, *The Nuclear Overhauser Effect in Structural and Conformational Analysis*, VCH, New York, 1989.
8. T. F. Havel, *Prog. Biophys. Mol. Biol.*, 1991, **56**, 43.
9. M. Nilges, G. M. Clore, and A. M. Gronenborn, *FEBS Lett.*, 1988, **229**, 317.
10. R. M. Scheek, W. F. van Gunsteren, and R. Kaptein, *Methods Enzymol.*, 1989, **177**, 204.
11. A. Brünger and M. Karplus, *Acc. Chem. Res.*, 1991, **24**, 54.
12. M. J. J. Blommers, C. B. Lucasius, G. Kateman, and R. Kaptein, *Biopolymers*, 1992, **32**, 45.
13. R. Pachter, R. B. Altman, and O. Jardetzky, *J. Magn. Reson.*, 1990, **89**, 578.
14. J. W. Keepers and T. L. James, *J. Magn. Reson.*, 1984, **57**, 404.
15. E. T. Olejniczak, R. T. Gampe, Jr., and S. W. Fesik, *J. Magn. Reson.*, 1986, **67**, 28.
16. R. Boelens, T. M. G. Koning, and R. Kaptein, *J. Mol. Struct.*, 1988, **173**, 299.
17. R. Boelens, T. M. G. Koning, G. A. van der Marel, J. H. van Boom, and R. Kaptein, *J. Magn. Reson.*, 1989, **82**, 290.
18. B. A. Borgias, M. Cochin, D. J. Kerwood, and T. L. James, *Prog. NMR Spectrosc.*, 1990, **22**, 83.

19. P. Koehl and J.-F. Lefèvre, *J. Magn. Reson.*, 1990, **86**, 565.
20. M. Madrid, E. Llinás, and M. Llinás, *J. Magn. Reson.*, 1991, **93**, 329.
21. F. J. M. Van de Ven, M. J. J. Blommers, R. E. Schouten, and C. W. Hilbers, *J. Magn. Reson.*, 1991, **94**, 140.
22. S. P. Edmonson, *J. Magn. Reson.*, 1992, **98**, 283.
23. B. R. Leeflang and L. M. J. Kroon-Batenburg, *J. Biomol. NMR*, 1992, **2**, 495.
24. P. Yip and D. A. Case, *J. Magn. Reson.*, 1989, **83**, 643.
25. K. Ösapay and D. Case, *J. Am. Chem. Soc.*, 1991, **113**, 9436.
26. D. S. Wishart, B. D. Sykes, and F. M. Richards, *J. Mol. Biol.*, 1991, **222**, 311.
27. M. P. Williamson, T. Asakura, E. Nakamura, and M. Demura, *J. Biomol. NMR*, 1992, **2**, 83.
28. A. C. de Dios, J. G. Pearson, and E. Oldfield, *Science*, 1993, **260**, 1491.
29. T. S. Harvey and W. F. van Gunsheren, *Techniques in Protein Chemistry*, Academic Press, New York, 1993, p. 615.
30. I. Solomon, *Phys. Rev.*, 1955, **99**, 559.
31. S. Macura and R. R. Ernst, *Mol. Phys.*, 1980, **41**, 95.
32. J. W. Peng and G. Wagner, *J. Magn. Reson.*, 1992, **98**, 308.
33. J. Peng and G. Wagner, *Biochemistry*, 1992, **31**, 8571.
34. E. T. Olejniczak, C. M. Dobson, M. Karplus, and R. M. Levy, *J. Am. Chem. Soc.*, 1984, **106**, 1923.
35. T. M. G. Koning, R. Boelens, G. A. van der Marel, J. H. van Boom, and R. Kaptein, *Biochemistry*, 1991, **30**, 3787.
36. G. Lipari and A. Szabo, *J. Am. Chem. Soc.*, 1982, **104**, 4546.
37. G. Lipari and A. Szabo, *J. Am. Chem. Soc.*, 1982, **104**, 4559.
38. T. M. G. Koning, R. Boelens, and R. Kaptein, *J. Magn. Reson.*, 1990, **90**, 111.
39. M. J. Forster, *J. Comput. Chem.*, 1990, **12**, 292.
40. D. Marion, M. Genest, and M. Ptak, *Biophys. Chem.*, 1987, **28**, 235.
41. A. Kumar, G. Wagner, R. R. Ernst, and K. Wüthrich, *J. Am. Chem. Soc.*, 1981, **103**, 3654.
42. G. Wagner and K. Wüthrich, *J. Magn. Reson.*, 1979, **33**, 675.
43. C. M. Dobson, E. T. Olejniczak, F. M. Poulsen, and R. G. Ratcliffe, *J. Magn. Reson.*, 1982, **48**, 97.
44. A. Kalk and H. J. C. Berendsen, *J. Magn. Reson.*, 1976, **24**, 343.
45. K. Wüthrich, *NMR of Proteins and Nucleic Acids*, Wiley, New York, 1986.
46. C. B. Post, R. P. Meadows, and D. G. Gorenstein, *J. Am. Chem. Soc.*, 1990, **112**, 6796.
47. P. D. Thomas, V. J. Basus, and T. L. James, *Proc. Natl. Acad. Sci. USA*, 1991, **88**, 1237.
48. A. M. J. J. Bonvin, J. A. C. Rullmann, R. Boelens, and R. Kaptein, *Proteins Struct. Funct. Genet.*, 1993, **15**, 385.
49. J. D. Baleja, J. Moult, and B. D. J. Sykes, *J. Magn. Reson.*, 1990, **87**, 375.
50. A. M. J. J. Bonvin, R. Boelens, and R. Kaptein, *J. Biomol. NMR*, 1991, **1**, 305.
51. J. E. Mertz, P. Güntert, K. Wüthrich, and W. Braun, *J. Biomol. NMR*, 1991, **1**, 257.
52. M. Nilges, J. Habazettl, A. T. Brünger, and T. A. Holak, *J. Mol. Biol.*, 1991, **219**, 499.
53. B. Stawarz, M. Genest, and D. Genest, *Biopolymers*, 1992, **32**, 633.
54. A. E. Torda, R. M. Scheek, and W. F. van Gunsteren, *Chem. Phys. Lett.*, 1989, **157**, 289.
55. R. M. Scheek, A. E. Torda, J. Kemmink, and W. F. van Gunsteren, in *Computational Aspects of the Study of Biological Macromolecules by NMR*, ed. J. C. Hoch, F. M. Poulsen, and C. Redfield, Plenum, New York, 1991, pp. 209–217.
56. A. E. Torda, R. M. Brunne, T. Huber, H. Kessler, and W. F. van Gunsteren, *J. Biomol. NMR*, 1993, **3**, 55.
57. A. M. J. J. Bonvin, R. Boelens, and R. Kaptein, *J. Biomol. NMR*, 1994, **4**, 143.
58. J. Pothier, J. Gabarro-Arpa, and M. Le Bret, *J. Comput. Chem.*, 1993, **14**, 226.
59. J. D. Baleja, *J. Magn. Reson.*, 1992, **96**, 619.
60. E. N. Nesterova and V. P. Chuprina, *J. Magn. Reson.*, 1993, **B101**, 94.
61. P. F. Yip, *J. Biomol. NMR*, 1993, **3**, 361.
62. R. Boelens, G. W. Vuister, T. M. G. Koning, and R. Kaptein, *J. Am. Chem. Soc.*, 1989, **111**, 8525.
63. H. Kessler, S. Seip, and J. Saulitis, *J. Biomol. NMR*, 1991, **1**, 83.
64. J. Habazettl, A. Ross, H. Oschkinat, and T. A. Holak, *J. Magn. Reson.*, 1992, **97**, 511.
65. A. M. J. J. Bonvin, R. Boelens, and R. Kaptein, *J. Magn. Reson.*, 1991, **95**, 626.
66. J. Habazettl, M. Schleicher, J. Otlewski, and T. A. Holak, *J. Mol. Biol.*, 1992, **228**, 156.
67. R. Bernstein, A. Ross, C. Cieslar, and T. A. Holak, *J. Magn. Reson.*, 1993, **B101**, 185.
68. L. M. Blumenthal, *Theory and Application of Distance Geometry*, Chelsea, New York, 1970.
69. G. M. Crippen and T. F. Havel, *Acta Crystallogr., Sect. A*, 1978, **34**, 282.
70. T. F. Havel, I. D. Kuntz, and G. M. Crippen, *Bull. Math. Biol.*, 1983, **45**, 665.
71. T. F. Havel and K. Wüthrich, *Bull. Math. Biol.*, 1984, **46**, 673.
72. W. Braun and N. Gō, *J. Mol. Biol.*, 1985, **186**, 611.
73. P. Güntert, W. Braun, and K. Wüthrich, *J. Mol. Biol.*, 1991, **217**, 517.
74. R. Kaptein, E. R. P. Zuiderweg, R. M. Scheek, R. Boelens, and W. F. van Gunsteren, *J. Mol. Biol.*, 1985, **182**, 179.
75. J. De Vlieg, R. Boelens, R. M. Scheek, R. Kaptein, and W. F. van Gunsteren, *Isr. J. Chem.*, 1986, **27**, 181.
76. T. A. Holak, D. Gondol, J. Otlewski, and T. Wilusz, *J. Mol. Biol.*, 1989, **210**, 635.
77. R. E. Bruccoleri and M. Karplus, *Biopolymers*, 1990, **29**, 1847.
78. R. C. Van Schaik, W. F. van Gunsteren, and H. J. C. Berendsen, *J. Comput.-Aided Mol. Des.*, 1992, **6**, 97.
79. G. M. Crippen, *J. Comput. Chem.*, 1982, **3**, 471.
80. R. C. Van Schaik, H. J. C. Berendsen, A. E. Torda, and W. F. van Gunsteren, *J. Mol. Biol.*, 1993, **234**, 751.
81. S. G. Hyberts, M. S. Goldberg, T. F. Havel, and G. Wagner, *Protein Sci.*, 1992, **1**, 736.
82. A. L. Morris, M. W. MacArthur, E. G. Hutchinson, and J. M. Thornton, *Proteins Struct. Funct. Genet.*, 1992, **12**, 345.
83. M. W. MacArthur and J. M. Thornton, *Proteins Struct. Funct. Genet.*, 1993, **17**, 232.
84. C. Gonzalez, J. A. C. Rullmann, A. M. J. J. Bonvin, R. Boelens, and R. Kaptein, *J. Magn. Reson.*, 1991, **91**, 659.
85. J. M. Withka, J. Srinivasan, and P. H. Bolton, *J. Magn. Reson.*, 1992, **98**, 611.
86. J. U. Bowie and R. T. Sauer, *Proc. Natl. Acad. Sci. USA*, 1989, **86**, 2152.
87. W. F. Van Gunsteren and H. J. C. Berendsen, *Groningen Molecular Simulation (GROMOS) Library Manual*, Biomos BV, Nijenborgh 16, 9747 AG Groningen, The Netherlands, 1987.

88. A. M. J. J. Bonvin, R. Boelens, and R. Kaptein, *Biopolymers*, 1994, **34**, 39.
89. J. N. Breg, J. H. J. van Opheusden, M. J. M. Burgering, R. Boelens, and R. Kaptein, *Nature (London)*, 1990, **346**, 586.

Biographical Sketches

Alexandre M. J. J. Bonvin. *b* 1964. B.S., 1989, Lausanne, Switzerland; Ph.D., 1993, Utrecht. Introduced to NMR by G. Bodenhausen. Postdoctoral associate of Professor Dr. A. T. Brünger, Yale University. Approx. 16 publications. Research interests include molecular modeling, development and application of new methods for biomolecular structure determination by NMR, and dynamic studies of proteins by molecular dynamics simulations.

R. Boelens. *b* 1951. B.S., 1977, University of Groningen, Ph.D., University of Amsterdam, Ph.D., 1984, biochemistry. Postdoctoral associate with R. Kaptein, Groningen. Associate professor at Utrecht University, 1987–present. Approx. 130 publications. Research specialties: NMR method development, structure determination of biomolecules by NMR and studies on protein–DNA interaction.

Robert Kaptein. *b* 1941. M.S., 1965, Ph.D., Leiden, 1971; postdoctoral fellow with Ray Freeman, Varian 1971–72; Shell Research Laboratory, Amsterdam, 1972–75; Groningen University, 1975–87; Utrecht University, Professor of Chemistry 1987–present. Research interests: biomolecular structure determination, NMR methodology, protein–DNA interactions.

Relaxation Matrix Refinement of Nucleic Acids

Jean-François Lefèvre and Patrice Koehl

UPR 9003, CNRS and Louis Pasteur University, Strasbourg, France

1	Introduction	1
2	Relaxation Matrix and NOE Intensities	2
3	Relaxation Matrix Refinement	2
4	Improvements	4
5	Related Articles	5
6	References	5

1 INTRODUCTION

Among the various techniques involved in the field of macromolecular structural determination, NMR spectroscopy has proven in the last decade to be a powerful tool for defining the folding of proteins,[1] as well as for structural studies of nucleic acid fragments in solution.[2] There is, however, a significant difference between the applications of NMR to the structural determinations of proteins and nucleic acids: while elucidation of the global secondary and tertiary structure of a protein still counts as a major achievement, for oligomeric nucleic acids this is a starting point rather than a goal. Secondary structures of nucleic acids (such as the helix type) are usually obvious from qualitative inspection of the NMR data (to the point that NMR studies of small duplexes has been qualified to be 'as easy as A, B, Z'[3]), and tertiary structures are usually not exhibited by the small duplexes investigated so far. Hence NMR is used to determine the finer details of the structure of nucleic acids, such as small local variations of the puckering of the sugar moieties and of helical parameters.

2D NMR nuclear Overhauser effect spectroscopy (NOESY) experiments are usually the major sources of structural information by providing interproton distances. A difficulty arises from the fact that the nuclear Overhauser effect (NOE) develops by magnetization transfer through a network of dipoles (so-called spin diffusion), and depends on fluctuations in the position and the length of the interproton vectors due to the overall as well as to internal motions. Hence dynamics and structural information are embedded in NOE intensities, and need to be deconvoluted.

The approximation is often made that internal motions have negligible effects on magnetization transfers. Any unknown interproton distance r_{ij} is then calculated from a reference distance r_{kl} by comparing the cross-relaxation rates σ_{ij} and σ_{kl} according to

$$r_{ij}/r_{kl} = (\sigma_{kl}/\sigma_{ij})^{1/6} \quad (1)$$

In NMR studies of nucleic acids, two reference distances are preferentially used, namely, cytosine H-5–H-6 (248 pm) and deoxyribose H-2′–H-2″ (179 pm). The cross-relaxation rates σ can be measured exactly as the initial NOE build-up rates. In practice, however, an estimate of the initial slope is obtained by measuring the NOE intensity after a reasonably short mixing time, leading to the so-called two-spin approximation, and NOEs rather than cross-relaxation rates σ are used in equation (1). Distances obtained from equation (1) have proven to be useful in determining the global folding of a protein, in which case the accuracy with which the distances are known is not crucial: in the structural reconstruction process, distances are only provided as upper and lower bounds, which are meant to include all possible misinterpretations. For example, weak NOEs are associated with uncertainties to account for large distances in relatively rigid regions or for short distances in very mobile regions. However, analysis of finer structural elements, such as those considered for nucleic acid fragments, cannot rely solely on this type of estimated distances, for several reasons. First, many of the structurally useful NOEs are not observed at short mixing times (e.g., H-1′ and H-3′ to H-8,6). In the case of long linear molecules, such as the DNA fragments studied so far, this could lead to erroneous patterns such as curved DNA through accumulation of errors.[2] Second, the two-spin approximation has been shown to yield incorrect estimates of distances.[2,4–8] Because of diffusion via H-2′, for instance, the H-3′ and the H-2″ are placed with respect to H-8,6 with an error amounting to more than 100 pm. Both distances, however, are essential to position the sugar moieties in DNA with respect to their bases. An illustration of the spin diffusion pathways in DNA is shown in Figure 1. Third, local motions, which play an important role in relaxation phenomena, have been shown to be important in nucleic acids, yielding, for example, different correlation times for sugar and bases.[9–11] equation (1) limits the interpretation of the relaxation data to structural information, discarding the dynamics of the molecule, which is known to play an important role with respect to its function.[12]

To overcome the above-mentioned problems, inherent to equation (1), several approaches that include the longitudinal relaxation of the whole spin system[4,6–8,13–20] have been suggested, mainly to compensate for spin diffusion effects, with some attempts to include dynamics. They all have in common that the full relaxation rate matrix **R** is calculated by solving the set of generalized Bloch equations (the full relaxation matrix is, in fact, a subset of the whole Redfield matrix, since it concerns only the relaxation of the longitudinal

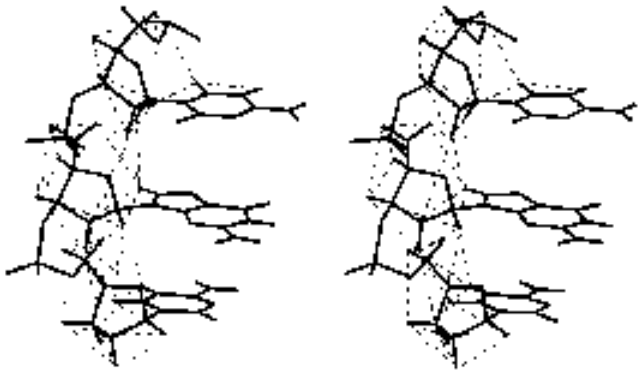

Figure 1 Stereoview of the trinucleotide d(CGC). Standard B-DNA geometry has been assumed. All interproton vectors whose norm is shorter than 400 pm are shown as dashed lines, illustrating the spin diffusion pathways

magnetization; 'full' refers to the fact that the complete spin system is included in the calculation). These methods, which were first developed for the analysis of NMR data of nucleic acids, have now been applied to proteins (see ***Protein Structures: Relaxation Matrix Refinement***.). In order to understand the basis of these methods, we shall first summarize the elements of the relaxation theory that are of importance for the interpretation of NOE data; then we shall present a brief description of the different relaxation matrix refinement techniques.

2 RELAXATION MATRIX AND NOE INTENSITIES

Under the assumption that cross correlation can be neglected, Kalk and Berendsen[21] have derived the so-called generalized Bloch equations, which govern the time dependence of the magnetization M_{zi} of each spin i within the molecule of interest. These sets of coupled differential equations can conveniently be expressed in matrix notation as[22]

$$\frac{\mathrm{d}}{\mathrm{d}t}\begin{bmatrix} M_1 \\ M_2 \\ \vdots \\ M_n \end{bmatrix} = -\begin{bmatrix} \rho_1 & \sigma_{12} & \dots & \sigma_{1n} \\ \sigma_{21} & \rho_2 & \dots & \sigma_{2n} \\ \vdots & \vdots & & \vdots \\ \sigma_{n1} & \sigma_{n2} & \dots & \rho_n \end{bmatrix}\begin{bmatrix} M_1 \\ M_2 \\ \vdots \\ M_n \end{bmatrix} \tag{2}$$

with $M_i = M_{zi} - M_{zi0}$. Here M_{zi0} is the z magnetization of spin i at equilibrium, ρ_i is the auto (longitudinal) relaxation rate of spin i, and σ_{ij} is the cross-relaxation rate between spin i and spin j. Assuming that relaxation mechanisms are dominated by dipolar interactions, the relaxation rates ρ_i and σ_{ij} for homonuclear proton relaxation in solution are given by

$$\rho_i = \alpha \sum_{j \neq i} [J_{ij}(0) + 3J_{ij}(\omega) + 6J_{ij}(2\omega)] \tag{3}$$

$$\sigma_{ij} = \alpha[6J_{ij}(2\omega) - J_{ij}(0)] \tag{4}$$

where α is a constant that depends on the gyromagnetic ratio of the nucleus (for protons, $\alpha = 5.69 \times 10^{-41}\ \mathrm{s}^{-2}\ \mathrm{m}^6$). The variable ω is the Larmor frequency of the proton, and $J_{ij}(\omega)$ are the spectral density functions, obtained as the cosine Fourier transforms of the time correlation functions, defined by (in the laboratory frame)

$$C_{ij}(t) = \left\langle \frac{P_2(\boldsymbol{\mu}(t) \cdot \boldsymbol{\mu}(0))}{r_{ij}^3(t) r_{ij}^3(0)} \right\rangle \tag{5}$$

where r_{ij} is the interproton distance between i and j, and $\boldsymbol{\mu}$ is a unit vector pointing from i to j. P_2 is the second-order Legendre polynomial defined by $P_2(x) = \frac{1}{2}(3x^2 - 1)$. If all the interproton vectors are assumed to be rigid and to move isotropically, the spectral density function takes the form

$$J_{ij}(\omega) = \frac{1}{r_{ij}^6} \frac{\tau_\mathrm{c}}{1 + (\omega\tau_\mathrm{c})^2} \tag{6}$$

where τ_c is the overall rotation correlation time.

Equation (2) can be rewritten as

$$\frac{\mathrm{d}}{\mathrm{d}t}\mathbf{M} = -\mathbf{R}\mathbf{M} \tag{7}$$

where $\mathbf{R}$ is the relaxation rate matrix. The solution of the set of generalized Bloch equations is then

$$\mathbf{M}(\tau_\mathrm{m}) = \exp(-\mathbf{R}\tau_\mathrm{m})\mathbf{M}(0) \tag{8}$$

These equations can be generalized for the analysis of 2D NOESY spectra,[22] in which case $\mathbf{M}(\tau_\mathrm{m})$ is a matrix proportional to the normalized NOE intensities recorded with a mixing time τ_m, and $\mathbf{M}(0)$ is the diagonal matrix containing the equilibrium z magnetization.

3 RELAXATION MATRIX REFINEMENT

As can be seen from equations (3)–(5) and (8), extracting structural and dynamical information from NOE intensities first requires generation of the relaxation matrix. The ideal and most direct way to calculate $\mathbf{R}$ is to take the logarithm[14] of equation (8), yielding

$$\mathbf{R} = -\frac{1}{\tau_\mathrm{m}} \ln[\mathbf{M}(\tau_\mathrm{m})\mathbf{M}(0)^{-1}] \tag{9}$$

This approach, however, requires that all NOE intensities be quantified; this condition will generally not be fulfilled owing to experimental limitations such as poor signal-to-noise ratios in the case of weak peaks and of peak overlaps, which in the case of DNA fragments are usually severe on the diagonal and in all regions concerning H-2′–H-2″. Even in the presence of small overlaps, this direct method was found not to be reliable for DNA studies.[23]

An alternative approach consists in testing model structures for the molecule of interest. The relaxation matrix of a given model structure can be calculated by assuming a particular model for the spectral density functions, from which NOE intensities are computed based on equation (8). These calculated values are then compared with the experimental NOE intensities, and the model structure that provides the best agreement is selected. The success of this trial-and-error approach is limited by the ability to generate appropriate trial structures.

Attention has been focused on improving both routes in order to circumvent their drawbacks, yielding two distinct sets of relaxation matrix refinement procedures.

3.1 Deriving the Relaxation Matrix from an Incomplete Set of NOE Data

A systematic search that compares the experimental NOE intensities with calculated values obtained for all possible conformations of the molecule would directly yield the family of structures compatible with the data. At the present state of computer technology, however, this strategy is computationally prohibitive, even for short DNA fragments of six base pairs. One route to circumvent this computing

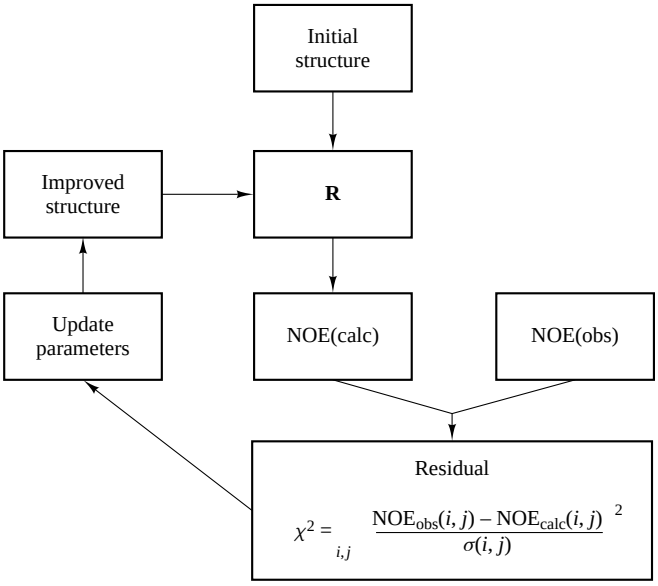

Figure 2 Flowchart of the methods of reconstruction of the relaxation matrix from an incomplete set of NOE intensities

limitation is to refine automatically the structure based on the available NOE intensities. A general flowchart of this approach is shown in Figure 2.

The goal of this method is to optimize iteratively a trial structure while minimizing the error χ^2 between the calculated and observed intensities:

$$\chi^2 = \sum_{i,j} \left[\frac{\mathrm{NOE_{obs}}(i,j) - \mathrm{NOE_{calc}}(i,j)}{\sigma(i,j)} \right]^2 \qquad (10)$$

where $\mathrm{NOE_{obs}}(i,j)$ and $\mathrm{NOE_{calc}}(i,j)$ are the observed and calculated NOEs for the pair of protons i and j, and $\sigma(i,j)$ is the standard deviation of that NOE estimated from the signal-to-noise ratio on the NOE spectrum. The full procedure comprises the following.

1. *Initial Model* For DNA, a reasonable starting structure is assumed, such as right-handed B DNA, especially if there is independent evidence of the nature of the gross structure (see ***Nucleic Acids: Spectra, Structures, and Dynamics*** and ***DNA: A-, B-, and Z-***).
2. *NOE Calculation* Based on this initial model, the relaxation matrix is calculated from equations (3) and (4), usually assuming the spectral density functions to be of the form described by equation (6). NOE values are then calculated either by numerical integration of the generalized Bloch equations, equation (2),[6,15] or directly from equation (8), which first requires the relaxation matrix to be diagonalized: $\mathbf{R} = \mathbf{P}\,\mathbf{D}\,\mathbf{P}^{-1}$. Then

$$\mathbf{M}(\tau_\mathrm{m}) = \mathbf{P} \exp(-\mathbf{D}\tau_\mathrm{m})\mathbf{P}^{-1}\mathbf{M}(0) \qquad (11)$$

3. *Structural Parameters to be Determined* Structural parameters of DNA molecules are commonly reported as torsion angles. The glycosidic torsion angle χ and the sugar pucker parameters P and $\theta_{\max}$ describe the structure of each nucleotide. The helical twist θ_t, the base pair roll θ_r, the propeller twist θ_p, and the base pair tilt t give the orientation of the bases with respect to one another. The helix displacement D and the local rise h describe the relative position of the helix axis and the vertical translation of each base pair. Methods of refinement based on the torsion angles usually do not include torsion angles in which phosphates are involved, since these angles are known to be subject to more extensive motional averaging than the rest of the molecule.[24,25] The main advantage of using torsion angles as variables compared with Cartesian coordinates resides in a significative reduction of the number of parameters, since all bond lengths and angles remain constant. Cartesian coordinates, however, have not been discarded, since they allow analytical calculations of the derivatives of the residual χ^2, as well as direct coupling with other techniques such as molecular dynamics (MD). This will be described below. Finally, distances themselves can be used as variables.
4. *Updating the Structural Parameters* In the torsion angle space, variables are modified according to the gradients of the residual χ^2; these gradients have so far been calculated only numerically for nucleic acids (analytical derivatives exist in the case of proteins[26]). A new trial structure is calculated from these new parameters. The procedure is iterated until convergence is achieved (i.e., there is negligible variation of χ^2 between two steps). The principle of this approach has been described in detail by Lefèvre et al.[6] and Borgias and James;[23] the latter have given the acronym COMATOSE to their program.

In principle, a similar procedure could be derived in Cartesian coordinate space, with the requirement that additional constraints be included to maintain the stereochemistry of the molecule. Though this approach would further benefit from analytical expressions for the gradients of the residual,[27] it has not yet been applied as such for structural refinement of nucleic acids. Alternative approaches have been proposed in which distances rather than Cartesian coordinates are updated, based on the relation

$$r_{ij}(\mathrm{new}) = r_{ij}(\mathrm{old}) \left[\frac{\mathrm{NOE_{calc}}(i,j)}{\mathrm{NOE_{obs}}(i,j)} \right]^{1/6} \qquad (12)$$

These distances can then be used to refine the positions of the protons directly, without consideration of the other atoms (program NO2DI[28]). The full molecule is built at the end of the iteration scheme. Another possibility is to include these distances in molecular mechanics or molecular dynamics calculations in order to derive a new reasonable trial structure, which is then used to derive the new set of calculated NOEs.[20]

All the methods presented above depend strongly on the model chosen for the internal dynamics of the molecule in order to calculate the relaxation matrix from its structure. An alternative approach is to use a least-squares optimization to fit the appropriate terms in the relaxation matrix directly to the experimental NOEs. The main point of this method is that it first handles the problem of spin diffusion rigorously, before getting to the details of the determination of the structure and dynamics of the molecule; these features are derived from the direct analysis of the relaxation rates ρ and σ. This method was reported to be successful for relatively small cross-relaxation networks involving subsets of the protons of a DNA molecule.[29,30]

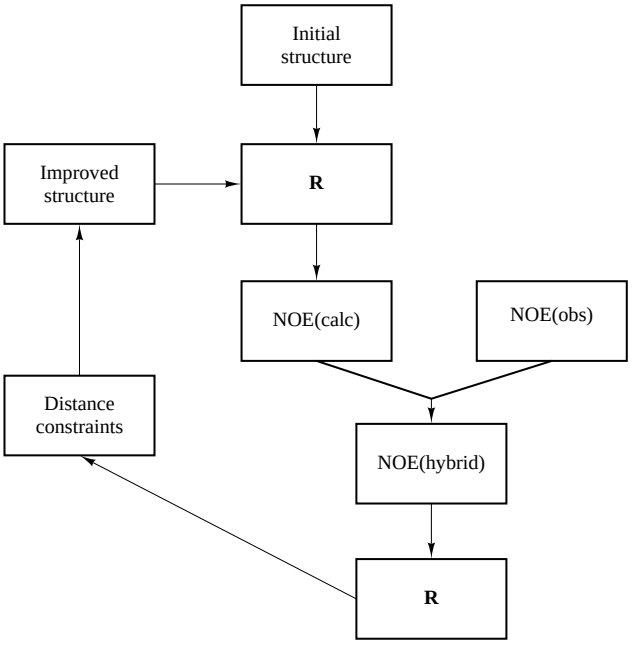

Figure 3 Flowchart of the hybrid matrix approach

3.2 Deriving the Relaxation Matrix from a Hybrid Set of Calculated and Observed NOE Intensities

The second route to circumvent the problem of missing NOE intensities is the so-called 'hybrid matrix approach',[16,17,31] illustrated in Figure 3. The hybrid matrix approach proceeds as follows. First, NOE values are calculated from a model structure, usually via equation (8). Next, after scaling the calculated NOE intensities to the experimental values, the NOEs for which measured values are available are substituted into the NOE matrix leaving the rest unchanged. Thus, a hybrid NOE matrix is constructed, which is complete and can therefore be used to back-calculate the relaxation matrix via equation (9). Distances are subsequently extracted from this matrix, assuming a model for the dynamics of the molecule. In the IRMA approach,[16,17] this set of refined distances is used immediately to refine the model, using restrained molecular dynamics calculations. This updated structure serves as a new trial structure for the next cycle. In the MARDIGRAS approach,[31] the updated set of distances is used again to calculate a 'model' NOE matrix for the next cycle. Iterations are pursued until good agreement is obtained between the model and the observed NOE values, measured, for example, through a residual [equation (10)]. In the MARDIGRAS approach, only relaxation rates that have a corresponding observed NOE are allowed to change. Both methods allow the incorporation of NOE data at several mixing times. Hybrid NOE matrices are then calculated for each mixing time, and the resulting relaxation matrices are averaged to yield the relaxation matrix used to estimate the distances.

Calculation of the relaxation matrix from the full NOE matrix based on equation (9) requires that all eigenvalues of the matrix $\mathbf{NOE}(\tau_m)[\mathbf{NOE}(0)]^{-1}$ be positive. This may not be the case when the hybrid NOE matrix is used. If a negative eigenvalue appears, either the corresponding mixing time is discarded or the eigenvalues are shifted so that all become positive.[31]

4 IMPROVEMENTS

The full relaxation matrix approaches have been shown to yield more reliable sets of distance constraints than can be obtained by the conventional initial rate analysis.[6,16,17,31] The effect of spin diffusion is taken into account in an accurate way either by solving the Bloch equations (Section 3.1) or by back-transformation of a hybrid calculated/experimental NOE matrix (Section 3.2). Application of these techniques, however, requires the quantification of a large number of NOEs, the definition of a model for the dynamics of the molecule, and a criterion for assessing the final model structures. These issues will be discussed below.

4.1 Quantification of NOE Data

Quantification of NMR experimental data is a crucial problem that is not specific to relaxation matrix refinements. A priori, because of the r^{-6} dependence, no great accuracy in the determination of the cross-relaxation rates is required; for example, an error of a factor of 2 in σ results in an error of about 10% in r. However, the situation is worse if one tries to extract dynamical information from the cross-relaxation rates, which depend linearly on the correlation times. Also, in cases where enough NOEs are available to constrain the molecule, good convergence toward a correct model can be expected. In cases in which the NOE data set is very incomplete, the convergence will become strongly dependent on the initial structure. Quantification usually proceeds through peak picking and numerical integration over a box containing the isolated cross peak of interest, or by a nonlinear least-squares fit in the frequency domain in the presence of overlap. Limitations of these procedures appear, however, for low signal-to-noise ratio, as well as in crowded or complicated spectra that show severe overlaps. In these cases, alternative approaches that have attracted considerable interest recently are linear prediction (LP)[32] and maximum entropy[33] methods, though no direct applications have yet been proposed.

4.2 Influence of the Dynamics of the Molecule

Spin diffusion affects the interpretation of experimental data in terms of relaxation rates, while dynamics affects the interpretation of the relaxation rates in terms of structural parameters. Most of the full relaxation matrix approaches presented above combine these two problems in order to derive the structure of the molecule directly from experimental data. It is worth mentioning that the effects of spin diffusion and dynamics can be separated in the process of analyzing NOE data,[29,30] though a model for the dynamics is still required in order to derive the structure of the molecule of interest. In the latter approach, however, information on the dynamics can be obtained from cross-relaxation rates involving protons separated by fixed distances, such as H-2′–H-2″ and H-5–H-6.[29]

In the calculation of the relaxation matrix from a known model structure, the molecule is usually assumed to be a rigid body undergoing only overall motion with a single correlation time τ_c. Under this assumption, the spectral density functions are described by equation (6). However, internal motions

induce changes in the cross-relaxation rates. Several methods have been suggested to incorporate the effect of local motion in the interpretation of NOE data for DNA molecules. In the case of the two-spin approximation, three different correlation times were chosen:[34]

1. one for the sugar–sugar, base–base, and sugar–base cross peaks not involving H-2′, H-2″, and methyl groups;
2. one for all the cross peaks involving H-2′ and H-2″;
3. one for cross peaks involving methyl groups.

In the case of full relaxation matrix calculations, a better fit to the NOE data could be obtained when small variations in the overall correlation time were allowed,[35] or when extra effective correlation times were added for the interproton vectors to H-2′ and H-2″, to account for possible anisotropy of the overall motion of the molecule,[20] related to the fact that DNA molecules are better represented by cylinders than by spheres. A protocol for the incorporation of these internal motions directly in the refinement of the relaxation matrix was also proposed.[36] In this method, systems where overall and fast internal motions occur are described by the model-free approach proposed by Lipari and Szabo.[37] This approach describes systems with three different parameters, namely, the overall correlation time τ_c, a generic correlation time τ_i to describe the rate of all fast internal motions, and a generalized order parameter S^2. S^2 varies between 0 for complete isotropic motion and 1 in the absence of local motion. The time correlation functions, equation (5), are rewritten in the form

$$C_{ij}(t) = S^2\langle r_{ij}^{-6}\rangle \exp\left(-\frac{t}{\tau_c}\right) + (1 - S^2)\langle r_{ij}^{-6}\rangle \exp\left(-\frac{t}{\tau_e}\right) \qquad (13)$$

where ${\tau_e}^{-1} = {\tau_c}^{-1} + {\tau_i}^{-1}$. The spectral density function is then given by

$$J_{ij}(\omega) = S^2\langle r_{ij}^{-6}\rangle \frac{\tau_c}{1 + (\omega\tau_c)^2} + (1 - S^2)\langle r_{ij}^{-6}\rangle \frac{\tau_e}{1 + (\omega\tau_e)^2} \qquad (14)$$

If the internal motions are in the motional narrowing limit ($\omega\tau_e \ll 1$) and are very fast compared with the overall motion ($\tau_i \ll \tau_c$), the second term in equation (14) can be neglected, yielding

$$J_{ij}(\omega) = S^2\langle r_{ij}^{-6}\rangle \frac{\tau_c}{1 + (\omega\tau_c)^2} \qquad (15)$$

Equation (15) is used instead of equation (6) to calculate the relaxation rates. In the absence of experimental values, both S^2 and $\langle r_{ij}^{-6}\rangle$ can be obtained from molecular dynamics simulations. The modified relaxation matrix refinement that uses this description of the internal dynamics consists in

1. determination of a first approximate structure based on an hybrid relaxation matrix approach, without inclusion of the fast internal motions;
2. free MD simulation in order to extract the generalized order parameters as well as the average distances;
3. a few more cycles of relaxation matrix refinement with inclusion of motion for further structure refinement.

Progress in this direction is expected, since the recent possibility of synthesizing ^{13}C-enriched nucleic acid fragments at a reasonable cost will help in extracting experimental values for the generalized order parameters.

4.3 Assessment of the Refined Structure

The common procedure to judge the quality of the final structure is a direct comparison of the theoretical and experimental NOE intensities, either by means of a residual χ^2, equation (10), or, for direct comparison with X-ray crystallography, by using the R factor defined by Gonzalez et al.:[38]

$$R = \frac{\sum_{i,j} |\mathrm{NOE}_{obs}(i, j) - \mathrm{NOE}_{calc}(i, j)|}{\sum_{i,j} \mathrm{NOE}_{obs}(i, j)} \qquad (16)$$

where the summation extends over all measured cross peaks i,j. However, neither the χ^2 residual nor the R factor include information on peaks whose intensities were too small to be detected, or on peaks that could not be quantified because of severe overlaps.

Another way of assessing the final structure is by simulation of the NOESY spectrum based on the calculated NOE intensities, and visual comparison of both simulated and experimental spectra. This procedure, which does not suffer the same drawbacks as the use of its R factor, has now been included in interactive relaxation matrix refinement procedures.[18, 36, 39]

5 RELATED ARTICLES

Biological Macromolecules: Structure Determination in Solution; Biological Macromolecules; Biological Macromolecules: NMR Parameters; Computer Assisted Structure Elucidation; Data Processing; DNA: A-, B-, and Z-; DNA Triplexes, Quadruplexes, and Aptamers; Drug–Nucleic Acid Interactions; Fourier Transform and Linear Prediction Methods; Maximum Entropy Reconstruction; Molecular Motions: T_1 Frequency Dispersion in Biological Systems; NOESY; Nuclear Overhauser Effect; Nucleic Acid Flexibility and Dynamics: Deuterium NMR; Nucleic Acid Structures in Solution: Sequence Dependence; Nucleic Acids: Base Stacking and Base Pairing Interactions; Nucleic Acids: Spectra, Structures, and Dynamics; Protein Dynamics from NMR Relaxation; Protein Structures: Relaxation Matrix Refinement; Relaxation Theory: Density Matrix Formulation; RNA Structure and Function: Modified Nucleosides.

6 REFERENCES

1. K. Wüthrich, *NMR of Proteins and Nucleic Acids*, Wiley, New York, 1986.
2. F. J. M. Van De Ven and C. W. Hilbers, *Eur. J. Biochem.*, 1988, **178**, 1.
3. J. S. Cohen, *Trends Biochem. Sci.*, 1987, **12**, 133.
4. J. W. Keepers and T. L. James, *J. Magn. Reson.*, 1984, **57**, 404.

5. G. M. Clore and A. M. Gronenborn, *J. Magn. Reson.*, 1985, **61**, 158.
6. J.-F. Lefèvre, A. N. Lane, and O. Jardetzky, *Biochemistry*, 1987, **26**, 5076.
7. E. P. Nikonowicz, V. Roongta, C. R. Jones, and D. G. Gorenstein, *Biochemistry*, 1989, **28**, 8714.
8. E. P. Nikonowicz, R. P. Meadows, and D. G. Gorenstein, *Biochemistry*, 1990, **29**, 4193.
9. P. H. Bolton and T. L. James, *Biochemistry*, 1980, **19**, 1388.
10. R. L. Rill, P. R. Hilliard, Jr., and G. C. Levy, *J. Biol. Chem.*, 1983, **258**, 250.
11. P. N. Borer, N. Zamatta, T. A. Holak, G. C. Levy, J. H. van Boom, and A. H.-J. Wang, *J. Biomol. Struct. Dyn.*, 1984, **1**, 1373.
12. M. Karplus and G. A. Petsko, *Nature (London)*, 1990, **347**, 631.
13. A. A. Bothner-By and J. H. Noggle, *J. Am. Chem. Soc.*, 1979, **101**, 5152.
14. E. T. Olejniczak, R. T. Gampe, Jr., and S. W. Fesik, *J. Magn. Reson.*, 1986, **67**, 28.
15. D. Marion, M. Genest, and M. Ptak, *Biophys. Chem.*, 1987, **28**, 235.
16. R. Boelens, T. M. G. Koning, and R. Kaptein, *J. Mol. Struct.*, 1988, **173**, 299.
17. R. Boelens, T. M. G. Koning, G. A. van der Marel, J. H. van Boom, and R. Kaptein, *J. Magn. Reson.*, 1989, **82**, 290.
18. W. Nerdal, D. R. Hare, and B. R. Ried, *Biochemistry*, 1989, **28**, 10 008.
19. C. B. Post, R. P. Meadows, and D. G. Gorenstein, *J. Am. Chem. Soc.*, 1990, **112**, 6796.
20. G. Lancelot, J.-L. Guesnet, and F. Vovelle, *Biochemistry*, 1989, **28**, 7871.
21. A. Kalk and H. J. C. Berendsen, *J. Magn. Reson.*, 1976, **24**, 343.
22. S. Macura and R. R. Ernst, *Mol. Phys.*, 1980, **41**, 95.
23. B. A. Borgias and T. L. James, *J. Magn. Reson.*, 1988, **79**, 493.
24. M. E. Hogan and O. Jardetzky, *Biochemistry*, 1980, **19**, 3460.
25. J. W. Keepers, P. A. Kollman, P. K. Weiner, and T. L. James, *Proc. Natl. Acad. Sci. USA*, 1982, **79**, 5537.
26. J. E. Mertz, P. Güntert, K. Wüthrich, and W. Braun, *J. Biol. NMR*, 1991, **1**, 257.
27. P. Yip and D. A. Case, *J. Magn. Reson.*, 1989, **83**, 643.
28. F. J. M. Van de Ven, M. J. J. Blommers, R. E. Schouten, and C. W. Hilbers, *J. Magn. Reson.*, 1991, **94**, 140.
29. P. Koehl and J.-F. Lefèvre, *J. Magn. Reson.*, 1990, **86**, 565.
30. P. Koehl and J.-F. Lefèvre, *Bull. Magn. Reson.*, 1990, **12**, 23.
31. B. A. Borgias and T. L. James, *J. Magn. Reson.*, 1990, **87**, 475.
32. H. Gesmar, J. J. Led, and F. Albigaard, in *Progress in Nuclear Magnetic Resonance Spectroscopy*, eds. J. W. Emsley, J. Feeney, and L. H. Sutcliffe, Pergamon Press, Oxford, 1990, Vol. 22, p. 255.
33. S. Sibisi, J. Skilling, R. G. Brereton, E. D. Laue, and J. Staunton, *Nature (London)*, 1984, **311**, 446.
34. G. M. Clore and A. M. Gronenborn, *FEBS Lett.*, 1985, **179**, 187.
35. M. S. Broido, T. L. James, G. Zon, and J. W. Keepers, *Eur. J. Biochem.*, 1985, **150**, 117.
36. T. M. G. Koning, R. Boelens, G. A. van der Marel, J. H. van Boom, and R. Kaptein, *Biochemistry*, 1991, **30**, 3787.
37. G. Lipari and A. Szabo, *J. Am. Chem. Soc.*, 1982, **104**, 4546.
38. C. Gonzalez, J. A. C. Rullmann, A. M. J. J. Bonvin, R. Boelens, and R. Kaptein, *J. Magn. Reson.*, 1991, **91**, 659.
39. H. Robinson and A. H.-J. Wang, *Biochemistry*, 1992, **31**, 3524.

Biographical Sketches

Jean-François Lefèvre. *b* 1948. M.S., 1972, Ph.D., 1980. Introduced to NMR by O. Jardetzky, during a postdoctoral stay, 1983–1985. Professor of Biophysics at the School of Biotechnology, Louis Pasteur University, Strasbourg, 1986–present. Director of the School since 1987. Approx. 50 publications. Research interests include structure determination and dynamic analysis of proteins and nucleic acids, mainly involved in mutagenesis.

Patrice Koehl. *b* 1961. M.S., 1984, Ph.D., 1989. Introduced to NMR by J. F. Lefèvre. Staff scientist of the CNRS Institute, 1989–present. Approx. 20 publications. Research interests include protein folding and applications of NMR to the analysis of motions in macromolecules.

D-Lactate Dehydrogenase

Gordon S. Rule
University of Virginia School of Medicine, Charlottesville, VA, USA

and

Chien Ho
Carnegie Mellon University, Pittsburgh, PA, USA

1	Introduction	1
2	Protein–Lipid Interactions	1
3	Topology of D-LDH	2
4	Dynamics of Trp Residues in D-LDH	3
5	Related Articles	6
6	References	6

1 INTRODUCTION

Information on the tertiary structure of membrane proteins has been difficult to obtain due to the heterogeneous environment of these proteins. Although crystallography has provided detailed information for a small number of membrane proteins, it is often difficult to obtain crystalline material for high-resolution diffraction studies. In the case of smaller peptides, such as gramicidin[1] and the M13 coat protein,[2] solid state NMR methods have proven capable of obtaining detailed structural information of the peptide within phospholipid bilayers. In addition, there have been numerous high-resolution solution NMR studies on small peptides and proteins bound to detergent micelles.[2,3]

The application of either solution phase NMR or solid state NMR to larger membrane proteins is fraught with difficulties. In the case of solid state NMR techniques, it is often difficult to obtain protein that is labeled at a small number of unique sites. The routine application of multidimensional NMR experiments, which are commonly used for structure determination, cannot be applied to large protein–lipid complexes because of the short spin–spin relaxation time. In view of these limitations, we and others[4–6] have explored the use of ^{19}F NMR as a method of obtaining information on the structure and dynamics of membrane associated proteins. Fluorine-19 is a particularly useful NMR nucleus to observe because it has high sensitivity, 100% natural abundance, a large dispersion of chemical shift, and is not normally found in biopolymers. The relaxation properties of the ^{19}F spin can be used to obtain information on the internal motion of amino acid residues within the protein molecule.

In order to apply ^{19}F NMR techniques to proteins, it is necessary to incorporate a fluorine atom into the membrane protein at a small number of sites. The incorporated ^{19}F spins would then serve as probes for the local environment and dynamics of regions of the protein. Fluorinated analogs of aromatic amino acids have been used to incorporate fluorine biosynthetically into several proteins without noticeable effects on protein function. Examples include alkaline phosphatase (F-Tyr),[7] lac repressor (F-Tyr),[8] λ-cro protein (F-Phe, F-Tyr),[9] D-lactate dehydrogenase (F-Trp),[5] D-galactose receptor protein (F-Trp),[6] and retinol binding protein (F-Trp).[10]

As a model system in which to apply ^{19}F NMR to the study of protein–lipid interactions, we have selected the membrane-associated enzyme D-lactate dehydrogenase (D-LDH) of *Escherichia coli*. This flavin containing enzyme has a molecular weight of 65 000 and catalyzes the oxidation of D-lactate to pyruvate in an electron transfer reaction that is coupled to the active transport of various amino acids and sugars into membrane vesicles.[11,12] The enzyme is located on the cytoplasmic face of the cell membrane.[13] The purified enzyme requires a lipid-like environment to prevent aggregation, and various lipids and detergents enhance its stability and activity.[5,12,14] Therefore, D-LDH appears to be an excellent model system in which to study protein–lipid interactions. To investigate these interactions, we have used ^{19}F NMR methods to address the following important questions: Is the structure of the protein altered by the presence of lipid? What is the topology of the protein–lipid complex? How are the motional properties of residues in D-LDH related to their microenvironment?

Before initiating NMR studies on D-LDH, it was necessary to obtain large amounts of fluorine labeled material. This was accomplished by overproduction of the enzyme in *E. coli* using recombinant DNA techniques.[15] D-LDH labeled with F-Phe or F-Tyr proved to be unsuitable for detailed ^{19}F NMR studies because the spectra of the labeled material contain large numbers of unresolved peaks. In contrast, ^{19}F NMR spectra obtained from 4F-, 5F-, and 6F-Trp labeled material were largely resolved. Since 5F-Trp labeled D-LDH produced the most resolved spectrum, it was used for the studies directed at investigating lipid induced conformational changes and mapping the topology of the enzyme. Nuclear spin relaxation measurements were performed with both 4F-Trp and 5F-Trp labeled material.

2 PROTEIN–LIPID INTERACTIONS

The effect of lipid on the conformation of D-LDH was assessed by acquiring the ^{19}F NMR spectra of 5F-Trp labeled D-LDH in the presence of different lipids. To determine the location of lipid-induced changes in the structure of D-LDH it is necessary to assign the resonance lines in the ^{19}F NMR spectrum of 5F-Trp labeled D-LDH. To accomplish this, a series of mutant enzymes were made in which each of the native Trp residues was replaced with Phe or Tyr. The resultant ^{19}F NMR spectrum of each mutant lacks a single resonance line, but is otherwise identical to that of the wild-type enzyme (Figure 1), suggesting that the mutation has not perturbed the environment of the remaining Trp residues. This method was originally used to assign ^{19}F resonance lines in F-Tyr labeled lac repressor,[8] and has been applied to other fluorine labeled proteins as well.[6]

Fluorine-19 NMR spectra of 5F-Trp labeled D-LDH in different lipid environments is shown in Figure 2. On the basis of chemical shift changes it appears that the conformation of D-LDH is similar in detergent micelles of Brij (heptaethylene glycol dodecyl ether), micelles of lysolecithin, and vesicles of DPPG (dipalmitoylphosphatidylglycerol). In

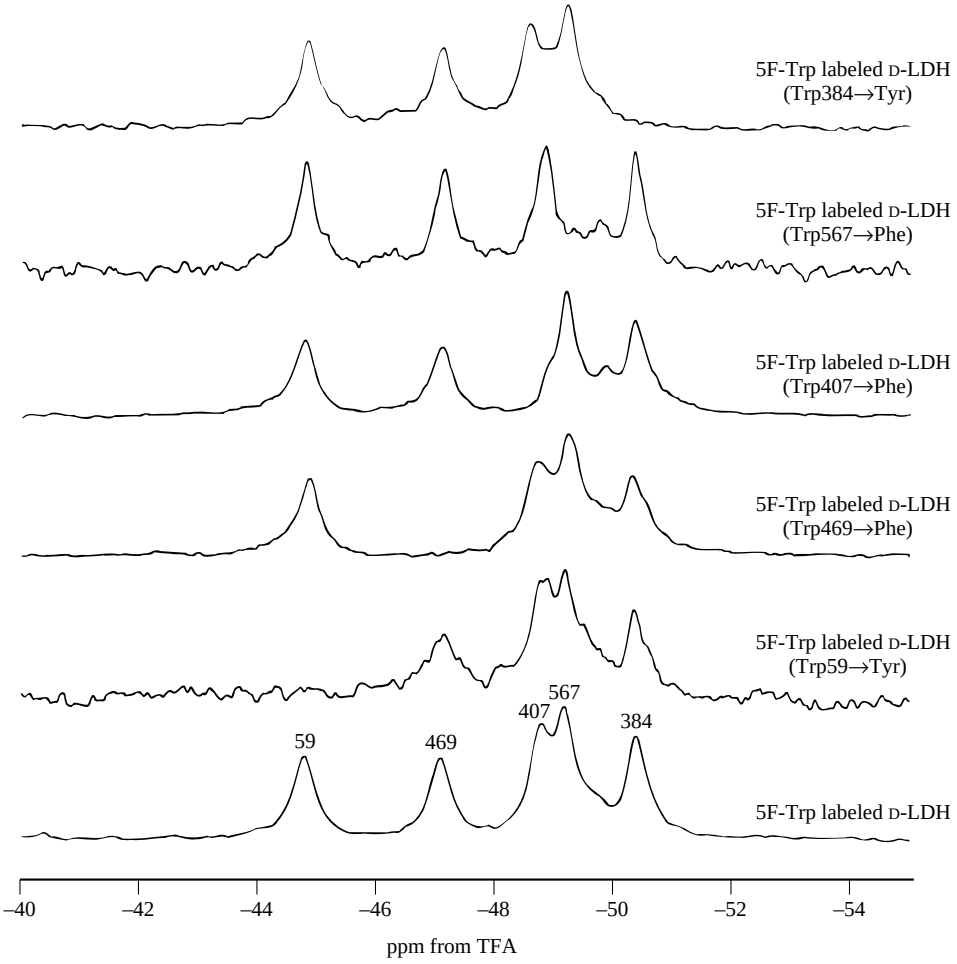

Figure 1 Assignment of ^{19}F NMR resonances for D-LDH labeled with 5F-Trp. Fluorine-19 NMR spectra were obtained at 282.4 MHz and at 42 °C in 10 mM phosphate buffer containing 100 mM lysolecithin and 1–2 mM D-LDH. (Reproduced by permission of Academic Press from Rule et al.[5])

contrast, chemical shift changes are noted in the presence of other detergents.

The ^{19}F resonances observed in the presence of DPPG are too broad to give spectra of useful resolution. However, adequate resolution of the resonances is obtained in the presence of lysolecithin because of the smaller size of this protein–lipid complex. Since the conformation of the protein appears to be similar in both of these lipids, studies performed in lysolecithin should provide information on D-LDH in a native environment.

3 TOPOLOGY OF D-LDH

The goal of these studies was to define the topology of D-LDH by determining the solvent exposure, lipid exposure, and sensitivity to substrate binding of each fluorinated residue in D-LDH. The ^{19}F NMR spectra of D-LDH can only provide information on regions of the protein which are in the vicinity of the native Trp residues (positions 59, 384, 407, 469, and 567). To provide information from other locations within the protein, additional Trp residues have been introduced into the protein by replacing hydrophobic residues with Trp. A total of 32 Trp substitution mutants have been constructed.[16–18] In some cases the substitution of a residue by Trp results in the production of either an inactive protein or a temperature sensitive folding mutant.[17] Presumably, replacement of some residues by Trp can disrupt the packing within the interior of the protein.[19]

Although some of the mutants were found to be inactive, a large number are not perturbed by the substitution of a residue by Trp. Spectra for nine enzymatically active Trp substitution mutants are shown in Figure 3. In all cases, it is possible to observe an additional spectral line that arises from the new Trp residue. In some cases, the resonance line from the added Trp residue is well resolved from those of the native Trp residues.

The native Trp residues and the active Trp substitution mutants can provide information for 27 positions which are uniformly distributed over the length of the protein. The solvent exposure of each residue has been quantified by measuring the change in chemical shift of the resonance line when the solvent is changed from H_2O to D_2O.[5,20] The proximity of each labeled site to the lipid phase can be assessed by measuring the paramagnetic broadening of the resonance lines when the nitroxide labeled fatty acids are included in the lipid phase. Figure 4 shows the effects of paramagnetic broadening on the spectrum from the Trp substitution mutant

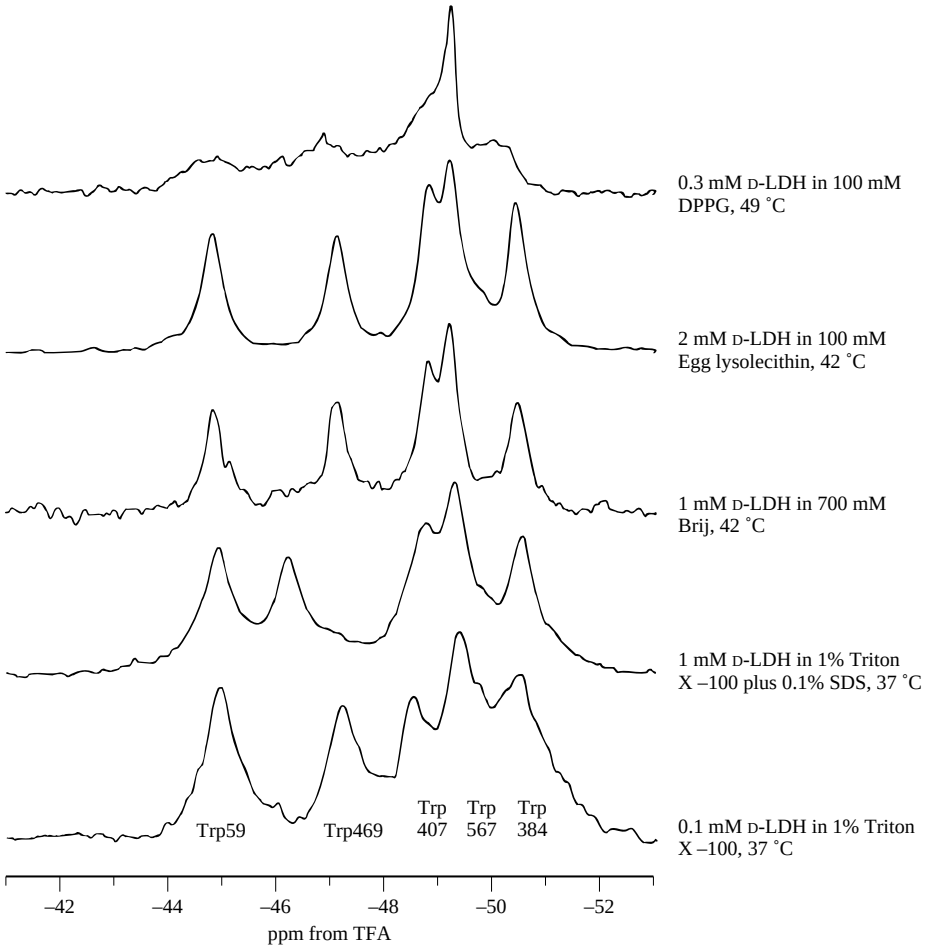

Figure 2 Fluorine-19 NMR spectra (282 MHz) of 5F-Trp labeled D-LDH in the presence of different lipids and detergents. In the Triton-X100 sample, it was necessary to use a low concentration of protein to prevent aggregation. (Reproduced by permission of Academic Press from Rule et al.[5])

F361. It is clear from this spectrum that this residue is close to the lipid bilayer.

The effect of substrate binding on the properties of the NMR resonances was also monitored to determine which areas of the protein may participate in catalysis. A particular example is that of Trp 469, whose resonance line undergoes a shift and broadening in the presence of substrate.[5] Figure 5 summarizes the results obtained for solvent isotopic shift, paramagnetic broadening, and substrate effects for all 27 locations throughout the molecule. This figure clearly demonstrates that the lipid binding domain of D-LDH has a unique characteristic that is distinct from other membrane proteins of known structure. The lipid binding domain of D-LDH appears to be composed of small discontinuous regions of the protein, containing residues 228, 243, 280, 309, 361, and 369.[18] This region of the protein is likely to be the site which transfers reducing equivalents to the electron transport chain.

4 DYNAMICS OF Trp RESIDUES IN -LDH

The relaxation properties of the ^{19}F nuclear spin can provide important information on protein dynamics. Both the dipolar interaction with adjacent protons and the CSA contribute to the relaxation of the ^{19}F spin. The effect of dipolar coupling on the spin–lattice (T_1) and spin–spin (T_2) relaxation times have been derived by Solomon.[21] Abragam[22] gives the following expressions for relaxation due to the CSA:

$$\frac{1}{T_1} = \frac{6}{40}\omega_0^2(\sigma_{zz} - \sigma_{\text{iso}})^2\left[1 + \frac{\eta^2}{3}\right]J(\omega_0) \tag{1}$$

$$\frac{1}{T_2} = \frac{1}{40}\omega_0^2(\sigma_{zz} - \sigma_{\text{iso}})^2\left[1 + \frac{\eta^2}{3}\right][2J(\omega_0) + 4J(0)] \tag{2}$$

where ω_0 is the Larmor frequency of the fluorine nucleus, ($\sigma_{zz} - \sigma_{\text{iso}}$) is the z component of the traceless part of the chemical shift tensor, η is the asymmetry parameter, and $J(\omega)$ is the spectral density function that describes the frequency spectrum of the random molecular motion. Since the contribution of the chemical shift tensor to relaxation is dependent on the square of the field, measurements of relaxation times at different field strengths can be used to determine the contribution of CSA to relaxation of the nuclear spin.

The analytical form of the spectral density function that is used in these calculations is dependent on which model is used to describe the motion of the fluorinated aromatic side

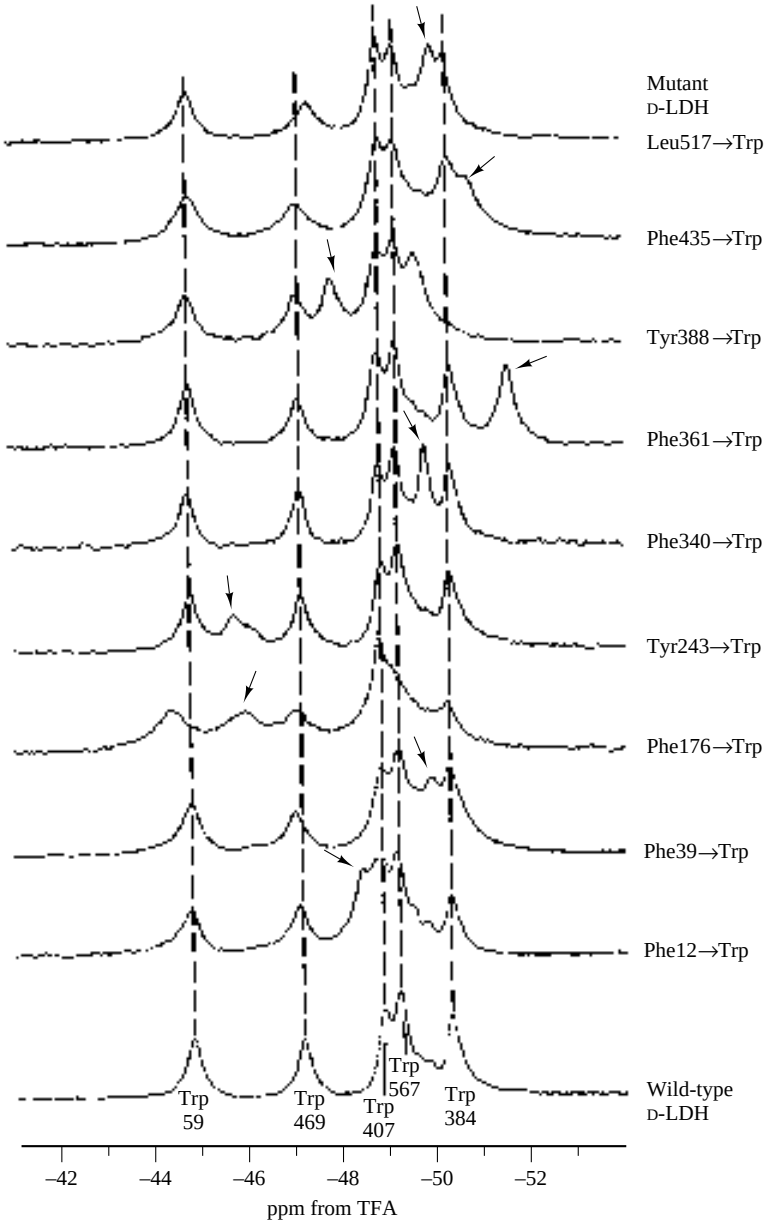

Figure 3 Fluorine-19 NMR spectra (282 MHz) of 5F-Trp labeled wild-type D-LDH and nine active Trp substitution mutants. The concentration of protein is approximately 1 mM in 100 mM lysolecithin, 10 mM phosphate, and 0.2 mM EDTA at pH 7.2 and 42 °C. The arrows indicate the additional resonance from the new Trp residue. (Reproduced by permission of Academic Press from Peersen et al.[16])

chain. Earlier work by Hull and Sykes[23] modeled the internal motion of the F-Tyr residues in alkaline phosphatase as axially symmetric diffusion about the $C_{\beta\gamma}$ bond. A similar approach was used by Dettman et al.[4] in the analysis of F-Phe and F-Tyr side-chain mobility in the M13 coat protein. In the case of D-LDH, the relaxation data were also interpreted within the context of specific molecular model of motion. This approach was taken because the relaxation properties of each positional isomer (i.e. 4F-Trp versus 5F-Trp) are uniquely sensitive to a particular type of motion.

We have considered two simple models of internal rotation: rotation about the $C_{\alpha\beta}$ bond and rotation about the $C_{\beta\gamma}$ bond. The spectral density functions for rotation about these bonds were obtained using the model dependent approach described by Wittebort and Szabo.[24] The effect of the rate of independent internal rotation about these two bonds on the T_1, T_2, and the heteronuclear (proton–fluorine) NOE is shown in Figure 6. These calculations assume isotropic rotation about the indicated bond; however, similar results are also obtained for large amplitude oscillations about the same axis. Although relaxation due to CSA and intraresidue heteronuclear dipolar coupling was considered in these calculations, it is not possible to calculate interresidue heteronuclear interactions; thus, these calculations should only be regarded as approximate. An important feature of the calculated relaxation parameters is that there are differences in the relaxation properties of 4F-Trp versus those observed with 5F-Trp. A comparison of the relaxation properties of each isomer provides a qualitative description of the type and rate of internal motion of Trp residues in D-LDH.

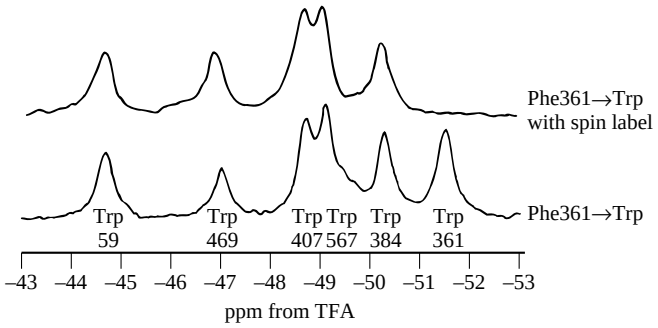

Figure 4 Fluorine-19 NMR spectra (282 MHz) of 5F-Trp labeled mutant D-LDH (Phe361 altered to Trp). Spectra were obtained in 100 mM lysolecithin, 10 mM phosphate, and 0.2 mM EDTA at pH 7.2 and 42 °C (bottom spectrum), or with the addition of 28 mM 8-doxylpalmitic acid (top spectrum). The arrow indicates the resonance that is severely broadened by the spin label. (Reproduced by permission of Academic Press from Peersen et al.[16])

Experimental data collected on 4F- and 5F-Trp D-LDH included the effect of magnetic field strength on T_1 and T_2, and the heteronuclear NOE. The heteronuclear NOE and contribution of the CSA to the linewidth are given in Table 1. All residues show heteronuclear NOE values which are greater than −1, suggesting internal motion of these Trp residues. Figure 6 shows that the rate of internal rotation ($\tau_{1,2}$) is not uniquely determined by measurement of the NOE. However, it has been shown[26] that the T_1 increases as the magnetic field strength is increased, suggesting that the rate of internal rotation of all of the Trp residues in D-LDH possesses relatively slow rates of internal rotation (i.e. $\tau_{1,2} < 10^{-9}$). The five Trp residues in D-LDH can be divided into three groups on the basis of a comparison of the measured NOE and linewidth due to the CSA. Trp residues at positions 59 and 469 show heteronuclear NOEs and CSA linewidths that are larger for 4F-Trp versus 5F-Trp. Calculated values of the NOE and linewidth [Figure 6(a)] suggest that these Trp residues are most

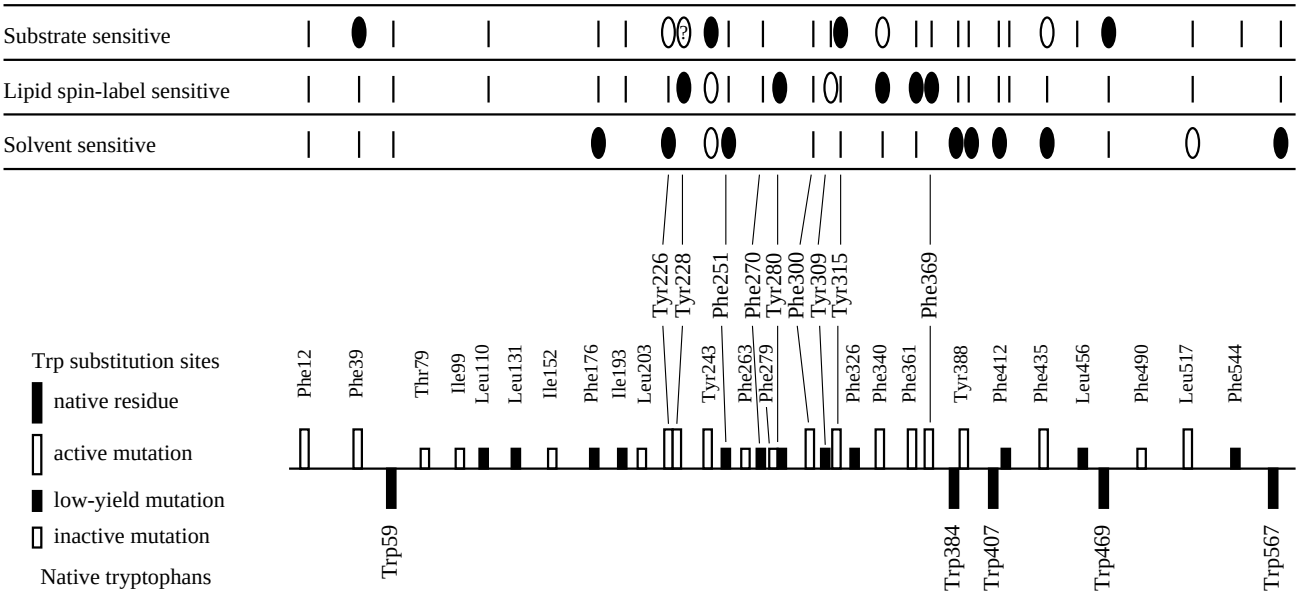

Figure 5 A summary of results from ^{19}F NMR observations of 5F-Trp labeled wild-type D-LDH and D-LDHs containing Trp substitution mutations. In general, open ovals indicate observed, but small, effects, and solid ovals indicate major effects. Substrate sensitivity: (○) 20–50% broadening, or <0.2 ppm shift; (●) >50% broadening, or >0.2 ppm shift. Sensitivity to spin labeled lysolecithin: (○) slight broadening; (●) loss of resonance from spectrum. Solvent exposure: (○) exposure index <0.25; (●) index >0.25 (index of 1.0 reflects shift of free 5F-Trp in solution). A vertical line indicates that no effect was seen. (Reproduced by permission of Cambridge University Press from Sun et al.[18])

Table 1 Relaxation Data for 4F- and 5F-Trp-labeled D-LDH

	Trp59	Trp384	Trp407	Trp469	Trp567
^{1}H–^{19}F NOE					
4F-Trp	−0.70	−0.90	−0.90	−0.70	−0.90
5F-Trp	−0.90	−0.80	−0.80	−1.00	−0.75
CSA linewidth[a]					
4F-Trp	105	100	155	100	170
5F-Trp	52	68	34	53	040

[a]Contribution of chemical shift anisotropy to the linewidth at 282 MHz.

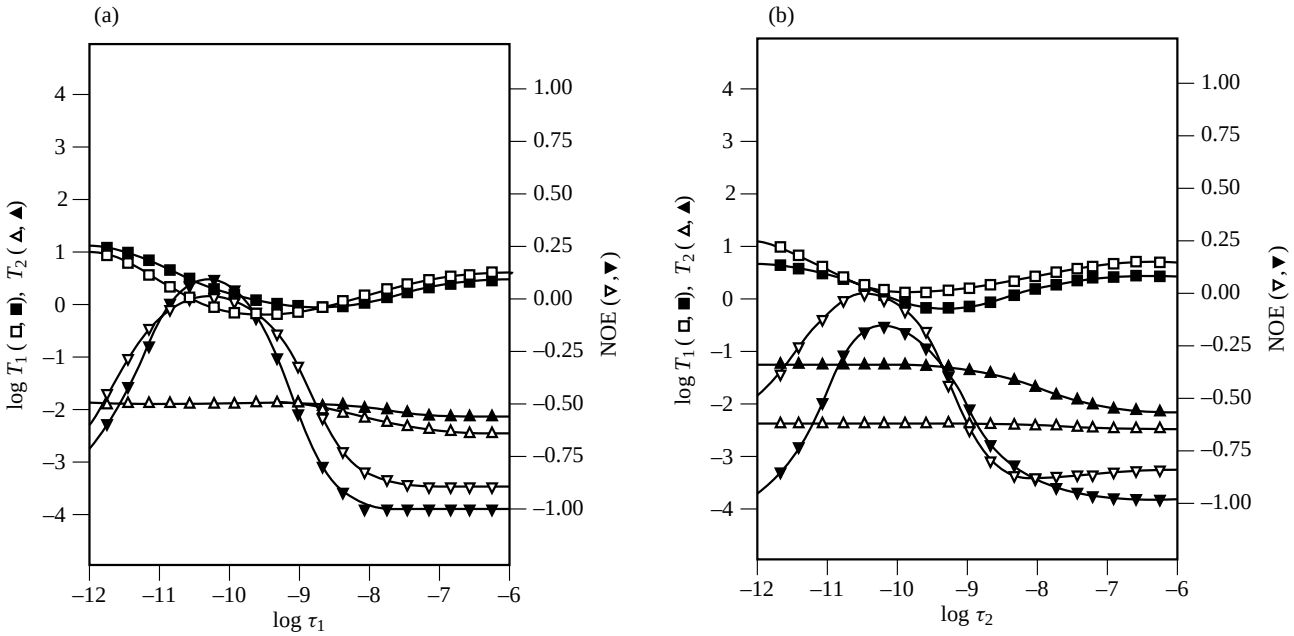

Figure 6 Effects of internal rotation on T_1, T_2, and heteronuclear NOE as a function of τ_1 and τ_2: (a) rotation about the $C_{\alpha\beta}$ bond with correlation time τ_1; (b) rotation about the $C_{\beta\gamma}$ bond with correlation time τ_2. The calculated T_1 (■, □), T_2 (▲, △), and the NOE (▼, ▽) are shown as functions of the correlation time for the internal rotation for 5F-Trp (solid symbols) and for 4F-Trp (open symbols). The correlation time for the overall rotation of the enzyme, τ, is 6×10^{-8} second and the ^{19}F frequency is 282.4 MHz. (Reproduced by permission of Elsevier Science Publishers from Ho et al.[25])

likely undergoing motion about the $C_{\alpha\beta}$ bond with a correlation time that is slower than 10^{-8} second. This finding supports the conjecture that these two residues are buried in the protein core (see Figure 5). Trp residues at positions 407 and 567 show the opposite effect; the measured values for 5F-Trp exceed those obtained for 4F-Trp. Figure 6(b) suggests that this second group of Trp residues is predominately undergoing rotation about the $C_{\beta\gamma}$ bond with a correlation time of 10^{-8}–10^{-9} second. Since these two residues are exposed to the solvent (see Figure 5), it is reasonable to expect a considerable amount of internal motion. In fact, the motion of Trp567 seems to be enhanced in the presence of DPPG since the resonance line from Trp567 is relatively sharp in the presence of DPPG (see Figure 1). Trp384 is a singular member of a class which shows a larger NOE for 4F-Trp but a narrower CSA linewidth for 5F-Trp. Clearly, the motion of Trp384 is not well described by the simple models of internal motions used here.

In summary we have demonstrated that ^{19}F NMR methods can provide considerable information from rather large membrane proteins in complex with detergent-like molecules. The utility of this method is greatly enhanced by the ability to use recombinant DNA methods to introduce additional NMR probes into the structure. These additional probes can be used to obtain information on the local environment and dynamics of the protein.

5 RELATED ARTICLES

Bacterial Chemotaxis Proteins: Fluorine-19 NMR; Bilayer Membranes: Proton and Fluorine-19 NMR; Fluorine-19 NMR; Protein Dynamics from NMR Relaxation; Protein Dynamics from Solid State NMR.

6 REFERENCES

1. W. Hu, K.-C. Lee, and T. A. Cross, *Biochemistry*, 1993, **32**, 7035.
2. K.-J. Shon, Y. Kim, L. A. Colnago, and S. J. Opella, *Science*, 1991, **252**, 1303.
3. J. C. Franklin, J. F. Ellena, S. Hayasinghe, L. P. Kelsh, and D. S. Cafiso, *Biochemistry*, 1994, **33**, 4036.
4. H. D. Dettman, J. H. Weiner, and B. D. Sykes, *Biochemistry*, 1984, **23**, 705.
5. G. S. Rule, E. A. Pratt, V. Simplaceanu, and C. Ho, *Biochemistry*, 1987, **26**, 549.
6. L. A. Luck and J. J. Falke, *Biochemistry*, 1991, **30**, 4248.
7. W. E. Hull and B. D. Sykes, *Biochemistry*, 1974, **3**, 3431.
8. M. A. C. Jarema, P. Lu, and J. H. Miller, *Proc. Natl. Acad. Sci. USA*, 1981, **78**, 2707.
9. K. T. Arndt, F. Boschelli, J. Cook, Y. Takeda, E. Tecza, and P. Lu, *J. Biol. Chem.*, 1983, **258**, 4177.
10. E. Li, S.-J. Qian, N. S. Winter, A. d'Avignon, M. S. Levin, and J. I. Gordon, *J. Biol. Chem.*, 1991, **266**, 3622.
11. E. M. Barnes, Jr. and H. R. Kaback, *J. Biol. Chem.*, 1971, **246**, 5518.
12. Y. Tanaka, Y. Anraku, and M. Futai, *J. Biochem.*, 1976, **80**, 821.
13. S. A. Short, H. R. Kaback, and L. D. Kohn, *J. Biol. Chem.*, 1975, **250**, 4291.
14. S. Korvatchev, W. L. C. Vaz, and H. Eibl, *J. Biol. Chem.*, 1981, **256**, 10369.
15. G. S. Rule, E. A. Pratt, C. C. Q. Chin, F. Wold, and C. Ho, *J. Bacteriol*, 1985, **161**, 1059.
16. O. B. Peersen, E. A. Pratt, H.-T. N. Truong, C. Ho, and G. S. Rule, *Biochemistry*, 1990, **29**, 3256.
17. H.-T. N. Truong, E. A. Pratt, G. S. Rule, P. Y. Hsue, and C. Ho, *Biochemistry*, 1991, **30**, 10722.

18. Z.-Y. Sun, H.-T. N. Truong, E. A. Pratt, D. C. Sutherland, C. E. Kulig, R. J. Homer, S. M. Groetsch, P. Y. Hsue, and C. Ho, *Protein Sci.*, 1993, **2**, 1938.
19. W. A. Lim and R. T. Sauer, *Nature*, 1989, **339**, 31.
20. D. S. Hagen, J. H. Weiner, and B. D. Sykes, *Biochemistry*, 1979, **18**, 2007.
21. I. Solomon, *Phys. Rev.*, 1955, **99**, 559.
22. A. A. Abragam, *Principles of Nuclear Magnetism*, Oxford University Press, Oxford, 1961.
23. W. E. Hull and B. D. Sykes, *J. Mol. Biol.*, 1975, **98**, 121.
24. R. J. Wittebort and A. Szabo, *J. Chem. Phys.*, 1978, **69**, 1722.
25. C. Ho, E. A. Pratt, and G. S. Rule, *Biochim. Biophys. Acta*, 1989, **988**, 173.
26. G. S. Rule, Ph.D. Thesis, Carnegie Mellon University, Pittsburgh, 1986.

Acknowledgments

Our work on D-lactate dehydrogenase has been supported by a research grant from the National Institutes of Health awarded to C. Ho (GM-26874).

Biographical Sketches

Gordon S. Rule. *b* 1956. B.S., 1979, Waterloo. M.S., 1981, Pennsylvania State University. Ph.D., 1986, Carnegie Mellon. Introduced to NMR by C. Ho. Postdoctoral work at Stanford with H. M. McConnell. Faculty in Biochemistry University of Virginia School of Medicine, 1988–present. Approx 30 publications. Research area: application of molecular biology and NMR to the study of protein structure and dynamics.

Chien Ho. *b* 1934. B.A., 1957, Williams. Ph.D., 1961, Yale University. Faculty in Biological Sciences, Carnegie Mellon University, 1981–present. Approx. 180 publications. Research interests include structure–function relationships in proteins and cell membranes, and applications of MRI and MRS to the investigation of organ functions of live animals and to tracking cell movements in live animals.

Enzymatic Transformations: Isotope Probes

A. Ian Scott

Texas A&M University, College Station, USA

1	Studying Enzyme Mechanism by ^{13}C NMR	1
2	The Quest for True Intermediate Structure: Cryoenzymology	2
3	Solid State NMR as a Probe for Enzyme–Substrate Structure	3
4	Cofactor Enrichment	5
5	Related Articles	7
6	References	7

1 STUDYING ENZYME MECHANISM BY ^{13}C NMR

Almost all enzymatic processes utilize multistep reactions during catalysis, and the characterization of each of these stages is essential if one is to understand enzyme mechanism at the molecular level. Earlier investigators used spectrophotometric methods for characterizing enzyme-catalyzed reactions, whereas inhibitors that form stable 'transition state analogs' were examined using other techniques that require long periods of data accumulation, for example, X-ray analysis. However, the use of NMR in enzymology is beginning to provide a novel and penetrating probe for elucidating enzyme mechanism by directly characterizing intermediates formed in catalysis. The studies of transition state analogs allow access to the unique properties of enzymes that enable them to stabilize labile intermediates and therefore achieve their remarkable catalytic efficiency. We discuss first the structure of an enzyme-inhibitor adduct of the serine protease trypsin and compare the results of direct observation by ^{13}C NMR with the structural information inferred by more classical techniques. We then review the powerful combination of NMR and cryoenzymology. The marriage of the two techniques whereby enzyme-catalyzed reactions are studied at subzero temperatures in aqueous organic solvents (cryosolvents), allows such reactions to be slowed down and can prolong the lifetime of enzyme–substrate intermediates.[1] Finally we discuss the use of ^{13}C-enriched cofactors to study molecular events at the active site.

Figure 1 shows the generally accepted mechanism for the hydrolysis of an amide function by a serine protease. To confirm this mechanistic pathway, the visualization and rigorous characterization of productive tetrahedral intermediates and acyl enzymes by ^{13}C NMR is the ultimate goal, and we now discuss the progress made so far, particularly with regard to the serine and thiol proteases.

In the domain of synthetic inhibitors, chloromethyl ketone derivatives of specific substrates are potent irreversible covalent inhibitors of the serine proteases, alkylating the active-center histidine at N-2. X-ray crystallographic studies led to the suggestion that, in addition to the above alkylation, there was

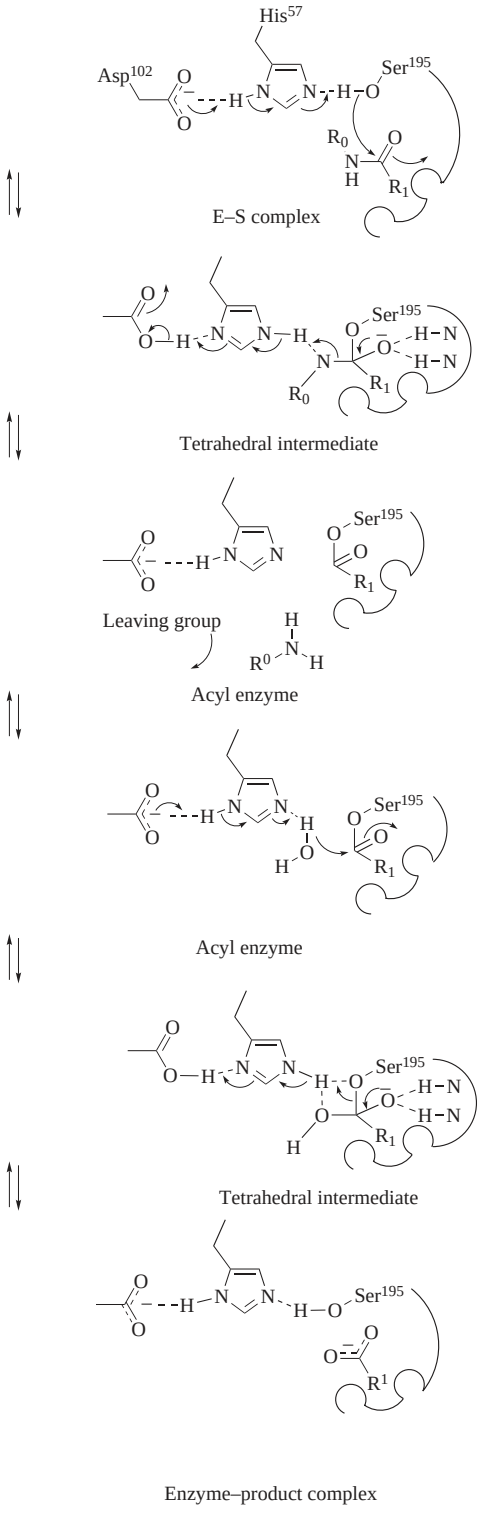

Figure 1 Serine protease mechanism

also nucleophilic attack by the active-center serine hydroxyl to form a hemiketal, which is stereochemically analogous to the tetrahedral intermediate purported to occur during catalysis.[2]

To test this suggestion, trypsin was inhibited with the highly specific reagent *N*-α-benzyloxycarbonyllysyl chloromethyl ketone ($RCOCH_2Cl$), labeled in the ketone carbon with 90% ^{13}C, for it was predicted that a tetrahedral adduct, if formed,

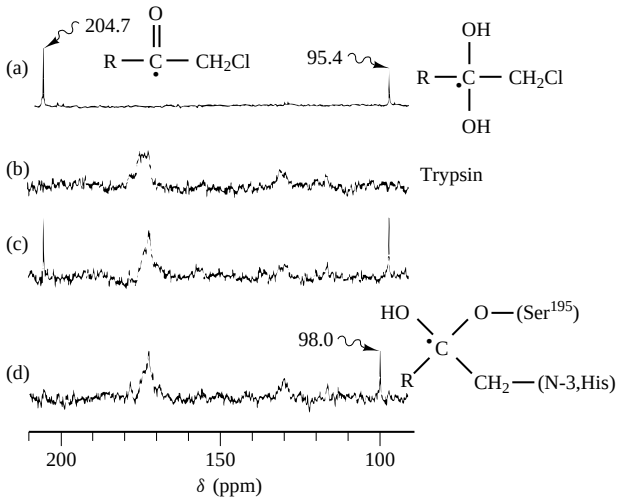

Figure 2 Formation of tetrahedral complex of trypsin with (*Z*)-Lys chloromethyl ketone (CMK)

would be directly observable by this technique. In aqueous solution (Figure 2) $RCOCH_2Cl$ exists as a mixture of the ketone (δ = 204.7 ppm) and its hydrate (δ = 95.4 ppm). At pH 3.2 no alkylation or inhibition of the enzyme is observed and the spectrum of [$^{13}C{=}O$] $RCOCH_2Cl$ is unperturbed [Figure 2(b) and 2(c)], showing that at low pH there is no detectable binding or tetrahedral adduct formation prior to alkylation. At pH 6.9 there is rapid, irreversible inhibition, and resonances due to both [$^{13}C{=}O$] $RCOCH_2Cl$ and its hydrate are replaced by a single resonance at 98.0 ppm [Figure 2(d)], an indication that the ^{13}C enriched carbonyl of the inhibitor is tetrahedrally coordinated in the inhibitor–enzyme adduct. Denaturation of the trypsin led to reappearance of a carbonyl resonance (205.5 ppm) and a decrease in the intensity of the resonance at 98.0 ppm. This demonstrates that the tetrahedral adduct formed by the attack of the serine hydroxyl on the inhibitor carbonyl and characterized by the resonance at 90.0 ppm requires an intact trypsin structure.[3]

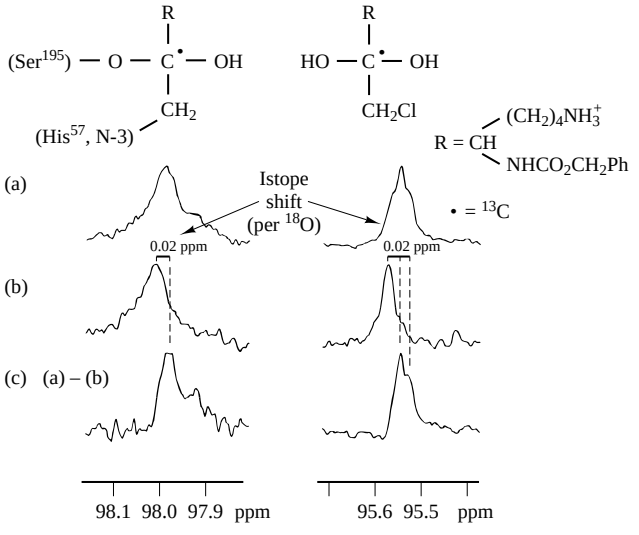

Figure 3 ^{18}O shifted ^{13}C NMR spectra of (*Z*)-Lys CMK complex with trypsin

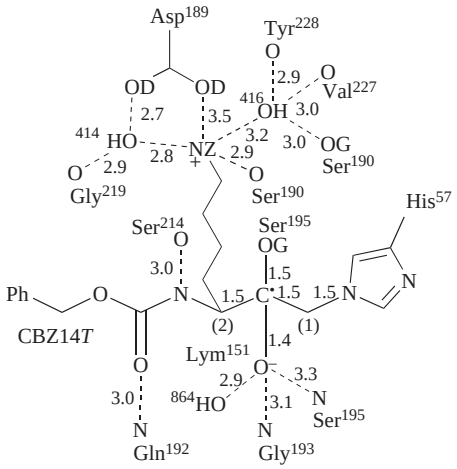

Figure 4 Bond distances in (*Z*)-Lys CMK with trypsin from X-ray data at 0.2 nm resolution

In the above experiments with [$^{13}C{=}O$] $RCOCH_2Cl$ and trypsin it is difficult to discount the possibility that the resonance at 98.0 ppm could result from hydration of the carbonyl of the covalently bound inhibitor. However, the use of ^{18}O isotopic shifts on the ^{13}C spectrum of the tetrahedral adduct shows that the adduct is indeed formed by nucleophilic attack of the Ser^{195} hydroxyl group (Figure 3), a result completely confirmed by X-ray diffraction studies as portrayed in Figure 4.[4]

2 THE QUEST FOR TRUE INTERMEDIATE STRUCTURE: CRYOENZYMOLOGY

The detection and characterization of a productive, short-lived acyl intermediate by ^{13}C NMR during catalysis with natural substrates at ambient temperature is not possible at present, because there is an inherent lack of sensitivity in ^{13}C NMR spectroscopy. Therefore, the lifetimes of these intermediates must be extended into the domain of the NMR experiment. One approach is to utilize cryoenzymological techniques to extend the lifetimes of such intermediates.

Since the ^{13}C NMR resonance of the carbonyl of a thioester is shifted 20–30 ppm from that of the oxygen analog, ^{13}C NMR spectroscopy should allow the direct monitoring of the formation and decay of a thioacyl intermediate during thiol protease catalysis. Using [$^{13}C{=}O$] *N*-benzoylimidazole (δ = 168.7 ppm) as substrate, it is possible to observe directly a thioacyl intermediate at δ = 195.9 ppm in the presence of the thiol protease, papain, under the cryoenzymological conditions of −20 °C in 25% aqueous dimethyl sulfoxide.[5] Moreover, the thioacyl species is clearly a productive intermediate since the decrease in its signal intensity is accompanied by an increase in the product resonances and by release of free enzyme determined by titration of its thiol group. The linewidth of the resonance at 195.9 ppm was 25 ± 2 Hz[5,6]. Similarly, the trypsin catalyzed hydrolysis (Figure 5) of the highly specific substrate *N*-α-benzyloxycarbonyl-L-lysine *p*-nitrophenyl ester [(*Z*)-Lys-*p*-NP] has been studied in detail under cryoenzymological conditions by both spectrophotometry and ^{13}C NMR spectroscopy.[6] The kinetic data from both techniques confirm

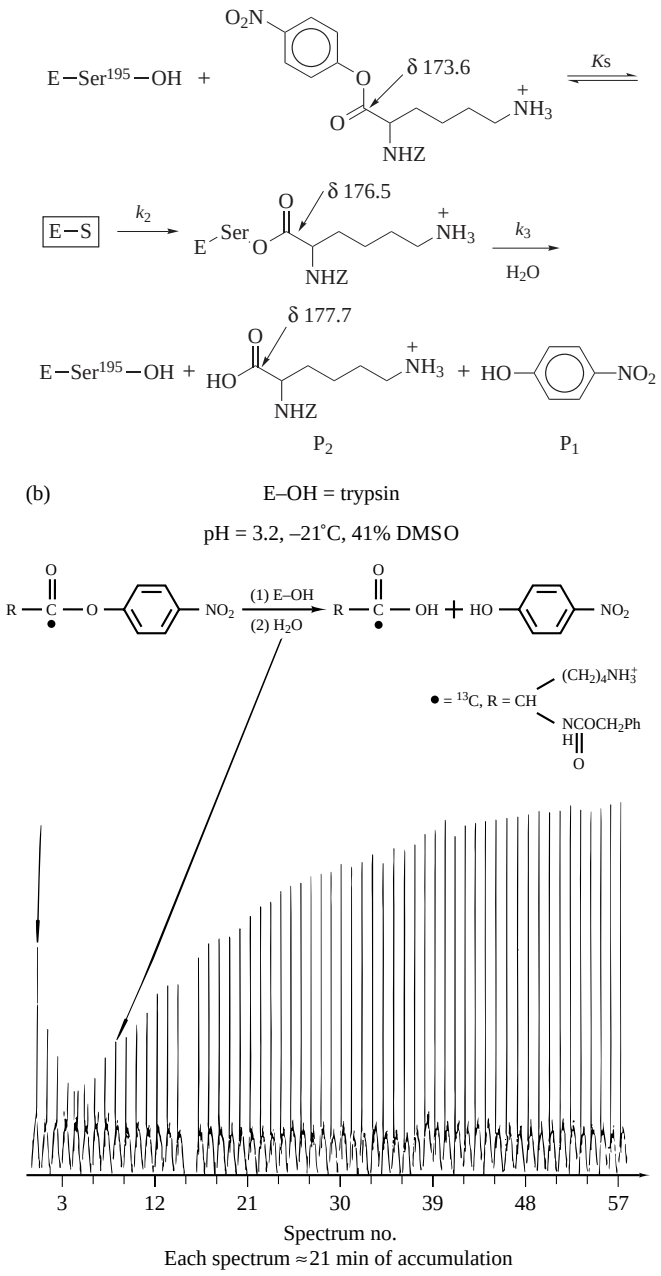

Figure 5 (a) Trypsin-catalyzed hydrolysis of (*Z*)-Lys-*p*-NP. (b) Time course of hydrolysis of (*Z*)-Lys-*p*-NP (^{13}C=O) by trypsin

that the kinetics and mechanism under cryoenzymological conditions are essentially the same as those determined at ambient temperatures by rapid reaction techniques. The hydrolysis of [^{13}C](*Z*)-Lys-*p*-NP [(S) in Figure 5, δ = 173.6 ppm] by trypsin was monitored by the decrease in intensity of this signal and the increase in the signal arising from the product (P_2 in Figure 5, δ = 177.7 ppm) at $-21\,^{\circ}$C in 41% aqueous dimethyl sulfoxide. The continued formation of product (P_2) after all the substrate has been consumed [Figure 5(b)] provides indirect evidence for an enzyme-bound intermediate whose linewidth is much greater than that of the free substrate or product and is therefore not directly observable in the individual ^{13}C NMR spectra shown in Figure 5. Improvement of the signal-to-noise ratio by summation of sets of the individual spectra in

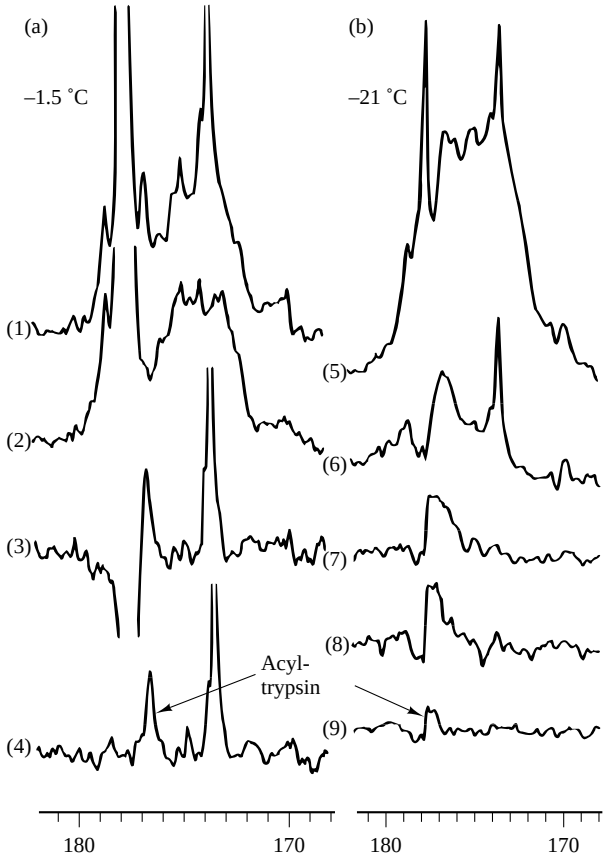

Figure 6 Difference NMR spectra at (a) $-1.5\,^{\circ}$C and (b) $-21\,^{\circ}$C, showing signals for acyltrypsin

Figure 5 made it possible to use difference techniques and allowed direct observation at $-21\,^{\circ}$C of a resonance (δ = 176.5 ppm) that was assignable to the acyl enzyme on the basis of its chemical shift and the kinetics of its breakdown–formation.

Experiments at $-1.5\,^{\circ}$C [Figure 6(a)] showed that the acyl intermediate was much more readily detected at this higher temperature, the resonance being clearly resolved in the individual spectra as a result of the smaller linewidth of the resonance at $-1.5\,^{\circ}$C compared with that at $-21\,^{\circ}$C, 22 ± 3 Hz and 100 ± 10 Hz respectively. This illustrates one of the main difficulties of a combined NMR–cryoenzymological approach in which the linewidth of enzyme-bound species increases dramatically as the cryosolvent viscosity increases on lowering the temperature. In recent studies with chymotrypsin modified by replacement of His-57 by *N*-methyl-His-57, stabilization of the acyl intermediate was achieved[7] at room temperature (Figure 7).

3 SOLID STATE NMR AS A PROBE FOR ENZYME–SUBSTRATE STRUCTURE

The basis for the NMR studies with proteases has relied heavily on the crystal structure determination of the enzyme and/or enzyme complex at the active site. Since the phase change from solid to solution may well involve considerable conformational alteration, the correlation of the two physical

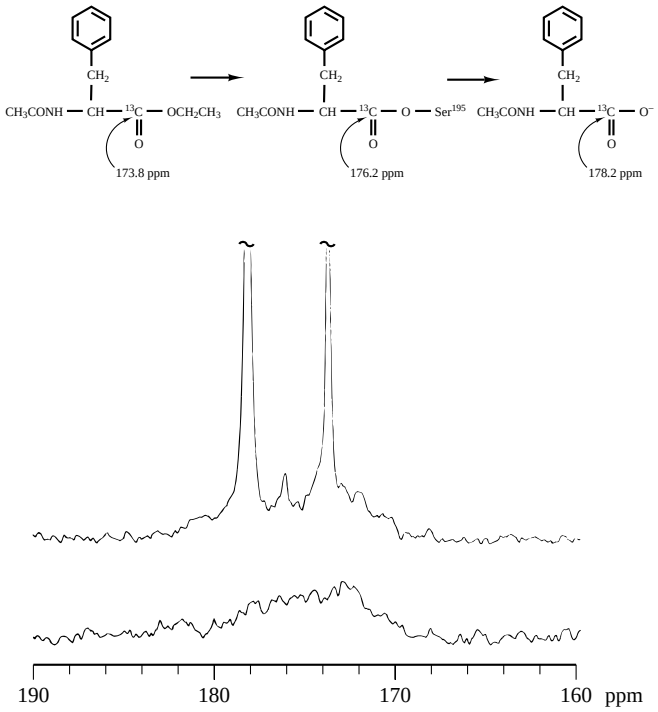

Figure 7 Hydrolysis of *N*-acetyl-L-Phe-OEt by *N*-3-methylhistidinyl-α-chymotrypsin at ambient temperature

methods (X-ray, NMR) in the same phase would be a desirable objective in furthering our understanding of enzyme mechanism. Our next theme concerns the application of solid state cross polarized magic angle spinning (CP MAS) NMR spectroscopy to the direct observation of the hydrolysis of a slow (pseudo) substrate catalyzed by an enzyme. MAS NMR has already been shown to be a powerful technique for the study of solids generally[8] and has been used extensively in inorganic systems.[9]

The crystal structures of several complexes of the metallo enzyme, carboxypeptidase A$^{\alpha}$ (CPA) (EC 3.4.17.1), have been examined in considerable detail.[10] The structure of the complex with glycyltyrosine (Gly-Tyr) has been refined to 0.2 nm resolution and reveals, inter alia, interactions between the amide carbonyl oxygen and the catalytically essential zinc, and between the amide nitrogen and the hydroxyl of Tyr-248 (Figure 8). The proposed mechanisms for hydrolysis of peptide and ester bonds by CPA have relied heavily on these crystal structures, but a clear distinction between the possible roles of glutamate-270 (Glu-270) in nucleophilic attack either by general base catalysis [Figure 8(a)] or by covalent anhydride formation [Figure 8(b)] remains a major unresolved problem. Indeed, it is not yet certain whether esters and amides are hydrolyzed by CPA via identical mechanisms.

Gly-Tyr was synthesized as both the [^{13}C]amido (90 atom % enrichment) and amido[^{13}C,^{15}N] (90 % atom enrichment, respectively) isotopomers by known methods. CPA soaked with Gly-Tyr crystals was examined using solid state NMR. The ^{13}C CP MAS NMR spectrum of the ^{13}C-enriched Gly-Tyr substrate [Figure 9(a)] displays residual ^{14}N,^{13}C quadrupolar coupling (δ = 176 ppm). However, the ^{13}C CP MAS difference spectrum of CPA and the CPA/Gly-Tyr complex [Figure 9(b)] displays a single resonance (δ = 178 ppm, linewidth at halfheight 60 Hz), revealing that, under the experimental

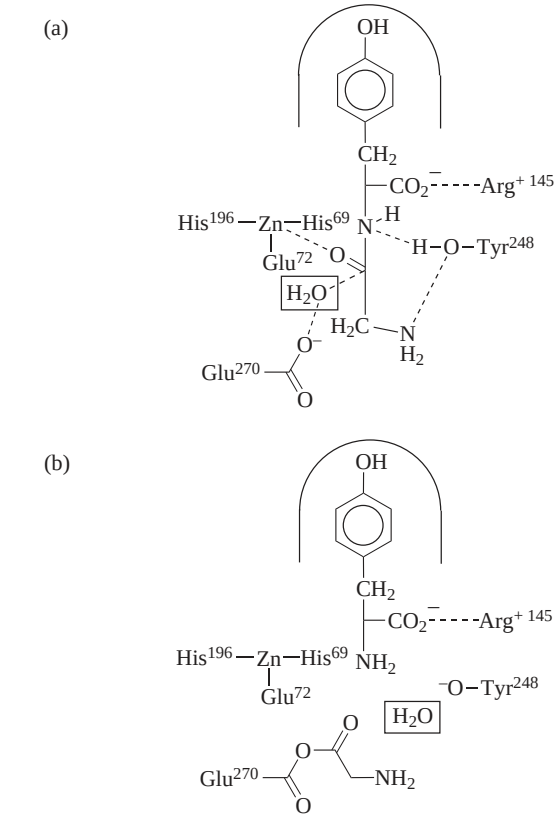

Figure 8 Two possible mechanisms for the hydrolysis of Gly-Tyr by CPAse

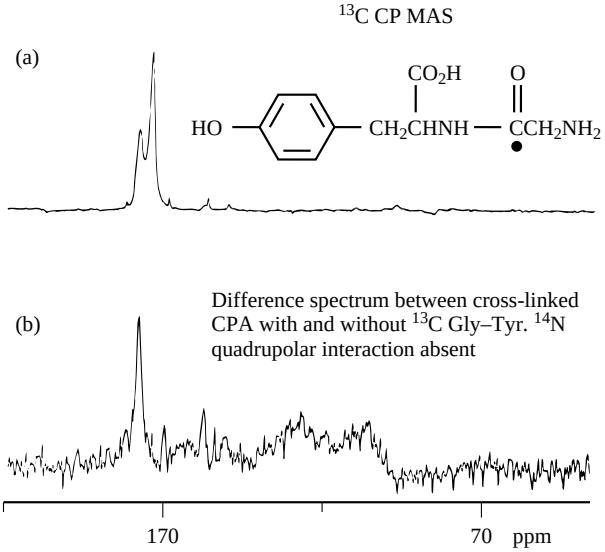

Figure 9 ^{13}C CP MAS spectrum of Gly-Tyr, showing the disappearance of quadrupolar coupling (^{14}N,^{13}C) after reaction with CPAse

conditions, the peptide bond of this slow reacting substrate has been cleaved to the extent of >90%. In order to confirm this result, doubly labeled amido [^{13}C,^{15}N]Gly-Tyr (not shown) was bound to CPA under identical conditions and the complex examined by ^{15}N NMR. The resonance of the substrate (δ = 120 ppm) is sufficiently broad (linewidth at halfheight 325 Hz) to conceal the ^{15}N,^{13}C one-bond scalar coupling

(J = 16 Hz). In the enzyme complex (not shown), the observed ^{15}N resonances correspond to the amide region of CPA (δ = 122 ppm, linewidth at halfheight = 400 Hz) and an amine (δ = 42 ppm, linewidth at halfheight = 250 Hz), respectively.

We infer from these experiments that we are observing either the first stable intermediate of the catalytic pathway, i.e. the anhydride of the cleaved glycine residue bound covalently to Glu-270 (Figure 8), or the bound glycine accompanied in either case by the second product, tyrosine (Figure 8) also bound to CPA, since in a separate experiment it could be shown that no unbound tyrosine or glycine was present in the complex. A distinction between the two glycine species (anhydride or acid) cannot be made at this stage since the ^{13}C chemical shifts of the carbonyl(s) in both the anhydride and the acid are within the observed chemical shift range. However, these preliminary experiments[11] clearly indicate the feasibility of simultaneous X-ray and CP MAS NMR studies, especially with slow substrates. In summary, a method of some generality for reaching the long-sought correlation between X-ray diffraction data, the resultant geometry of a substrate undergoing slow catalysis, and the corresponding NMR chemical shifts for selected atoms in the enriched substrate, obtained under identical conditions, is now available through the use of the CP MAS technique.

Recently, the application by Evans[12] of solid state NMR to freeze-quenched systems has revealed by ^{13}C enrichment of the substrate, the time course of the reaction catalyzed by 5-enolpyruvylshikimate synthase. This elegant study[12] paves the way for further correlation of structure between NMR and time resolved Laue X-ray diffraction.

From the discussion presented above, it is clear that the stage is now set for intensive research into the mechanism of enzyme action with cryoenzymology. Although most of the enzymes discussed above lie in the molecular weight range of 20–35 kDa, an upper figure of 100 kDa probably represents the maximum convenient size for ^{13}C NMR studies on currently available superconducting instruments with substrates and inhibitors. However, even with high molecular weight enzymes, labeling the coenzyme or a cofactor can give excellent results, as discussed in the two final examples.

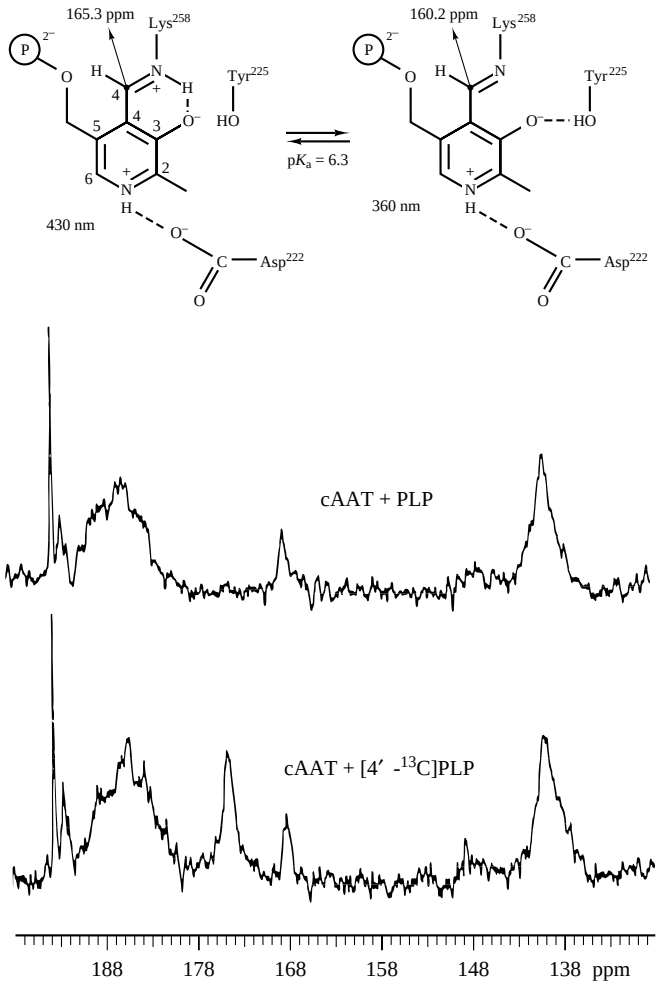

Figure 10 ^{13}C NMR spectrum of cytosolic AAT (cAAT) with (top) PLP (bottom) [4′-^{13}C]PLP, showing the bound cofactor signal at δ = 165.3 ppm

4 COFACTOR ENRICHMENT

1. The use of ^{13}C-labeled coenzyme pyridoxal phosphate (^{13}CHO-PLP) in the reactions catalyzed by cytosolic aspartate amino transferase (EC 2.6.1.1) (cAAT), a dimeric protein (M_r = 90 kDa), allows clear observation of both internal and external aldimine forms with inhibitors such as methyl aspartate, as shown in Figure 10.[13]
2. Tetrapyrrole biosynthesis, which is responsible for heme, chlorophyll and vitamin B_{12} formation, begins with the self-condensation of aminolevulinic acid (ALA) to porphobilinogen (PBG). Next PBG deaminase, encoded by *hemC*, catalyzes the tetramerization of PBG (**1**) to preuro'gen (hydroxymethylbilane, HMB; (**2**) which is cyclized with rearrangement to the unsymmetrical macrocycle uro'gen III (**3**) by uro'gen III synthase (Figure 11 and 12). In the absence of the latter enzyme, HMB (**2**) dehydrates spontaneously to uro'gen I (**4**), which, although strictly not a natural product, turns out to be a substrate for some of the methyltransferases of the vitamin B_{12} pathway.

Deaminase is an unusually helpful enzyme since a covalent bond is formed between each incoming substrate molecule and enzyme, thus allowing isolation of covalent complexes containing up to 3 PBG units (ES_1–ES_3). With cloned deaminase in hand it was found by ^{13}C NMR that a novel cofactor is covalently attached to one of the four cysteine residues of the enzyme (Cys-242) in the form of a substrate-derived dipyrromethane whose free α position becomes the site of attachment of the succeeding four moles of substrate during the catalytic cycle[14] (Figure 11 and 12).

Thus a mutant strain of *Escherichia coli* (*hemA*$^-$ requiring ALA for growth) in the presence of [5-^{13}C]Ala afforded highly enriched enzyme for NMR studies. At pH 8, the enriched carbon atoms of the dipyrromethane cofactor (py–CH_2–py) were clearly recognized at 24.0 ppm (py–CH_2–py), 26.7 ppm (py–CH_2–X), 118.3 ppm (α-free pyrrole) and 129.7 ppm (α-substituted pyrrole) [Figure 11(a)]. The signals are sharpened at pH 12 [Figure 11(b)] and the CH_2–X resonance is shifted to δ = 29.7 ppm in the unfolded enzyme. Comparison with synthetic models reveals that a shift of 26.7 ppm is in the range expected for an α-thiomethylpyrrole

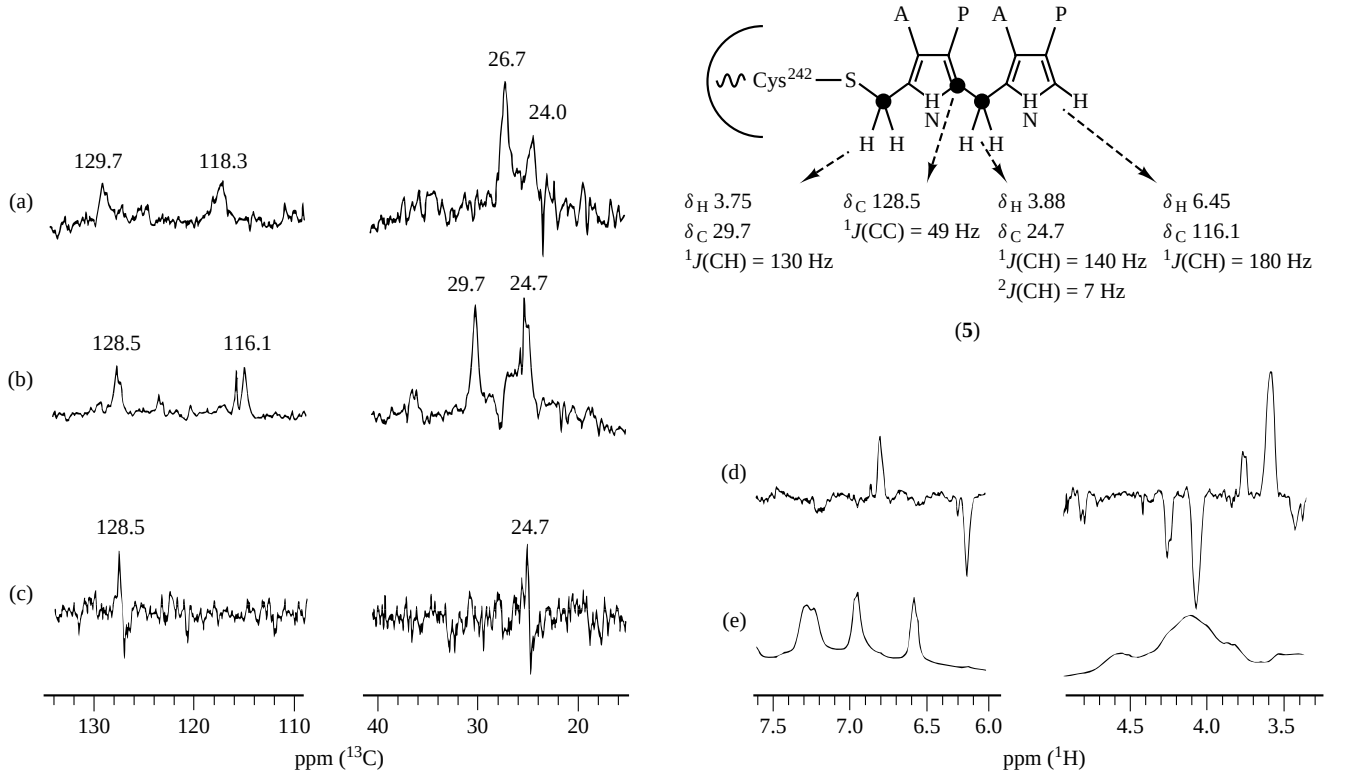

Figure 11 High field NMR spectra of *E. coli* PBG deaminase (~1 mM) specifically ^{13}C-enriched in the dipyrromethane cofactor via [5-^{13}C]Ala. (a) 125 MHz ^{13}C NMR difference spectrum between separate deaminase samples (pH 8) grown in the presence or absence of [5-^{13}C]Ala demonstrating the four Ala-derived ^{13}C-enriched carbon atoms. (b) Difference spectrum of samples as in (a), recorded at pH 12. Upon alkaline denaturation, the resonance assigned to thiomethyl carbon has been deshielded to δ = 29.7 ppm, which is in closer agreement to a model cysteine thiomethylpyrrole conjugate. (c) ^{13}C INADEQUATE spectrum (pH 12) of [5-^{13}C]Ala-derived deaminase demonstrating the coupling of adjacent carbon atoms, confirming the head-to-tail dipyrromethane structure. (d) Isotope-edited 300 MHz ^{1}H NMR spectrum (pH 12) of biosynthetically enriched deaminase (2 mM) showing the three pairs of signals originating from only those protons directly bound to the ^{13}C atoms derived from [5-^{13}C]Ala. The observed antiphase splittings are due to the one bond ^{13}C,^{1}H coupling. (e) Normal proton spectrum of same sample illustrating the degree of selection afforded by the pulse sequence for spectrum (d). Insert: structure of the dipyrromethane cofactor (**5**) and summary of ^{1}H and ^{13}C chemical shifts and coupling constants obtained at pH 12

(py−CH_2−SR). Confirmation of the dipyrromethane (rather than oligo pyrromethane) came from the ^{13}C INADEQUATE spectrum taken at pH 12 which reveals the expected coupling only between py−CH_2−py (δ = 24.7 ppm) and the adjacent substituted pyrrole carbon (δ = 128.5 ppm) [Figure 11(c)]. When the enriched deaminase was studied by ^{1}H detected heteronuclear filtered spectroscopy [Figure 11(d)], only five protons (in a total of nearly 2000) attached to ^{13}C-enriched nuclei were observed in accord with structure (**5**) (Figure 12). A specimen of deaminase was then covalently inhibited with the suicide inhibitor [2,11-$^{13}C_2$]-2-bromo-PBG (**8**) (Figure 12) to give a spectrum consistent only with structure (**9**). The site of covalent attachment of substrate (and inhibitor) is therefore the free α-pyrrole carbon of the dipyrromethane cofactor in the native enzyme, leading to the structural and mechanistic proposal for deaminase portrayed in Figure 12.[14]

Independent, complementary work in 1987−88 from two other laboratories[15,16] reached identical conclusions regarding the catalytic site. The ^{13}C-labeling defines the number of PBG units (two) attached in a head-to-tail motif to the native enzyme at pH 8 and reveals the identity of the nucleophilic group (Cys−SH) which anchors the dipyrromethane (and hence the growing oligopyrrolic chain) to the enzyme. Site specific mutagenesis and chemical cleavage were employed to determine that Cys-242 is the point of attachment of the cofactor.

The use of the α-carbon atom of a dipyrromethane as the nucleophilic group responsible for oligomerization of 4 mol of PBG (with loss of NH_3 at each successive encounter with an α-free pyrrole) is not only remarkable for the exquisite specificity and control involved, but is, as far as we know, a process unique in the annals of enzymology in that the substrate is actually used not only once, but twice, in the genesis of the active site cofactor! Even more remarkable is the fact that the apoenzyme is automatically transformed to the active holoenzyme by addition of two PBG units without the intervention of another enzyme. All of these events were 'viewed' by ^{13}C NMR spectroscopy.

This brief account has exemplified the application of the stable isotopes ^{13}C, ^{15}N and ^{18}O in probing enzymatic transformations in vitro. Many examples which are outside the scope of this article are concerned with the isotopic analysis of the products of biochemical conversions. These include applications of ^{2}H NMR,[17] ^{3}H NMR,[17−19] ^{31}P NMR,[20,21] and ^{1}H{^{13}C} heteronuclear filtered spectroscopy.[17,22]

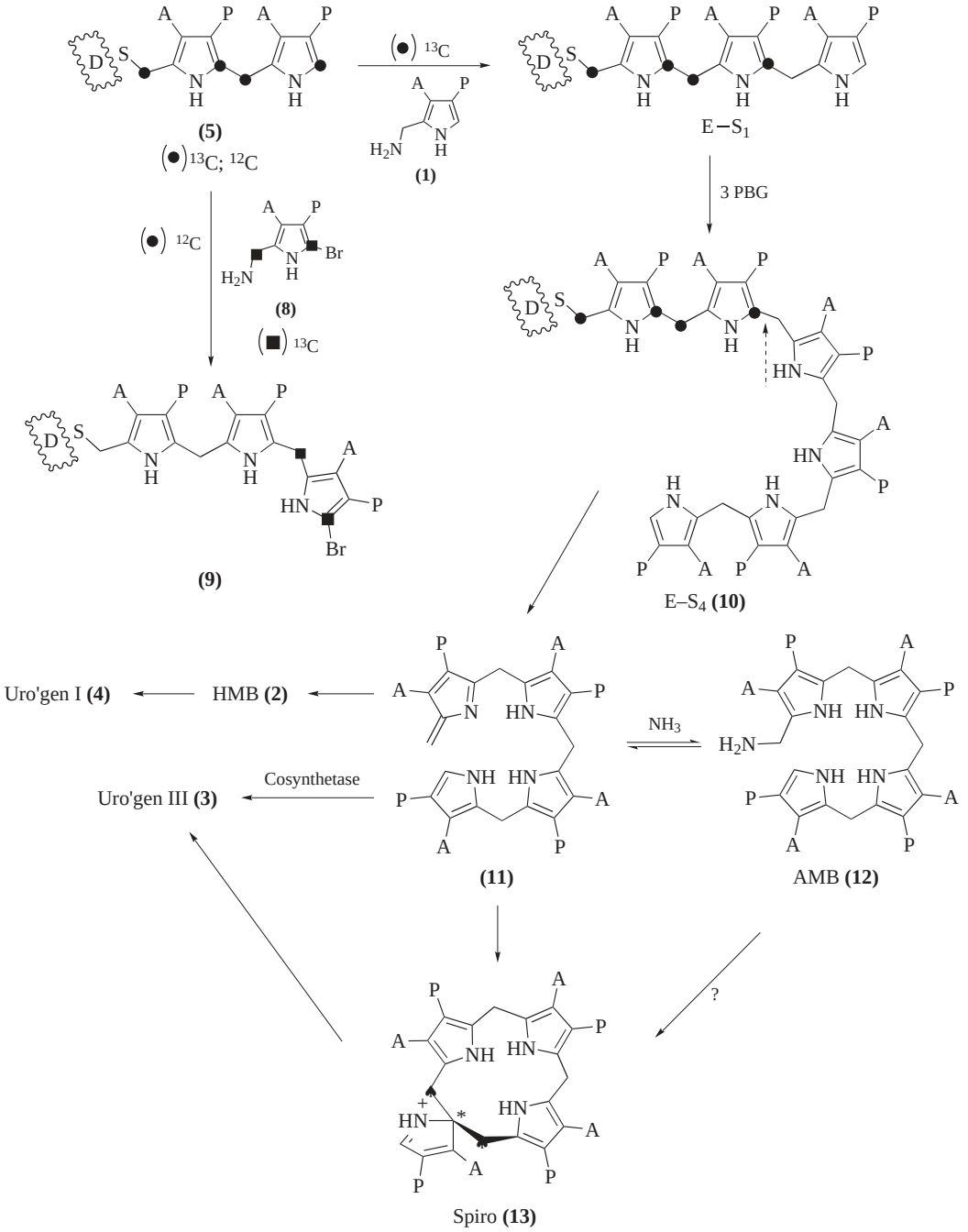

Figure 12 The remarkable dipyrromethane cofactor of PBG deaminase, covalently attached to Cys-242 of the enzyme and its role in tetrapyrrole assembly, showing the 'spiro' mechanism (**13**) for the action of uro'gen III synthase (cosynthetase)

5 RELATED ARTICLES

Biosynthesis and Metabolic Pathways: Carbon-13 and Nitrogen-15 NMR; Biosynthesis and Metabolic Pathways: Deuterium NMR; Vitamin B12.

6 REFERENCES

1. P. Douzou, *Cryobiochemistry*, Academic, New York, 1977.
2. T. L. Poulos, R. A. Alden, S. T. Frier, J. J. Birktoft, and J. Kraut, *J. Biol. Chem.*, 1976, **251**, 1097.
3. J. P. G. Malthouse, N. E. Mackenzie, A. S. F. Boyd, and A. I. Scott, *J. Am. Chem. Soc.*, 1983, **105**, 1685.
4. A. I. Scott, N. E. Mackenzie, J. P. G. Malthouse, W. U. Primrose, P. E. Fagerness, A. Brisson, L. Z. Qi, W. Bode, C. M. Carter, and Y. J. Jang, *Tetrahedron*, 1986, **42**, 3269.
5. J. P. G. Malthouse, M. P. Gamcsik, A. S. F. Boyd, N. E. Mackenzie, and A. I. Scott, *J. Am. Chem. Soc.*, 1982, **104**, 6811.
6. N. E. Mackenzie, J. P. G. Malthouse, and A. I. Scott, *Biochem. J.*, 1984, **219**, 437.
7. J. B. West, J. Scholten, N. J. Stolowich, J. C. Hogg, A. I. Scott, and C.-H. Wong, *J. Am. Chem. Soc.*, 1988, **110**, 3709.
8. E. R. Andrew, *Int. Rev. Phys. Chem.*, 1981, **1**, 195.

9. C. A. Fyfe, J. M. Thomas, J. Klinowski, and G. C. Gobbi, *Angew. Chem., Int. Ed. Engl.*, 1983, **22**, 259.
10. W. N. Lipscomb, *Acc. Chem. Res.*, 1982, **15**, 232.
11. N. E. Mackenzie, P. E. Fagerness, and A. I. Scott, *J. Chem. Soc., Chem. Commun.*, 1985, 635.
12. J. N. S. Evans, R. J. Appleyard, and W. A. Shuttleworth, *J. Am. Chem. Soc.*, 1993, **115**, 1588.
13. T. Higaki, S. Tanase, F. Nagashima, Y. Morino, A. I. Scott, H. J. Williams, and N. J. Stolowich, *Biochemistry*, 1991, **30**, 2519.
14. A. I. Scott, C. A. Roessner, N. J. Stolowich, P. Karuso, H. J. Williams, S. K. Grant, M. D. Gonzalez, and T. Hoshino, *Biochemistry*, 1988, **27**, 7984.
15. (a) M. J. Warren and P. M. Jordan, *FEBS Lett.*, 1987, **225**, 87; (b) M. J. Warren, and P. M. Jordan, *Biochemistry*, 1989, **27**, 9020.
16. (a) G. J. Hart, A. D. Miller, F. J. Leeper, and A. R. Battersby, *J. Chem. Soc., Chem. Commun.*, **1987**, 1762; (b) A. D. Miller, G. J. Hart, L. C. Packman, and A. R. Battersby, *Biochem. J.*, 1988, **254**, 915; (c) G. J. Hart, A. D. Miller, and A. R. Battersby, *Biochem. J.*, 1988, **252**, 909; (d) U. Beifuss, G. J. Hart, A. D. Miller, and A. R. Battersby, *Tetrahedron Lett.*, 1988, **29**, 2591.
17. J. C. Vederas, *Nat. Prod. Rep.* 1987, **4**, 277.
18. K. Gehring, P. G. Williams, J. G. Pelton, H. Morimoto, and D. E. Wemmer, *Biochemistry*, 1991, **30**, 5524.
19. H. G. Floss and S. Lee, *Acc. Chem. Res.*, 1993, **26**, 116.
20. R. L. Jarvest, G. Lave, and B. V. L. Potter, *J. Chem. Soc., Perkin Trans. 1*, 1981, 3186.
21. H. M. Siedel, S. Freeman, C. H. Schwalbe, and J. R. Knowles, *J. Am. Chem. Soc.*, 1990, **112**, 8149.
22. C. Ortiz, C. Tellier, H. Williams, N. J. Stolowich, and A. I. Scott, *Biochemistry*, 1991, **30**, 10 026.

Biographical Sketch

A. Ian Scott. *b* 1928. B.Sc., 1949, Ph.D., 1952, D.Sc., 1963, M.A.(Hon.), Yale University, 1968. Lecturer, Glasgow University, 1957–62; Professor, University of British Columbia, 1962–65, University of Sussex, 1965–68, and Yale University, 1968–77. Davidson Professor of Science and Distinguished Professor of Chemistry and Biochemistry, Texas A&M University, 1981–present. Director of Center for Biological NMR, 1982–present. Three books, 1 patent, and approx. 350 publications. Research specialties: natural product biosynthesis and NMR spectroscopy.

Enzyme-Catalyzed Exchange: Magnetization Transfer Measurements

Kevin M. Brindle

University of Cambridge, Cambridge, UK

1	Introduction	1
2	Theory and Experimental Methods	1
3	Fluxes Measured In Vivo	4
4	Concluding Remarks	6
5	Related Articles	6
6	References	6

1 INTRODUCTION

Magnetization transfer is a rapid reaction technique which can be used to measure enzyme-catalyzed fluxes with rate constants of the order of $1-10\,s^{-1}$. These measurements can be made not only in vitro but also in some cases in an intact living system, where this might be anything from microbial cells growing in culture to specific regions of the human brain. The techniques for measuring transfer of magnetization, which were discussed in detail and applied by Forsén and Hoffman,[1] were first applied to an enzyme-catalyzed reactions in vitro by Brown and Ogawa who measured exchange in the reaction catalyzed by adenylate kinase,[2] and by Brown and Cheshnovsky, who measured the rate of the reversible hydration of acetaldehyde catalyzed by carbonic anhydrase.[54] The first measurements made in vivo were also made by Brown and co-workers, who measured flux between inorganic phosphate (Pi) and adenosine triphosphage (ATP) in cells of the bacterium, *Escherichia coli*.[3] Since that time there have been numerous magnetization transfer studies of enzyme-catalyzed exchange both in vitro and in vivo. These have been discussed in a number of reviews.[4–7] I will concentrate here on applications of the technique in ^{31}P NMR measurements in vivo. Applications in whole body MR spectroscopy are also discussed elsewhere in the Encyclopedia.

2 THEORY AND EXPERIMENTAL METHODS

When the exchange rate constant is comparable to the spin–lattice relaxation rate and separate resonances are observed for the exchanging species then it is possible to determine the rate of exchange by measuring the transfer of nuclear polarization from one resonance to another. In ^{31}P NMR measurements in vivo, the spin–lattice relaxation rates are of the order of $0.1-1\,s^{-1}$.

Consider a two-site exchange system in which a nucleus exchanges between two sites, A and B.

$$\mathrm{A} \underset{k_{-1}}{\overset{k_{+1}}{\rightleftharpoons}} \mathrm{B} \qquad (1)$$

The z magnetizations of the A (M_A) and B (M_B) spins are described by the Bloch equations, which have been modified to include this exchange:

$$dM_A/dt = -\rho_A(M_A - M_0^A) - k_{+1}M_A + k_{-1}M_B \qquad (2)$$

$$dM_B/dt = -\rho_B(M_B - M_0^B) - k_{-1}M_B + k_{+1}M_A \qquad (3)$$

where $M_0{}^A$ and $M_0{}^B$ are the equilibrium z magnetizations of the A and B spins and ρ_A and ρ_B are their spin–lattice relaxation rates. The solutions of these equations are:

$$M_{A(t)} = C_1\exp(\lambda_+ t) + C_2\exp(\lambda_- t) + M_0^A \qquad (4)$$

$$M_{B(t)} = C_3\exp(\lambda_+ t) + C_4\exp(\lambda_- t) + M_0^B \qquad (5)$$

where $C_3 = C_1(\lambda_+ + \rho_A + k_{+1})/k_{-1}$ and $C_4 = C_2(\lambda_- + \rho_A + k_{+1})/k_{-1}$ and the constants C_1 and C_2 are determined by the values of M_A and M_B at $t = 0$. The quantities λ_+ and λ_- are given by:

$$\lambda_{+/-} = 1/2(-(\rho_A + k_{+1} + \rho_B + k_{-1}) + / - \{[(\rho_A + k_{+1}) - (\rho_B + k_{-1})]^2 + 4k_{+1}k_{-1}\}^{1/2}) \qquad (6)$$

Equations for exchange between three or more sites are of the same form as equations (2) and (3). Although there are no analytical solutions for systems containing more than four sites,[7] it is straightforward to solve the equations numerically.

There are several magnetization transfer experiments which can be used to measure the exchange rates in a simple two-site exchange system.[8]

2.1 Selective Inversion

If a selective 180° pulse is applied to the B spin then in general its resonance will undergo a nonexponential recovery towards its equilibrium value while the intensity of the A resonance undergoes a transient decrease in intensity. The z magnetization of the A spin at time t is given by:

$$M_{A(t)} - M_0^A = \frac{-2M_0^B k_{-1}}{\lambda_+ - \lambda_-}[\exp(\lambda_+ t) - \exp(\lambda_- t)] \qquad (7)$$

while the magnetization of the B spin is given by:

$$M_{B(t)} - M_0^B = \frac{-2M_0^B}{\lambda_+ - \lambda_-}[(\rho_A + k_{+1} + \lambda_+)\exp(\lambda_+ t) - (\rho_A + k_{+1} + \lambda_-)\exp(\lambda_- t)] \qquad (8)$$

The exchange rate constants can be obtained either by fitting the data to these solutions or initial rates can be measured to give $(\rho_B + k_{-1})$ for B and k_{+1} for A.[2,9] A selective inversion pulse can be obtained by using a relatively long, low power pulse. However for those spectrometers which lack the facility to produce low power pulses, selective inversion can also be obtained by using hard pulses in the DANTE sequence[10] or

by using a shortened one-dimensional (1D) version of the two-dimensional (2D) exchange experiment, which is described in Section 2.3. In the latter case the pulse sequence is: $\pi/2_x - t_1 - \pi/2_x$, where $t_1 = \frac{1}{2}\Delta\nu$ and $\Delta\nu$ is the difference in resonance frequencies of the A and B spins. If the transmitter frequency is set to the resonant frequency of the A spin then at the end of this sequence the A magnetization will lie along the $-z$ axis while the B magnetization is returned to the $+z$ axis.[11]

2.2 Selective Saturation

If the B spin is selectively irradiated (such that $M_B = 0$ at $t = 0$) for a time, t, then the observed intensity of the A resonance decays with a time constant $\rho_A + k_{+1}$ and reaches a new equilibrium value:

$$M^A_{(t=\infty)} = \frac{\rho_A M^A_0}{(\rho_A + k_{+1})} \tag{9}$$

Thus both ρ_A and k_{+1} can be calculated. The saturation pulse can be generated either by using a long, low power pulse or by using hard pulses in the DANTE sequence. Although instantaneous saturation is incompatible with the mechanism of saturation, it can be approximated by using a relatively large irradiating field strength.[12] The limit imposed on the amplitude of the saturating field is set by the requirement that the saturating pulse should be selective. Too large a saturating field will result in nonspecific saturation of the observed resonance leading to decreases in its steady-state magnetization ($M_\infty{}^A$) and apparent spin–lattice relaxation time.[13] Both effects will lead to an overestimation of the exchange rate. This experiment, which is sometimes referred to as the time-dependent saturation transfer experiment, has two variants which have also been used to measure enzyme-catalyzed exchange. In these experiments the steady state and equilibrium magnetizations of the nonirradiated spin ($M^A_{(t=\infty)}$ and $M_0{}^A$, respectively) are measured in order to obtain the ratio $\rho_A/(\rho_A + k_{+1})$ [see equation (9)]. The sum, $(\rho_A + k_{+1})$ is then determined in separate experiments by measuring the z magnetization of the A spin following either its inversion or saturation in the presence of saturation of the B spin. The A magnetization relaxes exponentially toward its steady-state value ($M^A_{(t=\infty)}$) with a time constant $(\rho_A + k_{+1})$. The relative accuracy of the kinetic parameters derived from these experiments in a given amount of time have been compared using simulated data.[14] The choice of which particular saturation transfer experiment to use depends on the rate constant to be measured and the T_1 of the observed resonance.

2.3 Two-Dimensional Exchange Experiments

The two-dimensional exchange experiment introduced by Jeener et al.[15] uses the following pulse sequence: $\pi/2 - t_1 - \pi/2 - t_m - \pi/2 - t_2$. The first two pulses frequency label the z magnetization. Transfer of this magnetization between the A and B spins due to cross relaxation or chemical exchange during the t_m period is then detected during the t_2 period following the third 90° pulse. These signals are recorded for regular increments of t_1 and the resulting matrix of free induction decays is then double Fourier transformed to produce a 2D spectrum. Magnetization that has exchanged between the A and B sites will appear as cross peaks while the diagonal peaks represent magnetization which has failed to migrate. Cross peaks arising from coherent magnetization transfer due to scalar coupling are eliminated by phase cycling the pulses.[16] The amplitudes of the peaks in the 2D spectrum are described by equations similar to those that describe signal intensities in the selective inversion experiment.[7] In early applications of the technique the exchange rate constants were estimated by recording 2D spectra at a series of t_m values and fitting the observed cross-peak intensities versus t_m to the appropriate exchange equation. Alternatively the rate constants can be estimated from the initial rate of cross-peak buildup, which is equal to k_{+1} (or k_{-1}). Recording a series of 2D spectra is extremely time consuming and therefore a method of analysis was developed to determine the rate constants from a single 2D exchange spectrum.

The 2D spectrum can be described by the following equation:

$$\mathbf{M} = \exp(\mathbf{R}t_m)\mathbf{M}_0 \tag{10}$$

where $\mathbf{M}$ is a matrix comprising the peak volumes in the spectrum and $\mathbf{R}$ is the matrix of exchange and relaxation rate constants. For the simple two-site exchange system described above, $\mathbf{R}$ has the form:

$$\mathbf{R} = -\begin{bmatrix} \rho_A + k_{+1} & -k_{-1} \\ -k_{+1} & \rho_B + k_{-1} \end{bmatrix} \tag{11}$$

$\mathbf{M}_0$ is a diagonal matrix representing the 2D spectrum obtained with $t_m = 0$. This is usually replaced with $\alpha\mathbf{S}_0$, where $\mathbf{S}_0$ is the diagonal matrix of mole fractions obtained from a fully relaxed 1D experiment and α is an unknown scaling factor. Replacing $\mathbf{M}_0$ with $\alpha\mathbf{S}_0$, which avoids collecting another 2D spectrum, gives rise to false values for the diagonal elements in the $\mathbf{R}$ matrix but leaves the off-diagonal elements, which specify the exchange rate constants, unaffected. This method, which has been termed 'back transformation'[17,18] and a 1D counterpart derived from it,[19] essentially involve fitting an exponential function to a data set consisting of only two time points. These are the magnetizations (signal intensities) of the exchanging species when $t_m = 0$ and when t_m is set at some other value. The value of t_m which will give the most precise estimate of the exchange rate constants, has been estimated to be equal to $1/(R + k)$, where R and k are the mean values of the relaxation and exchange rate constants, respectively.[20] The back transformation method has been used to estimate the exchange rate constants in the reactions catalyzed by adenylate kinase and phosphoglycerate mutase in vitro.[21]

Exchange rate constants can also be obtained from a single 2D exchange spectrum by using the 'accordion' experiment described by Bodenhausen and Ernst.[22] This is a modification of the 2D experiment in which the t_m period is incremented in steps of t_1 and the rate constants are obtained by analysis of the lineshapes in the resulting 2D spectrum. If, in the two-site exchange system discussed above, ρ_A and ρ_B and the concentrations of the A and B spins are equal then the diagonal peaks in the accordion spectrum will have a lineshape which is given by the sum of two Lorentzian lines with linewidths ρ and $(k_{+1} + k_{-1} + \rho)$ while the cross-peak lineshapes are given

by the difference between these two Lorentzian lines. This analysis of the accordion experiment was used to estimate the exchange rate constants in the reaction catalyzed by creatine kinase in vitro.[23] Analysis of the accordion experiment in a more typical case, where the populations of the exchanging spins are unequal and the relaxation rate constants are different has been considered by Kuchel.[7]

2.4 Comparison of 1D and 2D Methods

Two-dimensional methods have the advantage that in multisite exchange systems they can, in principle, detect all the exchanges in a single experiment. The 2D exchange experiment and its 1D counterpart also have the advantage that they use nonselective pulses and therefore avoid the problems associated with the limited selectivity of the irradiating field in the 1D experiments. All the methods described require some preliminary estimate of the exchange rate constant in order to optimize the experimental protocol, for example to choose the optimal t_m in the 2D experiments or the optimal saturation transfer protocol in the 1D experiments. For experiments in vivo, where limited sample viability precludes long data acquisition times, the 1D methods are preferred over the more time consuming 2D methods. This is reflected in the fact that although 2D exchange experiments have been performed,[24] the overwhelming majority of magnetization transfer measurements in vivo have employed 1D methods.

2.5 Effect of the Equilibrium Constant on Exchange Measurements

In the selective inversion and 2D experiments, which follow the z magnetization of the exchanging species after a transient perturbation, the amplitude of these changes depends on the mole fractions of both species. This is illustrated by equation (7) for the inversion transfer experiment. This is not the case in a saturation transfer experiment in which changes in the z magnetization of the A spin are independent of the concentration of the B spin [see equation (9)]. Thus a saturation transfer experiment may detect exchange between a metabolite present in high concentration and one present in low concentration, even if the latter is so low in concentration as to be undetectable in the NMR spectrum. This is illustrated by the saturation transfer spectra, obtained from the dog heart in vivo, shown in Figure 1. Saturation of the γ-phosphate resonance of ATP also results in saturation of the β-phosphate resonance of adenosine diphosphate (ADP), which is less than 1 ppm upfield and which is too low in concentration to be observable in these spectra. Exchange between the β-phosphate of ADP and the β-phosphate of ATP results in a decrease in the resonance intensity of the latter. The lower limit on the concentration of the metabolite to which flux can be measured is imposed by the amount of power required to achieve saturation of the nucleus in this site. For any given flux, as the concentration of the metabolite is decreased the residence time of the nucleus in this site will also decrease and the irradiating field required to achieve its saturation will increase. This was demonstrated experimentally with a study of ATP–ADP exchange catalyzed by creatine kinase in vitro.[25]

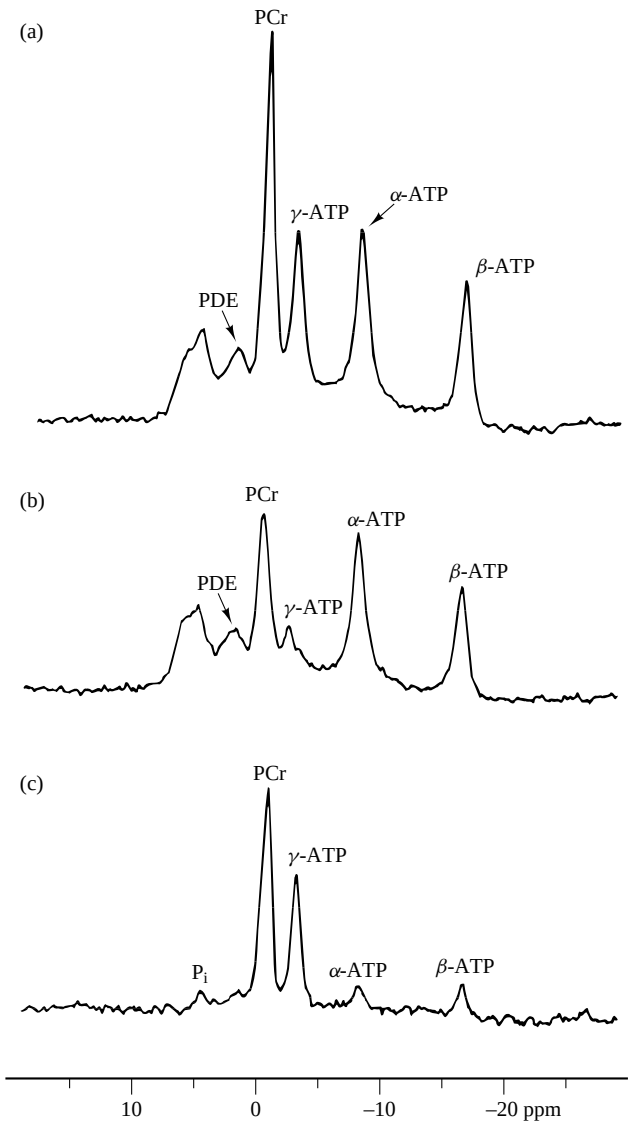

Figure 1 ^{31}P NMR saturation transfer spectra of the dog heart in vivo. The spectra were acquired using a surface coil placed over the heart. Saturation of the γ-phosphate resonance of ATP results in transfer of magnetization to the phosphocreatine and Pi resonances. This is manifest as a decrease in their resonance intensities [compare spectra (a) and (b)], which is clearly seen in the difference spectrum (c). The decrease in the β-phosphate resonance of ATP is due to exchange between ADP and ATP (see text). The decrease in the α-phosphate resonance, which has also been observed in a number of other studies and which cannot be explained by the lack of selectivity of the saturating field, is unexplained. Abbreviations: PDE, phosphodiester; PCr, phosphocreatine; γATP, γ-phosphate resonance of ATP; α-ATP, α-phosphate resonance of ATP; β-ATP, β-phosphate resonance of ATP. (Reproduced by permission of Academic Press, from K. M. Brindle, B. Rajagopalan, D. S. Williams, J. A. Detre, E. Simplaceanu, C. Ho, and G. K. Radda, *Biochem. Biophys. Res. Commun.*, 1988, **151**, 70)

2.6 Assumptions Made in Analyzing Magnetization Transfer Data

2.6.1 Two-Site Exchange

Magnetization transfer measurements of exchange between two substrates in an enzyme-catalyzed reaction are frequently

analyzed using the two-site exchange model described above. Enzyme-bound intermediates in the exchange reaction, which in general will be very low in concentration compared with the free substrates and therefore turning over very rapidly, can usually be ignored. However an intermediate could affect the measured exchange velocity if there was rapid loss of the magnetic label at this site, i.e. if the T_1 of the exchanging nucleus in this site were very short. Although modeling studies have shown that the T_1 would have to be very short,[25] and there appears to be no evidence for this from ^{31}P NMR studies of enzyme-bound substrates, there are now two independent reports that indicate that this may occur in the exchange between ATP and ADP catalyzed by creatine kinase in vitro.[25,26] These compared isotope exchange measurements with magnetization transfer measurements and showed that under some conditions the latter underestimated the exchange rate. However it should be emphasized that for the exchange most often measured in vivo, i.e. that between phosphocreatine and ATP, there was good agreement between the isotope exchange and magnetization transfer data.

2.6.2 Relationship Between Measured Exchange and Net Flux

Since the magnetization transfer experiment, like an isotope exchange experiment, only measures exchange between a pair of substrates there need be no direct relationship between this exchange flux and the metabolically relevant net flux catalyzed by the enzyme. Consider, for example, the reaction mechanism of creatine kinase, which is illustrated in Figure 2. Magnetization transfer measurements of exchange between ATP and ADP and between phosphocreatine and ATP and isotopic measurements of exchange between ATP and ADP, between PCr and ATP and between PCr and Cr have been shown to be similar under most conditions, consistent with rate-limiting interconversion of the two ternary complexes (E.MgADP.PCr and E.MgATP.Cr).[25,26] Therefore under these conditions it is valid to equate magnetization transfer measurements of PCr $\leftrightarrow$ ATP exchange with net flux in the reaction since the same step, the interconversion of the ternary complexes, is rate-limiting for all the exchanges and for the net flux catalyzed by the enzyme. However at high [PCr]/[Cr] ratios (above 2) the ATP $\leftrightarrow$ PCr exchange flux exceeds the ADP $\leftrightarrow$ ATP exchange flux, indicating that control has shifted from the interconversion of the ternary complexes to the steps of substrate–enzyme complex formation and breakdown.

Magnetization transfer measurements of steady-state ATP turnover appear to be measuring net flux. The evidence for this has come from the correspondence between P:O ratios

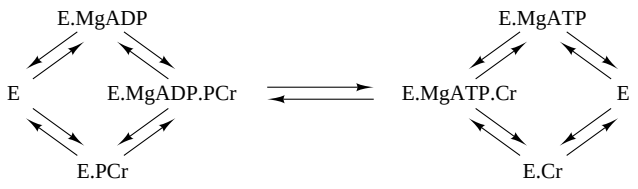

Figure 2 Reaction mechanism of creatine kinase. E represents free enzyme; PCr represents phosphocreatine and Cr represents creatine; MgADP and MgATP represent the Mg^{2+}-bound forms of ADP and ATP respectively

(moles of ATP synthesized: atoms of oxygen consumed) measured in the cell with those measured in suspensions of isolated mitochondria catalyzing net ATP synthesis (discussed in Section 3.2). However, evidence has been obtained recently that mitochondria in vivo can catalyze an ATP $\leftrightarrow$ Pi exchange reaction under some conditions.

3 FLUXES MEASURED IN VIVO

3.1 Creatine Kinase

Creatine kinase catalyses the reaction:

$$MgATP^{2-} + Cr \rightleftharpoons PCr^{2-} + MgADP^{-} + H^{+} \qquad (12)$$

The enzyme is abundant in muscle and neural tissue, where the reaction is normally near-to-equilibrium.[27] When an energy demand is placed on the tissue, the ATP concentration is maintained at the expense of phosphocreatine. Phosphocreatine thus acts as an energy store, buffering temporal changes in the ATP and ADP concentrations.

3.1.1 The Shuttle Hypothesis

A second role for the enzyme has been proposed based on the observation that the enzyme is spatially localized (reviewed by Wallimann et al.[27]). For example in muscle, concentrations of the enzyme are found at the myofibrils and at the mitochondria. In the latter case there is a distinct mitochondrial isoform which is located in the intermembrane space. According to the 'shuttle hypothesis' phosphocreatine also acts as a spatial energy buffer, shuttling energy between the sites of production, the mitochondria, to the sites of utilization, in muscle the myofibrillar Mg^{2+}-ATPase. In its simplest form phosphocreatine and creatine are thought to act as parallel diffusion pathways for the diffusion of ATP and ADP, respectively, between the mitochondria and myofibrils.[28] More elaborate models take into account the apparent functional interactions between the enzyme and other proteins in the muscle. For example there is good evidence that the mitochondrial isoform interacts directly with the adenine nucleotide translocase in the inner mitochondrial membrane, resulting in channeling of mitochondrially-generated ATP between the two proteins.[27] Inevitably ^{31}P NMR magnetization transfer measurements of creatine kinase kinetics in vivo have been used to look for evidence of the shuttle.

Studies in the perfused heart, which showed an increase in the reaction velocity with increased ATP turnover despite only small changes in the enzyme's steady state substrate concentrations, indicated a discrepancy with the solution properties of the enzyme.[29,30] A similar increase in creatine kinase flux with increased ATP turnover has also been observed in brain.[31] Measurements in neonatal rabbit hearts, at different stages of development, showed that the reaction velocity increased as the concentration of the mitochondrial isoform increased,[32] a result which is consistent with the shuttle hypothesis and with functional coupling between the mitochondrial isoform and the adenine nucleotide translocase. This study also showed, as expected from the solution properties of the enzyme, that flux increased with the increase

in creatine and phosphocreatine contents that occurred during development. These data may explain why in skeletal muscle, which contains only 2% mitochondrial creatine kinase activity, there is no increase in creatine kinase reaction velocity with increased work.[33,34] Further evidence for compartmentation of creatine kinase came from the observation that in a time-dependent saturation transfer experiment the decay of the phosphocreatine resonance was not always a single exponential. A kinetic model developed to explain these data attributed this to a nonsaturable mitochondrial pool of ATP in exchange with phosphocreatine in the reaction catalyzed by the mitochondrial isoform.[35] More recent work in the heart has shown that the presence of the mitochondrial isoform is not a prerequisite for the increase in creatine kinase flux with work. Increased flux was shown to result from changes in the enzyme's substrate concentrations. However there was, in addition, an unexplained change in the kinetic properties of the enzyme between rest and work.[36]

The role of creatine kinase in the shuttle has also been investigated by feeding animals creatine analogs which accumulate in cardiac and skeletal muscle and which inhibit the enzyme.[37,38] Magnetization transfer measurements of creatine kinase fluxes in these muscles, which were less than or comparable to the ATP turnover rates, showed that phosphocreatine could not be an obligatory intermediate in energy transduction. However it is now clear that during the long feeding periods required, skeletal muscle undergoes compensatory metabolic adaptations.[39] Furthermore in heart, it was subsequently shown that the presence of a creatine analog does in fact impair muscle function.[40]

Further information about the role of creatine kinase in muscle function will undoubtedly come from using NMR magnetization transfer techniques in conjunction with molecular genetic methods for manipulating the tissue concentrations of the enzyme. For example the role of the different isoforms in muscle function is being investigated by changing their expression in the skeletal muscle of transgenic mice.[41] Elimination of the M isozyme, using gene targeting techniques, was shown totally to eliminate magnetization transfer between phosphocreatine and ATP.[42] Remarkably the phosphocreatine levels declined normally during exercise. Presumably this was due to the residual mitochondrial creatine kinase activity present. Interestingly the muscle adapted to the absence of the M isoform and these adaptations show some similarities to those observed in muscle of analog-fed animals.

3.1.2 Differences in the Forward and Reverse Fluxes

Despite the fact that the reaction catalyzed by creatine kinase is normally near-to-equilibrium there have been numerous magnetization transfer studies which have shown that the forward and reverse fluxes are unequal. Two models have been proposed to explain this difference. One proposes that there are two pools of ATP, a large pool and a small pool which are both in exchange with phosphocreatine. Saturation of the observed γ-phosphate resonance of ATP allows measurement of flux from phosphocreatine to both pools of ATP. However the converse is not true since saturation of the phosphocreatine resonance will result in flux being measured predominantly between the large ATP pool and phosphocreatine. This model was elaborated in terms of the shuttle hypothesis, where the cytosolic ATP pool constitutes the large pool and the small pool is represented by ATP in the mitochondria and at the myofibrils.[43] In support of this proposal it was shown that the discrepancies in the forward and reverse fluxes reported in the literature increased as the rate of ATP synthesis increased. It was also pointed out that the forward and reverse fluxes measured in rat brain were equal if measured using a 2D exchange experiment but were unequal if measured using a saturation transfer experiment. As pointed out above, the saturation transfer experiment is capable of measuring exchange between metabolites present in very unequal concentrations whereas in a 2D exchange experiment, both exchanging pools need to be present at a significant concentration for the exchange to be observed. The second model considers the difference in the fluxes to be due to the fact that the γ-phosphate of ATP is in exchange with Pi as well as with phosphocreatine. Thus while exchange measurements of the flux from phosphocreatine to ATP can be analyzed using a two-site exchange model the reverse flux may be underestimated if not treated as a three-site exchange system, i.e. PCr $\leftrightarrow$ ATP $\leftrightarrow$ Pi. Much of the evidence which supports a compartmentation model is also compatible with this model (discussed by Brindle[6]). For example the difference in creatine kinase fluxes in this model would be expected to increase as the rate of ATP $\leftrightarrow$ Pi exchange increases. The elegant study of Ugurbil et al.[44] on the perfused working rat heart appeared to provide an answer as to which model was correct when it was shown that the forward and reverse fluxes were equal if the reverse flux was measured by saturating both the phosphocreatine and Pi resonances and employing a three-site exchange model for data analysis. However there are two problems with this experiment. As Ugurbil et al.[44] point out, the fractional reduction in the γ-phosphate resonance of ATP, when both the phosphocreatine and Pi resonances are saturated, should be equal to or less than the value observed when only the phosphocreatine resonance is saturated. This was not the case under one set of perfusion conditions. Another problem is that the measured ATP $\leftrightarrow$ Pi exchange is simply not fast enough to give the observed discrepancy.[45] An early study, which showed a difference in the forward and reverse fluxes despite the application of a correction factor which allowed for the observed exchange between ATP and Pi, concluded that the γ-phosphate of ATP must be in rapid exchange with other sites.[46]

There appears at present to be no completely satisfactory explanation for the discrepancy in the forward and reverse fluxes. However, in the context of compartmentation, perhaps tissue heterogeneity should also be considered. For example, in skeletal muscle measurements of enzyme levels in individual fibers have shown extreme heterogeneity, even between adjacent fibers.[47]

3.2 ATP Turnover

A significant limitation of magnetization transfer measurements in vivo is that very few enzyme-catalyzed fluxes are measurable. For example the spectra shown in Figure 1 illustrate almost all the exchanges that can be measured using ^{31}P NMR magnetization transfer measurements in vivo. However, in measuring the fluxes between Pi and ATP the technique can be used to determine arguably the most important fluxes in a living cell, ATP synthesis and hydrolysis. In early measurements of the flux between Pi and ATP it

was assumed that the flux was catalyzed solely by the mitochondrial F_1F_0 ATP synthase. However subsequent studies, in a number of systems including *E. coli*, yeast and the perfused heart, demonstrated that the coupled reaction catalyzed by the glycolytic enzymes, glyceraldehyde 3-phosphate dehydrogenase (GAPDH) and phosphoglycerate kinase (PGK) could also participate in this exchange reaction (reviewed by Brindle[6]). Elimination of this glycolytic exchange allows the Pi ↔ ATP exchange catalyzed by the mitochondria to be determined. For example, a detailed study of Pi → ATP and ATP → Pi fluxes in the perfused rat heart, in which the glycolytic exchange was inhibited, either by iodoacetate treatment or by depletion of glycolytic intermediates, showed that the P:O ratio was approximately 2.4.[48] The similarity of this value to that displayed by isolated mitochondria in vitro catalyzing net ATP synthesis suggests that the mitochondrial ATP synthase is operating unidirectionally in vivo and that the technique measures net ATP turnover. The technique can thus be used to assess the degree of mitochondrial coupling in vivo. For example measurements of P:O ratios in the postischemic perfused rat heart showed that mitochondrial uncoupling, which would lead to a decrease in the measured P:O ratio, could not be the cause of the observed postischemic depression in mechanical function.[49]

The measurements of Pi → ATP flux have also been used to examine the properties of the glycolytic enzymes. Studies of the perfused rat heart[49] and the dog heart in vivo[50] have shown that the activities of GAPDH and PGK are altered in the postischemic myocardium. Measurements of Pi → ATP flux in yeast cells, in which the concentration of PGK had been increased using molecular genetic techniques, allowed a detailed study of the kinetic properties of this enzyme in the intact cell. This showed that there were no unusual kinetic properties conferred on the enzyme by its cellular environment.[51]

Although the glycolytic exchange reaction can compromise magnetization transfer measurements of ATP turnover, particularly in the presence of glucose, this may be less of a problem in vivo. For example the glycolytic contribution to the measured Pi → ATP flux in the postischemic dog heart in vivo appeared to be much lower than that observed in postischemic glucose-perfused rat hearts.[49,50] In rat skeletal muscle in vivo, the measured Pi → ATP flux correlated well with the work performed. Although a glycolytic contribution could not be rigorously excluded the measured flux showed good agreement with ATP turnover rates estimated from oxygen consumption measurements in the perfused hind limb and the rates of phosphocreatine breakdown during a tetanus.[34]

Recent studies on yeast have shown that the measured Pi → ATP flux is increased in cells which have been genetically modified to overexpress an isoform of the mitochondrial adenine nucleotide translocase.[55] This increase in flux, which occurred in the absence of an increase in oxygen consumption, suggested that the mitochondria were catalysing predominantly an ATP ↔ Pi exchange reaction under these conditions rather than net ATP synthesis. This interpretation of the data is in accord with an earlier radioisotope study of ATP ↔ Pi exchange in isolated mammalian mitochnodria which showed that, at low rates of respiration, mitochondria can catalyze an ATP ↔ Pi exchange, but that at higher rates of respiration the Pi → ATP flux becomes unidirectional. Thus it is possible that in mammalian systems at low rates of respiration, even when the glycolytic contribution has been removed, the Pi → ATP flux measured in a magnetization transfer experiment might include some contribution from a mitochondrially catalyzed ATP ↔ Pi exchange.

4 CONCLUDING REMARKS

An interesting area, which I have not covered, is measurements of membrane transport (reviewed by Kuchel[7]). Of particular interest is a ^{19}F NMR study of 3-fluoro-3-deoxy-D-glucose transport across the red cell membrane.[52] However it is not yet clear whether this technique can be applied in other systems. Another interesting study employed the ^{31}P NMR saturation transfer experiment to measure ATP ↔ ADP exchange across the membrane of isolated mitochondria.[53] This showed that the exchange rates were more than 10 times faster than the rates previously determined using isotopic techniques and that they were almost 10 times faster than the ATP synthase (ATP ↔ Pi) exchange rates.

I have concentrated on ^{31}P NMR magnetization transfer measurements in vivo as this reflects my own interest, an interest which was initially stimulated by the potential of the technique to provide unique information on the kinetic properties of enzymes in vivo.

5 RELATED ARTICLES

Chemical Exchange Effects on Spectra; Enzymes Utilizing ATP: Kinases, ATPases and Polymerases; Peripheral Muscle Metabolism Studied by MRS; Phosphorus-31 Magnetization Transfer Studies In Vivo; Relaxation Effects of Chemical Exchange; Two-Dimensional Methods of Monitoring Exchange; Whole Body Studies: Impact of MRS.

6 REFERENCES

1. S. Forsén, and R. A. Hoffman, *J. Chem. Phys.*, 1963, **39**, 2892.
2. T. R. Brown and S. Ogawa, *Proc. Natl. Acad. Sci. U.S.A.*, 1977, **74**, 3627.
3. T. R. Brown, K. Ugurbil, and R. G. Shulman, *Proc. Natl. Acad. Sci. U.S.A.*, 1977, **74**, 5551.
4. J. R. Alger and R. G. Shulman, *Quart. Rev. Biophys.*, 1984, **17**, 83.
5. A. P. Koretsky and M. W. Weiner, in *Biomedical Magnetic Resonance*, eds. T. L. James and A. R. Margulis, Radiology Research and Education Foundation, San Francisco, 1984, p. 209.
6. K. M. Brindle, *Prog. NMR Spectrosc.*, 1988, **20**, 257.
7. P. W. Kuchel, *NMR Biomed.*, 1990, **3**, 102.
8. I. D. Campbell, C. M. Dobson, R. G. Ratcliffe, and R. J. P. Williams, *J. Magn. Reson.*, 1978, **29**, 397.
9. H. Degani, M. Laughlin, S. Campbell, and R. G. Shulman, *Biochemistry*, 1985, **24**, 5510.
10. G. A. Morris and R. Freeman, *J. Magn. Reson.*, 1978, **29**, 433.
11. G. Robinson, P. W. Kuchel, B. E. Chapman, D. M. Doddrell, and M. G. Irving, *J. Magn. Reson.*, 1985, **63**, 314.
12. C. M. Dobson, E. T. Olejniczak, F. M. Poulsen, and R. G. Ratcliffe, *J. Magn. Reson.*, 1982, **48**, 97.

13. W. Kuhn, W. Offermann, and D. Leibfritz, *J. Magn. Reson.*, 1986, **68**, 193.
14. M. Rydzy, R. Deslauriers, I. C. P. Smith, and J. K. Saunders, *Magn. Reson. Med.*, 1990, **15**, 260.
15. J. Jeener, B. H. Meier, P. Bachmann, and R. R. Ernst, *J. Chem. Phys.*, 1979, **71**, 4546.
16. S. Macura, Y. Huang, D. Suter, and R. R. Ernst, *J. Magn. Reson.*, 1981, **43**, 259.
17. C. L. Perrin and R. K. Gipe, *J. Am. Chem. Soc.*, 1984, **106**, 4036.
18. J. Bremer, G. L. Mendz, and W. J. Moore, *J. Am. Chem. Soc.*, 1984, **106**, 4691.
19. R. E. Engler, E. R. Johnston, and C. G. Wade, *J. Magn. Reson.*, 1988, **77**, 377.
20. C. L. Perrin, *J. Magn. Reson.*, 1989, **82**, 619.
21. G. L. Mendz, G. Robinson, and P. W. Kuchel, *J. Am. Chem. Soc.*, 1986, **108**, 169.
22. G. Bodenhausen and R. R. Ernst, *J. Am. Chem. Soc.*, 1982, **104**, 1304.
23. J. Boyd, K. M. Brindle, I. D. Campbell, and G. K. Radda, *J. Magn. Reson.*, 1984, **60**, 149.
24. R. S. Balaban, H. L. Kantor, and J. A. Ferretti, *J. Biol. Chem.*, 1983, **258**, 12 787.
25. K. M. Brindle, and G. K. Radda, *Biochim. Biophys. Acta*, 1985, **829**, 188.
26. V. V. Kupriyanov, R. S. Balaban, N. V. Lyulina, A. Ya. Steinschneider, and V. A. Saks, *Biochim. Biophys. Acta*, 1990, **1020**, 290.
27. T. Wallimann, M. Wyss, D. Brdiczka, K. Nicolay, and H. M. Eppenberger, *Biochem. J.*, 1992, **281**, 21.
28. R. A. Meyer, H. L. Sweeney, and M. J. Kushmerick, *Am. J. Physiol.*, 1984, **246**, C365.
29. V. V. Kupriyanov, A. Ya. Steinschneider, E. K. Ruuge, V. I. Kapel'ko, M. Ya. Zueva, V. L. Lakomkin, V. N. Smirnov, and V. A. Saks, *Biochim. Biophys. Acta*, 1984, **805**, 319.
30. J. A. Bittl and J. S. Ingwall, *J. Biol. Chem.*, 1985, **260**, 3512.
31. A. Sauter and M. Rudin, *J. Biol. Chem.*, 1993, **268**, 13 166.
32. S. B. Perry, J. McAuliffe, J. A. Balschi, P. R. Hickey, and J. S. Ingwall, *Biochemistry*, 1988, **27**, 2165.
33. R. Zahler, J. A. Bittl, and J. S. Ingwall, *Biophys. J.*, 1987, **51**, 883.
34. K. M. Brindle, M. J. Blackledge, R. A. J. Challiss, and G. K. Radda, *Biochemistry*, 1989, **28**, 4887.
35. R. Zahler and J. S. Ingwall, *Am. J. Physiol.*, 1992, **262**, H1022.
36. J. J. McAuliffe, S. B. Perry, E. E. Brooks, and J. S. Ingwall, *Biochemistry*, 1991, **30**, 2585.
37. E. A. Shoubridge, and G. K. Radda, *Biochim. Biophys. Acta*, 1984, **805**, 79.
38. E. A. Shoubridge, F. M. H. Jeffry, J. M. Keogh, G. K. Radda, and A.-M. L. Seymour, *Biochim. Biophys. Acta*, 1985, **847**, 25.
39. E. A. Shoubridge, R. A. J. Challiss, D. J. Hayes, and G. K. Radda, *Biochem. J.*, 1985, **232**, 125.
40. J. L. Zweier, W. E. Jacobus, B. Korecky, and Y. Brandejs-Barry, *J. Biol. Chem.*, 1991, **266**, 20 296.
41. M. J. Brosnan, S. P. Raman, L. Chen, and A. P. Koretsky, *Am. J. Physiol.*, 1993, **264**, C151.
42. J. van Deursen, A. Heerschap, F. Oerlemans, W. Ruitenbeek, P. Jap, H. ter Laak, and B. Weiringa, *Cell*, 1993, **74**, 621.
43. A. P. Koretsky, V. J. Basus, T. L. James, M. P. Klein, and M. W. Weiner, *Magn. Reson. Med.*, 1985, **2**, 586.
44. K. Ugurbil, M. Petein, R. Maidan, S. Michurski, and A. H. L. From, *Biochemistry*, 1986, **25**, 100.
45. K. M. Brindle and G. K. Radda, *Biochim. Biophys. Acta*, 1987, **928**, 45.
46. P. M. Matthews, J. L. Bland, D. G. Gadian, and G. K. Radda, *Biochim. Biophys. Acta*, 1982, **721**, 312.
47. C. V. Lowry, J. S. Kimmey, S. Felder, M. M.-Y. Chi, K. K. Kaiser, P. N. Passonneau, K. A. Kirk, and O. H. Lowry, *J. Biol. Chem.*, 1978, **253**, 8269.
48. P. B. Kingsley-Hickman, E. Y. Sako, P. Mohanakrishnan, P. M. L. Robitaille, A. H. L. From, J. Foker, and K. Ugurbil, *Biochemistry*, 1987, **26**, 7501.
49. E. Y. Sako, P. B. Kingsley-Hickman, A. H. L. From, J. Foker, and K. Uğurbil, *J. Biol. Chem.*, 1988, **263**, 10 600.
50. P.-M. Robitaille, H. Merkle, E. Sako, G. Lang, R. M. Clack, R. Bianco, A. H. L. From, J. Foker, and K. Uğurbil, *Magn. Reson. Med.*, 1990, **15**, 8.
51. K. M. Brindle, *Biochemistry*, 1988, **27**, 6187.
52. J. R. Potts, A. M. Hounslow, and P. W. Kuchel, *Biochem. J.*, 1990, **266**, 925.
53. P. T. Masiakos, G. D. Williams, D. A. Berkich, M. B. Smith, and K. F. LaNoue, *Biochemistry*, 1991, **30**, 8351.
54. D. Chesnnovsky and G. Navon, in *Nuclear Magnetic Resonance Spectroscopy in Molecular Biology*, ed. B. Pullman, Reidel, Dordrecht, 1978, p. 261.
55. K. Brindle, S. Fulton, J. Sheldon, and S. Williams, *Biochem. Soc. Trans.*, 1995, **23**, 374.

Biographical Sketch

Kevin M. Brindle. *b*. 1955. B.A., 1978, D.Phil., 1982, University of Oxford. He did his D.Phil. in Professor Iain Campbell's laboratory, where he worked on ^{1}H NMR studies of cells, then 4 years in Professor George Radda's laboratory before taking up a Royal Society University Research Fellowship in 1986. Lecturer at the University of Manchester, 1991, lectureship in Cambridge, 1993. Approx. 50 publications. Research interests: application of NMR techniques to study the properties of enzymes in vivo.

Motional Effects on Protein Structure: Acyl Carriers

James H. Prestegard
Yale University, New Haven, CT, USA

1	Introduction	1
2	Effects of Rapid Internal Motions	1
3	Effects of Slower Internal Motions	1
4	Initial Work on Acyl Carrier Protein	2
5	A Two-State Model for Acyl Carrier Protein	2
6	Supporting Evidence for a Multiple State Model	3
7	Overview	4
8	Related Articles	4
9	References	4

1 INTRODUCTION

The pioneering work of Wüthrich and co-workers on structure determination of bovine pancreatic trypsin inhibitor using NMR methods generated a great deal of excitement in the NMR and biochemical communities in the early 1980s.[1] This occurred partly because the work offered the prospect of protein structure elucidation in aqueous solution as opposed to in the confines of a crystalline environment. With successful application following successful application, however, there was a tendency to forget that a basic tenet of the early methodology imposed crystal-like constraints on structures which could have experienced much greater conformational flexibility in an aqueous environment. More precisely, the cross relaxation, or NOE data on which NMR structures were based were interpreted using a rigid, isotropically tumbling model for the protein in question. This model leads to the often quoted $1/r^6$ relationship between cross relaxation rates and internuclear distances r. We now know that this model is violated frequently, and, in retrospect, it may even seem surprising that the NMR structures determined show the quality and accuracy that they do. Some insight into the effects of violating the rigid model assumption, and the reasons why violation has made relatively little difference to the quality of many NMR structures is offered through our experiences with the structure determination of a protein that seems to have more than its fair share of motional freedom, acyl carrier protein (ACP).

ACP is a small protein (about 80 amino acids) which is found as a part of the fatty acid synthetase systems of most organisms.[2] It participates at many stages of lipid biosynthesis as a carrier of fatty acyl chains during the course of their elongation and modification. Despite the fact that it has been studied for more than 20 years, and in organisms such as *Escherichia coli* is among the most abundant proteins, no crystal structure had been produced at the point when NMR structural methods came on the scene, nor has a crystal structure been produced at the time of writing. Perhaps the very diverse class of interactions required of this protein, or the very long history of difficulties in producing isomorphic replacements for crystal studies, should have suggested a protein with more than a normal level of motional freedom. Perhaps some structural variability should have been suggested by the absence of disulfide bonds and the relatively high net negative charge on this small protein. Nevertheless, with so many successes in NMR structure determination of other small proteins, an attempt at an NMR structure for ACP seemed reasonable.

2 EFFECTS OF RAPID INTERNAL MOTIONS

There actually are some reasons to believe that certain classes of internal motions in proteins may not lead to severe violation of a rigid model. Motions which fall into this class include some of the very rapid motions produced by the cumulative effects of oscillations about bonds interconnecting proton pairs. In 1988, LeMaster et al.[3] introduced the simple model shown in Figure 1 in an attempt to illustrate the effects of these motions. The two protons are meant to move within the spheres in an uncorrelated fashion, sampling a centrosymmetric distribution on a timescale very short compared with that which dominates the cross-relaxation process (usually the timescale of protein tumbling). Under these conditions the dipolar interactions between the protons will be partially averaged. The averaging includes two terms, a distance term ($1/r^3$) and an angular term ($Y_0^2(\theta)$). These terms enter as a product in the spectral density function dominating cross relaxation. It is obvious that the first term will tend to increase with motion, since close distances of approach are weighted more heavily, and the second term will decrease as wider ranges of angles are sampled. What is not obvious is that the two terms exactly cancel for this very simple model, and relaxation effects prove to be identical to those for a rigid model with protons fixed at the centers of the spherical distributions. To the extent that internal motions are rapid, centrosymmetric, and uncorrelated, this may explain why a rigid model analysis works well in so many cases. Dynamics simulations based on works such as that of Kuriyan et al.[4] suggest that many internal motions approach this limit.

3 EFFECTS OF SLOWER INTERNAL MOTIONS

Unfortunately, not all internal motions fall into the category discussed above, and effects of these motions on

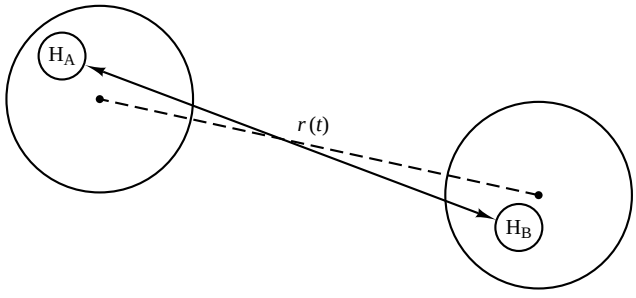

Figure 1 A simple model for rapid internal motions in proteins. Protons H_A and H_B move randomly in an uncorrelated fashion within their respective spheres

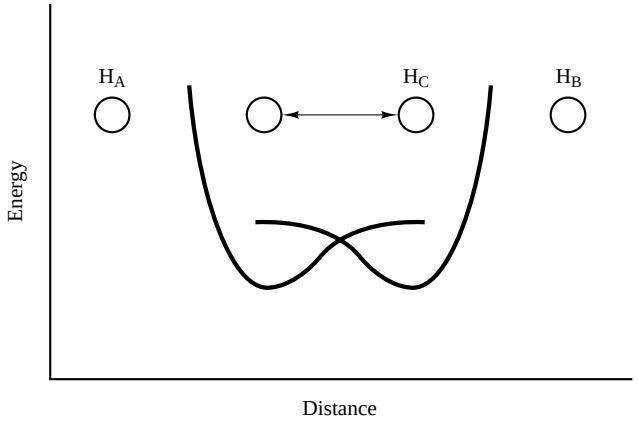

Figure 2 A simple model for slow internal motions in protein with a representation of penalty functions used as distance constraints

the interpretation of NOE data can be severe. Consider the limit in which internal motions are slow compared with overall tumbling of the protein. The motions do not then contribute to averaging of the dipolar interaction itself, but result in averaging of cross-relaxation effects experienced in the conformations sampled. In the absence of other motions, the cross-relaxation effects contribute in proportion to $1/r^6$. This strong distance dependence leads to dramatic effects.

Consider the case depicted in Figure 2. Two protons, A and B are fixed at a separation of 0.9 nm in all states sampled. Proton C finds itself 0.3 nm from A and 0.6 nm from B in one state, and 0.6 nm from A and 0.3 nm from B in another state. The two states are equally populated and interconversion between the states is sufficiently rapid to give rise to a single set of NMR resonances and NOE connectivities. NOEs between C and A and C and B will both be seen. The C−A NOE will be dominated by the first state and will have approximately 51% of the NOE that would have arisen if only the first state had been occupied. Similarly, the C−B NOE will be dominated by the second state and will have 51% of the NOE that would have arisen if only the second state had been occupied. If these NOEs were interpreted as if a single rigid state had existed, we would conclude that C is 0.336 nm from A and C is 0.336 nm from B. Since A and B are 0.9 nm apart, this is geometrically impossible. In searching for structures which satisfy a set of such averaged NOEs, we would either find that structures always violated some subset of NOEs, or distances corresponding to the 0.9 nm molecular constraint would be severely distorted producing high energy structures. This is the type of evidence for motion we initially found for ACP.

4 INITIAL WORK ON ACYL CARRIER PROTEIN

Initial work on ACP produced structures with substantial violations of NOE constraints in all cases.[5] The fact that these were so noticeable was in part due to the manner in which distance constraints were introduced. A penalty function (or pseudoenergy term) representing a constraint was added to the force field of a widely available molecular mechanics/molecular dynamics program and a search was executed for structures which simultaneously yielded low molecular energies and minimum penalties due to violation of NOE constraints.

The form of the penalty function was chosen to mimic more closely a true error function than the harmonic constraints commonly used at the time. In principle, the penalty function would be the square of the difference between a measured NOE [or $1/r^6$(exp)] and a NOE calculated from a trial structure [or $1/r^6$(cal)]. To improve convergence properties, a slightly modified form of this ideal penalty function was used. As illustrated in Figure 2, these penalty functions are highly asymmetric, rising abruptly when distances in trial structures are shorter than distances predicted from NOEs, and rising more slowly to a plateau when distances in trial structures are longer than distances predicted from NOEs. In the case of conflicting constraints, summation of these terms leads to double minimum functions in a way that harmonic constraints cannot. Searches then produce structures that tend to satisfy only one of the conflicting constraints at a time, leaving a large violation for the other constraints. Harmonic, or square well, constraints tend to produce structures that converge to a single distorted structure, with moderate violations of all constraints in a conflicting set.

Approaches using both harmonic constraints and highly asymmetric constraints were both used on ACP data.[5,6] Qualitatively similar structures were actually produced: three nearly parallel α-helices are observed with a very large loop connecting antiparallel helices I and II and a smaller loop connecting parallel helices II and III. The prosthetic group carrying the acyl chain is connected near the beginning of helix II, and acyl chains, when present, appear to lie between helices II and III.[7] Initially, we were fascinated with the opportunity to examine structures for ACP, and ignored the fact that the structures did not converge very well, especially with the more realistic penalty function (0.2−0.3 nm rms deviation of backbone atoms from the corresponding atoms of an average structure). On careful examination, however, the pattern of alternate violation of different NOEs was easily observed and the initial suggestion of a violation of the rigid model was made.[5]

5 A TWO-STATE MODEL FOR ACYL CARRIER PROTEIN

Dealing simultaneously with the effects of motion and structure on NOE values is a problem that is likely to recur as a wider variety of protein systems are studied. A first attempt to do this was made in the case of ACP. The penalty function approach mentioned above is easily generalized to the case where NOEs represent the average of NOEs seen in discrete structures. One simply replaces the calculated $1/r^6$ from a single trial structure with the average of $1/r^6$ from a pair of trial structures. During a search, pairs of structures whose average characteristics satisfy experimental observation are then produced. With limited NOE data and computational resources at the time, an exhaustive search could not be conducted, but using pairs of structures produced using a rigid model and minimizing these pairs with appropriate penalty functions, it was shown that structures with substantially reduced NOE distance violations and greatly improved molecular energies could be produced.[8]

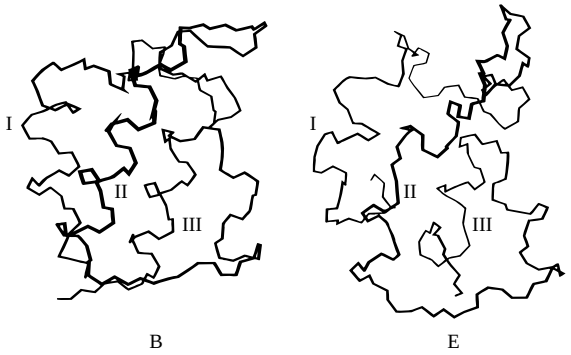

Figure 3 Backbone structures for two states sampled by ACP. Structures are based on 450 NOE constraints and 66 coupling constant constraints

Structures for one such pair are shown in Figure 3. These are from structures produced after further refinement using coupling constant data.[9] Structure B is energetically the more favorable and clearly shows the three helices mentioned above. The second structure (E) maintains a similar overall fold, but positioning of loops differs significantly and there is clear disruption of some of the helical structure, particularly that of helix II. At this point there was really no reason to believe that two and only two structures should contribute. Each may therefore represent the average of two or more structures and there is no reason to believe that either should have an absolutely ideal geometry.

6 SUPPORTING EVIDENCE FOR A MULTIPLE STATE MODEL

The search for supporting evidence for multiple conformations of ACP has occupied a good deal of time. The initial suggestion was not based on particularly strong evidence. Discrete resonances for different forms of *E. coli* ACP were not observed, only a single set of averaged resonances. It is also true that misassignment of some resonances could produce incompatibilities of NOE constraints in much the same way as occurs on averaging among conformational forms. Thus, a search for alternate explanations continues. Some support for multiple conformations has, however, come from data on ACPs from other species. ACP-I from spinach provides one piece of evidence for multiple conformations. In this case, a pair of resonances is seen for many of the assignable sites in the protein. These pairs are particularly noticeable in acylated forms of the protein, but also appear as major and minor components in nonacylated forms.[10] It has been possible in the nonacylated form of spinach ACP-I to show using ROESY that the pairs of resonances are not due to chemical heterogeneity but arise from conformational forms interconverting on the order of $1\,s^{-1}$.[11]

Direct support for multiple conformations for *E. coli* ACP has not been found, nor have conditions which clearly stabilize a single conformational form. Addition of divalent cations does stabilize the protein to thermal denaturation;[12,13] however, no improvements in structure have yet been realized. It is, however, interesting to note that during thermal denaturation of *E. coli* ACP, conditions can be selected under which either slow exchange, where discrete resonance for native and denatured forms are observed, or fast exchange, where a single set of averaged resonances are observed, exists.[13] The fast exchange situation is perhaps a little unusual for denaturation of a protein. But this situation does occur for *E. coli* ACP under the conditions of high levels of monovalent salts, where most of the initial structural data were collected.

Indirect support for the multiple state model has also come from attempts to monitor the stability of various helical structural elements. Clearly the model suggested in Figure 3 would require less than normal stability, at least for helix II. The use of amide proton exchange rates to monitor the stability of secondary structural elements is now well established.[14] Exchange of native protons for solvent deuteriums when a sample is freshly dissolved in ^2H_2O is believed to be precluded as long as amide protons are involved in hydrogen-bonding networks of common secondary structural elements. Under conditions where the base catalyzed rate of exchange in the open form of a structural element is slow compared with the rate of reformation of the structural element, rates corrected for variations in the base catalyzed exchange step provide a direct measure of the thermodynamic stability of the element.

The advent of extremely efficient methods for the collection of $^{15}N-^1H$ correlated experiments has provided an ideal means of monitoring amide exchange rates.[15] Figure 4 shows a comparison of amide exchange rates for sites in helix I, residues 3–15, and helix II, residues 36–50.[16] The timescales are adjusted to remove effects of variations in intrinsic rates for all except Glu-13. It is clear, first of all, that exchange of amide protons in ACP helices is relatively fast. Rates seen in other α-helical proteins of similar size are often more than an

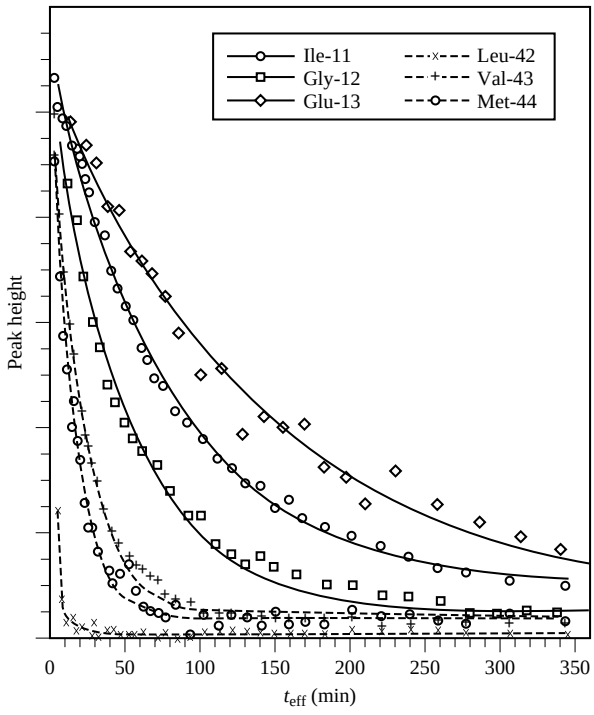

Figure 4 Loss of signal intensity of individual peaks for amide groups in a $^1H-^{15}N$ HSQC spectrum. Times are scaled relative to those of Glu-13 using the intrinsic exchange rate data of Molday et al.[23] The sample was approximately 3 mM ACP, 10 mM Ca^{2+}, pH 6.0; acquisition required 7 min per two-dimensional spectrum

order of magnitude slower. Second, exchange for residues in helix II is especially fast. Thus, it appears reasonable that ACP is a molecule with an unusual level of internal motion and that it is likely that multiple conformational states contribute to the NOEs measured in the course of structure determination.

ACP is of course not unique in having multiple conformational states and showing equilibration between them. Several examples of slow exchange among conformational forms are documented in the literature.[15,17,18] These cases are easily identified because of the appearance of discrete pairs of resonances for one or more chemically distinct sites in the protein. However, there is no reason to believe that there is anything less than a continuum of timescales for interconversion of conformational forms, and that there are numerous examples of fast exchange among conformational forms for which detection is less straightforward.

7 OVERVIEW

The need for dealing with structure determination in the presence of a variety of motional timescales has not gone unnoticed. Of a number of methods for dealing with the effects of motion on structural parameters, I will mention just a few. First, there is the time averaged constraint algorithm of Torda et al.[19,20] This algorithm uses molecular dynamics to sample different states, and averages over a characteristic decay time to generate a time averaged penalty function that can help direct the conformational search. It has been implemented for both NOE and coupling constant derived constraints. The algorithms are probably most applicable to the effects of motions on shorter timescales.

Second, there is a broadly based multiple conformation search algorithm proposed by Brüschweiler and co-workers.[21] This is based on identifying structures that satisfy subsets of distance constraints, and then combining the structures in pairs, triples, etc., to reproduce all NOE data. As yet, this has been applied only to relatively small systems, but it is applicable to motions which are too slow to deal with using molecular dynamics based algorithms. Finally, there are experimental approaches that can eliminate certain classes of exchange contributions to measured NOEs. These approaches have been described by Fejzo et al.[22] and have been applied to the case where motion is slow enough to yield discrete resonances.

In summary, a search for a three-dimensional structure of ACP carrier protein has been fruitful in that a first picture of this important carrier of acyl chains has been produced. Although it is relatively low in resolution, the picture provides a basis for understanding acyl chain interactions and protein–protein interactions that are fundamental to lipid biosynthesis. The search has, however, also brought to light the need to consider internal motions of proteins and the possible effects these motions might have on structures deduced from NMR data. It is obvious that the effects of motion on interpretation of NOE data are being increasingly considered and that methods which may provide alternative means of interpretation are likely to evolve in the future.

8 RELATED ARTICLES

Biological Macromolecules: Structure Determination in Solution; Biological Macromolecules; Hydrogen Exchange and Macromolecular Dynamics; Protein Dynamics from NMR Relaxation; Protein Structures: Relaxation Matrix Refinement.

9 REFERENCES

1. K. Wüthrich, G. Wider, G. Wagner, and W. Braun, *J. Mol. Biol.*, 1982, **155**, 311.
2. M. Rawlings and J. E. Cronan, Jr., *J. Biol. Chem.*, 1992, **267**, 5751.
3. D. M. LeMaster, L. E. Kay, A. T. Brünger, and J. H. Prestegard, *FEBS Lett.*, 1988, **236**, 71.
4. J. Kuriyan, G. A. Petsko, R. M. Levy, and M. Karplus, *J. Mol. Biol.*, 1986, **190**, 227.
5. T. A. Holak, S. K. Kearsley, Y. Kim, and J. H. Prestegard, *Biochemistry*, 1988, **27**, 6135.
6. T. A. Holak, M. Nilges, J. H. Prestegard, A. M. Gronenborn, and G. M. Clore, *Eur. J. Biochem.*, 1988, **175**, 9.
7. P.-J. Jones, E. A. Cioffi, and J. H. Prestegard, *J. Biol. Chem.*, 1987, **262**, 8963.
8. Y. Kim and J. H. Prestegard, *Biochemistry*, 1989, **28**, 8792.
9. Y. Kim and J. H. Prestegard, *Proteins*, 1990, **8**, 377.
10. Y. Kim, J. B. Ohlrogge, and J. H. Prestegard, *Biochem. Pharm.*, 1990, **40**, 7.
11. Y. Kim and J. H. Prestegard, *J. Am. Chem. Soc.*, 1990, **112**, 3707.
12. A. F. Frederick, L. E. Kay, and J. H. Prestegard, *FEBS Lett.*, 1988, **238**, 43.
13. L. A. Horvath, J. M. Sturtevant, and J. H. Prestegard, *Protein Sci.*, 1994, **3**, 103.
14. H. Roder, *Methods Enzymol. A*, 1989, **176**, 446.
15. P. C. Driscoll, A. M. Gronenborn, P. T. Wingfield, and G. M. Clore, *Biochemistry*, 1990, **29**, 4668.
16. M. Andrec, R. B. Hill, J. H. Prestegard, unpublished results.
17. P. A. Evans, R. A. Kautz, R. O. Fox, and C. M. Dobson, *Biochemistry*, 1989, **28**, 362.
18. S. Forsén, J. Kördel, T. Grundström, and W. J. Chazin, *Acc. Chem. Res.*, 1993, **26**, 7.
19. A. E. Torda, R. M. Brunne, T. Huber, H. Kessler, and W. F. van Gunsteren, *J. Biomol. NMR*, 1993, **3**, 55.
20. A. E. Torda, R. M. Scheek, and W. F. van Gunsteren, *J. Mol. Biol.*, 1990, **214**, 223.
21. M. J. Blackledge, R. Brüschweiler, C. Griesinger, J. M. Schmidt, P. Xu, and R. R. Ernst, *Biochemistry*, 1993, **32**, 10 960.
22. J. Fejzo, A. M. Krezel, W. M. Westler, S. Macura, and J. L. Markley, *Biochemistry*, 1991, **30**, 3807.
23. R. S. Molday, S. W. Englander, and R. G. Kallen, *Biochemistry*, 1972, **11**, 150.

Acknowledgments

This work was supported by a grant from the US Public Health Service, GM32243. The assistance of Michael Andrec and Mark Oswood in preparing figures and supplying data is also gratefully acknowledged.

Biographical Sketch

James H. Prestegard. *b* 1944. B.S., 1966, University of Minnesota; Ph.D., 1971, Caltech. Began NMR studies with Professor Sunney Chan in 1966, working on structures of nucleic acids and ion transport antibiotics. Faculty in Chemistry at Yale University, 1970–present. Approx. 130 publications. Research interests include application of NMR methods to structure elucidation of proteins in solution and glycolipids in oriented membrane arrays.

Proteases

J. T. Gerig
University of California, Santa Barbara, CA, USA

1	Introduction	1
2	Nature of the Catalytic Triad	2
3	Folding to Active Protein	3
4	Protease Dynamics	3
5	Inhibition of Proteases	4
6	New Proteases	6
7	Proteases in Organic Solvents	7
8	Summary	7
9	General References	7
10	Related Articles	7
11	References	7

Figure 1 Representation of the tertiary structures of subtilisin and α-chymotrypsin. The computer has drawn a ribbon through the polypeptide backbone of each. Side chains for the aspartic acid, histidine, and serine residues that are essential for catalysis are shown explicitly. (Drawings prepared by Mr. E. Y. Lau using information in the Brookhaven Protein Data Bank)

1 INTRODUCTION

Proteases are enzymes that catalyze the cleavage of peptide bonds in proteins [equation (1)]. The biological roles of proteases are incredibly diverse: they are essential to all processes that characterize a living organism, from its inception as an independent entity to the degradations of its tissues after death. Because their study has a long history, various nomenclatures have developed. The general terms protease, peptidase, peptide hydrolase, proteolytic enzyme, and proteinase are used interchangeably, although not always correctly so.

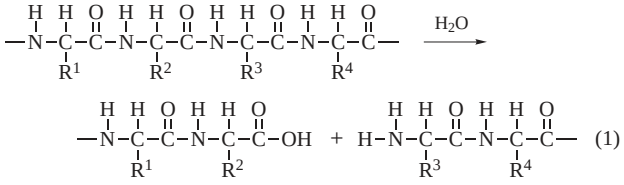

(1)

A wide variety of proteases have been isolated and characterized. Some proteases have specificity for cleaving the amino acid at the carboxyl or amino end from a protein; these are exopeptidases. Endopeptidases or proteinases act on peptide bonds within a protein chain. As understanding of the chemical natures of the proteases advanced, it became apparent that classification of these enzymes on the basis of similarities in their active sites, the mechanisms of their catalytic action, or their tertiary structures was useful.

Regardless of origin, serine proteases feature a triad of amino acids (aspartic acid, serine, histidine) in their active site. Commonly studied examples of this type of protease include trypsin, chymotrypsin, elastase, subtilisin, thrombin, and various components of the complement cascade. The fold of the polypeptide chain(s) that make(s) up such enzymes brings the critical triad of amino acids into close proximity, even though they may be highly separated in terms of their positions along the linear (primary) sequence. The drawings in Figure 1 depict the tertiary structures of α-chymotrypsin, a serine protease from the cow, and subtilisin, a serine protease from the bacterium *Bacillus amyloliquifaciens*. Because of the separation of these two organisms in evolution, homology between their primary sequences would not be expected and none is found. Given the lack of sequence homology, the very different tertiary structures for the enzymes indicated in Figure 1 are not unexpected. However, both enzymes function in essentially the same way and have the same arrangement of the aspartate–histidine–serine triad at their active sites.

Catalysis by serine proteases involves acylation of the serine residue in the triad by transfer of the acyl group of the substrate to the enzyme (Figure 2). In a latter phase of the process, the enzyme guides a water molecule in an attack on the carbonyl group of the acylated enzyme, hydrolyzing this species and regenerating the native (active) enzyme.

In cysteine proteases, the serine of the aspartate–serine–histidine triad is replaced by a cysteine residue—in effect the nucleophilic hydroxyl group (OH) of serine is changed to the more nucleophilic sulfhydryl group (SH). Many proteases isolated from plants have proven to be cysteine proteases, including papain from the papaya, bromelin from the pineapple, and ficin from different species of *Ficus*. Cysteine proteases from mammalian tissues include the cathepsins, several related enzymes, and the calpains, which are multisubunit, calcium-dependent proteases.

Aspartic proteases utilize a constellation of aspartic acid residues at their active sites to achieve catalysis, and usually have maximal activity at low pH. The mammalian enzymes renin, pepsin, and chymosin are examples of this class of proteases, but enzymes from bacterial and fungal sources have also been extensively studied. Proteases from retroviruses are aspartate proteases and one of these, the protease from HIV-1, is presently the target of much attention.[1]

Some exopeptidases include a coordinated metal atom as part of their active center. A representative of this class of metalloproteases is bovine carboxypeptidase A, which has specificity for cleaving the carboxyl terminal residue from a protein when that amino acid has an aromatic or aliphatic side chain.

Proteins are essential structural components of an organism; even the catalysts (enzymes) for a myriad of reactions that

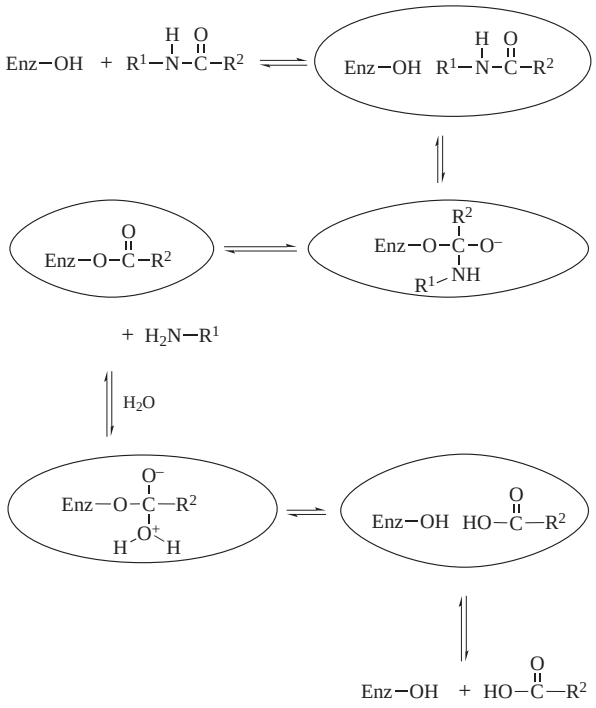

Figure 2 Mechanism of action of serine proteases. In the first step, substrate binds to the enzyme, here represented by the symbol Enz−OH, to give a Michaelis complex. Within the complex, the hydroxyl group of the serine residue attacks the carbonyl group of the substrate to give an intermediate in which the carbonyl carbon becomes tetrahedral. Departure of the amino part of the substrate leaves the acid part covalently bound to the enzyme—the serine hydroxyl group has been acylated. The acyl enzyme undergoes attack by a water molecule and is ultimately hydrolyzed to give a complex of the acid part of the substrate with the enzyme. This dissociates to give back the native enzyme. Changes in protein conformation and dynamics probably accompany each stage of the reaction and are indicated by alterations in the dashed structures. Details of the mechanism depend on the nature of the substrate and the enzyme

take place within the organism are proteins. The activity of protein-destroying enzymes (proteases) within the organism must therefore be controlled so the organism can exist. Several strategies for achieving regulation of protease activity have evolved. (i) A protease may be produced in an inactive, incipient form called a zymogen. The zymogen is converted into active enzyme by a limited attack of another protease, and cleavage of one or two peptide bonds of the zymogen is usually sufficient to convert it into active enzyme. (ii) Proteins which inhibit specific enzymes are present in many tissues. These inhibitors bind so tightly to their target enzyme that its active site is inaccessible to substrate and water molecules. (iii) The activities of some proteases are regulated or activated by the presence of metal ions, especially calcium and magnesium. (iv) Cellular proteins are continuously turning over; the halflife for a particular protein is typically between several minutes and several days. The amount, and thus the activity, of an enzyme that is present at a given location depends on the balance between the processes leading to its formation and degradation, both of which are themselves highly regulated.

The proteases for which most information is available generally range in size from about 25 kDa to 100 kDa, although proteinases with molecular weights of 800 000 kDa are known. Thus, except for viral proteases (ca. 14 kDa), the NMR technologies that have been developed over the past decade for the determination of the three-dimensional structures of proteins are unlikely to be productive with typical proteases, given the current state of the art.[2] The crystal structures of several dozen of the smaller proteases have been solved and these are the bases for virtually all information about three-dimensional structure that is available for these enzymes. However, there are inherent limits to what crystallography can tell about proteases and, as indicated by the examples below, NMR spectroscopy has contributed importantly to our understanding of many details of protease structure and function.

2 NATURE OF THE CATALYTIC TRIAD

The constancy in the appearance of the aspartate, serine, and histidine residues at the active site of serine proteases indicates that the processes of evolution have converged to a successful mechanism for catalysis, one that depends on the juxtaposition and interaction of the side chains of these amino acids. On the basis of the distances between heavy atoms and chemical intuition, it was proposed in 1969 that the structure shown in Figure 3 summarizes the interactions between these side-chains at neutral pH.[3] The carboxyl group of the aspartate was presumed to be ionized, and hydrogen bonds, which involve the serine hydroxyl hydrogen interacting with nitrogen-ϵ_2 of the imidazole ring of the histidine, and the hydrogen attached to nitrogen-δ_1 of the imidazole interacting with the negatively charged aspartate side chain, were inferred. The positioning of protons in the catalytic triad of serine proteases is critical to understanding the chemical and structural reasons for the catalytic effect of these enzymes. However, X-ray diffraction studies do not reveal the positions of the hydrogen atoms in protein crystals, and the location of the hydrogens in the catalytic triad has not been without controversy.

Using frequency sweep CW NMR spectroscopy, early workers observed a very broad resonance in the range 14–18 ppm from TMS in the ^{1}H NMR spectra of a number of serine proteases.[4] This signal disappeared when the solvent H_2O was replaced by D_2O and had an intensity corresponding to a single proton. It has been detected in chymotrypsinogen and trypsinogen, the zymogen precursors of chymotrypsin and trypsin, respectively, but not in proteins that do not have the catalytic triad. Assignment of this high-frequency (low-field) resonance to the proton in the hydrogen bond between histidine and aspartic acid was supported by the observation that chemical modifications of the histidine or serine residues

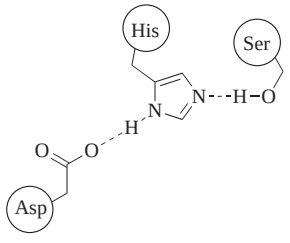

Figure 3 Representation of the catalytic triad of amino acids at the active sites of serine proteases, as inferred from X-ray crystallographic results

thought to prevent the formation of this hydrogen bond led to the disappearance of the signal. Unequivocal confirmation of the assignment came later from a study of α-lytic protease, a bacterial serine protease, in which nitrogen-δ_1 of the histidine imidazole was specifically labeled with nitrogen-15.[5] In this system a doublet is observed at the high-frequency position due to spin coupling with nitrogen-15.

The high-frequency resonance of serine proteases is about 100-times broader than backbone amide N–H signals from these proteins. Studies of this signal from porcine trypsin indicate that its width, but not its position, is strongly temperature-dependent. Such observations are consistent with the notion that broadening of the peak by some kind of exchange process is present. This exchange process is presumably the interconversion of protein species with magnetically distinguishable three-dimensional structures, and appears to take place on the ms timescale.[6]

Conflicting experimental results have made the ionization behavior of the histidine residue in the catalytic triad controversial. Depending on the protein examined, with increasing pH the high-frequency ^{1}H NMR signal from serine proteases and their zymogens moves from its position at about 18 ppm to a position near 15 ppm. The pK_a value of the group whose titration is detected by such experiments is near 7, consistent with the expected acid–base behavior of the imidazole ring of a histidine residue in a reasonably solvent-exposed environment.[7] Strong confirmation of normal ionization behavior for the histidine residue in the catalytic triad of serine proteases has come from ^{15}N NMR studies in which the nitrogens of the imidazole ring are labeled with nitrogen-15.[8]

Nitrogen-15 NMR spectroscopy with α-lytic protease in which one or both nitrogen atoms of the active-site histidine residue have been enriched with nitrogen-15 suggests that in solution a hydrogen bond exists between the histidine and the serine residues in the resting enzyme, as depicted in Figure 3.[9] This conclusion is at variance with several X-ray crystallographic studies of serine proteases which have been interpreted to show that the histidine and serine residues are too far apart and improperly aligned for appreciable hydrogen bonding between them. The discrepancy between the conclusions of the NMR studies of this enzyme in solution and X-ray studies of the crystalline protein have been resolved by ^{15}N CP MAS NMR experiments with the crystalline enzyme.[10] The nitrogen-15 spectrum of α-lytic protease is essentially identical in solution and in the solid state (Figure 4), indicating that the histidine–serine and aspartate–histidine hydrogen-bonding interactions are identical in the two states. It was determined that the source of the disagreement between the indications of the X-ray and NMR experiments is elevation of the histidine pK_a value to 7.9 in the solid state, so that at the pH used for the preparation of the samples examined by X-ray studies, the histidine residue is fully protonated and thus unable to participate in hydrogen bonding. Why the pK_a value of the histidine is elevated in the crystal in not clear, but this may be a consequence of the high concentration of salts present during the protein crystallization.

3 FOLDING TO ACTIVE PROTEIN

The three-dimensional structure of a protein is encoded by its amino acid sequence, although the mechanisms by which the polypeptide becomes folded into the correct three-dimensional structure remain obscure. In Nature, serine proteases are often synthesized as precursors that have additional polypeptide attached to the C-terminal or N-terminal amino acids of the enzyme. The 'extra' polypeptide has a role in folding the material to the functional structure. For example, subtilisin BPN′, an extracellular serine protease from a baccillus, requires a sequence of 77 extra amino acids at its N-terminal for correct folding. This sequence is only transiently linked to the enzyme and, after folding is completed, it is autocatalytically cleaved to produce the active enzyme. It has been shown that in vitro the peptide does not have to be covalently linked to the remainder of the structure in order to exert an effect on folding.

Circular dichroism (CD) experiments demonstrate that native (active) subtilisin BPN′ is unfolded by dissolving the enzyme in 6 M guanidine hydrochloride. The majority of the secondary structural elements (helices, sheets, turns) of the protein reform when the guanidine hydrochloride is removed.[11] An ^{1}H NMR spectrum of the unfolded-then-refolded protein is shown in Figure 5. Because of local magnetic anisotropies, proteins with developed tertiary structures exhibit appreciable dispersion of the chemical shifts of the backbone peptide/amide N–H protons and, to a lesser extent, the chemical shifts of methyl protons of alanine, valine, isoleucine, and leucine side chains. Thus, the ^{1}H NMR spectrum of native subtilisin BPN′ [Figure 5(a)], with the amide N–H resonances spread over about 4 ppm, is typical of a protein with a well-developed tertiary structure.[12] The corresponding spectrum of the unfolded-then-refolded protein [Figure 5(b)] shows little evidence of this shift dispersion and indicates that, despite the presence of secondary structures, there is little organization of these elements into a tertiary structure.

4 PROTEASE DYNAMICS

Tosyl fluoride, and other aromatic sulfonyl fluorides, react with the serine at the active site of serine proteases to afford a protein that is inactive by virtue of the formation of a sulfonate ester with this residue (**1**). This structure is a stable analog of the acylated enzyme intermediates that are transiently present during catalysis by the enzyme (cf. Figure 2). In the case of the tosyl derivative of α-chymotrypsin, crystallographic studies show that the tosyl ring fits snugly into a depression on the surface of the protein; it is this depression or 'tosyl pocket' that is thought to be largely responsible for the observed specificity of chymotrypsin for the cleavage of peptide bonds adjacent to amino acid residues carrying aromatic side chains. During catalysis, the side chains of the substrates must become sufficiently immobilized that the correct orientation of the stereoelectronic features of the active site essential for catalysis is achieved, but not to such an extent that the products of the reaction cannot rapidly depart from the enzyme.

Mobility of the tosyl ring of tosylchymotrypsin has been explored by studies of the nuclear spin relaxation of carbon-13, deuterium, and tritium nuclei that have been placed in the tosyl ring. At pH 4 the data indicate that the tosyl ring moves in and out of the tosyl pocket rapidly, spending on average only about one-half of the time within the pocket. The aromatic ring of the tosyl group is considerably more mobile than would be

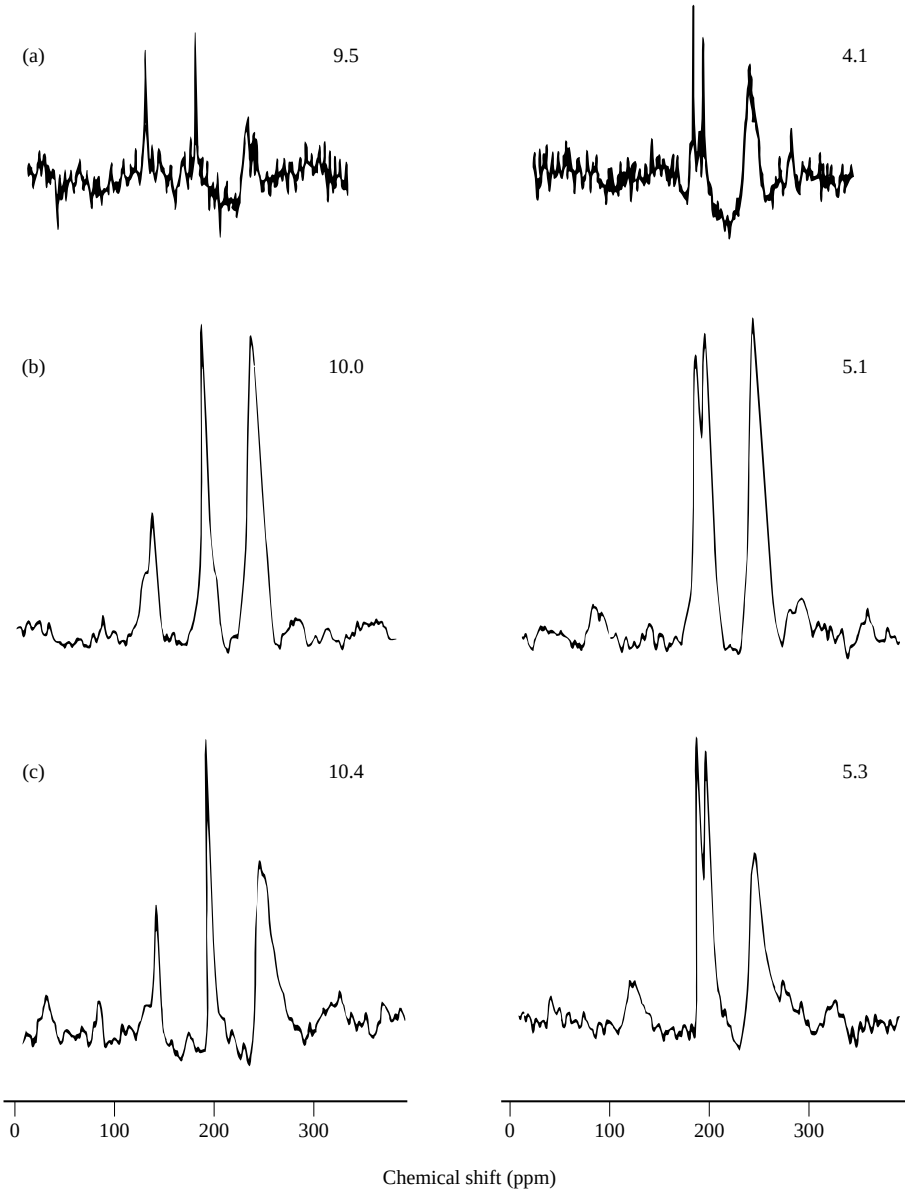

Figure 4 Nitrogen-15 NMR spectra of α-lytic protease in which the histidine residue has been doubly nitrogen-15 labeled. (a) Native protein in solution, (b) a frozen solution of the protein, (c) crystals of the protein. Spectra (b) and (c) were obtained with cross polarization; the signal at 255 ppm arises from nitrogen-15 at natural abundance in the amide groups of the protein backbone. The sample pH is indicated at the right of each spectrum[10]

expected for a group that resides exclusively in the tosyl pocket of the enzyme.[13]

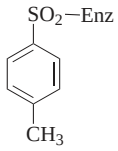

(1)

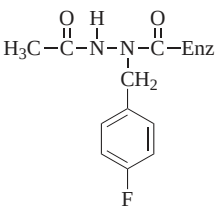

(2)

The relatively high mobility of the tosyl group in this model for acylated enzymes contrasts strongly with the mobility found for acylenzyme (**2**). In this case the analogy of the structure of the acylenzyme examined to the acylenzyme expected during the reaction of a specific substrate (such as one containing a phenylalanine residue) is much stronger and NMR relaxation measurements indicate that the fluorinated aromatic side chain of acylenzyme (**2**) is highly immobilized.[14]

5 INHIBITION OF PROTEASES

5.1 Protein Inhibitors of Proteases

The activity of some proteases in both plants and animals is regulated by polypeptide inhibitors that bind tightly to the active centers of enzymes. Such protein inhibitors present a

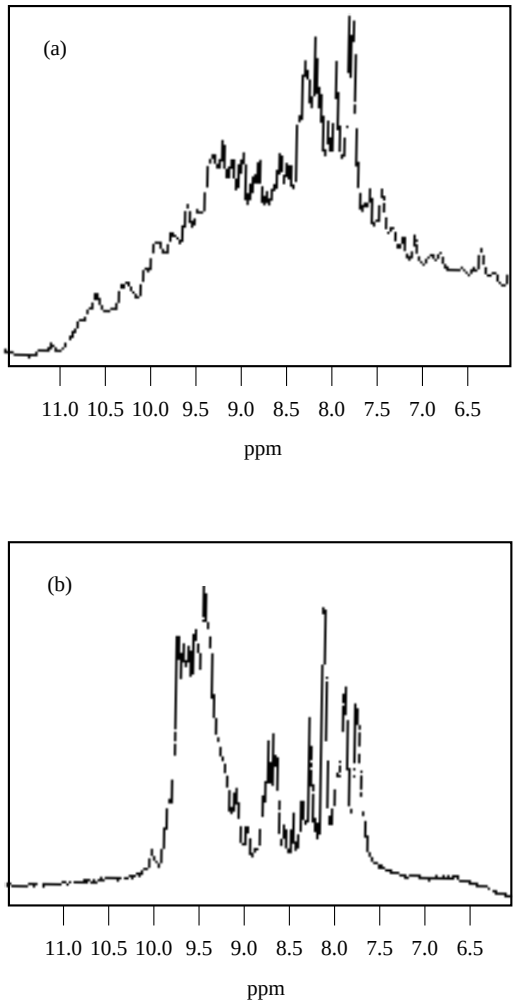

Figure 5 ^{1}H NMR spectrum of native subtilisin BPN′ at 500 MHz (a) and of subtilisin BPN′ that had been unfolded in 6 M guanidine hydrochloride, then refolded by removal of this denaturing agent (b)[12]

surface that is highly complementary to that of their target enzymes, and, while they may undergo attack by the protease, products of that reaction cannot diffuse away from each other and the protease because of the strength of the interactions at the protein surfaces. For some reason leguminous plants contain extraordinarily large quantities of serine protease inhibitors. The Bowman–Burk inhibitor from soybean, a polypeptide of 71 amino acids, is an example of such an inhibitor, although it is unusual in that it has two distinct protease-binding domains, one that is specific for interaction with trypsin and another specific for chymotrypsin. The tertiary structure of the Bowman–Burk inhibitor in solution has been determined from interproton distance and dihedral angle information afforded by standard two-dimensional ^{1}H NMR experiments.[15]

The rate at which a peptide N–H proton of a protein exchanges with protons of the solvent is diagnostic of the extent to which that N–H is exposed to the solvent. Those peptide groups buried within relatively static parts of the tertiary structure of a protein, or which reside at the interface between interacting protein molecules, are protected from the solvent and exhibit reduced N–H exchange rates. The rates of exchange with solvent for the N–H protons of the Bowman–Burk inhibitor in the absence and presence of bound chymotrypsin were determined by means of 2D ^{1}H NMR experiments which tracked the disappearance of N–H/C_{α}H NOE cross peaks with time. The rates of N–H exchange for the residues between positions 37 and 48 of the inhibitor, with two exceptions, were dramatically slowed within the protease–inhibitor complex, indicating that these residues reside within the surface where these two components make contact with one another. Computer modeling led to a proposed structure for the chymotrypsin–inhibitor complex that is consistent with the experimental N–H exchange rate data and is similar to structures of other serine protease–inhibitor complexes that have been determined by diffraction methods.[16]

5.2 Natural Small Molecule Protease Inhibitors

The microorganism *Actinomycetes* elaborates a group of highly effective tripeptide-based protease inhibitors. One of the major components is leupeptin, *N*-acetyl-L-leucyl-L-leucyl-L-argininal (**3**). Tight binding of this compound to serine proteases is reasonably presumed to be the result of formation of a hemiacetal by attack of the serine residue of the active site on the carbonyl group of the C-terminal aldehyde of leupeptin. An analogous process would take place when the inhibitor binds to thiol proteases.

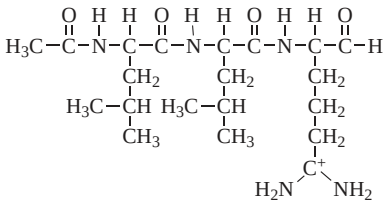

(3)

Attempts to demonstrate the existence of hemiacetals or hemithioacetals in these systems have produced conflicting results. ^{13}C NMR spectroscopy of leupeptin, labeled with carbon-13 at the aldehyde carbonyl, provides strong evidence that hemiacetal formation indeed occurs upon binding of leupeptin to the serine protease trypsin.[17] Four carbon resonances were observed for the enriched carbon in the absence of protein: 202.1, 90.3, 76.5, and 77.0 ppm, assigned to the aldehyde form of the inhibitor, the aldehyde hydrate, and the *R*- and *S*-configurations of a cyclic carbinolamine, respectively. In the presence of trypsin, two additional signals in the spectrum at 98.8 and 97.2 ppm were observed. Based on their carbon chemical shifts and the chemical shifts of protons near the bound leupeptin that gave rise to ^{1}H{^{1}H} NOEs (detected in carbon-13 isotope filtering experiments), these signals were assigned to tetrahedral species that result from the reaction of the active site serine hydroxyl with the aldehyde group of the inhibitor. The two signals observed for the adduct correspond to the *R*- and *S*-isomers resulting from attack of the serine residue on either side of the aldehyde group of the inhibitor.

Significantly, ^{13}C CP MAS experiments with the solid leupeptin–enzyme complex showed carbon-13 signals at 98.8 and 96.5 ppm, indicating that the tetrahedral enzyme–inhibitor complexes form in the solid state and that their structures

are very similar to those detected in solution by the NMR experiments mentioned.

5.3 Synthetic Small Molecule Inhibitors

Information about the protein-bound conformation of a small molecule is useful in the design of new, better binding ligands and, thus, is an important component in the rational design of new pharmaceutical agents. Isotope editing is one of several NMR approaches useful in defining the conformations of ligands bound to proteins. These editing or filtering procedures select for observation only those signals that arise from protons attached to a hetero nucleus and their scalar-coupled or relaxation-coupled partners.[18] Peptide analog (**4**) is an excellent inhibitor of the aspartate protease pepsin. A collection of specifically carbon-13 and nitrogen-15 labeled variants of this inhibitor has been used in isotope-edited experiments to detect NOEs between protons in different parts of the inhibitor and between protons of the inhibitor and the enzyme. These data showed that the inhibitor adopts an extended conformation when bound to pepsin.[19]

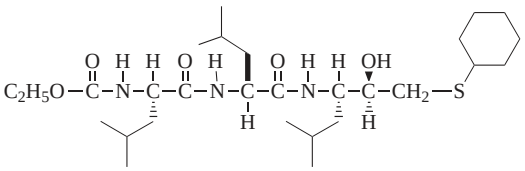

(4)

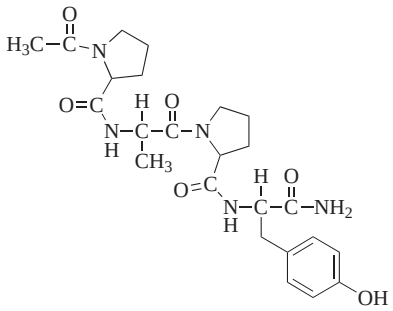

(5)

Another means of defining the structure of protease–small molecule complexes is through transferred NOEs. In this experiment the concentration of ligand can exceed that of its protein receptor, thus overcoming sensitivity limitations when the protein is present in inconveniently low concentrations. A requirement for this technique to be effective is that the rate of dissociation of the enzyme–small molecule complex be rapid enough that T_1 relaxation processes are at or near the fast exchange limit. The conformation of peptide (**5**) bound to the serine protease porcine pancreatic elastase was deduced from a set of 23 interproton distance constraints derived from two-dimensional transferred NOE experiments.[20]

Incorporation of difluoromethyl or trifluoromethyl ketones into substrate analogs can produce excellent inhibitors of serine or thiol proteases. The carbonyl group of these materials is rendered highly electrophilic by the electron-withdrawing effects of the adjacent fluorine atoms and is a likely target for attack by the reactive serine or cysteine at the active sites of these enzymes. An example is peptide analog (**6**) which is an inhibitor of chymotrypsin.[21]

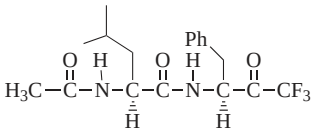

(6)

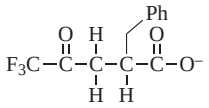

(7)

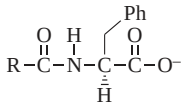

(8)

Fluorine chemical shifts in such structures are sensitive to hydration or hemiketal formation and enzyme binding. For compound (**6**), ^{19}F, ^{13}C, and ^{1}H NMR observations led to the conclusion that the keto group of the inhibitor is present in the enzyme environment as an ionized hemiketal, such that the enzyme is able to stabilize a tetrahedral oxyanion form of the inhibitor that is presumably analogous to the tetrahedral intermediates that form during catalysis (Figure 3).

Carboxypeptidase, a metalloexoprotease, is inhibited by 2-benzyl-4-oxo-5,5,5-trifluoropentanoic acid (**7**). Comparison with the structure of a peptide substrate of the enzyme (**8**) indicates that the electrophilic keto group in (**7**) is well positioned for undergoing attack by a nucleophilic group at the active site. However, X-ray crystallography has shown that, at least in the crystalline state, it is the ketone hydrate that is bound to the enzyme.

Fluorine NMR studies of the trifluoromethyl ketone show a single sharp resonance which has been assigned to the hydrate, a conclusion additionally supported by carbon-13 data. In the presence of carboxypeptidase two broad ^{19}F NMR signals were observed and assigned to the complex formed by the protein-bound trifluoromethyl ketone hydrate in the L-configuration and the complex in which hydrate is the D-enantiomer. Competition studies showed that 2-benzylsuccinate, a good competitive inhibitor of the enzyme, preferentially displaced the L-isomer.[22]

6 NEW PROTEASES

Conversion of the essential serine residue at the active center of serine proteases by chemical means to cysteine or selenocysteine has been achieved. These new enzymes remain catalytically active but a change of the OH group at the active site to SH or SeH alters the reactivity, specificity, or stability of the enzyme. Selenosubtilisin, produced by 'mutating' the active site serine residue of the protease subtilisin Carlsberg to selenocysteine, has been examined by ^{77}Se NMR.[23] Selenium chemical shifts span a 3400 ppm range and are extremely sensitive to the oxidation state. Protein crystallography is not useful in characterizing the oxidation state of selenium, and this system provides another example of how NMR observations can provide detailed information about proteases that is complementary to the results of diffraction experiments.

The enzyme was found by NMR to exist in selenolate, selenyl sulfide, and selenic acid forms. The first two of these are catalytically active. Like the serine proteases, these

selenium-containing enzymes exhibit highly deshielded proton resonances at roughly 18 ppm from TMS. This signal can be assigned with some confidence to the proton attached to nitrogen-δ_1 of the histidine residue at the active site. In contrast to native subtilisin, the seleninate and selenoate analogs show a second N–H resonance at 14–15 ppm which has been assigned to a proton bonded to nitrogen-ϵ_2 of this histidine. This proton is evidently positioned to engage in hydrogen bonding with the adjacent seleninate or selenolate group. Involvement in a strong hydrogen bond would be consistent with the resistance of this N–H hydrogen to exchange with solvent, as indicated by the ^{1}H NMR data. Studies of pH dependence indicated that the pK_a value of the active site histidine must be at least 3 pH units higher than the pK_a value of the corresponding histidine in the native, serine-containing enzyme.

Protein engineering technologies now make available an infinite variety of new proteases that differ from their native progenitors by one or more amino acids. It will interesting to see what NMR observations can reveal about the structural and functional consequences of these mutations.

7 PROTEASES IN ORGANIC SOLVENTS

There is burgeoning interest in the use of proteases as catalysts in organic solvents or other nonstandard media for the cleavage of bonds, or for the formation of bonds by forcing the enzymatic hydrolysis reaction to 'run backwards'.[24] Solid state ^{15}N NMR studies of histidine-labeled α-lytic protease crystals suspended in a variety of organic solvents suggest that the structural integrity of the active center of this protease remains unperturbed in several organic solvents, including acetone and octane, but appears to be lost when the enzyme is exposed to dimethyl sulfoxide. Alternation of the catalytic activity of this enzyme by organic solvents appears not to be always due to a loss of the critical orientations of the residues of the catalytic triad in these media but the result of other considerations.[25]

8 SUMMARY

Most proteases are too large to be realistic candidates for three-dimensional structure determination by NMR methods. However, NMR experiments have been used to provide important details of protease structure and function, and have been important in demonstrating the extent to which conclusions about protease structure and function based on crystallographic (solid state) results are applicable to the corresponding proteins in solution. NMR results can uniquely provide information about structural dynamics and the binding of large and small molecules to proteases that is not obtainable by crystallography.

9 GENERAL REFERENCES

R. H. Abeles, P. A. Frey, and W. P. Jencks, *Biochemistry*, Jones and Bartlett, Boston, MA, 1992.

A. J. Barrett (ed.), *Proteinases in Mammalian Cells and Tissues*, North-Holland, Amsterdam, 1977.

R. J. Beynon and J. S. Bond (eds.), *Proteolytic Enzymes: A Practical Approach*, IRL Press, Oxford, UK, 1989.

B. M. Dunn (ed.), *Structure and Function of Aspartic Proteases*, Plenum Press, New York, 1991.

A. Fersht, *Enzyme Structure and Mechanism*, Freeman, San Francisco, CA, 1977.

L. Polgár, *Mechanisms of Protease Action*, CRC Press, Boca Raton, FL, 1990.

10 RELATED ARTICLES

Amino Acids, Peptides and Proteins: Chemical Shifts; Biological Macromolecules; Biological Macromolecules: NMR Parameters; Pancreatic Trypsin Inhibitor; Peptides and Polypeptides; Protein Dynamics from NMR Relaxation; Protein Dynamics from Solid State NMR; Structures of Larger Proteins, Protein-Ligand, and Protein-DNA Complexes by Multi-Dimensional Heteronuclear NMR.

11 REFERENCES

1. A. Wlodawer and J. W. Erickson, *Annu. Rev. Biochem.*, 1993, **62**, 543.
2. G. Wagner, S. G. Hyberts, and T. F. Havel, *Annu. Rev. Biophys. Biomol. Struct.*, 1992, **21**, 167.
3. D. M. Blow, J. J. Birktoft, and B. S. Hartley, *Nature (London)*, 1969, **221**, 337.
4. G. Robillard and R. G. Shulman, *J. Mol. Biol.*, 1974, **86**, 519.
5. W. W. Bachovchin, *Proc. Natl. Acad. Sci. USA*, 1985, **82**, 7948.
6. J. L. Markley, *Biochemistry*, 1978, **17**, 4648.
7. J. L. Markley, in *Biological Applications of Magnetic Resonance*, ed. R. G. Shulman, Academic Press, New York, 1979.
8. W. W. Bachovchin and J. D. Roberts, *J. Am. Chem. Soc.*, 1978, **100**, 8041.
9. W. W. Bachovchin, *Biochemistry*, 1986, **25**, 7751.
10. S. O. Smith, S. Farr-Jones, R. G. Griffin, and W. W. Bachovchin, *Science*, 1989, **244**, 961.
11. J. Eder, M. Rheinnecker, and A. R. Fersht, *J. Mol. Biol.*, 1993, **233**, 293.
12. J. Eder, M. Rheinnecker, and A. R. Fersht, *Biochemistry*, 1993, **32**, 18.
13. T. M. O'Connell, J. T. Gerig, and P. G. Williams, *J. Am. Chem. Soc.*, 1993, **115**, 3048.
14. J. T. Gerig and S. J. Hammond, *J. Am. Chem. Soc.*, 1984, **106**, 8244.
15. M. H. Werner and D. E. Wemmer, *Biochemistry*, 1992, **31**, 999.
16. M. H. Werner and D. E. Wemmer, *J. Mol. Biol.*, 1992, **225**, 873.
17. C. Ortiz, C. Teller, H. Williams, N. J. Stolowich, and A. I. Scott, *Biochemistry*, 1991, **30**, 10 026.
18. S. W. Fesik, *J. Med. Chem.*, 1991, **34**, 2937.
19. S. W. Fesik, E. R. P. Zuiderweg, E. T. Olejniczak, and R. T. Gampe, Jr., *Biochem. Pharmacol.*, 1990, **40**, 161.
20. G. M. Clore, A. M. Gronenborn, G. Carlson, and E. F. Meyer, Jr., *J. Mol. Biol.*, 1986, **190**, 259.
21. T.-C. Liang and R. H. Abeles, *Biochemistry*, 1987, **26**, 7603.
22. C. Teater, D. Grobelny, and R. E. Galardy, *Biochem. Biophys. Res. Commun.*, 1988, **153**, 773.
23. K. L. House, R. B. Dunlap, J. D. Odom, Z.-P. Wu, and D. Hilvert, *J. Am. Chem. Soc.*, 1992, **114**, 8573.

24. P. A. Fitzpatrick, A. C. U. Steinmetz, D. Ringe, and A. M. Klibanov, *Proc. Natl. Acad. Sci. USA*, 1993, **90**, 8653.
25. P. A. Burke, S. O. Smith, W. W. Bachovchin, and A. M. Klibanov, *J. Am. Chem. Soc.*, 1989, **111**, 8290.

Biographical Sketch

J. T. Gerig. *b* 1938. B.A., 1960, College of Wooster, Ph.D., 1964, Brown University (supervisor: J. F. Neumer). Postdoctoral work, California Institute of Technology, 1964–66 (supervisor: J. D. Roberts). Faculty, University of California, Santa Barbara, 1966–present. Approximately 130 publications. Research interests include applications of NMR spectroscopy to studies of proteins and nucleic acids, in vivo NMR spectroscopy, and computer simulations of NMR phenomena.

Time-Resolved Solid State NMR of Enzyme–Substrate Interactions

Jeremy N. S. Evans
Washington State University, Pullman, WA, USA

1 Introduction 1
2 Which Types of Enzymes can be Studied by NMR? 1
3 Linewidths in Enzyme Complexes 2
4 Direct Observation of Enzyme–Substrate/Intermediate Complexes 2
5 Related Articles 6
6 References 6

1 INTRODUCTION

Although the introduction and development of multidimensional ^{1}H NMR techniques over the last 10 years has revolutionized the structural elucidation of proteins with $M_r \leq 35$ kDa, the majority of enzymes fall outside this molecular weight range. Thus for larger enzymes, the complete structure cannot currently be determined by NMR. But one of the distinguishing features of NMR spectroscopy as a technique for structural biology is its ability to provide crucial structural information about a specific part or region of a molecule. This sets NMR apart from other structural techniques such as X-ray crystallography, in which in general the whole structure must be completely solved before a selected region can be investigated. This ability to focus on structural regions of interest is no more important than in the field of protein function, where the relationship between structure and function is intimately connected at the enzyme active site. The use of heteronuclear MR, in particular nuclei such as ^{13}C, ^{15}N, ^{19}F, and ^{31}P, has been important in providing the means to focus on enzyme active sites for proteins whose $M_r = 25–100$ kDa.

In this article we will consider the ways in which such heteronuclear NMR approaches may be applied to the study of enzyme–substrate interactions, and specifically consider the approach of time-resolved solid state NMR spectroscopy, which was introduced recently by our laboratory.

2 WHICH TYPES OF ENZYMES CAN BE STUDIED BY NMR?

Not all enzymes are amenable to study by NMR spectroscopy. The limitations arise because of a number of factors, the two most important being: molecular weight, M_r, and also the k_{cat} of the enzyme. We will consider the effects of these limitations in sections 3 and 4. The types of functional information that can be obtained on enzymes may be summarized as follows:

1. The flux of isotopically labeled substrates to products through an enzyme-catalyzed pathway may be obtained by solution state NMR. This can lead to the identification of enzyme-free intermediates.
2. The structure of an isotopically labeled inhibitor bound to an enzyme may be determined by solution state ($M_r \leq 50$ kDa) or solid state ($M_r \leq 150$ kDa) NMR. This can be used in conjunction with protein structural methods by NMR or X-ray crystallography, for the identification of functional residues in the enzyme active site and a possible rôle in catalysis.
3. The structure of an enzyme–substrate or enzyme–intermediate complex of a multisubstrate enzyme with an insufficient number of substrates for the reaction to proceed can be carried out by solution state or solid state NMR.
4. The structure of an enzyme–substrate or enzyme–intermediate complex of a freely reversible enzyme can be determined by solution state or solid state NMR by balancing the concentrations of substrate and product, and allowing maximum accumulation of intermediate (depending on k_{cat}, K_M, and exchange rates).
5. The structure of an enzyme–substrate or enzyme–intermediate complex can be determined at low temperature by cryoenzymological solution state NMR and solid state NMR.

We will discuss these methods in more detail in Section 4.

In the foregoing list, the word ‘structure’ is used frequently, and it is important to realize the limits of the structural information that can be obtained. Clearly the molecular weight will affect the detail of the information obtainable, or put more formally, above $M_r = 35$ kDa, there is an inverse relationship between the number of distance restraints and molecular weight. The same sorts of considerations that apply to high-resolution ^{1}H NMR of proteins also, of course, apply to enzymes. Therefore alternative strategies have to be adopted to obtain structural information. The use of isotopic labels introduced at specific locations in the enzyme substrate or inhibitor molecule can be used for heteronuclear MR studies. But the detection of the resonance from such an isotope provides, in the first instance, only a chemical shift. This can be highly diagnostic: for example, if the enzyme catalyzes the cleavage of an amide bond via a tetrahedral sp^3 carbon, then the ^{13}C resonance would shift from around 200 ppm to around 100 ppm. But chemical shifts, a structure do not make! By analogy with the chemical shifts of model compounds, together with pH titration behavior, relaxation data, and J coupling data (e.g. for heteronuclei the spectrum can be obtained with and without ^{1}H decoupling), a structure can be deduced. However, the information that is most useful is distance or torsion angle restraints of some kind, from NOEs, transferred NOEs, paramagnetic relaxation enhancements, or dipolar couplings. Only with this information coupled with the other data, can the structure of a substrate, inhibitor, or intermediate be determined with any certainty.

The relationship of that ligand to the rest of the biomolecule poses a different type of problem, and yet again distance or torsion angle restraints are the data required to resolve it. Sometimes distance or torsion angle restraints can be used in conjunction with a low-resolution X-ray crystal structure, or an X-ray structure of the protein in the absence of ligand, in docking experiments. Above all it is the quality rather than the quantity of restraints that helps to define good structures for

larger enzyme–substrate or enzyme–intermediate complexes. This is in contrast to smaller protein structures, in which the quantity of relatively poor-quality distance restraints can generate remarkably accurate and in some cases precise structures.

3 LINEWIDTHS IN ENZYME COMPLEXES

In any NMR investigation of an enzyme complex, whether this involves heteronuclear studies of isotopically enriched substrates or intermediates, or homonuclear studies of the protein itself, the single most important factor crucial to successful detection of the resonance of interest is its linewidth. The linewidth of an NMR resonance is given by:

$$\Delta\nu_{\frac{1}{2}} = \frac{1}{\pi T_2^*} \tag{1}$$

where $\Delta\nu_{\frac{1}{2}}$ is the linewidth at halfheight, and T_2* is the apparent transverse relaxation time. Linewidths in enzyme complexes are determined essentially by two factors: (i) the overall rotational correlation time, τ_c, of the macromolecule, or (ii) chemical exchange. The rotational correlation time for globular proteins may be calculated using the Stokes–Einstein equation:

$$\tau_c = \tfrac{4}{3}\pi r^3 \frac{\eta}{k_B T} \tag{2}$$

where r is the molecular radius, η is the viscosity of the medium, k_B is Boltzmann's constant, and T is the temperature in kelvin. Assuming $M_r \propto r$,

$$\tau_c \approx M_r \times C \tag{3}$$

where C is typically 1.3×10^{-12} (calculated from T_1 values for backbone α-carbons at field strengths $\leq$2.4 T).[1] Note that this latter relation is *very* approximate.

Such an estimate of rotational correlation time is based on the assumption that the overall tumbling rate dominates the relaxation for nuclei in this molecule, even if it is a small molecule complexed with a large one such as an enzyme–substrate or enzyme–intermediate complex. There are exceptions to this, in which the local librational motion is greater than the tumbling. In these cases, mobile domains are detectable even in very large proteins.

4 DIRECT OBSERVATION OF ENZYME–SUBSTRATE/INTERMEDIATE COMPLEXES

The quest for an understanding of the molecular details of enzymatic catalysis has been a major motivation for much biochemical and biophysical research during the last decade. A crucial part of this endeavor has been the structural investigation of intermediates, which has played an important rôle in the elucidation of enzymatic reaction mechanisms. An enzymatic reaction mechanism can be said to be understood when (i) the enzyme-bound intermediate(s) can be detected and its structure determined; (ii) the kinetic competence of the enzyme has been demonstrated (i.e. the rate of formation and degradation are consistent with the forward and reverse reaction rates);[2] and (iii) the internal microscopic rate data are consistent with a reaction pathway in which all thermodynamic and kinetic states have been described. The use of ^{31}P, ^{13}C, and ^{15}N NMR in solution is a well-established technique for the study of enzymatic reaction mechanisms.[1,3–5]

The elucidation of the structure of an enzyme–substrate complex at various points along the reaction coordinate is one of the most sought-after goals of enzyme chemistry. Currently there are two approaches to stabilizing enzyme–intermediate complexes so that they can be examined by NMR: low-temperature solution state cryoenzymological NMR, and the recently introduced method of time-resolved solid state NMR spectroscopy.

4.1 Cryoenzymology

There are a considerable number of enzymatic reactions for which the catalytic rate is too fast for significant accumulation of intermediates during the reaction. In this case, the idea of lowering the temperature to slow the rate is straightforward. The kind of reduction in reaction rates can be quite significant.[6] To prevent freezing of an aqueous solution of an enzyme and substrate below 0 °C, cryosolvents are employed. In general the cryosolvent needs to be inert, and commonly 40–50% dimethyl sulfoxide (DMSO)–water is used. Unfortunately, the viscosity of this cryosolvent also increases at lower temperatures, resulting in increases in linewidth. For example there is a fourfold increase in linewidth in going from 0 to −20 °C in 40% DMSO–water. The use of a cryosolvent and low temperatures requires careful kinetic characterization of the enzymatic reaction under the new conditions, to ensure that the reaction pathway has not been altered. Furthermore, the current molecular weight limit is around 50 kDa.[6] This method has been applied to a number of enzymes, and application of solution state NMR spectroscopy to the study of enzyme–intermediate complexes at subzero temperatures can provide valuable data (chemical shift, relaxation times, J coupling, and NOEs).[7,8]

4.2 Time-Resolved Solid State NMR Spectroscopy

One way to circumvent some of the disadvantages of solution state cryoenzymology is to use the recently developed method of time-resolved solid state NMR spectroscopy.[9–11] In the past, study on intermediate species has depended upon their isolation from the reaction mixture and therefore limited to relatively stable, long-lived species. With the advent of spectroscopic techniques, it has become possible to investigate these intermediate species in situ during the reaction. However, the techniques that have gained the widest application have been those which furnish the least structural information, namely UV–visible spectroscopy, IR spectroscopy, Raman spectroscopy, and ESR spectroscopy. The two techniques that generate the most structural information, X-ray crystallography and NMR spectroscopy, also are among the slowest and most insensitive methods for the data collection. In the case of X-ray crystallography, the technique is wholly dependent upon obtaining suitable crystals, which is not a trivial undertaking. To date the best time-resolution achieved

with cryoenzymological methods[12] has been of the order of 0.5 h, although with the recent developments in Laue diffraction methods[13–16] time-resolved kinetic studies of enzymatic reactions have been reported[17] with time-resolutions of 1–3 s, and in theory it should be possible to carry out kinetics at time-resolutions in the millisecond regime.[18] However, there are intrinsic limitations to the time-resolved Laue diffraction methods, since diffusion of the substrate results in a kinetically inhomogeneous population of enzyme-bound intermediate states, and transient lattice disorder during substrate entry results in diffuse electron densities just at the time when the reaction takes place. These latter problems have been mitigated to some extent by employing caged substrate molecules, where a photo-releasable version of the substrate is cocrystallized with the enzyme, and photo-release of the substrate synchronized with X-ray irradiation.[19,20] Even with this approach, the Laue method only provides somewhat diffuse electron density maps for the substrate or intermediate, to which it is difficult to fit a precise structure. This is not too surprising, since during catalysis it is to be expected that the enzyme-bound substrate or intermediate are dynamic and undergoing significant molecular motion.

Although NMR spectroscopy has been used to study rapid reactions in solution, in particular by continuous-flow and stopped-flow methods,[21,22] the time-resolution is at very best about 20 ms and in practice of the order of 200 ms to >10 s. In time-resolved solid state NMR spectroscopy, the time-resolution achievable is of the order of about 2 ms. Other pre-steady-state techniques use quenching reagents to halt the reaction and then study the reaction mixture at leisure by various analytical techniques such as chromatography. The chemical quench-flow technique[23] has been used to identify one enzyme-intermediate for 5-enolpyruvylshikimate 3-phosphate (EPSP) synthase (EC 2.5.1.19) with subsequent analysis by solution state NMR spectroscopy.[24] EPSP synthase is a monomer with a molecular weight of 46 kDa and a key enzyme in the aromatic amino acid biosynthetic pathway that catalyzes the formation of EPSP [(**4**) Scheme 1] from shikimate 3-phosphate [S3P, (**1**)] and phosphoenolpyruvate [PEP, (**2**)] (see Scheme 1). The vulnerability of relatively unstable enzyme–intermediate complexes to a chemical quench is a major concern with this technique. It is important to realize that an intermediate that has been isolated could result from rearrangement or breakdown of another intermediate, which itself might be on the reaction pathway.[25] It would therefore seem preferable to detect the intermediate directly *whilst still bound to the enzyme*, and a less disruptive method of quenching is required in order to do this.

The idea of thermal quenching first came to light in the 1960s. The essential requirement of any rapid quench process is that it is fast compared with the reaction being studied. A technique was devised[26,27] to freeze rapidly a reaction solution at a rate on the order of 10^5 K s^{-1} and then to examine the frozen sample by ESR spectroscopy. The impetus behind the need for low temperatures was not only to quench the reaction and allow the use of slow and repetitive scanning techniques, but also because many paramagnetic centers can only be observed at low temperature.

Studies[28–30] of the effects of freezing on proteins have determined that the destructive aspect of the process is the formation of hexagonal ice. So long as the freezing process is fast ($\geq 10^5$ K s^{-1}) and/or cryoprotectants (e.g. glycerol) are used, the majority of enzyme activity can be retained throughout the freezing process. Furthermore the frozen water is probably largely amorphous,[31] with the protein itself acting in a similar manner to a cryoprotectant[31] thereby reducing the formation of hexagonal ice that is detrimental to the protein. We have also found that the effects of the rapid freezing technique[9,32] are consistent with minimal possible damage to the protein.

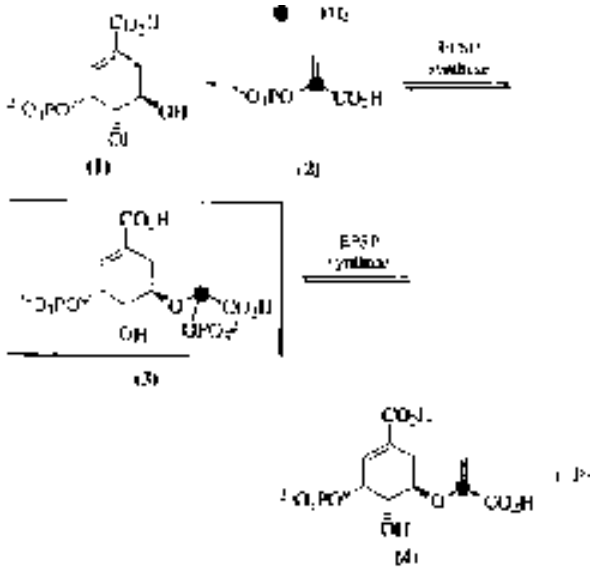

Scheme 1 Reaction catalysed by EPSP synthase

In contrast to cryoenzymological solution state NMR, with solid state NMR spectroscopy[33] line broadening due to chemical shift anisotropy and dipolar coupling can be reduced by CP MAS, so that there is theoretically no known molecular weight limit, since the rotational correlation time governs only the nuclear relaxation properties under MAS. The key therefore is the use of solid state NMR methods in conjunction with rapid freeze–quench methods, so that short-lived enzyme intermediates can be trapped. For this method, while knowledge of the pre-steady-state kinetics for the enzyme can be helpful, it is not a requirement, since the method can be used without prior knowledge in much the same way that other physical methods used to measure pre-steady-state kinetics start with initial guesses at the reaction time. Indeed time-resolved solid state NMR seems to be emerging as an alternative strategy for carrying out pre-steady-state kinetic analyses, which is superior to monitoring substrate consumption or product appearance by chromatographic techniques, since with these approaches there is always uncertainty as to the precise origin of the species being analyzed. Time-resolved solid state NMR spectroscopy essentially provides 'snapshots' of all the species, free and enzyme-bound, present at a particular time into the reaction. Furthermore, without the need for lengthy kinetic studies in cryosolvents, the method may be simpler and easier to use than cryoenzymological solution state NMR. The disadvantages are that considerable quantities of protein are required (on the order of 100 mg per time point), although with modern

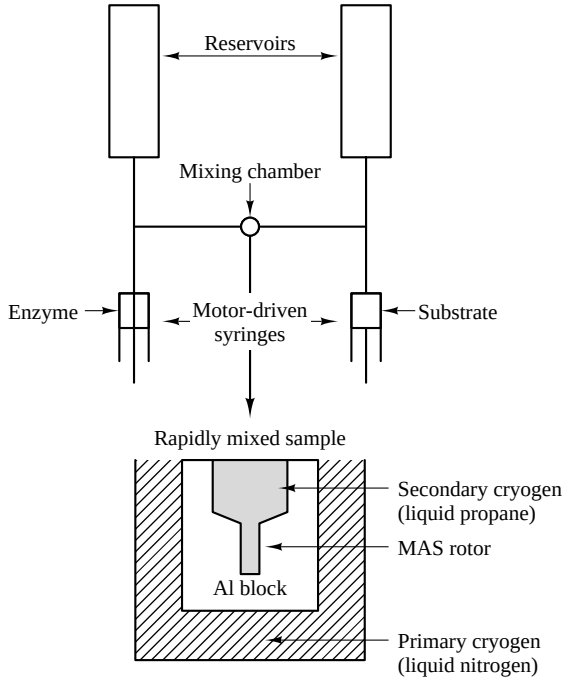

Figure 1 The apparatus used for rapid freeze–quench of intermediates in time-resolved solid state NMR

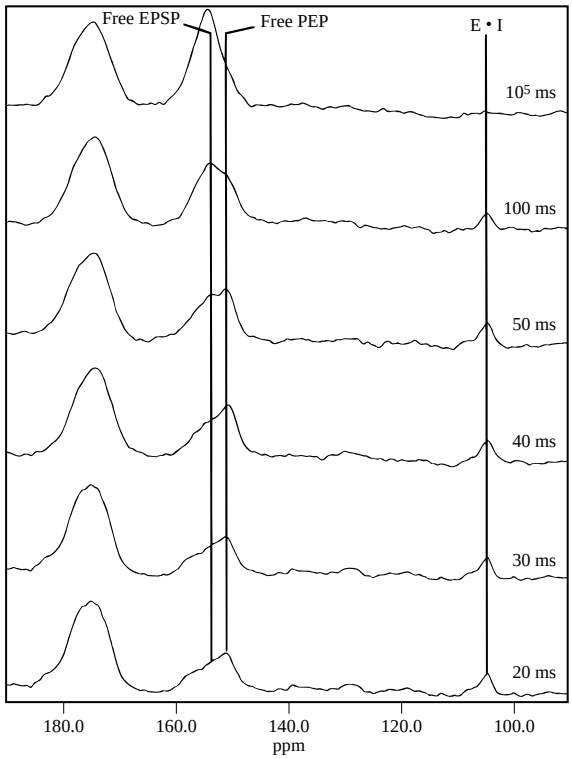

Figure 2 Carbon-13 TOSS CP MAS spectra of EPSP synthase (4 mM)/S3P (40 mM)/[2-^{13}C]PEP (40 mM) frozen mixtures, rapidly quenched in the forward direction at 20, 30, 40, 50, 100 ms and slow frozen after several minutes (10^5 ms). The spectra were acquired on the 7 mm probe in 12 000 scans using a 4 μs pulse width, 0.5 s contact time, and 2 s relaxation delay, and processed with 100 Hz line broadening and zero filling up to 8K data points. The spectra are shown with absolute intensity and normalized to the protein resonance at δ_C = 174.2 ppm. Reprinted with permission from Appleyard et al.[11] Copyright 1994 American Chemical Society

overexpression systems, this needs to be a limiting factor, and also a reaction with a k_{cat} of 10^{-5} s and a large activation enthalpy (e.g. -25 kJ mol^{-1}) will not be quenched even at $-75\,^{\circ}$C. The latter limitation is not too severe, given the number of enzymatic reactions that do not fall into this category.

The rapid freeze–quench method involves rapidly mixing enzyme and substrate together and freezing by spraying the mixture directly into a secondary cryogen such as liquid propane cooled to ~85 K (see Figure 1).

Figure 2 shows time-resolved solid state ^{13}C CP MAS NMR spectra of EPSP synthase mixed with [^{13}C]substrate under pre-steady-state conditions with the time elapsed from the start of the reaction indicated. The intermediate (E · I) is clearly visible at 104 ppm and its buildup demonstrated as the reaction proceeds. On allowing the pre-steady-state reaction to proceed for a few minutes, the turnover of intermediate (E · I) to product (E · EPSP) is evident. In addition to the resonance due to the E · I complex, the resonance due to the free product (EPSP) builds up at 155 ppm, and the free PEP decays at 151 ppm.

Although the E · I signal could be followed by direct integration, the enzyme-free [2-^{13}C]PEP and [8-^{13}C]EPSP could not. These two signals were therefore resolved by deconvoluting the overlapped resonances by peak fitting with fixed linewidths. The linewidths used were obtained from ^{13}C spectra of the substrates/products (Figure 2), and from averages of linewidths obtained from unfixed peak fits. The peak fitting routine determined the peak height and integral (assuming Lorentzian lineshape) for each time point, and the deconvoluted spectra obtained are shown in Figure 3. The chemical shifts obtained from the fits are δ_C([12-^{13}C]PEP) = 150.1 ppm and δ_C([8-^{13}C]EPSP) = 153.4 ppm. The peak intensities of all the individual species were normalized to the protein carbonyl resonance at δ_C = 174.2 ppm. This was performed to account for experimental variations in the sample volume due to different mixing programs and delay lines.

As noted for the chemical quench analysis,[23] the availability of software for the simulation of enzyme kinetics has revolutionized the fitting of pre-steady-state kinetic data since the entire data can be fitted to one mechanism and set of microscopic rate constants. The first stage of fitting the NMR integral data was to convert the arbitrary integral values into useable concentrations. Quantifiability of ^{13}C CP MAS NMR spectra has been addressed previously[34] and it is known that signal intensities are dependent on the kinetics of magnetization transfer during CP. At sufficiently long contact times spectra are approximately quantitative, even without normalization. In the case of EPSP synthase, the integral–concentration relationship can be determined from the direct NMR spectra of the free substrates and products, or an equilibrated enzyme solution by using the overall K_{eq} = 180. Of course there is a caveat[35] with this approach, which is that a good fit of experimental data to a proposed model using a kinetic simulation program, even over a wide range of experimental conditions, does not prove a mechanism to be correct.

In the forward direction, the integrals were standardized against the EPSP signal at equilibrium (Figure 2, 10^5 ms) and alone in frozen solution. A kinetic simulation

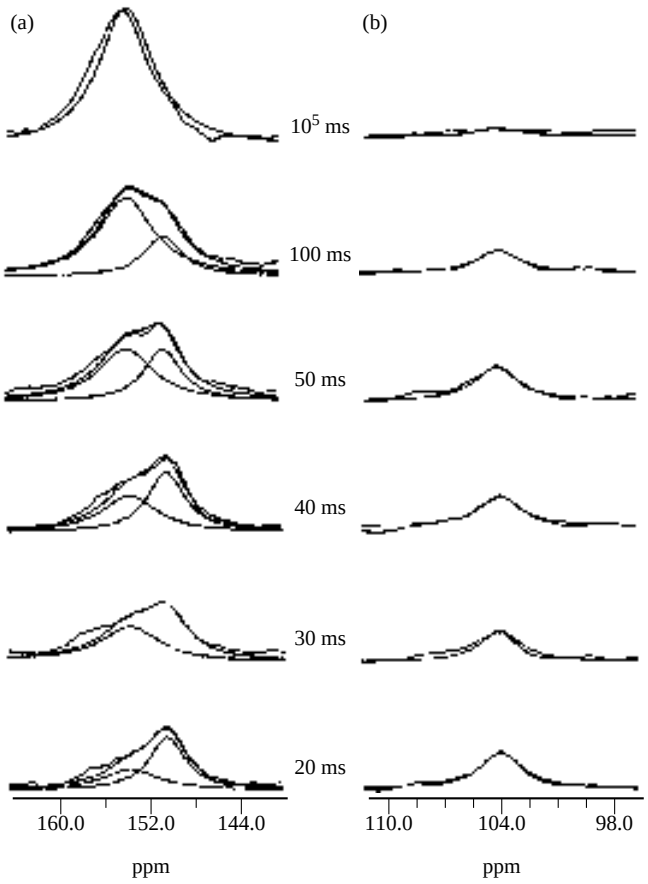

Figure 3 Peak fitting of the forward reaction of EPSP synthase for (a) enzyme-free [2-^{13}C]PEP and [8-^{13}C]EPSP and (b) the enzyme-bound intermediate (E · I). The fits were performed within FELIX using the simulated annealing algorithm. Constrained linewidths were used and these were estimated from averages of initial, unconstrained fits. Constrained peak positions were used for (a) in order to deconvolute the resonances successfully. Reprinted with permission from Appleyard et al.[11] Copyright 1994 American Chemical Society

was performed using the equilibrium ordered mechanism (Scheme 2) and the starting concentrations of 4 mM E · S3P, 36 mM S3P, and 40 mM [2-^{13}C]PEP. The previously determined kinetic rate constants[23] were used as a starting set, but the kinetic parameters could not be fitted to these converted concentrations either by manual interaction or with a computer fitting program. There was a good correlation between each set of experimental data and the corresponding simulation data, and the problem was the relative ratios between reaction species. By calculating early (10 ms) and final equilibrium concentrations for each species using a simulation, the integrals for each species were independently standardized. The resulting concentrations were then plotted along with the simulated data (Figure 4). A similar analysis was performed on the reaction species in the reverse direction.[11]

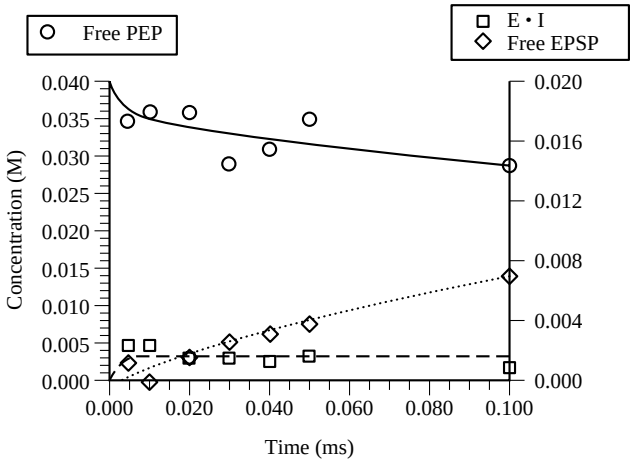

Figure 4 Plot of the experimental (points) and simulated (lines) concentrations of enzyme-free [2-^{13}C]PEP, enzyme-free [8-^{13}C]EPSP, and enzyme-bound intermediate (E · I) against the reaction time in the forward direction. Simulations performed using sequential ordered mechanism, full set of rate constants[24] and starting concentrations of 4 mM E · S3P, 36 mM S3P, and 40 mM [2-^{13}C]PEP. Reprinted with permission from Appleyard et al.[11] Copyright 1994 American Chemical Society

Laue X-ray diffraction and time-resolved solid state NMR obviously achieve similar goals, and each technique has its drawbacks. In the Laue method, large B factors are observed for mobile atoms, which lead to a blurred image of critical areas, e.g. substrates and active-site residues. It is also impossible to differentiate between the superimposed kinetic states in an electron density map. In the NMR method, chemical shift overlap of reaction species can be a problem but a change in hybridization in a reaction results in discrete chemical shift changes, allowing differentiation between kinetic states. The dipolar interaction can also be used, although it is limited because only pairwise internuclear distances can be measured at any one time. Recently, a number of solid state NMR pulse sequences have been developed[36–40] that can selectively reintroduce the dipolar interaction and allow the determination of very accurate distances.[41–43] The prospect of detailed internuclear distance measurements puts solid state NMR on the verge of a transformation similar to that which solution state NMR underwent with the introduction of two-dimensional techniques. Thus the Laue and NMR techniques complement rather than compete against one another. The strength of the former lies in generating a global picture, whereas the latter can focus on the enzyme active site and generate specific distance information.

Time-resolved solid state NMR spectroscopy provides a major technological advance in the study of enzymatic reaction mechanisms. One important consideration in any attempt to detect transient intermediates in addition to their lifetimes, is their pre-steady-state concentrations. This is dependent upon the kinetics and thermodynamic stability of intermediates of

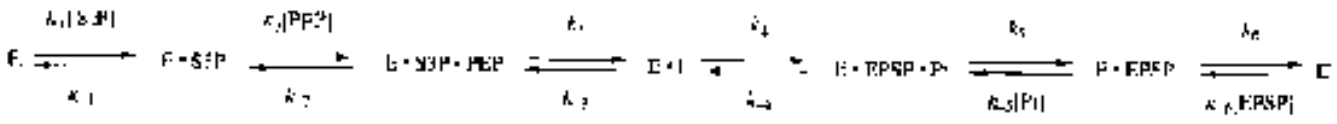

Scheme 2 Kinetic mechanism of EPSP synthase

each individual enzyme. Some enzymes, like EPSP synthase, have unusually stable intermediates. However, following the notions of Albery and Knowles,[44] we would expect that the majority of enzymes are evolving toward 'perfection', and stabilize highly unstable intermediates. For example, with triose phosphate isomerase (TIM) at equilibrium, the concentration of the postulated intermediate bound to the enzyme is approximately 5% of the total substrate concentration (with enzyme in excess). While the intermediate of TIM is probably beyond the limits of detection by time-resolved solid state NMR spectroscopy, a labeled intermediate bound to enzyme (at concentrations of 1–4 mM) greater than or equal to 10% of the protein concentration (with substrate in excess), can be detected using careful difference spectroscopy. While that excludes the 'perfect' enzymes, there remain a large number of enzymes for which this approach will still be very powerful. Furthermore, when coupled with the elegant solid state NMR distance-measurement methods that have been introduced recently (see ***REDOR and TEDOR***; ***Rotational Resonance in Biology***) time-resolved solid state NMR could be used to 'map out' molecular conformations of intermediates and enzyme-active-site–intermediate distances as an enzymatic reaction proceeds. This would provide the crucial missing structural details which Laue X-ray diffraction and allied techniques cannot provide, and enable the complete definition of the molecular events of enzyme catalysis.

5 RELATED ARTICLES

Carbon and Nitrogen Chemical Shifts of Solid State Enzymes; Cross Polarization in Rotating Solids: Spin-1/2 Nuclei; Cross Polarization in Solids; Enzymatic Transformations: Isotope Probes; Enzyme-Catalyzed Exchange: Magnetization Transfer Measurements; Magic Angle Spinning; REDOR and TEDOR; Rotating Solids; Rotational Resonance in Biology; Solid Biopolymers.

6 REFERENCES

1. J. P. G. Malthouse, *Prog. NMR Spectrosc.*, 1985, **18**, 1.
2. W. W. Cleland, *Biochemistry*, 1990, **29**, 3194.
3. J. N. S. Evans, G. Burton, P. E. Fagerness, N. E. Mackenzie, and A. I. Scott, *Biochemistry*, 1986, **25**, 905.
4. P. Rösch, *Prog. NMR Spectrosc.*, 1986, **18**, 123.
5. K. Kanamori and J. D. Roberts, *Acc. Chem. Res.*, 1983, **152**, 35.
6. J. N. S. Evans, in *Pulsed Magnetic Resonance: NMR, ESR and Optics (A Recognition of E. L. Hahn)*, ed. D. Bagguley, Oxford University Press, Oxford, 1992, pp. 123–173.
7. J. P. G. Malthouse, M. P. Gamcsik, A. S. F. Boyd, N. E. Mackenzie, and A. I. Scott, *J. Am. Chem. Soc.*, 1982, **104**, 6811.
8. N. E. Mackenzie, J. P. G. Malthouse, and A. I. Scott, *Biochem. J.*, 1984, **219**, 437.
9. R. J. Appleyard and J. N. S. Evans, *Bull. Magn. Reson.*, 1992, **14**, 81.
10. J. N. S. Evans, R. J. Appleyard, and W. A. Shuttleworth, *J. Am. Chem. Soc.*, 1993, **115**, 1588.
11. R. J. Appleyard, W. A. Shuttleworth, and J. N. S. Evans, *Biochemistry*, 1994, **33**, 6812.
12. P. Douzou and G. Petsko, *Adv. Protein Res.*, 1984, **36**, 245.
13. J. Hajdu, P. A. Machin, J. W. Campbell, T. J. Greenhough, I. J. Clifton, S. Zurek, S. Glover, L. N. Johnson and M. Elder, *Nature (London)*, 1987, **329**, 178.
14. G. K. Farber, P. Machin, S. C. Almo, G. A. Petsko and J. Hajdu, *Proc. Natl. Acad. Sci. U.S.A.*, 1988, **85**, 112.
15. J. Hajdu and L. N. Johnson, *Biochemistry*, 1990, **29**, 1669.
16. L. N. Johnson, *Protein Sci.*, 1992, **1**, 1237.
17. J. Hajdu, K. R. Acharya, D. I. Stuart, P. J. McLaughlin, D. Barford, N. G. Oikonomakos, H. Klein, and L. N. Johnson, *EMBO J.*, 1987, **6**, 539.
18. K. Moffat, *Annu. Rev. Biophys. Biophys. Chem.*, 1989, **18**, 309.
19. E. M. H. Duke, A. Hadfield, J. L. Martin, I. J. Clifton, J. Hajdu, L. N. Johnson, G. P. Reid, D. R. Trentham, I. Bruce, and G. W. J. Fleet, in *Protein Conformation*, *Ciba Foundation Symposium*, John Wiley, Chichester, 1991, p. 75.
20. B. L. Stoddard, P. Koenigs, N. Porter, K. Petratos, G. A. Petsko, and D. Ringe, *Proc. Natl. Acad. Sci. U.S.A.*, 1991, **88**, 5503.
21. C. A. Fyfe, M. Cocivera and S. W. H. Damji, *Acc. Chem. Res.*, 1978, **11**, 277.
22. J. J. Grimaldi and B. D. Sykes, *J. Am. Chem. Soc.*, 1975, **97**, 273.
23. K. S. Anderson, J. A. Sikorski, and K. A. Johnson, *Biochemistry*, 1988, **27**, 7395.
24. K. S. Anderson, J. A. Sikorski, A. J. Benesi, and K. A. Johnson, *J. Am. Chem. Soc.*, 1988, **110**, 6577.
25. A. Fersht, *Enzyme Structure and Function*, Freeman, New York, 1985, pp. 193–195.
26. R. C. Bray, *Biochem. J.*, 1961, **81**, 189.
27. D. P. Ballou and G. A. Palmer, *Anal. Chem.*, 1974, **46**, 1248.
28. H. Plattner and L. Bachmann, *Int. Rev. Cytol.*, 1982, **79**, 237.
29. W. B. Bald, *J. Microsc.*, 1985, **140**, 17.
30. E. Mayer, *J. Appl. Phys.*, 1985, **58**, 663.
31. L. Bachmann and E. Mayer, in *Cryotechniques in Biological Electron Microscopy*, eds. R. A. Steinbrecht and K. Zierold, Springer, Berlin, 1987, p. 3.; P. Douzou, *Cryobiochemistry: An Introduction*, Academic Press, New York, 1977.
32. R. J. Appleyard, and J. N. S. Evans, *J. Magn. Reson. Ser. B*, 1993 **102**, 245.
33. S. O. Smith, I. Palings, V. Copie, D. P. Raleigh, J. Courtin, J. A. Pardoen, J. Lugtenburg, R. A. Mathies, and R. G. Griffin, *Biochemistry*, 1987, **26**, 1606.
34. R. Voelkel, *Angew. Chem. Int. Ed. Engl.*, 1988, **27**, 1468.
35. C. Frieden, *Trends Biochem. Sci.*, 1993, **18**, 58.
36. D. P. Raleigh, M. H. Levitt, and R. G. Griffin, *Chem. Phys. Lett.*, 1988, **146**, 71.
37. T. Gullion, and J. Schaefer, *J. Magn. Reson.*, 1989, **81**, 196.
38. V. Copié, A. C. Kolbert, D. H. Drewry, P. A. Bartlett, T. G. Oas, and R. G. Griffin, *Biochemistry*, 1990, **29**, 9176.
39. S. M. Holl, R. A. McKay, T. Gullion, and J. Schaefer, *J. Magn. Reson.*, 1990, **89**, 620.
40. G. R. Marshall, D. D. Beusen, K. A. Kociolek, S. Redlinski, M. T. Leplawy, Y. Pan, and J. Schaefer, *J. Am. Chem. Soc.*, 1990, **112**, 963.
41. A. M. Christensen, and J. Schaefer, *Biochemistry*, 1993, **32**, 2868
42. J. R. Garbow, and A. McWherter, *J. Am. Chem. Soc.*, 1993, **115**, 238.
43. K. V. Lakshmi, M. Auger, J. Raap, J. Lugtenburg, R. G. Griffin, and J. Herzfeld, *J. Am. Chem. Soc.*, 1993, **115**, 8515.
44. W. J. Albery and J. R. Knowles, *Biochemistry*, 1976, **15**, 5631.

Acknowledgments

I would like to acknowledge the contributions of my co-workers: Richard Appleyard, Wendy Shuttleworth, Yan Li and Cecilia Ramilo in the development of time-resolved solid state NMR. This work was supported by the National Institutes of Health (GM43215), and the WSU NMR Center equipment was supported by NIH grant RR 0631401, NSF grant CHE-9115282, and Battelle Pacific Northwest Laboratories Contract No. 12-097718-A-L2.

Biographical Sketch

Jeremy N. S. Evans. *b* 1958. B.Sc., 1980, University College London; Ph.D., 1984, University of Edinburgh; postdoctoral research associate, Massachusetts Institute of Technology, 1984–1986; postdoctoral research fellow, 1986, University of Oxford; Honorary M.A., 1986, Brasenose College, University of Oxford; university lecturer in chemistry, and Tutorial Fellow of Brasenose College, University of Oxford and lecturer at Lady Margaret Hall, Oxford, 1986–1989. Associate Professor of Biochemistry and Biophysics, 1989–present, Associate Professor of Chemistry, 1989–1993, Director of Center of NMR Spectroscopy, 1991–present, Washington State University. Approx. 40 publications. Research interests include: new methods for determining the structure and dynamics of biomolecules by solid state NMR; time-resolved solid state NMR; structure and dynamics of protein–DNA complexes by solution state NMR; and enzymatic reaction mechanisms by NMR.

Dietary Changes Studied by MRS

Maria L. Barnard and Jimmy D. Bell
Royal Postgraduate Medical School, Hammersmith Hospital, London, UK

1	Introduction	1
2	Useful Nuclei for Dietary Studies	1
3	In Vivo NMR Spectroscopy	1
4	High-Resolution NMR Spectroscopy	4
5	Related Articles	5
6	References	5

1 INTRODUCTION

The importance of diet in both the preservation of health and treatment of disease is increasingly recognized. The major causes of morbidity and mortality in the Western world include cancer, coronary heart disease, diabetes mellitus, and obesity. Nutrition appears to have a major role both in their treatment and prevention.[1,2] There is therefore a growing need for the application of current scientific techniques to nutritional studies, to delineate the response of human metabolism to dietary alterations. The development and use of spectroscopy for nutritional studies is a major recent advance.

The last decade has seen increasing interest in the use of both in vivo and in vitro NMR spectroscopy for investigation of human and animal metabolism. Researchers are taking advantage of the nondestructive and noninvasive nature of the technique. These characteristics are particularly important for widespread, population-based studies of human nutrition, which often require serial examinations.

The initial applications of NMR to dietary studies were principally concerned with development of the NMR methodology, rather than focusing on specific nutritional and biochemical problems.[3,4] However, even at this early stage the potential of NMR spectroscopy when applied to lipid and glycogen metabolism could be envisaged. In this article we will review the recent use of in vivo and in vitro NMR spectroscopy for the investigation of the metabolic effects of diet.

2 USEFUL NUCLEI FOR DIETARY STUDIES

Carbon-13, ^{2}H, ^{1}H and ^{31}P NMR techniques have all been applied to study the effects of dietary manipulation in animals and humans.[3–9] Limited information can be obtained with in vivo ^{31}P and ^{1}H NMR spectroscopy as applied to nutrition. Phosphorus-31 NMR detects only phosphate-containing compounds; ^{1}H NMR suffers from a small chemical shift range, resulting in severe signal overlap and signals near the water resonance which cannot be readily detected. This has meant that ^{1}H and ^{31}P NMR techniques have principally been applied to dietary studies in vitro.[10–12] However, ^{2}H and ^{13}C NMR methods have been used in elegant in vivo metabolic studies.

The deuterium nucleus is quadrupolar ($I = 1$). It has both a low gyromagnetic ratio and natural abundance (0.015%), which leads to a very low sensitivity relative to proton spectroscopy (1.45×10^{-6}). These unfavourable properties are offset by its short relaxation times and high body content (12 mM), allowing its detection by natural abundance in vivo NMR spectroscopy. Furthermore, the tissue content can be readily increased by the use of deuterated water (D_2O), a fact that Brereton et al.[5] have utilized to great effect in lipid turnover studies.

Carbon-13 NMR spectroscopy in vivo has also been successfully applied in dietary studies.[3,4,8,9] Compared with ^{1}H NMR, ^{13}C NMR spectroscopy is very insensitive due to the low gyromagnetic ratio and low natural abundance (1.1%) of the ^{13}C nucleus. Its relative sensitivity is further reduced by the $^{1}H–^{13}C$ coupling which splits the ^{13}C signal, effectively reducing intensity. These problems are partially offset by the short relaxation times of most ^{13}C resonances, the use of decoupling techniques, and the high tissue content of important dietary-related, ^{13}C-containing compounds, including lipids and glycogen. Moreover, the very fact that ^{13}C has 1.1% natural abundance has been exploited by using ^{13}C-enriched metabolites in turnover studies, similar to classical ^{14}C tracer studies.

3 IN VIVO NMR SPECTROSCOPY

3.1 Lipid Metabolism

3.1.1 Carbon-13 NMR Spectroscopy

High-resolution ^{13}C NMR spectroscopy has found widespread use in the study of lipids in vitro.[13,14] In particular, the clear distinction of multiple different fatty acid groups allows this technique to be used, often quantitatively, in studies of dietary oils.[15–18] This degree of resolution cannot be achieved in vivo, which limits the utility of this technique in noninvasive human research. However, major lipid groups can be distinguished and, within these constraints, important clinical and biochemical work has been carried out using proton-coupled ^{13}C and proton-decoupled $^{13}C\{^{1}H\}$ NMR spectroscopy.

Canioni et al.[3] first showed that in vivo $^{13}C\{^{1}H\}$ NMR spectroscopy could detect differences in the lipid composition of adipose tissue and liver in rats fed a diet high in polyunsaturated fatty acids. Further work by Sillerud et al.[19] examined $^{13}C\{^{1}H\}$ NMR of triacylglycerols in rat adipocytes in vivo, advancing our knowledge particularly of signal assignment in biological systems. Moonen et al.[4] developed in vivo $^{13}C\{^{1}H\}$ NMR to characterize adipose tissue in human subjects. They confirmed that linoleic acid ($C_{18:2n-6}$), usually the principal polyunsaturated fatty acid present in human adipose tissue, dominated the polyunsaturated fatty acid carbon signal observed in vivo, allowing estimation of this stored essential fatty acid. A typical ^{13}C NMR spectrum of human adipose tissue is shown in Figure 1.

Barnard et al.[9] demonstrated the capability of in vivo $^{13}C\{^{1}H\}$ NMR spectroscopy to monitor the effect of diet on

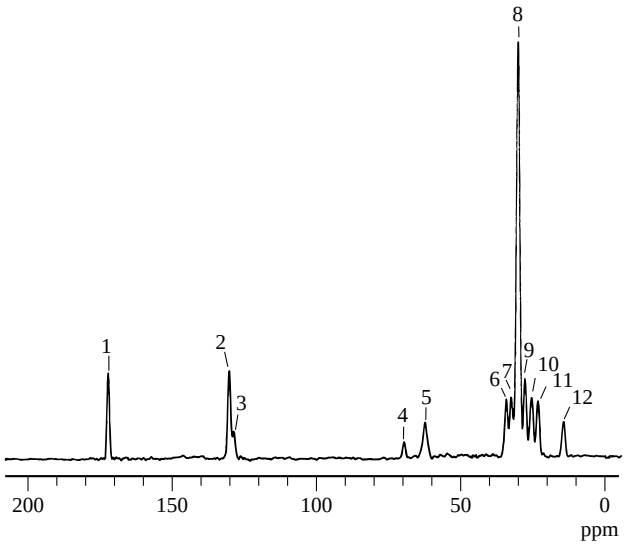

Figure 1 Natural abundance in vivo $^{13}C\{^1H\}$ NMR spectrum of human adipose tissue, dominated by signals from triacylglycerols. Peak assignment (referenced to $-\mathbf{C}H_3$): 1, **C**=O (171.79 ppm); 2, $-\mathbf{C}H{=}\mathbf{C}H-$(monounsaturated) and $-\mathbf{C}H{=}CHCH_2CH{=}\mathbf{C}H-$(polyunsaturated) (129.83 ppm); 3, $-CH{=}\mathbf{C}HCH_2\mathbf{C}H{=}CH-$(polyunsaturated) (128.13 ppm); 4, **C**-2 glycerol (69.21 ppm); 5, **C**-1, **C**-3 glycerol (62.05 ppm); 6, $-CH_2\mathbf{C}H_2CO_2R$ (33.93 ppm); 7, $-\mathbf{C}H_2CH_2CH_3$ (32.14 ppm); 8, $-(\mathbf{C}H_2)_n-$(29.69 ppm); 9, $-\mathbf{C}H_2CH{=}CH-$(27.39 ppm); 10, $-\mathbf{C}H_2CH_2CO_2R$ (25.04 ppm); 11, $-CH_2\mathbf{C}H_2CH_3$ (22.94 ppm); 12, $-CH_2\mathbf{C}H_3$ (14.1 ppm)

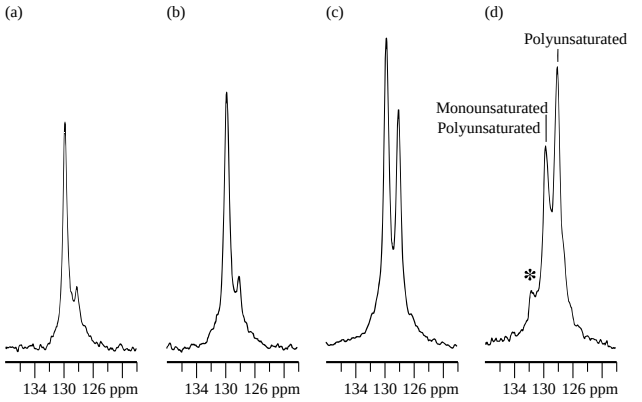

Figure 2 Olefinic region of natural abundance in vivo $^{13}C\{^1H\}$ NMR spectra of epididymal fat pad in rats fed fats high in different fatty acids. Unsaturated fatty acid carbon resonances appear in this region: monounsaturated ($-\mathbf{C}H{=}\mathbf{C}H-$) and polyunsaturated ($-\mathbf{C}H{=}CHCH_2CH{=}\mathbf{C}H-$) at 129.8 ppm; polyunsaturated ($-CH{=}\mathbf{C}H-CH_2\mathbf{C}H{=}CH-$) at 128.2 ppm. (a) Butter/lard diet–saturated fatty acids; (b) olive oil diet–monounsaturated fatty acids [oleic acid ($C_{18:1n-9}$)]; (c) sunflower oil–polyunsaturated fatty acids [linoleic acid ($C_{18:2n-6}$)]; (d) fish oil–($n-3$) polyunsaturated fatty acids [($C_{20:5n-3}$) and ($C_{22:6n-3}$)]. In these rats, adipose tissue lipid composition measured by NMR correlates to dietary content. Increasing dietary unsaturated and polyunsaturated fatty acid content produces similar changes in the adipose tissue, shown by an increasing total signal from **C**=**C** carbons and an increasing signal from polyunsaturated carbons at 128.2 ppm. Further, there appears to be a novel peak (*) at 132 ppm from unsaturated carbons at the $n-3$ position ($-CH{=}*\mathbf{C}HCH_2CH_3$), a double bond particularly found in the $n-3$ fatty acids of fish oil

adipose tissue in rats. In animals fed fats with different fatty acid patterns (butter/lard, olive oil, sunflower oil, fish oil), clear differences were found in the in vivo spectra, consistent with a significant effect of dietary fatty acid intake on the tissue fatty acid profile. Progressively increasing the total unsaturated and polyunsaturated fatty acid content in the diet was reflected in the adipose tissue composition (Figure 2), and results were correlated with in vitro spectroscopy and gas chromatography analyses. In humans, the turnover of fatty acids in adipose tissue is slow ($T_{\frac{1}{2}}$ = 600 d). The fatty acid profile of human subcutaneous fat therefore provides an index of the habitual dietary fatty acid intake over the previous 2–3 years.[20] This is of importance in long-term epidemiological surveys, but has previously been limited by the need for repeat tissue biopsies for fatty acid estimation. The application of in vivo ^{13}C NMR spectroscopy to the noninvasive analysis of adipose tissue composition is therefore of particular value for human nutritional studies.

Beckmann et al.[8] have used in vivo ^{13}C NMR to show a significant change in human adipose tissue fatty acid composition following a fat-reduced diet, with a correlation between diet and tissue monounsaturated fatty acids. No difference was found in the degree of polyunsaturation, and this may reflect the limited 6 month period of dietary change. Bryant et al.[21] chose to study vegan subjects as a defined population, with an established long-term diet, high in polyunsaturated fatty acids. A significantly increased adipose tissue total unsaturated and mono- and polyunsaturated fatty acid carbon content was shown in the ^{13}C spectra from the vegan group compared with omnivore controls (Figure 3). In addition, this was associated with a significant reduction in plasma concentrations of total cholesterol (4.55 ± 1.30 versus 5.39 ± 1.42 mmol l^{-1}, $p < 0.05$) and low-density lipoprotein (LDL) cholesterol (2.72 ± 1.06 versus 3.37 ± 1.34 mmol l^{-1}, $p < 0.05$) in the vegan subjects. The complex interactions between lipids in plasma and the body tissues are not fully defined, but are likely to be the subject of future NMR-based, dynamic studies of nutrition and lipid metabolism.

The interaction between diet and tissue lipids has been further studied by NMR in the liver. The liver has a pivotal role in lipid metabolism. Hepatic receptor-mediated LDL clearance is a major process controlling plasma LDL concentrations, and dietary saturated fat may increase plasma LDL levels by suppression of hepatic LDL receptor activity. The mechanisms underlying this effect are unclear, but it has been suggested that enrichment of hepatic membrane lipids with saturated fatty acids interferes with LDL receptor function.[22] Dietary substitution with polyunsaturated fatty acids may then increase hepatic LDL clearance and lower plasma LDL levels, possibly by increasing membrane fluidity.[23] Barnard et al.[24] used in vivo $^{13}C\{^1H\}$ NMR to examine the hepatic fatty acid profile in rats fed fats with different fatty acid patterns (butter/lard, sunflower oil, fish oil). The resolution of hepatic ^{13}C spectra is limited. The authors therefore used analysis by integration of signals across chemical shift ranges, and suggested expressing results by calculation of unsaturation and polyunsaturation indices (Table 1). A significant dietary effect was shown, with an increasing hepatic content of unsaturated fatty acids and an increasing degree of polyunsaturation as these fatty acids increased in the diet. However, in vitro $^{13}C\{^1H\}$ NMR studies of the liver lipid extracts showed a complex relationship,

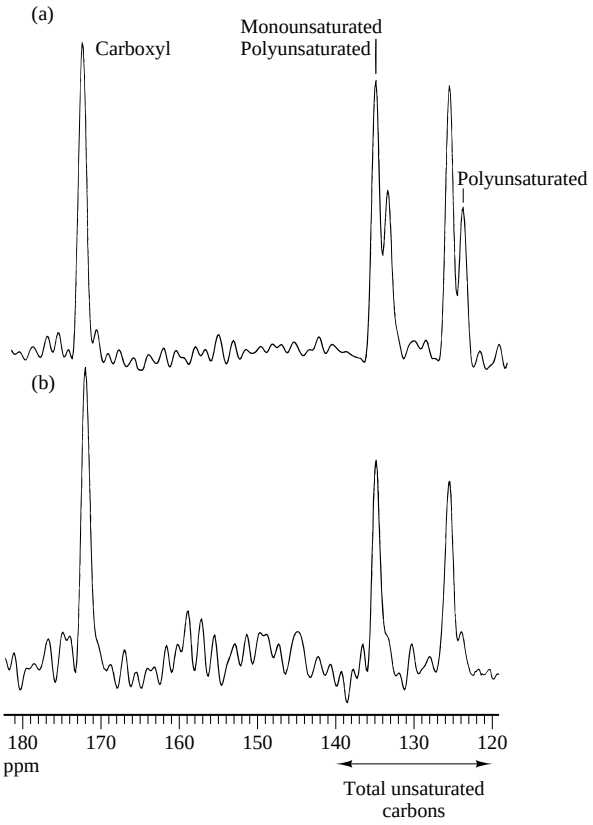

Figure 3 Olefinic region from natural abundance in vivo coupled ^{13}C NMR spectra of human thigh adipose tissue in (a) vegan and (b) omnivore subjects. Spectra are scaled to the carboxyl signal. The vegan subjects, compared to omnivores, have an increased adipose tissue content of both total unsaturated and polyunsaturated fatty acid carbons (polyunsaturated: 3.45 ± 0.87 versus 2.39 ± 0.55% of total fatty acid carbons, $p < 0.05$). This reflects at least 3 years' adherence to the vegan diet, which, in the absence of all animal products, is high in polyunsaturated fats (polyunsaturated: 33.13 ± 7.4 versus 25.2 ± 8.5% of total dietary fatty acids, $p < 0.05$)

with evidence of hepatic metabolism of the dietary fatty acids. Indeed, the liver is a major site of fatty acid uptake, desaturation, synthesis, storage, and secretion.

Investigation of the metabolism of specific dietary fatty acids is a largely unexplored possible future application of ^{13}C NMR spectroscopy. The use of ^{13}C-labeled fatty acids to trace metabolic pathways and kinetic rates is an exciting prospect. These studies may be restricted by the limited availability of labeled fatty acids, their oxidation after administration, and the sensitivity of the system, given the preexisting strong lipid signals. However, preliminary work has been performed by Cunnane et al.[25] and this demonstrated the ability of in vitro $^{13}C\{^1H\}$ NMR to detect carbon-specific incorporation of injected [U-^{13}C] eicosapentaenoic acid in extracted rat liver lipids.

3.1.2 Deuterium Spectroscopy

There is considerable interest in monitoring lipid turnover in both health and disease. A novel approach to the study of dynamic in vivo tissue lipid metabolism was developed by Brereton et al.[5] They investigated the use of in vivo ^2H NMR spectroscopy in mice. Administration of D_2O (10% v/v) in the drinking water for 3–4 d allowed the detection of deuterium-enriched tissue lipid resonances in spectra acquired in less than 2 min, as shown in Figure 4(a). The spectra consist of resonances from deuterated water (HOD) and the CHD groups of tissue lipids. Removal of D_2O from the drinking water led to clear changes in the intensity of both signals [Figure 4(b)]. The loss of deuterium from the water signal was significantly faster than from tissue lipids. The loss of deuterium from the lipid resonance was therefore proposed as a noninvasive measure of the rate of fat utilization. This method has since been applied to the study of fat utilization in obesity.

Obesity is one of the most common dietary disorders. It is characterized by excess adipose tissue and elevated levels of plasma nonesterified fatty acids. Furthermore, obesity is known to lead to glucose intolerance and insulin resistance. Fat turnover, as reflected by the levels of plasma nonesterified fatty acids, has been suggested as being implicated in this process. However, the lack of in vivo techniques for measuring fat utilization has greatly hampered progress in this area. Body fat turnover in mouse models of obesity and diabetes mellitus have been studied in vivo using the ^2H NMR technique.[26] Brereton et al.[26] showed that the rates of fat utilization in obese mice were significantly lower than the rates for nonobese mice (Figure 5) and the induction of diabetes did not affect utilization of fat as a metabolic fuel.

These studies clearly suggest that deuterium NMR spectroscopy provides researchers with a powerful method for noninvasively assessing fat turnover rates.

3.1.3 Proton Spectroscopy

The application of in vivo proton NMR spectroscopy to dietary studies has been rather limited. Indeed, many of the

Table 1 Hepatic Fatty Acid Profile by In Vivo $^{13}C\{^1H\}$ NMR Spectroscopy of Rats Fed Different Fats

Dietary Fat	Unsaturation Index[a]	Polyunsaturation Index[b]	Methylene–Methyl/%[c]	Olefinic/%[c]
Butter/lard	0.19 ± 0.04	0.90 ± 0.04	84.1 ± 0.91	15.9 ± 0.91
Sunflower oil	0.24 ± 0.01	1.04 ± 0.04	80.9 ± 0.31	19.1 ± 0.31
Fish oil	0.27 ± 0.01	1.32 ± 0.03	78.9 ± 0.79	21.1 ± 0.79

$p < 0.05$ for all differences between dietary groups.

[a]Unsaturation index = olefinic/methylene–methyl signal integration (measures the ratio of unsaturated to saturated fatty acid carbons).

[b]Polyunsaturation index = signal intensity at 128.2 ppm (=C–C–C=)/129.8 ppm (–C=C–) (measures the ratio of polyunsaturated to monounsaturated + polyunsaturated carbons).

[c]Olefinic and methylene–methyl signal area as the percentage of the total fatty acid signal integration (measures the percentage of fatty acid carbons that are unsaturated or saturated, respectively).

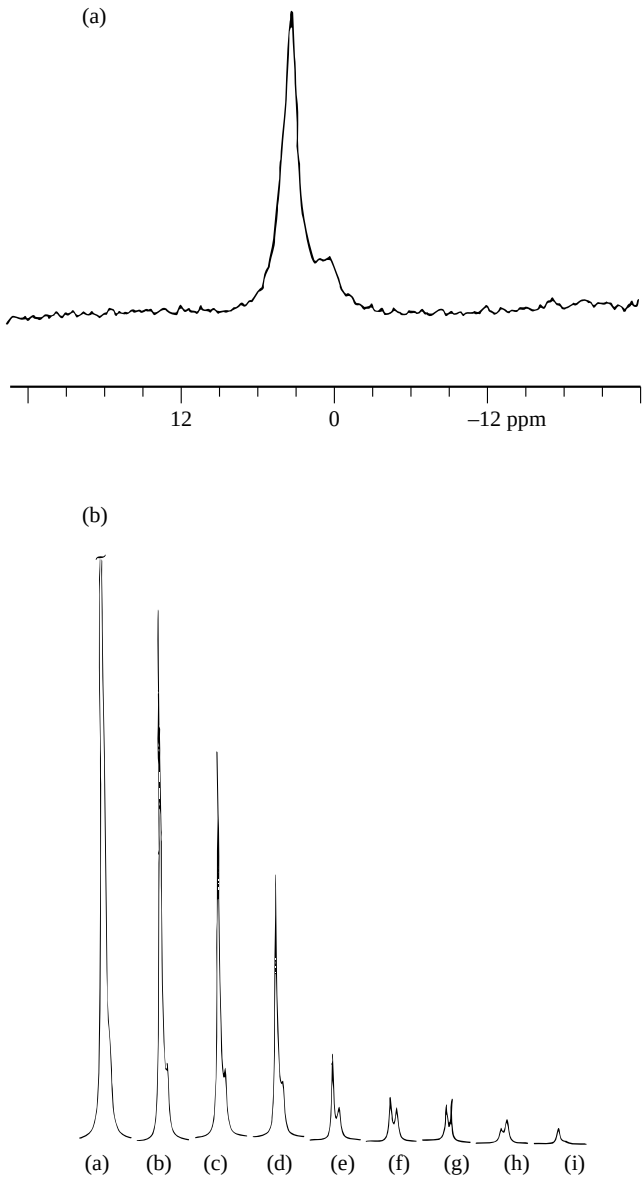

Figure 4 (a) Natural abundance ^{2}H NMR spectrum of a mouse. The CHD resonance is to high field at 1 ppm. Chemical shifts were referenced to the HOD resonance assigned to 4.8 ppm. (b) Deuterium NMR spectra of a mouse following the removal of 10% (v/v) of D_2O from its drinking water. The spectra were recorded (a) 1, (b) 4, (c) 5, (d) 8, (e) 11, (f) 15, (g) 16 and (h) 21 days after the resumption of normal drinking water. Spectrum (i) was recorded prior to the administration of D_2O to the drinking water (Adapted with permission of Heyden & Son Limited from I. M. Brereton, D. M. Doddrell, S. M. Oakenfull, D. Moss, and M. G. Irving, *NMR in Biomed.*, 1989, **2**, 55)

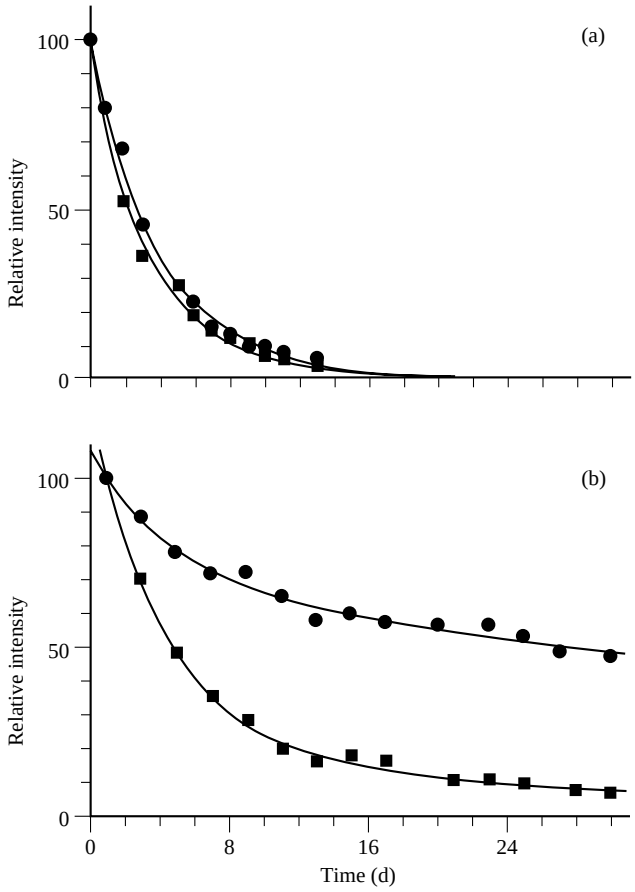

Figure 5 Plots of ^{2}H NMR signal intensity as a function of time showing (a) best fit single exponential decay curves for HOD and (b) best fit biexponential function for CHD intensities. The experimental data for control (solid square) and obese (solid circle) mice were used to calculate the body water and fat utilization rates. (Reproduced by permission of Heyden & Son Limited from I. M. Brereton, D. M. Doddrell, S. M. Oakenfull, D. Moss, and M. G. Irving, *NMR in Biomed.*, 1989, **2**, 55)

metabolites observed by ^{1}H NMR spectroscopy do not appear to be affected by diet, with the exception of lipids.[7] However, due to the small chemical shift range of ^{1}H resonances and the intense water signal, in vivo ^{1}H lipid studies have also been restricted. A potentially important alternative application of ^{1}H NMR is the use of fat imaging to determine quantitative fat distribution in human subjects.[27] Regional fat distribution has been correlated to serum lipids and coronary heart disease. Existing methods for measurement of body fat distribution are limited, and fat imaging may in future become the modality of choice in nutritional and metabolic studies evaluating the risk of coronary heart disease.

3.2 Glycogen Studies

Tissue glycogen values may be a marker of carbohydrate intake and could therefore be of value in dietary studies. Shulman and co-workers[28] have developed a ^{13}C NMR technique to provide a direct noninvasive method to measure liver and muscle glycogen concentration in humans. The time course of liver glycogen concentration, following standard test meals, has been carried out by ^{13}C NMR spectroscopy. This opens the possibility of following quantitative changes in glycogen storage with varying diets.[29,30]

4 HIGH-RESOLUTION NMR SPECTROSCOPY

The unique exploratory capability of NMR spectroscopy has been utilized to investigate the effects of diet on the metabolic profile of body fluids.[31] The ^{1}H NMR spectra of urine from

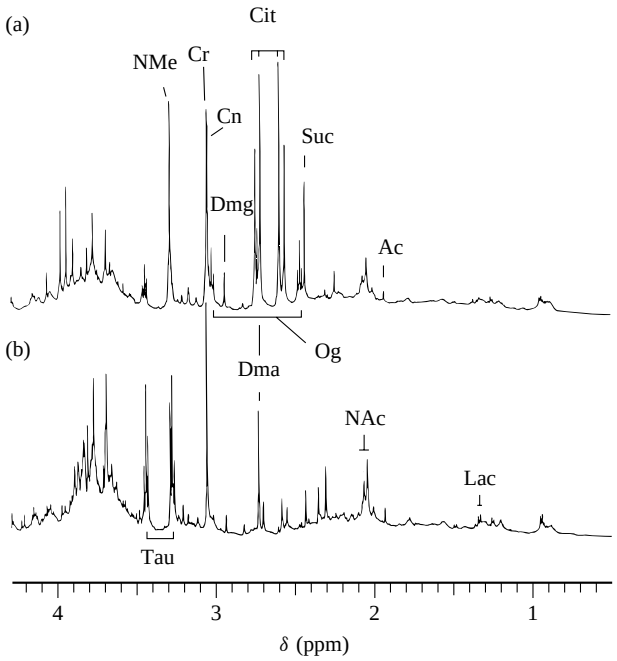

Figure 6 Proton NMR spectra at 500 MHz (aliphatic regions) of urine from 1-month-old rats fed either (a) chow or (b) casein diets. Assignments: Lac, lactate; Ac, acetate; NAc, *N*-acetyl groups of glycoproteins; Suc, succinate; Og, 2-oxoglutarate; Cit, citrate; Dma; dimethylamine; Dmg, dimethylglycine; Cr, creatinine; Cn, creatine; Tau, taurine; NMe, betaine plus trimethylamine *N*-oxide. (Reproduced by permission of Academic Press, Inc. from J. D. Bell, O. Lavender, V. C. Morris, and P. J. Sadler., *Magn. Reson. Med.* 1991, **17**, 414)

rats fed different diets are shown in Figure 6. Clear changes in the metabolic profile of the urine can be observed.[10] Rats fed casein diets for 1 month postweaning did not excrete 2-oxoglutarate, and excreted lower levels of hippurate, succinate, and citrate compared with age/sex-matched rats fed standard chow diets. The acquisition of these spectra took ∼2 min. This suggests that high-resolution NMR of urine or other body fluids could be utilized as a fast, multicomponent technique in human studies, for example to screen rapidly for multiple metabolic effects or to check dietary compliance.

Plasma concentrations of LDLs and high-density lipoproteins (HDLs) are well established markers for coronary heart disease risk assessment. Standard methods for quantification and compositional analysis of plasma lipoproteins require laborious and time-consuming physical separation based on particle size, density, or apolipoprotein content. Bell et al. have shown that NMR spectroscopy can be readily applied to study alterations in plasma lipoproteins associated with dietary manipulation, both in intact plasma or in the separated lipoprotein classes.[11,12] The effects of fish oil supplementation on the ^{1}H NMR profile of lipoproteins in intact plasma are illustrated in Figure 7. Changes in composition are shown by a new lipid resonance (peak 2A) arising from fish oil $n - 3/\omega - 3$ fatty acids incorporated into plasma lipoproteins, while the methylene $[-(C\mathbf{H}_2)_n-]$ signal (peak 3) is markedly reduced. Furthermore, T_2 analysis of the lipid resonances showed that these changes in lipid composition of the LDL particles are accompanied by alteration in the structural characteristics of these particles.

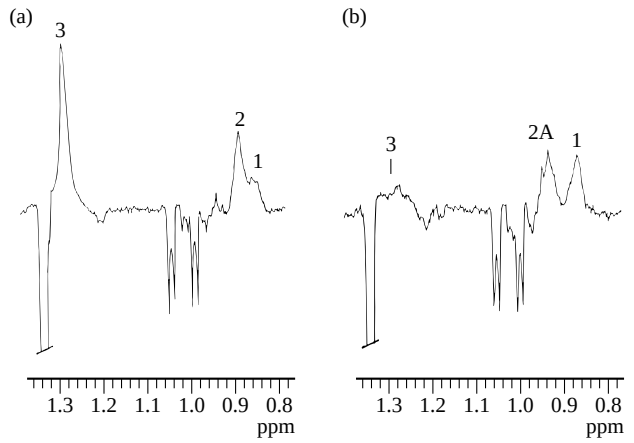

Figure 7 Expansions of spin echo ^{1}H NMR spectra of intact human plasma (a) before and (b) after 7 d of fish oil supplementation. Assignments: peaks 1 and 2, terminal $-C\mathbf{H}_3$ group from LDLs/HDLs and very low-density lipoproteins (VLDLs), respectively; peak 3, $-(C\mathbf{H}_2)_n-$of VLDLs. Peak 2A arises from $n - 3/\omega - 3$ fatty acids incorporated into plasma lipoproteins. (Reproduced by permission of Birkhauser Verlag from P. C. Dagnelie, J. D. Bell, M. L. Barnard, and S. C. R. Williams, in 'Omega-3 Fatty Acids: Metabolism and Biological Effects' ed. C. A. Drevon, I. Baksaas, and H. E. Krokan, Birkhauser Verlag, Basel/Switzerland, 1993, p. 27–34)

At present, sophisticated computer deconvolution methods (line-fitting analysis) are being developed to identify and quantify lipoprotein fractions in the ^{1}H NMR spectra of intact plasma samples (500 μl) within minutes.[32,33]

In this article we have reviewed the current state of NMR spectroscopy as applied to dietary studies. It is clear that this is a relatively new area of NMR research. However, it offers many exciting prospects for future research into diet and nutrition in humans.

5 RELATED ARTICLES

Analysis of High-Resolution Solution State Spectra; Brain Neoplasms Studied by MRI; Body Fluids; Chemical Shifts in Biochemical Systems; High-Field Whole Body Systems; Lipoproteins; Whole Body Studies: Impact of MRS.

6 REFERENCES

1. J. E. Kinsella, B. Lokesh, and R. A. Stone, *Am. J. Clin. Nutr.*, 1990, **52**, 1.
2. R. A. DeFronzo and E. Ferrannini, *Diabetes Care.*, 1991, **14**, 173.
3. P. Canioni, J. R. Alger, and R. G. Shulman, *Biochemistry*, 1983, **22**, 4974.
4. C. T. W. Moonen, R. J. Dimand, and K. L. Cox, *Magn. Reson. Med.*, 1988, **6**, 140.
5. I. M. Brereton, M. G. Irving, J. Field J, and D. M. Doddrell, *Biochem. Biophys. Res. Commun.*, 1986, **137**, 579.
6. P. C. Dagnelie, J. D. Bell, S. C. R. Williams, I. J. Cox, D. K. Menon, J. Sargentoni, and G. A. Coutts, *NMR Biomed.*, 1993, **6**, 2.

7. F. Schick, B. Eismann, W. I. Jung, H. Bongers, M. Bunse, and O. Lutz, *Magn. Reson. Med.*, 1993, **29**, 158.
8. N. Beckmann, J. J. Brocard, U. Keller, and J. Seelig, *Magn. Reson. Med.*, 1992, **27**, 97.
9. M. L. Barnard, J. D. Bell, S. C. R. Williams, T. A. B. Sanders, H. G. Parkes, K. K. Changani, J. S. Beech, M. L. Jackson, and S. R. Bloom, *Proceedings of the 11th Annual Meeting of the Society of Magnetic Resonance in Medicine, 1992*, p. 3339.
10. J. D. Bell, O. Lavender, V. C. Morris, and P. J. Sadler., *Magn. Reson. Med.*, 1991, **17**, 414.
11. J. D. Bell, J. C. C. Brown, R. E. Norman, P. J. Sadler, and D. R. Newell, *NMR Biomed.*, 1988, **1**, 90.
12. P. C. Dagnelie, J. D. Bell, M. L. Barnard, and S. C. R. William, in *Omega-3 Fatty Acids: Metabolism and Biological Effects*, ed. C. A. Drevon, I. Baksaas, and H. E. Krokan, Birkhauser Verlag, Basel, 1993, p. 27.
13. J. G. Batchelor, R. J. Cushley, and J. H. Prestegard, *J. Org. Chem.*, 1974, **39**, 1698.
14. J. Bus, I. Sies, and M. S. F. Lie Ken Jie, *Chem. Phys. Lipids*, 1976, **18**, 130.
15. F. D. Gunstone, M. R. Pollard, C. M. Scrimgeour, and H. S. Vedanayagam, *Chem. Phys. Lipids*, 1977, **18**, 115.
16. J. N. Shoolery, *Prog. NMR Spectrosc.*, 1977, **11**, 79.
17. N. G. Soon, *Lipids*, 1985, **20**, 778.
18. F. D. Gunstone, *Chem. Phys. Lipids*, 1991, **59**, 83.
19. L. O. Sillerud, C. H. Han, M. W. Bitensky, and A. A. Francendese, *J. Biol. Chem.*, 1986, **261**, 4380.
20. A. C. Beynen, R. J. J. Hermus, and J. G. A. J. Hautvast, *Am. J. Clin. Nutr.*, 1980, **33**, 81.
21. D. J. Bryant, J. D. Bell, E. L. Thomas, S. D. Taylor-Robinson, J. Simbrunner, J. Sargentoni, M. Burl, G. A. Coutts, G. Frost, M. L. Barnard, S. Cunnane, and R. A. Iles, *Proceedings of the 12th Annual Meeting of the Society of Magnetic Resonance in Medicine, 1993*, P. 1048.
22. S. M. Grundy, and M. A. Denke, *J. Lipid Res.*, 1990, **31**, 1149.
23. J. Loscalzo, J. Freedman, A. Rudd, I. Barsky-Vasserman, and D. E. Vaughan, *Arteriosclerosis*, 1987, **7**, 450.
24. M. L. Barnard, J. D. Bell, S. C. R. Williams, T. A. B. Sanders, and S. R. Bloom, *Proceedings of the 12th Annual Meeting of the Society of Magnetic Resonance in Medicine, 1993*, p. 92.
25. S. C. Cunnane, R. J. McDonagh, S. Narayan, and D. J. Kyle, *Lipids*, 1993, **28**, 273.
26. I. M. Brereton, D. M. Doddrell, S. M. Oakenfull, D. Moss, and M. G. Irving, *NMR Biomed.*, 1989, **2** 55.
27. R. Ross, L. Leger, D. Morris, J. De Guise, and R. Guardo, *J. Appl. Physiol.*, 1992, **72**, 787.
28. M. J. Avisoz, D. L. Rothman, E. Nadel, and R. G. Shulman. *Proc. Natl. Acad. Sci. USA*, 1988, **85**, 1634.
29. T. Jue, D. L. Rothman, B. A. Tavitian, and R. G. Shulman. *Proc. Natl. Acad. Sci. USA*, 1989, **86**, 1439.
30. M. Ishihara, H. Ikehira, S. Nishikawa, T. Hashimoto, K. Yamada, F. Shishido, T. Ogino, K. Cho, S. Kobayashi, M. Kawana, T. Matumoto, T. A. Iinuma, N. Arimizu, and Y. Tateno, *Am. J. Phys. Imag.*, 1992, **7**, 32.
31. J. D. Bell, J. C. C. Brown, and P. J. Sadler, *NMR Biomed.*, 1989, **2**, 246.
32. M. Ala-Korpela, Y. Hiltunen, J. Jokisaari, S. Eskelinen, K. Kiviniity, M. J. Savolainen, and Y. A. Kesaniemi. *NMR Biomed.*, 1993, **6**, 225.
33. J. D. Otvos, E. J. Jeyarajah, D. W. Bennett, and R. M. Krauss. *Clin. Chem.*, 1993, **38**, 1632.

Biographical Sketches

Maria L. Barnard. *b* 1960. B.Sc., 1981, M.B., Ch.B., 1984, University of Bristol, UK. Introduced to NMR by Graeme M. Bydder and Jimmy D. Bell, MRI Unit, Hammersmith Hospital during Medical Research Council (MRC) UK Training Fellowship with Stephen R. Bloom, Division of Endocrinology and Metabolism, Hammersmith Hospital, UK 1989–93. MRC (UK) Travelling Fellow to R.G. Shulman, Yale University, USA, 1992–93. Approx. 23 publications. Research interests: application of NMR spectroscopy to metabolic and nutritional studies.

Jimmy D. Bell. *b* 1958. B.Sc. Biochemistry 1982, University of Warwick. Ph.D. (supervisor P. J. Sadler), 1987, London. Senior NMR research fellow (with I. Young and D. G. Gadian), Hammersmith Hospital, 1989–93. Faculty in Biochemistry, Royal Postgraduate Medical School, 1993–present. Approx. 60 publications. Research interests include application of MRI/MRS in clinical research, and NMR spectroscopy to the chemistry of tissues and body fluids

Foods and Grains Studied by MRS and MRI

Suzanne L. Duce and Laurie D. Hall
University of Cambridge, UK

1	Introduction	1
2	Equipment	1
3	Spectroscopy	1
4	Imaging	1
5	Future Prospects	2
6	Related Articles	2
7	References	2

1 INTRODUCTION

From a chemical structure viewpoint, the building blocks of food are water, carbohydrates (particularly polysaccharides), lipids, and proteins. From the viewpoint of physical chemistry or materials science, these substances are combined together in a rich variety of structures ranging from essentially pure liquids, to solutions, gels, emulsions, foams, suspensions, solids, and porous media containing large amounts of water (as in fruit) and others which are dry or nearly so (e.g. biscuits). Furthermore, the molecules themselves contain one or more NMR-active nuclide (e.g. ^{1}H, ^{2}H, ^{13}C, ^{23}Na, or ^{31}P). As a result, foods are amenable to investigation by essentially the entire array of NMR methodology, including both solution- and solid state spectroscopy and NMR imaging.

2 EQUIPMENT

Whilst most of the NMR research in food science has been performed using high-resolution or solid state instrumentation, many industrial applications use low-cost, benchtop instruments specifically designed for a limited range of highly optimized applications.[1] The most widely used device is made by Bruker and operates at 10 and 20 MHz for samples up to 18 mm in diameter. Typical applications using such systems involve the determination of the solid-to-liquid ratio of fats, or the quantitation of water in foods. NMR imaging of food has mainly been done using 31-cm bore magnets operating at 2 T, or whole body clinical systems. The key technical requirement is that the gradient system be capable of implementing sequences with spin echo times of 5 ms or less.

3 SPECTROSCOPY

The most widespread use of proton spectroscopy in the food industry continues to be the determination of the solid-to-liquid ratio of fats.[2,3] The technique exploits the differences in the spin–spin relaxation times of protons in liquid and solid domains; such measurements are routinely performed using low field strength magnets. This is a rapid and reliable method for determining the oil and water content of seeds and can be used in breeding experiments and in optimizing storage and processing conditions.[4] Much of the early work on food involved ^{1}H relaxation studies of water[5,6,7] which gave insight to the location and mobility of water associated with foods, especially carbohydrates such as starch, and proteins. The diffusion coefficients of water and lipids can be determined by pulse field gradient NMR.[8] These experiments can also be used to investigate restrictions to free diffusion, and thereby allow the size of water domains in complex structures to be estimated (e.g. the size of water droplets in emulsions).

Measurements made at high field strengths of the deuteron resonances of wine and fruit juices have recently been used as a new approach to 'food authentication'. This elegant approach, called site-specific natural isotope fractionation (SNIF) NMR, is based on the fact that the distribution and ratio of ^{1}H and ^{2}H isotopes of low molecular weight molecules such as glucose, ethanol, and acetic acid depend on their biochemical origin.[9] For example, SNIF NMR can differentiate between ethanol produced from the sugar of grains and that from grape juice. Consequently, addition of beet or cane sugar to supplement a low sugar content grapes can be detected.

High field strength, highly homogeneous magnets are necessary for high-resolution, solution state NMR. This method is used to elucidate chemical structure. Typically, ^{1}H and ^{13}C spectra are acquired; however, ^{31}P, ^{23}Na, and ^{15}N nuclei are also useful in certain situations. For example, ^{31}P NMR is used to investigate metabolism in vivo as well as allowing cellular pH to be estimated.[10] Solid samples usually give rise to very broad featureless spectra; however, it is possible to acquire high-resolution spectra by cross polarization, magic angle spinning (CP MAS) NMR. Solution- and solid state ^{13}C NMR have been used to study whole intact seeds.[11,12] ^{15}N cross-polarization spectra have also been reported; for example, soya beans grown in ^{15}N enriched ammonium nitrate and amino acids have been studied.[13] High resolution solution- and solid state ^{13}C spectroscopy can be combined with ^{1}H relaxation studies to elucidate the microdynamics of the various domains in complex heterogeneous systems such as wheat gluten.[14]

4 IMAGING

It is relatively easy to obtain magnetic resonance (MR) images from most food products,[15–21] providing that the container is transparent to radiofrequency waves and is free of ferromagnetic components. Consequently, it is feasible to study food storage in the marketing container completely noninvasively. In addition to obtaining well-resolved NMR images of the internal structure of foods, the food scientist would like to make measurements from the images, for example correlating image intensity with a physical parameter such as water content, diffusion coefficient, or flow velocity. The ease with which a quantitative image[22] can be generated depends not only on the quantity of the NMR species present and their ^{1}H relaxation times, but also on the value of the echo time available. Thus it is relatively straightforward to produce proton density T_1 and T_2 maps for high water content foods such as fruit, vegetables, and many dairy and meat

products. Furthermore, since the water protons have relatively long T_2 values, their linewidths are sufficiently narrow that at 2 T or more chemical shift resolution between water and lipid resonances can be achieved by selective excitation.[23] By comparison, low moisture content foods, such as pasta, generally give such broad water resonances that the resolution of water from lipid signals is impossible; in most biscuits, for example, the MR image is dominated by the signal from the lipid.

Given the known dependence of NMR parameters on the physicochemical environment of the water and lipid molecules, it is clear that MRI should provide invaluable insight to structural changes that accompany food processing.[24,25] Examples to date include baking, freezing/thawing, drying, hydration, curing, heating in thermal or microwave ovens, or frying in oil. In addition, it is possible to visualize and quantitate the flow of liquids, including suspensions.[26] The circulation and diffusion of water within wheat grains has also been studied.[27,28]

MRI of fruits and vegetables provides excellent definition of the internal architecture of the object. Importantly, processes which disrupt the cellular structure can generally be visualized with great clarity. For example, bruising of fruit[16] and freeze/thawing[29] leads to a change in image contrast in the sample. Both these effects reflect two important changes. First, there is the local change in water distribution from intra- to intercellular space, which displaces air and thereby changes the distribution of susceptibility variations in the material.[30] Second, for some systems (e.g. celery), there can be anisotropy of diffusion rates and distances in the fresh material which is disrupted by cellular damage.

As the food system becomes 'dryer', the T_2 value of the water protons decreases. Consequently, it becomes progressively more difficult to perform any form of MRI measurement, let alone determine water content. For such systems, one-dimensional projections of spin density or ^{1}H relaxation times obtained without gradient switching can provide a one-dimensional map of water distribution. Depending on the physical shape of the object, such a projection may provide invaluable insight; for example, following the migration of water during the later stages of drying of spaghetti.

A simple example of chemical shift resolved imaging involves visualizing the separation of cream from whole milk. A valuable application is the ability to measure by this technique the water and lipid content in high moisture content samples such as sunflower oil emulsions and fresh meat.[31] An important use of chemical shift resolved imaging is mapping of the water and fat content of processed foods before, during, and after cooking. For example, chemical shift resolved studies of pork pies, fish in batter, and pizza, that were cooked in a microwave or thermal oven show distinct differences in the fat and water images related to their cooking regime. A similar study of the fat uptake during frying of chips is also revealing. In contrast, it is not possible to resolve the water and fat signals in an image of a biscuit; nevertheless, even in the hardest and driest of biscuits it is relatively easy to map the lipid distribution. The signal intensity of the MR image intensity from the lipid in chocolate[19] is very sensitive to the precise crystal, or liquid crystal, morphology of the lipid, and hence of the thermal treatment used to anneal the chocolate into a stable form which has desirable 'mouth feel'.

5 FUTURE PROSPECTS

The successful use of benchtop NMR spectrometers as a source of analytical data in the food laboratory is an encouraging augury for their wider use on the factory floor. Such applications will demand further improvements in 'ruggedization', together with interfacing either to automated batch sampling or, more likely, to continuous online, flow sampling. Fortunately, the technical components for such an instrument are already available, including low cost permanent magnets with a box or C-shaped structure, through which either a pipe or conveyor belt can pass. Furthermore, the development of 'inside-out NMR' in which the magnetic field is external to the magnet, means that it is feasible to construct a complete NMR magnet and probe which could be dipped into a container of food. Although the prospects for shop floor applications of NMR imaging are less obvious at this time, it is clear that demand will come from both increasing quality control standards and the need to develop new foods and optimize their processing and storage. A stimulus for this development is public demand for healthy, quality, ready-made foods which have low fat content and can be cooked in microwave ovens, yet have the texture and appeal of their traditional equivalents.

6 RELATED ARTICLES

Plants, Seeds, Roots, and Soils as Applications of Magnetic Resonance Microscopy; Relaxation Measurements in Imaging Studies; Tissue Water and Lipids: Chemical Shift Imaging and Other Methods

7 REFERENCES

1. Bruker Minispec Application Notes.
2. K. Van Putlte and J. Van den Erden, *J. Am. Oil Chem. Soc.*, 1974, **51**, 316.
3. M. C. M. Gibnau, *Trends Food Sci. Technol.*, 1992, **3**, 186.
4. P. N. Gambhir, *Trends Food Sci. Technol.*, 1992, **3**, 191.
5. H. Weisser, *'NMR Spectroscopy in The Food Industry'*, Bruker Minispec Application Note 7.
6. L. B. Rockland and G. F. Stewart (eds), *Water Activity: Influence on Food Quality*, Academic Press, New York, 1981.
7. B. P. Hills, S. F. Takacs, and P. S. Belton, *Food Chem.*, 1990, **37**, 95.
8. J. E. Tanner and E. O. Stejskal, *J. Chem. Phys.*, 1968, **49**, 1768.
9. C. Guillov, G. Remaud, and G. J. Martin, *Trends Food Sci. Technol.*, 1992, **3**, 197.
10. D. G. Gadian, *Nuclear Magnetic Resonance and its Applications to Living Systems*, Oxford University Press, Oxford, 1982.
11. J. Schaefer and E. O. Stejskal, *J. Am. Oil Chem. Soc.*, 1975, **52**, 366.
12. D. O'Donnell, J. J. H. Ackerman, and G. E. Maciel, *J. Agric. Food Chem.*, 1981, **29**, 514.
13. J. Schaefer, E. O. Stejskal, and R. A. McKay, *Biochem. Biophys. Res. Commun.*, 1979, **88**, 274.
14. P. S. Belton, S. L. Duce, I. J. Colquhoun, and A. S. Tatham, *Magn. Reson. Chem.*, 1988, **26**, 245.

15. S. Y. Wang, P. C. Wang, and M. Faust, *Sci. Hortic.*, 1988, **35**, 227.
16. P. Chen, M. J. McCarthy, and R. Kauten, *Trans. Am. Soc. Agric. Eng.*, 1989, **32**, 1747.
17. N. Ishida, T. Kobayashi, M. Koizumi, and H. Kano, *Agric. Biol. Chem.*, 1989, **53**, 2363.
18. J. B. German and M. J. McCarthy, *J. Agric. Food. Chem.*, 1989, **37**, 1321.
19. S. L. Duce, T. A. Carpenter, and L. D. Hall, *Lebensm. Wiss. u. Technol.*, 1990, **23**, 545.
20. S. L. Duce, T. A. Carpenter, and L. D. Hall, *Carbohydr. Res.*, 1990, **205**, Cl.
21. J. R. Heil, W. E. Perkins, and M. J. McCarthy, *J. Food Sci.*, 1990, **55**, 763.
22. J. Attard, L. Hall, N. Herrod, and S. Duce, *Phys. World*, 1991, **4**, 41.
23. H. Rumpel and J. M. Pope, *Concepts Magn. Reson.*, 1993, **5**, 43.
24. M. J. McCarthy and R. J. Kauten, *Trends Food Sci. Technol.*, 1990, Dec. **1**, 134.
25. G. W. Schrader, J. B. Litchfield, and S. J. Schmidt, *Food Technol.*, 1992, **46**, 77.
26. J. M. Ding, R. W. Lyczkowski, W. T. Sha, S. A. Altobelli, and E. Fukushima, *Powder Technol.*, 1993, **77**, 301.
27. C. F. Jenner, Y. Xia, C. D. Eccles, and P. T. Callaghan, *Nature*, 1988, **336**, 399.
28. C. D. Eccles, P. T. Callaghan, and C. F. Jenner, *Biophys. J.*, 1988, **53**, 77.
29. S. L. Duce, T. A. Carpenter, and L. D. Hall, *J. Food Eng.*, 1992, **16**, 165.
30. S. L. Duce, T. A. Carpenter, L. D. Hall, and B. P. Hills, *Magn. Reson. Imag.*, 1992, **10**, 289.
31. S. L. Duce, S. Ablett, T. M. Guiheneuf, M. A. Horsfield, and L. D. Hall, *J. Food Sci.*, 1994, **59**, 808.

Biographical Sketches

Suzanne L. Duce. *b* 1963. B.Sc., 1984. Scientific Officer, Institute of Food Research, Norwich (with Prof. Peter Belton), 1984–87. Ph.D., 1991, University of Cambridge. Postdoctoral research (with Prof. Laurie Hall), Herchel Smith Laboratory for Medicinal Chemistry, 1991–93. Presently in Cardiff. Approx. 20 publications. Research specialties: nonmedical MRI; solid and solution state carbon-13 NMR, and proton relaxation, in particular their application to food systems.

Laurie D. Hall. *b* 1938. B.Sc. 1959, Ph.D. 1962, Chemistry, University of Bristol, UK. Postdoctoral Fellow (with F. A. L. Anet) Ottawa University, 1962–63. Successively, Instructor, and Assistant, Associate and Full Professor, Department of Chemistry, University of British Columbia, Vancouver, Canada, 1962–84. Currently first holder of the Herchel Smith Chair of Medicinal Chemistry, University of Cambridge, UK (1984–present). Approx. 450 publications. Research specialties: carbohydrate chemistry, high resolution NMR spectroscopy, and medical and nonmedical applications of magnetic resonance imaging.

Cobalt(II)- and Nickel(II)-Substituted Proteins

Lucia Banci and Mario Piccioli
University of Florence, Florence, Italy

1	Introduction	1
2	The Electronic Properties of High Spin Cobalt(II) and Nickel(II) Ions	1
3	Metal Substitution and NMR Parameters	1
4	Cobalt(II)-Substituted Proteins	3
5	Nickel(II)-Substituted Proteins	5
6	Cobalt(II)- and Nickel(II)-Substitution in Magnetically Coupled Dimers	6
7	Conclusions	7
8	Related Articles	7
9	References	7

1 INTRODUCTION

Why is there a need for metal substitution? This approach in the investigation of metalloproteins has been, and is being, widely used in order to exploit the favorable spectroscopic properties of a suitable metal ion.[1–6] With regard to NMR, paramagnetic metal ions are used because they produce additional contributions to both the shift and relaxation parameters of the nuclei coupled to them [7–9] (see ***Electron–Nuclear Hyperfine Interactions***, ***Electron–Nuclear Multiple Resonance Spectroscopy***). The effect on the shift can be of sufficient size that, under certain circumstances, the signals due to such nuclei are well resolved from those of the rest of the protein. This increases the spectral resolution for those nuclei coupled with the paramagnetic center and, when the latter is in the active center of the molecule, very valuable biochemical information can be obtained.

Paramagnetic metal ions can be exploited as relaxation probes or shift probes depending essentially on their electron relaxation times. When the electron relaxation times are long, NMR lines are broad and the metal ion acts as relaxation probe (see ***Paramagnetic Relaxation in Solution***). When electron relaxation times are short, NMR lines are relatively sharp and the metal ion acts as a shift probe. We are only interested in shift probes here.

In order to have little line broadening, the coupling between the electron spin S and the nuclear spin I should be modulated by correlation times τ_c in the range 10^{-11}–10^{-13} s, depending on the number of unpaired electrons. As the rotational correlation times, τ_r, in macromolecules with molecular weights in the range 6000–50 000 are of the order of 10^{-8}–10^{-9} s, it follows that the possibility of obtaining high-resolution NMR spectra depends on the efficiency of the electron relaxation of the metal ion.

If a diamagnetic metal ion (typically Zn^{2+} but also Ca^{2+}, Cd^{2+}) or a paramagnetic metal ion with unfavorable relaxation properties (Cu^{2+}, Mn^{3+}, Mn^{2+}, high-spin Fe^{3+}) is present in a metalloprotein, its replacement with another metal ion with a similar ionic radius and similar coordination properties but favorable electron relaxation times gives rise to a metal-substituted protein whose metal ion surroundings can be investigated by NMR. Because of their favorable electronic properties with respect to NMR and their coordination chemistry, high-spin Co^{2+} and Ni^{2+} are among the most used and most suitable metal ions for substituting other metal ions, particularly Zn^{2+}. They are always high spin in tetrahedral geometry and, for Ni^{2+}, in octahedral geometry. Penta-coordinate ions are often high spin with oxygen and nitrogen donor atoms. In addition, octahedral Co^{2+} is often high spin.

The goal in the use of metal substitution is that of obtaining local information on the metal site through the analysis of the hyperfine (paramagnetic) shifts and of the nuclear relaxation rates of the nuclei of the metal ion ligands and of nearby residues. Furthermore, in the presence of inhibitors and pseudosubstrates, the NMR parameters provide information on the rearrangements induced by the binding of the molecule to the protein.

2 THE ELECTRONIC PROPERTIES OF HIGH SPIN COBALT(II) AND NICKEL(II) IONS

The Co^{2+} ion is a d^7 metal ion, the free ion having the ground state ^4F. In octahedral symmetry the ground state splits into $^4T_{1g}$, $^4T_{2g}$, $^4A_{2g}$, the ground state being $^4T_{1g}$. In the presence of low-symmetry components, spin–orbit coupling provides six Kramers doublets which are slightly separated. Conversely, in tetrahedral symmetry the ground state is the nondegenerate $^4A_2$ state. Hence, in O_h symmetry, low energy levels are available while in T_d symmetry the ground state is nondegenerate and excited levels are higher in energy. The presence of low-lying excited states in octahedral symmetry, arising from the splitting of the $^4T_{1g}$ ground level due to low-symmetry components, contributes to making electron relaxation more efficient in this geometry with respect to tetrahedral coordination and hence to shortening the electron relaxation times. Consequently, the τ_s values of a metal ion are dependent on the coordination geometry of the metal ion itself. For Co^{2+}, τ_s values of 10^{-13}–10^{-12} s have been found for hexa-coordinate ions, of around 10^{-12} s for penta-coordinate, and of around 10^{-11} s for tetrahedral chromophores.[9]

In the case of the Ni^{2+} (d^8) metal ion, the splitting of the free ion term ^3F provides a nondegenerate ($^3A_{2g}$) ground state for octahedral chromophores and, therefore electron relaxation mechanisms are not very efficient. In contrast, in tetrahedral chromophores a degenerate ($^3T_2$) ground state is available and therefore more efficient electron relaxation pathways are operative. Thus τ_s values of 3×10^{-12} s have been estimated for $Ni(H_2O)_6^{2+}$ [9] while tetrahedral Ni^{2+} experiences τ_s values in the range 10^{-12}–10^{-13} s at low magnetic fields. As a consequence, Ni^{2+} is a better probe for metal substitution in tetrahedral systems, while Co^{2+} is more suitable for penta- and hexa-coordinate chromophores. In the next sections we will provide examples of metalloproteins in which the native metal ion has been replaced with Co^{2+} and/or Ni^{2+} and we will illustrate the valuable information thus obtained.

3 METAL SUBSTITUTION AND NMR PARAMETERS

One large and relevant class of metalloproteins is that of the zinc enzymes[1–3] (see ***Carbonic Anhydrase***; ***Zinc Fingers***). Due to the similar coordination properties of the two metal ions, in many cases the cobalt(II)-substituted zinc proteins retain most of the biological properties of the native protein. Usually, substitution with Ni^{2+} produces derivatives with reduced biological activity. In addition, Fe^{2+}, Mn^{2+}, and Cu^{2+} have been replaced by Co^{2+} and also sometimes by Ni^{2+}.[6,10]

The extent of hyperfine shifts on the nuclei of residues directly bound to the paramagnetic metal ion depends on the metal ion itself and on the nature of the ligands (see ***Electron–Nuclear Hyperfine Interactions***). The contact contribution is related to the spin delocalization on the ligand nuclei, while the pseudocontact contribution depends on the magnetic susceptibility anisotropy of the metal ion which, in turn, is determined by the nature of the metal ion and by its coordination geometry. Table 1 reports the range of observed chemical shifts for protons of various ligands to cobalt(II) and nickel(II) in different coordination geometries and in biological molecules. In a few cases the two contributions, i.e. contact and pseudocontact contributions, have been factored out. However, for the nuclei of ligands directly coordinated to the metal ion, the contact contribution is, by far, the dominant. From Table 1, it appears that shifts of up to +300 ppm have been observed for the H-β protons of cysteines coordinated to Co^{2+} and Ni^{2+}.

The pseudocontact contribution to the shift in penta- and hexa-coordinate Co^{2+} chromophores is considerably larger than in tetrahedral coordination. The opposite occurs for Ni^{2+}, where large pseudocontact shifts are observed for tetrahedral coordination and negligible pseudocontact contributions are observed in hexa-coordinate systems. The presence of sizable pseudocontact contributions to the shift causes the appearance of several relatively sharp resonances in the +25 to −20 ppm region of penta- and hexa-coordinate Co^{2+} systems arising from protons up to 7–8 Å apart from the metal ion and not belonging to metal-coordinated residues. The hyperfine shifted signals can be investigated via 1D NOE (see ***Nuclear Overhauser Effect***) and/or 2D NMR spectroscopy in order to assign them unambiguously.

The increase in the nuclear relaxation rates due to coupling with the paramagnetic metal center occurs essentially through dipolar coupling for protons, while contact coupling can also appreciably affect nuclear relaxation in the case of other nuclei. In macromolecules, in the absence of chemical exchange, both couplings are modulated by the electron correlation times of the paramagnetic center.

A limitation in the application of high-resolution NMR in cobalt(II)- and nickel(II)-substituted proteins arises from the occurrence of substantial line broadening with increasing magnetic fields. Indeed, the contribution to transverse relaxation due to coupling of the nuclei with the static magnetic moment (Curie spin relaxation) (see ***Paramagnetic Relaxation in Solution***) must be taken into account.[11] This contribution can be relevant in metalloproteins, and its relevance increases with the number of unpaired electrons and, consequently, with the magnetic moment of the metal ion.[9] The spin state $S = \frac{3}{2}$ of cobalt(II) produces a sizable Curie spin relaxation contribution to the linewidth at high magnetic fields. The Curie spin relaxation term is modulated by τ_r and, therefore, increases with increasing molecular size. Furthermore, it depends on the square of the magnetic field. Hence, in unfavorable cases, i.e. large molecules at high magnetic fields, this contribution easily dominates transverse relaxation. As an example, consider a cobalt(II)-substituted protein of molecular weight 30 000 with τ_r of 1×10^{-8} s and a τ_s value of 5×10^{-12} s for Co^{2+}. For a proton 5 Å from the metal ion, the overall (dipolar + Curie) linewidth at 200 MHz is 78 Hz and the Curie spin contribution is 28 Hz (i.e. the latter accounts for 37% of the overall linewidth). At 600 MHz the overall linewidth for the same proton is 293 Hz and the Curie contribution is 249 Hz (85% of the overall linewidth). This example shows why, due to the strong field dependence of signal linewidths in cobalt(II)-containing proteins, the use of lower field spectrometers can be convenient and, sometimes, necessary.

The ^{1}H NMR spectra of an inhibitor (thiocyanate) adduct of cobalt(II)-substituted carbonic anhydrase (molecular weight, 32 000) (see later), shown in Figure 1 at different magnetic fields, provide a nice example of the above considerations. It can be seen, for example, that signal A′ is only detectable at 90 MHz, while signal E is still observable at 200 MHz but is broadened beyond detection at 600 MHz.

Two-dimensional experiments have been carried out on several cobalt(II)-substituted and nickel(II)-substituted macromolecules (see ***Multidimensional Spectroscopy: Concepts***), despite the presence of a paramagnetic center (see later for examples). In these experiments the mixing times were relatively short with respect to the relaxation of the nuclei but long enough such that transfer of magnetization or coherence occurred. The recycle times can also be set to be relatively short in order to increase the number of transients in the experiment time, thus improving the signal-to-noise ratio.

Recently, it has been pointed out[12] that cross correlation between dipolar relaxation and Curie spin relaxation [which can be sizable in cobalt(II)-containing macromolecules] can

Table 1 Chemical Shift Ranges (ppm) Experienced at Room Temperature in Solution by Protons of Residues Bound to a Cobalt(II) or a Nickel(II) in the Active Site of Metalloproteins with Different Coordination Geometries

Coordination geometry	Ligand and proton type			
	Cys G-β	His *ortho*-like	His *meta*-like	Asp H-β, Glu H-γ
Cobalt(II)				
Tetrahedral	300–200	150–40	70–35	80–30
Penta-coordinate	300–200	130–30	80–50	
Octahedral			70–50	
Nickel(II)				
Tetrahedral	300–150		80–20	
Penta-coordinate	240–190		80–35	

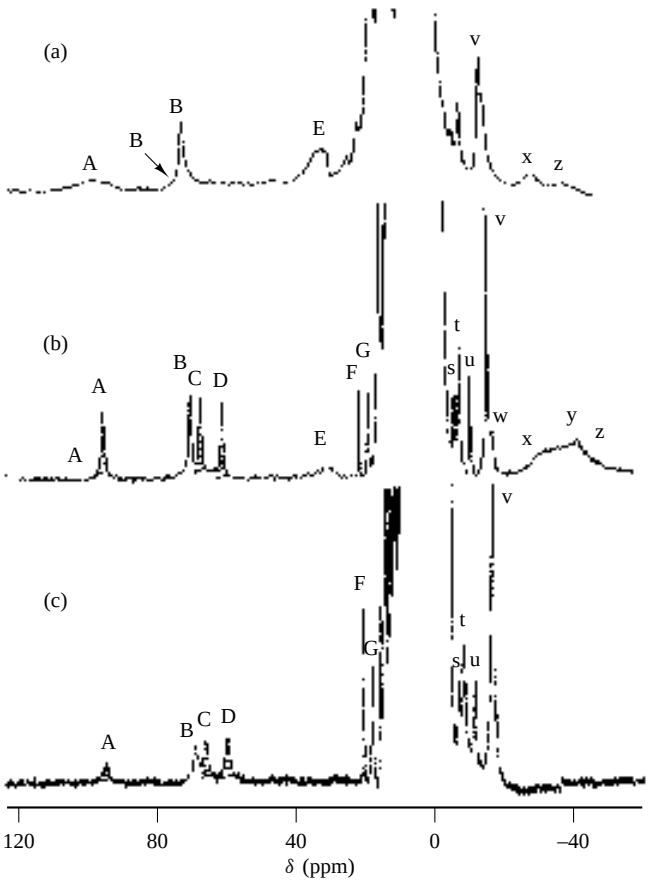

Figure 1 ^{1}H NMR spectra of the thiocyanate adduct of cobalt(II)-substituted carbonic anhydrase recorded at different magnetic fields: (a) 90 MHz, (b) 200 MHz, (c) 600 MHz. The spectrum shown in (a) was recorded in D_2O in order to detect the broad A′ signal otherwise covered by the A signal. 'Hatched' signals disappeared when the spectra were recorded in D_2O

give rise to cross peaks in COSY experiments even in the absence of scalar interaction between the protons. This mechanism is called relaxation allowed coherence transfer (RACT); it is absent in in-phase COSY or superCOSY experiments (see ***Relaxation Processes: Cross Correlation and Interference Terms***).

4 COBALT(II)-SUBSTITUTED PROTEINS

The first spectrum of a cobalt(II)-substituted protein for which an attempt at sequence specific assignment was reported was that of cobalt(II)-substituted carbonic anhydrase (CA).[13] CA is a zinc enzyme (see ***Carbonic Anhydrase***) which catalyzes the hydration of carbon dioxide.[14] The zinc ion is bound to three histidines with a roughly tetrahedral geometry. The fourth coordination position is accessible to the solvent or occupied by a water molecule. The latter molecule is transformed into a hydroxide group with a relatively low pK_a value. Substitution of the native zinc ion with cobalt(II) maintains about 50% of the enzymatic activity of the native protein. The cobalt(II)-substituted protein provides an NMR spectrum which shows some well resolved, high-frequency-shifted signals. They are due to the histidine protons in *meta*-like positions with respect to the cobalt. Some of these signals have been readily assigned to the NH protons of the histidine rings due to their exchange with the bulk solvent.

As can be seen from the spectrum of the native cobalt(II)-substituted protein, reported at the bottom of Figure 2, the ^{1}H NMR signals due to the protons of the cobalt ligands are relatively broad (ca. 300 Hz at 200 MHz) and shifted within a relatively narrow shift range (+53 to +63 ppm). In addition, very few signals of protons not belonging to metal ligands are resolved outside the diamagnetic envelope. This is due to the tetrahedral geometry of the cobalt ion in the native form of this enzyme, which is characterized by small magnetic anisotropy and relatively long electron relaxation times. Hence the pseudocontact contribution to the shift is small and only protons belonging to the metal ion ligands experience sizable hyperfine shifts. This means that information remains substantially limited to the coordinated residues.

When inhibitors bind cobalt(II) without displacing the coordinated solvent molecule, a five-coordinate adduct is obtained in which cobalt(II) experiences a much larger magnetic anisotropy and shorter electron relaxation times. This means that several protons belonging to residues close to the cobalt ion, but not directly coordinated to it, are shifted substantially and well resolved outside the diamagnetic envelope. Furthermore the lines are sharper (ca. 200 Hz at 200 MHz) than in the spectrum of the native form. ^{1}H NMR spectra of adducts with several inhibitors are reported in Figure 2. On these spectra, classical NMR techniques for spectral assignment such as NOE (see ***Nuclear Overhauser Effect***) and 2D NMR experiments (***COSY Two-Dimensional Experiments***; ***Multidimensional Spectroscopy: Concepts***; ***NOESY***) have been performed. They have led, for the adducts with nitrate, perchlorate and thiocyanate, to the assignment of the signals of the metal ligands and of several residues present around the active site.[13,16] Some of these assignments have been confirmed by analysis of the spectra of samples produced with selectively deuterated amino acids.[16]

The assignment of several protons experiencing only pseudocontact shifts has allowed the calculation, using a best-fitting procedure and the knowledge of the X-ray structure of the protein, of the anisotropy and the orientation of the magnetic susceptibility (χ) tensor. The latter information is relevant for the knowledge of the electronic structure of the cobalt ion in the adduct. Furthermore, it allows the calculation of the shifts for all the protons sensing some coupling with the metal ion, which can help in further assigning other signals.[13,16]

Extensive studies have also been performed on cobalt(II)-substituted carboxypeptidase (CPA) which is a zinc enzyme[17] where the five-coordinate metal ion is bound to two histidines, a water molecule, and a bidentate glutamate. Cobalt substitution increases the enzymatic activity of native CPA. The protein is soluble only at high ionic strengths, i.e. in viscous solutions. This provides long τ_r values and consequently large line broadening due to Curie spin relaxation. Indeed, no high-field NMR experiments have been performed on this system.

Despite these problems, cobalt(II)-substitution in CPA has provided useful information on the local structural features at the metal ion and on the enzyme reactivity. The ^{1}H NMR

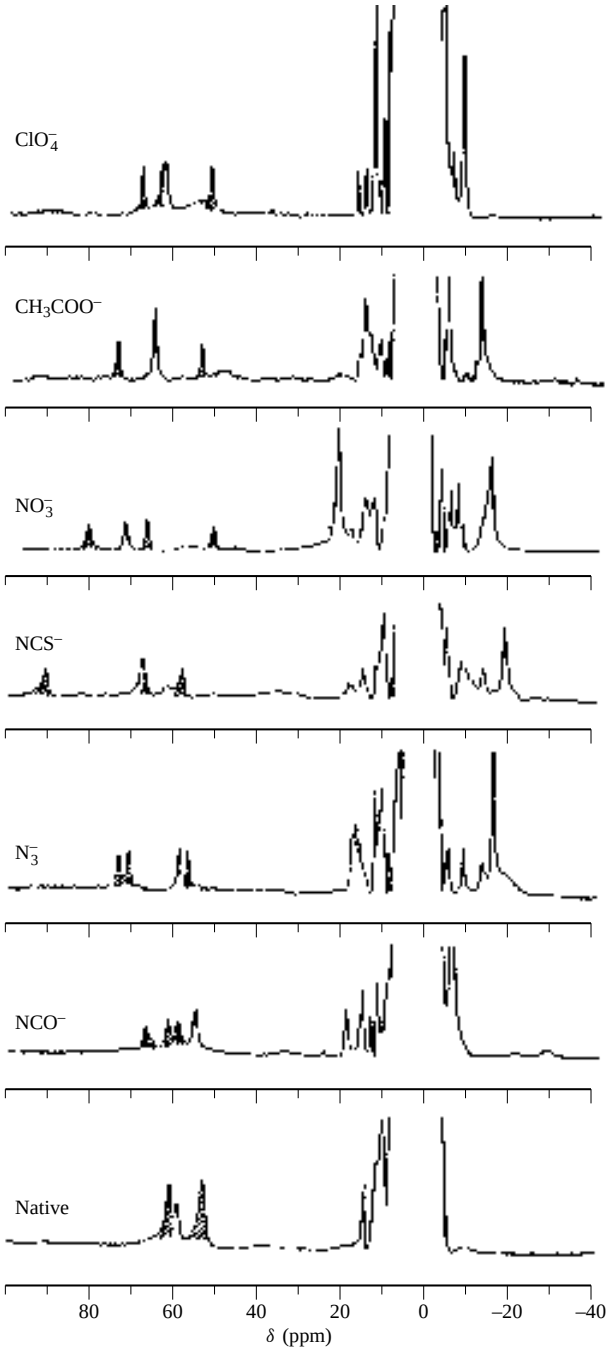

Figure 2 ^{1}H NMR spectra at 200 MHz of native and some anion adducts of cobalt-substituted carbonic anhydrase. 'Hatched' signals disappeared when the spectra were recorded in D_2O. (Reproduced by permission of Kluwer Academic Publishers from L. Banci, I. Bertini, C. Luchinat, and J. M. Moratal, in Enzymatic and Model Carboxylation and Reduction Reactions for Carbon Dioxide Utilization, eds. M. Aresta and J. V. Schloss, 1990, pp. 181–197)

spectrum of CoCPA (optimal field 90–200 MHz) shows three relatively sharp signals which have been assigned, through 1D NOE measurements, to *meta*-like protons of the two histidines. Two broader peaks have also been observed in the ^{1}H NMR spectrum of CoCPA and assigned, on the basis of their T_1 and T_2 values, to the two H-γ protons of the Co^{2+}-bound glutamate.

Information on the biochemistry of the enzyme was obtained by monitoring the changes in the ^{1}H NMR spectrum upon addition of inhibitors and substrate analogs.[18] For instance, it has been observed that some inhibitors such as carboxylic acids bind the enzyme in a 2:1 ratio. The first inhibitor molecule binds through its carboxylate group to an Arg residue (Arg-145) present in the catalytic cavity. The binding of this molecule in the cavity breaks the strong H-bond present between the zinc-bound water molecule and a Glu residue (Glu-270) present in the cavity, and makes the water molecule easily displaceable by a second molecule of inhibitor which binds the metal ion directly.

Cobalt substitution has been successfully performed on Cu_2Zn_2 superoxide dismutase (SOD hereafter).[19] This enzyme contains two metal centers connected by a histidinate bridge. Cobalt(II) can substitute zinc in its native site. Several systems, with no metal or with diamagnetic metal ions [Ag(I) or Cu(I)] in the copper site, have been investigated with the aim of characterizing the zinc ion-binding site. In such systems, cobalt(II) is coordinated by three histidines and a unidentate aspartate. The spectra of such derivatives are all similar to each other. Eight signals are hyperfine-shifted in the high-frequency region, i.e. the three *meta*-like exchangeable HN-ϵ2, the three nonexchangeable H-δ2 protons of the imidazole rings and the signals of the two H-β protons of the bound aspartate. The observation of three HN signals in the case of $Cu^I_2Co_2SOD$ provided the first direct evidence that the imidazole bridge between the two metal ions is broken when the copper ion is reduced.[20] Indeed, this finding is particularly remarkable in the light of recent X-ray studies on the reduced form of the native ($Cu^I_2Zn_2SOD$) protein which show, in the solid state, no bridge-breaking in this form of the enzyme. The spectrum of $Cu^I_2Co_2SOD$ has been investigated through 1D NOE and 2D NMR experiments at different magnetic fields[20] in order to: (i) assign the far-hyperfine-shifted signals (1D NOE at 200 MHz), (ii) assign the signals of residues belonging to the active site but not bound to the Co^{2+} ion (2D NOESY, 600 MHz), and (iii) use the pseudocontact shifts [available because of the assignment at point (ii)] to obtain information on the χ tensor anisotropy and directions of the Co^{2+} ion in the zinc site, analogous to the case of cobalt(II)-substituted CA.

An interesting example of the utility of metal substitution in proteins with large molecular weight (MW) is provided by cobalt substitution of the native zinc ion in liver alcohol dehydrogenase (LADH), a dimeric protein of MW ca. 80 000. The metal ligands are two cysteines, one histidine, and a water molecule. Even in the case of this large molecule, the signals of the two Cys H-β protons and of the three histidine protons (including the *ortho*-like proton) have been observed. Of course, the higher the molecular weight, the larger is the Curie spin relaxation term. Hence, such signals are best detected at 60 MHz![21]

Another example of a large protein for which cobalt substitution turned out to be useful with respect to obtaining information on the metal site is alkaline phosphatase (AP). AP is a large dimeric protein (MW 94 000) consisting of two identical subunits. Each contains three metal binding sites; in the native form two of these sites bind zinc while the third is specific for magnesium. Zinc has been substituted by cobalt(II) in its binding sites. Information on the metal ion ligands as well as on the metal uptake pathways has been obtained even on this large molecule.[22]

One of the most recent applications of cobalt(II) substitution has been performed on zinc finger peptide CP-1.[23] At variance with the previously reported cases, zinc finger proteins have already been studied extensively through high-resolution ^{1}H NMR in their native form due to their relatively low molecular weight (see ***Zinc Fingers***). However, cobalt(II) substitution has provided useful insights. Knowledge of the pseudocontact shifts of several resonances in the cobalt(II)-substituted protein has led the authors to calculate the χ tensor of the system. For a correct determination of the pseudocontact shifts, it is important to know the diamagnetic contributions to the shifts. The latter have been obtained by taking advantage of the assignment of the signals of the native protein.

Zinc proteins are not the only systems in which cobalt(II) substitution was successfully attempted. Iron has been substituted by cobalt(II) in several systems (see ***Iron—Sulfur Proteins***, ***Nonheme Iron Proteins***, ***Transferrins***). Indeed, in the absence of magnetic coupling with fast relaxing metal ions and in nonheme proteins, both high spin iron(III) and high spin iron(II) give rise to relatively broad ^{1}H NMR signals.[9] For this reason, although the ^{1}H NMR spectra of the iron(III)-containing protein Isopenicillin Synthase (INPS) have been recorded and several hyperfine-shifted signals observed, cobalt(II)-substituted INPS has been prepared in order to obtain hyperfine-shifted signals sharp enough to perform 1D NOE experiments. These have led to the tentative proposal of the structure of the active site (no X-ray data are available) and of a catalytic mechanism.[24] Similar considerations hold also for the signal linewidths in rubredoxin (Rd) (see ***Iron—Sulfur Proteins***) where the iron ion has a tetrahedral geometry and is coordinated to the sulfur atoms of the four cysteines. In this system, cobalt(II) and nickel(II) substitution was also performed. The ^{1}H NMR spectra are characterized by sharp and well-resolved signals, although no firm assignment is available for the spectra.[25]

Metallothioneins (MT) constitute a class of small proteins containing clusters of the type Cd_4S_{11} and Cd_3S_9. Titration of the apoprotein with cobalt(II) has been followed using NMR and has allowed the authors to study the uptake pathway of the metal ions. The Co_3S_9 cluster was first formed. The protein containing this cluster shows broad hyperfine signals, probably because the Co_3S_9 cluster experiences some fluxionality that broadens the lines beyond detection.[26] The ^{1}H NMR spectrum of the fully-substituted protein (Co_7MT) shows a large number of sharp, very high-frequency-shifted signals arising from the H-β protons of the cobalt(II)-coordinated cysteines. Such signals are shifted by up to +400 ppm. Detection of ^{1}H NMR signals at 600 MHz over such a large spectral width required the use of a fast ADC (9-bit digitizer over 10 MHz) (see ***Spectrometers: A General Overview***). An extensive pairwise assignment of the H-β cysteine protons was performed by 1D NOE and 2D NOESY experiments as well as by observing the temperature dependence of the shifts, interpreted on the basis of a magnetic coupling scheme among the metal ions.[26]

Substitution of the native iron(III) ion in transferrins (TRN, MW 90 000) (see ***Transferrins***) with cobalt(II) provided derivatives which showed, at 90 MHz, several high-frequency-shifted signals despite the large molecular weight of the protein.[27] The protein contains two metal binding sites which are not equivalent as revealed by ^{1}H NMR spectra. The observed signals were attributed to the presence of histidine and tyrosine residues as ligands to the metal ions. This example shows that the presence of a suitable metal ion can aid the characterization through NMR of even large proteins.

The blue copper protein azurin (Az) (see ***Copper Proteins***) has been investigated through ^{1}H NMR of the cobalt(II)- and nickel(II)-substituted derivatives.[28] The metal ion is pentacoordinate, its ligands being two histidines, one cysteine, one methionine, and the oxygen of the carbonyl group of a glycine residue. This protein has a relatively small molecular weight (16 000) which makes the Curie spin relaxation less efficient than in the systems previously described. The signals of the protons of the metal ion ligands are therefore relatively sharp. The H-β proton signals of the coordinated cysteine are shifted by more than +200 ppm while the signals of the ring protons of the two histidines fall in the usual 60–30 ppm region. The signals of two geminal proton pairs, which were tentatively assigned to the H-α protons of the metal-coordinated glycine and to the H-γ protons of the coordinated methionine, are observed with one signal shifted at low frequency and its geminal partner at high frequency for both pairs.[29] This behavior has not yet been rationalized, but it could be due to the different M–S(O)–C–H dihedral angles experienced by the two protons in each pair. This would make the spin density different on each of the two protons.

Experiments involving nuclei other than protons are much less common, even if quite promising. Heteronuclear multiple quantum coherence (HMQC) experiments (see ***Heteronuclear Shift Correlation Spectroscopy***) on ^{15}N-enriched samples have been performed on cobalt(II)-substituted CA,[6] and several scalar ^{15}N–^{1}H couplings between residues close to the cobalt ion have been detected.

5 NICKEL(II)-SUBSTITUTED PROTEINS

There are several examples in which nickel substitution has been performed on the same proteins where the native metal ion has also been replaced by cobalt. As previously discussed, nickel(II) is, in principle, more suitable for the investigation of tetrahedral centers and less useful in the case of hexacoordinate chromophores. Indeed, the nickel(II) ion in NiCPA in the presence of two moieties of D-phenylalanine induces broad lines and small pseudocontact shifts due to the small magnetic anisotropy.[30] In contrast, the ^{1}H NMR spectrum of NiCPA without any inhibitor shows sharp lines for the *meta*-like protons of the bound histidines,[30] the opposite of that observed for cobalt(II)-substituted CPA.

Nickel(II)-substituted CA has also been investigated through ^{1}H NMR, although the interest in such derivatives from the biochemical point of view is limited due to the severe reduction of activity. For those adducts of NiCA for which NMR studies have been performed, information similar to that obtained upon cobalt(II) substitution was achieved.[31]

In the case of tetrahedral chromophores such as Fe^{III}Rd and Cu^{II}Az, nickel(II) substitution produces derivatives with narrower lines relative to the corresponding cobalt(II) substituted derivatives.[32] In the case of zinc fingers, also, nickel(II) substitution produces narrower hyperfine-shifted ^{1}H NMR signals with respect to those observed in the cobalt(II) derivative. However, no assignment of the hyperfine-shifted signals has been attempted for the nickel derivative.[33]

Finally, a derivative with a nickel(II) in the zinc site of SOD and no metal in the copper site has been prepared and

characterized through NMR,[20] again obtaining information similar to that on the analogous cobalt(II) derivative.

6 COBALT(II)- AND NICKEL(II)-SUBSTITUTION IN MAGNETICALLY COUPLED DIMERS

Cobalt(II) and nickel(II) are not only efficient probes for NMR investigation in themselves, but they can also drastically reduce the electron relaxation rates of a slow-relaxing metal ion through magnetic coupling.[9] This coupling allows the slow-relaxing ion to relax through the efficient mechanisms of the fast-relaxing metal ion. The effect depends on the extent of the magnetic coupling constant; in the limit of $J/\hbar >> \tau_s{}^{-1}$ (where τ_s is referred to the fast-relaxing metal ion) the relaxation rate of the slow-relaxing metal ion approaches that of the fast-relaxing ion[9,34] (see ***Paramagnetic Relaxation in Solution***, ***Relaxation Theory: Density Matrix Formulation***). Under such conditions, even the signals of nuclei coupled to a slow-relaxing metal ion which, when isolated, would induce a dramatic increase in the linewidth, can be easily detected because they are sharp enough for the application of standard high-resolution NMR techniques.

An elegant application of the above considerations is provided by the replacement of native zinc ion in $Cu^{II}{}_2Zn_2SOD$ by cobalt(II) and nickel(II). The copper(II) ion is characterized by τ_s values of the order of 10^{-9} s which produce a dipolar contribution to the linewidth of a proton at 5 Å from copper (as for the *meta*-like protons of the coordinated histidines) of 2000 Hz. However, the magnetic coupling of copper with cobalt(II) or nickel(II), which relax much faster than copper(II), produces a drastic reduction of the relaxation times of the latter metal ion. The ^{1}H NMR spectra of Cu_2Co_2SOD and of Cu_2Ni_2SOD are reported as the upper traces in Figure 3.[20]

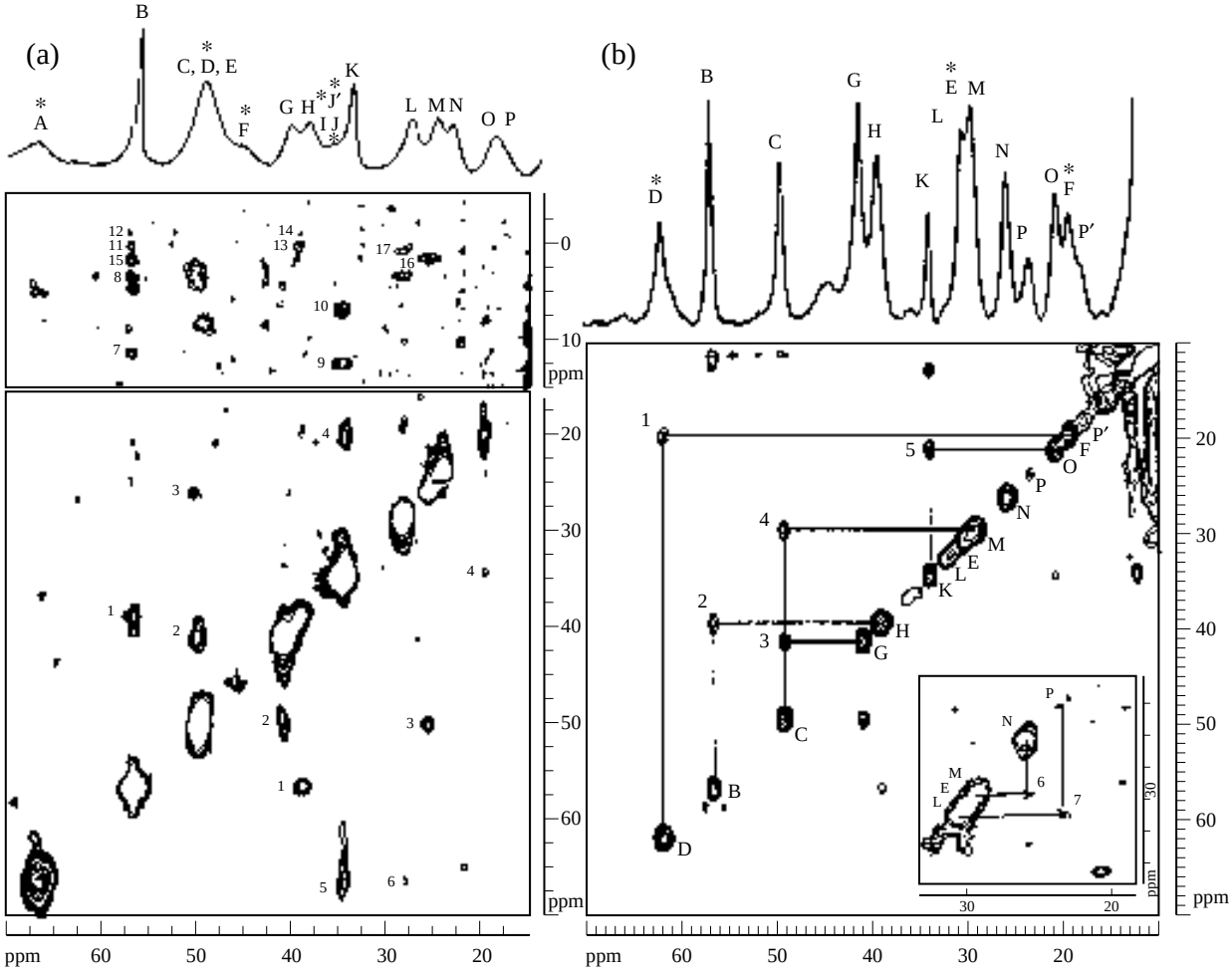

Figure 3 600 MHz NOESY spectra of Cu_2Co_2SOD (a) and Cu_2Ni_2SOD (b) in the region of hyperfine, high-frequency-shifted signals. The 1D spectra are also reported on the top of the NOESY maps. Signals marked by asterisks arise from protons of residues bound to the cobalt(II) or nickel(II) ions. Signal and cross peak labeling refer to the assignments summarized by Bertini et al.[20] Experimental conditions were: (a), lower map mixing time 4 ms, relaxation delay 80 ms, 256 experiments in F_1 and 512 experiment in F_2; upper map mixing time 15 ms, relaxation delay 150 ms (in order to better detect connectivities between hyperfine shifted signals and diamagnetic signals): (b), mixing time 15 ms, relaxation delay 80 ms, 512 experiments in F_1 and 1024 experiments in F_2. The inset in (b) shows a region of a NOESY spectrum recorded under the same experimental conditions at 300 MHz. All the observed connectivities in Cu_2Co_2SOD involve signals of copper-coordinated residues. In the NOESY map of Cu_2Ni_2SOD, connectivities 1–5 arise from intraresidue connectivities involving imidazole protons of residues bound either to Ni(II) (1) or Cu(II) (2–5). Connectivities 6 and 7 arise from interresidue contacts involving copper-coordinated histidines

It should be noted that the signals of the protons of the copper ligands are even sharper [due to the lower S value of copper(II) than of cobalt(II) and nickel(II)] than those of the cobalt or nickel ligands. All the metal–ligand proton signals, as well as several signals due to protons of residues located close to the two paramagnetic centers, have been firmly assigned through 1D NOE (see ***Nuclear Overhauser Effect***) and/or 2D NOESY (see ***NOESY*** experiments). In Figure 3 the NOESY spectra of Cu_2Co_2SOD and Cu_2Ni_2SOD are reported.[20,35,36] In these maps, besides many intraresidue connectivities, some interresidue connectivities are also detected between the copper ligand protons. In Cu_2Ni_2SOD some intraresidue connectivities have also been detected for nickel(II) ligand protons (see inset in Figure 3), while no connectivities between protons of residues coordinated to the cobalt(II) ion in Cu_2Co_2SOD could be observed. The latter effect is due to the very short T_2 values of the signals which render the broad NOESY cross peaks expected in these cases difficult to detect.

The signals of the protons in the copper site are sharper in Cu_2Ni_2SOD than in Cu_2Co_2SOD. This is the result of the shorter electron relaxation times of nickel(II) than of cobalt(II) in tetrahedral geometry. For the signals of the ligands of the zinc site, the spin state of Ni^{2+}, $S = 1$, makes the Curie contribution to their linewidth smaller than for those in the cobalt(II)-substituted derivative.

Cobalt(II) has also been used to replace the native copper(II) to obtain either Co_2Zn_2SOD or Co_2Co_2SOD; the above derivatives have been investigated through NMR and the signals of the metal-coordinated residues have been observed even if no detailed assignment was attempted.[20]

The ^{1}H NMR signals for metal–ligand protons have also been detected in Co_2Cu_2AP, for the ligands of copper ion,[22] and in iron(II)–cobalt(II) uteroferrin[37] (see ***Nonheme Iron Proteins***) for the ligands of the iron(II) ion. Indeed, the effect of the coupling is quite general. In all the proteins which contain two metal binding sites close enough that magnetic coupling can occur, NMR characterization of the metal sites can be successfully performed provided that one of the metal ions has short electron relaxation times.

Heteronuclear NMR spectroscopy has been rarely applied in the case of dimers. ^{15}N–^{1}H HMQC spectra (see ***Heteronuclear Shift Correlation Spectroscopy***) have been recorded on Cu_2Co_2SOD, detecting the ^{15}N–^{1}H scalar couplings for the copper-bound histidines.[38] This is the first case in which ^{15}N–^{1}H connectivities involving residues directly coordinated to the metal center of a paramagnetic protein have been observed.

7 CONCLUSIONS

Some of the examples discussed above clearly indicate that cobalt(II) substitution is *still* a powerful technique for the ^{1}H NMR spectroscopy of metalloproteins, although the actual capabilities of 'standard' multidimensional experiments are such that the 3D structure of proteins up to MW 30 000 can now be determined (see ***Biological Macromolecules: Structure Determination in Solution***, ***Structures of Larger Proteins, Protein-Ligand, and Protein-DNA Complexes by Multi-Dimensional Heteronuclear NMR***). In the case of proteins containing paramagnetic metal ions, which provide hyperfine-shifted signals which are too broad, Co^{2+} and/or Ni^{2+} substitutions allow a good structural characterization of the protein region around the metal center. In the case of relatively small proteins, standard NMR experimental procedures for diamagnetic systems can be successfully combined with the analysis of 2D NOESY and COSY maps designed for the detection of connectivities between the hyperfine shifted signals to obtain the overall 3D protein structure in solution. Hence, the 'paramagnetism' of the system is no longer a drawback for the complete characterization and for the determination of the solution structure. In the case of large proteins such results cannot be achieved, but valuable local information on the active site can be obtained. Finally, we would like to stress the relevance of the evaluation of the χ tensor anisotropy and directions in cobalt(II)-substituted systems. Analysis of pseudocontact shifts, as formerly performed in the case of heme proteins, has also provided satisfactory results in cobalt(II)-substituted systems. More frequent utilization of such an approach is expected in the future.

8 RELATED ARTICLES

Calcium-Binding Proteins; Carbonic Anhydrase; Copper Proteins; Electron–Nuclear Hyperfine Interactions; Iron—Sulfur Proteins; Metallothioneins; Nonheme Iron Proteins; Paramagnetic Relaxation in Solution; Transferrins; Zinc Fingers.

9 REFERENCES

1. I. Bertini and C. Luchinat, in *Metal Ions in Biological Systems*, ed. H. Sigel, Marcel Dekker, New York, 1983, 15, p. 101
2. I. Bertini, C. Luchinat, W. Maret, and M. Zeppezauer (eds.), *Zinc Enzymes*, Birkhauser, Boston, MA, 1986.
3. B. L. Vallee, A. Galdes, D. S. Auld, and J. F. Riordan, in *Zinc Enzymes*, ed. T. G. Spiro, Wiley-Interscience, New York, 1983, p. 25.
4. I. Bertini, H. B. Gray, S. J. Lippard, and J. S. Valentine (eds.) *Bioinorganic Chemistry*, University Science Books, Mill Valley, CA, 1994.
5. J. J. R. Frausto da Silva and R. J. P. Williams, *The Biological Chemistry of the Elements*, Oxford University Press, Oxford, UK, 1991.
6. J. S. Valentine and M. W. Pantoliano, in *Metal Ions in Biological Systems*, ed. H. Sigel, Marcel Dekker, New York, 1981, Vol. 3, p. 291.
7. G. N. La Mar, W. DeW Horrocks, Jr., and R. H. Holm (eds.), *NMR of Paramagnetic Molecules Principles and Applications*, Academic Press, New York, 1973.
8. I. Bertini and C. Luchinat, *NMR of Paramagnetic Molecules in Biological Systems*, Benjamin/Cummings, Menlo Park, CA, 1986.
9. L. Banci, I. Bertini, and C. Luchinat, *Nuclear and Electron Relaxation. The Magnetic Nucleus–Unpaired Electron Coupling in Solution*, VCH, Weinheim, 1991.
10. I. Bertini, P. Turano, and A. J. Vila, *Chem. Rev.*, 1993, **93**, 2833.
11. M. Gueron, *J. Magn. Reson.*, 1975, **19**, 58.
12. I. Bertini, C. Luchinat, and D. Tarchi, *Chem. Phys. Lett.*, 1993, **203**, 445.
13. L. Banci, L. B. Dugad, G. N. La Mar, K. A. Keating, C. Luchinat, and R. Pierattelli, *Biophys. J.*, 1992, **63**, 530.

14. S. Lindskog, in *Zinc Enzymes*, ed. T. G. Spiro, Wiley-Interscience, New York, 1983, p. 77.
15. L. Banci, I. Bertini, C. Luchinat, A. Donaire, M.-J. Martinez, and J. M. Moratal Mascarell, *Comments Inorg. Chem.*, 1990, **9**, 245.
16. I. Bertini, B.-H. Jonsson, C. Luchinat, R. Pierattelli, and A. J. Vila, *J. Magn. Reson. Ser. B*, 1994, **104**, 230
17. D. W. Christianson and J. D. Lipscomb, *Acc. Chem. Res.*, 1989, **22**, 62.
18. I. Bertini, C. Luchinat, L. Messori, R. Monnanni, D. S. Auld, and J. F. Riordan, *Biochemistry*, 1988, **27**, 8318.
19. (a) J. S. Valentine and M. W. Pantoliano, in *Copper Proteins*, ed. T. G. Spiro, Wiley, New York, 1981, p. 291; (b) I. Fridovich, *Adv. Enzymol. Relat. Areas Mol. Biol.*, 1986, **58**, 61.
20. I. Bertini, C. Luchinat, and M. Piccioli, *Prog. Nucl. Magn. Reson. Spectrosc.*, 1994, **26**, 91.
21. I. Bertini, M. Gerber, G. Lanini, C. Luchinat, W. Maret, S. Rawer, and M. Zeppezauer, *J. Am. Chem. Soc.*, 1984, **106**, 1826.
22. L. Banci, I. Bertini, C. Luchinat, M. S. Viezzoli, and Y. Wang, *Inorg. Chem.*, 1988, **27**, 1442.
23. L. V. Harper, B. T. Amann, V. K. Vinson, and J. M. Berg, *J. Am. Chem. Soc.*, 1993, **115**, 2577.
24. L. J. Ming, L. Que, Jr., A. Kriauciunas, C. A. Frolik, and V. J. Chen, *Biochemistry*, 1991, **30**, 11 653.
25. I. Moura, M. Teixeira, J. LeGall, and J. J. G. Moura, *J. Inorg. Biochem.*, 1991, **44**, 127.
26. I. Bertini, C. Luchinat, L. Messori, and M. Vašak, (a) *J. Am. Chem. Soc.*, 1989, **111**, 7296; (b) *J. Am. Chem. Soc.*, 1989, **111**, 7300; (c) *Eur. J. Biochem.*, 1993, **211**, 235.
27. L. Messori and M. Piccioli, *Inorg. Chim. Acta*, 1990, **174**, 137.
28. H. A. O. Hill, C. B. Storm, and R. P. Ambler, *Biochem. Biophys. Res. Commun.*, 1976, **70**, 783.
29. J. M. Moratal Mascarell, J. Salgado, A. Donaire, H. R. Jimenez, and J. Castells, *Inorg. Chem.*, 1993, **32**, 3587.
30. I. Bertini, A. Donaire, R. Monnanni, J. M. Moratal, and J. Salgado, *J. Chem. Soc., Dalton Trans.*, 1992, 1443.
31. J. M. Moratal, M.-J. Martinez Ferrer, A. Donaire, J. Castells, J. Salgado, and H. R. Jimenez, *J. Chem. Soc., Dalton Trans.*, 1991, 3393.
32. J. M. Moratal Mascarell, J. Salgado, A. Donaire, H. R. Jimenez, J. Castells, and M.-J. Martinez Ferrer, *Magn. Reson. Chem.*, 1993, **31**, S41.
33. B. A. Krizek and J. M. Berg, *Inorg. Chem.*, 1992, **31**, 2984.
34. L. Banci, I. Bertini, and C. Luchinat, *Struct. Bonding (Berlin)*, 1990, **72**, 113.
35. L. Banci, I. Bertini, C. Luchinat, M. Piccioli, and A. Scozzafava, *Gazz. Chim. Ital.*, 1993, **123**, 95.
36. I. Bertini, C. Luchinat, L. J. Ming, M. Piccioli, M. Sola, and J. S. Valentine, *Inorg. Chem.*, 1992, **31**, 4433.
37. R. C. Holz, L. Que, Jr., and L. J. Ming, *J. Am. Chem. Soc.*, 1992, **114**, 4434.
38. I. Bertini, C. Luchinat, R. Macinai, M. Piccioli, A. Scozzafava, and M. S. Viezzoli, *J. Magn. Reson. Series B*, 1994, **104**, 95.

Biographical Sketches

Lucia Banci. *b* 1954. Doctor in Chemistry, 1978, University of Florence. Faculty positions at University of Florence, 1982–present; Associate Professor of Nuclear Magnetic Resonance, 1987–present. More than 100 publications. Research fields: NMR of paramagnetic species, biological applications of NMR, molecular dynamics calculations on metalloproteins, bioinorganic and biophysical chemistry, theory of nuclear and electron relaxation.

Mario Piccioli. *b* 1960. Doctor in Chemistry, 1987, Ph.D. 1991, University of Florence (supervisor Lucia Banci). Researcher at University of Florence since 1991. Introduced to NMR by Ivano Bertini. 40 publications. Research fields: NMR of paramagnetic macromolecules, magnetic coupled systems, iron–sulfur proteins, solution structure of proteins, bioinorganic chemistry, biophysics.

Copper Proteins

Gerard W. Canters
Leiden University, Leiden, The Netherlands
and
Mart van de Kamp
Nijmegen University, Nijmegen, The Netherlands

1	Introduction	1
2	Blue Copper Proteins	1
3	Nonblue Copper Proteins	4
4	Related Articles	5
5	References	5

1 INTRODUCTION

The presence of a 3d transition metal in their interior makes Cu proteins challenging and interesting subjects of study by NMR techniques. In addition, in a number of cases the properties of the protein matrix make them eminently suitable for the application of advanced NMR spectroscopic techniques, despite the occasional inconvenience caused by the presence of a redox-active metal.

Although copper itself is NMR-visible this property has hardly been used in the study of copper proteins.[1] The two naturally occurring stable copper isotopes (^{63}Cu and ^{65}Cu, natural abundances 69.2% and 30.8%) have nonzero spin ($I = \frac{3}{2}$ for both isotopes), but the accompanying nuclear quadrupole moment is large enough to cause considerable relaxation and line broadening, except for cases where the metal environment is highly symmetric and the electrical field gradient is consequently zero. For coordination compounds the latter may sometimes be the case, but protein environments are usually of low symmetry and Cu NMR spectroscopy, therefore, has been of little practical value in the study of Cu proteins.

Copper in proteins may occur in more than one redox state: Cu(I) or Cu(II). Copper(I) is diamagnetic and produces no problems in the measurement and interpretation of NMR spectra. However, the metal is easily oxidized and changes over to the (paramagnetic) Cu(II) state, which may cause complications from a spectroscopic point of view. The electronic spin–lattice relaxation of Cu(II) is too slow (relaxation times of 1–3 ns) for Cu to be useful as a shift reagent. Instead, resonances from nuclei close to the metal are broadened beyond detection. This is often a nuisance, but it can be used to advantage in kinetic experiments where the rate of electron transfer to and from the Cu is measured (vide infra). The broadening effect may also be used as an additional help in the assignment of some peaks in the NMR spectrum of the protein. The metal then serves as a relaxation probe.

Thus the presence of Cu may impart some experimental obstacles to high-resolution studies of Cu proteins. NMR spectroscopists have tried to circumvent these by replacing the Cu with paramagnetic shift probes such as Ni(II) and Co(II), which have shorter electron spin relaxation times, or with diamagnetic redox-inactive metals such as Ag(I), Zn(II), Cd(II), and Hg(II).[2–5] Some of the latter nuclei are directly accessible to NMR spectroscopy (^{109}Ag, ^{113}Cd, ^{199}Hg).

Copper proteins have been distinguished on the basis of the structural and spectroscopic characteristics of their metal sites.[6,7] Type-I sites contain a single copper ion covalently anchored to the protein by three metal–ligand bonds, two of them provided by histidines that act as N-donors, and one by a cysteine that coordinates to the Cu via its S-γ atom. The Cu is located almost in the plane of the three ligands. A fourth ligand, usually a methionine, sometimes a glutamine, occupies one of the axial positions, while in the azurins an additional main-chain carbonyl oxygen may coordinate weakly at the opposite axial position. Type-I sites invariably function in electron transfer.

Type-II sites also contain a single Cu atom, often coordinated in a square planar configuration by four nitrogen/oxygen donors and one or two axial ligands, one of which may be a water molecule or the substrate. They are found, for instance, in various oxidases, often in conjunction with an organic cofactor.

Type-III sites contain a Cu_2 dimer which is fixed within the protein framework by six histidines. They function in the transport of oxygen (hemocyanins) or the activation of oxygen in oxidase or oxygenase reactions (tyrosinase).

For a long time the copper sites in the blue oxidases like ascorbate oxidase and laccase were thought to be of a composite of type-I, -II, and -III sites. Crystal structure determination of ascorbate oxidase has made it clear that at least in this oxidase the Cu atoms occur in the form of a single type-I site plus a trimer of Cu atoms arranged in an equilateral triangle, which may be considered as a new type of site (type-IV).

Finally, recent work on cytochrome a,a_3 oxidase and nitrous oxide reductase has provided evidence for the occurrence of a new type of Cu_2 dimer in which the Cu atoms are possibly bridged by a cysteine.[8,9]

Until very recently the size of most copper proteins precluded the study of their structure by means of high-resolution ^{1}H NMR techniques. Investigations were thus limited to studies of the metal site and its immediate surroundings, as in the case of proteins containing a type-I or a type-II Cu center. Only in the case of the so-called blue (type-I) copper proteins did the size of the proteins appear sufficiently small to allow extensive structural and mechanistic studies by high-resolution 2D and 3D NMR techniques. No elaborate NMR studies of proteins with type-III or type-IV sites seem to have been reported to date. Very recently the application of *rec*-DNA techniques has allowed the isolation of single domains of larger Cu-containing proteins, and the study of these domains by NMR techniques is presently being pursued by various groups.

In the following sections the progress achieved over the past two decades in the NMR study of Cu proteins is briefly reviewed.

2 BLUE COPPER PROTEINS

2.1 Introduction

The so-called small blue copper proteins (96–155 residues), which invariably contain a type-I Cu site, were described

for the first time at the end of the 1950s/beginning of the 1960s (for recent reviews see References 10 and 11).[10,11] The following subclasses are distinguished at present: proteins involved in bacterial respiratory electron transport (azurin, pseudoazurin, amicyanin, rusticyanin, and auracyanin),
photosynthetic plant and algal proteins (plastocyanin), and plant proteins with unknown function [either nonglycosylated: 'cucumber basic blue protein' (CBP) and plantacyanin; or glycosylated: stellacyanin, umecyanin, mavicyanin, and cucumber peeling cupredoxin (CPC)]. During the course of time it gradually transpired that their relatively small size (10–15 kDa), robustness under extremes of pH and temperature, ease of isolation and purification, and stability in solution at high concentrations made the blue copper proteins excellently suitable for detailed NMR investigations. Their attractiveness was further enhanced when the crystal structures of a number of them were solved at the end of the 1970s/beginning of the 1980s (plastocyanin,[12] azurin[13]). Later the structures of amicyanins (Amcs),[14,15] CBP,[16] and pseudoazurin were reported.[17,18]

The presence inside the protein of a metal capable of occurring in two oxidation states, one of which is paramagnetic, further heightened the appetite of NMR spectroscopists towards applying the tricks of their trade in unraveling the effect of the metal on the appearance of the NMR spectra. Most of the NMR studies have been performed on the azurins (Azus) from *Pseudomonas aeruginosa* and *Alcaligenes denitrificans*,[19,20] the plastocyanins (Pcs) from *Phaseolus vulgaris* (French bean),[21] spinach and *Scenedesmus obliquus*,[22,23] amicyanin (Amc) from *Thiobacillus versutus*,[24] and stellacyanin from *Rhus vernicifera*,[25] but brief reports have also been published of various other blue copper proteins.[26–30] Finally, it has recently been shown that the small blue copper proteins yield fairly easily to the application of *rec*-DNA and site-directed mutagenesis techniques and this has added a new dimension to their study.[11] For instance, the application of multidimensional heteronuclear MR techniques on isotopically-enriched (^{13}C and ^{15}N) proteins has now become available.

2.2 Copper Site Structure

Some of the first investigators to study copper proteins by NMR techniques were Blumberg et al.,[31] who around 1965 tried to assess the accessibility of the metal towards water molecules. They measured the relaxation enhancement of the bulk water protons as a function of the protein concentration and the oxidation state of the metal(s). In Pc, for instance, the Cu appeared inaccessible towards water. Application of this technique only required the study of the easily observable bulk water signal and not that of the protein. It would take 10 more years before spectrometers of sufficient resolution and sensitivity would become available to enable the successful tackling of the latter task. In the second half of the 1970s the first reports on the ^{1}H NMR spectra of various Pcs,[32–35] of *P. aeruginosa* Azu,[36–38] and of *R. vernicifera* stellacyanin appeared.[39] Also natural abundance ^{13}C NMR studies of Azu and Pc were reported around this time.[40,41] The spectra were much too complex to allow a detailed assignment of the signals, and attention primarily focused on the assignment by type of a few amino acids such as histidines and methionines, which give rise to easily identifiable singlet signals and (in the case of histidine) a characteristic pH titration behavior.

Since the four canonical ligands of a type-I Cu site comprise (apart from a cysteine) two histidines and a methionine, the structure of the Cu site in blue copper proteins rapidly became a popular subject of study by NMR techniques. By comparing the spectra of the Cu(II), Cu(I), apo-, and Hg(II)-substituted forms,[37] the ligands of the Cu could be identified correctly in Azu and Pc. Later on, these assignments were elaborated by 1D and 2D ^{1}H NMR and 2D $^{1}H\{^{113}Cd\}$ and $^{1}H\{^{13}C\}$ NMR studies.[42–48] The ^{1}H NMR signals of the metal ligands could be shifted outside the envelope of the regular NMR spectrum by replacing the Cu by paramagnetic shift probes such as the 3 d metal ions Co(II) and Ni(II).[48,49] This essentially provided clearly resolved signals from protons in the first coordination shell of the metal, but the unraveling of the various contact and pseudocontact contributions to the paramagnetic shifts proved too complicated to make this subterfuge much use in the analysis of the behavior and structure of the Cu site.

An illustration of the difficulties of this approach is provided by the study of Dahlin et al.[25] who made an elaborate attempt to identify the Cu ligands in the plant blue copper protein stellacyanin. The nature and coordinating properties of the fourth Cu ligand in this protein had long been an enigma, since the lack of methionines in the amino acid sequence provided indelible proof that the metal-binding site in stellacyanin was at least different in one respect from that in the Azus and Pcs. Despite careful analysis, the NMR results obtained on the Co(II)-substituted form of stellacyanin remained ambiguous. Subsequently, structural research on the related 'cucumber blue protein',[50] and site-directed mutagenesis studies on Azus,[51] have made it clear that the fourth ligand in stellacyanin is probably a glutamine.

The study of Ni(II) and Co(II)-substituted Azus has recently been taken up again by Moratal et al.[52,53] who are applying multidimensional NMR techniques to study paramagnetically shifted signals. This work may provide further insight into the malleability of the metal site, as probed already by NMR and XRD (X-ray diffraction) studies of wild-type and mutant blue copper proteins in their apo and holo forms, or with Cd(II), Hg(II), or Zn(II) substituted at the metal site.[10,11] The latter investigations have demonstrated that the metal site is preformed by the protein matrix, but does still retain some flexibility and is able to adapt somewhat to the metal that is substituted for the Cu.

Several attempts have been made to identify differences in structure and the Cu-binding mode of the metal sites between the Azus and the Pcs. Additional inspiration for this work came from XRD reports showing that the Cu site in Pc more closely resembled a distorted tetrahedron, while the coordination of the Cu in Azu was more like that of a trigonal bipyramid, with three strong almost in-plane ligands (two histidines and a cysteine) and two axial ligands, provided by a methionine sulfur (Met-121) and a backbone carbonyl oxygen (Gly-45).[6,11] Differences in chemical shift of the ^{113}Cd NMR signal of Cd-substituted Azu and Pc seemed diagnostic of a difference in electronic structure,[54,55] but the difference was not easy to interpret. Further, the early ^{13}C NMR studies of Azu implicated close proximity or possibly binding of a backbone carbonyl oxygen to the Cu.[40] Debate is still continuing regarding the amount of covalency involved in the Cu–S(Met) bond and the actual involvement of the Gly-45 carbonyl in determining the Cu-site properties in the Azus.

2.3 The Effects of pH

A clear difference between Pcs and Azus was provided by the pH titration behavior of the metal site. While the Cu site in the Azus is insensitive to pH, the geometry of the Cu site in the reduced form of the Pcs changes from fourfold to threefold towards low pH as one of the histidine ligands (His-87, *P. nigra* numbering) becomes protonated and dissociates from the Cu. This was beautifully documented by a series of XRD studies by Freeman et al.,[56] and confirmed later by ^{1}H NMR studies.[42,57,58] A similar effect is seen to occur in the Amcs described for the first time in the early 1980s, i.e. the blue copper proteins that act as electron acceptors of methylamine dehydrogenases in C_1 organisms. Thus the Amc from *T. versutus* was studied in detail by NMR spectroscopy, and the dissociation of the histidine ligand at low pH (His-96, *T. versutus* numbering) was shown to occur in two steps with different timescales.[59] As the change in coordination with pH is seen only for the reduced and not for the oxidized form of the protein, electron transfer at low pH is accompanied by a large change in conformation around the Cu. It is not surprising, therefore, that a slowing down of the electron transfer as catalyzed by Amc or Pc is observed under acidic conditions.[59] A similar lability of the Cu site probably occurs in the pseudoazurins.[60] It appears, therefore, as what was initially considered an anomaly in the case of Pc (a pH-dependent Cu-site structure) relative to Azus, seems to be the rule for small blue copper proteins and that the pH-insensitive Cu site of the Azus constitutes the anomaly.

A pH effect of a different kind was observed for Azu from *P. aeruginosa*, and for a long time its precise nature and mechanistic relevance remained a source of speculation. Almost from the very beginning of the NMR studies on the Azus it appeared that Azu from *P. aeruginosa* is involved in a pH-dependent equilibrium between two conformations which on the NMR timescale are in slow exchange.[37,46] From successive NMR studies it transpired that residue His-35 is responsible for this phenomenon and that the two conformations of the protein are related to the different states of protonation of His-35. Subsequent studies of the kinetics of the electron exchange between Azu and cytochrome C_{551} seemed to necessitate the assumption that Azu may occur in two states, one redox-active and the other one redox-inactive, and that the equilibrium between them was pH-dependent. The pK_a of this transition appeared to be the same as that of His-35. Since in the crystal structure His-35 is in van der Waals contact with the Cu ligand His-46, the hypothesis was advanced that (one of) the electron transfer pathway(s) in Azu runs through His-35 and His-46, and that His-35 might act as a switch depending on the pH of the surrounding medium. This hypothesis was subsequently tested by a large number of groups.[61]

Eventually, a combination of (a) NMR studies of the electron self-exchange (ESE) reaction of wild-type Azu and of Azus with mutations at residue 35 and in the hydrophobic patch surrounding the other histidine ligand (His-117),[62,63] (b) kinetic studies of the electron exchange between Azu mutants and physiological partners such as cytochrome C_{551} and nitrite reductase,[64] and (c) XRD studies of wild-type and mutant Azus[65,66] have led to the conclusion that His-35 is not in the electron transfer path to and from the Cu. Instead, Cu-ligand His-117, which pierces the protein surface at the position of the hydrophobic patch, provides the sole port of exit and entry for the electrons. Small changes in the chemical shifts of the protons in the first and second coordination shell of the metal as a function of protonation state of His-35 reflect a 180° flip in the Pro-36/Gly-37 peptide bond which is at H-bonding distance of the N-δ of His-35. The position of His-35 relative to the Cu site is hardly affected. Finally, the redox activity of the protein appears to be independent of pH.

The only parameter relevant to the redox properties of the Azu affected by the change in protonation of His-35 is the midpoint potential which drops by 60 mV if His-35 is deprotonated.[63] It is interesting to note that in Pc a pathway running through Cu ligand His-87 (*P. nigra* numbering) similar to the His-117 pathway in the Azus has been delineated, but that here a second, albeit less efficient route for electron transfer has been identified starting at the 'eastern side' of the protein at the Tyr-83 residue.[10,67,68]

2.4 Electron Transfer

The ESE rates of the blue copper proteins have attracted considerable attention apart from the metal site. It turned out that NMR methods are particularly suitable for the determination of these rates.[3,69,70] Due to small conformational differences the NMR spectra of the oxidised and reduced forms of a blue copper protein show numerous small differences. In addition, in the paramagnetic [Cu(II)] species, the signals from nuclei close to the Cu are broadened beyond detection. In a solution containing a mixture of the reduced and oxidized form, exchange of an electron may occur when an oxidized and a reduced molecule collide. As a result two observations can be made. First, as the exchange becomes faster, signals from the same proton which occur at different positions in the spectra of the oxidized and reduced protein begin to merge. Secondly, signals that are only observed for the diamagnetic species may begin to broaden.

The first phenomenon may be adequately analyzed with customary 'chemical exchange' theory and information about the ESE rate can be obtained directly. The second phenomenon can be analyzed most readily in the so-called strong pulse or slow exchange limit. This limit applies if during the time the protein is in the paramagnetic state the nuclear spins are dephased to a sufficient extent that any phase coherence left over from the period the protein was diamagnetic is wiped out. Thus, effectively only the (lifetime broadened) signal deriving from the diamagnetic protein is observed and the broadening in (rad s^{-1}) is directly equal to the inverse lifetime of the diamagnetic state. For the paramagnetic dephasing to be strong enough, the nucleus whose signal is studied should be close enough to the copper. In practice, the strong pulse condition is met for nuclei which are located on side chains of the Cu ligands. When nuclei further away from the Cu are used for this technique erroneous results may be obtained, as is illustrated by a study of Azu where the ESE-induced broadening of the His-35 proton signals was used to determine an ESE rate which was two orders of magnitude off the correct value.[71,72]

The high second order ESE rates (8×10^5 M^{-1} s^{-1}) observed for the Azus have been interpreted as indicating that formation of the association complex is thermodynamically favorable.[71,73,74] Current ideas are that the edges of the His-117 side chains in both Azus in the association complex

have to come sufficiently close for efficient electron transfer to occur, this being achieved when the two Azu molecules associate with their hydrophobic patches along each other. In the case of the Pcs a similar association complex has to be formed, but here the association is hampered by the presence of charged residues in or close to the hydrophobic ('northern') patch of the protein surface, which for most plant Pcs results in ESE rates of less than $1 \times 10^3\ M^{-1}\ s^{-1}$.[75,76] For the algal Pcs, which lack these charged residues in the hydrophobic patch, the ESE rates may reach values of $10^5\ M^{-1}\ s^{-1}$.[70] For Amc, which in some respects resembles the algal Pcs, rates on the order of $1 \times 10^5\ M^{-1}\ s^{-1}$ have been measured.[59] In line with these observations is that the ESE rates of the Azus are independent of ionic strength,[73] while those of the Pcs,[75] and to a smaller extent those of the Amcs,[59] increase when salts are added to the sample solution. Multivalent cations such as Mg(II) have appeared especially effective in promoting ESE.[75] Interestingly, redox-active compounds, such as ferricyanide, may catalyze the protein ESE reaction.[35,77]

To identify areas on the protein surface where other electron transfer proteins might possibly associate, the complexation of blue copper proteins with redox-inert paramagnetic transition metal compounds serving as charged analogs of protein partners have been studied.[22,57,58,78–80] By identifying and assigning the affected signals in the NMR spectrum, the location of the complex on the protein surface could sometimes be identified. In a similar way the association of blue copper proteins with proteins such as cytochrome *c* and cytochrome *f* have been studied directly. For this, the perturbation of the NMR spectrum of the blue copper protein that resulted from the admixture of the cytochrome and vice versa was investigated.[81–83] The inhibition of protein/protein complex formation by transition metal complexes was also studied in this manner. For this method to be successful it is of importance to dispose of a complete assignment of the NMR spectrum of the protein under study. Such assignments are now available for a number of cases.

2.5 Structural Studies

Complete NMR assignments for blue copper proteins started to become available in the second half of the 1980s. Two-dimensional ^{1}H NMR assignment studies have been performed on the Pcs from spinach,[22] *P. vulgaris* (French bean),[84,85] and the alga *S. obliquus*.[86] The assignment of the ^{1}H NMR spectrum of Amc from *T. versutus* has also been accomplished using 2D NMR techniques.[24] Finally from the analysis of 2D and 3D homo- and heteronuclear NMR experiments, complete ^{1}H and ^{15}N NMR assignments have become available for the Azus from *P. aeruginosa*[19] and *A. denitrificans*.[20] An interesting observation for the latter two proteins was that the differences in C-α–H chemical shifts did not average out to zero, contrary to the differences in amide proton chemical shifts. This is the subject of further study at the moment.

The secondary structures derived from the NMR results compared well with the published XRD structures in the case of the Pcs and Azus. For the Amc no XRD results were available initially, and the NMR results (later confirmed by more elaborate NMR studies and XRD investigations) showed an unusual extension of the N-terminus compared with the Pcs and Azus. Subsequent determination of the 3D structures of the Pcs from *S. obliquus*[23] and *P. vulgaris*[21] on the basis of the NMR results showed extensive similarity with the XRD-derived 3D structure of Pc from *P. nigra*. The NMR results formed a nice starting point for further structural investigations. Wright and coworkers studied the denaturation and refolding of Pc as well as the folding behavior of peptide fragments that were synthesized according to the natural amino acid sequence of the Pc. In this way a beginning could be made with the tentative delineation of the natural folding pathway(s) of Pc.[87,88] The 3D structure in solution of Amc from *T. versutus* was determined by NMR methods at the same time that an XRD study could be completed.[14,89] A detailed comparison of the two structures still has to be performed, but the overall structures do show a great deal of similarity.

3 NONBLUE COPPER PROTEINS

3.1 Superoxide Dismutase (SOD)

SOD is a eukaryotic homodimeric metalloenzyme (M_r approx. 30 kDa) which catalyzes the disproportionation of O_2^- to O_2 and H_2O_2.[90] Each monomer contains a structural Zn(II) site and a catalytic type-II Cu(II) site. An imidazolate bridges the two metal ions which are about 6 Å apart. The metal ions in the native enzyme $Cu(II)_2Zn(II)_2SOD$ can be readily removed or substituted. The crystal structures of bovine and spinach $Cu(II)_2Zn(II)_2SOD$[91,92] and of the $Cu(II)_2Co(II)_2$ derivative of bovine SOD[93] have been determined by X-ray crystallography. NMR experiments have been performed with bovine, human, and yeast SODs, which have similar catalytic, spectroscopic, and structural properties.

Because of their relatively large size, the assignment of all resonances in the ^{1}H NMR spectrum has not been achieved to date for any SOD. NMR experiments have been directed mainly at the study of the metal sites and their environment, including the interaction with exogenously added molecules like small anions and water. In the 1970s, work on SOD commenced by looking at the C-δ H and C-ϵ H resonances of His residues. The resonances of His ligands of the metal ions were tentatively identified by their broadening in the ^{1}H NMR spectrum of paramagnetic $Cu(II)_2Zn(II)_2SOD$ when compared with the spectrum of diamagnetic $Cu(I)_2Zn(II)_2SOD$,[94–96] and by the reduction of their C-α,H exchange rate.[97] His resonances were also investigated in the spectra of the diamagnetic forms E_2E_2SOD (E denotes an empty metal site), $E_2Zn(II)_2SOD$, and $Zn(II)_2Zn(II)_2SOD$. It appears that the metal-site conformation is preserved among these derivatives.

A breakthrough in the study of the metal sites of SOD was achieved when Bertini et al. investigated the metal derivative $Cu(II)_2Co(II)_2SOD$ by NMR spectroscopy.[90,98] Because of the magnetic coupling between Cu(II) and Co(II), which reduces the electron relaxation time of Cu(II), the resonances of protons near the Cu(II) ion are much less broadened than for $Cu(II)_2Zn(II)_2SOD$, and moreover experience large isotropic hyperfine shifts like the resonances of protons near the Co(II) ion. Similar observations have been made for $Cu(II)_2Ni(II)_2SOD$.[99] The metal-site ^{1}H resonances have been assigned, firstly by studying the effects of ^{1}H/^{2}H exchange on the 1D ^{1}H NMR spectrum and by analyzing 1D T_1, T_2 and ^{1}H NOE measurements,[90,99] and

secondly by the recent application of 2D ^{1}H NMR techniques (COSY, NOESY).[2,100–102] Using $Cu(II)_2Co(II)_2SOD$ and $Cu(I)_2Co(II)_2SOD$, it was shown that the breakage of the imidazolate bridge between the metal ions upon reduction of the copper occurs at the Cu side,[103] a result that had already been anticipated on the basis of ^{113}Cd NMR spectroscopy of $Cu(II)_2Cd(II)_2SOD$ and $Cu(I)_2Cd(II)_2SOD$.[104] From NMR experiments involving both protons and nuclei such as ^{13}C, ^{19}F, ^{31}P, and ^{35}Cl on SOD metal derivatives and SOD with mutations in the substrate-binding cavity, valuable insights were obtained regarding the interaction of the protein with substrate-mimicking and other anionic compounds such as CN^-, N_3^-, NCO^-, NCS^-, F^-, Cl^-, $H_2PO_4^-$, and HCO_2^-.[2,90,100,101,105–110] The accessibility of the Cu site in native and mutant $Cu(II)_2Zn(II)_2SOD$, and the effect of anion binding on it, has also been studied by measurements of the paramagnetic effect on the relaxation properties of solvent water.[90] The picture that arises from these studies is that some anions (in order of decreasing efficiency $CN^- > N_3^- > NCO^- > NCS^-$) bind to the Cu ion and displace a semicoordinated water molecule, thus reducing the solvent accessibility and affecting one of the Cu–His bonds. The effects of F^- and Cl^- binding are still smaller, making it questionable whether they bind to the Cu ion or to residues in its environment; phosphate and formate do not bind to the Cu ion but to residues near the copper. In addition to the Cu ion, one Arg and two Lys residues in the substrate-binding cavity have a particular effect in determining the affinity of SOD for anions.

3.2 Amine Oxidase (AO)

The eukaryotic copper-containing amine oxidases are dimeric metalloenzymes (M_r 170–190 kDa)[111] that have various functions, amongst others, in the metabolism of biogenic primary amines. Per dimer they contain two type-II Cu sites and one covalently bound organic cofactor with a quinone functionality. NMR studies of the protein have been confined to this cofactor and its orientation relative to the Cu site(s). ^{1}H NMR characterization of a small peptide from bovine serum AO that contained the phenylhydrazone-derivatized cofactor revealed it to be 6-hydroxydopa.[112] Using several fluorine-labeled phenylhydrazine derivatives, the distance between the organic cofactor at the amine-substrate-binding site of porcine plasma AO and one of its Cu(II) ions was inferred from the effect the paramagnetic Cu(II) exerts on the relaxation behavior of the fluorine nuclei as measured by ^{19}F NMR spectroscopy.[113] The organic cofactor and the Cu(II) ion appear to be within approximately 9 Å from each other.

3.3 Copper-Storage, -Transport and -Resistance Proteins

Several proteins involved in the storage and delivery of Cu ions, as well as in protection against Cu overload, are known. NMR reports concerning the Cu-containing forms of these proteins are scarce. Two examples which have been studied by NMR spectroscopy may be mentioned. In yeast, a 53-residue metallothionein (MT) involved in Cu resistance binds copper as Cu(I). Complete sequential ^{1}H NMR assignments have been made for the Cu(I)-containing MT as well as for the Ag(I)-substituted form.[114] The ligation pattern of the metal ions was derived from heteronuclear ^{1}H{^{109}Ag} HMQC spectroscopy.[114,115] It is noted that the 3D structures of several mammalian MTs have been determined with homo- and heteronuclear 2D NMR spectroscopy using the ^{112}Cd- or ^{113}Cd-substituted proteins.[116]

As a second example, the interaction of the high-M_r blood plasma protein albumin (67 kDa) with Cu(II), Co(II), and Ni(II) ions has been investigated by 1D and 2D ^{1}H NMR spectroscopy.[117,118] It appeared to be possible to detect such interactions at the mobile N-terminus, for which relatively sharp resonances are observed in the ^{1}H NMR spectrum of the metal-free protein.[119]

3.4 Other Cu Proteins

A very limited number of NMR reports on other Cu proteins or related model compounds has appeared in the literature. Here we mention two NMR studies that are concerned with Cu sites that have not been dealt with so far in this review. First, crystalline bovine heart cytochrome *c* oxidase (M_r 200 kDa), that contains so-called Cu_A and Cu_B sites, has been studied by solid state ^{13}C NMR spectroscopy.[120] The spectral resolution appeared to be better than that of dissolved or lyophilised samples and to be comparable with that of crystals of the much smaller protein lysozyme, without severe interference from the paramagnetic metal ions. Measurements of T_1 indicated that the backbone of cytochrome *c* oxidase is more flexible than that of lysozyme. Second, it has been reported that a dicopper dioxygen model compound for the dinuclear type-III Cu site in high-M_r metalloproteins such as hemocyanin exhibits very normal looking ^{1}H and ^{13}C NMR spectra, indicating strong coupling between the Cu(II) ions.[121]

4 RELATED ARTICLES

Biological Macromolecules: Structure Determination in Solution; Cadmium-113 NMR: A Surrogate Probe for Zinc and Calcium in Proteins; Cobalt(II)- and Nickel(II)-Substituted Proteins; Inorganic Nuclei: Low Sensitivity Transition Metals; Metallothioneins; Paramagnetic Relaxation in Solution; Quadrupolar Nuclei in Liquid Samples; Quadrupolar Transition Metal and Lanthanide Nuclei.

5 REFERENCES

1. J. Mason (ed.), *Multinuclear NMR*, Plenum Press, New York, 1987.
2. I. Bertini, P. Turano, and A. J. Vila, *Chem. Rev.*, 1993, **93**, 2833.
3. G. W. Canters, C. W. Hilbers, M. van de Kamp, and S. S. Wijmenga, *Methods Enzymol.*, 1993, **227**, 244.
4. L. M. Utschig, J. G. Wright, and T. V. O'Halloran, *Methods Enzymol.*, 1993, **226**, 71.
5. J. E. Coleman, *Methods Enzymol.*, 1993, **227**, 16.
6. E. T. Adman, *Adv. Protein Chem.*, 1991, **42**, 145.
7. N. Kitajima, *Adv. Inorg. Chem.*, 1992, **39**, 1.
8. W. E. Antholine, D. H. W. Kastrau, G. C. M. Steffens, G. Buse, W. G. Zumft, and P. H. M. Kroneck, *Eur. J. Biochem.*, 1992, **209**, 875.

9. B. G. Malmström and R. Aasa, *FEBS Lett.*, 1993, **325**, 49.
10. A. G. Sykes, *Adv. Inorg. Chem.*, 1991, **36**, 377.
11. G. W. Canters and G. Gilardi, *FEBS Lett.*, 1993, **325**, 39.
12. P. M. Colman, H. C. Freeman, J. M. Guss, M. Murata, V. A. Norris, J. A. M. Ramshaw, and M. P. Venkatappa, *Nature (London)*, 1978, **272**, 319.
13. E. T. Adman, R. E. Stenkamp, L. C. Sieker, and L. H. Jensen, *J. Mol. Biol.*, 1978, **123**, 35.
14. A. Romero, H. Nar, R. Huber, A. Messerschmidt, A. P. Kalverda, G. W. Canters, R. Durley, and F. S. Mathews, *J. Mol. Biol.*, 1994, **236**, 1196.
15. R. Durley, L. Chen, L. W. Lim, F. S. Mathews, and V. L. Davidson, *Protein Sci.*, 1993, **2**, 739.
16. J. M. Guss, E. A. Merritt, R. P. Phizackerley, B. Hedman, M. Murata, K. O. Hodgson, and H. C. Freeman, *Science*, 1988, **241**, 806.
17. E. T. Adman, S. Turley, R. Bramson, K. Petratos, D. Banner, D. Tsernoglou, T. Beppu, and H. Watanabe, *J. Biol. Chem.*, 1989, **264**, 87.
18. K. Petratos, Z. Dauter, and K. S. Wilson, *Acta Crystallogr.*, 1988, **B44**, 628.
19. M. van de Kamp, G. W. Canters, S. S. Wijmenga, A. Lommen, C. W. Hilbers, H. Nar, A. Messerschmidt, and R. Huber, *Biochemistry*, 1992, **31**, 10 194.
20. C. W. G. Hoitink, P. C. Driscoll, H. A. O. Hill, and G. W. Canters, *Biochemistry*, 1994, **33**, 3560.
21. J. M. Moore, C. A. Lepre, G. P. Gippert, W. J. Chazin, D. A. Case, and P. E. Wright, *J. Mol. Biol.*, 1991, **221**, 533.
22. P. C. Driscoll, H. A. O. Hill, and C. Redfield, *Eur. J. Biochem.*, 1987, **170**, 279.
23. J. M. Moore, D. A. Case, W. J. Chazin, G. P. Gippert, T. F. Havel, R. Powls, and P. E. Wright, *Science*, 1988, **240**, 314.
24. A. Lommen, S. Sijmenga, C. W. Hilbers, and G. W. Canters, *Eur. J. Biochem.*, 1991, **201**, 695.
25. S. Dahlin, B. Reinhammer, and J. Ångström, *Biochemistry*, 1989, **28**, 7224.
26. S. Mitra and R. Bersohn, *Proc. Natl. Acad. Sci. USA*, 1982, **79**, 6807.
27. G. King, T. A. Andary, H. C. Freeman, L. Gavrilovic, and P. E. Wright, *FEBS Lett.*, 1984, **166**, 288.
28. M. A. Babayan, L. Kh. Sarkissian, A. M. Nersissian, E. G. Sarukhanian, and R. M. Nalbandyan, *Biochem. Biophys. Res. Commun.*, 1983, **117**, 385.
29. A. M. Nersissian, M. A. Babayan, L. Kh. Sarkissian, E. G. Sarukhanian, and R. M. Nalbandyan, *Biochim. Biophys. Acta*, 1985, **830**, 195.
30. M. A. Babayan, A. M. Nersissian, and R. M. Nalbandyan, *FEBS Lett.*, 1988, **238**, 167.
31. W. E. Blumberg, J. Eisinger, P. Aisen, A. G. Morell, and I. H. Scheinberg, *J. Biol. Chem.*, 1963, **238**, 1675.
32. J. L. Markley, E. L. Ulrich, S. P. Berg, and D. W. Krogmann, *Biochemistry*, 1975, **14**, 4428.
33. H. C. Freeman, V. A. Norris, J. A. M. Ramshaw, and P. E. Wright, *FEBS Lett.*, 1978, **86**, 131.
34. H. A. O. Hill and B. E. Smith, *Biochem. Biophys. Res. Commun.*, 1978, **81**, 1201.
35. J. K. Beattie, D. J. Fensom, H. C. Freeman, E. Woodcock, H. A. O. Hill, and A. M. Stokes, *Biochim. Biophys. Acta*, 1975, **405**, 109.
36. K. Ugurbil and R. Bersohn, *Biochemistry*, 1977, **16**, 3016.
37. H. A. O. Hill and B. E. Smith, *J. Inorg. Biochem.*, 1979, **11**, 79.
38. H. A. O. Hill, J. C. Leer, B. E. Smith, C. B. Storm, and R. P. Ambler, *Biochem. Biophys. Res. Commun.*, 1976, **70**, 331.
39. H. A. O. Hill and W. K. Lee, *J. Inorg. Biochem.*, 1979, **11**, 101.
40. K. Ugurbil, R. S. Norton, A. Allerhand, and R. Bersohn, *Biochemistry*, 1977, **16**, 886.
41. J. L. Markley, E. L. Ulrich, and D. W. Krogmann, *Biochem. Biophys. Res. Commun.*, 1977, **78**, 106.
42. C. L. Kojiro and J. L. Markley, *FEBS Lett.*, 1983, **162**, 52.
43. G. King and P. E. Wright, *Biochem. Biophys. Res. Commun.*, 1982, **106**, 559.
44. D. H. Live, C. L. Kojiro, D. Cowbum, and J. L. Markley, *J. Am. Chem. Soc.*, 1985, **107**, 3043.
45. G. C. King and P. E. Wright, *Biochemistry*, 1986, **25**, 2364.
46. E. T. Adman, G. W. Canters, H. A. O. Hill, and N. A. Kitchen, *FEBS Lett.*, 1982, **143**, 287.
47. G. W. Canters, H. A. O. Hill, N. A. Kitchen, and E. T. Adman, *Eur. J. Biochem.*, 1984, **138**, 141.
48. H. A. O. Hill, B. E. Smith, C. B. Storm, and R. P. Ambler, *Biochem. Biophys. Res. Commun.*, 1976, **70**, 783.
49. J. A. Blaszak, E. L. Ulrich, J. L. Markley, and D. R. McMillin, *Biochemistry*, 1982, **21**, 6253.
50. B. A. Fields, J. M. Guss, and H. C. Freeman, *J. Mol. Biol.*, 1991, **222**, 1053.
51. A. Romero, C. W. G. Hoitink, H. Nar, R. Huber, A. Messerschmidt, and G. W. Canters, *J. Mol. Biol.*, 1993, **229**, 1007.
52. J.-M. Moratal, J. Salgado, A. Donaire, H. R. Jiménez, and J. Castells, *J. Chem. Soc., Chem. Commun.*, **1993**, 110.
53. J.-M. Moratal, J. Salgado, A. Donaire, H. R. Jiménez, and J. Castells, *Inorg. Chem.*, 1993, **32**, 3587.
54. H. R. Engeseth, D. R. McMillin, and J. D. Otvos, *J. Biol. Chem.*, 1984, **259**, 4822.
55. M. F. Summers, *Coord. Chem. Rev.*, 1988, **86**, 43.
56. J. M. Guss, P. R. Harrowell, M. Murata, V. A. Norris, and H. C. Freeman, *J. Mol. Biol.*, 1986, **192**, 361.
57. J. McGinnis, J. D. Sinclair-Day, A. G. Sykes, R. Powls, J. Moore, and P. E. Wright, *Inorg. Chem.*, 1988, **27**, 2306.
58. M. P. Jackman, J. D. Sinclair-Day, M. J. Sisley, A. G. Sykes, L. A. Denys, and P. E. Wright, *J. Am. Chem. Soc.*, 1987, **109**, 6443.
59. A. Lommen and G. W. Canters, *J. Biol. Chem.*, 1990, **265**, 2768.
60. E. T. Adman, personal communication.
61. E. T. Adman, *Top. Mol. Struct. Biol.*, 1985, **6**, 1.
62. M. van de Kamp, R. Floris, F. C. Hali, and G. W. Canters, *J. Am. Chem. Soc.*, 1990, **112**, 907.
63. M. van de Kamp, G. W. Canters, C. R. Andrew, J. Sanders-Loehr, C. J. Bender, J. Peisach, and I. Pecht, *Eur. J. Biochem.*, 1993, **218**, 229.
64. M. van de Kamp, M. C. Silvestrini, M. Brunori, J. Van Beeumen, F. C. Hali, and G. W. Canters, *Eur. J. Biochem.*, 1990, **194**, 109.
65. H. Nar, A. Messerschmidt, R. Huber, M. van de Kamp, and G. W. Canters, *J. Mol. Biol.*, 1991, **218**, 427.
66. H. Nar, A. Messerschmidt, R. Huber, M. van de Kamp, and G. W. Canters, *J. Mol. Biol.*, 1991, **221**, 765.
67. S. He, S. Modi, D. S. Bendall, and J. C. Gray, *EMBO J.*, 1991, **10**, 4011.
68. S. Modi, M. Nordling, L. G. Lundberg, O. Hansson, and D. S. Bendall, *Biochim. Biophys. Acta*, 1992, **1102**, 85.
69. G. W. Canters, H. A. O. Hill, N. A. Kitchen, and E. T. Adman, *J. Magn. Reson.*, 1984, **57**, 1.

70. C. Dennison, P. Kyritsis, W. McFarlane, and A. G. Sykes, *J. Chem. Soc., Dalton Trans.*, **1993**, 1959.
71. C. M. Groeneveld and G. W. Canters, *J. Biol. Chem.*, 1988, **263**, 167.
72. K. Ugurbil and S. Mitra, *Proc. Natl. Acad. Sci. USA*, 1985, **82**, 2039.
73. C. M. Groeneveld and G. W. Canters, *Eur. J. Biochem.*, 1985. **153**, 559.
74. C. M. Groeneveld, M. C. Ouwerling, C. Erkelens, and G. W. Canters, *J. Mol. Biol.*, 1988, **200**, 189.
75. F. A. Armstrong, P. C. Driscoll, and H. A. O. Hill, *FEBS Lett.*, 1985, **190**, 242.
76. D. G. A. H. de Silva, D. Beoku-Betts, P. Kyritsis, K. Govindaraju, R. Powls, N. P. Tomkinson, and A. G. Sykes, *J. Chem. Soc., Dalton Trans.*, **1992**, 2145.
77. A. Lommen, G. W. Canters, and J. van Beeumen, *Eur. J. Biochem.*, 1988, **176**, 213.
78. K. C. Cho, D. F. Blair, U. Banerjee, J. J. Hopfield, H. B. Gray, I. Pecht, and S. I. Chan, *Biochemistry*, 1984, **23**, 1858.
79. D. J. Cookson, M. T. Hayes, and P. E. Wright, *Nature (London)*, 1980, **283**, 682.
80. D. J. Cookson, M. T. Hayes, and P. E. Wright, *Biochim. Biophys. Acta*, 1980, **591**, 162.
81. L. Qin and N. M. Kostic, *Biochemistry*, 1993, **32**, 6073.
82. S. Bagby, P. C. Driscoll, K. G. Goodall, C. Redfield, and H. A. O. Hill, *Eur. J. Biochem.* 1990, **188**, 413.
83. G. C. King, R. A. Binstead, and P. E. Wright, *Biochim. Biophys. Acta*, 1985, **806**, 262.
84. W. J. Chazin, M. Rance, and P. E. Wright, *J. Mol. Biol.*, 1988, **202**, 603.
85. W. J. Chazin and P. E. Wright, *J. Mol. Biol.*, 1988, **202**, 623.
86. J. M. Moore, W. J. Chazin, R. Powls, and P. E. Wright, *Biochemistry*, 1988, **27**, 7806.
87. H. J. Dyson, J. R. Sayre, G. Merutka, H.-C. Shin, R. A. Lerner, and P. E. Wright, *J. Mol. Biol.*, 1992, **226**, 819.
88. S. Koide, H. J. Dyson, and P. E. Wright, *Biochemistry*, 1993, **32**, 12 299.
89. A. P. Kalverda, S. S. Wymenga, A. Lommen, F. J. M. van de Ven, C. W. Hilbers, and G. W. Canters, *J. Mol. Biol.*, 1994, **240**, 358.
90. I. Bertini, L. Banci, M. Piccioli, and C. Luchinat, *Coord. Chem. Rev.*, 1990, **100**, 67.
91. J. A. Tainer, E. D. Getzoff, K. M. Beem, J. S. Richardson, and D. C. Richardson, *J. Mol. Biol.*, 1982, **160**, 181.
92. Y. Kitagawa, N. Tanaka, Y. Hata, M. Kusunoki, G.-P. Lee, Y. Katsube, K. Asada, S. Aibara, and Y. Morita, *J. Biochemistry*, 1991, **109**, 477.
93. K. Djinovic, A. Coda, L. Antolini, G. Pelosi, A. Desideri, M. Falconi, G. Rotilio, and M. Bolognesi, *J. Mol. Biol.*, 1992, **226**, 227.
94. A. E. G. Cass, H. A. O. Hill, B. E. Smith, J. V. Bannister, and W. H. Bannister, *Biochemistry*, 1977, **16**, 3061.
95. J. D. Stoesz, D. P. Malinowski, and A. G. Redfield, *Biochemistry*, 1979, **18**, 4669.
96. H. A. O. Hill, W.-K. Lee, J. V. Bannister, and W. H. Bannister, *Biochem. J.*, 1980, **185**, 245.
97. A. E. G. Cass, H. A. O. Hill, J. V. Bannister, W. H. Bannister, V. Hasemann, and J. T. Johansen, *Biochem. J.*, 1979, **183**, 127.
98. I. Bertini, G. Lanini, C. Luchinat, L. Messori, R. Monnanni, and A. Scozzafava, *J. Am. Chem. Soc.*, 1985, **107**, 4391.
99. L.-J. Ming, L. Banci, C. Luchinat, I. Bertini, and J. S. Valentine, *Inorg. Chem.*, 1988, **27**, 4458.
100. I. Bertini, F. Capozzi, C. Luchinat, M. Piccioli, and M. S. Viezzoli, *Eur. J. Biochem.*, 1991, **197**, 691.
101. I. Bertini, C. Luchinat, L.-J. Ming, M. Piccioli, M. Sola, and J. S. Valentine, *Inorg. Chem.*, 1992, **31**, 4433.
102. M. Sette, M. Paci, A. Desideri, and G. Rotilio, *Eur. J. Biochem.*, 1993, **213**, 391.
103. I. Bertini, C. Luchinat, and R. Monnanni, *J. Am. Chem. Soc.* 1985, **107**, 2178.
104. D. B. Bailey, P. D. Ellis, and J. A. Fee, *Biochemistry*, 1980, **19**, 591.
105. L. Banci, I. Bertini, D. Cabelli, R. A. Hallewell, C. Luchinat, and M. S. Viezzoli, *Inorg. Chem.*, 1990, **29**, 2398.
106. L.-J. Ming and J. S. Valentine, *J. Am. Chem. Soc.*, 1990, **112**, 4256.
107. L.-J. Ming, and J. S. Valentine, *J. Am. Chem. Soc.*, 1990, **112**, 6374.
108. D. Mota de Freitas, L.-J. Ming, R. Ramasamy, and J. S. Valentine, *Inorg. Chem.*, 1990, **29**, 3512.
109. M. Paci, A. Desideri, M. Sette, and G. Rotilio, *Arch. Biochem. Biophys.*, 1991, **286**, 222.
110. M. Sette, M. Paci, A. Desideri, and G. Rotilio, *Biochemistry*, 1992, **31**, 12 410.
111. U. Bachrach, in *Structure and Function of Amine Oxidases*, ed. B. Mondovi, CRC Press, Boca Raton, FL, 1985, pp. 5–20.
112. S. M. Janes, D. Mu, D. Wemmer, A. J. Smith, S. Kaur, D. Maltby, A. L. Burlingame, and J. P. Klinman, *Science*, 1990, **248**, 981.
113. T. J. Williams and M. C. Falk, *J. Biol. Chem.*, 1986, **261**, 15 949.
114. S. S. Narula. D. R. Winge, and I. M. Armitage, *Biochemistry*, 1993, **32**, 6773.
115. S. S. Narula, R. K. Mehra, D. R. Winge, and I. M. Armitage, *J. Am. Chem. Soc.*, 1991, **113**, 9354.
116. K. Wüthrich, *Methods Enzymol.*, 1991, **205**, 502.
117. S. U. Patel, P. J. Sadler, A. Tucker, and J. H. Viles, *J. Am. Chem. Soc.*, 1993, **115**, 9285.
118. P. J. Sadler, A. Tucker, and J. H. Viles, *Eur. J. Biochem.*, 1994, **220**, 193.
119. P. J. Sadler and A. Tucker, *Eur. J. Biochem.*, 1992, **205**, 631.
120. S. Tuzi, S. K. Shinzawa-Itoh, T. Erata, A. Naito, S. Yoshikawa, and H. Saitô, *Eur. J. Biochem.*, 1992, **208**, 713.
121. Z. Tyeklár, R. R. Jacobson, N. Wei, N. N. Murthy, J. Zubieta, and K. D. Karlin, *J. Am. Chem. Soc.*, 1993, **115**, 2677.

Biographical Sketches

Gerard W. Canters. *b* 1940. M.A., 1966, Amsterdam University (with G.J. Hoitink), Ph.D., 1969, University of Nijmegen, The Netherlands (supervisor Bert de Boer). Postdoctoral work with Charles. S. Johnson, Jr. at University of North Carolina, Chapel Hill, NC, USA and with John van der Waals, Physics Department Leiden University. Lecturer, senior lecturer and Professor of Biophysical Chemistry subsequently at the Physics, Organic Chemistry, Inorganic Chemistry, and Biochemistry Departments of Leiden University, 1973–present. Visiting scientist, Oxford University, UK, 1981–82. Approx. 125 publications. Current research interest: structure/function of metalloproteins and engineering of metal sites in proteins.

Mart van de Kamp. *b* 1963. Ph.D. (supervisor Gerard W. Canters) 1993, Leiden University, The Netherlands. Postdoctoral work at the Nijmegen SON Research Centre with Cornelis W. Hilbers and Frank J. M. van de Ven. Approx. 20 publications. Research specialties: application of high-frequency NMR spectroscopy to the study of copper-containing proteins and modified polypeptides in solution.

Distance Geometry

Timothy F. Havel
Harvard Medical School, Boston, MA, USA

1	Introduction	1
2	Geometric Reasoning with Distance Information	1
3	Distance Geometry Algorithms	4
4	The Contributions of Distance Geometry to NMR	8
5	Related Articles	9
6	References	9

1 INTRODUCTION

Distance geometry is a general methodology which formulates conformational problems in terms of distance and chirality constraints.[1] It has been applied to such diverse problems as the conversion of two-dimensional chemical diagrams into three-dimensional structures, the systematic enumeration of all possible stereoisomers and conformers of small molecules, the docking of ligands to their receptors, and the construction of protein models by homology. It also plays a central role in present-day methods for determining the solution structures of proteins and other biological macromolecules from NMR data. There are several reasons for this. First, NMR spectroscopy, particularly the NOESY experiment, provides a wealth of data that are readily interpreted in terms of distance constraints. Second, although the problem of finding atomic coordinates consistent with distance constraints is a highly nonlinear one, unlike the problem of locating the global energy minimum it can nevertheless be solved quite reliably. Third, since the global minima of the functions that are minimized in distance geometry should have the value zero, the distance geometry formulation of the structure determination problem makes it relatively straightforward to find errors in the interpretation of the data.

2 GEOMETRIC REASONING WITH DISTANCE INFORMATION

Newcomers to distance geometry should be careful not to confuse it with the least-squares fits that are widely used in crystallography. Instead of seeking a *single* 'best fit' to the data as in the least-squares method, the goal of distance geometry is to understand better the set of all conformations consistent with the data as a whole. This is done by deriving new geometric facts about the molecule from those that are available experimentally, in a process known more generally as *geometric reasoning*. There are several ways of going about this, as described below.

2.1 Describing Molecular Conformation

A *distance geometry description* defines the set of possible conformations of a nonrigid molecule by means of lower and upper bounds on its interatomic distances, together with the chiralities of its rigid tetrahedra of atoms. The set of conformations consistent with these constraints itself is called *conformation space*. Such a description is usually not chemically complete, meaning that there may be conformations in the space that do not exist in appreciable concentration under the conditions of interest. It may also contain noncritical constraints, i.e. constraints that could be tightened without reducing the conformation space consistent with them, or it may contain redundant constraints, i.e. constraints that could be loosened or eliminated without enlarging the space.

The distance constraints may come from many sources. Clearly, the molecular formula (bond arrangement) is one of them, since both covalent bond lengths as well as the geminal distances which define the bond angles are determined essentially exactly by this information. Many other distances can also be fixed within larger rigid groups of atoms, e.g. aromatic ring systems. In addition, the distance between all pairs of atoms separated by four or more bonds may be assumed to be at least the sum of suitable hard sphere atomic radii, and other noncovalent interactions, e.g. hydrogen bonds, can also be modeled by means of distance constraints. Finally, distance constraints are available from many kinds of experiment, including optical fluorescence transfer, various noncrystallographic diffraction experiments and, of course, NMR spectroscopy. As a general rule, one should collect as many constraints as possible, since even redundant constraints are useful in distance geometry calculations.

The most obvious case in which chirality constraints are needed is at asymmetric carbon atoms, since the distances between their neighboring atoms cannot be used to distinguish enantiomers. It turns out that chirality constraints are also useful in many other cases. For example, prochiral centers should usually be constrained in distance geometry calculations, against the possibility that stereospecific assignments may be available, and chirality constraints among α-carbon atoms can be used to enforce the handedness of α-helices. Planarity can also be viewed as a sort of chirality constraint (neither left- nor right-handed), which is applicable to most double bonds. Finally, although the absolute value of a torsion angle about the 2,3-bond in a chain of four atoms can be determined by specifying the 1,4-distance, its sign can only be fixed by also constraining the chirality of the tetrahedron the vertices of which are these four atoms.

In solution, by far the richest source of distance constraints is the two-dimensional NMR experiment NOESY. Since the nuclear Overhauser effect (NOE) that this experiment measures is due to dipole–dipole interactions, the intensity of a cross peak in a NOESY spectrum is roughly proportional to the average inverse sixth power of the distance between a pair of protons in the molecule. This means that (provided a short enough mixing time is used to eliminate the possibility of indirect NOEs) the mere presence of such a cross peak implies that the maximum distance between the protons is quite small, 0.50 nm at the most. Because the NOE is also proportional to a factor that depends on the unknown average

rate at which the interproton vector reorients (and may, in addition, be influenced by many other sources of relaxation), a more quantitative interpretation of the cross-peak intensities is difficult. Fortunately, as discussed in the last section of this article, in the important special case of globular proteins a reasonably precise and well-defined structure can often be obtained without quantifying most of the NOESY cross-peak intensities.

2.2 Inconsistent Distance Constraints

The task of collecting, processing, and interpreting NMR data, particularly on large molecules such as proteins in solution, is a complex one which is susceptible to many sources of systematic as well as random error. The distance geometry approach attempts to distinguish between these two types of error by interpreting the data geometrically in terms of constraints that are intended to encompass the *full range* consistent with the intrinsic uncertainty of the measurements due to thermal noise, intramolecular motion, and similar phenomena. Assuming (as is often the case) that the data are sufficiently complete and precise to determine a nearly unique conformation, any serious errors in the interpretation of some of the data will usually cause the constraints as a whole to become mutually *inconsistent*. This means that it is impossible to satisfy the constraints by any single conformation, which in turn implies that one or more of the assumptions made in interpreting the data must be false. Although the inconsistencies can be arbitrarily complex, in most cases it is possible to isolate them to relatively small subsets of atoms, meaning that the constraints among those atoms are by themselves inconsistent with any three-dimensional structure.

Any method of detecting inconsistencies in the constraints also makes it possible to falsify structural hypotheses, and thereby opens up one possible route towards geometric reasoning. Certain relatively simple 'patterns' of inconsistent constraints can not only be detected, but also isolated, by a process known as 'bound smoothing' (see below). More often, however, inconsistency can only be detected by repeatedly trying to calculate a conformation consistent with the constraints, and failing. Since the currently available algorithms for doing this are quite reliable, this situation strongly implies that the constraints are inconsistent. Unfortunately, the minimization procedures commonly used to calculate conformations result in a compromise between violations of the correct as well as the incorrect constraints, which makes it relatively difficult to isolate inconsistency by this approach, although there is a significant correlation between the frequency and severity of constraint violations and the correctness of the constraints.

2.3 Bound Smoothing and Distance Limits

An important class of distance geometry algorithms are designed to perform *bound smoothing*. These play a central role in the so-called EMBED algorithm (see Section 3.4), but the distance limits that bound smoothing algorithms compute are of much broader interest, and hence are described here. A more complete description, together with a detailed presentation of the algorithms themselves, is available.[1]

The three-dimensional *distance limits* associated with any set of distance bounds are simply the minimum and maximum value that each distance can assume in any spatial structure the other distances of which all lie within their given bounds. Since the distance bounds available from NMR spectroscopy are necessarily imprecise and very sparse, computing the corresponding distance limits can reveal a great many consequences of the NMR data that are not obvious from direct inspection, thus providing another approach to geometric reasoning. The distance limits also enable one to detect redundant and critical distance constraints, since by definition the distance limits for redundant bounds are tighter than those bounds, while the distance limits for critical bounds are looser. Finally, the distance bounds as a whole are inconsistent if and only if the limits implied by the bounds among some subset of atoms violate the bounds, i.e. a lower bound exceeds its upper limit, or vice versa.

Unfortunately, the computation of the true three-dimensional distance limits is a difficult and unsolved problem, and only loose approximations are readily available. These are the limits implied by the bounds among subsets of three or four atoms at a time, which are known as the *triangle inequality and tetrangle inequality limits*, respectively (Figure 1). These can be computed in time proportional to at most the cube, and at least the fourth power, of the number of atoms, respectively. Although much weaker than the true three-dimensional limits, particularly with regard to the lower limits, they are capable of revealing considerable redundancy in many sets of distance constraints, and they often succeed in catching typographical errors committed during data entry that otherwise could be located only after careful proofreading or long calculation.

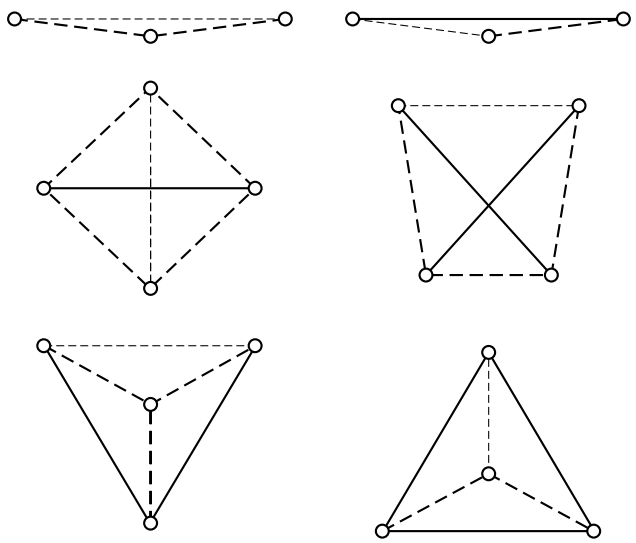

Figure 1 Schematic drawing of the triangle (top) and tetrangle (middle and bottom) limits; the upper limits are shown on the left half and the lower limits on the right. In these diagrams, solid lines indicate distances at their lower bounds, thick dotted lines indicate distances at their upper bounds, and thin dotted lines indicate the limit determined by this combination of bounds. Thus, for example, the upper left diagram indicates that the upper triangle inequality limit on the distance between the endpoints is obtained when the two distances to the midpoint are stretched to their upper bounds. The complete set of triangle or tetrangle limits may be obtained by iteratively replacing the bounds by the corresponding limits whenever these are tighter, until no further changes occur

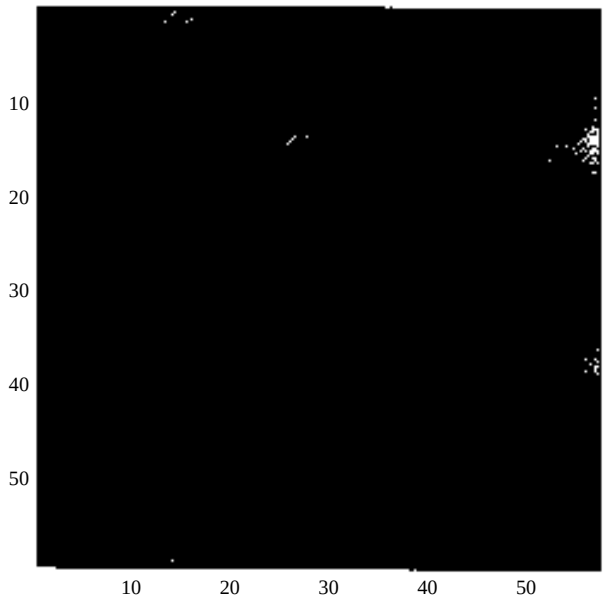

Figure 2 The triangle inequality limits among the α-carbon atoms of the 58 residue protein BPTI (above the diagonal), together with the distance matrix obtained from its crystal structure (below the diagonal). The rows and columns of this combined matrix are ordered in the same way as the corresponding residues in the BPTI sequence, and the cells are shaded according to the value of the corresponding limit or distance. The correlation between the upper limits and the distances is obvious

Another important use of the triangle (or tetrangle) limits is as a means of predicting various structural features prior actually to calculating any structures. Although this can, in principle, be done with any sort of molecule, we shall concentrate here on the important case of globular proteins subject to NOESY distance constraints. Contoured plots of the distances among the α-carbon atoms have long been used as a visual aid to recognizing the secondary structure 'topology' of globular proteins. Moreover, there exists a strong positive correlation between the upper triangle limits and the actual distances (even when only a few NOESY constraints per residue are available).[2] Therefore, contoured plots of the upper limits can serve much the same purpose as distance matrices, and it is possible to determine the chain fold and other basic features of a protein from NMR data at a very early stage in the analysis. This in turn should facilitate that analysis. Figure 2 shows an example of such a contour plot for the protein basic pancreatic trypsin inhibitor (BPTI), along with its distance matrix.

2.4 The Ensemble Approach

Bound smoothing constitutes an example of *deductive* geometric reasoning. Another, in some ways even more important approach may be called *inductive* geometric reasoning. Here, one computes an *ensemble* of conformations which satisfy the constraints, but are otherwise 'random'. Then, provided that this conformational ensemble is sufficiently large (meaning, for most purposes, 10 to 20 conformations), any geometric features that are uniformly present in all its members may safely be assumed to be necessary consequences of the constraints. The geometric features of interest are not limited to distances, but may include angles, chiralities, and far more subtle things such as the radius of gyration, surface accessibility or chain 'topology'. They may also include properties of the ensemble as a whole, such as the average or maximum 'difference' between any two conformations.

In structure determination by NMR spectroscopy, the most widely used measure of the difference between two conformations is the root mean square coordinate deviation (RMSD). This is simply the root mean square difference in their coordinate vectors (or equivalently, the root mean square distance between corresponding pairs of atoms) minimized over all translations and rotations of one conformation with respect to the other. This quantity may be computed among all the atoms, or among any desired subset (e.g. the α-carbons atoms of a protein). The average of the RMSD over all pairs of conformations in the ensemble is often used as a measure of the overall precision of an NMR structure determination, with 0.10 nm generally regarded as good, 0.20 nm as fair and 0.30 nm or more as poor. One should nevertheless be careful not to read too much into this single number. It is far more important to determine exactly how the conformations in the ensemble differ from one another than it is to determine by how much they differ on average. Fortunately, the translation and rotation which gives the RMSD also allows one to

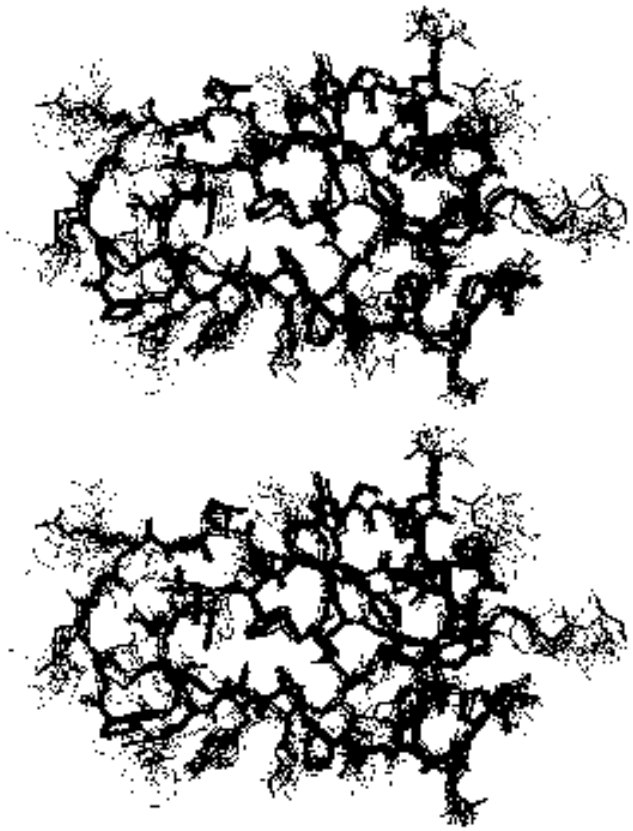

Figure 3 Stereoview of an ensemble of 25 BPTI conformations computed from a set of simulated NMR distance constraints using the program DGII.[4] These conformations (thin gray lines) have been superimposed on the crystal structure from which the constraints were derived (heavy black line) so as to minimize the RMSD to its α-carbon atoms, for an average RMSD of 0.085 nm

superimpose the structures so as to visualize easily their detailed differences by computer graphics (Figure 3).

Another commonly studied geometric feature is the torsion angles about single bonds. The precision of such cyclic parameters is best quantitated by means of an average value and 'order parameter', which is defined as follows. Given a single bond in the molecule, one puts a unit vector down in the plane for each conformation in the ensemble, whose angle with the x axis is equal to the value of the corresponding torsion angle in that conformation. On summing these unit vectors and dividing by the size of the ensemble, one obtains an average vector whose angle with the x axis is the average of the torsion angle, and whose length is the corresponding order parameter. This angular order parameter is unity only if the angle has exactly the same value in all conformations, and approaches zero as the angle becomes random.

3 DISTANCE GEOMETRY ALGORITHMS

Here the term 'distance geometry algorithm' is used somewhat loosely for any procedure that helps us to perform computer-aided geometric reasoning with distance and chirality constraints (including torsion angle constraints). Because of their utility in NMR studies of solution conformation, we concentrate here on algorithms for computing conformational ensembles. Several, rather different approaches have been taken to this problem, each of which has its advantages and disadvantages, but all of which have been successfully applied to large molecules. Rather than attempting an exhaustive survey, the discussion is limited to those algorithms which have been most widely used by NMR spectroscopists to date, or which appear particularly promising.

3.1 Restraints and Error Functions

A common feature of all these algorithms is that they rely on minimization of an error function, which measures the violations of the constraints.[1,3,4] As such, an error function is always non-negative, and zero if, and only if, all the constraints are fully satisfied. The construction of an error function involves translating the constraints into *restraints*, that is, into functions of a single geometric parameter that force that parameter to satisfy its constraint when they are minimized. The error function is then obtained as the sum over all restraints.

A simple example of such a function is

$$E(\boldsymbol{p}_1, \ldots, \boldsymbol{p}_N) = \sum \left[\max\left(0, \frac{d_{ij}^2}{u_{ij}^2} - 1\right) \right]^2 + \sum \left[\max\left(0, 1 - \frac{d_{ij}^2}{l_{ij}^2}\right) \right]^2 + \sum C_{ijkl}^2(\boldsymbol{p}_1, \ldots, \boldsymbol{p}_N) \qquad (1)$$

where u_{ij} and l_{ij} denote the upper and lower distance bounds, and $C_{ijkl}^2(\boldsymbol{p}_1, \ldots, \boldsymbol{p}_N)$ is a chirality restraint, which is described below. Squaring the distance restraints ensures that the function has continuous first derivatives, as required by many minimization algorithms, while scaling them by the inverse-squared bounds ensures that the various restraints receive roughly equal weight, which tends to make minimization of the error function somewhat easier. Ideally, however, the results should be independent of the assumed weights.

The chirality restraints, which are ordinarily needed only when Cartesian coordinates are used as the variables (see below), are usually defined as

$$C_{ijkl}^2(\boldsymbol{p}_1, \ldots, \boldsymbol{p}_N) = [\mathrm{vol}(\boldsymbol{p}_i, \boldsymbol{p}_j, \boldsymbol{p}_k, \boldsymbol{p}_l) - v_{ijkl}]^2 \qquad (2)$$

Here

$$\mathrm{vol}(\boldsymbol{p}_i, \boldsymbol{p}_j, \boldsymbol{p}_k, \boldsymbol{p}_l) = (\boldsymbol{p}_i - \boldsymbol{p}_l) \cdot [(\boldsymbol{p}_j - \boldsymbol{p}_l) \times (\boldsymbol{p}_k - \boldsymbol{p}_l)] \qquad (3)$$

is the oriented volume of the four atoms whose Cartesian coordinates are $\{\boldsymbol{p}_i, \boldsymbol{p}_j, \boldsymbol{p}_k, \boldsymbol{p}_l\}$, and v_{ijkl} is its target value. The well-known properties of the vector triple product imply that the oriented volume has absolute value equal to six times the volume of the tetrahedron spanned by the four atoms, and that its sign is positive for one chirality of this tetrahedron, negative for its mirror image, and zero whenever the atoms are coplanar.

There are two distinct ways of parameterizing the space of atomic configurations over which the minimizations must be carried out. The first uses three independent Cartesian coordinates for each atom, while the second uses the torsion angles about single bonds as the variables. The latter has the advantage of reducing the number of variables by about a factor of 10, which greatly improves the performance of many minimization algorithms. It also enables one to impose torsion angle constraints simply and directly, and maintains the covalent geometry automatically without the use of constraints on the bonded and geminal distances. As a consequence, however, it is not possible to correct violations of these constraints, which limits the methods that can be used to derive good starting structures for the minimizations. In addition, torsion angle optimizations are relatively complicated to implement, particularly if flexible rings are present in the molecules of interest. Both parameterizations are widely used in computational chemistry.

3.2 The Variable Target Function Algorithm

The variable target function algorithm was developed by Braun and Go̅[5] specifically for the purpose of computing the structures of proteins using distance constraints derived from NMR spectroscopy. By repeating the calculation many times, each time starting from a different set of randomly chosen torsion angles, one obtains the desired conformational ensemble. The method has been under continuous development since its introduction, and has become an effective tool for determining protein structures using distance and torsion angle constraints derived from NMR data. A survey of the early structures solved by this method is available.[6]

3.2.1 Avoiding Local Minima by Variable Target Functions

Even though torsion-based optimizations are quite efficient at converging to local minima, when used to solve distance geometry problems it is essential to find a global minimum of the error function. With large molecules such as proteins, the number of local minima is so large that this is highly unlikely to be achieved in any given run starting from a random conformation. The essential idea behind the variable target function approach is to avoid becoming trapped in local minima by initially minimizing a target (i.e. error!) function that restrains only the torsion angles together with the 'short-range' distances between neighboring amino acid residues, and gradually adding on longer and longer range restraints. In this way the 'short-range' or secondary structure is formed first, after which the secondary structural elements are docked together to form the tertiary structure, in a fashion that is analogous to the way in which proteins are widely believed to fold in solution. Although this heuristic method does not guarantee that a global minimum will be attained in any given run, it does increase the convergence ratio enough essentially to ensure that, with a little persistence, a global minimum with zero error will be found if one exists.

Because they require memory that grows only linearly with the size of the molecule, first-derivative based minimization methods such as conjugate gradients are generally used with the variable target function algorithm. The number of minimization iterations performed at each stage (restraint range) must be determined largely by trial and error, but does not seem to vary greatly from one protein to another. As a rule, it has been found more efficient to increase the range of the upper distance restraints obtained from NMR more rapidly than the lower distance restraints obtained as the sum of the hard-sphere radii (or, roughly equivalently, to weight the NMR restraints more strongly than the hard-sphere restraints in the initial stages), probably because the NMR restraints are far more effective at determining the tertiary structure than are the hard-sphere restraints. The method is particularly effective at determining the structures of proteins whose secondary structure consists primarily of α-helices, where the convergence ratio may approach 100%. With β-sheets or irregular structures, the convergence ratio can drop below 10%. This effectively lowers the efficiency of the method by a factor of 10, since nonconverging structures must be discarded and the minimization repeated until the desired number of conformations has been obtained.

3.2.2 Further Improvements in Speed and Reliability

The time required for each function/gradient evaluation is generally dominated by the time required to find all the hard-sphere overlaps, especially in the final stages of the variable target function algorithm when most of the hard-sphere restraints are considered. This can be greatly alleviated by using either grid-based or list-based methods to avoid checking most pairs of atoms for overlap. The hard-sphere overlap check, as well as much of the rest of the algorithm, has also been efficiently vectorized, so that each run can be performed very rapidly on a supercomputer.[7] The convergence ratio can be improved by choosing the torsion angles of the starting structure for the minimization from within their allowed ranges, rather than completely at random. These ranges can be reduced, and stereospecific assignments elucidated, by grid search methods which find those combinations of angles in each single residue that are consistent with the intraresidue distance constraints.[8] More recently, it has been suggested that the throughput can be greatly improved by imposing the ranges of angles observed in converged segments of nonconverged structures as constraints in subsequent calculations.[9] Finally, a minimization procedure has been proposed which, though apparently less efficient than conjugate gradients, yields error bounds on the torsion angles in the final conformations.[10]

3.3 Simulated Annealing and Related Methods

A second class of methods rely on a very general approach to global optimization problems known as simulated annealing. In this case, one treats the error function as an energy function, and uses either molecular dynamics or other methods to sample conformations with a Boltzmann distribution at a given absolute temperature. By slowly lowering the temperature, the distribution gradually narrows into a single energy minimum, and as in crystallization and similar physical processes this minimum will often be a global minimum. Because of the numerous error function calculations required, many of the above-mentioned methods of accelerating these calculations are also used in simulated annealing.

3.3.1 Dynamical Simulated Annealing

One way to generate conformations with a Boltzmann distribution is via molecular dynamics. This is a general method for simulating the evolution of molecular systems under the influence of a classical Hamiltonian $\mathcal{H}$, by iteratively solving Newton's equations of motion:

$$m_i \frac{\mathrm{d}^2 \boldsymbol{p}_i}{\mathrm{d}t^2} = -\nabla\mathcal{H} \tag{4}$$

This may be done by using either the 'leap-frog' algorithm

$$v_i[(2k+1)\Delta t/2] = v_i[(2k-1)\Delta t/2] - \Delta t \frac{\nabla\mathcal{H}}{m_i} \tag{5a}$$

$$\boldsymbol{p}_i[(k+1)\Delta t] = \boldsymbol{p}_i(k\Delta t) + \Delta t\, v_i[(2k+1)\Delta t/2] \tag{5b}$$

or the Verlet algorithm

$$\boldsymbol{p}_i[(k+1)\Delta t] = 2\boldsymbol{p}_i(k\Delta t) + \boldsymbol{p}_i[(k-1)\Delta t] - (\Delta t)^2 \frac{\nabla\mathcal{H}}{m_i} \tag{6}$$

In the first applications of this method to NMR structure determination problems,[11,12] the error due to the NMR restraints was added to an empirical energy function, and the combined function treated as the Hamiltonian of the system. This had several disadvantages. First, the strong forces between bonded and overlapping atoms necessitated the use of a small time step, which in turn meant that a large number of function and gradient evaluations were needed to reach equilibrium at any given temperature. Second, the function and gradient evaluations themselves required a relatively large quantity of computer time, because the forces involved in

empirical energy functions are relatively long range. Third, careful weighting of the NMR restraints was necessary in order to keep them from 'drowning out' the energy, or vice versa.

Despite these problems, by changing the weights of the short- and long-range restraints versus the energy as the annealing proceeded in a fashion similar to that used in the variable target function algorithm, impressive results were attained, including the folding of small proteins starting from a completely random array of atoms.[13] Subsequently, it was found that the efficiency and reliability of the calculations could be further improved by dropping the energy entirely, and treating a simple error function as the Hamiltonian.[14,15] In fact, in most cases the energy has little effect on the spread of the resulting conformational ensembles as measured by the average RMSD,[16] although it does tend to sharpen the distribution of the torsion angles noticeably. As a rule, however, this can be achieved more efficiently by energy minimization once the overall structure has been determined.[17]

Although in actual attempts to simulate the physical evolution of chemical systems it is essential to keep the time step small enough to accurately conserve the energy of the system, when molecular dynamics is used as a heuristic for simulated annealing we have found it advantageous to use the largest possible time step consistent with numerical stability.[4] A further improvement in efficiency can be attained by using the same mass for all the atoms, since numerical stability prevents the time step from being made much longer than the inverse rate of the fastest bond vibration. The temperature of the system can be controlled by rescaling the velocities, or by simulating a temperature bath via a temperature dependent viscosity term. Annealing has also been achieved by slowly making all the force constants larger, until the system becomes essentially rigid at a fixed temperature. While molecular dynamics can be performed using the torsion angles as the variables, such simulations are relatively uncommon and have only recently been applied to NMR structure determination problems. Further information on dynamical simulated annealing, and its applications to both NMR and crystallographic structure determination, may be found in recent reviews.[18]

3.3.2 Other Stochastic Optimization Methods

The classical method of generating atomic configurations with a Boltzmann distribution, known as the *Monte Carlo method*,[19] dates back to the earliest days of scientific computing. This method does not use gradient information, and is applicable to either Cartesian coordinates, torsion angles, or even to discrete (combinatorial) optimization problems.[20] While several applications of Monte Carlo based simulated annealing to energy minimization have been reported, only one application to NMR structure determination has been published to date.[21] The reason is that the usual implementations appear to be substantially less efficient than the dynamical simulated annealing method described above. The efficiency and reliability of the Monte Carlo method, however, hinges critically on the rate at which the temperature is lowered and the way in which the positions of the atoms are perturbed in each iteration. Recently, a variety of sophisticated methods have been developed for energy minimization purposes, which generate larger changes with a better chance of being accepted.[22–24] It therefore seems likely that a Monte Carlo procedure could be devised that performs reasonably efficiently with distance geometry problems.

Another class of stochastic minimization methods that appear suitable for distance geometry problems are known as *genetic algorithms*. Unlike the methods described above, which are based on a physical analogy, genetic algorithms are based on an analogy with the optimization of the 'fitness' of populations by natural selection. These methods have actually been available for some years,[25] but have only recently begun to attract widespread interest.[26] Once again, the basic procedure is simple, but the efficiency and reliability depend critically on how the basic steps are implemented. Using torsion angles as the variables, these procedures have recently been successfully applied to energy minimization problems,[27] as well as at least one distance geometry problem involving NMR data.[28] Genetic algorithms have the attractive feature of intrinsically computing ensembles of conformations, and hence, if reasonably good ways of implementing the basic steps can be found, they may prove to be an improvement over other torsion angle based algorithms.

3.4 The EMBED Algorithm and its Variations

The EMBED algorithm is a method of randomly generating the Cartesian coordinates of structures that roughly fit the distance constraints, and hence are good starting points for minimization by any method that is applicable to Cartesian coordinates. It was actually developed[3,29] prior to the development of two-dimensional NMR, as part of a larger effort to demonstrate the applicability of distance geometry to a wide variety of experimental and theoretical information.[30] Shortly thereafter, it was employed to determine the conformation of fragments of micelle-bound glucagon from NMR data,[31] and then to determine the first protein solution structure ever solved by NMR.[17] It has since been used in the determination of more protein, DNA, and other biomolecular structures than the space available here permits us to present.

Structure calculations with the EMBED algorithm consist of three basic steps:

1. Using bound smoothing algorithms to estimate the best possible limits on the distances from the sparse and imprecise set of distance bounds given as input.
2. Guessing a random set of distances from within the limits, and computing Cartesian coordinates such that the distances calculated from these coordinates are a best fit to this guess.
3. Optimizing these coordinates by minimization of an error function so that both the distance and chirality constraints are satisfied.

By repeating steps (2) and (3) with different random number seeds in step (2), one obtains the desired conformational ensemble. Although all three steps have traditionally been considered to be part of the EMBED algorithm, steps (1) and (3) are of independent interest (as described above). For this reason we prefer to restrict our usage of the term to step (2). Since any method for minimizing error functions with respect to Cartesian coordinates can be used in step (3), the EMBED algorithm should be understood as being complementary to these methods, rather than a substitute for them. Indeed, the combination of the EMBED algorithm with simulated annealing is presently one of the most efficient and reliable methods available for NMR structure determination.[4,32]

3.4.1 Random Distance Matrices by Metrization

Early implementations of the EMBED algorithm generated their random distance matrices by choosing the trial distances $[\tilde{d}_{ij}]$ independently of one another with a uniform distribution from within their limits. It was subsequently found that, when the density of distance constraints was quite low, the coordinates obtained in this way were uniformly expanded compared with those obtained by other methods. This undesirable tendency is eliminated by *metrization*, an extension of triangle inequality bound smoothing that enables one to choose random distance matrices which obey the triangle inequality from within the triangle inequality limits.[33,34] In principle, by making the trial distances more realistic, this should also improve the quality of the embedded coordinates.

Metrization itself is based on a characterization of the triangle inequality limits which shows that if any distance is set to any value between its triangle inequality limits, values exist for the remaining distances so that all the distances satisfy both the triangle inequality and the limits. Thus by alternately setting one distance to some random value between its limits, then setting the corresponding lower and upper bounds to that distance and updating the limits by this change, one will eventually obtain a complete distance matrix satisfying both the triangle inequality and the limits. Provided that one uses a data structure known as a 'shortest-paths tree' to store the limits involving one atom, these updates can be accomplished in time proportional to the number of atoms, so that the overall time required is proportional to its cube.

Because triangle bound smoothing is more effective at lowering upper bounds than it is at raising lower bounds, it is necessary to randomize the order in which the atoms are considered for each metrization, in order to avoid having some parts of the structure come out systematically more compact than others. In applications to distance constraints derived from NMR data, it is also desirable to control the distribution with which the distances are selected so as to obtain average values that asymptotically tend towards some fixed fraction of the upper limits, since this ensures a correlation between the distances and the upper limits similar to that observed in practice (see Figure 2).

3.4.2 Embedding Distance Matrices

The trial distances chosen randomly from within the distance limits in the previous step are essentially always inconsistent, and hence cannot be realized by any possible conformation of the molecule. Nevertheless, if we can find coordinates that are a 'best fit' to these distances, then since the distances satisfy the constraints, the coordinates ought to at least come close. It turns out that a certain type of best fit can be rapidly calculated by eigenvalue methods.

To see how this works, suppose we are given a matrix of squared distances among a set of $N + 1$ points $\boldsymbol{p}_0, \ldots \boldsymbol{p}_N$, in three-dimensional space:

$$\mathbf{D} = [d_{ij}^2] = [\|\boldsymbol{p}_i - \boldsymbol{p}_j\|^2] \tag{7}$$

The symmetric, $N \times N$ matrix of dot products of the vectors from the zeroth point to all the rest is usually called the *metric* or *Gram matrix* $\mathbf{G}$, and can be calculated directly from $\mathbf{D}$ via the well-known law of cosines:

$$\mathbf{G} = [(\boldsymbol{p}_i - \boldsymbol{p}_0) \cdot (\boldsymbol{p}_j - \boldsymbol{p}_0)] = \tfrac{1}{2}[d_{0i}^2 + d_{0j}^2 - d_{ij}^2] \tag{8}$$

Let $\mathbf{G} = \mathbf{U}\boldsymbol{\Lambda}\,\mathbf{U}^{\mathrm{T}}$ denote the eigenvalue decomposition of $\mathbf{G}$, where $\mathbf{U}$ is the orthogonal matrix whose columns are the eigenvectors of $\mathbf{G}$ and $\boldsymbol{\Lambda} = \mathbf{diag}(\lambda_1, \ldots, \lambda_N)$ is a diagonal matrix containing its real eigenvalues sorted by decreasing value. Since $\mathbf{G} = \mathbf{P}^{\mathrm{T}}\mathbf{P}$, where $\mathbf{P} = [\boldsymbol{p}_1 - \boldsymbol{p}_0, \ldots, \boldsymbol{p}_N - \boldsymbol{p}_0]$ is a $3 \times N$ matrix, the matrix $\mathbf{G}$ is positive semidefinite of rank at most 3, so that $\lambda_1 \geq \lambda_2 \geq \lambda_3 \geq 0$ and $\lambda_4, \ldots, \lambda_N = 0$. Thus if we define the 3×3 diagonal matrix $\boldsymbol{\Lambda}_3^{1/2} = \mathbf{diag}(\lambda_1^{1/2}, \lambda_2^{1/2}, \lambda_3^{1/2})$ together with the $3 \times N$ matrix:

$$\mathbf{Q} = [\boldsymbol{q}_1, \ldots, \boldsymbol{q}_N] = \boldsymbol{\Lambda}_3^{1/2}[\boldsymbol{u}_1, \boldsymbol{u}_2, \boldsymbol{u}_3]^{\mathrm{T}} = \boldsymbol{\Lambda}_3^{1/2}\mathbf{U}_3^{\mathrm{T}} \tag{9}$$

it follows that the points $\boldsymbol{q}_0 = 0$ and $\boldsymbol{q}_1, \ldots, \boldsymbol{q}_N$ have the same Gram matrix as $\boldsymbol{p}_0, \ldots, \boldsymbol{p}_N$:

$$\begin{aligned}\mathbf{G} &= (\mathbf{U}_3\boldsymbol{\Lambda}_3^{1/2})(\boldsymbol{\Lambda}_3^{1/2}\mathbf{U}_3^{\mathrm{T}}) = \mathbf{Q}^{\mathrm{T}}\mathbf{Q} = [\boldsymbol{q}_i \cdot \boldsymbol{q}_j] \\ &= [(\boldsymbol{q}_i - \boldsymbol{q}_0) \cdot (\boldsymbol{q}_j - \boldsymbol{q}_0)]\end{aligned} \tag{10}$$

They also have the same distance matrix, since $\|\boldsymbol{p}_i - \boldsymbol{p}_0\|^2 = g_{ii} = \|\boldsymbol{q}_i - \boldsymbol{q}_0\|^2$ for $i = 1, \ldots, N$, while for all $0 \neq i \neq j \neq 0$, we have:

$$\begin{aligned}&\|\boldsymbol{p}_i - \boldsymbol{p}_j\|^2 \\ &\quad = \|\boldsymbol{p}_i - \boldsymbol{p}_0\|^2 + \|\boldsymbol{p}_j - \boldsymbol{p}_0\|^2 - 2[(\boldsymbol{p}_i - \boldsymbol{p}_0) \cdot (\boldsymbol{p}_j - \boldsymbol{p}_0)] \\ &\quad = \|\boldsymbol{q}_i\|^2 + \|\boldsymbol{q}_j\|^2 - 2(\boldsymbol{q}_i \cdot \boldsymbol{q}_j) = \|\boldsymbol{q}_i - \boldsymbol{q}_j\|^2\end{aligned} \tag{11}$$

Therefore, the new points are the same as the old up to translation and/or rotation, so that $\boldsymbol{q}_0, \ldots, \boldsymbol{q}_N$ can be regarded as $\boldsymbol{p}_0, \ldots, \boldsymbol{p}_N$ in a new coordinate system. Moreover, it follows from the orthogonality of the eigenvectors that these new coordinates are principal axes coordinates.

Although principal axes coordinates can be found more efficiently by diagonalizing the inertial tensor, the above method is applicable even if we do not have any coordinates for the points, but only the distances among them. The problem is that if the distances are inconsistent, the approximate Gram matrix $\tilde{\mathbf{G}}$ computed from the squared trial distances $\tilde{\mathbf{D}} = [\tilde{d}_{ij}^2]$ according to equation (8) will not be positive semidefinite of rank 3, and hence cannot be represented as a matrix of dot products among three-dimensional vectors. It can be shown, however, that if one sets all but the three largest eigenvalues to zero, then the matrix $\mathbf{G}$ obtained via equation (10) will be an optimum least-squares fit to $\tilde{\mathbf{G}}$ over all positive semidefinite rank 3 matrices.[1] It follows that the squared distances calculated from the coordinates

$$\|\boldsymbol{q}_i - \boldsymbol{q}_j\|^2 = g_{ii} + g_{jj} - 2g_{ij} \approx \tilde{g}_{ii} + \tilde{g}_{jj} - 2\tilde{g}_{ij} = \tilde{d}_{ij}^2 \tag{12}$$

will likewise be similar to the squared trial distances $\tilde{\mathbf{D}}$.

Note that the diagonal elements of the approximate Gram matrix $\tilde{g}_{ii} = \tilde{d}_{0i}^2$, which are just the squared trial distances involving the zeroth point, affect the fit to all the other

distances. This disproportionate influence can be eliminated by creating an additional point located at the centroid of the remaining N points, and treating it as the zeroth point. This is possible because the distances from the centroid to the remaining points can be calculated directly from the distances among them via the equation[29]

$$\tilde{d}_{0i}^2 = \frac{1}{N}\sum_{j=1}^{N}\tilde{d}_{ij}^2 - \frac{1}{N^2}\sum_{j<k}^{N}\tilde{d}_{jk}^2 \qquad (13)$$

Even so, the EMBED algorithm does not produce exactly a least-squares fit between the trial distances and those calculated from the coordinates. The coordinates obtained by embedding, however, can easily be improved by minimization of an appropriately weighted least-squares residual, using a method known as *majorization*.[4]

Because a variety of extremely efficient methods exist to locate the largest few eigenvalues and eigenvectors of a symmetric matrix without completely diagnonalizing it, the EMBED algorithm is by far the fastest known way of finding reasonably good approximate coordinates to serve as starting points for further optimization.

3.4.3 Variations on Embedding

In the years since it was developed, the EMBED algorithm has been improved and extended in many ways, some of which have been touched on above. In this section several recent developments which promise to be useful in NMR structure determination are described.

The first of these methods is derived from early work by Crippen, who applied ideas from the EMBED algorithm to energy minimization.[1,35] Since the EMBED algorithm can be viewed geometrically as projecting a higher dimensional structure onto a three-dimensional subspace, Crippen proposed minimizing the energy of the structures in spaces of successively lower dimension, eventually reaching a very low energy minimum constrained to three dimensions. He calls this approach *energy embedding*. Because even the simple conjugate gradients minimization of error functions converges quite reliably in four dimensions, it appears that only four dimensions are needed in applications of this approach to distance geometry. Unfortunately, it also turns out that the reduction of a four-dimensional structure to three dimensions is the most difficult step of the procedure, probably because it is in this step that the chirality and diastereomeric configuration of the molecule is determined.

Several investigators have found that by applying dynamical simulated annealing to four-dimensional error functions in which the sum of the squares of the fourth coordinates is added to the error as an additional restraint, the local minima encountered in reducing the structure to a three-dimensional one which satisfies the distance and chirality constraints can be overcome.[4,14] At the same time, since atoms in the structure can pass through one another without the four-dimensional distance between them falling below the sum of their hard-sphere radii, the method appears to alleviate the local minimum problem encountered in three-dimensions significantly. Problems with local minima still occur, however, which can only be avoided by careful annealing.

Other, somewhat more analytic, approaches to reducing the dimension without violating the distance constraints are currently being explored. For example, in the *WARP procedure* recently developed by the author, this is done by using the elements of a 3×4 matrix $\mathbf{C}$ as the variables while holding the $4 \times N$ matrix of coordinates $\mathbf{P}$ fixed, thus seeking the minimum of the error function E over all projections and affine transformations:

$$\text{minimize } E(\mathbf{CP}) \quad \text{with respect to } \mathbf{C} \qquad (14)$$

This minimization involves only 12 variables, and converges very rapidly. Although the error is only reduced by about a factor of 2 on average, the change in the coordinates can be very large. Thus, this method appears to provide an inexpensive means of improving the coordinates obtained by embedding.

Another extension of the ideas behind the EMBED algorithm is found in the work of Glunt, Hayden and co-workers. These investigators have developed a method, called *modified alternating projections* (*MAP*), which reliably locates an $(N-1)$-dimensional structure that satisfies arbitrary self-consistent distance bounds.[36] This procedure involves repeated diagonalization of an $(N+1) \times (N+1)$ matrix, and hence is much more time consuming than EMBED. The MAP procedure, however, constitutes the most powerful general method yet developed for testing distance bounds for consistency, since if the bounds cannot be satisfied by an $(N-1)$-dimensional structure, they certainly cannot be satisfied by any three-dimensional structure. If it should prove possible to not only detect, but also isolate, inconsistencies by this method, it may be well worth the computer time required.

In addition, Glunt, Hayden and co-workers have developed an analogous procedure, called the *data box algorithm*, for refining three-dimensional structures versus both distance and chirality constraints.[37] This procedure may be summarized as follows:

1. Let $\tilde{\mathbf{D}}_0$ be a matrix of squared trial distances which satisfy the distance limits l_{ij}, u_{ij} (obtained from, for example, triangle bound smoothing), and use one iteration of MAP to find an $(N-1)$-dimensional structure $\mathbf{P}_0$ whose distances are a least-squares fit to $\tilde{\mathbf{D}}_0$.
2. Let $\mathbf{P}_1$ be a three-dimensional projection of $\mathbf{P}_0$, set $\tilde{\mathbf{D}}_1 = \tilde{\mathbf{D}}_0$ and $k = 1$.
3. Use a more efficient version of the majorization algorithm, called the *spectral gradient algorithm*, to obtain coordinates $\mathbf{P}_{k+1}$ whose distances $[d_{ij}] = [\|\boldsymbol{p}_i - \boldsymbol{p}_j\|]$ are a weighted least-squares fit to those in $\tilde{\mathbf{D}}_k$, and which minimize suitable chirality restraints.
4. Define $\tilde{\mathbf{D}}_{k+1} = [\tilde{d}_{ij}^2]$ according to

$$\tilde{d}_{ij} = \begin{cases} l_{ij} & \text{if } d_{ij} < l_{ij} \\ u_{ij} & \text{if } d_{ij} \rangle u_{ij} \\ d_{ij} & \text{otherwise} \end{cases} \qquad (15)$$

5. If the constraints are satisfied, stop; else set $k = k + 1$ and go to step (3).

With the most recent improvements in the spectral gradient algorithm, the efficiency and reliability of this procedure appears to be roughly comparable to the other methods discussed above.

4 THE CONTRIBUTIONS OF DISTANCE GEOMETRY TO NMR

Distance geometry has not only played an important role in NMR structure determinations, but has also been used to evaluate the efficacy of the geometric information available from NMR. This is done by simulating the constraints that could be obtained from NMR experiments of varying quality and completeness, computing a conformational ensemble for each such set of simulated constraints, and quantifying the precision of these ensembles by, for example, the RMSD (see Section 2.4). In this way, distance geometry has been able to assist NMR spectroscopists in deciding what kinds of experiment are most useful in determining structure, and thereby has played a role in the development of the experimental methodology. In this final section, we highlight some of the contributions of this approach to present-day methods for determining protein structure from NMR.

The original motivation for distance geometry was to develop a formalism for representing the structural information available from a wide variety of experimental and theoretical methods, together with computational methods for determining biomolecular conformation from this information.[30] As part of this larger effort, the simulation method described above was used to evaluate the distance constraints available from a number of possible experiments on protein structure, using a simple 'one point per residue' model (which was about all the computers available at that time could handle).[38] The most interesting result of this study was that it is better to know many distances imprecisely than it is to know a few distances precisely. In particular, a complete list of all contacts (<1 nm) and noncontacts (>1 nm) present in a globular α-carbon chain was found to be sufficient to determine all its distances to within only 0.1 nm on average. An important implication of these results, which had a substantial influence on subsequent events, is that the information available from the NOESY experiment should be a powerful constraint on the tertiary structure of proteins.

Because the density of constraints available from NOESY at that time was significantly lower than that used in these simulations, and because it was not immediately certain how well the results would extend to more detailed atomic models of proteins, a similar study was later performed using both a more detailed atomic model as well as constraint sets which mimicked those available from a wide variety of solution NMR experiments.[39] The conclusions of this latter study not only supported the earlier results, but were actually a good deal better than expected. The reason for this, as is now known, is that a more detailed atomic model enables one to represent the intrinsic rigidity of the polypeptide chain and the steric restrictions on how the interior side chains can be packed together much more accurately than a one-point-per-residue model. The results of this study also enabled us to formulate some general guidelines concerning the optimum strategy for determining a protein structure from NMR data, which may be summarized as follows:

1. In determining the large-scale tertiary structure of a protein's polypeptide backbone, it is much more important to maximize the quantity of interresidue distance constraints than it is to maximize the quality (i.e. precision) of those constraints; sequential, intraresidue and torsion angle constraints play only a secondary role in this regard.
2. In order to determine the 'local' conformation of short segments of the polypeptide chain and their side chains with adequate precision, relatively precise sequential and intraresidue distance constraints are needed; torsion angle constraints derived from coupling constants are also, of course, very useful.

Since stereospecific assignments were not usually available at the time these studies were performed, their effect was not evaluated at that time. Once they became widely available, however, further studies were performed which showed they made a surprisingly strong contribution to the precision, particularly of the local conformation.[4,8] In part this is due to the elimination of 'pseudoatoms' and the consequent corrections to the distance constraints, but a more significant contribution seems to be due to the directionality information that these assignments provide.

Even though sophisticated refinement methods involving 'back-calculation' of the NOESY cross-peak intensities are coming into use which promise further to enhance the precision of NMR structure determinations,[40] distance geometry may be expected to continue to play an important role in the overall structure determination process. In the first place, it is a suitable formalism in which to eliminate errors from the data, determine its intrinsic structural implications, and to establish the basic features of the conformation. In the second, since these more complex refinements are ill-conditioned and extremely prone to becoming trapped by local minima, the excellent starting conformations that distance geometry yields are essential if they are to succeed. Finally, whereas these refinements all assume that the solution 'structure' can be adequately summarized by a single conformation, in reality the solution structure is an ensemble of rapidly exchanging conformations. The conformational ensembles that distance geometry yields are therefore a potentially more accurate representation of the solution structure, and in time methods may be developed which enable us to generate or refine these ensembles so as to make them representative of the actual solution ensemble.[41]

Several more detailed reviews covering the applications of distance geometry to structure determination by NMR are available.[42–46]

5 RELATED ARTICLES

Biological Macromolecules: Structure Determination in Solution; Biological Macromolecules; NOESY; Nuclear Overhauser Effect; Protein Structures: Relaxation Matrix Refinement; Structures of Larger Proteins, Protein-Ligand, and Protein-DNA Complexes by Multi-Dimensional Heteronuclear NMR.

6 REFERENCES

1. G. M. Crippen and T. F. Havel, *Distance Geometry and Molecular Conformation*, Research Studies Press, Taunton, 1988.
2. C. M. Oshiro, J. Thomason, and I. D. Kuntz, *Biopolymers*, 1991, **31**, 1049.
3. T. F. Havel, I. D. Kuntz, and G. M. Crippen, *Bull. Math. Biol.*, 1983, **45**, 665.

4. T. F. Havel, *Prog. Biophys. Mol. Biol.*, 1991, **56**, 43.
5. W. Braun and N. Gō, *J. Mol. Biol.*, 1985, **186**, 611.
6. W. Braun, *Q. Rev. Biophys.*, 1987, **19**, 115.
7. P. Güntert, W. Braun, and K. Wüthrich, *J. Mol. Biol.*, 1991, **217**, 517.
8. P. Güntert, W. Braun, M. Billeter, and K. Wüthrich, *J. Am. Chem. Soc.*, 1989, **111**, 3997.
9. P. Güntert and K. Wüthrich, *J. Biomol. NMR*, 1991, **1**, 447.
10. P. Koehl, J.-F. Lefèvre, and O. Jardetzky, *J. Mol. Biol.*, 1992, **223**, 299.
11. R. Kaptein, E. R. P. Zuiderweg, R. M. Scheek, R. Boelens, and W. F. van Gunsteren, *J. Mol. Biol.*, 1985, **182**, 179.
12. G. M. Clore, A. M. Gronenborn, A. T. Brünger, and M. Karplus, *J. Mol. Biol.*, 1985, **186**, 435.
13. M. Nilges, G. M. Clore, and A. M. Gronenborn, *FEBS Lett.*, 1988, **239**, 129.
14. W. Nerdal, D. R. Hare, and B. R. Reid, *J. Mol. Biol.*, 1988, **201**, 717.
15. R. Kaptein, R. Boelens, R. M. Scheek, and W. F. van Gunsteren, *Biochemistry*, 1988, **27**, 5389.
16. A. M. Gronenborn and G. M. Clore, *Biochemistry*, 1989, **28**, 5978.
17. M. P. Williamson, T. F. Havel, and K. Wüthrich, *J. Mol. Biol.*, 1985, **182**, 295.
18. A. T. Brünger and M. Karplus, *Acc. Chem. Res.*, 1991, **24**, 54; A. T. Brünger and M. Nilges, *Q. Rev. Biophnys.*, 1993, **26**, 49.
19. M. H. Kalos and P. A. Whitlock, *Monte Carlo Methods*, Wiley, New York, 1986.
20. S. Kirkpatrick, C. D. Gelatt, Jr, and M. P. Vecchi, *Science*, 1983, **220**, 671.
21. D. Bassolino, F. Hirata, D. B. Kitchen, D. Kominos, A. Pardi, and R. M. Levy, *Int. J. Supercomput. Appl.*, 1988, **2**, 41.
22. D. Bouzida, S. Kumar, and R. H. Swendsen, *Phys. Rev. A*, 1992, **45**, 8894.
23. Z. Li and H. A. Scheraga, *Proc. Natl. Acad. Sci. USA*, 1987, **84**, 6611.
24. B. von Freyberg and W. Braun, *J. Comput. Chem.*, 1991, **12**, 1065.
25. J. H. Holland, *Adaptation in Natural and Artificial Systems*, University of Michigan Press, Ann Arbor, MI, 1975.
26. S. Forrest, *Science*, 1993, **261**, 872.
27. R. Unger and J. Moult, *J. Mol. Biol.*, 1993, **231**, 75.
28. M. J. J. Blommers, C. B. Lucasius, G. Kateman, and R. Kaptein, *Biopolymers*, 1992, **32**, 45.
29. G. M. Crippen and T. F. Havel, *Acta Crystallogr., Sect. A*, 1978, **34**, 282.
30. I. D. Kuntz, G. M. Crippen, and P. A. Kollman, *Biopolymers*, 1979, **18**, 939.
31. W. Braun, C. Boesch, L. R. Brown, N. Gō, and K. Wüthrich, *J. Mol. Biol.*, 1983, **169**, 921.
32. M. Nilges, G. M. Clore, and A. M. Gronenborn, *FEBS Lett.*, 1988, **229**, 317.
33. T. F. Havel and K. Wüthrich, *Bull. Math. Biol.*, 1984, **46**, 673.
34. T. F. Havel, *Biopolymers*, 1990, **29**, 1565.
35. G. M. Crippen, *J. Comput. Chem.*, 1984, **5**, 548.
36. W. Glunt, T. L. Hayden, and W.-M. Liu, *Bull. Math. Biol.*, 1991, **53**, 769.
37. W. Glunt, T. L. Hayden, and M. Raydan, *J. Comput. Chem.*, 1993, **14**, 114.
38. T. F. Havel, G. M. Crippen, and I. D. Kuntz, *Biopolymers*, 1979, **18**, 73.
39. T. F. Havel and K. Wüthrich, *J. Mol. Biol.*, 1985, **182**, 281.
40. P. Yip and D. A. Case, *J. Magn. Reson.*, 1989, **83**, 643.
41. J.-X. Yang and T. F. Havel, *J. Biomol. NMR*, 1993, **3**, 355.
42. K. Wüthrich, *Methods Enzymol.*, 1989, **177**, 125.
43. I. D. Kuntz, J. F. Thomason, and C. M. Oshiro, *Methods Enzymol.*, 1989, **177**, 159.
44. R. M. Scheek, W. F. van Gunsteren, and R. Kaptein, *Methods Enzymol.*, 1989, **177**, 204.
45. G. P. Gippert, P. F. Yip, P. E. Wright, and D. A. Case, *Biochem. Pharmacol.*, 1990, **40**, 15.
46. G. Wagner, S. G. Hyberts, and T. F. Havel, *Ann. Rev. Biophys. Biomol. Struct.*, 1992, **21**, 167.

Biographical Sketch

Timothy Franklin Havel. *b* 1953. B.S., Reed College, 1975; Ph.D. University of California at Berkeley, 1982. Introduced to distance geometry by G. M. Crippen and I. D. Kuntz, and to NMR by K. Wüthrich. Assistant Member, Research Institute of Scripps Clinic, San Diego, CA, 1985–88; Associate research scientist, University of Michigan, Ann Arbor, MI, 1988–90; Lecturer, Harvard Medical School, Boston, MA, 1990–present. Approx. 40 publications; with Professor Crippen the book 'Distance Geometry and Molecular Conformation', Research Studies Press, Taunton, 1988. Research interests include the theory of molecular conformation, and methods for determining conformation from NMR spectroscopy.

Enzymes Utilizing ATP: Kinases, ATPases and Polymerases

Albert S. Mildvan

Johns Hopkins School of Medicine, Baltimore, MD, USA

1	Introduction	1
2	NMR Parameters Useful in the Study of ATP-Utilizing Enzymes	1
3	Structure of Metal–ATP Complexes	2
4	Structure of Enzyme-Bound Metal–ATP Complexes	3
5	α-Substitution: DNA Polymerase I	3
6	β-Substitution: The Mut T Enzyme	5
7	γ-Substitution: cAMP-Dependent Protein Kinase	6
8	γ-Substitution: Adenylate Kinase	7
9	γ-Substitution: F1 ATPase, Active Site Peptide	7
10	Related Articles	8
11	References	8

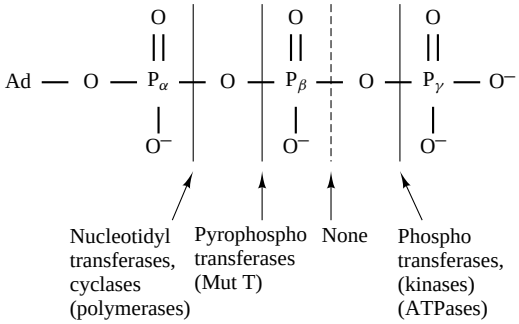

Figure 1 Sites of enzyme-catalyzed bond cleavage of ATP (modified from reference 1)

1 INTRODUCTION

Enzyme-catalyzed reactions of adenosine triphosphate (ATP) (Figure 1) are ubiquitous in biochemistry, occurring in almost all metabolic pathways. Chemically, such reactions are nucleophilic substitutions at either the α, β, or γ phosphorus atoms of ATP by an oxygen or, rarely, by an amine nitrogen.[1] Substitution at the P-α, which results in the departure of pyrophosphate as the leaving group, is common in biochemistry occurring on hundreds of enzymes including polymerases, cyclases, and synthetases. Substitution at P-β, which results in the leaving of AMP, is very rare with only seven known examples.[2] The rarity of these reactions may well result from the greater electron density at P-β as detected by its 13 ppm low-frequency (upfield) shift from P-α by ^{31}P NMR.[3] Substitution at P-γ which results in the leaving of ADP is very common, occurring on hundreds of enzymes including kinases, ATP hydrolases, and synthetases (Figure 1). All enzyme-catalyzed reactions of ATP require at least one divalent cation for activity and ATP is present in cells predominantly (~80%) as its Mg^{2+} complex.[4] Hence structural studies of ATP and its metal complexes were among the earliest biochemical applications of NMR.[3,5] Major questions addressed by NMR are whether the mechanism of substitution is dissociative [equation (1)] or associative [equation (2)] and the precise role of the divalent cation activator.

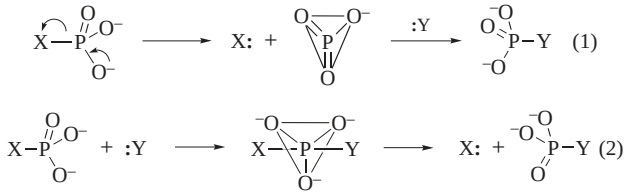

NMR methods have long been used to determine the conformations and arrangements of enzyme-bound substrates,[6] intersubstrate distances,[7] motion at enzyme active sites,[8] rates of exchange of bound with free substrate[9] and, more recently, the solution structures of ATP-utilizing enzymes[10–12] and of functional fragments of such enzymes which retain the ability to bind substrates.[13–16] The NMR docking procedure has been developed to locate the substrate binding site in the X-ray structure of several enzymes, including the ATP-utilizing enzymes adenylate kinase and DNA polymerase.[14,17–19]

2 NMR PARAMETERS USEFUL IN THE STUDY OF ATP-UTILIZING ENZYMES

In addition to the fundamental parameters of the NMR spectrum (chemical shifts, coupling constants, and intensities of resonances) that form the basis of resonance assignments, three relaxation rates are found to be especially valuable in the study of enzyme mechanisms. These are the longitudinal relaxation rate ($1/T_1$), which is used to measure metal–nucleus distances, the nuclear Overhauser effect (NOE), which is used to measure interproton distances, and the transverse relaxation rate ($1/T_2$), which is used to measure dissociation rates of enzyme–substrate and enzyme–product complexes.

Paramagnetic effects of transition metals on $1/T_1$ of protons, ^{31}P, ^{13}C, and ^{19}F have long been used to measure distances from the metals to these nuclei on enzymes, and enzyme-bound substrates, in the so-called paramagnetic probe-T_1 method.[9,20,21] The longitudinal relaxation rate ($1/T_1$), defined as the first order rate constant for orientation of a set of nuclear magnetic vectors along the direction of the magnetic field, is increased by the unpaired electrons of nearby transition metals or free radicals, by an amount inversely related to the sixth power of the distance (r) between the unpaired electrons and the nucleus. The relevant equation is

$$r = C\left[\left(\frac{qfT_{1P}T_{o.s.}}{T_{o.s.}-T_{1P}}-\tau_M\right)\left(\frac{3\tau_c}{1+\omega_I^2\tau_c^2}+\frac{7\tau_c}{1+\omega_S^2\tau_c^2}\right)\right]^{\frac{1}{6}} \quad (3)$$

where C is a product of known physical quantities, q is the relative stoichiometry of bound paramagnet and bound substrate, f is the concentration ratio of bound paramagnet to total substrate, T_{1P} is the paramagnetic contribution to

T_1, $T_{o.s.}$ is the outer-sphere relaxation time, τ_M is the lifetime of the complex, τ_c is the correlation time for dipolar interaction, ω_I is the nuclear precession frequency and ω_S is the electron precession frequency. As discussed in detail elsewhere,[20,21] the measurement of distances by this method requires the experimental determination of four other parameters in the relaxation equation, namely q, $T_{o.s.}$, τ_M, and τ_c, which can usually be done in the same or in a closely related experiment. Introduced into biochemistry in a study of MnATP interactions,[5] the paramagnetic probe-T_1 method was first tested and shown to give the correct distance in the simpler binary Mn^{2+}–F^- complex,[9] and was also extended to enzyme–metal–substrate complexes.[9] Since then, numerous comparisons of distances determined by this method with those determined by X-ray have shown its validity, when properly applied, in measuring distances as great as 2.4 nm.

The NOE can be used to measure the distance between pairs of magnetic nuclei. The NOE is defined as a change in the intensity of an NMR resonance observed after pre-irradiating another resonance. The magnitude of this change in resonance intensity, multiplied by the longitudinal relaxation rate of the resonance undergoing the change (the cross-relaxation rate) is, under certain circumstances, inversely proportional to the sixth power of the distance between the nuclei.[22–25] The relevant equation for a two spin system assuming instantaneous saturation of resonance B is

$$f_A(B)_t = \frac{\sigma_{AB}}{\rho_A}(1 - e^{-\rho_A t}) \quad (4)$$

where $f_A(B)_t$ is the fractional change in intensity of A after pre-irradiating B for time t, σ_{AB} is the cross-relaxation rate and ρ_A is the longitudinal relaxation rate ($1/T_{1A}$) of A. The experimentally measured values of $f_A(B)_t$ and ρ_A are fitted to equation (4) to evaluate σ_{AB} which is related to the internuclear distance between A and B (r_{AB}) by equation (5)

$$r_{AB} = \frac{\gamma^4 \hbar^2}{10 r_{AB}^6}\left(\frac{6\tau_r}{1 + 4\omega_1^2\tau_r^2} - \tau_r\right) \quad (5)$$

where γ is the gyromagnetic ratio, $\hbar$ is Planck's constant divided by 2π, τ_r is the time constant for reorientation of the internuclear vector r_{AB} and ω_I is the nuclear precession frequency. On taking a time derivative of equation (4) and setting $t = 0$ it is seen that the initial slope of $f_A(B)$ as a function of time directly gives σ_{AB}. Hence it is not always necessary to measure ρ_A if early time points are measured. Early time points are desirable for measuring interproton distances to avoid the effects of spin diffusion, since primary NOEs develop more rapidly than higher order effects.[25–27] The NOE method has been used qualitatively to detect proximities between pairs of protons,[23] and quantitatively to measure relative[26,27] and absolute interproton distances[17] ranging from 0.2 to 0.5 nm. The measurement of absolute interproton distances, which requires the determination of NOEs at two magnetic fields, has established the validity of this method since it yielded the correct interproton distance from H-1′ to H-2′ of MgATP.[17,26] A more comprehensive treatment of the data may be carried out, taking into account, where possible, all relaxation pathways[28] often with comparable results, within experimental error.

The transverse relaxation rate ($1/T_2$) is the rate constant for dephasing of nuclear magnetic vectors in a direction perpendicular to the applied magnetic field. Paramagnetic effects of enzyme-bound metals on $1/T_2$ of substrates have long been used to measure the exchange rates of ($1/\tau_M$) of enzyme-bound substrates with free substrates,[20] based on a relationship derived by Swift and Connick[29] which simplifies to

$$\frac{1}{fT_{2P}} = \frac{q}{T_{2M} + \tau_M} + \frac{1}{T_{o.s.}} \quad (6)$$

when the paramagnetic shift is small. In equation (6) T_{2M} is the transverse relaxation time in the paramagnetic complex. Analysis of the temperature dependence of $1/fT_{2P}$ is used to obtain the exchange rate or a lower limit to it.[20,21] These exchange rates are usually dominated by the rate of dissociation of the enzyme–substrate complex. Comparisons of the exchange rates of enzyme–substrate and enzyme–product complexes measured by $1/T_2$ with those determined by transient state and steady state kinetics provide a critical test of whether the complex, studied by NMR, dissociates rapidly enough to participate in catalysis.

The combined use of both the paramagnetic probe-T_1 method to measure metal–nucleus distances, and the NOE method to measure interproton distances, on an enzyme–bound flexible substrate, such as ATP, provides a rigorous way of defining both the conformation[26] of the bound substrate and the uniqueness of the conformation. Measurement of the dissociation rate of the enzyme–substrate complex by $1/T_2$ provides a test of its kinetic competence to participate in catalysis.[9,20,21]

The NMR docking procedure which is used to position the substrate such as ATP into the X-ray or NMR determined structure of an enzyme, consists of four steps:[17–19,30]

1. Determine the conformation of the enzyme-bound substrate by NMR measurements of metal–nucleus distances and interproton distances.
2. Measure distances from a paramagnetic reference point on the enzyme (or substrate) to assigned proton resonances of the substrate (or enzyme).
3. Identify amino acid residues of the enzyme within 0.5 nm of the bound substrate by intermolecular NOEs from assigned proton resonances of the enzyme to those of the substrate.
4. Use the distances from (2) and (3) to position the proper conformation of the substrate into the X-ray or NMR structure of the enzyme, removing steric overlaps by energy minimization of the complex.

An additional step, to confirm the location of the active site, is to design and synthesize a peptide, approximately 50 residues in length, based on the presumed location of the bound substrate, and to determine whether this peptide binds substrate with an affinity comparable to that of the enzyme. This step has been carried out with adenylate kinase[17], DNA polymerase,[14] and F1 ATPase.[15,16,31]

3 STRUCTURE OF METAL–ATP COMPLEXES

Because of the high concentrations of Mg^{2+} in cells, ranging from 3.5 to 8.5 mM, the cellular form of ATP is predominantly ($\geq$80%) MgATP, as determined by the ^{31}P chemical shifts of ATP in various cell types.[4] Hence for most ATP reactions, Mg^{2+} is the physiological activator although, in vitro, other

cations can substitute for Mg^{2+}. In free MgATP, as determined by ^{31}P chemical shifts[32,33] $^{2}J_{PP}$ coupling constants[33] and by T_1 values of ^{17}O bonded to phosphorus,[34] Mg^{2+} is simultaneously coordinated to all three phosphates, although somewhat more weakly to the α-phosphate. MnATP has a very similar structure as found by paramagnetic effects on T_1 of the phosphorus atoms.[5,35,36] The metal ions do not interact with the adenine ribose portion of ATP. Because of the flexibility of ATP, the structure of free metal–ATP in solution is a mixture of at least three conformations of the adenine ribose portion (Figure 2),[26] and four stereoisomers of the metal triphosphate portion, two at each of the chiral α- and β-phosphorus atoms.[37,38]

4 STRUCTURE OF ENZYME-BOUND METAL–ATP COMPLEXES

With enzyme-bound metal–ATP, the structure becomes much simpler, since the protein lattice constrains the conformations and stereoisomers of this flexible substrate usually to a single species.[26,35,36,39] Figure 2 summarizes the structures of metal–ATP found on several enzymes based on NMR as well as kinetic studies with substitution inert complexes of ATP with the trivalent metal ions Co(III) and Cr(III),[37] and with α- and β-thio–ATP complexes of hard and soft divalent cations.[38] As also indicated in Figure 2, those enzymes which significantly alter the glycosidic torsional angle of ATP from those found in the free nucleotide show high selectivity for a specific nucleotide base.

On enzyme-bound metal–ATP, the metal is always found to be coordinated to the γ-phosphate, almost always to the β-phosphate and sometimes to the α-phosphate as well. These locations of the metal ions on ATP have been found on all enzymes investigated, regardless of which phosphorus atom of ATP undergoes nucleophilic displacement and which bond undergoes cleavage in the catalyzed reaction. Hence the position of the metal does not determine the site of bond cleavage in ATP.[39–41]

The remainder of this article will consider individual examples of ATP enzymes which catalyze nucleophilic substitution at either the α, β, or γ phosphorus atoms.

5 α-SUBSTITUTION: DNA POLYMERASE I

The DNA polymerase reaction involves substitution at the α-P of deoxynucleoside triphosphate (dNTP) substrates by the 3′-OH group of the growing DNA strand or primer, with displacement of pyrophosphate. It utilizes four nucleotide substrates for elongation of the primer in a manner consistent with Watson–Crick base pairing between the incoming substrate and template. DNA polymerase I (pol I), the first enzyme found to catalyze such a reaction[42] is a single polypeptide of 928 amino acids consisting of three catalytic domains (Figure 3). The amino-terminal domain (residues 1 to 325) catalyzes a 5′,3′-exonuclease reaction, the middle domain (residues 326 to 524) catalyzes a proofreading 3′,5′-exonuclease which contributes to the fidelity of template copying, and the carboxy-terminal domain (residues 543 to 928) catalyzes the polymerase reaction. The middle- and carboxy-terminal domains (residues 326 to 928) together constitute the Klenow or large fragment of pol I for which an X-ray structure has been determined.[43,44] NMR studies of pol I and its large fragment have concentrated on the polymerase active site. An early measurement of distances from Mn^{2+} bound at the polymerase site to the substrates dTTP and dATP in abortive enzyme–Mn^{2+}–substrate complexes by ^{31}P and ^{1}H relaxation revealed metal coordination to the γ-phosphate and nucleotide conformations suggestive of B-form DNA.[35] B-like conformations of bound dTTP and dATP were confirmed in ternary Mg^{2+} complexes by NOE measurements of interproton distances which yielded high *anti* O-1′-*endo* substrate conformations.[45–47] The presence of templates (RNA rather than DNA templates were used to avoid their hydrolysis by the 3′,5′-exonuclease) had little effect on the conformations of bound dTTP or dATP. NOE studies also indicated the bound RNA templates $(rU)_{54}$, $(rA)_{50}$, and $(rC)_{37}$ to have B-like conformations on pol I. Because of their greater tendencies to form *syn* conformations, the substrates dGTP and ddGTP showed a mixture of *syn* (40%) and *anti* (60%) conformations on DNA polymerase. The binding of templates simplified these conformations to a single B-like, high *anti*-O-1′-*endo* species, suggesting base pairing between the template and the bound substrate.

Such conformational adjustments of the bound substrate and template into a B-like conformation could contribute to the low error rate in template replication achieved by this enzyme of approximately 10^{-6} fold, i.e. one error per 10^6 correct nucleotides incorporated. It has been estimated that Watson–Crick base pairing contributes a factor of $\sim 10^{-2}$ to the error rate, the proofreading 3′,5′-exonuclease contributes $\sim 10^{-1}$, and an error prevention step preceding incorporation contributes 10^{-3}. The nature of this error prevention step is under active investigation. Templates do not alter the relative affinities of pol I for complementary and noncomplementary substrates as found by competitive titrations monitored by NMR line broadening.[46,47] Hence the error prevention step increases the relative velocity of incorporation of the correct substrate over the incorrect substrate. The abortive enzyme–Mn–dTTP complex showed only γ-phosphate coordination[35] while the active complex shows β-coordination as well.[48] Hence a selective structural change occurring only with the correct substrate may involve β-coordination by the enzyme-bound divalent cation, closing the chelate ring to the leaving pyrophosphate group.[41,46] Model building of the B-like conformation of the MgdNTP substrate determined by NMR into B-DNA showed the α-P of the substrate to approach the 3′-OH of the primer terminus at a distance appropriate for an associative displacement (<0.49 nm), with inversion at phosphorus.[41,47] Such inversion, first predicted by NMR,[35] was subsequently established by stereochemical analysis of the polymerase reaction.[48]

Another question addressed by NMR was the amino acid environment of the active site for polymerization. Intermolecular NOEs from the enzyme to protons of the substrate dATP carried out by one-dimensional (1D) NMR studies at 250 MHz and recently confirmed by NOESY spectra at 600 MHz revealed the proximity of bound dATP to hydrophobic and aromatic residues, most likely Leu, Ile, and Tyr.[45–47] These results were consistent with photoaffinity labeling studies with 8-azido dATP[49] which modified Tyr-766 located in the sequence L-I-Y-G which is conserved among

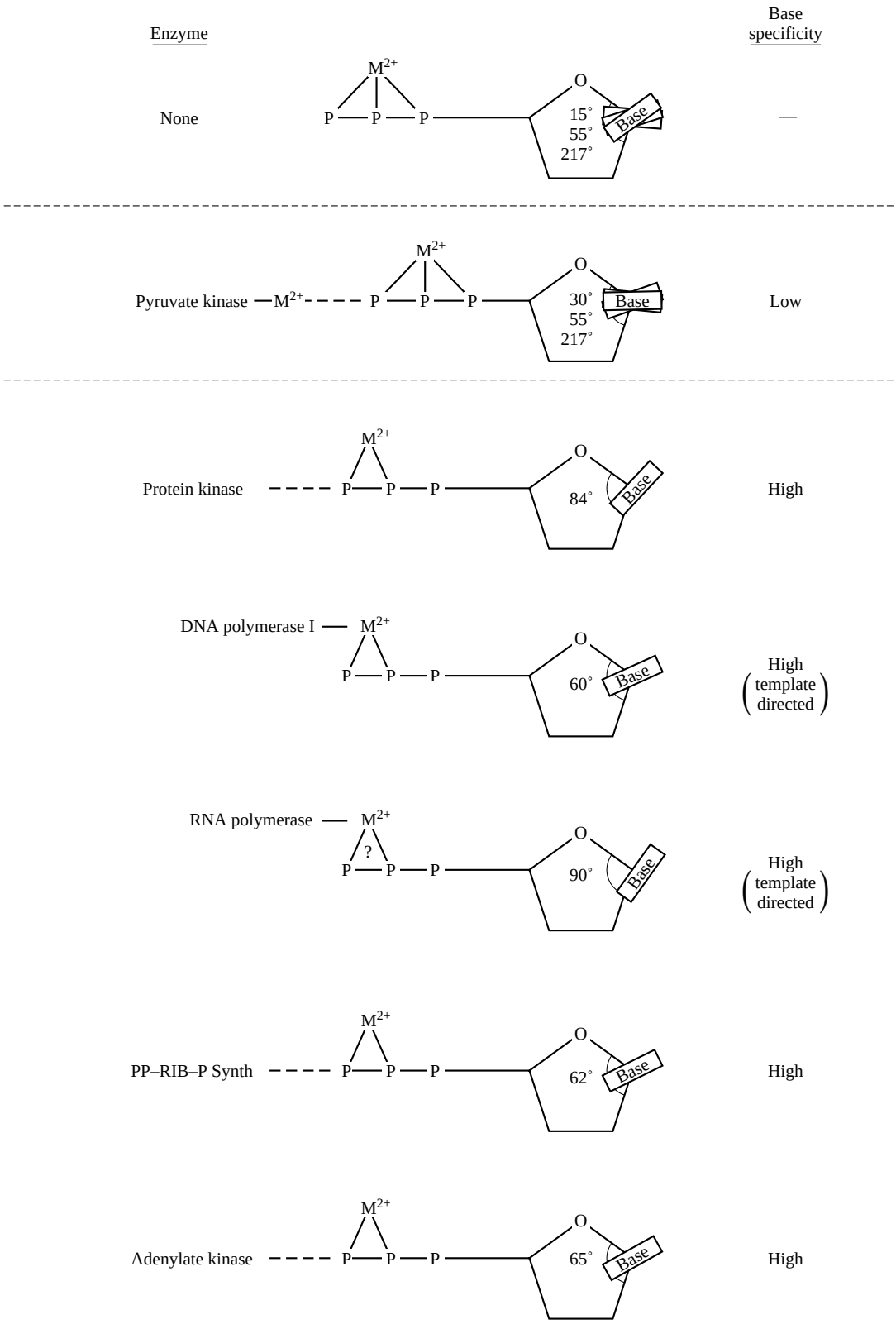

Figure 2 Conformations, expressed as glycosidic torsional angles, and location of metals on free and enzyme-bound ATP, and correlation of conformation with nucleotide base specificity as determined by kinetic studies (modified from reference 39)

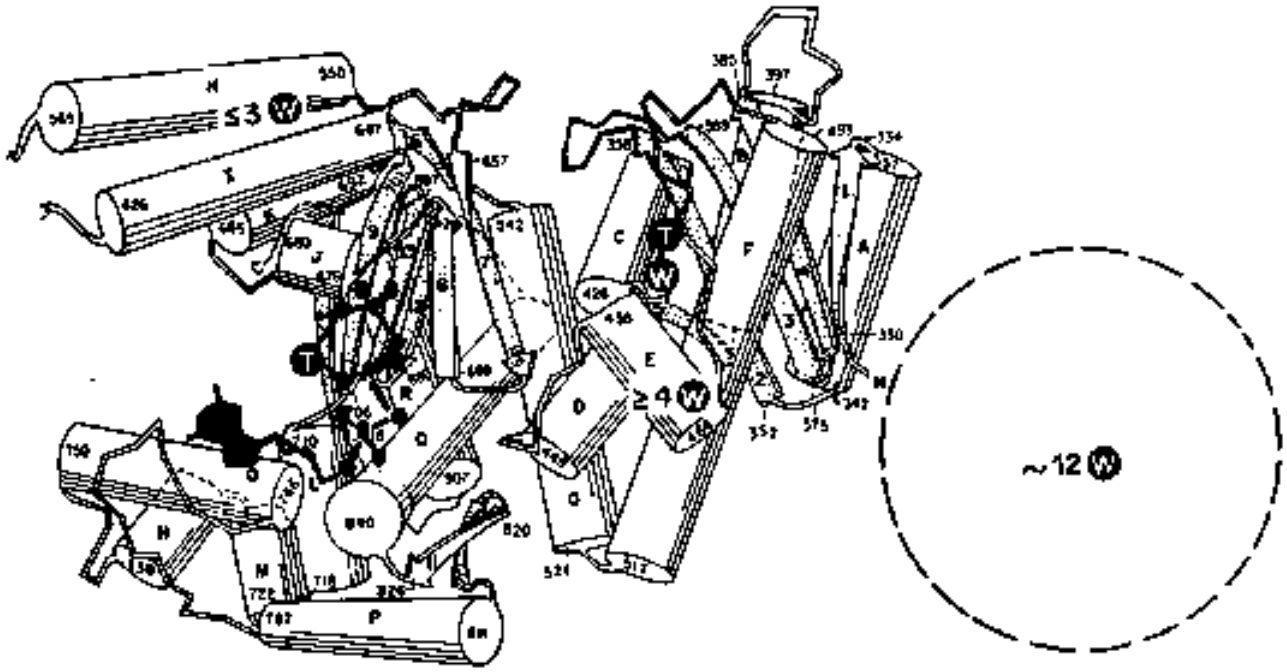

Figure 3 Position of the metal–nucleotide substrate in the X-ray structure of DNA polymerase I[43,44] based on transferred NOEs,[45–47] photoaffinity labeling,[49] and substrate binding properties of an active site peptide.[51] Also shown are the locations of tight (T) and weak (W) binding sites for divalent cations.[50] The broken circle depicts the 5′,3′-exonuclease domain

DNA polymerases. These and other chemical modification studies permitted docking of the substrate into the X-ray structure of the enzyme with the adenine ring along the O-helix where these residues are located (Figure 3).[47,50] NOEs from the enzyme to bound RNA templates were consistent with nearby Arg and/or Lys residues.

As an independent test of the substrate location, two peptides were synthesized and investigated for substrate binding.[51] Peptide I, based on residues 728 to 777 of the pol I sequence encompassed both the N and O helices (Figure 3). Peptide II, based on residues 840 to 888 contained the conserved sequence V-H-D-E, including His-881 which was photoaffinity labeled by TTP. It consisted of the Q helix and β strands 12 and 13 of the X-ray structure. While both peptides retained significant secondary structure as found by circular dichroism (CD), only peptide I was able to bind substrates and substrate analogs with affinities approaching those of the complete enzyme. Like the complete enzyme, peptide I also bound duplex DNA tightly, forming a ternary peptide–DNA–dNTP complex, providing strong evidence for the location of the polymerase active site (Figure 3).[51]

The solution structure of peptide I was determined by two-dimensional (2D) ^{1}H NMR[14] and, like other peptides, was found to consist of both extended and partially folded structures which equilibrated rapidly on the NMR timescale. The N-helix of the enzyme was replaced by four β-turns which may be intermediates in helix formation. The O-helix of the enzyme was replaced by a loop in the peptide. A residue-by-residue comparison of individual amino acid conformations revealed that only 36% of the enzyme conformation is retained by the peptide, a typical result for peptides. The homologous L-I-Y-G sequence, which was found by NOEs to water protons to be exposed to the solvent, contributes to the substrate binding site. An exposed cluster of cationic residues, three Arg and one Lys, probably represents the DNA binding site of the peptide.[51]

The conformations and arrangement of substrates at the active site of RNA polymerase have also been investigated by NMR and these studies have been reviewed.[52]

6 β-SUBSTITUTION: THE Mut T ENZYME

Of the seven known enzymes which catalyze nucleophilic substitution at the electron rich P-β of ATP,[2] most and possibly all require two divalent cations for catalytic activity, one directly coordinated by ATP, and the other by the enzyme.[53] The enzyme-bound metal also interacts with the metal–ATP complex, presumably to further activate the P-β for nucleophilic attack. The Mut T enzyme, the simplest of these enzymes, catalyzes the hydrolytic cleavage of nucleoside triphosphates to yield the nucleotide and pyrophosphate. While active with all NTPs, its biological role in *E. coli* and man is to cleave mutagenic dNTPs such as 8-oxo-dGTP which has a 10^3-fold lower K_M value than do other nucleotides.[54,55] When Mut T is inactivated by mutation, *E. coli* accumulates a large number of A · T → C · G transversions during DNA replication.[56,57]

When the Mut T-catalyzed hydrolysis of dGTP was carried out in H_2 ^{18}O, and monitored by ^{31}P NMR at 243 MHz, the label appeared in pyrophosphate as indicated by an 0.01 ppm low-frequency shift of the ^{31}P resonance of pyrophosphate, but not of dGMP, thus establishing nucleophilic substitution by H_2O at P-β.[2] Kinetic analyses of the Mn^{2+} and Mg^{2+} activated enzyme indicated a dual divalent cation requirement.[53] Binding studies with Mn^{2+} and with the non-hydrolyzable substrate analog, α,β-methylene adenosine triphosphate (AMPCPP),

monitored by $1/T_1$ of water protons, confirmed two Mn^{2+} binding sites, one on the enzyme and the other on the AMPCPP. Mutual tightening of binding of Mn^{2+} and MnAMPCPP to the enzyme, and the decrease in the enhanced longitudinal relaxation rate of water protons due to $E \cdot Mn^{2+}$, upon binding of MnAMPCPP, suggested a metal bridged $E-Mn^{2+}-AMPCPP-Mn^{2+}$ complex.[53]

The small size (129 residues) and stability of this enzyme permitted the study of its solution structure by heteronuclear multidimensional NMR.[11,12] ^{15}N labeling of the enzyme permitted $^{1}H[^{15}N]$ heteronuclear single quantum coherence (HSQC), $^{1}H[^{15}N]$TOCSY-HMQC, and $^{1}H[^{15}N]$NOESY-HMQC experiments, and ^{15}N and ^{13}C labeling permitted HNCA, HN(CO)CA, HNCO, constant time $^{1}H[^{13}C]$HSQC, HCACO, and HCA(CO)N experiments. These and other experiments led to the complete sequence-specific assignment of the backbone HN, N, C-α, H-α and CO resonances of the free enzyme,[11] and elucidated the secondary structure which consists of two α-helices, a five stranded, mixed β-sheet containing two β-turns, and four loops (Figure 4).[12] Mixed β-sheets are found in other highly stable proteins such as ubiquitin.[58]

The active site, as studied by changes in chemical shifts in the $^{1}H[^{15}N]$HSQC spectrum in response to the addition of Mg^{2+}, subtends loops I and III, the end of helix I and β-strands A and B. Subsequent titration with MgAMPCPP showed chemical shift changes in the same regions, but most notably in residues A27, M29, A30, N31, K39, and I40 of loop I. Titration with Mn^{2+}AMPCPP, a distance-dependent probe, resulted in the paramagnetic broadening of HN and ^{15}N cross peaks of residues G37, G38, and K39 of Loop I and G59 at the end of helix I.[12] In accord with these findings, residues in loop I and in the C-terminus of helix I show homologies with other anti-mutator enzymes, and mutations in loop I such as E34K and E38D markedly decrease enzymatic activity.[57]

NMR studies have also been made on the conformation and arrangement of substrates at the active site of phosphoribosyl pyrophosphate synthetase, another β-enzyme, and have been reviewed.[39]

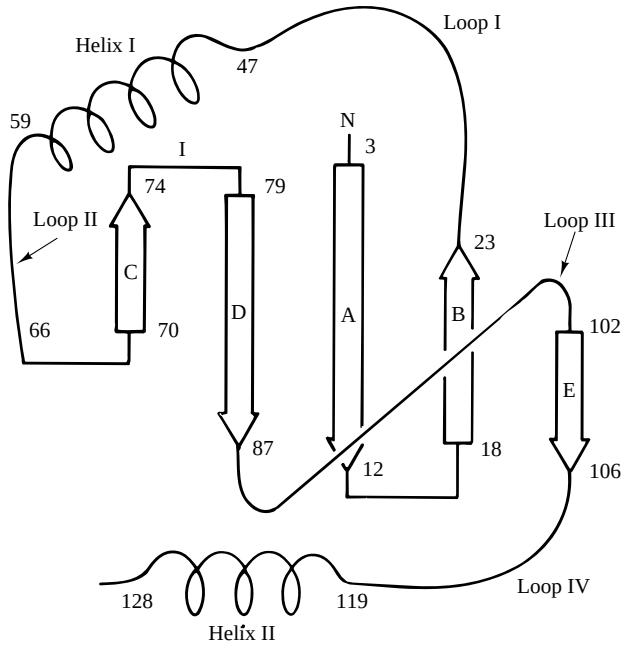

Figure 4 Diagram of the secondary structure of Mut T based on heteronuclear multidimensional NMR studies[11,12]

7 γ-SUBSTITUTION: cAMP-DEPENDENT PROTEIN KINASE

One of the most important members of this vast group of enzymes which catalyze substitution at P-γ of ATP is cAMP-dependent protein kinase, an enzyme which controls the rates of many other enzymes and of entire metabolic pathways.[59,60] The resting holoenzyme exists as an inhibited complex (R_2C_2) of the regulatory dimer (R_2) and two catalytic subunits (C). The binding of cAMP to four sites on the regulatory dimer increases the dissociation constant of R_2C_2 by $\sim 10^4$ fold resulting in the release of two molecules of the catalytic subunit which is the active enzyme.[60,61] This enzyme catalyzes the phosphorylation, by MgATP, of Ser and Thr residues on proteins and peptides with the preferred sequence -Arg-Arg-X-Ser-Y- in which X is almost any residue and Y is hydrophobic. Magnetic resonance studies of this enzyme have examined the role of the divalent cation,[62] the conformations and arrangement of enzyme-bound substrates,[26,63] the mechanism of phosphoryl transfer by the catalytic subunit,[64] the bound phosphorus of the regulatory subunit,[25] and the mechanism of inhibition of the catalytic subunit by the regulatory subunit.[61] The coordination scheme of the active ternary complex of the enzyme, metal, and ATP is a nucleotide bridge complex $E-ATP-M^{2+}$ as shown by kinetics and by Mn^{2+} and ATP binding studies monitored by $1/T_1$ of water protons.[62] The binding of Mn^{2+}ATP to the enzyme induced the formation of a second and weaker Mn^{2+} binding site which partially inhibited the enzyme. Mn^{2+} at this inhibitory site bridged the enzyme to the three phosphates of the metal–nucleotide substrate in a complex of the form

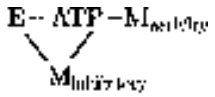

These two divalent cation binding sites were used separately as reference points from which distances were determined to both ATP and peptide substrates by the paramagnetic probe-T_1 method.[63,65] These distances, together with interproton distances measured by the NOE method[26] yielded a single, high *anti*-O-1′-*endo* conformation for bound $Co^{3+}(NH_3)_4$ ATP. Intersubstrate distances from two paramagnetic reference points, Mn^{2+} at the inhibitory site and Cr^{3+} at the activating site, were used to determine the conformation of the optimal heptapeptide substrate LRRASLG and its Tyr-4 and Ala-5 analogs. A total of 31 measured metal–proton distances were used in model building to explore the allowed conformations of the enzyme-bound heptapeptide substrate. The distances were incompatible with a helix, β-strand, β-bulge, or all possible β-turns within the bound heptapeptide. They were consistent only with two extended coil structures,[63] one of which could be ruled out by kinetic and model building studies of *N*-methylated peptides.[66] The *anti* conformation for bound ATP and the extended coil conformation for the bound substrate (Figure 5) were confirmed by X-ray diffraction.[67,68] Extended coil conformations of bound peptide and protein

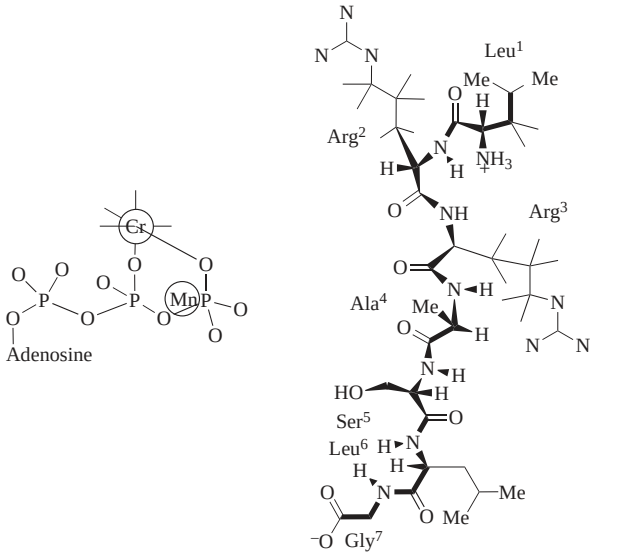

Figure 5 Coil conformation of the enzyme-bound heptapeptide substrate LRRASLG at the active site of cAMP-dependent protein kinase, based on NMR-determined distances from Cr^{3+}ATP and Mn^{2+}[63,66] (modified from reference 63)

substrates have been found at the active sites of many other enzymes including glyoxalase I, glutathione reductase, and each of the four classes of proteases. Such extended substrate conformations would permit greater interaction with the enzyme thereby contributing to enzyme specificity.[63]

^{31}P NMR studies of the regulatory dimer (R_2) revealed broad resonances assigned to tightly bound, highly immobilized cAMP and narrow resonances assigned to covalent, mobile phosphoserine signals. One of these phosphoserine signals was removed by the catalytic subunit and an ADP regenerating system, confirming that R_2 is a substrate of the catalytic subunit.[25] Accordingly, in R_2C_2 the access of peptide substrates to the active site was blocked while metal–ATP was freely accessible. On adding cAMP, which dissociated R_2C_2, peptide binding at the active site was detected by paramagnetic effects of Mn^{2+} on the relaxation rates of the peptide protons.[61] Thus the regulatory dimer is a tightly bound substrate which inhibits the catalytic subunit by occluding the peptide or protein-binding site but not the ATP-binding site.

8 γ-SUBSTITUTION: ADENYLATE KINASE

This small and ubiquitous enzyme which catalyzes the reaction

$$\mathrm{MgATP} + \mathrm{AMP} \rightleftharpoons \mathrm{MgADP} + \mathrm{ADP} \qquad (7)$$

has been studied by X-ray[69,70] and NMR.[10,13,17,71,72] An early NMR study of the ATP complex of adenylate kinase detected a NOE from the C-2 proton of His-36 to the adenine H-2 resonance of MgATP,[71] placing the binding site of ATP near two regions of amino acid sequence which were homologous with those found on numerous ATP-binding enzymes.[73] This proximity was confirmed by a distance of 12.9 ± 1.0 Å from Cr^{3+} of Cr^{3+}ATP to this histidine proton of the enzyme.[17] A synthetic peptide based on residues 1–45 of adenylate kinase which contained the first of these homologies GX_4GKGT was found to bind MgATP with an affinity and in a conformation very similar to those found on the complete enzyme.[17] The solution structure of this peptide, determined by 2D proton NMR methods,[13] revealed two transient helical regions and three stretches of β-strand. A residue-by-residue comparison with the corresponding region in the X-ray structure of the enzyme showed the retention of 42% of the secondary structure in the peptide. The binding of MgATP resulted in conformational changes in the peptide backbone with an overall decrease in its structural content, suggestive of the effects on the enzyme of binding MnATP.[69] The conformation of enzyme-bound AMP was found to be high-*anti*-3′-*endo*-2′-*exo* both by intramolecular NOEs and by intersubstrate distances from enzyme-bound Cr^{3+}AMPPCP. This high energy conformation was consistent with the high specificity of adenylate kinase for AMP.[72] The intersubstrate distances on the enzyme also yielded a reaction coordinate distance of ≥ 3 Å from the γ-phosphorus of Cr^{3+}AMPPCP to the entering phosphate oxygen of AMP, consistent with an associative mechanism of phosphoryl transfer.[72] The orientation of MgATP on the peptide[17] differs from that found on the complete enzyme.[10,70] This is not surprising since other portions of the binding site are not present in the peptide. The backbone NMR assignments of adenylate kinase, the solution secondary structure, and the binding site for the bisubstrate analog AP_5–A have been reported[10] and they generally agree with the crystal structure.[70]

9 γ-SUBSTITUTION: F1 ATPASE, ACTIVE SITE PEPTIDE

The synthesis of ATP from ADP and inorganic phosphate (Pi) in oxidative phosphorylation utilizes the enzyme F1 ATPase, which is driven in reverse by a proton electrochemical gradient generated by respiratory electron transport. The enzyme is huge (RMM 371 000) with an $\alpha_3\beta_3\gamma\delta\epsilon$ composition of subunits which are symmetrically arranged, as found by X-ray diffraction at 0.36 nm resolution.[74] As found by chemical modification and mutagenesis, the active sites for ATP hydrolysis and formation reside on each of the three β-subunits.[75] F1 ATPase shows two regions of sequence homology with other ATP or GTP binding enzymes adenylate kinase, *ras*, *rec*A, and myosin.[73] This homology and the location of the ATP-binding site on adenylate kinase by the NMR study of an appropriate peptide[17] led to the proposal that the active site of F1 ATPase corresponded to that of adenylate kinase.[76] Accordingly, a 50-residue peptide, PP-50, based on residues 141–190 of the β-subunit of F1 ATPase which contained the homologous sequence GX_4GKT was synthesized and was found to bind ATP tightly.[31] The solution structure of PP-50 was determined by 2D NMR at pH 4.0 which improved the solubility and retained the tight binding of ATP.[15] The structure was found to be labile, containing two transient β-turns and some transient tertiary structure detected by remote NOEs. The peptide–ATP complex was not soluble enough for study by NMR, but CD studies showed that ATP binding increased the structure of the peptide.[15] Titration of PP-50 with trifluoroethanol (TFE) increased the helix content

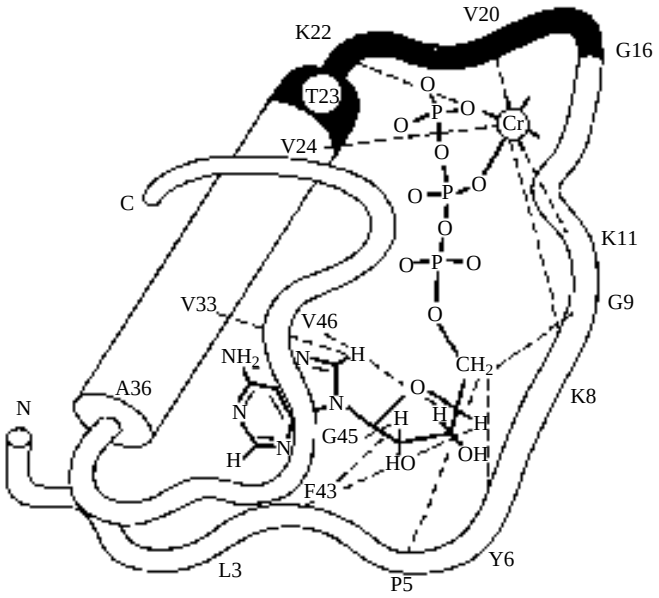

Figure 6 Diagram of the secondary structure and ATP-binding site of PP-50, a peptide based on residues 141–190 of F1 ATPase. Broken lines indicate proximities based on intermolecular ROEs and on paramagnetic effects of Cr^{3+}ATP on TOCSY spectra.[16] Shaded area shows GX_4GKT homology sequence

to 29% with an end point at 23.5% TFE, as detected by CD spectroscopy. TFE also increased the affinity of PP-50 for ATP to a value (K_D = 7.3 μM) approaching that of the intact enzyme (K_D = 1.2 μM) and increased the solubility of the PP-50–ATP complex, permitting the determination of its solution structure by 2D ^{1}H NMR.[16] The structure of PP-50 in 25% TFE consists of a coil (residues 1–8), an extended strand (residues 9–12), a loop (residues 13–22) containing the GX_4GKT homologous sequence (residues 16–23), a long α-helix (residues 23–36), a β-turn (residues 38–41) and a coil (residues 42–50) (Figure 6). No change in the structure of PP-50 occurred on the binding of ATP or MgATP, as detected by NOESY and CD spectra. NOEs and rotating frame Overhauser effects (ROEs) indicated an *anti* conformation for bound ATP. Intermolecular ROEs showed the adenine ribose portion to bind near the hydrophobic residues L3, P5, Y6, G9, V33, F43, G45, and V46. Paramagnetic effects of β,γ-bidentate Cr^{3+}ATP on TOCSY spectra of PP-50 showed the metal–triphosphate moiety to bind near K22 of the GX_4GKT loop, as found on adenylate kinase[17,70] and on an active site peptide based on adenylate kinase.[13,17] A hydrophobic environment for bound MgATP on F1, as found on PP-50,[16] would thermodynamically favor its formation from MgADP and Pi. The subsequent release of ATP from F1 could be driven conformationally by the discharge of the proton electrochemical gradient.[16,76] These structural findings are consisent with kinetic studies of site-directed mutants of F1 ATPase.[77]

10 RELATED ARTICLES

Biological Macromolecules: NMR Parameters; Fourier Transform Spectroscopy; Half-Filter Experiments: Proton–Carbon-13; Heteronuclear Shift Correlation Spectroscopy; Paramagnetic Relaxation in Solution; Peptide and Protein Secondary Structural Elements; Phosphorus-31 NMR; Protein Structures: Relaxation Matrix Refinement; Proteins and Protein Fragments: Folding; Relaxation Effects of Chemical Exchange; ROESY; Structures of Larger Proteins, Protein-Ligand, and Protein-DNA Complexes by Multi-Dimensional Heteronuclear NMR.

11 REFERENCES

1. M. Cohn, *J. Cell. Comp. Physiol.*, 1959, Suppl. 1, 17.
2. D. J. Weber, S. K. Bhatnagar, L. C. Bullions, M. J. Bessman, and A. S. Mildvan, *J. Biol. Chem.*, 1992, **267**, 16 939.
3. M. Cohn and T. R. Hughes, Jr., *J. Biol. Chem.*, 1960, **235**, 3250.
4. R. K. Gupta and W. D. Yushok, *Proc. Natl. Acad. Sci. U.S.A.*, 1980, **77**, 2487.
5. H. Sternlicht, R. G. Shulman, and E. W. Anderson, *J. Chem. Phys.*, 1965, **43**, 3133.
6. A. S. Mildvan, D. L. Sloan, C. H. Fung, R. K. Gupta, and E. Melamud, *J. Biol. Chem.*, 1976, **251**, 2431.
7. R. K. Gupta, C. H. Fung, and A. S. Mildvan, *J. Biol. Chem.*, 1976, **251**, 2421.
8. T. Nowak and A. S. Mildvan, *Biochemistry*, 1972, **11**, 2813.
9. A. S. Mildvan, J. S. Leigh, and M. Cohn, *Biochemistry*, 1967, **6**, 1805.
10. I.-J. L. Byeon, H. Yan, A. S. Edison, E. S. Mooberry, F. Abildgaard, J. L. Markley, and M. D. Tsai, *Biochemistry*, 1993, **32**, 12 508.
11. C. Abeygunawardana, D. J. Weber, D. N. Frick, M. J. Bessman, and A. S. Mildvan, *Biochemistry*, 1993, **32**, 13 071.
12. D. J. Weber, C. Abeygunawardana, M. J. Bessman, and A. S. Mildvan, *Biochemistry*, 1993, **32**, 13 081.
13. D. C. Fry, D. M. Byler, H. Susi, E. M. Brown, S. A. Kuby, and A. S. Mildvan, *Biochemistry*, 1988, **27**, 3588.
14. G. P. Mullen, J. B. Vaughn, Jr., and A. S. Mildvan, *Arch. Biochem. Biophys.*, 1993, **301**, 174.
15. W.-J. Chuang, C. Abeygunawardana, P. L. Pedersen, and A. S. Mildvan, *Biochemistry*, 1992, **31**, 7915.
16. W.-J. Chuang, C. Abeygunawardana, A. G. Gittis, P. L. Pedersen, and A. S. Mildvan, *Arch. Biochem. Biophys.*, 1995, **319**, 110.
17. D. C. Fry, S. A. Kuby, and A. S. Mildvan, *Biochemistry*, 1985, **24**, 4680.
18. A. Kuliopulos, E. M. Westbrook, P. Talalay, and A. S. Mildvan, *Biochemistry*, 1987, **26**, 3927.
19. D. J. Weber, A. G. Gittis, G. P. Mullen, C. Abeygunawardana, E. E. Lattman, and A. S. Mildvan, *Proteins: Struct. Funct. Genet.*, 1992, **13**, 275.
20. A. S. Mildvan, and R. K. Gupta, *Methods Enzymol.*, 1978, **49G**, 322.
21. A. S. Mildvan, J. Granot, G. M. Smith, and M. N. Liebman, *Adv. Inorg. Biochem.*, 1980, **2**, 211.
22. J. H. Noggle and R. E. Schirmer, in *The Nuclear Overhauser Effect*, Academic Press, New York, 1971, p. 41.
23. P. Balaram, A. A. Bothner-By, and E. Breslow, *J. Am. Chem. Soc.*, 1972, **94**, 4017.
24. G. Wagner and K. Wüthrich, *J. Magn. Reson.*, 1975, **33**, 675.
25. A. S. Mildvan, P. R. Rosevear, J. Granot, C. O'Brian, H. N. Bramson, and E. T. Kaiser, *Methods Enzymol.*, 1983, **99**, 93.
26. P. R. Rosevear, H. N. Bramson, C. O'Brian, E. T. Kaiser, and A. S. Mildvan, *Biochemistry*, 1983, **22**, 3439.

27. P. R. Rosevear and A. S. Mildvan, *Methods Enzymol.*, 1989, **177**, 333.
28. N. Murali, G. K. Jarori, S. B. Landy, and B. D. Nageswara Rao, *Biochemistry*, 1993, **32**, 12 941.
29. T. J. Swift and R. E. Connick, *J. Chem. Phys.*, 1962, **37**, 307.
30. D. J. Weber, E. H. Serpersu, A. G. Gittis, E. E. Lattman, and A. S. Mildvan, *Proteins: Struct. Funct. Genet.*, 1993, **17**, 20.
31. D. N. Garboczi, P. Shenbagamurthi, W. Kirk, J. Hullihen, and P. L. Pedersen, *J. Biol. Chem.*, 1988, **263**, 812.
32. M. Cohn and T. Hughes, Jr., *J. Biol. Chem.*, 1962, **237**, 176.
33. R. K. Gupta, and A. S. Mildvan, *J. Biol. Chem.*, 1977, **252**, 5967.
34. S. L. Huang and M.-D. Tsai, *Biochemistry*, 1982, **21**, 951.
35. D. L. Sloan, L. A. Loeb, A. S. Mildvan, and R. Feldmann, *J. Biol. Chem.*, 1975, **250**, 8913.
36. D. L. Sloan and A. S. Mildvan, *J. Biol. Chem.*, 1976, **251**, 2412.
37. W. W. Cleland and A. S. Mildvan, *Adv. Inorg. Biochem.*, 1979, **1**, 163.
38. E. K. Jaffe and M. Cohn, *J. Biol. Chem.*, 1979, **254**, 10 839.
39. A. S. Mildvan, *Philos. Trans. R. Soc. London, Ser. B*, 1981, **293**, 65.
40. A. S. Mildvan, *Adv. Enzymol.*, 1979, **49**, 103.
41. A. S. Mildvan and D. C. Fry, *Adv. Enzymol.*, 1987, **59**, 241.
42. A. Kornberg and T. A. Baker, *DNA Replication*, 2nd edn., W. H. Freeman, New York, 1992, p. 113.
43. D. L. Ollis, P. Brick, R. Hamlin, N. G. Xuong, and T. A. Steitz, *Nature (London)*, 1985, **313**, 762.
44. T. A. Steitz, L. Beese, P. S. Freemont, J. M. Friedman, and M. R. Sanderson, *Cold Spring Harbor Symp. Quant. Biol.*, 1987, **LII**, 465.
45. L. J. Ferrin and A. S. Mildvan, *Biochemistry*, 1985, **24**, 6904.
46. L. J. Ferrin and A. S. Mildvan, *Biochemistry*, 1986, **25**, 5131.
47. G. P. Mullen, J. B. Vaughn, Jr., P. Shenbagamurthi, and A. S. Mildvan, *Biochem. Pharm.*, 1990, **40**, 69.
48. P. M. J. Burgers and F. Eckstein, *J. Biol. Chem.*, 1979, **254**, 6889.
49. C. M. Joyce, D. L. Ollis, J. Rush, T. A. Steitz, W. H. Konigsberg, and N. D. F. Grindley, *UCLA Symp. Mol. Cell. Biol.*, 1985, **32**, 197.
50. G. P. Mullen, E. H. Serpersu, L. J. Ferrin, L. A. Loeb, and A. S. Mildvan, *J. Biol. Chem.*, 1990, **265**, 14 327.
51. G. P. Mullen, P. Shenbagamurthi, and A. S. Mildvan, *J. Biol. Chem.*, 1989, **264**, 19 637.
52. A. S. Mildvan, P. Stein, R. Koren, and B. Bean, *Frontiers of Biological Energetics*, L. Dutton, J. S. Leigh, and A. Scarpa, eds. Academic Press, New York, 1978, Vol. I, p. 769.
53. D. N. Frick, D. J. Weber, J. R. Gillespie, M. J. Bessman, and A. S. Mildvan, *J. Biol. Chem.*, 1994, **269**, 1794.
54. H. Maki and M. Sekiguchi, *Nature*, 1992, **355**, 273.
55. J.-Y. Mo, H. Maki, and M. Sekiguchi, *Proc. Natl. Acad. Sci. U.S.A.*, 1992, **89**, 11 021.
56. C. Yanofsky, E. C. Cox, and V. Horn, *Proc. Natl. Acad. Sci. U.S.A.*, 1966, **55**, 274.
57. L. C. Bullions, Ph.D. Dissertation, The Johns Hopkins University, Baltimore, MD, 1993, pp. 45, 111.
58. D. L. DiStefano and A. J. Wand, *Biochemistry*, 1987, **26**, 7272.
59. G. A. Robison, R. W. Butcher, and E. W. Sutherland, *Annu. Rev. Biochem.*, 1968, **37**, 149.
60. E. G. Krebs and J. A. Beavo, *Annu. Rev. Biochem.*, 1979, **48**, 923.
61. J. Granot, A. S. Mildvan, K. Hiyama, H. Kondo, and E. T. Kaiser, *J. Biol. Chem.*, 1980, **255**, 4569.
62. R.N. Armstrong, H. Kondo, J. Granot, E. T. Kaiser, and A. S. Mildvan, *Biochemistry*, 1979, **18**, 1230.
63. P. R. Rosevear, D. C. Fry, A. S. Mildvan, M. Doughty, C. O'Brian, and E. T. Kaiser, *Biochemistry*, 1984, **23**, 3161.
64. J. Granot, A. S. Mildvan, H. N. Bramson, and E. T. Kaiser, *Biochemistry*, 1980, **19**, 3537.
65. J. Granot, H. Kondo, R. N. Armstrong, A. S. Mildvan, and E. T. Kaiser, *Biochemistry*, 1979, **18**, 2339.
66. H. N. Bramson, N. E. Thomas, W. T. Miller, D. C. Fry, A. S. Mildvan, and E. T. Kaiser, *Biochemistry*, 1987, **26**, 4466.
67. D. R. Knighton, J. Zheng, L. F. Ten Eyck, V. A. Ashford, N. H. Xuong, S. S. Taylor, and J. M. Sowadski, *Science*, 1991, **253**, 407.
68. D. R. Knighton, J. Zheng, L. F. Ten Eyck, N. H. Xuong, S. S. Taylor and J. M. Sowadski, *Science*, 1991, **253**, 414.
69. E. F. Pai, W. Sachsenheimer, R. H. Schirmer, and G. E. Schulz, *J. Mol. Biol.*, 1977, **114**, 37.
70. C. W. Müller and G. E. Schulz, *J. Mol. Biol.*, 1992, **224**, 159.
71. G. M. Smith and A. S. Mildvan, *Biochemistry* 1982, **21**, 6119.
72. D. C. Fry, S. A. Kuby, and A. S. Mildvan, *Biochemistry*, 1987, **26**, 1645.
73. J. E. Walker, M. Saraste, M. J. Runswick, and N. J. Gay, *EMBO J.*, 1982, **1**, 945.
74. P. L. Pedersen and L. M. Amzel, *J. Biol. Chem.*, 1993, **268**, 9937.
75. H. S. Penefsky and R. L. Cross, *Adv. Enzymol.*, 1991, **64**, 173.
76. D. C. Fry, S. A. Kuby, and A. S. Mildvan, *Proc. Natl. Acad. Sci. U.S.A.*, 1986, **83**, 907.
77. A. E. Senior and M. K. Al-Shawi, *J. Biol. Chem.*, 1992, **267**, 21 471.

Biographical Sketch

Albert S. Mildvan. *b* 1932. A.B., Chemistry, University of Pennsylvania, M.D., Johns Hopkins School of Medicine. Postdoctoral work at NIH, Cambridge University, UK, and University of Pennsylvania, 1958–1965. Faculty, University of Pennsylvania and staff member, Institute for Cancer Research Fox Chase, 1965–1981. Professor of Biological Chemistry/Chemistry, Johns Hopkins School of Medicine–present. Approx. number of publications, 220. Current research specialties: application of kinetic and magnetic resonance methods to studies of mechanism of enzyme action.

Heme Peroxidases

James D. Satterlee
Washington State University, Pullman, WA, USA

1	Introduction	1
2	Peroxidase Chemistry	1
3	Proton Assignments	3
4	Mutant Enzymes	5
5	Nuclei Other than the Proton	6
6	Related Articles	6
7	References	6

1 INTRODUCTION

Peroxidases form a class of enzymes, an extensive subgroup of which consists of heme proteins. Out of the entire peroxidase superfamily, it is the heme peroxidases which have been most thoroughly studied by NMR, and they will be the focus of this article (Figure 1). Increasing attention has been devoted to NMR studies of heme peroxidases over the past decade, and no attempt will be made here to present a comprehensive review. Rather, selected examples, illustrative of specific problems that have been amenable to NMR study, will be presented. The majority of these examples will focus on proton NMR studies of horseradish peroxidase (HRP) and yeast cytochrome-*c* peroxidase (CcP), because these two proteins have been studied in the greatest detail to date. For NMR spectroscopists to appreciate both the problems and achievements facing those who work with peroxidases, a brief introduction to peroxidases, their chemistry, their structure and the effects of paramagnetism (characteristic of heme peroxidases) upon NMR spectra will be presented with appropriate references for those interested in details.

Peroxidases are widespread in nature,[1–5] catalyzing the hydrogen peroxide oxidation of such varied substrates as simple organic and inorganic compounds, lignin, coordination compounds, amino acids, halide ions, pseudohalide ions and ferrocytochrome *c*. The need for peroxidases apparently correlates with the common cellular production of hydrogen peroxide, a cytotoxic agent. In view of this it is not unusual to find peroxidases in many organisms, including animals, yeasts, fungi, plants, and bacteria. Initial NMR studies have emphasized HRP and CcP, probably due to the relative ease of isolating these two enzymes, their stability in solution, and, ultimately, the commercial availability of high purity preparations of HRP. All of the heme peroxidases so far identified possess molecular masses in the range of 30–150 kDa, making them a challenge for high resolution NMR spectroscopists.

2 PEROXIDASE CHEMISTRY

The general peroxidase mechanism was first formulated by Chance,[6] and is shown below:

$$\text{peroxidase} + H_2O_2 \rightarrow \text{peroxidase I} \qquad (1)$$

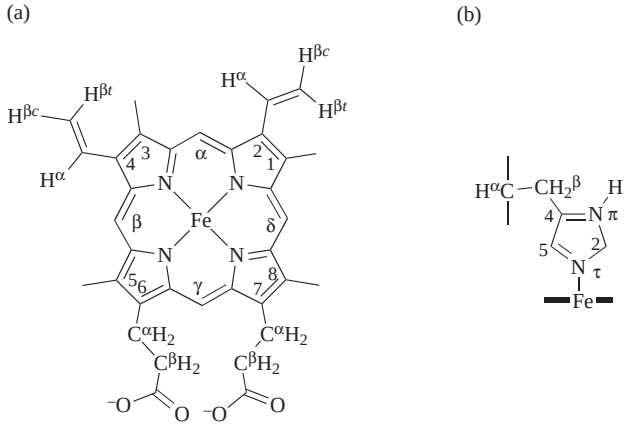

Figure 1 (a) Heme b structure and (b) coordination to the proximal histidine as it occurs in heme peroxidases. The widely used modified Fischer labeling scheme is used in (a). Several different labeling schemes are in use for histidine rings; shown in (b) is the IUPAC preferred scheme. In (b) the heme is shown edge-on as a heavy line. Many heme peroxidases contain heme b (e.g. horseradish peroxidase, cytochrome-*c* peroxidase, ligin peroxidase) or a simple derivative of heme b (e.g. lactoperoxidase, myeloperoxidase) at the enzyme active site

$$\text{peroxidase I} + AH_2 \rightarrow \text{peroxidase II} \qquad (2)$$

$$\text{peroxidase II} + AH_2 \rightarrow \text{peroxidase} \qquad (3)$$

Briefly, it can be described as follows. In equation (1) the resting state enzyme, which for HRP and CcP is a high spin ferriheme protein (Figures 1 and 2), reacts with hydrogen peroxide to form the initial oxidized enzyme intermediate, variously termed compound I or compound ES, depending upon the peroxidase. Compound I is oxidized two equivalents above the resting state enzyme. Equation (1), generating compound I, can also be achieved when the peroxidase is allowed to react with organic peroxy acids of the type ROOH in place of hydrogen peroxide. In equation (2), compound I is reduced by one equivalent when it oxidizes one molecule of its substrate, generally represented here by AH_2. The second enzyme intermediate generated in this step is called compound II, and is at an oxidation state elevated only one equivalent above the resting state enzyme. Finally, in equation (3), compound II is reduced to the resting state enzyme by oxidation of a second molecule of substrate.

Although equations (1)–(3) depict the general peroxidase enzymic cycle, the specific nature of the preferred substrate (AH_2) can vary from species to species. In particular, characterizing the interaction of peroxidases with their substrates is one of the problems that has recently attracted the attention of NMR spectroscopists. Other important problems addressed by early NMR studies included: (1) characterizing the heme active site; (2) making comprehensive proton assignments of hyperfine shifted resonances; (3) attempting proton assignments in the more crowded aromatic chemical shift region; (4) characterizing the enzyme intermediates, compound I and compound II; and (5) by these experiences defining the scope and limitations for modern NMR experiments on such medium-large sized paramagnetic macromolecules.

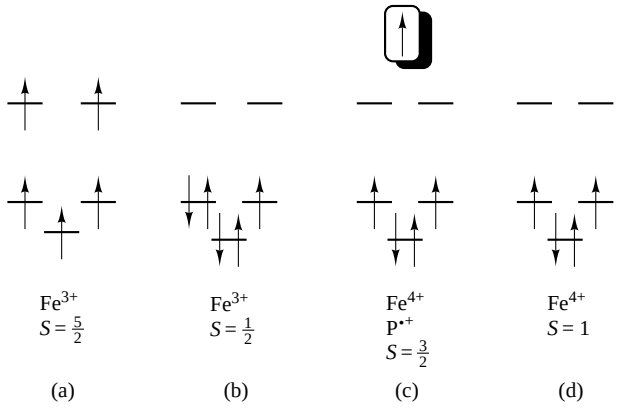

Figure 2 Peroxidase paramagnetism is demonstrated in this figure, which shows the electron configuration of heme iron ion d orbitals for various HRP and CcP intermediates. (a) Resting enzyme in the ferric high spin state. (b) Cyanide ligated, low spin enzyme derivative. (c) Compound I involves the Fe^{4+}=O heme plus a second oxidizing equivalent localized on the porphyrin in HRP and on Trp191 in CcP. (d) Compound II, with the Fe^{4+}=O heme

2.1 The Oxidized Enzyme Intermediates

How does a heme peroxidase store the oxidizing equivalents received during the initial hydrogen peroxide reaction step? This was one of the early questions facing peroxidase researchers, and a wide range of physical methods were applied to find the answer. In the case of HRP it is now generally accepted that HRP compound I consists of a ferryl heme iron ion (Fe^{4+}=O) and a porphyrin π cation radical[2,3] (Figure 2). In the case of CcP it is generally accepted that CcP compound I is a ferryl heme iron ion (Fe^{4+}=O) and a free radical resulting from the oxidation of Trp191, an amino acid adjacent to both the heme and the (proximal) heme-coordinating His175.[2,3]

For both HRP and CcP the second enzyme intermediate, compound II, is generally accepted as consisting of a ferryl heme iron ion (Fe^{4+}=O). However, at least in CcP there is evidence for the interconversion between two distinct compound II forms, that with the ferryl heme iron ion ($CcPII_F$) and that with a ferric heme and a free radical ($CcPII_R$) Other heme peroxidases exhibit similar characteristics for their individual oxidized intermediates, although the stability of peroxidase intermediates may vary widely.

Among the most intriguing properties of heme peroxidases is the comparatively stable heme iron +4 state of the oxidized intermediates. This is not a widely encountered formal oxidation state for iron, and it probably stimulated much of the early interest in these enzymes, raising such questions as how the enzyme structure stabilizes such a high oxidation state.

2.2 Effect of Heme Paramagnetism on NMR Spectra

In the ferriheme resting state and the two oxidized enzyme intermediates [equations (1)–(3)], heme peroxidases are paramagnetic by virtue of unpaired electrons in the heme iron ion d orbitals. A simple picture of the commonly encountered heme iron ion spin and oxidation states is given in Figure 2. Including the cyanide-ligated resting state enzyme, the commonly studied forms of peroxidases include three low spin derivatives and one high spin (the native resting state enzyme) form, all of which are paramagnetic. This further emphasizes the need to consider briefly paramagnetic effects on NMR spectra.

Molecular paramagnetism due to unpaired electron density formally associated with the heme iron ion produces dramatic effects in NMR spectra as a result of the large local magnetic fields associated with these unpaired electrons.[7–11] Unusually large, highly temperature dependent observed resonance shifts are found in paramagnetic molecules (Figure 3), and highly enhanced nuclear relaxation rates also occur as a consequence of nuclear magnetic moments coupling to the large unpaired-electron magnetic moments. The proton spectra shown for CcP compound I [Figure 3(a)], CcP [resting state, Figure 3(b)], and CcPCN [cyanide ligated, Figure 3(c)] illustrate the large shifts and linewidths that can occur. Electron–nuclear interactions and paramagnetic relaxation are treated elsewhere in this Encyclopedia, and it suffices here briefly to review the basic concepts as they are employed in interpreting NMR spectra of heme peroxidases.

2.2.1 The Hyperfine Shift[7–11]

The observed resonance shift (δ_{obs}) for a given molecule in a paramagnetic peroxidase is the sum of two parts: the shift it would have in a corresponding purely diamagnetic form of the same peroxidase (δ_{dia}) and the shift caused by the unpaired electrons (δ_{para}) [equation (4)]. The paramagnetic

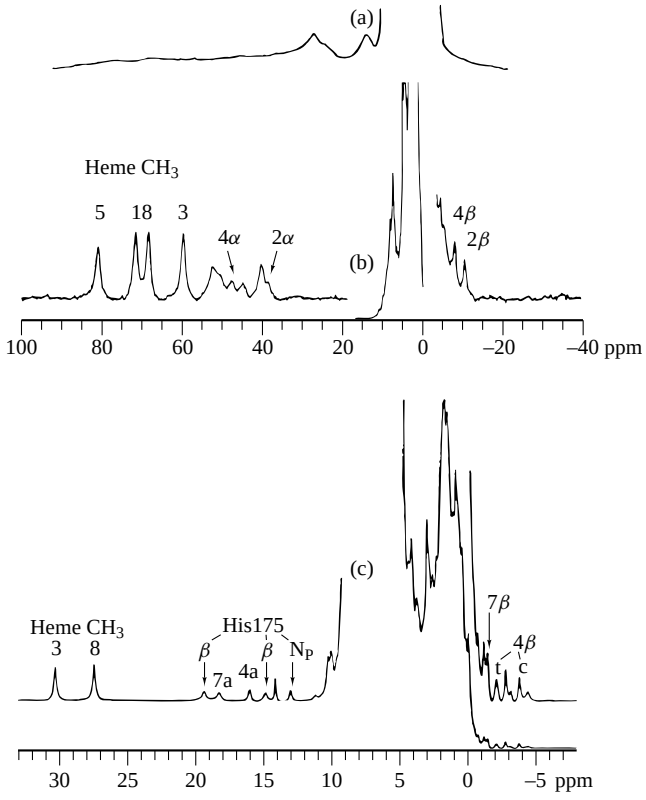

Figure 3 Proton NMR spectra of various forms of CcP: (a) Compound I, (b) resting state, and (c) the cyanide ligated enzyme (CcPCN). (a) and (b) were taken at 360 MHz in D_2O–buffer solutions, and share the same chemical shift scale. (c) was taken at 500 MHz in D_2O–buffer solution. Note the different chemical shift scales

shift (δ_{para}) has been referred to as the isotropic, or hyperfine shift and contains two terms, the contact shift (δ_{con}) and the pseudocontact, or dipolar shift (δ_{dip}) [equation (5)]. The contact shift is a consequence of metal–ligand covalency that results in delocalization of unpaired spin density from the heme iron ion onto its immediate ligands. This typically occurs by σ and/or π bonding. Previous work has shown that the extent of the contact shift is attenuated by the number of intervening bonds in the case of σ delocalization, whereas for π-type delocalization a significant effect may be found throughout the extent of the continuous π-bond network.

$$\delta_{obs} = \delta_{dia} + \delta_{para} \quad (4)$$

$$\delta_{para} = \delta_{con} + \delta_{dip} \quad (5)$$

The dipolar shift is a through-space interaction between the unpaired electron magnetic moments and the nuclear magnetic moments. It is distance dependent, falling off in intensity with the inverse third power of the direct distance between the unpaired electrons and the nucleus. In the highly delocalized heme iron ion ligation structure of peroxidase active sites (see Figure 1) there can be both iron centered dipolar shifts and ligand centered dipolar shifts, the latter deriving from delocalized unpaired electron spin density. The ligand centered dipolar shifts are typically the smaller of the two dipolar shifts. Detailed descriptions of the hyperfine shift equations have been presented.[7–11]

2.2.2 Paramagnetic Relaxation Effects

Electron paramagnetic moments can also provide an efficient relaxation pathway for nuclear magnetic moments, thereby enhancing nuclear relaxation rates. Just as there are contact and dipolar (pseudocontact) contributions to the observed shift there are corresponding contributions to nuclear relaxation.[7–11] Nuclei exhibiting strongly hyperfine shifted resonances also display unusually short longitudinal and transverse relaxation times. For paramagnetic proteins as large as the peroxidases, recovery of the nuclear magnetization of strongly hyperfine shifted resonances from inversion or saturation experiments is not characterized by a single exponential, thereby complicating interpretation of the term 'T_1' in these cases.[11] This is illustrated by the semilogarithmic plot of fractional magnetization recovery for nonselectively inverted CcP resonances shown in Figure 4. In the absence of cross relaxation, or spin diffusion, such a plot would be linear.[11–13] Nonlinearity in graphs like this emphasizes the multiple exponential relaxation behavior, which is exacerbated by increasing paramagnetic protein size and/or increasing the spectrometer field strength.[11–13]

2.2.3 Curie Spin Relaxation

Another phenomenon that affects the observability of hyperfine shifted resonances in large paramagnetic proteins such as peroxidases is the so-called Curie spin relaxation.[8,14,15] It is the result of coupling the rotational angular momentum of a protein to its time independent paramagnetic moment. The effect is one of 'anomalous' line broadening, indicating that it results in specific enhancement of nuclear transverse relaxation, and it increases as the second power of the magnetic field strength. The result is that larger proteins with larger paramagnetic moments (i.e. greater numbers of unpaired electrons) can exhibit severe line broadening, and it is common that such proteins may actually experience decreased resolution at higher fields.

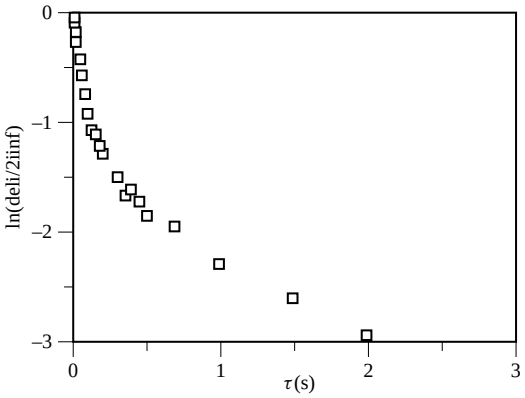

Figure 4 The result of nonselective inversion recovery experiments for the heme 8-CH_3 resonance of CcPCN plotted semilogarithmically. The fractional recovered magnetization intensity is plotted against the interpulse delay time (τ, in the sequence $180-\tau-90-$acq). Nonlinear behavior indicates that relaxation is not governed by a single exponential process, but involves significant spin diffusion

3 PROTON ASSIGNMENTS

3.1 Earliest Peroxidase Studies

The earliest reports of peroxidase NMR spectra focused on HRP and turnip peroxidases.[16–21] These studies provided spectra showing both strongly hyperfine shifted proton resonances and resonances in the broad overlapping envelope of protons between approximately −2 to 11 ppm. In this and other work reported prior to 1980, proton NMR was used to study processes involving the heme active site, primarily through monitoring hyperfine shifted resonances. These processes included pH dependence,[16–19] ligand binding,[16,18] formation and identification of the enzyme intermediates, compound I and compound II,[20] and calcium ion binding.[21]

Although illustrating the applicability of high-resolution NMR for studying fairly large (by NMR standards) paramagnetic proteins with large resonance linewidths, all of these early studies suffered from lack of specific resonance assignments. In part this was a result of the fact that chemical shift correlations, which are such helpful starting points for making resonance assignments in diamagnetic molecules, are not valid for strongly hyperfine shifted resonances. Also, at the time, few model systems had been developed that could provide any rationale for proposed assignments.

3.2 Definitive Proton Assignment Methods

The first unambiguous proton assignments were reported for resting state HRP, reduced HRP and HRPCN.[22–24] A single

proton belonging to the $N^{\pi}H$ of the heme-coordinating (see Figure 1) proximal histidine in each form was assigned. The results established the state of proximal histidine protonation for these various enzyme forms. This information was of functional importance for the reason that in the case of low spin HRPCN it indicated the validity of the idea that the enzyme stabilizes the low spin, oxidized intermediates by deprotonation of this histidine to form a histidinate ligand.

From such modest beginnings, many more specific assignments of hyperfine shifted proton resonances for CcP, HRP, lignin peroxidase, and, to a more limited extent, *Coprinus* peroxidase have been produced using a variety of techniques, including: (1) incorporation of specifically deuterated hemes,[25–29] (2) one-dimensional NOE experiments,[11,30,31] (3) two-dimensional spectroscopy,[11,32–37] and (4) deuterium NMR.[29] Particularly impressive are the NOE-based assignments made in such large enzymes as lactoperoxidase-CN (mass 78 kDa)[38] and myeloperoxidase-CN (mass ~150 kDa).[39] Among the many conclusions that were drawn from these studies, perhaps the most important is the fact that paramagnetism subverts spin diffusion and makes it possible for NOE experiments to be successful on very large proteins, for which NOE experiments would not be successful if they were diamagnetic.

Two other conclusions of note concerning techniques for making assignments in peroxidases have been published. One concerns the use of NOE rise curves for deriving internuclear distances.[40] This work showed that NOE rise curves, such as that shown in Figure 5 for HRPCN are only linear over the initial 1–5 ms of the mixing period, and, consequently, only the slope in that region quantitatively relates to internuclear distances. Figure 5 shows that NOEs achieve maximum intensities at ~10–20 ms for strongly hyperfine shifted resonances in peroxidases, which stresses the short time intervals inherent in work with paramagnetic peroxidases. A second pair of studies concerns the utility of COSY-type two-dimensional experiments as tools for making hyperfine resonance assignments in peroxidases.[41,42] The conclusion was reached that COSY displays complications such that cross peaks may be caused by sources other than the coherence transfer caused by scalar coupling. In particular it was shown that for two scalar coupled spins the cross correlation between internuclear dipole–dipole relaxation and the Curie spin relaxation is significant and often detected in COSY cross peaks.

3.3 Proton NMR Characterization of Oxidized Enzyme Intermediates

HRP compound I stores its oxidizing capacity centrally at the heme moiety as a porphyrin π cation radical/heme ferryl (Fe^{4+}=O) ion. This intermediate yields a comparatively rich proton NMR spectrum compared with HRP compound II, CcP compound I (see Figure 3), and CcP compound II, all of whose proton spectra are similarly composed of hard-to-interpret broad features[20,43,44] Although original NMR data were interpreted as indicating that a high spin Fe^{4+} heme was present in HRP compound I, subsequent studies, including model studies of iron porphyrins, clearly established the low spin, ferryl heme that is now accepted as the compound I intermediate structure.

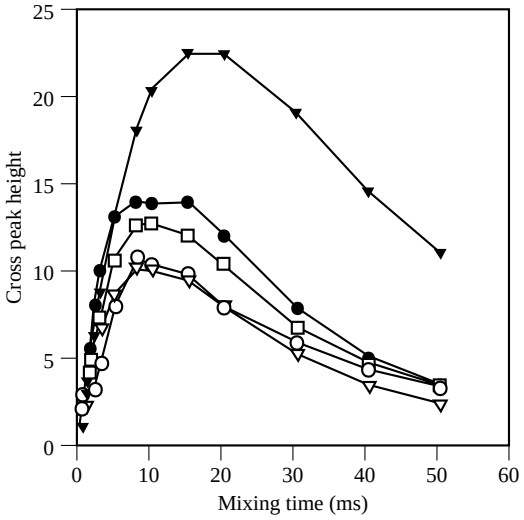

Figure 5 NOESY cross peak intensity versus mixing time for strongly coupled (geminal) proton pairs in HRPCN: $7H^{\alpha}-7H^{\alpha'}$ (▽); $4H^{\beta c}-4H^{\beta t}$ (▼); His170 $C^{\beta}H$-$C^{\beta}H'$ (□); Arg38 $C^{\beta}H-C^{\beta}H'$ (●); Arg38 $C^{\delta}H$-$C^{\delta}H'$ (○). The vertical scaling is identical for all data. The data are for the F_2 slices through the diagonal of the better resolved proton of the pair. (Reproduced by permission of the American Chemical Society from Sette et al.[40])

3.4 Peroxidase–Substrate Interactions

3.4.1 Horseradish Peroxidase

Peroxidases frequently catalyze oxidations of smaller substrates, typically organic or inorganic molecules. Among the many interesting questions left unresolved in this field are those concerning the mechanisms by which these oxidations take place. Thus, the thrust of much of the current research in this area is toward the elucidation of these mechanisms. Efforts have been made to understand the effects of substrate binding on the HRP and HRPCN hyperfine shift patterns and to locate the substrate binding site.[36,45,46] Proton NMR results and chemical data agree that substrates such as benzhydroxamic acid bind at the heme periphery in the vicinity of the heme 8-CH_3 group (see Figure 1).

3.4.2 Cytochrome-c Peroxidase from Saccharomyces cerevisiae

Although CcP is capable of catalyzing oxidations of small molecules, on the basis of kinetic discrimination the functional role of this molecule is presumed to be that of a catalyst for the H_2O_2 oxidation of mitochondrial ferrocytochrome *c*. Relative to equations (1)–(3), this means that following oxidation of CcP by H_2O_2 [equation (1)], CcP compound I oxidizes ferrocytochrome *c* [equation (2)]. This is thought to occur through the formation of a noncovalent electron transfer complex. In equation (3), CcP compound II, which results from the first electron transfer step [equation (2)], oxidizes another reduced cytochrome *c* molecule, again via the formation of an electron transfer complex. As a result of their size and solubility, CcP/cytochrome *c* complexes have emerged as a paradigm for the multitude of protein–protein electron transfer complexes.

Mixtures of Ccp, independently with both ferricytochrome *c* and ferrocytochrome *c*, spontaneously form noncovalent complexes in low ionic strength solutions. Proton NMR has been used to study these complexes because NMR spectroscopy, among all of the spectroscopic techniques applied to this problem so far, is uniquely the most sensitive to complex formation.[47–49] The capability to carry out these studies derives from the observation that ferricytochrome *c* hyperfine shifted proton resonances display significant complex-induced shifts (up to 2 ppm; Figure 6), although they are dependent upon the species of ferricytochrome *c*. The predominant complex stoichiometry found in solution is 1:1. Homonuclear proton NOESY two-dimensional spectra of these ∼47 kDa complexes have facilitated hyperfine shift assignments, particularly when both proteins were in low spin magnetic states (i.e. CcPCN/ferricytochrome *c*).

A fundamental dynamic property of these noncovalent complexes, the lifetime of a yeast iso-1 ferricytochrome *c* molecule bound to the peroxidase, was first directly measured by one-dimensional magnetization transfer experiments (Figure 7).[47] This series of measurements was facilitated by the observation of simultaneous sets of resonances for free (in solution) and CcP-bound forms of yeast iso-1 ferricytochrome *c* in 1:2 mixtures of CcP/iso-1 ferricytochrome *c* and CcPCN/iso-1 ferricytochrome *c* (see Figure 6). Lifetimes between 1 and 4 ms were found for yeast iso-1 ferricytochrome *c* bound to either CcP or CcPCN, depending upon temperature. Perhaps more importantly, the lifetimes were found to be concentration dependent, indicating that exchange of a molecule of iso-1 ferricytochrome *c* from CcP (or CcPCN) is not controlled by unimolecular dissociation. This has led to a reappraisal of the CcP mechanism of ferrocytochrome *c* oxidation.[50]

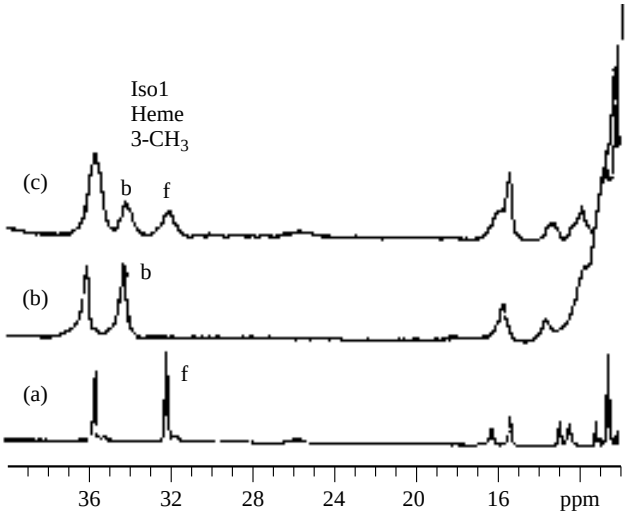

Figure 6 The high-frequency proton hyperfine shift region at 500 MHz of (a) yeast iso-1 ferricytochrome *c* alone in solution; (b) a 1:1 (mol/mol) mixture of CcP/yeast iso-1 ferricytochrome *c* in 10 mM potassium nitrate/D_2O; and (c) a 1:2 (mol/mol) mixture of CcP/yeast iso-1 ferricytochrome *c* in 10 mM potassium nitrate/D_2O. The iso-1 heme 8-methyl resonance appears at ∼36 ppm in (a), and the heme 3-CH_3 resonance appears at ∼32 ppm in (a). The linewidth increase and shift of the iso-1 resonances in (b) indicate noncovalent complex formation. In (c) the heme 3-CH_3 resonances of iso-1 free (in solution) and CcP bound are indicated by f and b, respectively. (Reproduced by permission of the American Chemical Society from Yi et al.[47])

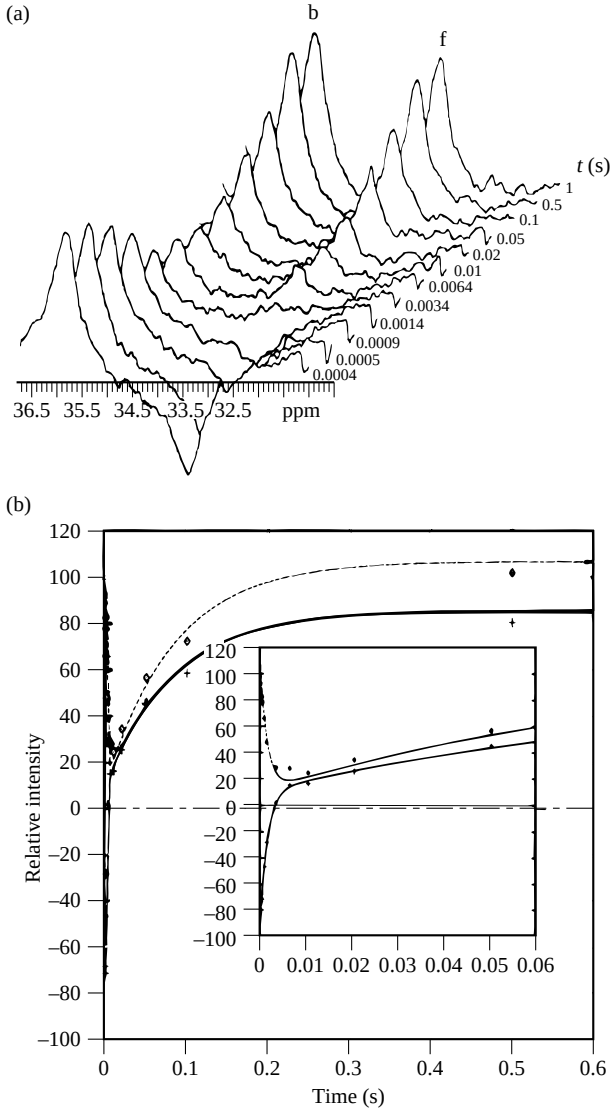

Figure 7 (a) Stack plot of a complete inversion transfer experiment for a 1:2 mixture of CcP (0.25 mM) and yeast iso-1 ferricytochrome *c* carried out at 5 °C. The free-form yeast iso-1 ferricytochrome *c* heme 3-CH_3 resonance was inverted. (b) Relaxation profile of this inversion transfer experiment plotted as peak intensity vs. magnetization transfer mixing time for both the inverted resonance [heme 3-CH_3(f)] and its exchange coupled partner [heme 3-CH_3(b)]. The dashed and solid lines are calculated from Monte Carlo/least squares fitting to the exchange modified Bloch equations. The inset depicts the behavior of both peaks at early exchange times where chemical exchange dominates the intensity. (Reproduced by permission of the American Chemical Society from Yi et al.[47])

4 MUTANT ENZYMES

Both HRP and CcP have been expressed in bacteria, and several mutants of each enzyme have been created for the purposes of NMR spectroscopy.[36,51] Both studies are similar in reporting that single mutations of amino acids

have dramatic effects upon the heme electronic structure and active site physical structure. What is emerging from these studies, and unpublished data from this laboratory, is a picture of HRP and CcP having carefully balanced active sites, perhaps primed specifically for the hydrogen peroxide reaction. Amino acid mutations, even those employing closely related amino acids (e.g. Glu → Gln), and even those more than one molecular layer removed from the heme site, have very significant effects on the peroxidase active site chemistry and spectroscopy.[51] Although mutations thus engender complicated spectral changes, making interpretations less than straightforward, it is anticipated that an increasing variety of peroxidase mutant enzymes will be studied by NMR in the future.

5 NUCLEI OTHER THAN THE PROTON

Although subject to less detailed interpretation than is possible for proton spectroscopy, there have been several reports of heteronuclear NMR studies of peroxidases. Typically these have involved isotope enrichment of a peroxidase heme ligand (e.g. CN^-, SCN^-). Detection of heme peroxidase derivatives using the heteronuclei ^{15}N,[52] ^{13}C,[53] ^{17}O,[54] ^{35}Cl,[55] ^{113}Cd,[56] and ^{2}H[29,57] has been reported.

Both HRP and CcP genes are currently being expressed in bacteria, and this renders stable isotope enrichment of both enzymes feasible. This, in turn, would allow application of higher-dimensional NMR experiments. To date, no reports of general or selective stable isotope enrichment of these enzymes has appeared. Still, examples of these enriched enzymes and the accompanying higher-dimensional NMR experiments are likely to appear in the near future. These experiments should provide expanded insights into the general applicability of modern NMR methods to paramagnetic proteins of this size.

6 RELATED ARTICLES

Amino Acids, Peptides and Proteins: Chemical Shifts; Biological Macromolecules; Chemical Exchange Effects on Spectra; COSY Two-Dimensional Experiments; Electron–Nuclear Hyperfine Interactions; Electron–Nuclear Multiple Resonance Spectroscopy; Enzymatic Transformations: Isotope Probes; Enzyme-Catalyzed Exchange: Magnetization Transfer Measurements; Hemoglobin; Iron—Sulfur Proteins; Mitochondrial Cytochrome c; Myoglobin; NOESY; Nonheme Iron Proteins; Nuclear Overhauser Effect; Protein Dynamics from NMR Relaxation; Relaxation Processes: Cross Correlation and Interference Terms.

7 REFERENCES

1. *Peroxidases in Chemistry and Biology*, eds. J. Everse, K. E. Everse, and M. B. Grisham, CRC Press, Boca Raton, 1991, Vols. I and II.
2. H. B. Dunford and J. S. Stillman, *Coord. Chem. Rev.*, 1976, **19**, 187.
3. H. Anni and T. Yonetani, in *Metal Ions in Biological Systems*, ed. H. Sigel and A. Sigel, Marcel Dekker, New York, 1992, Vol. 28, p. 219.
4. K. E. Hammel, in *Metal Ions in Biological Systems*, ed. H. Sigel and A. Sigel, Marcel Dekker, New York, 1992, Vol. 28, p. 41.
5. K. G. Welinder, *Curr. Opin. Struct. Biol.*, 1992, **2**, 388.
6. B. Chance, *Arch. Biochem. Biophys.*, 1949, **21**, 416.
7. *NMR in Paramagnetic Molecules*, eds. G. N. La Mar, W. D. Horrocks Jr., and R. H. Holm, Academic Press, New York, 1973.
8. J. D. Satterlee, *Annu. Rep. NMR Spectrosc.*, 1986, **17**, 79.
9. J. D. Satterlee, *Concepts Magn. Reson.*, 1990, **2**, 69, 119.
10. I. Bertini and C. Luchinat, *NMR of Paramagnetic Molecules in Biological Systems*, Benjamin/Cummings, Menlo Park, 1986.
11. G. N. La Mar, and J. S. de Ropp, in *Biological Magnetic Resonance*, ed. L. J. Berliner and J. Reuben, Plenum Press, New York, 1993, Vol. 12, p. 2.
12. J. Granot, *J. Magn. Res.*, 1982, **49**, 257.
13. A. Kalk and H. J. C. Berendsen, *J. Magn. Res.*, 1976, **24**, 343.
14. M. Gueron, *J. Magn. Res.*, 1975, **19**, 58.
15. A. J. Vega and D. Fiat, *Mol. Phys.*, 1976, **31**, 347.
16. R. J. P. Williams, P. E. Wright, G. Mazza, and J. R. Ricard, *Biochim. Biophys. Acta*, 1975, **412**, 127.
17. T. Iizuka, S. Ogawa, T. Inubushi, T. Yonezawa, and I. Morishima, *FEBS Lett.*, 1976, **64**, 156.
18. I. Morishima, S. Ogawa, T. Inubushi, T. Yonezawa, and T. Iizuka, *Biochemistry*, 1977, **16**, 5109.
19. I. Morishima, S. Ogawa, and T. Yonezawa, *Biochim. Biophys. Acta*, 1978, **537**, 293.
20. I. Morishima and S. Ogawa, *Biochemistry*, 1978, **17**, 4384
21. S. Ogawa, Y. Shiro, and I. Morishima, *Biochem. Biophys. Res. Commun.*, 1979, **90**, 674.
22. G. N. La Mar and J. S. de Ropp, *Biochem. Biophys. Res. Commun.*, 1979, **90**, 36.
23. J. S. de Ropp, V. Thanabal, and G. N. La Mar, *J. Am. Chem. Soc.*, 1985, **107**, 8268.
24. G. N. La Mar and J. S. de Ropp, *J. Am. Chem. Soc.*, 1982, **104**, 5203.
25. G. N. La Mar, J. S. de Ropp, K. M. Smith, and K. C. Langry, *J. Biol. Chem.*, 1980, **255**, 6646.
26. J. D. Satterlee, J. E. Erman, G. N. La Mar, K. M. Smith, and K. C. Langry, *Biochim. Biophys. Acta*, 1983, **743**, 246.
27. J. S. de Ropp, G. N. La Mar, K. M. Smith, and K. C. Langry, *J. Am. Chem. Soc.*, 1984, **106**, 4438.
28. J. D. Satterlee, J. E. Erman, G. N. La Mar, K. M. Smith, and K. C. Langry, *J. Am. Chem. Soc.*, 1983, **105**, 2099.
29. G. S. Lukat, K. R. Rodgers, M. N. Jabro, and H. M. Goff, *Biochemistry*, 1989, **28**, 3338.
30. V. Thanabal, J. S. de Ropp, and G. N. La Mar, *J. Am. Chem. Soc.*, 1988, **110**, 3027.
31. J. D. Satterlee, J. E. Erman, and J. S. de Ropp, *J. Biol. Chem.*, 1987, **262**, 11578.
32. J. S. de Ropp, L. P. Yu, and G. N. La Mar, *J. Biomol. NMR*, 1991, **1**, 175.
33. J. D. Satterlee and J. E. Erman, *Biochemistry*, 1991, **30**, 4398.
34. J. S. de Ropp, G. N. La Mar, H. Wariishi, and M. H. Gold, *J. Biol. Chem.*, 1991, **266**, 15 001.
35. L. Banci, I. Bertini, P. Turano, J. C. Ferrer, and A. G. Mauk, *Inorg. Chem.*, 1991, **30**, 4510.
36. N. C. Veitch, R. J. P. Williams, R. C. Bray, J. F. Burke, S. A. Sanders, R. N. F. Thorneley, and A. T. Smith, *Eur. J. Biochem.*, 1992, **207**, 521.
37. J. S. de Ropp and G. N. La Mar, *J. Am. Chem. Soc.*, 1991, **113**, 4348.
38. V. Thanabal and G. N. La Mar, *Biochemistry*, 1989, **28**, 7038.

39. L. B. Dugad, G. N. La Mar, H. C. Lee, M. Ikeda-Saito, K. S. Booth, and W. S. Caughey, *J. Biol. Chem.*, 1990, **265**, 7173.
40. M. Sette, J. S. de Ropp, G. Hernandez, and G. N. La Mar, *J. Am. Chem. Soc.*, 1993, **115**, 5237.
41. I. Bertini, C. Luchinat, and D. Tarchi, *Chem. Phys. Lett*, 1993, **203**, 445.
42. J. Qin, F. Delaglio, G. N. La Mar, and A. Bax, *J. Magn. Reson. B*, 1993, **102**, 332.
43. V. Thanabal, G. N. La Mar, and J. S. de Ropp, *Biochemistry*, 1988, **27**, 5400.
44. L. Latos-Grazynski, A. L. Balch, and G. N. La Mar, *Adv. Chem.*, 1982, **201**, 661.
45. G. N. La Mar, G. Hernández, and J. S. de Ropp, *Biochemistry*, 1992, **31**, 9158.
46. N. C. Veitch and R. J. P. Williams, *Biochemical, Molecular and Physiological Aspects of Plant Peroxidases*, University of Geneva, Geneva, 1991, p. 99.
47. Q. Yi, J. E. Erman, and J. D. Satterlee, *J. Am. Chem. Soc.*, 1994, **116**, 1981.
48. Q. Yi, J. E. Erman, and J. D. Satterlee, *Biochemistry*, 1993, **32**, 10 988.
49. S. J. Moench, S. Chroni, B.-S. Lou, J. E. Erman, and J. D. Satterlee, *Biochemistry*, 1992, **31**, 3661.
50. J. E. Erman and J. D. Satterlee, *Adv. Biophys. Chem.*, 1994, in press.
51. J. D. Satterlee, J. E. Erman, J. M. Mauro, and J. Kraut, *Biochemistry*, 1990, **29**, 8797.
52. S. Modi, D. V. Behere, and S. Mitra, *J. Biol. Chem.*, 1989, **264**, 19 677.
53. D. V. Behere, E. Gonzalez-Vergara, and H. M. Goff, *Biochem. Biophys. Res. Commun.*, 1985, **131**, 607.
54. K. D. Park, K. Guo, F. Adebodun, M. L. Chiu, S. G. Sligar, and E. Oldfield, *Biochemistry*, 1991, **30**, 2333.
55. G. E. Krejcarek, R. G. Bryant, R. J. Smith, and L. P. Hager, *Biochemistry*, 1976, **15**, 2508.
56. I. Morishima, M. Kurono, and Y. Shiro *J. Biol. Chem.*, 1986, **261**, 9391.
57. G. N. La Mar, V. Thanabal., R. D. Johnson, K. M. Smith, and D. W. Parish, *J. Biol. Chem.*, 1989, **264**, 5428.

Acknowledgments

Unpublished work from the author's laboratory cited herein has been supported by the National Institutes of Health (USA) grant RO1-GM 47645.

Biographical Sketch

James D. Satterlee. *b* 1948. B.A., 1970, M.S., 1971, Chemistry, Central Washington University, USA. Ph.D., 1975, Physical Chemistry, University of California, Davis, USA, where he was introduced to the study of paramagnetic molecules using NMR by G. N. La Mar. Postdoctoral research fellow with J. H. Richards at the California Institute of Technology. Faculty in Chemistry, Northern Illinois University, 1978–81, University of New Mexico, 1981–89, Washington State University, 1989–present. Approx. 100 publications. Research specialties: NMR of paramagnetic heme proteins, NMR of biologically active small peptides, protein engineering, biophysical chemistry.

Hemoglobin

Chien Ho

Carnegie Mellon University, Pittsburgh, PA, USA

1	Introduction	1
2	Methods	1
3	Results	2
4	Conclusions	9
5	References	10

1 INTRODUCTION

Hemoglobin (Hb) carries O_2 from the lungs to the tissues and returns CO_2 from the tissues to the lungs. Human normal adult Hb (Hb A) is a tetrameric protein of molecular mass ~65 000 Da, consisting of two α chains of 141 amino acid residues each and two β chains of 146 amino acid residues each. Each chain contains a heme group, which is an iron complex of protoporphyrin IX. Each of the four heme groups of Hb binds a ligand. The oxygen binding curve of Hb A exhibits a sigmoidal shape, indicating that when one O_2 molecule is bound, succeeding O_2 molecules are bound more readily. Thus, the oxygenation of Hb A is a cooperative process. The dependence of the oxygen affinity of Hb A on pH, which is known as the Bohr effect, is an important physiological property, resulting in a greater ease of unloading of O_2 when the muscles are acidic and more O_2 is needed. In addition to hydrogen ions, chloride, carbon dioxide, inorganic phosphate, 2,3-diphosphoglycerate (2,3-DPG), and inositol hexaphosphate (IHP) also influence the binding of O_2 or CO to Hb A. These compounds are known as heterotropic or allosteric effectors of Hb A. For a detailed description of Hb, see Dickerson and Geis.[1]

Under physiological conditions, the heme iron atoms of Hb are in the ferrous state [Fe(II)]. When O_2 is bound, each of the heme iron atoms of oxyhemoglobin (HbO_2) is in the low spin, diamagnetic ferrous state. In the absence of oxygen, each of the heme iron atoms of deoxy-Hb contains four unpaired electrons, and is in the high spin, paramagnetic ferrous state. Other forms of Hb, such as ferric Hb (methemoglobin, met-Hb), cyanomet-Hb, and azidomet-Hb, also contain unpaired electrons in their heme iron atoms, and are thus paramagnetic. Hyperfine interactions are produced between the unpaired electrons of the heme iron atoms and the protons in the porphyrins, as well as the protons of the nearby amino acid residues, i.e. in the vicinity of the heme groups of Hb. The π electrons in the porphyrin molecule can produce ring current shifts in the resonances from the protons in the porphyrins and the protons of the nearby amino acid residues. Because of these interactions, the proton chemical shift of an Hb molecule covers a very large spectral range, from about 20 ppm below the frequency of H_2O to about 90 ppm above the frequency of H_2O, depending on the spin state of the iron atoms and the nature of ligands attached to the heme groups (Figure 1).

Proton NMR spectroscopy has been shown to be a very powerful technique for investigating the structure–function relationship in Hb. It can monitor the binding of O_2 to the α and β chains of Hb A, and the tertiary and quaternary structural changes of the Hb molecule as a function of oxygenation under different experimental conditions. It has provided unique information about the structural changes associated with the cooperative oxygenation of Hb, the structural characteristics of partially ligated species of Hb (i.e. Hb with one, two, and three bound O_2 molecules), and the molecular basis for the Bohr effect of Hb A. These are among the central problems in contemporary Hb research. For details, see Ho and co-workers,[2–8] and the references therein. In this article, we give representative results from our ^{1}H NMR investigations of Hb.

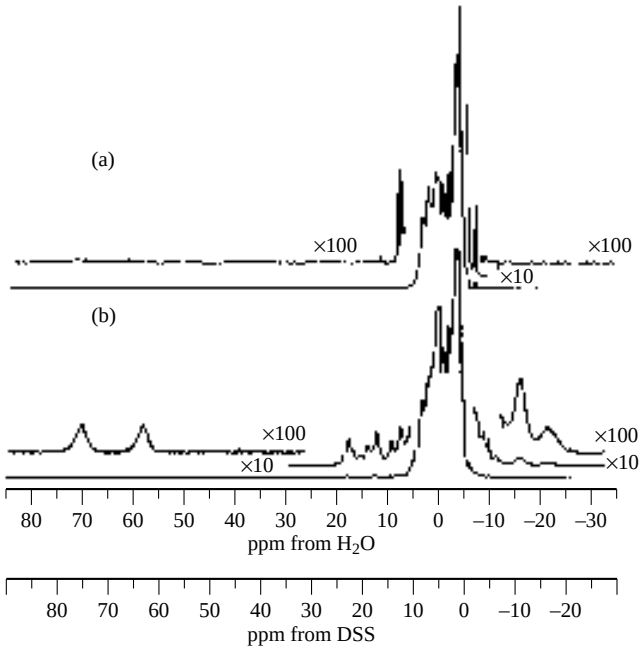

Figure 1 Proton NMR spectra (300 MHz) of 1.4 mM human normal adult hemoglobin (Hb A) in 0.1 M phosphate at pH 7.1 in H_2O at 29 °C over the spectral range from −30 to +90 ppm from H_2O and 2,2-dimethyl-2-silapentane-5-sulfonate (DSS): (a) oxy-Hb A and (b) deoxy-Hb A (×100 means that the spectrum is expanded 100 times from the original spectrum). (Reproduced by permission of Academic Press from Ho[2])

2 METHODS

2.1 Preparation of Hb Samples for ^{1}H NMR Studies

Hb A has been isolated from human blood samples obtained from the local blood bank. Human abnormal Hbs have been isolated from blood samples of individuals whose blood contains such mutant Hbs, provided for us by colleagues around the world. Now we are also able to produce human abnormal Hbs by site directed mutagenesis using our *Escherichia coli* expression system.[9a] The Hb samples for ^{1}H NMR studies can be prepared in either H_2O or D_2O media. Deoxy-, oxy-, or carbonmonoxy-Hb samples for ^{1}H NMR studies are prepared by procedures developed in our laboratory.[2,3,7]

2.2 Proton NMR Techniques

Any Fourier transform NMR spectrometer manufactured in the 1980s by major instrument companies is capable of obtaining ^{1}H NMR spectra of Hb. With a modern 7 T high-resolution NMR spectrometer operating at 300 MHz for ^{1}H, a satisfactory ^{1}H NMR spectrum (with a signal-to-noise ratio of ~20 or better) of a 0.3–0.5 ml sample of ~1 mM Hb contained in a 5 mm sample tube can be obtained in a few minutes.

To obtain ^{1}H NMR spectra of Hb samples in H_2O media, solvent suppression techniques are needed to reduce the dynamic range of the solvent protons in the sample. We have found that the jump-and-return pulse sequence developed by Plateau et al.[10] is very useful for obtaining ^{1}H resonances of Hb over the spectral range from 8 ppm below the frequency of H_2O to 22 ppm above the frequency of H_2O. To obtain very high-frequency hyperfine shifted exchangeable proton resonances from 50 to 90 ppm above the frequency of H_2O, we have recently developed a general method of selective excitation for shaped pulses and pulse sequences.[8a] When the Hb samples are prepared in D_2O media, standard pulse sequences available in a Fourier transform NMR spectrometer are capable of obtaining excellent ^{1}H NMR spectra of the Hb samples. We have found that the pulse sequence, developed by Hochmann and Kellerhals,[11] which selects the fastest relaxing resonances for observing while suppressing the slow relaxing ones (i.e. the diamagnetic proton resonances), is quite useful for obtaining the hyperfine shifted proton resonances of some forms of Hb over the spectral region from 5 to 30 ppm above the frequency of HDO.

The optimal magnetic field strength for ^{1}H NMR studies of Hb depends on both the spin state of the heme iron atoms of Hb and the nature of the measurement. For the hyperfine shifted proton resonances of deoxy-Hb and met-Hb, the linewidths increase with the square of the resonance frequency, whereas the resolution between the resonances only increases linearly with frequency.[12] Thus, there is a magnetic field at which both optimal sensitivity and optimal resolution can be obtained. For the hyperfine shifted proton resonances of deoxy-Hb, the optimal magnetic field appears to be around 7.0 T (or 300 MHz). Due to the chemical exchange contribution to the spin–spin relaxation, the linewidth of the C-2 proton resonances of histidyl residues of Hb also increases with the square of the resonance frequency.[13] There is no improvement in resolution in going from 300 to 600 MHz, and, thus, the His C-2 proton resonances of Hb can be readily obtained in a 300 MHz NMR spectrometer.[13] On the other hand, we have found that for diamagnetic proton resonances such as the exchangeable and ring-current shifted proton resonances, a 500 or 600 MHz NMR instrument gives better sensitivity and resolution than a 300 MHz spectrometer.

A commonly used proton chemical shift standard for ^{1}H NMR studies of proteins in aqueous solution is the proton resonance of the methyl group of the sodium salt of 2,2-dimethyl-2-silapentane-5-sulfonate (DSS). This resonance is +4.73 ppm above the frequency of the proton resonance of H_2O at 29 °C. Because all of our Hb samples contain H_2O (in the case of samples in D_2O, there is residual HDO present), it is convenient to take the proton resonance of H_2O in each sample as the internal reference. By taking account of the variation of the proton chemical shift of H_2O with temperature, we can always refer the proton chemical shift of H_2O to that of DSS. At the recommendation of IUPAC,[14] the chemical shift scale has been defined as positive in the region of the NMR spectrum at a higher frequency (lower field) than the resonance of a standard, and negative at a lower frequency. It should be noted that in our earlier publications we used the negative sign to indicate a chemical shift that was higher in frequency than that of the reference.

3 RESULTS

3.1 Proton NMR Spectra of Hb

The ^{1}H NMR spectrum of Hb can be divided into spectral regions that have been used to monitor structural (i.e. spectral) changes associated with the ligation of Hb A and the variation of the His C-2 proton resonances of Hb A as a function of pH. For details, see Figure 1 and Ho and co-workers.[2–7]

The greatest intensity of resonances in the spectra of oxy- and deoxy-Hb lies in the region between +5 and −5 ppm from HDO. Resonances in the most crowded spectral region, −1 to −5 ppm from HDO, arise from the protons of the large number of CH_2 and CH_3 groups in the aliphatic amino acid residues of oxy- and deoxy-Hb A. Resonances in the region +2 to +6 ppm from HDO arise from the aromatic amino acid residues of oxy- and deoxy-Hb A. The region from +2.8 to +3.8 ppm contains the C-2 protons of the histidyl residues, whereas the region from +1.8 to +2.8 ppm contains resonances from the C-4 protons of the histidyl residues as well as aromatic proton resonances from tryptophans, tyrosines, and phenylalanines. The C-2 proton resonances of the histidyl residues have been used to investigate the molecular basis of the Bohr effect of Hb A.[3–7]

Resonances from oxy-Hb A are limited to the region between +8.5 and −8 ppm. Resonances from +5 to +8.5 ppm from H_2O arise from the exchangeable proton resonances of oxy-Hb A. They are excellent markers for the subunit interfaces and the oxy quaternary structure.[15] Resonances in the region −5 to −8 ppm from H_2O arise from the ring-current shifted protons due to those protons located above and/or below the aromatic amino acid residues as well as the porphyrins of oxy-Hb A. They are very sensitive markers for the tertiary structure of the heme pocket[16–18] and have also been used to monitor the binding of O_2 to Hb A.[8b]

Resonances from the paramagnetic deoxy-Hb extend from +80 to −20 ppm. Resonances in the region +50 to +80 ppm from H_2O arise from the hyperfine shifted $N_\delta H$ exchangeable protons of the proximal histidyl residues of the α and β chains of deoxy-Hb A. They can be used to monitor the binding of O_2 to the α and β hemes of Hb A.[8b,19] Resonances in the region +5 to +20 ppm from H_2O of deoxy-Hb A are due to two sources. First, they arise from the protons of the heme groups and their nearby amino acid residues due to the hyperfine interactions between these protons and the unpaired electrons of the high spin ferrous heme iron atoms of deoxy-Hb A. They have been used to monitor the binding of O_2 to the α and β chains of deoxy-Hb A as well as the structural changes associated with the oxygenation of Hb.[20–22] Second, they arise from the exchangeable protons due to intra- and intermolecular hydrogen bonds in deoxy-Hb A. They have been used to monitor the changes in tertiary and quaternary structures as

a function of the oxygenation of Hb A.[15,20] Resonances in the region −6 to −20 ppm from H_2O arise from the ring-current shifted protons and the protons of the heme groups and their nearby amino acid residues due to the hyperfine interactions between these protons and the unpaired electrons of the high spin ferrous heme iron atoms of deoxy-Hb A.

3.2 Assignments of Proton Resonances of Hb

For proteins the size of Hb, a commonly used method for assigning proton resonances to specific amino acid residues is to compare the ^{1}H NMR spectra of normal and appropriate mutant or chemically modified molecules. This approach is shown in Figure 2, where the aromatic proton resonance region of the ^{1}H NMR spectrum of deoxy-Hb A is compared with those of mutant Hb Deer Lodge (β2His → Arg) and of enzymatically modified Hb (des-His(β146), i.e. β146His deleted). As a result of the replacement by arginine, a non-aromatic amino acid, of the histidyl residue at position β2, two resonances at +3.32 and +2.30 ppm from HDO are missing from the ^{1}H NMR spectrum of deoxy-Hb Deer Lodge as compared to that of deoxy-Hb A, both in 0.1 M bis(2-hydroxyethyl)iminotris(hydroxymethyl)methane (Bis−Tris) buffer in D_2O at pH 6.30. There are no other observable differences between these two spectra. Thus, these two resonances can be assigned to the two protons of β2His of deoxy-Hb A, the one at +3.32 ppm to the C-2 proton and the other at +2.30 ppm to the C-4 proton of the histidyl residue. Similarly, by comparing the ^{1}H NMR spectrum of deoxy-Hb A to that of deoxy-des-His(β146)Hb, both in 0.1 M Bis−Tris in D_2O at pH 6.30, the resonances at +3.80 and +2.76 ppm from HDO can be assigned to the C-2 and C-4 protons of β146His of deoxy-Hb A, respectively.

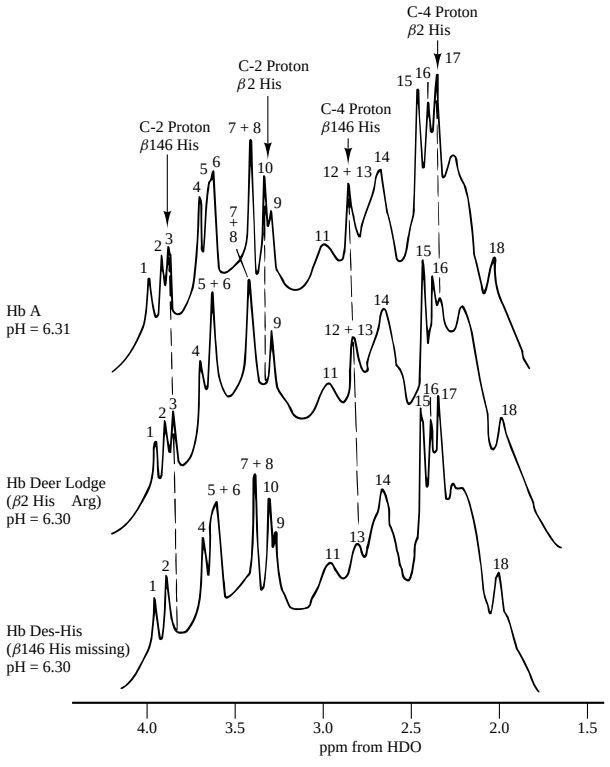

Figure 2 Aromatic proton resonances (250 MHz) of deoxy-Hb A, deoxy-Hb Deer Lodge (β2His → Arg), and deoxy-des-His(β146 deleted) in 0.1 M Bis−Tris in D_2O at pH 6.3 and 27 °C. Assignment of the proton resonances of the C-2 and C-4 protons of histidyl residues at β2 and β146 of deoxy-Hb A. (Reproduced by permission of Academic Press from Ho and Russu[3])

The above approach is weakened when a single mutation or chemical modification produces significant conformational alterations in other regions of the protein molecule. Such effects can produce changes in the ^{1}H NMR spectrum which make spectral assignments ambiguous. There are a number of ways to remedy this resonance assignment problem. First, one can use several mutant Hbs with a change in the same amino acid residue to clarify or confirm the assignment. This approach is becoming very feasible with the availability of a suitable expression system which can be used to produce any desired mutant Hbs.[9b,c] Second, one can use independent techniques to confirm the resonance assignment based on the mutant Hbs. One-dimensional NOE and 2D NMR techniques can be combined with X-ray structural information to make and confirm resonance assignments of Hb A.[18,23] Over the years, more than 70 proton resonances of Hb A have been assigned. The assignments of these resonances are tabulated in our recent reviews.[2,4]

3.3 The Cooperative Oxygenation of Hb

Two models have been offered to explain the sigmoidal nature of the oxygen binding curve of Hb A, one based on a concerted mechanism, proposed by Monod et al.,[24] and the other based on a sequential mechanism, proposed by Koshland et al.[25] The concerted mechanism postulates that, in the absence of ligand, there is an equilibrium between the low affinity deoxy conformation (T form) and the high affinity oxy conformation (R form), and that the transition from the T form to the R form is a concerted process, i.e. no intermediate or hybrid conformation RT exists. On the other hand, the sequential mechanism does not assume the existence of an equilibrium between the T and R forms in the absence of ligand, but postulates that the transition from the T to the R form is induced by the ligand binding, i.e. a sequential process. The intermediate species, RT, plays a very important role in the sequential mechanism. Both mechanisms can account for the oxygen binding curve of Hb A very well, in spite of the conceptual differences between them. This is not surprising in that, because of the highly cooperative oxygenation process, there are very few partially oxygenated species, i.e. $Hb(O_2)_1$, $Hb(O_2)_2$, and $Hb(O_2)_3$, present during the oxygenation process. However, it is only through a detailed characterization of the structural and functional properties of these partially oxygenated species that one can gain a full understanding of the structure−function relationships in Hb A.

Proton NMR studies of Hb during the past 35 years have provided new insights into the cooperative oxygenation of Hb A. Our approach has been twofold. First, we have monitored structural (spectral) markers of Hb A as a function of oxygenation under different experimental conditions. From these studies, we have gained information regarding the binding of O_2 to the α and β chains of Hb A and the structural changes associated with the cooperative oxygenation

of Hb A.[20–22] Second, we have used naturally occurring valency hybrid mutant Hbs (such as Hb M Milwaukee)[26,27] and synthetic cross-linked mixed valency hybrid Hbs[28,29] as models for partially oxygenated species. For recent reviews on this subject, see Ho and co-workers.[2,4]

3.3.1 Binding of O_2 to the α and β Chains of Hb and Associated Structural Changes

The ferrous hyperfine shifted proton resonances of deoxy-Hb A in the spectral region from +5 to +20 ppm from HDO and the ferrous hyperfine shifted $N_\delta H$ exchangeable proton resonances in the region from +55 to +75 ppm from H_2O provide unique markers for investigating the binding of O_2 to the α and β chains of Hb A. Since these are hyperfine shifted resonances, they disappear from the high-frequency region of the spectrum (or return to their normal diamagnetic resonance region) when the Hb molecule is converted to the diamagnetic oxy state on O_2 binding.

Figure 3 shows a representative series of the hyperfine shifted proton resonances over the spectral range +6 to +20 ppm from HDO as a function of oxygenation in D_2O at pH ~6.4 in the absence and presence of organic phosphates.[21] The resonances at about +12 and +18 ppm from HDO have been assigned to the α and β chains of deoxy-Hb A, respectively. Figure 4 gives a comparison of the relative intensities of the

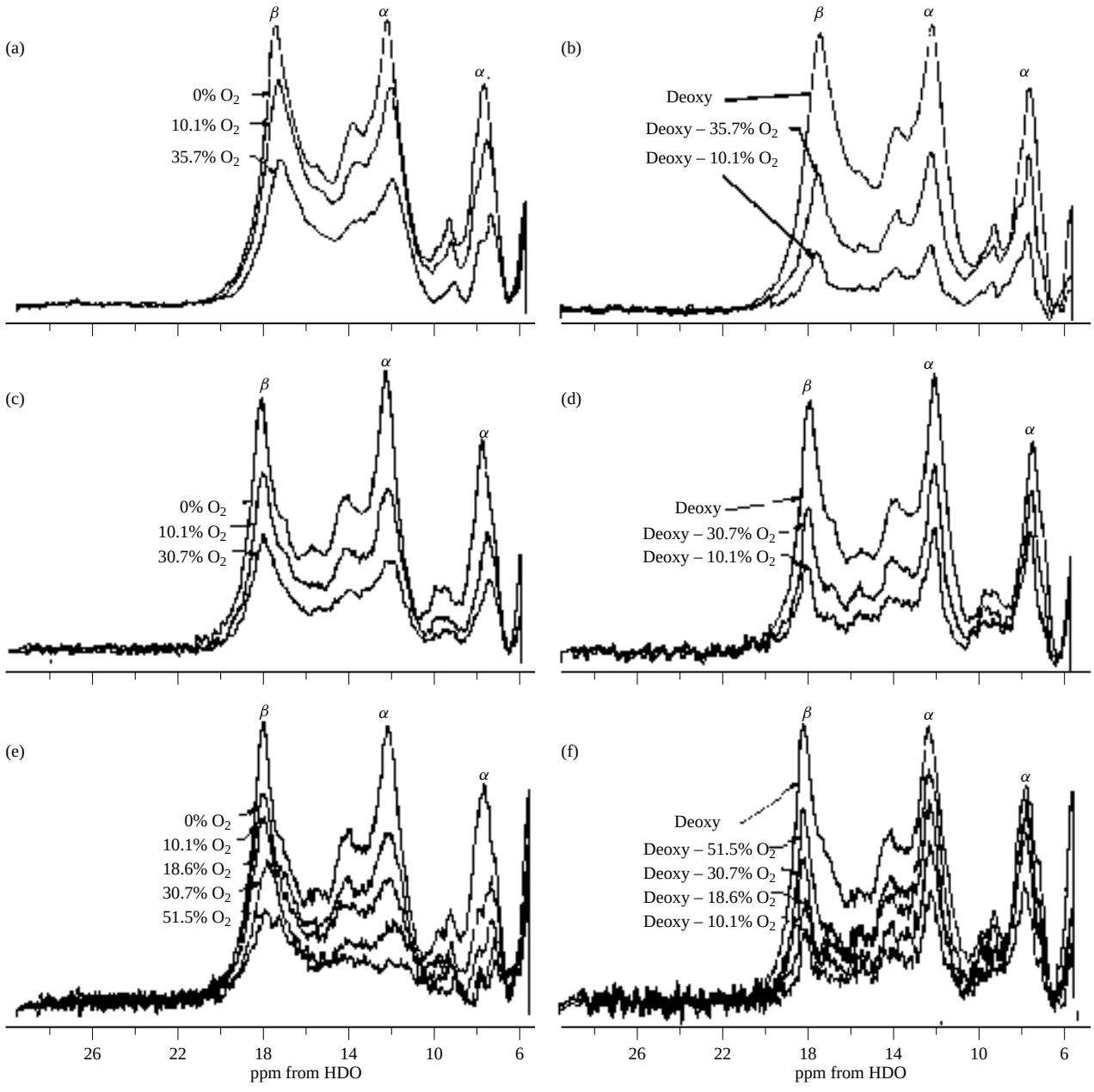

Figure 3 Proton NMR studies (250 MHz) of the oxygenation of Hb A in 0.1 M Bis–Tris in D_2O at 27 °C: (a) 18% Hb at pH 6.44; (b) difference spectra of 18% Hb A at pH 6.44; (c) 13% Hb A plus 35 mM 2,3-DPG at pH 6.34; (d) difference spectra of 13% Hb A plus 35 mM 2,3-DPG at pH 6.34; (e) 11.5% Hb A plus 10 mM IHP at pH 6.42; and (f) difference spectra of 11.5% Hb A plus 10 mM IHP at pH 6.42. It should be noted that pD = pH + 0.4. (Reproduced by permission of the American Chemical Society from Viggiano et al.[21])

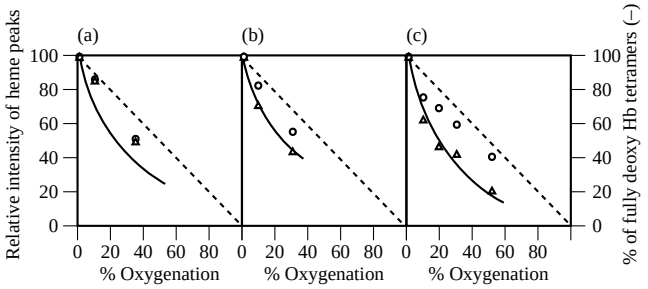

Figure 4 A comparison of the relative intensities of the α-heme resonance at 12 ppm (△) and the β-heme resonance at 18 ppm (○) with the percentage of fully deoxy-Hb tetramers (—) as a function of oxygenation: (a) in 0.1 M Bis–Tris at pH 6.44; (b) in 0.1 M Bis–Tris plus 35 mM 2,3-DPG at pH 6.34; and (c) in 0.1 M Bis–Tris plus 10 mM IHP at pH 6.42. The fraction of fully deoxy-Hb tetramers was calculated from the data of Tyuma et al.[30] (Reproduced by permission of the American Chemical Society from Viggiano et al.[21])

α-heme resonance at +12 ppm and the β-heme resonance at +18 ppm with the percentage of fully deoxy-Hb tetramers as a function of O_2 saturation in the absence and presence of organic phosphates. In the absence of organic phosphates, the areas of the +12 and +18 ppm resonances decrease at the same rate, i.e. the α and β chains of Hb A have similar affinity for O_2 [Figure 4(a)]. In the presence of organic phosphates, the area of the α peak at +12 ppm follows the behavior of the fully deoxy-Hb A populations, while the area of the +18 ppm β peak remains significantly larger than that of the +12 ppm α peak on oxygenation [Figure 4(b) and (c)]. This means that the presence of even one O_2 molecule in the Hb tetramer is enough to cause a decrease in the area of the +12 ppm α resonance, but not the +18 ppm β resonance. In the presence of IHP, the α chains have a much higher O_2 affinity than the β chains. As a first approximation, we can assume that, at low O_2 saturations, both the singly and doubly oxygenated species all have O_2 molecules bound on the α chains. The behavior of the +18 ppm β chain resonance, which is sensitive to both ligation and structural changes, shows that the number of modified β chains is less than the number of modified α chains.[21,22] The relative intensity of the +12 ppm α chain resonance follows the population of the fully deoxy-Hb tetramers, suggesting that all of the oxygenated species either have O_2 bound to the α chains or have some structural modifications in the unligated α chains. Thus, our ^{1}H NMR results suggest that a strong cooperativity must exist in the oxygenation of the α chains and that the oxygenation of one α chain affects the ligand affinity of the other unligated α chain within a tetrameric Hb molecule.[21,22] These results suggest that there are more than two affinity states in the Hb molecule on ligand binding. Thus, the structural changes at partial O_2 saturations in the presence of organic phosphates cannot be concerted as required by two-state allosteric models, even if extended to take into account the differences in affinity between the α and β chains as proposed by Ogata and McConnell.[31] These conclusions based on the behavior of the resonances at +12 and +18 ppm are also supported by experiments making use of other resonances.[2,20]

What relationship do the conclusions based on these in vitro experiments have to the situation in vivo? We have monitored the intensities of the hyperfine shifted $N_\delta H$ exchangeable proton resonances of the proximal histidyl residues of the α and β chains of deoxy-Hb at about +59 and +71 ppm from H_2O, respectively, as a function of O_2 saturation by using a soft 121 pulse sequence to suppress the H_2O signal in a fresh hemolysate at pH 6.6.[19] From the variation of the intensities of the resonances at about +59 and +71 ppm, we have concluded that the α chains of Hb A have a higher affinity for O_2 than the β chains. This is in agreement with the measurement of the relative intensities of the hyperfine shifted proton resonances at +12 and +18 ppm in the presence of organic phosphates. More recently, we have improved our pulse sequences for solvent suppression,[8] and our new pulse sequences allow us to monitor the binding of O_2 to Hb A inside intact red blood cells. Our results indicate that in fresh human red blood cells the α chains of Hb A have a higher affinity for O_2 than the β chains,[8b] in agreement with the results obtained from Hb A in solution in the presence of organic phosphates.

3.3.2 Models for Partially Ligated Species of Hb

The structural information about the partially ligated species of Hb A inferred from the previous section is indirect, i.e. it does not provide direct structural characteristics for the partially oxygenated species, $Hb(O_2)_1$, $Hb(O_2)_2$, and $Hb(O_2)_3$, formed during the oxygenation process. This is due to the fact that the oxygenation of Hb A is a highly cooperative process. Thus, there are very few partially oxygenated species present. There is also a rapid dimer exchange in the tetrameric Hb molecule, which makes it difficult to isolate intermediate species.

In this section, we describe our second approach for gaining structural information about partially ligated Hb species, using Hb M Milwaukee (β67Val $\rightarrow$ Glu, $\alpha_2\beta_2^+$) and cross-linked asymmetric mixed valency hybrid Hbs. As a result of the amino acid substitution β67Val $\rightarrow$ Glu, the two β chains of Hb M Milwaukee are in the high spin ferric state.[32] Thus, in deoxy-Hb M Milwaukee, the heme iron atoms in the α and β chains have different paramagnetic properties. The hyperfine shifted proton resonances of the high spin ferrous state of deoxy-Hb A occur in the spectral range from +5 to +20 ppm from H_2O, whereas those of the high spin ferric state occur in the spectral range from +10 to +90 ppm from H_2O. Using these ferric hyperfine shifted proton resonances of Hb M Milwaukee, it is possible not only to explore the structures of fully deoxygenated and fully oxygenated Hb M Milwaukee but also to observe the structural alterations at the ligand binding site of one type of subunit (β^+-hemes), which are associated with the binding of O_2 to the neighboring subunits (α-hemes). Thus, these ^{1}H NMR measurements can provide a direct probe of the structural manifestation of the 'heme–heme' interactions in Hb M Milwaukee.[26,27]

Figure 5 shows the variation of the ferric hyperfine shifted proton resonances of the β^+-hemes of Hb M Milwaukee as a function of oxygenation in 0.1 M Bis–Tris buffer at pH 6.6 and 30 °C. By analyzing the variation of the ferric hyperfine shifted proton resonances of Hb M Milwaukee as a function of oxygenation, we have concluded that the ferric hyperfine shifted proton resonance spectrum of singly oxygenated Hb M Milwaukee cannot be obtained as an average of the corresponding spectra of fully deoxygenated and fully oxygenated Hb M Milwaukee.[26,27] These ^{1}H NMR results indicate that during the course of oxygenation, unligated binding sites may adopt intermediate as well as deoxy-like and oxy-like conformations. This conclusion is not consistent

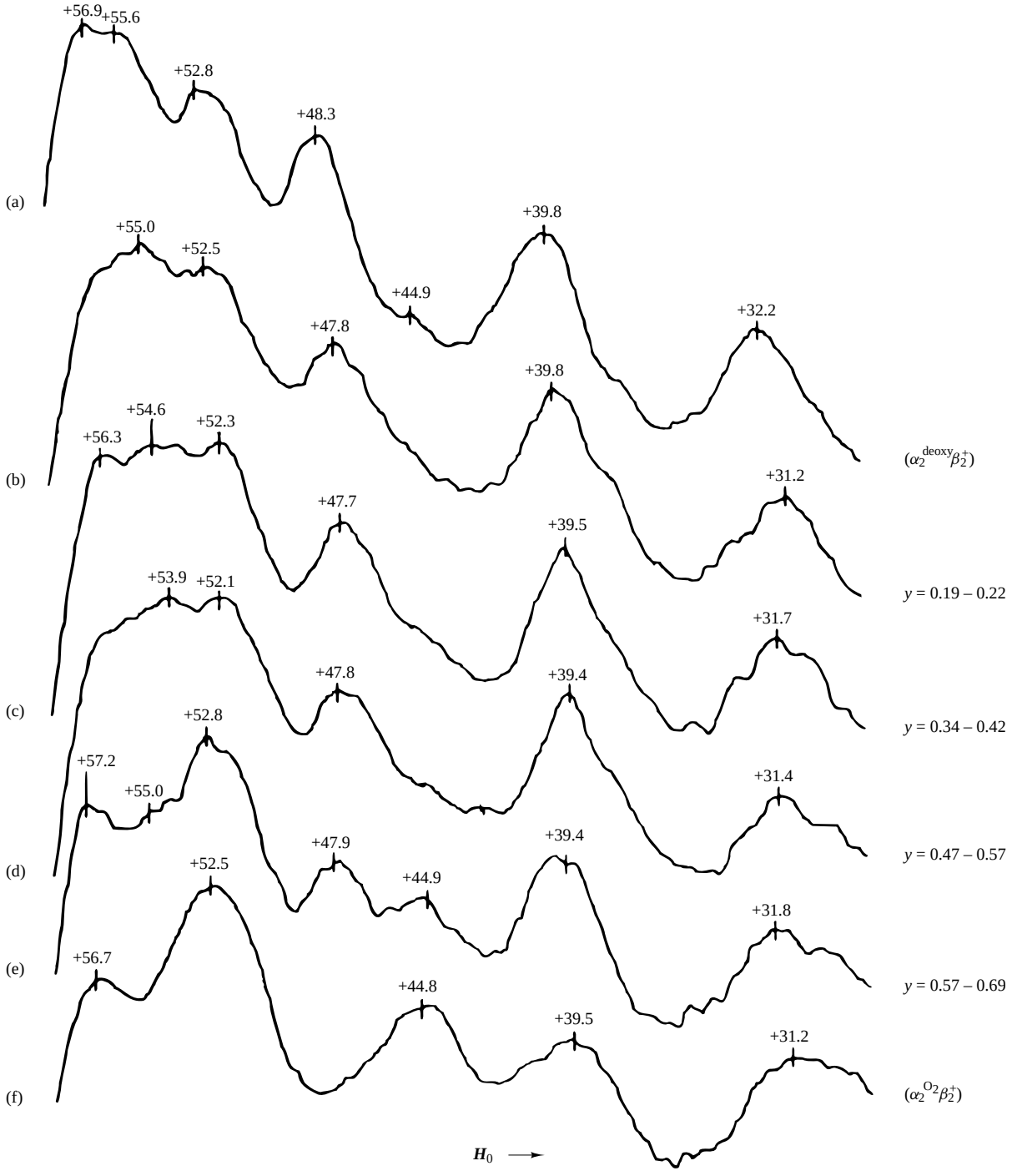

Figure 5 Ferric hyperfine shifted proton resonances (250 MHz) of the abnormal β chains of 15% Hb M Milwaukee (β67Val → Glu, $\alpha_2\beta_2^+$) as a function of oxygenation in 0.1 M Bis–Tris in D_2O at pH 6.6 and 30 °C. The proton chemical shifts are referenced to HDO. The range of fractional oxygenation (y) was based on P_{50} = 5 torr or P_{50} = 10 torr. (Reproduced by permission of the American Chemical Society from Fung et al.[27])

with the prediction of two-structure allosteric descriptions for the cooperative oxygenation of Hb. Thus, by implication, two-structure allosteric models cannot satisfactorily explain the structural changes of Hb A associated with the oxygenation process.

The exchange of two dissociated dimers of Hb can be prevented by introducing a cross-linking (XL) reagent, such as bis(3,5-dibromosalicyl)fumarate, which cross-links the Lys82 residues of the two β subunits.[33] This technique has enabled us to prepare various asymmetric cyanomet mixed valency hybrid Hbs, i.e. with one cyanomet heme in either an α or β subunit, or with two cyanomet hemes one in an α and one in a β chain within a tetrameric Hb molecule. Cyanomet heme has been used as a model for ligated heme in Hb research for a long time. Thus, we have prepared $(\alpha^{+CN}\beta)_A(\alpha\beta)_C$XL and $(\alpha\beta^{+CN})_A(\alpha\beta)_C$XL to serve as models for singly ligated species, and $(\alpha^{+CN}\beta^{+CN})_A(\alpha\beta)_C$XL and $(\alpha\beta^{+CN})_A(\alpha^{+CN}\beta)_C$XL to serve as models for doubly ligated

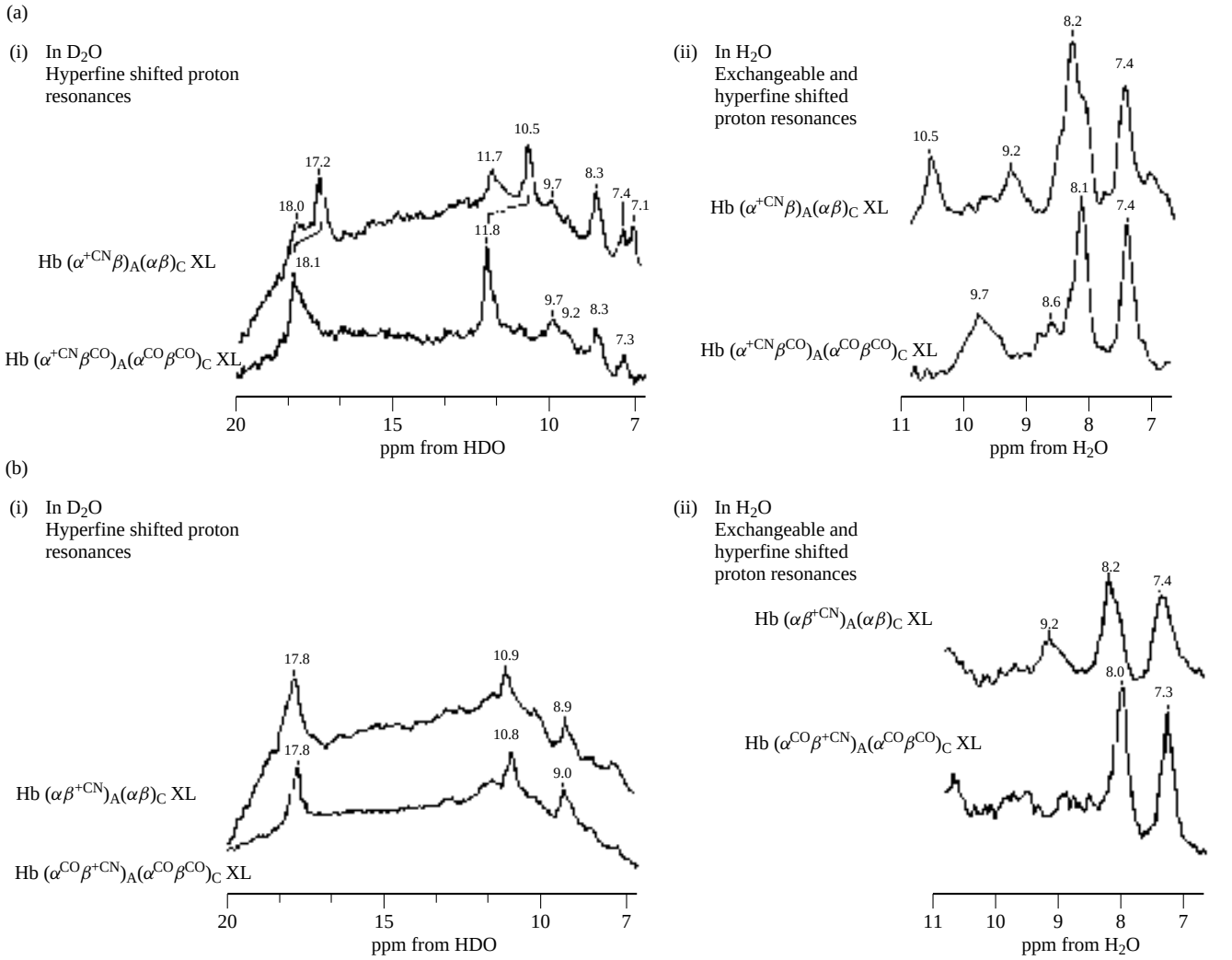

Figure 6 Proton NMR spectra (600 MHz) of cross-linked mixed valency asymmetric hybrid hemoglobins in 0.1 M phosphate at pH 6.8 and 21 °C in deoxy and CO forms: (a) Hb$(\alpha^{+CN}\beta)_A(\alpha\beta)_C$XL and (b) Hb$(\alpha\beta^{+CN})_A(\alpha\beta)_C$XL models for singly ligated species. (Reproduced by permission of the American Chemical Society from Miura and Ho[28])

species, the first one for the partially ligated $\alpha_1\beta_1$ dimer and the second one for the partially ligated $\alpha_1\beta_2$ dimer.

Figure 6 shows the 600 MHz ^{1}H NMR spectra of $(\alpha^{+CN}\beta)_A(\alpha\beta)_C$XL and $(\alpha\beta^{+CN})_A(\alpha\beta)_C$XL, the models for singly ligated Hbs. The sharp resonances shown in Figure 6(a)(i) and (b)(i) are due primarily to the low spin ferric hyperfine shifted proton resonances associated with the cyanomet chains, because the hyperfine shifted proton resonances due to the high spin ferrous chains are too broad (>1200 Hz) to be detectable under our measuring conditions.[12] The binding of CO to $(\alpha^{+CN}\beta)_A(\alpha\beta)_C$XL, the model for a ligated α chain, produces significant spectral changes in the low spin ferric hyperfine shifted proton resonances of the α^{+CN} chain, as shown in Figure 6(a)(i). On the other hand, the spectral changes of $(\alpha\beta^{+CN})_A(\alpha\beta)_C$XL, the model for a ligated β chain, in going from the deoxy to the CO form, are quite minor, as shown in Figure 6(b)(i), i.e. the resonances from the deoxy form are already in the positions found in the oxy-like quaternary structure.

Figure 6(a)(ii) and (b)(ii) give the proton resonances of $(\alpha^{+CN}\beta)_A(\alpha\beta)_C$XL and $(\alpha\beta^{+CN})_A(\alpha\beta)_C$XL in H_2O in both the deoxy and CO forms over the spectral region from +7 to +11 ppm from H_2O. These resonances are mainly the hyperfine shifted proton resonances associated with the low spin cyanomet chains and the exchangeable proton resonances. Again, the hyperfine shifted proton resonances due to the high spin ferrous chains are too broad to be observable under our measuring conditions.[12] The resonance at about +9.2 ppm in these spectra shows approximately half the intensity of the corresponding resonance in deoxy-Hb A or cross-linked Hb A.[28] This resonance disappears on going from the deoxy to the ligated form, and has been assigned to the intersubunit hydrogen bond between α42Tyr and β99Asp in the $\alpha_1\beta_2$ subunit interface, a deoxy quaternary structural marker.[15,28] The 50% reduction of the resonance at +9.2 ppm might suggest the equal coexistence of the two quaternary structures. However, the resonances from the cyanomet β chain as seen in Figure 6(b)(i) indicate that all are in the ligated form. Therefore, the results imply that at least one intermediate quaternary structure must be taken into account, in which about half of the hydrogen bonds responsible for the resonance at +9.2 ppm are altered.

We have also obtained similar 600 MHz ^{1}H NMR spectra of $(\alpha^{+CN}\beta^{+CN})_A(\alpha\beta)_C$XL and $(\alpha\beta^{+CN})_A(\alpha^{+CN}\beta)_C$XL in both deoxy and CO forms.[28] Overall, the 600 MHz ^{1}H NMR spectra of these two valency hybrid Hbs are quite similar to each other. There are small spectral changes in these two hybrid Hbs in going from the deoxy to the CO form. The most obvious difference between the cross-linked hybrid Hbs with two cyanomet chains and those with one cyanomet chain is the absence of the characteristic deoxy quaternary spectral marker at about +9.2 ppm from H_2O in the former hybrid Hbs. This suggests that the hybrid Hbs with two cyanomet chains per $\alpha\beta$ tetramer do not have the usual deoxy quaternary structure as manifested by the intersubunit hydrogen bond between α42Tyr and β99Asp.

Thus, the structural changes during the ligation process are not concerted, and two-structure allosteric models are not sufficient to describe fully the cooperation oxygenation of Hb A. It should be mentioned that spectral changes observed for the high spin ferric hyperfine shifted proton resonances of the β chains in Hb M Milwaukee on oxygenation of its α chains as described earlier in this section are consistent with the results on cross-linked asymmetric mixed valency hybrid Hbs with one cyanomet chain.

Ackers and co-workers[34] have carried out extensive thermodynamic measurements of cooperative free energies of quaternary assembly of Hb A, mutant Hbs, and Hbs with metal substituted porphyrins. They have concluded that singly ligated species such as $[(\alpha^{+CN}\beta)(\alpha\beta)]$ and $[(\alpha\beta^{+CN})(\alpha\beta)]$ and a doubly ligated species, $[(\alpha^{+CN}\beta^{+CN})(\alpha\beta)]$, have identical cooperative free energy and that they all belong to the T quaternary structure. These conclusions are inconsistent with our results as discussed in this section. Further work is needed to resolve these discrepancies.

3.4 The Molecular Basis for the Bohr Effect of Hb A

The Bohr effect is the change of the oxygen affinity of Hb A with pH. The alkaline Bohr effect results in the release of protons from the Hb molecule during the transition from the deoxy to the oxy state at a pH above 6.0. The acid Bohr effect results in the absorption of protons upon oxygenation below pH 6.0. Besides the alkaline and acid Bohr effects of Hb A, there is an additional Bohr effect that originates from the oxygen-linked interactions of the Hb molecule with solvent anions. It has been shown that the release of about half of the Bohr protons is due to a difference in chloride binding to the oxy and deoxy forms of Hb A.[35] Besides the α-amino terminal, the imidazole groups from the histidyl residues, because of their pK_a values in the physiologically relevant range, are the most likely amino acid residues of Hb for which changes in pK_a values on oxygenation and on anion binding could contribute significantly to the Bohr effect.

The involvement of the surface histidyl residues in the Bohr effect originates from the changes in their electrostatic environments accompanying the change in the conformation of the Hb molecule on ligation and/or on anion binding. Several histidyl residues of Hb A, in particular β2His and β146His, have been proposed, on the basis of X-ray diffraction data and the results on mutant and chemically modified Hbs, to play an important role in the Bohr effect. As shown in Figures 1 and 2, the C-2 proton resonances of the histidyl residues of Hb A are well separated from those of other proton resonances. There are 11–13 histidyl residues per Hb dimer (or 22–26 histidyl residues per Hb tetramer) that can be resolved and titrated individually by ^{1}H NMR spectroscopy in both deoxy and CO forms under a wide range of experimental conditions.[3–7] The pK_a values are determined by a nonlinear least-squares fit of the ^{1}H chemical shift as a function of $[H^+]$. From the pK_a values and the experimental values of the partial pressure of O_2 at 50% saturation obtained for a wide range of pH values, the hydrogen ions released per Hb molecule can be calculated under the assumption that the same 22–26 histidyl residues are observed in the deoxy and in the CO forms.

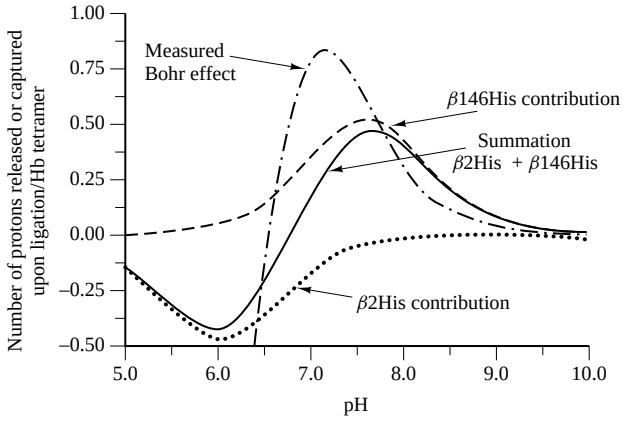

Figure 7 Alkaline Bohr effect of Hb A in D_2O in 0.1 M HEPES at 29 °C, and the contributions of β2His and β146His as calculated from the pK_a values determined by ^{1}H NMR spectroscopy. -·-, measured Bohr effect; ···, β2His contribution; ---, β146His contribution; —, sum of the contributions from β2His and β146His. (Reproduced by permission of the American Chemical Society from Busch et al.[7])

Figure 7 shows the measured Bohr effect of Hb A in chloride-free 0.1 M 4-(2-hydroxyethyl)-1-piperazineethanesulfonic acid (HEPES) at 29 °C and the protons calculated to be contributed by β2His and β146His. The summation of the contributions of β2His and β146His to the Bohr effect does not correspond to the total measured Bohr effect. It is clear that there are many more amino acid residues involved in the Bohr effect than β2His and β146His.

We have also used ^{1}H NMR spectroscopy to investigate the molecular mechanism of the Bohr effect in the presence of allosteric effectors such as chloride, inorganic phosphate, or 2,3-DPG.[6,7,36,37] The interactions of chloride and inorganic phosphate ions with the Hb molecule result in lowering the pK_a values of several surface histidyl residues and/or changes in the shapes of the H^+ binding curves. These results suggest that long-range electrostatic interactions between individual ionizable sites in Hb A could play an important role in the molecular mechanisms of the anion Bohr effect. The addition of an equimolar concentration of 2,3-DPG to the Hb A solution affects several His C-2 proton resonances in both the deoxy and CO forms. The largest effect is observed for the β2His and originates from an increase in the pK_a value of this histidyl residue in the presence of 2,3-DPG [Figure 8(a)]. In 0.1 M HEPES, β2His captures about 0.46 protons per Hb tetramer upon oxygenation at pH 6.0, and therefore contributes to the acid Bohr effect under these conditions. At pH 7.0, β2His absorbs about 0.17 protons per Hb tetramer, and thus makes a negative contribution to the

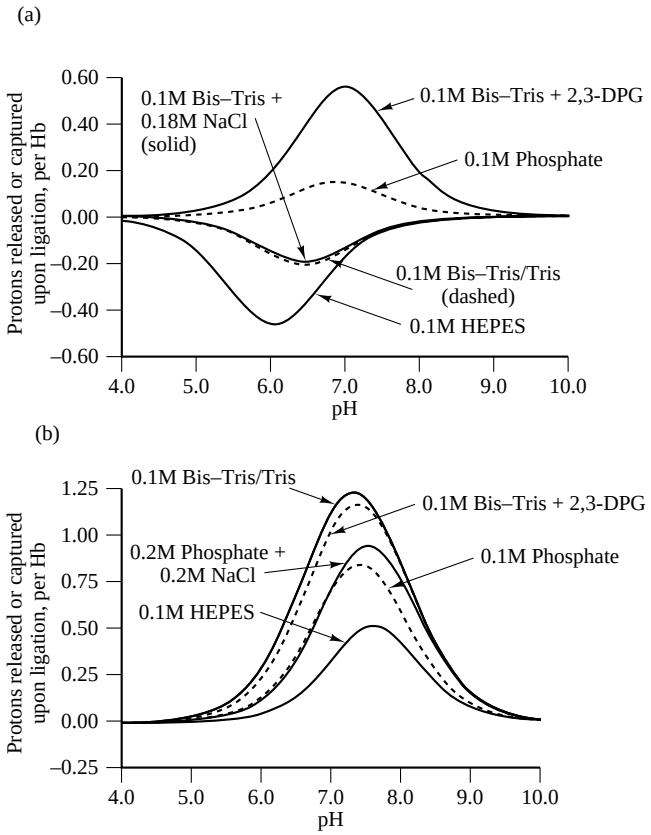

Figure 8 Contributions of (a) β2His and (b) β146His residues to the Bohr effect of Hb A under different experimental conditions. (Reproduced by permission of Elsevier Science Publishers from Busch and Ho[6])

overall alkaline Bohr effect. As seen in Figure 8(a), the curves for the 0.1 M Bis–Tris/Tris and 0.1 M Bis–Tris + 0.18 M NaCl conditions nearly superimpose, with β2His still capturing up to 0.20 protons per Hb tetramer upon ligation at about pH 6.5, thus still opposing the macroscopically observed Bohr effect. In the presence of 0.1 M phosphate, β2His releases up to 0.15 protons per Hb tetramer, making a small, but positive, contribution to the alkaline Bohr effect. The β2His residue releases up to 0.56 protons per Hb tetramer upon ligation in 0.1 M Bis–Tris + 2,3-DPG, a significant contribution to the alkaline Bohr effect.

Figure 8(b) shows the contributions of β146His to the Bohr effect. The contributions of this amino acid residue to the Bohr effect remain positive under the conditions studied, but the magnitude of its contribution can be significantly altered by different experimental conditions. Using pH 7.4 as a reference pH, β146His contributes 0.49 protons per Hb tetramer to the Bohr effect in 0.1 M HEPES, in 0.1 M phosphate, 0.85 protons per Hb tetramer, in 0.2 M phosphate + 0.2 M NaCl, 0.93 protons per Hb tetramer, in 0.1 M Bis–Tris + 2,3-DPG, 1.18 protons per Hb tetramer, and 1.24 protons per Hb tetramer in 0.1 M Bis–Tris. Our results also indicate that β146His is not a site for the binding of chloride or inorganic phosphate, yet these anions can significantly increase the contribution of this amino acid residue to the Bohr effect.

The examples of β2His and β146His clearly illustrate that the microscopic behavior of a specific group in Hb is determined by its site-specific chemical and electrostatic environments, defined by both the Hb structure and by the environment in which the Hb molecule resides. As a result, depending on solvent conditions, the individual behavior of a group could either contribute to the behavior seen macroscopically for the system, or oppose that behavior. Thus, the detailed molecular mechanism for the Bohr effect of Hb A is not unique, but is dependent on the nature of the solvent, both by direct interactions and by long-range electrostatic and/or conformational perturbations.[5–7]

In order to gain insights into the nature of the Bohr effect inside red blood cells (RBCs), we have compared the C-2 proton resonances of histidyl residues of purified Hb A, lysed RBCs, and intact RBCs.[4] The resonances from lysed cells are much better resolved than those of the intact cells. As a first step, we have carried out a preliminary investigation of the C-2 proton resonances of the histidyl residues of HbCO A in lysed cells and compared them to those of purified HbCO A under similar conditions. The pH titration curves of several C-2 proton resonances of histidyl residues in the lysed cells are very similar to those of HbCO A.[4] These preliminary results suggest that the study of lysed RBCs can provide useful information about the Bohr effect inside intact RBCs.

4 CONCLUSIONS

In this article we have given a few examples of the use of ^{1}H NMR to study the structure–function relationship in Hb A. Our results show that the structural changes associated with the cooperative oxygenation process are not concerted, and that within the deoxy quaternary state some cooperativity must be present during the oxygenation process. These results are not consistent with two-structure allosteric descriptions of the oxygenation of hemoglobin. Our ^{1}H NMR studies of the Bohr effect of Hb A illustrate that the microscopic behavior of a specific amino acid residue in Hb A is determined by the Hb structure and by the environment in which the Hb molecule resides. The variable role of a given amino acid residue under different solvent conditions has been demonstrated for β2His and β146His, and implies that the molecular basis for the Bohr effect of Hb A is not unique and depends on solvent conditions. Our ^{1}H NMR results clearly indicate that Hb is a very interactive molecule, i.e. perturbations at one site can be propagated to other parts of the molecule.

The Hb problem is certainly not yet solved. There are more exciting discoveries to be made by researchers in the coming years. With the recent success in creating a suitable expression system which can be used to produce any desired mutant hemoglobins, we have a unique opportunity to gain new insights into the molecular basis of signal transfer from a ligated subunit to its unligated partners within a tetrameric Hb molecule and to assign additional amino acid residues which contribute to the Bohr effect of Hb A. Hb is an excellent model for investigating the molecular basis of the properties of allosteric proteins and of signaling phenomena at the atomic level. Thus, NMR, in combination with appropriate engineered Hbs, offers an excellent approach to investigating these problems.

5 REFERENCES

1. R. E. Dickerson and I. Geis, *Hemoglobin: Structure, Function, Evolution, and Pathology*, Benjamin/Cummings, Menlo Park, CA, 1983.
2. C. Ho, *Adv. Protein Chem.*, 1992, **43**, 153.
3. C. Ho and I. M. Russu, *Methods Enzymol.*, 1981, **76**, 275.
4. C. Ho and J. R. Perussi, *Methods Enzymol.*, 1994, **232**, 97.
5. C. Ho and I. M. Russu, *Biochemistry*, 1987, **26**, 6299.
6. M. R. Busch and C. Ho, *Biophys. Chem.*, 1990, **37**, 313.
7. M. R. Busch, J. E. Mace, N. T. Ho, and C. Ho, *Biochemistry*, 1991, **30**, 1865.
8. (a) B. K. Fetler, V. Simplaceanu, N. S. VanderVen, I. J. Lowe, and C. Ho, *J. Magn. Reson. B*, 1993, **101**, 17; (b) B. K. Fetler, V. Simplaceanu, and C. Ho, *Biophys. J.*, 1995, **68**, 681.
9. (a) T.-J. Shen, N. T. Ho, V. Simplaceanu, M. Zou, B. N. Green, M. F. Tam, and C. Ho, *Proc. Natl. Acad. Sci. USA*, 1993, **90**, 8108; (b) M.-W. Kim, T.-J. Shen, D. P. Sun, N. T. Ho, M. Madrid, M. F. Tam, M. Zou, P. F. Cotton, and C. Ho, *Proc. Natl. Acad. Sci. USA*, 1994, 91, 11 547; (c) H.-W. Kim, T.-J. Shen, D. P. Sun, N. T. Ho, M. Madrid, and C. Ho, *J. Mol. Biol.*, 1995, **248**, 867.
10. P. Plateau, D. Dumas, and M. Guéron, *J. Magn. Reson.*, 1983, **54**, 46.
11. J. Hochmann and H. Kellerhals, *J. Magn. Reson.*, 1980, **38**, 23.
12. M. E. Johnson, L. W.-M. Fung, and C. Ho, *J. Am. Chem. Soc.*, 1977, **99**, 1245.
13. M. Madrid, V. Simplaceanu, N. T. Ho, and C. Ho, *J. Magn. Reson.*, 1990, **88**, 42.
14. *Pure Appl. Chem.*, 1972, **29**, 627.
15. L. W.-M. Fung and C. Ho, *Biochemistry*, 1975, **14**, 2526.
16. T. R. Lindstrom and C. Ho, *Biochemistry*, 1973, **12**, 134.
17. M. P. Mims, J. S. Olsen, I. M. Russu, S. Miura, T. E. Cedel, and C. Ho, *J. Biol. Chem.*, 1983, **258**, 6125.
18. C. Dalvit and C. Ho, *Biochemistry*, 1985, **24**, 3398.
19. C. Yao, V. Simplaceanu, A. K.-L. C. Lin, and C. Ho, *J. Magn. Reson.*, 1986, **66**, 43.
20. G. Viggiano and C. Ho, *Proc. Natl. Acad. Sci. USA*, 1979, 76, 3673.
21. G. Viggiano, N. T. Ho, and C. Ho, *Biochemistry*, 1979, **18**, 5238.
22. C. Ho, C.-H. J. Lam, S. Takahashi, and G. Viggiano, in *Hemoglobin and Oxygen Binding*, eds. C. Ho, W. A. Eaton, J. P. Collman, Q. H. Gibson, J. S. Leigh, Jr., E. Margoliash, K. Moffat, and W. R. Scheidt, Elsevier-North Holland, New York, 1982, p. 141.
23. I. M. Russu, N. T. Ho, and C. Ho, *Biochim. Biophys. Acta*, 1987, **914**, 40.
24. J. Monod, J. Wyman, and J.-P. Changeux, *J. Mol. Biol.*, 1965, **12**, 88.
25. D. E. Koshland, Jr., G. Némethy, and D. Filmer, *Biochemistry*, 1966, **5**, 365.
26. L. W.-M. Fung, A. P. Minton, and C. Ho, *Proc. Natl. Acad. Sci. USA*, 1976, 73, 1581.
27. L. W.-M. Fung,. A. P. Minton, T. R. Lindstrom, A. V. Pisciotta, and C. Ho, *Biochemistry*, 1977, **16**, 1452.
28. S. Miura and C. Ho, *Biochemistry*, 1982, **21**, 6280.
29. S. Miura, M. Ikeda-Saito, T. Yonetani, and C. Ho, *Biochemistry*, 1987, **26**, 2149.
30. I. Tyuma, K. Imai, and K. Shimizu, *Biochemistry*, 1973, **12**, 1491.
31. R. T. Ogata and H. M. McConnell, *Cold Spring Harbor Symp. Quant. Biol.*, 1971, **36**, 325.
32. A. V. Pisciotta, S. N. Ebbe, and J. E. Hinz, *J. Lab. Clin. Med.*, 1959, **54**, 73.
33. J. A. Walder, R. Y. Walder, and A. Arnone, *J. Mol. Biol.*, 1980, **141**, 195.
34. V. J. LiCata, P. M. Dalessio, and G. K. Ackers, *Proteins: Structure, Function, Genetics*, 1993, **17**, 279.
35. G. G. M. VanBeck, E. R. P. Zuiderweg, and S. H. DeBruin, *Eur. J. Biochem.*, 1979, **99**, 379.
36. I. M. Russu, S.-S. Wu, N. T. Ho, G. W. Kellogg, and C. Ho, *Biochemistry*, 1989, **28**, 5298.
37. I. M. Russu, S.-S. Wu, K. A. Bupp, N. T. Ho, and C. Ho, *Biochemistry*, 1990, **29**, 3785.

Acknowledgments

I wish to thank Dr E. Ann Pratt for suggestions to improve the writing of this article. Our research on hemoglobins and erythrocytes is supported by a research grant from the National Institutes of Health (HL-24525).

Biographical Sketch

Chien Ho. *b* 1934. B.A., 1957, Williams. Ph.D., 1961, Yale University. Faculty in Biological Sciences, Carnegie Mellon University, 1979–present. Approx. 190 publications. Research interests include structure–function relationships in proteins and cell membranes, and applications of MRI and MRS to the investigation of organ functions of live animals and to tracking cell movements in live animals.

Iron–Sulfur Proteins

Ivano Bertini
University of Florence, Florence, Italy

and

Claudio Luchinat
University of Bologna, Bologna, Italy

1	Introduction	1
2	NMR and Hyperfine Coupling in Various FeS Proteins	1
3	Structural Information on the Diamagnetic Part	4
4	Related Articles	4
5	References	4

1 INTRODUCTION

FeS proteins are defined as proteins containing sulfide ions bridging two or more iron ions.[1–4] We consider here those proteins having cysteines as the only protein ligands to associate with iron (Figure 1). We mention also proteins containing a single iron coordinated to four cysteines (rubredoxins). FeS proteins have been investigated through NMR since the start of investigations into paramagnetic systems in solution[5,6] (see ***Electron–Nuclear Hyperfine Interactions***; ***Electron–Nuclear Multiple Resonance Spectroscopy***, ***Nonheme Iron Proteins***, and ***Paramagnetic Relaxation in Solution***). Most of these molecules have short electronic relaxation times, and therefore have relatively long nuclear relaxation times, which make them suitable for high-resolution NMR studies. Short electronic relaxation times are due to one or more of the following reasons:[7,8] (i) the various iron ions experience sizeable antiferromagnetic coupling, which causes a decrease in magnetic susceptibility—therefore, the nuclear relaxation times are longer than expected in the absence of magnetic coupling; (ii) polymetallic systems involving more than two metals may have new relaxation mechanisms available with respect to the uncoupled systems; and (iii) when there are two ions with different valence, one will have shorter electronic relaxation times—in the present case, iron(II) has shorter electronic relaxation times than iron(III); when magnetic coupling occurs, the electronic relaxation times of iron(III) will become shorter, approaching those of iron(II).

The observation of the NMR signals of the cysteine ligand nuclei provides information on the nature of the iron ion to which the cysteine is bound and on the extent of magnetic coupling. Recently, NOE (see ***Nuclear Overhauser Effect***) and 2D studies have permitted the sequence specific assignments of the coordinated cysteines in a number of cases.[9–19] NMR, together with magnetic Mössbauer spectroscopy, thus permits the determination of the cysteine ligands bound to a given iron ion. Owing to the progress in spectrometer design together with the optimization of the spectral parameters, the attainment of 2D and 3D spectra (see ***Biological Macromolecules: Structure Determination in Solution*** and ***Multidimensional Spectroscopy: Concepts***) is now possible on these paramagnetic systems, and, notwithstanding the fact that the presence of the paramagnetic center still complicates the life of the spectroscopist, the resolution of the first 3D structures of proteins of the type discussed here is now at hand.[20]

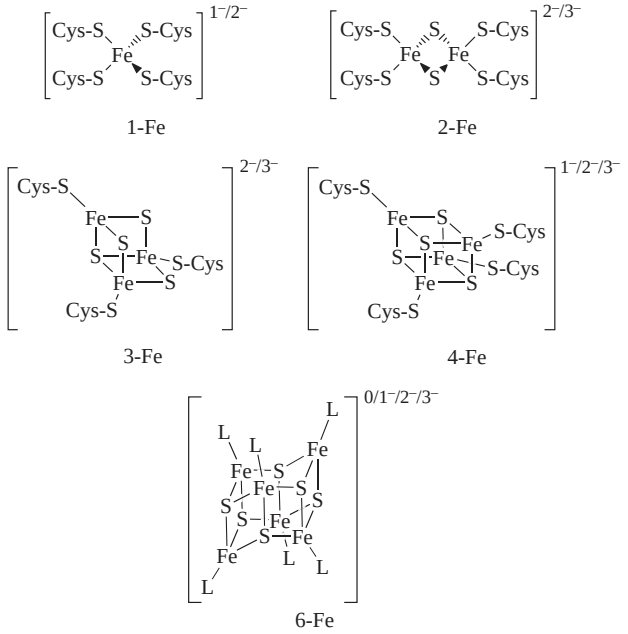

Figure 1 Iron coordination in rubredoxin (1-Fe) and in the most common iron–sulfur clusters (2-Fe, 3-Fe, 4-Fe, and 6-Fe) in proteins. The overall charges, related to the accessible oxidation states, are also shown

The following article deals first with the NMR parameters of the metal coordinated cysteines and nearby residues, and then with the more classical NMR investigations.

2 NMR AND HYPERFINE COUPLING IN VARIOUS FeS PROTEINS

The hyperfine coupling, as usual, contains contact, pseudocontact, and ligand centered contributions (see ***Electron–Nuclear Hyperfine Interactions*** and ***Electron–Nuclear Multiple Resonance Spectroscopy***). We refer here only to contact contributions, which presumably are dominant; extension to the other contributions, if needed, is easy.

2.1 $[Fe_2S_2]^{2+/1+}$-Containing Proteins

2.1.1 Oxidized $[Fe_2S_2]^{2+}$ Forms

The ^{1}H NMR spectrum shows a broad absorption around 40 ppm to high frequency which contains unresolved cysteine β-CH_2 signals (Figure 2).[21] The observability of the signal is due to the reduced paramagnetism, which results from the strong antiferromagnetic coupling. By using the formalism $\hat{\mathcal{H}} = J\hat{\boldsymbol{S}}_1 \cdot \hat{\boldsymbol{S}}_2$, the results are accounted for with a J value of about 300 cm^{-1}.[4] The ground state is diamagnetic. With increasing temperature, the hyperfine shifts increase because

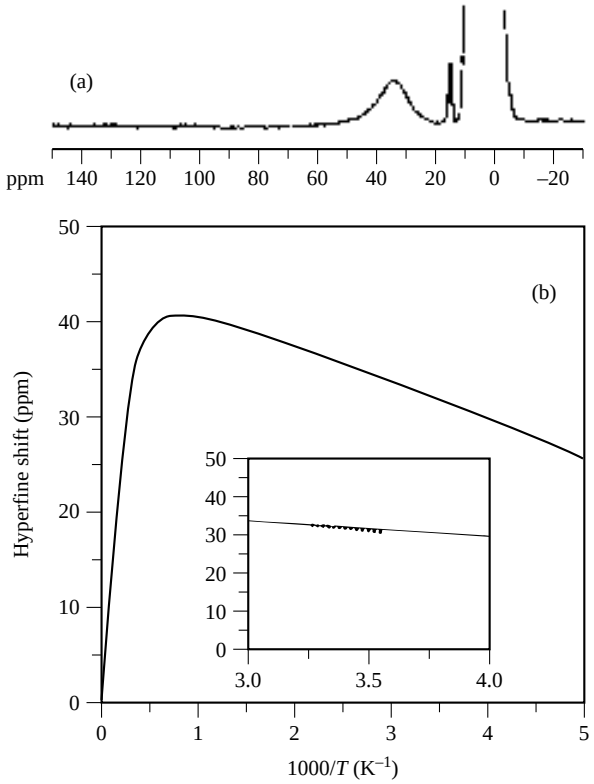

Figure 2 (a) Proton NMR spectrum (303 K, 200 MHz) of oxidized $[Fe_2S_2]^{2+}$ ferredoxin from spinach. (b) Calculated temperature dependence of the hyperfine shifts of β-CH_2 protons under antiferromagnetic coupling (J = 290 cm^{-1}) between the two iron ions, and experimental temperature dependence (inset)[4]

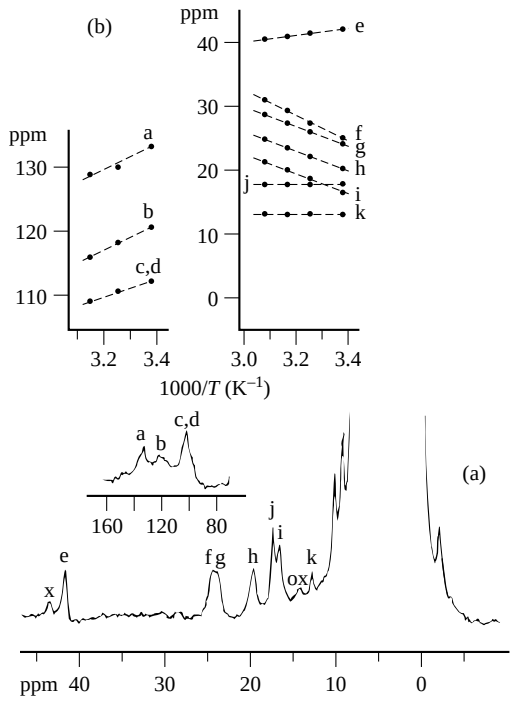

Figure 3 (a) Proton NMR spectrum (297 K, 300 MHz) of reduced $[Fe_2S_2]^{+}$ ferredoxin from spinach. (b) Experimental temperature dependence of the hyperfine shifts; signals a–d arise from β-CH_2 protons of cysteines coordinated to iron(III), while signals f–i arise from β-CH_2 protons of cysteines coordinated to iron(II)[22]

excited paramagnetic levels are more and more populated. This behavior is said to be of anti-Curie type. In the absence of magnetic coupling, as in the case of the oxidized protein rubredoxin, containing only iron(III), the cysteine β-CH_2 protons are indeed broadened beyond detection.

2.1.2 Reduced $[Fe_2S_2]^{+}$ Forms

The antiferromagnetic coupling between an iron(III) and an iron(II) ion gives a ground state with $S = \frac{1}{2}$. The ^1H NMR spectrum shows four signals between 100 and 140 ppm at high frequency (downfield), and several signals closer to the diamagnetic region (Figure 3).[22] The former have a temperature dependence of the Curie type, whereas the latter are of the anti-Curie type. It soon became evident, on the basis of the available theory,[23] that the signals with anti-Curie behavior belonged to the iron(II) domain, and the others to the iron(III) domain. This is because iron(III) with $S = \frac{5}{2}$ will force iron(II) with S = 2 to behave in a different way with respect to what would have happened in the absence of antiferromagnetic coupling. NMR, therefore, has shown that one of the two iron ions is more easily reduced, or is the only reducible ion (actually, one iron could be reduced at, for example, 90% and the other at 10%, the equilibrium between the two species being fast). In a number of proteins, two cysteines (e.g. Cys41 and Cys46 in *S. platensis* ferredoxin) are found to be close to each other and two protons can give inter-residue NOE (see ***Nuclear Overhauser Effect***). Such cysteines have been identified and recognized to be ligands of iron(II).[9,10] This biochemical information could be obtained only through NMR.

2.2 $[Fe_3S_4]^{1+/0}$-Containing Proteins

In the oxidized state the ground state is $S = \frac{1}{2}$. At the moment, two signals shifted well to high frequency have been observed which belong to one cysteine, plus two signals still at high frequency.[19,24,25] The sequence specific assignment of these signals in *D. gigas* ferredoxin II has been obtained recently[19] using the methodology described in Section 2.3. According to the present theory, we may have $S = \frac{5}{2}$ of one Fe^{3+} antiferromagnetically coupled to S = 2 of the other two Fe^{3+} ions. In other words, the magnetic coupling constants would be different among the three iron ions. The two signals of the cysteine bound to the $S = \frac{5}{2}$ Fe^{3+} are very much to high frequency, and four signals should be either at high frequency but close to the diamagnetic region, or at low frequency. The former signals should be of the Curie type.

The reduced form has S = 2, and no cysteine β-CH_2 signal has ever been observed. Probably, due to the large paramagnetism and unfavorable electronic relaxation times, the β-CH_2 signals are broadened beyond detection.

2.3 $[Fe_4S_4]^{3+}$-Containing Proteins

This cluster is present in oxidized HiPIPs. Formally, it contains one iron(II) and three iron(III). Actually, each cluster

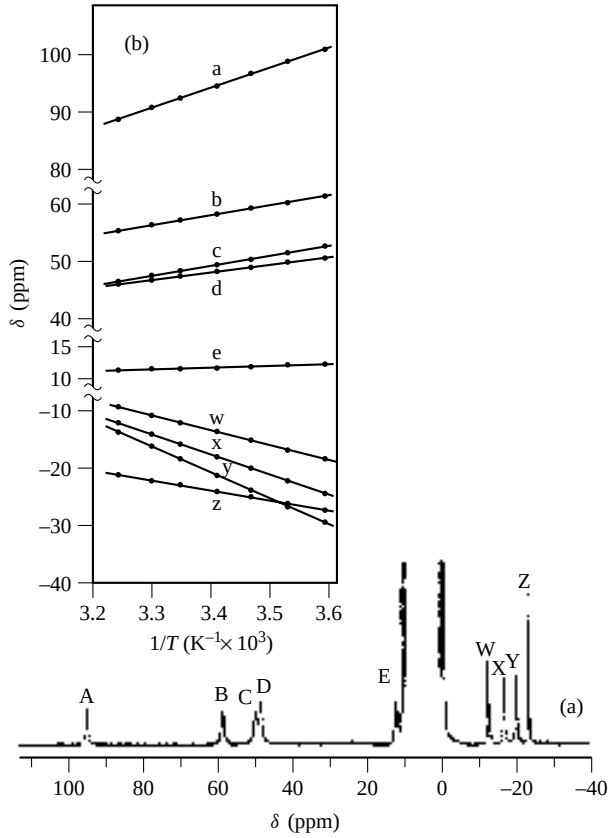

Figure 4 (a) Proton NMR spectrum (298 K, 600 MHz) of oxidized $[Fe_4S_4]^{3+}$ HiPIP II from *E. halophila*. (b) Experimental temperature dependence of the hyperfine shifts[4]

comprises a mixed valence pair with oxidation state +2.5 and two iron(III) ions. In the mixed valence pair, one electron is delocalized over two iron ions. Such a pair has a subspin larger than the iron(III) pair. The ground state is $S = \frac{1}{2}$. Therefore, the protons sensing the mixed valence pair are very much to high frequency, whereas the protons sensing the ion(III) pair are to low frequency.[12,13] The temperature dependence is shown in Figure 4. The occurrence of these valences is due to inequivalent antiferromagnetic couplings between pairs of iron ions and to electron delocalization within the mixed valence pair. The valence distribution within the cluster is determined by the protein frame. In the case of the HiPIP iso-II from *E. halophila* the residues bound to the mixed valence pair are Cys39 and Cys71, and those bound to the iron(III) ions are Cys42 and Cys55.[13] Of course, there are six different ways to delocalize one electron over two vertices of a cubane. It is believed that in another five HiPIPs investigated, a rapid equilibrium between two species differing for the valence distribution within the protein frame occurs.[11–16,26,27]

The sequence specific assignment is obtained by saturating each cysteine proton and observing NOE on nearby protons. Then, through NOESY (see ***NOESY***), COSY (see ***COSY Two-Dimensional Experiments***), or TOCSY (see ***TOCSY in ROESY and ROESY in TOCSY***) maps, the signals of the latter protons are recognized to belong to a given residue. If the X-ray structure (or a reliable structural model) is available, then the above connectivities are enough to perform the sequence specific assignment.[11–16]

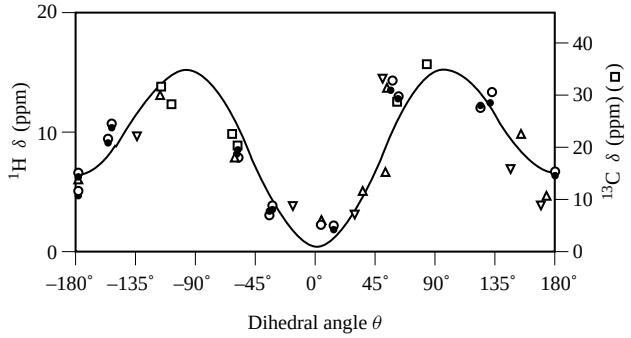

Figure 5 Plot of the hyperfine shifts of cysteine β-CH_2 protons (left) and α carbons (right-hand scale) for $[Fe_4S_4]^{2+}$ proteins, as a function of the Fe–S–C–H and Fe–S–C–C dihedral angles θ. Data refer to the following: oxidized *C. acidi urici* (●) and *C. pasteurianum* (○) ferredoxins; reduced *C. vinosum* (△) and *E. halophila* iso-II (▽) HiPIPs; and oxidized *C. acidi urici* (□, α carbon) ferredoxin[18]

2.4 $[Fe_4S_4]^{2+}$-Containing Proteins

Such polymetallic centers are present in reduced HiPIPs and oxidized ferredoxins. The iron ions have an oxidation state of +2.5. The ground state is diamagnetic, but appreciable paramagnetism arises from the population of the excited states. The shifts are all to high frequency and have an anti-Curie type of behavior.[21,28] The sequence specific assignment around the metal cluster is available for a number of HiPIPs[12,14] and two ferredoxins.[18] The system has been found ideal for investigating the angular dependence of the cysteine nuclei (protons and carbons) contact shifts.[18] It is found that such shifts depend on the M–S–C–X (X = ^{1}H,^{13}C) dihedral angle according to the following relationship:

$$\delta = a \sin^2 \theta + b \cos \theta + c \qquad (1)$$

where a = 10.9, b = −2.3, and c = 4.0 ppm.[4] In Figure 5 the relative plot is reported. Such dependence has been attributed to a predominant involvement of the π orbital of sulfur in the spin transmission.

2.5 $[Fe_4S_4]^{+}$-Containing Proteins

This cluster is present in reduced ferredoxins. The electronic properties have been again explained on the basis of a mixed valence pair ($S = \frac{9}{2}$) and two iron(II) ions (S = 4). The ground state is $S = \frac{1}{2}$, although in model compounds ground states with higher spins have been found. The overall picture is less clear than in the case of oxidized HiPIPs, because the antiferromagnetic coupling between pairs of iron ions is smaller and the excited levels are closer. All the β-CH_2 protons experience high frequency shifts, although the temperature dependences of the shifts are of both Curie and anti-Curie types.[29]

Several ferredoxins contain two Fe_4S_4 clusters. In this case they experience the equilibrium shown in Scheme 1. The equilibria between oxidized, reduced and intermediate species are slow, so that each of the three species gives a distinct pattern of NMR signals. Furthermore, saturation transfer between each pair of species is observed. The two

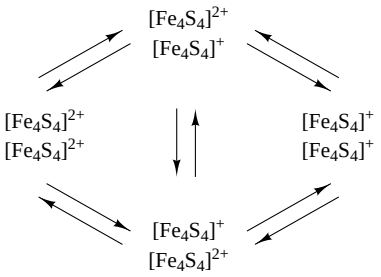

Scheme 1

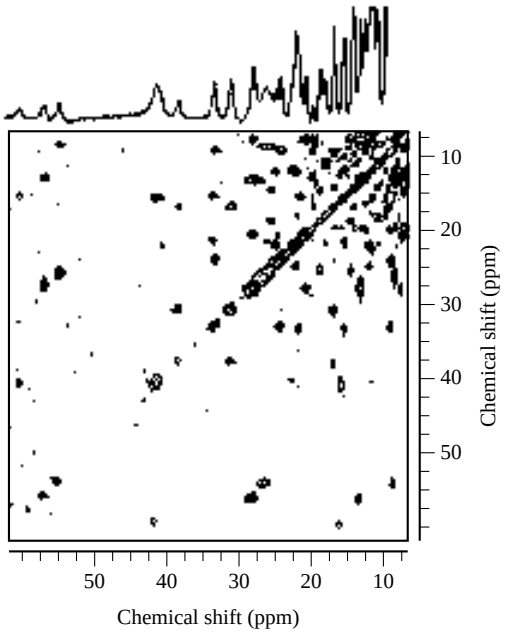

Figure 6 2D EXSY spectrum (293 K, 600 MHz) of 50% reduced *C. pasteurianum* ferredoxin. The two EXSY cross peaks from each of the most hyperfine shifted signals, belonging to the reduced form, correspond to the intermediate and oxidized forms[29]

species at intermediate oxidation states are in fast equilibrium; therefore, they give averaged signals whose position indicates the predominance of one species. The EXSY spectrum (see ***Chemical Exchange Effects on Spectra*** and ***Two-Dimensional Methods of Monitoring Exchange***) is shown in Figure 6.[29]

The sequence specific assignment of the bound cysteines is available for the proteins from *C. pasteurianum* and *C. acidi urici*.[18]

3 STRUCTURAL INFORMATION ON THE DIAMAGNETIC PART

From the above presentation it appears that FeS proteins are suitable examples with which to pursue the advancement of NMR in paramagnetic molecules, because the electronic relaxation times can be short and the paramagnetism small. Markley and others have pioneered the assignment of the protein part through ^{1}H, ^{13}C, and ^{15}N spectroscopies.[10,30,31] Most of these studies are typical diamagnetic studies. Carbon-13 and ^{15}N HETCOR (see ***Heteronuclear Shift Correlation Spectroscopy***) studies are available on natural and ^{15}N-labeled proteins, respectively.[32] In the latter case, 3D spectra ($^{15}N-^{1}H-^{1}H$) are now available.[20] In the case of the reduced HiPIP ($Fe_4S_4^{2+}$) from *C. vinosum*, 79 out of 85 residues have been assigned,[33] whereas in the case of ferredoxin ($Fe_2S_2^{+}$) from *Anabaena*, 81 out of 99 residues have been assigned and information on the secondary structure is available.[30] The difficulty remains that when a residue is close to the cluster often the sequence specific connectivities necessary for the assignment of that residue are lost. The Florence laboratory has successfully explored the possibility of overcoming this difficulty. The assignment of 71 residues out of 73 has now been reached for the recombinant HiPIP iso-I from *E. halophila*, and now the 3D structure is being refined based on 1000 NOE constraints.[20] Molecular dynamics approaches involving open shell metal ions have been developed.[13,34] The future of the NMR investigation of FeS proteins is now very promising, and biochemical information is now obtainable on the recently prepared mutants and on mixed metal proteins.

4 RELATED ARTICLES

Biological Macromolecules: Structure Determination in Solution; Electron–Nuclear Hyperfine Interactions; Electron–Nuclear Multiple Resonance Spectroscopy; Multidimensional Spectroscopy: Concepts; Nonheme Iron Proteins; Paramagnetic Relaxation in Solution; Transferrins.

5 REFERENCES

1. J. M. Berg and R. H. Holm, in *Iron–Sulfur Proteins*, ed. T. G. Spiro, Wiley-Interscience, New York, 1982, p. 1
2. H. Beinert, *FASEB J.*, 1990, **4**, 2483.
3. *Iron–Sulfur Proteins*, 1992, vol. *38, Advances in Inorganic Chemistry*, ed. R. Cammack, and A. G. Sykes, Academic Press.
4. I. Bertini, S. Ciurli, and C. Luchinat, *Struct. Bonding*, 1995, **83**, 1.
5. W. D. Phillips, in *NMR of Paramagnetic Molecules*, ed. G. N. La Mar, Jr., W. D. Horrocks, and R. H. Holm, Academic Press, New York, 1973.
6. I. Bertini and C. Luchinat, *NMR of Paramagnetic Molecules in Biological Systems*, Benjamin/Cummings, Menlo Park, CA, 1986.
7. L. Banci, I. Bertini, and C. Luchinat, *Nuclear and Electron Relaxation. The Magnetic Nucleus-Unpaired Electron Coupling in Solution*, VCH, Weinheim, 1991.
8. C. Luchinat and S. Ciurli, *Biol. Magn. Reson.*, 1993, **12**, 357.
9. L. B. Dugad, G. N. La Mar, L. Banci, and I. Bertini, *Biochemistry*, 1990, **29**, 2263.
10. B.-H. Oh and J. L. Markley, *Biochemistry*, 1990, **29**, 4012.
11. I. Bertini, F. Capozzi, C. Luchinat, M. Piccioli, and M. Vicens Oliver, *Inorg. Chim. Acta*, 1992, **198–200**, 483.
12. I. Bertini, F. Capozzi, S. Ciurli, C. Luchinat, L. Messori, and M. Piccioli, *J. Am. Chem. Soc.*, 1992, **114**, 3332.
13. L. Banci, I. Bertini, F. Capozzi, P. Carloni, S. Ciurli, C. Luchinat, and M. Piccioli, *J. Am. Chem. Soc.*, 1993, **115**, 3431.
14. I. Bertini, F. Capozzi, C. Luchinat, and M. Piccioli, *Eur. J. Biochem.*, 1993, **212**, 69.

15. L. Banci, I. Bertini, S. Ciurli, S. Ferretti, C. Luchinat, and M. Piccioli, *Biochemistry*, 1993, **32**, 9387.
16. I. Bertini, A. Gaudemer, C. Luchinat, and M. Piccioli, *Biochemistry*, 1993, **32**, 12 887.
17. D. G. Nettesheim, S. R. Harder, B. A. Feinberg, and J. D. Otvos, *Biochemistry*, 1992, **31**, 1234.
18. I. Bertini, F. Capozzi, C. Luchinat, M. Piccioli, and A. J. Vila, *J. Am. Chem. Soc.*, 1994, **116**, 651.
19. A. L. Macedo, P. N. Palma, I. Moura, J. LeGall, V. Wray, and J. J. G. Moura, *Magn. Reson. Chem.*, 1993, **31**, S59.
20. L. Banci, I. Bertini, L. D. Eltis, I. C. Felli, D. H. W. Kastrau, C. Luchinat, M. Piccioli, R. Pieratelli, and M. Smith, *Eur. J. Biochem.*, 1994, **225**, 715; L. Banci, I. Bertini, A. Dikiy, D. H. W. Kastrau, C. Luchinat, and P. Sompornpisut, *Biochemistry*, 1995, **34**, 20 619; I. Bertini, A. Dikiy, D. H. W. Kastrau, C. Luchinat, and P. Sompornpisut, *Biochemistry*, 1995, **34**, 9851; I. Bertini, L. D. Eltis, I. C. Felli, D. H. W. Kastrau, C. Luchinat, and M. Piccioli, *Chemistry*, in press; I. Bertini, A. Donaire, B. A. Feinberg, C. Luchinat, M. Piccioli, and H. Yuan, *Eur. J. Biochem.*, 1995, **232**, 192.
21. W. D. Phillips and M. Poe, in *Iron–Sulfur Proteins*, ed. W. Lovenberg, Academic Press, New York, 1977.
22. I. Bertini, G. Lanini, and C. Luchinat, *Inorg. Chem.*, 1984, **23**, 2729.
23. W. R. Dunham, G. Palmer, R. H. Sands, and A. J. Bearden, *Biochim. Biophys. Acta*, 1971, **253**, 373.
24. A. L. Macedo, I. Moura, J. J. G. Moura, J. LeGall, and B. H. Huynh, *Inorg. Chem.*, 1993, **32**, 1101.
25. S. C. Busse, G. N. La Mar, L. P. Yu, J. B. Howard, E. T. Smith, Z. H. Zhou, and M. W. W. Adams, *Biochemistry*, 1992, **31**, 11 952.
26. L. Banci, I. Bertini, F. Briganti, C. Luchinat, A. Scozzafava, and M. Vicens Oliver, *Inorg. Chem.*, 1991, **30**, 4517.
27. I. Bertini, S. Ciurli, A. Dikiy, and C. Luchinat, *J. Am. Chem. Soc.*, 1993, **115**, 12 020; I. Bertini, F. Capozzi, L. D. Eltis, I. C. Felli, C. Luchinat, and M. Piccioli, *Inorg. Chem.*, 1995, **34**, 2516.
28. M. Poe, W. D. Phillips, C. C. McDonald, and W. Lovenberg, *Proc. Natl. Acad. Sci. U.S.A.*, 1970, **65**, 797.
29. I. Bertini, F. Briganti, C. Luchinat, L. Messori, R. Monnanni, A. Scozzafava, and G. Vallini, *Eur. J. Biochem.*, 1992, **204**, 831.
30. B.-H. Oh and J. L. Markley, *Biochemistry*, 1990, **29**, 3993.
31. B.-H. Oh, E. S. Mooberry, and J. L. Markley, *Biochemistry*, 1990, **29**, 4004.
32. L. Skjeldal, W. M. Westler, B.-H. Oh, A. M. Krezel, H. M. Holden, B. L. Jacobson, I. Rayment, and J. L. Markley, *Biochemistry*, 1991, **30**, 7363.
33. J. Gaillard, J.-P. Albrand, J.-M. Moulis, and D. E. Wemmer, *Biochemistry*, 1992, **31**, 5632.
34. L. Banci, I. Bertini, P. Carloni, C. Luchinat, and P. L. Orioli, *J. Am. Chem. Soc.*, 1992, **114**, 10 683.

Biographical Sketches

Ivano Bertini. *b* 1940. Italian Doctor, 1964; free docent (1969), lecturer (1965) and Professor of Chemistry (1975) at the University of Florence, Italy. More than 300 publications; with C. Luchinat the book (1986), NMR of Paramagnetic Molecules in Biological Systems, Benjamin/Cummings, Menlo Park, CA, and with L. Banci and C. Luchinat the book (1991), Nuclear and Electron Relaxation, VCH, Germany. Research interests include the structure and dynamics of paramagnetic metalloproteins, nuclear relaxation, electron relaxation, protein chemistry, and environmental biotechnology.

Claudio Luchinat. *b* 1952. Italian Doctor, 1976, University of Florence. Introduced to NMR by I. Bertini. Faculty positions at Florence University, 1978–1986. Full Professor of Chemistry at Bologna University 1986–present. Nasini Award in Inorganic Chemistry in 1989. Approx. 200 publications. Research fields: NMR of paramagnetic species, theory of electron and nuclear relaxation, magnetic coupled systems, biological applications of NMR, bioinorganic, biophysical, environmental chemistry.

Metallodrugs

Hongzhe Sun

Department of Chemistry and Open Laboratory of Chemical Biology of the Institute of Molecular Technology for Drug Discovery and Synthesis, The University of Hong Kong, Hong Kong, P. R. China

1 Introduction 1
2 Platinum (and Other Metallo) Anticancer Drugs 1
3 Gold Anti-Arthritic Drugs 9
4 Lithium for Manic Depression 10
5 Bismuth Antiulcer (and Antimony Antileishmania) Agents 11
6 Summary 12
7 Related Articles in Volumes 1–8 12
8 References 12

1 INTRODUCTION

The use of metal containing compounds in medicine and health applications has been practiced for several thousand years.[1] The Egyptians used copper to sterilize water in 3000 BC and the Chinese were using gold in a variety of medicines 3500 years ago. In fact, the first modern chemotherapeutic agent was an organoarsenic compound (Erlich's arsphenamine), although modern pharmaceuticals are dominated by organic compounds. The success of cisplatin as an anticancer drug has largely stimulated the modern use of metal compounds for therapy and diagnosis. Beside platinum, clinically useful metal compounds include gold in antiarthritic agents, lithium for manic depression, antimony in antileishmaniasis, bismuth in antiulcer drugs, gadolinium (Gd^{3+}) as a magnetic resonance imaging contrast agent and technetium (^{99m}Tc) as radio-diagnostic agents (Table 1).[1–4] Not only do inorganic compounds extend the range of drugs available, but they are also successful in treating some diseases where organic compounds are not.

Both the metal and the bound ligands determine the biological activity of metallodrugs, not just the metal. The active species may not be that which is administered or tested in vitro, and it may be biotransformed by ligand substitution and/or redox reactions before it reaches the target sites. It is important to investigate both kinetic (ligand-exchange dynamics, mechanism and pathway) and thermodynamic aspects of the reactivity of a metal compound since biological systems are rarely at thermodynamic equilibrium. Modern multinuclear and multidimensional NMR spectroscopy is a very powerful method for investigation of the speciation of metal complexes in solution, and to a lesser extent in the solid-state, and is applicable for studies of the interaction of metal compounds with biomolecules under physiologically relevant conditions.

Although almost all of the available NMR techniques have been used for studying metallodrugs, ^{1}H NMR spectroscopy continues to be the most widely used method for monitoring the behavior of ligands and biomolecules. Other spin 1/2 nuclei such as ^{13}C, ^{15}N, ^{31}P and ^{195}Pt, and weak quadrupolar nuclei (e.g., ^{6}Li, ^{7}Li, ^{27}Al and ^{51}V, Table 2) have also quite often been used and ^{7}Li will be discussed in a later section. Most medicinally relevant metals are quadrupolar nuclei. Antimony, bismuth and gold have a limited number of useful NMR isotopes. This situation may improve at very high fields (e.g., 14.1 T and over), which are expected to dramatically sharpen the central transition ($m = 1/2$ to $-1/2$) of half-integer quadrupolar nuclei such as ^{27}Al ($I = 5/2$), ^{45}Sc ($I = 7/2$) and ^{71}Ga ($I = 3/2$), Table 2.[5] Other candidates include biologically important elements, e.g., ^{25}Mg, ^{43}Ca and ^{67}Zn. In the limit of slow isotopic molecular motion (e.g., macromolecules, $\omega\tau_c \gg 1$), the linewidth ($\Delta\nu_{1/2}$) of the central transition ($m = 1/2$ to $-1/2$) decreases with increasing magnetic field:

$$\Delta\nu_{1/2} = k\left[\frac{\chi^2}{\tau_c\nu_o^2}\right] \tag{1}$$

where χ is the quadrupolar coupling constant ($\chi = e^2qQ/h$), τ_c is the correlation time for fluctuations in the electric field gradient at the nucleus and ν_o is the resonance frequency which is proportional to the magnetic field. Decreasing temperature and increasing viscosity also give rise to a decrease in linewidths.[6] In these quadrupolar systems, the apparent shift is field-dependent, in contrast to $I = 1/2$ nuclei. The second-order dynamic frequency shift is given by:[7,8]

$$\Delta\delta_d = \delta_{obs} - \delta_{iso}\left(m = \frac{1}{2} \text{ to } \frac{-1}{2}\right) = k\left(\frac{\chi^2}{\nu_o^2}\right) \tag{2}$$

The chemical shift of ^{71}Ga in ovotransferrin, for example, is -103 ppm at 11.7 T but -57 ppm at 17.6 T.[5b]

This article provides examples of the application of NMR spectroscopy to the speciation of metallopharmaceuticals in solution and in the solid-state including biofluids and cells, and complexation to biomolecules (nucleic acids, peptides and proteins). Since the topic is vast, we focus on platinum anticancer, gold antiarthritic, lithium and bismuth antiulcer drugs. The reader is referred to related papers in this encyclopedia and elsewhere.[9]

2 PLATINUM (AND OTHER METALLO) ANTICANCER DRUGS

The accidental observation of the inhibition of bacterial division by *cis*-diamminedichloroplatinum(II) (cisplatin, *cis*-$Pt(NH_3)_2Cl_2$ or *cis*-DDP) in 1965 by Rosenberg led to the antiproliferative effects of this compound being applied to therapy of human tumours.[10–12] Today cisplatin is among the most active and widely used anticancer drugs, together with the second-generation drug carboplatin $Pt(NH_3)_2(CBDCA{-}O,O')$, where CBDCA is cyclobutane-1,1-dicarboxylate). Two new platinum compounds nedaplatin and oxaliplatin have recently been approved for clinical use in Japan and France, respectively (Scheme 1). Ru^{3+} compounds and the organometallic complex titanocene dichloride also have promising anticancer activities.

Table 1 Some metallodrugs and diagnostic agents

Compounds	Product	Use	Transformation events	Biological targets
Li_2CO_3	Camcolit	Manic depression	Widely distributed in body	Enzymes in inositol phosphate pathways
$Na_2[Fe^{II}(NO)(CN)_5]$	Nipride	Hypotensive crisis (vasodilator)	Release of CN^-, reaction with thiols	Release of NO to guanylate cyclase
Zn^{II} pyrithione	Omadine	Antimicrobial (antidandruff)		Skin
$^{67}Ga^{III}$ citrate	Neoscan	Diagnostic radio-imaging	Transferrin	Tumors and inflammatory lesions
$^{99m}Tc^{V}$-D,L-HM-PAO[a]	Ceretec	Diagnostic radio-imaging	Ligand exchange?	Brain
$^{99m}Tc^{I}[(C{\equiv}N{-}R)_6]^{+}$ [b]	Cardiolite	Diagnostic radio-imaging	Potassium channel?	Myocytes (heart)
Ag^{I} sulfadiazine	Flamazine	Antibacterial (burn wounds)	Protein binding	Enzymes (e.g., phosphomannose isomerase), cell walls?
$Na[Sb^{V}$ stibogluconate]	Pentostam	Antileishmanial	Unknown	Parasites in liver
$BaSO_4$	Baridol	X-ray contrast agent	None (insoluble in water)	Passage through GI tract
$[Gd^{III}(DTPA)](meglumine)_2$	Magnevist	MRI contrast agent	None	Extracellular water
$[Gd^{III}(DOTA)]^-$	Dotarem	MRI contrast agent	None	Extracellular water
cis-$[Pt^{II}Cl_2(NH_3)_2]$	Cisplatin	Anticancer	Hydrolysis, L-Met adducts and GSH	DNA
$Pt^{II}[(CBDCA)(NH_3)_2]$ [c]	Carboplatin	Anticancer	L-Met adducts, ring open and release of CBDCA, and GSH	DNA
Au^{I} thiomalate	Myocrisin	Antiarthritic drug	Thiol exchange, MT, albumin (Cys^{34}), oxidation to Au^{III}?	Lysosomes (aurosomes), thiol group of proteins
Et_3P Au^{I}(acetylthioglucose)	Auranofin	Oral antiarthritic drug	Phosphine oxidation, Au^{I} to Au^{III}?	Lysosomes (aurosomes), thiol group of proteins
Colloidal Bi^{III} citrate	De-Nol	Antiulcer and antimicrobial	GSH, MT and transferrin?	Block Fe^{III} uptake? enzymes in *Helicobacter pylori*?
Ranitidine Bi^{III} citrate	Pylorid	Antiulcer and antimicrobial	GSH, MT and transferrin?	Block Fe^{III} uptake? enzymes in *Helicobacter pylori*?

[a]HM-PAO is hexamethyl propyleneamine oxime.
[b]C≡N–R represents 2-methoxyisobutylisocyanide.
[c]CBDCA is 1,1-dicarboxycyclobutane.

Table 2 Useful NMR properties of selected elements

Nucleus	Spin	Natural abundance (%)	Quadrupole moment (10^{-28} m)	Receptivity/^{13}C	NMR Frequency (100 MHz ^{1}H)
^{6}Li	1	7.42	-6.4×10^{-4}	3.58	14.717
^{7}Li	3/2	92.58	-3.7×10^{-2}	1.54×10^3	38.864
^{13}C	1/2	1.108		1	25.145
^{14}N	1	99.63	1.6×10^{-2}	5.7	7.224
^{15}N	1/2	0.37		2.2×10^{-2}	10.136
^{25}Mg	5/2	10.00	0.1999	1.54	6.126
^{27}Al	5/2	100	0.140	1.17×10^3	26.077
^{31}P	1/2	100		3.77×10^2	40.480
^{51}V	7/2	99.76	-5.2×10^{-2}	2.16×10^3	26.350
^{67}Zn	5/2	4.11	0.150	0.665	6.252
^{69}Ga	3/2	60.40	0.168	2.38×10^2	24.040
^{71}Ga	3/2	39.60	0.106	3.19×10^2	30.495
^{109}Ag	1/2	48.18		0.276	4.653
^{195}Pt	1/2	33.8		19.1	21.414

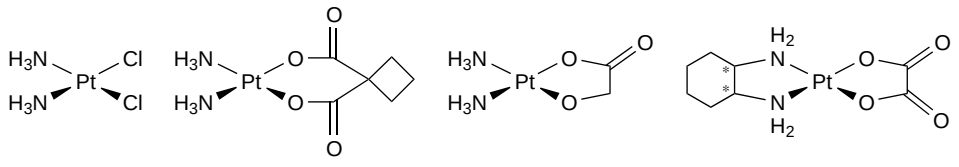

Scheme 1 Structures of clinically used platinum compounds. The carbons marked with asterisks are chiral carbons (Oxaliplatin contains *R*,*R*-1,2-diaminocyclohexane)

2.1 ^{195}Pt, ^{15}N NMR and Inverse [^{1}H, ^{15}N] NMR Spectroscopy

In addition to ^{1}H NMR, the use of ^{15}N and ^{195}Pt NMR spectroscopy has made an important impact, along with other biophysical techniques, in the understanding of the mode of action of platinum anticancer drugs. This includes the detection of intermediates arising during the hydrolysis process and in reactions with either DNA or amino acids (peptides and proteins), and metabolites in body fluids.[9] ^{195}Pt ($I = 1/2$) is a reasonably sensitive nucleus for NMR detection with natural abundance of 33.8% (Table 2) and a receptivity relative to ^{1}H of 3.4×10^{-3}. The spin-relaxation time for ^{195}Pt is usually in the range of 0.014–8.3 s, with most values less than 2 s.[13] The short relaxation times (T_1) are attributed to efficient relaxation via the chemical shift anisotropy (CSA) and spin-rotation (SR) contributions. The advantage of the increased sensitivity achievable at high magnetic field for ^{195}Pt is offset by the increase in linewidths due to CSA relaxation ($\propto B_0^2 \tau_c$). Similarly, ^{195}Pt satellites in either ^{1}H or ^{15}N spectra of Pt^{2+} complexes are often broadened beyond detection at high fields, again due to CSA relaxation of ^{195}Pt, which excludes the use of [^{1}H, ^{195}Pt] inverse detection to enhance the sensitivity of detection. The low detection limit (ca. 10 mM) precludes detection of natural abundance ^{195}Pt signals under biologically relevant conditions (e.g., in body fluids), but can be enhanced by isotopic enrichment of ^{195}Pt to >95%. A previous report has shown that DNA platination at millimolar concentrations can readily be studied with ^{195}Pt enrichment and both mono- and bi-functional guanine adducts were detected (Scheme 2 and Figure 1).[14] The rate-determining step for initial binding of cisplatin was found to be hydrolysis of the first chloride and similarly the rate-determining step for closure of the monofunctional species to form bifunctional adducts was found to be hydrolysis of the second chloride.

The chemical shift range of ^{195}Pt is very large (15 000 ppm and usually in the range from −6000 to 9000 ppm). Ready differentiation between Pt^{2+} and Pt^{4+} is usually possible. The former (Pt^{2+}) tends to have chemical shifts at the higher field while the latter resonates in the low-field end of the range. The ^{195}Pt chemical shift in monomeric compounds is usually highly sensitive to the nature of bound donor atoms and can

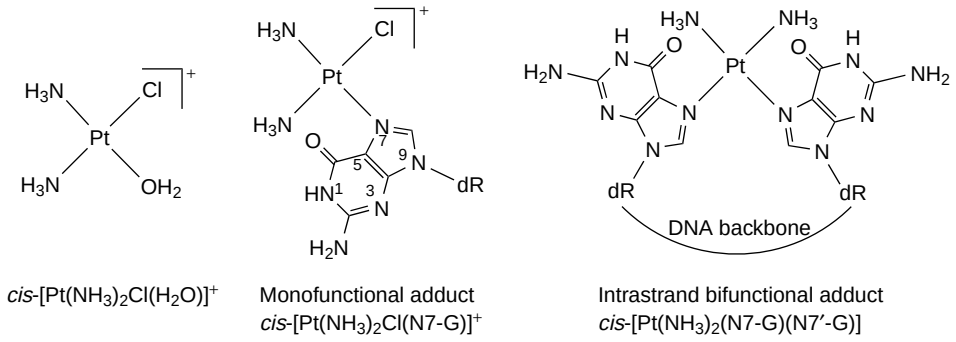

Scheme 2 Structures of cisplatin aqua-chloro intermediate, mono- and bi-functional DNA adducts

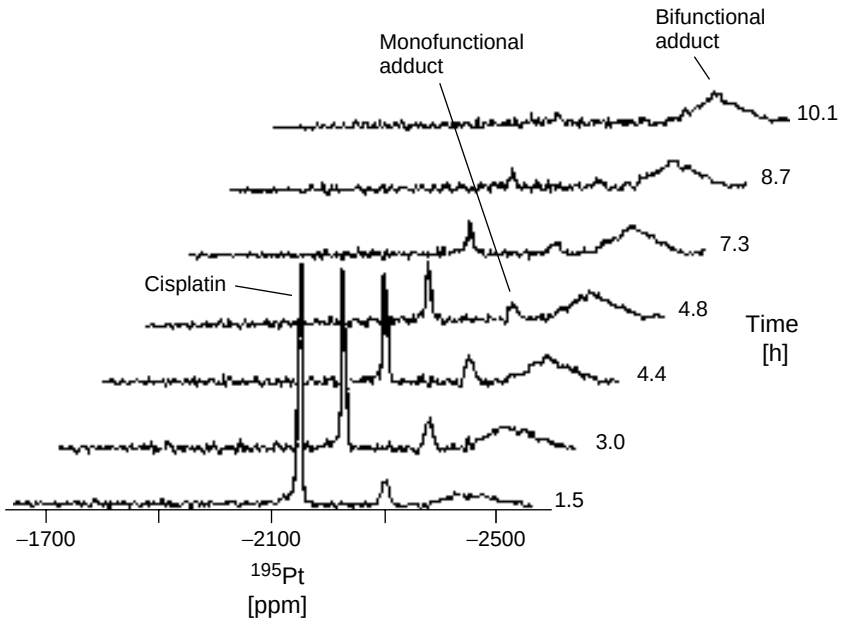

Figure 1 Time-dependent ^{195}Pt NMR spectra of the reaction between cisplatin and chicken erythrocyte DNA at 37 °C in 3 mM NaCl, 1 mM NaH_2PO_4. (Adapted with permission from Ref.[14])

Table 3 ^{195}Pt chemical shifts of *cis*-Pt complexes with different donor atoms

Cis-Pt complexes	$\delta(^{195}Pt)$ range[a]	References
cis-$[Pt(NH_3)_2Cl_2]$	−2048 to −2168[b]	**14,15**
cis-$[Pt(NH_3)_2Cl(O)]$	−1806 to −1841	**16**
cis-$[Pt(NH_3)_2Cl(N)]$	−2295 to −2369	**14,18,19**
cis-$[Pt(NH_3)_2(O)_2]$	−1570 to −1730	**15–17**
cis-$[Pt(NH_3)_2(N)_2]$	−2440 to −2661	**14,16,17**
cis-$[Pt(NH_3)_2(N)(O)]$	−2058 to −2147	**16,17**
cis-$[Pt(NH_3)_2(N)(S)]$	−2800 to −3218	**20,21**
cis-$[Pt(NH_3)_2(O)(S)]$	−2618 to −2800	**20,21**
cis-$[Pt(NH_3)_2(S)_2]$	−3200 to −3685	**20,21**

[a]Reference to Na_2PtCl_6.
[b]Slightly varies in different solvents, $\delta(^{195}Pt) = -2048$ (DMF), −2097 (DMSO) and −2149 (water).

be used as a diagnostic tool to distinguish various types of ligand binding to platinum (Table 3).[15–21] Moreover, the ^{195}Pt chemical shifts are very sensitive to complex geometry, e.g., geometrical isomers and diastereomers, and can be utilized in the detection of different intermediates formed during the reaction of platinum complexes with biomolecules. ^{195}Pt NMR shifts for conformers of bis-guanine derivatives differing only by rotation about the Pt–N7 bond can vary by as much as 13 ppm (see Scheme 2).[22] Sometimes even isotopomers are distinguishable: the ^{195}Pt isotope shift difference for Pt–^{35}Cl and Pt–^{37}Cl is 0.17 ppm and that for Pt–^{79}Br and Pt–^{81}Br is 0.03 ppm.[23] Therefore in principle it is possible to count the number of Cl and Br ligands bonded directly to Pt via the isotope-splitting pattern. But in practice it is difficult to resolve such multiple patterns because of line broadening, which is due to either relaxation mechanism or temperature drift. The latter is a problem since the chemical shift of ^{195}Pt is strongly temperature-dependent (up to 1 ppm/K).

^{14}N NMR spectroscopy can be useful for ammine ($-NH_3$) and amine ($-NH_2$,–NH) groups which coordinate to Pt. Since ^{14}N is a quadrupolar nucleus (Table 2), and quadrupolar relaxation is dominant when the environment of ^{14}N has a low symmetry. This leads to broad resonances and subsequently reduces the sensitivity. However, the quadrupolar nature of ^{14}N has the beneficial effect of shortening the relaxation rate and allowing rapid pulsing so that a large number of transients can be acquired. It is still possible to follow reactions of cisplatin in blood plasma and cell-culture media at millimolar drug concentrations and to monitor ammine release.[24]

^{15}N NMR is particularly useful in the study of the aqueous chemistry of cisplatin and other platinum ammine/amine compounds since ^{15}N-labeled compounds can readily be prepared. More importantly, both the ^{15}N NMR chemical shift (Figure 2) and the $^1J(^{15}N-^{195}Pt)$ coupling constant are sensitive to the nature of the *trans*-ligand in Pt–NH_3 (or Pt–NH_2) complexes which provide useful information for identifying the ligands in the coordination spheres of Pt^{2+} (and Pt^{4+}) (Figure 2). This technique has been used to characterize the reaction products of ^{15}N-labeled cisplatin.[25]

The low receptivity of ^{15}N (3.85×10^{-6} relative to ^{1}H) limits its usefulness for directly detected ^{15}N-NMR studies of cisplatin and related platinum ammine/amine complexes in biofluids. The sensitivity of detection can be improved to some extent by ^{15}N isotopic enrichment and further enhanced

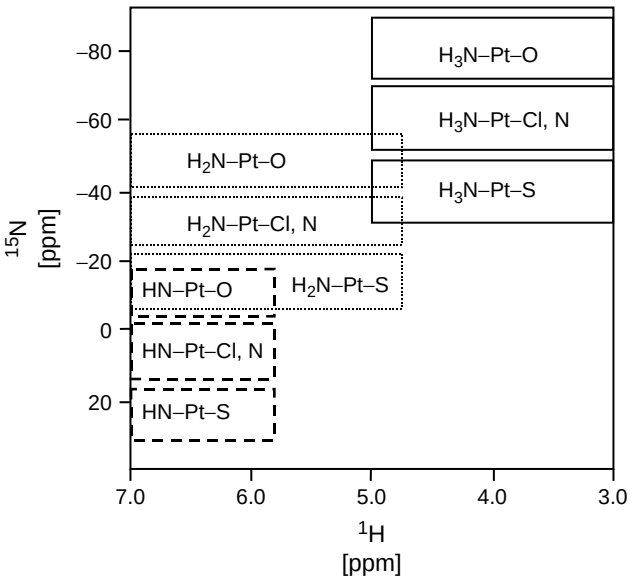

Figure 2 Variation of ^{1}H and ^{15}N chemical shifts with the *trans*-ligand in Pt^{II}–NH, Pt^{II}–NH_2 and Pt^{II}–NH_3 complexes. (Adapted with permission from Ref.[9b])

by polarization transfer from ^{1}H via for example, DEPT and INEPT experiments. But in practice, this enhancement of ^{15}N signal will be affected by the rate (k_{ex}) of exchange of protons between an ammine (and amine) and a solvent (e.g., water), and is hampered by rapid chemical exchange ($k_{ex} > J$). The maximum enhancement in ^{15}N signal via polarization transfer is only 9.8 (i.e., γ_{1H}/γ_{15N}). The repetition time of the pulse sequence is governed by the ^{1}H rather than the longer ^{15}N spin-lattice relaxation (T_1) which allows more rapid pulsing. ^{15}N{^{1}H} DEPT NMR techniques have been allowed the detection of rapidly changing intermediates in the reaction of ^{15}N labeled cisplatin with glutathione and also of ammine release following interaction of cisplatin with intracellular components of intact red blood cells at concentrations as low as 1 mM.[26] This method can be of values in situation where ^{1}H NMR resonances are very broad.

However, inverse ^{15}N methods (^{1}H{^{15}N}) are often preferred due to the greatly improved sensitivity for detection, by a theoretical maximum of 306 ($\{|\gamma_{1H}|/|\gamma_{15N}|\}^{5/2}$) with respect to directly detected ^{15}N. This technique is based on the large one-bond $^1J(^{15}N-^1H)$ coupling constant (ca. 70 Hz for $^{15}NH_3$) and it is necessary to work in H_2O (90% H_2O) since the NH protons normally exchange with deuterium rapidly in D_2O. The exchange of NH with solvent is much faster for Pt^{4+} than for Pt^{2+} complexes at neutral pH. Besides the high sensitivity, inverse detection also brings a simplification of complicated spectra since it selectively detects those protons directly attached to the labeled ^{15}N in the sample (e.g., Pt–NH_3), by use of the heteronuclear single (or multiple) quantum coherence transfer (HSQC or HMQC) pulse sequence. Each distinct type of Pt–NH resonance appears as a singlet, sometimes together with broadened ^{195}Pt satellites if ^{15}N decoupling is employed during the acquisition period (e.g., GARP method[27]). Water suppression can be achieved by the use of pulse sequences incorporating pulsed field gradient (which can be employed for both coherence selection and suppression of water signal).[28]

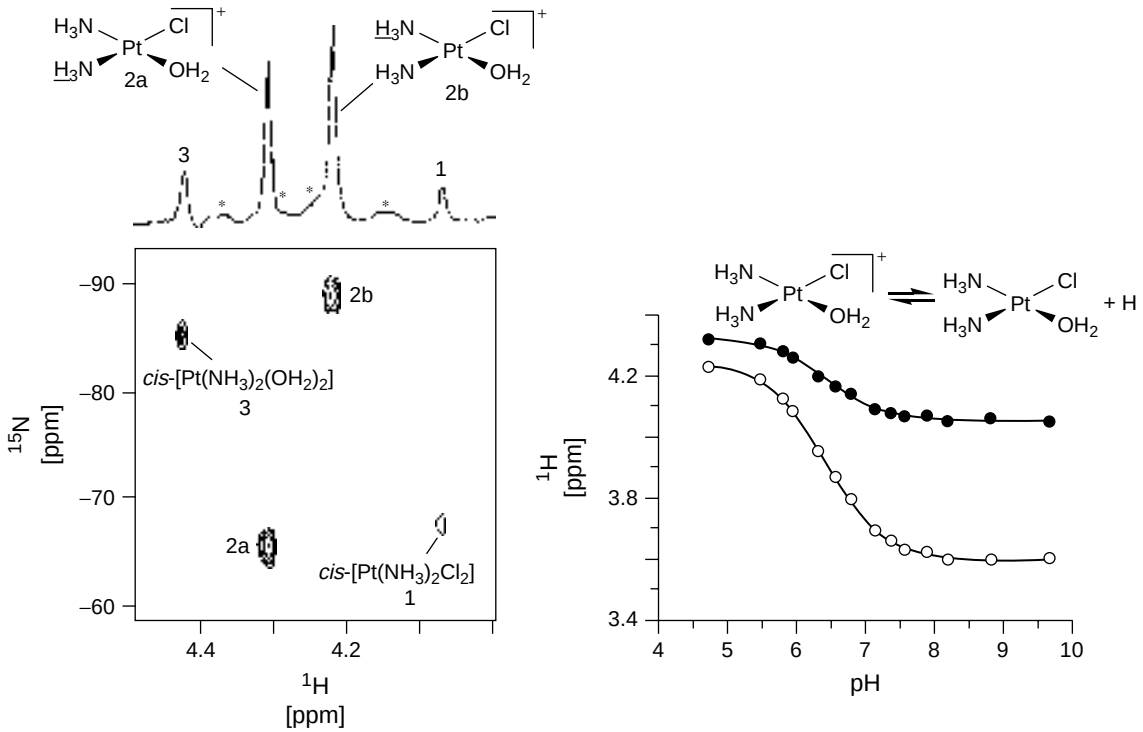

Figure 3 [^{1}H, ^{15}N] spectrum (left) of a 5 mM solution containing ^{15}N-cisplatin and its hydrolysis products in 95 : 5 = H_2O/D_2O at pH 4.72, 300 K. ^{195}Pt satellites are marked on the 1D ^{1}H spectrum with an asterisk. Plots of the ^{1}H shifts of Pt–NH_3 vs. pH allow direct determination of the pK_a values (right). (Adapted with permission from Ref.[29])

A one-dimensional ^{1}H spectrum (the first increment in a 2D experiment) contains only protons which are directly attached to the labeled ^{15}N in the sample (Pt–^{15}N<u>H</u>) and all others are eliminated. The combined detection of ^{1}H and ^{15}N in a reverse experiment, '2D [^{1}H, ^{15}N] HSQC NMR', is extremely powerful since the ^{15}N chemical shift range is large and diagnostic of the *trans*-ligand (Figure 2). The ^{195}Pt satellites in a 2D [^{1}H, ^{15}N] spectrum sometimes appears as diagonal peaks which correspond to the $^2J(^1\text{H}-^{195}\text{Pt})$ and $^1J(^{15}\text{N}-^{195}\text{Pt})$ coupling constants (again diagnostic) in the ^{1}H and ^{15}N dimensions, respectively (Figure 3) if they are not broadened beyond detection. The 2D [^{1}H, ^{15}N] method with ^{15}N-labeled platinum anticancer agents is particularly useful in studies of body fluids or cell culture media since thousands of overlapping ^{1}H resonances from other substances are filtered out. It takes just a few minutes to acquire a 2D [^{1}H, ^{15}N] spectrum at millimolar concentration and it is possible to detect ^{15}N-labeled species at concentrations as low as 20 μM.

2.2 Activation of Platinum Anticancer Drugs and Their Interaction with Nucleotides and DNA

It is widely accepted that the ultimate target for platinum anticancer drug is DNA and Pt–OH_2 bonds are much more reactive toward DNA and other biomolecules than Pt–Cl or Pt–OH bonds. The mechanism of action of cisplatin is believed to involve activation via hydrolysis inside cells where the concentration of chloride (Cl^-) (ca. 4 mM) is much lower than outside cells (ca. 104 mM). Therefore it is important to determinate the rates of hydrolysis and pK_a values of the hydrolysis products. By the use of 2D [^{1}H, ^{15}N] HMQC spectroscopy, the pK_a values can be rapidly measured at low concentration (Figure 3). By fitting the shift changes of ^{1}H NMR and ^{15}N-NMR as a function of pH, the pK_a values of the monoaqua *cis*-$[Pt(NH_3)_2Cl(H_2O)]^+$ (6.41) and diaqua adducts *cis*-$[Pt(NH_3)_2(H_2O)_2]^{2+}$ (5.37 and 7.21) were determined.[29] The equilibrium constant for the first stage of cisplatin hydrolysis was also determined to be 2.72 based on the resonance integration of reacted cisplatin, and the mono- and di-aqua adducts. Since all hydrolysis products can be readily distinguished in the spectrum, the problems associated with other methods are overcome. The pK_a values of aqua ligands of related platinum anticancer complexes such as *cis*- and *trans*-$[Pt(NH_3)(cyclohexamine)Cl_2]$, and *cis*-$[Pt(NH_3)(2\text{-Pic})Cl_2]$ (2-Pic is 2-methyl-pyridine), have also been determined by this [^{1}H, ^{15}N] NMR method.[30,31] The rate of hydrolysis for each chloride (Cl^-) ligand of *cis*-$[Pt(NH_3)(2\text{-Pic})Cl_2]$ was determined by the time-dependence of the [^{1}H, ^{15}N] NMR spectra for a period of over 20 h and was found to be slower than cisplatin.[31]

The reactions between ^{15}N-labeled cisplatin and guanosine-5′-monophosphate (5′-GMP) have also been investigated in aqueous solution by NMR spectroscopy.[32] The short-lived reactive species *cis*-$[Pt(NH_3)_2Cl(H_2O)]^+$ was detected during the early stages, followed by the formation of the mono- and bis-GMP adducts (Scheme 2). Hydrogen-bonding interactions were suggested to occur between N–H protons in Pt–NH_3 and deprotonated 5′-phosphate of GMP. Similar behavior was also observed between the N–H protons in ^{15}N-labeled ethylenediamine platinum complex $\{Pt(en)\}^{2+}$ with GMP and adenosine monophosphate (AMP).[33]

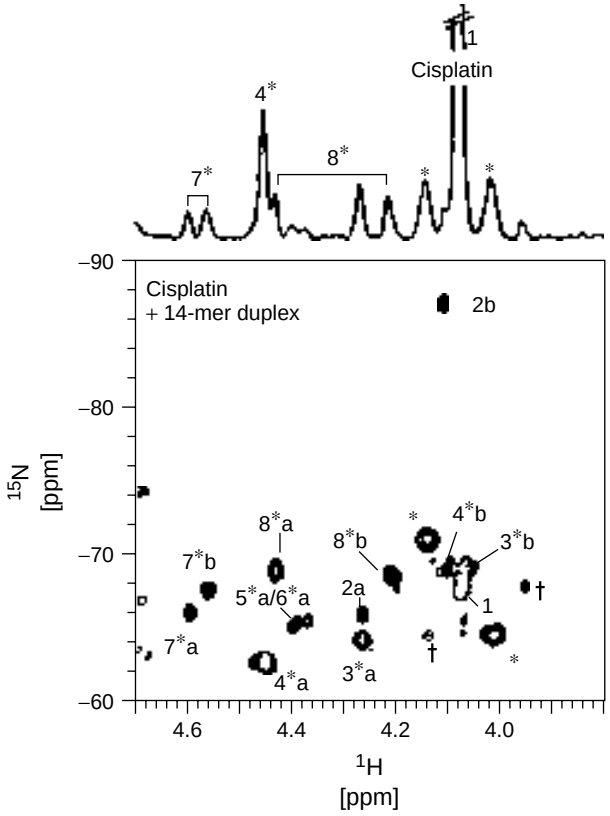

Figure 4 2D [^{1}H, ^{15}N] HSQC-NMR spectrum of 14-mer duplex d(ATACATG*G*TACATA)·d(TATGTACCATGTAT) after reaction with ^{15}N-cisplatin for 8 h. Labels: *, ^{195}Pt satellines; ‡, artefact. Peaks are assigned: **1**, cisplatin; **2**, *cis*-[Pt(NH$_3$)$_2$Cl(H$_2$O)]$^+$; **3**, *cis*-[Pt(NH$_3$)$_2$Cl(N(7)-G(7))]$^+$; **4**, *cis*-[Pt(NH$_3$)$_2$Cl(N(7)-G(8))]$^+$; **5/6**, *cis*-[Pt(NH$_3$)$_2$Cl(N(7)-G(18/25))]$^+$; **7,8**, *cis*-[Pt(NH$_3$)$_2$(N(7)-G(7))(N(7)-G(8))]$^+$ (distorted and kinked forms). (Adapted with permission from Ref.[35])

The detailed kinetics for the interaction of cisplatin with 10- and 14-mer oligonucleotides have been investigated. The major species in the pathways of platination of mono- and bi-functional adducts (both single- and double-strand GG adducts) can be simultaneously detected in a single [^{1}H, ^{15}N] NMR experiment (Figure 4).[34,35] The aqua-chloro intermediate which was usually present at micromolar concentrations, is readily monitored in these experiments and its lifetime was determined (ca. 8 min at 310 K) directly for the first time. Kinetic data obtained by [^{1}H, ^{15}N] NMR techniques are in close agreement with those determined by ^{195}Pt NMR spectroscopy (with enriched ^{195}Pt).[14] However, no aqua-chloro intermediate was detected previously by ^{195}Pt NMR during the course of the reaction with DNA. As expected, the reactions of cisplatin proceed via an aqua-chloro intermediate, and lead to two monofunctional adducts on the duplex and two on the GG-containing single strand. One of the GG residues is platinated three-fold faster than the other, which is in line with the results obtained by HPLC,[36] and ring closure to form a GG chelate on the duplex (3′-G) occurs also faster by about an order of magnitude for one monofunctional adduct than the other. Surprisingly, the 5′-G monofunctional adduct on the duplex has a very long lifetime (over 5 days at 298 K).[35,37] CD, ^{1}H and [^{1}H, ^{15}N] NMR data have shown that the 14-base GG-platinated DNA duplex d(ATACATG*G*TACATA)·d(TATGTACCATGTAT) where G*G* is platinated guanine (at N7) by the *cis*-[Pt(NH$_3$)$_2$]$^{2+}$, undergoes a reversible pH-induced structural transition (pK_a 4.8) between kinked-duplex and distorted forms. Binding of platinated duplex to the high-mobility-group protein 1 (HMG1) box A is at the concave face of the protein, and the kinked duplex may be converted to a different distorted form.[38] It is known that platinum forms bifunctional DNA adducts with the following order of sequence preference: –GG– > –AG– ≫ –GA– and that DNA platination is kinetically controlled. There is a clear preference for the formation of monofunctional adduct of cisplatin with –AG– over the –GA– sequence as judged from [^{1}H, ^{15}N] a HSQC NMR study. Closure to form the bifunctional adduct is more rapid in the former case than in the latter.[39] This could explain, at least in part, why –AG– bifunctional adducts are preferentially formed and few platinated –GA– adducts are observed.

2.3 Structures of Platinated Oligonucleotides

The anticancer activity of cisplatin and related complexes is believed to result from strong bonding of platinum to DNA affording mainly intrastrand –GG– and –AG– cross-links, the local structure of which are subsequently modified in such a way that apotosis is induced.[40] The presence of these DNA cross-links in cisplatin-treated cancer patients correlates with positive responses to treatment with the drug.[41] Such lesions have deleterious effects on DNA replication and transcription and cause mutations.[42,43] Previous studies have shown that platinated-DNA was recognized by proteins containing one or more high-mobility-group (HMG) domains[44–46] and structure-specific recognition protein 1.[47] The shielding of excision-repair caused by the binding of HMG proteins to DNA has been confirmed by both in vitro and in vivo experiments.[48,49] Elucidation of the structural distortion of the cisplatin (and related complexes) DNA adduct at the molecular level is definitely an important step toward understanding the activity of platinum anticancer drugs.

Various techniques especially those of X-ray crystallography and NMR spectroscopy, can be utilized to study the structure of platinated DNA adducts, but NMR spectroscopy is the focus of this paper. ^{1}H NMR is particularly useful for studying DNA and almost all of the modern NMR techniques can be used. Additional information can be obtained from studies with other nuclei such as ^{13}C, ^{15}N, ^{31}P and ^{195}Pt. Platinated DNA structures were determined based on observed 1D and 2D NMR data (e.g., NOE) with the aid of molecular mechanics and dynamics calculations, and have been reviewed previously.[50]

The structures of a number of platinated DNA adducts at either d(G*pG*) or d(A*pG*) sites have been solved and are listed in Table 3.[51–60] Platinum cross-link induced structural distortion seems to be a common feature. The solution structure of the platinated octameric duplex d(CCTG*G*TCC)·d(GGACCAGG) shows that it is unwound by ∼21°, and kinked by ∼58° toward the major groove at the d(G*pG*) site (Figure 5A).The minor groove is significantly widened and flattened at the platination site.[51] The overall features are similar to those observed for the crystal structure of the platinated dodecameric duplex.[61] The platinated duplex d(GCCG*G*ATCGC)·d(GCGATCCGGC) is also kinked by

Table 4 Lists of NMR structures of platinated DNA

Pt^{2+} complex	Sequence	Comments	References
cis-$[Pt(NH_3)_2]^{2+}$	d(CCTG*G*TCC)·d(GGACCAGG)	1,2-intrastrand cross-link d(G*pG*)	**51**
cis-$[Pt(NH_3)_2]^{2+}$	d(GCCG*G*ATCGC)·d(GCGATCCGGC)		**52**
cis-$[Pt(NH_3)$(4-amino-TEMPO)$]^{2+}$	d(CTCTCG*G*TCTC)·d(GAGACCGAGAG)		**56**
cis-$[Pt(NH_3)_2]^{2+}$	d(CCTCTG*G*TCTCC)·d(GGAGACCAGAGG)		**53**
cis-$[Pt(NH_3)_2]^{2+}$	d(ATACATG*G*TACATA)·d(TATGTACCATGTAT)		**54**
cis-$[Pt(NH_3)$(2-Pic)$]^{2+}$	d(ATACATG*G*TACATA)·d(TATGTACCATGTAT)		**55**
cis-$[Pt(NH_3)_2]^{2+}$	d(CTCA*G*CCTC)·d(GAGGCTGAG)	1,2-intrastrand cross-link d(A*pG*)	**57**
cis-$[Pt(NH_3)_2]^{2+}$	$d(CATAG*CTATG)_2$	1,2-interstrand cross-link	**58**
cis-$[Pt(NH_3)_2]^{2+}$	d(CCTCG*CTCTC)·d(GGAGCG*AGAG)	d(G*pG*)	**59**
cis-$[Pt(NH_3)_2]^{2+}$	d(CTCTAG*TG*CTCAC)·d(GTGAGCACTAGAG)	1,3-intrastrand cross-link d(G*pXpG*)	**60**

~60° toward the major groove at the Pt^{2+} coordination site and unwound by 12–19°.[52] The solution structure of the platinated dodecamer duplex was reported recently. The *cis*-$[Pt(NH_3)_2]^{2+}$–d(G*pG*) lesion causes the two adjacent –G*G*–bases to roll toward one another by 49°, leading to an overall helix kink by 78°.[53] The helix deformation in solution is greater than that in crystal, and the structural differences may be attributable to crystal packing interactions. The structure of a AT-rich DNA 14-mer d(ATACATG*G*TACATA)·d(TATGTACCATGTAT) was determined and it was suggested that the bend of DNA induced by cisplatin is sequence dependent.[54] Platination causes the overall DNA duplex to bend by ~52° toward the 3-end [with respect to the d(G*pG*) strand], in contrast to those GC-rich structures which bend toward the 5-end. The minor groove opposite the platination site is again widened and flattened. The solution structure of the d(G*pG*) platinated adduct of the nitroxide spin-labeled complex *cis*-$[Pt(NH_3)$(4-amino-TEMPO)$]^{2+}$ (TEMPO = 2, 2, 6, 6-tetramethylpiperidinyloxy) with the undecamer duplex has been determined by using conventional NMR methods (e.g., NOE studies) and long-range (10–20 Å) proton–electron distance constraints.[56] The use of long-range distance constraints did not affect the local geometry of the adduct only the global structure, but allows a better definition of the global structures of the duplexes. The platinated DNA duplex d(CTCA*G*CCTC)·d(GAGGCTGAG) cross-linked at the d(A*pG*) sequence by *cis*-$[Pt(NH_3)_2]^{2+}$ also bends to the double helix towards the major groove in a way similar to that observed for the d(G*pG*) crosslink.[52,57] Molecular modeling based on published NMR and X-ray data suggested that all duplexes in the three-base-pair d(XpG*pG*) and d(XpA*pG*) region are very similar and protein binding does not greatly change the structure of this region.[62]

Interstrand d(G*pG*) crosslinks formed by cisplatin with oligomers have also been studied.[58,59] They occur predominantly between two guanines on opposite strands, which requires a distance of ca. 2.8 Å between the two N7 atoms. As for the intrastrand crosslink, the interstrand crosslink also causes a kink in the DNA helix. However, unlike the intrastrand crosslink, the kink and unwound is toward the minor groove. The deoxyribose of the platinated deoxyguanosine (G) is inverted so that O4′ is pointing in the opposite direction to that of the remaining nucleotides. In addition, the complementary deoxycytidines (C), which were originally

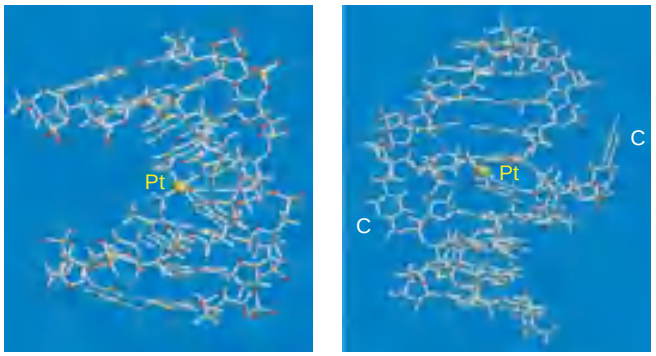

(A) (B)

Figure 5 NMR refined structures cisplatin-induced intrastrand (A) and interstrand cross-linked DNA duplex (B). The DNA is significantly altered from the B-form to accommodate cisplatin in (A), and the deoxycytosine residues originally base-paired to the platinated guanine have become extrahelical (B). Color code: C, green; H, metallic white; N, blue; O, red; P, orange; Pt, yellow. (Adapted with permission from Refs.[51,58])

base-paired to the platinated G are extruded and become extrahelical (Figure 5B).[58] The localized change from B-DNA to a left-handed Z-DNA structure around the platination site was also observed. *Cis*-$[Pt(NH_3)_2]^{2+}$ is also located in the minor groove of d(CCTCG*CTCTC)·d(GGAGCG*AGAG). The stacking of the two cross-linked guanines with the neighboring bases induces a kink of 40° toward the minor groove.

The 1,3-intrastrand d(G*XG*) (where X is C or T) cross-link minor adduct does not distort the global helical structure to the extent observed in the 1,2-intrastrand cross-link discussed above, but significantly disrupts local base-pairing and stacking at the 5′-end. The helix is bent by 24° and unwound by 19°. The platinum lesion causes a severe roll of 5′-G6 towards the major groove.[60]

2.4 Interaction with Amino Acids, Peptides and Proteins, and Their Metabolites in Biofluids

Increasing evidence has shown that platinum–peptide (amino acid and protein) interactions and particularly platinum–thioether interactions, play an important role in the mechanism of action of platinum drugs. The use of NMR

spectroscopy for studying these interactions has been summarized previously,[9] and Pt–methionine complexes with various isomers have been characterized by ^{13}C, ^{15}N, and ^{195}Pt NMR. In fact, it has been shown that platinum species can initially bind to thioether groups and then migrate to N7 of guanine.[63,64] ^{1}H and [^{1}H, ^{15}N] NMR spectroscopy has shown that L-methionine (Met) increases the rate of reaction of cisplatin with guanosine 5′-monophosphate (5′-GMP) at pH 7.[65] Therefore, methionines in peptides and proteins could play a role in the transfer of platinum onto DNA. Activation of carboplatin by reaction with L-Met derivatives could also provide an important pathway since carboplatin hydrolyses and interacts with chloride too slowly to account for its biological activity. Reaction with L-Met leads to a surprisingly stable ring-open intermediate with a half-life time 28 h at 310 K. By use of the 2D [^{1}H, ^{15}N] HSQC NMR method, a species with ^{1}H and ^{15}N shifts very similar to this intermediate was detected as a major metabolite in the urine samples from mice treated with ^{15}N-carboplatin.[66] This suggests that the ring-open intermediate is probably present in urine after carboplatin administration.

The thiolate-containing peptide glutathione (γ-L-Glu-L-Cys-Gly, GSH) is present in cells at mM concentrations. Various transient intermediates formed between the platinum complex and GSH during the reaction as judged by multinuclear NMR,[9b,67] and a novel dinuclear platinum GSH complex was also isolated and its structure was proposed based on ESI-MS and various advanced 2D NMR techniques.[68] In contrast to thioethers, the binding of Pt^{2+} to thiolate tends to be irreversible and ammine/amine ligands will finally be released from initial complex. Reactions between cisplatin and intracellular thiols such as GSH may therefore inactivate the drug and moreover the Pt–GSH complex can be pumped out of the cisplatin-resistant cells.

There are conflicting reports on the role of Pt–protein adducts in the mechanism of action. On the one hand, it has been postulated that the binding of cisplatin to protein is probably the cause of many of the drug's side-effects, while on the other hand several reports suggest that Pt^{2+}-albumin adducts may be anticancer active. One day after intravenous infusion of cisplatin, 65–98% of the platinum in blood plasma is protein bound.[69,70] Human serum albumin (66 kDa) is thought to be the major binding sites for cisplatin in human blood plasma. In contrast to previous reports, 1D and 2D [^{1}H, ^{15}N] NMR data suggest that ^{15}N-cisplatin mainly reacts with the methionine residues of albumin forming Met-S,N-macrocheltes together with minor monodentates Met-S adduct and Cys34, the only free thiol of the protein.[71] The iron binding protein transferrin (ca. 80 kDa) could deliver platinum to tumor cells, which are known to overexpress transferrin receptors. Diferric transferrin is taken up by cells via the known process of 'receptor-mediated endocytosis'. A combination of 2D [^{1}H, ^{13}C] and [^{1}H, ^{15}N] NMR spectroscopic studies using labeled transferrin (ε-[^{13}C]Met labeled protein) and ^{15}N-cisplatin has shown that preferred Pt^{2+} binding site appears to be Met256 with an additional site at the surface-exposed methionine.[72]

2.5 Other Metallo-anticancer Agents

Besides platinum, other metal complexes also have promising anticancer activity.[2,3] Gallium nitrate is known to exhibit anticancer activity and is now being used clinically for the treatment of cancer-induced hypercalcemia. The octahedral Ru^{3+} complexes (low spin d^5) are more active against metastases than primary tumors, and may be prodrugs which are bioreduced to Ru^{2+} species inside cells. Paramagnetically shifted ^{1}H NMR resonances are readily detected in ^{1}H spectra of Ru^{3+}

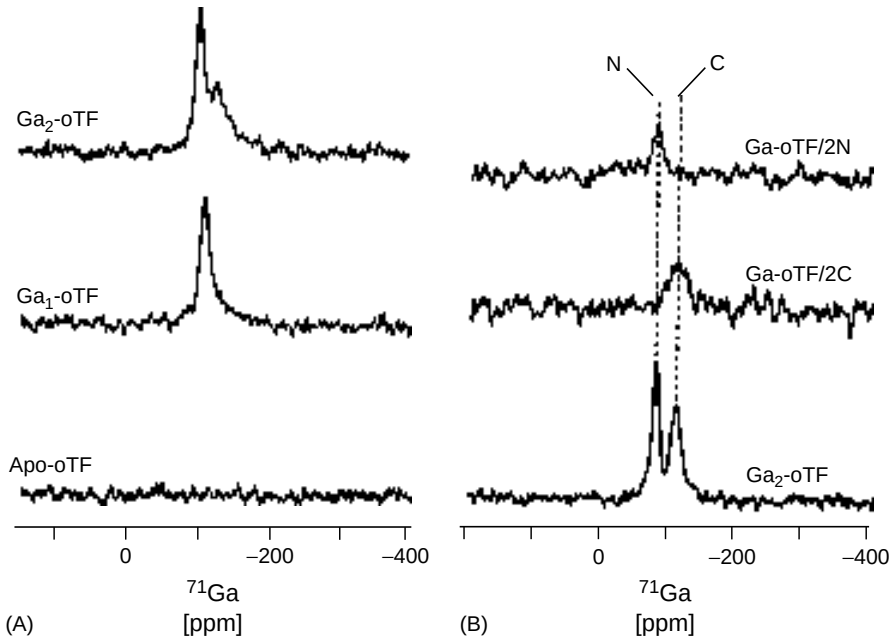

Figure 6 ^{71}Ga NMR spectra of ovotransferrin (1.3 mM, pH 7.6). (A) Before (bottom) and after addition of one (middle) and two mol equiv (top) of Ga^{3+} in the presence of 20 mM $NaHCO_3$. (B) ^{71}Ga NMR spectra of Ga_2-ovotransferrin (bottom), C-lobe of ovotransferrin (oTF/2C, 0.35 mM, 1.0 mol equiv of Ga^{3+}), and N-lobe of ovotransferrin (oTF/2N, 0.35 mM, 1.0 mol equiv. Of Ga^{3+}) in the presence of $Na_2C_2O_4$. (Adapted with permission from Ref.[75])

complexes and were used to determined the rate of hydrolysis of the anticancer agent *trans*-$[RuCl_4(Im)_2]^-$ where Im is imidazole.[73] Interestingly, both Ru^{3+} and Ga^{3+} are thought to be delivered by human transferrin (hTF).[2–4,74] It is known that many solid tumors express more transferrin receptor than normal cells. The binding properties of Ga^{3+} to ovotransferrin were investigated by ^{13}C and ^{71}Ga NMR. The latter technique is extremely useful at very high field once gallium has bound to large biomolecules.[5] Ga^{3+} interacts preferentially with the N-lobe of the protein when carbonate is present as the synergistic anion, but enters equally both the N- and C-lobes of the protein when oxalate is the anion (Figure 6).[75] The binding of Ru^{3+} complexes to lactoferrin is at the imidazole of His253, one of the iron ligands in the iron binding cleft of the N-lobe, and is reversible with Ru release at pH 4–5 or in the presence of a large excess of citrate or adenosine triphosphate (ATP).

The organometallic titanocene and another Ti^{4+} complex have entered phase II and I clinical trials for anticancer, respectively. We have demonstrated by UV and various NMR spectroscopies that the Ti^{4+} complex binds strongly to human serum transferrin at the specific iron (Fe^{3+}) site.[76] 2D [^1H, ^{13}C] studies of ε-[^{13}C]Met-hTF have shown that Ti^{4+} loads the C-lobe first followed by the N-lobe. Titanium (Ti^{4+}) bound transferrin effectively blocked cell uptakes of ^{59}Fe–hTF into BeWo cells,[77] which indicated that titanium transferrin could be recognized by transferrin receptor and be taken up into cells.

3 GOLD ANTI-ARTHRITIC DRUGS

Several injectable Au^+ thiolate drugs such as aurothiomalate and the oral drug auranofin are widely used for the treatment of difficult cases of rheumatoid arthritis and reviews on the medical use of gold have been published.[78–80] The injectable Au^+ complexes are polymers with thiolate sulfurs bridging to linear Au^+, in chain or cyclic structures. The crystal structure of aurothiomalate has shown that linear S–Au–S units are arranged into polymeric double-helical structures.[81] The structures of these polymers were found to be very sensitive to the ionic strength and pH of the solutions. Most of gold thiolate drugs often contain a small mol excess (10–15%) of thiol over gold.

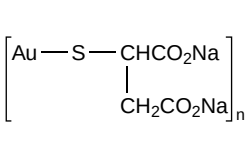

Aurothiomalate

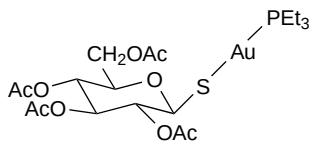

Auranofin

One feature of these linear Au^+ drugs is that they undergo facile thiolate exchange reactions and ^{13}C NMR studies have shown that thiols with lowest pK_a values bind most strongly to Au^+.[82] The administered drugs are probably not the active species. Gold(I) is a soft metal and therefore has a very high affinity for soft ligands such as thiolate sulfurs, but binds only weakly to nitrogen and hardly at all to oxygen. Consequently proteins (and enzymes) containing thiolate groups (Cys residues) particularly those with low pK_a values are targets for Au^+. In blood, a major site for gold transport is Cys34 of serum albumin which has a low pK_a (∼5). For the oral gold drug, ^{31}P NMR has been extensively used to probe speciations in proteins, bio-fluids and cells.[83–86] The ^{31}P chemical shift of bound phosphine (Au–PEt_3, where Et is ethyl) is sensitive to the nature of the coordinated ligands (X) and release of PEt_3 can readily be detected. The PEt_3 (and thiomalate) ligands of auranofin (and aurothiomalate, AuStm) are initially retained on binding of gold to albumin:

$$\text{Alb–Cys34–SH} + \text{auranofin}(\delta_{31P} = 37.0) \longrightarrow \text{Alb–Cys34–S–Au–PEt}_3(\delta_{31P} = 38.8)$$

Moreover, the ^{31}P chemical shift of bound phosphine in RS–Au–PR_3 was found to correlate with the pK_a of thiolates (SR),[82,86] ^1H and ^{31}P NMR studies have shown that the rate of binding of gold drugs to albumin appears to be determined by the rate of opening of the cleft in which Cys34 is situated.[87,88] Surprisingly, binding of auranofin and related gold compounds to Cys34 of albumin induces a structural transition, the effect of which can readily be observed by imidazole εCH^1H NMR resonances of His3 of the protein (Figure 7).[88,89] Such communication between His3 and Cys34 may be explained by small changes in the arrangement of intervening helices 1 and 2 of domain I of the protein. This may be mediated by a *cis-trans* isomerization of Pro35, changing the environment of Cys34 from a buried to an exposed form. The structural change can also be induced by blocking Cys34 as a disulfide, e.g., cystine. Such a structural transition of albumin induced by gold drugs has even been detected in intact blood plasma by ^1H NMR spectroscopy.[90] The exposed position of bound gold may have important implications for the transport and bioavailability of gold–drug metabolites.

Cyanide appears to play an important role in the metabolism of gold drugs. It can readily replace the thiomalate ligand from aurothiomalate in vitro and $Au(CN)_2^-$ has been shown to be a metabolite of gold drugs in vivo.[91,92] The enhanced uptake of gold into red blood cells of smokers is due to the formation of this species after inhalation of HCN in cigarette smoke. Interaction of aurothiomalate and cyanide (^{13}C-enriched CN^-) was followed by ^1H and ^{13}C NMR spectroscopy.[92] The mixed-ligand complex $[(Stm)Au(CN)]^-$ (Stm=S-bound thiomalate) readily forms as an intermediate when $[CN^-]/[\text{aurothiomalate}] < 2$, and $Au(CN)_2^-$ is the major species at higher ratio. Mixed-ligand complex of aurocyanide with other thiolates molecules such as glutathione, cysteine and captopril have also been reported.[92–95] Thiols and cyanide both bind to Au^+, although as expected, cyanide (CN^-) binds more strongly. Under biological conditions where [thiols] ≫ [HCN], substantial displacement of cyanide may take place. This may facilitate the accumulation of gold by red cells where the intracellular glutathione concentration is high (mM). An aurocyanide complex of albumin was recently studied by ^{13}C NMR spectroscopy and other techniques. There are two distinct binding mechanisms: the dominant mechanism is reversible association (non-specific binding) of intact $Au(CN)_2^-$ (δ_{13C} = 156.4) to albumin to form Alb·$[Au(CN)_2^-]_n$ (δ_{13C} = 154.7, broad signal).[96] The second binding mechanism is at Cys34 to form Alb-Cys34Au(CN) via a ligand exchange reaction which accounts for only a minor fraction of the bound-gold (ca. 11%).

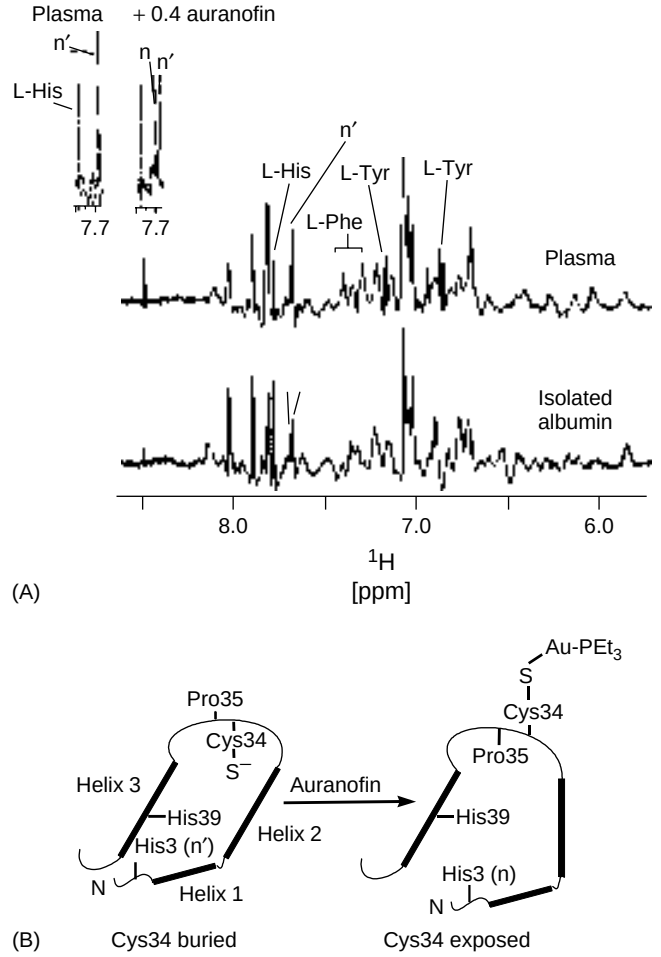

Figure 7 600 MHz ^{1}H spectrum of the aromatic region of a commercial sample of human albumin and fresh human blood plasma (A). The insert is Hε1 of His3 region of human blood plasma showing the n′ to n switch after addition of gold drug. (B) is the model for structural changes induced by gold in domain I of albumin. (Adapted with permission from Ref.[90])

4 LITHIUM FOR MANIC DEPRESSION

Lithium is an element discovered over 177 years ago (1817), but it was not until the seminal work of the Australian scientist, John Cade 50 years ago,[97] and subsequent clinical studies by Mogens Schou, that lithium was seen by modern psychiatry as an effective treatment for manic depression. Both lithium carbonate and citrate compounds are widely used as a prophylactic treatment for bipolar disorders.[98] Doses are normally gram quantities and the therapeutic level of lithium in serum is about 0.4–1.2 mM, and clinical efficacy usually takes 1–2 weeks to become established. Previous studies have shown that lithium was widely distributed in the body following oral administration due to its high lability and its weakness towards complexation.

Despite intensive research, the biochemical basis for lithium's therapeutic effects still remains to be fully elucidated. Lithium ions are small but highly hydrated and could interfere with Mg^{2+} biochemistry due to their comparably high charge densities, the so-called 'diagonal relationship' between Li^+ and Mg^{2+}. However, the favored mode of action of lithium is probably by interference with Ca^{2+} metabolism via inhibition of the inositol phosphate pathway.[99–101] Lithium also stimulates glutamate release and protects neurons by inhibiting N-methyl-D-asparate receptor-mediated calcium influx.[102,103] Determination of lithium is normally made by spectroscopic methods, e.g., atomic absorption and nuclear magnetic resonance. The former involves the disruption of samples (e.g., cells) and ensuing tedious separation. In addition, the atomic absorption measurements are not specific to the intracellular compartments. By contrast, NMR provides a non-invasive and direct way to investigate lithium in cells and tissues.[104]

Naturally occurring lithium consists of two isotopes ^{6}Li and ^{7}Li, with natural abundance 7.42 and 92.58%, respectively (Table 2). Both isotopes are weakly quadrupolar and the quadrupole moment of ^{6}Li is the smallest known while that of ^{7}Li is amongst the smallest, and they both give narrow resonance lines and have long spin-lattice relaxation times (T_1).[105] However, ^{7}Li is the choice for most biological studies because of its high sensitivity, higher natural abundance and more favorable relaxation as compared with ^{6}Li. The chemical shift range of ^{7}Li is small (ca. 15 ppm) due to its simple electronic structure and aqueous chemistry. The NMR spectrum of ^{7}Li generally contains a single peak corresponding to the overlapping signals from different environments, e.g., intra- and extra-cellular. It is possible to differentiate ^{7}Li signals from different compartments, for example, ions within the cells and those that are free in the extracellular bathing fluid, based either on their different relaxation properties or with the aid of shift reagent (e.g., dysprosium tripolyphosate), Figure 8.[106] Shift reagents, which are negatively charged lanthanide complexes and are insoluble in hydrophobic cell membrane, are repelled by the negatively charged head groups of phospholipids at the surface of cell membranes. In contrast to other alkali metals, ^{7}Li ($I = 2/3$) actually resembles a spin 1/2 nucleus and relaxation tends to be dominated by the dipolar mechanism.

The application of ^{7}Li and NMR of other alkali-metals to study the interaction of these metal ions with metalloproteins have been reviewed.[107] The chemical shifts of ^{6}Li, ^{7}Li and other alkali metal ions except Cs^+, are normally insensitive to either solvation or complexation by biomolecules. Li binds to myo-inositol monophosphatase, an enzyme that is inhibited by lithium and is thought to be the primary target for lithium therapy, and induces a downfield shift by <0.1 ppm and broadening of the ^{7}Li NMR signal. The binding constant at a single site was calculated to have a K_d of 1 mM, and lithium was found to compete with group II metal ions such as Mg^{2+} at that site.[108] NMR investigation of Li^+ binding to phospholipids and cell membrane have also been reported.

In order to get into the brain where the site of action of lithium is, Li^+ must be absorbed through the gastrointestinal tract into blood and pass the blood brain barrier. Clearly the membrane transport of lithium is a critical feature and several different NMR techniques have been used depending on the time-scale of the lithium transport process. The best model available for the study of Li^+ transport in human cells is the erythrocyte, which is also believed to be a good model for the blood brain barrier. Numerous NMR studies of Li^+ transport and environment in erythrocytes have been reported.[109,110] Depressed patients with a high $[Li]_i/[Li]_e$ ratio, where 'i' and 'e' represent intra- and extra-cellular concentration of lithium, were found to have a better therapeutic response that

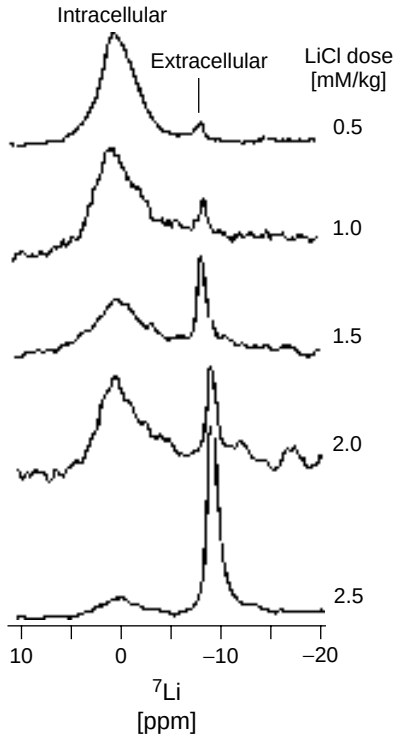

Figure 8 ^{7}Li NMR spectra of rat blood samples with added shift reagents (dysprosium tripolyphosphate, $Dy(ppp_i)_2^{7-}$). The peaks at 0 and ca. −10 ppm correspond to intracellular and extracellular ^{7}Li, respectively. The various doses of LiCl administered to the rats are indicated next to each spectrum. (Adapted with permission from Ref.[110b])

those patients with a lower ratio.[109] It was suggested that erythrocyte Li concentration could serve as a useful indicator of clinical response. However, subsequent studies were unable to substantiate the initial findings, and it is now generally accepted that this parameter is not clinically useful partly due to large interindividual variations in ionic transport process. It is known that a considerable amount of Li^+ enters the erythrocytes with the $[Li]_i/[Li]_e$ ratio typically at 0.3–0.6 which indicated that Li is actively extruded from the cells. Higher ratios have been reported recently in the low dose range in rats (Figure 8) and the coadministerated drug, thioridazine, has no effect on erythrocytes and plasma lithium levels.[110b,c]

In spite of extensive investigations of erythrocytes, little is known about the transport behavior of Li^+ in other cells and major differences are expected between erythrocytes and the excitable, nucleated cells of the central nervous system such as neurons and glia. Li^+ transport processes and intracellular concentrations in the brain have been approached by using human nerve 1321 N1 astrocytoma. ^{7}Li NMR spectroscopy showed that the uptake of Li^+ was approximately ten times faster than that into human erythrocytes and the steady-state was reached within 60 min. The low intracellular Li^+ concentration ($[Li]_i/[Li]_e \sim 0.3$) suggested the presence of an efflux mechanism in astrocytomas. Similar results have been obtained very recently for cultured human neuroblastoma SH-SY5Y cells.[112,113] Intra- and extra-cellular ^{7}Li resonances could be resolved in the presence of the shift reagent and relaxation measurements showed that Li^+ is immobilized more in human SH-SY5Y cells than in human erythrocytes. Significant increases in the first-order rate constants for Li^+ influx and efflux in the presence of veratridine (0.05 mM) suggested the Li^+ transport was mediated via Na^+ channels, a pathway not present in erythrocytes.[113] The studies of cultured central-nerve-system cells will also provide important information for in vivo study.

Direct investigation of Li^+ in the brain may be a better measure of efficacy or neurotoxicity than that in the serum. The spatial distribution of Li in the brain may also shed light on the still unknown mechanism of action of Li. Due to its relatively high sensitivity, the sufficiently high enough concentration of Li in tissues and most importantly the development of NMR spectroscopy in vivo, ^{7}Li NMR has successfully been used in recent years as a new tool to measure brain tissue lithium concentration.[104,114–117] Renshaw and coworkers' pioneering work demonstrated the feasibility of in vivo tissue measurements of lithium in animal and in human subjects.[118,119] In animals, efforts have been made to develop methods for measuring the pharmacokinetics of uptake in brain. It was found that the time constant for the uptake of a single dose of Li in rat brain was 48–98 min with signals that were uncontaminated by those from surrounding tissues.[120] Because of the high dose and long acquisition times used, the distribution of Li in the rat brain could be determined by ^{7}Li NMR imaging although the resolution of these imaging is overall quite poor.[121,122]

Most recent ^{7}Li work in vivo has focused on humans. Initial unlocalized studies measured the kinetics of uptake and elimination of ^{7}Li and compared serum and brain concentrations. Several studies have confirmed that the concentration of Li in brain is typically 0.1–0.6 mM and indicated brain/serum ratios of 0.4–0.7. Preliminary studies have attempted to examine a possible relationship between brain Li levels and therapeutic response, suggesting that Li brain levels may be of clinical relevance.[123–125] However, this question has yet to be properly addressed in patient samples large enough to provide a more clear answer. The potential for ^{7}Li in vivo NMR as an important tool for investigation of Li^+ refractoriness and predication of treatment outcome in bipolar disorder patients is currently being investigated.[116,126]

5 BISMUTH ANTIULCER (AND ANTIMONY ANTILEISHMANIA) AGENTS

Arsenic, antimony and bismuth have long been associated with medicine. Currently antimony compounds are used clinically for the treatment of leishmaniasis and bismuth compounds are widely used as antiulcer drugs (Table 1). Recently clinical studies in China demonstrated that the classical inorganic compound, arsenic trioxide (As_2O_3) can induce remission in patients with acute promyelocytic leukemia (APL, a rare blood cancer).[127,128] The induction of apoptosis and partial differentiation may be responsible for the activity of this metal.[129] Progress in the understanding the mode of action and design of drugs based on these elements are being greatly held up through lack of a suitable probe for the metal itself. NMR studies of these complexes have therefore relied on the observation of ligand nuclei such as ^{1}H and ^{13}C. The binding of citrate to Bi^{3+} in antiulcer complexes has been studied by ^{1}H, ^{13}C and [^{1}H, ^{13}C] NMR spectroscopy.[130–132] Citrate is a good bridging ligand and polymeric species are

formed in solution. The structures of bismuth citrate complexes are complicated, being dependent on pH, concentration, [Bi : citrate] ratio and the counter cations present. Different bismuth citrate species are in fast exchange on the NMR time-scale at pH < 6.2; the exchange rate decreases at pH > 6.2, and different species can be observed.[130,131] By means of diffusion-ordered 2D [^{1}H, ^{13}C] HSQC NMR spectroscopy together with isotope-labelling of citrate (^{13}C2/^{13}C4), a wide range of different types of bound citrate can readily be detected at low Bi concentrations (5 mM) in aqueous solutions of ranitidine bismuth citrate at pH* 7.4. There appears to be an equilibrium between free citrate, dinuclear species $[Bi(citrate)_2Bi]^{2-}$ and multinuclear bismuth citrate clusters at physiological pH values. The solid-state structure of the antiulcer drug, ranitidine bismuth citrate may be closely related to that of $Na_2[Bi_2(citrate)_2]\cdot 7H_2O$ in view of the similarity in their chemical compositions (Bi : citrate = 1 : 1), crystallization conditions (ca. pH 4), and solid-state ^{13}C NMR spectra.[133] Second coordination sphere interactions between coordinated citrate and ranitidine have been detected by ^{1}H NMR.[130]

Both antimony and bismuth form stable complexes with the tripeptide glutathione (GSH) with a stoichiometry $[Bi(GS)_3]$ or $[Sb(GS)_3]$. The rate of uptake of these metals into red blood cells and complexation with intracellular glutathione as determined by spin-echo ^{1}H NMR, is rapid for Sb^{3+} (minutes) and relatively slow for Bi^{3+} (hours).[134,135] Strong binding of Sb^{3+} to trypanothione $[T(SH)_2]$ was chemically characterized for the first time by ESI–MS spectrometry and NMR spectroscopy. In contrast to the glutathione complex, each Sb^{3+} coordinates to only one $T(SH)_2$ with two sulfurs being provided from Cys residues and probably an oxygen from water.[136]

Binding of bismuth to human transferrin was unexpectedly strong.[137,138] The uptake of Bi^{3+} by apo-transferrin from bismuth citrate complexes is very slow (hours at 310 K) and occurs in at least two steps, whereas transfer from bismuth nitrilotriacetate is rapid (min). ^{13}C NMR suggests that bismuth binds to transferrin along with carbonate (CO_3^{2-}) as the synergistic anion, which is similar to Fe^{3+}. Binding of Bi^{3+} occurs preferentially to the C-lobe of transferrin. This order of lobe-loading has been confirmed by 2D [^{1}H, ^{13}C] heteronuclear multiple-quantum coherence (HMQC) NMR studies using recombinant ε-[^{13}C]Met-hTF (ca. 0.3 mM) in which all Met residues are enriched with ^{13}C at the $-SCH_3$ group. The changes in shift of the ^{1}H and ^{13}C NMR resonances of Met can be used not only as a probe for determining the order of lobe-loading of transferrin with metal ions, but also as fingerprints of conformational changes induced by Bi^{3+} and other metal ions. Bi^{3+}, Fe^{3+}, Ga^{3+} and Al^{3+} probably induce similar conformational changes in hTF, since the changes in shifts of SCH_3 resonances (Met) are almost identical.[139] Due to the ^{13}C labeling of Met and the sensitivity enhancement obtainable by inverse detection, the possible metal binding (e.g., Bi^{3+}) to transferrin (ε-[^{13}C]Met-hTF) can readily detected in the presence of large excess of other proteins and even in blood plasma by 1D and 2D [^{1}H, ^{13}C] NMR spectroscopy.[140] Transferrin was found to be a potential mediator for Bi^{3+} transport in blood plasma, which may have implications for the mechanism of neurotoxicity of Bi^{3+} drugs.

6 SUMMARY

NMR spectroscopy is one of the most powerful techniques for the study of interactions of metallodrugs with molecules of biological importance. The chemical shifts of some nuclei such as ^{195}Pt are sensitive to either the oxidation state or to coordination sphere and provide information on the binding site of the metallodrug–biomolecule complex. With the development of NMR techniques and currently available high-fields (e.g., >17 T), more information is expected to be obtained from NMR experiments. The recent success of ^{67}Zn NMR in the study of a metalloprotein may shed light on other biologically relevant quadrupolar nuclei.[141] The use of inverse detection of ^{13}C or ^{15}N (e.g., 2D HSQC, HSQC-TOCSY, HSQC-NOESY) together with isotopically-labeled metallodrugs or biomolecules, allows studies to be conducted at physiologically relevant concentrations. The structures and dynamics of metallodrug-biomolecule complexes which have been investigated by 1D and 2D homo- and hetero-nuclear NMR techniques will continue to be an important field of study. Theoretically, drug discovery of inorganic compounds can also be screened based on structure-and-activity relationship NMR (SAR-NMR)[142] and we have demonstrated that metallodrug binding to the 80 kDa protein (transferrin) can readily be followed.[139,140] Screening the binding of inorganic compounds to larger proteins and enzymes should now be possible by the transverse relaxation-optimized spectroscopy (TROSY) experiment.[143] The combination of NMR techniques with chromatography (LC-NMR and HPLC-NMR) should be a powerful method for the identification of novel metallodrug metabolites.[144]

7 RELATED ARTICLES IN VOLUMES 1–8

Body Fluids, Volume 2, Contrast Agents in Whole Body Magnetic Resonance: An Overview, Volume 3, Lithium NMR, Volume 5, Nucleic Acids: Spectra, Structures, & Dynamics, Volume 5, Transferrins, Volume 8.

8 REFERENCES

1. (a) P. J. Sadler, *Adv. Inorg. Chem.*, 1991, **36**, 1; (b) *Metallopharmaceuticals (Top. Biol. Inorg. Chem.*, Vols. 1 and 2), Springer: Heidelberg, 1999; (c) N. P. Farrell, 'Uses of Inorganic Chemistry in Medicine', Royal Society of Chemistry: Cambridge, 1999.
2. (a) Z. Guo and P. J. Sadler, *Angew. Chem. Int. Edn.*, 1999, **38**, 1512; (b) Z. Guo and P. J. Sadler, *Adv. Inorg. Chem.*, 2000, **49**, 183.
3. Medicinal Inorganic Chemistry special issue of *Chem. Rev.*, 1999, **99**, 2201.
4. (a) M. J. Abrams and B. A. Murrer, *Science*, 1993, **261**, 725; (b) J. Reedijk, *Curr. Opin. Chem. Biol.*, 1999, **3**, 236.
5. (a) J. M. Aramini and H. J. Vogel, *Biochem. Cell. Biol.*, 1998, **76**, 210; (b) M. W. Germann, J. M. Aramini, and H. J. Vogel, *J. Am. Chem. Soc.*, 1994, **116**, 6971.
6. J. M. Aramini and H. J. Vogel, *J. Magn. Reson. Ser B*, 1996, **110**, 182.
7. P. O. Weslund and H. Wennerstrom, *J. Magn. Reson.*, 1982, **50**, 451.

8. (a) L. G. Werbelow, *J. Chem. Phys.*, 1979, **70**, 5381; (b) L. G. Werbelow and G. Pouzard, *J. Phys. Chem.*, 1981, **85**, 3887.
9. (a) S. J. Berners-Price and P. J. Sadler, *Coord. Chem. Rev.*, 1996, **151**, 1; (b) Y. Chen, Z. J. Guo, and P. J. Sadler, in 'Cisplatin – Chemistry and Biochemistry of a Leading Anticancer Drug', ed B. Lippert, Wiley-VCH: Weinheim, 1999; (c) S. O. Ana, Z. Kuklenyik, and L. G. Marzilli, *ibid.*
10. B. Rosenberg, L. van Camp, and T. Krigas, *Nature*, 1965, **205**, 698.
11. B. Rosenberg, L. van Camp, J. E. Trosko, and V. H. Mansour, *Nature*, 1969, **222**, 385.
12. (a) H. M. Pinto and J. H. Schornagel, 'Platinum and Other Coordination Compounds in Cancer Chemotherapy', Plenum: New York, 1996; (b) B. Lippert, 'Cisplatin – Chemistry and Biochemistry of a Leading Anticancer Drug', ed B. Lippert, Wiley-VCH: Weinheim, 1999.
13. P. S. Pregosin, *Annu. Rep. NMR Spectrosc.*, 1986, **17**, 285.
14. D. P. Bancroft, C. A. Lepre, and S. J. Lippard, *J. Am. Chem. Soc.*, 1990, **112**, 6860.
15. I. M. Ismail and P. J. Sadler, *ACS Symp. Ser.*, 1983, **209**, 171.
16. T. G. Appleton, J. R. Hall, and S. F. Ralph, *Aust. J. Chem.*, 1986, **39**, 1347.
17. T. G. Appleton, J. R. Hall, and S. F. Ralph, *Inorg. Chem.*, 1985, **24**, 673.
18. G. M. Clore and A. M. Gronenborn, *J. Am. Chem. Soc.*, 1982, **104**, 1369.
19. S. K. Miller and L. G. Marzilli, *Inorg. Chem.*, 1985, **24**, 2421.
20. T. G. Appleton, J. R. Hall, and S. F. Ralph, *Inorg. Chem.*, 1985, **24**, 4685.
21. T. G. Appleton, J. W. Connor, and J. R. Hall, *Inorg. Chem.*, 1988, **27**, 130.
22. S. T. Sullivan, A. Ciccarese, F. P. Fanizzi, and L. G. Marzilli, *Inorg. Chem.*, 2001, **40**, 455.
23. I. M. Ismail, S. J. S. Kerrison, and P. J. Sadler, *J. Chem. Soc. Chem. Commun.*, 1980, 1261.
24. R. E. Norman and P. J. Sadler, *Inorg. Chem.*, 1988, **27**, 3583.
25. T. G. Appleton, R. D. Berry, C. A. Davis, J. R. Hall, and H. A. Kimlin, *Inorg. Chem.*, 1984, **23**, 3514.
26. S. J. Berners-Price and P. W. Kuchel, *J. Inorg. Biochem.*, 1990, **38**, 327.
27. A. J. Shaka, P. B. Barker, and R. Freeman, *J. Magn. Reson.*, 1985, **64**, 547.
28. J. Stonehouse, G. L. Shaw, J. Keeler, and E. D. Laue, *J. Magn. Reson. Ser. A*, 1994, **107**, 174.
29. S. J. Berners-Price, T. A. Frenkiel, U. Frey, J. D. Ranford, and P. J. Sadler, *J. Chem. Soc. Chem. Commun.*, 1992, 789.
30. S. J. Barton, K. J. Barnham, A. Habtemariam, R. E. Sue, and P. J. Sadler, *Inorg. Chim. Acta*, 1998, **273**, 8.
31. Y. Chen, Z. Guo, S. Parsons, and P. J. Sadler, *Chem. Eur. J.*, 1998, **4**, 672.
32. S. J. Berners-Price, T. A. Frenkiel, J. D. Ranford, and P. J. Sadler, *J. Chem. Soc. Dalton. Trans.*, 1992, 2137.
33. S. J. Berners-Price, U. Frey, J. D. Ranford, and P. J. Sadler, *J. Am. Chem. Soc.*, 1993, **115**, 8649.
34. K. J. Barnham, S. J. Berners-Price, T. A. Frenkiel, U. Frey, and P. J. Sadler, *Angew. Chem. Int. Edn. Engl.*, 1995, **34**, 1874.
35. S. J. Berners-Price, K. J. Barnham, U. Frey, and P. J. Sadler, *Chem. Eur. J.*, 1996, **2**, 1283.
36. F. Gonnet, J. Kozelka, and J.-C. Chottard, *Angew. Chem. Int. Edn. Engl.*, 1992, **31**, 1483.
37. F. Reeder, Z. Guo, P. del S. Murdoch, A. Corazza, T. W. Hambley, S. J. Berners-Price, J.-C. Chottard, and P. J. Sadler, *Eur. J. Biochem.*, 1997, **249**, 370.
38. S. J. Berners-Price, A. Corazza, Z. Guo, K. J. Barnham, P. J. Sadler, Y. Ohyama, M. Leng, and D. Locker, *Eur. J. Biochem.*, 1997, **243**, 782.
39. M. S. Davies, S. J. Berners-Price, and W. Hambley, *J. Am. Chem. Soc.*, 1998, **120**, 11 380.
40. E. R. Jamieson and Lippard, *Chem. Rev.*, 1999, **99**, 2467.
41. E. Reed, R. F. Ozols, R. Tarone, S. H. Yuspa, and M. C. Poirier, *Proc. Natl. Acad. Sci. USA*, 1987, **84**, 5024.
42. Y. Corda, M. F. Anin, M. Leng, and D. Job, *Biochemistry*, 1992, **31**, 1904.
43. L. J. N. Bradley, K. J. Yarema, S. J. Lippard, and J. M. Essigmann, *Biochemistry*, 1993, **32**, 982.
44. C. S. Chow, C. M. Barnes, and S. J. Lippard, *Biochemistry*, 1995, **34**, 2956.
45. U. M. Ohndorf, J. P. Whitehead, N. L. Raju, and S. J. Lippard, *Biochemistry*, 1997, **36**, 14 807.
46. E. E. Trimmer, D. B. Zamble, S. J. Lippard, and J. M. Essigmann, *Biochemistry*, 1998, **37**, 352.
47. P. M. Pil and S. J. Lippard, *Science*, 1992, **256**, 234.
48. D. B. Zamble, D. Mu, J. T. Reardon, A. Sancar, and S. J. Lippard, *Biochemistry*, 1996, **35**, 10 004.
49. J.-C. Huang, D. B. Zamble, J. T. Reardon, S. J. Lippard, and A. Sancar, *Proc. Natl. Acad. Sci. USA*, 1994, **91**, 10 394.
50. S. O. Ano, Z. Kuklenyok, L. G. Marzilli, in 'Cisplatin – Chemistry and Biochemistry of a Leading Anticancer Drug', ed B. Lippert, Wiley-VCH: Weinheim, 1999.
51. D. Yang, S. S. G. E. van Boom, J. Reedijk, J. H. van Boom, and A. H.-J. Wang, *Biochemistry*, 1995, **34**, 12 912.
52. F. Herman, J. Kozelka, V. Stoven, E. Guittet, J.-P. Pirault, T. Huynh-Dinh, J. Igolen, J.-Y. Lallemand, and J.-C. Chottard, *Eur. J. Biochem.*, 1990, **194**, 119.
53. A. Gelasco and S. J. Lippard, *Biochemistry*, 1998, **37**, 9230.
54. J. A. Parkinson, Y. Chen, P. del S. Murdoch, Z. Guo, S. J. Berners-Price, T. Brown, and P. J. Sadler, *Chem. Eur. J.*, 2000, **6**, 3636.
55. Y. Chen, J. A. Parkinson, Z. Guo, T. Brown, and P. J. Sadler, *Angew. Chem. Int. Edn.*, 1999, **38**, 2060.
56. S. U. Dunham, S. U. Dunham, C. J. Turner, and S. J. Lippard, *J. Am. Chem. Soc.*, 1998, **120**, 5395.
57. M.-H. Fouchet, E. Guittet, J. A. H. Cognet, J. Kozelka, C. Gauthier, M. L. Bret, K. Zimmermann, and J.-C. Chottard, *J. Biol. Inorg. Chem.*, 1997, **2**, 83.
58. H. Huang, L. Zhu, B. R. Reid, G. P. Drobny, and P. B. Hopkins, *Science*, 1995, **270**, 1842.
59. F. Paquet, C. Pérez, M. Leng, G. Lancelot, and J.-M. Malinge, *J. Biomol. Struct. Dyn.*, 1996, **14**, 67.
60. C. J. van Garderen and L. P. A. van Houte, *Eur. J. Biochem.*, 1994, **225**, 1169.
61. P. M. Takahara, C. A. Frederick, and S. J. Lippard, *Nature*, 1995, **377**, 649.
62. L. G. Marzilli, J. S. Saad, Z. Kuklenyik, K. A. Keating, and Y. Xu, *J. Am. Chem. Soc.*, 2001, **123**, 2764.
63. J. M. Teuben, S. S. G. E. van Boom, and J. Reedijk, *J. Chem. Soc. Dalton Trans.*, 1997, 3979.
64. Z. Guo, T. W. Hambley, P. del S. Murdoch, and P. J. Sadler, *J. Chem. Soc. Dalton Trans.*, 1997, 469.
65. K. J. Barnham, M. I. Djuran, P. del S. Murdoch, J. D. Ranford, and P. J. Sadler, *J. Chem. Soc. Dalton Trans.*, 1997, 3721.
66. K. J. Barnham, U. Frey, P. del S. Murdoch, J. D. Ranford, and P. J. Sadler, *J. Am. Chem. Soc.*, 1994, **116**, 11 175.
67. T. G. Appleton, J. W. Connor, J. R. Hall, and P. D. Prenzler, *Inorg. Chem.*, 1989, **28**, 2030.
68. P. del S. Murdoch, N. A. Kratochwil, J. A. Parkinson, M. Patriarca, and P. J. Sadler, *Angew. Chem. Int. Edn.*, 1999, **38**, 2949.
69. J. J. Gullo, C. L. Litterst, P. J. Maguire, B. J. Sikis, D. F. Holth, and P. V. Woodley, *Cancer Chemother. Pharmacol.*, 1980, **5**, 21.
70. F. Kratz, in 'Metal Complexes in Cancer Chemotherapy', ed B. K. Keppler, VCH: Weinheim, Germany, 1993.
71. A. I. Ivanov, J. Christodoulou, J. A. Parkinson, K. J. Barnham, A. Tucker, J. Woodrow, and P. J. Sadler, *J. Biol. Chem.*, 1998, **273**, 14 721.

72. M. C. Cox, K. J. Barnham, T. A. Frenkiel, J. D. Hoeschele, A. B. Mason, Q.-Y. He, R. C. Woodworth, and P. J. Sadler, *J. Biol. Inorg. Chem.*, 1999, **4**, 621.
73. O. M. Ni Dhubhghaill, W. R. Hagen, B. K. Keppler, K.-G. Lipponer, and P. J. Sadler, *J. Chem. Soc. Dalton Trans.*, 1994, 3305.
74. F. Kratz, M. Hartmann, B. K. Keppler, and L. Messori, *J. Biol. Chem.*, 1994, **269**, 2581.
75. J. M. Aramini, D. D. McIntyre, and H. J. Vogel, *J. Am. Chem. Soc.*, 1994, **116**, 11 506.
76. H. Sun, H., H. Li, R. Weir, and P. J. Sadler, *Angew. Chem. Int. Edn.*, 1998, **37**, 1577.
77. M. Guo, H. Sun, H. J. McArdle, L. Gambling, and P. J. Sadler, *Biochemistry*, 2000, **39**, 10 023.
78. C. F. Shaw III, *Comments Inorg. Chem.*, 1989, **8**, 233.
79. (a) S. P. Fricker, *Gold Bull.*, 1996, **29**, 53; (b) S. L. Best and P. J. Sadler, *Gold Bull.*, 1996, **29**, 87; (c) P. J. Sadler, *Struct. Bonding*, 1984, **29**, 171.
80. C. F. Shaw III, *Chem. Rev.*, 1999, **99**, 2589.
81. R. Bau, *J. Am. Chem. Soc.*, 1998, **120**, 9380.
82. A. A. Isab and P. J. Sadler, *J. Chem. Soc. Dalton Trans.*, 1982, 135.
83. M. T. Razi, G. Otiko, and P. J. Sadler, *ACS Symp. Ser.*, 1983, **209**, 371.
84. J. R. Roberts, J. Xiao, B. Schliesman, D. J. Parsons, and C. F. Shaw III, *Inorg. Chem.*, 1996, **35**, 424.
85. P. J. Sadler and R. E. Sue, *Met. Based Drugs*, 1994, **1**, 107.
86. C. F. Shaw III, M. T. Coffer, J. Klingbeil, and C. K. Mirabelli, *J. Am. Chem. Soc.*, 1988, **110**, 729.
87. C. F. Shaw III, A. A. Isab, J. D. Hoeschele, M. Starich, J. Locke, P. Schulteis, and J. Xiao, *J. Am. Chem. Soc.*, 1994, **116**, 2254.
88. O. M. Ni Dhubhghaill, P. J. Sadler, and A. Tucker, *J. Am. Chem. Soc.*, 1992, **114**, 1118.
89. J. Christodoulou, P. J. Sadler, and A. Tucker, *Eur. J. Biochem.*, 1994, **225**, 363.
90. J. Christodoulou, P. J. Sadler, and A. Tucker, *FEBS Lett.*, 1995, **376**, 1.
91. R. C. Elder, Z. Zhao, Y. Zhang, J. G. Dorsey, E. V. Hess, and K. Tepperman, *J. Rheumatol.*, 1993, **20**, 268.
92. G. G. Graham, J. R. Bales, M. C. Grootveld, and P. J. Sadler, *J. Inorg. Biochem.*, 1985, **25**, 163.
93. G. Lewis and C. F. Shaw III, *Inorg. Chem.*, 1986, **25**, 58.
94. M. N. Akhtar, I. H. Gazi, A. A. Isab, A. R. Al-Arfaj, M. I. N. Wazeer, and M. S. Hussain, *J. Coord. Chem.*, 1995, **36**, 149.
95. A. A. Isab, I. H. Gazi, and A. R. Al-Arfaj, *J. Chem. Soc. Dalton Trans.*, 1993, 841.
96. A. J. Canumalla, S. Schraa, A. A. Isab, C. F. Shaw III, E. Gleichmann, L. Dunemann, and M. Turfeld, *J. Biol. Inorg. Chem.*, 1998, **3**, 9.
97. J. F. Cade, *Med. J. Aust.*, 1949, **36**, 349.
98. (a) L. H. Price and G. R. Heninger, *N. Engl. J. Med.*, 1994, **331**, 591; (b) N. J. Birch, 'Lithium: Inorganic Pharmacology and Psychiatric Use', IRL Press: Oxford, 1988.
99. J. R. Atack, H. B. Broughton, and S. J. Pollack, *Trends Neurosci.*, 1995, **18**, 343.
100. J. R. Atack, *Med. Res. Rev.*, 1997, **17**, 215.
101. G. Emilien, J. M. Maloteaux, A. Seghers, and G. Charles, *Arch. Int. Pharmacodyn.*, 1995, **330**, 251.
102. J. F. Dixon, G. V. Los, and L. E. Hokin, *Proc. Natl. Acad. Sci. USA*, 1994, **91**, 8358.
103. S. Nonaka, C. J. Hough, and D.-M. Chuang, *Proc. Natl. Acad. Sci. USA*, 1998, **95**, 2642.
104. (a) R. A. Komoroski, *Magn. Reson. Imaging*, 2000, **18**, 103; (b) F. G. Riddell, in 'Lithium: 50 years of Psychopharmacology. New Perspectives in Biomedical and Clinical Research', eds N. J. Birch, V. S. Gallicchio, and R. W. Becker, Weidner Publishing Group: Cheshire, CT, 2000; (c) F. G. Riddell, *J. Trace Microprobe. Technol.*, 1998, **16**, 99.
105. (a) C. Brevard and P. Granger, 'Handbook of High Resolution Multinuclear NMR', Wiley-Interscience Publication: New York, 1981; (b) J. E. Mason, 'Multinuclear NMR', 2nd edn, Plenum Press: London, 1989.
106. F. G. Riddell, in 'Lithium and the Cell: Pharmacology and Biochemistry', ed N. J. Birch, Academic Press: London, 1991, p. 85.
107. D. Mota de Freitas, *Methods Enzymol.*, 1993, **227**, 78.
108. V. Saudek, P. Vincendon, Q.-T. Do, R. A. Atkinson, V. Sklenár, P. D. Pelton, F. Piriou, and A. J. Ganzhorn, *Eur. J. Biochem.*, 1996, **240**, 288.
109. J. Mendels and A. Frazer, *J. Psychiat. Res.*, 1973, **10**, 9.
110. For example, (a) Q. Rong, M. Espanol, D. Mota de Freitas, and C. F. G. C. Geraldes, *Biochemistry*, 1993, **32**, 13 490; (b) S. Ramaprasad and V. W. Robbins, *Magn. Reson. Imaging*, 1998, **16**, 213; (c) S. Ramaprasad and V. W. Robbins, *Magn. Reson. Imaging*, 1998, **16**, 219.
111. J. Bramham, A. N. Carter, and F. G. Riddell, *J. Inorg. Biochem.*, 1996, **61**, 273.
112. J. Nikolakopoulos, C. Zacharich, D. Mota de Freitas, and C. F. G. C. Geraldes, *Inorg. Chim. Acta*, 1996, **251**, 201.
113. J. Nikolakopoulos, C. Zacharich, D. Mota de Freitas, E. B. Stubbs, R. Ramasamy, G. M. C. A. Castro, and C. F. G. C. Geraldes, *J. Neurochem.*, 1998, **71**, 1676.
114. T. Kato, S. Takahashi, and T. Inubushi, *Lithium*, 1994, **5**, 75.
115. P. F. Renshaw, G. S. Sachs, and R. G. Gonzalez, in 'NMR Spectroscopy in Psychiatric Brain Disorders', eds H. A. Nasrallah and J. W. Pettegrew, American Psychiatric Press: Washington, 1995.
116. J. C. Soares, F. Boada, and M. S. Keshavan, *Eur. Neuropsychopharmacol.*, 2000, **10**, 151.
117. (a) R. A. Komoroski, *Curr. Sci.*, 1999, **76**, 789; (b) R. A. Komoroski, *Anal. Chem.*, 1994, **66**, 1024A.
118. P. F. Renshaw, J. C. Haselgrove, J. S. Leigh, and B. Chance, *Magn. Reson. Med.*, 1985, **2**, 512.
119. P. F. Renshaw and S. Wicklund, *Biol. Psychiatry*, 1988, **23**, 465.
120. S. Ramaprasad, J. E. O. Newton, D. Cardwell, A. H. Fowler, and R. A. Komoroski, *Magn. Reson. Imaging*, 1992, **25**, 308.
121. R. A. Komoroski, J. M. Pearce, and J. E. O. Newton, *Magn. Reson. Med.*, 1997, **38**, 275.
122. R. A. Komoroski, J. M. Pearce, and J. E. O. Newton, *J. Magn. Reson.*, 1998, **133**, 98.
123. T. Kato, T. Inubushi, and S. Takahashi, *J. Clin. Psychopharmacol.*, 1994, **14**, 330.
124. T. Kato, K. Fujii, T. Shioiri, T. Inubushi, and S. Takahashi, *Prog. Neuropsychopharmacol. Biol. Psychiatry*, 1996, **20**, 87.
125. G. S. Sachs, P. F. Renshaw, B. Lafer, A. L. Stoll, A. R. Guimaraes, J. F. Rosenbaum, and R. G. Gonzalez, *Biol. Psychiatry*, 1995, **38**, 422.
126. J. C. Soares, F. Boada, S. Spencer, A. G. Mallinger, C. S. Dippold, K. F. Wells, E. Frank, M. S. Keshavan, S. Gershon, and D. J. Kupfer, *Biol. Psychiatry*, 2001, **49**, 437.
127. G. Q. Chen, X. G. Shi, W. Tang, S. M. Xiong, J. Zhu, X. Cai, Z. G. Han, J. H. Ni, G. Y. Shi, P. M. Jia, M. M. Liu, K. L. He, C. Niu, J. Ma, P. Zhang, T. D. Zhang, P. Paul, T. Naoe, K. Kitamura, W. Miller, S. Waxman, Z. Y. Wang, H. de The, S. J. Chen, and Z. Chen, *Blood*, 1997, **89**, 3345.
128. Z. X. Shen, G. Q. Chen, J. H. Ni, X. S. Li, S. M. Xiong, Q. Y. Qiu, J. Zhu, W. Tang, G. L. Sun, K. Q. Yang, Y. Chen, L. Zhou, Z. W. Fang, Y. T. Wang, J. Ma, P. Zhang, T. D. Zhang, S. J. Chen, Z. Chen, and Z. Y. Wang, *Blood*, 1997, **89**, 3354.
129. S. J. Soignet, P. Maslak, Z. G. Wang, S. Jhanwar, E. Calleja, L. J. Dardashti, D. Corso, A. De Blasio, J. Gabrilove, D. A. Scheinberg, P. P. Pandolfi, and R. P. Warrell, *N. Engl. J. Med.*, 1998, **339**, 1341.
130. P. J. Sadler and H. Sun, *J. Chem. Soc. Dalton Trans.*, 1995, 1395.

131. E. Asato, K. Katsura, M. Mikuriya, T. Fujii, and J. Reedijk, *Inorg. Chem.*, 1993, **32**, 5322.
132. J. A. Parkinson, H. Sun, and P. J. Sadler, *J. Chem. Soc. Chem. Commun.*, 1998, 881.
133. P. J. Barrie, M. I. Djuran, M. A. Mazid, M. McPartlin, P. J. Sadler, I. J. Scowen, and H. Sun, *J. Chem. Soc. Dalton Trans.*, 1996, 2417.
134. P. J. Sadler, H. Sun, and H. Li, *Chem. Eur. J.*, 1996, **2**, 701.
135. H. Sun, S.-C. Yan, and W.-S. Cheng, *Eur. J. Biochem.*, 2000, **267**, 5450.
136. S.-C. Yan, K. Ding, L. Zhang, and H. Sun, *Angew. Chem. Int. Edn.*, 2000, **39**, 4260.
137. H. Li, P. J. Sadler, and H. Sun, *J. Biol. Chem.*, 1996, **271**, 9483.
138. H. Sun, H. Li, A. B. Mason, R. C. Woodworth, and P. J. Sadler, *Biochem. J.*, 1999, **337**, 105.
139. H. Sun, M. C. Cox, H. Li, A. B. Mason, R. C. Woodworth, and P. J. Sadler, *FEBS Lett.*, 1998, **422**, 315.
140. H. Sun, H. Li, A. B. Mason, R. C. Woodworth, and P. J. Sadler, *J. Biol. Chem.*, 2001, **276**, 8829.
141. A. S. Lipton, G. W. Buchko, J. A. Sears, M. A. Kennedy, and P. D. Ellis, *J. Am. Chem. Soc.*, 2001, **123**, 992.
142. S. B. Shuker, P. J. Hajduk, R. P. Meadows, and S. W. Fesik, *Science*, 1996, **274**, 1531.
143. K. Pervushin, R. Riek, G. Wider, and K. Wüthrich, *Proc. Natl. Acads. Sci., USA*, 1997, **94**, 12 366.
144. J. C. Lindon, J. K. Nicholson, and I. D. Wilson, *J. Chromatogr. B*, 2000, **748**, 233.

Acknowledgements

We thank the University of Hong Kong (CRCG and UGC) Livzon Pharmaceutical Group and Area of Excellence Scheme of University Grants Committee (Hong Kong) for their support, and Dr. Geoffrey D. Brown for critical comments.

Biographical Sketch

Hongzhe Sun, *b* 1964. B.Sc. 1985, M.Sc. 1990, Ph.D., 1996, Postgraduate study (M.Sc.) at Wuhan Institute of Physics, the Chinese Academy of Sciences. Spent three years as a research associate and a lecturer at Nanjing University before undertaking Ph.D. research under the guidance of Peter J. Sadler at the University of London, Great Britain. Research fellow at the University of Edinburgh, 1996–1998. Assistant professor of chemistry, the University of Hong Kong, P. R. China, 1998–present. Over 30 publications. Current research interests: biological inorganic chemistry, structures and functions of metalloproteins.

Mitochondrial Cytochrome *c*

A. Joshua Wand
State University of New York at Buffalo, NY, USA

1	Introduction	1
2	Resonance Assignments	1
3	Structural Analysis	1
4	Dynamics and Stability	2
5	Complexes	3
6	Related Articles	4
7	References	4

1 INTRODUCTION

Mitochondrial cytochrome *c* is a small (12.4 kDa), soluble, basic protein that mediates single electron transfer between integral membrane protein complexes in the respiratory chain of eukaryotes.[1] Because of its stability, solubility and ease of preparation, cytochrome *c* has become one of the most thoroughly studied proteins, not only in terms of its biological function but also as a model system for studies of, for example, protein folding,[2] interprotein electron transfer,[3] molecular recognition,[4] antigenicity,[5] and protein dynamics (see below). As one of the first classes of proteins subjected to structural analysis by X-ray crystallographic techniques, a number of high-resolution models for the structures of *c*-type cytochromes have emerged.[6] These and other detailed structural studies have provided the basis for comprehensive evaluation of hypotheses concerning the fundamental nature of the electron transfer processes in proteins.[7] The mitochondrial cytochromes of the *c* type have been extensively examined by NMR methods. ^{1}H NMR based studies have a long history and find roots in the classic studies of Kowalsky,[8] Gupta and Redfield,[9] and McDonald and Philips.[10]

2 RESONANCE ASSIGNMENTS

Early ^{1}H resonance assignment studies were led by the pioneering work of Williams, Moore, and co-workers[11] and by Wüthrich and co-workers.[12] Much of that work focused on the assignment of the ^{1}H resonance of the reduced, or ferrous, form, ferrocytochrome *c*, in which the heme iron is diamagnetic. For ferrocytochrome *c*, the ^{1}H chemical shifts are restricted to between −4 and 11 ppm. In the efforts dealing with the ferric form, ferricytochrome *c*, where the low spin-$\frac{1}{2}$ iron provides an intrinsic paramagnetic perturbation, the initial efforts concentrated on paramagnetically shifted ^{1}H resonances dispersed in the chemical shift range of −40 to +40 ppm. In the early 1980s, the approaches to the resonance assignments became decidedly more aggressive and comprehensive. The work of Williams, Moore, and co-workers is particularly noteworthy for their application of a wide variety of analytical NMR techniques to what was then a seemingly impenetrable resonance assignment problem. In their initial ground-breaking efforts, these investigators were able, without the benefit of two-dimensional NMR techniques or extremely high magnetic fields, to assign a significant fraction of the side-chain ^{1}H resonances of both reduced and oxidized cytochrome *c* from a variety of species. Approaches used included comparison of ^{1}H NMR spectra of homologous cytochromes *c*, structure dependent interpretations of chemical shifts, and steady state and transient nuclear Overhauser effects (NOEs) and spin decoupling. Wüthrich and co-workers used a variety of NOE-based methods, including two-dimensional NOESY spectra, to characterize the role of axial ligand geometry on the setting of the redox potential of *c*-type cytochromes. Comprehensive ^{1}H resonance assignments were not completed until the work of Wand and co-workers with the essentially complete assignment of the ^{1}H NMR spectrum of the horse protein in both redox states.[13–15] Efforts with the reduced protein led to the formalized NOE-based pattern recognition method for analysis of ^{1}H NMR spectra of proteins termed the 'main chain directed resonance assignment strategy'.[16] These studies also resulted in the extensive characterization of the backbone conformation of the protein in its two redox states. The resonance assignments of the protein were extensively cross correlated by use of two-dimensional NOESY spectra of mixtures of the two redox states.[17]

Analysis of the carbon spectrum of cytochrome was initiated with the natural abundance studies done by Oldfield and Allerhand[18] and subsequently carried forward by Oldfield and others.[19] NMR studies using both ^{13}C and ^{15}N have been limited by the inability to cost-effectively isotopically enrich eukaryotic *c*-type cytochromes by recombinant DNA methods. Chemical modification of the protein has also allowed introduction of NMR active isotopes of fluorine[20] and iron.[21]

3 STRUCTURAL ANALYSIS

Focused structural studies have paralleled progress in the solution of the resonance assignment problem. Early work centered on structural issues regarding heme pocket packing[11] and axial ligand geometry,[12] which could be approached directly as the reporter ^{1}H resonances were generally well resolved. Particular emphasis was placed on comparisons of the coordination geometry at the heme iron and the electronic structure of ferric heme in homologous cytochromes *c*.[12] Detailed and relatively comprehensive structural analysis began with the characterization of the heme $\boldsymbol{g}$ tensor in the oxidized state and its use in detecting diamagnetic chemical shift changes (i.e. structure change) induced by a change in redox state.[22–24] These studies suggested the presence of localized and potentially significant structural differences between the two redox states, in contrast to the only subtle structural differences observed in models of the crystal structures of homologous cytochromes *c*. A more recent application of this approach combined both ^{1}H and ^{13}C chemical shift changes upon a change in redox state, allowing for a more explicit separation of paramagnetic and diamagnetic chemical shift effects.[24] Other NMR-based studies, primarily analysis of chemical shift perturbation and local NOE patterns, have also provided indications that the structure of cytochrome *c* is somewhat sensitive to conditions of salt type and concentration.[25,26]

The recent controversy surrounding the issue of the relative importance of the specific σ-bond pathway model for electron tunneling through the protein intervening between electron transfer donor and acceptor moieties, such as heme, raises the need for comprehensive structural detail under conditions where most experimental data on interprotein electron transfer chemistry are available, i.e. in solution under low ionic strength conditions. Truly comprehensive structural analysis of a mitochondrial *c*-type cytochrome has only recently been reported.[27–29] Using a variety of ^{1}H NMR-based techniques, Wand and co-workers have determined to very high precision the solution structures of reduced and oxidized horse heart cytochrome c by use of two- and three-dimensional ^{1}H NMR spectroscopy and hybrid distance geometry–dynamical simulated annealing calculations. Here, a significant limitation was the inability to label the protein with ^{13}C or ^{15}N or to use heteronuclear techniques to resolve and assign ^{1}H–^{1}H NOEs. Nevertheless, use of three-dimensional NOESY TOCSY spectra allowed the resolution and assignment of over 1900 and 1600 NOEs for the reduced and oxidized proteins, respectively. These restraints, when combined with ϕ torsion angle restraints determined by analysis of amide NH–C-αH *J* coupling constants, resulted in a family of structures which show all-residue rms deviations of the main chain atoms from the mean structure of better than 0.047 nm and 0.037 nm for the reduced and oxidized protein, respectively.

Stereo pairs of the backbone of the refined average structure of horse cytochrome *c* in each redox state are represented in Figures 1 and 2 as ribbon drawings.

These highly refined structures reveal several internal and surface features that may be important in the function, stability, and dynamical behavior of this protein. Some of these features have been noted previously with homologous proteins, while others have not. For example, a previously undocumented surface reorganization involving Ile81 appears to function as a molecular recognition device signaling the current redox state of the protein. On the main chain, the reduced protein displays unusual 3_{10} to α-helical transitions in the two of the three main helical segments of the protein. This leads to a bifurcated peptide carbonyl in the core of each helical segment.

In sum, the determination of the high-resolution models of the solution structures of oxidized and reduced cytochrome *c* by methods based on NMR has allowed a detailed comparison to be made between the solution structure of the protein in its two redox states and the corresponding structures of the

Figure 1 Ribbon diagram of the refined average solution structure of horse ferrocytochrome determined using NMR-based methods.[21] Drawn with the computer program MOLSCRIPT[40]

Figure 2 Ribbon diagram of the refined average solution structure of horse ferricytochrome determined using NMR-based methods.[22] Drawn with the computer program MOLSCRIPT[40]

homologous tuna protein in the high salt crystalline state. The latter structures have been used extensively in theoretical studies of solvent reorganization energies and other electron transfer parameters. An observed variance of the crystal structures with the low salt solution structures could therefore potentially be quite significant. Indeed, several differences have been detected between the solution and crystalline structures of the protein in both redox states.

Several detailed crystallographic studies of the structure of *c*-type cytochromes have revealed the presence of structural, deeply buried water molecules, which are apparently conserved across the cytochrome *c* family of proteins. In particular, one water molecule, located at a triad involving the side chains of residues Tyr67, Asn52 and Thr78 in the horse protein, has been suggested to be intimately linked to the setting of the redox potential of the heme. It is of considerable interest, therefore, to note that the aromatic ring of Tyr67, in both redox states, undergoes rotations on the millisecond timescale (see below). This necessarily raises several concerns about the residence time or even presence of water at this location in the protein under solution conditions. Similar comments can be made about the locations of the other three conserved structural water molecules found in the crystal structures of cytochrome *c* where there is considerable structural perturbation brought on by aromatic rings flipping at rates that are fast on the NMR chemical shift timescale. The existence of structural water in the interior of the solution structures of both oxidized and reduced horse heart cytochrome *c* has also been demonstrated using ^{1}H NMR spectroscopy. Using pseudo-three-dimensional NOESY TOCSY spectra, Qi and co-workers[29] have located six and five water molecules with residence times greater than a few hundred picoseconds in ferrocytochrome *c* and ferricytochrome *c*, respectively. Two water molecules are located in the heme crevice (see Figure 3). One of the water molecules is found to undergo a large change in position upon a change of oxidation state. Both these observations indicate that buried structural waters in the heme crevice, via microscopic dielectric effects, probably play a significant role in the setting of the solvent reorganization energy associated with electron transfer.

4 DYNAMICS AND STABILITY

The dynamics and stability of both redox states of cytochrome *c* have been probed extensively by NMR methods. Beginning with the earliest library of ^{1}H resonance

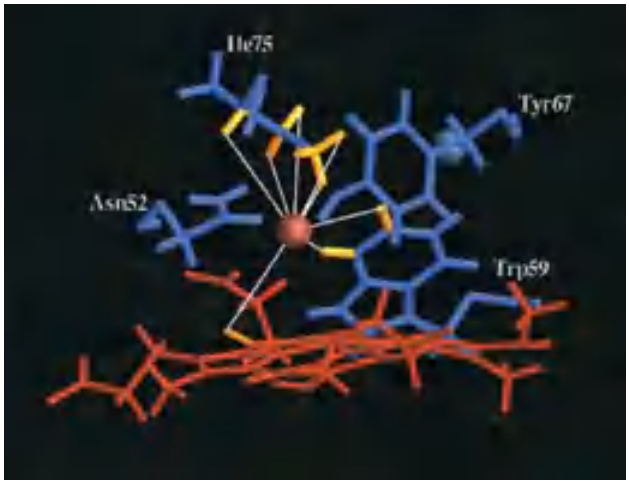

Figure 3 Heavy atom skeleton of several of the amino acid side chains surrounding one of the structural water molecules found in the interior of horse ferricytochrome *c*. Shown is the refined average structure derived from a family of highly refined structures having an average rms deviation from the mean structure of 0.051 ± 0.007 nm, for the main chain heavy atoms, and 0.106 ± 0.007 nm for all heavy atoms.[27] Details of the refinement of the structural model for oxidized horse cytochrome *c* are reported elsewhere.[27] Shown are the side chains of Asn52, Tyr67, Thr78, and the heme. Also shown are the amide NH groups of Lys79, Asn52, and Gly77, which provide NOE-based distance constraints to the water molecule. This particular water molecule is restrained in the model by five direct NOE-based restraints (indicated by white lines). Drawn with the computer program RIBBONS[41]

assignments, Moore, Williams, and co-workers have demonstrated that reduced cytochrome *c* is remarkably stable to both extremes of pH and temperature, maintaining extensive structure over pH 4–12 and from 4 °C to nearly 100 °C at pH 7.0.[30] The oxidized protein is somewhat less stable to extremes of pH and temperature.[31] The pH induced isomerization of cytochrome *c* has been studied extensively by ^{1}H NMR and is associated with a pK_a of approximately 9.5. At low pH, a so-called 'molten globule state' of the protein is achieved, which has been indirectly characterized by ^{1}H NMR methods and hydrogen exchange.[32] In addition to the characterization of the gross behavior of the protein, NMR has provided a great deal of insight into the activated processes leading to local motion arising from local instabilities. Large variation of the activation barriers associated with the flipping of phenylalanine and tyrosine aromatic rings about the $\beta-\gamma$ rotation axis has been examined extensively by means of both one-[30] and two-dimensional methods.[12] Indeed, while several aromatic rings are in fast exchange at temperatures below 20 °C, the ring of Tyr67 remains in intermediate exchange on the NMR chemical shift timescale, even at temperatures above 70 °C.

The rates of hydrogen exchange of the backbone amide hydrogen atoms of the protein have also been used as a sensitive measure of changes in local stability and dynamics.[33] Early observations of amide hydrogen exchange by NMR methods immediately indicated a wide range of local stabilities and dynamics on the main chain of the protein in the two redox states. With the completion of the ^{1}H resonance assignments of the backbone amide hydrogen atoms of the protein in its two redox states, it should be possible to use hydrogen exchange to pinpoint those parts of the protein that are functionally involved in setting of the redox potential of the heme, to identify the temporal relationships of hydrogen bonding during folding of the protein, to characterize non-native states of the protein, to identify the interaction surface in the complex with an antibody, and so on. With regard to local stability and dynamics, the hydrogen exchange data indicate a huge range of local equilibrium stabilities of the secondary structure hydrogen-bonding networks of the amino and carboxyl terminal helices, for example.[34,35]

5 COMPLEXES

The central role of cytochromes in electron transfer processes in general and in oxidative phosphorylation in mitochondria in particular has resulted in cytochrome *c* being the focal point of a large number of physiochemical investigations of interprotein electron transfer. Unfortunately, the main biological redox partners of cytochrome *c* are large, membrane-associated proteins, and have thus far not been subjected to direct investigation of their complexation with cytochrome *c* by solution NMR methods.

Two heterologous protein complexes involving cytochrome *c* have been studied in some detail by NMR methods. One is the complex formed between cytochrome *c* and cytochrome b_5. Though cytochrome b_5 is not a physiologically relevant redox partner of cytochrome *c*, their complexation and electron transfer properties have been used as a model system with which to probe the underlying physical issues of interprotein electron transfer. Burch and co-workers[36] have reported the one-dimensional ^{1}H and ^{13}C spectra of this complex and have noted only modest changes in the spectra. These authors attribute the subtlety of the spectral perturbation to an interaction domain which is primarily electrostatic and somewhat dynamic. A complete structural characterization of this complex by either NMR or crystallographic methods remains to be carried out. The second complex that has been extensively characterized by NMR methods is that between cytochrome *c* and cytochrome *c* peroxidase, a physiologically relevant complex. Satterlee and co-workers have studied this complex extensively.[37] One-dimensional NOE experiments combined with chemical shift perturbations proved valuable in the selective and efficient characterization of the protein–protein interface of this complex. However, as with the cytochrome *c*–cytochrome b_5 complex discussed above, the cytochrome *c* peroxidase–cytochrome *c* complex has not been defined comprehensively by NMR methods and remains a significant challenge of great biological significance.

The use of cytochrome *c* as a model protein for studying protein mediated electron transfer has resulted in the characterization of its interaction with a variety of inorganic complexes.[38] In addition, the interaction of cytochrome *c* with polyanions such as phosphate and adenosine triphosphate has also been examined. The latter has been argued to represent a feedback interaction point for the oxidative phosphorylation pathway of energy metabolism. These kinds of study are necessary to gain insight into the structural and electronic changes which govern the interaction and transfer of electrons between proteins. In particular, the balance between hydrophobic and electrostatic interactions can be probed by studies of the structural changes that occur upon changes in salt.[25,26]

A most interesting interaction of cytochrome *c* is that of binding to membrane or membrane mimetics. Though

extensively studied by other techniques, solution NMR methods have yet to be brought fully to bear on the characterization of the effects of membrane association on the structure of cytochrome *c*. With the exception of early work by Brown and Wüthrich,[39] which concentrated on the lipid portion of a vesicle–cytochrome *c* interaction, solution NMR methods have been used little in the characterization of the structural perturbations of the protein brought about by its association with a membrane-like surface. This promises to be a rich area of future investigation and will help complete the long history of the NMR-based description of the structure, dynamics, and function of this biologically critical protein.

6 RELATED ARTICLES

Biological Macromolecules: Structure Determination in Solution; Biological Macromolecules; Biological Macromolecules: NMR Parameters; Heme Peroxidases; Hydrogen Exchange and Macromolecular Dynamics; Paramagnetic Relaxation in Solution; Protein Dynamics from NMR Relaxation; Protein Dynamics from Solid State NMR; Structures of Larger Proteins, Protein-Ligand, and Protein-DNA Complexes by Multi-Dimensional Heteronuclear NMR.

7 REFERENCES

1. G. R. Moore and G. W. Pettigrew, *Cytochromes c: Evolutionary, Structural and Physiochemical Aspects*, Springer, New York, 1990.
2. See, for example, H. Roder, G. A. Elöve, and S. W. Englander, *Nature*, 1988, **335**, 700.
3. See, for example, A. Willie, M. McLean, R.-Q. Liu, S. Hilegn-Willis, A. J. Saunders, G. J. Pielak, S. G. Sligar, B. Durham, and F. Millet, *Biochemistry*, 1993, **32**, 7519, and references cited therein.
4. See, for example, K. K. Rodgers and S. G. Sligar, *J. Mol. Biol.*, 1991, **221**, 1453.
5. See, for example, R. Jemmerson and E. Margoliash, *Methods Enzymol.*, 1981, **74**, 244, and references cited therein.
6. See, for example, G. W. Bushnell, G. V. Louie, and G. D. Brayer, *J. Mol. Biol.*, 1990, **214**, 585, and references cited therein.
7. See, for example, D. S. Wuttke, M. J. Bjerrum, J. R. Winkler, and H. B. Gray, *Science*, 1992, **256**, 1007, and references cited therein.
8. A. Kowalsky, *J. Biol. Chem.*, 1962, **237**, 1807.
9. For one example of a series of papers by these authors, see R. K. Gupta and A. G. Redfield, *Science*, 1970, **169**, 1204.
10. C. C. McDonald and W. D. Philips, *Biochemistry*, 1973, **12**, 3170.
11. For the first of a ground-breaking series of papers, see G. R. Moore and R. J. P. Williams, *Eur. J. Biochem.*, 1980, **103**, 503.
12. See, for example, R. M. Keller and K. Wüthrich, *Biochim. Biophys. Acta*, 1991, **688**, 307, and references cited therein.
13. A. J. Wand and S. W. Englander, *Biochemistry*, 1985, **24**, 5290.
14. A. J. Wand, D. L. Di Stefano, Y. Feng, H. Roder, and S. W. Englander, *Biochemistry*, 1989, **28**, 186.
15. Y. Feng, H. Roder, S. W. Englander, A. J. Wand, and D. L. Di Stefano, *Biochemistry*, 1989, **28**, 195.
16. S. W. Englander and A. J. Wand, *Biochemistry*, 1987, **26**, 5953.
17. Y. Feng, A. J. Wand, H. Roder, and S. W. Englander, *Biophys. J.*, 1991, **59**, 323.
18. E. Oldfield and A. Allerhand, *Proc. Natl. Acad. Sci. USA*, 1973, **70**, 3531.
19. H. Santos and D. L. Turner, *Eur. J. Biochem.*, 1992, **206**, 721.
20. N. Staudenmayer, M. B. Smith, H. T. Smith, F. K. Spies, Jr., and F. Millett, *Biochemistry*, 1976, **15**, 3198.
21. J. Chung, H. C. Lee, and E. Oldfield, *J. Magn. Reson.*, 1990, **90**, 148.
22. G. Williams, N. J. Clayden, G. R. Moore, and R. J. P. Williams, *J. Mol. Biol.*, 1985, **183**, 447.
23. Y. Feng, H. Roder, and S. W. Englander, *Biochemistry*, 1990, **29**, 3494.
24. D. L. Turner and R. J. P. Williams, *Eur. J. Biochem.*, 1993, **211**, 555.
25. Y. Feng and S. W. Englander, *Biochemistry*, 1990, **29**, 3505.
26. S. J. Moench, T.-M. Shi, and J. D. Satterlee, *Eur. J. Biochem.*, 1991, **197**, 631.
27. P. X. Qi, D. L. Di Stefano, and A. J. Wand, *Biochemistry*, 1994, **33**, 6408.
28. P. X. Qi, R. A. Beckman, and A. J. Wand, *Biochemistry*, 1995, submitted.
29. P. X. Qi, J. L. Urbauer, E. F. Fuentes, M. F. Leopold, and A. J. Wand, *Nature Struc. Biol.*, 1994, **1**, 378.
30. G. R. Moore and R. J. P. Williams, *Eur. J. Biochem.*, 1980, **103**, 513.
31. G. R. Moore and R. J. P. Williams, *Eur. J. Biochem.*, 1980, **103**, 523.
32. M.-F. Jeng, S. W. Englander, G. A. Elöve, A. J. Wand, and H. Roder, *Biochemistry*, 1990, **29**, 10434.
33. D. J. Patel and L. L. Canuel, *Proc. Natl. Acad. Sci. USA*, 1976, **73**, 1398.
34. A. J. Wand, H. Roder, and S. W. Englander, *Biochemistry*, 1986, **25**, 1107.
35. A. J. Wand, Ph.D. Thesis, University of Pennsylvania, Philadelphia, PA, 1984.
36. A. M. Burch, S. E. J. Rigby, W. D. Funk, R. T. A. MacGillivray, M. R. Mauk, G. Mauk, and G. R. Moore, *Science*, 1990, **247**, 831.
37. S. J. Moench, S. Chroni, B.-S. Lou, J. E. Erman, and J. D. Satterlee, *Biochemistry*, 1992, **31**, 3661.
38. C. O. Arean, G. R. Moore, G. Williams, and R. J. P. Williams, *Eur. J. Biochem.*, 1988, **173**, 607.
39. L. R. Brown and K. Wüthrich, *Biochim. Biophys. Acta*, 1977, **468**, 389.
40. P. J. Kravlis, *J. Appl. Crystallogr.*, 1991, **24**, 946.
41. M. Carson, *J. Mol. Graphics*, 1987, **5**, 103.

Biographical Sketch

A. Joshua Wand. *b* 1957. B.Sc. (Hons), 1979, M.Sc., 1981, Carleton University; Ph.D., 1984, University of Pennsylvania. NSERC scholar, 1983–84; NSERC fellow, 1984–85. Associate member, 1985–90, and member, 1990–91, Institute for Cancer Research, Philadelphia. Associate Professor of Biochemistry and Biophysics, University of Illinois at Urbana–Champaign, 1991–95. Currently Professor of Biological Sciences, Biophysics, and Chemistry and Director of the Structural Biology Program, State University of New York at Buffalo. Research interests: heme- and calcium-binding proteins, protein stability, dynamics and folding, and use of NMR relaxation methods to characterize protein structure and dynamics.

Myoglobin

Gerd N. La Mar
University of California, Davis, CA, USA

1	Introduction	1
2	^{1}H NMR Spectral Properties	1
3	Studies on Diamagnetic Mb	2
4	Studies on Paramagnetic Mb	3
5	Related Articles	4
6	References	4

1 INTRODUCTION

Myoglobin, (Mb) is a small (15–18 kDa) protein containing a heme [Figure 1(a)], widely distributed in the animal kingdom, whose role is to store O_2 in muscle.[1] The reversible binding of O_2 by heme iron is one of the simplest in biochemistry, and intense study of both the reaction and structure of Mb have made it a major test case for the detailed elucidation of the relationship of function to structure and/or dynamics. Mb exhibits a remarkably conserved globular folding pattern of eight helices, A–H, with the heme wedged between helices E–F, in spite of the large variation in sequence and ligand affinity/dynamics. The only completely conserved residues are the axial (proximal) ligand His F8 (histidine) (position 8 on helix F), and a Phe CD1 (phenylalanine) in contact with the heme edge (position 1 of loop between helices C, D). The variation in ligation properties is attributed to the nature of the E helix residues in the distal pocket, in particular those at positions E7 and E11. To favor binding O_2 over the toxic adventitious CO, the protein exerts a stabilization by distal hydrogen bonding to the polar and bent Fe(II)O_2 unit [Figure 1(b)], and a destabilization by steric tilting of the nonpolar, linear Fe(II)CO unit [Figure 1(c)], which prefers to bind normal to the heme. The distal H-bond to O_2 [Figure 1(b)] is provided by His E7 in the large majority of mammalian Mbs, and in rare cases by glutamine (Gln); the latter residue is more common in invertebrate Mbs, and several have nonpolar E7 residues.[2] The E11 residue is invariably nonpolar [valine, isoleucine (Val, Ile)]. Both structural and functional properties of Mb are shared with hemoglobin, Hb, the related protein involved in O_2 transport, which is often found in oligomerized forms (see ***Hemoglobin***.).

Physiological active Mb has a ferrous, Fe(II), heme, designated Mb^{II}, which is high-spin in unligated or deoxy Mb^{II} and diamagnetic in the CO and O_2 ligated forms:

$$Mb^{II}[S = 2] + L \rightleftharpoons Mb^{II}L\,[S = 0 \quad \text{for } L = O_2, CO] \quad (1)$$

$Mb^{II}O_2$, however, is relatively unstable with respect to autoxidation to ferric Mb or metMb, designated Mb^{III}. While Mb^{III} is not a physiologically functional form, the electronic/magnetic and ligation properties of these necessarily paramagnetic variants serve as extraordinarily sensitive probes of important structural controls of function.[1] At acidic to neutral pH, high-spin Mb^{III} may possess a vacant sixth site or ligated H_2O, and readily reacts with small anionic ligands, X^-, according to:

$$Mb^{III}(\text{or } Mb^{III}H_2O)[S = \tfrac{5}{2}] + X^- \rightleftharpoons Mb^{III}X(+H_2O)$$
$$[S = \tfrac{5}{2} \quad \text{for X} = \text{OCN,F,N}_3;$$
$$S = \tfrac{1}{2} \quad \text{for X} = \text{CN,N}_3] \quad (2)$$

2 ^{1}H NMR SPECTRAL PROPERTIES

The active site chemical shifts for diamagnetic $Mb^{II}CO$ and $Mb^{II}O_2$, δ(dia), are dominated by the large ring current of the heme, δ_{rc},

$$\delta(\text{dia}) = \delta_{pep} + \delta_{rc} \quad (3)$$

where δ_{pep} is the peptide chemical shift as influenced by the secondary structure. The remainder of the derivatives are all paramagnetic, for which the observed shift, δ(para), is given by

$$\delta(\text{para}) = \delta_{dia} + \delta_{hf} \quad (4)$$

where δ_{dia} contains all diamagnetic influences (see ***Amino Acids, Peptides and Proteins: Chemical Shifts***). For practical purposes, δ_{dia} in equation (4) can be substituted by the value in equation (3). The hyperfine shift, δ_{hf}, has the two components:[3]

$$\delta_{hf} = \delta_{con} + \delta_{dip} \quad (5)$$

where the contact contribution, δ_{con}, reflects delocalized spin density onto the ligand and the dipolar contribution, δ_{dip}, reflects anisotropy of the paramagnetic susceptibility tensor, χ, and is given for proton i by:

$$\delta^i_{dip} = \Sigma^q \Delta\chi_q G F^i_q R(\alpha, \beta, \gamma) \quad (6)$$

where q = axial, rhombic, GF_q are geometric factors of proton i in iron-centered X-ray coordinates, and $R(\alpha,\beta,\gamma)$ are the Euler rotation angles that convert the iron-centered X-ray to the magnetic coordinate system $[x',y',z' \rightarrow x,y,z$ in Figure 1(a), 1(d)], where the susceptibility tensor, χ, is diagonal. Lastly, the paramagnetic influence on relaxation for proton i can be related to proximity to the iron, R_{Fe}, via:

$$T_1^{-1} \propto R_{Fe}^{-6} \quad (7)$$

The ^{1}H NMR spectra for the four readily accessible oxidated/spin states of Mb are illustrated in Figure 1(e)–(h). All paramagnetic forms exhibit hyperfine shifts and relaxation which increase with S, with the resolved (hyperfine shifted) signals observed outside the δ 0–10 ppm range necessarily arising from the active site.[4] The assignment of the largely overlapped resonances in diamagnetic MbCO (and MbO_2 when stable) are carried out by standard 2D methods, although heteronuclear labeling is necessary for a complete assignment because of the size of the protein.[5,6] In the paramagnetic derivatives, the initial assignments[4,7] were restricted to the

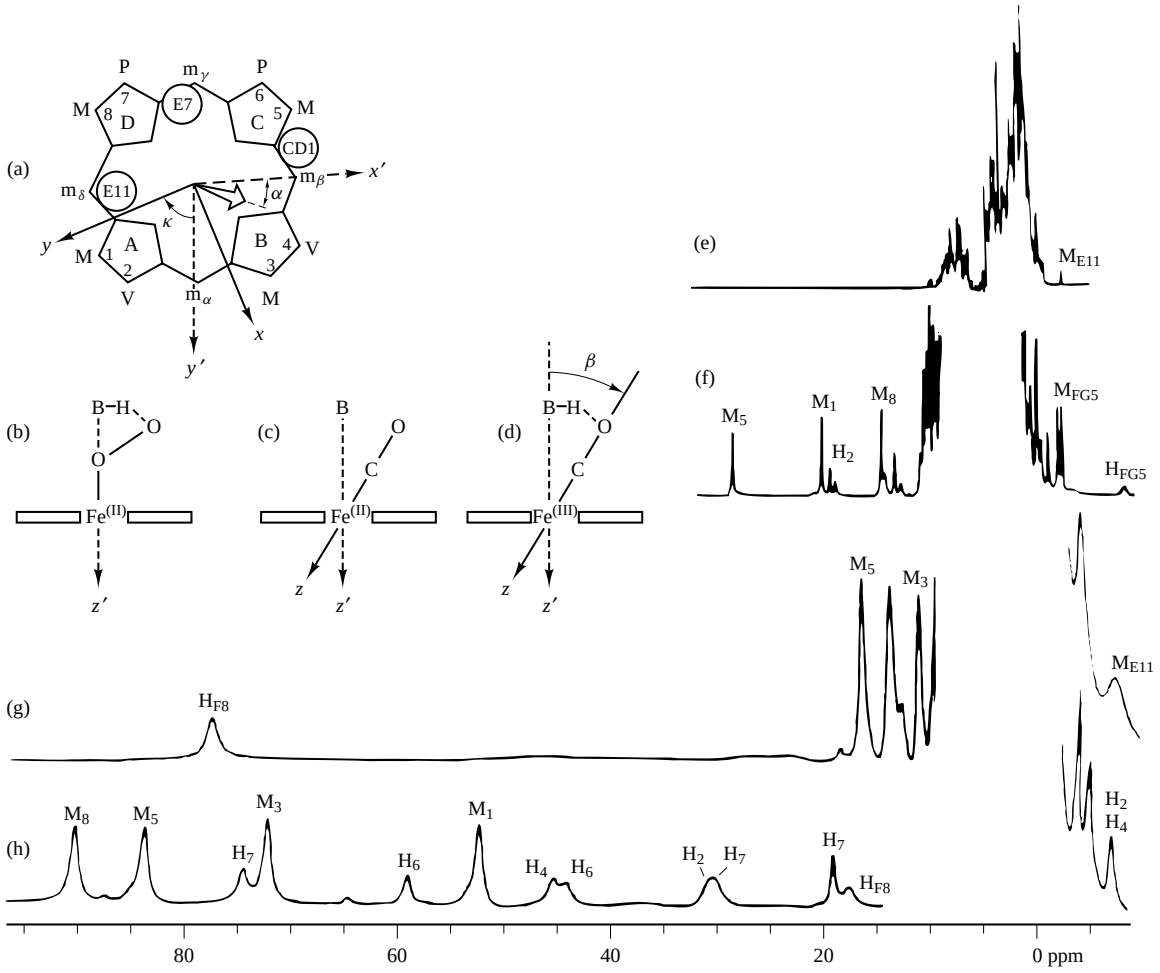

Figure 1 (a) Structure of the heme, as viewed from the distal side, with substituents M (methyl), V (vinyl), and P (propionate) at positions 1–8. The approximate position of distal residues E7, E11, and Phe CD1 in Mb are indicated. Edge-on views of the heme with; (b), iron(II)-coordinated O_2 that serves as a hydrogen-bond acceptor to the distal residue designated B–H; (c), iron(II)-coordinated CO which is tilted from the preferred heme normal by distal steric interactions (possibly with BH), but with no hydrogen bond with BH; and (d), iron(III)-coordinated CN^-, which is both tilted from the preferred heme normal due to steric interaction (like CO), and serves as a hydrogen-bond acceptor to the distal BH. The notation x',y',z' represents an iron-centered symmetry coordinate system with z' normal to the heme, and x,y,z are the coordinates in which the paramagnetic susceptibility tensor, χ, is diagonal (magnetic coordinate system). The coordinates x,y,z are related to x',y',z' by the Euler rotation angles α, β, γ so that $(x',y',z')R(\alpha, \beta, \gamma) \rightarrow (x,y,z)$. The quantity β defines the magnitude of the z axis tilt [shown in (d)], α defines the direction of tilt of the major magnetic or z axis tilt [shown in (a)], and the rhombic or in-plane magnetic axes, x,y, are related to x',y' by the angle $\kappa \sim \alpha+\gamma$[as shown in (a)]. The 360 MHz ^{1}H NMR spectra at 25°C of sperm whale Mb in different oxidation/spin states are illustrated in: (e) for diamagnetic (S = 0) $Mb^{II}CO$ in ^2H_2O, pH = 7.6; (f) for paramagnetic ($S = \frac{1}{2}$) $Mb^{III}CN$ in ^2H_2O, pH = 8.6; (g) for paramagnetic (S = 2) deoxy Mb^{II} in ^1H_2O, pH = 8.2; and (h) for paramagnetic ($S = \frac{5}{2}$) $Mb^{III}H_2O$ in ^2H_2O, pH = 6.5. The assigned signals are labeled M_i(methyl), H_i (single proton), where i is the position on the heme (i = 1–8), or the helical or loop position of an amino acid residue

heme (via isotope labeling) and the labile ring protons of the proximal F8 and distal E7 His [via paramagnetic relaxivity, see equation (7)]. Later, steady-state NOEs and 2D experiments, appropriately tailored for rapidly relaxed resonances, were shown to provide the necessary assignments in all derivatives.[8]

The most informative ^{1}H NMR data on Mb have resulted from comparative studies on either crystallographically characterized natural genetic variants, i.e. sperm whale and the sea hare *Aplysia limacina*, Mbs, or synthetic point mutants of a given Mb. Moreover, the wealth of information in the hyperfine shift, the enhanced resolution it imparts to active site residues, as well as the unique ability to detect directly the distal labile proton involved in H bonding to the ligand, have resulted in an emphasis on the ^{1}H NMR study of paramagnetic Mb derivatives.[4,7] In particular, $Mb^{III}CN$ is a valuable model for functional Mb because the ligand bond polarity makes it a probe for the distal H-bonding interaction of $Fe(II)O_2$, while the tilt of the preferred linear Fe(III)CN unit normal to the heme [Figure 1(d)] will sense the distal steric influences that would affect the Fe(II)CO unit. Hence, primarily results on paramagnetic derivatives will be discussed which provide unique information on distal H-bonding and the steric influence on the bound ligand [i.e. Fe(III)CN in Figure 1(d)]; early results have been summarized by Morrow and Gurd.[7]

3 STUDIES ON DIAMAGNETIC Mb

Because of its stability,[1] most ^{1}H NMR studies have been carried out on $Mb^{II}CO$ [spectrum in Figure 1(e)], whose

solution structure was found to be essentially the same as in the crystal;[5] the prominently resolved upfield ring-current-shifted Val E7 C-γH$_3$ provided one of the first resolved protein ^{1}H NMR signals.[7] Detailed assignment of titrating residues in sperm whale MbCO has provided important tests for theoretical models for pKs.[9,10] Comparison among several human Mb^{II}CO distal point mutants have shown that structural changes are localized to the perturbed residues.[11] The signals for enriched ^{57}Fe and ^{17}O in bound CO have also been detected (see ***Chemical Shifts in Biochemical Systems***).[12] Mb^{II}O$_2$ has been much less studied because of its instability toward autoxidation to Mb^{III}.

4 STUDIES ON PARAMAGNETIC Mb

4.1 Electronic Structure

Information on the electronic structure is derived directly from the contact shift.[3,4] In high-spin Mb^{II} and Mb^{III}, magnetic anisotropy, and hence the dipolar shifts, are relatively small.[13] Therefore, the dominant contact shift dictates that the strongly hyperfine-shifted and resolved signals arise from the iron-coordinated heme and axial His, which has been amply confirmed by detailed assignments.[4] The ^{6}A ground state for Mb^{III} results in contact shifts [Figure 1(h)] which are relatively insensitive to protein environment for a given ligation state,[4,13] but can serve as empirical probes to determine whether a water molecule is axially coordinated [spectrum in Figure 1(h)]. The heme contact shifts for deoxy Mb^{II} [Figure 1(g)] are very sensitive to the protein environment,[4] probably because of two contributing orbital states with different spin-delocalization patterns.[14] The axial His F8 contact shifts in high-spin Mb^{II}, on the other hand, are dominated by σ bonding with d_{z^2}. The imidazole ring NH shift, identified in the δ 60–90 ppm window by comparing ^{1}H$_2$O and ^{2}H$_2$O spectra [spectrum in Figure 1(g)], serves as a sensitive probe for axial bond strain,[4] which has been extensively applied to deoxy Hb (see ***Hemoglobin***).

The presence of a single unpaired spin in low-spin ($S = \frac{1}{2}$) iron(III) allows direct interpretation of the dominant contact shifts in terms of iron–porphyrin bonding.[15] The observation of characteristic π contact shifts for free hemin confirmed the E rather than A orbital ground state. In the free hemin, d_{xz}, d_{yz}, which interact solely with a pair of *trans*-pyrroles, respectively, are essentially degenerate and are fractionally occupied by an unpaired spin, giving rise to comparable contact shifts for the heme methyls of the four pyrroles.[15] Within Mb^{III}CN, however, the d_{xz}, d_{yz} degeneracy is lifted by the rhombic field of the protein, with the lone spin in the resulting orbital

$$\Psi = (\cos^2 \kappa)d_{xz} - (\sin^2 \kappa)\, d_{yz} \qquad (8)$$

with κ locating the rhombic axes [$\kappa = \sim\alpha + \gamma$ in equation (6) and Figure 1(a)]. The angle κ reflects primarily the orientation of the axial His F8 imidazole orientation relative to the heme.[13,15] Hence, large 1-CH$_3$ and 5-CH$_3$ (or 3-CH$_3$ and 8-CH$_3$) contact shifts are observed[4] [spectrum in Figure 1(e)] for His F8 oriented along pyrroles B, D (or A, C) in Figure 1(a). The characteristic pattern in heme contact shifts that reflects heme orientation relative to the His F8 provided the first evidence for the now generally observed phenomenon of heme orientational disorder about the α,γ-*meso* axis.[16]

4.2 Distal Hydrogen Bonding

The combination of large δ_{dip} [equation (6)] and significant paramagnetic relaxation [equation (7)] generally resolves and allows identification[17] of the heme pocket labile protons in Mb^{III}CN.[17–20] The detection of an isotope effect on heme contact shift, which is uniquely traceable[17] to the assigned distal side-chain NH, provides direct proof for the existence of the H bond to bound cyanide [shown in Figure 1(d)]. The H-bonding proton has been demonstrated to arise from the side chain of the E7 residue, His in sperm whale[17] and Gln in elephant,[18] but Arg E10 in *Aplysia*[19] and a sperm whale double mutant[20] Mb^{III}CN. For high-spin Mb^{III}, a strong solvent isotope sensitivity of the heme contact shift was shown to reflect the presence of a distal donor and acceptor H bond in Mb^{III}OH and Mb^{III}H$_2$O, respectively, which accounts for the affinity of these ligands at different pH values.[21]

4.3 Distal Steric Influence on Ligand Tilt

The necessarily dipolar shifts for the noncoordinated residues in the active site of an Mb complex with significant paramagnetic anisotropy can serve not only as important auxiliary constraints (in addition to NOEs) for determining active site structures,[13,18–20,22,23] but also allow the determination of the orientation of the paramagnetic susceptibility tensor, χ, in the molecular framework. The largest magnetic anisotropy for Mb is exhibited by low-spin Mb^{III}CN, where the out-of-plane g_z value is much larger that the two in-plane values; outside the protein matrix, the g_z value is normal to the heme. However, since cyanide is the strongest ligand in Mb^{III}CN, distortion of the Fe(III)CN unit from the heme normal will result in tilting of the major magnetic axis from the normal (z') by an angle β in Figure 1(d), and in a direction whose projection on the heme plane is defined by α [Figure 1(a)] in the Euler rotation $R(\alpha, \beta, \gamma)$ in equation (6).[13] The value of δ_{dip} for nonequivalent nuclei provided by 2D NMR analysis of Mb^{III}CN, together with the iron-centered X-ray coordinates for any derivative of Mb, allows a least-square search that uniquely yields $\Delta\chi_{ax}$, $\Delta\chi_{rh}$, and the three Euler angles α, β, γ. 2D NMR assignments of sperm whale and *Aplysia* Mb^{III}CN have yielded orientations of the magnetic z axis that are consistent with the crystallographically-determined Fe(III)CN units.[13,19] Moreover, it was shown that the anisotropy and Euler angles could be uniquely determined using experimental ^{1}H NMR data and X-ray coordinates only for the residue on the proximal side of the heme, for which both δ_{dia} and the coordinates for GF_q in equation (6) can be expected to be highly conserved in distal point mutants.[13] The latter conclusion allows the investigation of the influence of specific distal residues by site-directed mutagenesis in providing H bonding to, or sterically tilting of, the bound ligand.

Substitution of the His E7 by a glycine (Gly) or Val in Mb leads to an essentially unchanged Fe(III)CN tilt from that in WT ($\beta \sim 15^\circ$), but with a direction (α) rotated toward the vacancy created by removal of the tilting imidazole group[22] [$\alpha = 0 \rightarrow -40^\circ$ in Figure 1(a)]. Hence, contrary to the standard textbook example, the distal His does not cause ligand tilt in Mb^{II}CO, but does determine the direction of the tilt. On the other hand, decreasing the steric bulk of the E11 residue by the substitution of WT Val $\rightarrow$ alanine (Ala) leads to a significant

decrease in tilt magnitude but not direction.[23] The effect of double mutants at both the E7 and E11 position showed that the influence on tilt magnitude/direction of the individual residues is approximately additive. Once the magnetic axes have been determined for an $Mb^{III}CN$ distal point mutant based on the 2D NMR assigned δ_{dip} and the proximal δ_{dia} and X-ray coordinates, the δ_{dip} for the substituted distal residue can be analyzed by searching for the orientation(s) of the distal residue(s) that optimally account for the δ_{dip} [as well as iron-induced relaxivity, via equation (7), and the more conventional NOE constraints]. Detailed studies have been carried out on the His E7 $\rightarrow$ Val $Mb^{III}CN$ mutant,[22] which showed that lateral movements of the E helix by $\sim$0.8 Å and of Phe CD1 by 0.5 Å, each toward the iron, result in filling the void resulting from the reduced bulk of the E7 side chain.

In the case of sea hare *Aplysia* Mb, O_2 binding indicates a distal H-bound donor, despite the fact that it possesses an E7 Val. Determination of the magnetic axes[19] for *Aplysia* $Mb^{III}CN$ allowed a quantitative description of the distal pocket which showed that an arginine (Arg) at helical position E10 [occupied by a threonine (Thr) in sperm whale Mb] orients into the heme pocket and provides a H bond to the bound CN^- [and by inference, bound O_2 in $Mb^{II}O_2$]. The orientations of the distal residues determined from the dipolar shifts are essentially the same as those found in a parallel crystal diffraction study of that protein. Subsequently, it was possible to construct a double mutant sperm whale (His E7 $\rightarrow$ Val, E10 Thr $\rightarrow$ Arg) Mb to make a synthetic sperm whale Mb where the distal H bond is provided[20] by the Arg E10 with orientation similar to that in *Aplysia* Mb. The direction of tilt of the FeCN unit in E7 Val/E10 Arg $Mb^{II}CN$ differs from that on the E7 Val single mutant in a manner indicative of attractive H bonding between Arg E10 and the bound ligand in the former protein.

5 RELATED ARTICLES

Heme Peroxidases; Hemoglobin; Mitochondrial Cytochrome c; Paramagnetic Relaxation in Solution; Proteins and Protein Fragments: Folding.

6 REFERENCES

1. E. Antonini and M. Brunori, *Hemoglobin and Myoglobin in their Reactions with Ligands*, North-Holland, Amsterdam, 1971.
2. S. N. Vinogradov, D. A. Walz, B. Pohajdak, L. Moens, O. H. Kapp, T. Suzuki, and C. N. A. Trotman, *Comp. Biochem. Physiol. B*, 1993, **106**, 1.
3. P. J. Jesson, in *NMR of Paramagnetic Molecules*, eds. G. N. La Mar, W. P. Horrocks, Jr., and R. H. Holm, Academic Press, New York, 1973, pp. 1–52.
4. J. D. Satterlee, *Annu. Rep. NMR Spectrosc.*, 1986, **17**, 79.
5. C. Dalvit and P. E. Wright, *J. Mol. Biol.*, 1987, **194**, 313.
6. Y. Thériault, T. C. Pochapsky, C. Dalvit, M. L. Chiu, S. G. Sligar, and P. E. Wright, *J. Biomol. NMR*, 1994, **4**, 491.
7. J. S. Morrow and F. R. N. Gurd, *CRC Crit. Rev. Biochem.*, 1975, **3**, 221.
8. G. N. La Mar and J. S. de Ropp, in *Biological Magnetic Resonance*, eds. L. J. Berliner and J. Reuben, Plenum Press, New York, 1993, Vol. 12, pp. 1–78.
9. D. Bashford, D. A. Case, C. Dalvit, L. Tennant, and P. E. Wright, *Biochemistry*, 1993, **32**, 8045.
10. M. J. Cocco, Y.-H. Kao, A. T. Phillips, and J. T. J. Lecomte, *Biochemistry*, 1992, **31**, 6481.
11. R. Varadarajan, D. G. Lambright, and S. G. Boxer, *Biochemistry*, 1989, **28**, 3771.
12. H. C. Lee, J. K. Gard, T. L. Brown, and E. Oldfield, *J. Am. Chem. Soc.*, 1985, **107**, 4087; K. D. Park, K. Guo, F. Adebodun, M. L. Chiu, S. G. Sligar, and E. Oldfield, *Biochemistry*, 1991, **30**, 2333.
13. K. Rajarathnam, G. N. La Mar, M. L. Chiu, and S. G. Sligar, *J. Am. Chem. Soc.*, 1992, **114**, 9048.
14. G. N. La Mar, N. L. Davis, R. D. Johnson, W. S. Smith, J. B. Hauksson, D. L. Budd, F. Dalichow, K. C. Langry, I. K. Morris, and K. M. Smith, *J. Am. Chem. Soc.*, 1993, **115**, 3869.
15. R. G. Shulman, S. H. Glarum, and M. Karplus, *J. Mol. Biol.*, 1971, **57**, 93.
16. G. N. La Mar, U. Pande, J. B. Hauksson, R. K. Pandey, and K. M. Smith, *J. Am. Chem. Soc.*, 1989, **111**, 485.
17. J. T. J. Lecomte and G. N. La Mar, *J. Am. Chem. Soc.*, 1987, **109**, 7219.
18. K. Vyas, K. Rajarathnam, L. P. Yu, S. D. Emerson, G. N. La Mar, R. Krishnamoorthi, and H. Mizukami, *J. Biol. Chem.*, 1993, **268**, 14 826.
19. J. Qin, G. N. La Mar, F. Ascoli, and M. Brunori, *J. Mol. Biol.*, 1993, **231**, 1009.
20. J. Qin, G. N. La Mar, F. Cutruzzolá, C. Travaglini Allocatelli, A. Brancaccio, and M. Brunori, *Biophys. J.*, 1993, **65**, 2178.
21. J. Qin, U. Pande, G. N. La Mar, F. Ascoli, P. Ascenzi, F. Cutruzzolá, C. Travaglini-Allocatelli, and M. Brunori, *J. Biol. Chem.*, 1993, **268**, 24 012.
22. K. Rajarathnam, J. Qin, G. N. La Mar, M. L. Chiu, and S. G. Sligar, *Biochemistry*, 1993, **32**, 5670.
23. K. Rajarathnam, J. Qin, G. N. La Mar, M. L. Chiu, and S. G. Sligar, *Biochemistry*, 1994, **33**, 5943.

Acknowledgments

A grant from the National Institutes of Health (HL 16087) is gratefully acknowledged.

Biographical Sketch

Gerd N. La Mar. *b* 1937. B.S., 1960, Ph.D., 1964, Chemistry, Princeton University, USA. Postdoctoral student, 1964–65, University of Copenhagen, 1965–67, ETH, Zürich. Worked as research chemist for Shell Oil Company, 1967–71. Faculty in Chemistry, University of California, Davis, 1971–present. Approx. 300 publications. Current research specialty: NMR of paramagnetic proteins, structure function relationships of hemoproteins and iron–sulfur cluster proteins.

Nonheme Iron Proteins

Donald M. Kurtz Jr.

University of Georgia, Athens, GA, USA

1	Introduction	1
2	Synthetic Complexes	3
3	Catechol Dioxygenases	4
4	Purple Acid Phosphatases	5
5	Hemerythrin	7
6	Ribonucleotide Reductase	9
7	Summary and Future Directions	11
8	Related Articles	12
9	References	12

1 INTRODUCTION

The nonheme iron proteins listed in the Table of Contents constitute a representative sampling of a continually expanding class whose iron sites have a diverse range of structure and function. All of the proteins described in this article contain a nonheme mono- or diiron active site with O, N, or S ligands provided by amino acid side chains of the protein and/or by substrates. All such proteins for which ^{1}H NMR studies of the iron sites have been published through to the end of 1993 are included. Iron–sulfur proteins are dealt with in another article in this Encyclopedia and are, therefore, not included here (see ***Iron—Sulfur Proteins***).

With the recent expansion and diversity of known nonheme iron proteins has come a need for techniques to probe the structural and electronic factors which affect the reactivities of these iron sites. Starting in about 1982. ^{1}H NMR was shown to be a useful probe of these sites, and its usage has expanded since that time along with the number of proteins and advances in NMR technology. These studies were pioneered and developed largely by Que and co-workers.

The paramagnetism of the iron sites in these proteins has not discouraged the application of ^{1}H NMR. On the contrary, the large chemical shifts and altered ^{1}H relaxation times induced by this paramagnetism have provided extremely sensitive and selective probes of ligand type, coordination mode, and geometry, and have also delineated the magnetic properties of these iron sites. These insights would have been impossible without a theoretical and experimental framework for dealing with NMR of paramagnetic metal complexes.[1,2] This framework is most extensively developed for the ^{1}H, and this circumstance, along with the difficulty and expense of isotopically enriching proteins in nuclei such as ^{13}C, has made ^{1}H the focus of NMR investigations of nonheme iron proteins up to now. Therefore, this article describes the unique information which ^{1}H NMR can provide about paramagnetic nonheme iron sites in proteins. Only solution NMR of paramagnetic iron sites in proteins has so far been shown to be feasible, and, therefore, the following discussion applies to aqueous solutions near ambient temperatures. In this sense NMR has been complementary to other probes of nonheme iron sites, such as EPR and X-ray crystallography, which must use frozen solutions and crystals, respectively.

Application of theoretical principles and an experimental foundation for understanding paramagnetic effects on ^{1}H NMR of metalloproteins has been due largely to La Mar and colleagues and to Bertini and colleagues.[1,2] In order to orient the reader, some relevant theoretical and practical considerations that apply to ^{1}H NMR of paramagnetic Fe(II) and Fe(III) complexes are summarized in this section. [The reader should consult other chapters in this Encyclopedia for information on pulse sequences, techniques for water signal suppression, etc. (see, for example, ***Biological Macromolecules: NMR Parameters***). Many of the same principles discussed in ***Iron—Sulfur Proteins*** are equally relevant to the nonheme iron proteins discussed here.]

The extra magnetic field due to the paramagnetic transition metal ion either adds to or subtracts from the applied field at protons near the metal center. This additional field is responsible for the large high-frequency (downfield) (i.e., positive in sign) or low-frequency (upfield) (i.e., negative in sign) shifts, respectively, in NMR resonance positions relative to diamagnetic systems. The shift due to the paramagnetic center is referred to as an isotropic shift, δ^{iso}, which is the observed chemical shift minus a reference diamagnetic shift. The quantity δ^{iso} is the sum of contact (through-bond) and dipolar (through-space) contributions:

$$\delta^{\mathrm{iso}} = \delta^{\mathrm{con}} + \delta^{\mathrm{dip}} \tag{1}$$

High-spin Fe(II) and Fe(III) are by far the most common oxidation and spin states found in nonheme proteins, and so far the only states examined by NMR. The singlet orbital ground state of high-spin Fe(III) normally results in only contact contributions to the isotropie shifts. The orbital angular momentum associated with the quintet ground spin state of high-spin Fe(II) in a pseudooctahedral ligand field can result in significant dipolar contributions to the isotropic shifts. The dipolar contributions arise from the magnetic anisotropy of the complex and are analogous to (but much larger than) the well-known diamagnetic ring current effects on chemical shifts of aromatic protons. The anisotropy gives rise to internal magnetic fields centered at the metal ion, which, at the position of a proximal proton, can either add to or subtract from the applied field in the NMR experiment. For a system in which the molar magnetic susceptibility, χ, is axially symmetric (i.e., $\chi_\parallel \neq \chi_\perp$), the dipolar contribution depends on the angle, θ, between the nonbonded Fe–H distance vector, $\boldsymbol{r}$, and the principal magnetic susceptibility axis, $\chi_\parallel$, of the complex according to

$$\delta^{\mathrm{dip}} = (1/3N)(\chi_\parallel - \chi_\perp)(3\cos^2\theta - 1)r^{-3} \tag{2}$$

where N is Avogadro's number. Thus, both the magnitude and sign of the dipolar contribution are highly sensitive to the iron site geometry. The equation describing dipolar contributions to the isotropic shift contains both T^{-1} and T^{-2} temperature terms, with the latter term dominating for iron complexes.

The magnitude and sign of the contact contribution to the isotropic shift depends on the pathway of bonds and orbitals over which the unpaired spin is delocalized. Electron spin delocalization into the σ- or π-bond system of ligands to high-spin Fe(III) or Fe(II) usually occurs via ligand $\rightarrow$ metal antiparallel (i.e., opposed to the applied magnetic field) spin transfer, leaving net parallel (i.e., aligned with the applied field) spin on the ligating atom.[1] Subsequent spin delocalization through the σ-bond system of the ligand then

delivers parallel spin to the protons, which results in higher-frequency (i.e., positive in sign) contact shifts. These shifts usually drop off by roughly an order of magnitude with each intervening σ bond. Spin delocalization from the ligating atom through a ligand π system containing atom X cannot result in direct placement of unpaired spin density onto an X–H proton, since the X–H bond is orthogonal to the π system. Instead, spin polarization of the electron pair in the X–H bond results in net unpaired spin near the proton which is opposite in sign to that in the π orbital of atom X. Thus, delocalization of parallel or antiparallel spin into the X atom π orbital will result in low-frequency (negative) or high-frequency (positive) contact shifts, respectively, for the X–H proton. The spin density can alternate in sign around an aromatic ring, e.g., for a six-membered carbon ring, spin density at *ortho*- and *para*-carbon π orbitals is opposite in sign to that at the *meta*-carbon π orbitals. Furthermore, for π-spin delocalization, the magnitude of the contact contribution is not dependent on the number of intervening π bonds, but rather is a function of the relative π-electron densities on the various atoms in the π system.

Unpaired π-electron spin density on atom X can be delocalized onto X–C–H protons of methyl, methylene, or methine groups by a hyperconjugative mechanism. In this case the amount of spin delocalization depends on the torsion angle, θ_H, around the X–C bond between the long axis of the π orbital on X and the C–H bond axis, according to

$$\delta^{con} = k \cos^2 \theta_H \tag{3}$$

The proportionality constant, k, contains the product of an electron–nuclear hyperfine coupling constant for the hyperconjugative spin delocalization pathway and the magnitude of the unpaired π-spin density on X. For freely rotating groups, the averaged value, $\langle \cos^2 \theta_H \rangle$, is 0.5 (equivalent to $\theta_H = 45^\circ$). Thus, according to equation (3), the contact shift for restricted torsion angles can range from zero to twice the averaged free rotation value by the factor $2 \cos^2 \theta_H$. The sign of the delocalized spin on the X–C–H proton will be the same as that on the X atom π orbital. Therefore, for π-spin delocalization, –C–H and –H linkages to the same X atom of an aromatic ligand will have ^{1}H NMR contact shifts of opposite signs.

The contact contribution to the isotropic shifts of ligand protons is directly proportional to the molar magnetic susceptibility via the electron–nuclear hyperfine coupling constant. For a mononuclear high-spin Fe(II) or Fe(III) site, the contact contribution will show a T^{-1}, i.e., Curie, temperature dependence. For iron clusters, the contact contribution for an individual ligand is proportional to the molar magnetic susceptibility of the iron to which the ligand is attached, and, due to magnetic coupling between the unpaired electron spins, the susceptibility of each iron center in the cluster will not necessarily have a Curie temperature dependence. For diiron clusters (the only type encountered for the proteins discussed here) the magnetic coupling can be described by a spin Hamiltonian, $\hat{\mathcal{H}}_{ex} = -2J S_1 \cdot S_2$, where S_1 and S_2 represent the spin states of each iron in the cluster [either $\frac{5}{2}$ for high-spin Fe(III) or 2 for high-spin Fe(II)]. Antiferromagnetic coupling is most often encountered in diiron proteins. For such coupling $J < 0$ (by the convention used here), and a ladder of spin states, $S_{Tot} = [(S_1 - S_2), (S_1 - S_2 + 1), \ldots (S_1 + S_2)]$, is obtained, with each spin state in the ladder separated from the next lower state by $2S_{Tot}J$. For antiferromagnetic coupling, the state with lowest spin multiplicity is lowest in energy, and the higher states are thermally populated according to a Boltzmann distribution. Thus, for antiferromagnetic coupling, the molar magnetic susceptibility of each iron in the cluster, and, therefore, its ligand contact shifts, will be reduced from the values for mononuclear iron centers. The magnitude of J can be determined from least-squares fits of molar magnetic susceptibility, χ_M, versus absolute temperature, T, to the Van Vleck equation modified to account for the Boltzmann population of the spin states with J as a variable parameter. For $-J$ values less than approximately 200 cm^{-1}, nonzero states of the spin manifolds are populated in the region of room temperature. Since ligand proton contact shifts are proportional to χ_M, the temperature dependence of the contact shifts can also be used to estimate the value of J. For ^{1}H NMR, this method works well if, over the temperature range of the NMR measurement (10–60 °C for most nonheme iron proteins), χ_M varies significantly (so that $\Delta\delta^{con}/\Delta T$ is large enough to be reliably measured) and nearly all spin states of the ladder are appreciably populated (so that an averaged electron–nuclear hyperfine coupling constant can be used). These requirements are satisfied for weakly coupled systems, i.e., $-J < 30$ cm^{-1}.

For all paramagnetic metal complexes, broadening of the ^{1}H NMR resonances occurs due to shortening of the ^{1}H transverse relaxation time, T_2, relative to a diamagnetic system. In the absence of chemical exchange, the mechanism for shortening T_2 contains contact (T_{2F}), dipolar (T_{2D}), and Curie relaxation (T_{2C}) time components such that:

$$T_2^{-1} = T_{2F}^{-1} + T_{2D}^{-1} + T_{2C}^{-1} \tag{4}$$

Usually only the dipolar and Curie relaxation components make a significant contribution in nonheme iron systems. Both $T_{2D}{}^{-1}$ and $T_{2C}{}^{-1}$ contribute an r^{-6} dependence to $T_2{}^{-1}$, where r is the shortest through-space Fe–H distance. Thus, protons closest to the metal center exhibit the largest NMR linewidths. An empirical result of this distance dependence for nonheme high-spin Fe(III) centers in proteins is that protons closer than 5–7 Å from the metal ion are often not observable by NMR, i.e., the resonances are unobservably broadened into the baseline.[3–5] Thus, for example, His $C_\epsilon H$ (cf. Scheme 1) has not been observed by ^{1}H NMR when His is coordinated to Fe(III) in nonheme proteins.[3–5] The dipolar contribution to $T_2{}^{-1}$ is also a function of the electron spin moment on the metal ion, which is higher for high-spin Fe(III) [$S = \frac{5}{2}$ than for high-spin Fe(II) ($S = 2$)]. However, the magnitude

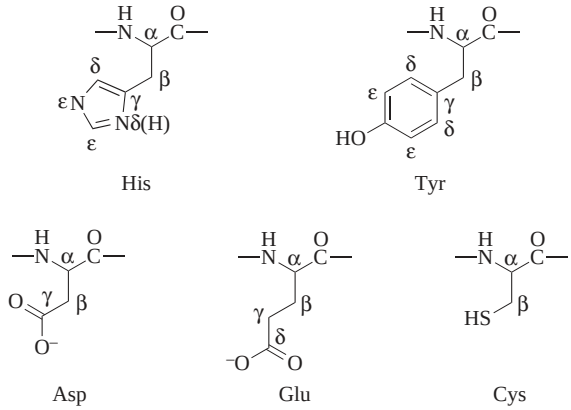

Scheme 1

of the spin moment does not by itself prevent observation of ligand resonances in either oxidation state. Finally, the dipolar contribution to T_2^{-1} is a function of τ_c, where $\tau_c^{-1} = \tau_R^{-1} + \tau_s^{-1}$, τ_R is the rotational correlation time and τ_s is the electron spin–lattice relaxation time of the paramagnetic metal ion. Depending on their relative magnitudes, either τ_R^{-1} or τ_s^{-1} can dominate τ_c^{-1}. In nonheme iron proteins, τ_s has been estimated to be 10^{-9}–10^{-10} s for high-spin Fe(III) and 10^{-11} s for high-spin Fe(II).[2,4] Therefore, given that $\tau_R > 10^{-9}$ s at accessible temperatures for even the smallest proteins, τ_s^{-1} should generally dominate τ_c^{-1} in nonheme iron proteins, in which case longer τ_s values should result in broader NMR resonances. In fact, some empirical observations suggest that τ_s is a major contributor to ^{1}H NMR linewidths in nonheme iron proteins. First, substitution of metal ions such as high-spin Fe(II) or Co(II), which have significantly shorter τ_s values than high-spin Fe(III), narrows the linewidths of isotropically shifted ^{1}H NMR resonances in these proteins.[5,6] This statement also applies to diiron clusters.[2,3] Thus, for a given distance from the metal, ^{1}H NMR linewidths are narrower for ligands to Fe(II) than to Fe(III) centers. Second, changing the coordination sphere around Fe(III) can affect the NMR linewidths. This phenomenon is due to a change in D, the axial zero field splitting parameter of the iron center. Larger values of D shorten τ_s, thereby narrowing the NMR resonances.[4] One possible explanation as to why ligand NMR resonances have not yet been observed for Fe(III) transferrin is an unusually low value of D for this site (see ***Transferrins***).

The contribution to T_2^{-1} due to Curie spin relaxation varies as the square of the applied magnetic field strength and is also a function of τ_R and of $[S_{Tot}(S_{Tot} + 1)]^2$. For proteins, τ_R is sufficiently long ($>10^{-9}$ s) that increasing the magnetic field strength in order to increase sensitivity and dispersion can lead to counterproductive broadening of resonances.[2] For nonheme iron proteins, magnetic field strengths corresponding to a radio-frequency range of 300–400 MHz for ^{1}H NMR have been found to be a convenient experimental compromise between sensitivity and Curie spin relaxation effects. (The frequent use of 300–400 MHz ^{1}H NMR spectrometers for studies of nonheme iron proteins probably reflects commercial availability. Higher resolution spectra could undoubtedly be obtained on lower frequency spectrometers, but such spectrometers often must be homebuilt or must have the electronics upgraded.) Approximately 0.5 mL of protein solution in the millimolar concentration range is required to obtain a spectrum in a reasonable time period (i.e., several hours) near ambient temperatures. Spectra of nonheme iron proteins from 6000 to 100 000 Da have been successfully obtained under these conditions. When Curie spin relaxation affects NMR linewidth, increasing the absolute temperature T, which decreases T_{2C}^{-1} by a factor of T^{-3}, can significantly narrow the resonances, effectively increasing the sensitivity.

For isotropically shifted resonances of nonheme iron proteins, the major contributor to the longitudinal relaxation time T_1 is usually dipolar relaxation. The dipolar relaxation rate, T_{1D}^{-1}, is also a function of r^{-6} and τ_s; therefore, T_1 measurements can be used to estimate Fe–H distances. (A rigorous treatment of the dipolar contributions to T_2^{-1} and T_1^{-1} cannot assume a point magnetic dipole centered at the iron, especially for conjugated ligands, i.e. the Fe–H distance parameter, τ, needs to be modified to account for the spin delocalization onto the ligand.[2]) For T_1 values greater than 5 ms, NOE connectivities can sometimes be made for the isotropically shifted resonances. These distance estimates and connectivities can help to create a self-consistent picture of resonance assignments in a complicated spectrum. Unfortunately, the 5 ms time limit for T_1 is often not exceeded for isotropically shifted resonances of the nonheme iron proteins discussed here, which has made determinations of NOE connectivities difficult.

2 SYNTHETIC COMPLEXES

^{1}H NMR studies of synthetic iron complexes have been an essential adjunct to NMR studies of the proteins. The synthetic models provide (i) chemical shift ranges for the iron ligands commonly found in nonheme proteins, thereby facilitating assignments of protein resonances, and (ii) more easily measured magnetic properties, such that certain of the observed protein contact shifts and their temperature dependences can confidently be used to approximate the magnetic susceptibility of the protein iron site. Table 1 lists the chemical shift ranges observed for complexes containing analogs of the only known protein ligands to high-spin Fe(III) and Fe(II) centers in nonheme proteins, namely, tyrosine (Tyr) phenoxo, aspartate (Asp) and glutamate (Glu) carboxylato, histidine (His) imidazolyl, and cysteine (Cys) thiolato. The carbon and nitrogen atom labeling scheme used for the protons in Table 1 and throughout this article is shown in Scheme 1.

Table 1 ^{1}H NMR Chemical Shifts (δ) for Amino Acid Ligands in Synthetic Mononuclear Nonheme High-Spin Fe(III) and Fe(II) Complexes[a]

Ligand proton	δ [Fe(III)]	δ[Fe(II)]
His:		
$N_\delta H$ or $N_\epsilon H$	97–104	57–68
$C_\delta H$ (N_δ-ligated)	78–82	47–63
$C_\beta H_2$ (N_ϵ-ligated)	$19f(\theta_H)$[b]	$7f(\theta_H)$
$C_\beta H_2$ (N_δ-ligated)	n.a.[c]	n.a.[c]
Tyr:		
$C_\epsilon H$	−101–(−94)	−15
$C_\delta H$	85–89	11
$C_\beta H_2$	$110f(\theta_H)$	$20f(\theta_H)$
Asp or Glu:		
$C_\beta H_2$ or $C_\gamma H_2$	$(25–125)f(\theta_H)$	$30f(\theta_H)$
Cys:		
$C_\beta H_2$	$(500–600)$[d]$f(\theta_H)$	$200f(\theta_H)$
$C_\alpha H$	n.a.[c]	10

[a]All data are *observed* chemical shifts in ppm relative to tetramethylsilane and are taken from work published elsewhere.[3–5,7]
[b]$f(\theta_H) \approx 2\cos^2\theta_H$ and is multiplied by the observed shift (or range of shifts) found for a freely rotating methyl group, for which $2\langle\cos^2\theta_H\rangle = 1$.
[c]No published data available.
[d]Estimated, cf. Que et al.[4]

The data in Table 1 serve as a reference frame for the protein data discussed below. Although the Fe(II) isotropic shifts generally have both contact and dipolar contributions, the contact contributions probably dominate most of the

isotropic shifts listed in Table 1. The contact contributions to the isotropic shifts are generally larger for ligands to Fe(III) than to Fe(II), and this observation is consistent with the larger magnetic moment of high spin Fe(III). The $f(\theta_H)$ factor indicates those shifts where the hyperconjugative mechanism of π-spin delocalization is operative. The relatively large range for the chemical shifts of Asp $C_\beta H_2$ and Glu $C_\gamma H_2$ (25–125 ppm) when coordinated to Fe(III) has been ascribed to variations in the carboxylate coordination mode, i.e., unidentate or bidentate and whether the carboxylate *syn* or *anti* lone pair coordinates to the metal. The *anti* lone pair is lower in basicity by a factor of $\approx 10^4$, which can result in a weaker Fe–O(carboxylate) bond and, therefore, a lower electron–nuclear hyperfine coupling constant. Surprisingly, there seem to be no confirmed assignments of Asp $C_\beta H_2$ or Glu $C_\gamma H_2$ ^{1}H NMR resonances when coordinated to a mononuclear Fe(III) site in a nonheme protein. It should be emphasized that the shifts in Table 1 are for mononuclear iron centers. Magnetic coupling between iron centers in a multinuclear site can alter these shifts drastically, due to the proportionality between the contact contribution and magnetic susceptibility of the iron centers, as discussed in the Introduction.

3 CATECHOL DIOXYGENASES

Catechol dioxygenases are bacterial enzymes which catalyze the oxidative cleavage of catechols to *cis,cis*-muconic acids according to

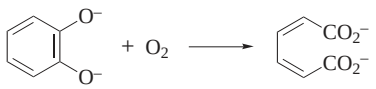

(5)

Prior to NMR studies, the active site of catechol dioxygenases was known from other spectroscopic results to consist of a mononuclear high-spin Fe(III) center containing one or two tyrosyl and other unidentified ligands, plus one or more labile sites for substrate coordination. These enzymes were also shown to remain in the Fe(III) oxidation state throughout the catalytic cycle. Catechol 1,2-dioxygenase (CTD) was chosen for NMR studies, due to its small size (63 000 Da) and abundance relative to other catechol dioxygenases. ^{1}H NMR has clarified two aspects of the CTD iron site: (i) the type and number of endogenous protein ligands; and (ii) the coordination modes of substrates and inhibitors. Some representative chemical shifts for isotropically shifted resonances of CTD and CTD–catecholate complexes are listed in Table 2, and representative spectra are shown in Figure 1.[4,8]

The CTD–catecholate complexes will not turn over in the absence of O_2 and the NMR solutions of these complexes were, therefore, anaerobic. The isotropically shifted resonances observed in ^{1}H NMR spectra of CTD can be divided into those due to endogenous ligands and those due to bound catechol substrates. Because the NMR spectra were obtained on the Fe(III) oxidation state of the enzyme, the isotropic shifts have only contact contributions. Therefore, assignments of resonances can be made by direct comparisons with shifts for the synthetic Fe(III) complexes listed in Table 1. From these comparisons it was noted that protons with an Fe–H

Table 2 Chemical Shifts for Endogenous and Exogenous Ligand ^{1}H NMR Resonances of Some CTD–Catecholate and Fe(III)(Salen)–Catecholate or –Phenolate Complexes[a]

CTD or Fe(III)(salen) complex		
Endogenous:		
native CTD	75, 48	32, 24
CTD–catechol	63, 52	35, 27, 22
CTD–4-methylcatechol	62, 53	34, 26, 21
Exogenous (4-CH$_3$):		
CTD–4-methylcatechol	105	
Fe(III)(salen)–4-methylcatechol	109 (O-1 isomer, unidentate) −27 (O-2 isomer, unidentate) 47 (chelated)	
Fe(III)(salen)–4-methylphenol	110	

[a]Chemical shifts in ppm at 30 °C referenced to tetramethylsilane; data from Que et al.[4,8]

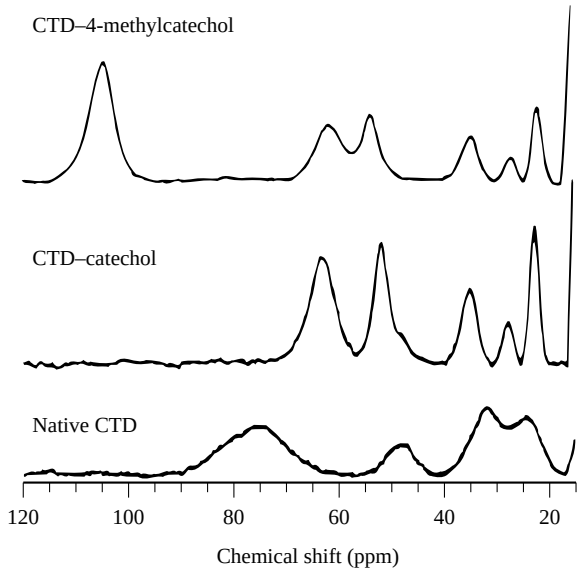

Figure 1 300 MHz ^{1}H NMR spectra of ≈2 mM CTD and CTD–catecholate complexes obtained in D_2O at pH 7.5 (uncorrected) at 30 °C. (Reproduced by permission of the American Chemical Society from L. Que, Jr., R. B. Lauffer, J. B. Lynch, B. P. Murch, and J. W. Pyrz, *J. Am. Chem. Soc.*, 1987, **109**, 5381)

distance less than 6 Å could not be observed for any of the CTD complexes, due to shortening of T_2 and concomitant broadening of the resonances. For example, all aromatic ring protons of both exogenous and endogenous ligands were unobservable. Thus, the isotropically shifted resonances in both the native CTD and CTD–catechol spectra (Figure 1) must be due exclusively to endogenous ligand protons which are ≥6 Å away from the iron. This distance restriction, plus comparisons with the shifts of the synthetic complexes in Table 1, results in assignments of the two higher-frequency resonances (i.e., those between 50 and 80 ppm) in the CTD and CTD–catechol spectra to $C_\beta H_2$ protons of tyrosine ligands and the two or three lower-frequency resonances to $C_\beta H_2$ protons of N_ϵ-coordinated histidine. Due to the dependence of these shifts on the torsion angle θ_H (defined in the Introduction), two distinct isotropically shifted resonances are expected for each

$C_\beta H_2$ group. These two resonances will not be resolved if the two torsion angles for the constituent C–H bonds are similar to each other. Alternatively, two dissimilar torsion angles could result in one resonance of each pair being obscured by protein resonances between 0 and 10 ppm. Since other spectroscopic evidence indicated the presence of two different tyrosine ligands, the two higher-frequency resonances were assigned to two different tyrosyl $C_\beta H_2$ groups. Similarly, the observation of three isotropically shifted histidine $C_\beta H_2$ resonances suggests at least two histidine ligands. An X-ray crystal structure of another catechol dioxygenase has since confirmed the presence of two tyrosine and two histidine ligands.[9] For reasons discussed in the Introduction, the relatively narrower linewidths for the CTD–catechol versus native CTD spectra were attributed to relatively higher values of the zero field splitting parameter, D, for the CTD–catechol iron sites. This conclusion is consistent with independent determinations of D values by Mössbauer spectroscopy.

The 6 Å observability restriction also applies to the coordinated catechol substrates of CTD. Thus, only those ring methyl protons in positions either *meta* or *para* to coordinated oxygen in CTD–methylcatecholate or –methylphenolate complexes are observable by NMR. The isotropic shifts observed for a series of Fe(III)(salen)–catecholate and –phenolate complexes [salen = 1,2-bis(salicylideneamino)ethane^{2-}] show that the unpaired spin on Fe(III) is delocalized through the π system of the coordinated catecholate or phenolate, which results in alternating signs of the spins at the ring carbon π orbitals.[4,8] This alternation in sign allows differentiation of the three possible coordination modes of 4-methylcatecholate to the iron center in CTD, namely, unidentate with either O-1 or O-2 coordinated or bidentate (O-1 and O-2 both coordinated). These three coordination modes are illustrated in Scheme 2 along with the observed 4-methyl ^{1}H NMR chemical shifts for the corresponding Fe(III)(salen)–4-methylcatecholate complexes.[8]

The 4-methyl chemical shift for the bidentate coordination mode is roughly the weighted average of the 4-methyl shifts for spin delocalization through both the O-1 and O-2 unidentate pathways. The 4-methyl resonance of the CTD–4-methylcatechol complex at 105 ppm (Table 2 and Figure 1, confirmed by CD_3 substitution) with no low-frequency resonance shows that 4-methylcatechol coordinates to the CTD iron center exclusively in the unidentate O-1 mode. Examination by NMR of a larger set of methyl-substituted phenols and catechols complexed to CTD confirms this interpretation. The unidentate coordination mode is believed to activate the catechol to oxidative cleavage relative to the bidentate coordination mode. Thus, these NMR studies provided a key insight into the catechol dioxygenase catalytic mechanism. These results also constitute a particularly elegant demonstration of how comparison with NMR data on synthetic complexes can be used to provide these insights.

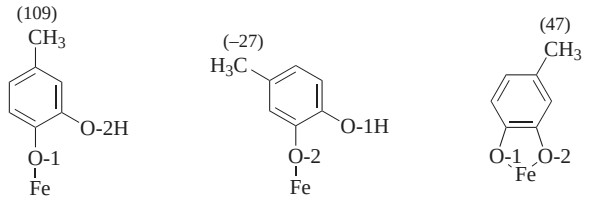

Scheme 2

4 PURPLE ACID PHOSPHATASES

These eukaryotic enzymes catalyze the hydrolysis of phosphate esters and have molecular weights of about 40 000 Da. The active site contains a pair of metal ions, with one or both of the metals being iron. Two proteins in this class have been characterized by ^{1}H NMR: uteroferrin (Uf), isolated from the uterine fluid of pregnant pigs, and a purple acid phosphatase isolated from beef spleen (BS-PAP).[3,10,11] In both of these enzymes the purple color has been established to be due to a tyrosine phenoxo → Fe(III) ligand-to-metal charge-transfer transition in an [Fe(II),Fe(III)] site. These mixed-valent forms (Uf_r and $BS\text{-}PAP_r$) are much more enzymatically active than the diiron(III) forms. The diiron(II) form is inactive and loses iron too rapidly to be useful for NMR.

The mixed-valent but not the diiron(III) oxidation levels have shown paramagnetically shifted ^{1}H NMR spectra up to now. This contrasting observability between the two oxidation levels is most likely due to the shorter τ_s of the mixed-valent cluster due its 50% Fe(II) character. Chemical shifts and assignments are listed in Table 3 for isotropically shifted ^{1}H NMR resonances of Uf_r and $BS\text{-}PAP_r$, and representative spectra are shown in Figure 2.[3,10]

For the diiron sites in Uf and BS-PAP, antiferromagnetic coupling lowers the averaged electron spin moment at each iron below that for mononuclear complexes (cf. Introduction). For Uf_r, antiferromagnetic coupling between the $S_1 = \frac{5}{2}$ Fe(III) and the $S_2 = 2$ Fe(II) results in a ladder of half-integer spin states from $S_{Tot} = \frac{1}{2}$ at lowest energy to $\frac{9}{2}$ at highest energy. The temperature dependence of the Uf_r resonances listed in Table 3 when fitted to the modified Van Vleck equation referred to in the Introduction led to $-J = 10\,cm^{-1}$,[11] consistent with weak antiferromagnetic coupling. This value of J is essentially identical to that subsequently obtained from direct measurements of magnetic susceptibilities versus temperature for Uf_r.[12] Using this value, the resulting population of states in the spin manifold at 30 °C (the temperature of the NMR experiment) is calculated to result in a molar susceptibility of the cluster and, therefore, ligand contact shifts which are approximately 17% lower than those

Table 3 Chemical Shifts (ppm) of Isotropically Shifted ^{1}H NMR Resonances for Uf_r and $BS\text{-}PAP_r$ at 30°C[a]

Resonance[b]	Assignment	Uf_r	$BS\text{-}PAP_r$
a	Fe(III)–Tyr–C_βH	86.6	69.5
b (ex)	Fe(III)–His–N_δH	88.4	83.2
c	Fe(III)–Tyr–C_δH	70.0	69.5
d	Fe(III)–Tyr–C_δH	62.4	69.5
e (ex)	Fe(II)–His–N_ϵH	44.0	39.9
f	?[c]	43.5	39.9
g	Fe(II)–His–C_δH	43.5	39.9
h	?[c]	29.5	30.0
i	Fe(III)–His–C_βH	23.4	24.0
j	Fe(III)–Tyr–C_βH	15.1	n.o.[d]
x (ex)	?	−24.5	n.o.
y	?[c]	−68.0	n.o.

[a]From Wang et al.[10]
[b]Cf. Figure 3 for labeling of resonances.
[c]See Figure 5 for possible assignment.
[d]Not observed.

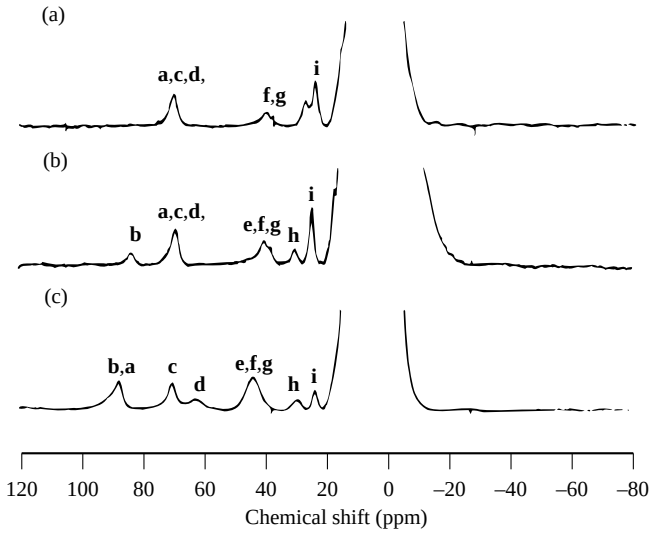

Figure 2 300 MHz ^{1}H NMR spectra of: (a) 1 mM BS-PAP$_r$ in D_2O, (b) 1 mM BS-PAP$_r$ in H_2O, and (c) 5 mM Uf$_r$ in H_2O (100 mM acetate buffer pH 4.9) at 30 °C. (Reproduced by permission of the American Chemical Society from Z. Wang, L.-J. Ming, L. Que, Jr., J. B. Vincent, M. W. Crowder, and B. A. Averill, *Biochemistry*, 1992, **31**, 5263)

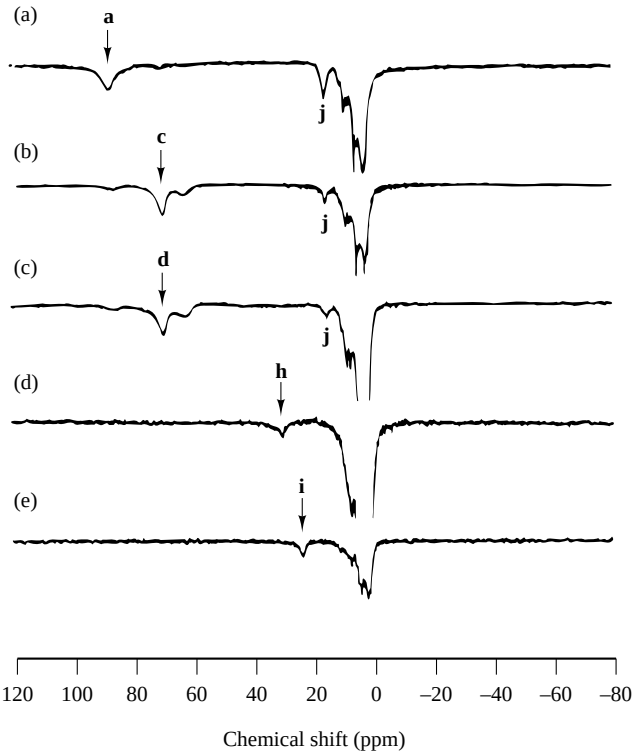

Figure 3 NOE difference spectra of Uf$_r$ in D_2O buffer at 300 MHz and 30 °C. Arrows indicate resonance irradiated. (Reproduced by permission of the American Chemical Society from Z. Wang, L.-J. Ming, L. Que, Jr., J. B. Vincent, M. W. Crowder, and B. A. Averill, *Biochemistry*, 1992, **31**, 5263)

of mononuclear complexes. Therefore, the isotropic shifts in Table 3 must be increased by 17% in order meaningfully to compare these shifts with those in Table 1.

Previous Raman resonance evidence had indicated only one tyrosine ligand per Fe(III). The assignments of the $C_\beta H_2$ resonances of this coordinated tyrosine illustrate both the difficulties involved in assigning resonances and the evidence which was accumulated for these assignments. One difficulty was mentioned above for CTD, namely the dependence of the $C_\beta H_2$ shifts on the torsion angle according to $110f(\theta_H)$ (cf. Table 1). Additional evidence was provided by T_1 measurements, which were used to estimate through-space Fe–H distances. Only resonance **a** in Figure 3 had a T_1 value (20 ms) appropriate for the Fe–H distance ($\geq$6.7 Å) expected for a tyrosine ligand $C_\beta H_2$ proton. All other resonances had significantly shorter T_1 values and, therefore, must be due to protons closer to one or both irons. As can be seen from Figure 3, saturation of resonance **a** in Uf$_r$ resulted in the largest NOE at resonance **j**. Thus, resonances **a** and **j** were assigned to the tyrosine ligand $C_\beta H_2$ protons of Uf$_r$. The large difference in chemical shift for resonances **a** and **j** indicates significantly different torsion angles for the two $C_\beta H_2$ protons. Based on these shifts, the torsion angles, θ_H as defined in equation (3), of the two C_β–H bond vectors with respect to the tyrosine phenyl ring normal were calculated to be 78° and 42°. Resonance **j** is difficult to observe except in the NOE difference spectrum, because it lies close to the diamagnetic envelope; in fact, resonance **j** is not observed in BS-PAP$_r$. The differences in chemical shifts of the **a,j** resonance pair between Uf$_r$ and BS-PAP$_r$ (cf. Table 3) are not due to differing amounts of spin delocalization onto the tyrosine rings in the two proteins, since the tyrosine $C_\gamma H$ protons (resonances **c** and **d** in Table 3 and Figure 2) have very similar chemical shifts in the two proteins. Rather the differences in the **a,j** resonance pair indicate different sets of torsion angles for the tyrosine ligand $C_\beta H_2$ protons in the two proteins.

Assignments of the remaining resonances in Table 3 were based on similar lines of evidence. The disappearance of resonances **b** and **e** in D_2O identifies them as belonging to His ligand NH protons. A proposed schematic structure of the Uf$_r$ and BS-PAP$_r$ diiron sites with hydrogens labeled according to their resonance assignments is shown in Figure 4. [The hydroxo bridge proton in the PAP$_r$ diiron site is thought to be too close to the iron atoms to be observable by NMR. Similarly, the N_δ-coordinated His residue has $C_\beta H_2$ protons (not explicitly indicated in Figure 4) which are thought to be too close to the Fe(II) to be observable.] Thus, these NMR studies of purple acid phosphatases illustrate the attempt to attain an internally consistent set of resonance assignments based on the cumulative results.

Table 3 and Figure 4 also show that the assignments are not yet complete. The suggested assignment of the low-frequency resonance **y** to the tyrosine ligand $C_\epsilon H$ (cf. Figure 4) is consistent with the expected alternation in sign of the unpaired spin delocalized through the π system of the aromatic ring. This assignment is also consistent with the proximity of this proton to Fe(III), and hence its unobservability in BS-PAP$_r$ spectra. Similarly, the relative proximity of the carboxymethylene protons shown in Figure 4 to the diiron site shortens both their T_1 and T_2 values, which makes the observation of their resonances in the NMR and NOE spectra discussed above difficult. A more recent approach to the observation and assignment of the carboxylate ligand resonances was based on replacement of Fe(II) in the diiron cluster of Uf$_r$ with Co(II).[13] The [Fe(III), Co(II)]Uf

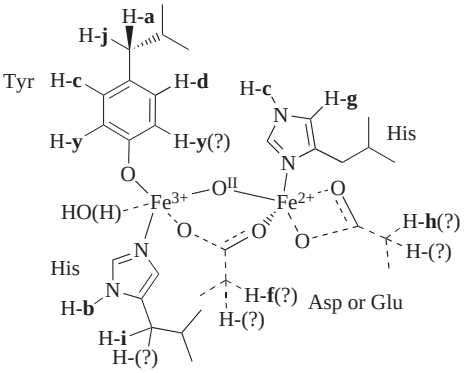

Figure 4 Schematic structure of the diiron site in Uf and BS-PAP with proposed NMR assignments. (Reproduced by permission of the American Chemical Society from Z. Wang, L.-J. Ming, L. Que, Jr., J. B. Vincent, M. W. Crowder, and B. A. Averill, *Biochemistry*, 1992, **31**, 5263)

retained 50% of the native enzyme activity, and replacement of Fe(II) with Co(II) shortened τ_s of the cluster, thereby lengthening the ligand proton T_1 values sufficiently for their observation in both 1D NOE and 2D NOESY spectra (see ***Cobalt(II)- and Nickel(II)-Substituted Proteins***). The NOESY spectrum of the [Fe(III),Co(II)]Uf showed clear connectivities of resonances at 64, 28.5, and 17.7 ppm, consistent with a YCH_2CH system where Y coordinates to the Co(II). Based on M−H distance estimates, it was concluded that only a carboxylate ligand could show the observed combination of proton T_1 values and NOE connectivities. These results provided the first direct evidence for a coordinated carboxylate in the purple acid phosphatases, and showed that NOESY spectra of paramagnetic nonheme iron sites in proteins are obtainable when proton T_1 values are greater than 10 ms.

5 HEMERYTHRIN

Hemerythrin (Hr), the oxygen carrier in certain marine invertebrates, also contains a diiron site whose structure is shown schematically in Scheme 3 for the [Fe(III),Fe(III)](met) oxidation level:[14]

N_ϵ from five histidine (His) residues provide terminal ligands, and carboxylates from glutamate (Glu) and aspartate (Asp) provide two bridging ligands. A bridging oxo ligand is provided by the solvent. The protein ligands do not change upon reduction to the [Fe(II),Fe(II)](deoxy) oxidation level, but the oxo bridge is converted to a hydroxo bridge. The diiron

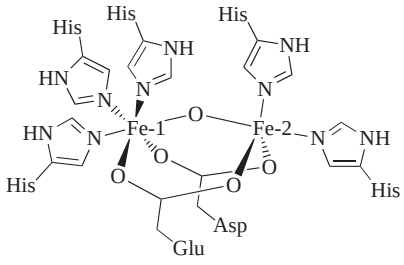

Scheme 3

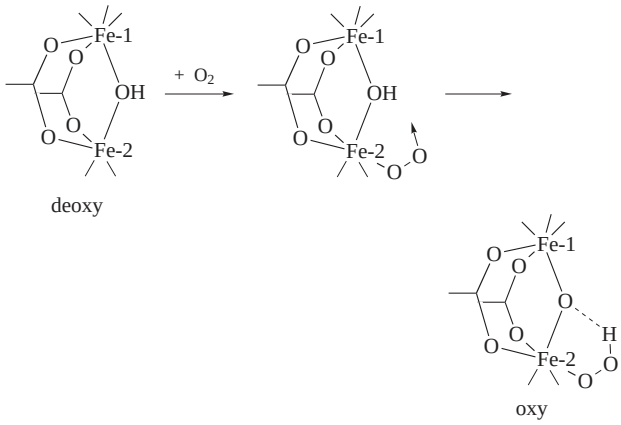

Scheme 4

site in Hr is, thus, richer in histidine ligands and poorer in oxygen ligands than that in Uf or BS-PAP.

The diiron site in Hr has probably been structurally, electronically, and chemically characterized in more detail than any other diiron protein. Nevertheless, ^{1}H NMR was able to clarify or confirm certain aspects of the diiron site structure and reactivity. Perhaps the most important aspect concerns the currently accepted oxygenation mechanism shown in Scheme 4.[14]

The oxyHr diiron site is best formulated as [Fe1(III)(μ-O)Fe2(III)O_2H^{-1}], i.e., like the met oxidation level, oxy formally contains an oxo-bridged diiron(III) site. The internal proton transfer which occurs upon interconversion of the deoxy and oxy forms has not been observed directly by any spectroscopic technique. However, ^{1}H NMR isotropic shifts can provide indirect measurements of magnetic susceptibility and, due to the expected differences in antiferromagnetic coupling mediated by an oxo versus a hydroxo bridge, can thereby provide evidence for the nature of the bridging ligands in deoxy- and oxyHr. As discussed above for the purple acid phosphatases, antiferromagnetic coupling in the Hr diiron site reduces the magnetic moments and, thereby, the ligand contact shifts below the values for mononuclear complexes. Antiferromagnetic coupling between the $S_1 = S_2 = \frac{5}{2}$ Fe(III) centers in oxy- and metHr or the $S_1 = S_2 = 2$ Fe(II) centers in deoxyHr leads to a ladder of integer spin states from $S_{Tot} = 0$ at lowest energy to $S_{Tot} = 5$ (met and oxy) or 4 (deoxy) at highest energy.[14]

Despite the relatively high molecular weight of Hr (an octamer of 108 000 Da), isotropically shifted resonances have been observed for deoxy-, oxy-, and metHrs.[15,16] ^{1}H NMR spectra of these three forms are shown in Figure 5, and Table 4 lists the chemical shifts of the isotropically shifted resonances for these three forms. As expected from the longer τ_s of Fe(III), the resonances are much narrower for deoxy-[Fe(II),Fe(II)] than for oxy- and metHrs [Fe(III),Fe(III)]. The His ligand $N_\delta H$ resonances were assigned based on their solvent exchangeability (cf. Scheme 2).

The $N_\delta H$ chemical shifts for deoxyHr are only slightly smaller than observed for mononuclear Fe(II) complexes (Table 1), indicating only a small antiferromagnetic interaction assuming that the isotropic shifts are predominantly contact in nature. Dipolar contributions are probably at least partially responsible for the relatively wide range of His ligand $N_\delta H$ chemical shifts (40−65 ppm). Nevertheless, the temperature

Table 4 Chemical Shifts of Paramagnetically Shifted ^{1}H NMR Resonances for Various Forms of Hemerythrin[a]

Hr form	Temperature (°C)	Chemical shifts (δ, ppm)	
		His ligand $N_\delta H$	Other
oxy	30	24, 20 (sh), 18 (sh), 13	11
met	30	24, 13	11
deoxy	40	62, 46, 43	14, 11, −1.9, −2.5, −3.1, −5.8
semi-metHrN_3	40	72, 54	20, 15, 13, −1.1

[a]From Maroney et al.[16]

dependence of the deoxyHr $N_\delta H$ shifts between 30 °C and 60 °C, when fitted to the modified Van Vleck equation referred to in the Introduction, led to values of $-J$ in the range of 10–20 cm^{-1}, i.e., consistent with weak antiferromagnetic coupling. This range for $-J$ is in good agreement with that determined by an Evans's NMR susceptibility study (−15 cm^{-1}),[16] and with that subsequently determined for deoxyHr by magnetic circular dichroism spectroscopy (12–38 cm^{-1}).[17] The range of $-J$ values determined for deoxyHr encompasses the value of −13 cm^{-1} reported for a synthetic (μ-hydroxo)bis(μ-carboxylato)diiron(II) complex, and is thus consistent with the deoxyHr diiron site structure shown in Scheme 4. The resonances at 11 and 14 ppm for deoxyHr can be tentatively assigned to His ligand $C_\beta H_2$ protons (cf. Table 1), especially if these shifts have some downfield dipolar contributions. The resonances to low frequency of zero listed in Table 3 are solvent nonexchangeable but their assignments remain a mystery; the low-frequency shifts are presumably due to dipolar contributions.

The His ligand $N_\delta H$ chemical shifts for oxy- and metHr (13–24 ppm) are much smaller than for mononuclear Fe(III) sites (Table 1), reflecting the relatively strong antiferromagnetic coupling in these forms. This strong coupling makes the temperature dependence of the isotropic shifts too flat for a reliable determination of J. However, the His ligand $N_\delta H$ chemical shifts for both oxy- and metHr are very similar to the terminal imidazolyl ligand NH chemical shifts (15 and 19 ppm) reported for a synthetic (μ-oxo)bis(μ-acetato)diiron(III) complex with $-J$ = 120 cm^{-1}.[7] The analogous (μ-hydroxo)bis(μ-acetato)diiron(III) complex has the imidazolyl NH chemical shifts to much higher frequency ($\geq$85 ppm), as expected from its much lower value of $-J$ ($\approx$17 cm^{-1}).[18] A similar observation can be made for the nonexchangeable resonance at 11 ppm for oxy- and metHr. This feature is assigned to one or more of the four $C_\beta H_2$ and $C_\gamma H_2$ protons of the bridging Asp and Glu carboxylate ligands (cf. Scheme 3). The aforementioned synthetic (μ-oxo)- and (μ-hydroxo)bis(μ-acetato)diiron(III) complexes exhibit acetate methyl resonances at 10 and 66 ppm, respectively.[7] Thus, the putative bridging carboxymethylene resonance at 11 ppm together with the His ligand $N_\delta H$ resonances between 24 and 13 ppm support an oxo- rather than hydroxo-bridged structure in oxyHr, i.e., the hydrogen-bonded proton is associated more strongly with the peroxo ligand than the oxo bridge, as shown in Scheme 4. These isotropic shifts are also qualitatively consistent with values of $-J$ = 77 and 134 cm^{-1} obtained for oxy- and metHr, respectively, in an earlier magnetic susceptibility study.[18] However, the similarity in the isotropic shifts of the oxy and met forms suggests that the difference in J between these two forms is less than 57 cm^{-1}. [The contact shifts of the bridging carboxymethylene protons are expected to depend on their torsion angles, θ_H, according to equation (3). Thus, given the acetate methyl resonance at 10 ppm for the synthetic oxo-bridged diiron(III) complex and a diamagnetic shift of 2 ppm for acetate, the bridging carboxymethylene proton isotropic shifts for an oxo-bridged diiron(III) site with $-J$ = 120 cm^{-1} should be $\approx$8(2 $\cos^2\theta_H$) or $\approx$0–16 ppm. The 11 ppm resonance for oxy- and metHr falls within this range (even after subtraction of a diamagnetic shift). A similar analysis indicates that an 11 ppm resonance is too far downfield to be assigned to $C_\beta H_2$ of N_ϵ-coordinated His ligands in a strongly antiferromagnetically coupled diiron(III) site.]

The Hr diiron site can also be prepared in a mixed-valent form, so-called 'semi-met' Hr. As for Uf_r, antiferromagnetic coupling leads to an $S_{Tot} = \frac{1}{2}$ ground state with a characteristic EPR spectrum. This mixed-valent diiron site is expected to have a shorter τ_s than does the diiron(III) site and therefore narrower isotropically shifted resonances, an expectation which is borne out by the spectra. The azide adduct of semi-metHr is particularly stable and was examined in some detail by NMR. Two solvent-exchangeable paramagnetically shifted resonances were observed for semi-metHrN_3 at 72 and 54 ppm (40 °C) with a respective intensity ratio of approximately 2:3 (cf. Figure 5). Based on the 2:3 ratio of His ligands to Fe-2:Fe-1 shown in Scheme 3, the 72 ppm resonance was assigned to the $N_\delta H$ of the two His ligands to Fe-2. Due to the larger paramagnetic shift, Fe-2 is assumed to be in the Fe(III) ($S = \frac{5}{2}$) state in semi-metHrN_3. Similarly, the 54 ppm resonance is assigned to the three His ligand N_δHs of Fe-1, which must then be in the Fe(II) (S = 2) state. Here again, due to antiferromagnetic coupling, the chemical shifts are smaller than those for mononuclear complexes (cf. Table 1). Possible dipolar contributions complicate a more quantitative analysis of the Fe(II) ligand resonance. On the other hand, the 72 ppm resonance assigned to the Fe(III) center should not have significant dipolar contributions and should, therefore, be proportional to the magnetic susceptibility of the Fe(III) center in the diiron cluster. Assuming an 8 ppm diamagnetic shift for histidine $N_\delta H$, the isotropic shift assigned to the Fe(III) center in semi-metHrN_3, 72 − 8 = 64 ppm, relative to the isotropic shift expected for mononuclear Fe(III), $\approx$102 − 8 = 94 ppm, translates to an approximate 32% reduction in susceptibility of the Fe(III) center in semi-metHrN_3 relative to that expected for mononuclear Fe(III). Using the modified Van Vleck equation, this reduction in susceptibility corresponds to a calculated $-J$ = 18 cm^{-1}.[16] Analysis of the temperature dependence of the 72 ppm resonance between 30 °C and 60 °C using the same equation led to a very similar value of $-J$. More recent magnetic circular dichroism studies yield

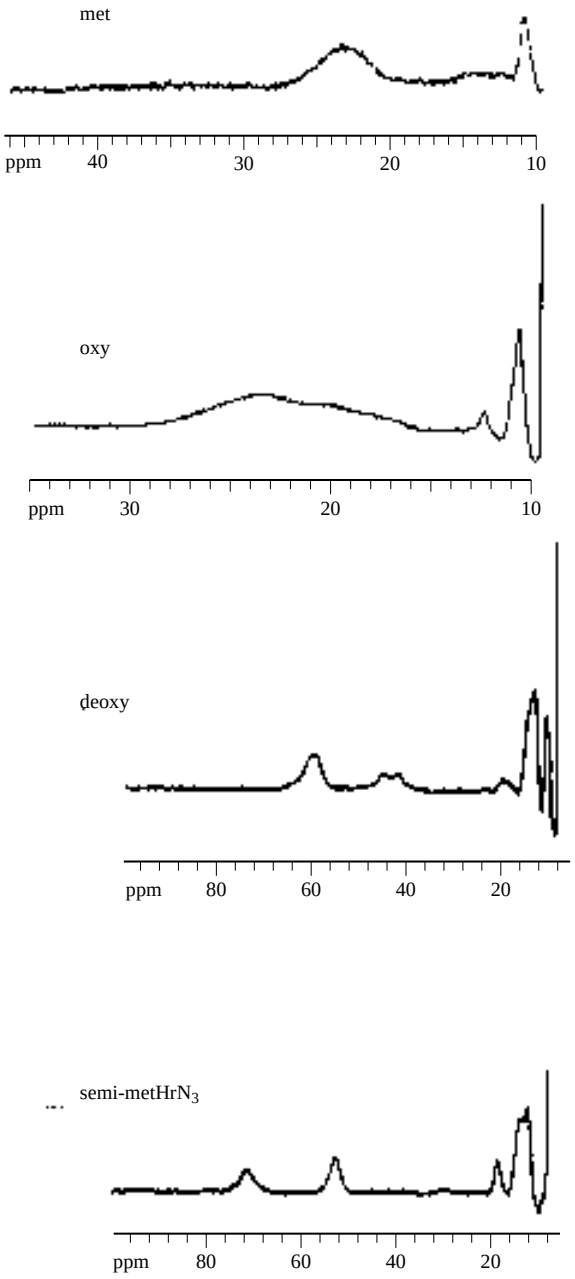

Figure 5 300 MHz ^{1}H NMR spectra in the high-frequency region of (from top to bottom) met- and oxyHr at 30 °C, and deoxyHr and semi-metHrN_3 at 40 °C. Note the differing ppm scales of the spectra. (Reproduced by permission of the American Chemical Society from M. J. Maroney, R. B. Lauffer, L. Que, Jr., and D. M. Kurtz, Jr., *J. Am. Chem. Soc.*, 1984, **106**, 6445, and M. J. Maroney, D. M. Kurtz, Jr., J. M. Nocek, L. L. Pearce, and L. Que, Jr., *J. Am. Chem. Soc.*, 1986, **108**, 6871)

$-J \approx 8\,\text{cm}^{-1}$ for the semi-met oxidation level of Hr.[17] This lower value may be due to inclusion of zero field splitting of the Fe(II) center, which was not taken into account in the NMR analyses. In any case, $-J$ values of $8-20\,\text{cm}^{-1}$ are thought to be too small for an oxo bridge and rather favor a hydroxo bridge between the Fe(II) and Fe(III) in the diiron site of semi-metHr. No resonances could be definitively assigned to the bridging carboxymethylene protons in semi-metHr.

Myohemerythrin is an O_2-carrying protein with a diiron site nearly identical to that in Hr, but myoHr is a monomer with a molecular weight ≈13 700 Da, i.e., one-eighth that of the octameric Hr. Despite the expected narrowing of resonances due to an increased rotational correlation time, no reports of ^{1}H NMR spectra of myoHr have yet appeared.

6 RIBONUCLEOTIDE REDUCTASE

Ribonucleotide reductases (RNRs) catalyze the reduction of ribonucleotides to 2′-deoxyribonucleotides, which represents the first committed step in DNA synthesis. The RNR which functions during aerobic metabolism in *E. coli* contains a diiron site in each subunit of a dimer called protein R2 ($M_r \approx$ 87 500).[14] The diiron site does not interact directly with the substrate, but instead generates a stable tyrosyl radical which is essential for substrate turnover. A metastable, highly-oxidizing diiron species resulting from reaction of the diiron(II) site in reduced R2 protein with O_2 abstracts a hydrogen atom from the hydroxy group of a proximal, nonligating tyrosyl residue, thereby creating the tyrosyl radical. An X-ray crystal structure is available for the diiron(III) form of the RNR-R2 protein (metR2), and the diiron site structure in this form is shown schematically in Scheme 5.[19]

The radical forming tyrosyl residue (not shown in Scheme 5) is located approximately 5 Å from Fe-1. The enzymatically active form of protein R2 is known to contain a diiron(III) site, presumably having the same structure as in metR2, but containing in addition the tyrosyl radical. As for Hr, the diiron site ligation in RNR-metR2 consists of a bridging oxo ligand from the solvent plus carboxylato and histidyl ligands from amino acid side chains. However, several distinct differences between the diiron sites in Hr and RNR are readily apparent. One rather than two carboxylate ligands bridges Fe-1 and Fe-2 in RNR-metR2. The terminal ligands consist of a mixture of carboxylates and histidyl imidazoles, with only two of the latter, one on each iron. In contrast to Hr, the His ligands in RNR are ligated through N_δ rather than N_ϵ. An X-ray crystal structure of the diiron(II) site in reduced RNR-R2 is not yet available, but the X-ray crystal structure of a dimanganese(II)-substituted form shows two *O*,*O*′-bridging carboxylates from two Glu residues as the only bridging ligands.[14] Isotropically shifted ^{1}H NMR resonances have been observed for both

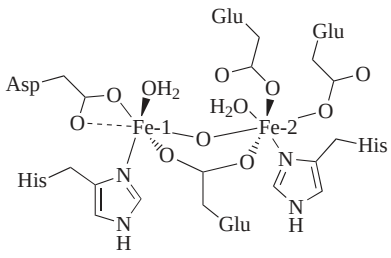

RNR-metR2

Scheme 5

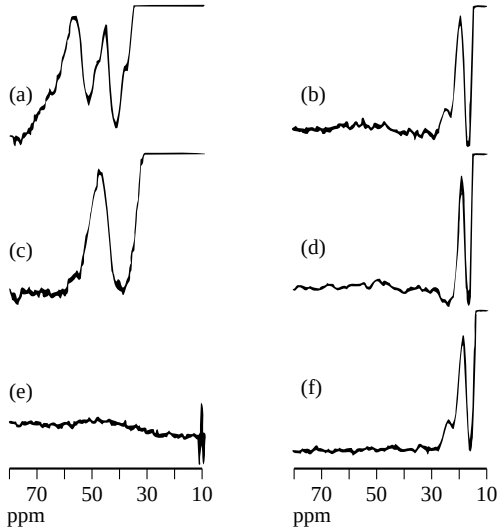

Figure 6 400 MHz ^{1}H NMR spectra of RNR-R2 protein: (a) reduced R2 in H_2O at 37 °C; (b) active R2 in H_2O at 37 °C; (c) reduced R2 in D_2O at 37 °C; (d) active R2 in D_2O at 30 °C; (e) apoR2 in H_2O at 25 °C; (f) reduced R2 after air oxidation in H_2O at 20 °C. (Reproduced by permission of the American Chemical Society from M. Sahlin, A. Gräslund, L. Petersson, A. Ehrenberg, and B.-M. Sjöberg, *Biochemistry*, 1989, **28**, 2618)

active R2 and reduced R2.[20] The spectra of these two forms are reproduced in Figure 6. The mixed-valent form has so far proven too unstable to be examined by NMR.

The active R2 spectrum shows one solvent-exchangeable resonance at 24 ppm, assigned to $N_\epsilon H$ of the coordinated His residues, and one nonexchangeable resonance at 19 ppm [cf. Figure 6(b), (d) and (f)]. From comparisons with the spectra of met- and oxyHr and synthetic complexes discussed in Section 5, the chemical shift of the His ligand $N_\epsilon H$ resonance suggests a strongly antiferromagnetically coupled diiron(III) site in active R2. The temperature dependences of both the 19 and 24 ppm resonances are essentially flat between 20 °C and 37 °C, as expected for a diiron(III) site with $-J > 100\,cm^{-1}$ and for the oxo-bridged structure shown in Scheme 5. The 19 ppm resonance has not yet been assigned. Given the strong antiferromagnetic coupling, 19 ppm is too large a shift for $C_\delta H$ of an N_δ-coordinated His ligand and is at the outer edge of the range expected for bridging carboxymethylene protons. Terminal carboxymethylene protons remain a possible assignment for the 19 ppm resonance.

The reduced R2 was obtained by addition of $Fe(II)_{(aq)}$ to apoR2, i.e., metal-free R2 whose spectrum is shown in Figure 6(e). The spectra of this reduced R2 are shown in Figure 6(a) and (c). Two isotropically shifted resonances are observed at 57 and 45 ppm, with the former being solvent-exchangeable and therefore assigned to the His ligand NH. Assuming the shift is predominantly contact in origin, an NH ligand resonance at 57 ppm falls within the range for mononuclear Fe(II) complexes (cf. Table 1) and indicates little or no magnetic coupling between the two Fe(II) centers of the reduced diiron site. This conclusion is supported by the temperature dependences of the isotropic shifts, which suggest $-J = 5 \pm 5\,cm^{-1}$. Comparisons with synthetic complexes indicate that a $-J$ value near zero is consistent with a bis(μ-carboxylato)diiron(II) core with no other bridging ligands,

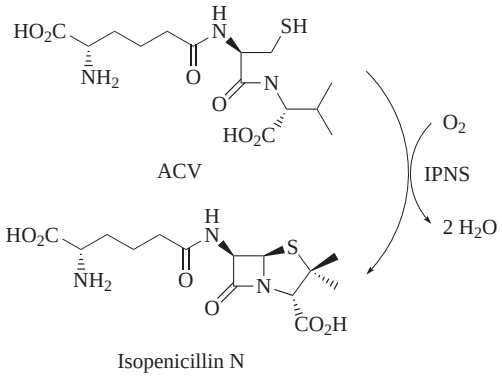

Scheme 6

as inferred from the structure of the Mn(II)-substituted R2 protein. The 45 ppm resonance has not been assigned; $C_\delta H$ of N_δ-coordinated His residues and $C_\gamma H_2$ of bridging Glu ligands are both consistent with the observed shift. Thus, although relatively limited compared with other diiron proteins, the available information on paramagnetically shifted ^{1}H NMR resonances of RNR-R2 fully support the diiron site structures in this enzyme which were determined by other means.

6.1 Isopenicillin N-Synthase

Isopenicillin N-synthase (IPNS) is found in some microorganisms and catalyzes the oxidative ring closure shown in Scheme 6, resulting in conversion of the substrate δ-(L-α-aminoadipoyl)-L-cysteinyl-D-valine (ACV) to isopenicillin N.

Oxygen is also a substrate for IPNS but is reduced completely to H_2O rather than incorporated into ACV. IPNS from *Cephalosporium acremonium* has a molecular weight of 38 400 Da and contains a mononuclear nonheme Fe(II) active site, which has been examined by ^{1}H NMR.[6] No Fe(III) form of IPNS has been reported. In the absence of O_2, the substrate ACV binds to the Fe(II) active site without transformation into product; therefore, ^{1}H NMR spectra of IPNS can be compared with that of the IPNS–ACV complex. Nitric oxide (NO) also binds to IPNS and to the IPNS–ACV complex, forming binary and ternary complexes, respectively, which are assumed to be analogous to the transient complexes formed with O_2. However, unlike those with O_2, the IPNS–NO complex and the IPNS–ACV–NO complex are sufficiently stable to allow examination by NMR. ^{1}H NMR spectra of these various IPNS complexes are shown in Figure 7. The intensities of the peaks were integrated against that of an external standard.

The Fe(II)IPNS spectrum [Figure 7(a)] shows a cluster of overlapping, solvent-exchangeable features centered near 65 ppm, which integrates to three protons. This shift falls in the range of $N_\delta H$ or $N_\epsilon H$ for His residues coordinated to Fe(II) (cf. Table 1) and the 65 ppm feature is therefore assigned to three His ligands. The solvent nonexchangeable resonance at 42 ppm with an intensity of two protons is within the range for a coordinated Asp $C_\beta H_2$ or Glu $C_\gamma H_2$ (cf. Table 1) whose constituent protons have sufficiently similar torsion angles that their resonances are not resolved. Further NMR evidence for a carboxylate ligand was obtained on an inactive form of IPNS in which Co(II) is substituted for Fe(II). The shorter τ_s of Co(II) facilitated NOE studies on the

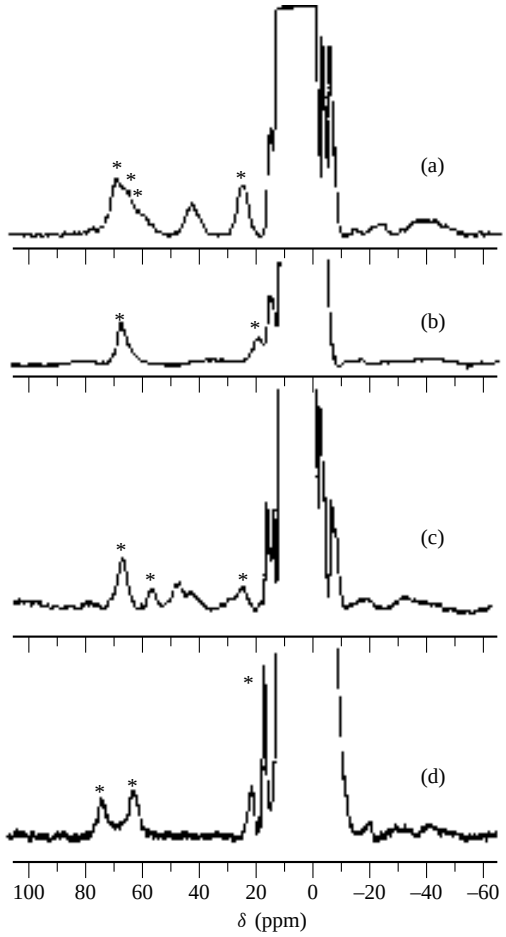

Figure 7 300-MHz ^{1}H NMR spectra of IPNS at 10 °C of (a) Fe(II)IPNS, (b) Fe(II)IPNS–NO complex, (c) Fe(II)IPNS–ACV complex under argon, and (d) Fe(II)IPNS–ACV–NO ternary complex under argon. All samples at pH 7 in H_2O. Starred peaks disappear in D_2O. (Reproduced by permission of the American Chemical Society from L.-J. Ming, L. Que, Jr., A. Kriauciunas, C. A. Frolik, and V. J. Chen, *Biochemistry*, 1991, **30**, 11 653)

isotropically shifted resonances, which showed clear evidence for a $YCH_2CH<$ spin system where Y coordinates to Co(II).[6] This result favors the assignment of the 42 ppm resonance of Fe(II)IPNS to a coordinated Asp $C_\beta H_2$ or Glu $C_\gamma H_2$ over a possible alternative assignment to $C_\delta H$ of two N_δ-coordinated His residues. Although irradiation of the 42 ppm resonance of Fe(II)IPNS did not reveal any NOE connectivities, this negative result is presumably due to the shorter T_1 values for Fe(II)IPNS than for Co(II)IPNS.

The solvent-exchangeable resonance near 24 ppm seen in all of the spectra in Figure 7 has no obvious assignment; it is well out of the range for the His ligand NH which is the only solvent-exchangeable proton listed in Table 1. Protons from water or hydroxide ligands to Fe(II) should resonate much farther to high frequency[21] and would be extremely broad due to their proximity to Fe(II). The 24 ppm solvent-exchangeable resonance could be due an uncommon protein ligand, such as *O*-coordinated amide or to a nonligand proton which is hydrogen bonded to the Asp ligand.

The substrate ACV (cf. Scheme 6) is known from other evidence to coordinate to Fe(II) through the sulfhydryl sulfur. Upon binding of ACV, the 65 ppm feature in Figure 7(a) splits into two resonances with a 2:1 intensity ratio [cf. Figure 7(c)]. These two resonances are assigned to the three His ligand NHs with the lower frequency, less intense resonance assigned to a His ligand whose Fe–N bond strength has been weakened by coordination of ACV. The 42 ppm resonance also splits into two features, and the mysterious solvent-exchangeable feature near 24 ppm is preserved. Thus, all of the protein ligands apparently remain coordinated upon ACV binding. Curiously, no paramagnetically shifted resonances were assigned to coordinated ACV. According to the data in Table 1, a resonance analogous to the $C_\beta H_2$ of coordinated cysteine near 200 ppm might be expected for sulfur-coordinated ACV. The Co(II)IPNS spectrum shows a resonance at 86 ppm, which was assigned to the Cys $C_\beta H_2$-like protons of sulfur-coordinated ACV. The shorter τ_s of Co(II) apparently favors observation of these proximal protons.

The Fe(II)IPNS–NO complex shows one solvent-exchangeable feature near 67 ppm [cf. Figure 7(b)] which integrates for three protons and is therefore logically assigned to the three His ligands whose resonances are observed at ≈65 ppm in the absence of NO [cf. Figure 7(a)]. The similarity in NH resonance positions and linewidths means that NO binding has not greatly perturbed either the spin delocalization onto the ligands or τ_s of the Fe(II), despite a change in spin state from $S = 2$ for high-spin Fe(II) to $S = \frac{3}{2}$ for [Fe(II)NO]. However, the solvent-nonexchangeable 42 ppm two-proton resonance seen in the Fe(II)IPNS spectrum [Figure 7(a)] has disappeared upon binding of NO. If, as discussed above, the 42 ppm resonance is due to the carboxymethylene protons of a coordinated Asp or Glu residue, then one explanation for the disappearance of this resonance is dissociation of the carboxylate ligand upon NO binding. However, one expects that neutral His ligands or water would be more readily displaced than a negatively charged carboxylate ligand. If the 42 ppm resonance is alternatively assigned to $C_\delta H$ of N_δ-coordinated His residues, then disappearance of this resonance due to dissociation of two His ligands should be accompanied by a decrease in intensity of the 65 ppm feature in Figure 7(a) assigned to the three His ligand NH's. However, this line of reasoning is inconsistent with the three-proton intensity of the 67 ppm feature in Figure 7(b). Therefore, the explanation favored by the authors for disappearance of the 42 ppm resonance upon NO binding is severe alteration but not displacement of a carboxylate ligand. One possible type of 'severe' alteration is conversion of carboxylate coordination from the *syn* to the *anti* lone pair, which, as discussed in Section 3, would tend to weaken the Fe–O(carboxylate) bond, and could thereby shift the ligand carboxymethylene resonance to a position under the diamagnetic proton envelope. This change in carboxylate coordination is illustrated in Figure 8.

The Fe(II)IPNS–ACV–NO complex [Figure 7(d)] also lacks the 42 ppm resonance and shows two solvent-exchangeable resonances of equal intensity at 62 and 74 ppm, which together integrate to two rather than three protons. This result is interpreted to mean that one of the His ligands has dissociated upon formation of the ternary complex. Figure 8 shows the proposed model for the structural changes in the IPNS active site upon binding of ACV and NO, which is consistent with the NMR and other spectroscopic results.

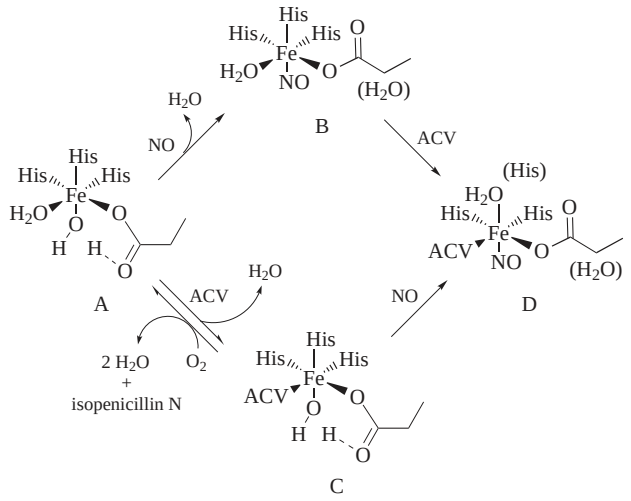

Figure 8 Proposed model for the changes in the IPNS active site upon binding of ACV and NO. (Reproduced by permission of the American Chemical Society from L.-J. Ming, L. Que, Jr., A. Kriauciunas, C. A. Frolik, and V. J. Chen, *Biochemistry*, 1991, **30**, 11 653)

7 SUMMARY AND FUTURE DIRECTIONS

^{1}H NMR of paramagnetic nonheme iron proteins has proven to be quite useful for the identification of ligand type and coordination geometry when used in conjunction with other spectroscopic data and chemical information, at least for proteins of $M_r \leq 100\ 000$ Da. One of the most important contributions of ^{1}H NMR has been in elucidation of the magnetic behavior of diiron clusters in nonheme proteins, which has assisted in assigning the bridging ligands. Definitive assignments of resonances have been hampered in some cases by the difficulty of conducting NOE and NOESY experiments on paramagnetic proteins containing nonheme, high-spin Fe(II) or Fe(III). However, as the technology improves and disperses, these methods are likely to be increasingly applied to nonheme iron proteins. As discussed for uteroferrin,[13] preparation of mixed-metal sites [e.g., Fe(III), Co(II)] with shorter τ_s values and resulting longer ligand proton T_1 values offer a promising approach for NOE and NOESY studies (see ***Cobalt(II)- and Nickel(II)-Substituted Proteins***). Also, as these proteins are increasingly cloned and overexpressed, isotopic labeling of residues may assist in assignments, especially of solvent nonexchangeable resonances (see ***Enzymatic Transformations: Isotope Probes***). Studies of these types are likely to yield increasingly quantitative and definitive analyses of the isotropically shifted ^{1}H NMR resonances of nonheme iron proteins.

Several other nonheme iron proteins would seem to be prime candidates for ^{1}H NMR studies of their iron sites. These proteins include myohemomerythrin, iron superoxide dismutases,[22] lipoxygenases,[23] nitrile hydratases,[24] iron-activated alcohol dehydrogenases,[25] stearoyl CoA Δ^9-desaturase,[26] and rubrerythrin.[27] (In fact, one- and two-dimensional ^{1}H NMR studies of iron superoxide dismutase have recently been reported.[28]) Thus, there is unlikely to be a shortage of novel proteins to which the powerful methods described above can potentially be applied.

8 RELATED ARTICLES

Cobalt(II)- and Nickel(II)-Substituted Proteins; Hemoglobin; Iron—Sulfur Proteins; Mitochondrial Cytochrome c; Myoglobin; Transferrins.

9 REFERENCES

1. G. N. La Mar, W. D. Horrocks, Jr., and R. H. Holm (eds.), *NMR of Paramagnetic Molecules. Principles and Applications*, Academic Press, New York, 1973. See especially Chap. 3 by La Mar.
2. I. Bertini and C. Luchinat, *NMR of Paramagnetic Molecules in Biological Systems*, Benjamin/Cummings, Menlo Park, CA, 1986. See especially Chaps. 2 and 3.
3. R. C. Scarrow, J. W. Pyrz, and L. Que, Jr., *J. Am. Chem. Soc.*, 1990, **112**, 657.
4. L. Que, Jr., R. B. Lauffer, J. B. Lynch, B. P. Murch, and J. W. Pyrz, *J. Am. Chem. Soc.*, 1987, **109**, 5381.
5. M. T. Werth, D. M. Kurtz, Jr., I. Moura, and J. LeGall, *J. Am. Chem. Soc.*, 1987, **109**, 273.
6. L.-J. Ming, L. Que, Jr., A. Kriauciunas, C. A. Frolik, and V. J. Chen, *Biochemistry*, 1991, **30**, 11 653.
7. F.-J. Wu and D. M. Kurtz, Jr. *J. Am. Chem. Soc.*, 1989, **111**, 6563.
8. L. Que, Jr., *J. Chem. Educ.*, 1985, **62**, 938.
9. D. H. Ohlendorf, J. D. Lipscomb, and P. C. Weber, *Nature (London)*, 1988, **336**, 403.
10. Z. Wang, L.-J. Ming, L. Que, Jr., J. B. Vincent, M. W. Crowder, and B. A. Averill, *Biochemistry*, 1992, **31**, 5263.
11. R. B. Lauffer, B. C. Antanaitis, P. Aisen, and L. Que, Jr., *J. Biol. Chem.*, 1983, **258**, 14 212.
12. E. P. Day, S. S. David, J. Peterson, W. R. Dunham, J. J. Bonvoisin, R. H. Sands, and L. Que, Jr., *J. Biol. Chem.*, 1988, **263**, 15 561.
13. R. C. Holz, L. Que, Jr., and L.-J. Ming, *J. Am. Chem. Soc.*, 1992, **114**, 4434.
14. D. M. Kurtz, Jr., in *Encyclopedia of Inorganic Chemistry*, ed. R. B. King, John Wiley & Sons, Chichester UK, 1994, p. 1847.
15. M. J. Maroney, R. B. Lauffer, L. Que, Jr., and D. M. Kurtz, Jr., *J. Am. Chem. Soc.*, 1984, **106**, 6445.
16. M. J. Maroney, D. M. Kurtz, Jr., J. M. Nocek, L. L. Pearce, and L. Que, Jr., *J. Am. Chem. Soc.*, 1986, **108**, 6871.
17. E. I. Solomon and Y. Zhang, *Acc. Chem. Res.*, 1992, **25**, 343.
18. D. M. Kurtz, Jr., *Chem. Rev.*, 1990, **90**, 585.
19. P. Nordlund and H. Eklund, *J. Mol. Biol.*, 1993, **232**, 123.
20. M. Sahlin, A. Gräslund, L. Petersson, A. Ehrenberg, and B.-M. Sjöberg, *Biochemistry*, 1989, **28**, 2618.
21. R. Lachicotte, A. Kitaygorodskiy, and K. S. Hagen, *J. Am. Chem. Soc.*, 1993, **115**, 8883.
22. B. L. Stoddard, P. L. Howell, D. Ringe, and G. A. Petsko, *Biochemistry*, 1990, **29**, 8885.
23. J. C. Boyington, B. J. Gaffney, and L. M. Amzel, *Science*, 1993, **260**, 1482.
24. H. Jin, I. M. Turner, Jr., M. J. Nelson, R. J. Gurbiel, P. E. Doan, and B. M. Hoffman, *J. Am. Chem. Soc.*, 1993, **115**, 5290.
25. E. K. Bakshi, P. Tse, K. S. Murray, G. R. Hanson, R. K. Scopes, and A. G. Wedd, *J. Am. Chem. Soc.*, 1989, **111**, 8707.
26. B. G. Fox, J. Shanklin, C. Somerville, and E. Münck, *Proc. Natl. Acad. Sci. USA*, 1993, **90**, 2486.
27. N. Ravi, B. C. Prickril, D. M. Kurtz, Jr., and B.-H. Huynh, *Biochemistry*, 1993, **32**, 8487.

28. L.-J. Ming, J. B. Lynch, R. C. Holz, and L. Que, Jr., *Inorg. Chem.*, 1994, **33**, 83.

Biographical Sketch

Donald M. Kurtz, Jr. *b* 1950. B.S., 1972, University of Akron, Ph.D., 1977, Northwestern University. Faculty in Chemistry and Biochemistry, Iowa State University, 1979–86; Faculty in Chemistry and Biochemistry and Center for Metalloenzyme Studies, University of Georgia, 1986–present. Approximately 90 publications. Research interests: inorganic chemistry, biochemistry and molecular biology associated with nonheme iron proteins.

Transferrins

Claudio Luchinat and Marco Sola
University of Bologna, Bologna, Italy

1	Introduction	1
2	The Role of NMR in the Chemistry of Transferrins: Achievements	2
3	The Role of NMR in the Chemistry of Transferrins: Future Prospects	7
4	Related Articles	8
5	References	8

1 INTRODUCTION

Transferrins are a family of metal binding glycoproteins which play a fundamental role in iron metabolism in vertebrates and invertebrates.[1] Transferrin from serum (Tf hereafter) acts as the principal iron carrier in plasma, binding the Fe^{3+} ion strongly and reversibly and shuttling it from the sites of metal uptake to those of iron–proteins biosynthesis and iron storage. Ovotransferrin from avian egg white (Otf), and lactoferrin (Ltf) found in many secretory fluids and in leukocytes, are mainly iron-sequestering proteins which exert a bacteriostatic and detoxifying function. Transferrins are monomeric proteins of about 700 residues with molecular weight close to 80 kDa. They are related by a sequence homology of about 50%. The X-ray structural information[2,3] indicates that the polypeptide chain is organized into two nearly equal-sized and about 40% homologous globular lobes connected by a short peptide segment, each containing one chain terminus (hence termed N-lobe and C-lobe), and one metal site (Figure 1). Each lobe is in turn structured into two domains. The metal lies at the bottom of the cleft between the two domains, about 10 Å from the protein surface. Both metals are bound by two tyrosines, one histidine, and one aspartate in a pseudooctahedral coordination which is completed by a bidentate carbonate ion hydrogen bonded to some protein groups (Figure 1).[2,3] X-ray data also indicate the absence of metal-coordinated water in the crystal.

The requirement of a concomitant (synergistic) binding of an anion (besides carbonate, carboxylate anions with a second donor group are also active) for specifically loading the metal in the two sites is a unique feature of the biochemistry of transferrins. In recent years X-ray crystallography and NMR have allowed the elucidation of several molecular details of the metal sites. It is apparent that the formation of the ternary complex at both sites proceeds through initial anion binding to the protein: the anion is most probably required to reduce the net positive charge in the binding cavity, due to the presence of a number of cationic residues, and for increasing the overall stability of the adduct by further anchoring the metal to the protein. Overall, it functions as a bridge between the metal and the protein. The synergistic anion appears to play a central role in the reactivity of the metal centers, acting as the key for the processes of metal uptake and release. The associated protein conformational changes are also being extensively studied, in particular the open–close equilibrium of the interdomain cleft at each lobe, with metal binding and removal occurring only in the open form.

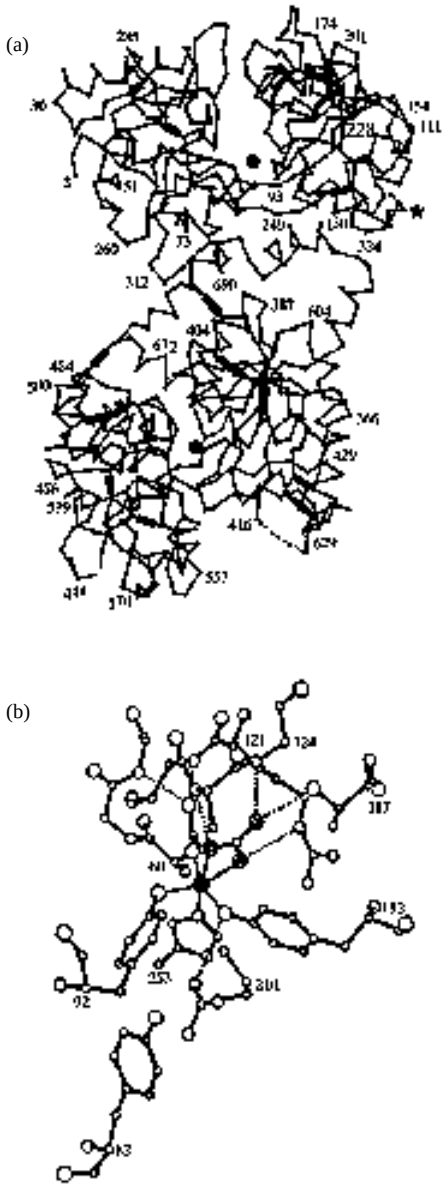

Figure 1 (a) C^{α} plot of the lactoferrin molecule showing its subdivision into two lobes, the N-lobe (top) and C-lobe (bottom). The iron atoms are shown as filled circles bound in the cleft between the two domains in each lobe. (b) The metal- and anion-binding site in lactoferrin (N-lobe). The carbonate anion is shown by hatched circles. Hydrogen bonds are indicated by dotted lines. (Reproduced by permission of Academic Press from B. F. Anderson, H. M. Baker, G. E. Norris, D. W. Rice, and E. N. Baker, *J. Mol. Biol.*, 1989, **209**, 711)

The two metal sites of transferrins are, in general, spectroscopically slightly inequivalent and differ, although most often not dramatically, in metal binding affinity. The relative binding strength of the two sites is sensitive to pH, synergistic anion, and ionic composition of the medium, and may vary toward different metals. However, the C-site almost invariably shows a greater metal affinity than the N-site at acidic pH. The structural bases of these differences are still not unequivocally

established (although the disulfide bridge content of the two lobes appears to be relevant in this respect). Their physiological relevance is also under investigation. The biological requirement for the structural 'doubleness' of transferrins is nowadays a central issue.

Transferrins can firmly bind a large number of transition, nontransition, and lanthanide ions. Several metals have served as spectroscopic probes for investigating the structural features of the metal sites, but some of the adducts also have a biological relevance since serum transferrin, being only about 30% saturated with iron in vivo, may function as an efficient carrier for metals other than iron.

2 THE ROLE OF NMR IN THE CHEMISTRY OF TRANSFERRINS: ACHIEVEMENTS

It should be recalled that for a protein of the size of transferrin full structural studies in solution (see ***Biological Macromolecules: Structure Determination in Solution***; ***Biological Macromolecules***; ***Biological Macromolecules: NMR Parameters***; ***Multidimensional Spectroscopy: Concepts***; ***Structures of Larger Proteins, Protein-Ligand, and Protein-DNA Complexes by Multi-Dimensional Heteronuclear NMR***) are not yet feasible. The NMR of transferrins was until recently mainly devoted to the elucidation of the molecular details of the ternary adducts at the metal sites with the following methodological approaches: (a) ^{13}C NMR of protein derivatives of diamagnetic metals with ^{13}C-enriched anions; (b) observation of protein-bound NMR active metal nuclei; (c) observation of ^{1}H NMR hyperfine-shifted resonances arising from the protons surrounding a bound paramagnetic metal (see ***Electron–Nuclear Hyperfine Interactions***; ***Cobalt(II)- and Nickel(II)-Substituted Proteins***; ***Electron– Nuclear Multiple Resonance Spectroscopy***); (d) NMRD profiles. Only in recent years, has one- and two-dimensional ^{1}H NMR at high field (see ***Multidimensional Spectroscopy: Concepts***) succeeded in handling, at least partially, the largely unresolved proton spectrum and proved to be of use in monitoring metal binding to the protein and the related conformational changes. In what follows we have outlined the contribution of NMR to the understanding of the main issues of the metallobiochemistry of transferrins.

2.1 Identification of the Metal-Binding Residues

The involvement of tyrosine residues in metal binding at both sites of transferrins, indicated by a number of spectroscopic and chemical modification studies, has been conclusively supported by ^{1}H NMR since the early 1970s from the shift induced in the corresponding resonances by Ga^{3+} binding, and their paramagnetic broadening upon Fe^{3+} binding (see ***Paramagnetic Relaxation in Solution***).[4] In addition, two histidines were also proposed as metal ligands from the detection of the C(2)H resonances which did not titrate with pH in the Ga^{3+} ternary complexes[5] of either intact or half molecules of Otf and human Tf[6,7] (Ga^{3+} has proved to be a good diamagnetic substitute for the Fe^{3+} ion, owing to the similarity of the ionic radius and to a similar binding affinity for transferrins). Metal binding of two histidines and two tyrosines was also consistent with the hyperfine shifted ^{1}H resonances in the mono- and bis-Co^{2+} derivatives of Otf.[8,9] The spread of the hyperfine shifted signals and their relatively long relaxation times[10] (see ***Paramagnetic Relaxation in Solution*** and ***Cobalt(II)- and Nickel(II)-Substituted Proteins***) suggested octahedral coordination around the metal ions.[8,9]

The X-ray structure later confirmed octahedral coordination and the presence of two tyrosine ligands, but showed that only one of histidine is involved in the metal binding site.[2,3] The identity of the additional nontitrating histidine in the Ga^{3+} derivative remains unknown, while the additional hyperfine shifted exchangeable proton in the spectrum of the Co^{2+} derivative could well arise, in retrospect, from one of the NH protons H bonded to the metal-coordinated carbonate ion.

Cadmium-113 NMR[11] (see ***Cadmium-113 NMR: A Surrogate Probe for Zinc and Calcium in Proteins***) and ^{205}Tl NMR data[12] (see ***Thallium NMR***) are in full agreement with the presence of only one histidine in the binding set. Aspartate coordination invariably went undetected, most probably due to the rather elusive ^{1}H NMR spectral changes in the crowded aliphatic region upon metal binding and the impossibility of metal NMR to discriminate it from other potential oxygen donors.

2.2 Exchangeable Protons in the Metal Sites

The issue of possible water coordination was tackled through water proton relaxation measurements. Early studies of water T_1 measurements in solutions of the Fe^{3+} adducts of Htf and Otf simply showed the accessibility of both sites to water molecules.[13,14] This was substantiated later by measurements of the field dependence of the longitudinal nuclear magnetic relaxation rates of water protons (NMRD profiles) on the iron adduct of Htf, also carried out for comparative purposes on the apoprotein and the diamagnetic analog containing Co^{3+}, which were interpreted as indicative of a water molecule only loosely bound to the metal in each site.[15,16] Analogously, one water molecule axially bound to the metal was also proposed for the Cu^{2+} derivative of Htf.[17] It was later shown that for slowly rotating protein complexes the anisotropic structure of the ligand fields of the complexed metals is not averaged out as it is for fast rotating aqua ions or small complexes.[18,19] The NMRD profiles for Cu^{2+} and VO^{2+} complexes of Htf were then evaluated with computations that included the anisotropic hyperfine interaction of metal ions with their own nuclei (see ***Electron–Nuclear Hyperfine Interactions***).[20] It was found that relaxation occurs through exchange of bulk water with a second coordination sphere water molecule. This was also confirmed for the Gd^{3+}–Htf complex[21] (see ***Gadolinium Chelates: Chemistry, Safety and Behavior***) and demonstrated later by the X-ray structure of human Ltf.[3] Recent[22] more quantitative interpretation of the NMRD data for Fe^{3+}–Htf,[23] taking into account zero field splitting of the iron ion,[18,19,24] suggests the presence of slowly exchanging protons (possibly from the protein) and of fast exchanging water at about 4–5 Å from the metal ion. NMRD data on Cu^{2+}–transferrin were also instrumental in demonstrating rotation-independent electronic relaxation mechanisms for Cu^{2+} in solution.[25]

2.3 Synergistic Anions in the Metal Sites

Elucidation of the anion binding arrangement in the metal sites was obtained from a number of ^{13}C NMR data using

Table 1 ^{13}C NMR Chemical Shifts for ^{13}C-Enriched Synergistic Anions in Various Metal–Transferrin Derivatives[a]

Derivative	Chemical shift[b]	
Carbonate derivatives		
Co^{3+}–Htf[27]	169.5	169.3
Al^{3+}–Otf[30]	165.7 (N)	165.5(C)
Al^{3+}–Htf[29]	165.4	
Ga^{3+}–Otf[29]	166.3	
Ga^{3+}–Htf[29]	166.5	
Tl^{3+}–Htf[12]	165.98 (N)	166.22 (C)
Tl^{3+}–Otf[12]	165.92	
Sc^{3+}–Otf[38]	166.74 (N)	166.61 (C)
Sc^{3+}–Htf[38]	167.19	166.76
Zn^{2+}–Otf[29]	168.2	
Zn^{2+}–Htf[29]	168.5	
Cd^{2+}–Otf[11]	168.2	
Cd^{2+}–Htf[11]	168.2	
Oxalate derivatives		
	C-1	C-2
Al^{3+}–Otf[30]	168.42 (C)	165.33 (C)
	168.47 (N)	165.89 (N)
Al^{3+}–Htf[36]	168.58	166.07
	168.40	165.33
Al^{3+}–Ltf[36]	168.55	166.0
	168.24	166.0
Ga^{3+}–Otf[29]	168.4 (C)	165.7 (C)
	168.4 (N)	166.2 (N)
Tl^{3+}–Otf[12]	167.80 (C)	165.35 (C)
	167.91 (N)	165.99 (N)
Tl^{3+}–Htf[12]	167.88 (N)	165.62 (N)
Sc^{3+}–Otf[38]	170.52 (C)	167.00 (C)
	170.60 (N)	167.68 (N)
Zn^{2+}–Otf[29]	169.6	
Cd^{2+}–Htf[32]	168.5 (C)	169.9 (N)

[a]Htf: human serum transferrin; Otf: ovotransferrin; Ltf: human lactoferrin. Assignments to the N- and C-site are reported in parentheses, when available.
[b]In ppm from Me_4Si.

^{13}C-enriched anions (mainly carbonate and oxalate) and/or NMR-active nuclei loaded in the protein sites. The spectral parameters and resonance assignments to individual sites, where available, have been collected in Table 1 and 2. The broadening beyond detection of the ^{13}C NMR resonance of isotopically-enriched bicarbonate bound to Fe^{3+}–Tf[26] allowed an estimate to be made of an upper limit of 9 Å for the Fe–^{13}C distance, which was later reduced to 4.5 Å[27] thanks to instrumental developments, consistent with the presence of the anion in the first coordination sphere of the metal. The latter study also indicated that the anion, most probably carbonate rather than bicarbonate as judged by the ^{13}C chemical shift value, was specifically bound in both metal binding sites of the diamagnetic Co^{3+} derivative and of the apoenzyme, giving rise in both cases to resonances in slow exchange with that of free bicarbonate (see ***Chemical Exchange Effects on Spectra***).[27] Specific anion binding to the apoprotein was taken as indicative that anion binding to the sites may precede metal binding, which is now indeed a widely accepted step in the mechanism of metal uptake of transferrins. A positively charged arginine residue was suggested as one of the anion binding groups for carbonate,[27] as later confirmed by X-ray data. The pH dependence of the ^1H NMR resonances of the histidine C(2)H protons in diamagnetic Ga(III) derivatives of Otf, Htf, and their half-molecules in the presence of dicarboxylic acids as synergistic anions indicated a histidine as the likely anion binding group in each site.[5–7,28] Interestingly, the X-ray structure of human Ltf allows for binding of anions larger than carbonate not to the arginine involved in the carbonate derivative, but to polar residues of a cavity beyond such a residue, which actually also includes a histidine residue.[3]

Further ^{13}C NMR studies of diamagnetic Al^{3+}–, Ga^{3+}– and Zn^{2+}–transferrin derivatives with carbonate and oxalate as the synergistic anion[29,30] were interpreted in terms of the anion bridging the metal and a positively charged group of the protein, in line with the 'interlocking-sites' model (Figure 2).[31] Oxalate bound in the Ga^{3+}– and Al^{3+}–Otf derivatives gave rise to two partially overlapped AB signal patterns.[29] The inequivalence of the two carbon atoms was assumed to arise from oxalate binding to the metal via only one carboxylate group, the other interacting with a positive residue of the site. Reference to ^{13}C chemical shift data of simple inorganic oxalate complexes allowed the assignment of the resonances of the protein-bound and metal-bound carbons of each oxalate molecule.[29,30] In the case of Zn^{2+}–[29] and Cd^{2+}–Otf–oxalate derivatives,[32] the effect of the metal on the shielding of the carbon atom is more similar to that of the protein residue, leading to the equivalence of the two carbon atoms (see ***Magnetic Equivalence***), hence to the observation of a single signal for each protein-bound anion.

Overall, although subject to a successive reevaluation (see below), these ^{13}C NMR data strongly supported the bridging arrangement of the synergistic anion prior to publication of the X-ray data.[2,3] Moreover, more recent ^{113}Cd NMR spectra of the ^{113}Cd–Otf derivative with glycine as the synergistic anion unequivocally indicated the binding of the amino group of the amino acid to the metal, fully in line with the interlocking sites model.[33]

Observation of the magnetic coupling between an $I = \frac{1}{2}$ metal and the carbon atom of the anion in both metal sites yielded conclusive spectroscopic evidence of a direct metal–ion linkage. In particular, this was achieved by using ^{205}Tl and ^{113}Cd ions loaded in one or both metal sites (Figure 3).[11,12,34] The ^2J coupling constants are collected in Table 2.

Thallium–transferrin derivatives allowed a reevaluation of the binding mode of oxalate, and led to further insight into the chemistry of the ternary adduct in the protein sites. The ^{13}C NMR signals of bound oxalate in each site of the $^{205}Tl^{3+}$ derivatives of human Tf and Otf are split into a doublet of doublets due to carbon–carbon and thallium–carbon coupling.[12] The comparable values of the ^{13}C–metal coupling constants for the two oxalate carbons (Table 2) indicate that the anion binds to the metal in a 1,2-bidentate mode at both sites. This is likely to be the case for all the oxalate adducts of transferrins with tripositive metals, as recently suggested from the similarity of the ^{13}C NMR spectral patterns for these adducts.[12] This view receives conclusive support from the X-ray structure of the Cu^{2+}–oxalate ternary adduct with the C-terminal half-molecule of Ltf,[35] which confirms the 1,2-bidentate bridging arrangement of the oxalate anion and indicates that the spectral inequivalence of the two carbon

Table 2 Spectral Parameters for Metal NMR Resonances and M–^{13}C Coupling Constants for Various Metal–Transferrin Derivatives[a]

Derivative	Chemical shift (ppm)[b]	$\Delta\nu_{\frac{1}{2}}$(Hz)	^2J(M,^{13}C) (Hz)
$^{27}Al^{3+}$–Otf–CO_3^{2-}[c] **30, 36, 37**	−2.3 (N)	140	
	−3.8 (C)	170	
$^{27}Al^{3+}$–Tf–CO_3^{2-}[c] **36**	−2.8	180	
$^{27}Al^{3+}$–Ltf–CO_3^{2-}[c] **36**	−4.3	200	
$^{27}Al^{3+}$–Otf–$C_2O_4^{2-}$[c] **30**	−4.4 (N)	170	
	−5.7 (C)	200	
$^{205}Tl^{3+}$–Htf–CO_3^{2-}[d] **34, 43**	2055 (C)	100	265
	2075 (N)	100	290
$^{205}Tl^{3+}$–Htf–CO_3^{2-}[e] **12**	2055 (C)		285
	2072 (N)		278
$^{205}Tl^{3+}$–Otf–CO_3^{2-}[e] **12**	2054 (C)		281
	2075 (N)		281
$^{205}Tl^{3+}$–Otf–$C_2O_4^{2-}$[e] **12**	2100 (C)		32, 21[f]
	2103 (N)		28, 14[f]
$^{205}Tl^{3+}$–Htf–$C_2O_4^{2-}$[e] **12**	–		27, 15[f,g]
$^{51}V^{5+}$–Htf–CO_3^{2-}[c] **39, 40**	−529.5 (C)	200	
	−531.5 (N)	310	
$^{45}Sc^{3+}$–Otf–CO_3^{2-}[c] **38**	77 (C)	940	
	85 (N)	740	
$^{45}Sc^{3+}$–Htf–CO_3^{2-}[c] **38**	76	1020	
$^{45}Sc^{3+}$–Otf–$C_2O_4^{2-}$[c] **38**	65 (C)	1030	
	70 (N)	1160	
$^{113}Cd^{2+}$–Otf–CO_3^{2-}[e] **11**	21.6	100	22
$^{113}Cd^{2+}$–Htf–CO_3^{2-}[e] **11**	11.7	100	20
$^{113}Cd^{2+}$–Htf–CO_3^{2-}[c] **54**	38.1 (N)	313	
	43.6 (C)	377	
$^{113}Cd^{2+}$–Otf–$C_2O_4^{2-}$[e] **32**	54 (C)	150	
	– (N)[h]		
$^{113}Cd^{2+}$–Otf–Gly[e] **33**	139	320	

[a]Htf: human serum transferrin; Otf: ovotransferrin; Ltf: human lactoferrin. Assignments to the N- and C-site are reported in parentheses.
[b]The following references were used: ^{27}Al: 1 M $Al(NO_3)_3$ in D_2O; ^{205}Tl: Tl^+ ion at infinite dilution; ^{51}V: $VOCl_3$; ^{45}Sc: 0.1 M $Sc(H_2O)_6^{3+}$; ^{113}Cd: 0.1 M $Cd(ClO_4)_2$ in D_2O. Assignment to the N- and C-site are reported in parentheses, when available.
[c]11.7 T.
[d]1.4 T.
[e]4.7 T.
[f]Inequivalent carbons.
[g]N-terminal half-molecule.
[h]Broadened beyond detection.

atoms in the ternary adducts with tripositive metals arises from differences in the protein residues H bonded to the two carboxylate groups. In the light of these results, the ^{13}C spectra of the $^{113}Cd^{2+}$–oxalate adduct of Otf, for which, unlike the carbonate derivative,[11] no ^{113}Cd–^{13}C coupling could be detected,[32] consistent with a longer metal–carbon distance, can also be interpreted in terms of the above anion arrangement.

Recent work on NMR of quadrupolar metal nuclei (^{51}V, ^{27}Al, and ^{45}Sc) (see ***Aluminum-27 NMR of Solutions***; ***Quadrupolar Transition Metal and Lanthanide Nuclei***) loaded in the sites of transferrins deserve a special mention.[12,30,36–40] For an $I = \frac{n}{2}$ nucleus (n = 3, 5, 7) firmly bound to a slowly rotating macromolecule, far from the extreme narrowing limit, it is shown that only the central $\frac{1}{2} \rightarrow -\frac{1}{2}$ nuclear spin transition can be observed (see ***Quadrupolar Interactions***) (Figure 4). Under these conditions the field dependence of the linewidth and chemical shift (see ***Dynamic Frequency Shift***) provides the values of the quadrupole coupling constant, χ, and of the rotational correlation time, τ_c, for the protein-bound metals, and hence yields information on the symmetry of the metal coordination environment. For example, independent of the synergistic anion, the Al^{3+} ion appears to be octahedrally coordinated in both sites, with a higher degree of symmetry in the N-site as compared to the C-site.[30] Moreover, the metal sites of the Sc^{3+}–Otf derivative show a higher symmetry than those in the homologous Al^{3+} derivative.[38]

Since detection of the resonances of these quadrupolar nuclei is facilitated by increasing the magnetic field and the molecular size of the protein, the technique is of general interest for probing the properties of the metal binding sites of large metalloproteins.

2.4 The (In)Equivalence of the Two Binding Sites

Early water proton relaxation measurements of Fe^{3+} binding to Otf, coupled with electrophoretic profiles, failed to detect the difference in iron binding ability of the two sites,[41] indicating a random distribution of iron in the two lobes.[14] Inequivalences can be detected with the aid of paramagnetic

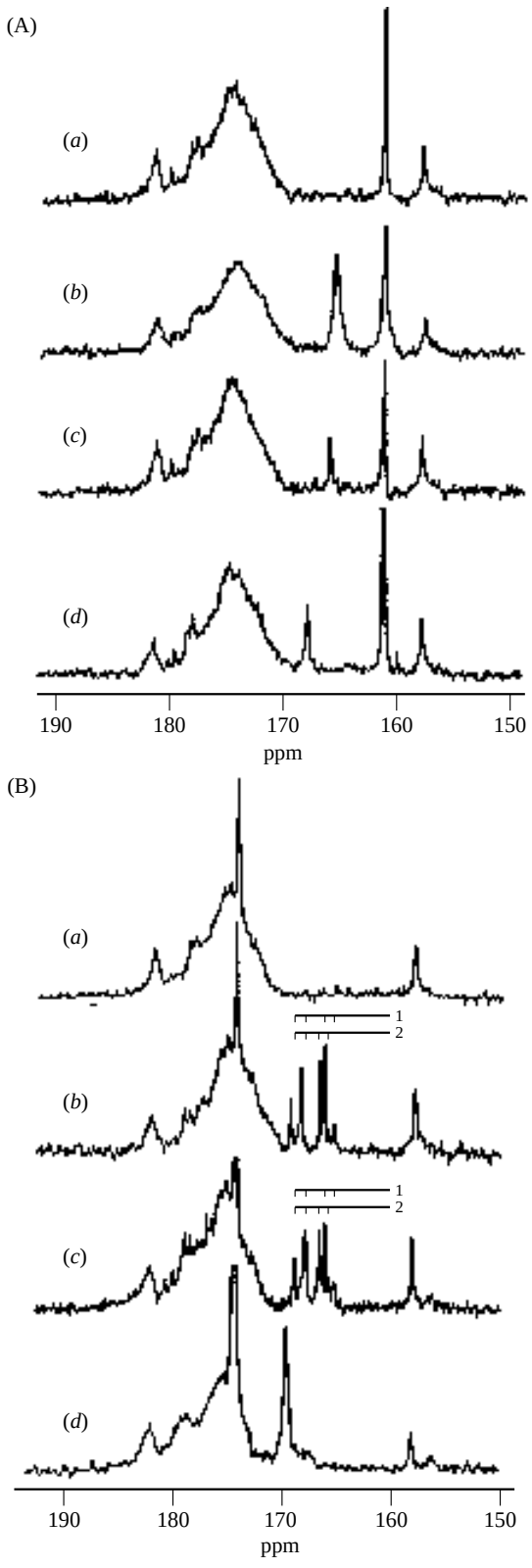

Figure 2 75.4 MHz ^{13}C NMR spectra of the carbonyl region of (A) Otf–carbonate–metal complexes and (B) Otf–oxalate–metal complexes in the presence of excess anion, pH 8 (protein concentration 1.5 mM): (*a*) apoprotein; (*b*) Al^{3+} derivatives; (*c*) Ga^{3+} derivatives; and (*d*) Zn^{2+} derivatives. (Reproduced by permission of the American Chemical Society from I. Bertini, C. Luchinat, L. Messori, A. Scozzafava, G. C. Pellacani, and M. Sola, *Inorg. Chem.*, 1986, **25**, 1782)

metals like Co^{2+} [8,9] and lanthanides,[42] taking advantage of the sensitivity of hyperfine shifts to even slight changes in the coordination sphere.[10] The advent of high-field Fourier transform spectrometers allowed the safe determination of site (in)equivalence simply from the presence of either one or two NMR signals (or signal patterns) due to the ^{13}C-labeled synergistic anion and/or NMR-active diamagnetic metals bound to the protein. A metal titration then generally indicated if sequential metal binding had occurred, and in some instances assignment of the NMR resonances to the individual sites allowed the site with higher metal affinity to be determined. This approach has been followed for the derivatives of Otf and Htf with Co^{3+}, Ga^{3+}, Al^{3+}, Tl^{3+}, Sc^{3+}, V^{5+}, Cd^{2+}, Zn^{2+} in combination with different synergistic anions, most often carbonate and oxalate. The NMR-active metals and the ^{13}C-labeled synergistic anion loaded in the two sites led to either overlapping peaks or distinct, but invariably closely spaced, resonances indicative of equivalent (within the resolution available) or slightly different chemical environments, respectively (Table 1 and 2). The higher metal affinity of the C-site over the N-site at acidic pH was, in general, exploited to obtain resonance assignment to individual sites, although recently the use of proteolytically-obtained half-molecules has proved to be a safer means for such an assignment. This was evidenced for the derivatives of human Tf and Otf with Al^{3+}, Tl^{3+}, and Sc^{3+}, for which the metal resonances and the ^{13}C signals of the synergistic anion in the bimetallic derivative were invariably found to exactly superimpose the signals of the two one-sited half-molecules.[12,30,36–38]

These extensive NMR data concurred to indicate that the relative properties of the two sites for a given transferrin vary with the nature of the metal, the synergistic anion, pH, and medium composition, and may differ from those of other transferrins. The following selected examples are worth mentioning. Aluminum–27 and ^{13}C NMR showed that in the presence of carbonate the two aluminum metal sites of Otf are slightly inequivalent and that Al^{3+} binds preferentially to the N-site at pH 8, while the site preference is reversed with oxalate.[30] In contrast, spectroscopically equivalent sites are detected in the homologous derivatives of human Tf and Ltf.[36] At pH values slightly above neutrality in the presence of carbonate, the Tl^{3+} ion was shown at an early stage,[43] unlike Al^{3+}, to bind more strongly to the C-site of human Tf, and more recently to bind with the same affinity to both sites of Otf.[12] Moreover, Sc^{3+} showed no site preference toward Otf with either carbonate or oxalate as synergistic anions,[38] and site inequivalence in the Cd^{2+} derivative of Tf with oxalate appeared more pronounced than in the homologous Zn^{2+} derivative.[11,32]

Although this overview demonstrates NMR to be a powerful tool for probing the differences in structural properties and binding affinity of the two metal sites, at present, as noted elsewhere,[44] it does not address unequivocally the question of the presence of a functional association between the lobes. The above-mentioned near-identity of the spectral properties of a given site in the half and intact transferrin molecules does not necessarily imply that the metal affinity of the sites remains unchanged upon proteolytic cleavage.

The application of resolution enhancement techniques, although allowing resolution of only a small fraction of the total proton resonances, particularly those belonging

to relatively mobile portions of the protein, has recently enabled one- and two-dimensional ^{1}H NMR (see ***COSY Two-Dimensional Experiments***; ***Multidimensional Spectroscopy: Concepts***; ***NOESY***) to monitor the binding of diamagnetic metals to whole and half-transferrin molecules.[45–47] Low-frequency methyl peaks probably experiencing aromatic ring current shifts, glycan *N*-acetyl and sugar ring protons, Lys/Arg ϵ/δ-CH_2 protons, and His C-2,H resonances could be resolved in the apo form of human Tf.[47] The disappearance of some of these peaks and the rise of new resonances in a slow exchange regime upon metal titration of the apo form of whole human Tf and its N-lobe (HTf/2N hereafter) allowed the detection of the sequential binding of Al^{3+} and Ga^{3+} to Tf, with preferential binding of the former metal to the N-site (in the presence of carbonate, pH 8.8),[46] and of the latter to the C-site (with oxalate as a synergistic anion, pH 7.2).[45] Examples of one- and two-dimensional proton spectra are illustrated in Figure 5.[45]

Since X-ray data indicate that the structural features of the N-lobe are likely to be closely similar in the intact protein and in the isolated lobe,[2] the lack of a perfect match between the spectral features of the apo form and the Al^{3+} adducts of Tf and Tf/2N was interpreted as indicative of an interaction between the lobes in the intact protein.[46] This approach also allowed a determination of the apparent binding constant of oxalate to apo-HTf/2N ($\log K = 4.04 \pm 0.09$) from the shift of some resonances induced by the weak binding of the anion, as a consequence of the fast exchange between the free and anion bound species on the NMR timescale.[45] Moreover, the time course of the paramagnetic broadening of the proton resonances in the Ga^{3+}–oxalate–HTf/2N adduct upon Fe^{3+} addition allowed the kinetics of Ga^{3+} displacement (k_{obs} = 0.162 h^{-1} at 310 K) to be determined.[45]

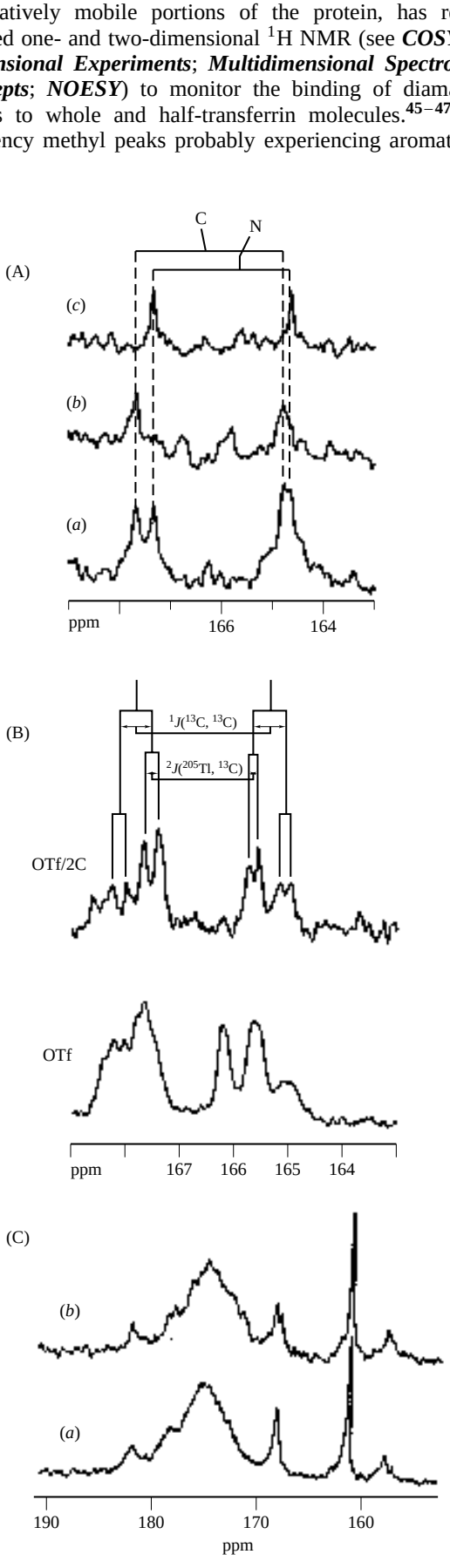

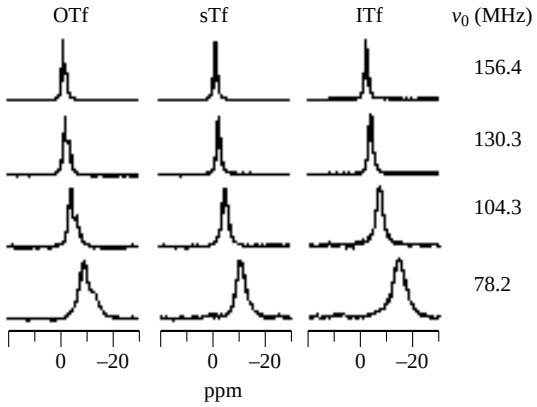

Figure 4 ^{27}Al NMR spectra of the Al_2 derivatives of Otf, human Tf, and human Ltf at different magnetic fields. (Reproduced by permission of the American Chemical Society from J. M. Aramini, M. W. Germann, and H. J. Vogel, *J. Am. Chem. Soc.*, 1993, **115**, 9750)

Figure 4 (A) Expanded carbonyl region of the 100.6 MHz ^{13}C NMR spectra of (*a*) Tl_2–Tf–CO_3^{2-} derivative; (*b*) Tl–Tf–carbonate derivative with Tl^{3+} loaded in the C-site; (*c*) Tl–Tf/2N–carbonate derivative. (Reproduced by permission of the American Chemical Society from J. M. Aramini, P. H. Krygsman, and H. J. Vogel, *Biochemistry*, 1994, **33**, 3304). (B) Expanded carbonyl regions of the 125.7 MHz ^{13}C NMR spectra of the Tl_2–Otf–oxalate derivative and of the Tl–Otf/2C–oxalate derivative. (Reproduced by permission of the American Chemical Society from J. M. Aramini, P. H. Krygsman, and H. J. Vogel, *Biochemistry*, 1994, **33,** 3304). (C) Carbonyl regions of the 50.3 MHz ^{13}C NMR spectrum of the Cd_2–Otf–carbonate derivatives containing (*a*) natural-abundance Cd^{2+} ion and (*b*) isotopically-enriched $^{113}Cd^{2+}$ ion. (Reproduced by permission of the American Chemical Society from M. Sola, *Inorg. Chem.*, 1990, **29**, 1113)

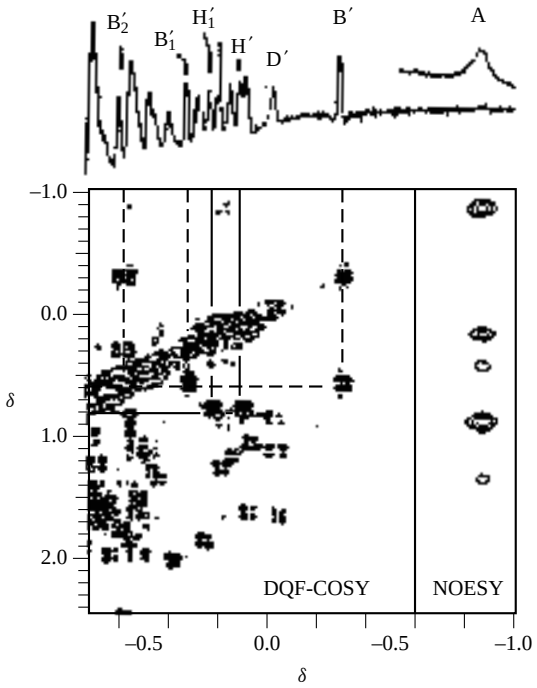

Figure 5 600-MHz phase-sensitive DQF-COSY ^{1}H NMR spectrum (subject to resolution enhancement) of the Ga^{3+}–Tf–oxalate adduct, together with a NOESY spectrum for the lowest frequency peak. (Reproduced by permission of the American Chemical Society from G. Kubal, A. B. Mason, S. U. Patel, P. J. Sadler, and R. C. Woodworth, *Biochemistry*, 1993, **32**, 3387)

2.5 Other Structural Features in Solution

Tentative assignments of the low-frequency methyl proton resonances to individual Leu, Val, and Ile residues were proposed for human Tf and its N-lobe through 2D COSY techniques (see ***COSY Two-Dimensional Experiments***) and calculation of the shifts induced by the ring currents of nearby aromatic groups (see ***Shielding: Overview of Theoretical Methods***).[45,46] The shifts of these resonances upon metal binding appear to be related to changes in their orientation toward the aromatic groups which reside in relatively mobile, yet structured hydrophobic domains possibly involved in conformational changes related to the closure of the interdomain cleft.[45] Unambiguous signal assignments and determinations of the precise movements of single residues are still unavailable, but much effort is being devoted toward this end.

Nonsynergistic anions like chloride, perchlorate, thiocyanate, and pyrophosphate are known to decrease the stability of various metal–transferrin derivatives, and, the chloride ion in particular, to affect the relative metal binding affinity of the sites.[48] They most probably bind to positively charged residues in the proximity of the metal site, altering the network of salt bridges and hydrogen bonds that stabilize the complex. The effect of perchlorate in decreasing the stability of the metal complexes was clearly monitored by the decrease of the ^{13}C and ^{113}Cd NMR resonances of the $^{113}Cd_2$–Otf–CO_3^{2-} adduct upon anion addition, due to dissociation of the complex.[11] Chlorine-35 and ^{14}N NMR linewidth measurements of chloride, perchlorate, and nitrate anion binding to human Tf in a fast exchange regime allowed the determination of a 2:1 stoichiometry for V^{5+} binding to the protein, since the formation of the ternary metal–carbonate complex at the sites determines the specific anion binding to the protein and hence leads to a decrease in quadrupolar relaxation (see ***Relaxation Theory for Quadrupolar Nuclei***).[49]

Proton NMR has also played an important role in the determination of the primary structure on the glycan moieties of a variety of transferrins and in the determination of solution conformation through 2D techniques.[50–53] Studies were carried out on glycopeptides obtained by proteolytic digestion or on the intact oligosaccharide chain detached from the protein by hydrazinolysis. Readers are referred to the original literature as far as the assignment procedures are concerned. However, it is worth mentioning that recent ^{1}H NMR studies on Ga^{3+} binding to human Tf indicate that metal binding alters the shift of the resonances of the *N*-acetylated sugar residues of both glycan chains, suggesting that the transmission of the perturbation to the carbohydrate chains may have significance for cell receptor recognition of the metal-loaded protein.[45]

3 THE ROLE OF NMR IN THE CHEMISTRY OF TRANSFERRINS: FUTURE PROSPECTS

The applicability of NMR techniques becomes less and less trivial with increase in molecular size. From this point of view, molecules of the size of transferrins represent a challenge. Multidimensional NMR, coupled with resolution enhancement techniques, of either intact and half-transferrin molecules, appear as a promising approach for detecting structural changes in the individual lobes upon metal uptake or release and ionization equilibria, and should be of use for monitoring the protein behavior toward the binding of a variety of metals and synergistic anions, under different conditions of pH and medium composition. The bottom line is to understand whether the two lobes undertake different roles in metal uptake and release processes, and whether they are functionally associated, and hence to address one of the most intriguing points of the biochemistry of transferrins related to their structural 'doubleness'. The advent of very high field spectrometers (750 MHz or higher) would greatly enhance the diagnostic power of this approach, together with the feasibility of NMR of quadrupolar metal nuclei which has proved highly sensitive to the structural features of the metal sites. The use of genetically-engineered proteins containing either amino acid substitutions, deletions, or labeled residues could also add essential information. Nitrogen-15 and/or ^{13}C selective and nonselective labeling is indeed providing a breakthrough to structural studies on medium sized proteins (see ***Heteronuclear Assignment Techniques***; ***Heteronuclear Shift Correlation Spectroscopy***).

Besides metal binding, NMR should also be a valuable means of monitoring the potential ability of transferrins to accommodate small molecules in the binding cleft.[3] Overall, the application of ^{1}H NMR to determine protein structure in solution, coupled with molecular dynamics calculations (although the size of transferrin would set this as a long-term project) appears to be the main research direction toward the elucidation of the structure–function relationships in this class of proteins.

4 RELATED ARTICLES

Calcium-Binding Proteins; Carbonic Anhydrase; Cobalt(II)- and Nickel(II)-Substituted Proteins; Copper Proteins; Field Cycling Experiments; Heme Peroxidases; Hemoglobin; Iron—Sulfur Proteins; Mitochondrial Cytochrome c; Myoglobin; Nonheme Iron Proteins; Proteases.

5 REFERENCES

1. D. C. Harris and P. Aisen, in *Physical Bioinorganic Chemistry*, ed. T. M. Loehr, VCH Publishers, New York, 1989, Vol. 2, p. 239
2. R. Sarra, R. Garratt, B. Gorinski, H. Jhoti, and P. Lindley, *Acta Crystallogr.*, 1990, **B46**, 763.
3. B. F. Anderson, H. M. Baker, G. E. Norris, D. W. Rice, and E. N. Baker, *J. Mol. Biol.*, 1989, **209**, 711.
4. R. C. Woodworth, K. G. Morallee, and R. J. P. Williams, *Biochemistry*, 1970, **9**, 839.
5. B. M. Alsaadi, R. J. P. Williams, and R. C. Woodworth, *J. Inorg. Biochem.*, 1981, **15**, 1.
6. A. A. Valcour and R. C. Woodworth, *Biochemistry*, 1987, **26**, 3120.
7. R. C. Woodworth, N. D. Butcher, S. A. Brown, and A. Brown Mason, *Biochemistry*, 1987, **26**, 3115.
8. I. Bertini, C. Luchinat, L. Messori, R. Monnanni, and A. Scozzafava, *J. Biol. Chem.*, 1986, **261**, 1139.
9. L. Messori and M. Piccioli, *Inorg. Chim. Acta*, 1990, **174**, 137.
10. I. Bertini and C. Luchinat, *NMR of Paramagnetic Molecules in Biological Systems*, Benjamin/Cummings, Menlo Park, CA, 1986.
11. M. Sola, *Inorg. Chem.*, 1990, **29**, 1113.
12. J. M. Aramini, P. H. Krygsman, and H. J. Vogel, *Biochemistry*, 1994, **33**, 3304.
13. A. Wishnia, *J. Chem. Phys.*, 1960, **32**, 871.
14. P. Aisen, A. Leibman, and H. A. Reich, *J. Biol. Chem.*, 1966, **241**, 1666.
15. S. H. Koenig and W. E. Schillinger, *J. Biol. Chem.*, 1969, **244**, 3283.
16. S. H. Koenig and W. E. Schillinger, *J. Biol. Chem.*, 1969, **244**, 6520.
17. B. P. Gaber, W. E. Schillinger, S. H. Koenig, and P. Aisen, *J. Biol. Chem.*, 1970, **245**, 4251.
18. I. Bertini, C. Luchinat, M. Mancini, and G. Spina, in *Magneto-Structural Correlations in Exchange-Coupled Systems*, ed. D. Gatteschi, O. Kahn, and R. D. Willet, Reidel, Dordrecht, 1985, p. 421.
19. L. Banci, I. Bertini, and C. Luchinat, *Nuclear and Electron Relaxation. The Magnetic Nucleus–Unpaired Electron Coupling in Solution*, VCH, Weinheim, 1991.
20. I. Bertini, F. Briganti, S. H. Koenig, and C. Luchinat, *Biochemistry*, 1985, **24**, 6287.
21. P. B. O'Hara and S. H. Koenig, *Biochemistry*, 1986, **25**, 1445.
22. I. Bertini, O. Galas, C. Luchinat, L. Messori, and G. Parigi, *J. Phys. Chem.*, in press.
23. S. H. Koenig and R. D. Brown, III, in *The Coordination Chemistry of Metalloenzymes*, ed. I. Bertini, R. S. Drago and C. Luchinat, Reidel, Dordrecht, 1983, p. 19.
24. I. Bertini, C. Luchinat, M. Mancini, and G. Spina, *J. Magn. Reson.*, 1984, **59**, 213.
25. I. Bertini, C. Luchinat, R. D. Brown, III, and S. H. Koenig, *J. Am. Chem. Soc.*, 1989, **111**, 3532.
26. D. C. Harris, G. A. Gray, and P. Aisen, *J. Biol. Chem.*, 1974, **249**, 5261.
27. J. A. Zweier, J. B. Wooten, and J. S. Cohen, *Biochemistry*, 1981, **20**, 3505.
28. R. C. Woodworth, *J. Inorg. Biochem.*, 1986, **28**, 245.
29. I. Bertini, C. Luchinat, L. Messori, A. Scozzafava, G. C. Pellacani, and M. Sola, *Inorg. Chem.*, 1986, **25**, 1782.
30. J. M. Aramini and H. J. Vogel, *J. Am. Chem. Soc.*, 1993, **115**, 245.
31. G. W. Bates and M. R. Schlabach, *J. Biol. Chem.*, 1975, **250**, 2177.
32. M. Sola, *Eur. J. Biochem.*, 1990, **194**, 349.
33. G. Battistuzzi and M. Sola, *Biochim. Biophys. Acta*, 1992, **1118**, 313.
34. I. Bertini, L. Messori, G. C. Pellacani, and M. Sola, *Inorg. Chem.*, 1988, **27**, 761.
35. M. S. Shongwe, C. A. Smith, E. W. Ainscough, H. M. Baker, A. M. Brodie, and E. N. Baker, *Biochemistry*, 1992, **31**, 4451.
36. J. M. Aramini, M. W. Germann, and H. J. Vogel, *J. Am. Chem. Soc.*, 1993, **115**, 9750.
37. J. M. Aramini and H. J. Vogel, *Bull. Magn. Reson.*, 1993, **15**, 84.
38. J. M. Aramini and H. J. Vogel, *J. Am. Chem. Soc.*, 1994, **116**, 1988.
39. A. Butler and H. Eckert, *J. Am. Chem. Soc.*, 1989, **111**, 2802.
40. A. Butler and M. J. Danzitz, *J. Am. Chem. Soc.*, 1987, **109**, 1864.
41. P. Aisen, A. Leibman, and J. Zweier, *J. Biol. Chem.*, 1978, **253**, 1930.
42. L. Messori and M. Piccioli, *J. Inorg. Biochem.*, 1991, **42**, 185
43. I. Bertini, C. Luchinat, and L. Messori, *J. Am. Chem. Soc.*, 1983, **105**, 1347.
44. M. Sola, *Chemtracts—Inorg. Chem.*, 1993, **5**, 201.
45. G. Kubal, A. B. Mason, S. U. Patel, P. J. Sadler, and R. C. Woodworth, *Biochemistry*, 1993, **32**, 3387.
46. G. Kubal, A. B. Mason, P. J. Sadler, A. Tucker, and R. C. Woodworth, *Biochem. J.*, 1992, **285**, 711.
47. G. Kubal and P. J. Sadler, *J. Am. Chem. Soc.*, 1992, **114**, 1117.
48. N. D. Chasteen, *Adv. Inorg. Biochem.*, 1983, **5**, 201.
49. N. D. Chasteen, J. K. Grady, and C. E. Holloway, *Inorg. Chem.*, 1986, **25**, 2754.
50. S. W. Homans, R. A. Dwek, D. L. Fernandes, and T. W. Rademacher, *Biochim. Biophys. Acta*, 1983, **760**, 256.
51. H. Van Halbeek, L. Dorland, J. F. G. Vliegenthart, G. Spik, A. Cheron, and J. Montreuil, *Biochim. Biophys. Acta*, 1981, **675**, 293.
52. L. Dorland, J. Haverkamp, J. F. G. Vliegenthart, G. Spik, B. Fournet, and J. Montreuil, *Eur. J. Biochem.*, 1979, **100**, 569.
53. L. Dorland, J. Haverkamp, B. L. Schut, J. F. G. Vliegenthart, G. Spik, G. Strecker, B. Fournet, and J. Montreuil, *FEBS Lett.*, 1977, **77**, 15.
54. W. Kiang, P. J. Sadler, and D. G. Reid, *Magn. Reson. Chem.*, 1993, **31**, 5110.

Biographical Sketches

Claudio Luchinat. *b* 1952. Doctor in Chemistry, 1976, University of Florence. Introduced to NMR by I. Bertini. Faculty positions at University of Florence, 1981–86. Professor of Chemistry, University of Bologna, 1986–present. More than 200 publications and two books. Research interests: NMR of paramagnetic species, theory of electron

and nuclear relaxation, biological applications of NMR, bioinorganic, biophysical and environmental chemistry.

Marco Sola. *b* 1957. B.S., 1984, University of Modena, Ph.D., 1987, University of Parma. Introduced to NMR by I. Bertini and C. Luchinat. Faculty in Chemistry, University of Modena, 1990–92. Associate Professor of Chemistry, University of Basilicata, 1992–1994. University of Bologna, 1994–present. More than 60 publications. Research interests: NMR of hydrolytic enzymes and metalloproteins involved in metal transport and electron transport, and NMR of model complexes.

Zinc Fingers

Michael F. Summers

University of Maryland, Baltimore County, Baltimore, MD, USA

1	Introduction	1
2	NH···S Hydrogen Bonding as a Determinant of Stability in Miniglobular Zinc-Containing Nucleic Acid Interactive Domains (NAIDs)	1
3	Classical **CCHH** Zinc Fingers	3
4	Retroviral **CCHC** Zinc Fingers	4
5	Steroid Hormone Receptor DNA-Binding Domains	4
6	GAL-4 DNA-Binding Domain	4
7	GATAa-1 DNA-Binding Domain	5
8	Met-tRNA Synthetase	5
9	Transcription Elongation Factor (TFIIS)	6
10	DNA Methyl Phosphotriester Repair Domain of Ada	6
11	RING Finger	6
12	LIM Motif	6
13	Summary	7
14	Related Articles	7
15	References	7

1 INTRODUCTION

The discovery in 1985 of 'zinc-binding fingers' in transcription factor IIIA from *Xenopus* oocytes[1,2] stimulated the development of a new field in bioinorganic chemistry that ultimately led to the identification of several novel classes of zinc-containing nucleic acid interactive protein domains (NAIDs). The term 'zinc finger' has been generally used to describe any miniglobular zinc-containing protein domain that functions in nucleic acid interactive processes. The 'classical **CCHH**' zinc finger[1,2] consists of a stretch of amino acids of the type: **C**-X_{2-5}-**C**-X_{12}-**H**-X_{2-4}-**H** (**CCHH**). Other zinc-containing NAIDs are often referred to as 'nonclassical zinc fingers'. Examples of such nonclassical zinc finger domains that have been studied by NMR include

1. the **CCHC** type (**C**-X_2-**C**-X_4-**H**-X_4-**C**), observed originally in retroviral nucleocapsid proteins but more recently found in proteins from other organisms, including frogs and humans;[3–5]
2. the cysteine-rich DNA-binding domain of GAL-4 (**C**-X_2-**C**-X_6-**C**-X_6-**C**-X_2-**C**-X_6-**C**),[6] which coordinates two atoms of zinc in a binuclear cluster that contains two bridging cysteines;
3. the steroid hormone receptor (SHR) family of DNA binding domains (DBDs),[7] in which two zinc atoms are bound via cysteines in two structurally nonequivalent but interacting **CCCC** modules of the type, **C**-X_2-**C**-X_{13}-**C**-X_2-**C** and **C**-X_5-**C**-X_9-**C**-X_2-**C**;
4. the DNA-binding domain of GATA-1, which binds zinc via a **C**-X_2-**C**-X_{17}-**C**-X_2-**C** sequence;[8]
5. the RING motif, which binds two atoms of zinc in independent sites via a **C**-X_2-**C**-X_{12}-**C**-X-**H**-X_2-**C**-X_2-**C**-X_{10}-**C**-X_2-**C** (or $\mathbf{C_3HC_4}$) sequence;[9]
6. the LIM motif, which also binds two equivalents of zinc in independent sites via a **C**-X_2-**C**-X_{16-23}-**H**-X_2-**C**-X_2-**C**-X_2-**C**-X_{16-21}-**C**-X_{2-3}-**C/H/D** ($\mathbf{C_2HC_5}$) sequence;[10,11]
7. the zinc ribbon motif observed in transcription elongation factor TFIIS that binds one atom of zinc in a **C**-X_2-**C**-X_{25}-**C**-X_2-**C** sequence;[12]
8. the zinc-containing domain of the tRNA synthetases;[13,14]
9. the zinc site of bacteriophage T4 gene-32 protein;[15,16]
10. the protein kinase C (PKC) zinc-binding domain;.[101]
11. the DNA methyl phosphotriester repair domain of Ada.[82]

Nuclear magnetic resonance spectroscopy has played a major role in advancing understanding of the structure and function of zinc-containing nucleic acid interactive domains. Indeed, the first structures of each class of zinc finger domain were determined originally by NMR methods, except for **GAL-4**, where the NMR[17,18] and X-ray structures[19] were reported simultaneously. Currently, there are at least 12 independent NMR structures reported for **CCHH** zinc finger domains,[20–25] six NMR structures of **CCHC** zinc finger domains and **CCHC**-containing proteins,[26–30,102] three NMR structures of the GAL-4-type DNA-binding domain,[17,18,103] and five NMR structures reported for steroid hormone receptor DNA-binding domains.[31–35] The structure of a **CCHC** zinc finger–nucleic acid complex has also been determined by NMR.[36] More recently, structures have been determined for the DNA-binding domain of GATA-1[8] and for the RING,[9] PKC,[101] Ada,[82] and LIM[37] zinc-binding domains by NMR methodologies. In addition, X-ray structures have been reported for DNA complexes with the **CCHH**-containing DNA-binding domains of the transcription factors Zif-286[38] and GLI[39] and with the DNA-binding domains of the GAL-4[19] and glucocorticoid receptor proteins.[40] In each of these domains, the essential zinc atoms do not participate directly in binding to nucleic acid, but rather function to stabilize a particular globular fold that allows amino acid side chains to make specific contacts with the nucleic acid.

The availability of structural data for a diverse class of zinc-containing NAIDs has enabled philosophical and experimental approaches to the question: why zinc fingers? Although current knowledge is not sufficient to address this question fully, one fact has become apparent; namely, all classes of Zn-NAIDs exist as highly stable, independently folded domains, despite the fact that the domains comprise a relatively small number of amino acid residues. Indeed, the **CCHC** retroviral-type motif comprises only 18 amino acid residues, and may represent the smallest known miniglobular protein domain. The 'zinc finger' motif thus appears to be Nature's choice for establishing stable, folded, miniglobular protein domains comprising a minimal number of amino acid residues. This prompts the following question: Why are zinc finger domains so stable?

By examination of the structures determined thus far for the different classes of Zn-NAIDs, common structural elements can be identified that may serve as the primary determinants of stability.[41–43] Specifically, all known Zn-NAIDS exhibit extensive hydrogen bonding between backbone amide protons and the cysteine sulfur atoms that are coordinated to zinc. NH···S hydrogen bonding was observed originally by Adman and co-workers[44] in the iron-binding domains of rubredoxins and ferredoxins, and, perhaps surprisingly, many of the structural elements observed originally in the iron domains of the iron–sulfur proteins are also observed in the zinc sites of the Zn-NAIDs.

2 NH···S HYDROGEN BONDING AS A DETERMINANT OF STABILITY IN MINIGLOBULAR ZINC-CONTAINING NUCLEIC ACID INTERACTIVE DOMAINS (NAIDs)

As indicated above, all of the known Zn-NAIDs that have been structurally characterized thus far contain NH···S hydrogen bonds between specific backbone amide protons and Zn-coordinated cysteine sulfurs. The local structural elements observed are often very similar to those observed in the iron-binding domain of rubredoxin (Rd). All rubredoxins contain two copies of a conserved iron-binding sequence, $X_{(i-2)}$-$X_{(i-1)}$-**C**$_{(i)}$-$X_{(i+1)}$-$X_{(i+2)}$-**C**$_{(i+3)}$-**G**$_{(i+4)}$-$X_{(i+5)}$ (where X is a variable amino acid), and high-resolution X-ray and NMR structures of proteins from *Clostridium pasteurianum*, *Desulfovibrio gigas*, *D. vulgaris*, *D. desulfuricans*, and *Pyrococcus furiosus*, reveal that the four Cys residues are coordinated to the single iron atom. The backbone conformations of the N- and C-terminal X-X-**C**-X-X-**C**-**G**-X-X-X residues are essentially identical. Adman and co-workers[44] discovered that three of the backbone amide protons within each of the **C**$_{(i)}$-$X_{(i+1)}$-$X_{(i+2)}$-**C**$_{(i+3)}$-**G**$_{(i+4)}$-$X_{(i+5)}$ loops are involved in amide-to-sulfur hydrogen bonding. The backbone amide protons of residues X(i + 2) and Cys(i + 3) are oriented in the direction of the Cys(i) side-chain sulfur atom, forming what are referred to as Types I and III tight turns, respectively (Figure 1). In addition, the backbone amide proton of residue X(i + 5) is oriented toward the side-chain sulfur atom of Cys(i + 3), forming a Type II NH···S tight turn. Rubredoxins also contain a conserved Gly residue at position (i + 4), and it was proposed that this residue is conserved in order to stabilize the Type II NH···S tight turn.[44] The glycine NH is positioned to hydrogen bond with the carbonyl of Cys(i), forming a Type II NH···O bond. Throughout this article, this conserved folding pattern (Figure 1) will be referred to as an 'Rd knuckle'.

To gain insights into the nature of the NH–S hydrogen bonding, NMR studies have been performed on Zn-, ^{113}Cd-, and ^{199}Hg-substituted rubredoxin from the extreme hyperthermophile, *Pyrococcus furiosus* (pf), a bacterium that grows optimally at 100 °C.[41,45–47] The ^{1}H–^{113}Cd heteronuclear spin echo difference (HSED) spectrum obtained for ^{113}Cd–PfRd exhibited four backbone NH signals corresponding to the Ile(7), Cys(8), Ile(40), and Cys(41) backbone NH protons, of which Ile(40) and Cys(41) are part of the metal-binding **C**XX**C**GX knuckle (**C**$_{38}$-X-I$_{40}$-**C**$_{41}$-G$_{42}$-A$_{43}$). The observed scalar couplings between ^{113}Cd and the NH protons of Ile(40) and Cys(41) do not occur through the peptide backbone, since the NH protons are eight and five bonds removed from the metal, respectively. The observed amide HSED signals are thus attributed to two-bond $^{2}J(^{113}\mathrm{Cd},^{1}\mathrm{H})$ scalar coupling mediated by NH···S(Cys) hydrogen bonds. These findings provide direct evidence that Types I and III NH···S hydrogen bonds exist in PfRd, and further demonstrate that these hydrogen bonds contain significant covalent character.

^{1}H–^{199}Hg HSED NMR experiments were also performed on the ^{199}Hg adduct to evaluate the influence of this larger metal on the nature of the NH···S hydrogen bonds.[41,47] A portion of the ^{1}H–^{199}Hg HSED spectrum is shown in Figure 2. As observed for the ^{113}Cd adduct, HSED signals were observed for the Ile(7,40) and Cys(8,41) backbone NH protons,[45] confirming the presence of the Types I and III NH···S turns. Interestingly, the magnitudes of the scalar couplings, determined using a novel pulse sequence that affords pure-phase HSED spectra,[47] were approximately twofold greater than the coupling constants determined for ^{113}Cd–PfRd. This finding confirms that the HSED signals result from scalar coupling rather than from a dipolar cross-correlation mechanism. In addition, a weak ^{1}H–^{199}Hg HSED signal [$^{2}J(^{199}\mathrm{Hg},^{1}\mathrm{H})$ = 0.4 Hz] was detected for the Tyr(10) backbone amide proton. Although a similar signal for the analogous Ala(43) amide could not be distinguished owing to signal overlap, the observation of a Tyr(10) NH HSED signal confirmed the existence of the Type II NH···S turn. Thus, for

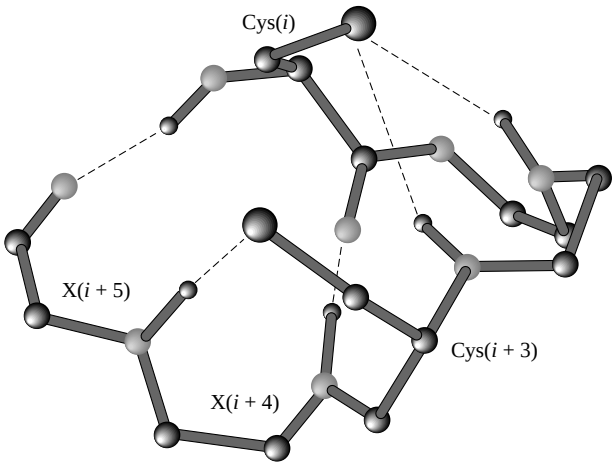

Figure 1 Structure of a 'rubredoxin knuckle' showing NH···S hydrogen bonds from the backbone amide protons of residues X(i + 2) and Cys(i + 3) to the S-γ sulfur of residue Cys(i), and from the backbone amide proton of residue X(i + 5) to the S-γ sulfur of residue Cys(i + 3). This folding pattern, which was observed originally in the iron-binding site of rubredoxin,[44,100] is commonly found in the zinc-binding sites of zinc fingers

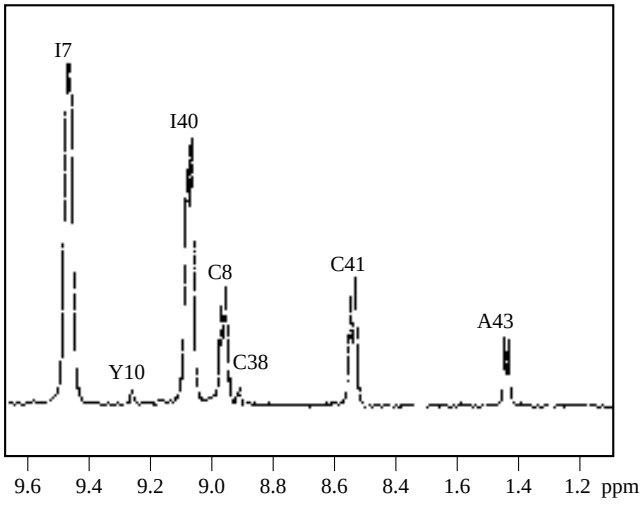

Figure 2 Portions of an ^{1}H–^{199}Hg heteronuclear spin echo difference spectrum obtained for ^{199}Hg-substituted rubredoxin from the hyperthermophile *P. furiosus*.[47] Difference signals are observed for backbone NH protons involved in Types I, II, and III NH···S hydrogen bonding, confirming the presence of these hydrogen bonds and demonstrating that these bonds contain significant covalent character

the ^{199}Hg adduct, where the magnitudes of the scalar couplings are greatest, HSED spectroscopy provided confirmation for the existence of all three types of NH···S tight turns (Figure 1).

As a side note, ^{1}H–^{113}Cd and ^{1}H–^{199}Hg scalar coupling was also observed between the metal and the Ala(43) methyl protons (Figure 2).[41,45,47] This scalar coupling is probably due to direct orbital overlap between the methyl protons of Ala(43) and the Cys(42) sulfur atom, since 6- and 11-bond ^{1}H–^{113}Cd scalar coupling mediated by the Ala(43) NH···S hydrogen bond or by the covalent bonds, respectively, is implausible. This finding has important implications for understanding intraprotein electron transfer, since (a) it suggests that 'through-space electron jumps' may be energetically more favorable than previously expected,[48–52] and (b) CH_3··S(Cys) overlap provides a direct electron transfer pathway between the metal center and the hydrophobic core of the protein.

3 CLASSICAL CCHH ZINC FINGERS

To date, more than a dozen classical **CCHH** zinc finger domains have been structurally characterized by NMR and X-ray crystallographic methods.[20–25] Except for a few cases, the experimentally derived **CCHH** zinc finger structures are consistent with a structure predicted on the basis of sequence comparisons with other metalloproteins, including rubredoxin.[53] Klevit and co-workers[54] were the first to provide experimental NMR evidence in support of the predicted model, and shortly thereafter, atomic coordinates for a peptide with sequence of the 31st zinc finger of the *Xenopus* protein, Xfin, were published by Wright and co-workers.[20]

The **CCHH** zinc finger consists of a three-turn helix and a short antiparallel β-sheet. The strands of the β-sheet are linked by the **C**XX**C**XX metal-binding turn. The **C**XX**C**XX turns for five representative **CCHH** zinc finger structures are shown in Figure 3. For comparison, relevant residues of the N-terminal **C**XX**C**XX turn of *C. pasteurianum* Rd, and the associated NH···S and NH···O hydrogen bonds, are included in this figure. These residues within zinc fingers Xfin-31, ADR-1 and Zif286-2,3 are folded in a manner similar to the folding of analogous residues in rubredoxins. All of these structures exhibit the Types I and III NH···S hydrogen bonding found in rubredoxins. However, only the zinc fingers of ADR1b and Zif-268 exhibit the Type II NH···S turn after the second Cys. The $\mathbf{C}_{(i+3)}$-X-X residues of the Xfin-31 structure were disordered, precluding classification of the potential NH···S hydrogen bonding for the X(i + 5) amide proton.

The **C**XX**C**XX loops of the Zif-268 and ADR-1 zinc fingers contain Type II NH···S turns after the second cysteine, whereas finger-3 of Zif-268 contains a Gly residue at position (i + 4). Finger-2 of Zif-268 and the ADR-1 zinc finger contain Met and Thr residues, respectively, at position (i + 4). Type II folding results in a positive ϕ value for the residue at position X(i + 4), and, as such, it was proposed early on that Type II NH···S folding should be stabilized by a glycine residue at position X(i + 4). This provided a rationale for the conservation of glycine residues at position X(i + 4) in the **C**XX**C**XX loops of all known rubredoxins.[55] As shown in Figure 1, Type II NH···S folding leads to hydrogen bonds between the X(i + 4) amide proton and the Cys(i) carbonyl and between the X(i + 5) amide proton and the Cys(i + 3) sulfur. Thus, the unfavorable steric interactions associated with the positive ϕ value may be offset by the additional hydrogen bond formed between the X(i + 4) amide and the Cys(i) carbonyl.[44] A positive ϕ value has also been observed for the Type II NH···S turn of residues **C**-A-G in the iron site of ferredoxin, where the Ala methyl group eclipses the Cys carbonyl.[44]

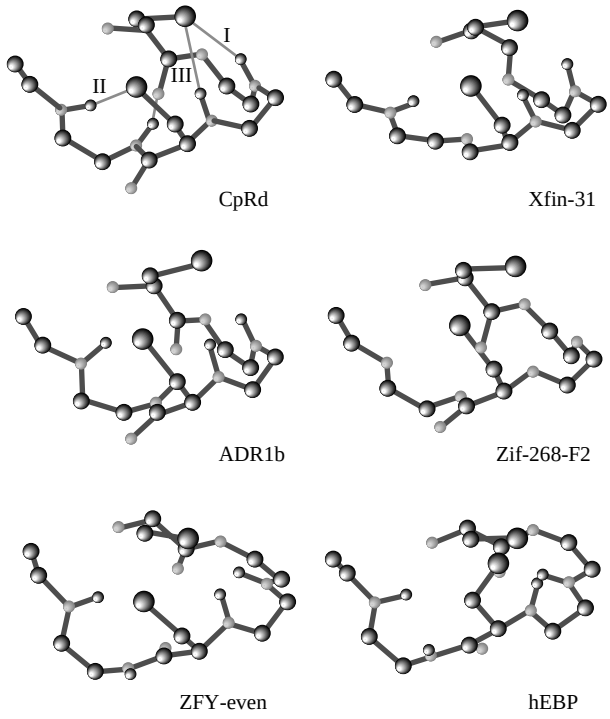

Figure 3 Comparison of the folding of the **C**XX**C**XX residues of representative classical-type **CCHH** zinc fingers with related residues of rubredoxin.[100] The folding of these residues in the Xfin-31,[20] ADR1b,[25] and Zif-268-2[38] zinc fingers is essentially identical to that observed in the X-ray structure of *C. pasteurianum* Rd. The ZFY-even finger domain[22–24] is similar, except that residues $\mathbf{C}_{(i+3)}$-$X_{(i+4)}$-$X_{(i+5)}$ form a Type I NH···S turn. The zinc fingers of the human enhancer DNA-binding domain[21] are unusual in that (i) the χ_1 value of the Cys(i + 3) residue precludes the formation of an NH···S hydrogen bond between the amide proton of X(i + 5) and the Cys(i + 3) sulfur, and (ii) the amide proton of X(i + 2) does not appear to form a hydrogen bond to the Cys(i) sulfur

The amide proton of the X(i + 5) residue of the ZFY-even finger and an even finger mutant are directed toward the β-carbon of the Cys(i) residue and not toward the sulfur atoms of residue Cys(i + 3).[22–24] In addition, the Cys(i + 3)-to-X(i + 4) peptide bond is oriented in a manner that would preclude hydrogen bonding to the Cys(i) carbonyl (Figure 3). Thus, although the folding observed for residues **C**-X-X-**C** of the ZFY-even finger domains are consistent with the rubredoxin fold, the conformation of the $\mathbf{C}_{(i+3)}$-X-X residues differs from that observed in rubredoxins. The folding observed for the zinc finger domains of the human enhancer protein DNA-binding domain (hEBP)[21,56] are unusual in that the side-chain orientation of the Cys(i + 3) residues precludes formation of a Type II NH···S turn, and amide orientations are generally inconsistent with NH···S hydrogen bonding.

In summary, with the exception of the human enhancer protein DNA binding domain, all of the classical **CCHH** zinc

finger structures exhibit Types I and III NH···S hydrogen bonds within the **C**-X-X-**C** knuckles. In addition, all **CCHH** zinc fingers except those of the hEBP and ZFY-even zinc finger domains exhibit an NH···S hydrogen bond from the X(i + 5) backbone amide to the Cys(i + 3) sulfur, forming either a Type I or II NH···S turn.

4 RETROVIRAL CCHC ZINC FINGERS

Retroviral genes encode a gag precursor polyprotein that functions in the recognition of viral RNA and in the assembly of virus particles.[57,58] Subsequent to assembly and budding, the gag polyproteins are cleaved by the viral protease to smaller proteins, including the nucleocapsid (NC) proteins. In 1981, Henderson and co-workers[5] at the Frederick Cancer Research and Development Center showed that retroviral gag and NC proteins contain at least one copy of an invariant amino acid sequence, **C**-X_2-**C**-X_4-**H**-X_4-**C**. This conserved sequence has recently been found in proteins ranging from plant viruses to frogs to humans, and thus may represent a common motif for binding single stranded nucleic acids.[59] For example, a nine tandem repeat of the conserved sequence is found in a protein encoded by the *Leishmania major* gene of the protozoan parasite *Leishmania*;[60] a seven-tandem repeat is found in human cellular nucleic acid binding protein (hCNBP) that binds to the sterol regulatory element;[61] and a single motif is present in a protein encoded by the *Xenopus-Posterior* (*Xpo*) gene of frog embryos.[62]

NMR structures have been determined for peptides with sequences of several **CCHC** zinc finger domains, as well as for the intact NC protein from HIV-1.[27–30,63] Like TFIIIA, overall folding of the NC protein consists of the independent **CCHC** zinc finger domains separated by a labile linker region. The global folding **CCHC** Zn-NAIDs consists of a short antiparallel β-sheet with an Rd knuckle, followed by a short β-like stretch that precedes a 3_{10} helix. Like **CCHH** zinc fingers and rubredoxin, the metal binding site of **CCHC** NAIDs fold with a number of NH···S hydrogen bonds, including a hydrogen bond between the side-chain NH of Asn(i + 2) and the Cys(i + 3) sulfur, and between the backbone NH protein of residue X(i + 15) and the Cys(i + 13) sulfur. In addition to these five NH···S hydrogen bonds, there are a total of six NH···O hydrogen bonds that further stabilize the **CCHC** zinc finger structure.[42]

5 STEROID HORMONE RECEPTOR DNA-BINDING DOMAINS

The steroid hormone receptor (SHR) superfamily is a class of transcription regulatory proteins whose activity is controlled by the binding of specific hormones. This class so far comprises more than a dozen proteins, including the glucocorticoid receptor, retinoic acid receptor β, progesterone receptor, estrogen receptor, and retinoid X receptor-α proteins. Typically, members of the SHR family bind as dimers to specific DNA hormone response elements (HREs),[64] forming a hormone–receptor complex that activates transcription.[65] To date, three-dimensional structures have been determined by NMR for five steroid hormone receptor DNA-binding domains,[31–35] and an X-ray structure of a DNA complex with the glucocorticoid receptor DNA binding domain has been reported.[40]

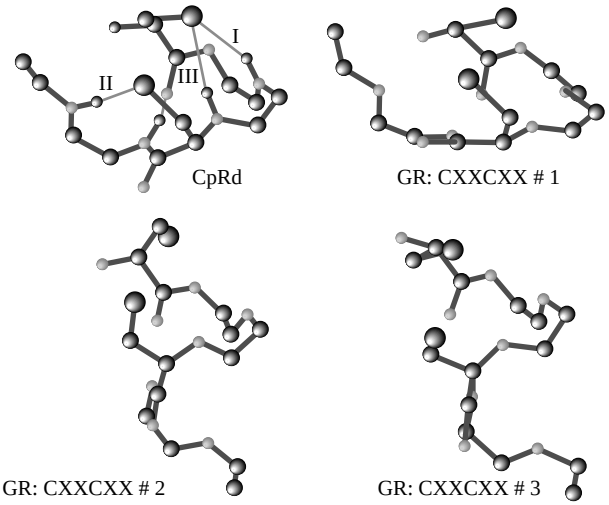

Figure 4 Comparison of the folding of the **C**XX**C**XX residues of the glucocorticoid receptor DNA-binding domain with related residues of *C. pasteurianum* Rd.[100] The GR protein contains three **C**XX**C**XX arrays. The folding of the N-terminal array (GR: CXXCXX # 1) is very similar to that observed in rubredoxins. The remaining arrays contain Types I and III NH···S turns within the **C**XX**C** knuckles common to rubredoxins; however, the $\mathbf{C}_{(i+3)}$-X-X residues do not form an NH···S turn, because of their involvement in α-helical conformations. Interestingly, the amide proton of residue X(i + 4) participates in a hydrogen bond to the Cys(i) carbonyl—an interaction that also occurs in rubredoxins

The steroid hormone receptor (SHR) DNA-binding domains contain two independent zinc sites, with each of the zinc atoms coordinated via four cysteine residues. Unlike classical **CCHH** zinc fingers, the two zinc atoms are incorporated into a single domain, with several contacts between residues that comprise the independent zinc sites. The N-terminal zinc coordination site of the SHR proteins contains two **C**XX**C** arrays, and the C-terminal zinc site contains one **C**XX**C** array. Luisi et al.[40] indicated that several backbone amide protons are involved in NH···S hydrogen bonding to the metal-coordinating sulfurs. Comparison of the three **C**XX**C** segments reveals a variation in χ_1 values of the cysteine side chains, with only the N-terminal knuckle exhibiting a Cys(i) side-chain orientation similar to that of rubredoxins (Figure 4). The backbone folding within each of the **C**XX**C** knuckles is generally consistent with the folding observed in rubredoxins, with backbone amide protons participating in Types I and III NH···S hydrogen bonding. The $\mathbf{C}_{(i+3)}$-X-X residues of the N-terminal **C**XX**C** knuckle form a Type II NH···S turn, with the X(i + 4) amide forming a hydrogen bond to the Cys(i) backbone carbonyl. The $\mathbf{C}_{(i+3)}$-X-X residues of the two subsequent **C**XX**C** segments do not form NH···S turns, owing to the fact that these residues reside within an α-helix (Figure 4). To summarize, the N-terminal **C**XX**C**XX array forms an Rd knuckle with Types I, II, and III NH···S turns, and the two subsequent arrays are similar in that they contain the Types I and III NH···S turns within the **C**XX**C** segment, but differ in that (i) the χ values of the Cys(i + 3) side chains are significantly different, and (ii) the $\mathbf{C}_{(i+3)}$-X-X residues do not form an NH···S turn.

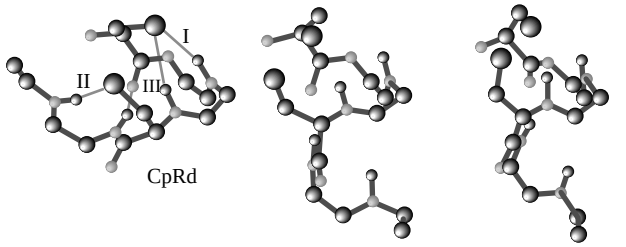

Figure 5 Comparison of the folding of the **C**XX**C**XX residues of the GAL-4 DNA-binding domain with related residues in *C. pasteurianum* Rd.[100] The folding of these residues is actually very similar to that observed for the two N-terminal **C**XX**C**XX stretches in the glucocorticoid receptor DNA-binding domain (see Figure 4)

6 GAL-4 DNA-BINDING DOMAIN

GAL-4 is a yeast transcription activator that binds to an upstream activating sequence (UAS_G) for the genes (*GAL-1* and *GAL-10*) encoding galactose-metabolizing enzymes.[19] The 881-amino-acid residue GAL-4 protein binds as a dimer to the UAS_G-DNA site.[66] In the absence of galactose, GAL-4 remains on the DNA, but is inactivated by a complex formed with another protein, GAL-80.[67,68] In the presence of galactose, a metabolite derived from galactose binds to and dissociates GAL-80, thus activating GAL-4.[66] The DNA-binding domain of GAL-4 is a 62-amino-acid sequence located on the N-terminus of the protein.[17] This sequence contains a cysteine-rich array, **C**-X_2-**C**-X_6-**C**-X_6-**C**-X_2-**C**-X_6-**C**, which is conserved among 13 known fungal transcription factors.[17] Unlike other Zn-NAIDs, the two zinc atoms of GAL-4 form a binuclear cluster that contains two bridging cysteines.[17,69]

Structures of the GAL-4 NAIDs have been determined by NMR.[17,18] and X-ray crystallographic[19] methods. The GAL-4 DBD contains two helix−turn−strand motifs that are packed around the $Zn(II)_2Cys_6$ binuclear cluster.[17] The structure has a twofold pseudosymmetry axis that passes between the two helices and the center of the $Zn(II)_2Cys_6$ binuclear cluster. The GAL-4 zinc-binding domain contains two **C**XX**C** arrays that participate in metal coordination. Both the N- and C-terminal **C**XX**C** arrays exhibit backbone folding that is generally consistent with the folding observed in rubredoxins. Amide protons of residues X(i + 2) and Cys(i + 3) are oriented in a manner consistent with Types I and III NH$\cdots$S hydrogen bonding to the Cys(i) sulfur (Figure 5). However, the χ_1 values of the Cys side chains differ from those of Rd by almost 180°. The $\mathbf{C}_{(i+3)}$-X-X residues comprise the N-terminal portions of α-helical stretches, and the associated backbone conformations preclude the formation of Type II NH$\cdots$S turns. The folding of these residues is similar to that observed for analogous residues in the steroid hormone receptor proteins where an α-helical conformation exists (Figure 4).

7 GATAa-1 DNA-BINDING DOMAIN

The DNA-binding domain of the transcription factor GATA-1 contains two conserved zinc binding sequences of the form **C**-X_2-**C**-X_{17}-**C**-X_2-**C**. Mutational studies indicated that the N-terminal motif may be unimportant for specific DNA binding,[70,71] although more recent studies indicate that sequence specificity is a function of both domains.[72]

The solution structure of the C-terminal GATA-DBD (residues 158−223) was determined recently by NMR methods.[8] The global folding of the peptide consists of a core (residues 2−51) that contains the zinc binding region, and an extended C-terminal tail (residues 52−59).[8] The folding of the majority of the core (residues 3−39) is very similar to the folding exhibited by the N-terminal **CCCC** zinc module of glucocorticoid receptor protein.[8] Interestingly, both the GATA-1 domain and the N-terminal **CCCC** module of GR participate directly in protein−nucleic acid interactions.

The N-terminal **C**XX**C**XX array of GATA-1 forms a classical Rd knuckle that contains Types I, II, and III NH$\cdots$S turns. The Type II turn is present despite the fact that the array lacks a Gly residue at position X(i + 4). In addition, the backbone NH of residue Cys(i + 21) forms a hydrogen bond to the Cys(i) sulfur, and the sulfur of Cys(i + 21) accepts a hydrogen bond from the backbone amide proton of Cys(i + 24).

8 MET-tRNA SYNTHETASE

Aminoacyl-tRNA synthetases are responsible for the correct esterification of tRNAs with the corresponding amino acid during protein translation.[73] A number of aminoacyl-tRNA synthetases have been analyzed and shown to display a zinc finger domain of the type **C**-X_2-**C**-X_9-**C**-X_2-**C**.[74] Among these enzymes are the methionyl-tRNA (met-tRNA), alanyl-tRNA, and isoleucyl-tRNA synthetases, all of which have been shown to contain zinc.[75−77] On the other hand, tyrosyl- and phenylalanyl-tRNA synthetases, which do not contain zinc finger domains, apparently do not contain zinc.[78]

Dardel and co-workers[73] have recently determined the three-dimensional structure of a peptide corresponding to the zinc coordination site of met-tRNA synthetase by NMR methods. The structure differs significantly from that determined by X-ray crystallography for the intact protein. The zinc binding site is located within residues 138−163 of the protein, and contains a single zinc atom coordinated via four cysteine residues. Unlike other Zn-NAIDs, the zinc binding region of met-tRNA synthetase does not contain any distinguishable helices or extended β-sheet structure. Instead, the domain contains a series of four consecutive tight turns separated by short loops. Turns 2 and 4 form Rd knuckles. Superposition of the backbone and Cys side-chain atoms of the X**C**XX**C**X residues of the met-tRNA synthetase metallopeptide with analogous residues of *C. pasteurianum* Rd and Zn(HIV-1−F1) afforded RMSD values of 65−90 pm.[73] The backbone amide protons of residues X(i + 2) and Cys(i + 3) are oriented in a manner consistent with Types I and III NH$\cdots$S hydrogen bonding. The N- and C-terminal Rd knuckles contain Gly and Lys residues, respectively, at position (i + 4). As expected, the backbone amide of residue X(i + 5) from the **C**XX**C**GX array forms a hydrogen bond to the Cys(i + 3) sulfur, with the backbone amide proton of Gly(i + 4) forming a hydrogen bond to the Cys(i) carbonyl. Thus, the $\mathbf{C}_{(i+3)}$-$G_{(i+4)}$-$X_{(i+5)}$ residues exist in a Type II NH$\cdots$S turn common to rubredoxins.

The backbone amide proton of the X(i + 5) residue from the N-terminal **C**XX**C**XX array also appears to form a hydrogen bond with the Cys(i + 3) sulfur. In addition, the backbone

amide proton of the lysine at position (i + 4) is oriented in the general direction of the Cys(i) backbone carbonyl. As such, the lysine at position (i + 4) possesses a positive ϕ value characteristic of Type II NH$\cdots$S tight turns. Thus, as observed in the zinc finger of Zif-268-F2 and ADR1b, the presence of a nonglycine residue at position X(i + 4) does not preclude the formation of a Type II NH$\cdots$S turn.

9 TRANSCRIPTION ELONGATION FACTOR (TFIIS)

Transcription elongation factor TFIIS is a protein that binds to the large subunit of RNA polymerase II in a paused elongation complex, and allows elongation through DNA pause and termination sites. It also facilitates transcription of sites blocked by sequence-specific DNA-binding proteins.[79] The 50-amino-acid zinc binding domain contains a **C**-X_2-**C**-X_{25}-**C**-X_2-**C** motif. The structure of a peptide with sequence of the TFIIS zinc binding site (residues 235–280) was determined recently by NMR methods.[80] Unlike other Zn-DBDs, the domain does not contain α-helical structure, but consists of a three-stranded antiparallel β-sheet. Two of the sheets are located between the **C**(15)-X_{25}-**C**(40) region, while the third exists after the second **C**(40)-X_2-**C**(43) array. TFIIS also contains three β-turns (residues 14–16, 30–32, and 42–44) two of which contain the zinc-binding cysteines.[80] The zinc atom is chelated via two Rd knuckles, both of which contain Types I, II, and III NH$\cdots$S turns [residues $\mathbf{C}_{(12)}$-X_2-$\mathbf{C}_{(15)}$-X-X and $\mathbf{C}_{(40)}$-X_2-$\mathbf{C}_{(43)}$-**G**-Asp(45)]. The N-terminal Rd knuckle contains a Type II NH$\cdots$S turn, even though the sequence lacks a glycine at residue 16.

10 DNA METHYL PHOSPHOTRIESTER REPAIR DOMAIN OF ADA

The Ada protein from *Escherichia coli* repairs methylated DNA by direct, irreversible transfer of a phosphotriester methyl group to a cysteine residue. The nucleophilic activity of the cysteine sulfur appears to be promoted by coordination to zinc.[81] Upon methylation, Ada binds specifically to DNA genes that confer resistance to methylating agents. The structure of an N-terminal 10 kDa fragment of Ada was determined by NMR methods.[82] This fragment, which retains DNA methyl phosphotriester repair activity, contains a single atom of zinc and exhibits a folding pattern that is unique by comparison with other known zinc finger domains. The structure consists of a three-stranded antiparallel β-sheet sandwiched between two α-helices. The atom of zinc is bound tetrahedrally by four cysteines, including the active-site Cys(69). Interestingly, no evidence was found for the presence of NH$\cdots$S hydrogen bonds. Thus, the backbone NH protons of residues near the sulfur atoms exhibited disorder and/or NH$\cdots$S distances incompatible with NH$\cdots$S hydrogen bonding, and none of these protons exhibited slow chemical exchange with water protons. Such hydrogen bonding might be expected to decrease the negative charge density on the cysteine sulfurs and render the active-site cysteine a poorer nucleophile.[82] It will be very interesting to determine if the methylated form of the protein contains NH$\cdots$S hydrogen bonds, since it is this form that exhibits sequence-specific DNA-binding properties.

11 RING FINGER

Over the past several years, more than 40 proteins have been identified from organisms including plants, fungi, viruses, and vertebrates that contain a '$\mathbf{C_3HC_4}$' or '**RING** finger' motif (**C**-X_2-**C**-X_{12}-**C**-X-**H**-X_2-**C**-X_2-**C**-X_{10}-**C**-X_2-**C**).[83,84] Proteins that contain a $\mathbf{C_3HC_4}$ motif are involved in numerous processes, including transcription, site-specific recombination, differentiation, and oncogenesis.[85]

The three-dimensional solution structure of a peptide of the sequence encompassing the $\mathbf{C_3HC_4}$ domain from a herpes virus protein was recently solved by Barlow and co-workers.[86] The two zinc atoms are bound in separate sites, with Cys(8) and (11) and Cys(29) and (32) coordinating to one zinc, and Cys(29), (43), (46) and His(26) coordinating to the second zinc atom. The peptide binds two zinc atoms and adopts a $\beta\beta\alpha\beta$ structure. Barlow and co-workers showed that the amphipathic α-helix is essential for *trans*- activation of gene expression. Interestingly, the N-terminal $\beta\beta\alpha$ portion of the protein is structurally very similar to that of classical **CCHH** zinc fingers.[86] Several backbone NH protons appear to be oriented to allow NH$\cdots$S hydrogen bonding with the metal-coordinating cysteines.

12 LIM MOTIF

A number of proteins with diverse functions and subcellular distributions display from one to three copies of a cysteine- and histidine-containing sequence called the **LIM** motif (**C**-X_2-**C**-X_{16-23}-**H**-X_2-**C**-X_2-**C**-X_2-**C**-X_{16-21}-**C**-X_{2-3}-**C**/**H**/**D**). This motif was first identified in three developmentally regulated transcription factors, *C. elegans* Lin-11, rat Isl-1, and *C. elegans* Mec-3.[10,11] Each of these gene products exhibits two copies of the **LIM** motif plus a DNA-binding homeodomain and potential transcriptional activation domains.[10,11] In addition to a growing collection of LIM homeodomain proteins,[10,11,87–90] the **LIM** motif is also found in a number of proteins that lack additional DNA-binding sequences.[91–96] For example, a cytoskeletal cysteine-rich protein (CRP) that has been implicated in cell growth control and differentiation contains two LIM domains as predominant sequence elements.[95,97,98] CRP interacts with another LIM protein called zyxin, which is co-localized with CRP in association with the actin cytoskeleton, particularly at sites of cell–substratum adhesion.[93,95] It has been postulated that zyxin and CRP may mediate communication between the cell membrane and the nucleus.[93]

The $\mathbf{C_2HC_5}$ LIM domain comprises tightly packed **CCHC** and **CCCC** zinc-binding modules. The folding and metal binding mode differ significantly from that of the $\mathbf{C_3HC_4}$ **RING** finger motif, which also binds two atoms of zinc via seven cysteines and a histidine residue.[9,99] The C-terminal **CCCC** module of the LIM domain folds in a manner essentially identical to that observed for the DNA-interactive **CCCC** modules of the GATA-1 and GR DBDs. Although previous biochemical studies have suggested that LIM domains may participate in protein–protein rather than protein–DNA interactions,[93] the demonstration that the LIM domain contains a substructure that is closely related to those of well-characterized DNA-binding domains raises the

possibility that the LIM domain may function in nucleic acid binding as well.

Heteronuclear spin echo difference (HSED) spectra were obtained for ^{113}Cd-substituted LIM to probe for NH$\cdots$S hydrogen bonding. Scalar coupling was observed between the backbone NH protons of residues Lys(147), Cys(148) and Lys(150) and ^{113}Cd in the **CCCC** site, and between the backbone NH proton of Arg(120) and ^{113}Cd in the CCHC site, supporting the NOE evidence that these residues form Rd knuckles. These and additional NH$\cdots$S hydrogen bonding patterns are similar to those observed in the GATA-1 DNA-binding domain.

13 SUMMARY

All of the zinc finger structures reviewed in this article contain at least one copy of a **C**XX**C** sequence at the metal binding site. As indicated above, many of these segments adopt similar backbone conformations when bound to zinc, with the NH protons of residues X(i + 2) and Cys(i + 3) oriented in a manner consistent with hydrogen bonding to the Cys(i) sulfur. In addition, many of the structures exhibit Type II NH$\cdots$S folding for the subsequent $\mathbf{C}_{(i+3)}$-$X_{(i+4)}$-$X_{(i+5)}$ residues. In fact, for most Zn-NAID structures, the folding of at least one **C**XX**C**XX segment matches that of the analogous iron-chelating residues in rubredoxins. The formation of a Type II NH$\cdots$S turn by residues $\mathbf{C}_{(i+3)}$-$X_{(i+4)}$-$X_{(i+5)}$ clearly does not depend on the presence of a Gly at position X(i + 4), even though the ϕ value for the X(i + 4) residue in a Type II NH$\cdots$S turn is positive. The NH$\cdots$O hydrogen bond between the X(i + 4) amide and the Cys(i) backbone carbonyl apparently compensates for the unfavorable steric interactions between the X(i + 4) side chain and the Cys(i + 3) carbonyl.[44] In several cases, the **C**XX**C**XX residues form a 'helix cap' at the N-terminal end of a helix. These structures still exhibit Types I and III NH$\cdots$S turns within the **C**XX**C** segment, although the conformation of the subsequent residues precludes formation of a Type II NH$\cdots$S hydrogen bond.

Heteronuclear ^{1}H–metal correlated NMR studies of ^{113}Cd- and ^{199}Hg-substituted forms of *P. furiosus* rubredoxin have provided the most detailed insights into the nature of the NH$\cdots$S hydrogen bonds in the metal center. Protons that participate in Types I, II, and III NH$\cdots$S hydrogen bonding exhibit NH$\cdots$S hydrogen-bond-mediated scalar coupling, providing direct evidence that these protons are indeed hydrogen bonded to the cysteine sulfurs and demonstrating that the NH$\cdots$S hydrogen bonds contain significant covalent character. NH$\cdots$S hydrogen-bond-mediated scalar coupling has also been observed in a ^{113}Cd-substituted LIM domain for NH protons with sufficiently long T_2 values.[37] NH$\cdots$S hydrogen-bond-mediated scalar coupling has been observed by Gardner, Coleman, and co-workers (personal communication) for ^{113}Cd-GAL-4.[103] Future studies with other classes of zinc domains are likely to lead to similar findings for what appear to be important determinants of stability in miniglobular Zn-NAIDs.

14 RELATED ARTICLES

Cadmium-113 NMR: A Surrogate Probe for Zinc and Calcium in Proteins; Coupling Through Space in Organic Chemistry; Inorganic Chemistry Applications; Iron—Sulfur Proteins.

15 REFERENCES

1. R. S. Brown, C. Sander, and P. Argos, *FEBS Lett.*, 1985, **186**, 271.
2. J. Miller, A. D. McLachlan, and A. Klug, *EMBO J.*, 1985, **4**, 1609.
3. T. B. Rajavashisth, A. K. Tayler, A. Andalibi, K. L. Svenson, and A. J. Lusis, *Science (Washington, DC)*, 1989, **245**, 640.
4. S. M. Sato and T. D. Sargent, *Development*, 1991, **112**, 747.
5. L. E. Henderson, T. D. Copeland, R. C. Sowder, G. W. Smythers, and S. Oroszlan, *J. Biol. Chem.*, 1981, **256**, 8400.
6. L. Keegan, G. Gill, and M. Ptashne, *Science (Washington, DC)*, 1986, **231**, 699.
7. P. H. Lohmar and D. O. Toft, *Biochem. Biophys. Res. Commun.*, 1975, **67**, 8.
8. J. G. Omichinski, G. M. Clore, O. Schaad, G. Felsenfeld, C. Trainor, E. Appella, S. J. Stahl, and A. M. Gronenborn, *Science (Washington, DC)*, 1993, **261**, 438.
9. P. N. Barlow, B. Luisi, A. Milner, M. Elliott, and R. Everett, *J. Mol. Biol.*, 1994, **237**, 201.
10. O. Karlsson, S. Thor, T. Norberg, H. Ohlsson, and T. Edlund, *Nature (London)*, 1990, **344**, 879.
11. G. Freyd, S. K. Kim, and H. R. Horvitz, *Nature (London)*, 1990, **344**, 876.
12. X. Qian, S. N. Gozani, H. Yoon, C. Jeon, K. Agarwal, and M. A. Weiss, *Biochemistry*, 1993, **32**, 9944.
13. L. H. Schulman, *Prog. Nucleic Acids Res. Mol. Biol.*, 1991, **41**, 23.
14. P. Schimmel, *Curr. Opin. Struct. Biol.*, 1992, **1**, 811.
15. D. P. Giedroc, B. A. Johnson, I. M. Armitage, and J. E. Coleman, *Biochemistry*, 1989, **28**, 2410.
16. D. P. Giedroc, H. Qiu, R. Kahn, G. C. King, and K. Chen, *Biochemistry*, 1992, **31**, 765.
17. P. J. Kraulis, A. R. C. Raine, P. L. Gadhavi, and E. D. Laue, *Nature (London)*, 1992, **356**, 448.
18. J. D. Baleja, R. Marmorstein, S. C. Harrison, and G. Wagner, *Nature (London)*, 1992, **356**, 450.
19. R. Marmorstein, M. Carey, M. Ptashne, and S. C. Harrison, *Nature (London)*, 1992, **356**, 408.
20. M. S. Lee, G. P. Gippert, K. A. Soman, D. A. Case, and P. E. Wright, *Science (Washington, DC)*, 1989, **245**, 635.
21. J. G. Omichinski, G. M. Clore, E. Appella, K. Sakaguchi, and A. M. Gronenborn, *Biochemistry*, 1990, **29**, 9324.
22. M. Kochoyan, T. F. Havel, D. T. Nguyen, C. E. Dahl, H. T. Keutmann, and M. A. Weiss, *Biochemistry*, 1991, **30**, 3371.
23. M. Kochoyan, H. T. Keutmann, and M. A. Weiss, *Biochemistry*, 1991, **30**, 7063.
24. M. Kochoyan, H. T. Keutmann, and M. A. Weiss, *Proc. Natl. Acad. Sci. USA*, 1991, **88**, 8455.
25. R. C. Hoffman, S. C. Horvath, and R. E. Klevit, *Protein Sci.*, 1993, **2**, 951.
26. M. F. Summers, T. L. South, B. Kim, and D. R. Hare, *Biochemistry*, 1990, **29**, 329.
27. T. L. South, P. R. Blake, D. R. Hare, and M. F. Summers, *Biochemistry*, 1991, **30**, 6342.
28. M. F. Summers, L. E. Henderson, M. R. Chance, J. W. Bess, Jr., T. L. South, P. R. Blake, I. Sagi, G. Perez-Alvarado, R. C. Sowder, III, D. R. Hare, and L. O. Arthur, *Protein Sci.*, 1992, **1**, 563.

29. J. G. Omichinski, G. M. Clore, K. Sakaguchi, E. Appella, and A. M. Gronenborn, *FEBS Lett.*, 1991, **292**, 25.
30. N. Morellet, N. Jullian, H. De Rocquigny, B. Maigret, J.-L. Darlix, and B. P. Roques, *EMBO J.*, 1992, **11**, 3059.
31. T. Hard, E. Kellenbach, R. Boelens, B. A. Maler, K. Dahlman, L. P. Freedman, J. Carlstedt-Duke, K. R. Yamamoto, J.-Å. Gustafsson, and R. Kaptein, *Science (Washington, DC)*, 1990, **249**, 157.
32. J. W. R. Schwabe, D. Neuhaus, and D. Rhodes, *Nature (London)*, 1990, **348**, 458.
33. R. M. A. Knegtel, M. Katahira, J. G. Schilthuis, A. M. J. J. Bonvin, R. Boelens, D. Eib, P. T. van der Saag, and R. Kaptein, *J. Biomol. NMR*, 1993, **3**, 1.
34. H. Baumann, K. Paulsen, H. Kovács, H. Berglund, A. P. H. Wright, J.-Å. Gustafsson, and T. Härd, *Biochemistry*, 1993, **32**, 13 463.
35. M. S. Lee, S. A. Kliewer, J. Provencal, P. E. Wright, and R. M. Evans, *Science (Washington, DC)*, 1993, **260**, 1117.
36. T. L. South and M. F. Summers, *Protein Sci.*, 1993, **2**, 3.
37. G. C. Perez-Alvarado, C. Miles, J. W. Michelsen, H. A. Louis, D. R. Winge, M. C. Beckerle, and M. F. Summers, *Nature Struct. Biol.*, 1994, **1**, in press.
38. N. P. Pavletich and C. O. Pabo, *Science (Washington, DC)*, 1991, **252**, 809.
39. N. P. Pavletich and C. O. Pabo, *Science (Washington, DC)*, 1993, **261**, 1701.
40. B. F. Luisi, W. X. Xu, Z. Otwinowshi, L. P. Freedman, K. R. Yamamoto, and P. B. Sigler, *Nature (London)*, 1991, **352**, 497.
41. P. B. Blake, B. Lee, M. F. Summers, J.-B. Park, Z. H. Zhou, and M. W. W. Adams, *New J. Chem.*, 1994, **18**, 387.
42. P. R. Blake and M. F. Summers, *Adv. Biophys. Chem.*, 1994, **4**, 1.
43. P. R. Blake and M. F. Summers, *Adv. Inorg. Biochem.*, 1994, **10**, 201.
44. E. Adman, E. D. Watenpaugh and L. H. Jensen, *Proc. Natl. Acad. Sci. USA*, 1975, **72**, 4854.
45. P. R. Blake, J.-B. Park, M. W. W. Adams, and M. F. Summers, *J. Am. Chem. Soc.*, 1992, **114**, 4931.
46. P. R. Blake, J.-B. Park, Z. H. Zhou, D. R. Hare, M. W. W. Adams, and M. F. Summers, *Protein Sci.*, 1992, **1**, 1508.
47. P. R. Blake, B. Lee, M. F. Summers, M. W. W. Adams, J.-B. Park, Z. H. Zhou, and A. Bax, *J. Biomol. NMR*, 1992, **2**, 527.
48. P. Dauber-Osguthorpe and D. J. Osguthorpe, *J. Am. Chem. Soc.*, 1990, **112**, 7921.
49. C. C. Moser, J. M. Keske, K. Warncke, R. S. Farid, and P. L. Dutton, *Nature (London)*, 1992, **355**, 796.
50. D. N. Beratan, J. N. Onuchic, J. N. Betts, B. E. Bowler, and H. B. Gray, *J. Am. Chem. Soc.*, 1990, **112**, 7915.
51. D. N. Beratan, J. N. Betts, and J. N. Onuchic, *Science (Washington, DC)*, 1991, **252**, 1285.
52. D. N. Beratan, J. N. Onuchic, J. R. Winkler, and H. B. Gray, *Science (Washington, DC)*, 1992, **258**, 1740.
53. L. M. Green and J. M. Berg, *Proc. Natl. Acad. Sci. USA*, 1990, **87**, 6403.
54. R. Klevit, J. R. Herriott, and S. J. Horvath, *Proteins: Struct., Funct., & Genet.*, 1990, **7**, 215.
55. E. Adman, K. D. Watenpaugh, and L. H. Jensen, *Proc. Natl. Acad. Sci. USA*, 1975, **72**, 4854.
56. J. G. Omichinski, G. M. Clore, M. Robien, K. Sakaguchi, E. Appella, and A. M. Gronenborn, *Biochemistry*, 1992, **31**, 3907.
57. D. P. Bolognesi, R. C. Montelaro, H. Frank, and W. Schäfer, *Science (Washington, DC)*, 1978, **199**, 183.
58. C. Dickson, R. Eisnman, R. Fan, E. Hunter, and N. Teich, in *The Molecular Biology of Tumor Viruses: RNA Tumor Viruses*, 2nd edn., eds. R. A. Weiss, N. Teich, H. Varmus, and J. Coffin, Cold Spring Harbor Laboratory, Cold Spring Harbor, NY, 1985.
59. M. F. Summers, *J. Cell. Biochem.*, 1991, **45**, 41.
60. J. R. Webb and W. R. McMaster, *J. Biol. Chem.*, 1993, **268**, 13 994.
61. T. B. Rajavashisth, A. K. Taylor, A. Andalibi, K. L. Svenson, L. Karen, and A. J. Lusis, *Science (Washington, DC)*, 1989, **245**, 640.
62. S. M. Sato and T. D. Sargent, *Development*, 1991, **112**, 747.
63. M. F. Summers, T. L. South, B. Kim, and D. R. Hare, *Biochemistry*, 1990, **29**, 329.
64. M. S. Lee, S. A. Kliewer, J. Provencal, P. E. Wright, and R. M. Evans, *Science (Washington, DC)*, 1993, **260**, 1117.
65. J. W. R. Schwabe, D. Neuhaus, and D. Rhodes, *Nature (London)*, 1990, **348**, 458.
66. K. H. Gardner, T. Pan, S. Narula, E. Rivera, and J. E. Coleman, *Biochemistry*, 1991, **30**, 11 292.
67. J. Ma and M. Ptashne, *Cell*, 1987, **48**, 847.
68. M. Johnston, *Nature (London)*, 1987, **328**, 353.
69. T. Pan and J. E. Coleman, *Biochemistry*, 1991, **30**, 4212.
70. H.-Y. Yang and T. Evans, *Mol. Cell. Biol.*, 1992, **12**, 4562.
71. D. I. K. Martin and S. H. Orkin, *Genes & Devel.*, 1990, **4**, 1886.
72. D. J. Whyatt, E. deBoer, and F. Grosveld, *EMBO J.*, 1993, **12**, 4993.
73. D. Fourmy, F. Dardel, and F. Blanquet, *J. Mol. Biol.*, 1993, **231**, 1078.
74. D. Fourmy, T. Meinnel, Y. Mechulan, and S. Blanquet, *J. Mol. Biol.*, 1993, **231**, 1068.
75. L. H. Posorske, M. Cohn, N. Yanagisawa, and D. S. Auld, *Biochim. Biophys. Acta*, 1979, **576**, 128.
76. J.-F. Mayaux and S. Blanquet, *Biochemistry*, 1981, **20**, 4647.
77. W. T. Miller, K. A. W. Hill, and P. Schimmel, *Biochemistry*, 1991, **30**, 6970.
78. J.-F. Mayaux and S. Blanquet, *Biochemistry*, 1981, **20**, 4647.
79. D. Reines and J. Mote Jr., *Proc. Natl. Acad. Sci. USA*, 1993, **90**, 1917.
80. X. Qian, S. N. Gozani, H. Yoon, C. Jeon, K. Agarwal, and M. A. Weiss, *Biochemistry*, 1993, **32**, 9944.
81. L. C. Myers, M. P. Terranova, A. E. Ferentz, G. Wagner, and G. L. Verdine, *Science (Washington, DC)*, 1993, **261**, 1164.
82. L. C. Myers, G. L. Verdine and G. Wagner, *Biochemistry*, 1993, **32**, 14 089.
83. P. S. Freemont, *Ann. NY Acad. Sci.*, 1993, **684**, 174.
84. R. D. Everett, P. Barlow, A. Milner, B. Luisi, A. Orr, G. Hope, and D. Lyon, *J. Mol. Biol.*, 1993, **234**, 1038.
85. R. D. Everett, P. Barlow, A. Milner, B. Luisi, A. Orr, G. Hope, and D. Lyon, *J. Mol. Biol.*, 1993, **234**, 1.
86. P. N. Barlow, B. Luisi, A. Milner, M. Elliott, and R. Everett, *J. Mol. Biol.*, 1994, **237**, 1201.
87. Y. Xu, M. Baldassare, P. Fisher, G. Rathbun, E. M. Oltz, G. D. Yancopoulos, T. M. Jessell, and F. W. Alt, *Proc. Natl. Acad. Sci. USA*, 1993, **90**, 227.
88. C. Bourgouin, S. E. Lundgren, and J. B. Thomas, *Neuron*, 1992, **9**, 549.
89. B. Cohen, M. E. McGuffin, C. Pfeifle, D. Segal, and S. M. Cohen, *Genes Devel.*, 1992, **6**, 715.
90. M. Taira, M. Jamrich, P. J. Good, and I. B. Dawid, *Genes Devel.*, 1992, **6**, 356.

91. T. Boehm, J. M. Greenberg, L. Buluwela, I. Lavenir, A. Forster, and T. H. Rabbitts, *EMBO J.*, 1990, **9**, 857.
92. E. H. Birkenmeier and J. I. Gordon, *Proc. Natl. Acad. Sci. USA*, 1986, **83**, 2516.
93. I. Sadler, A. W. Crawford, J. W. Michelsen, and M. C. Beckerle, *J. Cell Biol.*, 1992, **119**, 1573.
94. S. A. Liebhaber, J. G. Emery, M. Urbanek, X. Wang, and N. E. Cook, *Nucleic Acids Res.*, 1990, **18**, 3871.
95. A. W. Crawford, J. D. Pino, and M. C. Beckerle, *J. Cell. Biol.*, 1994, **124**, 117.
96. G. A. McGuire, R. D. Hockett, K. M. Pollock, M. F. Bartholdi, S. J. O'Brien, and S. J. Korsmeyer, *Mol. Cell. Biol.*, 1989, **9**, 2124.
97. X. Wang, G. Lee, S. A. Liebhaber, and N. E. Cooke, *J. Biol. Chem.*, 1992, **267**, 9176.
98. R. Weiskirchen and K. Bister, *Oncogene*, 1993, **8**, 2317.
99. R. D. Everett, P. Barlow, A. Milner, B. Luisi, A. Orr, G. Hope, and D. Lyon, *J. Mol. Biol.*, 1994, **234**, in press.
100. K. D. Watenpaugh, L. C. Sieker, and L. H. Jensen, *J. Mol. Biol.*, 1979, **131**, 509.
101. U. Hommel, M. Zurini, and M. Luyten, *Nature Struct. Biol.*, 1994, **1**, 383.
102. H. Déméné, N. Jullian, N. Morellet, H. de Rocquigny, F. Cornille, B. Maigret, and B. P. Roques, *J. Biomol. NMR*, 1994, **4**, 153.
103. K. H. Gardner, S. F. Anderson, and J. E. Coleman, *Nature Struct. Biol.*, 1995, **2**, 898.

Biographical Sketch

Michael F. Summers. *b* 1958. B.S., 1980, University of West Florida, Ph.D., 1984, Emory University. Postdoctoral training at NIH with Ad Bax, R. Andrew Byrd, William Egan. Introduced to NMR by Luigi G. Marzilli (Emory). Assistant professor, 1987–91, associate professor, 1991–present, University of Maryland, Baltimore County. Associate investigator, Howard Hughes Medical Institute, 1994–present. Approximately 70 publications in the areas of NMR and bioinorganic chemistry. Research interests include applications of NMR spectroscopy to studies of metalloproteins and macromolecular interactions.

Tritium NMR in Biology

Mark G. Kubinec and Philip G. Williams

Lawrence Berkeley National Laboratory, Berkeley, CA, USA

1	Introduction	1
2	Elucidation of Enzyme Stereochemistry	1
3	Protein–Ligand Interactions	4
4	Macromolecules Labeled With Tritium	7
5	Conclusion	8
6	Related Articles	8
7	References	8

1 INTRODUCTION

In the study of biologically active molecules, the effectiveness of NMR spectroscopy is limited by proton resolution. Even using modern techniques with ^{13}C- and ^{15}N-labeled molecules of uniform enrichment the upper molecular weight limit for NMR applications is ca. 40 kDa. Site specific or ligand labeling methods are the only alternative for systems over this 40 kDa limit, and are most useful in the study of catalytic or dynamic regions of macromolecules. These latter approaches eliminate the resolution and assignment limitations of uniform labeling while bringing to bear the power of NMR for the study of structural and dynamic problems.

Tritium is the most attractive NMR active nucleus available for site specific or ligand labeling. We have included some chemical and radiochemical properties of tritium in Table 1 and compared the NMR characteristics of ^{3}H with ^{1}H, ^{13}C, and ^{15}N in Table 2. Among the most important NMR properties of tritium are the high gyromagnetic ratio and low spin number ($\frac{1}{2}$), yielding the highest molar sensitivity of any nucleus. This is important in biological systems where sensitivity is limited by low solubility and/or catalytic yield of biological molecules. The low natural abundance of tritium ensures that the 'tritium window' on biological systems is not clouded by spurious signals, and few published ^{3}H NMR spectra have more than a half dozen signals to assign and monitor. Assignment is aided by the fact that tritons and protons have essentially identical chemical shifts.[1] Replacing one isotope of hydrogen with another allows basically native species to be studied by tritium NMR spectroscopy. In contrast, labeling with ^{19}F or some different *element* can completely change the substrate under investigation. In general, labeling with tritium leads to minor isotope effects on the labeled system, and the most serious, kinetic isotope effects, may be helpful in unraveling the mechanism of reactions at the labeled site (as discussed below).

Despite its many advantages, tritium NMR development has lagged behind that of other heteronuclei. Initially, hardware development and concern over highly radioactive samples hindered progress. Indeed, the first recorded tritium NMR spectra required many TBqs (curies) of material to obtain an adequate signal. Modern high-field spectrometers can readily detect 3.7 MBq (0.1 mCi) of tritium (i.e. ca. 2.5×10^{15} nuclei). This makes radiation safety a less dominant issue and yields a detection limit more suitable for biological samples. To contain the radiation, samples are often doubly sealed in Teflon tubes inside glass tubes. Since tritium is a weak β emitter ($E_{\max}$ = 18.6 keV), this approach totally blocks radiation while providing insurance against leakage or spilling of samples.[1] To understand the amounts of radioactivity typically encountered in tritium NMR experiments one must be familiar with the commonly used units, which are included in Table 1 along with several conversion factors. The most important equivalence is: 100% substitution of a tritium atom for a hydrogen atom in a molecule leads to a specific activity of 1064 GBq mmol^{-1} (28.76 Ci mmol^{-1}). For example, 250 μL of a 1 mM solution (0.25 μmol) of a substrate having 100% abundance of tritium at a single site contains ca. 266 MBq (7.2 mCi). For perspective, safety lights in aircraft have up to 370 GBq (10 Ci) of tritium, a marine compass may contain as much as 28 GBq (0.75 Ci), and commonly available night sights for rifles contain 2 GBq (50 mCi) of tritium.

The sensitivity of the tritium nucleus in modern spectrometers, coupled with advances in synthetic labeling techniques, have paved the way for the use of tritium NMR in biology. Today, most small biologically active molecules can be readily tritium-labeled, and the chemistry is often more straightforward than labeling the same molecule with either ^{13}C or ^{15}N. The tritiated molecules can be studied in conjunction with macromolecules in virtually any biological system accessible by NMR spectroscopy, including solutions of proteins and nucleic acids, cellular suspensions, and whole animals. Tritium NMR spectra can provide a remarkably simple and revealing window into the structure, chemistry, and dynamics of a biological system.

Three general applications of ^{3}H NMR are discussed below: Section 2 will cover enzyme mechanistic studies; Section 3 will review enzyme ligand interactions; and Section 4 will discuss macromolecular labeling.

2 ELUCIDATION OF ENZYME STEREOCHEMISTRY

For decades, radioactive tracer nuclei such as ^{14}C, ^{3}H, ^{32}P, and ^{35}S have been used to study metabolic pathways in cells by determination of the radiolabel position in a biological product or the stereochemistry of its addition. This often requires extensive chemical or enzymatic manipulation of the biosynthetic product. The complexity of these methods makes them difficult and error prone. Tritium NMR is the simple, rapid, accurate, and nondestructive product analysis technique researchers have sought: an NMR spectrum is acquired as opposed to chemical degradation or analysis. In addition to its relative simplicity, tritium NMR provides more detailed structural and stereochemical information than any other technique.

The group at Surrey University which pioneered ^{3}H NMR spectroscopy[1] first demonstrated the power of ^{3}H NMR in biology by following up ^{14}C work on the biosynthesis of penicillin with tritium labeling and tritium NMR. By growing bacteria on media supplemented with tritium-labeled acetate, they were able to determine unambiguously the fate of the methyl protons of acetate in the biosynthesis of the penicillin molecule.[2] This, and other early work, underscored many of the advantages of using tritium labeling coupled with ^{3}H NMR analysis. Since 1974 this approach has been applied

Table 1 General Physical and Chemical Data for Tritium, and Common Radioactivity Units[a]

Production	$^{6}Li(n, \alpha)^{3}H$
Radiation	β (100%); range = 4.5–6 mm in air, 6 μm in H_2O
β Energy	E_{max} = 18.6 keV, E_{mean} = 5.7 keV
Halflife	12.43 y (4540 d)
Maximum specific activity	1064 GBq milliatom^{-1} (28.76 Ci milliatom^{-1})

[a]37 gigabecquerels (GBq) = 1 curie (Ci) = 3.7 × 10^{10} disintegrations per second; 1 gray (Gy) = 10 000 erg g^{-1} = 100 rad (units of absorbed dose); 1 sievert (Sv) = 100 rem (units of radiation exposure).

Table 2 NMR Properties of ^{3}H and Common NMR Nuclei[a]

Nucleus	Natural abundance	Spin	γ	Resonant frequency	Relative sensitivity[b]
^{1}H	99.984	$\frac{1}{2}$	26.510	300.13	1.00
^{3}H	**<10^{-16}**	$\frac{1}{2}$	**28.5335**	**320.13**	**1.21**
^{13}C	1.10	$\frac{1}{2}$	6.7263	75.46	1.59 × 10^{-2}
^{15}N	0.37	$\frac{1}{2}$	−2.7116	30.40	1.04 × 10^{-3}

[a]7.1 T field.
[b]Sensitivity given for equal numbers of nuclei in the same field.

to much more subtle and complicated problems of enzyme stereochemistry. It has proven especially useful in instances of so-called 'cryptic' stereochemistry, where the fate of an individual H atom must be traced, as illustrated in Figure 1(a). Tritium NMR and a fascinating species known as a 'chiral methyl group' have emerged as the most powerful method for studying these reactions.

Chiral methyl groups are the smallest chiral entity ever synthesized.[3] They are created by attaching each of the isotopes of hydrogen, a proton, deuteron, and triton, to a single carbon atom. If a reaction occurs at this chiral center as in Figure 1(a), ^{3}H NMR analysis of the resulting methylene will give the stereochemical course of the reaction provided that the diastereotopic positions ['a' and 'b' in Figure 1(a)] are resolvable in the spectrum.

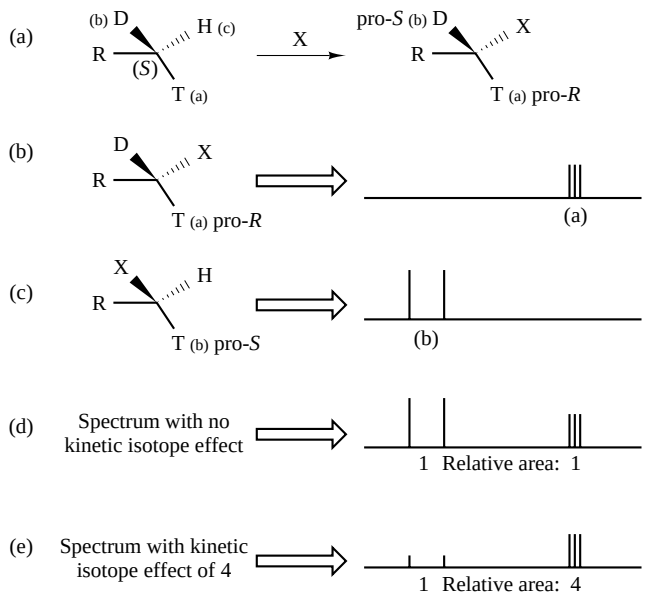

Figure 1 (a) A chiral methyl group undergoes a substitution reaction: D = deuterium, T = tritium. For a substitution with retention of configuration, the products detectable by ^{3}H NMR spectroscopy are shown in (b) and (c), along with idealized spectra. The effect of a kinetic isotope effect is shown in (d) and (e)

Figure 1(b)–(e) show a breakdown of an ideal substitution reaction to demonstrate how the NMR pattern of products from a chiral methyl reaction may be used to determine enzyme stereospecificity. Reaction of an (*S*) chiral methyl with retention of configuration is illustrated. Three isotopomeric species can result from the reaction, depending on which isotope of hydrogen is removed. Two of these species contain a tritium atom and may be observed by tritium NMR spectroscopy. One of these products, with a triton at the pro-*R* position, will give an NMR signal at chemical shift 'a', as shown in Figure 1(b). Here the proton was replaced leaving an (*R*) R–CDT–X species, and the ^{3}H signal is a triplet due to the triton–deuteron coupling (since ^{2}H is spin 1). The chemical shift of this species will also be affected by a deuterium isotope effect. A doublet will also occur in the tritium NMR spectrum from the other product, containing a triton in the pro-*S* position [at chemical shift 'b', Figure 1(c)]. In this species, the deuterium atom was replaced, giving (*S*) R–CHT–X. If the addition of X had occurred with inversion, the opposite pattern (a doublet at chemical shift 'a' and a triplet at 'b') would be observed. There is often a primary kinetic isotope effect in the substitution of X, and this will alter the intensity of the lines in the spectrum in a way that also reflects the stereochemistry of the reaction. If configuration is retained and there is a 'normal' kinetic isotope effect, the signal at 'a' will have a larger integral since it is kinetically more favorable to remove the proton [cf. Figure 1(d) and (e)]. The ratio of the intensities of the lines will directly yield the magnitude of the isotope effect. Thus both the intensity and coupling pattern of the lines in the ^{3}H NMR spectrum are indicative of the stereochemistry of the substitution. If racemization occurs the effect will be obvious, since the mixing of the product species leads to equal intensities at all labeled positions.

Analysis of enzyme stereochemistry using chiral methyl groups is becoming common.[3–8] Aside from the ability to resolve pro-*R* and pro-*S* chemical shifts, there are other technical requirements. It must be possible to synthesize the chiral tritiated substrate at sufficient specific activity. For probing reactions that are occurring in vivo or in cell-free extracts, a high level (5–50 GBq) is usually necessary to ensure sufficient uptake and yield for processing. Biosynthetic yield must also be high enough to provide product in the 4–400 MBq range for NMR analysis. This can be as much as 10^6-times more radioactivity than commonly used in a simple tracer experiment. In ^{13}C, ^{15}N, and ^{2}H spectroscopy of biomolecules, natural abundance signals may interfere with observation of the added label. In contrast, any tritium signals observed are directly related to the tritium originally introduced as labeled substrate. This feature facilitates the use of tritium NMR for in vivo studies, where tritium may be detected in several metabolites, including solvent.[9]

Another crucial and often difficult requirement of this technique is knowledge of the stereochemistry of the methyl group prior to reaction with the enzyme. Currently the most popular method involves the conversion of chiral acetate to acetyl coenzyme A, followed by digestion with malate synthase and fumarase. (This technology is very well described by Floss and Lee,[3] which also contains numerous primary references.) The percentage of tritium retention in the fumarase reaction is determined by liquid scintillation counting (LSC), and the enantiomeric excess in the starting acetate can then be calculated. The method depends on the ability to convert the subject chiral methyl group by a sequence of reactions of known stereochemistry into the methyl group of acetate. A more direct approach uses ^{3}H NMR to analyze *N*-methylated 2-methylpiperidine,[8] where the ability to transfer the chiral methyl species to 2-methylpiperidine builds on much of the same chemistry as the chiral acetate approach. The hindered rotation of the labeled *N*-methyl group makes the chemical shift of the triton dependent on the specific chirality of the methyl carbon. The only disadvantage of this approach compared with the enzymatic determination is the much larger quantities of tritium required for NMR analysis.

2.1 The Berberine Bridge Enzyme

A classic example of the application of chiral methyl groups for understanding cryptic stereochemistry is the study of the berberine bridge enzyme (BBE).[7] BBE catalyzes the ring-closure reaction shown in Figure 2 to yield scoulerine, which has axial (a) and equatorial (e) methylene hydrogens at the 8-position. These are well resolved ($\Delta\delta$ = 0.5 ppm) and their proton chemical shifts are known. The four possible product configurations, $^{3}H_a-^{1}H_e$, $^{3}H_a-^{2}H_e$, $^{3}H_e-^{1}H_a$, and $^{3}H_e-^{2}H_a$, should all be distinguishable in the ^{3}H NMR spectrum by a combination of their chemical shifts and splitting patterns. Labeled scoulerine was enzymatically synthesized by incubation of *S*-adenosylmethionine with nor-reticuline in the presence of nor-reticuline-*N*-methyltransferase, followed by incubation with BBE. Independent incubations were performed using *S*-adenosylmethionine having exclusively an (*S*)-methyl or (*R*)-methyl, and the ^{3}H NMR spectrum of the purified scoulerine from the (*S*) reaction is reproduced in Figure 3. Spectra were acquired with and without proton decoupling

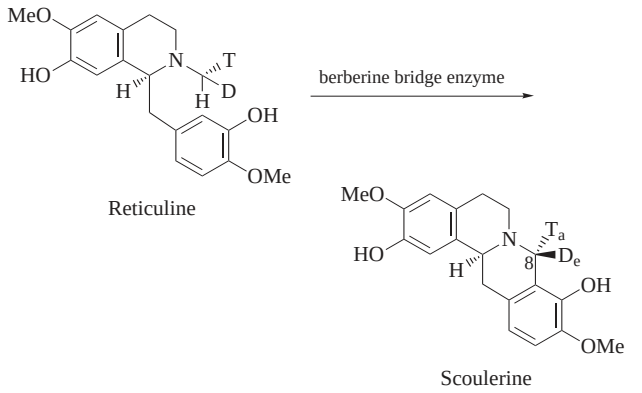

Figure 2 The biosynthesis of scoulerine by ring closure of a methyl group in reticuline, catalyzed by the berberine bridge enzyme

to help assign tritons coupled to protons, and the deuterium couplings were too small to be resolved at this field [*J*(T,D) = 2.3 Hz]. The most striking feature of these spectra is the abundance of tritium at the 8-axial position (pro-*R*). This peak is unchanged by proton decoupling, indicating that its geminal partner is a deuteron. The equatorial (pro-*S*) triton is coupled to a proton [*J*(T,H) = 15.3 Hz]. Since these are the only two tritiated species observed, the berberine bridge enzyme must be acting stereospecifically with exclusive *inversion* during the ring closure reaction. The 4:1 axial to equatorial intensity ratio is explained by a kinetic isotope effect, where $k_H/k_D = 4$.

In this study, 29.6 MBq (800 μCi) of tritium was introduced into the in vitro enzymatic system via tritiated *S*-adenosylmethionine, and 5.7 MBq (153 μCi) of scoulerine was purified. One tritium per molecule represents a specific activity of 1064 GBq mmol^{-1}, so 5.7 MBq of scoulerine is 5.3 nmol (ca. 3.2 $\times$ 10^{15} tritiated molecules). At this level of tritium abundance, 24 h of signal averaging (around 50 000 transients) were required to achieve each of the NMR spectra in Figure 3. This is comparable to the length of a standard 2D NMR experiment on a biological sample, and is therefore a small instrumental time commitment relative to the information obtained.

2.2 Cephalosporin C

In the BBE study described above, the amount of radioactivity employed was relatively small since enzymatic reactions were carried out in a cell-free extract. In contrast, studies with a true in vivo step may require tritium levels in the multiple curie range. The use of high levels of radioactivity is readily justified in cell systems where the enzymes involved may be unknown or difficult to purify, and elucidation of the biosynthetic route to Cephalosporin C is a good example (Figure 4).[6] In particular, both the pro-*R* and pro-*S* methyl groups of valine are stereospecifically derivatized in this synthesis, whereby the pro-*S* methyl (*) becomes the exocyclic ester (position 3′) and the pro-*R* methyl (¶) participates in ring expansion (position 2). The two proton abstractions are catalyzed by different enzymes with very similar properties. Both are 2-oxoglutarate dependent dioxygenases that require Fe(II) and a reducing agent. The stereochemistry of the proton abstractions in these reactions was studied in a very elegant set of experiments using valine molecules with either (*R*)

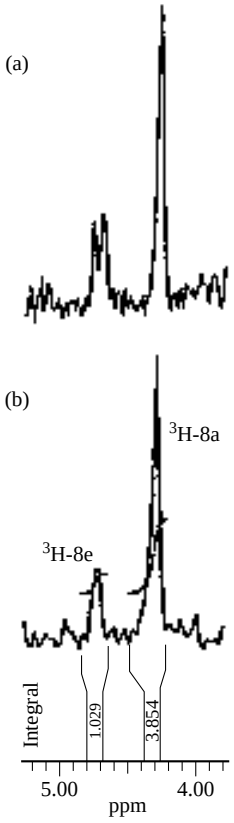

Figure 3 Tritium NMR spectra of scoulerine. The sample contained 5.7 MBq (153 μCi) of tritium in CD_3OD. (a) ^{1}H gated decoupled, WALTZ-16 ^{2}H broadband-decoupled, 47 347 transients. (b) Composite pulse broadband ^{1}H-decoupled, 76 472 transients. (Reprinted with permission from *J. Am. Chem. Soc.*, 1988, **110**, 7878. Copyright 1988 American Chemical Society)

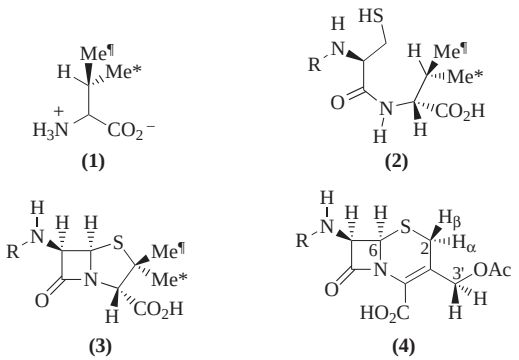

Figure 4 The biosynthesis of Cephalosporin C. The methyl groups of valine are stereospecifically incorporated into the product. This allows analysis of both methyl reactions in the same tritium NMR experiment (see text)

or (*S*) chiral methyl at either the pro-*R* (¶) or pro-*S* (*) positions. In this way, both enzyme mechanisms can be studied simultaneously in an in vivo synthesis. Each NMR study required ca. 90 GBq (2.5 Ci) of labeled valine substrates added in the cellular media in order to isolate 110 MBq (3 mCi) of cephalosporin (ca. 0.1% yield).

The ^{3}H NMR spectra of the isolated products are shown in Figure 5, and the combination of starting valine species for

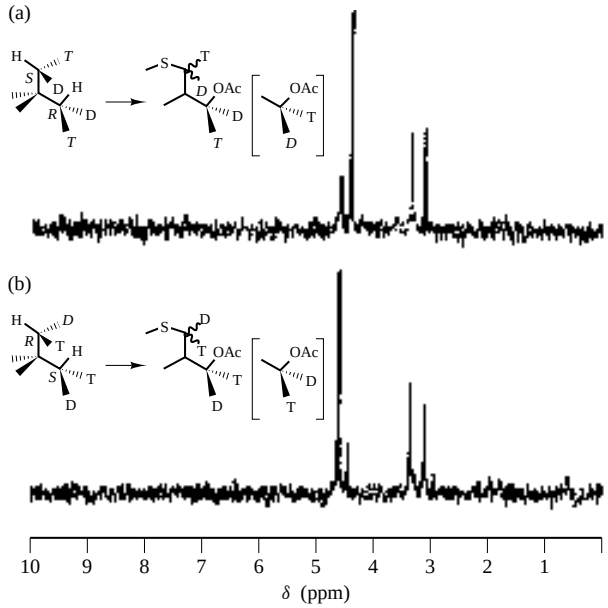

Figure 5 The ^{3}H NMR spectrum of Cephalosporin C derived from the starting species shown on each figure section. (Reprinted with permission from *Biochem. J.*, 1984, **222**, 777. Copyright 1984 Biochemical Society, London)

each sample is shown on the figure. The signals at 3.2 ppm and 3.4 ppm are the C-2 tritons, and clearly the ring expansion at the 2-position shows little stereochemical preference, since an equal mixture of the possible products is formed. This is consistent with a radical mechanism at this step in the biosynthesis.

The resonances at 4.6 ppm and 4.8 ppm arise from the C-3′ tritons, but were not stereospecifically assigned. In contrast to the ring expansion reaction, there is a strong stereochemical preference in reactions at the 3′-position, as shown by the dependence of the 4.8 ppm and 4.6 ppm signal intensities on the configuration of the pro-*S* methyl in the starting valine. The patterns are very similar to those observed in the BBE study described above (see Figure 3), but in this case the minor signal does not represent an R−CHT−X species since no proton coupling is observed. Since impurities have been ruled out, the remaining possibility is that the enzyme is only about 90% stereospecific, and a 'partial' preference is not uncommon in enzyme-catalyzed reactions.[10] When signals from the R−CHT−X species are not detected, the isotope effect (k_H/k_D) can only be estimated by the size of the spectral noise. In this case, k_H/k_D must be at least 5 for the R−CHT−X species to be unobservable.

The two similar enzymes studied here have clearly different modes of action in this biosynthetic pathway. The radioactivity and excellent NMR properties of tritium were essential in the synthesis of precursors, isolation of products, and final product analysis in this study.[6]

3 PROTEIN–LIGAND INTERACTIONS

In the study of protein−ligand interactions, the goal is both detailed structural information on binding sites and dynamic information on binding modes and kinetics.[11] There

are two major techniques for acquiring detailed structural information on protein structure; X-ray crystallography and NMR spectroscopy. Crystallography can give high-resolution structures but only limited information on dynamics. NMR is an excellent tool for dynamic studies but the size of the system that can be studied is limited, usually by proton resolution, to around 35–40 kDa. Tritium NMR can complement both these approaches. In cases where a crystal- or NMR-derived structural model exists, tritium NMR provides a method for probing dynamics that far exceeds data from crystallography and surpasses NMR with more conventional isotopes in its simplicity and application to larger protein systems. When NMR or crystal structural data are absent, useful information from ^{3}H chemical shifts, relaxation studies, and ^{3}H–^{1}H NOEs can be used to characterize the ligand binding site.

Here we review two works which are not only exemplary in their demonstration of the power of ^{3}H NMR in ligand binding investigations, but also show two distinct approaches to the problem which are used repeatedly in the literature.[12–16] We highly recommend these two studies for those interested in these techniques. The study of maltose binding protein shows how a ligand undergoing exchange at an intermediate rate can be analyzed by standard techniques, e.g. one-dimensional spectra, saturation transfer, and 2D EXSY spectroscopy.[13] Next we describe how the relaxation behavior of ^{3}H augmented extensive computer simulation in studying the dynamics of a small inhibitor peptide binding to bacterial collagenase.[14]

3.1 Maltose Binding Protein

Maltose binding protein (MBP) is involved in the transport of maltodextrins (maltose and its oligomers) across the periplasmic space in *E. coli*. MBP is a soluble, monomeric protein of 40 kDa, with known primary sequence, which has a dissociation constant for maltose of about 10^{-6} M, increasing somewhat for the longer maltose oligomers. Although there has been a crystal structure determined for MBP, there were questions remaining about the binding kinetics and possible differences in binding of the α and β anomers.

Maltose [Figure 6(d)] and longer maltodextrins were labeled, and tritium was incorporated to a level of 5–20% at the C-1 position. Hence, a limited percentage of ligand molecules were visible to tritium NMR detection. The labeled ligands were characterized by tritium and proton NMR techniques prior to binding studies. The proton-decoupled ^{3}H NMR spectrum of tritiated maltose in Figure 6(a) is representative of all the oligosaccharides, and shows lines from the α and β anomers at 5.15 ppm and 4.55 ppm (relative to DSS) respectively, with the expected intensity ratio of 40:60.

Initial investigations of the interaction of a labeled ligand and macromolecule invariably involve simple 1D NMR observations of a number of ligand/macromolecule mole ratios. When MBP (ca. 2.5 mM solution, in phosphate buffer at pH 7.0) is titrated with labeled maltose two lines appear, at 3.5 ppm and 3.4 ppm [Figure 6(b), 0.25 equiv.]. The lines are broadened relative to free maltose. This is a common effect in ligand binding studies, which results from the *bound* sugar molecules tumbling with the longer correlation time of the protein. As further additions are made exceeding a 1:1 mole ratio of maltose to MBP, additional peaks due to free maltose are observed at the same chemical shifts as in the absence of protein [Figure 6(b), 2 equiv.].

Very often several deductions can be drawn even from simple 1D ^{3}H NMR experiments. In this case, the observations are: (a) the large shifts of the bound resonances to lower frequency suggests that the labeled end of the maltose molecule makes direct contact with an aromatic residue in the protein binding site, probably tryptophan 230; (b) the degree of shift of the two anomers is different, which suggests an asymmetric environment around the binding site; and (c) the relative intensity of the bound peaks differs below and above stoichiometric addition. With excess protein, the intensities of the bound forms of the two anomers initially remain at their equilibrium solution value. If the intensities are followed over time, a gradual conversion of the β form into α is observed. When the sugar is present in excess, the *bound* α and *free* β peaks both exceed their equilibrium levels. Both of these observations indicate that there is significant anomeric specificity in binding.

The absolute identity of the bound resonances was determined by saturation transfer and 2D EXSY [Figure 6(c)] techniques, which confirmed that the α anomer is preferentially bound by the protein. These experiments were enhanced by the large chemical shift differences for bound and free sugar resonances, and the saturation transfer studies allowed independent determinations of the dissociation rate constants for α and β anomers. Both the identity of the bound species and the rate constant information is accessible from 2D EXSY experiments, where transfer of magnetization by chemical exchange between bound and free maltose gives rise to the observed cross peaks, and confirms the bound resonance at low frequency as the bound α anomer [Figure 6(c)].

Spectra of longer maltodextrins, containing three to six glucose units, in the presence of excess MBP contained resonances with varying linewidths and average chemical shifts, as a direct result of the range of binding affinities and chemical exchange rates prevalent for the various bound α and β species. Such an array of cases would have been impossible to understand without the simplification conferred by tritium labeling of the ligand and tritium NMR analysis.

In these studies tritium proved to be an excellent direct detection probe with which (a) clear anomeric specificity was observed in a situation where there were few alternative methods for unequivocally demonstrating it, (b) two types of binding (reducing end versus middle or remote) were deduced, this difference being undetectable by other means, and (c) the binding of longer oligomers was characterized with the same or **greater** ease than the maltose case. An added convenience was that the labeling chemistry was straightforward for all the ligands.

3.2 Bacterial Collagenase

As we have mentioned, the other common way to study protein–ligand interactions is by an analysis of the relaxation properties of tritium. An example of using ^{3}H NMR to study the dynamic and conformational aspects of an inhibitor interaction with bacterial collagenase is the most thorough example of this technique. The protein system was bacterial collagenase from *Achromobacter iophagus* (ca. 71 kDa), and the labeled inhibitor was succinyl-L-prolyl-L-alanine (K_i = 2.1 $\times$ 10^{-4} M), one of a range of competitive inhibitors under study.

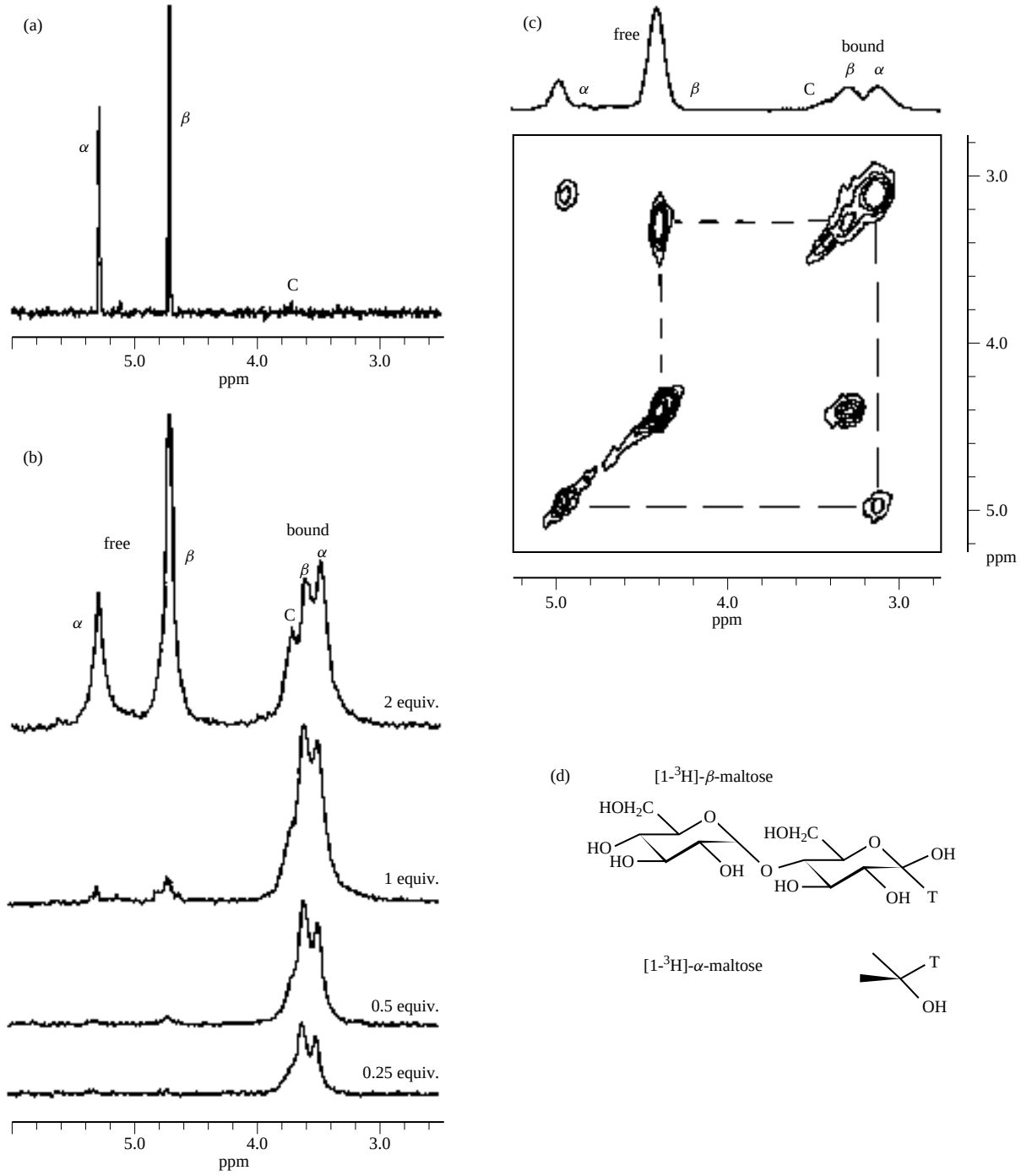

Figure 6 (a) $^{3}H[^{1}H]$ NMR spectrum of [1-^{3}H]maltose, (b) the titration of maltose binding protein with tritium-labeled maltose, (c) the 2D EXSY spectrum of excess maltose in the presence of maltose binding protein, (d) the structure of [1-^{3}H]maltose

The studies involved rigorous analysis of the relaxation behavior of selected spin systems in labeled inhibitor molecules in the absence and presence of bacterial collagenase. In contrast to the MBP/maltodextrin experiments described above, in this example the experimental data are only the starting point for extensive calculation and interpretation of physical models. Hence sample preparation included rigorous deoxygenation to facilitate accurate relaxation rate measurements, and repetitive determination of these parameters.

The solution behavior of the free ligand was first characterized, before proceeding to inhibition studies. Measurement of the relaxation properties of the tritium pair on the contiguous methylenes in the succinyl residue, and comparison with the relaxation behavior of the complementary protons of the analogously deuterated molecule, allowed the calculation of overall and internal correlation times. From these values, intertriton and interproton distances were estimated, rotamers proposed, and the fractional populations and coupling constants so derived were compared with the experimentally

determined parameters. In these two ways, both the motional (i.e. correlation times) and conformational (rotamer) populations of the free inhibitor were deduced.

Comparable relaxation measurements in the inhibitor/collagenase samples were conducted with a 20–30-fold excess of inhibitor (e.g. 97% free, 3% bound in many experiments), and the spectra showed the weighted average of the NMR parameters of these subspectra, i.e. the chemical shifts and linewidths, etc. We calculate that the tritium samples contained approximately 1000 MBq (27 mCi); [protein] = 40 μM, therefore [inhibitor] = 1.2 mM, assume 0.5 mL sample (= 0.6 μmol), specific activity = 45 mCi μmol^{-1}. By analysis of the cross relaxation of the Ala signals of the proton spectra of the inhibitor/collagenase sample, an indication of the motional freedom of this residue in the presence of protein could be gained, and this indicated that the α-proton had restricted motion. In a similar manner to the free inhibitor, relaxation measurements on the succinyl (Suc) methylenes in the presence of protein permitted the deduction of overall correlation times, internuclear distances, and a qualitative estimate of the order parameter (a measure of the internal mobility of the Suc) for the bound inhibitor. The similarity of tritium and proton cross-relaxation terms for the complementary methylene pairs suggests a similar geometry, and this is satisfied by the carbonyl and carboxy groups adopting a *trans* conformation when bound to the protein.

The natural substrate for this enzyme has the general sequence X–Gly–Pro–Y, and is cleaved at the peptide bond between X and Gly. The studies described above clearly showed that the carboxylate group of the inhibitor Suc residue has the strongest interaction with the enzyme, and that the carbonyl of the Ala residue appeared to be another anchoring site. Using these clues and detailed knowledge of the active site of other zinc proteinases, the structure of the inhibitor may be aligned with that of the natural substrate to identify important structural features. This approach was used to guide the design of improved inhibitors.

4 MACROMOLECULES LABELED WITH TRITIUM

Biological molecules are produced for NMR studies in a variety of ways. The most common are: solid phase synthesis for DNA, peptides, and smaller proteins; in vitro synthesis for RNA production; and in vivo or cellular expression systems, commonly used to prepare ^{13}C and ^{15}N uniformly enriched protein samples. Tritium labeling may be used in conjunction with each of these techniques. The cephalosporin example above demonstrates the in vivo method, while both DNA and RNA have been labeled at several sites demonstrating the use of solid phase and in vitro methods.

The self-complementary DNA dodecamer with sequence 5′ dCGCGAATTCGCG 3′ has been extensively studied. The proton spectrum is fully assigned and detailed X-ray crystal and NMR structures have been published. Both the crystal structure and recently published NMR data show interesting DNA–water interactions. This molecule has been labeled at the 2- and 8-positions of adenosine-5 (5′ dCGCG**A***ATTCGCG 3′) by addition of a tritiated phosphoramidite precursor at the appropriate step of the solid phase synthesis. Tritium NMR was expected to be helpful in the further investigation of water interactions since a major difficulty with the proton NMR studies is water suppression.

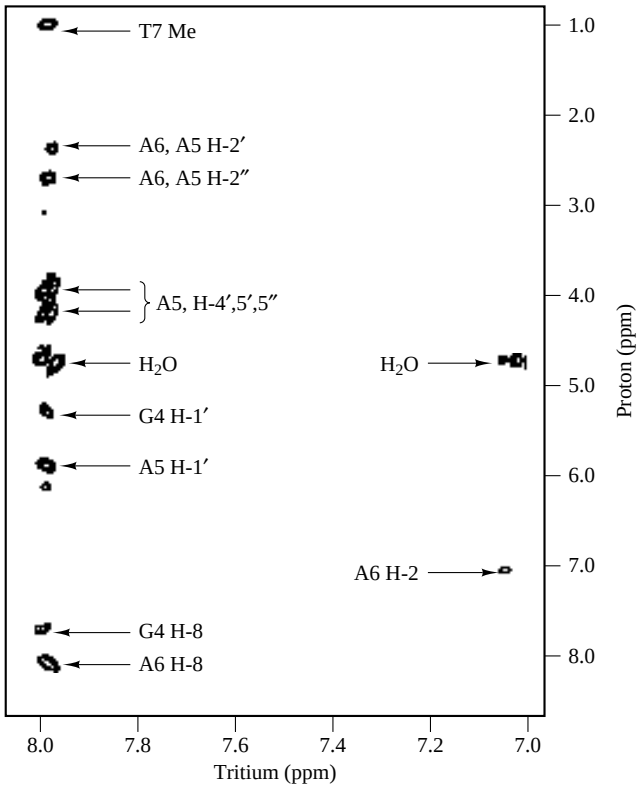

Figure 7 The 640-MHz tritium-detected ^{3}H–^{1}H NOESY spectrum of a ^{3}H-labeled DNA oligomer

The one-dimensional spectrum of the tritiated DNA has two lines at 8.1 ppm (8-position) and 7.2 ppm (2-position). Two-dimensional tritium-detected ^{3}H–^{1}H NOESY spectra of the molecule in H_2O solution showed all the expected intramolecular DNA proton cross peaks, plus cross peaks at the water chemical shift (Figure 7). No water suppression was necessary. In many respects the spectrum in Figure 7 represents a milestone in tritium NMR studies. It is the first and essentially the only heteronuclear ^{3}H–^{1}H NOESY collected on a macromolecule and fully assigned. Because it directly mirrors the proton spectrum, it demonstrates the fidelity of tritium NMR to proton NMR for the analysis of 'close in space' interactions.

The signal at the water chemical shift for both tritons is antiphase, while analogous proton data show purely in-phase cross peaks for this interaction. The major difference between the homo- and heteronuclear spectra is that the water is off-resonance in the tritium-detected experiments. This anomaly is explained by recent observations of multiple quantum interactions between solvent and solute when the solvent is off-resonance (see '***Concentrated Solution Effects***'). Although the multiple quantum nature of these cross peaks limits their usefulness in studying DNA–water interactions, their intensity and their acquisition without water suppression indicate that tritium NMR is an excellent method for further investigation of this multiple quantum phenomenon.

RNA has been a particularly difficult molecule to study by NMR methods. The poor dispersion of spectral lines in the ^{1}H, ^{13}C, and ^{15}N spectra has plagued the structural

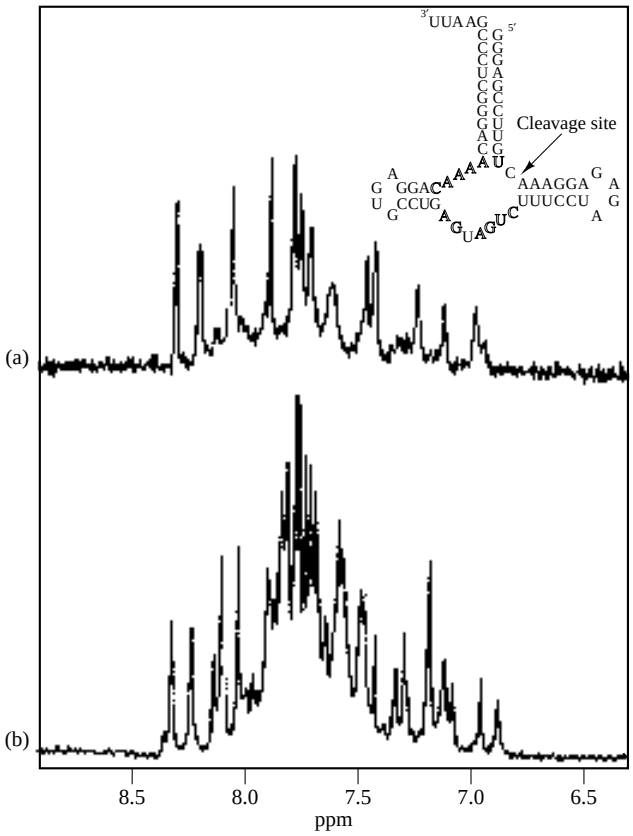

Figure 8 A comparison of the aromatic regions of (a) the ^{3}H (533 MHz) and (b) ^{1}H (600 MHz) NMR spectra of the 65 base RNA molecule shown in (a)

spectroscopist. Tritium NMR is an effective method for increasing resolution in RNA spectra. Figure 8 compares the ^{3}H NMR spectrum of a 64-base RNA molecule dissolved in H_2O and the corresponding proton spectrum of an analogous sample dissolved in D_2O (spectral conditions were not identical). The RNA molecule was labeled at the 2-position of each adenosine, giving tritium at 18 of the 75 aromatic sites in the molecule. The spectral simplification afforded by ^{3}H NMR is actually much more dramatic if it is compared with the proton spectrum in H_2O solution, where dozens of additional exchangeable protons also resonate in the region shown.

With these simpler spectra, it is clear from Figure 8 that the 18 labeled sites on the molecule are not equally represented. Temperature studies confirmed that a significant amount of conformational exchange is occurring in this molecule. Various assignment techniques, including one-dimensional tritium–proton NOE experiments, indicated that the highest degree of conformational exchange is in the central region of the molecule, which includes the bases most important for the self-cleaving properties of this RNA molecule. This conformational exchange is totally undetectable in the proton spectrum and would be difficult to analyze by a technique other than tritium NMR.

The DNA and RNA samples were labeled at high specific activity. The DNA was approximately 1500 GBq mmol^{-1} (40 Ci mmol^{-1}) at two sites and the RNA was more than 15 000 GBq mmol^{-1} (400 Ci mmol^{-1}) at 18 sites. These high levels of activity are beneficial for the rapid acquisition of spectra, but also accelerate radiation decomposition of the substrates. As a result, the samples discussed here had a useful lifetime of only 3 to 5 weeks. In cases where samples are concentration limited, high specific activity is the only alternative and a short sample lifetime should be expected. If the working concentration is not strictly limited by the properties of the sample, it is better to label at lower abundance and store the sample in dilute form, concentrating it only for NMR experiments. DNA and RNA labeling with tritium requires about the same amount of effort as the more common ^{13}C and ^{15}N techniques. In contrast to these nuclei, tritium is much more sensitive and can be directly detected without the need for water suppression.

5 CONCLUSION

The NMR properties of tritium are slightly better than those of ^{1}H, with essentially zero natural abundance. Hence it is possible to detect tritium with more sensitivity than the hydrogen it replaces, and spectral simplification is assured. Radioactivity is the only issue hindering the universal application of tritium in biological NMR studies.

6 RELATED ARTICLES

Biological Macromolecules: Structure Determination in Solution; Biological Macromolecules; Biological Macromolecules: NMR Parameters; Biosynthesis and Metabolic Pathways: Carbon-13 and Nitrogen-15 NMR; Biosynthesis and Metabolic Pathways: Deuterium NMR; Concentrated Solution Effects; DNA: A-, B-, and Z-; Enzymatic Transformations: Isotope Probes; Multidimensional Spectroscopy: Concepts; NOESY; Nucleic Acid Structures in Solution: Sequence Dependence; Nucleic Acids: Chemical Shifts; Nucleic Acids: Phosphorus-31 NMR; Nucleic Acids: Spectra, Structures, and Dynamics; Selective Relaxation Techniques in Biological NMR; Structures of Larger Proteins, Protein-Ligand, and Protein-DNA Complexes by Multi-Dimensional Heteronuclear NMR; Tritium NMR.

7 REFERENCES

1. E. A. Evans, D. C. Warrell, J. A. Elvidge, and J. R. Jones, *Handbook of Tritium NMR Spectroscopy and Applications*, Wiley, Chichester, 1985, pp. 1–249.
2. J. M. A. Al-Rawi, J. A. Elvidge, D. K. Jaiswal, J. R. Jones, and R. Thomas, *J. Chem. Soc., Chem. Commun.*, 1974, 220.
3. H. G. Floss and S. Lee, *Acc. Chem. Res.*, 1993, **26**, 116.
4. L. J. Altman, C. Y. Han, A. Bertolino, G. Handy, D. Laungani, W. Muller, S. Schwartz, D. Shanker, W. H. de Wolf, and F. Yang, *J. Am. Chem. Soc.*, 1978, **100**, 3235.
5. D. J. Aberhart, *Synth. Appl. Isot. Labeled Compd., Proc. Int. Symp.*, ed. W. P. Duncan and A. B. Susan, Elsevier, Amsterdam, 1983, p. 309.
6. C.-P. Pang, R. L. White, E. P. Abraham, D. H. G. Crout, M. Lutstorf, P. J. Morgan, and A. E. Derome, *Biochem. J.*, 1984, **222**, 777.

7. T. Frenzel, J. M. Beale, M. Kobayashi, M. H. Zenk, and H. G. Floss, *J. Am. Chem. Soc.*, 1988, **110**, 7878.
8. F. A. L. Anet, D. J. O'Leary, J. M. Beale, and H. G. Floss, *J. Am. Chem. Soc.*, 1989, **111**, 8935.
9. R. D. Newmark, S. Un, P. G. Williams, P. J. Carson, H. Morimoto, and M. P. Klein, *Proc. Natl. Acad. Sci. USA*, 1990, **87**, 583.
10. N. D. Priestley, H. G. Floss, W. A. Froland, J. D. Lipscomb, P. G. Williams, and H. Morimoto, *J. Am. Chem. Soc.*, 1992, **114**, 7561.
11. D. E. Wemmer and P. G. Williams, in *Methods in Enzymology*, ed. T. L. James and N. J. Oppenheimer, Academic Press, Orlando, FL, 1994, Vol. 239, p. 739.
12. J. N. S. Evans, G. Burton, P. E. Fagerness, N. E. Mackenzie, and A.I. Scott, *Biochemistry*, 1986, **25**, 905.
13. K. Gehring, P. G. Williams, J. G. Pelton, H. Morimoto, and D. E. Wemmer, *Biochemistry*, 1991, **30**, 5524.
14. V. Dive, A. Lai, G. Valensin, G. Saba, A. Yiotakis, and F. Toma, *Biopolymers*, 1991, **31**, 305.
15. A. Bergerat, W. Guschlbauer, and V. Fazakerley, *Proc. Natl. Acad. Sci. USA*, 1991, **88**, 6394.
16. T. M. O'Connell, J. T. Gerig, and P. G. Williams, *J. Am. Chem. Soc.*, 1993, **115**, 3048.

Acknowledgments

M.G.K. is supported by the Office of Energy Research, Office of Health and Environmental Research, Health Effects Research Division of the US Department of Energy under Contract DE-AC03-76SF00098, and through Instrumentation Grants from the US Department of Energy, DE FG05-86ER75281, and the National Science Foundation, DMB 86-09035. P.G.W. is supported by the Biomedical Research Technology Program, National Center for Research Resources, US National Institutes of Health, under Grant P41 RR01237, through Contract DE-AC03-76SF00098 with the US Department of Energy.

Biographical Sketches

Mark G. Kubinec. *b* 1964. B.S., 1986, biochemistry, B.S., 1987, chemistry, Michigan State University, USA, Ph.D., 1994, Chemistry, University of California, Berkeley, USA. Postdoctoral fellow, Lawrence Berkeley National Laboratory, 1995–present.

Philip G. Williams. *b* 1956. B.Sc., 1980, chemistry, Ph.D., 1984, Chemistry, University of New South Wales, Australia. Research Fellow, Ludwig Institute for Cancer Research, Sydney, Australia, 1984–85; staff scientist, Lawrence Berkeley Laboratory, USA, 1986–present. Approx. 70 publications Current research specialties: tritium labeling, tritium NMR.

Water Signal Suppression in NMR of Biomolecules

Maurice Guéron and Pierre Plateau
Ecole Polytechnique, Palaiseau, France

1	Introduction	1
2	Why Suppress the Solvent Signal?	3
3	Excitation Schemes for SSS	3
4	Experimental Aspects	7
5	Data Processing for SSS	9
6	Solvent Signal Suppression in 2D and 3D NMR	9
7	Conclusions	11
8	Related Articles	11
9	References	11

1 INTRODUCTION

1.1 Notation and Definition

An excitation sequence is made up of one or more pulses. It may be organized in subsequences of pulses. A selective pulse, subsequence, or sequence is one that excites spins in only a fraction of the spectral region of interest. Examples are a soft pulse and a DANTE subsequence. The prefix 'sub' may be omitted.

The term *saturation* is used to describe not only a state in which the longitudinal magnetization is zero throughout the sample, but any condition (e.g., that produced by forced nutation) that is operationally equivalent to uniform zero longitudinal magnetization.

1.2 Solvent Signal Suppression

It is often necessary to obtain proton NMR spectra of compounds whose concentration is in the millimolar range, dissolved in protonated solvents, such as H_2O rather than D_2O. This is the case for NMR of exchangeable protons, or in proton NMR in vivo. With nonselective pulse excitation, the high concentration of water protons, about 110 M, raises serious difficulties, such as saturation of the analog receiver or of the analog-to-digital converter, resulting in artifacts that could render the spectrum useless. It is therefore necessary to reduce the solvent signal.[1]

There are two stages in solvent signal suppression (SSS). The first is the reduction of the solvent contribution to the signal generated by the NMR probe, so as to prevent receiver saturation. This stage cannot be dispensed with. Methods for its implementation are of two types: those that perturb the solvent magnetization (e.g., by saturation), and those that leave it unchanged. The latter are preferred, or even indispensable, for the study of exchangeable protons.

The second stage consists in data postprocessing with the aim of further reduction of the residual solvent signal.

Suppression of the signal of the solvent, but not of the signals of the solutes, must use some difference between these. The most general difference is in the chemical shift, and most of this article is indeed devoted to SSS methods based on frequency differences between solvent and solutes.

However, any property distinguishing solvent from solute may be, and usually has been, recruited to aid in SSS. In the case of water, this includes

1. the small size of the molecule, leading to
   (a) fast rotational Brownian motion and hence long T_1,
   (b) fast translational Brownian motion and hence fast diffusion;
2. the equivalence of the two protons and consequent absence of J splitting;
3. the (obvious) lack of heteronuclear couplings to nitrogen or carbon.

An ideal SSS method would be universal, would suppress the solvent signal, and would leave all others unchanged. It would also be easy to implement, and would not be too demanding on the specifications of the spectrometer. In practice, the varieties of experimental situations and spectrometer limitations result in a large number of diverse cases, with different criteria for solvent suppression. Therefore, no SSS method is best for all cases at present. Despite this caveat, we shall risk general guidelines that apply to both 1D and nD NMR.

The first stage of SSS should reduce the solvent signal as required to avoid saturation of the receiver while keeping as small as possible any perturbations of the properties observable in the NMR spectrum, such as chemical exchange, NOE, signal-to-noise ratio and spectral (phase) distortions. Among frequency-selective SSS excitation sequences, the JR sequences described in Section 3.2.5 may be recommended on this basis.

All further reductions of the solvent signal should be left to data postprocessing. We recommend data processing in the frequency domain, including

1. the automatic subtraction of Lorentzians centered in a narrow window centered at the solvent frequency;
2. the automatic correction of spectral amplitude as required by the frequency-selective excitation procedure.

An elementary criterion for the quality of the SSS procedure is that NO linear phase correction or baseline correction should be needed, beyond those used on the same spectrometer in the case of excitation with a single 90° pulse.

1.3 A Single Long Pulse

In order to avoid excessive abstraction, we now describe a method of solvent signal suppression. It uses a single excitation pulse at the frequency of the spins of interest, such that they rotate by an angle θ away from Oz, whereas the solvent spins end up along Oz after the pulse.

A good description of the single long pulse method can be made in a *rotating frame*—one that rotates around the z axis at the excitation frequency (Figure 1a). In this frame, the excitation field $\boldsymbol{b}_1$ is static, and this is the effective field for a spin whose resonance frequency is equal to the excitation frequency. The effective field $\boldsymbol{b}_{\text{eff}}$ for the solvent spins, offset by $\omega/2\pi$ from the excitation frequency, has, besides the transverse component $\boldsymbol{b}_1$, a longitudinal component $(-\omega/\gamma)\boldsymbol{k}$,

where γ is the gyromagnetic ratio and $\boldsymbol{k}$ in the unit vector along the z axis. Each spin rotates around its effective field, at an angular frequency $\omega_{\text{eff}} = -\gamma|\boldsymbol{b}_{\text{eff}}|$.

At the end of a pulse lasting τ, the spins have rotated respectively by

$$\theta_{\text{resonant}} = -\gamma b_1 \tau \tag{1}$$

$$\theta_{\text{nonresonant}} = -\gamma \left[b_1^2 + \left(\frac{\omega}{\gamma}\right)^2 \right]^{1/2} \tau \tag{2}$$

Solvent signal suppression is obtained if $\theta_{\text{nonresonant}} = 2\pi$. Together with a choice of θ_{resonant}, this specifies the amplitude b_1 and duration τ of the pulse:

$$\tau = \frac{(4\pi^2 - \theta_{\text{resonant}}^2)^{1/2}}{|\omega|} \tag{3}$$

Equation (3) shows that the length of the pulse is a function of the frequency difference ω between the spins to be seen and those to be suppressed. More generally, for a strong variation of the excitation spectrum within a range ω_s, pulse lengths or intervals in the range of $2\pi/\omega_s$ are required. At 400 MHz, for a difference in chemical shift of 8 ppm, this corresponds to τ = 312 μs. To satisfy equation (1), a pulse of this length must be weak—or 'soft', as is commonly said.

The amplitude and phase of the transverse magnetization created by the soft pulse are shown in Figure 1(b) as functions of the frequency offset. The transverse magnetization is indeed zero at the solvent frequency, and maximum for the resonant spins. The phase of the transverse magnetization is approximately proportional to the frequency offset—the so-called linear phase shift.

This method has two qualities:

1. it is simple, and demands little of the spectrometer in terms of phase or amplitude modulation of the excitation pulse;
2. it restores the solvent magnetization to its original orientation.

It has two drawbacks:

1. the frequency of the excitation zero depends on the rf field amplitude [equation (2)], so that the degree of solvent signal suppression is susceptible to equipment drift;
2. compensation of the linear phase shift generates baseline distortions.

These features are important for SSS, and they will be considered anew as we examine principles and implementations of SSS.

1.4 Scope of This Article

Solvent signal suppression was originally developed in the framework of 1D NMR applications to chemistry and biochemistry. Nowadays, these applications often involve 2D and 3D NMR. SSS is also used in in vivo localized proton NMR spectroscopy, in which the rf field may be strongly inhomogeneous, and the water peak may have contributions not only from the volume of interest but also from large surrounding regions.

The emphasis of this article is on SSS fundamentals, which, despite differences in methodology, are the same in the three domains. Furthermore, the similarity in hardware and software

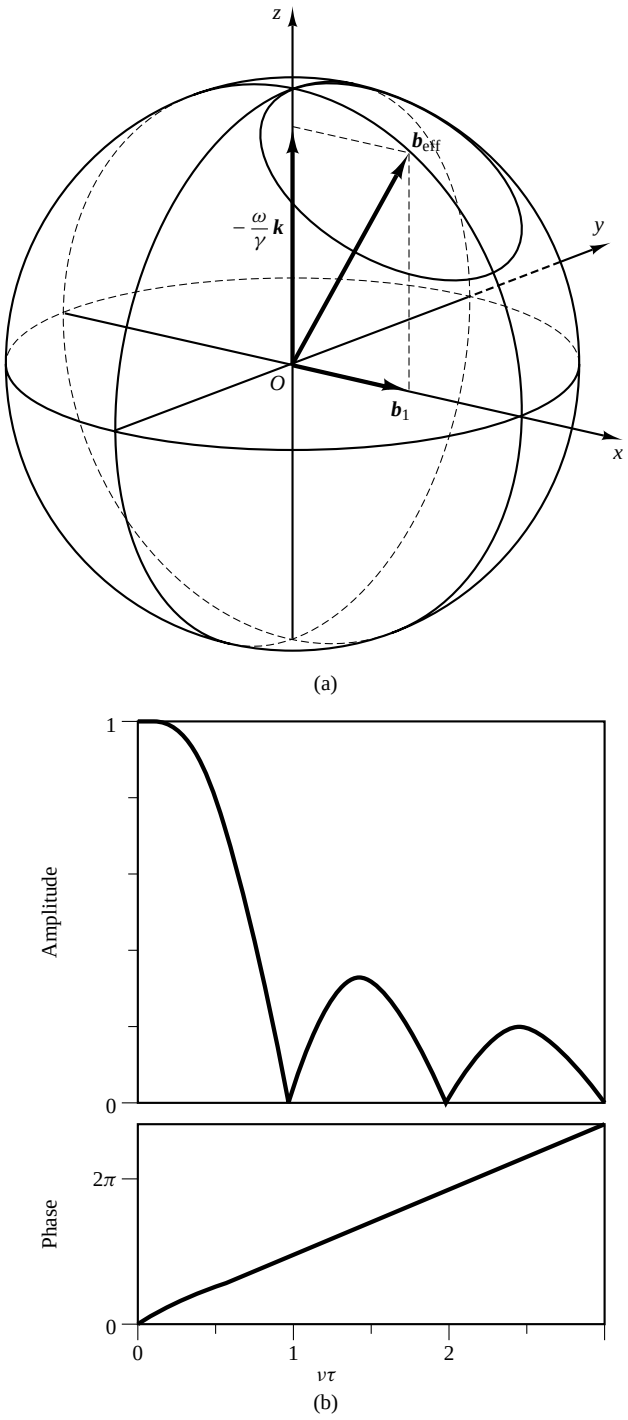

Figure 1 (a) The motion of the magnetic moment in the presence of a weak rotating field $\boldsymbol{b}_1$, as viewed in the frame rotating at the frequency of the field, aligned along Ox. The effective field $\boldsymbol{b}_{\text{eff}}$ is represented. Its components are $(-\omega/\gamma)\boldsymbol{k}$ and $\boldsymbol{b}_1$. The small circle is the trajectory of the magnetic moment, whose initial position is along the z axis. The scale is such that the lengths of the magnetic moment and of the effective field are equal. (b) Amplitude and phase of the transverse magnetic moment after a $\frac{1}{2}\pi$ pulse lasting τ, as a function of the frequency offset ν. The signal at $\nu = (\frac{15}{16})^{1/2}/\tau$ is suppressed (single long pulse technique). (Modified from M. Guéron, P. Plateau, and M. Decorps, in 'Progress in Nuclear Magnetic Resonance Spectroscopy', eds. J. W. Emsley, J. Feeney, and L. H. Sutcliffe, Pergamon Press, Oxford, 1991, Vol. 23, p. 138, Copyright 1991, with permission from Pergamon Press Ltd)

leads to comparable limitations on SSS. The discussion is mostly in terms of 1D NMR, and specific problems of 2D and 3D NMR are treated in a separate section. See also ***Water Suppression in Proton MRS of Humans and Animals***.

The question of SSS also arises in the context of subtractive techniques, as used for instance in homo- or heteronuclear editing techniques like reverse INEPT, or multiquantum NMR. The subtractive character may help considerably with respect to SSS. This is mostly outside the scope of the present article, as are tailored excitation,[2] the use of notch filters,[3] rapid scan FT NMR,[4] and stochastic excitation.[5]

The reader in need of more information on SSS is referred to the extensive original literature, to recent reviews,[6,7] and to related articles in this Encyclopedia.

2 WHY SUPPRESS THE SOLVENT SIGNAL?

Solvent signal suppression is required because it is impossible to acquire the free induction decay of the large solvent signal while maintaining maximum sensitivity for other signals.

2.1 Acquisition of the Free Precession

For good sensitivity, the noise issuing from the probe should be amplified to a value no less than one least significant bit of the analog-to-digital converter (ADC). Signals that are buried in the noise can then be recovered without loss in signal-to-noise ratio (S/N). The RMS thermal noise of a resistor r in a bandwidth $\Delta\nu$, $(4rk_{\mathrm{B}}T\ \Delta\nu)^{1/2}$, is 0.09 μV for 50 Ω and 10 kHz, and the appropriate receiver gain is then about 10^4 if the least significant bit of the ADC is 1 mV.

The maximum value of the FID must remain within the range of the ADC. It must therefore be less than 4096 times the noise for a 12-bit ADC, and 65 536 times for a 16-bit ADC. Since the noise increases with the bandwidth, the S/N of the FID, and together with it the required dynamic range of the receiver, may be reduced by increasing the bandwidth,[8] at no cost in the S/N of the spectrum.

The ratio of mean square signal to mean square noise $(\mathrm{S/N})^2$ at the beginning of the free precession following a $\frac{1}{2}\pi$ pulse is given by[7]

$$(\mathrm{S/N})^2 = \frac{mB_0/t_{\mathrm{R}}}{4Fk_{\mathrm{B}}T\,\Delta\nu} \tag{4}$$

where m is the magnetic moment within the probe, B_0 is the static field, and F is the noise factor of the receiver; t_{R} is the time for radiation damping[9] of a parallel-tuned circuit, given in SI units by

$$t_{\mathrm{R}}^{-1} = \frac{M\gamma\eta Q}{2\epsilon_0 c^2} \tag{5}$$

Here, $4\pi\epsilon_0 c^2 = 10^7$, M is the magnetization (the magnetic moment per unit volume), Q is the quality factor of the tuned circuit, and η is the filling factor. For water protons, M at equilibrium in a field B at room temperature is equal to $3.24 \times 10^{-3}B$, and $t_{\mathrm{R}}{}^{-1} = 168\eta QM$.

According to equation (4), the volt ratio $(\mathrm{S/N} \times 2\sqrt{2})$ of the *peak-to-peak* signal from 200 μL H_2O at 400 MHz to the RMS noise in a bandwidth of 10 kHz is about 3.8×10^5, or $2^{18.5}$, assuming that $Q\eta = 10$. Proper acquisition of the FID would thus require a 19-bit ADC together with a receiver having the same dynamic range. If a 12-bit ADC is used, the excitation procedure must reduce the water signal by a factor of at least 2^7, i.e., 128.

Note that the S/N of the FID is not equal to that of the spectrum. Indeed, the maximum value of the FID, right after a $\frac{1}{2}\pi$ pulse, corresponds to the integral of the spectrum, and is therefore independent of the linewidth, whereas the signal height in the spectrum is inversely proportional to it.

After attenuation by a factor of 128, sufficient for signal acquisition, the remaining water signal is still huge, but it may be reduced by postacquisition processing. Acquisition methods that provide a larger SSS factor than strictly required by the constraint of dynamic range are convenient, because they are more tolerant of spectrometer imperfections and may require less postacquisition processing. However, they have some problems. Typically, they use second- or third-order suppression, which creates a large region near the solvent frequency where the magnetic signals, but not the thermal noise of the probe, are reduced. The longer excitation sequence may affect measurements requiring multiple, closely spaced excitation pulses (spin echoes, inversion–recovery, 2D NMR, localized spectroscopy). It may also create spurious effects of cross polarization (NOE) and chemical exchange. Postacquisition processing suffers from none of these defects, and is therefore preferable in principle.

2.2 The 'Rolling Baseline'

Let us go back to the single long pulse described in Section 1. At the end of the pulse, the water magnetization is returned to the z axis, there is no transverse magnetization, and the amplitude of the water signal is zero.

Consider now a Bloch spin with central frequency ω_{C} close to, but distinct from that of the solvent. At the end of the excitation pulse, its magnetization will have a small transverse component. This will generate a FID, which will, as usual, decay exponentially according to T_2, and whose Fourier transform will therefore be the customary Lorentzian, or, in other words, the Bloch lineshape. The point is that this Lorentzian will have a finite, nonzero amplitude at the frequency of the solvent, that is, at the frequency of null excitation!

This shows that the solvent suppression scheme does not, strictly speaking, generate a frequency-dependent attenuation.[7] Rather, *it attenuates without distortion each Lorentzian line as a function of its central frequency: the suppression procedure acts on the entire Lorentzian*. In the same way, each Lorentzian is phase-shifted by a *constant* phase angle that is only a function of the central frequency.

This is not the same thing as a frequency-dependent phase shift,[1] and it cannot therefore be corrected by a true frequency-dependent phase shift of opposite value. Such a correction does not conserve Lorentzians, and this gives rise to the 'rolling baseline' defect that appears in Figure 2. This defect could be avoided by more sophisticated correction procedures.[7] Even better would be excitation procedures that do not produce a linear phase shift.

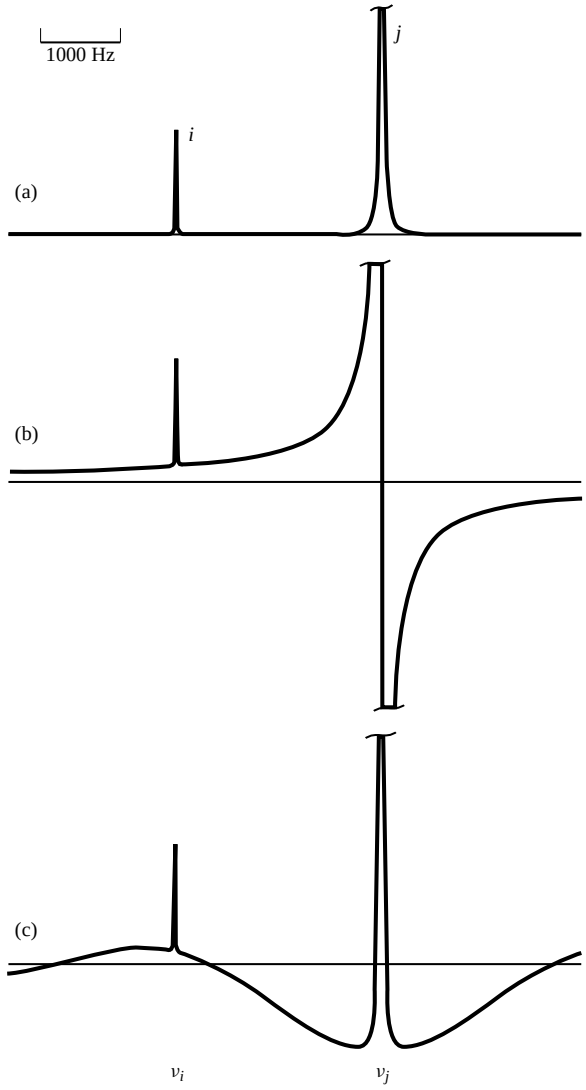

Figure 2 Simulated spectra of two Lorentzian lines (from species i and j), having the same width (5 Hz), and whose intensities are in the ratio of 1:100. The frequency separation is 2500 Hz. Only the absorption is shown. (a) The Fourier transform of the response to a hard pulse is the true spectrum, $S(\omega) = S_i(\omega) + S_j(\omega)$. (b) The Fourier transform $E(\omega)$ of the same response, except that acquisition begins 400 μs after the hard pulse. It is the sum of the two Lorentzians, with their phases offset by $\frac{1}{2}\pi$. The constant phase is chosen so that line i is phased in absorption. (c) The spectrum $D(\omega)$ that results from the application of a linear phase correction to $E(\omega)$, chosen so that each line is properly phased near its center. Since the phase varies with frequency, each line is distorted to a non-Lorentzian shape. The 'baseline roll' comes from the dispersion wing of the intense j line. (Reproduced from M. Guéron, P. Plateau, and M. Decorps, in 'Progress in Nuclear Magnetic Resonance Spectroscopy', eds. J. W. Emsley, J. Feeney, and L. H. Sutcliffe, Pergamon Press, Oxford, 1991, Vol. 23, p. 151, Copyright 1991, with permission from Pergamon Press Ltd)

3 EXCITATION SCHEMES FOR SSS

The number and variety of SSS methods may seem overwhelming, with new ones being published monthly. One may nevertheless attempt to clarify the situation, as follows.

1. Many methods are useful only in particular conditions.
2. Interesting new methods are usually those that take advantage of the new possibilities of modern spectrometers, in particular fast and flexible control of rf phase and amplitude, and, most importantly, the generation of pulsed gradients.
3. Methods with modest hardware requirements are accessible to more users, and they are less susceptible to hardware imperfections. This argues in favor of symmetric sequences, which help to compensate spectrometer imperfections; short sequences, which minimize spurious evolutions (e.g., radiation damping and magnetization transfer) during the sequence; and strong pulses.
4. The linear phase shift is a source of distortions that are only corrected with difficulty: it can and should be avoided.
5. Many SSS excitation methods lead to saturation of the solvent resonance, and this may change the magnetization of some solute protons (e.g., imino protons of nucleic acids) by way of NOE or chemical exchange. Methods that leave the solvent magnetization at equilibrium do not produce such side effects. They are therefore more generally applicable.

In this section, we present a selection of SSS methods that provide examples of the characteristics just described. They are separated into two classes: those that alter the solvent magnetization and those that do not.

3.1 Methods That Alter the Solvent Magnetization

SSS may be obtained by canceling the solvent magnetization. Solvent/solute discrimination may be based on a difference in the chemical shift, or in the rates of longitudinal or transverse relaxation or even of diffusion. Methods based on relaxation require a time in the range of T_1 or T_2. Methods based on the inhomogeneity of the main field B_0 or of the rf field b_1 may operate much faster. The required time is in the range of $(\gamma\delta)^{-1}$, where δ is the variation of the field over the sample.

Let us start with relaxation-based methods. In method (a) (Figure 3), the solvent magnetization is selectively saturated by a long and weak pulse at the solvent resonance frequency, after which the strong observation pulse is applied. In method (b), the solvent magnetization is selectively inverted by a weak pulse or by a series of intense pulses, the so-called DANTE sequence,[10] and residual transverse magnetization is destroyed with a gradient pulse. The observation pulse is applied when the longitudinal magnetization becomes null, after a time T_1 ln 2, where T_1 is the longitudinal relaxation time of the solvent. Method (c) (WEFT)[11,12] is a variant of (b). It is simple to set up in that it uses only strong, nonselective pulses. Because all spins are inverted by the first pulse, it works only if the *longitudinal* relaxation of the solvent is slower than that of the protons of interest. This will often be the case, because of the relatively small size of the water molecule, which results in a large *rotational* diffusion coefficient.

When the *transverse* relaxation of the solvent is faster than that of the spins of interest, one can achieve SSS by the WATR method.[13] This is a spin echo method, in which the refocusing π pulse occurs after a time much longer than the transverse relaxation time of water protons, which are therefore not refocused. Relaxation may be enhanced by paramagnetic ions,[14] or by proton exchange with ammonia or urea.[15] The

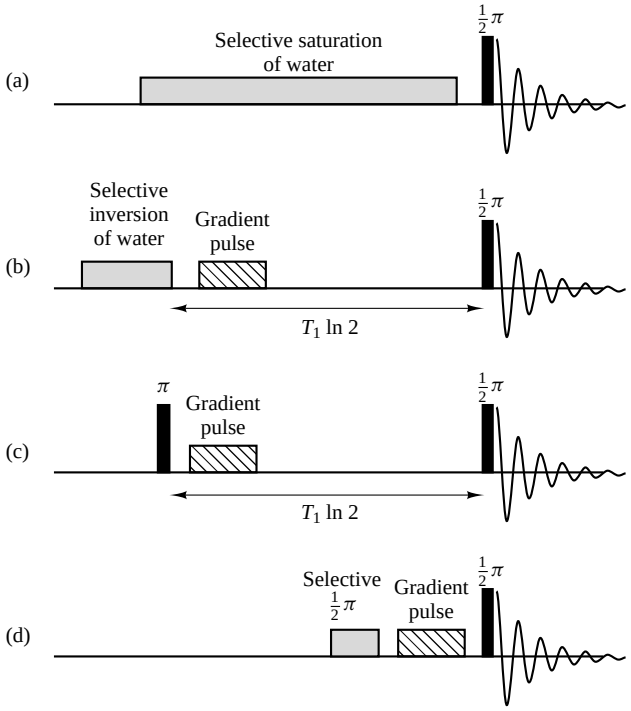

Figure 3 Four SSS sequences, based on saturation of the solvent signal. In methods (a) and (b), discrimination between solvent and solutes is achieved by frequency-selective excitation. In method (c), the water proton is selected by its long longitudinal relaxation time. Method (d), in contrast to (a)–(c), produces saturation quickly, independently of relaxation. (Modified from M. Guéron, P. Plateau, and M. Decorps, in 'Progress in Nuclear Magnetic Resonance Spectroscopy', eds. J. W. Emsley, J. Feeney, and L. H. Sutcliffe, Pergamon Press, Oxford, 1991, Vol. 23, p. 154, Copyright 1991, with permission from Pergamon Press Ltd)

method is also applied to the elimination of the signal from water or fat in biological tissues. Both WEFT and WATR have a flat spectral response, including at the solvent frequency.

Spurious effects of solvent saturation are reduced in methods that achieve solvent saturation quickly, independently of relaxation. In method (d) of Figure 3, a selective $\frac{1}{2}\pi$ pulse is followed by a gradient pulse ('homospoil'), which destroys the transverse magnetization.[16] With forced nutation[17] in an inhomogeneous rf field $b_1 \pm \delta b_1$, saturation is obtained in a time $(\gamma\ \delta b_1)^{-1}$. Forced nutation of the solvent spins may be combined with *spin locking* of the solute spins, so that all signals, including the solvent residual, end up in-phase. The method applies to 1D and 2D NMR and to in vivo spectroscopy.[18–21] This is also the case for the 'WATERGATE' (water-suppression by gradient-tailored excitation) method when the observed signal is a spin echo, from which the water proton signal is absent because the refocusing π pulse is selective.[22]

In the 'DRYCLEAN' method,[23] one uses the large *translational* diffusion coefficient of water as compared with macromolecules: the transverse water magnetization is selectively destroyed by the application of a pulsed magnetic field gradient during a spin echo sequence.[24] A beautiful extension of this concept has been made in the case of proton NMR of perfused cells,[25] for which SSS is particularly important, since the cells occupy only a small fraction (about 1%) of the total volume. Furthermore, the signals of the extracellular solutes must also be suppressed. The diffusion method discriminates between intra- and extracellular products, because the range of diffusion of the latter is restricted by the cell membrane. For an appropriate duration of the gradient pulse, signals from extracellular water and solute are suppressed, while the intracellular ones are unaffected by diffusion. The signal of the intramolecular water is suppressed by other characteristics of the excitation sequence, such as frequency selectivity.

3.2 Methods That Avoid Solvent Saturation

3.2.1 Long Pulses

A weak or long or selective pulse is one for which b_1 is smaller than the chemical shift range of the spectrum, so that the pulse acts differently on different spin species. These differences are used in the 'long pulse' suppression methods, such as the 'single long pulse' described in Section 1.

The excitation spectrum of a long pulse may be usefully modified by modulating its phase, as in Redfield's '214' pulse,[1] whose time sequence is $2\underline{1}4\underline{1}2$, the underlined numbers corresponding to times during which the phase is shifted by π. Its excitation spectrum has two closely spaced zeros. Similar sequences have a second-order zero.[7] This protects against instrumental imperfections, such as inhomogeneity or drift in field or in temperature, all of which generate water signals at frequencies differing slightly from the nominal excitation zero. The sequence is also less sensitive to rf field inhomogeneity. The cost is reduced sensitivity close to the solvent frequency.

3.2.2 Short Pulses; Binomial Sequences

Binomial sequences consist of sequences of pulses whose amplitudes are proportional to the binomial coefficients, separated by equal interpulse delays. The simplest binomial sequence is 1, 1 (two pulses of equal amplitude and phase, separated by a delay), at the frequency of maximum signal. An exact, as opposed to linear, description may be given in the rotating frame. The first pulse tilts the spins by, for instance, $\frac{1}{6}\pi$ in the direction of the y axis. During the delay, the solvent spins rotate by $\omega\tau = \pi$ and the spins to be observed are immobile. The second and last pulse, at time 0, brings the water protons back along Oz, while the spins to be observed end up tilted by $\frac{1}{3}\pi$ towards the y axis (Figure 4). Spins with intermediate chemical shifts are less tilted, and their transverse components have different directions, corresponding to a frequency-dependent phase shift.

The excitation may be described as two delta functions of opposite sign, at times $-\tau$ and 0. In the linear approximation, the spin response is determined by the Fourier transform of this sequence (the excitation spectrum), which is simply $e^{-i\omega\tau} + 1$, or $2e^{-i\omega\tau/2} \cos \frac{1}{2}\omega\tau$. The latter expression displays the frequency dependence of amplitude and phase. The amplitude is maximum for $\omega\tau = 0$, and zero for $\omega\tau = \pi$. The phase varies linearly from 0 to $\frac{1}{2}\pi$ in this frequency range.

This sequence has the following properties.

1. The evolution of the spins is easily described, because the excitation is a combination of hard pulses during which all spins rotate around the same pulse axis, and of waiting periods during which all spins rotate around the same Oz axis.

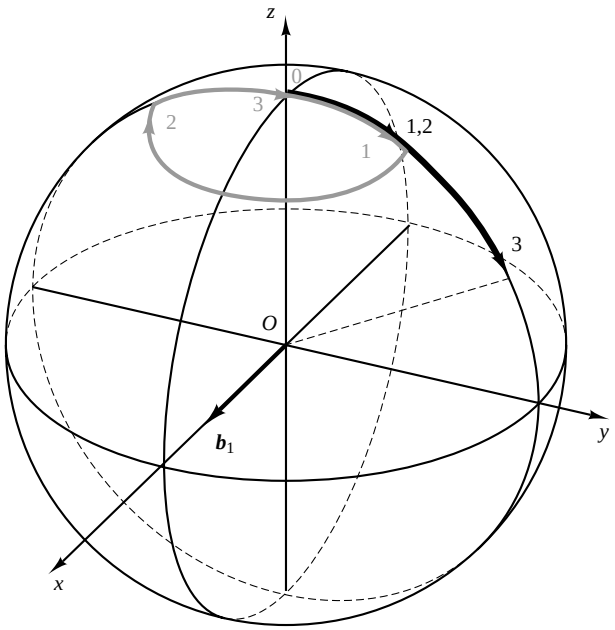

Figure 4 The simplest binomial SSS sequence: 1, 1. The gray line represents the motion of the solvent magnetization, ending in the *Oz* direction; the black line represents the motion of the magnetization of the resonant spins. (Modified from M. Guéron, P. Plateau, and M. Decorps, in 'Progress in Nuclear Magnetic Resonance Spectroscopy', eds. J. W. Emsley, J. Feeney, and L. H. Sutcliffe, Pergamon Press, Oxford, 1991, Vol. 23, p. 157, Copyright 1991, with permission from Pergamon Press Ltd)

2. Hard pulses provide excitation over a large spectral region.
3. Owing to the symmetry of the sequence, spatial inhomogeneity or long-term drift of the pulse amplitude does not change the frequency of the excitation zero.

In the linear approximation, a binomial sequence of order n provides suppression to the same order. The 1, −2, 1 (i.e., 1, −1, immediately followed by −1, 1) and 1, 2, 1 excitation sequences provide second-order suppression for all pulse angles.

The main drawback of the binomial sequences is the linear phase shift of the excitation spectrum. It is considerably reduced, without change of the amplitude response, in a *modified binomial sequence*, which consists of a binomial inserted between a $-\pi$ and a $+\pi$ pulse.[7,26,27] More complex hard pulse SSS sequences can be built on the basis of extensive computer searches.[28,29]

3.2.3 Combinations of Selective and Nonselective Subsequences

As an example, consider a sequence consisting of a soft pulse of angle θ, followed by a hard pulse of angle $-\theta$, both at the solvent frequency.[11] The response to the soft pulse has strong phase shifts, but it is limited to a narrow range around the solvent frequency. The subsequent hard pulse provides nonselective excitation without phase shift, and cancels the effect of the soft pulse on the solvent magnetization. This sequence therefore provides a nearly flat and phased response. In this way, the two functions of the excitation sequence, signal suppression in a narrow range and observation in a broad range, are well separated. On the other hand, the inherent asymmetry of the method makes it sensitive to hardware imperfections.

3.2.4 Echoes, Gradients and EXORCYCLE

The linear phase may be avoided by generation of a spin echo. An echo excitation sequence consists of two parts: the excitation subsequence E1, which generates transverse magnetization, and a refocusing subsequence E2. E1 and/or E2 may be designed to provide SSS.

If E1 is a selective binomial, it produces a linear phase shift whose sign corresponds to a *delay*. This is changed to one corresponding to an *advance* in the echo. The latter is easily compensated by waiting for an equal time following the echo center time, prior to the acquisition. Another procedure is to acquire the complete echo. Its Fourier transform has an imaginary component, but nevertheless it has no contribution from the dispersion of any spin signal, so that a frequency-dependent phase correction will not produce much baseline roll. The properties of complete echoes have been applied to magnetic resonance imaging and 2D NMR, and recently to in vivo proton spectroscopy.[30] They can also be used for phase correction of the free precession itself, as in the 'pseudoecho' method.[28,31] The order of the zero in the spectral response to an echo sequence may be uncomfortably high. For instance if E1 and E2 have a first-order zero at the solvent frequency, the zero of the echo response is third order.

An echo may be generated by a 90° pulse for E1 and a 180° pulse for E2. With other subsequences, spurious free precession contributions combine with the echo. Such deviations occur when the rf field is inhomogeneous, for instance in in vivo spectroscopy with surface coils, and with frequency-selective excitation for SSS. To obtain a pure echo under such conditions, one may use sequences in which the transverse magnetization is suppressed at appropriate times with a pulsed gradient. Or one may add successive acquisitions in which the excitation phases are shifted according to the EXORCYCLE scheme.[7,32]

3.2.5 Jump and Return (JR)

The 'jump and return' (JR) excitation sequence includes two $\frac{1}{2}\pi$ pulses of opposite phases, at the solvent frequency.[33] The first pulse brings all spins along *Oy* in the rotating frame (Figure 5). During the interval between the pulses, the water protons remain along *Oy* and the spins of interest precess by $\frac{1}{2}\pi$ in the equatorial *xOy* plane. The second pulse rotates the *xOy* plane into the vertical *xOz* plane, so that all spin species end up with their transverse component along $\pm Ox$. Hence, the phase is constant across the spectrum, except for a step of π at the solvent frequency (Figure 6a). The solvent magnetization ends up along *Oz*, providing first-order SSS. Spins for which $\omega\tau = \frac{1}{2}\pi$ end up along *Ox*, corresponding to maximum signal.

The three successive rotations of the magnetization that are produced by JR have the same effect as a single rotation of angle $\omega\tau$ around *Oy*. This result is valid whatever the original orientation of the magnetization. For instance, two successive JR excitations rotate the ($\omega\tau = \frac{1}{2}\pi$) spins by π while preserving SSS.

The most interesting property of JR is the *lack of linear phase shift*, a property that obtains only for a specific pulse angle, $\frac{1}{2}\pi$ (or multiples), in the case of a very large b_1 field. If

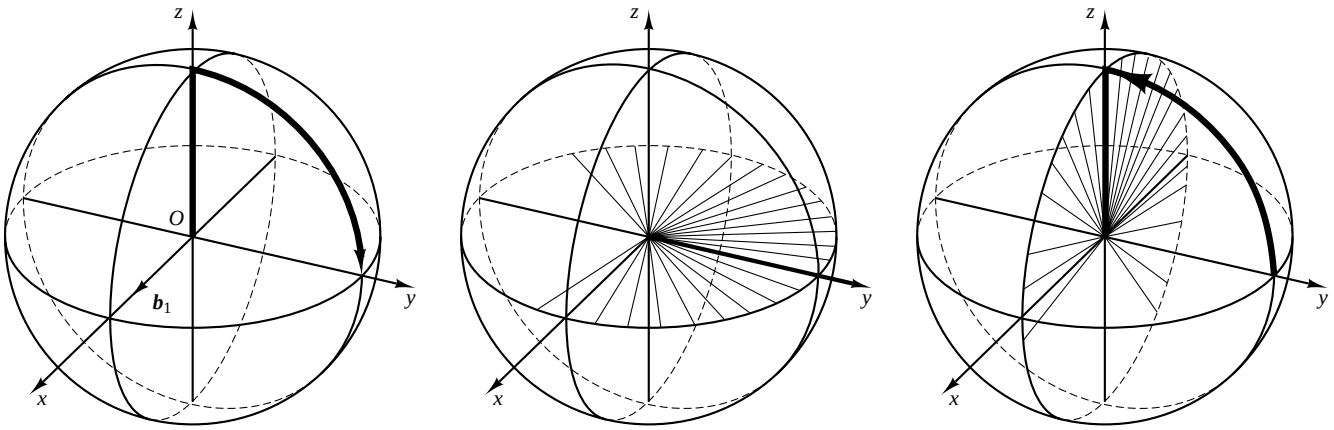

Figure 5 The 'jump and return' sequence. With the first $\frac{1}{2}\pi$ pulse, all spins jump to the *Oy* direction. During the waiting time τ, they rotate in the (x,y) plane by $\omega\tau$, ω being their frequency offset from the pulse frequency, which is the resonance frequency of the solvent. The second pulse, $-\frac{1}{2}\pi$, brings all spins in the (z,x) plane; hence, their transverse magnetizations are all along $\pm Ox$, so that there is no linear phase shift. The solvent spins return to the starting position along Oz. The effect of JR on each spin is a rotation by $\omega\tau$ around Oy. (Reproduced from M. Guéron, P. Plateau, and M. Decorps, in 'Progress in Nuclear Magnetic Resonance Spectroscopy', eds. J. W. Emsley, J. Feeney, and L. H. Sutcliffe, Pergamon Press, Oxford, 1991, Vol. 23, p. 160, Copyright 1991, with permission from Pergamon Press Ltd)

the angle differs slightly from this value, there will be a slight linear phase shift. But the SSS feature will not be affected. This makes the JR sequence robust with respect to spectrometer instability.

JR is the shortest known SSS sequence, being twice as short as the shortest binomial sequence, 1, −1: with JR, the spins of interest precess by $\frac{1}{2}\pi$ during the waiting period, whereas with 1, −1, the precession angle is π (Figure 4).

For spins whose frequency is close to that of maximum sensitivity, the rotation angle is close to $\frac{1}{2}\pi$. Thus, one can create an SSS version of any multipulse sequence of $\frac{1}{2}\pi$ pulses (or multiples) by simply replacing each pulse by a JR sequence. Application to 2D NMR is discussed in Section 6.

If the pulse angle is larger than $\frac{1}{2}\pi$, the JR sequence produces a phase shift corresponding to a negative delay, leading to a *spin echo*.[27]

The JR sequence is simple to adjust. The residual water signal should be observed on the free precession, whose phase and quadrature components should be available for display. The adjustment process is preferably carried out by analog controls in real time, rather than by computer-controlled procedures, whose response may be inconveniently slow. The *Ox* component is canceled by adjusting either the excitation frequency or the phase of one of the pulses. The *Oy* component is canceled by adjusting the length of one pulse. In this way, one corrects for hardware errors, as well as for movements of the water proton magnetization in the rotating frame due to frequency maladjustment, longitudinal relaxation, and radiation damping. JR has intrinsic compensation for transverse relaxation.

JR can be adapted to excitation frequencies distinct from the solvent frequency.

When the b_1 field is not very large, the JR response presents a quasilinear phase shift, and the frequency of maximum response is modified. These effects are avoided with the *power-adapted JR* (PJR) procedure,[27] whose frequency response is very close in phase and amplitude to that of JR with infinitely strong pulses. Let t_p be the length of a $\frac{1}{2}\pi$ pulse and let τ, as before, be equal to $\pi/2\omega_{max}$. Define a power parameter p by

$$p = t_p/\tau \tag{6}$$

In power-adapted JR, the pulse length is

$$t'_p = \frac{t_p}{1-(2/\pi)p} \tag{7}$$

and the interval τ' between the beginnings of the pulses is

$$\tau' = \tau(1-\tfrac{1}{3}p) \tag{8}$$

The JR sequence shares with the 1, −1 sequence a linear amplitude response for Larmor frequencies close to that of the solvent. This is a blessing, since it enables one to observe signals close to the solvent. Although solvent suppression is not as good as with higher-order sequences, this may be corrected after the acquisition. Alternatively, one may use SJR, a second-order modification of JR.[33]

4 EXPERIMENTAL ASPECTS

SSS is affected by instrumental imperfections of the excitation sequence, by relaxation and radiation damping during excitation, and by inhomogeneities in the static and rf fields. The practical analysis and adjustment of an SSS sequence require observation of the free induction decay in real time on an oscilloscope. A discussion of these matters may be found in Guéron et al.[7] Only a brief survey is given here.

Relaxation and radiation damping affect SSS by reorienting the magnetic moment of solvent spins during the excitation period. Radiation damping is the most significant, because its rate is usually the largest and because it may be inhomogeneous in the sample. Some SSS sequences (e.g., the binomial 1, −2, 1) automatically provide first-order compensation of radiation damping.

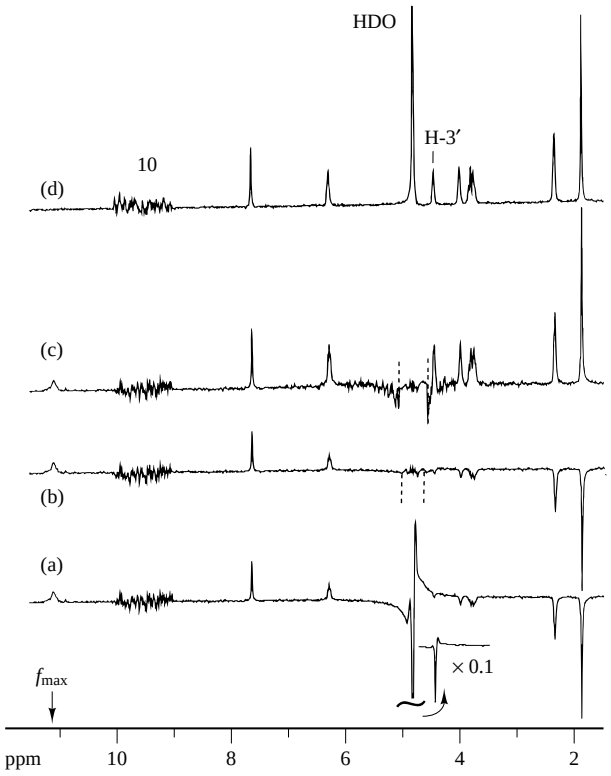

Figure 6 Proposed standard test for SSS. (a) JR spectrum of thymidine, 10 mM, in 90% H_2O, 10% D_2O. A single FID was collected. The length of a $\frac{1}{2}\pi$ pulse was 10 μs. The frequency of maximum sensitivity is at 11.1 ppm. No phase correction was applied, except for that used in the case of single pulse excitation. The imino proton signal (11.1 ppm) is broadened by exchange. Exponential multiplication provides 3 Hz broadening and insures that the peak heights are not sensitive to field inhomogeneity. By comparison with the H-5 signal at 7.7 ppm [spectra (a)–(d)], the suppression factor is about 1000. Proton frequency, 360 MHz; 5 mm outer-diameter sample tube; T = 20 °C, pH 4. Acquisition and data processing were performed with networked 80386 PC-type computers, running MS-DOS, with 20 MHz clock. (b) Spectrum derived from (a) by repeated subtraction (10 times) of a Lorentzian simulating the tallest peak within ±75 Hz of water (dotted lines). Total processing time 4 s. (c) Spectrum derived from (b) by correction of the JR amplitude response. The correction, which is not applied to the range within ±95 Hz of water (dotted lines), does not change the signal-to-noise ratio. (d) Spectrum of thymidine, 10 mM, in D_2O, following a single $\frac{1}{2}\pi$ pulse. Other conditions are as in (a). This spectrum is provided as a reference for evaluation of spectrum (c), which is the result of JR excitation and processing. In spectrum (c), (i) the maximum sensitivity is the same as in (d), (ii) relative signal amplitudes are respected, and (iii) the H-3′ signal at 4.45 ppm demonstates good observability and lack of artifacts near the water position (4.82 ppm). Spectrum (c) was obtained from the FID in about 6 s processing time. (Reproduced from M. Guéron, P. Plateau, and M. Decorps, in 'Progress in Nuclear Magnetic Resonance Spectroscopy', eds. J. W. Emsley, J. Feeney, and L. H. Sutcliffe, Pergamon Press, Oxford, 1991, Vol. 23, p. 135, Copyright 1991, with permission from Pergamon Press Ltd)

Static field inhomogeneities also affects SSS, particularly those such as Z^2 that give asymmetric lineshapes. It may also happen that small fractions of the sample suffer from large field offsets—either because they are rather far from the center of the sample or because of diamagnetic susceptibility anomalies. Examples are isolated drops on the sample tube wall, and the sample region located at the bottom of the sample tube. If they amount to 1% of the sample volume, they may limit the SSS factor to a few hundred. Even worse, they may generate artifactual lines in the spectrum. Appropriate probe designs help to reduce these problems. Sample tubes with a flat bottom and a long tail are recommended.[7]

4.1 Spectrometer Imperfections

Most SSS methods operate by compensation. For instance, one part of the excitation sequence moves the solvent magnetization away from Oz, another brings it back. Errors in *pulse amplitude*, *phase*, *timing* or *frequency* may ruin the compensation. Such errors may be static, or they may vary slowly (drift) or rapidly (fluctuations).

Static errors (e.g., of the phase) may be compensated for, if the spectrometer has provisions for appropriate adjustment. *Drift* of frequency, timing, or phase of the rf pulse generator should not be a problem in a spectrometer that is reasonably built and operated. The main sources of drift are the power amplifier, the temperature controller and the field/frequency lock. If the deuterated compound used for locking is not D_2O, the relative chemical shift of water will be changed by temperature drift, affecting SSS. Instrumental *fluctuations*, i.e., variations on the timescale of the SSS sequence, directly affect the compensation between pulses. They are easily observed as fluctuating differences between successive residual solvent signals following SSS excitation. For instance, we measured phase fluctuations of 1/1600 rad in the time between the two JR pulses. For a preliminary and easy measurement of the spectrometer fluctuations, one may look for fluctuations of the nominally null dispersion component of the free precession of a strong signal at the excitation frequency.[7]

4.2 Modern Spectrometers

Modern spectrometers have improved agility—meaning the capability of shaping rf excitation to high resolution in amplitude, phase, and frequency as a function of time. With the help of optimization techniques and/or on the basis of the Bloch equations, one may then impose desirable conditions on the excitation sequence. A recent example is a flexible procedure for the design of an excitation spectrum identical to any available NMR spectrum.[34] New SSS sequences may now be endowed with many more parameters, and they may be designed, for instance, with the aim of obtaining constant phase and amplitude accross the spectrum, except for a 'notch' at the solvent frequency.[35] Earlier SSS sequences can be revised by changing the pulse shape (from square to Gaussian, half-Gaussian, etc.) and phase. SSS will certainly benefit from the enhanced agility. However, the benefits should be limited, because pulse sequences with improved selectivity properties tend to be longer.

Probably more important for SSS is the improvement in stability and quality of the rf pulse generators, which should result in better results with a given SSS sequence.

Another important feature of modern spectrometers is the generation of a pulsed gradient of the main field, resulting in the destruction, and possibly the later recall, of any transverse magnetization existing at that time. SSS sequences using a

pulsed field gradient have been mentioned above, for example, the WATERGATE sequence (Section 3.1). Potential problems are the distortion of the pulsed field gradient by eddy currents and the perturbation of the field lock system during the pulse. An rf field gradient, which may provide the same benefits as a gradient of the main field, does not have these problems,[36] and could come into current use.

4.3 Evaluation Procedures and Test Samples

Detailed study of the performance of a method and of a spectrometer is usefully complemented by a global test, namely, the spectrum of a standard sample, designed to provide clear indications of the suppression factor, the sensitivity, and the type and amount of data processing required. We suggest a standard sample containing thymidine in H_2O, at a concentration of 10 mM. The excitation sequence should maximize the imino proton line, at -11.1 ppm. The spectrum should extend up to 1 ppm, exhibiting the aromatic, ribose, water, and methyl lines. A similar sample, but in D_2O, should be used for comparison. The spectrum should be examined, both before and after data processing, for reduction in sensitivity, artifacts, distortions of peaks and baseline, and reduction in visibility of lines close to the solvent line. Such defects are more important than the residual solvent signal per se. Figure 6 shows an application to the JR sequence.

5 DATA PROCESSING FOR SSS

The free precession resulting from SSS excitation, although it is within the dynamic range of the NMR receiver, may still contain a large solvent signal, which must be further reduced by postacquisition data processing. Data processing is invariably based on prior knowledge of the signal to be reduced (e.g., its frequency). It is carried out either in the time or frequency domain.

The elimination of a (solvent) signal on the basis of its frequency may be obtained with a frequency filter, which will strongly attenuate all of a Lorentzian centered at the filter frequency. For instance, subtracting from a FID its time-shifted copy filters out a signal at zero frequency.[37] Unfortunately, this convenient method introduces a linear phase shift.

A frequent defect of SSS spectra is the 'rolling baseline' resulting typically from linear phase correction acting on the solvent line. More or less empirical methods for baseline correction are usually provided on commercial equipment. The results are far from perfect. Worse, they may lead to systematic errors, for instance, in integration. To avoid this, the solvent signal should be eliminated before attempting linear phase correction. In our opinion, the best method is to treat the residual solvent signal as a collection of Lorentzians, which are simulated and subtracted recurrently, one at a time.[7] The procedure is fast and distortionless. It may be made entirely automatic (Figure 6). The general methods of maximum entropy[38] or linear prediction[39] may also be used.

In most SSS methods, the gain is a function of frequency, or, more precisely, the amplitude of a Lorentzian is a function of its center frequency. A frequency-dependent amplitude correction restores each Lorentzian peak to its correct height. This does produce distortions, but they are much less severe than those caused by phase correction.

Further spectral distortions in phase and amplitude arise owing to the noninfinite strength of the b_1 field (such effects motivate the use of PJR instead of JR). As a first step towards correcting these defects, it would be useful and possible to provide NMR spectrometers with software that would calculate amplitude and phase shift for an arbitrary excitation sequence.

6 SOLVENT SIGNAL SUPPRESSION IN 2D AND 3D NMR

This section, mainly contributed by A. G. Redfield of Brandeis University, is to a large extent based on limited personal experience. Therefore, references to recent excellent work may in some cases be inadvertently omitted.

6.1 General

We shall assume general familiarity with established methods and notations of 2D NMR.[40,41]

The solvent signal is not nearly so large a problem in 2D and 3D NMR as it is in 1D NMR, because, generally, one is interested only in cross peaks between two lines in the spectrum, and most often one of these is located far enough from the water peak to be observable with relatively simple means such as water presaturation. Cross peaks are commonly observable to protons of the amide and β-carbons, from protons of α-carbons that are within a few tens of hertz from the water resonance, and in some cases NOEs from peaks directly underneath water are observable. Furthermore, most 2D studies have been performed on extremely small biopolymers, i.e., proteins smaller than 15 kDa, or nucleic acid duplexes smaller than 15 base pairs. For these small molecules, the loss of signal by cross relaxation to saturated water[42] is relatively small. And, since the object of 2D NMR has often been primarily to determine structure, rather than study kinetics, the pH can often be chosen to minimize the other process of signal loss when water is saturated, namely, chemical exchange with water.

Furthermore, the nature of many 2D experiments is such as to cancel and filter out the direct effect of water signals and other large signals. Most heteronuclear 2D methods, and certain homonuclear methods such as double quantum filtered COSY,[41] are in this class. Especially for these experiments, the baseline roll far from water is not a problem. It is also often not a problem for many experiments, such as NOESY, where a large residual water self-peak does occur, because usually one of the two protons giving rise to interesting cross peaks is far from water, as mentioned above.

For these reasons, SSS methods have not been developed as intensively for 2D NMR as they have been, for example, by practitioners of in vivo NMR. Nevertheless, there is a need for continued development. Partly because each FID in a 2D data set results from the accumulation of only a few (typically 4–32) individual signals, averaging of random water signals due to random phase errors in selective sequences, or in water saturation, is not as effective as it is in some 1D experiments. These random signals result in random baseline variation in

each 1D spectrum obtained from the 2D data set by Fourier transformation (FT) with respect to the real-time dimension t_2, before FT in the second, evolution or t_1, dimension. As a result, there is an ugly stripe in the final 2D spectrum along the line corresponding to the solvent frequency in the f_1 dimension, exhibiting streaks extending roughly 1 ppm in the f_2 direction. Similar noise emanates from residual HDO in D_2O solvent, if HDO is not saturated, and from other strong signals such as buffer signals.

These streaks are known as 'phase noise', and they can often be reduced by computer flattening of the baseline of each spectrum after the FT in the t_2 dimension, or by other operations on the frequency domain spectrum based on the known frequency of water,[43] by time domain removal of the low-frequency water signal,[44] or by simple convolution difference weighting. The latter weighting produces undesirable troughs near the diagonal ridge. We often work with two 2D FTs of the same spectrum, one with heavy convolution difference weighting for finding cross peaks close to the water phase noise line, and another with little or no such weighting, to find peaks close to the diagonal. It is desirable to have software conveniently set up for such treatment. If convolution difference weighting is used, it is important to have a versatile weighting function for which the convolution difference weighting, at the beginning of the FID, can be varied independently from the line broadening or enhancement functions (affecting the middle of the FID) and from apodization (at the end of the FID). The commonly used shifted sine-bell function does not have this quality.

Water presaturation in 2D NMR is often performed in much the same way as in 1D NMR. It is often desirable to saturate water with a sequence (such as a spin lock pulse) that acts for a short time just before the start of the sequence, rather than a saturation pulse during the entire recovery time. Doing so decreases the number of protons that will be cross saturated by water, at the cost of a wider spectral region of saturation. After selective presaturation of water and, unavoidably, of α-protons whose frequency is close to, or even at, the water frequency, one can take advantage of the short cross-relaxation time within the protein compared with the T_1 of water to restore quickly the polarization of the α-protons. One can thus observe NOESY cross peaks to these protons.[45] Water saturation is also used in the middle of 2D or 3D sequences.[46] In heteronuclear sequences, one can saturate water once heteronuclear correlation has been established,[47] because water is not involved in the correlation. A simple modification of the excitation sequence for generating heteronuclear magnetization transfer provides a time window when the heteronuclear correlation is along Oz. At that time, a gradient pulse[10] can be used to destroy selectively transverse water proton magnetization. In such a scheme, SSS is based on the lack of J coupling of the water protons to the heteronucleus. There is no need for any frequency-selective sequence.[48,49]

Three-dimensional NMR offers no problems beyond 2D NMR, as far as the solvent signal is concerned.

6.2 Selective Excitation in 2D NMR

Water saturation is less desirable for studies of larger proteins,[42] studies at a pH far from the minimum (pH = 4) for the rate of proton exchange with solvent, and the study of nucleic acids, whose water accessibility and smaller diameter promote cross relaxation to water. In these cases, selective sequences are useful. We discuss the approach in some detail, because we think it may be useful for 3D NMR in larger proteins, where good signal-to-noise ratio will become a serious consideration.

6.2.1 Fully Selective Excitation

Fully selective 2D heteronuclear multiple quantum coherence NMR, or HMQC, may be implemented using a JR-type selective pulse sequence in place of every $\frac{1}{2}\pi$ or π proton pulse in the sequence.[50,51] This has the advantage that water, being unperturbed, can act as a magnetization reservoir for the macromolecular spin system. Perturbation of the exchangeable protons is also avoided—a matter of importance for NMR of nucleic acids, and sometimes of proteins. The JR sequence has the advantage of being short and of not generating phase dispersion. A selective pulse sequence with a broader zero, such as 214 (Section 3.2.1), may be even better, because it can be set to excite predominantly the high-frequency amide region and not the region of the aliphatic protons, to low frequency of water. This is useful, because, to some extent, these protons can act as a magnetization reservoir, like those of water. We have obtained HMQC spectra using 214 in place of each pulse, but have not yet established whether or not 214 is more useful than JR in practice.

In HMQC, as in many other procedures, a proton π sequence is required in order to refocus unwanted proton evolution. Generally, for this purpose, we have used either back-to-back JR pulse sequences, or—what is nearly the same—a JR sequence with roughly twice the spacing of the 'traditional' JR sequence. An alternative, which requires a good magnet and rf field, is to use carefully adjusted π pulses. If these pulses occurred in pairs in the sequence (accomplished, if necessary, by adding an initial π pulse), the water resonance would remain relatively unsaturated. We have not yet attempted to use this approach.

There were two unexpected aspects of our use of JR for proton $\frac{1}{2}\pi$ and π sequences in HMQC. First, we eventually discovered that the primary amide ($^{15}NH_2$) region of the protein spectrum has complicated side-peak artifacts when selective JR sequences are used, compared with the expected two peaks at the same ^{15}N shift that are actually observed when HMQC is performed with water presaturation and hard $\frac{1}{2}\pi$ and π pulses. We do not have a quantitative explanation for this difference. But, once recognized, it is useful for distinguishing the primary amide peaks of glutamine and asparagine side chains from peptide NH peaks.

A second unexpected result of the use of a selective π sequence in HMQC is that, because the sequence is also relatively ineffective for perturbing the α-protons (whose chemical shift is close to that of water), it suppresses a splitting in the ^{15}N dimension due to the coupling of the α-proton to nitrogen, which would otherwise degrade resolution.[52] It is generally desirable to avoid this splitting.

6.2.2 Mixed Excitation; Gradient Pulses

In some cases, fully selective excitation is undesirable because cross peaks to water or to α-protons will be suppressed. In these cases, it is often—perhaps always—possible

to use nonselective pulses as necessary within the first part of the sequence, and to use an SSS sequence in place of the last, read-out pulse. Before read-out, the large transverse water signal, which generally results from the first, 'hard' part of the sequence, must be destroyed—usually by application of gradient pulses placed so that they do not affect the evolution of the spins to be observed.

An example of this approach is the 'hard–soft NOESY' sequence,[53] in which the two encoding pulses are hard, the water signal is removed by relaxation or a gradient pulse during the mixing time, and SSS read-out follows. However, in high-field spectrometers equipped with efficient probes, there is a problem with this sequence when the first two pulses are phased so that they make the water magnetization negative: during acquisition, a residual water signal will then be amplified maser-like, by the phenomenon of radiation damping. For this phase combination, the SSS read-out subsequence should be replaced by one that, while not generating a transverse water signal, reverses the longitudinal water magnetization.[54]

A very useful example of mixed excitation is the use of a 'Z filter'[55] at the end of TOCSY (also called HOHAHA) or ROESY (also called CAMELSPIN) excitation. These are spin lock sequences, and it is difficult (but probably possible) and not very useful to make them water-selective. However, at the end of such a sequence, the magnetization can be flipped up to the z axis with a hard $\frac{1}{2}\pi$ pulse, and the residual transverse component of magnetization removed with a gradient pulse and/or appropriate phase cycling. Then, after a short homogeneity recovery delay, the final selective sequence is applied.[56] This is the method of choice to obtain amide–α-proton covalent correlations when water saturation is undesirable. The Z filter (as used here) functions exactly as the last two pulses of a Hahn stimulated echo.

The Z filter just described cannot generally be appended to a COSY or related sequence involving two-spin coherence. However, it seems likely that useful COSY and stimulated echo[57] homonuclear sequences could be assembled from combinations of selective pulses and gradient pulses.

Similar approaches have been applied to isotopically enriched proteins, in combination with heteronuclear selection, for the study of cross relaxation between amide and α-protons,[48] and also between amide protons and water.[58] In the latter work, frequency-selective subsequences are used to keep the solvent magnetization along the $+z$ axis except during the mixing period. Gradient pulses are used to destroy residual transverse magnetization, in order to avoid radiation damping artifacts and to enhance SSS. Applied in this way, they do not contribute to saturation of the solvent resonance. In particular, the final 'observe' subsequence is a WATERGATE-type sequence (Section 3.1) modified so as to avoid solvent saturation.

7 CONCLUSIONS

Proton NMR in protonated solvent used to be such a difficult proposition that it was carried out only if absolutely necessary—in particular for the study of exchangeable protons. Alternative approaches, such as NMR of nonexchangeable protons or of other nuclei, were much preferred. The situation has changed: SSS has become so simple that exchangeable protons are now a fruitful and relatively easy subject of investigation. It is now worthwhile to work in protonated water simply to avoid the H_2O-to-D_2O transfer of a precious protein. The mastering of NMR in protonated solvents leads to the highly sensitive reverse INEPT detection of ^{15}N, thus making possible studies of ^{15}N-labeled macromolecules that would have been impossible or very difficult previously. SSS is also applied to proton NMR spectroscopy of organs and organisms—a case where the solvent cannot be changed.

The value of signal solvent suppression stimulates methodological research, which is thriving if one gauges it by the number of publications. SSS methods also evolve as new equipment and processing software becomes available. They will benefit from enhanced stability of the rf phase and of the magnetic field; frequency-agile synthesizers would promote new variants; faster data processing would diminish the requirements on SSS excitation and acquisition.

Novel methods could emerge from two relatively recent developments, both stimulated by the needs of medical imaging and spectroscopy. One is the introduction of precise and flexible phase and amplitude control of the excitation pulses. This facilitates the design of excitation sequences that produce a spin response with complex, predesigned phase and amplitude properties.

The second—and in our opinion more important—development is the introduction of fast switching gradient coils. They are affecting all manners of NMR experiments, including those involving SSS. Switched gradients quickly eliminate transverse magnetization, so that a gradient pulse applied after a selective $\frac{1}{2}\pi$ sequence provides saturation of the solvent magnetic moment in a time short enough to avoid most difficulties due to spin exchange or chemical exchange. When used with echoes, gradients may eliminate the need for EXORCYCLE cycling. With these new possibilities, SSS methods using slow saturation, and those giving rise to a linear phase shift are, or should soon become, obsolete.

8 RELATED ARTICLES

Biological Macromolecules: Structure Determination in Solution; Bioreactors and Perfusion; Cell Suspensions; Complex Radiofrequency Pulses; Concentrated Solution Effects; Drug–Nucleic Acid Interactions; Field Gradients and Their Application; Hydrogen Exchange and Macromolecular Dynamics; Magnetization Transfer between Water and Macromolecules in Proton MRI; Nucleic Acids: Spectra, Structures, and Dynamics; Plant Physiology; Protein Hydration; Protein Structures: Relaxation Matrix Refinement; Shielding Theory: GIAO Method; Water Suppression in Proton MRS of Humans and Animals.

9 REFERENCES

1. A. G. Redfield, in *NMR Basic Principles and Progress*, eds. P. Diehl, E. Fluck, and R. Kosfeld, Springer-Verlag, Berlin, 1976, Vol. 13, p. 137
2. B. L. Tomlinson and H. D. W. Hill, *J. Chem. Phys.*, 1973, **59**, 1775.

3. A. G. Marshall, T. Marcus, and J. Sallos, *J. Magn. Reson.*, 1979, **35**, 227.
4. R. K. Gupta, J. A. Ferretti, and E. D. Becker, *J. Magn. Reson.*, 1974, **13**, 275.
5. R. R. Ernst, *J. Magn. Reson.*, 1970, **3**, 10.
6. P. J. Hore, *Meth. Enzymol.*, 1989, **176**, 64.
7. M. Guéron, P. Plateau, and M. Decorps, in *Progress in Nuclear Magnetic Resonance Spectroscopy*, eds. J. W. Emsley, J. Feeney, and L. H. Sutcliffe, Pergamon Press, Oxford, 1991, Vol. 23, p. 135.
8. M. A. Delsuc and J. Y. Lallemand, *J. Magn. Reson.*, 1986, **69**, 504.
9. A. Abragam, *The Principles of Nuclear Magnetism*, Clarendon Press, Oxford, 1961, Chap. III.
10. G. A. Morris and R. Freeman, *J. Magn. Reson.*, 1978, **29**, 433.
11. S. L. Patt and B. D. Sykes, *J. Chem. Phys.*, 1972, **56**, 3182.
12. F. W. Benz, J. Feeney, and G. C. K. Roberts, *J. Magn. Reson.*, 1972, **8**, 114.
13. D. L. Rabenstein and A. A. Isab, *J. Magn. Reson.*, 1979, **36**, 281.
14. R. G. Bryant and T. M. Eads, *J. Magn. Reson.*, 1985, **64**, 312.
15. D. L. Rabenstein and S. Fan, *Anal. Chem.*, 1986, **58**, 3178.
16. R. L. Vold, J. S. Waugh, M. P. Klein, and D. E. Phelps, *J. Chem. Phys.*, 1968, **48**, 3831.
17. D. I. Hoult, *J. Magn. Reson.*, 1976, **21**, 337.
18. P. Blondet, M. Decorps, J. P. Albrand, A. L. Benabid, and C. Remy, *J. Magn. Reson.*, 1986, **69**, 403.
19. V. Sklenář and A. Bax, *J. Magn. Reson.*, 1987, **75**, 378.
20. D. Canet, D. Boudot, and J. Brondeau, *J. Magn. Reson.*, 1988, **79**, 377.
21. Z. Starcčuk, L. Pučček, R. Fiala, and Z. Starcčuk, Jr., *J. Magn. Reson.*, 1988, **80**, 344.
22. M. Piotto, V. Saudek, and V. Sklenářč, *J. Biomol. NMR*, 1992, **2**, 661.
23. P. C. M. Van Zijl and C. T. W. Moonen, *J. Magn. Reson.*, 1990, **87**, 18.
24. P. Stilbs, in *Progress in Nuclear Magnetic Resonance Spectroscopy*, eds. J. W. Emsley, J. Feeney, and L. H. Sutcliffe, Pergamon Press, Oxford, 1987, Vol. 19, p. 1.
25. P. C. Van Zijl, C. T. W. Moonen, P. Faustino, J. Pekar, O. Kaplan, and J. Cohen, *Proc. Natl. Acad. Sci. USA*, 1991, **88**, 3228.
26. G. J. Galloway, L. J. Haseler, M. F. Marshman, D. H. Williams, and D. M. Doddrell, *J. Magn. Reson.*, 1987, **74**, 184.
27. M. Guéron, P. Plateau, A. Kettani, and M. Decorps, *J. Magn. Reson.*, 1992, **96**, 541.
28. M. H. Levitt, *J. Chem. Phys.*, 1988, **88**, 3481.
29. A. L. Davis and S. Wimperis, *J. Magn. Reson.*, 1989, **84**, 620.
30. A. A. de Graaf, W. M. M. J. Bovée, N. E. P. Deutz, and R. A. F. M. Chamuleau, *Magn. Reson. Imaging*, 1988, **6**, 255.
31. R. R. Ernst, G. Bodenhausen, and A. Wokaun, *Principles of Nuclear Magnetic Resonance in One and Two Dimensions*, Clarendon Press, Oxford, 1987, p. 333.
32. G. Bodenhausen, R. Freeman, and D. L. Turner, *J. Magn. Reson.*, 1977, **27**, 511.
33. P. Plateau and M. Guéron, *J. Am. Chem. Soc.*, 1982, **104**, 7310.
34. E Kupcče and R. Freeman, *J. Magn. Reson., Ser. A*, 1994, **106**, 135.
35. H. Liu, K. Weisz, and T. L. James, *J. Magn. Reson., Ser. A*, 1993, **105**, 184.
36. W. E. Maas and D. G. Cory, *J. Magn. Reson., Ser. A*, 1994, **106**, 256.
37. K. Roth, B. J. Kimber, and J. Feeney, *J. Magn. Reson.*, 1980, **41**, 302.
38. D. S. Stephenson, in *Progress in Nuclear Magnetic Resonance Spectrocopy*, eds. J. W. Emsley, J. Feeney, and L. H. Sutcliffe, Pergamon Press, Oxford, 1988, Vol. 20, p. 515.
39. H. Barkhuijsen, R. de Beer, W. M. M. J. Bovée, and D. Van Ormondt, *J. Magn. Reson.*, 1985, **61**, 465.
40. K. Wüthrich, *NMR of Proteins and Nucleic Acids*, Wiley-Interscience, New York, 1986.
41. R. R. Ernst, G. Bodenhausen, and A. Wokaun, *Principles of Nuclear Magnetic Resonance in One and Two Dimensions*, Clarendon Press, Oxford, 1987.
42. J. D. Stoesz, A. G. Redfield, and D. Malinowski, *FEBS Lett.*, 1978, **91**, 320.
43. P. Tsang, P. E. Wright, and M. Rance, *J. Magn. Reson.*, 1990, **88**, 210.
44. D. Marion, M. Ikura, and A. Bax, *J. Magn. Reson.*, 1989, **84**, 425.
45. S. C. Brown, P. L. Weber, and L. Mueller, *J. Magn. Reson.*, 1988, **77**, 166.
46. M. Ikura, L. E. Kaye, and A. Bax, *Biochemistry*, 1990, **29**, 4659.
47. G. Otting and K. Wüthrich, *J. Magn. Reson.*, 1988, **76**, 569.
48. A. Bax and S. S. Pochapsky, *J. Magn. Reson.*, 1992, **99**, 638.
49. G. Wider and K. Wüthrich, *J. Magn. Reson., Ser. B*, 1993, **102**, 239.
50. S. Roy, M. Z. Papastavros, V. Sanchez, and A. G. Redfield, *Biochemistry*, 1984, **23**, 4395.
51. E. P. Nikonowicz and A. Pardi, *J. Mol. Biol.*, 1993, **232**, 1141.
52. A. Bax, M. Ikura, L. E. Kay, D. A. Torchia, and R. Tschudin, *J. Magn. Reson.*, 1990, **86**, 304.
53. J. D. Cutnell, *J. Am. Chem. Soc.*, 1982, **104**, 362.
54. P. R. Blake and M. F. Summers, *J. Magn. Reson.*, 1990, **86**, 622.
55. M. Rance, *J. Magn. Reson.*, 1987, **74**, 557.
56. A. Bax, V. Sklenár, G. M. Clore, and A. M. Gronenborn, *J. Am. Chem. Soc.*, 1987, **109**, 6511.
57. A. G. Redfield, *Chem. Phys. Lett.*, 1983, **96**, 537.
58. S. Grzesiek and A. Bax, *J. Biomol. NMR*, 1993, **3**, 627.

Acknowledgments

This article is partly based on M. Guéron, P. Plateau, and M. Decorps, in 'Progress in Nuclear Magnetic Resonance Spectroscopy', eds. J. W. Emsley, J. Feeney, and L. H. Sutcliffe, Pergamon Press, Oxford, 1991, Vol. 23, p. 135, Copyright 1991, with kind permission from Pergamon Press Ltd. We are grateful to A. G. Redfield for contributing most of Section 6, and for many suggestions. We thank J. L. Leroy for performing the experiments and draftwork for Figure 6.

Biographical Sketches

Pierre Plateau. *b*. 1956. Graduate, Ecole Polytechnique. Ph.D., Metabolism of diadenosine tetraphosphate and related nucleotides. Affiliated to the Centre National de la Recherche Scientifique as Directeur de Recherches. Introduced to NMR by M. Guéron. Recent research interests: structure–function relationships and the genetic expression of aminoacyl-tRNA synthetases.

Maurice Guéron. *b* 1935. Graduate, Ecole Polytechnique. Ph.D., NMR–EPR study of indium antimonide (adviser: I. Solomon). Post-doctoral position at Bell Labs with R. G. Shulman. Presently Director, Groupe de Biophysique de l'Ecole Polytechnique, also affiliated to the Centre Nationale de la Recherche Scientifique as Directeur de Recherches. Recent research interests: the applications of NMR to molecular biophysics, physiology and medicine.

Plant Physiology

Justin K. M. Roberts
University of California, Riverside, CA, USA

1 Introduction 1
2 Nutrition and Metabolism 1
3 Responses to the Environment 2
4 Related Articles 5
5 References 5

1 INTRODUCTION

NMR spectroscopy has provided many new insights into the physiology of higher plants. There are a number of instances where NMR measurements of specific physiological parameters now constitute established methods. Other findings have been described by more limited numbers of investigators and/or with a limited number of plant systems, such that their importance and generality awaits future evaluation. The purpose of this chapter is to provide an overview of NMR studies of higher plants with respect to physiology. Hence the chapter is organized with respect to recognizable physiological functions.

The field of NMR spectroscopy of plants has been surveyed by several authors.[1–7] Practical aspects of specific NMR measurements have also been presented.[8–11] I have not cited every paper published in this field; the references provided will lead to the great majority.

2 NUTRITION AND METABOLISM

Since higher plants are autotrophs, the acquisition and metabolism of inorganic nutrients are processes that play a dominant role in determining plant performance. In addition, within the plant, the transport and partitioning of assimilated nutrients, such as sugars and amino acids, are central to plant growth and development. The following provides an overview of NMR investigations into these processes.

2.1 Carbon Assimilation and Metabolism

In 1975, Schaefer et al.[12] studied soybean ovules using in vivo ^{13}C NMR, observing metabolites derived from atmospheric $^{13}CO_2$, fixed via photosynthesis in the leaf and translocated to the growing ovule. Since then, attention has been mostly given to nonreductive inorganic carbon fixation and metabolism ('dark CO_2 fixation'). Here, carboxylic acid groups of organic and amino acids are monitored by ^{13}C NMR. Leaves of Crassulacean plants can fix inorganic carbon into malic acid in the dark such that by the end of the night the concentration of this acid can increase by more than 50 mM, with the chemical shifts of malate carboxylic acid resonances reflecting the pH in the vacuoles of the leaf cells.[13] Even though most of the malate that accumulates during the night is localized in vacuoles, Kalt et al.[14] found a considerable flux of malate back out of vacuoles, into the cytoplasm and mitochondria during this period of malate accumulation. This conclusion was drawn from observation of ^{13}C label in carbons 1 and 4 of malate. The initial carboxylation reactions label at carbon 4, whereas the mitochondrial enzyme fumarase will randomize the label between carbons 1 and 4; mass spectrometry demonstrated the existence of no more than one ^{13}C label per molecule.[15]

Dark, inorganic carbon fixation in maize roots has been studied by Chang and Roberts[16–18] who were able to resolve the distinct cytoplasmic and vacuolar malate pools. Since malate is synthesized and metabolized in the cytoplasm and mitochondria of plant cells, this NMR method is useful for monitoring the metabolically active pool of malate, which plays a critical role in many physiological processes.[19] Chang and Roberts[17] showed that the concentration of cytoplasmic malate varies with metabolic state, a result with implications for the regulation of such important enzymes as phospho*enol*pyruvate carboxylase, discussed later in Section 3.5. Gout et al.[20] were able to demonstrate that, in cultured sycamore cells, the concentration of cytoplasmic malate is much higher than that of citrate, reflecting the distinct reactions and forces that regulate transport of these two organic acids into and out of plant cell vacuoles. These authors also examined the intracellular location of fumarase in sycamore cells, and confirmed that randomization of label between malate carboxylic acid groups takes place in the mitochondria.

The in vivo activity of carbonic anhydrase has been estimated by two different NMR methods. Holtum et al.[21] used ^{18}O isotope shifts of [^{13}C]carboxylic acid signals in malate isolated from leaves of Crassulacean plants that had been fed $^{13}C^{18}O_2$; carbonic anhydrase activity is reflected in the replacement of ^{18}O by ^{16}O from leaf water. Chang and Roberts[18] used saturation transfer ^{13}C NMR to observe directly exchange of carbon between CO_2 and HCO_3^- in maize root tips. Both studies found a considerable excess of carbonic anhydrase activity over that of phospho*enol*pyruvate carboxylase, which catalyzes the dark fixation of bicarbonate. Hence, the hydration of CO_2 does not appear to limit phospho*enol*pyruvate carboxylase activity in vivo.

The definitive power of ^{13}C NMR to elucidate pathways of carbon metabolism is illustrated by the work of Keeling et al.[22] who followed the conversion of specifically labeled hexoses into starch in developing wheat grains. The question they addressed was whether or not hexose must first be converted to triose phosphates prior to transport into amyloplasts for starch synthesis. Such a pathway would randomize hexose carbons 1 and 6, 2 and 5, and 3 and 4. Keeling et al.[22] found the limited randomization of carbons in glucosyl residues of starch derived from [1-^{13}C] or [6-^{13}C]glucose to be similar to that in the hexose moieties of sucrose, which was taken to reflect randomization events in the cytoplasm. Hence, these investigators concluded that during starch biosynthesis in vivo, amyloplasts primarily import carbon as hexose phosphates, not triose phosphates. Viola et al.[23] reached similar conclusions in their studies with potato tubers and bean cotyledons. There is potential for applying in vitro positional analyses of isotope enrichments using NMR to questions of metabolic fluxes, by an approach that parallels radioisotope studies.[24]

2.2 Nitrogen Assimilation and Metabolism

Both stable isotopes of nitrogen, the naturally abundant ^{14}N and the rarer ^{15}N, give NMR signals and have been used to follow incorporation of inorganic nitrogen into amino acids and proteins. Use of both isotopes can provide somewhat complementary information, with ^{14}N spectra providing information on levels of the more abundant existing amino acid and inorganic pools,[25–28] while ^{15}N can be used to probe pathways of assimilation.[26,29] The resolution of in vivo ^{15}N spectra is generally better than that obtainable with ^{14}N. Thorpe et al.[26] observed the preferential uptake and assimilation of ammonium over nitrate in cultured spruce buds using ^{15}N NMR. Moreover, these investigators reported that external ammonium was required, in addition to nitrate, for induction of the enzymes of nitrate assimilation. Concerning the pathway of ammonium assimilation, ^{15}N NMR reports support the view that the glutamine synthetase–glutamate synthase pathway dominates over incorporation via glutamate dehydrogenase, since the first metabolite labeled with ^{15}N after feeding $^{15}HN_4^+$ is the amide nitrogen of glutamine.[26,29] Glutamate dehydrogenase appears to have a catabolic function,[29] a role mandated in part by very low cytoplasmic ammonium levels (which would necessarily limit ammonium assimilation via glutamate dehydrogenase) that have been estimated indirectly from cytoplasmic and vacuolar pH estimated using ^{31}P and ^{13}C NMR, and total intracellular ammonium measurements.[30] Intracellular ammonium is largely trapped in the acidic vacuoles because of the high permeability of biomembranes to NH_3, such that the ratio of NH_4^+ concentrations approaches the ratio of H^+ concentrations.

Solid state ^{13}C and ^{15}N NMR methods have been used by Schaefer and his colleagues to obtain a comprehensive picture of amino acid and ureide metabolism into storage protein of developing soybean cotyledons[31–36] (reviewed by Roberts[1,4]).

2.3 Cation Uptake

The transport and compartmentation of nonmetabolizable cations has been the subject of relatively few NMR studies, in contrast with the considerable amount of literature available on this agriculturally very important topic. This is due primarily to the electrical quadropole moment of the NMR-active Group 1 and 2 nuclei. The uptake of ^{23}Na by plant cells has been monitored using extracellular dysprosium shift reagent to separate intra- and extracellular sodium NMR signals.[37–39] The uptake and compartmentation of ^{133}Cs (a potential analog of potassium) can be studied without shift reagents, because the different environments of cytoplasm, vacuole, and external solution lead to distinct chemical shifts and relaxation times.[40,41]

The transport and compartmentation of Mn^{2+} has been followed indirectly, using signals from anions containing ^{31}P[42–44] or ^{13}C,[16,20] and signals from water in leaves.[45]

2.4 Phosphate Uptake and Metabolism

Phosphorus-31 NMR has been widely applied in plant physiology research, and a number of ^{31}P NMR studies are discussed in Section 1. The separation of cytoplasmic and vacuolar inorganic phosphate (Pi) signals in plant tissues[46] allows both the uptake and compartmentation of phosphate to be followed by NMR, together with the incorporation of phosphorus into the more abundant, freely mobile, low molecular weight metabolites such as nucleoside triphosphates, sugar phosphates, and sugar nucleotides.[47–49] Relatively few studies have been quantitative, using units recognizable by biochemists. Inspection of the following works provides one with a view of the complexities. Lee et al.[49] provide us with a valiant analysis of some published data on the concentration of cytoplasmic Pi. In 2 mm-long maize root tips, conversion of measured cytoplasmic Pi contents (μmol g^{-1} of tissue) to cytoplasmic concentrations does not involve application of large conversion factors, since cytoplasm occupies most of this tissue. Using an external reference compound in a sealed capillary, Roberts et al.[47] and Pfeffer et al.[43] (see also Lee et al.[49]) estimated the cytoplasmic Pi concentration in glucose-fed oxygenated maize root tips to be $\sim$2 mM. Using a reference compound contained in the perfusion medium and in the absence of exogenous glucose, Lee et al.[49] estimated a cytoplasmic Pi concentration of $\sim$6 mM. It is not clear if differences between these results arise from some methodological factor, possibly flow effects associated with use of a circulating external standard or the physiological condition of the root tips (sugar depletion and low oxygen status can increase cytoplasmic Pi concentrations by $\sim$50% and 250%, respectively[50]). Studies of cultured sycamore cells have led to cytoplasmic Pi estimates of 0.8–1.2 mM.[51] In nonilluminated spinach leaves, the analysis of Bligny et al.[52] indicates that the cytoplasmic (extrachloroplastic) Pi concentration is less than 2 mM.

The activities of several enzymes involved in phosphorus metabolism have been studied by ^{31}P NMR. The synthesis of adenosine triphosphate (ATP) from cytoplasmic Pi under steady-state conditions has been measured using saturation transfer NMR methods in maize root tips[50,53] and rice shoot tips.[54] This technique has also been applied to the exchange of phosphorus between glucose 1-phosphate and uridine diphosphoglucose (precursor to cell wall polysaccharides and sucrose).[55] Reactions slower than those just mentioned can be studied under non-steady-state conditions by following the intensities of specific resonances. Assignment of changes in a particular resonance to an individual biochemical reaction is complicated by the fact that often the unidirectional rates of synthesis and breakdown are both much higher than the rates of net synthesis or breakdown. Gout et al.[56] studied the transport of phosphorylcholine in cultured sycamore cells, demonstrating that this component of the xylem fluid is rapidly hydrolyzed in the cell wall, the products of hydrolysis being taken up separately, with the choline being phosphorylated in the cytoplasm by choline kinase.

3 RESPONSES TO THE ENVIRONMENT

The immobility of higher plants makes them prone to all manner of physical and biological insults, which they must therefore withstand for survival and success. Determination of the mechanisms by which higher plants withstand and adapt to different environments is of paramount importance for our understanding of natural, urban, and agricultural ecosystems.

The following sections outline how NMR has provided insight into plant responses to the environment.

3.1 Hypoxia

Low oxygen environments are commonly encountered by plant roots and entire, young seedlings when the soil becomes flooded, due to precipitation and runoff exceeding drainage. Hypoxia suppresses oxidative phosphorylation, so that plant tissues are forced to rely more on pathways of fermentation. A number of NMR studies have identified the importance of prevention of cytoplasmic acidosis if the plant is to survive prolonged periods of severe hypoxia,[57–62] and these studies have shown that a key factor is reduced fermentation to lactic acid (or the induction of a lactate excretion system), since these traits correlate strongly with survival. The apparent simplicity of this result, which has come from studies with divergent species and tissues, is perhaps surprising given that many reactions other than lactic acid synthesis can contribute to pH regulation in plants.[18,58,63–65] This result demonstrates that the relative importance of these many reactions that can influence intracellular pH remains to be evaluated critically.

Metabolic transformations in plant tissues during hypoxia have been studied by ^{13}C,[57,62,66] ^{1}H,[54,67,68] and ^{31}P NMR.[53,54,60]

Hooks et al.[69,70] described the physical state of nucleotides in maize root tips, using ^{31}P NMR and in vitro analytical techniques. Much of the cellular nucleoside diphosphate in oxygenated root tips is NMR-invisible, a significant proportion of which is due to immobilization on macromolecules, which have high affinities for ADP and guanosine 5′-diphosphate. Under hypoxia, the levels of NMR-visible, free nucleoside diphosphate increase several-fold, and much more than the levels of total cellular nucleoside diphosphate. In contrast, virtually all of the cellular nucleoside triphosphate in both hypoxic and oxygenated tissue is detectable by NMR. However, ^{31}P relaxation measurements of nucleotide resonances are consistent with the idea that when ATP levels are reduced by hypoxia, most of the ATP is associated with macromolecules (the bound nucleoside triphosphates being in rapid exchange with nucleotides in free solution). It was concluded that the free energy available to drive metabolism in oxygenated cells is much higher than that deduced from measurements of total cellular nucleotides, and similar to the values estimated by in vivo ^{31}P NMR. In contrast, for hypoxic cells, both in vivo NMR and extract analyses overestimate the available free energy of ATP hydrolysis (see also Roberts[65]). This view would account for the fact that processes such as protein synthesis and ion transport are so sensitive to hypoxia even though ATP levels often decrease by little more than 60%.

3.2 Starvation

Nonphotosynthetic plant tissues, and green cells in the dark, rely primarily on carbohydrates for their energetic needs. Either internal stores of starch, or sucrose donated by other cells via the phloem, feed into the glycolytic and pentose phosphate pathways. The effects of carbohydrate deprivation on phosphorus metabolism in cultured sycamore cells has been studied by Roby et al.[51] The restriction in carbohydrate metabolism could be followed in detail by observation of the decline in glucose 6-phosphate and uridine diphosphoglucose ^{31}P resonances. It was only when the signals from these metabolites were reduced considerably that nucleoside triphosphate began to fall, this latter change being accompanied by accumulation of phosphorylcholine in the cytoplasm. This response reflects cellular autophagy of membranes consumed for energy production during carbohydrate starvation. Natural abundance ^{13}C NMR studies of cell extracts during carbohydrate starvation indicated that the autophagy also involved catabolism of cellular protein, reflected in the elevated levels of many amino acids, the most prominent being asparagine.[71]

3.3 Salt

Soils in many regions of the world are naturally high in soluble salts. Moreover, many of the world's richest agricultural areas, which rely on extensive irrigation, face possible doom (the fate of civilization's past) from the salt residue left behind after prolonged evaporation of irrigation waters. Stress from salinity not only increases as a function of soil water salt concentration, but also with the concentration of specific ions. For example, the effects of high sodium ion are influenced by the presence of calcium, at the level of both soil structure and plant physiological response. There is also the difference between treatments involving almost instantaneous increases in salinity (salt shock), and those which employ more gradual applications of stress (this is an issue also in studies of plant responses to factors such as oxygen).

Roberts et al.[47] described the enhancement of Pi uptake in salt-treated (0.1 M NaCl/10 mM $CaCl_2$) maize root tips, from a solution containing 10 mM Pi. These authors estimated the cytoplasmic Pi concentration to be just under 2 mM. Hence the enhanced uptake may simply reflect increased passive influx of Pi, due to an increased permeability of the plasma membrane in the presence of salt. This treatment caused an increase in the cytoplasmic Pi concentration, and an increase in the level of cytoplasmic Pi relative to other cytoplasmic phosphates. This inability to regulate cytoplasmic Pi, in contrast to the behavior of nonstressed plant cells exposed to exogenous Pi,[48,72,73] may lead to the increase in Pi transport from roots to leaves which, in turn, can result in symptoms of phosphorus toxicity and reduced yield in salt-stressed maize plants fertilized with high levels of Pi.[47]

Spickett et al.[74] examined the effects of increased exogenous salt and nonionic osmotica on maize roots using ^{31}P NMR. These stresses induced increases in levels of phosphorylcholine, indicating breakdown of phosphatidylcholine (as observed in the starvation studies noted above), and vacuolar Pi, which was attributed to breakdown of NMR-invisible constituents such as nucleic acids and phospholipids. In contrast to vacuolar Pi, cytoplasmic Pi increased only transiently. These effects, and the observed cytoplasmic alkalinization, led the authors to postulate that a plasma-membrane-associated phospholipase is activated following a decrease in cell turgor, and that this and other enzymes may form part of the transduction system that senses, and may signal a response to, the stress. Spickett et al.[39] went on to study changes in intracellular pH in salt-stressed maize root tips using ^{31}P NMR. Since this tissue takes up significant quantities of sodium ion, which was followed by ^{23}Na NMR, these workers analyzed observed

changes in the chemical shifts of cytoplasmic and vacuolar Pi resonances with respect to changes in both pH and mineral ions, since both can significantly influence ^{31}P chemical shifts.[75] Despite these complications, Spickett et al.[39] were able to conclude that salt treatment led to a small cytoplasmic alkalinization (0.1−0.2 pH units) and a larger vacuolar alkalinization, as was also reported for barley by Fan et al.[76] These pH changes were interpreted as reflecting activation of the tonoplast H^+-ATPase, and operation of a tonoplast H^+/Na^+ antiporter.

3.4 Heat

The aerial parts of plants commonly experience wide variations in temperature, such that during the life of a plant only a small fraction of time may be spent at an optimum temperature. McCain et al.[77] have used ^1H NMR to monitor the integrity of the membrane that surrounds the chloroplast (the envelope). These investigators have shown that the ^1H NMR spectra of leaves of certain species (notably many trees) have two principal water signals: one from water in the chloroplast, the other from water in other compartments.[10] McCain et al.[77] found that with increasing temperature, the chloroplast water signal lost intensity and shifted upfield, further from the nonchloroplast signal, which increased in intensity. These changes occurred at a quite well-defined transition temperature range, and indicated a sudden loss of water from the chloroplast. These temperature-induced changes at the level of the envelope were not correlated with events associated with loss of thylakoid membrane function, followed by fluorescence, which indicates that these two spectroscopic approaches provide distinct perspectives on chloroplast function in intact leaves.

3.5 Extremes in Extracellular pH

The pH outside root cells will depend on the soil environment, influenced by such factors as lime content, fertilizer application, microbial activity, and aeration. The external pH of all plant cells may be impacted by levels of such factors as CO_2 and the pollutants of acid rain.

Two groups have carefully studied the regulation of intracellular pH in cultured cells exposed to different external pHs. Using ^{31}P NMR, Fox and Ratcliffe[78] found that cytoplasmic pH in oil palm and carrot cells was independent of external pH over the range of 5.5 to 8, if external pH was altered slowly. Outside of this range, responses were complex and time-dependent, including overcompensation during recovery from exposure to alkaline external pHs. Gout et al.[79] added to this knowledge by using both ^{13}C signals of citric acid and ^{31}Pi signals as intracellular pH indicators in sycamore cells, since these provide a sensitive picture over a wide range of pH values. Both cytoplasmic and vacuolar pH were quite independent of external pH over the range of 4.5 to 7.5, whereas outside of this range both intracellular compartments tended toward the external pH value, the effect at acidic pHs being sharper. Insight into the biochemical reactions underlying this pattern of intracellular pH regulation was provided by measurements of oxygen consumption. These measurements showed that respiration increased as external pH decreased from 7.5 to 4.5, this change being accompanied by a decrease in levels of nucleoside triphosphate, results which suggest that acidic extracellular pHs increase the demand for ATP, presumably due to activation of the plasma membrane H^+-ATPase which struggles to offset the influx of protons from the medium. The threshold seen at pH ∼4.5, below which tight regulation of intracellular pH was not maintained, occurred at the very pH where cell respiration was at the maximum. Hence, the failure of pH regulation at acidic pHs appears to reflect the demand for ATP by proton pumps exceeding the capacity of the cell to provide it. This attractive result implies that the exact range of extracellular pHs over which intracellular pH is maintained will depend on the cell type, and the physiological condition of the cells. Indeed, Gout et al.[79] show how Pi starvation has an impact on the ability of plant cells to respond to acidic environments.

The gradual rise in intracellular pH that occurs as extracellular pH increases above 8 is accompanied by a net synthesis of malate and citrate.[79] This result is anticipated by the classical literature, which describes the ability of plant cells to convert neutral sugars to carboxylic acids, thereby counteracting reactions that generate alkali (such as OH^- influx). An unsettled question on this phenomenon, however, is exactly what signals the activation of the enzymes responsible for organic acid synthesis, notably phospho*enol* pyruvate carboxylase. Gout et al.[79] speculated that it may be an increase in levels of cytoplasmic bicarbonate which activate this enzyme. This potential regulatory mechanism is one of several that have been proposed over the last few decades, and was explicitly examined by Chang and Roberts[18] in maize root tips, with respect to the activation of organic acid synthesis by exogenous potassium. They measured bicarbonate influx and the amount of cytoplasmic bicarbonate derived from both respiration and the external medium and found not only no differences in these parameters when phospho*enol* pyruvate carboxylase activity changed, but also that the concentration of cytoplasmic bicarbonate was approximately two orders of magnitude higher than the K_M of phospho*enol* pyruvate carboxylase for bicarbonate, measured in vitro. These results argue against the idea that organic acid synthesis in maize root tips is controlled by the availability of bicarbonate. It is possible that this may not be the case in cells that exhibit lower rates of respiration than maize root tips. It is also possible that the affinity of phospho*enol* pyruvate carboxylase for bicarbonate in vivo is not the same as that found by enzymologists.

Another sometimes popular hypothesis regarding the regulation of phospho*enol* pyruvate carboxylase invokes changes in intracellular pH as the key regulatory event. The status of this idea in the literature is unsettled, and is the subject of several discussions concerning both NMR and non-NMR data.[4,63,79]

If the extracellular space contains permeant acids or bases, then the effect of external pHs that are different from cytoplasmic pH can present a much greater challenge than the stresses just discussed. Guern et al.[80] imposed acid loads on cultured plant cells by adding to the medium aliquots of lipophilic acids, which penetrated the cells, liberating protons into the cytoplasm. Using ^{31}P NMR, these workers observed a large and rapid cytoplasmic pH drop, following addition of the acids. Significantly, after the initial drop in cytoplasmic pH, there was a partial recovery, a response of regulatory mechanisms that partially counteracts the effects of acid influx. Mathieu et al.[81] concluded that the principal

processes responsible for cytoplasmic pH regulation under conditions of acid load were consumption of intracellular malate ('metabolic consumption' of protons), proton extrusion via the plasma membrane H^+-ATPase, and other proton excretion mechanisms (see also Kurkdjian and Guern[63] for discussion).

3.6 Biological Agents

Plants are normally intimately affected by activities of other organisms including, at one end of the spectrum, the beneficial associations with symbiotic and free-living nitrogen-fixing bacteria, myccorhizal fungi, and pollinating insects, to the generally benign microbes that live on leaf surfaces and around root systems and, at the other end, herbivores, pathogens, and pests.

Rolin et al.[82] used ^{31}P NMR to study the symbiosis between soybean roots and the bacterium *Bradyrhizobium*, and were able to follow changes in vacuolar phosphate levels in root nodules under hypoxia or deprived of sugar. Subsequently, Pfeffer et al.[83] found that changes in vacuolar Pi signals under hypoxia were due to altered relaxation behavior of vacuolar ^{31}Pi in the cortical tissue of the nodule. These changes were postulated to arise from changes in viscosity, and occurred in parallel with changes in the water relaxation seen in images using NMR microscopy.[84] The observation of a signal from an unknown phosphodiester[82] led to the isolation and structural solution of a phosphorycholine-substituted glucan, produced by the bacterium.[85] This is a remarkable molecule, consisting of a 1.5 nm polyglucan ring, decorated on one side with a phosphorylcholine moiety. While the unusual structure of this molecule presumably is related to its function, its function is yet to be determined, although a role in osmoregulation has been suggested.

Horn et al.[86] examined the hypothesis that the response of plant cells to elicitors associated with pathogenic infection involves intracellular pH. These elicitors invoke a wide range of biochemical reactions that can constitute a global defensive response. Moreover, many of the reactions in this defensive response occur within just a few minutes. Both ^{31}P NMR and fluorescent dyes were used to follow intracellular pH immediately after addition of elicitors. They concluded that cultured soybean cells do not respond to elicitors by changing cytoplasmic and vacuolar pH.

4 RELATED ARTICLES

Biosynthesis and Metabolic Pathways: Carbon-13 and Nitrogen-15 NMR; Biosynthesis and Metabolic Pathways: Deuterium NMR; Cell Suspensions; Enzyme-Catalyzed Exchange: Magnetization Transfer Measurements; Plants, Seeds, Roots, and Soils as Applications of Magnetic Resonance Microscopy.

5 REFERENCES

1. J. K. M. Roberts, *Annu. Rev. Plant Physiol.*, 1984, **35**, 375.
2. B. C. Loughman and R. G. Ratcliffe, *Adv. Plant Nutr.*, 1984, **1**, 241.
3. F. Martin, *Physiol. Veg.*, 1985, **23**, 463.
4. J. K. M. Roberts, in *Plant Biochemistry*, ed. D. D. Davies, Academic Press, New York, 1987, Vol. 13, p. 181.
5. R. G. Ratcliffe, *Methods Enzymol.*, 1987, **148**, 683.
6. P. E. Pfeffer and W. V. Gerasimowicz (eds.), *Nuclear Magnetic Resonance in Agriculture*, CRC Press, Boca Raton, FL, 1989, 441.
7. R. G. Ratcliffe and J. K. M. Roberts, *Magn. Reson. Med.*, 1990, **4**, 77.
8. J. K. M. Roberts, in *Modern Methods of Plant Analysis*, eds. H. F. Linskens and J. F. Jackson, Springer, New York, 1986, p. 43.
9. J. K. M. Roberts, in *Modern Methods of Plant Analysis*, eds. H. F. Linskens and J. F. Jackson, Springer, New York, 1986, p. 106.
10. D. C. McCain, in *Modern Methods of Plant Analysis*, eds. H. F. Linskens and J. F. Jackson, Springer, New York, 1986, p. 127.
11. J. K. M. Roberts and J. H. Xia, in *Methods in Cell Biology*, eds. D. W. Galbraith, D. P. Bourque, and H. J. Bohnert, Academic Press, New York, 1995, Vol. 49, p. 243.
12. J. Schaefer, E. O. Stejskal, and C. F. Beard, *Plant Physiol*, 1975, **55**, 1048.
13. M. A. Stidham, D. E. Moreland, and J. N. Siedow, *Plant Physiol*, 1983, **73**, 517.
14. W. Kalt, C. B. Osmond, and J. N. Siedow, *Plant Physiol.*, 1990, **94**, 826.
15. C. B. Osmond, J. A. M. Holtum, M. H. O'Leary, C. A. Roeske, O. C. Wong, R. E. Summons, and P. N. Avadhani, *Planta*, 1988, **175**, 184.
16. K. Chang and J. K. M. Roberts, *Plant Physiol.*, 1989, **89**, 197.
17. K. Chang and J. K. M. Roberts, *Biochim. Biophys. Acta*, 1991, **1092**, 29.
18. K. Chang and J. K. M. Roberts, *Plant Physiol.*, 1992, **99**, 291.
19. C. Lance and P. Rustin. *Physiol. Veg.*, 1984, **22**, 625.
20. E. Gout, R. Bligny, N. Pascal, and R. Douce, *J. Biol. Chem.*, 1993, **268**, 3986.
21. J. A. M. Holtum, R. Summons, C. A. Roeske, H. N. Comins, and M. H. O'Leary, *J. Biol. Chem.*, 1984, **259**, 6870.
22. P. L. Keeling, J. R. Wood, R. H. Tyson, and I. G. Bridges. *Plant Physiol.*, 1988, **87**, 311.
23. R. Viola, H. V. Davies, and A. R. Chudeck, *Planta*, 1991, **183**, 202.
24. C. Salon, P. Raymond, and A. Pradet, *J. Biol. Chem.*, 1988, **263**, 12278.
25. P. S. Belton, R. B. Lee, and R. G. Ratcliffe, *J. Exp. Bot.*, 1985, **36**, 190.
26. T. A. Thorpe, K. Bagh, A. J. Cutler, D. I. Dunstan, D. D. McIntyre, and H. J. Vogel, *Plant Physiol.*, 1989, **91**, 193.
27. R. B. Lee, and R. G. Ratcliffe, *Planta*, 1991, **183**, 359.
28. R. B. Lee, J. V. Purves, R. G. Ratcliffe, and L. R. Saker, *J. Exp. Bot.*, 1992, **43**, 1385.
29. S. A. Robinson, A. P. Slade, G. G. Fox, R. Phillips, R. G. Ratcliffe, and G. R. Stewart, *Plant Physiol.*, 1991, **95**, 509.
30. J. K. M. Roberts and M. K. L. Pang, *Plant Physiol.*, 1992, **100**, 1571.
31. G. T. Coker, III, J. R. Garbow, and J. Schaefer, *Plant Physiol.*, 1987, **83**, 698.
32. T. A. Skokut, J. Manchester, and J. Schaefer, *Plant Physiol.*, 1985, **79**, 579.
33. G. T. Coker, III, and J. Schaefer, *Plant Physiol.*, 1985, **77**, 129.
34. T. A. Skokut, J. E. Varner, J. Schaefer, E. O. Stejskal, and R. A. McKay, *Plant Physiol.*, 1982, **69**, 308.
35. T. A. Skokut, J. E. Varner, J. Schaefer, E. O. Stejskal, and R. A. McKay, *Plant Physiol.*, 1982, **69**, 314.

36. J. Schaefer, T. A. Skokut, E. O. Stejskal, R. A. McKay, and J. E. Varner, *Proc. Natl. Acad. Sci. USA*, 1981, **78**, 5978.
37. L. O. Sillerud and J. W. Heyser, *Plant Physiol.*, 1984, **75**, 269.
38. W. V. Gerasimowicz, S.-I. Tu, and P. E. Pfeffer, *Plant Physiol.*, 1986, **81**, 925.
39. C. M. Spickett, N. Smirnoff, and R. G. Ratcliffe, *Plant Physiol.*, 1993, **102**, 629.
40. P. E. Pfeffer, D. B. Rolin, D. Brauer, S.-I. Tu, and T. F. Kumosinski, *Biochim. Biophys. Acta*, 1990, **1054**, 169.
41. P. E. Pfeffer, D. B. Rolin, J. H. Schmidt, S.-I. Tu, T. F. Kumosinski, and D. D. J. Douds, *J. Plant Nutr.*, 1992, **15**, 913.
42. M. J. Kime, R. G. Ratcliffe, and B. C. Loughman, *J. Exp. Bot.*, 1982, **33**, 670.
43. P. E. Pfeffer, S.-I. Tu, W. V. Gerasimowicz, and J. R. Cavanaugh, *Plant Physiol.*, 1986, **80**, 77.
44. C. Roby, R. Bligny, R. Douce, S.-I. Tu, and P. E. Pfeffer, *Biochem. J.*, 1988, **252**, 401.
45. D. C. McCain and J. L. Markley, *Plant Physiol.*, 1989, **90**, 1417.
46. J. K. M. Roberts, P. M. Ray, N. Wade-Jardetzky, and O. Jardetzky, *Nature (London)*, 1980, **283**, 870.
47. J. K. M. Roberts, C. S. Linker, A. G. Benqit, O. Jardetzky, and R. H. Nieman, *Plant Physiol.*, 1984, **75**, 947.
48. S.-I. Tu, J. R. Cavanaugh, and R. T. Boswell, *Plant Physiol.*, 1990, **93**, 778.
49. R. B. Lee, R. G. Ratcliffe, and T. E. Southon, *J. Exp. Bot.*, 1990, **41**, 1063.
50. J. K. M. Roberts, D. Wemmer, and O. Jardetzky, *Plant Physiol.*, 1984, **74**, 632.
51. C. Roby, J.-B. Martin, R. Bligny, and R. Douce, *J. Biol. Chem.*, 1987, **262**, 5000.
52. R. Bligny, P. Gardestrom, C. Roby, and R. Douce, *J. Biol. Chem.*, 1990, **265**, 1319.
53. J. K. M. Roberts, A. N. Lane, R. A. Clarke, and R. H. Nieman, *Arch. Biochem. Biophys.*, 1985, **240**, 712.
54. T. W.-M. Fan, A. N. Lane, and R. M. Higashi, *Arch. Biochem. Biophys.*, 1992, **294**, 314.
55. J. K. M. Roberts, *Biochim. Biophys. Acta*, 1990, **1051**, 29.
56. E. Gout, R. Bligny, C. Roby, and R. Douce, *Proc. Natl. Acad. Sci. USA*, 1990, **87**, 4280.
57. J. K. M. Roberts, J. Callis, D. Wemmer, V. Walbot, and O. Jardetzky, *Proc. Natl. Acad. Sci. USA*, 1984, **81**, 3379.
58. J. K. M. Roberts, J. Callis, O. Jardetzky, V. Walbot, and M. Freeling, *Proc. Natl. Acad. Sci. U.S.A.*, 1984, **81**, 6029.
59. J. K. M. Roberts, F. H. Andrade, and I. C. Anderson, *Plant Physiol.*, 1985, **77**, 492.
60. F. Menegus, L. Cattaruzza, M. Mattana, N. Beffagna, and E. Ragg, *Plant Physiol.*, 1991, **95**, 760.
61. R. A. Kennedy, M. E. Rumpho, and T. C. Fox, *Plant Physiol.*, 1992, **100**, 1.
62. J. H. Xia and J. K. M. Roberts, *Plant Physiol.*, 1994, **105**, 651.
63. A. Kurkdjian and J. Guern, *Annu. Rev. Plant Physiol. Plant Mol. Biol.*, 1989, **40**, 271.
64. V. Saint-Ges, C. Roby, R. Bligny, A. Pradet, and R. Douce, *Eur. J. Biochem.*, 1991, **200**, 477.
65. J. K. M. Roberts, in *Surviving Hypoxia: Mechanisms of Control and Adaptation*, eds. P. W. Hochachka, P. L. Lutz, T. Sick, M. Rosenthal, and G. van den Thillart, CRC Press, Boca Raton, FL, 1993, p. 187.
66. J. K. M. Roberts, M. A. Hooks, A. P. Miaullis, S. Edwards, and C. Webster, *Plant Physiol.*, 1992, **98**, 480.
67. T. W.-M. Fan, R. M. Higashi, and A. N. Lane, *Arch. Biochem. Biophys.*, 1986, **251**, 674.
68. T. W.-M. Fan, R. M. Higashi, and A. N. Lane, *Arch. Biochem. Biophys.*, 1988, **266**, 592.
69. M. A. Hooks, R. A. Clark, R. H. Nieman, and J. K. M. Roberts, *Plant Physiol.*, 1989, **89**, 963.
70. M. A. Hooks, G. C. Shearer, and J. K. M. Roberts, *Plant Physiol.*, 1994, **104**, 581.
71. P. Genix, R. Bligny, J. B. Martin, and R. Douce, *Plant Physiol.*, 1990, **94**, 717.
72. F. Rebeille, R. Bligny, J. B. Martin, and R. Douce, *Arch. Biochem. Biophys.*, 1983, **225**, 143.
73. R. B. Lee and R. G. Ratcliffe, *J. Exp. Bot.*, 1983, **34**, 1222.
74. C. M. Spickett, N. Smirnoff, and R. G. Ratcliffe, *Plant Physiol.*, 1992, **99**, 856.
75. J. K. M. Roberts, N. Wade-Jardetzky, and O. Jardetzky *Biochemistry*, 1981, **20**, 5389.
76. T. W.-M. Fan, R. M. Higashi, J. Norlyn, and E. Epstein, *Proc. Natl. Acad. Sci. USA*, 1989, **86**, 9856.
77. D. C. McCain, J. Croxdale, and J. L. Markley, *Plant Physiol.*, 1989, **90**, 606.
78. G. G. Fox and R. G. Ratcliffe, *Plant Physiol.*, 1990, **93**, 512.
79. E. Gout, R. Bligny, and R. Douce, *J. Biol. Chem.*, 1992, **267**, 13903.
80. J. Guern, Y. Mathieu, M. Pean, C. Pasquier, J.-C. Beloeil, and J. Y. Lallemand, *Plant Physiol.*, 1986, **82**, 840.
81. Y. Mathieu, J. Guern, M. Pean, C. Pasquier, J. C. Beloeil, and J. Y. Lallemand, *Plant Physiol.*, 1986, **82**, 846.
82. D. B. Rolin, R. T. Boswell, C. Sloger, S.-I. Tu, and P. E. Pfeffer, *Plant Physiol.*, 1989, **89**, 1238.
83. P. E. Pfeffer, D. B. Rolin, T. F. Kumosinski, J. S. MacFall, and J. H. Schmidt, *Plant Physiol.*, 1992, **100**, 1682.
84. J. S. MacFall, P. E. Pfeffer, D. B. Rolin, J. R. MacFall, and G. A. Johnson, *Plant Physiol.*, 1992, **100**, 1691.
85. D. B. Rolin, P. E. Pfeffer, S. F. Osman, B. S. Szwergold, F. Kappler, and A. J. Benesi, *Biochim. Biophys. Acta*, 1992, **1116**, 215.
86. M. A. Horn, R. P. Meadows, I. Apostol, C. R. Jones, D. G. Gorenstein, P. F. Heinstein, and P. S. Low, *Plant Physiol.*, 1992, **98**, 680.

Biographical Sketch

Justin K. M. Roberts. *b* 1956. B.A., University of Oxford, UK, Ph.D., Stanford University, USA; introduced to NMR by Oleg Jardetzky. Postdoctoral work at Stanford University. Faculty, Department of Biochemistry, University of California, 1985–present. Approx. 40 publications. Research specialties: metabolism and protein synthesis in plants, in vivo NMR.

Wood and Wood Chars

Mark S. Solum

University of Utah, Salt Lake City, UT, USA

1	Introduction	1
2	Whole Wood and its Major Components	1
3	Wood Chars	4
4	Related Articles	4
5	References	4

1 INTRODUCTION

Wood is a heterogeneous material composed roughly of 40–50% cellulose, 18–35% lignin, 15–35% hemicellulose, and a smaller amount, 1–10%, of miscellaneous material collectively called extractives.[1–4] The extractives are composed of tannins, starches, gums, fats, waxes, sugars, and resins. All of the carbohydrates, or what is left after removal of lignin and the extractives from wood, is called holocellulose. Whole wood has been studied by solid state NMR, and its components by both solid and liquid state NMR.[5] Chars or activated carbons made from pyrolysis of wood at temperatures of about 650 °C or less are also suitable for study by solid state NMR. This article will only deal with solid state NMR of wood and wood chars. Solid state NMR, because of its nondestructive nature, can be used to study wood without chemical modification of the wood components or with less modification than would be needed to solubilize them. Most solid state NMR studies have used the ^{13}C CP MAS technique for studies of whole woods or various components.[6] The usual problems of quantitation in CP MAS, which have been reviewed for coals, will also apply to woods and especially wood chars.[7] Quantitation problems have been discussed for wood with respect to the determination of carbohydrate and lignin content.[8,9]

Articles on NMR of wood or wood components in both liquid and solid states can be found in a variety of journals, some of which are hard to find, especially at nonagricultural schools. Some journals not referenced here in which NMR wood articles often appear are *Holzforschung*, *Tappi*, *Appita*, *Carbohydrate Research*, *The Journal of Wood Chemistry and Technology*, and *Mokuzai Gakkaishi*.

1.1 Experimental Considerations

Most solid state NMR data of wood or wood components have been obtained with a single-contact-time (τ_{cp}) CP MAS experiment[10] using contact times of 1 or 2 ms and pulse delays T_d of 0.5–10 s, with the longer times for pure cellulose. In the CP experiment, carbon magnetization is usually approximated as building up exponentially with a time constant T_{CH}, and dying out exponentially with a time constant $T_{1\rho}^H$. The experiment may be repeated, to increase the signal-to-noise ratio, with a time determined by T_1^H. For the data to represent the different carbon types fairly with one τ_{cp}, the following conditions should hold for each nucleus $T_{CH} \ll \tau_{cp} \ll T_{1\rho}^H$ and $T_d > 5\,T_1^H$. Several researchers[8,9,11,12] have measured these parameters for wood components, and in one case[9] a comparison has been made between the CP data and data from a single pulse experiment (SPE), which can be repeated in a time determined by the longer T_1^C.

The reported results for T_{CH} of the carbons in cellulose are 150 ms or shorter, with $T_{1\rho}^H$ values from 7 to 11 ms. For the nonprotonated aromatic carbons in lignin, T_{CH} values were found to be just under 0.5 ms, with $T_{1\rho}^H$ values from about 5 to 20 ms. The T_1^H value in cellulose was found to be 369 ms,[8] and the values for lignin were less than 41 ms. The most slowly polarizing group in wood was found to be the carboxyl resonance from an acetate group in hemicellulose, where the T_{CH} was 0.8 ms.[9] These researchers also compared CP experiments with contact times of 1 and 2 ms and a 1.5 s T_d with single pulse experiment (SPE) data using a 25 s T_d, and in all three experiments virtually all of the carbon was detected. However, at a contact time of 1 ms, the carboxyl region was underestimated in comparison to SPE data. These results agree with our data on coals, where carbonyl and carboxyl groups are the main functional groups underrepresented in CP experiments as compared with SPE. A 2 ms contact time and a 2 s pulse delay appears to be the best choice for the most quantitative data, although this might not be the maximum signal intensity.

2 WHOLE WOOD AND ITS MAJOR COMPONENTS

Wood can be studied by solid state NMR by looking at the intact wood or by breaking it into components such as cellulose, hemicellulose, and lignin. The different types of lignin are in fact defined by the procedure used to isolate them from the whole wood. Studying whole wood has the advantage that there is no modification of components as is the case in separation procedures. The different components all show characteristic resonances in the NMR spectrum, with some overlap of signals. One early NMR study on lodgepole pine shows spectra of the whole wood, the effect of ball milling on wood, two types of hollocellulose, two hemicelluloses, cellulose and five types of lignin isolated from the wood.[6]

2.1 Cellulose

Cellulose, the major constituent of wood, is a linear homopolysaccharide composed of β-D-glucopyranose units. The empirical formula for cellulose is $(C_6H_{10}O_5)_n$, where n is the number of glucose monomer units in the polymer chain and is about 10 000 in wood cellulose and 15 000 in cotton cellulose.[3] Cellulose is found in the form of microfibrils, which are the smallest structural units seen by an electron microscope. These microfibrils consist of a central core of parallel cellulose chains forming a crystalline region that is surrounded by amorphous cellulose and hemicellulose and encrusted and bound in the wood cell wall by lignin.[1,13] The size of microfibrils varies, depending on the source, with the highly crystalline[14] *Valonia macrophysa* having about a 20 nm cross section and the crystalline region running at least 50 nm in length.[13] The exact details of the fibrillar and

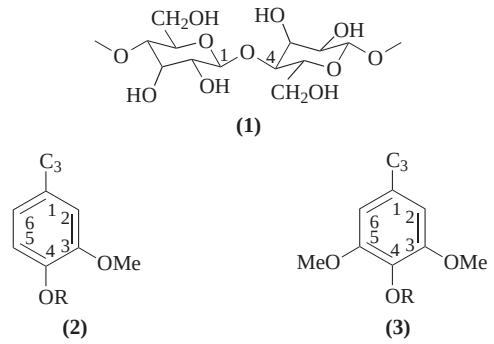

Figure 1 Basic structural units from wood components: cellobiose (**1**) unit in cellulose chain and guaiacyl (**2**) and syringyl (**3**) units from lignin

supramolecular crystal structure of cellulose is still open to debate.[1] All native celluloses have the same crystal structure called cellulose I, with four glucose units per unit cell and cellobiose (**1**) as the repeating unit in the chain direction with each glucose unit displaced 180° to give a twofold screw axis, (see Figure 1). There are at least three other crystal structures of cellulose (cellulose II, III, and IV). Cellulose II is more thermodynamically stable than cellulose I, because the crystal structure allows extra intermolecular hydrogen bonding between chains.

The ^{13}C CP MAS spectra of cellulose from three different sources is shown in Figure 2. The spectrum of amorphous cellulose has four broad lines. Lines in an amorphous material are usually broader than for crystalline material owing to chemical shift dispersion. The most deshielded line at 105.7 ppm is assigned to the anomeric C-1 carbon, and the next most deshielded line at 84.7 ppm can be assigned to the C-4 carbon of the glucosidic linkage. The large unresolved peak between 70 and 80 ppm is assigned to the three other

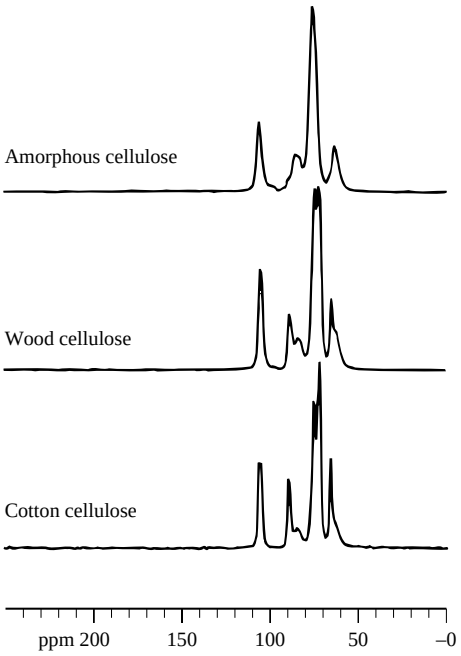

Figure 2 Carbon-13 CP MAS spectra of three types of cellulose. All spectra were run with a 2 ms contact time and 1 s pulse delay

ring carbons, C-2,3,5, and finally the nonring carbon, C-6, is assigned to the resonance at 63.1 ppm. The spectrum of powdered wood cellulose (Aldrich) is sharper than the amorphous cellulose, and two new sharp peaks at 89.6 and 65.9 ppm appear and can be assigned to carbons C-4 and C-6 of cellulose in the crystalline regions. The broad resonance between 70 and 80 ppm is now split also. The spectrum of cellulose from cotton is the most resolved of the three, with the anomeric carbon now showing a small splitting and with the sharp peaks at 90 and 66 ppm larger in comparison with broad shoulders at 84 and 64 ppm, showing this sample to be more crystalline than the wood cellulose. It should be noted that in cellulose the degree of crystallinity as measured by different techniques seems to vary with the technique[1,14] The NMR assignments for celluloses II and IV have also been given.[15]

2.2 Hemicellulose

Hemicelluloses are heterogeneous branched polysaccharides easily hydrolyzed by acid to their monomeric sugars consisting mainly of D-glucose, D-galactose, D-mannose, D-xylose, and L-arabinose. Also found are 4-*O*-methyl-D-glucuronic acid and galacturonic acid. The number of monomer units in a hemicellulose chain is about 200,[3] the chains are branched, and there are acetate, methoxy, and carboxylic acid functional groups not found in cellulose. The structures of hemicelluloses in hard woods are also different than in soft woods.[3] The ^{13}C CP MAS spectra of hemicelluloses A and B have also been assigned.[6] The general shape is somewhat similar to that of amorphous cellulose between 60 and 110 ppm, with the anomeric, C-1, carbon now at 103 ppm. Some additional resonances at 174 ppm are due to the acetate carboxyl groups, at 21.5 ppm from acetate methyls, and at 56 ppm from methoxy groups. Because clean separation of hemicellulose from lignin is difficult, small resonances from residual lignin can usually be seen in the aromatic region.

2.3 Lignin

Lignin is a highly aromatic irregular polymer of hydroxy- and methoxy-substituted phenylpropane units found in the middle lamella of plants, binding cells together, and in the secondary plant cell wall, encrusting cellulose microfibrils. Lignin in softwoods is composed mainly of guaiacyl units (**2**), while hardwood lignin is composed of syringyl (**3**) and guaiacyl units (**2**) (see Figure 1). Grass lignin is based on the *p*-hydroxyphenyl unit. However, most plants probably contain some of all three units. There are many methods used to isolate lignin from whole wood, and the name of the lignin is derived from the method (or the person who developed the method) used to isolate it. Because there are several types of ether and carbon–carbon linkages between phenylpropane units, there is great difficulty in isolating lignin without altering its chemical structure.

The ^{13}C CP MAS spectra of three different types of lignin (Aldrich) are shown in Figure 3. Kraft lignin is isolated from the spent liquor during Kraft pulping, organosolv lignin is isolated from a mixture of hardwood chips by aqueous ethanol in the presence of mineral acids, and hydrolytic lignin is

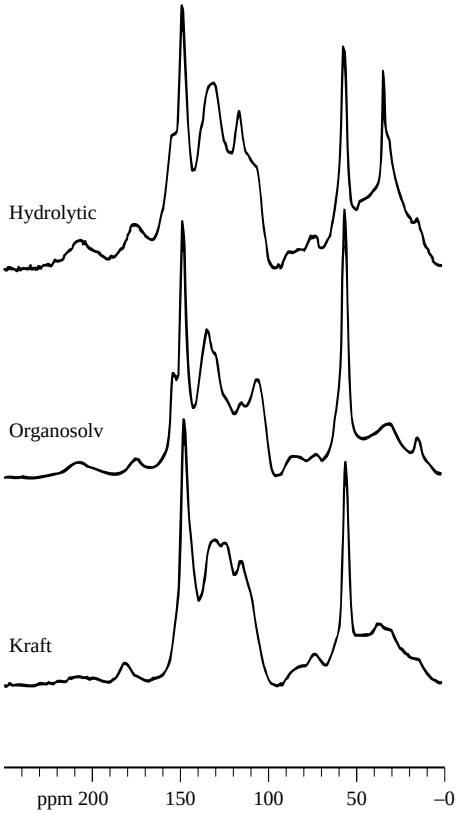

Figure 3 Carbon-13 CP MAS spectra of three types of lignin. All spectra were run with a 2 ms contact time and 1 s pulse delay

isolated from bagasse with superheated steam in the presence of acetic acid catalyst. In the NMR spectra, one can see major similarities and minor differences between the three lignins. All three show a very strong resonance between 50 and 60 ppm from methoxy groups on aromatic rings. The hydrolytic lignin also has a strong aliphatic resonance at 33.5 ppm from CH_2 groups not significant in the other two lignins. All three lignins show a resonance from carbonyl and carboxyl groups at about 206 ppm and 175–181 ppm respectively. The phenolic region between 145 and 153 ppm is very important in lignins, because (**2**) and (**3**) have slightly different resonances.[5] The 153 ppm peak is assigned to the C-3 and C-5 carbons of (**3**), and the 145 ppm and the 148 ppm peaks are from the C-4 and C-3 carbons of (**2**), respectively. All three lignins in Figure 3 show a strong resonance at 148 ppm from (**2**), but only the organsolv and hydrolytic lignins show significient intensity from (**3**) at 153 ppm. Because of the large amount of oxygen substitution in the aromatic rings, *ortho* and *para* effects shift significant aromatic intensity from the protonated carbons to the more shielded region between 100 and 120 ppm. Spectra of Klason, dioxane, periodate, enzymatic, and Brauns native lignin have been discussed elsewhere,[6] along with different Kraft preparations,[11] and comparisons between solid and liquid NMR spectra have also been given.[5]

2.4 Whole Wood

Some ^{13}C CP MAS spectra of whole woods are shown in Figure 4 for three hardwoods (white oak, yellow poplar, and

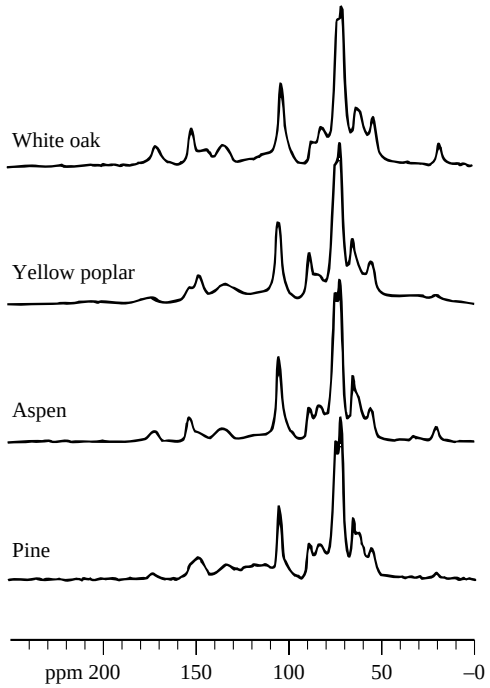

Figure 4 Carbon-13 CP MAS spectra of four whole woods, three hardwoods (white oak, yellow poplar, and aspen), and a softwood (pine). All spectra were run with a 2 ms contact time and 1 s pulse delay

aspen) and a softwood (pine). All spectra are dominated by the resonances from cellulose (and hemicellulose) between 60 and 90 ppm and the anomeric carbon at 105 ppm. The one major notable difference in this region is associated with the yellow poplar sample. Judging by the size of the 89 ppm peak compared with the 84 ppm peak and the size of the shoulder on the 66 ppm peak, the cellulose in this sample may be more crystalline than in the other three samples. All four woods show acetate resonances at 174 and 21 ppm from carboxyl and methyl groups in the hemicellulose (and possibly lignin). There is no significant carbonyl intensity in the spectra of any of the woods, and all samples show a strong methoxy resonance at 56 ppm. Another difference among the four woods is in the phenolic region between 145 and 155 ppm. The hardwoods, white oak, and aspen have a larger resonance at 153 ppm from (**3**) than the 148–145 ppm resonance from (**2**). The opposite is true for the softwood pine sample, but also for the hardwood yellow poplar sample, showing the variability of lignin in hardwoods.

If spectra are taken under quantitative conditions, solid state ^{13}C NMR can be used for the nondestructive determination of several structural parameters of whole (extractive free) woods. The parameters usually determined by solid state NMR are the total fraction of lignin in the wood,[7,11] OCH_3/R, the number of methoxy groups per aromatic ring, and $f_a^{a,H}$, the fraction of aromatic carbon that has a proton attached as determined from dipolar dephasing experiments.[8,16] These last two parameters give information on the basic lignin monomer unit and the ring substitution. One should note that in woods, the separation between the aromatic and aliphatic region is not as clean as in coals, owing to the carbohydrate C-1 carbons' deshielded resonance. While good results have been obtained by integrating the aromatic region from 109–110 ppm to the end of the aromatic range,[8,11] the most quantitative results

require some estimate of the lignin contribution under the C-1 carbohydrate peak and also carbohydrate overlap of the lignin methoxy peak at 56 ppm.[8]

3 WOOD CHARS

Pyrolysis is the application of heat to a material in the absence of oxygen to degrade the material into solid, liquid, and gasous phases. The remaining solid material, called char (or charcoal if the material was wood), has been historically used as a fuel. Sometimes, with chemical activation (H_3PO_4 or KOH), the pore structure of these chars (or activated carbons) can be increased, with the chars becoming highly adsorptive. The properties of these chars will depend on both the temperature and the time the wood has been heated. The products of pyrolysis of whole wood are basically what one would expect from pyrolysis of components separately. There have been very few reported studies of pyrolysis of wood[17–20] or wood components[18,19,21] by solid state NMR spectroscopy.

Spectra from four activated carbons[20] made by pyrolysis of white oak (see Figure 4) are shown in Figure 5. Two of the samples were soaked in phosphoric acid for 1 h before pyrolysis. The 150 °C sample was slowly heated to temperature and held there for 3 h. The other samples were heated to 170 °C over 2 h, held there for 30 min, and then taken to their final temperature and held for 1 h. The 250 °C thermal-only sample has an NMR spectrum very similar to that of the starting material, except that the carboxyl and methyl groups from the acetate groups on hemicellulose have decreased in intensity and new resonances are starting to appear between 110 and 150 ppm from new aromatic (or alkenic) moieties and at 0–50 ppm from new aliphatic groups. In contrast, the acid-treated wood has lost all carbohydrate resonances by 150 °C, the spectrum is highly aromatic with a large new phenolic resonance at 147.5 ppm, a new carbonyl peak has appeared at 204 ppm, and there are significient new aliphatic bands but with the lignin methoxy peak still visible. At 250 °C, the methoxy groups have left, aliphatic material has been lost or aromatized, carbonyl and carboxyl resonances have decreased, and the phenolic shoulder at about 150 ppm has been reduced in intensity. At 650 °C, only an aromatic peak can be seen. Underneath this peak, a very low intensity very wide band, probably from spins near free radicals, obscures any residual aliphatic material still present. The 650 °C spectrum is typical of that from the end product of pyrolysis of a carbonaceous material. On further heating, these types of material become too conductive to study by NMR.

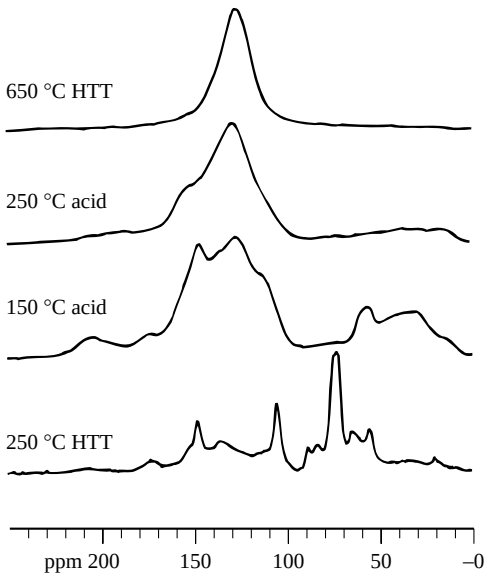

Figure 5 Carbon-13 CP MAS spectra of chars from white oak, showing final pyrolysis temperature. Two of the samples were treated with H_3PO_4 before pyrolysis. All spectra were run with a 2 ms contact time and 1 s pulse delay

4 RELATED ARTICLES

Amorphous Materials; Biological Macromolecules; Biological Macromolecules: NMR Parameters; Coal Structure from Solid State NMR; Cokes; Cross Polarization in Rotating Solids: Spin-1/2 Nuclei; Cross Polarization in Solids; Fossil Fuels; Magic Angle Spinning; Microporous Materials and Xenon-129 NMR; Solid Biopolymers.

5 REFERENCES

1. G. Tsoumis, *Science and Technology of Wood: Structure, Properties, Utilization*, Van Nostrand Reinhold, New York, 1991, Chap. 4
2. R. C. Pettersen, in *The Chemistry of Solid Wood*, ed. R. M. Rowell, American Chemical Society, Washington, DC, 1984, Chap. 2
3. E. Sjöström, *Wood Chemistry: Fundamentals and Applications*, 2nd edn., Academic Press, San Diego, 1993, Chaps. 3 and 4.
4. S. Saka, in *Wood and Cellulosic Chemistry*, eds. D. N.-S. Hon and N. Shiraishi, Marcel Dekker, New York, 1991, Chap. 2
5. M. A. Wilson, *NMR Techniques and Applications in Geochemistry and Soil Chemistry*, Pergamon Press, Oxford, 1987, Chap. 6
6. W. Kolodziejski, J. S. Frye, and G. E. Maciel, *Anal. Chem.*, 1982, **54**, 1419.
7. C. E. Snape, D. E. Axelson, R. E. Botto, J. J. Delpuech, P. Tekely, B. C. Gerstein, M. Pruski, G. E. Maciel, and M. A. Wilson, *Fuel*, 1989, **68**, 547.
8. A. L. Bates and P. G. Hatcher, *Org. Geochem.*, 1992, **18**, 407.
9. G. D. Love, C. E. Snape, and M. C. Jarvis, *Biopolymers*, 1992, **32**, 1187.
10. M. A. Wilson, *NMR Techniques and Applications in Geochemistry and Soil Chemistry*, Pergamon Press, Oxford, 1987, Chap. 4
11. J. F. Haw, G. E. Maciel, and H. A. Schroeder, *Anal. Chem.*, 1984, **56**, 1323.
12. R. H. Newman, in *Viscoelasticity of Biomaterials*, eds. W. G. Glasser and H. Hatakeyama, *ACS Symposium Series 489*, American Chemical Society, Washington, DC, 1992, Chap. 20
13. M. Fujita and H. Harada, in *Wood and Cellulosic Chemistry*, eds. D. N.-S. Hon and N. Shiraishi, Marcel Dekker, New York, 1991, Chap. 1
14. W. L. Earl and D. L. VanderHart, *Macromolecules*, 1981, **14**, 570.
15. R. L. Dudley, C. A. Fyfe, P. J. Stephenson, Y. Deslandes, G. K. Hamer, and Marchessault, *J. Am. Chem. Soc.*, 1983, **105**, 2469.
16. P. G. Hatcher, *Energy & Fuels*, 1988, **2**, 48.
17. W. L. Earl, in *Proceedings of 1981 International Conference on Residential Solid Fuels*, eds. J. A. Copper and D. Malek, Oregon Graduate Center, Beaverton, OR, 1982, 772.

18. Y. Sekiguchi, J. S. Frye, and F. Shafizadeh, *J. Appl. Polym. Sci.*, 1983, **28**, 3513.
19. F. Shafizadeh, in *The Chemistry of Solid Wood*, ed. R. M. Rowell, American Chemical Society, Washington, DC, 1984, Chap. 13
20. M. S. Solum, R. J. Pugmire, M. Jagtoyen, and F. Derbyshire, *Carbon*, 1995, **33**, 1247.
21. R. A. Wind, L. Li, G. E. Maciel, and J. B. Wooten, *J. Appl. Magn. Reson.*, 1993, **5**, 161.

Biographical Sketch

Mark S. Solum. *b* 1956. B.S., 1978, Ph.D., 1986, University of Utah. Research Associate Department of Chemistry and the Advanced Combustion Engineering Research Center (ACERC) at Brigham Young University & the University of Utah, 1986–present. Approx. 25 publications. Research interests include application of solid state NMR techniques for the study of coals, chars, woods, activated carbons and other fossil fuel materials with applications to modeling devolatilization processes and structure determinations.

Anisotropically Restricted Diffusion in MRI

Michael E. Moseley and Alex de Crespigny
Stanford University, CA, USA

1 INTRODUCTION

A dominant source of proton MR signal loss following radiofrequency excitation is caused by dephasing. While coherent flow will cause dephasing, other motions can contribute. One important mechanism of dephasing is that of a random *diffusion* of protons. This random phase shifting leads to signal loss because of phase cancelation. While T_1 and T_2 relaxation times reflect complicated frequency-dependent rotational and proton exchange processes, diffusion is caused solely by random proton displacements or translations through a tissue. Since the phenomenon of proton diffusion in vivo is complicated, the term 'apparent diffusion' described by the apparent diffusion coefficient, *ADC*, has been used to denote signal loss induced by random proton fluctuations. This applies to protons in water, phosphorus in high-energy metabolites, indeed to any MR-observable nucleus.[1–3]

Considering water proton displacements in pure isotropic solutions, where the probability that a water proton will diffuse in any given direction is equal, the rate of random proton phase cancellation due to diffusion will be same regardless of the direction observed. This is termed 'isotropic' diffusion and is seen in homogeneous environments. In ordered environments, such as that found in liquid crystals for example, the resulting diffusion coefficient will depend on the direction of the motion being considered and on any geometric anisotropy created by the nature of the microenvironment.[4,5] For water protons diffusing or moving within a tissue matrix, the observed diffusion rate and direction will reflect the molecular and macromolecular barriers or hindrances that the proton experiences during the translational process.

2 APPARENT DIFFUSION COEFFICIENTS AND OBSERVATION DIRECTION

Simply stated, proton apparent diffusion is slowed if the protons are hindered in their random motion.[6–8] Hindrances can be impermeable barriers that completely restrict diffusion. In living in vivo tissues, however, water protons are probably slowed solely by the presence of membranes, cell walls, and macromolecules due to differences in water proton permeability. More specifically, myelin fibers and neurofibrils in white matter tracts possess a special hindrance for water proton movement which is greater in one direction than another. This causes protons to diffuse faster along any direction of least resistance, in this case along the long axis of the tracts, causing the apparent diffusion coefficients to be anisotropic or directionally-dependent. It is important to note that in vivo proton diffusion is rarely restricted but is rather slowed by the presence and extent of permeable or semipermeable membranes. The complete concept of proton diffusion then is that of a tensor, where the diffusion rate or *ADC* value is a function of the diffusion direction in three-dimensional space.

As the tissue water protons constantly 'experience' the three-dimensional microenvironment through the processes of permeability, exchange, flow, and thermally-induced diffusion, their traveled path $\langle L \rangle$ along any one given direction (along the magnet bore direction, for example) can be estimated by:[9]

$$\langle L^2 \rangle = 2\Delta T(ADC) \tag{1}$$

where over an observation time of ΔT (s) the mean square displacement is expressed by an apparent diffusion coefficient, *ADC* (usually given in $m^2\ s^{-1}$ or $cm^2\ s^{-1}$). Typical proton diffusion coefficients, *ADC*, of $1\times10^{-5}\ cm^2\ s^{-1}$ are observed in cat cerebral gray matter,[10] the average mean square displacement along that one given observation direction $\langle L \rangle$ becomes $(2 \times 40\ ms \times 10^{-5}\ cm^2\ s^{-1})^{\frac{1}{2}}$ or 9 μm, observed over an effective observation time, (ΔT), of 40 ms.

To date, most diffusion-weighted MR imaging and spectroscopy sequences have been based upon a spin echo Stejskal–Tanner (ST) sequence,[11–13] either as the sequence itself or as a magnetization preparation set of prepulses, prior to another MR sampling scheme. Since the two ST 'diffusion-sensitizing' gradient pulses are symmetrical, all proton spin dephasing caused by the first diffusion-sensitizing gradient pulse will be refocused (spin-rephased) by the second diffusion-sensitizing gradient pulse for stationary spins. Randomly-moving spins (because of flow, perfusion, diffusion, etc.) will not completely refocus and will attenuate the observed echo or echo train. Note that mild coherent motions will result in phase shifts and not in signal attenuation without phase cancellation.

The observed echo or echo train signal intensity $S(Gi)$ can be expressed as:

$$S(Gi) = S(0)\mathrm{e}^{-bD} \tag{2}$$

where the b value is defined[12,13] by equation (3):

$$b = \gamma^2\delta^2G_\delta^2(\Delta - \delta/3) \tag{3}$$

and $S(0)$ is the signal obtained without applied diffusion-sensitizing gradient pulses, γ is the gyromagnetic ratio, δ and G_δ are the duration and the amplitude of the diffusion-sensitizing ST gradient pulses along a given direction, Δ is the time interval between the leading edges of the diffusion-sensitizing gradients pulses and D is the water apparent diffusion coefficient (often expressed as the *ADC* value).[12,13] Measurement of apparent diffusion from MR images would require plotting the natural logarithm of the image intensities against the b value. The slope of this observed monoexponential decay directly leads to a diffusion coefficient.[11]

There exist three major advantages to using a 'pulsed' gradient approach for measuring in vivo diffusion. One is that the stronger pulsed gradient diffusion-sensitizing pulses overcome poor magnet homogeneity (which upon reflection, is a sort of residual magnetic field gradient itself).[11] Also, because the diffusion-sensitizing gradients are relatively short pulses, the time during which the sequence is sensitive to diffusion, ($\Delta - \delta/3$), can be accurately controlled. From a knowledge of this obser-

vation time, ($\Delta - \delta/3$), the mean path length can be estimated from the above Einstein displacement equation given the measured diffusion coefficient [equation (1)]. A final advantage is that the direction of the diffusion-sensitizing gradient pulses can be controlled accurately. All MRI scanners possess three orthogonal and linear magnetic field gradient coils, any or all of which can be pulsed to produce the diffusion sensitization, the effective angle of which is then the geometric sum of the pulsed gradients. This opens the path to mapping of the apparent diffusion tensor.[14,15]

The complete concept of proton diffusion is then that of a tensor[14,15] where the diffusion rate or *ADC* value is a function of the diffusion direction in three-dimensional space. Thus the tensor for free, isotropic, diffusion can be visualized as a sphere, with the same *ADC* in all directions, while the anisotropic diffusion of a white matter tract can be viewed as an ellipsoid tilted at some angle to the three principal axes, depending on the particular fiber orientation. Diffusion is then fastest along the principal or long axis of the ellipsoid, and takes a lower (but equal) value along the two orthogonal axes. The 'trace' of this ellipsoidal diffusion tensor is just the average of the *ADC* values measured along any three orthogonal directions, and is independent of fiber orientation thus yielding a useful measure of the average rate of diffusion without the complications of fiber directionality.

3 MAPPING AND THE ORIGIN OF THE APPARENT DIFFUSION ANISOTROPY

The *b* value-dependent diffusion effects on image intensity can be displayed in different ways. A diffusion-weighted image contains typically T_1-, T_2-, and diffusion-weighting, the amount of the diffusion-weighting being dependent on the *b* value. Within diffusion-weighted images, relative faster intravoxel motion will be observed as increased attenuation of the signal from that voxel, and consequently an observed hypointensity from that voxel as the *b* value is increased. Conversely, slower motions or diffusion leads to smaller signal attenuation. The observed result is that of regional relative hyperintensity. This is best seen in lipid regions outside the brain where lipid protons experience little or no diffusion because of the molecular size and environment of the long chain hydrocarbons.

A pure diffusion of *ADC* image is calculated from the acquisition of two or more images of varying *b* values. *ADC* images eliminate T_1- and T_2-weighting; voxel intensities reflect only the apparent diffusion.[12,13] The *ADC* images are produced by fitting equation (2) to a series of two or more diffusion-weighted images of varying *b* value. The *ADC* images are then displayed with the voxel intensity related or scaled to the rate of diffusion. Visualization of cerebral details is sometimes easier from diffusion-weighted images, which are devoid of cerebrospinal fluid (CSF) hyperintensity because of the relatively faster apparent diffusion of water protons in CSF. In the corresponding *ADC* images, the pronounced CSF hyperintensity (reflecting faster apparent diffusion) can often limit the visualization of more subtle *ADC* differences in gray and white matter.

An appropriate example of ordered or anisotropic diffusion can be seen in proton diffusion-weighted images of fibrous vegetables or fruits. Apparent diffusion along the direction of ordered fibers (measured by application of the diffusion-sensitizing gradient parallel to the long axis), renders the diffusion-weighted intravoxel intensity within the fibers hypointense, implying fast diffusion of water protons along the fibers (since rapid diffusion produces signal attenuation on diffusion-weighted images). Corresponding images acquired with the diffusion-sensitizing gradient perpendicular to the long axis of the fibers result in very hyperintense image intensity within the fibers, implying relatively slow proton diffusion (little echo loss) along this direction. The translational distances traveled by water protons perpendicular and parallel to fibrous matter during the MR observation time ($\Delta - \delta/3$) of roughly 20–50 ms is estimated to be 5–13 μm (respectively). If water proton displacements in any given direction are significantly shorter that the statistical diameter of a structure of barriers along that direction, then little or no anisotropy will be observed. Anisotropy is apparent when the water protons within a voxel can sample the microenvironment adequately.

The rationale behind diffusional anisotropy in an ordered structure is that water protons within a matrix statistically prefer to move *along* ordered structures rather than *across* them (by the principle of least resistance). In other words, average proton displacements along the fibers are greater due to fewer barriers being present in this direction. Proton displacements are shorter across the fibers due to barriers presented by the very orientation of the fibers themselves. When the diffusion-sensitizing gradient direction coincides with the direction of least hindrance, the apparent diffusion appears greater and the observed *ADC* is larger.

Anisotropy of diffusion was first suggested as a possible explanation for the large regional differences in in vivo human white matter apparent diffusion coefficients by Thomsen et al.[16] More recent descriptions of the existence of and characterization of in vivo anisotropy have subsequently appeared.[10,17,18]

In axial and coronal diffusion-weighted images in animal models,[10] the directional dependence of the white matter apparent diffusion is not observed in regions of gray matter. Within the corpus callosum, however, apparent diffusion can be as slow as $0.4 \pm 0.1 \times 10^{-5}$ cm^2 s^{-1} (across the short axis of the tract) and as high as $1.3 \pm 0.1 \times 10^{-5}$ cm^2 s^{-1} (along the long axis of the corpus callosum). This suggests faster proton diffusion in white matter along the direction of the long axis of the tract. From the observed image intensities and knowledge of the diffusion-sensitizing gradient direction, one can then ascertain the orientation of individual white matter tracts. The translational distances traveled by water protons perpendicular and parallel to the white matter orientation during ($\Delta - \delta/3 =$) 40 ms can be estimated to be 6 and 11 μm respectively, suggesting that axonal diameters may be determinable from such measurements.

4 CLINICAL IMPLICATIONS

The in vivo directional diffusion-weighted images observed in human volunteers indicate that water proton diffusion anisotropy is best observed in the large diameter, fast-conducting motor and somatosensory nerve fibers (Figures 1–5). Significant anisotropy is observed in adult volunteers in all white matter tracts such as the corpus callosum, splenium, and in-

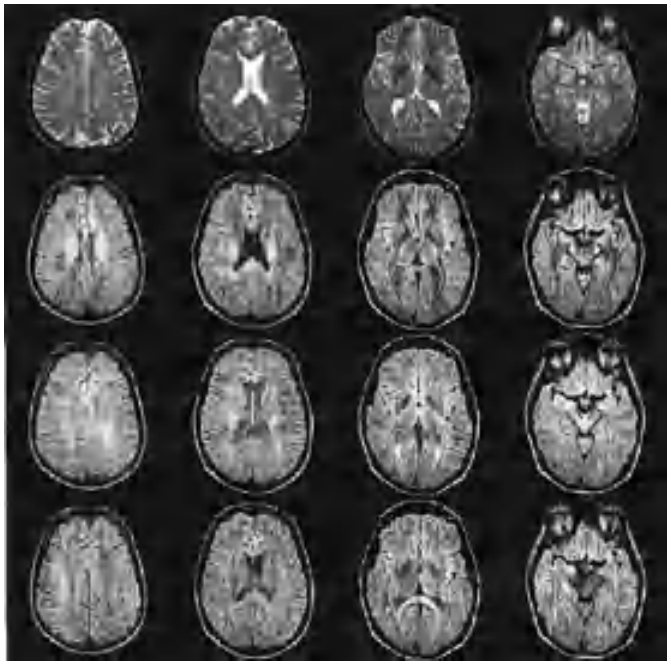

Figure 1 Axial, multislice diffusion-weighted images of a human volunteer acquired on a GE Signa at 1.5 T. Top row: minimal diffusion-weighting (b = 12 s mm^{-2}). Second row: diffusion-sensitizing gradient applied along AP direction (up–down in images), b = 512 s mm^{-2}. Third row: diffusion-sensitizing gradient applied along LR direction (left–right in images), b = 512 s mm^{-2}. Bottom row: diffusion-sensitizing gradient applied along IS direction (through-plane in images), b = 512 s mm^{-2}. All images were acquired with TR = 2× cardiac cycle (~1500 ms), TE = 102 ms and 124 ms (second echo used for navigation), 1 NEX. Gradient durations δ = 45 ms, gradient separation Δ = 62 ms, gradient strengths = 1 mT m^{-1} (1 G cm^{-1}), FOV = 24 cm, 128 × 256 matrix size, and scan times = 4.3 min for eight slices per TR. Navigation achieved by correction of navigational echo magnitude. CSF suppression not applied. All images are scaled except top row. On these images, containing T_1-, T_2-, proton density-, and diffusion-weighting, relative regions of hypointensity denote rapid apparent diffusion of protons. Regions of relative hyperintensity demarcate slower diffusion. Note little or no anisotropic effects in gray matter or lipids (which display very slow apparent diffusion). TR, repetition time; TE, echo time; NEX, average; FOV field of view

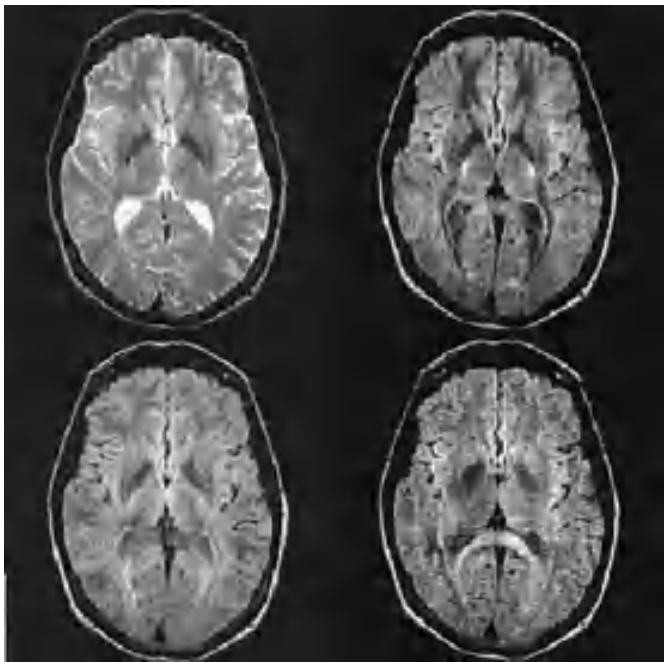

Figure 2 Diffusion-weighted images chosen from one slice and taken from images in Figure 1. Top left: minimally diffusion-weighted; top right: diffusion-sensitizing gradient applied along AP direction (up–down in images), b = 512 s mm^{-2}. Bottom left: diffusion-sensitizing gradient applied along LR direction (left–right in images), b = 512 s mm^{-2}. Bottom right: diffusion-sensitizing gradient applied along IS direction (through-plane in images), b = 512 s mm^{-2}. Note regional hypointensity in white matter tracts when applied diffusion-sensitizing gradient direction is parallel to white matter orientation. This is best seen in the image at top right, in the lower limbs of the splenum of the corpus callosum

ternal capsules. In addition, myelinated tracts in spinal cord,[10] optic (A. de Crespigny, unpublished data), and peripheral nerves[20] appear to be associated with significant anisotropic effects.

Several pioneering studies verifying white matter diffusional anisotropy in normal and abnormal human and neonate subjects have been presented.[18,21–25] It has been shown that the newborn brain demonstrates isotropic diffusion of water molecules.[22,23] As the brain matures, diffusion becomes anisotropic, being greater along the longitudinal axes of the major axonal bundles of the cerebral white matter than perpendicular to them.

This anisotropic ordering of water motion most likely occurs along the long axis of the individual neurofibrils as well as along or within the axons isolated by the myelin sheath. Studies indicate that the presence of myelin is not necessary for ordering of proton apparent diffusion since anisotropic proton mobility is seen in nerves lacking microtubules and fast axonal transport.[26] It is reasonable to assume that the development of anisotropy is related to the development of myelin sheaths; however, the temporal evolution of anisotropy seems to precede that of myelination as described by most authors.[27] Additionally, diffusional anisotropy has been proved to occur in nonmyelinated nerve bundles.[26] Another possibility is that diffusion anisotropy develops in relation to the maturation of the microtubules, intraaxonal organelles that facilitate axonal transport.[28,29] Thus, diffusion-weighted imaging (DWI) seems to be useful in the real time assessment of cerebral maturation.

The use of diffusion-weighted imaging for the determination of water proton apparent diffusion anisotropy may aid in the study of peripheral CNS tissues, which exhibit water proton diffusional anisotropy effects. One novel application, termed 'MR neurography'[20] can increase tissue contrast by using MR diffusion-weighting in a variety of directions to evaluate the diffusion tensor found in nerve tissue. An important adjunct to neurography is the use of fat saturation to reduce hyperintense artifacts due to the slow mobility of protons in lipid tissues and in the use of maximum intensity projection (MIP) methods to track nerve tissue in a MR angiography-like fashion.

Most clinical usage of diffusion-weighted MRI has been hampered by two significant problems, gradient strength and motion artifacts. Many clinical scanners possess gradients capable of strengths of no more than 10 mT m^{-1} (1 G cm^{-1}), limiting b values to roughly 300 s mm^{-2} along any given direction. These limitations typically require pulsing two or all

three gradients together for longer durations (with increases in *TE* to well over 100 ms) to push the *b* value to above roughly 500 s mm^{-2}, above which diffusion effects can be clearly seen above the inherent T_2-weighting. This in turn limits the signal-to-noise ratio (SNR) and degrades image quality, an important factor in diffusion imaging since good diffusion-weighting will itself attenuate SNR exponentially.

More importantly, longer *TE* values lead to significant motional artifacts. Linear excursions of just a few millimeters can easily ruin images where diffusion-weighted tissue contrast arises from proton displacements on the order of microns. The solutions employed to date have included restraint of the head with rigid holders or vacuum cushions that seal the head in the coil. These are uncomfortable and are difficult to implement on uncooperative patients, particularly when several images are required to map the apparent diffusion tensor or to synthesize *ADC* images.

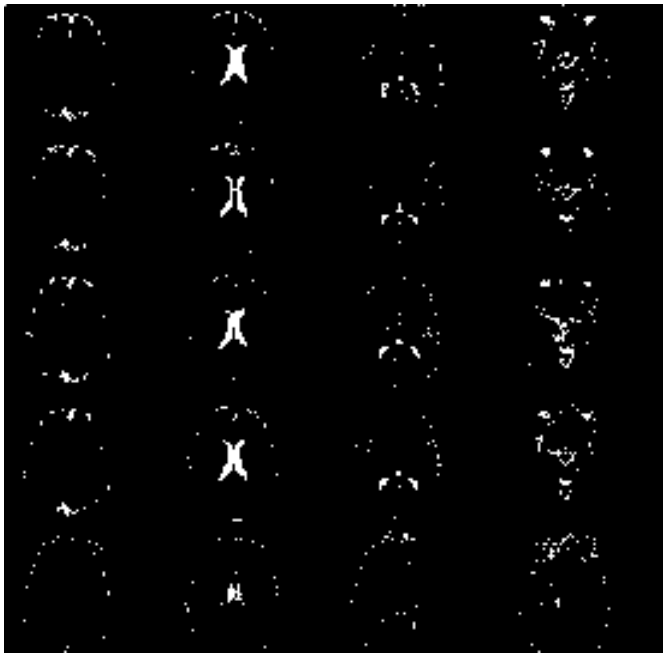

Figure 3 Series of three diffusion-weighted images were acquired at *b* values of 12, 350, and 512 s mm^{-2} to produce the pure diffusion (*ADC*) images shown here for the three gradient axes and for the same four slices shown in Figure 1. Top row: diffusion-sensitizing gradient applied along AP direction (up–down in images). Second row: diffusion-sensitizing gradient applied along LR direction (left–right in images). Third row: diffusion-sensitizing gradient applied along IS direction (through-plane in images). Note that regional hyperintensity on *ADC* images indicates rapid apparent diffusion. CSF hyperintensity is an example of fast apparent motion or diffusion, so much so that smaller variations in gray and white matter are masked out and difficult to appreciate. For this reason, diffusion-weighted or other image synthesis is needed. Fourth row: images of the 'trace' of the diffusion tensor determined for each of the slices shown in the top three rows. The trace of the tensor is essentially an average of the diffusion images from the three principal axes and is useful for removing orientation effects from diffusion-weighted or *ADC* images. The trace image is useful for discrimination of *ADC* alterations due to stroke or other cerebrovascular diseases,[19] which is often difficult because of regional *ADC* differences due to white matter anisotropy. Bottom row: the synthesized 'standard deviation' images[19] taken from the *ADC* images and the trace image. The SD image is essentially a pixel-by-pixel map of the deviations from the trace and can be very useful for the identification of white matter tracts and discrimination from stroke or regional gray matter

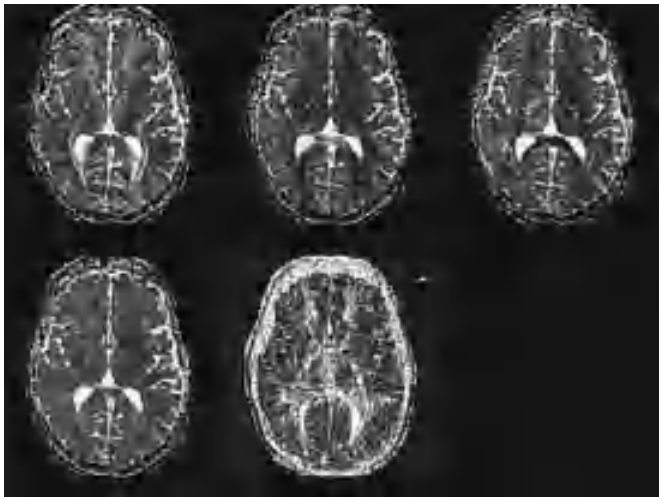

Figure 4 Enlargements from the *ADC* and anisotropy maps for one slice taken from the images shown in Figure 3. Top left: *ADC* image with diffusion-sensitizing gradient applied along AP direction (up–down in images). Top middle: *ADC* image with diffusion-sensitizing gradient applied along LR direction (left–right in images). Top right: *ADC* image with diffusion-sensitizing gradient applied along IS direction (through-plane in images). Bottom left: trace image. Bottom middle: standard deviation image

Fast-scan and high-speed MRI capable of acquiring diffusion-weighted images in seconds or less requires typically large gradient strengths (not currently present on most clinical scanners) and has been limited to relatively low-resolution images which make proper visualization of the individual white matter tracts very difficult. The use of multiple shots or echo trains in

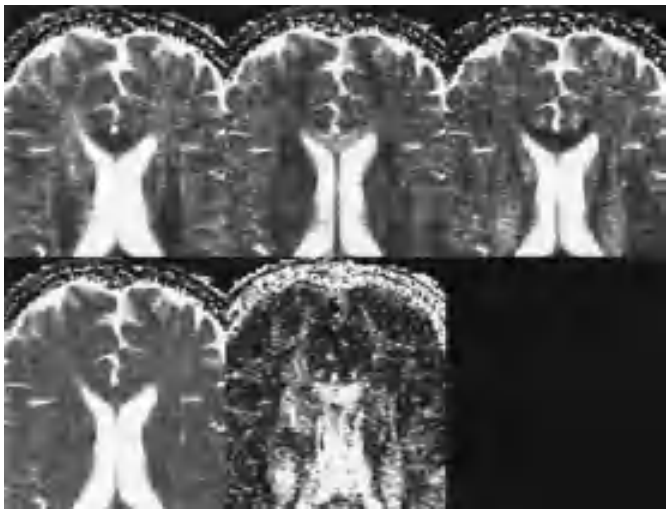

Figure 5 Enlargements of another slice from the image set in Figure 3; image layout is as for Figure 4. This slice clearly shows the genu of the corpus callosum in the center of the *ADC* images (top row), which is not seen in the trace image (bottom left) but stands out in the anisotropy image (bottom middle) due to the strong orientation effects of the corpus callosum

high-speed imaging to improve resolution or SNR will in turn render the images again sensitive to motional artifacts.

Phase navigation[30,31] combined with a conventional single or multi echo imaging sequence has great potential for clinical application. It involves simple modifications of standard clinical pulse sequences using additional spin- or gradient-echoes acquired without phase encoding to map and correct each phase-encoded line or train of *k*-space. This can yield relatively motion-free images of excellent resolution with limited gradient strengths at the expense of conventional scan times. Uncooperative patients can create motion artifacts not easily correctable with linear phase navigation methods (A. de Crespigny, unpublished data). However, with motion correction or navigation, a multishot approach (using EPI, RARE, or spiral *k*-space coverage) could become the optimal apparent diffusion imaging technique, using conventional gradients to build resolution in much shorter scan times. This would be fast enough to acquire a series of images with increasing *b* value or varying gradient direction in order to generate an *ADC* or an orientation map.

Utilization of this unique MRI technique for determining the orientation of white matter through the measurement of water proton apparent diffusion has the potential greatly to improve our understanding and assessment of demyelination disorders, white matter infarcts with associated edema development,[32] neoplasms involving white matter tracts, and of neonatal brain and spinal cord development. Significant proton anisotropic effects have also been observed in human arm muscle, [33] opening up the potential of using this technique to map performance or pathology. Finally, images devoid of white matter orientation effects can be synthesized by mapping the trace of the tensor enabling better visualization and earlier detection of ischemia in the CNS.[19]

5 RELATED ARTICLES

Diffusion: Clinical Utility of MRI Studies; Image Formation Methods; Intracranial Infections; Magnetic Resonance Imaging of White Matter Disease; Spin Warp Data Acquisition.

6 REFERENCES

1. G. E. Wesbey, M. E. Moseley, and R. L. Ehman, *Invest. Radiol.*, 1985, **19**, 484.
2. C. T. W. Moonen, P. C. M. van Zijl, D. LeBihan, and D. Despres, *Magn. Reson. Med.*, 1990, **13**, 467.
3. M. E. Moseley and P. Stilbs, *Chem. Scr.*, 1980, **15**, 215.
4. M. E. Moseley and A. Loewenstein, *Mol. Cryst. Liq. Cryst.*, 1982, **90**, 117.
5. M. E. Moseley, *J. Phys. Chem.*, 1983, **87**, 18.
6. E. O. Stejskal and J. E. Tanner, *J. Chem. Phys.*, 1965, **43**, 3579.
7. J. E. Tanner and E. O. Stejskal, *J. Chem. Phys.*, 1968, **49**, 1768.
8. R. L. Cooper, D. B. Chang, A. C. Young, C. J. Martin, and D. Ancker-Johnson, *Biophys. J.*, 1974, **14**, 161.
9. A. Einstein, 'Investigations on the Theory of the Brownian Movement', Dover Publications, New York, 1956.
10. M. E. Moseley, Y. Cohen, J. Kucharczyk, J. Mintorovitch, H. S. Agari, N. F. Kenland, J. Tsurula, and D. Norman, *Radiology*, 1990, **176**, 439.
11. E. O. Stejskal and J. E. Tanner, *J. Chem. Phys.*, 1965, **42**, 288.
12. D. LeBihan, E. Breton, D. Lallemand, P. Grenier, E. Cabanis, and M. Laval-Jeantet, *Radiology*, 1986, **161**, 401.
13. D. LeBihan, E. Breton, D. Lallemand, M. Aubin, J. Vignaud, and M. Laval-Jeantet, *Radiology*, 1988, **168**, 497.
14. P. J. Basser, J. Mattiello, and D. LeBihan, *J. Magn. Reson. Ser. B*, 1994, **103**(3), 247.
15. J. Mattiello, P. J. Basser, and D. LeBihan, *Magn. Reson., Med. B*, 1997, **37**(2), 292.
16. C. Thomsen, O. Henriksen, and P. Ring, *Acta Radiol.*, 1987, **28**, 353.
17. D. Chien, R. B. Buxton, K. K. Kwong, and B. R. Rosen, *J. Comput. Assist. Tomogr.*, 1990, **14**, 514.
18. W. M. Chew, J. Tsuruda, and M. E. Moseley, *Radiology*, 1990, **177**, S121.
19. P. van Gelderen, M. M. de Vleeschouwer, D. DesPres, J. Pekar, P. C. M. van Zijl, and C. T. W. Moonen, *Magn. Reson. Med.*, 1994, **31**, 154.
20. F. A. Howe, A. G. Filler, B. A. Bell, and J. R. Griffiths, *Magn. Reson. Med.*, 1992, **28**, 328.
21. T. L. Chenevert, J. A. Brunberg, and J. Pipe, *Radiology*, 1990, **177**, 401.
22. H. Sakuma, Y. Nomura, K. Takeda, T. Tagami, T. Nakagawa, Y. Tamagawa, Y. Ishi, and T. Tsukomoto, *Radiology*, 1991, **180**, 229.
23. M. A. Rutherford, F. M. Cowan, A. Y. Manzur, L. M. Dubowitz, M. Pennock, J. V. Majnal, I. R. Young, and G. M. Bydder, *J. Comput. Assist. Tomogr.*, 1991, **15**, 188.
24. M. Doran, J. V. Hajnal, N. Van Bruggen, M. D. King, I. R. Young, and G. M. Bydder, *J. Comput. Assist. Tomogr.*, 1990, **14**, 865.
25. J. V. Hajnal, M. Doran, and G. M. Bydder, in 'Magnetic Resonance Imaging', eds. D. D. Stark and W. G. Bradley, Mosby, St. Louis, MO, 1991, Vol. 2, p. 1081.
26. C. Beaulieu and P. S. Allen, *Proc. 11th Ann Mtg. Soc. Magn. Reson. Med.*, Berlin, 1992, p. 1728.
27. A. J. Barkovich and D. M. Wimberger, in 'Magnetic Resonance Neuroimaging', eds. J. Kucharczyk, M. Mosley, and A. J. Barkovich, CRC Press, Boca Raton, FL, 1993.
28. F. Espejo and J. Alvarez, *J. Comp. Neurol.*, 1986, **250**, 65.
29. V. Faundez and J. Alvarez, *J. Comp. Neurol.*, 1986, **250**, 73.
30. R. A. Ordidge, J. A. Helpern, Z. Qing, and R. A. Knight, *Proc. 11th Ann Mtg. Soc. Magn. Reson. Med.*, Berlin, 1992, p. 1902.
31. R. Asato, T. Tsukamoto, R. Okumura, Y. Miki, E. Yoshitome, and J. Konishi, *Proc. 11th Ann Mtg. Soc. Magn. Reson. Med.*, Berlin, 1992, p. 1226.
32. T. Ebisu, S. Naruse, Y. Horikawa, S. Ueda, C. Tanaka, M. Uto, M. Umeda, and T. Higuchi, *J. Magn. Reson. Imaging*, 1993, **3**, 863.
33. M. E. Moseley, and M. F. Wendland, *Proc. 10th Ann Mtg. Soc. Magn. Reson. Med.*, San Francisco, 1991, p. 108.

Biographical Sketches

M. E. Moseley. *b* 1951. B.S., 1973, North Carolina State University, Ph.D., 1980, Uppsala University. Postdoctoral work at Weizmann Institute of Science, Rehovot (with Z. Luz). Faculty at UCSF, 1985–93; Stanford, 1993–present. Approx. 150 publications. Research interests include MR methods of mapping diffusion, perfusion and functional physiology.

A. de Crespigny. *b* 1965. Ph.D., 1991, Cambridge University. Postdoctoral work at UCSF. Approx. 22 publications. Research interests include MR methods of mapping anisotropy in neonates, high-speed MRI, and image display and fusion.

Brain Parenchyma Motion Observed by MRI

Van J. Wedeen
Harvard Medical School, USA

and

Brigitte Ponceleti
Massachusetts General Hospital, MA, USA

1 INTRODUCTION

MRI studies of brain motion afford a unique window onto the mechanical homeostasis of the central nervous system (CNS). Velocity-sensitive MRI techniques may be based upon modulation of the magnitude or phase of the NMR image data, and have the capacity to detect the distributions of velocities, the displacements, or the material strainrates within the brain parenchyma. Having the capacity to resolve tissue displacements on the scale of micrometers, limited in practice by proton diffusion, NMR movies have mapped the physiological pulsation of the brain and spinal cord with the heartbeat and have measured brain parenchymal deformations due to everyday cranial accelerations. Clinical applications are projected to include the prediction of response to surgical treatment for a tethered spinal cord, and, potentially, the diagnosis of normal-pressure hydrocephalus. Brain motion studies will be of value in elucidating the mechanisms of CNS trauma of both exogenous and endogenous forms.

2 BRAIN MOTION

Physiological brain motion reflects the reaction of the brain parenchyma, spinal cord, and cerebrospinal fluid (CSF) to changes in arterial and venous pressure and volume with the cardiac pulse and respiration.[1] According to the Monro–Kellie doctrine, cranial entry of an arterial blood volume bolus with each systole must be matched by an equal egress of blood, CSF, and brain parenchyma from this incompliant compartment.[2–4] Ultimately, parenchymal egress is effected by the movement of the cervical cord caudally through the foramen magnum.

A detailed picture of the physiological brain motion has gradually emerged. DuBoulay postulated that CSF pulsation is pumped by the brain parenchyma, specifically the compression of the third ventricle by a medial motion of the thalami.[5] MRI has since confirmed this and has been instrumental in the emergence of a more complete view. Anatomically, brain parenchymal pulsation may now be seen chiefly as a radial inflow of brain tissue inward and downward toward the foramen magnum: a herniation in miniature.[6–10] For a superb treatment of multiaxial ciné velocity data, see Greitz et al.[8] Most rapid motion is seen in the cervical cord and brain stem, which descend at velocities as great as 5–10 mm s^{-1}. By contrast, the cerebral mantle is almost immobile with respect to the calvarium. Velocities of intermediate size and complex 3D form are present in central deep gray and midbrain structures, among them the compressive motion of the thalami postulated by DuBoulay. Superimposed on the cardiac pulsation is a respiratory pulsation of a much smaller size.[2] Observations of brain parenchymal strain patterns (see Section 5.1) suggest that variation in vascular turgor, particularly of the large arteries, may influence the observed parenchymal motion. MRI measurement of CNS motion may be confounded by head movements of musculoskeletal or cardiac-ballistic origins.[3]

3 OVERVIEW OF MRI OF CNS MOTION

CNS motion has been assessed by a variety of NMR imaging techniques. The earliest MRI demonstration of CNS motion was offered by Feinberg and Mark, who in 1987 presented echocardiogram (ECG)-gated movies of Fourier velocity spectra along selected 1D lines within the head, as shown in Figure 1.[6,11] (For pioneering work on Fourier transform imaging spectra, antecedent to the present techniques and to phase contrast MRA, see Moran.[12]) Later investigators have estimated mean velocity using reduced numbers of velocity phase encoding steps and increased spatial or temporal resolution in conventional 2D multishot MRI,[13–15] echo planar MRI,[10] and real-time 1D-selective line MRI ('M-mode' NMR).[16] The technique of NMR 'interferography' of Hennig is a variant type of velocity encoding, based on a spatial modulation of local signal magnitude rather than phase.[17] A quite different approach to CNS pulsation was taken by Lee, Wang, and Mezrich, who measured pulsatile changes in the volume of the lateral ventricles using conventional MRI.[18]

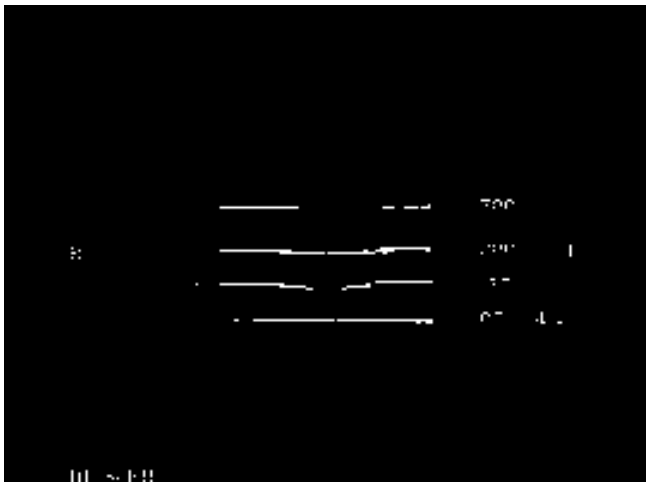

Figure 1 Fourier-encoded ciné velocity study for a selected line of tissue at the level of the foramen of Monroe. Cardiac gate delays from the R-wave are denoted. Cranio caudal velocities are depicted on the vertical axis, with single-pixel resolution of 0.4 mm s^{-1}. Line selection was performed using orthogonal slice selects. The basic downward ''piston'' motion of the midbrain is demonstrated. (Reproduced by permission from Feinberg and Mark[6])

4 MOTION-SENSITIVE ECHO PLANAR MRI OF BRAIN MOTION

The displacements associated with brain motion range from a typical maximum of 1–2 mm in the cervical cord down to unmeasurably small values in the cerebral mantle. Consequently, brain motion justifies the highest feasible levels of motion sensitivity. MRI can achieve high velocity sensitivities by the method of magnetic gradient phase encoding, familiar in magnetic resonance angiography (MRA) and diffusion imaging and more recently in the imaging of myocardial motion.[19,20] A pulsed gradient $\boldsymbol{G}$ is applied such that $\int_0^{TE}\boldsymbol{G}(t)\,dt = 0$ to induce a phase shift ϕ for velocity $\boldsymbol{V}$ of $\phi = \boldsymbol{k}_v \cdot \boldsymbol{V}$, where $\boldsymbol{k}_v = \int_0^{TE}\gamma\boldsymbol{G}(t)\,t\,dt$.

The velocity resolution of a phase-sensitive MRI experiment is approximately $\Delta\boldsymbol{V} = N/\boldsymbol{k}_v S$, where N is the desired number of standard deviations of discrimination and S is the signal-to-noise ratio (SNR) of the MRI phase over the region in question, typically equal to π times the SNR of the MRI magnitude.[21] If the velocity changes over time, the phase shift ϕ represents the time-average velocity weighted by the integral of the gradient: $E(T) = \int_0^T \boldsymbol{G}(t)\,dt$.[10]

4.1 Subtraction of Head Motion

Rigid motion of the brain and skull can be an important confounding factor in high-sensitivity studies of brain motion.[10] Head motion is caused by cardiac pulsation, respiration, and involuntary activity of skeletal muscles seen even in cooperative subjects with good head fixation. Echo planar MRI has demonstrated that head motions of 1 mm s^{-1} may occur even under relatively optimal conditions. Using ordinary means of head fixation, extrinsic skull motion and intrinsic CNS motion in the supratentorial region appear to be of similar magnitudes, but may be out of phase. In the cervical region, the craniocaudal motion of the cord is several-fold greater than extrinsic motion.

The effects of rigid head motion in studies of brain parenchyma motion can be conveniently removed by mathematical means.[10] Using the fact that a rigid motion defines a linear function, velocities of the skull are measured, and brain motion due to this rigid motion estimated by linear interpolation (brain parenchymal strain rate may be corrected for rigid motion by subtracting from each component $\partial V_i/\partial X_j$ times its mean value over the skull).[22] When this rigid component of motion is subtracted out, the specific motion of the brain relative to the skull is revealed.

4.2 Limitations

MRI velocity sensitivity is ultimately limited by molecular diffusion and by the spatiotemporal characteristics of the motion pattern under study. Signal attenuation due to tissue water self-diffusion limits the intensities and durations of the gradient pulses that may be usefully applied. A gradient pulse of intensity G and duration δ establishes in the tissue parallel isophase planes of spatial period $\gamma G\delta$ diffusional attenuation becomes severe as the Einstein diffusion length $(2D\delta)^{1/2}$, where D is the diffusivity, approaches the isophase lamellar spacing.[23–25]

A second limit to velocity sensitivity is imposed by signal attenuation due to velocity gradients within each voxel. Velocity gradients may result from rigid rotation or material shear. In the simplest case, velocity and phase are linear functions of position. In this case, image magnitude will be attenuated by a Fourier coefficient of the spatial profile of the voxel.[22] Typically, the voxel profile has the form of a rectangular function in the slice direction (z) and a sincfunction in each in-plane coordinate (x and y). Then the attenuation due to shear, A_{SH}, becomes simply

$$A_{SH} = \text{rect}\,(\partial\phi/\partial x)\ \text{rect}\,(\partial\phi/\partial y)\ \text{sinc}\,(\partial\phi/\partial z) \qquad (1)$$

when the spatial coordinates (x, y, z) are expressed in units of pixel diameters, ϕ is in cycles and $\text{rect}\,(u) = 1$ if $|u| < \frac{1}{2}$, 0 otherwise. Equation (1) implies that attenuation due to in-plane velocity shear is all-or-none: 0% attenuation when $|\partial\phi/\partial x_i| < \frac{1}{2}$ cycle/pixel and 100% attenuation when $|\partial\phi/\partial x_i| > \frac{1}{2}$ cycle/pixel. No definite evidence of shear attenuation has to date been demonstrated in brain parenchyma, although such attenuation has been seen in the CSF in zones of high-shear such as the aqueduct.[26]

4.3 Normal Pulsatile Brain Motion

Qualitatively, the intrinsic brain motion consists of a primary systolic downstroke of the brainstem, which moves like a plunger within the relatively fixed cerebral mantle, followed by a slower diastolic recovery toward the initial configuration. In synchrony with this axial motion, the thalami move inward bilaterally to compress the third ventricle. Anteroposterior velocities are typically less than 25% of maximum craniocaudal or mediolateral velocities.

Figure 2 shows the three components of intrinsic brain parenchyma velocity in axial slices in a normal volunteer. The slices are at the midventricular level, and ciné data were acquired with 50 ms temporal resolution. Gray scale images show the magnitude and mediolateral, craniocaudal, and anteroposterior velocity component images 100 ms after the ECG R-wave. The curves plot the velocity components as functions of time for the elliptical regions of interest indicated. The net craniocaudal displacement 100 ms after the R-wave is shown as a 3D surface in Figure 3. Craniocaudal velocity in a midline sagittal plane is shown in Figure 4. The velocity curves [Figure 2(b)] show a monophasic or biphasic motion burst 50–200 ms after the ECG R-wave, synchronous with the systolic arterial pulse wave arrival, and subsequently in diastole much smaller velocities of recovery (diastolic RMS velocity < 20% systolic). The velocity images demonstrate the rapid caudal descent and of central structures, and the medial compressive motion of the thalami; anteroposterior velocities are relatively small.

In normal volunteers, absolute CNS motion proves to be reproducible between heartbeats ±15% (SD). It follows that conventional multishot MRI with an ECG trigger would produce reasonably accurate maps of CNS motions.

4.4 Tethered Spinal Cord

Under normal conditions, the spinal cord participates in the pulsatile movement of the CNS, with significant vertical motion seen throughout cervical and upper thoracic levels. Physiological cord motion is normally rapid, with velocities of up to 10 mm s^{-1}, and may exhibit several cycles of damped oscillation, possibly related to elastic recoil of the dentate ligaments.[27]

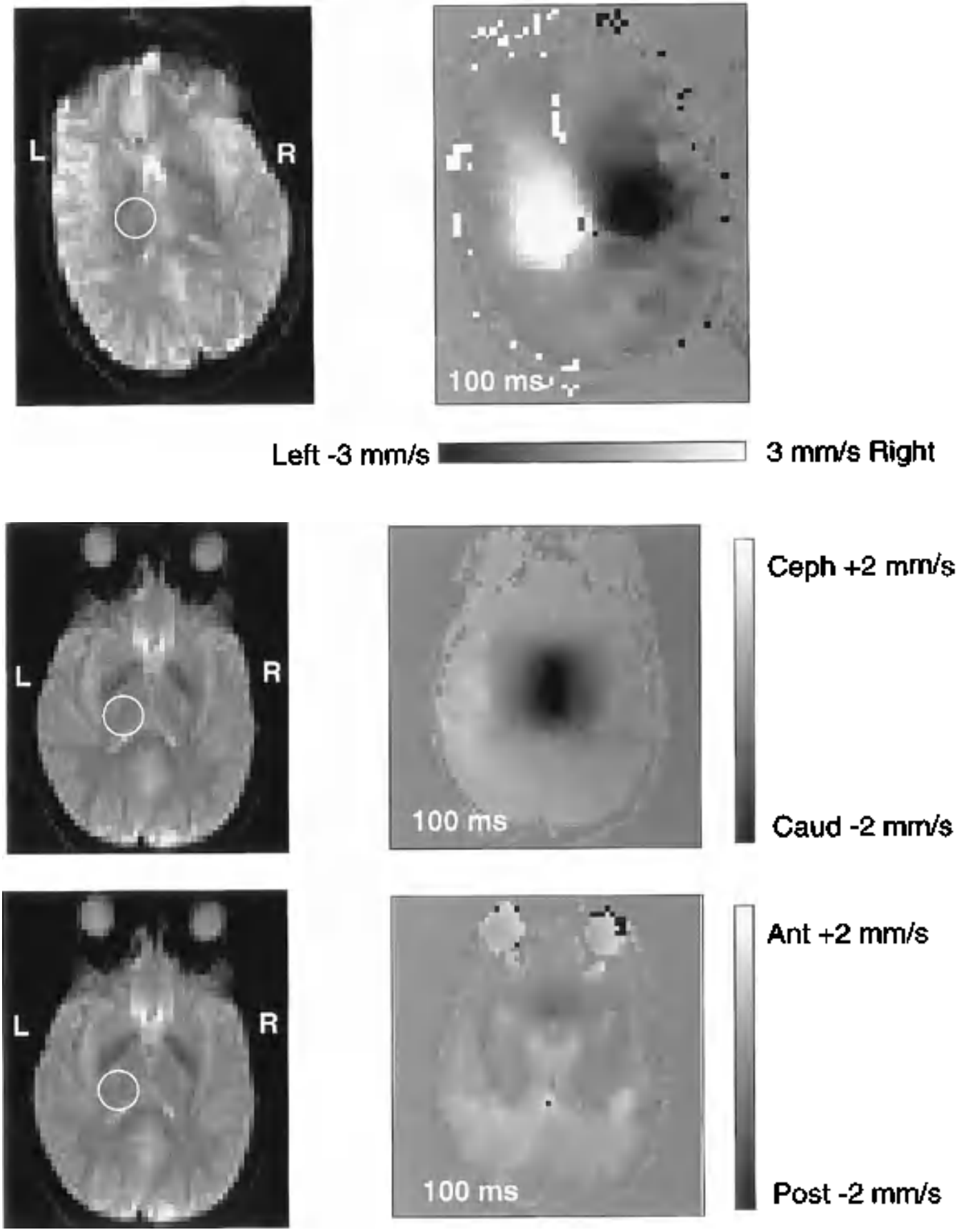
L
R
100 ms
Left -3 mm/s
3 mm/s Right
L
R
100 ms
Ceph +2 mm/s
Caud -2 mm/s
L
R
100 ms
Ant +2 mm/s
Post -2 mm/s

Figure 2(a)

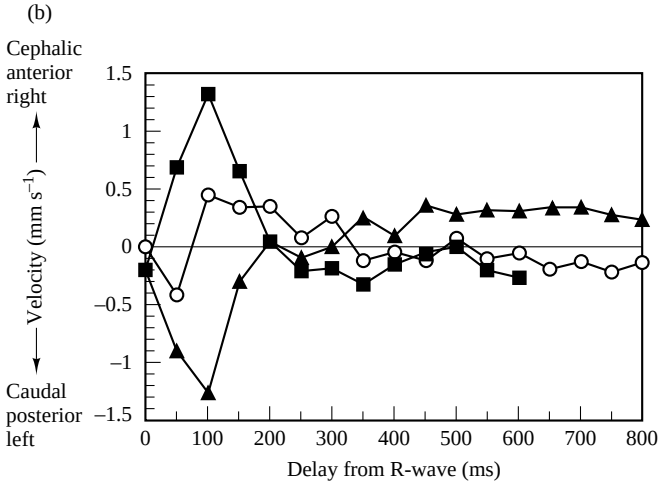

Figure 2 (a) Images of intrinsic brain velocity components for axial slices at the midventricular level in a normal subject 100 ms after the ECG R-wave, the approximate moment of peak parenchymal pulsatile velocities. To the left are the magnitude images; to the right are the mediolateral, craniocaudal and anteroposterior velocity component images with scales. The craniocaudal velocity map shows the rapid central descent (dark gray to black), and the mediolateral image shows the rapid bilateral medial velocities of the thalami (white–black dipole). The bottom image shows the anteroposterior velocity component. (b) The velocity–time curves for the left thalamic ROI designated by the circle. Parenchymal velocities are highest between 50 and 200 ms after the ECG R-wave during cardiac systole; much slower velocities of parenchymal recovery are seen beyond about 200 ms after the R-wave, during diastole. ▲, cephalocaudal; ○, anteroposterior; ■, left–right

During normal development, the vertebral column undergoes greater craniocaudal growth than the spinal cord, and so the distal cord appears to ascend within the spinal canal. If the ascent of the cord is hindered by a mass, bone spur, or fibrous band, the cord may become stretched, which may lead by ischemia to symptoms of paresis, paresthesias, and loss of sphincter control. This syndrome is called the 'tethered cord', and is treated surgically. Given the normal physiological motion of the cord, it is reasonable to inquire whether changes in the normal pattern of motion could be a diagnostic marker of tethering.

Investigators at The Johns Hopkins University School of Medicine and Georgetown have shown that motion of the cervical cord is a good predictor of clinical response to surgery

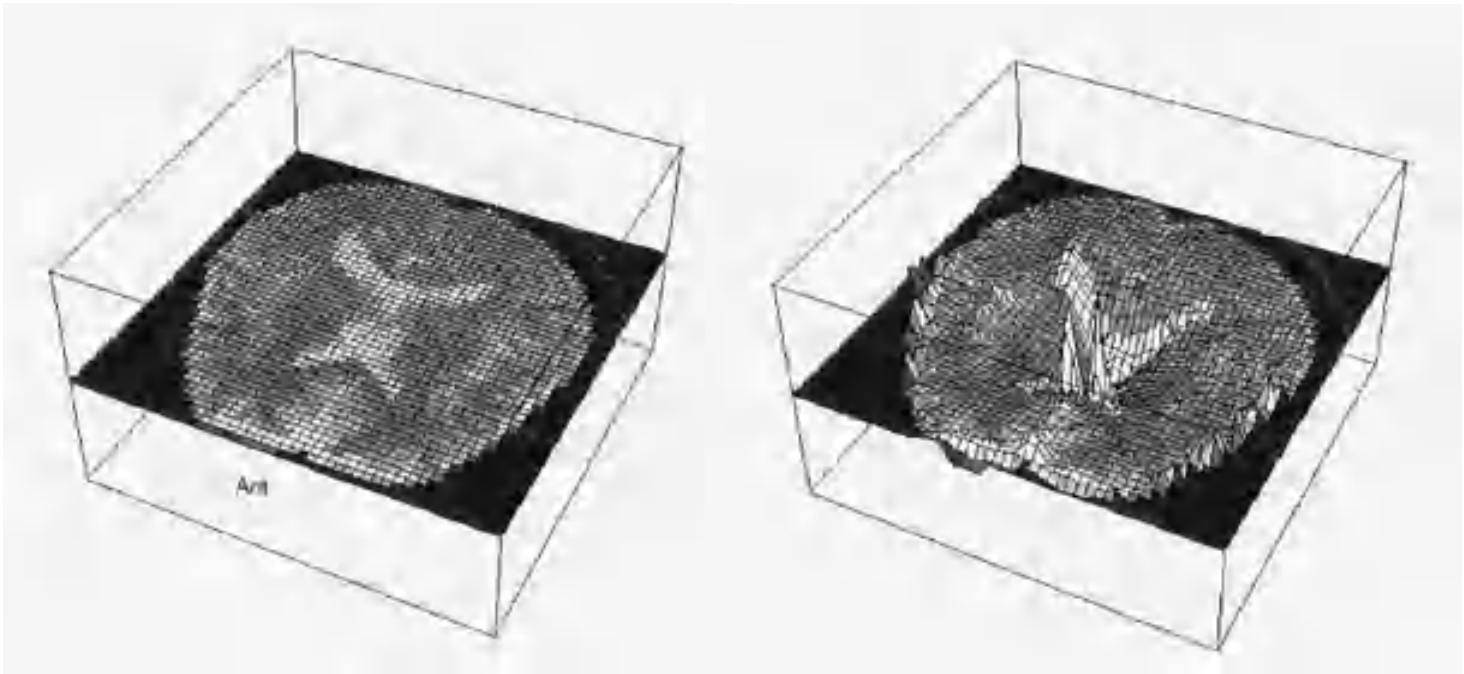

Figure 3 Net craniocaudal displacement of an axial slice 300 ms after the R-wave. Displacement is represented by the surface height, with a full scale of ±3 mm. Image magnitude has been texture mapped onto the 3D surface. The predominant displacement is a monophasic downward movement of central structures; this figure corresponds to maximal displacement. Bidirectional CSF motion is seen in the horns of the lateral ventricles

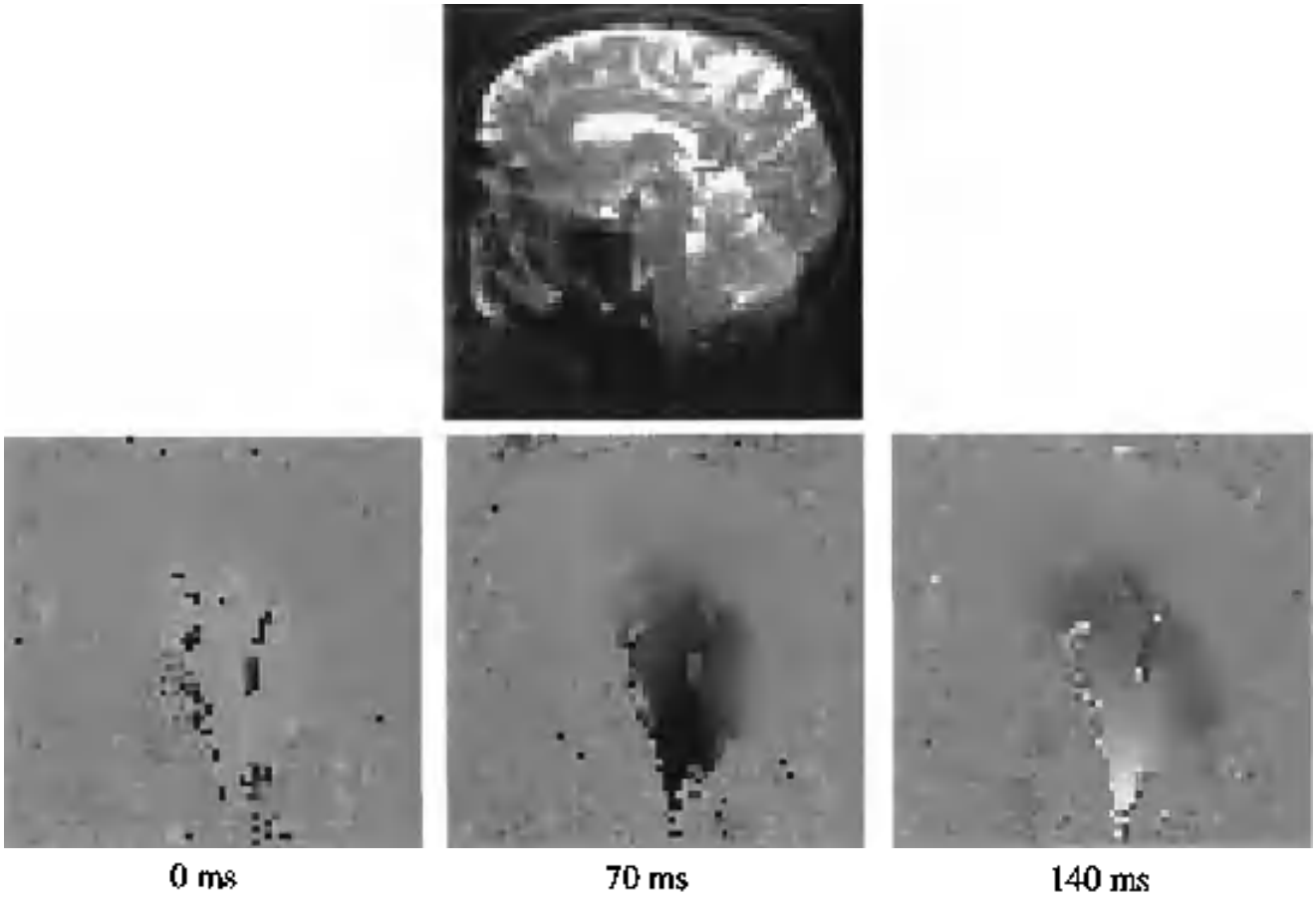

Figure 4 Craniocaudal velocity in a midline sagittal slice. A magnitude image is at the top, and gray-coded images of craniocaudal velocity triggered at various times after the R-wave are shown at the bottom. Velocities in general increase with proximity to the foramen magnum, this downstroke systolic and is synchronous with the known systolic egress of CSF from the calvarium. Maximal velocities in the upper cervical cord are about $3\,\mathrm{mm\,s^{-1}}$ caudally

for a tethered spinal cord.[7,13] If cord motion is normal, the patient is unlikely to benefit from surgical untethering, and an alternative etiology for neuropathic symptoms should be sought. Based on an experience of over 400 patients, MRI CNS motion studies are now standard at the Massachusetts General Hospital in cases of suspected tethering.

4.5 Normal-Pressure Hydrocephalus (NPH)

NPH is a syndrome of uncertain etiology whose classic form includes dementia, ataxic gait, and urinary incontinence.[28] Accurate diagnosis is imperative, as treatment can fully restore neurological function, whereas failure to treat may lead to progressive neurological dysfunction and death. At present, NPH diagnosis remains problematic, with no set of clinical or laboratory criteria clearly able to predict the individual response to CSF shunting.[29,30]

Prompted by recognition of the abnormal CSF dynamics in NPH,[29,31] MRI studies of brain motion in NPH have been undertaken. Wahkloo et al. found brain motion in NPH patients to have greater amplitude and complexity than in age-matched controls.[32] This finding is particularly interesting because of the support it lends to hypotheses linking the neurophysiology of the NPH syndrome with endogenous mechanical trauma.[33]

5 NMR IMAGING OF PARENCHYMAL STRAIN RATES

Strain defines the degree of contraction and elongation at each point in a material during deformation. Velocity-sensitive NMR imaging can be used to reconstruct images of the distribution of physiological strain rates within tissues, including the myocardium and the brain parenchyma, as described here. By defining the pattern of tissue deformation at each location, strain imaging may shed light on both the mechanical causes and the specific neural effects of disorders of the mechanical homeostasis in the CNS. In an elastic material, strain is proportional to stress, which is the internal force per unit area, the constant of proportionality being the elasticity (in general, a fourth-order tensor).

Strain rates are described by a strain rate tensor $\mathbf{S}$ whose components S_{ij} are defined by the directional derivatives $\partial/\partial x_j$ of velocity components V_i according to

$$S_{ij} = 1/2\left(\frac{\partial V_i}{\partial x_j} + \frac{\partial V_j}{\partial x_i}\right) \quad (2)$$

The rate of tissue elongation or contraction in the direction of a unit vector $\boldsymbol{v}$ is simply: $\boldsymbol{v}^{\mathrm{T}}\cdot\boldsymbol{S}\cdot\boldsymbol{v}$. Measurement of the complete 3D strain rate tensor $\boldsymbol{S}$ by equation (2) requires acquisition of complete 3D spatial and velocity data. As such complete acquisitions have not yet been performed in the brain, images have been produced that reconstruct tensor components based upon one or two components of velocity.[20]

To portray strain rate tensor fields usefully, novel display methods are needed. Let λ_i and $\boldsymbol{E}_i$ denote the eigenvalues and eigenvectors of the strain rate tensor, respectively, and let f be a positive constant such that $|f\lambda_i| \ll 1$ for all observed $\boldsymbol{S}$. Then the value of $\boldsymbol{S}$ at each location can be depicted by means of a small rhomboid whose axes are given by the four vectors

$$(1 \pm f\lambda_i)\boldsymbol{E}_i \quad (3)$$

Intuitively, this rhomboid shows the configuration of a unit square after $\boldsymbol{S}$ has acted upon it for a time equal to f. These rhomboids show the magnitude and direction of strain rate at each location; their long axes indicate the directions of most rapid stretch. Alternatively, a color code may be used to display the values of tensor invariants of the strain rate.

5.1 Normal Brain Parenchymal Strain Rates Due to Physiological Pulsation

Normal systolic parenchymal in-plane strain rate patterns are shown in Figure 5. In-plane (x and y) components of velocity were encoded in a gated ciné echo planar acquisition, and strain rates were computed according to equation (2). Data were acquired using a velocity sensitivity $|\boldsymbol{k}_v| = 3.7$ rad s mm^{-1} (gradient pulse intensity $G = 0.085$ mT m^{-1}, duration $\delta =$ 35 ms, separation $\Delta = 40$ ms). Given an MRI magnitude SNR per pixel of 25:1, this experiment should have the capacity to resolve velocity differences of 0.02 mm s^{-1} per pixel ($P <$ 0.05). Defining the 'strain rate' sensitivity $\boldsymbol{k}_s$ so that the phase shift per pixel equals $\boldsymbol{k}_s\cdot\boldsymbol{S}$; then $\boldsymbol{k}_s = R\boldsymbol{k}_v$ where R refers to the dimensions of the voxel. In the experiments described, the strain sensitivity for in-plane strains is $|\boldsymbol{k}_s| = 3.7$ rad s^{-1} mm^{-1} (for 3 mm = 11 rad s). MRI motion sensitization in effect magnifies strain rates by the ratio of the strain rate sensitivity $|\boldsymbol{k}_s|$ to the motion observation period Δ; here, $|\boldsymbol{k}_s|/\Delta =$ 275:1.

The display shows a strain rate rhomboid, constructed according to equation (3), and uses color to depict the trace, Tr ($\boldsymbol{S}$) = $\lambda_1 + \lambda_2$. The trace represents the rate of compression or dilation of area within the 2D image plane. Because tissue is incompressible, in-plane area change implies compression or extension in the through-plane direction (i.e. Tr ($\boldsymbol{S}$) + $\partial V_z/\partial z =$

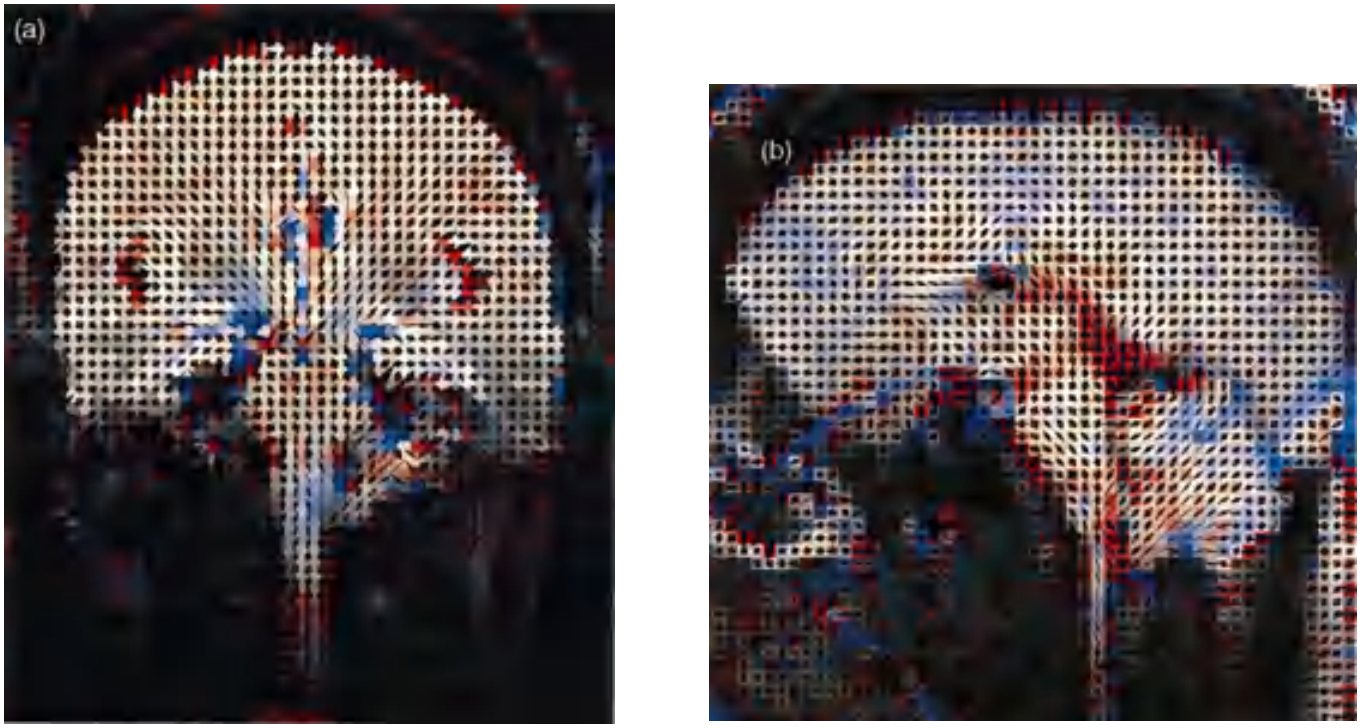

Figure 5 Images of in-plane 2D strain rates of the brain parenchyma in a normal subject in (a) coronal–oblique and (b) sagittal planes 150 ms after the ECG R-wave, corresponding to the rapid parenchymal motion of cardiac systole. A rhomboid graphic at each pixel shows the magnitude and orientation of the 2D strain rate tensor $\boldsymbol{S}$ at that location [according to equation (3) with $f = 4$ s]. Color indicates the rate of change of in-plane area, the trace of $\boldsymbol{S}$, with red denoting expansion [Tr($\boldsymbol{S}$) > 0] and blue shrinkage [Tr($\boldsymbol{S}$) < 0]. The predominant inflow of brain parenchyma toward the foramen magnum is striking in both image planes. The coronal slice shows prominent downward tissue elongation in and near the internal capsule; the sagittal slice shows downward and forward deformation of the cerebellum and midbrain, and vertical stretching of the upper cervical cord, also seen in the coronal image. Compression of the thalami upon the region of the third ventricle is evident in the strain rhomboids in the coronal image and is also evident in the sagittal image, where red hues of in-plane expansion near the third ventricle (at center) suggest compression in the through-plane direction

0). Color hue indicates the sign of Tr ($\boldsymbol{S}$) at each location, with red corresponding to positive and blue to negative. Color saturation is proportional to $|\mathrm{Tr}\ (\boldsymbol{S})|$, with full saturation at $|\mathrm{Tr}\ (\boldsymbol{S})| \geqslant 0.05$ rad s^{-1}.

Figure 5 shows coronal and sagittal images of strain rate 150 ms after the ECG R-wave. Strain rate rhomboids demonstrate the predominant elongation of parenchyma toward the foramen magnum. In the coronal image, there is seen a dramatic elongation in the region of the upper cervical cord, internal capsule, and corona radiata; in the sagittal image such elongation is seen in the cerebellum and midbrain. Maximal strain rates in these zones are on the order of 0.1 rad s^{-1}. The red color in the region of the third ventricle in the sagittal image, denoting Tr ($\boldsymbol{S}$) > 0, demonstrates the through-plane compressive motion of the thalami in this zone. Small strain rates are seen in the cerebral mantle. Ciné velocity studies have shown, and strain rate ciné studies have confirmed, that motion in the territory of the basilar circulation precedes that in the middle cerebral territory cerebellar motion.[9] Of interest, we see in the coronal image dilational strain patterns deep in the Sylvian fissures bilaterally. We can speculate that this reflects pulsatile motion of the middle cerebral vessels due to pulsatile turgor, the stiffening of the 'vascular endoskeleton'.[34]

5.2 Brain Parenchymal Shear Due to Small Cranial Accelerations

The human brain is an organ uniquely vulnerable to acceleration injury. Acceleration injury is associated with a variety of clinical syndromes, including acute concussion syndromes of mild to profound severity and delayed effects, as in the dementia pugilistica or 'punch drunk' syndrome. An attractive unifying hypothesis is that these syndromes may be caused by acceleration-induced shear injury to deep cerebral white matter. This idea was advanced on theoretical grounds by Holburn, and soon received strong support in the experiments of Pudenz and Shelden, who, placing transparent windows into the skulls of monkeys, directly observed the swirling motion of the cerebral cortex due to cranial acceleration.[35,36] Clinicopathological correlations in patients with severe concussion have demonstrated prominent damage to deep white matter tracts including the corpus callosum, cerebellar peduncles, and corticospinal tracts.[37] Particularly intriguing were the findings of hemorrhage at gray–white matter boundaries, suggesting elastic impedance mismatch as a cause of trauma. Similar lesion patterns have been seen in animal models of concussive nonpenetrating head injury.[38] These experiments, however, have become increasingly difficult to justify due to concerns for animal welfare.

MRI may afford the opportunity to characterize the response of the human brain to mild acceleration noninvasively, and, from this, perhaps to extrapolate the phenomenology of trauma. To investigate this, coronal images sensitive to anteroposterior velocity were acquired while a normal subject shook the head 'No' twice per second for 10 s. Contributions of rigid head motion were subtracted as described above, and data were processed to demonstrate the $\partial V_z/\partial x$ component of parenchymal shear, where z is the through-plane coordinate and x is the horizontal coordinate. Figure 6 shows intrinsic parenchymal strain rates at three points in the head shake cycle. Acceleration-induced shear rates in this experiment are at most 0.1 rad s^{-1}. This study demonstrates concentrations of strain adjacent to the falx, consistent with transmission of angular acceleration from the falx to the hemispheres. Shearing strain is seen to concentrate in parasagittal bands deep to the temporal lobes, and torsional strain to concentrate at the spinomedullary junction.

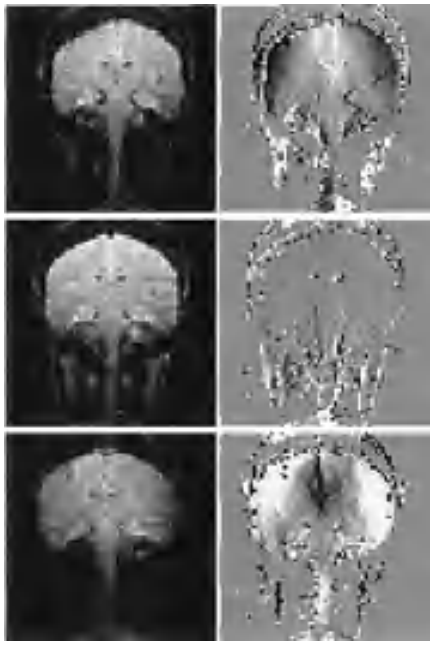

Figure 6 Brain parenchymal strain rates due to voluntary head shake. Images acquired during (a) clockwise cranial acceleration, (b) zero acceleration, and (c) counter-clockwise acceleration. The magnitude images are shown to the left and the strain rate images are to the right. The strain rate gray scale is proportional to $\partial V_z/\partial x$, where x is the horizontal and z is the through-plane direction. Locally increased $\partial V_z/\partial x$, indicative of localized rotation or shearing strain, are seen adjacent to the falx, in bilateral vertical bands deep to the temporal lobes, and at the spinomedullary junction where the brainstem seems to twist slowly upon the upper cervical cord

6 EFFECTS OF PARENCHYMA MOTION ON MRI OF PERFUSION AND DIFFUSION

Motion of the head and brain can interfere with studies of cerebral diffusion and cerebral function. Functional NMR studies of cerebral hemodynamic activation based on T_1 inflow or T_2* deoxyhemoglobin effects must detect changes in signal magnitude of 1%.[39] These measurements, whether made with conventional or echo planar MRI, can be confounded by parenchymal inflow[40–42] related to cardiac and respiratory motions.[43,44] Cerebral diffusion measurements are exquisitely motion-sensitive; when acquired using conventional multishot MRI, these studies are easily degraded by uncontrolled cerebral motion leading to phase inconsistency among Fourier data lines. This has been addressed by cardiac gating,[45] data post-processing,[46] compensation for measured motion using 'navigator pulses',[47] and by the adoption of single-shot acquisition techniques. Interestingly, whole-head motion has

overshadowed the effect of intrinsic brain motion in studies to date, suggesting the relative ineffectiveness of head fixation.

7 PROSPECTS

Motion-sensitive MRI opens a novel window onto the complex phenomena of brain parenchyma motion. This emerging picture of brain motion, however, represents only a first step of a program to understand the underlying biophysics of brain motion. At issue is the desire to know intracerebral distributions of mechanical stress. At a basic level, the distributions of stress may reveal the sites of action of the cardiovascular impulse and of resistance to it. Clinically, stress concentrations may account for the specificity of the neurological syndromes related to derangements of CNS dynamics (e.g. the relation of NPH to gait disturbance), and help predict the outcomes of intervention (e.g. how and when does fenestration of the optic nerve sheath alleviate the visual deficit of pseudotumor cerebrii). One promising avenue of study is exemplified by the work of Pelc and Enzmann, who have measured concurrent intracerebral volume changes of brain parenchyma, blood, and CSF,[15] an important step toward the unification of brain motion with CSF dynamics in the spine and with the physiology of arterial pulse wave propagation.[48–50]

8 RELATED ARTICLES

Assessment of Regional Blood Flow and Volume by Kinetic Analysis of Contrast-Dilution Curves; Methods and Applications of Diffusion MRI; Marker Grids for Observing Motion in MRI; Phase Contrast MRA; Time-of-Flight Method of MRA.

9 REFERENCES

1. J. E. A. O'Connell, *Brain*, 1943, **66**, 204.
2. A. Monro, 'Observations on the Structure and Function of the Nervous System', Creech and Johnson, Edinburgh, 1783.
3. G. Kellie, *Trans. Med. Chir. Soc. Edinburgh*, 1824, **1**, 84.
4. L. B. Flexner, J. H. Clark, and L. H. Weed, *Am. J. Phys.*, 1933, **101**, 292.
5. G. H. DuBoulay, *Br. J. Radiol.*, 1966, **39**, 255.
6. D. A. Feinberg and A. S. Mark, *Radiology*, 1987, **163**, 793.
7. D. C. McCullough, L. M. Levy, G. DiChiro, and D. L. Johnson, *Pediatr. Neurosurg.*, 1990, **16**, 3.
8. D. Greitz, R. Wirestam, A. Franck, B. Nordell, C. Thomsen, and F. Stahlberg, *Neuroradiology*, 1992, **34**, 370.
9. D. R. Enzmann and N. J. Pelc, *Radiology*, 1992, **185**, 653.
10. B. P. Poncelet, V. J. Wedeen, R. M. Weisskoff, and M. S. Cohen, *Radiology*, 1992, **185**,
11. D. A. Feinberg, J. C. Hoenninger, L. E. Crooks, L. Kaufman, J. C. Watts, and M. Arakawa, *Radiology*, 1985, **156**, 734.
12. P. Moran, *JMIR*, 1982, **1**, 197.
13. L. M. Levy, G. Di Chiro, D. C. McCullough, A. J. Dwyer, D. L. Johnson, and S. S. L. Yang, *Radiology*, 1988, **169**, 773.
14. R. Wirestam, D. Greitz, C. Thomsen, F. Ståhlberg, F. Nordell, and M. Stubgaard, *Proc. IXth Ann Mtg. Soc. Magn. Reson. Med.*, New York, 1990, p. 1107.
15. D. E. Enzmann, M. R. Ross, and N. J. Pelc, *Proc. Xth Ann Mtg. Soc. Magn. Reson. Med.*, San Francisco, 1991, p. 155.
16. S. E. Maier, C. J. Hardy, and F. A. Jolesz, *Proc. XIIth Ann Mtg. Soc. Magn. Reson. Med.*, New York, 1993, p. 151.
17. J. Henning, D. Ott, T. Adam, and H. Friedburg, *JMIR*, 1990, **8**, 543.
18. E. Lee, J.-Z. Wang, and R. Mezrich, *Am. J. Neuroradiol*, 1989, **10**, 1145.
19. N. J. Pelc, R. J. Herfkins, and L. R. Pelc, *JMIR*, 1991, **1**, 181.
20. V. J. Wedeen, *Magn. Reson. Med.*, 1992, **27**, 52.
21. N. J. Pelc and M. A. Bernstein, *Proc. IXth Ann Mtg. Soc. Magn. Reson. Med.*, New York, 1990, p. 475.
22. V. J. Wedeen, R. M. Weisskoff, and B. P. Poncelet, *Magn. Reson. Med.*, 1994, July.
23. V. J. Wedeen, B. R. Rosen, and T. J. Brady, 'The Magnetic Resonance Annual', Raven Press, New York, 1987, p. 174.
24. P. T. Callaghan and C. D. Eccles, *JMIR*, 1988, **71**, 1.
25. D. G. Cory and A. N. Garroway, *Magn. Reson. Med.*, 1990, **14**, 435.
26. W. G. Bradley, Jr, A. R. Whittermore, K. E. Kortman, A. S. Watanabe, M. Homyak, L. Teresi, and S. J. Davis, *Radiology*, 1991, **178**, 459.
27. D. J. Mikulis, M. L. Wood, B. Poncelet, O. A. M. Zerdoner, and D. E. Bohning, *Proc. XIth Ann Mtg. Soc. Magn. Reson. Med.*, Berlin, 1992, p. 626.
28. R. D. Adams, C. M. Fisher, S. Hakim, R. G. Ojemann, and W. H. Sweet, *N. Engl. J. Med.*, 1965, **273**, 117.
29. R. P. Friedland, *J. Am. Med. Assoc.*, 1989, **262**, 2577.
30. N. R. Graff-Radford, J. C. Godersky, and M. P. Jones, *Neurology*, 1989, **39**, 1601.
31. H. D. Portnoy, M. Chopp, C. Branch, and M. B. Shannon, *J. Neurosurg.*, 1982, **56**, 666.
32. A. K. Wahkloo, F. Jungling, and J. Hennig, *Proc. XIth Ann Mtg. Soc. Magn. Reson. Med.*, Berlin, 1992, p. 627.
33. C. M. Fisher, *Neurology*, 1982, **32**, 1358.
34. K. R. Davis, Personal communication, 1992.
35. A. H. S. Holburn, *Lancet*, 1943, **ii**, 438.
36. R. H. Pudenz and C. H. Shelden, *J. Neurosurg.*, 1946, **3**, 487.
37. S. J. Strich, *Lancet*, 1961, 443.
38. T. A. Genarelli et al., *Acta Neuropath. Suppl.*, 1981, **7**, 23.
39. K. K. Kwong, J. W. Belliveau, D. A. Chesler, I. E. Goldberg, R. M. Weisskoff, B. P. Poncelet, D. N. Kennedy, B. E. Hoppel, M. S. Cohen, and R. Turner, *Proc. Natl. Natl. Acad. Sci., USA*, 1992, **89**, 5675.
40. J. R. Singer, *Science*, 1959, **130**, 1652.
41. L. Axel, *Am. J. Roentgenol.*, 1984, **143**, 1157.
42. F. W. Wehrli, J. R. MacFall, L. Axel, D. Shutts, G. H. Glover, and R. J. Herfkins, *Noninvasive Med. Imaging*, 1984, **1**, 127.
43. P. Jezzard, D. Le Bihan, C. Cuenod, L. Pannier, A. Prinster, and R. Turner, *Proc. XIIth Ann Mtg. Soc. Magn. Reson. Med.*, New York, 1993, p. 1392.
44. R. M. Weisskoff, J. Baker, J. Beleiveau, T. L. Davis, K. K. Kwong, M. S. Cohen, and B. R. Rosen, *Proc. XIIth Ann Mtg. Soc. Magn. Reson. Med.*, New York, 1993, p. 7.
45. D. Chien, R. B. Buxton, K. K. Kwong, T. J. Brady, and B. R. Rosen, *J. Comput. Assist. Tomogr.*, 1990, **14**, 514.
46. J. J. M. Cuppen, J. P. Groen, J. J. E. In den Klef, and H. A. Tuithof, *Proc. IVth Ann Mtg. Soc. Magn. Reson. Med.*, London, 1985, p. 962.
47. W. S. Kim, C. W. Mun, D. J. Kim, and Z. H. Cho, *Magn. Reson. Med.*, 1990, **13**, 25.
48. M. Chopp and H. D. Portonoy, *J. Neurosurg.*, 1980, **53**, 516.
49. B. Berman and G. Agarwal, *Surg. Neurol.*, 1984, **22**, 83.
50. M. Kosteljanetz, *Acta Neurolog. Scand.*, 1987, **75**, 5.

Biographical Sketches

Van J. Wedeen. *b* B.A. (Mathematics), Harvard College, USA, 1977. M.D., Albert Einstein College of Medicine, USA, 1981. Certification

in Nuclear Medicine, 1993. Introduced to NMR by T. J. Brady, B. R. Rosen, and I. Pykett. Department of Radiology, Massachusetts General Hospital, 1983–present. Approx. 30 publications. Research specialties: the theory and application of MRI to the study of motion and flow, cardiovascular MRI, mathematical issues in neurocognitive functional MRI.

Brigitte P. Poncelet. *b* B.S. (Physics), Free University of Brussels, Belgium. Introduced to NMR by C. Segebarth and P. van Dijk. Ph.D. candidate, Free University of Brussels, 1989–present. Research fellow in Radiology, Massachusetts General Hospital, USA, 1990–present. Approx. 10 publications. Research specialties: the MRI study of motion and flow, functional MRI.

Diffusion and Perfusion in MRI

Denis Le Bihan

Warren G. Magnuson Clinical Center, Bethesda, MD, USA

1	Introduction	1
2	Diffusion MRI	1
3	Perfusion MRI	6
4	Related Articles	11
5	References	11

1 INTRODUCTION

The effects of diffusion on the NMR signal have been deeply analyzed and powerful diffusion measurement techniques using NMR have been extensively used in physics and chemistry. The recent application of such principles, coupled to NMR imaging (MRI) in the field of medical sciences, represents a spectacular and somewhat unpredicted development. The measurement of molecular displacements in biological tissues in vivo is of enormous interest in terms of its potential applications—from the determination of the molecular organization in tissues, to the emergency management of stroke patients, to the monitoring of laser surgery. MRI is the only means available today of approaching the molecular diffusion process in vivo noninvasively. In this article the basic principles of diffusion measurements made using NMR are presented, together with a description of the various methods that have been proposed for producing images of diffusion. Some technical considerations are discussed, followed by a description of the effects on diffusion measurements of the microdynamics and microstructure of biological tissues. Emphasis will be given to the difficulties encountered when implementing diffusion imaging, and the significance of diffusion measurements in biological tissues.

It has been proposed that, because of its relative safety, its high spatial and temporal resolution, its ability to acquire images in any orientation, and its greater availability compared to other modalities such as positron emission tomography (PET), MRI can be used to image perfusion. Two approaches have been developed that allow MRI to be used to image quantities related to perfusion. One approach mimics conventional nuclear medicine methods, but uses radioactively inert external tracers. The other approaches are more original and MRI specific, using blood directly as an endogenous natural tracer. Such methods offer new insights, for instance valuable information can be obtained by monitoring variations in blood oxygenation in human brain cortex during activation tasks. This article covers the physical principles and fields of applications of these techniques, both tracer and blood pool agent based approaches and methods specific to NMR where flowing blood is magnetically labeled. Finally, a large section of this article is devoted to the 'blood oxygen level dependent' (BOLD) contrast approach which has resulted in the recent and fascinating incursion of MRI into the field of functional brain imaging. With MRI it is now possible to monitor completely noninvasively and with unmatched combined spatial and temporal resolution the activity of the brain during mental processes and the execution of cognitive tasks.

2 DIFFUSION MRI

2.1 Diffusion and NMR

The effect of diffusion on the NMR signal can be understood from the bipolar pulsed gradient spin echo experiment (echo time TE) suggested by Stejskal and Tanner[1] (Figure 1). The first gradient pulse induces a phase shift φ_1 of the spin transverse magnetization, which depends on the spin position z_1:

$$\varphi_1 = \gamma G \delta z_1 \tag{1}$$

where γ is the gyromagnetic ratio, G is the gradient strength along the z axis, δ is the gradient duration. The time interval between the pulse onsets is denoted by Δ. After the 180° rf pulse, φ_1 is inverted to $-\varphi_1$. The second pulse will produce a phase shift φ_2:

$$\varphi_2 = \gamma G \delta z_2 \tag{2}$$

where z_2 is the spin position during the second pulse. The net transverse magnetization is:

$$M_{xy}/M_0 = \exp[\mathrm{i}(\varphi_2 - \varphi_1)] = \exp[\mathrm{i}\gamma G \delta (z_2 - z_1)] \tag{3}$$

where all relaxation effects have been included in M_0.

Obviously, for 'static' spins $z_1 = z_2$, so the bipolar gradient pair is easily evaluated. For 'moving' spins, however, there is a net dephasing which will depend on the spin history during the time interval Δ between the pulses. Indeed, we must now consider a population of spins, which may have different motion histories. If $P(z_2, z_1, \Delta)\, \mathrm{d}z_2$ is the conditional

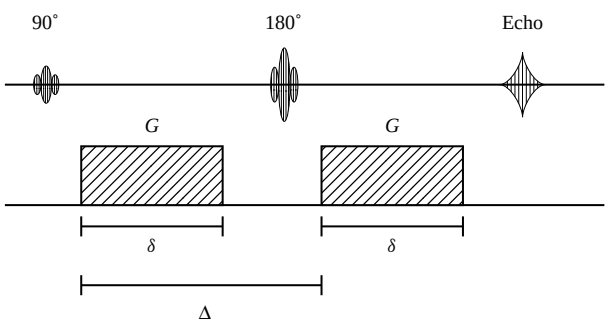

Figure 1 Stejskal and Tanner diffusion spin echo sequence. Gradients pulses G are separated by a time interval Δ; their duration is δ

probability of finding a spin initially at z_1 between positions z_2 and $z_2 + dz_2$ after a time interval Δ, the amplitude attenuation is:

$$M_{xy}/M_0 = \int \exp[i\gamma G\delta(z_2 - z_1)]P(z_2, z_1, \Delta)\, dz_2 \qquad (4)$$

In the case of the diffusion process, one has:

$$P(z_2, z_1, \Delta) = (4\pi\Delta D)^{-1/2} \exp[-(z_1 - z_2)^2/4\Delta D] \qquad (5)$$

where D is the diffusion coefficient. Combining equations (4) and (5), the signal attenuation is:

$$M_{xy}/M_0 = \exp[-(\gamma G\delta)^2 \Delta D] \qquad (6)$$

In practice, as δ is usually not negligible compared with Δ, movement during the application of the gradient pulses can no longer be neglected (see below). Also, the contribution of other gradient pulses, such as the imaging pulses, must be taken into account.[2] Solving the Bloch–Torrey equation,[3] one obtains:

$$M_{xy}/M_0 = \exp\left(-\left\{\gamma^2 \int_0^{TE}\left[\int_0^t G(t')\, dt'\right]^2 dt\right\} D\right)$$
$$\equiv \exp(-b \cdot D) \qquad (7)$$

This relationship is valid for any gradient pulse combination, provided the sign of G is inverted for all gradient pulses following the 180° pulse. This expression may become analytically complex when many gradient pulses are involved, as in MRI. Therefore, it is useful to characterize the sensitivity of MRI sequences to diffusion using the 'gradient factor' b.[2,4] One must remember, however, that this equation is valid only for diffusion in an infinite and homogeneous medium. If diffusion is restricted or anisotropic, the signal attenuation must be calculated using a more general formalism based on diffusion tensors.[5]

2.2 The Different Approaches

Almost any NMR sequence can be designed to measure diffusion.

2.2.1 Constant Field Gradient Spin Echo Method

In the presence of a simple constant linear gradient G_0, the echo attenuation is:[6,7]

$$M(nTE)/M_0 = \exp(-\gamma^2 G_0^2 DTE^3/12n) \qquad (8)$$

where n is the number of echoes in a multiple echo experiment. This simple approach is difficult to combine with NMR imaging because the presence of a constant gradient during the rf pulses of the imaging sequence severely impairs the selected slice profile. In addition, the relaxation time T_2 of the medium should not be too short, so that enough diffusion attenuation occurs during TE.

2.2.1.1 Bipolar Gradient Pulse Spin Echo Technique. This technique, suggested by Stejskal and Tanner,[1] is by far the most widely used sequence in NMR diffusion measurements. Taking into account spin diffusion during δ, equation (6) becomes:

$$M/M_0 = \exp[-\gamma^2 G^2 D\delta^2(\Delta - \delta/3)] \qquad (9)$$

The diffusion time T_d can be formally defined as $(\Delta - \delta/3)$, but its physical significance is clear only when the gradient pulse duration δ is sufficiently short compared with Δ. Tissues with short T_2 values require short TEs which may not allow sufficiently long diffusion times to produce a large enough diffusion effect.

2.2.2 Stimulated Echo Technique

A stimulated echo is generated from a sequence consisting of three rf pulses separated by time intervals τ_1 and τ_2. Gradient pulses must be inserted within the first and the third periods of the stimulated echo sequence (Figure 2). The diffusion time now includes τ_2 and can be much longer than with the spin echo sequence, because only longitudinal relaxation occurs during this time interval. The Stejskal–Tanner relationship [equation (9)] still applies, provided that the period τ_2 is included in Δ.[8] The longer diffusion time is useful for studying very slow diffusion rates, or in compensating for the unavailability of large gradients.[9] Unfortunately the signal is reduced by one-half compared with the spin echo signal.

2.2.3 Gradient Echo Technique

The effect of diffusion on the amplitude of a gradient echo formed by a bipolar gradient pulse pair of reversed polarity does not differ from that of a spin echo sequence.[2] However, if the gradient echo is part of a steady state free precession (SSFP) sequence, where some degree of phase coherence is propagated throughout successive cycles, multiple echo paths with different diffusion times and different diffusion weightings must be considered.[10] In MRI, the

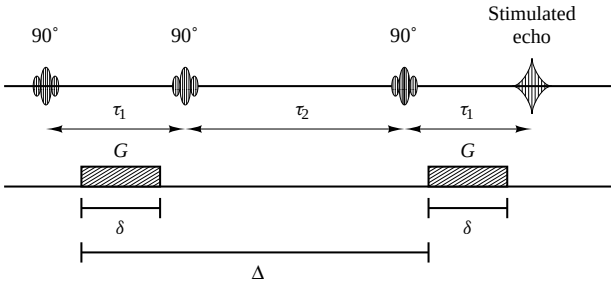

Figure 2 Diffusion-weighted stimulated echo sequence. The stimulated echo results from the spin excitation by three rf pulses separated by time intervals τ_1 and τ_2. During τ_2, relaxation is driven by T_1 and not T_2. Diffusion effects can be enhanced by placing gradient pulses within the τ_1 periods, where transverse magnetization is sensitive to field inhomogeneities

contrast-enhanced (CE-fast) scheme has been proposed.[11–13] Unfortunately, this sequence remains very sensitive to motion artifacts.[14] Moreover, the effects of diffusion and relaxation are intermingled so that diffusion measurements are always contaminated to some degree by relaxation effects.[15]

2.2.4 Diffusion Measurements with B_1 Field Gradients

Diffusion measurements can also be achieved by means of the rf field ($\boldsymbol{B}_1$) produced by an NMR rf coil oriented perpendicularly to the main transmit/receive NMR coil.[16,17] With rf gradients, extremely short switching times can be achieved, since there are no eddy currents. Furthermore, substantial gradient strength may be produced from the rf transmitter, allowing the measurement of very low diffusion coefficients.

2.3 Combining Diffusion NMR with MRI

'Diffusion-weighted' images are obtained by inserting gradient pulses into any NMR imaging sequence. For quantification it is necessary to determine the degree of diffusion weighting, which is achieved by calculating the factor b [equation (7)] associated with the acquisition parameters. Without additional gradients, typical spin echo imaging sequences have intrinsically very low b values, typically less than 1 s mm $^{-2}$, so that diffusion effects are completely negligible (for water, $D = 2 \times 10^{-3}$ mm^2 s^{-1} at room temperature and the attenuation is less than 1%).[2,18] When inserting gradient pulses for diffusion, however, the combination of the imaging and diffusion gradients produce cross terms in the b factors.[2,19] These cross terms will depend on the time course of these gradient pulses and may be significant, so that the Stejskal–Tanner relation [equation (9)] is incorrect in most cases. Using the b factor values associated with each image, it is possible to compute diffusion images, i.e. images where the diffusion coefficient is determined for each pixel according to equation (7).[2,4,9,18] The computation of such diffusion images is obtained by fitting the signal intensity of each pixel of a series of images differently sensitized to diffusion (i.e. with different b values) with equation (7) (Figure 3).

Using the spin echo sequence, it is possible to vary the strength or the duration of the diffusion-sensitizing gradients, or their direction, in order to enhance anisotropic diffusion effects.[2] The spin echo two-dimensional FT method is certainly the simplest to implement.[4,18,20] Other sequences[2] that have been investigated are stimulated echo sequences; line-integral projection reconstruction; variants of the SSFP technique; 'turbo' sequences; and echo planar imaging.[21,22] These schemes have been suggested to overcome, at least partly, some of the problems encountered with the spin echo two-dimensional FT method.

With echo planar imaging (EPI), the entire set of echoes needed to form an image is collected within a single acquisition period (single shot) of 25–100 ms. This is obtained by switching the echo signal formation in a train of gradient echoes, by means of a large gradient the polarity of which is very rapidly inverted as many times as is required to achieve the desired image resolution.[23] EPI may easily be sensitized to diffusion[21,22] (Figure 4).

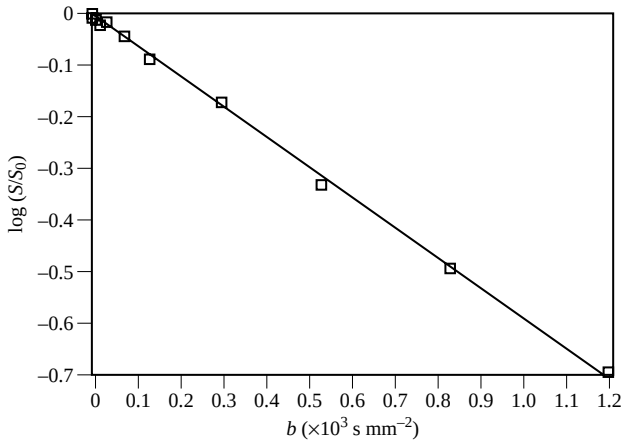

Figure 3 Plot of the logarithm of the signal intensity in brain white matter against the gradient factor b. The plot is linear, and the slope is equal to the diffusion coefficient ($D = 0.60 \pm 0.01 \times 10^{-3}$ mm^2 s^{-1})

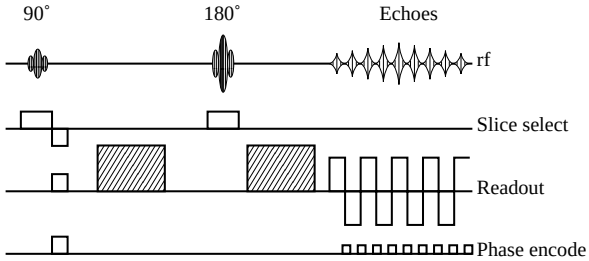

Figure 4 Diffusion echo planar imaging sequence. The spin echo is split into a series of gradient echoes by quickly switching the readout gradient. Sensitization to diffusion of an echo planar imaging sequence can be easily achieved by additional gradient pulses (hatched boxes)

Sensitization consists of providing a pair of large compensated gradients for a period of time before rapid gradient switching and data acquisition. The refocusing may be achieved either by simply reversing the polarity of the gradient halfway through the period over which it is applied, or by inserting a 180° rf refocusing pulse at the midpoint without reversing the gradient polarity.

With EPI, motion artifacts are virtually eliminated. The accuracy on diffusion achieved with EPI is generally extremely good, as many images differently sensitized to diffusion can be generated due to the very short acquisition time (typically less than 100 ms). The EPI technique is the method of choice for in vivo diffusion imaging, although it is very vulnerable to susceptibility artifacts, which are responsible for image distortion or signal dropout, and to chemical shift artifacts which require efficient fat suppression. Diffusion-EPI has been successfully used to measure the diffusion of water in the human brain in volunteers and patients[21] (Figure 5).

2.4 Experimental Considerations in Diffusion MRI

2.4.1 Gradient Requirements

Any mismatch between the diffusion sensitizing gradient pulses may cause artifactual signal losses, due to improper spin

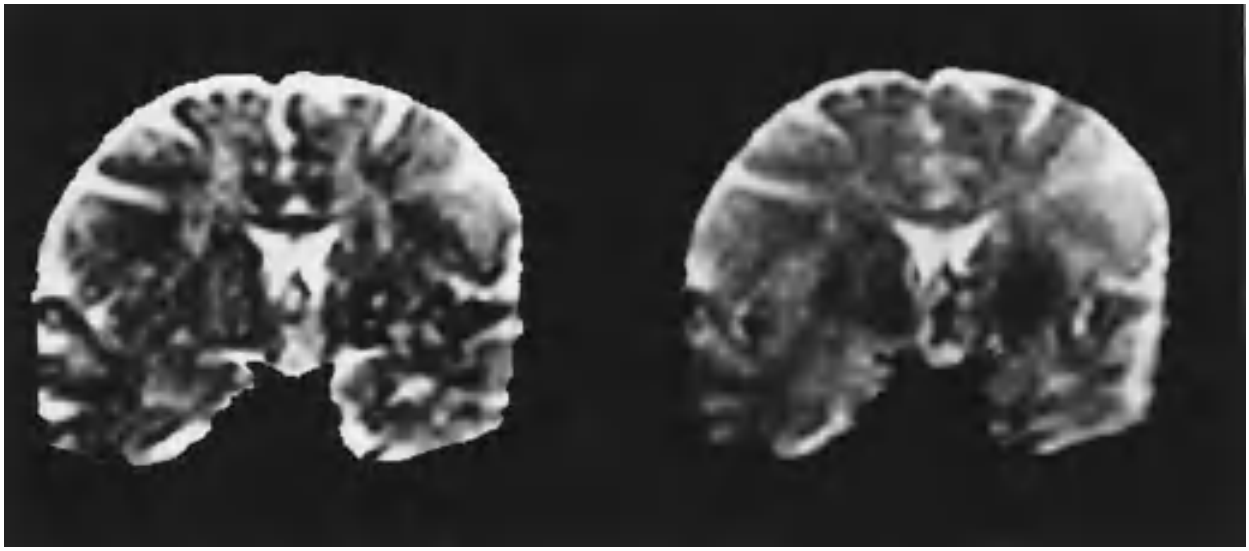

Figure 5 Diffusion images calculated from a set of 16 diffusion-weighted coronal echo planar images of the brain of a normal volunteer. These are 64 × 64 pixel images with a field of view of 16 cm and thus an in-plane resolution of 2.5 × 2.5 mm. The section thickness was 10 mm. The diffusion gradients varied from 0 to 38 mT m^{-1} in the z direction, the duration of each lobe was 20 ms, and their separation was 6 ms (b = 0 to 872 s mm^{-2}). The acquisition time for each image was about 50 ms. Note that diffusion is highest in ventricular cavities containing cerebrospinal fluid (free water). Because of diffusion anisotropy, diffusion in corpus callosum is very low, while vertical frontal white matter tracts have higher diffusion (see Table 1)

rephasing. Two major sources of problems are commonly seen. One is gradient instability, which may arise when gradient amplifiers are driven hard for fast switching of large gradient intensities. Variations from shot to shot of the bipolar gradient balance results in widely distributed ghost artifacts. While such an artifact does not occur when a single-shot technique such as EPI is used, it is still essential to have high quality gradient amplifiers with some reserve capacity for accurate diffusion imaging. The second problem results from eddy currents generated mainly in the cryostat when switching rapidly large gradient pulses. Eddy currents may also be a major cause of gradient pulse mismatch, leading to signal loss. The best solution to this problem is undoubtedly to remove eddy currents at source by using actively shielded gradient coils, which have no fringe fields and therefore do not generate eddy currents. The use of a gradient coil of small dimensions, which remains at a fair distance from the magnet core and with which it is easier to generate large gradient amplitudes, is certainly an attractive alternative.[21]

2.4.2 Motion Artifacts

As the sequences used are deliberately sensitized to motion by the addition of large gradients, a major problem occurring with in vivo imaging of diffusion arises from irregular motion of the object. Artifacts result from discontinuities that occur between successive cycles of an imaging sequence. Results of such temporal incoherence are commonly visible as 'ghosts' along the phase-encoding direction. These 'ghosts' are particularly intense in the presence of the diffusion gradients and render the diffusion measurements meaningless. Cardiac gating has been used to mitigate this problem, but even this motion is not strictly cyclic. It is difficult to compensate diffusion imaging sequences for motion, since the use of successive bipolar gradient pulses considerably reduces the value of the gradient factor b.[2] Chenevert et al.[24] have suggested eliminating any phase encoding from the acquisition by sacrificing one dimension of the image, which is then reduced to a single line. Ultimately, however, the best way to avoid motion artifacts is to use a single-shot technique, such as EPI, and to secure patients comfortably within the magnet using cushions or inflating devices.

2.5 Diffusion in Biological Systems

The diffusion coefficient of water in tissues has been found to be 2–10 times less than that of pure water (Table 1). This can be largely understood considering that water molecules are obliged to divert tortuously around obstructions presented by fibers, intracellular organelles, or macromolecules. Biological systems thus differ greatly from an 'infinitely large medium'; they are very heterogeneous and made of multiple subcompartments (microstructure). Depending on the permeability of the barriers that limit these compartments, we have to consider exchanges and transport

Table 1 Diffusion Coefficients of Water in Human Brain[a]

	$\times 10^3$ mm^2 s^{-1}
Cerebrospinal fluid	2.94 ± 0.05
Gray matter	0.76 ± 0.03
White matter	
Corpus callosum	0.22 ± 0.22
Axial fibers	1.07 ± 0.06
Transverse fibers	0.64 ± 0.05

[a]Measurements obtained in normal volunteers using a diffusion sensitized EPI sequence.[21] Direction of fibers refers to z axis (direction of the diffusion sensitizing gradient pulses).

between them (microdynamics). A classical treatment of the NMR signal may not then reflect properly the tissue structure or properties. In these conditions diffusion coefficients may become meaningless if the measurement timescale or the measurement direction are not provided. The main difficulty is that the structure of the medium is generally unknown in detail.

2.5.1 Restricted Diffusion

Diffusion is restricted when boundaries in the medium prevent molecules from moving freely.[2,25,26] When measurement times are very short, most molecules do not have enough time to reach boundaries, and so they behave as if diffusing freely. Once the diffusion time increases, an increasing fraction of molecules will strike the boundaries, and diffusion will deviate from the free behavior. The diffusion distance, calculated as for free diffusion using Einstein's relation $\langle \zeta^2 \rangle = 2 D T_d$, shows a curvature and, finally, a levelling-off when the diffusion distance reaches the size of the restricting compartment. The effects of restriction, which depend on the shape of the restricting volumes and the types of restriction,[2] will thus appear in the NMR signal for diffusion times such that molecular displacements are of the order of the size of the restricting volumes.

When the restrictive barriers become permeable to diffusing molecules, the restricted diffusion pattern changes. An example has been given by Tanner[27] for the case of equally spaced, plane, and permeable barriers. When the diffusion time is increased, the apparent diffusion coefficient decreases, as expected for restricted diffusion, but saturates at a level which depends on the permeability constant.

2.5.2 Anisotropic Diffusion

Diffusion in tissues may also be anisotropic if hindrance or restriction is not the same for different directions of motion. The measured diffusion coefficient then varies according to the direction of measurement. Examples include muscle[28] and brain white matter (see Figure 6).[29]

To consider anisotropy, the diffusion 'coefficient' must be replaced by a tensor, $\boldsymbol{D}$.[1,5] The diagonal terms of the diffusion tensor D_{xx}, D_{yy}, and D_{zz} represent molecular mobility along the axes x, y, and z of the laboratory frame of reference, while the off-diagonal terms indicate how displacements are coupled in directions which are mutually perpendicular. The echo attenuation must be rewritten as:

$$M/M_0 = \exp\left(- \sum_{i=x,y,z} \sum_{j=x,y,z} b_{ij} D_{ij} \right) \qquad (10)$$

where b_{ij} are components of a matrix $\mathbf{b}$ and D_{ij} are components of the diffusion tensor.[5] Off-diagonal terms in the diffusion tensor may be important when the gradient directions do not coincide with the orthotropic directions of the tissue. The echo attenuation then depends on a combination of the diagonal and nondiagonal terms of the diffusion tensor.

The three orthotropic axes of the tissue coincide with the eigenvectors of $\boldsymbol{D}$. The diffusivities along these principal directions are the eigenvalues of $\boldsymbol{D}$. The main direction of the tissue, e.g. the fiber-tract direction for muscle of white matter, is given by the eigenvector with the largest principal diffusivity. Also associated with $\boldsymbol{D}$ are *scalar invariants*, such as Tr($\boldsymbol{D}$), which are independent of the orientation of the sample with respect to the laboratory frame of reference; they depend only on the tissue microstructure.[5]

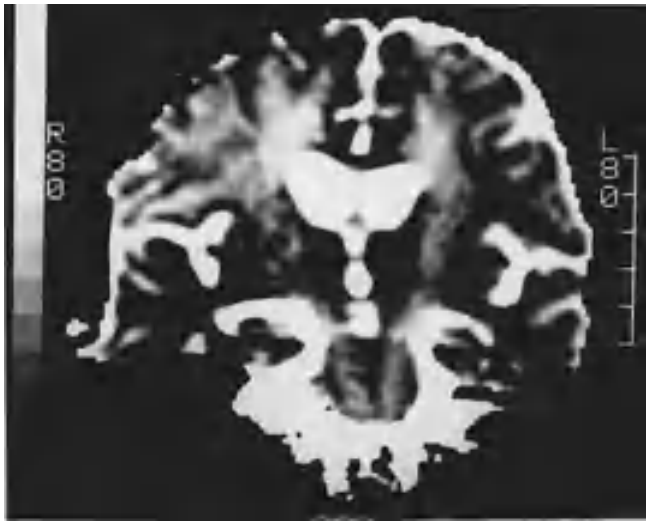

Figure 6 Diffusion image showing anisotropic diffusion in white matter. Excellent contrast is achieved, although T_1 and T_2 effects have been removed. Corpus callosum and temporal white matter fibers, which are horizontal, are dark. Vertical corona radiata frontal fibers and internal capsule fibers are bright. In brainstem, vertical fast-conducting motor and somatosensory tracts are also bright

In white matter, the results of the measurements depend on the respective orientation of the myelin fiber tracts and the gradient direction at each different image location. Diffusion coefficients are significantly lower when the myelin fiber tracts are perpendicular to the direction of the magnetic field gradient used to measure molecular displacements (Figure 6). Considering that most NMR visible water is in the axons, a simple model would be to consider that water molecules are enclosed in the axonal spaces and that water diffusion outside the axons is prevented by the myelin sheath. Recent diffusion experiments have not been able to show complete restricted diffusion, since the diffusion distance increases linearly with the square root of the diffusion time, as for free diffusion[30] (Figure 7). The reduced value of the diffusion coefficient across myelin fibers can thus only reflect a decreased water mobility through the successive lipid layers.

2.5.3 Diffusion in Multiple Compartment Systems

Most diffusion measurements in biological tissues refer to an 'apparent' diffusion coefficient (ADC), and it is generally considered that diffusion in the measurement volume (the 'voxel', in imaging) has a unique diffusion coefficient:

$$D_a = \sum_i \rho_i D_i \qquad (11)$$

This simplification may not always be legitimate, since most tissues are made of multiple subcompartments—at the least, intracellular and extracellular compartments. Assuming measurement times are short, so that diffusion is unrestricted

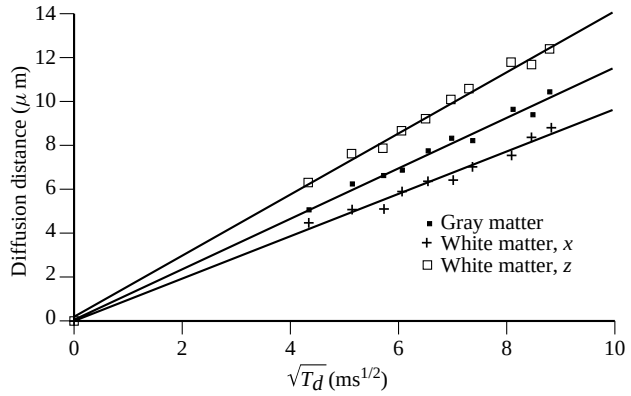

Figure 7 Plot of the diffusion distance against diffusion time in gray and white matter. The diffusion distance was obtained from the diffusion coefficient using Einstein's relationship. There is no leveling-off of the diffusion distance, suggesting that water diffusion is not completely restricted

in each subcompartment i, and there is no exchange, the signal attenuation is:

$$M/M_0 = \sum_i \rho_i \exp(-bD_i) \tag{12}$$

where ρ_i is the density of molecules diffusing in compartment i, and D_i is the associated diffusion coefficient. In this case, the 'apparent' diffusion coefficient that would be measured would depend on the range used for b and would not reflect properly the diffusion in the voxel. Measurements with low b values would then be more sensitive to fast diffusion components. The ideal approach would be to separate all subcompartments by fitting the data with a multiexponential decay. Unfortunately, the values for D_i are often low and not very different from each other, so that very large b values and very high signal-to-noise ratios would be required.

2.6 Conclusion

Diffusion thus appears to be a powerful source of contrast for tissue characterization or functional studies. It has been shown that there is no correlation between the diffusion coefficient and the relaxation times T_1 and T_2. T_1 and T_2 may be normal or elevated in diseased states, while diffusion is lowered, as shown in early brain ischemia.[31–33] Other applications include temperature imaging, a technique based on the sensitivity of diffusion coefficients to temperature[34] (Figure 8). Temperature imaging is especially useful for monitoring interventional procedures.

3 PERFUSION MRI

Classical techniques used to measure and image perfusion can be split into three categories: methods based on diffusible tracers (Figure 1); methods based on intravascular tracers (blood pool tracers); and deposition techniques (microspheres) (Figure 9). Conventional perfusion measurement techniques based on radionuclide tracers have led to the identification

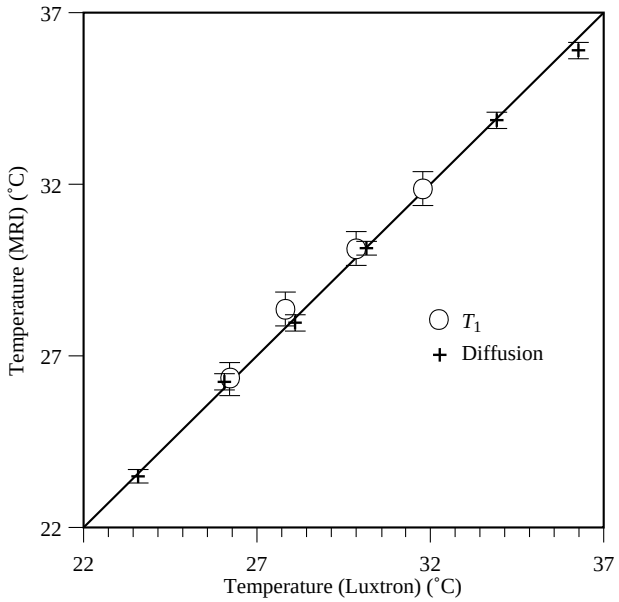

Figure 8 Comparison of temperature measurements using T_1 and diffusion MRI, and using probes (Luxtron) in a phantom. The accuracy was found to be 0.2°C with diffusion and 0.5°C with T_1

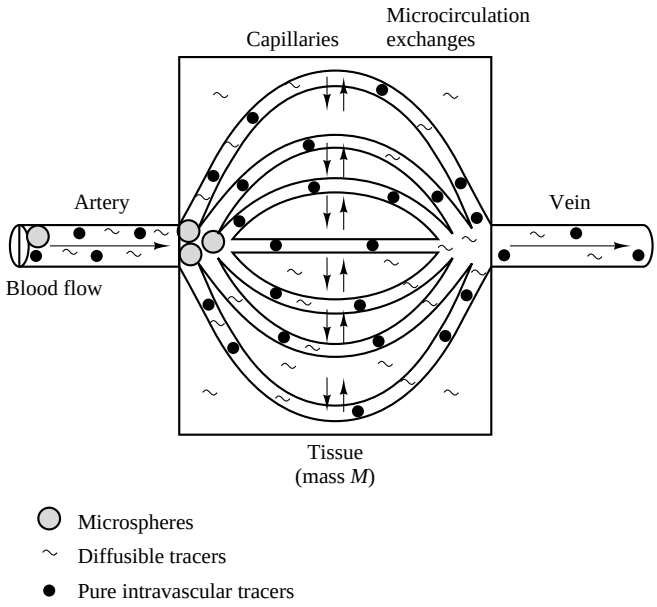

Figure 9 Principles of conventional perfusion measurements. Microspheres are particulates which, because of their size, are trapped at the entry of the capillary network; a count of their deposition pattern gives the flow rate. Diffusible tracers cross the capillary wall; their concentration in the tissue reflects blood flow. Intravascular tracers remain inside the capillary compartment and may be used to evaluate blood flow (under some assumptions)

of 'perfusion' with 'blood flow' in the tissue. However, perfusion has also often been used simply to denote the degree (density) of normal or abnormal microvasculature in a tissue as seen, for instance, with conventional catheter angiography.

3.1 Diffusible Tracers

Blood flow measurements using diffusible tracers were first introduced by Kety and Schmidt.[35] Blood flow can, in principle, be determined from two parameters: the arterial input $C_a(t)$, which is assumed to be uniform across all voxels, and the tissue tracer concentration, measured by means of the external imaging detector. The tracer tissue concentration at time T, $C_0(T)$, is related to the normalized arterial flow F (in mL min^{-1} per 100 g of tissue):

$$C_0(T) = (F/\lambda)\exp[-(F/\lambda)T]\int_0^T C_a(t)\exp[(F/\lambda)T]\,dt \tag{13}$$

where λ is the blood/tissue partition coefficient of the tracer.

With NMR, the tracers are nonproton nuclei, such as ^{19}F compounds, D_2O or $H_2{}^{17}O$; so far these have been used in animal studies. Tissue concentration is determined from integrated spectral line areas with spectroscopy techniques or from pixel signal intensities with MRI methods after tracer has been administered, and the arterial input function is derived from blood samples or, in some cases, from monitoring the NMR signal in a peripheral artery (either on-line or off-line). In general, one has to deal with multiple compartment fitting, e.g. gray/white matter in the brain, signal contamination from surrounding muscles, and tracer recirculation.

^{19}F has a sensitivity and a resonant frequency which are close to those of the proton, and is thus easily observed by NMR. Most studies have used inhalation of inert Freon gases, such as FC22 ($CHClF_2$)[36] or FC23,[37–39] which appear to be less toxic and induce fewer changes in brain physiology.

Deuterium is used as a tracer injected intraarterially in the form of deuterated water (D_2O), which quickly exchanges protons with the surrounding water to become HOD.[40] HOD behaves very similarly to normal water, and the potential toxicity is limited at low concentration. The low sensitivity of the nucleus and its short T_2 result in low signal-to-noise ratios.

^{17}O is a stable isotope of natural abundance of 0.0037%, is chemically equivalent to ^{16}O and has a very low toxicity, even at somewhat high concentrations. The current limitation to its use is its low availability and high cost. While the ^{17}O NMR signal has been observed directly,[41] other workers have based their approach on the scalar coupling of ^{17}O which relaxes water protons efficiently.[42,43] Much higher signal-to-noise ratios may thus be reached by observing ^{17}O water through proton–hydrogen MRI (Figure 10). ^{17}O may also be administered as $H_2{}^{17}O$ and used similarly to $H_2{}^{15}O$ with PET to evaluate perfusion, or as a gas to evaluate tissue oxygen extraction.[41]

3.2 'Blood Pool' Agents

If a nondiffusible NMR paramagnetic agent, such as gadolinium diethylenetriaminepentaacetic acid (Gd-DTPA), is injected into the blood stream in the form of a bolus, the difference in magnetic susceptibility between the tissue and the blood where the contrast agent is compartmentalized results in internal magnetic field gradients, which extend far beyond the capillary limits and, therefore, represent a significant amplification effect over the simple relaxivity effect. These gradients are responsible for spin dephasing which leads to significant signal loss, especially with long echo time gradient echo sequences and high field strengths (Figure 11).

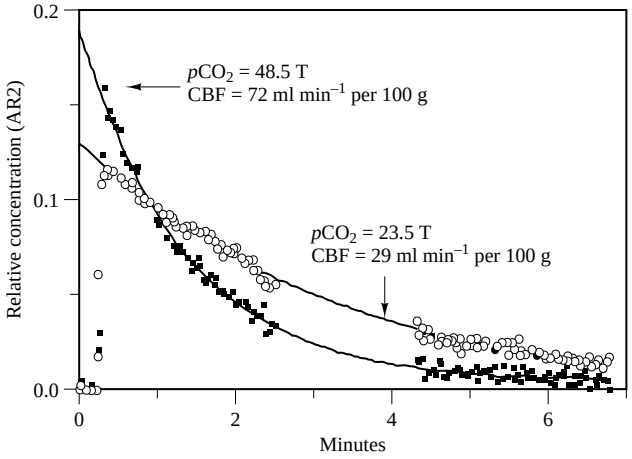

Figure 10 Perfusion measurements based on relaxivity effects of [^{17}O]water. Cerebral blood flow (CBF) was found to increase with pCO_2, as expected (from ref. 43, with permission)

At 'clinical' concentrations, i.e. 0.1 mM kg^{-1}, the relationship between the tissue agent concentration and the NMR signal loss is experimentally linear:[44]

$$\Delta R_2^* = \Delta(1/T_2^*) = k[\mathrm{Gd}] \tag{14}$$

The constant k has been empirically determined in the brain, but potential variations between tissues, and especially abnormal tissues, remains an important issue.

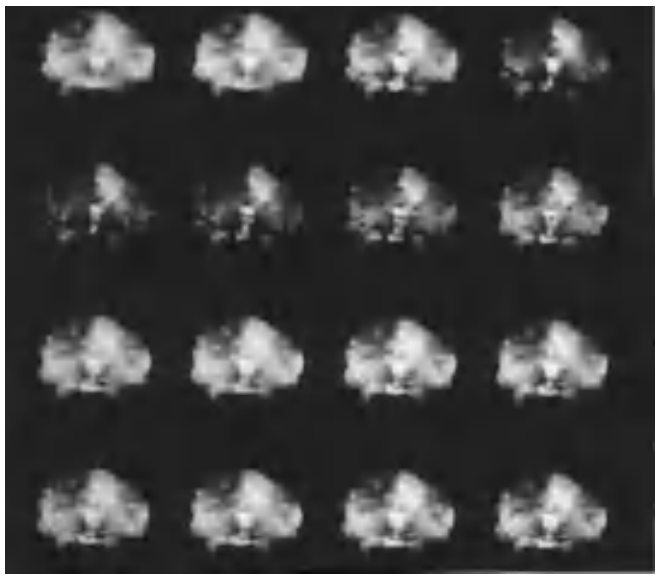

Figure 11 Set of 16 echo planar images acquired after injection of a bolus of Gd-DTPA. Images were obtained at 1-s intervals. The transit of the contrast agent bolus through the brain capillaries produces a signal drop which lasts a few seconds. This drop is higher in gray matter than in white matter. The limited signal drop in the low grade astrocytoma suggests that the tumor has a low capillary density (blood volume)

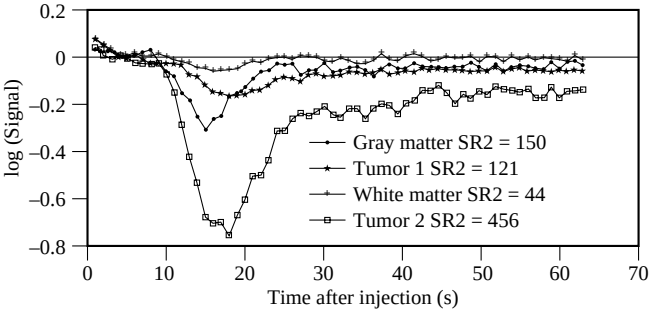

Figure 12 Typical magnetic resonance signal time course study after injection of a bolus of Gd-DTPA in a patient with a high-grade glioma. Each curve corresponds to a given region of interest. The necrotic center of the tumor is completely avascularized. The tumor wall has a very large blood volume. Note that, due to the breakdown of the blood–brain barrier in the tumor, the contrast agent starts leaking inside the tumor, where T_1 effects (which counteract the susceptibility-related signal drop) may lead to underestimation of the blood volume SR2, area under first-pass curve [proportional to cerebral blood volume (CBV)].

As with other blood pool tracer approaches,[45] information on perfusion (i.e. blood flow, blood volume, or mean transit time) may, in theory, be derived from the tissue concentration–time curve. In practice, the local blood volume V derived from the magnetic resonance signal time course is proportional to the area (integral) under the tissue concentration–time curve:

$$V \propto F_a/Q \cdot \int S(t)\,dt \tag{15}$$

where Q is the total amount of tracer injected as a tight bolus, and F_a is the arterial blood flow. Only the relative blood volume is determined but, assuming the same blood comes from a common feeding artery, comparison can be made between different parts of the brain (Figure 12). Several difficulties have to be overcome when integrating the tissue concentration over time, such as the recirculation of the tracer.[46]

As for the blood flow, in principle the recirculation of the tracer could be determined using the Stewart–Hamilton theorem:

$$F_a = V/\mathrm{MTT} \tag{16}$$

where MTT is the mean transit time, i.e. the average time required by the tracer to pass through the tissue.[47] Ideally, the tracer should be introduced into the vascular compartment as an impulse bolus. In practice, the mean transit time could be determined by deconvolving the tissue concentration–time curve by the arterial input function obtained by monitoring the contrast agent concentration in a feeding artery using MRI (Figure 13).

Without the knowledge of the arterial input function, the area under the tissue tracer concentration–time course only gives the regional blood volume, and not blood flow.[48] This technique has been used clinically to produce semiquantitative maps of the regional cerebral volume, for instance in brain tumors (Figure 14). Under some circumstances, however, such as brain activation studies, blood volume evaluation may provide useful information on hemodynamic changes.[49]

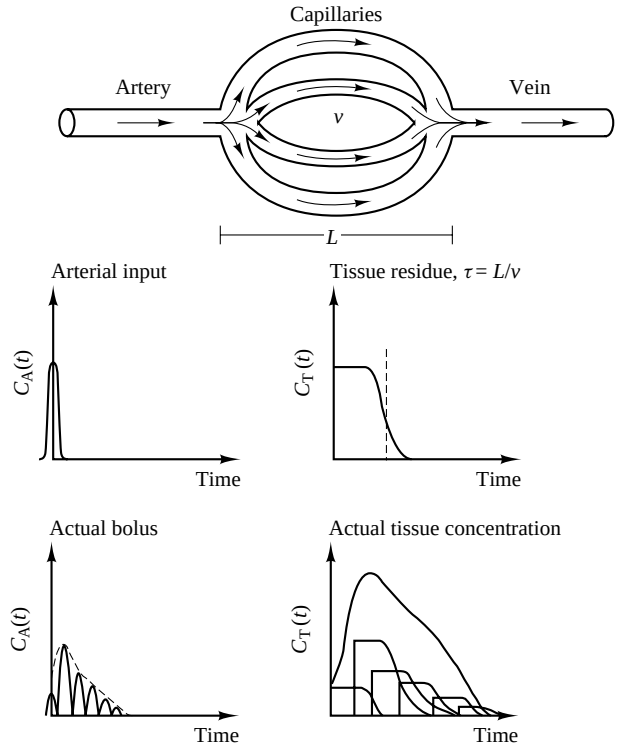

Figure 13 Diagram showing that the actual tissue concentration time course is the product of convolution of the tissue residue function and the arterial input function. (Adapted from Axel[45])

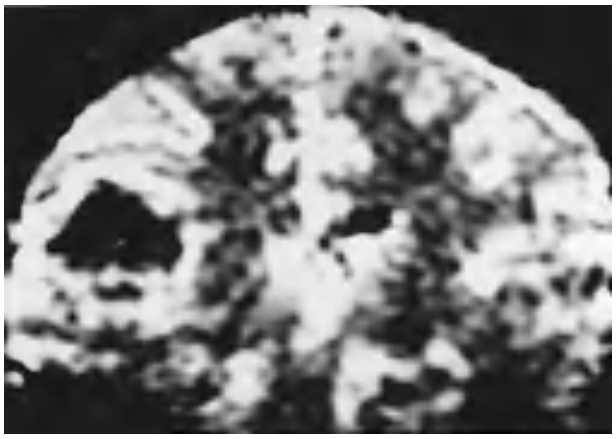

Figure 14 Blood volume map calculated from a set of echo planar images obtained during the transit of a bolus of Gd-DTPA. The tumor shows a rim with very high blood volume, while the necrotic center remains black. The blood volume is 2–4 times larger in gray matter than in white matter

3.3 Magnetic Labeling

3.3.1 Methods Based on Phase Shifts

Spins moving in the presence of a magnetic field gradient get out of phase. Depending on the capillary geometry and circulation conditions on the one hand, and the MRI acquisition parameters on the other, perfusion can be viewed

as a predominantly incoherent motion (intravoxel incoherent motion, IVIM)[50] or a predominantly coherent motion (intravoxel coherent motion, IVCM).[51]

3.3.1.1 IVIM. When the capillary bed is sufficiently tortuous, phase shifts of flowing spins are distributed within each voxel and result in signal attenuation. A simple approach considers microcirculation as a pseudodiffusion process.[50] The signal attenuation A depends then on a 'pseudodiffusion coefficient' D^*:

$$A \propto \exp(-bD^*) \tag{17}$$

$D^* = lv/6$, where l is the mean capillary segment length, and v is the average blood velocity; b is the gradient factor defined in equation (7). Pseudodiffusion has, in practice, to be separated from bulk water diffusion, which requires a high signal-to-noise ratio[52] and hardware stability, given the very small blood volume fraction f in the brain (2–4%). The use of EPI allows one to obtain a large number of images in a short time and significantly reduces the occurrence of motion artifacts[21] (Figure 15).

The IVIM parameters, f and D^*, may be related to actual perfusion in terms of blood flow F under some assumptions about capillary network organization:[53]

$$F = 6f\,D^*/(\rho l_t l) \tag{18}$$

where ρ is tissue density and l_t is the average total capillary length (between the arteriole and the venule).

An interesting and successful approach is to use ^{19}F blood substitutes (perfluorocarbons), which remain in the vascular compartment.[54] Paramagnetic contrast agents may also be used to enhance signal from flowing blood.[55]

3.3.1.2 IVCM. Considering now the coherent part of microscopic flow, even echo rephasing has been used in an attempt to observe perfusion in first and second echo difference images,[56] but variations in T_2 tend to mask the effects of perfusion. A more powerful technique uses velocity compensation. It is possible to devise two sequences with the same echo time, one of which refocuses the effects of blood moving with constant velocity along capillaries ('flow compensated'), while the other gives an additional attenuation resulting from this motion. A difference image then highlights the effects of perfusion. This effect has been shown in a model of rat brain ischemia, where the perfusion deficit is clearly visible as the disappearance of the difference between the two images.[57] This technique, however, requires excellent hardware stability and high signal-to-noise ratio. The order of flow compensation by gradient nulling may be increased to take into consideration the tortuosity of the capillary network.

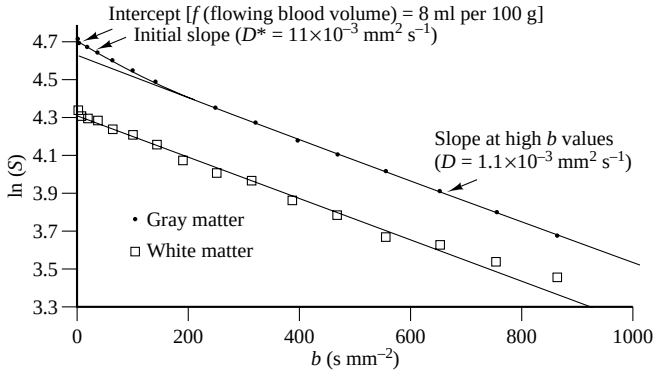

Figure 15 Plot of the logarithm of the signal decay versus gradient b factor in the presence of IVIM (experiment carried out at 1.5 T on a 70-year-old human volunteer using IVIM EPI). A series of 16 differently diffusion-sensitized spin echo images was collected. For white matter, the plot follows a straight line, as expected for a pure diffusion process. The slope of the straight line gives the diffusion coefficient D. For gray matter, the plot clearly shows a curvature effect for low b values. This curvature has been ascribed to microcirculation effects. The straight line obtained for large b values gives the diffusion coefficient. The deviation from the diffusion asymptote, as measured at the intercept, gives the perfusion fraction f. D*, blood velocity

3.3.2 Arterial Water Spin Labeling

In the experiment proposed by Williams et al.[58] to look at brain perfusion, a series of rf inversion pulses is used to saturate continuously or invert spins of arterial blood water protons. The inflow of these inverted spins in the imaging volume results in a small signal loss S/S_0, which depends on blood flow F:

$$F = (\lambda/T_{1\text{app}})(S/S_0 - 1)/2\alpha' \tag{19}$$

where λ is the brain/blood partition coefficient, α' is the effective degree of arterial inversion, and $T_{1\text{app}}$ is the apparent spin–lattice relaxation time in the presence of arterial inversion.

In practice, one has also to consider T_1 recovery of labeled flowing spins between the excitation and the detection slices, and cross relaxation between tissue water and macromolecules. A critical parameter is the degree of arterial spin labeling α', which depends on the flow velocity and the technique used to label spins. Steady-state spin inversion has been successfully achieved using adiabatic fast passage (AFP) spin inversion.

Quantitative perfusion maps have been obtained with this technique at high magnetic fields in animals, which have a short distance between neck and brain. High magnetic fields may be required to achieve a sufficient signal-to-noise ratio and dispose of longer T_1 values. A variant of this technique is to invert or saturate spins in the imaged slice and to monitor entry of fresh spins. Results may not be quantitative, but variations in blood flow during brain activation tasks may be observed.[59]

3.3.3 Blood Oxygenation Level Dependent (BOLD) Contrast

Although the approach based on Gd-DTPA was a significant breakthrough for functional brain imaging, it had several limitations, in particular the requirement to use an external contrast agent. The number of measurements is therefore limited (for instance, to one baseline and one activation image) and brain function cannot be evaluated in real time. Based on earlier works describing the magnetic properties of hemoglobin[60] and their effect on the magnetic resonance signal,[61] it was recently suggested that deoxyhemoglobin (which is paramagnetic, although oxyhemoglobin is not) in red blood cells could be used as an endogenous contrast material.[62,63] Kwong et al.,[59] closely followed by others,[64,65] showed that MRI could be used to monitor in real time the local modulation of the level of blood oxygenation associated

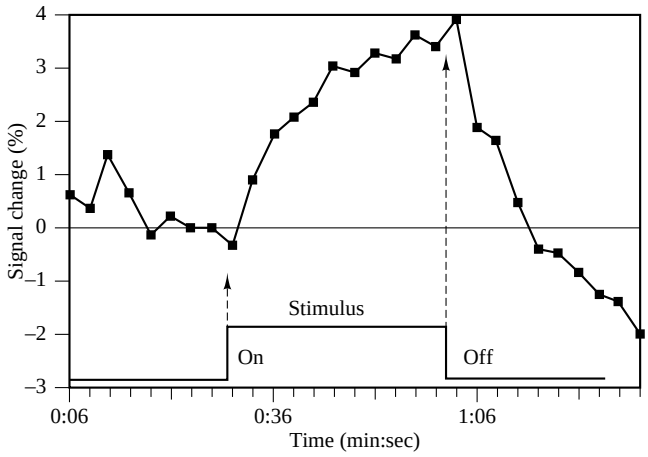

Figure 16 Typical magnetic resonance (MR) signal time course study during brain activation by a visual stimulus using the BOLD method (1.5 T). Gradient echo EPI images were obtained at 3-s intervals. During the stimulus the MR signal increases. The amplitude of the signal change is usually small, but largely exceeds baseline fluctuations. After stimulation, the MR signal sometimes goes below baseline. There is a delay of several seconds between the beginning of the activation task and the MR signal change, due to the delayed hemodynamic response over the neuronal response

with brain activity on an individual basis, without the need for intersubject averaging.

During brain activation tasks, there is a large local increase in blood flow which overcomes a small increase in tissue oxygen uptake. There is, therefore, a surplus of oxyhemoglobin over deoxyhemoglobin, resulting in a reduction of the susceptibility effects and thus in increased MRI signal (Figure 16). The effect is usually small (a few per cent) and depends on the sequence parameters, the voxel size, and the field strength.[66,67] Recent articles have demonstrated the tremendous potential of MRI to aid in our understanding of how the brain works, with unmatched combined spatial and temporal resolution[68–71] (Figure 17).

Besides exploration of the normal brain, potential clinical applications include presurgical mapping,[72] monitoring of recovery after stroke or head trauma, and monitoring the fate of neuropharmacological agents.[73] Presurgical mapping consists in functional evaluation of brain tissue to be removed or spared during surgery, for instance in cases of intractable complex partial seizures if language is to be spared during lobectomy. So far, hemispheric language dominance is determined from invasive and risky tests, such as the Wada test which is based on intracarotid amobarbital injection, and electrical cortical recording through electrodes positioned intraoperatively. It is clear that functional MRI (FMRI) language studies have the potential to replace such invasive tests.[68,74] On the other hand, FMRI could also be used to visualize epileptic foci with, or even without, associated clinical seizure. The use of FMRI for monitoring of functional recovery after stroke or head trauma appears especially important for patients with hemiplegia or aphasia. Studies may be repeated at will on individuals during the recovery period without concerns about irradiation.

MRI could also be used to visualize regions of the brain where receptors have been activated or inhibited by neuropharmacological agents through effects on blood flow and blood oxygenation, as we recently suggested using

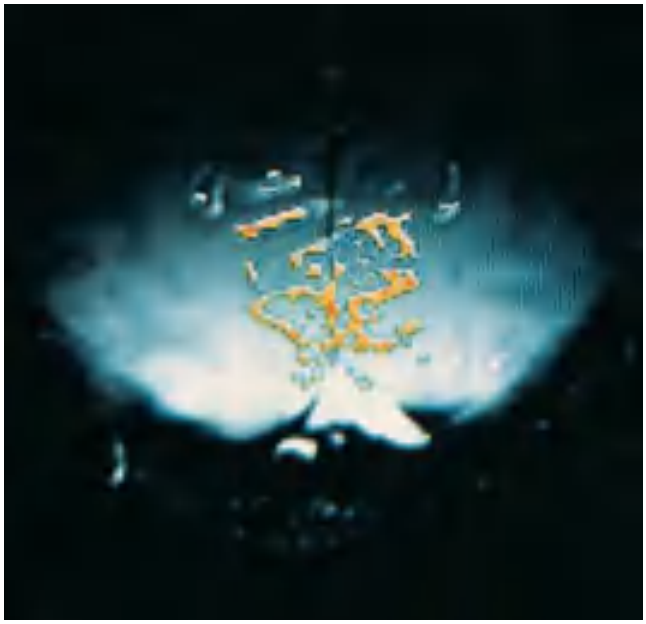

Figure 17 Activation map of the visual cortex. Activation maps can be calculated by identifying pixels where significant magnetic resonance signal change occurred during stimulation. The degree of activation is shown using a color scale. The raw BOLD images were obtained using a spoiled-GRASS gradient echo (SPGR) sequence with a spatial resolution of 0.8 mm × 1.6 mm. The activation map is overlayed on a high resolution anatomical image to show the exact location of activation

neurochemical activation by arecholine in monkey brain.[73] Also, the modulation by such drugs of the response of the brain to specific stimuli or cognitive tasks could be evaluated.

There are, of course, some limitations when using FMRI. Patient cooperation is particularly necessary. Not only is their active participation required for the activation tasks, but they are also required to stay absolutely immobile during scanning in order to avoid misregistration artifacts. Registration algorithms are being evaluated, as well as sophisticated statistical analysis packages. Another concern regards the size of the vessels (veinules or feeding arteries) responsible for the effect. If the vessels are not small enough, they may correspond to a fairly large territory, so that the area of activation may differ from the location where activation is seen on the images.

3.4 Conclusion

MRI appears to be a very promising imaging modality for looking at microcirculation and perfusion. Compared with other approaches, MRI may provide images of high temporal and spatial resolution totally noninvasively. However, today, methods which give the best spatial and/or temporal resolution are not always quantitative, at least in terms of blood flow or other physiological parameters, often due to the lack of an adequate model. On the other hand, there are techniques, most of them using the basic principles of more conventional methods, which are potentially quantitative, but remain difficult to implement and give images with limited spatial and/or temporal resolution. It is likely that progress

will be made in both directions, so that physiologists and clinicians will soon have available to them methods which give quantitative information on perfusion with unmatched spatial and temporal resolution.

4 RELATED ARTICLES

Anisotropically Restricted Diffusion in MRI; Brain: Sensory Activation Monitored by Induced Hemodynamic Changes with Echo Planar MRI; Diffusion: Clinical Utility of MRI Studies; Whole Body Magnetic Resonance Angiography.

5 REFERENCES

1. E. O. Stejskal and J. E. Tanner, *J. Chem. Phys.*, 1965, **42**, 288.
2. D. Le Bihan, *Magn. Reson. Q.*, 1991, **7**, 1.
3. H. C. Torrey, *Phys. Rev.*, 1965, **104**, 653.
4. D. Le Bihan, E. Breton, D. Lallemand, P. Grenier, E. A. Cabanis, and M. Laval-Jeantet, *Radiology*, 1986, **161**, 401.
5. P. J. Basser, J. Mattiello, and D. Le Bihan, *J. Magn. Reson.*, 1994, in press.
6. E. L. Hahn, *Phys. Rev.*, 1950, **80**, 580.
7. H. Y. Carr and E. M. Purcell, *Phys. Rev.*, 1954, **94**, 630.
8. J. E. Tanner, *J. Chem. Phys.*, 1970, **52**, 2523.
9. K. D. Merboldt, W. Hanicke, and J. Frahm, *J. Magn. Reson.*, 1985, **64**, 479.
10. R. Kaiser, E. Bartholdi, and R. R. Ernst. *J. Chem. Phys.*, 1974, **60**, 2966.
11. D. Le Bihan, *Magn. Reson. Med.*, 1988, **7**, 346.
12. D. Le Bihan, R. Turner, and J. R. MacFall, *Magn. Reson. Med.*, 1989, **10**, 324.
13. K. D. Merboldt, W. Hanicke, M. L. Gyngell, J. Frahm, and H. Bruhn, *J. Magn. Reson.*, 1989, **82**, 115.
14. K. D. Merboldt, H. Bruhn, J. Frahm, M. L. Gyngell, W. Hanicke, and M. Deimling, *Magn. Reson. Med.*, 1989, **9**, 423.
15. E. X. Wu and R. B. Buxton, *J. Magn. Reson.*, 1990, **90**, 243.
16. D. Canet, B. Diter, A. Belmajdoub, J. Braondeau, J. C. Boubel, and K. Elbayed, *J. Magn. Reson.*, 1989, **81**, 1.
17. G. S. Karczmar, D. B. Twieg, T. J. Lawry, G. B. Matson, and M. W. Weiner, *Magn. Reson. Med.*, 1988, **7**, 111.
18. D. Le Bihan and E. Breton. *CR Acad. Sci. Paris*, 1985, **301**, 1109.
19. M. Neeman, J. P. Freyer, and L. O. Sillerud, *J. Magn. Reson.*, 1990, **90**, 303.
20. D. G. Taylor and M. C. Bushell, *Phys. Med. Biol.*, 1985, **30**, 345.
21. R. Turner, D. Le Bihan, J. Maier, R. Vavrek, L. K. Hedges, and J. Pekar, *Radiology*, 1990, **177**, 407.
22. R. Turner and D. Le Bihan, *J. Magn. Reson.*, 1990, **86**, 445.
23. P. Mansfield, *J. Phys. C: Solid State Phys.*, 1977, **10**, L55.
24. T. L. Chenevert, J. G. Pipe, D. M. Williams, and J. A. Brunberg, *Magn. Reson. Med.*, 1990, **17**, 197.
25. E. O. Stejskal, *J. Chem. Phys.*, 1965, **43**, 3597.
26. R. L. Cooper, D. B. Chang, A. C. Young, C. J. Martin, and D. Ancker-Johnson, *Biophys. J.*, 1974, **14**, 161.
27. J. E. Tanner, *J. Chem. Phys.*, 1978, **69**, 1748.
28. G. G. Cleveland, D. C. Chang, C. F. Hazlewood, and H. E. Rovschach, *Biophys. J.*, 1976, **16**, 1043.
29. M. E. Moseley, Y. Cohen, J. Kucharczyk, J. Mintorovitch, H. S. Asgari, M. F. Wendland, J. Tsuruda, D. Norman, and P. Weinstein, *Radiology*, 1990, **176**, 439.
30. D. Le Bihan, R. Turner, and P. Douek, *NeuroReport*, 1993, **4**, 887.
31. M. E. Moseley, J. Kucharczyk, J. Mintorovitch, Y. Cohen, J. Kurhanewicz, N. Derucin, H. Asgari, and D. Normou, *Am. J. Neuroradiol.*, 1990, **11**, 423.
32. S. Warach, D. Chien, W. Li, M. Ronthal, and R. R. Edelman, *Neurology*, 1992, **42**, 1717.
33. D. Le Bihan, R. Turner, P. Douek, and N. Patronas, *Am. J. Radiol.*, 1992, **159**, 591.
34. D. Le Bihan, J. Delannoy, and R. Levin, *Radiology*, 1989, **171**, 853.
35. S. S. Kety and C. F. Schmidt, *Am. J. Physiol.*, 1945, **143**, 53.
36. N. M. Bolas, A. J. Petros, D. Bergel, and G. K. Radda, *Proc. Soc. Magn. Reson. Med. 1985 Meet.*, p. 315.
37. S. Eleff, M. Schnall, L. Ligetti, M. Osbakken, H. Subramanian, B. Chance, and J. S. Leigh, *Magn. Reson. Med.*, 1988, **7**, 412.
38. D. Barranco, L. N. Sutton, S. Florin, J. Greenberg, T. Sinnwell, L. Ligetti, and A. C. McLaughlin, *J. Cereb. Blood Flow Metab.*, 1989, **9**, 886.
39. J. R. Ewing, C. A. Branch, S. C. Fagan, J. A. Helpern, R. T. Simkins, S. M. Butt, and K. M. A. Welch, *Stroke*, 1990, **21**, 100.
40. J. J. H. Ackerman, C. S. Ewy, N. N. Becker, and R. A. Shalwitz, *Proc. Natl. Acad. Sci. USA*, 1987, **84**, 4099.
41. J. Pekar, L. Ligeti, Z. Ruttner, R. C. Lyon, T. M. Sinnwell, P. van Gelderen, D. Fiat, C. T. W. Moonen, and A. C. McLaughlin, *Magn. Reson. Med.*, 1991, **21**, 313.
42. A. L. Hopkins, E. M. Haacke, J. Tkach, R. G. Barr, and C. B. Bratton, *Magn. Reson. Med.*, 1988, **7**, 222.
43. K. K. Kwong, A. L. Hopkins, J. W. Belliveau, D. A. Chesler, L. M. Porkka, R. C. McKinstry, D. A. Finelli, G. J. Hunter, J. B. Moore, R. G. Barr, and B. R. Rosen, *Magn. Reson. Med.*, 1991, **22**, 154.
44. C. R. Fisel, J. L. Ackerman, R. B. Buxton, L. Garrido, J. W. Belliveau, B. R. Rosen, and T. J. Brady, *Magn. Reson. Med.*, 1991, **17**, 336.
45. L. Axel, *Radiology*, 1980, **137**, 679.
46. J. W. Belliveau, B. R. Rosen, H. L. Kantor, R. R. Rzedzian, D. N. Kennedy, R. C. McKinstry, J. M. Vevea, M. S. Cohen, I. L. Pykett, and T. J. Brady, *Magn. Reson. Med.*, 1990, **14**, 538.
47. K. L. Zierler, *Circ. Res.*, 1962, **10**, 393.
48. N. A. Lassen, *J. Cereb. Blood Flow Metab.*, 1984, **4**, 633.
49. J. W. Belliveau, D. N. Kennedy, R. C. McKinstry, R. M. Buchbinder, R. M. Weisskoff, S. M. Cohen, J. M. Vevea, T. J. Brady, and B. R. Bosen, *Science*, 1991, **254**, 716.
50. D. Le Bihan, E. Breton, D. Lallemand, M. L. Aubin, J. Vignaud, and M. Laval-Jeantet, *Radiology*, 1988, **168**, 497.
51. I. R. Young, A. S. Hall, D. J. Bryant, D. G. T. Thomas, S. S. Gill, M. S. Dubowitz, F. Cowan, and J. M. Pennock, *J. Comput. Assist. Tomogr.*, 1988, **12**, 727.
52. J. Pekar, P. C. M. van Zijl, and C. T. W. Moonen, *Magn. Reson. Med.*, 1992, **23**, 122.
53. D. Le Bihan and R. Turner, *Magn. Reson. Med.*, 1992, **27**, 171.
54. J. J. Neil and J. J. H. Ackerman, *J. Magn. Reson.*, 1992, **97**, 194.
55. J. J. Neil, L. A. Scherrer, and J. J. H. Ackerman, *J. Magn. Reson.*, 1991, **95**, 607.
56. C. B. Ahn, S. Y. Lee, O. Nalcioglu, and Z. H. Cho, *Med. Phys.*, 1987, **14**, 43.
57. J. H. Maki, J. R. MacFall, and G. A. Johnson, *Magn. Reson. Med.*, 1991, **17**, 95.

58. D. S. Williams, J. A. Detre, J. S. Leigh, and A. P. Koretsky, *Proc. Natl. Acad. Sci. USA*, 1992, **89**, 212.
59. K. K. Kwong, J. W. Belliveau, D. A. Chesler, I. E. Goldberg, R. M. Weisskoff, B. P. Poncelet, D. N. Kennedy, B. E. Hoppel, M. S. Cohen, R. Turner, H. M. Cheng, T. J. Brady, and B. R. Rosen, *Proc. Natl. Acad. Sci. USA*, 1992, **89**, 5675.
60. L. Pauling and C. D. Coryell, *Proc. Natl. Acad. Sci. USA*, 1936, **22**, 210.
61. K. R. Thulborn, J. C. Waterton, P. M. Matthews, and G. K. Radda, *Biochim. Biophys. Acta*, 1982, **714**, 265.
62. S. Ogawa, T. M. Lee, A. S. Nayak, and P. Glynn, *Magn. Reson. Med.*, 1990, **14**, 68.
63. R. Turner, D. Le Bihan, C. T. W. Moonen, D. Despres, and J. Frank, *Magn. Reson. Med.*, 1991, **22**, 159.
64. P. A. Bandettini, E. C. Wong, R. S. Hinks, R. S. Tikofsky, and J. S. Hyde, *Magn. Reson. Med.*, 1992, **25**, 390.
65. S. Ogawa, D. W. Tank, R. Menon, J. M. Ellerman, S. G. Kim, H. Merkle, and K. Ugurbil, *Proc. Natl. Acad. Sci. USA*, 1992, **89**, 5951.
66. J. Frahm, H. Bruhn, K. D. Merboldt, and W. Hanicke, *J. Magn. Reson. Imag.*, 1992, **5**, 501.
67. R. Turner, P. Jezzard, H. Wen, K. K. Kwong, D. Le Bihan, T. Zeffiro, and R. S. Balaban, *Magn. Reson. Med.*, 1993, **29**, 277.
68. G. McCarthy, A. M. Blamire, D. L. Rothman, R. Gruetter, and R. G. Schulman, *Proc. Natl. Acad. Sci. USA*, 1993, **90**, 4952.
69. D. Le Bihan, R. Turner, T. A. Zeffiro, C. A. Cuenod, P. Jezzard, and V. Bonnerot, *Proc. Natl. Acad. Sci. USA*, 1993, **90**, 1 1802.
70. S. Kim, J. Ashe, K. Hendrich, J. M. Ellermann, H. Merkle, K. Urgubil, and A. P. Georgopoulos, *Science*, 1993, **261**, 615.
71. W. Schneider, D. C. Noll, and J. D. Cohen, *Nature*, 1993, **365**, 150.
72. C. R. Jack, R. M. Thompson, R. K. Butts, F. W. Sharbrough, P. J. Kelly, D. P. Hanson, S. J. Rieckrer, R. L. Ehmon, N. J. Hangianoreou, and G. D. Cascino, *Radiology*, 1994, **190**, 85.
73. C. A. Cuenod, M. C. J. Chang, T. Arai, L. Pannier, S. Posse, D. DesPres, J. A. Frank, S. Rapoport, and D. Le Bihan, *Proc. Soc. Magn. Reson. Med. 1993 Meet.*, p. 1387.
74. L. Rueckert, I. Appollonio, J. Grafman, P. Jezzard, R. Johnson, and D. Le Bihan D, *J. Neuroimag*, 1994, **4**, 67.

Biographical Sketch

Denis Le Bihan. *b* 1957. Ph.D., 1987, Physics, M.D., 1984, Radiology, University of Paris, France. Chief, Diagnostic Radiology Research Section, National Institutes of Health, Clinical Associate Professor of Radiology, Georgetown University, USA. Approx. 250 articles, book chapters and abstracts. Research specialties: diffusion, temperature, interventional, perfusion and functional MRI.

Diffusion: Clinical Utility of MRI Studies

Ole Henriksen

Danish Research Center of Magnetic Resonance, Hvidovre University Hospital, Denmark

1 INTRODUCTION

Tissue characterization by MRI has been a subject of great interest because the multiparameter dependence of the MRI signal makes it possible to improve the differentiation between various pathologies in vivo, which may lead to an improved specificity of clinical MRI investigations. So far, these approaches have mostly been based on signal contrast behavior due to differences in proton densities, and T_1 and T_2 relaxation behavior between different tissue types. In recent years, methods for studying diffusion processes in vivo by means of MRI have been developed, and possible clinical applications are currently under investigation. The studies published so far have mostly been directed to imaging of diffusion processes of water in the human brain. The results are very promising with respect to future clinical utility. These studies will be described in this article, outlining possible major areas of application for diffusion studies in clinical practice.

2 MRI MEASUREMENTS OF WATER DIFFUSION IN BIOLOGICAL TISSUES IN VIVO

A detailed description of the factors which influence the diffusion of water molecules in biological tissues is given in other articles (see the list of related articles). Only those aspects relevant for the interpretation of clinical in vivo diffusion studies will therefore be considered here.

2.1 The Concept of Restricted Diffusion

Translational molecular diffusion processes are a phenomenon in which molecules in a fluid of infinite extent move along random paths, colliding with and moving past each other. Diffusion can be described in statistical terms. The diffusion coefficient, D, describes the mobility at the molecular level, and has the unit of length squared per unit of time. D is specific for a given molecule, and varies with viscosity and temperature. For the free diffusion of water molecules in water the diffusion coefficient D is approximately 3×10^{-9} m^2 s^{-2} at 37 °C. If the diffusion coefficient of water in a given tissue is less than this value at 37 °C, and it varies with the diffusion time, the diffusion is said to be restricted, and depends on a number of factors related to the microstructure of the tissue in question, which will be described briefly below.

The water diffusion in the cytosol may be hindered by the presence of barriers such as cell membranes, intracellular organelles, the presence of macromolecules, electrical charges, etc. The consequence is that the diffusion path of the water molecule becomes geometry-dependent, and the concept of a diffusion coefficient depending only on the properties of the diffusion medium breaks down. The practical consequence is that the diffusion coefficients obtained in MRI studies also include prolonged diffusion paths encountering such barriers (tortuosity), and they should thus be regarded as 'apparent diffusion coefficients', and are denoted D^* in the following discussion. The signal contrast in diffusion-weighted imaging depends on the design of the pulse sequence because D^* depends on the time (diffusion time) in which the diffusion processes influence the signal obtained by diffusion-sensitized pulse sequences. If the diffusion time is very short, the probability that a water molecule meets a barrier is low compared with that of diffusion over a longer period of time. Thus, D^* decreases monotonically from values close to D for short diffusion times to a constant smaller value as the diffusion time is extended to very long periods.

The fractional signal attenuation, A, due to diffusion in a given time, Δ, in pulsed gradient experiments, neglecting the small effects of the imaging gradients, can be written as

$$A = \exp[-bD^*(\Delta)] \tag{1}$$

where b is the diffusion attenuation factor in units of time per length squared [equal to $\gamma^2 G^2 \delta^2(\Delta - \delta/3)$] and $D^*(\Delta)$ is the apparent diffusion coefficient at the diffusion time, Δ (δ is the effective gradient duration and Δ is the time between the leading edges of the pulses). Thus, in images displaying D^*, tissues with high D^* will appear with a high signal intensity. In diffusion-weighted images the situation is the opposite, as tissues with high D^* values tend to appear with low signal intensity, but the interpretation is more difficult because the signal will also be influenced by T_1- and T_2-weighting factors. Even though the D^* in cerebrospinal fluid (CSF) is very high and equals D, the signal appears bright in diffusion-weighted images using a diffusion-sensitized spin echo sequence because the T_2 of CSF is very long compared with that of the brain tissue.

2.2 Sources of Errors

Apart from imperfections in the MRI equipment, macroscopic movements are a main source of error in diffusion studies in vivo. Patient movements may be minimized by careful fixation, but one still has to take physiological movements induced by arterial pulsation, respiration, etc., into account. Studies of brain motion using the phase contrast method[1] have indicated an average velocity of about 0.5 mm s^{-1} during the cardiac cycle, corresponding to distances of at least 10 μm in 20 ms, which are very similar to the expected values for the apparent average diffusion distance with Δ of 20 ms.

Cardiac and respiratory synchronization and compensation for first order bulk movements by gradient moment nulling techniques reduce the movement problems considerably when spin echo sequences are used.[2,3] Another way is to use single-shot sequences with very short imaging times.[3]

Table 1 Clinical MRI studies of diffusion in human brain tissues

Tissue	Apparent diffusion coefficient $D^*/(10^{-9}\ m^2\ s^{-1})$	References
CSF	2.9–3.5	3,4,5,6
White matter	0.2–1.7	4,7,10,11
Perpendicular	0.2–0.9	2,7
Parallel	0.8–1.5	2,7
Gray matter	0.7–2.3	3,6,8,9,10

3 CLINICAL MRI STUDIES OF DIFFUSION IN BRAIN

3.1 Normal Subjects

So far the vast majority of in vivo diffusion studies applied to human beings have been carried out on the brain. The reasons are that the brain movements are small, and the relatively long T_2 values of brain tissue make it possible to achieve a reasonable signal-to-noise ratio in high-resolution images (voxel size 8 mm^3). Relatively few studies where quantitative measurements of the apparent diffusion coefficient have been performed in healthy humans have been published so far. The results are summarized in Table 1. The main findings are that the apparent diffusion coefficient is reduced in gray and white matter compared with the diffusion coefficient of water molecules in water at 37 °C (Figure 1). Studies of white matter indicate that the diffusion is anisotropic, as the apparent diffusion coefficient is smaller for diffusion perpendicular to than parallel to the direction of the axons.[11] Another important finding is that the diffusion appears to be restricted in white matter perpendicular to the direction of the nerve fibers as D^* decreases for diffusion times above 26 ms, which corresponds to an average diffusion distance of about 4–5 μm.[5] No sign of restricted diffusion is seen in the direction of the fibers up to distances of 9 μm.[5] The same seems to be true for gray matter.[5] The apparent diffusion coefficients obtained in CSF may be regarded as a kind of internal control of the validity of the quantitative measurements, since the expected values should be equal to the diffusion coefficient of water molecules in water at 37 °C ($D = 3 \times 10^{-9}\ m^2\ s^{-1}$). In the early study of Thomsen et al.,[8] D^* in CSF is higher than the expected value of free diffusion in water, indicating that bulk movements contributed to the measurement. In a later study where compensation for movements of constant velocity is incorporated, D^* in CSF corresponds to the expected value.[2]

3.1.1 Age Dependency

Gideon et al.[6] have observed that the apparent diffusion coefficient for water in deep white matter increases with age from $0.7 \times 10^{-9}\ m^2\ s^{-1}$ (age ~20 years) to approximately $1.0 \times 10^{-9}\ m^2\ s^{-1}$ (age 60–75 years), using a flow-compensated, diffusion-sensitized spin echo sequence with a diffusion time of 19 ms (Figure 2). This relationship between water diffusion and age has not been seen in gray matter.[6] Measurements on

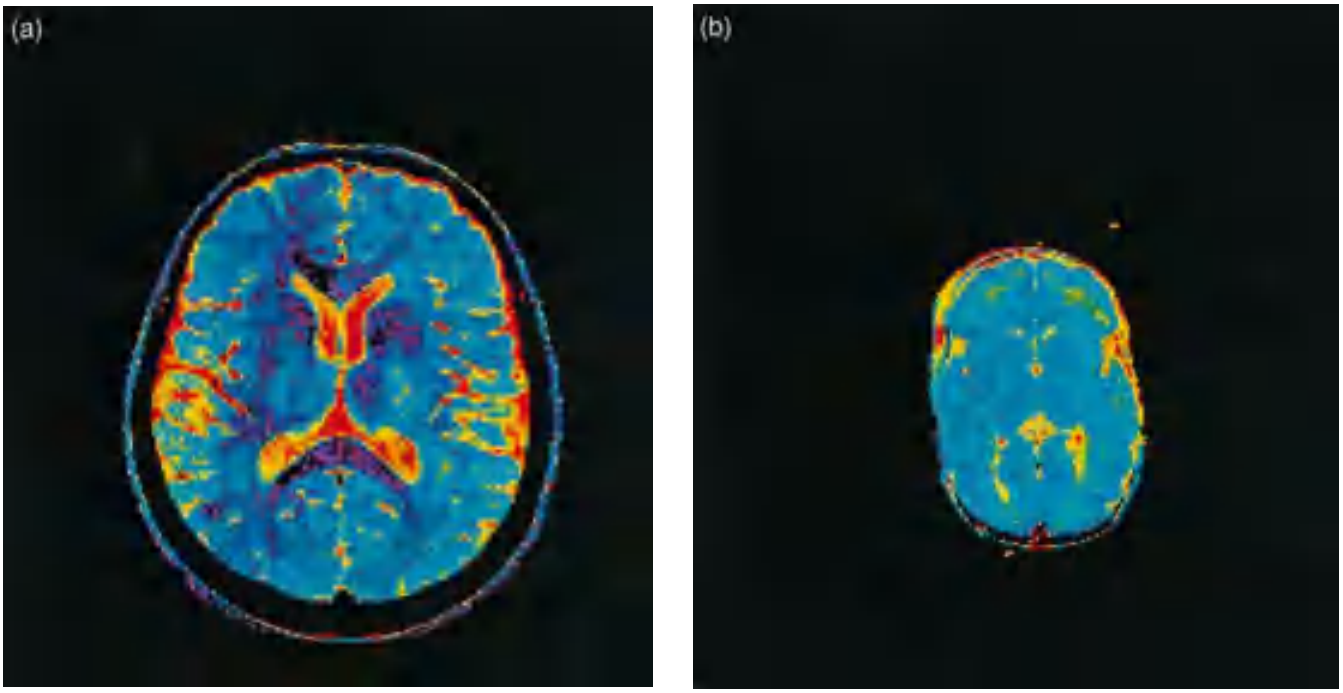

Figure 1 Images of the calculated apparent diffusion coefficient of water in the brain of (a) an adult healthy volunteer and of (b) a premature neonate (gestational age 33 weeks). The calculated images are based on diffusion-weighted spin echo sequences with compensation for first-order bulk movements. ECG triggering was performed as well. The color scale shown to the right of the images is linear, corresponding to $D^* = 0$ (magenta) to $D^* = 3.5 \times 10^{-9}\ m^2\ s^{-1}$ (red) which corresponds to the free diffusion coefficient of water in water at 37 °C. The voxel size is $1 \times 1 \times 8\ mm^3$. Note the relatively low D^* in white matter perpendicular to the fiber direction in the adult brain and that D^* is considerably less than in the CSF, which corresponds to the free diffusion of water molecules in water. In contrast to the adult brain, the D^* in white matter is higher than in gray matter in the neonatal premature brain

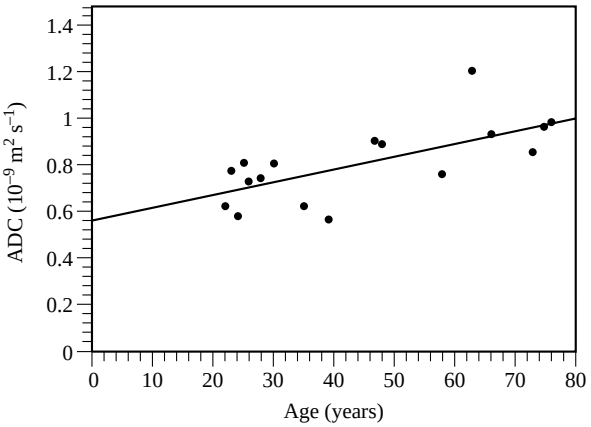

Figure 2 D^* of water in periventricular white matter of healthy subjects plotted against age. Regression analysis shows a significant correlation between D^* and age. (Adapted from Gideon et al.[6])

neonates and small infants suggest that the degree of water diffusion anisotropy in frontal white matter and optic radiation is less in neonates than in young adults.[12] No clear difference is seen between the neonates and adults when D^* is measured parallel to the direction of the fibers.[12]

3.1.2 Diffusion-weighted Imaging

The studies mentioned so far in which the apparent water diffusion in human brain has been estimated in quantitative terms indicate that the water diffusion in white matter is restricted and there is an appreciable degree of anisotropy. The possible mechanisms underlying the diffusion anisotropy in brain white matter is discussed in ***Anisotropically Restricted Diffusion in MRI***, but the observations in neonates[12] suggest that the myelin sheaths may at least be partly responsible. The practical consequence is that anisotropically restricted diffusion creates a signal contrast between nerve fiber bundles running in different directions in relation to those of the diffusion-sensitizing gradients. This has been shown in a number of studies where major ascending and descending projection tracts are visualized.[5,13] It should be recalled that nerve fibers running perpendicular appear brighter than those running in parallel with the direction of the diffusion-sensitizing gradients.

3.2 Brain Pathologies

3.2.1 Brain Ischemia

A number of animal studies show that the apparent diffusion of water is reduced in experimentally induced ischemic areas of the brain.[14–16] These alterations seem to be detectable within the first half hour after the onset of brain ischemia, and occur a long time before changes are detectable in T_2-weighted images.[15,17] In diffusion-weighted images, focal ischemic areas appear brighter than normal brain tissue in a gray–white scale, because the smaller apparent diffusion coefficient of water causes less reduction of the signal due to diffusion processes. The animal studies also indicate good agreement between the anatomical spreading of focal brain ischemia as visualized by diffusion-weighted imaging, perfusion-related imaging of the passage of a gadolinium compound (input function is not taken into account), and histological evaluation based on staining with Evans blue.[14,17] Diffusion-weighted imaging of photochemically induced ischemia in rat brain shows hyperintense signals corresponding to the ischemic area on the first day. During the following days the signal intensity fades, indicating that the diffusion of water becomes less impeded in the subacute stage.[16]

Taken together, the animal studies mentioned above clearly demonstrate that the apparent diffusion of water is reduced in ischemic brain tissue and that these alterations occur in the very early phase. The reason for the impeded diffusion of water is unclear at present. It cannot be explained by a decrease in tissue temperature because this has to drop about 10 °C in order to explain the observed decrease in the apparent diffusion coefficient of water of about 30%. It seems to be associated with energy failure secondary to severe ischemia.[18] The impediment of diffusion probably reflects alterations of the water balance between tissue compartments, swelling of membranes, and accumulation of macromolecules.

Only a few studies of water diffusion in the brain of stroke patients have been published. As early as 1987 Thomsen et al.[8] had presented evidence suggesting that the apparent diffusion coefficient of water is reduced in subacute brain infarcts. Warach et al.[19] have studied 32 patients with stroke using a high-speed diffusion-weighted stimulated echo sequence (turbo-STEAM). The time after the onset of symptoms ranged between 1 h and about 4 months. Diffusion-weighted images confirm the results of the animal studies described above, as a hyperintense signal is seen in the ischemic area, and these changes can be seen in the very acute stage where no changes are seen in T_2-weighted images (Figure 3). In accordance with this, parametric images of the calculated apparent diffusion coefficient of water show that this is reduced compared with the contralateral side in the acute and subacute stages, whereas the apparent diffusion coefficient in infarcted tissue is increased in the chronic stage (Figure 4). The absolute values of D^* may have been influenced as bulk movements due to gross head movements, brain movements caused by arterial pulsation,[1,2,20] and respiration may not have been sufficiently controlled. However, another study using a diffusion-sensitized spin echo pulse sequence and cardiac triggering also suggests a reduced apparent diffusion of water in ischemic areas following acute stroke.[20] These results show a considerable interindividual variation, and they do not indicate a significant correlation between D^* and the duration of ischemia.

Taken together, the experimental animal and human studies have established that the apparent diffusion coefficient of water is reduced in brain tissue subjected to severe acute ischemia, and that these alterations can be visualized at a very early stage. The evidence obtained suggests that the apparent water diffusion coefficient increases within the lesion to supranormal values in the chronic stage of stroke. As mentioned before, the exact pathophysiological events underlying these observations are still poorly understood. When the diffusion values obtained in these often elderly patients are compared with those obtained in healthy volunteers, the latter should be carefully age matched because the apparent diffusion coefficients in white matter have been shown to increase with age[6] (cf Figure 2). Further studies on anisotropy as well as on the relationship between water diffusion characteristics and regional cerebral perfusion are warranted in order to obtain a better understanding of the underlying pathophysiological mechanisms in acute

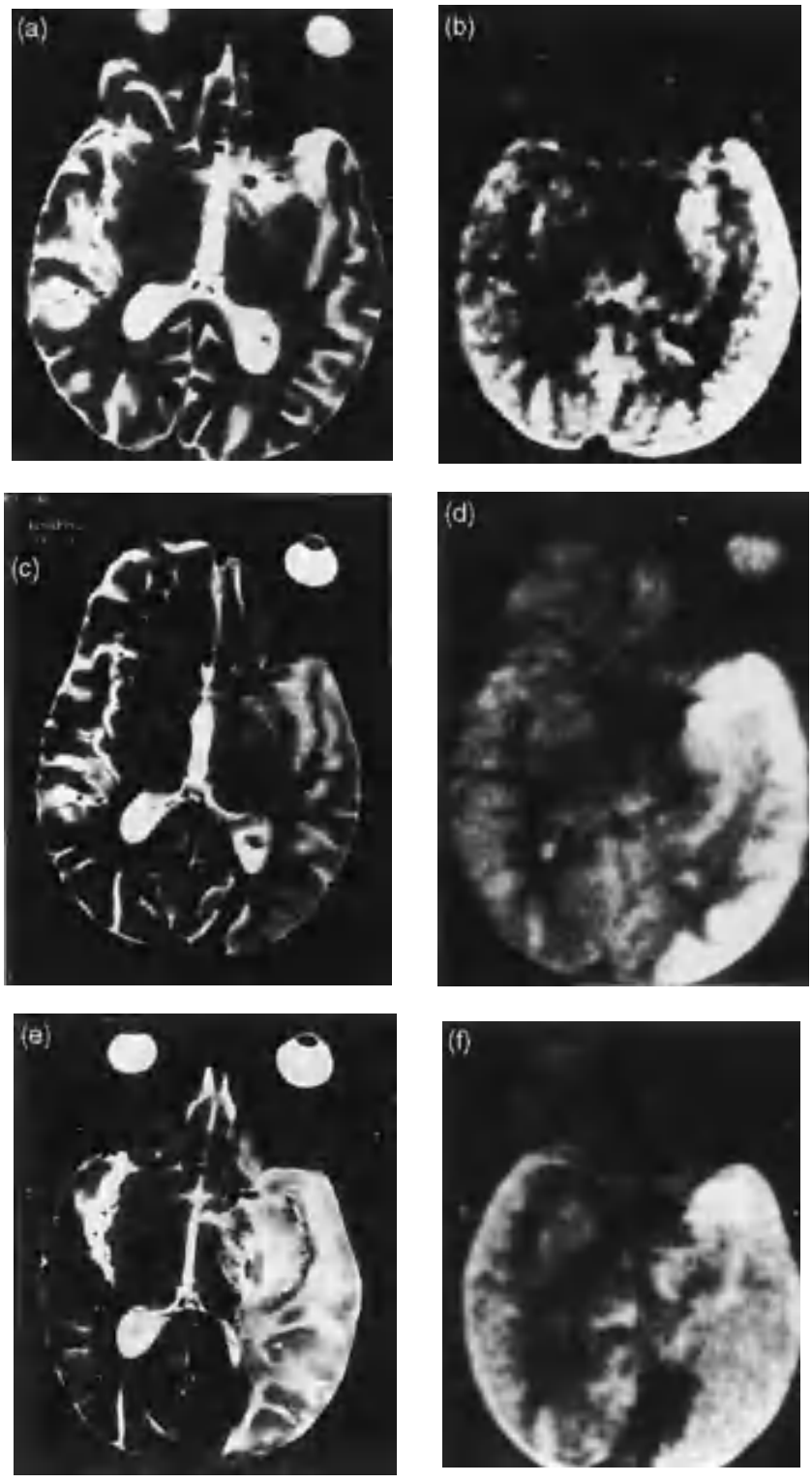

Figure 3 T_2-weighted (left) and corresponding diffusion-weighted (right) images obtained (a, b) 105 min, (c, d) 13 h, (e, f) 9 days after an acute stroke incident. Note that the ischemic tissue located in the left hemisphere can already be clearly visualized approximately 1.5 h after the clinical attack, where no changes are seen in the T_2-weighted image. (Reproduced by permission from Warach et al.[19])

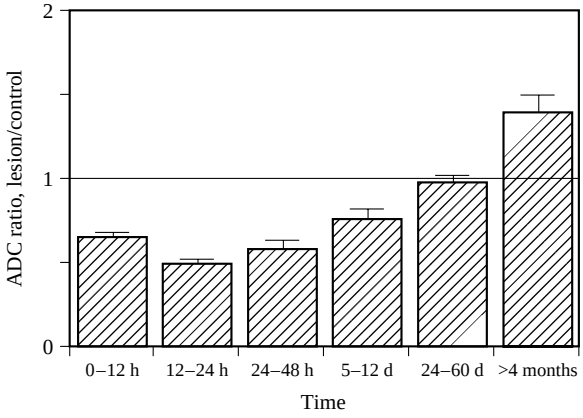

Figure 4 Calculated apparent diffusion coefficients (ADC) ratios of water in ischemic and contralateral nonischemic brain tissue plotted against time after a stroke incident. Note that the ratios seem to increase from values <1 in the acute and subacute stages to values >1 in the chronic stage. (Adapted from Warach et al.[19])

cerebral ischemia, and to be able to evaluate the prognostic information in diffusion-weighted images of brain ischemia with respect to tissue survival.

3.2.2 White Matter Disorders

Quantitative water diffusion studies indicate that the apparent diffusion coefficient is increased in *multiple sclerosis lesions* as compared with healthy age-matched volunteers,[21] in agreement with preliminary results published by Larsson et al.,[22] (Figure 5). Possible influences by movement due to brain pulsation and flow phenomena have been taken into account by using a flow refocusing sequence and cardiac triggering. It is of interest that the apparent diffusion coefficient is higher in acute lesions than in chronic but stable lesions, and that there is a significant increase in D^* in apparently normal white matter in the conventional spin echo images[21] (Figure 6). Finally, no relationship between the apparent diffusion coefficient and the T_2 relaxation rate measured by means of a multi-spin echo technique is seen, stressing that these phenomena depend on different mechanisms.[21] Diffusion-weighted imaging of a patient with chronic multiple sclerosis shows a high signal in the lesion compared with apparently normal white matter.[21] Since D^* of water is increased, as shown by Christiansen et al.,[21] a low signal should be expected in the diffusion-weighted images. The most likely reason for this is that the T_2 weighting dominates compared with the effect of increased diffusion in lesions with high T_2 values when pulsed gradient, diffusion-sensitized spin echo pulse sequences are used.

Even though our experience is relatively limited, the results obtained so far are promising with respect to differentiation between acute and chronic multiple sclerosis lesions.[21] The higher D^* value in acute than in chronic lesions may reflect an increase in water content due to edema and demyelinization in acute lesions, whereas gliosis dominates in the chronic stage.

To what extent diffusion studies may contribute to the differential diagnosis between lesions due to multiple sclerosis and other diseases including, for example, subcortical infarcts and viral infections, is still too early to say, as systematic comparative diffusion studies are still lacking. A single case study suggests that diffusion-weighted imaging may give further information in patients with *progressive multifocal leukoencephalopathy*.[13]

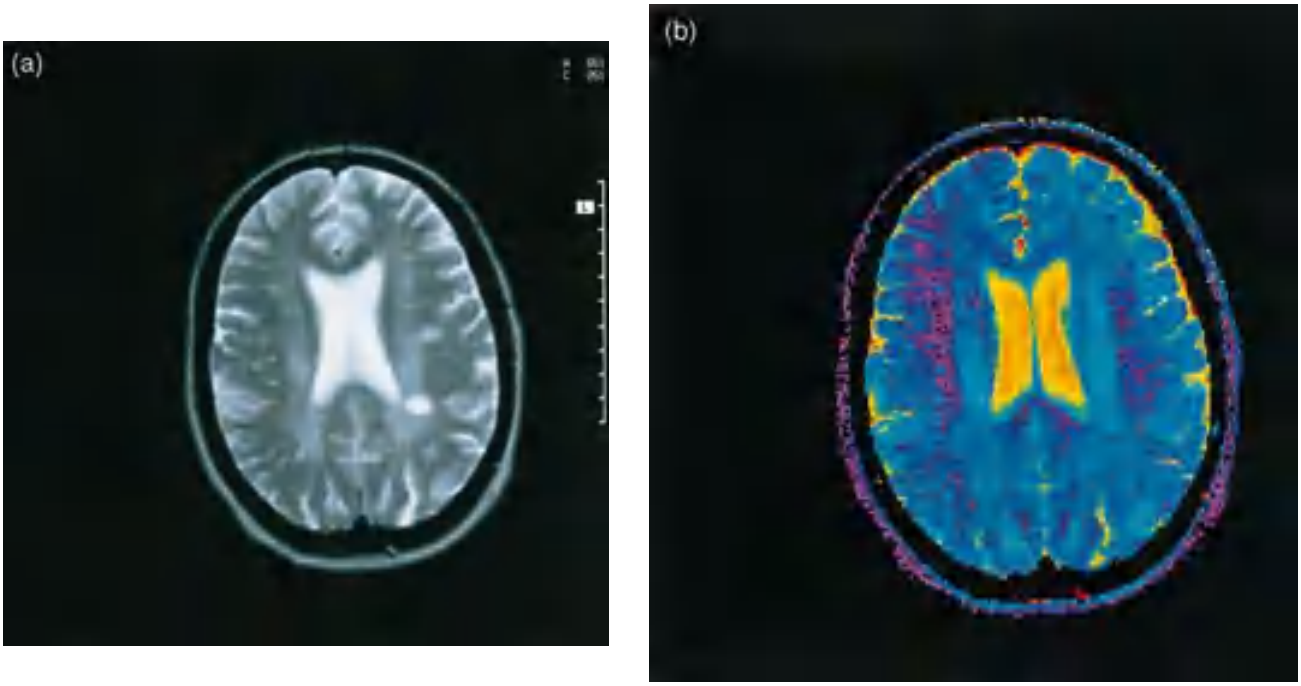

Figure 5 (a) T_2-weighted and (b) calculated apparent water diffusion coefficient images obtained in a patient with an acute attack of multiple sclerosis. The color scale shown to the right is similar to that described for Figure 1. Note the increase in diffusion corresponding to the acute lesion seen at the left posterior horn of the lateral ventricles. There also seems to be an increased diffusion in the apparently normal periventricular white matter. (Reproduced by permission from Christiansen et al.[21])

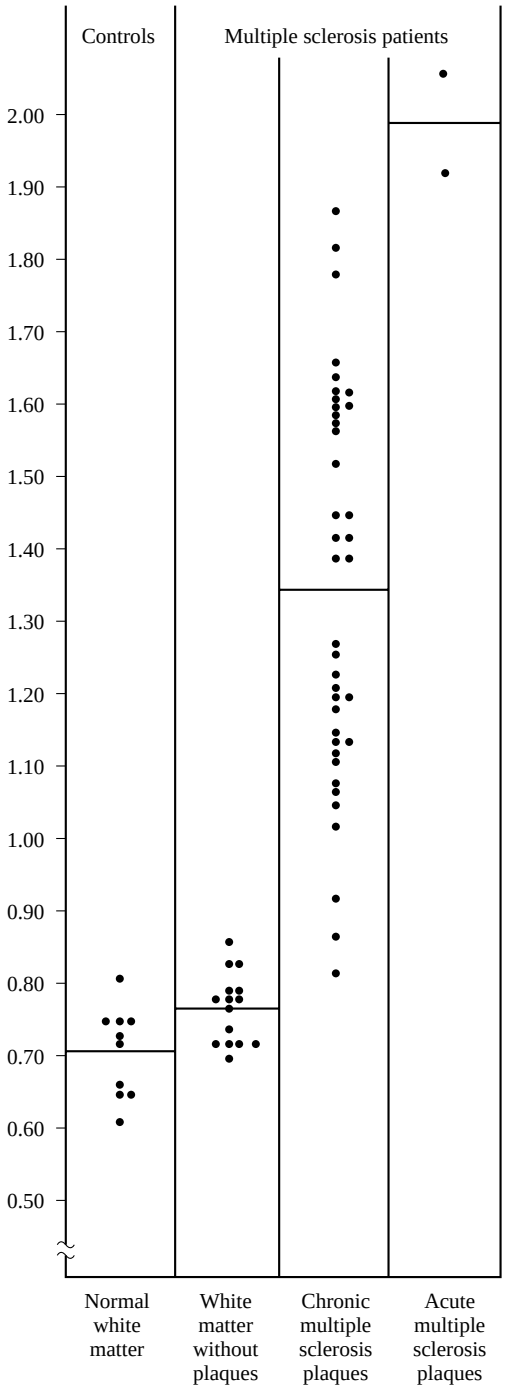

Figure 6 Apparent diffusion coefficient of water in white matter obtained in age-matched controls (left) and patients with chronic and acute multiple sclerosis lesions. Note that the average diffusion coefficient obtained in apparently normal white matter of multiple sclerosis patients is significantly increased compared with the control group. (Adapted from Christiansen et al.[21])

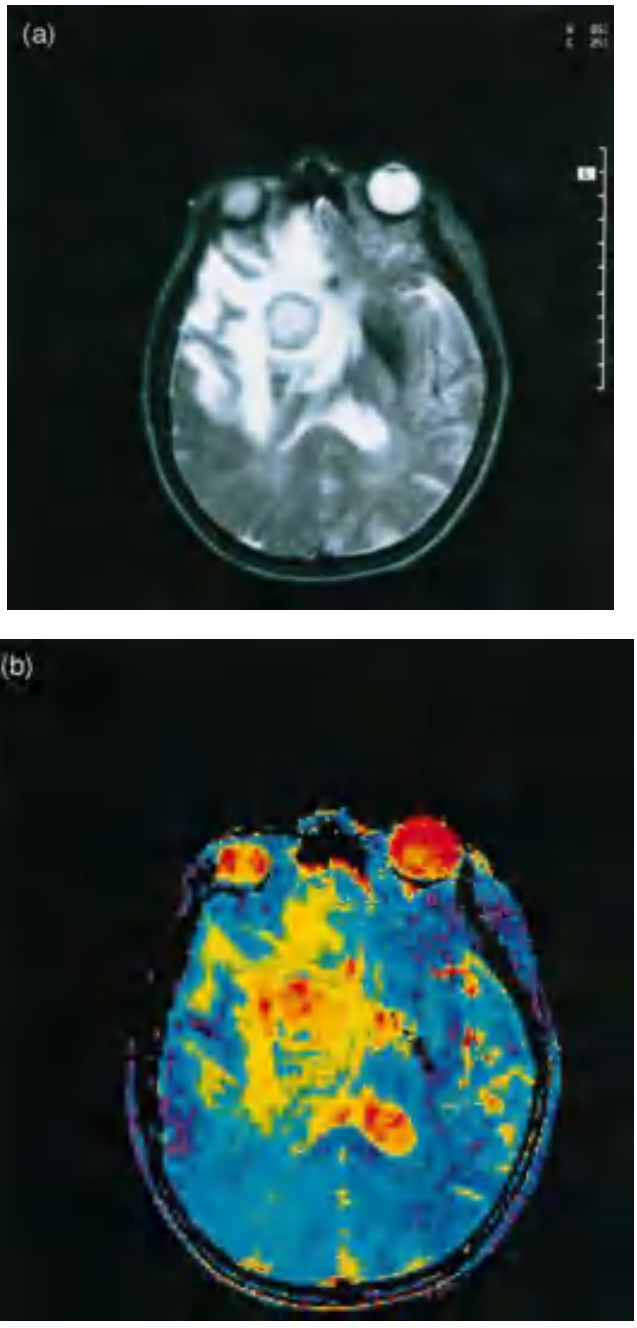

Figure 7 (a) T_2-weighted and (b) calculated apparent water diffusion coefficient images, obtained from a patient with a cystic astrocytoma. Note that D^* in the central part of the tumor is close to the free diffusion of water in water, indicating a cystic component of the lesion containing free fluid

3.2.3 Intracranial Tumors

Only a few studies on a limited number of patients with intracranial tumors have been reported so far.[5,23,24] The findings suggest both an increase and decrease in D^* within, as well as between, tumors compared with normal brain tissue (Figure 7). The increase in D^* is most prominent in cystic parts of the tumor approaching that of CSF and water. Diffusion measurements seem to make it possible to differentiate between solid tumor tissue and cystic lesions having the same appearance on conventional T_1- and T_2-weighted images due to a high content of paramagnetic protein. In the

latter case, diffusion studies will reveal D^* values corresponding to cyst fluid.[25] Diffusion studies may also improve the assessment of the delineation between epidermoid tumor and adjacent CSF.[23]

The extent to which diffusion studies may improve the tissue characterization of solid brain tumors is as yet unclear. Another important clinical aspect is whether diffusion studies allow differentiation between solid tumor and surrounding edema. Anecdotal evidence suggests that the signals from presumed edema in diffusion-weighted images are isointense with the solid tumor components but the edema may be associated with a higher degree of diffusion anisotropy.[13] It is, however, much too early to draw any definite conclusions.

3.2.4 *Disturbances in CSF Hydrodynamics*

Preliminary studies indicate that the apparent diffusion coefficient of water is significantly higher in white as well as gray matter of patients with *normal-pressure hydrocephalus* than in a group of healthy age-matched controls[26] (Figure 8). Surprisingly, the diffusion coefficients in the CSF of the patients seem also to be higher than in the controls, even though the diffusion-sensitive pulse sequences were compensated for first-order motion, and ECG triggering was performed. Since pulsatile motion of CSF is increased in these patients,[27] a higher degree of complex flow patterns may have contributed to the signal loss. This may explain the apparent elevation of the diffusion coefficients in CSF of patients with normal-pressure hydrocephalus. Examination of two patients with *high-pressure hydrocephalus* also suggests a higher apparent diffusion coefficients in both white and gray matter compared with normal subjects.[26] The increase in the apparent diffusion of water in brain white matter of patients with normal-pressure hydrocephalus may reflect the loss of myelin sheaths, especially in the periventricular regions.

Soelberg Sørensen et al.[28] have observed a pronounced increase in the apparent diffusion coefficient of water in patients with *benign intracranial hypertension* or *pseudotumor cerebri*. The alterations in water diffusion are most pronounced in the periventricular white matter. In some cases the calculated apparent diffusion coefficient exceeds that of free diffusion of water in water, indicating that the obtained diffusion values may to some extent have been influenced by pulsatile movements of the brain as well as by convective water movements in the brain tissue. In a later study where first order movement was corrected for in the pulse sequence, Gideon et al.[26] confirm that the apparent diffusion is increased in periventricular white matter of patients with benign intracranial hypertension, whereas no significant changes are seen in gray matter (Figure 9). Thus, it seems that the increased apparent diffusion coefficient of water in gray matter observed by Soelberg Sørensen et al.[28] can most likely be ascribed to pulsatile brain movements, which may be more pronounced in these patients than in healthy volunteers. Quantitative measurements of T_1 and T_2 of gray and white matter, respectively, show no differences between patients with benign intracranial hypertension and healthy volunteers.[28] In accordance with this, T_1- and T_2-weighted images do not show any abnormalities, indicating that quantitative diffusion imaging is much more sensitive to alterations in intra- and extracellular water balance and dynamics.

3.2.5 *Brain Edema*

Sevick et al.[29] have studied the influence of *cytotoxic edema* secondary to hyponatremia on the apparent diffusion

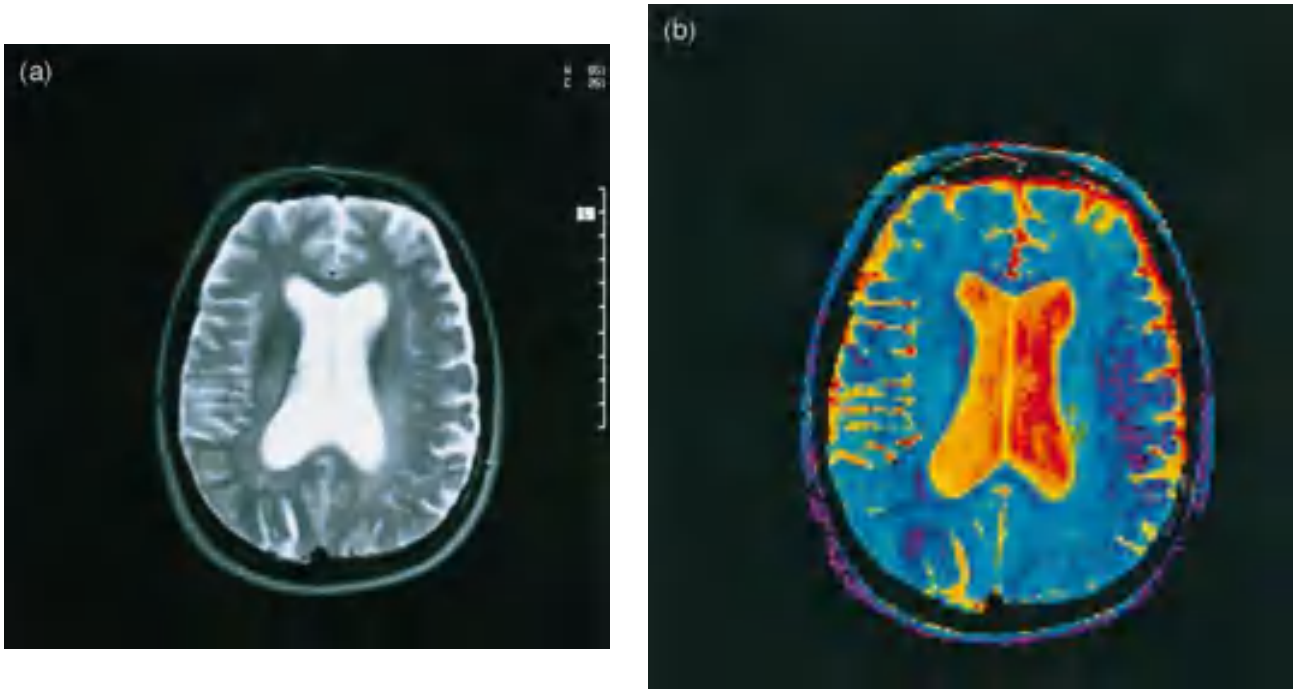

Figure 8 (a) T_2-weighted and (b) calculated apparent water diffusion coefficient images obtained from a patient with normal-pressure hydrocephalus. There is an increased diffusion in the periventricular white matter as compared with normal subjects. (Reproduced by permission from Gideon et al.[6])

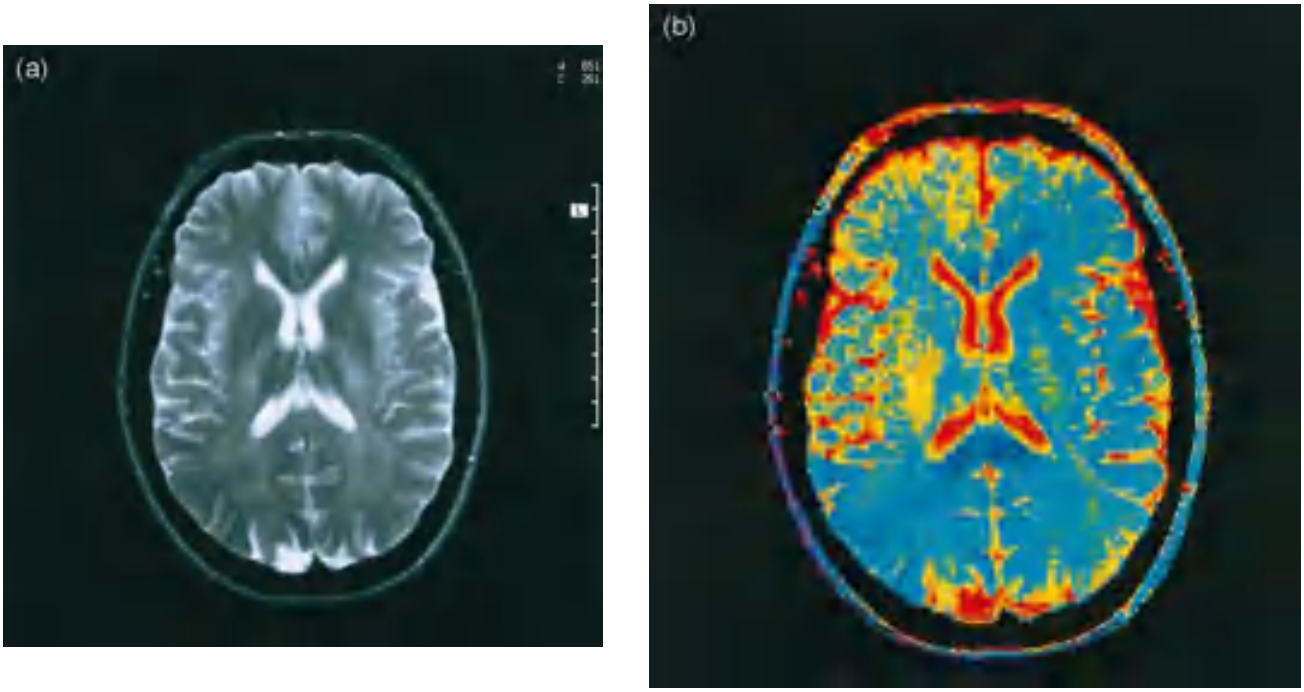

Figure 9 (a) T_2-weighted and (b) calculated apparent water diffusion coefficient images obtained in a patient with benign intracranial hypertension. Note the marked increase in D^* in the periventricular white matter in the diffusion images, whereas the T_2-weighted image appears normal. (Reproduced by permission from Gideon et al.[6])

coefficient of water in rat brain. The results suggest that cytotoxic edema reduces the apparent diffusion coefficient of water in the brain by about 10%, and there seems to be an inverse relationship between the calculated D^* value and the total water content of the brain tissue. It cannot, however, be totally excluded that the results may at least partly have been influenced by a concomitant reduction in pulsatile movements of the edematous brain, since no cardiac triggering or compensation for first order movements was performed. Anyway, the relatively small decrease in the apparent diffusion coefficient observed in cytotoxic brain edema does not explain the alterations seen in acute brain ischemia described in a previous section.

A number of studies indicate that the apparent diffusion coefficient of water is higher in tumor-induced *vasogenic brain edema* than in normal gray and white matter[13] (cf Figure 6).

Taken together, the preliminary evidence suggests that quantitative diffusion studies may make it possible to differentiate between cytotoxic (D^* reduced) and vasogenic brain edema (D^* increased).

3.2.6 Pediatric Disorders

The experience with diffusion studies of infants is very limited at present. Rutherford et al.[30] have recently published a study in which they examined 31 neonates and infants with various disorders of the brain. They did not calculate the apparent diffusion coefficient. *Cysts* and *fluid collections* are recognized by their hypointense signals, indicating an increase in the D^* value of water. Low signal intensities are seen in *chronic infarcts*, consistent with a relatively free isotropic diffusion, whereas the signals are low in *intracerebral hematomas*, suggesting restricted isotropic diffusion. Patients with *leukodystrophy* associated with congenital muscle dystrophy reveal an anisotropic diffusion pattern. In three cases, abnormalities can be seen in the diffusion-weighted images despite conventional imaging being normal. Finally, abnormalities in the corticospinal tract are frequently seen in children with a history of *birth asphyxia*.

Even though the retrospective character of the study does not allow any definite conclusions to be drawn, the results are very promising, indicating that diffusion studies may contribute to the diagnosis of a number of pediatric brain disorders. Before reaching that point, however, a large number of systematic studies with quantitative measurements of the apparent diffusion coefficient of water are warranted in order to interpret the signal changes which are seen in the diffusion-weighted images.

4 OTHER ORGANS

Only a very limited number of diffusion studies of organs other than the brain are available at present. The reason is that diffusion studies may be hampered by considerable gross movements of the organ, caused by respiration and arterial pulsation.

Evidence of anisotropic water diffusion has been obtained in *human skeletal muscle*. The apparent diffusion coefficients of water range from 1.1×10^{-9} to $1.5 \times 10^{-9}\,m^2\,s^{-1}$ perpendicular to and are about $2 \times 10^{-9}\,m^2\,s^{-1}$ parallel to the muscle fibers, giving an anisotropic ratio of about 0.7.[31,32]

The ability to map changes in tissue temperature noninvasively in vivo in been investigated in human skeletal muscle during hyperthermia.[33–35] Noninvasive mapping of tissue temperatures in vivo may offer great clinical potential in the control of hyperthermia therapy. The question is whether diffusion measurements as described above are sufficiently accurate and reproducible. A study by Morvan et al.[35] suggests that it is possible to measure temperature differences of approximately 2 °C. This approach should be compared with an alternative method where changes in resonance frequencies induced by alterations in tissue temperature are measured.[36] The latter method may turn out to be more sensitive and reproducible.

Preliminary studies indicate that it may be possible to obtain meaningful diffusion-weighted images of *human kidneys in vivo* by means of an ultrafast diffusion-sensitized echo planar imaging sequence.[37] It is much too early to speculate on the clinical significance, however, because water transport in the kidney is very complex. Furthermore, substantial sources of error due to motion have to be taken into account. Ultrafast techniques combined with breath holding may be a part of the solution.

5 DIFFUSION-WEIGHTED SPECTROSCOPY

Recent developments in localized spectroscopic techniques have made it possible to take advantage of chemical shift information to extend diffusion measurements to include molecules other than water. By means of ^{31}P spectroscopy it is possible to study the diffusion of various phosphorus compounds, including phosphocreatine, in skeletal muscle.[38] Diffusion characteristics of *N*-acetylaspartate, total creatine, and choline-containing compounds have been measured in anesthetized rat brain,[39] and recently also in human brain,[40] using a diffusion-sensitized localized proton spectroscopic sequence with water suppression. The calculated apparent diffusion coefficients (mean ± 1 SD) of *N*-acetylaspartate, choline-containing compounds, and total creatine in normal human brain are $(0.18 \pm 0.02) \times 10^{-9}$, $(0.13 \pm 0.03) \times 10^{-9}$, and $(0.15 \pm 0.03) \times 10^{-9}\,m^2\,s^{-1}$, respectively.[40]

Applications of diffusion-weighted spectroscopic techniques are very interesting because compounds which do not penetrate the cell membranes can be used to study the intracellular medium, including viscosity, cell dimensions, etc. At present, the drawback is relatively poor spatial resolution, which means that the calculated D^* values represent a weighted average of diffusion coefficients in a mixture of tissue types consisting of many different cell types.

6 CLINICAL UTILITY OF MRI DIFFUSION STUDIES: A GENERAL VIEW

Although clinical experience with diffusion imaging is rather limited, it is possible to outline some general trends with respect to clinical utility. So far the method has almost exclusively been applied to the brain, because problems due to movement can be dealt with, and secondly, the relatively high T_2 values make it possible to achieve a reasonable signal-to-noise ratio at the long echo times which are necessary in order to obtain sufficient diffusion sensitivity.

One of the most striking areas for the use of diffusion-weighted imaging is early visualization of brain ischemia. This will most likely have a great impact on treatment strategies, where success depends critically on a very early start to intervention. Further research is needed in order to evaluate the prognostic information of alterations in diffusion characteristics, with particular emphasis on questions related to the penumbra zones.[41,42] Studies on anisotropy during the course of infarction may give new information about pathophysiological mechanisms operating during severe brain ischemia.

Secondly, diffusion studies may contribute to tissue characterization in the brain and thus improve the specificity of MRI investigations, taking advantage of the information related to anisotropy. Such studies may contribute to the separation of solid tumors and edema, identification of fluid compartments, and maybe also to differentiation between cytotoxic and vasoactive edema. Quantitative diffusion imaging is very sensitive to subtle changes in water balance and viscosity, as observed in patients with benign intracranial hypertension, where imaging by all other imaging modalities, including radio isotope techniques, is normal.

Thirdly, it is most likely that diffusion studies will contribute significantly to the characterization of brain white matter disorders. Alterations in diffusion anisotropy may give information of lesions in specific nerve tracts. Quantitative measurements of the apparent diffusion coefficients may contribute, for example, to the differentiation between acute and chronic multiple sclerosis lesions.

Diffusion-weighted spectroscopy may offer unique information about specific molecules. The study of chemical compounds which do not penetrate cell membranes and other structures makes it possible to obtain information about cell dimensions, intracellular fluid viscosity, etc.

It is important to avoid errors due to motion in diffusion studies. Cardiac gating and compensating for first-order movements are mandatory unless single acquisition techniques such as echo planar imaging are used. Quantitative measurements of apparent diffusion coefficients in pathologies are needed in order to obtain the knowledge necessary for interpretating the diffusion-weighted images where the signal intensity is also influenced by proton density, and T_1 and T_2 relaxation.

Thus, diffusion-weighted imaging is a very challenging field which offers great potential for biomedical research and diagnosis. Systematic clinical studies are now required in order to define the clinical indications for diffusion-weighted imaging by magnetic resonance.

7 RELATED ARTICLES

Anisotropically Restricted Diffusion in MRI; Brain MRS of Infants and Children; Susceptibility and Diffusion Effects in NMR Microscopy.

8 REFERENCES

1. D. Greitz, R. Wirestam, A. Franck. B Nordell, C. Thomsen, and F. Ståhlberg. *Neuroradiol.*, 1992, **34**, 370.

2. H. B. W. Larsson, M. Stubgaard, C. Thomsen, and The Scandinavian Flow Group, *Proc. 9th Ann Mtg. Soc. Magn. Reson. Med.*, New York, 1990, p. 389.
3. D. Le Bihan, R. Turner, C. T. W. Moonen, and J. Pekar, *JMRI*, 1991, **1**, 7.
4. D. Chien, R. B. Buxton, K. K. Kwong, T. J. Brady, and B. R. Rosen, *J. Comput. Assist. Tomogr.*, 1990, **14**, 514.
5. D. Le Bihan, R. Turner, and P. Douek, and N. Patronas, *Am. J. Roentgenol.*, 1992, **159**, 591.
6. P. Gideon, C. Thomsen, and O. Henriksen, *JMRI*, **4**, 185.
7. P. Douek, R. Turner, J. Pekar, N. Patronas, and D. Le Bihan, *J. Comput. Assist. Tomogr.*, 1991, **15**, 923.
8. C. Thomsen, O. Henriksen, and P. Ring, *Acta Radiol.*, 1987, **28**, 353.
9. D. Le Bihan, E. Breton, D. Lallemand, P. Grenier, E. Cabanis, and M. Laval-Jeantet, *Radiology*, 1986, **161**, 375.
10. K. Harada, N. Funita, K. Sakurai, Y. Akai, S. Kim, N. Nakanishi, and T. Kozuka, *Proc. 9th Ann Mtg. Soc. Magn. Reson. Med.*, New York, 1990, 375.
11. T. L. Chenevert, J. A. Brunberg, and J. G. Pipe, *Radiology*, 1990, **177**, 401.
12. H. Sakuma, Y, Nomura, K. Takeda, T. Tagami, T. Nakagawa, Y, Tamagawa, Y Ishii, and T. Tsukamoto, *Radiology*, 1991, **180**, 229.
13. J. V. Hajnal, M. Doran, A. S. Hall, A. G. Collins, A. Oatridge, J. M. Pennock, I. R. Young, and G. M. Bydder, *J. Comput. Assist. Tomogr.*, 1991, **15**, 1.
14. M. E. Moseley, J. Kucharczyk, J. Mintorovitch, Y. Cohen, J. Kurhanewicz, N. Derugin, H. Asgari, and D. Norman, *Am. J. Neuroroentg.*, 1990, **11**, 423.
15. M. E. Moseley, Y. Cohen, J. Mintorovitch, L Chileuitt, H. Shimizu, J. Kucharczyk, M. F. Wendland, and P. R. Weinstein, *Magn. Reson. Med.*, 1990, **14**, 330.
16. N. van Bruggen, B. M. Cullen, M. D. King, M. Doran, S. R. Williams, D. G. Gadian, and J. E. Cremer, *Stroke*, 1992, **23**, 576.
17. M. Maeda, S. Itoh, H. Ide, T. Matsuda, H. Kobayashi, T. Kubota, and Y. Ishii, *Radiology*, 1993, **189**, 227.
18. A. L. Busza, K. L. Allen, M. D. King, N. van Bruggen, S. R. Williams, and D. G. Gadian, *Stroke*, 1992, **23**, 1602.
19. S. Warach, D. Chien, W. Li, M. Ronthal, and R. R. Edelman, *Neurology*, 1992, **42**, 1717.
20. D. Chien, K. K. Kwong, D. R. Gress, F. S. Buoanno, R. B. Buxton, and B. R. Rosen, *Am. J. Neuroroentg.*, 1992, **13**, 1097.
21. P. Christiansen, P. Gideon, C. Thomsen, M. Stubgaard, O. Henriksen, and H. B. W. Larsson, *Acta Neurol. Scand.*, 1993, **87**, 195.
22. H. B. W. Larsson, C. Thomsen, J. Frederiksen, M. Stubgaard, and O. Henriksen, *Magn. Reson. Imag.*, 1992, **10**, 7.
23. J. S. Tsuruda, W. M. Chew, M. E. Moseley, and D. Norman, *Am. J. Neuroroentg.*, 1990, **11**, 925.
24. J. S. Tsuruda, W. M. Chiew, M. E. Moseley, and D. Norman, *Magn. Reson. Med.* 1991, **19**, 316.
25. M. Maeda, Y. Kawamura, Y. Tamagawa, T. Matsuda, S. Itoh, H. Kimura, T. Iwasaki, N. Hayashi, K. Yamamoto, and Y. Ishii, *J. Comput. Assist. Tomogr.* 1992, **16**, 514.
26. P. Gideon, C. Thomsen, F. Ståhlberg, O. Henriksen, P. Soelberg Sørensen, and F. Gjerris, *Proc. XIth Ann Mtg. Soc. Magn. Reson. Med.*, Berlin, 1992, p. 1609.
27. P. Gideon, F. Ståhlberg, C. Thomsen, F. Gjerris, P. Soelberg Sørensen, and O. Henriksen, *Neuroradiology*, 1994, **36**, 210.
28. P. Soelberg Sørensen, C. Thomsen, F. Gjerris, J. Schmidt, L. Kjaer, and O. Henriksen, *Neurol. Research*, 1989, **11**, 160.
29. R. J. Sevick, F. Kanda, J. Mintorovitch, A. I. Arieff, J. Kucharczyk, J. S. Tsuruda, D. Norman, and M. E. Moseley, *Radiology*, 1992, **185**, 687.
30. M. A. Rutherford, F. M. Cowan, A. Y. Manzur, L. M. S. Dubowitz, J. M. Pennock, J. V. Hajnal, I. R. Young, and G. M. Bydder, *J. Comput. Assist. Tomogr.* 1991, **15**, 108.
31. M. E. Moseley and M. F. Wendland, *Proc. Xth Ann Mtg. Soc. Magn. Reson. Med.*, San Francisco, 1991, 108.
32. D. Morvan, A. Leroy-Willig, P. Jehenson, C. A. Cuenod, and A. Syrota, *Radiology*, 1992, **185**, 871.
33. D. Le Bihan, J. Delannoy, and R. L. Levin, *Radiology*, 1989, **171**, 853.
34. A. S. Hall, M. V. Prior, J. W. Hand, I. R. Young, and R. J. Dickinson, *J. Comput. Assist. Tomogr.*, 1990, **14**, 430.
35. D. Morvan, A. Leroy-Willig, A. Malgouyres, C. A. Cuenod, P. Jehenson, and A. Syrota, *Magn. Reson. Med.*, 1993, **29**, 371.
36. J. de Poorter, C. de Wagter, C. Thomsen, Y. de Deene, F. Stöhlberg, and E. Acten, *J. Magn. Reson.*, 1995, **33**(1), 74.
37. R. Turner, D. Le Bihan, J. Maier, R. Vavrek, and J. Baich, *Proc. 9th Ann Mtg. Soc. Magn. Reson. Med.*, New York, 1990, 1136.
38. C. T. W. Moonen, P. C. M. van Zijl, D. Le Bihan, and D. Des Pres, *Magn. Reson. Med.*, 1990, **13**, 467.
39. K.-D. Merboldt, D. Hörstermann, W. Hänicke, H. Bruhn, and J. Frahm, *Magn. Reson. Med.*, 1993, **29**, 125.
40. S. Posse, C. A. Cuenod, and D. Le Bihan, *Radiology*, 1993, **188**, 719.
41. M. J. Quast, N. C. Huang, G. R. Hillman, and T. A. Kent, *Magn. Reson. Imag.*, 1993, **11**, 465.
42. J. Seega and B. Elger, *Magn. Reson. Imag.*, 1993, **11**, 401.

Biographical Sketch

Ole Henriksen. *b* 1944. M.D., 1973. Specialist, Clinical Physiology and Nuclear Medicine, 1982. Doctor, Medical Science, 1977. Professor, MRI, 1990. Director, The Danish Research Center of Magnetic Resonance, 1985–present. Approx. 100 publications on MRI since 1985. Research interests are mainly in vivo studies of physiological and pathophysiological mechanisms in humans using MRI techniques including diffusion, flow perfusion, and spectroscopy measurements.

Methods and Applications of Diffusion MRI

Denis Le Bihan
Service Hospitalier Frédéric Joliot, CEA, Orsay, France

1 INTRODUCTION

Diffusion is the process by which matter is transported from one part of a system to another as a result of random molecular motion, also called Brownian motion. This motion, of thermal origin, results in the macroscopic flux of different molecular species, which can be observed in nonuniform systems and is characterized by a diffusion coefficient. Classically, diffusion coefficients may be determined by measuring the concentration of molecular species at different times using either physical or chemical methods based on the classical first Fick Law.[1] Such approaches rely on the introduction of a tracer in the medium, as similar as possible to the studied molecular species, and then monitoring the concentration of the tracer in the medium by chemical or radiotracer techniques.[2] Microscopic displacements on the scale of millimeters can be seen with such tracers over diffusion times of minutes. Such tracer methods have been successfully applied to biological systems, such as the brain[3] but are, of course, extremely invasive. An alternative in studying diffusion is to monitor the random walks of molecules. On a statistical scale, the diffusion reflects the mean-square distance traveled by molecules in a given interval of time ($m^2\ s^{-1}$). Diffusion NMR, which relies on these principles, is the only method today available to provide noninvasively such information on molecular displacements which occur over diffusion distances that extend largely beyond elementary molecular jumps, justifying the considerable success of diffusion NMR in physics and chemistry, and more recently in biology.[4] Taking typical values for water diffusion ~1×10^{-3} $mm^2\ s^{-1}$) and diffusion time (~20 ms) achievable on conventional MRI equipment free water molecules diffuse over distances on the order of 6 μm, which is about the size of many tissue structures. NMR has, in principle, a displacement sensitivity of around 100 nm.[5] Because of its noninvasive nature, it is especially suited to probing the molecular dynamics and structural information of biological systems, as well as transport processes. The recent combination of such principles with MRI[6–8] represents a spectacular and somewhat unpredicted development in the field of medical sciences. Measuring molecular displacements in biological tissues in vivo may have enormous value, from the determination of the molecular organization in tissues to the emergency management of stroke patients or the monitoring of laser surgery. In this chapter, the basic principles of diffusion measurements with NMR will be presented, as well as the various methods that have been proposed to produce images of diffusion. Some technical considerations will be discussed, followed by a description of the effects on diffusion measurements of microdynamic and microstructure in biological tissues. Emphasis will be given to the difficulties encountered when implementing diffusion imaging and the potential of diffusion measurements for clinical applications.

2 DIFFUSION MRI

Although the effects of diffusion on the NMR signal have been described very early,[9,10] most diffusion NMR studies started after the seminal work of Stejskal and Tanner, who introduced the bipolar pulse field gradient method (Figure 1).[11] This approach not only provides much better control over what is actually measured but also simplifies the understanding of the encoding of the diffusion process in the NMR signal. The purpose of these gradient pulses, the duration and the separation of which are classically represented, respectively, as δ and Δ, is to label spins carried by diffusing molecules magnetically. To some extent, these labeled spins are like the endogenous tracers that can be monitored with classical diffusion measurement tracer methods. However, the behavior of these labeled spins in an NMR experiment leads to more peculiar and specific results that are unique to diffusion NMR, and diffusion data obtained with NMR may not always be directly comparable with those obtained by other means.

The first gradient pulse induces a phase shift φ_1 of the spin transverse magnetization, which depends on the spin position z_1:

$$\varphi = \gamma G \delta z_1 \tag{1}$$

where γ is the gyromagnetic ratio and G is the gradient strength (here, along the z axis). After the 180° rf pulse, φ_1 is inverted to $-\varphi_1$. The second pulse will produce a phase shift φ_2:

$$\varphi_2 = \gamma G \delta z_2 \tag{2}$$

where z_2 is the spin position during the second pulse. The net transverse magnetization Mxy is:

$$Mxy/M_0 = \exp[\mathrm{i}(\varphi_2 - \varphi_1)] = \exp[\mathrm{i}\gamma G \delta (z_2 - z_1)] \tag{3}$$

where all relaxation effects have been incorporated into M_0.

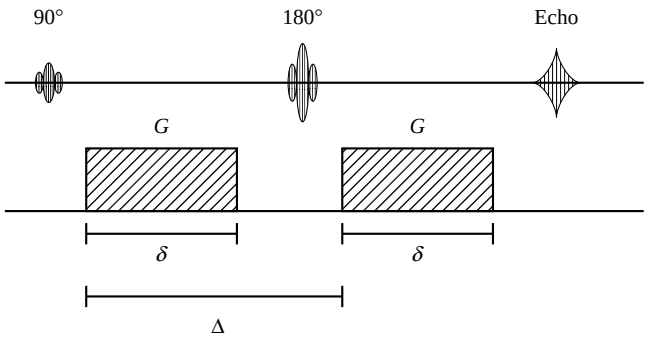

Figure 1 Stejskal and Tanner diffusion spin-echo sequence. Gradient pulses, G, are separated by a time interval Δ. Their duration is δ

For References see p. 16

Obviously for 'static' spins, z_1=z_2 and the bipolar gradient pair has no effect. For 'moving' spins, however, there is a net dephasing that will depend on the spin history during the time interval Δ between the pulses. Indeed, we must now consider a population of spins, which may have different motion histories. This leads to an attenuation of the *Mxy* and the resulting signal. Assuming δ<<Δ (negligible displacement during δ), these equations give a time-dependent part that represents the attenuation owing to diffusion, *A*:

$$A = \int \mathrm{d}\, z_1 P(z_1) \int \exp[\mathrm{i}\gamma\delta G(z_2 - z_1)] P(z_2, z_1, \Delta) \mathrm{d}\, z_2 \qquad (4)$$

where $P(z_1)$ is the probability for a labeled spin to be at initial position z_1 and $P(z_2, z_1, \Delta)$ is the diffusion propagator, i.e., $P(z_2, z_1, \Delta)\mathrm{d}z_2$ is the conditional probability to find a labeled spin initially at position z_1 in position z_2 after a time interval Δ. For a true, isotropic diffusion process:

$$\partial P(z_2, z_1, t)/\partial t = D\nabla^2 P(z_2, z_1, t) \qquad (5)$$

and *P* is Gaussian, at t=Δ:

$$P(z_2, z_1, \Delta) = (4\pi\Delta D)^{-1/2} \exp[-(z_2 - z_1)^2/4\Delta D] \qquad (6)$$

where *D* is the diffusion coefficient.

Combining Equations (1) and (2) gives:

$$A = \exp[-(\gamma\delta G)^2 \Delta D] \equiv \exp[-(\gamma\delta G)^2 \langle z^2 \rangle/2] \qquad (7)$$

where the root mean square diffusion displacement $\langle z^2 \rangle$ that occurred during the diffusion time Δ is easily interchangeable with *D* according to Einstein's equation, $\langle z^2 \rangle$=$2DT_\mathrm{d}$. Diffusion coefficients or root mean square diffusion distances are classically obtained by varying either *G* or δ and by measuring the slope of the semilogarithmic plot of the signal intensity versus $(\delta G)^2$. However, it is the diffusion path that the NMR experiment is actually sensitive to, not the diffusion coefficient. Therefore, in this simple bipolar gradient experiment, clear information on spin displacements can directly be obtained from the signal attenuation *A*, assuming *P* is Gaussian. This model is valid only for diffusion in an infinite and homogeneous medium. If diffusion is restricted or anisotropic (see below), the signal attenuation must be calculated using a more general formalism based on diffusion tensors.[12]

2.1 Diffusion and the NMR Signal: Different Approaches

Almost any NMR sequence can be designed to measure diffusion.

2.1.1 Constant Field Gradient Spin Echo Method

In the presence of a simple constant linear gradient G_0, the echo attenuation is:[9,10]

$$A(nTE) = \exp(-\gamma^2 G_0^2 DTE^3/12n) \qquad (8)$$

where *TE* is the echo time and *n* the echo number in a multiple echo experiment. This simple approach is difficult to combine with NMR imaging because the presence of a constant gradient during the rf pulses of the imaging sequence severely impairs the selected slice profile. In addition, the relaxation time T_2 of the medium must not be too short to allow enough diffusion attenuation to occur during *TE*.

2.1.2 Bipolar Gradient Pulse Spin Echo Technique

The bipolar gradient pulse spin echo technique is, by far, the sequence most widely used for NMR diffusion measurements. In practice, as δ is usually not negligible compared with Δ, movement during the application of the gradient pulses can no longer be neglected. Taking into account spin diffusion during δ, Equation (7) becomes:[11]

$$A = \exp[-\gamma^2 G^2 D\delta^2(\Delta - \delta/3)] \qquad (9)$$

The diffusion time can be formally defined as $(\Delta - \delta/3)$, but its physical significance is clear only when δ is sufficiently short compared with Δ. Tissues with short T_2 times require short *TE* values, which may not allow sufficiently long diffusion times to produce enough diffusion effects.

2.1.3 Stimulated Echo Technique

A stimulated echo is generated from a sequence consisting of three rf pulses separated by time intervals τ_1 and τ_2. Gradient pulses must be inserted within the first and the third periods of the stimulated echo sequence (Figure 2).

The diffusion time now includes τ_2 and can be much longer than with the spin echo sequence without T_2-related signal decay because only longitudinal relaxation occurs during this time interval. The Stejskal–Tanner relation [Equation (9)] still applies, provided that the period τ_2 is included in Δ.[13] The longer diffusion time is useful for studying very slow diffusion rates or for compensating for the unavailability of large gradients.[7] Unfortunately, the signal is reduced by 50% compared with the spin echo signal.

2.1.4 Gradient Echo Technique

The effect of diffusion on the amplitude of a gradient echo formed by a bipolar gradient pulse pair of reversed polarity does not differ from that of a spin echo sequence.[14] However, if the gradient echo is part of a steady-state free precession (SSFP) sequence, where some degree of phase coherence is

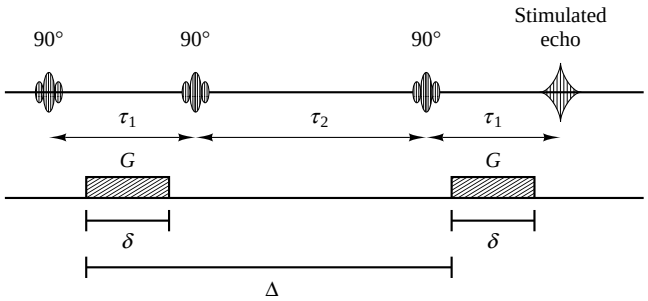

Figure 2 Diffusion-stimulated echo sequence. The stimulated echo results from the spin excitation by three rf pulses separated by time intervals τ_1 and τ_2. During τ_2, relaxation is driven by T_1 and not T_2. Diffusion effects can be enhanced by placing gradient pulses within the τ_1 periods, where transverse magnetization is sensitive to field inhomogeneities

propagated throughout successive cycles, multiple echo paths with different diffusion times and different diffusion weighting must be considered.[15] In MRI, the contrast-enhanced (CE-Fast) scheme has been proposed.[16–18] Unfortunately, this sequence remains very sensitive to motion artifacts.[19] Moreover, the effects of diffusion and relaxation are mingled so that diffusion measurements are always contaminated to some degree by relaxation effects.[20]

2.1.5 *Diffusion Measurements with $\boldsymbol{B}_1$ Field Gradients*

Diffusion measurements can also be achieved by means of the rf ($\boldsymbol{B}_1$) field produced by a NMR rf coil oriented perpendicularly to the main transmit/receive NMR coil.[21–24] With rf gradients, extremely short switching times can be achieved since there are no eddy currents. Furthermore, substantial gradient strength may be produced from the rf transmitter, allowing measurements of very low diffusion coefficients.

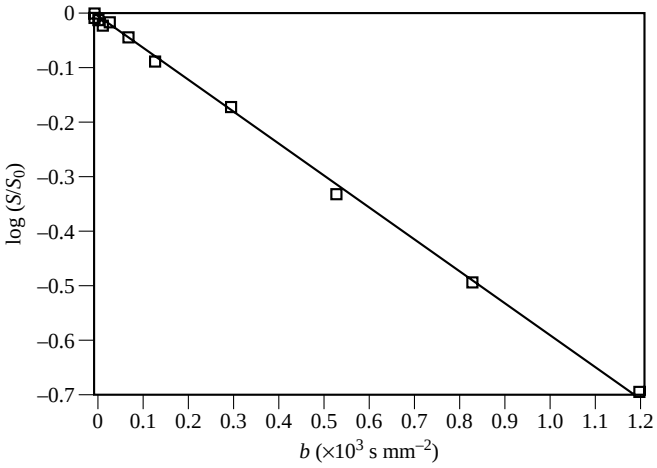

Figure 3 The relationship of the logarithm of the signal intensity in brain white matter with the gradient factor b is linear; the slope is equal to the diffusion coefficient D=0.60 (±0.01) 10^{-3} mm^2 s^{-1}

2.2 Combining Diffusion NMR with MRI

2.2.1 *Principles*

Diffusion-weighted (DW) images are obtained by inserting gradient pulses into any NMR imaging sequence. For quantification, it is necessary to determine the degree of diffusion weighting of the sequence. When inserting gradient pulses for diffusion, however, the combination of the imaging and the diffusion gradient pulses produces cross-terms. These cross-terms, which depend on the sequence design, may also lead to significant diffusion-related attenuation effects,[14,25] which must be taken into account; consequently the Stejskal–Tanner relation [Equation (9)] is incorrect in most cases. A more general formalism must then be developed to solve the Bloch–Torrey equation.[26] Solutions may become analytically complex,[27] and it has been suggested that all gradient effects should be combined in a term generally known as the 'b factor':[14,28]

$$b = \gamma^2 \int_0^{TE} \left[\int_0^t \boldsymbol{G}(t')\mathrm{d}\,t' \right]^2 \mathrm{d}\,t \qquad (10)$$

The signal attenuation for, unrestricted, isotropic diffusion is then reduced to a simple, convenient expression:

$$A = \exp(-bD) \qquad (11)$$

This b factor characterizes the diffusion sensitivity of the sequence, as TE characterizes the degree of T_2 weighting of a spin echo sequence. Without additional gradients, typical spin echo imaging sequences have intrinsically very low b values, typically less than 1 s mm^{-2}; consequently diffusion effects are negligible (for pure water at room temperature the attenuation is less than 1%).[14,29]

As the raw signal depends not only on diffusion but also on other MR parameters, such as T_1 or T_2, a quantitative determination of the diffusion coefficient requires at least two images acquired with different diffusion sensitivities (i.e., b factor values), but better accuracy is obtained when more than two images are used (see below). With the b factor values associated with each image, it is possible to compute diffusion images, i.e., images where the diffusion coefficient is determined for each pixel. The computation of such diffusion images is obtained by fitting the signal intensity of each pixel obtained for different b factor values with Equation (11)[4,6,7,14,28] using a regression analysis (Figure 3).

On diffusion images, diffusion values are displayed using a gray scale where brightness corresponds to high, fast diffusion and darkness to low, slow diffusion (Figure 4). To save on acquisition and processing time, some investigators have proposed to limit the diffusion studies to the analysis of the raw images obtained with some degree of diffusion sensitivity or weighting. For this reason, these images are called DW images. Contrast in these images is opposite to that found in true diffusion images: regions with high diffusion have more pronounced MRI signal attenuation and appear dark, while regions with low diffusion appear bright. The DW image may be convenient to use, but its content is affected by many parameters other than diffusion, as it is also usually strongly T_1 and T_2 weighted. As these parameters may not have the same behavior as diffusion, variations in image intensity may be difficult to interpret. For instance, acute stroke lesions have decreased diffusion (see below) and appear bright on DW images, while subacute infarcted areas, which are associated with increased diffusion, may also appear bright on DW images because T_2 has increased (T_2 'shine-through' effect). DW images may be convenient to use in clinical practice, but, whenever possible, absolute diffusion images should be preferred.

2.2.2 *Diffusion MRI Sequences*

Using the spin echo sequence, it is possible to vary the strength or the duration of the diffusion-sensitizing gradients or their direction in order to enhance anisotropic diffusion effects[14] (see below). The spin echo two-dimensional Fourier (2DFT) method is certainly the simplest to implement.[6,8,28,29] Other sequences[4] that have been investigated are stimulated echo sequences,[7] line-integral projection reconstruction,[30–32] variants of the SSFP technique; and 'turbo' sequences such as HASTE,[33] TurboFlash[34] and fast spin echo.[35] These schemes have been suggested to overcome, at least partially, some of the problems encountered with the spin echo 2DFT method.

For References see p. 16

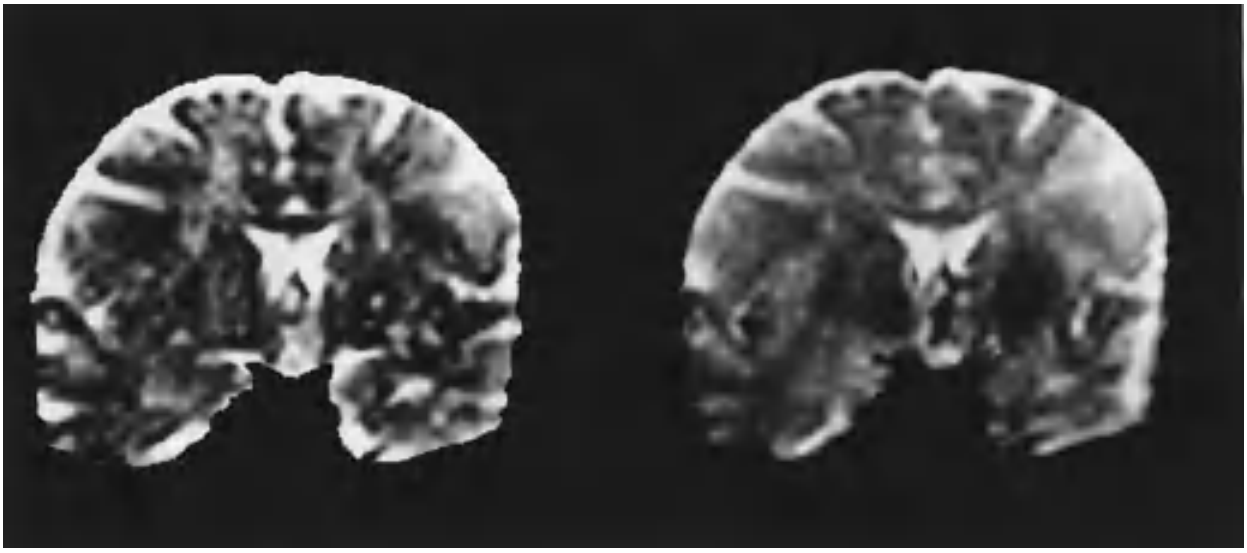

Figure 4 Diffusion image (left) calculated from a set of 16 diffusion-weighted coronal echo-planar images of the brain of a normal volunteer. These are 64×64 pixel images with a field of view of 16 cm and, therefore, an in-plane resolution of 2.5 mm $\times$ 2.5 mm. The section thickness was 10 mm. The diffusion gradients varied from 0 to 38 mT m^{-1} in the z direction; the duration of each lobe was 20 ms and their separation was 6 ms (b=0 to 872 s mm^{-2}). The acquisition time for each image was about 50 ms. Note that diffusion is the highest in ventricular cavities containing cerebrospinal fluid (free water). Because of diffusion anisotropy, diffusion along the x axis in corpus callosum is very low, while vertical frontal white matter tracts has the higher diffusion (see Table 1)

However, echo planar imaging (EPI) remains generally the imaging method of choice.[36–39] With EPI, the entire set of echoes needed to form an image is collected within a single acquisition period (single shot) of 25–100 ms. This is obtained by switching the echo signal formation in a train of gradient echoes by means of a large gradient in which polarity is very rapidly inverted as many times as is required to achieve the desired image resolution.[40] EPI may easily be sensitized to diffusion (Figure 5).[36–39]

Sensitization consists of providing a pair of large compensated gradients for a period of time before rapid gradient switching and data acquisition. The refocusing may be achieved either by simply reversing the polarity of the gradient halfway through the period over which it is applied or by inserting a 180° rf refocusing pulse at the midpoint without reversing the gradient polarity.

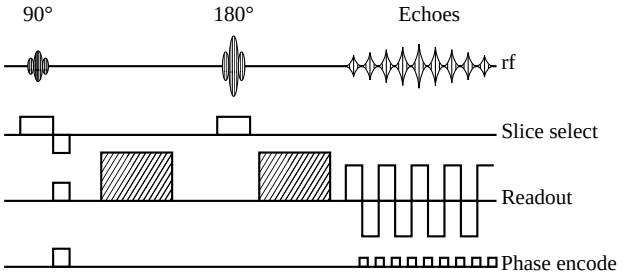

Figure 5 Diffusion echo planar imaging sequence. The spin echo is split into a series of gradient echoes by quickly switching the readout gradient. Sensitization to diffusion of an echo planar imaging sequence can be easily achieved by additional gradient pulses (dashed boxes)

With EPI, motion artifacts are virtually eliminated. The accuracy of assessments of diffusion achieved with EPI is generally extremely good, as many images differently sensitized to diffusion can be generated because of the very short acquisition time (typically less than 100 ms). The EPI technique is the method of choice for in vivo diffusion imaging, although it is very vulnerable to susceptibility artifacts, which are responsible for image distortion or signal dropout and to chemical shift artifacts, which require efficient fat suppression. Despite this, diffusion-EPI has become widely available on many clinical scanners and has been successfully used for measuring diffusion of water in the human brain in volunteers (Figure 4)[37,41] and patients (see below).

Recently, alternative fast acquisition schemes, such as BURST[42,43] and spiral MRI,[44] have been proposed to overcome some EPI artifacts, such as ghosting or susceptibility artifacts.

2.2.3 *Sequence Optimization*

Although the b factor can be exactly determined for any pulse sequence,[27,45] the diffusion time is impossible to define accurately for a MR sequence where gradient pulses of finite duration are scattered all over the pulse sequence. A mixture of diffusion-related events with differently weighted contributions are obtained depending on their sequence in time with respect to the many pulse gradients. That is why it has been suggested that the parameter derived from the NMR signal attenuation using Equation (7) should be called an 'apparent diffusion coefficient' (ADC).[28] MR sequences should be designed to minimize these problems, i.e., by placing gradient pulses to get as close as possible to the simple Stejskal–Tanner bipolar pulse sequence. However, the use of the ADC term remains justified,

as biological tissues usually differ significantly from the ideal 'free, unlimited, isotropic' medium.

Another issue is to optimize the values and the number of b factors to be used. A simple calculation[4] shows that the best accuracy for the diffusion coefficient is obtained from a set of two acquisitions if the two b factors, b_1 and b_2 differ by about $1/D$.[46] In the brain, this translates to (b_2-b_1)~1000 to 1500 s mm^{-2}. If more than two acquisitions are to be used, error propagation theory[47] shows that it is better to accumulate n_1 and n_2 measurements at each of the small and large b factors, b_1 and b_2, than to use a range of b factors. The accuracy dD/D can be obtained from the raw image signal-to-noise ratio (SNR):

$$\mathrm{d}D/D = [1/n_1 + \exp[2D(b_1 - b_2)]/n_2]^{1/2}/[(\mathrm{SNR})D(b_1 - b_2)] \quad (12)$$

Acquisition performed with linear sets of b value ranges remains, however, extremely useful to validate the sequence/hardware quality and to assess the nature of the diffusion process or the presence of multiple diffusion compartments as it allows the exponential diffusion attenuation to be visualized according to Equation (11).

2.3 Experimental Considerations in Diffusion MRI

2.3.1 Gradient Hardware

Since the minimum length of molecular diffusion paths detectable with gradient-pulsed NMR is primarily determined by the intensity of the gradient pulses, hardware must be capable of providing stable gradients of the utmost intensity.[48] This requirement may be extremely challenging when considering whole-body instruments designed for clinical studies. The lack of gradient power is usually compensated by using somewhat long gradient pulse widths; as a result, the classical condition $\delta \ll \Delta$ is not satisfied. The case of such finite pulse widths is significantly more difficult to treat and to interpret compared with the situation with δ-sharp pulses. If the duration of the pulses is ignored, significant underestimation of the diffusion distances may result.[49] For instance, to achieve at least a 20% signal attenuation and limit signal loss from transverse relaxation, the minimum diffusion coefficient $D_{\min}$ measurable is 37×10^{-3} mm^2 s^{-1} using $\delta=\Delta/10$, $\Delta=T_2=100$ ms, and $G_{\max}=10$ mT m^{-1}, which is more than 16 times the diffusion coefficient of free water![14] Maximum sensitivity is achieved when $\delta=\Delta$ (equivalent to a constant gradient) and $\Delta=T_2/2$. Then $D_{\min}$ is 0.4×10^{-3} mm^2 s^{-1}. There are partial solutions to this problem, such as using stimulated echoes to increase the effective diffusion time without penalizing the signal by T_2 relaxation effects,[13] or, better, by building high-performance gradient coils (e.g., up to 50, 100 or even 200 mT m^{-1}). Safety should not be too much a concern, considering that slew rates will remain low, as there is no need to switch such gradient coils very rapidly (which also limits eddy currents). Hence, diffusion effects during the application of the gradient pulses can no longer be neglected, although their contribution to the overall signal attenuation does not scale the same way with time as for diffusion occurring between pulses. The diffusion time then becomes more difficult to define, although $(\Delta-\delta/3)$ is often taken instead of Δ as the efficient diffusion time.[11]

Another concern is that any mismatch between the diffusion-sensitizing gradient pulses may cause artifactual signal losses through an improper spin rephasing. Two major sources of problem are commonly seen. One is gradient instability, which may arise when gradient amplifiers are driven hard for fast switching of large gradient intensities. Variations from shot to shot of the bipolar gradient balance result in widely distributed ghost artifacts. While such artifacts do not occur when a single-shot technique such as EPI is used, it is still essential to have high-quality gradient amplifiers with some reserve capacity for accurate diffusion imaging. The second problem results from eddy currents generated mainly in the cryostat when switching large gradient pulses rapidly. Eddy currents may also be a major cause of image distortion and misregistration between images obtained with different b values, leading to ADC miscalculation. The best solution to this problem is undoubtedly to remove eddy currents at the source by using actively shielded gradient coils, which have no fringe fields and, therefore, do not generate eddy currents. The use of a gradient coil of small dimensions, which remains at a fair distance from the magnet core and with which it is easier to generate large gradient amplitudes, is certainly an attracting alternative.[21] If residual eddy current effects persist, other approaches can be combined.[50–52]

In summary, there is clearly a need for very-high-performance gradient coils. With the hardware that is now becoming available,[53,54] shorter diffusion times or larger b values can be reached while maintaining high SNR, giving access to slow diffusion components (e.g., intracellular water, metabolites).

2.3.2 Motion Artifacts

As the sequences used are deliberately sensitized to motion by the addition of large gradients, a major problem occurring with in vivo imaging of diffusion arises from motion of the object. Artifacts result from discontinuities that occur between successive cycles of an imaging sequence. Results of such temporal incoherence are commonly visible as 'ghosts' along the phase-encoding direction. These ghosts are particularly intense in the presence of the diffusion gradients and render the diffusion measurements meaningless. Cardiac gating has been used to mitigate this problem, but even this motion is not strictly cyclic. It is difficult to compensate diffusion imaging sequences for motion, since the use of successive bipolar gradient pulses considerably reduces the value of the b factor.[4,14] Chenevert et al. have suggested eliminating any phase encoding from the acquisition by sacrificing one dimension of the image, which is then reduced to a single line.[55,56] Ultimately, however, the best way to avoid motion artifacts is to use a single-shot technique, such as EPI, and to secure patients comfortably within the magnet using cushions or inflating devices. In spite of this, motion artifacts may persist, especially when multiple shots are used, as with diffusion spectroscopy (see below) or segmented EPI. Motion effects can be estimated by monitoring the phase of the signal and corrected.[57,58] Navigator echoes have been used with some success by several investigators.[59–62]

For References see p. 16

2.3.3 Background Inhomogeneities

In addition to the magnetic field gradient pulses, residual field inhomogeneities arising from the imperfect shimming of the magnet and from inhomogeneities in the sample must be considered. These inhomogeneities result from susceptibility variations, especially at high field, and may not be negligible.[63] By adding a constant, linear gradient G_0, it is clear that two contributions of the residual gradients coexist.[11] One is a unique contribution (term in G_0^2); the other results from a cross-term between the residual and the applied gradients (GG_0 term).[14] While the first contribution can easily be eliminated from a series study where only G is varied, the second term is more difficult to handle. There are however, diffusion pulse sequences that have been designed to reduce significantly or to eliminate effects of background gradients.[64–70] Most of them are based on multiple rf pulses. For instance, cross-terms can be completely eliminated by alternating the gradient pulses between the successive 180° rf pulses of a quadrupole spin echo sequence.[71]

If cross-terms with the background gradients are not eliminated, the logarithm of A is no longer linear with the b factor and the ADC overestimates the true diffusion coefficient.[25] The ADC will, furthermore, appear as a function of the diffusion time. The examination of the linearity of the relationship between log A and b is therefore, the first step in interpreting any NMR diffusion study in biological tissues, although there are several possible causes that would explain a deviation from linearity. Notably, similar nonlinear behavior will be seen if the b factor is miscalculated, i.e., cross-terms coming from all applied (diffusion and imaging) gradient pulses are not appropriately considered in the calculation.[27] The b factor must be carefully calculated before the presence of background gradients can be assessed.

However, finding a linear plot for log A versus b does not exclude background gradients. First, the effect may be small. Second, the interpretation of the data may become very complicated when gradients are nonuniform or nonlinear and slowly varying in space, as in the case of capillaries filled with materials with a high susceptibility constant (e.g. contrast agent). Simulations and experiments have shown, in this case, that the ADC is decreased and that the parameter to consider is the variance of the internal gradients.[72,73]

The ultimate test to evaluate background gradients, however, is to vary TE while δ and Δ are kept constant. The measured ADC should normally be independent of TE. Otherwise, the contribution of background gradients must be suspected. Furthermore, as self-induced gradients may depend on the orientation of the sample with respect to the direction of $\boldsymbol{B}_0$, they may cause isotropic diffusion to appear anisotropic.[65] In this case also, the measured diffusion coefficient depends on the diffusion time.

Once it is established that background gradients are present, it may be desirable to estimate them from the attenuation behavior in order to obtain information on the structure of the medium. For instance, in the ideal case where the internal gradients result from inhomogeneities caused by the presence of closely packed particles, a rough estimation of the mean size R, of these particles can be obtained from:[74]

$$R \approx 6\chi_0 B_0 / G_0 \tag{13}$$

where χ_0 is the magnetic susceptibility constant. Furthermore, these susceptibility effects may be of biological interest,[75] as variations in the oxygenation level in brain capillaries and small vessels following brain activity have been shown to induce susceptibility effects measurable by T_2^*.[76,77] A significant drop of the measured ADC has also been observed during status epilepticus,[78] cortical electroshocks[79] and spreading depression.[80–82] In all cases, large increases in oxygenated blood flow could result in important reductions in local internal gradients and apparent variations to diffusion, although cytotoxic edema and cell swelling associated with energy failure has been mainly evoked as the reason for this diffusion drop.

2.4 Other Approaches to Diffusion

2.4.1 Diffusion Tensor Imaging

Diffusion is a three-dimensional process. However, the molecular mobility may not be the same in all directions. This anisotropy may be a result of the physical arrangement of the medium (liquid crystal) or the presence of obstacles that limit diffusion in some directions. The result is that the ADC appears different when pulse gradients are imposed in different directions; this has been observed in muscle[83] and, more recently, in brain white matter.[37,56,84]

The proper way to study anisotropic diffusion is to consider the diffusion tensor.[1,11] Diffusion is no longer characterized by a single scalar coefficient but by a tensor $\underline{\boldsymbol{D}}$, which fully describes molecular mobility along each axis and the correlation between these axes:

$$\underline{\boldsymbol{D}} = \begin{matrix} D_{xx} & D_{xy} & D_{xz} \\ D_{yx} & D_{yy} & D_{yz} \\ D_{zx} & D_{zy} & D_{zz} \end{matrix} \tag{14}$$

In the reference frame [x', y', z'] that coincides with the principal or main directions of diffusivity, the off-diagonal terms do not exist and the tensor is reduced only to its diagonal terms $D_{x'x'}$, $D_{y'y'}$, $D_{z'z'}$, which represent molecular mobility along axes x', y', and z', respectively. The echo attenuation then becomes:

$$A = \exp(-b_{x'x'}D_{x'x'} - b_{y'y'}D_{y'y'} - b_{z'z'}D_{z'z'}) \tag{15}$$

where b_{ii} are the elements of the $\underline{\boldsymbol{b}}$ matrix (which now replaces the b factor) expressed in the coordinates of this reference frame.

In practice, measurements are made in the reference frame [x, y, z] of the gradients, which usually does not coincide with that of the tissue. Therefore, one must also consider the coupling of the nondiagonal elements b_{ij} of the $\underline{\boldsymbol{b}}$ matrix with the nondiagonal terms D_{ij} ($i \neq j$), of the diffusion tensor (now expressed in the gradient frame), which reflect correlation between molecular displacements in perpendicular directions:[85]

$$A = \exp\left(-\sum_{i=x,y,z}\sum_{j=x,y,z} b_{ij}D_{ij}\right) \tag{16}$$

Calculation of the value of $\underline{\boldsymbol{b}}$ may quickly become very complicated when many gradient pulses are used,[45] however, the full

determination of the diffusion tensor is necessary to assess anisotropic diffusion properly and fully.

To determine the diffusion tensor, DW images are collected along several gradient directions. As the diffusion tensor must be symmetric, measurements along only six directions are mandatory (instead of nine), along with an image acquired without diffusion sensitivity (b=0). A typical set of gradient combinations that preserves uniform space sampling and similar b values along each direction is as follows (coefficients for gradient pulses along the x, y, z axes, normalized to a given amplitude, G):

$$[(1/\sqrt{2},0,1/\sqrt{2});(-1/\sqrt{2},0,1/\sqrt{2});(0,1/\sqrt{2},1/\sqrt{2});$$

$$(0,1/\sqrt{2},-1/\sqrt{2});(1/\sqrt{2},1/\sqrt{2},0);(-1/\sqrt{2},1\sqrt{2},0)]$$

This minimal set of images may be repeated for averaging, as the SNR may be low[12,85] In the case of 'axial symmetry', only four directions are necessary (tetrahedral encoding),[86] as suggested for the spine.[87] The acquisition time and the number of images to process is then reduced, but efforts should be made to collect data along as many directions in space as possible to avoid sampling direction biases for applications such as the determination of fiber orientation and gain in SNR (see below).[88] A second step is to estimate the D_{ij} values from the set of diffusion/orientation-weighted images, generally by multiple linear regression, using Equation (23) below. The final step is to determine the main direction of diffusivities in each voxel and the diffusion values associated with these directions. This is equivalent to determine the reference frame [x', y', z'] where the off-diagonal terms of $\boldsymbol{D}$ are null. This 'diagonalization' of the diffusion tensor provides 'eigen-vectors' and 'eigen-values', λ, which correspond, respectively, to the main diffusion directions and associated diffusivities,[12,85] (the eigen-diffusivities λ are not to be confused with the tortuosity factors; see below).

As it is difficult to display tensor data with images (multiple images would be necessary), the use of 'diffusion ellipsoids' has been proposed.[12,85] Ellipsoids are a three-dimensional representation of the diffusion distance covered in space by molecules in a given diffusion time (T_d). These ellipsoids, which can be displayed for each voxel of the image, are easily calculated from the eigen-diffusivities λ_1, λ_2, and λ_3 (corresponding to $D_{x'x'}$, $D_{y'y'}$, and $D_{z'z'}$):

$$x'^2/(2\lambda_1 T_d) + y'^2/(2\lambda_2 T_d) + z'^2/(2\lambda_3 T_d) = 1 \qquad (17)$$

where x', y', and z' refer to the frame of the main diffusion direction of the tensor. These eigen-diffusivities represent the unidimensional diffusion coefficients in the main directions of diffusivity of the medium. The main axis of the ellipsoid gives the main diffusion direction in the voxel (coinciding with the direction of the fibers), while the eccentricity of the ellipsoid provides information about the degree of anisotropy and its symmetry (isotropic diffusion would be seen as a sphere). The length of the ellipsoids in any direction in space is given by the diffusion distance covered in this direction. In other words, the ellipsoid can also be seen as the three-dimensional surface of constant mean squared displacement of the diffusing molecules.

Recent work has demonstrated the feasibility of diffusion tensor imaging (DTI) in animal models, as well as in the human brain.[41,86,89,90]

2.4.2 *The Diffusion Propagator and* q*-space Imaging*

In the case where diffusion deviates from the Gaussian model, as with restricted diffusion (see below), it becomes extremely difficult to get any meaningful information on molecular displacements from the measured NMR signals. The distribution of the propagator is no longer Gaussian; consequently the value obtained for the diffusion coefficient using Equation (11) may not necessarily properly reflect tissue structure of properties. Diffusion coefficients may become, in these conditions, meaningless. The main difficulty is that the medium structure is generally not known in detail and modeling is required. In particular, one must be cautious in the use of Fick's Law and derived relations. The probability distribution driven by the diffusion process (Equation (6)] may now significantly deviate from a Gaussian distribution; as a result the relationship between A and b is no longer exponential as would be expected from Equation (7). A successful analysis should, therefore, start from a reformulation of the probability distribution, taking into account the medium structure and particular boundary or limit conditions. Hence, more useful information may be obtained by directly inferring molecular displacements from the MR signal attenuation without going through a diffusion coefficient formulation. Molecular displacement profiles, or more exactly their probability density distribution, can be obtained using q-space imaging.[91,92] This does not differ, in principle, from diffusion imaging. Assuming $P(z_1)$ is homogeneous throughout the medium, Equation (4) can be rewritten by substituting the relative diffusion displacement z for (z_2-z_1) and by calling q the quantity $(\gamma\delta G)$ as:

$$A(q,\Delta) = \int \exp[iqz] P(z,\Delta)\,\mathrm{d}z \qquad (18)$$

It now appears that $P(z,\Delta)$ is just the Fourier transform of the attenuation $A(q,\Delta)$. By inverting Equation (15), direct and unequivocal data on molecular displacements can be obtained. In practice, data are collected for a series of different gradient strengths and an inverse Fourier transform is applied to the corresponding set of signal attenuation values. The experiment can be repeated with different values of Δ in order to characterize the probability distribution for different diffusion times.[93] With q-space imaging, a more comprehensive picture of the system under study is obtained than when using a unique ADC.[92] It then becomes straightforward to verify whether $P(z,\Delta)$ is a Gaussian distribution and to determine the value of the diffusion time when the value of $P(z,\Delta)$ may start to deviate from a Gaussian behavior, suggesting that molecules have reached another structural order in the medium, or to obtain the molecular displacement distribution in different conditions. Localized q-space imaging has been used, for instance, to obtain water-displacement profiles from normal and ischemic mouse brain, showing an increase of the fraction of molecules undergoing displacements of less than 10 μm.[94] Such findings are very useful for examining the microstructural changes occuring during acute brain ischemia (see below).

For References see p. 16

2.4.3 *Diffusion Spectroscopy*

Water may not be the most suitable molecule for diffusion measurements in biological tissues because of its ubiquity and the permeability of most tissue interfaces, such as membranes, to water molecules. Consequently, diffusion measurements of larger molecules that are more specific to a tissue or compartment appear to be more promising for tissue characterization. However, such measurements are technically more challenging, because of the low concentration of such molecules and their relatively low diffusion coefficients. Further, this requirement for signal averaging, and, therefore, long acquisition times, makes in vivo diffusion spectroscopy particularly sensitive to motion.[57,95]

Recent progress made in in vivo Fourier NMR spectroscopy allows the extension of diffusion measurements to molecules other than water. For a given species, the chemical shift can be used to determine independent diffusion coefficients of compounds in complex mixtures.[96] Diffusion of phosphocreatine, for instance can be studied by ^{31}P spectroscopy.[97,98] Phosphocreatine is a true intracellular space probe, in contrast to water, which diffuses across cell membranes; as a result it can be used to observe true restricted diffusion. Phosphocreatine may be used to provide unique information on the intracellular medium, such as viscosity or geometry. Similarly, diffusion of *N*-acetylaspartate (NAR) and *myo*-inositol may provide useful information on neuronal and glial cell populations, respectively. Monitoring of exchanges of metabolites or drugs through cell membranes could also benefit from diffusion filter techniques designed to separate intracellular from extracellular compounds.[99] Although diffusion coefficients of metabolites are low because of their size, for nuclear species with spin >1/2 or for coupled-spin systems, multiple quantum experiments are less demanding on gradient hardware because the effective gradient amplitudes are increased by the power of the coherence order (n). With n=2, a fourfold increase in the diffusion effect would occur. Such spectral editing techniques have been used for selective measurement of diffusion properties of *J*-coupled compounds such as lactate.[100,101]

3 DIFFUSION IN BIOLOGICAL SYSTEMS: EFFECTS OF MICRODYNAMICS AND MICROSTRUCTURE

Significant technical progress has been achieved in biological systems to ensure that meaningful data can be acquired with minimal artifacts. However, even in the ideal case with perfect data, the interpretation of diffusion NMR experiments performed in biological tissues remains challenging. The diffusion coefficient of water in tissues has been found to be two to ten times less than that of pure water (Table 1).[14] This can be largely understood by considering that water molecules are obliged to divert tortuously around obstructions presented by fibers, intracellular organelles, or macromolecules. Water molecules may be confined in bounded compartments or retained by attractive centers or surfaces. Biological systems, therefore, differ greatly from an 'infinitely large medium'. They are very heterogeneous and made of multiple subcompartments (microstructure). Depending on the permeability of the barriers that limit these compartments, exchanges and transport between them (microdynamics) may occur. A classic treatment of the NMR signal may not then reflect properly tissue structure or properties. Water molecules will 'sense' all these obstacles only if the time over which diffusion is measured is made sufficiently long that significant interaction of the water molecules with cellular compartments may occur. The concept of 'diffusion time' is, therefore, central to any diffusion study in biological tissues. While it may appear that using long diffusion times may reveal more tissue interactions, it is perhaps even more interesting to make the diffusion time as short as possible, up to the point where the diffusion coefficient will reach its value in pure water. By doing so, and plotting measured diffusion coefficients versus diffusion times, the many mechanisms contributing to in vivo diffusion may be revealed and identified. This approach, which will benefit from the newly developed gradient hardware allowing very large gradient strength, may be compared in some ways to that used in NMR dispersion studies, where multiple elementary relaxation mechanisms can be identified and separated by studying dispersion curves.[102] Diffusion coefficients may become, in these conditions, meaningless if the measurement time scale or the measurement direction are not provided.

Table 1 Diffusion Coefficients of Water in Human Brain

	Mean diffusivity (10^{-3} mm s^{-1})	Anisotropy (1−volume ratio)
Cerebrospinal fluid	3.19 ± 0.10	0.02 ± 0.01
Gray matter (frontal cortex)	0.83 ± 0.05	0.08 ± 0.05
Caudate nucleus	0.67 ± 0.02	0.08 ± 0.03
White matter		
Pyramidal tract	0.71 ± 0.04	0.93 ± 0.04
Corpus callosum (splenium)	0.69 ± 0.05	0.86 ± 0.05
Internal capsule	0.64 ± 0.03	0.70 ± 0.08
Centrum semiovale	0.65 ± 0.02	0.27 ± 0.03

Measurements (mean ± SD) were obtained in normal volunteers using diffusion tensor MRI. (With permission from Pierpaoli et al.[41])

The main difficulty is that the medium structure is generally unknown in detail. The issue is, therefore, to infer meaningful information on tissue from the measured NMR signals. Initially, this problem could be reversed to consider how known tissue features relevant to tissue microstructure and dynamics affect diffusion NMR signals. Diffusion NMR has been used to study fluid-filled porous media and derive information on microstructure (shape of the pore space) and fluid permeability (porosity).[103–105] It is clear that many of the questions addressed in those studies are relevant to diffusion measurements in biological media.[5] Differences in diffusion coefficient and available diffusion space can be used to distinguish compartments and exchanges between them.[99]

3.1 Effect of Temperature

The first obvious effect on diffusion is that of temperature, as diffusion directly results from the molecular thermal motion. The diffusion sensitivity to temperature is high, about 2.4% for 1°C change (Figure 6),[106,107] consequently temperature must be carefully controlled in diffusion MRI experiments. Based on the strong and unique relationship that exists between temperature and molecular diffusion, diffusion imaging has been proposed for the real-time and noninvasive monitoring of tem-

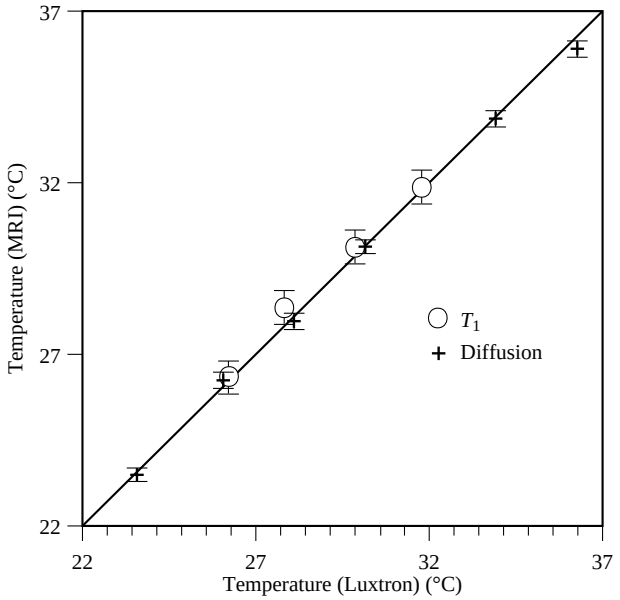

Figure 6 Comparison of temperature measurements using T_1 and diffusion MRI, and using probes (Luxtron) in a phantom. The accuracy was found to be 0.2°C with diffusion and 0.5°C with T_1

perature. Noninvasive and nondestructive temperature imaging in biological systems may be particularly useful to monitor hyperthermia treatments in real-time, whether using rf electrical fields[108] or focused ultrasound.[109,110] It could also be used to study and control tissue interactions in surgical and medical laser procedures. However, in the context of this chapter, the diffusion–temperature relationship also provides some indication about diffusion mechanisms in tissues.

This relationship has been established semi-empirically in liquids[1] and verified experimentally.[106,111]

$$D = D_0 \exp(-E_a/kT) \tag{19}$$

where k is the Boltzmann constant, T is the temperature, D_0 is the diffusion that would be obtained at an infinite temperature, and E_a is introduced as the translational diffusion activation energy, which is approximately equal to the energy required to break hydrogen bonds, both in pure water and in vivo (E_a=0.2 eV).[107,111]

This important result can be understood by considering that the mechanism at the molecular scale for water to move, and thus diffuse, involves continuous breaking and reforming of hydrogen bonds. The fact that E_a is identical for water molecules diffusing in vitro and in vivo is not really surprising as the laws of physics at this level should not be different.

3.2 Restricted Diffusion

Diffusion is restricted when boundaries in the medium prevent molecules from moving freely.[112,113] Restriction must be related to the experimental parameters. When measurement times are very short, most molecules do not have enough time to reach boundaries and so they behave as if diffusing freely. Once the diffusion time increases, an increasing fraction of molecules will strike the boundaries, and diffusion will deviate from the free, Gaussian behavior. Hence, the usual way to check for restricted diffusion is to plot the diffusion distance, calculated as for free diffusion using Einstein's equation, as a function of the square root of the diffusion time. In the case of restricted diffusion, this plot shows a curvature and finally a leveling off when the diffusion distance reaches the size of the restricting compartment. The effects of restriction will, therefore, appear in the NMR signal for diffusion times such that molecular displacements are in the order of the size of the restricting volumes. These effects will depend on the type of restriction (impermeable or permeable barriers, attractive centers, etc.), the shape of the restricting volumes (spherical, cylindrical, parallel walls, etc.), and the type of NMR experiment (constant or pulsed gradients). As a result, there is not a unique analytical expression that could describe any configuration. A simple example is represented by molecules diffusing between two impermeable parallel walls separated by a distance a.[112] If the theoretical, free diffusion distance greatly exceeds a, the echo attenuation A in the case of the bipolar gradient pulse experiment significantly deviates from an exponential decay and becomes independent of the diffusion time,[112] implying that molecules are trapped in the direction of the applied gradient:

$$A = [\sin(\gamma\delta G\, a/2)/(\gamma\delta G\, a/2)]^2 \tag{20}$$

Another interesting, but somewhat more complicated, case is represented by diffusion restricted in a spherical cavity of radius R_0. In the limit where the theoretical, free diffusion distance largely exceeds R_0, the attenuation is again independent of the diffusion time[112,114] and the measured ADC decreases when the diffusion time is increased:

$$A = \exp[-(\gamma\delta G)^2 R_0^2/5] \tag{21}$$

corresponding to an asymptotic ADC value, D_{asymp} of $R_0^2/5$. The factor 5 would be replaced by 3 if diffusion was confined to the surface of the sphere.

Whatever the geometry of the restrictive medium, the deviation from linearity in the semi-log plot of the signal attenuation versus b is crucial to determine whether diffusion is restricted, although other causes may be responsible, such as diffusion in inhomogeneous systems or anisotropic diffusion. The ultimate test is to show that the measured diffusion coefficient or the signal attenuation varies when the diffusion time is changed. Such studies can theoretically lead to the determination of the geometry and size of the restricting boundaries, as with the q-space concept. To avoid restricted diffusion effects, the diffusion time must be decreased to ensure that the diffusion distance during that period remains less than the size R of the restricted region. Unfortunately, the diffusion effect in these conditions becomes small unless considerable gradient intensities are used. A further complication is that in biological tissues walls may not be reflecting boundaries but rather occur as partially absorbing borders.[115]

3.3 Permeable Barriers

When the restrictive barriers become permeable to diffusing molecules, the restricted diffusion pattern changes. The mathematical treatment of diffusion in systems partitioned by

For References see p. 16

permeable barriers is far from simple. An example was given by Tanner for equally spaced, plane barriers having a permeability constant κ.[116] For short diffusion times, the ADC is D_0. When the diffusion time increases, the ADC decreases, as expected for restricted diffusion, but saturates at D_{asymp}, which depends on the permeability constant:

$$D_{\text{asymp}} = D_0/(1 + D_0/\kappa a) \qquad (22)$$

where a is the barrier spacing. This spacing can be estimated by the equivalent free diffusion distance that would be obtained from Einstein's equation with $D=(D_0+D_{\text{asymp}})/2$ as the diffusion coefficient and $T_{d_{1/2}}$, the corresponding diffusion time.[117] The plot of D versus T_d then shows a typical sigmoid pattern and it becomes possible to estimate the barrier permeability κ by fitting the data with Equation (22).[118] This approach is, however, very optimistic, as the geometrical arrangement of the medium is generally not known. In particular, this formalism does not apply to the case where the system consists of spherical cavities separated by permeable barriers.

3.4 Hindered Diffusion

True 'restricted' diffusion, which occurs in bounded media and leads to a decrease of diffusion with the diffusion time should be distinguished from 'hindered' diffusion. With hindered diffusion, diffusion is decreased by the presence of obstacles but there is no limit to the diffusion distance; consequently diffusion does not change with the diffusion time (once the hindered diffusion regime has been reached). Perhaps the most powerful concept associated with hindered diffusion is that of 'tortuosity', a concept that has been widely used in solid porous media studies and more recently in brain diffusion experiments using external tracers.[119–121] The idea is that because of the presence of obstacles such as fibers, macromolecules, and organelles water molecules must travel longer paths to cover any given distance. In other words, molecules can no longer go straight from A to B, but must diffuse around structures that are impermeable to them (Figure 7). This situation results in a longer diffusion time to diffuse from A to B, or to an apparent decrease in the diffusion distance covered in a given diffusion time and in the measured ADC. This 'hindered'

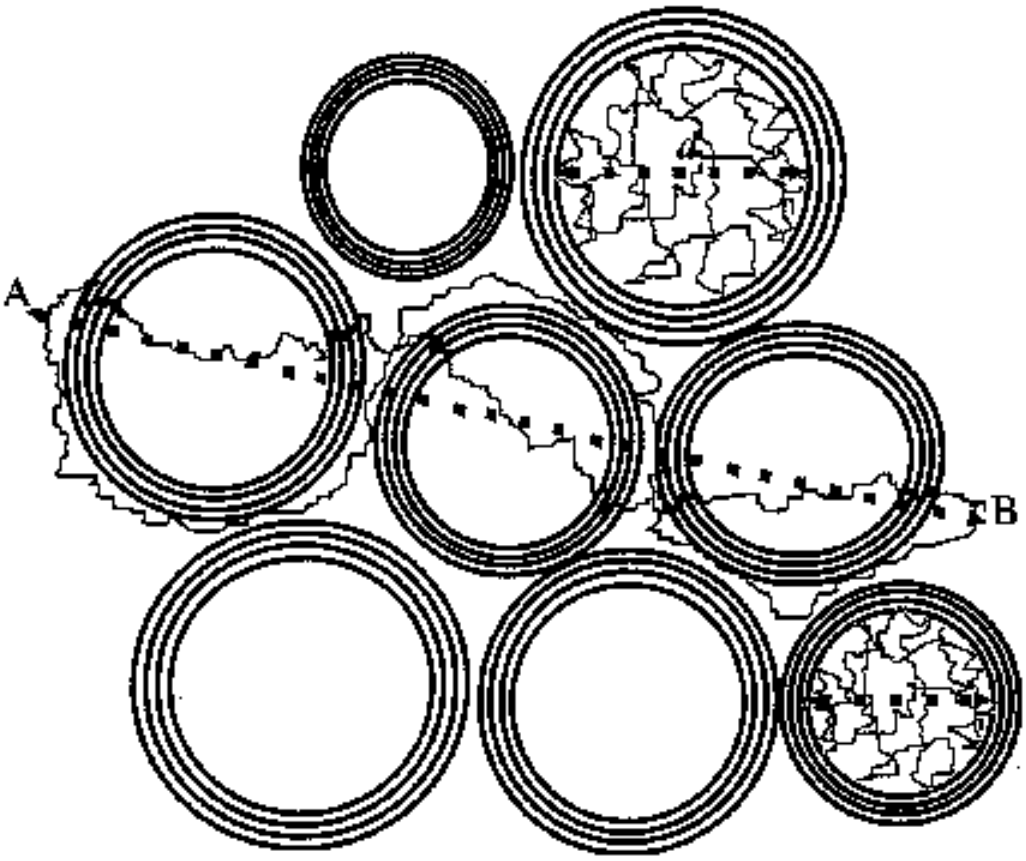

Figure 7 Restricted and hindered diffusion in white matter. Several models have been suggested to explain white matter diffusion anisotropy. First, diffusion may simply be totally restricted in axons (diameter, d). Plots of diffusion distance versus diffusion time (as in Figure 8, below) however, do not support this hypothesis. One may also take into account permeability of membranes and myelin to water. Going from A to B, water molecules would have to cross several interfaces. However, one may argue that those results may also be compatible with a 'tortuosity' or 'hindrance' model, where water molecules going from A to B would have to move around fibers. As there is no limit to diffusion, this model is totally compatible with Figure 8 if extracellular water diffusion predominates

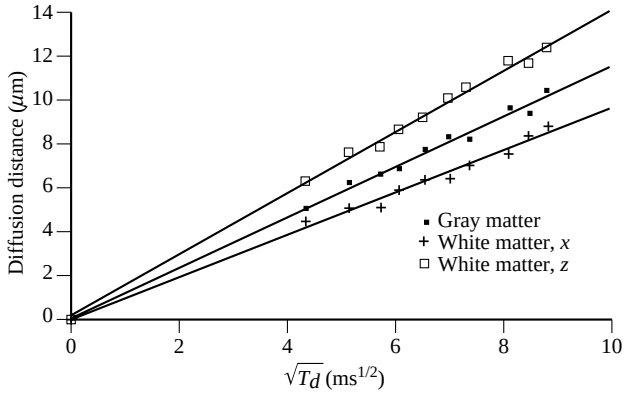

Figure 8 Plot of the diffusion distance against diffusion time in gray and white matter. The diffusion distance was obtained from the diffusion coefficient using Einstein's relation. There is no leveling off of the diffusion distance, suggesting that water diffusion is not completely restricted

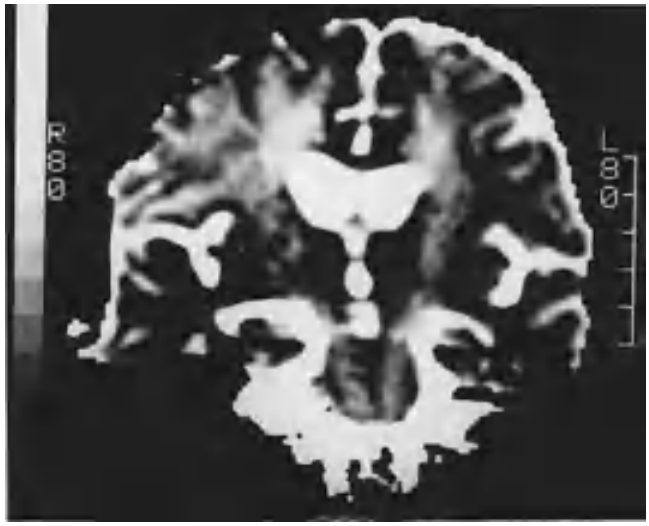

Figure 9 Diffusion image showing anisotropic diffusion in white matter. Excellent contrast is achieved, although T_1 and T_2 effects have been removed. Corpus callosum and temporal white matter fibers, which are horizontal, are dark. Vertical corona radiata frontal fibers and internal capsule fibers are bright. In brainstem, vertical fast-conducting motor and somatosensory tracts are also bright

diffusion effect is classically expressed quantitatively using a 'tortuosity' coefficient, λ, such that:

$$\mathrm{ADC} = D/\lambda^2 \tag{23}$$

where D would be the diffusion coefficient observed in the absence of obstacles.

Furthermore, as there is no real barrier, molecules can, in principle, diffuse over very large distances compared with those seen in restricted diffusion. Therefore, no curvature would be seen in the plot of the diffusion distance versus the square root of the diffusion time. Similarly, the measured ADC would not depend on the diffusion time, unless the diffusion time is very short, and hindered diffusion paths would not differ significantly from free diffusion paths (Figure 8). It would then be difficult to distinguish between hindered diffusion and diffusion restricted by permeable barriers.

3.5 Anisotropic Diffusion

Diffusion in tissues may be different for different directions of motion; this anisotropy will give rise to variations in the measured diffusion coefficient with the direction of measurement. Diffusion anisotropy has been observed in muscle,[83] in brain white matter,[37,56,84] (Figure 9) and, recently, in gray matter.[122,123] It may result from restriction of diffusion inside fibers (intracellular water) or from an increased tortuosity when diffusion occurs around fibers (extracellular water). Diffusion can be both anisotropic and unrestricted. This behavior is well known in nematic liquid crystals[124] and can be found in the water lamellar phase of amphiphilic lyotropic systems.[125]

Using DTI, it appears that diffusion data can be analyzed in three ways to provide information on tissue microstructure and architecture for each voxel or region of interest:[126] the mean diffusivity, which characterizes the overall mean-squared displacement of molecules (average ellipsoid size) and the overall presence of obstacles to diffusion; the degree of anisotropy, which describes how much molecular displacements vary in space (ellipsoid eccentricity) and is related to the presence of oriented structures; and the main direction of diffusivities (main ellipsoid axes), which is linked to the orientation in space of the structures. These three DTI 'meta-parameters' can all be derived from complete knowledge of the diffusion tensor. However because of the complexity of data acquisition and processing for full DTI, and the sensitivity to noise of the determination of the diffusion tensor eigen values, simplified approaches have been proposed.

3.5.1 *Mean Diffusivity*

To obtain an overall evaluation of the diffusion in a voxel or region, anisotropic diffusion effects must be avoided and the result limited to an 'invariant', i.e., a quantity that is independent of the orientation of the reference frame.[12,86] Among several combinations of the tensor elements, the trace of the diffusion tensor,

$$\mathrm{Tr}(\boldsymbol{D}) = D_{xx} + D_{yy} + D_{zz} \tag{24}$$

is such an invariant. The mean diffusivity is then given by $\mathrm{Tr}(\boldsymbol{D})/3$. A slightly different definition of the trace has proved useful in assessing the diffusion drop in brain ischemia[127] (see below).

Unfortunately, the correct estimation of $\mathrm{Tr}(\boldsymbol{D})$ still requires the complete determination of the diffusion tensor. Diffusion coefficients obtained by separately acquiring data with gradient pulses added along the x, y, and z axes cannot be used as these measured coefficients usually do not coincide with D_{xx}, D_{yy}, and D_{zz}, respectively. The reason is that the diffusion attenuation that results, for instance from inserting gradients on the x axis, is $A=\exp[-b_{xx}D_{xx}+2b_{xy}D_{xy}+2b_{xz}D_{xz}]$ and not simply $\exp[-b_{xx}D_{xx}]$ unless diffusion is isotropic (no nondiagonal terms) or there are no gradient pulses at all on the other axes (y and z, here) (no localization) during the diffusion measurement time.

For References see p. 16

To avoid this problem and to simplify the approach, several groups have designed sequences based on multiple echoes or acquisitions with tetrahedral gradient configurations to cancel nondiagonal term contributions to the MRI signal directly.[86,128–130]

3.5.2 *Diffusion Anisotropy Indices*

Several scalar indices have been proposed to characterize diffusion anisotropy. Initially, simple indices calculated from DW images[84] or ADC values obtained in perpendicular directions were used, such as ADC_x/ADC_y and displayed using a color,[131] scale. Other groups have devised indices mixing measurements along the x, y, and z directions, such as maximum [ADC_x, ADC_y, ADC_z]/minimum [ADC_x, ADC_y, ADC_z] or the standard deviation of ADC_x, ADC_y, and ADC_z divided by their mean value.[127] Unfortunately, none of these indices is really objective as they do not correspond to a single meaningful physical parameter; more importantly, they are clearly dependent on the choice of directions made for the measurements. The degree of anisotropy would then vary upon the respective orientation of the gradient hardware and the tissue frames of reference and would generally be underestimated. Here again invariant indices must be found to avoid such biases and provide objective, intrinsic structural information.[132]

Invariant indices are made of combinations of the terms of the diagonalized diffusion tensor, i.e., the eigen-values λ_1,λ_2, and λ_3. The most commonly used invariant indices are the relative anisotropy, RA, the fractional anisotropy, FA, and the volume ratio, VR:

$$\mathrm{RA} = \sqrt{(\lambda_1 - \langle\lambda\rangle)^2 + (\lambda_2 - \langle\lambda\rangle)^2 + (\lambda_3 - \langle\lambda\rangle)^2}/\sqrt{3\langle\lambda\rangle} \tag{25}$$

where $\langle\lambda\rangle = (\lambda_1 + \lambda_2 + \lambda_3)/3$

$$\mathrm{FA} = \sqrt{3[(\lambda_1 - \langle\lambda\rangle)^2 + (\lambda_2 - \langle\lambda\rangle)^2 + (\lambda_3 - \langle\lambda\rangle)^2]}/\sqrt{2(\lambda_1^2 + \lambda_2^2 + \lambda_3^2)} \tag{26}$$

$$\mathrm{VR} = \lambda_1\lambda_2\lambda_3/\langle\lambda\rangle^3 \tag{27}$$

RA, a normalized standard deviation, also represents the ratio of the anisotropic part of $\underline{\boldsymbol{D}}$ to its isotropic part. FA measures the fraction of the 'magnitude' of $\underline{\boldsymbol{D}}$ that can be ascribed to anisotropic diffusion. FA and RA vary between 0 (isotropic diffusion) and 1 ($\sqrt{2}$ for RA) (infinite anisotropy). As for VR, which represents the ratio of the ellipsoid volume to the volume of a sphere of radius $\langle\lambda\rangle$, its range is from 1 (isotropic diffusion) to 0; as a result some authors prefer to use (1−VR).[133]

Once these indices have been defined, it is possible to evaluate them directly from DW images, i.e., without the need to calculate the diffusion tensor.[134] For instance, A_σ which is very similar to RA, has been proposed as:[135]

$$A_\sigma = \sqrt{\sum_{i=x,y,z} (D_{ii} - \langle D\rangle)^2 + (D_{xy}^2 + D_{xz}^2 + D_{yz}^2/\sqrt{6}\langle D\rangle} \tag{28}$$

with $\langle D\rangle = \sum_{i=x,y,z} D_{ii}/3$.

For list of General Abbreviations see end-papers

Also, images directly sensitive to anisotropy indices, or anisotropically weighted images, can be obtained.[136] Finally, the concept of these *intravoxel* anisotropy indices can be extended to a family of *intervoxel* or 'lattice' measures of diffusion anisotropy, which allows neighboring voxels to be considered together, in a region of interest, without losing anisotropy effects resulting from different fiber orientations across voxels.[133] Clinically relevant images of anisotropy indices have been obtained in the human brain (Table 1).[41,137]

3.5.3 *Fiber Orientation Mapping*

The last family of parameters that can be extracted from the DTI concept relates to the mapping of the orientation in space of tissue structure. The assumption is that the direction of the fibers is colinear with the direction of the eigen-vector associated with the largest eigen-diffusivity. This approach opens a completely new way to obtain directly in vivo information on the organization in space of tissues such as muscle, myocardium, and brain or spine white matter, which is of considerable interest, clinically and functionally. Direction orientation can be derived from DTI directly from diffusion/orientation-weighted images or through the calculation of the diffusion tensor. A first issue is to display fiber orientation on a voxel-by-voxel basis. The use of color maps was first suggested,[131] followed by representation by ellipsoids,[12,133] octahedra[138] or vectors pointing in the fiber direction.[139,140] A second issue is to assess connectivity from DTI data in order to visualize anatomical connections between different parts of the brain on an individual basis. Studies of neuronal connectivity are tremendously important to the interpretation of functional MRI data and for establishing how activated foci are linked together through networks.[141,142] This issue is difficult, as continuity of fiber orientation from voxel to voxel has to be inferred. Fiber orientation may appear to be varying because of the occurrence of noise in the data. In a given voxel fibers may be merging, branching or dividing. In addition, several fascicles may cross in a given voxel, which cannot be detected with the diffusion-tensor approach in its present form. Structures that exhibit anisotropic diffusion at the molecular level can be isotropically oriented at the microscopic level, resulting in a 'powder average' effect that is difficult to resolve.[143] The semilog plot of the signal attenuation versus b may not be linear in this case.[125] This deviation from linearity can be ascribed to anisotropy and not to restricted diffusion because the diffusion measurements are independent of the diffusion time. Several groups have recently approached the difficult problem of inferring connectivity from DTI data in the rat brain[144] in vitro and in the living human brain[145] (Figure 10).

3.6 Diffusion in Multiple Compartment Systems

Most diffusion measurements in biological tissues refer to an ADC and yet it is generally considered that diffusion in the measurement volume (voxel) has a unique diffusion coefficient. This simplification may not always be legitimate, since partial volume effects may occur and most tissues are made of multiple subcompartments (with at least intracellular and extracellular components). Assuming measurement times are short and diffusion is unrestricted in each subcompartment i, and that there is no exchange, the signal attenuation is:

$$A = \sum_i \rho_i \exp(-bD_i) \tag{29}$$

where ρ_i is the density of molecules diffusing in compartment i, and D_i the associated diffusion coefficient. In this case, the ADC that would be measured would depend on the range used for the b values and would not reflect properly the diffusion in the voxel. Measurements with low b values would then be more sensitive to fast diffusion components. The ideal approach would be to separate all subcompartments by fitting the data with a multiexponential decay. Unfortunately, the values for D_i are often low and not very different from each other; consequently very large b values and very high SNR would be required.

Relaxation effects must also be considered if compartments have different relaxation rates.[146] If all spins do not have the same transverse relaxation during the pulse sequence, Equation

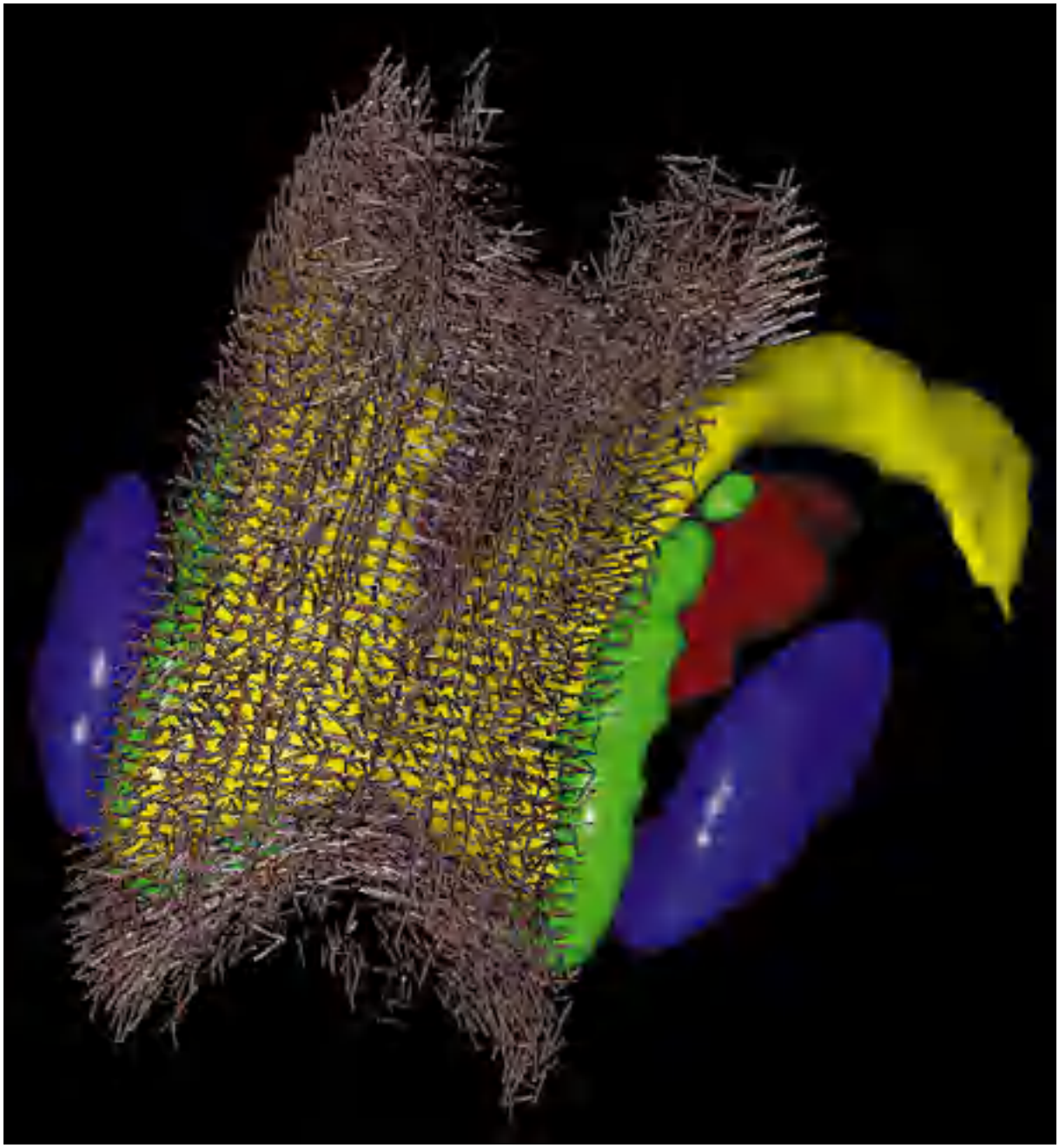

Figure 10 Diffusion tensor imaging and fiber orientation mapping in the brain of a normal volunteer at 1.5 T. The direction of the white matter fibers can be determined from the eigen vectors of the diffusion tensor for each voxel and superimposed on a 3D rendering of internal brain structures. (Contribution of J.F. Mangin, C. Clark, C. Poupon, D. Le Bihan)

For References see p. 16

(5) must be complemented with a decay term:[115]

$$\partial P(z_2, z_1 t)/\partial t = D\nabla^2 P(z_2, z_1 t) - P(z_2, z_1, t)/T_2 \qquad (30)$$

For two compartments, assuming measurement times are short and, therefore, exchanges are small, the diffusion signal is given by:

$$S = F_1 \exp(-bD_1) + F_2 \exp(-bD_2) \qquad (31)$$

where b is the sequence diffusion factor, D_1, D_2 are the diffusion coefficients and F_1, F_2 are relative weights to the signal of the two compartments. Estimates of F_1, F_2 and D_1, D_2 are obtained by fitting a series of signals acquired with multiple b values. For a spin echo sequence with $TR>>T_1$, F depends on the volume fraction f and the relaxation time T_2 of each compartment:

$$F = f \exp(-TE/T_2) \qquad (32)$$

Two diffusion compartments have been found in the rat brain.[147] Assignment of these compartments to extra- and intracellular water is not, however, straightforward, as the values found for F_1 and F_2 are apparently opposite to the known volume fractions for the intra- and extracellular spaces (82.5% and 17.5%, respectively). A first explanation for this discrepancy is that T_2 effects must be taken into account when converting F values into f values. A second factor is that the exchange rate may not be negligible. It has been shown that if the residence rate in each compartment is considered, the contribution of the fast diffusing component is overestimated.[148] It is, therefore, not yet certain that the two compartments that have been observed do correspond to the intra- and extracellular compartments.

The situation is even more complex when measurement times are longer. First, restricted diffusion may be seen in the smallest subcompartments. Second, molecular exchanges may occur between communicating compartments. As a result, the analytic treatment becomes difficult. Applying the central limit theorem for statistically distributed compartments in the case of long diffusion times, the use of a single apparent diffusion constant D_a can be justified:

$$D_a = \sum_i \rho_i D_i \qquad (33)$$

This result is also consistent with NMR dispersion studies,[102] which consider that cell membranes can be ignored on the NMR time scale. In intermediate situations, the geometrical arrangement and the diffusion coefficients of each compartment must be considered as well as their rates of exchange.[149] The comprehensive analysis of the diffusion attenuation curves obtained with different diffusion times may lead to an accurate description of the medium microstructure.

It is clear that the ADC depends on the range used for the b values and would not reflect properly diffusion in the tissue. Measurements with low b values (less than 1000 s mm^{-2}) would be more sensitive to fast diffusion components, such as those occurring in the extracellular compartment. In clinical studies and most animal experiments, especially when data are fitted to a single exponential, diffusion patterns observed in tissues have to be explained by features of the extracellular space, although this compartment is physically small. Changes in the ADC calculated in these conditions should be interpreted in terms of changes in the diffusion coefficient of the extracellular space (tortuosity) and in its fractional volume relative to the intracellular volume. This explains why diffusion has appeared as a sensitive marker of the changes in the extracellular/intracellular volume ratio, as observed in brain ischemia, spreading depression,[80–82] status epilepticus,[78] or extraphysiological manipulations of the cell size through osmotic agents.[150] Using large b values, it becomes increasingly possible to assess separately the intra- and extracellular compartments and their relative volumes in vitro[151] and in vivo, as attempted in the rat brain[147] and the human brain.[152]

3.7 Metabolites

Data on magnitudes and even directional anisotropy of diffusion coefficients of molecules such as choline, creatine/phosphocreatine and NAA in animals,[97,153,154] and human brain[95] have been made available. Although diffusion rates of metabolites in pure water are lower than that of water because of the difference in molecular weight and hydration layers, the ADC values of these metabolites in brain are considerably smaller. Typical values from a series of 10 normal volunteers (18 cm^3 voxels located in white matter, diffusion time 240 ms) are 0.13×10^{-3} mm^2 s^{-1} for choline and creatine and 0.18×10^{-3} mm^2 s^{-1} for NAA compared with 1.24×10^{-3} mm^2 s^{-1} for choline and 0.85×10^{-3} mm^2 s^{-1} for NAA at 35°C in vitro.[155] The fact that metabolites, as well as molecules such as fluorodeoxyglucose 6-phosphate,[156] with different molecular weights had very similar ADC values in vivo is striking and remains to be explained. The very low values of the ADC obtained with long diffusion times are, of course, compatible with restriction of these metabolites in compartments that were about the same size. For instance, recent experiments varying the diffusion times have shown that diffusion of NAA is considerably restricted in a manner compatible with two compartments, one of 7–8 μm and one of approximately 1 μm, possibly representing the cell bodies and the intra-axonal space.[157] However, intracellular obstacles may also play an important role, as water molecules could diffuse easily in small spaces between small obstacles, such as mitochondria, organelles or macromolecules, while larger metabolites would 'feel' a more obstructed medium. Tortuosity factors may, therefore, be larger for metabolites than for water and this would explain, at least partially, the diffusion decrease for intracellular metabolites that has been observed during ischemia.[158,159]

3.8 Summary: Application to Brain White Matter

The concepts of restriction, hindrance, tortuosity, and multiple compartments are particularly useful to understand diffusion findings in brain white matter. Water diffusion is highly anisotropic in white matter[37,56,84] and this anisotropy is observed even before fibers are myelinated, though at a lesser degree.[137,160–166] ADC values obtained by measurements made parallel and perpendicularly to the fibers do not seem to depend on the diffusion time[167,168] at least for diffusion times longer than 20 ms (see Figure 8).

Initial reports suggested that the anisotropic water diffusion could be explained by restriction of the water molecules to the axons (anisotropically restricted diffusion) by the myelin sheath.[169,170] However, although restricted diffusion has been seen for intra-axonal metabolites, such as NAA, or for truly intra-axonal water,[171] it now appears that most studies were performed with relatively low b values and are mostly sensitive to the extracellular, interaxonal space. In this condition, diffusion anisotropy in white matter should be linked to the anisotropic tortuosity of the interstitial space between the fibers: diffusion would be more impeded perpendicular to the fibers because of their geometric arrangement (Figure 7).[167]

Considering a bundle where fibers are organized in the most compact way, molecules would have to actually travel over a distance of $\pi d/2$, where d is the fiber diameter, for an apparent diffusion distance equal to the fiber diameter. Therefore, on average, the ADC measured perpendicularly to the fibers would be reduced, whatever the diffusion time, to:

$$\mathrm{ADC} = (2/\pi)^2 D_0 \approx 0.4 D_0 \qquad (34)$$

where the reference value, D_0, is the diffusion value measured parallel to the fibers. This ratio of about 0.4 fits reasonably very well with literature data,[167] although much larger ratios have been reported.[133] This rough model also implies that the tortuosity factor would be anisotropic in white matter with a $\lambda_{\mathrm{perpendicular}}/\lambda_{\mathrm{parallel}}$ ratio of $\pi/2$ (≈ 1.15). Unfortunately no systematic measurements of λ have yet been made in white matter using ionic extracellular tracers,[2,119] although anisotropy has been seen.[172] Another interesting point about this model is that it is compatible with the fact that no true restricted effects are observed when the diffusion time is increased, as there are no actual boundaries to diffusing molecules. Also, the parallel organization of the fibers may be sufficient to explain the presence of anisotropy before myelination. However, as the axonal membranes should be more permeable to water than the myelin sheaths, the degree of anisotropy should be less pronounced in the absence of myelin, as significant exchanges with the axonal spaces should occur. Oriented filaments within the axoplasm do not seem to play an important role.[173] Fiber orientation mapping and connectivity studies derived from anisotropic diffusion in white matter will clearly benefit from a better understanding of the respective contributions of intra-axonal and extra-axonal compartments to anisotropy mechanisms.[174]

4 CLINICAL APPLICATIONS

Diffusion imaging is a truly quantitative method. The diffusion coefficient is a physical parameter that directly reflects the physical properties of the tissues in terms of the random translational movement of the molecules under study (most often water molecules, but sometimes metabolites. The diffusion coefficient does not depend on the field strength of the magnet or the pulse sequence used, which is not the case for the other classical MRI parameters such as T_1 or T_2. Diffusion coefficients obtained at different times in a given patient, or in different patients, or in different hospitals can be compared without any need for normalization.

4.1 Central Nervous System

The most clinically relevant field of application of diffusion MRI is in the nervous system. Diffusion MRI has already appeared as a breakthrough in two areas: early brain ischemia and white matter diseases.

During the acute stage of brain ischemia, water diffusion is decreased in the ischemic territory by as much as 50%, as shown in cat brain models.[175] This diffusion slowdown is linked to the cytotoxic edema that results from the energetic failure of the cellular membrane Na^+/K^+ pumping system. The exact mechanism by which diffusion is reduced is still unclear (increase of the slow-diffusion intracellular volume fraction, changes in membrane permeability,[176] or shrinkage of the extracellular space resulting in increased tortuosity for water molecules.[177,178] have been suggested). Diffusion MRI has been extensively used in animal models to establish and test new therapeutic approaches. These results have been confirmed in patients with stroke, offering the potential to highlight ischemic regions within the first hours of the ischemic event, when brain tissue might still be salvageable,[179,180] well before conventional MRI becomes abnormal (vasogenic edema). Combined with perfusion MRI, diffusion MRI is under clinical evaluation as a tool to help clinicians to optimize their therapeutic approach to individual patients,[181] to monitor patient progress on an objective basis, and to predict clinical outcome.[182–185]

In white matter, DTI has already shown its potential in diseases such as multiple sclerosis[186–188] leukoencephalopathy,[189] Wallerian degeneration, Alzheimer disease,[190,191] and Creutzfeld–Jacob disease.[192–194] Mean diffusivity indices, such as the trace of the diffusion tensor, reflect overall water content, while anisotropy indices indicate myelin fiber integrity. It has been shown that the degree of diffusion anisotropy in white matter increases during the myelination process,[137,162,195] and diffusion MRI could be used to assess brain maturation in children,[196] newborns, or premature babies.[137,197] Abnormal connectivity in frontal white matter based on DTI data has also been reported in schizophrenic patients.[198] The potential of diffusion MRI has also been studied in brain tumor grading,[199–201] trauma,[202] hypertensive hydrocephalus,[203] AIDS,[204] eclampsia,[205] leukoaraiosis,[206,207] and the spinal cord.[87,185,208,209]

4.2 Body

The use of diffusion imaging has been less successful in areas of the body apart from the brain because of the occurrence of strong respiratory motion artifacts and of the short T_2 values of body tissues, which require shorter TE than in the brain and, therefore, leaves less room for the diffusion gradient pulses. These obstacles, however, can sometimes be overcome with ad hoc MR sequences and hardware. Potential for tissue characterization has been shown in the extremity muscles,[210] the spine,[211,212] the breast,[54,213,214] the kidney, and the liver.[215–218] Muscle fiber orientation can be approached using DTI in organs such as the tongue[219] or the heart. Myocardium DTI[220,221] has tremendous potential for providing data on heart contractility, a very important parameter, but remains technically very challenging to perform in vivo because of heart motion. Other applications include temperature imaging

For References see p. 16

through the sensitivity of diffusion coefficients to temperature.[107,108,210,222]

5 CONCLUSION

Many tissue features at the microscopic level may influence NMR diffusion measurements. So far, many theoretical analyses of the effect of restriction, membrane permeability, hindrance, anisotropy, or tissue inhomogeneity have been published. These analyses underline how much care is necessary to conduct diffusion NMR studies properly and to interpret the results. Although the results of these analyses have been applied to characterize nonliving systems, such as porous media, much work remains to be done to produce accurate information on microstructure and microdynamics in vivo in biological systems. Powerful tools, such as diffusion spectroscopy of metabolites, DTI or *q*-space imaging, that are still under development are expected to provide such information.

6 RELATED ARTICLES

Anisotropically Restricted Diffusion in MRI; Diffusion: Clinical Utility of MRI Studies; Ischemic Stroke; Male Pelvis Studies Using MRI.

7 REFERENCES

1. W. Jost, 'Diffusion in Solids, Liquids and Gases', Academic Press, San Diego, 1960.
2. C. Nicholson, 'Diffusion and Perfusion Magnetic Resonance Imaging. Applications to Functional MRI', ed. D. Le Bihan, Raven Press, New York, 1995, p. 127
3. O. B. Paulson, M. M. Hertz, T. G. Bolwig, and N. A. Lassen, *Microvasc. Res.*, 1977, **13**, 113.
4. D. Le Bihan (ed.), 'Diffusion and Perfusion Magnetic Resonance Imaging. Applications to Functional MRI', Raven Press, New York, 1995.
5. P. T. Callaghan, 'Principles of Nuclear Magnetic Resonance Microscopy', Oxford University Press, Oxford, 1991.
6. D. Le Bihan and E. Breton, *C. R. Acad. Sci. Paris, Series II*, 1985, **T.301**, 1109.
7. K. D. Merboldt, W. Hanicke, and J. Frahn, *J. Magn. Reson.*, 1985, **64**, 479.
8. D. G. Taylor and M. C. Bushell, *Phys. Med. Biol.*, 1985, **30**, 345.
9. E. L. Hahn, *Phys. Rev.*, 1950, **80**, 580.
10. H. Y. Carr and E. M. Purcell, *Phys. Rev.*, 1954, **94**, 630.
11. E. O. Stejskal and J. E. Tanner, *J. Chem. Phys.*, 1965, **42**, 288.
12. P. J. Basser, J. Mattiello, and D. Le Bihan, *Biophys. J.*, 1994, **66**, 259.
13. J. E. Tanner, *J. Chem. Phys.*, 1970, **52**, 2523.
14. D. Le Bihan, *Magn. Reson. Q.*, 1991, **7**, 1.
15. R. Kaiser, E. Bartholdi, and R. R. Ernst, *J. Chem. Phys.*, 1974, **60**, 2966.
16. D. Le Bihan, *Magn. Reson. Med.*, 1988, **7**, 346.
17. D. Le Bihan, R. Turner, and J. R. MacFall, *Magn. Reson. Med.*, 1989, **10**, 324.
18. K. D. Merboldt, W. Hanicke, M. L. Gyngell, J. Frahm, and H. Bruhn, *J. Magn. Reson.*, 1989, **82**, 115.
19. K. D. Merboldt, H. Bruhn, J. Frahm, M. L. Gyngell, W. Hanicke, and M. Deimling, *Magn. Reson. Med.*, 1989, **9**, 423.
20. E. X. Wu and R. B. Buxton, *J. Magn. Reson.*, 1990, **90**, 243.
21. D. Canet, B. Diter, A. Belmajdoub, J. Braondeau, J. C. Boubel, and K. Elbayed, *J. Magn. Reson.*, 1989, **81**, 1.
22. G. S. Karczmar, D. B. Twieg, T. J. Lawry, and M. W. Weiner, *Magn. Reson. Med.*, 1988, **7**, 111.
23. F. Humbert, M. Valtier, A. Retournard, and D. Canet, *J. Magn. Reson.*, 1998, **134**, 245.
24. F. Humbert, B. Diter, and D. Canet, *J. Magn. Reson.*, 1996, **A123**, 242.
25. M. Neeman, J. P. Freyer, and L. O. Sillerud, *J. Magn. Reson.*, 1990, **90**, 303.
26. H. C. Torrey, *Phys. Rev.*, 1965, **104**, 563.
27. J. Mattiello, P. J. Basser, and D. Le Bihan, *J. Magn. Reson.*, 1994, **108**, 131.
28. D. Le Bihan, E. Breton, D. Lallemand, P. Grenier, and E. A. Cabanis, *Radiology*, 1986, **161**, 401.
29. G. A. Ojemann, *J. Neurosci.*, 1991, **11**, 2281.
30. R. V. Mulkern and R. G. S. Spencer, *Magn. Reson. Imag.*, 1988, **6**, 623.
31. H. Gubjartsson, S. E. Maier, and F. A. Jolesz, *Magn. Reson. Med.*, 1997, **38**, 101.
32. S. E. Maier, H. Gudbjartsson, S. Patz, L. Hsu, K. O. Lövblad, R. R. Edelman, S. Warach, and F. A. Jolesz, *Am. J. Roentgenol.*, 1998, **171**, 85.
33. K. O. Lövblad, P. M. Jakob, Q. Chen, A. E. Baird, G. Schlaug, S. Warach, and R. R. Edelman, *Am. J. Neuroradiol.*, 1998, **19**, 201.
34. D. L. Thomas, G. S. Pell, M. F. Lythgoe, D. G. Gadian, and R. J. Ordidge, *Magn. Reson. Med.*, 1998, **39**, 950.
35. F. Schick, *Magn. Reson. Med.*, 1997, **38**, 638.
36. R. Turner and D. Le Bihan, *J. Magn. Reson.*, 1990, **86**, 445.
37. R. Turner, D. Le Bihan, J. Maier, R. Vavrek, L. K. Hedges, and J. Pekar, *Radiology*, 1990, **177**, 407.
38. R. C. McKinstry, R. M. Weisskoff, M. S. Cohen, J. M. Vevea, K. K. Kwong, R. R. Rzedzian, T. J. Brady, and R. R. Rosen, *Proc. IXth Annu. Mtg. Soc. Magn. Reson. Med.*, New York, 1990, p. 5.
39. H. R. Avram and L. E. Crooks, *Proc. VIIth Annu. Mtg. Soc. Magn. Reson. Med.*, San Francisco, 1988, p. 80.
40. P. Mansfield, *J. Phys. C.*, 1977, **10**, L55.
41. C. Pierpaoli, P. Jezzard, P. J. Basser, A. Barnett, and G. DiChiro, *Radiology*, 1996, **201**, 637.
42. J. S. Doran, P. Jakob, and M. Décorps, *Magn. Reson. Med.*, 1996, **35**, 547.
43. J. S. Doran and M. Décorps, *J. Magn. Reson.*, 1995, **117**, 311.
44. L. Li, *Magn. Reson. Med.*, 1999, **41**, 143.
45. J. Mattiello, P. J. Basser, and D. Le Bihan, in 'Diffusion and Perfusion Magnetic Resonance Imaging. Applications to Functional MRI', ed. D. Le Bihan, Raven Press, New York, 1995, p. 77.
46. J. H. Burdette, A. D. Elster, and P. E. Ricci, *J. Comput. Assist. Tomogr.*, 1998, **22**, 792.
47. D. Xing, N. G. Papadakis, C. L. Huang, V. M. Lee, T. A. Carpenter, and L. D. Hall, *Magn. Reson. Imag.*, 1997, **15**, 771.
48. R. M. Vavrek and J. R. MacFall, in 'Diffusion and Perfusion Magnetic Resonance Imaging. Applications to Functional MRI', ed. D. Le Bihan, Raven Press, New York, 1995, p. 67.
49. P. P. Mitra and B. I. Halperin, *J. Magn. Reson.*, 1995, **113**, 94.
50. J. C. Haselgrove and J. R. Moore, *Magn. Reson. Med.*, 1996, **36**, 960.
51. P. Jezzard, A. S. Barnett, and C. Pierpaoli, *Magn. Reson. Med.*, 1998, **39**, 801.
52. F. Calamante, *Magn. Reson. Med.*, 1999, **41**, 95.

For list of General Abbreviations see end-papers

53. M. R. Thompson, R. Venkatesan, K. Kuppusamy, A. Celik, W. L. Lin, D. K. Kido, and E. M. Haacke, *Radiology*, 1999, **210**, 253.
54. C. F. Maier, H. N. Nikolov, K. C. Chu, B. A. Chronick, and B. K. Rutt, *Magn. Reson. Med.*, 1998, **39**, 392.
55. T. L. Chenevert and J. G. Pipe, *Magn. Reson. Med.*, 1991, **19**, 261.
56. T. L. Chenevert, J. A. Brunberg, and J. G. Pipe, *Radiology*, 1990, **177**, 401.
57. S. Posse, C. A. Cuenod, and D. Le Bihan, *J. Magn. Reson.*, 1993, **102**, 222.
58. A. M. Ulug, P. B. Barker, and P. C. M. van Zijl, *Magn. Reson. Med.*, 1995, **34**, 476.
59. R. J. Ordidge, J. A. Helpern, Z. X. Qing, A. Knight, and V. Nagesh, *Magn. Reson. Imag.*, 1994, **12**, 455.
60. A. W. Anderson and J. C. Gore, *Magn. Reson. Med.*, 1994, **32**, 379.
61. A. J. de Crespigny, M. P. Marks, D. R. Enzmann, and M. E. Moseley, *Magn. Reson. Med.*, 1995, **30**, 720.
62. M. P. Marks, A. De Crespigny, D. Lentz, D. Enzmann, G. W. Albers, and M. E. Moseley, *Radiology*, 1996, **199**, 403.
63. Z. H. Endre, B. E. Chapman, and P. W. Kuchel, *Biochim. Biophys. Acta*, 1984, **804**, 137.
64. D. W. Williams, E. F. W. Seymour, and R. M. Cotts, *J. Magn. Reson.*, 1978, **31**, 271.
65. J. D. Trudeau, W. T. Dixon, and J. Hawkins, *J. Magn. Reson.*, 1995, **B108**, 22.
66. R. F. Karlicek and I. J. Lowe, *J. Magn. Reson.*, 1980, **37**, 75.
67. W. D. Williams, E. F. W. Seymour, and R. M. Cotts, *J. Magn. Reson.*, 1978, **31**, 271.
68. M. I. Hrovat and C. G. Wade, *J. Magn. Reson.*, 1981, **44**, 62.
69. R. M. Cotts, M. J. R. Hoch, T. Sun, and J. T. Marker, *J. Magn. Reson.*, 1989, **83**, 252.
70. L. L. Latour, L. Li, and C. H. Sotak, *J. Magn. Reson.*, 1993, **101**, 72.
71. E. von Meerwall and M. Kamat, *J. Magn. Reson.*, 1989, **83**, 308.
72. R. P. Kennan, J. Zhong and J. C. Gore, *Magn. Reson. Med.*, 1994, **31**, 9.
73. R. P. Kennan, J. Zhong, and J. C. Gore, in 'Diffusion and Perfusion Magnetic Resonance Imaging. Applications to Functional MRI', ed. D. Le Bihan, Raven Press, New York, 1995, p. 110.
74. J. S. Murdey and R. M. Cotts, *J. Chem. Phys.*, 1968, **48**, 4938.
75. S. Majumdar and J. C. Gore, *J. Magn. Reson.*, 1988, **78**, 41.
76. R. M. Weisskoff, C. S. Zuo, J. L. Boxerman, and B. R. Rosen, *Magn. Reson. Med.*, 1994, **31**, 601.
77. J. L. Boxerman, L. M. Hamberg, B. R. Rosen, and R. M. Weisskoff, *Magn. Reson. Med.*, 1995, **34**, 555.
78. J. Zhong, O. A. C. Petroff, J. W. Prichard, and J. C. Gore, *Magn. Reson. Med.*, 1993, **30**, 241.
79. J. Zhong, O. A. C. Petroff, L. A. Pleban, J. C. Gore, and J. W. Prichard, *Magn. Reson. Med.*, 1997, **37**, 1.
80. L. L. Latour, Y. Hasegawa, J. E. Formato, M. Fisher, and C. H. Sotak, *Magn. Reson. Med.*, 1994, **32**, 189.
81. Y. Hasegawa, L. L. Latour, J. E. Formato, C. H. Sotak, and M. Fisher, *J. Cereb. Blood Flow Metab.*, 1995, **15**, 179.
82. E. Busch, M. Hoehn-Berlage, M. Eis, M. L. Gyngell, and K.-A. Hossmann, *NMR Biomed.*, 1995, **8**, 59.
83. G. G. Cleveland, D. C. Chang, and C. F. Hazelwood, *Biophys. J.*, 1976, **16**, 1043.
84. M. E. Moseley, Y. Cohen, and J. Kucharczyk, *Radiology*, 1990, **176**, 439.
85. P. J. Basser, J. Mattiello, and D. Le Bihan, *J. Magn. Reson.*, 1994, **103**, 247.
86. T. E. Contouro, R. C. McKinstry, E. Akbudakr, and B. H. Robinson, *Magn. Reson. Med.*, 1995, **35**, 399.
87. V. Gulani, G. A. Iwamoto, H. Jiang, J. S. Shimony, A. G. Webb, and P. C. Lauterbur, *Magn. Reson. Med.*, 1997, **38**, 868.
88. N. G. Papadakis, D. Xing, C. L. H. Huang, L. D. Hall, and T. A. Carpenter, *J. Magn. Reson.*, 1999, **137**, 67.
89. P. J. Basser, J. Mattiello, R. Turner, and D. Le Bihan, *Proc. XIIth Annu. Mtg. Soc. Magn. Reson. Med.*, New York, 1993, p. 584.
90. T. L. Davis, V. J. Wedeen, R. M. Weisskoff, and B. R. Rose, *Proc. XIIth Annu. Mtg. Soc. Magn. Reson. Med.*, New York, 1993, p. 289.
91. P. T. Callaghan, *J. Magn. Reson.*, 1990, **88**, 493.
92. D. G. Cory and A. N. Garroway, *Magn. Reson. Med.*, 1990, **14**, 435.
93. M. D. King, J. Houseman, S. A. Roussel, N. Van Bruggen, S. R. Williams, and D. G. Gadian, *Magn. Reson. Med.*, 1994, **32**, 707.
94. M. D. King, J. Houseman, D. G. Gadian, and A. Connelly, *Magn. Reson. Med.*, 1997, **38**, 930.
95. S. Posse, C. A. Cuenod, and D. Le Bihan, *Radiology*, 1993, **188**, 719.
96. T. L. James and G. G McDonald, *J. Magn. Reson.*, 1973, **11**, 58.
97. C. T. W. Moonen, P. C. M. van Zijl, D. Le Bihan, and D. Despres, *Magn. Reson. Med.*, 1990, **13**, 467.
98. K. Yoshizaki, Y. Seo, H. Nishikawa, and T. Morimoto, *Biophys. J.*, 1982, **38**, 209.
99. P. C. M. van Zijl, C. T. W. Moonen, P. Faustino, J. Pekar, O. Kaplan, and J. S. Cohen, *Proc. Natl. Acad. Sci., USA*, 1991, **88**, 3228.
100. L. E. Kay and J. H. Prestegard, *J. Magn. Reson.*, 1986, **67**, 103.
101. C. H. Sotak, *J. Magn. Reson.*, 1990, **90**, 198.
102. S. H. Koenig, R. D. Brown, M. Spiller, and N. Lundbom, *Magn. Reson. Med.*, 1990, **14**, 482.
103. M. D. Hurlimann, K. G. Helmer, L. L. Latour, and C. H. Sotak, *J. Magn. Reson.*, 1994, **111**, 169.
104. P. T. Callaghan, A. Coy, T. P. J. Halpin, D. MacGowan, K. J. Packer, and F. O. Zelaya, *J. Chem. Phys.*, 1992, **97**, 651.
105. D. J. Bergman and K. J. Dunn, *Phys. Rev.*, 1995, **51**, 3401.
106. R. Mills, *J. Phys. C.*, 1973, **77**, 685.
107. D. Le Bihan, J. Delannoy, and R. Levin, *Radiology*, 1989, **171**, 853.
108. J. Delannoy, D. Le Bihan, D. I. Hoult, and R. L. Levin, *Med. Phys.*, 1990, **17**, 855.
109. K. Hynynen, A. Darkazanli, and E. Unger, *Med. Phys.*, 1993, **20**, 7.
110. H. E. Cline, K. Hynynen, R. D. Watkins, W. J. Adams, J. F. Schenck, R. H. Ettinger, W. R. Freund, J. P. Vetro, and F. A. Jolesz, *Magn. Reson. Imag.*, 1995, **194**, 731.
111. J. H. Simpson and H. Y. Carr, *Phys. Rev.*, 1958, **111**, 1201.
112. E. O. Stejskal, *J. Chem. Phys.*, 1965, **43**, 3597.
113. J. E. Tanner, *Biophys. J.*, 1979, **28**, 107.
114. C. H. Neuman, *J. Chem. Phys.*, 1974, **60**, 4508.
115. A. V. Barzykin, K. Hayamizu, W. S. Price, and M. Tachiya, *J. Magn. Reson.*, 1995, **114**, 39.
116. J. E. Tanner, *J. Chem. Phys.*, 1978, **69**, 1748.
117. R. L. Cooper, D. B. Chang, and A. C. Young, *Biophys. J.*, 1974, **14**, 161.
118. E. von Meerwall and R. D. Ferguson, *J. Chem. Phys.*, 1981, **74**, 6956.
119. C. Nicholson and J. M. Philipps, *J. Physiol.*, 1981, **321**, 225.
120. C. Nicholson and E. Sykova, *Trends Neurosci.*, 1998, **21**, 470.
121. D. A. Rusakov and D. M. Kullmann, *Proc. Natl. Acad. Sci., USA*, 1998, **95**, 8975.
122. M. F. Lythgoe, A. L. Busza, F. Calamante, C. H. Sotak, M. D. King, A. C. Bingham, S. R. Williams, and D. G. Gadian, *Magn. Reson. Med.*, 1997, **38**, 662.
123. M. Hoehn Berlage, M. Eis, and B. Schmitz, *NMR Biomed.*, 1999, **12**, 45.

For References see p. 16

124. M. E. Moseley, *J. Chem. Phys.*, 1983, **87**, 18.
125. P. T. Callaghan and O. Soderman, *J. Chem. Phys.*, 1983, **87**, 1737.
126. P. J. Basser, 'Imaging Brain Structure and Function', New York Academy of Sciences, New York, 1997, p. 123.
127. P. van Gelderen, M. H. M. De Vleeschouwer, D. Des Pres, J. Pekar, P. C. M. Van Zijl, and C. T. W. Moonen, *Magn. Reson. Med.*, 1994, **31**, 154.
128. S. Mori and P. C. M. van Zijl, *Magn. Reson. Med.*, 1995, **33**, 41.
129. T. Chun, A. M. Ulug, and P. C. M. van Zijl, *Magn. Reson. Med.*, 1998, **40**, 622.
130. E. W. Hsu and S. Mori, *Magn. Reson. Med.*, 1995, **34**, 194.
131. P. Douek, R. Turner, J. Pekar, N. J. Patronas, and D. Le Bihan, *J. Comput. Assist. Tomogr.*, 1991, **15**, 923.
132. P. J. Basser and C. Pierpaoli, *J. Magn. Reson.*, 1996, **B111**, 209.
133. C. Pierpaoli and P. J. Basser, *Magn. Reson. Med.*, 1996, **36**, 893.
134. P. J. Basser and C. Pierpaoli, *Magn. Reson. Med.*, 1998, **39**, 928.
135. T. E. Conturo, R. C. McKinstry, E. Akbudak, and B. H. Robinson, *Magn. Reson. Med.*, 1996, **35**, 399.
136. R. I. Shrager and P. J. Basser, *Magn. Reson. Med.*, 1998, **40**, 160.
137. J. J. Neil, S. I. Shiran, R. C. McKinstry, et al., *Radiology*, 1998, **209**, 57.
138. R. J. Gilbert, T. G. Reese, S. J. Daftary, R. N. Smith, R. M. Weisskoff, and V. J. Wedeen, *Am. J. Physiol.*, 1998, **38**, G363.
139. N. Makris, A. J. Worth, A. G. Sorensen, et al., *Ann. Neurol.*, 1997, **42**, 951.
140. D. J. Werring, C. A. Clark, G. J. Barker, D. H. Miller, G. J. M. Parker, M. J. Brammer, E. T. Bullmore, V. P. Giampietro, and A. J. Thompson, *J. Neurol. Neurosurg. Psychiatr.*, 1998, **65**, 863.
141. D. J. Werring, C. A. Clark, G. J. M. Parker, D. H. Miller, A. I. Thompson, and G. J. Barker, *Neuroimage*, 1999, **9**, 352.
142. J. W. Meyer, N. Makris, J. F. Bates, V. S. Caviness, and D. N. Kennedy, *Neuroimage*, 1999, **9**, 1.
143. J. Karger and H. Pfeifer, *Magn. Reson. Imag.*, 1994, **12**, 235.
144. S. Mori, B. J. Crain, V. P. Chacko, and P. C. M. van Zijl, *Ann. Neurol.*, 1999, **45**, 265.
145. C. Poupon, J. F. Mangin, V. Frouin, J. Régis, F. Poupon, M. Pachot-Clouard, D. Le Bihan, and T. Bloch, 'Regularization of MR Diffusion Tensor Maps for Tracking Brain White Matter Bundles', Springer-Verlag, 1998, p. 489.
146. E. D. von Meerwall, *J. Magn. Reson.*, 1982, **50**, 409.
147. T. Niendorf, R. M. Dijkhuizen, D. G. Norris, M. van Lookeren Campagne, and K. Nicolay, *Magn. Reson. Med.*, 1996, **36**, 847.
148. J. G. Li, G. J. Stanisz, and R. M. Henkelman, *Magn. Reson. Med.*, 1998, **40**, 79.
149. G. P. Zientara and J. H. Freed, *J. Chem. Phys.*, 1980, **72**, 1285.
150. J. Pfeuffer, U. Flogel, and D. Leibfritz, *NMR Biomed.*, 1998, **11**, 11.
151. U. Pilatus, H. Shim, D. Artemov, D. Davis, P. C. van Zijl, and J. D. Glickson, *Magn. Reson. Med.*, 1997, **37**, 825.
152. R. V. Mulkern, H. Gudbjartsson, C. F. Weston, et al., *NMR Biomed.*, 1999, **12**, 51.
153. K. D. Merboldt, D. Hörstermann, W. Hänicke, H. Bruhn, and J. Frahm, *Magn. Reson. Med.*, 1993, **29**, 125.
154. S. Posse, C. A. Cuenod, and D. Le Bihan, in 'Diffusion and Perfusion Magnetic Resonance Imaging. Applications to Functional MRI', ed. D. Le Bihan, Raven Press, New York, 1995, p. 57.
155. M. K. Nishijima, R. C. Koehler, and P. D. Hurn, *Am. J. Physiol.*, 1989, **257**, H1860.
156. T. Q. Duong, J. J. Ackerman, H. S. Ying, and J. J. Neil, *Magn. Reson. Med.*, 1998, **40**, 1.
157. Y. Assaf and Y. Cohen, *J. Magn. Reson.*, 1998, **131**, 69.
158. M. Wick, Y. Nagatoma, F. Prielmeier, and J. Frahm, *Stroke*, 1995, **26**, 1930.
159. A. van der Toorn, R. M. Dijkhuizen, C. A. F. Tulleken, and K. Nicolay, *Magn. Reson. Med.*, 1996, **36**, 914.
160. M. A. Rutherford, F. M. Cowan, and A. Y. Manzur, *J. Comput. Assist. Tomogr.*, 1991, **15**, 188.
161. P. B. Toft, H. Leth, B. Peitersen, H. C. Lou, and C. Thomsen, *J. Comput. Assist. Tomogr.*, 1996, **20**, 1006.
162. C. Baratti, A. S. Barnett, and C. Pierpaoli, *Radiology*, 1999, **210**, 133.
163. I. Vorisek and E. Sykov, *J. Neurophysiol.*, 1997, **78**, 912.
164. D. Prayer, T. Roberts, A. J. Barkovich, L. Prayer, J. Kucharczyk, M. Moseley, and A. Arieff, *Neuroradiology*, 1997, **39**, 320.
165. K. Takeda, Y. Nomura, H. Sakuma, T. A. Tagami, Y. Okuda, and T. Nakagawa, *J. Comput. Assist. Tomogr.*, 1997, **21**, 1.
166. C. Beaulieu, F. R. Fenrich, and P. S. Allen, *Magn. Reson. Imaging.*, 1998, **16**, 1201.
167. D. Le Bihan, R. Turner, and P. Douek, *NeuroReport*, 1993, **4**, 887.
168. C. T. W. Moonen, J. Pekar, M. H. M. De Vleeschouwer, P. Van Gelderen, P. C. M. Van Zijl, and D. Des Pres, *Magn. Reson. Med.*, 1991, **19**, 327.
169. J. V. Hajnal, M. Doran, and A. S. Hall, *J. Comput. Assist. Tomogr.*, 1991, **15**, 1.
170. M. A. Rutherford, F. M. Conan, and A. Y. Manzur, *Radiology*, 1991, **180**, 229.
171. Y. Assaf and Y. Cohen, *J. Magn. Reson.*, 1996, **B112**, 151.
172. C. Nicholson and E. Sykova, *Trends Neurosci.*, 1998, **21**, 207.
173. C. Beaulieu and P. S. Allen, *Magn. Reson. Med.*, 1994, **32**, 579.
174. G. J. Stanisz, A. Szafer, G. A. Wright, and R. M. Henkelman, *Magn. Reson. Med.*, 1997, **37**, 103.
175. M. E. Moseley, J. Kucharеczyk, J. Mintorovitch, Y. Cohen, J. Kurhanewicz, N. Derucin, H. Asgari, and D. Normou, *Am. J. Neuroradiol.*, 1990, **11**, 423.
176. L. L. Latour, K. Svoboda, P. P. Mitra, and C. H. Sotak, *Proc. Natl. Acad. Sci., USA*, 1994, **91**, 1229.
177. D. G. Norris, T. Niendorf, and D. Leibfritz, *NMR Biomed.*, 1994, **7**, 304.
178. J. Pfeuffer, W. Dreher, E. Sykova and D. Leibfritz, *Magn. Reson. Imag.*, 1998, **16**, 1023.
179. A. G. Sorensen, F. S. Buonanno, R. G. Gonzalez, et al., *Radiology*, 1996, **199**, 391.
180. S. Warach, D. Chien, W. Li, M. Ronthal, and R. R. Edelman, *Neurology*, 1992, **42**, 1717.
181. S. Warach, M. Boska, and K. M. A. Welch, *Stroke*, 1997, **28**, 481.
182. K. O. Lövblad, A. E. Baird, G. Schlaug, et al., *Ann. Neurol.*, 1997, **42**, 164.
183. R. G. Gonzalez, P. W. Schaefer, F. S. Buonanno, L. H. Schwamm, R. F. Budzik, G. Rordorf, B. Wang, A. G. Sorensen, and W. J. Koroshetz, *Radiology*, 1999, **210**, 155.
184. S. Warach, M. Boska, and K. M. Welch, *Stroke*, 1997, **28**, 481.
185. W. Dreher, B. Köhn, M. L. Gyngell, E. Busch, T. Niendorf, K. A. Hossmann, and D. Leibfritz, *Magn. Reson. Med.*, 1998, **39**, 878.
186. J. Ono, K. Harada, T. Mano, K. Sakurai, and S. Okada, *Pediatr. Neurol.*, 1997, **16**, 63.
187. T. Iwasawa, H. Matoba, A. Ogi, H. Kurihara, K. Saito, T. Yoshida, S. Matsubara, and A. Nozaki, *Magn. Reson. Med.*, 1997, **38**, 484.
188. M. A. Horsfield, H. B. Larsson, D. K. Jones, and A. Gass, *J. Neurol. Neurosurg. Psychiatry*, 1998, **64(Suppl 1)**, S80.
189. H. Ay, F. S. Buonanno, P. W. Schaefer, D. A. Le, B. Wang, R. G. Gonzalez, and W. J. Koroshetz, *Neurology*, 1998, **51**, 1369.
190. H. Hanyu, H. Shindo, D. Kakizaki, K. Abe, T. Iwamoto, and M. Takasaki, *Gerontology*, 1997, **43**, 343.

For list of General Abbreviations see end-papers

191. H. Hanyu, H. Sakurai, T. Iwamoto, M. Takasaki, H. Shindo, and K. Abe, *J. Neurol. Sci.*, 1998, **156**, 195.
192. M. M. Bahn, D. K. Kido, W. L. Lin, and A. L. Pearlman, *Arch. Neurol.*, 1997, **54**, 1411.
193. S. Kropp, M. Finkenstaedt, C. Laske, W. SchulzSchaeffer, I. Zerr, A. Kretschmar, and S. Poser, *J. Neurol.*, 1999, **246**, 66.
194. P. Demaerel, L. Heiner, W. Robberecht, R. Sciot, and G. Wilms, *Neurology*, 1999, **52**, 205.
195. T. Q. Li, Z. G. Chen, and T. Hindmarsh, *Acta Radiol.*, 1998, **39**, 460.
196. R. A. Zimmerman, J. C. Haselgrove, Z. Y. Wang, J. V. Hunter, M. C. Morriss, A. Hoydu, and L. T. Bilaniuk, *Brain Dev.*, 1998, **20**, 275.
197. P. S. Huppi, S. E. Maier, S. Peled, G. P. Zientara, P. D. Barnes, F. A. Jolesz, and J. J. Volpe, *Pediatr. Res.*, 1998, **44**, 585.
198. M. S. Buchsbaum, C. Y. Tang, S. Peled, et al., *Neuroreport*, 1998, **9**, 425.
199. D. Le Bihan, P. Douek, M. Argyropoulou, R, Turner, N. Patronas, and M. Fulham, *Top. Magn. Reson. Imag.*, 1993, **5**, 25.
200. K. Ikezaki, M. Takahashi, H. Koga, J. Kawai, Z. Kovächs, T. Inamura, and M. Fukui, *Acta Neurochir. Suppl. (Wien)*, 1997, **70**, 170.
201. K. Krabbe, P. Gideon, P. Wagn, U. Hansen, C. Thomsen, and F. Madsen, *Neuroradiology*, 1997, **39**, 483.
202. P. Barzo, A. Marmarou, P. Fatouros, K. Hayasaki, and F. Corwin, *J. Neurosurg.*, 1997, **87**, 900.
203. R. B. Schwartz, R. V. Mulkern, H. Gudbjartsson, and F. Jolesz, *Am. J. Neuroradiol.*, 1998, **19**, 859.
204. L. Chang and T. Ernst, *Neuroimaging Clin. North Am.*, 1997, **7**, 409.
205. P. W. Schaefer, F. S. Buonanno, R. G. Gonzalez, and L. H. Schwamm, *Stroke*, 1997, **28**, 1082.
206. K. Okada, L. H. Wu, and S. Kobayashi, *Stroke*, 1999, **30**, 478.
207. D. K. Jones, D. Lythgoe, M. A. Horsfield, A. Simmons, S. C. R. Williams, and H. S. Markus, *Stroke*, 1999, **30**, 393.
208. J. C. Ford, D. B. Hackney, E. Lavi, M. Phillips, and U. Patel, *JMRI*, 1998, **8**, 775.
209. B. A. Inglis, L. Yang, E. D. Wirth, D. Plant, and T. H. Mareci, *Magn. Reson. Imag.*, 1997, **15**, 441.
210. D. Morvan, *Magn. Reson. Imag.*, 1995, **13**, 193.
211. A. Baur, A. Stabler, R. Bruning, R. Bartl, A. Krodel, M. Reiser, and M. Deimling, *Radiology*, 1998, **207**, 349.
212. G. Akansel, V. M. Haughton, R. A. Papke, S. Censky, *Am. J. Neuroradiol.*, 1997, 318, 443.
213. S. A. Englander, A. M. Ulug, R. Brem, J. D. Glickson, and P. C. M. van Zijl, *NMR Biomed.*, 1997, **10**, 348.
214. C. F. Maier, Y. Paran, P. Bendel, B. K. Rutt, and H. Degani, *Magn. Reson. Med.*, 1997, **37**, 576.
215. T. Namimoto, Y. Yamashita, S. Sumi, Y. Tang, and M. Takahashi, *Radiology*, 1997, **204**, 739.
216. T. Ichikawa, H. Haradome, J. Hachiya, T. Nitatori, and T. Araki, *Am. J. Roentgenol.*, 1998, **170**, 397.
217. Y. Yamashita, Y. Tang, and M. Takahashi, *JMRI*, 1998, **8**, 367.
218. I. Yamada, W. Aung, Y. Himeno, T. Nakagawa, and H. Shibuya, *Radiology*, 1999, **210**, 617.
219. R. J. Gilbert, T. G. Reese, S. J. Daftary, R. N. Smith, R. M. Weisskoff, and V. J. Wedeen, *Am. J. Physiol.*, 1998, **275**, G363.
220. D. F. Scollan, A. Holmes, R. Winslow, and J. Forder, *Am. J. Physiol.*, 1998, **44**, H2308.
221. E. W. Hus, A. L. Muzikant, S. A. Matulevicius, R. C. Penland, and C. S. Henriquez, *Am. J. Physiol.*, 1998, **274**, H1627.
222. Y. Zhang, T. V. Samulski, W. T. Joines, J. Mattiello, R. L. Lebin, and D. Le Bihan, *Int. J. Hyperthermia*, 1992, **8**, 263.

Biographical Sketch

Denis Le Bihan. *b* 1957. Ph.D., 1987, Physics, M.D., 1984, Radiology, University of Paris, France. Former Chief of the Radiology Research Section, Clinical Center, NIH, Bethesda, USA. Presently Research Director, French Atomic Energy Commission, Director, Anatomical and Functional Neuroimaging Laboratory, Orsay, France, and Clinical Professor of Radiology, Harvard University, Cambridge, USA. Corresponding Member, French Academy of Sciences. Approx. 400 articles, book chapters, abstracts and patents. Research interests: diffusion, perfusion and functional MRI.

For References see p. 16

Brain MRS of Human Subjects

James W. Prichard
Yale University, New Haven, CT, USA

1 INTRODUCTION

A biomedical revolution based on NMR technology is under way. Many of the NMR methods described in this Encyclopedia are already in use for medical research and diagnosis, and many others will find such application soon. As the full impact of mature NMR methods becomes evident in the latter 1990s, it will be measured on the same scale with such things as microscopy and genetics. Two well-established characteristics of biomedical NMR technology ensure this outcome: it is remarkably noninvasive (see ***Health and Safety Aspects of Human MR Studies***) and it is remarkably versatile, as attested in many other chapters. In each respect separately, it exceeds most other technologies available for the study of living tissue. By their combination, it stands alone.

This chapter deals with human brain research done by the branch of biomedical NMR technology designated magnetic resonance spectroscopy (MRS) to distinguish it from magnetic resonance imaging (MRI), which makes pictures of anatomical structure from the water proton signal. MRS obtains chemically specific information from biological tissue by the measurement of much smaller signals from ^{1}H, ^{31}P, ^{13}C, ^{17}O, and other magnetic nuclei in a variety of compounds. It is extending the range of biomedically useful NMR measurements to practical applications that would have courted dismissal as visionary a decade ago. In 1994, signals from more than two dozen compounds can be detected routinely in the human brain, and many more are in prospect. All report on biochemical phenomena previously accessible only by surgical removal of tissue or at autopsy. As various forms of MRS supported by MRI reach technical maturity, their collective contributions to an understanding of normal and deranged biochemistry in the brain will amount to nothing less than a new neurobiological discipline comparable in scope to today's neurochemistry, neuroanatomy, and neuropathology combined. All stages of normal human brain development and disease processes—including intrauterine stages—will be open to inspection along the many axes MRS can measure.

The MRS studies mentioned in this chapter are intended to help scientists and physicians interested in the brain to evaluate the above assertions, which may appear extravagant to readers who are exploring modern NMR for the first time. Many more studies appropriate for that purpose have been published than can be cited. Selection among them was intended to favor efforts that illuminate each other or set new problems by failing to do so, but it cannot have escaped all of the author's biases.

2 ^{1}H AND ^{31}P SPECTRA

Most human brain MRS research to date has used these two nuclei. Figures 1 and 2 illustrate the normal features and some disease-related abnormalities of brain ^{1}H and ^{31}P spectra with simulations that are free of the wide technical variation among spectra in original publications. Differences in acquisition parameters and data processing can cause spectra that are biologically equivalent to look quite different from each other. For readers new to either NMR or neuroscience, the variation can easily distract attention from features of biological importance.

The simulated spectra in Figures 1 and 2 were generated by Mathematica© and annotated in Adobe Illustrator©. Within each figure, random noise is of the same intensity in all spectra. Resonance variables were adjusted to mimic the appearance typical of many published spectra, in which less intense resonances are not evident because of such factors as long spin echo times, J coupling, and processing methods. The resonances shown are usually identifiable in all spectra from normal adult brain. The disease-related variations are large ones that have been reported by more than one group. They are presented together to emphasize their potential for metabolic fingerprinting of different disease processes.

3 NORMAL BRAIN FUNCTION: LACTATE IN HUMAN SENSORY SYSTEMS

A signal from lactate is detectable in ^{1}H spectra from the normal human brain.[1] Stimulation of the human visual[2–4] and auditory[5] systems can cause increases in lactate observable by ^{1}H MRS in the primary cortical receiving areas. These findings are consistent with positron emission tomography (PET) data showing that similar stimulation can increase glucose uptake more than oxygen extraction in the regions affected.[6] The PET workers interpreted their observations as evidence for preferential activation of nonoxidative glycolysis. The MRS data strengthen that view.

The notable aspect of this research area is the evidence from at least five different PET and NMR groups showing that glycolysis can increase more than respiration in response to some kinds of activation within the normal range of brain function. The phenomenon is well known in skeletal muscle. Selective activation of muscle cells with differing capacities for glycolysis and respiration is a normal feature of muscle function, and heterogeneous distribution of glycolytic and respiratory enzymes has long been employed for histochemical characterization of individual muscle cells. Evidence for similarly heterogeneous enzyme distribution already exists at the level of cell groups in the animal brain.[7] Like muscle cells, neurons and possibly glia may well have variable capacity for glycolysis and respiration related to their physiological functions.

These PET and MRS data prompt the question of what adaptive utility lactate elevation resulting from brain activity might have. Two novel possibilities that can be tested by experiment are the following:

(1) *Lactate may be a local energy storage medium that is increased in anticipation of sudden high energy demand.* Ammunition stacked beside cannons defending a fort is more useful than ammunition in a remote storehouse if the fort is

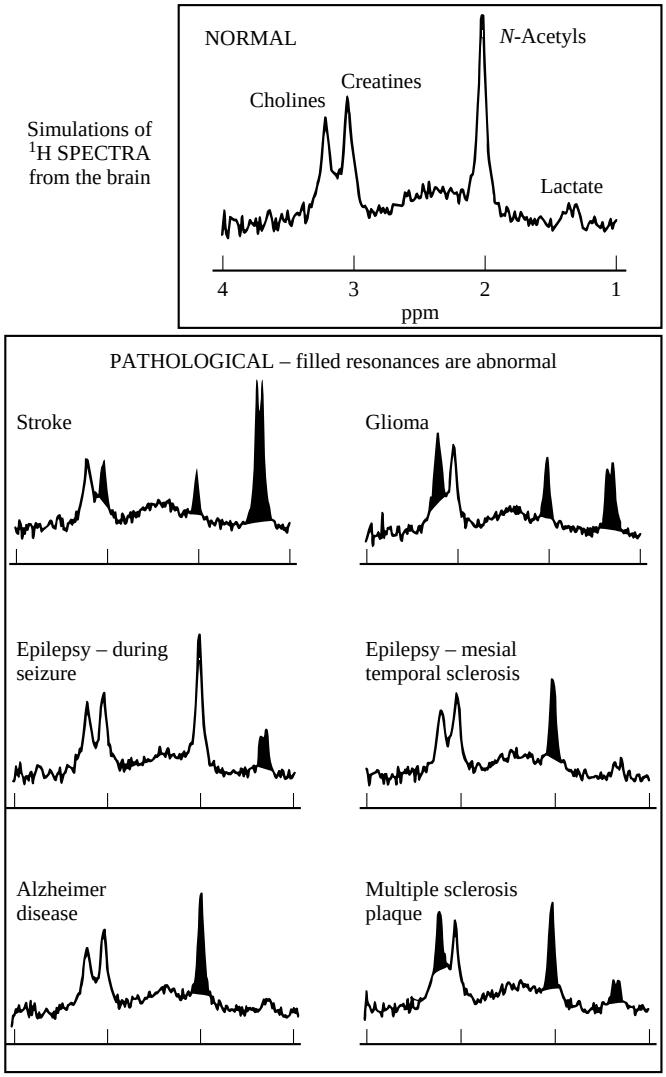

Figure 1 Simulated ^{1}H spectra from brain, created in Mathematica© and annotated in Adobe Illustrator©. Alterations typically caused by six pathological conditions are contrasted with each other and to normal. Spectral variables were adjusted to mimic the appearance common in published spectra. Random noise and each unfilled resonance are of the same intensity in all spectra. The 'normal' spectrum represents resonances from choline-containing compounds (cholines), creatine and phosphocreatine (creatines), *N*-acetyl-containing compounds, mostly *N*-acetylaspartate (*N*-acetyls), and lactate methyl protons (lactate). Glutamate and glutamine signals are represented as unresolved low-intensity resonances between 2 and 3 ppm. The 'pathological' spectra were created by varying the intensities of signals reported to be affected by the disease states indicated by labels on each spectrum. The abnormalities shown are the ones most often associated with each condition, but they are not all present in every case. The elevated lactate signal in four spectra displays the characteristic 7 Hz splitting caused by *J* coupling to the C-2 proton

suddenly attacked. Suspicion of imminent attack would certainly cause the fort's defenders to move extra ammunition from the storehouse to the cannons, to shorten the response time and lengthen the duration of maximum firing. In the brain, neurons can suddenly be called upon to fire hundreds of action potentials a second and surrounding cells to recycle transmitter at proportional rates. The immediate metabolic burden of this intense activity falls principally on synaptic terminals, which are quite small and in consequence have low ratios of cytoplasmic volume to the area of excitable surface membrane that they must support. In such a structure, the Krebs cycle can respond to sudden maximum energy demand more quickly if it is not limited by the time necessary for activation of glycolysis, which is long on the scale of intense neuronal discharge and transmitter release. Local lactate elevation by previous activity would prime synaptic terminals to deliver their maximum response to sudden demand while glycolytic rate is increasing. Existing techniques for the measurement of glucose and oxygen uptake and lactate concentration would not detect most instances of this process, because the ones that can be used in vivo, including MRS, report on overall changes in volumes of tissue much larger than the scattered locations at which such priming would ordinarily occur, and the others are bedeviled by the possibility of agonal artifact. Only when it occurs in many cells at the same time—as during sensory barrages and seizure discharge—could such a process be detected by present methods.

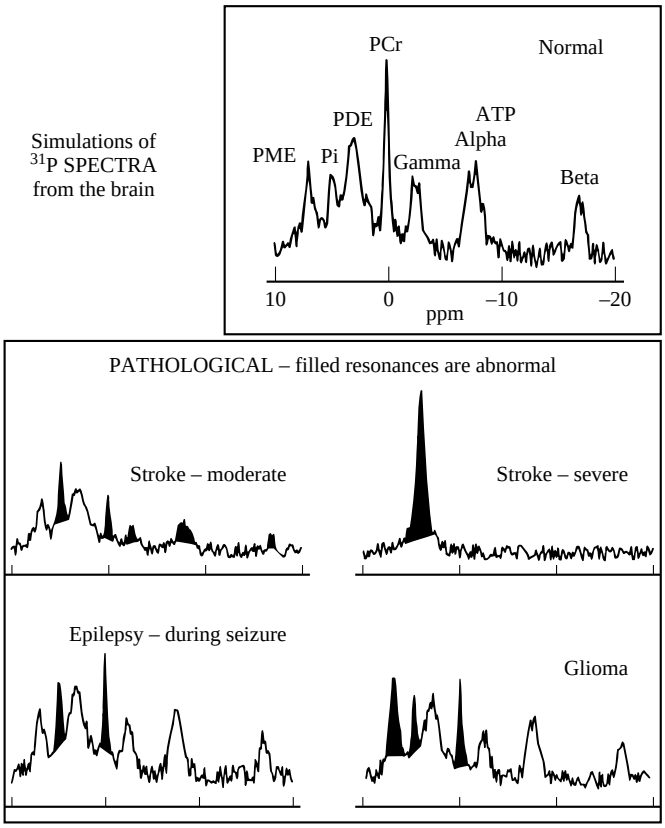

Figure 2 Simulated ^{31}P spectra from normal and diseased brain, created and presented by the same procedures used for Figure 1. The resonances represented are from phosphomonoesters (PME), inorganic phosphate (Pi), phosphodiesters (PDE), phosphocreatine (PCr) and the α, β, and γ phosphates of adenosine triphosphate (ATP). In the 'stroke - severe' example, all of the signal present is Pi, indicating total loss of high-energy phosphate compounds

(2) *Lactate may have a signaling function in the brain*. Lactate is well suited to be a neuromodulator—a substance which alters the excitability of local neural ensembles. It is produced at increased rates whenever glycolysis accelerates in response to neural activity. It accumulates during pathological activation caused by ischemia or lack of oxygen, and, as described above, during some kinds of activation in the physiological range. If—upon escape from the active cell that produced it—it reduced the excitability of adjacent cells, it could both inhibit seizure discharge and 'sharpen' transmission along multifiber pathways, a process known to occur by other mechanisms. A finding consistent with this idea is available: in *Torpedo* electroplax, lactate in concentrations that can be produced by brain activation inhibited release of acetylcholine.[8]

4 STROKE

Stroke is the commonest major brain disease and a principal medical burden on society through the lost productivity it causes and its consumption of resources by extended disability. It is a natural place to test the benefits of new biomedical technology.

MRS observations on human stroke are far enough advanced to allow initial assessment of the role MRS will come to have in patient management. Lactate and *N*-acetyl (NA) resonances in the ^{1}H spectrum and intracellular pH (pHi) derived from the ^{31}P spectrum appear to have the best prospects for clinical utility.

4.1 ^{1}H MRS in Stroke

Figure 1 illustrates the kind of change commonly observed in ^{1}H spectra of human brain infarction: loss of the NA signal and elevation of the signal from lactate. Loss of NA signal should ensue from death of neurons, which are the only cells in mature brain thought to contain *N*-acetylaspartate (NAA), the principal source of the NA resonance. The NA signal was depressed both in the first few days after stroke onset and several weeks later in six patients studied at least twice.[9] In 10 patients studied within 60 h of stroke onset, it was reduced relative to the homologous region of the contralateral hemisphere in all but two; in seven of the same patients, repeat examination 1–2 weeks later showed additional decline at an overall rate calculated at $-29\% \pm 9\%$ per week.[10] Similar findings have been reported by other groups.[11–13]

Decline of the NA signal in the first days after a stroke surely reflects, in part, clearing of debris from neurons killed at the outset, but it may also be evidence of continuing neuronal loss after the acute period, possibly in the ischemic penumbra.[14] Therapy which prevents delayed neuronal loss would presumably also reduce eventual fixed deficit. Monitoring of the NA signal may prove useful as a surrogate endpoint for evaluation of therapies intended to reduce continuing neuronal loss in the subacute period.

Lactate elevation by acute infarction is readily detectable by ^{1}H MRS (Figure 1). However, the first report of increased lactate associated with stroke[14] was on patients studied months after the stroke occurred. Many observers including the present writer doubted that stroke-associated lactate elevation would persist so long, but subsequent observations by several groups have shown that it does. Serial study of individual patients demonstrated continuous lactate elevation for weeks after stroke in most and for several months in some.[9] Again, similar observations have been made by other groups.[11–13]

Multiple mechanisms of lactate elevation must be at work over so long a period. A newly infarcted region of brain accumulates lactate to a concentration of 15–30 mM within minutes of losing its blood supply, as glucose and glycogen in unperfused tissue are metabolized in the absence of oxygen, which is exhausted in the first few seconds. If the region is never reperfused, the lactate in it can dissipate only by diffusion, but the process would not take weeks to months in the presence of active tissue repair processes. Other possible sources of elevated lactate associated with infarction include adjacent regions of surviving but impaired tissue referred to as an 'ischemic penumbra',[15] infiltrating cells involved in the tissue's reaction to injury, and altered metabolism of surviving brain. MRS has provided evidence for the second of these:[16] the brain of a patient studied two weeks after a stroke and autopsied a week later had large numbers of macrophages in the regions where ^{1}H MRS had shown elevated lactate. The role of altered metabolism is conjectural at present; the long-term metabolic response of brain tissue that survives ischemic insult is not well understood.

Lactate that accumulates in the killed core of an infarct is metabolically inert, while that in an ischemic penumbra turns over, albeit probably at a rate different from that of normal brain tissue. The anatomical boundary between pools of lactate in these two states need not be sharp; the pools may even be anatomically interdigitated. Their relative sizes reflect the proportion of killed to surviving tissue early in the history of the lesion, and may therefore indicate how a particular lesion is likely to evolve. An advanced form of combined ^{1}H/^{13}C MRS that has been shown to be feasible in humans can make a pertinent measurement. Inert and metabolically active lactate associated with a human stroke can be distinguished from each other by determining how much of the total stroke-associated lactate pool can be labeled with ^{13}C from blood glucose. Explanation of this remarkable possibility requires a brief description of the NMR properties of ^{13}C.

4.2 ^{13}C MRS

Carbon in Nature is nearly 99% ^{12}C, which is not magnetic and hence gives no NMR signal. The stable magnetic isotope ^{13}C is 1.1% naturally abundant. Its potential for biological studies was appreciated early in the second decade of empirical NMR work. In 1958, the following passage was written by P. C. Lauterbur:[17]

> 'Most practical applications of ^{13}C spectra must await some improvement in the signal-to-noise ratio. *One application that might be made immediately is in the use of ^{13}C as an isotopic tracer in reactions*. Various chemical forms of carbon could be identified by their chemical shifts and fine structures, even in complex mixtures, after the introduction of a compound enriched in ^{13}C. *Even some biological systems might be studied by this technique*.' (Emphases added.)

These words are the conceptual origin of biomedical ^{13}C MRS. In 1957, their author had published the first report of ^{13}C chemical shifts,[18] which was followed shortly by another.[19] Years became decades while NMR technology evolved to a stage at which Lauterbur's idea could be explored by ^{13}C labeling studies, first on enzyme systems and functioning cells,[20] later on intact animal liver,[21] animal brain,[22] and human brain.[23,24] The potential adumbrated by these studies is so great that even the most advanced of them belong to what later generations of biomedical scientists will regard as the early history of ^{13}C MRS. Lauterbur was remarkably prescient.

In living subjects including humans, natural abundance ^{13}C MRS has much still unexploited potential for characterization of normal and pathological variation among tissues, but the most inviting opportunity that ^{13}C MRS presents to biomedical workers is ^{13}C enrichment of molecules observable in vivo. As demonstrated more than two decades ago in *Candida utilis*,[25] feeding a ^{13}C-enriched nutrient to a living organism provides the simultaneous advantages of increased signal-to-noise ratio for observation of molecules that receive the ^{13}C through metabolic processes and a nondestructive means of measuring the rates of those processes. The adult brain normally derives nearly all of its energy from glucose, most of which it converts to two molecules of lactate; if the glucose was enriched in ^{13}C at the C-1 position, one of the lactates receives ^{13}C glucose in its methyl position. Further metabolism in the Krebs cycle creates several other ^{13}C-labeled molecules observable in vivo, the most prominent of which is 4-^{13}C-glutamate. After animal experiments demonstrated that 1-^{13}C-glucose, 3-^{13}C-lactate, and ^{13}C-labeled amino acids could be detected in living brain by ^{13}C MRS,[22] similar observations were made in the human.[24]

4.3 Detection of ^{13}C by ^{1}H MRS

Direct ^{13}C MRS has the disadvantage for in vivo work of long acquisition times due to the low sensitivity of ^{13}C compared to ^{1}H. In samples containing enough ^{1}H–^{13}C bonds, the presence of the ^{13}C can be detected in ^{1}H spectra by the characteristic way in which it splits the signal from protons bonded to it. Exploitation of this phenomenon confers proton sensitivity on NMR measurement of ^{13}C in some positions of intact, functioning molecules. The principle was used in studies of organic molecular structure as early as the 1960s.[20] Later, technological advances and diligent effort allowed its successful adaptation to observation of ^{13}C-labeled compounds in the brains of living animals[26] and humans.[23] By the use of appropriate models, cerebral metabolic rates can be calculated from the time course of ^{13}C accumulation in observable metabolic pools.[27] These and related NMR methods are still in the early stages of development; in their fully mature forms, they are likely to be the preeminent means of measuring metabolic rates in the living human brain.

4.4 Labeling of Stroke-Elevated Lactate with ^{13}C

In stroke, ^{13}C labeling can make the important distinction between lactate which is trapped in a nonmetabolizing compartment and lactate that is persistently elevated in the presence of competent metabolic machinery. This strategy was used to show that shock-elevated lactate in rabbit brain[28] is all metabolically active,[29] and it is equally applicable to assessment of stroke-elevated lactate in the human, as has been demonstrated.[30]

However, the prospect for the routine use of this very sophisticated technique in emergency stroke evaluation depends on other things. Carbon-13 labeling of the kind described can certainly provide information about how much of a fresh stroke is an ischemic penumbra,[14] but rapid evolution of MRI may provide equivalent information from simpler measurements. The best candidates are diffusion weighted imaging (DWI)[31] (see ***Diffusion: Clinical Utility of MRI Studies***) and magnetization transfer contrast imaging (see ***Magnetization Transfer Contrast: Clinical Applications***). The point here is that if ^{13}C labeling of stroke-elevated lactate proves to be a sufficiently novel predictor of a fresh infarct's later course to justify its relative complexity, its minor risk, and a few hundred dollars for each patient, it can be widely implemented.

4.5 ^{31}P MRS in Stroke

Figure 2 illustrates two degrees of loss of energy stores and elevation of inorganic phosphate that can be caused by stroke. Intracellular acidosis is measurable from the resonant frequency of the inorganic phosphate signal, but the frequency difference is too small to be evident in the figure.

The first ^{31}P MRS study of human stroke found normal metabolite ratios with reduced total phosphorus signal in chronic stroke, consistent with the replacement of infarcted tissue by cerebrospinal and interstitial fluid.[32] After developing the capability to study acutely ill patients in a magnet—a decidedly nontrivial acheivement—a group at Henry Ford Hospital in Detroit used it to monitor ^{31}P changes from the acute to the subacute period.[33] Phosphocreatine and ATP were reduced in the acute period, and inorganic phosphate was elevated, as shown in Figure 2. Intracellular pH was acidotic. All of these changes are consistent with the traditional understanding of stroke pathophysiology, but they did not correlate well with clinical measures. Alkalosis replaced acidosis within a few days. The authors suggested that effective therapy might have to be instituted during the period of acidosis.

An estimate of tissue Mg^{2+} concentration can be made from information in ^{31}P spectra.[34] In stroke, Mg^{2+} was elevated in the acidotic period; it might be a pathophysiological factor or a marker of cellular injury.[35]

^{1}H and ^{31}P spectra can both be obtained in the same session. Combined $^{1}H/^{31}P$ observations are a powerful way of analyzing relationships among a wide range of brain metabolites, as was first demonstrated in animal work on hypoglycemia.[36] Despite rather considerable technical obstacles to doing this in human stroke patients, two groups have accomplished it,[37,38] and the results are illuminating. Both groups found that stroke-associated lactate and pH were usually not inversely correlated. In combined $^{1}H/^{31}P$ observations ranging from the acute to the chronic period, the more common association was of elevated lactate with alkalosis, rather than acidosis or normal pH. Because ^{31}P and ^{1}H spectra come from tissue volumes that are not the same size and are both large compared with the dimensions of any of the several metabolic compartments they contain, MRS-observable metabolites should not be expected to behave as though they were in a well-stirred test tube. Dissociation of lactate from pH has been observed in ex-

perimental status epilepticus by NMR[39] and, by biochemical techniques, in tumors and one day after global ischemia.[40]

5 EPILEPSY

5.1 ^{31}P MRS in Epilepsy

Several animal studies on seizure phenomena in the early years of in vivo MRS demonstrated that the PCr/Pi (Figure 2) decline well established by traditional biochemical research could be observed in the the living brain.[41] Due to the limited bore size of available spectrometers, the first MRS observations on the epileptic human brain were ^{31}P spectra from infants.[42] Findings during seizures were as expected: the PCr/Pi ratio was decreased about 50%, as shown in Figure 2, and it returned to normal after seizure discharge ceased. Infants who had the lowest ratios during seizures developed long-term neurological sequelae.

The development of spectrometers with bores large enough for adults was quickly followed by studies of chronic temporal lobe epilepsy, which is a major problem in modern epilepsy management. Two groups have published data on enough patients to allow comparison of results, which are somewhat different. One found alkaline pHi associated with the seizure focus in eight patients, seven of which also had increased Pi and decreased PME.[43,44] The other group reported low PCr/Pi ratios without other changes.[45] Further work will be necessary to determine whether the discrepancy reflects technical factors of differences between patient populations.

5.2 ^{1}H MRS in Epilepsy

The principal component of the NA signal in ^{1}H spectra of normal brain is from NAA, which occurs mainly if not exclusively in neurons. Reduction of the NA signal implying loss of neurons is a common feature of chronically epileptogenic brain tissue, having been documented in two papers,[46,47] and in six preliminary reports by these groups and others at the Annual Meeting of The Society of Magnetic Resonance in Medicine in 1993. The phenomenon is illustrated in Figure 1.

These data have the important implication that chemically specific ^{1}H MRS abnormalities may be detectable in vivo before structural changes in patients with chronic temporal lobe epilepsy, which is commonly associated with a neuropathological state known as mesial temporal sclerosis and can often be relieved by surgery. MRI techniques that appear to be especially sensitive to this pathology have been reported,[48,49] but even if they become routine, noninvasive preoperative detection of chemical abnormality is likely to improve accurate selection of the tissue to be resected for relief of complex partial epilepsy. MRS will be especially important for that purpose if the NA signal proves to be the first NMR quantity to change as mesial temporal sclerosis develops. Noninvasive electroencephalographic and NMR techniques together may soon eliminate the need for implantation of intracranial electrodes to determine which patients with this kind of intractable epilepsy can benefit from surgery.

Observation by ^{1}H MRS of two patients with a form of chronic localized epileptogenic encephalitis known as Rasmussen's syndrome produced the first report of elevated lactate associated with seizure discharge in human brain.[46] Lactate elevation caused by seizure discharge is illustrated in Figure 1.

Monitoring of signals from γ-aminobutyric acid and glutamine in the human brain by newly developed ^{1}H MRS methods[50] has allowed direct observation of the effects of vigabatrin, a new antiepileptic drug.[51] Such observation of drug effects directly in the living target organ opens a new era in neuropharmacology.

6 DEMENTIA

Primary dementia—decline of mental function not secondary to tumors, trauma, drugs, or other obvious causes—is about one-half dementia of the Alzheimer type (hereinafter 'Alzheimer disease'). Vascular, infectious, and other dementias are much less common. Alzheimer disease is a condition of unknown etiology that is defined by its characteristic neuropathology, although the diagnosis can usually be made correctly in life from its distinctive constellation of clinical and laboratory abnormalities. The protracted disability that it causes places a large burden on society, motivating intense research effort which now includes MRS.

6.1 ^{31}P Studies of Alzheimer Disease

Published ^{31}P data on Alzheimer patients do not agree with each other. Conflicting claims about what changes, if any, are present have persisted for several years. A series of studies recently summarized[52] reported that PME and Pi were above normal in the brains of Alzheimer patients, while another group found no clear ^{31}P changes associated with the disease.[53,54] No obvious difference in patient selection or characterization accounts for the difference. Technical factors might; the two studies used somewhat different ^{31}P acquisition methods.

6.2 ^{1}H Studies of Alzheimer Disease

In contrast to the ^{31}P findings, ^{1}H MRS done by several groups has produced general agreement that a reduced NA signal is characteristic of Alzheimer disease (see Figure 1). Preliminary reports of nine studies of living Alzheimer patients all describe decreased NA signals (*Proc. 12th Ann Mtg. (Int) Soc. Magn. Reson. Med.*, New York, 1993). These very consistent data urge the conclusion that NA is characteristically reduced in Alzheimer disease, apparently in proportion to the severity of neuron loss.

7 BRAIN TUMORS

The cellular heterogeneity of brain tumors is a substantial impediment to progress in understanding neoplasia in the nervous system by in vivo techniques, as PET workers have known for years. The heterogeneity is far below the anatomical resolution of current MRS techniques, and technical improvements that appear feasible offer no hope that the gap can be closed. Its effects were evident in an early ^{31}P MRS study of

brain tumors, which commented on the 'striking diversity' of the metabolic patterns observed.[55] Later studies associated decreased PCr, alkaline pH, increased PME, and altered PDE signals with heightened aggressivity of gliomas.[56,57] One constellation of ^{31}P changes that can occur in gliomas is illustrated in Figure 2.

More detailed observation of metabolic properties of brain tumors is possible by ^{1}H MRS due to its finer anatomical resolution. In the form of chemical shift imaging (CSI), it allows variations within single lesions to be detected. A study that combined ^{1}H CSI with PET found that regions of high lactate tended to coincide with regions of high glucose uptake.[58] Later work with improved techniques by the same group revealed a more complicated situation: high lactate was also associated with loculations of extracellular fluid.[59] Another group able to study patients with both ^{1}H CSI and PET reported similar variability and metabolic findings.[60,61] Variable reductions in NA and increased choline signals were observed by both groups. These changes and the elevated lactate seen in some brain tumors are illustrated in Figure 1.

Metabolic maps made from ^{31}P have lower anatomical resolution than ^{1}H maps, due to the lower sensitivity of ^{31}P, but they are capable of showing metabolite distributions across major brain structures and defects caused by large lesions (also see the related ***Chemical Shift Imaging***).[62,63] The information about energy state, pH, and phospholipids available in ^{31}P spectra is so valuable for the understanding of many disease states that continued vigorous efforts to refine ^{31}P CSI are certain.

8 MULTIPLE SCLEROSIS

Demonstration of the extensive, clinically silent pathology of cerebral white matter in multiple sclerosis was among the first major new findings of MRI in the nervous system. MRS of the disease was not practical until several years later, for the usual reason that MRS signals are of much lower intensity. By 1993, NMR technology had advanced to the point that nine preliminary reports on ^{1}H MRS studies of multiple sclerosis appeared in that year's *Proc. 12th Ann Mtg. (Int) Soc. Magn. Reson. Med*. Reduced NA and increased choline signals associated with plaques were the most common findings. Elevated lactate was also observed; it may reflect the presence of highly glycolytic white cells, as in subacute cerebral infarction.[16] All three changes are illustrated in Figure 1.

These metabolic abnormalities were followed over a period of months in a single multiple sclerosis patient with an unusually large cerebral plaque.[64] Metabolic aspects of plaque evolution have not previously been accessible for study in human patients. The combination of MRI and chemically specific MRS will produce new understanding of the pathophysiology of multiple sclerosis, as they are used together to obtain new information on the natural history and therapeutic responsiveness of the disease in individual patients. All of the data reported by Arnold and colleagues[64] are new information bearing on the underlying cellular and molecular biology of episodic demyelination. The opening of so wide a window on a pathophysiological process is certain to improve understanding of it.

9 THE FUTURE OF HUMAN BRAIN MRS

The chemical specificity of MRS guarantees a major role for it in neurobiology. That property, together with the noninvasiveness that it shares with all NMR methods, offers scope for the investigation of the normal human brain that has no close precedent in the history of any earlier technology. Detailed biochemical characterization of the living human brain at all its stages of development and decline is coming within the reach of noninvasive, chemically specific MRS. Investigation of how the human brain works when it is normal and when it is diseased will move more rapidly, and in new directions, with abundant benefit to both science and medicine.

9.1 Science

Neurochemistry is a difficult discipline, because nervous tissue is well protected and highly intolerant of the kind of disruption required for study by standard chemical techniques. MRS can reduce that barrier considerably by providing abundant neurochemical data from the living organ, free of agonal artifact and remeasurable as often as necessary in the same individual. The MRS studies of normal function and metabolic rates mentioned above are early examples of work that will grow into a new dimension of neurochemistry touching nearly every aspect of human brain biology. While MRS can measure only a small fraction of the compounds present in living brain, information about that fraction is unique because previously it was not available at all. Neurobiologists can now look through the window of several dozen MRS-measurable compounds at the biochemical milieu of which they are part. As the number of compounds observable in vivo grows, MRS will become an increasingly powerful complement to cellular and molecular methods in neurobiological research.

9.2 Medicine

In the late 1990s, no routine clinical application of MRS is yet standard practice of the kind that every hospital must provide, like X-ray equipment and electrocardiographs, but MRI has not reached that point either. Both will. Diagnostic MRI is so much more versatile and efficient than earlier technologies that its emergence as the premier medical imaging method of the latter 1990s is certain. Implementation of MRS (small signal capability) on standard clinical MRI machines is no longer a large step in either technique or money. The widespread availability of MRI machines needed for efficient medical diagnosis will facilitate the introduction of MRS into routine clinical practice as rapidly as MRS research demonstrates useful applications.

The most important prospect that MRS offers clinical medicine is chemically specific characterization of disease processes at all of their stages. Noninvasive longitudinal MRS data that provide new understanding of how pathophysiological processes evolve are unique. They will affect medicine no less than the data from microscopic and chemical study of removed brain tissue that are much of the basis for modern conceptions of disease. MRS-defined biochemical profiles that distinguish ischemic, neoplastic, inflammatory, degenerative, and other pathophysiological categories from each other in vivo will emerge, as will profiles that identify specific diseases. Many

MRS measurements will be useful in monitoring the effects of therapy. As this body of knowledge grows, the use of specific MRS measurements in the management of individual patients will become routine.

10 RECENT PROGRESS

This article was first written in 1994. In the four intervening years, MRS of the human brain has advanced rapidly, as have nearly all biomedical applications of NMR technology. Most of the advances in MRS have been along paths predictable from the work described in the article, which continues to provide useful orientation to the origins of a field that is both revolutionary and still young.

However, in several areas recent progress is either novel or extensive to a degree that the article does not adequately indicate. The following recent citations, which are mostly reviews, will help the interested reader find relevant literature.

10.1 Spectroscopic Imaging

This procedure, also known as chemical shift imaging, allows mapping of metabolites in two dimensions. The major technical problems that it presents have been the object of intense development efforts in recent years,[65,66] and it has been used by several groups in clinical research studies on brain tumors,[67] multiple sclerosis,[68] and various aspects of brain metabolism.[69,70]

10.2 High-field Magnets

Spectrometers suitable for human studies at fields as high as 4.1 T have been used in research for several years, and instruments with fields up to 8 T are under development. Notable examples of the neurobiologic opportunities opened by work at 4 T include improved observation of glucose[71] and amino acid[69] resonances in the human brain.

10.3 Measurement of Brain pH in ^{1}H Spectra

Human ^{1}H MRS at 2.1 T has shown that a titrating signal from homocarnosine can provide a measure of cytosolic pH in neurons with high concentrations of that compound, probably a subset specialized for synaptic release of γ-aminobutyric acid.[72] A general review of brain pH measurements by MRS has appeared.[73]

11 RELATED ARTICLES

Anisotropically Restricted Diffusion in MRI; Brain Infection and Degenerative Disease Studied by Proton MRS; Brain MRS of Infants and Children; Brain Neoplasms Studied by MRI; Chemical Shift Imaging; Diffusion: Clinical Utility of MRI Studies; Echo-Planar Imaging; Health and Safety Aspects of Human MR Studies; Localization and Registration Issues Important for Serial MRS Studies of Focal Brain Lesions; Single Voxel Localized Proton NMR Spectroscopy of Human Brain In Vivo; Sodium-23 Magnetic Resonance of Human Subjects; Structural and Functional MR in Epilepsy; Systemically Induced Encephalopathies: Newer Clinical Applications of MRS; Whole Body Studies: Impact of MRS.

12 REFERENCES

1. C. C. Hanstock, D. L. Rothman, J. W. Prichard, T. and R. G. Shulman, *Proc. Natl. Acad. Sci. USA*, 1988, **85**, 1821.
2. J. Prichard, D. Rothman, E. Novotny, O. Petroff, T. Kuwabara, M. Avison, A. Howseman, C. Hanstock, and R. Shulman, *Proc. Natl. Acad. Sci. USA*, 1991, **88**, 5829.
3. D. Sappey-Marinier, G. Calabrese, G. Fein, J. Hugg, C. Biggins, and M. Weiner, *J. Cereb. Blood Flow Metab.*, 1992, **12**, 584.
4. B. G. Jenkins, J. W. Belliveau, and B. R. Rosen, *Proc. 11th Ann Mtg. (Int) Soc. Magn. Reson. Med.*, Berlin, 1992, 2145.
5. M. Singh, *IEEE Trans. Nucl. Sci.*, 1992, **39**, 1161.
6. P. T. Fox, M. E. Raichle, M. A. Mintun, and C. Dence, *Science*, 1988, **241**, 462.
7. I. W. Borowsky and R. C. Collins, *J. Comp. Neurol.*, 1989, **288**, 401.
8. Y. M. Gaudry-Talarmain, *Eur. J. Pharmacol.*, 1986, **129**, 235.
9. G. D. Graham, A. M. Blamire, A. M. Howseman, D. L. Rothman, P. B. Fayad, L. M. Brass, O. A. Petroff, R. G. Shulman, and J. W. Prichard, *Stroke*, 1992, **23**, 333.
10. G. D. Graham, A. M. Blamire, D. L. Rothman, L. M. Brass, P. B. Fayad, O. A. C. Petroff, and J. W. Prichard, *Stroke*, 1993, **24**, 1891.
11. J. H. Duijn, G. B. Matson, A. A. Maudsley, J. W. Hugg, and M. W. Weiner, *Radiology*, 1992, **183**, 711.
12. C. C. Ford, R. H. Griffey, N. A. Matwiyoff, and G. A. Rosenberg, *Neurology*, 1992, **42**, 1408.
13. P. Gideon, B. Sperling, P. Arlien-Soborg, T. S. Olsen, and O. Henriksen, *Stroke*, 1994, **25**, 967.
14. J. W. Berkelbach van der Sprenkel, P. R. Luyten, P. C. van Rijen, C. A. Tulleken, and J. A. den Hollander, *Stroke*, 1988, **19**, 1556.
15. J. W. Prichard, in 'Molecular and Cellular Approaches to the Treatment of Brain Disease', ed. S. G. Waxman, Raven Press, New York, 1993, pp. 153–174.
16. O. A. Petroff, G. D. Graham, A. M. Blamire, R. M. al, D. L. Rothman, P. B. Fayad, L. M. Brass, R. G. Shulman, and J. W. Prichard, *Neurology*, 1992, **42**, 1349.
17. P. C. Lauterbur, *Ann. N.Y. Acad. Sci.*, 1958, **70**, 841.
18. P. C. Lauterbur, *J. Chem. Phys.*, 1957, **26**, 217.
19. C. H. Holm, *J. Chem. Phys.*, 1957, **26**, 707.
20. N. A. Matwiyoff, and D. G. Ott, *Science*, 1973, **181**, 1125.
21. J. R. Alger, L. O. Sillerud, K. L. Behar, R. J. Gillies, R. G. Shulman, R. E. Gordon, D. Shae, and P. E. Hanley, *Science*, 1981, **214**, 660.
22. K. L. Behar, O. A. C. Petroff, J. W. Prichard, J. R. Alger, and R. G. Shulman, *Magn. Reson. Med.*, 1986, **3**, 911.
23. D. L. Rothman, E. J. Novotny, G. I. Shulman, A. M. Howseman, O. A. C. Petroff, G. Mason, T. Nixon, C. C. Hanstock, J. W. Prichard, and R. G. Shulman, *Proc. Natl. Acad. Sci. USA*, 1992, **89**, 9603.
24. R. Gruetter, E. J. Novotny, S. D. Boulware, D. L. Rothman, G. F. Mason, G. I. Shulman, R. G. Shulman, and W. V. Tamborlane, *Proc. Natl. Acad. Sci. USA*, 1992, **89**, 1109.
25. R. T. Eakin, L. O. Morgan, C. T. Gregg, and N. A. Matwiyoff, *FEBS Lett.*, 1972, **28**, 259.
26. D. L. Rothman, K. L. Behar, H. P. Hetherington, J. A. den Hollander, M. R. Bendall, O. A. C. Petroff, and R. G. Shulman, *Proc. Natl. Acad. Sci. USA*, 1985, **82**, 1633.
27. G. F. Mason, D. L. Rothman, K. L. Behar, and R. G. Shulman, *J. Cereb. Blood Flow Metab.*, 1992, **12**, 434.
28. J. W. Prichard, O. A. Petroff, T. Ogino, and R. G. Shulman, *Ann. N.Y. Acad. Sci.*, 1987, **508**, 54.

29. O. A. C. Petroff, E. J. Novotny, M. Avison, D. L. Rothman, J. R. Alger, T. Ogino, G. I. Shulman, and J. W. Prichard, *J. Cereb. Blood Flow Metab.*, 1992, **12**, 1022.
30. D. L. Rothman, A. M. Howseman, G. D. Graham, O. A. C. Petroff, G. Lantos, P. B. Fayad, L. M. Brass, G. I. Shulman, R. G. Shulman, and J. W. Prichard, *Magn. Reson. Med.*, 1991, **21**, 302.
31. S. Warach, D. Chien, W. Li, M. B. Ronthal, and R. R. Edelman, *Neurology*, 1992, **42**, 1717.
32. P. A. Bottomley, B. P. Drayer, and L. S. Smith, *Radiology*, 1986, **160**, 763.
33. S. R. Levine, J. A. Helpern, K. M. Welch, A. M. Vande Linde, K. L. Sawaya, E. E. Brown, N. M. Ramadan, R. K. Deveshwar, and R. J. Ordidge, *Radiology*, 1992, **185**, 537.
34. H. R. Halvorson, A. M. Vande Linde, J. A. Helpern, and K. M. Welch, *NMR Biomed.*, 1992, **5**, 53.
35. J. A. Helpern, A. Vande Linde, K. M. Welch, S. R. Levine, L. R. Schultz, R. J. Ordidge, H. R. Halvorson, and J. W. Hugg, *Neurology*, 1993, **43**, 1577.
36. K. L. Behar, J. A. den Hollander, O. A. C. Petroff, H. Hetherington, J. W. Prichard, and R. G. Shulman, *J. Neurochem.*, 1985, **44**, 1045.
37. J. W. Hugg, J. H. Duijn, G. B. Matson, A. A. Maudsley, J. S. Tsuruda, D. F. Gelinas, and M. W. Weiner, *J. Cereb. Blood Flow Metab.*, 1992, **12**, 734.
38. P. Gideon, B. Sperling, O. Henriksen, N. A. Lassen, T. Skyhøj, T. S. Olsen, P. Sidenius, and P. Arlien-Soborg, *Proc. 12th Ann Mtg. Soc. Magn. Reson. Med.*, New York, 1993, 1484.
39. O. A. C. Petroff, J. W. Prichard, T. Ogino, M. J. Avison, J. R. Alger, and R. G. Shulman, *Ann. Neurol.*, 1986, **20**, 185.
40. W. Paschen, B. Djuricic, G. Mies, R. Schmidt-Kastner, and F. Linn, *J. Neurochem.*, 1987, **48**, 154.
41. J. W. Prichard, *Epilepsia*, 1994, **35**(Suppl 6), S14.
42. D. P. Younkin, P. M. Delivoria, J. Maris, E. Donlon, R. Clancy, and B. Chance, *Ann. Neurol.*, 1986, **20**, 513.
43. J. W. Hugg, G. B. Matson, D. B. Tweig, A. A. Maudsley, D. Sappey-Marinier, and M. W. Weiner, *Magn. Reson. Imag.*, 1992, **10**, 227.
44. K. D. Laxer, B. Hubesch, M. D. Sappey-Marinier, and M. W. Weiner, *Epilepsia*, 1992, **33**, 618.
45. R. Kuzniecky, G. A. Elgavish, H. P. Hetherington, W. T. Evanochko, and G. M. Pohost, *Neurology*, 1992, **42**, 1586.
46. P. M. Matthews, F. Andermann, and D. L. Arnold, *Neurology*, 1990, **40**, 985.
47. G. Layer, F. Traber, U. Muller-Lisse, J. Bunke, C. E. Elger, and M. Reiser, *Radiologe*, 1993, **33**, 178.
48. G. D. Jackson, S. F. Berkovic, J. S. Duncan, and A. Connelly, *Am. J. Neuroradiol.*, 1993, **14**, 753.
49. G. D. Jackson, A. Connelly, J. S. Duncan, R. A. Grunewald, and D. G. Gadian, *Neurology*, 1993, **43**, 1793.
50. D. L. Rothman, O. A. Petroff, K. L. Behar, and R. H. Mattson, *Proc. Natl. Acad. Sci. USA*, 1993, **90**, 5662.
51. O. Petroff, D. Rothman, K. Behar, and R. Mattson, *Proc. 12th Ann Mtg. Soc. Magn. Reson. Med.*, New York, 1993, 434.
52. J. N. Kanfer, J. W. Pettegrew, J. Moossy, and D. G. McCartney, *Neurochem. Res.*, 1993, **18**, 331.
53. P. A. Bottomley, J. P. Cousins, D. L. Pendrey, W. A. Wagle, C. J. Hardy, F. A. Eames, R. J. McCaffrey, and D. A. Thompson, *Radiology*, 1992, **183**, 695.
54. D. G. Murphy, P. A. Bottomley, J. A. Salerno, C. DeCarli, M. J. Mentis, C. L. Grady, D. Teichberg, K. R. Giacometti, J. M. Rosenberg, C. J. Hardy, M. B. Schapiro, S. I. Rapoport, J. R. Alger, and B. Horwitz, *Arch. Gen. Psychiatr.*, 1993, **50**, 341.
55. R. D. Oberhaensli, J. D. Hilton, P. J. Bore, L. J. Hands, R. P. Rampling, and G. K. Radda, *Lancet*, 1986, **2**, 8.
56. J. Jeske, K. Herholz, W. Heindel, and W. D. Heiss, *Onkologie*, 1989, **1**, 42.
57. W. D. Heiss, W. Heindel, K. Herholz, J. Rudolf, J. Bunke, J. Jeske, and G. Friedmann, *J. Nucl. Med.*, 1990, **31**, 302.
58. P. R. Luyten, A. J. Marien, W. van G. P. Heindel, K. den H. J. Herholz, G. Friedmann, and W. D. Heiss, *Radiology*, 1990, **176**, 791.
59. K. Herholz, W. Heindel, P. R. Luyten, J. A. denHollander, U. Pietrzyk, J. Voges, H. Kugel, G. Friedmann, and W. D. Heiss, *Ann. Neurol.*, 1992, **31**, 319.
60. J. R. Alger, J. A. Frank, A. Bizzi, M. J. Fulham, B. X. DeSouza, M. O. Duhaney, S. W. Inscoe, J. L. Black, P. C. Van Zijl, C. T. Moonen, and G. Di Chiro, *Radiology*, 1990, **177**, 633.
61. M. J. Fulham, A. Bizzi, M. J. Dietz, H. H. Shih, R. Raman, G. S. Sobering, J. A. Frank, A. J. Dwyer J. R. Alger, and G. Di Chiro, *Radiology*, 1992, **185**, 675.
62. T. R. Brown, *NMR Biomed.*, 1992, 5, 238.
63. B. J. Murphy, R. Stoyanova, R. Srinivasan, T. Willard, D. Vigneron, S. Nelson, J. S. Taylor, and T. R. Brown, *NMR Biomed.*, 1993, **6**, 173.
64. D. L. Arnold, M. D. Matthews, G. S. O. C. J. Francis, and J. P. Antel, *Ann. Neurol.*, 1992, **31**, 235.
65. S. J. Nelson, D. B. Vigneron, J. Star-Lack, and J. Kurhanewicz, *NMR Biomed.*, 1997, **10**, 411.
66. R. V. Mulkern, H. Chao, J. L. Bowers, and D. Holtzman, *Ann. N. Y. Acad. Sci.*, 1997, **820**, 97.
67. M. C. Preul, Z. Caramanos, R. Leblanc, J. G. Villemure, and D. L. Arnold, *NMR Biomed.*, 1998, **11**, 192.
68. D. L. Arnold, J. S. Wolinsky, P. M. Matthews, and A. Falini, *J. Neurol. Neurosurg. Psychiat.*, 1998, **64**(Suppl. 1), S94.
69. H. P. Hetherington, J. W. Pan, W. J. Chu, G. F. Mason, and B. R. Newcomer, *NMR Biomed.*, 1997, **10**, 360.
70. P. C. van Zijl and P. B. Barker, *Ann. N. Y. Acad. Sci.*, 1997, **820**, 75.
71. R. Gruetter, M. Garwood, K. Ugurbil, and E. R. Seaquist, *Magn. Reson. Med.*, 1996, **36**, 1.
72. D. L. Rothman, K. L. Behar, J. W. Prichard, and O. A. Petroff, *Magn. Reson. Med.*, 1997, **38**, 924.
73. J. W. Prichard, D. L. Rothman, and O. A. C. Petroff, in 'pH and brain function', eds K. Kaila and B. R. Ransom, John Wiley, New York, 1998, p. 149.

Acknowledgements

The author's own work was supported by USPHS Grants NS 27883, DK 34576, and NS 21708.

Biographical Sketch

J. W. Prichard. *b* 1934. A.B., 1955, Philosophy, Washington University, St. Louis, M.D., 1959 Harvard Medical School, Boston. Clinical and postdoctoral training at Bellevue Hospital (New York), The National Hospital for Nervous Diseases (Queen Square, London), Yale (New Haven), and The National Institutes of Health (Bethesda). Research career in neurology electrophysiology prior to 1981. Entered NMR research then through collaboration with Yale spectroscopists in development and validation of NMR methods for study of the brain in vivo. Approx. 110 publications, half in NMR. Principal research interests: application of NMR methods to clinical neurology and their relationship to cerebral electrophysiology.

Brain: Sensory Activation Monitored by Induced Hemodynamic Changes with Echo Planar MRI

Peter A. Bandettini, Jeffrey R. Binder, Edgar E. DeYoe and James S. Hyde

Medical College of Wisconsin, Milwaukee, WI, USA

1	Introduction	1
2	Postprocessing Methodology	2
3	Pulse Sequence and Hardware	2
4	Auditory Stimuli	2
5	Visual Stimuli	2
6	Conclusions	3
7	Related Articles	4
8	References	4

1 INTRODUCTION

In recent years, it has been demonstrated that MRI is capable of detecting changes in cerebral blood volume,[1] flow,[2] and oxygenation,[2–5] that accompany an increase in neuronal activity. MRI methods that observe these activation-induced changes have been termed functional MRI (FMRI).

The most widely used FMRI method for the noninvasive mapping of human brain activity is based on blood oxygenation level dependent (BOLD) contrast.[6] A localized signal increase in activated cortical regions is generally observed using a time-course collection of T_2*-weighted images. A working model of this phenomenon is that an increase in neuronal activity causes local vasodilatation, which in turn causes blood flow to increase in such a manner that the amount of paramagnetic deoxyhemoglobin in the local vasculature is reduced. This reduction causes an increase in spin coherence and, therefore, an increase in signal when using T_2- or T_2*-weighted pulse sequences.

Support for the hypothesized BOLD contrast mechanism, as it related to FMRI, comes from several studies. Local cerebral blood oxygenation has been observed to increase with neuronal activity.[7–10] Brain tissue T_2, T_2*, and T_2' have been shown to be decreased and increased by cerebral blood oxygenation decreases and increases, respectively.[6,11–15] In addition, brain activation has been shown to increase T_2, T_2*, and T_2',[16–20] in proportions that show general agreement with mathematical simulations based on simplified models of the cerebral vasculature.[21,22]

The applicability of FMRI depends on the degree to which the induced signal enhancement magnitude, location, and timing can be correlated with underlying neuronal activation. The signal enhancement magnitude is not only affected by MRI parameters, but is also dependent on hemodynamic factors (i.e. blood volume, oxygenation, vessel orientation, and radii), which vary significantly from voxel to voxel. Correlation between BOLD signal enhancement magnitude and cerebral blood flow has, nevertheless, been observed. Visual cortex activation studies have shown that BOLD signal enhancement has essentially the same flicker frequency dependency[2] as that of cerebral blood flow changes observed using positron emission tomography (PET).[23]

The FMRI signal enhancement location and distribution is also an issue. The upper limit of spatial resolution of FMRI may be influenced by the degree to which an activation induced modulation of the velocity or oxygenation of rapidly inflowing spins or large collecting veins may contribute to the signal change. Generally, the larger the collecting vessel, the more spatially removed the signal change is from the area of neuronal activation. Such vessel size weighting might depend strongly on the pulse sequence, field strength, and resolution used.[16–26] Nevertheless, studies have shown that FMRI can reveal activity localized to patches of cortex smaller than 1.5 mm.[27]

The temporal resolution of FMRI depends on the latency and consistency of the activation-induced signal change. Rise latency of 8–9 s from stimulus onset to maximal signal change and a fall latency of 9–10 s from stimulus cessation to baseline signal have been reported.[2,28,29] The hemodynamic response time sets upper limits on the functional temporal resolution. A significant increase from baseline is generally observed to take place within 2–3 s after stimulus onset.[2,28,29] Activation durations of less than 1 s are detectable[30,31] and relative differences (in the rise time from adjacent regions or from different experiments) in the onset of signal enhancement are discriminable to within a second.[32]

Platforms on which FMRI are performed vary considerably. Primary differences are in field strength, pulse sequence, gradient and radiofrequency coil hardware, and postprocessing methods. The many trade-offs that exist between platform types have not been completely characterized, but it is clear that FMRI based on BOLD contrast benefits from high field strength, high system stability, high signal-to-noise, (S/N) ratio, and minimal pulsatile motion sensitivity. From reported results, it appears that these criteria are most readily met using echo planar imaging. Nevertheless, other techniques may be suitable. Initial successes in the performance of FMRI using BOLD contrast were published by groups using either EPI at 1.5 T,[2,3] and 4 T,[16] or fast multishot gradient-recalled imaging techniques at 4 T,[4] and at 2 T.[5] Results have since been reported using fast multishot gradient-recalled imaging techniques at 1.5 T.[33–35] Pulsatile brain, cerebrospinal fluid, and blood motion apparently cause nonrepeatable ghosting patterns in sequential images obtained by conventional multishot techniques,[36,37] thus adding significantly to the image signal variation in time. Multishot spiral-scan techniques have lower sensitivity to these contaminating pulsatile effects,[36,37] and have been used successfully to perform high resolution FMRI at 1.5 T.[27]

The use of a time course of images in conjunction with control over activation timing allows for the application of postprocessing methods which include the use of z maps,[38] and other statistical techniques.[35] In addition, other methods, including Fourier analysis,[39] temporal cross correlation,[39] and time–frequency analysis[40] have been successfully applied. While significant signal changes are easily observed using the most conservative statistical tests, a standardized method by which functional images are created has not been established.

Using EPI, studies of the fluctuations in the susceptibility-weighted signal from a quiescent brain have been carried out,[41] not only to determine the nature of the noise for application to statistical tests, but also to obtain potentially useful physiological information, and to determine the actual relationship between functional contrast to noise and field strength.[42]

Because of the ease of use and accessibility of FMRI, many areas of the brain and many different tasks have already been studied. Studies that have been carried out include those of primary cortical regions including visual cortex,[2,4,5,16,29,35,43] motor cortex,[2,3,26,33,34,39,44–46] and auditory cortex.[47] Studies of higher cognitive function, including word generation,[48,49] higher visual processing,[35,43] visual recall,[50] complex motor control,[46] and single word semantic processing,[51] have also been performed.

In this article, applications of FMRI to the mapping of cortex activated by sensory stimulation are summarized using time-course collection of gradient recalled echo planar images at 1.5 T.[3,39] and temporal crosscorrelation postprocessing techniques.[39] Specifically, auditory cortex regions were differentially activated by noise and speech sounds, and visual cortex regions were selectively activated by visual stimuli of different eccentricity.

2 POSTPROCESSING METHODOLOGY

Stimuli are presented in a repetitive on/off fashion for several cycles throughout each time course. Foci of brain activation are identified by crosscorrelation of the time course of each voxel with a reference vector resembling the expected activation-induced response.[39] In general, a reference vector may be obtained by: (a) choosing the voxel containing what appears to be the 'best' temporal response; (b) averaging, in time, the activation cycles in a 'best temporal response' voxel and then duplicating the time-averaged cycle for the length of the time course; (c) averaging in space several of the 'best temporal response' voxels; (d) synthesizing a reference vector; or (e) choosing a vector obtained from principal component analysis of the time course. Pixels having a temporal correlation coefficient below a given threshold (typically 0.4–0.6) are removed. After thresholding, the vector product of the reference vector with each of the surviving time courses is calculated to yield an index of change in the signal magnitude. These 'activation' images are then colorized and superimposed on high resolution anatomical scans of the same slice obtained in the same imaging session.

3 PULSE SEQUENCE AND HARDWARE

All studies presented in this article were performed using single-shot 64 × 64 gradient-recalled EPI (TE = 40 ms) on a clinical 1.5-T GE Signa scanner. To perform EPI without additional stress to the standard gradient amplifiers, we used an insertable balanced torque three-axis head gradient coil designed for rapid gradient switching.[52] To obtain high-quality images throughout the entire brain volume, a shielded quadrature elliptical endcapped transmit/receive birdcage radiofrequency coil was used.[53] Typically, single- or multi-slice time-course series of 64–1024 images were obtained with a TR of 0.5–3 s, flip angle of 65–90°, field of view (FOV) of 24 cm, and slice thickness of 4–10 mm.

4 AUDITORY STIMULI

This study[47] presents findings using FMRI of brain regions involved in auditory speech perception. Specifically, regions activated by speech sounds (words and pseudowords) and nonspeech sounds (noise) were compared.

Five right-handed subjects were tested. Symmetric lateral sagittal slices (slice thickness 10 mm) of the left and right hemispheres were obtained, centered at positions 8 mm medial to the most lateral point of the temporal lobe on each side. In each time-course series, 64 sequential images were collected (TR = 3 s), during which activation alternated with baseline every 9 s (6 images per cycle, 18 s per cycle, 10 cycles). During baseline periods, subjects heard only the ambient scanner noise. During activation periods, prepared digitized auditory stimuli were delivered to the subject via air conduction through a semi-rigid 1-cm-bore plastic tube. The tube conducted the sound stimulus approximately 20 feet from control room wall to the subject, at which point a Y-connector split the tube for binaural stimulation through a tightly fitting headset with occlusive earplugs to reduce scanner noise exposure.

Subjects passively listened to stimuli; no response was required. Stimuli differed in both semantic and acoustic (frequency modulation) content. White noise presentation was compared to presentation of nouns (e.g. 'barn'), and pseudowords (e.g. 'narb') with stimuli matched for duration, presentation rate, average sound pressure level, and spectral range. All voxels having a temporal correlation coefficient to a sinusoidal reference vector below 0.5 were removed. The activation images were superimposed on high resolution scans of the same slices.

Figure 1 illustrates typical results from two of the subjects studied with white noise, pseudowords, and words, respectively. In these and all other subjects studied, the area activated by white noise was considerably smaller than that activated by speech sounds, and was restricted to the dorsal aspect of the superior temporal gyrus. In most instances, this region coincided with or included the transverse temporal (Heschl's) gyrus. Presentation of speech sounds activated a larger region, including more anterior and posterior areas of the dorsal superior temporal gyrus, as well as cortex in or near the superior temporal sulcus bilaterally.

Both words and pseudowords differed significantly from noise bilaterally, while no significant differences were seen between word and pseudoword conditions. Activity occurred symmetrically in the left and right temporal lobes. Unlike white noise, therefore, processing of speech sounds appears to elicit extensive participation of auditory association areas, even when the subject is not engaged in any 'active' task.

5 VISUAL STIMULI

Much of the utility of FMRI depends on its ability to depict spatial patterns of neural activity. To test this capacity in the visual system, FMRI was used for retinotopic mapping of primary visual cortex activation.[43]

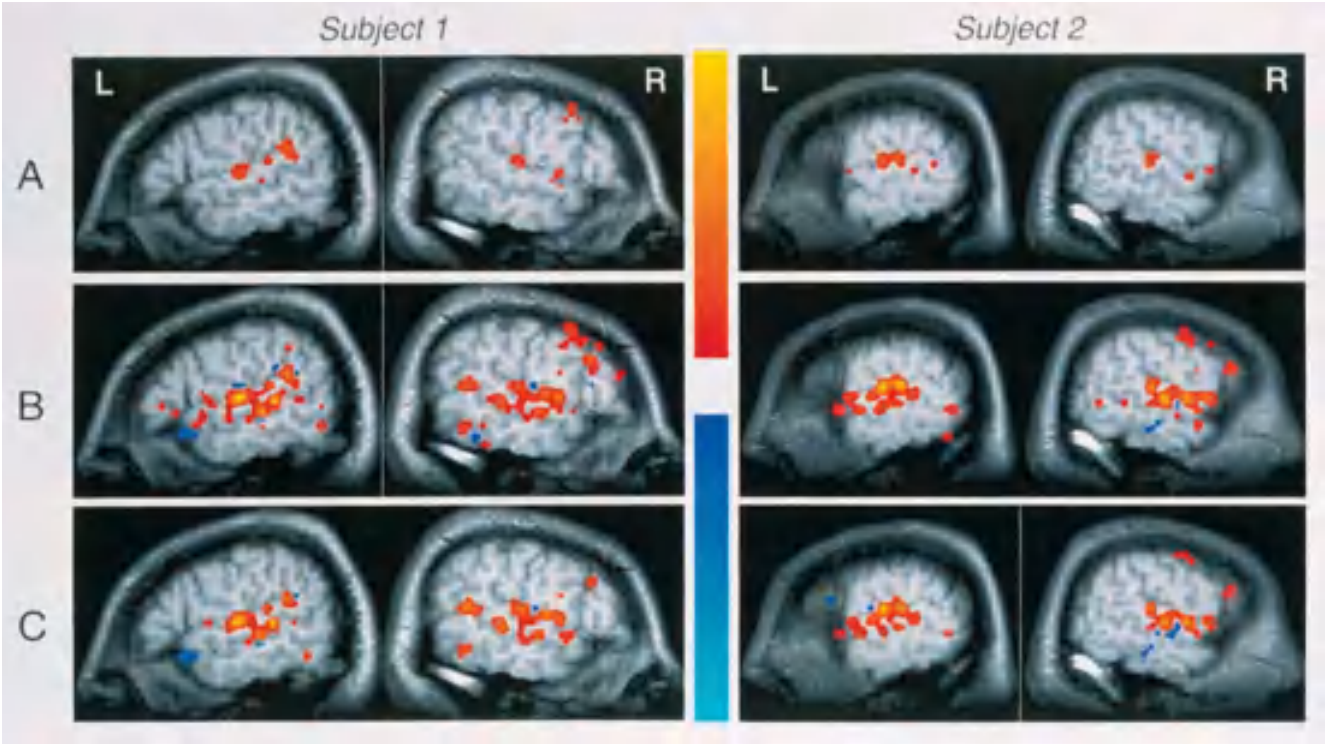

Figure 1 Sagittal images of the left and right temporal lobes of two subjects. Demonstrated are regions activated during passive listening to (A) white noise, (B) pseudowords, and (C) words. The area activated by white noise was smaller than the area activated by either pseudowords or words. The area activated by pseudowords was generally the same size and shape as the area activated by words. Reproduced with permission of the American Neurological Association, 1994)

Dynamic, computer graphics-based visual images were directly projected onto the subjects' retinae. The image generator was a modified Sharp XG2000U video projector driven by Cambridge Instruments VSG video graphics board installed in a personal computer. The image plane was then viewed through a custom optical system that included a wide field, magnifying eyepiece, a 45° prism, and additional objective lenses for adjusting magnification and minimizing chromatic aberration. Two sets of imaging optics were combined to provide full binocular viewing.[54]

To map the retinotopic organization of the visual cortex, three highly trained subjects viewed a small white fixation dot on a uniform black or gray field subtending 60° of visual angle. A black-and-white checkered annulus surrounding the fixation point was presented for 5 on/off cycles of 10 s on and 10 s off. Time-course series (TR = 2 s) of 100 images (slice thickness 8 mm) were used. When on, the checkered pattern was either counter-phase modulated or flickered at 6–8 Hz. Six successively larger annuli were tested. The width of each annulus as well as the check size were scaled in proportion to eccentricity. Only voxels having a correlation coefficient above 0.55 with respect to a chosen reference vector were used in the creation of functional images. All functional images were then superimposed on high resolution anatomical scans.

Figure 2 illustrates the relative sizes of the annuli and shows the corresponding brain activation images. In these experiments, the subject passively viewed the stimuli and was not required to respond to them. A small checkerboard annulus presented at the fixation point elicited activation in striate cortex only at the occipital poles bilaterally. Annuli presented at increasing eccentricities activated successively more anterior regions of the calcarine sulcus. The most eccentric stimulus activated only the anterior calcarine cortex while sparing the occipital poles. Detailed examination of the sequence of activity foci in Figure 2, shows a progression that closely follows the folded cortical mantle within the calcarine sulcus. While such a precise progression is not always observed, these data do show that, under optimal conditions, a detailed mapping of the visual field representation is possible with FMRI. Resolution is not limited by the coarseness of the distribution of large blood vessels, even though such vessels may sometimes introduce artifacts.

6 CONCLUSIONS

MRI of human brain activation using BOLD contrast is a relatively new functional brain imaging method. Accompanying the novelty of the technique are many unknowns regarding the upper limits of spatial and temporal resolution as well as an unclear understanding of physiological and the biophysical mechanisms that regulate hemodynamic changes. In addition, the ways in which the hemodynamic changes affect the magnetic resonance signal are incompletely understood. Nevertheless, the applications described here and elsewhere empirically establish the utility of this approach.

These studies demonstrate observation by FMRI of human brain activation by sensory stimulation. Regions activated in temporal lobes by various speech and nonspeech auditory stimuli were observed. In addition, retinotopic organization of the

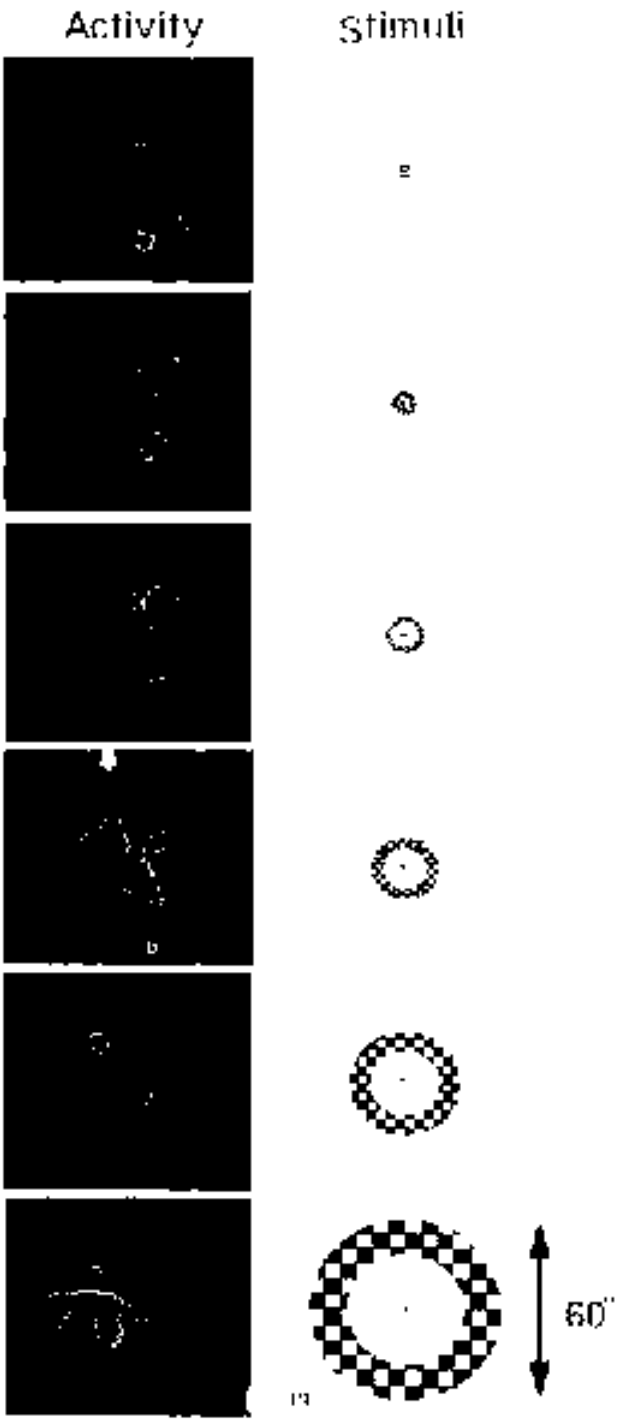

Figure 2 Axial brain activation images created by passive viewing of visual stimuli with six different eccentricities while fixating at the center. The active foci traveled in an anterior direction along the calcarine fissure as the stimulus became more peripheral

primary visual cortex was observed using stimuli of varying visual field eccentricity. Additionally, in our laboratory, preliminary studies involving activation by tactile, aromatic, and taste stimuli are in progress.

FMRI is a new technique that holds great promise in uncovering unique and useful information about brain function and physiology.

7 RELATED ARTICLES

Diffusion and Perfusion in MRI; Echo-Planar Imaging; Functional MRI: Theory and Practice; Functional Neuroimaging Artifacts; Hemoglobin; Susceptibility Effects in Whole Body Experiments

8 REFERENCES

1. J. W. Belliveau, D. N. Kennedy, R. C. McKinstry, B. R. Buchbinder, R. M. Weisskoff, M. S. Cohen, J. M. Vevea, T. J. Brady, and B. R. Rosen, *Science*, 1991, **254**, 716.
2. K. K. Kwong, J. W. Belliveau, D. A. Chesler, I. E. Goldberg, R. M. Weisskoff, B. P. Poncelet, D. N. Kennedy, B. E. Hoppel, M. S. Cohen, R. Turner, H. M. Cheng, T. J. Brady, and B. R. Rosen, *Proc. Natl. Acad. Sci. USA*, 1992, **89**, 5675.
3. P. A. Bandettini, E. C. Wong, R. S. Hinks, R. S. Tikofsky, and J. S. Hyde, *Magn. Reson. Med.*, 1992, **25**, 390.
4. S. Ogawa, D. W. Tank, R. Menon, J. M. Ellermann, S.-G. Kim, H. Merkle, and K. Ugurbil, *Proc. Natl. Acad. Sci. USA*, 1992, **89**, 5951.
5. J. Frahm, H. Bruhn, K.-D. Merboldt, and W. Hanicke, *J. Magn. Reson. Imaging*, 1992, **2**, 501.
6. S. Ogawa, T. M. Lee, A. R. Kay, and D. W. Tank, *Proc. Natl. Acad. Sci. USA*, 1990, **87**, 9868.
7. A. Grinvald, R. D. Frostig, R. M. Siegel, and E. Bratfeld, *Proc. Natl. Acad. Sci. USA*, 1991, **88**, 11559.
8. P. T. Fox and M. E. Raichle, *Proc. Natl. Acad. Sci. USA*, 1986, **83**, 1140.
9. R. D. Frostig, E. E. Lieke, D. Y. Ts'o, and A. Grinvald, *Proc. Natl. Acad. Sci. USA*, 1990, **87**, 6082.
10. A. Villringer, J. Planck, C. Hock, L. Schleinkofer, and U. Dirnagl, *Neurosci. Lett.*, 1993, **154**, 101.
11. R. Turner, D. Le Bihan, C. T. Moonen, D. Despres, and J. Frank, *Magn. Reson. Med.*, 1991, **22**, 159.
12. B. E. Hoppel, R. M. Weisskoff, K. R. Thulborn, J. B. Moore, K. K. Kwong, and B. R. Rosen, *Magn. Reson. Med.*, 1993, **30**, 715.
13. M. K. Stehling, F. Schmitt, and R. Ladebeck, *J. Magn. Reson. Imaging*., 1993, **3**, 471.
14. A. J. DeCrespigny, M. F. Wendland, N. Derugin, E. Kozniewska, and M. E. Moseley, *Magn. Reson. Med.*, 1992, **27**, 391.
15. P. Jezzard, F. Heineman, J. Taylor, D. Taylor, H. Wen, R. S. Balaban, and R. Turner, *NMR Biomed.*, 1994, **7**, 35.
16. R. Turner, P. Jezzard, H. Wen, K. K. Kwong, D. Le Bihan, T. Zeffiro, and R. S. Balaban, *Magn. Reson. Med.*, 1993, **29**, 277.
17. R. S. Menon, S. Ogawa, D. W. Tank, and K. Ugurbil, *Magn. Reson. Med.*, 1993, **30**, 380.
18. B. E. Hoppel, J. R. Baker, R. M. Weisskoff, and B. R. Rosen, *Proc. Soc. Magn. Reson. Med. 1993 Meet*., p. 1384.
19. P. A. Bandettini, E. C. Wong, A. Jesmanowicz, R. S. Hinks, and J. S. Hyde, *NMR Biomed.*, 1994, **7**, 12.
20. P. A. Bandettini, E. C. Wong, A. Jesmanowicz, R. S. Hinks, and J. S. Hyde, *Proc. Soc. Magn. Reson. Med. 1993 Meet*., p. 169.
21. S. Ogawa, R. S. Menon, D. W. Tank, S.-G. Kim, H. Merkle, J. M. Ellermann, and K. Ugurbil, *Biophys. J.*, 1993, **64**, 803.
22. R. P. Kennan, J. Zhong, and J. C. Gore, *Magn. Reson. Med.*, 1994, **31**, 9.
23. P. T. Fox and M. E. Raichle, *J. Neurophysiol.*, 1984, **51**, 1109.
24. J. Frahm, K.-D. Merboldt, and W. Hanicke, *Proceedings, 12th Annual Scientific Meeting*, Society of Magnetic Resonance Medicine, New York, 1993, p. 1427.

25. J. H. Duyn, C. T. W. Moonen, R. W. de Boer, G. M. van Yperen, and P. R. Luyten, *Proc. Soc. Magn. Reson. Med. 1993 Meet*., p. 168.
26. S. Lai, A. L. Hopkins, E. M. Haacke, D. Li, B. A. Wasserman, P. Buckley, L. Friedman, H. Meltzer, P. Hedera, and R. Friedland, *Magn. Reson. Med.*, 1993, **30**, 387.
27. S. A. Engel, D. E. Rumelhart, B. A. Wandell, A. T. Lee, G. H. Glover, E. J. Chichilnisky, and M. N. Shadlen, *Nature (Lond.)*, 1994, **369**, 525.
28. E. A. DeYoe, J. Neitz, P. A. Bandettini, E. C. Wong, and J. S. Hyde, *Proc. Soc. Magn. Reson. Med. 1991 Meet*., p. 1824.
29. A. M. Blamire, S. Ogawa, K. Ugurbil, D. Rothman, G. McCarthy, J. M. Ellermann, F. Hyder, Z. Rattner, and R. G. Shulman, *Proc. Natl. Acad. Sci. USA*, 1992, **89**, 11069.
30. P. A. Bandettini, E. C. Wong, E. A. DeYoe, J. R. Binder, S. M. Rao, D. Birzer, L. D. Estkowski, A. Jesmanowicz, R. S. Hinks, and J. S. Hyde, *Proc. Soc. Magn. Reson. Med. 1993 Meet*., p. 1382.
31. J. W. Belliveau, J. R. Baker, K. K. Kwong B. R. Rosen, J. S. George, C. J. Aine, J. D. Lewine, J. A. Sanders, G. V. Simpson, and J. Foxe, *Proc. Soc. Magn. Reson. Med. 1993 Meet*., p. 6.
32. J. R. Binder, A. Jesmanowicz, S. M. Rao, P. A. Bandettini, T. A. Hammeke, and J. S. Hyde, *Proc. Soc. Magn. Reson. Med. 1993 Meet*., p. 1383.
33. Y. Cao, V. L. Towle, D. N. Levin, and J. M. Balter, *J. Magn. Reson. Imaging*, 1993, **3**, 869.
34. A. Connelly, G. D. Jackson, R. S. Frackowiak, J. W. Belliveau, F. Vargha-Khadem, and D. G. Gadian, *Radiology*, 1993, **188**, 125.
35. W. Schneider, D. C. Noll, and J. D. Cohen, *Nature*, 1993, **365**, 150.
36. G. H. Glover and J. M. Pauly, *Magn. Reson. Med.*, 1992, **28**, 275.
37. G. H. Glover, A. T. Lee, and C. H. Meyers, *Proc. Soc. Magn. Reson. Med. 1993 Meet*., p. 197.
38. D. Le Bihan, P. Jezzard, R. Turner, C. A. Cuenod, L. Pannier, and A. Prinster, *Proc. Soc. Magn. Reson. Med. 1993 Meet*., p. 11.
39. P. A. Bandettini, A. Jesmanowicz, E. C. Wong, and J. S. Hyde, *Magn. Reson. Med.*, 1993, **30**, 161.
40. B. Biswal, P. A. Bandettini, A. Jesmanowicz, and J. S. Hyde, *Proc. Soc. Magn. Reson. Med. 1993 Meet*., p. 722.
41. R. M. Weisskoff, J. Baker, J. Belliveau, T. L. Davis, K. K. Kwong, M. S. Cohen, and B. R. Rosen, *Proc. Soc. Magn. Reson. Med. 1993 Meet*., p. 7.
42. P. Jezzard, D. Le Bihan, C. Cuenod, L. Pannier, A. Prinster, and R. Turner, *Proc. Soc. Magn. Reson. Med. 1993 Meet*., p. 1392.
43. E. A. DeYoe, P. A. Bandettini, J. Neitz, D. L. Miller, and P. Winans, *J. Neurosci. Meth.*, 1994, **54**, 171.
44. S.-G. Kim, J. Ashe, A. P. Georgopoulos, H. Merkle, J. M. Ellermann, R. S. Menon, S. Ogawa, and K. Ugurbil, *J. Neurophysiol.*, 1993, **69**, 297.
45. S.-G. Kim, J. Ashe, K. Hendrich, J. M. Ellermann, H. Merkle, K. Ugurbil, and A. P. Georgopoulos, *Science*, 1993, **261**, 615.
46. S. M. Rao, J. R. Binder, P. A. Bandettini, T. A. Hammeke, F. Z. Yetkin, A. Jesmanowicz, L. M. Lisk, G. L. Morris. W. M. Meuller, L. D. Estkowski, E. C. Wong, V. M. Haughton, and J. S. Hyde, *Neurology*, 1993, **43**, 2311.
47. J. R. Binder, S. M. Rao, T. A. Hammeke, F. Z. Yetkin, A. Jesmanowicz, P. A. Bandettini, E. C. Wong, L. D. Estkowski, M. D. Goldstein, V. M. Haughton, and J. S. Hyde, *Ann. Neurol.*, in press.
48. G. McCarthy, A. M. Blamire, D. L. Rothman, R. Gruetter, and R. S. Shulman, *Proc. Natl. Acad. Sci. USA*, 1993, **90**, 4952.
49. R. M. Hinke, X. Hu, A. E. Stillman, S.-G. Kim, H. Merkle, R. Salmi, and K. Ugurbil, *Neuroreport*, 1993, **4**, 675.
50. D. Le Bihan, R. Turner, T. Zeffiro, C. A. Cuenod, P. Jezzard, and V. Bonnerot, *Proc. Natl. Acad. Sci. USA*, 1993, **90**, 11802.
51. J. R. Binder, S. M. Rao, T. A. Hammeke, J. A. Frost, P. A. Bandettini, A. Jesmanowicz, and J. S. Hyde, *Arch. Neurol.*, 1995, **52**, 593.
52. E. C. Wong, P. A. Bandettini, and J. S. Hyde. *Proc. Soc. Magn. Reson. Med. 1991 Meet*., p. 105.
53. E. C. Wong, E. Boskamp, and J. S. Hyde, *Proc. Soc. Magn. Reson. Med. 1992 Meet., 3 vol.3*, p. 4015.
54. E. A. DeYoe, J. Neitz, D. Miller, and J. Wieser, *Proc. Soc. Magn. Reson. Med. 1993 Meet*., p, 1394.

Acknowledgments

This work was supported in part, by grants CA41464 and RR01008 from the National Institute of Health. P.A.B. thanks GE Medical Systems for financial support. In adition, the support of R. Scott Hinks at GE Medical Systems and of Donald Dickerson, Lloyd D. Estkowski, Andrew S. Greene, Thomas A. Hammeke, Victor M. Haughton, Andre Jesmanowicz, George L. Morris, Wade M. Meuller, Joel B. Myklebust, David Miller, Jay Neitz, Steven M. Rao, Elliot Stein, Eric C. Wong, F. Zerrin Yetkin, and Jeffrey R. Zigun, at the Medical College of Wisconsin, are gratefully appreciated.

Biographical Sketches

Peter A. Bandettini. *b* 1966. B.S., 1989, Ph.D., 1994, Biophysics, Medical College of Wisconsin, USA (supervisors James S. Hyde and R. Scott Hinks). Postdoctoral fellow, Massachusetts General Hospital NMR Center, 1994–95. Approx. 15 publications. Research specialties: functional MRI contrast mechanisms, postprocessing techniques, and applications.

Jeffrey R. Binder. *b* 1958. B.M., 1980, M.D., 1986, University of Nebraska, USA. Neurology Residency, 1987–90,. Neurological Institute of New York. Fellow in cerebrovascular disease, 1990–92. Neurological Institute (with J. P. Mohr). Currently Assistant Professor of Neurology, Medical College of Wisconsin, USA. Approx. 15 publications. Research specialties: behavioral neurology, neuroscience applications of functional MRI, cerebrovascular disease.

Edgar A. DeYoe III. *b* 1950. B.S. Electrical Engineering, 1972; Ph.D. 1983, Experimental Psychology; Ph.D. 1983, Neuroscience, University of Rochester, USA (Advisor: Robert W. Doty). Postdoctoral fellowship at California Institute of Technology (Supervisor: David Van Essen). Currently assistant professor in Department of Cellular Biology and Anatomy with adjunct appointment to Department of Biophysics at the Medical College of Wisconsin, Milwaukee, WI. Approx. 21 publications. Research interests: Neural mechanisms of visual perception—anatomy and physiology; Functional magnetic resonance imaging (FMRI) of the human visual system; development of systems for testing normal vision and visual system; development of systems for testing normal vision and visual dysfunction during FMRI.

James S. Hyde. *b* 1932. B.S., 1954, Ph.D., 1959, Physics, M.I.T, Cambridge, MA, USA. Member of the scientific staff, Varian Associates, 1959–75, working under the direction of W. A. Anderson and M. E. Packard. Professor of Biophysics, Medical College of Wisconsin, 1975–present. Approx. 275 publications, 27 patents. Research specialties: ESR spectroscopy, ENDOR, muscloskeletal MRI, surface coils, functional MRI, electron and nuclear spin physics, and magnetic resonance instrumentation.

Fluorine-19 MRS: General Overview and Anesthesia

David K. Menon
University of Cambridge, UK

1 INTRODUCTION

Fluorine-19 has 100% natural abundance and possesses a spin of $\frac{1}{2}$ and an NMR sensitivity of 80–85% relative to protons. Consequently, fluorine-containing compounds produce NMR signals that are nearly as easily detected as proton signals. The range of chemical shifts for ^{19}F compounds is about 1000 ppm, far greater than that observed for ^{1}H spectroscopy, leading to much greater spectral dispersion. These attributes, coupled with the fact that ^{19}F magnetic resonance (MR) does not require solvent suppression, would be expected to make it an ideal nucleus for study in biological systems. Unfortunately, no naturally occurring molecules of biological consequence contain adequate concentrations of MR-visible ^{19}F (bone and teeth contain a substantial amount of ^{19}F, but this is contained in compounds that possess extremely short T_2 values). However, several pharmacologically active compounds contain fluorine, and ^{19}F magnetic resonance spectroscopy (MRS) has been used for the study of the biodistribution, pharmacokinetics, and metabolism of several drugs.[1] Other groups have also used ^{19}F-containing compounds as tracers for blood,[2] either to image tissue blood flow (perfusion) or intravascular volume (angiography). In addition, ^{19}F chemical shifts and relaxation parameters can be greatly influenced by the physical and chemical environment, and ^{19}F containing molecules in biological systems exhibit significant and variable ^{19}F{^{1}H} nuclear Overhauser effects (NOEs) which depend on their chemical environment and mobility.[3] These properties allow ^{19}F MR to be used to probe molecular interactions in biological systems.

Section 2 of this article provides an overview of the applications of in vivo ^{19}F MR to biological systems, while Section 3 covers the application of ^{19}F MR to research in anesthesia.

2 APPLICATIONS OF ^{19}F MR: AN OVERVIEW

In the following discussion illustrative examples are described, the aim being to outline the principles of applications of ^{19}F MR. The discussion will focus on experiments that have involved whole body in vivo MR either in experimental animals or in humans, but occasional reference will be made to in vitro studies of tissue preparations or cell cultures to illustrate a potential in vivo application.

2.1 Biodistribution and Pharmacokinetics

^{19}F MRS has been used to study the biodistribution of volatile anesthetic agents and antimitotic compounds, and studies addressing this area are discussed in some detail in later sections of this article. In addition, the technique has also been used to study the metabolism of other drugs, two examples of which are discussed here.

Karson et al.[4] studied subjects being treated with the antidepressant agent fluoxitine, and found brain concentrations of 1.3–5.7 μg mL^{-1} on a daily dose of 40 mg day^{-1} in volunteers. They found acquisition of signals from patients more difficult, but suggested a correlation between dose and measured brain concentrations. In a more recent paper,[5] the same group describe the use of a quadrature coil for localized ^{19}F MRS of fluoxitine in patients and reported on T_1 and T_2 values for the fluoxitine resonance, which was predominantly intracerebral in location. Ex vivo ^{19}F MRS of brain obtained from patients at autopsy showed that at least part of the in vivo resonance was due to the active metabolite norfluoxitine, and in vitro analysis of lipid extracts of brain showed far higher concentrations (12.3–18.6 μg mL^{-1}) than were observed in vivo, suggesting that some of the compound may be NMR invisible in vivo. These studies clearly demonstrate that, while ^{19}F MRS is technically suitable for clinical pharmacokinetic research, in vivo MRS needs to be underpinned in its initial phases by ex vivo and in vitro data. Relevant clinical studies might investigate the relationship of brain concentrations to drug response, and the behavior of brain concentrations in relation to changes in dosage schedules.

Lee et al.[6] used ^{19}F MRS to study the rate of absorption of the nonsteroidal antiinflammatory agent flubiprofen from a topical preparation in an animal model. This technique may be easily transferred to human studies, and may provide substantial advantages over traditional methods (which either involve excised human skin or require the use of radioisotope labeling) for studying transcutaneous drug absorption.

2.2 Metabolism

Most work reported in the literature has concentrated on the metabolism of drugs, and several examples are discussed in later sections in the context of volatile anesthetic agents and antimitotics. However, ^{19}F MRS may also be used to study the metabolism of modified physiological substrate molecules.

Some recent studies have investigated the use of fluorinated glucose analogs, such as 2-fluoro-2-deoxy-D-glucose (2-FDG), in imaging glucose utilization in intact animals.[7–9] Such studies provide a regional map of glucose utilization in a manner analogous to ^{18}FDG positron emission tomography (PET), but without the need to expose subjects to radiation.[7] In addition, ^{19}F MRS also provides the ability to interrogate individual metabolic pathways by detecting and quantifying downstream metabolites. Thus, 3-fluoro-3-deoxy-D-glucose (3-FDG) has been used to study glucose metabolism to sorbitol via the aldose reductase pathway,[9] a process that is thought to be intimately involved in the pathogenesis of diabetic cataract and peripheral neuropathy. This is of particular relevance because of the need to evaluate new aldose reductase inhibitors which may be of use in postponing or avoiding the long-term complications of diabetes mellitus. Unfortunately, while many animal studies are underway, the large doses of FDG required, coupled with the potential toxicity of the molecule, dictate that clinical studies are not likely to be possible in the immediate future.

2.3 Insights into Molecular Mechanisms of Drug Action and Metabolism

The interaction of ^{19}F-containing compounds with other molecules at their site of action may be elucidated by studying changes in NMR properties, including T_1, T_2, and NOE values. Such information may provide insight into the mechanisms of action or metabolism of drugs. For example, the demonstration of short T_2 environments for volatile anesthetics in the brain in some studies implies that the agents may be immobilized at their site of residence (see later), and that this environment is substantially different from that in adipose tissue, where these agents possess long T_2 values. This distinction may be of considerable importance in validating putative mechanisms of action of volatile anesthetic agents.

The T_1 relaxation of fluorinated compounds in biological systems is dominated by ^{1}H–^{19}F interactions,[10] and the resulting NOEs can provide useful information regarding these interactions.[3] In small molecules, irradiation of the proton frequency often results in an enhancement of signal intensity (a positive NOE). In other systems, where the ^{19}F nucleus is bound to a large molecule (e.g. a protein), the NOE is typically negative (i.e. there is a reduction in signal intensity with irradiation of the proton frequency). In situations where the ^{19}F nucleus under study is part of a small molecule which attaches reversibly to a macromolecule, the observed NOE depends on the mole fraction of the small molecule that is bound and its rate of dissociation from the complex. In many biological systems the observed effects are dominated by macromolecular binding, even when the bound fraction is small and the rate of dissociation slow. Jacobson et al.[3] have used these effects to investigate the interaction of a cytochrome P450 inducer and a novel herbicide with macromolecules in the liver using in vivo ^{19}F MRS, and the technique may be applicable to many more experimental situations. Direct transfer to human research must be preceded by studies that estimate energy deposition produced by ^{1}H irradiation, but this is unlikely to be major problem, since similar issues have been addressed in the context of ^{13}C and ^{31}P MRS.

2.4 Information Regarding Physicochemical Environment

The T_1 of perfluorocarbons varies with, and may thus provide information regarding, their chemical and physical environment. The paramagnetic O_2 molecule reduces their T_1 from 1–4 to 0.3–0.5 s in linear proportion to the local partial pressure of oxygen.[11] When administered intravenously, these compounds are sequestered in tissues, where their T_1 value provides a measure of pO_2. Alternatively, the compound may be directly introduced into the site of interest (e.g. the vitreous humor). This technique has been used to estimate tissue pO_2 in experimental tumors, vitreous humor in animals and humans, and in animal myocardium.

Unfortunately, the T_1 of fluorocarbons also varies with temperature, making estimation of pO_2 difficult in experimental situations such as brain ischemia where there may be simultaneous changes in temperature. Berkowitz et al.[12] suggest the use of the compound perfluorotributylamine (FTBA) in this situation. While the T_1 value of FTBA changes with pO_2 and temperature, the chemical shift of its ^{19}F resonance is independent of pO_2, but shows a linear change with temperature. ^{19}F MRS of this compound can thus provide an independent measure of the tissue temperature from chemical shift data, and the resulting information can be used to correct T_1 data to provide independent and valid measures of pO_2.

The chemical shift of other ^{19}F compounds is sensitive to pH, and ^{19}F MRS has been used to measure pH in biological systems. For example, Beech and Iles[13] used the chemical shift of exogenously administered F-Quene 1 to estimate intracellular pH (pH_i) in rat liver in vivo. While the technique was practicable, it did not work consistently, and they found small differences when comparisons were made to estimates of pH_i from ^{31}P MRS (using the chemical shift of Pi).

Finally, when ^{19}F is covalently attached to various chelators (e.g. 5,5′-difluoro-1,2-bis(*o*-aminophenoxy)ethane-*N*,*N*,*N*′,*N*′-tetraacetic acid (5-FBAPTA)), the ^{19}F chemical shift of the resultant compound is sensitive to binding by cations, and the local concentration of many cations (of which calcium is the most biologically important) can be estimated by measuring the relative concentration of the bound species. 5-FBAPTA and other fluorinated chelates have been used to study intracellular Ca^{2+} concentrations in cell preparations and tissue slices,[14] and more recent studies have used the techniques to quantify other cations.[15] However, no in vivo study has been reported.

2.5 Imaging of Large Vessel Flow and Tissue Perfusion

The perfluorocarbons have been used as ‘contrast agents’ for ^{19}F angiography, with varying degrees of success.[2,16] While their distribution in tissues provides a measure of local tissue blood flow, they do not give a true estimate of perfusion since they are retained in the intravascular compartment, and are not freely diffusible tracers. However, ^{19}F-containing gases and vapors are freely diffusible and can be used as tracers for estimating brain perfusion. Rudin and Sauter[17] used the washout of halothane to estimate cerebral blood flow (CBF) in rats. However, halothane is known to be a potent cerebral vasodilator and increases CBF in the doses used in this study. Consequently, its use to determine CBF is inappropriate. However, Pekar et al.[18] administered the inert diffusible gas trifluoromethane via the inhalational route in cats, and estimated CBF from wash-in and wash-out data. Their results suggest that the measurement of rCBF may be possible using this technique, with a spatial resolution of 0.4 mL, at least in experimental animals.

3 ^{19}F MRS STUDIES OF FLUORINATED ANESTHETIC AGENTS

3.1 Clinical and Pharmacological Context

Recent ^{19}F MRS studies of fluorinated anesthetics have been the source of some controversy, as results from some groups challenge generally held notions of anesthetic action. Two main issues are pertinent: (a) theories regarding the site of action of anesthetic agents; and (b) the duration of residence of modern anesthetic agents in the brain. Conventional viewpoints on these issues are briefly described below, in order to put the following discussion into some sort of context.

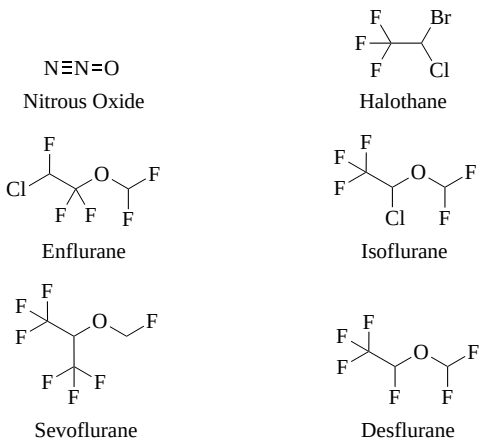

Figure 1 Chemical structures of general anesthetic agents in common clinical use

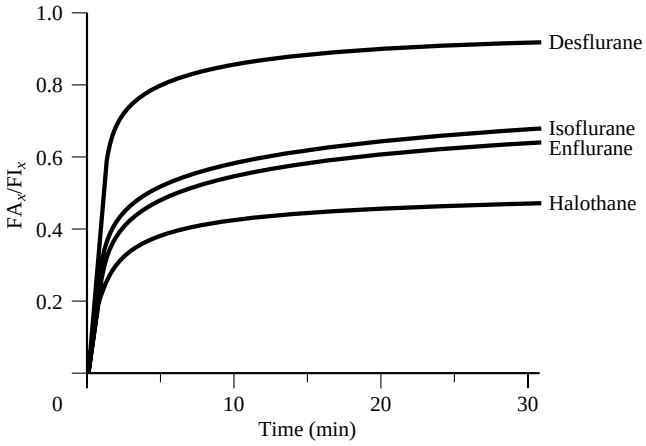

Figure 2 Increase in the alveolar fractional concentration (FA_x) toward that of inspired fractional concentration (FI_x) with time, compared for different fluorinated volatile agents. Note that the less soluble agents (isoflurane and desflurane) show a more rapid rise

General anesthetic agents vary widely in chemical structure (Figure 1), but still continue to have surprisingly similar behavioral effects. However, we have little information on how and where they act in the brain. Two opposing theories claim very different sites of anesthetic action.[19] One school of thought attributes general anesthesia to action at a nonspecific hydrophobic site in the lipid bilayer of cell membranes which is 'disordered' by the entry of the anesthetic molecule.[20] The opposing school of thought suggests that these agents may act at specific stereoselective hydrophilic sites on membrane proteins.[21] Data that suggest molecular specificity of the interaction between anesthetic agents and the brain would provide support to the second theory.[21]

The fluorinated volatile agents constitute the most widely used class of general anesthetics in the world, and individual agents that are presently in use (Figure 1) include halothane, enflurane, isoflurane, sevoflurane, and desflurane.[22] These compounds are characterized, on clinical grounds, by an apparently rapid onset and offset of action. Conventionally, the rapidity of wash-in and wash-out of an anesthetic agent is thought to vary inversely with its solubility in blood and tissue.[22] On this basis, the agents mentioned above rank as follows: desflurane > sevoflurane > isoflurane > enflurane > halothane, where halothane has the highest blood gas solubility, and hence slowest wash-in and wash-out characteristics[22] (Figure 2). Nevertheless, even with halothane, the offset of clinical anesthesia is relatively rapid, with patients awakening within a few minutes of ceasing administration of the agent. However, patients are reported to continue to have subtle psychomotor impairments for several hours to days after general anesthesia.[23]

3.2 Pharmacokinetics of Fluorinated Anesthetics: Is Anesthetic Residence Prolonged in the Brain?

Over the last 10 years there have been numerous papers from several groups that have used ^{19}F MRS to study anesthetic action in the brain. These address two main issues; the first of which is discussed in this section; the second issue is discussed in Section 3.3.

The first in vivo surface coil study of fluorinated anesthetics demonstrated the feasibility of such studies, and suggested that the compounds could be detected in the brain for substantially longer than had been expected.[24] Further studies from Wyrwicz et al.[25] conducted with 2.8 cm surface coil on the scalp, suggested that, following a 2-h exposure to 1% halothane, halothane was washed out of rabbit brain with a biexponential temporal profile (Figure 3). The initial rapid decay had a time constant of approximately 25 min, while the later slower washout phase had a time constant of 320 min. These findings were confirmed by in vitro ^{19}F MRS of extracts of excised rabbit brain at different intervals after the cessation of anesthesia (Figure 4). Although figures for washout half-times were not presented for the in vitro data, they were reported to show an 'elimination profile similar to that observed in intact animals'. These in vitro studies provided better spectral resolution than in vivo studies, and showed that, starting at 90 min after cessation of halothane anesthesia, brain halothane could be resolved into two resonances: a doublet with a 5.6 Hz proton J coupling that was attributed to the trifluoromethyl resonance of halothane, and a second peak 0.7 ppm downfield whose proportion increased with time, such that it represented 40% of the residual ^{19}F signal by 6 h. These two resonances were also differentiated by their relaxation properties. The halothane resonance showed a T_1 of 1.3 s and a T_2 of 3.8 ms, while the new singlet resonance had a T_1 of 2.8 s and a T_2 of 10.6 ms, suggesting that the two resonances were in different chemical environments. Further subcellular fractionation showed that the singlet resonance was confined to the cytosol, while the halothane trifluoromethyl resonance was widely present, and was loosely bound, being dissociated from cellular components by washing with 0.32 M sucrose. The authors concluded that the new singlet resonance represented a nonvolatile metabolite of halothane, possibly trifluoroacetate.

These findings were surprising, since they implied prolonged halothane residence in the brain, a concept that flew in the face of conventional perfusion-limited models of anesthetic elimination.[26] The possibility that a nonvolatile metabolite might be responsible for the prolonged ^{19}F signal provides some explanation for these findings, but did not account for the fact that even 6 h after anesthesia, 60% of the observed ^{19}F signal in excised brain appeared to arise from the trifluoro-

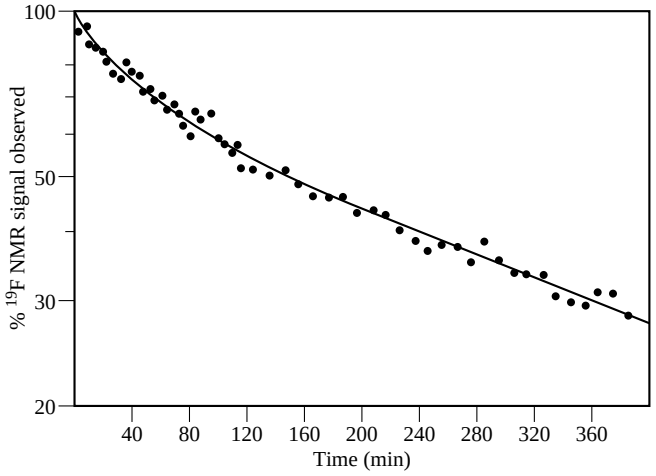

Figure 3 A representative time course of decay of the ^{19}F signal from halothane during recovery from anesthesia. Spectra were obtained during a pulse-and-collect experiment with a surface coil placed over the head of a rabbit after a 120-min exposure to 1% halothane. All signal intensities are expressed as a percentage of the initial signal obtained. (Reproduced with permission from A. M. Wyrwicz, C. B. Conboy, B. G. Nichols, K. R. Ryback, and P. Eisle, *Biochim. Biophys. Acta*, 1987, **929**, 271)

methyl resonance of unmetabolized halothane.[25] Furthermore, this theory could not explain the fact that in a similar experiment Wyrwicz et al.[27] observed similar two-compartment elimination for isoflurane (Figure 5), a compound that is only minimally (<1%) metabolized.[28] The initial decay phase for both halothane and isoflurane were similar ($t_{1/2}$ of 25 and 26 min, respectively), but the later elimination of halothane was significantly slower than isoflurane ($t_{1/2}$ of 320 and 174 min, respectively). The authors suggested that the slow, late elimination of halothane could be attributed to its greater tissue solubility and the presence of nonvolatile metabolites.

While the two pharmacokinetic compartments might represent brain tissue with varying perfusion (e.g. gray and white matter), the $t_{1/2}$ values were at odds with data obtained from non-NMR techniques. Cohen et al.[29] administered labeled halothane intravenously, and found minimal (<10%) retention of radiolabel after 20 min. Similarly, Wolff[30] found that 97% of a subanesthetic dose of halothane was eliminated within 3 h. However, it has been argued by Topham and Longshaw[31] that the pharmacokinetics of halothane may be significantly dependent on the route of administration and the dose administered. Consequently, the preceeding two experiments may be irrelevant to the process of clinical anesthesia. Indeed, Divakaran et al.[32] used gas chromatography to measure halothane levels in excised brain, and found elimination rates that correlate well with the figures obtained by Wyrwicz et al. However, Strum et al.[33] used gas chromatography to measure residual concentrations of isoflurane in rabbit tissue following 90 min of 1.3% isoflurane administration, and showed that brain concentrations of isoflurane were reduced to about 10% by 90 min.

In an effort to address these discrepancies, the research group at the University of California studied elimination of halothane and isoflurane in animal models. They hypothesized that much of the delayed elimination in published in vivo studies arose from contaminating signals in extracranial tissue, where volatile anesthetics tend to be retained, owning to lower perfusion. Accordingly, they used a spatially selective depth pulse in an effort to obtain a selective signal from deeper brain tissue during ^{19}F MRS studies of halothane elimination in rats.[34] They found that the ^{19}F NMR signal from halothane decreased to 40% of its initial value by 34 min (in contrast to about 240 min as reported by Wyrwicz et al.[25]). Several factors may have explained this discrepancy. First, halothane elimination may be significantly faster in rats when compared with rabbits. Second, the depth pulse imposed an acquisition delay of about 0.5 ms, and may have resulted in significant loss of signal from the short T_2 component. In a separate paper,[35] the same group reported data on isoflurane elimination in rabbits with two protocols, both obtained with pulse-and-collect sequences (Figure 6). In the first set of experiments they used

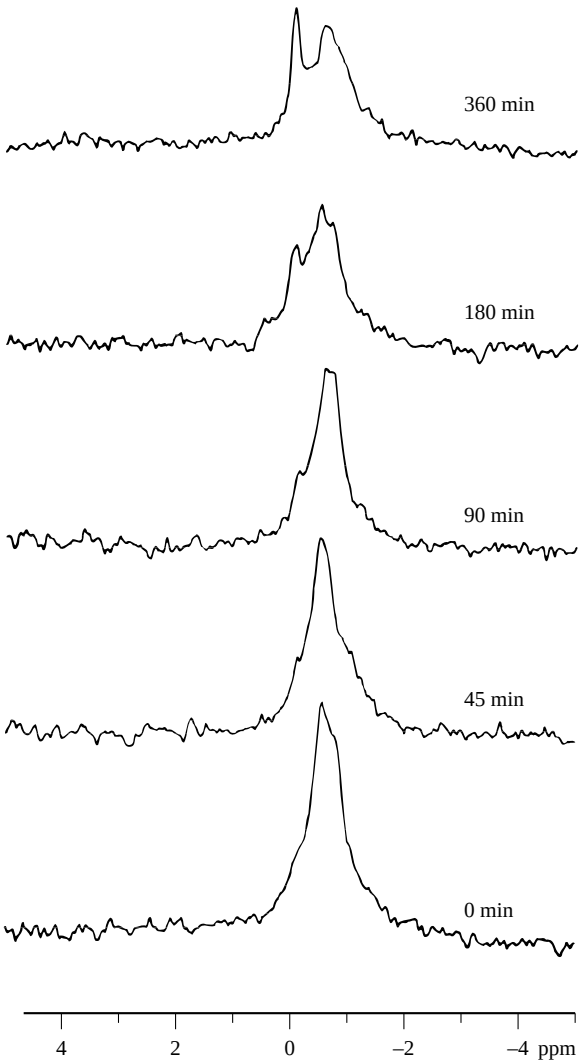

Figure 4 High-resolution ^{19}F MRS experiments on excised rabbit brain removed after varying periods of recovery (between 0 and 6 h) following halothane anesthesia. Chemical shifts are reported relative to an external 5 mM trifluoroacetic acid standard. Note the appearance of a new resonance in the 90-min spectrum, attributed to trifluoroacetic acid. (Reproduced with permission from A. M. Wyrwicz, C. B. Conboy, B. G. Nichols, K. R. Ryback, and P. Eisle, *Biochim. Biophys. Acta*, 1987, **929**, 271)

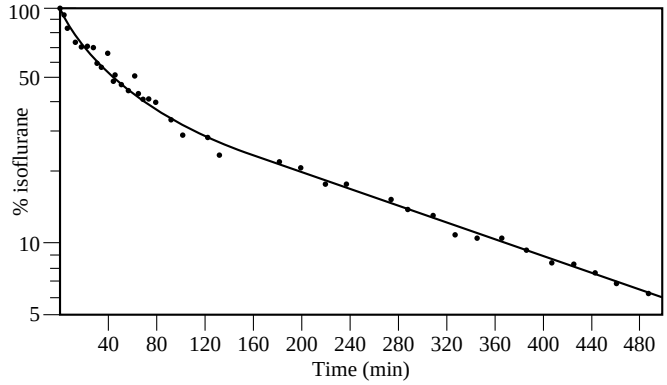

Figure 5 A representative time course of decay of the ^{19}F signal from isoflurane during recovery from anesthesia. Spectra were obtained during a pulse-and-collect experiment with a surface coil placed over the head of a rabbit after a 90-min exposure to 1.5% isoflurane. All signal intensities are expressed as a percentage of the initial signal obtained. (Reproduced with permission from A. M. Wyrwicz, C. B. Conboy, K. R. Ryback, B. G. Nichols, and P. Eisele, *Biochim. Biophys. Acta*, 1987, **927**, 86)

a 3 cm surface coil over the scalp, similar to that employed by Wyrwicz et al.,[27] and found similar kinetics for isoflurane elimination. In another experiment they placed a 1 cm surface coil directly over the exposed dura in rabbits. This study revealed a monoexponential decay of isoflurane concentrations in the brain, with a reduction to 15% of initial values by 90 min. These data agreed well with findings of Strum et al.,[33] who used non-NMR methods and showed a reduction to 10% of initial values by 90 min. The University of California group concluded that the later prolonged elimination kinetics for isoflurane observed by Wyrwicz et al. arose from signal contamination by isoflurane in extracerebral tissues.

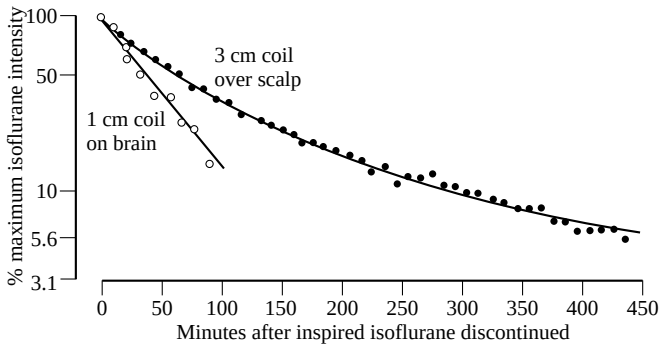

Figure 6 Time course of decay of the ^{19}F signal from isoflurane during recovery from anesthesia. Spectra were obtained during a pulse-and-collect experiment with a surface coil placed over the head of a rabbit after a 90-min exposure to 1.5% isoflurane. All signal intensities are expressed, on a log scale, as a percentage of the initial signal obtained. (○) Signal obtained from a 1.0 cm diameter surface coil placed directly over the dura in craniectomized animals, fitted to a single exponential decay. (●) Signal obtained from a similar experiment, acquired using a 3.0 cm diameter surface coil placed over the intact scalp of the rabbit; the line represents the optimum least-squares fit for a biexponential decay. (Reproduced with permission from P. Mills, D. I. Sessler, M. Moseley, W. Chew, B. Pereora, T. L. James, and L. Litt, *Anesthesiology*, 1987, **67**, 169)

The papers discussed above show that the issue of the spatial localization of the ^{19}F signal from anesthetic agents is an important one. Attempts have been made to clarify this point using ^{19}F MRI studies. While both spin echo[36] and gradient echo[37] sequences have been used to image halothane and enflurane in anesthetized animals, the echo times for these imaging studies have been 9 and 10 ms, respectively. As the T_2 of volatile anesthetics in the brain is short (typically 3–4 ms),[25] it is not surprising that these studies were unable to demonstrate any anesthetic in the brain, despite being conducted while the animal was still anesthetized. On the other hand, they clearly demonstrate fairly high concentrations of fluorinated agent in extracerebral tissues. When these distributions were compared with either ^{1}H lipid imaging[36] or ^{13}C imaging,[37] it appeared that the anesthetics localized in lipid rich areas in adipose tissue stores, glands, and muscle. Localized spectroscopy of volatile anesthetic agents therefore demands techniques that do not involve appreciable delays in data acquisition.

Wyrwicz and Conboy[38] used rotating frame zeumatography (RFZ) to examine the distribution of halothane in the rat head. Localized spectra were obtained from animals that were allowed to recover for varying periods after 90 min of anesthesia with 1% halothane (Figure 7). The localization of signals was necessarily imperfect since RFZ localizes signals along a single axis only. However, the ^{19}F spectra obtained immediately after anesthesia demonstrated very little variation in chemical shift across most of the rat head, but a heterogeneous distribution of ^{19}F signal across the animal's head with apparently lower peak heights in the 'brain' slices [Figures 7(a) and (b)]. The authors did not report on variations in T_2 or linewidths across the blocks of spectra, so estimates of signal intensity are impossible to obtain. RFZ experiments after 4.5 and 6.5 h of recovery from anesthesia showed signals from both halothane and halothane metabolite in all areas of the head [Figures 7(c) and (d)]. With time, the proportion of ^{19}F signal arising from halothane decreased, but this reduction followed a heterogeneous pattern across the head with more rapid reductions being seen in the 'brain' slices. Nevertheless, spectra obtained at 6.5 h (390 min) continued to show clearly detectable peaks from halothane in 'brain' slices. As the metabolite signal contribution increased, its distribution also changed, with a larger proportion of the ^{19}F signal arising from the brain. By 10 h after anesthesia, virtually all the ^{19}F signal arose from the metabolite resonance, and was mainly confined to 'brain' slices. No information regarding relative changes in signal intensity over time in different regions was provided, so even crude estimates of regional elimination halflives are impossible.

In a more recent study, Lockhart et al.[39] measured the cerebral uptake and elimination of halothane, isoflurane, and desflurane from rabbit brain, using a 1 cm surface coil positioned over the exposed dura. They found that rates of change of cerebral concentrations of anesthetic paralleled alveolar levels, and both cerebral uptake and elimination of desflurane were 3 times as fast as for halothane and 1.7 times as fast as for isoflurane (Figure 8). These findings would fit with standard clinical and pharmacokinetic premises, since desflurane has a rapid onset and offset of action owing to its lower blood and tissue solubility. The data for the elimination of isoflurane were similar to those

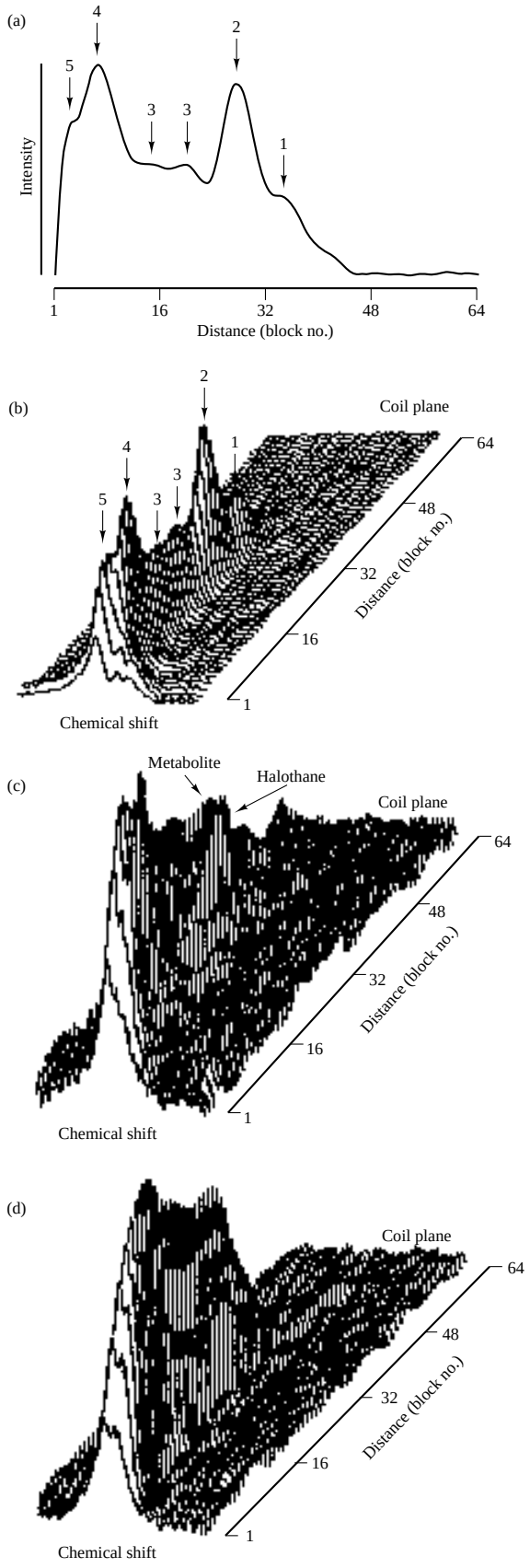

obtained from the previous University of California study, with a monoexponential decay and only 10% of initial levels retained in the brain 90 min after discontinuation of isoflurane. The data also clearly demonstrate a hysteresis between alveolar and cerebral levels of all three volatile agents; alveolar concentrations were higher during the uptake phase, while cerebral concentrations were higher during the elimination phase (Figure 9). This is consistent with conventional pharmacokinetic modeling. However, it was found that the degree of hysteresis was identical for all three agents, suggesting that the rates of transfer between brain and blood are governed by factors other than blood and tissue solubility.

Chen et al.[40] studied elimination of isoflurane from the rat brain as a function of age using ^{19}F MRS with a surface coil. They found a biphasic elimination of isoflurane in both age groups with $t_{1/2}$ values of 7–9 and 100–115 min for the fast and slow components, respectively. The $t_{1/2}$ estimates for the fast compartment are consistent with data for elimination of isoflurane from the brain obtained using other techniques. Consequently, the authors attributed the slow component to washout of isoflurane from intracranial fatty tissue. They also found that older rats showed a slower elimination of isoflurane than younger rats, a difference that the authors attributed to impaired cardiovascular function.

What inferences can we draw from this review of ^{19}F MRS studies of the cerebral pharmacokinetics of anesthetic agents? Clearly, ^{19}F MRS provides a convenient technique for investigating these questions, but several issues need to be addressed. These include efficient spatial localization without acquisition delays, which will result in the loss of signal from short T_2 components. While many of the studies that reported prolonged anesthetic residence in the brain may have been flawed due to contamination by signal from extracerebral tissues, three points cannot be ignored. First, many MR studies tend to suggest slower anesthetic elimination from the brain when compared to non-NMR techniques. However, two more recent studies[39,40] suggest brain isoflurane kinetics that are similar to those obtained from non-NMR techniques. Second, the RFZ studies strongly suggest the presence of residual unmetabolized anesthetic in the brain as long as 6.5 h after anesthesia.[38] Finally, prolonged residence of at least some proportion of halothane is supported by the in vitro studies of brain extracts per-

Figure 7 Results of localized ^{19}F MRS using rotating frame zeumatography performed following administration of 1.5% halothane for 90 min. (a) One-dimensional projection across the rabbit head (from above downwards) showing the location of different blocks of spectra: 1, soft tissue (skin and muscle); 2, brain, muscle, and calvarium; 3, brain; 4, brain, muscle, and calvarium; 5, tissue below the cranium. (b) Stacked, spatially resolved spectra obtained immediately after discontinuing anesthesia, blocks are numbered as in (a). (c) Stacked, spatially resolved spectra obtained 4.5 h after cessation of anesthesia. Note the appearance of a new resonance to the left of the halothane resonance, which is attributed to trifluoroacetic acid. (d) Stacked, spatially resolved spectra obtained 6.5 h after cessation of anesthesia. Note the decrease in intensity of the halothane resonance, and the increase in the intensity of the metabolite resonance. (Reproduced with permission from A. M. Wyrwicz and C. B. Conboy, *Magn. Reson. Med.*, 1989, **9**, 219)

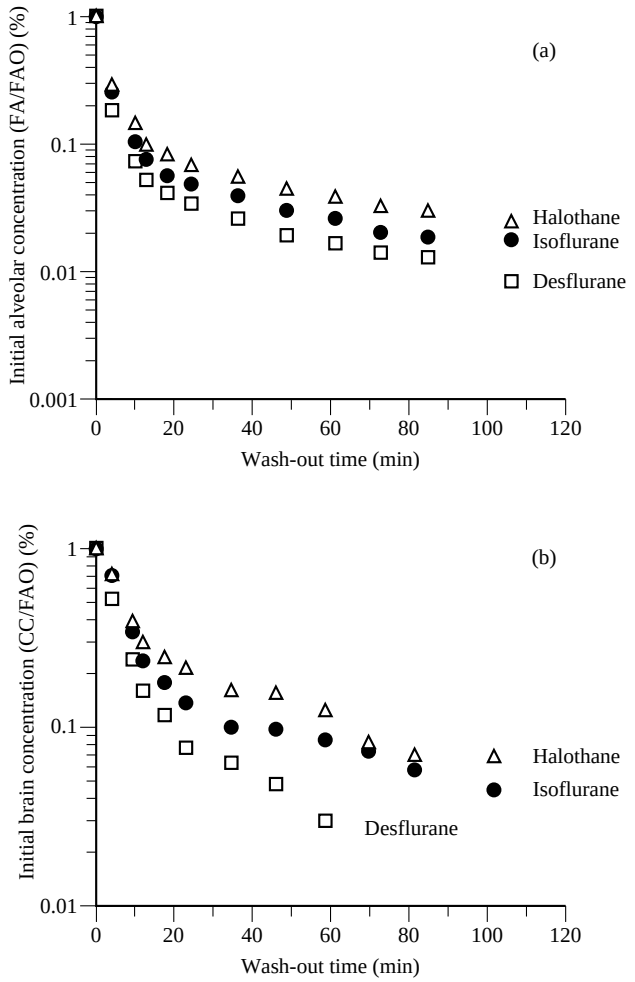

Figure 8 (a) Alveolar washout obtained from gas chromatography, and (b) cerebral washout obtained from in vivo ^{19}F MRS of anesthetic agent following anesthesia with desflurane (□), isoflurane (●), and halothane (△). (Reproduced with permission from S. M. Lockhart, Y. Cohen, N. Yasuda, B. Freire, S. Taheri, L. Litt, and E. I. Eger II, *Anesthesiology*, 1991, **74**, 575)

formed by Wyrwicz et al.[25] However, as several of the later studies have shown, this may be an extremely small proportion of the initial concentrations.

These small quantities of residual cerebral anesthetic are important for two reasons. First, they may provide an explanation for the minor but prolonged psychomotor deficits that are recognized to persist for up to days after general anesthesia.[23] Second, elucidation of the mechanisms that result in prolonged anesthetic retention may provide clues regarding the mechanisms of anesthetic action.

3.3 Sites of Anesthetic Residence in the Brain: Physical Environment and its Significance, Saturability

Many authors have reported that volatile anesthetics in the brain exhibit shorter T_2 values than when they are dissolved in lipid solvents or adipose tissue. These findings have been interpreted as implying immobilization of the fluorinated anesthetic molecules, and have led to speculation that the short T_2 environment may be intimately related to the process of anesthesia. These latter speculations were further fuelled by the results of a study by Evers et al.[41] in which T_2 values of four fluorinated anesthetic agents (methoxyflurane, enflurane, isoflurane, and fluoroxene) and one nonanesthetic fluorinated hydrocarbon (hexafluoroethane) in the brain were compared. The T_2 values of the four anesthetic agents were significantly shorter than in adipose tissue (0.5–4.5 versus 200–400 ms, respectively) and correlated linearly with the anesthetic potency of these agents (Figure 10). The nonanesthetic fluorocarbon exhibited a substantially higher T_2 (18.5 ms) in brain tissue.

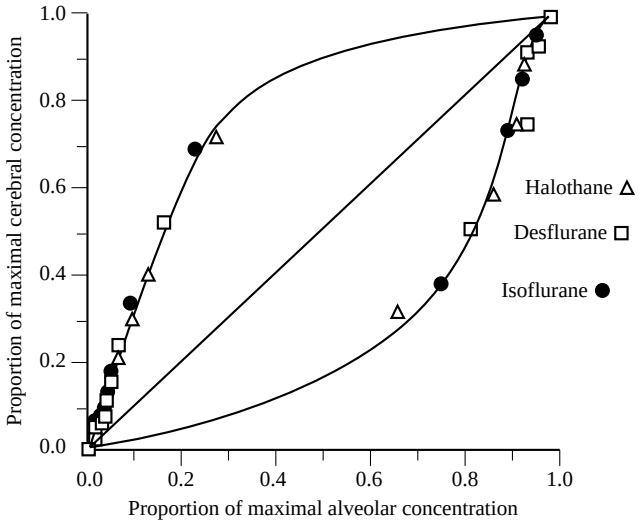

Figure 9 Plot of the relationship between cerebral and alveolar concentrations of volatile anesthetics during induction of and recovery from anesthesia (lower and upper halves of ellipsoid, respectively). Both parts of the curve deviate from the line of identity (straight line), suggesting a significant hysteresis between alveolar and brain levels of anesthesia. Note the unexpected result showing that all three anesthetic agents studied seem to fit to the same curve. (Reproduced with permission from S. H. Lockhart, Y. Cohen, N. Yasuda, B. Freire, S. Taheri, L. Litt, and E. I. Eger II, *Anesthesiology*, 1991, **74**, 575)

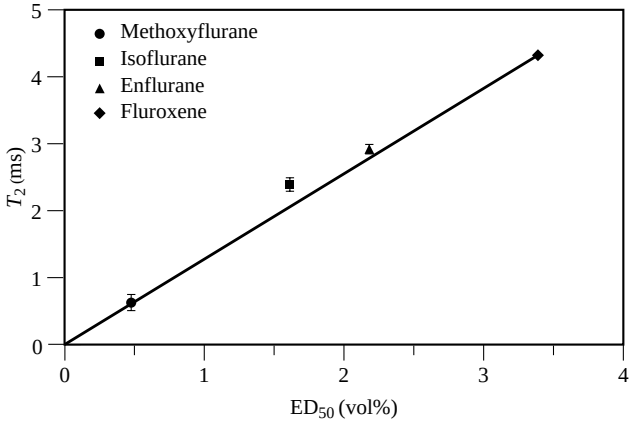

Figure 10 Relationship of anesthetic potency (measured as ED_{50}) to ^{19}F spin–spin relaxation times of fluorinated volatile anesthetics in the brain. (Reproduced with permission from A. S. Evers, J. C. Haycock, and D. A. d'Avignon, *Biochem. Biophys. Res. Commun.*, 1988, **151**, 1039)

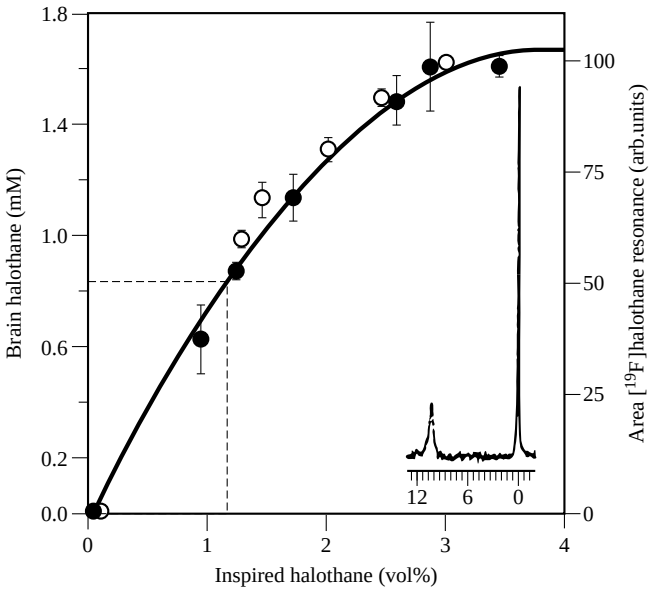

Figure 11 Brain halothane concentrations in rats as a function of inspired halothane concentrations, measured using either in vivo ^{19}F MRS (○) or ex vivo ^{19}F MRS (●) of excised brain. The horizontal dashed line indicates the half-maximal concentration of brain halothane concentration achieved in this experiment. This value (about 1.2%) corresponds closely to the ED_{50} for halothane in rats. The inset shows a representative ^{19}F MR spectrum from the ex vivo experiments. The resonance at 0 ppm arises from methoxyflurane in an external standard, while the peak at 10.2 ppm corresponds to halothane in the brain. (Reproduced with permission from A. S. Evers, B. A. Berkowitz, and D. A. d'Avignon, *Nature*, 1987, **328**, 157)

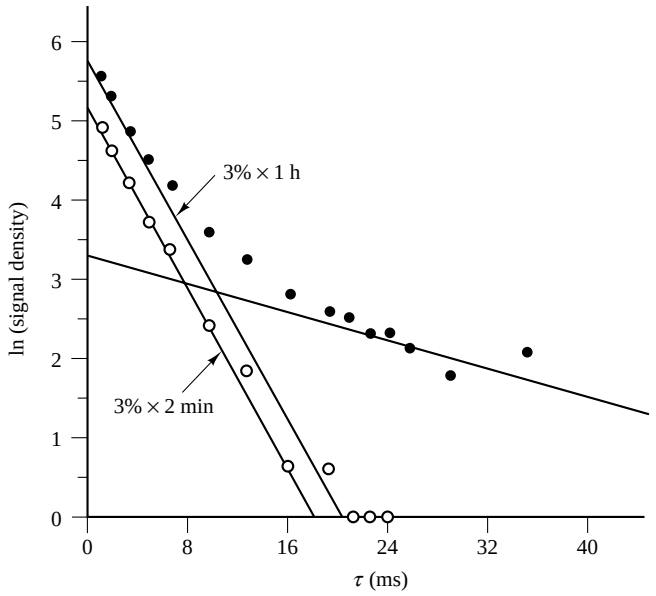

Figure 12 Decay of the ^{19}F MR signal from brain halothane in rats as a function of echo time (expressed as τ) in a Carr–Purcell–Meiboom–Gill sequence from rats exposed to 3% halothane for 2 min (○) or 1 h (●). Note the biexponential T_2 decay of the signal from rats exposed to halothane for 1 h, and the minimal increase in the amount of signal with short T_2 characteristics with longer exposure. (Reproduced with permission from A. S. Evers, B. A. Berkowitz, and D. A. d'Avignon, *Nature*, 1987, **328**, 157)

These data were interpreted as supporting the premise that the short T_2 environment represented a molecular site of anesthetic action.

In a later study, Evers et al.[42a] studied spontaneously breathing rats, anesthetized with halothane, using high resolution in vitro ^{19}F MRS of excised brain at different anesthetic concentrations and in vivo MRS of whole animals at 4.7 T. These experiments showed increasing cerebral levels of anesthetic with increasing inspired concentrations of halothane up to 2.5%. However, little or no further increases in cerebral halothane concentrations were observed when inspired halothane concentrations were increased from 2.5% to 4% (Figure 11). These data were interpreted as evidence for abundant saturable binding sites for halothane, a concept that did not support a nonspecific hydrophobic site of action of volatile anesthetic agents. Evers et al. also measured the T_2 relaxation parameters for the brain halothane resonance, and found that there were at least two components, with one T_2 value of about 3.6 ms (short T_2) and a second one of about 43 ms (long T_2). They also showed that the short T_2 site represented 85% of the halothane molecules present in the brain, and was preferentially occupied during the initial period of induction of anesthesia (Figure 12). Continuing anesthetic administration beyond this point seemed to occupy the long T_2 site. These findings were thought to provide further proof for the importance of the short T_2 site in the process of anesthesia. Unfortunately, these conclusions had to be revised owing to further experimental results.

First, both Evers et al.[42b] and Litt et al.[43] reported that the apparent saturability of brain halothane concentrations was a physiological artifact, being the consequence of respiratory depression at high inspired concentrations of halothane in spontaneously breathing animals. When the studies were repeated with artificially ventilated animals, the cerebral anesthetic concentrations scaled linearly with inspired concentrations of halothane (Figure 13). Furthermore, the short T_2 environment was not specific to brain,[44] but was also found in other tissues, including red blood cells, liver, and kidney, while the long T_2 behavior was exhibited by halothane in serum.

These more recent results have prompted a thorough review of the original paper by Evers et al.,[41] and have led to a reappraisal of the pharmacological relevance of the T_2 behavior of volatile anesthetic agents in the brain. The area clearly requires further study.

3.4 Metabolism of Fluorinated Agents

Many of the previous ^{19}F MRS studies of halothane provided some data on the production of metabolites of the agent. Other groups have used the technique to study directly the metabolism of volatile anesthetics in the liver.[46–48] This issue is of considerable importance, since reactive metabolites of halothane and other agents are thought to act as haptens and lead to rare but fatal immunologically mediated liver failure.[49] For example, Preece et al.[50] studied the metabolism of enflurane in the liver of rats anesthetized with thiobarbitone. They demonstrated an elimination $t_{1/2}$ of 76 min for enflurane in the rat liver, and showed that this figure could be reduced to 39

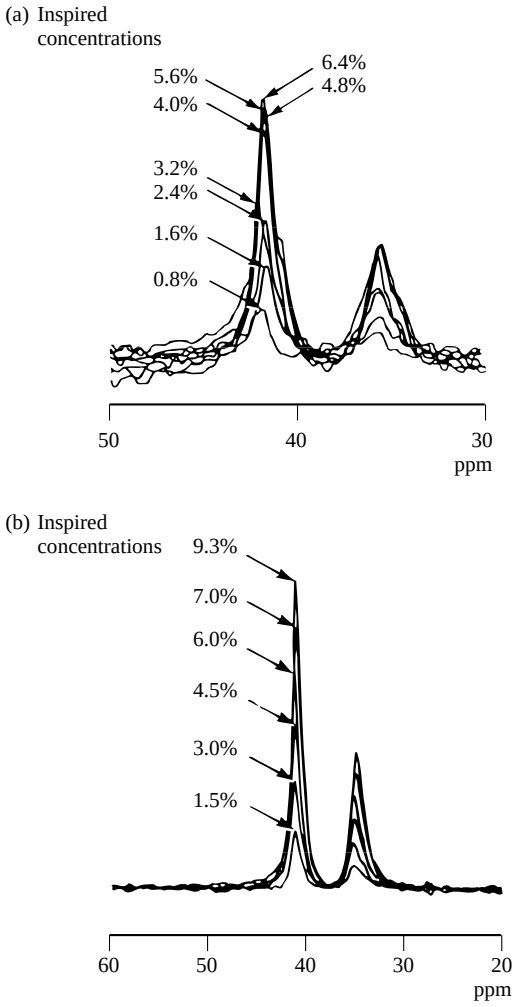

Figure 13 Superimposed ^{19}F MR spectra of brain isoflurane obtained at 4.7 T at different inspired concentrations of the agent, in spontaneously breathing (a) and artificially ventilated (b) animals. The apparent saturability of brain isoflurane at high inspired concentrations seen in (a) is a reflection of respiratory depression, since the spectra in (b) show a linear increase in brain halothane levels with inspired concentration. (Reproduced with permission from S. H. Lockhart, Y. Cohen, N. Yasuda, F. Kim, L. Litt, E. I. Eger II, L.-H. Chang, and T. James, *Anesthesiology*, 1990, **73**, 455)

min by pretreatment with isoniazid, which is known to enhance hepatic metabolism of enflurane (Figure 14). Similar studies may be useful in delineating pharmacogenetic differences in metabolism between individuals, or in elucidating the effects of drugs that enhance or inhibit the metabolism of volatile anesthetic agents. Data obtained from such studies may be quantitatively different, as in the studies by Preece et al.,[50] or show qualitative differences in metabolic pathways in different individuals or induced by different agents. Such processes could result in an increase or decrease in the production of toxic metabolites.

3.5 Clinical Studies

Clinical ^{19}F MRS studies of volatile anesthetics may have substantial advantages, since they enable the assessment of

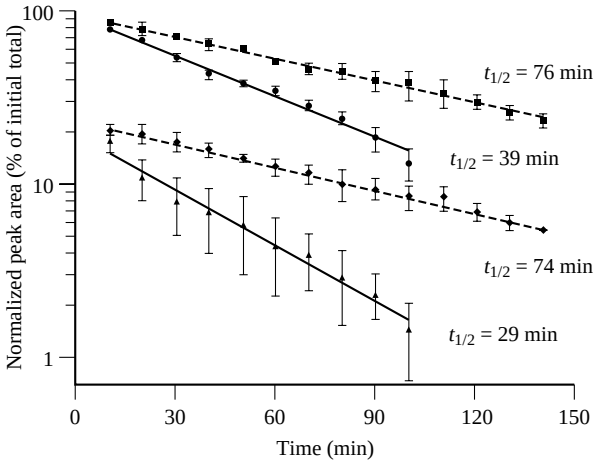

Figure 14 Decrease in the normalized signal intensities (as a percentage of the initial total) of enflurane in the liver with time. The plots show the decay of the major and minor resonances in control (■, ◆) and isoniazid pretreated rats (●, ▲). Points and bars represent the mean ± SEM of four rats; the calculated $t_{1/2}$ values for signal decay are also shown. (Reproduced with permission from N. E. Preece, J. Challands, and S. C. Williams, *NMR Biomed.*, 1992, **5**, 101)

subtle cognitive dysfunction produced by trace residual anesthetic concentrations, and may be technically easier since the human head is larger, and the improved signal-to-noise ratio may enable more effective and specific volume selection. However, such studies also present considerable logistic and ethical problems. Menon et al.[51] reported the use of ^{19}F MRS to study halothane in the brain of eight patients recovering from halothane anesthesia of short duration. A 6 cm surface receiver coil was used, and resonances attributable to halothane were observed in these patients up to 90 min after withdrawal of the anesthetic agent (Figure 15). Localized spectroscopy with two-

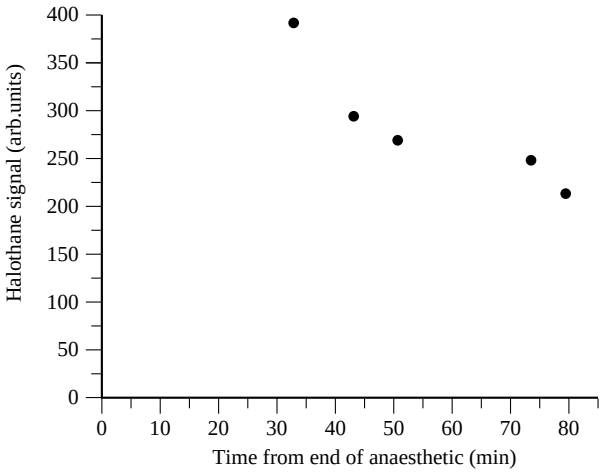

Figure 15 Decay of the ^{19}F signal intensity (arbitrary units) of halothane resonance with time after anesthesia in a patient where a single ^{19}F resonance was observed, and localized to the brain using a two-dimensional CSI sequence. (Reproduced with permission from D. K. Menon, G. G. Lockwood, C. J. Peden, I. J. Cox, J. Sargentoni, and J. D. Bell, *Magn. Reson. Med.*, 1993, **30**, 680)

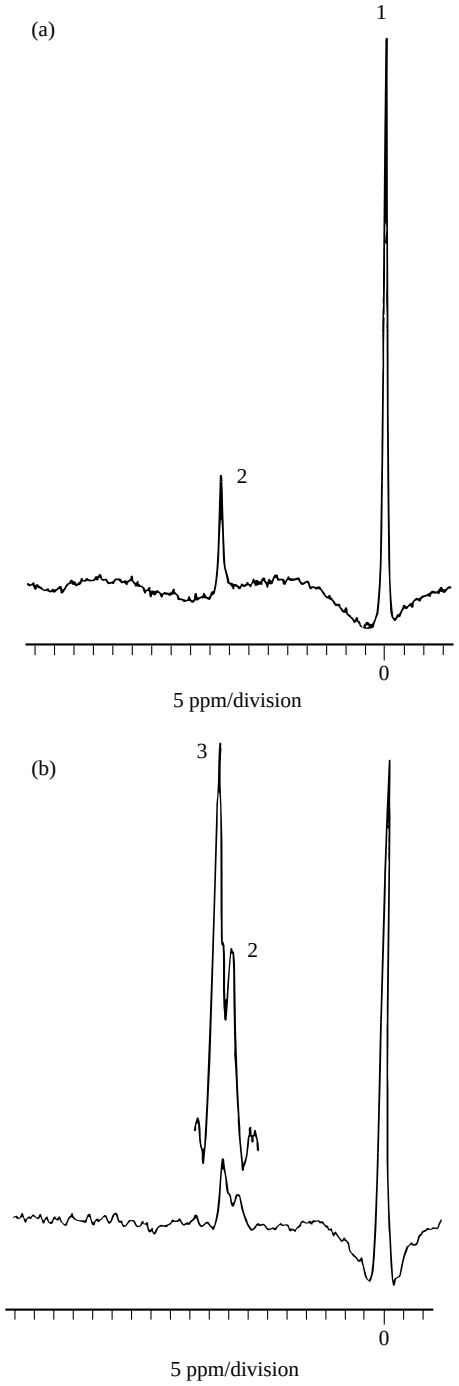

Figure 16 Spectra acquired from the whole sensitive volume of a surface receiver coil in two patients recovering from halothane anesthesia. In both spectra the large resonance at 0 ppm arises from an external NaF standard. (a) The single resonance at +43 ppm is from halothane. (b) The two resonances at +38 and +41 ppm are clearly seen in the inset, where the peaks are enlarged. (Reproduced with permission from D. K. Menon, G. G. Lockwood, C. J. Peden, I. J. Cox, J. Sargentoni, and J. D. Bell, *Magn. Reson. Med.*, 1993, **30**, 680)

dimensional chemical shift imaging (CSI) showed that, although some of the signal arose from extracranial tissues, a substantial proportion arose from brain. The signal-to-noise ratio for an unlocalized spectrum was typically 20 with data collection times of 2 min.

In seven patients a single resonance was seen with a mean (± SD) chemical shift of +43.3 (± 1.8) ppm, referenced to NaF at 0 ppm [Figure 16(a)]. This chemical shift is comparable to that observed in animal studies of halothane anesthesia. This resonance exhibited a T_1 value of 0.5–1 s, and a T_2* (estimated from the linewidth of the resonance) value of 3.5–10 ms. In one patient two resonances were observed with chemical shifts of +38 and +41 ppm [Figure 16(b)]. These two resonances may represent halothane in two different chemical environments within the brain, since phantom studies showed that the chemical shift of halothane in different environments (such as water, olive oil, methanol, and lecithin) could vary to an extent that accounted for the two resonances seen. The two resonances observed in this patient had different T_1 values and linewidths (and, by implication, different T_2* values). Intriguingly, the two-dimensional CSI localization in this patient suggested that the broader resonance at +38 ppm was confined to the brain, while the narrow resonance at +41 ppm arose from overlying scalp (Figure 17). Although susceptibility effects could not be excluded, it is at least possible that these two resonances represent halothane in two different tissues.

While the results discussed above do not resolve the problems discussed in earlier sections, they do demonstrate the feasibility of in vivo ^{19}F MRS studies of fluroinated volatile agents in humans, and confirm several findings observed in animal studies. In further studies, Lockwood et al.[52,53] have used ^{19}F MRS to study the pharmacokinetics of isoflurane in volunteers. They found two-compartment kinetics within the

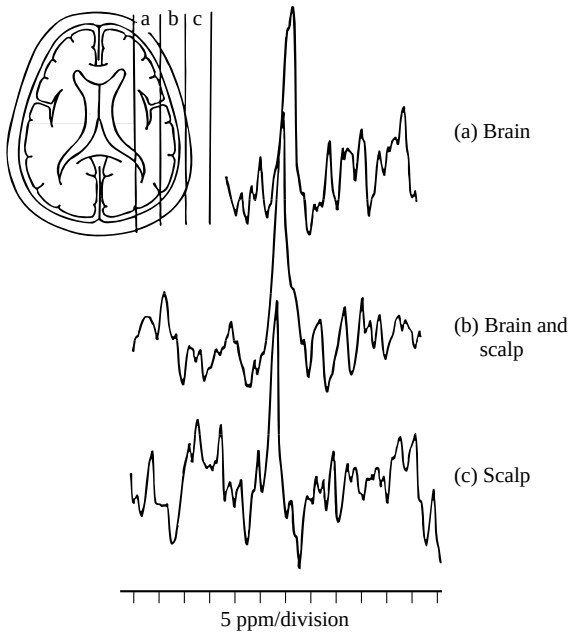

Figure 17 Spectra from three contiguous planes of the head acquired during the course of a two-dimensional CSI sequence, the location of which is shown on the line diagram of a transverse image of the head. Note that the resonances from superficial and deep slices have different chemical shifts (+38 and +41 ppm, respectively) and linewidths. (Reproduced with permission from D. K. Menon, G. G. Lockwood, C. J. Peden, I. J. Cox, J. Sargentoni, and J. D. Bell, *Magn. Reson. Med.*, 1993, **30**, 680)

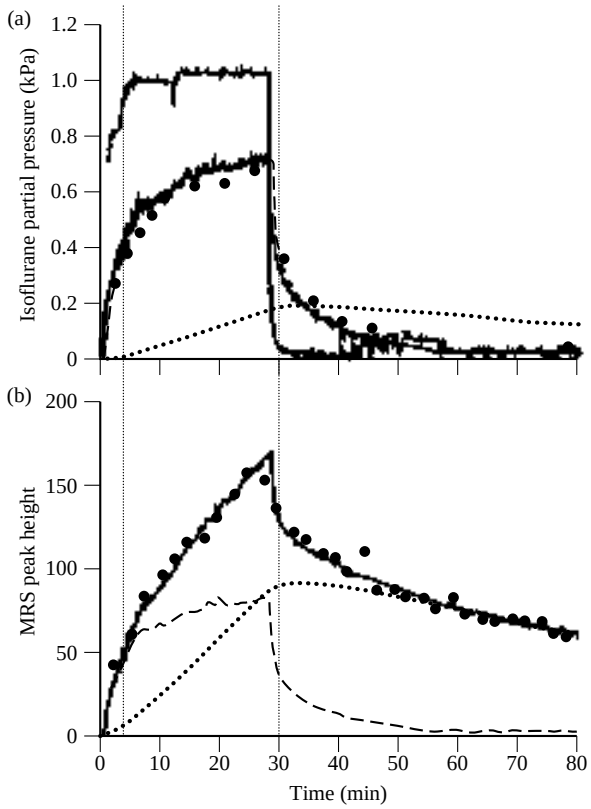

Figure 18 Isoflurane anesthesia in a volunteer during wash-in and wash-out.[53] The subject was unresponsive to verbal stimuli during the period between the two vertical dotted lines. (a) Partial pressure of isoflurane measured in inspired gas (upper continuous line), expired gas (lower continuous line) and arterial blood (solid circles). (b) Actual ^{19}F MRS data in arbitrary units (solid circles) and the summed intensities from the two-compartment model calculated for the data (continuous line). The fast (broken line) and slow (dotted line) components of the model are calculated from the MR data. In (a) the calculated fast-compartment trace is largely identical with the experimental data and is not visible. (Reproduced by kind permission of Oxford University Press from G. G. Lockwood, D. P. Dob, D. J. Bryant, J. A. Wilson, J. Sargentoni, S. M. Sapsed-Byrne, D. N. Harris and D. K. Menon, Magnetic resonance spectroscopy of isoflurane kinetics in humans, Part II: Functional localisation. *British Journal of Anaesthesia*, **79**, 586–9 (1999).)

head with equilibrium half-times of 3.5 min and approximately 1 h with respect to expired isoflurane concentrations.[52] Using critical fusion flicker frequency as an objective measure of the cerebral effect of isoflurane, they found evidence to identify the fast component as in brain tissue. Responsiveness to command was lost at a brain partial pressure of 0.3% isoflurane.[52] It was concluded that these measurements exactly matched the predictions of the classical perfusion-limited model. These compartments showed decay half-times of 9.5 and 130 min, but the signal was too weak to localize the compartments spatially. If the fast compartment is assumed to be the brain then these results match the predictions of the classical perfusion-limited pharmacokinetic model of inhalation anesthesia (Figure 18).[53]

4 RELATED ARTICLES

Brain MRS of Human Subjects; Cation Movements across Cell Walls of Intact Tissues Using MRS; pH Measurement In Vivo in Whole Body Systems; Temperature Measurement Using In Vivo NMR; Whole Body Studies: Impact of MRS.

5 REFERENCES

1. M. C. Malet-Marino and R. Martino, *Biochimie*, 1992, **74**, 785.
2. P. M. Joseph, J. E. Fishman, B. Mukherji, and H. A. Sloviter, *J. Comput. Assist. Tomogr.*, 1985, **9**, 1012.
3. A. R. Jacobsons, L. A. Sylvia, D. L. Veenstra, and J. T. Gerig, *J. Magn. Reson.*, 1992, **96**, 387.
4. C. N. Karson, J. E. Newton, P. Mohanakrishnan, J. Sprigg, and R. A. Komoroski, *Psychiatr. Res.*, 1992, **45**, 95.
5. R. A. Komoroski, J. E. O. Newton, D. Cardwell, J. Sprigg, J. Pearce, and C. N. Karson, *Magn. Reson. Med.*, 1994, **31**, 204.
6. D. J. Lee, C. T. Burt, and R. L. Koch, *J. Invest. Dermatol.*, 1992, **99**, 431.
7. T. Nakada, I. L. Kwee, B. V. Griffey, and R. H. Griffey, *Magn. Reson. Imag.*, 1988, **6**, 633.
8. T. Nakada, I. L. Kwee, B. V. Griffey, and R. H. Griffey, *Radiology*, 1988, **168**, 823.
9. T. Nakada, I. L. Kwee, P. J. Card, N. A. Matwiyoff, B. V. Griffey, and R. H. Griffey, *Magn. Reson. Med.*, 1988, **6**, 307.
10. J. T. Grieg, *Methods Enzymol.*, 1989, **177**, 1.
11. L. C. Clark Jr, J. L. Ackerman, S. R. Thomas, R. W. Millard, R. E. Hoffman, R. G. Pratt, H. RagleCole, R. A. Kinsey, and R. Janakiraman, *Adv. Exp. Med. Biol.*, 1984, **180**, 835.
12. B. A. Berkowitz, J. T. Handa, and C. A. Wilson, *NMR Biomed.*, 1992, **5**, 65.
13. J. S. Beech and R. A. Iles, *Magn. Reson. Med.*, 1991, **19**, 386.
14. H. S. Bachelard, R. S. Badar-Goffer, K. J. Brooks, S. J. Dolin, and P. G. Morris, *J. Neurochem.*, 1988, **51**, 1311.
15. R. Badar-Goffer, P. Morris, N. Thatcher, and H. Bachelard, *J. Neurochem.*, 1994, **62**, 2488.
16. P. M. Joseph, Y. Yuas, H. L. Kundel, B. Mukherji, and H. A. Sloviter, *Invest. Radiol.*, 1985, **20**, 504.
17. M. Rudin and A. Sauter, *NMR Biomed.*, 1989, **2**, 98.
18. J. Pekar, L. Ligeti, T. Sinnwell, C. T. Moonen, J. A. Frank, and A. C. McLaughlin, *J. Cereb. Blood Flow Metab.*, 1994, **14**, 656.
19. J. K. Alifimoff and K. W. Miller, 'Principles and Practice of Anesthesiology', M. C. Rogers, J. H. Tinker, B. G. Covino, and D. E. Longnecker ed., Mosby, St Louis, 1993, pp. 1035–1052.
20. K. W. Miller, *Int. Rev. Neurobiol.*, 1985, **27**, 1.
21. N. P. Franks and W. R. Lieb, *Nature*, 1994, **367**, 607.
22. D. E. Longnecker and F. L. Miller, 'Principles and Practice of Anesthesiology', ed. M. C. Rogers, J. H. Tinker, B. G. Covino, and D. E. Longnecker, Mosby, St Louis, 1993, pp. 1053–1086.
23. M. Herbert, T. E. J. Healy, J. B. Bourke, I. R. Fletcher, and J. M. Rose, *Br. Med. J.*, 1983, **286**, 1539.
24. A. Wyrwicz, M. H. Pszenny, J. C. Schofield, P. C. Tillman, R. E. Gordon, and P. A. Martin, *Science*, 1983, **222**, 428.
25. A. M. Wyrwicz, C. B. Conboy, B. G. Nichols, K. R. Ryback, and P. Eisle, *Biochim. Biophys. Acta*, 1987, **929**, 271.
26. E. I. Eger II, 'Anaesthetic Uptake and Action', Williams & Wilkins, Baltimore, 1974, p. 230.
27. A. M. Wyrwicz, C. B. Conboy, K. R. Ryback, B. G. Nichols, and P. Eisele, *Biochim. Biophys. Acta*, 1987, **927**, 86.
28. J. H. Lewis, H. J. Zimmerman, K. G. Ishak, and F. G. Mulluk, *Ann. Int. Med.*, 1983, **98**, 984.
29. E. N. Cohen, K. L. Chow, and L. M. Mathers, *Anesthesiology*, 1972, **37**, 324.

30. M. S. Wolff, *J. Toxicol. Environ. Health*, 1977, **2**, 1079.
31. J. C. Topham and S. Longshaw, *Anesthesiology*, 1972, **37**, 311.
32. P. Divakaran, F. Joiner, B. M. Rigor, and R. C. Wiggins, *J. Neurochem.*, 1980, **34**, 1543.
33. D. P. Strum, B. H. Johnson, and E. I. Eger II, *Science*, 1986, **234**, 1586.
34. L. Litt, R. Gonzalez-Mendez, T. L. James, D. I. Sessler, P. Mills, W. Chew, M. Moseley, B. Pereira, J. W. Severinghaus, and W. K. Hamilton, *Anesthesiology*, 1987, **67**, 161.
35. P. Mills, D. I. Sessler, M. Moseley, W. Chew, B. Pereora, T. L. James, and L. Litt, *Anesthesiology*, 1987, **67**, 169.
36. T. L. James, L.-H. Chang, W. Chew, R. Gonzalez-Mendez, L. Litt, P. Mills, M. Moseley, B. Pereira, D. I. Sessler, and P. R. Weinstein, *Ann. NY. Acad. Sci.*, 1987, **508**, 64.
37. T. Hashimoto, H. Ikehira, H. Fukuda, Y. Ueshima, and Y. Tateno, *Magn. Reson. Imag.*, 1991, **9**, 577.
38. A. M. Wyrwicz and C. B. Conboy, *Magn. Reson. Med.*, 1989, **9**, 219.
39. S. H. Lockhart, Y. Cohen, N. Yasuda, B. Freire, S. Taheri, L. Litt, and E. I. Eger II, *Anesthesiology*, 1991, **74**, 575.
40. M. Chen, J. I. Olsen, J. A. Stolk, M. P. Schweizer, M. Sha, and I. Ueda, *NMR Biomed.*, 1992, **5**, 121.
41. A. S. Evers, J. C. Haycock, and D. A. d'Avignon, *Biochem. Biophys. Res. Commun.*, 1988, **151**, 1039.
42. (a) A. S. Evers, B. A. Berkowitz, and D. A. d'Avignon, *Nature*, 1987, **328**, 157; (b) correction: 1989, **341**, 766.
43. S. H. Lockhart, Y. Cohen, N. Yasuda, F. Kim, L. Litt, E. I. Eger II, L.-H Chang, and T. James, *Anesthesiology*, 1990, **73**, 455.
44. H. J. C. Yeh, E. J. Moody, and P. Skolnick, *Nature*, 1990, **346**, 227.
45. H. Zimmerman, *Hepatology*, 1991, **13**, 1251.
46. D. S. Selinsky, M. Thompson, and R. E. London, *Biochem. Pharmacol.*, 1987, **36**, 413.
47. B. S. Selinsky, M. E. Perlman, and R. E. London, *Mol. Pharmacol.*, 1988, **33**, 559.
48. B. S. Selinsky, M. E. Perlman, and R. E. London, *Mol. Pharmacol.*, 1988, **33**, 567.
49. H. Zimmerman, *Hepatology*, 1991, **13**, 1251.
50. N. E. Preece, J. Challands, and S. C. R. Williams, *NMR Biomed.* 1992, **5**, 101.
51. D. K. Menon, G. G. Lockwood, C. J. Peden, I. J. Cox, J. Sargentoni, G. A. Coutts, and J. G. Whitesam, *Magn. Reson Med.*, 1993, **30**, 680.
52. G. G. Lockwood, D. P. Dob, D. J. Bryant, J. A. Wilson, J. Sargentoni, S. M. Sapsed-Byrne, D. N. Harris, and D. K. Menon, *Br. J. Anaesth.*, 1997, **79**, 581.
53. G. G. Lockwood, D. P. Dob, D. J. Bryant, J. A. Wilson, J. Sargentoni, S. M. Sapsed-Byrne, D. W. Harris, and D. K. Menon, *Br. J. Anaesth.*, 1997, **79**, 586.

Biographical Sketch

David Krishna Menon. *b* 1956. M.B.B.S. 1977, M.D. 1982, M.R.C.P. 1984, F.R.C.A. 1988, Ph.D. 1995, F. Ac. Med. Sci. UK 1998, F.R.C.P. 1999; internal medicine residency, Jawaharlal Institute, Pondicherry, India 1978–1983; Medical Registrar, Professorial Medical Unit, Leeds General Infirmary 1985–86; Registrar in Anaesthesia, Royal Free Hospital, London 1987–1988; MRC Research Fellow, NMR Unit, Hammersmith Hospital 1989–91. Presently: lecturer in anaesthesia, Cambridge University, and Director, Neurosciences Critical Care Unit, Addenbrooke's Hospital, Cambridge, UK. Current research interests: metabolic imaging of acute brain injury and brain inflammation following ischemia and trauma.

Functional MRI at High Fields: Practice and Utility

Kamil Ugurbil, Wei Chen, Xiaoping Hu, Seong-Gi Kim, Xiao-Hung Zhu

Center for Magnetic Resonance Research, University of Minnesota, MN, USA

and

Seiji Ogawa

Bell Laboratories, Lucent Technologies, Murray Hill, NJ, USA

1 INTRODUCTION

In the middle of the 19th century, a central debate about brain function revolved about the issue of whether the human brain processed all of its task as a single entity or function was compartmentalized. At about that time, an argument for the existence of regional specialization of human brain function was presented by Pierre Paul Broca.[1] Broca examined a patient who was unable to speak as a result of a stroke but was otherwise normal. Based on an autopsy performed subsequent to the patient's death, Broca concluded that the seat of the damage was an egg-sized lesion located in the inferior frontal gyrus of the frontal lobe in the left hemisphere; this general area is now commonly referred to as Broca's area, although its precise topographical extent remains ambiguous. This type of study and, later, intraoperative mapping efforts with electrodes were, until recently, the primary source of our information on functional compartmentation in the human brain.

Recent techniques using NMR permitted the acquisition of such information much more rapidly and with greater spatial accuracy, fueling explosive developments in the investigation of human brain function. For example, the language area first identified by Broca can now be visualized with unprecedented spatial resolution using functional MRI (fMRI), in data collection times that last only a few minutes. Figure 1 displays the three-dimensional result of such a study.[2] The functional map generated is superimposed on the anatomical image during a covert language task. In these figures, the gray scale anatomic images are either opaque, permitting the visualization of activation only on the outer cortical surface, or rendered partially transparent so that activation in the interior of the brain and within its numerous folds (sulci) are visible, albeit with diminished intensity.

These images are based on BOLD (blood oxygen level-dependent contrast), first described by Ogawa in rat brain studies[3–5] and subsequently applied to generate functional images in human brain.[6–8] Today, images like those shown in Figure 1 can be generated by the 1.5 T scanners that are often found in hospitals, provided that the scanner is equipped with appropriate hardware to perform fast imaging. These are relatively 'low' resolution images, in the several millimeter spatial domain, obtained with averaging over many executions of the same task by a single individual. However, there have been studies beyond this type of imaging using significantly higher magnetic fields.

Shortly before the introduction of BOLD-based fMRI, efforts were initiated in three laboratories, Universities of Minnesota and Alabama, and the National Institutes of Health, to explore the possibility of using high magnetic fields (4 T) for human MRI. However, these high-field studies were initially met with skepticism, and the possibility of human imaging at magnetic fields much higher than 1.5 T was seriously questioned. This skepticism was not based on the existence of any experimental evidence; rather, it followed from concepts and theoretical considerations regarding the interaction of high-frequency electromagnetic waves with the conductive human body. These considerations had led prominent investigators in the field of MRI research, as early as 1979, to suggest that human imaging would not be possible beyond 10 MHz (~0.24 T).[9] Of course, even clinical imaging is now performed at magnetic fields much higher than 0.24 T (up to 1.5 T), and recent work at 3 and 4 T has demonstrated that exquisite anatomical and functional imaging of the human head is achievable at these high fields. The efforts toward the development of fMRI at our site was performed only at 4 T, coinciding with the effort to introduce and explore the use of these high magnetic fields.

It is generally stated that the contrast-to-noise ratio (CNR) for the BOLD effect and hence for detection of activated areas increases at high fields, hence higher fields are better for fMRI. This may indeed be the case for some field strengths. A clear demonstration of this is illustrated in Figure 2, where mapping of the various functionally distinct regions within the visual cortex at 1.5 and 3 T depict larger areas of activation at the higher field strength. These are images of the flattened cortex. Similar functional maps have been published by Tootell and colleagues previously, mainly at 1.5 T.[10–15]

However, the field dependence of the BOLD-based fMRI is rather complex. At high fields, for example, the fractional signal change coupled to alterations in neuronal activity may actually become smaller than that observed at lower magnetic fields such as 1.5 T; however, the specificity of signal changes detected by MR in relation to the actual site of neuronal activation may be substantially improved. Such trade-offs between CNR and specificity will also depend on the details of data acquisition. Therefore, consideration of the BOLD mechanism is imperative in understanding the underlying field dependence of fMRI. This chapter starts with such a discussion and subsequently gives a few selected examples of accomplishments that remain unique to high-field fMRI.

2 MECHANISTIC CONSIDERATIONS RELEVANT TO FIELD DEPENDENCE

2.1 Extravascular Blood Oxygen Level-dependent Effects

Modeling of the effect of susceptibility gradients across vascular boundaries on MR signals have been considered by several groups, with similar conclusions.[16–24] If one considers an infinite cylinder as an approximation for a blood vessel with magnetic susceptibility difference $\Delta\chi$, then the magnetic field expressed in angular frequency at any point in space will be perturbed from the applied magnetic field ω_0.[16] Inside the

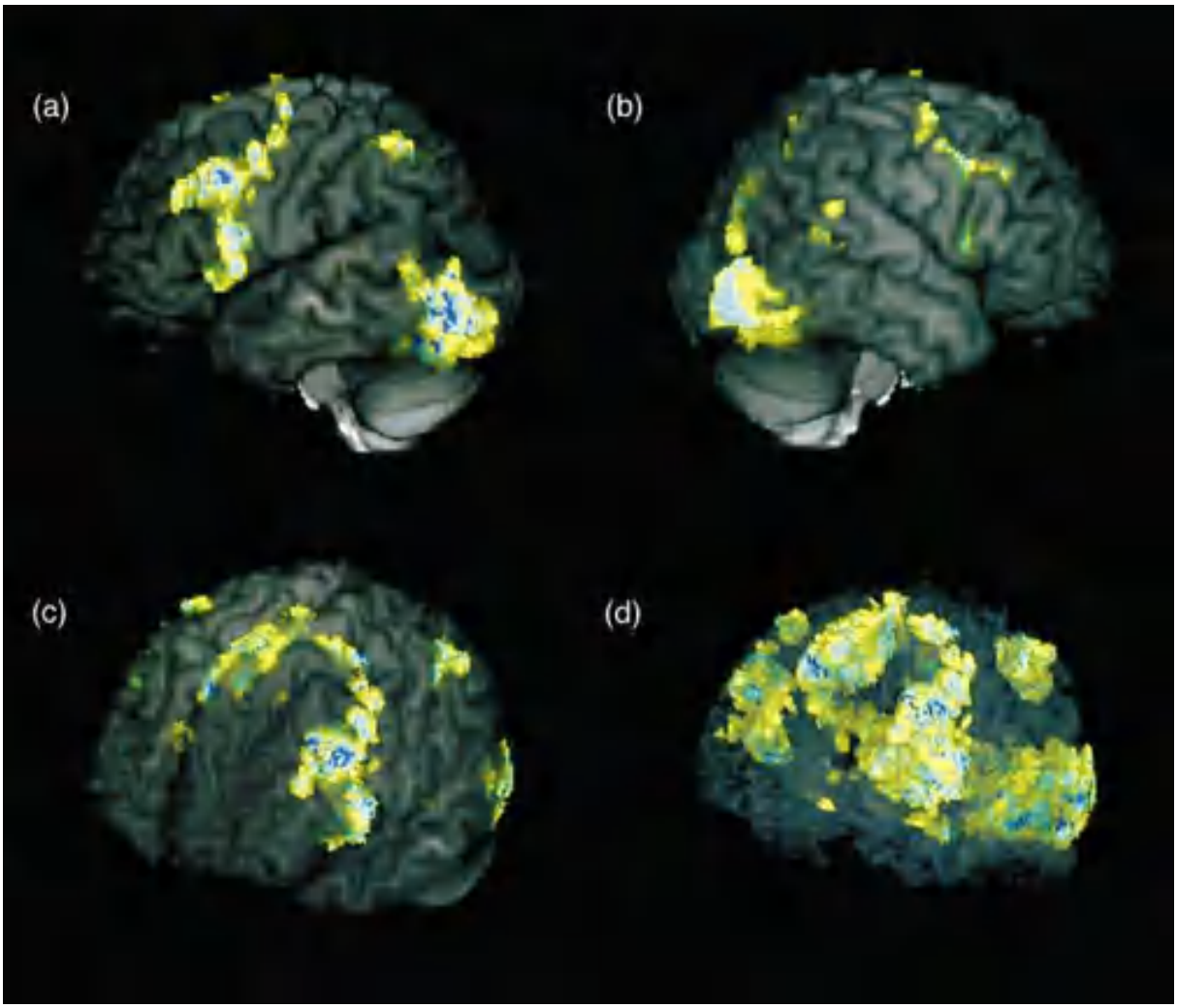

Figure 1 Three-dimensional, whole brain images of activation during a language task based on word generation from a phoneme. Subjects were presented phonemes and were asked to think of as many English words as they could that contained the phoneme until the presentation of the next phoneme. The gray scale picture is the anatomical image. In color is the superimposed functional map. Brain images shown are (a) left hemispheres (b) right hemispheres, and (c) at an angle where the left hemisphere and top of the brain are both partially seen. The extensive frontal cortex activity depicted in (a) largely defines the area of Broca and extends to area 46 as well. In (a)–(c), the anatomical images are opaque; consequently only activated regions that lie predominantly on the cortical surface are seen. Image (d) is identical to (c) except that the anatomical image was rendered partially transparent in order to 'look through' and see the activated regions that would normally be blocked from the view by overlapping cortex (e.g., regions within sulci). In these particular views, activity in the medial part of the brain and other areas are also apparent, albeit with diminished intensity, in addition to the extensive activity in the left hemisphere frontal cortex. (With permission from Erhard et al.[2])

cylinder, the perturbation, $\Delta\omega_B$, will be given by:

$$\Delta\omega_B^{in} = 2\pi\Delta\chi_0(1 - Y)\omega_0\{\cos^2(\theta) - 1/3\} \qquad (1)$$

At any point outside the cylinder, the magnetic field will vary, depending on the distance and orientation relative to the blood vessel and the external magnetic field direction, according to the equation:

$$\Delta\omega_B^{out} = 2\pi\Delta\chi_0(1 - Y)\omega_0\{r_b/r\}^2\sin^2(\theta)\cos(2\phi) \qquad (2)$$

In these equations, $\Delta\chi_0$ is the maximum susceptibility difference expected in the presence of fully deoxygenated blood, Y is the fraction of oxygenated blood present, r_b is the cylinder radius, and r is the distance from the point of interest to the center of the cylinder in the plane normal to the cylinder (Figure 3). Note that outside the cylinder the magnetic field changes rapidly over a distance comparable to two or three times the cylinder radius; at a distance equal to the diameter of the cylinder from the cylinder center, $\Delta\omega_B^{out}$ is already down to 25% of its value at the cylinder boundary.

If such a blood vessel is present in a given voxel, the magnetic field within this voxel will be inhomogeneous. The effect of this inhomogeneity in tissues can be understood in terms of *dynamic* and *static averaging*, the former arising as a result of the diffusive motion of the water molecules.

First, let us ignore the blood in the intravascular space (i.e., inside the cylinder) and focus on the *extravascular space* only. In BOLD-based fMRI, data are collected after excitation and an echo delay time *TE* in a gradient or a spin echo sequence.

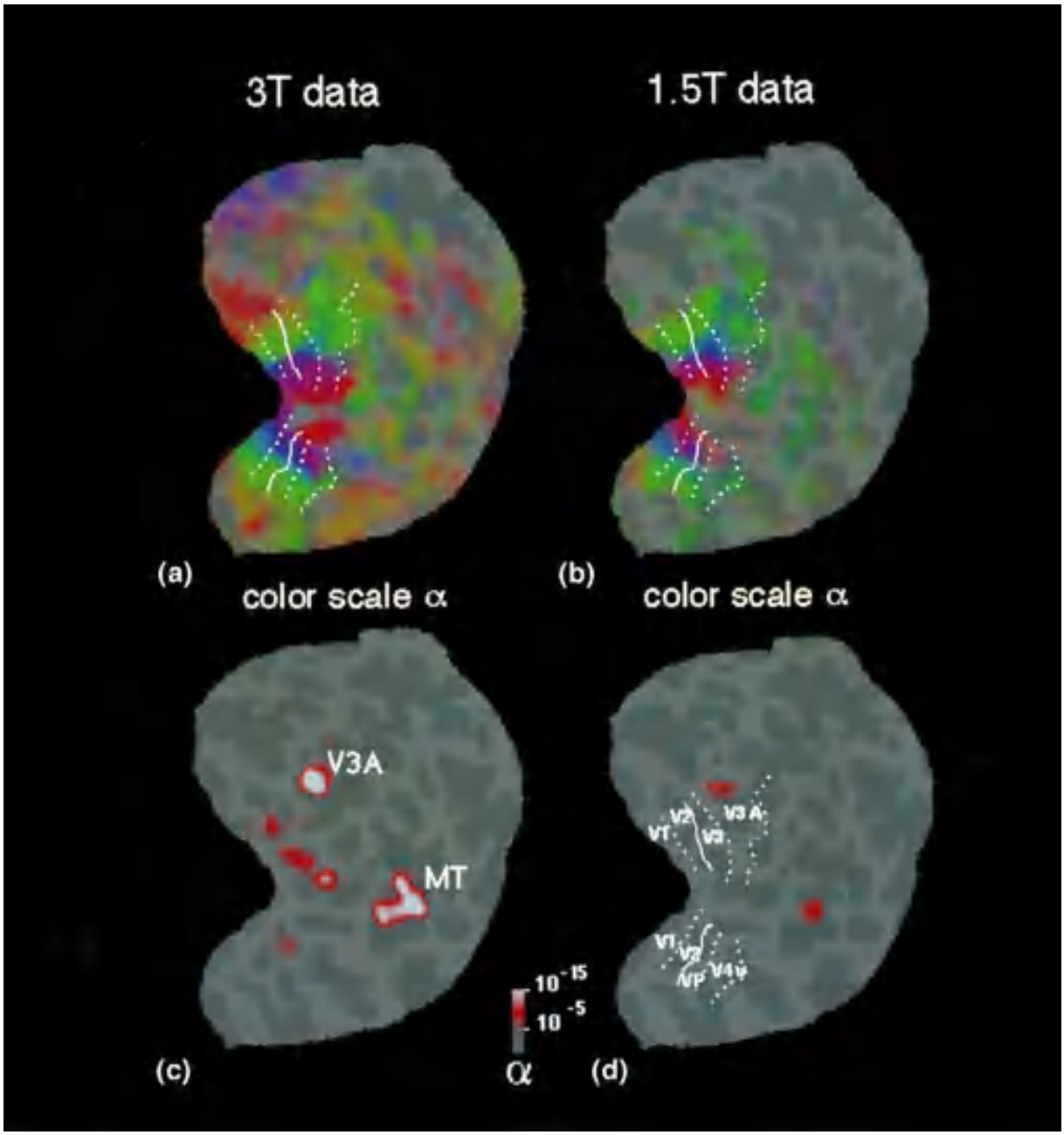

Figure 2 Mapping eccentricity and motion versus stationary stimulus in the visual cortex. Images are presented as a flattened cortex. (a), (b) Data from an experimental mapping eccentricity; (c), (d) low-contrast moving stimulus versus stationary stimulus that activates areas MT and V3a. (a), (c) Data at 3 T, with statistical significances ranging from 10^{-5} to 10^{-15}. (b), (d) Data at 1.5 T analyzed with the same statistical criteria as in (a) and (c). Comparison of (a) and (c) and of (b) and (d) show the effects of magnetic field strength at the same statistical significance. (Figure supplied by N. Hadjikhani and R. Tootell)

Typical *TE* values used depend on the field strength and the specifics of the pulse sequence but, in general, range from ~30 to ~100 ms. If the typical diffusion distances during the delay *TE* are comparable to the distances spanned by the magnetic field gradients, then during this delay the magnetic field inhomogeneities will be dynamically time-averaged. Therefore, blood vessel size compared with the diffusion distances in this 30–100 ms time domain becomes a critical parameter in the BOLD effect (Figure 4). In this time scale, small blood vessels (e.g., capillaries) that contain deoxyhemoglobin will contribute to the dynamic averaging and result in a signal decay that will be characterized with a change in T_2 time.[17,18,25] In a spin echo experiment with a single refocusing pulse in the middle of the delay period, the dynamic averaging that has taken place during the first half of the echo will not be recovered. Of course, applying many refocusing pulses, as in a Carr–Purcell pulse train, or applying a large $\boldsymbol{B}_1$ field (relative to the magnitude of the magnetic field inhomogeneity) for spin-locking during this delay will reduce or even eliminate this signal loss through dynamic averaging. In a gradient echo measurement,

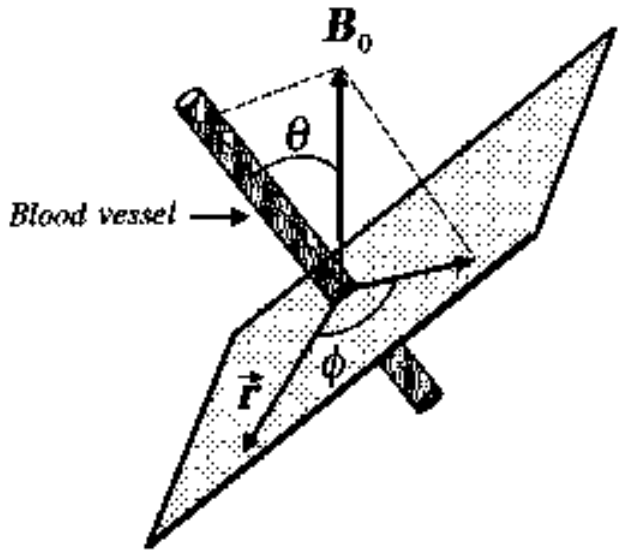

Figure 3 A cylinder representing a blood vessel and the parameters that determine magnetic field at a point outside of the cylinder when the susceptibilities inside and outside the cylinder are not the same

dynamic averaging will occur during the entire delay *TE*. If the imaging voxel contains only small blood vessels at a density such that one half the average distance between them is comparable to diffusion distances (as is the case in the brain where capillaries are separated on the average by 25 μm[26]), then the entire signal from the voxel will be affected by dynamic averaging.

In considering the movement of water molecules around blood vessels, we need not be concerned with the exchange that ultimately takes place between intra- and extravascular water across capillary walls. Typical lifetime of the water in capillaries exceeds 500 ms,[27–29] significantly longer than the typical T_2 and T_2^* values in the brain tissue and longer than the period *TE* typically employed in fMRI studies.

For larger blood vessels, complete dynamic averaging for the entire voxel will not be possible. Instead, there will be 'local' or 'partial' dynamic averaging over a subsection of the volume spanned by the magnetic field gradients generated by the blood vessel. However, there will be signal loss from the voxel through static averaging if refocusing pulses are not used or asymmetric spin echoes are employed. Following the excitation and rotation onto the plane transverse to the external magnetic field, a water molecule at a given point in space relative to the blood vessel will see a 'locally' time-averaged magnetic field that will vary with proximity to the large blood vessel. Therefore, the signal in the voxel will then be described by:

$$S(t) = \sum_k c_k \mathrm{e}^{-TE/T_{2k}} (\mathrm{e}^{-i\bar{\omega}_k TE}) \qquad (3)$$

where the summation is performed over the parameter k, which designates small volume elements within the voxel, and c_k is a constant; the time-averaged magnetic field experienced within these small volume elements is $\bar{\omega}_k$ in angular frequency units. The summation over k, therefore, covers the entire voxel. Because $\bar{\omega}_k TE$ varies across the voxel, the signal will be

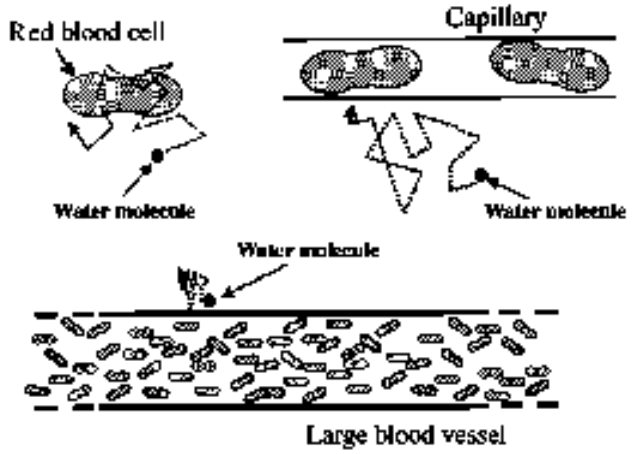

Figure 4 Dynamic and static averaging regimes based on diffusion distances relative to the size of a compartment that differs in magnetic susceptibility from the surrounding tissue. The magnetic field gradients are most prominent in the vicinity of the compartments with different susceptibility, i.e., red blood cells, capillaries, and large blood vessels. For large blood vessels, diffusion distances are not large compared with vessel radius, and hence they do not lead to dynamic averaging

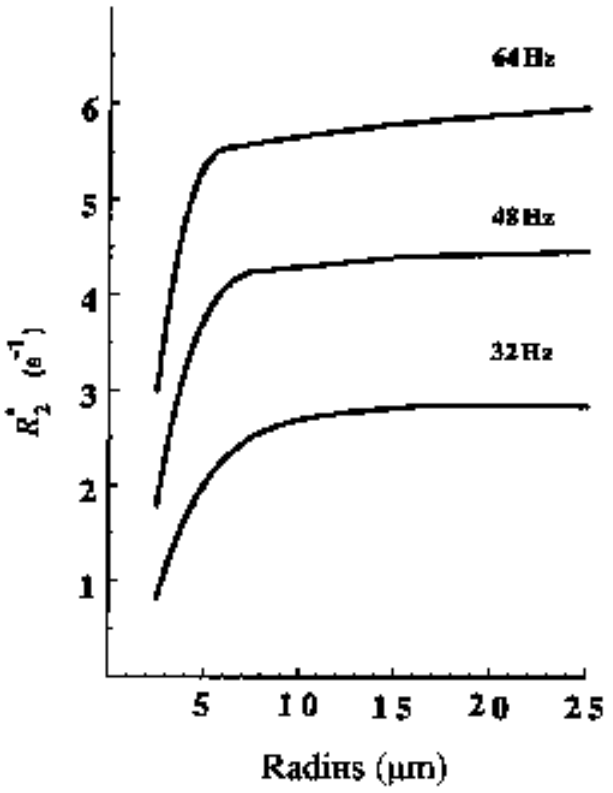

Figure 5 The susceptibility-induced R_2^* ($1/T_2^*$) in the presence of water diffusion plotted as a function of cylinder radius at three different values of frequency shifts. *TE* is 40 ms and the fractional 'blood volume' (i.e., volume within cylinder relative to voxel volume) is 0.02. (With permission from Ogawa et al.[18])

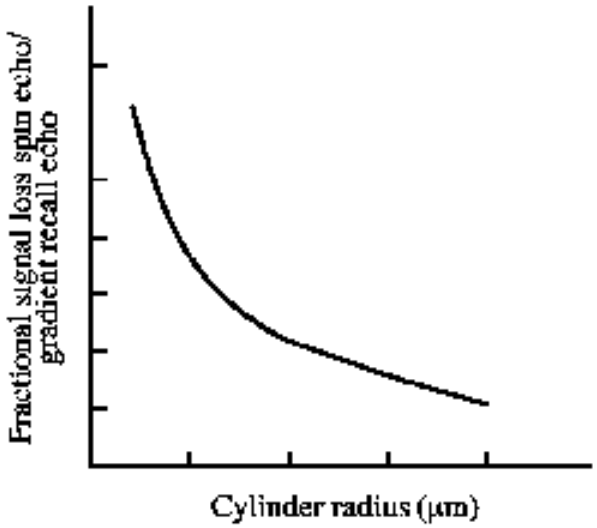

Figure 6 The fractional signal loss ($\Delta S/S$) for spin echo versus a gradient echo image acquisition as a function of cylinder radius *TE*, 40 ms; frequency shift owing to susceptibility difference, 40 Hz; fractional 'blood volume' (i.e., volume within cylinder relative to voxel volume), 0.02. (With permission from Ogawa et al.[18])

'dephased' and diminish with increasing *TE*. This signal loss occurs from static averaging. In this domain, if the variation $\bar{\omega}_k$ over the voxel is relatively large, signal decay can be approximated with a single exponential time constant T_2^*.

Figure 5 illustrates R_2^* (i.e., $1/T_2^*$) as a function of the radius of the cylinder from modeling studies by Ogawa et al.[18] In this calculation, all other relaxation mechanisms that can contribute to transverse relaxation of water protons are ignored; only the effect of the susceptibility difference between the cylinders and their surrounding is considered. The imaging voxel was divided into many cubes ($>10^6$) with an edge dimension L, each of which contained a single cylinder of length L. The volume of the cylinder (i.e., 'blood volume' b_v) relative to the volume of the cube is given by $(\pi r_b{}^2 L)/L^3$. Figure 5 displays the results as a function of cylinder radius and for a frequency shift ($\Delta\chi_0(1-Y)\omega_0$) equal to 32, 48, and 64 Hz, b_v=0.02 (simulating the capillary blood volume to total tissue volume ratio in the brain,[26] and *TE* of 40 ms (often used in studies at 4 T). Given the maximal susceptibility difference between fully oxygenated and fully deoxygenated blood[5] and taking Y to be 0.6, typical of venous blood in the brain, the frequency difference $\Delta\chi_0(1-Y)\omega_0$ is calculated to be 43 Hz at 4 T. The data in Figure 5 demonstrate that at a radius less than ~5 to 10 μm, depending on the magnitude of the frequency shift, R_2^* decreases because of dynamic averaging; the cylinder radius where this R_2^* decrease becomes apparent is smaller at larger frequency shifts as expected. Above ~10 μm, R_2^* is approximately independent of the radius as the static regime dominates for all $\Delta\chi_0(1-Y)\omega_0$ values considered in these calculations. These modeling efforts also suggest that deoxyhemoglobin-containing microvessels in the brain [i.e., capillaries (5 μm mean diameter) and venules (which can be 2–20 μm in diameter[30])] would be in the 'dynamic' averaging regime. Note that the frequency difference between the intra- and extra-cylinder compartments depends both on the applied external magnetic field $\boldsymbol{B}_0$ and on the magnetic susceptibility difference $\Delta\chi$ between the cylinder and its surrounding. Consequently, either at very high magnetic fields or at very large values of $\Delta\chi$, the radius at which a transition occurs from static to dynamic averaging will shift to values smaller than the capillary size. Such large values of $\Delta\chi$ can be achieved even at 1.5 T with bolus injections of contrast agents.

Figure 6 illustrates the dynamic versus static averaging regimes and their dependence on cylinder radius (i.e., blood vessel radius) in a different way. In a spin echo study, static averaging will not come into play because the refocusing pulse will undo the 'dephasing' and 'rephase' the spins. Therefore, spin echoes will only be sensitive to small cylinder radii. For gradient recalled echoes, both dynamic and static averaging are, in principle, operative. However, for small cylinder radii, only the dynamic averaging regime will apply. Therefore, a plot of the ratio of fractional signal loss during *TE* (i.e. $\Delta S/S$) for a spin echo versus a gradient recalled echo will have a curve approaching unity as the cylinder radius approaches zero. At the other extreme, this ratio will diminish with increasing cylinder radius as dynamic averaging disappears and a static averaging regime dominates.

The net result of these calculations (again so far not considering the intravascular effects) yields the following terms for contributions to R_2^*:

$$R_2^* = \alpha\{\Delta\chi_0\omega_0(1-Y)\}b_{vl} \quad \text{(large vessels)} \tag{4}$$

$$R_2^* = \eta\{\Delta\chi_0\omega_0(1-Y)\}^2 b_{vs}p \quad \text{(small vessels)} \tag{5}$$

where α and η are constants, ω_0 is the external magnetic field in frequency units (rad/s) (i.e., $\omega_0=\gamma\boldsymbol{B}_0$), $\Delta\chi_0\omega_0(1-Y)$ is the frequency shift owing to the susceptibility difference between the cylinder simulating the deoxyhemoglobin-containing blood vessel, b_{vl} is the blood volume for large blood vessels (veins and venules with a radius greater than ~5 μm for 4 T) and b_{vs} is the small vessel blood volume (capillaries and small venules, less than ~5 μm in radius, that permit dynamic averaging), and p is the fraction of active small vessels (i.e., filled with deoxyhemoglobin-containing red blood cells).

An important feature of Equation (5) is the fact that it varies as the square of the external magnetic field for small vessels where the effect is dominated by dynamic averaging. In contrast, the dependence on the external magnetic field is linear for large blood vessels because they are in the static averaging domain. Note, however, that even for the capillaries the quadratic dependence of the extravascular BOLD effect on ω_0 will not persist forever with increasing external magnetic field. At some very high external magnetic field strength, the frequency shift across the luminal boundaries of the blood vessel will be sufficiently large to displace even the capillaries into the static averaging domain, and hence to linear dependence on the applied magnetic field. At the present time, there is no experimental evidence as to what that field strength is, although results from our laboratory demonstrate that at 9.4 T there still exists an extravascular BOLD effect owing to dynamic averaging during activation (presented below).

Another important point that can be surmised from Equations (4) and (5) is that the BOLD effect will be proportional to three physiologic parameters: regional cerebral

blood flow (CBF) and oxygen consumption rate ($CMRO_2$) [since $(1-Y)=CMRO_2/CBF$] and regional blood volume. Neuronal activity is coupled to all of these physiologic parameters. It has been suggested that regional CBF increases while $CMRO_2$ in the same area is not elevated commensurably,[31–33] resulting in decreased extraction fraction and lower deoxyhemoglobin content per unit volume of brain tissue.

Another important prediction of the modeling studies is that there are large and small vessel extravascular BOLD effects. This has implications with respect to the specificity of functional images generated by the BOLD effect. While capillaries are uniformly distributed in tissue and are sufficiently high in density, large venous vessels are not; consequently BOLD effects associated with large vessels will not be as closely correlated with the actual site of neuronal activity. This issue will be discussed in greater detail below.

2.2 Intravascular Blood Oxygen Level-dependent Effects

In the blood, hemoglobin is also compartmentalized within red blood cells and when the deoxy form is present, there are field gradients around the red cells. However, because the dimensions of red cells are very small compared with diffusion distances, the effect is dynamically averaged and becomes a T_2 effect only. The dynamic averaging in this case also involves exchange across the red blood cell membrane, which is highly permeable to water. Consequently, in the presence of deoxyhemoglobin-containing red blood cells, the T_2 value of blood decreases. This effect was noted by Thulborn and was shown to increase quadratically with field strength as expected from dynamic averaging owing to diffusion in the presence of field gradients.[34,35] Therefore, even when we neglect the extravascular effect described above, the T_2 time of blood itself will change when the deoxyhemoglobin content is altered by elevated neuronal activity, and this will lead to a signal change in a T_2- or T_2^*-weighted image. This effect will be present wherever the deoxyhemoglobin content has changed, potentially both in large and small blood vessels.

As discussed previously, an increase in cerebral blood volume (CBV) results in signal loss in the extravascular BOLD effect. If the extravascular BOLD effect is neglected and only the intravascular contribution is considered, the increase in CBV with elevated neuronal activity can be more complex. Essentially, the ratio of blood to tissue volume will increase in a given voxel when CBV is elevated during increased neuronal activity. If the blood T_2 time is longer than that of tissue, then the CBV increase will lead to a signal *increase* rather than the decrease that is always expected from the extravascular BOLD effect. At 1.5 T, blood T_2 can be calculated from:[36]

$$(1/T_2) = 4.02 + 41.5(1 - Y)^2 \qquad (6)$$

which yields ~250 ms for arterial blood ($Y \approx 1$), and 94, 129, and 176 ms for venous blood with Y=0.6, 0.7, and 0.8, respectively. Experimental determinations give human arterial and venous blood T_2 times of 254±26 ms and 181±23 ms, respectively, at 1.5 T.[37] Compared with these blood T_2 values, cerebral tissues display T_2 values that range from ~70 to 90 ms at 1.5 T,[38] where the longest value is associated with cortical gray matter. These investigators measured T_2 values at 1.4 T. These values are expected to be also valid for 1.5 T given the relatively slow variation of T_2 with magnetic field strength for water in the brain. For example T_2 of cortical gray matter is 63±6.2 ms at 4 T[39] as opposed to 87±2 ms reported for 1.4 T.[38] At 1.5 T, the value of T_2 of both arterial and venous blood is longer than that of gray matter where the blood volume and alterations in blood volume coupled to neuronal activity are most significant.

Taking into account that the coefficient 41.5 in Equation (6) should be proportional to the square of the static field (except at very high magnetic fields), the T_2 time for venous blood can be calculated at other field strengths. At the same Y values, the predicted blood values for T_2 are approximately 4, 7, and 14 ms, respectively, for 9.4 T, in agreement with the experimentally measured values of ~7 to 8 ms in rat venous blood for a Y value in the 0.7 to 0.8 range (unpublished data from our laboratory). This rapid decrease in venous blood T_2 with increasing magnetic fields has significant implications for high-field fMRI studies and will be discussed below. At 4 T, where high-field human fMRI studies have so far been performed, blood T_2 is estimated to be 20, 31 and 63 ms for Y=0.6, 0.7 and 0.8, respectively, using Equation (6); these values are comparable to or significantly less than the gray matter T_2 time of 63±6.2 ms.[39]

Blood contribution comes into the BOLD phenomenon in a second special way when blood occupies a large fraction of the volume of the voxel, in other words when a large blood vessel occurs in the voxel. When deoxyhemoglobin is present in the blood, the blood water will result in dynamic averaging in the gradients surrounding the red blood cells and it will behave as if it encounters the uniform magnetic field given by Equation (1). This will differ from the magnetic field experienced by the rest of the voxel. In the immediate vicinity of the blood vessel, the magnetic field will vary and it will approach a constant value in tissue distant from the blood vessel. For simplicity, we can neglect the gradients near the blood vessel and consider the voxel to be composed of two large bulk magnetic moments, one associated with blood and the rest with the extravascular volume. These magnetic moments will precess at slightly different frequencies, the difference in frequency given by Equation (1); therefore, the signal from the voxel will decrease with time as the two moments lose phase coherence. In this scenario, the signal can even oscillate as the phase between the two magnetic moments increases and then decreases. We will refer to this as a type 2 blood effect in fMRI. When a voxel only contains capillaries, the blood volume is ~2%;[26] hence, the type 2 blood effect cannot exist for such a voxel. However, when a large blood vessel or vessels are present in the voxel, blood volume can significantly increase and become comparable to or even exceed the tissue volume in the voxel. If, of course, the voxel is smaller than the blood vessel dimensions, and the entire voxel is occupied by blood, then here too the type 2 effect does not come into play.

Note that the type 2 blood effect and the extravascular BOLD effect in the static averaging regime are similar in nature because they both involve signal modulation owing to dephasing of magnetization within a voxel. The main difference is the presence of a large blood component and the lack of sufficient variation in resonance frequency within the voxel to approximate the signal modulation as an exponential signal decay in the type 2 blood effect. Similar to the extravascular BOLD effect in the static averaging domain, the type 2 blood

effect will be refocused in a symmetric spin echo and thus nullified. Consequently, it will *not* be present in purely T_2-weighted BOLD and functional images derived from it.

Another important point is that this type 2 effect will diminish and even disappear at high magnetic fields because the T_2 value of blood gets very short and blood signal contribution becomes negligible.

2.3 Blood Oxygen Level Effects Detected in T_2 and T_2^* by fMRI

The origin of the signal intensity changes that are detected in T_2 versus T_2^*-based BOLD fMRI images, and hence the dependence on magnetic field of these effects, differ significantly, as can be surmised from the above discussion. These differences are summarized here.

The T_2^*-based BOLD signal can arise from both intravascular (blood) and extravascular effects originating from both large and small blood vessels. The relative contributions of these effects will depend on the magnetic field strength. In a T_2-based BOLD fMRI map, the signal changes come from intravascular effects (i.e., blood T_2 changes), hence from both large and small blood vessels, and from an extravascular effect associated only with microvessels such as capillaries and small venules. The major difference is that the extravascular BOLD effect in a T_2 image can only arise from the microvasculature, whereas in T_2^* images, it can originate from blood vessels of all sizes.

It is often suggested that T_2-based fMRI avoids a large vessel contribution. This claim is *not* correct because it ignores the intravascular blood-associated BOLD effect. At field strengths of 1.5 T, or even 4 T, there clearly exists a significant blood contribution to the BOLD effect during increased neuronal activity. At 1.5 T, T_2-based fMRI maps are predominantly if not exclusively affiliated with blood T_2 changes, hence with intravascular space, as discussed in the next section. Such blood contribution can originate from both large and small blood vessels. Only at very high fields (e.g., 9.4 Tesla) is T_2-based BOLD fMRI largely associated with the capillaries because intravascular blood contributions are suppressed by the very short T_2 value of blood (discussed in greater detail in the next section).

2.4 Experimental Studies

Early in the history of fMRI, it was demonstrated experimentally that the BOLD effect in human brain functional maps contained contributions from macroscopic venous blood vessels (i.e., vessels of ~0.5 mm or larger that can be visualized in MRI images) as well as from regions where no such macroscopic vessels were identified.[40] This has profound implications for the effective spatial specificity and spatial resolution that can be achieved with fMRI since large blood vessels do not exist at high density in the brain, where capillaries are common. Therefore, functional maps based on the macrovasculature can be significantly distant from the actual site of increased neuronal activity and thus misleading *if* high-resolution mapping in the millimeter or smaller scale is desired. The effect of the blood vessel size on BOLD will depend on magnetic field strength and the relative contributions of intra- and extravascular effects. These relationships can be experimentally evaluated.

The issue of extra- and intravascular BOLD effects has been experimentally examined using a Stejskal and Tanner[41] gradient pair of either the same or opposite polarity, depending on whether gradient or spin echoes are used, respectively. Such gradients were first used to examine molecular diffusion; therefore, their use to alter the image signal intensity is often referred to as 'diffusion weighting' even though there are additional perturbations that arise from the use of such gradients.

In experiments employing the Stejskal–Tanner gradients, the important parameters are the magnitude and the duration of the gradient pulses and the time separation between them. Frequently, the results are evaluated in terms of a parameter b, which is equal to $(\gamma G\delta)^2\,(\Delta - \delta/3)$ where γ is the gyromagnetic ratio (rad s^{-1} G^{-1}), G is the magnetic field gradient magnitude (G cm^{-1}), δ is the duration of the gradient pulse, and Δ is the separation in time of the onset of the two gradient pulses (where 1 G=10^{-4} mT). In simple isotropic diffusion, the MR signal in the presence of Stejskal–Tanner gradient, decays according to $\exp(-bD)$ where D is the diffusion constant. For flowing spins, b does not have such an immediately obvious physical meaning. If there is flow, the spins will acquire a phase that will depend on their velocity along the direction of the gradient and the gradient magnitude. Within vasculature, however, blood velocities are not uniform especially for vessels of large diameter. Furthermore, the blood vessels may change directions within a voxel, and there may be several different blood vessels with different flow rates and/or different orientations relative to the gradient direction. Since the blood signal detected from the voxel will be the sum of all these, the net result can be nulling of signal from flowing spins through dephasing.

The ability to nullify the intravascular signals by use of Stejskal–Tanner pulsed gradients provides the means to distinguish between intra- and extravascular BOLD effects in functional images. Such experiments have been performed at 1.5 and 4 T on humans. The studies at 1.5 T have indicated that most of the BOLD-based signal increase during elevated neuronal activity is eliminated by Stejskal–Tanner gradients, leading to the conclusion that most of the fMRI signal at 1.5 T arises from intravascular effects.[42,43] This intravascular BOLD effect may be associated with macroscopic blood vessels since it is debatable whether the gradient pulses used can suppress intravascular signals from microscopic blood vessels such as capillaries and small venules.[44] As discussed above, the intravascular BOLD effect in functional brain imaging can arise from the change in blood T_2 time or from what we described as the type 2 blood effect. The latter is refocused by symmetric spin echoes and, therefore, can only be present in gradient recalled echo or asymmetric spin echo measurements. Given the fact that symmetric spin echo fMRI experiments at 1.5 T yield very weak effects compared with gradient recalled echo studies, the data acquired with suppressing the blood component suggests that most of the fMRI signal at 1.5 T arises from type 2 blood effects. The same conclusion was reached in high-resolution two-, or three-dimensional gradient recalled echo studies of motor cortex activation.[45]

The effect of the Stejskal–Tanner gradients on brain tissue signal intensity at 4 T is illustrated in Figure 7a for a spin echo sequence. When activation studies were performed with such gradients at this field strength, ~60% of the 'activated' pixels disappeared at small b values but the remaining pixels persisted

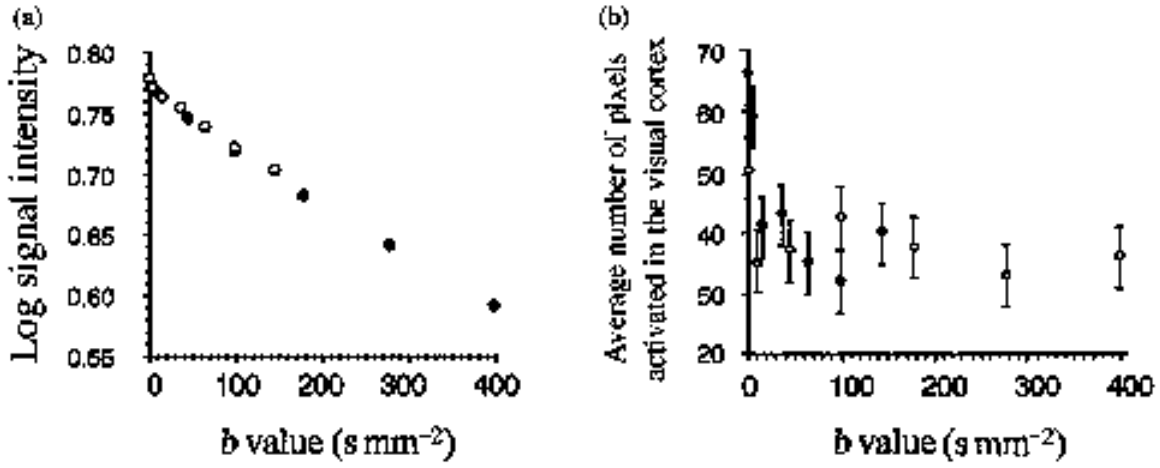

Figure 7 (a) The effect on signal intensity of variations in the value of b in the human brain under diffusion weighting in a spin echo sequence. (b) Number of activated pixels in the human visual cortex during visual stimulation at 4 T before and during application of bipolar gradients with increasing b value. The sequence was a spin echo sequence yielding T_2-weighted BOLD images. Residual signal intensity that persists at high b values can come only from the microvasculature. Data were from four subjects (○) or one subject (●). (With permission from Menon et al.[46])

as the gradient strength was increased to very large b values (Figure 7b). This suggests that at 4 T extravascular and/or capillary-level intravascular BOLD effects exist during activation as well as a significant intravascular contribution associated with the macrovasculature. Note that we have grouped extravascular and capillary-level intravascular effects together because it is not clear whether these gradients are sufficient to nullify the intravascular signal from capillaries.

At 9.4 T, the effects of the Stejskal–Tanner gradients become even more interesting. In a T_2-weighted fMRI study conducted in the rat brain (forepaw stimulation, symmetric spin echo with one 180° pulse), activation does not alter at all with changes from very small to very high b values (Figure 8).[47] The T_2-based BOLD effects can only come from the blood through a change in the blood T_2 or from extravascular effects associated with capillaries and comparably sized venules. The gradient pair will suppress the blood effect, except possibly in capillaries and postcapillary small venules. Therefore, it can be concluded that at this very high magnetic field there exists a strong and dominant BOLD effect originating from microscopic vessels. Intravascular effects associated with a blood T_2 change is a priori not expected to be significant at this field strength because the T_2 value of venous blood is very short at 9.4 T (~5 ms),[47] as discussed above. Even arterial blood has a short T_2 time at this high magnetic field strength (~30 ms).[47]

3 FUNCTIONAL IMAGING BASED ON CEREBRAL BLOOD FLOW

BOLD contrast relies on the interplay between CBF and $CMRO_2$ as well as blood volume, and, as such, it represents a complex response controlled by several parameters.[18,21,23–25,48,49] Recent MR techniques, however, can also generate images based on quantitative measures of changes in CBF coupled with neuronal activity.[7,50–54] These CBF techniques rely on tagging the blood spins differentially within and outside of a well-defined volume. For example, in the FAIR technique[51–53] frequency-selective inversion pulses are used to invert the longitudinal magnetization within a 'slab' along one direction (typically axial); in the absence of blood flow, the spins relax back to thermal equilibrium only by spin-lattice relaxation mechanisms characterized with the time constant T_1. If flow is present, however, the relaxation becomes effectively faster as unperturbed spins outside the inverted slab flow in and replenish the net magnetization within the slab. Consequently, the effective spin-lattice relaxation in FAIR as well as other, similar flow-sensitive techniques[48,51,53–58] becomes characterized by a shorter time constant, T_1^*, which is related to blood flow. It also follows naturally that if the inversion pulse in FAIR does not define a slab but inverts everything in the whole body (i.e., it is nonselective), blood flow does not enter into the problem. Therefore, in the FAIR technique, two images are acquired consecutively, each after a fixed delay period subsequent to the inversion pulse; in one, the inversion pulse is slab selective and in the other it is nonselective. The difference image generated from this pair is a flow-sensitive image.

One of the unique aspects of CBF-based functional maps is that macrovascular flow components can be selectively suppressed while sensitivity to microvascular flow and tissue perfusion changes is enhanced. In an experimental approach such as FAIR, this selective microvascular sensitivity is accomplished by changing the delay time after the initial inversion pulse and the subsequent signal excitation before image acquisition. In CBF-based functional imaging, longer delays (>1 s) emphasize microvascular flow and perfusion whereas shorter delays yield predominantly large vessel images.[51,59] The former, of course, is highly desirable for generating functional maps. Herein lies the magnetic field dependence of CBF-based functional images. The T_1 time of tissue water gets significantly longer at high magnetic fields. Consequently, it is easier

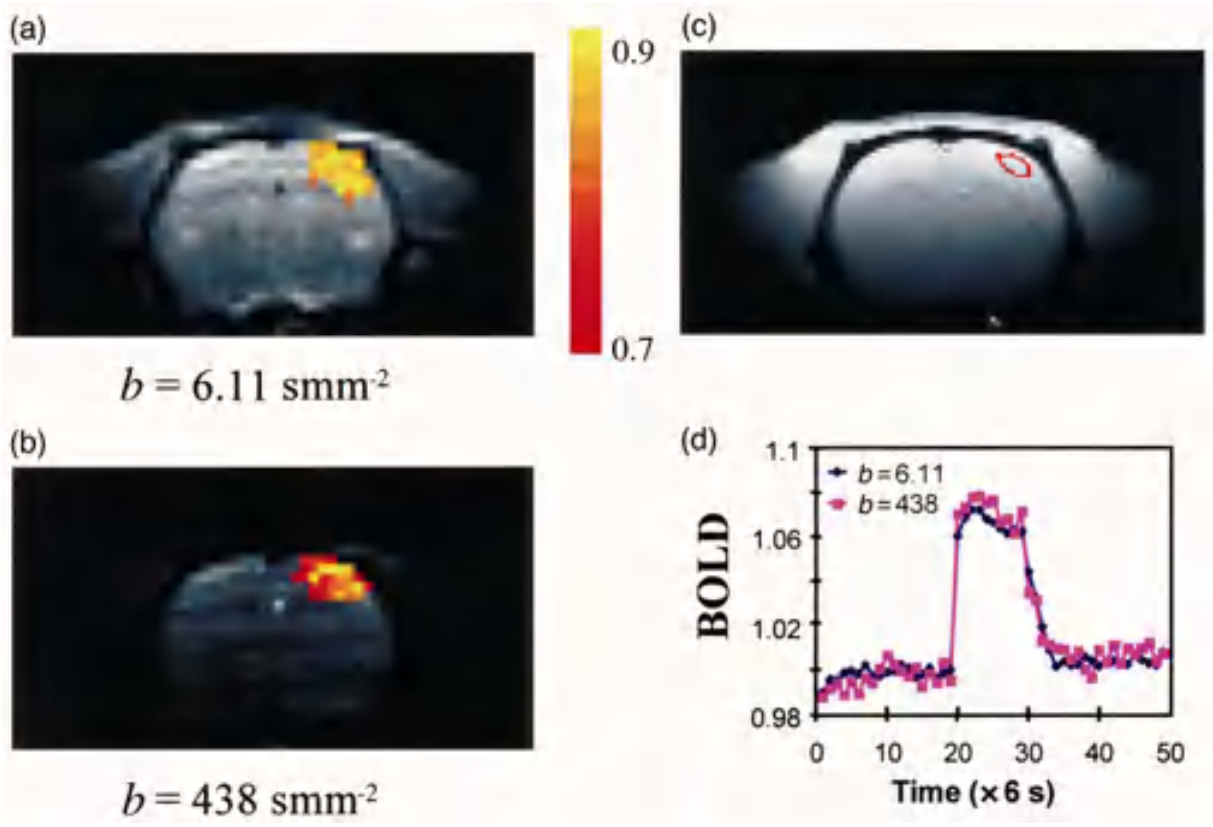

Figure 8 Diffusion-weighted spin echo fMRI maps at 9.4 T with b values of 6.1 (a) and 438 s mm^{-2} (b) overlaid on one of the original consecutively acquired echo planar images (BOLD and diffusion weighted) collected during the functional imaging study. Coronal single-slice single-shot spin echo planar images of rat brain were acquired with a matrix size of 64 × 32, a Field of View of 3.0 cm × 1.5 cm, a slice thickness of 2 mm, and *TE* of 30 ms. Somatosensory stimulation was used. The color bar indicates a maximum cross-correlation value from 0.7 to 0.9. Signal intensity (shown in background) was significantly reduced by bipolar gradients, as expected owing to diffusion. Localized activation is observed at the somatosensory cortex in the contralateral side of a stimulated forepaw. Foci of activation site (color) agree very well in both fMRI maps. (c) A Turbo FLASH image shows the region of interest. (d) Time courses of diffusion-weighted images within the region of interest. If the macrovascular contribution was significant, relative BOLD signal changes would decrease when a higher b value was used. However, relative signal changes remained the same in both images, suggesting that extravascular and microvascular components predominantly contribute to spin echo BOLD at 9.4 T

to detect the 'microvascular' flow and perfusion and suppress the macrovascular component (see Tsekos et al.[59]).

In view of the macrovascular problems that can deleteriously affect BOLD images, the question arises as to why CBF-based images are not the preferred approach in generating functional maps. The answer is that the CNR is higher in BOLD images, and, in particular, rapid acquisition techniques covering the whole or a large subsection of the brain are yet to be developed with CBF-based methods. Unlike the CBF-based techniques, however, BOLD images can be acquired rapidly over the whole brain. Consequently, this approach remains the main method employed in fMRI applications.

4 SPATIAL SPECIFITY

In fMRI studies, there are two reasons for concern regarding spatial specificity; one is the sensitivity to different size blood vessels and the presence of a macrovascular contribution, and the second is the spatial specificity of the physiologic and metabolic events that ultimately yield the functional images.

4.1 Early Blood Oxygen Level-dependent Responses

Optical measurements in animal experiments have demonstrated that the onset of task-related activation first results in signal changes interpreted as caused by an increase in deoxyhemoglobin content.[60,61] This deoxyhemoglobin increase peaks at ~3 s after task onset and is subsequently reversed, ultimately resulting in a relatively large decrease in overall deoxyhemoglobin content. If $CMRO_2$ is elevated because of energy requirements of increased neuronal transmission, oxygen extraction and consequently the deoxyhemoglobin level will also be elevated provided the blood flow remains constant. In contrast, a CBF increase alone without any alterations in $CMRO_2$ will cause only a decrease in deoxyhemoglobin; if there is a difference in the metabolic and hemodynamic response times of these two processes, with the latter lagging behind, the time dependence of deoxyhemoglobin content in the 'activated' region will resemble the biphasic curve illustrated in Figure 9. Presence of early deoxygenation has been recently reported based on direct measurements of blood partial pressure of oxygen,[62] indicating that there indeed exists an

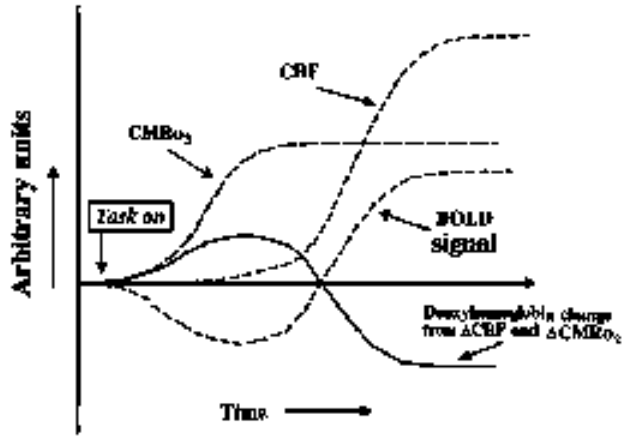

Figure 9 Hypothetical time courses of cerebral blood flow (CBF) and oxygen consumption rate ($CMRO_2$) that would predict an early negative BOLD response

early increase in $CMRO_2$ that precedes the onset of enhancement in blood flow.

The early deoxyhemoglobin increase can also arise from a rapid elevation in blood volume before the onset of blood flow augmentation; such a volume increase would actually result in elevated oxy- and deoxyhemoglobin contents. A subsequent rush of oxygenated blood through enhanced blood flow would then decrease the deoxyhemoglobin level, provided oxygen utilization does not increase commensurately with CBF. The possible occurrence of such a rapid volume increase has been suggested by recent studies in the rat brain.[63]

Malonek and Grinvald have argued that the early response is spatially more specific and defines better the columnar structure in the cat visual cortex examined in that study.[61] In contrast, they suggest that the CBF increase is not as specific, flooding not only the active but also inactive columns and surpassing in spatial extent the actual area of activation by several millimeters. These claims suggest that the BOLD effect associated with the hyperoxygenated, high-flow phase during increased neuronal activity will also be spatially nonspecific over several millimeters, reflecting the spatial distribution of the CBF response. The question arises whether the early response associated with increased deoxyhemoglobin can also be detected as a negative signal change in BOLD-weighted MRI and whether this response can be used as a means of obtaining functional images with the MR approach.

An early negative response to activation was first reported by Hennig and colleagues using a MR spectroscopy method, monitoring signal from a relatively large voxel but with high temporal resolution.[64] Subsequently, first using averaging of data from a number of subjects[65] and later with single subjects, imaging studies documented the presence of a small but detectable early negative signal change, a 'dip', at high magnetic fields.[66–70] Recently, the presence of this initial response was also observed in fMRI studies conducted in monkeys at 4.7 T;[71] the magnitude and the time course was very similar to the human data obtained at 4 T.

Figure 10 illustrates the time dependence of BOLD contrast fMRI signal changes observed in the human visual cortex during and subsequent to a brief visual stimulation that lasted 2.4, 3.6, and 4.8 s.[67] In this study, T_2^*-weighted, gradient-recalled echo planar images were acquired rapidly covering only a few slices in the visual cortex, thus sacrificing spatial extent of coverage and spatial resolution in favor of time resolution. Furthermore, the brief stimuli were repeated several times (four to ten) and images were collected in synchrony with the stimulus presentation so that they could be averaged. The data revealed that during and following the brief visual stimulation period the BOLD-based fMRI signal initially decreased; this decrease was reversed at about 3 s, resulting subsequently in a large signal intensity increase (Figure 10). For the longer stimulation period, a signal intensity decrease below baseline was also seen towards the end of the time course; this 'late-phase', poststimulation decrease has been observed before, even in the very first fMRI papers, and may reflect a difference in the post-task temporal responses of blood volume[72] and/or $CMRO_2$ values[73] returning to basal levels much more slowly than did the blood flow.

Figure 11 displays visual stimulation activation maps in the sagittal plane constructed from these data with the negative signal changes color coded in blue/purple colors and the positive response in red/yellow colors. Examining the images constructed from data collected during the early (negative) and the late (positive) response, we see that the early response is restricted to the anatomically well-defined visual area V1 (primary visual cortex) along the calcarine fissure while the later 'positive' BOLD image displays apparent 'activation' in areas distant from this region; in this study, these distant areas represent artifacts associated with the MR methodology, namely the macrovascular inflow effect, which has been already discussed. The macrovascular inflow effect was not suppressed in these images because they were rapidly acquired and were obtained using a surface coil both for signal detection and excitation; consequently, it was practically impossible to achieve the condition of 'full relaxation' between images that would have eliminated these artifacts without significantly sacrificing signal-to-noise ratio (SNR). The macrovascular inflow effect does not appear in the early images because it is absent owing to the slower hemodynamic response time. If the macrovascular effects are ignored and the functional maps around the calcarine fissure are compared, they are similar for the early negative and the later positive BOLD images. This observation has implications with respect to the spatial specificity of the functional maps generated by fMRI. It suggests that, provided the macrovascular 'inflow' artifacts are eliminated, the spatial specificity of the early negative BOLD-based maps and the later ΔCBF-dominated positive BOLD images are very similar at the resolution of this study (~3 to 4 mm isotropic). However, this study does not yet answer the question of spatial specificity raised by Malonek and Grinvald[61] because the study is not conducted at a sufficiently high spatial resolution. It is likely that higher magnetic fields will be necessary to achieve greater spatial resolution with this early response because it is a very weak effect. The fact that it is detectable by BOLD-based fMRI, however, is significant both from a mechanistic point of view and for future developments in fMRI.

The early negative response has been examined further[74] and demonstrated to be linearly dependent on *TE*. The percentage signal change varied from individual to individual in the nine subjects studied, ranging between 0.38 and 0.95% at 21 ms *TE* and 0.93 and 3.2% at 45 ms *TE* at 4 T; however, in

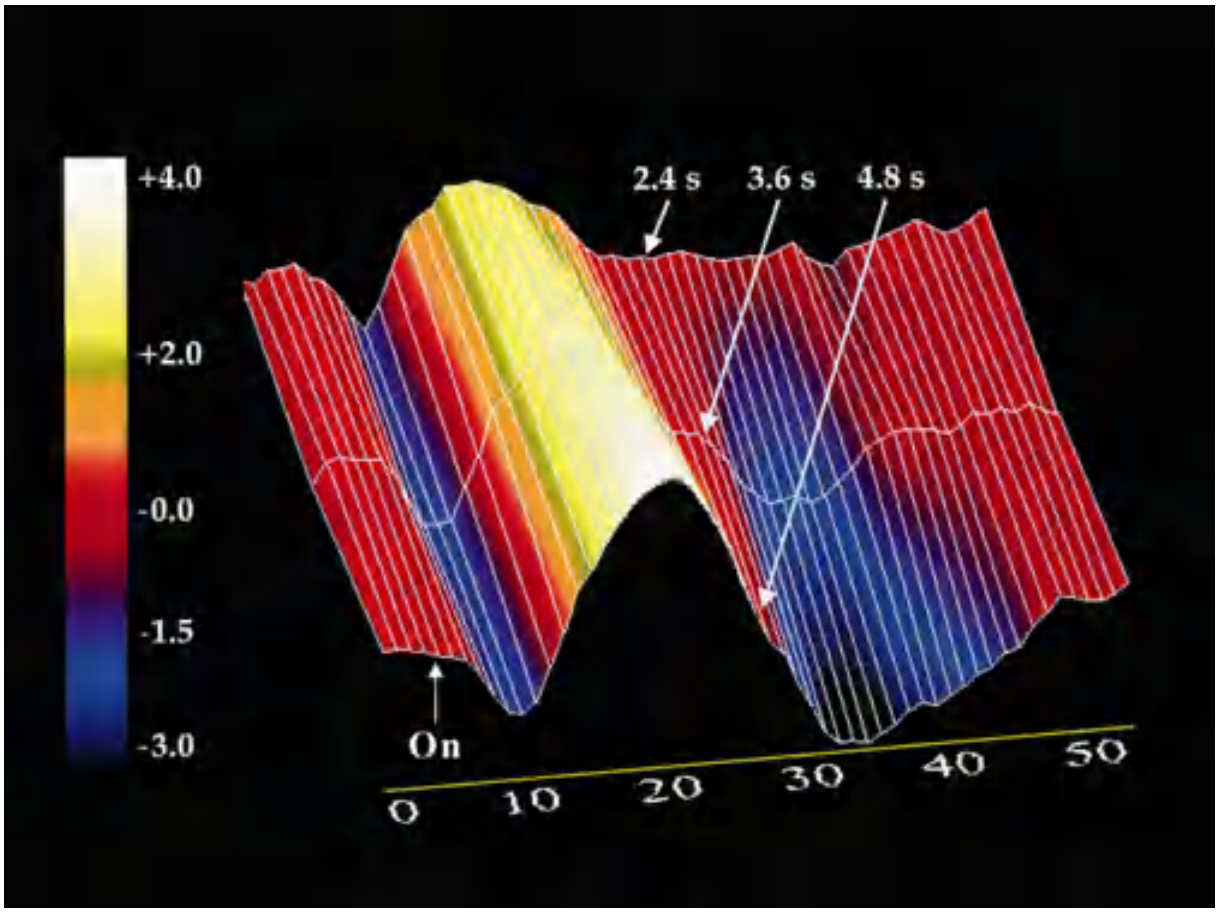

Figure 10 Signal intensity time course for activated areas in the primary visual cortex (V1) for three different periods of brief visual stimulation. Initially, the signal decreased to a valley, which is the early negative response or dip; subsequently, the signal increased leading to a peak that corresponded to the positive BOLD effect employed in functional images. This positive BOLD effect is much larger in magnitude than the early negative BOLD effect. Note that the poststimulation undershoot is seen prominently only when the visual stimulation duration is 3.6 ms or larger. (With permission from Hu et al.[67])

each case, a linear dependence on *TE* was strongly evident. Figure 12 illustrates this linear dependence in a way that accounts for the intersubject variability. The presence of this linear response with *TE* is a priori expected if the initial negative change arises from a BOLD effect reflecting an increase in regional cerebral deoxyhemoglobin content.

If the early response arises from an elevated $CMRO_2$ prior to the onset of an increase in blood flow, then initial stages of this early response will be associated with the capillary bed. At later times, this deoxyhemoglobin alteration will show up in the venules and veins as a result of blood flow. Capillary BOLD effects scale as the square of the magnetic field, which would explain why this early negative response has not been detected or has been reported to be very small at 1.5 T. A recent study in our group was able to identify a small early response at 1.5 T in the visual cortex; comparison with the 4 T data suggests that the ratio of the peaks corresponding to the early negative and subsequent positive responses increased linearly with field strength. Given the large macrovascular contribution at both 1.5 and 4 T to the late hyperoxygenated state, only a linear dependence on $\boldsymbol{B}_0$ is expected for this positive BOLD response. This suggests that the early response must increase quadratically with the magnetic field.

4.2 High-Resolution Imaging

The issue of spatial specificity and resolution of fMRI can also be addressed using specific experiments to map functionally distinct structures with well-defined organization and topography in the human brain. Early experiments introducing the fMRI methodology employed such a strategy and examined the hemispheric lateralization in brain function.[6–8,75] For example, simple motor tasks are expected to be lateralized ipsilaterally in the cerebellum;[75] in other words, a simple motor task with the left or the right hand should predominantly activate the left or the right cerebellar hemisphere, respectively. This is in direct contrast to what is expected and observed in V1. However, detection of functional specialization with respect to hemispheric laterality only reveals the existence of a very coarse level of spatial specificity in a spatial domain that can be characterized as several centimeters; certainly, this level of specificity was demonstrated in the very first studies introducing fMRI.[6–8] On a much finer spatial scale (e.g., millimeter and submillimeter), it is possible to examine activation of small subcortical nuclei and even that of lower-level neuronal functional organizations such as the ocular dominance columns (ODCs).

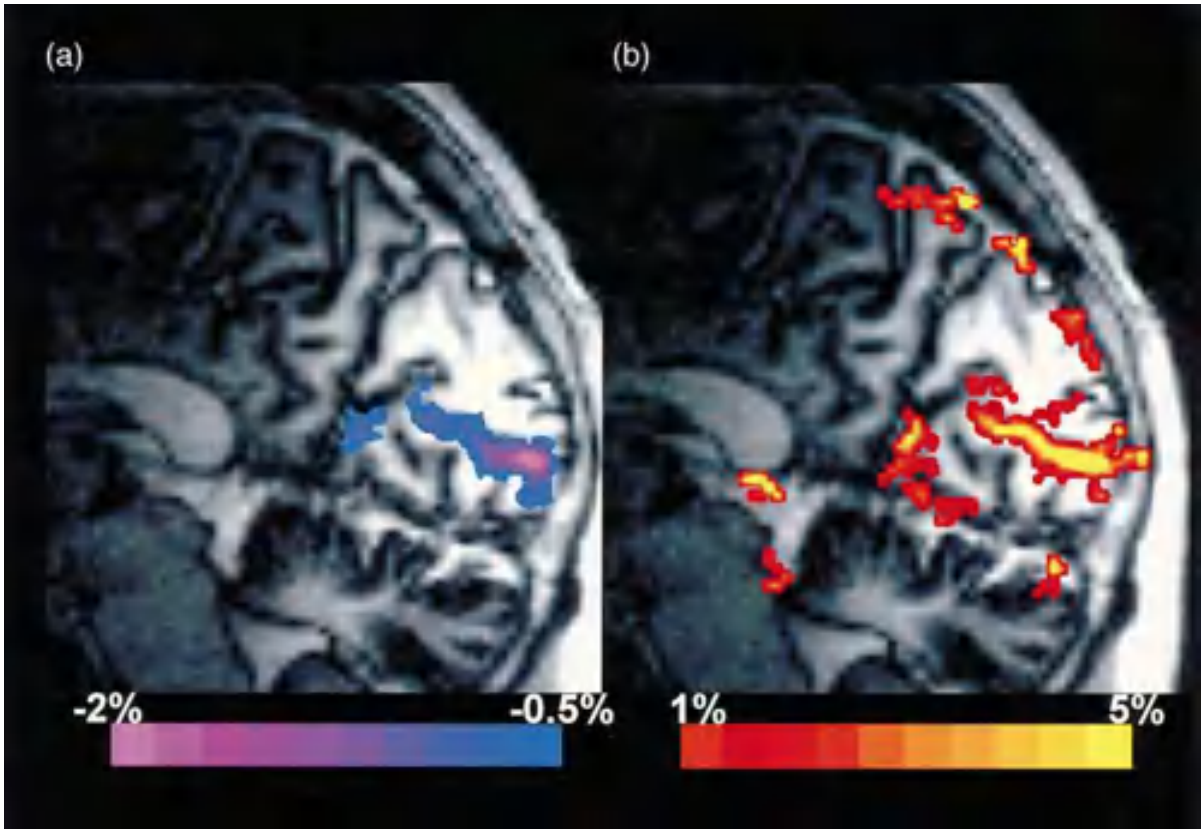

Figure 11 Functional images of visual stimulation constructed from (a) the early negative response (color coded in blue) and (b) the peak of the subsequent positive response (color coded in yellow/red). (With permission from Hu et al.[67])

The thalamus provides an excellent case for evaluating the question whether structures that are only a few millimeters in size can be accurately mapped by fMRI methodology. The thalamus contains several distinct, anatomically well-defined regions or nuclei. These nuclei serve as relay points for a remarkably large number of pathways. For example, retinal output projects mainly to the lateral geniculate nucleus (LGN), a small, subcentimeter nucleus located posteriorly and ventrally within the thalamus. In turn, the LGN activates V1.[76–80] Detection of LGN activation by fMRI has previously been reported at 1.5 and 4 T field strength.[81–83]

The LGN is functionally and spatially segregated and compartmentalized. Each of six LGN layers receives inputs from the specific visual field via the retina and then retinotopically signals to V1.[84] The specificity and resolution of fMRI can be examined by testing the feasibility of mapping the retinotopic organization within this small nucleus. We have recently conducted such a study using a checkerboard visual stimulus covering different sections of the visual field.[85] In particular, either upper or lower hemifield stimulation against a dark control period was utilized. This is expected to activate LGN bilaterally but not uniformly. Spatial differentiation reflecting the retinotopical relationship between the upper and lower visual fields was detected and distinguished within the LGN. This is illustrated as composite maps for four individual subjects in Figure 13. The LGN activation induced by the upper visual field stimulation (green and red pixels) was more inferior in location (closer to the hippocampal formation) compared with that induced by the lower visual field stimulation (yellow

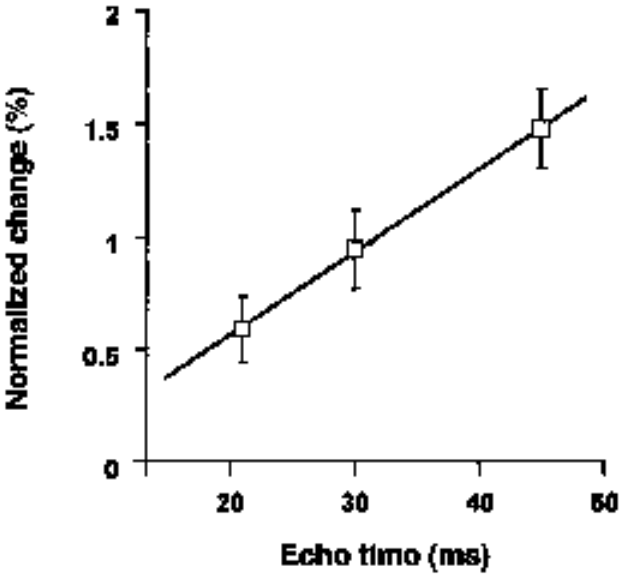

Figure 12 Echo time dependence of the early negative response (dip) to activation. For each of nine individuals studied, an average percentage change was calculated for the three echo delays used. Subsequently, the percentage change for the dip at each echo time was divided by this average for that individual. Then, the 'normalized' percentage change at each echo time was averaged across the nine subjects studied. The data points represent the mean and standard deviation obtained from this procedure. The line is a linear fit to the data. (With permission from Yacoub et al.[74])

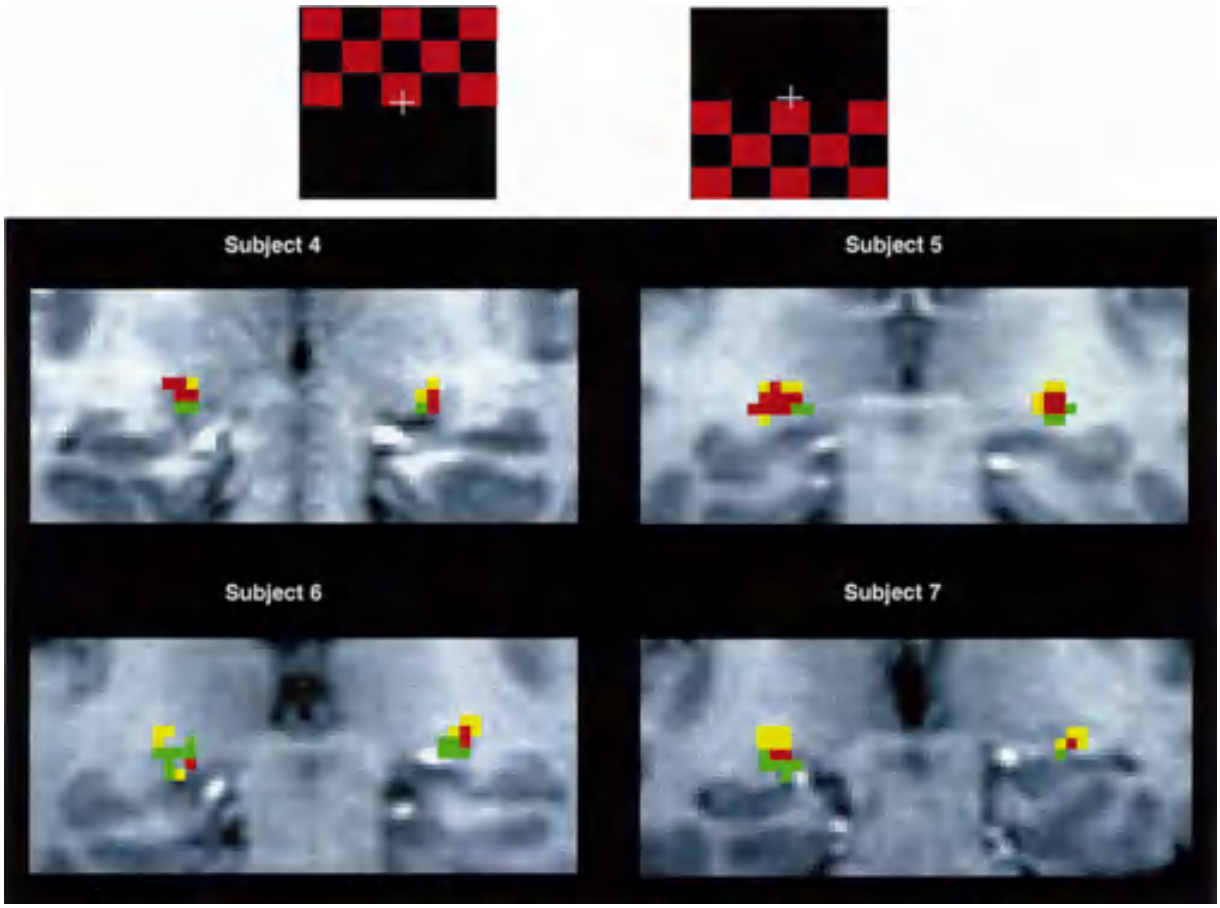

Figure 13 High-resolution fMRI mapping of lateral geniculate nucleus activation during the upper-field and lower-field red/black checkerboard visual stimulations (illustrated at the top of the figure). Images are in the coronal orientation. The activations in color represent composite fMRI maps obtained by combining the activation maps generated by upper-visual field versus a dark control period and lower visual stimulation versus a dark control period. The red pixels represent the overlap between these two activation maps. Yellow and green identify pixels activated only by the lower- and upper-field stimulation, respectively. (Adapted from Chen et al.[85])

and red pixels). This relationship is consistent with data obtained in the non-human primate visual system, which has been extensively studied using microelectrode recording[86] and selective lesions.[87,88] Our results also illustrate that the LGN in humans behaves similarly to V1.[10] However, the upper and lower visual field representations in V1 are anatomically separated by the calcarine fissure and are distinguishable without overlap. In contrast, they are continuous in LGN layers. This contributes to the partial overlap of LGN activation between the upper and lower visual fields (Figure 13).

From the LGN, geniculostriate projections to V1 continue to carry left or right eye input separately and terminate in layer IVC of V1, where they are arranged in a system of roughly parallel alternating stripes known as ODCs. In non-human primates and other vertebrates (e.g., cats), the organization of these columns has been studied by histological stains, autoradiography, and microelectrode recordings[80,89,90] and by optical imaging of intrinsic signals.[60,61,91–93] In humans, the ODCs have been demonstrated at autopsy in the striate cortex by histochemical staining for cytochrome oxidase;[94,95] however, a noninvasive technique for examining human striate cortex organization on the scale of cortical functional subunits has not been available.

The hemodynamic-response mechanism that allows visualization of orientation columns and ODCs in awake monkeys by optical imaging of intrinsic signals demonstrates that corticovascular responses to visual stimuli can be localized to the columnar level in several mammalian species. In particular, the optical data demonstrate that, while the CBF response may not be specific at the ODC level,[61] a deoxyhemoglobin difference across the active and inactive columns is generated presumably because of the enhanced $CMRO_2$ in the active but not the inactive column (Figure 14). This deoxyhemoglobin difference between the two columns should, in principle, be detectable by BOLD-based fMRI provided the technique has sufficient specificity as well as sensitivity (SNR) to achieve the required high spatial resolution. For example, if large vessel contributions dominate the BOLD contrast observed, specificity will be inadequate to detect ODCs.

For fMRI studies using clinically available hardware, ~3 mm in-plane resolution and ~5 mm slices are typical because of the limited SNR available without extensive data averaging. Using the same high-resolution fMRI pulse sequence with imaging hardware and parameters optimized at three different field strengths, we have found that the SNR at 4 T is at least four times higher than at the much more commonly available 1.5 T

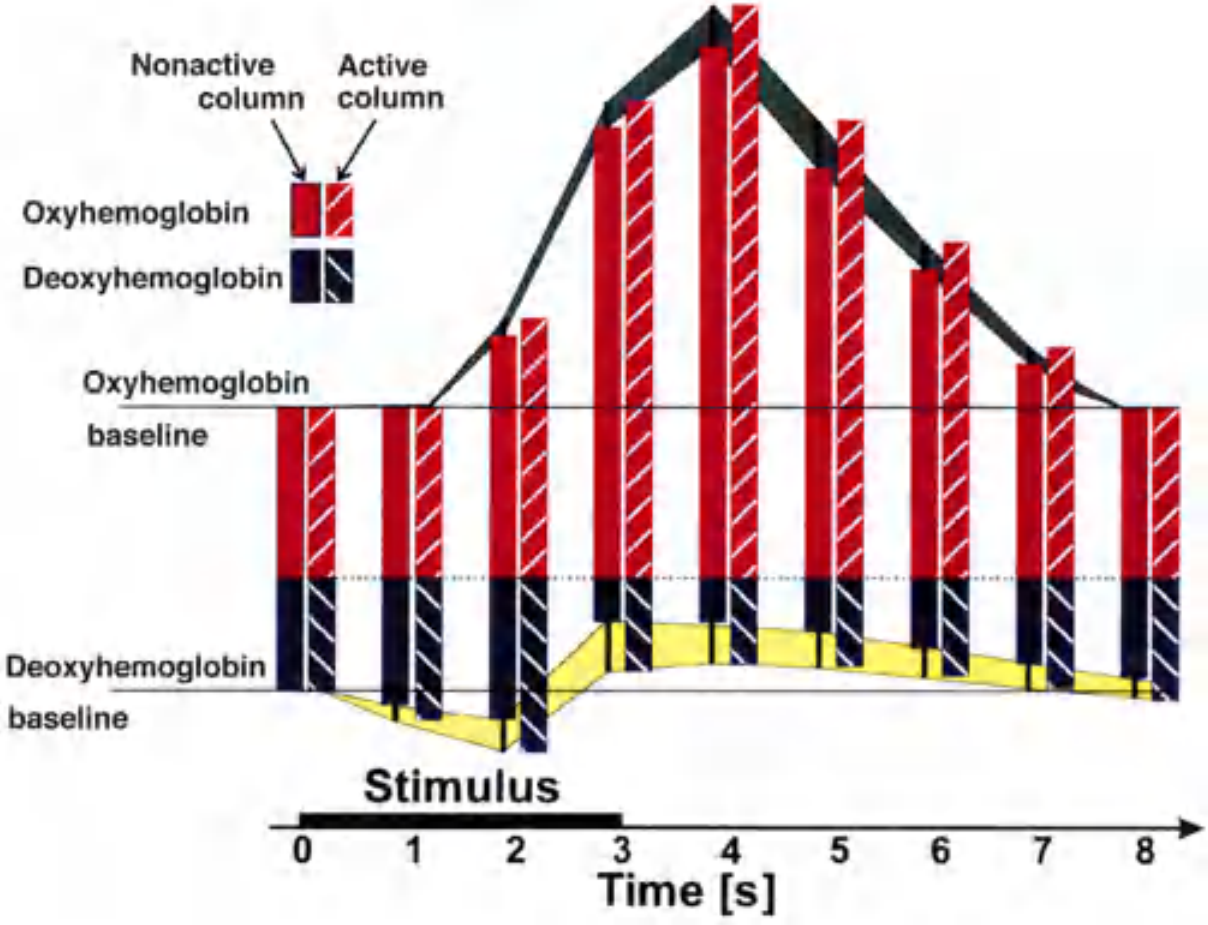

Figure 14 Deoxy- and oxyhemoglobin response as a function of time during a brief period of visual stimulation in active and inactive columns in the cat visual cortex. The figure represents a summary of findings by Maloneck and Grinvald.[61]

field strength.[96,97] This increase is sufficiently large to attempt imaging of ODCs in human V1, which are approximately 0.8–1 mm on a side for a column and 5–10 mm long.[94,95] Using a simple visual paradigm in combination with an optimized rf coil, head restraints, subvoxel image registration, and the enhanced SNR provided by 4 T field strength, it has been possible to demonstrate adjacent image pixels in human V1 that respond primarily to left or right eye photic input.[98–101]

Figure 15a demonstrates a magnified picture of cortical ribbon along a sulcus in V1. The image plane is along the calcarine fissure and columns appear as rectangles of approximately 1 mm×1 mm separated by ~1 mm in the cortical gray matter. The color map represents pixels that had higher signal intensity during left eye monocular photic stimulation than during right eye simulation. The dimensions of the 'activated' pixels are approximately 1 mm×1 mm or slightly smaller and are reproducible.[98,99] The technique in this study was to first use a binocular stimulation and then to use alternating left and right monocular stimulation. The data were, however, analyzed by looking for statistically significant differences in pixel intensities for only the monocular stimulation period, ignoring the binocular stimulation completely. The pixels identified as activated during either the left or right eye monocular stimulation also showed activation for the binocular period, as they should if they indeed represent ODCs as opposed to random statistical correlations.

Figure 15b demonstrates ODCs in the human brain from a more recent study at 4 T by Menon and colleagues.[102] These images are obtained in the sagittal plane adjacent to the interhemispheric fissure and the ODCs are visualized as they appear on the cortical surface in this region of the visual cortex. The blue and red colors illustrate the columns associated with the two eyes. The columns are now seen along their long axis rather than in cross-section.

These data demonstrate for the first time that mapping of functional subunits in humans is possible in a noninvasive manner. The fMRI time courses show that the hemodynamic response at the 'hyperoxygenation phase' can be used at 4 T as a direct indicator of neuronal activity in cortical columns. This opens up the possibility of mapping specialized populations of neurons in humans that are not accessible to electrophysiological or other methods of invasive mapping. However, they do not yet resolve the issue of whether CBF increase coupled to increased neuronal activity and consequently BOLD response is spatially specific and selective at the column level. The column images illustrated in Figure 15 were obtained using alternating monocular stimulation. Therefore, columns would be detectable as long as there was a *difference* in the deoxyhe-

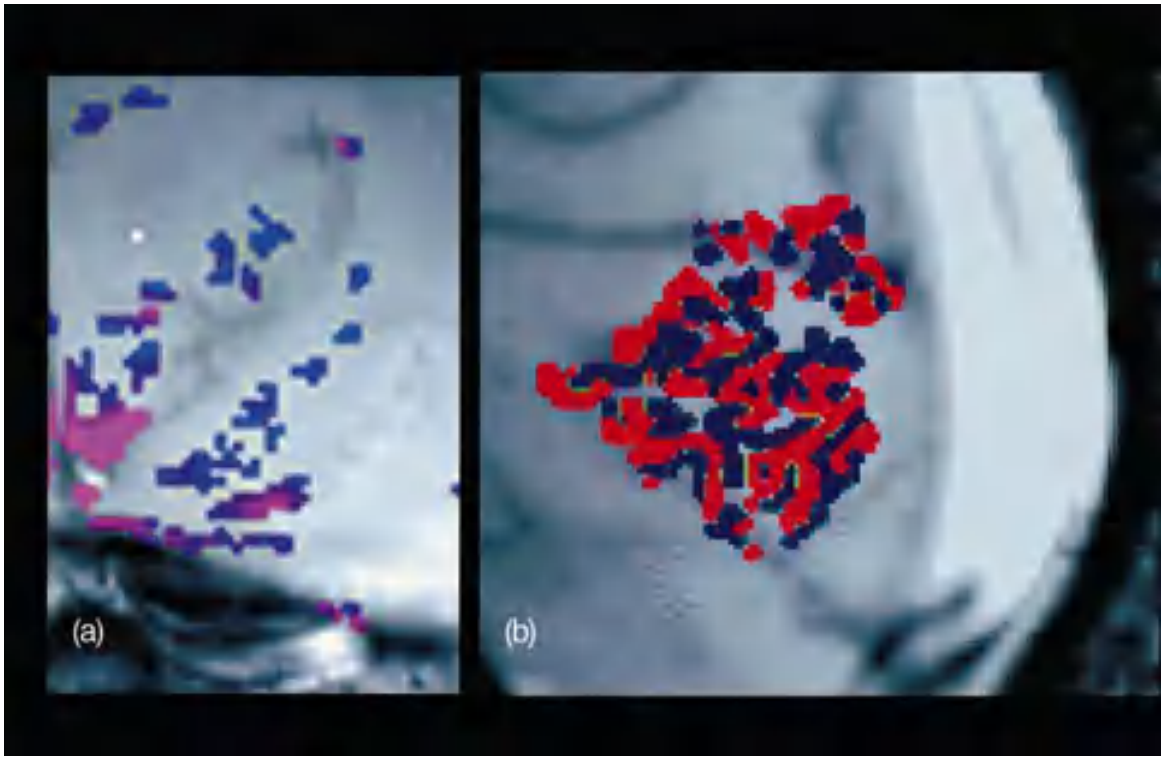

Figure 15 Detection of human ocular dominance columns (ODCs) during alternating monocular stimulation at 4 T. (a) Data obtained on a plane parallel to the calcarine fissure that intersects the ODCs perpendicular to their long axis. In this view, the ODCs should appear approximately as squares of 1×1 mm cross-section, separated by ~1 mm. There is a curving sulcus lined by the ODCs. (With permission from Menon et al.[99]) (b) A more recent study at 4 T showing a sagittal plane adjacent to the interhemispheric fissure; the ODCs are visualized as they appear on the cortical surface. The blue and red colors illustrate the columns associated with different eyes. (With permission from Menon and Kim[101] and Goodyear and Menon[102])

moglobin content of the inactive and active columns, and hence a difference in the BOLD effect, even if the deoxyhemoglobin content changed for *both* active and inactive columns, as illustrated in Malonek and Grinvald (Figure 14).[61]

The results summarized above demonstrate that, despite the presence of several potential problems, fMRI at 4 T has the specificity and sensitivity to map organizations in the millimeter or slightly smaller scale with the use of appropriate paradigms. This is unprecedented in human brain studies. We must emphasize the high-field aspect of all of the afore-mentioned high-resolution studies; to date, the ODCs have not been detected at lower field strengths.

5 SINGLE-TRIAL FUNCTIONAL MRI

Most fMRI studies utilize a 'block' design where periods of a control state are interleaved with periods of task performance and/or sensory stimulation. The control period itself may also require the subject to perform a task and/or be subjected to sensory stimulation. The images are generated by examining the difference between the control and the tasking periods. Each of these periods are relatively long, typically a minute or more, and the subject executes the task many times. The picture that emerges from such a study is a time average that blurs important information regarding the temporal evolution of the neuronal activity in different parts of the brain. Equally important, cognitive effects such as learning, alteration in strategy, etc. that evolve with repeated executions are also averaged into the final image generated.

fMRI is actually a realtime measurement. Single-slice fMRI images can be acquired in tens of milliseconds, adequate to monitor neuronal responses. Unfortunately, the temporal response of fMRI signals is dictated by the response of the vascular system, which is characterized with a time constant of seconds. This was demonstrated in one of the early fMRI studies[103] and subsequently confirmed in numerous other reports.[67,104–108] However, even within this temporal regime, useful information on brain function can be obtained since numerous tasks and processes exist that necessarily engage the human brain for prolonged periods. In this temporal domain, signal changes in the fMRI images track the temporal evolution of stimulation or mental task performance very well, albeit with a shift in time or a delay that lasts several seconds. This capability permits the acquisition of fMRI data gated to a particular time point in stimulus onset or the instruction–execution sequence. In either case, this type of fMRI data collection is referred to as event-related fMRI.

In event-related fMRI, two distinct types of experiments have been performed. Buckner et al. acquired images gated to the onset of a task in a paradigm so that the temporal evolution of the fMRI signal during and following the execution of the task could be temporally co-registered and averaged following repeated executions of the same task.[109] However, such aver-

aging loses unique information associated with each execution of the task; subjects do not perform the same way each time because both brain function and performance is modulated by effects such as learning, alterations in strategy, errors, and habituation. In addition, when averages of single trials are performed, it is not possible to conclude much about the temporal differences that may be observed among different regions of the brain; such a difference was reported in the study by Buckner et al., where activation in left prefrontal areas involved in language were delayed ~2 s relative to extrastriate areas during a word generation task.[109] Of course, the human brain performs this task much faster than 2 s, and this time difference cannot really be attributed to differences in brain activation. Rather, differences must exist in the hemodynamic response of the fMRI signal in different regions of the brain. This distinction, however, cannot be made from the data alone in this study, and the interpretation of the results would be ambiguous in less obvious cases when this approach is utilized.

The second type of experiment was a true single-trial fMRI study achieved with the use of high magnetic fields (4 T).[105,106,110–113] Intentionally and specifically, it was demonstrated that (at least at 4 T) there exists enough sensitivity to monitor fMRI signal evolution in a single execution of a task without averaging over many trials. This point is important. With this capability, it is then possible to perform many such single trial executions of a task and *not average them but rather to store them separately* and subsequently analyze and correlate the fMRI data with differences in aspect of the subject's performance (e.g., response time, errors, etc.). In this way, the hemodynamic response time differences can also be factored out and distinguished from temporal behavior of neuronal activity. An alternative approach is to average such single trials but using performance or response criteria to pool together only those response that are similar.

An example of a true single-trial study conducted at 4 T monitored the evolution of fMRI signals in the human brain before, during, and subsequent to an instruction and execution of a motor task (Figure 16). Both the single-trial fMRI signal intensity time courses in motor areas and the electromyograph (EMG) changes detected in the muscle are shown. The EMG showed no movements during the motor preparation period between Instruction and GO. Activation of the primary motor area and of the supplementary and premotor areas were observed during motor execution and preparation. These data are virtually identical to electrode recordings taken from the corresponding areas in a monkey cortex during execution of the same task, except that the fMRI data are displaced in time by seconds relative to the actual time of neuronal activity. The data presented in Figure 16 also illustrate the sensitivity of the high-field fMRI method. Like the electrode recordings from primates, the fMRI data demonstrate that V1 is active during the motor preparation period. This, however, has been a controversial issue with humans because position emission tomographic studies did not reveal activation during such motor preparation.[114] In the high-field fMRI study, this activation is detectable in a single execution of the task.

This type of true single-trial experiment was also utilized to correlate aspects of activation with task performance.[106,113] The paradigm employed was the 'mental rotation' task of Shepard and Metzler:[115] The subjects were presented with drawings of

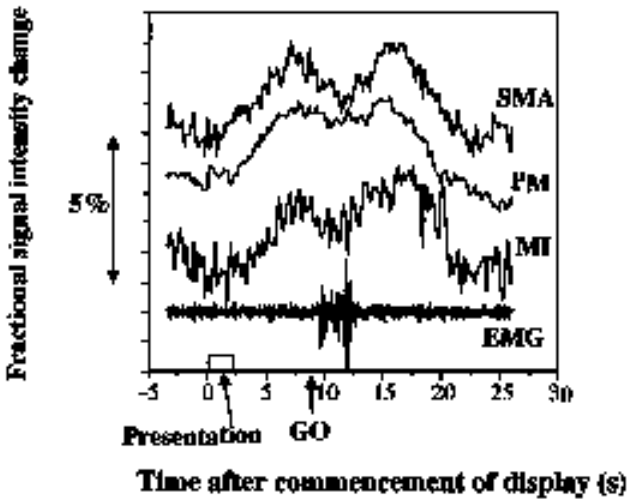

Figure 16 A single-subject, single-trial fMRI (without averaging) study showing time courses in three regions of the brain together with the electromyograph (EMG) recording of muscle movement during a visually instructed delayed cued four-finger movement task. The presentation lasted 2.1 s and the GO signal was given at 9.1 s. M1, contralateral primary motor area; PM, bilateral premotor area; SMA, bilateral supplementary motor area. (With permission from Richter et al.[111])

three-dimensional objects, examples of which are illustrated in Figure 17. In each task, a pair of objects were presented; they were either identical or mirror images and they were rotated relative to each other through varying degrees. The subject had to identify whether the pair was identical or a mirror image and report it by pressing one of two buttons. In this task, subject's response time depended on the angle through which the two objects were rotated relative to each other. The experiment started with the subject looking at similar but identical two-dimensional objects. When ready, the subject commenced the scanning process by pressing a button. The three-dimensional objects were shown and the subject made a decision; after a suitable delay to allow for the hemodynamic response to return to basal levels, the process was repeated. Figure 18 displays signal intensity curves from the parietal lobe from two trials where the response time of the subject was different. The width of the response was evaluated for correct response only with respect to the response time. In each individual, linear correlation was found. However, the intercept corresponding to a response time of zero was significantly different for the different individuals, presumably reflecting fundamental differences in the hemodynamic response to elevated neuronal activity among individuals. When this subject-dependent variable was subtracted, each single-trial, single-subject data point for all subjects yielded an excellent correlation with response time (Figure 19).

One potential confounding problem with such single-trial fMRI studies is the presence of various types of spatiotemporal patterns in the fMRI signals even under basal 'resting' conditions. The T_2^*-weighted MRI signals fluctuate with heart beat and respiration, although fluctuations can be removed from the fMRI data.[116–121] When cardiac and respiratory fluctuations are suppressed, fMRI signal from resting human brain still exhibits low-frequency oscillations at about 0.1 Hz.[121–124] Near-infrared

Figure 17 The paradigm in a true single-trial 'mental rotation' study. (With permission from Richter et al.[107])

optical studies also show this slow oscillation. Therefore, techniques that can separate the fMRI data into its various components (e.g., Mitra et al.[121]) and in the process significantly improve effective SNR for detection of function will play a crucial role in mapping brain function, particularly in single-trial fMRI studies with temporal resolution.

6 CONCLUSION

Since its introduction, fMRI has rapidly evolved to become the most significant method for investigating human brain function, and unique accomplishments have been realized at high magnetic fields. However, it must be realized that high magnetic field MRI instruments are not optimized and refined machines as clinical scanners. Presence of a high-field magnet does not guarantee superior functional imaging results; instead, advantages that are inherent in the high field for functional mapping can easily be lost through instrumentation imperfections. Therefore, improvement in high-field instrumentation are essential for future expansion of these fMRI applications. Additional refinements in data collection schemes, motion correction, and statistical methods for data analysis, which are areas that are being actively pursued, will undoubtedly improve the already impressive capabilities of this methodology.

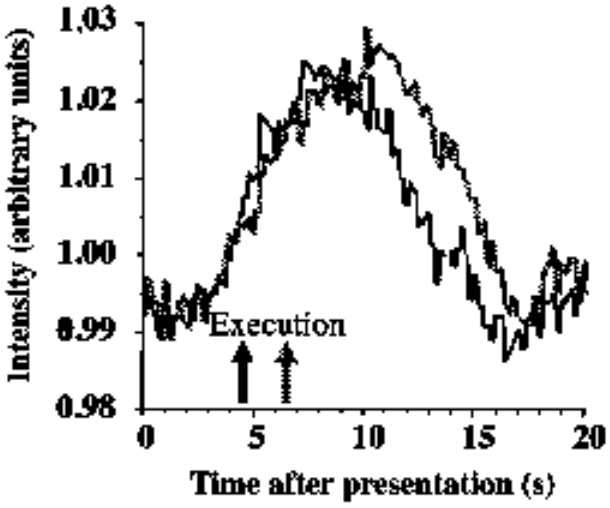

Figure 18 The T_2^*-weighted BOLD response in the parietal lobe for two different single trials (no averaging) for the paradigm outlined in Figure 17. The arrows indicate the time at which the subject responded. (With permission from Richter et al.[106])

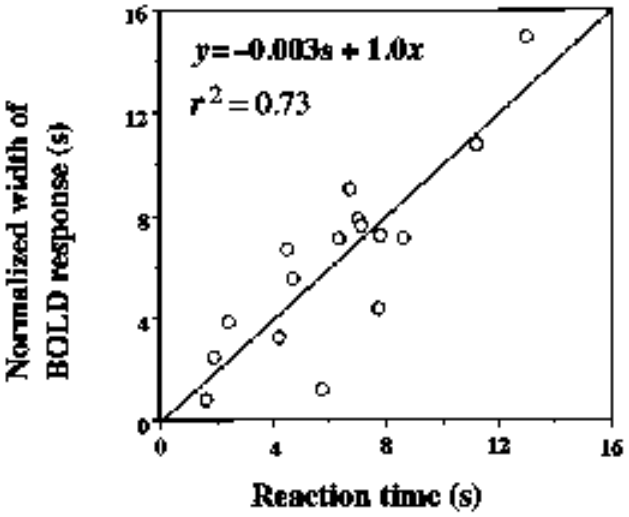

Figure 19 The width of the fMRI response (in Figure 18) versus performance data from all subjects subsequent to removal of the time zero intercept. Each point represents a true single trial in a single subject (no averaging). (With permission from Richter et al.[107])

7 RELATED ARTICLES

Hemodynamic Changes owing to Sensory Activation of the Brain Monitored by Echo-Planar Imaging; Image Processing of Functional MRI Data.

8 REFERENCES

1. P. Broca and C. E. Brown-Sequard, 'Proprietes et fonctions de la moelle epiniere: Rapport quelques experiences de M. Borwn-Sequard'. (Lu a loa Soceite de biologies le 21 Juillet). Bonaventure et Ducessois. 1855.
2. P. Erhard, P. Strick, J. Strupp, A. K. Helms Tillery, S. Naeve-Velguth, and K. Ugurbil, unpublished results, 1998.
3. S. Ogawa, T.-M. Lee, A. R. Kay, and D. W. Tank, *Proc. Natl. Acad. Sci., USA*, 1990, **87**, 9868.
4. S. Ogawa, T.-M. Lee, A. S. Nayak, and P. Glynn, *Magn. Reson. Med.*, 1990, **14**, 68.
5. S. Ogawa and T. M. Lee, *Magn. Reson. Med.*, 1990, **16**, 9.
6. P. A. Bandettini, E. C. Wong, R. S. Hinks, R. S. Tikofsky, and J. S. Hyde, *Magn. Reson. Med.*, 1992, **25**, 390.
7. K. K. Kwong, J. W. Belliveau, D. A. Chesler et al., *Proc. Natl. Acad. Sci., USA*, 1992, **89**, 5675.
8. S. Ogawa, D. W. Tank, R. Menon, J. M. Ellermann, S. G. Kim, H. Merkle, and K. Ugurbil, *Proc. Natl. Acad. Sci., USA*, 1992, **89**, 5951.
9. D. I. Hoult and P. C. Lauterbur, *J. Magn. Reson.*, 1979, **34**, 425.
10. M. I. Sereno, A. M. Dale, J. B. Reppas, K. K. Kwong, J. W. Belliveau, T. J. Brady, B. R. Rosen, and R. B. H. Tootell, *Science*, 1995, **268**, 889.
11. R. B. H. Tootell, J. B. Reppas, A. M. Dale, R. B. Look, M. I. Sereno, R. Malach, T. J. Brady, and B. R. Rosen, *Nature*, 1995, **375**, 139.
12. R. B. H. Tootell, J. B. Reppas, K. K. Kwong, R. Malach, R. T. Born, T. J. Brady, B. R. Rosen, and J. W. Belliveau, *J. Neurosci.*, 1995, **15**, 3215.
13. R. G. H. Tootell, A. M. Dale, M. I. Sereno, and R. Malach, *Trends Neurosci.*, 1996, **19**, 481.
14. J. B. Reppas, S. Niyogi, A. M. Dale, M. I. Sereno, and R. B. Tootell, *Nature*, 1997, **388**, 175.
15. R. B. Tootell, J. D. Mendola, N. K. Hadjikhani, P. J. Ledden, A. K. Liu, J. B. Reppas, M. I. Sereno, and A. M. Dale, *J. Neurosci.*, 1997, **17**, 7060.
16. C. S. Springer and Y. Xu, *New Devel. Contrast Agent Res.*, 1991, 13.
17. J. L. Boxerman, R. M. Weisskoff, B. E. Hoppel, and B. R. Rosen, in *Proc. XIIth Annu. Mtg Soc. Magn. Reson. Med.*, New York, 1993, 389.
18. S. Ogawa, R. S. Menon, D. W. Tank, S.-G. Kim, H. Merkle, J. M. Ellermann, and K. Ugurbil, *Biophys. J.*, 1993, **64**, 800.
19. R. M. Weisskoff, J. L. Boxerman, C. S. Zuo, and B. R. Rosen, 'Functional MRI of the Brain', Arlington, Virginia, 1993.
20. E. C. Wong and P. A. Bandettini, in *Proc. XIIth Annu. Mtg Soc. Magn. Reson. Med.*, New York, 1993, 10.
21. R. P. Kennan, J. Zhong, and J. C. Gore, *Magn. Reson. Med.*, 1994, **31**, 9.
22. D. A. Yablonskiy and E. M. Haacke, *Magn. Reson. Med.*, 1994, **32**, 749.
23. J. L. Boxerman, L. M. Hamberg, B. R. Rosen, and R. M. Weisskoff, *Magn. Reson. Med.*, 1995, **34**, 555.
24. S. Ogawa, R. S. Menon, S. G. Kim, and K. Ugurbil, *Annu. Rev. Biophys. Biomol. Struct.*, 1998, **27**, 447.
25. R. M. Weisskoff, C. S. Zuo, J. L. Boxerman, and B. R. Rosen, *Magn. Reson. Med.*, 1994, **31**, 601.
26. G. Pawlik, A. Rackl, and R. J. Bing, *Brain Res.*, 1981, **208**, 35.
27. J. O. Eichling, M. E. Raichle, R. L. Grubb, and M. M. Ter-Pogossian, *Circ. Res.*, 1974, **35**, 358.
28. O. B. Paulson, M. M. Hertz, T. G. Bolwig, and N. A. Lassen, *Acta Neurol. Scand.*, 1977, **64(Suppl.)**, 492.
29. O. B. Paulson, M. M. Hertz, T. G. Bolwig, and N. A. Lassen, *Microvasc. Res.*, 1977, **13**, 113.
30. A. C. Burton, *Fed. Proc.*, 1966, **25**, 1753.
31. P. T. Fox and M. E. Raichle, *Proc. Natl. Acad. Sci., USA*, 1986, **83**, 1140.
32. M. E. Raichle, 'Handbook of Physiology—The Nervous System', 1987, 643.
33. P. T. Fox, M. E. Raichle, M. A. Mintun, and C. Dence, *Science*, 1988, **241**, 462.
34. K. R. Thulborn, J. C. Waterton, P. M. Mathews, and G. K. Radda, *Biochim. Biophys. Acta*, 1982, **714**, 265.
35. K. R. Thulborn, J. C. Waterton, and P. M. Matthews, *Biochim. Biophys. Acta*, 1992, **714**, 265.
36. G. A. Wright, B. S. Hu, and A. Macovski, *JMRI*, 1991, **1**, 275.
37. M. Barth and E. Moser, *Cell. Mol. Biol.*, 1997, **43**, 783.
38. F. W. Wehrli, J. R. MacFall, D. Schutts, R. Breger, and R. J. Herfkens, *J. Comput. Assist. Tomogr.*, 1984, **8**, 369.
39. P. Jezzard, S. Duewell, and R. S. Balaban, *Radiology*, 1996, **199**, 773.
40. R. S. Menon, S. Ogawa, D. W. Tank, and K. Ugurbil, *Magn. Reson. Med.*, 1993, **30**, 380.
41. E. O. Stejskal and J. E. Tanner, *J. Chem. Phys.*, 1965, **42**, 288.
42. J. L. Boxerman, P. A. Bandettini, K. K. Kwong, J. R. Baker, T. L. Davis, B. R. Rosen, and R. M. Weisskoff, *Magn. Reson. Med.*, 1995, **34**, 4.
43. A. W. Song, E. C. Wong, S. G. Tan, and J. S. Hyde, *Magn. Reson. Med.*, 1996, **35**, 155.
44. R. M. Henkelman, J. J. Neil, and Q. S. Xiang, *Magn. Reson. Med.*, 1994, **32**, 464.
45. E. M. Haacke, A. Hopkins, and S. Lai et al., *NMR Biomed.*, 1994, **7**, 54.
46. R. S. Menon, X. Hu, G. Adriany, P. Andersen, S. Ogawa, and K. Ugurbil, in *Proc. IInd Annu. Mtg (Int.) Soc. Magn. Reson.*, San Francisco, 1994, **2**, 622.
47. S.-P. Lee, A. C. Silva, K. Ugurbil, and S.-G. Kim, *Magn. Reson. Med.*, 1999, **42**, 919.
48. R. B. Buxton and L. R. Frank, *J. Cereb. Blood Flow Metab.*, 1997, **17**, 64.
49. P. C. van Zijl, S. M. Eleff, J. A. Ulatowski, J. M. Oja, A. M. Ulug, R. J. Traystman, and R. A. Kauppinen, *Nature Med.*, 1998, **4**, 159.
50. R. E. Edelman, B. Siewer, D. G. Darby, V. Thangaraj, A. C. Nobre, M. M. Mesulam, and S. Warach, *Radiology*, 1994, **192**, 513.
51. S.-G. Kim, *Magn. Reson. Med.*, 1995, **34**, 293.
52. S.-G. Kim and N. V. Tsekos, *Magn. Reson. Med.*, 1997, **37**, 425.
53. S. G. Kim and K. Ugurbil, *Magn. Reson. Med.*, 1997, **38**, 59.
54. E. C. Wong, R. B. Buxton, and L. R. Frank, *Magn. Reson. Med.*, 1998, **39**, 702.
55. J. A. Detre, J. S. Leigh, D. S. Williams, and A. P. Koretsky, *Magn. Reson. Med.*, 1992, **23**, 37.
56. J. A. Detre, W. Zhang, D. A. Roberts, A. C. Silva, D. S. Williams, D. J. Grandis, A. P. Koretsky, and J. S. Leigh, *NMR Biomed.*, 1994, **7**, 75.
57. D. A. Roberts, J. A. Detre, L. Bolinger, E. K. Insko, and J. S. Leigh, *Proc. Natl. Acad. Sci., USA*, 1994, **91**, 33.
58. K. K. Kwong, D. A. Chesler, R. M. Weisskoff, K. M. Donahue, T. L. Davis, L. Ostergaard, T. A. Campbell, and B. R. Rosen, *Magn. Reson. Med.*, 1995, **34**, 878.
59. N. V. Tsekos, F. Zhang, H. Merkle, M. Nagayama, C. Iadecola, and S. G. Kim, *Magn. Reson. Med.*, 1998, **39**, 564.
60. R. D. Frostig, E. E. Lieke, D. Y. Ts'o, and A. Grinvald, *Proc. Natl. Acad. Sci., USA*, 1990, **87**, 6082.
61. D. Malonek and A. Grinvald, *Science*, 1996, **272**, 551.

62. I. Venzetta and A. Grinvald, *Neurosci. Lett.*, 1998 **Suppl. 51**, S42.
63. J. B. Mandeville, J. J. A. Marota, C. Ayata, M. Moskowitz, B. R. Rosen, and R. M. Weisskoff, in *Proc. VIth Annu. Mtg (Int.) Soc. Magn. Reson. Med.*, Sydney, 1998, p. 1422.
64. T. Ernst and J. Hennig, *Magn. Reson. Med.*, 1994, **32**, 146.
65. R. S. Menon, S. Ogawa, X. Hu, J. P. Strupp, P. Anderson, and K. Ugurbil, *Magn. Reson. Med.*, 1995, **33**, 453.
66. T. H. Le and X. Hu, in *Proc. IVth Annu. Mtg (Int.) Soc. Magn. Reson. Med.*, New York, 1996, p. 285.
67. X. Hu, T. H. Le, and K. Ugurbil, *Magn. Reson. Med.*, 1997, **37**, 877.
68. J. McIntosh, Y. Zhang, S. Kidambi, T. Harshbarger, G. Mason, G. M. Pohost, and D. Twieg, in *Proc. IVth Annu. Mtg (Int.) Soc. Magn. Reson. Med.*, New York, 1996, **1**, p. 284.
69. G. G. Moore, Y. T. Zhang, and D. B. Twieg, in *Proc. Vth Annu. Mtg (Int.) Soc. Magn. Reson. Med.*, Vancouver, 1997, **1**, p. 377.
70. D. B. Twieg, G. G. Moore, and Y. T. Zhang, in *Proc. Vth Annu. Mtg (Int.) Soc. Magn. Reson. Med.*, Vancouver, 1997, **1**, p. 1647.
71. N. K. Logothetis, H. Gugenberger, S. Peled, and J. Pauls, *Nature Neurosci.*, 1999, **2**, 555.
72. J. B. Mandeville, J. J. Marota, B. E. Kosofsky, J. R. Keltner, R. Weissleder, B. R. Rosen, and R. M. Weisskoff, *Magn. Reson. Med.*, 1998, **39**, 615.
73. J. Frahm, K. D. Kruger, K. D. Merboldt, and A. Kleinschmidt, *Magn. Reson. Med.*, 1996, **35**, 143.
74. E. Yacoub, T.H. Le, K. Ugurbil, and X. Hu, *Magn. Reson. Med.*, 1999, **41**, 436.
75. J. M. Ellermann, D. Flament, S.-G. Kim, Q.-G. Fu, H. Merkle, T. J. Ebner, and K. Ugurbil, *NMR Biomed.*, 1994, **7**, 63.
76. D. H. Hubel and T. N. Wiesel, *J. Physiol. (Lond.)*, 1968, **195**, 215.
77. D. H. Hubel and T. N. Wiesel, *J. Comp. Neurol.*, 1972, **146**, 421.
78. D. H. Hubel, N. Wiesel, and D. M. K. Lam, *Brain Res.*, 1974, **79**, 273.
79. P. Rakic, *Nature*, 1976, **261**, 467.
80. D. H. Hubel and T. N. Wiesel, in *Proc. R. Soc. Lond. Ser. B*, 1977, **198**, 1.
81. A. Kleinschmidt, K. D. Merboldt, W. Hanicke, H. Steinmetz, and J. Frahm, *J. Cereb. Blood Flow Metab.*, 1994, **14**, 952.
82. C. Buchel, R. Turner, and K. Friston, *Magn. Reson. Med.*, 1997, **38**, 691.
83. W. Chen, T. Kato, X. H. Zhu, J. Strupp, S. Ogawa, and K. Ugurbil, *Magn. Reson. Med.*, 1998, **39**, 89.
84. S. Zeki, 'A Vision of the Brain', Oxford, Blackwell Scientific, 1993.
85. W. Chen, X. H. Zhu, K. R. Thulborn, and K. Ugurbil, *Proc. Natl. Acad. Sci., USA*, 1999, **96**, 2430.
86. J. G. Malpeli and F. H. Baker, *J. Comp. Neurol.*, 1975, **161**, 569.
87. P. H. Schiller, N. K. Logothetis, and E. R. Charles, *Vis. Neurosci.*, 1990, **5**, 321.
88. P. H. Schiller, N. K. Logothetis, and E. R. Charles, *Nature*, 1990, **343**, 68.
89. C. Kennedy, M. H. Des Rosiers, and O. Sakurada, *Proc. Natl. Acad. Sci., USA*, 1976, **73**, 4230.
90. S. LeVay, M. Connolly, and J. Houde, *J. Neurosci.*, 1985, **5**, 486.
91. A. Grinvald, E. Lieke, R. D. Frostig, C. D. Gilbert, and T. N. Wiesel, *Nature*, 1986, **324**, 361.
92. D. Y. Ts'o, R. D. Frostig, E. E. Lieke, and A. Grinvald, *Science*, 1990, **249**, 417.
93. A. Grinvald, R. D. Frostig, R. M. Siegel, and E. Bartfeld, *Proc. Natl. Acad. Sci., USA*, 1991, **88**, 11559.
94. J. C. Horton and E. T. Hedley-White, *Phil. Trans. R. Soc. Lond. Ser. B*, 1984, **304**, 255.
95. J. C. Horton, L. R. Dagi, and E. P. McCrane, *Arch. Opthalmol.*, 1990, **108**, 1025.
96. J. S. Gati, R. S. Menon, K. Ugurbil, and B. K. Rutt, in *Proc. IIIrd Annu. Mtg (Int.) Soc. Magn. Reson.*, Nice, 1995, p. 772.
97. J. S. Gati, R. S. Menon, K. Ugurbil, and B. K. Rutt, *Magn. Reson. Med.*, 1997, **38**, 296.
98. R. S. Menon, S. Ogawa, and K. Ugurbil, *Neuroimage*, 1996, **3**, S357.
99. R. S. Menon, S. Ogawa, J. P. Strupp, and K. Ugurbil, *J. Neurophysiol.*, 1997, **77**, 2780.
100. R. S. Menon and B. G. Goodyear, *Magn. Reson. Med.*, 1999, **41**, 230.
101. R. S. Menon and S.-G. Kim, *Trends Cognit. Neurosci.*, 1999, **3**, 207.
102. B. G. Goodyear and R. S. Menon, Submitted, 1999.
103. A. M. Blamire, S. Ogawa, K. Ugurbil, D. Rothman, G. McCarthy, J. M. Ellermann, F. Hyder, Z. Rattner, and R. G. Shulman, *Proc. Natl. Acad. Sci., USA*, 1992, **89**, 11069.
104. R. L. Savoy, P. A. Bandettini, K. M. O'Craven, K. K. Kwong, T. L. Davis, J. R. Baker, J.W. Belliveau, R. M. Weisskoff, and B. R. Rosen, *Proc. IIIrd Annu. Mtg (Int.) Soc. Magn. Reson. Med.*, Nice, 1995, p. 450.
105. S.-G. Kim, W. Richter, and K. Ugurbil, *Magn. Reson. Med.*, 1997, **37**, 631.
106. W. Richter, P. M. Andersen, A. P. Georgopoulos, and S.-G. Kim, *Neuroreport*, 1997, **8**, 1257.
107. W. Richter, K. Ugurbil, A. P. Georgopoulos, and S.-G. Kim, *Neuroreport*, 1997, **8**, 3697.
108. R. S. Menon, D. C. Luknowsky, and J. S. Gati, *Proc. Natl. Acad. Sci., USA*, 1998, **95**, 10902.
109. R. L. Buckner, P. A. Bandettini, K. M. O'Craven, R. L. Savoy, S. E. Petersen, M. E. Raichle, and B. R. Rosen, *Proc. Natl. Acad. Sci. USA*, 1996, **93**, 14878.
110. S.-G. Kim and W. Richter, *Proc. IVth Annu. Mtg (Int.) Soc. Magn. Reson. Med.*, New York, 1996, p. 289.
111. W. Richter and S.-G. Kim, *Proc. Soc. Neurosci.*, 1996, **1**, 22.
112. W. Richter, K. Ugurbil, and S.-G. Kim, *Neuroimage*, 1996, **3**, S38.
113. W. Richter, A. P. Georgopoulos, K. Ugurbil, and S.-G. Kim, *Proc. Vth Annu. Mtg (Int.) Soc. Magn. Reson. Med.*, Vancouver, 1997, p. 357.
114. J. Decety, R. Kawashima, B. Gulyas, and P. E. Roland, *Neuroreport*, 1992, **3**, 761.
115. R. N. Shepard and J. Metzler, *Science*, 1971, **171**, 701.
116. X. Hu and S.-G. Kim, *Magn. Reson. Med.*, 1994, **31**, 495.
117. J. S. Hyde, B. Biswal, A. W. Song, and S. G. Tan, *Proceedings of the 2nd Annual Midwest Functional MRI Workshop, Madison, WI*, 1994, p. 73.
118. X. Hu, T. H. Le, T. Parrish, and P. Erhard, *Magn. Reson. Med.*, 1995, **34**, 201.
119. P. P. Mitra, D. J. Thompson, S. Ogawa, X. Hu, and K. Ugurbil, *Proc. IIIrd Annu. Mtg (Int.) Soc. Magn. Reson. Med.*, Nice, 1995, p. 817.
120. B. Biswal, E. A. DeYoe, and J. S. Hyde, *Magn. Reson. Med.*, 1996, **35**, 117.
121. P. P. Mitra, S. Ogawa, X. Hu, and K. Ugurbil, *Magn. Reson. Med.*, 1997, **37**, 511.
122. B. Biswal, F. Z. Yetkin, V. M. Haughton, and J. S. Hyde, *Magn. Reson. Med.*, 1995, **34**, 537.

123. S. Ogawa, P. P. Mitra, X. Hu, and K. Ugurbil, 'Recent Advances in MEG and functional MRI', (*EEG J.* Suppl. 47), eds. I. Hashimoto, Y. C. Okada, and S. Ogawa, International Federation of EEG Societies, Limerick, 1996, p. 5.
124. B. Biswal, A. Hudetz, F. Yetkin, V. M. Haughton, and J. S. Hyde, *J. Cereb. Blood Flow Metab.*, 1997, **17**, 301.

Acknowledgements

Work reported here from the Center for Magnetic Resonance University of Minnesota was supported by NIH P41 RR08079, an NIH Regional Resource grant, and NIH NS32191.

Biographical Sketches

Kamil Ugurbil. *b* 1949. A.B. Physics, 1971, Ph.D. Chemical Physics, Columbia University, New York, 1976. Postdoctoral Fellowship, Bell Laboratories, 1976–79, Assistant Professor Biochemistry, Columbia University, New York, 1979–82, Associate Professor Biochemistry, University of Minnesota, Minneapolis, 1982–85, Professor in Biochemistry, Radiology, Medicine, and Neurosciences, University of Minnesota, 1985–present, Director Center for Magnetic Resonance Research (CMRR), University of Minnesota, 1991–present, and holder of Margaret & H.O. Peterson Chair of Neuroradiology, Department of Radiology, University of Minnesota, 1996–present. Approx. 160 publications. Current research interests: high field magnetic resonance imaging and spectroscopy with particular focus on functional imaging in the brain and myocardial bioenergetics.

Wei Chen. *b* 1959. B.S. Physical Chemistry, Fudan University, Shanghai, China, 1981, Ph.D. Physical Chemistry, Washington University, St. Louis, 1991. Postdoctoral Associate, Yale University, New Haven, 1991–94. Assistant Professor, Radiology, University of Minnesota, 1994–99, Associate Professor of Radiology, 1989–present. Approx. 50 publications. Current research interests: function and metabolism study of brain and heart using magnetic resonance imaging/spectroscopy.

Xiaoping Hu. *b* 1961. B.S. Physics, University of Science of Technology of China, Hefei, China, 1982, Ph.D. Medical Physics, University of Chicago, Chicago, 1988. Postdoctoral Associate, University of Chicago, 1988–90, Assistant Professor Radiology 1990–94, Associate Professor Radiology 1994–98, Professor Radiology 1998–present, University of Minnesota Minneapolis. Approx. 80 publications. Current research interests: methodological development, mechanistic studies, and applications of functional magnetic resonance imaging at high magnetic fields.

Seong-Gi Kim. *b* 1958. B.E. Applied Chemistry, Kyungpook National University, Korea, 1980, Ph.D. Chemistry, Washington University, St. Louis, 1988. Postdoctoral Associate, Washington University, St. Louis and University of Washington, Seattle, 1988–91, Research Associate, Radiology, University of Minnesota, 1991–94, Assistant Professor, Radiology, University of Minnesota, 1994–98, Associate Professor of Radiology, 1988–present. Approx. 70 publications. Current research interests: physiological and functional MRI studies of animal and human brain.

Seiji Ogawa. *b* 1934. B.S. Applied Physics, University of Tokyo, 1957, Ph.D. Chemical Physics, Stanford University, 1967, Postdoctoral Fellowship, Stanford University, 1967–68, Postdoctoral Fellowship, AT&T Bell Laboratories, 1968–69, Member of Technical Staff, AT&T Bell Laboratories, 1969–83, Distinguished Member of Technical Staff, AT&T Bell Laboratories, 1984–96, Distinguished Member of Technical Staff, Bell Laboratories, Lucent Technologies, 1996–present. Approx. 70 publications. Current research interests: functional magnetic resonance imaging of the brain.

Xiao-Hong Zhu. *b* 1964. B.S. Chemistry, Fudan University, Shanghai, China, 1985, Ph.D. Chemistry, University of Missouri-St. Louis, St. Louis, 1991. Postdoctoral trainee, Yale University, Connecticut, 1991–94. Postdoctoral associate, University of Minnesota, 1994–98, Research Associate, University of Minnesota, 1998–present. Approx. 30 publications. Current research interests: magnetic resonance spectroscopy and functional imaging of brain at high field.

Functional MRI: Theory and Practice

Robert Turner
Institute of Neurology, London, UK
and
David G. Gadian
Institute of Child Health, London, UK

1	Introduction	1
2	Contrast Mechanisms in Functional MRI	1
3	Imaging Methods	3
4	Sources of Artifact	3
5	Image Analysis	4
6	Brain Functions Studied	4
7	Discussion	6
8	Related Articles	6
9	References	6

1 INTRODUCTION

Since 1990, interest has grown rapidly in MRI methods for mapping human brain function. These methods have good spatial and temporal resolution, and are completely noninvasive. As a result, repeated single-subject studies are feasible, allowing new types of experiments in cognitive neuroscience to be formulated. In addition, there are many potential clinical applications.

Functional brain mapping involves the visualization of local physiological changes within the brain that are associated with activation of the visual, motor, or other brain systems. The technique that has so far contributed most to functional brain mapping is positron emission tomography (PET).[1] These PET studies rely on the detection of changes in local hemodynamics that are associated with cerebral activation; in particular, there are changes in regional cerebral blood flow that can be mapped with PET through the use of ^{15}O-labeled water. The MRI studies of functional activation that have recently been described also rely on hemodynamic changes, and on the detection of signals from water. However, in contrast to PET, the signal is from the protons of the water and the effects are observed without any need for radioisotope labeling. Instead, the detection of activation relies on perturbations of the water magnetization that are associated with the hemodynamic changes.

The first brain activation study using functional MRI involved the administration of the paramagnetic contrast agent Gd-DTPA to act as a marker of cerebral blood volume.[2] This investigation of the human visual cortex used a visual stimulus paradigm that, on the basis of PET studies, produces changes in regional cerebral blood flow of about 30–50%. Echo planar MR images were collected at intervals of 750 ms, before, during and after injection of Gd-DTPA, which was administered as a bolus into the antecubital vein. As the Gd-DTPA passed through the brain, it produced a transient reduction in water signal intensity because of its magnetic susceptibility effects. From the time course of the signal changes, it was possible to generate images that reflected relative cerebral blood volume. The imaging procedure was carried out under control conditions, and also during visual stimulation produced by goggles that generated 8 Hz patterned flashes. Subtraction of the control from the activated blood volume image revealed those areas in which there was a change in blood volume associated with the task activation. These areas corresponded to the primary visual cortex.

As it happened, this initial activation study was very rapidly superseded by an alternative MRI approach which had the major advantage that no extrinsic contrast agent was required. It had been known for some time that there were several mechanisms whereby changes in blood flow, volume, and oxygenation can influence signal intensities without any requirement for exogenous agents, and it soon became apparent that activated regions of the human brain could be visualized using such intrinsic contrast mechanisms. In these studies, particular interest has focused on T_2*-weighted signal intensity changes that have been attributed primarily to changes in local venous blood oxygenation, in particular to the effects generated by the paramagnetic iron centers of deoxyhemoglobin. There is a long history to NMR studies of this compound, and some of the salient points are described briefly below.

2 CONTRAST MECHANISMS IN FUNCTIONAL MRI

2.1 Blood Oxygenation Level Dependent (BOLD) Effects

It has long been known that the magnetic state of hemoglobin in red cells is dependent on oxygen saturation; with deoxygenation of hemoglobin, the electron spin of the heme Fe^{2+} changes from a diamagnetic state to a paramagnetic state. As a result, deoxygenated blood is more paramagnetic than oxygenated blood, the difference being about 0.2 ppm. There are magnetic susceptibility effects associated with this paramagnetism, and therefore local field gradients are generated in and around the blood vessels. These cause signal attenuation in T_2*-weighted images, which is not confined just to water within the vessels; it can extend significantly into the surrounding tissue. As a result, there may be substantial signal changes associated with changes in oxygenation state, even if the blood volume is relatively small.

In the early 1990s, a number of animal imaging studies were published, in which it was demonstrated that these magnetic susceptibility effects could be exploited as a means of detecting oxygenation changes in the brain[3–5] (see Figure 1). In particular, T_2*-weighted images showed a reduction in signal intensity under conditions of reduced oxygenation, i.e. under conditions where there are increased susceptibility effects associated with the presence of deoxyhemoglobin. Before very long, studies were carried out in humans, using T_2*-weighted imaging sequences[6–8] that showed focal changes in signal intensity in response to visual tasks. In the work of Kwong et al.,[6] subjects experienced visual stimulation for periods of 30 s,

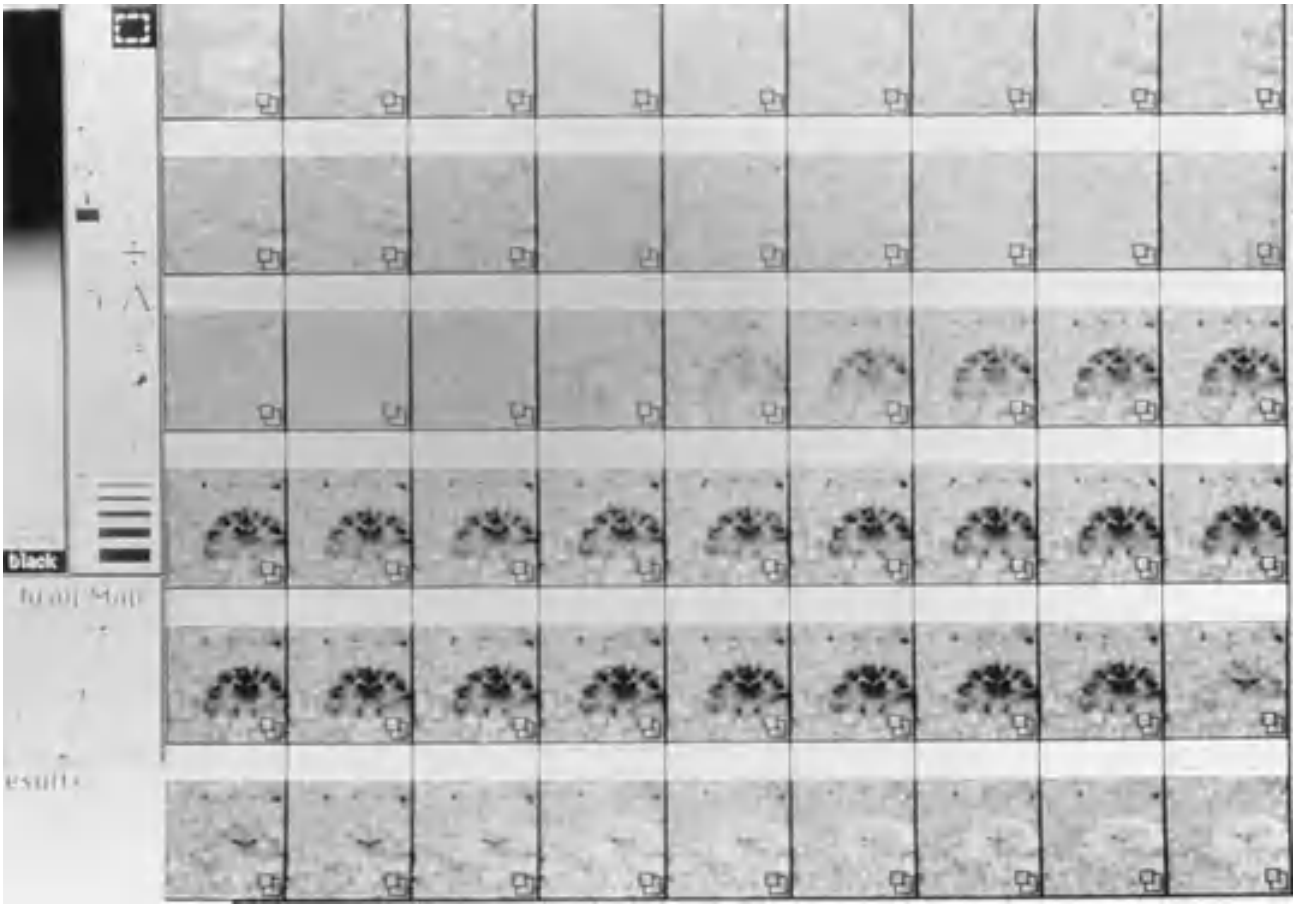

Figure 1 Sequential coronal difference images of a cat brain, at 3-intervals. The cat was subjected to respiratory anoxia from images 20–40. Image 20 was subtracted from each of the others to give this demonstration of contrast changes. The development of hypoxemia is well seen as a darkening, predominantly in gray matter, and the overshoot on recovery is also clearly visible. The first image shows enhancement of cerebrospinal fluid due to the completely unsaturated condition of the spins at the outset of scanning. Images were obtained using a 2.0 T GE Omega, 45 cm bore, MR scanner. (Reproduced by permission from Turner et al.[5])

interspersed by equal periods of darkness, while echo planar gradient echo images of a section passing through the primary visual cortex were obtained at 3 s intervals. When a control image was subtracted from each of the time-series of images, the resulting difference images showed unequivocal increases in intensity in the visual cortex, correlating very well with the visual stimulus. A lag time of 6–9 s was noted between onset of stimulation and rise to maximum of the difference signal, reflecting the timescale of the hemodynamic changes associated with activation.

It is significant that a rise in signal can be observed during visual stimulation, indicating a relative decrease in the concentration of paramagnetic deoxyhemoglobin. This confirms earlier work using PET[9] in which the measured rise in oxygen uptake rate during visual stimulation was found to be much smaller than the rise in blood flow. Earlier observations during neurosurgery (see, for example, Penfield[10]) had also demonstrated that the blood leaving active cortical regions is brighter red, i.e. more oxygenated, than normal, as a result of this mismatch between demand and supply.

The contrast in T_2*-weighted images is generated because gradient echoes do not refocus the dephasing effects of local field homogeneities associated with the presence of deoxyhemoglobin. If spin echoes are used instead of gradient echoes, then such dephasing effects will be refocused, provided that there is no significant diffusion of the water molecules through the field gradients. This explains why T_2*-weighted images are more sensitive than T_2-weighted images to the effects of brain activation. However, if the water molecules diffuse through local field gradients during the echo time TE, then this will result in imperfect refocusing and hence to signal loss in T_2-weighted spin echo sequences[11] (see also, earlier ^{1}H NMR studies of red cell metabolism[12]). Because water molecules can only diffuse a small distance in an echo time that may be of the order of 60 ms, this diffusion-dependent mechanism of signal loss should be more effective when the distances that characterize the gradients are small. Within the blood vessels themselves, these distances are indeed small, because the localization of deoxyhemoglobin to red cells results in local field gradients in the periphery of each individual cell. In the adjacent tissue, however, the dimensions characterizing these local gradients should be determined by the dimensions of the vessels. Therefore it can be anticipated that, in comparison with large draining vessels, small vessels such as capillaries should produce relatively large diffusion-dependent T_2 effects in the adjacent tissue. This has been explored as a means of distinguishing between the effects of large and small vessels (see below). However, it needs to

be borne in mind that changes in oxygenation in vessels of size comparable to a voxel will result in large signal intensity changes even in T_2-weighted images.

2.2 Flow Effects

In theory, the water signal intensity can be affected by many hemodynamic effects, including changes in blood arterial oxygenation, blood volume, blood flow, hematocrit, tissue oxygen uptake, and possibly blood velocity. Indeed, the initial study of Kwong et al.[6] highlighted not only T_2*-dependent effects, but also T_1-dependent effects that could be attributed to the direct influence of changes in local blood flow that were associated with activation. There is considerable interest in the influence of blood flow on signal changes associated with task activation, and numerous investigations have been concerned with distinguishing between flow and oxygenation effects (see, for example, Frahm et al.[13]).

One approach to visualizing flow effects involves the use of arterial spin tagging, using saturation or inversion of inflowing spins as a magnetic label. For example, if spins in the neck region are selectively inverted, then arterial flow will carry these labeled spins into the brain tissue and hence influence the observed signal from brain water. Comparison of the data obtained with and without this labeling procedure permits measurements of regional perfusion to be made. The signal change resulting from the magnetic labeling depends upon a number of factors, including the perfusion rate, the T_1 value of the tissue water, and any relaxation of the labeled spins during the time that they take to travel from the labeling plane to the detection volume. This approach has been used for the quantitative measurement of cerebral perfusion, initially in small animals, and more recently in man.[14] Although the method has a number of well-recognized problems, it does offer a very promising approach to the noninvasive investigation of cerebral perfusion and of changes in perfusion associated with task activation and with disease processes.

A related method, termed EPISTAR, has recently been used to obtain qualitative maps of cerebral blood flow, with spatial resolution of $2 \times 2 \times 2$ mm.[15] This method is an echo planar imaging modification of a time-of-flight angiography technique. It involves the alternate acquisition of two echo planar images with and without a radiofrequency inversion pulse applied to inflowing arterial spins. Image subtraction provides a picture of large proximal vessels when short inflow times are used, while progressively more distal portions of the tagged vessels are seen as the inflow time is lengthened. At these longer inflow times, the images represent a qualitative map of cerebral blood flow. The acquisition of such images also provides a means of visualizing activated regions of the brain.

3 IMAGING METHODS

Functional MRI studies generally involve the acquisition of data during a series of interleaved periods of rest and stimulation, each of these periods typically lasting about 30 s. Rapid imaging methods are therefore required. These divide into two categories: methods that use a series of low flip-angle excitation pulses (e.g. FLASH, Turbo-FLASH etc.),[16] and methods which use a single excitation pulse (echo planar imaging).[17] While both have proved successful, there is an increased tendency toward the use of echo planar imaging, which permits imaging of a complete slice in a time of 60–100 ms. With an imaging time of 100 ms, a complete multislice data set covering the whole brain can be obtained very rapidly (data from 30 slices could be acquired in 3 s), and it seems likely that multislice echo planar imaging will become the preferred method for the majority of functional MRI studies of the brain.

4 SOURCES OF ARTIFACT

In any magnetic resonance study, it is important to appreciate the various ways in which artifacts can influence the appearance of spectra or images. This is particularly true in the case of functional brain mapping methods, which suffer from certain problems which can give false positive results, or obscure the effect altogether. It must be understood that the signal changes of interest are usually not much larger than the thermal and physiological noise that inevitably accompany MR images of living tissue, so that equipment stability is of great importance. But two other issues have been the subject of controversy in the literature. These relate to the precision of localization of neural activity, and to artifactual image differences associated with subject motion.

4.1 Localization

Changes in signal intensity may be observed as a result of hemodynamic changes that are associated not only with capillaries, but also with larger draining vessels (see Lai et al.[18]). The draining vessels may be situated a long way 'downstream' of the activated tissue, and on task activation they may give rise to changes in signal intensity in regions that do not correspond directly to the regions that are actually activated, particularly with MRI sequences that are sensitive to flow velocity. For this reason, it is essential to establish, by one means or another, that the location of the observed signal changes does indeed reflect the focally activated regions. There are several ways in which this might be achieved. One method is to combine functional MRI with angiographic techniques, so that the regions of increase in signal intensity can be compared directly with the anatomical location of the draining vessels. Alternatively, the signal from these vessels may be suppressed by using imaging sequences that give reduced signal from regions of high flow. In addition, multislice techniques that effectively give a three-dimensional activation pattern should help to establish the source of the signal increase. Finally, it has been pointed out that the combination of T_2-weighted and T_2*-weighted imaging should help to distinguish between large and small vessels (see above), T_2-weighted and T_2*-weighted effects becoming more similar as vessels become smaller.[19,20] In practice, there is a lot to be said for visualizing both the activated regions and the hemodynamic changes in the draining vessels, and the best approaches will no doubt preserve both types of information.

Further information about the possible importance of downstream effects, and also about the extent to which delivery of blood to brain tissue is spatially matched to

the increased demand, is available from other techniques. In particular, optical imaging methods, using a cranial window in animal models, or intraoperatively in human subjects, can provide information of direct relevance to the interpretation of functional MRI data.[21,22]

4.2 Subject Motion

To visualize task-related regions of increased signal, the earliest functional MRI studies relied on single or averaged image differences between experimental and control conditions. While this method has the merit of explicitness and simplicity, it takes no account of spatial variations in image noise, and it is extremely vulnerable to head motion temporally correlated with the experimental task.[23] Normalization of the image difference by division of the difference at each pixel by the standard error of the mean in that pixel, to give a z score, accounts for artifacts caused by large intensity fluctuations related to cardiac or respiratory cycle. Misregistration artifact, however, may continue to confound the results. Clearly, either the brain must be rigidly fixed in place during each experiment, or a robust means of reregistration of images must be employed. Rigid head fixation may entail considerable discomfort, though a number of workers have successfully used bite bars. Image reregistration can be performed either by noting fiducial changes in head position during a study, and applying the required rotations and translations to the images afterwards, or by using internal image features and least-squares search procedures to determine post hoc the corrections needed. The iterative algorithm of Woods et al.[24] has been successfully used by a number of workers (e.g. Tyszka et al.[25]), and very recently a faster, more robust, and more accurate algorithm has been developed.[26] Any such algorithm requires the acquisition of multislice image data to specify fully the three translations and three rotations characteristic of solid body displacement. This encourages the use of echo planar imaging (EPI) methods for functional MRI which, as mentioned above, can obtain images of the complete brain within 3 s.

5 IMAGE ANALYSIS

Once images have been coregistered, there are a variety of methods for extracting significant activated regions. Maps of F score, z score or Student's t score can be used, but only for images acquired with a repeat time of more than about 10 s, since the slowness of the hemodynamic response (about 6–10 s) introduces temporal correlations into the data, which reduces the number of degrees of freedom in each image. When images are acquired more rapidly, it is preferable to calculate the cross correlation between the time series data in each pixel with a suitably smoothed representation of the time variation of the task, the so-called contrast function.[27,28] As a rule of thumb, a correlation coefficient r of >0.5 can be considered highly significant.

A number of workers have explored the use of non-parametric measures of signal change significance. Use of Kolmogorov–Smirnov statistics has attracted attention, but as the character of the image intensity distributions in functional MRI becomes more fully investigated, this approach is likely to become less popular. Of greater importance is the increase in statistical power obtainable by including the spatial correlation between activated pixels,[29] which has not yet been fully explored in the context of functional MRI.

6 BRAIN FUNCTIONS STUDIED

Since the discovery of BOLD contrast in 1989, MR studies of human brain function have expanded very rapidly. As an index of this growth, at the Annual Meeting of the Society for Magnetic Resonance in Medicine in 1991 there was one presentation mentioning (and introducing) functional MRI. In 1992, at the next meeting, there were 21 presentations dealing with functional MRI, and 94 in 1993. At the corresponding meeting in 1994 there were more than 120 such presentations. Much of this early research has been published only in the form of long refereed abstracts for these meetings. Similar growth rates have occurred in submissions to the Society for

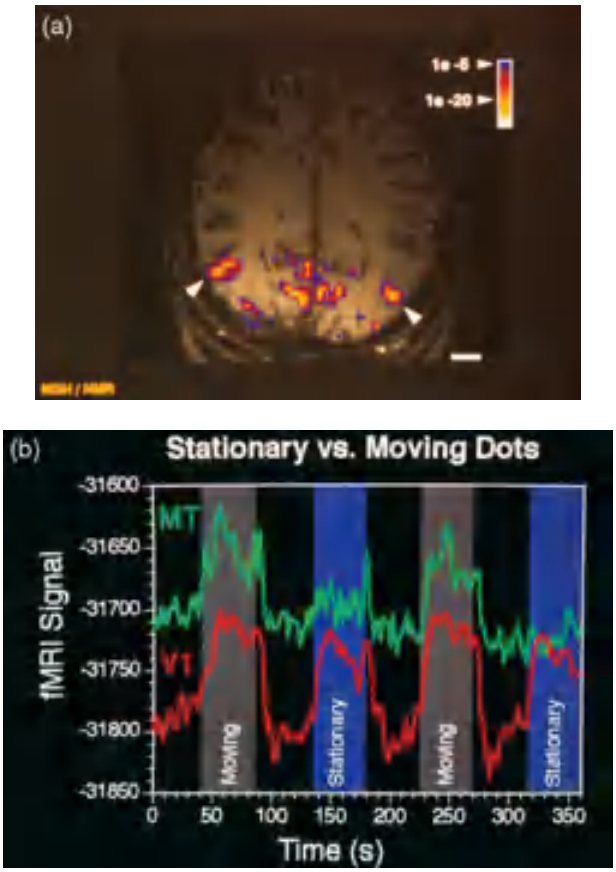

Figure 2 Areas V5/MT of occipital cortex specialized for motion perception. Protocol consisted of alternate presentations of still and moving visual grids, separated by rest periods of darkness. Multislice functional MRI was performed using echo planar imaging (*TR* 3 s, *TE* 40 ms) at 1.5 T, with a surface radiofrequency receiver coil at the back of the head to improve signal-to-noise ratio. (a) Map of echo planar imaging functional data, processed to give a Kolmogorov–Smirnov statistic, superimposed on a high-resolution structural MR oblique axial scan. Areas responding specifically to the moving grid are indicated by arrows. (b) Plots of time course data of regions of interest in V1 and in V5, showing the lack of response in V5 to a static object. (Figure provided by R. Tootell)

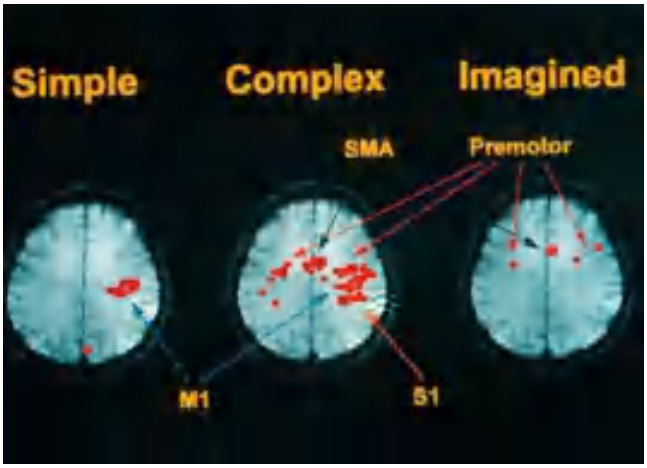

Figure 3 Brain activations in axial slices obtained with echo planar imaging at 1.5 T. The simple task consisted of flexing and extending all four digits together, while the complex task involved tapping each finger to the thumb sequentially in a repeating sequence. The imagined task required subjects mentally to rehearse this complex task without actual finger motion. Active areas were determined using a correlation technique, and were superimposed in color on a gray-scale high-resolution structural scan. (Figure provided by Rao et al.[34] summarizing their results) (SMA denotes supplementary motor area; M1 denotes primary motor cortex; S1 denotes primary somatosensory cortex)

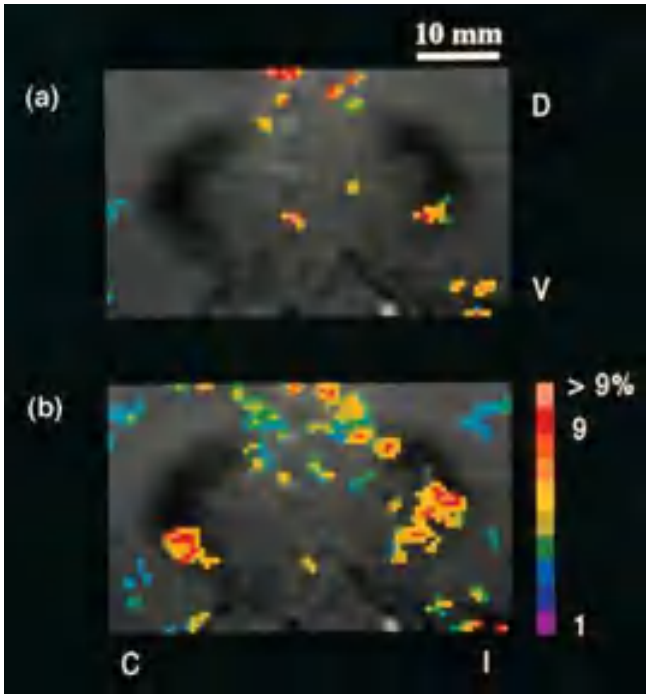

Figure 4 Functional maps of dentate activation during visually guided finger movements (a) and a cognitive puzzle task (b). The color-coded functional map is superimposed on a T_2*-weighted image in gray scale. The dentate nuclei in the cerebellum are dark crescent-shaped regions with low background signal due to iron deposit. C, dentate contralateral to the moving limb; I, dentate ipsilateral to the moving limb; D, dorsal; V, ventral. For tasks, a small lightweight pegboard with nine holes was used. Subjects simply moved pegs for visually guided movements and tried to solve a pegboard puzzle for the cognitive task. All seven subjects examined showed a large bilateral activation during the cognitive task. The activated area was 3–4 times greater than that seen during the visually guided movements. These support the concept that the computational power of the cerebellum is applied not only to the control of movements, but also to cognitive functions. Data were obtained using a FLASH-type functional MRI sequence at 4.0 T. (Reproduced with permission from Kim et al.[36])

Neuroscience annual meetings. In view of the current relative crudity of tools for registration and statistical analysis of functional MRI data, as already noted, the findings in many of these studies must be regarded at this stage as provisional but highly suggestive. For these reasons, we provide just a brief summary of the findings so far.

The study of the primary visual and motor cortices provides an appropriate means of establishing and validating this new method of functional neuroimaging, partly because these systems are relatively well characterized. Numerous studies have now been reported, including, for example, investigations of hemispheric asymmetry and handedness.[30] Another advantage of investigating these cortical areas is that the hemodynamic changes (and hence signal intensity changes) associated with the visual and motor tasks are likely to be considerably greater than those associated with higher cognitive functions. One of the main requirements is to establish the extent to which such higher functions are accessible to investigation by MRI. Initial studies, for example observations involving word generation,[31–33] mental imagery (e.g imagining of motor and visual tasks[34,35]) and other cognitive tasks (see, for example, Kim et al.[36]) appear encouraging, as illustrated by the studies shown in Figures 2–5. However, a great deal more work still needs to be carried out in order to establish the sensitivity of MRI to the wide range of cognitive tasks that are of interest to the neuroscience community.

The demonstration that standard 1.5 tesla systems can be used for at least some applications of functional imaging, including simple motor and visual task activation studies (see, for example, Connelly et al.[38]) has greatly facilitated the use of functional MRI for clinical as well as the more neuroscientific applications. One clinical area of interest relates to neurosurgical removal of lesions that are close to the primary sensory or motor cortex. It can often be difficult to predict the exact location of these primary cortical areas, due to normal biological variation and the distorting effects of the lesion itself. In order to permit maximal resection of such lesions, cortical mapping is performed. Until now, this has required direct electrical stimulation of the brain, often during an awake craniotomy. Using functional MRI, it is now possible to carry out noninvasive presurgical mapping of the sensory and motor cortex.[39] The functional MRI maps can be validated by comparison with the standard intraoperative cortical mapping procedures, and once the MRI method has been extensively validated in this way, then it could have major implications with respect to preoperative planning and to counseling of patients with lesions in these areas of the brain.

Functional MRI could also be of value in the investigation of patients with epilepsy, for preliminary studies have shown that the technique can be used to map the cortical activation that occurs during focal seizures. In these studies of a boy suffering from frequent partial motor seizures, functional MRI revealed sequential cortical activation in structurally abnormal regions of the brain.[40] The activation was observed with

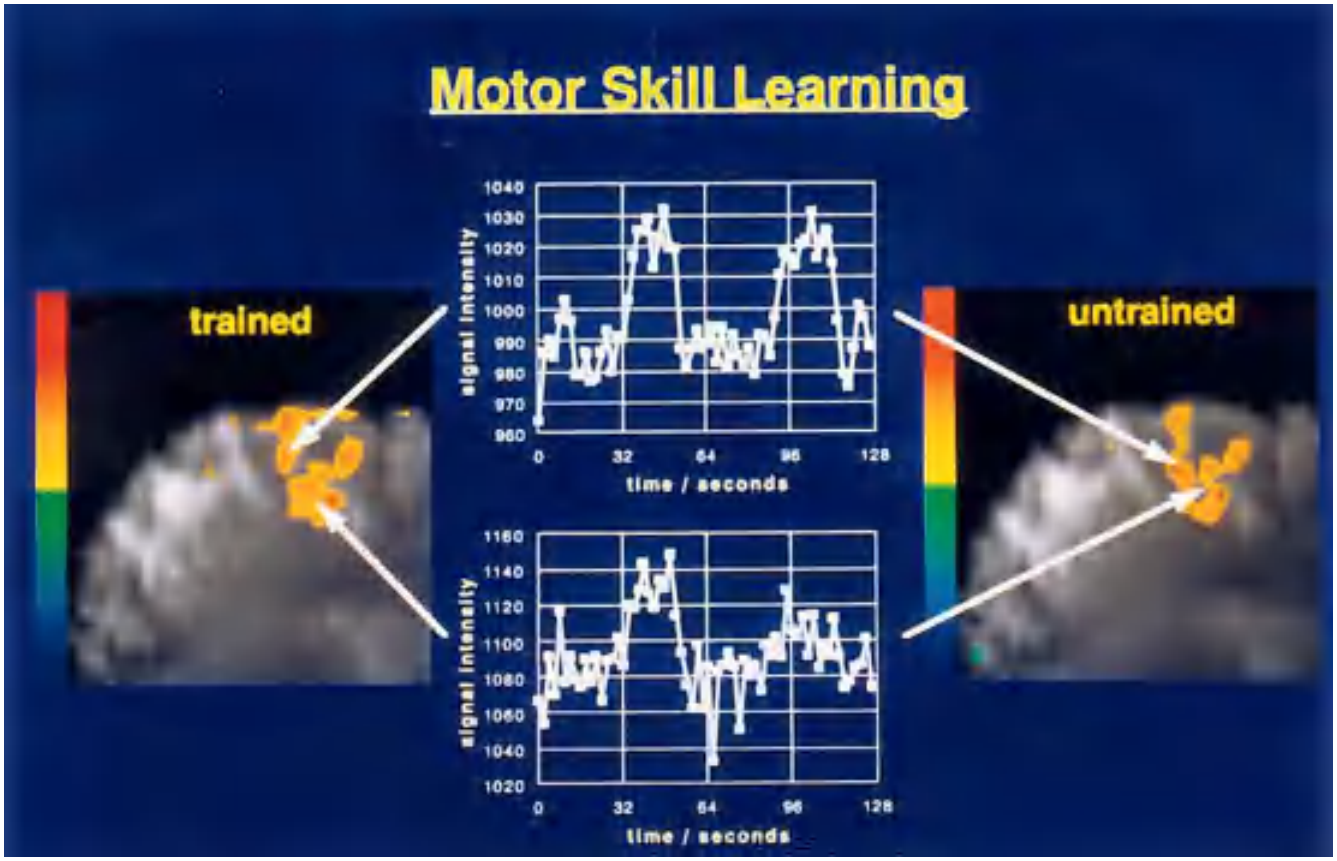

Figure 5 Effect of hand training on area of activated motor cortex.[37] Two finger-tapping tasks were performed during the same functional MRI study, one unrehearsed and the other practised for 10 min per day. After 2–4 weeks the trained task activated a greater number of pixels, as shown. Echo planar imaging data (*TR* 2 s, *TE* 25 ms) at 4 T are projected as a *z* map in color on a high-resolution structural scan. Also shown are time course data from an area of cortex that activated much more for the trained task than for the untrained task, and from an area where the amplitudes of activation were more equal

each of five consecutive clinical seizures, and was also seen during a period that was not associated with a detectable clinical seizure. This latter finding, together with the time dependence of the signal changes that were observed, opens up the possibility of using functional MRI to detect not only the seizures themselves, but also subclinical or interictal events. The technique may therefore find relatively widespread application in the investigation of patients with intractable seizure disorders.

7 DISCUSSION

The scope of magnetic resonance functional neuroimaging is clearly very wide. Variations in the cerebral division of labor, both between subjects and over the course of time within a single subject, can be studied noninvasively with a hitherto unparalleled combination of temporal and spatial resolution. However, the small size of the signal changes results in vulnerability to misregistration artifact, and good reregistration software is essential. Vast quantities of image data can be generated rapidly using echo planar imaging methods (of the order of two gigabytes per day) so that fast-throughput computing facilities and major archiving capabilities are needed.

Be this as it may, a new era in human brain mapping is beginning. Research into the numerous areas of neuroscience and neurology will be accelerated by the relative ease, noninvasiveness, and good spatial and temporal resolution of these techniques.

8 RELATED ARTICLES

Diffusion and Perfusion in MRI; Echo-Planar Imaging; Structural and Functional MR in Epilepsy; Whole Body Magnetic Resonance Angiography; Functional Neuroimaging Artifacts; Head and Neck Investigations by MRI.

9 REFERENCES

1. D. J. Chadwick and J. Whelan, *Ciba Found. Symp.*, 1991, **163**, 1.
2. J. W. Belliveau, D. N. Kennedy, R. C. McKinstry, B. R. Buchbinder, R. M. Weisskoff, M. S. Cohen, J. M. Vevea, T. J. Brady, and B. R. Rosen, *Science*, 1991, **254**, 716.
3. S. Ogawa, T-M. Lee, A. S. Nayak, and P. Glynn, *Magn. Reson. Med.*, 1990, **14**, 68.
4. S. Ogawa and T.-M. Lee, *Magn. Reson. Med.*, 1990, **16**, 9.

5. R. Turner, D. LeBihan, C. T. W. Moonen, D. Despres, and J. Frank, *Magn. Reson. Med.*, 1991, **22**, 159.
6. K. K. Kwong, J. W. Belliveau, D. A. Chesler, I. E. Goldberg, R. M. Weisskoff, B. P. Poncelet, D. N. Kennedy, B. E. Hoppel, M. S. Cohen, R. Turner, H.-M. Cheng, T. J. Brady, and B. R. Rosen, *Proc. Natl. Acad. Sci. U. S. A.*, 1992, **89**, 5675.
7. S. Ogawa, D. W. Tank, R. Menon, J. M. Ellermann, S.-G. Kim, H. Merkle, and K. Ugurbil, *Proc. Natl. Acad. Sci. U. S. A.*, 1992, **89**, 5952.
8. P. A. Bandettini, E. C. Wong, R. S. Hinks, R. S. Tikofsky, and J. S. Hyde, *Magn. Reson. Med.*, 1992, **25**, 390.
9. P. T. Fox and M. E. Raichle, *Proc. Natl. Acad. Sci. U. S. A.*, 1986, **83**, 1140.
10. W. Penfield, *Ann. Intern. Med.*, 1933, **7**, 303.
11. K. R. Thulborn, J. C. Waterton, P. M. Matthews, and G. K. Radda, *Biochim. Biophys. Acta*, 1982, **714**, 265.
12. K. M. Brindle, F. F. Brown, I. D. Campbell, C. Grathwohl, and P. W. Kuchel, *Biochem. J.*, 1979, **180**, 37.
13. J. Frahm, K.-D. Merboldt, W. Hänicke, A. Kleinschmidt, and H. Boecker, *NMR Biomed.*, 1994, **7**, 45.
14. D. Roberts, J. A. Detre, L. Bolinger, E. K. Insko, and J. S. Leigh, Jr., *Proc. Natl. Acad. Sci. U. S. A.*, 1994, **91**, 33.
15. R. R. Edelman, B. Siewert, D. G. Darby, V. Thangaraj, A. C. Nobre, M.-M. Mesulam, and S. Warach, *Radiology*, 1994, **192**, 513.
16. J. Frahm, M. L. Gyngell, and W. Hanicke, in *Magnetic Resonance Imaging* eds. D. D. Stark and W. G. Bradley, Jr., Mosby Year Book, St. Louis, 1992, pp. 165.
17. M. K. Stehling, R. Turner, and P. Mansfield, *Science*, 1991, **254**, 43.
18. S. Lai, A. L. Hopkins, E. M. Haacke, D. Li, B. A. Wasserman, P. Buckley, L. Friedman, H. Meltzer, P. Hedera, and R. Friedland, *Magn. Reson. Med.*, 1993, **30**, 387.
19. S. Ogawa, R. S. Menon, D. W. Tank, S.-G. Kim, H. Merkle, J. M. Ellermann, and K. Ugurbil, *Biophys. J.*, 1993, **64**, 803.
20. R. M. Weisskoff, C. S. Zuo, J. L. Boxerman, and B. R. Rosen, *Magn. Reson. Med.*, 1994, **31**, 601.
21. R. D. Frostig, E. E. Lieke, D. Y. Ts'o, and A. Grinvald, *Proc. Natl. Acad. Sci. U. S. A.*, 1990, **87**, 6082.
22. R. Turner and A. Grinvald, *2nd Mtg., Proc. Soc. Magn. Reson., San Francisco, 1994*, 430.
23. J. V. Hajnal, R. Myers, A. Oatridge, J. E. Schwieso, I. R. Young, and G. M. Bydder, *Magn. Reson. Med.*, 1994, **31**, 283.
24. R. P. Woods, S. R. Cherry, and J. C. Mazziotta, *J. Comput. Asst. Tomogr.*, 1992, **16**(4), 620.
25. J. M. Tyszka, S. T. Grafton, W. Chew, R. P. Woods, and P. M. Colletti, *Ann. Neurol.*, 1994, **35**, 746.
26. K. J. Friston, J. Ashburner, C. D. Frith, J.-B. Poline, J. D. Heather, and R. S. J. Frackowiak, *Hum. Brain Mapping*, in press.
27. P. A. Bandettini, A. Jesmanowicz, E. C. Wong, and J. S. Hyde, *Magn. Reson. Med.*, 1993, **30**, 161.
28. K. F. Friston, P. Jezzard, and R. Turner, *Hum. Brain Mapping*, 1994, **1**, 153.
29. W. Schneider, D. C. Noll, and J. D. Cohen, *Nature (London)*, 1993, **365**, 150.
30. S.-G. Kim, J. Ashe, K. Hendrich, J. M. Ellermann, H. Merkle, K. Ugurbil, and A. P. Georgopolis, *Science*, **261**, 615.
31. G. McCarthy, A. M. Blamire, D. L. Rothman, R. Gruetter, and R. G. Shulman, *Proc. Natl. Acad. Sci. U. S. A.*, 1993, **90**, 4952.
32. R. M. Hinke, X. Hu, A. E. Stillman, S.-G. Kim, H. Merkle, R. Salmi, and K. Ugurbil, *Neuroreport*, 1993, **4**, 675.
33. L. Rueckert, I. Appollonio, J. Grafman, P. Jezzard, R. Johnson, D. Le Bihan, and R. Turner, *J. Neuroimaging*, 1994, **4**, 67.
34. S. M. Rao, J. R. Binder, P. A. Bandettini, T. A. Hammeke, F. Z. Yetkin, G. L. Morris, W. M. Mueller, and L. D. Estkowski, *Neurology*, 1993, **43**, 2311.
35. D. Le Bihan, R. Turner, T. Zeffiro, C.-A. Cuenod, P. Jezzard, and V. Bonnerot, *Proc. Natl. Acad. Sci. U. S. A.*, 1993, **90**, 11 802.
36. S.-G. Kim, K. Ugurbil, and P. L. Strick, *Science*, 1994, **265**, 949.
37. P. Jezzard, A. Karni, G. Meyer, M. Adams, A. Prinster, L. Ungerleider, and R. Turner, *2nd Mtg. Proc. Am. Soc. Magn. Reson. San Francisco, CA, 1994*, p. 330.
38. A. Connelly, G. D. Jackson, R. S. J. Frackowiak, J. W. Belliveau, F. Vargha-Khadem, and D. G. Gadian, *Radiology*, 1993, **188**, 125.
39. C. R. Jack, R. M. Thompson, F. W. Sharbrough, P. J. Kelly, D. P. Hanson, R. K. Butts, N. J. Hangiandreou, S. J. Riederer, R. L. Ehman, and G. D. Cascino, *Radiology*, 1994, **190**, 1.
40. G. D. Jackson, A. Connelly, J. H. Cross, I. Gordon, and D. G. Gadian, *Neurology*, 1994, **44**, 850.

Acknowledgments

We thank the Wellcome Trust for their support.

Biographical Sketches

Robert Turner. *b* 1946. B.A., 1968, Cornell University, Ph.D., 1972, Simon Fraser University, B.C., Canada. Postdoctoral work in NMR of liquid crystals, University of Cambridge, UK, 1973–75; Lecturer in Physics, University of Nottingham, UK (working with Peter Mansfield on MRI hardware and software), 1975–88 visiting scientist, NIH, Bethesda, MD, 1988–93; Institute of Neurology, London, UK, 1993–present. Approx. 70 publications. Current research interests include gradient coil design, applications of echo-planar MRI, and functional imaging of human brain.

David G. Gadian. *b* 1950. B.A., 1971, Physics, D. Phil., 1975, University of Oxford, UK (supervisor Rex Richards). Postdoctoral research with Rex Richards and George Radda in Oxford. Moved in 1983 to the Royal College of Surgeons in London. Currently Rank Professor of Biophysics and Head of the RCS Unit of Biophysics and of the Radiology and Physics Unit at the Institute of Child Health, London. Approx. 140 publications. Research interests: development and application of magnetic resonance techniques for noninvasive investigation of brain metabolism and physiology.

Functional Neuroimaging Artifacts

Joseph V. Hajnal
Hammersmith Hospital, London, UK

1	Introduction	1
2	Recognition of Activation-Induced Signal Changes	1
3	The Problem of Subject Motion	2
4	Image Registration	3
5	Evidence for Stimulus Correlated Motion	3
6	Correction of Misregistration Artifacts	5
7	Conclusion	9
8	Related Articles	9
9	References	9

1 INTRODUCTION

Functional neuroimaging with MRI (fMRI) may open up enormous possibilities for the study of human brain function in health and disease.[1,2] It offers the combination of being noninvasive with the potential for high spatial and moderate temporal resolution.

Most functional MRI studies involve the acquisition of a series of images over time while the subject performs a task or experiences a stimulus. Images acquired with the subject in different states are then compared in order to detect signal changes associated with brain activation. The origin of such changes is widely thought to be associated with a localized hemodynamic response to increased neuronal activity. This response is thought to produce signal changes by two principal mechanisms: (a) changes in blood oxygenation state resulting in susceptibility mediated signal changes [the blood oxygen level dependent (BOLD) effect];[3] and (b) signal changes associated with increased blood throughput.[4] The signal changes attributed to these effects range from 1–2% up to 20–30%, depending on the MRI technique employed and the strength of the $\boldsymbol{B}_0$ field.[5,6]

Thus the task in functional MRI studies is to detect very small localized signal changes in a series of images of nominally the same anatomical structures. A key feature in this endeavor is the suppression of the wealth of anatomical detail that has hitherto been the hallmark of MRI in order to reveal functionally mediated signal variations. This change of emphasis has introduced a class of artifacts that are quite distinct from the imperfections usually seen on conventional in vivo magnetic resonance (MR) images.

This article is concerned with the artifacts that may occur in fMRI studies including ways in which they may be identified or reduced.

2 RECOGNITION OF ACTIVATION-INDUCED SIGNAL CHANGES

Detection of activation-induced signal changes generally relies on correlating changes in the signals from individual image pixels or groups of pixels with the temporal structure of the activation protocol under study. The basic methodology employed owes much to studies of brain activity using positron emission tomography (PET),[7] a technique with which functional MRI shows some similarities as well as some essential differences.

The majority of PET activation studies rely on detecting blood flow changes made visible by the injection of radioactive water. The data obtained typically display both a low effect-to-noise ratio and a large effect-to-resting-signal ratio. Thus the methodology employed is designed to detect a small coherent signal that may be buried deep in random noise. Statistical methods and spatial averaging are employed to discriminate against the noise,[8] and signals that correlate with the activation protocol are taken to reflect activation-induced physiological changes.

In contrast, functional MRI is characterized by a small effect-to-resting-signal ratio with a high overall signal-to-noise ratio. Thus, although it is necessary to distinguish the desired effect from random noise, for which statistical methods akin to those employed in PET may be appropriate,[9,10] it is also essential to differentiate signals induced by activation from all other sources of change in the resting anatomical signal. This latter task requires a different approach because the competing signal changes may also be temporally coherent with the activation paradigm. In addition, the resting signals also have pronounced spatial structure, so that spatial averaging (smoothing) may not preferentially reduce them as would be the case for random noise.

Coherent signal changes that may confound functional MRI studies can arise from a variety of sources. Both respiration and cardiac pulsations can cause signal changes in brain images.[11] Changes in the subject's state of arousal during activation studies thus may lead to signal changes that correlate with the task protocol. Large effects may be produced simply by changes in the subject's position during the course of a study. The structural content of MR images may result in steep intensity gradients at interfaces between tissues, so that a slight head movement between the baseline and the activated images may result in a substantial signal variation. If subject motion is correlated with the task paradigm, the signal change may become task locked. As a result, it is insufficient to rely solely on coherence with the task under study as a sine qua non of a genuine activation.

Recognition of artifacts is hampered by the suppression of anatomical details which removes many of the signs that radiologists conventionally rely on to detect them. Processing procedures that remove these landmarks may lead to confusion. For example, the discovery that detected signals are actually from the scalp or ventricles provides an obvious indication that something is amiss. It is important not simply to disregard these contributions to the overall activation map, but to recognize that whatever mechanism has produced them may also be contributing to less obviously erroneous signals.

Even when activation signals are apparently appropriately located, detailed study of the local anatomy is often revealing. For example, direct visualization of the local cortical structure can be invaluable for checking if 'cortical activation' signals cross tissue boundaries or do not in fact follow the line of the cortex at all. Figure 1 illustrates this for a hemifield visual stimulation experiment designed to detect susceptibility changes associated with the BOLD effect. Long echo time field

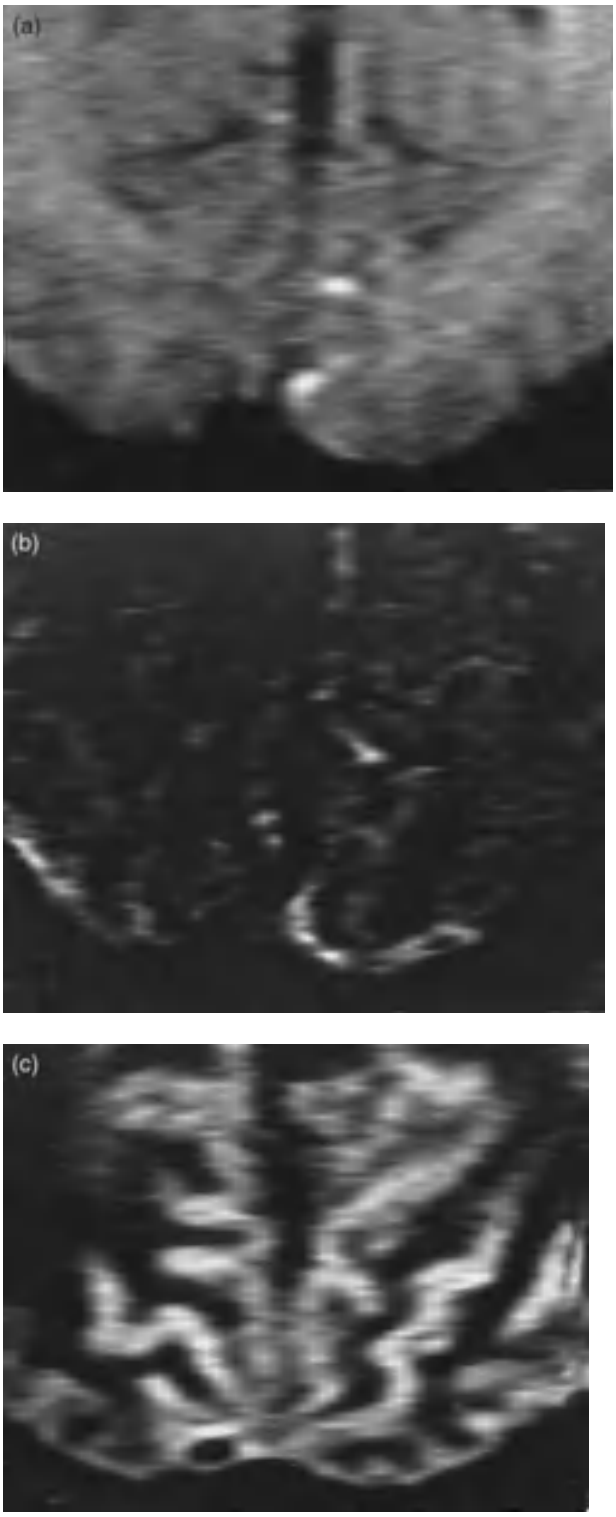

Figure 1 A visual stimulation study in which (a) an oblique transverse slice was repeatedly imaged with a field echo sequence (*TR* 150, *TE* 100, flip angle 65°, 18 cm FOV, 64 × 256 matrix) while the subject experienced periods of hemifield visual stimulation and darkness. (b) A difference image reveals apparent activation in only one hemisphere as expected. However, (c) use of a double inversion recovery sequence (*TR* 6080, TI_A 2600, TI_B 245, *TE* 16) to image selectively the cortex at the same resolution reveals that the "activation" signals in (b) follow the outline of the brain as visualised in (a) rather than the more complex cortical structure (c)

echo images acquired during the activation study [Figure 1(a)] do not provide clear differentiation of the cortex, so that the difference image (illumination of half the visual field minus darkness) appears to show a plausible activation signal in one occipital cortex [Figure 1(b)]. However, acquisition of images at the same resolution, but designed to display the cortex alone [Figure 1(c)], reveals that the 'active' region follows the outline of the brain and not the highly convoluted cortex. The difference image shown in Figure 1(b) is thus most unlikely to represent cortical activation, and further analysis showed it to be artifactual.

The process of recognizing genuine evidence for activation and rejecting other signal changes is still evolving. A cautious approach is indicated at present in which potential sources of error are identified and their effects at least quantified if they cannot be reduced or eliminated.

3 THE PROBLEM OF SUBJECT MOTION

Subject motion affects most MRI techniques to a greater or lesser extent. In most cases problems arise because of changes in subject position during the acquisition of image data. This may lead to gross motion artifacts or simply to an apparent reduction in the signal-to-noise ratio (see also ***Whole Body Magnetic Resonance Artifacts***). Many techniques have been developed to minimize these effects, and some are now being applied to improve the quality of the individual images obtained in functional MRI studies.[12] The long *TE* field echo sequences used to detect BOLD changes are particularly vulnerable to instabilities of various kinds. Fast imaging techniques such as EPI are, in general, less vulnerable to image artifacts produced by motion of the subject during the scan.

Another kind of motion artifact is of particular importance in functional MRI. If the subject changes position between scans the anatomical content will change from one image to the next. This may result in artifactual signal changes even though the individual images are themselves relatively free from motion artifacts. It has been shown that subjects generally move to some degree during functional MRI studies and that this motion frequently has components that are correlated with the stimulus protocol.[13] The result of such stimulus-correlated displacement is that the intensity in some pixels varies synchronously with the stimulus. Analyses designed to detect correlated signal changes extract these motion-induced effects along with any genuine activation effects.

A simple calculation illustrates the magnitude of the likely effects of changes in position. The signal intensity change ΔI caused by a small spatial displacement Δx in a region of an image where there is a pixel intensity gradient ($\mathrm{d}I/\mathrm{d}x$) is approximately

$$\Delta I \simeq \frac{\mathrm{d}I}{\mathrm{d}x}\Delta x \qquad (1)$$

If the intensity difference between adjacent pixels is 20% and the subject has moved by 1/10 of a pixel, a signal change of 2% will result. This is the same magnitude as the expected signal change from brain activation, so that clearly only a much smaller shift could be tolerated without some form of correction being necessary. With typical imaging parameters (16–22 cm field of view, 64–128 phase encode steps), 1/10

pixel represents about 300 μm or less. The restraint necessary to prevent motions of this size cannot be reliably achieved by noninvasive head-holding techniques.

4 IMAGE REGISTRATION

Fortunately, the wealth of structural (anatomical) information contained in MR images allows subject movements to be detected retrospectively and corrected. Image registration algorithms that can match MR images to a tiny fraction of a pixel are now available. Hitherto, most techniques have been designed for cross-modality image matching [MRI to computerized tomography (CT), PET to MRI, etc.],[14,15] and frequently operator intervention has been required to select landmarks. However, Woods et al.[16,17] have developed a simple, fully automatic procedure that can be used for intramodality matching, and their approach is now being refined specifically for MRI to MRI registration.

5 EVIDENCE FOR STIMULUS CORRELATED MOTION

Changes in subject position during brain activation studies may result in gross misregistration artifacts which can easily be recognized and may have little to do with the task under study. However, smaller more subtle movements are commonplace and their effects may be more difficult to recognize by image inspection alone.

The nature of subject motion during functional MRI examinations has been studied for both motor and visual activation paradigms.[13] In these studies subjects were imaged using long *TE* rapid gradient echo sequences with a surface coil for signal reception. Repeated single-slice images of appropriate anatomical regions were acquired at a rate of one every 20 s. The stimulus condition was changed every five images. For the motor studies, the subjects performed finger to thumb touching continuously with one hand for the duration of five images and then changed hands for the next five images, and so on. At the end of the experiment all the images acquired with the left hand exercising were subtracted from all those with the right hand exercising and the results summed to form a cumulative difference image.

Figure 2 shows an example of the results obtained. The anatomical slice which was acquired in the coronal plane is shown in Figure 2(a) and the cumulative difference image is shown in Figure 2(b). The highlighted region in Figure 2(b) (arrow) shows where there was a localized signal change that correlated with the stimulus protocol; it increased when the right hand was active and fell when the left hand was active. The 'active' region is in an appropriate cortical location for the task being performed.

To examine the subject's motion during the study, an image registration technique[16] was used to find the rigid body translations and rotations that were required to match the head position in each of the images obtained with that in a single base image. This resulted in the time series data shown in Figure 2(d). The top graph shows left–right shifts from image to image, the middle graph shows head–foot displacements, and the bottom graph shows in-plane rotations of the head.

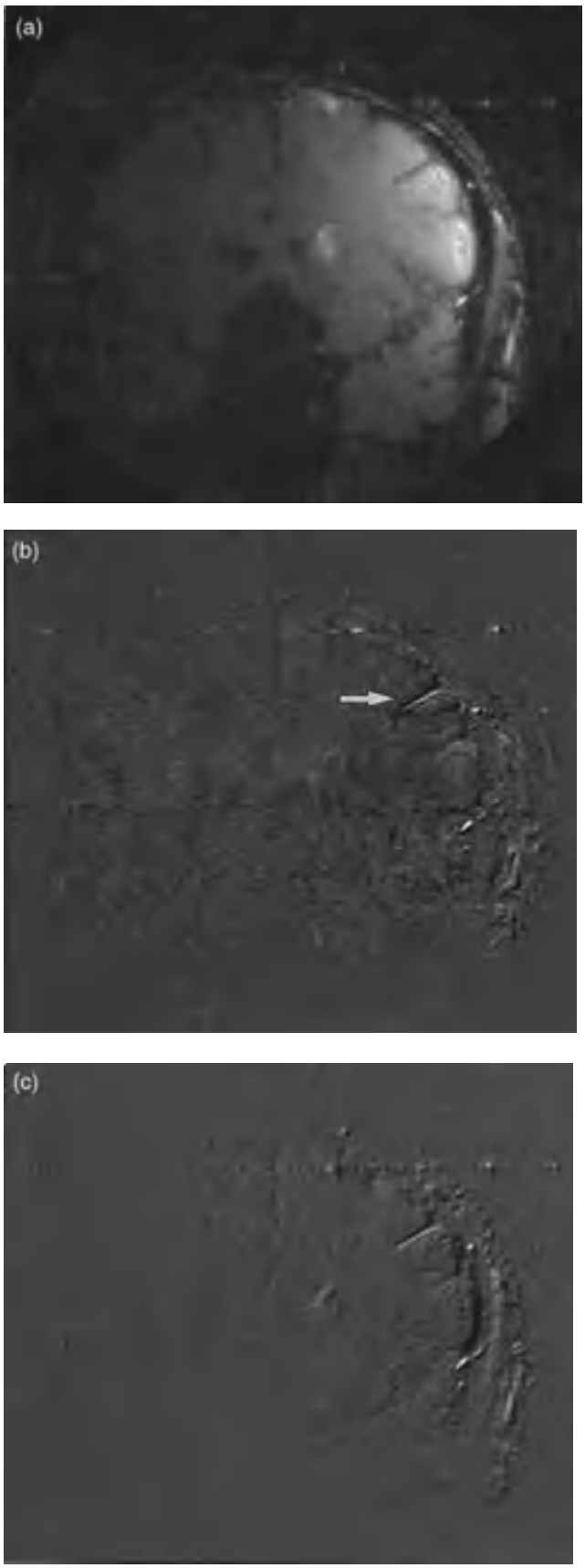

Figure 2

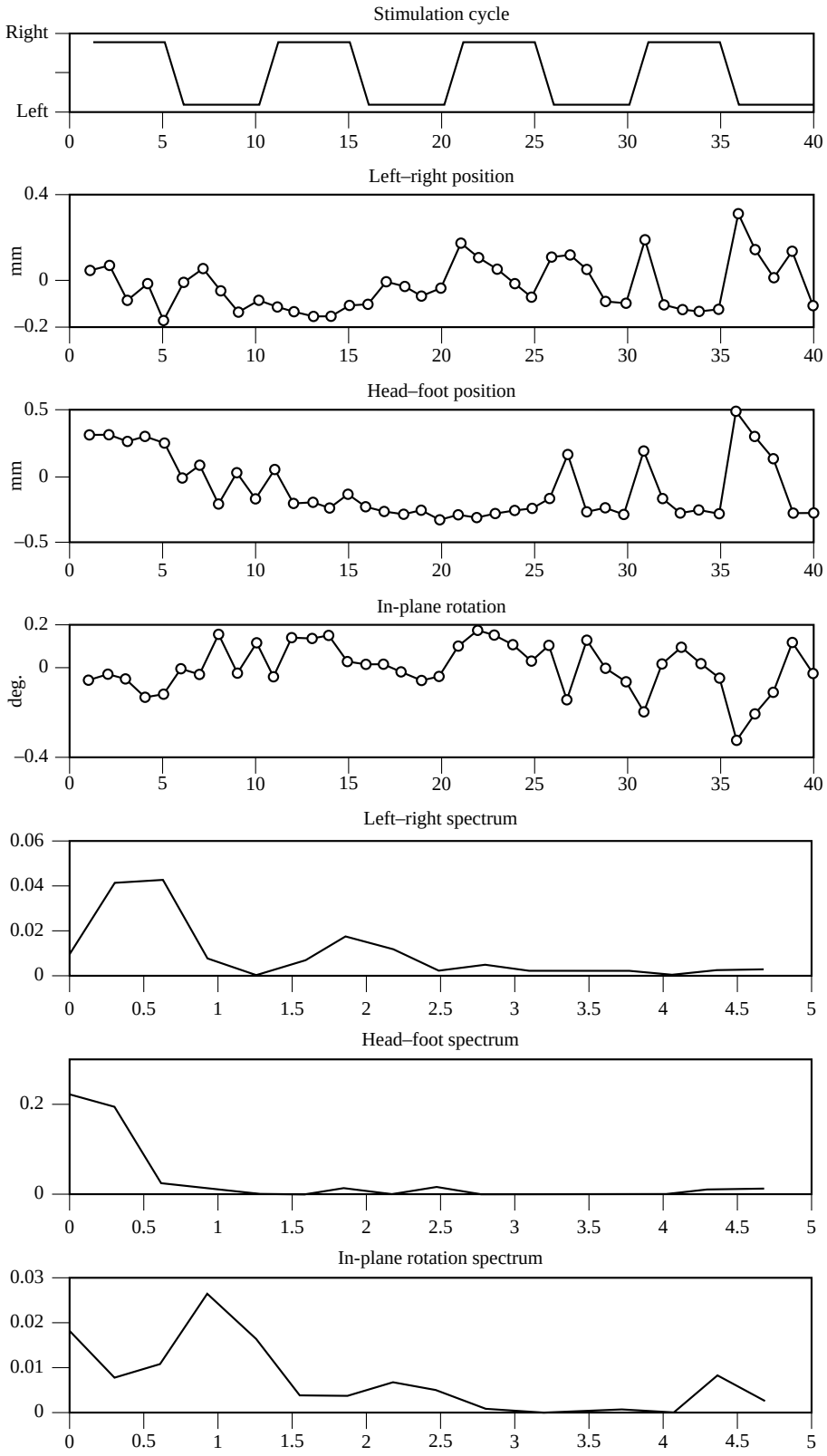

Figure 2 (a) Anatomical image of the coronal slice chosen for a motor stimulation study. (b) The cumulative difference image, right hand action minus left hand action, reveals a focal high signal region in an appropriate anatomical location (arrow). However, (c) a strikingly similar pattern of focal signal change can be demonstrated to have been produced purely as a result of small changes in position of the subject during the study. (d) The position changes, as determined by an image registration technique, are plotted against image number (time). They reveal that small displacements tend to occur as the hand being exercised is changed (i.e. at multiples of five images). (e) A power spectral analysis of the movement time series in (d) reveals dominant peaks associated with the periodicity of the stimulus protocol

The magnitude of these displacements was less than 0.5 mm for translations and 0.3° for rotation.

Although the motion is small, there is evidence that the positional changes occur in concert with the task [Figure 2(d) note the left–right shifts at images 20,25,30,35]. To investigate this more systematically a power spectrum analysis was performed [Figure 2(e)],[18] to reveal the dominant periodic components of the motion. In this analysis the unit of frequency was normalized so that unity corresponds to one motion cycle per stimulus cycle of 10 images. There is a particularly pronounced peak at 1 for the in-plane rotation, indicating that the subject had a tendency to nod their head from side to side in time with each change of hand. The peak at 2 in the left–right displacement spectrum shows that the subject was moving in a way that correlated with changes of hand, irrespective of which hand was being exercised.

To investigate the effect of the stimulus-correlated motion on individual pixel intensities in the difference image [Figure 2(b)], a synthetic data set was created. This was done by taking a single base image from the original functional series, replicating it, and then using the data obtained by coregistration to reposition the replicated images to match the position of each of the other images in the series. The resulting set of images matched the original experimental data by retaining the subject's anatomy and history of their motion, but specifically excluded other sources of signal change such as changes in blood flow or oxygenation state. The calculated cumulative difference image from the synthetic data set is shown in Figure 2(c) and replicates the highlighted region in Figure 2(b) that appeared to be due to brain activation.

Figure 2 thus illustrates that subject motion can correlate with the stimulus and cause signal changes that may easily be mistaken for evidence of brain activation. Similar analyses of four motor stimulation studies and four hemifield visual stimulation studies showed that stimulus-correlated motion was present in each case.[13]

6 CORRECTION OF MISREGISTRATION ARTIFACTS

The presence of signals that arise from changes in subject position during the course of a functional MRI study may not in itself be a problem, provided that the artifactual contribution can be recognized and dealt with in an appropriate manner.

Estimating the maximum displacement that may have occurred allows the magnitude of potential displacement artifacts to be quantified. Using the study shown in Figure 2 as an example, if the subject was known to have moved by less than Δx of a pixel from left to right, Δy from head to foot and to have tilted the head by less than $\Delta\theta$ radians in plane about a point (x_0, y_0), then the maximum displacement-induced signal (ΔI) for a pixel at (x, y) can be estimated as:

$$\Delta I(x,y) = \sqrt{\left\{\left[\frac{\partial I(x,y)}{\partial x}\Delta x\right]^2 + \left[\frac{\partial I(x,y)}{\partial y}\Delta y\right]^2 + \left[\left\{-(y-y_0)\frac{\partial I(x,y)}{\partial x} + (x-x_0)\frac{\partial I(x,y)}{\partial y}\right\}\Delta\theta\right]^2\right\}} \quad (2)$$

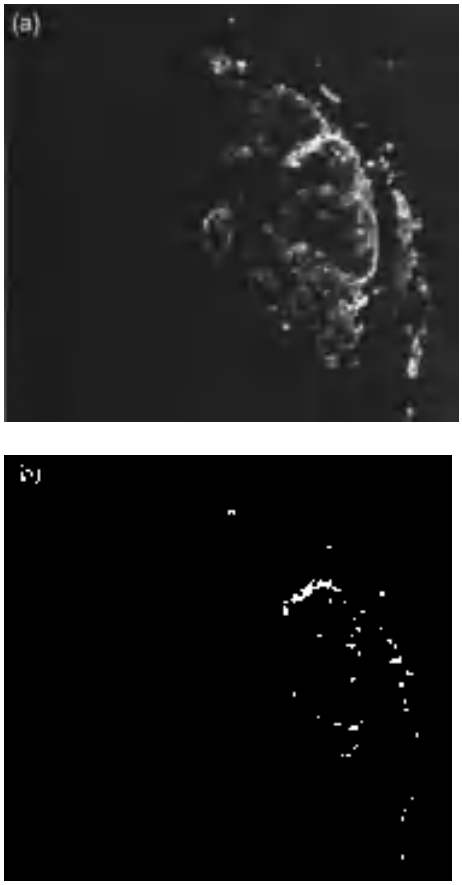

Figure 3 Vulnerability maps produced from Figure 2(a) which reveal the spatial distribution of all potential signal changes that could occur as a result of displacements of $\Delta x = \Delta y = 1/10$ pixel and $\Delta\theta = 0.02$ rad (a) and $\Delta x = \Delta y = 0$ and $\Delta\theta = 0.02$ rad (b)

Applying this formula to the image shown in Figure 2(a) with $\Delta x = \Delta y = 1/10$ pixel and $\Delta\theta = 0.002$ rad, and dividing ΔI by the resting pixel intensity, results in the image shown in Figure 3(a). Note that most of the cortex is vulnerable to motion-induced changes, with typical signal changes of 10–20%, even for the small displacements considered. The image shown in Figure 3(a), which we refer to as a 'vulnerability map', indicates the potential combined effect of all possible movements up to the chosen maximum displacement in x, y, and θ. Figure 3(b) shows another vulnerability map, but this time calculated with $\Delta x = \Delta y = 0$ so that it shows the distribution of signal change induced by pure rotations of the head. Note that the most prominent features are the same as those that are highlighted in Figure 2(b) and (c).

Vulnerability maps may be used as a thresholding device to subtract out potential motion effects. A signal change in a given pixel that was larger than the vulnerability for that pixel could then confidently be assigned to a cause other than motion. This approach is rather crude since, as can be seen from Figure 3, even modest displacements would lead to threshold criteria that would be unlikely to be exceeded by the expected genuine activation signals. A more rigorous approach is to quantify the exact displacements and correct for them, leaving a data set that can more confidently be analysed for evidence of genuine brain activation.

The image registration techniques already described provide a means of doing this; however, special care is required to ensure that the process of registration does not itself introduce artifacts. Since subpixel displacements are required, it is necessary to interpolate the image data to generate new interstitial pixel values.

6.1 Image Interpolation

Image matching is frequently performed using linear interpolation[19] (see, for example, Woods et al.[16]). The effect that this has on MRI data can be determined with a simple experiment. An MR image, for example the T_1-weighted image shown in Figure 4(a), is rotated using a computer, and new interpolated pixel values calculated to produce the image shown in Figure 4(b). The rotated image is then rotated back to its original orientation and the difference between the original image and the doubly interpolated image is calculated. Figure 4(c) shows the result for linear interpolation. Substantial intensity errors have been introduced because the interpolation function does not match the structure of the image data.

Much more faithful interpolation can be achieved by making use of the fact that MR data are strictly band limited and, therefore, their in-plane point spread function is the sinc function.[20] Using sinc interpolation[21] to rotate the images shown in Figures 4(a) and (b) produces much smaller differences [Figure 4(d)], with the maximum error now being less than 1% of the maximum signal.

6.2 In-Plane Registration

Sinc interpolation can form the basis of an in-plane misregistration correction scheme in which images are positionally matched with subvoxel precision and then compared in order

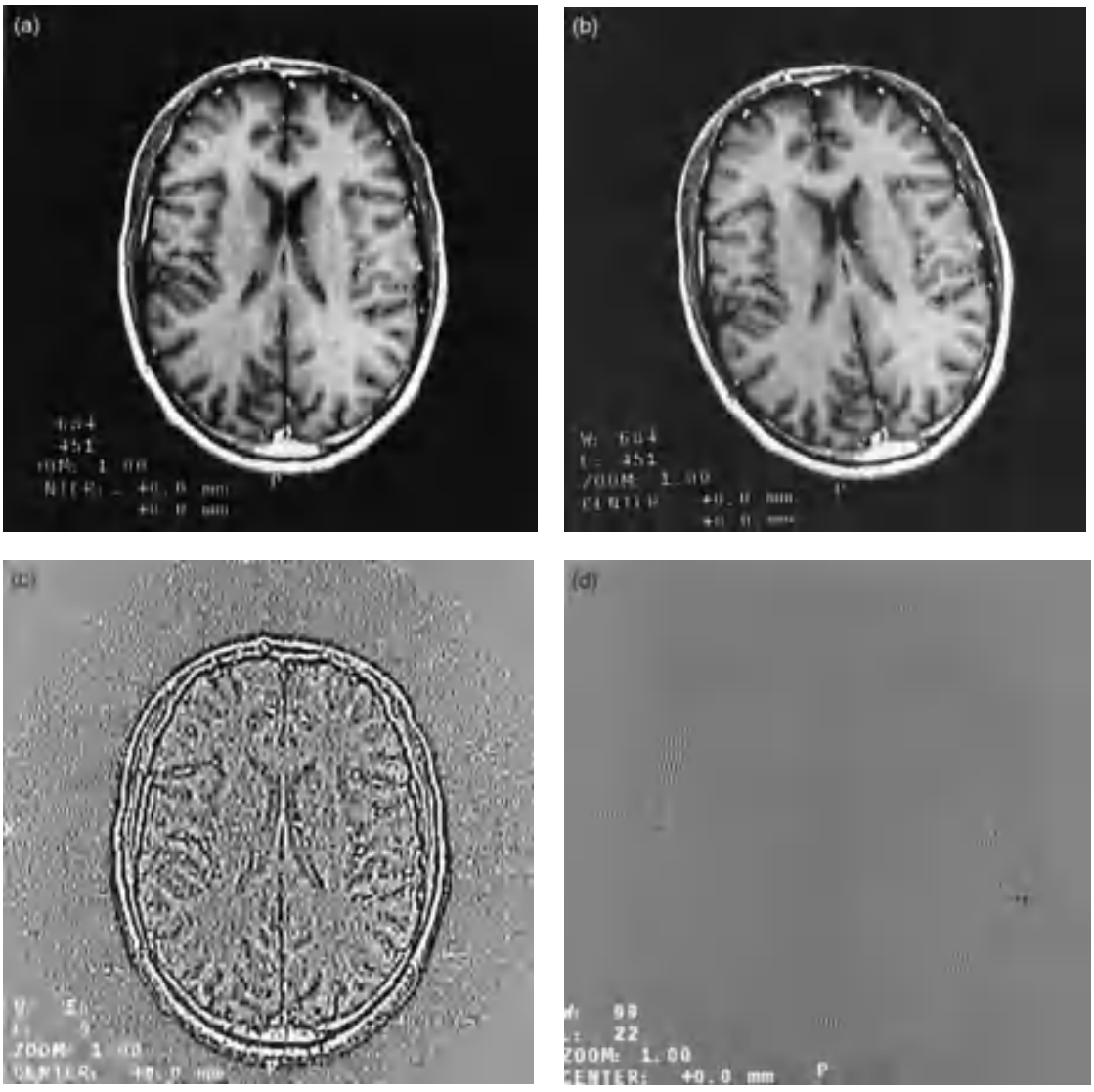

Figure 4 Displacement of image data by a fraction of a pixel requires image interpolation, which may introduce errors. These errors can be detected (a) by rotating a sample image by 10° to produce a second image (b) and then rotating (b) back to the original position. The final image, which has been interpolated twice, can then be subtracted from (a) to reveal any errors. Linear interpolation introduces substantial errors particularly at edges (c), whereas sinc interpolation is much more faithful to the original data structure (d)

to detect changes that are independent of the transformations employed.

A least-squares minimization procedure can be used to determine the required positional transformations. We employ the Levenberg–Marquart algorithm[22] to minimize

$$\chi^2 = \frac{\sum}{\text{pixels}} \frac{(I_A - I_B)^2}{N} \tag{3}$$

where I_A and I_B are the intensities of corresponding pixels in the two images being matched, and N is the number of pixels included in the calculation of χ^2. Minimization is achieved by rigid body rotation and translation of image A using sinc interpolation to generate new values for I_A.

Figure 5 illustrates the image registration procedure. A phantom [Figure 5(a)] was imaged twice with an in-plane displacement of approximately 2.5 pixels between the images. A difference image showing the effect of the displacement is shown in Figure 5(b). After χ^2 minimization, shifting one image to match the other using sinc interpolation results in the difference image shown in Figure 5(c). The procedure has succeeded in reducing displacement-induced differences to the level of the background noise.

For in vivo studies, a further refinement is generally required because subject movement can introduce image differences caused by the differential displacement of soft tissues. It is therefore advisable to restrict the registration to those parts of the image containing the tissue of interest. This can readily be achieved by segmenting[23] one of the images.

6.3 Full Three-Dimensional Registration

The example illustrated in Figure 5 was restricted to in-plane displacements. In a living subject, we must expect full three-dimensional movement to occur, and thus single-slice data do not provide sufficient information. Conventional multislice techniques can nominally provide the required

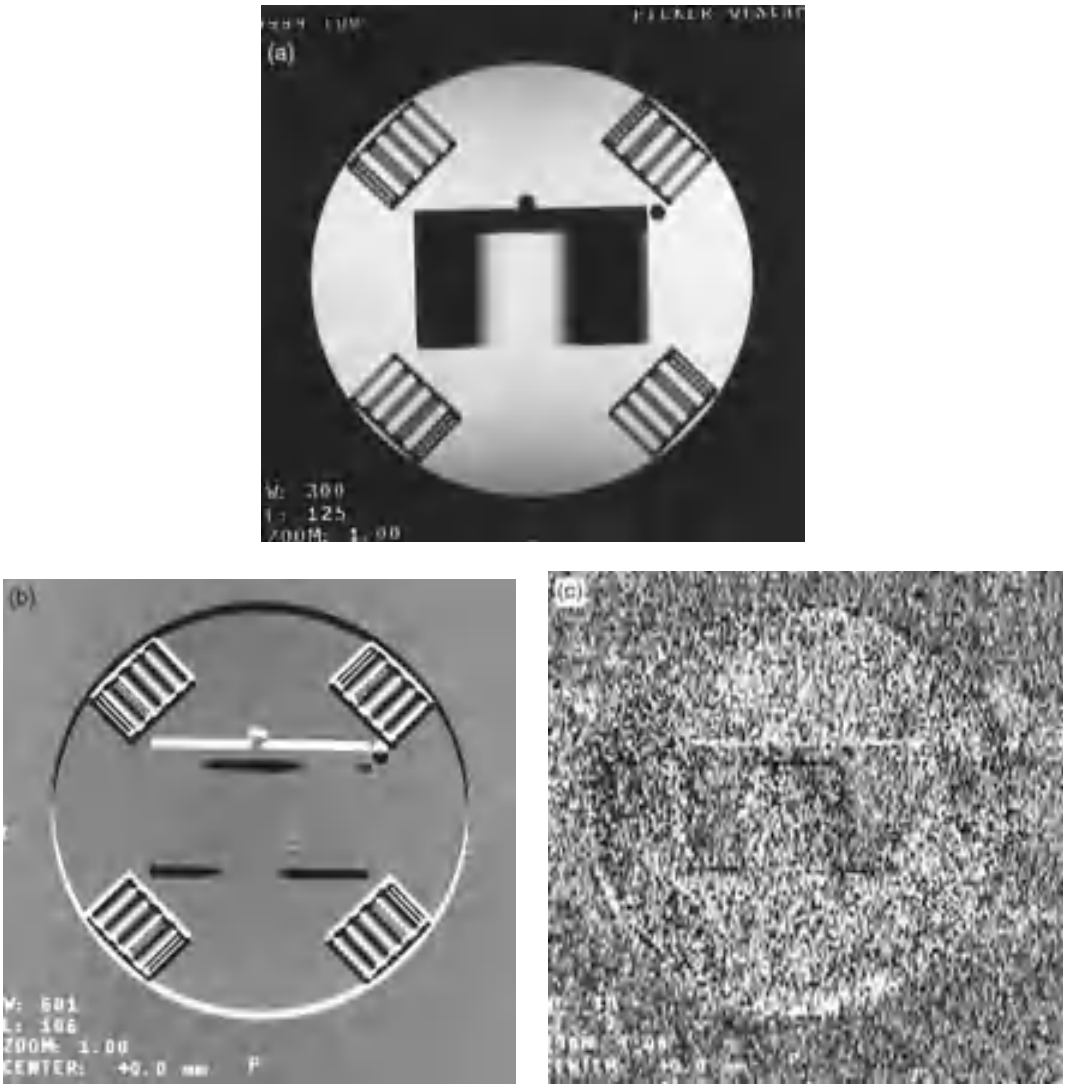

Figure 5 Image registration allows subject displacement to be corrected. (a) A phantom imaged twice with a differential offset of 2.5 mm results in substantial misregistration signals when the two images are subtracted (b). (c) Using an automatic image registration algorithm to determine the spatial shift required and sinc interpolation to reposition one image at the location of the other, reduces differences to the level of the background noise

spatial coverage, but problems can arise with uncertainties of data content at the boundaries between slices. The fidelity with which multislice data can be interpolated in the through-slice direction depends on the details of the slice profile. An idealized profile with uniform sensitivity in the selected slice and zero outside is uninterpolable because each slice is represented by independent isolated data.

True three-dimensional volume data acquisitions (see also ***Image Formation Methods***), in which phase encoding is used in the slice direction, are band limited in all directions and therefore can be faithfully interpolated using the sinc function. This type of acquisition is thus ideally suited to correction of arbitrary displacements. It has the drawback of being rather slower than the single-slice methods more commonly employed in functional MRI.

Figure 6 illustrates a motor stimulation study designed to detect changes in blood flow in draining veins, using three-dimensional acquisitions to image 40 slices. The subject performed hand exercises with one hand for the duration of a scan, changed hands for the next scan, and so on, for a total of six scans. Figure 6(a) shows one slice from one of the 40 slice sets. A cumulative difference image of the same slice [Figure 6(b)] shows obvious misregistration effects. In Figure 6(c) the images were registered before subtraction. Gross difference signals have now been eliminated from the brain, but some vessels can still be seen (arrow) as well as the scalp. Segmenting the image so that only the brain was used to calculate the transformations required for positional matching, but then transforming the original complete images, results in precise cancellation of signals from the brain and cerebral

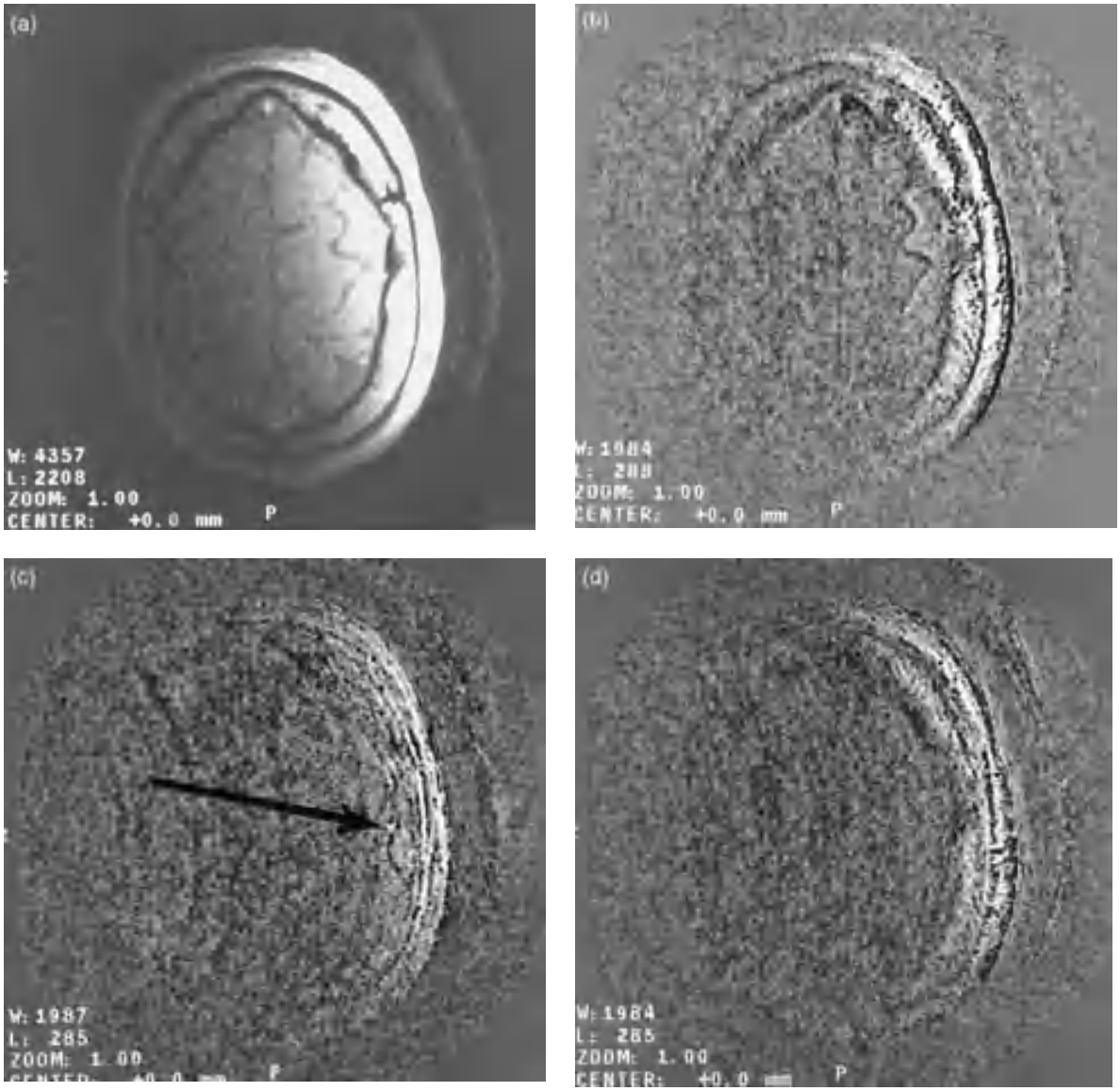

Figure 6 A motor stimulation study in which each hand was exercised in turn as images were acquired repeatedly using an inflow sensitive 3D sequence (*TR* 40, *TE* 8, flip angle 20°, 192 × 256 matrix, 21 cm FOV, 40 slices of 1 mm) and a surface coil placed adjacent to the dominant hemisphere of the brain. (a) A single slice from the series and (b) cumulative difference image (right hand activation minus left hand activation). In (c) the images have been registered before subtraction and some vessels can still be seen (arrows) as well as the scalp. (d) Segmenting the image so that only the brain is used for detecting how the subject moved, but retaining all the information in the positionally matched images results in complete cancellation of brain and cortical vessel signals but leaves larger residual signals from the scalp

vessels but leaves residual signals in the scalp [Figure 6(d)]. This indicates that the relative positions of the brain and scalp have altered. However, although a task was being performed, no significant signal changes were detected in the brain or its draining vessels when these were precisely matched for position.

7 CONCLUSION

Functional neuroimaging using MRI is a new and challenging area of research. The detection of signal changes that correlate with the applied stimulus protocol is not in itself sufficient evidence for localized brain activation as there are other sources of such signals. Most notably, subject movement during the course of an examination can result in task locked signal changes that may not be discriminated against by correlation and statistical analyses. Single-slice studies are particularly vulnerable because of the lack of information about tissues adjacent to the slice, which makes it difficult to detect the effects of through-slice movement. Image registration provides a means of correcting for the effect of interimage displacements, but great care is required to ensure that the correction procedure itself does not introduce spurious results.

8 RELATED ARTICLES

Brain: Sensory Activation Monitored by Induced Hemodynamic Changes with Echo Planar MRI; Image Formation Methods; Whole Body Magnetic Resonance Artifacts.

9 REFERENCES

1. K. K. Kwong, J. W. Belliveau, D. A. Chesler, I. A. Goldberg, R. M. Weisskoff, B. P. Poncelet, D. N. Kennedy, B. E. Hoppel, M. S. Cohen, R. Turner, H.-M. Cheng, T. J. Brady, and B. R. Rosen, *Proc. Natl. Acad. Sci. USA*, 1992, **89**, 5675.
2. S.-G. Kim, J. Ashe, K. Hendrich, J. M. Ellermann, H. Merkle, K. Ugurbil, and A. P. Georgopoulo, *Science*, 1993, **261**, 615.
3. S. Ogawa, T. M. Lee, A. R. Kay, and D. W. Tank, *Proc. Natl. Acad. Sci. USA*, 1990, **87**, 9868.
4. S. Lai, A. L. Hopkins, E. M. Haacke, D. Li, B. A. Wasserman, P. Buckley, L. Friedman, H. Meltzer, P. Hedera, and R. Friedland, *Magn. Reson. Med.*, 1993, **30**, 387.
5. R. Turner, P. Jezzard, H. Wen, K. K. Kwong, D. Le Bihan, T. Zeffiro, and B. Balaban, *Magn. Reson. Med.*, 1992, **25**, 390.
6. A. Connelly, G. D. Jackson, R. J. Frackowiak, J. W. Belliveau, F. Vargha-Khadem, and D. G. Gadian, *Radiology*, 1993, **188**, 125.
7. R. Myers, T. J. Spinks, and D. J. Brooks, in *Quantitative Methods in Neuroanatomy*, ed. M. G. Steward, Wiley, Chichester, 1992, p. 117.
8. K. J. Friston and R. S. J. Frackowiack, in *Brain Work and Mental Activity. Quantitative Studies with Radioactive Tracers*, ed. N. A. Lassen, D. H. Ingvar, M. E. Raichle, and L. Friberg, Munskgaard, Copenhagen, 1991, p. 267.
9. P. A. Bandettini, A. Jesmanowicz, E. C. Wong, and J. Hyde, *Magn. Reson. Med.*, 1993, **30**, 161.
10. R. T. Constable, G. McCarthy, T. Allison, A. W. Anderson, and J. C. Gore, *Magn. Reson. Imag.*, 1993, **11**, 451.
11. R. M. Weisskoff, J. Baker, J. Belliveau, T. L. Davis, K. K. Kwong, M. S. Cohen, and B. R. Rosen, in *Proceedings of the 12th Annual Meeting, SMRM, New York*, Society of Magnetic Resonance in Medicine, Berkeley, CA, 1993, p. 7.
12. X. Hu and S.-G. Kim, *Magn. Reson. Med.*, 1994, **31**, 495.
13. J. V. Hajnal, R. Myers, A. Oatridge, J. E. Schwieso, I. R. Young, and G. M. Bydder, *Magn. Reson. Med.*, 1994, **31**, 283.
14. D. L. G. Hill, D. J. Hawkes, J. E. Crossman, M. J. Gleeson, T. C. Cox, E. E. Bracey, A. J. Strong, and P. Graves, *Br. J. Radiol.*, 1991, **64**, 1030.
15. C. A. Pelizzari, G. T. Y. Chen, D. R. Spelbring, R. R. Weichselbaum, and C. T. Chen, *J. Comput. Assist. Tomogr.*, 1988, **13**, 20.
16. R. P. Woods, S. R. Cherry, and J. C. Mazziotta, *J. Comput. Assist. Tomogr.*, 1992, **16**, 620.
17. R. P. Woods, J. C. Mazziotta, and S. R. Cherry, *J. Comput. Assist. Tomogr.*, 1993, **17**, 536.
18. P. Bloomfield, *Fourier Analysis of Time Series—An Introduction*, Wiley, Chichester, 1976.
19. E. Kreysig, *Advanced Engineering Mathematics*, 4th edn, Wiley, Chichester, 1979, p. 774.
20. A. K. Jain, *Fundamentals of Digital Image Processing*, Prentice-Hall, Englewood Cliffs, NJ, 1992, p. 84.
21. A. K. Jain, *Fundamentals of Digital Image Processing*, Prentice-Hall, Englewood Cliffs, NJ, 1992, p. 89.
22. W. H. Press, S. A. Tenkolsky, W. T. Vetterling, and B. P. Flannery, *Numerical Recipes in C*, 2nd edn, Cambridge University Press, Cambridge, 1992, p. 683.
23. D. H. Ballard and C. M. Brown, *Computer Vision*, Prentice-Hall, Englewood Cliffs, NJ, 1982.

Biographical Sketch

Joseph V. Hajnal. *b* 1958. B.Sc., Ph.D., 1984, University of Bristol, UK. Postdoctoral research fellow, Department of Physics, University of Bristol, 1984–86. Postdoctoral research fellow, School of Physics, University of Melbourne, Australia, 1986–89. Research scientist, GEC Hirst Research Centre, and Honorary Senior Lecturer in Diagnostic Radiology, Royal Postgraduate Medical School, Hammersmith Hospital, 1990–present. Approx. 80 publications. Current research speciality: in vivo MRI techniques and applications.

Hemodynamic Changes Owing to Sensory Activation of the Brain Monitored by Echo-Planar Imaging

Peter A. Bandettini, Jeffrey R. Binder, Edgar E. DeYoe, and James S. Hyde

Medical College of Wisconsin, Milwaukee, WI, USA

1 INTRODUCTION

In recent years, it has been demonstrated that MRI is capable of detecting changes in cerebral blood volume,[1] flow,[2] and oxygenation,[2–5] that accompany an increase in neuronal activity. MRI methods that observe these activation-induced changes have been termed functional MRI (fMRI).

The most widely used fMRI method for the noninvasive mapping of human brain activity is based on blood oxygenation level dependent (BOLD) contrast.[6] A localized signal increase in activated cortical regions is generally observed using a time-course collection of T_2*-weighted images. A working model of this phenomenon is that an increase in neuronal activity causes local vasodilatation, which in turn causes blood flow to increase in such a manner that the amount of paramagnetic deoxyhemoglobin in the local vasculature is reduced. This reduction causes an increase in spin coherence and, therefore, an increase in signal when using T_2- and T_2*-weighted pulse sequences.

Support for the hypothesized BOLD contrast mechanism, as it relates to fMRI, comes from several studies. Local cerebral blood oxygenation has been observed to increase with neuronal activity.[7–10] Brain tissue T_2, T_2*, and T_2' have been shown to be decreased and increased by cerebral blood oxygenation decreases and increases, respectively.[6,11–15] In addition, brain activation has been shown to increase T_2, T_2*, and T_2',[16–20] in proportions that show general agreement with mathematical simulations based on simplified models of the cerebral vasculature.[21,22]

The applicability of fMRI depends on the degree to which the induced signal enhancement magnitude, location, and timing can be correlated with underlying neuronal activation. The signal enhancement magnitude is not only affected by MRI parameters, but is also dependent on hemodynamic factors (i.e. blood volume, oxygenation, vessel orientation, and radii), which vary significantly from voxel to voxel. Correlation between BOLD signal enhancement magnitude and cerebral blood flow has, nevertheless, been observed. Visual cortex activation studies have shown that BOLD signal enhancement has essentially the same flicker frequency dependency[2] as that of cerebral blood flow changes observed using positron emission tomography (PET).[23]

The fMRI signal enhancement location and distribution is also an issue. The upper limit of spatial resolution of fMRI may be influenced by the degree to which an activation-induced modulation of the velocity or oxygenation of rapidly inflowing spins or large collecting veins may contribute to the signal change. Generally, the larger the collecting vessel, the more spatially removed the signal change is from the area of neuronal activation. Such vessel size weighting might depend strongly on the pulse sequence, field strength, and resolution used.[16–26] Nevertheless, studies have shown that fMRI can reveal activity localized to patches of cortex smaller than 1.5 mm.[27]

The temporal resolution of fMRI depends on the latency and consistency of the activation-induced signal change. Rise latency of 8–9 s from stimulus onset to maximal signal change and a fall latency of 9–10 s from stimulus cessation to baseline signal have been reported.[2,28,29] The hemodynamic response time sets upper limits on the functional temporal resolution. A significant increase from baseline is generally observed to take place within 2–3 s after stimulus onset.[2,28,29] Activation durations of less than 1 s are detectable[30,31] and relative differences (in the rise time from adjacent regions or from different experiments) in the onset of signal enhancement may be discriminated to within a second.[32]

Platforms on which fMRI are performed vary considerably. Primary differences are in field strength, pulse sequence, gradient and radiofrequency coil hardware, and postprocessing methods. The many trade-offs that exist between platform types have not been completely characterized, but it is clear that fMRI based on BOLD contrast benefits from high field strength, high system stability, high signal-to-noise ratio (SNR), and minimal pulsatile motion sensitivity. From reported results, it appears that these criteria are most readily met using echo planar imaging. Nevertheless, other techniques may be suitable. Initial successes in the performance of fMRI using BOLD contrast were published by groups using either EPI at 1.5 T,[2,3] and 4 T,[16] or fast multishot gradient-recalled imaging techniques at 4 T,[4] and at 2 T.[5] Results have since been reported using fast multishot gradient-recalled imaging techniques at 1.5 T.[33–35] Pulsatile brain, cerebrospinal fluid, and blood motion apparently cause nonrepeatable ghosting patterns in sequential images obtained by conventional multishot techniques,[36,37] thus adding significantly to the image signal variation in time. Multishot spiral-scan techniques have lower sensitivity to these contaminating pulsatile effects,[36,37] and have been used successfully to perform high resolution fMRI at 1.5 T.[27]

The use of a time course of images in conjunction with control over activation timing allows for the application of postprocessing methods which include the use of z maps,[38] and other statistical techniques.[35] In addition, other methods, including Fourier analysis,[39] temporal cross correlation,[39] and time–frequency analysis[40] have been successfully applied. While significant signal changes are easily observed using the most conservative statistical tests, a standardized method by which functional images are created has not been established. Using EPI, studies of the fluctuations in the susceptibility-weighted signal from a quiescent brain have been carried out,[41] not only to determine the nature of the noise for application to statistical tests, but also to obtain potentially useful physiological information, and to determine the actual relationship between functional contrast to noise and field strength.[42]

Because of the ease of use and accessibility of fMRI, many areas of the brain and many different tasks have already been studied. Studies that have been carried out include those of primary cortical regions including visual cortex,[2,4,5,16,29,35,43] motor cortex,[2,3,26,33,34,39,44–46] and auditory cortex.[47] Studies of higher cognitive function, including word generation,[48,49] higher visual processing,[35,43] visual recall,[50] complex motor control,[46] and single word semantic processing,[51] have also been performed.

In this article, applications of fMRI to the mapping of cortex activated by sensory stimulation are summarized using time-course collection of gradient-recalled echo planar images at 1.5 T.[3,39] and temporal cross correlation postprocessing techniques.[39] Specifically, auditory cortex regions were differentially activated by noise and speech sounds, and visual cortex regions were selectively activated by visual stimuli of different eccentricity.

2 POSTPROCESSING METHODOLOGY

Stimuli are presented in a repetitive on/off fashion for several cycles throughout each time course. Foci of brain activation are identified by cross correlation of the time course of each voxel with a reference vector resembling the expected activation-induced response.[39] In general, a reference vector may be obtained by: (a) choosing the voxel containing what appears to be the 'best' temporal response; (b) averaging, in time, the activation cycles in a 'best temporal response' voxel and then duplicating the time-averaged cycle for the length of the time course; (c) averaging in space several of the 'best temporal response' voxels; (d) synthesizing a reference vector; or (e) choosing a vector obtained from principal component analysis of the time course. Pixels having a temporal correlation coefficient below a given threshold (typically 0.4–0.6) are removed. After thresholding, the vector product of the reference vector with each of the surviving time courses is calculated to yield an index of change in the signal magnitude. These 'activation' images are then colorized and superimposed on high resolution anatomical scans of the same slice obtained in the same imaging session.

3 PULSE SEQUENCE AND HARDWARE

All studies presented in this article were performed using single-shot 64 $\times$ 64 gradient-recalled EPI (TE = 40 ms) on a clinical 1.5-T GE Signa scanner. To perform EPI without additional stress to the standard gradient amplifiers, we used an insertable balanced torque three-axis head gradient coil designed for rapid gradient switching.[52] To obtain high-quality images throughout the entire brain volume, a shielded quadrature elliptical endcapped transmit/receive birdcage radiofrequency coil was used.[53] Typically, single- or multi-slice time-course series of 64–1024 images were obtained with a TR of 0.5–3 s, flip angle of 65–90°, field of view (FOV) of 24 cm, and slice thickness of 4–10 mm.

4 AUDITORY STIMULI

This study[47] presents findings using fMRI of brain regions involved in auditory speech perception. Specifically, regions activated by speech sounds (words and pseudowords) and nonspeech sounds (noise) were compared.

Five right-handed subjects were tested. Symmetric lateral sagittal slices (slice thickness 10 mm) of the left and right hemispheres were obtained, centered at positions 8 mm medial to the most lateral point of the temporal lobe on each side. In each time-course series, 64 sequential images were collected (TR = 3 s), during which activation alternated with baseline every 9 s (6 images per cycle, 18 s per cycle, 10 cycles). During baseline periods, subjects heard only the ambient scanner noise. During activation periods, prepared digitized auditory stimuli were delivered to the subject via air conduction through a semi-rigid 1-cm-bore plastic tube. The tube conducted the sound stimulus approximately 20 feet (6 m) from control room wall to the subject, at which point a Y-connector split the tube for binaural stimulation through a tightly fitting headset with occlusive earplugs to reduce scanner noise exposure.

Subjects passively listened to stimuli; no response was required. Stimuli differed in both semantic and acoustic (frequency modulation) content. White noise presentation was compared to presentation of nouns (e.g. 'barn'), and pseudowords (e.g. 'narb') with stimuli matched for duration, presentation rate, average sound pressure level, and spectral range. All voxels having a temporal correlation coefficient to a sinusoidal reference vector below 0.5 were removed. The activation images were superimposed on high resolution scans of the same slices.

Figure 1 illustrates typical results from two of the subjects studied with white noise, pseudowords, and words, respectively. In these and all other subjects studied, the area activated by white noise was considerably smaller than that activated by speech sounds, and was restricted to the dorsal aspect of the superior temporal gyrus. In most instances, this region coincided with or included the transverse temporal (Heschl's) gyrus. Presentation of speech sounds activated a larger region, including more anterior and posterior areas of the dorsal superior temporal gyrus, as well as cortex in or near the superior temporal sulcus bilaterally.

Both words and pseudowords differed significantly from noise bilaterally, while no significant differences were seen between word and pseudoword conditions. Activity occurred symmetrically in the left and right temporal lobes. Unlike white noise, therefore, processing of speech sounds appears to elicit extensive participation of auditory association areas, even when the subject is not engaged in any 'active' task.

5 VISUAL STIMULI

Much of the utility of fMRI depends on its ability to depict spatial patterns of neural activity. To test this capacity in the visual system, fMRI was used for retinotopic mapping of primary visual cortex activation.[43]

Dynamic, computer graphics-based visual images were directly projected onto the subjects' retinae. The image generator was a modified Sharp XG2000U video projector driven by

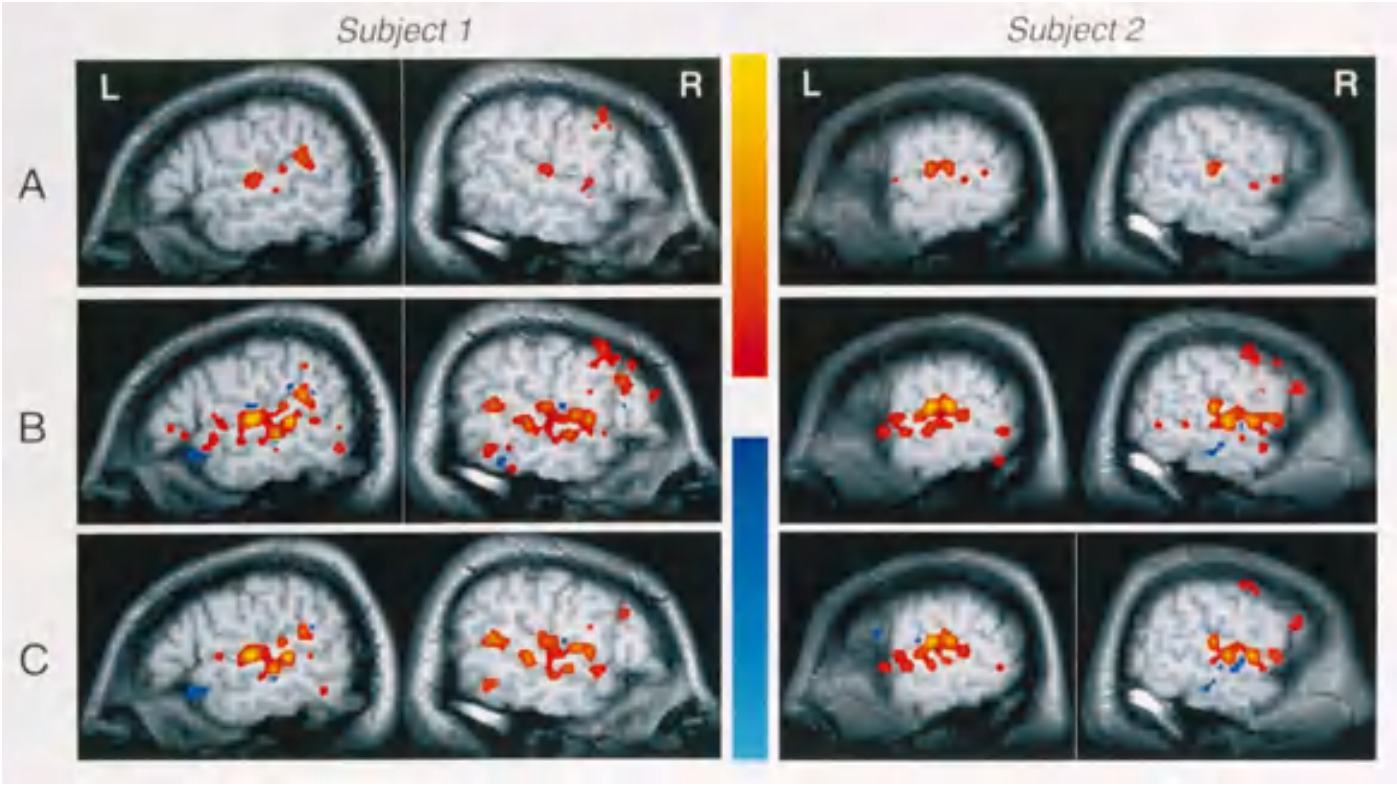

Figure 1 Sagittal images of the left and right temporal lobes of two subjects. Demonstrated are regions activated during passive listening to (A) white noise, (B) pseudowords, and (C) words. The area activated by white noise was smaller than the area activated by either pseudowords or words. The area activated by pseudowords was generally the same size and shape as the area activated by words. (Reproduced with permission of the American Neurological Association, 1994)

Cambridge Instruments VSG video graphics board installed in a personal computer. The image plane was then viewed through a custom optical system that included a wide field, magnifying eyepiece, a 45° prism, and additional objective lenses for adjusting magnification and minimizing chromatic aberration. Two sets of imaging optics were combined to provide full binocular viewing.[54]

To map the retinotopic organization of the visual cortex, three highly trained subjects viewed a small white fixation dot on a uniform black or gray field subtending 60° of visual angle. A black-and-white checkered annulus surrounding the fixation point was presented for 5 on/off cycles of 10 s on and 10 s off. Time-course series (TR = 2 s) of 100 images (slice thickness 8 mm) were used. When on, the checkered pattern was either counter-phase modulated or flickered at 6–8 Hz. Six successively larger annuli were tested. The width of each annulus as well as the check size were scaled in proportion to eccentricity. Only voxels having a correlation coefficient above 0.55 with respect to a chosen reference vector were used in the creation of functional images. All functional images were then superimposed on high resolution anatomical scans.

Figure 2 illustrates the relative sizes of the annuli and shows the corresponding brain activation images. In these experiments, the subject passively viewed the stimuli and was not required to respond to them. A small checkerboard annulus presented at the fixation point elicited activation in striate cortex only at the occipital poles bilaterally. Annuli presented at increasing eccentricities activated successively more anterior regions of the calcarine sulcus. The most eccentric stimulus activated only the anterior calcarine cortex while sparing the occipital poles. Detailed examination of the sequence of activity foci in Figure 2, shows a progression that closely follows the folded cortical mantle within the calcarine sulcus. While such a precise progression is not always observed, these data do show that, under optimal conditions, a detailed mapping of the visual field representation is possible with fMRI. Resolution is not limited by the coarseness of the distribution of large blood vessels, even though such vessels may sometimes introduce artifacts.

6 CONCLUSIONS

MRI of human brain activation using BOLD contrast is a relatively new functional brain imaging method. Accompanying the novelty of the technique are many unknowns regarding the upper limits of spatial and temporal resolution as well as an unclear understanding of physiological and the biophysical mechanisms that regulate hemodynamic changes. In addition, the ways in which the hemodynamic changes affect the magnetic resonance signal are incompletely understood. Never-

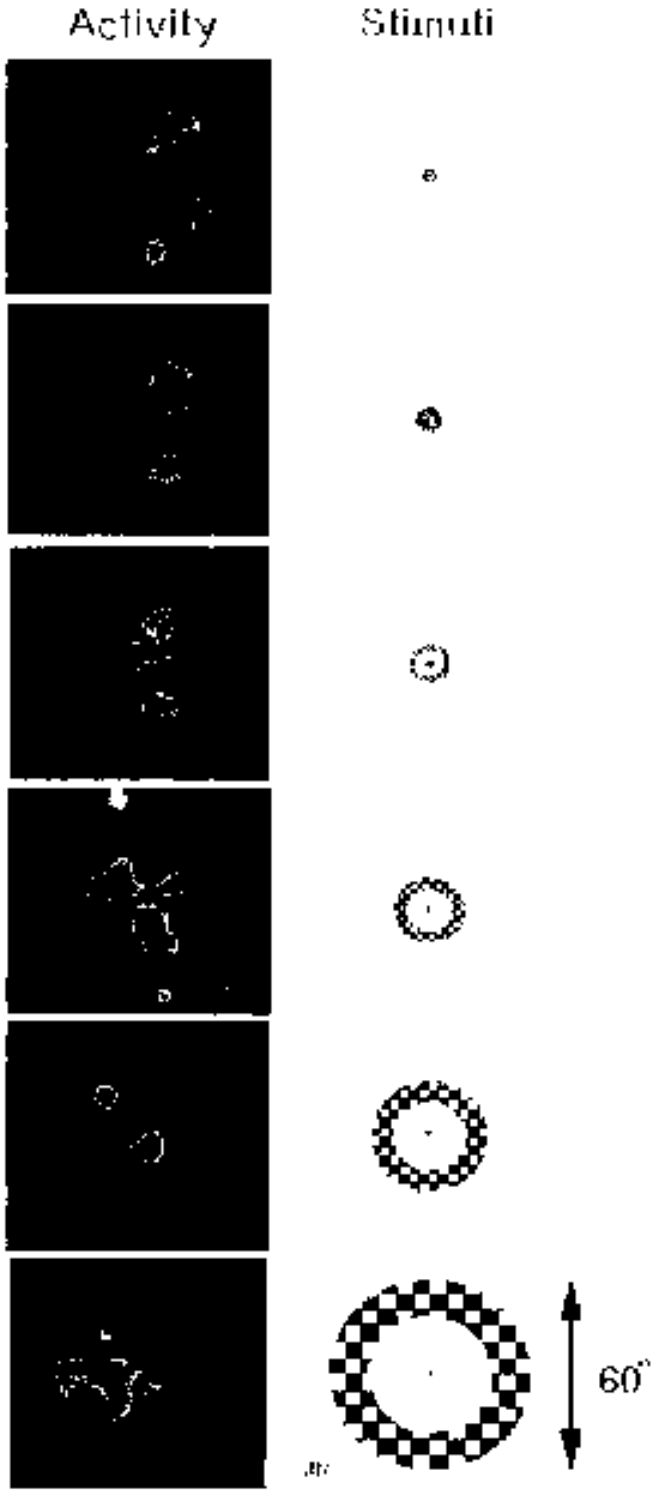

Figure 2 Axial brain activation images created by passive viewing of visual stimuli with six different eccentricities while fixating at the center. The active foci traveled in an anterior direction along the calcarine fissure as the stimulus became more peripheral

theless, the applications described here and elsewhere empirically establish the utility of this approach.

These studies demonstrate observation by fMRI of human brain activation by sensory stimulation. Regions activated in temporal lobes by various speech and nonspeech auditory stimuli were observed. In addition, retinotopic organization of the primary visual cortex was observed using stimuli of varying visual field eccentricity. Additionally, in our laboratory, preliminary studies involving activation by tactile, aromatic, and taste stimuli are in progress.

fMRI is a technique that holds great promise in uncovering unique and useful information about brain function and physiology.

7 RELATED ARTICLES

Echo-Planar Imaging; Methods and Applications of Diffusion MRI; MR-Guided Therapy in the Brain; Susceptibility Effects in Whole Body Experiments.

8 REFERENCES

1. J. W. Belliveau, D. N. Kennedy, R. C. McKinstry, B. R. Buchbinder, R. M. Weisskoff, M. S. Cohen, J. M. Vevea, T. J. Brady, and B. R. Rosen, *Science*, 1991, **254**, 716.
2. K. K. Kwong, J. W. Belliveau, D. A. Chesler, I. E. Goldberg, R. M. Weisskoff, B. P. Poncelet, D. N. Kennedy, B. E. Hoppel, M. S. Cohen, R. Turner, H. M. Cheng, T. J. Brady, and B. R. Rosen, *Proc. Natl. Acad. Sci. USA*, 1992, **89**, 5675.
3. P. A. Bandettini, E. C. Wong, R. S. Hinks, R. S. Tikofsky, and J. S. Hyde, *Magn. Reson. Med.*, 1992, **25**, 390.
4. S. Ogawa, D. W. Tank, R. Menon, J. M. Ellermann, S.-G. Kim, H. Merkle, and K. Ugurbil, *Proc. Natl. Acad. Sci. USA*, 1992, **89**, 5951.
5. J. Frahm, H. Bruhn, K.-D. Merboldt, and W. Hanicke, *JMRI*, 1992, **2**, 501.
6. S. Ogawa, T. M. Lee, A. R. Kay, and D. W. Tank, *Proc. Natl. Acad. Sci. USA*, 1990, **87**, 9868.
7. A. Grinvald, R. D. Frostig, R. M. Siegel, and E. Bratfeld, *Proc. Natl. Acad. Sci. USA*, 1991, **88**, 11559.
8. P. T. Fox and M. E. Raichle, *Proc. Natl. Acad. Sci. USA*, 1986, **83**, 1140.
9. R. D. Frostig, E. E. Lieke, D. Y. Ts'o, and A. Grinvald, *Proc. Natl. Acad. Sci. USA,* 1990, **87**, 6082.
10. A. Villringer, J. Planck, C. Hock, L. Schleinkofer, and U. Dirnagl, *Neurosci. Lett.*, 1993, **154**, 101.
11. R. Turner, D. Le Bihan, C. T. Moonen, D. Despres, and J. Frank, *Magn. Reson. Med.*, 1991, **22**, 159.
12. B. E. Hoppel, R. M. Weisskoff, K. R. Thulborn, J. B. Moore, K. K. Kwong, and B. R. Rosen, *Magn. Reson. Med.*, 1993, **30**, 715.
13. M. K. Stehling, F. Schmitt, and R. Ladebeck, *JMRI*, 1993, **3**, 471.
14. A. J. DeCrespigny, M. F. Wendland, N. Derugin, E. Kozniewska, and M. E. Moseley, *Magn. Reson. Med.*, 1992, **27**, 391.
15. P. Jezzard, F. Heineman, J. Taylor, D. Taylor, H. Wen, R. S. Balaban, and R. Turner, *NMR Biomed.*, 1994, **7**, 35.
16. R. Turner, P. Jezzard, H. Wen, K. K. Kwong, D. Le Bihan, T. Zeffiro, and R. S. Balaban, *Magn. Reson. Med.*, 1993, **29**, 277.
17. R. S. Menon, S. Ogawa, D. W. Tank, and K. Ugurbil, *Magn. Reson. Med.,* 1993, **30**, 380.
18. B. E. Hoppel, J. R. Baker, R. M. Weisskoff, and B. R. Rosen, *Proc. XIIth Annu. Mtg. Soc. Magn. Reson. Med.*, New York, 1993, p. 1384.

19. P. A. Bandettini, E. C. Wong, A. Jesmanowicz, R. S. Hinks, and J. S. Hyde, *NMR Biomed.*, 1994, **7**, 12.
20. P. A. Bandettini, E. C. Wong, A. Jesmanowicz, R. S. Hinks, and J. S. Hyde, *Proc. XIIth Annu. Mtg. Soc. Magn. Reson. Med.*, New York, 1993, p. 169.
21. S. Ogawa, R. S. Menon, D. W. Tank, S.-G. Kim, H. Merkle, J. M. Ellermann, and K. Ugurbil, *Biophys. J.*, 1993, **64**, 803.
22. R. P. Kennan, J. Zhong, and J. C. Gore, *Magn. Reson. Med.*, 1994, **31**, 9.
23. P. T. Fox and M. E. Raichle, *J. Neurophysiol.*, 1984, **51**, 1109.
24. J. Frahm, K.-D. Merboldt, and W. Hanicke, *Proc. XIIth Annu. Mtg. Soc. Magn. Reson. Med.*, New York, 1993, p. 1427.
25. J. H. Duyn, C. T. W. Moonen, R. W. de Boer, G. M. van Yperen, and P. R. Luyten, *Proc. XIIth Annu. Mtg. Soc. Magn. Reson. Med.*, New York, 1993, p. 168.
26. S. Lai, A. L. Hopkins, E. M. Haacke, D. Li, B. A. Wasserman, P. Buckley, L. Friedman, H. Meltzer, P. Hedera, and R. Friedland, *Magn. Reson. Med.,* 1993, **30**, 387.
27. S. A. Engel, D. E. Rumelhart, B. A. Wandell, A. T. Lee, G. H. Glover, E. J. Chichilnisky, and M. N. Shadlen, *Nature*, 1994, **369**, 525.
28. E. A. DeYoe, J. Neitz, P. A. Bandettini, E. C. Wong, and J. S. Hyde, *Proc. Xth Annu. Mtg. Soc. Magn. Reson. Med.*, San Francisco, 1991, p. 1824.
29. A. M. Blamire, S. Ogawa, K. Ugurbil, D. Rothman, G. McCarthy, J. M. Ellermann, F. Hyder, Z. Rattner, and R. G. Shulman, *Proc. Natl. Acad. Sci. USA*, 1992, **89**, 11069.
30. P. A. Bandettini, E. C. Wong, E. A. DeYoe, J. R. Binder, S. M. Rao, D. Birzer, L. D. Estkowski, A. Jesmanowicz, R. S. Hinks, and J. S. Hyde, *Proc. XIIth Annu. Mtg. Soc. Magn. Reson. Med.*, New York, 1993, p. 1382.
31. J. W. Belliveau, J. R. Baker, K. K. Kwong B. R. Rosen, J. S. George, C. J. Aine, J. D. Lewine, J. A. Sanders, G. V. Simpson, and J. Foxe, *Proc. XIIth Annu. Mtg. Soc. Magn. Reson. Med.*, New York, 1993, p. 6.
32. J. R. Binder, A. Jesmanowicz, S. M. Rao, P. A. Bandettini, T. A. Hammeke, and J. S. Hyde, *Proc. XIIth Annu. Mtg. Soc. Magn. Reson. Med.*, New York, 1993, p. 1383.
33. Y. Cao, V. L. Towle, D. N. Levin, and J. M. Balter, *JMRI*, 1993, **3**, 869.
34. A. Connelly, G. D. Jackson, R. S. Frackowiak, J. W. Belliveau, F. Vargha-Khadem, and D. G. Gadian, *Radiology*, 1993, **188**, 125.
35. W. Schneider, D. C. Noll, and J. D. Cohen, *Nature*, 1993, **365**, 150.
36. G. H. Glover and J. M. Pauly, *Magn. Reson. Med.*, 1992, **28**, 275.
37. G. H. Glover, A. T. Lee, and C. H. Meyers, *Proc. XIIth Annu. Mtg. Soc. Magn. Reson. Med.*, New York, 1993, p. 197.
38. D. Le Bihan, P. Jezzard, R. Turner, C. A. Cuenod, L. Pannier, and A. Prinster, *Proc. XIIth Annu. Mtg. Soc. Magn. Reson. Med.*, New York, 1993, p. 11.
39. P. A. Bandettini, A. Jesmanowicz, E. C. Wong, and J. S. Hyde, *Magn. Reson. Med.*, 1993, **30**, 161.
40. B. Biswal, P. A. Bandettini, A. Jesmanowicz, and J. S. Hyde, *Proc. XIIth Annu. Mtg. Soc. Magn. Reson. Med.*, New York, 1993, p. 722.
41. R. M. Weisskoff, J. Baker, J. Belliveau, T. L. Davis, K. K. Kwong, M. S. Cohen, and B. R. Rosen, *Proc. XIIth Annu. Mtg. Soc. Magn. Reson. Med.*, New York, 1993, p. 7.
42. P. Jezzard, D. Le Bihan, C. Cuenod, L. Pannier, A. Prinster, and R. Turner, *Proc. XIIth Annu. Mtg. Soc. Magn. Reson. Med.*, New York, 1993, p. 1392.
43. E. A. DeYoe, P. A. Bandettini, J. Neitz, D. L. Miller, and P. Winans, *J. Neurosci. Meth.*, 1994, **54**, 171.
44. S.-G. Kim, J. Ashe, A. P. Georgopoulos, H. Merkle, J. M. Ellermann, R. S. Menon, S. Ogawa, and K. Ugurbil, *J. Neurophysiol.*, 1993, **69**, 297.
45. S.-G. Kim, J. Ashe, K. Hendrich, J. M. Ellermann, H. Merkle, K. Ugurbil, and A. P. Georgopoulos, *Science*, 1993, **261**, 615.
46. S. M. Rao, J. R. Binder, P. A. Bandettini, T. A. Hammeke, F. Z. Yetkin, A. Jesmanowicz, L. M. Lisk, G. L. Morris. W. M. Meuller, L. D. Estkowski, E. C. Wong, V. M. Haughton, and J. S. Hyde, *Neurology*, 1993, **43**, 2311.
47. J. R. Binder, S. M. Rao, T. A. Hammeke, F. Z. Yetkin, A. Jesmanowicz, P. A. Bandettini, E. C. Wong, L. D. Estkowski, M. D. Goldstein, V. M. Haughton, and J. S. Hyde, *Ann. Neurol.*, 1994, **35**, 672.
48. G. McCarthy, A. M. Blamire, D. L. Rothman, R. Gruetter, and R. S. Shulman, *Proc. Natl. Acad. Sci. USA*, 1993, **90**, 4952.
49. R. M. Hinke, X. Hu, A. E. Stillman, S.-G. Kim, H. Merkle, R. Salmi, and K. Ugurbil, *Neuroreport*, 1993, **4**, 675.
50. D. Le Bihan, R. Turner, T. Zeffiro, C. A. Cuenod, P. Jezzard, and V. Bonnerot, *Proc. Natl. Acad. Sci. USA*, 1993, **90**, 11802.
51. J. R. Binder, S. M. Rao, T. A. Hammeke, J. A. Frost, P. A. Bandettini, A. Jesmanowicz, and J. S. Hyde, *Arch. Neurol.*, 1995, **52**, 593.
52. E. C. Wong, P. A. Bandettini, and J. S. Hyde. *Proc. Xth Annu. Mtg. Soc. Magn. Reson. Med.*, San Francisco, 1991, p. 105.
53. E. C. Wong, E. Boskamp, and J. S. Hyde, *Proc. XIth Annu. Mtg. Soc. Magn. Reson. Med.*, Berlin, 1992, p. 4015.
54. E. A. DeYoe, J. Neitz, D. Miller, and J. Wieser, *Proc. XIIth Annu. Mtg. Soc. Magn. Reson. Med.*, New York, 1993, p, 1394.

Acknowledgements

This work was supported in part, by grants CA41464 and RR01008 from the National Institute of Health. P.A.B. thanks GE Medical Systems for financial support. In adition, the support of R. Scott Hinks at GE Medical Systems and of Donald Dickerson, Lloyd D. Estkowski, Andrew S. Greene, Thomas A. Hammeke, Victor M. Haughton, Andre Jesmanowicz, George L. Morris, Wade M. Meuller, Joel B. Myklebust, David Miller, Jay Neitz, Steven M. Rao, Elliot Stein, Eric C. Wong, F. Zerrin Yetkin, and Jeffrey R. Zigun, at the Medical College of Wisconsin, are gratefully appreciated.

Biographical Sketches

Peter A. Bandettini. *b* 1966. B.S., 1989, Ph.D., 1994, Biophysics, Medical College of Wisconsin, USA (supervisors James S. Hyde and R. Scott Hinks). Postdoctoral fellow, Massachusetts General Hospital NMR Center, 1994–95. Approx. 15 publications. Research specialties: functional MRI contrast mechanisms, postprocessing techniques, and applications.

Jeffrey R. Binder. *b* 1958. B.M., 1980, M.D., 1986, University of Nebraska, USA. Neurology Residency, 1987–90. Neurological Institute of New York. Fellow in cerebrovascular disease, 1990–92. Neurological Institute (with J. P. Mohr). Currently Assistant Professor of Neurology, Medical College of Wisconsin, USA. Approx. 15 publications. Research specialties: behavioral neurology, neuroscience applications of functional MRI, cerebrovascular disease.

Edgar A. DeYoe III. *b* 1950. B.S. Electrical Engineering, 1972; Ph.D. 1983, Experimental Psychology; Ph.D. 1983, Neuroscience, University of Rochester, USA (Advisor: Robert W. Doty). Postdoctoral fellowship at California Institute of Technology (Supervisor: David Van Essen). Currently assistant professor in Department of Cellular Biology and Anatomy with adjunct appointment to Department of Biophysics at the Medical College of Wisconsin, Milwaukee, WI. Approx. 21 publications. Research interests: Neural mechanisms of visual perception—anatomy and physiology; Functional magnetic resonance imaging (fMRI) of the human visual system; development of systems for testing normal vision and visual system; development of systems for testing normal vision and visual dysfunction during fMRI.

James S. Hyde. *b* 1932. B.S., 1954, Ph.D., 1959, Physics, M.I.T, Cambridge, MA, USA. Member of the scientific staff, Varian Associates, 1959–75, working under the direction of W. A. Anderson and M. E. Packard. Professor of Biophysics, Medical College of Wisconsin, 1975–present. Approx. 275 publications, 27 patents. Research specialties: ESR spectroscopy, ENDOR, musculoskeletal MRI, surface coils, functional MRI, electron and nuclear spin physics, and magnetic resonance instrumentation.

Postoperative Trauma Observed by MRI

David N. F. Harris
Royal Postgraduate Medical School, London, UK

1 INTRODUCTION

This article reviews the use of magnetic resonance imaging (MRI) in patients undergoing major cardiac and vascular surgery, with particular emphasis on the problems presented when imaging patients immediately after major surgery.

Up to 80% of patients develop neuropsychological defects following coronary artery bypass surgery (CABS), with 38% persisting at 1 year; this is thought to indicate permanent damage. Of CABS patients, 1–2% develop overt strokes with a higher incidence reported following valve surgery. The cause of the defects is not known, but cerebral emboli of both air and microaggregates, hypoperfusion, and release of cytokines from the trauma to blood cells by the cardiopulmonary bypass circuit have been implicated. It is not yet clear whether these defects are specifically related to cardiopulmonary bypass as the incidence of neuropsychological defects in noncardiac surgery varies widely in reported studies, and it is difficult to find a satisfactory control group for CABS patients.

Neuropsychological testing shows a high variability between patients, and performance on tests improves with practice (learning): different investigators also produce different results. Accuracy can be improved by using multiple tests and a battery of 10 is commonly used, but this reduces the sensitivity and makes assessment of subtle defects difficult. X-Ray computerized tomography (CAT) scanning is the most widely used test for detecting cerebral trauma; it shows abnormalities in patients who have suffered major neurological events, but often does not show such anomalies in patients with less severe deficits. The development of MRI offers the attractive possibility for sensitive and objective assessment of cerebral structure and function noninvasively.

2 CARDIAC SURGERY

2.1 Focal Defects

Schmidt et al.[1] investigated patients with 1.5 T MRI before and 1–3 weeks after CABS and showed an increase in focal defects—infarcts, lacunar lesions, and cortical atrophy. In 50 patients, Peden et al.[2] showed a high incidence of defects in the preoperative scans of CABS patients, with a significant increase in focal defects in 35% of patients 1 week after surgery; 20% of the defects persisted at 8 weeks. New defects were more common in those who had preoperative defects, and imaging defects were associated with neuropsychological deficits.

2.2 Swelling

To assess the incidence in the early postoperative phase we looked at six patients before, immediately after the end of surgery before going to Intensive Care, and 1 week after surgery.[3] All patients showed marked cerebral edema on the immediate postoperative images, which returned to normal when imaged 1–3 weeks later (Figure 1). The cause of this swelling was not known, but it was suggested that it might reflect cerebral ischemia at the end of bypass as shown by jugular bulb desaturation.

2.3 High-energy Phosphates

To see if there was any evidence of ischemia, we studied eight patients with MR spectroscopy immediately after cardiac surgery, four with ^{1}H spectroscopy and four with ^{31}P spectroscopy. There was no visible lactate either globally or regionally, the ratio of phosphocreatine to ATP was maintained, and there was no intracellular acidosis. However, phosphocreatine/inorganic phosphate was increased immediately after the operation, which suggests rebound replacement of energy stores following recovery from temporary cerebral ischemia during cardiopulmonary bypass: intraoperative studies would be needed to test this hypothesis further.[4]

3 MAJOR VASCULAR SURGERY

3.1 Aortic Aneurysm

It has been noted that many patients become confused 2–3 d after successful aortic aneurysm surgery. This was thought to be due to hypoxia over the first postoperative nights, but MR images in three patients who also exhibited confusion on neuropsychological testing showed cerebral swelling on the second and third postoperative day similar to that found after CABS, though to a smaller degree. One patient also showed cerebral swelling immediately after the operation which had returned to normal 14 h later.

3.2 Carotid Endarterectomy

We studied six patients immediately after carotid endarterectomy to see if cerebral edema was localized to the operative side. Four patients showed significant swelling, but no lateralizing signs were seen on FLAIR imaging.

With subtraction imaging, two patients with previous strokes showed deviation of the ventricles away from the infarct.

4 TECHNICAL REQUIREMENTS FOR EARLY POSTOPERATIVE SCANS

When imaging patients in the early postoperative period, great care must be taken to ensure the safety of the patients. As with any MR scan of the head, the patient must be still, with their head enclosed in a coil and inaccessible in the mag-

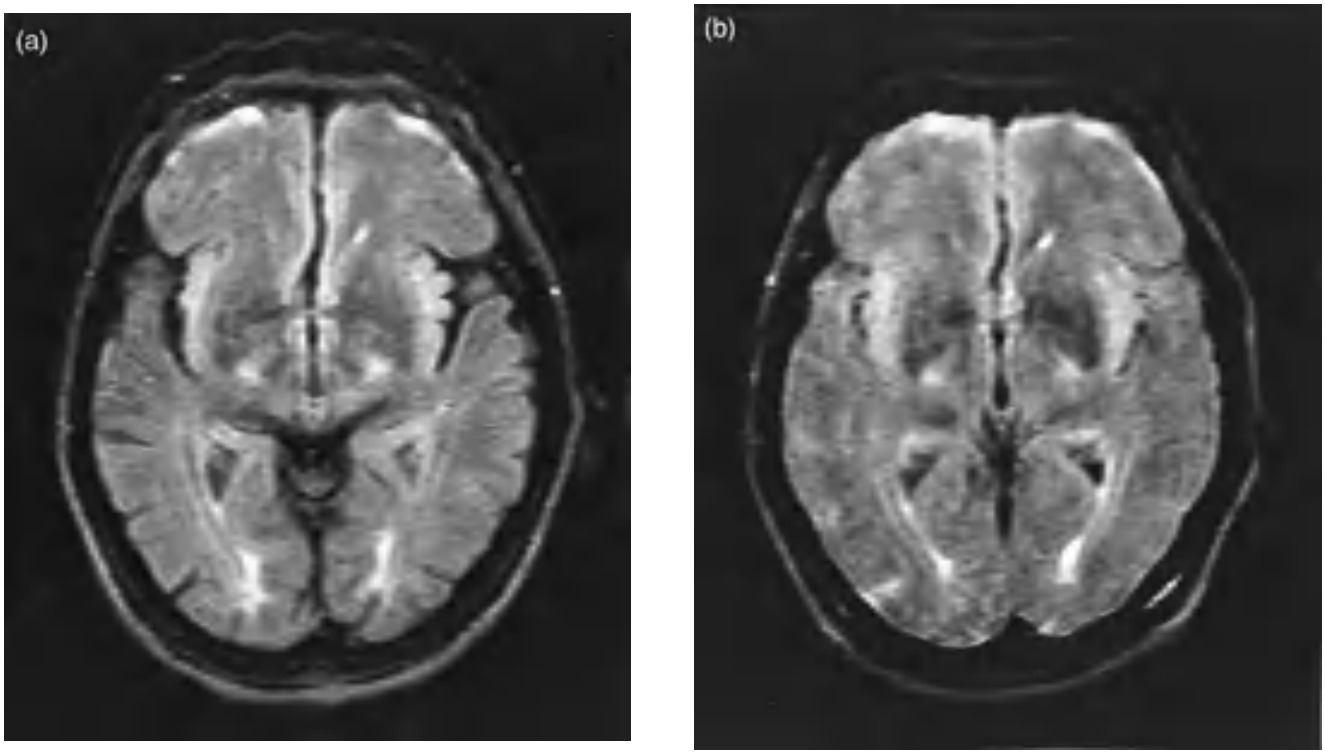

Figure 1 FLAIR (6000/160/2100) sequences before cardiac surgery (a) and 40 min after the end of cardiopulmonary bypass (b) in a 62-year-old patient. Sulci are clearly seen in (a) and are almost obliterated in (b)

net during the scan. Following any anesthetic there is a risk of nausea and vomiting, respiratory obstruction, or depression, as well as cardiovascular collapse. The incidence of complications depends on the length and severity of the operation, and patients are closely monitored in the recovery room by highly trained staff for between 30 min and 8 h following routine surgery so that such complications can be prevented or treated rapidly: this requires instant access to the patient. When discharged from the recovery area, the patient is considered to be safe under occasional and possibly unskilled observation.

Any of the above complications could be fatal if they occurred unnoticed during a scan when access is by no means instant. There is therefore a 'no-go' time after an operation, similar to the recovery time, during which it is difficult to examine patients safely with MR. After this time imaging can be performed, but it would be advisable to monitor the ECG and oxygen saturation (SaO_2) throughout the scan within 24 h of any operation; this is clearly an arbitrary limit. If the operation was major or prolonged, then measurement of blood pressure should be considered, and it should be possible to transfuse intravenous fluids at any desired rate. Usually this would require a suitably trained member of staff (anesthetist, critical care nurse) present in the magnet room.

If it is important to acquire MR scans within this time, it is safer to keep the patient under anesthesia throughout the scan and the transport to and from the MR unit; this requires the 'metal check' to be performed before the operation. Critically-ill patients can be transferred safely, but it requires a protocol with close attention to detail and safety. For the images immediately following CABS and aortic aneurysm surgery, patients were required to be hemodynamically stable, with no likelihood of requiring cardiac pacing or massive transfusion.

The system described by Peden et al.[2] was used with minor modifications. All cables were enclosed together in tubing so that 'spaghetti knitting' and disconnections could be avoided. All intravenous extensions and infusions were attached and primed in the operating room to minimize hemodynamic changes, and anesthesia was maintained by infusion (fentanyl/propofol). Sufficient supplies of intravenous fluids (crystalloid, colloid, and blood) with a pressure infuser were available in the magnet room, and suitable vasoactive drugs were brought with the patient from the operating room (OR). The patient was transferred from the operating table to an MR compatible trolley and to the MR magnet couch using a flexible roller to ensure a controlled, smooth transfer; monitoring of ECG, invasive blood pressure, and oxygen saturation was interrupted for less than 10 s.

Intermittent positive pressure ventilation was provided using a jet ventilator[5] with pressure sensed at the endotracheal tube to avoid compression losses in tidal volume over the 5 m from head to ventilator. Capnography was used to confirm the adequacy of ventilation and to warn of disconnections in the circuit as standard pressure sensing alarms do not work reliably over that distance. The patient's airway is not visible during the scan and disconnections are easily possible as the patient is moved into the magnet bore; if unnoticed this would be catastrophic. Two anesthesiologists remained in the magnet room throughout the procedure, continuing the same monitoring that had been provided in the operating room.

With this protocol it has been possible to investigate patients immediately following major cardiac and vascular sur-

gery while providing the same excellence of care that they had received in the operating room (and a similar system should be considered for subsequent studies). This has produced new and interesting information on postoperative cerebral edema.

5 SUMMARY

It is difficult to study cerebral function in the anesthetized, early postoperative, and critically ill patient; yet it is an area of great interest. MRI offers interesting information on cerebral function and structure, but these studies present difficult problems for patient safety. Monitoring should be available for ECG, invasive and noninvasive blood pressures, pulse oximetry, and capnography throughout the scans. Anesthesia/sedation must be maintained during transfer to and from the MR unit; this is usually best provided by intravenous infusion. Intermittent positive pressure ventilation must be available over a distance of 3–5 m, which requires care in the choice of ventilator. It is important to have extensions on all intravenous lines to enable fluids to be transfused and changed during a scan, and all lines and cables should be routed to avoid snagging during movement of the patient. As the patient's airway is hidden during scans, an anesthetically trained member of staff should be present throughout, and evacuation procedures established and practised.

With these protocols, MRI scanning can be offered safely to critically-ill patients, and has provided interesting new information on cerebral edema immediately after cardiopulmonary bypass surgery.

6 RELATED ARTICLES

Cardiac Gating Practice; Patient Life Support and Monitoring Facilities for Whole Body MRI.

7 REFERENCES

1. R. Schmidt, F. Fazekas, H. Offenbacher, H. Machler, N. Freidi, F. Payer, B. Rigler, M. J. Harrison, and H. Leehner, *Neurology*, 1993, **43**, 775.
2. C. J. Peden, D. K. Menon, A. S. Hall, J. Sargentoni, and J. G. Whitwam, *Anaesthesia*, 1992, **47**, 508.
3. D. N. F. Harris, S. M. Bailey, P. L. C. Smith, K. M. Taylor, A. Oatridge, and G. M. Bydder, *Lancet*, 1993, **342**, 586.
4. D. N. Harris, A. Oatridge, D. Dob, P. L. Smith, K. M. Taylor, and G. M. Bydder, *Anesthesiology*, 1998, **88**, 340.
5. J. G. Whitwam, M. K. Chakrabarti, W. H. Konarzewski, and H. Askitopoulou, *Br. J. Anaesth.*, 1983, **55**, 1017.

Biographical Sketch

D. N. F. Harris. *b* 1949. M.B., Ch.B., 1974, M.D., 1982, Bristol, FRCA, 1984. Research fellow, Nuclear Cardiology, Southampton, 1979–82. Senior lecturer, anesthesia, Royal Postgraduate Medical School, London, 1991–present. Approx. 50 publications. Research interests: cerebral damage following major surgery, using MRI to correlate with neuropsychological assessment of cerebral impairment.

Abdominal MRA

Paolo Pavone, Andrea Laghi, Carlo Catalano, Valeria Panebianco, Francesco Fraioli, Isabella Baeli, and Roberto Passariello

University of Rome, 'La Sapienza', Italy

1 INTRODUCTION

The study of abdominal vessels by MRA is a new and interesting perspective available in a routine clinical examination. The main problem which has limited such applications of MRA is the sensitivity of this method to motion artifacts due to breathing, cardiac motion, peristalsis, and pulsatile blood flow. However, the improvement in technical equipment has made it possible to reduce these problems and to obtain an excellent evaluation of abdominal vessels.[1,2]

To date, both the time-of-flight (TOF) and phase contrast (PC) techniques are used and each has its own advantages and disadvantages.[3–5] The TOF method has a faster acquisition time and a higher signal-to-noise ratio (SNR), but it is very sensitive to saturation effects; as a consequence it is only possible to work with small volumes, particularly when a 3D technique is employed.[6]

Recently, a new method of study using a dynamic intravenous injection of gadolinium-DTPA in conjunction with a 3D TOF acquisition technique has been developed.[7] The use of gadolinium shortens the blood relaxation time and overcomes in-flow saturation; hence it is possible to image arteries with a low flow velocity and large volumes. These vessels can therefore be imaged in any direction without saturation problem, i.e. using a coronal plane for the aorta and so reducing the acquisition time. However, the overlapping of venous structures occurs and presaturation pulses are not effective.

The phase contrast technique can be used over large fields of view because of its lack of sensitivity to the spin saturation effect. Other advantages are the complete cancellation of stationary tissues and the possibility of quantifying flow velocity. By comparison, PC techniques require longer acquisition times and are very sensitive to motion artifacts, especially if such motion is not constant during image acquisition.

In the evaluation of abdominal vessels, contrast-enhanced MRA is currently considered the only technique able to provide anatomical images of all major vessels, allowing an optimal image quality, with improved diagnosis.[6] Using this technique, all the datasets needed can be acquired during a breath-hold, provided that enhanced gradient systems are available to reduce repetition and echo time dramatically.

This overcomes the old problem with the conventional TOF or PC methods in which long acquisition times and the complexity of flow effects resulted in a myriad of artifacts, rendering a considerable fraction of examinations unreadable.

Furthermore, arterial blood is clearly visualized because it contains the paramagnetic contrast agents. The presence of paramagnetic agents such as a gadolinium chelate rapidly reduces the T_1 relaxation time of blood from 1400 ms to 200–400 ms depending on the dose and the rate of injection.

Obviously the visualization of blood depends on the presence of contrast in the arterial system while the 3D imaging data are being collected; this makes the technique very sensitive to the timing of the intravenous contrast administration relative to data acquisition.[7]

Great efforts have been made in recent years to improve further the image quality of enhanced MRA. These have been aimed at the improvement of the pulse sequences on the one hand and the contrast agents used on the other.

Improvement of the pulse sequence for enhanced MRA must involve one single and important issue: minimizing dephasing phenomena, thus reducing the signal loss related to phase dispersion of flowing spins, mostly evident in stenotic (jet flow) and tortuous vessels (turbulent flow). These effects are, in fact, still evident even when enhanced techniques are used, despite the fact that these newer sequences visualize directly the effect of the contrast agent (T_1 shortening) rather than the flow phenomena. Reduction of phase dispersion is achieved by using either optimized gradient rephasing pulses or, in a more effective way, by reducing the echo time of the pulse sequence. With current commercial equipment, a minimum echo time of 1.5 ms can be used, and the improvement achieved in moving to this from the 3 ms available on older equipment is really dramatic, with more consistent evidence about small vessels and better definition of the true diameter of every vessel imaged by MRA. Moving to shorter echo time has only one important requisite: that the gradient characteristics of the equipment are optimized. Current equipment must have a gradient strength of at least 20 mT m^{-1} and a rise time of 400–800 μs.[8] Specialized equipments for use in the cardiovascular system are being produced that have a gradient strength of 40 mT m^{-1}, although they are currently being offered only for research purposes.

Another way to improve the image quality in enhanced MRA is to use more effective contrast agents. Conventional gadolinium chelates have basic pharmacokinetics, with intravascular–extracellular diffusion. In practice, these agents pass rapidly through the capillary membrane and very rapidly (within 5 min) reach pseudoequilibium between the vascular and the interstitial concentration. There are two ways to improve the characteristics of the contrast agent for enhanced MRA: by using a contrast agent with the same pharmacokinetic characteristics but having an increased relaxivity (the capacity to influence the local magnetism and, therefore, the T_1 relaxation time of blood), or by using contrast agents with prolonged blood half-life, having a lower capacity to diffuse through the capillary membrane.

The first approach is used with a new gadolinium chelate Gd-Bopta (Multihance, Bracco). This contrast agent was initially proposed only for hepatobiliary use, because of its consistent biliary excretion, but has now also been applied for general purposes, because of its good characteristics. In particular, in the vascular system, this contrast agent is able to provide a very high enhancement of the vascular structure because its relaxivity is almost twice as great as that of other gadolinium chelates in human plasma (R1 9.7 versus 4.9 for Gd-DTPA). Early studies have demonstrated that evaluation of abdominal vessels by enhanced MRA is improved by this contrast agent. The second approach is to use contrast agents that are not able to cross the capillary membrane rapidly. The first class of such contrast agents are the macromolecular com-

pounds, where a long molecular chain with large molecular weight is bonded to gadolinium. Schering has proposed a gadolinium chelate covalently bound to a polymer composed of polylysin (Gadomer 17). This compound has a molecular weight of 30–35 kDa, with high relaxivity, good acute tolerance, low viscosity, and low osmolarity. In early studies, this contrast agent has been able to improve the enhancement of vessels and to provide prolonged evidence of the vascular system in enhanced MRA. The second class of contrast agent that is not able to cross the capillary membrane rapidly is represented by one single molecule: MS 325, first synthesized by EPIX and currently produced by Mallinkrodt. This contrast agent is rapidly bound to human serum albumin after being injected into the vascular system, with a strong but short-lasting link. In fact, after a few hours all the contrast agent injected is free from this link and is excreted through the kidneys. The result is that this agent provides a very high enhancement of the vascular system that is prolonged in time. The advantage of using intravascular agents is that the whole vascular system can be imaged more safely, with images being acquired in different anatomic areas, without the need for giving repeated injections of contrast agent at each anatomic level. In conclusion, there is no doubt that contrast-enhanced MRA is the technique of choice for abdominal MRA. Hardware improvements are to be expected and the use of newer contrast agents will definitely contribute to increasing the image quality and clinical value of this technique.

2 CLINICAL APPLICATIONS

2.1 Abdominal Aorta

The main clinical application of aortic MRA is the study of aortic aneurysms in terms of the extent and size of the pathology as well as the involvement of collateral vessels, identification of either an aortic stenosis or a thrombus in an atherosclerotic vessel and evaluation of either the patency or the complications of a graft.[9]

In the study of aortic aneurysms MRA is complementary to conventional spin echo images. In fact, a complete evaluation of the diameter of the lesion is possible only after a study performed using spin echo sequences. However, MRA has a major role in defining the size of the true lumen, in depicting the neck of the aneurysm, and a potential role in the quantification of the blood flow. Figure 1 illustrates the utility of MRA in the evaluation of an aortic aneurysm. By reconstructing the images with maximum intensity projection (MIP), it is possible to obtain a clear definition of the relationship between the aneurysm and the other vessels arising from the aorta. One study[10] showed a sensitivity of 67% and a specificity of 96% for MRA in the identification of proximal stenosis of the renal artery involved by the aneurysm (Figure 2), and a sensitivity of 67% and a specificity of 100% for stenosis of the celiac trunk and of the superior mesenteric artery.

Enhanced MRA is particularly useful in the evaluation of abdominal aortic aneurysms. In fact, the presence of blood turbulence has limited to a large extent the use of nonenhanced techniques, with areas of flow void related to spin dephasing. With enhanced MRA all these problems are overcome, and the use of a coronal acquisition makes it possible to image the whole aorta and iliaco-femular district in one single field of view (FOV of 50 cm can easily be used). The absence of excretion toxicity from gadolinium compounds also permits a complete study in patients with suspected renal arterial stenosis or involvement. Currently, noninvasive 3D imaging studies (either CT or MRI) are recommended for the evaluation of abdominal aortic aneurysms, avoiding the use of invasive catheter angiography. In particular, the aim is to determine the treatment that is to be performed in each patient; endovascular placement of aortic stent grafts can be developed as the treatment of abdominal aortic aneurysms, and all the data needed to evaluate if the graft can be placed can be collected.

A study has compared the results of MRA and CTA (CT X-ray angiography) for evaluating the information needed for graft placement.[11] Both techniques agreed with catheter angiography (as gold standard) in the measurement of the abdominal aorta at the level of its largest diameter and at the level of the renal artery ostium. Another measurement that was obtained consistently with good agreement with both methods was the definition of the distance between the renal arterial ostium and the origin of the aneurysm. For tube graft placement, a distal nonaneurysmatic segment of at least 15 mm is mandatory. This distance was also measured equally well by CTA and MRA (Figures 3 and 4).

Another important issue is the evaluation of accessory renal arteries. In initial studies, MRA had generally performed very poorly, with sensitivities lying between 28 and 92%. More recent studies have reported an accuracy of 100%. The importance of breath-hold MRA is shown in all these studies. In general, 12% of patients with abdominal aortic aneurysms present with accessory renal arteries, and information about them is crucial for proper treatment planning. CTA and MRA now also offer similar results in this field.

Other information that is provided by MRA concerns the patency of the mesenteric artery: in some cases the inferior mesenteric artery may be patent and this can cause revascularization of the aneurysmal lumen through reverse flow. The status of the iliac vessels has also to be evaluated. The possibility of stenosis has to be considered, since the endovascular stent graft is of fixed expanded diameter once introduced (18 F requires a minimum vessel diameter of 6 mm). Involvement of the iliac arteries through aneurysmal dilatation does not prevent the placement of a stent graft, but size and location should be considered carefully in deciding on the type of graft to be used and the best approach to its location.

Material arising from thromboses adhering to the walls can result in underestimation of aortic diameter and misinterpretation of the proximal extent of an abdominal aortic aneurysm. Evaluation of images acquired in the axial and coronal planes with gradient echo sequences straight after the MRA sequences (when contrast agent is still enhancing the vascular lumen) permits a detailed evaluation of the thrombus.

Some advantages for MRA do exist compared with CTA: the use of safer contrast agents, which can be used as well in patients with initial renal insufficiency; the use of nonionizing radiation; the possibility of acquiring images directly in the coronal plane, with a more consistent longitudinal (or z axis) resolution; and faster postprocessing analysis (as a 3D MRA dataset is composed of far fewer images than those provided by CTA). However, MRA also has some drawbacks, including

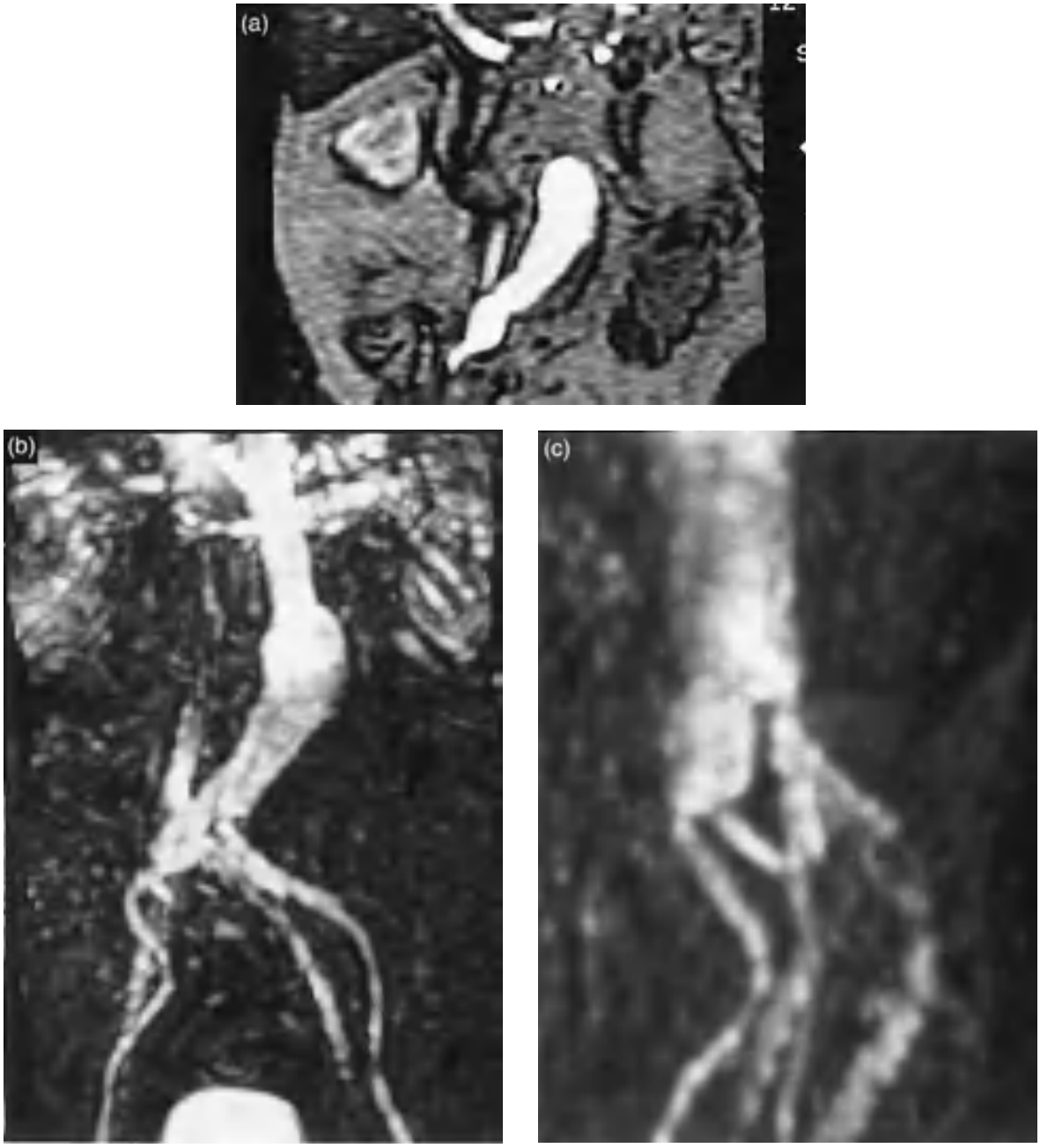

Figure 1 Abdominal aortic aneurysm; evaluation with the 3D TOF technique after gadolinium injection. (a) Single coronal slice depicting the true lumen of the aneurysm; the image also allows the thrombolytic part to be recognized. (b) MIP reconstruction of the same aneurysm; good visualization of the abdominal aorta from the renal arteries to the iliac vessels is obtained. (c) Magnification of the iliac bifurcation with evidence of involvement of the right common iliac artery and a tight stenosis at the origin of the left common iliac artery

the usual contraindications for MR in general (such as implanted pacemakers). Further, inaccuracy in the detection of small accessory renal arteries must be considered, although this problem may be overcome by continuing technical improvements that allow imaging with better spatial resolution and visualization of very small vessels.

Another field of application for MRA is in the evaluation of leaks after the placement of endovascular stent grafts.[12] Follow-up of endovascular grafts is required in order to evaluate the success of the treatment and the development of complications. In the early phase after placement of an endovascular graft, it is important to ensure that the procedure has led to technical success and that there is no leakage of blood between the graft and the native lumen of the aneurysm, which is better known as endoleak. The two major complications observed in the first series reported by Moore[13] were stent fractures (23%) and endoleaks (44%); 23% of the endoleaks had spontaneous closure. Stent fractures have been corrected fol-

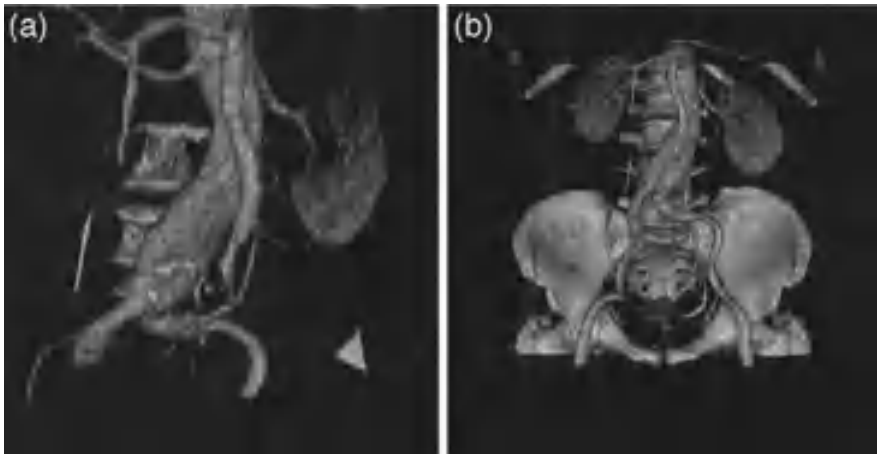

Figure 2 Volume-rendering reconstruction clearly visualizes the celiac trunk, mesenteric artery and both renal arteries in a patient with aneurysm

lowing a modification in the stent hook design by the manufacturer. However, the endoleaks remain a significant problem and may be associated with an increase in aneurysmal diameter at 1 year.[14]

In the long-term follow-up of aneurysms treated with a stent graft, it is necessary to monitor the caliber of the lumen of the aneurysm at regular intervals. In fact there have been several case reports of ruptured aneurysms after stent-graft repair. A noninvasive technique is required to monitor all these potential complications, and catheter angiography should be limited to the role of guidance of inventional procedures needed to correct such complications. Ultrasound may be able to provide consistent information with high accuracy in defining the presence of leaks or in evaluating the caliber and patency of the aorta and of the iliac vessels.[15] The value of CT has also been advocated;[16] with current helical acquisition it is possible to reconstruct angiographic projection images. CT is considered to be the required investigation for the EUROSTAR registry.[17]

With MRA, both types of endoleak can be easily detected by the evaluation of areas of increased signal intensity detected after contrast agent injection. Moreover, 3D images provided by MRA are able to define both the patency and morphology of the stent graft and its relative position compared with the origin of the renal arteries.

Figure 3 CT axial image with the aneurysm lumen surrounded by thrombolytic material

2.2 Renal Arteries

Several types of examination have been used during the past few years for the evaluation of renovascular hypertension, but many have been abandoned because of their invasivity. Although digital subtraction angiography (DSA) and conventional angiography have become increasingly important because of the success of percutaneous procedures, they still remain too invasive as screening method procedures.

It is now possible to propose MRA of the renal arteries as an accurate, noninvasive diagnostic procedure in the evaluation of renal artery stenosis, especially of the ostium of the renal vessel.[18] An example of MRA of the renal arteries is shown in Figure 5. Recent data show the high accuracy of MRA, which is similar in this case to conventional angiography in detecting both the normal and accessory renal arteries as well as the anomalous vessels. According to the literature, MRA has a sensitivity varying between 89% and 94% and a specificity of between 95% and 97%.[19,20]

The evaluation of renal arteries has been performed principally with DSA, ultrasound, and conventional CT during the past few years.

Different etiologies are implicated in renovascular disease and, in most cases, the renal arteries are affected as part of the entire vascular system. Because of the continuous advances in percutaneous endoluminal therapies, the best possible imaging method is required in the detection of renovascular diseases.

According to the literature, MRA allows the visualization of all the main arteries as well as accessory arteries. In the detection of stenosis, the MRA sensitivity and specificity amounted

Figure 4 Maximum intensity projections (MIP) show the extension of the aneurysm and the renal involvement

to 93% and 90%, respectively, with a negative predictive value of 96%.[21,22]

In contrast to other noninvasive techniques such as scintigraphy or ultrasound, contrast-enhanced 3D MRA allows visualization of accessory renal arteries with a high degree of accuracy. The visualization of accessory arteries is especially important in the evaluation of renal transplant donors. Imaging must be completely accurate before surgical revascularization or nephrectomy in living-related renal donors can be contemplated.

As far as atherosclerotic lesions are concerned, the diagnostic performance of 3D MRA is still limited, particularly when all forms of stenosis are considered; in fact, as seen in the literature, there have been a considerable number of false-positive and false-negative findings.[23] Therefore, the gold standard diagnostic procedure for detecting arterial stenosis still remains angiography, though this is an invasive examination that exposes the patient to ionizing radiation as well as iodinated contrast material, which may cause allergic reactions and/or nephrotoxicity. Therefore, according to the literature,[24] contrast-enhanced 3D MRA is, as yet, only a promising approach to obtaining contrast arteriography but is comparable to arteriography in the assessment of renal artery morphology and pathologic states. It does not involve the risk of arterial catheterization, ionizing radiation, or nephrotoxic contrast material.

2.3 MR Venography (MRV)

Studies of abdominal veins are an interesting application of MRA. It is possible to evaluate the normal and pathologic anatomy of the portal system, including the splenic vein, the superior mesenteric vein (SMV), and the eventual collateral vessels.[25] The relatively slow and homogeneous venous blood

Figure 5 Axial MIP reconstruction of renal arteries; good evaluation of the distal part of the vessels is also obtained

flow allows high-quality images to be obtained in almost all patients. The large FOV permits the imaging of the whole spleno-portal axis and the collateral vessels at the same time. This option is not available in any other imaging technique such as DSA, duplex scan, or color Doppler ultrasonography.

The main technical difficulties arising from respiratory and peristaltic motion, and to the different flow direction and velocity in abdominal vessels, have now been overcome by new image acquisition procedures. The breath-hold coronal TOF technique is the preferred method with which to image the abdominal veins. An image can be acquired in about 8 s and in a few minutes all the abdominal vessels can be displayed. It is, therefore, possible to obtain a selected evaluation of the portal vein or any of the other vessels by acquiring the images in the plane corresponding to the vessel to be studied. Because of saturation effects, all the vessels not in that plane will not be depicted.

To obtain a more selective evaluation of the venous system, it is possible to use more sophisticated techniques such as bolus tracking and selective presaturation. Those two options allow the clinician to define accurately the flow direction in a vessel and to distinguish a thrombus from flowing blood. Furthermore, they permit the selective suppression of the signal coming from specific arterial vessels or veins. After acquisition of the data, a postprocessing MIP technique can be used to reconstruct the images. Thus, it is possible to rotate the vessels and to show them on the monitor in the most useful projection and it is also possible to recognize strange anatomic variants in this way.

Portal hypertension represents one of the major fields of application of MR venography (MRV) in the abdomen (Figure 6). Because of the large FOV, MRV allows the whole spleno-portal axis and its collateral vessels to be shown at the same time in almost all patients. It is possible to evaluate the diameter of the portal vein and, with adequate techniques, to obtain quantitative information about the blood flow. Compared with color Doppler ultrasonography, which can actually be considered to be the method of choice for the screening and follow-up of patients with portal hypertension, MRV is not operator-dependent; it is not influenced by the presence of ascites, which is very common in these patients, or by colic meteorism and patient habitus, all of which disturb a sonographic examination.

Another recent clinical indication for MRV is the evaluation of complex venous disease in cases of liver transplantation. MRV is very accurate and has a good correlation with DSA and duplex ultrasound. Moreover, MRV displays images in different orientations: thus the reconstructed images can be easily interpreted by the surgeon and complex structures can be demonstrated better than by any alternative imaging method.

Following liver transplantation, complications may arise as a result of anastomosis failure or stenosis. In this case the examination technique is ultrasonography, which has an important limitation in depicting the anastomosis. MRV can also show the condition through the paramagnetic effects of the material in the anastomosis, which creates a lack of signal. Additionally, anastomosis on the hepatic artery can be depicted by MRA in a high percentage of patients.

Finally, another recent field of application for MRV is the study of the patency of both surgical and percutaneous shunts of the ortho-systemic structure (TIPS). MRV makes it possible to obtain a noninvasive postsurgical follow-up. The anastomosis can be identified, flow direction established, and both size and patency of the shunts evaluated. After TIPS procedures the position of the stent can also be accurately determined.

There are a few pitfalls and limitations in the use of MRV in the portal system. At a venous confluence, such as the junction of superior mesenteric and splenic veins, a signal void may occur simulating a thrombus. In order not to misunderstand this artifact, gradient echo images can be acquired in different orientations through the questionable area. Changing the slice orientation can also be useful sometimes so as to

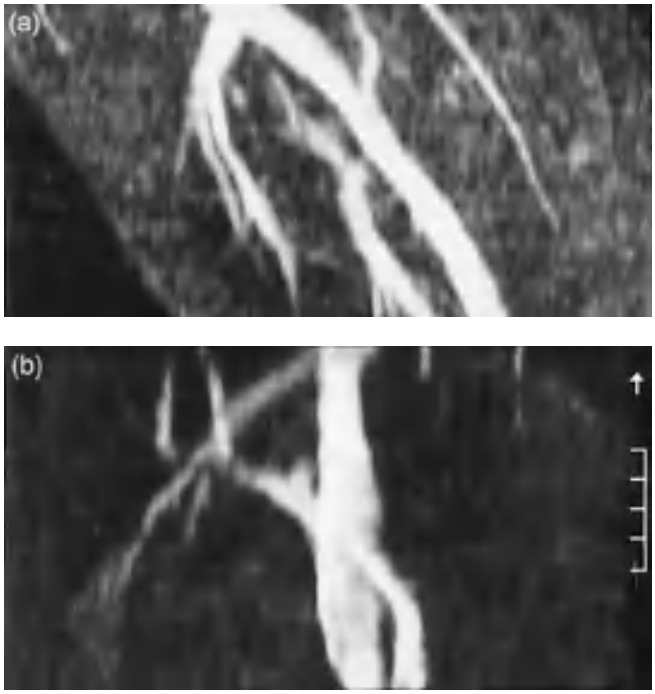

Figure 6 2D TOF MR venography. (a) MIP reconstruction shows the inferior vena cava (IVC) with the hepatic vessels and the portal vein. (b) Good evaluation of the portal vein and its bifurcation. The IVC and one hepatic vessel are also depicted

avoid the in-plane saturation effect. Usually, this is not as common for the portal system as it is for the aorta or the inferior vena cava, but a verticalization of the portal axis together with slow flow, as in a cirrhotic patient, may impair signal acquisition.

In conclusion, MRV of the portal system is extremely accurate and complete for the evaluation of these vessels. The large field of view, the insensitivity to patient habitus and the graphic presentation format make it very useful for preoperative assessment in patients with portal hypertension.

3 RELATED ARTICLES

Liver, Pancreas, Spleen, and Kidney MRI; Peripheral Vasculature MRA; Phase Contrast MRA; Time-of-Flight Method of MRA.

4 REFERENCES

1. R. R. Edelman, H. P. Mattle, D. J. Atkinson, and H. M. Hoogewoud, *Am. J. Roentgenol.*, 1990, **154**, 937.
2. H. Bosmans, G. Marchal, P. van Hecke, and P. Vanhoenacker, *Clin. Imag.*, 1992, **16**, 152.
3. D. G. Nishimura, *Magn. Reson. Med.*, 1990, **14**, 194.
4. C. L. Dumoulin, S. P. Souza, M. F. Walker, and W. Wagle, *Magn. Reson. Med.*, 1989, **9**, 139.
5. C. L. Dumoulin, E. K. Yucel, P. Vock, S. P. Souza, F. Terrier, F. L. Steinberg, and H. Weymuller, *J. Comput. Assist. Tomogr.*, 1990, **14**, 779.
6. J. S. Lewin, G. Laub, and R. Hausmann, *Radiology*, 1991, **179**, 261.
7. J. L. Creasy, R. R. Price, T. Presbrey, D. Goins, C. L. Partain, and R. M. Kessler, *Radiology*, 1990, **175**, 280.
8. A. N. Shetty, K. G. Bis, T. G. Vrachliotis, M. Kirsch, A. Shirkhoda, and R. Ellwood, *JMRI*, 1998, **8**, 603.
9. R. Passariello, P. Pavone, C. Catalano, A. Laghi, L. Marsili, and M. Di Girolamo, *Ann. Chir. Gynaecol.*, 1993, **82**, 87.
10. J. A. Kaufman, E. K. Yucel, A. C. Waltman, S. C. Geller, C. A. Athanosoulis, and M. R. Prince, *Radiology*, 1993, **189(P)**, 174.
11. A. Siegfried, M. D. Thurnher, R. Dorffner, P. Polterauer, and J. Lammer, *Radiology*, 1997, **205**, 341.
12. L. Engellau, E. M. Larsson, U. Albrechtsson, T. Jonung, E. Ribbe, J. Thorne, Z. Zdanowski, and L. Norgren, *Eur. J. Vasc. Endovasc. Surg.*, 1998, **15**, 212.
13. W. S. Moore, *J. Endovasc. Surg.*, 1997, **4**, 182.
14. J. S. Matsumura, *J. Vasc. Surg.*, 1998, **4**, 606.
15. J. Golzarian, L. Dussaussois, H. T. Abada, P. A. Gevenois, D. van Gansbeke, J. Ferreira, and J. Struyven, *Am. J. Roentgenol.*, 1998, **171**, 329.
16. D. T. Sato, C. D. Goff, R. T. Gregory, K. D. Robinson, K. A. Carter, B. R. Herts, H. B. Vilsack, R. G. Gayle, F. N. Parent III, R. J. de Masi, and G. H. Maier, *J. Vasc. Surg.*, 1998, **28**, 657.
17. P. L. Harris, *J. Endovasc. Surg.*, 1997, **4**, 72.
18. M. Strotzer, C. M. Pruell, A. Geissler, S. M. Kohler, B. R. Kraemer, and J. Gmeinwieser, *Radiology*, 1993, **189P**, 189.
19. T. M. Grist, T. W. Kennell, I. A. Sproat, E. M. Flath, J. C. McDermott, and M. M. Majkiwcyz, *Radiology*, 1993, **189P**, 190.
20. T. F. Hany, D. A. Leung, T. Pfammatter, and J. F. Debatin, *Invest. Radiol.*, 1998, **33**, 653.
21. S. Miller, F. Schick, S. H. Duda, T. Nagele, U. Hahn, F. Teufl, M. Muller-Schimpfle, C. M. Erley, J. M. Albes, and C. D. Claussen, *Magn. Reson. Imag.*, 1998, **16**, 1005.
22. D. Kim, R. R. Edelman, K. C. Kent, D. J. Porter, and J. J. Skillman, *Radiology*, 1990, **174**, 727.
23. M. R. Prince, *JMRI*, 1998, **8**, 511.
24. D. B. Stafford-Johnson, C. A. Lerner, M. R. Prince, S. N. Kazanjian, D. L. Narasimham, A. B. Leichtman, and K. J. Cho. *Magn. Reson. Imag.*, 1997, **15**, 13.
25. H. B. Gehl, K. Bohndorf, K. C. Klose, and R. W. Gunther, *J. Comput. Assist. Tomogr.*, 1990, **14**, 619.

Biographical Sketches

P. Pavone, *b* 1957. M.D., 1981, Rome. Studies on CT and vascular and interventional radiology, 1981–87. Researcher on MRI at the University of L'Aquila, Italy, 1988–93; researcher at University of Rome 'La Sapienza', 1993–present. Approx. 300 publications. Current research specialties; experimental and clinical studies of the abdominal organs and vascular system by MRI.

A. Laghi. *b* 1967. M.D., 1992, Rome. Resident, University of Rome 'La Sapienza', 1992–present. Approx. 60 publications. Current research specialties: experimental and clinical studies of the abdominal organs and vascular system by MRI.

C. Catalano. *b* 1965. M.D., 1990, Rome. Residency, University of L'Aquila, 1990–1994. Fellow, University of Rome 'La Sapienza', 1994–present. Approx. 120 publications. Current research specialties: experimental and clinical studies of the abdominal organs and vascular system by MRI.

V. Panebianco. *b* 1967. M.D., 1994, Rome. Resident, University of Rome 'La Sapienza', 1993–present. Approx. 30 publications. Current research specialties: clinical studies of the abdominal organs by MRI.

F. Fraioli. *b* 1973. M.D., 1998, Rome. Residency University of Rome 'La Sapienza', 1993–present. Approx. 10 publications. Current research specialties: experimental and clinical studies of the abdominal and vascular system by MRI.

I. Baeli. *b* 1974. M.D. 1999, Rome. Residency University of Rome 'La Sapienza', 1993–present. Approx. 10 publications. Current research specialties: experimental and clinical studies of the abdominal and vascular system by MRI.

R. Passariello. *b* 1942. M.D. 1965, Rome. Residency University Padua, 1965–1967. Full Professor of Radiology, University of L'Aquila, 1986–1991. Full Professor of Radiology and Chairman of the 2nd Department of Radiology, University of Rome 'La Sapienza', 1991–present. Approx. 500 publications. Organization of more than 65 Congresses. 1994–present Vice-President of the European Congress of Radiology '95 and '97. Chairman of the European Seminars on Diagnostic and Interventional Radiology, 1990–present. Member of the Executive Board of the NICER Programme. 1990–present.

Assessment of Regional Blood Flow and Volume by Kinetic Analysis of Contrast-Dilution Curves

Johannes C. Böck and Roland Felix
Freie Universität Berlin, Germany

1 INTRODUCTION

The success of clinical magnetic resonance imaging (MRI) is based on its superb anatomic and contrast resolution, in particular in the central nervous system. However, MRI was initially unable to contribute to the field of perfusion imaging because of two factors: the lack of MRI contrast media and insufficient temporal resolution of the pulse sequences.

Contrast media are now available. The first agent in clinical use was gadolinium–DTPA, a well-tolerated ionic paramagnetic contrast agent developed by Schering AG, Berlin and first used in humans at our Institution in 1983.[1] After intravenous injection, gadolinium–DTPA is distributed in the extracellular space with the notable exception of the central nervous system, where the extravasation of gadolinium–DTPA into the interstitial space is effectively prevented by the intact blood/brain barrier. No such barrier prevents leakage of gadolinium–DTPA in the normal myocardium.

The limitation of temporal resolution has been overcome by the development of pulse sequences such as gradient echo and echo planar imaging. These pulse sequences allow for acquisition times ranging from 0.5–20 images per second, sufficient to follow the first passage of a contrast bolus through an organ.

In 1986, Haase et al.[2] published a report which pioneered contrast enhanced perfusion MRI. In an experimental model, they combined the intravenous bolus injection of the first available paramagnetic contrast agent, gadolinium–DTPA, and a new rapid image acquisition strategy 'fast low angle shot' (FLASH). When a series of images was acquired in the same slice position after contrast bolus injection ('FLASH MR movie') a reversible signal intensity decrease was observed in the brain which apparently coincided with the first pass of the contrast medium through the brain.

Unfortunately, the interpretation of the contrast kinetic is limited because of the physical properties of currently available contrast agents, which distribute either in the intravascular space (in the intact brain) or, in addition, in the interstitial space (in the myocardium but also in cerebral pathologies with disruption of the blood/brain barrier). From a rigorous mathematical standpoint only relative cerebral blood *volume* can be calculated on the basis of concentration–time curves measured in the brain[3]—cerebral blood *flow* can only be estimated.[3,4] Since gadolinium–DTPA is not a strictly intravascular contrast medium in other organs than the brain, both blood flow and volume cannot be derived from gadolinium–DTPA kinetics measured in the myocardium and the kidneys.

By contrast, organ blood flow can be quantitatively assessed using diffusible contrast media such as deuterium oxide[5] or $H_2{}^{17}O$.[6] However, these techniques will not be addressed in depth in this article since clinical experience is still lacking, probably because the methodology requires an injection either directly into the tissue or into the feeding artery. A less invasive approach, intravenous injection, would require the measurement of the concentration–time curve in the feeding artery and deconvolution of the arterial and tissue curves.[7] Such techniques offer the same advantages as positron emission tomography in that blood flow can be measured in absolute terms (mL min^{-1} per 100 g of tissue).

2 PRINCIPLES

Conventional contrast enhanced MRI using paramagnetic agents such as gadolinium–DTPA relies on dipole–dipole interactions between the nuclear spins of local protons and unpaired electrons of the contrast molecules. These interactions shorten the T_1 relaxation times and thereby increase signal intensity in the interstitial space *minutes* (the time required for contrast extravasation) after injection. If, however, the contrast is rapidly injected as a bolus, and if an appropriate (susceptibility-sensitive) pulse sequence is used, then a signal intensity *decrease* is observed within *seconds* after injection. The underlying mechanism is the compartmentalization of the contrast material in the vasculature (at least in the brain) with consecutively high contrast concentration gradients between the intravascular and interstitial compartments. (Positive) susceptibility is the property of paramagnetic substances to produce an intrinsic magnetic field when exposed to an extrinsic magnetic field. Because the magnetic susceptibility of gadolinium–DTPA is different to that of biological tissues, the contrast concentration gradients translate into regional (intravoxel) magnetic field gradients.

Intravoxel magnetic field inhomogeneity broadens the resonance frequency spectrum with subsequent dephasing and signal loss. Since gradient echo pulse sequences do not refocus static magnetic field inhomogeneities, signal intensity is directly affected by this process, in particular when the echo time is long (on the order of 20 ms). Spin echo pulse sequences do refocus *static* inhomogeneities and are therefore only sensitive to dephasing of mobile spins (diffusion of water molecules); again, the sensitivity increases with the echo time.

The signal intensity decrease is reversed as the contrast bolus passes the brain (first pass); however, a second (third, etc.) passage of the contrast (systemic contrast recirculation) is usually observed *before* the baseline signal intensity has been reached.

For further computations (e.g. blood volume), indicator dilution theory requires a concentration–time curve which can be computed for every voxel on the basis of the measured signal intensities by logarithmic transformation:[8]

$$c(t) = -\ln[S(t)/S(t_0)]/(k_2 TE) \qquad (1)$$

(c = concentration, S = signal intensity, t = time, t_0 = time of injection, k_2 = constant depending on system and tissue properties, TE = echo time).

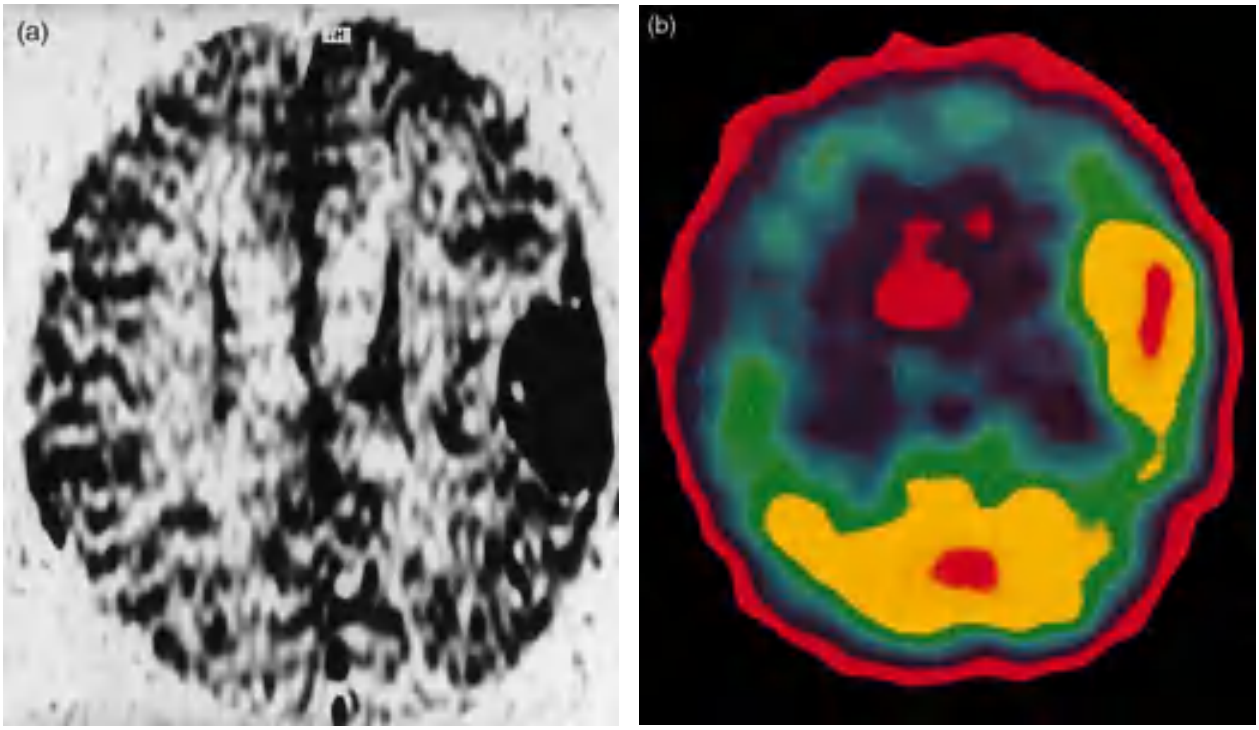

Figure 1 Sixty-one year old man with focal seizures of the right arm and speech arrest. Left parietal mass with homogeneous hyperperfusion pattern documented by MRI and confirmed by the radionuclide reference technique. Histology: meningiomatous and angiomatous meningioma. (a) T_2*-weighted first-pass study (subtraction image); (b) radionuclide study (HMPAO–SPECT)

The postprocessing algorithm is based on the hypothesis that the area under the concentration–time curve recorded in every voxel reflects regional cerebral blood volume.[9] This assumption is correct for the first pass of the contrast bolus and requires numerical elimination of recirculating contrast. This is achieved with sufficient accuracy by a nonlinear least-squares fit procedure using a γ-variate or some other algebraic function as a model for the cerebral contrast transit in the absence of systemic contrast recirculation. Finally, a parameter image is generated in which the brightness of each voxel reflects the area of the concentration–time curve and thus regional cerebral blood volume.

In the myocardium, the contrast extravasates into the interstitial space. This already occurs to a substantial degree during the first pass;[10] the area under the concentration–time curve therefore does not correspond to a well-defined biologic compartment, but reflects the intravascular and a variable portion of the interstitial compartment. Myocardial blood volume can therefore not be derived from the concentration–time curve of small molecules[11] like gadolinium–DTPA. The use of a macromolecular agent with a molecular weight above 20 000 Da such as gadolinium–DTPA–polylysine[12] would be required for this purpose, but macromolecular agents are not yet available for clinical use.

As already mentioned, there is no rigorous theoretical concept for the construction of parameter images from concentration–time curves which reflect regional cerebral or myocardial blood flow. Some approaches are based on mean transit time concepts although the correct regional mean transit times cannot be determined using intravascular contrast agents.[3,4] In fact, the mean transit time calculated from the tissue concentration–time curve alone (without consideration of the arterial input function) overestimates the true organ mean transit time (which is on the order of only a few seconds in the brain) by more than 100%. Correction for the dispersion of the contrast bolus outside of the brain (finite injection duration, passage from the peripheral vein to the brain) would require numerical deconvolution of the tissue curves with the arterial input function. Although the arterial input function can be measured[13] it is not the correct input function for every voxel. Finally, since the volume of distribution of gadolinium–DTPA-type contrast material is restricted, the inverse of the (correct) mean transit time would not represent blood flow in terms of [mL min^{-1} per 100 g tissue] but blood flow per unit blood volume [mL min^{-1} per ml blood]. Despite these limitations, some investigators have used transit time approaches with some success.[14–17]

Another approach is to calculate a subtraction image where the image acquired at the time of maximum cerebral contrast concentration is subtracted from an image acquired before any contrast has reached the brain on a voxel-by-voxel basis [Figure 1(a)].[18] The underlying theoretical concept is valid under certain experimental conditions[19] and requires the consideration of the arterial input function. Fortunately, the arterial input function can be neglected as long as the image contains its own reference (e.g. the normal contralateral hemisphere), since the arterial input function is identical for all voxels under considerations in this concept. Subtraction images appear to reflect regional cerebral blood flow as assessed by an established radionuclide reference technique (HMPAO–SPECT) in the vast majority of patients with cerebral infarcts[18] and in all patients with homogeneous

intracranial tumors [Figures 1(a) and (b)].[20] Discrepant results between the radionuclide method and first-pass subtraction images were found in inhomogeneous tumors (vital tumor/necrosis/edema). However, the discrepancy did not appear to result from the inability of MRI to depict adequately regional cerebral blood flow in these tumors but from the lower spatial resolution of SPECT (voxel volume = 1500 mm^3) versus MRI (voxel volume = 50 mm^3).

3 CEREBRAL PERFUSION IMAGING

Clinical experience with contrast enhanced MR perfusion imaging is steadily increasing. A number of recent reports focus on cerebral ischemia, intracranial tumors, and arteriovenous malformations.

In cerebral infarcts, regional cerebral blood flow is usually decreased but a hyperperfusion pattern is identified in some cases.[18,21] While the prognostic significance of the hyperperfusion pattern in subacute infarcts has yet to be established, one might speculate that evidence of reperfusion indicates a better clinical outcome.

The grade of malignancy of intraaxial tumors appears to be correlated with the perfusion pattern. Low-grade astrocytomas are characterized by decreased blood volume when compared with contralateral gray matter. High-grade astrocytomas show either a homogeneous increase of blood volume or signs of marked inhomogeneity. These findings parallel—to a certain degree—the extent of the blood/brain barrier disruption as demonstrated by contrast enhancement on T_1-weighted (or cranial computerized tomography—CCT) images. However, it is important to remember that the blood/brain barrier and regional cerebral perfusion are two distinct features which obey different underlying regulating and disturbing mechanisms.[22]

Multiple biopsies of intraaxial tumors have shown that high-grade tumors are composed of tissues with different histological grading. It is obvious that biopsies should be obtained from the most malignant part of the tumor. These areas are often characterized by increased metabolism, increased tumor blood flow, and volume. Perfusion imaging should therefore be considered for optimal biopsy guiding.[23] The differentiation of radiation necrosis after therapy of high-grade intraaxial tumors from recurrent tumor is cumbersome because both present with mass effect, necrosis and blood/brain barrier disruption. However, initial clinical results indicate that blood volume is homogeneously decreased in radiation necrosis, while an inhomogeneous pattern with areas of high regional blood volume can be demonstrated in recurrences.[23]

Arteriovenous malformations are quite easily demonstrated by MRI, including magnetic resonance angiography. However, due to inherent limitations of magnetic resonance angiography, the success of interventional therapy by embolization tends to be overestimated. In a recent study[24] we showed that contrast enhanced perfusion imaging is by far the most sensitive MRI technique to demonstrate residual pathologic vasculature after embolization. Perfusion imaging is also highly useful to demonstrate reopening of previously occluded pathways and is therefore part of our standard protocol in the evaluation and follow-up of arteriovenous malformations.

4 MYOCARDIAL PERFUSION IMAGING

Initial experience with gadolinium–DTPA at our Institution demonstrated increased enhancement in acute infarcts but no significant enhancement in subacute and chronic infarcts.[25] Since spin echo pulse sequences with an acquisition time of more than 5 min were used in these studies, the enhancement did not reflect blood flow but contrast extravasation into the interstitial space which is mainly a function of microvascular permeability. Other MR contrast media such as dysprosium, manganese, macromolecular gadolinium compounds, and superparamagnetic agents have been successfully studied.[26,27]

Atkinson and co-workers performed bolus injection experiments using a T_1-weighted pulse sequence;[28] they described a transient signal intensity increase during the first pass of the contrast material in normal myocardium of experimental animals and volunteers, but no signal intensity change after experimental occlusion of the left coronary artery. In a subsequent study, similar effects were seen in patients with coronary artery disease.[29] No attempt was made in these studies to quantify the effects in terms of myocardial blood flow.

Wilke et al. have used a kinetic model involving the mean transit time concept to obtain blood flow estimates in an experimental model. Blood flow was measured by a radiomicrosphere reference technique. A correlation coefficient of $r = 0.89$ was found between the MRI estimate of flow (the inverse of mean transit time) and the reference technique. It must be noted, however, that changes in myocardial blood volume are not accounted for in that model. Since myocardial blood volume is highly variable, myocardial blood flow estimates based on mean transit time alone are likely to be much less reliable in a clinical setting.

5 PERFUSION IMAGING OF OTHER ORGANS

Next to the brain and heart, perfusion imaging of the kidneys might be of clinical interest. Imaging of renal blood flow is quite complex because flow and function (=excretion) are tightly related. Gadolinium–DTPA is freely filtrated in the glomerulus and neither secreted nor reabsorbed in the tubular system.[30] Due to water reabsorption in the tubules, the concentration of gadolinium–DTPA increases by up to a factor of 100 from the initial plasma concentration. This wide range of concentrations is unique in the kidneys and has important effects on the observed signal intensity: at lower concentrations, signal intensity increases due to T_1 shortening; at higher concentrations, signal intensity decreases due to T_2 shortening. Obviously, this nonlinearity complicates the interpretation of signal intensity versus time curves measured in the kidneys. Nevertheless, three phases can be distinguished after contrast bolus injection: a vascular, a tubular, and a ductal phase.[31] Due to the complexity of both renal physiology and the contrast mechanisms, assessment of renal blood flow will remain one of the most challenging tasks in MR imaging of organ blood flow.

The methodology discussed in this article also applies to perfusion imaging of other tissues. It must be noted, however, that the quality of the primary data (the concentration versus time curve) depends on the contrast concentration obtained during the first pass after bolus injection; tissues with low re-

gional blood flow and volume are therefore unlikely to be candidates for the assessment of perfusion by contrast bolus experiments.

6 FUNCTIONAL IMAGING OF THE HUMAN CORTEX

Functional imaging of the brain refers to the detection of stimulated cortical activity. The stimulus may be an optical, motor, or sensory paradigm; even ideation of motion or a visual pattern can act as a stimulus. Cortical stimulation entails alterations of regional cerebral blood flow, blood volume, oxygenation, and metabolism which can be detected by MRI. Classically a domain of nuclear medicine, in particular of positron emission tomography, MRI has been very successful in detecting evidence of cortical activation.[32] The methodology relies upon the above-described contrast bolus experiment which is performed under resting conditions and during stimulation. The computed blood volume images are subtracted from one another; the subtraction image represents areas of locally altered perfusion due to cortical stimulation.

7 RELATED ARTICLES

Blood Flow: Quantitative Measurement by MRI; Hemodynamic Changes owing to Sensory Activation of the Brain Monitored by Echo-Planar Imaging; Gadolinium Chelate Contrast Agents in MRI: Clinical Applications; Gadolinium Chelates: Chemistry, Safety, and Behavior; Susceptibility Effects in Whole Body Experiments.

8 REFERENCES

1. W. Schörner, R. Felix, M. Laniado, L. Lange, H. J. Weinmann, C. Claussen, W. Fiegler, U. Speck, and E. Katzner, *Fortschr. Röntgenstr.*, 1984, **140**, 493.
2. A. Haase, D. Matthaei, W. Hänicke, and J. Frahm, *Radiology*, 1986, **160**, 537.
3. N. A. Lassen, *J. Cerebr. Blood Flow Metab.*, 1984, **4**, 633.
4. R. M. Weisskoff, D. Chesler, J. L. Boxerman, and B. R. Rosen, *Magn. Reson. Med.*, 1993, **29**, 553.
5. J. J. H. Ackerman, C. S. Ewy, S. G. Kim, and R. A. Shalwitz, *Ann. N. Y. Acad. Sci.*, 1987, **508**, 89.
6. K. K. Kwong, A. L. Hopkins, J. W. Belliveau, D. A. Chesler, L. M. Porkka, R. C. McKinstry, D. A. Finelli, G. J. Hunter, J. B. Moore, B. R. Rosen, and R. G. Barr, *Magn. Reson. Med.*, 1991, **22**, 154.
7. N. A. Lassen and W. Perl, 'Tracer Kinetic Methods in Medical Physiology', Raven Press, New York, 1979.
8. B. R. Rosen, J. W. Belliveau, J. R. Vevea, and T. J. Brady, *Magn. Reson. Med.*, 1990, **14**, 249.
9. L. Axel, *Radiology*, 1990, **177**, 679.
10. J. A. Rumberger and M. R. Bell, *Invest. Radiol.*, 1992, **27**, S40.
11. J. M. Canty, R. M. Judd, A. S. Brody, and F. J. Klocke, *Circulation*, 1991, **84**, 2071.
12. M. Saeed, M. F. Wendland, T. Masui, A. J. Connolly, N. Derugin, R. C. Brasch, and C. B. Higgins, *Radiology*, 1991, **180**, 153.
13. W. H. Perman, M. H. Gado, K. B. Larson, and J. S. Perlmutter, *Magn. Reson. Med.*, 1992, **28**, 74.
14. J. W. Belliveau, B. R. Rosen, G. J. Hunter, E. Tasdemiroglu, R. MacFarlane, P. Boccalini, L. M. Hamberg, M. A. Moskowitz, and S. H. Simon, *Stroke*, 1993, **24**, 444.
15. N. Wilke, C. Simm, J. Zhang, J. Ellermann, X. Ya, H. Merkle, G. Path, H. Lüdemann, R. J. Bache, and K. Ugurbil, *Magn. Reson. Med.*, 1993, **29**, 485.
16. K. A. Rempp, G. Brix, F. Wenz, C. R. Becker, F. Guckel, and W. J. Lorenz, *Radiology*, 1994, **193**, 637.
17. J. C. Böck, O. Henrikson, A. H. G. Götze, W. Wlodarczyk, B. Sander, and R. Felix, *Invest. Radiol.*, 1995, **30**, 693.
18. J. C. Böck, B. Sander, J. Hierholzer, M. Cordes, J. Haustein, W. Schörner, and R. Felix, *Fortschr. Röntgenstr.*, 1992, **156**, 382.
19. N. A. Mullani and K. L. Gould, *J. Nucl. Med.*, 1983, **24**, 577.
20. J. C. Böck, B. Sander, J. Hierholzer, J. Haustein, M. Scholz, K. H. Radke, W. Schörner, W. Lanksch, and R. Felix, *Fortschr. Röntgenstr.*, 1992, **157**, 378.
21. R. R. Edelman, H. P. Mattle, D. J. Atkinson, T. Hill, J. P. Finn, C. Mayman, M. Ronthal, H. M. Hoogewoud, and J. Kleefield, *Radiology*, 1990, **176**, 211.
22. J. C. Böck, B. Sander, K. H. Radke, J. Haustein, C. Zwicker, and R. Felix, *Adv. MRI Contrast*, 1993, **1**, 76.
23. B. R. Rosen, J. W. Belliveau, A. J. Aronen, D. Kennedy, B. R. Buchbinder, A. Fischman, M. Gruber, J. Glas, R. M. Weisskoff, M. S. Cohen, F. H. Hochberg, and T. J. Brady, *Magn. Reson. Med.*, 1991, **22**, 293.
24. J. C. Böck, H. P. Molsen, B. Sander, and R. Felix, *Fortschr. Röntgenstr.*, 1992, **157**, 471.
25. H. W. Eichstaedt, R. Felix, F. C. Dougherty, M. Langer, W. Rutsch, and H. Schmutzler, *Clin. Cardiol.*, 1986, **9**, 527.
26. A. D. Watson, S. M. Rocklage, and M. J. Carvlin, in 'Magnetic Resonance Imaging', 2nd edn. ed. D. D. Stark and W. G. Bradley, Mosby Year Book, St. Louis, MO, 1992, Vol. 1, Chap. 14.
27. C. B. Higgins, G. Caputo, M. F. Wendland, and M. Saeed, *Invest. Radiol.*, 1992, **27**, S66.
28. D. J. Atkinson, D. Burstein, and R. Edelman, *Radiology*, 1990, **174**, 757.
29. W. J. Manning, D. J. Atkinson, W. Grossman, S. Paulin, and R. R. Edelman, *J. Am. Coll. Cardiol.*, 1991, **18**, 959.
30. C. H. Lorenz, T. A. Powers, and C. L. Partain, *Invest. Radiol.*, 1992, **27**, S109.
31. P. L. Choyke, J. A. Frank, M. E. Girton, S. W. Inscoe, M. J. Carvlin, J. L. Black, H. A. Austin, and A. J. Dwyer, *Radiology*, 1989, **170**, 713.
32. J. W. Belliveau, D. N. Kennedy, R. C. McKinstry, B. R. Buchbinder, R. M. Weisskoff, M. S. Cohen, J. M. Vevea, T. J. Brady, and B. R. Rosen, *Science*, 1991, **254**, 716.

Biographical Sketches

Johannes C. Böck. *b* 1957. M.D., 1987, Göttingen. Introduced to MRI by R. Felix in 1989. Research fellow, Departments of Surgery, Radiology and Nuclear Medicine, University of California, San Francisco, 1987–89; Strahlenklinik und Poliklinik, Virchow-Klinikum, Medizinische Fakultät der Humboldt-Universität zu Berlin, 1989–present. Approximately 60 publications. Research interests include cerebral perfusion imaging by NMR, MR contrast media, MR angiography, and pulmonary imaging by NMR.

Roland Felix. *b* 1938. M.D., 1962, Munich. 1962–78; Departments of Surgery, Freiburg; Gynecology, Hamburg; Medicine, Mainz; Physiology, Bonn; Medicine, Kiel; Radiology, Bonn. Professor of Clinical Radiology and Chairman, Strahlenklinik und Poliklinik (Department of Diagnostic Radiology, Nuclear Medicine, and Radiooncology), Virchow-Klinikum, Medizinische Fakultät der Humboldt-Universität zu Berlin, 1978–present. Approximately 900 publications. Research interests cover contrast enhanced CT and MRI, telecommunication, and radiooncology including therapeutic hyperthermia.

Cerebral Perfusion Imaging by Exogenous Contrast Agents

Leif Østergaard
Århus University Hospital, Århus, Denmark

1 INTRODUCTION

Cerebral blood flow (CBF) and cerebral blood volume (CBV) are traditionally used as physiologic indices of cerebral function. Positron emission tomography (PET), single photon emission computed tomography (SPECT) and stable xenon-enhanced computed tomography (Xe-CT) are frequently used for determining relative or absolute CBF, as well as flow changes in response to pharmacologic stimuli or functional activation.

With the increasing role of magnetic resonance imaging (MRI) in the diagnosis of cerebral pathologies, techniques to derive cerebral perfusion indices have also emerged. Rosen and co-workers[1–4] derived maps of relative CBV by dynamic bolus tracking of susceptibility contrast agents, a technique known as perfusion imaging. Theoretical analysis of bolus-tracking experiments has subsequently been extended to allow measurements of CBF. In this article, the theoretical foundation of perfusion imaging by exogenous contrast agents is reviewed, together with areas of potential clinical use for the techniques.

2 THEORY

2.1 Contrast Mechanisms

The derivation of physiologic parameters from dynamic MR images requires detailed tracer kinetic analysis of tissue concentration–time curves obtained during passage of a bolus of contrast agent. Establishing the relation between signal changes observed with a given pulse sequence and the corresponding tissue contrast agent concentration is, therefore, necessary to derive quantitative information. Consequently, the study of interactions between contrast agents and tissue represents the foundation of perfusion imaging and remains a field of intense research. Although a full overview of this area is beyond the scope of this article, certain findings are of central importance to the application and understanding of perfusion imaging.

2.1.1 Susceptibility Contrast

Most cerebral perfusion imaging is carried out using dynamic susceptibility contrast imaging: tracking the passage of a rapidly injected paramagnetic gadolinium-based chelate. In the presence of an intact blood–brain barrier, the intravascular compartmentalization of a paramagnetic contrast agent with high magnetic moment creates large, microscopic susceptibility gradients, with resulting signal loss in T_2 and T_2^*-weighted images. The dynamics in the presence of a leaky blood–brain barrier will be further explored in Section 2.7.

The microscopic susceptibility gradients cause local changes in water resonance frequency and in water frequency line width, with resultant signal loss and phase distortions for pulse sequences without full refocusing of static field inhomogeneities (gradient echoes, asymmetric spin echoes). For pulse sequences *with* full refocusing of static field inhomogeneities (spin echoes), these phenomena do not cause appreciable signal loss. Instead, signal loss is observed at long echo times (*TE*) because there is sufficient time for water to diffuse through areas of different magnetic fields (i.e. among contrast-filled vessels) and thereby dephase. This diffusion-related signal loss is a complex function of *TE*, the distribution and density of vessel sizes, and the concentration and magnetic properties of the contrast agent. Weisskoff, Boxerman, Fisel and co-workers performed a detailed analysis of these effects in the context of cerebral physiology, using Monte Carlo modeling as well as empirical data.[5–7] Two results are particularly important in terms of interpreting perfusion imaging data. First, owing to the properties of susceptibility contrast mechanisms, spin echo measurements are mainly sensitive to vessels of a similar size to the water diffusion length (~10 μm), whereas gradient echo measurements are equally sensitive to all vessel sizes. Figure 1 illustrates the change in transverse relaxation rate for gradient echo (ΔR_2^*) and spin echo (ΔR_2) caused by different concentrations of gadolinium and deoxyhemoglobin. Second, an approximately linear relationship exists between tissue contrast agent concentration and change in the T_2 relaxation rate

$$\Delta R_2(t) \propto C_t(t) \tag{1}$$

where for gradient and spin echo sequences, signal intensity $S(t)$ depends in an exponential fashion upon ΔR_2 and the longitudinal relaxation rate change ΔR_1

$$S(t) = S(t_0)(1 - \exp^{TR\cdot\Delta R_1(t)})\exp^{TE\cdot\Delta R_2(t)} \tag{2}$$

where $S(t_0)$ is the baseline signal intensity and TR is the repetition time. If R_1 remains constant, this provides the desired relation between concentration and signal intensity

$$C_t(t) = -k\log\left(\frac{S(t)}{S(t_0)}\right)/TE \tag{3}$$

The constant k depends on the magnetic properties of the contrast agent, as well as its distribution space (plasma fraction).

The assumption of linearity in Equation 1 has since been further confirmed by indirect measurements *in vivo*;[8] preliminary studies suggest that, in the brain, the microvascular CBV 'visible' by spin echo planar imaging is approximately 45% of the 'total' CBV as observed by PET.[9]

It is particularly important to bear in mind that tissue and major vessel hematocrit differ in the brain because of rheologic effects.[10,11] This must be taken into account when simultaneously applying noninvasively determined tissue and arterial

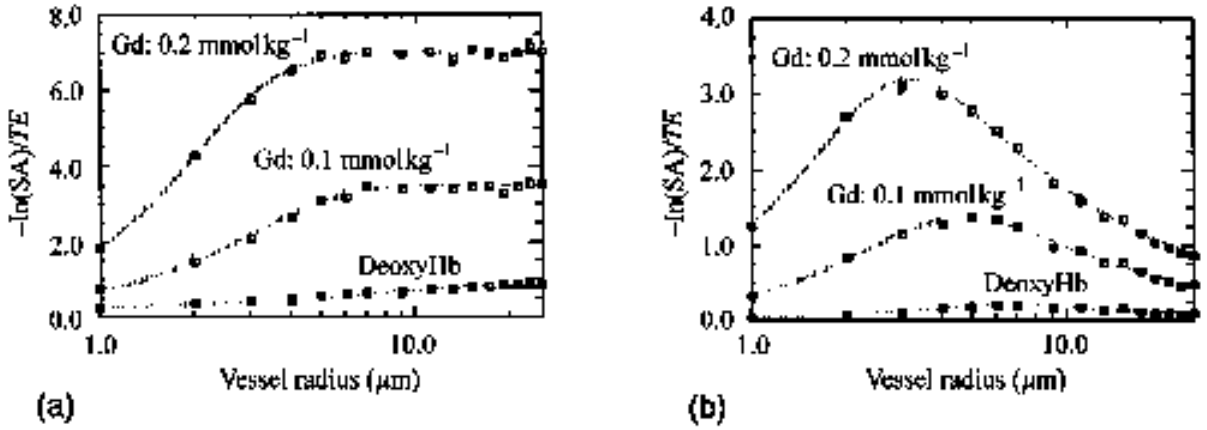

Figure 1 Changes in the transverse relaxation rates (as derived from Equations 1 and 3) for (a) gradient echo [ΔR_2^*; echo time (*TE*) 60 ms] and (b) spin echo (ΔR_2; *TE* 100 ms) sequences as a function of vessel size. Curves are shown for typical gadolinium (Gd) doses used in cerebral perfusion imaging (0.1–0.2 mmol kg^{-1}) and typical cerebral vascular volume fraction. Also shown are corresponding curves for the weakly paramagnetic deoxyhemoglobin (Deoxy Hb) used in functional MRI. Whereas spin echo measurements peak for small vessel sizes, gradient echo values reach a plateau and remain equally sensitive to all vessel sizes. In addition, ΔR_2^* values exceed ΔR_2 values for all vessel sizes. (With permission from Boxerman *et al.* 1995[5])

concentration levels (Sections 2.2. and 2.3). In general, microvascular hematocrit is a complicated function of vessel size, flow, and pathophysiologic conditions and ranges from 40 to 100% of the systemic blood hematocrit.[12]

2.2 Cerebral Blood Volume Measurements

Figure 2 shows a typical dynamic susceptibility contrast imaging experiment. Upon injection of contrast agent into an

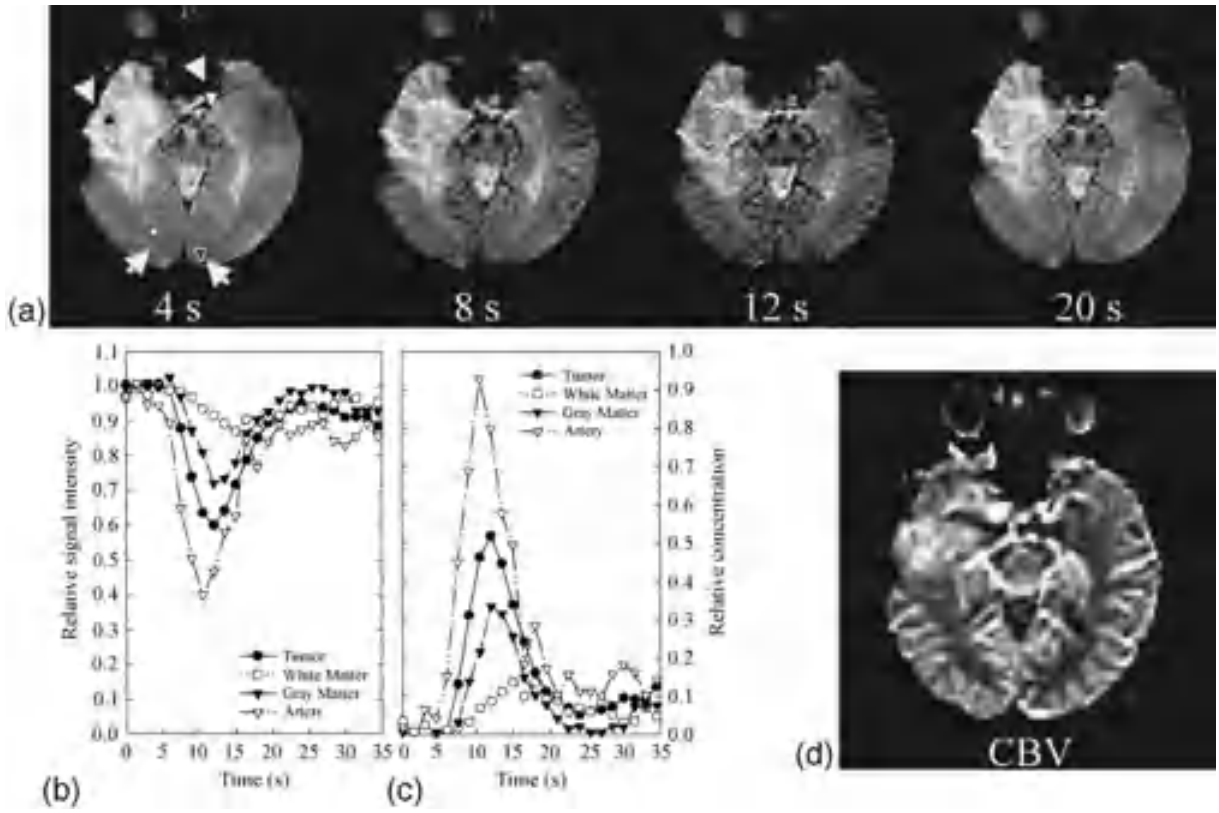

Figure 2 Typical bolus tracking experiment. (a) MRI images at different time points (indicated in seconds) during a Gd-chelate bolus passage. Arrows highlight symbols, which are defined in the graphs. (b) Following intravenous injection, contrast agent appears early in the arteries, causing appreciable signal loss. Tissue signal loss varies according to regional blood volume. This study was obtained from a patient with a brain tumor and shows high blood volume (CBV) in the temporal lobe (see Section 3.3). (c) The corresponding concentration–time curves are derived from Equations 1 and 3. (d) These tissue curves are integrated using Equation 4 to generate maps of CBV.

antecubital vein, the contrast agent reaches the brain, causing a substantial signal loss. The transit of the bolus is very rapid; consequently, rapid imaging (typically 1 image every 1.5 s) is required in order to capture the first pass of the bolus using fast low angle shot (FLASH) or multislice echo planar image sequences.

By detecting the arterial as well as the total tissue concentration as a function of time during a single transit, the CBV can be determined from the ratio of the areas under the tissue concentration–time and arterial concentration–time curves, respectively:[13–16]

$$\mathrm{CBV} = \frac{\int_{-\infty}^{\infty} C_\mathrm{t}(\tau)\,\mathrm{d}\tau}{\int_{-\infty}^{\infty} C_\mathrm{a}(\tau)\,\mathrm{d}\tau} \tag{4}$$

where $C_\mathrm{a}(\tau)$ and $C_\mathrm{t}(\tau)$ are the arterial and tissue contrast agent concentrations respectively.

It is inherently difficult to obtain arterial concentrations by dynamic susceptibility contrast MRI (see Section 2.5); consequently, uniform arterial concentration profiles in all arterial blood reaching the tissue is often assumed. The denominator of Equation 4 is thereby constant across regions, and relative CBV can be determined by simply integrating the area under the concentration–time curve,[2–4] often by the use of a gamma variate function to correct for tracer recirculation.[17]

2.3 The Transport Function and Mean Transit Time

Figure 3 shows a schematic vascular residue. An infinitely sharp input is injected into the bloodstream of a tissue element at time t=0. The tracer follows the bloodstream through arterioles, capillaries, and venules, finally leaving the tissue vasculature through the vein. The associated probability density function of transit times is denoted by $h(t)$, the transport function. For an arterial input $C_\mathrm{a}(t)$ with a finite duration, the venous output tracer concentration, $C_\mathrm{v}(t)$, is described by the convolution of the local transport function by the arterial input function:

$$C_\mathrm{v}(t) = C_\mathrm{a}(t) \otimes h(t) \equiv F_\mathrm{t} \int_0^t C_\mathrm{a}(\tau) h(t-\tau)\,\mathrm{d}\tau \tag{5}$$

where $\otimes$ denotes convolution and F_t is tissue flow. The mean transit time (MTT) for the tracer particles is defined as the first moment of the transport function:

$$\mathrm{MTT} \equiv \frac{\int_{-\infty}^{\infty} \tau h(\tau)\,\mathrm{d}\tau}{\int_{-\infty}^{\infty} h(\tau)\,\mathrm{d}\tau} \tag{6}$$

As pointed out by Weisskoff *et al*. the distinction between MTT and the first moment of the tissue concentration–time curve is crucial in attempts to measure transit times using intravascular tracers.[18] The calculation of MTT, therefore, requires knowledge of the transport function or CBF, as, by the central volume theorem.[14]

$$\mathrm{MTT} = \frac{\mathrm{CBV}}{F_\mathrm{t}} \tag{7}$$

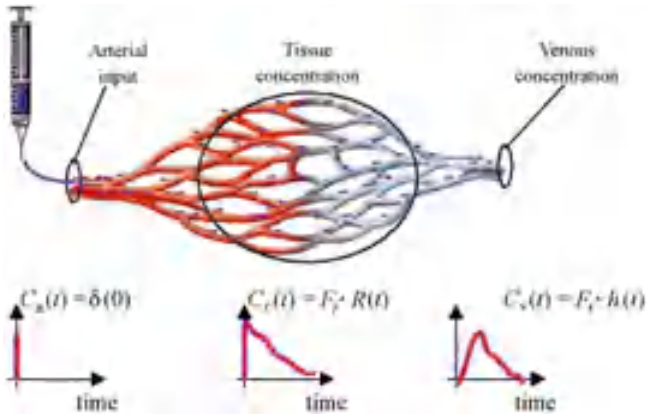

Figure 3 Idealized, infinitely sharp bolus injection into the bloodstream of a schematic tissue volume. The tissue concentration as a function of time ($C_t(t)$) is in this case given by the flow (F_t) multiplied by the residue function $R(t)$. Notice $R(0)$=1 and $R(\infty)$=0. The tracer concentration in the vein is determined by the transport function, $h(t)$, which is given by the time derivative of $R(t)$: $h(t)$=$-R'(t)$. In actual experiments, the bolus reaching the brain will have a finite duration. The tissue concentration–time curve then becomes a convolved signal of the impulse response above (i.e. $F_tR(t)$) with the arterial input shape (Equation 9).

2.4 The Residue Function: Cerebral Blood Flow

For tomographic measurements of tissue tracer concentrations, the local retention is described by the residue function $R(t)$, the fraction of injected tracer still present in the vasculature at time t; this is defined in terms of the transport function as

$$R(t) \equiv \left[1 - \int_0^t h(\tau)\,\mathrm{d}\tau\right] \tag{8}$$

Note that by the definition of $h(t)$ as a probability density function, $R(0)$=1 and $R(\infty)$=0, just as $R(t)$ is a positive, decreasing function of time.

As shown in Figure 3, the concentration $C_\mathrm{VOI}(t)$ of tracer within a given volume of interest can now be written

$$C_\mathrm{VOI}(t) = F_\mathrm{t} \int_0^t C_\mathrm{a}(\tau) R(t-\tau)\,\mathrm{d}\tau \tag{9}$$

The equation states that the tissue concentration–time curve is given by an impulse response function, $F_tR(t)$, convolved with the arterial input function, $C_a(t)$. In other words (as $R(0)$=1): the initial height of the deconvolved concentration–time curve equals the flow, F_t.

There are two main approaches to solve Equation 9 to determine regional flow. The model-dependent techniques use specific analytical expressions chosen to describe the shape of the residue function. In model-independent approaches, straight deconvolution is performed in every image pixel, solving Equation 9 for the impulse response function.

2.4.1 Model-independent Approach

In the model-independent approach, Equation 9 is solved for the impulse response function by standard mathematical deconvolution techniques, typically a transform approach or a linear algebraic approach.

In the Fourier transform approach,[19,20] Equation 9 is rewritten

$$\mathrm{F}\{F_\mathrm{t}\cdot R(t)\otimes C_\mathrm{a}(t)\}=\mathrm{F}\{C_\mathrm{t}(t)\}\Rightarrow F_\mathrm{t}\cdot R(t)=\mathrm{F}^{-1}\left\{\frac{\mathrm{F}\{C_\mathrm{t}(t)\}}{\mathrm{F}\{C_\mathrm{a}(t)\}}\right\} \tag{10}$$

where F and F^{-1} denote the discrete and inverse discrete Fourier transform, respectively.

In the linear algebraic approach, Equation 9 is rewritten into a matrix equation.[21] Assuming that tissue and arterial concentrations are measured at equidistant time points t_1, $t_2=t_1+\Delta t$, …, t_N, the tissue concentration $C(t_j)$ at time t_j in Equation 9 is reformulated as a matrix equation by noting

$$C_\mathrm{t}(t_j)=F_\mathrm{t}\int_0^{t_j}C_\mathrm{a}(\tau)R(t_j-\tau)\,\mathrm{d}\tau\approx F_\mathrm{t}\Delta t\sum_{i=0}^{j}C_\mathrm{a}(t_i)R(t_j-t_i)$$

This is equivalent to

$$\begin{pmatrix}C_\mathrm{t}(t_1)\\C_\mathrm{t}(t_2)\\\cdots\\C_\mathrm{t}(t_\mathrm{N})\end{pmatrix}=F_\mathrm{t}\cdot\Delta t\begin{pmatrix}C_\mathrm{a}(t_1)&0&\cdots&0\\C_\mathrm{a}(t_2)&C_\mathrm{a}(t_1)&\cdots&0\\\cdots&\cdots&\cdots&\cdots\\C_\mathrm{a}(t_\mathrm{N})&C_\mathrm{a}(t_{\mathrm{N}-1})&\cdots&C_\mathrm{a}(t_1)\end{pmatrix}\bullet\begin{pmatrix}R(t_1)\\R(t_2)\\\cdots\\R(t_\mathrm{N})\end{pmatrix} \tag{11}$$

which can then, theoretically, be inverted to yield $F_\mathrm{t}\cdot R(t)$

Stable solutions to Equations 10 and 11 can only be obtained by applying techniques to suppress experimental noise. For the Fourier transform, this is achieved by applying a filter to the higher frequencies in the frequency (transformed) domain, assuming this can be done without losing physiologic information. For matrix equations such as Equation 11, noise is often suppressed by regularization (forcing the solution to satisfy a priori, user-defined conditions, or otherwise be well behaved)[22] or by singular value decomposition.[23,24] The optimal choice of some transform and linear algebraic approaches was studied by Østergaard *et al*. using Monte Carlo simulations.[24] It was found that the Fourier transform has an inherent problem in reproducing the discontinuity of the residue function at t=0, bearing in mind that

$$\lim_{t\to 0^+}R(t)=1$$

whereas

$$\lim_{t\to 0^-}R(t)=0$$

This discontinuity is represented at high frequencies in the transformed data and is, therefore, easily lost in subsequent filtering. As reliable determination of the initial height of the response function is essential in determining flow, this property, in theory, introduces a tendency for F_t to be overestimated, and biased by the underlying vascular structure. Despite this drawback, the Fourier transform approach has the attraction of, theoretically, being insensitive to any delays between the arterial input function and the tissue arrival, as may occur in cerebrovascular disease. Preliminary results indicate that, in normal volunteers, the Fourier transform dependence upon vascular structure does not lead to appreciable differences in rCBF estimates from those obtained by the singular value decomposition approach.[25]

In the linear algebraic approaches, regularization showed an inherent dependency on signal-to-noise ratio (and, therefore, on rCBV). Deconvolution by singular value decomposition showed, however, a remarkable independence of vascular structure and CBV, yielding reasonably accurate CBF estimates even at the signal-to-noise ratio of pixel-by-pixel clinical echo planar imaging measurements. The major disadvantage of the linear algebraic approaches is a tendency to underestimate flow when tissue tracer arrival is delayed relative to the arterial input function, a problem not associated with the transform approaches.

The deconvolution techniques make no assumptions regarding the vascular structure. Instead, regional vascular transit-time characteristics can be determined along with tissue flow by studying the residue function. Given the potential metabolic information of the residue function (see Section 2.6. on flow heterogeneity), this approach may be desirable in some cases.

Even though a straight delay of tracer arrival can, in theory, be accounted for, model-less approaches cannot distinguish tracer dispersion in feeding vessels from tracer retention in the capillary bed: large vessel dispersion will be interpreted as a low flow, although actual tissue flow is normal.[26] This is a more fundamental limitation that cannot be circumvented unless a specific model of major vessel dispersion is assumed. This will be described further below.

2.4.2 Model-dependent Approach

Models of tracer transport and retention must be chosen very carefully in order not to lose generality and thereby bias the resulting flow values.[27] Larson *et al*. suggested an exponential residue model, assuming the microvasculature to behave like a single, well-mixed compartment.[28] Although residue functions determined by model-less approaches (Section 2.4.1) often appear exponential, this model tends to bias resulting flow values in cases where the underlying residue function is nonexponential.[26] Østergaard *et al*. modified and applied a model of macrovascular transport and microvascular retention in the brain.[29] The model, originally introduced to describe tracer transport and retention in the heart,[30–32] utilizes vascular transport operators, allowing detailed modeling of the delay and dispersion of the arterial input owing to the passage through the artery downstream of the measurement site.

Vonken *et al*. recently suggested a promising, more general family of analytical functions to fit residue functions, with the further advantage of allowing for delayed tracer arrival relative to the measured arterial input.[33,34]

Whereas the model-less approach offers simultaneous determination of flow and vascular residue function, the vascular model approach requires a model of major vessel transport as

well as of microvascular retention. Major vessel dispersion and microvascular retention can then to some extent be distinguished, stabilizing CBF estimates. However, abnormal capillary perfusion patterns (and consequent deviation from the normal flow heterogeneity) are likely to affect flow estimates by this approach.[18,27]

2.5 Quantification Issues

The formalism above produces absolute values for CBF and CBV provided arterial and tissue concentrations are experimentally determined in identical units. This, however, represents a number of practical problems in actual clinical applications. First, in order to obtain arterial and tissue concentrations in similar units, the hematocrit difference between the micro- and macrovasculature (and thereby the difference in plasma volume) must be taken into account (see Section 2.1.1).[20] Second, absolute arterial tracer concentration measurements are difficult to obtain from image data because of the inherently limited resolution of MRI relative to vessel sizes. Several studies have applied FLASH-type imaging sequences, allowing measurements of arterial levels in a separate, low slice with a short *TE*; this avoids complete loss of vascular signal during the bolus passage.[18,20,35] These studies yielded somewhat high values for absolute CBF, possibly as a result of the choice of the deconvolution approach, or because of partial volume and averaging effects. A recent study by Schreiber *et al*. obtained absolute values in good agreement with accepted flow rates.[36] In multi-slice echo planar imaging experiments, a single echo is generally used, optimizing tissue signal loss but often causing complete signal loss at major vessels. Therefore, smaller arterial branches with partial volume effects with surrounding tissue are used. The shape rather than the absolute amplitude of the arterial input function is obtained in these experiments. For comparison of results in different subjects, an internal reference must be chosen that is believed to have little intersubject variability, for example white matter or cerebellum. In an attempt to obtain absolute flow values from echo planar imaging, Østergaard *et al*. assumed proportionality between the area of the arterial input function and the injected contrast dose, using water clearance PET as a calibration method. This approach provided reproducible absolute CBF measurements in animal hypercapnia studies[9] and in humans.[37] It may, however, be too crude a method for general use in patients with severe cardiac or cerebrovascular disease.

2.6 Flow Heterogeneity: Metabolic Significance of the Residue Function

As diffusible solutes such as oxygen pass through the capillary bed, they are extracted by the tissue. The extraction fraction E (fraction of substance extracted during a single pass) of a solute is given by:[38,39]

$$E = (1 - \mathrm{e}^{-(PS/F_\mathrm{t})}) \tag{12}$$

where P is the permeability and S the surface area of the capillary endothelium. When the mean flow is very small compared with PS, extraction is near unity; when flow approaches or exceeds PS, extraction becomes incomplete.

Assuming that the capillary bed can be subdivided into a number of parallel microvessels with identical PS, and with individual relative flow rates f (flow divided by the mean flow F_t), Equation 12 generalizes to Equation 13 where $w(f)$ is the *flow heterogeneity*, the probability density function of relative flows. In this situation, the extraction fraction becomes:

$$E = \int_0^\infty w(f)(1 - \mathrm{e}^{-(PS/fF_\mathrm{t})})\,\mathrm{d}f \tag{13}$$

Assuming the PS product for a given molecule and tissue is essentially constant, the flow and associated flow heterogeneity become the prime determinants of solute extraction when PS is large (i.e. extraction is determined by flow rather than permeability). In particular, if flow is fixed (e.g. in acute stroke), extraction can only be modified by altering flow heterogeneity.

The residue function and the flow heterogeneity are related through the distribution of transit times (see Section 2.3). The transport function is the slope of the residue function

$$h(t) = -\frac{\mathrm{d}R}{\mathrm{d}t} \tag{14}$$

and the distribution of flows is by the central volume theorem[14] given by

$$w(f) = -\frac{T}{f} \cdot h(T) \tag{15}$$

where T is the associated transit time for a relative flow of f. Combining Equations 14 and 15 will give flow heterogeneity in terms of the residue function. Flow and flow heterogeneity, in turn, can be used to determine the extraction fraction by Equation 13.

2.7 Bolus Tracking when the Blood–Brain Barrier is Leaky

For high-grade CNS tumors and in diseases such as multiple sclerosis, the blood–brain barrier breaks down, and vessels become permeable to standard gadolinium chelates. The compartmentalization necessary to perform dynamic susceptibility contrast studies partly breaks down and the T_1-shortening properties of the contrast agents become prominent (Figure 4). This problem has been circumvented in three ways. First, dysprosium-based contrast agents, which have little T_1 enhancement, can be used rather than gadolinium-based contrast agents. As this inevitably affects subsequent conventional diagnostic imaging based on traditional T_1 enhancement, this approach is now uncommon. Second, a pre-dose of gadolinium-based contrast agent can be applied, saturating the interstitial space and thereby minimizing first-pass clearance during the subsequent bolus passage.[40] In the following, a third approach, namely modeling the simultaneous T_1 and T_2 enhancement, is described.

2.7.1 Tracer Extraction: Flow versus Permeability

The total tissue concentration as a function of time as contrast agent passes from the bloodstream into the surrounding extravascular space can be broken down into an intravascular, $C_\mathrm{iv}(t)$, and an extravascular, $C_\mathrm{ev}(t)$, component as follows:

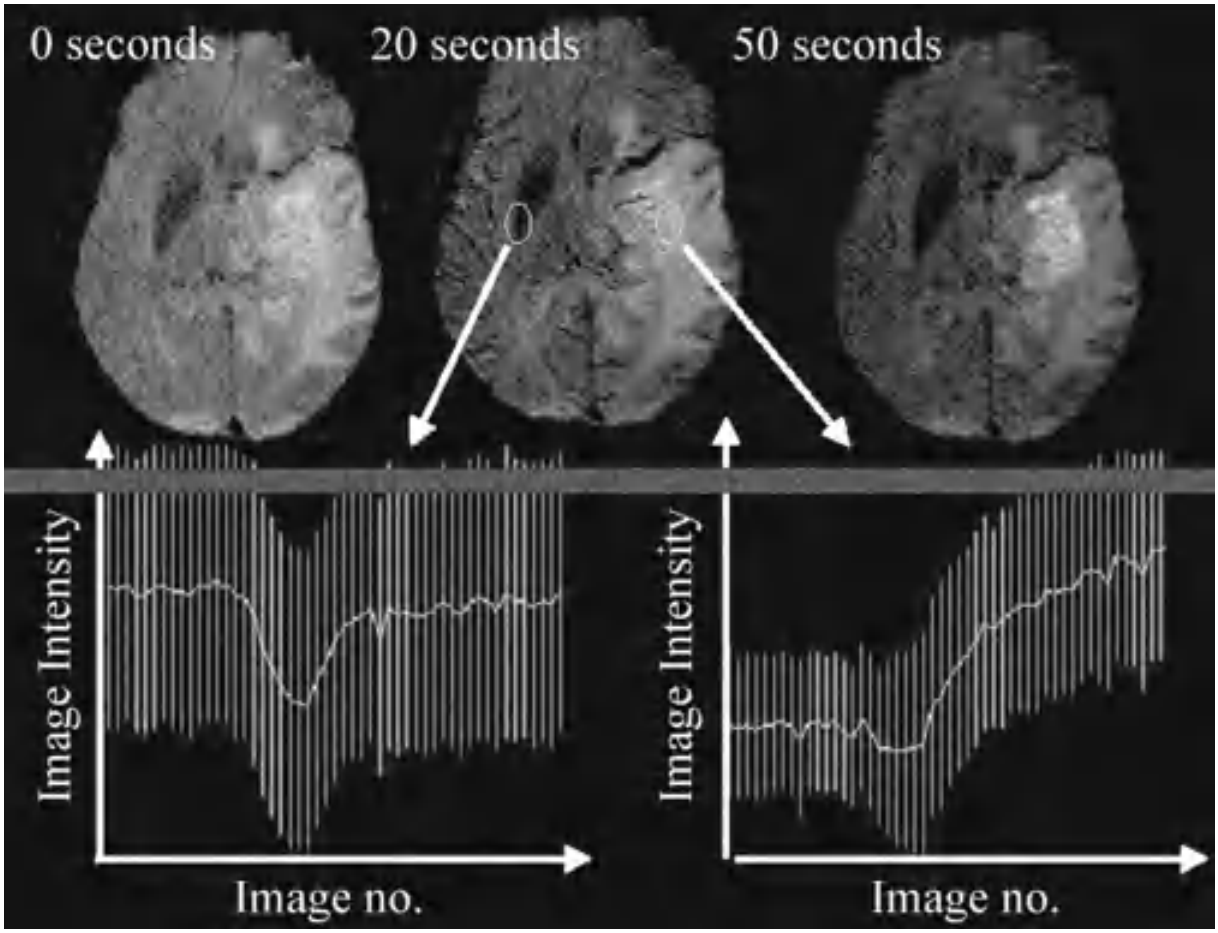

Figure 4 Dynamic susceptibility contrast imaging in a patient with an astrocytoma grade III with leakage of gadolinium contrast across the blood–brain barrier. In normal tissue, signal loss is observed during the bolus passage (graph, lower left). Notice the T_1 enhancement in the tumor owing to contrast leakage (upper right), dominating over the normal signal loss caused by the T_2 shortening from compartmentalization of the gadolinium (lower right). If not corrected for, this would cause an underestimation of cerebral blood volume. (Courtesy Dr. J. D. Rabinov)

$$C_{\mathrm{t}}(t) = C_{\mathrm{ev}}(t) + C_{\mathrm{iv}}(t) = K_1 \cdot \int_0^t C_{\mathrm{a}}(\tau) \cdot \mathrm{e}^{-k_2(t-\tau)}\, \mathrm{d}\tau$$

$$+ F_{\mathrm{t}} \int_0^t C_{\mathrm{a}}(\tau) \cdot R(t-\tau)\, \mathrm{d}\tau \qquad (16)$$

where K_1 is the unidirectional clearance rate of tracer from blood to tissue and k_2 is the clearance rate from tissue to blood. The latter is given by K_1/V_{d}, where V_{d} is the distribution space for the tracer; for most contrast agents this is extravascular, extracellular space. The last term in Equation 16 is that given in Equation 9 to describe the concentration of intravascular tracer within a volume of interest. The first and second terms in Equation 16 are very similar; in transport into the extravascular space, the residue function is assumed to be that of a well-mixed compartment, namely an exponential. The terms K_1 and V_{d} in Equation 16 (the latter as part of k_2) are equivalent to F_{t} and CBV, respectively, in Equations 7 and 9.

Neglecting for a while the intravascular term in Equation 16, the physiologic interpretation of the unidirectional clearance K_1 depends somewhat on its magnitude. Bearing in mind that the extraction fraction is the unidirectional clearance divided by the tissue flow, Equation 12 can be rewritten

$$K_1 = F_{\mathrm{t}}(1 - \mathrm{e}^{-(PS/F_{\mathrm{t}})}) \qquad (17)$$

When the term *PS* is much smaller than the mean flow, transport into the tissue is limited by the vascular permeability and surface area, and, from Equation 17, K_1 is approximately equal to *PS*, i.e. it is a measure of capillary surface area and capillary permeability. When *PS* is much greater than mean flow, clearance is independent of permeability and only flow through the tissues limits the appearance of tracer in the tissue. In this flow-limited case, K_1 approximates to mean flow. Interpretation of measured clearance rates, therefore, requires careful inspection as to whether these are comparable to likely flow rates. If, on the one hand, clearance values represent *PS*, they may serve to characterize vascular density and integrity. However, on the other hand, if they represent flow, the correlation with vascular characteristics is less clear, and they may be an indirect measurement of the supply of nutrients to the tissue.

2.7.2 *Correction for Permeability*

As gadolinium-chelate leaks into the tissue (first term in Equation 16), the T_1 shortening effects of the contrast agent

become dominant, ultimately overwhelming the signal loss resulting from the T_2 decrease associated with compartmentalization of the agent. This causes a net increase in signal intensity (Figure 4). Unless the effects of contrast leakage on T_1 are corrected for, the signal loss will result in underestimation of CBV.

Weisskoff *et al.* introduced an approximation to Equation 16 allowing simultaneous mapping of CBV and the permeability of the blood–brain barrier to gadolinium-chelates.[41] The intravascular concentration term in Equation 17 was assumed to be proportional to the vascular signal in a nonleaky reference volume, $C_c(t)$. Assuming this vascular concentration constitutes the input function to the extravascular compartment in Equation 16, and further assuming that backdiffusion is negligible (k_2=0) during the short time of a bolus transit, the combined change in transverse relaxation rate, $\Delta R_{2,\text{total}}$ (as derived from Equations 1 and 3) can be shown to simplify to

$$\Delta R_{2,\text{total}}(t) = A \int_0^t C_c(\tau)\,d\tau + B{\cdot}C_c(t) \qquad (18)$$

where A is proportional to K_1 and B to CBV, thus allowing simultaneous determination of permeability and CBV even in the presence of contrast leakage. Østergaard *et al.* presented an extension of this model, maintaining the second term in Equation 16 and allowing simultaneous measurement of permeability, CBF, and CBV.[42]

2.8 Other Hemodynamic Indices

The derivation of flow and transit time from bolus tracking requires derivation of arterial input tracer levels. In some cases, this may not be practical, just as the inherent complexity of deconvolution approaches may preclude the use of these techniques in some situations. Parameters that can be derived directly from the tissue concentration–time curves include time-to-peak (time from injection to maximum concentration is reached), arrival time (arrival time of tracer in the pixel), full width at half maximum of the tissue bolus shape, and first moment of the peak. Although the dependence of these parameters upon MTT and CBF is strongly affected by the vascular structure and the arterial input function,[18] they often suffice to delineate pathologic changes and provide important qualitative information in many diseases. It appears, however, that the derivation of CBF, CBV, and MTT from kinetic principles somewhat improves specificity and sensitivity of clinical studies, facilitating inter- and intrasubject comparison.[43]

3 APPLICATIONS

Much of the success of cerebral perfusion imaging lies in the fact that it allows the association of high-quality structural conventional MRI with physiologic parameters of importance in diagnosing and assessing outcome in major diseases. In the following discussion, major areas of impact for perfusion imaging are outlined, along with the rationale of its use.

3.1 Acute Stroke

3.1.1 Background

Acute stroke is the third leading cause of death in the Western World and the major cause of adult disability. As the incidence of the disease increases exponentially with age, the increase in mean age will cause the incidence to approximately double within the first half of the 21st century. In light of these severe personal and socioeconomic consequences, therapeutic strategies are emerging, that seek to limit tissue damage in the acute phase of the disease. For all types of pharmacologic intervention, treatment must be given promptly, as neuronal death from ischemia progresses rapidly after symptom onset. Currently, recombinant tissue-type plasminogen activator is approved by the US Food and Drug Administration for administration within 3 h of symptom onset (later administration of the drug is associated with risk owing to intracranial hemorrhage). Studies by PET and diffusion-weighted imaging (DWI, see below), however, indicate that neuronal death continues beyond 3 h, probably as long as 24 h in some patients. There is, therefore, an urgent need for imaging techniques to guide treatment, especially in terms of pointing to the presence of tissue at risk of infarction and selecting patients who would benefit from aggressive treatment. This poses a special challenge to diagnostic methods, as conventional CT and MRI are insensitive to the extent of neuronal death or extent of metabolic derangement within the first critical hours after symptom onset.

3.1.2 The Role of Diffusion Weighted Imaging

DWI (see ***Methods and Applications of Diffusion MRI***) has become widely accepted as the method of choice for demonstrating severe ischemia in acute experimental situations as well as in human stroke. It is believed that as the sodium–potassium pump breaks down as a result of the severe energy depletion, there is a subsequent loss of water homeostasis and cells swell. As total water diffusivity is dominated by water in the extracellular space, this reduction in extracellular space results in a marked reduction in the apparent diffusion coefficient of water, which corresponds to signal increase in DWI. Although there is evidence from animal studies that the apparent diffusion coefficient decreases gradually with the severity and duration of ischemia, and may indeed be reversible if tissue is reperfused early on, there are only sporadic reports of spontaneous reversal of DWI abnormalities in humans.

After onset of ischemia, irreversible tissue damage occurs rapidly, and abnormalities have been observed by DWI within minutes in animals[44] as well as in humans.[45] DWI abnormalities seen in patients imaged early after symptom onset often spread substantially within the following 24 h,[46–49] demonstrating further neuronal loss. It is hoped that perfusion weighted imaging (PWI) will enable prediction of this subsequent spread of tissue damage and, thus, improve patient management.

3.1.3 Perfusion Weighted Imaging: Rationale and Findings

The role of PWI in cerebral ischemia lies mainly in identifying areas where blood flow and oxygen supply are compromised to such an extent that subsequent tissue damage is imminent.

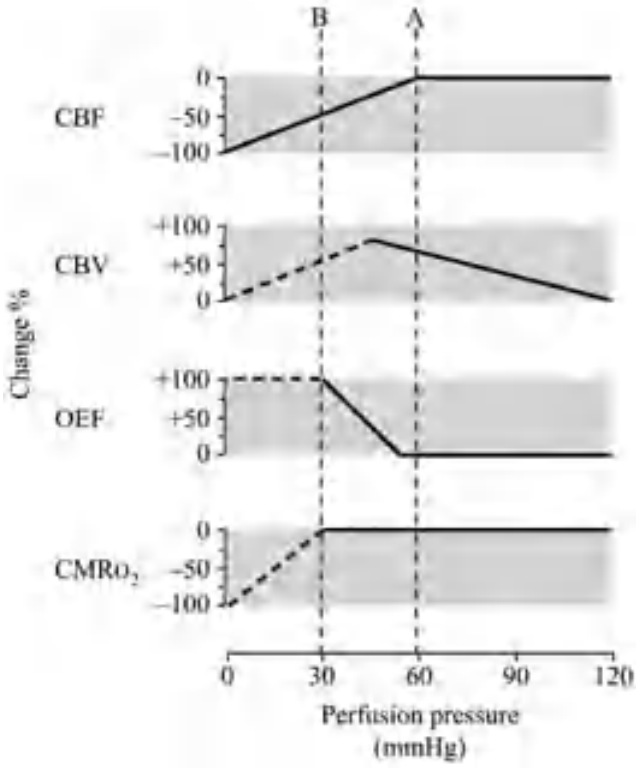

Figure 5 Changes in cerebral blood flow (CBF), blood volume (CBV), metabolic rate for oxygen ($CMRO_2$), and oxygen extraction fraction (OEF) as a function of perfusion pressure. A, perfusion pressure at which CBF can no longer be maintained. B, the perfusion pressure at which tissue oxygen demands can no longer be met by the blood supply. (With permission from Powers, 1991[51]).

Figure 5 shows a schematic outline of the hemodynamic and metabolic events that can lead to irreversible tissue death owing to a sudden decrease of perfusion pressure in acute stroke.[50] Through cerebral autoregulation, CBF remains constant at perfusion pressures above approximately 60 mmHg, through a compensatory increase in CBV. Below this perfusion pressure, CBF can no longer be maintained, and with a further decrease in CBF, CBV ultimately decreases. As cortical CBF falls below roughly half of normal values, oxygen supply is no longer sufficient to drive metabolic needs, and the patient experiences neurological deficits. Brain tissue can only withstand this energy depletion for a limited time. With prolonged ischemia or further decrease in CBF (down to roughly 25% of normal flow rates), irreversible damage is imminent. MTT is the CBV:CBF ratio (Figure 5) and is roughly inversely proportional to the perfusion pressure.[51–54] As MTT thereby increases steeply as perfusion pressure drops, it has been proposed as a sensitive marker (together with CBF and CBV) of the severity of the hemodynamic impairment in patients who have suffered an acute stroke or have carotid stenosis (Section 3.2).

As discussed in Section 3.1.2, abnormalities by DWI increase within the first 24 h after infarction. Studies have further established that abnormal perfusion patterns can be observed by PWI in patients with acute stroke; the volume of tissue showing PWI abnormalities often exceeds that of abnormal DWI, which is referred to as a *perfusion–diffusion mismatch*. More importantly, infarct growth (i.e. growth of DWI lesion) almost exclusively occurs into areas of PWI–DWI mismatch.

Sorensen *et al*. investigated a group of 23 patients using PWI and DWI within 12 h of symptom onset of stroke.[55] In two thirds, the infarct subsequently grew significantly and lesion volumes by DWI at follow up exceeded the initial values by more than 15%. One third of patients displayed a decrease CBV exceeding the DWI abnormality, and half the patients showed decreased CBF beyond the DWI-determined lesion. In both cases, more than 90% of patients displaying such PWI–DWI mismatches experienced lesion growth, demonstrated on subsequent follow-up scans (Figure 6). The study confirmed the presence of increased CBV around DWI-determined lesions in some patients, as implied by Figure 5. Furthermore, one patient was found to have a DWI abnormality exceeding in size the PWI abnormality, suggesting the combined modalities may be used in detecting spontaneous reperfusion prior to institution of treatment.

Although DWI–PWI mismatch represents a predictor of infarct growth, the volume of MTT or CBF overestimated final infarct size by almost a factor of two; by comparison CBV and DWI seemed to underestimate final infarct size somewhat.[55] In the effort to be able to predict final infarct sizes, this has led to attempts not only to detect the presence of PWI abnormalities but also to build predictive models, thereby identifying levels of CBV, CBF, and MTT associated with extreme risk of subsequent infarction.[56] It is likely that effective prediction will require a combination of these parameters, rather than a single parameter (c.f. Figure 5), together with data such as duration of symptoms, blood pressure, and temperature.

The observation that a PWI–DWI volume mismatch suggests risk of subsequent infarction has been suggested as a tool in patient management. Sunshine *et al*. demonstrated that acute measurement by DWI and PWI is feasible in patients immediately after stroke.[57] Based on DWI, time-to-peak PWI, and duration of symptoms, patients in this study were stratified into groups with no infarct, lacunar infarcts, and cortical infarcts; on the basis of this grouping, patients were selected for conservative treatment, intravenous thrombolysis, or angiography with intra-arterial thrombolysis, respectively. This triage procedure enabled the risk of thrombolysis or invasive diagnostic procedures to be avoided in some patients while maintaining a more aggressive approach in others.

3.1.4 Flow Heterogeneity in Acute Stroke

In Figure 5, the cerebral metabolic rate of oxygen and the oxygen extraction fraction are shown. With limited blood flow, the relative lack of oxygen is compensated by extracting a higher fraction of the blood oxygen pool.[58] Classically, oxygen extraction is measured by PET as the ratio between regional oxygen clearance and CBF. Using invasive techniques in animal models, it can be shown that a graded decrease in perfusion pressure causes progressive loss of rapidly flowing red blood cells in the brain, thus decreasing total flow heterogeneity and causing increased oxygen extraction (see Section 2.6).[59] The importance of heterogeneity in cerebral physiology is also reviewed by Kuschinsky *et al*.[60]

Østergaard *et al*. examined flow heterogeneity in normal volunteers and in patients within 12 h of symptom onset in strokes.[29,61] In normal brain tissue, the distribution of relative

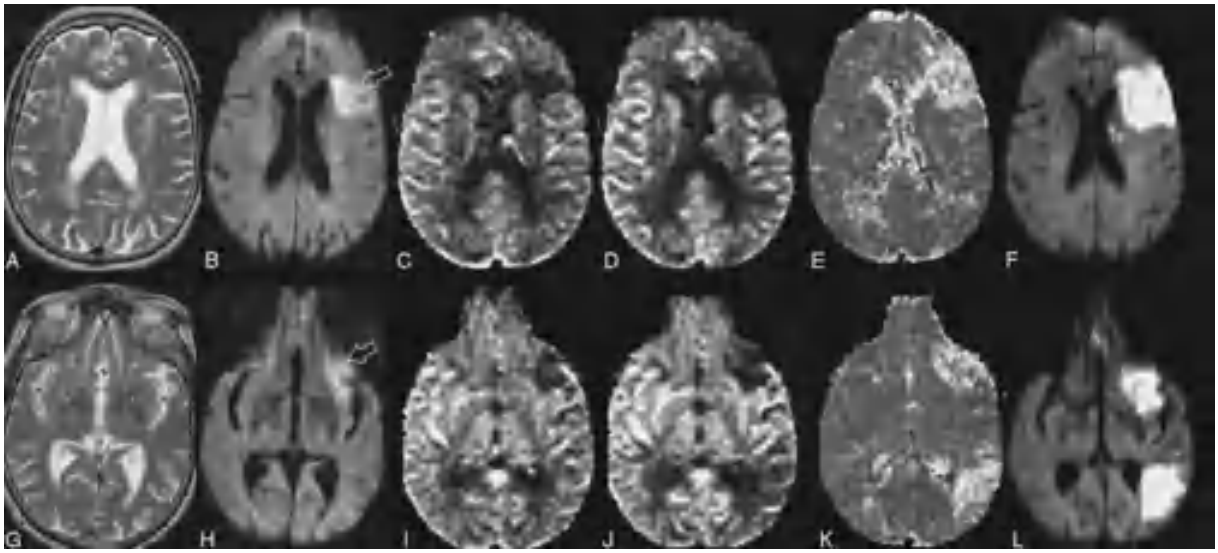

Figure 6 MR images at two levels from a 78-year-old female, 3 h after acute onset of aphasia during a cardiac catheterization routine. A, G, Structural MR images. Diffusion weighted images (B, H) show irreversible cell death in a small anterior region (arrows). Perfusion weighted imaging showed low cerebral blood volume (CBV) (C, I) and blood flow (CBF) in both anterior and posterior watershed areas. Note the mismatch between areas of low CBV and CBF, respectively, easily visible as a prolongation of plasma mean transit times (E, K). Note the correspondence with the final infarct size on subacute diffusion weighted images (F, L) (With permission from Sorensen *et al*., 1999[55]).

flows was found to be markedly skewed towards high flow rates, in agreement with observations using invasive techniques. Within regions of increased MTT, subregions showed loss of the high-flow component of the flow distribution, causing increased homogeneity of flow velocities,[61] in agreement with animal studies.[59] In parametric maps quantifying statistically significant acute deviation of flow heterogeneity from that of normal tissue, areas of extreme homogenization of capillary flows predicted final infarct size on follow-up scans in 10 out of 11 patients (Figure 7). Although this finding is surprising and needs further validation, it suggests that heterogeneity measurements by high signal-to-noise ratio PWI may be a value in assessing acute stroke.

3.2 Carotid Stenosis

High-grade stenosis of the internal carotid arteries is associated with high risk of ischemic events, accounting for a significant fraction of acute strokes. Despite the high risk of stroke in patients with carotid stenosis, surgical treatment by carotid endarterectomy has often yielded only marginal reductions in the subsequent incidence of ischemic events, indicating a need for methods to identify subgroups of high-risk patients.

The pathophysiologic events ultimately leading to neurologic symptoms and tissue damage are similar to those described for stroke (see Section 3.1.3). PET studies have demonstrated that severe stenosis causes a marked compensatory increase in CBV.[62] The degree of decrease in the CBF:CBV ratio (1/MTT) has been used as an indicator of regional perfusion pressure: low values (down to 50% of normal ratios) corresponding to hazardous hemodynamic impairment.[62,63] However, some results suggest that oxygen extraction fraction assessed by PET may correlate more closely with the degree of hemodynamic impairment than does the CBF:CBV ratio.[64]

The hemodynamic severity of carotid stenosis may also be assessed by monitoring the brain's reserve capacity, i.e. its ability to respond to stimuli increasing CBF, such as breathing carbon dioxide or therapy with acetazolamide (a carbonic anhydrase inhibitor causing a similar increase in arterial carbon dioxide partial pressure). In a group of eight patients with known carotid occlusion, Schreiber *et al*. found decreased CBF in six and increased MTT in seven patients; five patients showed a decreased cerebrovascular reserve capacity as determined by an acetazolamide challenge.[36] The study suggests that MR, which is also capable of providing accurate delineation of vascular stenosis by MR angiography, may provide a powerful tool in assessing the hemodynamic severity of carotid stenosis, thus improving the identification of patients who may benefit from endarterectomy or stenting.

3.3 Cerebral Neoplasms

Tumor growth is limited by the ability of a neoplasm to stimulate surrounding tissue to form new blood vessels. Tumor angiogenesis by release of humoral factors (vascular endothelial growth factor) is one of the hallmarks of tumor growth and the target of novel approaches to treat human neoplasms. Noninvasive methods to assess the size, density, and integrity of tumor microvessels are, therefore, essential to detect malignancies, understand tumor growth, and to target and monitor new therapeutic approaches.[65]

3.3.1 Tumor Vessel Density

The specific sensitivity of spin echo, echo planar imaging to microvessels provides a unique potential to study the proliferation of capillary sized vessels in tumor angiogenesis. As the

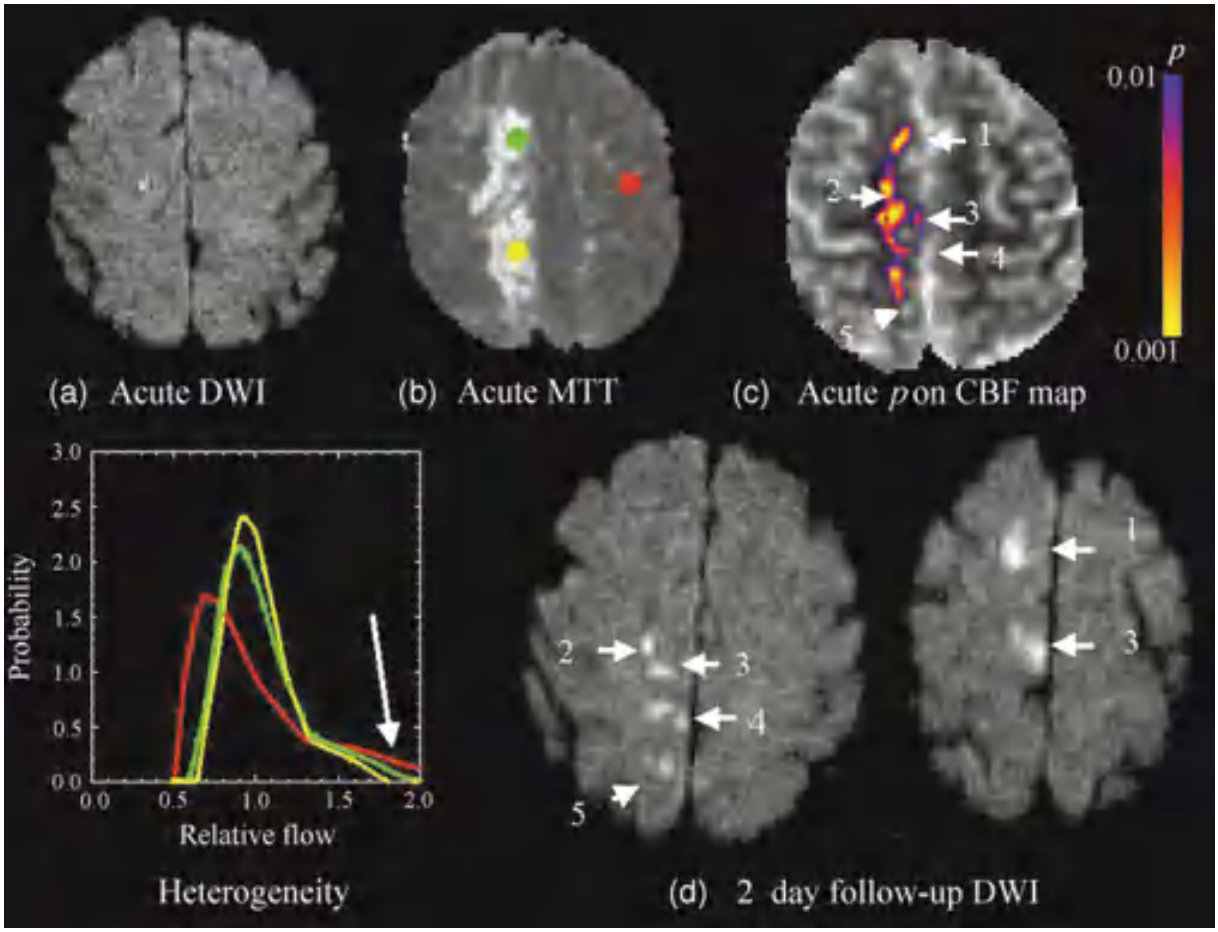

Figure 7 Initial diffusion weighted images (DWI) from a patient 5.5 h after onset of symptoms compatible with acute stroke (a). The patient suffers from a partial anterior cerebral artery (ACA) occlusion: note the prolonged mean transit time (MTT) in ACA territory (b) and that no acute DWI abnormalities are seen, indicating potential reversibility of the symptoms. The graph shows plots of flow heterogeneity probability density functions for normal MTT (red area indicated on MTT map) and two areas showing prolonged MTT (green, yellow areas). Note the narrow flow distributions in areas displaying prolonged MTT relative to normal tissue. This presumably results in higher oxygen extraction fraction. Areas of abnormal flow heterogeneity (1–5; defined as $p<0.01$ by a Kolmogorov–Smirnov test comparing the pixels flow heterogeneity with that of normal tissue) are shown on a cerebral blood flow map (c). Note the striking correspondence with the final pattern of neuronal death (indicated by numbers to show areas in (b)) on the follow-up DWI (d).

ability to form new vessels is closely related to the growth potential and thereby aggressiveness of the tumor, the relation between histologic tumor grade and regional CBV has been studied extensively. Aronen *et al*. studied 19 patients with cerebral glioma and showed that CBV correlated with tumor grade as determined by biopsy or surgery.[40] In addition, a positive correlation was found between CBV and microscopic vascularity as well as with mitotic activity (Figure 8).

These studies also suggested a close correlation between microvascular CBV and the unidirectional clearance of fluorodeoxy glucose (FDG) as measured by PET, the gold standard for noninvasive staging and prediction of outcome in cerebral neoplasms (Figure 8). This correspondence may not be entirely coincidental: FDG transport across cerebral microvessels is limited by endothelial transporters and is, therefore, related to vascular surface area. Its uptake therefore to some extent represents a measurement of capillary density,[66] as do spin echo CBV measurements.

Subsequent reports have confirmed that CBV mapping may aid in noninvasive staging of tumors.[67,68] and in the differential diagnosis of neoplasms and infectious changes.[69] CBV mapping in conjunction with conventional imaging may aid diagnosis by allowing accurate biopsy planning[31,67] and can be used for assessment of the effects of treatment such as radiotherapy.[70] Consequently, MR perfusion imaging may provide a tool for the important, but often difficult, distinction between radiation necrosis and tumor regrowth.[71,72]

Dennie *et al*. recently proposed an experimental methodology whereby the combined use of gradient and spin echo techniques for PWI could be used for more accurate, quantitative characterization of vascular morphology in tumor angiogenesis.[73]

With further development of these techniques, there is reason to believe that CBV mapping may become an important supplement to conventional MRI, particularly in delineating and staging tumors, in defining appropriate biopsy sites, in the

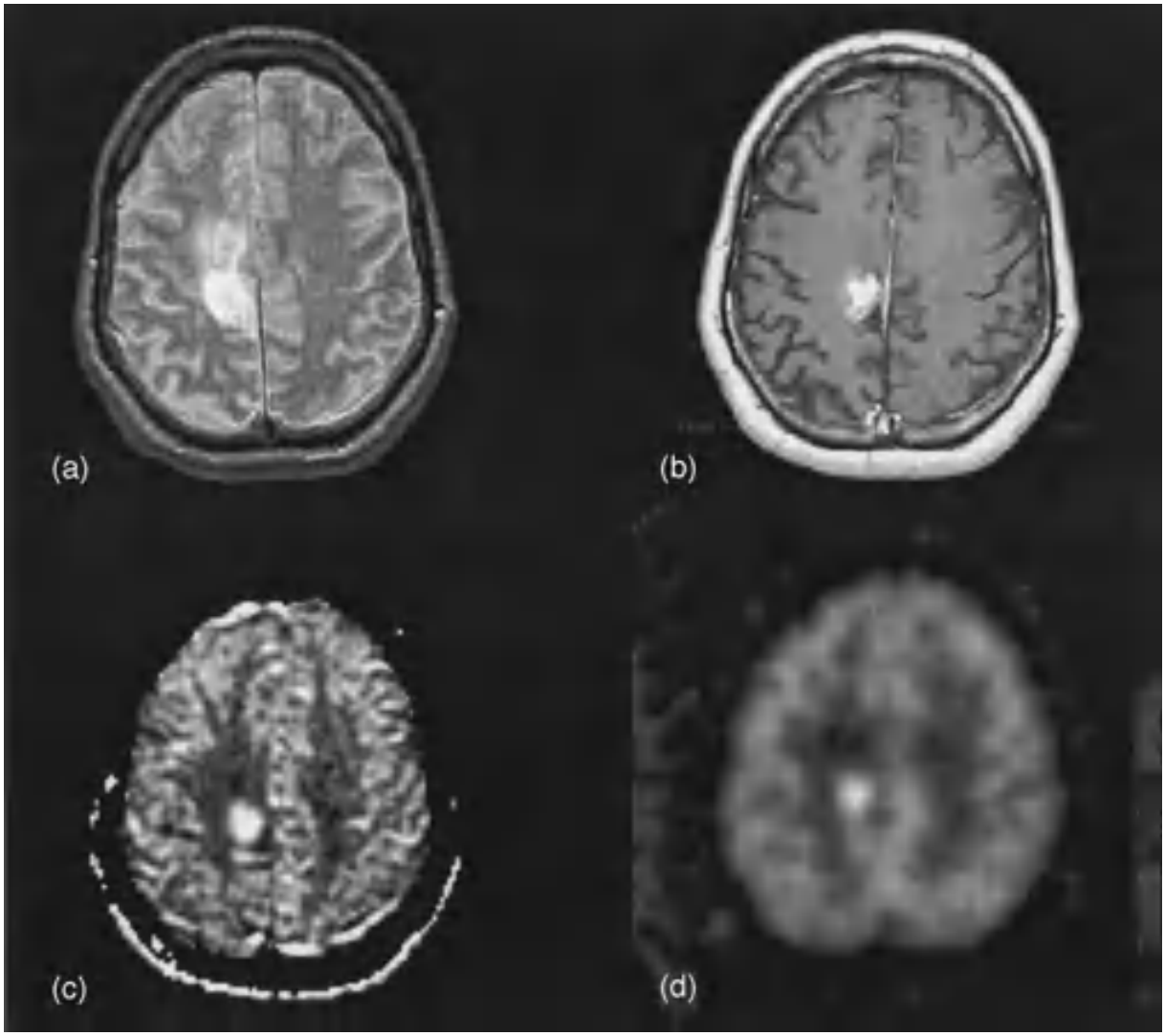

Figure 8 MR of the brain in a patient with a grade III astrocytoma. (a) The T_2-weighted image showing a small, contrast-enhancing lesion within the tumor volume, indicating edema. (b) A postcontrast T_1-weighted image. (c) The CBV map identifies a region of significantly increased microvascular blood volume within the region of contrast leakage. (d) A PET scan using fluorodeoxyglucose to assess capillary density. There is a striking correspondence between the CBV map (c) and the area of high fluorodeoxyglucose uptake. (Courtesy of Prof. Hannu Aronen)

assessment of angiogenesis, and, finally, in monitoring conventional as well as novel, anti-angiogenic therapies.

4 RELATED ARTICLES

Anisotropically Restricted Diffusion in MRI; Diffusion: Clinical Utility of MRI Studies; Hemodynamic Changes owing to Sensory Activation of the Brain Monitored by Echo-Planar Imaging; Ischemic Stroke; Methods and Applications of Diffusion MRI.

5 REFERENCES

1. J.W. Belliveau, D.N.J. Kennedy, R.C. McKinstry, B.R. Buchbinder, R.M. Weisskoff, M.S. Cohen, J.M. Vevea, T.J. Brady, B.R. Rosen, *Science*, 1991, **254**: 716.
2. B. R. Rosen, J. W. Belliveau, H. J. Aronen, D. Kennedy, B. R. Buchbinder, A. Fischman, M. Gruber, J. Glas, R. M. Weisskoff, M. S. Cohen, F. H. Hochberg, T. J. Brady, *Magn. Reson. Med.*, 1991, **22**: 293.
3. B. R. Rosen, J. W. Belliveau, B. R. Buchbinder, R. C. McKinstry, L. M. Porkka, D. N. Kennedy, M. S. Neuder, C. R. Fisel, H. J. Aronen, K. K. Kwong, R. M. Weiskoff, M. S. Cohen, T. J. Brady, *Magn. Reson. Med.*, 1991, **19**: 285.
4. B. R. Rosen, J. W. Belliveau, J. M. Vevea, T. J. Brady, *Magn. Reson. Med.*, 1990, **14**: 249.
5. J. L. Boxerman, L. M. Hamberg, B. R. Rosen, R. M. Weisskoff, 1995, *Magn. Reson. Med.*, **34**: 555.
6. C. R. Fisel, J. L. Ackerman, R. B. Buxton, L. Garrido, J. W. Belliveau, B. R. Rosen, T. J. Brady, *Magn. Reson. Med.*, 1991, **17**: 336.
7. R. M. Weisskoff, C. S. Zuo, J. L. Boxerman, B. R. Rosen, *Magn. Reson. Med.*, 1994, **31**: 601.
8. C. Z. Simonsen, L. Østergaard, P. Vestergaard-Poulsen, L. Røhl, A. Bjørnerud, C. Gyldensted, *JMRI*, 1999, **9**: 342.

9. L. Østergaard, D. F. Smith, P. Vestergaard-Poulsen, S. B. Hansen, A. Gee, A. Gjedde, C. Gyldensted, *J. Cereb. Blood Flow Metab.*, 1998, **18**: 425.
10. A. A. Lammertsma, D. J. Brooks, R. P. Beaney, D. R. Turton, M. J. Kensett, J. D. Heather, J. Marshall, T. Jones, *J. Cereb. Blood Flow Metab.*, 1984, **4**: 317.
11. O. A. Larsen, N. A. Lassen, *J. Apply. Phys.*, 1964, **19**: 571.
12. P. Gaehtgens, *Biorheology*, 1980, **17**: 183.
13. P. Meier, K. L. Zierler, *J. Apply. Phys.*, 1954, **6**: 731.
14. G. N. Stewart, *J. Physiol. (Lond.)*, 1894, **15**: 1.
15. K. L. Zierler, *Circ. Res.*, 1962, **10**: 393.
16. K. L. Zierler, *Circ. Res.*, 1965, **16**: 309
17. H. K. Thompson Jr, F. Starmer, R. E. Whalen, H. D. McIntosh, *Circ. Res.*, 1964, **14**: 502.
18. R. M. Weisskoff, D. Chesler, J. L. Boxerman, B. R. Rosen, *Magn. Reson. Med.*, 1993, **29**: 553.
19. G. T. Gobbel, J. R. Fike, *Phys. Med. Biol.*, 1994, **39**: 1833.
20. K. A. Rempp, G. Brix, F. Wenz, C. R. Becker, F. Guckel, W. J. Lorenz, *Radiology*, 1994, **193**: 637.
21. M. E. Valentinuzzi, V. E. Montaldo, *Med. Biol. Eng.*, 1975, **13**: 123.
22. T. A. Bronikowski, C. A. Dawson, J. H. Linehan, *Int. J. Comput.*, 1983, **14**: 411.
23. H. S. Van Huffel, J. Vandewalle, R.M. De, J. L. Willems, *Med. Biol. Eng. Comput.*, 1987, **25**: 26.
24. H. L. Liu, Y. Pu, Y. Liu, L. Nickerson, T. Andrews, P. T. Fox, J. H. Gao, *Magn. Reson. Med.*, 1999, **42**: 167.
25. R. Wirestam, L. Andersson, L. Østergaard, F. Stahlberg, *Proc. VIIth Annu. Mtg. (Int.) Soc. Magn. Reson. Med.*, Philadelphia, 1999, p. 605.
26. L. Østergaard, R. M. Weisskoff, D. A. Chesler, C. Gyldensted, B. R. Rosen, *Magn. Reson. Med.*, 1996, **36**: 715.
27. N. A. Lassen, *J. Cereb. Blood Flow Metab.*, 1984, **4**: 633.
28. K. B. Larson, W. H. Perman, J. S. Perlmutter, M. H. Gado, K. L. Zierler, *J. Theor. Biol.*, 1994, **170**: 1.
29. L. Østergaard, D. Chesler, R. M. Weisskoff, A. G. Sorensen, B. R. Rosen, *J. Cereb. Blood Flow Metab.*, 1999, **19**: 690.
30. R. B. King, A. Deussen, G. M. Raymond, J. B. Bassingthwaighte, *Am. J. Physiol.*, 1993, **265**: H2196.
31. R. B. King, G. M. Ramond, J. B. Bassingthwaighte, *Ann. Biomed. Eng.*, 1996, **24**: 352.
32. K. Kroll, N. Wilke, H. M. Jerosch, Y. Wang, Y. Zhang, R. J. Bache, J. B. Bassingthwaighte, *Am. J. Physiol.*, 1996, **271**: H1643.
33. E. P. Vonken, F. J. Beekman, C. J. Bakker, M. A. Viergever, *Magn. Reson. Med.*, 1999, **41**: 343.
34. E. P. Vonken, M. J. Osch, C. J. Bakker, M. A. Viergever, *JMRI*, 1999, **10**: 109.
35. W. H. Perman, M. H. Gado, K. B. Larson, J. S. Perlmutter, *Magn. Res. Med.*, 1992, **28**: 74.
36. W. G. Schreiber, F. Guckel, P. Stritzke, P. Schmiedek, A. Schwartz, G. Brix, *J. Cereb. Blood Flow Metab.*, 1998, **18**: 1143.
37. L. Østergaard, P. Johannsen, P. H. Poulsen, P. Vestergaard-Poulsen, H. Asboe, A. Gee, S. B. Hansen, C. E. Cold, A. Gjedde, C. Gyldensted, *J. Cereb. Blood Flow Metab.*, 1998, **18**: 935.
38. C. Crone, *Acta Physiol. Scand*, 1963, **58**: 292.
39. E. M. Renkin, *Am. J. Physiol.*, 1959, **197**: 1211.
40. H. J. Aronen, I. E. Gazit, D. N. Louis, B. R. Buchbinder, F. S. Pardo, R. M. Weisskoff, G. R. Harsh, G. R. Cosgrove, E. F. Halpern, F. H. Hochberg, *Radiology*, 1994, **191**: 41.
41. R. M. Weisskoff, J. L. Boxerman, A. G. Sorensen, S. F. Kulke, T. A. Campbell, B. R. Rosen, *Proc. Soc. Magn. Reson.*, 1994, **1**: 279.
42. L. Østergaard, J. D. Rabinov, B. R. Rosen, C. Gyldensted, *Proc. IVth Annu. Mtg. (Int.) Soc. Magn. Reson, Med.*, New York, 1996, p. 1307.
43. K. Yamada, A. G. Sorensen, G. Gonzalez, W. A. Copen, O. Wu, C. J. Bakker, L. Østergaard, B. R. Rosen, *Proc. 36th Annu. Mtg. Soc. Neuroradiol.*, 1998, p. 213.
44. M. E. Moseley, Y. Cohen, J. Mintorovitch, L. Chileuitt, H. Shimizu, J. Kucharczyk, M. F. Wendland, P. R. Weinstein, *Magn. Reson. Med.*, 1990, **14**: 330
45. Y. Yoneda, K. Tokui, T. Hanihara, H. Kitagaki, M. Tabuchi, E. Mori, *Ann. Neurol.*, 1999, **45**: 794.
46. A. E. Baird, A. Benfield, G. Schlaug, B. Siewert, K. O. Lovblad, R. R. Edelman, S. Warach, *Ann. Neurol,*, 1997, **41**: 581.
47. C. Beaulieu, A. de Crespigny, D. C. Tong, M. E. Moseley, G. W. Albers, M. P. Marks, *Ann. Neurol.*, 1999, **46**: 568.
48. J. O. Karonen, R. L. Vanninen, Y. Liu, L. Østergaard, J. T. Kuikka, J. Nuutinen, E. J. Vanninen, P. L. Partanen, P. A. Vainio, K. Korhonen, J. Perkio, R. Roivainen, J. Sivenius, H. J. Aronen, *Stroke*, 1999, **30**: 1583.
49. L. H. Schwamm, W. J. Koroshetz, A. G. Sorensen, B. Wang, W. A. Copen, R. Budzik, G. Rordorf, F. S. Buonanno, P. W. Schaefer, R. G. Gonzalez, *Stroke*, 1998, **29**: 2268.
50. W. J. Powers, *Ann. Neurol.*, 1991, **29**: 231.
51. W.-D. Heiss, I. Podreka, Cerebrovascular disease. In: H.N. Wagner, Z. Szabo, J.W. Buchanan (eds). *Principles of Nuclear Medicine*, 2nd edition. W.B. Saunders Co., Philadelphia, 1995, pp. 531.
52. J. C. Baron, M. G. Bousser, A. Rey, A. Guillard, D. Comar, P. Castigne, *Stroke*, 1981, **12**: 454.
53. P. Schumann, O. Touzani, A. R. Young, J. C. Baron, R. Morello, E. T. MacKenzie, *Brain*, 1998, **121**: 1369.
54. G. Zaharchuk, J. B. Mandeville, A. A. J. Bogdanov, R. Weissleder, B. R. Rosen, J. J. Marota, *Stroke*, 1999, **30**: 2197.
55. A. G. Sorensen, W. A. Copen, L. Østergaard, F. S. Buonanno, R. G. Gonzalez, G. Rordorf, B. R. Rosen, L. H. Schwamm, R. M. Weisskoff, W. J. Koroshetz, *Radiology*, 1999, **210**: 519.
56. O. Wu, A. G. Sorensen, D. Bakker, F. Buonanno, W. A. Copen, G. Gonzalez, C. Harmath, L. Østergaard, B. R. Rosen, L. H. Schwamm, G. Rordorf, R. M. Weisskoff, W. M. Wells, K. Yamada, G. Zaharchuk, W. J. Koroshetz, *Proc. VIth Annu. Mtg. (Int.) Soc. Magn. Reson. Med.*, Sydney, 1998, p. 235.
57. J. L. Sunshine, R. W. Tarr, C. F. Lanzieri, D. M. Landis, W. R. Selman, J. S. Lewin, *Radiology*, 1999, **212**: 325
58. R. J. Wise, S. Bernardi, R. S. Frackowiak, N. J. Legg, T. Jones, *Brain*, 1983, **106**: 197.
59. A. G. Hudetz, G. Feher, J. P. Kampine, *Microvasc. Res.*, 1996, **51**: 131.
60. W. Kuschinsky, O. B. Paulson, *Cerebrovasc. Brain Metab. Rev.*, 1992, **4**: 261.
61. L. Østergaard, A. G. Sorensen, D. Chesler, R. M. Weisskoff, W. J. Koroshetz, C. Gyldensted, B. R. Rosen, *J. Cereb. Blood Flow Metab.*, 1999, **19** (Suppl. 1), S621.
62. J. M. Gibbs, R. J. Wise, K. L. Leenders, T. Jones, *Lancet*, 1984, **i**: 310.
63. W. J. Powers, G. A. Press, R. L. J. Grubb, M. H. Gado, M. E. Raichle, *Ann. Intern. Med.*, 1987, **106**: 27.
64. M. Itoh, J. Hatazawa, C. Pozzelli, H. Fukuda, Y. Abe, T. Fujiwara, K. Kubota, K. Yamaguchi, T. Sato, T. Matsuzawa, *Neuroradiology*, 1987, **29**: 416.
65. N. Ferrara, K. Alitalo, *Nature Med.*, 1999, **5**: 1359.
66. A. Gjedde, H. Kuwabara, A. M. Hakim, *J. Cereb. Blood Flow Metab.*, 1990, **10**: 317.
67. E. A. Knopp, S. Cha, G. Johnson, A. Mazumdar, J. G. Golfinos, D. Zagzag, D. C. Miller, P. J. Kelly, I. I. Kricheff, *Radiology*, 1996, **211**: 791.
68. T. Sugahara, Y. Korogi, M. Kochi, I. Ikushima, T. Hirai, T. Okuda, Y. Shigematsu, L. Liang, Y. Ge, Y. Ushio, M. Takahashi, *Am. J. Roentgenol.*, 1998, **171**: 1479.
69. T. M. Ernst, L. Chang, M. D. Witt, H. A. Aronow, M. E. Cornford, I. Walot, M. A. Goldberg, *Radiology*, 1998, **208**: 663.

70. F. Wenz, K. Rempp, T. Hess, J. Debus, G. Brix, R. Engenhart, M. V. Knopp, K. G. Van Kaick, M. Wannenmacher, *Am. J. Roentgenol.*, 1996, **166**: 187.
71. H. J. Aronen, J. Glass, F. S. Pardo, J. W. Belliveau, H. L. Gruber, B. R. Buchbinder, I. E. Gazit, R. M. Linggood, A. J. Fischman, B. R. Rosen, *Acta Radiol.*, 1995, **36**: 520.
72. T. Siegal, R. Rubinstein, T. Tzuk-Shina, J. M. Gomori, *J. Neurosurg.*, 1997, **86**: 22.
73. J. Dennie, J. B. Mandeville, J. L. Boxerman, S. D. Packard, B. R. Rosen, R. M. Weisskoff, *Magn. Reson. Med.*, 1998, **40**: 793.

Biographical Sketch

Leif Østergaard, *b* 1965. B.Sc. 1987, Physics and Mathematics, M.Sc., 1992, Astrophysics, M.D., 1994, Århus University, Århus, Denmark. Formerly Research Fellow, MGH-NMR Center, Department of Radiology, Massachusetts General Hospital, Charlestown, Massachusetts, USA. Presently Research Director, Magnetic Resonance Imaging, Department of Neuroradiology and Intern, Grenaa General Hospital, Grenaa, Denmark. Approx. 140 publications. Research interests: perfusion, diffusion, water exchange phenomena and functional MRI.

CSF Velocity Imaging

William G. Bradley, Jr
Long Beach Memorial Medical Center, CA, USA

1 INTRODUCTION

Cerebrospinal fluid (CSF) is produced by the choroid plexus within the ventricles of the brain at a rate of 500 ml per day. It flows out of the foramina of Lushka and Magendie in the fourth ventricle and is absorbed by the arachnoid villi on either side of the superior sagittal sinus.[1] Superimposed on this slow, steady egress of CSF from the ventricular system are much more prominent cardiac pulsations resulting from systolic expansion and diastolic contraction of the brain. When the local CSF velocity is sufficiently high, e.g. through the narrow aqueduct of Sylvius, a 'CSF flow void'[2,3] is normally produced, similar to that seen with rapidly flowing blood.[4] When there is obstruction to CSF flow, the flow void is not observed.[3] Obstruction proximal to the outlet foramina of the fourth ventricle is termed 'obstructive hydrocephalus'; obstruction between the outlet foramina of the fourth ventricle and the arachoid villi is termed 'communicating hydrocephalus'. Communicating hydrocephalus most often follows subarachoid hemorrhage or meningitis; however, a number of elderly patients may present with a radiographic pattern of communicating hydrocephalus without a history of either of these preceding events. Such hydrocephalus is termed 'occult' or 'idiopathic'.[5,6] Since the mean intraventricular pressure is normal, it has also been called 'normal pressure hydrocephalus' (NPH).

Classically, NPH patients present with a clinical triad of gait apraxia, dementia, and incontinence.[5–7] Although the mean intraventricular pressure is normal in these patients, the pulse pressure, i.e. the change in CSF pressure over the cardiac cycle, is much greater than normal. A 'waterhammer' pulse has been described in such patients when their intraventricular pressure is monitored.[8,9] Until now the diagnosis of NPH has been made on the basis of a radiographic picture of ventricles enlarged out of proportion to any cortical sulcal enlargement (to distinguish NPH from atrophy).

Prior to the advent of MRI, this radiographic picture and the appropriate clinical triad alone were not sufficient to predict which patients would respond to the primary treatment for NPH, i.e. ventriculoperitoneal (VP) shunting. Recently, the magnitude of the aqueductal CSF flow void (Figure 1) has been used to predict which patients with clinical NPH will respond to shunting.[10] The CSF flow void is a normal phenomenon, resulting from the pulsatile motion of CSF back and forth through the ventricular system over the cardiac cycle.[11] In the normal patient, there is space over the cortical convexities occupied by the cortical veins and the CSF in the subarachnoid space (Figure 2). When the brain expands during systole, it expands outward, compressing the cortical veins (leading to subsequent venous outflow), and it expands inward, compressing the lateral ventricles (leading to outflow of CSF through the aqueduct which produces the normal flow void).[10] In communicating hydrocephalus, the brain has already expanded against the inner table of the calvarium, so further outward expansion is not possible. Thus, during systole all cerebral expansion is directed inward, compressing the lateral ventricles, leading to increased outflow of CSF through the aqueduct. This is the etiology for the increased CSF flow void[7] in patients with communicating hydrocephalus and normal cerebral blood flow (Figure 2). When the blood supply to the brain decreases due to atrophy, the main force behind the CSF pump decreases and the CSF flow void is consequently also reduced. In a recent study, there was a significant correlation between an increased CSF flow void, i.e. one extending from the third ventricle through the obex of the fourth ventricle, and a successful response to ventriculoperitoneal shunting.[7] Patients with clinical NPH who did *not* have a hyperdynamic flow void, on the other hand, failed to respond to shunting. This association was significant at the $p < 0.003$ level.[10] Thus, in the setting of an appropriate clinical triad for NPH and ventricular enlargement out of proportion to cortical sulcal dilatation, the presence of an increased aqueductal CSF flow void on MRI should prompt the neurosurgeon to perform a VP shunt. It should be emphasized, however, that younger patients with communicating hydrocephalus and intact cerebral blood supply may also have hyperdynamic CSF flow. Thus, the sign is not specific for NPH. Since NPH is a disease of elderly patients, it appears that symptoms follow a combined insult related to the ventricular enlargement and also to decreased perfusion of the periventricular region, i.e. the same process that leads to deep white matter ischemia and infarction.[12]

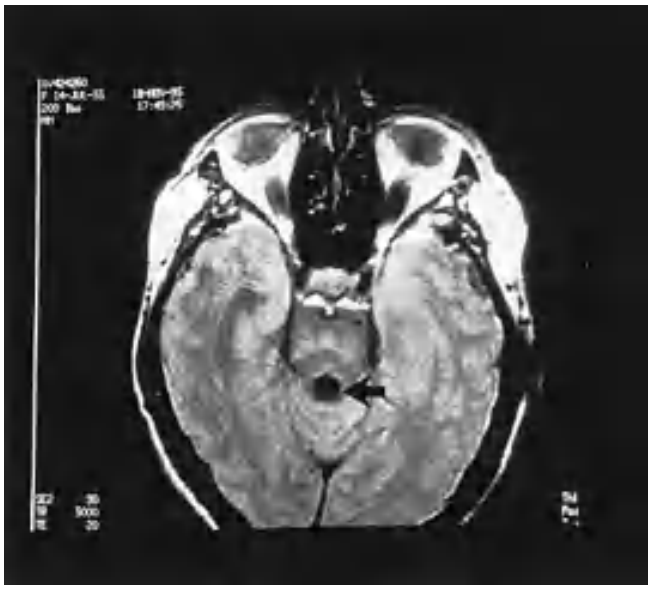

Figure 1 CSF flow void in normal pressure hydrocephalus. Proton density-weighted axial image through the upper fourth ventricle demonstrates marked CSF flow void (arrow)

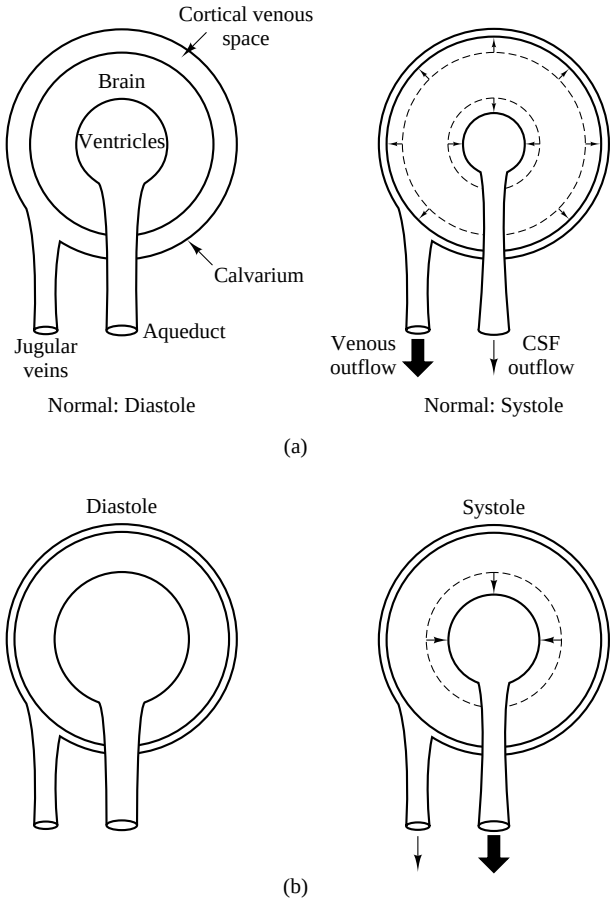

Figure 2 Schematic representation of CSF flow mechanism. (a) In normal patients, systolic expansion of cerebral hemispheres occurs outward, compressing cortical veins and, to a lesser extent, inward, compressing the lateral ventricles. (b) In communicating hydrocephalus, the brain has already expanded against the inner table of the calvarium. Since outward expansion of the brain is no longer possible, the entire increase in volume due to systolic expansion is directed inwards, towards the lateral ventricles. The combination of this greater inward displacement and the mild aqueductal enlargement that accompanies communicating hydrocephalus leads to hyperdynamic CSF flow

2 MR TECHNIQUES USED TO MEASURE CSF FLOW

A number of magnetic resonance (MR) observations and techniques have been employed to take advantage of signal changes associated with CSF flow. The aqueductal CSF flow void (Figure 1) noted on routine MR images was the first indication of CSF motion.[2,3] Subsequently, the CSF flow void was shown to be related to the cardiac cycle.[13] Although a CSF flow void may be appreciated on routine spin echo and gradient echo MR images, the degree of signal loss is not consistent, nor does it change in a linear fashion with velocity.[1] Thus by using the CSF flow void sign alone, it may be difficult to appreciate when CSF flow is mildly abnormal. When a CSF flow void is not visualized at all in areas where it is normally expected (e.g. the aqueduct), however, inferences can be made concerning obstruction.[3] Axial, single slice, gradient echo techniques which maximize flow-related enhancement[4] (entry phenomenon) have also been used[14] to evaluate aqueductal patency. However, the best observations of CSF flow have been obtained using dedicated techniques, gated to the cardiac cycle.

In 1985, Feinberg and Mark[15,16] used MR 'velocity density imaging' to measure the velocity of CSF through the aqueduct as a function of the cardiac cycle. Subsequently Edelman et al.[17] used saturation pulses and bolus tracking techniques, while Axel and Dougherty.[18] used spatial modulation of magnetization (SPAMM) to measure CSF velocity. Today, most investigators are using phase contrast techniques.[19–21]

The phase contrast CSF velocity imaging techniques[19–21] can be divided on the basis of the form of cardiac gating used, i.e. prospective or retrospective,[22] and on the basis of background phase determination.[23] Most investigators[19,20] determine the background phase from an additional acquisition. This approach necessitates obtaining two interleaved acquisitions and then subtracting them. We make the assumption of zero net flow[21] over the cardiac cycle and calculate the background phase (which entails a single acquisition in one-half the time).

The relationship between the phase shift θ and velocity v is given by:

$$\theta = \gamma \int_0^t G(t) v t \, \mathrm{d}t \tag{1}$$

where γ is the gyromagnetic ratio, $G(t)$ is the gradient strength as a function of time t, and t is the elapsed time.[24] Thus for an appropriate gradient pulse of strength G and duration t, a linear relationship should exist between the phase shift (from zero to $\pm 180^\circ$, depending on the direction of flow) and the actual CSF velocity. A new parameter, the V_{enc}, is the aliasing or 'encoding' velocity, which leads to a 180° phase shift.

With prospective cardiac gating, acquisition starts at a predetermined time interval after the R wave and continues at approximately 50–75 ms intervals to within about 200 ms of the next R wave (to allow for respiratory variation).[19] Since there is no sampling of CSF motion during the final 100 or 200 ms of the R–R interval (when flow is in a rostral or retrograde direction), there appears to be a large net flow of CSF in the systolic direction (i.e. craniocaudal) over this partially sampled cardiac cycle.[21]

With retrospective cardiac gating,[22] the computer keeps track of the R wave and data are acquired throughout the cardiac cycle and then retrospectively 'binned' into a predetermined number of frames.[22] The entire cardiac cycle is sampled; therefore, there is no time for eddy currents to build up, as they do during the 200 ms dead time when prospective cardiac gating is used.[21]

We routinely use two retrospective cardiac gated techniques:[21] a 'routine resolution' sagittal acquisition in the midline (see Figure 3); and a 'high-resolution' axial acquisition through the aqueduct (see Figure 4). In the sagittal technique, a 4 mm slice is acquired in the midsagittal plane (Figure 3) with velocity sensitization along the read-out axis (which is also the craniocaudal axis of the patient). Cardiac gating is performed with ECG leads rather than using finger plethysmography,

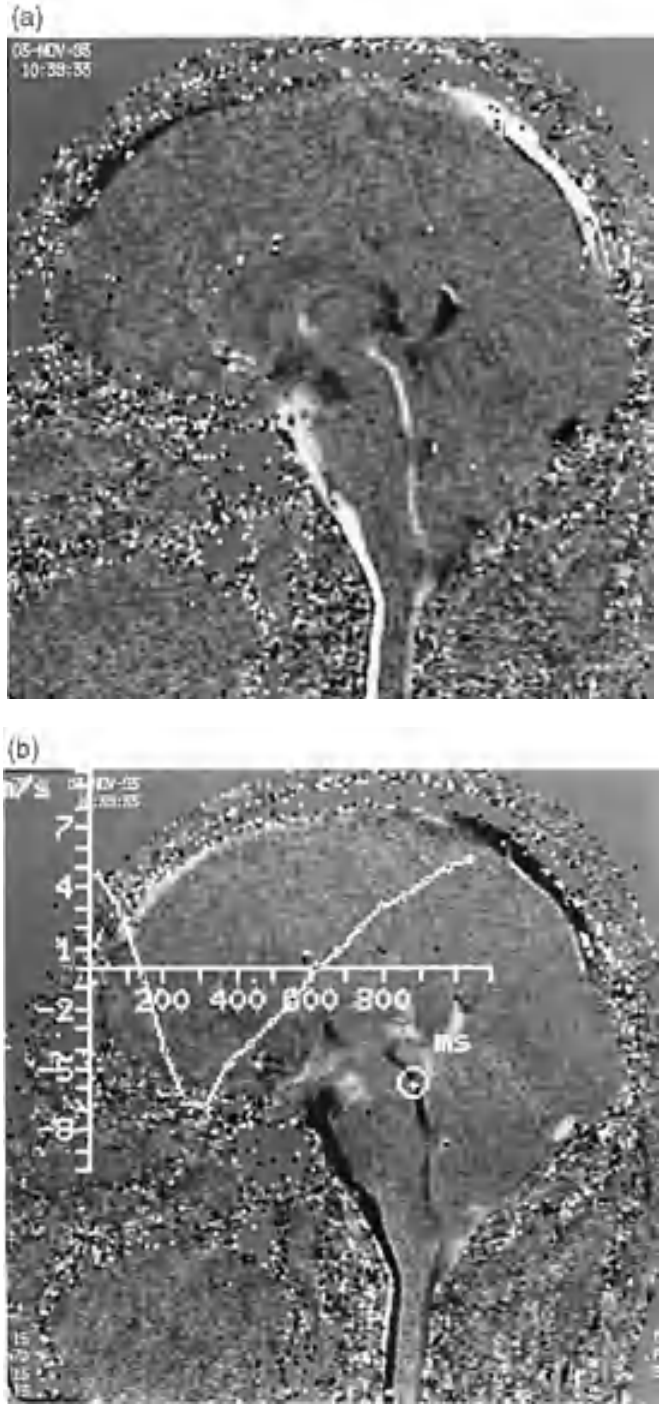

Figure 3 Sagittal phase contrast technique. (a) During systole, CSF flow is downward (craniocaudal), as indicated by shades of white. (b) During diastole, CSF flow is upward (caudocraniad), as indicated by shades of black. By placing a cursor over any point in the image, the velocity can be obtained as a function of the cardiac cycle

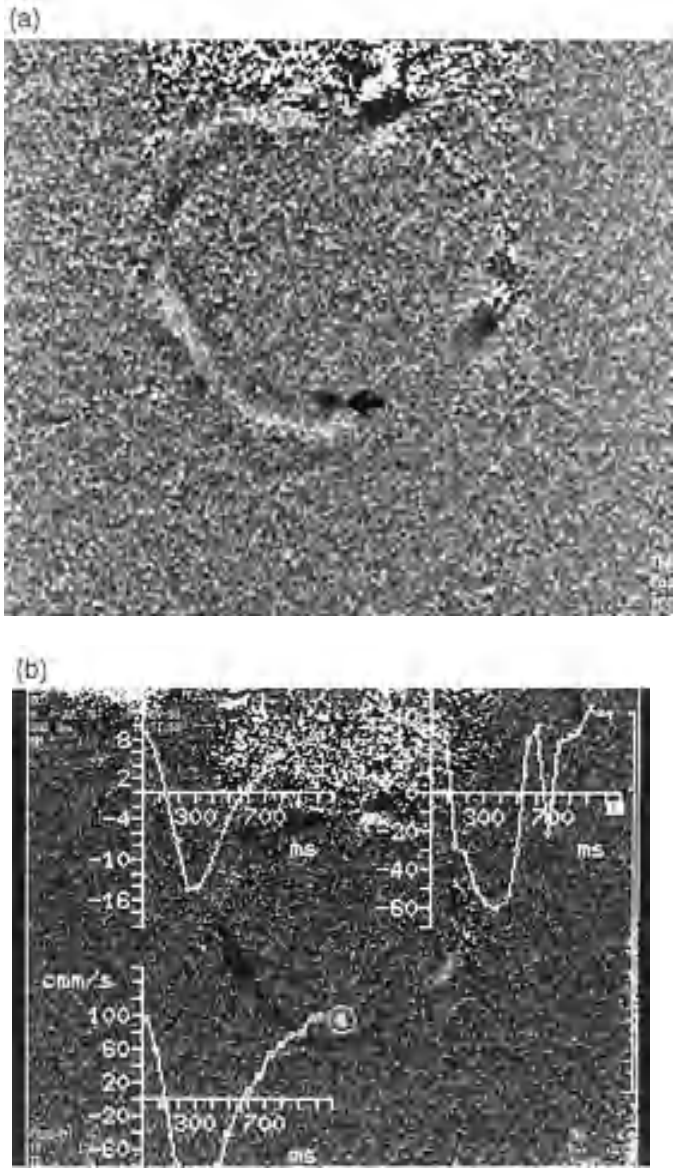

Figure 4 Axial phase contrast technique. (a) High-resolution axial image obtained during diastole indicates upward flow (black) in the aqueduct (arrow). (b) During systole, flow is downward (white). The mean velocity (left upper), peak velocity (right upper), and volumetric flow rates (left lower) through the aqueduct are shown as a function of the cardiac cycle

since the systolic motion of the brain may actually precede the systolic pulse in the finger.[21] The basic technique is a flow-compensated, two-dimensional fast imaging with steady precession (FISP) with a repetition time (*TR*) of 70 ms, a echo delay time (*TE*) of 13 ms, and a 15° flip angle (Figure 3). A 192 × 256 matrix is acquired over a 25-cm field of view, providing in-plane spatial resolution of approximately 1 mm. The aliasing velocity is 100 mm s^{-1}. Such images are used routinely in the head to document midsagittal CSF flow. Using a single excitation and 32 acquisitions before phase advance, this sagittal technique takes 7 min. When a cursor is placed over any point on the phase contrast velocity image, craniocaudal CSF velocities can be measured and plotted versus the phase of the cardiac cycle, allowing comparison of phase relationships of CSF motion at different points in the ventricular system and subarachnoid space[21] (Figure 3).

The measured velocity through the aqueduct on this sagittal acquisition also reflects the stationary tissue in the midbrain on either side of the aqueduct in a 4 mm thick slice. Therefore,

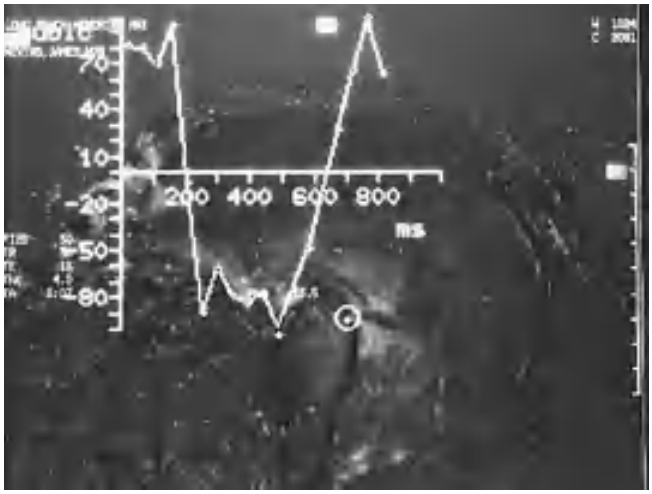

Figure 5 In this 78-year-old man with clinical NPH, hyperdynamic flow is demonstrated through the aqueduct with the qualitative sagittal technique

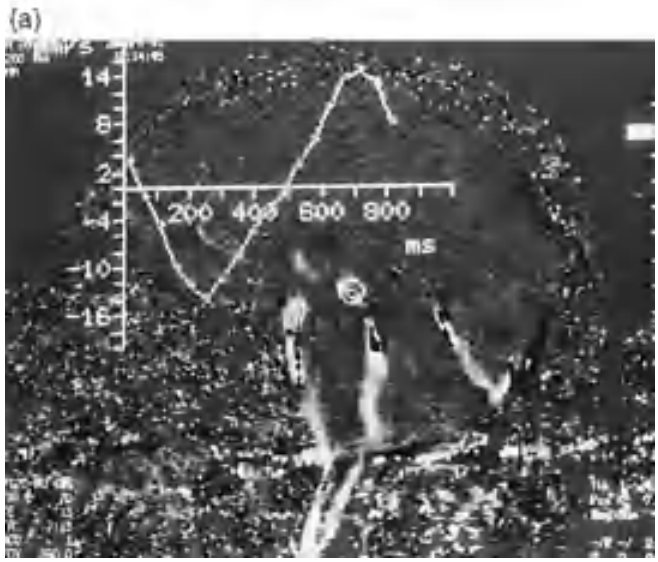

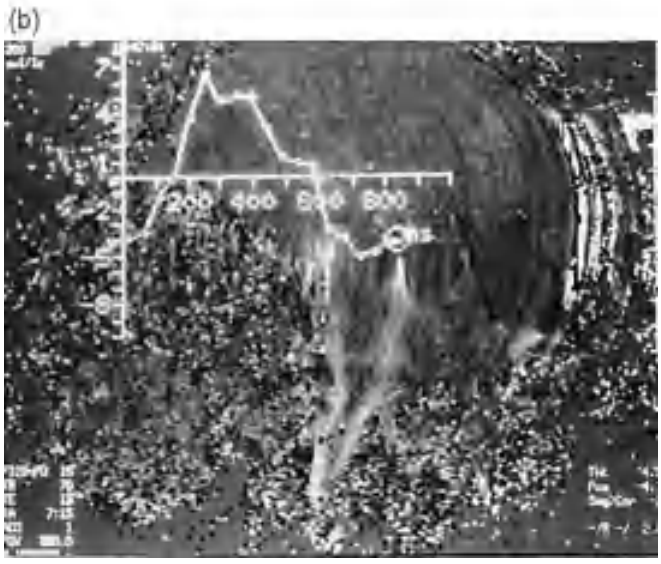

Figure 6 Shunt malfunction in NPH. (a) A 73-year-old man shunted initially for NPH one year previously now presents with recurrent symptoms and 'normal' flow pattern through the aqueduct. (b) Two months later, when the shunt has been revised and the patient is again asymptomatic, the CSF flow pattern through the aqueduct is reversed (as expected with normal shunt function)

the velocity is artifactually reduced due to partial volume effects.[21] To circumvent these effects, the high resolution axial technique was developed.[21] In this technique, an angled axial slice is positioned perpendicular to the aqueduct so that the CSF is viewed en face, without inclusion of adjacent stationary tissue (Figure 4). Velocity sensitization is provided by the slice-select gradient, i.e. for through-plane flow. We currently use a 512 × 512 (half Fourier) matrix over a 16 cm field of view, providing pixels 0.3 mm on a side. Thirty such pixels can be placed in the average 2-mm diameter aqueduct. Like the sagittal technique, this is a modified two-dimensional FISP with a 15° flip angle, a *TR* of 100 ms, and a *TE* of 16 ms. With a single excitation and 32 acquisitions per phase step, it takes 14 min.[21] An aliasing velocity of 200 mm s^{-1} is routinely used. Integrating the volumetric flow rate over the cardiac cycle, an aqueductal CSF 'stroke volume' can be calculated.[21] Using a pulsatile flow phantom velocity, volumetric flow measurements have recently been validated.[25]

3 NORMAL CSF FLOW IN THE BRAIN

In normals, the maximal downward wave of CSF movement through the aqueduct occurs 175–200 ms following the R wave; however, it is usually preceded by CSF flow out of the fourth ventricle through the foramen of Magendie.[20] Mixing occurs in the middle of the fourth ventricle, resulting in turbulence.[21] Midway through the cardiac cycle, a diastolic cephalad (retrograde) wave of CSF can be seen pulsing through the aqueduct.[20] Variable degrees of CSF flow within the posterior third ventricle are observed and, occasionally, flow at the level of the foramen of Monro is also seen in normals. Flow is less often observed in the lateral ventricles, however, due to the larger diameters involved. As a result of volume changes in the brain during the cardiac cycle, CSF also flows to and fro in the basal cisterns.[21]

Flow out of the inferior portion of the fourth ventricle through the foramen of Magendie is not simply a continuation of the flow coming in from the aqueduct. Such asynchrony may result from pulsations of the choroid plexus of the fourth ventricle.[20] In fact, the caudally directed CSF pulse wave is observed to start first in the fourth ventricle, followed approximately 100 ms later by caudal flow in the aqueduct.[20] Cranial flow of CSF back through the aqueduct may still be occurring when the first downward pulsation through the foramen of Magendie is seen. Clearly, therefore, this cephalad aqueductal CSF flow is not simply the result of retrograde flow from the basal cisterns into the fourth ventricle and upwards.[20] The probable reasons for these normal

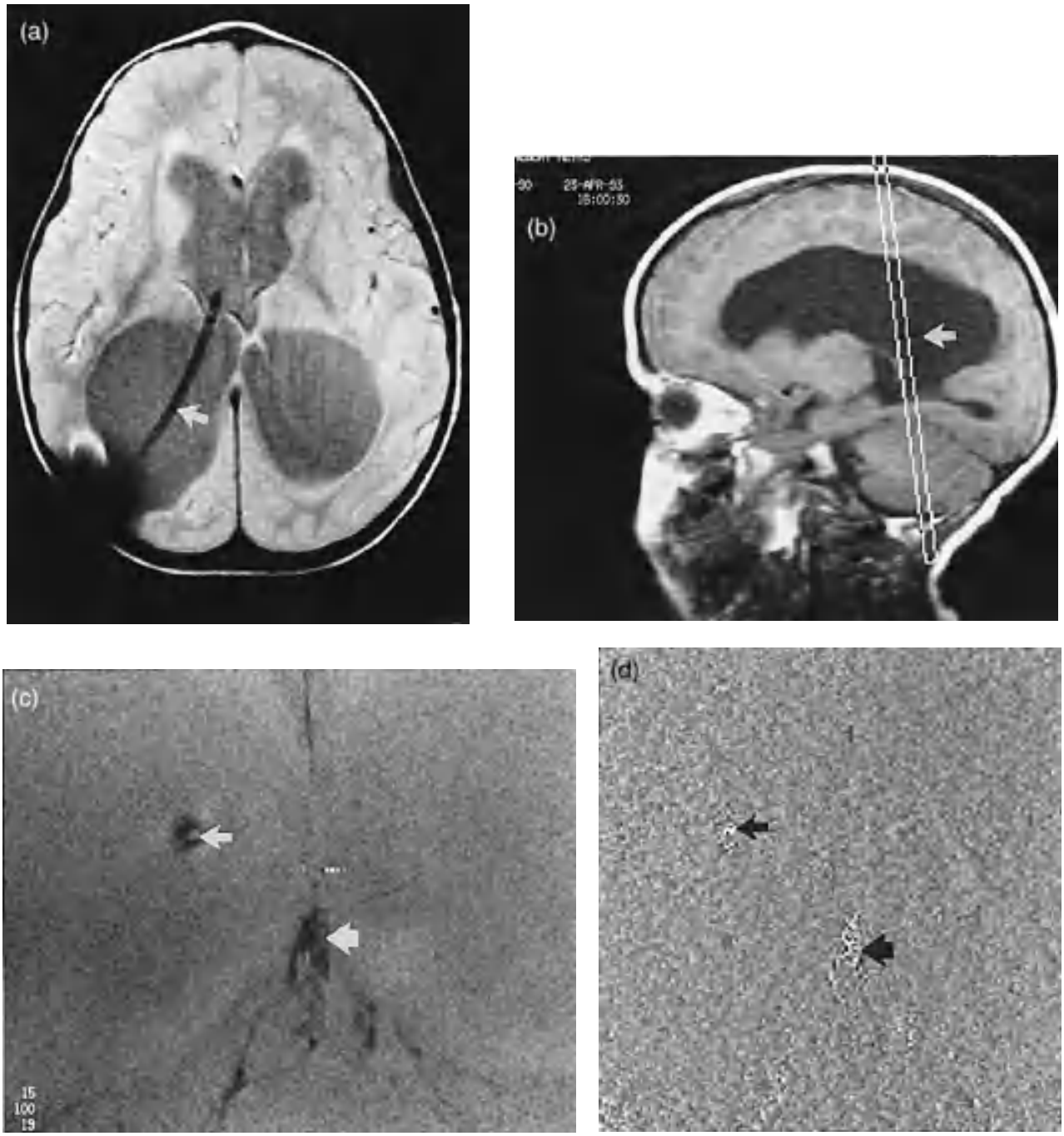

Figure 7 Normal shunt function. (a) A shunt tube (arrow) is noted in a 2-year-old boy with obstructive hydrocephalus. (b) This right parasagittal section demonstrates the position of the high-resolution acquisition plane perpendicular to the dark shunt tube (arrow). (c) A 'magnitude' image from a high-resolution coronal acquisition, angled perpendicular to the shunt tube (small arrow); the image also demonstrates the quadrigeminal plate cistern (large arrow). (d) A phase contrast image again demonstrates the quadrigeminal plate cistern (large arrow) and high signal intensity (small arrow) in the shunt, corresponding to forward flow

variations are multiple, but relate most likely to the size of the nearby vascular structures, the compliance of surrounding brain and spinal cord, the anatomy of the CSF spaces, the volume and vascularity of the choroid plexus, and the resultant systemic hydrodynamics.[20]

4 ABNORMAL CSF FLOW IN THE BRAIN

Using the qualitative sagittal technique, the hyperdynamic CSF flow of NPH (Figure 5) can be distinguished from the hypodynamic flow of atrophy. Even more accurate is the high

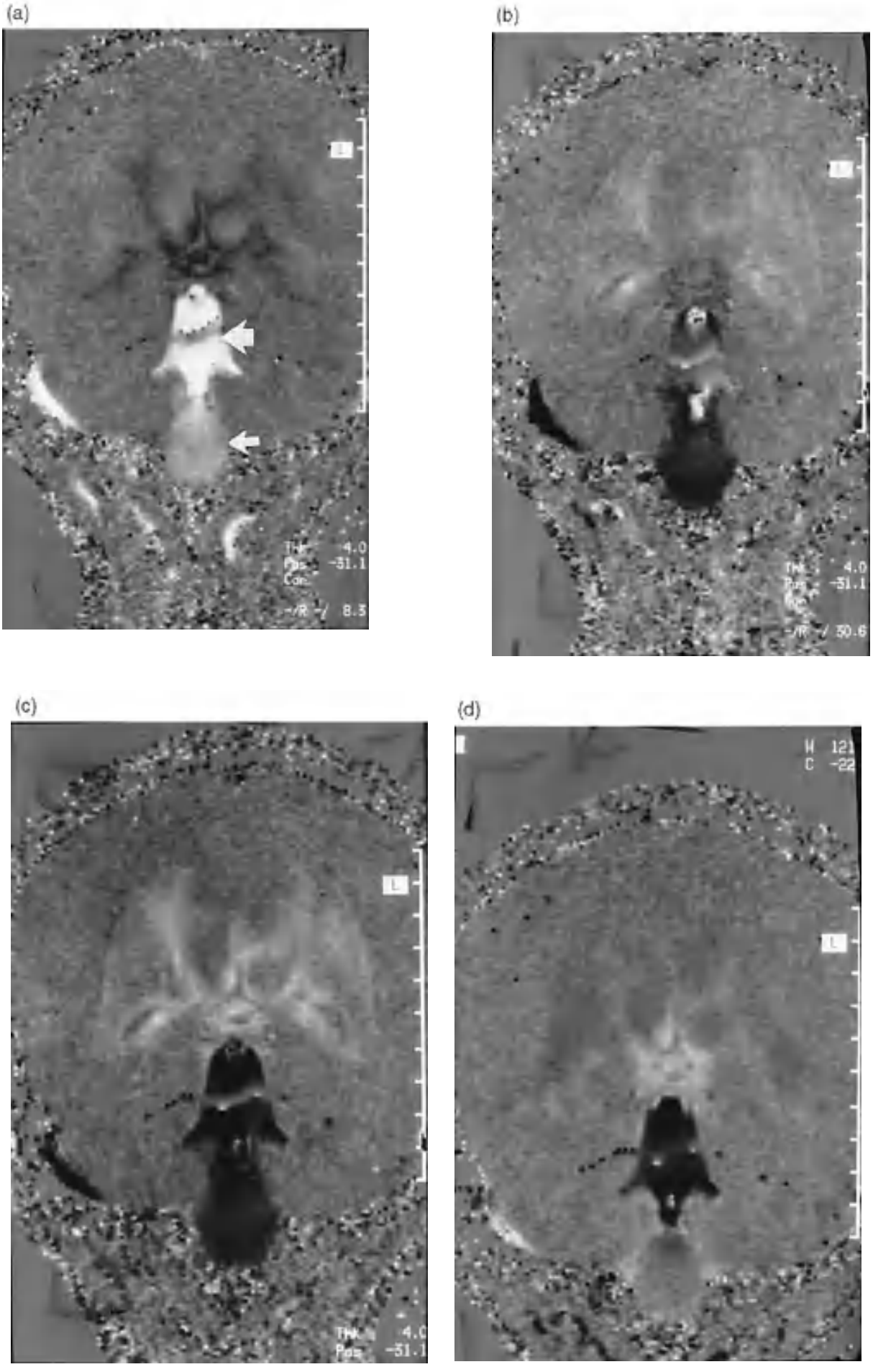
(a)
(b)
(c)
(d)

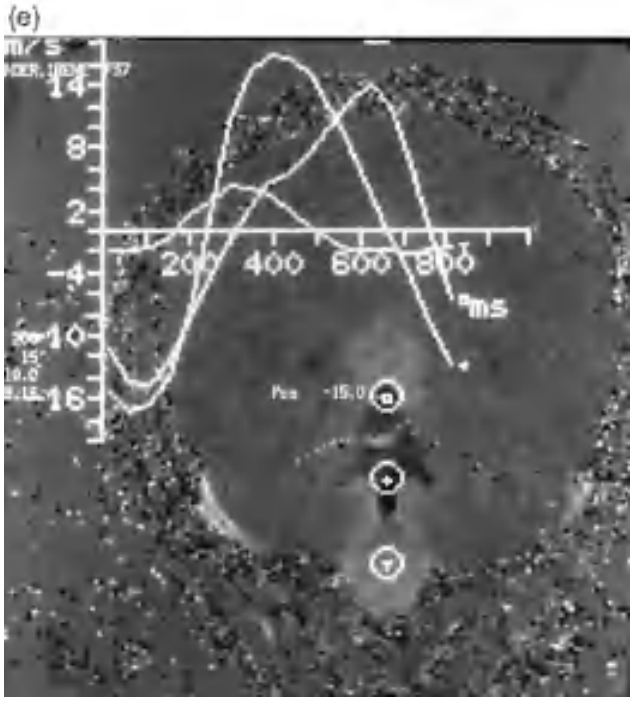

Figure 8 The 'rebound sign' in an arachnoid cyst. The qualitative (sagittal) technique has been rotated into the coronal plane with velocity encoding along the craniocaudal read-out axis. White, downward flow; black, upward flow (no flow is gray). (a) During systole, flow in the fourth ventricle (large arrow) is down while flow in the arachnoid cyst (small arrow) has stopped due to maximal deformation by the surrounding CSF. (b) 200 ms later, flow in the fourth ventricle has stopped (turning gray), while flow in the cyst has already started heading up (turning black). (c) 200 ms later, both the flow in the cyst and that in the fourth ventricle are up. (d) 100 ms later, the cyst has become maximally deformed and has stopped flowing (turning gray), while flow continues in the caudocraniad direction in the fourth ventricle. (e) By placing cursors on the fourth ventricle and the cyst, motion in the cyst is seen to be of lower amplitude and 90° phase-advanced relative to the flow within the fourth ventricle

resolution axial technique which provides a measurement of the aqueductal CSF stroke volume. In a recent study of 20 patients with clinically suspected NPH, 14 were found to have hyperdynamic CSF flow, i.e. stroke volumes greater than 40 μL, while six were found to have hypodynamic flow.[26] Of the patients with hyperdynamic flow, 13 of 14 responded favorably to the ventriculoperitoneal shunt. (The one patient who did not was known to have chronic multiple sclerosis.) Thus this technique has an excellent positive predictive value. Of the six patients who had hypodynamic flow, three responded to shunting and three did not, probably reflecting the presence of concomitant atrophy in these patients. Interestingly, of the 14 patients with hyperdynamic flow (as determined by the measured stroke volume), only seven (50%) had hyperdynamic CSF flow voids on their routine MR images. This most likely reflects the current widespread use of first-order flow compensation on the proton density-weighted images which was not available on the 1984 images in the earlier study.[10] Thus, quantitative CSF velocity imaging is an even better technique than routine MRI to determine the presence of shunt-responsive normal pressure hydrocephalus.

CSF velocity imaging is also useful in the evaluation of potential shunt malfunction.[27] In patients who have been shunted for communicating hydrocephalus, the normal pattern of CSF flow through the aqueduct is exactly 180° out of phase with normal with respect to the cardiac cycle, i.e. CSF flows caudocraniad during systole and craniocaudad during diastole (Figure 6). This probably reflects the fact that the shunt tube is the lowest resistance pathway to outflow of CSF following systolic expansion of both the cerebrum and the cerebellum. In patients with either obstructive or communicating hydrocephalus, the high-resolution axial technique can also be used to assess flow through the shunt tube itself (Figure 7). In cases of normal shunt function, CSF motion tends to be intermittent and unidirectional, rather than sinusoidal (as is normally seen through the aqueduct), reflecting the presence of the one-way valve.

Since the plane and position of both CSF velocity imaging techniques can be modified, they can also be used to distinguish cysts from enlarged CSF spaces. Within a cyst, the motion of CSF appears to rebound against the flowing CSF around it. This 'cyst rebound sign'[28] is the combination of decreased CSF velocity (within the cyst) 90° phase-advanced relative to the motion of the surrounding CSF (Figure 8).

5 RELATED ARTICLES

Brain Parenchyma Motion Observed by MRI; Marker Grids for Observing Motion in MRI; Phase Contrast MRA; Whole Body Magnetic Resonance Angiography.

6 REFERENCES

1. W. G. Bradley and R. M. Quencer, in 'Magnetic Resonance Imaging', 2nd edn, eds D. D. Stark and W. G. Bradley. Mosby-Yearbook, St Louis, MO, 1992, Chap. 28.
2. W. G. Bradley, K. E. Kortman, and B. Burgoyne, *Radiology*, 1986, **159**, 611.
3. J. L. Sherman and C. M. Citrin, *Am. J. Neuroradiol.,* 1986, **7**, 3.
4. W. G. Bradley and V. Waluch, *Radiology*, 1985, **154**, 443.
5. S. Hakim, Thesis No. 957, Javerian University, School of Medicine, Bogota, Columbia, 1964.
6. R. D. Adams, C. M. Fisher, S. Hakim, R. G. Ojemann, and W. H. Sweet, *N. Engl. J. Med.*, 1965, **273**, 117.
7. S. Hakim, J. G. Venegas, and J. D. Burton, *Surg. Neurol.* 1976, **5**, 187.
8. J. Ekstedt and H. Friden, in 'Hydrocephalus' eds. K. Shapiro, A. Marmarou, and H. Portnoy, Raven, New York, 1984.
9. E. L. Foltz, in '*Hydrocephalus*', eds. K. Shapiro, A. Marmarou, and H. Portnoy, Raven, New York, 1984.
10. W. G. Bradley, A. R. Whittemore, K. E. Kortman, A. S. Watanabe, M. Homyak, L. M. Teresi, and S. J. Davis, *Radiology*, 1991, **178**, 459.
11. G. H. DuBoulay, *Br. J. Radiology.*, 1966, **39**, 255.
12. W. G. Bradley, A. R. Whittemore, A. S. Watanabe, S. J. Davis, L. M. Teresi, and M. Homyak, *Am. J. Neuroradiol.*, 1991, **12**, 31.
13. C. M. Citrin, J. L. Sherman, R. E. Gangarosa, and D. Scanlon, *Am. J. Roentgenol.*, 1987, **148**, 205.
14. S. W. Atlas, A. S. Mark, and E. K. Fram, *Radiology*, 1988, **169**, 449.
15. D. A. Feinberg, L. E. Crooks, P. Sheldon, J. Hoenninger, J. C. Watts, and M. Arakawa, *Magn. Reson. Med.*, 1985, **2**, 555.
16. D. A. Feinberg and A. S. Mark, *Radiology*, 1987, **163**, 793.
17. R. R. Edelman, H. P. Mattle, J. Kleefield, and M. S. Silver, *Radiology* 1989, **171**, 551.
18. L. Axel and L. Dougherty, *Radiology*, 1989, **171**, 841.
19. R. M. Quencer, M. J. Post, and R. S. Hinks, *Radiology*, 1990, **32**, 371.
20. D. R. Enzmann and N. J. Pelc, *Radiology*, 1991, **178**, 467.
21. W. R. Nitz, W. G. Bradley Jr., A. S. Watanabe, R. R. Lee, B. Burgoyne, R. M. O'Sullivan, and M. D. Herbst, *Radiology*, 1992, **183**, 395.
22. T. A. Spraggins, *Magn. Reson. Imaging*, 1990, **8**, 676.
23. D. N. Firmin, G. L. Nayler, P. J. Kilner, and D. B. Longmore, *Magn. Reson. Med.*, 1990, **14**, 230.
24. P. R. Moran, *Magn. Reson. Imaging*, 1982, **1**, 197.
25. W. J. Mullin, D. Atkinson, R. Hashemi, J. Yu, and W. G. Bradley, *J. Magn. Reson. Imaging*, 1993, **3**, 55.
26. W. G. Bradley, D. Scalzo, J. Queralt, W. N. Nitz, D. J. Atkinson, and P. Wong, *Radiology,* 1996, **198**, 523.
27. W. G. Bradley, D. Atkinson, D.-Y. Chen, W. R. Nitz, and W. J. Mullin, *Radiology,* 1993, **189**, 223.
28. M. D. Herbst, W. G. Bradley, W. R. Nitz, B. Burgoyne, R. R. Lee, and R. M. O'Sullivan, *Radiology*, 1991, **181**, 287.

Biographical Sketch

William G. Bradley, Jr. *b* 1948. B.S., Chemical Engineering Caltech, 1970; Ph.D., Chemical Engineering, Princeton, 1974; M.D. UCSF 1977; Internship UCSF, 1978; Radiology Residency UCSF, 1981. Introduced to NMR by J. D. Roberts in 1968 and to MRI by L. Crooks in 1979. Approx. 150 publications and 10 textbooks including 'Magnetic Resonance Imaging' with David D. Stark. President, SMRI 1988–89. Currently Director of MRI and Radiology Research, Long Beach Memorial Medical Center, and Professor of Radiology, University of California at Irvine.

Head and Neck Studies Using MRA

Paul M. Ruggieri, Jean A. Tkach, and Thomas J. Masaryk

Cleveland Clinic Foundation, Cleveland, OH, USA

1 INTRODUCTION

Magnetic resonance angiography (MRA) is most commonly applied to the evaluation of cerebrovascular disease as neurological examinations continue to be the mainstay of clinical MRI. In addition, the rapid blood flow through the extra-/intracranial cerebral vasculature, the paucity of gross physiological motion, and the existing coil technology make these vessels ideally suited to vascular MRI. MRA is especially appealing since it provides a morphological representation of the vasculature as a relatively rapid, noninvasive alternative to the existing vascular imaging modalities. During the same examination, conventional spin echo images of the brain parenchyma are acquired to assess the consequences of the underlying vascular pathology.

1.1 Carotid MRA: Technical Considerations

Two basic types of MRA sequences are commonly employed to study the cerebral vasculature: phase contrast (PC) and time-of-flight (TOF).[1,2] The PC technique provides optimal suppression of the background stationary tissues via subtraction of alternating flow encoded images, and can be designed to be highly sensitive to blood moving at specific velocities. Appropriately calibrated sequences can also be designed to measure flow velocities. However, this technique demands longer acquisition and postprocessing times than the TOF studies of comparable spatial resolution. The phase sensitivity of this method also makes it more vulnerable to intravascular signal loss due to complex motion (e.g. carotid bifurcation stenosis) and/or local field inhomogeneities (e.g. carotid siphon, densely calcified atherosclerotic plaque).[3] Consequently, the PC study is not commonly used to evaluate the carotid bifurcations in routine clinical work. A 2D PC study is useful as a quick scout view for subsequent positioning of the 2D or 3D TOF volumes and to confirm vessel patency. The 2D PC technique may also prove to be useful for making flow velocity measurements in the region of a carotid stenosis (similar to duplex ultrasound studies).

The TOF techniques take advantage of the rapid, constant inflow of fresh unsaturated spins to provide the necessary contrast relative to the adjacent stationary tissues. In lieu of subtraction mask acquisitions, angiographic images are rendered using computer postprocessing algorithms which may then create multiple MRA images from a single data set. The TOF methods are capable of minimizing intravoxel phase dispersion (and intravascular signal loss) by incorporating very small voxels and very short echo times with motion refocusing gradients.[4] Alternatively, the TOF sequences are not as sensitive to slow flow as the PC techniques. The TOF images also have less effective background suppression. Because the TOF studies are inherently T_1-weighted, and the commonly used postprocessing method (maximum intensity projection or MIP) cannot necessarily distinguish bright vessels from other tissues with short T_1 relaxation times (e.g. fat, subacute hemorrhage), the vessels in the volume may be obscured by adjacent tissues. The MIP reconstruction technique may introduce additional artifacts in all MRA images. Small vessels may frequently be visible in the original slices but are not represented in the MRA image because of: (1) variation in background intensities; (2) marginal flow-related enhancement; and (3) partial volume averaging artifacts.[5]

Neither the PC nor the TOF technique can provide the contrast and spatial resolution needed to identify very subtle contour abnormalities which would be important in confirming mild vascular dysplasias (e.g. fibromuscular disease) or vasculitis that would only be evident using conventional arteriography. These limitations are predominantly related to signal-to-noise ratio (S/N) issues and the hardware (e.g. gradients, computer memory, processing speed) constraints imposed on the MRA pulse sequences. The two techniques are also unable to provide the same dynamic information as with catheter angiography.

1.2 Carotid MRA: Clinical Significance

MRA has the potential to make its greatest impact on routine clinical work in the evaluation of carotid bifurcation atherosclerotic disease. Justification for imaging the carotid bifurcations is based on the conclusions of the North American Symptomatic Carotid Endarterectomy Trial (NASCET) and the European Carotid Surgery Trial (ECST). These controlled randomized clinical studies support the clinical utility of carotid endarterectomies in symptomatic patients with severe (>70%) carotid bifurcation stenosis, and set well defined standards for the preoperative evaluation of these patients (angiographic demonstration, specific measurements of the stenosis, significant tandem lesions).[6–10]

Ideally, it would be preferable to replace the conventional catheter arteriogram with a noninvasive alternative, thereby avoiding the potential risks of the invasive study. As many of the symptomatic patients with cerebrovascular disease are evaluated by spin echo MRI to assess the severity of the parenchymal sequelae, MRA of the carotid and intracranial vasculature would be a logical (noninvasive) extension of such studies. However, this makes the assumption that MRA can provide the same information as the invasive study and has similar sensitivity and specificity. The questions that remain to be proven in large scale, prospective clinical trials include the following: (1) can MRA characterize carotid stenoses of 70–99% severity, (2) distinguish complete occlusion from severe stenosis, and (3) exclude tandem stenoses as accurately as catheter angiography? Among these questions, the issue with the least objective data is the ability of MRA to exclude the presence of tandem stenoses, most commonly in the carotid siphon. The presence of distal stenoses have been associated with an increased risk for cerebrovascular and cardiac complications, suggesting a subpopulation with more malignant

atherosclerosis.[11,12] Moreover, although 3D TOF and PC MRA continue to improve, there are frequently artifacts mimicking stenoses of the carotid siphons due to complex flow and/or local field inhomogeneities.[13,14] In the evaluation of carotid bifurcation disease, MRA is currently most appropriately assigned the role of a screening study for significant atherosclerotic disease which would be best followed up by conventional angiography, preoperatively.

1.3 Carotid MRA: Technical Considerations

In 2D TOF imaging, the carotid arteries are visualized by acquiring a series of thin 2D axial gradient echo images sequentially (superior to inferior) against the direction of flow. The high signal from the venous structures (particularly the jugular vein) can obscure the carotid bifurcation, but a traveling saturation pulse is placed superior to each excitation slice to eliminate the signal from the caudally directed venous flow.[15] The motion-induced dephasing (intravascular signal loss) is minimized through a combination of constant velocity flow compensation gradients along the slice-select and frequency-encoding directions, the shortest possible echo times (8.0–9.0 ms with conventional gradients), and the smallest possible voxels (1.5–3.0 mm slice thickness and 1.0 mm in-plane resolution).

The major advantage of 2D TOF sequences relate to their sensitivity to slow flow as the spins must only move a short distance (1.5–3.0 mm 2D slice) within each *TR* interval to ensure high intravascular signal in each slice. Consequently, these sequences are readily able to distinguish a severe stenosis from an occlusion. A disadvantage of the 2D technique is the stair-step misregistration artifact or vessel discontinuities in the final MRA arteriogram images that arise due to gross patient motion during the acquisition of the individual slices. More importantly, the 2D sequences demand high gradient amplitudes to define the thin 2D slices, which, in turn, place significant restrictions on the minimum echo time and in-plane voxel dimensions. The high gradient amplitudes accentuate any spin dephasing due to motion which is not corrected by the flow compensating gradients. As a result, severe stenoses are often seen as 'flow voids' or vascular interruptions. In spite of this, 2D TOF MRA has been demonstrated to be a highly sensitive and very acceptable screening study.[16]

3D TOF sequences incorporate the same strategies for vessel visualization as their 2D counterparts, but the rf pulse excites a thick slab of tissue during each *TR* interval and the thin slices within the volume are defined by a second phase-encoding gradient along the slice-select direction. The examination time increases in proportion to the number of phase-encoding steps in the second direction (number of slices), but there is also a proportional increase in the S/N when contrasted to comparable size voxels in 2D sequences. As a result of the reduced gradient demands, the 3D sequences permit shorter echo times (4.5–7.0 ms) and higher spatial resolution (<1.0 mm^3) with comparable refocusing pulses when contrasted to the 2D TOF sequences. These factors combine to minimize the degree of intravoxel phase dispersion and signal loss within the vessel.[17] The phase errors increase quadratically with time in the setting of higher order motion terms so intravascular signal loss is especially likely within and immediately distal to a stenosis, within a focal tortuosity, and in some normal vessel bifurcations. Since the greatest amount of dephasing occurs during the application of the gradients, the phase errors are most effectively suppressed by minimizing the duration, amplitude, and timing of the gradients.[18] Additional flow compensation gradients can be incorporated to correct for the higher order motion terms but only at the expense of significantly stronger and longer gradients before the echo. The signal loss with the longer gradients more than offsets the minimal improvement derived from the supplementary motion compensation. Because these sequences are all gradient echo acquisitions, the intravascular signal is also reduced by T_2* phenomena. This effect is similarly reduced with small voxels and short echo times.[19]

The rapid unidirectional flow in the carotid arteries is particularly well suited to a 3D TOF acquisition. This technique also has its limitations which primarily relate to the saturation of flowing spins (e.g. slow antegrade flow distal to a severe stenosis). Spatially variable rf pulses (lower flip angle as the spins enter the volume and higher flip angles distally in the volume) have proven particularly helpful in this regard. The vessel/soft tissue contrast is somewhat reduced at the caudal end of the volume, but the contrast increases superiorly and the spins can flow further into the volume before becoming saturated without increasing the *TR*. Higher flip angles at the cranial end also increase the saturation of the stationary tissues for a given *TR*. The advantages of this rf pulse are particularly noticeable with slow flow such as in an elderly patient with poor cardiac output, a very small vessel lumen, or distal to a severe stenosis.

Failure to adequately suppress the background stationary tissues is a limitation of any TOF technique, but particularly the 3D technique in view of the lower signal of the blood (relative to 2D TOF). Excitation with higher flip angles improves the flow-related enhancement but accentuates the problem of spin saturation in 3D acquisitions. Shorter repetition times enhance the background suppression while causing more saturation of the flowing spins. In the neck, fat is the most problematic, as its short T_1 relaxation time and high spin density causes it to appear bright on the final MRA images. Since there tends to be a large amount of perivascular and subcutaneous fat in older patients (the group most likely to be studied for carotid atherosclerotic disease), the fat can largely obscure the underlying vessels. Reconstructing a subvolume that is limited to the region immediately surrounding the vessels excludes much of the stationary tissue from the reconstruction but does not eliminate the problem. Incorporating additional fat suppression pulses into these sequences will reduce the signal of the fat without affecting the vessel signal and can significantly improve the vessel/soft tissue contrast-to-noise level.[20] In practice, these pulses can be unreliable in clinical studies since local field inhomogeneities in the neck may cause inhomogeneous fat suppression or even water (blood) suppression.

In light of the above arguments, a most promising clinical method is the stacked overlapping 3D volume technique, which combines many of the advantages of the 2D and 3D studies.[21] Relatively small volumes minimize the problem of spin saturation while the lower gradient demands of the 3D sequences allow for very short echo times and small voxels. Moreover, the stacked volume approach can be implemented with higher flip angles and/or shorter *TR* values than are possible with a large single 3D volume so the vessel/soft tissue contrast is

enhanced. If the stacked volumes incorporate the specialized rf pulses as discussed above, intermediate sized volumes can be used to improve the postprocessing, increase the anatomical coverage, and reduce the overall examination time.

1.4 Carotid MRA: Clinical Applications—Carotid Bifurcation

A number of studies have evaluated the clinical efficacy of 2D TOF MRA for imaging the carotid bifurcations, the largest of which was a study by Laster et al. in which the images from 101 patients were compared with conventional catheter angiography and, in some cases, Doppler ultrasound.[22,23] As in any MRA technique, the degree of lumenal narrowing tends to be accentuated compared with the conventional arteriogram images. Because of the limitations in echo time and voxel size with the 2D technique, the dephasing caused by higher order motion terms induces more prominent intravascular signal loss and therefore greater apparent narrowing of the lumen than with the 3D technique. In the case of a severe stenosis, there is frequently a flow void or complete absence of signal in the involved segment so the morphology of the stenosis cannot be defined at all. The reader simply concludes that the vessel is severely stenotic because there is complete loss of signal in that segment with reappearance of the vessel distally. Whereas the MRA images agreed with the catheter studies in up to 75% of cases, overestimation of the stenosis was seen in up to 44%.[24,25] As expected, the highest percentage of these errors was evident in those studies with relatively long echo times and large voxel dimensions. The most significant error, however, was seen in those cases of moderate stenoses which were labeled as 'severe' on MRA. This was a problem even with a slice thickness of 1.5 mm and echo times of approximately 9.0 ms.[24] If MRA is used as the sole imaging study preoperatively, a carotid endarterectomy may be recommended inappropriately. It can be argued that Doppler ultrasound could be performed in conjunction with the MRA, but the ultrasound also has potential pitfalls such as operator dependence, machine variability, vessel tortuosity and plaque calcification leading to nondiagnostic studies, overestimation of stenoses, and (although less commonly with color flow systems) misdiagnoses of complete occlusion at the bifurcation.

Although it is difficult to depict the morphology of severe stenoses, the sensitivity of the 2D TOF technique to slow flow generally makes it readily able to distinguish a severe stenosis from an occlusion if the slice thickness is sufficiently small, the *TR* is sufficiently long, and a long enough segment of the vessel is evaluated to include a segment in which the flow has returned to a laminar profile.[22] Nevertheless, in a few cases, MRA overestimates a critical stenosis as an occlusion which has important clinical implications as the patient is no longer considered a surgical candidate if the vessel is occluded.

The 2D TOF studies have also been compared to Doppler ultrasound examinations of the carotid bifurcations. The only noticeable difference was that the MRA studies tended to be less likely to misdiagnose a severe stenosis as an occlusion, but there was ultimately no statistically significant difference in accuracy between the two modalities.[24,26] Both studies tended to overestimate the degree of carotid stenosis. Even when the results of the two examinations are in agreement, they still do not necessarily correlate with the invasive arteriogram and may not have the accuracy to replace the conventional study.[24–26]

Other groups have primarily relied upon 3D TOF imaging in patient studies because of a lesser degree of flow-related dephasing and, consequently, improved characterization of carotid stenoses. When single-volume 3D TOF MRA was compared to intra-arterial digital subtraction angiography (IADSA) using a caliper technique, ROC analysis showed that technically adequate 3D TOF MRA images can be interpreted consistently, show a very strong correlation with IADSA, and that 3D TOF MRA may be a sensitive screening examination for extracranial carotid stenoses.[27] In spite of the advantages of the 3D sequence parameters, the more severe stenoses may still be accentuated due to higher order motion in the region of the stenosis. As alluded to above, another obvious limitation of the 3D technique is its potential to misrepresent a severe stenosis as an occlusion so 2D and 3D TOF carotid MRA investigations have been combined in patient examinations to avoid this pitfall.[28]

Even when the 2D and 3D TOF studies are combined, it seems unlikely at this time that MRA, duplex ultrasound, or the combination of the two can replace conventional angiography in patients who are being considered for surgery. It would be more appropriate for these modalities to serve as a screening examination, and, if a significant stenosis is detected, an invasive diagnostic study can be performed for further evaluation prior to surgical intervention. Based on the guidelines set by the NASCET study, it is now not only necessary to measure accurately the lumenal narrowing but it is also necessary to exclude the presence of a tandem stenosis elsewhere in the carotid circulation.[6] Moreover, it is important to measure the stenosis in a consistent fashion and to have the capability to distinguish different gradations of severe lumenal compromise since the NASCET study demonstrated a greater benefit of the endarterectomies with increasing severity of the stenoses. While the 3D TOF technique characterizes the morphology of the stenotic segment more accurately than 2D studies, both tend to exaggerate the degree of narrowing and may show complete signal void within the stenosis (particularly in the 2D studies) (Figure 1).

Further improvements should be realized with improved gradient capabilities which will permit shorter echo times, higher resolution, and reduced intravoxel dephasing at the site of severe stenoses.[18,29]

1.5 Carotid MRA: Clinical Applications—Carotid Dissection

Dissection of the carotid artery is not an infrequent cause of stroke but tends to occur in younger adults than strokes relating to atherosclerotic disease. If the clinical suspicion is low, a carotid dissection is only one possible explanation for the patient's clinical presentation, and/or there is a relative contraindication to conventional angiography. MRI in conjunction with MRA serves as a noninvasive alternative to evaluate for dissection and to identify simultaneously the extent of parenchymal sequelae. Catheter angiography, however, remains the gold standard, and is the most reliable means by which the underlying etiology can be identified (e.g. fibromuscular dysplasia). The conventional study may also be the only method

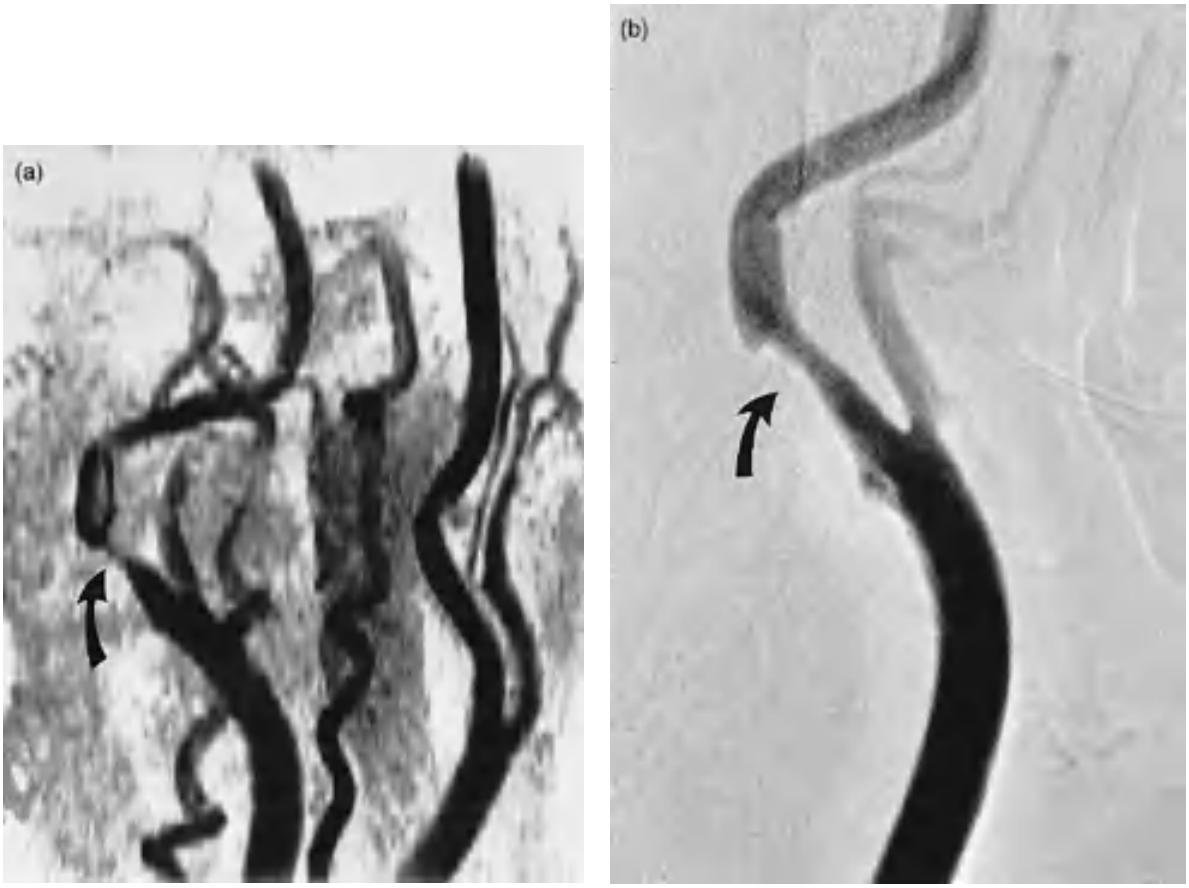

Figure 1 (a) Stacked overlapping volume acquisition of the carotid bifurcations shows no significant saturation despite the tortuosity of the vessels and the proximal stenosis of the internal carotid artery. (b) The degree of stenosis (arrow) is less severe in the conventional arteriogram, likely due to the long gradient duration for the MRA acquisition

of fully appreciating the extent of collateral filling of the intracranial circulation if the alternative routes are circuitous with slow flow in small vessels. Alternatively, it is also possible to have a false-negative catheter study if the vessel is completely occluded (nonfilling) or the dissection is subadventitial (normal size and configuration of the lumen) and the MRI/MRA study may be the best way to confirm the diagnosis by demonstrating the perilumenal blood products.[30] In routine T_1- and T_2-weighted spin echo imaging the dissection is generally detected as a crescentic area of hyperintensity around a narrowed lumen of the cervical internal carotid artery.[31] In particular, an axial T_1-weighted spin echo study using fat saturation and an inferior spatial saturation pulse suppresses the signal of the perivascular fat and intraluminal flow-related enhancement, thereby increasing the conspicuity of the hyperintense (short T_1) periluminal hemorrhage.[32]

MRA is used to complement conventional spin echo imaging in the evaluation of patients with suspected carotid dissections.[33] As in IADSA studies, the internal carotid artery may appear narrowed and there may be poor flow-related enhancement proximally if the outflow through the internal carotid artery is severely impaired. The dissection is often imaged when the periluminal hemorrhage contains methemoglobin, so the vessel lumen can appear artifactually widened on the MRA since the hyperintense thrombus is similar in intensity to the flow-related enhancement in the true lumen. Because of the variability in the state of evolution of the thrombus, the hemorrhagic by-products are either hyperintense or hypointense relative to the lumen. If the distinction between lumen and hemorrhage is not apparent on the projection arteriogram images, the two lumena and the intervening flap are usually evident in the source images for the MRA.

1.6 Intracranial MRA: Technical Considerations

The intracranial circulation presents problems similar to those seen in the evaluation of the extracranial cerebral vasculature except the studies are further complicated by smaller vessels, field inhomogeneities, and reduced through-plane flow. The 3D sequences seem particularly well suited to this situation as they not only provide the high spatial resolution needed to visualize the smaller vessels but they also provide the reconstruction capabilities (maximum intensity projection) necessary to display the complex intracranial vascular geometry. Intracranially, local field inhomogeneities exist at air–soft tissue and bone–soft tissue interfaces while higher order motion terms occur at focal vessel tortuosities, bifurcations, and lumenal stenoses. Both of those factors are limited by small voxels and short echo times. In comparison to the 2D sequences, the 3D acquisitions are better able to demonstrate the large component

of in-plane flow intracranially (with appropriate adjustments in the *TR* and flip angle to avoid saturation).

The reduced flow velocities and large component of in-plane flow are still somewhat limiting in the 3D acquisitions as these factors aggravate the problem of spin saturation, thereby reducing the vessel–soft tissue contrast particularly in the distal volume. Adjustments in the conventional imaging parameters provide only limited benefit. The incorporation of magnetization transfer saturation in all intracranial TOF MRA studies has become routine.[34] Since the off-resonance saturation pulse suppresses the signal of the bound water molecules, and the bound component is largely restricted to the brain parenchyma, the magnetization transfer saturation effectively enhances the vessel–soft tissue contrast. Additional vascular contrast may be obtained by incorporating the spatially varying rf pulses for excitation designed to limit the problem of spin saturation. Because of the slower flow rates in the intracranial arteries, the most promising TOF technique seems to be the stacked volume approach, which combines the advantages of 2D and 3D TOF acquisitions.[21]

Phase contrast sequences are also commonly used to evaluate the intracranial circulation. The vessel geometry and small size of the arteries make the 3D acquisition necessary for most purposes but, for comparable spatial resolution and flow sensitization along all three planes, the acquisition time is longer and the postprocessing more complex for the 3D PC technique. Alternatively, 2D acquisitions may provide similar flow information relatively quickly, but at the expense of limited anatomical coverage. A problem common to both phase contrast techniques is the need for some a priori knowledge of the range of velocities present within a given patient or lesion. Inappropriate choice of the velocity-encoding gradient can cause poor visualization of the small and/or peripheral vessels with slow flow if the chosen velocity-encoding gradient is too weak, or aliasing of flow information and signal loss if the chosen velocity range is too low. On the other hand, the freedom to choose different velocity encodings provides options that are not possible or more cumbersome in a TOF acquisition such as the direction of blood flow (e.g. collateral flow in the circle of Willis).[35,36] Alternatively, directional information is easily attainable in the PC acquisition without performing a separate study. The PC studies also readily provide the capability to measure flow velocities and volume flow rates of individual vessels. Lastly, if 2D PC studies are performed in a cardiac gated cine mode, the flow dynamics in various vascular lesions can be studied at different, specified velocity ranges which is only possible in a very limited fashion with TOF techniques.

1.6.1 Intracranial MRA: Aneurysms

The statistics relative to subarachnoid hemorrhage from a ruptured intracranial aneurysm remain devastating—greater than 50% mortality and major morbidity.[37] Given the low operative morbidity and mortality of surgery on unruptured aneurysms, it is appealing to consider the possibility of using MRA as a screening test. It would be especially applicable in patient groups where there is an increased incidence or a high anxiety level for an aneurysm, such as patients with a strong family history, polycystic kidney disease, aortic coarctation, fibromuscular disease, and collagen vascular disease. Based on the decision analysis of Levy et al., the risk of an aneurysm even in these groups does not warrant the screening of all these patients with conventional arteriography.[38] It is possible, however, to perform an accurate noninvasive pretest that would increase the prevalence in subgroups which could then be studied by conventional arteriography for further evaluation. Based on the results of MRA in the evaluation of intracranial aneurysms, MRA exceeds the criteria of sensitivity and specificity for the noninvasive pretest outlined by Levy et al.[37,39] It is possible to use high resolution contrast enhanced computerized tomography (CT) to study these patients, but the sensitivity and specificity have not been studied, and the requirement of intravenous iodinated contrast and the beam hardening artifact from the skull base are potentially limiting, which make MRA preferable.[40] Currently, TOF MRA is frequently used as a screening test in these groups or in stable patients with a subacute onset of symptoms in which an intracranial aneurysm is only one of a number of potential explanations for the clinical presentation and the suspicion of an aneurysm is not high enough to warrant a conventional arteriogram (Figure 2). However, the patients who present acutely with a subarachnoid hemorrhage are best served by a nonenhanced head CT followed by conventional catheter angiography.

Retrospective studies have been conducted to test the accuracy of the 3D TOF MRA method for the detection of intracranial aneurysms as compared to IADSA examinations.[39,41,42] Aneurysms as small as 3–4 mm have been detected using 3D TOF and 3D PC techniques. In a series of 21 angiographically confirmed aneurysms in 19 patients, the authors demonstrated an increase in sensitivity from 67% when evaluating the 3D TOF MRA projection images alone, to 86% when the MRA arteriogram images were evaluated along with the source images from the 3D data set and the spin echo images. Using the MIP images, the individual slices, and the spin echo study, the sensitivity was calculated to be 95% for the detection of at least one aneurysm in a patient such that the study would lead to the referral for a conventional arteriogram for further evaluation preoperatively.

Recognizing the limitations of these MRA acquisitions becomes particularly important when choosing the method of postprocessing, interpreting the images, and recommending a conventional arteriogram as a follow-up study or in place of MRA. Larger aneurysms or aneurysms compressing the parent vessel may reduce the extent of inflow and washout of fresh unsaturated spins within the aneurysm lumen, which causes an apparent reduction of the size of the aneurysm on TOF studies.[41] This is less of a problem with a PC acquisition if the preliminary spin echo study reveals a giant intracranial aneurysm, so that a low velocity encoding range can be selected for PC MRA.[42] On the other hand, these lesions are also obvious on the spin echo study owing to the prominent flow artifacts, intimate relationship with the adjacent basilar vessels, and (if present) the contained blood products.

The stagnant flow within a large aneurysm tends to promote thrombus formation which partially fills the aneurysm lumen. Since the TOF sequences are inherently T_1 and spin density weighted, both the thrombus and the patent lumen may be visible on the MIP images, depending on the state of evolution of the thrombus just as in conventional IADSA. This will cause an underestimation of the overall aneurysm size in PC studies because of the strong background suppression. In the case of

subarachnoid hemorrhage, the aneurysm and the parent vessel may not be observed altogether.

Although the gross relationships with the parent vessel may be visible, identification of the aneurysm neck may be difficult at times when evaluating the projection images and occasionally with conventional cerebral angiography. In these cases, evaluation of the 3D TOF source images and multiplanar reconstructions of the original slices create 'angiotomograms' to delineate more clearly both the aneurysm and its point of origin. Alternatively, reconstructing vessels from small subvolumes that contain only the vessels of interest provides images with better definition (reduces the artifact inherent to the MIP algorithm) and eliminates the problems relating to vessel overlap.[5] This is especially helpful with aneurysms arising from a tortuous carotid siphon or in determining which branch the aneurysm arises from if it occurs at a bifurcation (e.g. middle cerebral artery bifurcation/trifurcation). More importantly, routine evaluation of the source images and planar reconstructions of the axial slices reduces the likelihood of missing small aneurysms that may otherwise be missed by reviewing only the projection MRA images.

Identifying the relationship of the aneurysm to the parent vessel may also be difficult if the aneurysm arises from an arterial segment that is incompletely visualized due to motion induced dephasing. This is most commonly seen in the carotid siphon, particularly if the supraclinoid segment is immediately apposed to the juxtasellar segment so the turn of the siphon is rather tight. Because of a greater tendency towards motion induced dephasing, this should be more problematic with PC than TOF acquisitions. Shorter gradient times and smaller voxels significantly reduce the phase dispersion and signal loss in these vessels.[19–21]

MRA can also be applied to the long term postoperative follow-up of aneurysm patients treated via an endovascular route (e.g. balloon occlusion) or noninvasive follow-up of a known, untreated aneurysm (Figure 2). Susceptibility artifacts from the nonferromagnetic aneurysm clips preclude the evaluation of aneurysms treated by surgical clipping but would not prohibit the use of MRA to evaluate for intracranial aneurysms elsewhere.

1.6.2 Intracranial MRA: Arterial Occlusive Disease

Patients with symptoms of cerebral ischemia are frequently examined by MRI to assess the extent of parenchymal ischemic disease. The morphology and signal characteristics of the vessel lumena can only suggest stenosis and slow flow or occlusion, whereas MRA can directly identify the site and severity of the underlying stenosis. Not infrequently, the patient has already had a Doppler ultrasound study of the carotid bifurcations, and the ischemic symptoms are not explained by the mild narrowing in the carotid bifurcations. MRA provides an additional noninvasive study which can be performed at the same time as the spin echo study to evaluate the morphology of the intracranial vessels. Alternatively, in a patient with severe stenosis, MRA provides the means by which the physician can evaluate the degree of collateral flow to the circulation that is severely compromised in the extracranial circulation. As compared with transcranial Doppler ultrasound studies, MRA is better able to evaluate the posterior fossa circulation and provides an anatomical display of the intracranial vasculature that is not possible with the transcranial Doppler technique.[43,44] The MRA findings can alert the clinician to the nature and location of the occlusive disease and a conventional

Figure 2 (a) This 55-year-old woman is known to have a basilar tip aneurysm and is presenting for noninvasive follow-up. The aneurysm is seen as a rounded hypointense focus (arrow) in the interpeduncular cistern. (b) The 3D TOF MRA image confirms the aneurysms (arrow), including its size and orientation with respect to the parent vessel

angiographic study could then be performed to confirm the full extent of pathology prior to starting therapy if the MR/MRA findings do not explain the clinical situation or if surgical or endovascular therapy is being considered. Alternatively, a negative study might avert the need for an invasive diagnostic examination altogether. The hope for the future is that MRA can effectively evaluate for tandem stenoses in the distal internal carotid arteries in patients being considered for carotid endarterectomies and, in combination with a similar noninvasive study of the carotid bifurcations, can obviate the need for an invasive study preoperatively (i.e. noninvasively meet the NASCET criteria).

Initial studies have been restricted to the evaluation of the larger vessels such as the carotid siphon, the proximal anterior and middle cerebral arteries, the distal vertebral arteries, and the basilar trunk. This is, in part, related to the spatial resolution limitations of these sequences and the small vessel caliber of the intracranial vasculature. Narrowing of the distal peripheral vessels, typical of cerebral vasculitis, cannot be effectively evaluated with MRA, and requires a conventional arteriogram. Flow rates also impose restrictions in the TOF acquisitions as only the larger arteries of the circle of Willis will have flow which is rapid enough that the flow-related enhancement will likely 'opacify' the vessel distal to the stenosis. This is not as problematic with the PC sequences if the physician has a priori knowledge about the expected range of flow velocities in the vessels.

3D TOF MRA is readily able to display normal vessels and to distinguish normal from stenotic vessels. In one study, the sensitivity for identifying stenoses in the distal vertebral and basilar arteries was shown to be 100% whereas the specificity of the study was not nearly as high.[44] When 3D TOF MRA was compared with the IADSA studies, the degree of stenosis was exaggerated in as many as 63% of the MRA images. When correlated with the results of other clinical studies, this error was likely accentuated to some extent by the chosen voxel dimensions, the small but highly variable caliber of the distal vertebral arteries, and the separation of the stenoses into five categories.[44] Reviewing the original 3D source images was found to be helpful for distinguishing occlusion from slow flow in a severely stenotic or hypoplastic vessel. This distinction was further aided by incorporating selected 2D TOF slices because of their improved sensitivity to slow flow.

Knowledge of the degree of collateral flow between different vascular territories may have a significant impact on the physician's therapeutic decisions. Often times, the method of cross filling is obvious on the standard TOF MRA acquisition. For example, if one internal carotid artery is occluded but there is still good flow to the corresponding anterior circulation, the flow is more likely through the patient's large anterior communicating artery than the diminutive posterior communicating arteries. It is not as easy to draw these conclusions when the potential collateral vessels are more uniform in size or they are all diminutive. The slow flow and small size of leptomeningeal collateral vessels prevents their visualization. Evaluation of the source images from PC studies clearly demonstrates the direction of flow in major vascular trunks, making the pattern of collateral flow obvious.[36] Moreover, PC studies also provide the potential to make flow velocity and flow volume measurements. Alternatively, examining the corresponding phase images from a TOF study can also confirm the direction of blood flow in main vascular trunks. The relative contributions from the other vascular territories can also be identified in a TOF study through the use of appropriately positioned saturation pulses.[35] A narrow saturation slab, which is perpendicular to a 2D TOF slice or narrow 3D TOF volume, can be oriented to eliminate the flow-related enhancement from any one or any combination of the main vascular trunks to identify the source of collateral flow to a given vascular distribution. For example, selectively saturating the contralateral internal carotid artery will demonstrate the relative contribution from the posterior circulation to the remaining internal carotid artery distribution in question.

1.6.3 Intracranial MRA: Vascular Malformations

Intracranial vascular malformations are generally easy to identify on the routine spin echo study of the head. Capillary telangiectasias are usually discovered incidentally at autopsy while cavernous angiomas are most commonly detected as subcortical foci of mottled hyperintensity on the T_1- and T_2-weighted sequences with a peripheral rim of ferritin and hemosiderin deposition on the T_2 images from prior hemorrhage.[45] In both cases, the flow through these lesions is so slow that their abnormal vessels cannot be visualized by any MRA technique. (In fact, TOF MRA images can be misleading since the short T_1 of hemorrhage in a cavernous angioma can mimic the high flow vascular nidus of an arteriovenous malformation.) Venous angiomas are also readily identified on the spin echo study as a caput of veins draining into a large medullary vein extending from a point near the ependymal surface to the cortex. While the sensitivity to slow flow in the 2D TOF or PC studies would make these veins visible with MRA, their characteristic spin echo appearance makes this unnecessary.

High flow arteriovenous malformations are also easily diagnosed on the conventional spin echo parenchymal study. The vascular nidus appears as a cluster of serpiginous flow voids because of the relatively fast flow through these vessels. The factors that are considered important predictors of surgical resectability are also readily appreciated, including the size of the nidus, its relationship to eloquent areas of the brain, and the presence of deep venous drainage.[46] If there is a direct arteriovenous fistula, there will be no intervening nidus but the enlarged feeding arteries and draining veins will still be easily identified. There may also be associated parenchymal findings related to hemorrhage, ischemic steal, secondary venous thrombosis, or prior surgical, embolization and/or radiation therapy. The arteriovenous malformations can be identified with TOF or PC MRA, but the images generally do little more than reinforce the 3D spatial relationships of the vascular nidus with the circle of Willis and identify the main feeding arteries and draining veins.

Conversely, one situation in which MRA is essential in the work-up is in the evaluation of suspected dural vascular malformations which make up approximately 15% of the arteriovenous malformations. Frequently, the dural malformations are not visible at all on the spin echo study because of the small size and lack of contrast between the flow voids and the adjacent hypointense skull base.[47] The only clues to the presence of the malformation may be the clinical history, the presence of enlarged draining cortical veins, or secondary findings such as dural venous thrombosis, subdural or parenchymal

hematomas, and venous infarcts. On occasion, subtle peripheral flow voids or focal prominence of a dural venous sinus may be present, but these are often identified only in retrospect, once the MRA study makes the diagnosis obvious. MRA is often able to identify the vascular nidus along the dura, enlarged branches of the external carotid and/or vertebral arteries, and possibly enlarged draining veins or dural sinuses if there is a direct arteriovenous fistula present. It is essential to evaluate the source images from the MRA acquisition, as the findings may even be subtle on the projection MRA. Intravenous gadolinium can be used with 3D TOF MRA to evaluate better small feeding arteries and draining veins, but a study of dural fistulas failed to identify venous constriction. A study of dural fistulas with 3D TOF MRA was unable to identify venous constriction when gadolinium was used to reduce the problems of spin saturation and better identify the slow flow in the small feeding arteries and draining veins.[48]

Ultimately, conventional catheter angiography will be performed on any patient with an arteriovenous malformation to characterize it prior to therapy. Only the invasive arteriogram provides the spatial resolution necessary to identify all of the afferent and efferent vessels. While the MRA acquisition can identify aneurysms along the afferent vessels, these too should be further evaluated by a conventional arteriogram preoperatively. Lastly, only the catheter study provides the temporal resolution to assess the arteriovenous circulation time, to identify individual vessels with the greatest degree of arteriovenous shunting and, in the case of a direct fistula, to localize the point of communication between the arterial and venous systems.

The MRA acquisitions can be designed to provide a limited degree of physiological information about the vascular malformations. Thin saturation slabs can be applied to a 2D or thin volume 3D TOF acquisition to eliminate the flow-related enhancement from one vascular trunk and monitor the relative intensity and/or size of the malformation in the final image. In this way, it is possible to determine if the malformation is fed by more than one vascular distribution (collateral flow) and to assess the relative contributions from the different vascular territories.[35] The PC acquisitions can also be designed to supply similar information by applying a series of different velocity-encoding gradients in a stepwise fashion to demonstrate different components of the malformation.[35] A low velocity-encoding range (e.g. 10–20 cm s^{-1}) would demonstrate draining veins with low to medium velocities whereas higher velocity-encoding ranges (e.g. 60–100 cm s^{-1}) would preferentially demonstrate the nidus, larger veins, and feeding arteries with more rapid flow.[42] In this fashion, it is possible to provide a velocity flow map of the vascular malformation. Such information may be clinically useful if serial studies indicate a change in flow dynamics which may be predictive of hemorrhage, but this remains to be tested.

In spite of the advantages, saturation of flowing spins is perhaps the most significant limitation of the 3D TOF technique. This limits visualization of the small feeding arteries (slower flow) distally in the volume, all but the largest early draining veins, and potentially part of the vascular nidus itself if there is relatively slow flow through the nidus and it is located distally in the volume. The 2D TOF studies are less susceptible to spin saturation and provide better contrast-to-noise levels across the imaging volume. Alternatively, 2D TOF images are more limited by flow-induced dephasing and may not visualize portions of the afferent and efferent vessels depending on the direction along which the slices are acquired relative to the course of these vessels. The problem of spin saturation is reduced with intravenous gadolinium, but this also increases the intensity of the background tissues, which may be quite limiting if the malformation is situated along the skull base (e.g. many dural vascular malformations). The best compromise between the TOF techniques is the stacked overlapping volume approach.[21] If the malformation is located within the parenchyma, a paramagnetic contrast medium could be added to improve venous visualization, while the stacked volume approach improves arterial visualization.[49]

1.6.4 Intracranial MRA: Venous Sinus Thrombosis/Occlusion

Dural venous sinus thrombosis and secondary parenchymal findings (e.g. edema, hemorrhagic venous infarct) can be detected on conventional spin echo images although the findings are not always obvious and may be misleading. The most sensitive spin echo study to evaluate the venous sinuses is a T_2 weighted sequence in which the slices are oriented perpendicular to the direction of flow in the sinus in question (e.g. coronal for the superior sagittal and straight sinuses). With such a long echo time, blood flowing perpendicular to the slice normally causes a flow void as it is least apt to experience the 90 and 180° pulses and remain in the imaging plane at readout unless the sinus is thrombosed or occluded. An occluded sinus will fail to demonstrate a flow void or may be frankly hyperintense on the T_1- and T_2-weighted images. Slow flow may also cause an intermediate to high signal within the sinus and simulate thrombus. In the case of acute/early subacute thrombus, the hypointense thrombus may simulate a flow void on a T_2-weighted image.[50] In the situations where the spin echo findings of thrombosis are ambiguous or an adjacent mass appears to have invaded and occluded the sinus, MRA venograms can be most helpful in confirming or excluding thrombosis/occlusion without resorting to an invasive study.

A 2D technique would be the most sensitive TOF study to evaluate the slow flow in the dural sinuses.[51] Coronal slices acquired sequentially, from posterior to anterior, should ensure flow-related enhancement in the major dural sinuses since the flow is largely in the reverse direction except the posterior portion of the superior sagittal sinus. This same strategy can be followed with fewer slices and a shorter examination time if the slices were acquired in an oblique coronal plane (e.g. rotated 75° towards the sagittal plane). In view of the relatively slow normal velocities in these veins, the slice thickness for these 2D slices should be minimized, the *TR* maintained relatively long, and a low-to-intermediate flip angle should be used (e.g. 30°) to avoid spin saturation. Hyperintense thrombus could simulate flow-related enhancement, but this is easily distinguished when correlated with the findings on the spin echo study. The prior administration of intravenous gadolinium would make it difficult to distinguish a normal sinus from contrast enhancement along the periphery of a thrombosed sinus. A more important potential error relates to the limitations of the technique. There may be insufficient flow-related enhancement in a small sinus with slow flow, leading to a false-positive study. Similarly, an oblique coronal acquisition will insure flow-related enhancement in one transverse sinus, but

this is not necessarily the case in the opposite transverse sinus. In either case, evaluating the individual slices or reconstructing a small subvolume eliminates the reconstruction artifact and usually makes it possible to distinguish patency from occlusion.

Phase contrast techniques are especially well suited to this application because of strong background suppression and the ability to adjust the sequence so it is sensitive to very slow flow (10–20 cm s^{-1}).[52,53] While the sensitivity of the 2D TOF study is sufficient for most routine clinical work, the sensitivity is somewhat greater with PC, and it may be possible to detect flow in a recanalized sinus when the TOF images would suggest occlusion. The relatively large size of these sinuses, laminar flow profiles, and predominantly unidirectional flow make it easy to study these veins with two quick 2D PC acquisitions. A thick 2D slab can be selected in the midline sagittal plane, with velocity sensitization along the anterior/posterior direction, to assess the patency of the deep and superficial midline veins. A second thick axial slab in the posterior fossa with sensitization in a similar direction will evaluate the patency of the transverse and sigmoid sinuses.

2 RELATED ARTICLES

Abdominal MRA; Peripheral Vasculature MRA; Phase Contrast MRA; Time-of-Flight Method of MRA; Whole Body Magnetic Resonance Angiography.

3 REFERENCES

1. C. L. Dumoulin, *Neuroimaging Clin. N. Am.*, 1992, **2**, 657.
2. G. A. Laub and W. A. Kaiser, *J. Comput. Assist. Tomogr.*, 1988, **12**, 377.
3. C. L. Dumoulin, S. P. Souza, M. F. Walker, and W. Wagle, *Magn. Reson. Med.*, 1989, **9**, 139.
4. G. W. Lenz, E. M. Haacke, T. J. Masaryk, and G. A. Laub, *Radiology*, 1988, **166**, 875.
5. C. M. Anderson, D. Saloner, J. S. Tsuruda, L. G. Shapeero, and R. E. Lee, *Am. J. Radiol.*, 1990, **154**, 623.
6. The North American Symptomatic Carotid Endarterectomy Trial (NASCET) Steering Committee, *Stroke*, 1991, **22**, 711.
7. V. J. Howard, J. Grizzle, H. C. Diener, R. W. Hobson, M. R. Mayberg, and J. F. Toole, *Stroke*, 1992, **23**, 583.
8. European Carotid Surgery Trialists' Collaborative Group, *Lancet*, 1991, **337**, 1235.
9. Editorial, *Lancet*, 1991, **337**, 1255.
10. North American Symptomatic Carotid Endarterectomy Trial Investigators, *Stroke*, 1991, **22**, 816.
11. J. J. Schuler, P. Flanigan, L. T. Lim, T. Keifer, L. R. Williams, and A. J. Behrend, *Surgery*, 1982, **92**, 1058.
12. D. J. Marzewski, A. J. Furlan, P. St. Louis, J. R. Little, M. T. Modic, and G. Williams, *Stroke*, 1982, **13**, 821.
13. T. J. Masaryk, M. T. Modic, J. S. Ross, P. M. Ruggieri, G. A. Laub, G. W. Lenz, E. M. Haacke, W. R. Selman, M. Wiznitzer, and S. I. Harik. *Radiology*, 1989, **171**, 793.
14. J. Huston, D. A. Rufenacht, R. L. Ehman, and D. O. Wiebers, *Radiology*, 1991, **181**, 721.
15. P. J. Keller, B. P. Drayer, E. K. Fram, K. D. Williams, C. L. Dumoulin, and S. P. Souza, *Radiology*, 1989, **173**, 527.
16. J. E. Heiserman, B. P. Drayer, E. K. Fram, P. J. Keller, C. R. Bird, J. A. Hodak, and R. A. Flom, *Radiology*, 1992, **182**, 761.
17. G. W. Lenz, E. M. Haacke, T. J. Masaryk, and G. A. Lamb, *Radiology*, 1988, **166**, 875.
18. A. J. Evans, D. B. Richardson, R. Tien, J. R. MacFall, L. W. Hedlund, E. R. Heinz, O. Boyko, and H. D. Sostman, *Am. J. Neuroradiol.*, 1993, **14**, 721.
19. E. M. Haacke, J. A. Tkach, and T. B. Parrish, *Radiology*, 1989, **170**, 457.
20. J. A. Tkach, P. M. Ruggieri, J. S. Ross, M. T. Modic, J. J. Dillinger, and T. J. Masaryk, *J. Magn. Res. Imaging*, 1993, **3**, 811.
21. D. D. Blatter, D. L. Parker, S. S. Ahn, A. L. Bahr, R. O. Robison, R. B. Schwartz, F. A. Jolesz, and R. S. Boyer, *Radiology*, 1992, **183**, 379.
22. R. E. Laster Jr., J. D. Acker, H. H. Halford III, and T. C. Nauert, *Am. J. Neuroradiol.*, 1993, **14**, 681.
23. B. C. Bowen, R. M. Quencer, P. Margosian, and P. M. Pattany, *Am. J. Roentgenol.*, 1994, **162**, 9.
24. R. L. Mittl, M. Broderick, J. P. Carpenter, H. I. Goldberg, J. Listerud, M. M. Mishkin, H. D. Berkowitz, and S. W. Atlas, *Stroke*, 1994, **25**, 4.
25. T. S. Riles, E. M. Eidelman, A. W. Litt, R. S. Pinto, F. Oldford, and G. W. S. Schwartzenberg, *Stroke*, 1992, **23**, 341.
26. J. Huston III, B. D. Lewis, D. O. Wiebers, F. B. Meyer, S. J. Riederer, and A. L. Weaver, *Radiology*, 1993, **186**, 339.
27. T. J. Masaryk, J. S. Ross, M. T. Modic, G. W. Lenz, and E. M. Haacke, *Radiology*, 1988, **166**, 461.
28. C. M. Anderson, D. Saloner, R. E. Lee, V. J. Griswold, L. G. Shapeero, J. H. Rapp, S. Nagarkar, X. Pan, and G. A. Gooding, *Am. J. Neuroradiol.*, 1992, **13**, 989.
29. J. A. Tkach, P. M. Ruggieri, J. J. Dillinger, J. S. Ross, M. T. Modic, and T. J. Masaryk, *J. Magn. Reson. Imaging*, 1993, **3**, 365.
30. M. Assaf, P. J. Sweeney, G. Kosmorsky, and T. J. Masaryk, *Can. J. Neurol. Sci.*, 1993, **20**, 62.
31. H. I. Goldberg, R. I. Grossman, J. M. Gomori, A. K. Asbury, L. T. Bilaniuk, and R. A. Zimmerman, *Radiology*, 1986, **158**, 157.
32. R. Pacini, J. Simon, L. Ketonen, D. Kido, and K. Kieburtz, *Am. J. Neuroradiol.*, 1991, **12**, 360.
33. C. Levy, J. P. Laissy, V. Raveau, P. Amarenco, V. Servois, M. G. Bousser, and J. M. Tubiana, *Radiology*, 1994, **190**, 97.
34. R. R. Edelman S. S. Ahn, D. Chien, W. Li, A. Goldmann, M. Mantello, J. Kramer, and J. Kleefield, *Radiology*, 1992, **184**, 395.
35. R. R. Edelman, H. P. Mattle, G. V. O'Reilly, K. U. Wentz, C. Liu, and B. Zhao, *Stroke*, 1990, **21**, 56.
36. P. Turski and F. Korosec. *Neuroimaging Clin. N. Am.*, 1992, **2**, 785.
37. T. J. Ingall, J. P. Whisnant, D. O. Wiebers, and W. M. O'Fallon, *Stroke*, 1989, **20**, 718.
38. A. S. Levey, S. G. Pauker, and J. P. Kassirer, *N. Engl. J. Med.*, 1983, **308**, 986.
39. J. S. Ross, T. J. Masaryk, M. T. Modic, P. M. Ruggieri, E. M. Haacke, and W. R. Selman, *Am. J. Neuroradiol.*, 1990, **11**, 449.
40. A. B. Chapman, D. Rubinstein, R. Hughes, J. C. Stears, M. P. Earnest, A. M. Johnson, P. A. Gabow, and W. D. Kaehny. *N. Engl. J. Med.*, 1992, **327**, 916.
41. R. J. Sevick, J. S. Tsuruda, and P. Schmalbrock, *J. Comput. Assist. Tomogr.*, 1990, **14**, 874.
42. J. Huston, D. A. Rufenacht, R. L. Ehman, and D. O. Wiebers, *Radiology*, 1991, **181**, 721.
43. J. E. Heiserman, B. P. Drayer, P. J. Keller, and E. K. Fram, *Radiology*, 1992, **185**, 667.
44. K. U. Wentz, J. Rother, A. Schwartz, H. P. Mattle, R. Suchalla and R. R. Edelman, *Radiology*, 1994, **190**, 105.
45. S. Atlas, *Radiol. Clin. N. Am.*, 1988, **26**, 821.
46. R. F. Spetzler, and N. A. Martin, *J. Neurosurg.*, 1986, **65**, 476.
47. J. K. DeMarco, W. P. Dillon, V. V. Halbach, and J. S. Tsuruda. *Radiology*, 1990, **175**, 193.

48. J. Chen, J. S. Tsuruda, and V. V. Halbach, *Radiology*, 1992, **183**, 265.
49. G. Marchal, H. Bosmans, L. Van Fraeyenhoven, G. Wilms, P. Van Hecke, C. Plets, and A. L. Baert, *Radiology*, 1990, **175**, 443.
50. G. Sze, B. Simmons, G. Krol, R. Walker, R. D. Zimmerman, and M. D. Deck, *Am. J. Neuroradiol.*, 1988, **9**, 679.
51. H. P. Mattle, K. U. Wentz, R. R. Edelman, B. Wallner, J. P. Finn, P. Barnes, D. J. Atkinson, J. Kleefield, and H. M. Hoogewoud, *Radiology*, 1991, **178**, 453.
52. D. J. Rippe, O. B. Boyko, C. E. Spritzer, W. J. Meisler, C. L. Dumoulin, S. P. Souza, and E. R. Heinz, *Am. J. Neuroradiol.*, 1990, **11**, 199.
53. J. S. Tsuruda, A. Shimakawa, N. J. Pelc, and D. Saloner, *Am. J. Neuroradiol.*, 1991, **12**, 481.

Biographical Sketches

Paul M. Ruggieri. *b* 1956. B.S., 1978, M.S., 1979, Bucknell University, Lewisburg, PA, USA. M.D., 1984, UMDNJ-Rutgers Medical School, Piscataway, NJ, USA. Radiology residency at University Hospitals of Cleveland, Neuroradiology fellowship at Cleveland Clinic Foundation including pediatric neuroradiology at Cincinnati Children's Hospital, research fellowship with Siemens Medical Engineering Group in Erlangen, Germany (supervisor Gerhard Laub). 1990–present, Associate Staff, Sections of Neuroradiology and Pediatric Radiology, Cleveland Clinic Foundation, Cleveland, OH, USA. Approx. 25 publications. Current specialties: neuroradiology, pediatric neuroradiology, MRI flow imaging.

Jean A. Tkach. *b* 1961. B.S.E., 1982, M.S., 1985, Ph.D., 1988 (Biomedical Engineering), Case Western Reserve University, Cleveland, Ohio, USA. 1990–present, Head of MR Imaging Research at the Cleveland Clinic Foundation, Cleveland, Ohio, USA. Approx. 30 publications. Current research specialties: MRA, functional MRI, cardiac MRI, flow quantification, magnetization transfer saturation MRI and steady state MRI techniques.

Thomas J. Masaryk. *b* 1955. B.S., 1978, M.D., 1981, Medical College of Ohio, Toledo, Ohio, USA. Radiology residency at the Cleveland Clinic Foundation, Neuroradiology fellowship at the Cleveland Clinic Foundation. 1990–present, Head of Neuroradiology, the Cleveland Clinic Foundation, Cleveland, Ohio, USA. Approx. 92 publications. Current specialties: neuroradiology, interventional neuroradiology, MRI flow imaging.

Peripheral Vasculature MRA

Cathy Maldjian
Mount Sinai Medical Center, New York, NY, USA

and

Mitchell D. Schnall
University of Pennsylvania Medical Center, Philadelphia, PA, USA

1 INTRODUCTION

While conventional angiography has been the 'gold standard' in the evaluation of peripheral vascular disease, recent technical advances have made magnetic resonance angiography (MRA) a favorable alternative in many instances. Multiplanar imaging capabilities and noninvasive acquisition of data provide distinct advantages over contrast angiography. Overnight hospital stays, and potential morbidity from contrast injection and from obtaining arterial access may be avoided with MRA. Furthermore, distal runoff may be obscured by inadequate contrast filling in up to 70% of cases.[1–4] This has mainly been attributed to contrast dilution in intramuscular collaterals before reaching the reconstituted vessels of interest. MRA allows cross-sectional imaging, which facilitates the evaluation of the vessel lumen for stenotic lesions. Impaired detection of stenotic lesions due to interference from overlying bone is not a problem, although it may be in contrast angiography. Quantitation of flow, in particular by cine-phase contrast, is also possible with MRA. Three-dimensional data sets may be obtained by MRA. Gravimetric layering of contrast, which may prevent filling in anterior branches of slow-flowing vessels, is obviated with MRA. Pulsatility artifacts tend not be a problem in studying collateral reconstitution past a high level stenotic lesion, since these vessels often adopt a monophasic rather than a triphasic wave pattern. However, with the advent of digital subtraction angiography, a higher level of technical proficiency and accuracy can be achieved. Inplane resolution is superior with cut-film angiography compared with MRA. Skeletal bony anatomy, sequential demonstration of retrograde flow, metal artifacts, and total length of vascular anatomy, may be better appreciated with contrast angiography. Also, contraindications to MR, such as pacemakers, defibrillators, and metallic prosthetic valves, prohibit its use in these instances.

Various artifacts of MRA will be discussed later in further detail. Bearing all this in mind, MRA may play an integral part in the presurgical evaluation of lower-extremity ischemia by providing the surgeon with the arterial anatomy in a noninvasive manner. It may afford decreased intraoperative times. Stenosis, occlusions, and native target outflow vessels favorable for bypass procedures may be identified noninvasively. In addition, reconstituted vessels may potentially be seen to better advantage.

2 TECHNIQUES

Currently, the predominant technique for imaging the peripheral vasculature consists of two-dimensional (2D) time-of-flight (TOF). Single sections are imaged perpendicular to the plane of flow. Short *TR* is utilized to saturate stationary spins, which imparts high intensity to flowing blood where spins are unsaturated. This flow-related enhancement allows visualization of the peripheral vasculature [Figure 1(a)]. Further selection of the arterial or venous system can be accomplished by utilizing a saturation band [Figure 1(b)].

A saturation band positioned distally to the imaging section would provide an arterial study. This relationship would be reversed in the head and neck, where venous blood generally travels inferiorly rather than superiorly and arterial blood courses superiorly rather than inferiorly. During arterial diastole, there is a component of flow reversal which allows arterial blood to enter the presaturation slab during systole and subsequently the imaging section during diastolic reversal of flow if the slab is positioned close enough to the imaging section. This creates undesirable dark, horizontal, stripe artifacts. For this reason, a saturation gap is often utilized. A saturation gap is a distance placed between the saturation pulse and the

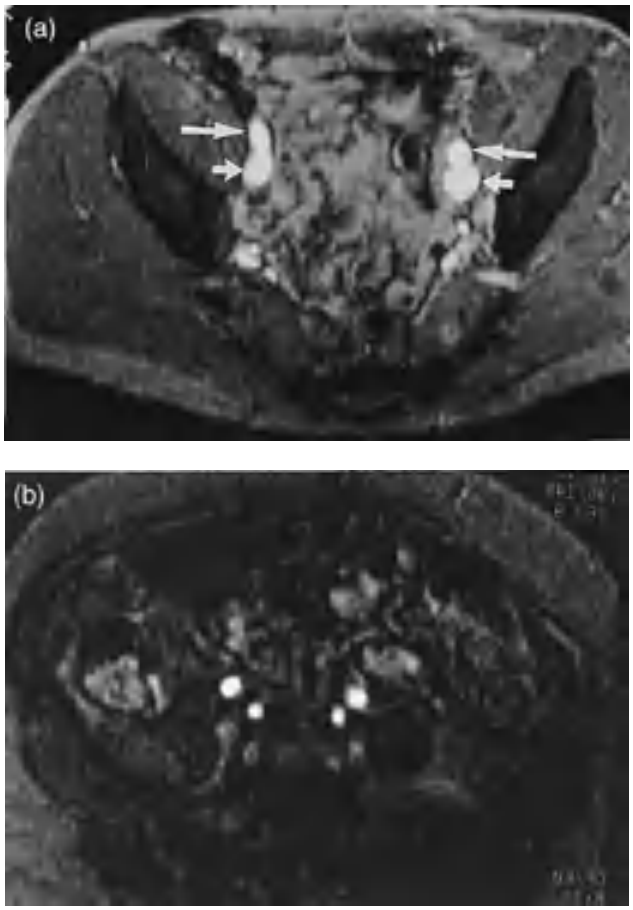

Figure 1 Single slice from a 2D TOF angiogram taken: (a) without saturation bands demonstrating both arteries (larger arrows) and veins (smaller arrows); (b) with inferior saturation. The venous structures have been saturated out and only arterial structures remain

Figure 2 MIP projection obtained from a 2D TOF arteriogram in the region of the calf, demonstrating high-signal arterial vessels (large arrow) and lower signal venous vessels (small arrow). The veins are visible due to the wide saturation gap (2 cm) used in this case

imaging plane. The larger the gap, the less likely that retrograde arterial flow from the saturation slab will reach the imaging section. On the other hand, a larger gap would also enable venous blood within the gap to enter the imaging slice without first being saturated. Therefore, some venous blood may also be inadvertently imaged and potentially confused for arterial flow. This phenomenon is called 'venous bleed-through' (Figure 2). It is therefore evident that the size of the saturation gap is critical and that the optimal saturation gap size may vary depending upon the arterial and venous flow rates at the particular site of interest. In addition to the above techniques, we also utilize flow compensation at our institution.

The 2D axial images obtained are stacked on top of each other to create a three-dimensional (3D) data set. Projection angiograms are created by the MIP algorithm. A ray is projected through this 3D data set, and each pixel in the projection is designated a value based on the maximum intensity encountered within the pixel.

At our institution, we utilize a *TR* of 33–36 ms, a *TE* of 6.2–7.7 ms, and a 60° flip angle. Our 2D TOF imaging protocol entails imaging at several stations. The pelvis is imaged with a 32 cm field-of-view (FOV), 2.5 mm thickness, 128×256 matrix, and a body coil. No skip is utilized. Distal thigh, knee, leg, ankle, and foot are imaged with an extremity coil at a 16 cm field of view. Ninety 2 mm images per station are obtained with the knee coil. The pelvis and one lower extremity are imaged in approximately 1.5 h. Station 1 is at the forefoot, where the dorsal and plantar arches form from the dorsalis pedis and posterior tibial arteries [Figure 3(a)]. Upper and lower margins of the coil are marked to ensure that all vessels are examined, which in the General Electric knee coil is up to 20 cm long. In patients with peripheral vascular disease, the flow distally tends to be nonpulsatile, thus a narrower saturation gap is utilized. This also limits venous bleed-through. The arches frequently cannot be seen, since they course horizontally and become saturated. Retrograde flow, sometimes seen in the dorsalis pedis, susceptible to saturation by the inferior saturation slab, may create the impression of stenosis on the MIP.

The second station examines the anterior tibial, posterior tibial, and peroneal arteries [Figure 3(b)]. Calcaneal and perforator branches arise from the peroneal artery, and these course posteriorly and anteriorly, respectively. The calcaneal artery (communicator branch) may function as a collateral to the plantar aspect of the foot, while the perforator branch coursing through the interosseous membrane may function as a dorsal collateral. The posterior tibial artery bifurcates into medial and lateral plantar arteries at the ankle.

The third station ends at the mid-calf [Figure 3(c)]. The posterior tibial artery is most medial and usually anterior to the peroneal artery. The anterior tibial artery is located very superficially at the talus, where the dorsalis pedis forms, and it travels in the tibialis anterior muscle within the anterior compartment. The peroneal artery parallels the fibula. Intramuscular collaterals may accompany disease at the trifurcation. Venous bleed-through may mimic such arterial collaterals.

The fourth station, at the knee, is where the popliteal artery and the trifurcation are evaluated [Figure 3(d)]. Basis images are critical, especially for assessing stenosis of the anterior tibial artery. This area represents the most variable for the number of vessels seen. Anatomic variation, occlusion, and collaterals all contribute to this phenomenon. The length of the region examined is also variable due to individual height discrepancies.

The fifth station examines the common femoral artery to the superficial femoral artery (SFA)–popliteal artery junction [Figure 3(e)]. The SFA is medial and superficial. The profunda femoral artery is posterior and lateral in location, and terminates at the mid-thigh with associated muscular branches. The SFA has no muscular branches. Hunter's canal is contained in this series. Stenoses at this level are common. Faster arterial inflow and venous outflow at this station are conducive to a shorter *TR* (33 ms) and a larger saturation gap (1 cm), respectively.

The sixth station (pelvis) covers the distal abdominal aorta to the common femoral arteries [Figure 3(f)]. The aorta normally bifurcates into the common iliac arteries, which further bifurcate into internal and external iliac arteries. The common femoral arteries subsequently give rise to the deep and superficial femoral arteries. The faster flowing veins at this level require an even larger saturation gap (2 cm) at this station.

3 CLINICAL DATA

Clinical data thus far has shown 2D TOF MRA to be a promising technique. Mulligan et al. studied 140 lesions and found a 71% correlation between 2D TOF MRA and conventional angiography of the abdominal aorta and distal-runoff vessels.[5] MRA alone proved inaccurate in six out of 140 cases for planning a surgical approach. As this was one of the early studies in this area, these inaccuracies to some extent may reflect inadequacies of the early techniques. Later studies by other investigators produced more promising results, probably

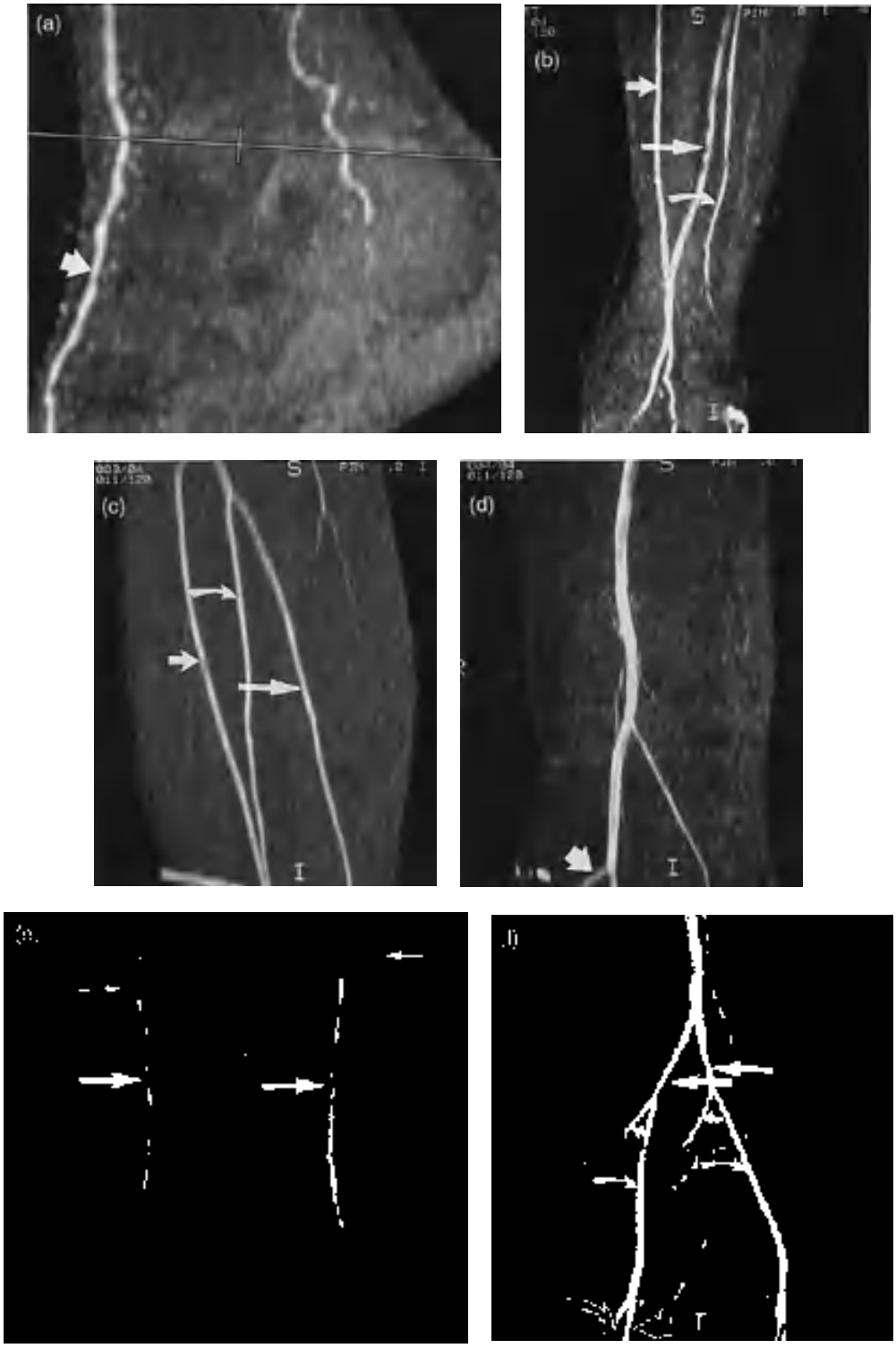

Figure 3 Two-dimensional TOF projection: (a) through the hind foot, demonstrating the dorsalis pedis artery dorsally; (b) anteriorly through the ankle. The anterior tibial (small arrow), peroneal (curved arrow), and posterior tibial arteries (large arrow) are demonstrated; (c) anteriorly in the region of the mid-calf, demonstrating the anterior tibial artery (small arrow) and tibial peroneal trunk bifurcating into posterior tibial (large arrow) and peroneal arteries (curved arrow); (d) through the region of the knee, demonstrating the popliteal artery and the take-off of the anterior tibial artery (arrow); (e) obtained with the body coil, demonstrating the superficial femoral arteries bilaterally from upper thigh through Hunter's canal (large arrows). The distal profunda femoral arteries are also identified (small arrows); (f) through the pelvis, demonstrating the aorta, common iliac arteries (largest arrows), internal (small curved arrows) and external iliac (larger curved arrows) arteries, and common deep (curved open arrow) and superficial (open arrow) femoral arteries. Note the excellent visualization of the femoral artery bifurcation

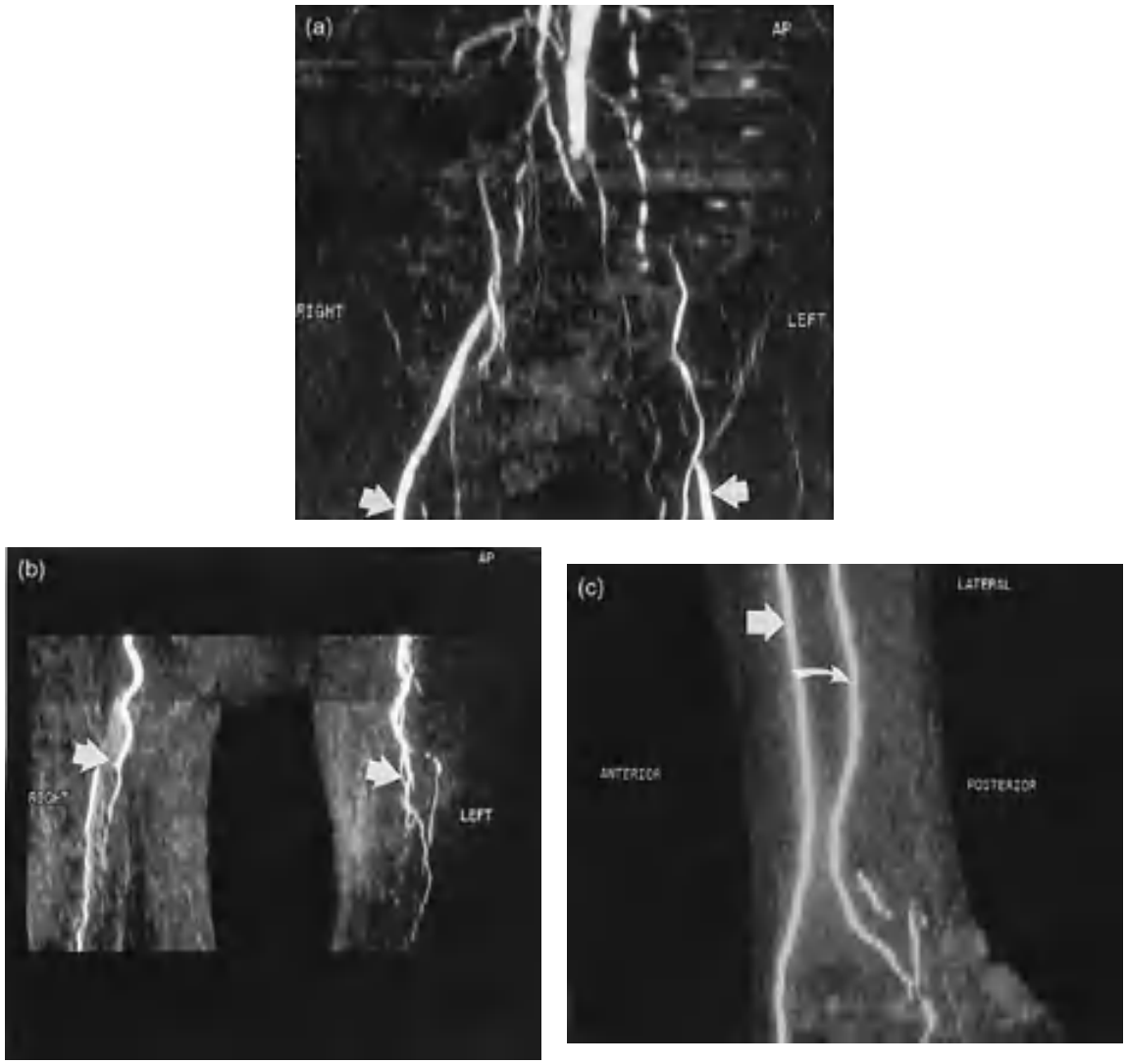

Figure 4 Representative images from the magnetic resonance arteriogram of a patient who presents with lymph-threatening ischemia. (a) Images through the pelvis demonstrating bilateral iliac artery occlusion and reconstruction of the SFA bilaterally (arrows). (b) Images obtained through the upper thighs. Bilateral superficial femoral artery occlusions are demonstrated (arrows). (c) Images through the lower left calf. The presence of an anterior tibial artery crossing the ankle to form the dorsalis pedis (arrow) and a peroneal artery (curved arrow) with a calcaneal branch crossing the ankle to form the plantar arches is demonstrated. On the basis of these MR images, this patient went on to have revascularization procedure without contrast angiogram

due to technical advancements. Color-duplex ultrasound (US) demonstrated 93% concurrence for infrainguinal disease. While MRA was superior to US in evaluating the iliac regions due to limited visualization with US in that area, image quality with MRA was inconsistent. Workers concluded that both duplex US and MRA were suboptimal for surgical planning. Owen et al. found that most of the discordance between 2D TOF MRA and conventional angiography was due to enhanced detection of runoff vessels on MRA[6] (Figure 4). Interventional planning was altered in 16% of cases (12 patients) due to improved visualization with MRA of stenosis and vessels not seen on conventional angiography.

Carpenter et al. studied 51 patients with peripheral vascular disease.[7] Two-dimensional TOF MRA evaluation demonstrated that in 48% of cases, MRA provided additional information to contrast angiography without loss of other information. In 22% of cases, the MRA data were responsible for altering surgical treatment. Target vessels were observed in 18% of cases on MRA that were undetected on contrast angiography. Identification of these target vessels enabled the surgeons to perform limb-salvaging procedures. Similarly, two cases (4%) demonstrated MRA findings of target runoff vessels which were not seen on conventional angiography, where the information was used to formulate a better interventional plan for bypass grafting. These investigators demonstrated superior sensitivity of MRA compared with contrast angiography in evaluating distal runoff vessels.[8] Other workers also found that 2D TOF suppressed veins better than the 3D techniques.[9]

In evaluating for stenosis, Chien et al.[9] suggest black-blood techniques to prevent nonvisualization of turbulent spins from

phase incoherence.[5] Bright-blood methods, on the other hand, may overestimate a stenosis due to phase incoherence.

Mulligan et al. evaluated stenosis from MIP, which simulates the unidimensionality of angiographic studies; however, axial-basis images are more accurate for such assessments.[5] Also, since they utilize the large FOV, the in-plane resolution of the basis images is worsened. This also compromises the resolution of the MIP.

Cambria et al. reported 98% concurrence between 2D TOF MRA and contrast angiography in 178 patients with a 100% concurrence below the inguinal ligament.[10] Intraoperative confirmation was obtained in the seven bypass grafts performed on the basis of the MRA data alone. Hertz et al. also reported a high correlation between 2D TOF MRA and contrast angiography in assessing arterial stenosis in 19 patients[11] (Figure 5). For the popliteal to the dorsalis pedis area, Carpenter et al.[7] showed MRA to be superior to conventional angiography, with a 48% discordance rate between the two techniques.[6] This difference appeared to be more progressively pronounced the further distally one examined. Up to 50% of stenosis may be overlooked with conventional angiography if the plaque is en face with no available edge for imaging.

We have found 2D TOF MRA to be accurate in assessing peripheral stenosis. Cross-sectional images are particularly useful, in that they may demonstrate more information than contrast angiography. We showed good agreement in blinded interobserver interpretation (91%).[11] Also, lesions distal and proximal to stenosis were seen equally well with MRA, with no appreciable discrepancy between the two.[11] We investigated 41 patients for aorto–iliac disease.[12] Only six cases showed a discrepancy between MRA and contrast angiography. Two of these proved to be false-positive on MRA, and two proved to be false-negative. The other two underestimated a greater than 50% stenosis seen on angiography. In the pelvis and lower extremity, we obtained a 62% concordance in a 103-patient series, with no false-positives or false-negatives on MRA.[13] Contrast angiography failed to show 162 open segments that were confirmed surgically.

We have found MRA to be reliable in assessing vessel patency. Baum et al. demonstrated a 0.7 correlation coefficient between contrast angiography and 2D TOF MRA for determining the parameters of a stenosis.[14] We compared contrast angiography with MRA results in 60 patients with peripheral vascular disease. ROC-curve analysis of one blinded observer demonstrated that location and patency yielded a high correlation between angiography and MRA at our institution.[15]

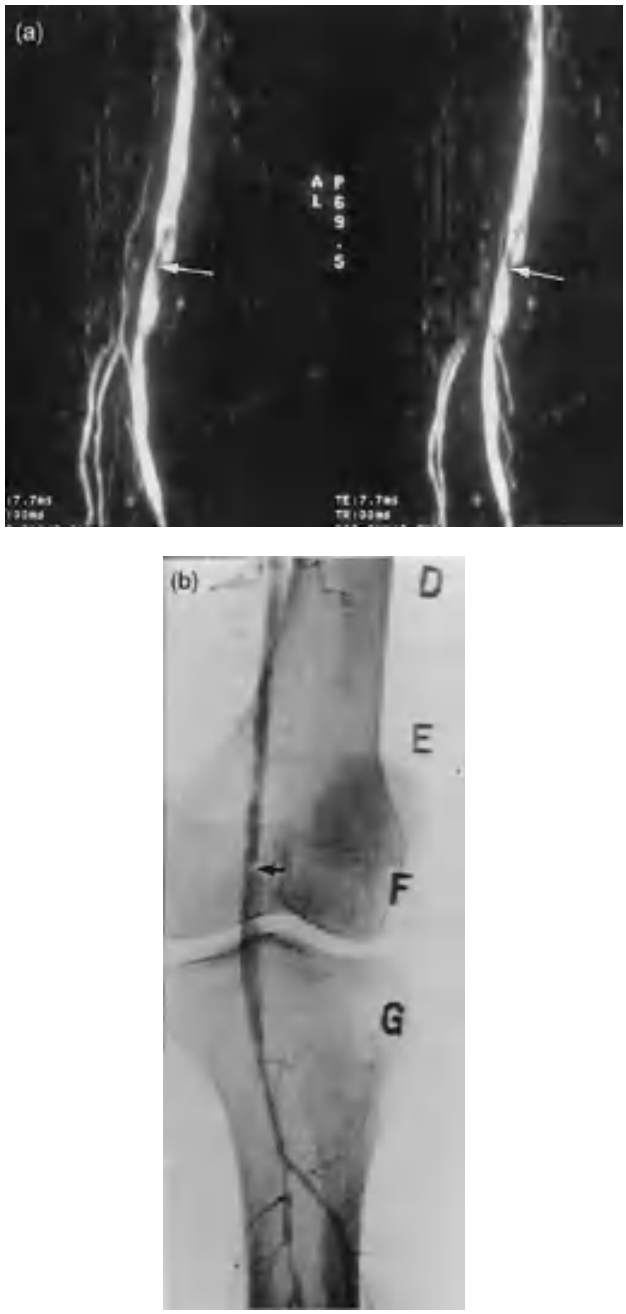

Figure 5 Two-dimensional TOF arteriogram: (a) on a patient who had recently had an angioplasty, demonstrating recurrent stenosis with an intimal flap (arrows); (b) obtained 1 week prior, demonstrating the stenosis (arrow)

4 PHASE CONTRAST (PC)

Phase contrast techniques utilize motion as an imaging tool, whereby flow is detected in all three axes. A technique relying on phase discrepancy, which measures phase shift of moving spins to determine their velocities, was proposed by Bryant et al.[16] Other investigators demonstrated that cardiac gating imparts accuracy to the calculated arterial flow rates.[17] Various phases of arterial flow could also be better segregated and evaluated. Applications of PC in peripheral vascular disease soon followed. A 2D TOF with PC velocity-sensitive technique demonstrated significantly increased velocities at systole in diseased peripheral vessels after angioplasty, whereas normal vessels demonstrated no alteration in flow.[18] A one spatial- and one-dimensional-variant of PC may enhance tracing of the triphasic flow in the popliteal artery.[19]

In our recent experience with two-axis cine-PC angiography for arterial wave patterns in diseased vessels, we have observed monophasicity beyond points of critical stenosis. Simultaneous measurements of velocities at several sites may be implemented with a combined excitation technique to obtain cine-PC data in one dimension, with cardiac gating to generate a second dimension (time).[20] Measurements of arterial compliance are made

possible. Addressing arterial compliance is useful in atherosclerotic disease, where compliance is decreased and arterial waveforms are altered. Recently, investigators have demonstrated similar velocity measurements in common iliac arteries with a cine-PC technique with a surgically attached US flow probe on the artery.[21] Velocity-encoded cine MRA was compared with color-coded US in ten healthy subjects above and below the trifurcation and showed good correlation.[22] The classic triphasic pattern was seen. These investigators suggest that velocity-encoded cine MRA may help to evaluate the hemodynamic significance of a stenotic lesion.[23] This information may complement anatomical information obtained from standard 2D TOF MRA. They suggest that a single MRA examination may derive all the information that previously might have been obtained by performing both contrast angiography and duplex US. ECG-triggered 2D PC techniques, where velocity encoding varies with the cardiac cycle, may improve the contrast-to-noise ratio, most notably in small vessels, where up to 260% improved signal has been noted.[24] In summary, PC techniques appear to be very promising.

5 3D MRA

While we do not advocate the use of 3D techniques, we will briefly describe their applications. While in 2D imaging, many slices are imaged in sequence, in 3D imaging a volume is imaged. Acquisition of data from a larger volume, as in 3D TOF, enhances spatial resolution and therefore increases S/N. Imaging times are also decreased. Flow compensation is easier with 3D rather than 2D TOF MRA due to the increased gradient amplitude required for slice selection in 2D TOF. In 3D techniques, resolution along the *Y* and *Z* axes is obtained by phase-encoding techniques. Therefore, the slice selection gradient is relatively unburdened. In contradistinction, an extra lobe on the gradient waveform would be necessary to implement flow compensation with 2D techniques, and this would consequently increase the *TE*. Therefore, shorter *TE*s are possible with a 3D modality when utilizing flow compensation in comparison with a 2D modality. So, less dephasing of moving spins occurs with 3D flow compensation. Smaller voxel sizes may also be utilized with 3D imaging. The main disadvantages of 3D imaging techniques, which significantly hinder their usefulness, include decreased sensitivity to slow flows and prolonged reconstruction times of a 3D volume-based data set. In the 3D method, slow flow may incur saturation as it traverses further into the saturation slab. By the same reasoning, venous blood would saturate more readily compared with arterial blood. Therefore 3D MRA may be of greater value in imaging fast flowing and small vessels. Its primary benefits have been seen in the area of neurovascular imaging.

6 ARTIFACTS

Clip artifacts and orthopedic prostheses and artifacts related to susceptibility differences at various interfaces may simulate stenosis or occlusion of a vessel (Figure 6). Local magnetic field variations may be large enough to cause phase dispersion, yielding a net signal intensity vector of zero. Frequently, there is an associated high-signal intensity rind near the metal or air

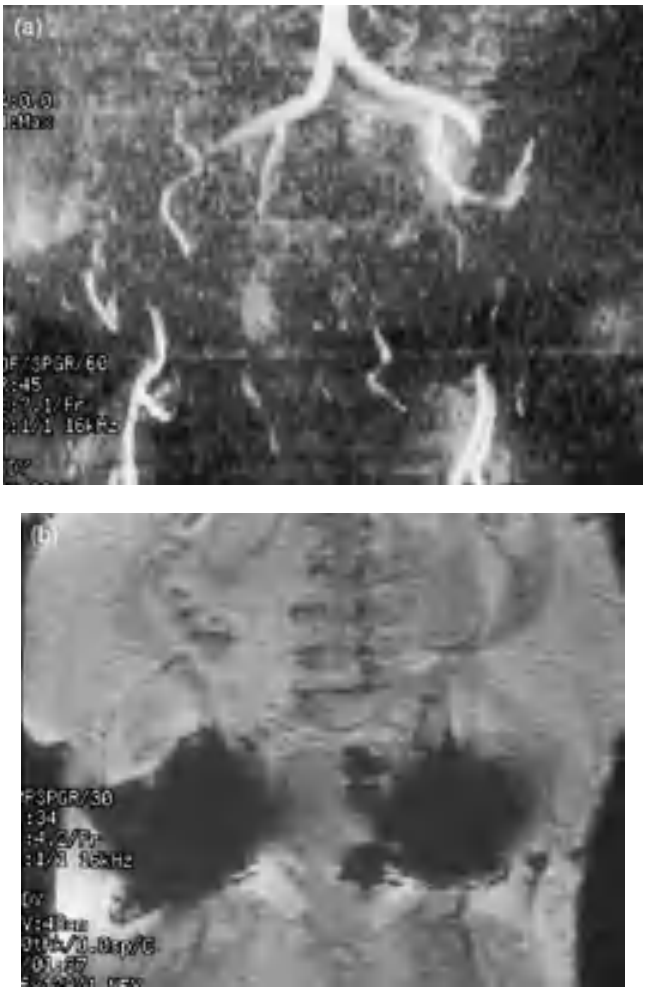

Figure 6 (a) Frontal projection from a 2D TOF arteriogram through the pelvis demonstrating complete absence of iliac arteries distal to the common iliac artery bilaterally. (b) Coronal scout image demonstrating large artifacts due to the presence of hip prostheses bilaterally

due to misregistration in frequency and slice selection directions as a result of magnetic susceptibility. Gradient echo sequences are particularly vulnerable to these effects.

Due to the length of the examination movement may occur in some patients. Displacement may appear as one translocated, or multiple translocated, slices on the MIP (Figure 7). Motion may create the appearance of a vascular lesion, and individual sections must be reviewed. Peristalsis or respiratory motion may confer high signal intensity on bowel material by 'refreshing stationary spins'. Muscle contraction may confer increased signal intensity to muscle in the same fashion as flowing motion in vessels produces flow-related enhancement.

As discussed previously, pulsatile flow may generate dark, horizontal bands on the MIP, as each section is not obtained at identical times in the cardiac cycle. Thus, varying signal intensities are obtained in each section. This banding artifact, or 'Venetian-blind effect,' is more pronounced in vessels with triphasic flow (Figure 8). Cardiac gating and an increased saturation gap are two ways of counteracting these effects. Phase ghosting, also produced by vessel pulsatility, may be

Figure 7 Lateral MIP projection demonstrating the effect of motion on the MR arteriogram. Displacement of segments of the vessel can simulate stenosis (arrows). Motion can be confirmed by observing motion of the skin line (small arrows)

counteracted with EKG gating. Apparent absence of retrograde arterial flow may occur with the use of a saturation slab which is primarily intended to saturate venous flow. Arterial pulsatility may be confirmed by removing the saturation slab or by acquiring velocity-encoded information.

Turbulence artifacts near a site of stenosis, with its dephasing effects, causes high flow with spin-phase incoherence. However, this is not much of a problem peripherally where flow is less pulsatile. Inspection of axial images for high-grade stenosis would explain the findings.

Potential pitfalls of MIP images occur when a high signal intensity interferes with visualization of a blood vessel, such as from a blood clot. Conversely, a filling defect may become nonapparent if it is surrounded by high signal intensity flowing blood. Also, when section thickness exceeds that of in-plane resolution, normal horizontal flow may appear obstructed on the MIP. In the same vein, pseudobeating may occur with tortuous oblique vessels. This may manifest as a 'stair-step' artifact on the MIP. This may be counteracted by thinner slices, slice overlap, and reacquisition perpendicular to the vessel. Inplane or 'horizontal' flow refers to areas where, due to the orientation or tortuosity of a vessel, flow occurs in a roughly horizontal rather than vertical plane. Since flow in the horizontal plane would not be detected because of saturation, the vascular anatomy would be obscured or underrepresented as stenotic. Examples of this include the anterior tibial artery take-off, which is roughly horizontal or perpendicular to the popliteal artery, and tortuous iliac bifurcations.

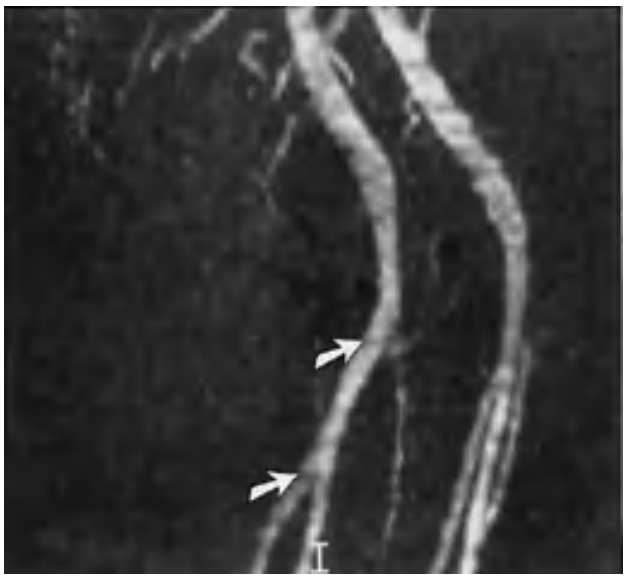

Figure 8 Oblique magnetic resonance arteriogram projection through the pelvis demonstrating high and low signal stripes (arrows) representing banding from pulsatile flow

7 RELATED ARTICLES

Abdominal MRA; Head and Neck Studies Using MRA; Phase Contrast MRA; Time-of-Flight Method of MRA.

8 REFERENCES

1. K. R. Patel, L. Semel, and R. H. Clauss, *J. Vasc. Surg.*, 1988, **7**, 531.
2. J. B. Ricco, W. H. Pearce, J. S. T. Yao, W. R. Flinn, and J. J. Bergan, *Ann. Surg.*, 1983, **198**, 646.
3. R. Scarpato, R. Gembarowicz, S. Farber, T. F. O'Donnell, J. J. Kelly, A. D. Callow, and R. A. Deterling, *Arch. Surg.*, 1981, **116**, 1053.
4. D. P. Flanigan, L. R. Williams, T. Keifer, J. J. Schuler, and A. J. Behrend, *Surgery*, 1982, **92**, 627.
5. S. A. Mulligan, T. Matsuda, P. Lanzer, G. M. Gross, W. D. Routh, F. S. Keller, D. B. Koslin, L. L. Berland, M. D. Fields, and M. Doyle, *Radiology*, 1991, **178**, 695.
6. R. S. Owen, R. A. Baum, J. P. Carpenter, G. A. Holland, and C. Cope, *Radiology*, 1993, **187**, 627.
7. J. P. Carpenter, R. S. Owen, R. A. Baum, C. Cope, C. F. Barker, H. D. Berkowitz, M. A. Golden, and L. J. Perloff, *J. Vasc. Surg.*, 1992, **16**, 807.
8. R. S. Owen, M. Sheline, J. Listerud, and H. Y. Kressel, *Proc. Xth Ann. Mtg. Soc. Magn. Reson. Med., San Francisco, 1991*, p. 138.
9. D. Chien, A. Goldmann, and R. R. Edelman, *Proc. XIth Ann. Mtg. Soc. Magn. Reson. Med., New York, 1992*, p. 3111.
10. R. P. Cambria, E. K. Yucel, D. C. Brewster, G. L'Italien, J. P. Gertler, G. M. Lamuragha, J. A. Kaufman, A. C. Waltman, and W. M. Abbott, *J. Vasc. Surg.*, 1993, **17**, 1050.
11. S. M. Hertz, R. A. Baum, R. S. Owen, G. A. Holland, D. R. Logan, and J. P. Carpenter, *Am. J. Surg.*, 1993, **166**, 112.
12. R. A. Baum, G. A. Holland, D. R. Logan, J. P. Carpenter, and C. Cope, *J. Vasc. Intervent. Radiol.*, 1993, **4**, 59.
13. R. A. Baum, G. A. Holland, D. R. Logan, J. P. Carpenter, and C. Cope, *J. Vasc. Intervent. Radiol.*, 1993, **4**, 15.

14. R. A. Baum, G. A. Holland, D. R. Logan, S. Hertz, J. P. Carpenter, R. S. Owen, and C. Cope, *J. Vasc. Intervent. Radiol.*, 1993, **4**, 60.
15. M. L. Schiebler, J. Listerud, G. A. Holland, R. Owen, R. Baum, and H. Kressel, *Invest. Radiol.*, 1992, **27**, S90.
16. D. J. Bryant, J. A. Payne, D. N. Firman, and D. B. Longmore, *J. Comput. Assist. Tomogr.*, 1984, **8**, 588.
17. G. L. Naylor, D. N. Firman, and D. B. Longmore, *J. Comput. Assist. Tomogr.*, 1986, **10**, 715.
18. M. Koch, S. E. Maier, I. Baumgartner, K. D. Hagspiel, C. Von Weymarn, P. Boesinger, A. Bollinger, and G. K. Von Schultess, *Proc. Xth Ann. Mtg. Soc. Magn. Reson. Med., San Francisco, 1991*, p. 137.
19. V. Dousset, F. W. Wehrli, A. Louie, and J. Listerud, *Radiology*, 1991, **179**, 437.
20. C. L. Dumoulin, D. J. Doorly, and C. G. Caro, *Magn. Reson. Med.*, 1993, **29**, 44.
21. L. R. Pelc, N. J. Pelc, S. C. Rayhill, L. J. Castro, G. H. Glover, R. J. Herfkens, D. C. Miller, and R. B. Jeffrey, *Radiology*, 1992, **185**, 809.
22. G. R. Caputo, T. Masui, G. A. Gooding, J. M. Chang, and C. Higgins, *Radiology*, 1992, **182**, 387.
23. G. R. Caputo, C. B. Higgins, *Invest. Radiol.*, 1992, **27**, S97–S102.
24. J. S. Swan, D. M. Weber, T. M. Grist, M. M. Wojtowycz, F. R. Kovosec, and C. A. Mistretta, *Radiology*, 1992, **184**, 813.

Biographical Sketches

Cathy Maldjian. *b* 1965. B.A. Columbia University, New York, 1986; M.D. University of Medicine and Dentistry of New Jersey, 1990. Diagnostic Radiology Residency, Mount Sinai Medical Center (New York), 1995. Magnetic Resonance Imaging Fellowship at the Hospital of the University of Pennsylvania following residency. Approx. 10 publications. Research interests include clinical applications of MRI.

Mitchell D. Schnall. B.A., physics, University of Pennsylvania, 1982, M.D., Ph.D., University of Pennsylvania, 1986. Residency in Radiology at the Hospital of the University of Pennsylvania, 1991. Assistant Professor of Radiology at the University of Pennsylvania 1991–1994. Currently Associate Professor of Radiology and Chief of the MRI Section.

Phase Contrast MRA

Charles L. Dumoulin

General Electric Research and Development Center, Schenectady, NY, USA

and

Patrick A. Turski

University of Wisconsin, Madison, WI, USA

1 INTRODUCTION

Recent advances in X-ray, ultrasonic, nuclear, and NMR technologies are making the role of diagnostic radiology increasingly important in the practice of modern medicine. The rapid development of magnetic resonance methods in particular has been most striking. MR has several advantages over X-ray, and MR methods have replaced X-ray methods for many applications. One example of this is the development of MR methods for the visualization of blood vessels within the body. Today this modality is known as magnetic resonance angiography (MRA).

The significance of MRA in medicine cannot be fully appreciated unless one is aware of the competing methods for the generation of blood vessel images. Before the advent of MRA, clinicians generated vascular images using ionizing radiation in the X-ray spectrum. While X-rays of an appropriate energy easily penetrate the body, there is essentially no difference in the X-ray attenuation of blood and surrounding tissue. To overcome this problem, diagnosticians replace blood in a selected vessel with an X-ray-opaque liquid. This contrast media is somewhat toxic and uncomfortable for the patient. In addition, it is typically delivered to the selected blood vessel by a catheter placed into the patient. In light of concerns regarding the ionizing radiation, the toxic effects of the contrast media and a low, but nonzero, mortality rate, the diagnostic benefit of X-ray angiography must be weighed against the risks to the patient.

An alternative to X-rays in vascular radiology is the use of ultrasound. Ultrasonic vascular images are made by observing the reflection of acoustic energy at high frequency. The acoustic attenuation and reflection properties of blood are different from surrounding tissue and frequently provide sufficient contrast to permit the visualization of a vessel. Doppler frequency shifts in the ultrasonic signal can also be used to highlight moving blood. While ultrasonic measurements carry none of the risks of X-ray methods, they are limited in their applications to only a few clinical applications. For example, vessels that are obscured by bone cannot be observed. Vessels deep within the body, or hidden by a thick layer of adipose tissue, are also difficult or impossible to detect. Another aspect of ultrasonic detection is that the resulting images are heavily dependent on the skills of the operator, since the ultrasonic probe must be manipulated at the surface of the patient.

Magnetic resonance angiography overcomes many of the problems of X-ray angiography and ultrasonic imaging. The MRA techniques employed today fall into two classes of technique that are defined by the two different ways in which macroscopic motion of nuclear spins influences the creation and detection of an NMR signal.

The first class of methods relies on the macroscopic displacement of longitudinal magnetization. The phenomenon was first observed and used by Singer and others long before the advent of MR imaging.[1–3] Today, MRA methods of this type are frequently referred to as 'time-of-flight' methods (see ***Time-of-Flight Method of MRA***).

The second class of MRA methods relies on a very different phenomenon. These methods exploit the change in the phase of transverse spin magnetization which occurs when nuclear spins move along a magnetic field gradient. The phenomenon was first reported by Hahn[4] in 1960, and was recognized as a major source of artifacts in the early development of MRI.[5,6] The utility of motion-induced phase shifts for the detection of flow was also recognized[7,8] and many phase-sensitive MRA methods have since been proposed and demonstrated. This article will attempt to describe the more widely used methods of phase-sensitive MRA and provide an overview of the unique aspects of this class of imaging methods.

2 PRINCIPLES OF PHASE DETECTION OF MOTION

2.1 Bipolar Gradient Pulses

The fundamental phenomenon which is the source of many motion-induced artifacts in MRI and the source of motion-based contrast in MR angiograms is the effect that a magnetic field gradient pulse has on transverse spin magnetization. This effect is illustrated in Figure 1. In Figure 1, longitudinal spin magnetization is first generated by an excitation rf pulse. A flow-encoding magnetic field gradient pulse is then applied. This flow-encoding pulse induces a phase shift which is proportional to velocity. Phase-sensitive MRA methods use this phase shift to discriminate between moving nuclear spins and those that are stationary.

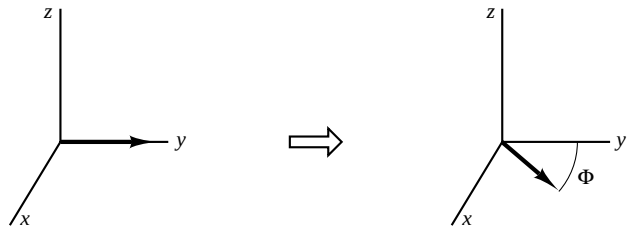

(a) Create transverse magnetization (b) Apply flow-encoding magnetic field gradient pulses (c) Phase shift now proportional to velocity

Figure 1 Velocity-induced phase shifts. All phase-sensitive velocity imaging and measurement with magnetic resonance follows these steps. First, transverse spin magnetization within the sample is generated by applying a radiofrequency pulse at the Larmor frequency. A flow-encoding gradient pulse is then applied. This flow-encoding gradient pulse induces a phase shift which is directly proportional to velocity

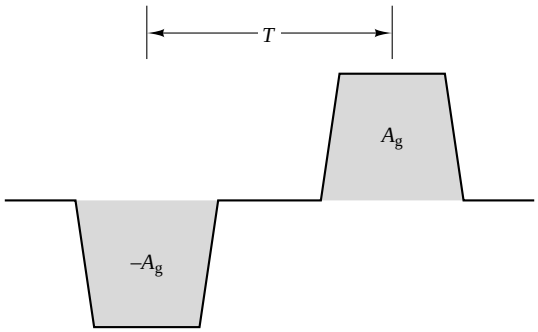

Figure 2 The bipolar flow-encoding gradient pulse. The first lobe dephases transverse magnetization by an amount proportional to position. The second lobe rephases the magnetization. If the magnetization moves in the interval between the pulses, however, the cancelation of the induced phase shift is incomplete. The residual phase shift is proportional to velocity

The simplest flow-encoding magnetic field gradient pulse is shown in Figure 2. This pulse consists of two lobes, separated by a time interval, T. These gradient lobes are applied in the same direction, but with opposite polarity. The unsigned area of each lobe, A_g, is identical. The phase shift induced by velocity, Φ, can be expressed as:

$$\Phi = \gamma VTA_g \tag{1}$$

where γ is the gyromagnetic ratio of the nuclear spin, and V is the velocity of motion.

The effect of a flow-encoding gradient on transverse spin magnetization is illustrated in Figure 3. In Figure 3, two bodies of nuclear spins are shown. The first body is located some distance from the center of the magnetic field gradient and remains stationary during the flow-encoding gradient pulse. The second body of nuclear spins is also located along the magnetic field gradient, but is moved during the time interval between the gradient lobes.

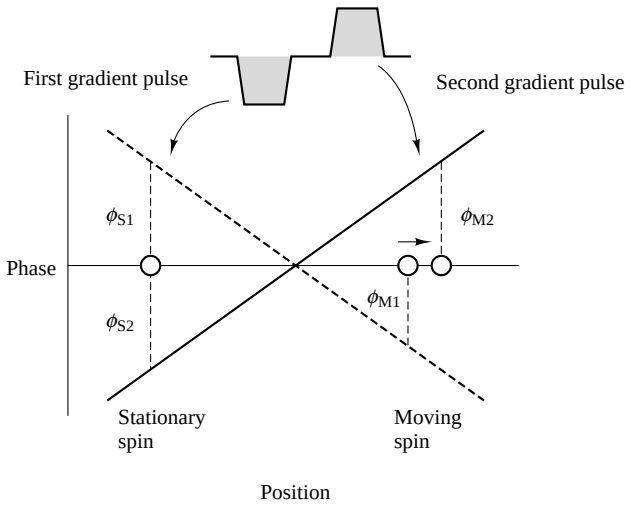

Figure 3 The effect of a bipolar gradient pulse on the phase of stationary and moving spin magnetization. The first magnetic field gradient lobe of the bipolar pulse induces a phase shift that is proportional to position. The second lobe also induces a phase shift, but this phase shift has the opposite sign. The phase shifts induced in stationary nuclei by the first and second lobes, Φ_{S1} and Φ_{S2}, cancel upon subtraction. The phase shifts for moving nuclei, Φ_{M1} and Φ_{M2}, on the other hand, are not equal and thus do not entirely cancel. The residual phase shift is proportional to the nuclei's velocity

Before application of the first lobe of the flow-encoding gradient, transverse spin magnetization is generated and exists with a phase shift, which for the sake of simplicity is assumed to be zero. The application of the first gradient lobe causes the strength of the magnetic field to be proportional to position for the duration of the lobe. Since the Larmor frequency of the transverse spin magnetization is directly proportional to the strength of the magnetic field, during the application of the lobe, nuclear spins will have a resonant frequency that is proportional to location. After the lobe is finished, the magnetic field is homogeneous once again (i.e. all transverse spin magnetization resonates at the same frequency), but the transverse spin magnetization will have acquired a phase shift. This phase shift is proportional to the strength and duration of the lobe, and is also proportional to the location of the nuclear spin along the applied magnetic field gradient.

The phase shift induced by the first lobe in Figure 3 can be undone by the application of a second lobe having equal amplitude and duration, but having opposite polarity. If the nuclear spins do not move during the interval between the gradient lobes, the phase shifts induced by the first lobe will be canceled by the second lobe. If, on the other hand, the nuclear spins move during the interval between gradient lobes, the phase shift induced by the first lobe will not be exactly canceled by the phase shift induced by the second lobe. The residual phase shift will be proportional to the distance the nuclear spins have moved and hence will be proportional to the velocity of the nuclear spins.

2.2 Higher Order Gradient Pulse Waveforms

A bipolar magnetic field gradient pulse is only one member of a series of magnetic field gradient pulse waveforms which induce phase shifts in transverse spin magnetization. Single-lobed gradient pulses induce phase shifts that are proportional to position and are used to encode position in conventional MRI. Bipolar gradient pulses are simply two spatial-encoding gradient pulses applied at slightly different times so that changes in position during the bipolar pulse give phase shifts that are proportional to velocity. Higher orders of motion such as acceleration and jerk can be detected with more complicated gradient waveforms, which can be constructed with linear combinations of simpler gradient waveforms. An illustration of this concept is shown in Figure 4.

2.3 Detecting Velocity with Phase

Once transverse spin magnetization has been given a phase shift that is proportional to velocity, several strategies can be employed to selectively detect signals arising from moving nuclear spins in the presence of signals from stationary spins. Since flow-encoding gradient pulses are only one of many potential sources of phase shifts in transverse spin magnetization, the direct detection of phase itself is usually impractical. Fortunately, phase shifts induced by phenomena other than flow can

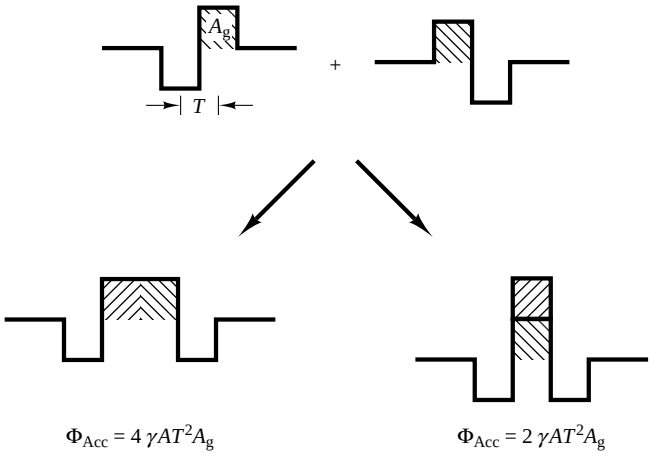

Figure 4 Construction of an acceleration (Acc)-encoding magnetic field gradient pulse waveform by combining two velocity-encoding waveforms. Note that the two different waveforms induce different phase shifts

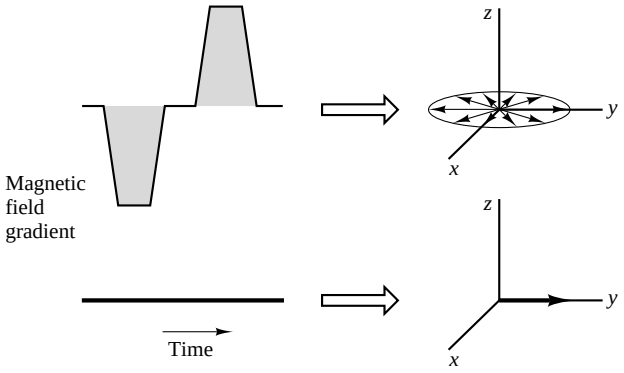

Figure 5 Use of phase cancelation to modulate the amplitude of the MR signal. With this strategy data are acquired under two conditions. The first data set is acquired under conditions which cause loss of signal due to phase cancelation caused by motion. The second data set is acquired under identical conditions to the first, except that the phase cancelation is not performed. The two acquired data sets are identical except for that part arising from motion

easily be removed through a variety of modulation schemes. For example, an early method described by Wedeen et al.[9] relied on the modulation of velocity that occurs in arteries. With this method, two complex images were obtained. Each image was acquired with a flow-encoding gradient. The first image was acquired during the period of peak velocity in the cardiac cycle (systole) and the second was acquired during a period of low flow (diastole). During periods of high velocity, large phase shifts were induced in the MR signals. These phase shifts were frequently so large that distributions of velocity within an image voxel would cause attenuation of the MR signal by phase cancelation. Since the only aspect of the detected MR signal that was different in each acquisition was the phase cancelation arising from velocity, only signals from moving blood were retained upon subtraction of the two images.

A major disadvantage of the cardiac gated scheme described above was that only pulsatile blood flow could be visualized. One strategy that was designed to overcome this limitation employed an amplitude modulation of the flow-encoding gradient waveform.[10,11] As with Wedeen's technique, moving blood was distinguished from stationary tissue by phase cancelation arising from a distribution of velocities as shown in Figure 5.

An alternative modulation scheme that has found widespread use[12–16] is outlined in Figure 6. With this method, two sets of data are acquired under identical conditions, except for the polarity of the flow-encoding gradient pulses. The amplitude of each flow-encoding gradient is kept small to minimize phase cancelation caused by velocity distributions within a pixel, and yet is large enough to cause a detectable phase shift in the MR signal.

Velocity information contained within MR signals detected with modulated flow-encoding gradient pulses can be extracted in several ways.[17] The simplest method is to subtract the magnitude of each image data set. This is only useful, however, if the data are amplitude-modulated (i.e. the modulation scheme causes phase cancelation of MR signals for one of the acquired data sets). More commonly, the extraction of velocity information is performed by complex arithmetic on the image data.

Two methods for the extraction of velocity information are currently in use. The first method is the computation of the magnitude of the complex difference. A vector representation of the generation of complex difference data is shown in Figure 7. Images acquired in this way have an angiographic appearance in which stationary features have little or no signal intensity, and moving blood appears bright. Complex difference data are relatively insensitive to the presence of stationary spin magnetization within the voxel, but provide pixel intensities that are not linearly related to velocity as shown in Figure 8. The relationship between pixel intensity, I, and velocity is:

$$I = K\ \mathrm{abs}[\sin(\gamma VTA_g)] \qquad (2)$$

where K is a constant of proportionality. The problem of nonlinearity is frequently minimized by choosing flow-encoding gra-

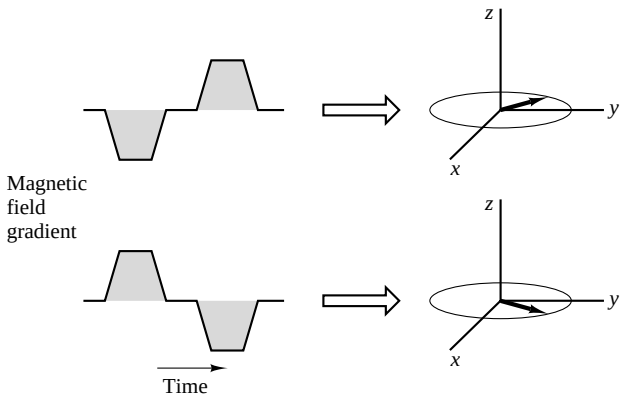

Figure 6 Phase modulation of the MR signal. With this strategy data are acquired under two conditions. The first data set is acquired with a flow-encoding gradient pulse which induces a discrete phase shift due to motion. The second data set is acquired under identical conditions to the first, except that the polarity of the flow-encoding gradient pulse is reversed. The two acquired data sets are identical except for that part arising from motion

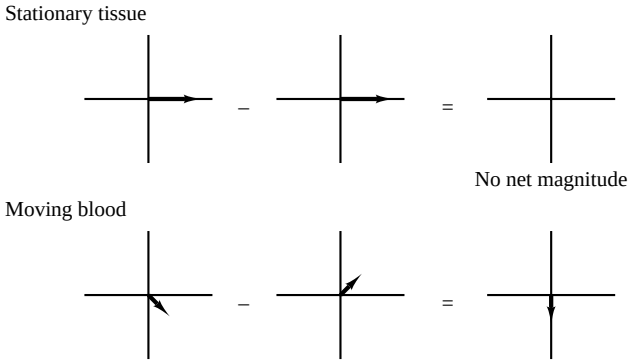

Figure 7 Vector representation of complex subtraction in phase contrast angiography. Two data sets are collected. The first is collected with a bipolar gradient pulse (e.g. a positive lobe followed by a negative lobe) which induces a phase shift that is proportional to velocity. The second is collected in an identical fashion except that the polarity of the bipolar gradient is reversed (e.g. a negative lobe followed by a positive lobe). The complex difference of these two data sets is then calculated. Note that the complex difference of stationary tissue is zero, but that of moving blood is represented by a nonzero length vector

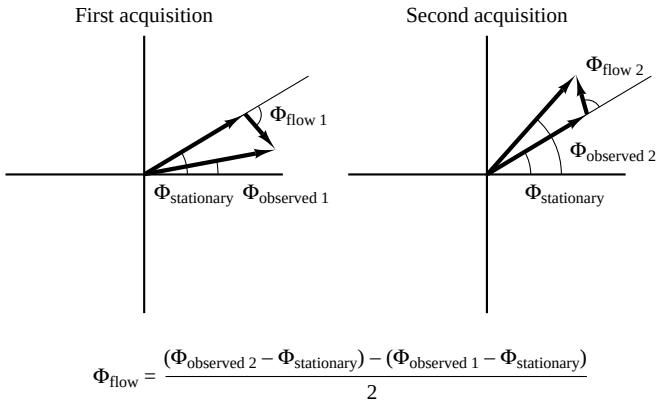

Figure 9 Vector representation of phase difference computations in phase contrast angiography. Two data sets are collected. The first is collected with a bipolar gradient pulse (e.g. a positive lobe followed by a negative lobe) which induces a phase shift that is proportional to velocity. The second is collected in an identical fashion except that the polarity of the bipolar gradient is reversed (e.g. a negative lobe followed by a positive lobe). The difference of the phases of these two data sets is then calculated. Note that if the data contain contributions from both stationary tissue and flowing blood (as shown), then the phase shift of the stationary tissue must be removed before the phase difference due to flow can be calculated

dient pulses that are only strong enough to cause a 1 rad phase shift for the highest expected velocity. Under this condition, the assumption:

$$x \approx \sin(x) \tag{3}$$

holds and the pixel intensity becomes approximately proportional to velocity.

The second method for the extraction of velocity information from complex data is outlined in Figure 9. With this method, the phase of data in each data set is computed. The difference between the phase of the first and second data set is then computed to give a phase difference data set. The intensity of each pixel in the final image is set equal to the phase difference. The pixel intensity of phase difference data is linearly proportional to velocity, but its dependence on velocity is discontinuous and has a periodicity of π as shown in Figure 10. Note that when phase differences are computed it is important to remove static phase shifts arising from resonance offset conditions in order to maintain the expected relationship between velocity and phase.

When pixel intensity is set equal to the phase difference of the acquired data, the images have a unique appearance. Stationary tissue and regions devoid of signal typically appear gray in color. Blood flowing in the direction of the flow-encoding gradient pulse, however, has bright signal intensity which is proportional to velocity. Blood flowing in the opposite direction appears dark.

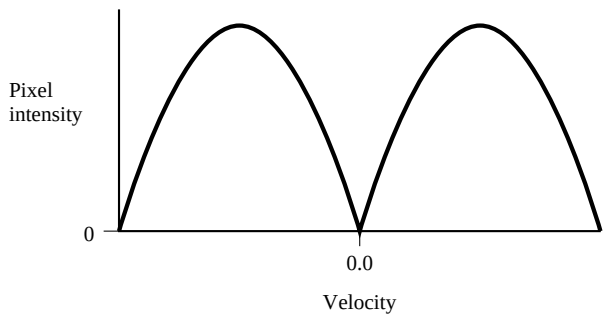

Figure 8 The relationship between velocity and image pixel intensity when complex differences are employed. The magnitude of the complex difference does not include directional information and is only approximately linear with respect to velocity as long as the velocity-induced phase shift is small. If the phase shift is too large, it becomes indistinguishable from a smaller phase shift (an effect called aliasing)

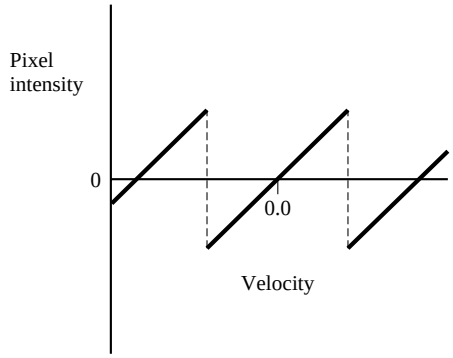

Figure 10 Relationship between velocity and image pixel intensity when phase differences are employed. Note that phase shifts are directly proportional to velocity. If the phase shift is too large, however, it becomes indistinguishable from a smaller phase shift. Note that phase difference displays produce a more linear response than magnitude displays, but have more severe discontinuities in the event of velocity aliasing

A phase difference display is frequently used when a quantitative velocity image is desired. To ensure the quantitative nature of the image, however, phase offsets arising from sources other than velocity must be removed. These sources include resonance offset conditions such as transmitter offsets, field inhomogeneities, chemical shift phenomena, and eddy current effects.

2.4 Strategies for Vessel Selectivity

In clinical practice it is frequently useful to limit the number and nature of the blood vessels imaged in an angiogram. In X-ray angiography this is accomplished by injecting the contrast media into the selected vessel using a catheter. Since MRA uses the motion of blood for contrast, a selective injection is not possible. Fortunately, several strategies exist to permit the selective detection of blood vessels.

Perhaps the most frequently used strategy for selectively detecting vessels is the use of saturation zones around the region of interest. Saturation zones are regions that are subjected to strong rf pulses, typically having a flip angle of between 90 and 135°. These pulses are applied repeatedly, and cause the longitudinal magnetization of tissue within the zone to become saturated. Blood traveling through the zone also becomes saturated. Blood leaving the saturation zone and entering the region of interest is made invisible since transverse spin magnetization cannot be created when longitudinal magnetization has been destroyed. Once the blood has been in the region of interest for a while, however, its longitudinal magnetization reaches a new steady state, and the blood may become visible. Saturation zones are useful in many clinical applications, particularly those in which the targeted vessel crosses from the saturation zone to the region of interest only once.

A second mechanism that can be employed to selectively detect vessels with phase-sensitive MRA relies on differences in blood velocity. This is possible because the size of the flow-encoding gradient pulses can be tailored to cause maximum phase shifts for a selected range of velocities. Smaller flow-encoding gradient pulses will induce phase shifts in only the highest velocities, and have little effect on slowly moving blood. Since arteries typically carry relatively high velocity blood and veins have lower velocity blood, phase-sensitive angiograms using small flow-encoding gradient pulses usually highlight arterial structures. Venous structures can be highlighted by increasing the strength of the flow-encoding gradient pulses. Increasing the strength of the flow-encoding pulses will cause the phase shifts arising from higher velocities to exceed π and the pixel intensity of arterial structures will no longer be proportional to velocity.

In the body, arterial blood tends to be pulsatile while venous blood flows more smoothly. The nature of arterial pulsatility depends on the location of the artery within the body and is heavily influenced by the presence of stenosis. This is illustrated in Figure 11. Data acquisition strategies that highlight pulsatile flow and suppress steady flow can be devised if data are acquired synchronously with the cardiac cycle. For example, pulsatile flow can be highlighted in an angiogram by acquiring images at multiple points in the cardiac cycle and computing the standard deviation of each pixel.

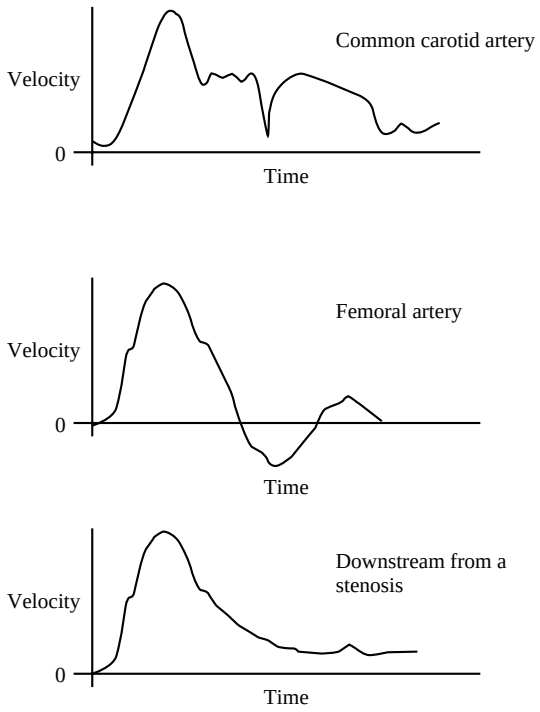

Figure 11 Blood velocity during the cardiac cycle in several locations within the body. Note that the velocity profile is dramatically different in different vessels and is influenced by vessel disease

2.5 Multiplexed Detection of Multiple Flow Components

The flow-encoding gradient pulses used in phase-sensitive MRA induce phase shifts that are proportional only to the component of velocity that is parallel to the direction of the applied magnetic field gradient. Consequently, to construct an angiogram that contains information for all components of velocity, data from three orthogonal flow-sensitive directions must be acquired. Since each flow-sensitive direction requires that data be collected twice, a total of six acquisitions are required.

The information present in a six-excitation phase contrast angiogram has only four components (i.e. stationary tissue and velocity in three orthogonal directions). It is possible to acquire this information more efficiently using a four-excitation multiplexing scheme. One such scheme[18–20] is based on the Hadamard transform. With this method four excitations are performed, each having flow-encoding gradient pulses applied in all three orthogonal directions simultaneously. The combination of flow-encoding pulse polarities is unique in each excitation. One possible combination of flow-encoding pulse polarities is:

	Gradient axis		
Excitation	X	Y	Z
1	+	+	+
2	−	−	+
3	−	+	−
4	+	−	−

where + and − denote the polarity of the applied flow-encoding gradient pulse. The four components of information can be extracted by computing appropriate linear combinations of the acquired data. For the modulation scheme shown above, the linear combinations take the form:

$$\text{Stationary tissue} = Ex_1 + Ex_2 + Ex_3 + Ex_4 \quad (4)$$

$$X \text{ flow component} = -Ex_1 + Ex_2 + Ex_3 - Ex_4 \quad (5)$$

$$Y \text{ flow component} = -Ex_1 + Ex_2 - Ex_3 + Ex_4 \quad (6)$$

$$Z \text{ flow component} = -Ex_1 - Ex_2 + Ex_3 + Ex_4 \quad (7)$$

where Ex_i represents data from the ith excitation.

3 IMPORTANT ATTRIBUTES OF PHASE CONTRAST MRA

There are several important attributes that distinguish phase-sensitive MRA from time-of-flight MRA and from X-ray angiography. For example, each datum collected in a phase-sensitive procedure is sensitive only to a single component of flow. Thus, if a complete angiographic image is required, data must be collected at least four times to obtain all three velocity components and the stationary tissue component. This is in contrast to the single detection required for most time-of-flight procedures. A phase-sensitive angiogram does not necessarily take four times longer to collect than a time-of-flight angiogram, however, since the optimum repetition time, *TR*, for a phase-sensitive angiogram is the minimum available on the system (e.g. 16 ms) whereas the optimum repetition time for a time-of-flight angiogram is longer (e.g. 40–50 ms) to permit the inflow of nonsaturated spin magnetization.

A second attribute of phase-sensitive angiography is that image acquisition is relatively independent of the field-of-view. This is because the source of image contrast in a phase-sensitive angiogram is motion. With phase-sensitive MRA, images of slowly moving blood in small vessels can be acquired within small fields-of-view as easily as higher velocity blood travelling in larger vessels within a large field-of-view. Time-of-flight angiography, however, is constrained by the requirements of vessel geometry and blood velocity to ensure that the inflow of relaxed blood into the region of interest is optimized.

Because the only source of image contrast in a phase-sensitive MR angiogram is motion, excellent suppression of background signals from stationary tissue is possible. Full suppression of background tissue with time-of-flight methods, however, is difficult since the source of image contrast in time-of-flight methods is differential levels of spin saturation. Consequently, the saturation of spin magnetization to suppress stationary tissue signal in time-of-flight angiography also suppresses signals from moving blood. Another consequence of the time-of-flight contrast mechanism is that tissue having short T_1 [e.g. mucus and neoplasms after an injection of Gd-diethylenetriaminepentaacetic acid (Gd-DTPA)] can appear with the same pixel intensity as moving blood. Different levels of spin saturation among tissues can also occur in phase-sensitive angiography, but this does not affect the suppression of stationary tissue, and partially saturated blood appears with only a reduced signal intensity.

One attribute of phase-sensitive methods that has found extensive use is their quantitative nature. Several nonangiographic methods are currently in use. These include thin-slice methods in which vessels are imaged in cross section and the intensity of each pixel of the image is made proportional to the flow-induced phase shift.[21–23] An alternative approach is the conversion of one image dimension into a velocity dimension.[24–27] Images acquired in this fashion are not affected by artifacts arising from background phase shifts and are similar in appearance to Doppler ultrasonic images.

Another characteristic of phase-sensitive MR angiographic methods is that they are heavily dependent on the quality of the instrument. This is particularly true with respect to phase stability since phase shifts are used to detect and measure motion. Perhaps the most common source of phase instability in an MRI system is eddy currents. These eddy currents are induced in metallic structures within the magnet by magnetic field gradient pulses. Phase instability can also occur in the transmitter and receiver subsystems of the instrument. Fortunately, most modern MRI systems are stable enough to perform phase-sensitive angiography.

4 PHASE-SENSITIVE FLOW IMAGING PULSE SEQUENCES

4.1 Two-Dimensional Phase Contrast MRA

The earliest implementations of phase-sensitive MRA[9,12] were similar to X-ray methods in that they provided two-dimensional (2D) projections of the region of interest. In these methods the thickness of the imaged volume was often made to be the full thickness of the patient. If slice selection was employed at all, it was often used to excite a thick slab of magnetization orthogonal to the image plane. Today 2D phase contrast MRA is rarely performed as a full projection. Instead, one or more thick slices are typically obtained from the region of interest.

The speed of 2D phase contrast procedures can be advantageously used in a number of ways. For example, speed can be used to shorten the overall patient examination time. Quite often, however, it is useful to acquire additional data to provide more diagnostic information. With 2D phase contrast MRA, this might include additional view angles or slice locations. Alternatively, certain types of artifacts can be minimized by acquiring additional data. For example, phase-encoding artifacts arising from changes in blood velocity during the cardiac cycle can be minimized by detecting the average velocity-induced phase shift rather than one detected at an arbitrary instant in time. This can be done by acquiring data with a relatively large NEX. For example, with a repetition time, *TR*, of 50 ms and a heart rate of 60 beats per minute, choosing NEX to be about 20 will cause velocity variations during the cardiac cycle to be averaged.

4.2 Cine Phase Contrast MRA

An early variant of 2D phase contrast MRA was the use of cardiac gating and the detection of images at multiple points in the cardiac cycle.[14,15] Cine MRA is particularly useful in imaging peripheral arteries since blood flow in these vessels is typically triphasic and moves forward, backward, and remains still at different points of each cardiac cycle. Arterial flow dynamics can be exploited to differentiate arterial flow from venous flow.

Thin-slice cine phase contrast imaging in which the phase of each pixel is displayed[21–23] has become widely used in the past few years. These images provide a quantitative measure of blood velocities during the cardiac cycle and have been applied in the head,[28] aorta,[29] renal,[30] mesenteric,[31] and peripheral vessels.[32]

4.3 Three-Dimensional (3D) Phase Contrast MRA

Two-dimensional phase contrast angiograms have several limitations that can be overcome by the collection of the data in three dimensions.[16] Unlike a projection angiogram, a typical 3D angiogram has approximately isotropic voxels. Phase variations across a voxel are minimized because the voxel dimensions are small. Perhaps the most significant advantage, however, is that the data can be analyzed retrospectively in a number of ways. For example, 2D projections can be generated for any view angle. Selected subsets of the acquired data can be extracted to remove features that interfere with the presentation of features of interest. With 3D MRA it is also easy to generate cross-sections of vessels.

4.4 Fourier Velocity Encoding

Fourier velocity-encoding pulse sequences are a form of phase-sensitive velocity imaging in which the velocity of spin magnetization is represented as a positional displacement rather than as a phase shift in the image. These pulse sequences are equivalent to conventional spin warp imaging pulse sequences, except that the spatially localizing phase-encoding gradient pulses are replaced with bipolar flow-encoding gradient waveforms. In other words, a Fourier velocity-encoded image has a phase-encoded dimension in which displacement of signal depends on spin velocity rather than on spin position. Pixel intensity in these images is determined by the sensitivity of the imaging system and the strength of the detected MR signal. The phase of each pixel, however, is determined by resonance offset conditions such as transmitter offsets, field inhomogeneities, and susceptibility effects. As with conventional MR imaging, this phase information is typically ignored.

Figure 12 shows an example of Fourier velocity-encoding applied in the human abdomen. In this image the horizontal dimension is a spatial dimension corresponding to the subject's left/right axis. The vertical axis, however, is a velocity dimension corresponding to the component of velocity parallel with the subject's inferior/superior axis. Excitation of spin magnetization was limited in this image to a 5 mm axial slice. Note that the distribution of velocities within the aorta is narrow, but the distribution of velocities within the vena cava is relatively broad.

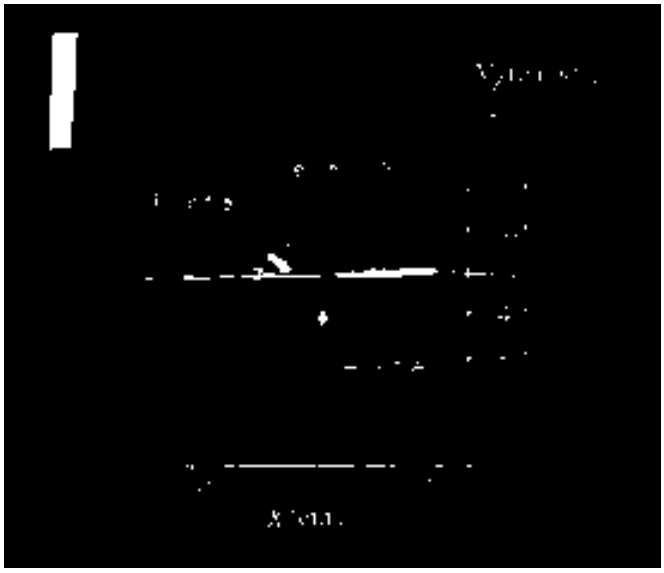

Figure 12 Fourier velocity-encoded image of the abdomen. In this image one spatial dimension and one velocity dimension have been collected. Images of this form can be used to measure the distributions of velocity within a vessel. Since they use a phase-encoding mechanism to detect velocity, these images have a velocity precision and accuracy equivalent to that of spatial measurements in conventional imaging. (Reproduced by permission from C. L. Dumoulin et al.[27])

5 POSTPROCESSING

Many of the MRA methods in current use acquire data in three dimensions. For example, a 3D phase contrast angiogram has three spatial dimensions. Cine 2D phase contrast angiograms are also 3D, but consist of two spatial dimensions and a temporal dimension. Unfortunately, 3D data cannot be displayed directly with the hardware available in most institutions. Rather, a 2D subset of the 3D data set must be extracted and put into a suitable form such as film for diagnosis. Several methods currently in use are outlined below.

5.1 Maximum Intensity Projection

Filming thin-slice extractions of a 3D data set is straightforward and often useful. Projection images in which one of the three dimensions is collapsed, however, are usually more helpful. The simplest and most commonly used projection algorithm is the Maximum Intensity Projection (MIP) method. With MIP a 'ray' is sent through the 3D data set to create each pixel in the projection. The maximum pixel intensity value found along the ray determines the pixel value in the projection image as shown in Figure 13. An important aspect of MIP is that vessels close to the viewer are indistinguishable from vessels further away. Depth information can be recovered, however, by sequentially displaying several MIP projections at a variety of view angles to create the illusion of a 3D object.

5.2 Subvolume Reconstruction

In an ideal MR angiogram the pixel intensities of blood vessels and stationary tissue are different enough to guarantee

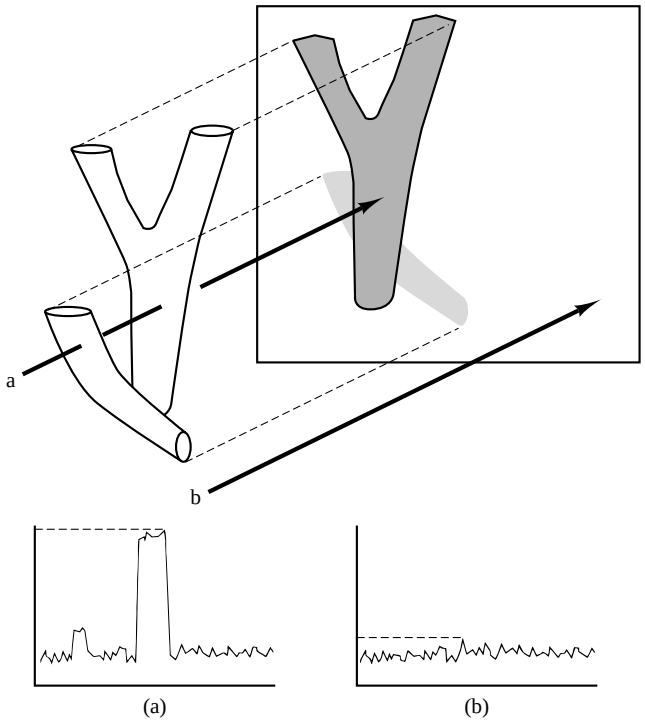

Figure 13 Projection of the maximum intensity pixel to extract a 2D image from a 3D data set. In this procedure 'rays' are sent through the 3D object. A 2D projection is created by reducing the data encountered by each 'ray' to a single value. With the *m*aximum *i*tensity *p*rojection (MIP) algorithm, the value of the most intense pixel is chosen for the projection image. Here two 'rays' are shown. The first 'ray' (a) encounters the bright signal in a vessel and selects the most intense pixel. The second 'ray' (b) also selects the brightest pixel, but this pixel contains noise

that only vessels are detected with an MIP algorithm. Complete suppression of stationary tissue, particularly for time-of-flight procedures, is often impossible, however, and the MIP algorithm projects the most intense pixels of the stationary tissue background. This makes small vascular features having relatively low pixel intensity more difficult to detect. Fortunately, the appearance of nonsuppressed tissue can be minimized by applying the MIP algorithm only over a selected subvolume of data. In addition to improving vessel contrast in the projection image, subvolume reconstructions can be used to remove overlapping blood vessels to enhance the appearance of the vessels of interest.

5.3 Temporal Filtering

Data that are acquired with a temporal dimension can also be subjected to projection procedures. The appearance of all vessels within a dynamic image can be enhanced by applying the MIP algorithm in the temporal dimension. Alternatively, the standard deviation of pixel intensity, rather than the maximum pixel intensity, along the ray can be determined to highlight dynamic features, such as arteries. Features that are more constant during the cardiac cycle, such as veins and background, are suppressed. Arterial blood flow downstream from an occlusion or high-grade stenosis, however, may no longer be pulsatile and a standard deviation projection may suppress rather than enhance the appearance of the vessel.

6 APPLICATIONS

Phase contrast MRA is frequently used in clinical evaluations to display pathologic flow conditions. The principle reasons for using phase contrast methods are: (1) to improve vessel detection by subtracting the background signal and (2) to utilize the velocity/phase relationship to provide physiological information regarding blood flow. The flexibility of phase contrast methods makes them somewhat more complex to use than time-of-flight methods in the clinical environment. Nevertheless, phase contrast methods are becoming increasingly valuable for the evaluation of patients with suspected vascular disease.

6.1 The Role of Flow-Encoding Strength in Phase Contrast MRA

The amplitude of the bipolar flow-encoding gradient pulse determines the amount of velocity encoding. A larger amplitude will sensitize the MR angiogram to low velocities. Conversely, a small amplitude will produce an angiogram that emphasizes higher velocities.[33] One can therefore create phase contrast angiograms that display pathologic conditions by selecting a velocity encoding that closely approximates the pathologic flow state. Encoding for slower flow velocities can improve detection of slow flow within venous structures such as the dural sinuses or deep cerebral veins. Encoding for slow flow can also improve visualization of small arterial structures as illustrated in Figure 14. In general, when one wants to optimize visualization of intracranial arterial structures a velocity encoding of 30 cm s^{-1} is preferable to improve detection of the slow blood flow along the vessel wall and to help define small vessels and pathologic vessels with reduced flow velocities. Similarly when phase contrast techniques are used to identify aneurysms, it is important to use a low-velocity encoding in order to optimize visualization of slow vortex flow in the central portions of the aneurysm.[35] Phase wrap (or flow aliasing) is not a serious problem in phase contrast 'speed' imaging (i.e. when the magnitude of the data is displayed), because the higher velocity spins typically occur in the center of the vessel and the vessel morphology will still be well delineated by visualization of the slower flow along the edges of the vessel.

By selecting a higher velocity encoding (100–150 cm s^{-1}) and using phase-difference reconstruction, images can be obtained that preserve the quantitative phase/velocity relationships and emphasize higher velocity flow structures. This can be advantageous for identifying high-flow arteries that supply arteriovenous malformations or higher velocity inflow jets associated with intracranial aneurysms. Phase-difference images also permit the sign of the flow-induced phase shift to be encoded as pixel intensity. This is particularly useful for determining the direction of flow within vessels.

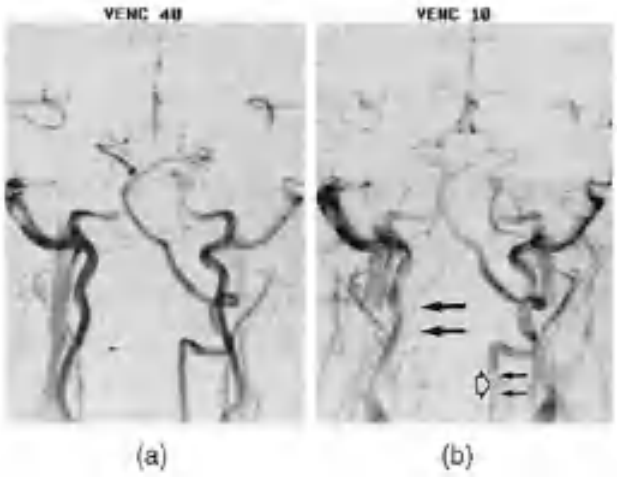

Figure 14 Coronal 2D phase contrast angiogram of the vertebral arteries at two velocity encodings. (a) This image was obtained with a velocity encoding of 40 cm s^{-1}. The right vertebral artery is not visualized and was initially thought to be occluded. (b) The angiogram was repeated with a velocity encoding of 10 cm s^{-1}. The slow flow in the small, right vertebral artery is now visualized (large arrows). The slow flow along the wall of the left vertebral artery is also demonstrated (small arrows). Note that the central higher velocity flow has aliased and appears as reduced signal intensity (open arrow). (Reproduced by permission of Raven Press from C. A. Anderson et al.[34])

6.2 MRA and T_1 Relaxation Agents

Blood flowing into the region of interest reaches a steady state having reduced signal intensity after experiencing multiple rf pulses. This saturation of slowly moving blood is particularly problematic for time-of-flight MRA since the intensity of blood is ultimately reduced to that of the surrounding background tissue. Saturation of slowly moving blood can also be a problem with phase contrast MRA, but since the background signal intensity in a phase contrast angiogram is zero, saturation merely reduces the signal-to-noise ratio of the blood signal and the vessel is usually still visible. Nevertheless, slowly moving blood would be easier to detect if the equilibrium magnetization could be increased. This can be accomplished by shortening the T_1 of blood by administering a relaxation agent such as Gd-DTPA.

With a T_1 relaxation agent in the bloodstream, flowing blood reaches a steady state, which gives a stronger MR signal. Higher concentrations of the relaxation agent result in a shorter T_1 and a corresponding increase in the steady state magnetization. For Gd-DTPA this relationship holds for concentrations up to 0.5 mM kg^{-1}. At higher doses the T_2 shortening effects become dominant and the MR signal intensity begins to decrease.[35,36]

The effects of intravenous contrast enhancement for phase contrast methods is related to velocity encoding. At higher velocity encodings slow flow has relatively low signal intensity and is poorly visualized. In this instance, intravenous contrast material will significantly improve the detection of slow flow. This is particularly advantageous in four clinical situations.

6.2.1 Small Arteries

Frequently small arteries with minimal flow are difficult to detect. This is due to saturation of slowly moving blood as it passes through the imaging volume. An incorrect diagnosis of vascular occlusion might be made when in fact the vessel is patent. By administering intravenous contrast material the signal intensity associated with the slowly moving blood increases by a factor of two, making the vessel easier to detect. This increase in signal results in an increase of the dynamic range of detectable velocities. An example of increased sensitivity to slow flow after injection of a T_1 relaxation agent is shown in Figure 15.

6.2.2 Venous Structures

Imaging venous structures is improved by the use of intravenous contrast material by decreasing the saturation of slow venous flow especially along the wall of the vein. This is particularly important in cases of dural sinus thrombosis where collateral flow may be difficult to detect due to its very slow flow rates.

6.2.3 Complicated Flow

Vortex flow within aneurysms may also result in signal loss due to saturation effects. By shortening the T_1 of blood, the lumen of the aneurysm may be better defined.

6.2.4 Increased Spatial Resolution

Increasing spatial resolution results in reduced signal-to-noise for most MRA acquisitions. Intravenous contrast enhancement enables more highly resolved matrices and smaller fields-of-view to be used by increasing the signal associated with small vessels.

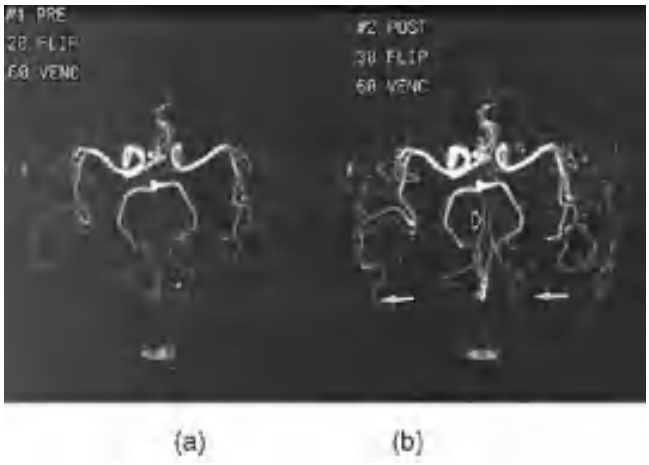

Figure 15 Gd-DTPA-enhanced phase contrast MRA. (a) The nonenhanced axial phase contrast angiogram was obtained using a 256×256 matrix and a field-of-view of 20 cm. (b) After the administration of Gd-DTPA at a dose of 0.1 mM kg^{-1}, the scan was repeated using identical imaging parameters. Smaller arterial branches (arrows) as well as venous structures (open arrow) can now be identified

6.3 Clinical Applications in the Head and Neck

Phase contrast angiography has proven useful in the head,[37,38] neck,[39] abdomen,[40,41] and peripheral vessels.[42,43] Rather than provide a complete atlas of examples, only applications in the head will be discussed below.

6.3.1 Cerebral Ischemia

The ability to quantify flow velocity and flow volumes with phase contrast MRA has added a new dimension to the MRA evaluation of neurological disease. In addition to demonstrating vascular morphology, phase contrast MRA can now determine the adequacy and character of blood flow for specific vessels. The goals of the MRA examination are to identify compromised blood flow and to determine the severity and etiology of the flow reduction. Usually, reduced or absent flow within the internal carotid, vertebral, basilar, anterior, middle, and posterior cerebral arteries can be identified with a high degree of accuracy.

There are four pathologic flow conditions that are generally recognized as leading to cerebral ischemia or infarction. The first is global hypoperfusion due to sustained hypotension. The second is thrombosis of the small perforating arteries leading to infarction of deep structures such as the basal ganglia or white matter. The third category is embolic disease in which atherosclerotic material or thrombus dislodges from a preexisting atheromatous lesion, producing flow compromise distally in smaller branch vessels. The last condition is the complete thrombosis of a major vessel resulting in decreased or absent distal perfusion.[44,45] MRA can frequently determine which of these mechanisms is responsible for the patient's ischemic event in a fashion analogous to X-ray angiography.[46–48]

Patients may present with anterior circulation, large artery ischemic events (i.e. motor or sensory deficits) requiring attention to the carotid bifurcations (Figure 16), the proximal middle cerebral arteries, and possibly the aortic arch. Other patients may present with ischemic events related to the larger posterior circulation vessels (i.e. ataxia, dizziness, nausea, cranial nerve dysfunction). In this instance, the proximal and distal vertebral arteries and basilar artery must be evaluated (Figure 17). For patients presenting with embolic events, the embolic material may arise from the heart or the proximal arterial system. If the transient ischemic attacks occur in multiple vascular territories, a cardiac source for emboli should be sought. If previous transient ischemic attacks have occurred in the same vascular territory, a localized proximal vascular lesion is the most likely etiology.[49]

Intracranial MRA examination can be approached in several ways. The most commonly used method is a 3D time-of-flight acquisition which includes the circle of Willis, the proximal middle cerebral arteries, and the distal basilar artery. This approach is effective for evaluating the proximal vessels. Unfortunately, time-of-flight angiography is not particularly sensitive to slow flow, and there may be instances in which vessel patency is overlooked due to saturation of the slow flow distal to an area of severe stenosis. An alternative approach is to obtain a 2D or a 3D phase contrast angiogram with low velocity encoding (e.g. 20 cm s^{-1}).[50] These images can define the vascular morphology in the region of reduced flow. In addition, cine phase contrast studies can be performed to display flow direction[50] and to permit quantitative measurements of flow and velocity. In selective instances, this can be helpful for defining the hemodynamic effects of vascular lesions.

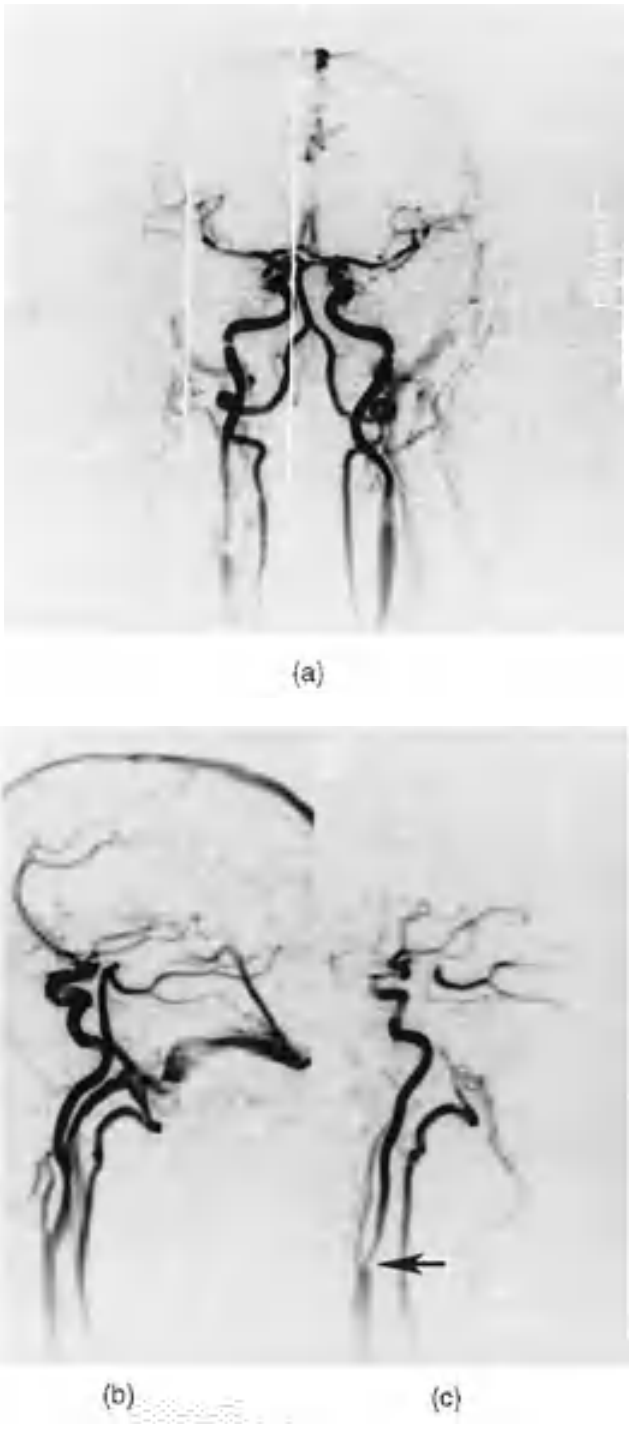

Figure 16 Right internal carotid artery stenosis demonstrated by 2D phase contrast MRA. (a) The coronal 2D phase contrast image demonstrates a stenosis of the proximal right internal carotid artery. Flow is symmetric in both internal carotid arteries. Sagittal 2D phase contrast MRA images clearly define (b) the normal left internal carotid artery, and (c) the stenotic proximal right carotid artery (arrow)

MRA evaluation of the extracranial carotid arteries is currently a source of controversy.[51,52] Most investigators rely on single slab or multiple slab 3D time-of-flight MRA to define

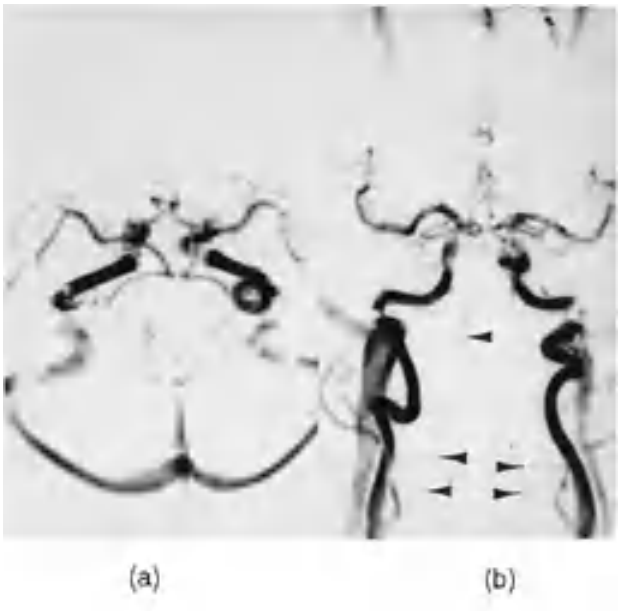

Figure 17 Basilar artery occlusion demonstrated by phase contrast MRA. (a) The axial and (b) the coronal phase contrast angiograms indicate absence of flow within the basilar artery and only minimal flow in the right and left vertebral arteries (arrows)

the degree of vessel compromise.[53] Some authors have recommended performing a 2D time-of-flight study whenever a carotid occlusion is encountered to avoid missing a nearly occluded internal carotid artery.[54,55] Unfortunately, high velocities caused by a severe stenosis may cause a signal loss in 2D time-of-flight angiography. Carefully controlled trials will ultimately be needed to define precisely the accuracy of MRA for defining carotid stenosis. There is no question, however, that MRA is capable of providing high-resolution images that are adequate for many clinical management decisions.

6.3.2 *Vascular Malformations*

Arteriovenous malformations (AVMs) are most commonly supratentorial where a large component of the AVM is located superficially in the pia. The malformation occasionally has a wedge shape with the apex of the wedge directed toward the ventricular system. The amount of parenchymal component of the AVM is variable. Occasionally vascular malformations may have both dural and pial components and are thus termed mixed AVMs. Malformations completely restricted to the dura are termed dural AVMs. Spinal vascular malformations are most often dural in location and frequently contain direct arteriovenous fistulas.[56]

The nidus of the AVM may be variable and difficult to characterize accurately. The nidus has been defined as 'that part of the malformation interposed between the recognizable feeding arteries and the larger terminal draining veins'. The nidus represents the area of arteriovenous shunting within the malformation. It is therefore the low-resistance portion of the malformation and is thus responsible for the hemodynamic changes related to the malformation. The venous drainage begins as the multiple vascular channels coalesce into one large

Figure 18 MRA of an AVM prior to stereotactic radiosurgery. (a) The phase contrast angiogram (velocity encoding = 80 cm s^{-1}) demonstrates enlargement of the right pericallosal artery (arrow). (b) A second phase contrast angiogram (velocity encoding = 20 cm s^{-1}) reveals deep venous drainage into the vein of Galen. Cortical venous drainage along the medial aspect of the right parietal lobe is also noted (arrows). (c) Following the phase contrast angiograms a 3D time-of-flight acquisition was obtained. The axial projection demonstrates the pericallosal feeder to the AVM, as well as the AVM nidus (arrows)

venous structure. The ability to define the size and location of the AVM nidus is essential for the proper selection of patients for surgery, endovascular therapy, or focused radiation therapy.

For patients with AVMs, the MR angiographic evaluation attempts to (1) identify the arterial supply to the AVM (Figure 18), (2) determine the size and location of the AVM nidus, (3) define the location and morphology of the venous drainage (Figure 19), (4) identify high flow aneurysms, and (5) attempt to detect the presence of fistulas within the AVM. The patient is initially evaluated by obtaining spin echo images. Typically sagittal T_1-weighted and axial fast spin echo T_2-weighted images are obtained. Sagittal 2D phase contrast angiograms are acquired with multiple velocity encodings (e.g. 80 and 20 cm

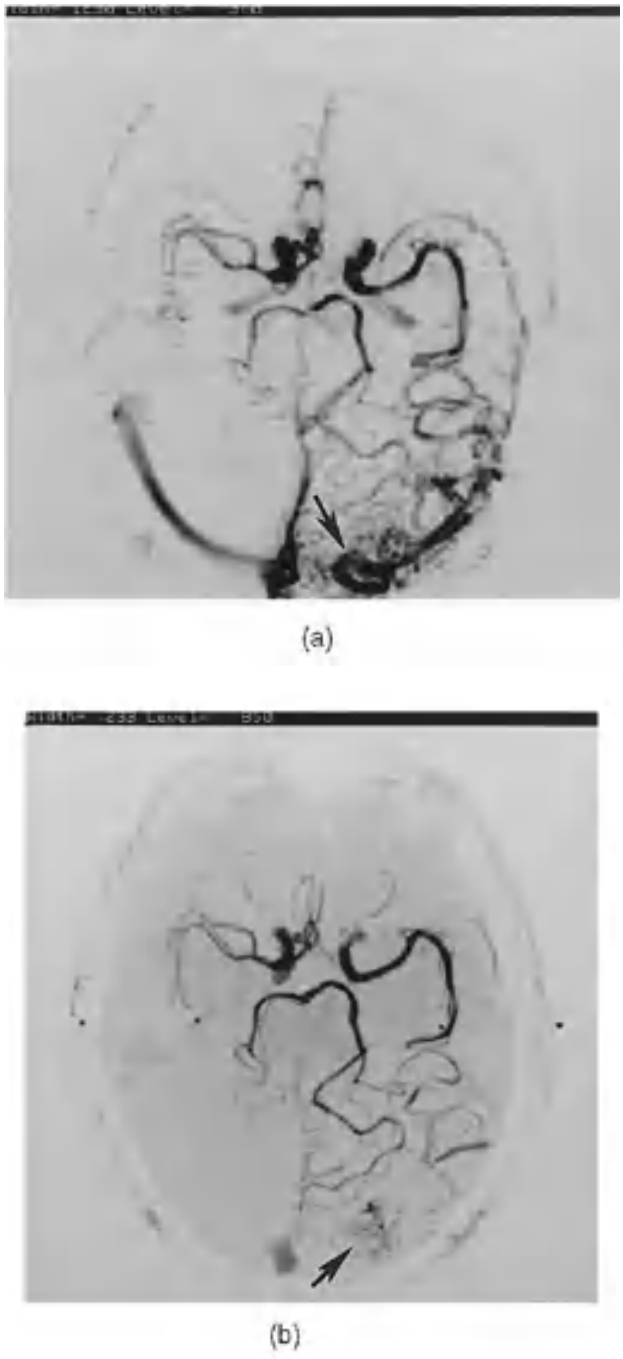

Figure 19 Occipital lobe AVM. (a) The phase contrast MRA study demonstrated an enlarged angular branch of the middle cerebral artery and enlargement of the right posterior cerebral artery. There are dilated cortical veins overlying the vascular malformation, with superficial venous drainage extending into the transverse sinus (arrow). (b) The 3D time-of-flight study was obtained without intravenous contrast material. The nidus of the vascular malformation is identified (arrow) and the posterior cerebral and middle cerebral artery feeders are clearly delineated

s^{-1}). By generating images that emphasize fast and slow velocities it is possible qualitatively to assess blood flow within the AVM. Additional advantages of this approach are that the arterial supply is well defined at the higher velocity encodings and the venous drainage is delineated at the lower velocity encodings. High flow rates may also be quantitated by cine phase contrast MRA techniques.

6.3.3 Intracranial Aneurysms

MRA is also becoming an important modality for identifying and characterizing intracranial aneurysms. Although MRA has outstanding potential as a noninvasive method for identifying intracranial aneurysms, the present limitations of MRA require that it be used cautiously in this patient population. Failure to detect an intracranial aneurysm may result in inappropriate therapy and subsequent devastating subarachnoid hemorrhage. The identification of intracranial aneurysms prior to hemorrhage is of critical importance because nearly half of all patients presenting with acute subarachnoid hemorrhage will die within the first 30 days of rupture.

Although the morphology of intracranial aneurysms is best delineated by 3D time-of-flight MRA, additional information regarding the flow dynamics of the aneurysm can be obtained by using phase contrast techniques[57] as shown in Figure 20. A useful approach is to obtain a 2D phase contrast angiogram in a plane that profiles the aneurysm and parent vessel. This is conveniently done by reviewing a 3D time-of-flight angiogram. The velocity encoding of the phase contrast angiogram can be selected to emphasize the faster inflow jet or the slower circulating central vortex flow. Another advantage of the phase contrast angiogram is that high signal intensity thrombus does not appear in the angiographic image, thus better delineating the residual lumen. In addition, time-resolved cine phase contrast angiograms can be acquired to define variations in the size and configuration of the aneurysm during the cardiac cycle (Figure 21). Occasionally, a portion of the aneurysm wall will bulge during systole, suggesting that this portion of the aneurysm wall may be more likely to rupture. Thus phase contrast

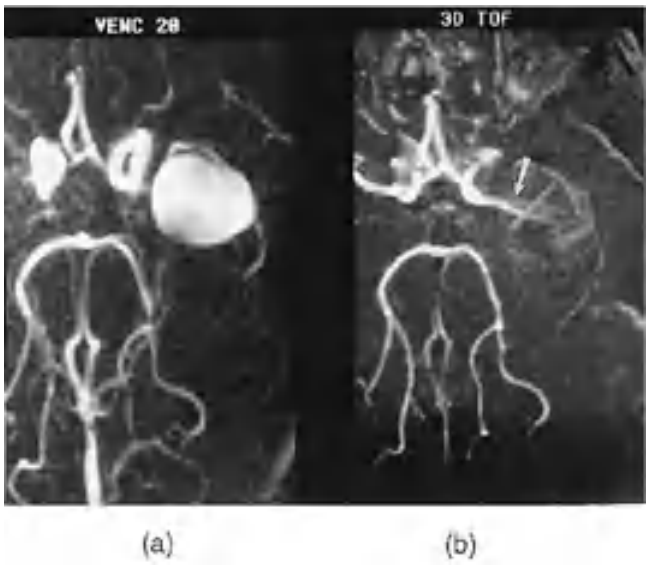

Figure 20 Giant middle cerebral artery aneurysm. (a) The axial 2D phase contrast MR angiogram demonstrates slow vortical flow within the aneurysm (velocity encoding = 20 cm s^{-1}). (b) The axial 3D time-of-flight angiogram displays only the high velocity inflow jet (arrow); the slow flow within the aneurysm is not visible due to saturation

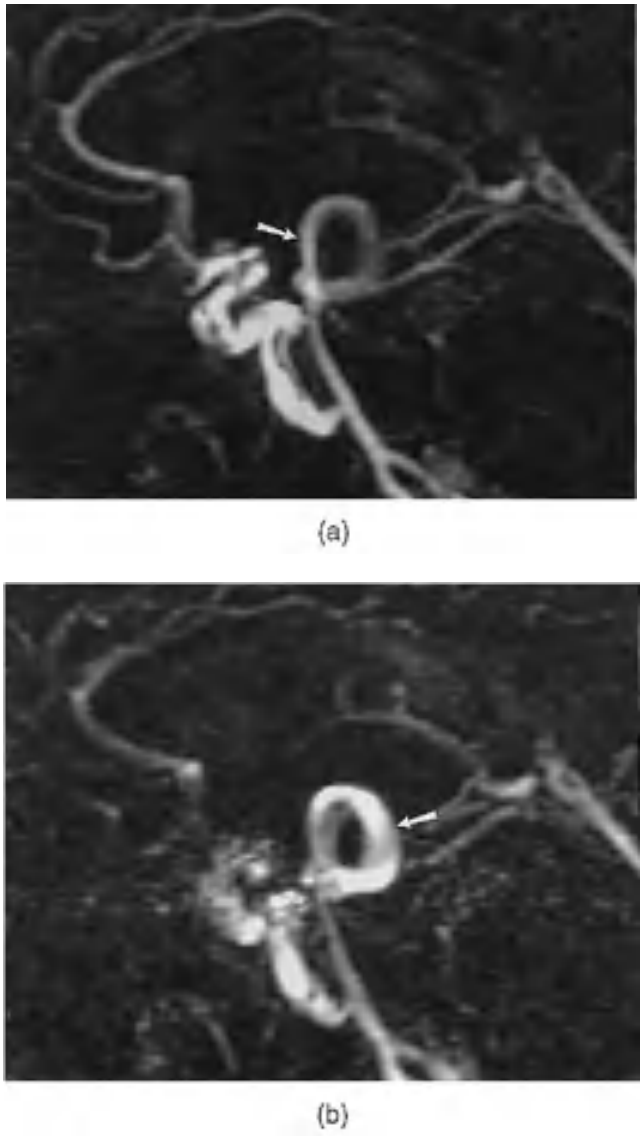

Figure 21 Change in aneurysm size during the cardiac cycle. (a) The cine 2D phase contrast image was obtained during systole and represents one of 16 images obtained during the cardiac cycle. Note the high signal intensity inflow jet (arrow). (b) During diastole the slow flow along the wall of the aneurysm can be appreciated (arrow)

MRA plays an important adjunctive role in 3D time-of-flight MRA for the presurgical workup of patients with intracranial aneurysms.

6.3.4 Cerebral Venous Thrombosis

Complex difference 2D phase contrast angiography is a fast and effective method for imaging blood flow within the dural sinuses. The phase contrast angiogram can be made sensitive to venous flow rates by selecting a relatively low velocity encoding (e.g. 20 cm s^{-1}) as illustrated in Figure 22. Clinically useful images that clearly demonstrate the dural sinuses can be obtained in approximately 4 min. A midline sagittal phase contrast angiogram displays flow in the sagittal sinus as well as the internal cerebral veins, vein of Galen and straight sinus. Phase contrast angiograms can also be obtained in the axial plane to detect flow in the lateral sinuses and jugular veins. In this projection, the confluence of the dural sinuses is well visualized as well as the transverse and sigmoid segments of the lateral sinus. Phase contrast angiography has several desirable features that favor successful imaging of the dural sinuses. Phase contrast angiograms are sensitive to flow in all directions facilitating imaging of complex geometries such as the sigmoid sinus. There is also better visualization of inplane flow due to the subtraction of background tissue. Most importantly, high signal intensity thrombus is subtracted from the flow image along with the other stationary soft tissues. The result is an MR venogram that is sensitive to slow flow and only displays moving blood.

7 CONCLUSIONS

Cardiovascular disease is the leading cause of death in the industrialized world. Consequently, considerable medical resources are employed each year in its diagnosis and treatment. Before the advent of magnetic resonance imaging, diagnosticians relied primarily on invasive X-ray methods to visualize vascular anatomy. Unfortunately, X-ray methods are uncomfortable and present a risk to patient health. A frequently used alternative to X-ray angiography is ultrasonic imaging. While ultrasonic methods are risk-free, they are limited to a few clinical applications, and are heavily dependent on the skill of the operator.

Magnetic resonance angiography has become an important imaging modality for the diagnosis of vascular disease because it overcomes many of the limitations of X-ray and ultrasonic imaging methods. For example, MRA presents the patient with the same degree of risk as conventional MRI. Unlike

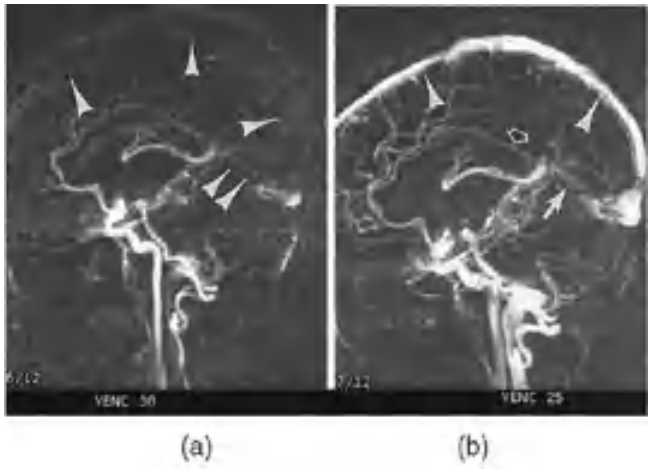

Figure 22 Sagittal sinus thrombosis and recanalization. (a) The sagittal phase contrast angiogram obtained at a velocity encoding of 30 cm s^{-1} reveals absence of flow in the sagittal sinus and straight sinus (arrowheads). (b) The follow-up phase contrast angiogram obtained 1 month following anticoagulant therapy demonstrates recanalization of the sagittal sinus (arrowheads). There is, however, persistent thrombus within the straight sinus (arrow). Note that the inferior sagittal sinus is visible (open arrowhead)

ultrasonic methods, MRA is applicable to a wide variety of blood vessels within the body and does not require a highly skilled operator.

Magnetic resonance angiography has several features that make it more suitable than X-ray angiography for many clinical situations. For example, patients with compromised renal function may be better served with MRA since the injection of X-ray contrast media employed in X-ray angiography can cause renal failure. The absence of ionization radiation is an attractive aspect of MRA and is particularly important for pediatric applications.

Magnetic resonance angiography also provides information that is difficult or impossible to obtain with X-rays. In addition to providing cross-sectional images of blood vessels, MRA can provide details of blood flow dynamics and quantitative measurements of blood velocity. Perhaps the most significant aspect of MRA, however, is that the technology is still young and prospects for future development in applications and techniques are excellent.

8 RELATED ARTICLES

Abdominal MRA; Time-of-Flight Method of MRA; Whole Body Magnetic Resonance Angiography.

9 REFERENCES

1. J. R. Singer, *Science*, 1959, **130**, 1652.
2. O. Morse and J. R. Singer, *Science*, 1970, **170**, 440.
3. T. Grover and J. R. Singer, *J. Appl. Phys.*, 1971, **42**, 938.
4. E. L. Hahn, *J. Geophys. Res.*, 1960, **65**, 776.
5. V. Waluch and W. G. Bradley, *J. Comput. Assist. Tomogr.*, 1984, **8**, 594.
6. P. M. Pattany, J. J. Phillips, L. C. Chiu, J. D. Lipcomon, J. L. Duerk, J. M. McNally, and S. N. Mohapaka, *J. Comput. Assist. Tomogr.*, 1987, **11**, 369.
7. P. R. Moran, *Magn. Reson. Imag.*, 1982, **1**, 197.
8. M. O'Donnell, *Med. Phys.*, 1985, **12**, 59.
9. V. J. Wedeen, R. A. Meuli, R. R. Edelman, S. C. Geller, L. R. Frank, T. J. Breely, and B. R. Rosen, *Science*, 1985, **230**, 946.
10. L. Axel and D. Morton, *J. Comput. Assist. Tomogr.*, 1987, **11**, 31.
11. G. A. Laub and W. A. Kaiser, *J. Comput. Assist. Tomogr.*, 1988, **12**, 377.
12. C. L. Dumoulin and H. R. Hart, *Radiology*, 1986, **161**, 717.
13. C. L. Dumoulin, S. P. Souza, and H. R. Hart, *Magn. Reson. Med.*, 1987, **5**, 238.
14. C. L. Dumoulin, S. P. Souza, M. F. Walker, and E. Yoshitome, *Magn. Reson. Med.*, 1988, **6**, 275.
15. S. P. Souza and C. L. Dumoulin, *Dyn. Cardiovasc. Imaging*, 1987, **1**, 126.
16. C. L. Dumoulin, S. P. Souza, M. F. Walker, and W. Wagle, *Magn. Reson. Med.*, 1989, **9**, 139.
17. M. A. Bernstein and Y. Ikezaki, *JMRI*, 1991, **1**, 725.
18. C. L. Dumoulin, S. P. Souza, R. D. Darrow, N. J. Pelc, W. J. Adams, and S. A. Ash, *JMRI*, 1991, **1**, 399.
19. N. J. Pelc, M. A. Bernstein, A. Shimakawa, and G. H. Glover, *JMRI*, 1991, **1**, 405.
20. R. Hausmann, J. S. Lewin, and G. Laub, *JMRI*, 1991, **1**, 415.
21. P. van Dijk, *J. Comput. Assist. Tomogr.*, 1984, **8**, 429.
22. D. J. Bryant, J. A. Payne, D. N. Firmin, and D. B. Longmore, *J. Comput. Assist. Tomogr.*, 1984, **8**, 588.
23. I. R. Young, G. M. Bydder, and J. A. Payne, *Magn. Reson. Med.*, 1986, **3**, 175.
24. D. A. Feinberg, L. E. Crooks, P. Sheldon, J. Hoenninger 3rd, J. Watts, and M. Arakawa, *Magn. Reson. Med.*, 1985, **2**, 555.
25. J. Hennig, M. Muri, P. Brunner, and H. Friedburg, *Radiology*, 1988, **166**, 237.
26. S. P. Souza, F. L. Steinberg, C. Caro, C. Dumoulin, and E. K. Yucel, *Proc. VIIIth. Ann Mtg. Soc. Magn. Reson. Med.*, Amsterdam, 1989, p. 102.
27. C. L. Dumoulin, S. P. Souza, C. J. Hardy, and S. A. Ash, *Magn. Reson. Med.*, 1991, **21**, 242.
28. M. C. Henry-Feugeas, I. Idy-Peretti, B. Blanchet, D. Hassme, G. Zannoli, and E. Schouman-Clarys, *Magn. Reson. Imag.*, 1993, **11**, 1107.
29. G. L. Nayler, D. N. Firmin, and D. B. Longmore, *J. Comput. Assist. Tomogr.*, 1986, **10**, 715.
30. J. F. Debatin, R. H. Ting, H. Wegmuller, F. G. Sommer, J. O. Fredrickson, T. J. Brasnen, B. S. Bowmen, B. D. Myers, R. J. Herfkens, and N. J. Pelc, *Radiology*, 1994, **190**, 371.
31. K. C. P. Li, W. S. Whitney, C. H. McDonnell, J. O. Fredrikson, N. J. Pelc, R. L. Dalman, and R. B. Jeffrey, Jr., *Radiology*, 1994, **190**, 175.
32. M. B. M. Hofman, M. Kouwenhoven, M. Sprenger, A. C. van Roseum, J. Volk, and N. Westerhof, *Magn. Reson. Med.*, 1993, **29**, 648.
33. W. A. Wagle, C. L. Dumoulin, S. P. Souza, and H. Cline, *Am. J. Neuroradiol.*, 1989, **10**, 911.
34. C. A. Anderson, R. R. Edelman, and P. A. Turski, 'Clinical Magnetic Resonance Angiography', Raven Press, New York, 1993.
35. W. Lin, E. M. Haacke, A. S. Smith, and M. E. Clampitt, *JMRI*, 1992, **2**, 277.
36. G. Marchal, H. Bosmans, and S. McLachlan, in 'Magnetic Resonance Angiography', eds. E. J. Potchen, E. M. Haacke, J. E. Siebert, and A. Gottschalk, Saunders, Philadelphia, 1992, p. 305.
37. J. R. Pernicone, J. E. Siebert, E. J. Potchen, A. Pera, C. L. Dumoulin, and S. P. Souza, *Am. J. Roentgenol.*, 1990, **155**, 167.
38. F. Nussel, H. Wegmuller, and P. Huber, *Neuroradiology*, 1991, **33**, 56.
39. D. K. Kido, J. B. Barsotti, L. Z. Rice, B. M. Lottenberg, R. J. Panzer, S. P. Souza, and C. L. Dumoulin, *Neuroradiology*, 1991, **33**, 48.
40. P. Vock, F. Terrier, H. Wegmüller, F. Nahler, P. Gertsch, S. P. Souza, and C. L. Dumoulin, *Br. J. Radiol.*, 1991, **64**, 10.
41. C. L. Dumoulin, F. L. Steinberg, E. K. Yucel, and R. J. Darrow, *J. Comput. Assist. Tomogr.*, 1993, **17**, 328.
42. F. L. Steinberg, E. K. Yucel, C. L. Dumoulin, and S. P. Souza, *Magn. Reson. Med.*, 1990, **14**, 315.
43. P. Lanzer, D. Bohning, J. Groen, G. Gross, N. Nanola, and G. Pohost, *Magn. Reson. Med.*, 1990, **15**, 372.
44. L. R. Caplan and S. M. Wolpert, *Am. J. Neuroradiol.*, 1991, **12**, 593.
45. H. J. M. Barnett, *N. Engl. J. Med.*, 1991, **325**, 445.
46. S. Warach, W. Li, M. Ronthal, and R. R. Edelman, *Radiology*, 1992, **182**, 41.
47. D. D. Blatter, D. L. Parker, S. S. Ahn, A. L. Bahr, R. O. Robinson, R. B. Schwartz, F. A. Jolesz, and R. S. Bayer, *Radiology*, 1992, **183**, 379.
48. J. E. Heiserman, B. P. Drayer, P. J. Keller, and E. K. Fram, *Radiology*, 1992, **185**, 667.
49. L. R. Caplan, *J. Am. Med. Assoc.*, 1991, **266**, 2413.
50. D. Crosby, P. Turski, and W. Davis, *Neuroimaging Clin. North Am.*, 1992, **2**(3), 509.
51. T. J. Masaryk and N. A. Obuchowski, *Radiology*, 1993, **186**, 325.
52. J. F. Polak, R. L. Bajakian, D. H. O'Leary, M. R. Anderson, M. C. Donaldson, and F. A. Jolesz, *Radiology*, 1992, **182**, 35.
53. A. M. Masaryk, J. S. Ross, M. C. DiCello, M. T. Modic, L. Paranandi, and T. J. Masaryk, *Radiology*, 1991, **179**, 797.

54. C. Anderson, D. Saloner, R. E. Lee, V. S. Growidel, L. G. Shapeero, J. M. Rapp, S. Nogarkar, X. Pan, and G. A. Gooding, *Am. J. Neuroradiol.*, 1992, **13**, 989.
55. J. E. Heiserman, B. P. Drayer, E. K. Fram, P. S. Keller, C. R. Birol, J. A. Hodak, and R. A. Flom, *Radiology*, 1992, **182**, 761.
56. W. F. McCormick, in 'Intracranial Arteriovenous Malformations', eds. C. B. Wilson and B. M. Stein, Williams, and Wilkins, Baltimore, 1984.
57. J. Huston, D. A. Rufenacht, R. L. Ehman, and D. O. Wiebers, *Radiology*, 1991, **181**, 721.

Biographical Sketches

Charles L. Dumoulin. *b* 1956. B.S., 1977; Ph.D., 1981, Florida State University. Adjunct Faculty in Chemistry at Syracuse University, 1981–1984. Research scientist at General Electric Research and Development Center 1984–present. Associate Professor of Radiology, Albany Medical College, 1987–present. Approx. 60 publications. Research interests include analytical chemistry, NMR spectroscopy, MRI, and magnetic resonance flow measurement and imaging.

Patrick A. Turski. *b* 1950. B.S., 1971, chemistry, University of Illinois; M.D., 1975, Rush Medical College, Chicago, IL. Internship in internal medicine and radiology residency at the University of Wisconsin. Training in Neuroradiology at the University of California, and the Foundation Rothschild Cancer Center, Paris. Currently Professor of Radiology and Neurosciences, University of Wisconsin Medical School and Chief of the Neuroradiology Section at the University of Wisconsin Hospital and Clinic.

Time-of-Flight Method of MRA

Gerhard Laub
Siemens AG., Erlangen, Germany

1 BASIC PHYSICS

Most of the techniques currently used for magnetic resonance angiography (MRA) are based on one of the following basic physical principles: time-of-flight and phase shift effects. Time-of-flight (TOF) is related to the macroscopic motion of spins with a different history into the imaging volume.[1,2] Phase shift effects are based on the motion of spins along the directions of the magnetic field gradients which are used for the spatial encoding of the spins.[3,4]

Both effects are incorporated into imaging sequences for the purpose of flow visualization. Figure 1 demonstrates the idea of inflow enhancement which is the basic effect for TOF MRA. The blood flow is assumed to be perpendicular to the imaging plane [or volume in the case of a three-dimensional (3D) study]. For repetition times shorter than the longitudinal relaxation time T_1, the signal of tissue within the slice will be reduced due to partial saturation effects. Blood flow will move spins from outside the slice which have not been subjected to the spatially selective rf pulses into the imaging volume. These unsaturated or fully relaxed spins have full equilibrium magnetization and, therefore, upon entering the slice, will produce a much stronger signal than stationary spins assuming that a gradient echo sequence is applied to avoid outflow effects otherwise seen with spin echo sequences.[5,6] This effect has also been referred to as the 'entry slice phenomenon'.

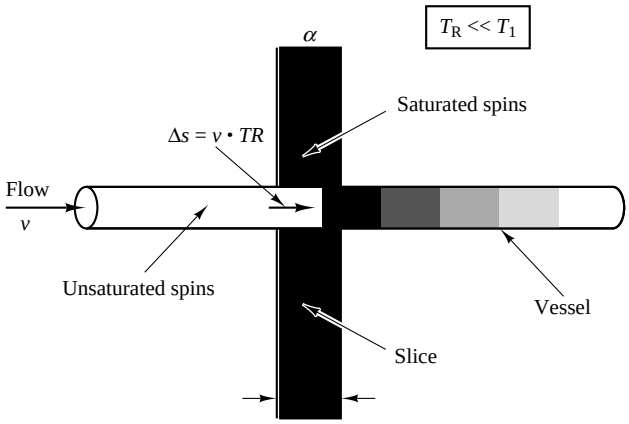

Figure 1 Principle of inflow enhancement. The longitudinal magnetization M_z of spins in the imaging slice is reduced due to partial saturation for $TR << T_1$. Inflowing spins have equilibrium magnetization $\boldsymbol{M}_o$ and, therefore, will produce more signal intensity. The displacement of the spins for each TR interval is Δs

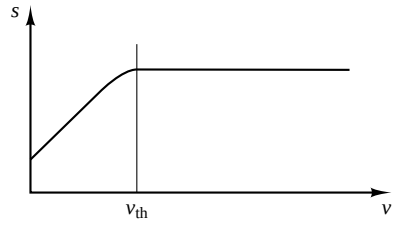

Figure 2 Relative signal enhancement of inflow enhancement as a function of blood flow velocity. As velocity increases, the signal gradually increases to reach a plateau beyond which no further signal enhancement occurs

A simple model helps to get a more quantitative aspect of inflow enhancement. According to Figure 1 a critical velocity v_{th} can be defined as

$$v_{th} = s/TR \tag{1}$$

Spins flowing at velocities smaller than v_{th} will see several rf pulses depending on their actual speed, and consequently, the longitudinal magnetization will decay. Accordingly, less signal will be produced. With velocities larger than v_{th} the spins will see only one rf pulse, resulting in maximal signal enhancement. The overall signal enhancement as a function of the spin's velocity is plotted in Figure 2.

The second flow effect, flow-induced phase shifts, is a consequence of the phase memory of the spin system. When traveling along the direction of magnetic field gradients, the excited spins will experience additional phase shifts which depend on the motion of spins. Techniques which make use of the flow-induced phase shifts are usually referred to as phase contrast MRA.[7,8] In the case of TOF MRA phase effects are eliminated as much as possible by using a flow-compensated gradient waveform in combination with short echo times as shown in Figure 3. Both the slice select and the readout gradients are flow-compensated to minimize flow-induced phase shifts. The signal from blood flowing into the slice is maxi-

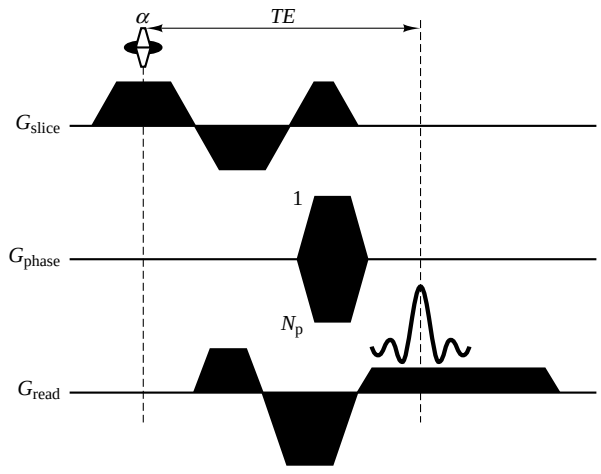

Figure 3 Typical timing diagram of a flow-compensated gradient echo sequence. Asymmetric echo sampling is used for shorter echo times

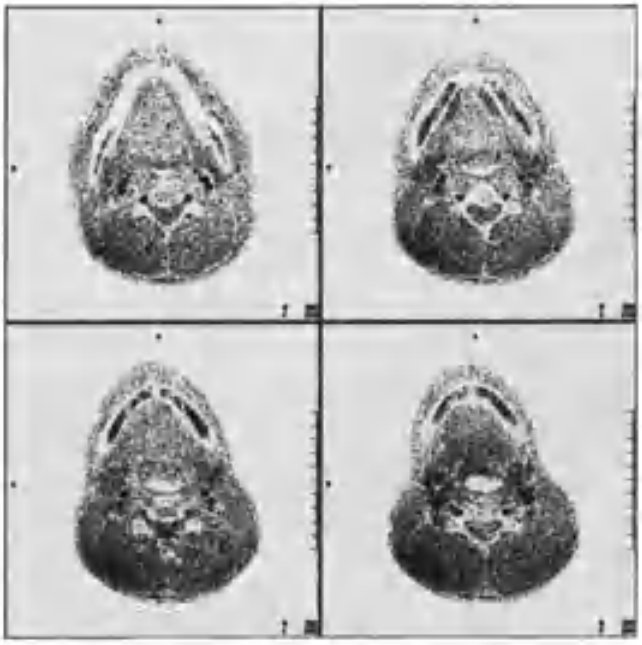

Figure 4 Four images acquired at different positions in the neck. A FLASH sequence with *TR*/*TE*/*a* = 30 ms/9 ms/40° is used to saturate stationary spins in the slice and produce high signal from inflowing blood. Slice thickness is 2.5 mm with 0.5 mm overlap, and a total of 60 slices is acquired to cover a section of 120 mm of the neck vessels

mized by a proper selection of sequence parameters. In most cases a pulse repetition time *TR* of 30–40 ms along with tip angles of 40° results in sufficient saturation of biological tissues, as demonstrated in Figure 4. According to equation (1) thin slices help to avoid spin saturation within the slice in the case of slow blood flow. For a *TR* of 30 ms, and a slice thickness of 3 mm, a blood flow velocity of 10 cm s^{-1} is sufficient to replace all of the spins in the slice within one *TR* interval, resulting in good vessel/background contrast. Additional presaturation pulses are applied on either side of the slice to suppress either arterial or venous inflow enhancement.

2 POSTPROCESSING OF 3D DATA SETS

In principle, with this technique any vessel segment can be imaged by cutting through the vessel perpendicular to the flow direction. With repetitive increments of the slice position a 3D data set of the complete vessel tree can be measured. (see Figure 4 for example). For the observer, this form of representation requires experience in order to obtain the correct 3D spatial impression. Obviously, postprocessing methods should be used to extract two-dimensional (2D) projections of vessel structures from the 3D volume information. With these methods spatial impressions can be obtained in two ways: by showing a sequence of projective images with different projection angles, or by coding of the depth information onto the surface of the displayed objects.[9,10]

Since the surfaces of most vessels are relatively small, the first method, multiple projections with different angles, has proven more useful in practice. The starting point for this method

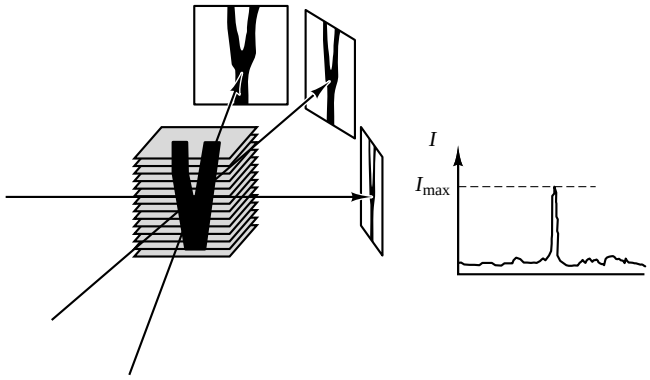

Figure 5 Schematic representation of the maximum intensity projection (MIP) method

must be a 3D data set in which the structures to be extracted are associated with a characteristic range of signal intensity levels. In this case a projective image can be calculated by penetrating the data volume with a set of parallel projection rays and selecting along each of these rays only the data point that represents the intensity maximum as demonstrated in Figure 5. The inflow enhancement and proper pulse sequence parameters (flip angle, pulse repetition time, and flow compensation on) ensure that the maximum intensity is always associated with a blood vessel, as long as the projection ray intersects at least one. All of the other projection rays will just pick up a background pixel out of the 3D data set. As a result, Figure 6 demonstrates a complete projection image calculated from one 3D data set.

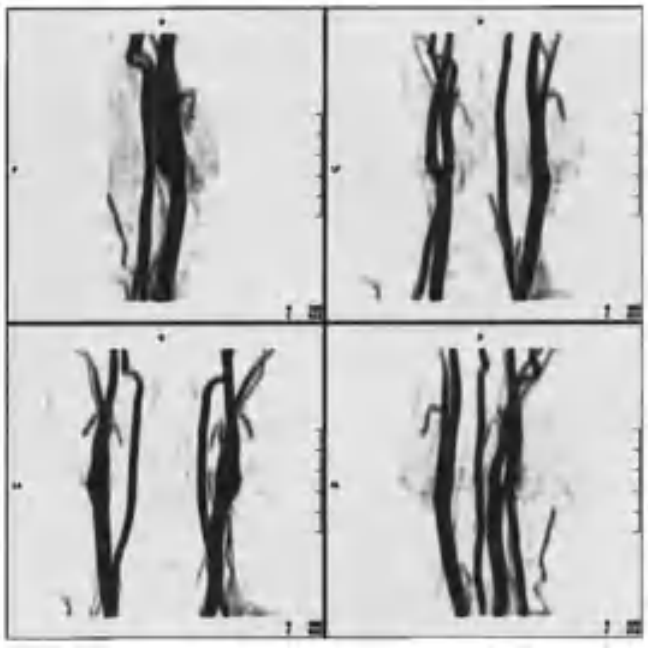

Figure 6 Calculated MIP from the 3D data set of the carotid artery. Sixty slices were acquired in sequential order and transverse orientation with 160 × 256 matrix and 3/4 rectangular field-of-view. Total acquisition time was 4 min 48 s for all 60 slices

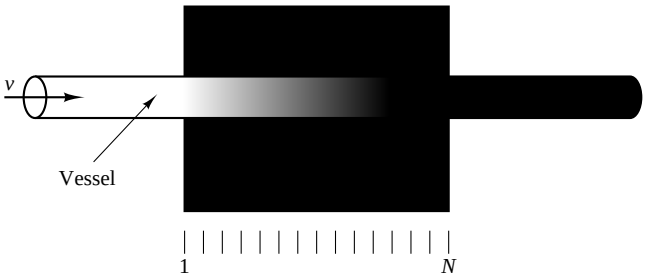

Figure 7 Three-dimensional fast FFT imaging techniques in TOF MRA. The whole volume of slab thickness D is excited by an rf pulse, and is then subdivided into N partitions by the use of an additional phase-encoding gradient. The contrast of blood vessels is maximal at the entrance plane of the imaging volume, and decreases constantly toward the exit plane due to spin saturation

By varying the projection angle multiple projective images can be obtained retrospectively which allow the observer to obtain the correct spatial impression of the 3D information. By displaying a number of projections with projection increments of only a few degrees in a rapid fashion, the impression of a continuously rotated object will be generated which allows a correct 3D visualization of such complex structures as a vessel tree.

Improvement of the spatial resolution along with an improvement of the signal-to-noise ratio can be achieved with 3D imaging techniques. As shown in Figure 7, the whole volume is excited simultaneously, and will then be subdivided into thin partitions or slices by using an additional phase-encoding scheme in the slice select direction. Unlike 2D imaging, where the slice resolution is defined by the excitation profile of the radiofrequency pulse, the slice resolution is defined by spatially-encoding magnetic field gradients and can be less than 1 mm. In 3D, or volume imaging, complete compensation of the flow-induced phase shifts is also necessary to avoid flow artifacts in the form of signal losses and ghosting.[11,12] For this purpose flow compensation is applied in conjunction with short echo times similar to 2D techniques.

The acquisition time T_A for a 3D data set is defined as

$$T_A = TR \cdot N_p \cdot N_s \qquad (2)$$

where TR denotes the pulse repetition time of the sequence, and N_p, N_s are the number of phase-encoding steps in the phase-encoding and slab select directions, respectively. In most of the clinical protocols the repetition times vary between 20 and 40 ms and the typical matrix size is 192 $\times$ 256 with a $\frac{3}{4}$ rectangular field of view and 64 partitions along the slab select direction, resulting in acquisition times of between 4 and 8 min.

One of the major limitations of 3D TOF MRA is the loss of vessel contrast as spins penetrate into the imaging volume. This effect is due to progressive saturation when spins experience the rf excitation pulses in the imaging volume. As can be seen from Figure 8 the transverse magnetization decreases with the number of rf pulses, and the difference between blood and stationary tissue is reduced rapidly. A more effective use of the magnetization is possible when using variable flip angles across the slab.[13] At the entrance plane when spins enter with equilibrium magnetization a relatively small flip angle of, for example, 10° will still provide sufficient signal, without reducing the longitudinal magnetization too much. Next, the flip angle is increased a little to maintain, or even increase, the signal from blood spins on their way through the volume, and so forth. In principle, it is possible to shape the flip angle distribution over the entire imaging volume according to the specific flow velocity and vessel coverage.

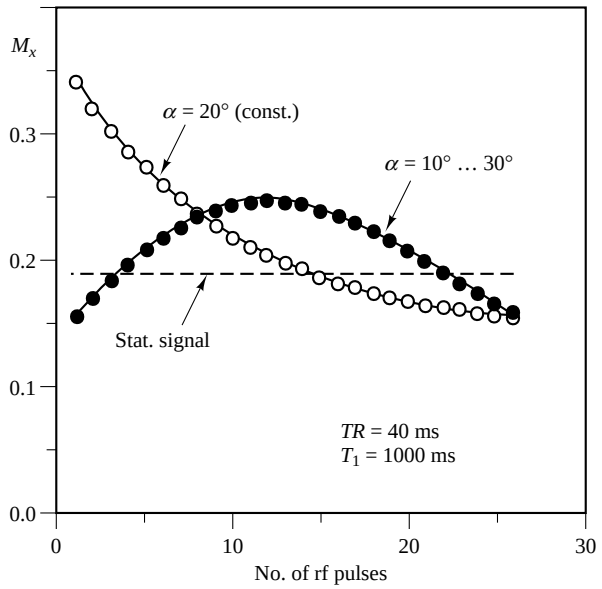

Figure 8 Transverse magnetization of spins as a function of rf pulses. For constant flip angles throughout the imaging volume there is a constant decrease until the magnetization has approached its steady state value. In the case of a variable flip angle the signal reaches its maximum after about 12 excitations. As a result the contrast of blood is maintained over a longer distance in the imaging volume. Stat = stationary

A further improvement is possible by the application of magnetization transfer pulses (magnetization transfer contrast, MTC).[14] The idea is to use off-resonance rf pulses which do not directly affect the mobile protons which usually create the signal in MRI. Protons with restricted mobility, however, do get saturated, and because of magnetization or chemical exchange processes some of the magnetization will be transferred in some biological tissues, such as gray or white matter, resulting in a partial saturation. Blood will not be affected by the MTC pulses, and as a result, there will be more contrast between blood and background. This technique is particularly useful in the brain as demonstrated in Figure 9, as the background signal from gray and white matter tissue is significantly reduced.

3 DISCUSSION

The results of preliminary clinical studies indicate that this MRA technique can provide accurate, reproducible flow images in different anatomical regions of the body.[15] Applications of TOF MRA for the assessment of intracranial vascular disease in the brain are shown in Figure 10. This technique is noninvasive and can be performed in conjunction with 2D spin echo or

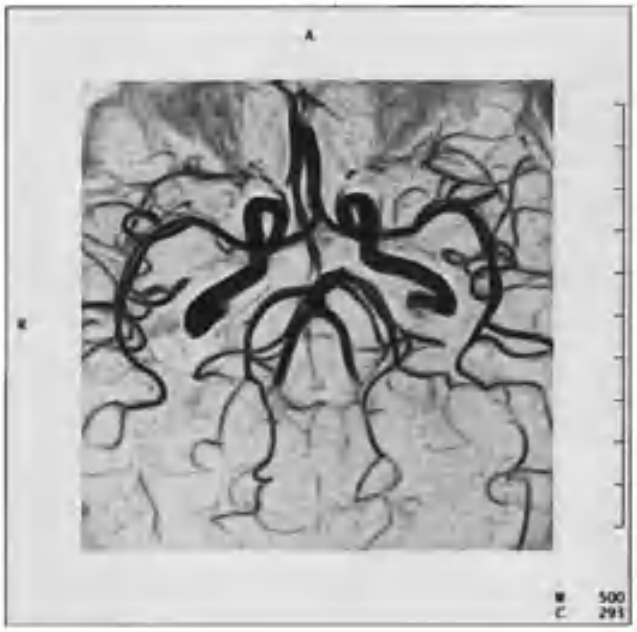

Figure 9 Maximum intensity projection image of the intracranial vasculature. The images were acquired with a 3D FISP sequence including MTC partial saturation and TONE (*TR/TE/a* = 40 ms/6.5 ms/ 10–30°). Total scan time was 8–20 min

gradient echo imaging, with only a 5–10 min extension of the examination time.

The unique advantages of this technique include the capacity to provide multiple projections of anatomically complex vascular abnormalities with a single data acquisition. It appears that this capability may increase both the sensitivity and the specificity of MRA in some patients with cerebrovascular disease when MRA is performed in conjunction with routine spin echo imaging of the brain. While the acceptance of the 3D inflow MRA technique will depend on its sensitivity and specificity in disease diagnosis, as determined by means of prospective clinical trials relative to other screening modalities, the preliminary clinical results suggest that this MRA technique can serve as a screening tool for the identification of normal vasculature as well as stenosis and/or occlusions produced by atherosclerotic disease. It can be performed in conjunction with MRI of the brain, with only a small increase in examination time, and provides both vascular and parenchymal evaluation of cerebrovascular disease in a single setting.

4 RELATED ARTICLES

Head and Neck Studies Using MRA; Phase Contrast MRA; Whole Body Magnetic Resonance Angiography.

5 REFERENCES

1. W. S. Hinshaw, P. A. Bottomley, and G. N. Holland, *Nature* (London), 1977, **270**, 722.
2. L. Axel, *Am. J. R.*, 1984, **143**, 1157.
3. E. L. Hahn, *Phys. Rev.*, 1950, **80**, 580.
4. P. R. Moran, *Magn. Reson. Imag.*, 1982, **1**, 197.
5. F. W. Wehrli, A. Shimakawa, G. T. Gullberg, and J. R. MacFall, *Radiology*, 1986, **160**, 781.
6. L. E. Crooks, C. M. Mills, P. L. Davis, M. Brant-Zawadzki, J. Hoenninger, M. Arakawa, J. Watts, and L. Kaufman, *Radiology*, 1982, **144**, 843.

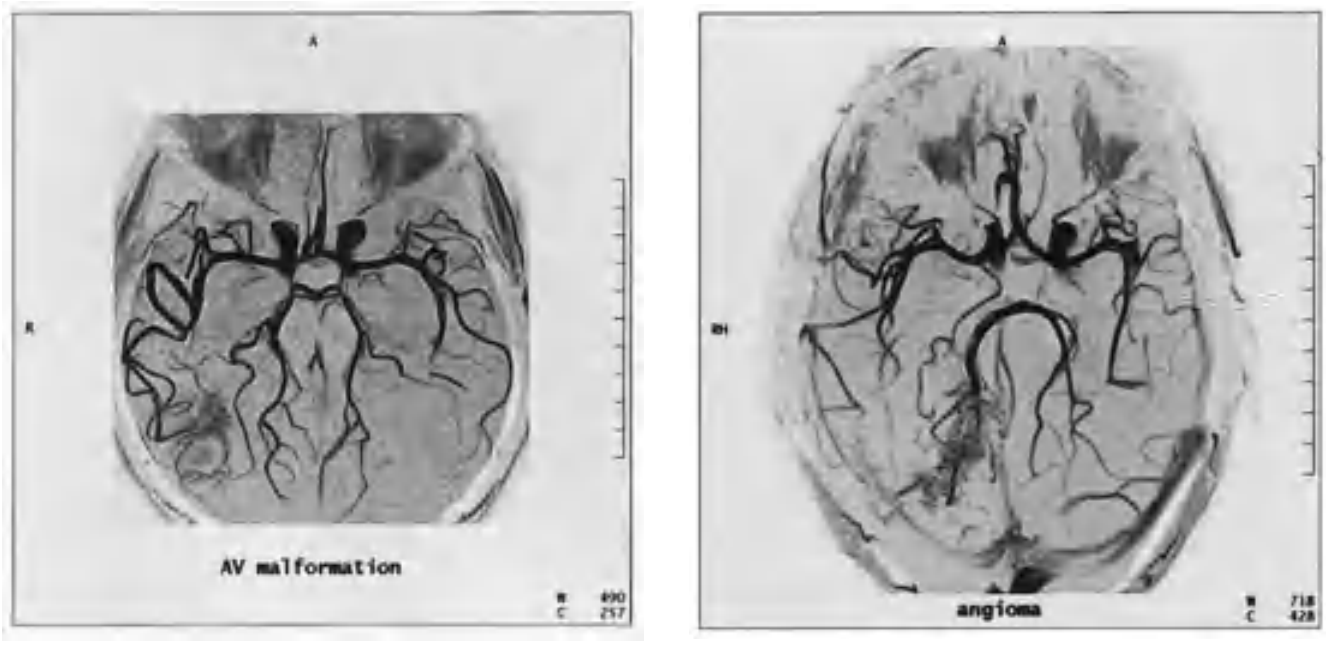

Figure 10 Clinical applications of TOF MRA. Left: arteriovenous malformation. Right: angioma. Both images were acquired with a 3D FISP sequence in 9 min. Axial MIPs are shown to demonstrate the vascular lesions

7. L. Axel and D. Morton, *J Comput. Assist. Tomogr.*, 1987, **11**, 31.
8. C. L. Dumoulin, S. P. Souza, and M. F. Walker, *Magn. Reson. Med.*, 1989, **9**, 139.
9. G. A. Laub, *Magn. Reson. Med.*, 1990, **14**, 222.
10. H. E. Cline, C. L. Dumoulin, W. E. Lorensen, H. E. Clini, C. L. Dumoulin, W. E. Lorensen, S. P. Sonzo, and A. J. Adams, *Magn. Reson. Med.*, 1991, **18**, 384.
11. T. J. Masaryk, M. T. Modic, J. S. Ross, P. M. Ruggier, G. A. Laub, G. W. Lenz, E. M. Haacke, W. R. Selmon, M. Wiznitzer, and S. I. Sarik, *Radiology*, 1989, **171**, 793.
12. T. J. Masaryk, M. T. Modic, P. M. Ruggieri, J. S. Ross, G. Loub, G. L. S. Kenz, J. A. Tkach, E. M. Haacke, W. R. Selmon, and S. I. Hank, *Radiology*, 1989, **171**, 801.
13. D. Atkinson, M. Brant-Zawadzki, and G. Laub, *Radiology*, 1994, **190**, 890.
14. S. D. Wolff and R. S. Balaban, *Magn. Reson. Med.*, 1989, **10**, 135.
15. E. J. Potchen, E. M. Haacke, J. E. Siebert, and A. Gottschalk, 'Magnetic Resonance Angiography: Concepts and Applications', Mosby, St. Louis, MO, 1993.

Biographical Sketch

Gerhard A. Laub. *b* 1951. Ph.D., 1982, University of Stuttgart, Germany. Faculty of Physical Electronics, University of Stuttgart, 1982–1985. MR applications development, Siemens Medical Systems, Erlangen, 1986–present. Research interests include the theory and application of flow phenomena in MRI, postprocessing of MR data, and fast imaging techniques.

Whole Body Magnetic Resonance Angiography

E. Mark Haacke, Weili Lin, and Debiao Li
Washington University, St. Louis, MO, USA

1 INTRODUCTION

The first seeds of whole body magnetic resonance began with the simple concept of spatial encoding using gradients in Paul Lauterbur's seminal 1973 paper.[1] It only took several years for it to be implemented on systems large enough for the human body, and developed rapidly owing to the several decades of previous study in chemistry and physics. Many of the concepts from steady-state free precession[2] to adiabatic fast passage[3] would play a role in the understanding of how to deal with motion [usually of blood, but equally simply cerebrospinal fluid (CSF) flow] during a magnetic resonance experiment. The key to the present day success of MR angiography (MRA) lay in the discovery of how moving spins could be motion compensated.[4–8] The advent of faster and faster computers and the role of image processing were key to the advances in MRA.[9] Although the basic concepts of magnetic resonance whole body flow imaging are well understood today, there is still room for basic evaluation and applications from the biological to clinical sciences.

In this short article on whole body flow imaging, we will review the history behind bulk flow studies in the eras of pre-imaging and during imaging to show how technological and scientific advances led to the formation of dealing with motion as we understand it today. We begin by studying the effects of motion on the signal in terms of amplitude and phase, how it could be dealt with or corrected, the ongoing debate of whether phase contrast or time-of-flight (TOF) imaging is to be preferred, and what future directions remain to be investigated. This overview should serve as a good introduction to the more technical aspects of each of these areas.

2 THE EFFECTS OF MOTION

The first measurements and theory for magnetic resonance were based on the assumption that the spins were stationary. It was several years before the issues of motion were first addressed by Suryan[10] in 1951, and several more years before the flurry of papers appeared in the mid-1950s on diffusion.[11] At this time a real effort was made to incorporate the effects of diffusion on the signal measured, and it was not long before the theory for the equations of motion were modified to deal with these phenomena.[12] Bulk effects in blood were considered toward the end of the decade by Singer[13] and Bowman,[14] who could be credited with the first TOF magnetic resonance experiments on blood. This TOF effect relates to the fact that the inflowing blood appeared brighter than it would have had it remained in the excitation region, and, hence, it was viewed as having an effective T_1 smaller than that of stationary blood. It must be remembered that all the experiments evaluating the signals were from projections over the entire excited region (whether it was a small vial of material or a mouse tail) and that no imaging per se was done at that time. This fact had severe consequences on the subsequent development of flow methods and the ability to assess accurately what was happening. Nevertheless, brave attempts were made to detect and quantify flow. The effects were well enough understood from the amplitude changes that it was possible to design a flowmeter using magnetic resonance equipment.[15]

Two papers have significant historical relevance. The first is that by Hahn in 1960, where he recognized the fact that motion through a gradient would lead to phase dispersion at the echo.[16] For a simple bipolar pulse (peak gradient amplitude, G, negative lobe of duration τ, positive lobe following of duration τ, constant velocity flow v) the phase at the echo is $\gamma G v \tau^2$ where γ is the gyromagnetic ratio. The key points to extract from this simple formula are the linear behavior with v and the quadratic behavior with time. The second key paper in retrospect is that of Packer[17] in 1969 (later rediscovered by Waluch and Bradley[18]). He investigated the signal behavior when multiple pulses were used in the presence of gradients. He discovered the most important fact that the flowing spins rephased at the even echoes. This was the precursor to future imaging papers which rediscovered this phenomenon[4–8] and others which extended the concept to correct for the fact that motion during the gradients led to a phase change. The first was subsequently revisited in the imaging world by Moran[19] in 1982 and the second by Constantinesco[4] in 1984. These two papers set the foundation for future advances in the field of MRA.

2.1 Time-of-Flight Effects

Early experiments with spin echo imaging noticed the 'flow void' effect or lack of signal from blood. This was at the time considered anomalous (or paradoxical) enhancement since blood has a spin density of 0.8 relative to water. It was quickly realized that those spins that did not see both the 90° and 180° pulses were not refocused and did not contribute to the signal. This is known today as the wash-out effect, and it depends very much on the direction of the flow relative to the slice acquisitions and the flow rate itself. The same phenomenon using gradient echoes leads to a wash-in effect where stationary tissue is saturated and inflowing blood is brighter than naively anticipated. This concept dominates today for much of MRA methodology to enhance the signal from moving blood. For a fast (short TR) gradient echo sequence, when a 2D slice or plane is excited, blood which was excited flows out of the slice and sees no more rf pulses during the experiment (or at least we will assume so, an assumption which is usually valid). For 2D imaging and constant blood flow, the blood will be imaged at the same location in each case. The signal seen will then be a sum over all sections of the blood each of which has seen a different number of rf pulses. For a 3D scan, the signal will be that of the blood in a given section which has seen that number of rf pulses associated with the time from its entry into the 3D volume and the repeat time.[20] Specifically, the number of rf pulses is $n = [t/TR]$ where $t = d/v$ with d the distance traveled, v the speed and [ ] the integer part of the argument.

For blood which flows through the entire slice, each new rf pulse excites unsaturated or fresh blood, and hence this blood has the maximum possible signal. For a flip angle of 90°, the signal is a maximum at 1.0 units relative to the spin density of the blood. Figures 1 and 2 show the expected signal response for two different T_1 values for blood, the first of 1200 ms for pristine blood and the second for 300 ms for blood doped with a sufficient amount of T_1 reducing contrast agent. From these curves we see two most important features for imaging blood. The first is that at low flip angles of about 15–20° the best contrast between blood and stationary tissue is achieved at 1.5 T even for fairly slow flow (hence most TOF imaging in the head is done with these low values). The second is that the use of contrast agents can dramatically enhance the contrast between even stationary blood and background tissue (assuming that gray matter is the background tissue with a T_1 of about 950 ms at 1.5 T, quite close to that of blood).

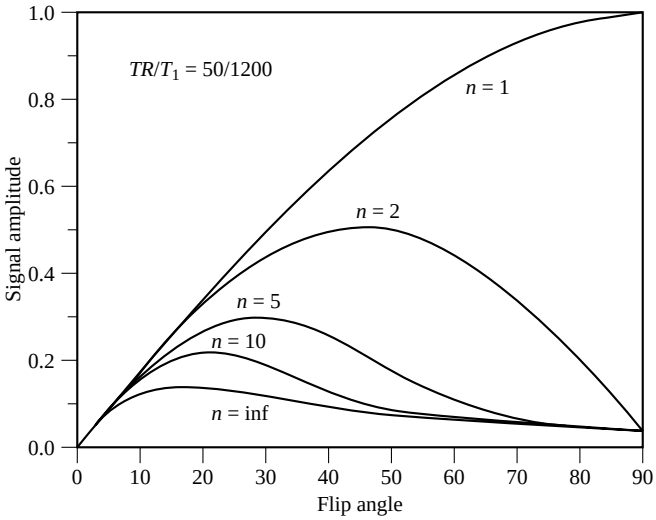

Figure 1 Blood signal as a function of flip angle for different numbers of rf pulses (n) for T_1/TR = 24

2.2 2D versus 3D TOF

From the above arguments, it is clear that thin slices are best to obtain maximum signal for slow flow[21] (for example, with TR = 40 ms and a 2 mm thick slice, flow greater than 5 cm s^{-1} presents with a maximum signal). This is still considered the best way to image veins in the leg.[22] In these images, both arteries and veins will be bright. To avoid confusion between the two, a saturation pulse is usually applied upstream to saturate arteries or downstream to saturate veins (the latter is used when imaging the carotid arteries in the neck). However, 2D TOF suffers from longer echo times (although some cures for this may exist through higher gradient strengths[23] or rf design[24]), and a longer acquisition time for thin slices due to the need to overlap slices for full spatial coverage. Saturation pulses can saturate retrograde flow, and through-plane resolution is not as good as a 3D acquisition. On the other hand, slow flow is easily seen and a small region of interest can be rapidly covered. The use of 3D imaging overcomes many of the above problems as it allows for short echo times and thin contiguous slices. It has the problem that blood appears nonuniformly throughout the region of interest because of the spin saturation. This is partly overcome using a variable flip angle spatially[25] (obtained by applying an rf pulse designed to increase along one direction, usually the direction of flow, so that saturation effects are reduced; this method is referred to as TONE or tilted optimized nonsaturating excitation), multiple thin slabs,[26] magnetization transfer saturation or MTS,[27,28] and contrast agents.[29,30] The use of MTS is good because it does not require injection of a contrast agent and it can suppress the background brain parenchyma[27,28] by about 25% or myocardium[31] by up to 50% while leaving the signal from blood virtually intact. MTS pulses have two problems: they add more power deposition to the sequences so care must be taken in their design and implementation, and they do not suppress lipid signal. The advantages of using a contrast agent are that the scan can be run faster, or better resolution can be obtained, or a larger field-of-view (FOV) can be obtained without saturation effects. The problems are that both arteries and veins become bright, and the signal from regions of the blood–brain barrier breakdown can obscure vessel information; for both these reasons, vessel tracking is needed[32–34] to separate the vessels of interest from other vessels or tissues.

2.3 Phase Effects

The presence of motion during the application of a gradient pulse causes a phase shift of the signal from the moving tissue at the echo. For a simple bipolar pulse of duration and amplitude G, the phase is simply $\gamma G v \tau^2$ where v is the speed along the direction of the gradient G. In fact, for any symmetrically placed gradient pulses about a 180° pulse at time t' [i.e. a time reversed pulse where $G(t') = G(2t' - t)$ for $t > t'$], the phase for constant velocity spins will be zero at $t = 2t'$. This shift in phase is not necessarily a problem. For constant velocity plug flow for every phase encoding step (where the flow is only along the read direction), the final image in the region of the flow will have a nonzero phase as described above and the correct amplitude on a magnitude image. In practice, for nonpulsatile laminar flow, spins develop a different phase as a

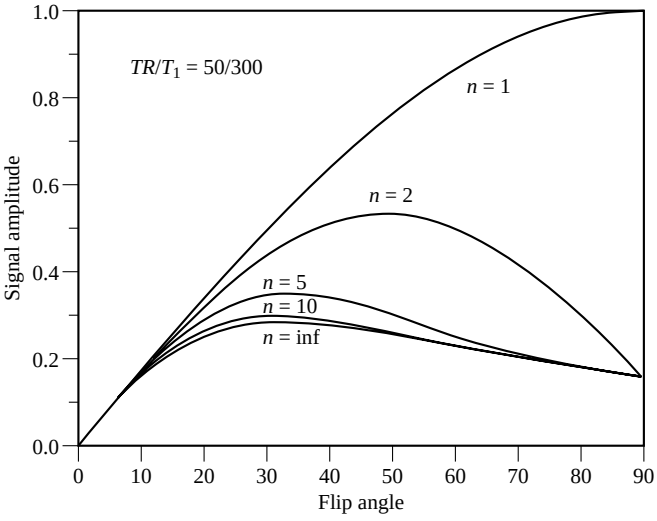

Figure 2 As in Figure 1 but for T_1/TR = 6 for blood with a triple dose of gadolinium diethylenetriaminepentaacetic acid (Gd-DTPA)

function of position, and the signal in a voxel is reduced accordingly. For example, in a 1D analogy, if the flow varies linearly across a voxel, the signal will be reduced to $(\sin\theta)/\theta$ of its original value for a phase dispersion of 2θ. For a phase dispersion of 180°, the signal will fall to $2/\pi$ of its initial value (only a 30% signal loss). Both velocity and acceleration can create large velocity gradients in blood flow (in areas near stenoses or curved flow). Interestingly, the loss of signal has been recognized quite early, and in spin echoes was partly due to the outflow of the blood between the 90° and 180° pulses, and created a flow void. Today the dephasing and in-flow/out-flow phenomena are also used to create what are referred to as 'black blood' images. These are often very useful in delineating vessel wall. The disadvantage of this method is the poorer contrast-to-noise ratio of blood versus background in rapid imaging. The inflow enhancement (wash-in effect) of the bright blood methods offers a potentially much higher contrast-to-noise ratio between vessel and surrounding tissue.

Even for plug flow, phase is a problem if the flow is pulsatile. Now the phase changes from line to line and creates what is referred to as ghosting. This can be understood as a periodic change in signal which creates a periodic effect on the sampling and hence creates aliasing of the image. The graphs Figures 1 and 2 indicate how severe a problem this is when the flip angle is large, as now the signal jumps rapidly depending on how many rf pulses the blood sees (and therefore on how fast the blood is flowing[20]). Clearly, this problem is avoided at low flip angles where the signal becomes more spin density weighted and the differences in flow are less observable.

Pulsatility can be handled quite well by triggering off the cardiac cycle. Now if a bipolar pulse is added to a conventional sequence and G is chosen so that the phase changes by less than π for all velocities, it is easy to use just the phase image to determine the blood velocity in the direction of the gradient. In principle, three such experiments must be run to determine the full velocity vector. It then becomes possible to predict from the sequence structure and the geometry how many rf pulses would be seen during the experiment and therefore what the magnitude of the signal should be. This would allow for a self-consistency check between phase and magnitude of the images. Little work has yet been done in this direction, although when it is accomplished it will have brought together the initial historical focus on amplitude flow imaging discussed in the introduction with the flow quantification efforts begun after the advent of MRI.

3 MOTION COMPENSATION

The real beginnings of MRA came with the recognition that there were effects on the signal from flow. These were only brought under control by the redesign of the gradient structure to fix the phase at the echo to be zero even in the presence of motion. First-order motion compensation refers to compensating for constant velocity flow[4–8] so that the phase at the echo is zero. This is effected by using at least three gradient lobes in both the read and slice select direction so that the zeroth and first moment of the gradients is zero at the echo. Higher order terms such as acceleration and jerk are then usually not zero (although even order terms can be in some cases[35,36]). The choice of timings and amplitudes makes this a complicated optimization problem.[37] It has been suggested[20] and shown[38,39] that the best choice to make in the design of these sequences when acceleration effects are present is to keep the duration of the gradients as short as possible. In an uncompensated sequence, acceleration effects grow as time cubed, but in a velocity compensated sequence they grow as only time squared. This is still fast enough to warrant collecting the data with an asymmetric echo[40] rather than adding a fourth pulse and compensating for acceleration as well. In summary, the sequence is designed so that

$$\int_0^{TE} G_{\mathrm{r}}(t)\,\mathrm{d}t = 0 \tag{1}$$

and

$$\int_0^{TE} tG_{\mathrm{r}}(t)\,\mathrm{d}t = 0 \tag{2}$$

for the readout gradient, G_{r} and

$$\int_T G_{\mathrm{pe}}(t)\,\mathrm{d}t = T\,\Delta G_{\mathrm{pe}} \tag{3}$$

and

$$\int_T tG_{\mathrm{pe}}(t)\,\mathrm{d}t = 0 \tag{4}$$

for the phase-encoding gradient.[41] Here, T is the time from the beginning of the first phase-encoding table to the end of the second phase-encoding table, and G_{pe} is the usual phase-encoding increment.

An example 3D sequence which has partial motion compensation in all axes is given in Figure 3. This sequence is ideal for phase-encoding in that it also compensates for position shift or spin misregistration. For example, since the phase encoding gradient is shifted temporally from the echo, the spins are encoded at a different location than they are read out at and, therefore, they appear shifted in the image from their actual location. (This gives the appearance of a black hole where the vessels should have been and the vessels appear extra bright because they now lie on top of some other tissue—a fact which has ironically proved useful for visualizing vessels.) By velocity compensating in the phase-encoding direction as discussed above, there will be no misregistration artifacts; an important point if the magnetic resonance images are to be used as a reference for neurosurgical applications.

4 FLOW MEASUREMENT

The observation of flow is quite a different challenge to its measurement. Early attempts to measure flow rates used the effective change in T_1, as the faster the flow, the less saturated it was and hence the shorter the effective T_1. These amplitude approaches rarely proved useful. The concept of flow to visualize and quantify blood flow also began rather early. In 1959, Singer described a method of quantifying blood flow in a mouse's tail by using a receiver downstream of the transmit-

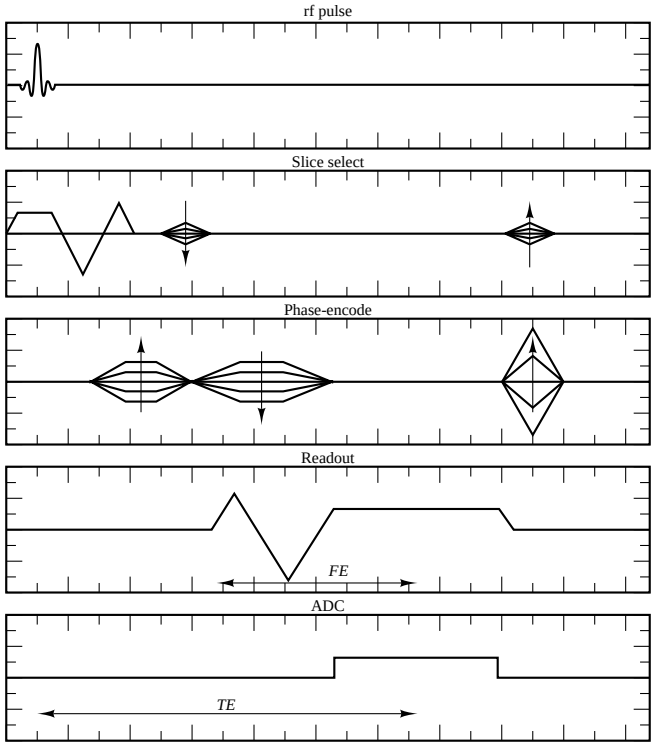

Figure 3 A 3D sequence diagram showing velocity compensation at the echo in both read and phase-encoding directions. The slice select tab file could have added to it a second tab file and the partition encoding could then be velocity compensated. *FE* refers to the time from the onset of the read gradient to the echo. ADC refers to the analogue to digital conversion of the signal to finite sampled data during the acquisition period

ter.[13] The time delay between the spin excitation and signal reception was used to measure the flow velocity. The method was then further modified and applied to human arms and fingers.[42,43] It was used again in imaging for adiabatic excitation of inflowing blood[44] and for exciting and refocusing just blood using a 180° pulse (orthogonal to and in the direction of the blood flow) in a spin echo experiment.[45,46] This gave an image showing how far the blood had moved between its encoding after the 90° pulse and where it was finally read out. For laminar flow, the fastest flow moved furthest into the image, and the standard crescent shape was seen in this type of image. The same type of approach was later implemented using fast imaging sequences by employing a saturation pulse instead of a 180° pulse.[47] Although this is well described as part of the same concept, in retrospect one did not follow on the heels of the other but was rediscovered from a different perspective when saturation pulses were used to eliminate signal from unwanted tissue. By nulling the blood before the conventional excitation pulse and acquiring the data in a cardiac triggered mode, the saturated blood could be followed throughout the cardiac cycle. The complement of the bright blood image using the spin echo approach was seen with the crescent shape now being dark. Another variant of this method can be used to create a bright bolus of blood by using a magnetization preparation type of sequence to null or reduce the signal from the background tissue and then dynamically to acquire the data throughout the cardiac cycle or just continuously to watch the inflow of blood. This is best accomplished using a rapid 2D acquisition approach such as a short *TR* method or echo planar imaging with blood inverted outside the slice. In these cases, the blood signal changes from negative to positive as time progresses and the longitudinal magnetization recovers (this approach is limited by the T_1 of blood to a few seconds).

4.1 1D Velocity Information

One of the concerns about MRA is that it does not give functional information. In this section, different methods of giving velocity information are discussed. One method projected to give velocity information quickly is the Fourier flow quantification technique first introduced by Moran.[19] He recognized that because of the linear dependence of the phase on the velocity and the gradient that a set of experiments changing the strength of an applied bipolar gradient, for example, would phase encode the velocity in that direction. Collecting in a 1D velocity and 1D transverse spatial direction through the neck gives a nice display as a function of the cardiac cycle of the different positive and negative velocity components in all the vessels cutting across the excited region.[48] The resulting image shows velocity versus position with the amplitude of the signal representing the number of spins at that location with that velocity. This can also be accomplished in a much simpler way by exciting just a plane[49] or cylinder[50] and projecting all information along the read axis. The flow is then sensitized to one direction (usually along the slice select direction using the bipolar gradient scheme discussed earlier), and the phase is used to map directly the velocity of all spins summed over the projection. This is often used in the aorta or to see heart valves in motion. It can have a time resolution of 20 ms and does not require cardiac triggering. It has difficulties if arteries and veins overlap as vessel phase data become confounded. We will return to this method in the future directions section.

4.2 2D or 3D Phase Contrast Imaging

The most common and best investigated approach to flow quantification today is phase contrast imaging pioneered by Dumoulin.[51,52] By not fully compensating the blood motion, a remnant phase remains which is proportional to the velocity. Using a sequence with one bipolar pulse giving a positive phase and a second sequence with a polarity inverted bipolar pulse giving a negative phase, the subtraction eliminates stationary tissue and leaves tissue with a nonzero velocity. This is the conventional approach used in 2D imaging and goes back to the early work of Moran[19] and, somewhat later, Bryant.[53] However, the bipolar pulse can be applied in all three directions and not at all so that the experiment is repeated four times and full 3D velocity information can be extracted. If the gradient amplitude chosen is too small, aliasing of the phase will occur. If the resolution is high enough, the aliasing can be unwrapped, but this is rarely done today (because of the processing time and difficulties in passing through or around regions in the image with no signal and because the phase is complicated by field inhomogeneity phase effects in gradient echo imaging). This is actually the best way to collect the data in terms of the signal-to-noise ratio (S/N) as a higher phase has a higher S/N. Phase contrast images can be acquired in two or

three dimensions. Their main disadvantage is the length of time it takes to acquire information in all three directions and the fact that this is a necessity. 3D phase contrast imaging is less sensitive to inflow but still loses signal from the saturation phenomena. Nevertheless, small vessels with very slow flow (much less than 5 cm s^{-1}) can be seen quite well with this approach, as can CSF.[54] Today the use of 2D phase contrast imaging is the most common to obtain flow rates by using the velocity information orthogonal to the excited plane and a high-resolution cross-section for the vessels. Since many pixels should be available for a given area, this limits its application to vessels with diameters several times the available pixel size. A further limitation comes from the fact that a fixed maximum phase is usually encoded for, so that any values of velocity above this maximum lead to aliasing in the image. This implies that, if there is a broad range of velocity information present, several scans would need to be run to obtain the optimal S/N.[55]

5 MRA OF THE ENTIRE BODY

5.1 Contrast Optimization

Both TOF and phase contrast methods need to be optimized depending on the regions being imaged. The optimization is not just one of getting the best S/N, but rather the best contrast-to-noise ratio or, one step further, object visibility. Phase contrast offers the best suppression of background tissue and the best S/N when the subtraction of two phase images is performed. The lower velocities are the hardest to see as the image intensity is proportional to the velocity. Nevertheless, phase contrast can do a good job with slow flow if the gradient causing dephasing is made very large. It does suffer from velocity changes in time (pulsatility) which causes ghosting (except in a cine mode where the images are gated to the cardiac cycle). TOF can give good contrast in a variety of ways. These will be discussed individually in the different body part discussions to appear below. Suffice it to say at this time that the major improvements in this approach come from magnetization transfer contrast and the use of contrast agents.

Lastly, there are other contrast mechanisms available such as black blood[56,57] and steady-state free precession imaging (to map the tissue properties of blood rather than its flow[58]). In the latter case the challenge is to make the signal insensitive to the flow and then using spin density or T_1/T_2 to recognize blood from background tissue. In this section we will address the different areas of the body presently covered by MRA applications.

5.2 Head and Neck MRA

Currently MRA is most widely used for imaging the head and neck. Nevertheless, as mentioned above, there still remain problems. The four most dominant ones include: loss of signal from disturbed or very fast flow (such as in regions of curved flow or tight stenoses); spin saturation caused by stationary blood or very slow flow (such as for obstructed flow or flow in the carotid bulb, for example); insufficient resolution (such as in the intracranial or carotid bifurcation studies to verify accurately if a stenosis is 75% or higher; and an insufficient S/N (for when high resolution is used). Solutions to these problems are still under development, and for the previous four points include: the use of shorter gradient timings to generate the echo; the use of spatially varying (or TONE) pulses, MTS, fat saturation and contrast agents to improve the contrast-to-noise ratio; the use of a smaller FOV or partial Fourier reconstruction methods to improve resolution; and the designing of new coils and, again, the use of contrast agents for a better S/N. Fat saturation itself has been a major problem since it requires a very uniform field to avoid saturating water instead. Without the use of segmentation methods fat otherwise blocks information in a maximum intensity projection (MIP) because of its remnant high signal (especially after the use of an MTS pulse, which suppresses gray matter/white matter in the head or muscle in the neck). Some other methods are also under development which will use many of the above improvements but whose purpose is to get 'black blood' images for highlighting vessel wall to examine plaque with high resolution and a spectroscopic analysis, as well as methods for functional imaging to see dynamic local blood flow with and without contrast agents. Ideally, one would like to cover a large region of interest very quickly, but this usually leads to blood saturation. The combination of the above methods would make it feasible to cover the entire head or neck in 5–10 minutes. At the moment the high contrast and high resolution aspects are accomplished using the multiple thin slab method in a transverse orientation.

This latter method, the use of the MIP algorithm, and the use of contrast agents all also require the use of vessel tracking or blood segmentation postprocessing to extract the best representation of the blood vessels from the images. The multislab technique requires significant overlapping of adjacent 3D slabs because of the tapering off of the rf profile at the slab edges. Using segmentation it becomes possible to extract the vessels from the background in most slices even given the spatial variation of signal intensity, and to digitize the images. Merging the newly processed data now eliminates the border artifacts otherwise evident in the final MIP images (Figure 4). The MIP itself causes a loss in the contrast-to-noise ratio, but if applied to the segmented data over a dilated region about the vessel tracked information this becomes less of a problem and, in fact, opens the door to other types of projections such as a straight sum, for example. These methods are becoming automated, so that the user only needs to input a single seed point in most cases [this is true for the major vessels in the head (Figure 5) and neck (Figure 6), and even for the cardiac system]. Other types of displays such as surface or volume rendering can also be used to advantage, and these will be dealt with in other sections in this treatise.

5.3 Cardiovascular Imaging

The application of MRA techniques to the heart is relatively new compared to that in the head and neck, owing to the special challenges and technical difficulties in magnetic resonance flow imaging of the heart. The motion of the heart during cardiac and respiratory cycles is the major obstacle for consistent magnetic resonance images. Some kind of motion compensation is usually needed to overcome this problem. Prospective or retrospective electrocardiogram (ECG) triggering is

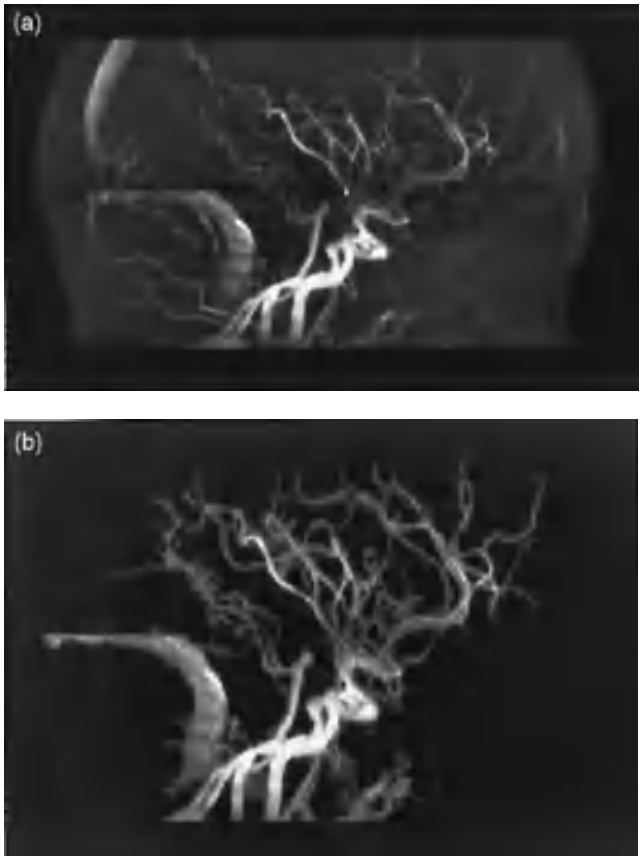

Figure 4 Intracranial study with a high-resolution two slab acquisition (a) without and (b) with vessel tracking. The MIP has obscure information in (a) which is brought out after vessel tracking in (b). The image parameters were: TR = 35 ms, MAT = 160 × 256 with a 5/8 rectangular FOV, FA = 15° and slice thickness = 1 mm with 64 partitions

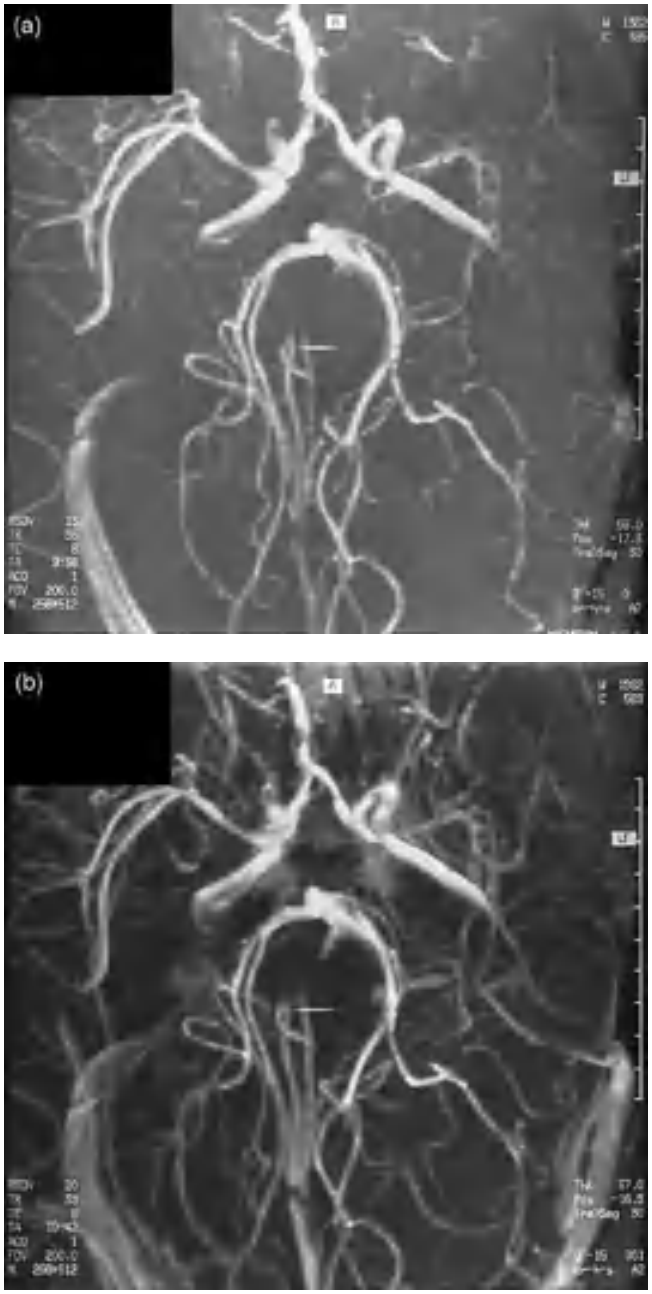

Figure 5 Comparison study of the intracranial vascular system (a) without and (b) with the contrast agent Gd-DTPA. A single dose of 0.1 mmol kg^{-1} was used. Saturated slow flow blood is now enhanced, especially for smaller vessels

used in almost all imaging cases to obtain cine images (images obtained throughout the cardiac cycle one after the other) or to minimize the cardiac motion effects. The respiratory motion effects are usually reduced or eliminated by prospective or retrospective respiratory gating, multiple signal averaging, or breath-holding. The major areas of magnetic resonance flow imaging application in the heart include the coronary arteries, great vessels, cardiac chambers and valves.

5.3.1 Coronary Arteries

In addition to their movement, coronary arteries have a small size. Thus, a high S/N and spatial resolution are required to visualize the coronary arteries reliably. Further, the coronary arteries are surrounded by epicardial fat, which tends to have a strong signal. Some kind of fat saturation is needed to increase the conspicuity of the coronary arteries. Early attempts at coronary MRA used multislice, multiphase, spin echo,[59] 2D gradient echo cine,[60,61] and inversion–recovery techniques.[62] Recent efforts have been on segmented 2D gradient echo acquisition,[63,64] fast spiral echo planar acquisition,[65] and 3D acquisition.[66–69] 2D scans are usually acquired within a single breath-hold, thus eliminating the respiratory motion effects. However, 2D images have relatively thick slices and evaluation of images may be complicated by the discontinuity of the slices acquired from different breath-holds since coronary arteries are highly tortuous. The acquisition of the 2D images also requires more patient cooperation and experience from the operator. Fast 3D scans with fat saturation create thin and contiguous slices, and can be easily postprocessed to visualize the coronary arteries (Figure 7). 3D scans have a better S/N and higher resolution than 2D images, and do not require breath-holding. However, image blurring will occur, reducing the effective resolution. Both hardware (echo planar system,

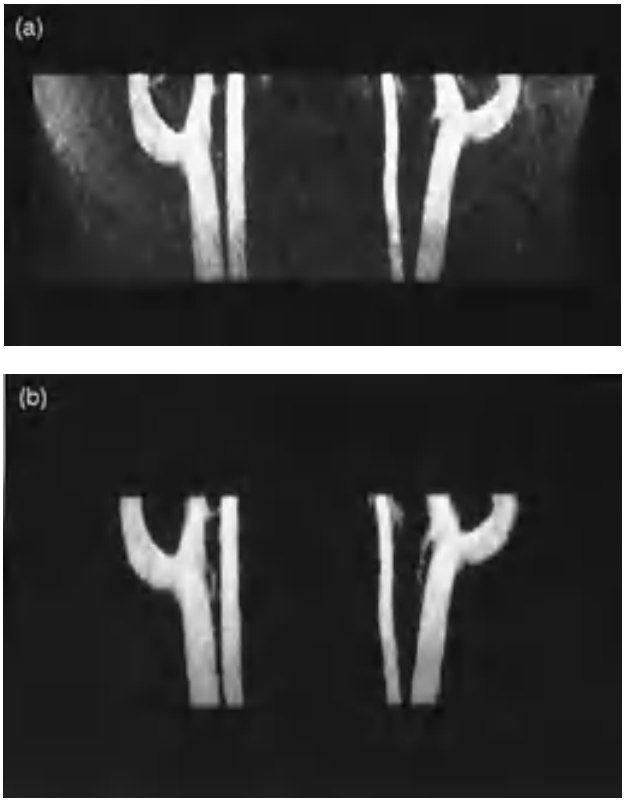

Figure 6 High resolution carotid artery study (a) without and (b) with vessel tracking. The imaging parameters were: *TR* = 31 ms, *TE* = 7 ms, FA = 20°, MAT = 256 × 512 and TH = 1 mm

high/faster gradient capability, better coils, respiratory gating) and software advancement (sequence development and postprocessing such as retrospective respiratory gating[70,71]) will further improve the performance of coronary MRA. These improvements will lead to faster coronary artery imaging using 3D retrospective[72–75] or 3D breath-hold[76–79] techniques and greater coverage of the heart.

Using a segmented gradient echo sequence, Burstein first reported on the feasibility of measuring coronary artery flow in isolated and in vivo hearts.[80] A phase contrast modification of this method allowed quantification of the coronary artery flow velocity within a breath-hold.[81] TOF quantification of the coronary flow with echo planar imaging was demonstrated to provide real time cine images.[82] Currently the spatial resolution of these techniques is still not adequate for accurate blood volume and, therefore, blood flow calculation.

5.3.2 Great Vessels

The anatomy of great vessels can be demonstrated by spin echo images.[83,84] The blood is dark due to wash-out effects, and the vessel wall is highlighted. 2D and 3D TOF MRA sequences have also been used to evaluate the great vessels. Common great vessel diseases include dissection and congenital diseases. 3D sequences may have the advantage when complicated vascular abnormality is involved because of the postprocessing capability of 3D images. Cine phase contrast methods are commonly used to evaluate the blood flow in the aorta.[85,86] Blood flow information is important to study the flow patterns and to evaluate the functional significance of great vessel diseases. The same methods were also used to assess the vena caval flow.[87]

5.3.3 Cardiac Chambers and Valves

Cine gradient echo sequences have been used to visualize the cardiac pools to evaluate cardiac function.[88] Magnetization transfer saturation is applied to enhance the blood/myocardium contrast.[89] Cardiac parameters such as ejection fraction, stroke volume, and cardiac output can then be calculated from the images. A segmented gradient echo sequence was also used to acquire cine images within a breath-hold to eliminate the motion of the heart induced by respiration. Signal void jets in the cardiac pools may indicate abnormalities of valves such as regurgitation and stenosis. Phase images of the cine scan can provide additional information about the motion of blood and myocardium during the cardiac cycle. Specifically, jet velocity mapping was used to assess valve stenosis.[90]

5.3.4 Pulmonary Arteries

Pulmonary artery flow imaging is a difficult task because of motion, magnetic susceptibility variations due to air–tissue interfaces in the lung, and the overlapping of arteries and veins. TOF gradient echo techniques are used in imaging the pulmonary vasculature. 2D scans are run within a single breath-hold.[91–93] These images have an enhanced blood signal due to adequate inflow and minimum motion artifacts.

A 3D syncopated sequence was proposed[91–94] to visualize the pulmonary vasculature. Multiple signal averaging is used to eliminate the ghosting artifacts due to motion and demonstrate the location where vessels stay most of the time. By adding an inversion pulse before data acquisition, a 'black blood' scan is obtained. A combination of 'bright blood' and 'black blood' scans will be able to differentiate normal blood and emboli, which should have high intensity in both scans. The advantage of 3D imaging is that the images can be postprocessed by MIP to evaluate the whole vasculature. An example MIP image generated from an ECG-triggered 3D 'bright blood' scan is shown in Figure 8.

Patients with a single lung transplantation are studied using phase contrast velocity mapping.[95] The blood volume and flow pattern of the native and transplanted lungs are compared and could be used to monitor these patients.

5.4 Renal Arteries

Image artifacts associated with cardiac, respiratory, and bowel motion, and the inherent complex flow patterns and directions of the renal arteries are the major challenges for renal artery flow imaging. Reasonable success has been achieved in imaging the renal arteries using both 2D[96–99] and 3D phase contrast methods.[100] These methods are sensitive to slow flow and can achieve good background suppression. However, they are sensitive to pulsatile and nonuniform flow and tissue motion, and are time consuming.

2D TOF methods[96,101] have been applied to acquire MRA images of the renal arteries with breath-holding. The major problems with these techniques are the thick slices and the possible slice misregistration between separate breath-holds.

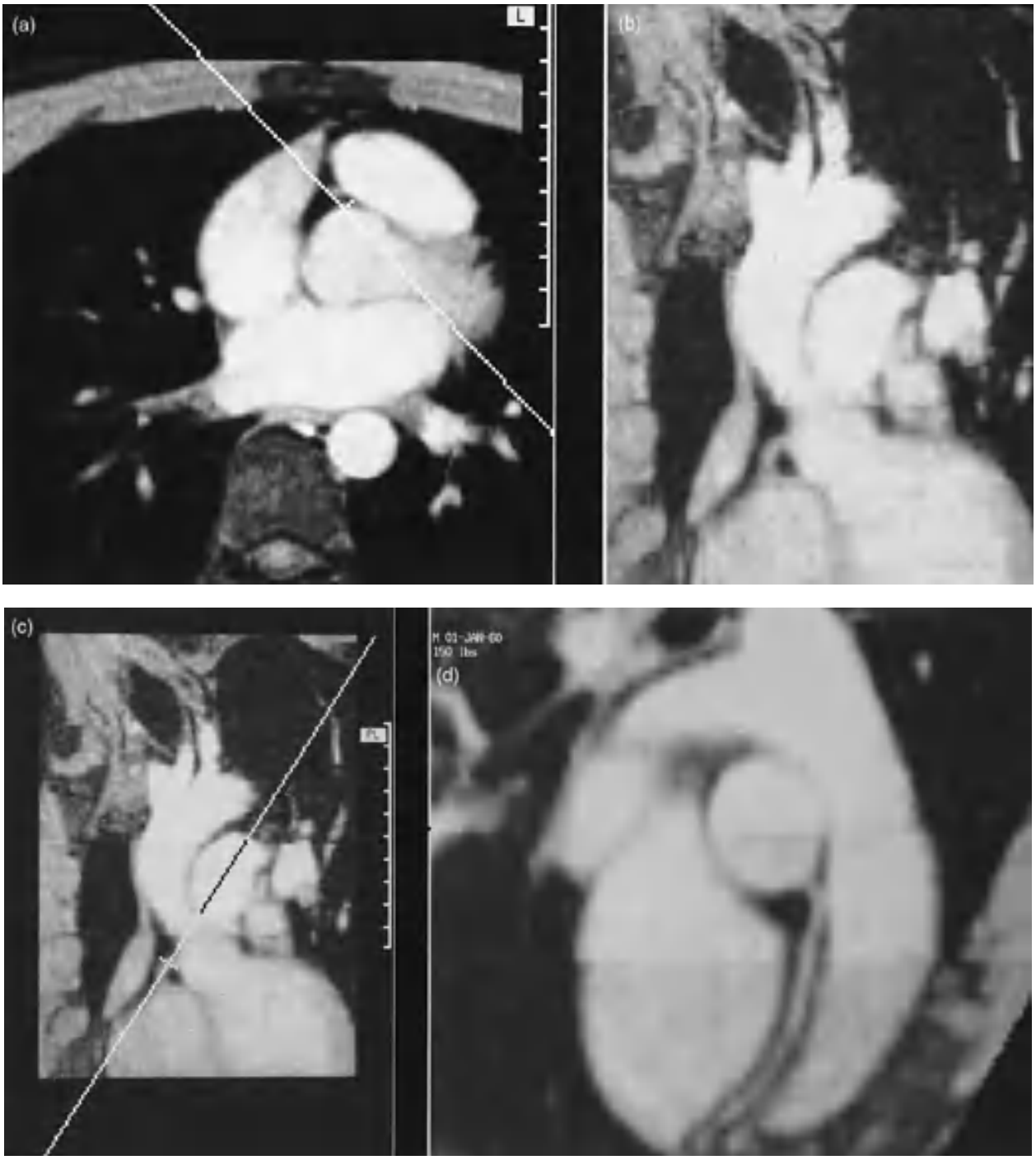

Figure 7 Three slabs (each 64 mm thick with 32 partitions) were acquired using a 3D technique. First a multiplanar reconstruction (MPR) (b) was obtained along the line illustrated in (a). The origin of the right coronary artery at the aortic root was clearly identified in (b). A second MPR (d) was obtained along the line illustrated in (c). A segment of the right coronary artery is visualized in (d)

3D TOF imaging[102–106] has also been used, but the motion induced blurring and ghosting severely degrade the image quality.

Background suppression increases the blood–tissue contrast and helps to delineate vascular details better. It also reduces vessel boundary blurring and ghosting artifacts from the physiological motion of the background tissue. Magnetization transfer saturation can be used to suppress background with little effect on blood signal. While MTS is quite effective in enhancing vascular contrast in evaluating intracranial arteries, it suffers from high power deposition when used in body imaging. A selective inversion recovery, rapid gradient echo sequence[107] was proposed to suppress the background and background induced motion artifacts. Data acquisition takes

Figure 8 An MIP image of the pulmonary vasculature generated from an ECG-triggered 3D scan with 32 partitions, each 2 mm thick

place during diastole so that blood intravoxel dephasing due to pulsatile flow is minimized. An MIP image generated from this sequence is shown in Figure 9.

The contrast agent gadolinium diethylenetriaminepentaacetic acid (Gd-DTPA) has been successfully used in enhancing the vascular contrast in imaging the abdominal arteries. A continuous injection instead of a bolus was utilized to enhance arteries but not veins.[108] Two studies measured the renal blood flow using cine phase contrast methods.[109,110] The flow measurements correlate closely with renal clearance of *p*-aminohippurate. The same sequence was also used to measure the volumetric flow rates in the portal venous system.[111] Technical improvement and better hardware are needed to improve the spatial resolution further.

5.5 Peripheral Imaging

Imaging of slow flow is difficult because of the saturation of blood. The use of an intravascular contrast agent makes it possible to collect rapid, 3D, projective, coronal images of both legs in roughly 30 s. With 25 mT m^{-1} gradients and a rise time of 300 μs, an in-plane resolution of 1 mm by 1 mm and a through plane resolution of 2 mm with 32 slices is possible in roughly 30 s with a *TR* of 5 ms.[112,113] Higher resolution covering the entire leg is possible for scans of several minutes but then arteries and veins become equally bright. Figure 10a shows a rapid early first-pass scan of the vessels in which only arteries are enhanced, followed by a steady-state scan (Figure 10b) showing the enhanced veins as well (because the contrast agent has reached the same equilibrium value in both arteries and veins).

Figure 9 An MIP image of renal arteries from a 3D diastolic acquisition and selective inversion recovery background suppression. The original data set has 32 partitions, each 1.25 mm thick

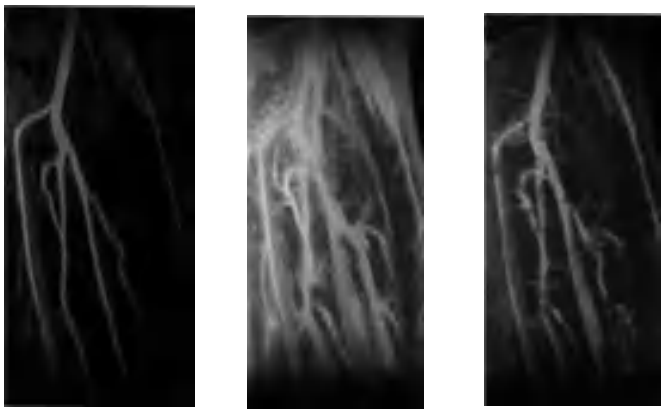

(a) (b) (c)

Figure 10 An example set of 3D limited volume-of-interest maximum intensity projection images in the leg post contrast agent injection. (a) Image collected during the arterial phase over 30 s with 50 slices and a resolution of 1 mm × 1 mm × 2 mm. (b) Image collected afterward for a period of roughly 10 min with 100 slices and a resolution of 1 mm × 1 mm × 1 mm. (c) Image is a processed version of the central image using the phase difference between veins and arteries to suppress the venous signal

Three methods have been proposed to deal with this problem. The first is vessel tracking (mentioned above) and the second and third are developing methods using the T_2 and phase differences between arteries and veins. The shorter T_2 of venous blood can be used to suppress signals from veins while keeping those from arteries bright. This was accomplished in the 1980s using long echoes.[114] In the late 1990s, using a T_2 preparation pulse and a spiral acquisition, reasonably fast high-resolution data can be collected[115] where arteries are significantly brighter than veins and surrounding muscle. Alternatively, the phase can be used to suppress venous signal.[116] This is possible because the venous blood has a different susceptibility from the surrounding tissue for vessels parallel to the static field (this difference is caused by the deoxyhemoglobin in the veins). Figure 10c shows the suppression of venous blood using this method (see below).

5.6 Venographic Imaging in the Brain

Angiography is a general term for imaging vessels, including both arteries and veins. Arteries are usually the focus of MRA studies, since they carry the crucial morphologic information as to the supply of blood to the tissue. However, if one

Figure 11 A minimum intensity projection image from a $TE = 40$ ms, $TR = 57$ ms, 3D, gradient echo image projected over seven images. The resolution is 0.5 mm × 0.5 mm × 2.0 mm. The acquisition time was 10 min and 32 partitions (slices) were collected in total. The peripheral

is interested in whether or not the tissue actually performed its function and used the oxygen delivered to it, then the venous image is important. The use of intravascular contrast agents makes it possible to visualize both arteries and veins. How to separate them remains the problem. However, one method exists that can highlight small venous structures even without a contrast agent. This method uses a high resolution, long *TE*, 3D gradient echo approach to reduce susceptibility effects caused by static field inhomogeneities, and to highlight the field differences between arteries and veins[117,118] caused by the differences in deoxyhemoglobin content. The field difference between veins and arteries is about 0.3 p.p.m. for veins parallel to the static field and leads to an out-of-phase relationship between them that occurs for a *TE* of roughly 50 ms. This π phase shift leads to a cancellation effect between the background tissue and the veins. Further, the phase image itself reveals the same π phase shift and can be used to suppress the venous signal simply by scaling the phase image to unity where the phase is zero and to zero when the phase is π; the resulting phase mask is then multiplied by the magnitude image. Figure 11 demonstrates the level of cancellation and the visualization of small venous structures in the brain. This approach has proven valuable for the study of venous lesions and other vascular abnormalities.

6 FUTURE DIRECTIONS

Future developments depend on what remains unanswered using the present techniques and what new directions remain to be investigated. In the former category, the use of short (possibly velocity compensated) gradient echoes, enhanced contrast for TOF imaging, faster imaging, and phase unwrapped images for an improved S/N for phase contrast quantitative flow imaging are major areas for continued research. In the latter category, major new directions include the use of intravascular or higher relaxivity contrast agents, echo planar flow imaging, fluid dynamic applications, the use of phase coil arrays, the acquisition of larger matrix sizes (1024 or even 2048) and better postprocessing and display techniques. As far as whether TOF or phase contrast is better, this may become a moot point as both methods become less competitive and more complementary due to the increased speed of acquisition possible with new systems today. With both high resolution images and functional information, MRA promises to be the ideal way to obtain most vascular information noninvasively.

7 RELATED ARTICLES

Abdominal MRA; Head and Neck Studies Using MRA; Phase Contrast MRA; Time-of-Flight Method of MRA.

8 REFERENCES

1. P. C. Lauterbur, *Nature*, 1973, **242**, 190.
2. S. Patz and R. C. Hawkes, *Magn. Reson. Med.*, 1986, **3**, 140.
3. W. T. Dixon, L. N. Du, D. D. Faul, M. Gado, and S. Rossnick, *Magn. Reson. Med.*, 1986, **3**, 454.
4. A. Constantinesco, J. J. Mallet, A. Bonmartin, C. Lallot, and A. Briguet, *Magn. Reson. Imaging*, 1984, **2**, 335.
5. D. G. Nishimura, A. Macovski, and J. M. Pauly, *IEEE Trans. Med. Imaging*, 1986, **5**, 140.
6. E. M. Haacke and G. W. Lenz, *Am. J. Radiol.*, 1987, **148**, 1251.
7. L. Axel and D. Morton, *J. Comput. Assist. Tomogr.*, 1987, **11**, 31.
8. G. L. Nayler, D. N. Firmin, and D. B. Longmore, *J. Comput. Assist. Tomogr.*, 1986, **10**, 715.
9. G. A. Laub and W. A. Kaiser, *J. Comput. Assist. Tomogr.*, 1988, **12**(3), 377.
10. G. Suryan, *Proc. Indian Acad. Sci.*, 1951, **33**, 107.
11. H. Y. Carr and E. M. Purcell, *Phys. Rev.*, 1954, **94**, 630.
12. H. C. Torrey, *Phys. Rev.*, 1956, **104**, 563.
13. J. R. Singer, *Science*, 1959, **130**, 1652.
14. R. L. Bowman, and V. Kudravcev, *IRE Trans. Med. Elec.*, 1959, **6**, 267.
15. R. E. Halbach, J. H. Battocletti, S. X. Salles-Cunha, and A. Sances, *Med. Phys.*, 1981, **8**, 444.
16. E. L. Hahn, *J. Geophys. Res.* 1960, **65**, 776.
17. K. J. Packer, *Mol. Phys.*, 1969, **17**, 355.
18. V. Waluch and W. G. Bradley, *J. Comput. Assist. Tomogr.*, 1984, **8**, 594.
19. P. R. Moran, *Magn. Reson. Imaging*, 1982, **1**, 197.
20. E. M. Haacke, T. J. Masaryk, P. A. Wielopolski, F. R. Zypman, J. A. Thach, S. Amartus, J. Mitchell, M. Clampitt, and C. Paschal, *Magn. Reson. Med.*, 1990, **14**, 202.
21. P. J. Keller, B. P. Drayer, E. K. Fram, K. D. Williams, C. L. Dumoulin, and S. P. Souza, *Radiology*, 1989, **173**, 527.
22. R. S. Owen, J. P. Carpenter, R. A. Baum, L. J. Perloff, and C. Cope, *N. Engl. J. Med.*, 1992, **326**, 1577.
23. J. A. Tkach, P. M. Ruggieri, J. J. Dillinger, J. S. Rose, M. T. Modic, and T. J. Masaryk, *J. Magn. Reson. Imaging*, 1993, **3**, 365.

24. J. I. Jackson, D. G. Nishimura, and A. Macovski, *Magn. Reson. Med.*, 1992, **25**, 128.
25. D. Purdy, G. Cadena, and G. Laub, *Proc. XIth Ann Mtg. Soc. Magn. Reson. Med.*, Berlin, 1992, p. 882.
26. D. L. Parker, C. Yuan, and D. D. Blatter, *Magn. Reson. Med.*, 1991, **17**, 434.
27. G. B. Pike, B. S. Hu, G. H. Glover, and D. R. Enzmann, *Magn. Reson. Med.*, 1992, **25**, 372.
28. R. R. Edelman, S. S. Ahn, D. Chien, W. Li, A. Goldmann, M. Mantello, J. Krames, and J. Kleefield, *Radiology*, 1992, **184**, 395.
29. G. Marchal, H. Bosmans, P. van Hecke, U. Speck, P. Aerts, P. Vanhoenacker, and A. L. Baert, *Am. J. Roentgenol.*, 1990, **155**, 407.
30. W. Lin, E. M. Haacke, A. S. Smith, and M. E. Clampitt, *J. Magn. Reson. Imaging*, 1992, **2**, 277.
31. T. D. Scholz, T. L. Ceckler, and R. S. Balaban, *Magn. Reson. Med.* 1993, **29**, 352.
32. H. E. Cline, C. L. Dumoulin, W. E. Lorensen, S. P. Souza, and W. J. Adams, *Magn. Reson. Med.* 1991, **18**, 384.
33. W. Lin, E. M. Haacke, T. J. Masaryk, and A. S. Smith, *JMRI*, 1992, **2**, 519.
34. D. Saloner, W. A. Hanson, J. S. Tsuruda, R. van Tyen, C. M. Anderson, and R. E. Lee, *JMRI*, 1991, **1**, 423.
35. P. M. Pattany, R. Marino, and J. M. McNally, *Magn. Reson. Imaging*, 1986, **4**, 154.
36. G. L. Naylor, D. N. Firmin, and D. B. Longmore, *J. Comput. Assist. Tomogr.*, 1986, **10**, 715.
37. L. R. Frank, A. P. Crawley, and R. B. Buxton, *Magn. Reson. Med.*, 1992, **25**, 299.
38. O. P. Simonetti, J. L. Duerk, and V. Chankong, *Magn. Reson. Med.*, 1993, **23**, 498.
39. S. N. Urchuk and D. B. Plewes, *JMRI,* 1992, **2**, 453.
40. P. J. Kilner, D. N. Firmin, R. S. Rees, J. Martinez, D. J. Pennell, R. H. Mohiaddin, S. R. Underwood, and D. B. Longmar, *Radiology*, 1991, **178**(1), 229.
41. E. M. Haacke, E. D. Lindskog, and W. Lin, *J. Magn. Reson.* 1991, **92**, 126.
42. J. R. Singer, *Electronics*, 1960, **33**, 77.
43. O. C. Morse, and J. R. Singer, *Science*, 1970, **170**, 440.
44. W. T. Dixon, L. N. Du, and M. Gado, *Magn. Reson. Med.*, 1986, **3**, 454.
45. L. Axel, A. Shimakawa, and J. MacFall, *Magn. Reson. Imaging*, 1986, **4**, 199.
46. K. Shimizu, T. Matsuda, T. Sakurai, A. Fujita, H. Ohara, S. Okamura, S. Hashimoto, H. Mano, C. Kawai, and M. Kiri, *Radiology*, 1986, **159**, 195.
47. R. R. Edelman, H. P. Mattle, J. Kleefield, and M. S. Silver, *Radiology*, 1989, **171**, 551.
48. J. Hennig, M. Mueri, P. Brunner, and H. Friedburg, *Radiology*, 1988, **166**, 237.
49. E. M. Haacke, A. S. Smith, W. Lin, J. S. Lewin, D. A. Finelli, and J. L. Duerk, *Top. Magn. Reson. Imaging*, 1991, **3**, 34.
50. C. L. Dumoulin, S. P. Souza, C. J. Hardy, and S. A. Ash, *Magn. Reson. Med.* 1991, **21**, 242.
51. C. L. Dumoulin, S. P. Souza, M. F. Walker, and E. Yoshitome, *Magn. Reson. Med.*, 1988, **6**, 275.
52. C. L. Dumoulin, S. P. Souza, M. F. Walker, and W. Wagle, *Magn. Reson. Med.*, 1989, **9**, 139.
53. D. J. Bryant, J. A. Payne, D. N. Firmin, and D. B. Longmore, *J. Comp. Assist. Tomogr.*, 1984, **8**, 588.
54. C. Thomsen, F. Stahlberg, M. Stubgaard, and B. Nordell, *Radiology*, 1990, **177**, 659.
55. N. J. Pelc, M. A. Bernstein, A. Shimakawa, and G. H. Glover, *J. Magn. Reson. Imaging*, 1991, **1**, 405.
56. R. R. Edelman, D. Chien, and D. Kim, *Radiology*, 1991, **181**, 655.
57. W. Lin, R. R. Edelman, E. M. Haacke, in 'Magnetic Resonance Angiography: Concepts and Applications', ed. E. J. Potchen, E. M. Haacke, J. E. Siebert, and A. Gottshalk, Mosby-Yearbook, St. Louis, Ch. 8, 1993.
58. D. LeBihan, R. Turner, and J. R. MacFall, *Magn. Reson. Med.*, 1989, **10**, 324.
59. S. Paulin, G. K. von Schulthess, E. Fossel, and H. P. Krayenbuehl, *Am. J. Radiol.*, 1987, **148**, 665.
60. Z. H. Cho, C. W. Mun, and R. M. Friedenberg, *Magn. Reson. Med.*, 1991, **20**, 134.
61. C. L. Dumoulin, S. P. Souza, R. D. Darrow, and W. J. Adams, *J. Comput. Assist. Tomogr.* 1991, **15**, 705.
62. S. J. Wang, B. S. Hu, A. Macovski, and D. G. Nishimura, *Magn. Reson. Med.*, 1991, **18**, 417.
63. R. R. Edelman, W. J. Manning, D. Burstein, and S. Paulin, *Radiology*, 1991, **181**, 641.
64. W. J. Manning, W. Li, and R. R. Edelman, *N. Engl. J. Med.*, 1993, **328**, 828.
65. C. H. Meyer, B. S. Hu, D. G. Nishimura, and A. Macovski, *Magn. Reson. Med.*, 1992, **28**, 202.
66. R. J. Alfidi, T. J. Masaryk, E. M. Haacke, G. W. Lenz, J. S. Ross, M. T. Modic, A. D. Nelson, J. P. Li Puma, and A. M. Cohen, *Am. J. Roentgenol.*, 1987, **149**, 1097.
67. G. W. Lenz, E. M. Haacke, and R. D. White, *Magn. Reson. Imaging*, 1989, **7**, 445.
68. D. Li, C. B. Paschal, E. M. Haacke, and L. P. Alder, *Radiology*, 1993, **181**, 401.
69. C. B. Paschal, E. M. Haacke, and L. P. Adler, *JMRI*, 1993, **3**, 491.
70. M. Hofman, C. B. Paschal, D. Li, and E. M. Haacke, *J. Comput. Assist. Tomogr.*, 1995, **19**, 56.
71. Y. Wang, R. C. Grimm, and P. J. Rossman, *Magn. Reson. Med.*, 1995, **35**, 11.
72. M. B. M. Hofman, C. B. Paschal, D. Li, E. M. Haacke, A. C. Van Rossum, and M. Sprenger, *J. Comput. Assist. Tomogr.*, 1995, **19**, 56.
73. Y. Wang, P. J. Rossman, R. C. Grimm, S. J. Riederer, and R. L. Ehman, *Radiology*, 1996, **198**, 55.
74. D. Li, S. Kaushikkar, E. M. Haacke, *et al*., *Radiology*, 1996, **201**, 857.
75. P. K. Woodard, D. Li, E. M. Haacke, *et al*., *Am. J. Roentgenol.*, 1998, **170**, 883.
76. P. A. Wielopolski, W. J. Manning, and R. R. Edelman, *JMRI*, 1995, **5**, 403.
77. J. W. Goldfarb and R. R. Edelman, *Radiology*, 1998, **206**, 830.
78. J. Zheng, D. Li, K. T. Bae, P. K. Woodard, and E. M. Haacke, *J. Cardiovasc. Magn. Reson.*, 1998, **1**, 33.
79. D. Li, B. Dolan, R. C. Walovitch, and R. B. Lauffer, *Magn. Reson, Med.*, 1998, **39**, 1014.
80. D. Burstein, *J. Magn. Reson. Imaging*, 1991, **1**, 337.
81. R. R. Edelman, W. J. Manning, E. Gervino, and W. Li, *J. Magn. Reson. Imaging*, 1993, **3**, 699.
82. B. P. Poncelet, R. M. Weisskoff, V. J. Wedeen, T. J. Brady, and H. Kantor, *Magn. Reson. Med.*, 1993, **30**, 447.
83. C. B. Higgins, B. F. Byrd, M. T. McNamara, P. Lanzer, M. J. Lipton, E. Botvinick, N. B. Schiller, L. E. Crooks, and L. Kaufman, *Radiology*, 1985, **155**, 671.
84. R. D. White, C. B. Paschal, J. A. Tkach, and M. J. Carvlin, *Top. Magn. Reson. Imaging*, 1990, **2**(2), 31.

85. H. G. Bogren, R. H. Mohiaddin, R. K. Klipstein, D. N. Firmin, R. S. Underwood, R. S. Rees, and D. B. Longmore, *Am. Heart J.*, 1989, **118**, 234.
86. H. G. Bogren, R. K. Klipstein, D. N. Firmin, R. H. Mohiaddin, S. R. Underwood, R. S. Rees, and D. B. Longmore, *Am. Heart J.*, 1989, **117**, 1214.
87. R. H. Mohiaddin, S. L. Wann, R. Underwood, D. N. Firmin, R. S. Rees, and D. B. Longmore, *Radiology*, 1990, **177**, 537.
88. U. Sechtem, P. W. Pflugfelder, R. D. White, R. G. Gould, W. Holt, M. J. Lipton, and C. B. Higgins, *Am. J. Roentgenol.*, 1987, **148**, 239.
89. S. Kaushikkar, D. Li, W. Lin, E. M. Haacke, D. Wilson, L. Adler, R. Stengall, *Proc. XIIth Ann Mtg. Soc. Magn. Reson. Med.*, New York, 1993, p. 502.
90. P. J. Kilner, D. N. Firmin, R. S. O. Rees, J. Martinez, D. J. Pennell, R. H. Mohiaddin, S. R. Underwood, and D. B. Longman, *Radiology*, 1991, **178**, 229.
91. H. Hatabu, W. B. Gefter, H. Y. Kressel, L. Axel, and R. E. Lenkinski, *Radiology*, 1989, **171**, 391.
92. T. K. F. Foo, J. R. MacFall, C. E. Hayes, H. D. Sostman, and B. E. Slayman, *Radiology*, 1992, **183**, 473.
93. T. M. Grist, H. D. Sostman, J. R. MacFall, T. K. Foo, C. E. Spritzer, and L. W. Wittig, *Radiology*, 1993, **189**, 523.
94. P. A. Wielopolski, E. M. Haacke, and L. P. Adler, *Radiology*, 1992, **183**, 465.
95. R. H. Mohiaddin, R. Paz, S. Theodoropoulos, D. L. Firmin, D. B. Longmore, and M. H. Yacoub,, *J. Thorac. Cardiovasc. Surg.*, 1991, **101**, 1016.
96. J. F. Debatin, C. E. Spritzer, T. M. Grist, C. Beam, L. P. Svetkey, G. E. Newman, and H. D. Sostman, *Am. J. Roentgenol.*, 1991, **157**, 981.
97. C. L. Dumoulin, E. K. Yucel, P. Vock, S. P. Souza, F. Terrier, F. L. Steinberg, and H. Weymueller, *J. Comput. Assist. Tomogr.* 1990, **14**, 779.
98. F. L. Steinberg, E. K. Yucel, C. L. Dumoulin, and S. P. Souza, *Magn. Reson. Med.*, 1990, **14**, 315.
99. E. Farrugia, B. F. King, and T. S. Larson, *Mayo Clin. Proc.*, 1993, **68**, 157.
100. P. Vock, F. Terrier, H. Wegmueller, F. Mahler, P. Gertsch, S. P. Souza, and C. L. Dumoulin, *Br. J. Radiol.*, 1991, **64**, 10.
101. D. Kim, R. R. Edelman, K. C. Kent, D. H. Porter, and J. J. Skillman, *Radiology*, 1989, **174**, 727.
102. J. Borrello, D. Li, T. Vesely, E. P. Vinning, J. J. Brown, and E. M. Haacke, *Radiology*, 1995, **197**, 793.
103. J. S. Lewin, G. Laub, and R. Hausmann, *Radiology*, 1991, **179**, 261.
104. P. A. Hardy, J. A. Tkach, G. K. Lammert, and M. G. Zelch, *J. Magn. Reson. Imaging*, 1993, **3**, 58.
105. H. J. Smith and S. J. Bakke, *Acta Radiol.*, 1993, **34**, 150.
106. E. K. Yucel, J. A. Kaufman, M. Prince, H. Bazari, L. S. T. Fang and A. C. Waltman, *Magn. Reson. Imaging*, 1993, **11**, 925.
107. D. Li, E. M. Haacke, J. P. Mugler, S. Berr, and J. R. Brookeman, *Magn. Reson. Med.*, 1994, **31**, 414.
108. M. R. Prince, E. K. Yucel, J. A. Kaufman, D. C. Harrison, and S. C. Geller, *JMRI*, 1993, **3**, 877.
109. B. Lundin, T. G. Cooper, R. A. Meyer, and E. J. Potchen, *Magn. Reson. Imaging*, 1993, **11**, 51.
110. R. L. Wolf, B. F. King, V. E. Torres, D. M. Wilson, and E. L. Ehman, *Am. J. Roentgenol.*, 1993, **161**, 995.
111. D. J. Burkart, C. D. Johnson, M. J. Morton, R. L. Wolf, and R. L. Ehman, *Am. J. Roentgenol.*, 1993, **160**, 1113.
112. M. R. Prince, D. Li, Narasimham, W. T. Jacoby, *et al*., *Am. J. Roentgenol.*, 1996, **166**, 1387.
113. T. M. Grist, F. R. Korosec, D. C. Peters, *et al*., *Radiology*, 1998, **207**, 539.
114. P. J. Keller and D. Saloner, in 'Magnetic Resonance Angiography: Concepts and Applications', eds. E. J. Potchen, E. M. Haacke, J. E. Siebert, and A. Gottshalk, Mosby-Yearbook, St Louis, PA, 1993, Ch. 7.
115. J. H. Brittain, E. W. Olcott, A. Szuba, G. E. Gold, G. A. Wright, P. Irarrazaval, and D. G. Nishimura, *Magn. Reson, Med.*, 1997, **38**, 343.
116. Y. Wang, Y. Yu, T. Bae, D. Li, W. Lin, and E. M. Haacke, 1998 Xth Annual Workshop on MRA, Park City, Utah, p. 24.
117. J. R. Reichenbach, R. Feiwell, K. Kuppusamy, M. Bahn, and E. M. Haacke, *Magn. Reson, Imag.*, 1997, **16**, 281.
118. J. R. Reichenbach, R. Venkatesan, D. J. Schillinger, D. K. Kido, and E. M. Haacke, *Radiology*, 1997, **204**, 272.

Biographical Sketches

E. Mark Haacke. *b* 1951. B.S., 1973, M.Sc., 1975, Ph.D., 1978, University of Toronto. Introduced to NMR by Neil Holland with Picker Int. in 1983. Faculty at Case Western Reserve University, Department of Radiology, 1985–93. Faculty at Washington University, Mallinckrodt Institute of Radiology, 1993–present. Approx. 100 publications. Research interests include MR in functional imaging, angiography, cardiovascular imaging, fast imaging methods, and image reconstruction methods.

Weili Lin. *b* 1963. M.S., 1990, Ph.D., 1993 Case Western Reserve University. Faculty at Washington University, 1993–present. Approx. 50 publications. Research interests include MR in functional imaging, angiography, signal processing, and stroke.

Debiao Li. *b* 1962. Ph.D., 1992, University of Virginia. Research associate at Case Western Reserve University, 1992–93. Faculty at Washington University, 1993–present. Approx. 50 publications. Research interests include MR in cardiac imaging, angiography, and fast imaging techniques.

Blood Flow: Quantitative Measurement by MRI

David N. Firmin

National Heart and Lung Institute, University of London, UK

and

Raad H. Mohiaddin

Royal Brompton Hospital, London, UK

1 INTRODUCTION

The study of flow with nuclear magnetic resonance (NMR) has a long history, although the early research work merely set out to analyze the flow effects on the signal without detailing a particular application. Hahn,[1] for example, was the first to note the effect of diffusion while the first to study the effect of coherent flow was Suryan.[2] Several years later methods of flow measurement were presented, a number of which were designed for the measurement of blood flow. The methods all used either flow-related phase shifts or time-of-flight principles, where the latter could involve tagging or saturation and wash-in effects. Following the introduction of NMR imaging techniques, a number of methods were described, again applying the same principles, but for obtaining flow information in the form of an image.

2 EARLY QUALITATIVE IN VIVO STUDIES

Much of the initial work concentrated on understanding the appearance of a flow on an image and the artifacts it can cause; these can often be indicative of the type of flow present and can therefore give important information in the diagnosis of a particular disorder. Examples of flow phenomena studied include: signal dephasing,[3] wash-in/wash-out with different sequences,[4–6] even echo rephasing,[7] and signal misregistration effects.[8] Pulsatile flow can also alter the appearance of the image by the formation of nonstructured flow artifacts. These result because the motion of blood during the application of imaging gradients results in a phase shift of the blood signal which is added to the spatial phase encoding. If the motion of blood changes from one acquisition to another, the resultant phase shift will introduce a varying error to the spatial phase encoding. The Fourier transform will then get 'confused' and the blood signal will end up being spread out along the phase encoding axis. Perman et al.[9] investigated this type of flow artifact and demonstrated that even echo rephasing corrected the error and removed the artifact as long as the motion was reasonably simple (i.e. it did not contain significant acceleration or other high-order derivatives of position).

3 EARLY QUANTITATIVE IN VIVO STUDIES

The quest for a method quantitatively to image blood flow in vivo was first realized in the early 1980s, initially using time-of-flight methods and soon afterwards phase methods.

3.1 Time-of-Flight Methods

Singer and Crooks[6] initially used a saturation wash-in technique in an attempt to measure flow in the internal jugular veins. They employed the same principles as first Garroway[10] and then Thulborn et al.[11] had previously used in vitro. The method involved first saturating the slice and then leaving an interval before acquiring image data from the slice; the longer the time interval τ the greater the inflow of fully magnetized spins and the higher the signal on the image. The two main problems with these methods were that only low flow velocities could realistically be measured with practical slice thicknesses, and also many other factors could affect the amplitude of the blood signal.

Later work on this type of method tended to be more related to angiography, although some quantitative flow measurements were demonstrated.[12,13] However, the advent of 3D imaging techniques has enabled ungated measurements of constant flows or averaged pulsatile flows to be carried out by using the time-of-flight principles as described below.

The first true time-of-flight (TOF) method of blood flow imaging was described by Feinberg et al.[14] Their approach was to use a variation on a double echo spin echo sequence; the first 180° selected slice was displaced by 3 mm from the 90° selected slice, and the second was displaced by 9 mm. The first 180° selection overlapped sufficiently with the 90° selection to produce a good anatomical image. The second 180° pulse selection did not overlap with that of the 90° or the first 180° pulse selection, and hence produced no anatomical image but gave a high signal from the blood that had experienced all the preceding rf pulses (i.e. that had passed between the different selected planes). Flow in the carotid and vertebral arteries of a volunteer's neck was identified with the technique.

One-dimensional methods that directly imaged blood movement over a known time were described by both Shimizu et al.[15] and Axel et al.[16] The methods consisted of slice selection and frequency encoding being applied in the same axis. In this way material that had moved in this axis between selection and reading would be displaced relative to the stationary material. This technique is therefore making use of an effect that is often seen as a problem in other methods of flow imaging. With the flow information encoded in one axis as described, the other one or two axes may be spatially encoded by use of phase-encoding gradients. Shimizu et al.[15] tested the technique on a U-tube phantom where, by varying the velocity and the echo time (TE) to produce different flow displacements, they found very good correlation between these displacements and true flow. The technique was demonstrated in vivo[17] where it was repeated rapidly throughout the heart cycle so that pulsatile flow information could be acquired in a reasonable time. One of the main advantages of the technique was its ability to image very high velocities.

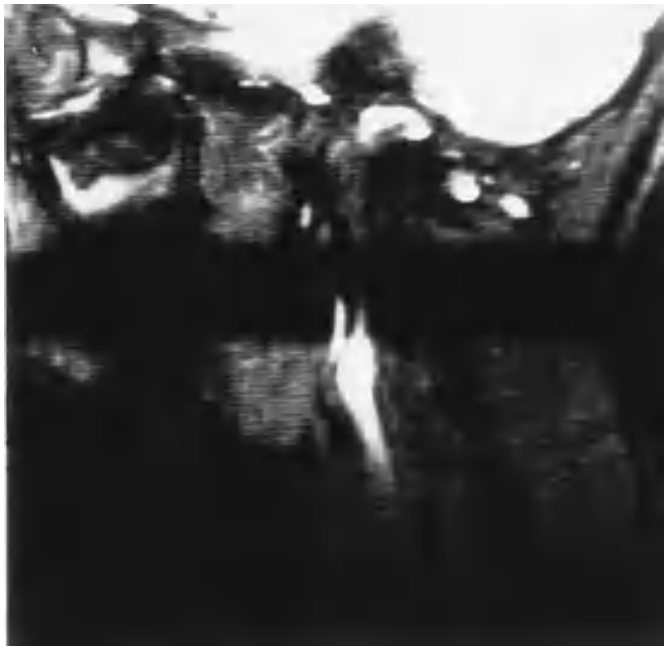

Figure 1 Inflow of arterial blood (up) and venous blood (down) into a presaturation band in a 2D cardiac gated image. The saturation has taken place just above the carotid bifurcation during systole. The time between the saturation pulse and the echo time is 18 ms. The distance the blood has moved is slightly more than 1.2 cm, resulting in a velocity of about 60 cm s^{-1}. (Reproduced with permission of Aspen Publishers from E. M. Haacke, A. S. Smith, W. Lin, J. S. Lewin, D. A. Finelli, and J. L. Duerk, *Top. Magn. Reson. Imaging*, 1991, **3**, 34)

Methods have also been developed combining the time-of-flight and wash-in/wash-out principles. Two general approaches using slice saturation in an orthogonal plane to that of the image have been used. The first utilizes the pulse to saturate tissues within a band across the image so that magnetized blood flowing into the region can be imaged and flow quantified by measuring the distance of inflow over the time between saturation and image acquisition. Results have been demonstrated using two-dimensional cardiac gated (Figure 1) and three-dimensional ungated methods (Figure 2). The second approach is to saturate a band of tissue, for example in a transverse plane, and then follow the progress of this dark band in the coronal or sagittal planes.[18]

The main limitation of these saturation techniques is that they are limited by the T_1 value of the tissue. The signal from the saturated blood or tissue will increase towards equilibrium with time, eventually making it difficult to measure accurately the distances traveled. Also, motion during the sampling gradients can result in signal distortion and thus affect the image.[19] For arterial flow measurements where cardiac gating is required, only two-dimensional images can realistically be acquired. This limits our ability to study flow details as the flow profile can only be acquired in one dimension at the most.

3.2 Phase Methods

In 1982, Moran[20] suggested the introduction of bipolar velocity phase-encoding pulses, such as had previously been used

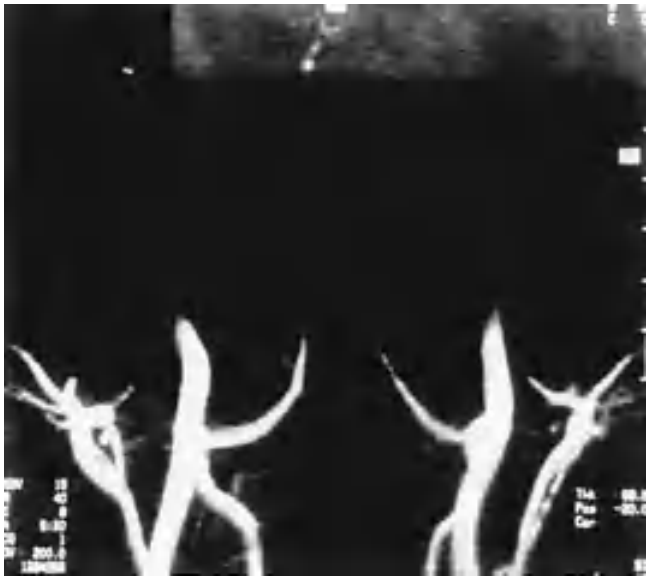

Figure 2 Inflow during a 3D TOF experiment carried out in the upper neck/head region reveals many arterial vessels. The peak flow represented in the internal carotid is more than 1 m s^{-1}. (Reproduced with permission of Mosby-Year Book, Inc. from D. N. Firmin, C. L. Dumoulin, and R. H. Mohiaddin, in 'Magnetic Resonance Angiography, Concepts and Applications', ed. E. J. Potchen, E. M. Haacke, J. E. Siebert, and A. Gottschalk, 1993)

in nonimaging experiments, in order to introduce velocity phase-encoding to the data. Phase methods of flow imaging that were later developed using this suggested theory fell broadly into two categories:

1. Fourier flow imaging methods that phase-encoded flow velocity so that a number of flow phase-encoding steps would separate the different flow velocities present in a particular region.
2. Phase-mapping methods that mapped the phase of the signal directly in order to measure the flow.

Both categories of methods are based on the same theory that the NMR signal from a sample of spins moving in the direction of a bipolar magnetic gradient pulse pair (Figure 3) will accumulate a phase shift given by:

$$\phi = \gamma_v \Delta A_g \tag{1}$$

where γ is the gyromagnetic ratio, v is the velocity, Δ is the time between the centers of the lobes of the gradient pulse, and

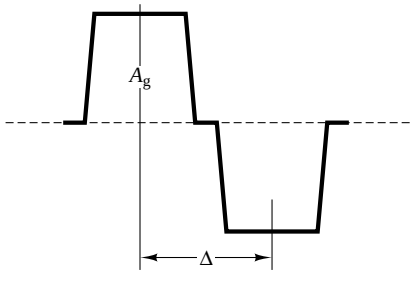

Figure 3 A bipolar magnetic gradient profile as used to produce velocity-dependent phase shifts

A_g is the area of one gradient lobe. The phase shift is therefore directly related to the velocity for a particular gradient wave form.

3.2.1 *Fourier Flow Methods*

The first to demonstrate experimentally the method of Fourier flow imaging were Redpath et al.[21] when they used eight flow phase-encoding steps to image a circle of fluid-filled tubing that was rotated in the image plane. Different segments of the circle were seen on the eight resultant images, each corresponding to a different velocity range in the direction of the flow phase-encoding gradient. Feinberg et al.[22] applied the method both in vitro and in vivo, but increased the velocity resolution and simplified the reconstruction by increasing the number of flow phase-encoding steps and removing the spatial phase encoding. The phantom results proved the accuracy of the method and the in vivo study, while showing the flow in the descending aorta, also highlighted the problem of a very high signal from stationary tissue imaged in the spatial dimension. In 1988, Hennig et al.[23] described a development of this method where the signal from stationary tissue was saturated and the sequence repeated much more rapidly. The main problem with the technique, particularly when pulsatile flow is being studied, is that the time required to obtain a reasonably high resolution in the velocity axis precludes the use of more than one spatial dimension.

3.2.2 *Phase Mapping Methods*

In 1984, both van Dijk[24] and Bryant et al.[25] demonstrated the use of velocity phase mapping to measure flow velocity directly from the phase of the signal originating from each imaging voxel. These phase–mapping methods were made clinically more useful, partly by the use of a field echo sequence[26,27] and, most importantly, by the introduction of velocity compensated gradient waveforms.[28,29] The improvements enabled the sequence to be repeated rapidly and prevented the characteristic signal loss due to shear flow when uncompensated gradient waveforms were employed. The technique has been validated in vivo[30] and has already provided useful information in clinical and physiological flow studies.[31]

The accuracy of the techniques depends on numerous factors,[32] although validation of the phase velocity mapping method has been demonstrated both in vitro and in vivo. In vitro measurements have been made by imaging a disk of doped water (1 mM $CuSO_4$) rotating at known rate and by comparing measurements of the flow of doped water through tubes with true flows. The in vivo validation[30] showed a very good correlation between the measurement of the stroke volume of the heart carried out by the phase mapping technique and a previously validated multislice volume method.

3.2.3 *Rapid Flow Imaging Methods*

The previously described methods acquire data over a long period of time in comparison to the cardiac cycle, and rapid variations in flow cannot be followed. In order to study flow dynamics, very rapid flow imaging techniques have been developed, either by imaging only one spatial dimension or by combining a phase mapping type approach with a very fast imaging method such as echo planar.[33]

The more obvious approach in many respects is to remove the slow spatial phase-encoding process and to image in only one spatial dimension. One such method, RACE (Real time ACquisition and velocity Evaluation),[33] was developed to measure flow perpendicular to the slice. The technique can be repeated rapidly throughout the cardiac cycle in order to give near real time flow information. Figure 4 shows examples of flow images acquired using the RACE technique. One problem with this type of approach is that data are acquired from a projection through the patient; this means that any signal overlapping with the flow signal will combine and introduce errors to the flow measurement. Several strategies have been suggested for localizing the signal in order to avoid this: they include spatial presaturation, projection dephasing (applying a gradient to suppress stationary tissue), collecting a cylinder of data, and multiple oblique measurements.

For 2D spatial resolution with velocity information, a very rapid technique such as echo planar is required. The echo planar method is technically difficult and not possible on many current standard machines. However, methods have been developed to minimize the technical difficulties and Figure 5 shows echo planar velocity images of a normal neck acquired in 40 ms of two consecutive cardiac cycles using such a method. Figure 6 shows a comparison of echo planar velocity measurements with those obtained using field even echo rephasing (FEER)[28] velocity mapping. The two techniques agree well although it should be remembered that one is an average over time and the other is not. An additional problem is that the conventional echo planar sequence has a relatively high phase sensitivity to flow in the phase-encode (blip) direction, even if additional flow compensation is applied. This has been used to advantage for more qualitative flow imaging, showing flow disturbances for example. Recent studies have concentrated on reducing the phase sensitivity and increasing the image matrices; one such approach is to use spiral echo planar where the phase sensitivity is reduced because the sampling starts at the center of *k*-space.[34–36] An alternative is to combine phase mapping with subsecond FLASH techniques; here the limitation is the duration of the acquisition (>100 ms) and the relatively low spatial resolution.

Less rapid and higher resolution acquisitions can be made on standard MR imaging equipment by acquiring *k*-space in an interleaved fashion. FLASH, echo planar, or spiral imaging may be acquired in such a so-called segmented *k*-space approach. Cardiac gated images can be acquired over a period of approximately 16 cardiac cycles so that, although dynamic changes in flow cannot be monitored with this approach, images can be acquired in a breath-hold. The problems of respiration that have precluded imaging details such as the coronary arteries can thus be reduced or removed, and more reliable coronary flow measurements made feasible.[37]

4 CLINICAL OBSERVATIONS AND APPLICATIONS

As described in the previous sections, magnetic resonance imaging (MRI) offers several methods for measuring blood

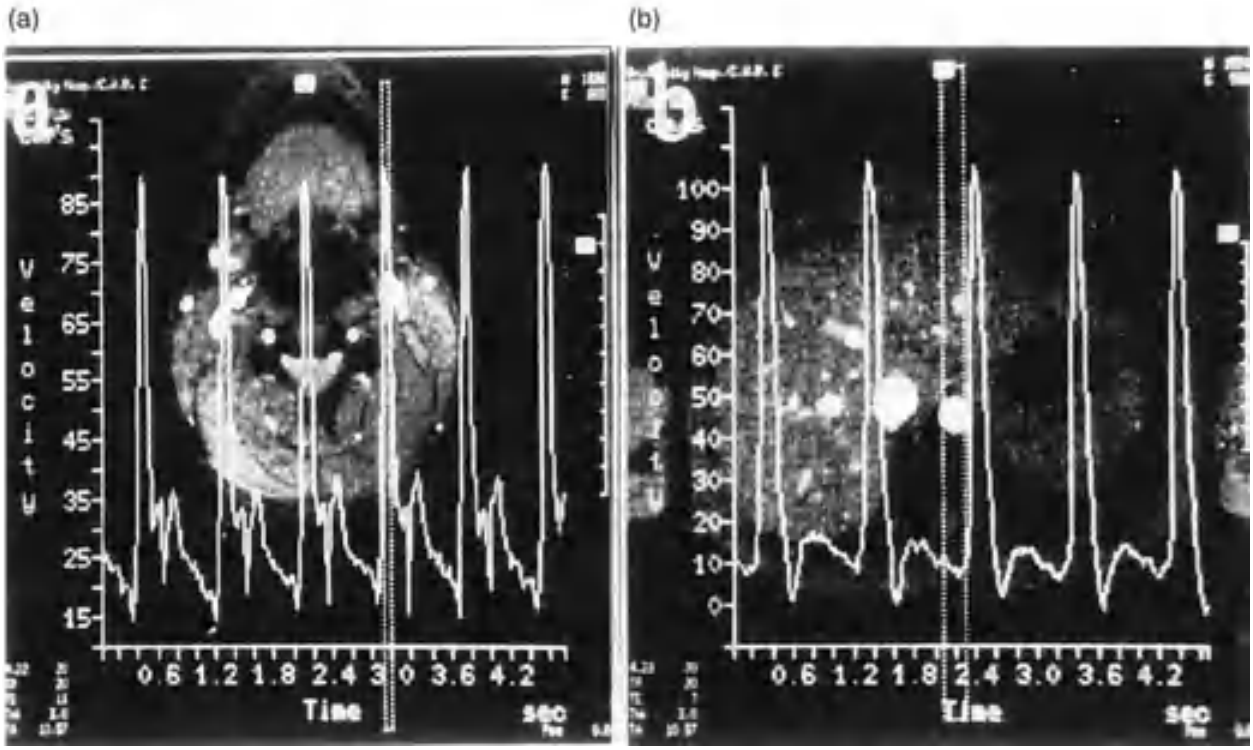

Figure 4 RACE profile through (a) five cardiac cycles in the neck and (b) four cardiac cycles in the abdomen. The carotid velocity is similar to that seen with Doppler ultrasound, never quite dropping to zero. The aortic flow is rapid and drops to zero and then returns to a fairly constant low flow rate. (Reproduced with permission of Aspen Publishers from E. M. Haacke, A. S. Smith, W. Lin, J. S. Lewin, D. A. Finelli, and J. L. Duerk, *Top. Magn. Reson. Imaging*, 1991, **3**, 34)

flow which have greatly enhanced the potential capability of MRI as a physiological tool in cardiology. As yet the majority of clinical use has been with the method of phase shift velocity mapping, and for this reason alone many of the following observations and applications will concentrate on this approach.

4.1 Thoracic Aorta

Quantitative analysis of aortic flow using MRI has been a subject of considerable interest in health and disease. Normal systolic flow in the ascending aorta is plug flow with a skewed velocity profile which has higher velocities around

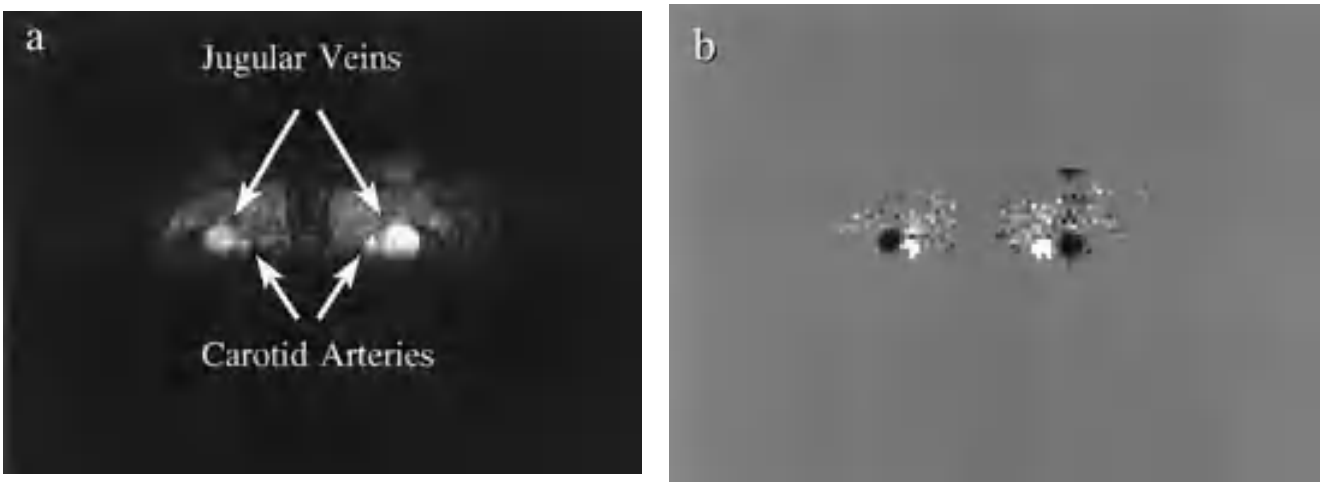

Figure 5 (a) A magnitude reconstruction of echo planar data acquired with one excitation. The selected region includes the carotid arteries (short arrows) and jugular veins (long arrows) which can be seen exhibiting high blood signal. (b) An example of a velocity phase map reconstructed from data acquired with one excitation of each of a modified and unmodified EPI flow sequence. Flow in the carotid arteries can be seen tending toward white whilst that in the jugular veins tends toward black with stationary material mid-gray. (Reproduced with permission of Academic Press from D. N. Firmin, G. L. Nayler, P. J. Kilner, and D. B. Longmore, *Magn. Reson. Med.*, 1990, **14**, 230)

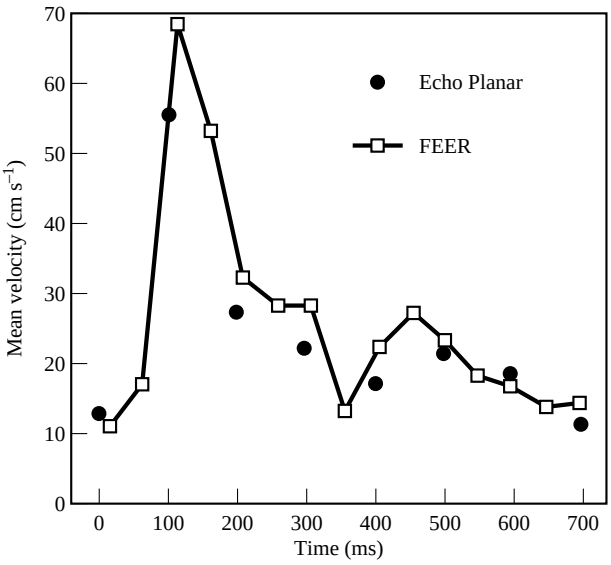

Figure 6 A comparison of the flow versus time plots for the right carotid artery of a normal volunteer obtained from echo planar velocity images and FEER velocity images. The close comparison between the two plots suggests that echo planar velocity measurements are as accurate as the FEER measurements. It should be noted, however, that the two types of flow information are somewhat different. (Reproduced with permission of Academic Press from D. N. Firmin, G. L. Nayler, P. J. Kilner, and D. B. Longmore, *Magn. Reson. Med.*, 1990, **14**, 230)

the inside of the arch. Throughout diastole the blood continues to move with simultaneous forward and reverse channels as is demonstrated in Figure 7.[38] In patients with coronary artery disease, the reverse flow channel is smaller and may enter any of the coronary sinuses.[39] In aortic valve regurgitation, the magnitude of the reverse flow is understandably increased (Figure 8 and Figure 9) and aortic or pulmonary regurgitation may be quantified from the backflow of blood in the proximal great vessels assessed by velocity mapping.[40]

4.1.1 Aortic Flow Wave Velocity

Aortic flow wave velocity can be calculated by MR velocity mapping from the delay between the leading edge or onset of the flow wave in the ascending and descending limbs of the thoracic aorta.[41,42] This parameter is closely related to aortic compliance[41] which may prove to be useful for the detection and monitoring of arterial disease.

4.1.2 Aortic Dissection

Aortic dissection is readily detected by spin echo imaging and its extent can be displayed, including the involvement of other vessels.[43] However, a thin intimal flap may not be shown in these images unless static blood in the false lumen provides natural contrast with the true lumen. If there is any doubt, then the flap will be more easily seen using a gradient echo sequence, and velocity mapping will confirm the diagnosis by demonstrating the differential flow velocities in each lumen (Figure 10).[44]

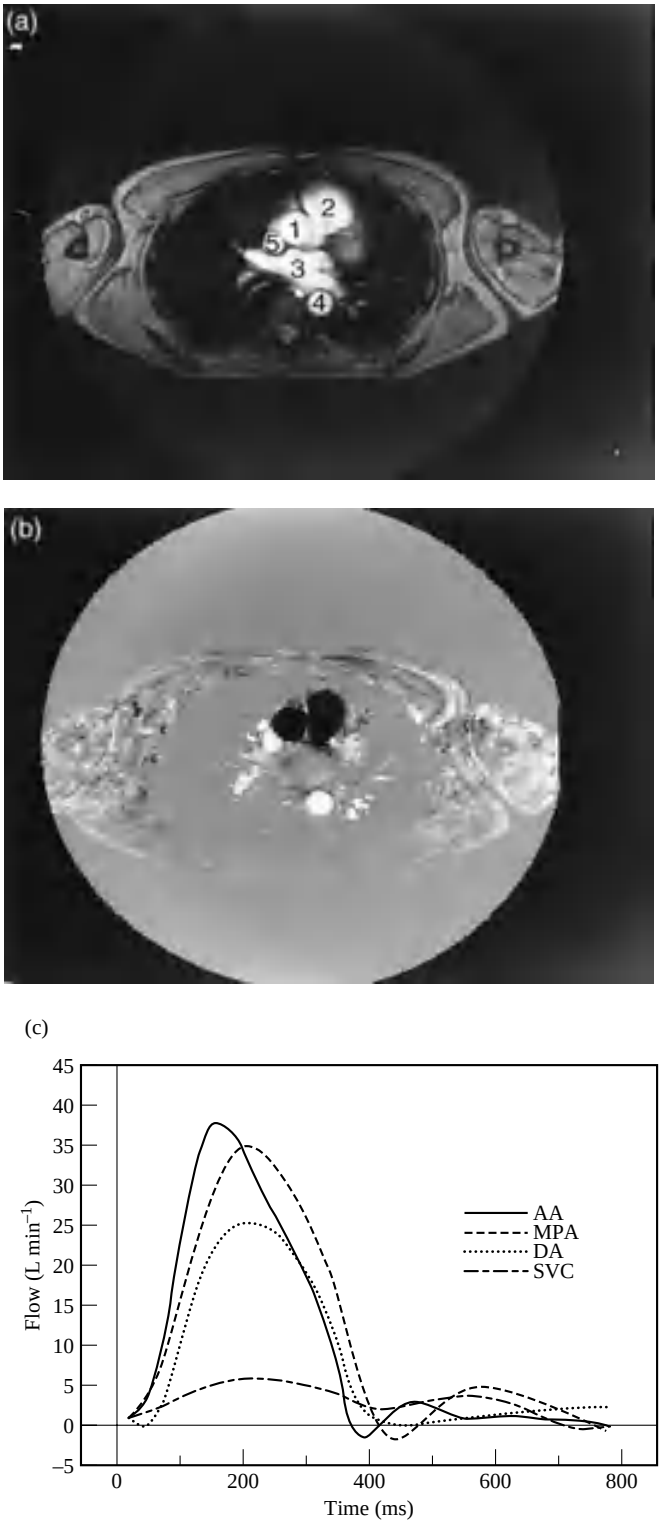

Figure 7 (a) A mid-systolic gradient echo image in a transverse plane through the great vessels of a healthy volunteer with (b) the corresponding velocity map. (c) The instantaneous flow volume curves of the ascending aorta (AA), main pulmonary artery (MPA), descending aorta (DA), and superior vena cava (SVC) calculated from the complete cine velocity map acquired in the same plane: 1, ascending aorta; 2, main pulmonary artery; 3, left atrium; 4, descending aorta; 5, superior vena cava. (Reproduced with permission of the American Heart Association from R. H. Mohiaddin and D. B. Longmore, *Circulation*, 1993, **88**, 264)

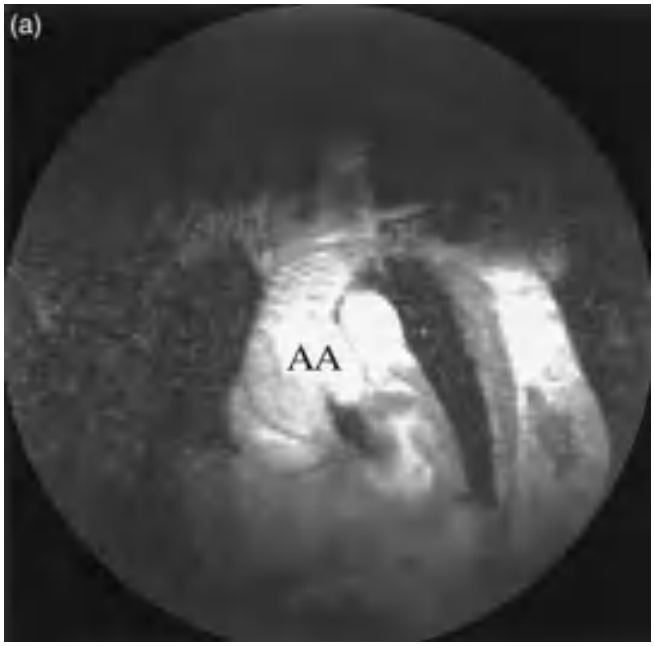

(b)

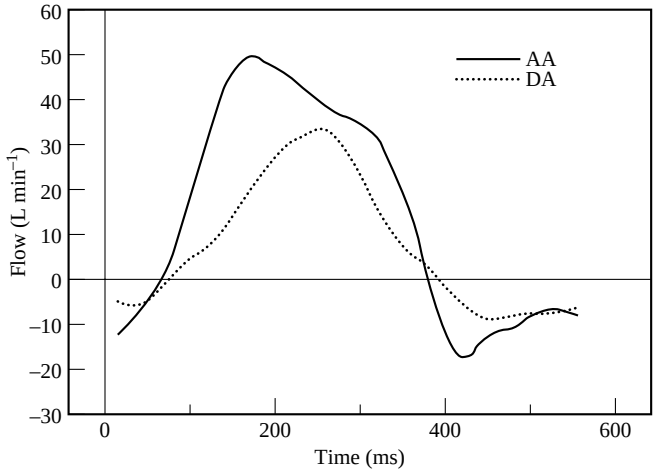

Figure 8 (a) Gradient echo images in a coronal plane acquired during ventricular diastole in a patient with Marfan's syndrome and aortic valve regurgitation. (b) Flow volume curves in the ascending aorta (AA) and descending thoracic aorta (DA) measured from the complete cine acquisition acquired in a transverse plane perpendicular to the AA and DA. Note the large retrograde net flow during diastole. (Reproduced with permission of the American Heart Association from R. H. Mohiaddin and D. B. Longmore, *Circulation*, 1993, **88**, 264)

4.2 Central Pulmonary Arteries

The retrosternal position of the central pulmonary arteries makes it difficult to assess pulmonary blood flow by Doppler echocardiography, especially in the presence of skeletal or lung abnormalities. Pulmonary flow profiles have been studied less well in patients but MR velocity mapping has confirmed an abnormally early forward systolic peak and increased reverse diastolic flow in patients with pulmonary hypertension.[45,46]

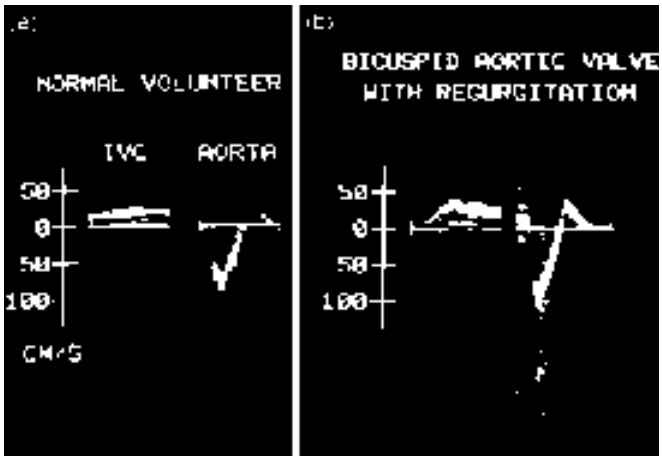

Figure 9 Fourier velocity measurements using a thin-slice excitation in the abdomen of (a) a healthy volunteer and (b) a volunteer with a bicuspid aortic valve regurgitation. (Reprinted with permission of Mosby Publishers from D. N. Firmin, C. L. Dumoulin, and R. H. Mohiaddin, in 'Magnetic Resonance Angiography, Concepts and Applications', ed. E. J. Potchen, E. M. Haacke, J. E. Siebert, and A. Gottschalk, 1993)

This abnormal pattern (Figure 11) may be caused by reflected waves from the distal vasculature which has a high impedance. Patients with a single lung transplant are unique in that the cardiac output is ejected into two pulmonary vascular beds with different characteristics, and in these patients the differential blood flow depends on the relative resistance in each lung. Velocity mapping can assess the total and differential pulmonary blood flow which may be useful for monitoring these patients (Figure 12).[47]

4.3 Caval Veins

The caval veins are relatively large, and reliable velocity maps and flow measurements can readily be obtained.[48] The normal pattern of caval flow has two forward peaks in ventricular systole and diastole (Figure 7), but this pattern is disturbed by disease. Any condition that causes impaired filling of the right ventricle reduces the diastolic peak, a pattern seen in constrictive and restrictive cardiac disease (Figure 13).[48] Tricuspid regurgitation attenuates the systolic peak of caval flow, sometimes to the extent that reverse flow occurs (Figure 14).[48] MR is commonly requested for the assessment of pericardial disease and therefore the ability to measure caval flow is an important adjunct, providing an estimate of the functional significance of the disease. In patients with obstruction of the superior vena cava, absence of flow can be confirmed and reverse flow in the azygous vein can be measured (Figure 15).[48]

4.4 Pulmonary Veins

Normal pulmonary venous flow measured by MR velocity mapping shows two peaks of forward flow, one during ventricular systole and the other in diastole.[49,50] A small back flow also occurs during atrial systole. A non-

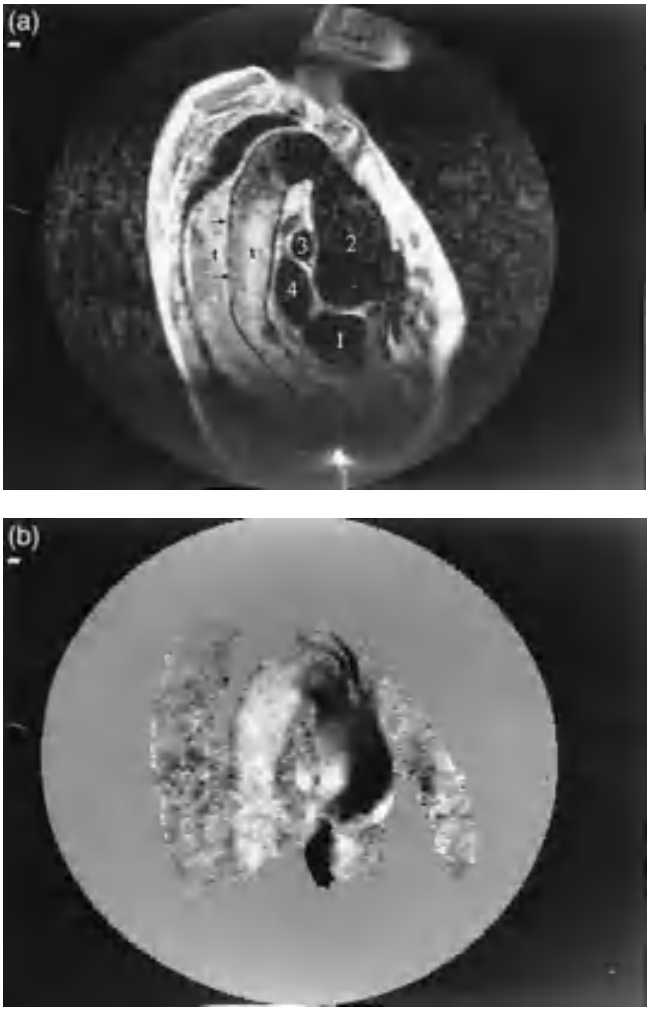

Figure 10 (a) A spin echo image in an oblique plane through the ascending aorta, aortic arch, and descending thoracic aorta showing a dilated atherosclerotic thoracic aorta with an intimal flap (arrows) separating the true lumen [t] from the thrombosed false lumen [f]. (b) The systolic velocity image shows high velocity in the true lumen and zero velocity in the false lumen: 1, Left ventricle; 2, ascending aorta; 3, right pulmonary artery; 4, left atrium. (Reproduced with permission of the American Heart Association from R. H. Mohiaddin and D. B. Longmore, *Circulation*, 1993, **88**, 264)

compliant left ventricle produces high left atrial pressure during atrial systole, causing the retrograde flow in the pulmonary veins to become larger than the flow through the mitral valve. An attenuated systolic forward flow peak has been demonstrated in patients with mitral valve regurgitation and the degree of this attenuation correlates well with the severity of regurgitation.[51]

4.5 Portal Vein

The nature of the Fourier flow imaging technique, in that it only resolves one spatial dimension, requires that some form of signal localization is applied. Figure 16 demonstrates a method of using a 2D selective rf pulse to excite a cylinder of tissue. Spatial resolution can then be obtained along the axis of the cylinder by use of the frequency-encoding gradient. The image, acquired in 9 s, displays flow in the portal vein and inferior vena cava.

4.6 Valvular Stenosis

A stenotic valve may be assessed by measuring the flow velocity in the jet of blood passing through the stenosis. In the case of a given flow, an increasingly narrow stenosis leads to an increase in the velocity of flow through the orifice. The relationship between the velocity of the jet and the difference between the pressures on either side of the stenosis can be approximated by the modified Bernoulli equation which in its simplest form is:

$$\Delta P = 4V^2 \tag{2}$$

where ΔP is the pressure drop across the stenosis in mmHg and V is the velocity in m s^{-1}.

Accurate velocity mapping of stenotic jets by MRI requires the use of very short echo times.[49,52,53] The velocity map may be through-plane with the jet passing perpendicularly through the chosen imaging plane, or in-plane when the imaging plane is chosen to encompass the length of the jet (Figure 17). In-plane imaging yields a greater number of pixels for the analysis of velocity, but if the jet is small in-plane imaging is less reliable because of partial volume effects and movement of the jet out of the imaging plane. It is preferable to acquire data in both planes.

4.7 Flow in the Coronary Arteries

The development of fast imaging techniques has improved the ability of MRI to image directly the proximal portions of both the left and right coronary arteries, but these are not comparable in quality with X-ray angiograms.[54,55] It is doubtful however that the place for MR is simply as another method of demonstrating coronary anatomy, subject to interpretation but revealing no information about flow in the vessels. The feasibility of MRI for the measurement of flow in the epicardial coronary arteries has been demonstrated (Figure 18).[37,56] Coronary artery bypass grafts can be assessed using MR velocity mapping.[57] However, flow measurement within the grafts is not always possible because of signal loss due to sternal suture and clips left after surgery.

4.8 Peripheral Arteries

Peripheral atherosclerosis produces clinical problems either by reducing blood flow or by the release of emboli from ulcerated plaques. Arterial stenosis can be detected and its severity can be assessed from measurement of changes in the velocity profile across the stenosis using MR velocity mapping (Figure 19). The flow ratio in paired vessels, like the iliac arteries, is greater than 0.85 in healthy volunteers (Figure 20) and less

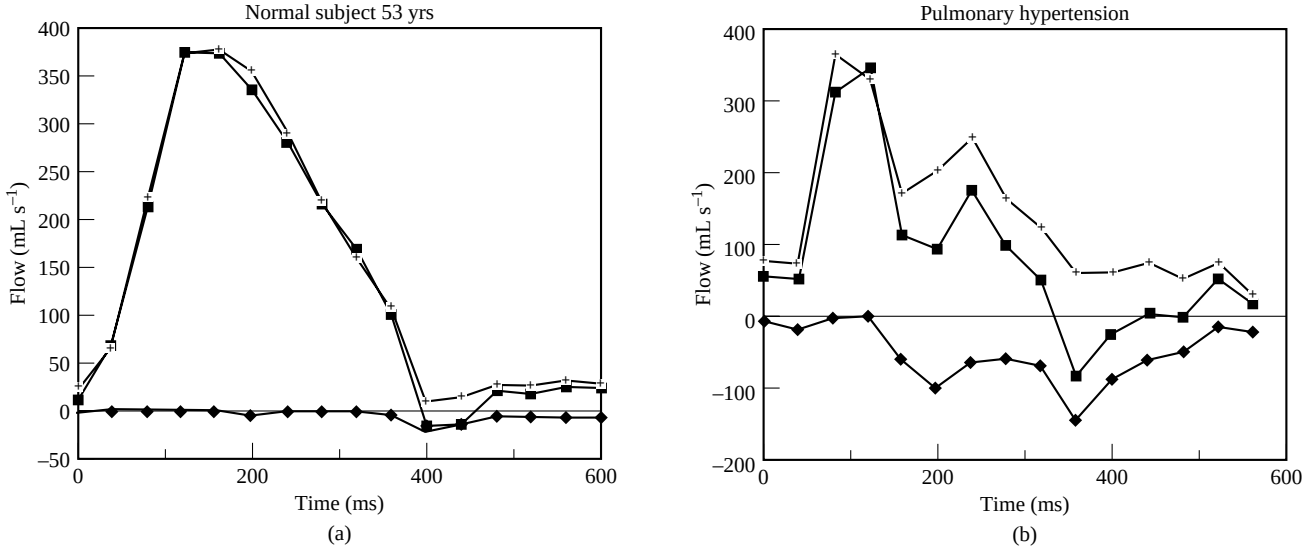

Figure 11 Main pulmonary artery flow volume curves measured by cine resonance velocity mapping (a) in a normal subject and (b) in a patient with pulmonary arterial hypertension: ■ = net flow; + = forward flow, ◆ = reverse flow. In the patient studied, the net flow, forward, and reverse flow were irregular and the reverse flow was relatively large. (Reproduced with permission of Mosby-Year Book, Inc. from H. G. Bogren, R. H. Klipstein, R. H. Mohiaddin, D. N. Firmin, S. R. Underwood, R. S. O. Rees, and D. B. Longmore, *Am. Heart J.*, 1989, **118**, 990)

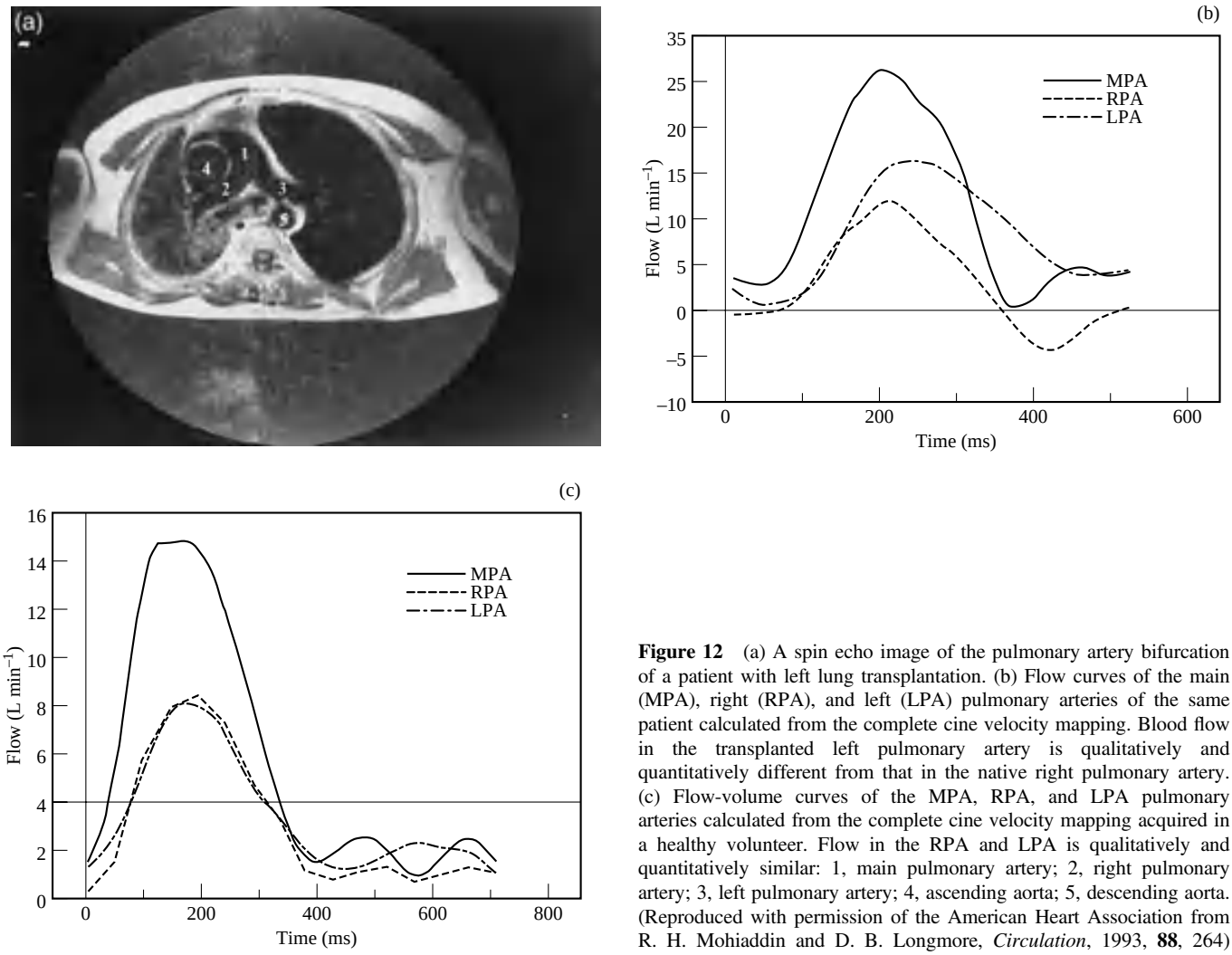

Figure 12 (a) A spin echo image of the pulmonary artery bifurcation of a patient with left lung transplantation. (b) Flow curves of the main (MPA), right (RPA), and left (LPA) pulmonary arteries of the same patient calculated from the complete cine velocity mapping. Blood flow in the transplanted left pulmonary artery is qualitatively and quantitatively different from that in the native right pulmonary artery. (c) Flow-volume curves of the MPA, RPA, and LPA pulmonary arteries calculated from the complete cine velocity mapping acquired in a healthy volunteer. Flow in the RPA and LPA is qualitatively and quantitatively similar: 1, main pulmonary artery; 2, right pulmonary artery; 3, left pulmonary artery; 4, ascending aorta; 5, descending aorta. (Reproduced with permission of the American Heart Association from R. H. Mohiaddin and D. B. Longmore, *Circulation*, 1993, **88**, 264)

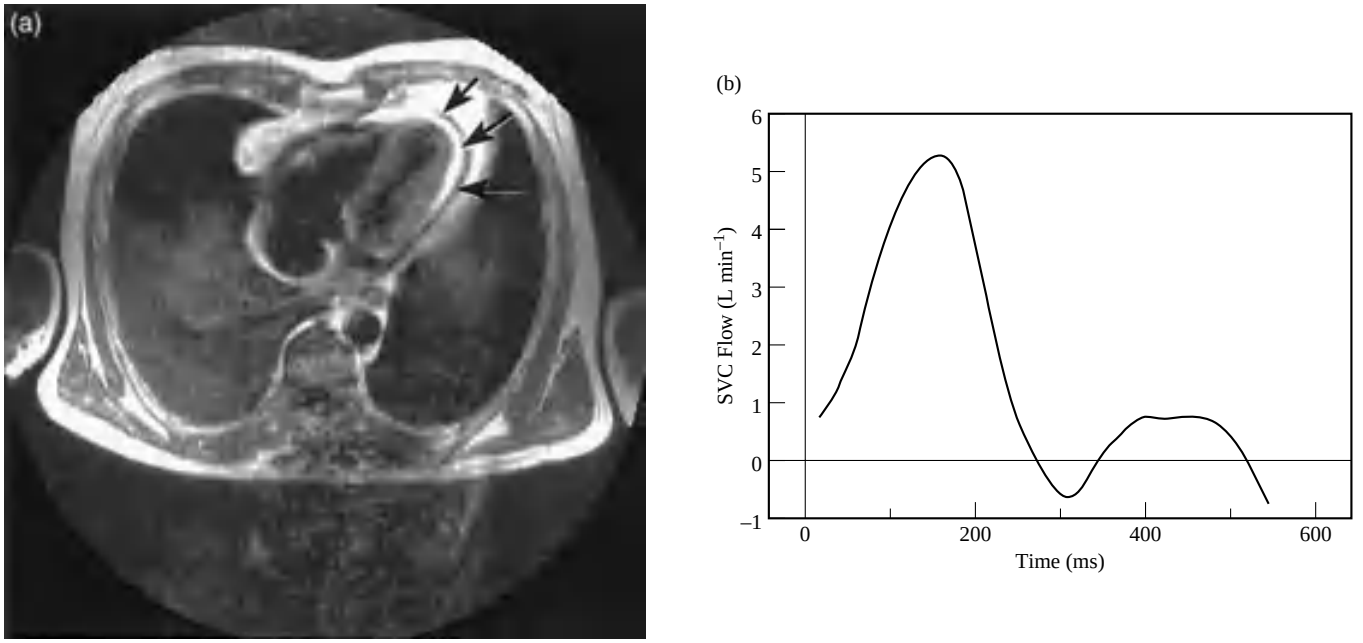

Figure 13 (a) A spin echo image in a transverse plane at mid-ventricular level in a patient with constrictive pericarditis showing pericardial thickening (arrows). (b) Superior vena caval flow curve of the previous patient measured from the complete cine velocity map acquisition throughout the cardiac cycle. The diastolic peak is attenuated which implies impaired right ventricular filling: 1, left ventricle; 2, right ventricle; 3, right atrium. (Reproduced with permission of the American Heart Association from R. H. Mohiaddin and D. B. Longmore, *Circulation*, 1993, **88**, 264)

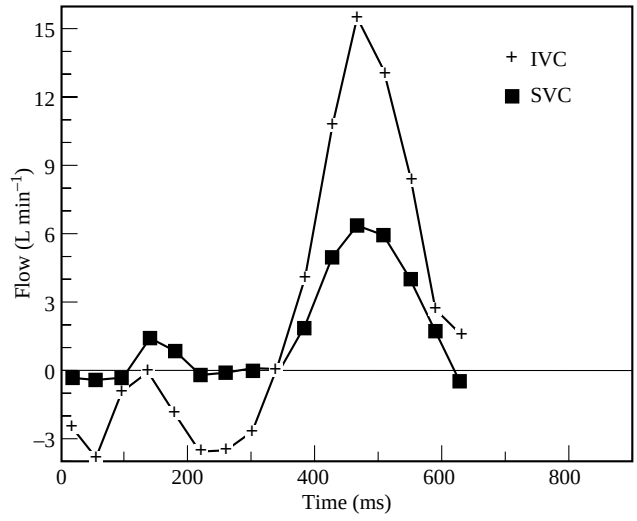

Figure 14 Superior and inferior vena caval flow curves in a patient with tricuspid valve regurgitation. The systolic peak is attenuated and there is retrograde flow in the inferior vena cava in systole. (Reproduced with permission of RSNA Publications from R. H. Mohiaddin, S. L. Wann, S. R. Underwood, D. N. Firmin, R. S. O. Rees, and D. B. Longmore, *Radiology*, 1990, **177**, 537)

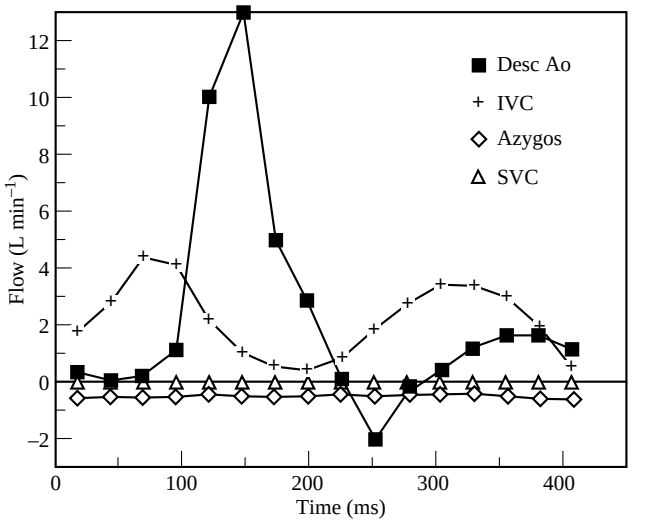

Figure 15 Flow curves in the superior and inferior venae cavae in a patient with a rhabdomyosarcoma and obstruction of the superior vena cava showing high flow with a normal pattern in the inferior vena cava, absent flow in the superior vena cava, and retrograde flow in the azygos vein. (Reproduced with permission of RSNA Publications from R. H. Mohiaddin, S. L. Wann, S. R. Underwood, D. N. Firmin, R. S. O. Rees, and D. B. Longmore, *Radiology*, 1990, **177**, 537)

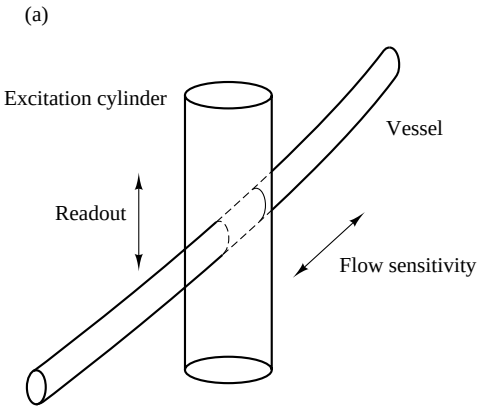

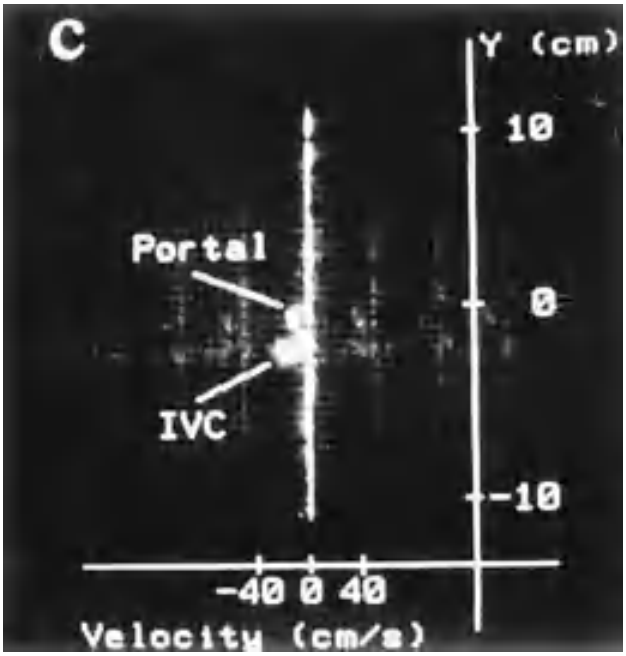

Figure 16 Images from a velocity quantification protocol. (a) Geometry of the procedure. The patient is placed in a supine position. The axis of the cylindric excitation is in the patient's anterioposterior (AP) direction. The direction of the flow-encoding gradient is oblique to the major axes and is chosen to be aligned with the portal vein. The frequency-encoding axis is chosen to be coincident with the axis of the cylindric excitation pulse. (b) Coronal pilot image (acquisition time 20s for five images). (c) Quantitative velocity image in which the horizontal axis is in velocity units and the vertical axis represents spatial displacement of the measured flow along the AP dimension. (Reprinted with permission of Mosby Publishers from D. N. Firmin, C. L. Dumoulin, and R. H. Mohiaddin, in 'Magnetic Resonance Angiography, Concepts and Applications', ed. E. J. Potchen, E. M. Haacke, J. E. Siebert and A. Gottschalk, 1993)

Figure 17 (a) A gradient echo image and (b) a corresponding velocity map in a patient with aortic stenosis. The unusual oblique plane was necessary to orient the abnormal jet direction vertically for velocity encoding. Velocity profile displayed in the center of the jet recorded a peak velocity of 3.3 m s^{-1} (44 mmHg): 1, the left ventricle; 2, ascending aorta; 3, pulmonary artery; 4, right atrium. (Reproduced with permission of the American Heart Association from R. H. Mohiaddin and D. B. Longmore, *Circulation*, 1993, **88**, 264)

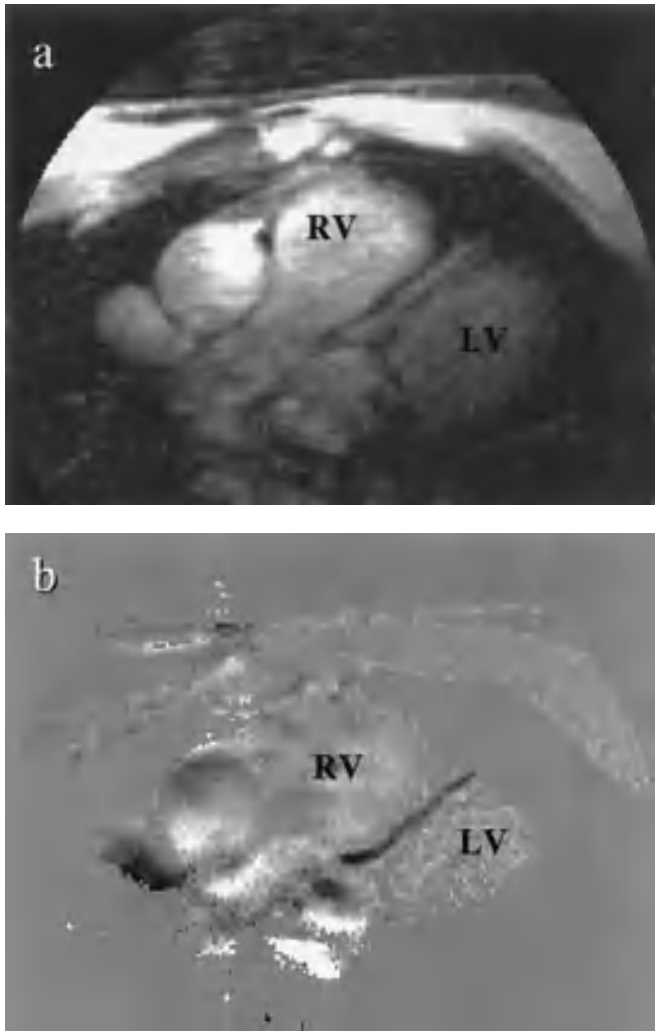

Figure 18 (a) In-plane early diastolic magnitude images and (b) velocity map of a normal left anterior descending coronary artery (LAD). The peak flow was measured at 12 cm s^{-1}. (LV, left ventricle; RV, right ventricle). (Reproduced with permission of Williams & Wilkins from J. Keegan, D. N. Firmin, P. D. Gatehouse, and D. B. Longmore, *Magn. Reson. Med*., 1994, **31**, 526)

than 0.85 in patients with tight stenosis of one iliac artery [Figure 21(a)].[58] In patients studied pre- and postangioplasty, the preangioplasty ratio was 0.31 and postangioplasty improved to 0.79 [Figure 21(b)]. This finding was supported by improvement in the walking distance and in the peripheral Doppler pressure measurement (the posterior tibial/brachial artery index was right = 1, left = 0.88 on the preangioplasty recordings and right = 1, left = 0.96 on the postangioplasty recordings).[58]

4.9 Congenital Heart Disease

MR velocity mapping has been very successful in grown-up patients with congenital heart disease.[52,59,60,61] Intra and extra cardiac shunting can be measured in a number of ways by MR velocity mapping. Flow directly through atrial and ventricular defects can be visualized [Figures 22(a) and (b)], but the best method has been to measure the pulmonary (*Qp*) to systemic (*Qs*) ratio directly from aortic and pulmonary flow [Figure 22(c)].[60] Other structures of interest for the measurement of flow are surgically created shunts and conduits, and baffle obstruction following the Mustard procedure (see section 5, *). The technique is also useful for following up patients after Fontan's operation and its modifications (see section 5, †). The hemodynamic significance of aortic coarctation or recoarctation can be assessed noninvasively by MR velocity mapping.[59] The modified Bernoulli equation can be used to calculate the pressure difference across the diseased

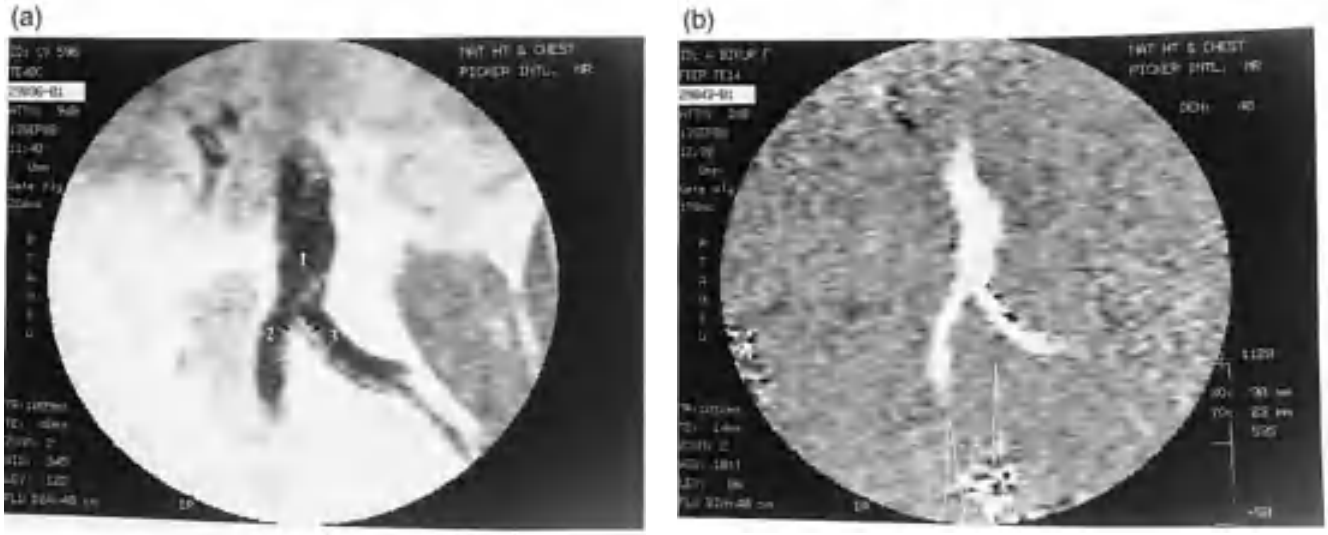

Figure 19 Multiple atheromatous plaques causing stenoses of both common iliac arteries and the origin of the left internal and external iliac arteries (arrows). (a) Spin echo image. (b) Magnetic resonance velocity map in the same plane as (a) showing velocity profiles across [1] the abdominal aorta, [2] the right, and [3] the left iliac arteries. There is increased peak velocity in both iliac arteries compared with the aorta. The peak velocity is greater in the left iliac artery which demonstrates that the stenosis on the left is greater than that on the right. (Reproduced with permission from R. H. Mohiaddin, C. Sampson, D. N. Firmin, and D. B. Longmore, *Eur. J. Vasc. Surg.*, 1991, **5**, 383)

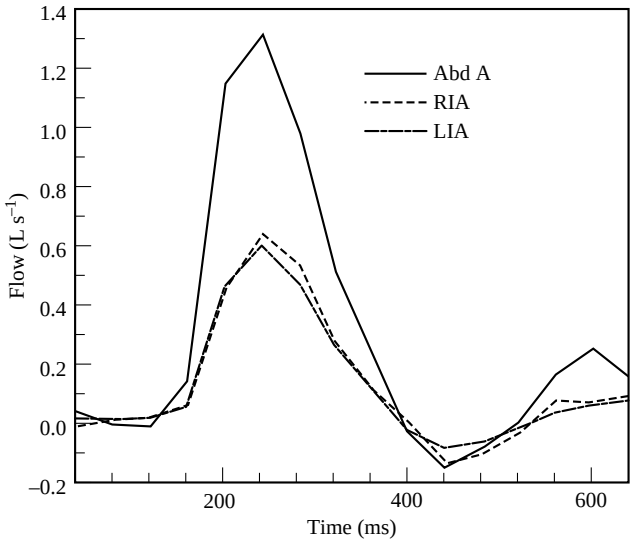

Figure 20 Flow curve in the abdominal aorta, and right and left iliac arteries of a volunteer. Flow is qualitatively similar in the three arteries and quantitatively similar in the R and L iliac arteries. (Reproduced with permission from R. H. Mohiaddin, C. Sampson, D. N. Firmin, and D. B. Longmore, *Eur. J. Vasc. Surg.*, 1991, **5**, 383)

segment from peak jet velocity in the coarctation. Abnormalities in aortic volume flow and aortic flow waveforms distal to the coarctation can also be measured and could represent an additional index for monitoring the hemodynamic significance of coarctation or recoarctation in patients (Figure 23).[59]

5 NOTES

*Mustard's operation was designed to redirect the inflow streams of blood in patients with congenital disease of transposition of the great arteries. The atrial septum is removed and a saddle-shaped baffle (Dacron or pericardial) is placed within the atria to direct the systemic venous blood through the mitral valve to the left ventricle, and pulmonary artery and pulmonary venous blood to traverse the tricuspid valve to the right ventricle and aorta.

†Fontan's operation was designed to redirect systemic venous blood in patients with tricuspid atresia to the pulmonary arterial circulation. The right atrial appendage is usually connected to the pulmonary trunk. Modifications of Fontan's operation have been used for other complex cardiac malformations.

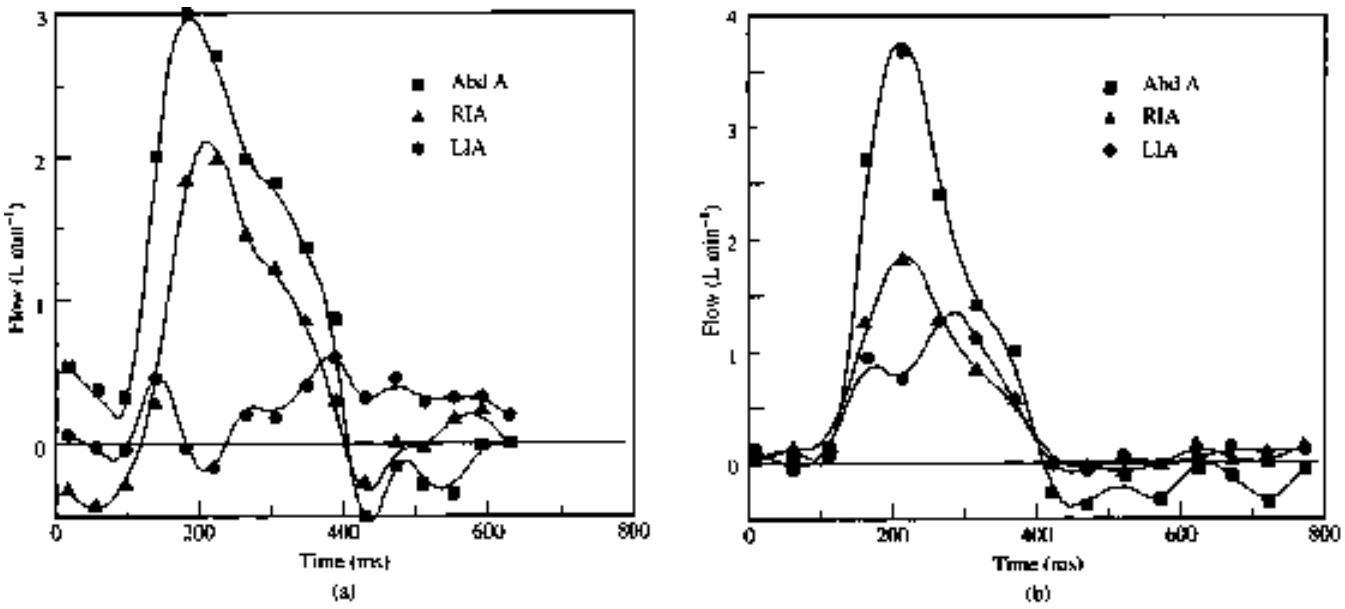

Figure 21 Flow in the abdominal aorta and R and L iliac arteries of a patient (a) before angioplasty and (b) after angioplasty. The flow in the left artery has improved and it is interesting to note that the flow in the right artery has decreased. (Reproduced with permission from R. H. Mohiaddin, C. Sampson, D. N. Firmin, and D. B. Longmore, *Eur. J. Vasc. Surg.*, 1991, **5**, 383)

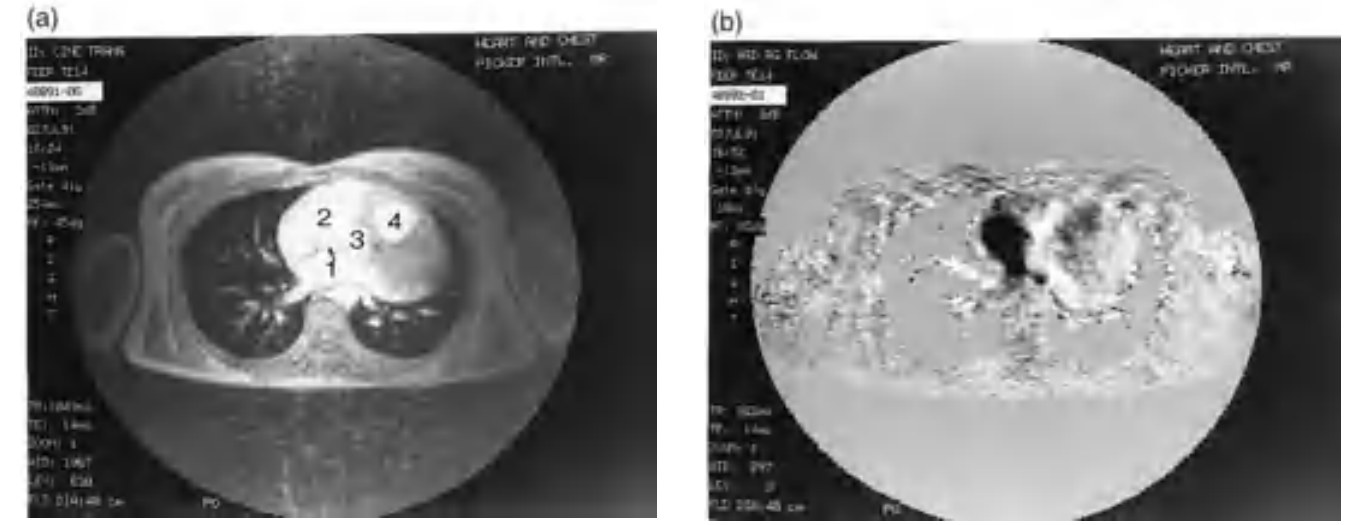

(c)

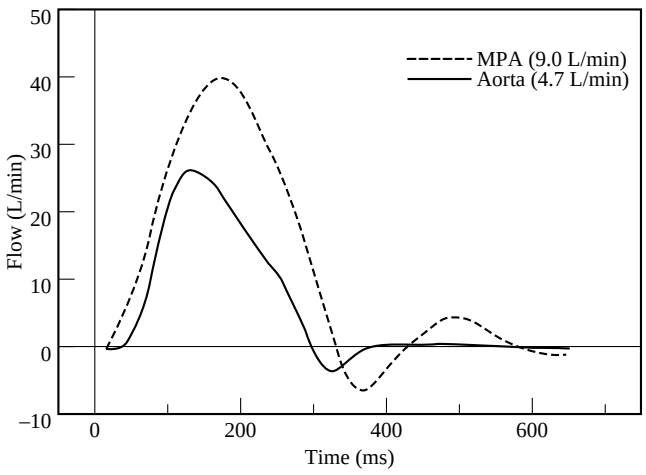

Figure 22 (a) Gradient echo image showing a large atrial septal defect (arrow). (b) Velocity map of the same slice encoded from bottom to top of the image (posterior to anterior). The left-to-right shunt through the defect is seen black. (c) Flow volume curve of the main pulmonary artery (*Qp*) and the ascending aorta (*Qs*) in the same patient (*Qp*/*Qs* ratio = 1.9): 1, left atrium; 2, right atrium; 3, aorta; 4, main pulmonary artery. (Reproduced with permission of the American Heart Association from R. H. Mohiaddin, and D. B. Longmore, *Circulation*, 1993, **88**, 264)

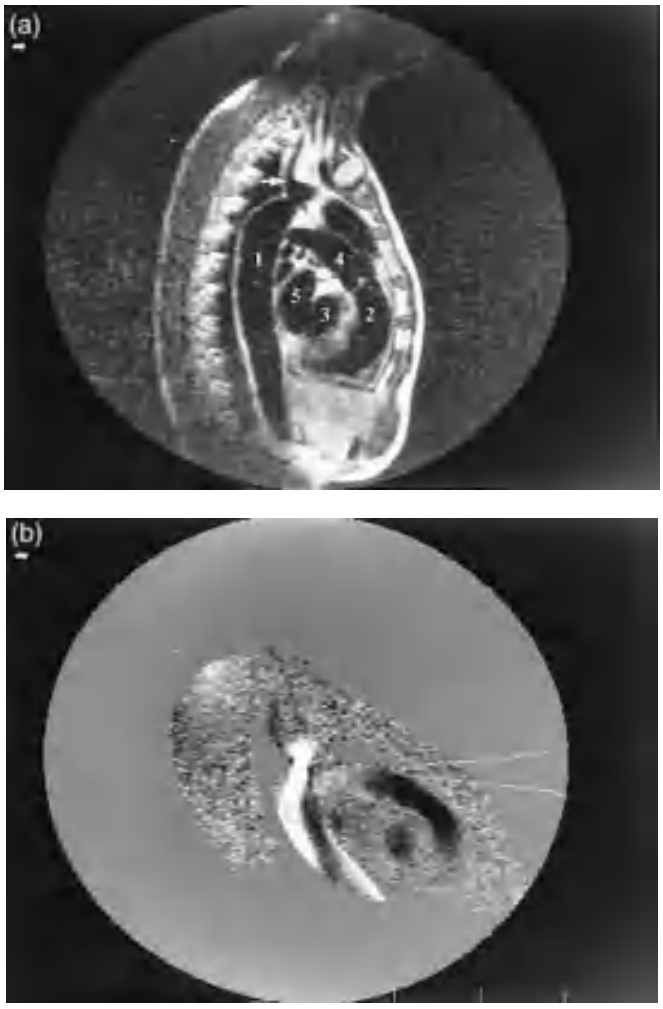

Figure 23 (a) A spin echo image (TE 40 ms) acquired in a sagittal plane in a patient with aortic coarctation (large arrow) and (b) a corresponding velocity map acquired during systole with velocity encoding displayed vertically on the image. The sagittal plane was rotated during velocity map acquisition to align the velocity-encoding direction with the jet. The velocity maps indicate zero velocity as mid-gray, caudal velocities in lighter shades of gray, and cranial velocities in darker shades of gray. Coarctation jet velocity is seen in white with a velocity profile (m s^{-1}) displayed in the center of the jet. A reverse flow is seen in black anterior to the jet: 1, descending aorta, left subclavian artery (small arrow); 2, right ventricle; 3, left ventricle; 4, pulmonary trunk; 5, left atrium. (Reproduced with permission of Elsevier Science from R. H. Mohiaddin, P. J. Kilner, R. S. O. Rees, and D. B. Longmore, *J. Am. Coll. Cardiol.*, 1993, **22**, 1515)

6 RELATED ARTICLES

Time-of-Flight Method of MRA; Whole Body Magnetic Resonance Angiography.

7 REFERENCES

1. E. L. Hahn, *Phys. Rev.*, 1950, **80**, 580.
2. G. Suryan, *Proc. Indian Acad. Sci.*, 1951, **33A**, 107.
3. J. P. Grant and C. Back, *Med. Phys.*, 1982, **9**, 188.
4. C. R. George, G. Jacobs, W. J. MacIntyre, R. J. Lorig, R. T. Go, Y. Nose, and T. F. Meaney, *Radiology*, 1984, **151**, 421.
5. W. G. Bradley, V. Waluch, K. S. Lai, E. J. Fernandez, and C. Spahter, *AJR*, 1984, **143**, 1167.
6. J. R. Singer and L. E. Crooks, *Science*, 1983, **221**, 654.
7. V. Waluch and W. G. Bradley, *J. Comput. Assist. Tomogr.*, 1984, **8**, 594.
8. G. K. Von Schulthess and C. B. Higgins, *Radiology*, 1985, **157**, 687.
9. W. H. Perman, P. R. Moran, R. A. Moran, and M. A. Bernstein, *J. Comput. Assist. Tomogr.*, 1986, **10**, 473.
10. A. N. Garroway, *J. Phys. D.*, 1974, **7**, L159.
11. K. R. Thulborn, J. C. Waterton, and G. K. Radda, *J. Magn. Reson.*, 1981, **45**, 188.
12. F. W. Wehrli, A. Shimakawa, G. T. Gullberg and J. R. MacFall, *Radiology*, 1986, **160**, 781.
13. J. Henning, M. Mueri, H. Friedburg, and P. Brunner, *J. Comput. Assist. Tomogr.*, 1987, **11**, 872.
14. D. A. Feinberg, L. E. Crooks, J. Hoenninger, M. Arakawa, and J. Watts, *Radiology*, 1984, **153**, 177.
15. K. Shimizu, T. Matsuda, T. Sakurai, A. Fujita, H. Ohara, S. Okamura, S. Hashimoto, H. Mano, C. Kawai, and M. Kiri, *Radiology*, 1986, **159**, 195.
16. L. Axel, A. Shimakawa, and J. MacFall, *Magn. Reson. Imaging*, 1986, **4**, 199.
17. T. Matsuda, K. Shimizu, T. Sakurai, A. Fujita, H. Ohara, S. Okamura, S. Hashimoto, S. Tamaki, and C. Kawai, *Radiology*, 1987, **162**, 857.
18. R. R. Edelman, H. P. Mattle, J. Kleefield, and M. S. Silver, *Radiology*, 1989, **171**, 551.
19. S. H. Izen and E. M. Haacke, *IEEE Trans. Med. Imaging*, 1990, **MI-9**, 450.
20. P. R. Moran, *Magn. Rescon. Imaging*, 1982, **1**, 197.
21. T. W. Redpath, D. G. Norris, R. A. Jones, and M. S. Hutchinson, *Phys. Med. Biol.*, 1984, **29**, 891.
22. D. A. Feinberg, L. E. Crooks, P. Sheldon, J. Hoenninger, III, J. Watts, and M. Arakawa, *Magn. Reson. Med.*, 1985, **2**, 555.
23. J. Hennig, M. Mueri, P. Brunner, and H. Friedburg, *Radiology*, 1988, **166**, 237.
24. P. van Dijk, *J. Comput. Assist. Tomogr.*, 1984, **8**, 429.
25. D. J. Bryant, J. A. Payne, D. N. Firmin, and D. B. Longmore, *J. Comput. Assist. Tomogr.*, 1984, **8**, 588.
26. I. R. Young, G. M. Bydder, and J. A. Payne, *Magn. Reson. Med.*, 1986, **3**, 175.
27. J. P. Ridgway, and M. A. Smith, *Br. J. Radiol.*, 1986, **59**, 603.
28. G. L. Nayler, D. N. Firmin, and D. B. Longmore, *J. Comput. Assist. Tomogr.*, 1986, **10**, 715.
29. E. M. Haacke, and G. W. Lenz, *AJR*, 1987, **148**, 1251.
30. D. N. Firmin, G. L. Nayler, R. H. Klipstein, S. R. Underwood, R. S. O. Rees, and D. B. Longmore, *J. Comput. Assist. Tomogr.*, 1987, **11**, 751.
31. S. R. Underwood, D. N. Firmin, R. H. Klipstein, R. S. O. Rees, and D. B. Longmore, *Br. Heart J.*, 1987, **57**, 404.
32. D. N. Firmin, G. L. Nayler, P. J. Kilner, and D. B. Longmore, *Magn. Reson. Med.*, 1990, **14**, 230.
33. D. N. Firmin, R. H. Klipstein, G. L. Hounsfield, M. P. Paley, and D. B. Longmore, *Magn. Reson. Med.*, 1989, **12**, 316.
34. C. B. Ahn, J. H. Kim, and Z. H. Cho, *Trans. Med. Imaging*, 1986, **MI-5**, 2.
35. C. H. Meyer, B. S. Hu, D. G. Nishimura, and A. Macovski, *Magn. Reson. Imaging*, 1992, **28**, 202.
36. P. D. Gatehouse, D. N. Firmin, S. Collins, and D. B. Longmore, *Magn. Reson. Med.*, 1994, **31**, 1.
37. J. Keegan, D. N. Firmin, P. D. Gatehouse, and D. B. Longmore, *Magn. Reson. Med.*, 1994, **31**, 526.

38. R. H. Klipstein, D. N. Firmin, S. R. Underwood, R. S. O. Rees, and D. B. Longmore, *Br. Heart J.*, 1987, **58**, 316.
39. H. G. Bogren, R. H. Mohiaddin, R. H. Klipstein, D. N. Firmin, S. R. Underwood, R. S. O. Rees, and D. B. Longmore, *Am. Heart J.*, 1989, **118**, 234.
40. M. C. Dulce, G. H. Mostbeck, M. O'Sullivan, M. Cheitlin, G. R. Caputo, and C. B. Higgins, *Radiology*, 1992, **185**, 235.
41. R. H. Mohiaddin, D. N. Firmin, and D. B. Longmore, *J. Appl. Physiol.*, 1993, **74**, 492.
42. C. L. Dumoulin, D. J. Doorly, and C. G. Caro, *Magn. Reson. Med.*, 1993, **29**, 44.
43. C. A. Nienaber, R. P. Spielmann, Y. von Kodolitsch, V. Siglow, A. Piepho, T. Jaup, V. Nicolas, P. Weber, H. Triebel, and W. Bleifeld, *Circulation*, 1992, **85**, 434.
44. H. G. Bogren, S. R. Underwood, D. N. Firmin, R. H. Mohiaddin, R. H. Klipstein, R. S. O. Rees, and D. B. Longmore, *Br. J. Radiol.*, 1988, **61**, 456.
45. H. G. Bogren, R. H. Klipstein, R. H. Mohiaddin, D. N. Firmin, S. R. Underwood, R. S. O. Rees, and D. B. Longmore, *Am. Heart J.*, 1989, **118**, 990.
46. C. Kondo, G. R. Caputo, T. Masui, E. Foster, M. O'Sullivan, M. S. Stulbag, J. Golden, K. Catterjee, and C. B. Higgins, *Radiology*, 1992, **183**, 751.
47. R. H. Mohiaddin, R. Paz, S. Theodoropulus, D. N. Firmin, D. B. Longmore, and M. H. Yacoub, *J. Thorac. Cardiovasc. Surg.*, 1991, **101**, 1016.
48. R. H. Mohiaddin, S. L. Wann, S. R. Underwood, D. N. Firmin, R. S. O. Rees, and D. B. Longmore, *Radiology*, 1990, **177**, 537.
49. R. H. Mohiaddin, M. Amanuma, P. J. Kilner, D. J. Pennell, C. C. Manzara, and D. B. Longmore, *J. Comput. Assist. Tomogr.*, 1991, **15**, 237.
50. R. H. Mohiaddin, M. Amanuma, and D. B. Longmore, *Am. J. Noninvasive Cardiol.*, 1992, **6**, 13.
51. A. van Rossum, K. H. Sprenger, and F. C. Peels, *Eur. Heart J.*, 1991, **12**, 117.
52. P. J. Kilner, D. N. Firmin, R. S. O. Rees, J. E. Martinez, D. J. Pennell, R. H. Mohiaddin, S. R. Underwood, and D. B. Longmore, *Radiology*, 1991, **178**, 229.
53. P. J. Kilner, C. C. Manzara, R. H. Mohiaddin, P. J. Pennell, M. G. St John Sutton, D. N. Firmin, and D. B. Longmore, *Circulation*, 1993, **87**, 1239.
54. R. R. Edelman, W. J. Manning, D. Burstein, and S. Paulin, *Radiology*, 1991, **181**, 641.
55. S. J. Wang, D. G. Nishimura, and A. Macovski, *Magn. Reson. Med.*, 1992, **23**, 109.
56. R. R. Edelman, W. J. Manning, E. Gervino, and W. Li, *J. Magn. Reson. Imaging*, 1993, **3**, 699.
57. J. F. Debatin, A. Strong, H. D. Sostman, R. Negro-Vilar, S. S. Paine, J. M. Douglas, and N. J. Pelc, *J. Magn. Reson. Imag.*, 1993, **3**, 443.
58. R. H. Mohiaddin, C. Sampson, D. N. Firmin, and D. B. Longmore, *Eur. J. Vasc. Surg.*, 1991, **5**, 383.
59. R. H. Mohiaddin, P. J. Kilner, R. S. O. Rees, and D. B. Longmore, *J. Am. Coll. Cardiol.*, 1993, **22**, 1515.
60. R. S. O. Rees, D. N. Firmin, R. H. Mohiaddin, S. R. Underwood, and D. B. Longmore, *Am. J. Cardiol.*, 1989, **64**, 953.
61. J. E. Martinez, R. H. Mohiaddin, P. J. Kilner, K. Khaw, R. S. O. Rees, J. Somerville, and D. B. Longmore, *J. Am. Coll. Cardiol.*, 1992, **20**, 338.

Biographical Sketches

David N. Firmin. *b* 1955. B.Sc., 1978, M.Phil., 1982, Ph.D., 1989, Magnetic Resonance Imaging of Blood Flow, University of London. Introduced to NMR By D. B. Longmore, National Heart and Chest Hospital, London. Senior Lecturer, National Heart and Lung Institute, University of London, 1982–present. Approx. 210 publications. Research specialties: rapid, flow, and cardiovascular imaging by use of magnetic resonance.

Raad H. Mohiaddin. *b* 1957. After graduation with M.B., Ch.B., 1981, Mosul-Iraq, received training in cardiology, M.Sc., 1985, Ph.D., 1994, Structural and Functional Evaluation of Atherosclerotic Vascular Disease by Magnetic Resonance Imaging, University of London, London. Introduced to NMR by D. B. Longmore, National Heart and Chest Hospital, London. Approx. 200 publications. Research specialties: magnetic resonance imaging as applied to congenital and acquired cardiovascular diseases.

Breast MRI

Sylvia H. Heywang-Köbrunner
University of Halle, Germany

Hans Oellinger
Universitäts-Klinikum Rudolf-Virchow, Freie Universität Berlin, Germany

1 INTRODUCTION

On the basis of the high soft tissue contrast of MRI and based on suspected differences of T_1 and T_2 values between benign and malignant breast tissues, MRI was initially considered to be a particularly promising tool for breast imaging. Unfortunately, the expected tissue characterization by MRI could not be demonstrated despite intense further research; signal intensities on various pulse sequences, and in vivo calculated T_1 and T_2 values, varied significantly in both benign and malignant tissues. Both MR parameters and signal intensities seemed to correlate well with the water/content, cells or fibrosis within the corresponding tissues, but did not allow a reliable distinction between benign and malignant tissues. This has proven true until today, even after the application of more sophisticated evaluation such as computer-aided evaluation methods.[1–5] For this reason, plain MRI (= MRI without contrast agent) does not play a role in the detection and diagnosis of breast malignancy nowadays. The disappointing results mentioned above, however, initiated work concerning the use of contrast agents for MR of the breast and the very encouraging results caused its further exploration.[6–8] Today contrast-enhanced MRI of the breast is developing as an important additional tool for breast diagnostics, providing new information which is different from that of conventional imaging and is thus most valuable in certain problem areas of conventional breast diagnostics.[9–28]

In one special area, however, both tomographic imaging and the high soft tissue contrast of plain MRI has proved helpful; this special area concerns the evaluation of the integrity of silicone implants.[29–33] This chapter will provide an overview of these two major applications of breast MRI; plain MRI for the evaluation of implant integrity and contrast-enhanced (CE) MRI of the breast.

2 PLAIN MRI — DETECTION AND DIAGNOSIS OF IMPLANT FAILURE

Based on the latest knowledge concerning potential hazards caused by leaking or ruptured implants and free silicone, the detection of possible implant failure has become an important new demand. The capabilities of conventional methods such as mammography and ultrasound for detecting extra- and particularly intracapsular leakage are very limited. Hence the use of MRI in this field has been evaluated.

At present, various combinations of pulse sequences are still being tested. These use differences of T_1, of T_2, and of the reasonance frequency of silicon compared with the surrounding fat, fibrosis, or glandular tissue.[29–33] In general, a combination of at least three pulse sequences is recommended. These should, for example, include a T_1-weighted pulse sequence with and without fat suppression, and one with silicone or water suppression as well as a fast high-resolution T_2-weighted pulse sequence. The suppression of fat, water, or silicone can be obtained by spectrally selective presaturation pulses or by signal nulling with IR sequences. In order to cut potential ruptures orthogonally, these pulse sequences are usually applied in different planes (coronal, transverse, and/or sagittal). For the detection of discrete ruptures, at least one of the pulse sequences should allow slice thicknesses below 2–3 mm. For the other pulse sequences, a slice thickness below 5 mm appears optimal.

The implant itself is generally covered by a fine shell, which in intact implants can usually not be recognized since it is directly attached to the capsule of fibrous tissue which surrounds the implant. When the shell of the implant is ruptured, silicone can leak. Depending on whether the leakage of silicone is confined to the area surrounded by the fibrous capsule, or whether the leak is beyond the fibrous capsule (about 5% of the ruptures), the rupture is called intra– or extracapsular.

The following signs indicating a rupture have so far been described (Figure 1):

1. Linguine sign: The shell is ruptured, silicone remains predominantly within the fibrous capsule, and the collapsed shell floats within the silicone. The tomographic slices show wavy dark lines within the silicone, which represent the collapsed implant shell floating within the silicone. The wavy lines are called ‘linguine’.

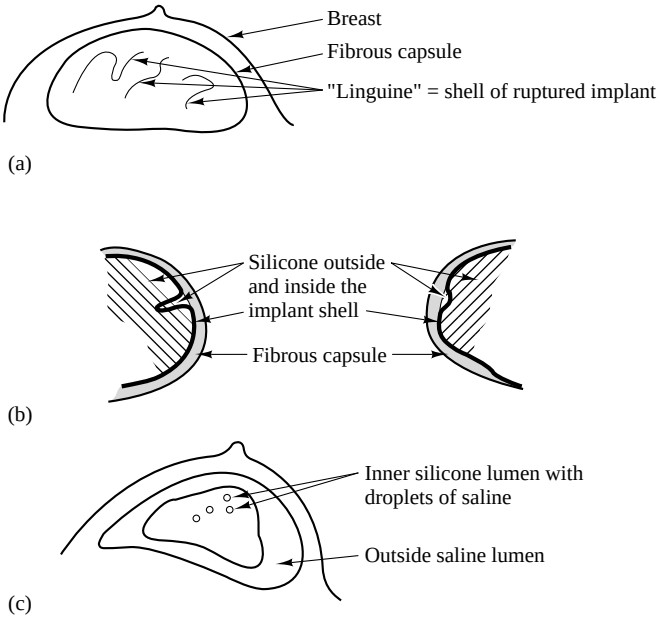

Figure 1 Morphological MR signs of implant rupture: (a) ‘linguine sign’; (b) ‘keyhole sign’ or ‘reverse c-sign’ (right), and (c) ‘droplet sign’ in double lumen implant

2. When silicone enters between the shell and the fibrous capsule, silicone becomes visible outside the shell. Depending on the shape of the shell in this area, this sign is called 'c-sign' or 'keyhole sign'.
3. In double lumen implants, saline may enter the silicone lumen of the implant. Since saline and silicone gel do not mix, small droplets become visible; this sign is called the 'droplet sign' or the 'salad oil' sign.
4. Finally small droplets of silicone can be visualized outside the capsule. This sign indicates extracapsular rupture.

To date, with careful examination techniques using several pulse sequences and thin slices, very good sensitivities (above 80%) and specificities (above 90%) have been reported.[29–33]

3 CONTRAST-ENHANCED MRI OF THE BREAST

Based on the unsatisfying results of plain MRI mentioned above, CE MRI of the female breast has been performed and investigated by us since 1985.[6–8,16,17,21,22,28] Other workers have followed and contributed significantly.[9–15,18–20,23–27] Today, contrast-enhanced MRI is gaining increasing importance as an additional tool for breast diagnostics.

3.1 Principles of Contrast-Enhanced MRI of the Breast

The complete breast is examined with thin and contiguous slices before and after the i.v. application of Gd–DTPA. By comparison of the corresponding pre- and postcontrast slices, tissue enhancement can be detected or excluded.

The fact that the large majority, possibly all, invasive breast malignancies do enhance is supported by the following fundamental data:[34–40] (i) an increased number and size of vessels has also been encountered histologically in and around breast malignancies, as studies with special vascular staining show; (ii) according to in vivo animal experiments, vessel sprouting seems to be a prerequisite for tumor growth beyond a size of about 2–3 mm; (iii) tumor growth seems to depend on both increased vascularity and increased vascular permeability; (iv) both increased vascularity and vascular permeability are induced by socalled angiogenesis and permeability factors, numbers of which have already been identified; (v) cells from both invasive and numerous in situ carcinomas were able to induce vascular sprouting when transplanted on an animal cornea, while cells from normal breast tissue could not induce such changes; (vi) it has also been reported that cells from several benign entities were equally well able to produce identical or similar angiogenesis and permeability factors leading to similar vascular changes as in malignancy. Benign changes with similar capabilities included some proliferative dysplasias, healing wounds, and benign tumors.

The above-mentioned observations support may of the MR findings. They may also serve to explain both the reported excellent sensitivity and the limited specificity of CE MRI.

3.2 Techniques

For prognostic reasons, it is generally agreed that breast imaging techniques should be able to image carcinomas of 5 mm and above reliably. Furthermore, it is also desirable to detect in situ carcinomas which usually grow within the ducts where they may extend within areas of very variable size. The ducts themselves, however, rarely exceed 1–3 mm in diameter and may be surrounded by uninvolved nonenhancing tissue. Hence with a tomographic imaging modality such as MRI it is important to minimize slice thickness so as to improve resolution and contrast.

In order to achieve sufficient signal-to-noise ratio, a dedicated single or double breast coil has to be used. Cardiac motion artifacts also need to be eliminated. At present, the best way to achieve the latter is by switching phase and frequency encoding gradients, so that the artifacts cross the axillas instead of the breast. An alternative is the use of coronal slices, where most of the artifacts neither cross the breast nor the axillas. (The use of local presaturation is not useful, since generally larger areas are extinguished than would be disturbed by artifacts. In our experience flow compensation increases echo time without sufficient effect on artifact elimination.)

In order to obtain sufficiently small slices without gaps, 3D imaging is strongly recommended. In this way it is possible, for example, to image the breast with 32 transverse slices of 4 mm slice thickness within slightly more than 1 min. By using a rectangular field of view and coronal slices, either the imaging time can be further reduced by a factor of two, or 64 slices of 2-mm slice thickness are possible within the same imaging time. Thus with present 3D techniques both high temporal resolution or high spatial resolution are possible.

However, when choosing between high spatial and high temporal resolution it should be remembered that with a 5-mm slice thickness in the worst case a 5-mm lesion may only be half contained within two neighboring slices. This means that only half of the signal increase can be measured in each neighboring slice. Hence 2-mm or thinner slices will probably allow better results, particularly with regard to the detection of intraductal enhancement. The optimum temporal resolution is still controversial.[9–17]

As far as the choice of pulse sequences is concerned, the highest sensitivity to Gd–DTPA and hence the best contrast of enhancing lesions can be achieved with 3D gradient echo sequences such as FLASH or spoiled GRASS or with some fat saturation techniques like RODEO or spoiled GRASS with fat saturation.[23–25] Due to their low sensitivity to Gd–DTPA, SE sequences can no longer be recommended.

Since enhancement might be confused with a fat lobule on the postcontrast image alone, elimination of the fat signal has been suggested as a means of improving the detectability of enhancing lesions. Elimination of the fat signal can be achieved in two different ways.

1. On T_1-weighted fat suppression sequences, ideally only enhancing tissues display high signal intensity while dysplasia and suppressed fat exhibit low or no signal intensity. The disadvantage of fat suppression techniques is that they are more sensitive to magnetic field inhomogeneities. Within such inhomogeneities, which may be caused by the patient or the breast coil, enhancement might be underestimated or missed. Thus, greater technical prerequisites need to be fulfilled, i.e. more experience and very careful quality control are necessary.

2. Since fat does not enhance, like all other nonenhancing tissues it is ideally eliminated on subtraction images. Software has now been developed which allows routine subtraction of

all corresponding pre- and postcontrast slices (2 × 64 slices) within about 1 min. The major disadvantage which has been ascribed to this technique relates to problems which occur when the patient moves. In our experience, this problem occurs with less than 5–10% of all patients with currently available very short imaging times. Motion and its inherent problems are at least readily recognized with this technique

Three-dimensional MIP reconstruction is possible for both fat suppressed and subtracted images. It has been suggested as a means of improving the distinction of enhancing vessels from enhancing ducts.[27]

As far as optimum dosage is concerned, to date only one dose comparison study has been published.[28] In this study, we demonstrated that significantly better results were obtained with FLASH-3D using the higher dosage of 0.16 mmol of Gd–DTPA per kg as compared with the widely used lower dosage of 0.1 mmol of Gd–DTPA per kg. In fact, three out of 54 carcinomatous foci would have been overlooked with the lower dosage. Histologically, these three foci were all smaller than the applied slice thickness of 4 mm.

3.3 Results

The results of CE MRI of the breast are based worldwide on the examination of over 5000 patients.[6–28] Despite still remaining differences in technique and image interpretation, the following results have been confirmed: (a) the great majority of invasive carcinomas are enhanced (see Figure 2); (b) no significant enhancement is usually seen in normal breast tissue, in nonproliferative dysplasia, sclerosed benign tumors, old scarring, and cysts; and (c) variable enhancement, which might cause false positive calls, has been encountered in some proliferative dysplasias, in nonsclerosed benign tumors, and in inflammatory changes.

In over 700 biopsy-proven tissues which we have examined with FLASH-3D, about 75% of the dysplasias enhanced only a little and it was possible to define a threshold so that all carcinomas enhanced more than by this threshold.[16,17]

We also evaluated the shape of enhancement and roughly estimated the speed of enhancement in these 700 tissues. In a similar manner to mammography, we found that an irregular outline of an enhancing lesion was indeed highly suggestive of malignancy, but neither diffuse nor well-circumscribed enhancement could reliably exclude malignancy (for example, 16% of the diffusely enhancing tissues and 21% of our postoperatively examined well circumscribed lesions, in fact, turned out to be malignant). When the speed of enhancement was estimated from two postcontrast studies (first measurement: 1–5 min post injection; second measurement 6–11 min post injection), fast enhancement was highly suggestive of malignancy but unfortunately delayed enhancement could not rule out malignancy reliably. This result has been confirmed by another separate dynamic study in 79 patients, where selected slices were imaged every 30 s after i.v. injection of Gd–DTPA.[7,16,17]

As to the potential of dynamic contrast studies, controversial results are still being discussed. While Kaiser[9,10] reports a sensitivity and specificity of 97% with dynamic contrast-enhanced MRI, other authors have not been able to reproduce these results, reporting both fast enhancing benign tissues and (what is much more important) slowly enhancing malignancies.[12–17] In our experience the use of a slow enhancement speed as a criterion of benignity is comparable to increasing the threshold above which enhancement is considered to be possibly malignant, i.e., specificity can be improved at the cost of sensitivity.

Since the development of very fast pulse sequences such as Turbo-FLASH or echo planar imaging, it has become possible to image the first pass of a contrast agent within a tissue. Initial results with Turbo-FLASH have been promising.[26] The optimum use of this additional information needs to be carefully determined, in view of its effect on both sensitivity and specificity. When the results of various authors are compared[6–28] (Table 1), excellent sensitivity values overall have been reported for CE MRI. Indeed, the sensitivity exceeds that of conventional imaging. Differences can be explained by different techniques (sometimes thick slices with gaps, the choice of pulse sequence, the dosage of Gd–DTPA), by different guidelines for interpretation, and by different patient selection. On comparison with conventional imaging alone, the sensitivity was however, improved in general. This diagnostic gain was, however, most prominent within mammographically dense and/or distorted tissue, while in fatty breasts and in cases with microcalcifications little or no diagnostic gain was achieved.

Table 1 Sensitivities and Specificities of Enhanced MRI, as Reported in the Literature

Author	Year	Sensitivity of MRI (%)	Specificity of MRI (%)	Sensitivity of Conv.[a] (%)	Specificity of Conv.[a] (%)
Allgayer (1)[c]	1991	90	40	ni	ni
Fischer (2)	1992	95	89	ni	ni
Gilles (3)	1993	93.3	63.1	ni	ni
Harms (3)	1993	94	37	ni	ni
Heywang-Köbrunner (1)	1993	98.6[b]	65.0	60	45
Heywang-Köbrunner (3)	1993	99.5[b]	28.0	82	18
Kaiser (1)	1992	97[b]	97	ni	ni
Lewis-Jones (1)	1991	100	91	100	60
Oellinger (4)	1993	88	80	83	75

[a]Conv. = Sensitivity/Specificity of conventional imaging.
[b]Sensitivity/Specificity based on MR and conventional imaging.
[c](1), problem cases; (2) retrospective study; (3) preoperative patients; (4) evaluation of multicentricity.
ni = not indicated.

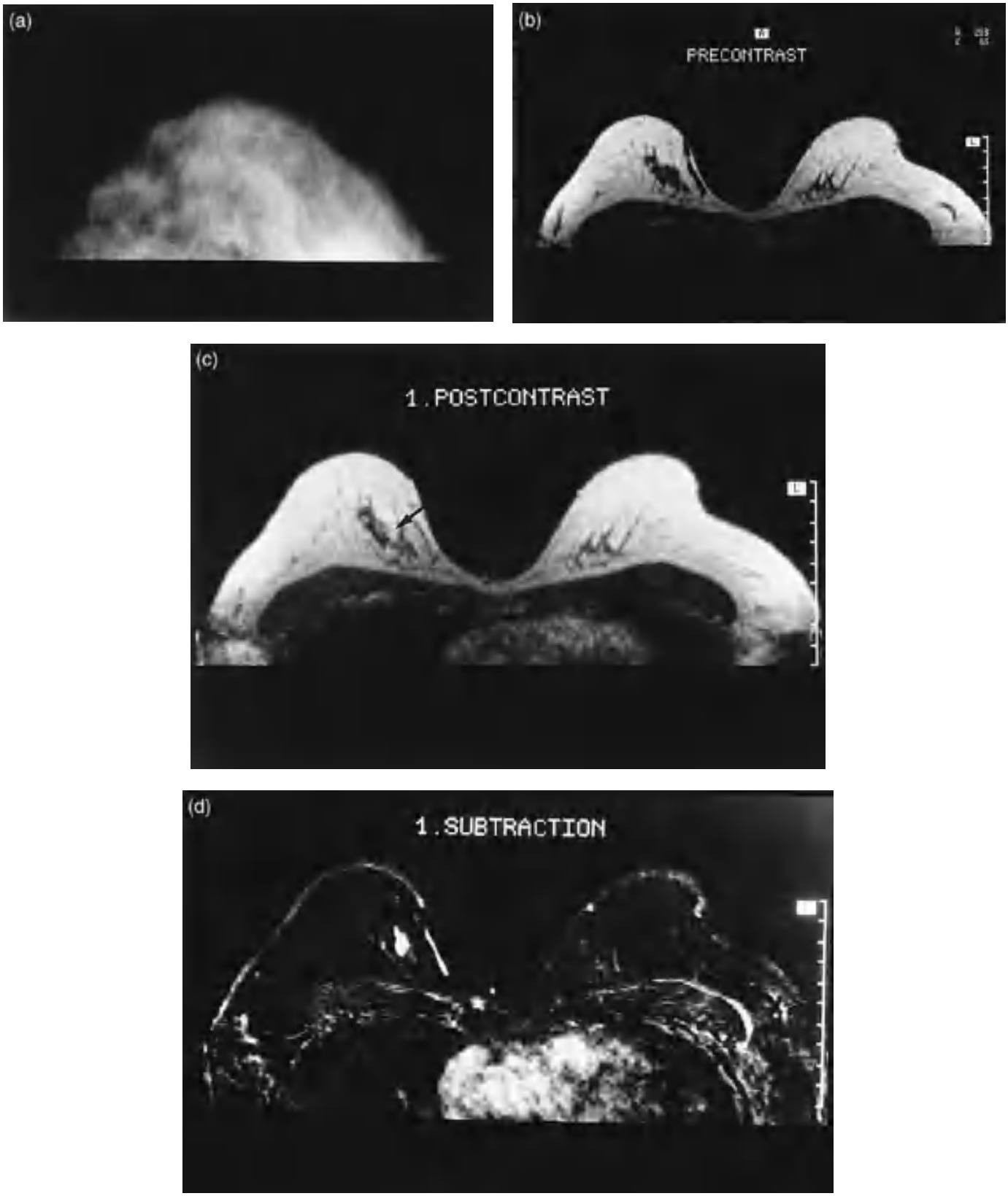

Figure 2 Mammography versus MRI in cases of very dense breasts. (a) Mammography of a 43 year old patient, cranio-caudal view. Very dense right breast, no radiological evidence of malignancy. (b) MR image before injection of the contrast agent; anatomical region of the upper quadrants. Basically fatty tissue and small areas of parenchyma in the upper inner quadrants of both sides. (c) MR image after application of the contrast agent gadolinium–DTPA with moderately strong signal intensity rise in the parenchyma of the inner quadrant of the patient's right breast (see arrow). Same position as in the precontrast MR image shown in (b). (d) The use of the subtraction method (postcontrast minus precontrast) allows the postcontrast enhancement of carcinomas to be seen much better. This method is especially useful in the case of small carcinomas. The histology revealed an invasive ductal carcinoma

With respect to microcalcifications and in situ carcinomas, the following may be stated. Mostly due to patient preselection, experience concerning the capabilities of MRI in this field is still limited to date. Some authors reported misses. Although our in situ carcinomas did enhance, some did so diffusely and many slowly. Thus, detection of in situ carcinomas and their differentiation from proliferative dysplasias is certainly also a question of threshold and interpretation. Those 50–60% of in situ carcinomas which contain microcalcifications are already excellently visualized by mammography. Even though improvement of the mammographic specificity in this field is still desirable, we do not recommend MRI in this case for the following reasons:

1. It is not known as yet whether all in situ carcinomas are sufficiently vascularized to be detectable by contrast-enhanced MRI.
2. Further research must show whether in situ carcinomas can be included in the enhancement thresholds of MRI without risking too many false positive calls. In our own experience, numerous false positive calls occurred particularly in cases with mammographic microcalcifications.
3. Due to the additional possibility of partial volume effects, excellent thin slice techniques will be necessary together with extremely careful application of any threshold.

Thus, we do not recommend reliance on MRI in this field at present and we do not recommend application of MRI as a means of answering these questions. Instead diagnostic decisions should be based on careful analysis of the mammogram and possibly other diagnostic tests such as transcutaneous biopsy.

As far as noncalcified in situ carcinomas are concerned, it is important to mention that seven out of our 21 in situ carcinomas were detected by MRI alone. The in situ carcinomas detected by MRI frequently became apparent as a focal area of enhancement and sometimes enhancement with a ductlike shape.

While the sensitivity results of CE MRI have been very satisfying, improvement of specificity has been a major concern (Table 1). Overall the following possibilities are being discussed:

(i) All available information including that of shape and speed of enhancement should be used for the final diagnosis. Because of the existence of both diffusely and slowly enhancing carcinomas, it is necessary to warn against overinterpretation of shape or speed of enhancement. Optimization of interpretation guidelines in this field (using optimum techniques) will therefore be an important task for the near future.

(ii) In addition, all available information including that of mammography and clinical examination should be used for the final diagnosis. MRI is not a stand-alone method!

(iii) In order to avoid unnecessary biopsy of MR-detected small benign enhancing lesions, MR follow-up of benign-appearing lesions (predominantly well-circumscribed round or oval lesions, which are likely to be small fibroadenomas) is recommended. MR-guided stereotaxic transcutaneaous biopsy should be considered for indeterminate benign-appearing lesions. First experiences with such devices are presently being acquired.

(iv) Finally unnecessary costs should be avoided and optimum diagnostic gain attempted by using MRI exclusively for those indications where definite advantages compared with conventional imaging can be expected.

On the basis of our own experiences over 2000 contrast-enhanced MR studies of the breast, we do not recommend contrast-enhanced MRI for the following indications: (a) evaluation of microcalcifications (see above), and (b) evaluation of those cases where diffuse enhancement is to be expected in any event, since in these cases malignancy can never be excluded in principle. Such cases include clinically obvious inflammatory changes, patients with secretory disease, and patients with known enhancing dysplasia from previous studies.

As an additional method however, CE MRI has been most helpful in diagnostic problems within mammographically dense or distorted tissue. Most interesting indications in these breasts include the search for primary tumors (not detected by conventional imaging) and the exclusion of multicentricity or contralateral involvement in patients with small tumors and very dense tissue (see Figure 2).[15–17,24] Contrast-enhanced MRI is particularly useful for patients with severe scarring after surgery, after radiation therapy, and after silicone implant.[16,20–22] It must, however, be added that MRI should not be used within the first 3–6 months after surgery or within the first 12 months after radiotherapy (RT), since post-therapeutic diffuse enhancement usually impairs evaluation during that period.

3.4 Conclusions and Outlook

The use of a contrast agent is obligatory for MR detection and diagnosis of malignancy. Contrast-enhanced MRI is gaining increasing importance as an additional tool for breast diagnostics. However, because of the increasing interest in the method, optimization and standardization of interpretation is an urgent task for the near future.

In order to develop optimized criteria for interpretation, an international multicenter study is presently being started. The study is supported by Siemens Corporation, Schering, and Berlex Corporations, and includes only centers with a high reputation in both breast imaging and MRI based on histologically proven data only. Both the optimization of interpretation guidelines, and in a second prospective trial the determination of wellfounded and generally recognized accuracy data, are the major goals of this study. These data, as well as further research by other groups, will help to define the optimum role which MRI should play in integrated diagnostic work-up.

MRI is thus gaining its place in breast diagnostics. It must be our concern to use MRI optimally only for those indications where definite diagnostic gain can be achieved for the patient without risking false negative calls and without causing an unacceptable number of false positive calls, which might cause unnecessary concern, costs for additional clarification, or even surgery. Further development and improvements of the technique are still proceeding.

4 RELATED ARTICLES

Cardiac Gating Practice; Echo-Planar Imaging; Gadolinium Chelate Contrast Agents in MRI: Clinical Applications; Gadolinium Chelates: Chemistry, Safety, and Behavior; Whole Body Magnetic Resonance: Fast Low-Angle Acquisition Methods.

5 REFERENCES

1. W. A. Murphy and J. K. Gohagan, 'Magnetic Resonance Imaging', ed. D. D. Stark and W. G. Bradley, Jr., C. V. Mosby, St. Louis, MO, 1987, pp. 861–886.
2. J. I. Wiener, A. C. Chako, C. W. Merten, S. Gross, E. L. Coffey, and H. L. Stein, *Radiology*, 1986, **160**, 299.
3. F. S. Alcorn, D. A. Turner, J. W. Clark, et al., *Radiographics*, 1985, **5**, 631.
4. S. H. Heywang, R. Bassermann, G. Fenzl, W. Nathrath, D. Hahn, R. Beck, I. Krischke, and W. Eiermann, *Eur. J. Radiol.*, 1987, **3**, 175.
5. J. K. Gohagan, A. E. Tome, E. Spitznagel, et al., *Radiology*, 1994.
6. S. H. Heywang, D. Hahn, H. Schmid, I. Krischke, W. Eiermann, R. Bassermann, and J. Lissner, *J. Comput. Assist. Tomogr.*, 1986, **10**, 199.
7. S. H. Heywang, T. Hilbertz, E. Pruss, A. Wolf, W. Permanetter, W. Eiermann, and J. Lissner, *Digitale Bilddiagn.*, 1988, 7.
8. S. H. Heywang, A. Wolf, E. Pruss, T. Hilbertz, W. Eiermann, and W. Permanetter, *Radiology*, 1989, **171**, 95.
9. W. A. Kaiser and E. Zeitler, *Radiology*, 1989, **170**, 681.
10. W. A. Kaiser, *Diagn. Imaging Int.*, 1992, 44.
11. J. P. Stack, A. M. Redmond, M. B. Codd, P. A. Derran, and J. T. Ennis, *Radiology*, 1990, **174**, 491.
12. F. W. Flickinger, J. D. Allison, R. Sherry, and J. C. Wright, *Proc. XIth Ann Mtg. Soc. Magn. Reson. Med.*, Berlin, 1992, p. 955.
13. M. D. Schnall, S. Orel, and L. Muenz, *Proc. XIth Ann Mtg. Soc. Magn. Reson. Med.*, Berlin, 1992, p. 120.
14. U. Fischer, D. von Heyden, R. Vosshenrich, I. Vieweg, and E. Grabbe, *RoeFo*, 1993, **158**, 287.
15. H. Oellinger, S. Heins, B. Sander, et al., *Eur. Radiol.*, 1993, **3**, 223.
16. S. H. Heywang-Köbrunner, 'Contrast-enhanced MRI of the Breast', Karger, Basel/Munchen, 1990.
17. S. H. Heywang-Köbrunner, *Electromedica*, 1991, **61**, 43.
18. B. Allgayer, P. Lukas, W. Loos, and K. Mühlbauer, *Roentgenpraxis*, 1991, **44**, 368.
19. D. Rubens, S. Totterman, A. K. Chacko, K. Kothari, W. Logan-Young, J. Szumowski, J. H. Simon, and E. Zacharich, *AJR*, 1991, **157**, 267.
20. H. G. Lewis-Jones, G. H. Whitehouse, and S. J. Leinster, *Clin. Radiol.*, 1991, **43**, 197.
21. S. H. Heywang-Köbrunner, A. Schlegel, R. Beck, T. Wendt, W. Kellner, B. Lammetzsch, M. Untch, and W. B. Nathrath, *J. Comput. Assist. Tomogr.*, 1993, **17**, 891.
22. S. H. Heywang-Köbrunner, T. Hilbertz, R. Beck et al., *J. Comput. Assist. Tomogr.*, 1990, **14**, 348.
23. W. B. Pierce, S. E. Harms, D. P. Flamig, R. H. Giffey, W. P. Evans, and J. G. Hugins, *Radiology*, 1991, **181**, 757.
24. S. E. Harms, D. P. Flamig, K. L. Hesley, M. D. Meiches, R. A. Jensen, W. P. Evans, D. A. Savina, and R. V. Wells, *Radiology*, 1993, **187**, 493.
25. W. Whitney, R. J. Herfkens, J. Silverman, D. Ikeda, J. Brumbaugh, S. Jeffrey, L. Esserman, J. Frederickson, C. Meyer, and G. Glover, *Proc. XIIth Ann Mtg. Soc. Magn. Reson. Med.*, New York, 1993, p. 856.
26. C. Boetes, R. D. Mus, J. O. Barentsz, J. H. Hendriks, R. Holland, and J. H. Ruijs, *Radiology*, 1993, **189**, 301.
27. H. Oellinger, B. Sander, U. Quednau, J. Hadijuana, H. Schoenegg, and F. Felix, *JMRI*, 1993, **3**, 109.
28. S. H. Heywang-Köbrunner, J. Haustein, C. Pohl, W. M. Bauer, W. Eirmann, W. Permanetter, *Radiology*, 1994, **191**, 639.
29. R. F. Brem, C. M. C. Tempany, and E. A. Zerhouni, *J. Comput. Assist. Tomogr.*, 1992 **16**, 157.
30. D. P. Gorczyca, S. Sinha, and C. Y. Ahn, *Radiology*, 1992, **185**, 407.
31. L. I. Everson, H. Parantainen, A. E. Stillman, T. Dethi, M. C. Toshager, and B. Cunningham, *Radiology*, 1993, **189**, 301.
32. W. A. Berg, N. D. Anderson, B. W. Chang, E. A. Zerhouni, and T. E. Kuhlman, *Proc. XIIth Ann Mtg. Soc. Magn. Reson. Med.*, New York, 1993, p. 123.
33. S. Mukundan, W. T. Dixon, R. C. Nelson, D. C. Monticciolo, and J. Bostwick, *Radiology*, 1993, **189**, 301.
34. A. Ottinetti and A. Sapino, *Breast Cancer Res. Treat.*, 1988, **11**, 241.
35. C. H. Blood and B. R. Zetter, *Biochim. Biophys. Acta*, 1990, **1032**, 89,
36. H. M. Jensen, J. Chen, M. R. De Vault, and A. E. Lewis, *Science*, 1982, **218**, 293.
37. N. Weidner, J. P. Semple, W. R. Welch, and J. Folkman, *N. Engl. J. Med.*, 1991, **324**, 1.
38. M. A. Gimbrone, S. B. Leapman, R. S. Cotran, and J. Folkman, *J. Exp. Med.*, 1972, **136**, 261.
39. I. F. Tannock, *Br. Cancer Res.*, 1968, **22**, 258.
40. D. T. Connolly, D. M. Heuvelman, R. Nelson, J. V. Olander, B. L. Eppley, J. J. Delfino, N. R. Siegel, R. M. Leimgruber, and J. Feder, *J. Clin. Invest.*, 1989, **84**, 1470.

Biographical Sketches

S. H. Heywang-Köbrunner. *b* 1956. Dr.med., 1982 University of Munich. Fellowship in breast imaging in the US (Georgetown University, Emory University, Betty Ford Breast Diagnosis Center, Washington DC) 1982–83. Radiology residency with special training in CT and MRI, University of Munich (Prof. Dr. J. Lissner); staff member and assistant professor, University of Munich, 1990–92, assistant professor, University of Leipzig, 1993, associate professor, University of Halle, 1994–present. Approx. 150 publications. Research specialties: since 1985, investigation of CE MRI of the breast clinical MRI, breast imaging.

H. Oellinger. *b* 1948. Dr.med., 1989, Free University of Berlin. M.S.M.E. New Jersey Institute of Technology, Fulbright Fellow, 1974–76; site engineer for conventional and nuclear power plants (Siemens, Erlangen, Germany) 1976–82; Radiology Department (Strahlenklinik und Poliklinik, FUB, Prof. Dr. Dr h.c.. R. Felix) with special training in CT and MRI, 1989–present. Research interests: clinical MRI, breast and pelvic imaging.

Cardiac Gating Practice

David N. Firmin
National Heart and Lung Institute, University of London, UK

1 INTRODUCTION

Conventional magnetic resonance images or spectra are acquired over a period that is much longer than the cardiac cycle and for this reason some method of referencing to the cardiac cycle is required. If cardiac images or spectra were to be acquired without any reference to the cardiac motion, then the position of the heart would vary from one view or signal acquisition to another and artifacts and blurring of the image or signal contamination of the spectrum would result. Although the referencing techniques are often referred to as cardiac gating, strictly speaking they would be better referred to as cardiac synchronization. Gating is a technique used in radionuclide ventriculography, for example, when the acquisition occurs continuously but the cardiac events are used to time the opening and closing of an acquisition 'gate' or 'gates', so that the image or images that are built up relate to specific parts of the cardiac cycle.

There have been two approaches to cardiac synchronization of the MR acquisition: the first, known as prospective cardiac gating or cardiac triggering, was initially developed and used for early cardiac MR scanning and can be used for any type of MR imaging sequence. The second, known as retrospective gating, has been developed for synchronizing fast repetition cine acquisitions to the cardiac cycle. Both techniques have their own advantages and disadvantages as will be discussed below.

2 REQUIREMENT OF CARDIAC GATING

The importance of synchronizing the MR acquisition to the cardiac cycle is illustrated in Figure 1 which shows an example of spin echo images of the heart acquired with (a) and without (b) cardiac triggering. In this case, lack of gating generates artifacts resulting from view-to-view variations in the position of the heart and blood flowing through it. Cardiac synchronization is not only important for cardiac imaging; other organs in the body pulsate due to pressure changes in the arterial vascular systems and image quality has been shown to improve with cardiac gating. Single shot techniques such as echo planar imaging, where the acquisition time is relatively short in comparison to the cardiac cycle, require cardiac triggering when the relationship between the image and the time in the cardiac cycle is of interest, as would be the case for echo planar imaging of the heart.[1] Also for imaging of the spinal cord where CSF pulsates with the cardiac cycle[2] and techniques such as diffusion imaging[3] are particularly sensitive to motion, some form of cardiac triggering or gating is required.

3 METHODS OF CARDIAC MONITORING

There have been a number of approaches to monitoring the cardiac cycle including various forms of pulse sensor, the electrocardiogram (ECG), and magnetic resonance methods of rapidly imaging the position of the heart. The pulse sensors include those that monitor the changes in infrared reflection or absorption in the vascular bed and are normally placed on the finger or the ear lobe and continuous wave Doppler probes directed at any 'near surface' artery. Both of these methods monitor the pulsatility of blood flow and can be set up to detect the slope or the amplitude of the waveform. In general, pulse sensors are not used unless the electrocardiographic waveform is unusable. The main problem with the methods are that timing errors can occur, both because the waveforms are less well defined than the ECG, in that there are no high-frequency portions to compare with the QRS complex, and because physiological factors can affect the shape of the waveform. An additional problem is that there can be a significant delay between the beginning of cardiac contraction and the associated flow pulse that is being detected. One advantage, however, is that the signal is affected less by the static magnetic field, and the rf and gradient pulses that can interfere with the ECG waveform; the latter two are problematic, especially when sequences are repeated very rapidly.

The safety implications are similar for ECG and pulse sensor monitoring although the hazards are somewhat greater for the ECG system because of the requirement of electrical contacts made directly to the skin. It is possible for the transmitted rf signal to be coupled into the leads of the system to such an extent that their temperature is raised enough to cause local burning. To avoid this risk, large loops are avoided and the leads are kept away from the patient's skin as much as possible.

Transmission of the electrocardiogram out of the magnet also requires care as cables running out of the magnet can act as an aerial and transmit radiofrequency noise into the scanning region. To overcome this, the electrocardiogram can either be converted to an optical signal and carried out along a fiber-optic cable[4] or transmitted by radiotelemetry at a frequency that does not interfere with the MR signal.[5] In 1990, Spraggins described a method of cardiac gating that required no external monitoring device. The method involved alternating between the acquisition of image and timing data, the latter being non-phase-encoded and designed to give a 1D image to monitor the changing size of the heart, that could later be used to reorder the image data retrospectively.[6]

4 ARTIFACTS ON THE ELECTROCARDIOGRAM

Recording an electrocardiogram in a magnetic resonance scanner during a scan is not a simple matter and the waveform bears little relationship to the one that would be obtained away from the magnetic field. The static field has a number of effects, and the changing gradient and rf fields applied during the imaging introduce additional artifacts. The flow of blood (a conductor) through the heart and great vessels in the presence of the static magnetic field results in a varying induced potential that is superimposed on the electrocardiogram. The main effect is during the systolic part of the heart cycle when blood

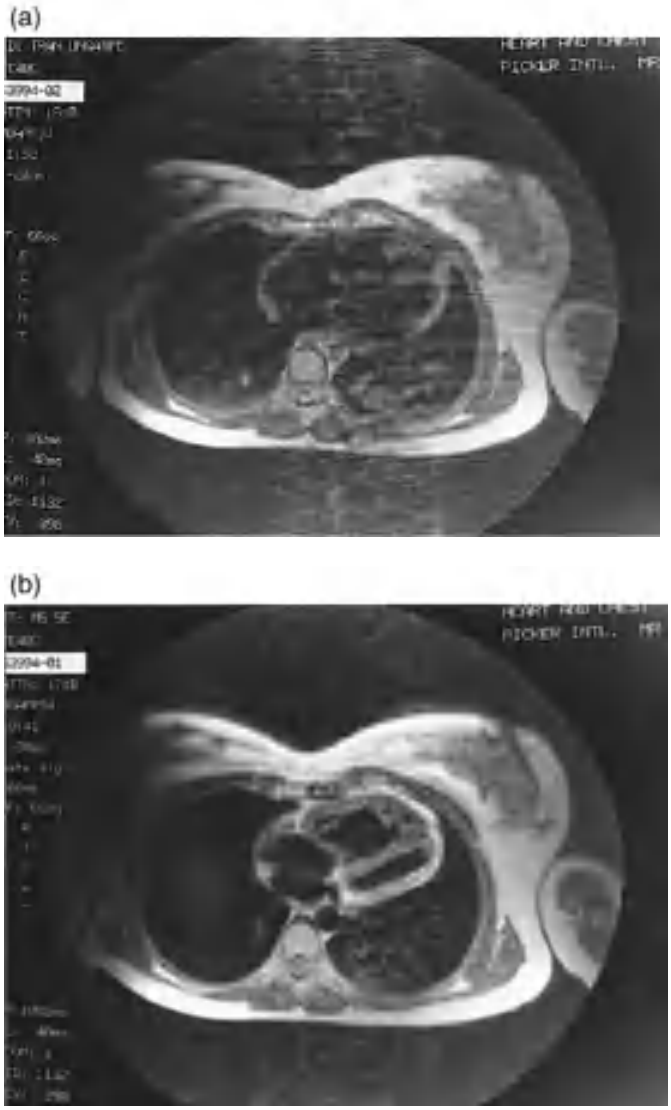

Figure 1 Illustration of the importance of cardiac gating when imaging the heart. The figure compares transverse spin echo images of the heart (a) ungated and (b) gated to the end-systolic part of the cardiac cycle

is flowing most rapidly out of the heart and in the aorta, and the size of the T wave is most noticeably affected. The effect is governed by the Faraday–Neumann law which states that if a conductor cuts a magnetic flux, ϕ, the induced potential difference, V, is proportional to the rate of change of flux, $d\phi/dt$, so that the effect is greatest when there is a large component of flow perpendicular to the field (crossing lines of flux); the direction of the induced potential is perpendicular to both of these. The size of the potential is also directly related to the strength of the magnetic field so that the artifacts are much more pronounced at high field strengths. As far as the detection of the QRS complex of the electrocardiogram is concerned, generally the detection systems monitor the rate of change of the signal and not the overall amplitude. Even though the increased T wave is accompanied by an increased rate of change of the signal, the rate of change found during the QRS complex is normally significantly greater. Another artifact caused by the presence of the static magnetic field is that of induced potentials that result if the ECG leads are moved during the scan. Some care is required to choose electrode sites that minimize the potential of such a problem.

The switched magnetic field gradients that are used during all imaging sequences also introduce rapidly changing potentials that can severely interfere with the electrocardiogram. The size of these depends on the rate of change of magnetic flux through the conductor loop presented to the field and upon the area of the loop. The size of the artifacts can be reduced, therefore, by twisting the cables up to the patient and placing the electrodes close together. The latter of these is somewhat self-defeating in that placing the electrodes closer together also reduces the amplitude of the detected QRS complex. Most ECG amplifiers that are used in MR systems are modified so that they detect the rapidly changing potentials and clamp or hold the waveform for their duration. For the majority of magnetic resonance sequences, this allows the ECG waveform to be monitored as the gradient switching occupies a relatively small proportion of time. However, for very fast sequences such as echo planar imaging, the gradients are switched so rapidly that the waveform is obscured throughout the acquisition.

The radiofrequency pulse may also cause problems if it couples into the ECG leads or amplifier circuitry. Some amplifier systems are controlled by a microprocessor and such systems have to be very well shielded from the rf to avoid signal disruption.

5 ELECTROCARDIOGRAM ELECTRODE AND LEAD POSITIONING

There a number of factors that are relevant when choosing the positions to place the ECG electrodes. These factors include the requirement to get a good reliably detectable QRS signal, to minimize artifacts due to breathing, to minimize the potential for artifacts on the image due to the metallic content of the ECG electrodes, and to minimize any potential coupling between the rf signals and the cables of the ECG system.

Dimick and colleagues have shown that the vector of the blood flow induced potential normally points anteriorly and slightly down the body.[7] The QRS complex vector, on the other hand, usually points to the left, posteriorly and down so that a left-sided or posterior lead is recommended to maximize the ratio between this signal and the artifactual one. One approach that is used to achieve this is to place the two active electrodes one on the right shoulder and the other on the lower left side of the chest, with the common electrode often positioned on the left shoulder (Figure 2). An alternative is to place the electrodes in similar positions on the back; although the detected signal is not quite as strong, the potential for motion artifacts due to respiration are reduced.

The material of which the electrodes and cables are made is also relevant. These are not normally ferromagnetic, but their metallic content can induce artifacts by altering the magnetic field locally. In spin echo imaging the artifacts are very superficial and can normally be ignored, but field echo images are much more affected (Figure 3). Positioning of an electrode or lead over the region of interest should therefore be avoided unless specialized electrodes and leads containing minimal or no metal (i.e. carbon compounds) are used.

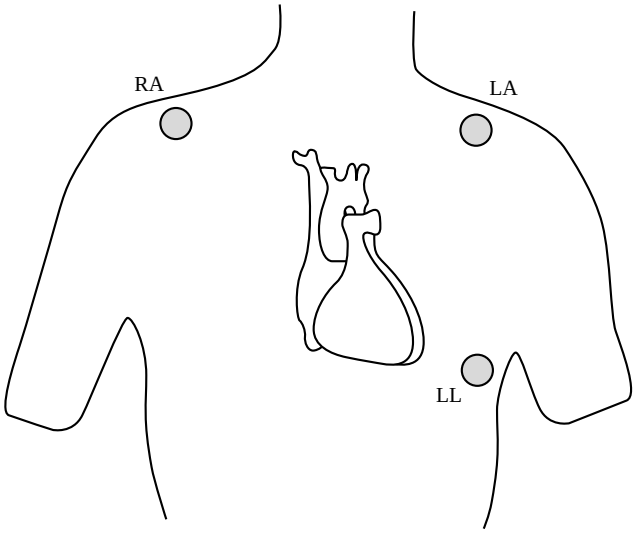

Figure 2 Typical positions of the electrodes for recording the electrocardiogram during magnetic resonance imaging. Similar positions on the back can be used, at the expense of a weaker signal, to reduce motion artifacts due to respiration. (Reproduced by permission of Blackwell Scientific Publications, from 'Magnetic Resonance of the Cardiovascular System', ed. S. R. Underwood and D. N. Firmin)

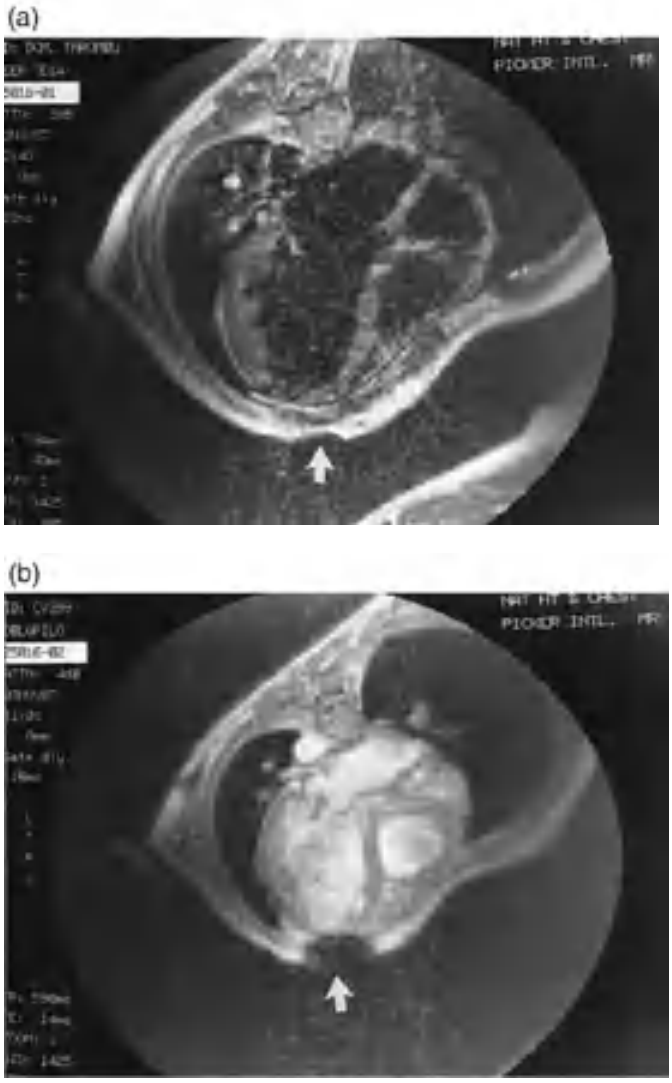

Figure 3 Artifacts produced by metallic electrocardiogram electrode positions on the chest near the apex of the heart (large arrow). On the spin echo image (a) the artifacts are very much smaller than on the gradient echo image (b). (Reproduced by permission of Blackwell Scientific Publications, from 'Magnetic Resonance of the Cardiovascular System', ed. S. R. Underwood and D. N. Firmin)

6 PROSPECTIVE AND RETROSPECTIVE GATING

Both prospective and retrospective forms of gating involve monitoring the ECG or other cardiac-related signal with the regular detection of a prominent part, such as the QRS complex of the ECG or the arterial flow pulse of a pulsimeter waveform.

With the prospective system, the detection is used to initiate one or a number of sequence repetitions following a predefined delay and separated by a repetition time *TR* [Figure 4(a)].[4,8] The sequence repetitions can be of the same phase encoding acquisition for a number of different slices, the same phase encoding acquisition for a number of frames from a cine scan, or a number of different phase encoding acquisitions contributing towards one image. If the sequence can be repeated very quickly, then a complete image can be acquired within a fraction of a cardiac cycle; in this case, a delay is used following the cardiac detection to the start of the sequence repetitions to define the period of the cardiac cycle over which the image is acquired. For extremely fast techniques such as echo planar, several images can be acquired within a cardiac cycle and, rather as for the phase encoding steps of the slower methods, either multiple slices or multiple cine frames can be acquired at defined times following the cardiac detection.

One problem with this prospective method of triggering is that of cardiac arrythmia, which invalidates the assumption that the cardiac cycles used to construct the image are identical. Artifacts can result for two different reasons: firstly the position and shape of the heart may vary from beat to beat, and secondly the time between excitation can be different from one beat to the next, a fact that can cause an amplitude modulation of the acquired signal. In practice, however, normal sinus arrhythmia and infrequent ectopic beats of the heart do not seriously interfere with image quality. For cine field gradient echo imaging, however, the enforced requirement to leave a period of delay between the last frame and the next trigger results in a relatively high signal (sometimes known as the lightning artifact) on the first frame of the cine because of the increased longitudinal relaxation that occurs during the delay. This also means that part of the heart cycle cannot be imaged, this being the end-diastolic part when using the R-wave of the ECG as a trigger.

The retrospective method of cardiac gating was developed to enable cine field echo images to be acquired throughout the entire cardiac cycle, to remove the lightning artifact and to reduce the other artifacts that result because of cardiac arrhythmia.[9–11] The method involves the continuous repetition of the sequence at a constant *TR* whilst also monitoring and recording a cardiac waveform. There are two ways of implementing the technique: firstly by advancing the phase encoding at a regular

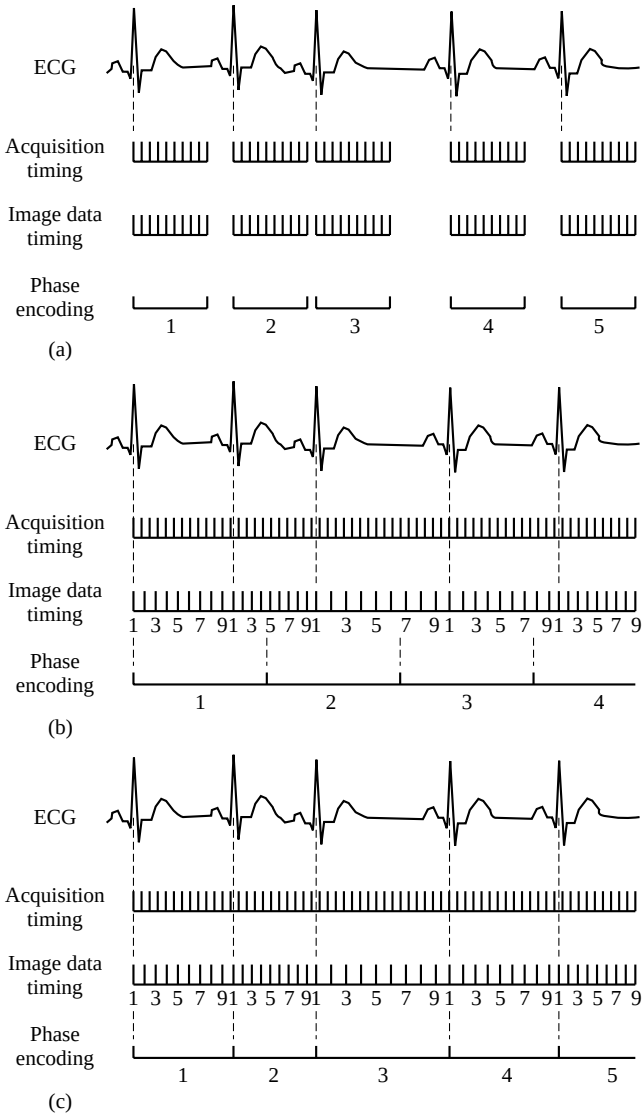

Figure 4 Diagram comparing the different methods of cardiac gating for a cine acquisition. Cardiac triggering (a) cannot adequately cover the diastolic part of the heart cycle and has a variable delay between the last frame on one heart cycle and the first frame of the next. For the first retrospective gating method (b) the phase encoding is incremented at regular intevals that are ca. 20% longer than the average cardiac cycle. The majority of heart cycles are therefore oversampled and data for one phase encoding may well be made up from two different heart cycles. For the second retrospective gating method (c) the phase encoding is incremented on the fly immediately after the R wave detection

interval that is longer than the longest cardiac cycle [Figure 4(b)] or secondly by changing the phase encoding step immediately after each cardiac detection [Figure 4(c)]. The first method is the easier to implement; the cardiac cycle is monitored for a period of approximately 30 s and the mean cardiac cycle duration calculated. Then, from the *TR* of the predefined cine sequence, the number of time frames that will fit into the mean cardiac cycle plus 20% is calculated; the phase encoding is then stepped regularly after this number of frames. The phase encoding steps now occur at arbitrary times in the cardiac cycle and data reordering is necessary before image reconstruction. The disadvantage of this approach is that the scan time is

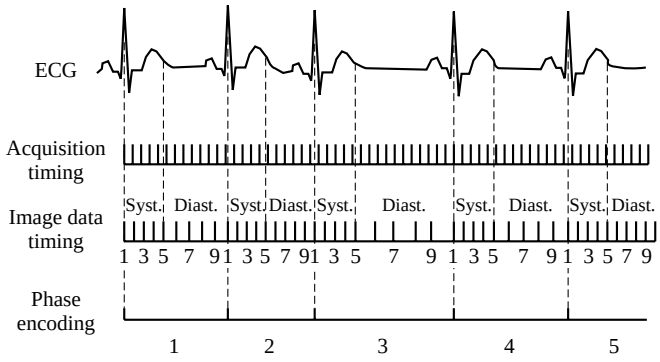

Figure 5 Diagram to illustrate how retrospective gating with data interpolation can be used to compensate for the nonproportionate variability in the cardiac cycle. The reconstructed systolic frames have a constant *TR* whereas for the diastolic frames the *TR* is varied

extended by approximately 20% and the data for particular phase encoding steps are likely to be acquired over two different cardiac cycles. The second method of retrospective gating overcomes these problems: the phase encoding gradient is incremented immediately after each cardiac detection and, depending on the cardiac duration, a variable number of sequence repetitions and data acquisitions may be employed for each phase encoding gradient. The technique requires very flexible hardware enabling the phase encoding gradient to be incremented on the fly, an option not available on the majority of systems.

Both retrospective methods require data interpolation to reconstruct a defined number of images within the cardiac cycle at time points that may lie between those that were actually acquired. Normally, simple linear data interpolation is used although least square interpolation schemes using variable time windows have been investigated; the wider the time window the higher the S/N, but the greater the temporal averaging and consequential image blurring. The simple interpolation method is generally acceptable if image frames are acquired with a reasonably high temporal resolution. The fact that the cardiac cycle varies in a nonproportionate manner, such that the systolic part varies in length less than the diastolic part, can be taken into account with this method of interpolation before reconstruction (Figure 5).

A heart in atrial fibrillation or exhibiting frequent ectopic beats can present a problem for either prospective or retrospective gating, although for cardiac triggering and the second

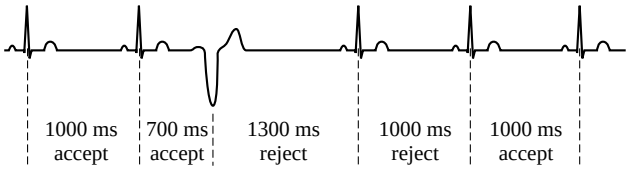

Figure 6 Arrhythmia rejection. The user defines a window of beat lengths that will be accepted. The data acquisition on the beat following one that falls outside this window is rejected and the effect is to reject the acquisition of the ectopic beat and the following sinus beat. (Reproduced by permission of Blackwell Scientific Publications, from 'Magnetic Resonance of the Cardiovascular System', ed. S. R. Underwood and D. N. Firmin)

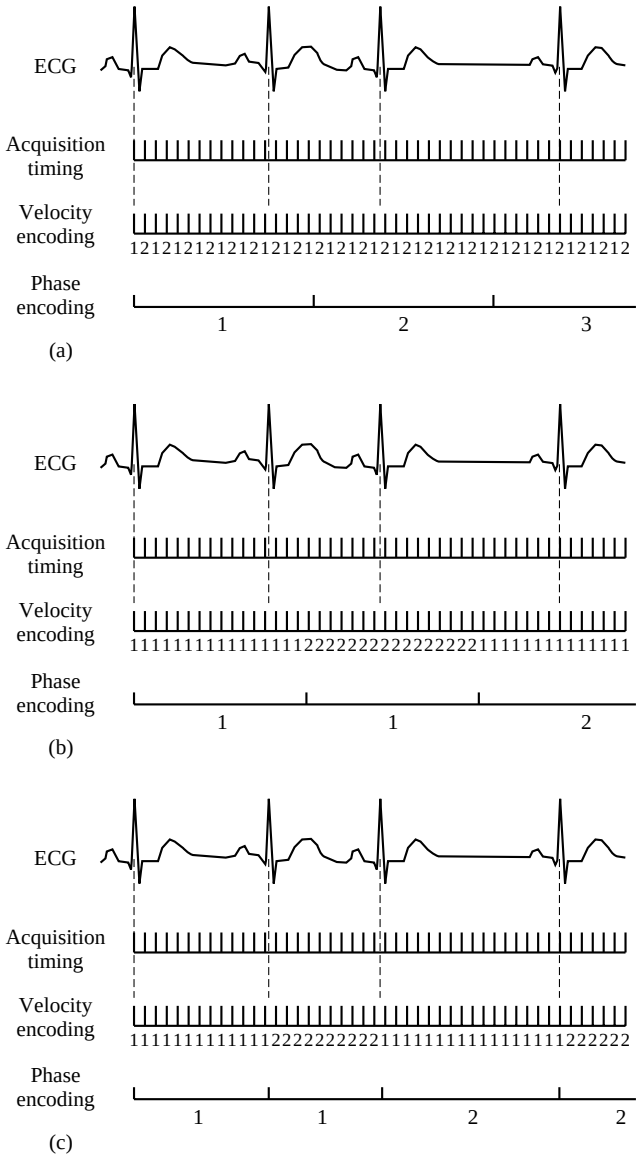

Figure 7 Illustration of the methods of acquiring velocity encoded data with retrospective gating. The velocity encoding is normally alternated on successive acquisitions (a); however, this can result in some high-frequency filtering of the pulsatile flow waveform. Alternating the velocity encoding after a fixed number of phase encoding steps removes the problem but is inefficient (b), and efficiency can be improved by alternating velocity encoding on the fly on successive cardiac cycles (c)

method of retrospective gating it is possible to suspend data acquisition and incrementing the phase encoding for a number of beats after a cycle of abnormal length (Figure 6).

7 IMPLICATIONS OF THE GATING TYPE ON THE ACCURACY OF BLOOD FLOW MAPPING

The potential of magnetic resonance to measure blood flow is of particular importance to studies of the cardiovascular system. Although many techniques have been described, the method of phase velocity mapping[12–14] has been shown to be particularly useful clinically.[15] The method of gating has been shown to have implications on the accuracy of pulsatile blood flow measurement using phase velocity mapping.[16,17]

The phase velocity mapping technique, when used to measure flow in a particular direction, involves the simultaneous acquisition of two scans with a different phase sensitivity to velocity in that direction. Phase images are reconstructed and these are subtracted to form the phase velocity map. When prospective gating is used, the data are acquired for the different velocity sensitivities on successive cardiac cycles. This enables high temporal resolution flow data to be acquired throughout the majority of the cardiac cycle. With retrospective gating, in order to minimize the scan time, a method of alternately acquiring the different velocity sensitivity data on successive sequence repetitions has been used [Figure 7(a)]. This has the effect of doubling the *TR* of the sequences and has been shown to result in a high-frequency filtering of the pulsatile blood flow waveform. Methods of reducing or removing this error include using a shorter *TR*, minimizing the interpolation window, and running two separate scans with the order of velocity encoding reversed before resorting the data appropriately.[16] Alternatively, the method of acquisition could be changed so that the velocity sensitivity of the sequence is changed less frequently, on successive cardiac cycles or on successive periods 20% longer than the mean cardiac cycle, depending on the method of retrospective gating that is being used [Figure 7(b) and (c)].

8 RELATED ARTICLES

Cardiovascular NMR to Study Function; Echo-Planar Imaging; Health and Safety Aspects of Human MR Studies; Heart: Clinical Applications of MRI; Motion Artifacts: Mechanism and Control; NMR Spectroscopy of the Human Heart; Pulsatility Artifacts Due to Blood Flow and Tissue Motion and Their Control; Whole Body Magnetic Resonance Artifacts.

9 REFERENCES

1. R. J. Ordidge, A. Howseman, R. Coxon, R. Turner, B. Chapman, P. Glover, M. Stehling, and P. Mansfield, *Magn. Reson. Med.*, 1989, **10**, 227.
2. G. Bergstrand, M. Bergstrom, B. Nordell, F. Stahlberg, A. A. Ericsson, A. Hemmingsson, G. Sperber, K. A. Thuomas, and B. Jung, *J. Comput. Assist. Tomogr.*, 1985, **9**, 1003.
3. J. V. Hajnal, M. Doran, A. S. Hall, A. G. Collins, A. Oatridge, J. M. Pennock, I. R. Young, and G. M. Bydder, *J. Comput. Assist. Tomogr.*, 1991, **15**, 1.
4. P. Lanzer, E. H. Botvinick, N. B. Schiller, L. E. Crooks, M. Arakawa, L. Kaufman, P. L. Davis, R. Herfkens, M. J. Lipton, and C. B. Higgins, *Radiology*, 1984, **150**, 121.
5. R. E. Wendt, R. Rokey, G. W. Vick, and D. L. Johnston, *Magn. Reson. Imag.*, 1988, **6**, 89.
6. T. A. Spraggins, *Magn. Reson. Imag.*, 1990, **8**, 675.
7. R. N. Dimick, L. W. Hedlund, R. J. Herfkens, E. K. Fram, and J. Utz, *Invest. Radiol.*, 1987, **22**, 17.
8. P. van Dijk, *Diagn. Imag. Clin. Med.*, 1984, **53**, 29.
9. G. H. Glover and N. J. Pelc, in 'Magnetic Resonance Annual', ed. H. Y. Kressel, Raven Press, New York, 1988, p. 299.

10. G. W. Lenz, E. M. Haacke, and R. D. White, *Magn. Reson. Imag.*, 1989, **7**, 445.
11. D. E. Bohning, B. Carter, S. S. Liu, and G. M. Pohost, *Magn. Reson. Med.*, 1990, **16**, 303.
12. D. J. Bryant, J. A. Payne, D. N. Firmin, and D. B. Longmore, *J. Comput. Assist. Tomogr.*, 1984, **8**, 588.
13. P. van Dijk, *J. Comput. Assist. Tomogr.*, 1984, **8**, 429.
14. G. L. Nayler, D. N. Firmin, and D. B. Longmore, *J. Comput. Assist. Tomogr.*, 1986, **10**, 715.
15. S. R. Underwood, D. N. Firmin, R. H. Klipstein, R. S. O. Rees, and D. B. Longmore, *Br. Heart J.*, 1987, **57**, 404.
16. M. H. Buonocore and H. Bogren, *Magn. Reson. Med.*, 1992, **26**, 141.
17. L. Søndergaard, F. Ståhlberg, C. Thomsen, T. A. Spraggins, E. Gymoese, L. Malmgren, E. Müller, and O. Henriksen, *Magn. Reson. Imag.*, 1993, **11**, 533.

Biographical Sketch

David N. Firmin. *b* 1955. B.Sc., 1978, M.Phil., 1982, Ph.D., 1989, Magnetic Resonance Imaging of Blood Flow, University of London. Introduced to NMR by D. B. Longmore, National Heart and Chest Hospital, London. Senior Lecturer, National Heart and Lung Institute, University of London, 1982–present. Approx. 210 publications. Research specialties: rapid flow, and cardiovascular imaging by use of magnetic resonance.

Cardiovascular NMR to Study Function

Donald B. Longmore
Royal Brompton Hospital, London, UK

1 INTRODUCTION

Approximately half of those reading this volume will die of cardiovascular disease, a further quarter will die of cancer, and 12% of lung disease. The diagnosis of these diseases are all now within the capabilities of NMR. However, vast intellectual and financial resources have been, and are being, applied to magnetic resonance technology, ignoring these major causes of death. Only a handful of the world's 9800 NMR machines are available to cardiologists, oncologists, and lung specialists. Presently NMR is used to study less than 3.5% of all disease. Open access rapid cardiovascular and lung imagers with facilities for intervention including laser and ultrasound surgery are technically feasible and needed urgently. Furthermore, the diagnostic power and, from the patient's point of view, the simplicity of a functional cardiovascular NMR examination, means that, for the first time, the ultimate medical objective of preventing the commonest diseases could be realized. The potential of functional evaluation of the cardiovascular system is for population screening to enable an understanding of the natural history of atheromatous disease, the commonest cause of death in the western world. Detection of presymptomatic cardiovascular disease enables both secondary prevention monitoring the efficacy of therapeutic and preventive measures using repeated functional NMR studies. Demographic evidence reveals the changing incidence of the disease in the same population over time and the varying incidence from place to place in the same ethnic groups (see section 8). This, coupled with experimental evidence, shows atheroma to have causative factors—and therefore to be preventable.[1–4] While the heart and circulation are being studied, it is only a small step to include screening for breast cancer[5] (***Breast MRI***) and, with the new ultra-short (50 μs to 500 μs) *TE* sequences, to study the lung (***Lung and Mediastinum MRI***).

Contemporary cardiovascular diagnosis relies on an expensive and time-consuming combination of clinical examination, chest radiography, electrocardiography (ECG), stress ECG, echo cardiography, nuclear medicine studies with and without pharmacological stress and invasive cardiac catherization, which carries a small but important mortality and morbidity. Unsuccessful attempts have been made to evaluate the cardiovascular system avoiding cardiac catherization using external recording devices such as apex cardiography, ballisto cardiography, ECG, impedance cardiography, etc. Now the balance has been profoundly altered following advances in nuclear medicine techniques, X-ray computed tomography, and echo cardiography. NMR is the most powerful diagnostic instrument yet conceived and this, combined with echo cardiography, means that virtually every cardiac diagnosis that previously required invasion can now be made noninvasively and cost-effectively, without mortality or morbidity. Until recently the exception was coronary artery disease. The NMR alternative to the coronary angiogram is dealt with elsewhere.

2 TECHNICAL REQUIREMENTS FOR CARDIOVASCULAR NMR

In order to study cardiovascular function, magnetic resonance techniques additional to those for imaging motionless parts of the body are required. Essential enhancements are cardiac gating, velocity mapping (***Cardiac Gating Practice***), rapid imaging, and velocity encoded rapid imaging (***Whole Body MRI: Strategies for Improving Imaging Efficiency***) in all planes.[6–8]

2.1 Imaging Strategy

A comprehensive heart NMR study is achieved in minimal time using a simple strategy. A transverse (transaxial) image of the chest is used to measure the angle of the heart to the left. A scan in the plane through the long axis of the left ventricle produces a vertical long axis (VLA) image through the left atrium and the left ventricle. From this, the downward angle of the heart is measured and a double oblique image from below produced to provide a horizontal long axis (HLA) view [Figure 1(a)] showing the five functional chambers of the heart and the coronary arteries in cross-section. Image planes can be selected perpendicular to the HLA to produce the short axis (SA) image [Figure 1(b)].

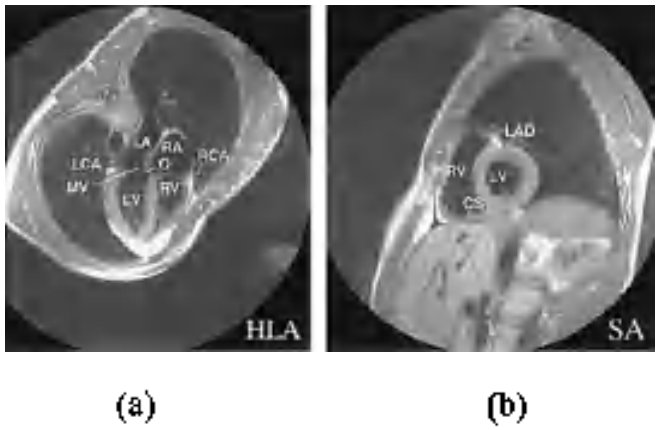

Figure 1 (a) The spin echo HLA image shows the right atrium (RA), the right ventricle (RV), the left atrium (LA), the left ventricle (LV) and the left ventricular outflow tract (O). The tricuspid valve which is not indicated is at the same level as the mitral valve marked (MV). The right coronary artery (RCA) and the left coronary artery (LCA) are also seen in cross-section. Fat at the apex of the heart is prominent. (b) The spin echo SA image shows the 'doughnut'-shaped left ventricular muscle (LV) with the right ventricle (RV) anterior to it. The left anterior descending coronary artery (LAD) is seen in the upper interventricular groove and the coronary sinus (CS) in the lower interventricular groove

2.2 Rapid Imaging applied to the Cardiovascular System

Two rapid imaging techniques are currently available[9,10] (dealt with in detail in ***Blood Flow: Quantitative Measurement by MRI***). Orders of magnitude of reduction of acquisition times for NMR imaging were first achieved by Mansfield and Pykett[8] with the one-shot echo planar 'Snapshot' (EPI) technique. The advantage of EPI for the cardiovascular system is that data acquisition can follow preparation pulses required to study cardiovascular function for diffusion, chemical shift imaging, and velocity encoding. The alternative to EPI with velocity mapping is the fast low angle shot (FLASH) technique with velocity mapping. EPI has a better signal-to-noise ratio (SNR) and can freeze movement, which is vital in the neonate. Less than 50 ms acquisition time is needed to obtain a velocity encoded image. The FLASH technique uses a total acquisition time of over 300 ms. There is no stage in the cardiac cycle of an infant when the heart is relatively still for this long. Furthermore, at all stages throughout life the filling and contraction of the heart varies from beat to beat. This variability is never more marked than in the neonate with congenital disease. EPI is more suitable for the measurement of aperiodic movements (irregularly irregular) than FLASH, which relies on periodicity and the heart being in the same position and at the same stage of contraction for 16 or more heart beats. However, despite these disadvantages, because the gross appearance of a FLASH image is mainly determined by the data from a relatively few central phase encoding steps acquired in the first 50 ms or so of a total acquisition of over 300 ms, acceptable FLASH velocity encoded imaging is possible; FLASH is also less demanding on the gradients, the rf, data collection, etc., and it can be implemented on standard machines with relatively simple modification.

Either technique can be used to find a jet, measure its velocity and, from the velocity measurement, calculate the gradient and therefore the severity of the lesion using a modified Bernoulli equation.[11] Velocity mapping combined with good anatomical imaging usually reveals more useful functional information about congenital and acquired disease than can be obtained from a cardiac catheter angiogram.

2.3 Volume Measurements

The volumes of all the cardiac chambers, notably the ventricles, can be measured accurately from two multislice sets of transverse, or HLA, or SA images, one set taken at end systole (when the volumes are least) and the other at end diastole (when the heart is fullest). Usually 10–12 slices are sufficient to cover the whole of the heart. The areas of the cardiac cavities can be measured manually or by automatic edge detection or area growth techniques. Ventricular volume measurements are obtained by summing the areas of the images covering the ventricles in systole or diastole. The thickness of the slices is known and the volume of each slice calculated. Summation of the various slice volumes gives the total cavity volume.[12]

A 'shorthand' method of measuring stroke volume uses area length calculations of VLA and HLA systolic and diastolic images assuming the ventricles to approximate to a cone. The end diastolic volume is calculated from the formula:

$$\frac{\text{area of diastolic VLA} \times \text{area of diastolic HLA}}{\text{minimum diastolic length apex to valve plane}} \times 0.85 \qquad (1)$$

and the end systolic volume from the formula:

$$\frac{\text{area of systolic VLA} \times \text{area of systolic HLA}}{\text{minimum length apex to valve plane}} \times 0.85 \qquad (2)$$

This method is only valid if the ventricles are contracting evenly.

2.3.1 Clinical Significance of Volume Measurements

Subtraction of the systolic volume from the diastolic volume produces an accurate measure of stroke volume, which when multiplied by the heart rate gives the cardiac output. Continued life depends on the way the heart is functioning rather than on the output at a moment in time. An efficient heart retains a small residual volume of blood which when compared with the stroke volume gives the ejection fraction. A low ejection fraction carries a poor prognosis.

2.3.2 The Four Way Comparison

Volume measurements have been validated by comparing the stroke volumes of the right and left ventricles which in normal subjects is unity. The stroke volumes have also been compared with the aortic and pulmonary artery flows. Three measurements (right ventricular output, pulmonary artery flow, and left ventricular output) correspond to within 2%. Aortic flow is 5–10% below the other measurements due to the 'take off' of coronary flow.

Functional assessment of the cardiovascular system can be applied to all types of disease. In this article the classical 'surgical sieve' is used, dividing disease into congenital and acquired, and further dividing acquired disease into traumatic, inflammatory, neoplastic, etc. There is a 'gray area' where it is difficult to distinguish between diseases we are born with and those we acquire, possibly because we are genetically vulnerable.

3 FUNCTIONAL ASSESSMENT OF CONGENITAL HEART DISEASE

Approximately three in every 1000 live births manifest one of the commoner congenital heart diseases, pulmonary artery stenosis, atrial septal defect, patent ductus arteriosis, and tetralogy of Fallot, though there is a significant incidence of many other complex forms of congenital disease. NMR functional imaging can detect and quantify the threat to life and form a vital part of the management in all these conditions. Three discrete groups of patients require functional assessment. These are: neonates and infants; children, when the less catastrophic abnormalities begin to manifest themselves; and 'grown up' congenital heart disease usually to follow up the results of surgical intervention.

3.1 Neonates and Infants

The small size of an infant and its inability to lie still, combined with the complexity of many congenital abnormalities,

necessitates a rapid imaging technique and the use of special surface coils or a head coil.

3.2 Functional Imaging in Children

Functional techniques have given an insight into the compensatory mechanisms which can allow an infant with gross cardiac abnormalities to survive to childhood when operative intervention is easier and safer. The ideal diagnostic techniques for children are a combination of rapid imaging used in neonates and infants and the standard adult functional imaging methods.

3.3 'Grown Up' Congenital Heart Disease (GUCH)

NMR is the only available technique for the repeated long-term follow-up of adolescents and young adults who have undergone successful surgery. It is vital in postoperative cases to include velocity mapping searching for deterioration, because calcified obstructions are not visualized on anatomical images and can only be demonstrated by blood velocity mapping.[13]

NMR is uniquely able to detect the afferent and efferent vessels to congenital arteriovenous (AV) malformations, helping the surgeon to plan an operation. In cases with multiple AV malformations (Klippel, Tralawney syndrome) the measurement of the total blood flow through all the afferent or efferent vessels to the AV malformations can predict the impending onset of high-output heart failure.[14]

3.4 The Late Effects of Congenital Heart Disease

3.4.1 Valve Disease

Valve disease may be acquired or present as a late manifestation of congenital heart disease. A small proportion of the population are born with a bicuspid aortic valve which will usually function normally until the patient reaches the fourth decade of life, by which time calcification causing stenosis and regurgitation results from the abnormal vibrations and stresses on the two cusps. NMR can be used to measure the jet velocity and to calculate the gradient and to measure the regurgitant fraction. This regurgitation can be quantified directly using velocity mapping or by comparing the ratio of the stroke volumes of the right and left ventricles.

3.4.2 Septal Defects

Pulmonary valve stenosis and atrial septal defect are the commonest congenital deformities of the heart, but they may not prove to be significant until adolescence or early adult life when the gradients across the pulmonary valve become significant and can be measured from the jet velocity. The shunt across the septal defect can be measured by the volume method or by velocity mapping. It is important to determine the amount of blood shunting from the left (higher pressure side of the heart) to the right (lower pressure side). It is not uncommon for the shunt ratio to be as high as 4:1, with four times as much blood flowing through the lungs as the body. This shunt gradually and irreversibly damages the lungs, increasing their resistance to flow and eventually reversing the shunt and making closure of the defect irrelevant and dangerous. If only one defect is present in the absence of valve regurgitation, the shunt can be measured by comparison of the outputs of the two sides of the heart. Velocity mapping measuring the shunt directly is more reliable.

4 FUNCTIONAL ASSESSMENT OF ACQUIRED HEART DISEASE

4.1 Traumatic Cardiovascular Disease

The commonest traumatic cardiovascular lesion due to road traffic and other accidents is a partial tear of the aorta causing a dissecting aneurysm. These can be detected with a computed tomography (CT) scan or an anatomical MR image which reveal the presence of the dissection. A dissection usually travels down the length of the aorta and sometimes it extends back towards the origin of the coronary arteries. Before any repair can be attempted it is essential to use velocity mapping to determine where the blood is flowing, and which branches to vital organs arise from the true lumen and which from the false lumen.[15]

Tears and penetrating injuries such as stab wounds to the heart and the associated blood in the pericardium can be seen on spin echo and better on gradient echo images. Blood flowing in and out of false aneurysms indicates their size, and more significantly, differentiates them from pericardial cysts.

4.2 Inflammatory and Toxic Damage to the Heart

4.2.1 Valve Disease

The mitral and aortic valves may be damaged by bacterial infection on an already damaged or abnormal valve, or by rheumatic fever which for the past decades has been uncommon in the western world. Hypersensitivity to *Streptococcus* spp. still commonly causes valve disease in developing countries and there is now a resurgence, notably in the USA. Thickened valve cusps can be seen on 'black blood' images or as filling defects on white blood images. However, life depends on the normal function of valves, and appearance may not correlate with the severity of their malfunction. Turbulent and regurgitant flow associated with stenosis and regurgitation due to rheumatic fever, etc. can be visualized as areas of signal loss on gradient echo images. If velocity mapping is not available, a remarkably accurate assessment of the volume of a regurgitant jet can be made from the proportion of the chamber occupied by the jet and the duration of the back flow.[16] Stenosis and regurgitation are best measured directly using velocity mapping with short echo times. A *TE* of 3 ms to the second echo can capture velocities of up to 6 m s^{-1}: the highest velocity attained through a stenotic valve. Multivalve disease invalidates comparison of stroke volumes from the two sides of the heart. The same multislice technique can be used to measure ventricular mass, which is increased in congenital cardiomyopathies.

4.2.2 Heart Muscle Disease

Heart muscle can be affected directly by viral illnesses such as influenza, the ME virus and glandular fever. Conditions such as post partum cardiomyopathy and inflammatory/allergic

infiltrative processes such as rheumatic fever also impair muscle function. Alcohol, drugs, and industrial toxic substances can also cause generalized dysfunction of the myocardium. In florid cases, cine NMR imaging is sufficient to demonstrate the dilated poorly contracting heart with a low ejection fraction. In less obvious cases, measurement of global ventricular function, as described below, is required.

4.3 Neoplastic Disease

Primary malignant tumors of the heart muscle are uncommon. They can be seen invading the muscle on multislice NMR images. Their effects on cardiac function can be determined by measuring global and regional function (see sections 4.4.2 and 4.4.3). Benign tumors and developmental cysts are commoner and do not usually have a significant effect on heart function, but repeated studies are necessary to check them for malignant change. Tumors in the atria can float through the atrioventricular valves during artrial systole and be blown back into the atria during ventricular systole, causing cardiac dysfunction by obstructing the valves and by displacing blood in a pumping chamber. Anatomical images do not distinguish well between intracardiac blood clot and intracavity tumor on spin echo images and gradient echo, and velocity mapping techniques are needed to reveal the presence of clot. Tumors in the right atrium may appear to have an obvious connection to the atrial wall but are frequently extensions of tumors in other parts of the vascular system which have grown along the great veins into the atrium. An 'NMR search' can locate the origin of the tumor. The hemodynamic significance of intracavity space-occupying lesions can be determined by velocity mapping. More frequently the heart is invaded by a local tumor such as a lung cancer with hilar glandular involvement. In these cases cardiac function can be impaired in three ways: by stiffening of the wall, by reduction of chamber size due to the mass of tumor tissue, or directly by tumor replacing contractile elements of the heart.

4.4 Degenerative Heart Disease

Most cardiovascular deaths, and hence about 40% of all deaths, are due to various forms of degenerative heart disease of which the commonest are hypertension and atherosclerotic disease.

4.4.1 Hypertension and Ventricular Mass

The reduction of ventricular mass following effective treatment of hypertension can be monitored using the multislice method (section 2.3). The muscle hypertrophy caused by high blood pressure can be quantified using the same multislice technique as for ventricular volumes.[17]

Studies of the caval or pulmonary venous flow which normally exhibit two similar flow peaks, one in systole and one in diastole, can be used to distinguish between ventricular function which is abnormal due to valvar regurgitation which causes an enhanced second peak 'constriction' of the heart by pericardial effusion or scar tissue around it. 'Restriction' due to stiffness of the heart itself, usually as a result of an inadequate blood supply due to coronary artery disease, correlates with an enlarged first peak.

Ventricular function can be studied globally or regionally.

4.4.2 Global Ventricular Function

Ventricular function measurements are clinically most relevant, but the heart has four chambers and the techniques described here are equally relevant to the atria. Global ventricular function measured in the resting state is frequently within normal limits, but the patient's disability indicates that there is inadequate cardiac output during exercise associated with normal activities.

Pharmacological stress (section 4.4.4) can reveal occult abnormalties of global function in two ways: by changes in velocity and acceleration of blood in the aorta, or by changes of stroke volume and ejection fraction.[18]

In the normal heart, increasing doses of a pharmacological stress (section 4.4.4) agent such as dobutamine cause an increase in aortic blood flow, velocity, and acceleration. In the abnormal heart, increasing the dose produces increased performance up to a much lower limit than in the normal heart, which has large reserves of power, and there is a 'fall off' in performance at dose levels which in the normal heart would still increase velocity. The dose level at which the 'fall off' occurs is an indication of the extent of the myocardial damage.

When the resting global function is at the lower end of normal limits, and pharmacological stress (section 4.4.4) indicates myocardial dysfunction with exercise, this may be because regions of the ventricle are contracting suboptimally, not contracting, or even moving paradoxically, bulging during systole thereby further disadvantaging the remaining normal heart muscle. In these cases it is necessary to study regional ventricular function.

4.4.3 Regional Ventricular Function

Multislice VLA, HLA, or, most usefully, SA views of the heart can be used to assess regional thickening and movement of the heart wall during contraction. If these appear normal but the clinical history suggests otherwise, then pharmacological stress is required.

The inner surface of the heart muscle is under maximum stress during cardiac contraction and is remote from the blood supply which enters the heart from its outer surface. The earliest sign that the heart is becoming injured is the failure of the subendocardial muscle fibers to 'actively relax' to enable filling at the beginning of diastole. Later in the disease process, contraction of these muscle fibers is also impaired. Velocity mapping of the inner surface of the heart in the direction of the long axis of the heart provides a sensitive measure of the elasticity and capability of the heart to fill actively. Later in the disease process, the same velocity mapping technique can be used as an accurate measure of the local failure of contraction.[19]

4.4.4 Pharmacological Stress

To mimic normal exercise, pharmacological stress using inotropic agents to increase cardiac work are used. Intravenous dobutamine, which has a half-life of less than 100 s, is an example of a safer, effective agent than the long-acting coronary vasodilator dipyramidole (Persantin), which is more

commonly used. Any angina caused by the dobutamine infusion passes off within 90 s of stopping the infusion.[20]

Pharmacological stress agents highlight areas which fail to contract normally, and indicate which coronary artery territory is receiving an inadequate blood supply. During simulated exercise there is good correlation between areas which do not thicken and move during systole and bolus tracking of a 'pseudo blood pool' magnetic resonance contrast agent. Both correlate well with nuclear medicine techniques.[21]

Measurements such as global and regional ventricular function demonstrate the effect, rather than the cause, of reduced ventricular function, which is most commonly a result of a diminished blood supply caused by atheromatous disease partially blocking the coronary arteries.

4.5 Atheromatous Disease

Atheromatous disease is progressive, and from demographic studies and animal experimentation is known to be reversible in its early presymptomatic stages (see section 8). The reader, hopefully a normal subject, requires answers to three fundamental questions about atheromatous disease. (a) Have I *got* it? (b) Are the *atheromatous* plaques of a type which can ulcerate and cause sudden death? (c) Can MR monitor the *efficacy* of preventive and therapeutic measures? An NMR machine capable of chemical shift imaging and velocity mapping is capable of answering all these questions.

4.5.1 Arterial Compliance

(a) *Have I got arterial disease*?: Atheromatous disease, mainly in the coronary arteries in the male and the carotid arteries in the female, appears not to coexist with a normal compliant arterial system. For this reason, measurements of aortic compliance, or its reciprocal the velocity of the onset of the arterial pulse wave along the aorta, can be used as a screening test to determine whether the subject is normal or an arteriopath.[22] Aortic compliance can be determined by NMR directly by measuring the volume of the arch of the aorta at peak systole when it is most dilated, and at the end of diastole when its elastic recoil reduces it to its smallest volume. It can be derived indirectly with similar accuracy by measuring the onset of the arterial pulse wave in the ascending aorta and at the end of the arch of the aorta during peak systolic flow. In a normal subject under the age of 55, the pulse wave takes an average of 32 ms to traverse the arch, whereas if the transit time of the leading edge of the pulse wave takes less than 12 ms diffuse arterial disease is present. This simple screening test divides subjects under the age of 55 into three groups: athletes who have remained fit; the average normal; and arteriopaths. Over this age the normal age-related aortic dilatation and reduction of arterial compliance is such that all subjects appear to be arteriopaths.

4.5.2 Chemical Shift Imaging

(b) *Are the atheromatous plaques of a type which can ulcerate and cause sudden death*?: If the patient is shown to be an arteriopath by the screening tests outlined above, arterial plaques in the larger vessels can be found on spin echo images of the vessel walls (Figure 2). The presence of the plaque can be confirmed and artefacts excluded by detecting acceleration of blood upstream of the obstruction, increased velocity across it, and deceleration downstream of it.

Water and fat images of the plaque can be acquired by using Dixon's selective reading of fat and water or Hinks' selective excitation of fat and water. A subtraction image indicates the percentage of lipid present.[23] Figures 3(a) and (b) show an atheromatous plaque with low lipid content. The range of lipid content in a plaque varies from zero up to a maximum of 28%. Figures 4(a) and (b) show a plaque with a high lipid content. A fibrous plaque [Figures 5(a) and (b)] with no or very low lipid content, though it impairs the circulation, is unlikely to cause sudden death. A plaque with a high lipid content puts the subject at risk because the plaque may rupture and ulcerate, precipitating acute thrombosis on its surface and, frequently, sudden death.

At the present stage of development, chemical shift imaging is only applicable to larger vessels, and the resolution is inadequate for NMR studies of coronary arteries based on single breathhold imaging acquiring 16 turbo-FLASH images. Furthermore, fat suppression techniques are needed in order to produce accurate images of the coronary arteries and velocity measurements in them, because phase changes due to the presence of fat surrounding the vessels invalidate the Dixon technique. Coronary velocity mapping is however adequate for the determination of the hemodynamic significance of coronary plaques by measuring the increased velocity across the plaque taking 24 heart beats (a breathhold duration within the capabilities of most subjects). The way ahead for coronary imaging depends on the development of velocity encoded echo planar and spiral imaging, both techniques with potentially sufficient resolution to enable analysis of coronary plaques. At present the inference has to be made that the lipid content of plaques in the coronary arteries is similar to that in plaques elsewhere in the circulation, as is usually the case.

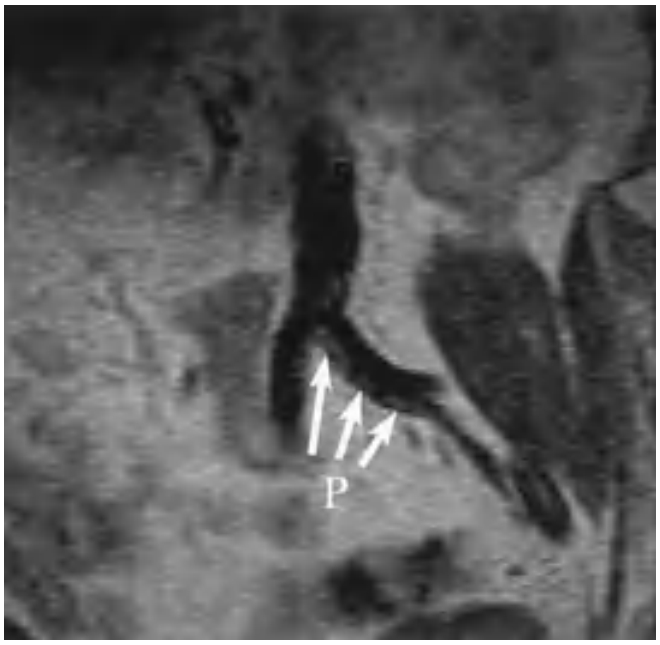

Figure 2 Atheromatous plaques (P) in the aorta of a 59-year-old male seen on a black blood spin echo image

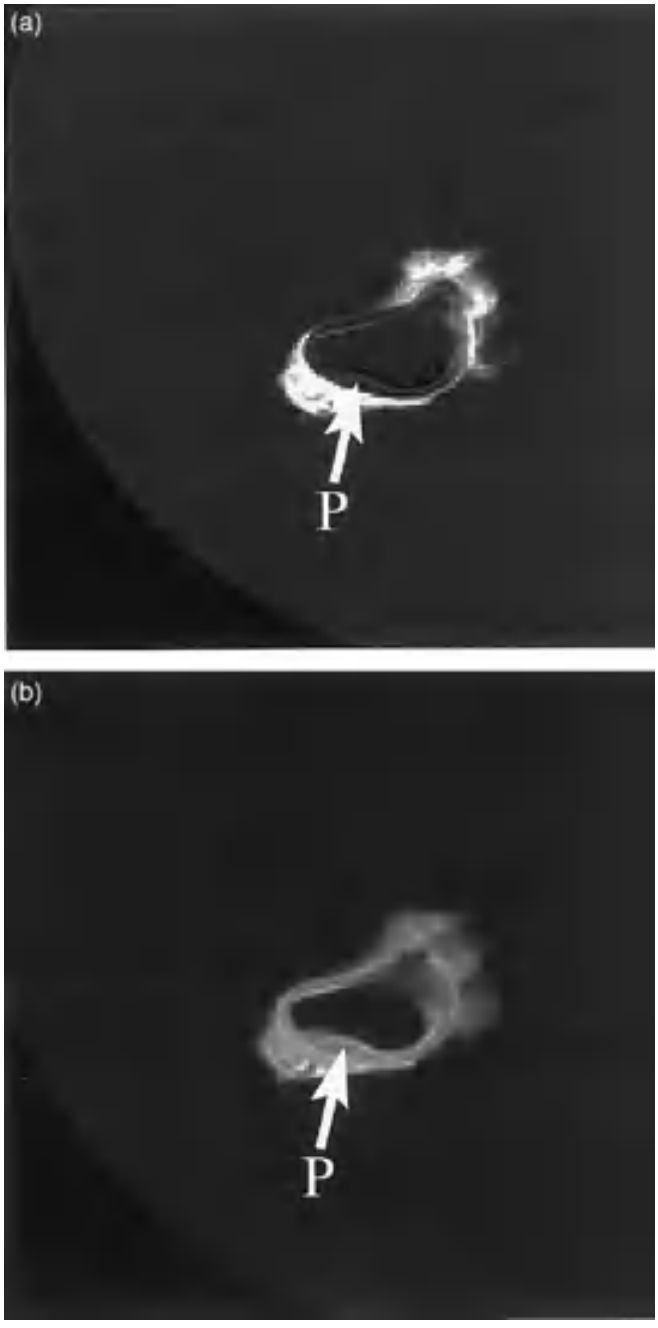

Figure 3 (a) A spin echo image of an atheromatous plaque (P) in a cadaveric specimen of aorta. (b) The image produced by subtraction of the fat and water images. There is no signal in the plaque which contains no lipid, confirmed by histology

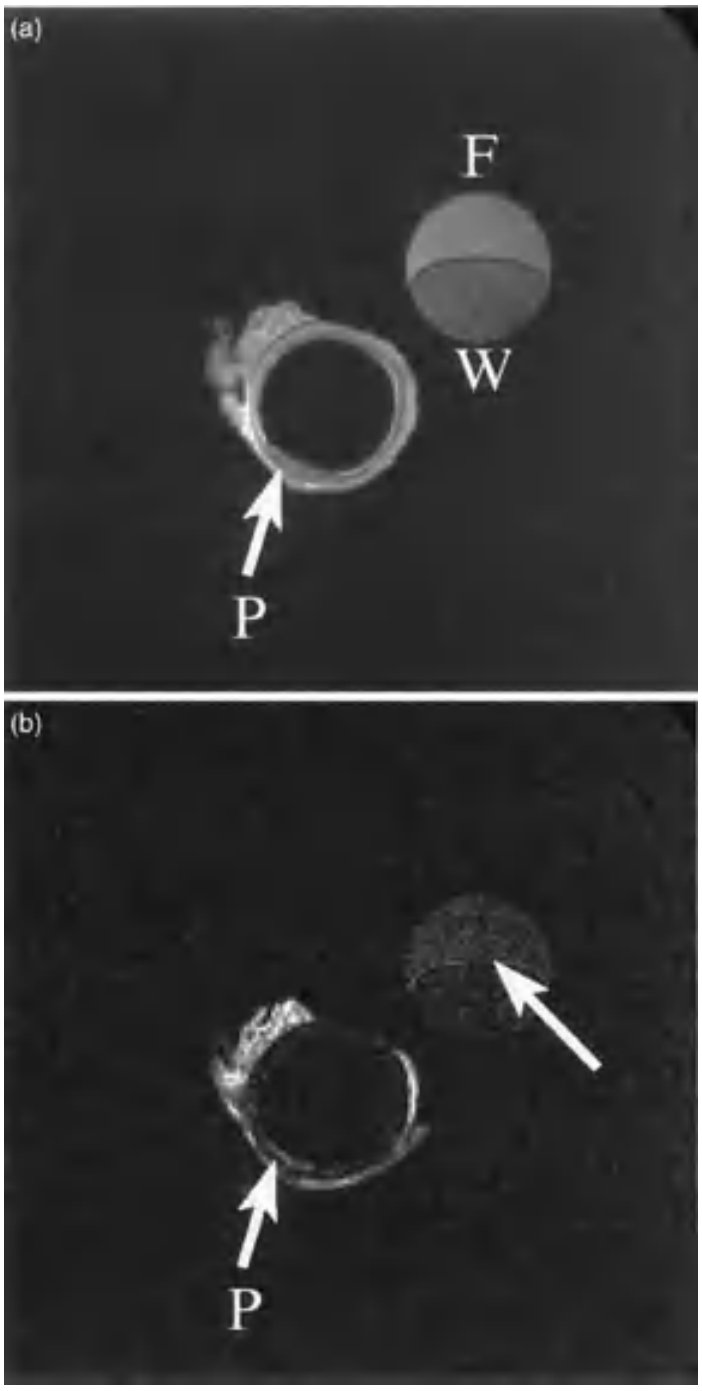

Figure 4 (a) Spin echo cross-sectional images of a cadaveric specimen of human aorta with an atheromatous plaque (P) and a test tube with fat floating on water (W + F). (b) The images produced by subtraction of fat and water images. The plaque (P) and the periaortic fat have high signals corresponding with the high lipid content in the histology specimen. There is a line of high signal on the interface between the fat and water in the test tube (arrowed)

4.5.3 Monitoring Atheroma using Functional NMR

(c) *Can NMR monitor the efficacy of preventive and therapeutic measures?*: Experiments with artificially induced atheroma in animals show that plaques regress with starvation (see section 8). Simple preventive measures including strict diet and exercise have also been shown to cause regression of atheromatous plaques. In subjects with very high cholesterol and other lipid levels, lipid-lowering agents may be necessary to augment the simple preventive regime. The advantages of NMR are that functional studies can be repeated regularly to monitor the progress of preventive measures.

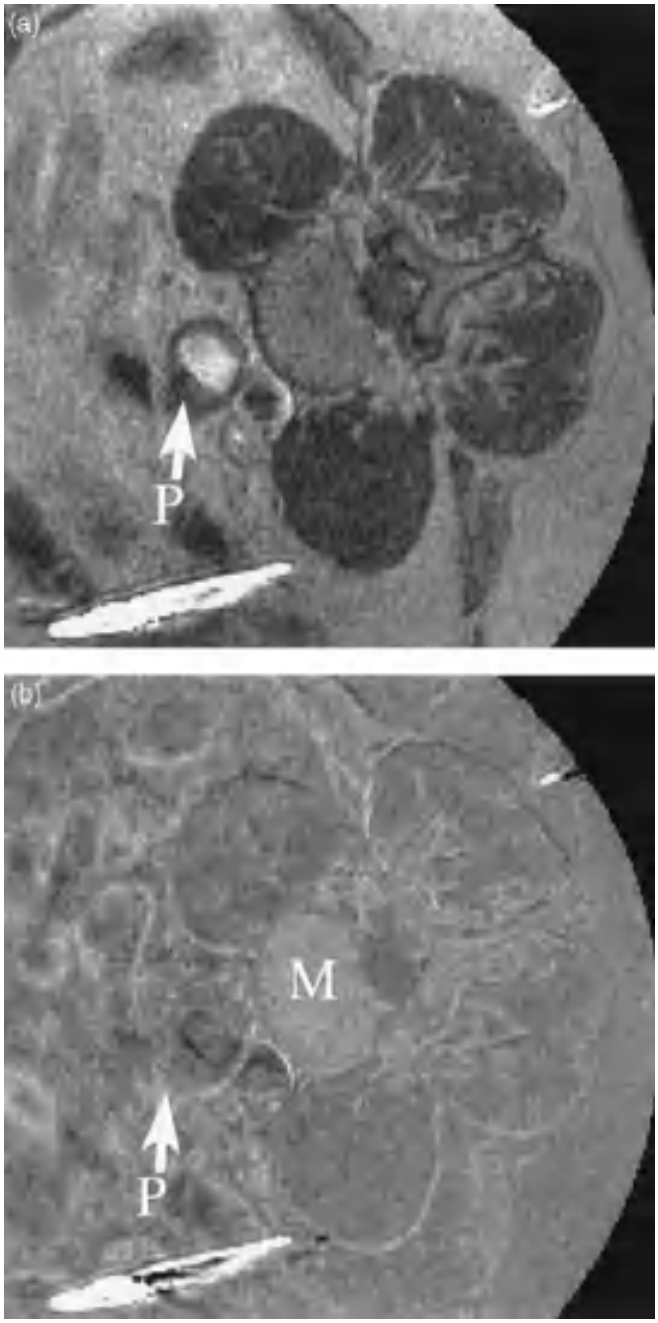

Figure 5 (a) A spin echo image of the abdominal aorta in a 61-year-old male showing a typical asymmetric plaque (P). (b) The image produced by subtraction of fat and water images. The plaque (P) has a lower signal than the marrow (M) in the vertebral body which contains fat in a similar proportion to a lipid-rich plaque; therefore this is a fibrous plaque which will not rupture and cause sudden death

5 THE FUTURE

More versatile magnetic resonance machines capable of echo planar imaging and spiral velocity mapping will become available. These machines will use a new generation of open-access magnets in which ultrasound and laser intervention will be done using direct NMR vision. Ultrasound surgery with NMR vision has the advantage that the ultrasound energy can be applied at a low level using the changes to the NMR signal with increased temperature to confirm that the ultrasound transducers are focused on the area of interest. The ultrasound energy can then be increased to ablate the lesion. The massive intellectual pool of knowledge of NMR will be switched from less common diseases to cardiology, oncology, and to the lung. Proper training in cardiovascular NMR is required, not so much for imagers, as for cardiologists and experts in vascular disease.

6 CONCLUSIONS

Functional NMR evaluation of the cardiovascular system using volume measurements, velocity encoded rapid imaging, and chemical shift imaging is capable of making the diagnosis in congenital and acquired cardiovascular disease which, between them, cause the largest number of deaths of any disease in the western world and massive morbidity and suffering. Furthermore, for the first time in the history of medicine, there is the opportunity to apply preventive measures to eradicate the epidemic of preventable arterial disease.

7 RELATED ARTICLES

Blood Flow: Quantitative Measurement by MRI; Breast MRI; Echo-Planar Imaging; Heart: Clinical Applications of MRI; Lung and Mediastinum MRI; Whole Body Magnetic Resonance: Fast Low-Angle Acquisition Methods.

8 BACKGROUND NOTE

Atheromatous disease was unknown in Central Europe after World War I. Autopsy studies at the London Hospital from 1908–40 showed a steady increase in coronary artery disease. Casualties in the starving population of the siege of Leningrad in World War II showed no arterial disease; likewise there was no atheromatous disease in the survivors of concentration camps. Young soldiers killed in the Korean and Vietnam Wars showed massive diffuse disease. Experimental atheroma in laboratory animals regresses with starvation. Atheromatous disease does not coexist with wasting diseases. It also varies not only from time to time but from place to place. There are wide variations in its incidence in apparently genetically similar populations in different countries. There is no relationship between the 'spend' on health care and the incidence of disease. The USA spends the highest proportion of its GDP on health care and the UK nearly the lowest. Both countries are amongst those with the highest incidence. France, a high spender, and Japan, the lowest, share the lowest incidence of occlusive vascular disease.

9 REFERENCES

1. D. B. Longmore, *Diagn. Imag.*, 1988, 399.

2. Physiology and Treatment of Starvation: Experiences in Warstarved Europe, Report of Societies 818, *Br. Med. J.*, June 9, 1945.
3. J. Brozek, S. Wells, and A. Keys, 'Medical Aspects of Semistarvation in Leningrad (Seige 1941–42)'.
4. P. Mollison, *Br. Med. J.*, January 1946.
5. B. A. Porter and J. P. Smith, *Magn. Reson.*, 1993.
6. G. L. Nayler, D. N. Firmin, and D. B. Longmore, *J. Comput. Assist. Tomogr.*, 1986, **10**, 715.
7. D. J. Bryant, J. A. Payne, D. N. Firmin, and D. B. Longmore, *J. Comput. Assist. Tomogr.*, 1984, **8**, 588.
8. P. Mansfield and I. L. Pykett, *J. Magn. Reson.*, 1978, **29**, 355.
9. J. Frahm, A. Haase, and D. Matthaei, *Magn. Reson. Med.*, 1986, **3**, 321.
10. D. N. Firmin, P. D. Gatehouse, and D. B. Longmore, *Proc. XIth Annu. Mtg. Soc. Magn. Reson. Med.*, Berlin, 1992, 2915.
11. P. J. Kilner, C. C. Manzara, R. H. Mohiaddin, D. J. Pennell, M. G. St. J. Sutton, D. N. Firmin, S. R. Underwood, and D. B. Longmore, *Circulation*, 1993, **87**, 1239.
12. D. B. Longmore, R. H. Klipsten, S. R. Underwood, D. N. Firmin, G. N. Hounsfield, M. Watanabe, C. Bland, K. Fox, P. A. Poole-Wilson. R. S. O. Rees, D. N. Denison, A. M. McNeilly, and E. D. Burman, *Lancet*, 1985, **i**, 1360.
13. P. J. Kilner, D. N. Firmin, J. Martinez, J. Somerville, S. R. Underwood, R. S. O. Rees, and D. B. Longmore, *Eur. Heart J.*, 1991, **12**(Suppl.), 284.
14. M. Huber, D. B. Longmore, D. N. Firmin, J. Assheuer, H. Bewermeyer, and W. D. Heiss, *Digit. Bilddagnos.*, 1989, **9**, 1.
15. H. G. Bogren, S. R. Underwood, D. N. Firmin, R. H. Mohiaddin, R. H. Klipstein, R. S. O. Rees, and D. B. Longmore, *Br. J. Radiol.*, 1988, **61**, 456.
16. R. H. Mohiaddin and D. J. Pennell, in 'Percutaneous Balloon Valvuloplasty', ed. T. O. Cheng, Igaku-Shoin Medical Publishers, New York, 1992, pp. 185–213.
17. S. M. Forbat, S. P. Karwatowski, P. D. Gatehouse, D. N. Firmin, S. R. Underwood, and D. B. Longmore, *Br. J. Radiol*, 1993, **66**, 957.
18. D. J. Pennell, S. R. Underwood, and D. B. Longmore, *J. Comput. Assist. Tomogr.*, 1990, **14**, 167.
19. S. P. Karwatowski, R. H. Mohiaddin, G. Z. Yang, D. N. Firmin, M. G. St. J. Sutton, S. R. Underwood, and D. B. Longmore, *JMRI*, 1994, **4**, 151.
20. D. J. Pennell, S. R. Underwood, C. C. Manzara, R. H. Swanton, J. M. Walker, P. J. Ell, and D. B. Longmore, *Am. J. Cardiol.*, 1992, **70**, 34.
21. D. J. Pennell, S. R. Underwood, P. J. Ell, R. H. Swanton, J. M. Walker, and D. B. Longmore, *Br. Heart J.*, 1990, **64**, 362.
22. R. H. Mohiaddin, S. R. Underwood, H. G. Bogren, D. N. Firmin, R. H. Klipstein, R. S. O. Rees, and D. B. Longmore, *Br. Heart J.*, 1989, **62**, 90.
23. R. H. Mohiaddin, D. N. Firmin, S. R. Underwood, A. K. Abdulla, R. H. Klipstein, R. S. O. Rees, and D. B. Longmore, *Br. Heart J.*, 1989, **62**, 81.

Coronary Artery Disease Evaluated by MRI

Robert R. Edelman and Warren J. Manning
Beth Israel Hospital, Boston, MA, USA

1 Related Articles 3
2 References 3

Magnetic resonance imaging has had a profound clinical impact in several areas, including the brain, spine, and joints. A variety of technical advances have expanded the applications of MRI into areas where motion can be problematic, such as the abdomen. Fast imaging techniques also permit good quality images of the heart to be acquired, either for the demonstration of anatomy or for the measurement of function. Nonetheless, the clinical impact of MRI in the heart has only been modest. Aside from the technical challenges involved in imaging the beating heart, alternative, less expensive, and more readily available imaging modalities, such as ultrasound and radionuclide scintigraphy, can usually provide the desired information.

There is one area where alternative noninvasive imaging tests fall short, i.e. in the assessment of myocardial ischemia. Cardiovascular disease remains the leading cause of death in the United States with an estimated 1.2 million myocardial infarctions and 600 000 deaths per year attributed to coronary artery disease.[1] Minimally invasive tests for myocardial ischemia include single photon emission tomography (SPECT)[2,3] and positron emission tomography (PET).[4,5] These tests reveal perfusion abnormalities, but do not depict the coronary artery stenoses that cause them nor do they provide direct measurements of coronary artery blood flow. Transthoracic and transesophageal echocardiography can depict portions of the coronary arteries, but not sufficiently for routine clinical use.[6–8] While transesophageal echocardiography does not require contrast injection, it does require esophageal intubation and has associated risks of death, esophageal perforation/laceration, aspiration/hypoxia, and arrhythmias.[9]

The 'gold standard' for the evaluation of the coronary arteries is contrast angiography with over 500 000 diagnostic cardiac catheterizations performed annually in the United States. Despite the development of multiple noninvasive tests for the detection of myocardial ischemia, up to 20% of these coronary angiograms reveal insignificant coronary artery disease.[10] Information derived from such angiograms, however, is the standard by which mechanical interventions and many medical therapies are planned. In addition, prognostic information is also gained from data regarding coronary artery patency.

Hospital charges alone for cardiac catheterizations have been estimated at over $1.8 billion annually. In addition, coronary angiography carries with it a low, though finite major complication rate—death (0.12–0.20%), cerebrovascular accident (0.03–0.20%), myocardial infarction (0.0–0.25%) and a minor complication rate—vascular complication, local infection (0.57–1.6%), or arrhythmias (0.30–0.63%).[11–13] The high cost and associated risk make routine coronary angiography inappropriate for use as a screening test. Furthermore, while semiquantitative techniques exist for estimating the flow restriction caused by a coronary artery stenosis based on the conventional angiogram,[14] they do not provide a quantitative measure of coronary artery blood flow.

Magnetic resonance (MR) imaging is well suited for evaluating the heart, with excellent soft-tissue contrast and the ability to image the heart in double-oblique tomographic sections. Complex cardiac anatomy[15] and systolic function[16] have already been elucidated using MR imaging techniques. Magnetic resonance angiography is currently being used in several clinical applications, including screening for intracranial aneurysms,[17] detection of stenoses of the extracranial carotid arteries,[18] vertebro-basilar system, and renal arteries.[19] If the techniques of MR angiography could be extended successfully to the heart, then MR might be used to predetermine which patients should go on for coronary catheterization, to follow high-risk patients noninvasively, to quantify flow reserve so as to determine the physiological significance of a stenosis, or ultimately as a cost-effective substitute for catheterization.

Human coronary arteries are small in caliber. The left main coronary artery is typically 4–6 mm in diameter[20] while the left anterior descending and left circumflex coronary arteries are generally 3–4 mm at their origins and taper distally. The right coronary artery supplying less myocardium is smaller than the left main, and is typically 3–4 mm proximally. High-resolution MR angiography of arteries of similar caliber (e.g. circle of Willis) to epicardial coronary vessels has been successful, but reproducible coronary angiography has remained elusive due to the effects of significant cardiac and respiratory motion. Standard ECG-gated spin echo and gradient echo cine images only occasionally show portions of the coronary arteries, and these images are not adequate for detailed evaluation.[21]

There are several fast imaging methods that have been used for coronary artery imaging. Three-dimensional gradient echo methods[22] permit thin sections and short *TE*, thereby minimizing partial volume averaging and flow-related dephasing. With 3D approaches, however, saturation effects are more severe than with 2D approaches, resulting in suboptimal flow contrast particularly in the setting of low flow velocities. Unfortunately, long scan time for 3D acquisitions (at least several minutes for ECG-gated studies) precludes breath-holding, so that significant blurring from respiratory motion will occur.

Subtraction methods also have potential value for coronary artery imaging. One approach involves the interleaved acquisition of a pair of projection (thick section) images, of which one has a spatially localized inversion pulse applied to the aortic root to tag the coronary inflow.[23] Since only the signal intensity of the coronary arteries is altered by the inversion pulse, background and cardiac chamber signals are eliminated by image subtraction. Potential drawbacks of this method are the need for prolonged breath-holding periods (e.g. 24 s or longer), inadvertent saturation of other structures such as blood within the left atrium, dependence of flow contrast on the R–R interval, and potential misregistration resulting in imperfect subtraction. The method also assumes that blood within the major epicardial coronary arteries is completely displaced

within one R–R interval by blood from the aortic root. The use of a thick section also has the drawback of increased intravoxel dephasing compared with the use of thin sections. Nonetheless, encouraging preliminary results have been demonstrated in healthy volunteers.

Conventional gradient echo pulse sequences used for cine cardiac imaging consist of a radiofrequency pulse followed by a gradient refocused echo. The data acquisition is synchronized to the cardiac cycle. One line of data (one phase-encoding step) is acquired for each phase of the cardiac cycle within one R–R interval. As a result, the time required to acquire 128 lines of data (the amount required for a 128 × 256 matrix image) is 128 × R–R interval. For a 1-s interval, the imaging time is approximately 2 min, too long for a breath-hold. In order to acquire the images within a breath-hold interval, the sequence is modified so that up to 10 lines of data are acquired in rapid sequence within a 100 ms time period.[24] This group of lines is called one segment, and the imaging technique is called *segmented turboflash* or *breath-hold cine*. In our experience, there is relatively little blurring of coronary artery detail for segment durations up to 100 ms, but the blurring worsens as the duration is further increased. Imaging is performed during diastole, when cardiac motion is least and coronary flow velocities are high. One segment is acquired during each heart beat, and a series of these segments, acquired over multiple heart beats, are then combined to create a whole image. For instance, 16 segments, each consisting of eight lines of data, would be combined so as to complete a 128 × 256 matrix. The imaging time would be 16 heart beats, on the order of 16 s or less. Cine imaging is also feasible by acquiring segments in rapid sequence (one segment per cardiac phase) within each breath-hold.

Flow velocities in the coronary arteries of resting subjects are rather low, on the order of 10–30 cm s^{-1}. As a result, it is difficult to develop adequate flow contrast in the coronaries, compared to the adjoining myocardium, on the basis of inflow effects alone. This is a particular problem when the coronary arteries are imaged longitudinally. However, the epicardial portions of the coronary arteries are typically surrounded by fat. It is possible to apply fat suppression pulses (binomial or chemical shift selective) to diminish the signal intensity of the epicardial fat. By combining the segmented turboflash method with fat suppression techniques, the proximal and more distal portions of the epicardial coronary arteries are routinely depicted.

We have begun clinical studies of MR coronary angiography (Figure 1 and 2).[25] Sensitivity and specificity for coronary artery disease are in the 80–90% range, which is comparable with thallium scintigraphy. One problem has been poor flow contrast resulting from slow flow distal to a severe stenosis, making it difficult to distinguish a stenosis from an

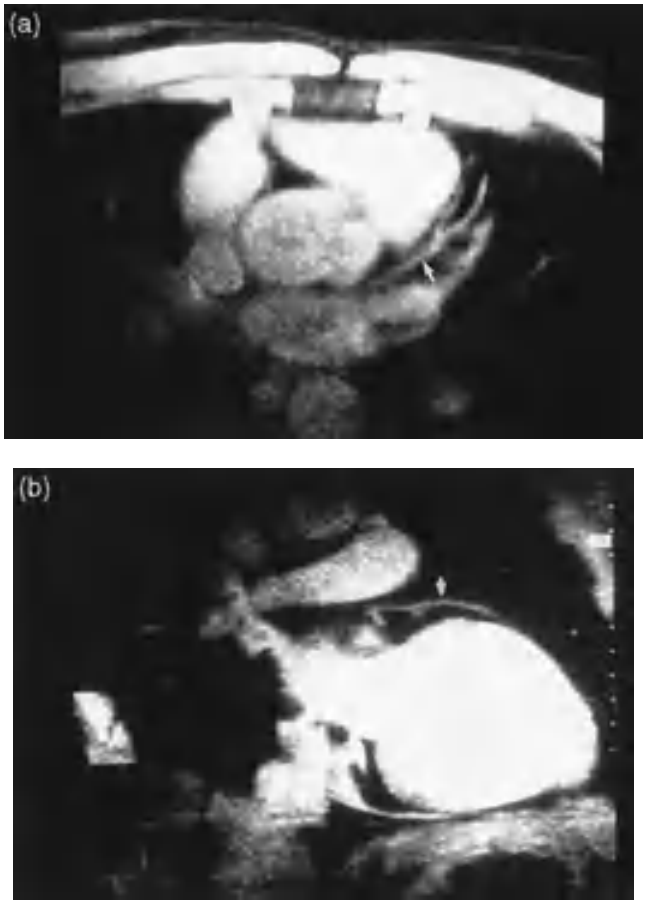

Figure 1 Left anterior descending coronary artery. (a) Axial segmented turboFLASH image shows the left anterior descending coronary artery (arrow) and a septal branch. (b) Oblique view in another subject shows the left anterior descending coronary artery (arrow) and a septal branch

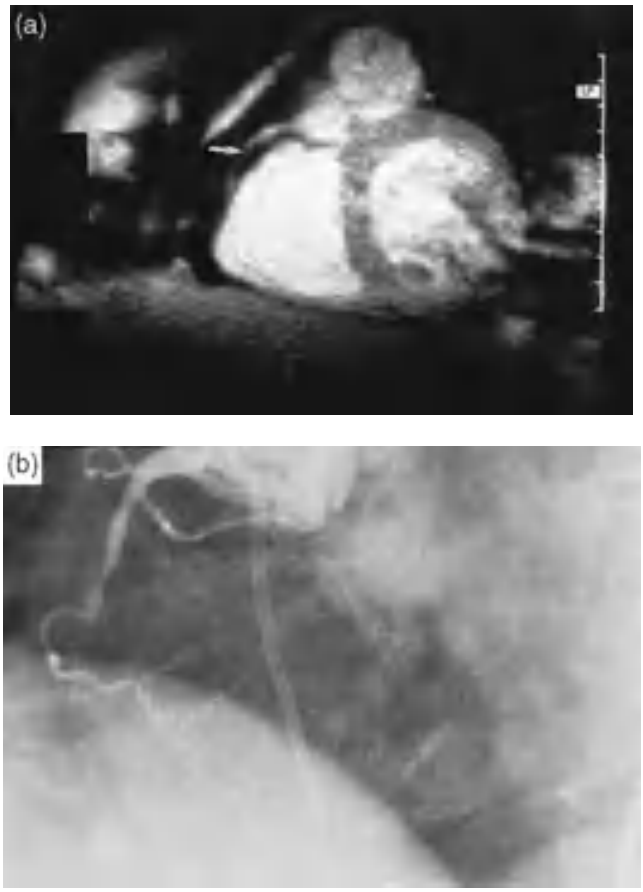

Figure 2 Severe stenosis of the right coronary artery. (a) MR angiogram shows the lesion (arrow). (b) Coronary catheterization

occlusion. This problem might be ameliorated by the use of contrast agents. Blood pool contrast agents are currently under development that could greatly improve the quality of coronary artery images.

Compared with our original technique, we have recently obtained a greater than 50% improvement in signal-to-noise ratio by lowering the sampling bandwidth of the sequence from 195 Hz pixel^{-1} to 78 Hz pixel^{-1}, keeping the echo time at 7 ms. This was possible because of enhancements in the gradient capabilities of our MRI system. The signal-to-noise ratio improvement has allowed us to position the patient supine within the body coil, which is better tolerated than the prone positioning previously required with a flat surface coil. Further 2–3-fold signal-to-noise improvements will be possible with the introduction of circularly polarized whole-volume phased-array coils.

Flow velocity measurements can be done by using a phase contrast modification of segmented turboFLASH, in which two segmented turboFLASH images are acquired in a single breath-hold.[26] In one sequence, the slice-selective gradient incorporates a three-lobed, velocity-compensated waveform that is insensitive to flow; in the other, a bilobed waveform is applied resulting in a measurable shift in the phase of the MR signal of flowing blood. The gradients were calibrated to permit flow velocity measurements up to 150 cm s^{-1}. A 96 × 256 acquisition matrix is used with pixel dimensions of 1.4 mm × 0.8 mm. Four images are produced by this sequence, comprising magnitude and phase reconstructions of the flow-insensitive and flow-sensitive data. The flow-insensitive magnitude image shows vessel anatomy, whereas subtraction of the flow-insensitive and flow-sensitive phase images produces a phase difference image in which the phase shift is proportional to the flow velocity along the direction of slice selection. Image subtraction eliminates background phase shifts unrelated to blood flow.

The method was tested in 12 subjects studied at rest and four studied before and during pharmacologic stress using intravenous adenosine. Flow velocities at rest in the midportion of the right coronary artery were 9.9 ± 3.5 cm s^{-1} (n = 12); in the proximal left anterior descending artery they were significantly higher, measuring 20.5 ± 5.2 cm s^{-1} (n = 6). With adenosine, flow velocities typically increased at least fourfold. These results indicate that noninvasive measurement of coronary artery flow velocities is feasible using MR angiography. Table 1 summarizes the current performance of MR coronary angiography in our clinical practice.

Finally, entirely new imaging techniques are likely to be developed that are advantageous compared with segmented turboFLASH. The fastest known method for creating an MR image is called echo planar imaging (EPI).[27] The most commonly used EPI method, called blipped EPI, oscillates the read-out gradient so that a series of gradient echoes are generated. Each gradient echo is separately phase-encoded by a short duration gradient pulse (the blip); alternatively, a constant amplitude phase-encoding gradient can be applied for the entire read-out period. Using specially designed gradient coils, EPI can generate a series of 64 echoes in as little as 32 ms. Thus a 64 × 128 matrix image can be acquired in 1/30th of a second, which is sufficiently short to freeze any kind of physiologic motion, including that of the heart. We have had promising results imaging the coronary arteries recently using an echo planar MR angiography method that circumvents the problem of vessel tortuousity by using thick slices and suppression of background tissue signal.

Table 1 Sensitivity and Specificity of the MR Coronary Angiographic Technique to Correctly Classify a Vessel as having Significant Disease.[a] Sensitivity/specificity for Individual Vessels are as Listed.[b]

	No. (%) with disease	Sensitivity (%)	Specificity (%)	PV (+)	PV (−)
Left main	2 (5)	100	100	1.00	1.00
LAD	23 (64)	87	92	0.95	0.80
LCX	7 (20)	71	90	0.63	0.93
RCA	20 (53)	100	78	0.83	1.00
Patient	29 (74)	97	70	0.90	0.88

[a]Sensitivity = 90%; specificity = 90%.
[b]LAD = left anterior descending coronary artery; LCX = left circumflex coronary artery; RCA = right coronary artery; PV (+) = predictive value positive; PV (−) = predictive value negative.

1 RELATED ARTICLES

Abdominal MRA; Whole Body Magnetic Resonance Angiography; Head and Neck Studies Using MRA; Phase Contrast MRA; Time-of-Flight Method of MRA.

2 REFERENCES

1. S. S. Yang, L. G. Bentivoglio, V. Maranhao, and H. Goldberg (eds.) *Cardiac Catheterization Data to Hemodynamic Parameters*, 3rd edn., F. A. Davis, Philadelphia, PA, 1988, p. 256.
2. B. L. Holman, S. C. Moore, P. M. Shulkin, C. M. Kirsch, R. J. English, and T. C. Hill, *Invest. Radiol.*, 1983, **18**, 322.
3. J. H. Cladwell, D. L. Williams, G. D. Harp, J. D. R. Stratton, and J. L. Ritchie, *Circulation*, 1984, **70**, 1048.
4. R. C. Marshall, J. H. Tillisch, M. E. Phelps, S. C. Huang, R. Carson, E. Henze, and M. R. Schelbert, *Circulation*, 1983, **67**, 766.
5. R. Brunken, J. H. Tillisch, M. Scwarger, J. S. Childs. R. Marshall, M. Mandelkern, M. E. Phelps, and H. R. Schelbert, *Circulation*, 1986, **73**, 951.
6. C. C. Chen, J. Morganroth, S. Ogawa, and T. J. Mardelli, *Circulation*, 1980, **62**, 288.
7. S. Ogawa, C. C. Chen, F. E. Hubbard, F. S. Pauletto, T. J. Mardelli, J. Morganroth, L. S. Dreifus, M. Akashi, and Y. Nakamura, *Am. J. Cardiol.*, 1980, **45**, 301.
8. F. B. Pearce, K. H. Sheikh, N. P. deBruijn, and J. Kisslo, *J. Am. Soc. Echo*, 1989, **2**, 276.
9. W. B. Daniel, R. Erbel, W. Kasper, C. A. Visser, R. Engberding, O. R. Sutherland, E. Arribe, P. Hanroth, and B. Maisch et al., *Circulation*, 1991, **83**, 817.
10. L. W. Johnson, E. C. Lozner, S. Johnson, R. Kron, A. D. Pichard, G. W. Vetrovec, and T. J. Nota, *Cathet. Cardiovasc. Diagn.*, 1989, **17**, 5.
11. K. Davis, J. W. Kennedy, H. G. Kemp, M. P. Judkins, A. J. Gosselin, and T. Killip, *Circulation*, 1979, **59**, 1105.
12. J. W. Kennedy/ Registry Committee of the Society for Cardiac Angiography, *Cathet. Cardiovasc. Diagn.*, 1982, **8**, 5.
13. R. M. Wyman, R. D. Safian, V. Portway, S. J. Shilman, R. G. McKay, and D. S. Bain, *J. Am. Coll. Cardiol.*, 1988, **12**, 1400.

14. K. L. Gould, *Cardiovasc. Intervent. Radiol.*, 1990, **13**, 5.
15. D. Didier, C. B. Higgins, M. R. Fisher, L. Osaki, N. H. Silverman, and M. D. Cheitlin, *Radiology*, 1986, **158**, 227.
16. C. B. Higgins, W. Holt, P. Pflugfelder, and U. Sechtem, *Magn. Reson. Med.*, 1988, **6**, 121.
17. P. M. Ruggieri, G. A. Laub, T. J. Masaryk, and M. T. Modic, *Radiology*, 1989, **171**, 785.
18. T. J. Masaryk, M. T. Modic, P. M. Ruggieri, J. S. Ross, G. Laub, G. W. Lenz, J. A. Tkaeh, E. M. Haacke, W. R. Selman, and S. I. Harik, *Radiology*, 1989, **171**, 801.
19. K. C. Kent, R. R. Edelman, D. Kim, T. I. Steinman, D. H. Porter, and J. J. Skillman, *J. Vasc. Surg.*, 1991, **13**, 311.
20. S. Paulin, *Acta Radiologica*, 1964(Suppl.), 125.
21. S. Paulin, G. K. von Schulthess, E. Fossel, and H. P. Krayenbuehl, *Am. J. Roentgen.*, 1987, **148**, 665.
22. C. B. Paschal, E. M. Haacke, L. P. Adler, W. Lin, A. Sketty, and R. J. Alfidii, *Proc. 9th Annu. Meet. Soc. Magn. Reson. Med., New York, Aug. 18–24, 1990*, p. 278.
23. S. J. Wang, B. S. Hu, A. Marcovski, and D. G. Nishimura, *Magn. Reson. Med.*, 1991, **18**, 417.
24. R. R. Edelman, W. J. Manning, D. Burstein, and S. Paulin, *Radiology*, 1991, **181**, 641.
25. W. J. Manning, W. Li, and R. R. Edelman, *N. Engl. J. Med.*, 1993, **328**, 828.
26. R. R. Edelman, W. J. Manning, E. Gervino, and W. Li, *J. Magn. Reson. Imag.*, 1993, **3**, 699.
27. M. K. Stehling, R. Turner, and P. Mansfield, *Science*, 1991, **254**, 43.

Heart: Clinical Applications of MRI

Scott D. Flamm and Charles B. Higgins
University of California at San Francisco, San Francisco, CA, USA

1 INTRODUCTION

The first electrocardiographically gated magnetic resonance images of the human heart were shown in 1984. In the decade that followed several important techniques have been developed which facilitate the use of MRI for the evaluation of cardiovascular morphology, contractile function, myocardial tissue characterization, and blood flow. With these techniques, MRI has been found to be effective for the investigation of a variety of acquired and congenital cardiovascular diseases. This role of MRI in relation to preexisting cardiac imaging techniques continues to evolve.

The clearly defined indications for the effective use of MRI in acquired heart disease include the evaluation of pericardial disease, right ventricular dysplasia, thoracic aortic disease, intra- and extracardiac masses, cardiomyopathies, valvular heart disease, ischemic myocardial disease, and the morphology of the coronary arteries.

The indications for the application of MRI in congenital heart disease include the assessment of pulmonary artery morphology, coarctation of the aorta, vascular rings, complex congenital heart disease, and postoperative evaluation.

2 IMAGING TECHNIQUES

A multitude of sequences are available for cardiac imaging (Table 1). These include spin echo and multiplanar multiphasic techniques for morphological information of both cardiac and extracardiac structures (e.g. the great vessels). Anatomical information also can be obtained using electrocardiogram (ECG)-gated cine gradient echo (cine GRE) and newer, fast gradient echo techniques that sample segmented *k*-space during a single breath-hold (breath-hold cine GRE). These latter two techniques are also useful for acquiring multiple, ECG referenced images of the heart, in either long or short axis projections similar to echocardiography, which may be electronically 'looped' and viewed in a cinematic format to evaluate global ventricular function and segmental wall motion. Velocity-encoded cine MRI techniques can assess quantitatively blood flow velocity and flow volume within the heart to evaluate intracardiac shunts, and valvular pathology and function. This same technique may also be used in the great vessels to determine pulmonary and aortic blood flow, including differential flow to the right and left pulmonary arteries, as well as to estimate gradients across areas of stenosis such as in coarctation of the aorta.

For multislice spin echo MRI, ECG gating is required to 'freeze' the motion of the heart, and respiratory compensation further improves image quality (see also ***Cardiac Gating Practice*** and ***Motion Artifacts: Mechanism and Control***). In adults, typical sequences include ECG gating T_1-weighted images of 7–10 mm slice thickness obtained in the axial plane, with supplemental images acquired in the sagittal, and oblique sagittal, axial, and coronal planes, as dictated by the particular clinical concern.

In adults and children, body coils are used most commonly. Flexible phased array surface coils are gaining in use for both general and special purposes, as they provide greater resolution and image contrast as a result of improved signal-to-noise ratios. For some infants and small children a head coil may be practical, and will result in the greatest resolution and signal-to-noise ratio for the relatively small areas of interest.[1]

3 LEVEL OF CURRENT CLINICAL ACTIVITY

Cardiovascular MRI is used primarily for detection and delineation of anatomical abnormalities according to a recent survey of members of the Society for Magnetic Resonance

Table 1 Techniques for MRI of the Heart

Technique	Application
ECG-gated spin echo	Anatomy and morphology
Cine GRE	Anatomy; atrial and ventricular dimensions and volumes; global and regional ventricular function
Fast (turbo) GRE	Anatomy; myocardial perfusion; rapid imaging of great vessels
Breath-hold, segmented *k*-space GRE	Anatomy including coronary arteries; myocardial perfusion; global and regional ventricular function
Velocity encoded cine MRI	Valvular function (quantification of regurgitation, and estimation of peak valvular gradient), measurement of stroke volume and cardiac output of each ventricle, quantification of shunts, measurements of differential flow in right and left pulmonary arteries, quantification of gradients at stenoses of the pulmonary arteries or coarctation of the aorta
Echo planar	Global and regional function of left and right ventricles, quantification of regional myocardial blood volume and perfusion

Imaging. Of the responding centers, 46% reported exclusively clinical work, 3% exclusively research, and 51% both clinical and research. The majority of MRI studies are performed in the evaluation of thoracic aortic disease, congenital heart disease, and cardiac masses. While most studies are performed for morphological information, half of the centers also accomplish functional studies, usually for ventricular and/or valvular function, in conjunction with anatomical studies.[2]

4 ACQUIRED HEART DISEASE

4.1 Pericardial Disease

Differentiating constrictive pericarditis from restrictive pericarditis is the most frequent indication for applying MRI in pericardial disease. This is an important distinction because both diseases cause similar hemodynamic abnormalities, and are usually indistinguishable on cardiac catheterization. Only constrictive pericarditis can be alleviated by surgery. Constrictive pericarditis is seen most commonly after cardiothoracic surgery, and radiation therapy. On spin echo sequences it is manifested by local or generalized thickening of the pericardium to 4 mm or greater. This thickening is more readily evident over the right ventricle and right atrium. Associated findings include enlargement of the right atrium, inferior vena cava and hepatic veins, pericardial effusion, and tubular narrowing of the right ventricle. The reported diagnostic accuracy of MRI in establishing the diagnosis is 93%.[3]

MRI also can be used to examine the pericardium and its contents for evidence of effusion or hemorrhage, and mass lesions. Echocardiography is a fast, effective technique to determine the presence and general quantity of pericardial effusions, but can be less accurate in discerning hemorrhagic from nonhemorrhagic effusion, or determining the extent and location of loculated effusions, particularly in the posterior and basal portions of the heart. Spin echo MRI can easily determine the anatomical location and size of effusions, as well as the extent of loculations in all portions of the heart. It also has the advantage of more easily identifying the presence of pericardial masses, which may represent metastatic tumors responsible for hemorrhagic and/or recurrent effusion. The hemorrhagic nature of effusions can be identified with T_1-weighted spin echo sequences as high signal intensity, in contrast to the very low signal intensity of nonhemorrhagic pericardial effusions.

4.2 Right Ventricular Dysplasia

Right ventricular dysplasia is a relatively uncommon disorder generally occurring in young people, and manifesting as potentially life threatening arrhythmias originating from the right ventricle. The diagnosis is predicated on the identification of fatty infiltration or fibrosis replacing the right ventricular myocardium. The diagnosis of right ventricular dysplasia is difficult to establish even with electrophysiological studies and myocardial biopsy.

The primary diagnostic feature on MRI is transmural fat within the free wall of the right ventricle, but the spectrum of findings includes 'islands' of fat within, or abnormal thinning of, the right ventricular free wall, regional or global contraction abnormalities of the right ventricle, and aneurysmal outpouching of the right ventricular outflow tract during systole.[4] Axial spin echo images focused on the right ventricular free wall are used to demonstrate myocardial fat, and cine GRE sequences obtained in the axial or horizontal long axis are useful to evaluate regional right ventricular contraction abnormalities. The utility of MRI in establishing the diagnosis noninvasively was recently documented in a group of patients with biopsy proven right ventricular dysplasia. Those patients with inducible right ventricular arrhythmias were significantly more likely to have identifiable fat within the myocardium, contraction abnormalities of the right ventricle, and/or a lower ejection fraction.[5]

The course of patients with right ventricular dysplasia typically has been followed with periodic right heart angiography and myocardial biopsy, which entails a significant degree of risk. MRI appears to be an effective technique for identifying at least a subset of patients with right ventricular dysplasia, and may become the procedure of choice for follow-up.

4.3 Thoracic Aortic Disease

Aneurysm and dissection are the most common indications for MRI of the thoracic aorta. Spin echo sequences are used to demonstrate the morphology of thoracic aortic aneurysms, which may occur as a result of atherosclerosis, trauma, or Marfan's syndrome, or may be mycotic or syphilitic in origin. In aortic dissection the intimal flap can often be identified on spin echo images, but is more readily seen with GRE and cine GRE sequences (Figure 1). These techniques also are effective in correctly identifying the true and false lumens, and differentiating slow flow versus thrombus within the false lumen. Additionally, MRI can identify the presence of hematoma within the wall of the aorta.[6] This cannot be defined with X-ray angiography.

MRI is a highly sensitive and specific technique for the detection of aortic dissection that can identify both the intra- and extravascular space, and the walls of the aorta. Conventional angiography has been considered the gold standard, but requires an invasive procedure, may incompletely identify the false lumen and its extent, and is unable to evaluate fully the walls of the aorta, and the extravascular space. MRI has proven to be superior to X-ray angiography and transthoracic echocardiography.

MRI has been compared to transesophageal echocardiography, which is also a highly sensitive technique, and has the advantage of being portable, permitting its use in critical and unstable patients unable to leave the intensive care setting. Multiple studies have demonstrated a similar high sensitivity (98–100%) for both methods, but MRI has a significantly higher specificity (98–100%) than transesophageal echocardiography (68–77%) in high risk populations.[7,8]

Evaluation of the thoracic aorta usually requires approximately 20–30 min using standard cine GRE sequences. Newer sequences, particularly segmented *k*-space breath-hold cine GRE sequences, can acquire each slice in 12–16 s, providing images of the entire thoracic aorta in approximately 5 min. The study can be extended to the abdominal aorta to evaluate for potential involvement of the mesenteric vessels with the addition of a few minutes of imaging time.

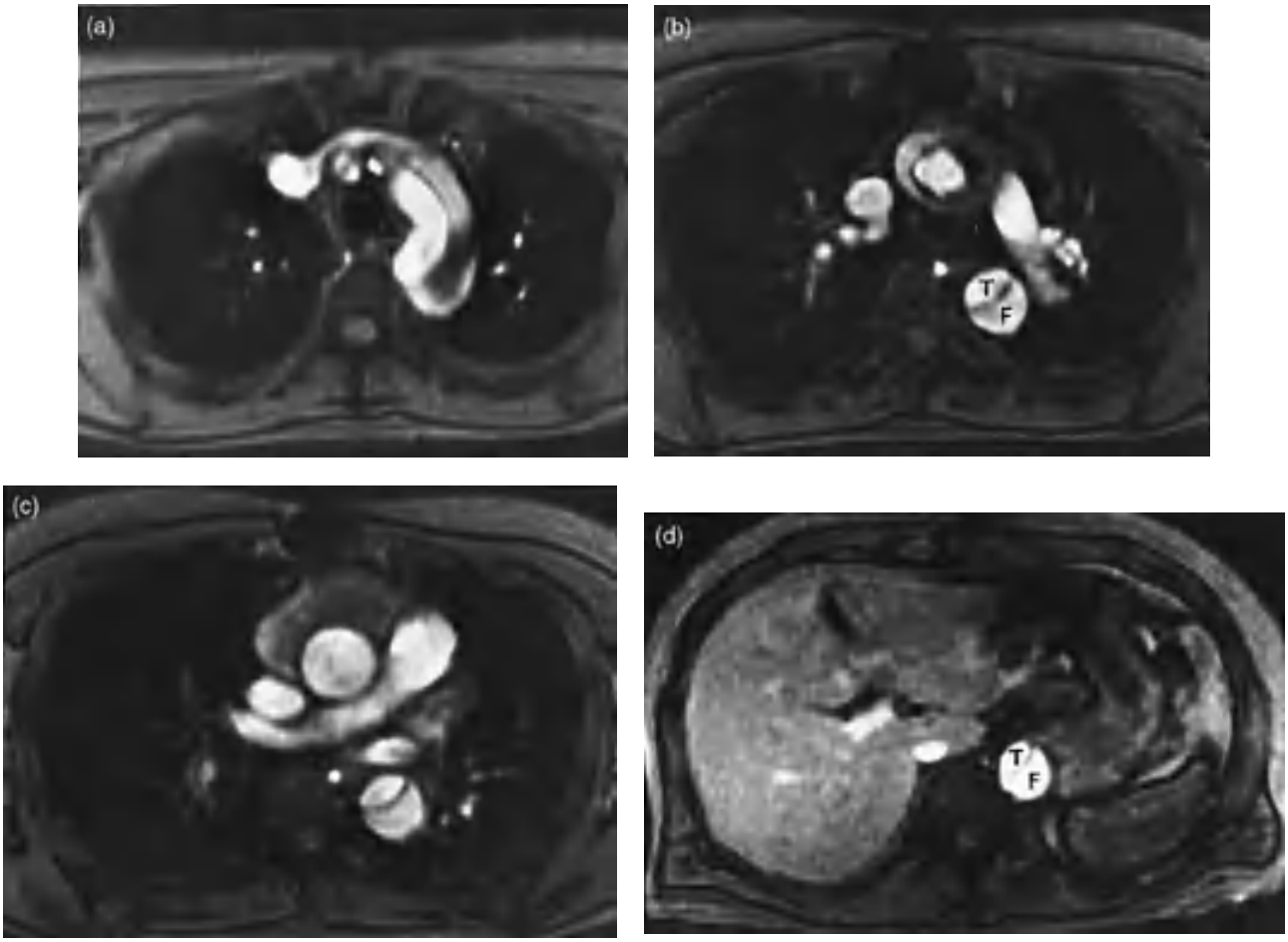

Figure 1 Series of selected images from a patient with a type A aortic dissection involving the aortic arch, descending thoracic aorta, and abdominal aorta. These are images acquired using a breath-hold segmented *k*-space cine MRI sequence acquired at the level of (a) the aortic arch, (b) the left pulmonary artery, (c) the main and right pulmonary artery, and (d) the upper abdomen. Note the compression of the true lumen by the false lumen. The bright signal within the false lumen confirms the presence of flow. T, true lumen; F, false lumen

4.4 Intracardiac Masses

Tumor, thrombus, and valvular vegetations (as occur in bacterial endocarditis) are the primary considerations when there is concern for an intracardiac mass. There are no studies demonstrating the benefit of MRI for valvular vegetations; echocardiography remains the most effective noninvasive technique for this determination.

MRI is effective for evaluating intracardiac masses, and in most instances can differentiate between tumor and thrombus.[9] Spin echo sequences are usually adequate to identify the size and location of intracardiac masses. Both tumors and thrombus tend to be isointense to myocardium on spin echo images; however, some thrombi may have a low signal intensity and be indistinguishable from the ventricular cavity without the additional application of cine GRE sequences.[10] Cine GRE sequences are particularly useful in that they permit identification of the majority of masses, and typically are successful in differentiating thrombus from tumor.[11] The most common tumors include myxomas (usually left atrial), rhabdomyomas (usually right ventricular), and metastases from primary carcinoma of the breast or lung, or melanoma. On cine GRE images tumors tend to be intermediate in signal intensity, with myocardium being low–intermediate in intensity, while thrombus is frequently very low in signal intensity. In the case of relatively fresh thrombus, high signal intensity may be present on cine GRE images. These signal characteristics hold true in the majority of instances; however, some tumors, particularly myxomas which have bled internally, may contain increased amounts of hemosiderin, making them very low signal intensity on GRE images.

4.5 Cardiomyopathy

There are four recognized types of cardiomyopathy—hypertrophic, congestive (or dilated), restrictive, and obliterative—each of which has a distinct constellation of morphological and functional features. The etiology of the myocardial abnormality is varied. Most forms are idiopathic in nature, but chronic injury from ischemia or toxins, or infiltrative disorders are responsible for a minority of cases. The hypertrophic and congestive forms have been studied extensively with MRI; less is known about the obliterative form as it is very rare, and encountered primarily in Africa.

Hypertrophic cardiomyopathy usually manifests as global hypertrophy of the left ventricular myocardium, though many

variants have been documented with MRI, including focal or diffuse septal hypertrophy, and midventricular and apical forms.[12] Cine GRE, acquired in either the long or short axis, has been used to quantify left ventricular mass, volumes, and ejection fraction in this disease. MRI has shown high accuracy and interstudy reproducibility for quantifying left ventricular volumes and mass, providing a precise technique for serial assessment during treatment.[13,14] Patients with hypertrophic cardiomyopathy also demonstrate abnormal diastolic and systolic function. The overall heart size remains normal, but the end-diastolic volume and filling rates are reduced in both the left and right ventricles.[15] Systolic function is hyperdynamic, and near obliteration of the ventricular cavity, particularly at the apex, is a characteristic feature (Figure 2).

In congestive cardiomyopathy the overall cardiac dimensions are increased, and there is left ventricular dilation. The idiopathic forms have normal myocardial thickness, and as a result the myocardial mass is greater than normal. In patients with chronic injury or ischemic etiology the myocardium may be globally or focally thinned. As in the hypertrophic form, cine MRI in congestive cardiomyopathy can quantify the ventricular volumes and mass, and assess ventricular function and wall stress.[16] Recent studies have demonstrated the effectiveness of using serial MRI examinations to follow patients with congestive cardiomyopathy undergoing treatment with angiotensin-converting enzyme inhibitor therapy.[17,18]

Restrictive cardiomyopathy may have either normal or thickened myocardium, and normal, increased, or decreased left ventricular end-diastolic volume. The salient characteristic functional feature is markedly reduced diastolic compliance, which is similar to that seen in constrictive pericarditis. Constrictive pericarditis, however, may be differentiated by the

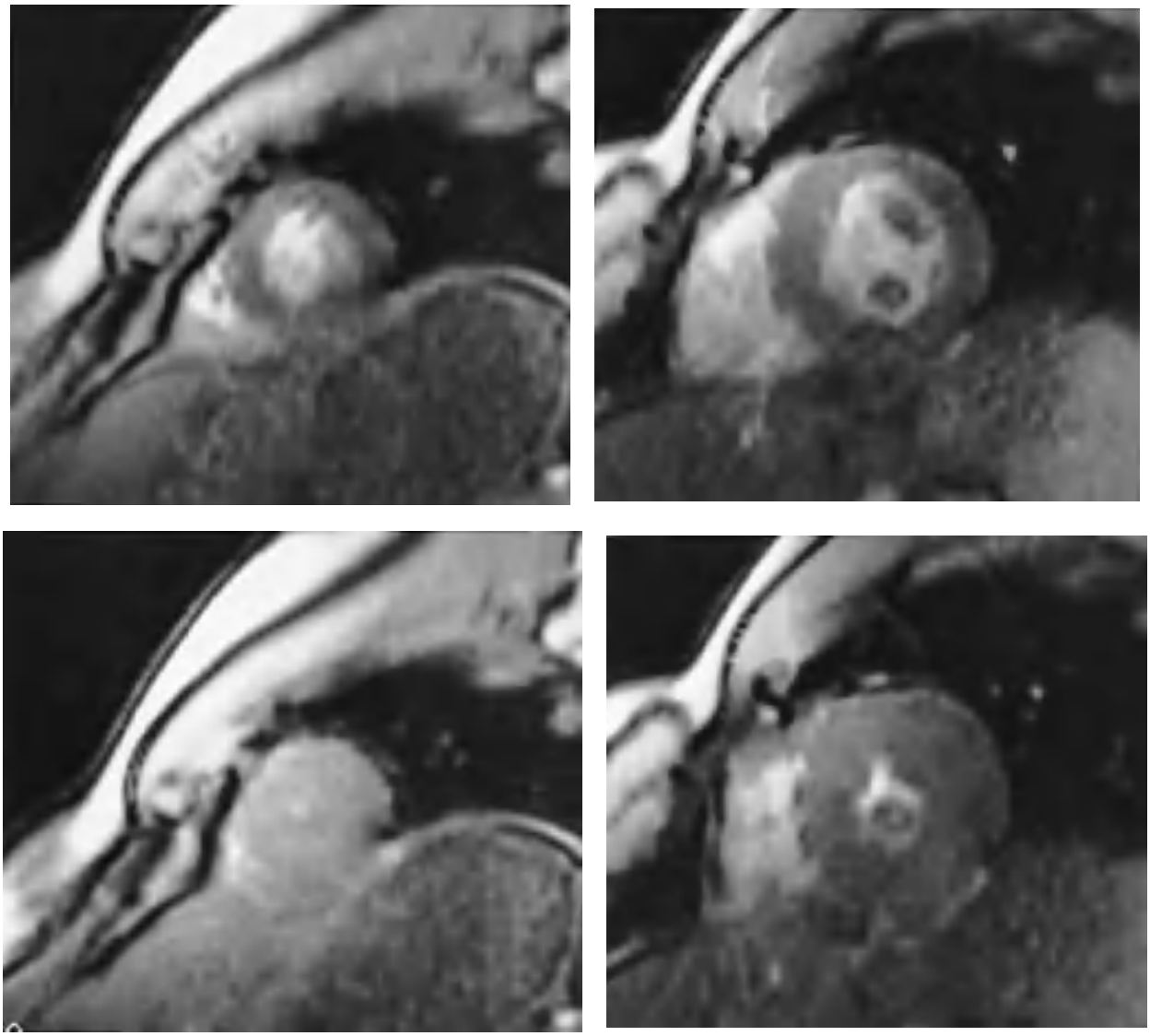

Figure 2 Short axis images of the heart in a patient with hypertrophic cardiomyopathy. The upper row of images were acquired in diastole (the images on the left are from near the apex, and the images on the right from the mid-venticular region), and directly below each is the respective systolic image, demonstrating marked, global thickening of the left ventricular myocardium, and obliteration of the apical cavity during systole. The sequence used is a breath-hold segmented *k*-space cine MRI

abnormally thickened pericardium (>4 mm), usually noted over the right side of the heart. Patients who have restrictive cardiomyopathy with thickened myocardium (such as in amyloidosis) may be differentiated from those with hypertrophic cardiomyopathy based on the reduced systolic function in the former, compared with the hyperdynamic function in the latter.[19]

4.6 Valvular Heart Disease

MRI using cine GRE sequences can identify the severity, extent, and direction of the turbulent jet of blood across stenoses of the aortic, pulmonic, mitral, and tricuspid valves. Turbulence, on cine GRE images is shown as a signal void against the background of bright signal intensity blood in the great vessels or ventricle. Using these images as a reference, the peak velocity of the turbulent jet may be determined with velocity-encoded cine MRI images obtained perpendicular to the long axis of the turbulent jet near the valve's orifice. Velocity-encoded cine MRI can determine the peak velocity of stenotic jets with accuracy up to 6 m s^{-1}.[20] By using the modified Bernoulli equation [gradient (mmHg) = 4 $\times$ (peak velocity (m s^{-1}))^2], the peak gradient across the stenosis can be calculated; this is one of the important clinical indicators used in determining the effectiveness of medical therapy, and, when necessary, timing of valve replacement surgery. Recent work has demonstrated the usefulness of this technique in both the aortic[21] and mitral[22] valves.

Cine GRE sequences also have been used to measure the extent and direction of the regurgitant jet in aortic and mitral insufficiency. Quantification of the volume of regurgitant flow may be acquired using velocity-encoded cine MRI sequences where the cardiac cycle (each R–R interval) is divided into 16 phases, and flow is measured at each phase of the cycle. In the case of aortic regurgitation, an imaging slice is acquired perpendicular to the long axis of the aorta proximal to the origin of the innominate artery. The data at each of the 16 phases can be plotted versus time, and the forward, reverse, and total flow calculated.[23] This method has the advantage of determining absolute flow, and has high interstudy reproducibility.[24] Regurgitant volume across the mitral valve has been calculated by measuring the amount of left ventricular inflow during diastole (velocity-encoded cine MRI slice across the mitral valve) and subtracting the left ventricular outflow during systole (imaging slice in the ascending aorta).[25]

4.7 Ischemic Heart Disease

MRI has the potential to become an important technique to differentiate normal from ischemic or infarcted myocardium by combining information about morphology, function, and perfusion in a single study. Of these three the largest hurdle has been determining global and regional myocardial perfusion in a rapid, reproducible manner under conditions reflecting both the basal state, and stress.

The earliest attempts at differentiating ischemic from normal myocardium focused on acute infarctions because of the edema that occurs secondary to vascular leak at the site of damage. Increased water in tissue results in increased signal on T_2-weighted scans in areas of acute infarction due to T_2 prolongation.[26] Subsequently, MRI contrast agents have been used to improve the distinction between acute and subacute infarctions, and normal myocardium. Contrast enhancement (greater than the adjacent normal myocardium) has been noted uniformly in many reperfused areas of myocardium, or only peripherally in areas of infarction in which the central zones had necrosis, hemorrhage, or marked edema that limited or ceased blood flow centrally.[27,28]

Detecting areas of stress induced ischemic myocardium has been approached using contrast-prepared fast imaging techniques. Recent studies have demonstrated the feasibility of monitoring the passage of a bolus of MRI contrast agent through the myocardium using rapid, sequential images.[29–32] Myocardium supplied by coronary arteries with angiographically proven significant stenoses demonstrates lower peak signal intensity after contrast administration, and a lower rate of signal increase than normal myocardium.[29] Ischemic myocardium, induced with the administration of dipyridamole, a pharmacological stress agent, also demonstrates lower peak signal intensity as compared with normal myocardium.[30] At present, imaging is limited to a few imaging planes for each study, but with the development of echo planar imaging, dynamic acquisition of the entire heart during the first pass of MRI contrast media will be feasible (see Figure 3; also ***Echo-Planar Imaging***).

Ischemic myocardium also may be identified by functional wall motion abnormalities observed on cine GRE sequences acquired in the basal state or during pharmacological stress. Areas of threatened myocardium demonstrate decreased contractility during dipyridamole infusion.[33] One study found the sensitivity/specificity (percent values) for localization of stenotic vessels at 78/100 for the left anterior descending, 73/100 for the left circumflex, and 88/87 for the right coronary artery.[34] This technique has also been compared to radionuclide scanning using ^{99m}Tc–methoxyisobutyl isonitrile SPECT (MIBI SPECT), with no significant differences detected in sensitivity for lesion localization.[35] Dobutamine is another pharmacological stressor that has been used to assess wall motion abnormalities with cine GRE sequences. Dobutamine MRI studies have demonstrated close agreement with findings on dobutamine thallium-201 SPECT,[36] and a sensitivity and specificity of 81 and 100%, respectively, using coronary arteriography as the gold standard.[37]

4.8 Coronary Arteries

MRA techniques have recently been used for imaging of the coronary arteries.[38–40] The coronary arteries present a formidable challenge for MRI, because they are small structures whose motion within the thorax is complex, being influenced by the spiral contraction of the heart, expansion of the chest, and descent of the diaphragm.

The proximal and midportions of the coronary arteries have been demonstrated by MRA with a fat-suppressed, cine GRE technique using segmented *k*-space and breath-holding. In a group of 19 normal volunteers, and six patients with recent angiograms, the left anterior descending and right coronary arteries were identified in 100%, the left main in 96%, and the left circumflex in 76%.[41] A subsequent study using a similar MRA technique in 39 patients with angiographically identified coronary stenoses demonstrated a sensitivity and specificity of 90 and 92% for detection of significant ($\geqslant$50% narrowing) lesions.[42]

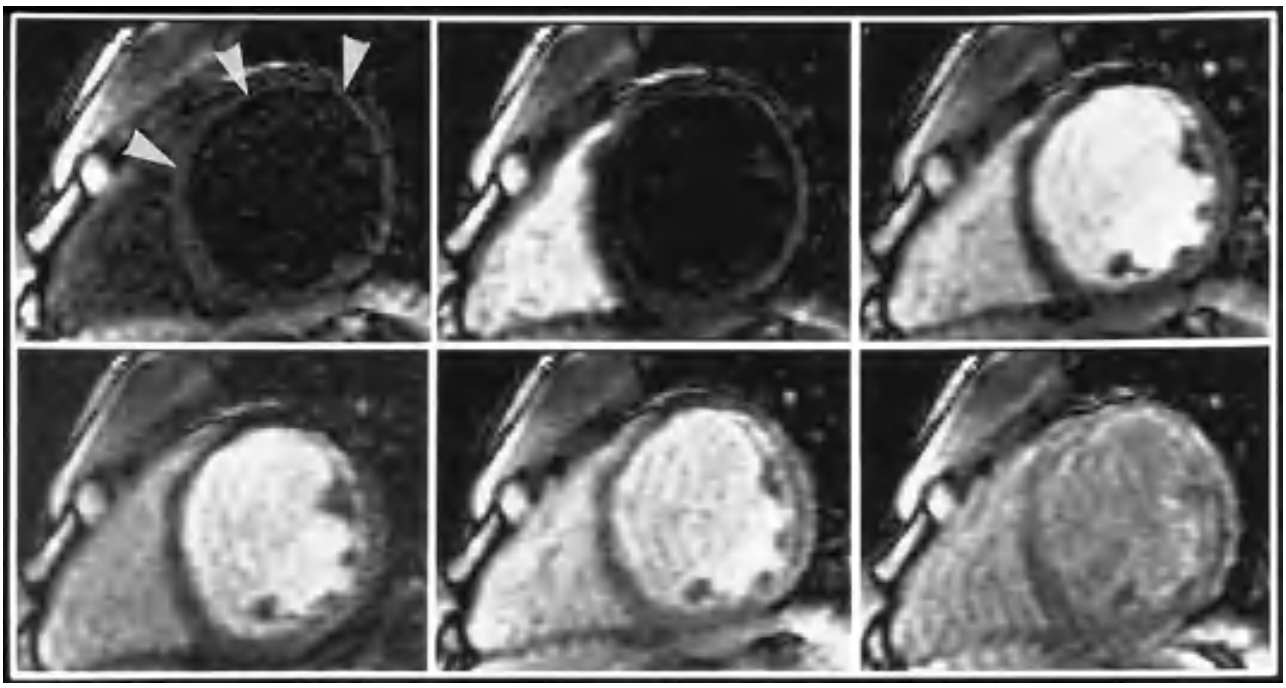

Figure 3 Series of short axis images of the heart acquired repetitively at the same level over a 90 s period during bolus administration of contrast media. The transit of contrast material increases signal intensity first in the right ventricular blood pool, then left ventricular blood pool, and finally the myocardium of the right and left ventricles. The patient has had an infarction in the anterior and anteroseptal distribution (arrowheads); note the delayed rise in signal intensity compared to the adjacent normal myocardium

The use of complex, oblique planes has permitted visualization of more than 8 cm lengths of the right coronary artery and left anterior descending coronary artery (Figure 4).[38] Other recent advances include non-breath-hold three-dimensional imaging using fat saturation and magnetization transfer contrast techniques. Initial work has demonstrated the first 3–10 cm of the left and right coronary arteries from a single 7–10 min acquisition.[43] Further improvements in scanning time, image

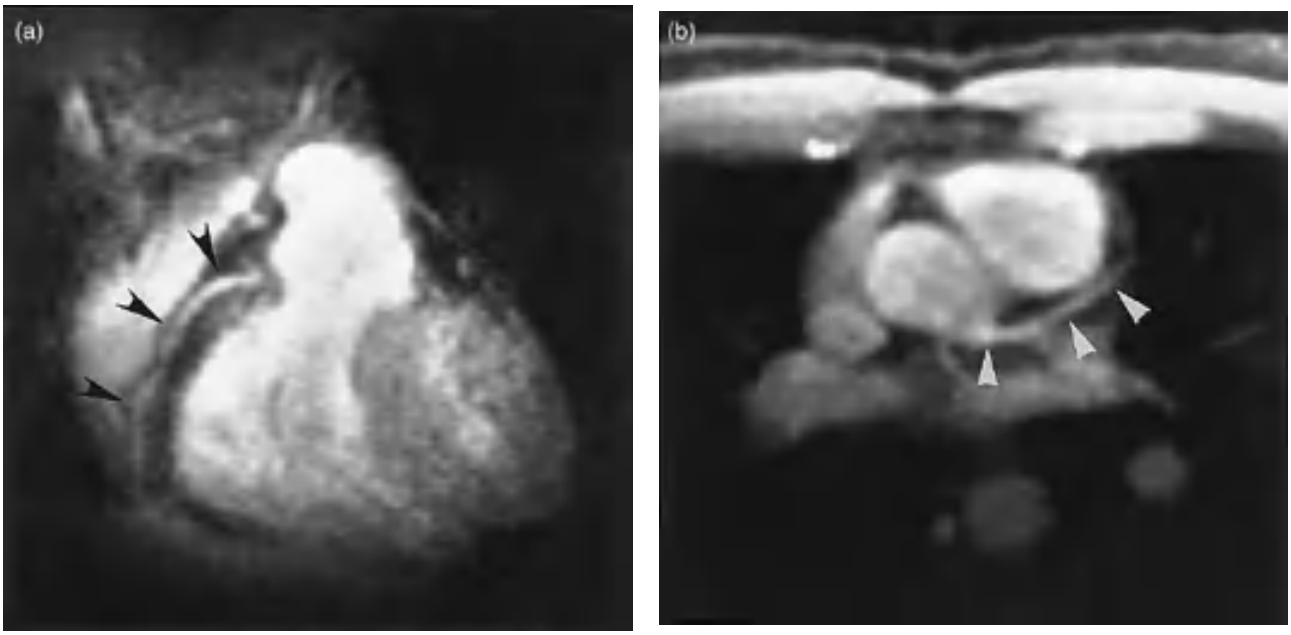

Figure 4 MRA of the coronary arteries using a breath-hold segmented *k*-space cine sequence. (a) An oblique coronal image demonstrating the proximal and midportions of the right coronary artery (arrowheads). (b) An axial image showing the left main and proximal left anterior descending coronary arteries (arrowheads)

resolution, and surface coil technology may result in a complete magnetic resonance angiogram of the coronary arteries.

5 CONGENITAL HEART DISEASE

5.1 Coarctation of the Aorta

MRI can provide excellent anatomic visualization of the aorta. Images are acquired first in the axial plane using a spin echo sequence, and then using these images as a reference a set of oblique sagittal images are acquired parallel to the plane of, and including, the ascending and descending aorta. These two sets of images can adequately describe the anatomical location and severity of the stenosis, including involvement of arch vessels, and degree of poststenotic dilation. A cine GRE sequence in the same oblique sagittal plane can demonstrate the jet of turbulent flow along the descending thoracic aorta just distal to the site of coarctation.[44] The gradient across the stenosis can be estimated from the peak velocity (using the modified Bernoulli equation described previously); measurements performed with velocity-encoded cine MRI reveal a close correlation ($r = 0.95$) with values obtained by continuous wave Doppler ultrasound.[45] The length of the turbulent jet has been correlated with the severity of stenosis, a factor important in gauging the appropriate timing of initial corrective surgical procedure, or subsequent repair in recoarctation.

At present, determining the optimal time for corrective surgery has been based on a combination of clinical findings and the echocardiographically determined gradient across the coarctation, both of which are only loosely correlated with the severity of stenosis. Recent work has revealed a unique ability of MRI in the evaluation of coarctation of the aorta. Velocity-encoded cine MRI was used to measure blood flow in the descending thoracic aorta just distal to the coarctation and at the level of the diaphragm, with the difference in flow representing the contribution from collateral vessels (Figure 5). While normal individuals have an average 8% decrease in blood flow along the descending thoracic aorta, patients with significant coarctations have an average 80% increase in flow.[46] This technique represents the only currently available noninvasive method to measure the extent of collateral development, and their contribution in supplying blood to the abdominal aorta.

5.2 Pulmonary Arteries

The evaluation of pulmonary arterial anatomy, orientation, size, and flow is critical to the management of children with lesions affecting the pulmonary arteries such as tetralogy of Fallot, and pulmonary atresia and stenosis.[47]

The pulmonary arteries are best visualized using 3–5 mm ECG-gated spin echo images in the axial plane, followed by oblique sagittal images through the pulmonary infundibulum, and/or right and left pulmonary arteries. MRI can define accurately the location and severity of narrowing in the right ventricular outflow tract and main pulmonary artery, as well as associated poststenotic dilation.[48,49] In a series of 12 patients who had undergone the arterial switch operation MRI correctly identified 92% of the pulmonary artery stenoses, while echocardiography identified only 58%. Moreover, MRI was superior in identifying peripheral pulmonary stenoses, as echocardiography visualized only seven of the 17 peripheral stenoses seen by MRI.[50]

Pulmonary atresia is identified by a fibrous and/or muscular band at the expected junction of the main pulmonary artery and the right ventricular outflow tract, on both axial and sagittal images. Determining the presence or absence of the main pulmonary artery and continuity of the right and left pulmonary arteries is crucial information for surgical planning. At least two studies, using angiography as the gold standard, have confirmed the ability of MRI to determine correctly the status of main, left and right pulmonary arteries, without the need for an invasive procedure.[51,52]

Quantitative, physiological information regarding flow within the pulmonary arteries can be obtained using velocity-encoded cine MRI images. This technique can accurately quantify both total, and right and left lung differential blood flow,[53] and correlates well with radionuclide lung scanning for the evaluation of relative blood flow to the left and right lungs.[54] This information is useful for determining the severity of stenoses and their effect on total and differential pulmonary blood flow (Figure 6). In addition, it may prove particularly valuable in serially assessing flow at sites of stenosis after balloon valvuloplasty, or surgical repair.

5.3 Vascular Rings

MRI is ideal to define the aortic arch and great vessel relationships because of its multiplanar capabilities and ability to image the adjacent air-filled trachea and esophagus, both of which may be compressed by the vascular structures. Spin echo sequences are typically employed in the axial and sagittal planes to demonstrate the commonly encountered abnormalities which include double aortic arch, right aortic arch with mirror image branching, right aortic arch with aberrant left subclavian artery, left aortic arch with aberrant left subclavian artery, and pulmonary sling. The sagittal images often best demonstrate the compression on both the trachea and esophagus. Coronal images may provide further information regarding double aortic arches.

Imaging may also be performed using magnetic resonance angiography, with either time-of-flight or phase contrast techniques.[55,56] Both techniques produce signal primarily from moving blood resulting in images that reflect the intravascular space, similar to conventional contrast angiograms, but without the need for contrast or an invasive procedure. These sequences have a further advantage in that the images may be reconstructed into a three-dimensional format, and viewed from any desired angle. Further postprocessing permits close examination of a particular area of interest for detailed analysis.

5.4 Complex Congenital Heart Disease

Complex congenital heart disease requires definition of the complicated anatomical relationships of the heart. MRI permits segmental analysis of complex congenital heart disease by providing tomograms encompassing the great vessels, heart, and infradiaphragmatic structures. Axial spin echo sequences are

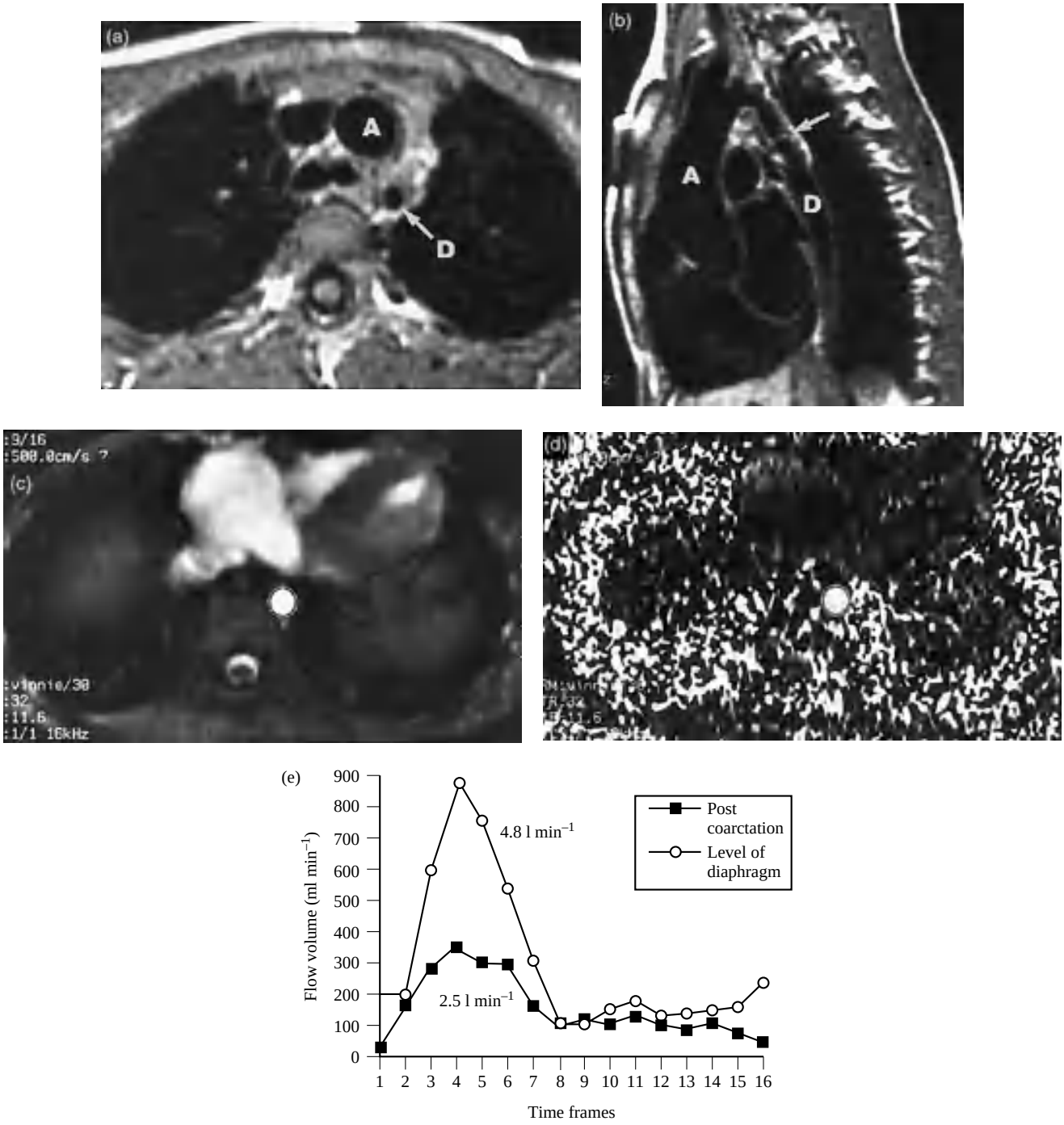

Figure 5 Patient with coarctation of the aorta. (a, b) ECG-gated spin echo images acquired in the axial and oblique sagittal projections, respectively. (c, d) Magnitude and phase images, respectively, from a VEC sequence acquired at the level of the diaphragm. Regions-of-interest have been placed over the aorta. (e) A flow curve can be derived, and blood flow at that level calculated (as described in the text). Similar information is obtained from a slice positioned just distal to the site of coarctation. The difference in blood flow between the sites in the descending thoracic aorta is a direct measure of the contribution of collateral blood flow to the abdominal aorta. A, ascending aorta; D, descending aorta; arrow, coarctation

usually sufficient to define the anatomy, with sagittal, coronal, and oblique imaging planes used to further complement the anatomical information.

A segmental approach is used to define the anatomy beginning with determination of the abdominal situs, and the relationship of the inferior vena cava and aorta. After this, the pattern of blood flow through the heart and great vessels is determined starting with the systemic and pulmonary venous connections, and then identifying the atrial situs, and presence and position of the atrioventricular valves. Next, the ventricular anatomy, and ventriculoarterial connections and great artery relationship are determined.

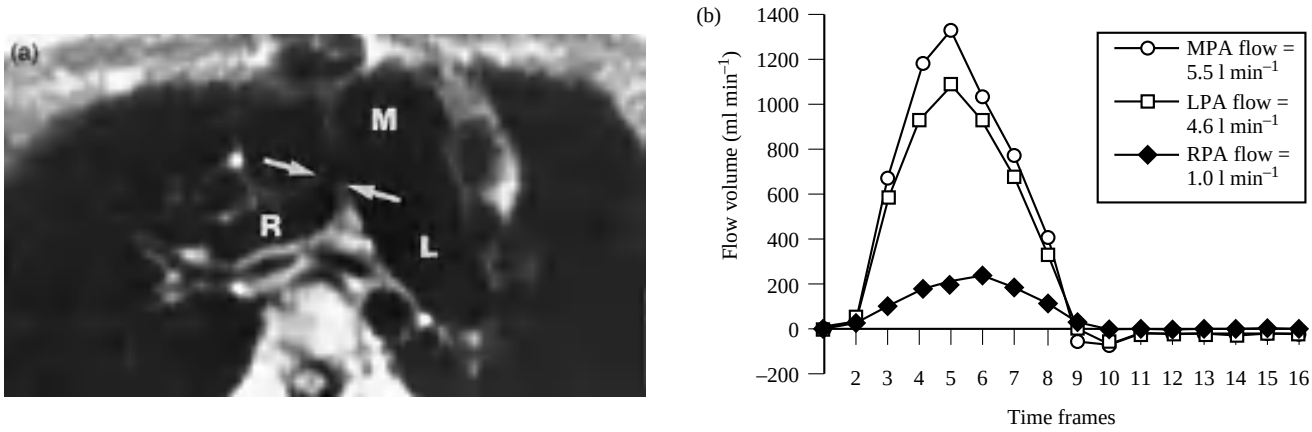

Figure 6 (a) Axial spin echo image of a patient with stenosis (between arrows) of the proximal right pulmonary artery. VEC MRI can be performed perpendicular to the main, and proximal right and left pulmonary arteries, and the total blood flow to the lungs, and differential blood flow to each lung calculated. (b) The different flows calculated for each of the respective arteries are demonstrated here. R, right pulmonary artery; L, left pulmonary artery; M, main pulmonary artery

The absolute and relative sizes of the ventricular system including quantification of ventricular mass, and the quantity and spatial extent of septal tissue are all well defined by MRI.[57–59] Many complex lesions have been evaluated correctly with MRI including double-outlet right ventricle,[60,61] double-outlet left ventricle,[62] double-inlet ventricle,[63] single ventricle and atrioventricular canal,[64] partial and total anomalous pulmonary venous connection,[65,66] and Ebstein's anomaly.[67] In a study of 29 patients with complex lesions, MRI was shown to be more informative for defining complex congenital heart disease than conventional angiography.[64] Receiver operating characteristic curves have been derived for MRI at a specificity level of 90%, demonstrating 100% sensitivity for evaluating great vessel relationships, ventricular septal defects, visceroatrial situs, and ventricular loop, 95% for right ventricular outflow tract obstructions, 94% for thoracic aortic anomalies, and 91% for atrial septal defects.[68]

5.5 Postoperative Evaluation

The metallic clips, wires, stents, shunts, and prosthetic valves used in interventional and surgical correction of congenital heart disease are sometimes problematic for MRI. On magnetic resonance images these devices may result in paramagnetic artifacts that degrade image quality, but fortunately, in most instances, they do not affect significantly the diagnostic utility of the study. The characteristics of noninvasiveness, lack of ionizing radiation, and good interstudy reproducibility are all distinct advantages for an imaging study intended to be used serially in children.

Congenital obstruction at the level of the main pulmonary artery, right ventricular outflow tract, or tricuspid valve requires a corrective procedure that involves construction of an atriopulmonary connection (Fontan procedure) or ventriculopulmonary conduit (Rastelli procedure) using native tissue and/or homograft material. These procedures can be complicated by insidious stenosis of the conduit, or the anastomotic site(s), and will benefit from periodic imaging examinations in addition to clinical follow up. The Fontan procedure has been evaluated with the spin echo technique alone.[69] Addition of velocity-encoded cine MRI can provide further information regarding quantification of blood flow through the connection into the pulmonary arteries. This technique has demonstrated the normal biphasic pattern of blood flow, similar to venous flow, seen in atriopulmonary Fontans, or the normal monophasic pattern, seen in atrioventricular Fontans, thus confirming the success of the operation.[70] Rastelli conduits may also be complicated by stenosis, which is often difficult to evaluate with echocardiography because of the anterior location of the conduit in the chest. The velocity-encoded cine MRI technique has been applied in these patients to measure the gradient and to localize accurately the site of obstruction, providing a measure of the severity of the lesion which was superior to echocardiography.[71] The Norwood[72] and Jatene[50,73] procedures have been evaluated similarly, and MRI has been shown to be equivalent to angiography, and superior to echocardiography, respectively.

Extracardiac conduits such as the Glenn (superior vena cava to the right pulmonary artery) and Blalock–Taussig (subclavian artery to the ipsilateral pulmonary artery) shunts also can be evaluated easily with spin echo techniques, often in a single imaging plane. Serial imaging studies are valuable to evaluate for size, course, and patency of these shunts, as well as growth of the pulmonary arteries.[63,74]

6 THE FUTURE

The technology relevant to MRI of the heart continues to evolve. Consequently, the application of MRI in cardiovascular disease can be expected to increase further in the next several years.

7 RELATED ARTICLES

Cardiac Gating Practice; Cardiovascular NMR to Study Function; Echo-Planar Imaging; Lung and Mediastinum MRI;

Motion Artifacts: Mechanism and Control; NMR Spectroscopy of the Human Heart.

8 REFERENCES

1. M. Erlichman, *Health Technol. Assess. Report*, 1990, **4**, 1.
2. R. D. White, R. L. Ehman, and J. C. Weinreb, *JMRI*, 1992, **2**, 365.
3. T. Masui, G. R. Caputo, J. C. Bowersox, and C. B. Higgins, *J. Comput. Assist. Tomogr.*, 1995.
4. L. M. Blake, M. M. Scheinman, and C. B. Higgins, *Am. J. Roentgenol.*, 1994, **162**, 809.
5. W. Auffermann, T. Wichter, G. Breithardt, K. Joachimsen, and P. E. Peters, *Am. J. Roentgenol.*, 1993, **161**, 549.
6. E. K. Yucel, F. L. Steinberg, T. K. Egglin, S. C. Geller, A. C. Waltman, and C. A. Athanasoulis, *Radiology*, 1990, **177**, 779.
7. C. A. Nienaber, Y. von Kodolitsch, V. Nicolas, V. Siglow, A. Piepho, C. Brockhoff, D. H. Koschyk, and R. P. Spielmann, *N. Engl. J. Med.*, 1993, **328**, 1.
8. C. A. Nienaber, R. P. Spielmann, Y. von Kodolitsch, V. Siglow, A. Piepho, T. Jaup, V. Nicolas, P. Weber, H. J. Triebel, and W. Bleifeld, *Circulation*, 1992, **85**, 434.
9. N. Fujita, G. R. Caputo, and C. B. Higgins, *Am. J. Card. Imaging*, 1994, **23**, 959.
10. M. Jungehulsing, U. Sechtem, P. Theissen, H. H. Hilger, and H. Schicha, *Radiology*, 1992, **182**, 225.
11. K. C. Seelos, G. R. Caputo, C. L. Carrol, H. Hricak, and C. B. Higgins, *J. Comput. Assist. Tomogr.*, 1992, **16**, 169.
12. J. H. Park, Y. M. Kim, J. W. Chung, Y. B. Park, J. K. Han, and M. C. Han, *Radiology*, 1992, **185**, 441.
13. J. D. Allison, F. W. Flickinger, J. C. Wright, D. G. Falls, L. M. Prisant, T. W. VonDohlen, and M. J. Frank, *Magn. Reson. Imag.*, 1993, **11**, 329.
14. R. C. Semelka, E. Tomei, S. Wagner, J. Mayo, G. Caputo, M. O'Sullivan, W. W. Parmley, K. Chatterjee, C. Wolfe, and C. B. Higgins, *Am. Heart J.*, 1990, **119**, 1367.
15. J. Suzuki, J. M. Chang, G. R. Caputo, and C. B. Higgins, *J. Am. Coll. Cardiol.*, 1991, **18**, 120.
16. J. Suzuki, G. R. Caputo, T. Masui, J. M. Chang, M. O'Sullivan, and C. B. Higgins, *Am. Heart J.*, 1991, **122**, 1035.
17. N. E. Doherty, K. C. Seelos, J. Suzuki, G. R. Caputo, M. O'Sullivan, S. M. Sobol, P. Cavero, K. Chatterjee, W. W. Parmley, and C. B. Higgins, *J. Am. Coll. Cardiol.*, 1992, **19**, 1294.
18. N. Fujita, J. Hartiala, M. O'Sullivan, D. Steiman, K. Chatterjee, W. W. Parmley, and C. B. Higgins, *Am. Heart J.*, 1993, **125**, 171.
19. T. Masui, S. Finck, and C. B. Higgins, *Radiology*, 1992, **182**, 369.
20. P. J. Kilner, D. N. Firmin, R. S. Rees, J. Martinez, D. J. Pennell, R. H. Mohiaddin, S. R. Underwood, and D. B. Longmore, *Radiology*, 1991, **178**, 229.
21. A. C. Eichenberger, R. Jenni, and G. K. von Schulthess, *Am. J. Roentgenol.*, 1993, **160**, 971.
22. P. A. Heidenreich, J. C. Steffens, N. Fujita, M. O'Sullivan, G. R. Caputo, E. Foster, and C. B. Higgins, *Am. J. Cardiol.*, 1994, **75**, 365.
23. N. Honda, K. Machida, M. Hashimoto, T. Mamiya, T. Takahashi, T. Kamano, A. Kashimada, Y. Inoue, S. Tanaka, and N. Yoshimoto, *Radiology*, 1993, **186**, 189.
24. M. C. Dulce, G. H. Mostbeck, M. O'Sullivan, M. Cheitlin, G. R. Caputo, and C. B. Higgins, *Radiology*, 1992, **185**, 235.
25. N. Fujita, A. F. Chazouilleres, J. J. Hartiala, M. O'Sullivan, P. Heidenreich, J. D. Kaplan, H. Sakuma, E. Foster, G. R. Caputo, and C. B. Higgins, *J. Am. Coll. Cardiol.*, 1994, **23**, 951.
26. M. T. McNamara, C. B. Higgins, N. Schechtmann, E. Botvinick, M. J. Lipton, K. Chatterjee, and E. G. Amparo, *Circulation*, 1985, **71**, 717.
27. A. de Roos, A. C. van Rossum, E. van der Wall, S. Postema, J. Doornbos, N. Matheijssen, P. R. van Dijkman, F. C. Visser, and A. E. van Voorthuisen, *Radiology*, 1989, **172**, 717.
28. M. C. Dulce, A. J. Duerinckx, J. Hartiala, G. R. Caputo, M. O'Sullivan, M. D. Cheitlin, and C. B. Higgins, *Am. J. Roentgenol.*, 1993, **160**, 963.
29. W. J. Manning, D. J. Atkinson, W. Grossman, S. Paulin, and R. R. Edelman, *J. Am. Coll. Cardiol.*, 1991, **18**, 959.
30. S. Schaefer, R. van Tyen, and D. Saloner, *Radiology*, 1992, **185**, 795.
31. M. A. Klein, B. D. Collier, R. S. Hellman, and V. S. Bamrah, *Am. J. Roentgenol.*, 1993, **161**, 257.
32. F. P. van Rugge, J. J. Boreel, E. E. van der Wall, P. R. van Dijkman, A. van der Laarse, J. Doornbos, A. de Roos, J. A. den Boer, A. V. Bruschke, and A. E. van Voorthuisen, *J. Comput. Assist. Tomogr.*, 1991, **15**, 959.
33. D. J. Pennell, S. R. Underwood, P. J. Ell, R. H. Swanton, J. M. Walker, and D. B. Longmore, *Br. Heart J.*, 1990, **64**, 362.
34. F. M. Baer, K. Smolarz, M. Jungehulsing, P. Theissen, U. Sechtem, H. Schicha, and H. H. Hilger, *Am. J. Cardiol.*, 1992, **69**, 51.
35. F. M. Baer, K. Smolarz, P. Theissen, E. Voth, H. Schicha, and U. Sechtem, *Int. J. Card. Imaging*, 1993, **9**, 133.
36. D. J. Pennell, S. R. Underwood, C. C. Manzara, R. H. Swanton, J. M. Walker, P. J. Ell, and D. B. Longmore, *Am. J. Cardiol.*, 1992, **70**, 34.
37. F. P. van Rugge, E. E. van der Wall, A. de Roos, and A. V. Bruschke, *J. Am. Coll. Cardiol.*, 1993, **22**, 431.
38. H. Sakuma, G. R. Caputo, J. C. Steffens, A. Shimakawa, T. K. F. Foo, and C. B. Higgins, *Radiology*, 1993, **189**(P), 278 (abstract).
39. R. R. Edelman, W. J. Manning, D. Burstein, and S. Paulin, *Radiology*, 1991, **181**, 641.
40. R. R. Edelman, W. J. Manning, J. Pearlman, and W. Li, *Radiology*, 1993, **187**, 719.
41. W. J. Manning, W. Li, N. G. Boyle, and R. R. Edelman, *Circulation*, 1993, **87**, 94.
42. W. J. Manning, W. Li, and R. R. Edelman, *N. Engl. J. Med.*, 1993, **328**, 828.
43. D. Li, C. B. Paschal, E. M. Haacke, and L. P. Adler, *Radiology*, 1993, **187**, 401.
44. S. Rees, J. Somerville, C. Ward, J. Martinez, R. H. Mohiaddin, R. Underwood, and D. B. Longmore, *Radiology*, 1989, **173**, 499.
45. R. H. Mohiaddin, P. J. Kilner, S. Rees, and D. B. Longmore, *J. Am. Coll. Cardiol.*, 1993, **22**, 1515.
46. J. C. Steffens, M. W. Bourne, H. Sakuma, M. O'Sullivan, G. R. Caputo, and C. B. Higgins, *Radiology*, 1993, **189**(P), 302 (abstract).
47. A. S. Gomes, *Radiol. Clin. North Am.*, 1989, **27**, 1171.
48. P. R. Julsrud, R. L. Ehman, D. J. Hagler, and D. M. Ilstrup, *Radiology*, 1989, **173**, 503.
49. A. S. Gomes, J. F. Lois, and R. G. Williams, *Radiology*, 1990, **174**, 51.
50. F. Blankenberg, J. Rhee, C. Hardy, G. Helton, S. S. Higgins, and C. B. Higgins, *J. Comput. Assist. Tomogr.*, 1994, **18**, 749.
51. D. A. Lynch and C. B. Higgins, *J. Comput. Assist. Tomogr.*, 1990, **14**, 187.
52. J. M. Parsons, E. J. Baker, A. Hayes, E. J. Ladusans, S. A. Qureshi, R. H. Anderson, M. N. Maisey, and M. Tynan, *Int. J. Cardiol.*, 1990, **28**, 73.
53. G. R. Caputo, C. Kondo, T. Masui, S. J. Geraci, E. Foster, M. M. O'Sullivan, and C. B. Higgins, *Radiology*, 1991, **180**, 693.
54. J. M. Silverman, P. J. Julien, R. J. Herfkens, and N. J. Pelc, *Radiology*, 1993, **189**, 699.
55. K. S. Azarow, R. H. Pearl, M. A. Hoffman, R. Zurcher, F. H. Edwards, and A. J. Cohen, *Ann. Thorac. Surg.*, 1992, **53**, 882.
56. R. B. Jaffe, *Semin. Ultrasound. CT MR*, 1990, **11**, 206.

57. E. J. Baker, V. Ayton, M. A. Smith, J. M. Parsons, E. J. Ladusans, R. H. Anderson, M. N. Maisey, M. Tynan, N. L. Fagg, and P. B. Deverall, *Br. Heart J.*, 1989, **62**, 305.
58. G. R. Caputo, J. Suzuki, C. Kondo, H. Cho, R. A. Quaife, C. B. Higgins, and D. L. Parker, *Radiology*, 1990, **177**, 773.
59. N. E. Doherty, N. Fujita, G. R. Caputo, and C. B. Higgins, *Am. J. Cardiol.*, 1992, **69**, 1223.
60. J. R. Mayo, D. Roberson, B. Sommerhoff, and C. B. Higgins, *J. Comput. Assist. Tomogr.*, 1990, **14**, 336.
61. J. M. Parsons, E. J. Baker, R. H. Anderson, E. J. Ladusans, A. Hayes, N. Fagg, A. Cook, S. A. Qureshi, P. B. Deverall, and M. N. Maisey, *J. Am. Coll. Cardiol.*, 1991, **18**, 168.
62. S. A. Rebergen, G. L. Guit, and A. de Roos, *Br. Heart J.*, 1991, **66**, 381.
63. I. C. Huggon, E. J. Baker, M. N. Maisey, A. P. Kakadekar, P. Graves, S. A. Qureshi, and M. Tynan, *Br. Heart J.*, 1992, **68**, 313.
64. B. A. Kersting-Sommerhoff, L. Diethelm, P. Stanger, R. Dery, S. M. Higashino, S. S. Higgins, and C. B. Higgins, *Am. Heart J.*, 1990, **120**, 133.
65. T. M. Vesely, P. R. Julsrud, J. J. Brown, and D. J. Hagler, *J. Comput. Assist. Tomogr.*, 1991, **15**, 752.
66. B. Kastler, A. Livolsi, P. Germain, A. Gangi, A. Klinkert, J. L. Dietemann, D. Willard, and A. Wackenheim, *Pediatr. Radiol.*, 1992, **22**, 262.
67. B. Kastler, A. Livolsi, H. Zhu, E. Roy, G. Zollner, and J. L. Dietemann, *J. Comput. Assist. Tomogr.*, 1990, **14**, 825.
68. B. A. Kersting-Sommerhoff, L. Diethelm, D. F. Teitel, C. P. Sommerhoff, S. S. Higgins, S. S. Higashino, and C. B. Higgins, *Am. Heart J.*, 1989, **118**, 155.
69. B. A. Kersting-Sommerhoff, K. C. Seelos, C. Hardy, C. Kondo, S. S. Higgins, and C. B. Higgins, *Am. J. Roentgenol.*, 1990, **155**, 259.
70. S. A. Rebergen, J. Ottenkamp, J. Doornbos, E. E. van der Wall, J. G. Chin, and A. de Roos, *J. Am. Coll. Cardiol.*, 1993, **21**, 123.
71. J. E. Martinez, R. H. Mohiaddin, P. J. Kilner, K. Khaw, S. Rees, J. Somerville, and D. B. Longmore, *J. Am. Coll. Cardiol.*, 1992, **20**, 338.
72. C. Kondo, C. Hardy, S. S. Higgins, J. N. Young, and C. B. Higgins, *J. Am. Coll. Cardiol.*, 1991, **18**, 817.
73. C. E. Hardy, G. J. Helton, C. Kondo, S. S. Higgins, N. J. Young, and C. B. Higgins, *Am. Heart J.*, 1994, **128**, 326.
74. B. Kastler, A. Livolsi, P. Germain, G. Zollner, and J. L. Dietemann, *Int. J. Card. Imaging*, 1991, **7**, 1.

Biographical Sketches

Scott D. Flamm. *b* 1960. B.A., 1982, University of California, Berkeley. M.D., 1988, George Washington University, USA. Residency training in diagnostic radiology, University of California, Los Angeles. Fellowship training in cardiovascular imaging and MRI (supervisor Charles B. Higgins), University of California, San Francisco. Currently clinical instructor in cardiovascular imaging/MRI, University of California, San Francisco, Approx. 10 publications. Research specialties: MRI of acquired and congenital cardiac disease, MRA, and quantitative vascular flow measurements.

Charles B. Higgins. *b* 1944. B.S., 1963, Villanova University. M.D., 1967, Jefferson Medical College, USA. Residency training in surgery, University of California, Los Angeles, and in diagnostic radiology, University of California, San Diego. Fellowship training in cardiovascular radiology, Stanford University. Research training at the Cardiovascular Research Laboratory (supervisor Eugene Braunwald), University of California, San Diego. Currently Professor of Radiology, and Chief, Magnetic Resonance Imaging and Cardiac Imaging Sections, University of California, San Francisco. Approx. 450 publications. Research specialties: MRI of acquired and congenital cardiac disease, and strategies for detection of myocardial ischemia using MR contrast media.

Lung and Mediastinum MRI

Robert J. Herfkens
Stanford University School of Medicine, CA, USA

The utilization of MRI techniques for visualization of lung and mediastinal abnormalities has been greeted with great enthusiasm due to the excellent contrast resolution of MRI. However, the complex motions associated with those respiratory and cardiac events have posed significant challenges to the utilization of MRI for visualizing pulmonary and mediastinal abnormalities. The utilization of motion compensation techniques have greatly improved the image quality of MRI, and its intrinsic qualities have indeed provided unique diagnostic information about thoracic disease.

In order to compensate for the complex motions associated with the heart motion and blood flow, methods for coordinating the acquisition of the images in concert with the cardiac cycle have been developed.[1] Gating or triggering of the acquisition to the cardiac cycle has been obtained through a number of methods; primarily, electrocardiographic (ECG) gating methods have been employed.[2,3] In addition, methods of plethysmographic or pulse oximeter methods have been utilized, but these are somewhat less precise in coordinating the acquisition with the cardiac cycle. The ECG signal triggers the magnetic resonance (MR) scanner as providing a consistent point in the cardiac cycle for initiating multislice or cine imaging. This, however, provides a limitation in imaging of the chest, as the R–R interval determines the repetition time of the scan. This provides a significant limitation to the flexibility of presenting imaging contrast. For an average heart rate of 60 beats per minute, the minimum repetition time would be 1000 ms. Depending upon the patient's physiologic status, the heart rate may vary quite greatly, thus having a significant effect on the overall image contrast, due to varying *TR* times.

Respiratory motion, which is also periodic, causes significant artifacts in MRI. These have a strong impact on chest images. The simplest solution to respiratory artifacts originally was to provide multiple signal averages, which blur the respiratory motion and, in general, improve the signal-to-noise ratio. These increases in imaging time, associated with respiratory averaging, are somewhat inappropriate on modern systems. Techniques that coordinate the phase encoding of the image acquisition with the respiratory cycle, so-called 'respiratory ordered phase encoding' or 'respiratory compensation', can significantly reduce the amount of respiratory artifacts without unduly increasing the imaging time. Recent fast imaging techniques with fast repetition times as short as 10 ms have allowed breath-held images of the chest. Although these images may introduce some blurring of the cardiac silhouette, improved definition of mediastinal and diaphragmatic structures have been realized.

Basic spin echo techniques gated to the cardiac cycle will provide relatively unique contrast within the mediastinum. The basic contrast associated with relative T_1-weighted imaging shows fat as a relatively high signal intensity, with normal mediastinal structures, such as the esophagus and heart, with intermediate signal intensity.[4] The intrinsic flow sensitivity spin echo images show a relative decrease in signal intensity of the vascular structures. In gated spin echo imaging, however, the signal intensity of major vessels may vary, depending upon when the specific image is obtained in the cardiac cycle. Those images obtained during systole have a relatively strong signal void, and those obtained during diastole may have significant intravascular signal, because of the relatively slow flow. Utilization of flow sensitive sequences, such as gradient-recalled imaging techniques, have improved the ability to differentiate intravascular slow flow signal from soft-tissue signals. Gradient-recalled images show an intrinsic sensitivity to flowing blood due to flow related enhancement, thus demonstrating an increase in signal intensity associated with flow. By utilizing gating with gradient-recalled sequences, phase-encoding signals can be advanced with each cardiac cycle, thus providing a cine image throughout the cardiac cycle, generating sensitivity to flow. In addition, phase contrast techniques have been applied to the cine technique, allowing the demonstration of velocity changes throughout the cardiac cycle (Figure 1). These phase contrast techniques have been used to characterize flow in major vascular structures and may be important in characterizing pulmonary artery flow abnormalities[5] (Figure 2).

When using spin echo sequences, the repetition time is determined by the R–R interval. In order to obtain T_2-weighted images in the chest, techniques which would allow for the gating of the acquisition to multiple heart beats, which is every third or every fourth heart beat, allow for the acquisition of T_2-weighted data. In general, the utilization of T_1-weighted data has been superior for anatomic definition. The intrinsic contrast, as previously noted, where fat is bright and muscle and esophagus are dark, leave any other intermediate signal intensities as being pathologic. The relatively high contrast between flowing blood in spin echo images and other soft tissues also allows for excellent contrast to characterize other pathologic entities related to vascular involvement or improved definition of the spatial relationship associated with the relative signal void of vascular structures (Figure 3).

The ability of MR to generate any plane has been a significant advantage over conventional techniques, such as computerized tomography (CT). The use of coronal planes has significantly enhanced the visualization of abnormalities and the apices of the lungs, and has improved the visualization of lesions associated with the diaphragm. The ability to utilize oblique planes has been extremely helpful in characterizing pathologies associated with the aorta or other structures.[6]

Another major element which degrades images within the thorax is the susceptibility associated with the multiple air–water interfaces in the pulmonary parenchyma. This marked change in susceptibility has resulted in a very poor delineation of other abnormalities within the lungs themselves. A number of recent techniques have provided significant improvement in the visualization of pulmonary abnormalities; however, they still appear to be significantly less sensitive than CT for detecting pulmonary pathologies.[7–9] The development of fast spin

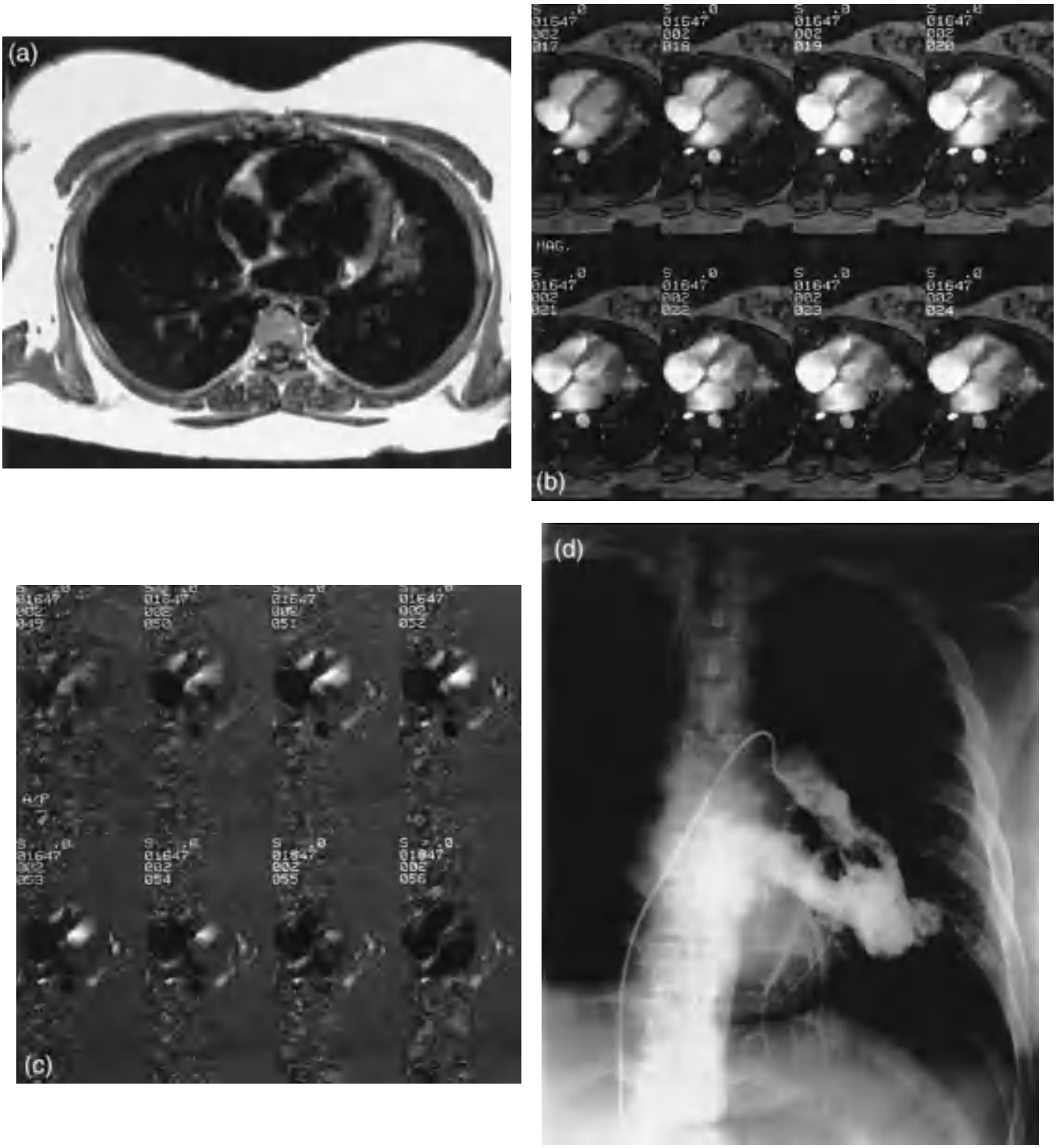

Figure 1 (a) A gated T_1-weighted spin echo image showing prominent soft tissue density along the lateral wall of the heart. This mass in a 32-year-old female was identified on chest X-ray. (b) Eight frames of a cine gradient-recalled imaging sequence from diastole through systole. The mass noted in (a) is shown with signal variations suggesting flow. (c) A cine phase contrast imaging sequence encoded in the superior to inferior direction corresponding to the image shown in (b). Note the significant change in signal intensity during systolic contraction in both the superior and inferior directions in the region of the mass, suggesting that this mass is a pulmonary arterial–venous malformation. (d) A pulmonary angiogram confirming the presence of a pulmonary arterial–venous malformation

Figure 2 Flow analysis of the right pulmonary artery flow pattern in a patient after lung transplant. This is the native lung and shows a pulsatile flow profile going from positive to negative throughout the cardiac cycle, showing a low net total flow to the lung. Such pulmonary flow analysis may be helpful in determining vascular compliance of the lung, as well as in relative ratios in blood flow in postoperative patients

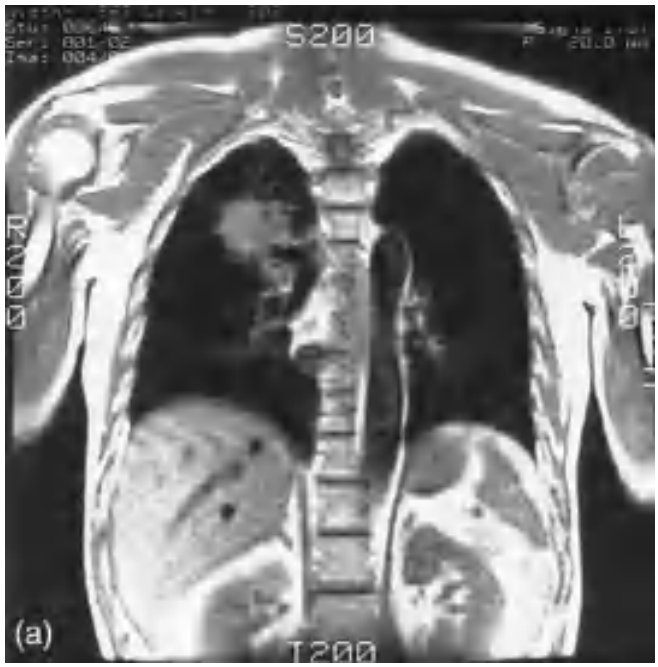

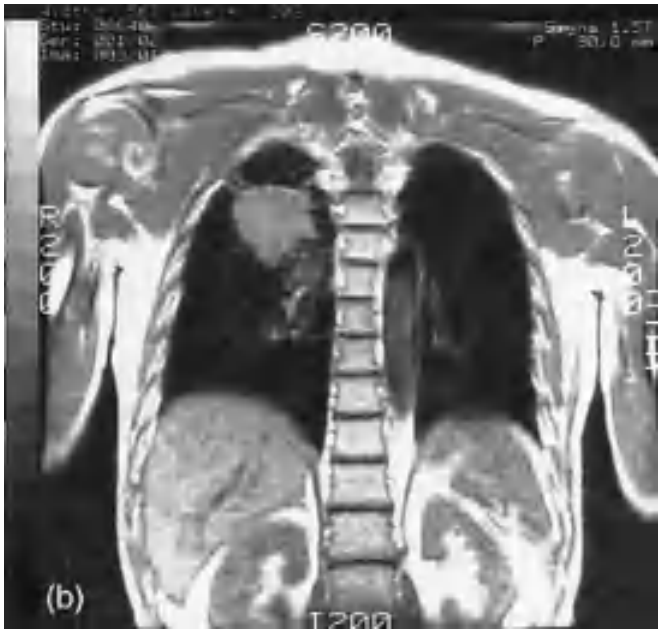

Figure 3 (a) A coronal-gated spin echo image showing the intimate relationship of a bronchiogenic carcinoma with the right upper lobe bronchus. (b) A gated spin echo image posterior to (a), showing a larger portion of the mass and possible association with the chest wall

echo imaging techniques has recently been shown to increase the sensitivity to pulmonary parenchyma abnormalities, such as metastasis. However, CT is significantly superior. Projection–reconstruction techniques can utilize extremely short echo times (as short as 100 μs), and thus allow imaging of the pulmonary parenchyma or lung water associated with the pulmonary parenchyma[10] (Figure 4). These techniques remain somewhat experimental but will allow for the demonstration of pulmonary parenchymal signals, which are less sensitive to the susceptibility generated within the lung. These signals represent excellent maps of lung water and show exceptional promise in improving MR's ability for characterizing subtle intrapulmonary abnormalities.

The utilization of paramagnetic contrast agents has also advanced the abilities of thoracic MRI to characterize a number of lesions.[11] The T_1 shortening effects of paramagnetic materials have provided the ability to enhance the differentiation of atelectatic from existing tumors as well as characterizing nonperfused cystic structures.

MRI has been valuable in characterizing a number of signal intensities related to tissues. The specific signal characteristics of hemorrhage have allowed the identification of short T_1 changes associated with methemoglobin in order to characterize hemorrhagic processes from pulmonary parenchymal diseases. Pulmonary hemorrhage appears as a relatively short T_1 of bright signal intensity on T_1-weighted images. Hemorrhage into the mediastinum or associated with aortic dissections can be characterized due to the signal intensity changes associated with hemoglobin as it changes from oxyhemoglobin to deoxyhemoglobin to methemoglobin.

The mediastinum contains relatively simple contrast relationships for MRI. The esophagus and heart remain intermediate in signal intensity, contrasted to the relatively high signal intensity on T_1-weighted images of thoracic fat. The normal thymus appears as a signal of intermediate intensity; it generally decreases in size with age, and increases in signal intensity with fatty replacement. Of note is the fact that the thymus may rebound in adulthood due to some physiologic stress, thus providing an intermediate anterior mediastinal sig-

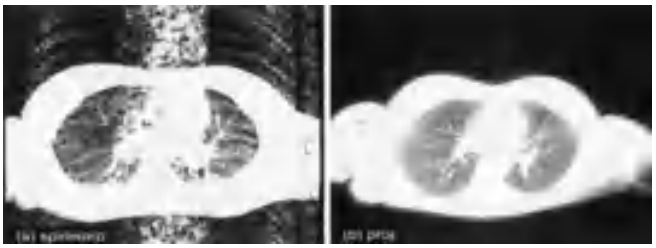

Figure 4 Comparison of images obtained with (a) conventional T_1-weighted gated (1 R–R) multislice spinwarp ($TR \approx 750$ ms, $TE = 15$ ms, 256×2 NEX, scan time 7.6 min, using respiratory compensation and spatial presaturation) and (b) multislice Hadamard projection reconstruction ($TR = 200$ ms, $TE = 0.25$ ms, 512 views $\times$ 8 NEX, scan time 4 min). The images have been windowed to show the lung parenchyma, which causes the flow artifacts in (a), to appear abnormally intense. Note that the projection–reconstruction acquisition has intrinsically lower respiratory and flow artifacts, even without the compensation methods employed in (a), and despite the reduced scan time. The lack of respiratory motion artifacts with the projection–reconstruction sequence is critical to the successful visualization of lung parenchyma

nal intensity. This, in general, can be differentiated from most pathologic processes on the basis of morphology. Although MRI provides excellent tissue characterization, the ability of MRI in differentiating between benign and malignant changes within the thymus itself is somewhat limited. CT and MRI both provide an excellent technique for evaluating anatomic changes associated with thymic disorders.[12–14]

MRI provides an excellent method for identifying and characterizing abnormalities in the pulmonary hyla. The sensitivity to flow associated with spin echo imaging and the increase in signal intensity from gradient-recalled images provide an excellent format for identifying soft tissue abnormalities in the hyla. MRI appears to be significantly more sensitive than CT for the detection of these abnormalities; however, the characterization of these may be somewhat difficult.[15–17] The pathologic nature of hilar and mediastinal lymph nodes remains largely based on the size of the individual lesions. MRI provides an excellent format for visualizing lymphadenopathy. The ability to image in the coronal plane has increased the sensitivity for the detection of aortapulmonary window adenopathy. The major advantage of MRI over CT is that the intrinsic contrast relationships allow identification of the lymph nodes and their separation from major vascular structures without the need to administer an iodinated contrast agent. Characterization of pathologies by T_1- and T_2-weighted images, however, has been somewhat disappointing. Both inflammatory and neoplastic adenopathy appear to have prolonged T_2 times. The primary mechanism for distinguishing between benign and malignant adenopathy remains that of lymph node morphology and size.[18,19] Staging of bronchiogenic carcinoma with MRI has provided an excellent means of detecting mediastinal lymph nodes on an anatomic basis. Characterization of lymphomas has also benefited significantly from the detection of mediastinal lymphadenopathy, due to the excellent contrast characteristics of MRI. The relative T_2 prolongation associated with lymphomas has been identified, but its use remains limited due to the lack of ability to characterize changes other than those based on size (Figure 5). The evaluation of patients with recurrent lymphoma has been suggested to be improved by the ability of MRI to characterize increased water content of nodes. In most treated lymphomas, there is a generalized decrease in size and signal intensity related to therapy. The recurrence of lymphoma can be characterized by either an increase in size or an increase in signal intensity. The increase in signal intensity in T_2-weighted images has been suggested to be grounds for suspecting recurrence, and individual patients with changes in signal intensity or size should be assessed for recurrent disease.[20]

The evaluation of bronchiogenic carcinoma is important in determining therapy and prognosis. MRI and CT both provide excellent anatomic images of the primary tumor as well as the ability to characterize the presence of lymphadenopathy. A specific problem for which MRI may provide improved specificity is in the associated changes in atelectasis associated with proximal bronchiogenic lesions.[21,22] MRI has been suggested to be an excellent method for differentiation of obstructed atelectasis from the primary mass. The utilization of paramagnetic contrast material appears to provide significantly improved information over CT, and aids in differentiating mass from atelectasis[23,24] (Figure 6).

Mediastinal cysts can often be confused with neoplastic lesions. The specific characteristics of very long T_2 and very long T_1 associated with mediastinal cysts enable these lesions to be characterized by MRI. The relative homogeneity associated with these benign congenital cysts and their anatomic location provides specific clues as to their etiology. Mediastinal cysts can be divided into duplication cysts, neurenteric cysts, and pleuroparenchymal cysts. In general, they are specifically characterized by their long T_1 and long T_2 and relatively sharp margins. The additional use of an intravenous paramagnetic contrast material will characterize these lesions as being avascular.

Esophageal carcinoma represents a continuing diagnostic dilemma. The presence of the primary mass can easily be identified by the relative increase in soft tissue density associated with the esophagus. MRI provides an excellent method for the staging of esophageal cancer and characterizing the association with vascular structures. The obliteration of fat planes about the aorta and other adjacent vascular structures, such as the left atrium, can be extremely helpful in planning therapy. These changes, however, do not appear to have significantly impacted on the ultimate outcome of esophageal cancer (Figure 7).

Approximately 10% of parathyroid glands are ectopic. Two thirds of these appear to arise in the anterior mediastinum. In the presence of hyperparathyroidism unresponsive to resection of the cervical components of the thyroid glands, the mediastinum becomes the primary source. The behavior of hyperplastic parathyroid glands on MRI is characterized by a markedly prolonged T_2 relaxation time. This makes the identification of T_1- and T_2-weighted images extremely important. It should be noted that the identification of a markedly prolonged T_2 signal in the mediastinum should be separated from relatively slow flow in thoracic veins by the utilization of some form of gradient-recalled imaging sequence.

The excellent contrast characteristics of MRI provide an excellent means of staging of thoracic neoplasms. The sensitivity to direct invasion of vascular structures by obliteration of

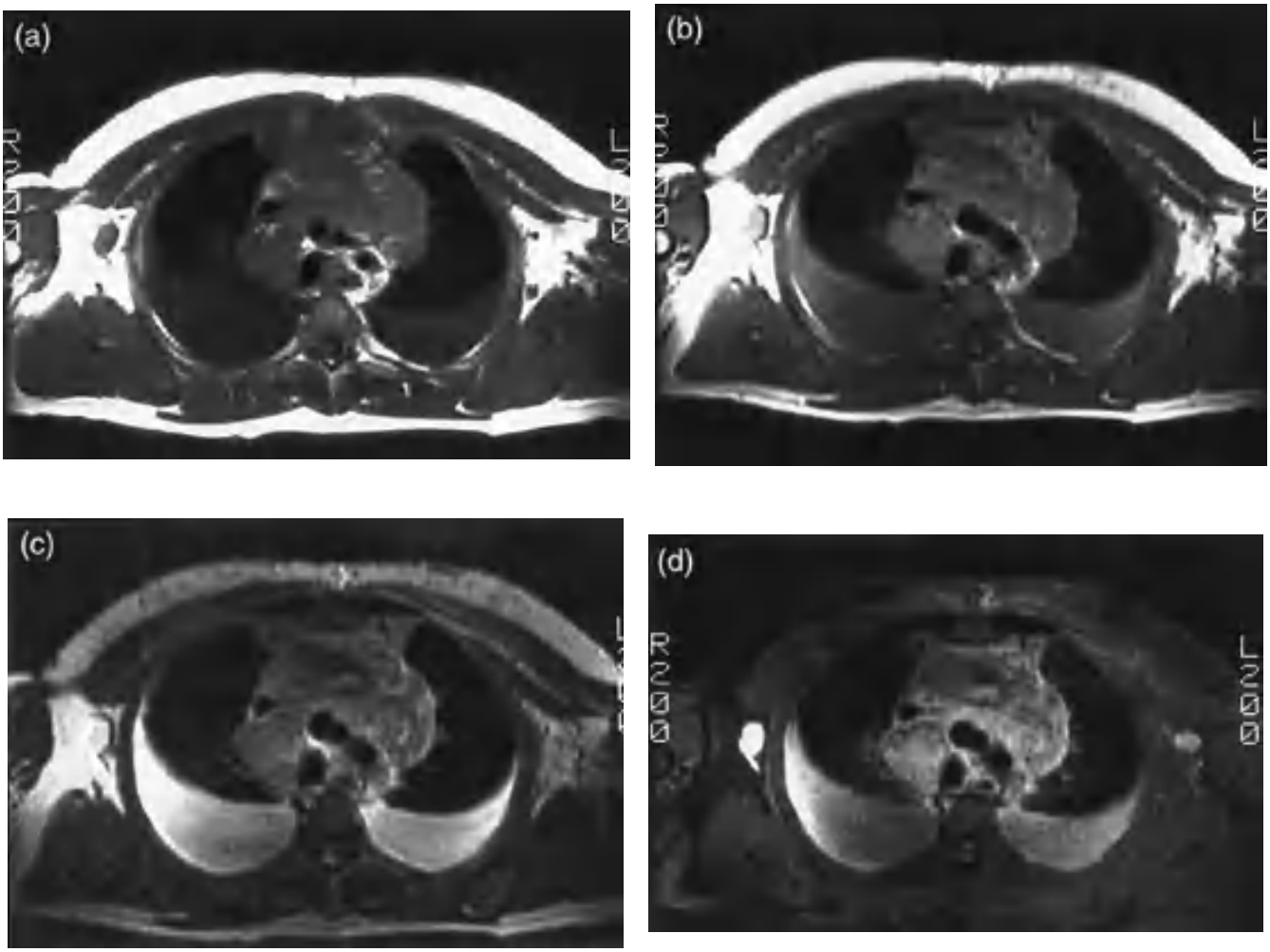

Figure 5 (a) A gated T_1-weighted spin echo image through the upper mediastinum. (b) A spin density gated image through the upper mediastinum. (c) A T_2-weighted gated image through the upper mediastinum. (d) A fat-suppressed, fast spin echo image through the upper mediastinum. Note the bulky adenopathy in the anterior mediastinum and the right paratracheal space. In addition, note the large lymph node in the right axilla. There are bilateral pleural effusions present, which give significantly variable signal intensities, as do all these images, to the relatively long T_1 and T_2 of the effusion, which is affected strongly by flow secondary to cardiac and respiratory motion. Note the difference in the degree of conspicuousness of the axillary node in the fat-suppressed image (d) and the significant difference in the signal characteristics of the mediastinal adenopathy. The fast spin echo image associated with both fat suppression and magnetization transfer effects will have significantly different contrast in this mediastinal adenopathy. The ability to characterize adenopathy, due to signal changes, remains a complex issue

associated short T_1 fat planes provides an excellent method (Figure 8). The ability of MRI to characterize changes along the thoracic wall provides a unique opportunity to demonstrate thoracic wall invasion. The short T_1 associated with subpleural fat and the relatively long T_1 of thoracic neoplasms give MRI great sensitivity in detecting thoracic wall invasion (Figure 9). These changes in thoracic wall invasion observed in both lymphoma and bronchiogenic carcinomas may significantly change therapy.[25] Either identification of the lesion as being nonresectable or the provision of information about thoracic wall invasions may significantly alter the radiation therapy planning. Similarly, the ability to provide coronal images of Pancoast's tumors may provide important information about resectability and therapy.[26,27]

Pleural effusions are easily identified in MRI scans. The signal intensities were originally thought to provide important information about transudative versus exudative behavior of pleural effusions. However, the strong effect of flow within the pleural effusions provides the dominant mechanism for signal changes in spin echo imaging. Free flowing pleural effusion may even appear as a signal void on spin echo images, and can easily be identified as areas of increased signal intensity and gradient-recalled images due to their flow related enhancement.[28]

Pulmonary artery abnormalities, such as the presence of pulmonary emboli, have been identified as areas of increased signal intensity on spin echo images. MRI represents an excellent method for characterizing the presence of central pulmonary emboli. In general, chronic pulmonary emboli have intermediate signal intensity on both T_1- and T_2-weighted images. However, the presence of acute pulmonary emboli may be characterized by the presence of an extremely high

intensity signal on T_2- and T_1-weighted images due to the presence of methemoglobin in the thrombi (Figure 10). The flow sensitivity of MRI has been utilized to characterize pulmonary arteriovenous malformations. The relatively intermediate signal intensity seen on T_1-weighted images may be present due to relatively slow flow. The sensitivity of gradient-recalled images or phase contrast methods has allowed the characterization of these pulmonary parenchyma abnormalities by demonstrating the flow within them (Figure 1).

In summary, the excellent contrast characteristics of MRI, associated with its sensitivity to flow, make it an excellent method for identifying and characterizing pulmonary and mediastinal pathologies. The relatively limited spatial resolution within the pulmonary parenchyma is a significant limitation; however, the superb contrast sensitivities have ensured the place of MRI in the identification and characterization of thoracic pathologies.

1 RELATED ARTICLES

Breast MRI; Heart: Clinical Applications of MRI; Whole Body Magnetic Resonance Angiography.

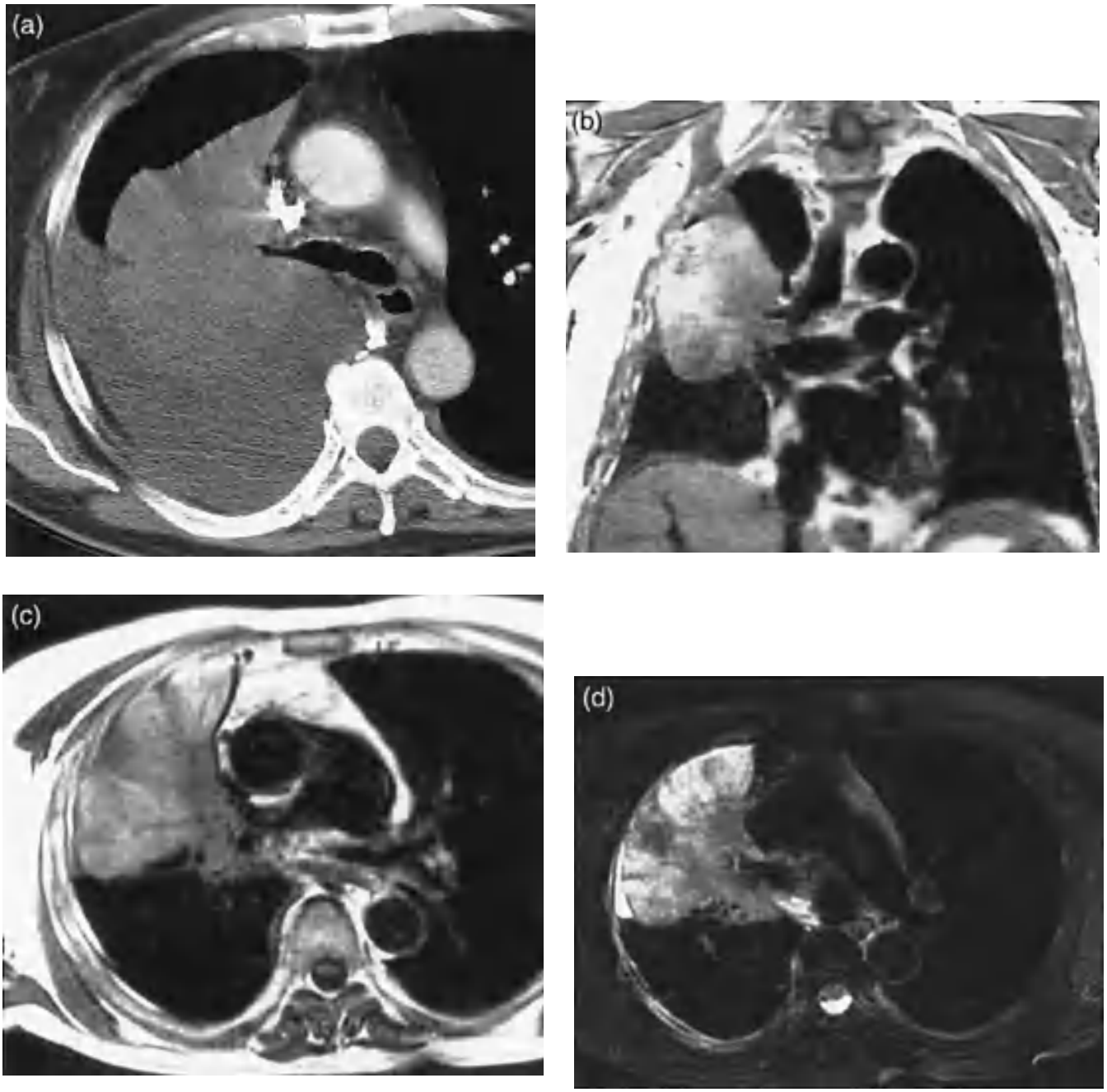

Figure 6 (a)–(d)

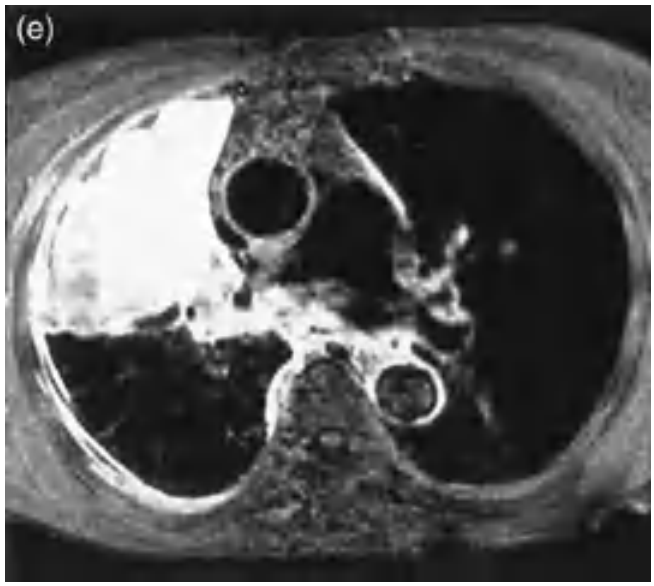

Figure 6 (a) A CT scan obtained from a patient presenting with a right-sided mass and large pleural effusion. (b) A gated coronal image through the same patient as in (a) following a thoracentesis. This image still shows a rather prominent mass, with occlusion of the right upper lobe bronchus. The question of primary mass versus atelectasis is often raised. (c) A gated transverse spin echo image through the mass. Note the relatively high signal intensity of this 'T_1-weighted image' in the periphery of this mass, the finding which is described in atelectatic lung. (d) A fat-saturated fast spin echo image showing marked heterogeneity in the mass but relatively clear delineation between the peripheral components and more central low intensity mass. (e) A T_1-weighted fat-saturated gated fast spin echo image through the same region as in (d) showing marked enhancement of the mass, as well as the adjacent pleura on this side

Figure 7 A gated transverse spin echo image through the midthorax shows a subcarinal mass associated with relatively subtle esophageal carcinoma. There is a fat plane between the aorta and mediastinal soft tissue, suggesting no definite invasion. Of more importance are the soft tissue densities in each lung field. These relatively hazy, ill-defined nodules are characteristic of metastatic disease on MRI. CT remains the primary method of screening for pulmonary metastases

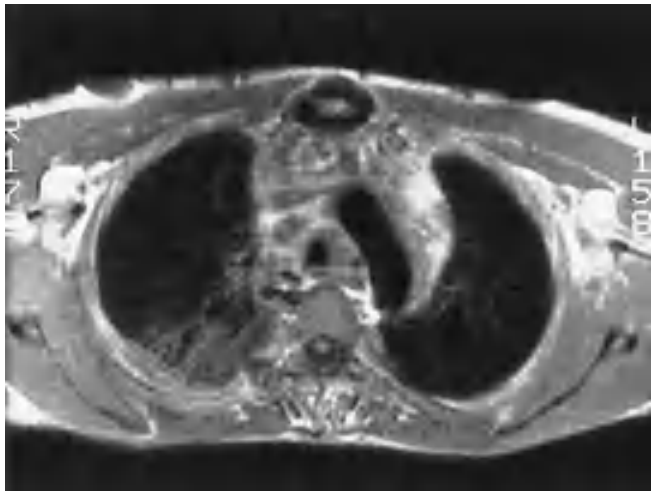

Figure 8 A gated spin echo image through the upper mediastinum shows prominent anterior mediastinal adenopathy as well as a prominent para-aortic node. On the right-hand side there is pulmonary parenchymal consolidation and fibrotic changes secondary to prior radiation therapy. Shoddy mediastinal adenopathy is present. Of note is the absence of a significant signal void in the superior vena cava, due to vena caval occlusion

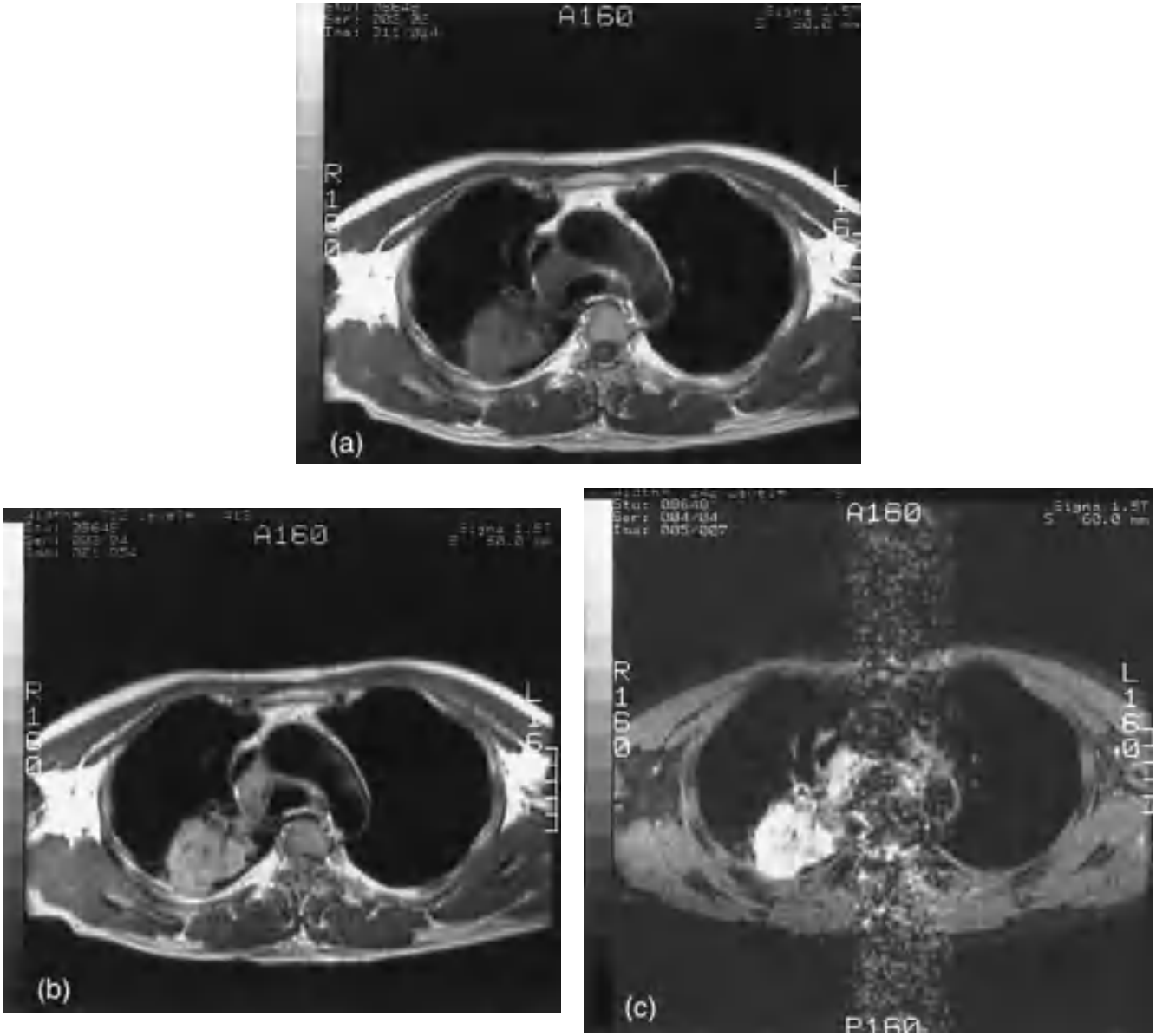

Figure 9 (a) A gated spin echo image through a bronchiogenic carcinoma of the right upper lobe. (b) A gated spin-density-weighted image through the carcinoma. (c) A STIR image obtained through the upper mediastinum. Note the excellent delineation on all images of the primary mass in relation to the pulmonary parenchyma. Paratracheal adenopathy is clearly visible on the spin echo images, but is somewhat obscured on the STIR images. The STIR image does, however, provide much better detail of the mass and its intimate association with the chest wall, suggesting chest wall invasion. In addition, the significant motion artifacts present on the STIR image are due to the relative difficulty of gating inversion–recovery images. The STIR images themselves are useful in investigating chest wall invasion but, due to the relative temporal inefficiency, may not be appropriate for all patients

Figure 10 A gated T_1-weighted transverse image through the aortic arch, showing a very high signal intensity area on the left upper lung corresponding to a subacute pulmonary embolus

2 REFERENCES

1. L. Axel, R. M. Summers, H. Y. Kressel, and C. Charles, *Radiology*, 1986, **160**, 795.
2. L. Hedlund, R. Herfkens, J. Deitz, R. Blinder, R. Nassar, E. Coleman, E. Effman, and C. Putman, *Proc. IVth Ann Mtg. Soc. Magn. Reson. Med.*, London, 1985, **1**, 583.
3. C. B. Higgins, E. H. Botvinick, P. Lanzer, R. J. Herfkens, M. J. Lipton, L. E. Goorn, and L. Kaufman, *Cardiol. Clin.*, 1983, **1**, 527.
4. G. Gamus and D. Sostman, *Am. Rev. Respir. Dis.*, 1989, **139**, 254.
5. N. J. Pelc, R. J. Herfkens, A. Shimakawa, and D. R. Enzmann, *Magn. Reson. Q.*, 1991, **7**, 229.
6. P. Y. Poon, M. J. Bronskill, R. M. Henkelman, D. F. Redeout, M. S. Sholman, G. L. Weisbrod, M. I. Steinhardt, M. J. Dunlap, A. R. J. Ginsberg, and R. Feld, *Radiology*, 1987, **196**, 651.
7. S. L. Primack, J. R. Mayo, T. E. Hartman, R. R. Miller, and N. L. Müller, *J. Comput. Assist. Tomogr.*, 1994, **18**, 233.
8. N. L. Müller, J. R. Mayo, and C. V. Zwirewich, *Am. J. Roentgenol.*, 1992, **158**, 1205.
9. E. H. Moore, W. R. Webb, N. L. Müller, and R. Sollitto, *Am. J. Roentgenol.*, 1986, **146**, 1123.
10. C. J. Bergin, J. M. Pauly, and A. Macovski, *Radiology*, 1991, **179**, 777.
11. C. J. Herold, J. E. Kuhlman, and E. A. Zerhouni, *Radiology*, 1991, **178**, 715.
12. G. M. Glazer, M. B. Orringer, T. L. Chenevert, J. A. Borrello, M. W. Penner, L. E. Quint, K. C. Li, and A. M. Arsers, *Radiology*, 1988, **168**, 429.
13. G. M. Glazer, *Chest*, 1989, **96** (Suppl. 1), 44S.
14. W. R. Webb, M. Sarin, E. A. Zerhouni, R. T. Heelan, G. M. Glazer, and C. Gatsonis, *J. Comput. Assist. Tomogr.*, 1993, **17**, 841.
15. W. R. Webb, C. Gatsonis, E. A. Zerhouni, et al., *Radiology*, 1991, **178**, 705.
16. W. B. Gefter, *Semin. Roentgenol.*, 1990, **25**, 73.
17. O. Musset, P. Grenier, M. F. Carette, G. Frija, M. P. Hauuy, H. T. Desbleds, P. Giraird, J. M. Bigot, and D. Lallemand, *Radiology*, 1986, **160**, 607.
18. G. M. Glazer, B. H. Gross, A. M. Aisen, L. E. Quint, I. R. Francis, and M. B. Orringer, *Am. J. Roentgenol.*, 1985, **145**, 245.
19. H. S. Glazer, R. G. Levitt, J. K. T. Lee, B. Emami, S. Gronemeyer, and W. A. Murphy, *Am. J. Roentgenol.*, 1984, **143**, 729.
20. R. S. Nyman, S. M. Rehn, B. L. Glinelius, M. E. Hagberg, A. L. Memmingtson, and C. J. Sundstrom, *Radiology*, 1989, **170**, 435.
21. J. A. Verschakelen, P. Demaerel, J. Coolen, M. Demeols, G. Marshal, and A. L. Baert, *Am. J. Roentgenol.*, 1989, **152**, 965.
22. C. J. Herold, J. E. Kuhlman, and E. A. Zerhouni, *Radiology*, 1991, **178**, 715.
23. P. M. Bourgouin, T. C. McLoud, J. F. Fitzgibbon, E. J. Mark, J. A. Shepard, E. M. Moore, E. Rummeny, and T. J. Brady, *J. Thorac. Imag.*, 1991, **6**, 22.
24. J. Tobler, R. C. Levitt, H. S. Glazer, J. Moran, E. Crouch, and R. G. Evens, *Invest. Radiol.*, 1987, **22**, 538.
25. R. T. Heelan, B. E. Demas, J. F. Caravelli, N. Martini, M. S. Bains, P. M. McCormack, M. Burt, D. M. Panicek, and A. Mitzner, *Radiology*, 1989, **170**, 637.
26. D. R. Pennes, G. M. Glazer, K. J. Wimbish, B. H. Gross, R. W. Long, and M. B. Orringer, *Am. J. Roentgenol.*, 1985, **144**, 507.
27. A. M. Haggar, J. L. Pearlberg, J. W. Froelich, D. O. Hearshen, G. H. Beure, J. W. Lewis, Jr., G. W. Schkuder, C. Wood, and P. Gniewck, *Am. J. Roentgenol.*, 1987, **148**, 1075.
28. P. Vock, L. W. Hedlund, R. J. Herfkens, E. L. Effmann, M. A. Brown, and C. E. Putman, *Invest. Radiol.*, 1987, **22**, 382.

Biographical Sketch

Robert J. Herfkens. *b* 1949. M.D., 1974, Loyola University, Stritch School of Medicine. Associate Professor and Director of MRI, Stanford University School of Medicine, 1989. Principal investigator on research grants sponsored by Government and private industry. Approx. 100 scientific papers, presented at over 100 national meetings; several textbooks. Main research interest: the development of applications and new techniques directed towards body imaging, most specifically those related to cardiovascular diseases.

Marker Grids for Observing Motion in MRI

Leon Axel

University of Pennsylvania, Philadelphia, PA, USA

1 INTRODUCTION

Early in the development of NMR, it was noticed that motion could affect the NMR signal.[1] It was quickly understood that this reflected the fact that moving material carries its magnetization with it. If the magnetization is perturbed locally, that perturbed magnetization is carried with the material as it moves. This principle was applied in some early applications of NMR to the measurement of fluid flow.[2–4]

With the development of MRI, selective excitation was applied to the region to be imaged. The resulting local perturbation of magnetization within the slice being imaged led to intensity changes in the images of flowing blood or cerebrospinal fluid, due to 'time-of-flight' (TOF) effects.[5,6] (See also articles on Flow in this Encyclopedia, listed in the Related Articles below.) These TOF effects due to selective slice excitation can be used for qualitative or quantitative evaluation of flow through the plane of the image. We will review here some aspects of using regional perturbation of the magnetization in planes *perpendicular* to the image to create magnetic tags. Subsequent imaging allows us to display directly the motion (of fluid or tissue) in the plane of the image during the time between tag production and image data acquisition, as a corresponding displacement of the tags in the image. We will review some aspects of tag production, approaches to tagged image analysis, and initial applications. While the phase shifts acquired by excited spins moving along magnetic field gradients can also affect their signal, we will not consider these effects here.

2 TAG PRODUCTION

When perturbed, the altered magnetization (excitation or saturation) in a tag will persist for times of the order of the relaxation time. An excitation tag can be produced with initial excitation of a plane perpendicular to the imaging plane and subsequent conventional position encoding in the imaging plane. These excited spins will be seen as a bright stripe in the image, representing the intersection of the initially excited plane with the imaging plane. Any displacement of the spins in the plane of the image between the times of initial excitation and subsequent position encoding will be seen as a corresponding displacement of the tagged stripe. This approach has been used to demonstrate fluid flow, with the excited spins detected either as a conventional spin echo[7] or as a gradient echo.[8] If conventional spin echo detection is used, the refocusing rf pulse can be used to select the plane to be imaged. With gradient echo excitation tagging, a two-dimensionally selective 'spike' excitation could be used to restrict the tagging plane. The motion sensitivity of tagging depends on the time between excitation and readout. This, in turn, is limited by transverse relaxation to be of the order of the T_2 relaxation time, or T_2^* for gradient echo readout.

An alternative way to create tags is with local production of saturation or inversion in a plane or planes perpendicular to the image plane. The altered longitudinal magnetization will result in stripes with a correspondingly altered image intensity in a subsequent image acquisition, representing the intersections of the tagged planes with the imaging plane. Any displacement in the image plane between the times of tagging and imaging will be seen as a corresponding displacement of the tagged stripe in the image. In this case, tag persistence is limited by longitudinal relaxation so that displacement can be tracked for times of the order of the T_1 relaxation time (with initial inversion leading to longer tag persistence than initial saturation).

The local perturbation of magnetization can be created selectively. Selective tagging is analogous to slice selection excitation, with an rf excitation pulse with tailored frequency content applied in the presence of a magnetic field gradient, in order to excite only a desired plane perpendicular to the gradient. If only longitudinal magnetization tagging is desired, any remnant transverse magnetization from the tagging can be 'spoiled' by applying a further magnetic field gradient prior to excitation of the imaging plane. Multiple tagging planes can be created by applying the tagging process repeatedly at several locations or by tailoring the rf pulse to excite several locations simultaneously.[9] The latter approach can allow more rapid production of tagging patterns, but may require more rf power. By following selective inversion tagging with a nonselective inversion pulse, we can create a tag pattern with bright stripes (where the magnetization has been driven back up toward equilibrium) against a darker background.[10] Separate images of different tagging patterns can be combined to give the effect of having used a more complex tagging pattern.[11]

The tagging pattern can also be created nonselectively. In this case, the magnetic field gradient is applied *between* nonselective rf excitation pulses.[12,13] The resulting periodic phase variation along the direction of the gradient leads to a net periodic modulation of the magnetization along the direction of the gradient, or spatial modulation of magnetization (SPAMM). This is precisely analogous to the use of binomial pulses[14] and related techniques in NMR spectroscopy for solvent suppression; in spectroscopy the corresponding periodicity of the suppression is usually chosen to be greater than the relevant spectral bandwidth. This spatially modulated magnetization, in turn, will be seen in a final image as a periodic stripe pattern along the direction of the tagging gradient. The spacing of the stripes will be determined by the strength and duration of the gradient pulses; the orientation of the stripes will be determined by the orientation of the tagging gradient. The relative position of the tag pattern along the gradient direction can be shifted by shifting the relative phases of the rf pulses. By using multiple rf pulses with suitable relative intensities, we can control the intensity profile of the resulting tagging pattern.

The result of one application of SPAMM is a set of parallel tagging stripes. Creating a second set at right angles to the first can produce a tagging grid.[13] Images with tagging patterns of opposite polarity can be combined to increase the effective amplitude of the tags.[15] Tags can also be created with tagging planes that are not perpendicular to the imaging plane, although the stripes may be blurred due to partial volume effects with the oblique intersection of the tagging plane with the slice being imaged.[16,17] The SPAMM principle can be used with a continuous gradient if the rf pulses have sufficiently broad spectral content (are 'hard' enough) to excite the region to be tagged in the presence of the gradient.[18] The SPAMM principle can also be applied in combination with selective excitation tagging to create periodic amplitude modulation along the tag.[19]

Saturation or inversion tags can be used as a preconditioning sequence incorporated into any imaging pulse sequence, much as a conventional inversion pulse can be used to add T_1 relaxation time weighting to images. For example, with cardiac-gated imaging, the cardiac-derived trigger can be used to control initiation of the tagging, and then imaging data can be acquired at subsequent desired delays into the cycle (Figure 1). The tag pattern will reflect any motion of the underlying tissue between the times of tagging and imaging. If used in conjunction with a rapid enough imaging technique, images can be acquired with suspended respiration, removing image degradation due to respiratory motion.[11,20,21] With a further decrease in imaging time, motion of soft tissue structures can be evaluated with a voluntary motion initiated at the time of tagging (e.g. in response to the audible sound of the gradients used in the tagging sequence)[10] and a 'one-shot' image acquired when the new position has stabilized but before the tags have faded too much.

3 TAGGED IMAGE ANALYSIS

Much qualitative motion information can be gained from visual inspection of the deformation of the tag pattern (Figure 2), particularly with a dynamic 'cine' display of images acquired with progressive delays after the tagging. However, there is the potential for further extraction of quantitative measures of motion from analysis of the displacement and deformation of the tags.

Motion can be considered as composed of rigid body motion (displacement and rotation) and deformation ('strain'). The rigid body displacement is a property of material points. It is defined as the motion of the points relative to an external reference system, for example, the centroid of a ventricle (at a fixed time or moving with the ventricle), and will be affected by bulk motion of the structure of which a particular point is a part. In contrast, the 'strain' is a property of the material in a small region about a given point. It is defined as the relative change in length of material line segments passing through the point. As it depends only on the deformation of this region, it will be independent of the choice of external reference system. Another important difference between displacement and strain, as properties describing motion, is that whereas displacement is a vector quantity described by a magnitude and a direction, strain is a higher-dimensional *tensor* quantity that is orientation dependent. While a line segment oriented in one direction may be stretched a given fractional amount, other line segments passing through the same point in different directions will, in general, be stretched different fractional amounts, or even shrunk.

Although it would seem difficult or impossible to describe efficiently the full strain tensor, the strain in a small region around a point can be conveniently summarized by the 'princi-

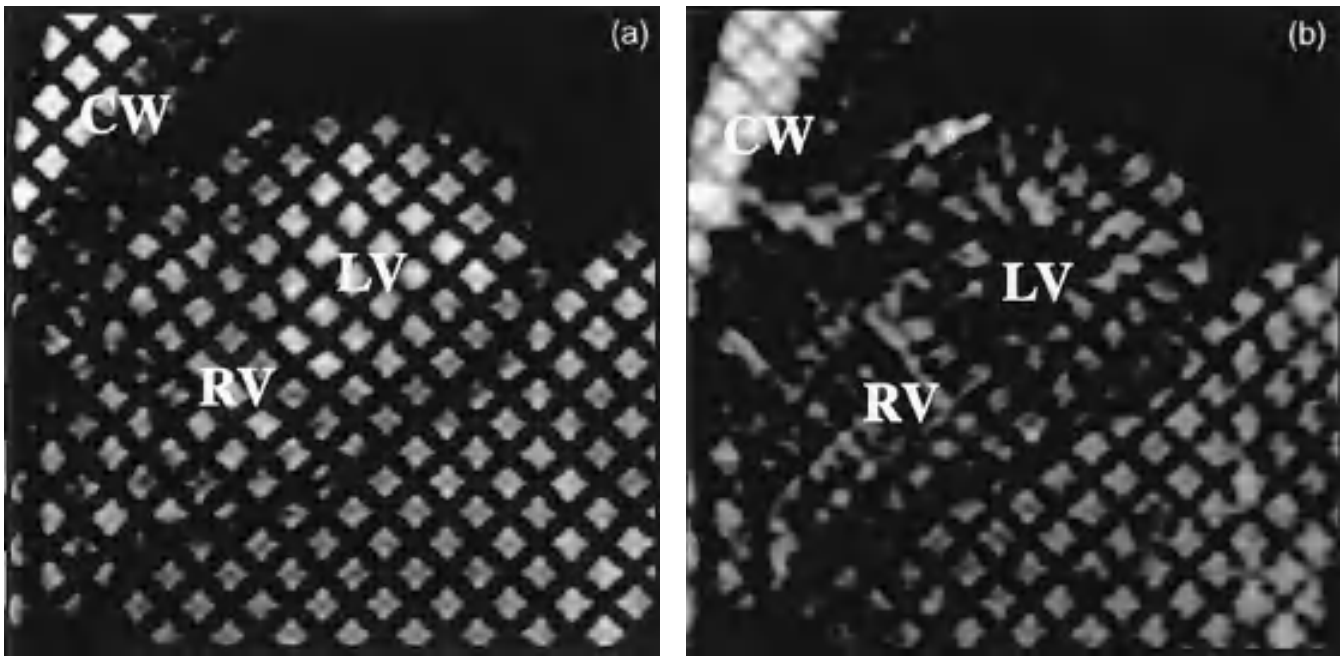

Figure 1 Tagged short axis images of the heart, (a) immediately after tagging at end diastole and (b) at end systole: chest wall (CW), right ventricle (RV), left ventricle (LV)

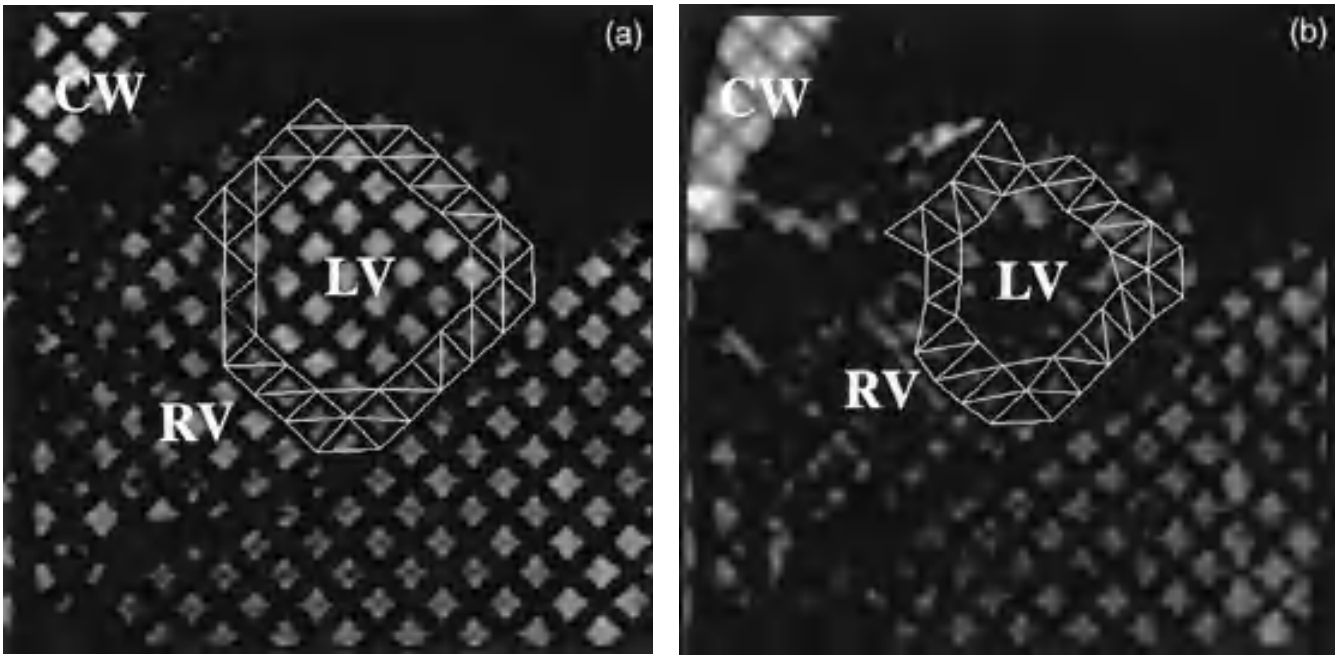

Figure 2 Superimposed positions of tag lines measured from images in Figure 1

pal strains' at the point. In general, a hypothetical unit sphere (circle in two dimensions) about the point in an initial state will be transformed by motion into an ellipsoid (ellipse in two dimensions). The three major axes of the ellipsoid (or two axes of the ellipse) will suffice to define the final length of any initial line segment. The lengths of these axes for an initial unit length are the 'eigenvalues' of the strain; their directions give the 'eigenvectors'.

For homogeneous deformation within a given region defined by a two-dimensional tagging grid, the rigid body motion and deformation motion variables can be calculated from the motion of the grid points. In particular, for a two-dimensional homogeneous deformation, the motion of the corners of a triangular region is sufficient to define the rigid body motion and strain within the triangle.[22,23] An alternative approach to calculating the motion variables within a tagged region is to use finite element methods to fit the motion between the tags to a smoothly varying function of position; this model of the motion permits calculating the rigid body motion and strain at each point without requiring the assumption of homogeneous strain within each portion of the tagging grid. The motion data from two orthogonal sets of tagged images can be combined into one unified three-dimensional (3D) finite-element model and used to calculate 3D strains.[24] Note that in calculating motion from tagging grid points, it is generally not wise to use the coordinates of the intersections of tag lines with the boundaries of a moving object as distinct tagged landmarks, because through-plane motion of an obliquely oriented or tapered object can result in artifactual motion due to the change of the intersection of the boundary of the object with the fixed imaging plane. When the amplitude of the motion is of the order of the spacing between tags, care must be taken to avoid confusing one tag for another in the deformed state. If this is a problem, additional images with a more widely spaced grid or at intermediate times can help resolve the ambiguity.

Tracking the sequential positions of multiple points in a tagging grid through multiple imaging slice locations can be a time-consuming and tedious process. The use of computer programs specifically designed for tag analysis can significantly speed up the analysis process[25]. In particular, techniques to make the process of extraction of tag position from the images more automated can be very useful. These approaches can include means to match the tags to a 'template' of a model tag or tag grid intersection.[26–28] Alternatively, various edge or contour tracking techniques can be used to track the tags.[29,30]

Having derived a large amount of regional motion data from tagged images, we are faced with the problem of how to present it in a readily assimilated form. Visual display of the local values of motion variables as 'functional images' is an efficient and appealing approach to this problem, made practical by the continuously improving performance/cost ratio of computers with graphical displays. Scalar quantities, such as the magnitude of the displacement, can be relatively easily displayed, for example, as pseudocolor overlays on the images. Even here, however, the task of displaying the time evolution of motion in a three-dimensional object may require interactive dynamic display on a computer screen to convey fully the nature of the motion. Vector motion quantities, such as directed displacement, may require overlaying the display with symbols such as arrays of directed arrows. Higher order motion quan-

tities, such as strain eigenvectors, are intrinsically difficult to display fully on a flat screen or page, particularly for three-dimensional motions. Tensor properties may require display as lower order components such as the strain eigenvalues.

The reliability of tagged imaging studies as markers of the underlying motion has been validated with imaging studies of phantoms with independently known motions. This includes both phantoms undergoing only rigid body motion[31] and phantoms undergoing deformation.[32] As expected, the tags do move with the underlying material.

4 APPLICATIONS

The development of tagged imaging methods and of methods for the analysis of the resulting images is still ongoing. However, experience is being gained with initial applications to a variety of motion studies, including flow imaging, regional heart wall motion, and other soft tissue deformation.

A simple, but very useful, application of tagged imaging to flow studies is simply to detect the presence of flow. Although the usual TOF and phase shift effects of motion seen in conventional MRI are generally sufficient to distinguish flowing blood from static thrombus in MR images, it is not uncommon to have difficulty distinguishing slow flow from thombus. Tagging methods provide a straightforward way to increase the sensitivity of MRI to slow flows. If grid saturation tags are created in the region of question as part of a cardiac-gated imaging sequence, and a delay of 200 ms or so is allowed to elapse between tagging and image data acquisition, any fluid motion of the order of a pixel or more during this interval will result in a visible shift and distortion of the tag pattern, or even complete smearing out of the tag pattern due to shearing motions of the fluid.[12] For example, in pulmonary artery embolization, the resulting slow flow can be difficult to distinguish from the emboli; SPAMM can be very helpful in defining the emboli.[33]

The problem of visualizing patterns of fluid flow is a long standing and important one, with many different solutions such as the injection of opaque tracers into transparent flowing fluids. The use of tagged MRI provides a new and potentially powerful tool for the study of flow patterns. The tagging process does not disturb the flow in any way, MR tagging can be employed with opaque fluids, there is no distortion due to refraction, and images are obtained in registered 3D sectional planes. In addition to biological fluid flow applications, there may be useful engineering and industrial applications.[34,35]

An important area of potential application is to the study of regional heart-wall motion. Traditional imaging methods of studying cardiac function have been invasive or limited in the kinds of motion data they provide. The lack of trackable landmarks within the heart wall, and the few surface landmarks, have largely limited heart-wall motion analysis to the study of the motion of the endocardial surface or of wall thickening. This analysis has been further limited by the uncertainty about what is the appropriate reference system against which to measure the surface motion, and by the potential error due to through-plane motion of the curved and tapering heart wall. Within-wall and nonradial components of heart-wall motion can be evaluated at selected points through biplane imaging of radioopaque markers embedded in the heart wall, but the difficulty of tracking many markers and the invasive nature of the embedding process has limited such studies to relatively few markers and precluded routine clinical application of these methods. In contrast, tagged MRI is completely noninvasive and permits a full tensor analysis of motion patterns within the heart wall.

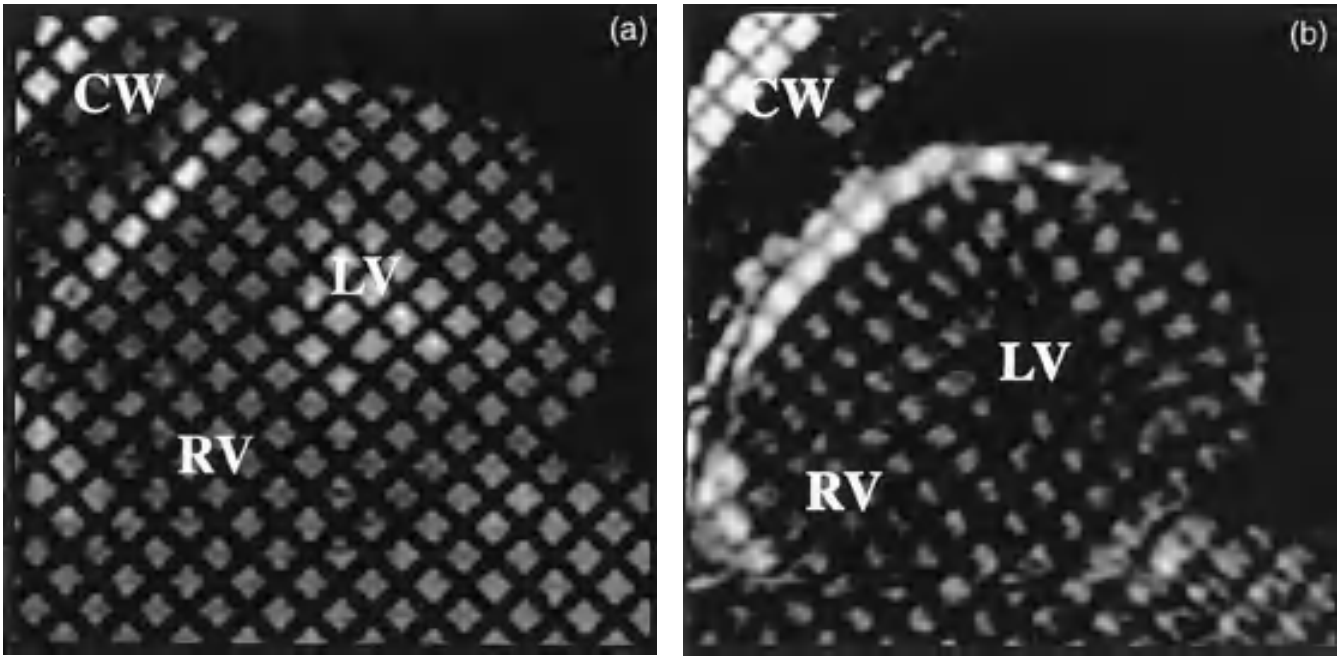

Figure 3 As in Figure 1, but for a patient with diffuse hypertrophic cardiomyopathy

As the cardiac motion data provided by MRI are new, initial applications of tagged MRI to the heart have studied the normal patterns of regional wall motion.[36,37] Application to the study of abnormal motion patterns in hypertrophy due to pressure overload[38] or hypertrophic cardiomyopathy[39] is attractive both because of their clinical importance and because of the relative ease of studying motion within thicker heart walls (Figure 3). Ischemic heart disease is another area of potential significance, as MRI-derived strain measures may provide a more precise and sensitive way to characterize regional contractile dysfunction than conventional wall motion studies. This may lead to a better understanding of phenomena such as the impairment of function seen in the perinfarct zone.

Other soft tissue structures, such as skeletal muscle, may be studied in a manner similar to the heart wall. They can be imaged either with repetitive motions using a modified, tagged, cardiac imaging sequence and an appropriate trigger signal,[17] or with a 'one-shot' tagged imaging sequence.[10] While it is still early in the development of these areas of application, the power of tagged MRI to provide a noninvasive means to analyze other 'hidden' motions should lead to a new understanding of normal and abnormal function, and hopefully to a useful new diagnostic tool.

5 RELATED ARTICLES

Heart: Clinical Applications of MRI; Selective Excitation in MRI and MR Spectroscopy; Water Suppression in Proton MRS of Humans and Animals; Whole Body Magnetic Resonance Angiography.

6 REFERENCES

1. G. Suryan, *Proc. Indian Acad. Sci. Sect. A*, 1951, **33**, 107.
2. J. R. Singer, *Science*, 1959, **130**, 1652.
3. A. N. Garroway, *J. Phys. D*, 1974, **7**, L159.
4. J. H. Battocletti, R. E. Halbach, S. X. Salles-Cunha, and A. Scances, *Med. Phys.*, 1981, **8**, 435.
5. I. R. Young, M. Burl, G. J. Clarke, A. S. Hall, T. Pasmore, A. G. Collori, D. T. Smith, J. S. Orr, G. M. Bydeler, F. H. Doyle, R. H. Greenshan, and R. E. Steiner, *Am. J. Roentgenol.*, 1981, **137**, 895.
6. L. Axel, *Am. J. Radiol.*, 1984, **143**, 1157.
7. L. Axel, A. Shimakawa, and J. MacFall, *Magn. Reson. Imag.*, 1986, **4**, 199.
8. T. Matsuda, K. Shimizu, T. Sakurai, T. Matsuda, K. Shimizu, T. Sakurai, A. Fujita, H. Ohara, S. Okamura, S. Hashimoto, S. Tomaki, and C. Kowai, *Radiology*, 1987, **162**, 857.
9. E. A. Zerhouni, D. M. Parish, W. J. Rogers, A. Yang, E. P. Shapiro, *Radiology*, 1988, **168**, 59.
10. M. Niitsu, N. G. Campeau, A. E. Holsinger-Bampton, S. J. Riederer, and R. L. Ehman, *J. Magn. Reson. Imag.*, 1992, **2**, 155.
11. E. R. McVeigh and E. Atalar, *Magn. Reson. Med.*, 1992, **28**, 318.
12. L. Axel and L. Dougherty, *Radiology*, 1989, **171**, 841.
13. L. Axel and L. Dougherty, *Radiology*, 1989, **172**, 349.
14. P. J. Hore, *Magn. Reson.*, 1983, **55**, 283.
15. S. E. Fischer, G. C. McKinnon, S. E. Maier, and P. Boesiger, *Magn. Reson. Med.*, 1993, **30**, 191.
16. L. Axel and L. Dougherty, *Radiology*, 1989; **173**(P), 223.
17. J. G. Pipe, J. L. Boes, and T. L. Chenevert, *Radiology*, 1991, **181**, 591.
18. T. J. Mosher and M. B. Smith, *Magn. Reson. Med.*, 1990, **15**, 334.
19. B. Bolster, Jr., E. R. McVeigh, and E. A. Zerhouni, *Radiology*, 1990, **177**, 769.
20. L. Axel, Z. A. Fayad, and L. Dougherty, *Radiology*, 1992, **185**(P), 223.
21. Z. A. Fayad, D. L. Kraitchman, and L. Axel, 'Magnetic resonance tagging: Conventional spin echo versus fast breath-hold gradient-echo imaging using phased-array coils', in *Proc. 12th Ann Mtg. Soc. Magn. Reson. Med.*, New York, 1993, p. 1217.
22. G. D. Meier, M. C. Ziskin, W. P. Santamore, and A. A. Bove *IEEE Trans. Biomed. Eng.*, 1980, **27**, 319.
23. L. Axel, R. Gonçalves, and D. Bloomgarden, *Radiology*, 1992, **183**(3), 745.
24. A. A. Young and L. Axel, *Radiology*, 1992, **185**, 241.
25. L. Axel, D. Bloomgarden, C.-N. Chang, D. Kraitchman, and A. A. Young, 'SPAMMVU: a program for the analysis of dynamic tagged MRI', *Proc. 12th Ann Mtg. Soc. Magn. Reson. Med.*, New York, 1993, p. 724
26. D. Fisher, 'Automated tracking of cardiac wall motion using magnetic resonance markers', Dissertation, University of Iowa, 1990.
27. D. L. Kraitchman, L. Axel, and A. A. Young, 'Springs: a fast method for detection and correspondance of cardiac magnetic resonance tags', *Proc. 12th Ann Mtg. Soc. Magn. Reson. Med.*, New York, 1993, p. 725.
28. M. A. Guttman, J. L. Prince, and E. R. McVeigh, *IEEE Trans. Med. Imag.*, in press.
29. M. Kass, A. Witkin, and D. Terzopoulos, *Int. J. Comput. Vis.*, 1987, **1**, 321.
30. D. Kraitchman, A. A. Young, and L. Axel, 'Active contour models for tracking magnetic resonance tags', Proc. of the 15th Annu. Int. Conf. of the IEEE Eng. in Med. and Biol. Soc., San Diego, CA, 1993, pp. 166, 167.
31. E. R. McVeigh and E. A. Zerhouni, *Radiology*, 1991, **180**, 677.
32. A. A. Young, L. Axel, L. Dougherty, D. K. Bogen, and C. S. Parenteau, *Radiology*, 1993, **188**, 101.
33. H. Hatabu, W. B. Gefter, L. Axel, H. I. Palevsky, C. Cope, N. Reichek, L. Dougherty, J. Listerud, and H. Y. Kressel, *Radiology*, 1994, **190**, 791.
34. M. V. Icenogle, A. Caprihan, and E. Fukushima, *J. Magn. Reson.*, 1992, **100**, 376.
35. M. Tyszka, R. C. Hawkes, and L. D. Hall, *J. Magn. Reson.*, 1992, **97**, 391.
36. N. R. Clark, N. Reichek, P. Bergey, E. A. Hoffman, D. Brownson, L. Palmon, and L. Axel, *Circulation*, 1991, **84**, 67.
37. A. A. Young, H. Imai, C.-N. Chang, and L. Axel, *Circulation*, 1994, **89**(2), 740.
38. L. C. Palmon, N. Reichek, S. B. Yeon, N. R. Clark, D. Brownson, E. Hoffman, and L. Axel, *Circulation*, 1994, **89**(1), 122.
39. A. A. Young, C. M. Kramer, V. A. Ferrari, L. Axel, and N. Reichek, *Circulation*, 1994, **90**, 854.

Biographical Sketch

L. Axel. *b* 1947. B.S. Syracuse University, 1967; Ph.D. Princeton University, 1971; M.D., University of California at San Francisco, 1976. Department of Radiology, Hospital University of Pennsylvania, 1981–present. Approx. 110 publications. Research interests include development of NMR imaging methods to study cardiovascular function.

NMR Spectroscopy of the Human Heart

Paul A. Bottomley

Johns Hopkins University, Baltimore, MD, USA

1 INTRODUCTION

The heart is the largest consumer of energy per gram of tissue, and defects involving energy metabolism, including energy supply and demand, are central to much disease of the heart. It is inevitable, therefore, that human cardiac spectroscopy has focused on the energy metabolites that are NMR detectable. Phosphorus (^{31}P) NMR spectroscopy (MRS) can see adenosine triphosphate (ATP), the fundamental energy currency of the body, and phosphocreatine (PCr), a reservoir of cellular energy, in the heart, as well as the metabolic by-product inorganic phosphate (P_i). The signal-to-noise ratio is about 1×10^{-5} or 2×10^{-5} of that of the proton (^{1}H) NMR signal from muscle water (from the same volume), at the same magnetic field strength.[1,2] PCr and ATP cannot therefore be imaged with the same spatial resolution, signal-to-noise ratio, and scan time as tissue water protons in the same magnetic field. However, with compromises in spatial resolution and scan time, PCr and ATP can be seen in anterior wall volume elements (voxels) as small as 8 mL in the anterior myocardium.[3]

PCr and ATP are linked via the creatine kinase (CK) reaction:

$$\mathrm{PCr} + \mathrm{ADP} \rightleftharpoons \mathrm{ATP} + \mathrm{creatine} \quad (1)$$

whereupon inorganic phosphate (P_i) may be formed as

$$\mathrm{ATP} \rightarrow \mathrm{ADP} + \mathrm{P_i} + \mathrm{energy} \quad (2)$$

The total creatine pool (CR) comprising unphosphorylated (Cr) plus PCr is also detectable in the heart via its *N*-methyl resonance at 3.0 parts per million (p.p.m.) using ^{1}H MRS, with a current resolution of 3–9 ml in scan times of <10 min.[4] Consequently, a combination of ^{1}H and ^{31}P MRS could potentially provide a near-complete picture of CK metabolism in the heart. Under anaerobic conditions, such as may occur in ischemic heart disease in regions of the heart supplied by blocked arteries,[5] a transient mismatch between oxygen supply and demand can cause excess PCr consumption to maintain adequate ATP, along with possible elevations in P_i. This is manifested as reductions in PCr/ATP, PCr/P_i, and/or ATP/P_i in the corresponding ^{31}P NMS during the ischemic episode. The rapid depletion of ATP and PCr levels assayed after coronary occlusion or low-flow ischemia has been demonstrated in animal models.[6] Biochemical assays of biopsies taken at surgery have also demonstrated chronic reductions in the levels of PCr, Cr, and creatine kinase activity in patients with dilated cardiomyopathy (DCM), hypertrophy, and coronary artery disease (CAD).[7,8] These findings link changes in energy metabolism to contractile dysfunction, but in the absence of evidence of active ischemia.[9] Thus, the levels and ratios of PCr, ATP, CR, Cr, and P_i measured by ^{1}H and ^{31}P MRS may be useful indices of supply-side myocardial energy metabolism.

To date, ^{31}P NMR has been applied extensively in studies of patients with cardiomyopathies, including DCM, hypertrophic cardiomyopathy (HCM), and pressure overload left ventricular hypertrophy (LVH); patients with transplanted hearts, in an attempt to assess histological rejection; and patients with CAD and myocardial infarction, including exercise stress testing of patients with reversible ischemia. The literature on ^{31}P NMR of the heart has recently been reviewed in detail.[10] Abnormalities of varying extents in the phosphate metabolites have been reported in all of these disease states. In particular, the variability of findings in cardiomyopathy, and the results from transplanted hearts, suggest the existence of confounding variables that are as yet incompletely understood. However, quantitative studies are approaching a consensus on the true PCr/ATP ratio for human heart, and there are preliminary values reported for the PCr and ATP concentrations, the intracellular pH, and the forward CK reaction rate, and flux. Quantification of P_i has proved difficult because of the presence of neighbouring blood 2,3-diphosphoglycerate (DPG) resonances. Partial saturation effects and contamination from blood and chest muscles are probably the main sources of discrepancy amongst reported myocardial ^{31}P NMR PCr/ATP data.

^{1}H NMR spectra from the human heart are dominated by water and fat resonances, but metabolites such as CR can be measured either relative to water, or as concentrations.[4] CR appears to be depleted in myocardial infarction,[4] and alterations are also anticipated in cardiomyopathy and heart failure.[9]

NMR spectroscopy studies of the human heart with nuclei other than ^{31}P or ^{1}H are scarce. Carbon (^{13}C) NMR potentially provides access to glycolytic and citric acid cycle metabolites such as lactate and glutamate but has the disadvantage of low NMR sensitivity and a 1.1% natural isotopic abundance. This effectively prevents their detection at natural abundance with current technology without resorting to ^{13}C-enriched substrates.[2] Fatty acid resonances are the main contributors to the natural abundance ^{13}C human heart spectrum, and pericardial fat is probably a dominant contaminant, but glycogen may be discernible with ^{1}H decoupling and NOE.[11] While strictly not spectroscopy since there is usually only a single resonance, sodium (^{23}Na) NMR has been performed in human heart[12,13] and has potential for detecting sodium increases in reperfused infarction where sodium–potassium pump function is lost.[14]

2 METHODS

2.1 Localization

Localized ^{31}P NMR spectroscopy of the human heart was first reported in 1985.[1] That study, and all those since, employed surface detection coils placed on the chest closest to the anterior myocardium. Myocardium was distinguished from chest wall using MRI slice selection (the depth resolved surface coil spectroscopy, or DRESS, technique), and ^{1}H MRI was

used for tissue identification. While an unlocalized surface coil study of the chest of an infant with congenital cardiomegaly was also reported in 1985,[15] the first studies of heart patients with localized spectroscopy protocols were not published until 1987.[16,17] These were limited to two to four patients with hypertrophic cardiomyopathy or recent myocardial infarction, and localization was afforded by rotating frame zeugmatography (RFZ), which uses $\boldsymbol{B}_1$ gradients, or by the DRESS technique.

Full three-dimensional MRI gradient localization of ^{31}P NMR spectra to single voxels in the heart via the image selected in vivo spectroscopy (ISIS) technique appeared in 1988.[18] Multiple voxel, chemical shift imaging (CSI) studies of the heart using MRI phase-encoding gradients in one or more dimensions were published around 1990.[5,18,19] These spectroscopy localization techniques are reviewed in greater detail elsewhere (see ***Chemical Shift Imaging***, ***Selective Excitation in MRI and MR Spectroscopy***, and ***Single Voxel Whole Body Phosphorus MRS***), and have various advantages and disadvantages. For example, a problem with three-dimensional CSI is that the large number of phase-encoding steps required to encode the entire sample volume sets a minimum scan time, which may not be compatible with clinical study protocols of limited duration such as in stress testing for myocardial ischemia. One-dimensional CSI and RFZ can be completed faster, but at the expense of the fuzzy localization afforded by the surface coil in the two dimensions that are not gradient encoded. An example of a one-dimensional CSI data set and the corre-

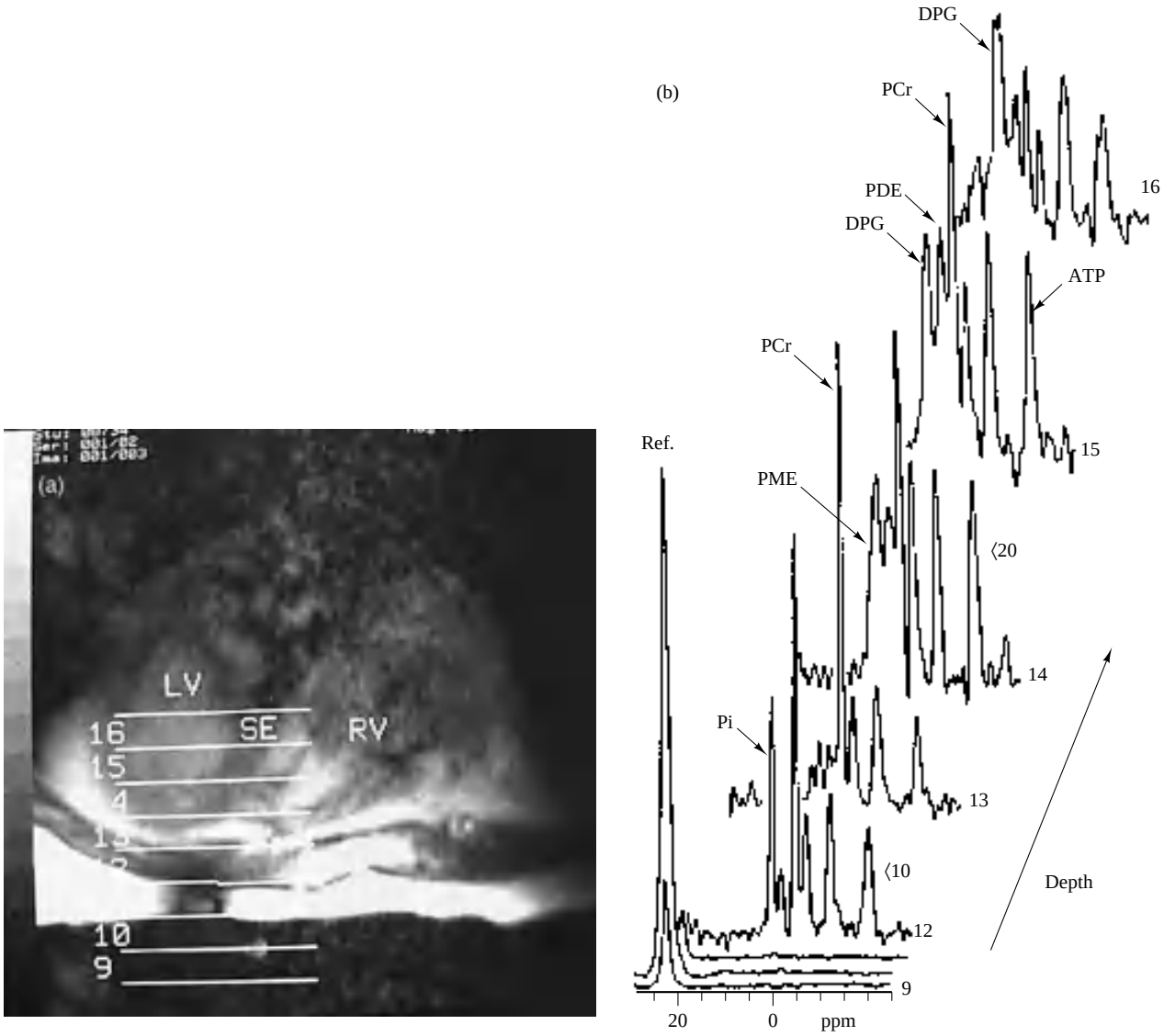

Figure 1 (a) Typical axial ^{1}H surface coil image of the chest and heart of a normal volunteer, annotated to show the location of eight 1 cm thick coronal slices localized in the spectroscopy exam. (b) Cardiac-gated one-dimensional CSI surface coil ^{31}P NMR spectra from the slices show a reference peak from a vial embedded in the coil (slices 9, 10), chest muscle (slices 12, 13), and myocardium (slices 14–16). Scan time for the spectra was about 12 min, in a clinical 1.5 T scanner. (Reproduced by permission of the Radiological Society of North America from Bottomley et al.[20])

sponding annotated cardiac image is shown in Figure 1.[20] Use of single voxel methods such as DRESS or ISIS requires accurate selection of a suspected region of abnormality a priori: incorrect voxel selection for a stress test, for example, could result in a missed finding for reversible ischemia.

^{1}H NMR spectroscopy studies of myocardial CR in patients to date have been performed using the single voxel point-resolved surface coil spectroscopy method (PRESS)[21] and the stimulated echo method (STEAM)[22] with water suppression. Each method localizes a spin-echo or stimulated echo NMR signal to a voxel defined in all three dimensions by the use of three spatially selective NMR pulses (90°–180°–180° for PRESS; 90°–90°–90° for STEAM).

2.2 Coils and NOE

A typical experimental cardiac ^{31}P NMR surface coil probe is pictured in Figure 2.[23] When the sample is the dominant source of the noise detected by the surface coil, the coil diameter should be chosen roughly equal to the depth of the tissue of interest. This leads to heart ^{31}P detectors with typical diameters of 6–12 cm for the anterior wall to mid-wall. Preferably, the signal is excited with a separate, larger rf coil to minimize spatially dependent distortions due to $\boldsymbol{B}_1$ inhomogeneity.[23] Additional ^{1}H MRI coils ensure correct ^{31}P detection coil placement, which is critical because of the limited range of sensitivity of the surface coil, and possible avoidable contamination from nearby tissue, especially chest muscle.

Sensitivity improvements of up to about $\sqrt{2}$ compared with the best positioned surface coil, and the need for careful positioning is relaxed if phased-array surface detection coils are used.[24] This technology is in use in MRI,[25] and has been implemented in ^{31}P studies of normal volunteers,[24] but not yet in patient studies.

Other factors offering potential sensitivity gains are the use of a prone, as opposed to supine, patient orientation, to bring the heart closer to the detection coil(s);[23] synchronization of NMR acquisitions to the cardiac cycle (see ***Cardiac Gating Practice***); and ^{1}H NOE.[26] At 1.5 T, NOEs of $\eta = 0.61 \pm 0.25$ for PCr, $\eta = 0.6 \pm 0.3$ for γ-ATP, and $\eta = 0.3 \pm 0.2$ for β-ATP have been reported for the human heart.[26] Because of the differences in η for PCr and ATP, the NOE may distort the PCr/ATP ratio by up to 20%, necessitating a correction for quantitative intersite comparisons.[26]

3 QUANTIFICATION

3.1 Myocardial PCr/ATP Ratio

If the PCr/ATP ratio is the most important metabolic index that ^{31}P NMR can reliably detect in the heart, it is important to establish its normal range for inter- and intralaboratory comparisons. However, published values from healthy volunteers range from 0.9 ± 0.3[22] to 2.1 ± 0.4.[28] Why the difference? There are two main causes. First, data are distorted to varying extents by partial saturation effects that result from the use of pulse sequence repetition periods, *TR*, that are comparable to or less than the T_1 values of PCr and ATP. Differences in the T_1 values of the two moieties produce differential distortion of PCr/ATP.[29] The 95% confidence intervals for published T_1 values are given in Table 1.[17,19,26,30–35] With a ratio of the T_1

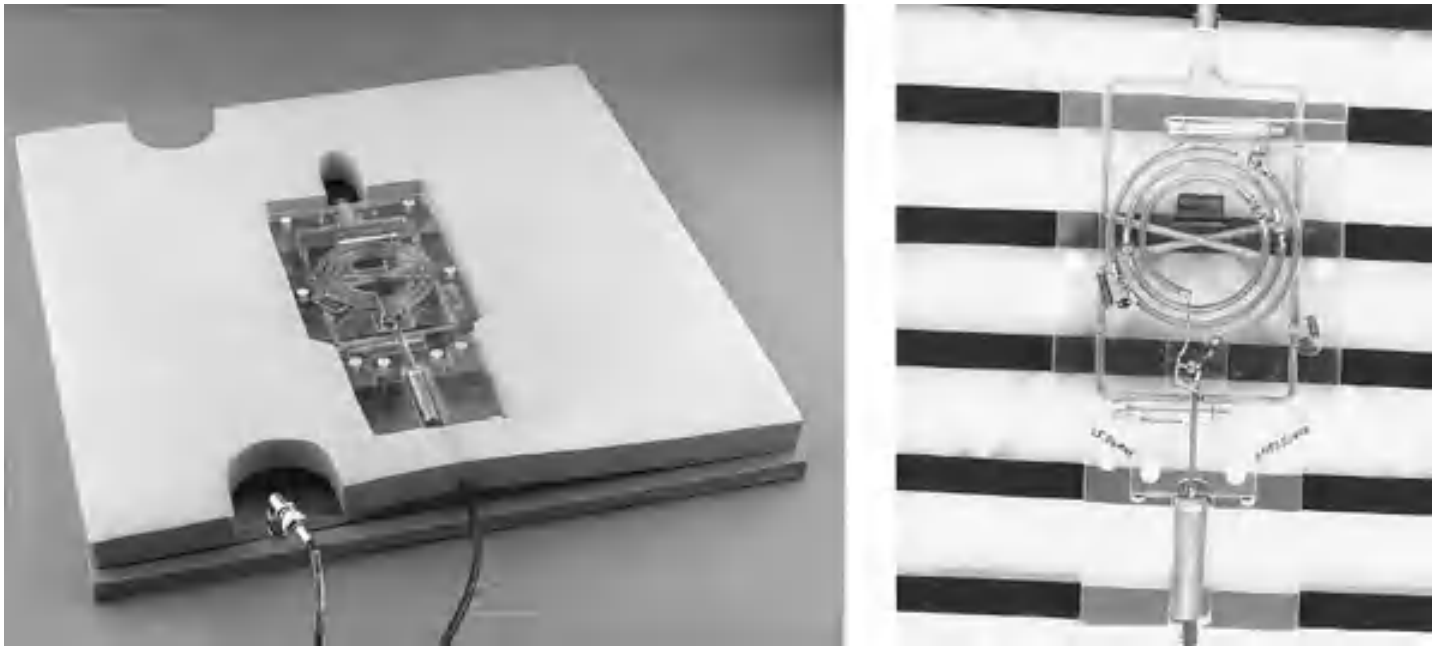

Figure 2 The cardiac ^{31}P NMR surface coil probe used to acquire the localized ^{31}P and ^{1}H NMR data in Figure 1.[23] The patient lies prone on the padded coil set (left), which is positioned on the patient table in the center of the whole body NMR magnet. The coil set comprises a square base with a 0.40 × 0.40 m ^{31}P transmit coil (lower left), and a smaller probe containing a 0.065 m mean diameter spiral ^{31}P detector coil, and a 0.08 × 0.13 m figure-8 ^{1}H receiver coil, used for imaging and shimming (right). Black strips (right) are Velcro, permitting the smaller probe to be positioned at will. Passive diode circuitry minimizes coil interactions[23]

Table 1 Phosphorus-31 NMR Measurements of Phosphate Metabolites in Normal Volunteers

Parameter	Value	Reference
T_1(PCr)	4.37 ± 0.48[a]	30
T_1(γ-ATP)	2.52 ± 0.45[a]	30
T_1(β-ATP)	2.28 ± 0.54[a]	30
[PCr]	11 ± 3 μmol (g wet wt)$^{-1}$	19
	12 ± 4.3 μmol (g wet wt)$^{-1}$	31
	10 ± 2 μmol (g wet wt)$^{-1}$	32
[ATP]	6.9 ± 1.6 μmol (g wet wt)$^{-1}$	19
	7.7 ± 3.0 μmol (g wet wt)$^{-1}$	31
	5.8 ± 1.6 μmol (g wet wt)$^{-1}$	32
P_i/PCr	<0.25	17
	0.14 ± 0.06	33
pH	7.15 ± 0.2	17
	7.15 ± 0.03	33
CK forward rate	0.5 ± 0.2 s^{-1}	34
CK forward flux	6 ± 3 μmol (g wet wt s)$^{-1}$	34
NOE of PCr at 1.5 T	0.61 ± 0.25	26
	0.6 ± 0.1	35
NOE of ATP at 1.5 T	0.6 ± 0.3 (γ-ATP)	26
	0.3 ± 0.2 (β-ATP)	26
	0.4 ± 0.2 (γ- and β-ATP)	35

CK, creatine kinase; γ-ATP and β-ATP, γ- and β- phosphates of ATP.
[a]95% confidence intervals.

values of PCr and ATP of about 1.9, the distortion or saturation factor, F, by which the PCr/ATP ratio measured in the short TR experiment must be multiplied by to yield the true myocardial PCr/ATP ratio, will vary between 1 and ~2, depending on TR and the NMR pulse flip angles.[29] Thus, measurements that are corrected for partial saturation can differ from those that have not, by up to a factor of about two.

Correction of experimental PCr/ATP values for partial saturation can be done by two methods. First, F can be calculated using known myocardial T_1 values and a measurement of the experimental NMR pulse flip angle (e.g. with equation (2) of Bottomley et al.).[29] Due to time constraints, T_1 values are usually either measured on a separate group of individuals, or else published values are adopted. Second, F may be measured directly from the ratio of spectra acquired under partially saturated conditions and fully relaxed conditions. The unlocalized, uniformly excited signal detected by a surface coil on the chest is sufficiently sensitive to permit the measurement of saturation factors in about 6 min, which can easily be incorporated into the study protocol.[5,29] This use of an unlocalized saturation factor depends on the assumption that T_1(PCr)/T_1(ATP) is essentially the same in the chest and heart tissue that contribute to the unlocalized spectrum.[29] The assumption is consistent with the available data,[30] and errors resulting from differences in the ratio can be minimized by using small or Ernst flip angles for excitation.

The second, lesser source of scatter in the reported myocardial PCr/ATP values is that of blood which contains ATP but no PCr. This reduces the apparent PCr/ATP ratio in voxels that intersect the ventricles.[36] The PCr/ATP ratio can be corrected for blood ATP contamination by measuring the amount of blood using the blood DPG signal present in the spectrum as a marker. DPG has a characteristic doublet at 5.4 and 6.3 ppm, near P_i[17] and other phosphomonoesters (PMs). The amount of ATP added by blood is estimated from

$$\text{corrected ATP} = \text{contaminated ATP} - 0.5 \times ([\text{ATP}]/[\text{DPG}]) \times \text{total DPG signal} \quad (3)$$

where [ATP]/[DPG] ≈ 0.30,[33,37–39] and remembering that DPG has two phosphates.

Blood ATP corrections typically increase PCr/ATP values by a relatively small amount, $13 \pm 6\%$.[20,33,36,39,40] Potential problems with the correction may arise from differences between the T_1 of ATP and DPG for short TR protocols (possibly offset, however, by the effect of inflowing unsaturated blood), variations in the blood ATP/DPG ratio with localization method and patients,[41] and possible contamination of DPG by P_i or PMEs, which would tend to cause overestimation of the amount of blood contamination.

Considering only those human studies in which both saturation and blood corrections were performed[20,31,33,36,40,42–48] or in which blood contamination was ruled out,[3] a consensus is emerging on the normal myocardial PCr/ATP value, as evident in Table 2. The mean value is 1.81 ± 0.14, omitting the highest and lowest values. This should represent the best current estimate for the true PCr/ATP ratio in the normal human heart, since tissue ATP and PCr appear to be 100% NMR visible.[49,50]

3.2 PCr and ATP Concentrations

Tissue [PCr] and [ATP] can be determined by combining the fully corrected PCr/ATP ratio from a voxel, with a measurement of the NMR signal from a concentration reference and a measurement of the volume of myocardium present in the voxel. The reference may lie outside of the subject, which requires that corrections be made for differences in field strength and sensitivity of the NMR coils at the two locations.[16] Alternatively, a reference located at the same position as the heart may be observed in a separate experiment in

Table 2 Some Corrected Normal Human Myocardial PCr/ATP Ratios

Value	Field (T)	Reference
1.80 ± 0.21	1.5	36
1.93 ± 0.21	1.5	20
1.8 ± 0.1	4.0	3
1.95 ± 0.45	1.5	40
1.65 ± 0.26	1.5	33
1.85 ± 0.28	1.5	42
1.8 ± 1	1.5	31
1.71 ± 0.13	1.5	39
1.98 ± 0.07	1.5	43
2.02 ± 0.11	1.5	44
1.42 ± 0.18	1.5	45
1.61 ± 0.18	1.5	46
2.46 ± 0.53	1.5	47
1.6 ± 0.3	2.0	48

which differences in coil loading are taken into account.[31] The tissue volumes must again be estimated by MRI, which may introduce weighting errors when the coil sensitivity is nonuniform across the localized volume.

A quantification method that does not require tissue volumetry employs measurements of the ^{1}H signal from water, s_W, as a concentration reference, using the identical localization sequence.[32] The water signal is recorded with the same ^{31}P coil used to measure the PCr and ATP metabolite signals, s_P; as a result, both ^{31}P and ^{1}H spectra are acquired with essentially the same B_1 profile. This is possible because of the enormous concentration advantage of the water signal compared with the metabolites. The method requires calibration with a phosphate reference to determine the ratio of the ^{31}P signal per phosphate to the ^{1}H signal per proton, C_{PH}, as well as knowledge of the myocardial tissue water content [W], which appears to be relatively constant.[4] The metabolite concentration in a voxel is calculated from:

$$[\mathrm{P}] = \frac{2s_P[\mathrm{W}]C_{PH}}{s_W} \times \left(\frac{F_P E_P}{F_W E_W}\right) \quad (4)$$

where $F_P F_W$ are the saturation factors and E the factors accounting for signal decay during TE (e.g. $E = \exp\{TE/T_2^*\}$ where T_2^* is the transverse signal decay time) with subscripts W for water, P for the metabolite (subscript P). The factor of 2 accounts for the two protons on water. The value of C_{PH} is determined in a separate experiment using a standard solution of phosphate.[32] The tissue water signal can be corrected for contamination from water in ventricular blood and in pericardial fat via a ^{31}P DPG measurement and a measurement of the fat resonance in the ^{1}H spectrum, respectively. The contaminating water signal from ventricular blood is:

$$S(\mathrm{blood}) = \frac{S(\mathrm{DPG})W_B C_{PH}}{[\mathrm{DPG}]} \times \left(\frac{F_{DPG}E_{DPG}}{E_B}\right) \quad (5)$$

The contaminating water signal from fat is $LS(CH_2)$, where $S(CH_2)$ is the lipid ^{1}H signal, and L is the water content of fat, which is about 15%.[32] The corrected water signal to use in equation (4) is:

$$S_W = (\text{measured water signal}) - S(\mathrm{blood}) - LS(CH_2). \quad (6)$$

Concentrations reported to date for the human heart are in fair agreement and are summarized in Table 1.

3.3 Total Myocardial Creatine

The detection of the *N*-methyl ^{1}H resonance of CR at 3.0 ppm provides a means of quantifying myocardial CR.[4] Unlike PCr/ATP ratios, CR cannot be reliably measured as a ratio from a single ^{1}H acquisition relative either to water, which is normally suppressed, or to fat resonances, which are often variable because of contamination from pericardial fat. A solution is to acquire two consecutive ^{1}H spectra under the same conditions, with and without water suppression. The CR peak in the water-suppressed spectrum is measured relative to the water peak in the unsuppressed spectrum. Because ^{1}H sensitivity is high and because the ^{1}H T_1 values are shorter than for ^{31}P, the experiment can essentially be done fully relaxed. The CR/water ratios measured with the same STEAM or PRESS timing parameters can be used for patient comparative studies.[4] The normal CR/water ratio is about 1.3×10^{-3}. Such ratios can be translated into absolute concentration measurements using the known myocardial tissue water content and correcting for the signal loss caused by the STEAM or PRESS echo delay, represented by the E factors as in equation (4):[4]

$$[\mathrm{CR}] = \frac{2S_{CR}[\mathrm{W}]}{3S_W} \times \left(\frac{F_{CR}E_{CR}}{F_W E_W}\right) \quad (7)$$

with the extra factor of 3 for the *N*-methyl protons.

The initial ^{1}H NMR estimate for normal human heart [CR] is 28 ± 6 μmol (g wet wt)$^{-1}$, which is consistent with canine and human necropsy studies.[4] Concentrations reported to date for the human heart are in agreement, and summarized in Table 1.

3.4 P_i, pH, and Creatine Kinase Reaction Kinetics

Intracellular pH can be measured from the chemical shift of the P_i resonance, which varies from 3.7 to 5.2 ppm relative to PCr over a pH range of 6.0–7.3.[51] In the normal heart, P_i is small and difficult to resolve unambiguously from blood DPG. It is probably better described by inequalities[17] (Table 1). Even with ^{1}H decoupling, which may reduce the linewidths of the DPG signals and permit a less ambiguous determination of any neighboring P_i, P_i still appears undetectable in about half of the normal subjects studied.[33] When detectable, the normal myocardial pH is about 7.15 (Table 1). It is also possible that P_i is partially NMR invisible.[49,50] It is unlikely, however, that P_i and pH measurements are contaminated by P_i in blood,[52] since P_i is imperceptible in ^{31}P spectra from human blood[39,41] and the [P_i] in whole human blood is listed as only 0.08 mM.[53]

The flux of PCr through the creatine kinase reaction [see equation (1)] in the heart can be measured using the saturation transfer NMR experiment.[34] The experiment involves acquisition of ^{31}P spectra while the γ-phosphate resonance of ATP is being saturated, for example, by application of a long rf pulse tuned to its resonant frequency. When ATP is saturated, the PCr signal declines as PCr is converted to ATP via the forward reaction, in the absence of any refreshment by unsaturated phosphates produced via the reverse reaction. The ratio of PCr signals measured with and without saturation is directly proportional to the first-order rate constant, in units of the T_1 of PCr in the presence of the saturating radiation. Studies in a 4 T whole body instrument indicate that about half of the PCr is turned over per second (Table 1), consistent with data from animals.[34]

4 PATIENT STUDIES

Some data from human heart ^{31}P NMR studies of patients are summarized in Table 3.[5,17,20,28,31,33,36,39,40,42–44,47,48,54,55]

4.1 Cardiomyopathy

Evidence anticipating reductions in myocardial high energy phosphates in human cardiomyopathy and hypertrophic disease comes from ^{31}P NMR studies of animal models,[56–61] and

Table 3 Summary of Some Findings for Myocardial PCr/ATP in Patients

PCr/ATP Patients	Controls	Comments	Reference
Cardiomyopathy studies showing significant changes (see text)			
1.3 ± 0.3*	2.1 ± 0.4	MD, BB, CA patients	28
1.4 ± 0.4*	2.1 ± 0.4	HCM patients	28
1.3 ± 0.3***	1.7 ± 0.3	NYHA class 0–II HCM patients	•
1.1 ± 0.4**	1.7 ± 0.3	HCM patients	39
1.1 ± 0.3**	1.6 ± 0.2[a]	NYHA class II–III LVH patients	54
1.5 ± 0.31*	1.8 ± 0.2	NYHA class II–IV DCM patients	36
1.4 ± 0.5***	1.9 ± 0.4[a]	NYHA class ⩾III DCM patients	40
1.3 ± 0.5	1.94 ± 0.11	DCM with NYHA class II–III, high mortality	43
1.5 ± 0.1*	2.0 ± 0.1	Aortic valve disease, NYHA class III	44
1.3 ± 0.3**	1.6 ± 0.3	Patients with severe mitral valve disease	48
2 ± 0.4***	2.4 ± 0.5	HCM patients	47
Heart transplant patients			
1.6 ± 0.5**	1.9 ± 0.2	All transplant patients	20
1.6 ± 0.5***	1.9 ± 0.4[a]	Patients with rejection (myocyte necrosis)	20
Myocardial infarction			
1.7 ± 0.4 (normal)	1.6 ± 0.4	P_i/ATP elevated 5–9 days-post-MI	17
normal		[PCr][b], [ATP][d] reduced in old MI	55
1.8 ± 0.5	2.0 ± 0.5	Patients studied 0.5–24 months post-MI	40
1.2 ± 0.3**	1.85 ± 0.28	Patients with fixed ^{201}Tl defects	42
0.9 ± 0.4***	1.8 ± 1.0	Fixed ^{201}Tl defects; [PCr], [ATP] reduced***	31
Ischemia			
0.9 ± 0.2*	1.5 ± 0.3[a]	During isometric exercise stress testing	5
1.0 ± 0.3*	1.6 ± 0.2[a]	Isometric exercise, reversible ^{201}Tl defects	42

Values are mean ±SD. Data from abstracts are omitted. MD, muscular dystrophy; BB, cardiac beri-beri; CA, cardiac amyloidosis; MI, myocardial infarction. Controls were normal, or LVH patients not in heart failure (indicated by [a]),[54] patients with dilated cardiomyopathy NYHA class <III failure,[46] or patients with no rejection.[62]
Statistical analysis versus controls or at rest:[5] *$P < 0.001$; **$P < 0.01$; ***$P < 0.05$.

biochemical analyses of patient biopsies taken at surgery.[7,8] Human in vivo ^{31}P NMR studies have demonstrated statistically significant reductions in anterior myocardial PCr/ATP ratios in a group of patients with cardiomyopathies due to specific disease (muscular dystrophy, beri-beri, amyloidosis);[28] in patients with HCM;[28,33,39,47] in patients with valve disease who were undergoing treatment for heart failure;[44,48,54] and in patients with DCM who were in heart failure [New York Heart Association (NYHA) clinical classification for heart failure ⩾II].[36,40,43] One report found a significant negative correlation between the NYHA classification for failure, and the myocardial PCr/ATP ratio.[40] Also, in patients whose NYHA classification was improved by drug therapy, myocardial PCr/ATP values recovered,[40] while patients with significantly reduced PCr/ATP ratios had a poorer survival rate compared with patients with normal PCr/ATP ratios, suggesting that the ratio may be of prognostic value.[43]

A number of other studies have reported no statistically significant changes in myocardial PCr/ATP in LVH,[27,28] or DCM,[27,28,33,62,63] although possible correlations between reduced myocardial PCr/ATP ratio and the NYHA heart failure classification[40] were not explicitly ruled out by these studies. The findings are reviewed in detail elsewhere.[10] Except for the NYHA classification, PCr/ATP ratios have generally correlated weakly with etiology and functional indices of disease severity such as the left ventricular ejection fraction or fractional shortening although such links may be proved with ongoing studies.[48]

The factors responsible for the differences in the significant findings for PCr/ATP ratios in cardiomyopathies are probably (i) variations in the range and severity of heart failure in patient study populations, and (ii) variations in statistical sensitivity. Regarding the former, it appears that averaging results from patients in mild and severe failure, or from a group of patients in predominantly mild failure, can mask significant PCr/ATP changes,[40] and that abnormalities might only be seen in subsets of patients in more advanced stages of heart failure.[54] With respect to the second factor, it should be noted that in all studies of HCM, DCM, and LVH so far, the mean myocardial PCr/ATP ratios were lower by 2–54% relative to the corresponding normal control groups with varying statistical significance.[10]

The ^{31}P NMR data linking PCr/ATP changes to heart failure would indicate that abnormal myocardial PCr/ATP ratios may first become detectable in DCM and LVH between NYHA classes II and III,[40,54] which is the point at which physical activity is limited by fatigue, and accompanying symptoms such as palpitation, or dyspnea. This is consistent with studies that conclude that the ability of the cell to sustain adequate levels of ATP is compromised only in the more advanced stages of

failure.[64] One hypothesis is that the reduced energy reserve, as demonstrated by the reduction in myocardial PCr/ATP ratios seen by ^{31}P NMR, and by the decreases in myocardial creatine and creatine kinase activity evident in surgical biopsies, may limit the ability of the heart to do work, and lead to contractile dysfunction.[9] On the other hand, in at least two studies of HCM,[15,33] the PCr/ATP ratio was reduced in the absence of a link to heart failure, so it is possible that there are differences between HCM, and DCM and LVH.

In the clinic, ^{31}P NMR might help identify patients in heart failure where physical activity or diagnosis is complicated by other conditions, including age[54] and lung disease. In patients with valve disease, the detection of metabolic abnormalities might find use in surgical planning to minimize permanent injury and maximize benefit.[65] Further work is needed to define where, specifically, the benefits lie.

4.2 Heart Transplant Patients

The idea that changes in myocardial metabolite ratios might predict histological rejection in human heart transplants stems from animal ^{31}P NMR studies, usually of nonimmunosuppressed allografts, which showed metabolic changes prior to the occurrence of histological evidence for acute rejection in the first week or so posttransplantation.[66–70] In the management of heart transplant patients, the standard criterion for assessing the existence of significant allograft rejection of severity sufficient to warrant augmentation of immunosuppressive therapy is histological evidence for myocyte necrosis in endomyocardial biopsies acquired during regular cardiac catheterization procedures. While some earlier conference reports on ^{31}P NMR studies in transplant patients dating from 1988 show reduced myocardial PCr/ATP and PCr/P_i ratios in transplanted hearts, the success with which ^{31}P NMR can reliably predict the outcome of histological evaluations is mixed.

The first published paper on 19 ^{31}P NMR examinations of patients studied up to 5.5 years posttransplantation did find significantly lower resting anterior myocardial PCr/ATP ratios relative to normal controls, consistent with the animal studies.[10,20] However, the results showed agreement between ^{31}P NMR abnormalities and histological evidence for necrosis in only about 60–70% of examinations,[20] suggesting that ^{31}P NMR is not a precise predictor of significant histological rejection in many transplant patients.

To date there is no firm evidence linking the finding of significant reductions in the myocardial PCr/ATP (and possibly PCr/P_i) ratio in transplanted hearts to other factors such as hypertrophy, or CAD involving the major vessels. However, one conference report of 13 transplant recipients on 71 occasions found reduced PCr/ATP ratios in the first few weeks after transplantation, suggesting that lower creatine levels or injury or edema following surgery may be possible causes.[71] The observation that PCr/ATP ratios may not precisely predict histological rejection is likely to reflect fundamental differences between histological and metabolic indices. In particular, myocyte necrosis would not cause altered PCr/ATP ratios because dead cells can contribute no high energy phosphates, whereas necrosis is important in histological evaluation. If the PCr/ATP reduction is associated with rejection, it may reflect an earlier phase of the process, which would not be inconsistent with the observed PCr/ATP reduction in the early weeks postsurgery because rejection episodes tend to be more frequent during this period. A much more frequent schedule of NMR examinations and biopsies would be needed to test this hypothesis. Nevertheless, the occurrence of reductions in the high energy phosphate metabolism of a majority of transplant patients is a concern meriting further study.

4.3 Coronary Artery Disease

4.3.1 Myocardial Infarction

Published papers to date show no significant alterations in resting myocardial PCr/ATP ratios in myocardial infarction.[17,40,46,55] Two reports do show significantly reduced resting PCr/ATP in patients with infarction and irreversible ^{201}Tl defects by radionuclide imaging.[31,42] It is unclear whether other factors such as heart failure and/or cardiomopathy may play a role in these patients and could explain the different findings.[10] In recent anterior myocardial infarction, significant elevations in P_i levels can be detected within the first week or so after onset,[17] which is consistent with canine ^{31}P NMR studies showing elevated P_i levels persisting for several days postcoronary occlusion, as a byproduct of PCr and ATP consumption.[72] Biochemical analyses of animal hearts also show that essentially all the ATP and PCr is depleted within the first few hours of ischemic injury that results in cell death.[6] Thus again, as dead cells can contribute no high energy phosphates, it is likely that the normal resting PCr/ATP ratios derive from a mixture of metabolically normal tissue, scar tissue and, possibly, jeopardized myocardium adjacent to, or interspersed with, the infarction. Accordingly the infarction itself may best be characterized by the absence of any contribution to the spectrum.

Evidence for the possible use of ^{31}P NMR for assessing myocardial viability, is provided by a study of 29 patients with recent myocardial infarction.[46] This revealed no changes in PCr/ATP ratios in patients with myocardial stunning after reperfusion, suggesting that relative levels of high-energy phosphates are not depleted in stunned human myocardium.

There is now ^{31}P NMR evidence that the metabolite concentrations are reduced in infarction itself.[31,55] This includes the observation of a significant negative correlation between ATP levels and the size of perfusion deficits in the heart, as quantified by thallium ^{201}Tl radionuclide imaging,[55] and reductions in [PCr] and [ATP] in patients with fixed ^{201}Tl defects compared with those with reversible defects.[31] Concentration measurements made by ^{31}P NMR must be treated cautiously, however, since the tissue volume present in the voxel may be reduced by any wall thinning that occurs after infarction. This may partially offset the signal loss due to infarction, depending on how tissue volume is accounted for in the concentration measurements. Nevertheless, the observations[31,55] are consistent with a model for infarction wherein the myocardial PCr and ATP levels are reduced in the heart spectrum in proportion to the volume of infarcted tissue that intersects the voxel.[10]

Reductions of about 60% in myocardial [CR] can also be detected with water-referenced ^{1}H NMR in patients with myocardial infarction.[4] The results are consistent with animal studies and the concept of metabolic depletion in infarction. Because the resolution and sensitivity are better with ^{1}H NMR than with ^{31}P NMR (and because the CR resonance has three

protons compared with the single phosphate group of PCr), ^{1}H NMR could provide a useful metabolic means for distinguishing healthy from infarcted nonviable myocardium.

4.3.2 *Myocardial Ischemia*

In patients with ischemic heart disease involving severe stenosis of the anterior vessels the resting anterior myocardial PCr/ATP ratio is normal,[40] or nearly so.[5] To observe metabolic change corresponding to reversible ischemia, safe and effective stress protocols that can be performed in the NMR magnet for the duration of a localized ^{31}P NMR examination are necessary. Three types of stress have been tried: aerobic exercise involving the lifting of weights with the legs;[73] an isometric exercise, performed, for example, with a handgrip dynamometer;[5,42] and stress induced by pharmaceutical agents such as dobutamine.[45,63] The increase in cardiac work-load indexed by the heart rate–blood pressure product in these protocols is about 70% for an aerobic leg exercise lifting 5 kg weights;[73] about 30–35% with the isometric hand-grip exercise at 30% of the subjects maximum force;[5] and up to 130% (2.3-fold) with dobutamine infusion.[45,63] While producing a lesser increase in cardiac work, the isometric exercise protocol can produce reflex coronary vasoconstriction in stenosed vessels. It also minimizes motion problems during NMR acquisition compared with aerobic exercise, and, in addition, produces vasoconstriction in patients with critical coronary disease.[5] It is also well tolerated by CAD patients, and can be immediately terminated should complications arise.

Phosphorus-31 NMR exercise stress testing of healthy volunteers who are free of significant CAD appears to elicit no significant alterations in anterior myocardial PCr/ATP ratios, with a 30–70% increase in rate–pressure product.[5,73] Dobutamine stress testing at 230% rate–pressure product produced no significant change in seven normal controls, although a recent study of 20 healthy volunteers elicited a statistically significant 14% reduction in myocardial PCr/ATP at a 300% rate–pressure product.[45]

There are two papers reporting ^{31}P findings from isometric hand-grip stress testing of patients with documented anterior wall ischemia.[5,42] In the first hand-grip exercise, the PCr/ATP ratio decreased by 37% in a group of 16 patients with severe anterior stenoses (Figure 3).[5] After exercise, metabolite ratios recovered to near-normal, pre-exercise values. Eleven healthy control subjects, and nine patients with nonischemic heart disease (cardiomyopathy or valve disease) exhibited no PCr/ATP changes during the same exercise, suggesting that the stress-induced changes in PCr/ATP are specific to CAD. Five CAD patients underwent repeat ^{31}P NMR stress-testing after successful revascularization therapy.[5] Prior to therapy, stress provoked a 33% decrease in PCr/ATP in these patients, as in the larger group. Exercise stress testing performed posttherapy produced no change, indicating that the metabolic abnormality resolves with successful clinical outcome.

The second report found a similar 40% decrease in the PCr/ATP ratio in patients with reversible anterior wall ischemia that was confirmed by exercise ^{201}Tl radionuclide imaging.[42] Twelve patients with fixed ^{201}Tl defects indicative of myocardial infarction, as well as normal controls, exhibited no exercise induced PCr/ATP changes. This, and the observation that dobutamine stress testing induced no significant reduction in myocardial PCr/ATP, on average, in patients with DCM,[63]

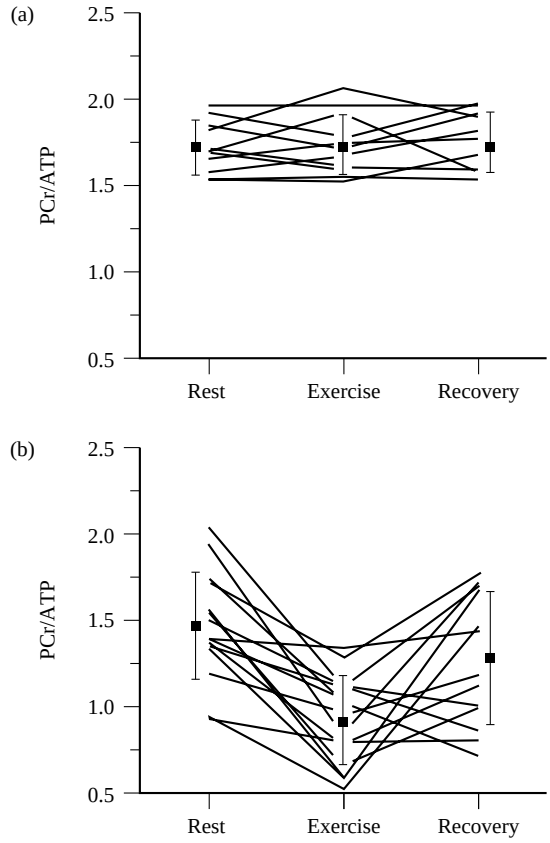

Figure 3 Transient changes in the anterior myocardial PCr/ATP ratio in (a) control subjects free of CAD, and (b) patients with CAD involving the anterior wall, in response to continuous isometric handgrip exercise at 30% of the subjects maximum force.[5] Error bars show means ±SD. (Reproduced by permission of *New England Journal of Medicine* from Weiss et al.[5])

is further evidence that the stress-induced changes may be specific for ischemia.

Present ^{31}P NMR studies are limited to the anterior wall. Whether ^{31}P NMR stress testing might play a role in the evaluation of ischemia in the clinic may depend in part on extending ^{31}P NMR to other regions of the heart, which will necessitate further improvements in sensitivity such as those afforded by NOE and phased array detection coils. Comparative studies of sensitivity relative to existing clinical modalities would then be needed.

4.3.3 *Cardiac Model*

In summary, the ^{31}P studies of myocardial infarction and reversible ischemia suggest a model in which the cardiac spectrum from a voxel comprises of up to four components: (i) myocardium either with an essentially normal resting PCr/ATP ratio or, possibly, a reduced resting PCr/ATP ratio due to complications arising from chronic infarction such as heart failure or cardiomyopathy; (ii) jeopardized myocardium whose PCr/ATP ratio decreases with stress testing; (iii) scar tissue with lower ATP and PCr concentrations; and (iv) infarcted myocar-

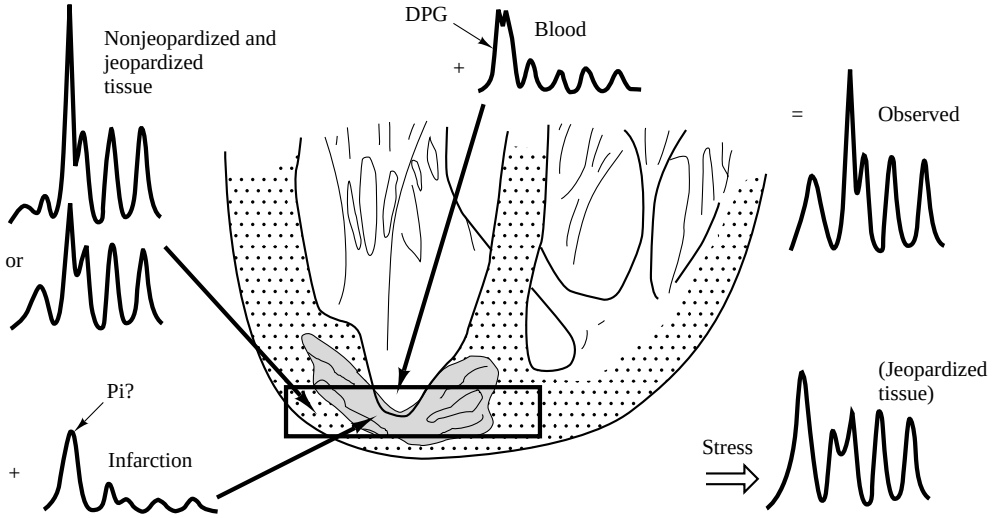

Figure 4 Model for the observed cardiac spectrum as the integral of four potentially distinguishable components: (i) myocardium either with an essentially normal resting PCr/ATP or, possibly, a reduced resting PCr/ATP ratio associated with heart failure; (ii) jeopardized myocardium, possibly only distinguishable from normal or failing heart by stress testing; (iii) a mixture of infarction with no PCr or ATP but perhaps some residual P_i shortly after infarction, and scar tissue, presumably with lower ATP and PCr concentrations; and (iv) contaminating signal from blood[10]

dium with no PCr, ATP, or CR but possibly some residual P_i persisting several days after infarction. Appropriate choice of the ^{31}P or ^{1}H NMR protocols may resolve these components: measurements of the metabolite concentrations at rest may index the fraction of scar tissue and infarction present in a selected volume, while jeopardized myocardium may be indexed by stress testing (Figure 4).[10]

5 RELATED ARTICLES

Cardiac Gating Practice; Cardiovascular NMR to Study Function; Chemical Shift Imaging; Heart: Clinical Applications of MRI; Magnetization Transfer between Water and Macromolecules in Proton MRI; Proton Decoupling During In Vivo Whole Body Phosphorus MRS; Proton Decoupling in Whole Body Carbon-13 MRS; Rotating Frame Methods for Spectroscopic Localization; Selective Excitation in MRI and MR Spectroscopy; Single Voxel Whole Body Phosphorus MRS.

6 REFERENCES

1. P. A. Bottomley, *Science*, 1985, **229**, 769.
2. P. A. Bottomley, *Radiol.* 1989, **170**, 1.
3. R. S. Menon, K. Hendrich, X. Hu, and K. Ugurbil, *Magn. Reson. Med.*, 1992, **26**, 368.
4. P. A. Bottomley and R. G. Weiss, *Lancet*, 1998, **351**, 714.
5. R. G. Weiss, P. A. Bottomley, C. J. Hardy, and G. Gerstenblith, *N. Engl. J. Med.*, 1990, **323**, 1593.
6. R. B. Jennings and K. A. Reimer, *Am. J. Pathol.*, 1981, **102**, 241.
7. J. L. Swain, R. L. Sabina, R. B. Peyton, R. N. Jones, A. S. Wechsler, and E. W. Holmes, *Proc. Natl. Acad. Sci. USA*, 1982, **79**, 655.
8. J. S. Ingwall, M. F. Kramer, M. A. Fifer, B. H. Lorell, R. Shemin, W. Grossman, and P. D. Allen, *N. Engl. J. Med.*, 1985, **313**, 1050.
9. J. S. Ingwall, *Circulation*, 1993, **87**(Suppl. VII), VII-58.
10. P. A. Bottomley, *Radiology*, 1994, **191**, 593.
11. P. A. Bottomley, C. J. Hardy, P. B. Roemer, and O. M. Mueller, *Magn. Reson. Med.*, 1989, **12**, 348.
12. J. B. Ra, S. K. Hilal, C. H. Oh, and J. K. Mun, *Magn. Reson. Med.*, 1988, **7**, 11.
13. T. B. Parish, D. S. Fieno, S. W. Fitzgerald, and R. M. Judd, *Magn. Reson. Med.*, 1997, **38**, 653.
14. R. J. Kim, J. O. A. C. Lima, E. L. Chen, S. B. Reeder, F. J. Klocke, E. A. Zerhouni, and R. M. Judd, *Circulation*, 1997, **95**, 1877.
15. J. R. Whitman, B. Chance, H. Bode, J. Maris, J. Haselgrove, R. Kelley, B. J. Clark, and A. H. Harken, *J. Am. Coll. Cardiol.*, 1985, **5**, 745.
16. B. Rajagopalan, M. J. Blackledge, W. J. McKenna, N. Bolas, and G. K. Radda, *Ann. N.Y. Acad. Sci.*, 1987, **508**, 321.
17. P. A. Bottomley, R. J. Herfkens, L. S. Smith, and T. M. Bashore, *Radiology*, 1987, **165**, 703.
18. S. Schaefer, J. Gober, M. Valenza, G. S. Karczmar, G. B. Matson, S. A. Camacho, E. H. Botvinick, B. Massie, and M. W. Weiner, *J. Am. Coll. Cardiol.*, 1988, **12**, 1449.
19. P. A. Bottomley, C. J. Hardy, and P. B. Roemer, *Magn. Reson. Med.*, 1990, **14**, 425.
20. P. A. Bottomley, R. G. Weiss, C. J. Hardy, and W. A. Baumgartner, *Radiology*, 1991, **181**, 67.
21. P. A. Bottomley, US patent, 4 480 228, Oct. 30, 1984.
22. J. Frahm, H. Bruhn, M. L. Gyngell, K. D. Merbold, W. Hanicke, and R. Sauter, *Magn. Reson. Med.*, 1989, **9**, 79.
23. P. A. Bottomley and C. J. Hardy, *Philos. Trans. R. Soc. London, Ser. A*, 1990, **333**, 531.
24. C. J. Hardy, P. A. Bottomley, K. W. Rohling, and P. B. Roemer, *Magn. Reson. Med.*, 1992, **28**, 54.
25. P. B. Roemer, W. A. Edelstein, C. E. Hayes, S. P. Souza, and O. M. Mueller, *Magn. Reson. Med.*, 1990, **16**, 192.

26. P. A. Bottomley and C. J. Hardy, *Magn. Reson. Med.*, 1992, **24**, 384.
27. S. Schaefer, J. R. Gober, G. G. Schwartz, D. B. Twieg, M. W. Weiner, and B. Massie, *Am. J. Cardiol.* 1990, **65**, 1154.
28. Y. Masuda, Y. Tateno, H. Ikehira, T. Hashimoto, F. Shishido, M. Sekiya, Y. Imazeki, H. Imai, S. Watanabe, and Y. Inagaki, *Jap. Circ. J.*, 1992, **56**, 620.
29. P. A. Bottomley, C. J. Hardy, and R. G. Weiss, *J. Magn. Reson.*, 1991, **95**, 341.
30. P. A. Bottomley and R. Ouwerkerk, *Magn. Reson. Med.*, 1994, **32**, 137.
31. T. Yabe, K. Mitsunami, T. Inubushi, and M. Kinoshita, *Circulation*, 1995, **92**, 15.
32. P. A. Bottomley, E. A. Atalar, and R. G. Weiss, *Magn. Reson. Med.*, 1996, **35**, 664.
33. A. de Roos, J. Doornbos, P. R. Luyten, L. J. M. P. Oosterwaal, E. E. van der Wall, and J. A. den Hollander, *J. Magn. Reson. Imaging*, 1992, **2**, 711.
34. P. A. Bottomley and C. J. Hardy, *J. Magn. Reson.*, 1992, **99**, 443.
35. H. Kolem, R. Sauter, M. Friedrich, M. Schneider, and K. Wicklow, in 'Cardiovascular Applications of Magnetic Resonance', ed. G. M. Pohost, Futura, Mt. Kisco, NY, 1993, p. 417.
36. C. J. Hardy, R. G. Weiss, P. A. Bottomley, and G. Gerstenblith, *Am. Heart J.*, 1991, **122**, 795.
37. S. Minakami, C. Suzuki, T. Saito, and H. Yoshikawa, *J. Biochem.*, 1965, **58**, 543.
38. E. Beutler, in 'Hematology', 3rd edn., eds. W. J. Williams, E. Beutler, A. J. Erslev, and M. A. Lichtman, McGraw-Hill, New York, 1983, p. 283.
39. H. Sakuma, K. Takeda, T. Tagami, T. Nakagawa, S. Okamoto, T. Konishi, and T. Nakano, *Am. Heart J.*, 1993, **125**, 1323.
40. S. Neubauer, T. Krahe, R. Schindler, M. Horn, H. Hillenbrand, C. Entzeroth, H. Mader, E. P. Kromer, G. A. J. Riegger, K. Lackner, and G. Ertl, *Circulation*, 1992, **86**, 1810.
41. M. Horn, S. Neubauer, M. Bomhard, M. Kadgien, K. Schnackerz, and G. Ertl, *Magma*, 1993, **1**, 55–60.
42. T. Yabe, K. Mitsunami, M. Okada, S. Morikawa, T. Inubushi, and M. Kinoshita, *Circulation*, 1994, **89**, 1709.
43. S. Neubauer, M. Horn, M. Cramer, K. Harre, J. B. Newell, W. Peters, T. Pabst, G. Ertl, D. Hahn, J. S. Ingwall, and K. Kochsiek, *Circulation*, 1997, **96**, 2190.
44. S. Neubauer, M. Horn, T. Pabst, K. Harre, H. Stromer, G. Bertsch, J. Sandstede, G. Ertl, D. Hahn, and K. Kochsiek, *J. Invest. Med.*, 1997, **45**, 453.
45. H. J. Lamb, H. P. Beyerbacht, R. Ouwerkerk, J. Doornbos, B. M. Pluim, E. E. van der Wall, A. van der Laarse, and A. de Roos, *Circulation*, 1997, **96**, 2969.
46. R. Kalil-Filho, C. P. de Albuquerque, R. G. Weiss, A. Mocelim, G. Bellotti, G. Cerri, and F. Pileggi, *J. Am. Coll. Cardiol.*, 1997, **130**, 1228.
47. W. Jung, L. Sieverding, J. Breuer, T. Hoess, S. Widmaier, O. Schmidt, M. Bunse, F. van Erckelens, J. Apitz, O. Lutz, and G. J. Dietze, *Circulation*, 1998, **97**, 2536.
48. M. A. Conway, P. A. Bottomley, R. Ouwerkerk, G. K. Radda, and B. Rajagopalan, *Circulation*, 1998, **97**, 1716.
49. S. M. Humphrey and P. B. Garlick, *Am. J. Physiol.*, 1991, **260**, H6.
50. P. B. Garlick and R. M. Townsend, *Am. J. Physiol.*, 1992, **263**, H497.
51. D. G. Gadian, 'Nuclear Magnetic Resonance and its Applications to Living Systems', Oxford University Press, Oxford, 1982, p. 30.
52. K. M. Brindle, B. Rajagopalan, N. M. Bolas, and G. K. Radda, *J. Magn. Reson.*, 1987, **74**, 356.
53. D. L. Altman and D. A. Dittmer, *FASEB*, 1961, **21**, 29.
54. M. A. Conway, J. Allis, R. Ouwerkerk, T. Niioka, B. Rajagopalan, and G. K. Radda GK, *Lancet*, 1991, **338**, 973.
55. K. Mitsunami, M. Okada, T. Inoue, M. Hachisuka, M. Kinoshita, and T. Inubishi, *Jap. Circ. J.*, 1992, **56**, 614.
56. W. Markiewicz, S. Wu, W. W. Parmley, C. B. Higgins, R. Sievers, T. L. James, J. Wikman-Coffelt, and G. Jasmin, *Circ. Res.*, 1986, **59**, 597.
57. S. A. Camacho, J. Wikman-Coffelt, S. T. Wu, T. A. Watters, E. H. Botvinick, R. Sievers, T. L. James, G. Jasmin, and W. W. Parmley, *Circulation*, 1988, **77**, 712.
58. S. Wu, R. White, J. Wikman-Coffelt, R. Sievers, M. Wendland, J. Garrett, C. B. Higgins, T. James, and W. W. Parmley, *Circulation*, 1987, **75**, 1058.
59. K. Nicolay, W. P. Aue, J. Seelig, C. J. A. van Echteld, T. J. C. Ruigrok, and B. de Kruijff, *Biochim. Biophys. Acta*, 1987, **929**, 5.
60. S. J. Kopp, L. M. Klevay, and J. M. Feliksik, *Am. J. Physiol.*, 1983, **245**, H855.
61. N. Afzal, P. K. Ganguly, K. S. Dhalla, G. N. P$_i$erce, P. K. Singal, and N. S. Dhalla, *Diabetes*, 1988, **37**, 936.
62. W. Auffermann, W. M. Chew, C. L. Wolfe, N. J. Tavares, W. W. Parmley, R. C. Semelka, T. Donnelly, K. Chatterjee, and C. B. Higgins, *Radiology*, 1991, **179**, 253.
63. S. Schaefer, G. G. Schwartz, S. K. Steinman, D. J. Meyerhoff, B. M. Massie, and W. M. Weiner, *Magn. Reson. Med.*, 1992, **25**, 260.
64. S. M. Krause, *Heart Failure*, 1988, 267.
65. Editorial, *Lancet*, 1991, **338**, 981.
66. R. C. Canby, W. T. Evanochko, L. V. Barrett, J. K. Kirklin, D. C. McGiffen, T. T. Sakai, M. E. Brown, R. E. Foster, R. C. Reeves, and G. M. Pohost, *J. Am. Coll. Cardiol.*, 1987, **9**, 1067.
67. C. E. Haug, J. L. Shapiro, L. Chan, and R. Weil, *Transplantation*, 1987, **44**, 175.
68. C. D. Fraser, V. P. Chacko, W. E. Jacobus, R. L. Soulen, G. M. Hutchins, B. A. Reitz, and W. A. Baumgartner, *Transplantation*, 1988, **46**, 346.
69. C. D. Fraser, V. P. Chacko, W. E. Jacobus, P. Mueller, R. L. Soulen, G. M. Hutchins, B. A. Reitz, and W. A. Baumgartner, *J. Heart Transplant.*, 1990, **9**, 197.
70. C. D. Fraser, V. P. Chacko, W. E. Jacobus, G. M. Hutchins, J. Glickson, B. A. Reitz, and W. A. Baumgartner, *Transplantation*, 1989, **48**, 1068.
71. J. O. van Dobbenburgh, N. de Jonge, C. Klopping, J. R. Lahpor, S. R. Woolley, and C. J. A. van Echteld, *Proc. XIIth Ann Mtg. Soc. Magn. Reson. Med.*, New York, 1993, **3**, 1093.
72. P. A. Bottomley, L. S. Smith, S. Brazzamano, L. W. Hedlund, R. W. Redington, and R. J. Herfkens, *Magn. Reson. Med.*, 1987, **5**, 129.
73. M. A. Conway, J. D. Bristow, M. J. Blackledge, B. Rajagopalan, and G. K. Radda, *Br. Heart J.*, 1991, **65**, 25.

Acknowledgements

I would like to thank R. G. Weiss, M. Conway, and B. Rajagopalan for many helpful discussions.

Biographical Sketch

Paul A. Bottomley. *b* 1953. B.Sc. Hon., 1974, Ph.D. 1978, University of Nottingham, UK, with E. Raymond Andrew and Waldo Hinshaw. Research Associate at Johns Hopkins Medical Institutions, 1978–1980. Physicist, G.E. Research and Development Center, 1980–1994. Presently Russell H. Morgan Professor and Director, Division of MR Research, Dept of Radiology, Johns Hopkins University, Baltimore, U.S.A. Approx. 120 publications, 130 conference reports, 27 patents. Gold Medal, Society of Magnetic Resonance in Medicine, 1989; G.E. Coolidge Medal and Fellow, 1990. Research specialties: in vivo NMR imaging, localized spectroscopy, tissue relaxation times, MRI, human cardiac NMR spectroscopy.

Brain Infection and Degenerative Disease Studied by Proton MRS

Robert E. Lenkinski, Dolores López-Villegas, and Supoch Tunlayadechanont

University of Pennsylvania, Philadelphia, PA, USA

1 INFECTIONS

1.1 Creutzfeldt–Jakob Disease (CJD)

Bruhn et al.[1] showed in an initial case report of CJD that there was significant loss of *N*-acetylaspartate (NAA) in both white matter (40%) and gray matter (30%). The level of inositol, presumably myo-inositol (MI), was higher than normal (30%) in white matter. The conventional magnetic resonance (MRI) images of this patient showed only mild cortical atrophy and hyperintensities in the lentiform nuclei. These authors suggested that proton MRS might be useful in the early detection of CJD.

Graham et al.[2] have studied two patients with biopsy proven CJD using in vivo MRS. High-resolution NMR spectroscopy was also carried out on an extract of a biopsy specimen of a third patient with CJD.[2] These NMR results were compared with neuronal cell counts. Marked decreases in the levels of NAA (detected in vivo) were observed at later stages of disease in two patients. However in the early stages of CJD smaller decreases were observed (15% and 27%) in the level of NAA. The NMR spectrum obtained from the biopsy sample taken from a third patient showed little or no reduction in the levels of metabolites. In contrast with the previous case report of Bruhn et al.[1] Graham et al. suggested that there should be little or no change in the levels of metabolites in the early stages of CJD. This suggestion was supported by referring to the known pathophysiology of CJD which indicates that neurons are lost relatively late in the disease process.

1.2 Herpes Simplex Encephalitis (HSE)

Menon et al.[3] showed in an early case report that the ratio of NAA to choline (NAA/Cho) was reduced in an 11 year old boy. This reduction observed at eight weeks after the onset of symptoms was found to be unaltered on follow-up examination (16 weeks), indicating that there was no progressive neuronal loss. This observation was consistent with the clinical evaluation of the patient.

As part of an MRI study of HSE involving eight patients, Demaerel et al.[4] obtained proton spectra from two patients with HSE. The proton spectra from one of the HSE subjects are shown in Figure 1.

Note the reduction in NAA observed in the affected region as compared with the contralateral temporal lobe. There is also a significant amount of lactate observed. The authors interpret the observation of lactate to indicate the presence of an infarct.

1.3 Intracranial Tuberculomas

Gupta et al.[5] have reported the results of localized proton MRS carried out on two patients with intracranial tuberculo-

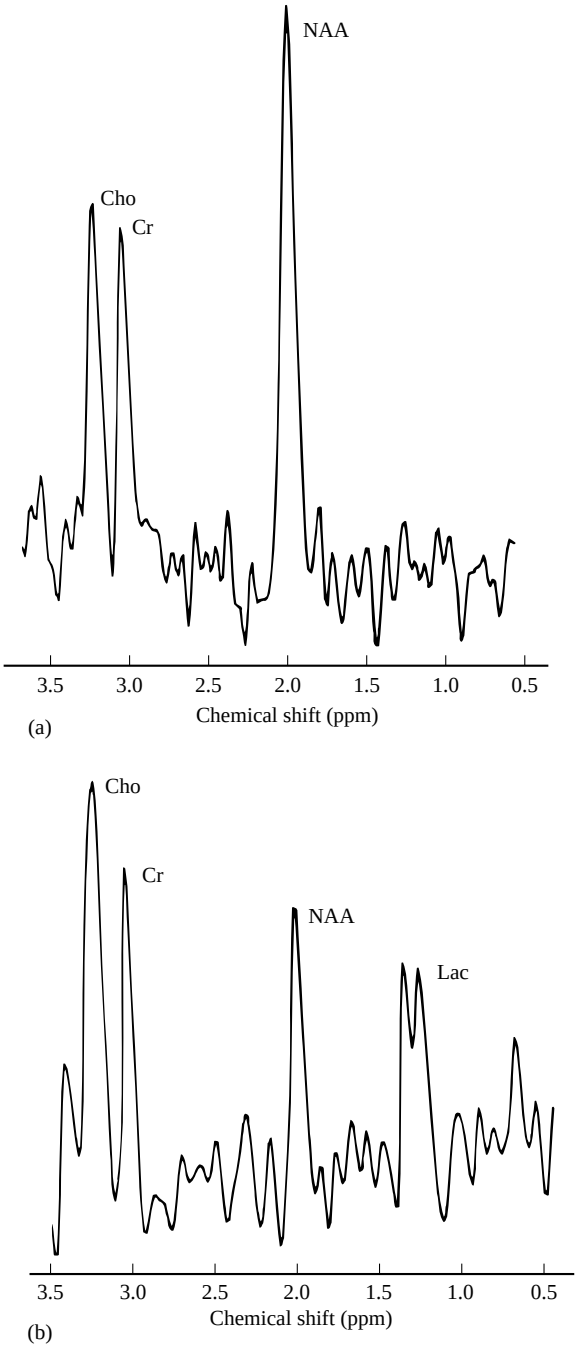

Figure 1 Solvent-suppressed proton spectra obtained using the STEAM sequence at 1.5 T (*TR* = 3000 ms, *TE* = 270 ms) from a 27 cm^3 voxel located at (a) the left and (b) the right temporal lobe. Each spectrum is the sum of 256 acquisitions. Reproduced with permission from Demaerel et al.[4]

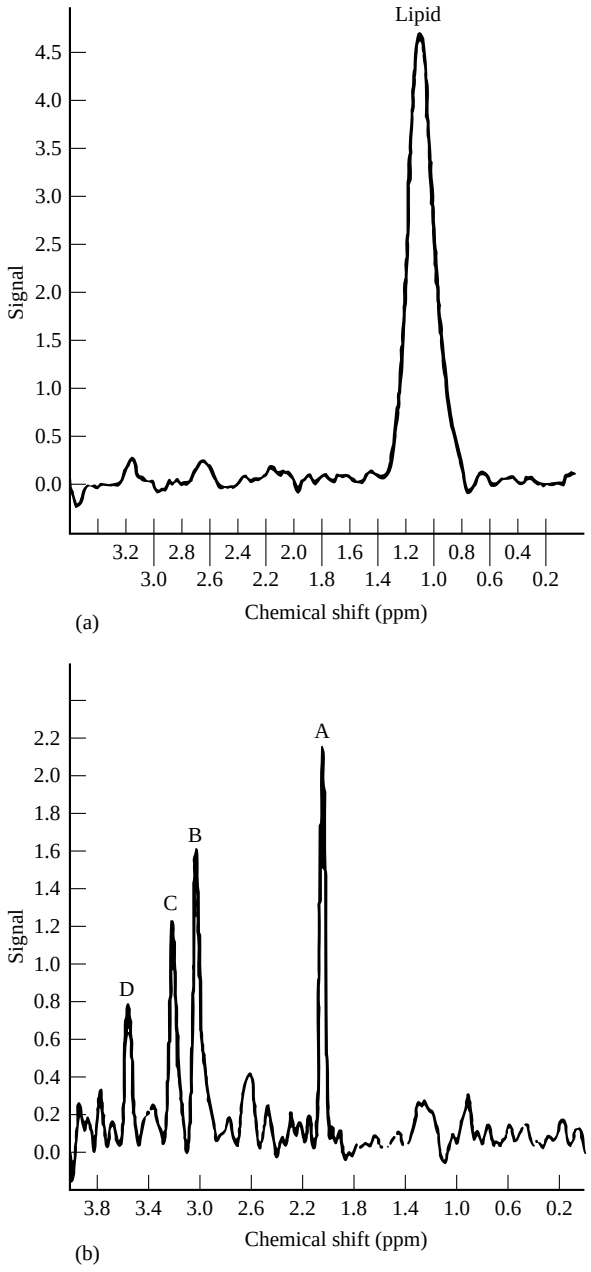

Figure 2 Solvent-suppressed proton spectra obtained using the STEAM sequence at 2.0 T (*TR* = 5000 ms, *TE* = 20 ms) from an 8 cm^3 voxel located (a) in a tuberculoma and (b) in a contralateral normal brain. Each spectrum is the sum of 128 acquisitions. Reproduced with permission from Gupta et al.[5]

mas. A large resonance was observed between 0.7–1.6 ppm (see Figure 2) which was assigned to the $(CH_2)_n$ group of saturated fatty acids. The presence of this peak was attributed to the large lipid fraction present in the tubercule bacillus.

1.4 Human Immunodeficiency Virus (HIV) Infection

Menon et al.[6] reported the first spectroscopic study of the brains in patients infected by Human Immunodeficiency Virus (HIV). The authors examined two patients with AIDS [Centers for Disease Control classification (CDC) Group IV] and evidence of focal CNS pathology. A multiple-echo spectroscopy acquisition (MESA) sequence with a *TR* of 2000 ms and *TE* of 270 ms was employed. The spectra were collected from a 64 cm^3 voxel in the right parietal region. Although these patients had abnormal MRI, the spectra were taken in areas of normal appearing white matter. In both cases the spectra showed a marked reduction in the ratio of NAA/Cho and NAA/creatine (NAA/Cr) when compared with control subjects. The authors proposed that the spectral changes in these regions which appear normal on MRI may be attributed to other causes but is most likely to be due to primary HIV infection. The authors first demonstrated the ability of proton MRS to detect brain abnormalities in HIV-infected patients at a stage when it is undetectable by imaging and proposed a possible role for the early selection of patients for treatment with antiviral drugs.

The same group examined 11 patients with HIV infection and varying stages of AIDS dementia complex (ADC) (actually known as HIV-1-associated cognitive/motor complex).[7] In this study, patients with pathology seen on MR imaging that could not be directly attributed to HIV infection of the brain were excluded from the study. Spectra were obtained from 27 to 64 cm^3 voxels in the parieto–temporal regions using the same sequence as in the previous study. Spectra from patients with moderate (Stage 2) to severe ADC (Stage 3), when compared with spectra from normal volunteers, exhibited significant reductions in NAA/Cr ratio and a tendency to increased Cho/Cr ratio, although this last trend did not reach statistical significance. Spectra from patients with no ADC (Stage 0) or early ADC (Stage 1) were not significantly different from normal volunteers (see Figures 3 and 4).

Many of the patients in this study exhibited abnormalities on MRI, but apart from the presence of atrophy, which was seen in all of the patients with moderate to severe ADC, MRI did not seem to discriminate between patients with and without ADC. The authors concluded that although the NAA/Cr ratio may not be an early or sensitive marker of ADC, it may be relatively specific since all of the patients with significantly low values of this ratio had a clinical diagnosis of ADC.

Meyerhoff et al.[8] examined 14 HIV seropositive patients, 10 with varying degrees of cognitive impairment and four who were cognitively asymptomatic. Spectra were obtained from nine 2.5 cm^3 volumes in the centrum semiovale and the mesial cortex in each patient. Significantly reduced NAA/Cho and NAA/Cr ratios were observed in cognitively impaired subjects versus normal controls, without significant regional differences between the voxels studied. No significant differences were found between groups with cognitive impairment and asymptomatic groups or between asymtomatic and control groups.

This study reported diffuse reductions in NAA in individuals with cognitive impairment due to HIV. Contrary to previous studies, most of the patients in this study had normal appearing MRI (80%) suggesting that proton MRS is more sensitive than imaging in assessing the effects of HIV infection on the brain.

Jarvik et al.[9] examined 11 HIV seropositive patients without clinical, radiological, or laboratory evidence of CNS infections other than HIV. Proton spectra were acquired with the stimulated echo acquisition mode (STEAM), *TR* of 2000 ms, *TE* of

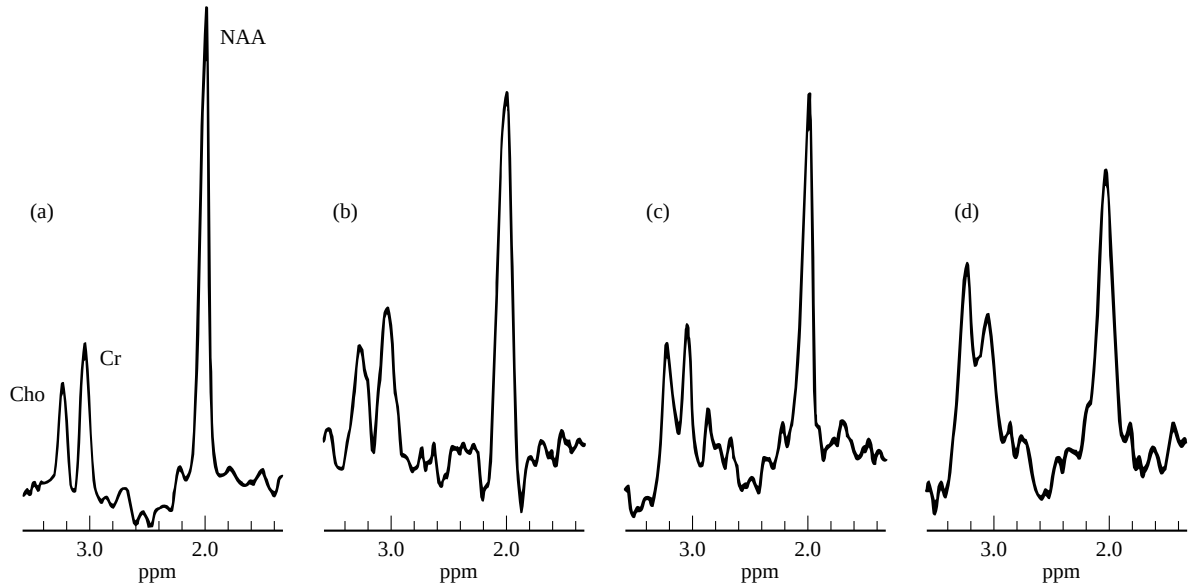

Figure 3 Solvent-suppressed proton spectra obtained from a 27 cm^3 voxel located in the parietal lobe from a healthy volunteer and three patients with HIV infection. The spectra were obtained with a double-echo sequence, *TR* = 2000 ms, *TE* = 270 ms. Each spectrum is the sum of 128 acquisitions. The spectra are displayed with creatine scaled similarly. The spectra are from (a) a healthy volunteer, (b) a patient with ADC Stage 0, (c) a patient with ADC Stage 1, and (d) a patient with ADC Stage 3. Reproduced with permission from Menon et al.[7]

19 ms, and *TM* of 10.6 ms. Voxels of 3.4–8 cm^3 were chosen to cover areas of abnormal white matter signal intensity if present, or centrum semiovale if the white matter appeared normal at imaging. Analysis of the images showed that there was a significant difference between the patients and control subjects with respect to atrophy, although no significant difference was found between the appearance of the white matter in patients and control subjects. Analysis of the spectra showed that the NAA/Cr ratio was significantly lower and Cho/Cr and marker peak/Cr ratios significantly higher in patients as compared with control subject. The authors calculated an aggregate score that combined these three ratios. This aggregate score proved to be a good discriminator between the patient and control populations ($P = 0.001$) (see Figure 5).

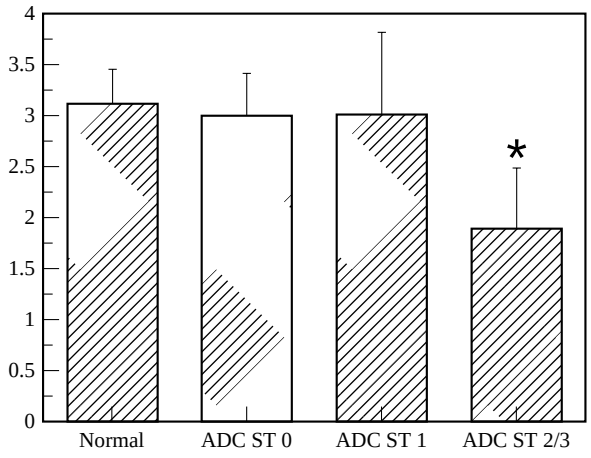

Figure 4 A comparison of the NAA/Cr ratios in normals and patients with different stages of ADC. The bars represent 1 SD. The NAA/Cr ratio is significantly reduced in the ADC Stage 2 and 3 as compared with any of the other groups ($P < 0.05$). Reproduced with permission from Menon et al.[7]

The aggregate scores were abnormal (>2 SDs from the mean of the control subjects) in 13 out of 15 patient spectra (87%), while 8 out of 11 patients (73%) had abnormal MR images. Moreover, only one out of 10 control spectra (10%) was abnormal while four out of 11 controls (36%) had abnormal imaging. These results suggested that MRS may be more sensitive and specific than MR imaging in detecting CNS involvement in HIV-infected patients.

Chong et al.[10] reported the largest study in which proton MRS was performed in 103 HIV seropositive patients and 23 control subjects. Spectra were collected from an 8 cm^3 voxel placed in a normal parieto–occipital region of the brain using a 90°, 180°, 180° spin echo sequence (PRESS), *TR* of 1600 ms and *TE* of 135 ms. In the first part of the study, the spectra of HIV seropositive patients were compared and correlated with clinical, inmunologic, and radiologic measures of HIV infection. A significant reduction in the NAA/Cr ratio was seen in patients with late-stage disease (CDC Group IV). The NAA/Cr and NAA/Cho ratios were also reduced in patients with CD4 counts <200 mm^{-3} and in patients with neurologic signs. Significant increases in Cho/Cr ratios were seen in patients with low CD4 counts and abnormal MR images. Reduced NAA ratios correlated with diffuse but not focal MR imaging abnormalities. In the second part of the study, the authors evaluated the utility of combining the results of MR imaging and spectroscopy, finding that the combination of both modalities provides closer relationships to clinical and immunologic measures of disease than either modality alone. Moreover, abnormal spectra correlated more with abnormal neurologic finding than did abnormal MR images, suggesting that spec-

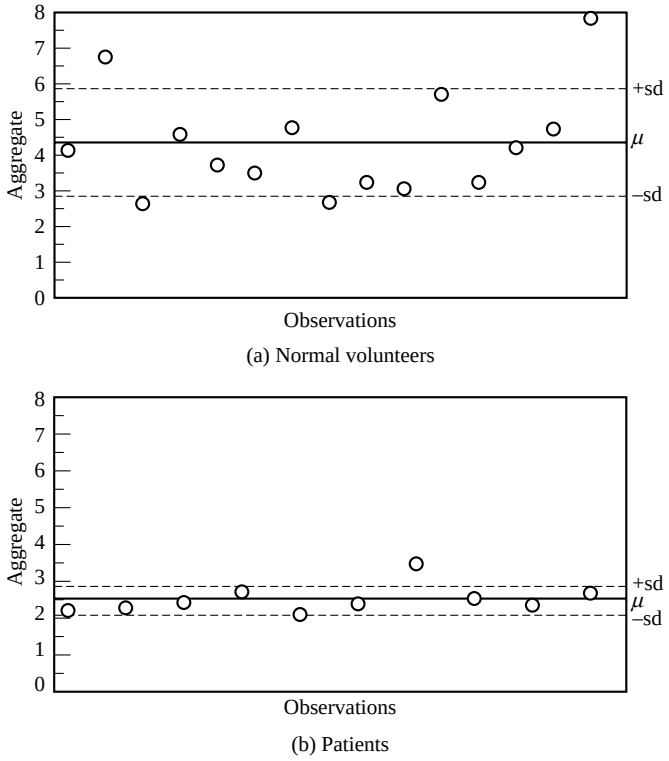

Figure 5 Aggregate spectral scores (Cr/NAA + Cho/Cr + marker/Cr) obtained from normal volunteers and patients with HIV infection. The mean and 1 SD lines are indicated. Note the almost complete separation between the two groups. See Jarvik et al. for experimental details[9]

troscopy may be sensitive to changes in cerebral chemistry that are clinically relevant and are not apparent on MR images.

The same authors[11] studied 43 HIV seropositive patients, including 26 who had clinical or radiologic evidence of late-stage disease (CDC Group IV) and 17 in the early stages of infection (CDC Groups II and III). Using the same sequence as described above, spectra were obtained from a 8 cm^3 voxel placed in a normal parieto-occipital region of the brain. When patients grouped by different criteria were compared, a significant reduction in the NAA/(NAA + Cho + Cr) ratio was found in patients in the late stage of the disease as compared with those in early stage disease. This ratio was lower in patients with HIV-1-associated cognitive/motor complex as compared with patients who were neurologically healthy. Also this ratio was decreased in patients with abnormal MR images (diffuse white matter abnormalities) as compared with those with normal appearing white matter. When patients were compared with healthy control subjects, the NAA/(NAA + Cho + Cr) ratios were significantly higher in control subjects than in CDC Group II and III patients and also significantly higher than in all seropositive patients with normal MR imaging. The authors noted, however, that the control group was younger and so these last results may be influenced by the expected decrease in NAA levels which parallel neuronal loss with age. The authors reported the first follow-up spectroscopic study performed in 15 patients between three and eight months after their initial studies. A significant reduction in the NAA/(NAA + Cho + Cr) ratio was observed at follow-up study when compared with the initial examinations.

The results of all of the MRS studies of HIV infection are summarized in Table 1.

A common finding in all of the studies on HIV infection of the brain is the reduced level of NAA. Although NAA, which resonates at 2.0 ppm, is the most prominent resonance in the brain proton spectrum, its precise biochemical function is not clear. It has been suggested that NAA is involved in the regulation of lipid synthesis, the regulation of protein synthesis, or as a storage buffer for aspartate. Since NAA is largely confined to neurons it has been proposed as a neuronal marker. Hence, decreases in the level of NAA may be interpreted as a sign of neuronal loss or injury. This finding is consistent with the pathologic evidence of neuronal loss reported in HIV infected patients. Another common finding, although not present in all of the studies, is the increase in Cho/Cr ratio. Choline, which resonates at 3.2 ppm, is an important precursor of cell membrane synthesis and is often found to be elevated in tissues that are rapidly regenerating or undergoing membrane disruption. The significance of the elevation in Cho/Cr ratio remains uncertain. A possible interpretation for this increase in HIV infected patients is that the increased Cho may not directly arise from changes in neurons but may result from metabolic alterations in glial or inflammatory cells.[7] An alternative interpretation is that the increase in Cho/Cr ratio combined with the increase in marker/Cr ratio, also observed in these patients, may reflect myelin damage.[9] Choline phosphoglycerides contribute 11.2% of myelin lipids, with phosphatidylcholine being the most abundant. Therefore, as myelin damage occurs, free choline may be released increasing the choline resonance detected by MRS. The 'marker peak' region between 2.1–2.6 ppm may be a combination of nonspecific amino acids and possibly myelin catabolites which may increase with myelin breakdown. Both explanations for the increase in Cho/Cr ratio are consistent with the neuropathologic finding of inflammatory infiltrates and white matter abnormalities in the brain of HIV infected patients. An alternative explanation proposed for the increase in this ratio is the decrease in Cr resonance.[10] This resonance at 3.0 ppm reflects the concentration of the total creatine pool (PCr and Cr). The level of this peak remains stable under many conditions in the brain. The decrease in creatine pool may indicate impairment of cellular metabolism in the brain of these patients and is supported by the decrease in PCr peak observed in phosphorus MRS studies.

Abnormal proton spectra may be found in normal-appearing white matter on imaging, suggesting that MRS may be more sensitive than MRI in detecting CNS involvement in HIV infected patients. Moreover, MRS seems to be a better discriminator between the patient and control populations than MRI, suggesting that MRS may be also more specific. When individuals displaying different manifestations of illness were compared, the abnormalities in the spectra correlated with the presence and the severity of the cognitive impairment and with clinical and immunologic measures of late-stage disease. These findings suggest that MRS may serve as an indicator of the degree of CNS involvement. Therefore, MRS may serve to monitor the course of disease progression and may have a prognostic role regarding CNS involvement. This modality may provide a sensitive method for the early detection of HIV migration to the CNS. Finally, MRS can be employed in longitudinal studies to monitor the response to therapy and thus may lead to individual optimized treatment effectiveness.

Table 1 A Summary of the Proton MRS Findings in HIV infection

Study	Patients (p) Controls (c)	Stage[a]		Clinical evidence of CNS involvement		MRI findings[c]		MRS sequence and parameters	MRS findings	Groups statistically distinguished by MRS
Menon et al. (1990)	2p/6c	late-stage	2	cogn. imp. + focal signs	1 1	focals lesions not attributed to HIV	2	MESA *TR* 2000 ms *TE* 270 ms V = 64 cm^3 normal parietal region	↓NAA/Cho ↓NAA/Cr	patients/controls
Menon et al. (1992)	11p/8c	late-stage	10	cogn. imp. (ADC)	7	abnormal	9	MESA *TR* 2000 ms *TE* 270 ms	↓NAA/Cr	ADC Stage 2/3/ controls
		early-stage	1	no cogn. imp	4	normal	2	V = 27–64 cm^3 parieto-temporal region	↑Cho/Cr (NS)	
Meyerhoff et al. (1993)	14p/7c	late-stage	4	cogn. imp.	10	abnormal	3	CSI	↓NAA/Cr	cogn. impair/ controls
		early-stage	10	no cogn. imp	4	normal	11	V = 2.5 cm^3 centrum semiovale and mesial cortex	↓NAA/Cho	
Jarvik et al. (1993)	11p/8c	late-stage	4	cogn. imp.	9	abnormal	8	STEAM *TR* 2000 ms *TE* 19 ms *TM* 10.6 ms	↓NAA/Cr	patients/ controls
		early-stage	7	no cogn. imp.	2	normal	3	V = 3.4–8 cm^3abnormal white matter or centrum semiovale	↑Cho/Cr ↑ Marker peak/Cr	
Chong et al. (1993)[d]	103p/23c	late-stage	70	neurologic signs	19	abnormal	34[e]	PRESS *TR* 1600 ms *TE* 135 ms	↓NAA/Cr	late-stage/early-stage
		early-stage	22	no neurologic signs	31	normal	36	V = 8 cm^3 normal parieto-occipital region	↓NAA/Cho ↑Cho/Cr	<CD4 count/>CD4 count neurologic signs/no neurologic signs abnormal MRI/ normal MRI
Chong et al. (1994)[d]	43p/8c	late-stage	26	cogn. imp. (HIV-1-associated		abnormal	9	PRESS *TR* 1600 ms *TE* 135 ms	↓NAA/NAA + Cho + Cr	late-stage/early stage
		early-stage	17	cognitive/motor complex) no cogn. imp.	6 14	normal	34	V = 8 cm^3 normal parieto-occipital region		cogn imp/no cogn imp abnormal MRI/ normal MRI early-stage/controls normal MRI patients/controls

[a]Stage: late stage refers to CDC Group IV, early stage to CDC Groups II and III. [b]ADC refers to the aids dementia complex, actually known as HIV-1-associated cognitive/motor complex. Cogn. imp. is an abbreviation for cognitive impairment. [c]Abnormal MRI: abnormalities were either GM atrophy or WM signal changes. [d]Not all of the subjects had complete neurological examinations. [e]The remaining patients (33) were excluded because they exhibited focal lesions on MRI.

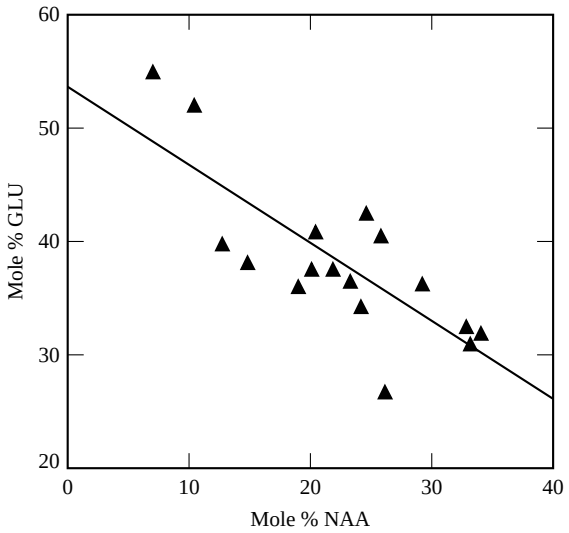

Figure 6 The variation in the mol% of glutamate with the mol% of NAA in the NMR spectra of extracts of brain samples from patients with AD. See Klunk et al. for experimental details[12]

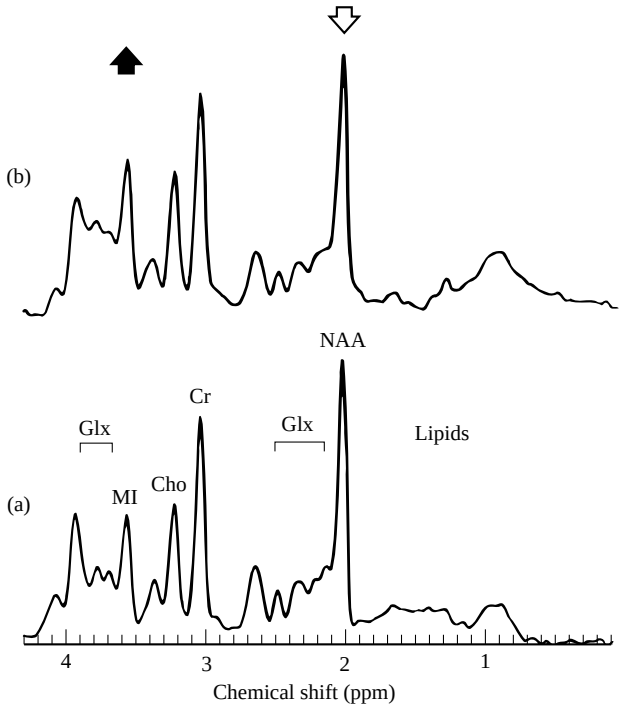

Figure 7 Representative summed solvent-suppressed proton spectra obtained using the STEAM sequence (*TR* = 1500 ms, *TE* = 30 ms) from (a) normal volunteers (n = 8) and (b) patients with AD (n = 8). Reproduced with permission from Miller et al.[13]

2 DEGENERATIVE DISEASES

2.1 Alzheimer's Disease (AD)

2.1.1 In Vitro Studies of AD

Klunk et al.[12] determined the mole ratios of several amino acid metabolites in perchloric extracts of 12 AD and five control brain samples from either the junction of the superior and middle frontal cortex or the superior temporal cortex. NAA and γ-aminobutyric acid (GABA) were found to be lower in AD. The NAA levels also had a negative correlation to the numbers of senile placques (SP) and neurofibrillary tangles (NFT). As shown in Figure 6, glutamate levels were greater in AD and had an inverse correlation with NAA levels. The authors suggested that these findings applied to in vivo studies and reflected neuronal loss, while the remaining neurons were exposed to the potentially excitatotoxic effect of glutamate.

2.1.2 In Vivo Studies of AD

Miller et al.[13] used the STEAM sequence, at field strength of 1.5 T and *TE* 30 ms, to acquire proton spectra from 10–15 ml voxels in white matter located in the parietal area (WM) and gray matter in the occipital cortex (GM). Summed spectra are shown in Figure 7. They reported an increased myoinositol/creatine (MI/Cr) ratio, which suggested abnormalities in the inositol polyphosphate messenger pathway, and reduced NAA/Cr in AD compared to controls. The difference in NAA/Cr level was small but statistically significant in both WM and GM voxels. The increase in MI/Cr was more prominent, especially in GM. However, there was no correlation between the severity of the disease and spectroscopic findings.

Shiino et al.[14] studied a patient group (n = 9) with primary degenerative dementia (PDD) which included seven patients with probable AD, three normal pressure hydrocephalus (NPH), and healthy controls. The DRY STEAM technique was applied with a *TR* of 2500 ms, *TE* of 19 ms, and *TM* of 5.7 ms. The NAA/Cr was significantly reduced in patients with PDD, with no significant brain atrophy or reduction in regional blood flow detected by SPECT. There was no reduction of NAA/Cr in PH. These authors concluded that, in the appropriate clinical setting, proton MRS was a useful measure for the early detection and study of PDD (see Figure 8).

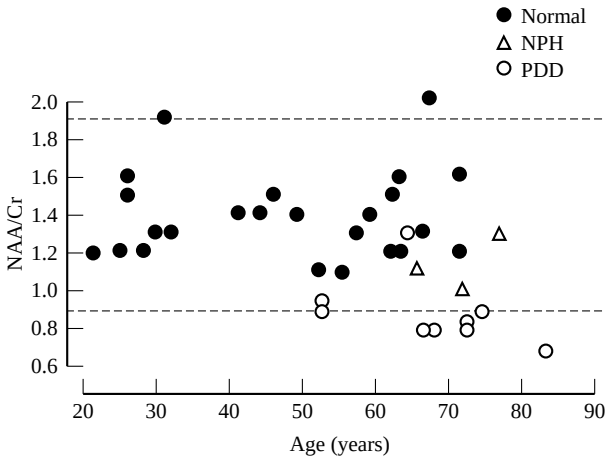

Figure 8 A correlation plot of NAA/Cr versus age. Normals are designated by filled circles. Patients with primary degenerative dementia (PDD) are designated with open circles and patients with normal pressure hydrocephalus are designated by triangles. See Shiino et al.[14] for experimental details

2.2 Parkinson's Disease (PD)

Shiino et al.[14] examined two patients with PD using proton MRS. Spectra were acquired from a 27 cm^3 voxel located in the insular area of the brain. A decrease in the NAA/Cr ratio was observed in the two patients with PD when compared with control subjects. Even though the mean age in the control group was lower, the authors observed that there were no age-related changes in the mean area ratio of NAA/Cr in this group. Both PD patients examined in this study exhibited marked atrophy on MRI, and since the spectra were obtained from voxels placed in the insular area these results should be interpreted with caution.

2.3 Huntington's Disease (HD)

Jenkins et al.[15] reported the results of a proton MRS study in a series of HD patients. Sixteen patients with clinical signs of definite HD and confirmed family history and two individuals without neurologic affectation but with linked DNA markers, indicating a high probability to have inherited the HD gene, were examined. Proton spectroscopy was performed using a STEAM sequence with *TR* of 2000 ms, *TE* of 272 ms, and *TM* of 10 ms. Spectra were collected from a 15.6 cm^3 voxel placed over the visual cortex and from a 5.4–20 cm^3 voxel placed in basal ganglia. A 5 inch surface coil was used to study the occipital cortex and the quadrature head coil was used for studies of the basal ganglia. Elevated lactate levels were observed in the occipital cortex in all of the symptomatic patients when compared with normal controls. The lactate level correlated with the duration of illness. Lactate levels were normal in the two asymptomatic subjects with high probability of having the HD gene. In the basal ganglia, the levels of NAA were decreased and the levels of Cho elevated relative to creatine. Several patients also showed elevated lactate levels in the basal ganglia.

The authors suggested that the increase in lactate may be explained by a defect in oxidative phosphorylation in HD. This possibility is supported by biochemical studies that have reported reduced mitochondrial enzyme activity in HD patients, and ultrastructural studies that have shown abnormalities in the mitochondria of these patients. The reduced NAA and increased Cho were interpreted in these patients as resulting from neuronal loss and gliosis. The authors suggested that lactate likely precedes neuronal death and that this may be the explanation for the more variable lactate elevation in the basal ganglia where evidence of more neuronal loss and gliosis was found. On this basis, they proposed that the elevated lactate may provide a simple marker to monitor the progression of the disease and possible therapies for HD patients.

High-resolution proton MRS was employed by Nicoli et al.[16] to study CSF and serum metabolic samples obtained from patients with HD. Serum and CSF samples were collected from 11 patients suffering HD and 12 reference patients suffering miscellaneous neurological diseases. A significant increase in the pyruvate concentration in CSF was found in patients with HD. This finding may be explained by the decrease of pyruvate-dehydrogenase and Kreb's cycle enzyme activity observed in HD patients. This observation is consistent, as was the finding of elevated lactate reported by Jenkins et al.,[15] with the hypothesis of the existence of a defect in oxidative phosphorylation present in this disease.

3 RELATED ARTICLES

Brain MRS of Human Subjects; Brain Neoplasms in Humans Studied by Phosphorus-31 NMR Spectroscopy; Localization and Registration Issues Important for Serial MRS Studies of Focal Brain Lesions; Systemically Induced Encephalopathies: Newer Clinical Applications of MRS.

4 REFERENCES

1. H. Bruhn, T. Weber, V. Thorwirth, and J. Frahm, *Lancet*, 1991, **337**, 1610.
2. G. D. Graham, O. A. Petroff, A. M. Blamire, G. Rajkowska, P. Goldman-Rakic, and J. W. Prichard, *Neurology*, 1993, **43**, 2065.
3. D. K. Menon, J. Sargentoni, C. J. Peden, J. D. Bell, I. J. Cox, G. A. Coutts, C. Baudouin, and C. G. Newman, *J. Comput. Assist. Tomogr.*, 1990, **14**, 449.
4. Ph. Demaerel, G. Wilms, W. Robberecht, K. Johannik, P. Van Hecke, H. Carlton, and A. L. Baert, *Neuroradiology*, 1992, **34**, 490.
5. R. K. Gupta, R. Pandey, E. M. Kahn, P. Mittal, R. B. Gujral, and D. K. Chhabra, *Magn. Reson. Imag.* 1993, **11**, 443.
6. D. K. Menon, C. J. Baudouin, D. Tomlinson, and C. Hoyle, *J. Comput. Assist. Tomogr.*, 1990, **14**, 882.
7. D. K. Menon, J. G. Ainsworth, I. J. Cox, R. C. Coker, J. Sargentoni, G. A. Coutts, C. J. Baudouin, A. E. Kocsis, and J. R. Harris, *J. Comput. Assist. Tomogr.*, 1992, **16**, 538.
8. D. J. Meyerhoff, S. Mackay, L. Bachman, N. Poole, W. P. Dillon, M. W. Weiner, and G. Fein, *Neurology*, 1993, **43**, 509.
9. J. G. Jarvik, R. E. Lenkinski, R. I. Grossman, J. M. Gomori, M. D. Schnall, and I. Frank, *Radiology*, 1993, **186**, 739.
10. W. K. Chong, B. Sweeney, I. D. Wilkinson, M. Paley, M. A. Hall-Craggs, B. E. Kendall, J. K. Shepard, M. Beecham, R. F. Miller, I. V. D. Weller, S. P. Newman, and M. J. G. Harrison, *Radiology*, 1993, **188**, 119.
11. W. K. Chong, M. Paley, I. D. Wilkinson, M. A. Hall-Craggs, B. Sweeney, M. J. G. Harrison, R. F. Miller, and B. E. Kendall, *AJNR*, 1994, **15**, 21.
12. W. E. Klunk, K. Panchalingam, J. Moossy, R. J. McClure, J. W. Pettigrew, *Neurology*, 1992, **42**, 1578.
13. B. L. Miller, R. A. Moats, T. Shonk, T. Ernst, S. Woolley, and B. D. Ross, *Radiology*, 1993, **187**, 433.
14. A. Shiino, M. Matsuda, S. Morikawa, T. Inubushi, I. Akiguchi, and J. Handa, *Surg. Neurol.*, 1993, **39**, 143.
15. B. G. Jenkins, W. J. Koroshetz, M. F. Beal, and B. R. Rosen, *Neurology*, 1993, **43**, 2689.
16. F. Nicoli, J. Vion-Dury, J. M. Maloteaux, C. Delwaide, S. Confort-Gouny, M. Sciaky, and P. Cozzone, *Neurosci. Lett.*, 1993, **154**, 47.

Acknowledgements

Supported in part by NIH grant NS 31464 (Robert E. Lenkinski). Dr. López-Villegas would like to acknowledge support by the Ministry of Health of Spain (FIS: BAE 94/5033). Dr. Tunlayadechanont would like to acknowledge support from Ramathibodi Hospital in Thailand.

Biographical Sketches

Robert E. Lenkinski. *b* 1947. B.Sc., 1969, University of Toronto, Ph.D., 1973, University of Houston. Postdoctoral Fellow, Weizmann Institute of Science, Isotope Department, Rehovot, Israel, 1973–75. Faculty at University of Houston, 1975–76; Comprehensive Cancer Center, University of Alabama in Birmingham, 1976–80; Department of Chemistry, University of Guelph, Ontario, Canada, 1980–86; University of Pennsylvania, 1986–present. Approx. 92 publications. Research interests include clinical MRS particularly in the diagnosis and staging of disease.

Dolores López-Villegas. *b* 1964. M.D., 1988, University of Barcelona, Medical School. Intern in Medicine, Hopital Clinic, University of Barcelona, 1988. Resident in Medicine, Hopital de la Santa Creu i Sant Pau, Autonomous University of Barcelona, 1989. Resident in Neurology in the same hospital, 1990–92. Research Fellow in MRS (supported by the Ministry of Health of Spain), University of Pennsylvania, Department of Radiology, 1993–present. Approx. 10 publications. Research interests include application of MRS to investigation of neurological diseases.

Supoch Tunlayadechanont. *b* 1962. M.D., 1986, Ramathibodi Hospital, Mahidol University. Residency training in Neurology, Ramathibodi Hospital, 1989–92; Graduate Diplomate in Clinical Science, 1990, Mahidol University; Diplomate the Thai Board of Neurology, 1992, Thai Medical Council. Training in MRI and MRS, Institute of Magnetic Resonance, University of Innsbruck, Austria, 1993. Research Fellow in MRS, University of Pennsylvania, 1993–present. Approx. 10 publications. Research interests include clinical MRS particularly in neurological disease.

Brain MRS of Infants and Children

Ernest B. Cady
University College London Hospitals, UK

and

E. Osmund R. Reynolds
University College London Medical School, UK

1 INTRODUCTION

Magnetic resonance spectroscopy (MRS) was first introduced into pediatrics in the early 1980s as a method for the noninvasive investigation of perinatal brain injury.[1] This injury is often due to cerebral periventricular hemorrhage (PVH) in preterm infants (born before 37 weeks of gestation) or to hypoxia-ischemia in both preterm and term infants. It is responsible for permanent neurodevelopmental impairments in about 10% of disabled children of school age. In the 1970s, X-ray computerized tomography (CT) and, more especially, ultrasound imaging using portable equipment at the cotside, were found to be useful for investigating the incidence, pathogenesis, and prognostic significance of PVH, but long-term follow-up studies indicated that hypoxia-ischemia, often causing periventricular leukomalacia, was a more important cause than PVH of permanent disabilities in preterm infants.[2] In term infants, hypoxia-ischemia was the mechanism by which 'birth asphyxia' (critically impaired gas exchange during labor) damaged the brain. Overall, hypoxia-ischemia turned out to be the most prevalent cause of serious perinatal brain injury, so there was an obvious need for noninvasive investigation of cerebral oxidative metabolism, and hence of the pathogenesis and evolution of hypoxic-ischemic brain injury. MRS was thought to provide a suitable, noninvasive, method for obtaining biochemical information from the otherwise inaccessible neonatal brain.[3–5]

In the early 1980s, ^{31}P MRS had already been used to investigate oxidative metabolism in human skeletal muscle in vivo and the first in vivo spectra had been obtained from mammalian brain.[6] However, studies of newborn infants had to await the development of superconducting magnets with a sufficiently wide bore (approximately 20 cm) and a high enough field strength for spectroscopic work. These magnets (intended primarily for studies of human limb muscles), became available in the early 1980s, and investigations of the brain in newborn infants started shortly thereafter.[1,7] The first in vivo spectra from the human brain were obtained from a preterm baby at University College London in 1982 using the ^{31}P nucleus.[1] It rapidly became clear that metabolites involved in energy metabolism [e.g. adenosine triphosphate (ATP), phosphocreatine (PCr), and inorganic phosphate (Pi)] as well as those related to more fixed cellular components, namely phosphomonoesters (PMEs) and phosphodiesters (PDEs), were easily detected. Intracellular pH (pH_i) could also be measured. Obvious spectral abnormalities were soon found in the brains of infants with hypoxic ischemic injury.[1,7] ^{31}P spectra have also been obtained from the brains of older children and developmental changes have been elucidated. In addition, ^{1}H spectra have demonstrated products of anerobic glycolysis such as lactate (Lac), various amino acids (e.g. glutamate and glutamine), and other brain metabolites, including those containing choline (Cho; related to membrane metabolism) and *N*-acetylaspartate (NAA; a putative neuronal marker). Localization of spectra to specific regions of the brain was initially crude, relying solely on the sensitive volume of a surface coil. Recently, techniques have been developed that enable spectra to be acquired from well defined volumes of tissue, so deeper and focal lesions can be investigated.

The purposes of this article are to summarize the methods used for MRS of the brain in infants and children, to describe what has been learnt about normal brain development, and then to consider the role of MRS, particularly in the investigation of hypoxic ischemic brain injury.

2 PATIENT MANAGEMENT

MRS studies of the brains of infants and children are safe provided that current recommendations are observed,[8] though the requirements for physiological support and monitoring are often much greater than for adults.

Newborn infants, who may be in an unstable condition, have to be conveyed and studied in a specially designed transport incubator incorporating a nonmagnetic, cylindrical pod that encloses the baby and is suitable for insertion into the magnet. Conventional facilities for temperature control, monitoring, and mechanical ventilation are provided.[9,10] Monitoring of heart rate [by electrocardiogram (ECG) or ultrasound Doppler flow], blood pressure, arterial oxygen saturation (by pulse oximetry), end-tidal CO_2, transcutaneous pO_2 and pCO_2, and body temperature (by skin and/or rectal sensors) should be available. Intravenous infusions may have to be provided. Newborn infants can often be studied satisfactorily whilst naturally asleep following a feed. However, sedation with, for example, chloral hydrate is often required for studies of older children. Especially for the newborn, the head must be gently immobilized during studies using, for example, a polythene bag containing expanded polystyrene beads and which can be evacuated. Clinical apparatus must be carefully designed to take into account the large range of size of infants and children. It is important that the data acquisition protocol is such that useful information can be obtained even if small movements take place.

Interactions between magnetic fields (both static and transient) and the pulsed rf, and the monitoring equipment needed for patient care, require consideration. Some sensors contain ferromagnetic components that can impair the homogeneity of the magnetic field. Many manufacturers of monitoring equipment can supply special magnetic resonance compatible devices. Alternatively, it may be possible to position ferromagnetic components so that their effects are unimportant. Some sensors may pick up rf interference, thereby decreasing the signal-to-noise ratio and transient rf and pulsed magnetic fields may overload ECG and other devices. The accidental formation

of conductive loops by sensor cables must be avoided. This is in order to eliminate the risk of burns that could be caused if currents are induced by transient rf and pulsed gradient fields.[11] Microprocessors, included in many newer monitors, emit rf interference and thus special rf Faraday shields and filters are required. Also, the spectrometer must be safe in the presence of the high inspired oxygen concentrations needed by some patients. Probes (rf) must be tested to ensure that transmitter pulses do not cause arcing; they must be in sealed containers which, as a further precaution, can be flushed with a relatively inert gas such as N_2.

3 DATA ACQUISITION

Using surface coils with diameters in the range 5–7 cm and without further localization techniques, good quality ^{31}P spectra can be obtained from 10–50 mL of the cerebral cortex of the newborn infant. These spectra have very little contamination from other tissues since skin and fat contain little ^{31}P, cranial muscle is sparse, and the cranial bones are poorly mineralized and have relatively immobile ^{31}P nuclei. For basic studies of the normal brain and abnormalities associated with nonfocal brain injury, valuable information has been obtained without better spectroscopic localization. However, the sensitive volume provided solely by a surface coil is not well defined. For investigations of focal metabolism, particularly deep in the brain, and in older infants and children who have better developed cranial musculature, and also for ^{1}H studies, in which fat contamination can be a problem, spectroscopic localization techniques are essential. Many volume localization methods exist which have been used successfully for studies of infants and children. These techniques all employ pulsed magnetic field gradients to obtain low-contamination spectra from a well defined voxel positioned with reference to MRI scout images. In these multipulse techniques, rf power is higher than for 'single pulse' surface coil methods and consequently greater attention to safety is mandatory.

Image-selected in vivo spectroscopy (ISIS; see ***Single Voxel Whole Body Phosphorus MRS***)[12] has been used for ^{31}P studies of the developing brain[13] and, in order to combine MRI with localized ^{31}P MRS, double-tunable probes dedicated to the examination of children's brains have been developed.[14] For neonatal applications, standard probeheads are usually too large and give poor signal-to-noise ratio with the tiny voxels (about 1 mL) often necessary when studying the smaller anatomy. Localized ^{1}H spectra from infants and older children have been acquired using both the point resolved spectroscopy (PRESS) and stimulated echo amplitude mode (STEAM) techniques (see ***Single Voxel Localized Proton NMR Spectroscopy of Human Brain In Vivo***).[15] MR spectroscopic imaging[16] (see ***Chemical Shift Imaging***) has not been as widely applied as the single voxel methods. Absolute concentrations (i.e. in millimoles per kilogram wet weight, or millimoles per liter) of ^{31}P metabolites in developing brain have been estimated both by PRESS with brain water as an internal reference,[17] and by ISIS with an external reference.[18] The absolute concentrations of ^{1}H metabolites are more difficult to estimate, due largely to the dependences of peak areas on T_2 relaxation and, in the case of multiplets, on phase modulation. However, some information about developmental changes has been acquired using an external reference[19] or brain water as an internal reference.[17,20]

4 NORMAL BRAIN DEVELOPMENT IN INFANTS AND CHILDREN

Information about the relative and absolute concentrations of metabolites detectable by ^{31}P and ^{1}H MRS in the developing human brain has been acquired at several centers worldwide with good agreement of results.

4.1 The Neonatal Brain

The major ^{31}P energy related resonances in spectra from skeletal muscle had been securely assigned when the first studies of the neonatal brain were carried out. Peaks attributable to γ-, α-, and β-nucleotide triphosphate (NTP), PCr, and Pi, all of which are involved in energy metabolism, were also detected in the brains of newborn infants (see Figure 1). Magnesium complexed ATP is the main contributor to cerebral NTP, with guanosine, uridine, and cytidine triphosphates making up about a quarter of the remaining NTP pool;[21] the γ- and α-NTP resonances have small contributions from nucleotide diphosphates; and an often unresolved nicotinamide adenine dinucleotide (NAD + NADH) quartet resonates on the right-hand shoulder of α-NTP.[22] Within the physiological range, the PCr resonant frequency is independent of both pH_i (it only shifts significantly at very low pH) and metal ion concentration; it is often used as a chemical shift reference (assigned as 0 ppm).

Only a single Pi resonance (peak 2) is visible in the ^{31}P spectra shown in Figure 1. Its chemical shift relative to PCr (δ_{Pi}) depends strongly on the concentration ratio of its acidic and basic species ($pK_a \approx 6.8$) and hence pH_i can be estimated from the Henderson–Hasselbalch equation:[23]

$$pH_i = 6.77 + \log_{10}[(\delta_{Pi} - 3.29)/(5.68 - \delta_{Pi})] \quad (1)$$

Estimation of pH_i is accurate to about 0.1 pH units. At high field strengths ($\geqslant$4.7 T), the Pi peak can often be resolved into extra- and intracellular[24] and perhaps also mitochondrial components,[25] implying the presence of compartments of different pH.

When the first ^{31}P spectra were acquired from the neonatal brain, problems arose with the interpretation and assignment of prominent resonances other than those particularly involved in energy metabolism. The PME and the moderately broad, unresolved PDE peaks were both surprisingly large, and surface coil spectra were superimposed on a broad hump [see Figure 1(c)]. Chromatography and ^{31}P and ^{1}H MRS of extracts of neonatal mammalian brain have identified phosphoethanolamine (PEt) as the main contributor to the PME peak[26] which also includes phosphocholine (PC) and several smaller resonances, due for example to phosphoserine and phosphoinositol.[22] These PMEs are involved in phospholipid metabolism, including the synthesis of myelin.

The moderately broad resonance at about 2.9 ppm [see Figures 1(a) and 1(b), peak 3] is largely attributable to cross linked PDEs in membrane bilayer phospholipids and also to a small pool of mobile phospholipid breakdown products

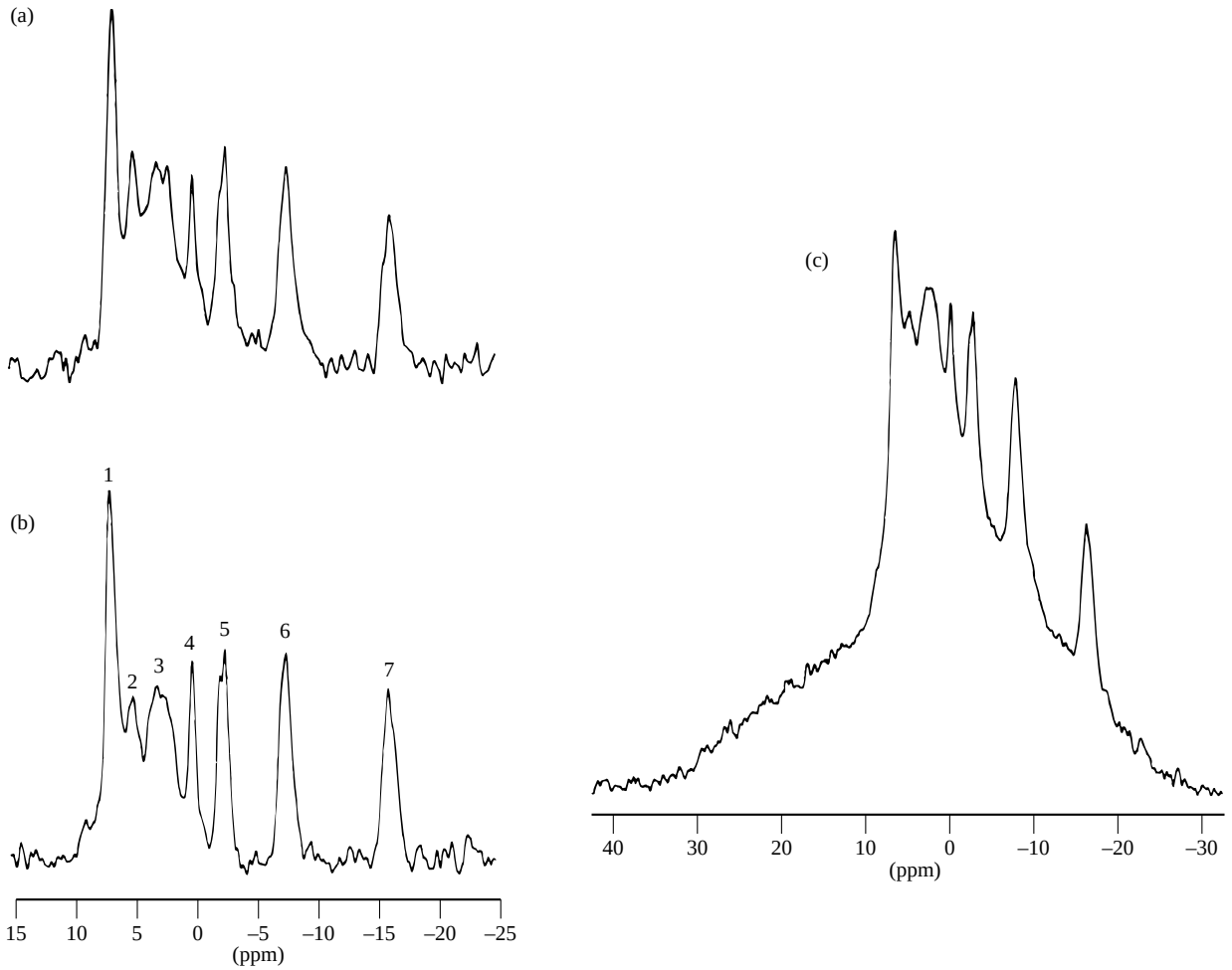

Figure 1 ^{31}P spectra acquired from the temporo-parietal cortex of (a) a preterm infant of gestational plus postnatal age (GPA) 31 weeks; (b) an infant born and studied at full term. Pi is relatively smaller and PCr larger in spectrum (b) as compared with spectrum (a). Spectrum (c) is from the same infant as (b) but without removal by postacquisition processing of the broad underlying hump which was due to relatively immobile ^{31}P in bone and membrane phospholipids. Peak identifications: (1) PME; (2) Pi; (3) PDE; (4) PCr; (5) γ-NTP; (6) α-NTP; (7) β-NTP. (Reproduced by permission of Plenum Press from E. B. Cady, 'Clinical Magnetic Resonance Spectroscopy', New York, 1990, p. 86)

[glycerolphosphorylethanolamine (GPE) and glycerolphosphorylcholine (GPC)]. The membrane bilayer phospholipids exhibit chemical shift anisotropy leading to a reduced signal-to-noise ratio at higher field strengths (e.g. 4.7–7 T). The very broad underlying signal, shown in Figure 1(c), is due to more rigidly bound ^{31}P nuclei mainly in membrane phospholipids and myelin.

Well resolved ^{1}H spectra can be acquired from the brains of newborn infants if long echo times (*TE*) are used (e.g. 270 ms). In Figure 2 an in vivo spectrum from a normal newborn infant is compared with an in vitro high-resolution spectrum of adult rat brain extract.[27] The major in vivo peaks originate from Cho, Cr, and NAA; a smaller but clearly detectable Lac methyl resonance is also present. In the extract spectrum, Cho is seen to include GPC, PC, and taurine, and NAA is adjacent to glutamate, glutamine, and γ-aminobutyric acid (GABA). At shorter *TE* times (e.g. about 25 ms), T_2 relaxation and phase modulation are less important and numerous peaks are easily detected; however, ^{1}H spectra become more difficult to analyze. This problem is further complicated by the presence of many broad overlapping resonances from fatty acids (from extravoxel contamination and perhaps also free fatty acids) and macromolecules (e.g. proteins). Unlike ^{31}P metabolites, whose biochemical pathways are largely known, many ^{1}H resonances other than Lac still pose problems of interpretation.[28] For example, although NAA is widely regarded as an intraneuronal marker, its biochemical role remains unclear and NAA has also been found in oligodendrocyte progenitor cells.[29]

4.2 Changes with Age

Age-dependent changes in the concentration ratios and absolute concentrations of ^{31}P and ^{1}H metabolites have been defined in several studies. A major reason for doing these investigations has been to establish normal age-related values so that metabolic abnormalities may be securely identified. Attention has focused on the rapid changes taking place in the last 3 months of gestation as determined in preterm and term infants studied during the first days of life. Investigations of development during later childhood have also been undertaken. Figure

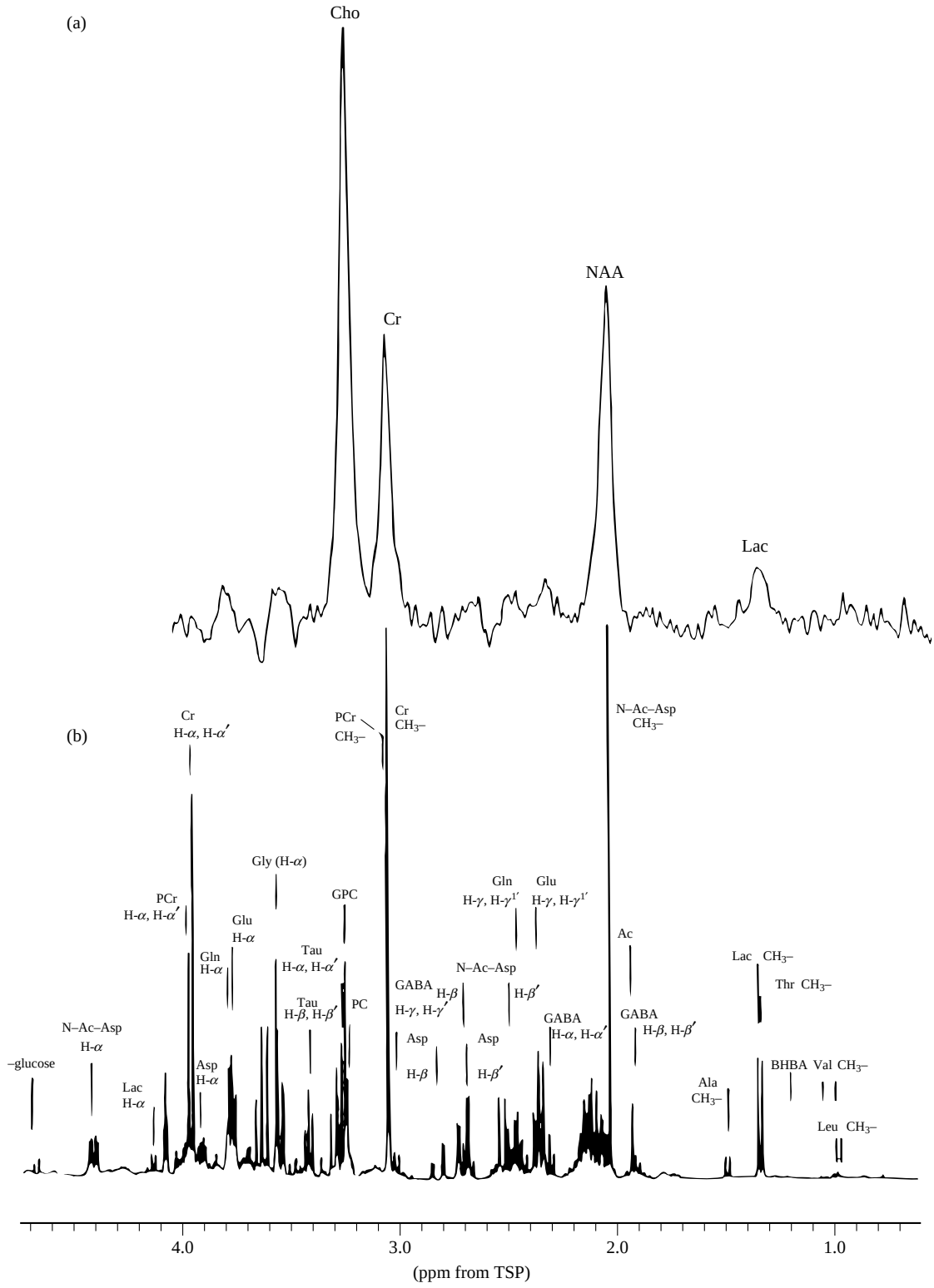

Figure 2 An in vivo ^{1}H PRESS spectrum from the thalamic region of a normal newborn infant of GPA 35 weeks (a) compared with an in vitro spectrum of an extract of adult rat brain (b). Spectrum (a) was collected at 100 MHz and the acquisition conditions were: *TE* 270 ms; repetition time (*TR*) 2 s, 128 averaged echoes; and an 8 mL voxel. Resonance identifications: Cho, choline containing compounds; Cr, creatine + phosphocreatine; NAA, *N*-acetylaspartate; Lac, lactate. Spectrum (b) was obtained at 360 MHz with *TR* 3 s and a 90° flip angle (water-suppressed single pulse sequence). [Spectrum (a) was obtained in collaboration with A. Lorek, J. Penrice, J. S. Wyatt, R. Aldridge, and M. Wylezinska. Spectrum (b) is reproduced by permission of Elsevier Science Publishers from S. Cerdan, R. Parrilla, J. Santoro, and M. Rico, *FEBS Lett.*, 1985, **187**, 167]

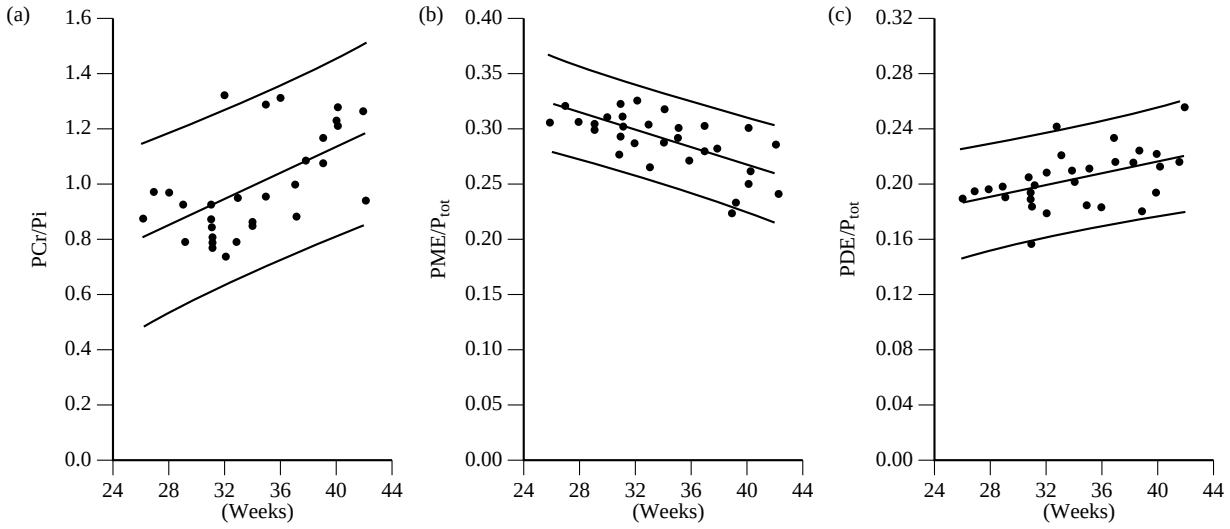

Figure 3 Relations between ^{31}P metabolite concentration ratios in the temporo-parietal cortex and GPA in 30 infants of appropriate weight for gestational age. Regression lines and 95% confidence limits are shown. (Reproduced by permission of International Pediatric Research Foundation Inc. from D. Azzopardi, J. S. Wyatt, P. A. Hamilton, E. B. Cady, D. T. Delpy, P. L. Hope, and E. O. R. Reynolds, *Pediatr. Res.*, 1989, **25**, 440)

3 and Table 1 give ^{31}P surface coil data from the temporo-parietal cortex of 30 infants of appropriate weight for gestational age (AGA) studied at a median postnatal age of 4 days.[30] It can be seen that, with increasing gestational plus postnatal age (GPA), [PCr]/[Pi] and [PDE]/[total mobile phosphorus (P_{tot})] increased, whereas [PME]/[P_{tot}] fell. These alterations, together with an increase in [PCr]/[NTP], continue during the first months of life, but then the changes slow down as adulthood is approached (see Figures 4 and 5).[13] Adult values are attained by about 4 years. Values from normal, small-for-gestational-age (SGA; i.e. with birthweights below the 3rd centile for gestation) infants were similar to those from AGA infants.[30] [PCr]/[Pi] is directly related to the phosphorylation potential and to the free energy change of hydrolysis of ATP. The increase in [PCr]/[Pi] with age may be attributable to a greater need for an energy reserve in the mature brain and perhaps also to less efficient oxidative phosphorylation in the immature one. In the newborn human infant, [PCr]/[Pi] is similar to that in other altricious species, such as the newborn rat,[31] but smaller than in precocious animals such as the lamb.[32]

The large amplitude of the PME resonance in the neonatal period is due to high [PEt].[33,34] This metabolite may have an important role as a phospholipid precursor related to increased synthesis of membrane phospholipids and myelin at this time. Of the ^{31}P resonances only PME shows a change in relaxation with development; T_1 decreases from a neonatal value of about

Table 1 Relationships between Metabolite Concentration Ratios and pH_i, in the temporo-parietal cortex and Gestational plus Postnatal age in 30 Infants of Appropriate Weight for Gestational Age[a]

	x	*c*	*r*	*p*	28 weeks	42 weeks
PCr/Pi	0.024	0.190	0.58	<0.001	0.85 ± 0.33	1.18 ± 0.33
NTP/P_{tot}	0.001	0.075	0.19	NS	0.09 ± 0.03	0.10 ± 0.03
PCr/P_{tot}	0.001	0.051	0.56	<0.01	0.09 ± 0.02	0.11 ± 0.02
Pi/P_{tot}	−0.001	0.128	−0.40	<0.05	0.10 ± 0.02	0.09 ± 0.02
PME/P_{tot}	−0.004	0.429	−0.68	<0.001	0.32 ± 0.04	0.26 ± 0.04
PDE/P_{tot}	0.002	0.131	0.47	<0.01	0.19 ± 0.04	0.22 ± 0.04
PCr/NTP	0.009	0.717	0.20	NS	0.79 ± 0.42	1.09 ± 0.42
Pi/NTP	−0.013	1.482	−0.24	NS	1.13 ± 0.50	0.95 ± 0.50
PME/NTP	−0.050	4.887	−0.37	<0.05	3.49 ± 1.23	2.79 ± 1.25
PDE/NTP	0.016	1.658	0.15	NS	2.11 ± 1.03	2.34 ± 1.05
Hump/NTP[b]	1.011	−7.790	0.49	<0.05	20.5 ± 20.5	34.7 ± 21.6
pH_i[c]	−0.003	7.233	0.12	NS	7.14 ± 0.28	7.09 ± 0.28

[a]*x*, Slope; *c*, ordinate intercept from the regression; *p*, significance of the correlation coefficient *r*. Data for 28 and 42 weeks are mean values ±95% confidence intervals from the regressions. [b]$n = 24$. [c]$n = 23$; values for the remaining infants were not calculated, because spectra were not well resolved. (Reproduced by permission of International Pediatric Research Foundation Inc. from D. Azzopardi, J. S. Wyatt, P. A. Hamilton, E. B. Cady, D. T. Delpy, P. L. Hope, and E. O. R. Reynolds, *Pediatr. Res.*, 1989, **25**, 440)

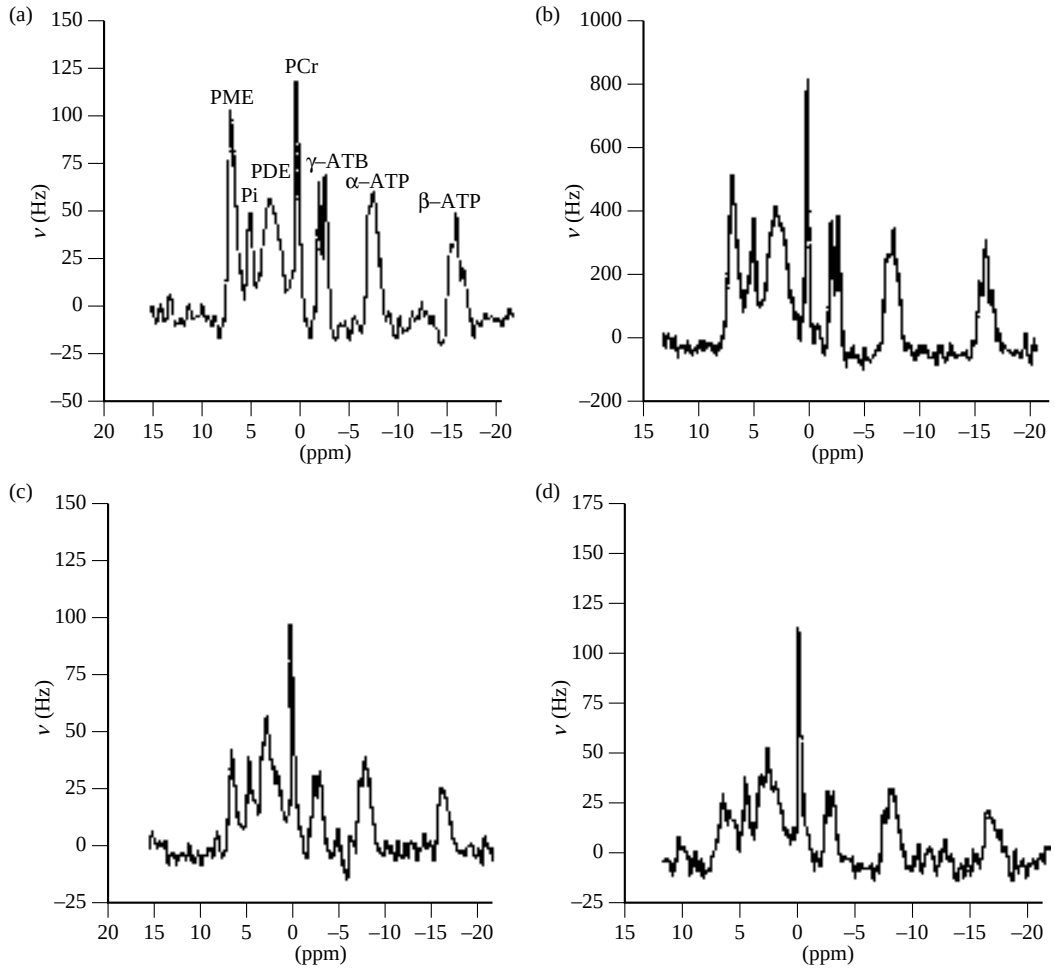

Figure 4 ^{31}P ISIS spectra from the paraventricular region of the human brain at postnatal ages of 1 month (a), 4 months (b), 30 months (c), and 15 years (d). The spectra were obtained at 1.5 T using a sensitive volume varying from 54 mL in infants to 72 mL in older children. *TR* was 3.75 s and 256 FIDs were averaged. Significant developmental changes occurred within the first few years of life. (Reproduced by permission of The Radiological Society of North America from M. S. Van der Knaap, J. van der Grond, P. C. van Rijen, J. A. J. Faber, J. Valk, and K. Willemse, *Radiology*, 1990, **176**, 509)

1.8 ms to about 1.2 ms in adulthood.[18] This fall is probably due to alterations in the constituents of the peak, notably the reduction in PEt. No change has been detected in pH_i during maturation ($pH_i \simeq 7.10$).[13,30]

Measurements of the absolute concentrations of ^{31}P metabolites in the newborn human brain obtained by PRESS[17] and ISIS[18] techniques have shown disagreements. For example, with the ISIS technique, the apparent [NTP] was much less than estimated with the PRESS method. These discrepancies could be due to a number of factors, including the acquisition of data from different parts of the brain. Furthermore, ISIS and PRESS estimates of [PDE] may be affected by relaxation during the delays and the pulses of the acquisition sequence; the cross-linked membrane bilayer fraction of PDE has a T_2 of about 3 ms.[35]

As with ^{31}P metabolites, the relative peak areas[13,19,36] and absolute concentrations[17,19] of ^{1}H metabolites change with increasing age (see Figures 6–8). NAA/Cr increases and Cho/Cr decreases up to about 3 years when the rate of change declines. [NAA] and [Cr] both appear to increase with age, whereas both [Cho] and [myoinositol] decrease.[17,19,37] The relatively low NAA signal seen in younger subjects and the increase with age are supported by biochemical studies, indicating that [NAA] increases greatly during mammalian brain development.[38] Since NAA is mainly located in neurons, this increase may reflect neuronal maturation. The Cho peak contains signals from PCh, GPC and other metabolites; changes in its amplitude probably relate to alterations in the PME and PDE peaks in ^{31}P spectra. Recent evidence suggests that Lac is detectable in the brains of normal newborn infants [see Figure 2(a)] and is higher in preterm and SGA infants. The implied greater reliance on anerobic glycolysis in preterm and SGA infants may relate to their reduced values for [PCr]/[Pi].[17,36]

5 CEREBRAL PATHOLOGY

^{31}P MRS has proved particularly valuable for the investigation of hypoxic-ischemic brain injury, especially in newborn infants. Most of the data have been acquired from infants who

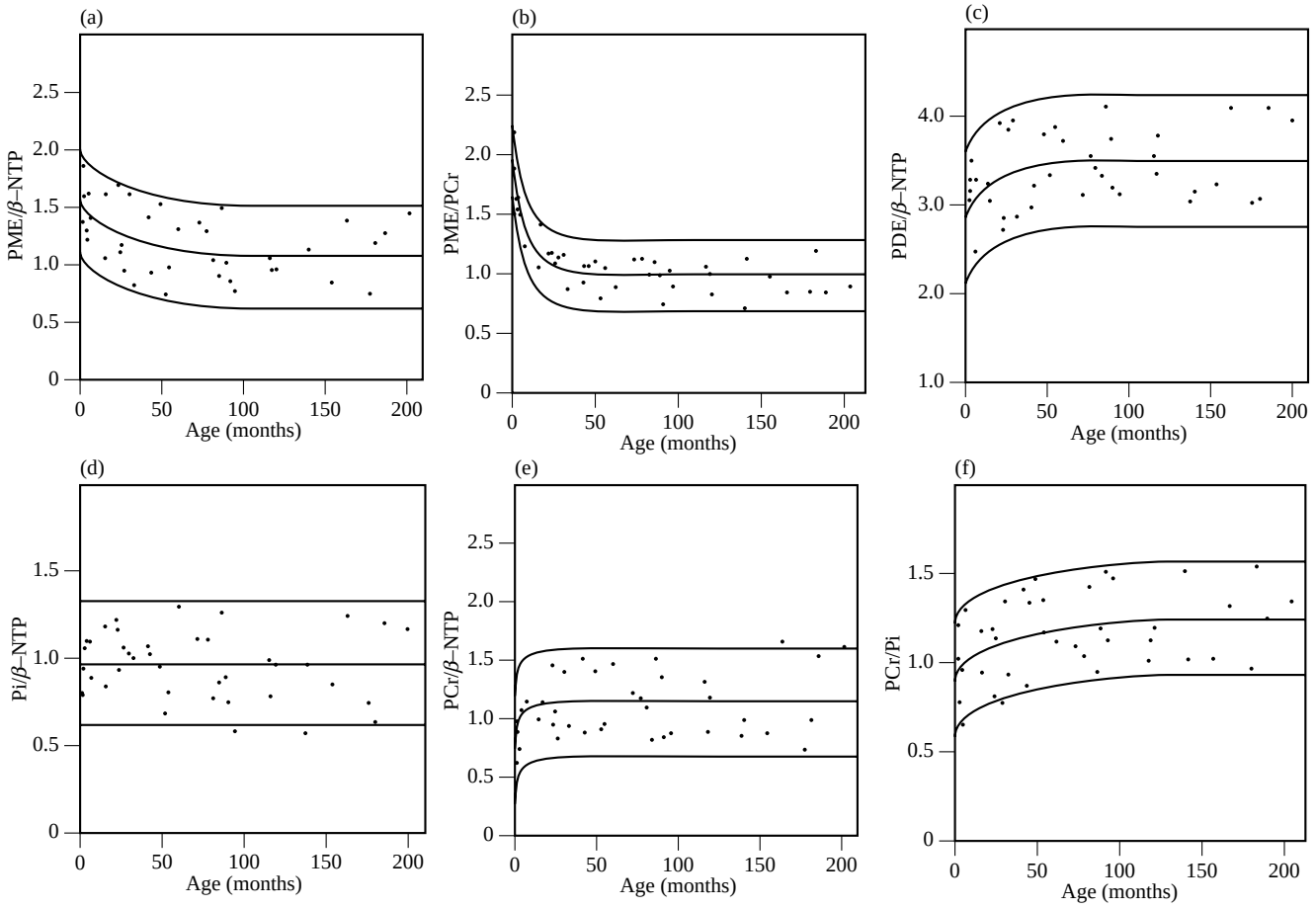

Figure 5 Relationships between age and PME/β-NTP (a), PME/PCr (b), PDE/β-NTP (c), Pi/β-NTP (d), PCr/β-NTP (e), and PCr/Pi (f) in the paraventricular region. Regression lines and 2.5 and 97.5 percentile lines are shown. (Reproduced by permission of The Radiological Society of North America from M. S. Van der Knaap, J. van der Grond, P. C. van Rijen, J. A. J. Faber, J. Valk, and K. Willemse, *Radiology*, 1990, **176**, 509)

have suffered birth asphyxia, but similar results have been obtained in those with periventricular leukomalacia and other forms of hypoxic ischemic injury. More recently, ^{1}H MRS has been used for monitoring abnormal glycolytic pathway activity (via increased Lac) and neuronal degeneration (via decreased NAA).

5.1 Perinatal-Hypoxia Ischemia

Studies of babies with suspected cerebral hypoxic-ischemic injury were initiated on the premise that in conditions where the supply of oxygen to the brain was curtailed, or the mitochondrial mechanisms for its consumption were damaged, [ATP] would tend to fall. It was expected that the decrease in [ATP] would initially be very small because, unless [PCr] is grossly depleted, [ATP] is buffered by the creatine kinase reaction[39] which maintains it close to normal, but at the expense of a fall in [PCr] and a reciprocal rise in [Pi]. It was hypothesized that [PCr]/[Pi] in the brains of infants with hypoxic ischemic injury would be reduced and that, in extreme circumstances, [ATP] might also be low. Surprisingly, studies of severely birth-asphyxiated babies have shown that cerebral ^{31}P spectra were often normal on the first day of life.[40] Subsequently [PCr]/[Pi] gradually fell, with a nadir at 2–4 days of age (see Figure 9 and Table 2), in spite of normal arterial oxygen saturation, blood pressure, and blood glucose. In the most affected infants, [NTP] then fell and death ensued. In contrast to the profound intracellular acidosis seen in experimental hypoxia-ischemia,[32] pH_i tended to be slightly alkaline. (It is of interest that PCr and NTP were almost undetectable in two infants with inborn metabolic errors, propionic acidemia and arginosuccinic aciduria.[41] However, cerebral pH_i was profoundly acidic in these infants.) In survivors, the spectra usually returned to normal within about 2 weeks, but the overall ^{31}P signal amplitude was often reduced, indicating loss of brain cells.

Since the lowest observed [PCr]/[Pi] values were strongly related to long-term prognosis (see below) and because of the long timescale of the postnatal biochemical changes, in order not to miss useful information it is important that spectra are obtained on several occasions during the first 2–4 days of life during which metabolic abnormalities are at their greatest. An explanation for the observed sequence of spectral changes is that the brain suffered an acute episode of hypoxia-ischemia before birth causing 'primary' energy failure, which was reversed by resuscitation at delivery, so that the energy state of

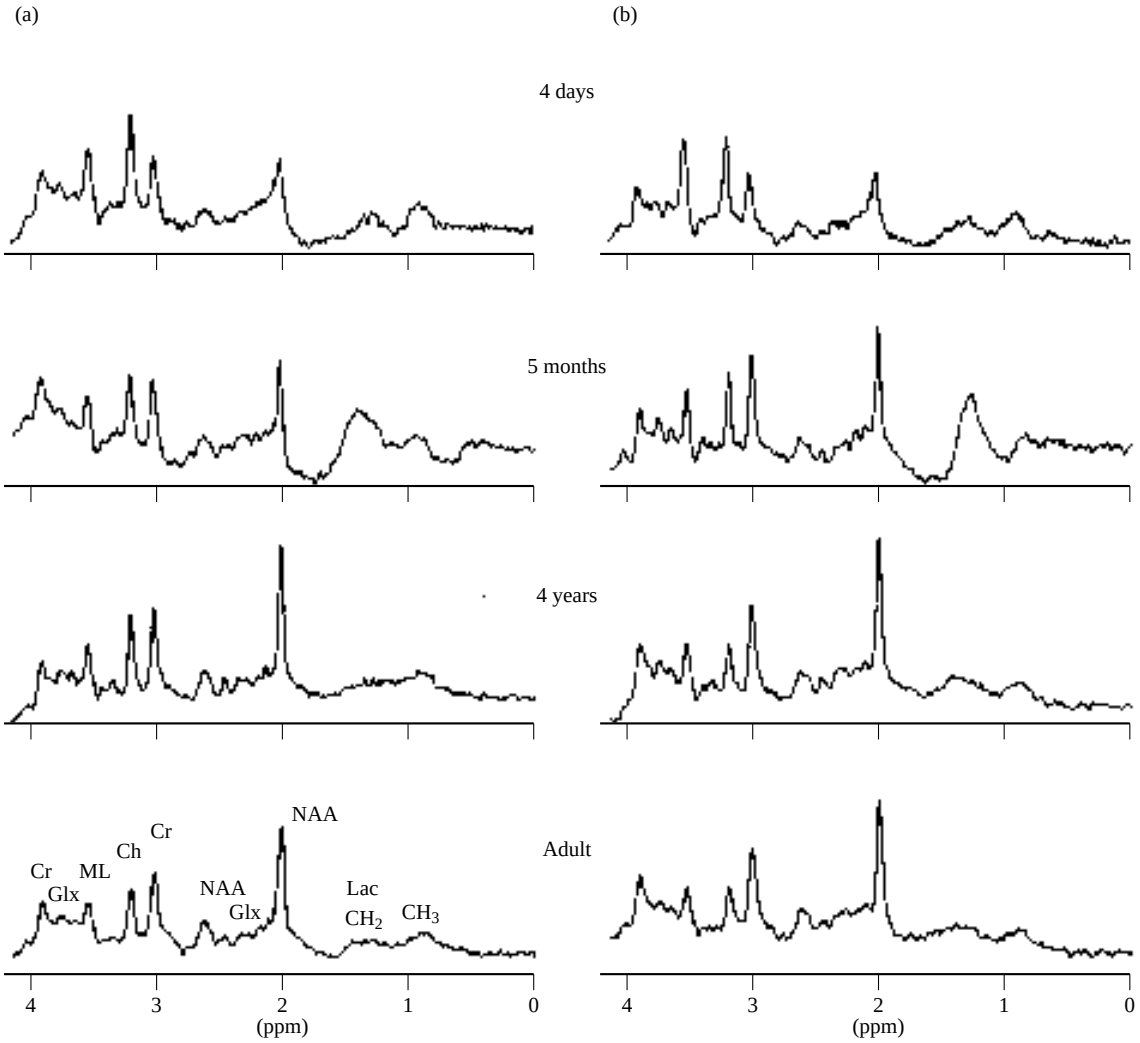

Figure 6 ^{1}H STEAM spectra obtained from (a) the parietooccipital cortex (predominantly white matter) and (b) the midline occipital cortex (mostly gray matter) of human brain at the ages of 4 days, 5 months, 4 years and from an adult. Amplitude scales have been adjusted so that absolute differences depending on both development and location can be visualized directly. Acquisition conditions: *TR* 2.87 s; mixing time (*TM*) 13 ms; *TE* 272 ms. Peak assignments: Ch, choline containing compounds; Cr, creatine + phosphocreatine; NAA, *N*-acetylaspartate; Glx, glutamate and glutamine; MI, myoinositol; Lac, lactate; CH_2/CH_3, lipid. (Reproduced by permission of Williams and Wilkins from R. Kreis, T. Ernst, and B. D. Ross, *Magn. Reson. Med.*, 1993, **30**, 424)

the brain returned to normal. The subsequent changes in ^{31}P spectra have been attributed to a 'secondary' impairment or failure of energy generation set off by the primary phase or events associated with it.[41] Studies using near-infrared spectroscopy (NIRS) in infants developing secondary energy failure have shown that both cerebral blood flow and blood volume are increased; continuing inadequate oxygen or substrate supply is therefore not likely to be causal.

Many mechanisms have been suggested to account for the progression from primary to secondary energy failure, which is associated with delayed neuronal death. For example, one possibility is that excitatory neurotransmitters, particularly glutamate, which are released at the synapses in response to acute hypoxia ischemia may, by stimulating *N*-methyl-D-aspartate (NMDA) and other receptors, cause massive calcium entry to cells and damage to the mitochondrial electron transport chain. Other possible mechanisms include those involving prostanoids, nitric oxide, free radicals, immune mechanisms, phagocytes, growth factors, and impaired protein synthesis. Because of the relation between secondary energy failure and long-term prognosis, much effort is being made to explore the mechanisms involved and how to interrupt them, with a view to the cerebroprotective treatment of asphyxiated infants. The same mechanisms are likely to be involved in stroke in adults.

Some evidence is emerging from animal studies of the feasibility of cerebroprotection. The development of secondary energy failure has been modeled in the newborn piglet, giving ^{31}P MRS results closely resembling those seen in birth-asphyxiated human infants.[42] This model is suitable

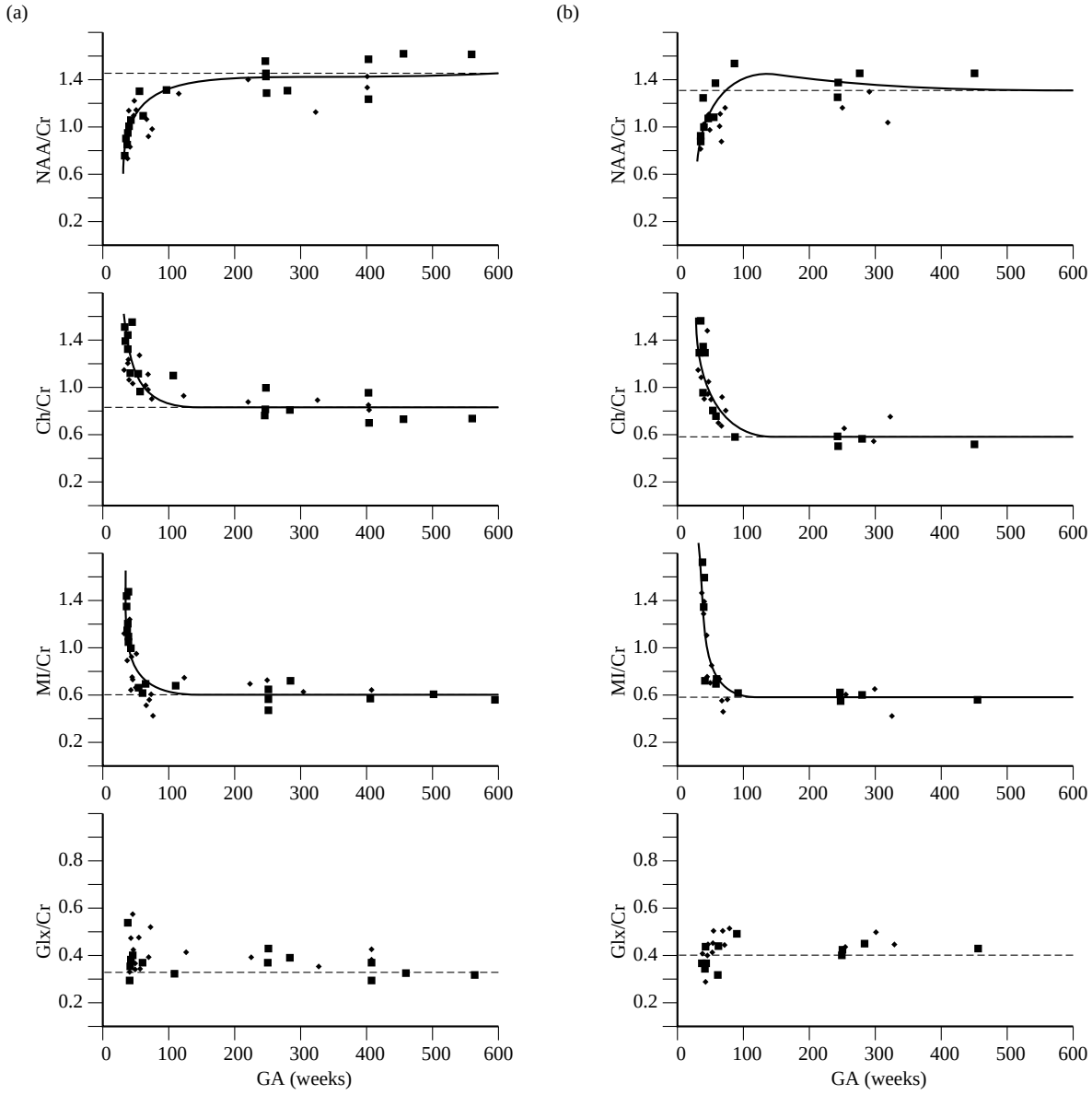

Figure 7 Relations between gestational age (GA) and cerebral peak-amplitude ratios at the same anatomical locations as in Figure 6. Acquisition conditions and resonance identifications are as in Figure 6. Cho/Cr and MI have been fitted to a monoexponential function, whereas the NAA/Cr fit is biexponential. (Reproduced by permission of Williams and Wilkins from R. Kreis, T. Ernst, and B. D. Ross, *Magn. Reson. Med.*, 1993, **30**, 424)

for testing clinically feasible cerebroprotective strategies, with the amelioration of secondary energy failure, as measured by ^{31}P and ^{1}H MRS, providing an initial end-point. Recently, mild hypothermia, applied after a severe cerebral hypoxic–ischemic insult, was shown to be markedly cerebroprotective in this model,[43] whereas intravenous magnesium sulfate was ineffective.[44]

^{1}H MRS studies of infants with hypoxic-ischemia brain injury[36,45,46] show that increased Lac (due to failure of oxidative phosphorylation and consequent anerobic glycolysis), and occasionally also reduced NAA (due to neuronal death), may be detected (see Figure 10). The Lac/NAA peak area ratio is often high and this index may prove a sensitive marker of cerebral injury. Reduced [NAA] has also been seen in newborn infants with a variety of nonfocal pathologies,[19] and in children with generalized demyelination.[47] Abnormal ^{1}H spectra have been found in older children with a variety of inborn errors of metabolism, including increased NAA in Canavan's disease (see Figure 11), and increased Lac in Leigh, Schilder, and Cockayne disease, and also in neuroaxonal dystrophy.[47]

5.2 Prognosis

The prognostic significance of secondary energy failure has been investigated by Azzopardi et al.[40] They studied 61 infants recruited because of evidence or suspicion of hypoxic

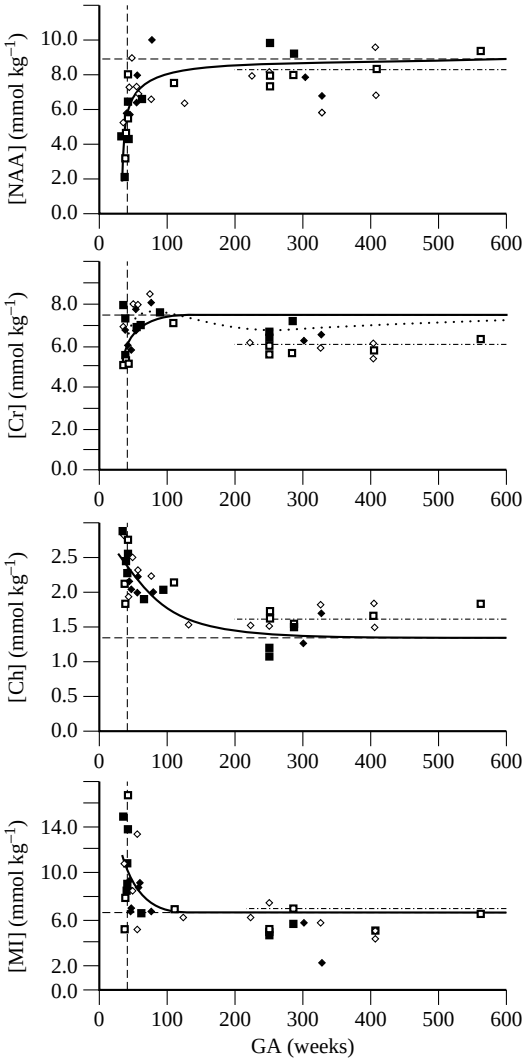

Figure 8 Absolute concentrations (mmol/kg brain tissue) of the main cerebral metabolites detectable by in vivo ^{1}H MRS. Unfilled symbols are data from parietal white matter [location (a) in Figure 6]; filled symbols are data from occipital gray matter [location (b) in Figure 6]. (□, ■) Data points from both normal infants and subjects with no primary cerebral pathology; (◇, ◆) data points from infants with essentially normal neurological status for whom the eventual diagnosis was considered immaterial to the cerebral metabolite profile. The solid lines are best fits to the data; biexponential for [NAA] and monoexponential for [Cr], [Cho], and [MI]. (The dotted curve in the [Cr] plot is triexponential and appears to fit the data better.) The vertical dashed lines indicate term at 40.5 weeks gestational age. The horizontal dashed lines show the mean adult values measured at location (a) in Figure 6. (Reproduced by permission of Williams and Wilkins from R. Kreis, T. Ernst, and B. D. Ross, *Magn. Reson. Med.*, 1993, **30**, 424)

ischemic brain injury, many of whom had sustained birth asphyxia. Clear evidence was found that the chances of survival and the severity of neurodevelopmental impairments at 1 year of age were directly related to the maximum detected extent of energy failure during the first days of life, quantified as the minimum observed value for [PCr]/[Pi] (see Table 2 and Figure 12). Furthermore, if [NTP]/[P_{tot}] fell, death was almost inevitable.

As a continuation of the same study, Roth et al.[48] recruited a further group of birth-asphyxiated infants, so that data from a total of 52 such infants were available for analysis. These infants had been in very poor condition at birth; their mean arterial base excess in cord blood shortly after delivery was -20 mmol L^{-1}, 38 had fits, and 26 required mechanical ventilation. The relation between minimum recorded [PCr]/[Pi] in the first days of life and neurodevelopmental outcome is illustrated in Figure 13. These data extend those of Azzopardi et al. and confirm the bad prognosis of secondary energy failure. The sensitivity, specificity and positive predictive value for death or multiple disabling impairments of values of [PCr]/[Pi] more than 2 SD below normal were 72%, 92%, and 91%, respectively. Roth et al. also found a relationship between minimum observed [PCr]/[Pi] and head growth. Although the infants had normal head circumferences at birth, head growth was slowest, leading to microcephaly, in those whose values for [PCr]/[Pi] fell the most. Further follow-up indicated that the severities of adverse outcomes at age 4 years were also closely related to the extent of cerebral energy impairment in the first week of life.[49]

The results of these studies may be summed up as showing that secondary energy failure leads both to neurodevelopmental disabilities and to microcephaly. The worse the energy failure, the worse the outcome is likely to be.

^{31}P spectra from the brains of infants with increased echo densities on ultrasound scans are also often abnormal, showing reduced values for [PCr]/[Pi] and sometimes [NTP]/[P_{tot}] (see Table 2).[40,50] Such echo densities are usually due to hypoxic ischemic injury or to hemorrhage. ^{31}P spectroscopy can be useful for segregating infants whose echo densities carry a relatively good, from those implying a bad, prognosis.

Data are becoming available which indicate that abnormal ^{1}H spectra also imply a bad prognosis.[36,45] Observation of raised Lac and of reduced NAA appear predictive of an unfavorable outcome. Further investigations, including long-term follow-up, are required before definitive statements can be made.

6 CONCLUSIONS

The first in vivo MRS studies of the human brain were in newborn infants. Since these studies were carried out, investigations of older children and adults have been undertaken and developmental changes have been defined for ^{31}P and ^{1}H metabolites. For example, [PCr]/[Pi] rises with age, indicating increased phosphorylation potential, and [PME]/[PDE] falls. ^{31}P MRS has proved particularly useful for investigating the cerebral metabolic consequences of severe birth-asphyxia. Spectra are often normal shortly after birth, but then [PCr]/[Pi] and, in severe cases, [NTP]/[P_{tot}] gradually falls, reaching minimum values at 2–4 days of age. The extent of the falls in [PCr]/[Pi] and [NTP]/[P_{tot}] are strongly related to the likelihood of long-term neurodevelopmental impairments or death. These changes in ^{31}P metabolite concentrations have been termed 'secondary' cerebral energy failure, on the hypothesis that they were initiated by an episode of 'primary' energy failure taking

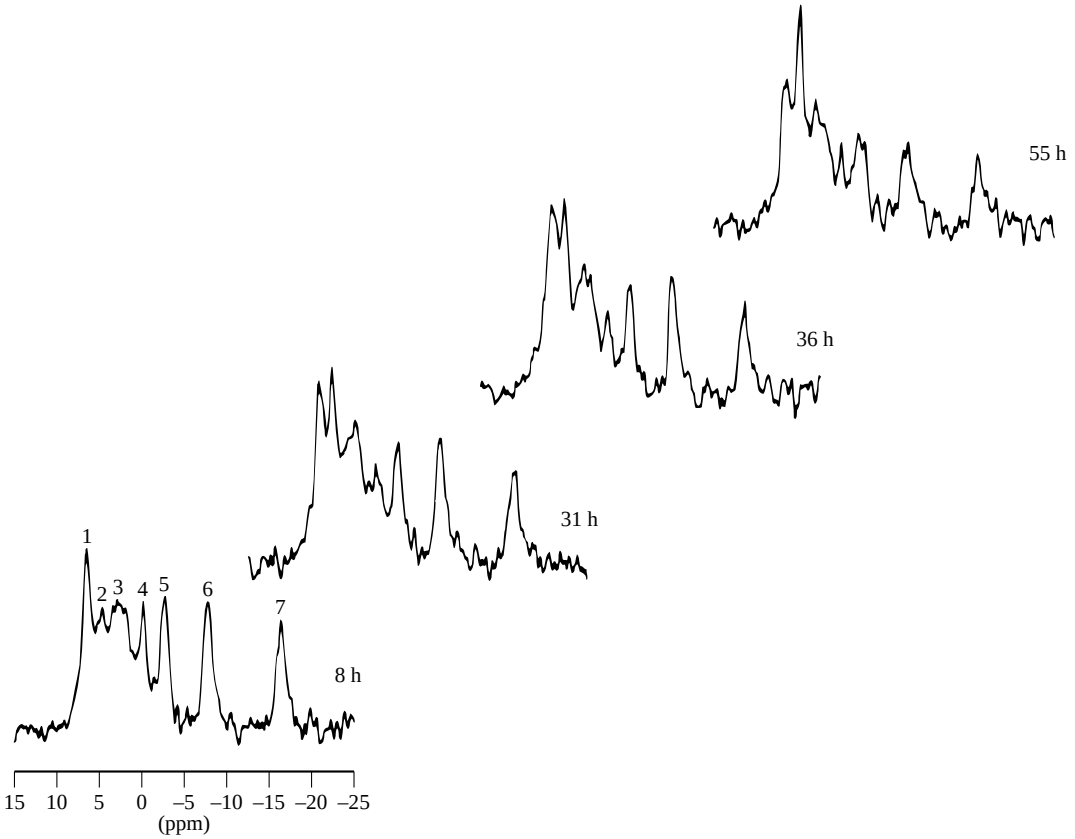

Figure 9 ^{31}P spectra from the temporo-parietal cortex of a birth-asphyxiated infant born at 37 weeks gestation. The postnatal ages at the times of study are given. Peak assignments are as in Figure 1. At age 8 h, [PCr]/[Pi] was 0.99, [NTP]/[P_{tot}] was 0.09 and pH_i was 7.06; pH_i increased to a maximum of 7.28 at 36 h. The minimum [PCr]/[Pi] was 0.32 at 55 h, when [NTP]/[P_{tot}] was 0.04 and pH_i was 6.99. The infant died aged 60 h. (Reproduced by permission of International Pediatric Research Foundation Inc. from D. Azzopardi, J. S. Wyatt, E. B. Cady, D. T. Delpy, J. Baudin, A. L. Stewart, P. L. Hope, P. A. Hamilton, and E. O. R. Reynolds, *Pediatr. Res.*, 1989, **25**, 445)

Table 2 Age-dependent Standard Deviation Scores (SDS) for Phosphorus Metabolite Concentration Ratios and pH_i in the temporo-parietal cortex of Newborn Infants Suspected of Hypoxic–ischemic Brain Injury[a]

	All infants (n = 61)	Birth asphyxia (n = 40)	Postnatal asphyxia (n = 5)	Increased cerebral echodensities (n = 16)
PCr/Pi	−2.14 ± 2.10[b]	−2.14 ± 2.19[b]	−0.03 ± 0.76	−2.04 ± 1.78[b]
NTP/P_{tot}	−0.98 ± 1.86[c]	−1.17 ± 1.82[c]	−0.01 ± 1.03	−0.83 ± 1.99
PCr/P_{tot}	−1.72 ± 2.58[b]	−1.79 ± 2.59[b]	0.33 ± 1.04	−2.19 ± 2.52[b]
Pi/P_{tot}	5.40 ± 8.77[b]	5.97 ± 8.91[b]	0.69 ± 0.99	5.51 ± 9.06[c]
PME/P_{tot}	0.42 ± 1.69	0.63 ± 1.58	−0.79 ± 1.26	0.30 ± 1.83
PDE/P_{tot}	0.44 ± 1.43	−0.60 ± 1.44[d]	0.39 ± 0.50	−0.32 ± 1.47
PCr/NTP	0.52 ± 2.98	0.65 ± 3.14	0.15 ± 0.66	0.31 ± 2.91
Pi/NTP	7.21 ± 16.41[b]	8.96 ± 17.94[b]	0.35 ± 1.06	4.94 ± 13.27[c]
PME/NTP	1.94 ± 4.40[d]	2.49 ± 4.71[c]	−0.26 ± 1.11	1.25 ± 3.72
PDE/NTP	1.02 ± 3.84	1.43 ± 4.48	0.17 ± 0.77	0.23 ± 1.81
pH_i	0.05 ± 1.47 (n = 55)	0.23 ± 0.97 (n = 36)	−0.28 ± 0.22 (n = 5)	0.00 ± 2.21 (n = 14)

[a]Values are those obtained when PCr/Pi was at its lowest. Mean values for SDS ± SD vs the normal control infants (see Table 1) are given. [b]$p < 0.001$. [c]$p < 0.01$. [d]$p < 0.05$. (Reproduced by permission of International Pediatric Research Foundation Inc. from D. Azzopardi, J. S. Wyatt, E. B. Cady, D. T. Delpy, J. Baudin, A. L. Stewart, P. L. Hope, P. A. Hamilton, and E. O. R. Reynolds, *Pediatr. Res.*, 1989, **25**, 445)

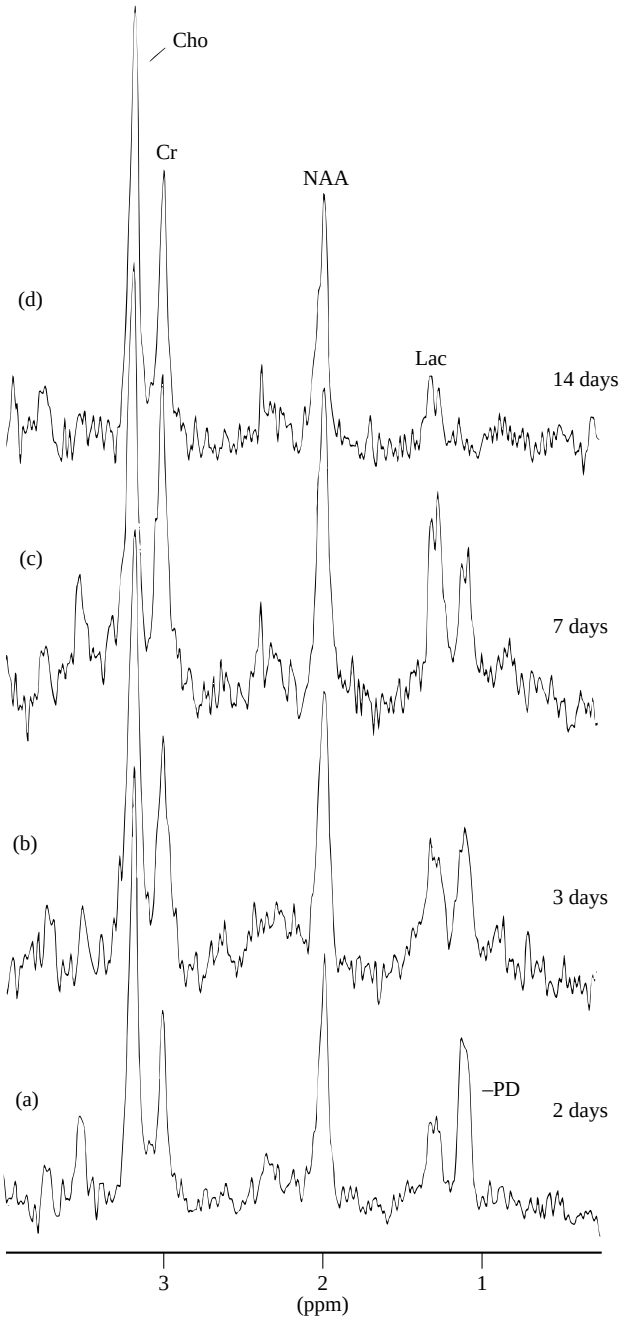

Figure 10 ^{1}H PRESS spectra acquired at 100 MHz from the thalamus of a severely birth-asphyxiated term infant. The ages at which the spectra were acquired are shown. Acquisition conditions: *TE* 270 ms; *TR* 2 s; 128 averaged echoes; 8 mL voxel. The lactate peak at about 1.3 ppm is greatly increased when compared with normal infants [see Figure 2(a)], although this may be partly due to raised free fatty acids. The peak at about 1.1 ppm is due to propan-1,2-diol (PD; the injection medium for phenobarbitone and phenytoin preparations). (Reproduced by permission of Williams and Wilkins from E. B. Cady, A. Lorek, J. Penrice, E. O. R. Reynolds, R. A. Iles, S. P. Burns, G. A. Coutts, and F. M. Cowan, *Magn. Reson. Med.*, 1994, **32**, 764)

place shortly before or during delivery. The prognostic information acquired by ^{31}P MRS is valuable for guiding the clinical care of infants suspected of hypoxic ischemic brain injury. In the future, the prevention of secondary energy failure, as measured by MRS, may be used to test the efficacy of cerebroprotective strategies. ^{1}H spectroscopy has demonstrated increased Lac/NAA peak area ratios in the brains of asphyxiated infants and this may also have prognostic significance.

Recent technological developments will enhance the value of MRS to clinical pediatrics. Five major areas have potential for immediate improvement: the development of special neonatal head probes to increase the signal-to-noise ratio; optimized acquisition methods to enhance the quality and variety of spectroscopic information; spectroscopic quantification; and spectral editing to detect resonances that would otherwise be difficult to resolve. Spectroscopic imaging for metabolite

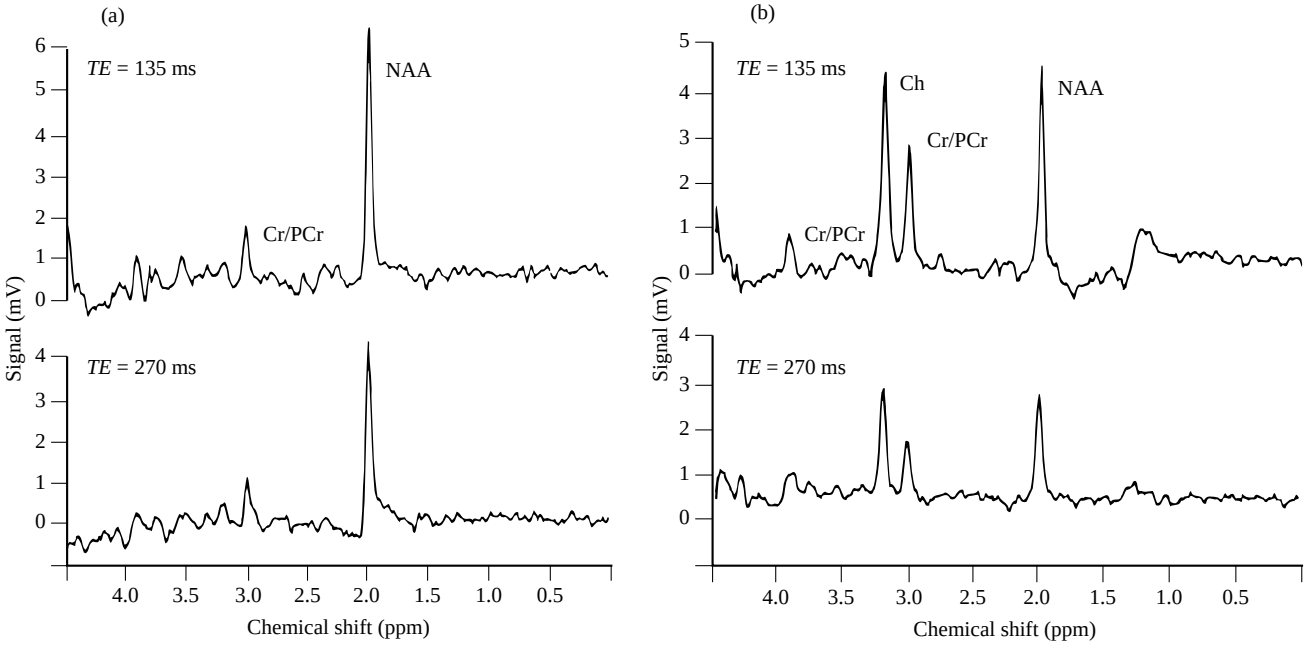

Figure 11 ^{1}H PRESS spectra from occipital voxels in the brain of a 7-month-old child with Canavan disease (a) and in that of an age-matched, normal control (b). Spectrum (a) shows increased *N*-acetylaspartate (NAA) signal, and the resonance from choline-containing compounds (Cho) is almost undetectable. Canavan disease has been linked with high body fluid levels of NAA caused by aspartoacylase deficiency. The disease also affects myelin sheaths due to a defect of myelin formation and/or glial metabolism, and this may be the reason for the low Cho signal. (Reproduced by permission of The Radiological Society of North America from W. Grodd, I. Krageloh-Mann, U. Klose, and R. Sauter, *Radiology*, 1991, **181**, 173)

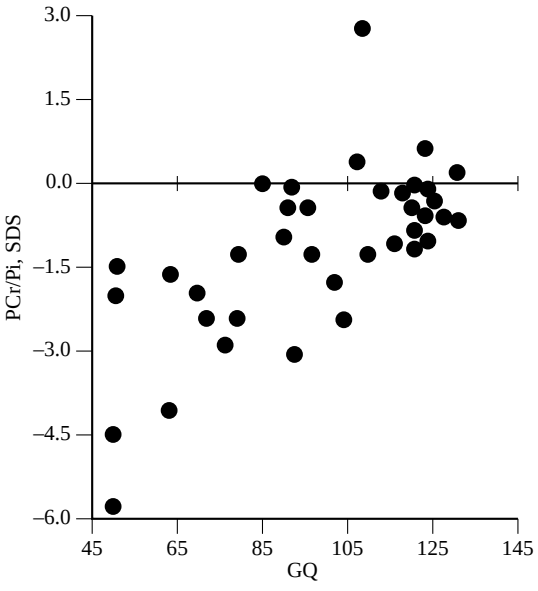

Figure 12 The relationship between minimum observed PCr/Pi in the temporo-parietal cortex expressed as standard deviation score (SDS) vs normal infants and the Griffiths general quotient (GQ) assessed at age 1 year in 38 infants surviving after hypoxic ischemic brain injury. Scores below 50 are recorded as 50 ($r = 0.67$, $p < 0.001$). (Reproduced by permission of International Pediatric Research Foundation Inc. from D. Azzopardi, J. S. Wyatt, E. B. Cady, D. T. Delpy, J. Baudin, A. L. Stewart, P. L. Hope, P. A. Hamilton, and E. O. R. Reynolds, *Pediatr. Res.*, 1989, **25**, 445)

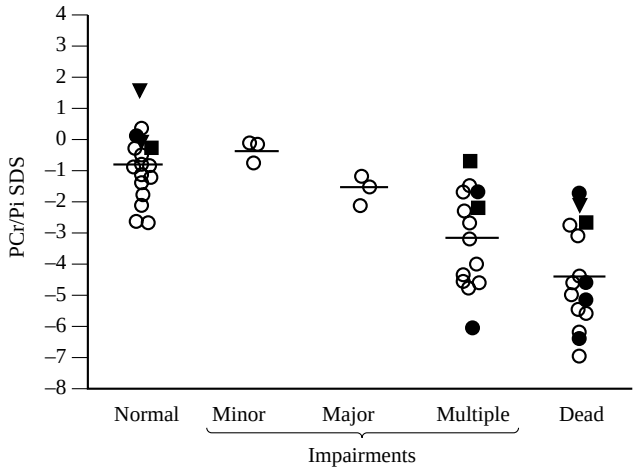

Figure 13 Minimum observed age-related PCr/Pi standard deviation score (SDS) in the temporo-parietal cortex of birth-asphyxiated newborn infants and neurodevelopmental outcome at age 1 year: (○) term AGA infants; (●) term SGA infants; (▼) preterm AGA infants; (■) preterm SEA infants. (Reproduced by permission of Mac Keith Press from S. C. Roth, D. Azzopardi, A. D. Edwards, J. Baudin, E. B. Cady, J. Townsend, D. T. Delpy, A. L. Stewart, J. S. Wyatt, and E. O. R. Reynolds, *Dev. Med. Child Neurol.*, 1992, **34**, 285)

mapping and direct comparison of MRI and spatial MRS data should help to improve the quality of the information available and further develop MRS as an acceptable and valuable clinical tool.

7 RELATED ARTICLES

Brain Infection and Degenerative Disease Studied by Proton MRS; Brain MRS of Human Subjects; Localization and Registration Issues Important for Serial MRS Studies of Focal Brain Lesions; MRI in Clinical Medicine; Patient Life Support and Monitoring Facilities for Whole Body MRI; Single Voxel Localized Proton NMR Spectroscopy of Human Brain In Vivo; Single Voxel Whole Body Phosphorus MRS; Tissue and Cell Extracts MRS.

8 REFERENCES

1. E. B. Cady, A. M. de L. Costello, M. J. Dawson, D. T. Delpy, P. L. Hope, E. O. R. Reynolds, P. S. Tofts, and D. R. Wilkie, *Lancet*, 1983 **i**, 1059.
2. A. L. Stewart, R. J. Thorburn, P. L. Hope, M. Goldsmith, A. P. Lipscomb, and E. O. R. Reynolds, *Arch. Dis. Child.*, 1983, **58**, 598.
3. E. B. Cady, J. Hennig, and E. Martin, in 'Imaging Techniques of the CNS of Neonates', ed. J. Haddad, D. Christmann, and J. Messer, Springer, Berlin, 1991, Chap. 6.
4. E. B. Cady, in 'Magnetic Resonance Spectroscopy in Biology and Medicine', ed. J. D. de Certaines, W. M. M. J. Bovee, and F. Podo, Pergamon, Oxford, 1992, Chap. 23.
5. E. B. Cady, C. Boesch, and E. Martin, in 'Perinatal Asphyxia', ed. J. Haddad and E. Saliba, Springer, Berlin, 1993, Chap. 13.
6. A review of this early in vivo work is given in: E. B. Cady, 'Clinical Magnetic Resonance Spectroscopy', Plenum, New York, 1990.
7. D. P. Younkin, M. Delivoria-Papadopoulos, J. C. Leonard, V. H. Subramanian, S. Eleff, J. S. Leigh, and B. Chance, *Ann. Neurol.*, 1984, **16**, 581.
8. Department of Health (United Kingdom), 'Guidelines for Magnetic Resonance Diagnostic Equipment in Clinical Use', HMSO, Norwich, 1993.
9. A. Chu, D. T. Delpy, and S. Thalayasingam, in 'Fetal and Neonatal Physiological Measurements', ed. P. Rolfe, Butterworths, London, 1986, Chap. 59.
10. C. Boesch and E. Martin, *Radiology*, 1988, **168**, 481.
11. F. G. Shellock and G. L. Slimp, *Am. J. Roentgenol.*, 1989, **153**, 1105.
12. R. J. Ordidge, A. Connelly, and J. A. B. Lohman, *J. Magn. Reson.*, 1986, **66**, 283.
13. M. S. Van der Knaap, J. van der Grond, P. C. van Rijen, J. A. J. Faber, J. Valk, and K. Willemse, *Radiology*, 1990, **176**, 509.
14. R. Gruetter, C. Boesch, M. Muri, E. Martin, and K. Wuthrich, *Magn. Reson. Med.*, 1990, **15**, 128.
15. C. T. W. Moonen, M. von Kienlin, P. C. M. van Zijl, J. Cohen, J. Gillen, P. Daly, and G. Wolf, *NMR Biomed.*, 1989, **2**, 201.
16. J. H. Duyn and C. T. W. Moonen, *Magn. Reson. Med.*, 1993, **30**, 409.
17. E. B. Cady, J. Penrice, P. N. Amess, A. Lorek, M. Wylezinska, R. F. Aldridge, F. Franconi, J. S. Wyatt, and E. O. R. Reynolds, *Magn. Reson. Med.*, 1996, **36**, 878.
18. R. Buchli, E. Martin, P. Boesiger, and H. Rumpel, *Pediatr. Res.*, 1994, **35**, 431.
19. R. Kreis, T. Ernst, and B. D. Ross, *Magn. Reson. Med.*, 1993, **30**, 424.
20. P. Christiansen, O. Henriksen, M. Stubgaard, P. Gideon, and H. B. W. Larsson, *Magn. Reson. Imaging*, 1993, **11**, 107.
21. A. G. Chapman, E. Westerberg, and B. K. Siesjö, *J. Neurochem.*, 1981, **36**, 179.
22. T. Glonek, S. J. Kopp, E. Kot, J. W. Pettegrew, W. H. Harrison, and M. M. Cohen, *J. Neurochem.*, 1982, **39**, 1210.
23. O. A. C. Petroff, J. W. Prichard, K. L. Behar, J. R. Alger, J. A. den Hollander, and R. G. Shulman, *Neurology*, 1985, **35**, 781.
24. R. C. Robbins, R. S. Balaban, and J. A. Swain, *J. Thorac. Cardiovasc. Surg.*, 1990, **99**, 878.
25. P. B. Garlick, S. Soboll, and G. R. Bullock, *NMR Biomed.*, 1992, **5**, 29.
26. J. W. Pettegrew, S. J. Kopp, J. Dadok, N. J. Minshew, J. M. Feliksik, T. Glonek, and M. M. Cohen, *J. Magn. Reson.*, 1986, **67**, 443.
27. S. Cerdan, R. Parrilla, J. Santoro, and M. Rico, *FEBS Lett.*, 1985, **187**, 167.
28. Reviews of biochemical aspects of the resonances seen in ^{1}H brain spectra are given, in: B. L. Miller and B. D. Ross, *NMR. Biomed.*, 1991, **4**, 47, 59.
29. J. Urenjak, S. R. Williams, D. G. Gadian, and M. Noble, *J. Neurosci.*, 1993, **13**, 981.
30. D. Azzopardi, J. S. Wyatt, P. A. Hamilton, E. B. Cady, D. T. Delpy, P. L. Hope, and E. O. R. Reynolds, *Pediatr. Res.*, 1989, **25**, 440.
31. P. Tofts and S. Wray, *J. Physiol. (London)*, 1985, **359**, 417.
32. P. L. Hope, E. B. Cady, A. Chu, D. T. Delpy, R. M. Gardiner, and E. O. R. Reynolds, *J. Neurochem.*, 1987, **49**, 75.
33. H. C. Agrawal and W. A. Himwich, in 'Developmental Neurobiology', ed. W. A. Himwich, C. C. Thomas, Springfield, IL, 1970, Chap. 9.
34. N. Okumura, S. Otsuki, and A. Kameyama, *J. Biochem.*, 1960, **47**, 315.
35. W.-I. Jung, S. Widmaier, M. Bunse, U. Seeger, K. Straubinger, F. Schick, K. Kuper, G. Dietze, and O. Lutz, *Magn. Reson. Med.*, 1993, **30**, 741.
36. J. Penrice, E. B. Cady, A. Lorek, M. Wylezinska, P. N. Amess, R. F. Aldridge, A. L. Stewart, J. S. Wyatt, and E. O. R. Reynolds, *Pediatr. Res.*, 1996, **40**, 6.
37. P. S. Huppi, S. Posse, F. Lazeyras, R. Burri, E. Bossi, and N. Herschkowitz, *Pediatr. Res.*, 1991, **30**, 574.
38. H. H. Tallan, *J. Biol. Chem.*, 1957, **223**, 41.
39. B. K. Siesjö, 'Brain Energy Metabolism', Wiley, New York, 1978.
40. D. Azzopardi, J. S. Wyatt, E. B. Cady, D. T. Delpy, J. Baudin, A. L. Stewart, P. L. Hope, P. A. Hamilton, and E. O. R. Reynolds, *Pediatr. Res.*, 1989, **25**, 445.
41. P. L. Hope, A. M. de L. Costello, E. B. Cady, D. T. Delpy, P. S. Tofts, A. Chu, P. A. Hamilton, E. O. R. Reynolds, and D. R. Wilkie, *Lancet*, 1984, **ii**, 366.
42. A. Lorek, Y. Takei, E. B. Cady, J. S. Wyatt, J. Penrice, A. D. Edwards, D. Peebles, M. Wylezinska, H. Owen-Reece, V. Kirkbride, C. Cooper, R. F. Aldridge, S. C. Roth, G. Brown, D. T. Delpy, and E. O. R. Reynolds, *Pediatr. Res.*, 1994, **36**, 699.
43. M. Thoresen, J. Penrice, A. Lorek, E. B. Cady, M. Wylezinska, V. Kirkbride, C. E. Cooper, G. C. Brown, A. D. Edwards, J. S. Wyatt, and E. O. R. Reynolds, *Pediatr. Res*, 1995, **37**, 667.
44. J. Penrice, P. N. Amess, S. Punwani, M. Wylezinska, L. Tyszczuk, P. D'Souza, A. D. Edwards, E. B. Cady, J. S. Wyatt, and E. O. R. Reynolds, *Pediatr. Res.*, 1997, **41**, 1.
45. E. B. Cady, *Neurochem. Res.*, 1966, **21**, 1043.
46. E. B. Cady, P. Amess, J. Penrice, M. Wylezinska, V. Sams, and J. S. Wyatt, *Magn. Reson. Imaging*, 1997, **15**, 605.
47. W. Grodd, I. Krageloh-Mann, U. Klose, and R. Sauter, *Radiology*, 1991, **181**, 173.

48. S. C. Roth, A. D. Edwards, E. B. Cady, D. T. Delpy, J. S. Wyatt, D. Azzopardi, J. Baudin, J. Townsend, A. L. Stewart, and E. O. R. Reynolds, *Dev. Med. Child Neurol.*, 1992, **34**, 285.
49. S. Roth, J. Baudin, E. B. Cady, K. Johal, J. Townsend, J. S. Wyatt, E. O. R. Reynolds, and A. L. Stewart, *Dev. Med. Child Neurol.*, 1997, **39**, 718.
50. P. A. Hamilton, P. L. Hope, E. B. Cady, D. T. Delpy, J. S. Wyatt, and E. O. R. Reynolds, *Lancet*, 1986, **i**, 1242.

Biographical Sketches

Ernest B. Cady. *b* 1952. B.Sc. (astronomy), University College London, 1973; Dip. Adv. Sc. Studies (radio astronomy), Manchester University, 1974. Introduced to NMR by Prof. D. R. Wilkie FRS. Medical Physicist, University College London Hospitals, 1978–present. Approx. 100 publications, including the book *Clinical Magnetic Resonance Spectroscopy*. Research interests: probe design, data analysis, absolute quantification, and neonatal brain metabolism.

E. Osmund R. Reynolds. *b* 1933. B.Sc. (physiology), 1955, M.B., B.S., 1958, M.D., 1965, London University; M.R.C.P., 1966, F.R.C.P., 1975, F.R.C.O.G. (*ad eundem*), 1983; F.R.S., 1993; C.B.E., 1995; Hon. F.R.C.P.C.H., 1997; Professor of Neonatal Pediatrics, University College London Medical School, 1976–96 (emeritus). Approx. 300 publications. Research interests: noninvasive investigation of perinatal brain injury, in particular employing ultrasound imaging, NMR spectroscopy, and near-infrared spectroscopy.

Central Nervous System Degenerative Disease Observed by MRI

Frank J. Lexa

Leonard Davis Institute of Health Economics, University of Pennsylvania, Philadelphia, PA, USA

1 INTRODUCTION

The degenerative diseases encompass some of the most interesting and important pathological entities in clinical medicine. In the past decade, MR imaging (MRI) has emerged as the premier radiological method for examining the brain and spinal cord. MRI has many advantages over computerized tomography (CT) for the detection of subtle changes in white and gray matter structures. This has led to the ability finally to detect and characterize some of these diseases early in their course without resorting to invasive techniques. This section will discuss the use of MRI to detect and characterize neural degeneration, beginning with the general case of the processes of Wallerian degeneration, which are common to many types of brain injury, and then move on to discuss the salient clinical and imaging features of the most important and best characterized of the neurodegenerative disorders. In the interest of brevity, only the most important clinical and imaging facets of the diseases will be covered. The reader is referred to two standard texts which are able to provide a more comprehensive discussion and bibliography.[1,2]

2 WALLERIAN DEGENERATION: THE NEURONAL REACTION TO INJURY

Waller is credited for making the first histological description of the series of events which occur in the distal axonal segment following a proximal injury.[3–5] This can occur after a wide variety of insults to the brain or spinal cord and thus represents an important marker of significant central nervous system (CNS) damage. The earliest phase is cessation of axonal transport, and collapse of the axonal segment.[6] The myelin begins to fragment, and the Schmidt–Lanterman incisures open up. This is followed by reaction of the surrounding tissue with cellular proliferation and edema, during which the myelin is chemically degraded and removed. This eventually leads to formation of a gliotic scar.

Until the advent of MRI, it was difficult or impossible to detect degeneration of axonal pathways using antemortem imaging techniques. CT is usually only capable of detecting significant volume loss in end-stage cases. Early reports of the MRI appearance of Wallerian degeneration described T_1 and T_2 prolongation along corticofugal pathways in patients with acquired lesions such as strokes and Schilder's disease.[7–13] In these reports, the lesions were at least several months old when they had these signal characteristics, although these changes have been reported to be observable earlier.[14] Observations from the first month were reported in which no abnormality could be detected.[15] High signal intensity in the dentatorubral–thalamic tract has been reported after dentate nucleus resection.[16]

Other reports described a more complex pattern with no detectable signal changes in approximately the first month, a transient period of hypointensity on long *TR* images at approximately 1 month, followed by normalization of that hypointensity and later development of the more familiar T_1 and T_2 prolongation effects at approximately the 3–4 month mark.[17–18] Recent work suggests that fast spin echo (FSE) imaging shows this early hypointense phase of Wallerian degeneration more conspicuously than conventional proton density imaging.[19] In clinical medicine, this has important implications for the diagnosis and treatment of brain injury.

Animal models have been used to address the controversies raised by the above studies. Magnetic resonance spectroscopy of peripheral nerves showed significant increases in T_1 and T_2 relaxation times 15 days after sectioning the sciatic nerve.[20] Imaging of the tibial nerve confirmed that the T_2 signal intensity was elevated on long *TR/TE* images at day 15 in a crush injury model.[21] Histological confirmation of Wallerian degeneration was obtained in a feline model of radiation injury. These areas showed high signal intensity on long *TR/TE* images over 200 days after radiation injury.[22]

Newer techniques utilizing magnetization transfer techniques appear very promising for the early detection and separation of some of these changes. Using a cortical ablation model, Lexa et al. were able to demonstrate changes as early as the first week after injury (Figure 1).[23] Magnetization transfer images detected degenerating tracts at a distance from the primary injury site before conventional spin echo images or even routine light microscopy showed significant evidence of injury. Electron microscopy confirmed that the first phase of Wallerian degeneration was underway (Figure 2). Myelin degeneration and cellular degeneration were not detectable by light-microscopic techniques until significantly later. Moreover, the biphasic nature of the early changes in magnetization transfer suggests that it may be possible to separate some of the processes occurring in early axonal injury with magnetization transfer (Figure 3).

3 DEGENERATIVE DEMENTING ILLNESSES: ALZHEIMER'S AND PICK'S DISEASES

Alzheimer's disease is both the commonest cause of dementing illness as well as one of the most common causes of death in the industrialized countries. Both pathological and radiological studies demonstrate extensive atrophy, particularly of the hippocampus.[24,25]

Pick's disease is a much rarer dementing illness with similar cognitive deficits to Alzheimer's disease; however, abnormal behaviors, apathy, abulia, and the Klüver–Bucy syndrome are more common.[26] The disease appears to be transmitted in a dominant, although modified, fashion, and is more common in females.

Neuroradiological studies and gross pathology show findings of marked atrophy affecting the frontal and anterior

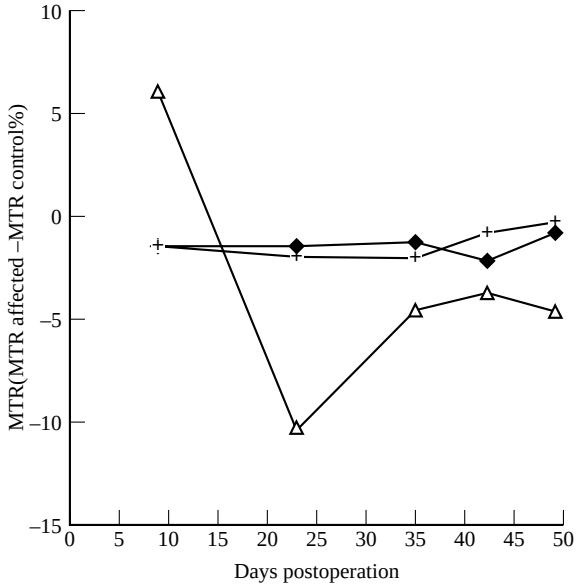

Figure 1 Demonstration of changes in magnetization transfer in a feline model of Wallerian degeneration at 1.5 T. The *x* axis shows the number of days postplacement of a cortical lesion. The *y* axis shows the change in the magnetization transfer ratio (MTR) of the affected side relative to a control in three structures: the degenerating superolateral white matter (△), remote white matter (◆), and the ipsilateral lateral geniculate nucleus (+). The ipsilateral white matter tracts show an early rise and later fall in magnetization transfer as early degeneration progresses. (Reproduced by permission of The American Society of Neuroradiology from Lexa et al.[23])

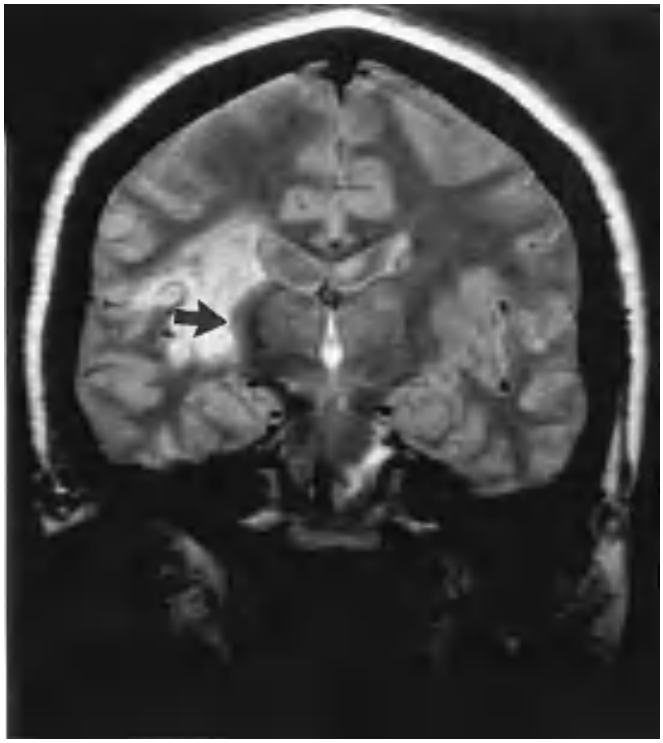

Figure 3 Long *TR* FSE images in a woman 4 weeks after a middle cerebral artery stroke showing evidence of Wallerian degeneration in the ipsilateral corticospinal tract with marked signal loss (arrow) relative to the unaffected side

temporal lobes with relative sparing of the parietal lobes and sparing of the posterior portion of the superior temporal gyrus and the occipital regions.[26] Alzheimer's disease appears to have associations with other degenerative diseases of the CNS–most notably Parkinson's disease (see below). In some reports, close to half of those patients with Alzheimer's disease have evidence of the degenerative changes associated with Parkinson's disease.[27,28]

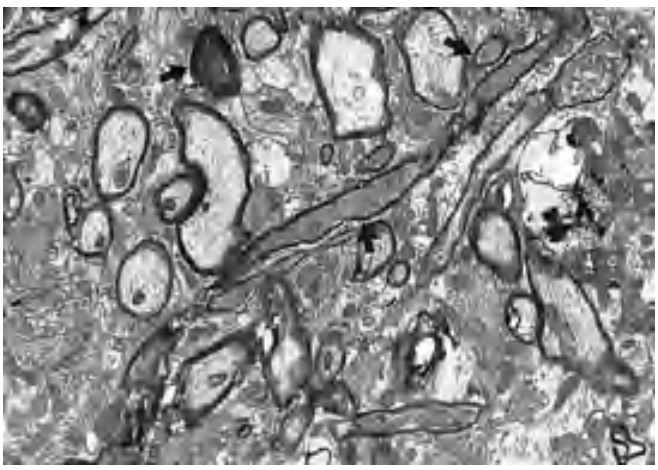

Figure 2 Electron micrograph of white matter immediately superior to the lateral geniculate nucleus 8 days after ablation of the cortical sites of visual processing. Arrows mark examples of early degeneration with axonal collapse and increased cytoplasmic staining. (Reproduced by permission of The American Society of Neuroradiology from Lexa et al.[23])

4 NORMAL PRESSURE HYDROCEPHALUS

Hydrocephalus can occur secondary to a wide variety of etiologies. This discussion will be limited to the 'degenerative' form of normal pressure hydrocephalus (NPH).

The syndrome of NPH is seen predominately in older patients, and includes a triad of clinical findings—dementia, gait ataxia, and urinary incontinence. The underlying mechanism which leads to NPH is controversial and includes theories related to diminished absorption from prior hemorrhage or inflammatory disease, changes in the physical properties of the ventricular walls, or, rarely, a preexisting congenital form of hydrocephalus. Patients may respond to shunting, and favorable factors include response to a preliminary trial of cerebrospinal fluid removal, presentation with gait disturbance, and short duration of symptoms.[29] NPH and white matter ischemic disease appear to be significantly related, including a direct correlation of the severity of the diseases.[30]

On cross-sectional imaging techniques, NPH may overlap significantly in appearance with other diseases in this age group. In particular, the overlap with atrophy from other causes is problematic. The most useful features are those found in

other forms of hydrocephalus: thinning and elevation of the corpus callosum, and distention of the third ventricle.[31]

MRI may provide an additional clue by allowing detection and quantification of flow in the cerebral aqueduct. The magnitude of flow in this structure is increased in the setting of NPH, and is probably secondary to the diminished compliance of the ventricular system.[32]

5 DEGENERATION OF THE CENTRAL GRAY MATTER STRUCTURES

5.1 Huntington's Chorea

Huntington's chorea is an autosomal dominant degenerative disease which has been localized to chromosome 4.[33] Presentation is in the fourth and fifth decades, with choreathetosis and dementia. Neuroradiological studies confirm characteristic atrophy of the caudate and putamen as well as more generalized atrophy.[34] On MRI, abnormal signal intensity on long *TR*/*TE* images may be present in the striatum.

In addition to reductions in the caudate and putamen, detailed volumetric studies show volume loss in the thalamus and mesial temporal lobes.[35] In mildly affected individuals, the putaminal measurement appears to be sensitive and specific.[36]

5.2 Wilson's Disease (Hepatolenticular Degeneration)

Wilson's disease is a genetic deficiency of ceruloplasmin, which leads to toxic copper deposition particularly in the liver and the lenticular nuclei of the brain. It is an autosomal recessive disorder which localizes to chromosome 13.[37] Clinical manifestations include liver disease, movement disorders of tremor, ataxia, dysarthria and rigidity, and psychiatric symptoms. The Kayser–Flesicher ring of copper deposition in Descemet's membrane is characteristic, while the definitive diagnosis is made by low serum ceruloplasmin, increased urinary copper, and elevated liver copper levels.

Atrophy, particularly of the gray matter, is a hallmark of Wilson's disease. Focal white matter lesions may occur which are hypointense on short *TR*, but of variable intensity on long *TR*.[38] These lesions appear to have a reversible component during appropriate therapy.[38–40] Clinical neurological symptoms appear to correlate with the presence of radiological abnormalities. The location of lesions can be useful in predicting the type of neurological manifestation.[41]

5.3 Parkinson's Disease

Parkinson's syndrome, or Parkinsonism, is a broad clinical term referring to a cluster of symptoms due to loss of the majority of the dopaminergic efferent projections of the substantia nigra. The predominant clinical symptom is an involuntary tremor with rigidity and akinesia. The syndrome can be caused by a wide variety of etiologies, including stroke, trauma, inflammatory processes (particularly an epidemic which occurred after World War I, von Economo's encephalitis, now rarely with viral illnesses such as Cocksackie B, Japanese B and St. Louis viral encephalitides), drug effects, and associations with other degenerative diseases such as progressive supranuclear palsy, striatonigral degeneration, and Parkinson's disease. The final common pathway is loss of the dopaminergic effects of these nigral projections on the striatal structures.

Parkinson's disease is a true degenerative disease of the CNS with idiopathic loss of nigral–striatal projections. This entity is common, with an age of onset in the 50–60 years range, affecting approximately 1 in 1000 of people over the age of 50 years.[27] The disease is progressive, probably due in part to ongoing loss of nigrostrial function. Early in the course of the disease, patients may respond well to a variety of medications, often with progressive resistance as the degeneration advances.

On pathological examination, there are characteristic cell inclusions called Lewy bodies in the neurons of the substantia nigra, as well as in several related regions of the brain. MRI of Parkinson's disease patients reveals a decrement in the width of the pars compacta of the substantia nigra. This finding is shared with diseases leading to Parkinsonism such as striatonigral degeneration and progressive supranuclear palsy. Atrophy of the brain is also a characteristic that Parkinson's disease shares with other degenerative disorders, although sometimes this can be of a relatively small magnitude.

5.4 Striatonigral Degeneration

This degenerative disease presents with similar symptoms to Parkinson's disease. The primary differences rest with the much greater early involvement of the striatum (the putamen more than the caudate), which may in part explain the poor response to traditional Parkinsonism pharmacotherapy. This putaminal involvement may be detected on MRI with greater than normal hypointensity of the putamen on T_2-weighted sequences. The magnitude of this finding has been reported to correlate with the severity of clinical involvement.[42] A second area of detectable involvement occurs in the substantia nigra, with loss of width of the pars compacta.

5.5 Progressive Supranuclear Palsy

Named for the presence of supranuclear ophthalmoplegia of vertical gaze, this syndrome includes manifestations of pseudobulbar palsy, rigidity, extrapyramidal signs, and dementia, presenting in late middle age and in the elderly population. This degenerative disease localizes predominantly to the midbrain. In particular, the superior colliculi are atrophic, constituting a relatively specific MRI sign of the disease. Neurofibrillary tangles can be detected in the periaqueductal gray matter of the mesencephalon with gliosis–similar to the findings in Alzheimer's disease.[43,44] Changes in this region can be seen on MRI, with high signal intensity on relatively T_2-weighted sequences.[43] As in the other degenerative diseases related to Parkinson's disease, there is diminished size of the pars compacta.

6 DEGENERATION OF THE CEREBELLUM AND BRAIN STEM

There are several degenerative diseases which have a propensity to attack the structures of the posterior fossa (Figure 4).

Figure 4 Sagittal T_1-weighted MRI scan demonstrating idiopathic vermian atrophy in a patient with marked cerebellar symptoms

6.1 Down's Syndrome

Down's syndrome is a very important cause of inherited mental retardation. Supranormal amounts of the genetic material on chromosome 21 usually from nondisjunction are the underlying cause. MRI measurements show a global reduction in both gray and white matter. Interestingly, Down's syndrome is a very important risk factor for the ultimate development of Alzheimer's disease, with close to 100% of Down's patients developing a pathology similar to Alzheimer's disease in later life. The gene for the production of the amyloid-β protein which has been linked to some of the pathology in Alzheimer's disease also maps to chromosome 21. Reports of older patients with Down's syndrome (up to 64 years old) show significant widening of the temporal horns on MRI–similar to what has been reported in patients affected by Alzheimer's disease.[45] Finally, NMR spectroscopic analysis has shown a rapid decline in *N*-acetylaspartate (NAA)/choline in older Down's patients, which correlates well with onset of clinical symptoms and precedes atrophic changes.[46]

6.2 Fragile X and Rett's Syndrome

The fragile X syndrome is a rare genetic cause of mental retardation. The syndrome is characterized by autism, repetitive movements, and hyperactive, self-destructive behaviors. The most profound expression is in males, but female carriers also show mild clinical and neuroradiological features of the disease. MRI reports have shown atrophy of the cerebellar vermis with concomitant enlargement of the fourth ventricle.[47]

In contrast, Rett's syndrome is a disease of girls which manifests also with autism and stereotyped movements with loss of language and motor skills. The brain appears to have a globally decreased volume, particularly in the frontal lobes. This probably occurs from a combination of congenital hypoplasia and perhaps ongoing degeneration—particularly in the cerebellum. The cerebellar loss is controversial, and other groups have shown greater effects on loss of gray matter volume.

6.3 Autism

Autism has been reported to be associated with findings of focal loss of volume in the superior vermian lobules (declive, folium, and tuber), as well as more generalized volume loss in other parts of the brain.[48] This finding has been contested by others.[49]

6.4 Olivopontocerebellar Degeneration

This rare neurodegenerative disorder can be inherited or sporadic. Ataxia is the presenting sign, and can occur at any age. Because of the nonspecific nature of the presentation, MRI may be particularly useful in providing a specific diagnosis. Pathological and imaging findings include marked loss of volume in the body of the pons, middle cerebellar peduncles, cerebellum, and inferior olive. The pathways which interconnect these structures may show abnormal increased signal intensity on long *TR* sequences.[50] This probably depends on the stage of axonal degeneration.

6.5 Cerebellar Cortical Degeneration

Cerebellar cortical degeneration can present either with an early onset familial form or a late-onset sporadic form. There is a slowly progressive ataxia affecting the limbs, the trunk, and speech. Pathological examination and imaging studies both show marked cerebellar atrophy, particularly in the anterior vermis.

6.6 Acetazolamide-Responsive Familial Paroxysmal Ataxia

This unusual disorder is characterized by recurrent attacks of cerebellar symptoms which are associated with anterior vermian atrophy in the cerebellum.

6.7 Friedreich's Ataxia

Presenting in the second decade of life, this genetic degenerative disorder (localizing to chromosome 9 with multiple inheritance patterns) leads to a progressive ataxia. This leads to gait ataxia and difficulty with speech, as well as kyphoscoliosis, probably on a muscular basis. In addition, to the degeneration of the spinocerebellar tracts, there is loss of the posterior columns of the spinal cord. The spinal cord is atrophic, particularly in the posterior and lateral columns. The majority of subjects also have cerebellar atrophy; however, this is less pronounced than other processes which affect the cerebellum.

7 CONCLUSIONS

MR imaging has revolutionized the detection and diagnosis of many of the neurodegenerative diseases. The patterns of

atrophy and Wallerian degeneration in these entities often allow a specific diagnosis to be made noninvasively. Moreover, in the near future, advances in MRI such as magnetization transfer techniques may allow much earlier detection and characterization of the degenerative processes within the neuron which lead to these tragic diseases.

8 RELATED ARTICLES

Brain Neoplasms Studied by MRI; Hemorrhage in the Brain and Neck Observed by MRI; Intracranial Infections; Magnetic Resonance Imaging of White Matter Disease; Structural and Functional MR in Epilepsy.

9 REFERENCES

1. R. D. Adams and M. Victor, 'Principles of Neurology', McGraw Hill, New York, 1989.
2. S. W. Atlas, 'Magnetic Resonance Imaging of the Brain and Spine', Raven Press, 1991.
3. A. V. Waller, *Philos. Trans. R. Soc. London*, 1850, **140**, 423.
4. R. J. Rossiter, 'Chemical Pathology of the Nervous System', ed. J. Folch-Pi, Pergamon Press, New York, 1961.
5. P. M. Daniel and S. J. Strich, *Acta Neuropathol. (Berlin)*, 1969, **12**, 314.
6. H. Webster and F. De, *Ann. N.Y. Acad. Sci.*, 1964, **122**, 29.
7. L. D. DeWitt, J. P. Kistler, D. C. Miller, E. P. Richardson Jr., and F. S. Buonanno, *Stroke*, 1987, **18**, 342.
8. S. R. Cobb and C. M. Mehringer, *Radiology*, 1987, **162**, 521.
9. M. J. Kuhn, K. A. Johnson, and K. R. Davis, *Radiology*, 1988, **168**, 199.
10. M. Bouchareb, T. Moulin, F. Cattin, J. L. Dretemann, A. Rack, H. Verdot, and J. F. Bonneville, *J. Neuroradiol.*, 1988, **1988**, 238.
11. A. Uchino, K. Onomura, and M. Ohno, *Radiat. Med.*, 1989, **7**, 74.
12. J. E. Pujol, J. L. Mari-Vilata, C. Junque, P. Vendrell, J. Fernandez, and A. Capdevila, *Stroke*, 1990, **21**, 404.
13. T. Orita, T. Tsurutani, A. Izumihara, and T. Matsunaga, *J. Comput. Assist. Tomogr.*, 1991, **15**, 802.
14. Y. Inoue, Y. Matsumura, T. Fukuda, Y. Nemoto, N. Shirahata, T. Suzuki, M. Shakudo, S. Yawata, S. Tanaka, and K. Takemoto, *Am. J. Roentgenol.*, 1990, **11**, 897.
15. A. Danek, M. Bauer, and W. Fries, *Eur. J. Neurosci.*, 1990, **2**, 112.
16. N. P. Bontozoglou, D. W. Chakeres, G. F. Martin, M. A. Brogen, and R. B. McGhee, *Radiology*, 1991, **180**, 223.
17. M. J. Kuhn, D. J. Mikulis, D. M. Ayoub, B. E. Kosofsky, K. R. Davis, and J. M. Taveras, *Radiology*, 1989, **172**, 179.
18. A. Uchino, H. Imada, and M. Ohno, *Neuroradiology*, 1990, **32**, 191.
19. N. Kumar, and F. J. Lexa, in preparation.
20. F. A. Jolesz, J. F. Polak, P. W. Ruenzel, and D. F. Adams, *Radiology*, 1984, **152**, 85.
21. D. S. Titelbaum, J. L. Frazier, R. I. Grossman, P. M. Joseph, L. T. Yu, E. A. Kassab, W. F. Mickey, D. laRossa, and M. J. Brown, *Am. J. Roentgenol.*, 1989, **10**, 741.
22. R. I. Grossman, C. M. Hecht-Leavitt, S. M. Evans, R. E. Lenkinski, G. A. Holland, J. J. van-Winkle, J. T. McGrath, W. J. Curran, A. Shetty, and P. M. Joseph, *Radiology*, 1988, **169**, 305.
23. F. J. Lexa, R. I. Grossman, and A. C. Rosenquist, *Am. J. Roentgenol.*, 1994, **15**, 201.
24. M. L. Schmidt, V. M.-Y. Lee, and J. Q. Trojanowski, *Lab. Invest.*, 1989, **60**, 513.
25. J. W. Dahlbeck, K. W. McCluney, J. W. Yeakley, M. J. Fenstermacher, C. Bonmati, G. van-Horn, and J. Aldeg, *Am. J. Roentgenol.*, 1991, **12**, 931.
26. J. L. Cummings, and L. W. Duchen, *Neurology*, 1981, **31**, 1415.
27. A. Barbeau, 'Handbook of Clinical Neurology', Elsevier, Amsterdam, 1986, Vol. 49, p. 87.
28. E. B. Larson, B. V. Reifler, S. M. Sumi, C. G. Confield, and N. M. Chinn, *Arch. Intern. Med.*, 1986, **146**, 1917.
29. C. Wikkelso, H. Andersson, C. Blomstrand, M. Matousek, and P. Svenelson, *Neuroradiology*, 1989, **31**, 160.
30. W. G. Bradley Jr., A. R. Whittemore, A. S. Watanabe, S. T. Davis, L. M. Teresi, and M. Komyak, *Am. J. Roentgenol.*, 1991, **12**, 31.
31. T. El Gammal, M. B. Allen, B. S. Brooks, and E. K. Mark, *Am. J. Roentgenol.*, 1987, **8**, 591.
32. W. G. Bradley Jr., K. E. Kortman, and B. Burgoyne, *Radiology*, 1986, **159**, 611.
33. J. F. Gusella, N. S. Wexler, P. M. Conneally, S. L. Naylor, M. A. Anderson, R. E. Tanzi, P. C. Watkins, K. Ottina, M. R. Wallace, and A. Y. Sakaguchi, *Nature*, 1983, **306**, 234.
34. S. T. Grafton, J. C. Mazziotta, J. J. Pahl, P. St. George Hyslop, J. L. Haines, J. Gusella, J. M. Hoffman, L. R. Baxter, and M. E. Phelps, *Arch. Neurol.*, 1992, **49**, 1161.
35. T. L. Jernigan, D. P. Salmon, N. Butters, and J. R. Hesselink, *Biol. Psychol*, 1991, **29**, 68.
36. G. J. Harris, G. D. Pearlson, C. E. Peyser, E. H. Aylward, J. Roberts, P. E. Barta, G. A. Chose, and S. E. Folstein, *Ann. Neurol.*, 1992, **31**, 69.
37. S. Starosta-Rubinstein, A. B. Young, K. Kluin, G. Hill, A. M. Aisen, T. Gabrielsem, and G. J. Brewer, *Arch. Neurol.*, 1984, **44**, 365.
38. L. Prayer, D. Wimberger, J. Kramer, G. Grimm, K. Oder, and H. Imhof, *Neuroradiology*, 1990, **32**, 211.
39. H. Nazer, J. Brismar, M. Z. Al-Kawi, T. S. Gunasekaran, and K. H. Jorulf, *Neuroradiology*, 1993, **35**, 130.
40. K. A. Thuomas, S. M. Aquilonius, K. Bergstrom, and K. Westermark, *Neuroradiology*, 1993, **35**, 134.
41. W. Oder, L. Prayer, G. Grimm, J. Spatt, P. Ferenci, K. Holleger, B. Schneider, A. Gangl, and L. Deeke, *Neurology*, 1993, **43**, 120.
42. R. Brown, R. J. Polinsky, G. Di Chiro, B. Postakia, L. Wener, and J. J. Simmons, *J. Neurol. Neurosurg. Psychiatry*, 1987, **50**, 913.
43. M. Savoiardo, L. Strada, F. Girotti, L. D'Incerti, M. Sherna, P. Soliveri, and A. Bolzarini, *J. Comput. Assist. Tomogr.*, 1989, **13**, 555.
44. M. L. Schmidt, V. M.-Y. Lee, J. Q. Trojanowski, and H. Hurtig, *Lab. Invest.*, 1988, **59**,
45. M. LeMay and N. Alvarez, *Neuroradiology*, 1990, **32**, 104.
46. T. Murata, Y. Koshino, M. Omori, I. Murati, M. Nishio, T. Horie, Y. Umezawa, K. Isaki, H. Kimura, and S. Itoh, *Biol. Psychol.*, 1993, **34**, 290.
47. E. H. Aylward and A. Reiss, *J. Psychiatr. Res.*, 1991, **25**, 159.
48. E. Courchesne, G. Press, and R. Yeung-Courchesne, *Am. J. Roentgenol.*, 1993, **160**, 387.
49. M. A. Nowell, D. B. Hackney, A. S. Muraki, and M. Coleman, *JMRI*, 1990, **8**, 811.
50. M. Savoiardo, L. Strada, F. Girotti, R. A. Zimmerman, M. Grisoli, D. Testa, and R. Petrillo, *Radiology*, 1990, **174**, 693.

Biographical Sketch

Frank J. Lexa. *b* 1958. A.B. (Biology), Harvard University, USA, 1980. M.S. (Physiology), 1982, M.D. 1985, Stanford University School of Medicine, USA. Postgraduate medical training in internal medicine, Brigham and Women's Hospital, Harvard Medical School,

and diagnostic radiology/neuroradiology, Hospital of the University of Pennsylvania, USA. Currently Fellow, Leonard Davis Institute of Health Care Economics and Graduate MBA Candidate, Class of '99, The Wharton School Director, Medical Acquisitions, BTG International. Approx. 30 publications. Current research specialties: early detection and characterization of axonal degeneration using magnetization transfer techniques, MRI contrast agent development for advanced medical applications.

Cranial Nerves Investigated by MRI

Anton N. Hasso
University of California, Irvine, CA, USA

and

Peggy J. Fritzsche
Loma Linda University, Loma Linda, CA, USA

1 INTRODUCTION

The reader of this article will gain an understanding of the normal pathways of the cranial nerves and be able to correlate the function with the course of each nerve. The functional anatomy will also be addressed in conjunction with the clinical manifestations of pathologic entities. Tumors, infections, and inflammations of the cranial nerves will be discussed separately.

2 NORMAL ANATOMY

2.1 Cranial Nerve I (Olfactory)

Smell is consciously perceived in the gray matter covering the medial and lateral striae of the olfactory gyri. The lateral striae travel from the inferior medial aspect of the temporal lobe (pyriform area) and the medial striae from the medial and inferior aspects of the frontal lobe (subcallosal region) to the olfactory trigone located at the anterior perforated substance. The intermediate stria is not significant in humans, but joins the lateral and medial striae at the trigone to extend anteriorly as the olfactory tract. The olfactory tract terminates in the olfactory bulb. The olfactory bulbs are located inferior to the olfactory sulci (Figure 1). The olfactory sulci separate the gyri rectus from the medial orbitofrontal gyri.

Sensory nerve bundles exit the olfactory bulbs via the cribriform plate of the skull to separate into multiple neurosensory cells which reside in the nasal epithelium. The function of the olfactory nerve is to provide olfaction. Neuropathy of the first cranial nerve manifests as anosmia, or acute loss of olfaction. Anosmia is usually unilateral, and typically occurs secondary to pathologic processes arising in the nasal cavities. Intracranial neoplasms, infections, arterial disease, or congenital anomalies also can cause anosmia.[1]

2.2 Cranial Nerve II (Optic)

The optic fibers originate in the calcarine portion of the occipital cortex and travel superiorly, inferiorly, and laterally to the occipital horn of the ventricle. The optic fibers then become the optic radiations as they course over the temporal horn of the lateral ventricle and the tail of the caudate nucleus to enter the lateral geniculate body of the thalamus [Figure 2(a)]. Bilateral optic tracts then exit the lateral geniculate bodies and meet in the midline to form the optic chiasm. From the optic chiasm ventrally, the optic fibers then divide into the bilateral optic nerves coursing initially into the cranial openings of the optic canals. The optic nerves exit the orbital openings of the optic canals and extend forward in a sinusoidal manner to enter the globes at the optic nerve heads.

Lesions involving the intraorbital and prechiasmal portions of the optic nerve result in total monocular blindness. The sudden onset of a monocular deficit suggests a possible vascular or demyelinating process. The slow onset of a monocular optic neuropathy may be caused by a lesion intrinsic to the optic nerve sheath or secondary to extrinsic compression by an adjacent mass.

The fibers from the outer (temporal) portion of both visual fields cross at the optic chiasm and thus are carried via the optic tracts to the contralateral calcarine cortex of the occipital lobes. The fibers from the medial (nasal) portion of the visual fields do not cross at the optic chiasm and are projected to the ipsilateral visual cortex. Lesions involving the central portion of the chiasm particularly produce bitemporal hemianopsias. Lesions along the optic tracts result in loss of vision in the ipsilateral (uncrossed) nasal field and contralateral (crossed) temporal field. Since the retrochiasmal segment of the visual pathway recognizes the opposite visual field, a retrochiasmal lesion leads to a homonomous hemianopsia contralateral to the lesion. Contralateral hemianopsias may be produced by lesions involving any portion of the retrochiasmal optic pathways including the lateral geniculate bodies, the optic radiations, or the occipital cortices.[1–3]

2.3 Cranial Nerve III (Oculomotor)

The motor component of cranial nerve III originates in the motor cortex of the cerebrum. The fibers then travel centrally

Figure 1 Normal anatomy of the olfactory bulbs. The olfactory bulbs (arrows) are located inferior to the olfactory sulci which separate the gyrus rectus from the medial orbitofrontal gyrus

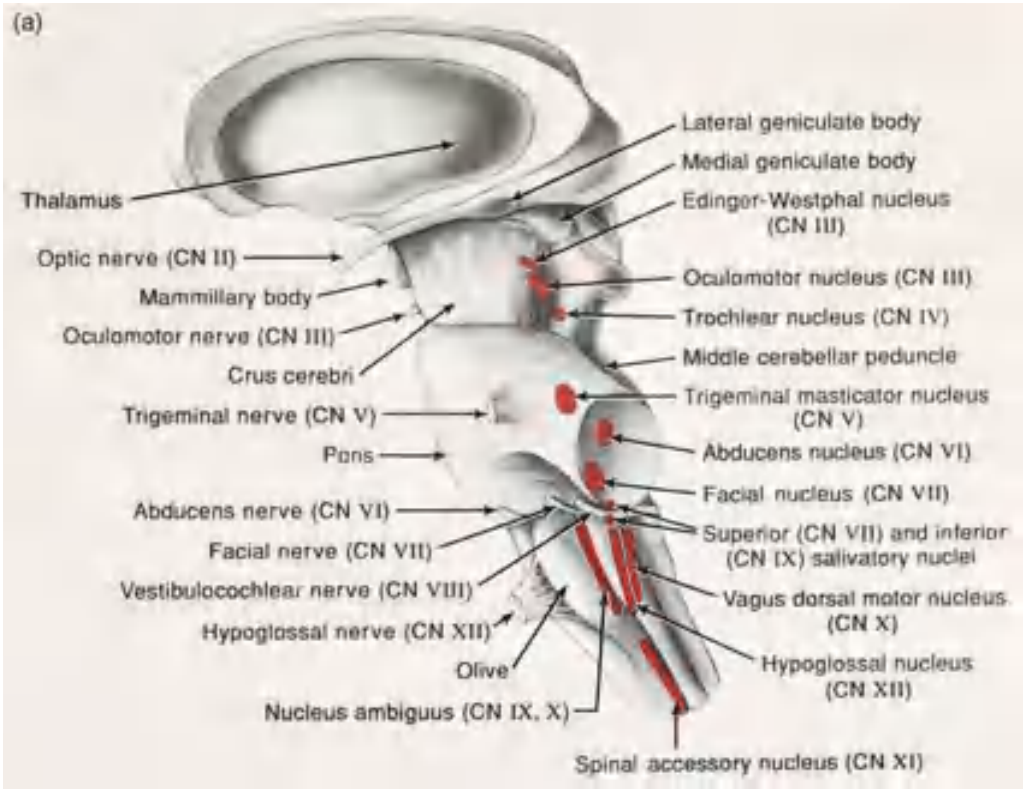
(a)
Thalamus
Optic nerve (CN II)
Mammillary body
Oculomotor nerve (CN III)
Crus cerebri
Trigeminal nerve (CN V)
Pons
Abducens nerve (CN VI)
Facial nerve (CN VII)
Vestibulocochlear nerve (CN VIII)
Hypoglossal nerve (CN XII)
Olive
Nucleus ambiguus (CN IX, X)
Lateral geniculate body
Medial geniculate body
Edinger-Westphal nucleus (CN III)
Oculomotor nucleus (CN III)
Trochlear nucleus (CN IV)
Middle cerebellar peduncle
Trigeminal masticator nucleus (CN V)
Abducens nucleus (CN VI)
Facial nucleus (CN VII)
Superior (CN VII) and inferior (CN IX) salivatory nuclei
Vagus dorsal motor nucleus (CN X)
Hypoglossal nucleus (CN XII)
Spinal accessory nucleus (CN XI)

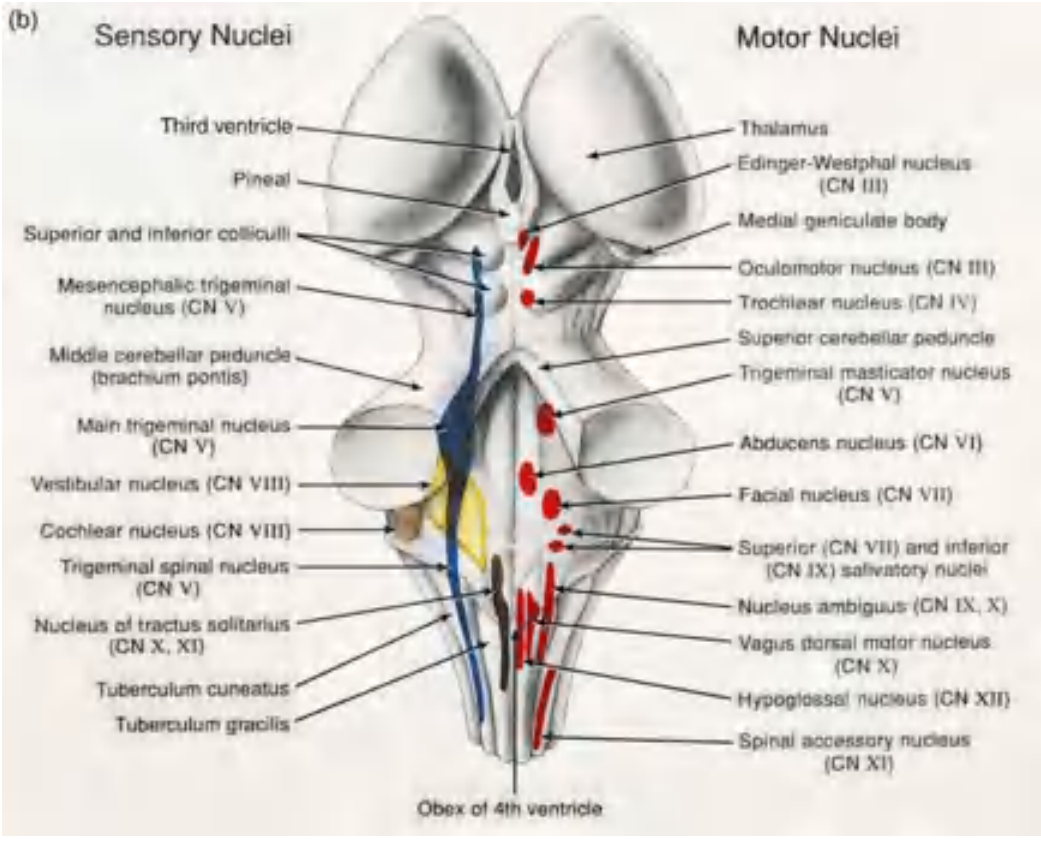
(b)
Sensory Nuclei
Motor Nuclei
Third ventricle
Pineal
Superior and inferior colliculli
Mesencephalic trigeminal nucleus (CN V)
Middle cerebellar peduncle (brachium pontis)
Main trigeminal nucleus (CN V)
Vestibular nucleus (CN VIII)
Cochlear nucleus (CN VIII)
Trigeminal spinal nucleus (CN V)
Nucleus of tractus solitarius (CN X, XI)
Tuberculum cuneatus
Tuberculum gracilis
Obex of 4th ventricle
Thalamus
Edinger-Westphal nucleus (CN III)
Medial geniculate body
Oculomotor nucleus (CN III)
Trochlear nucleus (CN IV)
Superior cerebellar peduncle
Trigeminal masticator nucleus (CN V)
Abducens nucleus (CN VI)
Facial nucleus (CN VII)
Superior (CN VII) and inferior (CN IX) salivatory nuclei
Nucleus ambiguus (CN IX, X)
Vagus dorsal motor nucleus (CN X)
Hypoglossal nucleus (CN XII)
Spinal accessory nucleus (CN XI)

Figure 2 (a, b)

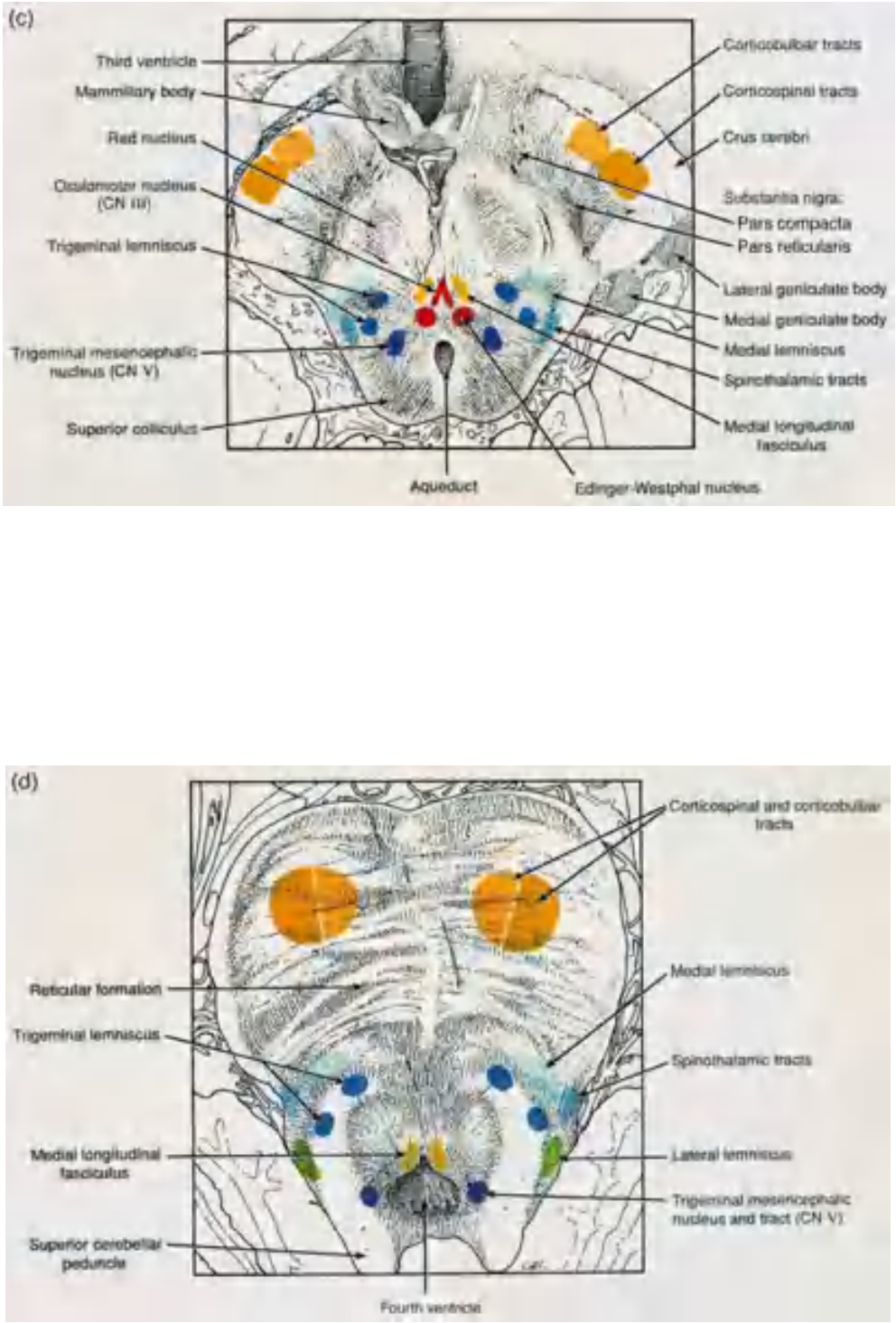
(c)
Third ventricle
Mammillary body
Red nucleus
Oculomotor nucleus (CN III)
Trigeminal lemniscus
Trigeminal mesencephalic nucleus (CN V)
Superior colliculus
Aqueduct
Edinger-Westphal nucleus
Corticobulbar tracts
Corticospinal tracts
Crus cerebri
Substantia nigra:
Pars compacta
Pars reticularis
Lateral geniculate body
Medial geniculate body
Medial lemniscus
Spinothalamic tracts
Medial longitudinal fasciculus
(d)
Corticospinal and corticobulbar tracts
Reticular formation
Trigeminal lemniscus
Medial longitudinal fasciculus
Superior cerebellar peduncle
Fourth ventricle
Medial lemniscus
Spinothalamic tracts
Lateral lemniscus
Trigeminal mesencephalic nucleus and tract (CN V)

Figure 2 (c, d)

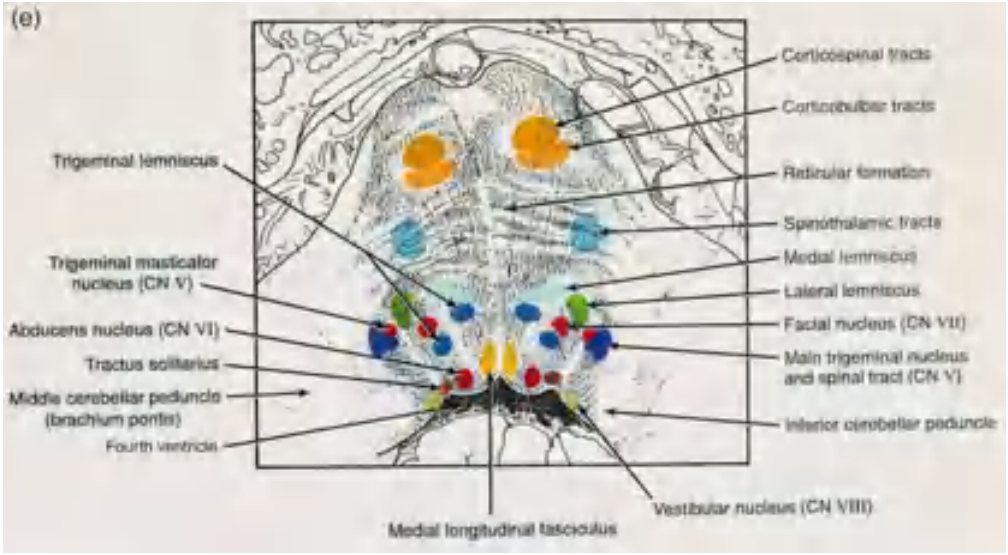

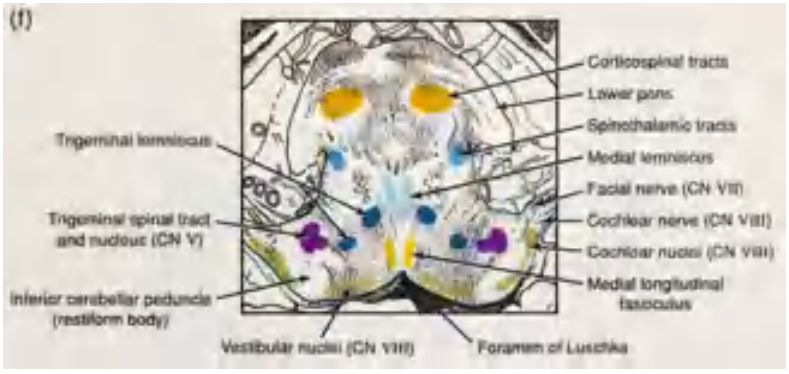

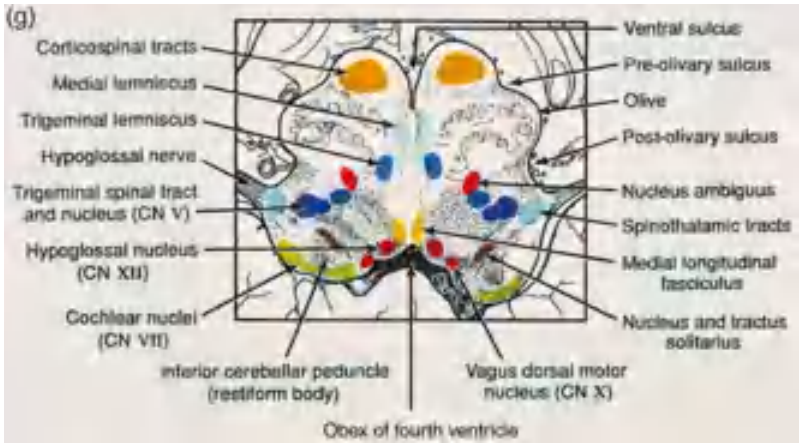

Figure 2 Illustrations of normal anatomy of brainstem and cranial nerves. (a) Lateral view of brainstem with motor nuclei. (b) Posterior view of brainstem with sensory and motor nuclei. (c) Normal axial anatomy of the brainstem at the level of the midbrain. (d) Normal axial anatomy of the brainstem at the level of the pontine isthmus. (e) Normal axial anatomy of the brainstem at the pons. (f) Normal axial anatomy of the brainstem at the upper medulla. (g) Normal axial anatomy of the brainstem at the middle medulla. CN, cranial nerve. Reproduced with permission from W. G. Bradley, Jr, *Radiology*, 1991, **179**, 319

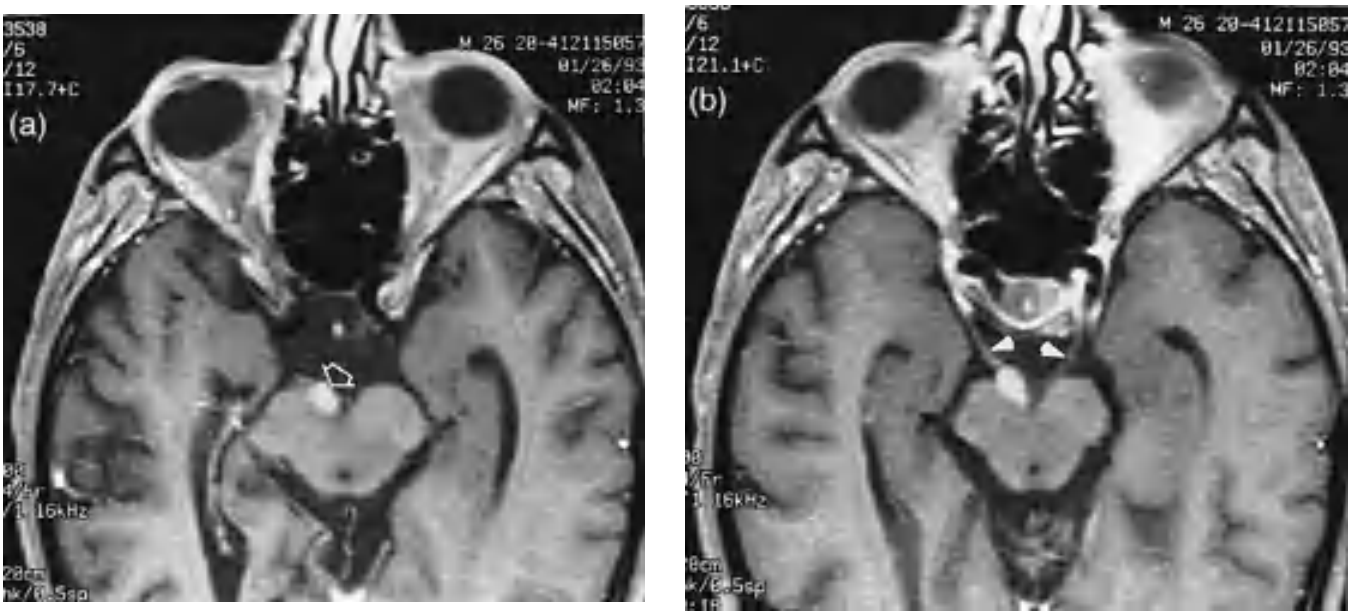

Figure 3 Lymphomatous meningitis in a patient with AIDS. Axial enhanced images with fat saturation pulses. (a) Note the focal nodule in the right side of the interpeduncular cistern (arrow). (b) The characteristic V-shape of the oculomotor nerves in the prepontine cistern is well shown (arrows)

through the internal capsule to the ipsilateral superior colliculus. The fibers cross between the red nuclei in the dorsal tegmental decussation and continue distally in the paramedian raphe to synapse in the pontine reticular formation. The fibers then ascend in the medial longitudinal fasciculus to the oculomotor nucleus which is situated in the paramedian midbrain tegmentum ventral to the aqueduct of Sylvius at the level of the superior colliculus. At this level, additional fibers from the parasympathetic nucleus, paramedian nucleus, Perlia's nucleus, and Edinger–Westphal nucleus join the motor fibers. These combined fibers bow laterally to extend through the medial aspect of the red nucleus and the cerebral peduncle (Figure 2). Fibers then exit from the brainstem anteriorly at the pontomedullary junction near the midline where the two nerves form parallel structures in a V-configuration as they extend through the interpeduncular fossa (Figure 3).

The oculomotor nerves then travel between the superior cerebellar and posterior cerebral arteries through the prepontine cistern. Each cranial nerve III then penetrates the dura of the cavernous sinus and rises superiorly along the lateral wall of the cavernous sinus adjacent to the fourth cranial nerve and above the sixth cranial nerve and ophthalmic division of the fifth cranial nerve. The parasympathetic and motor fibers are in close proximity, and altogether the nerves penetrate the superior orbital fissure to reach the orbital structures.

The motor fibers provide the somatic motor function to the medial rectus, inferior rectus, superior rectus, and inferior oblique extraocular muscles. Lesions of this portion of the oculomotor nerve lead to a downward abducted eye, due to the unopposed action of the superior oblique and lateral rectus muscles. The oculomotor nerve also supplies the levator palpebrae superioris, which elevates the eyelid. Lesions of this portion of cranial nerve III also result in lid droop or ptosis. The visceral motor fibers from the Edinger–Westphal nucleus provide parasympathetic motor function to the pupillary constrictor and ciliary muscles. Lesions of this portion of the oculomotor nerve result in pupillary dilatation due to unopposed sympathetic input and failure to accommodate. Isolated third-nerve palsies are regarded as either complete (including parasympathetic involvement) or incomplete (due to lack of parasympathetic involvement).[1–3]

2.4 Cranial Nerve IV (Trochlear)

The motor impulses of cranial nerve IV originate in the motor cortex and then extend centrally via the internal capsule to the ipsilateral superior colliculus. The fibers cross between the red nuclei in the dorsal tegmental decussation and travel caudally in the paramedial raphe to synapse in the pontine reticular formation. The fibers then ascend in the medial longitudinal fasciculus to reach the motor nucleus. The fourth cranial nerve nucleus is located in the tegmentum of the mesencephalon at the level of the inferior colliculus immediately caudal to the third nerve nucleus. Fibers from the nucleus loop posteriorly to decussate in the tectum of the lower midbrain beneath the inferior colliculi. This pathway forms a sickle-shaped arch around the aqueduct of Sylvius (Figure 2).

The trochlear nerve exits from the dorsal aspect of the brainstem, emerging from the superior medullary vellum just beneath the inferior colliculus. The nerve extends around the cerebral peduncle between the superior cerebellar and posterior cerebral arteries, just lateral to the third cranial nerve (Figure 4). The nerve then pierces the dura of the cavernous sinus coursing along the superior margin adjacent to the oculomotor nerve and the ophthalmic portion of the trigeminal nerve en route to the superior orbital fissure.

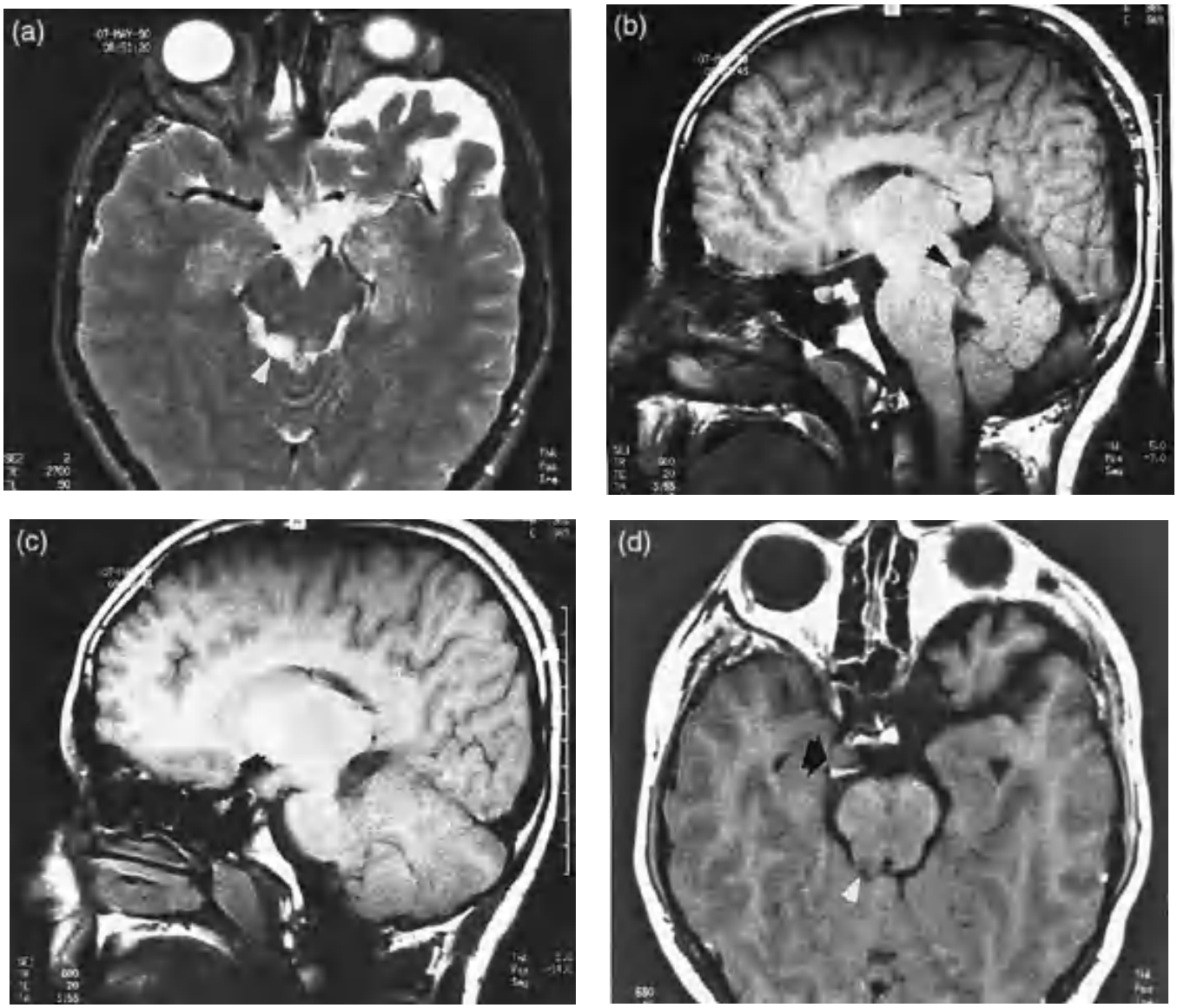

Figure 4 Tectal and right trochlear nerve tumor in a patient with neurofibromatosis I. (a) Axial image at the level of the inferior colliculus. There is a hyperintense mass in the right tectum encompassing the nucleus of cranial nerve IV. Note the incidental dysplasia of the left sphenoid wing which is commonly seen in patients with NF-1. (b and c) Sagittal unenhanced images. There is a hypointense tumor expanding the inferior colliculus [arrow, (b)]. Note the expansion of the right trochlear nerve in the prepontine cistern [broad arrow, (c)]. (d) Axial enhanced image. The tumor foci in the tectal plate (white arrow) and in the right prepontine cistern (black arrow) do not enhance significantly. A hamartoma or low grade glioma is suspected. Note the uninvolved oculomotor nerves in the prepontine cistern

The fourth cranial nerve innervates the superior oblique muscle in the orbit. Lesions of the trochlear nerve or its nucleus result in outward rotation of the affected eye. Because the trochlear nerve has the longest intracranial course (7.5 cm), it has the greatest chance of injury from trauma or surgery in the region of the midbrain.[1,3,4]

2.5 Cranial Nerve V (Sensory Trigeminal)

The sensory impulses from the upper, middle, and lower part of the face extend to the gasserian ganglion via the ophthalmic (V1), maxillary (V2), and mandibular (V3) branches of cranial nerve V. These branches enter the skull via the superior orbital fissure, foramen rotundum and foramen ovale, respectively. The ophthalmic and maxillary divisions extend through the cavernous sinus, while the mandibular branch bypasses the cavernous sinus and directly enters the trigeminal (gasserian) ganglion. This ganglion lies in the inferior portion of Meckel's cavity and contains the cell bodies of numerous afferent sensory fibers. Facial numbness and burning (tic douloureux) represent signs and symptoms caused by sensory trigeminal neuropathies.

Sensory impulses from the face then leave the trigeminal ganglion to enter the midlateral pons through the prepontine cistern. As they enter the brainstem, branches go to the three sensory nuclei: the principal sensory nucleus, the mesencepha-

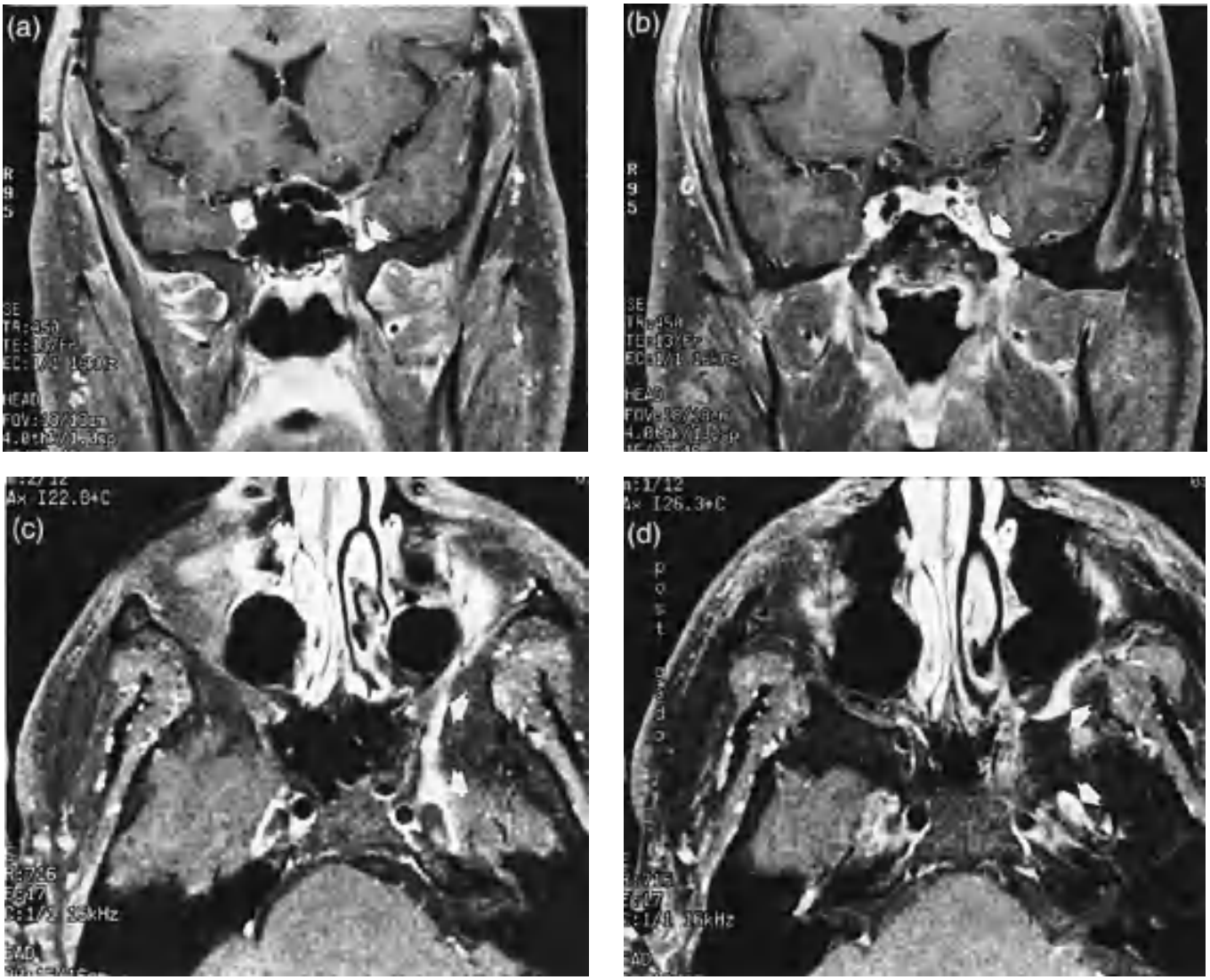

Figure 5 Plexiform neurofibroma involving the left trigeminal nerve. Adult patient with neurofibromatosis I. Enhanced images with fat saturation pulses. (a and b) Coronal images demonstrate the expansion and enhancement in the left maxillary division [arrow, (a)] and mandibular division [arrow, (b)] of the trigeminal nerve. (c and d) Axial images demonstrate the course of the left axillary nerve from the trigeminal ganglion through the foramen rotundum [arrows, (c)]. Note the expansion of the tumor into the left foramen ovale and pterygopalatine fossa [arrows, (d)]

lic nucleus, and the spinal nucleus. Pain and temperature fibers descend to the C2–C3 cord level where they synapse in the spinal nucleus of cranial nerve V. These fibers then cross the midline ascending in the ventral trigeminal lemmiscus to reach the ventral posteromedial nucleus of the thalamus. The thalamocortical tract then carries the fibers via the internal capsule to the sensory cortex. The sensory impulses that mediate proprioception from the face, particularly of the mandible, synapse in the mesencephalic nucleus of cranial nerve V which extends superiorly into the periaqueductal gray matter of the midbrain. This portion of the sensory nucleus is composed of the sensory neurons that travel with the mandibular nerve. Sensory nerves that mediate touch and pressure from the face synapse in the principal sensory nucleus of cranial nerve V and travel to the ventral posteromedial nucleus of the thalamus via the contralateral dorsal trigeminal lemmiscus. The extension to the sensory cortex is via the thalamocortical tract which passes through the internal capsule (Figure 2).[1–3,5]

2.6 Cranial Nerve V (Motor Trigeminal)

The impulses for the motor components of cranial nerve V originate in the motor cortex of the cerebral hemisphere. The pathway then extends through the genu of the internal capsule and the cerebral peduncle (along the corticobulbar tract) to the motor nucleus which is situated medial to the principal sensory nucleus. The fused motor and sensory components of the fifth nerve emerge from the ventrolateral pons, coursing through the anterior portion of the cerebellopontine angle cistern near the apex of the medial petrous ridge. The nerve fibers then pierce the dura of Meckel's cavity and enter the trigeminal ganglion. At the distal aspect of Meckel's cavity, the motor fibers of the mandibular nerve exit at the inferolateral surface and extend through the foramen ovale (Figure 5). The motor division of the mandibular nerve supplies the muscles of mastication plus other small muscles (tensor villi palatini, mylohyoid, anterior belly of the digastric and tensor tympani).

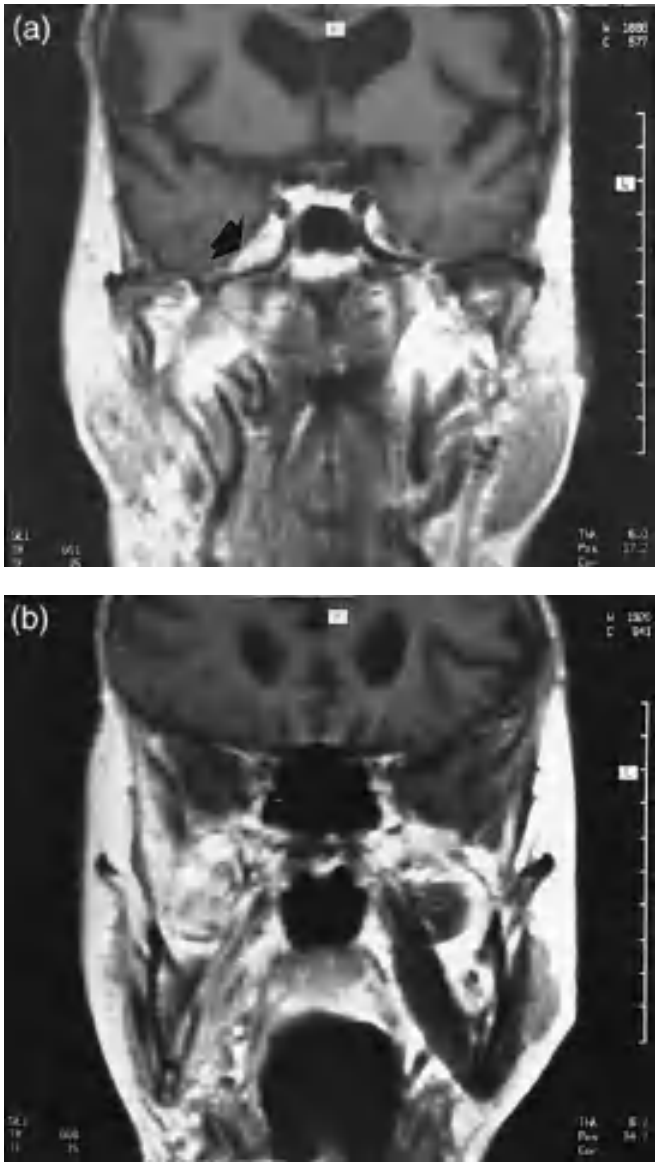

Figure 6 Perineural extension of squamous cell carcinoma. Adult patient with previous known facial cancer. Coronal enhanced images. (a) Note the lateral deviation of the cavernous sinus wall and enhancement along the right trigeminal ganglion (arrow). (b) There is marked denervation atrophy of the right muscles of mastication. The fat which replaces the muscle shows moderate diffuse enhancement

The exit point of the motor trigeminal nerve from the brainstem is also the entry point of the sensory trigeminal nerve. This area is termed the 'root entry zone' of the sensory trigeminal nerve and is subject to vascular compression by dolichoectatic vessels or aneurysms which may cause tic douloureux or other trigeminal neuropathies. Alternatively, an ipsilateral or contralateral posterior fossa tumor or other mass lesion can torque the brainstem and cause a distention of this root entry zone. If the motor trigeminal portion is affected by a pathologic process, weakness of the muscles of mastication (with or without denervation atrophy) can occur (Figure 6).[1–3,5]

2.7 Cranial Nerve VI (Abducens)

The impulses of cranial nerve VI originate in the motor cortex of the cerebral hemisphere. The fibers extend through the internal capsule and the corticobulbar tract to the ipsilateral superior colliculus. At this point, the fibers cross between the red nuclei in the dorsal tegmental decussation. They then extend caudally in the paramedian raphe of the brainstem to synapse in the pontine reticular formation. Both ipsilateral and contralateral fibers ascend in the medial longitudinal fasciculus to reach the brainstem nucleus of the abducens nerve which lies in the pons immediately anterior to the fourth ventricle. These fibers pass through the pontine tegmentum and exits anteriorly from the brainstem at the pontomedullary junction. The abducens nerve then courses superiorly and slightly laterally along the clivus. At the base of the dorsum sella, the sixth cranial nerve courses anteriorly piercing the dura through Dorello's canal to enter the cavernous sinus. The nerve then extends obliquely through the cavernous sinus just inferior and medial to cranial nerves III and IV, immediately adjacent to the cavernous portion of the internal carotid artery. Cranial nerve VI then exits anteriorly through the cavernous sinus to enter the superior oblique fissure en route to the lateral rectus muscle (Figure 2).

An isolated lateral rectus palsy is the most common lesion of the cranial nerves supplying the extraocular muscles. Injury to the abducens nerve produces paralysis of the ipsilateral lateral rectus muscle, with resultant horizontal diplopia. The unopposed pull of the medial rectus muscle causes the eye to turn inward (adduct), thereby producing internal strabismus.[1–3]

2.8 Cranial Nerve VII (Facial)

The motor impulses of cranial nerve VII originate in the motor cortex of the cerebral hemisphere and extend via the genu of the internal capsule and cerebral peduncle to the brainstem nucleus. The motor nucleus of cranial nerve VII is situated in the caudal one-third of the ventral pontine tegmentum. Fibers from the ipsilateral and contralateral sides meet in this brainstem nucleus. From the nucleus, the fibers extend posteriorly toward the floor of the fourth ventricle and loop around the nucleus of cranial nerve VI (abducens). This portion of the facial nerve contributes to the facial colliculus, a mound of tissue that protrudes internally towards the floor of the fourth ventricle. Extending from the loop, cranial nerve VII emerges from the brainstem at the anterolateral aspect of the pontomedullary junction. The nerve then extends laterally in the cerebellopontine angle cistern reaching the anterior superior quadrant of the internal auditory canal. The facial nerve extends through the temporal bone to the fundus of the internal auditory canal. It then exits to join the geniculate ganglion within the roof of the petrous bone (Figure 7). At this point, there is a synapse with the sensory neurons for taste to the anterior two-thirds of the tongue and the cutaneous fibers for light touch in the region of the external ear.

The superior salivatory nucleus in the pons is the site of origin of the parasympathetic fibers that terminate in and stimulate the lacrimal, sublingual, and submandibular glands. The nucleus solitarius represents the end point of the fibers that convey taste sensation from the anterior two-thirds (via cranial

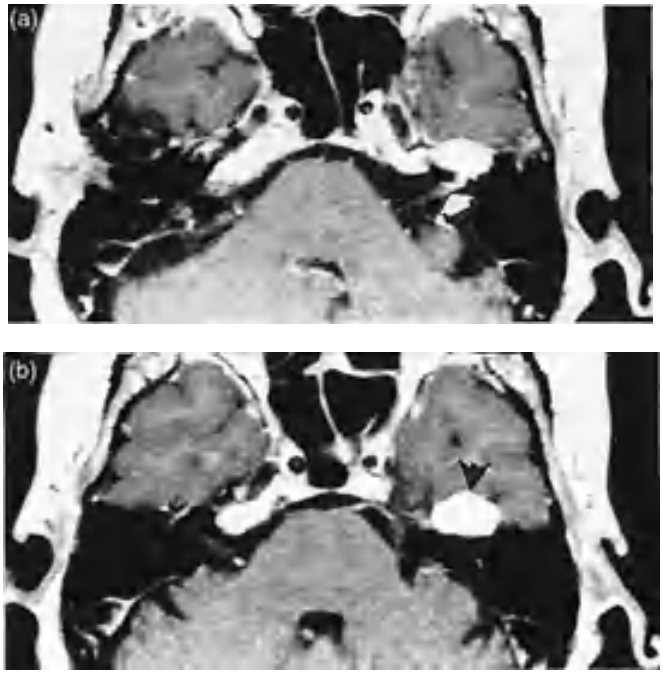

Figure 7 Axial enhanced images of the geniculate ganglion and proximal facial nerve schwannoma. (a) Note the tumor enhancement extending through the fundus of the left internal auditory canal to the geniculate ganglion (arrow). (b) The expansion of the tumor along the surface of the left petrous bone into the middle cranial fossa can be clearly seen (arrow)

nerve VII) and from the posterior third (via cranial nerve IX) of the tongue. The cell bodies of these taste fibers are found in the geniculate ganglion. The impulses from these nuclei form the intermediate nerve fibers which join the motor root of the facial nerve as it exits the brainstem (Figure 2).

From the region of the geniculate ganglion, the secretomotor fibers project forward as the greater superficial petrosal nerve which joins some parasympathetic fibers from the carotid artery to form the nerve of the pterygoid canal. The pterygoid canal will transmit the nerve to the pterygopalatine fossa from where the parasympathetic components synapse and fibers extend to affect lacrimation and salivation.

From the geniculate ganglion, the facial motor fibers and taste fibers form a 180° turn and are directed posteriorly, at the anterior genu of the facial nerve. Extending posteriorly, these fibers lie at the medial aspect of the tympanic cavity medial to the ossicular chain and below the lateral semicircular canal. At the posterior aspect of the middle ear, the motor and taste fibers extend inferiorly at the posterior genu of the facial nerve to enter the stylomastoid foramen. At this point, the stapedial nerve exits to supply the stapedial muscle which controls the mobility of the ossicles. The chorda tympani fibers for taste also separate from the seventh nerve within the stylomastoid foramen extending via the petrotympanic fissure and eventually joining the lingual branch of the mandibular nerve to participate in the sensory fibers for taste to the anterior two-thirds of the tongue. The seventh nerve then exits the stylomastoid foramen into the parotid gland and extends anteriorly to innervate the muscles of facial expression as well as the posterior belly of the digastric, the stylohyoid, and the platysma muscles.

Lesions of the facial nerve result in a facial palsy, which can be either peripheral or central. Central paralysis refers to a supranuclear injury that becomes manifest as paralysis of the contralateral muscles of facial expression, with sparing of the muscles of the forehead. Peripheral facial nerve function implies injury to the facial nerve from the level of the brainstem nucleus to the end of its motor fibers. All the ipsilateral muscles of facial expression are paralyzed in a peripheral injury. Dysfunction of the facial nerve branches within the greater superficial petrosal nerve is manifested as an impairment of ipsilateral lacrimation. Dysfunction of the stapedius branch of the facial nerve is manifested by hyperacusis. Dysfunction of the chorda tympani nerve causes loss of taste from the anterior two-thirds of the tongue. An impression on the 'root exit zone' of the facial nerve from the brainstem by a vascular anomaly may lead to spasmodic contractures of the ipsilateral muscles of facial expression (facial tic) (Figure 8).[1–3,6]

2.9 Cranial Nerve VIII (Vestibular)

Movement impulses are modulated by the hair cells within the utricle, saccule, and three semicircular canals and transmitted through the superior and inferior vestibular nerves (Figure 9). The combined vestibular nerve courses along with the cochlear nerve and facial nerve within the internal auditory canal. The superior and inferior vestibular divisions enter the brainstem at the pontomedullary junction after crossing the cerebellopontine angle cistern. These fibers extend into the vestibular nuclear complex with postganglionic fibers carrying information regarding equilibrium to many coordination sites including the folliculonodular lobe of the cerebellum, the vestibulospinal tract, both medial longitudinal fasciculi and other pathways which affect the control of the eyes and the muscles of balance (Figure 2).[1–3]

2.10 Cranial Nerve VIII (Cochlear)

Sound waves from the external environment are converted to energy in the inner ear in the form of vibratory impulses at the oval window of the vestibule. The kinetic impulses are propagated as fluid waves in the cochlea. These impulses are then converted to electrical impulses along the spiral organ of Corti. The auditory signals are then transmitted via the spiral ganglion in the cochlear nerve through the internal auditory canal and cerebellopontine angle to the origin of cranial nerve VIII at the ventrolateral pontomedullary junction. There are two cochlear nuclei (dorsal and ventral) located lateral to the inferior cerebellar peduncles in the upper medulla. The dorsal cochlear nucleus carries high frequencies, while the ventral cochlear nucleus connects low frequencies. Somewhat more than half of the fibers from these nuclei cross to the contralateral superior olivary nucleus to form the trapezoid body. From the trapezoid body, the fibers enter the posteriorly located lateral lemniscus to ascend to the inferior colliculus in the midbrain. From the inferior colliculus, the fibers travel to the medial geniculate body of the thalamus and then, via the auditory radiations to the superior temporal gyrus (Figure 2).

Clinical manifestations of acoustic pathway injury depend on the level of the injury. Lesions of the cochlear portion of the eighth nerve result in hearing loss and tinnitus (ringing or roaring in the ear). If unilateral sensorineural hearing loss is

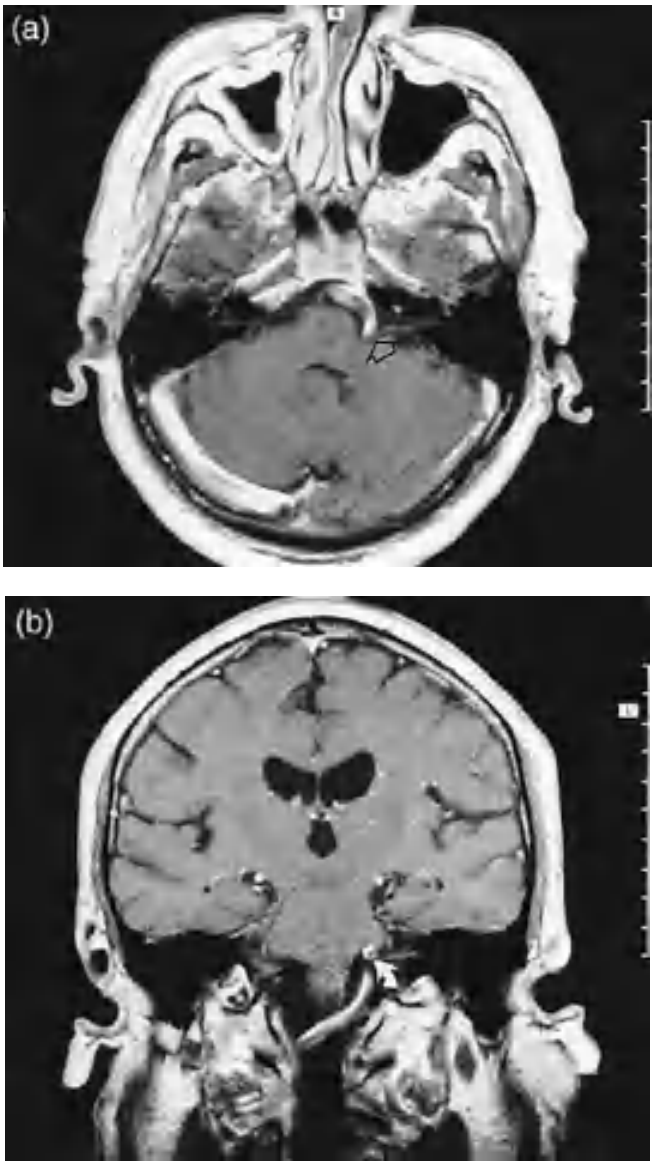

Figure 8 Enhanced images of dolichoectasia of the basilar artery compressing the root exit zone of the left facial nerve. (a) This axial view shows an indentation by the basilar artery on the brainstem at the origin of the left facial nerve (open arrow). (b) This coronal view documents the tortuous course of the left basilar artery, including the brainstem compression at the origin of the facial nerve (arrow)

present, the injury has occurred somewhere between the cochlea and the cochlear nuclei of the brainstem. Unilateral involvement of the auditory pathway above the cochlear nuclei usually causes bilateral hearing loss due to the multiple crossings through the acoustic pathways. The hearing loss is greater in the ear contralateral to the site of the lesion. Cortical acoustic pathway lesions, which rarely cause disruption of auditory function, may result in auditory agnosia.[1–3,7]

2.11 Cranial Nerve IX (Glossopharyngeal)

Impulses from the motor cortex of the cerebral hemisphere extend to the genu of the internal capsule and subsequently follow the corticobulbar tract through the midbrain to the nucleus ambiguus. The fibers extend to the posterior olivary sulcus leaving the medulla at this point to extend anterolaterally to the superior and inferior glossopharyngeal ganglia situated in the jugular foramen. The fibers then travel inferiorly to supply the stylopharyngeus and constrictor muscles of the pharynx. In addition to this motor component to the muscles, there is a solitary nucleus for sensory fibers and a salivatory nucleus for parasympathetic fibers. These nuclei represent the primary sensory neurons for general visceral and special sensation, including taste, for the posterior third of the tongue (Figure 2).

The sensory portion of the glossopharyngeal nerve joins the motor portion which then extend together into the pars nervosa of the jugular foramen (Figure 10). There is a small tympanic branch (Jacobson's nerve) which supplies sensation to the middle ear and eustachian tube as well as parasympathetic fibers to the parotid gland. A small visceral branch supplies the carotid sinus and carotid body which controls the pressor and chemoreceptor functions. Pharyngeal sensory branches supply the posterior oropharynx and soft palate. The lingual branch includes fibers for both sensation and taste for the posterior third of the tongue.

Clinical manifestations of ninth nerve dysfunction include otalgia (referred pain along the tympanic branch to the ear), dysphagia (stylopharyngeus muscle dysfunction), and tachycardia or bradycardia with hypotension (sinus nerve dysfunction). Other symptoms definitely related to ninth nerve injury are loss of the afferent limb of the gag reflex and loss of taste to the posterior third of the tongue.[1–3]

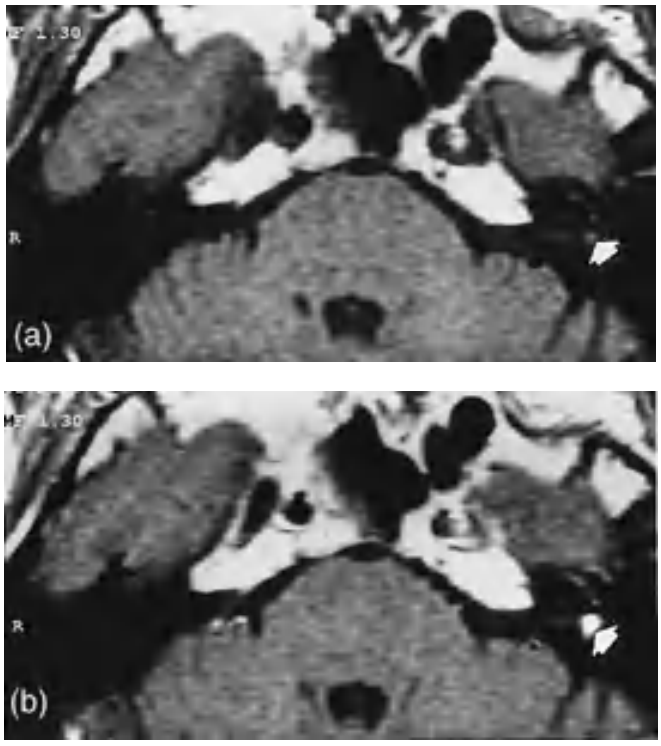

Figure 9 Vestibular schwannoma of the left utricle and saccule. (a) Unenhanced axial image. The small tumor of the membranous labyrinth is difficult to identify within the left petrous temporal bone (arrow). (b) Enhanced axial image. The bulbous tumor in the left vestibule is clearly shown (arrow)

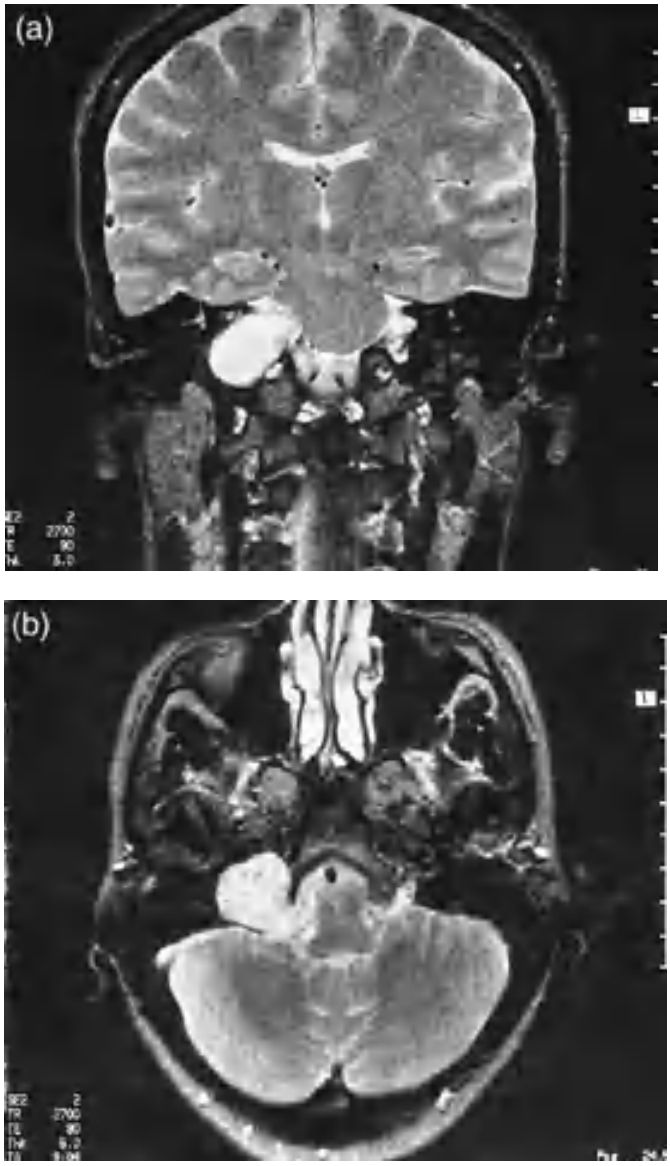

Figure 10 Schwannoma of the right glossopharyngeal nerve in the jugular foramen. (a) Coronal image. The homogeneously hyperintense tumor smoothly expands the right jugular foramen. The apex of the tumor is along the brainstem with its inferior portion extending through the right side of the skull base. (b) Axial image. The homogeneously hyperintense tumor mass in the right side of the skull base is clearly seen on this T_2-weighted image

2.12 Cranial Nerve X (Vagus)

Impulses from the motor cortex of the cerebral hemisphere travel through the genu of the internal capsule and cerebral peduncle via the corticobulbar tract to the nucleus ambiguus. The fibers extend to the posterior olivary sulcus slightly more lateral than cranial nerve IX exiting the medulla in the groove between the inferior peduncle and olive. Cranial nerve X continues an anterolateral course with its companion nerves (cranial nerve IX and the bulbar portion of cranial nerve XI) through the perimedullary cistern. The vagus nerve and bulbar portion of the eleventh cranial nerve enter the anterior aspect of the pars vascularis of the jugular foramen. As previously discussed, the ninth cranial nerve enters the pars nervosa of the jugular foramen. After exiting the jugular foramen, the vagus nerve plunges like a plumb line along the posterolateral aspect of the carotid artery to the aortopulmonic window of the mediastinum on the left side and to the clavicle on the right side. The right recurrent laryngeal branch turns cephalad around the right subclavian artery, while the left recurrent laryngeal branch turns cephalad by looping through the aortopulmonic window. Both recurrent laryngeal nerves reach the larynx via the tracheoesophageal groove. Sensory fibers of the vagus nerve begin in the thoracoabdominal viscera and chemoreceptors at the aortic arch. These then synapse in the solitary nucleus (pure sensory fibers) and the dorsal motor nucleus (parasympathetic secretomotor fibers) (Figure 2).

Injury to the vagus nerve below the hyoid bone causes manifestations of recurrent laryngeal nerve malfunction and include hoarseness, aspiration, and cervical dysphagia. Injury to the vagus nerve above the hyoid bone results in the above symptoms in combination with oropharyngeal symptoms of uvular deviation and loss of the efferent limb of the gag reflex secondary to pharyngeal plexus malfunction. Proximal vagal neuropathy usually involves some combination of cranial nerves IX, X, XI, and XII.[1–3,8]

2.13 Cranial Nerve XI (Spinal Accessory)

Impulses from the motor cortex of the cerebral hemisphere extend through the genu of the internal capsule and cerebral peduncle via the corticobulbar tract to the nucleus ambiguus. The motor fibers of the bulbar portion of the spinal accessory nerve are joined by additional fibers which arise from the anterior horn cells of the first five cervical cord segments. The fibers from the spinal nucleus have ascended through the foramen magnum. Together, the combined fibers from the bulbar and spinal portions of the spinal accessory nerve pass anteriorly to exit from the medulla at the posterior olivary sulcus. The eleventh cranial nerve joins the companion cranial nerves IX and X to pass through the perimesencephalic cistern. The spinal accessory nerve then leaves the skull via the posterior portion of the pars vascularis of the jugular foramen. From the skull base, the eleventh cranial nerve enters the carotid space and then quickly diverges posterolaterally to descend along the medial aspect of the sternocleidomastoid muscle. It then continues its course across the posterior triangle of the neck to terminate in the trapezius muscle.

Clinical manifestations of spinal accessory nerve injury are often found in conjunction with ninth, tenth, and twelfth nerve symptoms. When isolated, the symptoms will consist of shoulder droop and an inability to lift the arm.[1–3]

2.14 Cranial Nerve XII (Hypoglossal)

Impulses from the motor cortex travel via the corona radiata through the genu of the internal capsule and cerebral peduncle via the corticobulbar tract to reach the hypoglossal nucleus, which is found in a paramedian location in the floor of the fourth ventricle. Hypoglossal nerve root fibers as well as fibers from the nucleus ambiguus exit forward from the medulla passing lateral to the medial lemniscus. The fibers exit from the

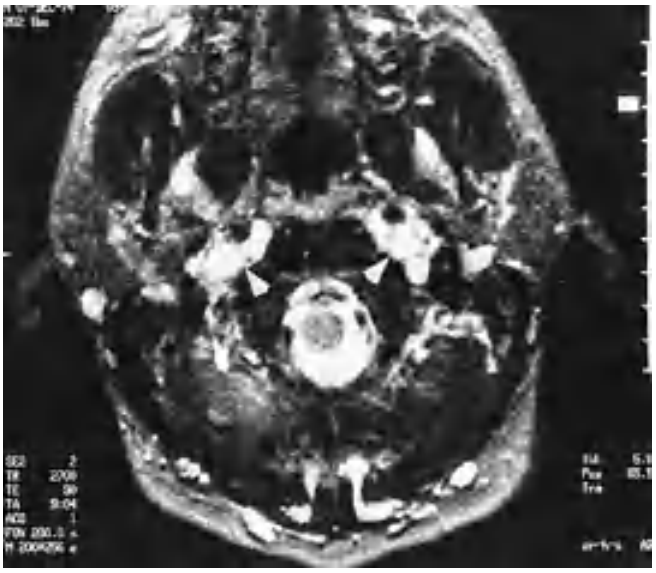

Figure 11 Multiple neurofibromas in a patient with neurofibromatosis I. There are bilateral neurofibromas in the carotid spaces which surround the carotid arteries. The lesions are readily identified by their high signal intensity (arrows). Additional smaller neurofibromas are seen in the posterior scalp region

brainstem in the sulcus between the pyramid and olive as multiple small rootlets. The rootlets extend anteriorly to form the hypoglossal nerve extending anterolaterally through the hypoglossal canal. Once exited from the skull base, the fibers descend inferiorly in the carotid space lying medial to cranial nerves IX, X, and XI and passing lateral to the carotid bifurcation. The hypoglossal nerve then continues forward to enter the posterior portion of the sublingual space of the oral cavity. From here it curves upward medially to the submandibular salivary glands to supply the intrinsic and extrinsic muscles of the tongue and the infrahyoid strap muscles.

Clinical manifestations of hypoglossal nerve injury include deviation of the tongue toward the side of the lesion on protrusion. Tongue atrophy, including both the intrinsic and extrinsic muscles will be evident in chronic lesions. Fasciculations of the tongue muscles may also be seen.[1–3]

3 TUMORS OF CRANIAL NERVES

3.1 Neural Tumors

Schwannoma and neurofibroma are the two most common tumors of the cranial and peripheral nerves. Both tumors are derived from Schwann cells, but present quite differently. Schwannomas are usually solitary masses arising from more proximal nerves, while neurofibromas may be multiple, and usually arise in more distal nerves (Figure 11). Histologically, schwannomas show areas of high and low cellularity known as Antoni-A and Antoni-B areas, respectively, while neurofibromas show spindle cells with wavy nuclei not seen in schwannomas. Another differentiation between these two tumors is the presence of a capsule around schwannomas, whereas neurofibromas are usually not encapsulated. In many cases, schwannomas can be removed by surgery without transecting the nerve. Neurofibromas, however, are part of the nerve which has to be excised with the tumor.

3.2 Schwannoma (Neurilemoma)

Schwannoma is a benign tumor which arises from the Schwann cells surrounding the cranial nerves, peripheral nerves and sympathetic plexus. The Schwann cells represent structures that both encircle the axons of the nerves and provide the nerves with mechanical support and their myelin sheaths. Histologically, a schwannoma contains a cellular component (formed from the Antoni-A cells) and a myxoid component (formed from the Antoni-B cells). The presence of these components and the absence of nerve fibers in the body of the tumor allow the pathologist to differentiate a schwannoma from a neurofibroma.

Schwannomas of the olfactory system and visual pathway are rare, since cranial nerves I and II are not true cranial nerves, but rather are embryologic invaginations of fiber tracts from the telencephalon and diencephalon. The remaining cranial nerves and the upper spinal nerves are the sites of origin of the majority of schwannomas. These tumors are more common in women aged 30–60 years. The signs and symptoms vary according to the specific site of origin.

Schwannomas of cranial nerves III, IV and VI may be seen along the cisternal, cavernous or intraorbital course of these nerves. Symptoms include diplopia, ophthalmoplegia or proptosis, depending upon the site of greatest mass effect. These tumors may be visualized on MRI as they course through the cranial canals. Bulbous expansion of the canals at the site of a lesion is considered pathognomonic; however, differentiation of schwannomas from various malignancies extending along nerve roots may be difficult.

Schwannomas of the trigeminal ganglion and trigeminal nerve usually cause progressive facial numbness, pain, and paresthesias. Some trigeminal tumors can attain a considerable size in the absence of facial pain or numbness, since they may arise from the nerve sheath and secondarily compress the nerve fibers. Schwannomas involving the trigeminal nerve are divided into three anatomical divisions: preganglionic, ganglionic, and postganglionic. Lesions that originate from the trigeminal ganglion typically straddle the incisura with a component extending into the cavernous sinus (postganglionic) and another portion extending into the prepontine cistern (preganglionic) (Figure 12).[9–12]

Facial nerve schwannomas may present with facial nerve palsy and/or hearing loss, or may be relatively asymptomatic. The development of facial nerve schwannomas from the nerve sheaths allows some of these tumors to enlarge and decompress into the adjacent air-containing cavities of the temporal bone without producing symptoms. Schwannomas originating from the geniculate ganglion typically become quite large without producing facial nerve dysfunction. These lesions may expand into the superior surface of the temporal bone and present as middle fossa masses (Figures 7 and 13).

Acoustic nerve schwannomas originate from the vestibulocochlear nerve along its course from the vestibule and cochlea, internal auditory canal, and cerebellopontine angle cistern. These tumors represent 5–10% of all primary intracranial neoplasms and approximately 85–90% of all cerebellopontine

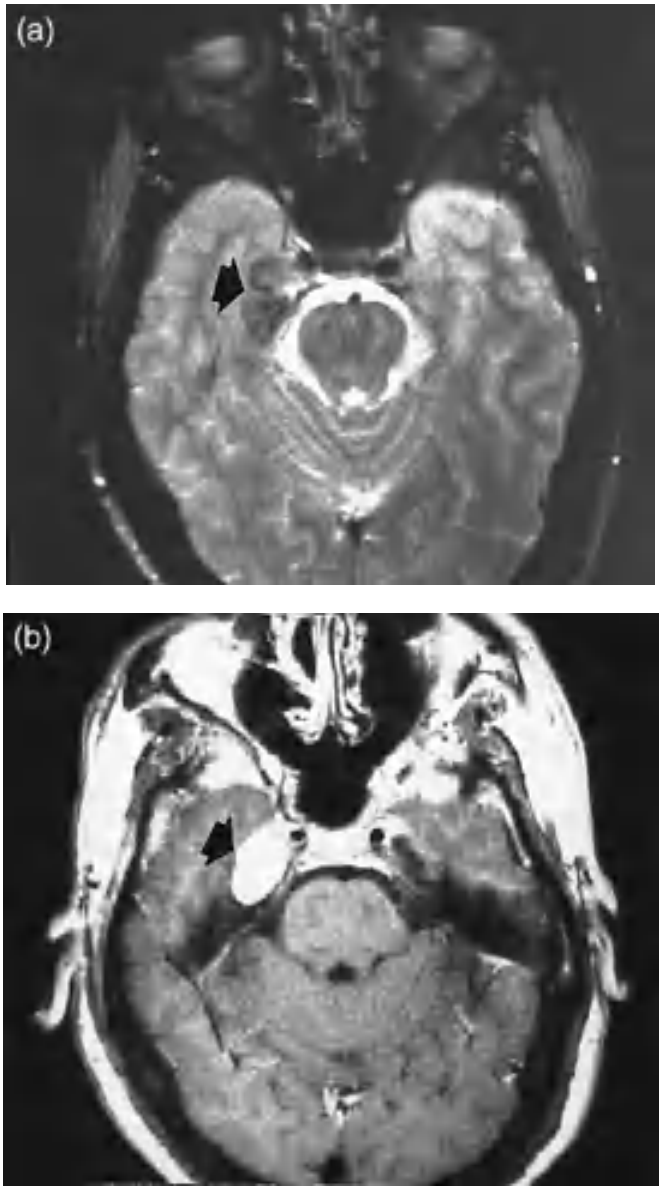

Figure 12 Schwannoma of the right trigeminal ganglion. (a) There is a primarily hypointense lesion in the right Meckel's cave and trigeminal ganglion region (arrow). (b) This enhanced view documents homogeneous enhancement of the tumor mass (arrow)

angle tumors. The clinical symptoms of acoustic nerve schwannoma are typically unilateral or asymmetric neurosensory hearing loss. These symptoms are directly related to the size of the tumor. As the tumor enlarges and fills the internal auditory canal, it compresses the cochlear nerve, causing neurosensory hearing loss and tinnitus, which are the most common initial symptoms (Figure 13). The early hearing loss is of the high-frequency variety, which may be related to the anatomic arrangement of the high frequency fibers around the periphery of the nerve. The hearing loss is typically gradual and progressive, but may have an acute onset. Vestibular dysfunction, such as dizziness and disequilibrium, are relatively uncommon presenting symptoms, even though 85% of acoustic nerve schwannomas arise from the vestibular nerves. Small intracanalicular lesions may be either relatively asymptomatic or may cause progressive symptoms. Some larger neoplasms may develop intramural or extramural hemorrhage with the sudden onset of headache, nausea, and vomiting. True central vertigo may be associated with brainstem involvement. Facial nerve dysfunction may be related to compression of the seventh nerve.

Jugular foramen schwannomas can originate from different sites along cranial nerves IX, X or XI. Early symptoms consist of loss of taste in the posterior third of the tongue (glossopharyngeal nerve), paralysis of the vocal cord and palate (vagus nerve), and paresis of the trapezius and sternocleidomastoid muscles (spinal accessory nerve). Proximal schwannomas may extend into the inferior portion of the posterior fossa, producing hearing loss, vertigo, ataxia, hoarseness, and swallowing difficulties (Figure 10). Schwannomas of the twelfth nerve usually cause hemiatrophy and paresis of the tongue. Some large tumors of the jugular foramen can extend into the hypoglossal canal and large hypoglossal schwannomas may expand into the adjacent jugular foramen. Concomitant involvement of cranial nerves IX, X, XI, and XII is rare, but may be seen with bulky tumors. Additional disturbances of posterior fossa function may include gait abnormalities, swallowing difficulties, dizziness, and vomiting. In the neck, schwannomas are the most common neoplasm of the carotid space and the second most common lesion of the parapharyngeal space. Clinical presentation is a painless, slow growing mass in the anterolateral neck or posterolateral oropharynx. These lesions may become painful with associated neuropathies if they continue to grow and compress the nerves.[11–13]

The MRI appearance of all schwannomas is similar. The key differentiating point is the location of the central portion of the tumor within or near the nerve of origin. Schwannomas are fairly fusiform in appearance and well circumscribed because of their associated capsule. There may be smooth and uniform enlargement of the cranial canal through which the nerve is transmitted. The signal intensities, however, differ dramatically with respect to the size of the tumor. Smaller tumors usually appear homogeneous (since they are predominantly of the Antoni-A cell type), while larger tumors demonstrate heterogeneity and variable signal intensities owing to the presence of hemorrhage, necrosis, and cystic degeneration (Figure 13). Larger tumors typically contain many Antoni-B type cells. These schwannomas can have foci of high and low signal intensities on both the T_1- and T_2-weighted images. The presence of intramural cysts will characteristically produce foci of high signal intensity on the T_2-weighted images (Figure 14).[9,12]

One MRI study suggested that cystic changes in acoustic nerve schwannomas may be related to either intramural cysts (Figures 13 and 14) or extramural arachnoid cysts (Figure 15). The intramural cysts showed high signal intensity on the T_2-weighted images, which was thought to be due to necrotic material, blood, or colloid-rich fluid. The extramural cysts showed high signal intensity related to higher protein and/or colloid contents secreted by the tumor. The extramural cysts were thought to originate from peritumoral adhesions which caused a pseudoduplication by the trapping effect of fluid between the leptomeninges and the schwannoma.[14]

Enhancement following gadolinium contrast administration is also variable, although it is typically rapid due to extravasation of contrast into the extracellular compartment of the often

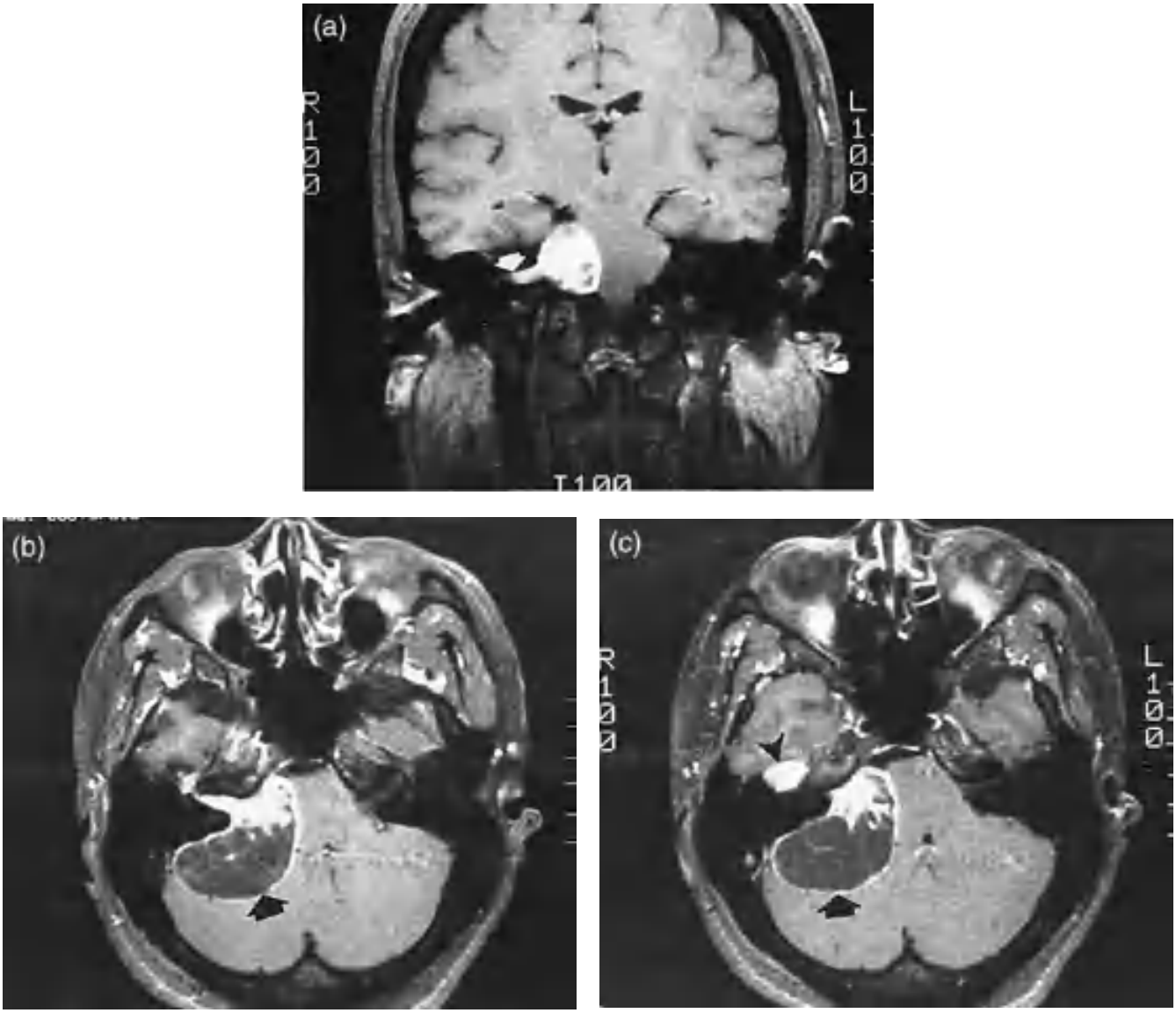

Figure 13 Large schwannomas of the right seventh and eighth cranial nerves extending from the geniculate ganglion to the cerebellopontine angle (CPA). The patient had marked hearing loss, but only minimal facial nerve dysfunction. Enhanced images with fat saturation pulses. (a) This coronal image shows the tumor in the right CPA and internal auditory canal (arrow). (b and c) Axial images. The portion of the tumor in the right CPA shows both solid and cystic components (arrows). The solid component extends through the right internal auditory canal where it merges with a companion tumor in the right geniculate ganglion [arrow, (c)]

vascular schwannoma. In nearly all cases, there is a sharp demarcation between the margin of the tumor and the adjacent structures. Enhancement of the cranial nerves or their ganglia without an associated soft tissue mass is consistent with cranial nerve neuritis and/or ganglionitis rather than a neoplasm. Sarcomas, hemangiomas, or paragangliomas may have similar MRI enhancement characteristics and need to be considered in the differential diagnosis of schwannomas.[12,15]

3.3 Neurofibroma

A neurofibroma contains neural elements with a fibrous core. This tumor may arise from the cranial, spinal, or peripheral nerves. The patient's symptoms depend upon the nerve of involvement and may be similar to the symptoms associated with a schwannoma. In the extracranial head and neck, neurofibromas may present as subcutaneous soft tissue nodules in the skin or as a mass lesion in the carotid or parapharyngeal spaces (Figure 11). In such cases, the clinical symptoms result from tumor bulk and may include dysphagia or difficulty turning the neck. Some neurofibromas cause pain or other focal neurologic deficits.

Most neurofibromas are seen in young adult patients. Approximately 10% of patients with neurofibromas have neurofibromatosis type I (NF-1 or von Recklinghausen's disease). Two types of neurofibroma are known to be associated with NF-1. Multiple or single solid lesions may be seen along the cranial, spinal, or peripheral nerves (Figure 11). Another type of lesion presents as an infiltrating soft tissue mass with extension along the cranial nerves through the orbits, skull base, or

Figure 14 Acoustic nerve schwannoma with solid and intramural cystic components. (a) This axial image shows the heterogeneous mass in the left internal auditory canal and cerebellopontine angle cistern. The cystic component of the tumor merges with the bright signal intensity of the cerebrospinal fluid. (b) This axial enhanced image shows the solid and cystic components. Note that the cystic portion shows peripheral enhancement confirming an intramural cyst (arrow)

posterior fossa. This so-called 'plexiform' neurofibroma encases the muscles and soft tissues along the course of the nerves (Figure 5).[16]

The MRI characteristics of neurofibromas are quite varied and simulate schwannomas in many cases. Neurofibromas project an intermediate signal intensity on the T_1- and proton-density-weighted images. They sometimes have a 'salt and pepper' appearance whenever there is intense vascularity within the stroma of the tumor. The T_2-weighted images are variable, depending on whether the tumor is cystic or solid in nature. Variable enhancement is seen following gadolinium administration due to the presence of cystic areas, calcifications, or vascularity. The margins of a neurofibroma appear less distinct than the margins of a schwannoma, because neurofibromas lack a capsule. In many cases, it may not be possible to differentiate a neurofibroma from a schwannoma on MRI characteristics.[12,15]

3.4 Malignant Schwannoma

Many terms have been used to describe a malignant schwannoma, including malignant neurofibroma, neurofibrosarcoma, neurosarcoma, neurogenic sarcoma, malignant neurilemoma, and malignant nerve sheath tumor. Many malignant schwannomas contain interlacing fascicles of spindle cells in a herring-bone pattern, as typically seen in fibrosarcomas. Unlike fibrosarcomas, however, on electron microscopy malignant schwannomas are seen to contain basement membranes. The light microscopic findings include high cellularity, pleomorphism, high incidence of mitotic figures, presence of necrosis, and presence of histologic invasion. There is no capsule around a malignant fibrosarcoma.[16]

Malignant schwannomas are highly malignant lesions that recur following local excision in 50–80% of patients. The histologic grade is the most important factor in determining prognosis and is the primary factor considered in staging. Five-year survival rates in one study of 17 patients over the course of 37 years was 47%. Wide and aggressive excision with or without adjuvant radiation therapy is considered the best treatment alternative. Generally, patients with malignant schwannomas of the head and neck have a poorer prognosis than do those with similar tumors of the extremities, which can be treated with amputation. One factor contributing to the poor prognosis of this tumor is its resistance to radiation therapy.

The incidence of malignant schwannomas is approximately 5–10% of all sarcomas and 2–12% of all nerve sheath tumors. Patients with NF-1 have a 5–30% chance of developing a de novo malignant neurogenic tumor. The typical NF-1 patient with a malignant neural tumor is 20–50 years old. The 5-year survival rate in patients with NF-1 is 15–30%. Recurrences and metastases may occur as late as 5–10 years following treatment.

The tumor initially causes a fusiform, nodular swelling of the involved nerve and ultimately diffusely infiltrates the nerve. It then spreads into the surrounding soft tissues and often contains areas of hemorrhage or necrosis (Figure 16). The tumor may cause neurologic symptoms such as pain, paresthesias, atrophy, and muscle weakness. Occasionally, a symptomless mass along a nerve distribution is seen.[12,15,16]

The MRI appearance is of a tubular mass along the involved nerve with regional extension into the skull base (cranial nerve) or cervical soft tissues. The signal intensity is varied, but is typically hypointense on the T_1-weighted images and hyperintense on the T_2-weighted images. Gadolinium contrast administration helps to outline the margins of the tumor including extension beyond the site of origin into the spinal canal or cranial cavity (Figure 17)[12,15]

3.5 Cranial Nerve Seeding

Both metastatic neoplasms and primary malignant tumors of the central nervous system can disseminate via the subarachnoid cisternal pathways to distant locations. This type of

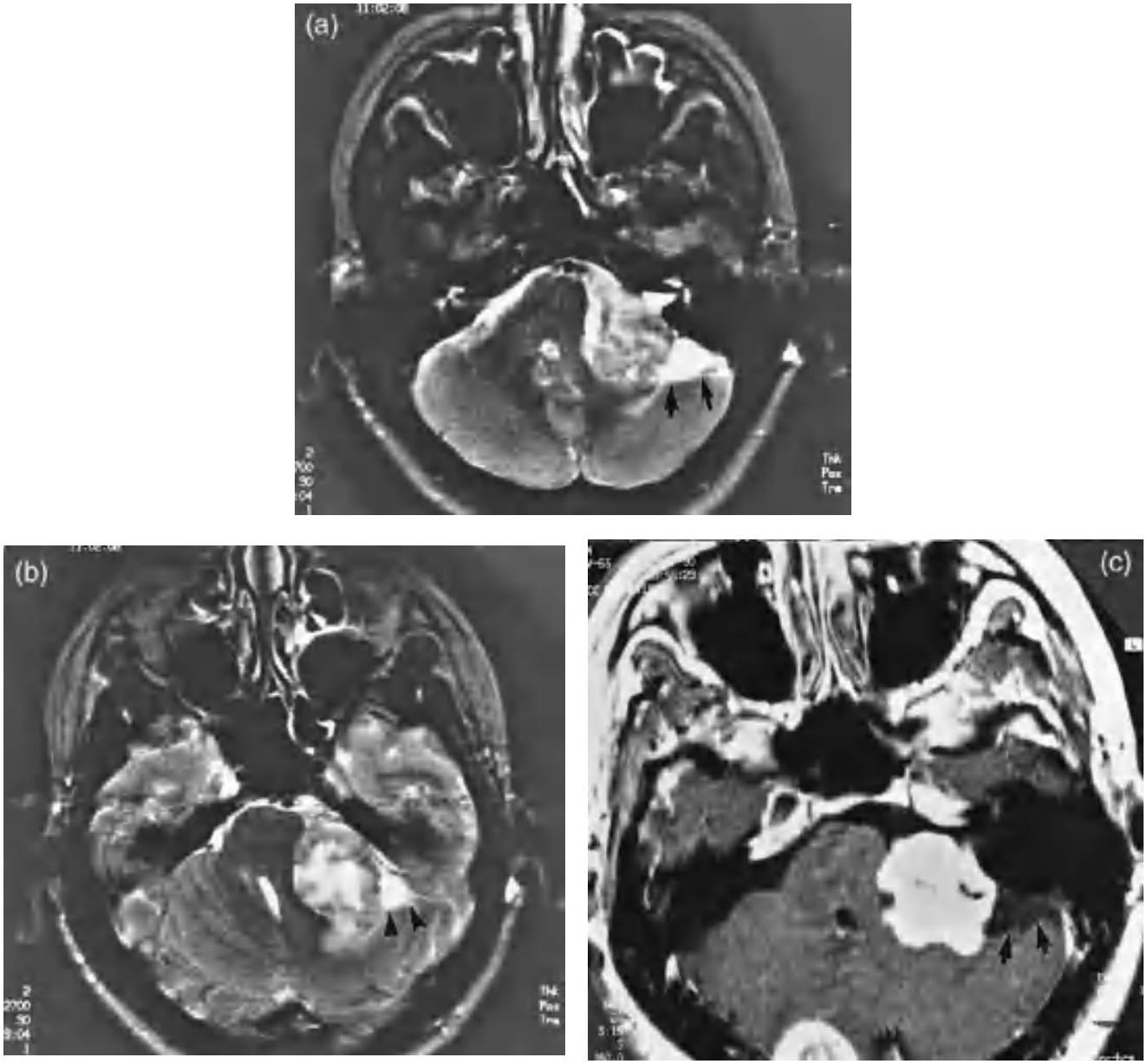

Figure 15 Acoustic nerve schwannoma with a small arachnoid cyst in the left cerebellopontine angle. (a and b) The large tumor is highly heterogeneous and deforms the left side of the brainstem and cerebellum. Note the homogeneously bright signal in the small left arachnoid cyst (arrows). (c) This image shows enhancement of the tumor. The arachnoid cyst, however, is extramural and does not enhance (arrows)

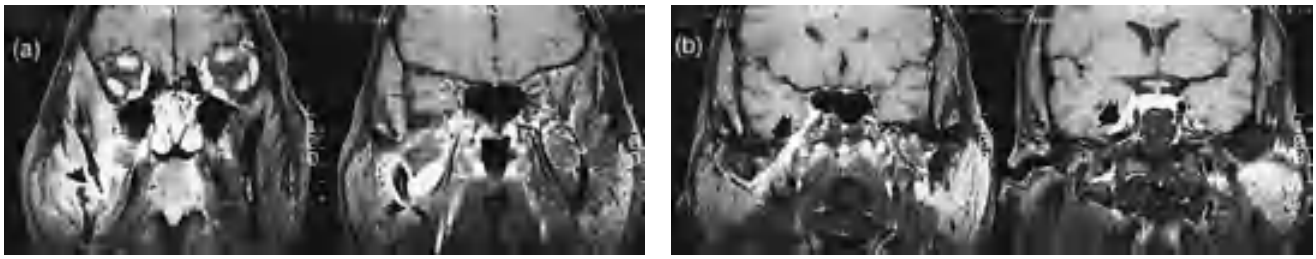

Figure 16 Malignant schwannoma of the right trigeminal and inferior alveolar nerves. Coronal enhanced images with fat saturation pulses. (a) This composite image documents the extensive infiltration of the tumor in the right muscles of mastication. There is a pathologic fracture of the right ramus of the mandible (arrows). (b) This composite view documents the extension of the tumor in a tubular manner through the right foramen ovale into the right trigeminal ganglion (arrows)

Figure 17 Coronal enhanced images of a malignant schwannoma of the right brachial plexus with intraspinal extension. (a and b) The tumor fills the region of the scalene muscles and brachial plexus. There is downward extrapleural extension [arrow, (a)]. Note a small intraspinal portion along the cervical nerve roots [arrow, (b)]

metastatic spread may be manifested as either a diffuse spread along the leptomeningeal surfaces of the brain or loculated deposits of tumor nodules along specific sites within the subarachnoid spaces such as the cranial nerves. The most common dissemination in children is from primitive neuroectodermal tumors and ependymomas. The most common cause of seeding in adults is from a glioblastoma multiforme. The incidence of seeding from a glioblastoma is less than 5% in all age groups. Other tumors that can seed to the leptomeninges or cranial nerves are sarcomas, carcinomas, and adenocarcinomas. Leptomeningeal metastases from various lymphoproliferative tumors are also common in both children and adults. Metastatic lymphomatous foci may be deposited adjacent to the cranial nerves along their courses through the posterior and middle cranial fossae (Figures 3 and 18).[16,17]

Intracranial leptomeningeal metastases tend to be diffuse along the subarachnoid spaces and cranial nerves. Microscopically, the tumor cells infiltrate the leptomeninges as a single layer or as thicker, multilayered aggregates. The earliest infiltration is along cortical vessels and is limited to the perivascular Virchow–Robin spaces. Clinically, patients most often present with a variety of symptoms, which are usually multifocal. Headache, change of mental status, cranial nerve deficits, and gait disturbances are the most common.

These metastatic deposits are visualized best on the T_1-weighted postcontrast images, particularly if fat saturation

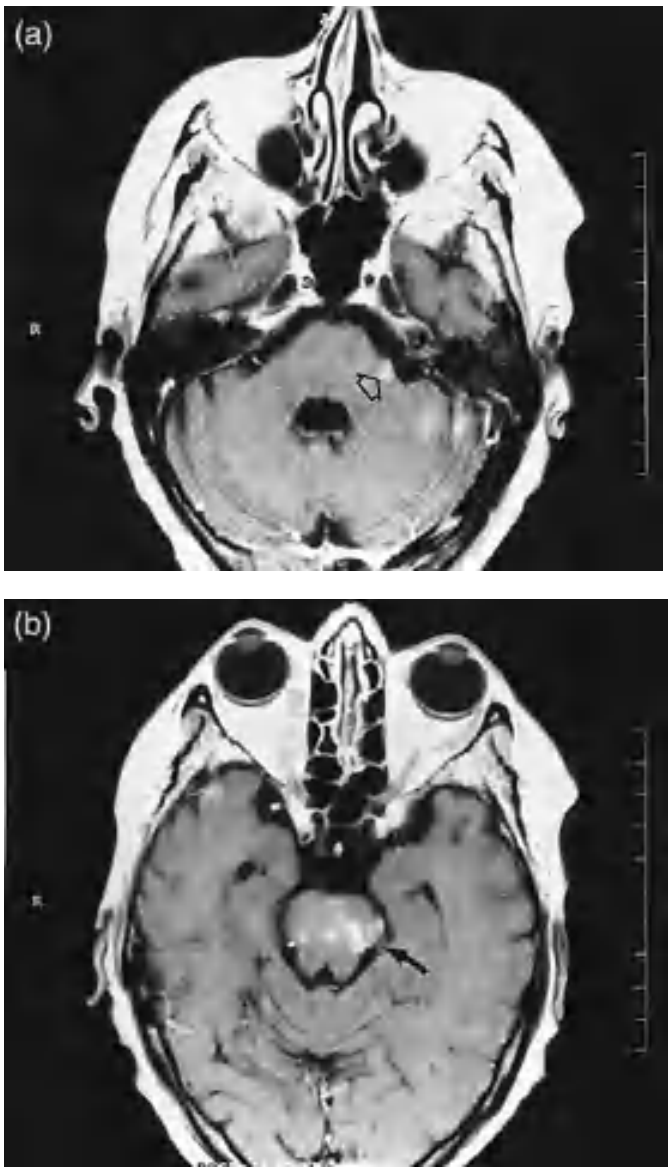

Figure 18 Lymphomatous meningitis of the brainstem and cranial nerves. Axial enhanced images. There is a focal tumor nodule in the left cerebellopontine angle region [arrow, (a)]. There is diffuse infiltration of the midbrain and enhancement along the left trochlear nerve [arrow, (b)]

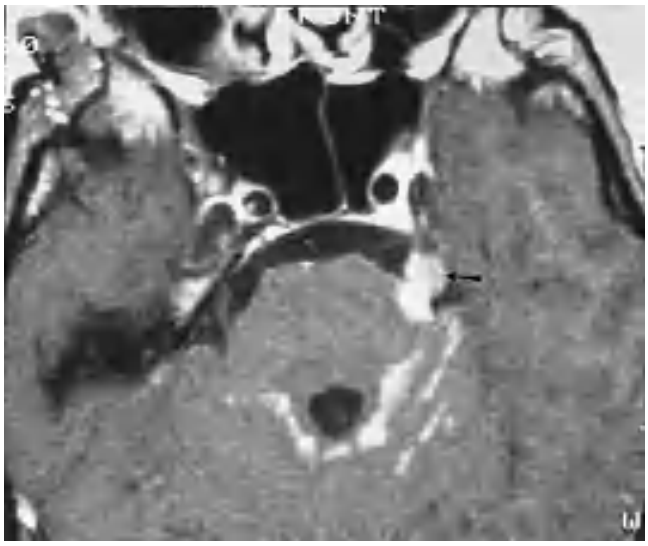

Figure 19 Axial enhanced image of seeding of metastatic adenocarcinoma to the subarachnoid spaces and cranial nerves. There are sheets and nodules of tumor surrounding the midpons and cerebellar folia. A large focal nodule occupies the origin and preganglionic portions of the left trigeminal nerve (arrow)

techniques are utilized. The areas of nodular or linear enhancement follow the contours of the meningeal surfaces or cranial nerves as they traverse through the cerebrospinal fluid (Figure 19). The T_2-weighted images are less sensitive because of the surrounding high signal intensity of the cerebrospinal fluid.[12,15]

3.6 Perineural Spread of Malignant Neoplasms

Perineural tumor extension is a form of metastatic disease in which primary tumors spread along neural pathways and gain access to noncontiguous regions. Since the treatment and prognosis are altered when perineural spread is identified, proper evaluation is critical. The infiltration of the nerves by tumor is best seen on gadolinium enhanced MRI.[18,19]

Perineural tumor spread is visible as smooth thickening of the cranial or spinal nerves and/or concentric expansion of the foramina and fissures through which the nerves traverse. Involvement of the maxillary and mandibular divisions of the trigeminal nerve is common because of the large size of these branches and their strategic passage through the pterygopalatine fossa. In cases of perineural spread to the trigeminal ganglion, there may be replacement of the normal trigeminal cistern hypointensity by an isointense or enhancing soft tissue mass (Figure 20). Other signs of trigeminal ganglion involvement include lateral bulging of the cavernous sinus dural membranes and atrophy of the masticator muscles supplied by the trigeminal nerve branches (Figure 6). Perineural metastatic disease may occur along the course of the facial nerve, most commonly resulting from neoplasms of the parotid gland, particularly adenoid cystic carcinoma.[15,18,19]

4 INFECTIONS AND INFLAMMATIONS OF CRANIAL NERVES

Infections of the cranial nerves commonly are caused by a latent virus such as herpes simplex I or varicella zoster. These neurotropic viruses tend to affect the cell bodies of the sensory neurons, in which they may reside for many years. Reactivation of the dormant virus results in a swelling of the involved ganglion or of the involved nerve. After contrast medium administration, there may be enhancement in the ganglion or along the course of an infected nerve.[15,20]

The most common viral mononeuritis is Bell's palsy, which is thought to be caused by reactivation of a herpes simplex virus in the geniculate ganglion. Following gadolinium administration, there may be enhancement along the entire course of the facial nerve from the internal auditory canal through the mastoid foramen. More commonly, the portion of the facial nerve in the region adjacent to the geniculate ganglion is enhanced as a result of entrapment of the seventh cranial nerve in the fallopian canal (Figure 21). Herpes simplex trigeminal neuritis and ganglionitis have been described, revealing involvement of the fifth cranial nerve on contrast enhanced MRI (Figure 22).[21,22]

The clinical prevalence of herpetic involvement of the cranial nerves is most likely underestimated. However, in patients infected with the human immunodeficiency virus (HIV), it is fairly common to recognize postgadolinium enhancement along one, two or more cranial nerves. The mechanism is similar to that of herpes simplex virus, since the HIV virus is also neurotropic and directly invades sensory ganglia and their associated nerves.[20,21]

5 OPTIC NERVE AND SHEATH DISORDERS

Primary disorders of the optic nerve and optic nerve sheath typically cause visual disturbances and occasionally proptosis in cases of large neoplasms. The most common primary neoplasms of the optic nerve include gliomas (astrocytomas and hamartomas) or meningiomas. There may be a paraoptic component of optic nerve tumors, which is characteristically seen in patients with neurofibromatosis type I. The paraoptic component results from perineural arachnoidal gliomatosis, consisting of proteinaceous material that seeds and spreads within the optic nerve subarachnoid space and is a portion of the tumor. This process may result in optic nerve elongation and resultant kinking of the nerve just posterior to the posterior portion of the globe. There is no correlation between the size of the lesion and visual loss.

Extension of tumors into the optic chiasm, optic tracts, and lateral geniculate bodies of the thalami is more accurately depicted on MRI than computed tomography (CT). The size and shape of the optic canals are best assessed in the axial projection, while the size and shape of the optic nerves are best appreciated on coronal and oblique sagittal images. Many optic nerve tumors exhibit fusiform homogeneous enhancement (Figure 23). Unenhanced portions of optic nerve tumors may represent the sites of gliomatosis, rather than a true neoplasm. Biopsy is essential to make the correct diagnosis,[23,24]

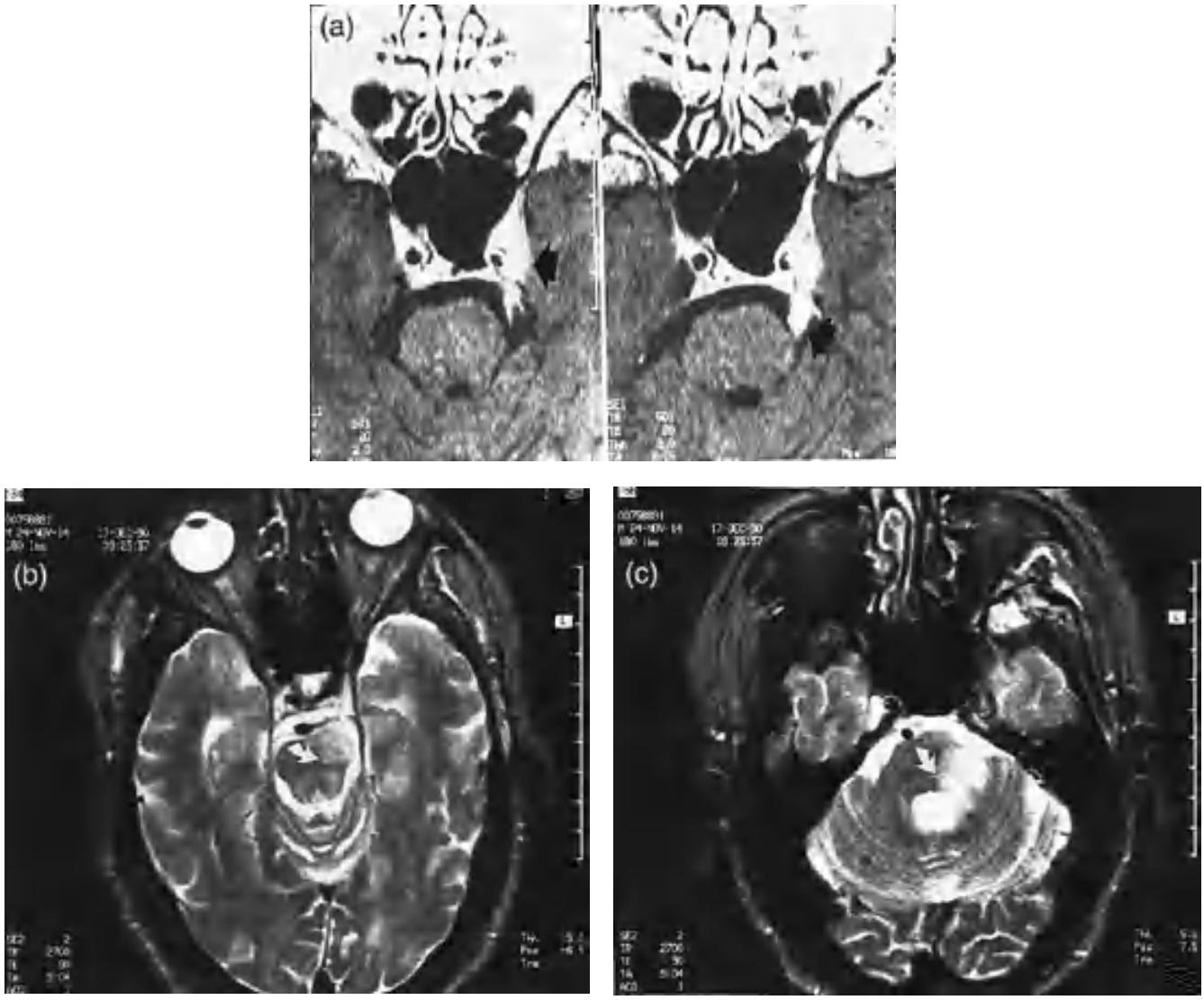

Figure 20 Perineural spread of squamous cell carcinoma. (a) This axial enhanced composite image shows bulging of the left side of the cavernous sinus and tumor extension into the preganglionic portion of the left trigeminal nerve (arrows). (b and c) Axial images. There is well defined edema and tumor infiltration into the left cerebral peduncle, pons, and middle cerebellar peduncle (arrows). The wide extent through the brainstem correlates with the long nuclei of the fifth cranial nerve

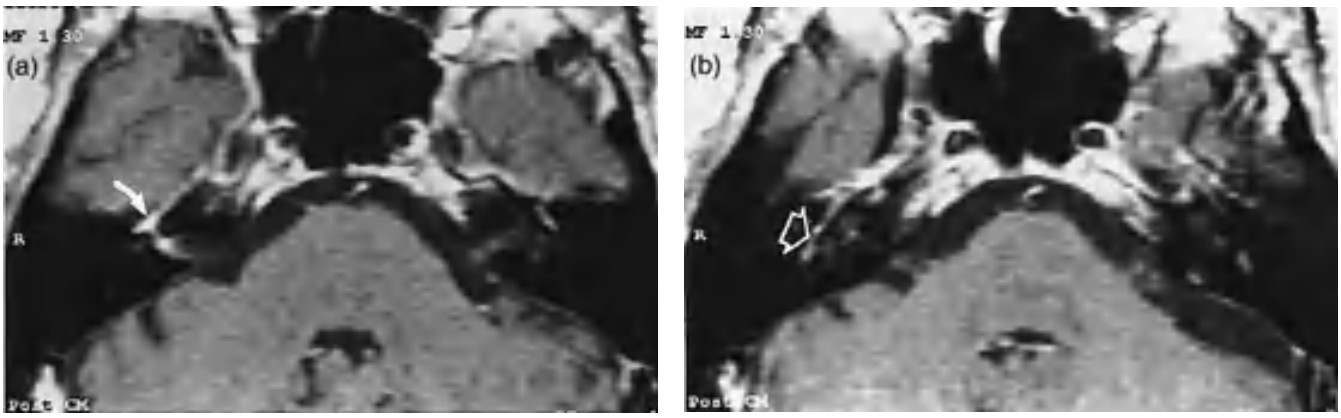

Figure 21 Facial neuritis and geniculate ganglionitis in a patient with Bell's palsy. Axial enhanced images. (a) Note the enhancement in the fundus of the right internal auditory canal with extension into the adjacent geniculate ganglion (arrow). (b) There is enhancement along the tympanic segment of the right facial nerve (arrow)

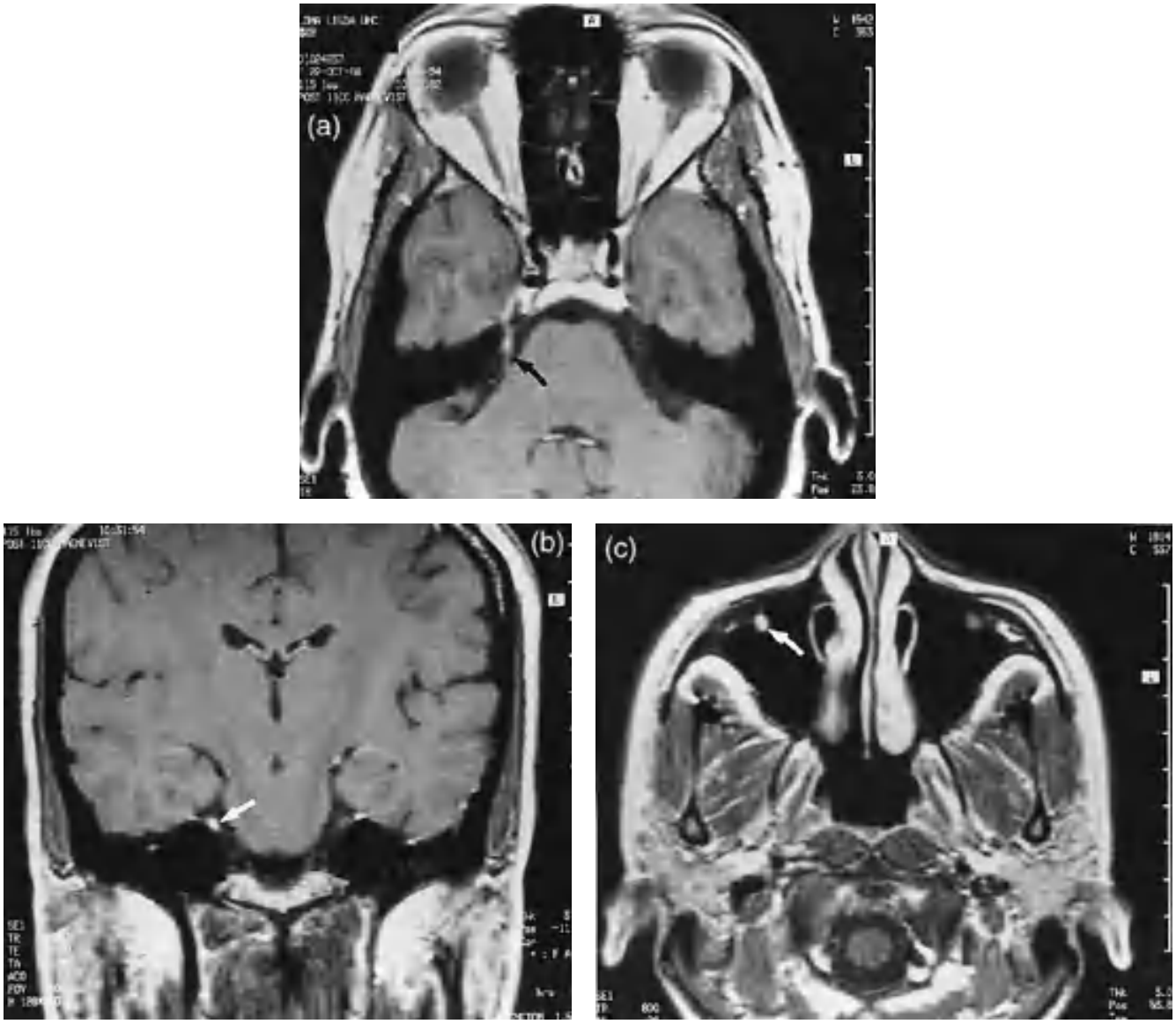

Figure 22 Enhanced images of viral trigeminal neuritis in a patient with trigeminal neuropathy. (a) There is enhancement along the preganglionic portion of the right trigeminal nerve (arrow). (b) This coronal view confirms the enhancement of the cisternal portion of the right trigeminal nerve (arrow). (c) The enhancement extends along the infraorbital division of the right maxillary nerve into the infraorbital groove (arrow)

Meningiomas are the most common optic nerve sheath tumors; they usually arise from the arachnoidal coverings of the optic nerve. Visual loss and optic atrophy are the usual presenting symptoms. Most cases are seen in middle-aged or elderly patients, more often in women. The tumor may be cuff-like surrounding the optic nerves or eccentrically located on only one side of the nerve. CT scans will often demonstrate calcifications and show typical postcontrast enhancement parallel to the length of the optic nerves. MR scans readily depict the irregular thickening along the optic nerves and spread into adjacent meninges on the postcontrast scans (Figure 24). Parallel optic cysts may be identified surrounding the optic nerve immediately distal to the meningioma. The process causes trapping of the cerebrospinal fluid in the subarachnoid space and can add to the mass effect and proptosis.[23,25]

Optic neuritis is seen on MRI as focal or diffuse enlargement of the optic nerve associated with abnormal signal intensities and enhancement (Figure 25). This is caused by immunological inflammation of the optic nerve, which affects the myelin sheaths with relative preservation of the axons. As optic neuritis is the initial manifestation of multiple sclerosis in about 20% of patients and may occur at some point in the disease in approximately 50%, the role of MRI in the evaluation of acute optic neuritis is changing. A multicenter trial was developed to assess the efficacy of corticosteroid treatment for acute optic neuritis. This study showed that the utility of MRI in establishing the diagnosis of optic neuritis was limited; however, with additional views of the cranial cavity, abnormal MRI scans could differentiate those patients who would later develop multiple sclerosis from those that would not. Thus, MRI is a predictor of multiple sclerosis as it can help to identify a subgroup of patients whose risk of developing the disease appears to be low and it can provide prognostic data about the development of multiple sclerosis after optic neuritis.[23,26]

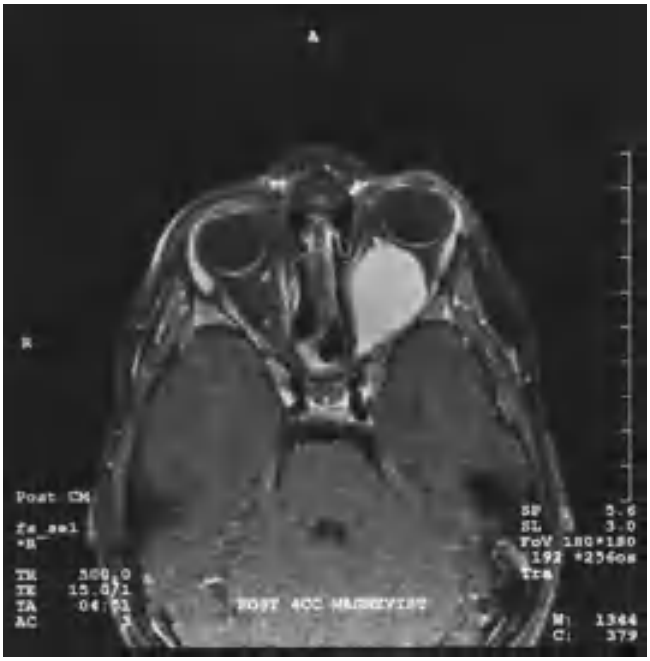

Figure 23 A 4-year-old boy with large left optic nerve glioma. There is a pear-shaped densely enhancing tumor mass in the left orbit causing mild proptosis. Note extension of the tumor into the orbital opening of the left optic nerve canal

The papilledema associated with the pseudotumor cerebri may be detected on CT or MRI scans as enlargement of the optic nerve sheaths. If severe, there is a reversal of the optic nerve head with bulging forward into the posterior wall of the globe. This phenomenon is more readily detected on CT than MRI because of the chemical shift artifact inherent to the MR studies. There is some correlation between the severity of the visual loss and the detection of enlarged nerves with reversed nerve heads. Patients with more severe visual loss demonstrate more frequent and more severe reversal of the optic nerve head.[27]

5.1 Optic Nerve Neuropathies

Isolated visual disturbances may result from a variety of optic nerve neuropathies, caused by radiation, chemotherapy, compressive phenomena, or ischemia.[28–30] Radiation-induced optic neuropathy (RON) is a rare catastrophic complication of radiation therapy regimens used to treat a variety of neoplasms of the skull base, sella, and parasellar regions (Figure 26). There is typically a latency period of 6 to 36 months following treatment. Clinically, the nerve head may appear normal, but gadolinium-enhanced MRI will show patchy, linear, or confluent enhancement along the portions of the optic nerve, chiasm, or optic tract.[25,28] These findings precisely correlate as the cause of delayed visual loss following radiation therapy. Treatment of RON with corticosteroids may be helpful, although optic atrophy may develop with permanent visual loss.[28]

Compressive optic nerve neuropathies can be seen with a variety of lesions in the orbital apex [including Idiopathic Orbital Pseudotumor (IOP), thyroid ophthalmopathy with muscular hypertrophy, and edema causing compression of the intraocular portion of the optic nerve] or other systemic diseases with common orbital manifestations, such as sarcoidosis or Wegener's granulomatosis.[29–36]

Compression of the optic nerve may occur as a result of cavernous carotid fistulae, arteriovenous malformations, or orbital varices. Such vascular anomalies may produce retrograde flow through the ophthalmic vessels, with subsequent dilatation of the orbital veins and passive congestion of the orbital tissues. This leads to progressive increases in the intraocular pressure and subsequent decreases in visual acuity

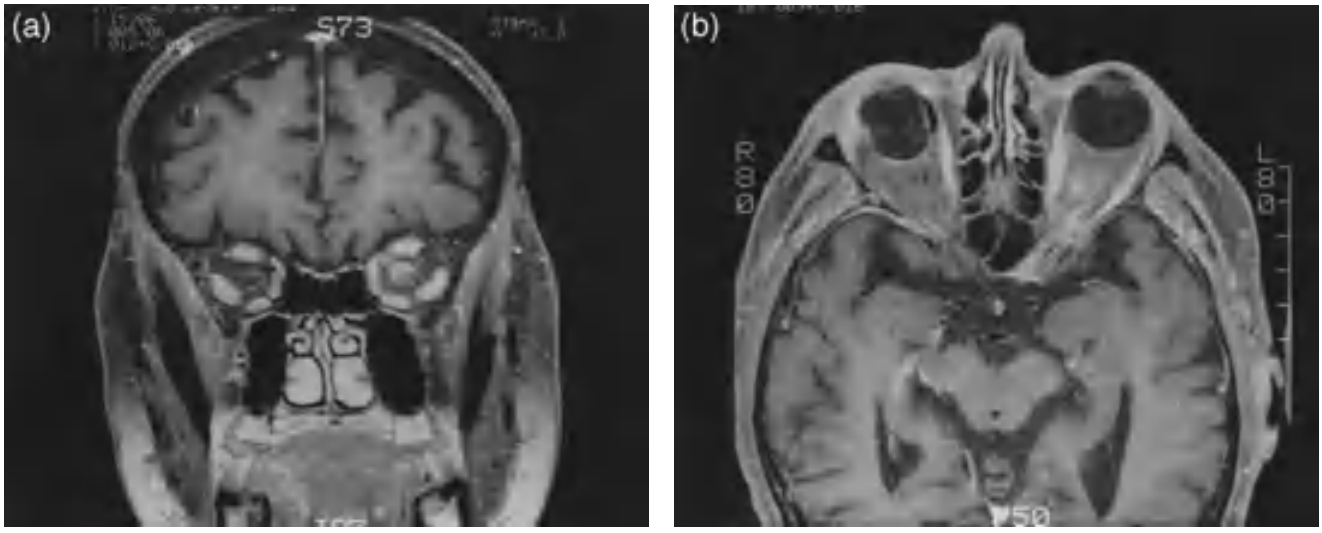

Figure 24 An 80-year-old female with left optic sheath meningioma. (a) Coronal enhanced view shows an enlarged left optic nerve with near complete enhancement of the lesion. (b) Axial enhanced MR scan shows the extent of the tumor in a 'railroad track' manner about the left optic nerve, with extension into the intracanalicular portion of the left optic nerve. Incidental note is made of a retinal banding procedure around the right globe

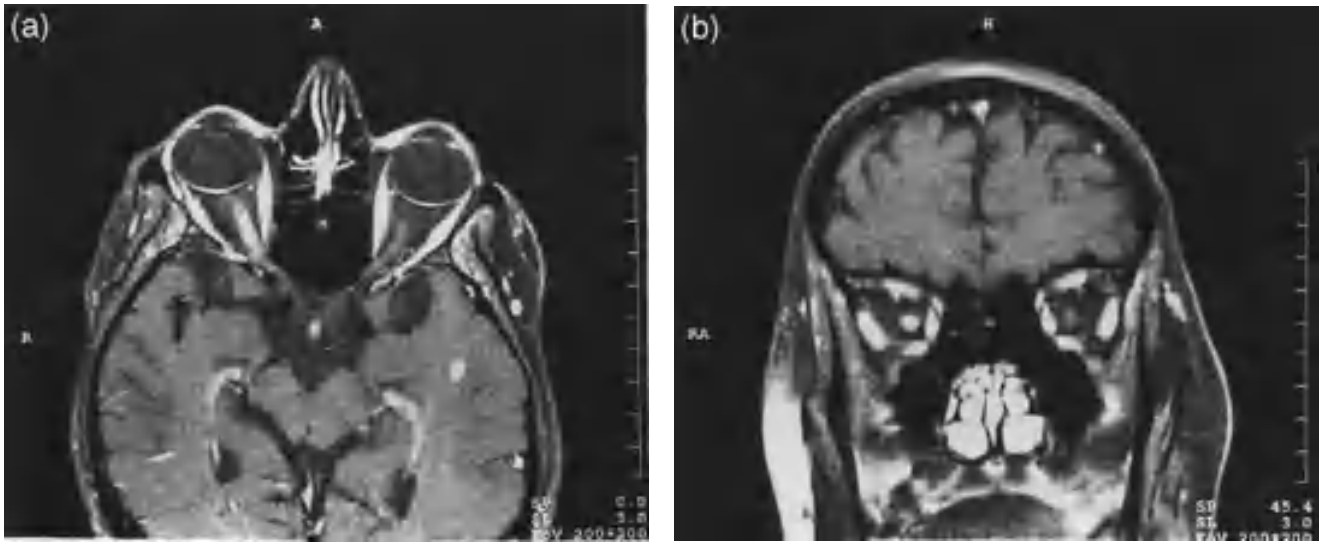

Figure 25 Right optic nerve neuritis in a 40-year-old female. (a) Axial enhanced MR scan showing no enlargement of the right optic nerve. There is enhancement along a major portion of the intraorbital part of the optic nerve. (b) Coronal enhanced scan showing the normal size but enhancing nerve in the right eye

leading to blindness. Spontaneous thrombosis of the ophthalmic veins occasionally occurs and may aggravate the mass effect within the apex of the orbit and the compressive neuropathy.[23,33]

MRI will demonstrate the dilated ophthalmic veins, facial veins, and other regional venous structures along with enlargement of the cavernous sinus. Large edematous extraocular muscles and other periorbital structures may be identified. These findings are optimally seen with MRI, particularly as the addition of MR angiography allows for flow assessments along with the static morphologic changes. In some cases, conventional angiography may be required to make the definitive diagnosis, although most commonly this is used in conjunction with therapeutic interventional procedures.

6 VERTIGO AND HEARING LOSS

6.1 Dizziness and Vertigo

Dizziness is a common clinical complaint. It accounts for 1% of visits to US office-based physicians. Vertigo is a form of dizziness in which there is an illusion of movement (rotation, tilt, or linear translation). Vertigo occurs through an imbalance of tonic vestibular signals; consequently, it is a hallucination of movement and represents a symptom of a disturbed vestibular system.[37,38]

The complete vestibular system comprises the end organs in the temporal bone, the vestibular components of the VIIIth cranial nerve, and the central connections in the brainstem. The end organs in the temporal bones are the cristae of the three semicircular canals, which respond to movement of the head, and the macula of the utricle, which records the position of the head. The semicircular canals record dynamic actions while the utricle records static function. Vertigo is subdivided into peripheral vertigo (caused by failure of the end organs) or central vertigo (caused by failure of the vestibular nerves or central connections to the brainstem and the cerebellum.[38,39]

6.2 Peripheral Vestibular Disorders

Patients with benign positional vertigo describe episodic vertigo lasting less than a minute, brought on by movements of the head and without other associated symptoms. There are no radiological findings in patients with benign positional vertigo.[37,39]

In Meniere's disease, paroxysmal attacks of whirling vertigo are usually accompanied by nausea; the attacks are transient in nature, lasting a few hours but not days. The severe episodic vertigo is accompanied by tinnitus, fluctuating hearing loss, and a feeling of fullness in the affected ear or ears. Typically, hearing decreases and tinnitus increases during the attack. Hearing may improve between attacks in early stages of the disease. Generally, the hearing loss begins unilaterally and affects primarily the lower frequencies, with mid and high frequencies being affected in later stages of the disease.[37–39]

Meniere's disease is most common in middle age and may become bilateral in up to 50% of the affected patients. The etiology of Meniere's disease is a failure of the mechanism regulating the production and disposal of endolymph, resulting in recurrent attacks of endolymphatic hydrops. Since the endolymphatic duct and sac are the sites of resorption of endolymph, these structures play an important role in the pathogenesis of endolymphatic hydrops. The success of various surgical procedures in relieving the symptoms of Meniere's disease has led to great interest in using CT and/or MRI to evaluate the vestibular aqueduct and the endolymphatic duct and sac.[39–41]

Unfortunately, there is no unanimity on the value of imaging in cases of Meniere's disease. Some investigators have used CT or MRI to evaluate the potential success of shunt surgery, based on showing patency of the vestibular aqueduct.[39,41]

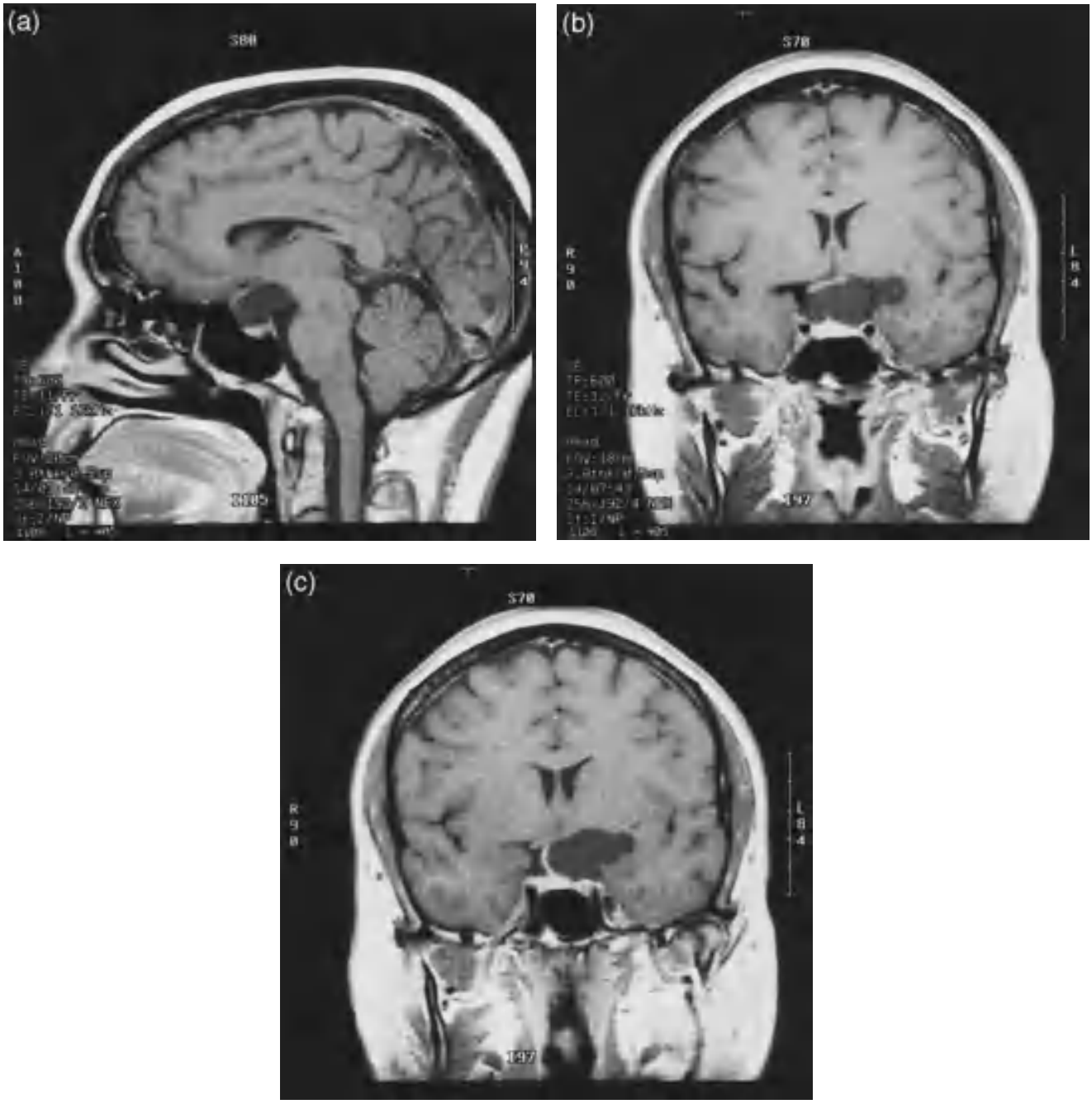

Figure 26 Parasellar and suprasellar Rathke's pouch cyst. (a) Fragile unenhanced scan showing the mass causing elevation of the optic chiasm. (b) Coronal enhanced scan at the level of the chiasm. Note that the non-enhanced cyst causes elevation and deformity of the optic chiasm. (c) Coronal enhanced scan at the level of the pituitary stock shows displacement of the stock to the right by the left parasellar mass

Other investigators, however, report that the size, shape, and patency of the vestibular aqueduct are of no value in predicting surgical results in shunt procedures or in predicting occurrence of bilateral disease.[40] MRI with its ability to detect the endolymphatic duct and sac, separate from the bony vestibular aqueduct, may offer more useful information than can CT.[41] The value of CT and MRI may be in their ability to exclude associated infectious or neoplastic disease processes.[38,39]

Vestibular neuronitis is a clinical diagnosis based on an aggregate of specific symptoms. The disease is characterized by an acute onset of severe vertigo, lasting several days, followed by gradual improvement of several weeks. Hearing is typically unaffected. The history includes onset of vertigo following an illness such as an upper respiratory infection. Most patients become completely symptom free following central compensation.[39] Vestibular labyrinthitis is similar in that the disease presents with the acute symptoms of vertigo, but this disease is always associated with hearing loss. Labyrinthitis is usually viral in origin but may result from acute or chronic bacterial middle ear infections. Unlike viral labyrinthitis,

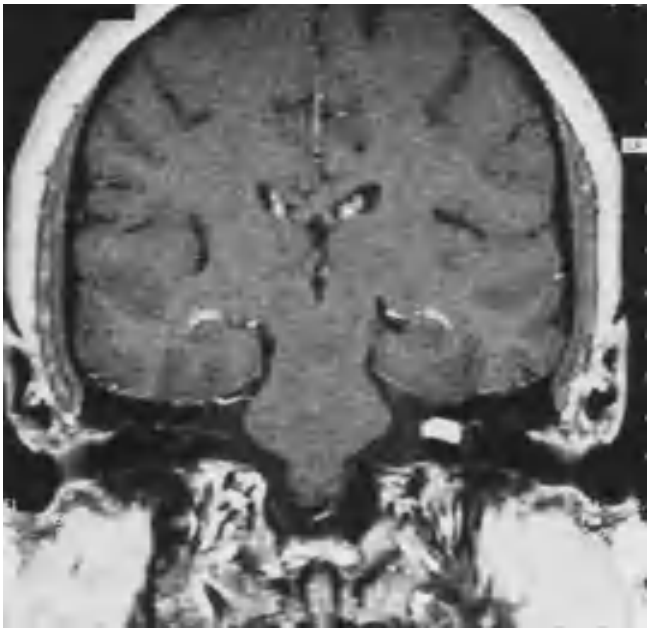

Figure 27 Tumor of the left internal auditory canal. Enhanced coronal image documents a linear enhancing tumor that fills the left auditory canal

labyrinthitis associated with suppurative ear disease may progress to develop partial or complete occlusion of the lumen of the affected labyrinth.[38,39] Early on, the obstructed lumen may be detected by MRI through loss of the signal intensity of the fluid contents. Later, more complete obliteration of all the labyrinthine structures occurs, leading to labyrinthitis obliterans, which is readily diagnosed on CT or conventional tomography.[42]

With MRI, there may be postgadolinium enhancement of the labyrinthine structures or vestibular nerves during the acute or subacute stages of vestibular neuronitis and/or labyrinthitis.[43,44] Such results must be interpreted with care, since sudden labyrinthine dysfunction may be caused by spontaneous hemorrhage or injury, which result in abnormal signal intensities within the labyrinthine structures secondary to the presence of blood products.[45]

Diseases of the internal auditory canal and cerebellopontine angle are generally not characterized by severe attacks of vertigo but rather with intermittent dizziness and/or exacerbated periods of dizziness.[37,39] A variety of benign or malignant tumors of the petrous temporal bone, such as paragangliomas, carcinomas, or metastatic tumors, may directly involve the labyrinthine structures, causing vertigo. Such processes are readily evaluated with MRI (Figures 27–29).

6.3 Central Vestibular Disorders

Lesions of the brainstem or cerebellum that result in central vertigo can readily be diagnosed by MRI. Vascular insufficiency in the vertebrobasilar circulation is a common cause of vertigo in patients over 50 years of age. Thrombosis of the

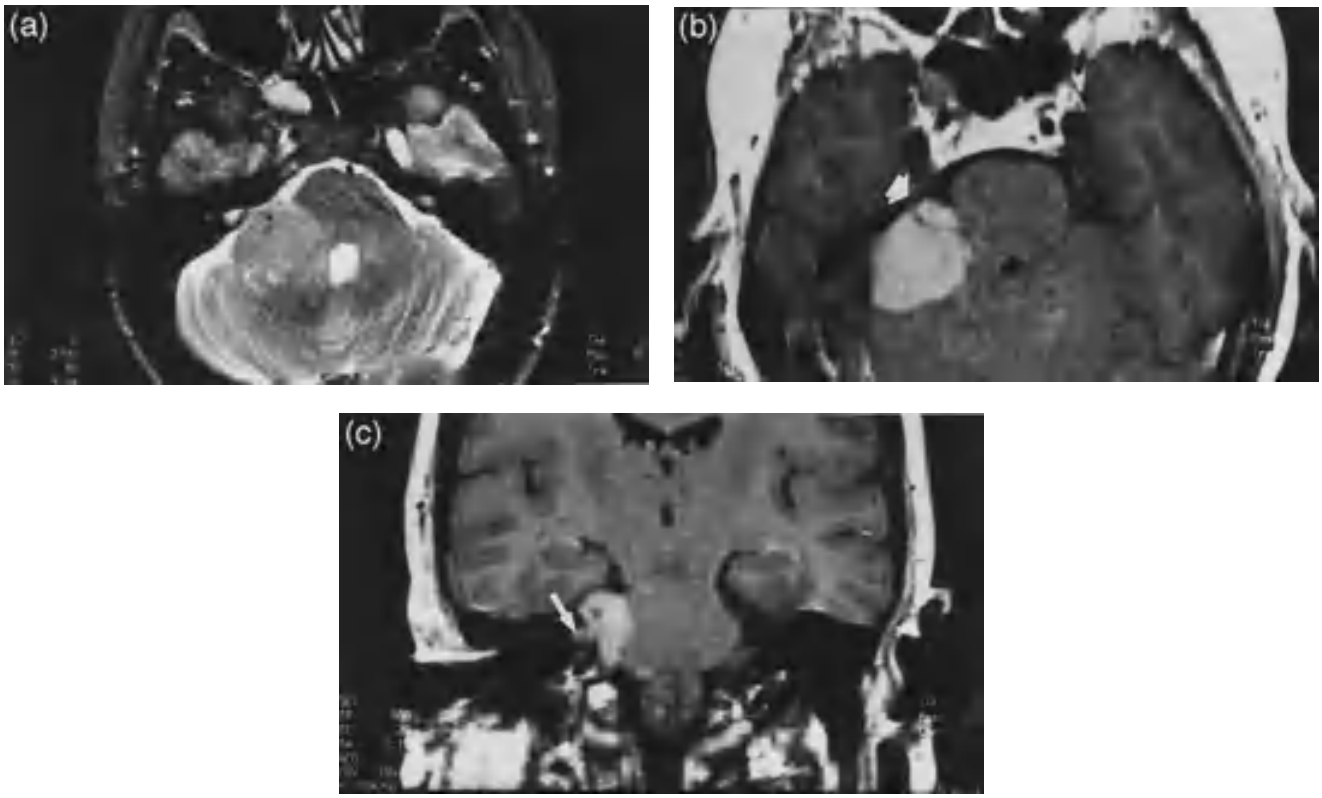

Figure 28 Meningioma of the right cerebellopontine angle. (a) Axial MR scan without contrast. The nearly isointense tumor can be seen to indent the left cerebellopontine angle. (b) Enhanced axial CT scan showing the full extent of the tumor mass. Note that the mass bends up to the level of the left fifth nerve (arrowhead). (c) Enhanced coronal image shows that mass to extend into the internal auditory canal, simulating an acoustic nerve tumor

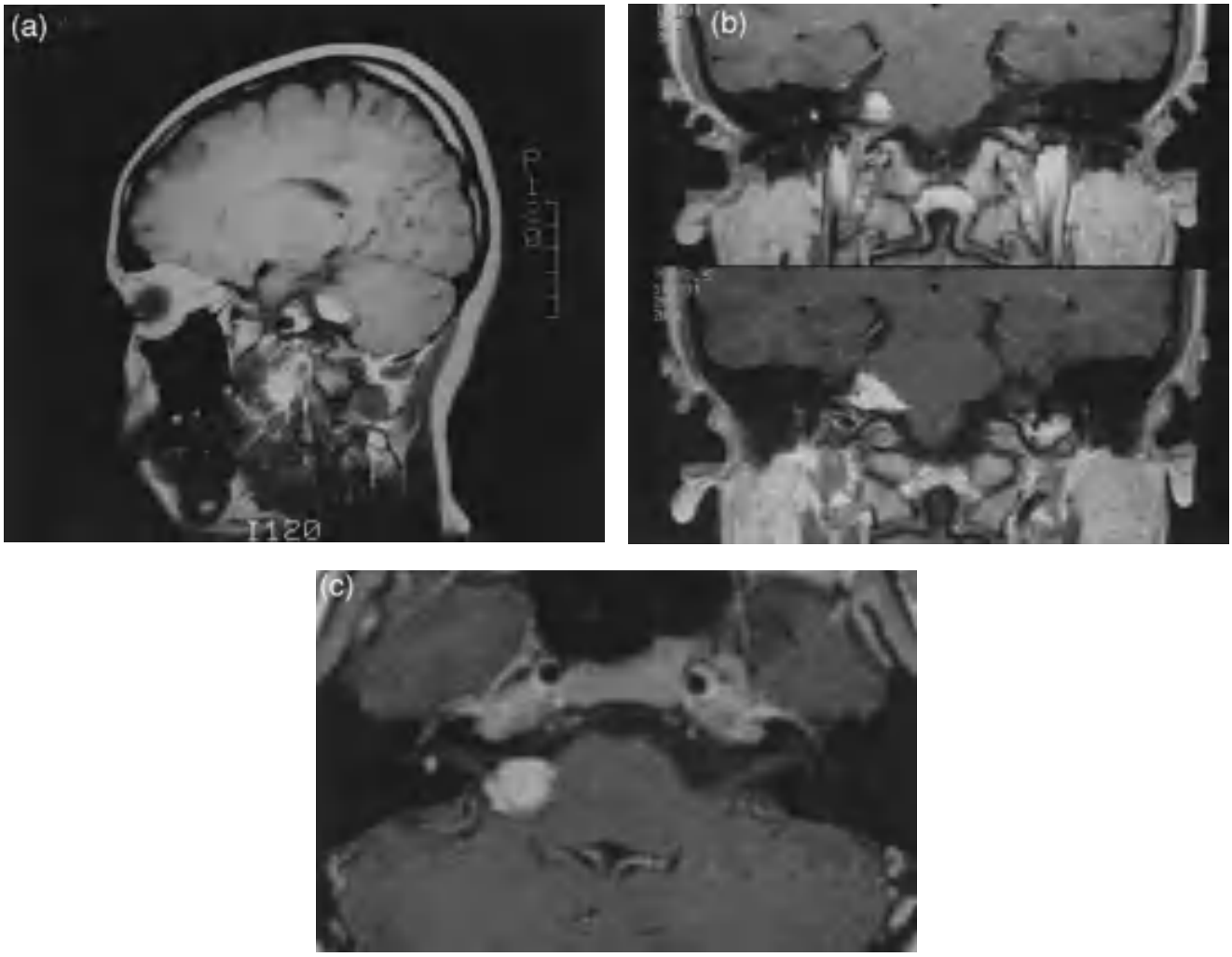

Figure 29 Lipoma of the right cerebellopontine angle and vestibule. (a) Saggital unenhanced image shows the fat intensity mass in the cerebellopontine angle. (b) Coronal unenhanced images document the lesion in the right cerebellopontine angle with a small focus of a high signal in the region of the right vestibule. (c) Axial enhanced CT scan again shows the tumor masses both in the cerebellopontine angle and the vestibule. The patient complained of severe dizziness that was more likely related to the small lesion in the vestibule

labyrinthine artery or infarction of the lateral medulla from vertebral or posterior inferior cerebellar artery insufficiency may cause severe vertigo. The subclavian steal syndrome can cause a variety of symptoms, including vertigo.[38,46,47] Such conditions can be carefully evaluated with MR angiography or conventional angiography of the posterior fossa vasculature.

A variety of other central nervous diseases may produce vertigo or dizziness. These include seizure disorders, multiple sclerosis, ataxic diseases, head injuries, or any cause for increased intracranial pressure. Vertigo may result from stroke and transient ischemic attacks may present as episodic dizziness.[39]

Various metabolic disorders may result in dizziness. These include thyroid disorders, hyperlipidemia, diabetes, and hypoglycemia. Autoimmune diseases or diseases that affect the proprioceptive system may be the cause of vertigo. In many cases, the possibility of function neurotic symptoms must be considered in patients in whom no diseases can be found. Finally cervical spondylosis is thought to cause vertigo by disc degeneration and narrowing of the disc space, which affects the nerves in close proximity, or by osteophyte formation, which compresses the blood vessels. In such cases, conventional radiographs and/or cross-sectional imaging procedures may be helpful.[38,39,42]

6.4 Sensorineural Hearing Loss

Sensorineural hearing loss may be sudden, fluctuating, or progressive. Sudden sensorineural hearing loss is a manifestation of viral infections, vascular occlusive diseases, or inner ear membrane ruptures.[48–52] As discussed above, there may be vertigo associated with these conditions, which would help to define whether the lesion is peripheral or central. In order to discriminate idiopathic or viral infections from other causes of sensorineural hearing loss, auditory brainstem responses and gadolinium enhanced MRI may be utilized.[48–50] Patients with cochleitis or cochlear nerve neuritis typically have abnormal

auditory brainstem responses and may be helped by a tapering course of oral corticosteroids.[49,50] Whether gadolinium enhanced MRI shows enhancement of the cochlear nerve or cochlea is not a helpful indicator for or against using corticosteroid therapy. However, one study suggests that sudden deafness associated with MRI changes is more difficult to cure with steroid therapy than that without associated MRI changes.[49]

Fluctuating neurosensory hearing loss is a difficult disease to assess properly. The audiometric examination does, of course, indicate the level of dysfunction but not the likely cause. In patients where MRI indicates large vestibular aqueducts (apertures greater than 4 mm), this may indicate a fluctuating frequency loss more often than low frequency loss. Fluctuating sensorineural hearing loss resulting from an enlarged vestibular aqueduct appears to be more common in children and young adults, which is an important point in differentiating this disease from Meniere's disease in which the majority of patients are middle aged or older. The vestibular aqueduct of patients with Meniere's disease may be small rather than large.[38,39]

There is speculation on the causes of a sudden drop in hearing in patients with large vestibular aqueducts.[53] Two possible causes are reflux of hyperosmolar fluid from the endolymphatic sac to the inner ear and rupture of the membranous labyrinth or a perilymphatic fistula caused by transmission of intracranial pressure to the inner ear through the enlarged vestibular aqueduct. It is well recognized that patients sustaining relative minor head trauma, or patients who are subjected to extreme barotrauma (scuba diving), may have aggravated episodes of hearing loss. Consequently, it may be worthwhile to image the temporal bones in order to detect enlarged vestibular aqueducts and thus advise the patients or their parents of the dangers of contact sports or activities that entail extreme barometric pressure changes. The imaging findings must be correlated with audiometry, since the fluctuating sensorineural hearing loss of large vestibular aqueduct patients does not resemble the low frequency changes characteristic of Meniere's disease which may also be associated with fluctuating hearing loss.[54,55]

The pathophysiologic basis of disease in patients with isolated large vestibular aqueducts may differ from that in patients whose large aqueducts are associated with other inner ear malformations. Patients with complex inner ear malformations may be subject to recurrent episodes of meningitis and/or the 'gusher' syndrome, resulting in a dead ear at the time or surgical intervention such as a stapedectomy.[52,54]

Asymmetric sensorineural hearing loss or gradually declining unilateral sensorineural hearing loss is a common symptom that may be ascribed to a variety of pathologic processes. Initial evaluation attempts to find the site of the lesion (i.e. cochlear or retrocochlear). All retrocochlear lesions are associated with an abnormal auditory brainstem response, which is often obtained prior to an imaging study. Whether auditory brainstem response testing should be eliminated as a cost-saving measure is a subject of considerable debate. It seems unlikely that clinicians will refer patients directly to MRI without at least preliminary audiometric and/or auditory brain response testing.[48,50,56]

A complete MR study of the head should be performed in addition to the studies of the internal auditory canal and temporal bones. The MR examination should include complete evaluation of the central nuclei in the brainstem as well as the auditory pathways extending upwards into the cerebral hemispheres.[7] Whether or not gadolinium contrast enhancement is routinely utilized depends on a variety of factors including coil size, field of view, field strength, and pulse sequences. CT is diagnostic in lesions 1–1.5 cm or greater in diameter but does not readily detect small brainstem lesions such as infarctions or demyelination.[7,56]

7 RELATED ARTICLES

Eye, Orbit, Ear, Nose, and Throat Studies Using MRI; Gadolinium Chelate Contrast Agents in MRI: Clinical Applications; Head and Neck Investigations by MRI.

8 REFERENCES

1. L. A. Hayman, L. A. Rolak, J. M. Gundzik, and R. B. Lufkin, in 'Clinical Brain Imaging', ed. L. Anne Hayman, Mosby, St. Louis, 1992, Chap. 8.
2. W. G. Bradley, Jr, *Radiology*, 1991, **179**, 319.
3. W. M. Kelly, *Neuroimaging Clin. North Am.*, 1993, **3**, 1.
4. L. R. Gentry, R. C. Mehta, R. E. Appen, and J. E. Weinstein, *Am. J. Neuroradiol.*, 1991, **12**, 707.
5. L. G. Hutchins, H. R. Harnsberger, C. W. Hardin, W. P. Dillon, W. R. Smoker, and A. G. Osborn, *Am. J. Neuroradiol.*, 1989, **10**, 1031.
6. S. S. Gebarski, S. A. Telian, and J. K. Niparko, *Radiology*, 1992, **183**, 391.
7. S. S. Gebarski, D. L. Tucci, and S. A. Telian, *Am. J. Neuroradiol.*, 1993, **14**, 1311.
8. C. J. Jacobs, H. R. Harnsberger, R. B. Lufkin, A. G. Osborn, W. R. Smoker, and J. L. Parkin, *Radiology*, 1987, **164**, 97.
9. A. N. Hasso and D. S. Smith, *Semin. Ultrasound, CT, MR*, 1989, **10**, 280.
10. L. G. Hutchins, H. R. Harnsberger, J. M. Jacobs, and R. I. Apfelbaum, *Radiology*, 1990, **175**, 837.
11. N. Martin, O. Sterkers, D. Mompoint, and N. Nahum, *Neuroradiology*, 1992, **34**, 62.
12. A. N. Hasso, in 'MRI Atlas of the Head and Neck', Martin Dunitz, London, 1993, Chaps 1 and 6.
13. M. F. Mafee, C. S. Lachenauer, A. Kumar, P. M. Arnold, R. A. Buckingham, and G. E. Valvassori, *Radiology*, 1990, **174**, 395.
14. E. T. Tali, W. T. C. Yuh, H. D. Nguyen, G. Feng, T. M. Koci, J. R. Jinkins, R. A. Robinson, and, A. N. Hasso, *Am. J. Neuroradiol.*, 1993, **14**, 1241.
15. A. N. Hasso and K. D. Brown *J. Med. Radiol. Imag.*, 1993, **3**, 247.
16. D. S. Russell and L. J. Rubinstein, in 'Pathology of Tumours of the Nervous System', Williams & Wilkins, Baltimore, OH, 1989, Chap. 5.
17. Y. Y. Lee, R. D. Tien, J. M. Bruner, C. A. DePena, and P. VanTassel, *Am. J. Roentgenol.*, 1990, **154**, 351.
18. F. J. Laine, I. F. Braun, M. E. Jensen, L. Nadel, and P. M. Som, *Radiology*, 1990, **17**, 65.
19. G. D. Parker and H. R. Harnsberger, *RadioGraphics*, 1991, **11**, 383.
20. R. D. Tien, G. J. Felsberg, and A. K. Osumi, *Am. J. Roentgenol.*, 1993, **161**, 167.
21. A. Vahlne, S. Edstrom, P. Arstila, M. Beran, H. Ejnell, O. Nylen, and E. Lycke, *Arch. Otolaryngol.*, 1981, **107**, 79.

22. R. Tien, W. P. Dillon, and R. K. Jackler, *Am. J. Neuroradiol.*, 1990, **11**, 735.
23. L. T. Bilaniuk, R. A. Zimmerman, and T. H. Newton, in 'Modern Neuroradiology, Vol. 4. Radiology of the Eye and Orbit', ed. T. H. Newton, L. T. Bilaniuk. Clavadell Press, New York, pp. 5.1–5.84.
24. S. R. Kodsi, D. J. Shetlar, R. J. Campbell, J. A. Garrity, and G. B. Bartley, *Am. J. Ophthalmol.,* 1994, **117**, 177.
25. B. J. Goldsmith, S. A. Rosenthal, W. M. Wara, and D. A. Larson, *Radiology*, 1992, **185**, 71.
26. M. C. Brodsky and R. W. Beck, *Radiology*, 1994, **192**, 22.
27. W. A. Gibby, M. S. Cohen, H. I. Goldberg, and R. C. Sergott, *Am. J. Roentgenol.*, 1993, **160**, 143.
28. J. Guy, A. Mancuso, R. Beck, M. Moster, L. A. Sedwick, R. G. Quisling A. L. Rhoton Jr, E. E. Protzko and J. Schiffman, *J. Neursurg.*, 1991, **74**, 426.
29. N. Hosten, B. Sander, and M. Cordes, *Radiology*, 1989, **172**, 759.
30. H. Tonami, H. Tamamura, K. Kimizu, A. Takarada, T. Okimura, I. Yamamoto, and K. Sasaki, *Am. J. Roentgenol.*, 1990, **154**, 385.
31. R. F. Carmody, M. F. Mafee, J. A. Goodwin, K. Small, and C. Haery, *Am. J. Neuroradiol.*, 1994, **15**, 775.
32. N. A. Courcoutsakis, C. A. Langford, M. C. Sneller, T. R. Cupps, K. Gorman, and N. Patronas, *J. Comput. Assist. Tomogr.*, 1997, **21**, 452.
33. A. S. Cytryn, A. M. Putterman, G. L. Schneck, E. Beckman, and G. E. Valvassori, *Ophthal. Plastic Recons. Surg.*, 1997, **13**, 129.
34. P. de Potter, J. A. Shields, and C. L. Shields, *MRI of the Eye and Orbit*, J. B. Lippincott Company, Philadelphia, PA, USA, 1995
35. R. A. Nugent, R. I. Belkin, J. M. Neigel, J, Rootman, W. D. Robertson, J. Spinelli, and D. A. Graeb, *Radiology*, 1990, **177**, 675.
36. T. Ohnishi, S. Noguchi, N. Murakami, J. Tajiri, M. Harao, H. Kawamoto, H. Hoshi, S. Jinnouchi, S. Futami, S. Nagamachi, and K. Watanabe, *Radiology*, 1994, **190**, 857.
37. S. R. McGee, *West. J. Med.*, 1995, **162**, 37.
38. P. D. Phelps and G. A. S. Lloyd in 'Radiology of the Ear', Blackwell Scientific, Boston, MA, 1983, pp. 137–141.
39. J. R. E. Dickins and S. S. Graham, *Ear Hearing*, 1986, **7**, 133.
40. E. M. Kraus and P. J. DuBois, *Arch. Otolaryngol.*, 1979, **105**, 91.
41. F. W. J., Albers, R. V. Van Weissenbruch, and J. W. Casselman, *Acta Otolaryngol.*, 1994, **114**, 595.
42. A. N. Hasso and J. A. Ledington, *Otolaryngol. Clin. North Am.*, 1988, **21**, 219.
43. S. Seltzer and A. S. Mark, *Am. J. Neuroradiol.*, 1991, **12**, 13.
44. A. S. Mark, S. Seltzer, J. Nelson-Drake, J. C. Chapman, D. C. Fitzgerald, and A. J. Gulya, *Ann. Otol. Rhinol. Laryngol.*, 1992, **101**, 459.
45. J. L. Weissman, H. D. Curtin, B. E. Hirsch, and W. L. Hirsch Jr, *Am. J. Neuroradiol.*, 1992, **13**, 1183.
46. S. Kikuchi, K. Kaga, T. Yamasoba, R. Higo, T. O'uchi, and A. Tokumaru, *Acta Otolaryngol.*, 1993, **113**, 257.
47. B. Norving, N. Magnusson, and S. Holtås, *Acta Neurol. Scand.*, 1995, **91**, 43.
48. R. A. Hendrix, R. M. DeDio, and A. P. Sclafani, *Otolaryngol. Head Neck Surg.*, 1990, **103**, 593.
49. K. Kano, T. Tono, Y. Ushisako, T. Morimitsu, Y. Suzuki, and T. Kodama, *Acta Otolaryngol.*, 1994, **514**, 32.
50. N. Y. Busaba and S. D. Rauch, *Otolaryngol. Head Neck Surg.*, 1995, **113**, 271.
51. M.-H. Huang, C.-C. Huang, S. J. Ryu, and N.-S. Chu, *Stroke*, 1993, **24**, 132.
52. J. S. Reilly, *Laryngoscope*, 1989, **99**, 393.
53. G. E. Valvassori and J. D. Clemis, *Laryngoscope*, 1978, **88**, 723.
54. M. F. Mafee, D. Charletta, A. Kumar, and H. Belmont, *Am. J. Neuroradiol.*, 1992, **13**, 805.
55. T. Okumura, H. Takahashi, I. Honjo, A. Takagi, and K. Mitamura, *Laryngoscope*, 1995, **105**, 289.
56. S. H. Selesnick, R. K. Jackler, and L. W. Pitts, *Laryngoscope*, 1993, **103**, 431.

Acknowledgements

The authors sincerely thank W. G. Bradley, Jr, M.D., Ph.D., for reviewing the manuscript and for granting permission to reproduce Figure 2.

Biographical Sketches

Anton N. Hasso. *b* 1940. B.S., 1962, M.D., 1967, Loma Linda University. Faculty, UCLA, 1972–74. Faculty, Loma Linda University, 1974–96, Professor and Chairman, Department of Radiological Sciences, University of California, Irvine, 1996–present. Approx. 130 publications including 15 in NMR; senior author of *MRI Atlas of the Head and Neck* (1993) and *MRI of Brain: Neoplastic Disease* (1991); co-author of *MRI of the Brain, Head and Neck, A Text Atlas* (1985). Research interests include applications of NMR in neuroradiology/head and neck radiology, particularly magnetic resonance angiography and the use of gadolinium contrast agents.

Peggy J. Fritzsche. *b* 1941. B.S., Andrews University, 1962; M.D., Loma Linda University, 1966. Faculty, UCLA, 1973–74. Faculty, Loma Linda University, 1974–91, Medical Director, Riverside MRI, 1991–present. Approx. 85 publications including eight in NMR; co-author of *MRI of the Body* (1992). Research interests include applications of NMR in genitourinary and abdominal radiology, breast imaging and pelvic imaging.

Degenerative Disk Disease Studied by MRI

Michael T. Modic

Cleveland Clinic Foundation, OH, USA

1 INTRODUCTION

Degeneration of the intervertebral disk complex is a process that begins early in life and is a consequence of a variety of environmental factors as well as normal aging. The pathophysiology of this disorder is complicated and poorly understood. It has been stated[1] that degeneration as commonly applied to the intervertebral disk covers such a wide variety of clinical, radiologic, and pathologic manifestations as to be really 'only a symbol of our ignorance'.

It is estimated that low back pain affects 5% of the adult population each year and that the lifetime incidence of LBP in adults is 60–80%.[2] Fortunately, the natural history of back pain is such that the vast majority of back pain sufferers improve with little or no medical intervention; only 14% of patients have episodes of pain lasting more than 2 weeks.[3] Despite the self-limited nature of most LBP, the total societal costs of LBP have been estimated at US$16–100 billion annually,[2] and, as back pain is the second leading cause of physician visits among American adults, it is estimated to account for more than US$10 billion in direct medical care costs each year.[4] Much of the direct cost of treating patients with LBP is related to diagnostic tests;[5] it is estimated that MRI alone contributes US$2 billion dollars in direct medical care costs (Modic MT, 1993, projected estimate).

The sequelae of disk degeneration remain among the leading causes of functional incapacity in both sexes and are an all too common source of chronic disability in the working years. However, by the age of 50 years, 85–95% of adults show evidence of degenerative disk disease at autopsy;[6] thus the jump from identifying an anatomic derangement to proposing a symptom complex must be made with caution, since to date only a moderate correlation has been found between imaging evidence of disk degeneration and symptomatology.[7] There is no unifying theory regarding the cause of disk degeneration. It is likely that degeneration and aging are multifactorial processes that encompass a wide spectrum of changes and sequelae. Nevertheless, in patients in whom surgical therapy is planned, or where the diagnosis remains elusive and patient treatment and outcome is dependent upon a more definitive diagnosis, imaging studies are an important component in the evaluation of patients with symptoms of disk disease.

2 MORPHOLOGY

The contrast sensitivity and multiplanar imaging capability of proton magnetic resonance (MR) place this modality in a position to provide a unique noninvasive means of imaging intervertebral disks. The implementation of surface coil technology,[8] cardiac gating,[9] gradient refocusing,[10] paramagnetic contrast agents,[11] saturation pulses,[12] gradient echo volume imaging, turbo (fast) T_2-weighted spin echo sequences, and magnetization transfer techniques continue to refine the capability of MRI for degenerative disk disease. When a combination of imaging planes and pulse sequence parameters is used, the anatomy of the intervertebral disk (Figure 1), spinal nerves, dural sac, and adjacent structures can be clearly depicted. From a morphological aspect, MRI may be the most accurate means of evaluating the intervertebral disk. Accordingly, most research to date has been directed clinically towards optimizing anatomic image display in a fashion similar to that of computerized tomography (CT) for assessment of disk contour.[13–19] Unlike CT and conventional radiography, however, which are dependent on information related to electron density, proton MR signals are influenced by the T_1 and T_2 relaxation times, and by proton density, providing greater tissue contrast. Thus the role of this technique may go beyond gross anatomic appraisal to actual tissue characterization of pathology and biochemical change.[20]

The relationship among the vertebral body, endplate, and disk has been studied[21–24] using both degenerated and chymopapain-treated disks as models. Signal intensity changes in vertebral body marrow adjacent to the endplates of degenerated disks are a common observation in MRI. Work using T_2-weighted spin echo sequences[20] further suggests that MRI is capable of detecting changes in the nucleus pulposus and anulus fibrosus relative to degeneration and aging based on a loss of signal presumed to be secondary to known changes in hydration that occur within the intervertebral disk (Figure 2). However, the correlation is not straightforward, since differences in signal intensity appear to be somewhat exaggerated for the degree of water loss noted with degeneration (about 15%).[25] At present the role that specific biochemical changes (proteoglycan ratios, aggregating of complexes) play in the altered signal intensity is not well understood. In fact, the important factor may not be the total quantity of water but the state that the water is in. Sodium images suggest that the T_2 signal intensity in the disk tracks the concentration and regions of high glycosamino glycans (GAG) percentages. Thus it seems likely that the health and status of the proteoglycans determine the signal intensity.

The vacuum phenomenon within a degenerative disk is represented on spin echo images as areas of signal void.[26] Gradient echo sequences demonstrate this better than do conventional spin echo sequences, plain radiographs and CT. This is due to the magnetic susceptibility effects caused by the intradiskal gas collection. Whereas the presence of gas within the disk is usually suggestive of degenerative disease rather than an infected process, spinal infection may (rarely) be accompanied by intradiskal or intraosseous gas.[27] A gas density cleft within a transverse separation of the vertebral body appearing in extension and disappearing in flexion is characteristic of the vacuum phenomenon within a region of ischemic vertebral collapse. Rarely, the phenomenon has been identified with vertebral body neoplasms such as multiple myeloma.[28–32]

Hyperintense intervertebral disks are not an infrequent finding on T_1-weighted MR images of the spine, and it has been suggested[33] that the relatively 'bright' intervertebral disk may reflect diffuse abnormality and loss of normal signal in the

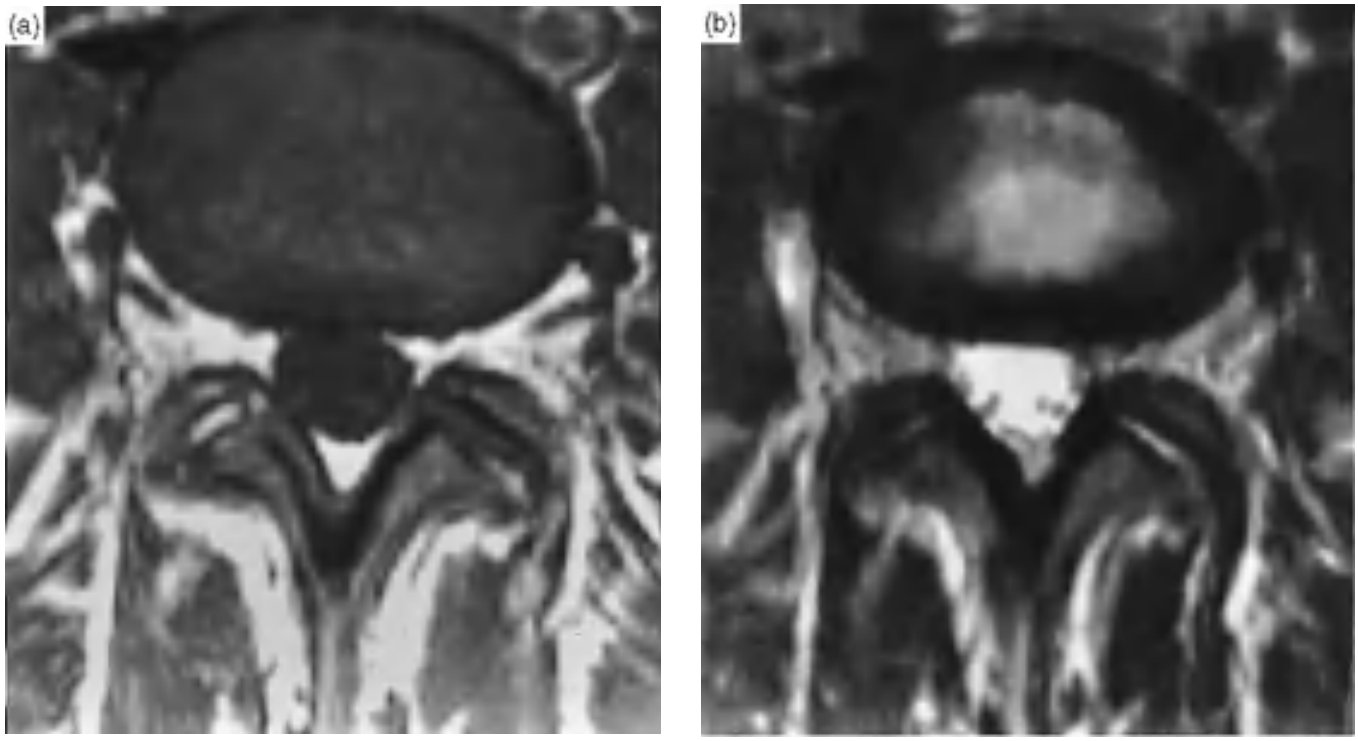

Figure 1 Axial L3–L4 disk: (a) and (b) are normal. Axial T_1-weighted spin echo (500/17), and T_2-weighted spin echo (2000/90) images through the axial midplane of the intervertebral disk. On the T_1-weighted axial image (a) the disk has a homogeneous soft tissue signal intensity. On the T_2-weighted image (b) three distinct components of the disk can be identified: first, a decreased signal intensity is noted in the outer annulus and ligamentous region; second, the inner annulus has a slightly increased signal intensity, and third, the region of the nucleus pulposus has the highest signal intensity consistent with the highest concentration of proteoglycans

marrow of the adjacent vertebral bodies. Calcification has usually been described on MR images as a region of decreased or absent signal. The loss of signal is attributed to a low mobile proton density as well as, in the case of gradient echo imaging, to its sensitivity to the heterogeneous magnetic susceptibility found in calcified tissue.

There is, however, variability of signal intensity of calcium on various sequences; the type and concentration of calcification are probably important factors. Multiple examples of a hyperintense signal on T_1-weighted spin echo images in areas that contain calcification on CT have been reported in the literature. These hyperintensities have been attributed to the paramagnetic effects of methemoglobin,[34–36] melanin,[37] and trace elements,[38,39] as well as to the T_1-shortening effects of lipids and cholesterol,[40] proteins,[41,42] and laminar necrosis associated with infarction and calcification.[43–47] Focal or diffuse areas of hyperintensity on T_1-weighted spin echo sequences may also be encountered in the intervertebral disk. Hyperintensities that are affected by fat-suppression techniques have also been noted within intervertebral disks.[48] These are presumably related to areas of ossification with formation of a lipid marrow in the ossified disk space; they also appear calcified on conventional studies.

3 SEQUELAE OF DISK DEGENERATION

Disk herniation, especially in the lumbar and thoracic regions, is probably better depicted by MRI than by other modalities.[14–19,49,50] It is, again, important to bear in mind that not all morphological changes are a cause of symptoms. In a prospective study of individuals who never had low back pain, sciatica or neurogenic claudication,[51] one-third of the subjects were found to have substantial abnormalities. In patients who were less than 60 years of age, 20% had a herniated nucleus pulposus. In the group that was 60 years or older, findings were abnormal on 57% of the scans. Thirty-six per cent of the subjects had a herniated nucleus pulposus, and 21% had spinal stenosis. More recent studies[52,53] have confirmed the observation that disk bulges and protrusions are common findings on MRI in the asymptomatic population. These latter studies, however, suggest that frank disk extrusion is rare; a disk bulge was observed to be age related, but disk protrusion was not.

Multidimensional imaging allows the direct acquisition of orthogonal views covering long segments of the spine, without requiring secondary reconstructions. Alternatively, three-dimensional datasets can be acquired with or without contrast, which allows multiplanar reformation with variable partition thicknesses for improved overall spatial resolution and reduced examination times. The outer anulus–posterior longitudinal ligament (PLL) complex can usually be seen as an area of decreased signal relative to the inner anulus–nucleus pulposus, which helps in characterizing the type of herniation (protrusion, extrusion and/or sequestration).[54] This ability to characterize and differentiate the various subgroups of disk herniation has been proposed to have certain diagnostic and therapeutic ramifications, particularly in the lumbar region.

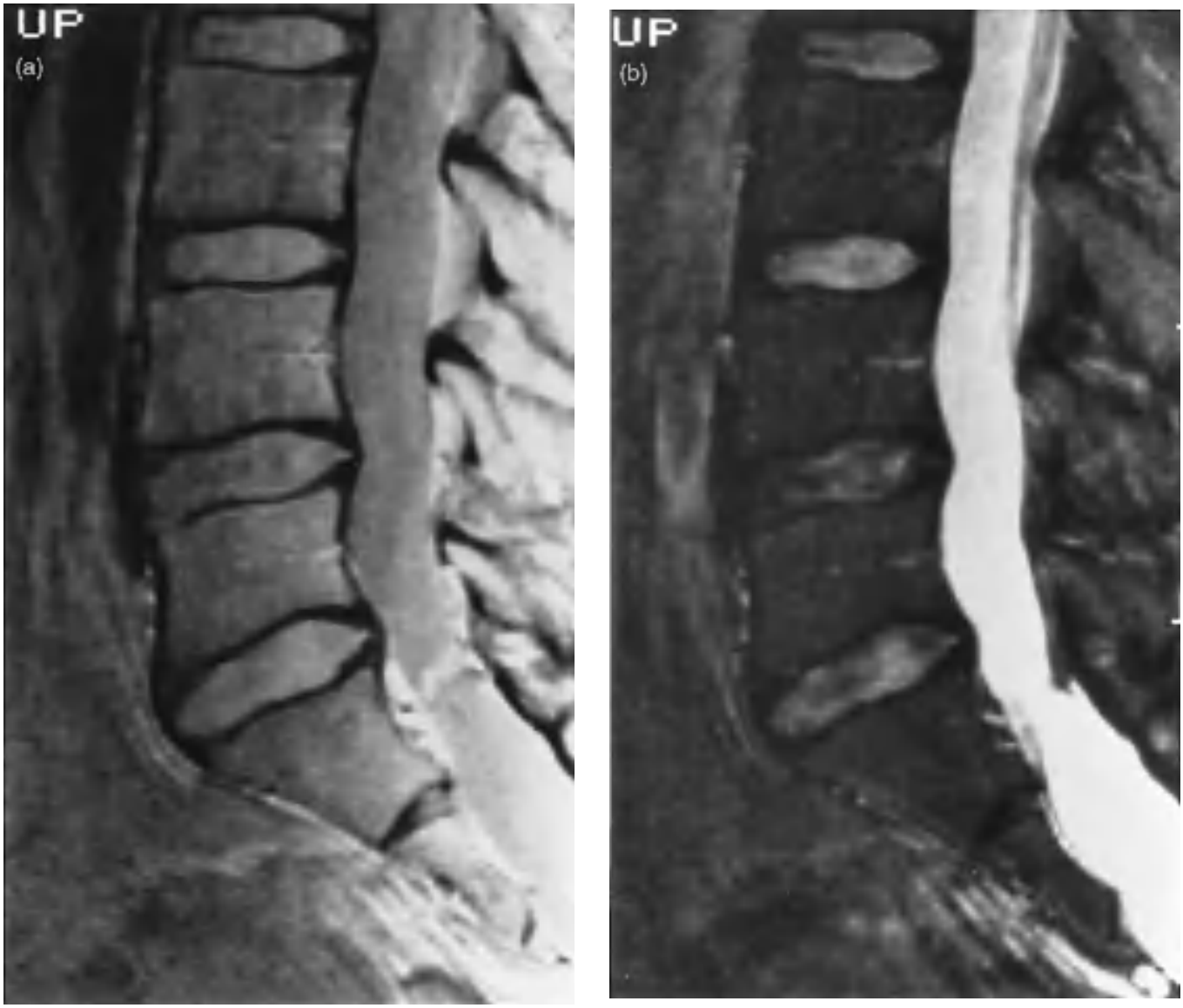

Figure 2 Spin echo and gradient sagittal images. (a) Intermediate spin echo (2000/20). (b) T_2 weighted spin echo (2000/90). (c) FLASH (50/13/10 degrees). (d) FLASH (50/13/60 degrees). (b) There is decreased signal intensity in the L4–L5 and L5–S1 disk, consistent with degeneration. The L2–L3 and L3–L4 disks have a normal signal intensity. The signal intensity changes consistent with degeneration are not as well appreciated from sequences (a), (c) and (d). (Reproduced with permission from *Magnetic Resonance Imaging of the Spine*, 2nd edn, Chap. 2, p. (52, Fig. 2-14)

Abnormal disks can be classified as an anular bulge or herniated (protruded, extruded, or free fragment). Concurrently, herniated disk disease should be described by contour, size, location, and presence or absence of enhancement.

4 BULGE

An anular bulge is a result of disk degeneration with a grossly intact, albeit lax, anulus, usually recognized as a generalized extension of the disk margin beyond the margins of the adjacent vertebral endplates, regardless of the signal of the interspace. An index of disk bulging using sagittal anatomic sections from 149 lumbar disks[55] has been studied. The largest disk bulgings were always associated with radial tears of the anulus, which contradicts the previously held concept that the anulus fibrosus remains intact with a bulging disk.

Some investigators would recognize the anular tear as an intermediate category between bulge and herniation. The significance of the anular tear, however, remains extremely unclear; it is perhaps best considered as a sequela of disk degeneration rather than as a discrete category that may imply some type of clinical significance. On nonenhanced T_2-weighted MR images anular tears are best appreciated as an area of high signal extending into the area of decreased signal of the anulus–ligamentous complex (Figure 3).

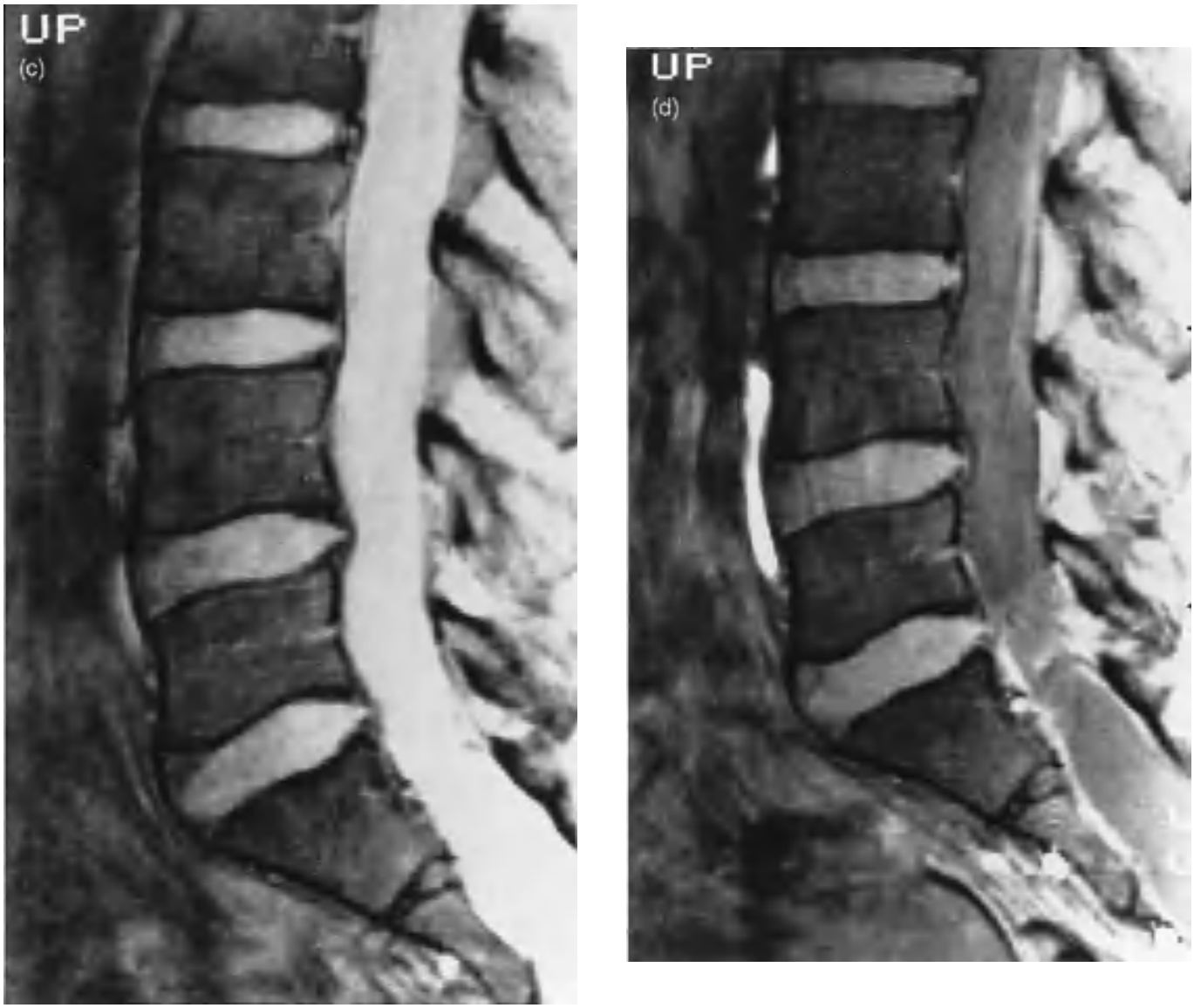

Figure 2 continued

5 LUMBAR DISK HERNIATIONS

Obviously some degree of anular disruption is an intrinsic component of any disk herniation.

A protrusion represents herniation of nuclear material through a defect in the anulus, producing a focal or broad-based extension of the disk margin. The extension is less than that which occurs with an extrusion. At least some fibers of the overlying anulus and PLL remain intact, and the disk is described as 'contained'. The signal intensity of the parent nucleus is usually decreased.

The next two categories, extrusion and sequestration, represent herniations that are no longer contained by the overlying anulus and ligament (Figure 4). In an extrusion, nuclear material becomes an anterior extradural mass that remains attached to the nucleus of origin, often via a high-signal pedicle on the T_2-weighted image. The signal intensity of the extruded portion may be increased or decreased. The disk usually appears contained by the PLL and remaining contiguous portions of the anulus, which show up as curvilinear areas of decreased signal.

The term 'free fragment' or 'sequestrated disk' refers to disk material external to the anulus fibrosus and no longer contiguous with the parent nucleus. A frequent finding with both extruded and free fragments is the presence of a high signal intensity extradural defect often surrounded by a curvilinear area of decreased signal that is distinct from the interspace of origin.

Whereas all of the foregoing has become a part of our clinical lore, it is not at all clear whether these findings are clinically relevant. It has been proposed, for example, that differentiating between various degrees of herniation is critically

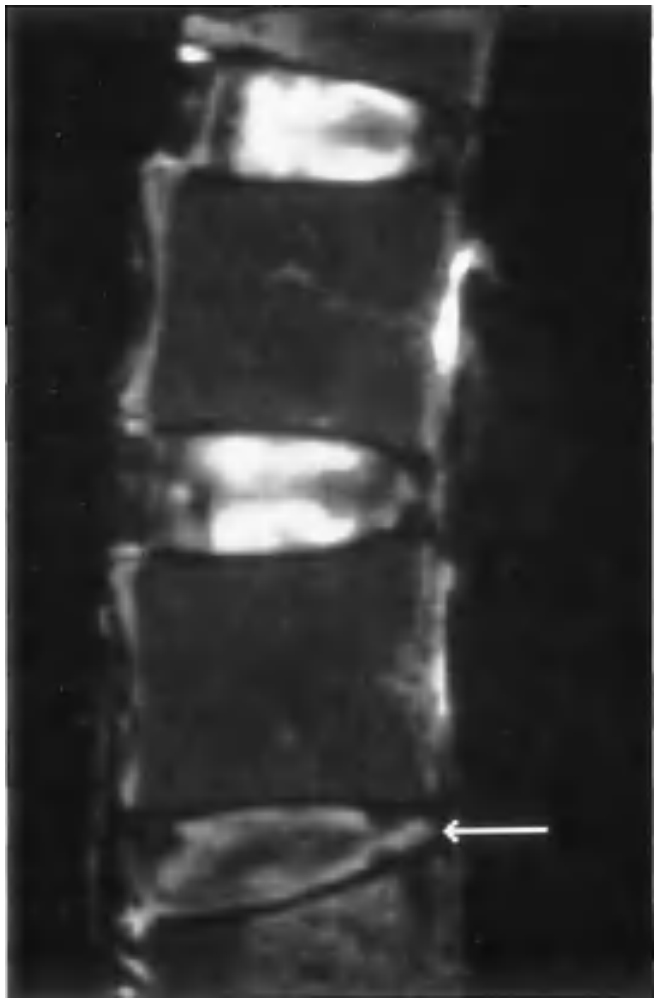

Figure 3 Sagittal T_2-weighted spin echo image (2000/90) through a cadaveric spine. Note the loss of signal intensity at the L4–L5 disk and the region of high signal extending into the anulus–ligament complex (arrow). This represents an annular tear. (Reproduced with permission from *Magnetic Resonance Imaging of the Spine*, 2nd edn, Chap. 3, p. 96, Fig. 3-16)

important; yet the reality of the situation is that any disk herniation most likely represents a spectrum or continuum rather than a discrete entity with specific clinical relationships. One may view the continuum of herniated disk disease as starting with anular disruption, proceeding to a small focal herniation that does not break through the anulus–ligamentous complex, and winding up as a frank herniation (extrusion) that does indeed dissect through the anulus–posterior ligamentous complex.

Traversing nerve roots within the thecal sac above a particular level of impingement from a herniated disk or stenosis have been noted to be enlarged compared to the contralateral side. This may be a reflection of nerve root edema. Enhancement of traversing nerve roots within the thecal sac has also been reported[56] on MRI, the majority of cases being associated with focally protruding disk pathology. A significant number of these patients, however, had isolated enhancement of multiple nerve roots without significant associated anatomic pathology. The mechanism of such enhancement may be related to the blood–nerve barrier of this spinal nerve root, which is altered by compression.[57] It has also been suggested that the enhancement may be related to the vascular anatomy as a variation of normal, rather than as a pathologic reaction.[58]

In a prospective evaluation of surface coil MRI, CT, and myelography for lumbar herniated disk disease and canal stenosis[16] there was 82.6% agreement between MRI and surgical findings regarding type and location of disease, 83% agreement between CT and surgical findings, and 71.8% agreement between myelography and surgical findings. In another study,[59] the accuracy of CT, myelography, CT-myelography and MRI for lumbar herniated nucleus pulposus was compared prospectively in 59 patients, all of whom underwent surgical exploration. MRI was the most accurate (76.5%), CT-myelography next (76%), and then CT (73%) and myelography (71%). The false-positive rate was lowest for MRI, at 13%, followed by myelography and CT.[59] Similar data from a carefully controlled prospective study in Wisconsin[60] suggest the same equivalence for plain CT, CT-myelography, and MRI.

The natural history of lumbar disk herniation has engendered recent interest and MRI has been an excellent tool for these investigations. Multiple studies have demonstrated that the size of the disk herniation can change with time, and studies of patients treated conservatively have demonstrated that the majority will show a reduction in disk herniation size of 30–100%. The larger herniations show the most significant decrease in size. A resulting impression has also been that patients who do well conservatively will show this reduction in herniation size, yet the correlation of disk changes with time and symptoms resolution has not yet been carefully worked out.

As part of a long term natural history study, patients with acute radiculopathy were evaluated clinically and with contrast enhanced MRI to determine if there was a correlation between presenting symptoms and the type, size, location and enhancement of the disk herniations at presentation. In this group, 72% had a herniated disk at one or more levels at presentation. There was excellent agreement between MRI and clinical findings for level and size, but no correlation of pain and disability with disk size, type or enhancement. At the 6-week follow-up, 36% of large herniated disks demonstrated a significant reduction in size (Figure 5), but there was no difference in clinical outcome based on disk size, change, or type. At 6 months, 60% of herniated disks had reduced significantly in size, but again there was no correlation of pain and disability with disk size, change, or type.

Enhancement of herniated disk was almost a constant feature. The degree of enhancement was variable and probably related to granulation tissue which develops around and through herniated disk. The granulation tissue response itself may comprise a fair percentage of the herniated disk mass. One possible explanation for the change of a disk with time then is that the granulation tissue undergoes cicatrization and retraction, a normal phenomenon for reparative tissue.

Although less common than lumbar or cervical herniations, thoracic herniations have been noted more frequently with the advancement of imaging techniques.[19] A higher prevalence of

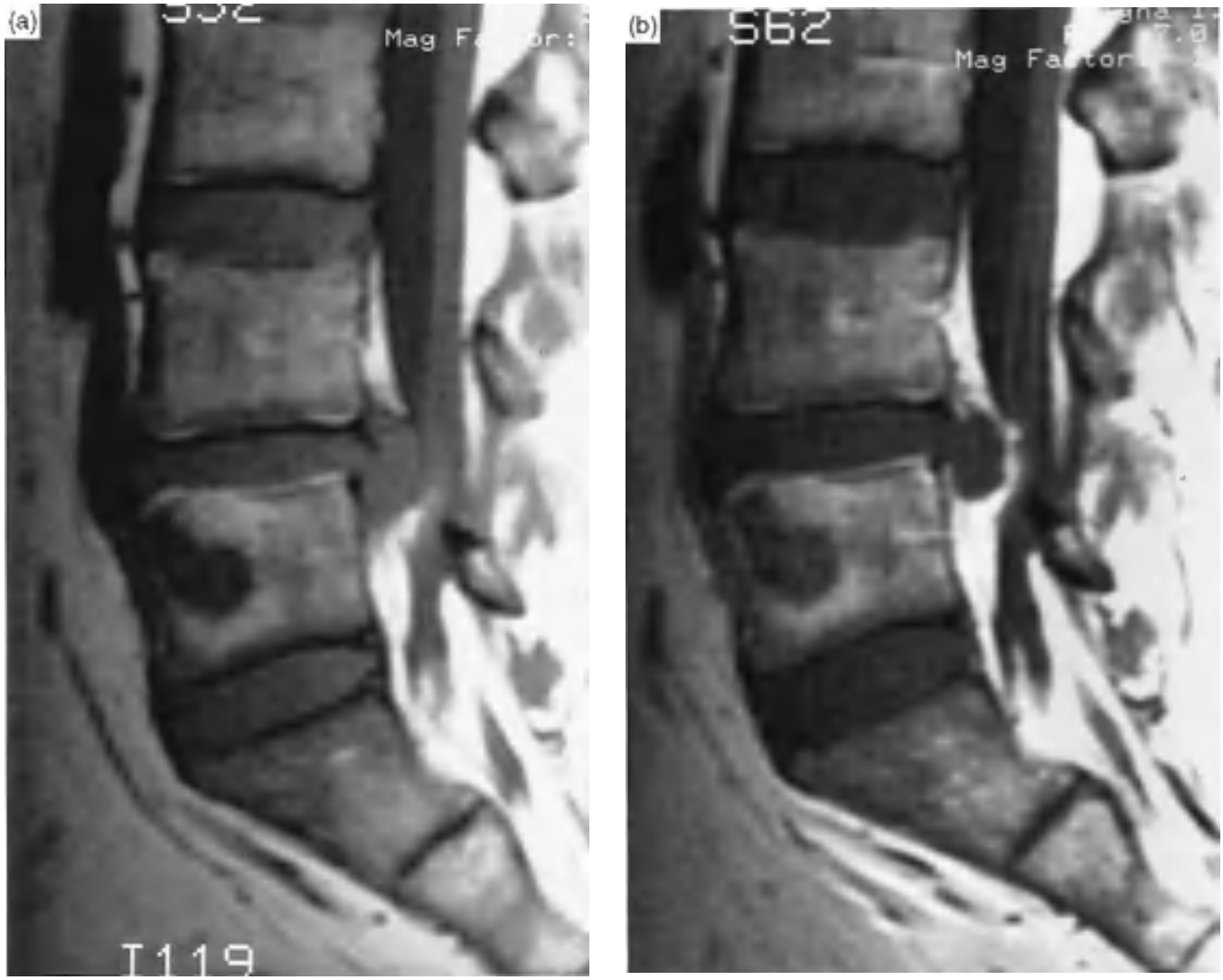

Figure 4 L4–L5 disk herniation. (a) Pre- and (b) post-contrast sagittal T_1-weighted spin echo images demonstrate an extradural mass at the L4–L5 disk level. Axial T_1-weighted spin echo (500/17 images) before (c) and after (d) contrast show the peripheral enhancement of disk material, which is also appreciated on the sagittal images. The enhancing areas of granulation tissue contribute to the overall size of the mass. (Reproduced with permission from *Magnetic Resonance Imaging of the Spine*, 2nd edn, Chap. 3, p. 102, Fig. 3-26)

asymptomatic morphologic change is also present in the thoracic spine.

Symptomatic cervical disk herniations are most common in young patients (third and fourth decades) and frequently occur without recognized trauma. In a prospective study of patients with no symptoms of cervical disease,[61] 10% of subjects less than 40 years of age had a herniated nucleus pulposus and 4% had foraminal stenosis. Of the subjects who were older than 40 years of age, 5% had a herniated nucleus pulposus, 3% a bulging disk, and 20% foraminal stenosis. Narrowing of the disk space, degeneration of a disk, spurs, or compression of the cord were noted at one or more levels in 25% of the subjects less than 40 years of age and in almost 60% of those who were older than 40.

Cervical disk herniation, especially when central or large, is well appreciated on routine sagittal and axial MR images. Again, thin slices (3 mm or less) are critical for accurate diagnosis. This may necessitate the use of three-dimensional volume sequences with partitions of 2 mm or less and/or reconstructions in other planes. The T_2 signal intensity of intervertebral disks in the cervical region is not as helpful as that in the lumbar region for identifying the presence or absence of degeneration. Cervical disk herniation is usually identified on sagittal images as an anterior or anterior–lateral extradural defect that may indent or compress the cervical cord. In a prospective study to compare the accuracy of surface coil MRI with metrizamide myelography (MM) and CT with metrizamide (CTM),[17] there was surgical agreement in 74% of patients with surface coil MRI, 85% with CTM, and 67% with MM. When surface coil MRI and CTM were used jointly, 90% agreement with surgical findings was seen, and when CTM and MM were used jointly there was 92% agreement. In gen-

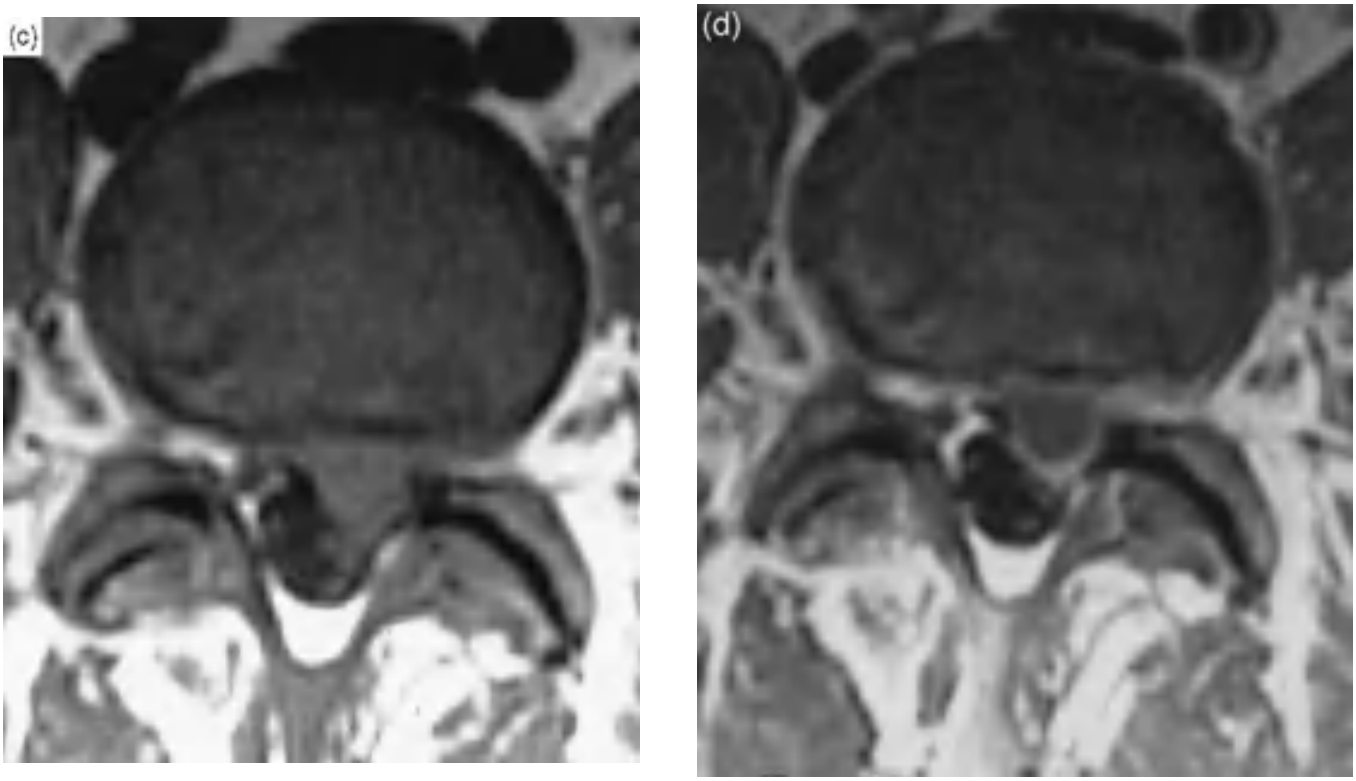

Figure 4 continued

eral, surface coil MRI was as sensitive as CTM for identifying disease level, but not as specific for type of disease.

In another study comparing MRI and CT, plain film myelography, and CT-myelography in 35 patients operated on for cervical radiculopathy and myelopathy,[62] MRI correctly predicted 88% of the surgically proved lesions. The corresponding rates were 81% for CT myelography, 58% for plain myelography, and 50% for CT.

Although we would maintain that most evaluations of the cervical spine for extradural disease can be done in an adequate fashion using spin echo T_1-weighted sagittal and axial images, the introduction of fast gradient echo images with small flip angles (less than 15°) has improved the accuracy of the examination by increasing the conspicuousness of extradural defects. Recent work[63–65] has confirmed the value of this technique. This capability, coupled with the potential of utilizing very short *TR*s (50 ms or less), has provided the stimulus for using volume imaging in the evaluation of extradural disease, in the hope of shortening the examination time and decreasing slice thickness.

The disadvantages of gradient echo imaging relate to problems with field inhomogeneity and contrast detectability of pathologic processes within the cord itself. Furthermore, depending upon the echo time, the ability accurately to characterize morphologic defects, foraminal narrowing, and bony ridges is inferior to that for viewing bone by CT.

An adjunct to conventional MRI in evaluating degenerative disk disease is the utilization of gadolinium diethylenetriaminepentaacetic acid (Gd-DTPA). Studies with virgin disks and postoperative disk herniation[11] indicate that it is the most accurate means of separating epidural fibrosis and disk tissue. There is consistent enhancement of peridiskal fibrosis early (less than 15 min after injection), and variable enhancement occurs in herniated or degenerated parent disks late (30 min after injection). Enhancement of intervertebral disks does not appear to occur in the normal state and is probably a sequela of the degenerative process.[11,66] Thus it seems likely that Gd-DTPA may play a role in identifying the sequelae of degenerative disk disease by enhancing the reactive granulation tissue that forms secondary to disruption of the disk and associated structures.

In addition to changes within the disk, including herniation, secondary changes are noted both in animal models and in humans following disk degeneration. The stability of a motion segment depends on the integrity of all its components. Diseases occurring in this area are circumferential, with that in one joint affecting another, and degeneration of one disk leads to a loss of disk height and forces the facet joints into malalignment, so-called 'rostrocaudal subluxation'. This leads to increased biomechanical forces at the facet joint with increasing joint relaxation and instability, secondary facet and arthritic changes, and potential fractures. Similarly, abnormal movements allowed by disk degeneration and facet changes add stress to the posterior ligaments and can result in hypertrophy. A vicious degenerative cycle is established which includes degenerative disk disease, facet arthrosis, ligamentous and capsular hypertrophy, spinal instability, and lumbar stenosis.[67]

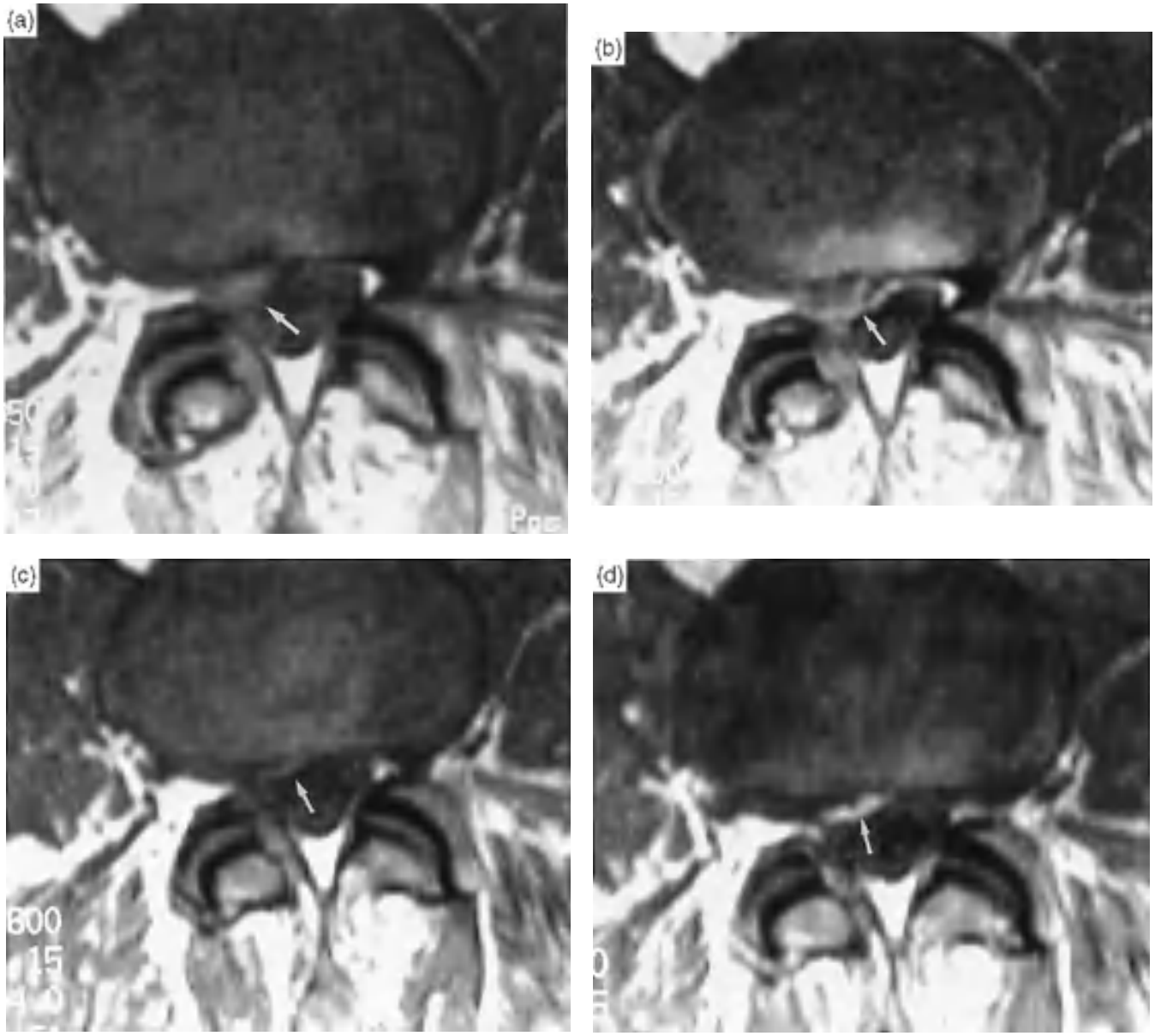

Figure 5 L3–L4 disk herniation. (a) Pre- and (b) post-contrast axial T_1-weighted spin echo images through the L3–L4 disk in a patient who presented with the onset of acute right-sided radiculopathy. A moderate sized extradural mass is identified on the right which shows peripheral enhancement following the administration of contrast. (c) (d) Axial T_1-weighted spin echo (500/17) images at the same level as (a) and (b) following 6 weeks of conservative management. There is a marked reduction in the size of the extradural mass, although there is still some enhancement in this region

6 SPINAL STENOSIS

Spinal stenosis results from an overall diminution of the spinal canal, lateral recesses, or neural foramina. It occurs more commonly in the lumbar and cervical regions. The symptoms are usually a reflection of the compressive pathology.

In the lumbar spine, central stenosis tends to occur at multiple levels but is most frequent and usually most severe at the L4–L5 level, where it may occur alone.

The transverse and sagittal dimensions of the central neural canal are best depicted by integrating orthogonal (e.g. axial and sagittal) planes. Gradient echo images with low flip angles or more T_2-weighted spin echo sequences provide the best views of thecal sac dimensions by furnishing a gray-scale inversion of the cerebrospinal fluid and extradural elements.[63,64]

Peripheral stenosis is best appreciated on T_1-weighted images, which maintain the separation between neural structures and epidural fat quite well. The signal intensity between neural elements and fat is less well seen on more T_2-weighted and gradient echo images, although bony overgrowth can be identified.

In the cervical spine degenerative changes affect all major spinal articulations, including the intervertebral disks, apophy-

seal joints, ligamentous connections between vertebral bodies, and the vertebral bodies themselves.

The suggestion has been made[68] that myelopathy or stenosis is associated with an average canal diameter of less than 12 mm. Care must be taken, however, when using gradient echo images since the degree of spinal narrowing can be overestimated because of susceptibility effects. Another method suggested for determining cervical spinal stenosis[69] is the vertebral body/canal ratio, which has been suggested to correct for body size. A spinal canal/vertebral body ratio of less than 0.82 would indicate significant cervical spinal stenosis. MRI and myelographic CT studies appear to be equivalent in measuring the degree of cord compression. There may be a correlation between compression and the amount of neurologic dysfunction.[70]

Although there are no good studies to indicate that MRI has led to improved therapeutic choices, there is at present sufficient evidence to suggest that MRI is adequate for most therapeutic planning to allow physicians to stop further testing, obviating the need for a myelogram or CT scan.[71,72]

7 FACET JOINTS

Although facet arthrosis constitutes an important cause of acquired lumbar stenosis, degenerative change can occur independently of it and may be a cause of low back pain and radiculopathy.[67,73]

On MRI the facet joints are best evaluated by visually integrating sagittal and axial images. Again, osteophytes are easier to identify on gradient echo or spin echo images with long relaxation times. Those that contain marrow are also better demarcated than are those that are sclerotic, which can be confused with the adjacent capsular ligamentous structures. Altered signal intensity in bone marrow consistent with fatty replacement has also been reported to be commonly associated.[74] The articular cartilage can be directly visualized on both T_1 and T_2-weighted spin echo images, but thinning is difficult to measure accurately because of variable axial obliquity and chemical shift artifact from the adjacent facet. Gradient echo examinations have demonstrated that they provide better conspicuousness of the articular cartilage itself as distinct from adjacent osseous structures.

In summary, degenerative disk changes appear to be a normal consequence of the aging process. MRI is an excellent modality for depicting them. However, the clinical relevance of these morphologic changes remains to be established and the value of MRI as a prognostic indicator for patient outcome needs to be studied more fully. At the present time, one can clearly recommend MRI as the single best presurgical decision-making tool, but its role in the evaluation of patients who are going to be treated in a conservative fashion appears to be much more limited.

8 RELATED ARTICLES

Contrast Agents in Magnetic Resonance: Operating Mechanisms; Contrast Agents in Whole Body Magnetic Resonance: An Overview; Gadolinium Chelate Contrast Agents in MRI: Clinical Applications; Head and Neck Investigations by MRI; Lung and Mediastinum MRI.

9 REFERENCES

1. K. P. H. Pritzker, *Orthop. Clin. North Am.* 1977, **8**, 66.
2. J. W. Frymoyer and W. L. Cats-Baril, *Orthop. Clin. North Am.,* 1991, **22**, 263.
3. R. A. Deyo and Y. J. Tsui-Wu, *Spine*, 1987, **12**, 264.
4. B. K. Cypress, *Am. J. Public Health*, 1983, **73**, 389.
5. R. A. Deyo, *J. Gen. Intern. Med.* 1986, **1**, 328.
6. R. J. Quinet and N. M. Hadler, *Semin. Arthritis Rheum.* 1979, **8**, 261.
7. A. A. White and S. L. Gordon, *Spine*, 1982, **7**, 141.
8. L. Axel, *J. Comput. Assist. Tomogr.*, 1984, **8**, 381.
9. D. R. Enzmann, J. B. Rubin, and A. Wright, *Radiology*, 1987, **162**, 763.
10. E. M. Haacke and G. Lenz, *Am. J. Roentgenol.* 1987, **148**, 1251.
11. M. G. Hueftle, M. T. Modic, J. S. Ross, T. J. Masaryk, J. R. Carter, R. G. Wilber, H. H. Bohlman, P. M. Steinberg, and R. B. Delamartor, *Radiology* 1988, **167**, 817.
12. R. R. Edelman, D. J. Atkinson, M. S. Silver, F. L. Hoaiza, and W. S. Warren, *Radiology* 1988, **166**, 231.
13. N. I. Chafetz, H. K. Genant, K. L. Moon, C. A. Helms, and J. M. Morris, *Am. J. Roentgenol.*, 1983, **141**, 1153.
14. R. R. Edelman, G. M. Shoukimas, D. D. Stark, R. R. Davis, P. F. New, S. Saini, D. I. Rosenthal, G. L. Wismer, and T. J. Brady, *Am. J. Roentgenol.*, 1985, **144**, 1123.
15. K. R. Maravilla, H. P. Lesh, J. C. Weinreb, D. K. Selby, and V. Mooney, *Am. J. Neuroradiol.*, 1985, **6**, 237.
16. M. T. Modic, T. J. Masaryk, F. Boumphrey, M. Goormastic, and G. Bell, *Am. J. Roentgenol.*, 1986, **147**, 757.
17. M. T. Modic, T. J. Masaryk, G. P. Mulopolos, C. V. Bundschuh, J. J. Han, and H. Bohlman, *Radiology*, 1986, **161**, 753.
18. M. T. Modic, T. J. Masaryk, J. S. Ross, G. P. Mulopolos, C. V. Bundschuh, and H. Bohlman, *Radiology*, 1987, **163,** 227.
19. J. S. Ross, N. Perez-Reyes, T. J. Masaryk, M. Bohlman, and M. T. Modic, *Radiology*, 1987, **165** 511.
20. M. T. Modic, W. Pavlicek, M. A. Weinstein, F. Boumphrey, F. Ngo, R. Hardy, and P. M. Duchesneau, *Radiology*, 1984, **152**, 103.
21. A. deRoos, H. Kressel, C. Spritzer, and M. Dalinka, *Am. J. Roentgenol.*, 1987, **149**, 531.
22. M. T. Modic, P. M. Steinberg, J. S. Ross, T. J. Masaryk, and J. R. Carter, *Radiology*, 1988, **166**, 193.
23. J. Aoki, I. Yamamoto, N. Kitamura, T. Sone, H. Iroh, K. Torizuka, and K. Takasu, *Radiology*, 1987, **164**, 411.
24. T. J. Masaryk, F. Boumphrey, M. T. Modic, C. Tamborrello, J. S. Ross, and M. D. Brown, *J. Comput. Assist. Tomogr.* 1986, **10**, 917.
25. V. M. Haughton, *Radiology*, 1988, **166**, 297.
26. N. Grenier, R. I. Grossman, M. L. Schiebler, B. A. Yeager, H. I. Goldberg and H. Y. Kressel, *Radiology*, 1987, **164**, 861.
27. D. K. Bielecki, D. Sartoris, D. Resnick, K. Van Lom, J. Fierer, and P. Haghighi, *Am. J. Roentgenol.*, 1986, **147**, 83.
28. W. Kumpan, E. Salomonowitz, G. Seidl, and G. R. Wittich, *Skeletal Radiol.* 1986, **15**, 444.
29. D. Resnick, G. Niwayama, J. Guerra, V. Vint, and J. Usselman, *Radiology*, 1981, **139**, 341.
30. L. G. Naul, G. J. Peet, and W. B. Maupin, *Radiology*, 1989, **172**, 219.
31. B. E. Maldague, H. M. Noel, and J. J. Malghem, *Radiology*, 1978, **129**, 23.
32. F. Gagnerie, B. Taillan, L. Euller-Ziegler, and G. Ziegler, *Clin. Rheumatol.*, 1987, **6**, 597.

33. M. Castillo, J. A. Malko, and J. C. Hoffman, *Am. J. Neuroradiol.*, 1990, **11**, 23.
34. J. M. Gomori, R. I. Grossman, H. I. Goldberg, R. A. Zimmerman, and L. T. Bilaniuk, *Radiology*, 1985, **157**, 87.
35. J. M. Gomori, R. I. Grossman, D. B. Hackney, H. I. Goldberg, R. A. Zimmerman, and L. T., Bilaniuk *Am. J. Neuroradiol.*, 1987, **8**, 1019; *Am. J. Roentgenol.*, 1988.
36. H. Nabatame, N. Fujimoto, K. Nakamura, Y. Imura, Y. Dodo, H. Fukuyama, and J. Kimura, *J. Comput. Assist. Tomogr.*, 1990, **14**, 521.
37. S. A. Mirowitz, K. Sartor, and M. Gado, *Am. J. Neuroradiol.*, 1989, **10**, 1159; *Am. J. Roentgenol.*, 1990, **154**, 369.
38. S. A. Mirowitz, T. J. Westrich, and J. D. Hirsch, *Radiology*, 1991, **181**, 117.
39. S. A. Mirowitz and T. J. Westrich, *Radiology*, 1992, **185**, 535.
40. P. P. Maeder, S. L. Holtas, L. N. Basibuyuk, L. A. Salford, V. A. Tapper, and A. Bruh, *Am. J. Neuroradiol.*, 1990, **11**, 575.
41. P. M. Som, W. P. Dillon G. D. Fullerton, R. A. Zimmerman, B. Rajagopalan, and Z. Marom, *Radiology*, 1989, **172**, 515.
42. K. Abe, H. Hasegawa, Y. Kobayashi, H. Fujimura, S. Yorifuji, and S. Biton, *Neuroradiology*, 1990, **32**, 166.
43. O. B. Boyko, P. C. Burger, J. D. Shelburne, and P. Ingram, *Am. J. Neuroradiol.*, 1992, **13**, 1439.
44. R. M. Henkelman, J. F. Watts, and W. Kucharczyk, *Radiology*, 1991, **179**, 199.
45. L. A. Dell, M. S. Brown, W. W. Orrison, C. G. Eckel, and N. A. Matwiyoff. *Am. J. Neuroradiol.*, 1988, **9**, 1145.
46. R. D. Tien, J. R. Hesselink, and A. Duberg, *Am. J. Neuroradiol.*, 1990, **11**, 1251.
47. Y. Araki, T. Furukawa, K. Tsuda, T. Yamamoto and I. Tsukaguchi, *Neuroradiology*, 1990, **32**, 325.
48. B. A. Bangert, M. T. Modic, J. S. Ross, N. A. Obuchowski, J. Perl, P. M. Ruggieri, and T. J. Masaryk, *Radiology*, 1995.
49. R. P. Jackson, J. E. Cain, R. R. Jacobs, B. R. Cooper, and G. E. McManus, *Spine*, 1989, **14**, 1362.
50. J. S. Ross, M. T. Modic, T. J. Masaryk, J. Carter, R. E. Marcus, and H. Bohlman, *Am. J. Neuroradiol.*, 1989, **10**, 1243.
51. S. D. Boden, D. O. Davis, T. S. Dina, N. J. Patronas, and S. W. Wiesel, *J. Bone Joint Surg (Am.)*, 1990, **72**, 403.
52. M. C. Jensen et al., *N. Engl. J. Med. 2*, 1994, **331**, 69.
53. D. Fardon, S. Pinkerton, R. Balderston, S. Garfin, R. Nasca, and R. Salib, *Spine*, 1993, **18**, 274.
54. T. J. Masaryk, J. S. Ross, M. T. Modic, F. Boumphrey, H. Bohlman, and G. Wilberg, *Am. J. Neuroradiol.*, 1988, **150**, 1155.
55. S. W. Yu, V. M. Haughton, L. A. Sether, and M. Wagner, *Radiology*, 1988, **169**, 761.
56. J. R. Jinkins, *Am. J. Neuroradiol.*, 1993, **14**, 193.
57. S, Kobayashi, H. Yoshizawa, and Y. Hachiya in '18th Annual Meeting of the International Society for the Study of the Lumbar Spine, 1991'.
58. R. Quencer *Am. J. Neuroradiol.*, 1994,
59. R. P. Jackson, J. E. Cain, R. R. Jacobs, B. R. Cooper, and C. E. McManus, *Spine* 1989, **14**, 1362.
60. J. R. Thornbury, D. G. Fryback, P. A. Turski, M. J. Jarid, J. V. McDonald, B. R. Bernlich, L. R. Gentry, J. F. Saekott, E. J. Dosbach, and P. A. Martin, *Radiology*, 1993, **186**, 731.
61. S. D. Boden, P. R. McCowin, D. O. Davis, T. S. Dina, A. S. Mark, and S. Wiesel, *J. Bone Joint Surg. (Am.)*, 1990, **72**, 1178.
62. B. M. Brown, R. H. Schwartz, E. Frank, and N. K. Blank, *Am. J. Neuroradiol.*, 1988, **9**, 859.
63. M. C. Hedberg, B. P. Drayer, R. A. Flom, J. A. Modak and C. R. Bird, *Am. J. Roentgenol.*, 1988, **150**, 683.
64. D. R. Enzmann, and J. B. Rubin, *Radiology*, 1988, **166**, 467.
65. D. M. Yousem, S. W. Atlas, H. I. Goldberg, and R. I. Grossman, *Am. J. Neuroradiol.*, 1991, **12**, 229.
66. E. E. Awwad, D. S. Martin, K. R. Smith, and R. D. Bucholz, *J. Comput. Assist. Tomogr.*, 1990, **14**, 415.
67. D. Schellinger, L. Wener, B. D. Ragsdale, and N. J. Patronas, *RadioGraphics*, 1987, **7**, 944.
68. T. B. Freeman and C. R. Martinez, *Perspect. Neurol. Surg.*, 1992, **3**, 34.
69. H. Pavlov, J. S. Torg, B. Robie, and C. Jahre, *Radiology*, 1987, **164**, 771.
70. T. Fukushima, T. Ikata, Y. Taoka, and S. Takata, *Spine*, 1991, **16**, (Suppl. 10), 5534.
71. P. F. Statham, D. M. Hadley, P. MacPherson, R. A. Johnston, I. Bone, and G. M. Teasdale, *J. Neurol. Neurosurg. Psychiatry.*, 1991, **54**, 484.
72. B. M. Brown, R. H. Schwartz, E. Frank, and N. K. Blank, *Am. J. Roentgenol.*, 1988, **151**, 205.
73. R. I. Harris and I. McNab, *J. Bone Joint Surg. (Br.)*, 1954, **36**, 304.
74. N. Grenier, H. Y. Kressel, M. L. Schiebler, R. I. Grossman, and M. K. Dalinka, *Radiology*, 1987, **165**, 517.

Biographical Sketch

Michael T. Modic received his M.D. degree from Case Western Reserve School of Medicine in 1975. He completed his residency in radiology and fellowship in neuroradiology at the Cleveland Clinic Foundation. He spent a year as assistant professor of Radiology and as a staff neuroradiologist at University Hospitals in Cleveland from 1979–1980 and in 1980 returned to the Cleveland clinic as a staff neuroradiologist. In 1982 he was appointed head of the section of Magnetic Resonance. In 1985 he returned to Case Western Reserve School of Medicine/University Hospitals as Director of Magnetic Resonance and Neuroradiology, positions he held through 1989. During that time he also held the rank of Professor of Radiology, Neurology, and General Medical Sciences. In 1988 he was given a joint appointment as Professor of Neurosurgery as well. In 1989, Dr. Modic returned to the Cleveland Clinic Foundation as Chairman of Radiology and in 1993 was appointed as Professor of Radiology, Ohio State University. Dr. Modic has served on the Editorial Boards of the journals Radiology, American Journal of Neuroradiology, Neurology, Magnetic Resonance in Medicine, and Magnetic Resonance Imaging. He has served as a member of the Board of Trustees of the Society of Magnetic Resonance in Medicine and Board of Directors of the Society of Magnetic Resonance Imaging. He was President of the Society of Magnetic Resonance in Medicine for the 1992–1993 year and was the recipient of the Society Gold Medal in Clinical Science for his research activities related to the spine in 1991. He is co-author of the text 'Magnetic Resonance Imaging of the Spine' which is in its second edition and is the author or co-author of over 125 peer reviewed articles related to neuroradiology.

Eye, Orbit, Ear, Nose, and Throat Studies Using MRI

Mahmood F. Mafee
University of Illinois at Chicago, Chicago, IL, USA

1 MRI OF THE EYE

1.1 Introduction

The eye consists of three primary layers: (1) the sclera, or outer layer, composed primarily of collagen-elastic tissue; (2) the uvea or middle layer, a richly vascular and pigmented tissue consisting of the iris, ciliary body, and choroid; and (3) the retina or inner layer, the neurosensory stratum of the eye.[1] The Tenon's capsule (bulbar fascia) is a fibroelastic membrane that covers the sclera and envelops the eyeball. Tenon's capsule encloses the posterior four-fifths of the eyeball separating it from the orbital fat. Tenon's capsule is separated from the sclera by the potential Tenon's space.[2,3]

1.2 Anatomy of the Globe

1.2.1 Anterior and Posterior Segments of the Globe

The ciliary body and the iris divide the globe into an anterior and a posterior segment. The anterior segment which includes the anterior and posterior chambers is the space lying between the cornea and the crystalline lens. The posterior (vitreous) segment contains the vitreous chamber (body), which acts as a biologic shock absorber. The vitreous chamber is a gel-like, transparent, extracellular matrix, composed of a meshwork of 0.2% collagen fibrils interspersed with 0.2% hyaluronic acid polymers, 98–99% water, and small amounts of soluble protein.[4,5]

1.2.2 Lens

The lens is one of the least hydrated organs of the body containing only 66% water.[5] The remainder is composed of long, thin cells (lens fibers) whose main cytoplasmic content is protein.

1.2.3 Sclera

The sclera, the outer, white, leathery coat of the globe is primarily composed of cellular bundles of collagen. Its external surface lies adjacent to Tenon's capsule. Its internal surface blends with the uveal tissues.

1.2.4 Uvea (Iris, Ciliary Body and Choroid)

The uvea lies between the sclera and retina and provides vascular supply to the eye and regulates ocular temperature. The choroid is a portion of the uvea that lies between the sclera and the retinal pigment epithelium (RPE). The ciliary body is a direct anterior continuation of the choroid, and the iris is a further extension of the ciliary body itself.

1.2.5 Retina

The external surface of the retina is in contact with the choroid and the internal surface is adjacent to the vitreous body; posteriorly, the retina is continuous with the optic nerve. Grossly the retina has two layers: (1) the inner layer is the sensory retina, composed of photoreceptors, first and second order neurons (ganglion cells) and neuroglial elements and (2) the outer layer is the RPE, which consists of a single lamina of cells whose nuclei are adjacent to the basal membrane of the choroid, the so-called Bruch's membrane.

1.3 MRI Anatomy of the Globe

The globe is unique in that it contains the most (vitreous) and the least (lens) water concentration of all the tissues in the body.[4,5] The eye is an ideal organ to be evaluated by MRI because the wide variations in water content produce different water proton relaxation times of the various tissues. The eye can be imaged using head coil or surface coil. Images obtained with surface coil provide better spatial resolution. A routine MRI of the eye usually includes single echo short repetition time (*TR*), short echo time (*TE*) (*TR*/*TE*, 400–600/20–25 ms), sagittal and axial views and an axial view SE double echo (*TR*/*TE*, 2000/20–25; 70–100 ms) pulse sequences. Following the intravenous (i.v.) administration of gadolinium diethylenetriaminepentaacetic acid (Gd-DTPA), single echo, short *TR*, short *TE* images in axial and other views are obtained with or without fat suppression techniques. The section thickness for MRI of the eye should be 3 mm. The normal lens has long T_1 and short T_2 relaxation properties on MRI (Figure 1). The nucleus of the lens has both lower water content and shorter T_2 than the cortex of the lens. The sclera has a low signal intensity on various pulse sequences which is probably related to the short T_2 caused by a greater proportion of bound water.[5] Differentiation of individual layers of the retina, choroid, and posterior hyaloid membrane is impossible by MRI in the normal eye; however, in pathological conditions, detachment of different layers of the eye can be visualized on MR images.

1.4 MRI of Ocular Pathology

MRI has served as an important diagnostic method in ophthalmology for the last decade.[2,6–14] Excellent contrast between various normal structures and high sensitivity in detection of pathologic states is due to the intrinsic differences in proton density and in proton relaxation times.[2,4]

1.5 Posterior Hyaloid, Retinal, and Choroidal Detachment

The posterior hyaloid space is a potential space between the posterior hyaloid (vitreous) membrane and the sensory retina. The posterior hyaloid membrane is thin and is invisible on MRI. It becomes visible when blood or other fluid fills the potential posterior hyaloid space. On MRI, a detached posterior hyaloid membrane is seen as a thin membrane within the globe, in front of the optic disk.

Retinal detachment results from separation of the sensory retina from the RPE with accumulation of fluid in the potential subretinal space.

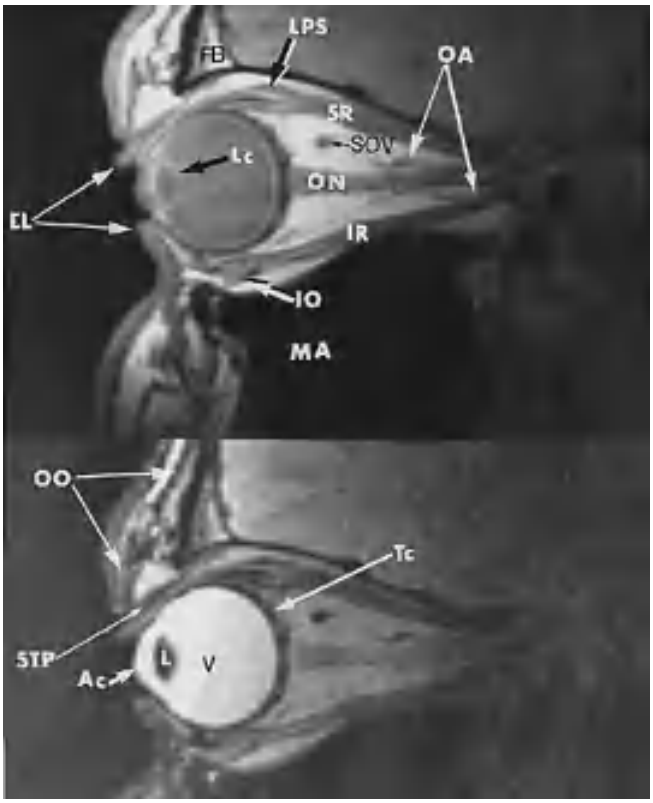

Figure 1 Normal MRI anatomy of the eye and orbit. Sagittal PW (top) and T_2W (bottom) MR images. Ac = anterior chamber, EL = eyelids, FB = frontal bone, IO = inferior oblique muscle, IR = inferior rectus muscle, L = lens, Lc = lens capsule, LPS = levator palbebra superioris, MA = maxillary antrum, OA = ophthalmic artery, ON = optic nerve, OO = fibers of the orbicularis oculi muscle, SOV = superior ophthalmic vein, SR = superior rectus muscle, STP = superior tarsal plate, Tc = Tenon's capsule

Since the retina is very thin, it cannot be directly visualized on MRI scans. However, it may be shown when it is outlined by significant contrast differences between the subretinal effusion and the vitreous chamber. On axial MRI, the detached retina is seen as a V-shaped structure, with its apex at the optic disk and its extremities toward the ora serrata just behind the ciliary body, where the sensory retina ends. On coronal MR scans, retinal detachment appears as a characteristic folded membrane. The subretinal exudate is rich in protein, therefore has higher MR signals than the vitreous cavity on T_1- and often on T_2-weighted MR images.

Choroidal detachment results from the accumulation of fluid (serous) or blood (hemorrhagic choroidal detachment) within the potential space between the choroid and the sclera. MRI is an excellent technique in the evaluation of choroidal detachment, particularly when ultrasonography or computerized tomography (CT) in conjunction with the clinical examination have not provided sufficient information. Serous choroidal detachment appears as a semilunar or ring-shaped area of higher MR signal than vitreous on T_1- and T_2-weighted MR images.[9] The appearance of choroidal detachment on MR images may be confused with retinal detachment. However, choroidal detachment is often restricted by the anchoring effect of the vortex veins and short posterior ciliary arteries. This restriction results in a characteristic appearance in which the leaves of the detached choroid, unlike the detached retina, frequently do not extend to the region of the optic disc.

The MRI appearance of hemorrhagic posterior hyaloid, retinal and choroidal detachments varies with the age and the degree of organization of the hemorrhage. A hematoma less than 48 h old usually appears iso- to slightly hypointense relative to the normal vitreous body on T_1-weighted (T_1W) and proton-weighted (PW) MR images, but is markedly hypointense on T_2-weighted (T_2W) images. When the hematoma is approximately 5 days old, it appears relatively hyperintense on PW and T_1W images but is hypointense on T_2W images. At this stage, hematoma may be confused with an ocular melanoma.[6,8,9] The hematoma usually continues to increase in signal intensity on T_1W, PW, and T_2W images and usually becomes markedly hyperintense by day 14 on all MR pulse sequences.

1.6 Retinoblastoma

Retinoblastoma, the most common intraocular tumor of childhood, is a highly malignant retinal tumor. The tumor arises from neuroectodermal cells (nuclear layer of the retina) destined to become retinal photoreceptors.[2,10] Leukokoria, a pink–white or yellow–white pupillary reflex (cat's eye), is the most common presenting sign of retinoblastoma. Computerized tomography is most sensitive in demonstrating the presence of the typical deoxyribonucleic acid (DNA)–calcium complexes within the tumor.[2,10] Magnetic resonance imaging is not as specific as CT scanning in the diagnosis of retinoblastoma due to its lack of sensitivity in detecting calcification. However, it is more specific than CT in differentiating retinoblastoma from other lesions that simulate retinoblastoma clinically, such as persistent hyperplastic primary vitreous (PHPV), Coats' disease, retinopathy of prematurity (ROP), toxocariasis, retinal detachment, and other so-called pseudogliomas and leukokorias.[2,10,12,13] Lesions less than 2–3 mm in thickness are not recognized as discrete areas by MR technology to date. At times lesions less than 3 mm thick may be better visualized on post Gd-DTPA contrast MR scans due to increased contrast resolution. On MRI, retinoblastomas appear slight to moderately hyperintense to vitreous on T_1W and slightly or moderately hypointense to vitreous on T_2W MR scans. Even extensive calcification noted on CT scans may be missed in all MR pulse sequences. Retinoblastomas demonstrate moderate to marked contrast enhancement following i.v. administration of Gd-DTPA contrast material. Involvement of the Tenon's capsule, optic nerve and retrobulbar space is best evaluated on post Gd-DTPA fat-suppression T_1W MR images. MRI including Gd-DTPA contrast study appears to be the study of choice for the evaluation of intracranial spread of retinoblastoma and the association of bilateral retinoblastoma, suprasellar and pineal primitive neuroectodermal tumors (tetra lateral retinoblastoma).[14]

1.7 Persistent Hyperplastic Primary Vitreous (PHPV)

Persistent hyperplastic primary vitreous is caused by failure of the embryonic hyaloid vascular system to regress normally. The ocular malformation can reflect either an isolated congeni-

tal defect or may be a manifestation of more extensive ocular or systemic involvement.[2,15,16] The MRI findings of PHPV include: (1) microphthalmos, (2) lack of calcification, (3) posterior hyaloid or retinal detachment, (4) tubular, cylindrical or other discrete intravitreal images suggestive of persistence of fetal tissue, (5) fluid level within the globe, reflecting the presence of serosanguinous fluid in either the subhyaloid or subretinal space, (6) enhancement of abnormal intravitreal tissue following i.v. administration of Gd-DTPA contrast material, (7) altered signal of lens of the involved eye compared with the other normal eye.

1.8 Coats' Disease

Coats' disease is a primary vascular anomaly of the retina, characterized by idiopathic retinal telangiectasia and exudative retinal detachment (exudative retinopathy). It is almost always unilateral and generally affects boys of 4 to 6 years of age, although it may be seen in younger children. In the early stage of the disease, MRI may yield little information. In the later stages, the exudative retinal detachment is seen as hyperintense images on all MRI pulse sequences. At times, due to lipoproteinaceous exudate, typically seen in Coats' disease, the subretinal exudate may be less hyperintense than the vitreous body on T_2W MR scans. The leaves of the detached retina in Coats' disease may be very thickened and may show moderate to significant enhancement following i.v. administration of Gd-DTPA contrast material.

1.9 Retinopathy of Prematurity (ROP)

Retinopathy of prematurity, formerly termed retrolental fibroplasia, is believed to be related to a combination of developmental (prematurity) and environmental (supplemental oxygen therapy) factors that prevent normal retinal vasculogenesis. The MRI findings of the early stage of ROP are nonspecific. The eyes may be microphthalmic. In the more advanced stages the differential diagnoses include PHPV, retinoblastoma, endophthalmitis as well as a number of pathologic conditions in which retinal detachment is a common feature.[2,17] Retinoblastoma has rarely been reported in microphthalmic eyes with or without ROP or PHPV.

1.10 Ocular Toxocariasis

Toxocariasis results from ingestion of eggs of the nematode, *Toxocara canis*. The death of the larva results in a wide spectrum of intraocular inflammatory reactions. MRI is superior to CT for the evaluation of ocular toxocariasis. The MR findings of ocular toxocariasis consist of localized or diffuse intravitreal mass with moderate to marked contrast enhancement. The subretinal exudate has variable hyperintense signal on T_1W, PW, and T_2W MR scans.[17]

1.11 Malignant Uveal Melanoma

Malignant uveal melanoma is the most common intraocular tumor in adults. They are uncommon in blacks, the white:black ratio being about 15 : 1[6] Metastasis primarily involves the liver. Uveal melanomas and other intraocular lesions more than 3 mm in thickness are usually well visualized on MR scans.[6,17] Smaller lesions are better studied with ultrasonography. The MR characteristics of melanotic lesions are thought to be related to the paramagnetic proton relaxation by stable radicals in melanin.[18] The stable radicals cause a proton relaxation enhancement that shortens both T_1 and T_2 relaxation times.[11] Hence, uveal melanomas appear as areas of moderately to markedly high signal (greater signal intensity than vitreous) on T_1W and PW MR images. On T_2W images, melanomas appear as areas of moderately to markedly low signal (lesser signal intensity than vitreous). These MR characteristics are similar to those of retinoblastoma. Some of the melanomas may not be hypointense on T_2W images. Melanomas demonstrate moderate enhancement following i.v. administration of Gd-DTPA contrast media (Figure 2). Exudative retinal detachment, associated with choroidal melanoma is seen on MRI as dependent areas of moderate to high intensity on T_1W, PW and T_2W images. Organized exudative chronic retinal detachment and hemorrhagic subretinal fluids may simulate melanoma on MRI scans. Invasion of the sclera, extension of tumor into the Tenon's capsule or optic disk and extraocular invasion can be best detected by MR scans, particularly on post Gd-DTPA fat-suppression T_1W MR images.

1.12 Choroidal Hemangioma

Choroidal hemangiomas are congenital vascular hamartomas. Two different forms have been described: a circumscribed or solitary type and a diffuse angiomatosis.[19] Diffuse choroidal hemangiomas are usually seen in association with Sturge–Weber disease. Choroidal hemangiomas can be diagnosed by ophthalmoscopy, fluorescein angiography, ultrasonography or CT. However, misdiagnoses are not uncommon, particularly when the angiomas are concealed by a detachment of the retina.[2] On MRI, choroidal hemangiomas appear hypointense to slightly hyperintense to vitreous on T_1W images and hyperintense on T_2W images. They show intense enhancement on post Gd-DTPA T_1W MR scans. MRI scans are, therefore, extremely

Figure 2 Malignant choroidal melanoma. Axial T_1W postcontrast MR image. A hyperintense enhancing mass (solid arrows) is demonstrated. The melanoma has caused retinal detachment (hollow arrow). The tumor can be easily differentiated from subretinal exudate

useful in differentiating choroidal hemangiomas from choroidal melanomas.

1.13 Uveal Metastases

A most common source of secondary carcinoma within the eye is from breast or lung. Metastatic lesions of the uvea extend chiefly in the plane of the choroid, causing relatively little increase in its thickness. Unlike uveal melanomas, which tend to form a protuberant mass, uveal metastases usually have a mottled appearance and a diffuse outline on MRI scans. Most uveal metastases appear as areas of low signal on T_1W MR scans. On T_2W images, metastases appear as areas of high signal intensity. A mucin-producing metastatic lesion (adenocarcinoma) may simulate a uveal melanoma because the proteinaceous fluid tends to decrease T_1 and T_2 relaxation times.[2] Uveal metastatic carcinoid lesions may simulate uveal melanomas on MRI scans.[20] Uveal metastases demonstrate moderate to marked enhancement following i.v. administration of Gd-DTPA contrast material. Exudative retinal detachment associated with uveal metastases can be best differentiated from metastasis on postcontrast T_1W images.

1.13.1 Choroidal Hemorrhage and Detachment

Choroidal hemorrhage and detachment may be easily mistaken for choroidal tumors.[2,8,9] MRI is invaluable in differentiating choroidal detachments from uveal melanomas.[8]

1.13.2 Other Uveal Tumors

Neurofibroma and schwannoma of the choroid and ciliary body, adenoma, leiomyoma, and lymphoreticular proliferative disorders of the uveal tract are rare lesions involving the choroid and ciliary body which can cause diagnostic confusion with uveal melanoma. If these lesions are large enough (3 mm or more) they can be detected by MRI.[10]

2 MRI OF THE ORBIT

2.1 Introduction

The orbits are two recesses that contain the globes, the extrinsic ocular muscles, the blood vessels, lymphatic, nerves (II, III, IV, and V), adipose and connective tissues, and most of the lacrimal apparatus.[1] The orbit is bounded by the periosteum (periorbita) and separated from the globe by Tenon's capsule. Anteriorly are the orbital septum and the lids. The orbital cavity is pyramidal; its apex is directed posteriorly and medially and its base is directed anteriorly and laterally as the orbital opening. Its bony walls separate it from the anterior cranial fossa superiorly, the ethmoid and sphenoid sinuses and nasal cavity medially, the maxillary sinuses inferiorly, and the lateral surface of the face and temporal fossa laterally and posteriorly. At the apex of the orbit, the optic canal and the superior and inferior orbital fissures allow various structures to enter and leave the orbit.[1,21]

2.2 Anatomy of the Orbit

2.2.1 Orbital Septum and Eyelids

The orbital septum is a weak, membranous sheet that forms the fibrous layer of the eyelids and is attached to the margins of the bony orbit where it is continuous with the periorbita. Each eyelid or palpebra from without inwards consists of skin, subcutaneous areolar tissue, fibers of the orbicularis oculi, tarsus, and orbital septum.

2.2.2 Orbital Fatty Reticulum, Extraocular Muscles, and Optic Nerve

Within the orbit all structures are embedded in a fatty reticulum. The fibroelastic tissue that makes up the reticulum divides the fat into lobes and lobules.[21] The six striated extraocular muscles, including the four recti and the two oblique muscles, control eye movement. The rectus muscles arise from the annulus of Zinn, which is a tunnel-shaped tendinous ring that encloses the optic foramen and the medial end of the superior orbital fissure.[22]

The optic nerve is a nerve fiber tract that conveys visual sensation. It traverses the optic canal with the ophthalmic artery. The optic nerve is covered by three layers, the pia mater, the arachnoid, and the dura, all of which sheathe the nerve.

2.2.3 Lacrimal Apparatus

The lacrimal gland lies in the superolateral angle of the orbit in the lacrimal fossa. Tears produced by the gland are drained into the lacrimal sac. The lacrimal sac lies in the lacrimal groove, located in the anterior-inferomedial angle of the orbit. From the sac, the tears drain through the nasolacrimal duct into the inferior meatus of the corresponding nasal cavity.

2.3 MRI Techniques

Excellent natural contrast between various orbital tissues (water, fat, muscles, and nerves) makes the orbit an ideal organ to study by MRI. The three-dimensional capability of MRI along with its superior contrast resolution is of great assistance in localizing orbital pathology. Using a head coil, a routine MRI of the orbit usually includes a single echo short *TR*, short *TE* (*TR*/*TE*, 500–800/20–25 ms), SE sagittal view, an axial SE double echo (*TR*/*TE*, 2000–2500/20–25, 70–100 ms) and a single echo, short *TR*, short *TE*, SE axial or coronal view. Following the intravenous i.v. administration of Gd-DTPA, single echo, short *TR*, short *TE* images are obtained with or without fat-suppression techniques. Images obtained with a surface coil provide better spatial resolution; however, the apical lesions and intracranial extension of the orbital lesions may not be fully evaluated because of signal dropout, proportional to the distance from the surface coil. We use the surface coil for those lesions situated in the anterior orbit. In general, the orbital MRI study and the use of paramagnetic contrast material should be tailored according to the suspected problem of individual patients.[22]

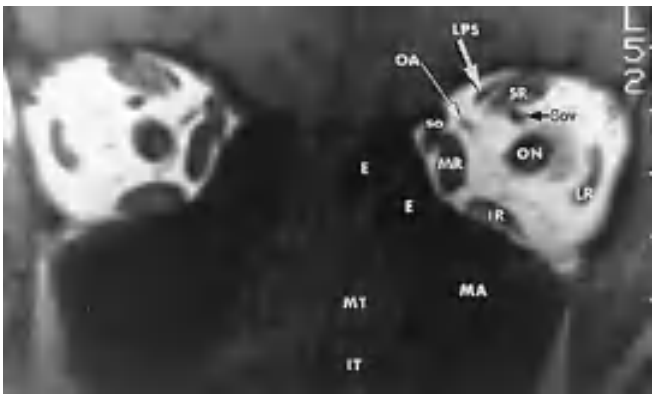

Figure 3 Normal orbital anatomy. Coronal 3 mm thick MR scan, demonstrating various anatomical structures of the orbits, nasal and paranasal sinuses. E = ethmoidal sinus, IR = inferior rectus muscle, IT = inferior turbinate, LPS = levator palbebra superioris, LR = lateral rectus muscle, MA = maxillary antrum, MR = medial rectus muscle, MT = middle turbinate, OA = ophthalmic artery, ON = optic nerve, so = superior oblique muscle, Sov = superior ophthalmic vein, SR = superior rectus muscle

2.4 MRI Anatomy of the Orbit

MRI provides the best cross sectional imaging anatomy of the orbit. The SE, short *TR* and short *TE* pulse sequences provide the most spatial resolution with exquisite anatomical details.[22] The extraocular muscles, the intermuscular septae, the optic nerve, superior ophthalmic vein, ophthalmic artery, the lacrimal gland, lacrimal sac, and nasolacrimal duct are very well visualized on routine MR images (Figure 3). Smaller structures such as divisions of the ophthalmic and third cranial nerves, lacrimal vein and artery, and even ciliary vessels can be visualized on high resolution MR images, obtained with a surface coil. The orbital septum, structures of the eyelids including tarsal plates, the annulus of Zinn, and most of the tendinous portion of the extraocular muscles can be best visualized on images obtained with a surface coil.[22]

2.5 MRI of Orbital Pathology

2.5.1 Developmental Orbital Cysts

MRI is particularly helpful in the evaluation of congenital anomalies of the orbit and optic system. The most frequent developmental cysts involving the orbit and periorbital structures are epidermoid and dermoid cysts and teratomas. Epidermoid and dermoid cysts appear hypointense to brain on T_1W and hyperintense on T_2W MR images. Portions of the dermoids which contain fatty tissue appear hyperintense on T_1W and hypointense on T_2W images. Epidermoid and dermoid cysts do not show enhancement with Gd-DTPA.

2.5.2 Inflammatory Conditions

Preseptal and postseptal orbital inflammation, subperiosteal phlegmon and abscess, ophthalmic vein and cavernous sinus thrombosis can be demonstrated by MRI. The main contribution of MRI to the diagnosis of sinonaso-orbital infections is its clear demonstration of the relationship between nasal, sinus, orbital and cranial disease.[22]

2.5.3 Idiopathic Orbital Inflammations (Pseudotumors)

Pseudotumors are defined as nonspecific, idiopathic, orbital inflammatory conditions for which no local identifiable cause or systemic disease can be found.[22–24] Classically the rapid development of unilateral, painful ophthalmoplegia, proptosis and chemosis, with a rapid and lasting response to steroid therapy in an otherwise healthy patient, is highly suggestive of the diagnosis of pseudotumor. On MRI, pseudotumors usually appear as an infiltrative process which is isointense or hypointense to muscles on T_1W and hyperintense on T_2W images. On MRI, the enhancement of pseudotumors with Gd-DTPA is best demonstrated on fat-suppressed T_1W images. There are no specific imaging characteristics or clinical signs to establish the diagnosis of pseudotumor with absolute certainty. Idiopathic orbital myositis may simulate thyroid myopathy. However, typically, enlargement of the muscles in thyroid myopathy involves the muscle belly, sparing its tendinous portion.

2.6 Orbital Tumors

2.6.1 Lymphoma

Lymphomas, the most common malignant orbital tumors in adults, are solid tumors of the immune system. Most are composed of monoclonal B cells. The most common cytologic forms of malignant lymphoma involving the orbit are histiocytic and lymphocytic in various degrees of differentiation. True lymphoid tissue in the eye is found in the subconjunctival and lacrimal gland. This explains why most orbital lymphomas are commonly seen in the anterior portion of the orbit. The MRI findings of orbital lymphomas are usually nonspecific and at times are impossible to differentiate from those of orbital pseudotumors. Both pseudotumors and lymphomas may have an intermediate or hypointense signal in T_1W images (Figure 4) and appear isointense or hyperintense and even hypointense (although less common) to fat in T_2W images (Figure 4). Both pseudotumors and lymphomas demonstrate moderate contrast enhancement on postcontrast MRI scans.

2.6.2 Rhabdomyosarcoma

Rhabdomyosarcoma is the most common malignant mesenchymal tumor of childhood, as well as the most common primary malignant tumor of the orbit in children.[22,25] The tumor is notorious for producing a rapidly developing unilateral proptosis. Any rapidly developing proptosis in childhood must presumptively be diagnosed as rhabdomyosarcoma. The differential diagnosis also includes leukemia and metastatic deposits (neuroblastoma), Langerhans histiocytosis, ruptured dermoid cyst, hemorrhage in a pre-existing lymphangioma, subperiosteal infection and hematoma after trauma. Rhabdomyosarcomas are both aggressive bone-destroying lesions and bone-pushing lesions. Rhabdomyosarcoma appears hypointense to brain on T_1W and isointense to slightly hyperintense to brain on T_2W images. The use of paramagnetic contrast media results in moderate to marked enhancement.[25] Magnetic resonance imaging is the most sensitive imaging study to differentiate rhabdomyosarcoma from most simulating lesions.[22,25]

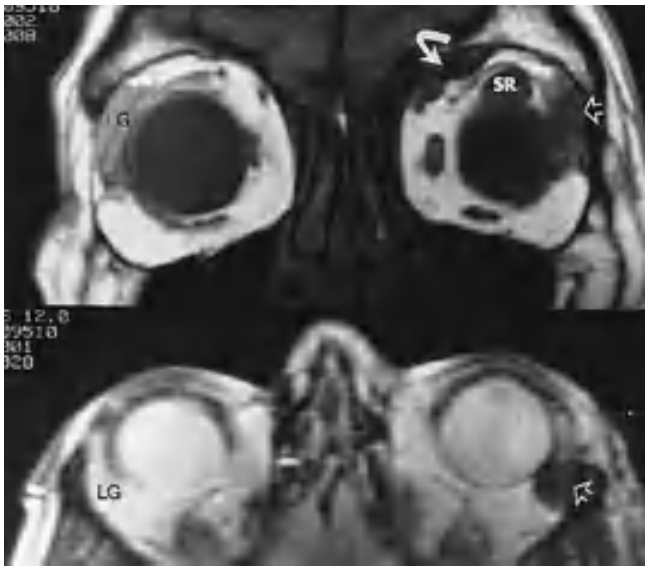

Figure 4 Small cell lymphoma of the orbit. Coronal T_1W (top) and axial T_2W (bottom) MR scans demonstrating normal right lacrimal gland (LG) and abnormal left lacrimal gland (hollow arrows) due to involvement by lymphoma. Notice lymphomatous involvement of left superior rectus muscle (SR) as well as extraconal fat (curved arrow)

2.6.3 Hemangiomas and Lymphangiomas

Capillary hemangiomas are the most common orbital vascular tumors that occur in infants during the first year of life. The tumor often increases in size for 6 to 10 months and then gradually involutes. On MRI, capillary hemangiomas have long T_1 and long T_2 characteristics. At times, prominent vessels can be identified within the lesion. They demonstrate marked contrast enhancement. On MR angiography, the vascular blush may not be appreciated.

Cavernous hemangiomas, the most common orbital vascular tumor in adults, appear as well-defined masses, frequently occurring within the intraconal space. On MRI, they appear as well-defined, sharply marginated, homogeneous, rounded, ovoid, or lobulated masses, which appear hypointense to brain on T_1W and hyperintense on T_2W images. They demonstrate moderate to marked contrast enhancement on MRI. The MRI characteristics of orbital schwannomas and hemangiopericytomas may be similar to cavernous hemangiomas.[22,26]

Orbital lymphangiomas occur in children and young adults. Lymphangiomas may have distinct borders but are typically diffuse and not well capsulated. Spontaneous hemorrhage within the lesion is common.[22,26] On MRI scans lymphangiomas are seen as homogeneous or heterogeneous, and hypointense to relatively hyperintense on T_1W and, usually, heterogeneously very hyperintense on T_2W scans. Their MRI characteristics usually help to differentiate them from hemangiomas, pseudotumors, rhabdomyosarcoma and many other lesions.[22,26]

2.6.4 Optic Nerve Sheath Meningioma

Optic nerve sheath meningioma (ONSM) arises from the meningoendothelial cells of the arachnoid that are situated along the optic nerve sheath. Meningiomas are usually seen in middle-aged and elderly women. ONSM presents as very slowly progressive axial proptosis and loss of vision. On MRI scans, ONSM can be seen as localized or fusiform enlargement of the optic nerve. ONSM frequently appears hypointense on T_1W and hyperintense on T_2W images as compared with the brain. ONSM demonstrates moderate to marked enhancement on post Gd-DTPA MR scans.[22] Postcontrast fat-suppressed T_1W MR scans are the most sensitive images to detect ONSM. Involvement of the optic nerve by sarcoidosis may result in focal or diffuse enlargement of the optic nerve, mimicking an optic nerve meningioma on all MR pulse sequences.

2.6.5 Optic Nerve Glioma

Optic nerve glioma is a tumor arising from the neuroglia (glial cells) of the optic nerve. It is usually a tumor of childhood (2 to 8 years of age). In general, optic nerve glioma in children is considered a benign, well-differentiated, slowly growing, and noninvasive astrocytoma (pilocystic astrocytoma). However, optic nerve glioma in adults is a rare but invasive malignant astrocytoma (usually glioblastoma multiformis). Bilateral optic nerve gliomas are characteristic of neurofibromatosis type 1 (NF1). Optic nerve gliomas are seen on MRI as a well-defined, fusiform enlargement of the optic nerve. Diffuse, tortuous enlargement of the optic nerve with a characteristic kinking and buckling appearance is a characteristic feature of the childhood form of optic glioma. On T_1W MR scans, gliomas appear isointense or slightly hyperintense compared with the white matter. On T_2W images they appear hyperintense compared with the white matter.[22] The use of paramagnetic contrast media results in moderate to marked enhancement. MRI remains the study of choice for the evaluation of optic gliomas. Intracranial extension of optic nerve gliomas and associated intracranial pathological changes in patients with neurofibromatosis can be best appreciated on MRI scans.[22]

2.7 Optic Neuritis

Optic neuritis is an acute inflammatory process involving the optic nerve. The process may be idiopathic, immune-mediated, metabolic, and infective in nature.[27,28] Multiple sclerosis is the most common cause of optic neuritis;[28,29] visual loss is typically unilateral in patients with demyelinative optic neuritis. A recent study by Beck et al.[29] has shown that intravenous methylprednisolone followed by oral prednisone will speed the recovery of visual loss due to optic neuritis. On MR, the optic nerve in patients with optic neuritis may infrequently appear diffusely enlarged. On T_2W MR scans, the involved optic nerve may be slightly or moderately more hyperintense than the one on the normal side. Most patients with acute idiopathic optic neuritis and with no other neurologic disorder have the same areas of high-intensity signal in the cerebral white matter on T_2W MR scans that are found in patients with multiple sclerosis. In patients with optic neuritis, contrast enhancement on MRI is often subtle or present in a short segment of the optic nerve. It is best demonstrated by comparing pre- and post-contrast T_1W MR images or on postcontrast fat-suppresed T_1W MR scans.[22]

2.8 Lacrimal Gland Tumors

Epithelial tumors represent approximately 50% of masses involving the lacrimal gland. Half of these are pleomorphic (benign mixed) adenomas; the other half are malignant.[30] Of the malignant tumors, adenoid cystic (adenocystic) are the most common.[31] The nonepithelial masses of lacrimal gland fossa include lymphoid-inflammatory lesions, that is, benign dacryoadenitis, pseudotumor, and malignant lymphoma.[31] MRI is the study of choice for the evaluation of lacrimal gland tumors. Benign, mixed tumors appear as well-defined encapsulated masses and have long T_1 and long T_2 MR signal characteristics. The tumor may be homogeneous or heterogeneous. The use of paramagnetic contrast material results in moderate to marked enhancement. The heterogeneity within the tumor may be better appreciated on T_2W and postcontrast T_1W MR images. Malignant lacrimal gland tumors may show poor margins and an infiltrative character. Invasion of the surrounding tissues and intracranial extension can be best evaluated on MRI scans.[22,31]

3 MRI OF THE EAR

3.1 Introduction: Anatomy of the Ear

The ear is essentially a distance receptor concerned with the collection, conduction, modification, amplification and parametric analysis of the complex soundwaves which impinge on the head. The ear is subdivided into three major areas: the outer ear, the middle ear, and the inner ear. Each region has a specific function. The outer ear channels sound to the tympanic membrane (ear drum). The middle ear is an air-filled space (tympanic cavity), connected via the eustachian tube to the nasopharynx. Lying across the tympanic cavity are three small bones; the malleus, the incus and the stapes. The stapes footplate touches a membrane called the oval window, located between the middle ear and the inner ear.[32] A second membrane-covered opening called the round window is located in the cochlea below the oval window. This connects the inner ear with the middle ear and maintains a constant (perilymphatic fluid) pressure within the cochlea. The essential function of the tympanic cavity and its ossicles is the efficient transfer of energy from the air to the perilymphatic fluids which surround the cochlea.[32] The inner ear contains sensory receptors for hearing and balance. It consists of three main parts: the cochlea, the vestibule, and the semicircular canals. The inner ear is composed of the membranous labyrinth and the osseous labyrinth. The membranous labyrinth has two major subdivisions, a sensory portion called the sensory labyrinth and a nonsensory portion designated as the nonsensory labyrinth. The sensory labyrinth lies within the petrous portion of the temporal bone. It contains two intercommunicating portions: (1) the cochlear labyrinth that consists of the cochlea and is concerned with hearing, and (2) the vestibular labyrinth that contains the three semicircular canals, the saccule and utricle, (two small sacs), occupying the vestibule, all of which are concerned with equilibrium. These hollow chambers are filled with fluid, known as endolymph, that resembles intracellular fluid. The nonsensory element of the membranous labyrinth is formed by the endolymphatic duct and sac, whose main function is believed to be the degradation and absorption of the endolymph, produced in the sensory labyrinth, i.e. the cochlea and vestibule. All of the structures of the membranous labyrinth are enclosed within hollowed-out bony cavities that are considerably larger than their membranous contents. These bony cavities assume the same shape as the membranous chambers and are referred to as the osseous labyrinth. The bony cavities of the osseous labyrinth contain fluid, known as perilymph, that bathes the external surface of the membranous labyrinth.

The sound vibrations travel through the middle ear and then through the ossicular chain to the oval window. This in turn sets the perilymph in the cochlear labyrinth in motion. Stimulated by the fluid motion, sensory receptors (hair cells) in the cochlea generate nerve impulses that are transmitted by the cochlear nerve and auditory pathway to the auditory center in the temporal lobe of the brain. Impulses generated in the sensory cells of the semicircular canals and vestibule are carried to the brain by the vestibular nerve.

The essential function of the vestibular labyrinth is to provide the central nervous system (CNS) with a constant flow of information concerning the static position of the head in space, or its state of linear or angular acceleration or deceleration.[32,33]

3.2 Acoustic and Facial Nerves

Acoustic nerve consists of the cochlear nerve and the vestibular nerves (superior and inferior). These are joined into a common trunk that enters the internal auditory canal with the facial nerve. The facial nerve then travels within the temporal bone for some 33 mm through a tortuous bony canal, known as the fallopian canal, before it enters the parotid gland.

3.3 MRI Anatomy of the Ear

MRI remains the study of choice for imaging evaluation of the membranous labyrinth, and the vestibulo-cochlear and facial nerves. The osseous labyrinth, cortical bones, and the air filled mastoid cells appear hypointense in all pulse sequences. The endolymphatic and perilymphatic fluid within and surrounding the membranous labyrinth provides MR signal, resulting in visualization of the membranous labyrinth on various MR pulse sequences (Figure 5). MRI remains the study of choice for the evaluation of the membranous labyrinth, and the vestibulo-cochlear and facial nerves. Cochlear and vestibular divisions of the acoustic nerve and the entire course of facial nerve including its parotid segment can be visualized with exquisite details on MR scans.

3.4 Pathology using MRI of the Ear

The main contribution of MRI to the diagnosis of ear disorders is its clear demonstration of the membranous labyrinth, cochlear, vestibular, and facial nerves. The use of paramagnetic contrast material enhances the sensitivity and at times specificity of MRI in the evaluation of certain pathological conditions. Gd-DTPA contrast has been shown to play an important role in the detection of inflammatory (Figure 6), autoimmune, and neoplastic diseases of the membranous labyrinth as well as soft tissue tumors and inflammatory and infiltrative processes of the ear.[34,35]

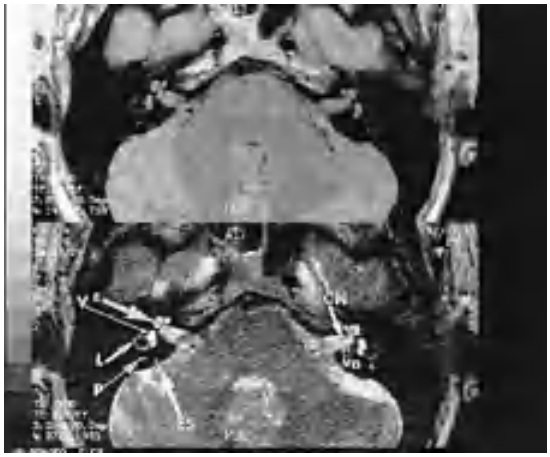

Figure 5 Normal anatomy of the ear: 3 mm axial proton-weighted (top) and T_2W (bottom) MR scans. The cochlea (c), vestibule (V), lateral semicircular canal (L), posterior semicircular canal (P), endolympathic sac (ES), cochlear nerve (CN) and inferior vestibular nerve (vn) are shown

3.5 Developmental Anomalies of the Ear

Computerized tomography scanning remains the study of choice for the evaluation of ear anomalies. MRI provides little information in the evaluation of patients with anomalies of the external and middle ears. In these patients MRI may be used to evaluate the facial nerve. Inner ear anomalies such as Mondini anomaly, large vestibular aqueduct, and Michel anomaly are best evaluated on CT scans. In Mondini anomaly, MRI reveals fluid-filled cystic dilatation of the membranous labyrinth. In patients with large vestibular aqueduct, MRI reveals fluid-filled cystic dilatation of the endolymphatic duct and sac.[33]

3.6 Inflammatory Conditions of the Ear

CT remains the study of choice for the evaluation of acute and chronic otomastoiditis and their complications, including acquired cholesteatomas.[34] The main contribution of MRI to the evaluation of the inflammatory conditions of the ear is its clear demonstration of the involvement of membranous labyrinth and associated intracranial complications (Figure 6). T_1-weighted MRI sequences obtained following the use of paramagnetic contrast material are most informative, as they readily demonstrate abnormal intralabyrinthine enhancement (Figure 6). In patients with vestibulocochlear or facial neuronitis, MRI may demonstrate moderate to marked contrast enhancement of the involved nerve (Figure 7).

3.7 Cholesteatomas and Cholesterol Granulomas

Cholesteatomas of the ear may be congenital or acquired. Histologically the pathology of congenital cholesteatomas is similar to that of the acquired varieties, namely, a cavity, lined with keratinizing stratified squamous epithelium which encapsulates desquamated epithelial cells, keratomatous materials, and minimal cholestrin.

Cholesterol granulomas of the ear are believed to be a tissue response to hemorrhage and an irritant foreign body, i.e. cholesterol crystals and other blood byproducts. Cholesteatomas and cholesterol granulomas of the petrous apex are the most common expansile, slowly destructive, lesions of the petrous bone.[34] On CT scans they are very difficult to differentiate from each other. However, on MRI, cholesteatomas have a long T_1 and long T_2 characteristics, whereas, cholesterol granulomas have a short T_1 and long T_2 characteristic. Both lesions if not infected demonstrate no contrast enhancement. CT scanning is superior to MRI for the detection of middle ear cholesteatomas.[34] MRI however, is superior to CT scanning for the evaluation of infected cholesteatomas, petrous apex and intradural cerebellopontine (CPA) cholesteatomas (epidermoids), as well as for the evaluation of cholesteatomatous involvement of the facial nerve, membranous labyrinth, and intracranial structures.

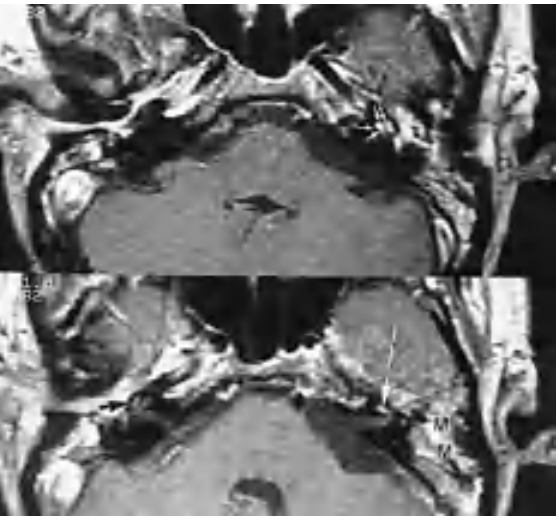

Figure 6 Acute otomastoiditis and labyrinthitis: 3 mm axial post-Gd-DTPA T_1W MR scans. There is marked enhancement of granulation tissues within the mastoid air cells (M). Notice marked enhancement of left membranous cochlea (white, short and long arrows). There is slight enhancement of the right cochlea (black arrow); patient had bilateral acute otomastoiditis, left more so than right

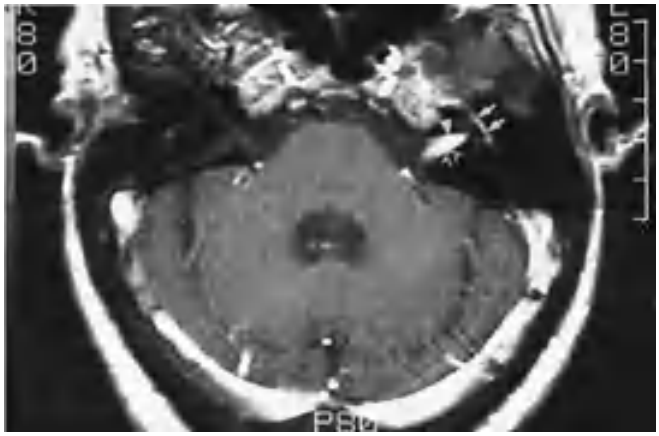

Figure 7 Ramsey hunt syndrome: 3 mm axial post-Gd-DTPA T_1W MR scan. There is marked enhancement of the meatal segment (arrow head) and tympanic segment (solid arrows) of the facial nerve. Note enhancement of the superior vestibular nerve (hollow arrow)

3.8 Tumors of the Ear

The diagnostic approach to evaluating a patient suspected of having a lesion of acoustic and facial nerves or a CPA tumor has changed as the resolution of MRI has improved and as the sensitivity and specificity of MRI has been established. MRI remains the initial imaging study of choice for the evaluation of acoustic and facial neuromas, and most CPA tumors. The most common tumors of the temporal bone are Schwann-cell tumors that arise from the vestibular divisions of the acoustic nerve; as such, they are actually vestibular schwannomas. Bilateral vestibular schwannomas are characteristic of neurofibromatosis type 2 (NF2).

Vestibular schwannomas are the most common CPA masses.[36] Meningiomas are the second and epidermoid cysts are the third most common CPA masses. Magnetic resonance imaging is the most useful diagnostic test to diagnose as well as to differentiate these CPA masses.[37] The use of paramagnetic contrast material significantly increases the sensitivity of MRI. Tumors as small as 2 mm in size can be detected along the course of facial and acoustic nerves. The use of paramagnetic contrast has allowed for the first time the detection of tiny intralabyrinthine schwannomas,[38] and inflammatory processes of the facial nerve which were extremely difficult to diagnose even with high-resolution CT scan.[39–41] Paragangliomas or chemodectomas (glomus tumors) are the second most common tumors of the temporal bone.[42] Paragangliomas appear as regions of hypointensity on T_1W and hyperintensity on T_2W MR scans.[42] There are frequently areas of signal void related to rapid arterial flow present in the matrix of these hypervascular tumors. Paragangliomas demonstrate significant enhancement following intravenous (i.v.) administration of paramagnetic contrast material.[42] Other benign and malignant tumors that involve the ear, including adenoma, carcinomas, adenocarcinomas, papillary adenocarcinomas, adenoid cystic carcinomas, rhabdomyosarcomas, chondrosarcomas, osteosarcomas, osteoclastomas, chordomas, and other mesenchymal tumors can be adequately evaluated by MRI.

4 MRI OF THE NASAL CAVITY AND PARANASAL SINUSES

4.1 Introduction

The nasal cavity, the first of the respiratory passages, extends from the roof of the mouth upwards to the base of the skull. It is divided by the nasal septum into two halves which open on the face through the nostrils, and communicates behind with the nasopharynx.[43] The lateral wall of the nasal cavity is irregular, owing to the presence of three bony projections, the inferior, middle, and superior nasal conchae (turbinates). The conchae project downward and slightly medially and divide the passageway into meatuses, or channels of air. The inferior meatus receives the orifice of the nasolacrimal duct. The middle meatus receives the opening of the ipsilateral anterior ethmoidal air cells, frontonasal duct of the frontal sinus and the ostium of the maxillary sinus. The superior meatus receives the opening of the ipsilateral posterior ethmoidal air cells. A narrow interval, the spheno-ethmoidal recess, separates the superior turbinate from the anterior surface of the body of the sphenoid, through which each sphenoidal sinus opens into the nasal cavity.[43] The nasal mucous membrane lines the nasal cavity. It is continuous with the mucous membrane of the nasopharynx and paranasal sinuses.

The paranasal sinuses are air-filled cavities and include the frontal, ethmoidal, sphenoidal and maxillary sinuses. They are lined with upper respiratory mucosa, continuous with that of the nasal cavity.[43] The frontal sinuses are rudimentary or absent at birth, they are usually fairly well developed by the seventh or eighth years, and they reach their full size after puberty. The ethmoidal sinuses are small, but of clinical importance, at birth; they grow rapidly between the sixth and eighth years and after puberty.[43] The sphenoidal sinuses are present at birth, as minute cavities within the body of the sphenoid bone, but their main development takes place between the third and tenth years and after puberty. The maxillary sinuses are present as minute cavities at birth, but do not, however, reach full size until after the eruption of all the permanent teeth. The natural opening of the maxillary sinus is high above its floor and communicates with the lower part of the hiatus semilunaris to be drained into the middle meatus.

4.2 MRI Anatomy of Nasal and Paranasal Sinuses

The nasal cavity and paranasal sinuses can be visualized by MRI, using head coil or surface coil. Images obtained with head coil are preferred because of the size and deep location of posterior sinonasal cavities. The cortical bone and air of the sinonasal structures do not provide MR signal, and therefore they appear hypointense in all pulse sequences. The mucosa of nasal structures, however, appear as intermediate signal on T_1W and increased signal (hyperintense) on T_2W images. The normal mucosa of the paranasal sinuses are very thin and cannot be visualized on MR scans.

4.3 MRI of Sinonasal Pathology

4.3.1 Congenital Anomalies

Magnetic resonance imaging remains the study of choice for the evaluation of congenital sinonasal anomalies such as sphenoidal, sphenoethmoidal, ethmoidal, frontonasal, and intraorbital encephaloceles. Magnetic resonance imaging is very useful for the evaluation of intranasal–extranasal dermoids and nasal gliomas.

4.3.2 Inflammatory Conditions

Standard sinus roentgenograms, CT and, more recently, MRI are currently the most used imaging methods to assess paranasal pathology.[44] Computerized tomography remains the imaging study of choice for appropriate evaluation of patients with acute sinusitis associated with complications such as subperiosteal or orbital abscesses and for patients with chronic sinusitis.[44,45] Magnetic resonance imaging is also very sensitive in the evaluation of acute sinonasal pathology. The main contribution of MRI to the diagnosis of sinonasal-orbital infections is its clear demonstration of the relationship between nasal, sinus, orbital and cranial diseases. Orbital cellulitis, subperiosteal phlegmon and abscess can be readily visualized on MR scans. Magnetic resonance imaging is superior to CT in

demonstrating sinogenic complications such as thrombosis of the superior ophthalmic vein, thrombosis of the cavernous sinus, and intracranial complications such as epidural abscess, focal or diffuse encephalitis and brain abscesses.

4.3.3 Tumors

Magnetic resonance imaging provides excellent delineation of tumor from surrounding soft tissue, inflammatory tissue, and retained secretions within the sinuses.[46–52] It might be anticipated that the typical appearance of edema or retained secretions within the sinuses on MR images would be of low intensity on T_1W and high intensity on T_2W images, reflecting the high water content associated with the excessive interstitial fluid or retained secretions. However, because of the frequent chronic nature of these benign processes in patients who have a nasal cavity or paranasal sinus tumor, especially in those patients in whom an advanced tumor has been diagnosed, sufficient time has elapsed to allow for the concentration of high water affinity mucoproteins and the absorption of free water. This leads to various degrees of shortening of both T_1 and T_2 relaxation times.[45] The areas of complete desiccation appear as low signal on T_1W, PW, and T_2W MR images.

Sinonasal carcinomas are highly cellular tumors with little free water; as such, they appear as low to intermediate signal intensity on T_1- and T_2W images (Figure 8). Inflammatory diseases have intermediate signal intensity on T_1W and high signal intensity on T_2W images [Figure 8(b)]. Benign pathological processes within the nasal cavity and paranasal sinuses, such as polyps, papillomas, low grade adenocarcinomas, (minor salivary gland tumors), and schwannomas have higher signal intensity than carcinomas on T_2W images (Figure 9). The use of paramagnetic contrast material often offers additional information.[52] In most instances, Gd-DTPA contrast enhancement of the tumor is less than the enhancement of the normal mucosa and associated inflammatory changes. Gd-DTPA is extremely helpful in detecting intracranial extension of a sinonasal tumor.

Magnetic resonance imaging has proved valuable in the diagnosis of most other tumors of the sinonasal cavity such as rhabdomyosarcomas, lymphomas, angiomas, angiofibromas, hemangiopericytomas, chondrosarcomas, osteogenic sarcomas malignant melanomas, and metastases.[45]

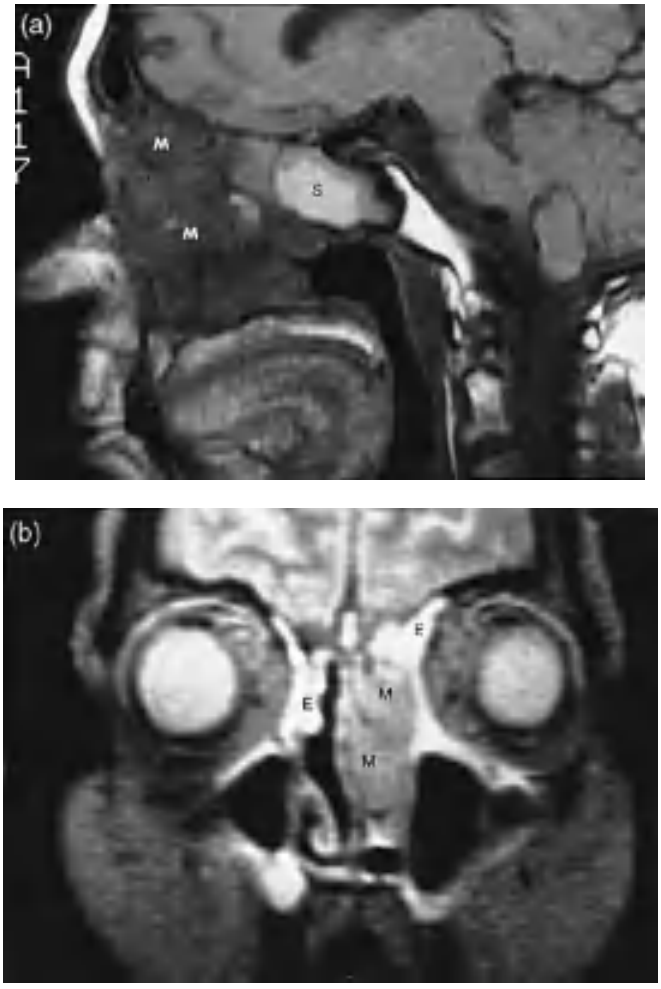

Figure 8 (a) Sinonasal squamous cell carcinoma. Sagittal T_1W MR image. A hypointense mass (M) is demonstrated, involving the nasal cavity and ethmoidal sinus. The tumor has caused obstruction of the ostium of the sphenoid sinus, resulting in hyperintense retained secretions within the adjacent sphenoid sinus (S). (b) Coronal T_2W MR images. A relatively hypointense mass (M) is demonstrated, compared with hyperintense retained secretions in the ethmoidal sinuses (E)

5 MRI OF THE NECK

5.1 Introduction: Anatomy of the Neck

The neck is the junctional region between the head and thorax and upper limbs. Its rostral limits are the base of the skull posteriorly and the inferior border of the mandible anteriorly. Caudally it is bounded by the thoracic inlet and pectoral girdle (clavicle, manubrium of sternum, acromion and spine of the scapula), a plane which parallels the first rib. The neck contains the cervical vertebrae and muscles, the pharynx, the larynx, cervical esophagus, cervical trachea, thyroid gland, salivary glands lymph nodes, and vessels and nerves that either supply the various organs of the neck or are in transit between the head, thorax, and upper limbs.[53]

5.2 MRI Techniques

Our protocol for the upper neck (above the angle of the mandible) uses a head coil and a neck coil for the lower neck. The nasopharynx, parapharyngeal space, infratemporal fossa, masticatory space, oropharynx, tongue, and salivary glands are ideally suited for evaluation by head coil. The larynx is best evaluated by using a surface coil. Thyroid gland and parathyroid glands and lower neck may be evaluated by both head and surface coils. A routine MRI of the neck should include at least a sagittal T_1W localizer and axial SE double echo pulse sequences. At times, additional coronal T_1W or T_2W images may be obtained. The use of Gd-DTPA contrast material, gradient echo images, and fat-suppression pulse sequences should be tailored according to the clinical information and initial evaluation of the sagittal T_1W and axial SE double echo pulse sequences.

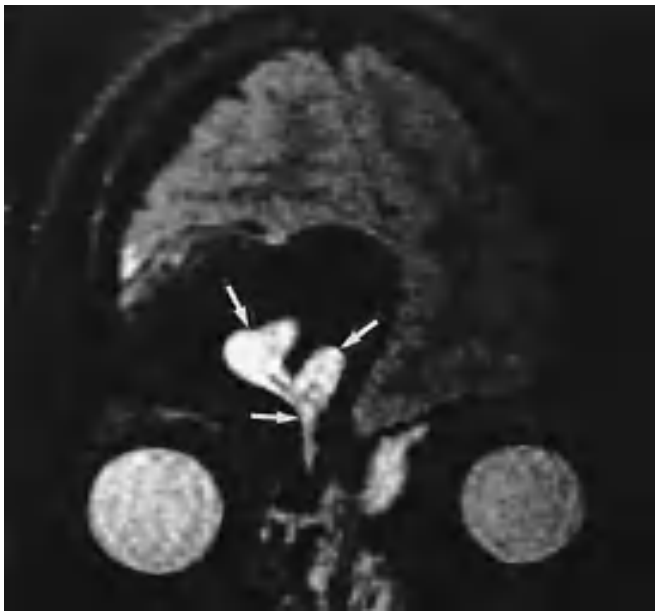

Figure 9 Frontal sinus polyp. Coronal T_2W MR image. A hyperintense polyp (arrows) is demonstrated within an otherwise aerated frontal sinus. The signal intensity of the polyp (benign process) is greater than that of the carcinoma (malignant process), seen in Figure 8(b)

5.3 MRI Anatomy of the Neck

Magnetic resonance imaging offers the best soft tissue contrast resolution and therefore remains the study of choice for imaging the anatomy of the soft tissue of the neck.[54] The larynx, pharynx, tongue, floor of the mouth, salivary glands, thyroid gland, parapharyngeal space, infratemporal fossa, masticatory space, and vascular structures of the neck can be visualized with exquisite anatomical detail.[54–56]

5.4 MRI Pathology of the Neck

5.4.1 Developmental Neck Cysts

Magnetic resonance imaging is extremely helpful in the evaluation of congenital anomalies of the neck.[55] The most frequent developmental conditions involving the neck are brachial cleft anomalies, cystic hygromas (lymphangiomas), dermoids and epidermoids, and teratomas. Most of these lesions have characteristic MRI findings that should help the radiologists make the diagnosis.[55]

5.4.2 Inflammatory Conditions

The main contribution of MRI to the diagnosis of neck infections is its clear demonstration of the relationship between various potential spaces within the neck and adjacent structures

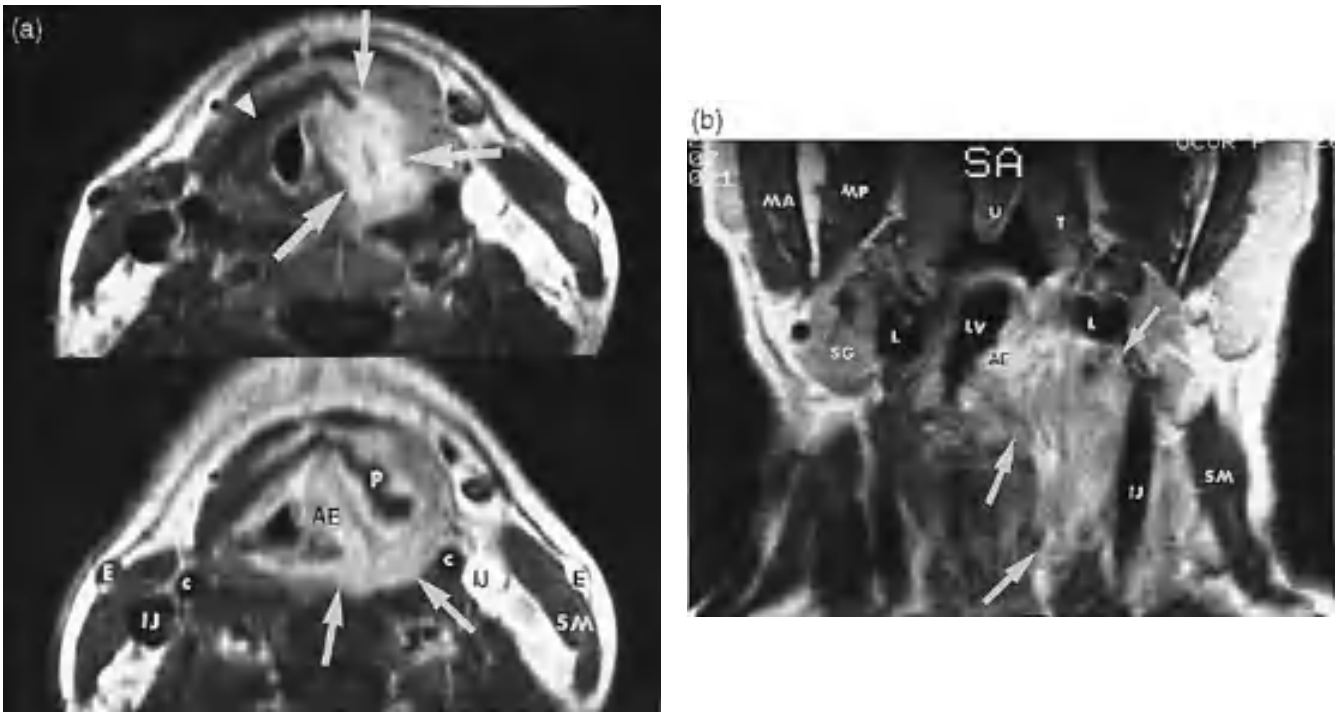

Figure 10 (a) Chronic laryngeal and perilaryngeal infection: 5 mm axial post-Gd-DTPA T_1W MR scans. A large enhancing inflammatory induration (arrows) is demonstrated, associated with marked thickening of the left aryepiglottic fold (AE), and an area of fluid loculation, proved to be pus (P), in the paralaryngeal space. Notice the normal right thyroid cartilage (arrowhead) and partial destruction on the left side. c = common carotid, E = external jugular vein, IJ = internal jugular vein, P = pus, SM = sternocleidomastoid muscle. (b) Coronal post-Gd-DTPA MR scan (4 mm). This coronal MR image demonstrates the caudal and cephalad extension of laryngeal and paralaryngeal inflammation (arrows). Notice marked thickening of the left aryepiglottic fold (AE), lateral displacement of the left internal jugular vein (IJ), and bilateral laryngoceles (L). LV = laryngeal vestibule, MA = masseter muscle, MP = medial pterygoid muscle, SG = submandibular gland, SM = sternocleidomastoid muscle, T = palatine tonsil, U = uvula

including base of the skull and intracranial structures. Soft tissue induration, edema, and fluid collections (pus) can be readily demonstrated on MRI (Figure 10). Magnetic resonance imaging is highly sensitive for the detection of early and late inflammatory changes of the bone marrow of the bony structures of the head and neck as well as the temporo-mandibular joint.

5.5 Neck Tumors

Magnetic resonance imaging is capable of depicting most benign and malignant tumors of the neck. On MRI, most tumors have long T_1 and T_2 characteristics.[54–57] The T_2W images are most valuable for detecting differences in signal intensity of the pathological process.[54–60] Magnetic resonance imaging remains the study of choice for imaging evaluation of nasopharyngeal, and parapharyngeal, salivary gland tumors. In most patients with laryngeal tumor, MRI appears to be more appropriate than a computerized tomography (CT) scan for evaluating the extent of laryngeal tumor.[57] Involvement of the pre-epiglottic space, paralaryngeal space, postcricoid region, as well as cartilage invasion by laryngeal tumor can be readily visualized on MR scans.[57] Magnetic resonance imaging is as sensitive as CT for demonstrating nodal (lymph) diseases of the neck.[59] Gd-DTPA contrast studies have been shown to play an important part in the detection and diagnosis of certain lesions of the neck.[61]

6 RELATED ARTICLES

Cranial Nerves Investigated by MRI; Head and Neck Investigations by MRI; Hemorrhage in the Brain and Neck Observed by MRI; Temperomandibular Joint MRI.

7 REFERENCES

1. R. Warwick and P. L. Williams, eds. 'Gray's Anatomy', 35th edn. (British), Saunders, Philadelphia, 1973.
2. M. F. Mafee, in 'Radiology of the Eye and Orbit', eds. T. H. Newton and L. T. Bilaniuk, Raven Press, New York, 1990 p. 2. 1–23.1.
3. M. F. Reeh, J. L. Wobij and J. D. Wirtschafter, 'Ophthalmic Anatomy: A Manual With Some Clinical Applications', American Academy of Ophthlmology, San Francisco, 1981, p. 11.
4. J. B. Aguayo, B. Glaser, A. Mildvan, H. M. Cheng, R. G. Gonzalez, and T. Brady, *Invest. Ophthalmol. Visual Sci.*, 1985, **26**, 692.
5. B. J. terPenning, H. M. Cheng, P. Barnett, J. Seddon, D. Sang, M. Latina, J. B. Aguayo, R. G. Gonzalez and T. Brady, *J. Comput. Assist. Tomogr.*, 1986, **10**, 551.
6. M. F. Mafee, G. A. Peyman, J. E. Grisolano, M. E. Fletcher, D. G. Spigos, F. W. Wehrli, F. Rasouli, and V. Capek, *Radiology*, 1986, **160**, 773.
7. M. F. Mafee, G. A. Peyman, J. H. Peace, S. B. Cohen, and M. W. Mitchell, *Ophthalmology*, 1987, **94**, 341.
8. M. F. Mafee, B. Linder, G. A. Peyman, B. G. Langer, K. H. Choi, and V. Capek, *Radiology*, 1988, **168**, 781.
9. M. F. Mafee and G. A. Peyman, *Radiol. Clin. North Am.*, 1987, **25**, 487.
10. M. F. Mafee, M. F. Goldberg, S. B. Cohen, E. D. Gotsis, M. Safran, L. Chekuri, and B. Raofi, *Ophthalmology*, 1989, **96**, 965.
11. J. M. Gomori, R. I. Grossman, J. A. Shields, J. J. Augsburger, P. M. Joseph, and D. DeSimeone, *Radiology*, 1986, **158**, 443.
12. R. G. Peyster, J. J. Augsburger, J. A. Shields, B. L. Hershey, R. Eagle, and M. E. Haskin, *Radiology*, 1988, **168**, 773.
13. B. G. Haik, L. Saint Louis, M. E. Smith, R. M. Ellsworth, D. H. Abramson, P. Cahill, M. Deck, and J. Coleman, *Ophthalmology*, 1985, **92**, 1143.
14. M. F. Mafee, in, 'Head and Neck Disorders (Fourth Series) Test and Syllabus', ed. P. M. Som, American College of Radiology, Reston, VA, 1992, p. 71.
15. M. F. Mafee, M. F. Goldberg, G. E. Valvassori, and V. Capek. *Radiology*, 1982, **145**, 713.
16. M. F. Mafee and M. F. Goldberg, *Radiol. Clin. North Am.*, 1987, **25**, 683.
17. M. F. Mafee, *Radiol. Clin. North Am.* 1998, **36**, 1083.
18. R. Damadian, K. Zaner, D. Hor, and T. Dimaio, *Physiol. Chem. Phys.* 1973, **5**, 381.
19. M. F. Mafee, D. J. Ainbinder, A. A. Hidayat, and S. M. Friedman, *Int. J. Neuroradiol.* 1995, **1**, 67.
20. R. G. Peyster, M. D. Shapiro, and B. G. Haik, *Radiol. Clin. North Am.* 1987, **25**, 647.
20. R. Warwick and P. L. Williams, eds. 'Gray's Anatomy', 35th edn. (British), Saunders, Philadelphia, 1973, p. 262–264.
21. M. F. Reeh, J. L. Wobig, and J. D. Wirtschafter, 'Ophthalmic Anatomy: A Manual with Some Clinical Applications', American Academy of Ophthalmology, San Francisco, 1981, p. 11.
22. M. F. Mafee, in 'Imaging of the head and neck', eds. G. E. Valvassori, M. F. Mafee, and B. L. Carter, Thieme, Stuttgart, 1995, p. 158.
23. F. C. Blodi and J. D. Gass, *Trans. Am. Acad. Opthalmol. Otolaryngol.*, 1967, **71**, 303.
24. A. E. Flanders, M. F. Mafee, and V. M. Rao, *J. Comput. Assist. Tomogr*, 1989, **13**, 40.
25. M. F. Mafee, E. Pai, and B. Philip, *Radiol. Clin. North Am.*, 1998, **36,** 215.
26. M. F. Mafee, A. Putterman, G. E. Valvassori, M. Campos, and V. Capek, *Radiol. Clin. North Am.*, 1987, **25**, 529.
27. S. Lessell, *N. Engl. J. Med.*, 1992, **329**, 634.
28. G. C. Ebers, *Arch. Neurol.*, 1985, **42**, 702.
29. R. W. Beck, P. A. Cleary, M. M. Anderson, J. L. Keltner, W. T. Shults, D. I. Kaufman, E. G. Buckley, J. J. Corbett, M. J. Kupersmith, and N. R. Miller, *N. Engl. J. Med.*, 1992, **326**, 581.
30. M. F. Mafee and B. G. Haik, *Radiol. Clin. North Am.*, 1987, **25**, 767.
31. M. F. Mafee, D. P. Edward, K. Keller, and S. Darodi, *Radiol. Clin. North Am.*, 1998, **37**, 219.
32. R. Warwick and P. L. Williams, eds. 'Gray's Anatomy', 35th edn. (British), Saunders, Philadelphia, 1973, p. 1134.
33. M. F. Mafee, D. Charletta, A. Kumar, and H. Belmont, *Am. J. Neuroradiol.*, 1992, **13**, 805.
34. M. F. Mafee, *J. Otolaryngol.*, 1993, **22**, 240.
35. A. S. Mark and D. Fitzgerald, *Am. J. Neuroradiol.*, 1993, **14**, 991.
36. M. F. Mafee, *Otolaryngol. Clin. North Am.*, 1995, **28**, 407.
37. G. E. Valvassori, *Otolaryngol. Clin. North Am.*, 1988, **21**, 337.
38. M. Brogan and D. W. Chakeres, *Am. J. Neuroradiol.*, 1990, **11**, 407.
39. M. F. Mafee, G. E. Valvassori, A. Kumar, et al. *Otolaryngol. Clin. North Am.*, 1988, **21**, 349.
40. M. F. Mafee, C. S. Lachenauer, A. Kumar, P. M. Arnold, R. A. Buckingham, and G. E. Valvassori, *Radiology*, 1990, **174**, 395.
41. D. L. Daniels, L. F. Czervionke, S. J. Millen, T. J. Haberkamp, G. A. Meyer, L. E. Hendrix, L. P. Mark, A. L. Williams, and V. M. Haughton. *Radiology*, 1989, **171**, 807.
42. P. D. Phelps, *Clin. Radiol.*, 1990, **41**, 301.
43. eds. R. Warwick and P. L. Williams, 'Gray's Anatomy', 35th edn. (British), Saunders, Philadelphia, 1973, p. 1087.
44. M. F. Mafee, *J. Am. Med. Assoc.*, 1993, **269**, 2608.

45. P. M. Som and H. D. Curtin, *Radiol. Clin. North Am.*, 1993, **31**, 33.
46. J. M. Chow, J. P. Leonetti, and M. F. Mafee, *Radiol. Clin. North Am.*, 1993, **31**, 61.
47. M. F. Mafee, *Radiol. Clin. North Am.*, 1993, **31**, 75.
48. P. M. Som, M. D. Shapiro, H. F. Biller, C. Sasaki, and W. Lawson, *Radiology*, 1988, **167**, 803.
49. G. A. S. Lloyd, V. J. Lund, P. O. Phelps, and D. J. Howard, *Br. J. Radiol.*, 1987, **60**, 957.
50. M. G. M. Hunink, R. G. M. de Slegte, G. J. Gerritsen, and H. Speelman, *Neuroradiology*, 1990, **32**, 220.
51. P. van Tassell and Y. Y. Lee, *J. Comput. Assist. Tomogr.*, 1991, **15**, 387.
52. C. F. Lanzieri, M. Shah, D. Krauss, and P. Lavertu, *Radiology*, 1991, **178**, 425.
53. J. A. Gosling, P. F. Harris, and J. R. Humpherson, eds. 'Atlas of Human Anatomy with Integrated Text', Lippincott, Philadelphia, 1985.
54. M. F. Mafee, F. Rasouli, D. G. Spigos, G. E. Valvassori, H. Friedman, and M. Capek, *Otolaryngol. Clin. North Am.*, 1986, **19**, 523.
55. M. F. Mafee, in 'Head and Neck Imaging', eds. G. E. Valvassori, R. A. Buckingham, B. L. Carter, W. N. Hanafee, and M. F. Mafee, Thieme Medical, New York, 1988, p. 253.
56. R. B. Lufkin and W. N. Hanafee, *Invest. Radiol.*, 1988, **23**, 162.
57. J. A. Castelijns, R. P. Golding, C. Van Schaik, J. Valk, and G. B. Snow, *Radiology*, 1990, **174**, 669.
58. H. D. Curtin, *Radiology*, 1989, **173**, 1.
59. P. M. Som, *Am. J. Radiol.*, 1992, **158**, 961.
60. L. M. Teresi, R. B. Lufkin, D. G. Worthman, E. Abemayor, and W. N. Hanafee, *Radiology*, 1989, **163**, 405.
61. T. Vogl, S. Dresel, L. T. Bilaniuk, G. Grever, K. Kang, and J. Lissner, *Am. J. Neuroradiol.*, 1990, **154**, 585.

Biographical Sketch

Mahmood F. Mafee. *b* 1941. M.D., 1969 Tehran University, Iran; Resident in Radiology, 1973, Albert Einstein University Hospital, New York; Resident in Radiology, University of Illinois Hospital at Chicago, 1974–76, Fellowship in Neuroradiology-Head and Neck, University of Illinois Hospital and Eye and Ear Infirmary, 1976–1977. Faculty in Radiology, Illinois State University 1976–present. Approx. 170 publications. Research interests: the clinical applications of MRI in the diagnosis of head and neck disorders and neuro-otological and neuro-ophthalmological disorders.

Head and Neck Investigations by MRI

Yoshimi Anzai
University of Michigan, USA

and

Robert Lufkin
University of California, Los Angeles, CA, USA

1 INTRODUCTION

MRI has revolutionized head and neck imaging and has replaced computerized tomography (CT) as the study of choice for many lesions of the extracranial head and neck. MRI easily surpasses CT in its ability to differentiate subtle differences in soft tissue boundaries and extensions of tumors of the head and neck. The beam hardening artifacts on CT images from dental amalgam and dense cortical bone of the mandible, skull base, shoulders, and other areas are also not a problem with MRI. Multiplanar imaging capabilities and lack of ionizing radiation make MRI the preferred imaging study for many head and neck processes.

The exceptions where CT is still indicated are many inflammatory diseases, congenital malformations of the temporal bone, fibro-osseous lesions, and fractures. In patients with a contraindication to MRI, difficult or confusing cases where the MRI findings are inconclusive, or in situations where MRI is not available, CT is often very valuable. In the paranasal sinuses and middle ear disease where lesions are often defined by their relationship to thin cortical bone and air, CT is the study of choice. However, MRI is the preferred imaging modality for the majority of neoplastic conditions in most areas of the head and neck.

Cancers in the head and neck are often more accessible by visual inspection or palpation than similar lesions in brain, lung, abdomen, and pelvis. Therefore the role of any imaging modality in the evaluation of head and neck cancer is usually to define the deep extension of tumors, rather than to detect their presence. Mucosal changes are usually best evaluated by direct inspection during physical examination. Some submucosal tumors do not show findings other than fullness or bulging on physical examination. MRI is a powerful tool for the determination of deep disease extension and the relationship of the tumor to significant structures such as major vessels and nerves, which helps define therapeutic options.

2 TECHNIQUE

Surface coils greatly increase the MRI signal-to-noise ratio and allow higher spatial resolution of most examinations of the head and neck. While acceptable studies of the sinuses and naso- and oropharynx may be obtained with the standard head coil, the use of surface coils for examination of the larynx, hypopharynx, neck, and temporal bone is practically essential.[1,2]

The new bilateral phased array surface coil provides high resolution with a higher signal-to-noise ratio compared with standard surface coils. Each phased array coil element has its own preamplifier, receiver channel, and digitizer, allowing the collection of data and generation of images individually and subsequent combination into a composite image. This approach is now routinely used in many centers for MRI of the temporal bone and temporomandibular joint (Figure 1).

While specialized surface rf coils are important factors that make quality magnetic resonance images of the head and neck possible, perhaps the most significant factor in the superiority of MRI over CT scanning in this area is the high soft tissue contrast resolution of MRI. Unlike the central nervous system where virtually no MRI signal from fat is present, the abundance of fat–water interfaces in the extracranial head and neck, which literally defines the anatomy of this region, greatly influences the selection of pulse sequences for optimum image contrast.

Although there is considerable variation in imaging approaches to the head and neck, a standard MRI sequence would include T_1- and T_2-weighted axial images, and T_1-weighted coronal images for most lesions. T_1-weighted sagittal images are necessary for the larynx, mastoid portion of the facial nerve, and midline lesions.

Currently, T_2-weighted fast spin echo (FSE) imaging has replaced the regular T_2-weighted spin echo image for most studies of the head and neck at many centers.[3] In FSE acquisition, multiple refocused echoes are generated during a single *TR* (usually 8–16 echoes train), resulting in a short scan time and a better signal-to-noise ratio. The reduced scan time allows higher image matrix acquisition, such as 512 instead of 256, for improved spatial resolution. The drawbacks of FSE include fewer slices obtained for the same *TR* and less sensitivity to susceptibility effects.

Other parameters commonly used in head and neck MRI are an FOV (field of view) of 18–20 cm and slice thickness of 3–4 mm. A 192×256 matrix is routinely used in most of head and neck MRI, except for high resolution temporal bone MRI where a 384×512 matrix is used.

The role of gadolinium contrast agents in MRI examinations of the head and neck has been investigated.[4] Although gadolinium does enhance most head and neck tumors, it may also obscure the tumor margin in some cases because of the presence of enhancement within normal tissue resulting in reduced fat/tumor contrast. Fat suppression gadolinium enhancement MRI, therefore, was introduced to improve the lesion conspicuity following contrast administration. This technique is most valuable in regions with large amounts of fat, such as the orbit. In other regions of the head and neck the advantages of this technique are less well defined.

Although gadolinium administration adds information about whether the suspected tumor does or does not enhance, the clinical relevance of this information has been questioned in some cases. When intracranial extension is present, however, gadolinium can clearly improve the detection of the blood–brain barrier and leptomeningeal pathology. For these reasons many centers now limit their use of gadolinium to studies of the orbit and other regions close to the skull base where leptomeningeal and perineural pathology is a possibility.

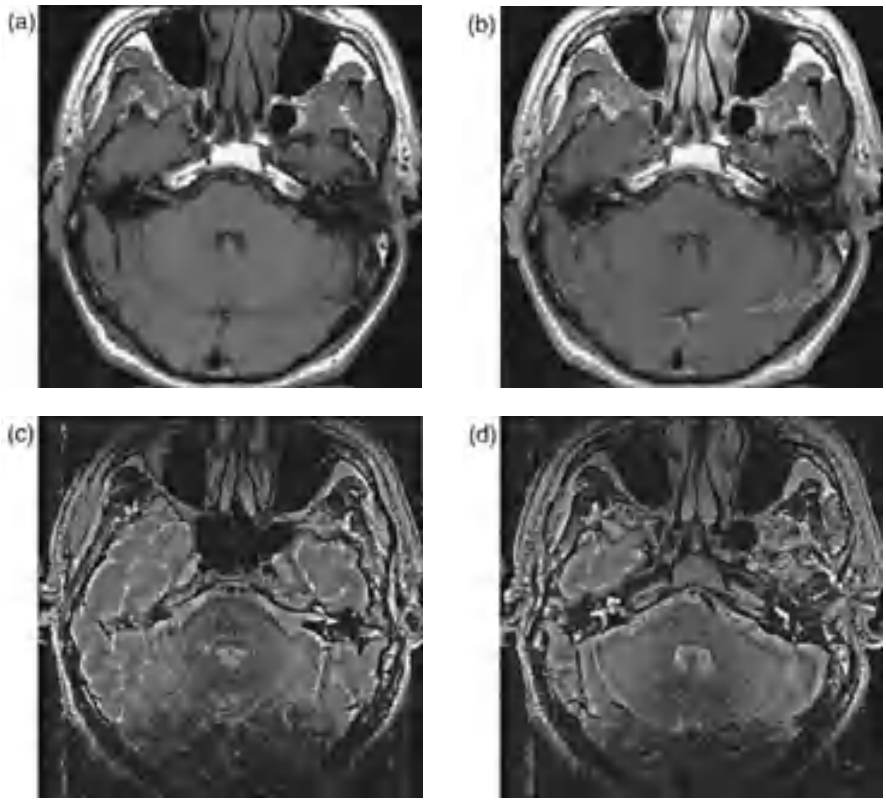

Figure 1 Intracanalicular acoustic neuroma. (a) Axial T_1-weighted image without contrast barely resolves the abnormality. (b) Following contrast administration, there is dense enhancement by the tumor. (c) High resolution (512 matrix) surface coil T_2-weighted axial image through the contralateral side shows clearcut depiction of the normal internal auditory canal contents. (d) View through the abnormal side shows the tumor without the use of a contrast agent. Some investigators are now questioning the added value of the contrast study

3 TEMPORAL BONE

MRI is the modality of choice to evaluate sensorineural hearing loss and to a large extent to evaluate the facial nerve in its course through the temporal bone. High-resolution technique is critically important in the imaging of the temporal bone.[5] In our institution, a bilateral phased array coil is used with 3 mm interleaved slices. T_1-weighted spin echo and T_2-weighted FSE images as well as gadolinium enhanced T_1-weighted images are obtained. Gadolinium may also help in the detection of small intracanalicular acoustic tumors, although the possibility of inflammatory enhancement simulating a neoplasm must always be considered.[6]

The most common CP angle tumor is the acoustic neuroma that appears as an enhancing mass often extending into the internal acoustic canal (IAC) (Figure 2). While gadolinium enhanced MRI clearly delineates the tumor extension and improves detection of the intracanalicular acoustic neuroma, recent studies using high-resolution T_2-weighted images now question its value.[7]

Meningioma is the second most common CP angle tumor, and characteristically shows broad dural attachment. They are isointense to the cerebral cortex on T_2-weighted images in the majority of cases. Hyperostosis and dural thickening are often associated with meningioma. Following gadolinium administration, meningioma typically shows enhancing dural extension of the tumor.

Epidermoid (primary cholesteatoma) is a congenital lesion resulting from inclusion of ectoderm during early fetal life. The epidermoid contains keratin debris and solid cholesterin. The signal intensity of the tumor depends on the proportion of these two elements. When keratin debris predominates, the tumor appears of low signal on T_1- and of high signal on T_2-weighted images. The cholesterin portion gives a high signal on T_1-weighted images. The absence of gadolinium enhancement is characteristic.

CT remains the imaging study of choice at the present time for inflammatory disease and most other conditions resulting in conductive hearing loss. Important information about the status of the ossicles and bony covering of the facial nerve canal is still best obtained with CT. CT can also best visualize tumors and metabolic diseases affecting the middle ear and mastoid air cells. For the remainder of lesions of the temporal bone, CT and MRI will continue to play complementary roles in the imaging workup. Depending on the location and particular pathology, each of the imaging modalities will contribute information.

4 SALIVARY GLANDS

The preferred method of imaging the salivary glands has evolved with new developments in imaging technology as well as clinical needs. While sialography is still used to evaluate in-

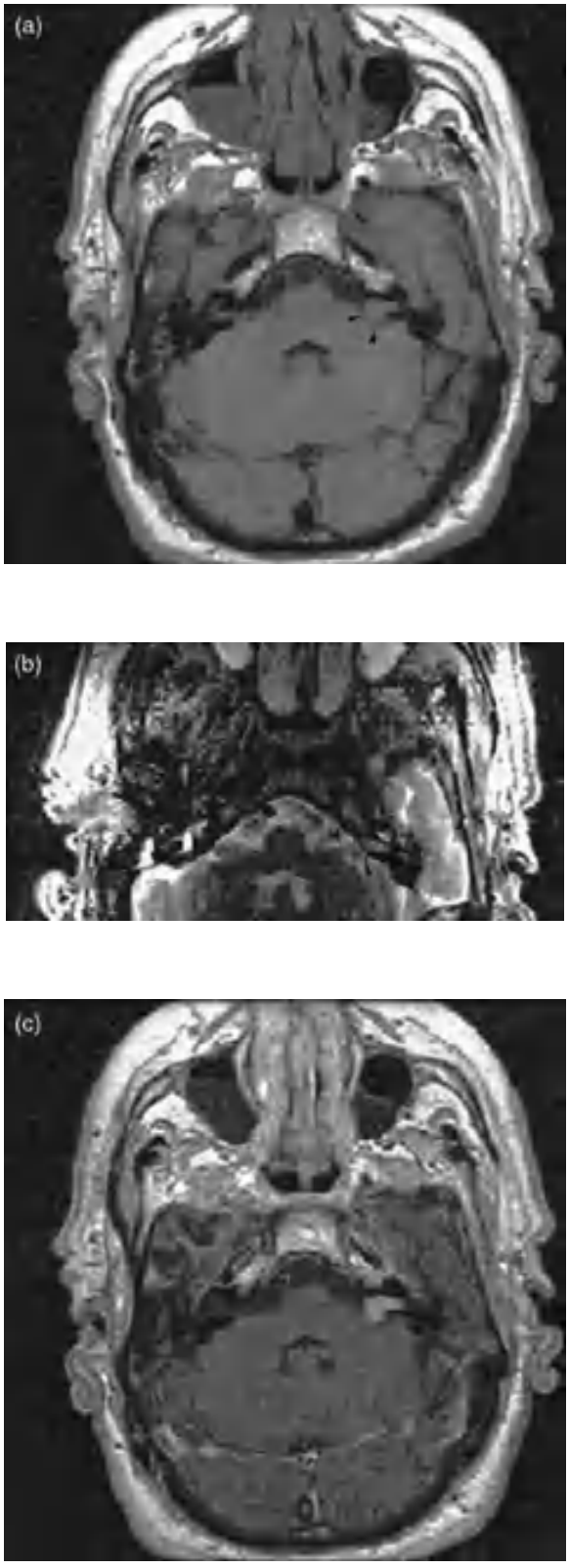

Figure 2 Acoustic neuroma. This middle-aged man presented with left sided sensorineural hearing loss. (a) Axial T_1-weighted image shows a rounded soft tissue mass (arrowed) centered over the right internal auditory canal extending to the cerebellopontine angle. (b) Axial T_2-weighted image shows similar findings. (c) Axial T_1-weighted image following contrast administration shows uniform enhancement

flammatory or autoimmune diseases of the salivary glands, MRI has replaced sialo CT scanning for the imaging evaluation of the majority of masses in the major salivary glands.[8–10]

While 80% of major salivary gland tumors occur in the parotid gland, inflammatory lesions are the most common in the submandibular gland. The sublingual gland is the smallest major salivary gland. Tumors originating from the sublingual gland are relatively rare. Therefore, MRI is most frequently indicated for evaluation of parotid masses.

T_1-weighted images in the axial plane provide excellent contrast among most tumors, parotid gland, and parapharyngeal fat, allowing differentiation of an intraparotid from extraparotid gland masses (Figure 3). These views are supplemented with coronal or sagittal views when there is a suggestion of temporal bone involvement. Although poor tumor margin and low signal intensity on T_2-weighted images has been reported to predict the high grade of malignancies in parotid gland tumors to some extent this is not universally accepted, and determinations of histology by imaging studies is generally not possible. This is in part due to the unusual, and variety of, histology found in parotid tumors. Fortunately, fine needle aspiration (FNA) is a simple, lower cost and relatively noninvasive method to determine the nature of the tumor, and has been widely applied in large clinical series.

The real advantage of MRI in evaluating parotid masses is its ability to determine more accurately whether the intraparotid tumor is within the superficial or deep lobe. The superficial and deep lobes of the parotid gland are not based on an actual anatomical structure but, rather, are defined by their location relative to the main trunk of the facial nerve. Coronal images are sometimes useful to determine the distance of the parotid mass from the stylomastoid foramen, which is crucial information for a surgeon. Malignant tumors in close relation to the facial nerve may require excision of part of that structure and subsequent microsurgical repair or transposition of nerve VII. Access to larger, deeper lesions may require division and reflection of the ramus of the mandible. This valuable information is easily obtained with MRI.[11–13]

5 PARANASAL SINUSES

As stated before, MRI is primarily indicated for sinus tumors rather than inflammatory or fibro-osseous diseases. Although cortical bone and air do not return a signal on MRI, cortical bone can often be visualized as a lower signal between the layers of high signal soft tissue and mucosa covering the sinus wall. MRI allows excellent delineation of solid tissue masses surrounded by secretions within the paranasal sinuses.[14,15] Erosions of the bony walls can be demonstrated on MRI as the absence of signal void normally present in cortical bone (Figure 4). For extensions beyond the bony sinuses, MRI is the clear study of choice because it differentiates skeletal muscle from tumor extension. In cases where there is a question of extension to the anterior or middle cranial fossa, MRI with gadolinium enhancement remains the study of choice.

MRI is also valuable for repeated follow-up studies for diseases of children such as juvenile angiofibroma where multiple studies are required and radiation dose becomes a factor. The high soft tissue contrast capabilities of MRI in distinguishing low protein fluids, high protein fluids, soft tissues, and normal

Figure 3 MRI guided aspiration cytology of a parotid mass. Several attempts at needle biopsy in the clinic without imaging guidance were uninformative. (a) Axial T_1-weighted image shows the superficial parotid mass (arrowed). (b) Axial T_2-weighted image shows heterogeneous areas of high signal which are nonspecific. This may be seen with a variety of benign and malignant conditions. (c) Axial T_1-weighted image following MRI compatible needle placement shows the linear signal defect of the needle entering the mass (arrowed). The cytology revealed adenocarcinoma

musculature make MRI ideal to differentiate sinus tumor from secondary obstructed sinuses.[14]

One possible pitfall encountered in MRI of inflammatory sinus disease is signal void seen in patients with desiccated lesions such as fungus infection. Unlike nonfungus sinusitis, mycetoma is of low signal intensity on both T_1- and T_2-weighted images, simulating well pneumatized normal sinuses. This is due to the presence of paramagnetic substances such as manganese, iron, and calcium as well as desiccated debris within mycetoma which do not contain any free water. The fungus infection can be clearly demonstrated on CT, which is another reason that the mainstay for imaging inflammatory sinus disease will continue to be CT.

6 NASOPHARYNX

The lack of motion and abundant facial planes of the nasopharynx result in high quality MRI.[16] Retropharyngeal adenopathy, tumor infiltration beyond the pharyngobasilar fascia, and hypertrophic lymphoid tissue are all better identified on MRI than on CT. The main goal of MRI examination is to evaluate the extension of primary tumor as well as nodal metastases. T_1-weighted images are usually adequate for examining the nasopharynx because of the abundance of loose areolar tissue between various muscle groups and bundles. Tumors can be identified as low signal regions on T_1-weighted images and high signal on T_2-weighted images in these loose areolar planes (Figure 5).

The configuration of the nasopharynx is dominated by a very tough fascial membrane called the pharyngobasilar fascia. This tough fascia represents a continuation of the pharyngeal constrictor muscles and extends from the base of the skull down to the level of the hard palate. Its function is to maintain the airway as an open channel for breathing during normal activities and during chewing. Only malignant tumors and very aggressive inflammatory processes such as mucormycosis will pass from the mucosa of the nasopharynx through the pharyngobasilar fascia to involve the structures within the parapharyngeal space. MRI can routinely show the pharyngobasilar fascia and destruction of this tough fascia which indicates the aggressive nature of mass.

The nasopharynx remains an area that is obscure to casual clinical examination due to gag reflex or poor patient cooperation. Its proximity to the skull base makes cancers in this region particularly devastating. Most malignancies of the nasopharynx are squamous cell carcinoma. The presenting symptoms of nasopharyngeal carcinoma vary widely. The most common complaints of patients presenting with nasopharyngeal tumors are nasal obstruction, local invasion of cranial nerves, serous otitis media, and cervical lymph node metastases. MRI is particularly well suited to complement the clinical examination in this situation. Other nasopharyngeal tumors, such as lymphoma, plasmacytoma, and occasionally rhabdomyosarcomas are also encountered. These tumors tend to be bulkier and infiltrate more widely than squamous carcinoma.

If a patient has symptoms of cranial nerve involvement, the skull base, jugular foramen, and the cavernous sinus should be thoroughly studied with MRI with administration of gadolinium. In particular, the direct coronal and sagittal MR scans are valuable to assess craniocaudal extension of tumor in skull

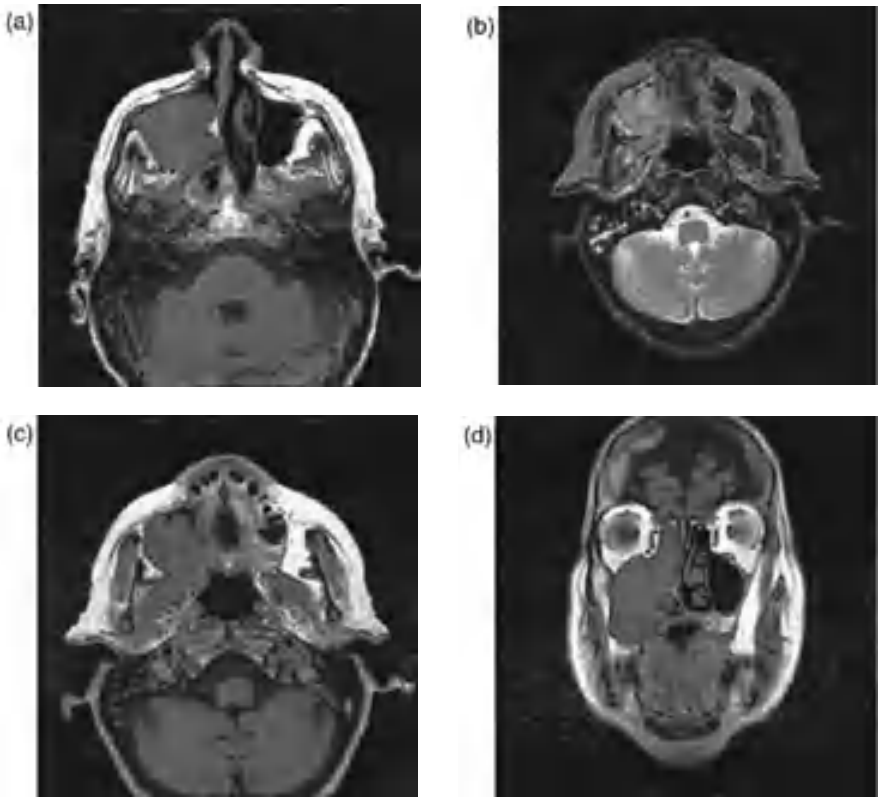

Figure 4 Maxillary sinus carcinoma. (a) Axial T_1-weighted image shows opacification of the maxillary sinus with associated bone destruction. The amount of extension posteriorly is unclear. (b) Axial T_2-weighted image at the same level shows improved muscle/tumor contrast. (c) Axial T_1-weighted image at a higher level shows invasion of the pterygopalatine fossa. (d) Coronal T_1-weighted image better defines the craniocaudal extension of the mass which involves the ethmoid sinus

base involvement, which can help to define radiation ports. Abnormalities of the skull base are detected by replacement of the normal low signal cortical bone and normal high signal bone marrow with the invading neoplasm.

The tensor veli palatini muscle is enveloped in a fascial plane of its own which divides the parapharyngeal space into two compartments.[17] The tensor veli palatini muscle fascia passes posterior to the styloid process and divides the space into a lateral compartment which is called the pre-styloid space and a medial compartment which is called the post-styloid space. This helps narrow down the list of differential diagnosis, since depending on the anatomical location the possible pathologies are different. For example, the majority of pre-styloid space masses are salivary gland tumors, and most post-styloid masses are of neurovascular origin, such as neuroma and paraganglioma. Metastatic tumor can be seen in both compartments. The capability of multiplanar imaging and the far superior soft tissue resolution make MRI the clear imaging study of choice to evaluate the nasopharynx and the adjacent spaces.

7 TONGUE AND OROPHARYNX

In general, MRI produces superior soft tissue detail in evaluating the tongue and oropharynx compared with CT.[18,19] Lack of artifacts from dental amalgam and beam hardening artifacts from the mandible on MRI also eliminates two major shortcomings of CT in the examination of this area. Moreover, the ability of MRI to obtain direct coronal and sagittal scan planes is a distinct advantage in recognizing intrinsic tongue musculature and assessing tumor volume and spread for treatment planning. MRI is therefore considered the study of choice in this area.

Squamous cell carcinomas account for well over 90% of the malignancies of the tongue. The remaining lesions are lymphomas, rhabdomyosarcomas, adenocarcinoma, adenoid cystic carcinoma originating from the minor salivary gland, and an assortment of benign tumors and inflammatory processes.

Squamous cell carcinomas of the tongue, tonsillar bed and posterior pharyngeal wall are the lesions most likely to require radiological imaging. The main purpose of the MRI study is to evaluate the extent of the primary tumor and nodal spread. Occasionally an infiltrating tumor of these regions may have spread to the nasopharynx or the supraglottic larynx so that additional imaging is needed prior to surgical management.

The tongue is one area in the head and neck where T_2-weighted pulse sequences are extremely valuable (Figure 6). The musculature of the tongue is of low signal on both T_1- and T_2-weighted images. Tumors produce a very high signal on T_2-weighted images, resulting in excellent delineation of tumor margins. Anatomical details of the midline are best obtained by coronal T_1-weighted images. The midline lingual septum

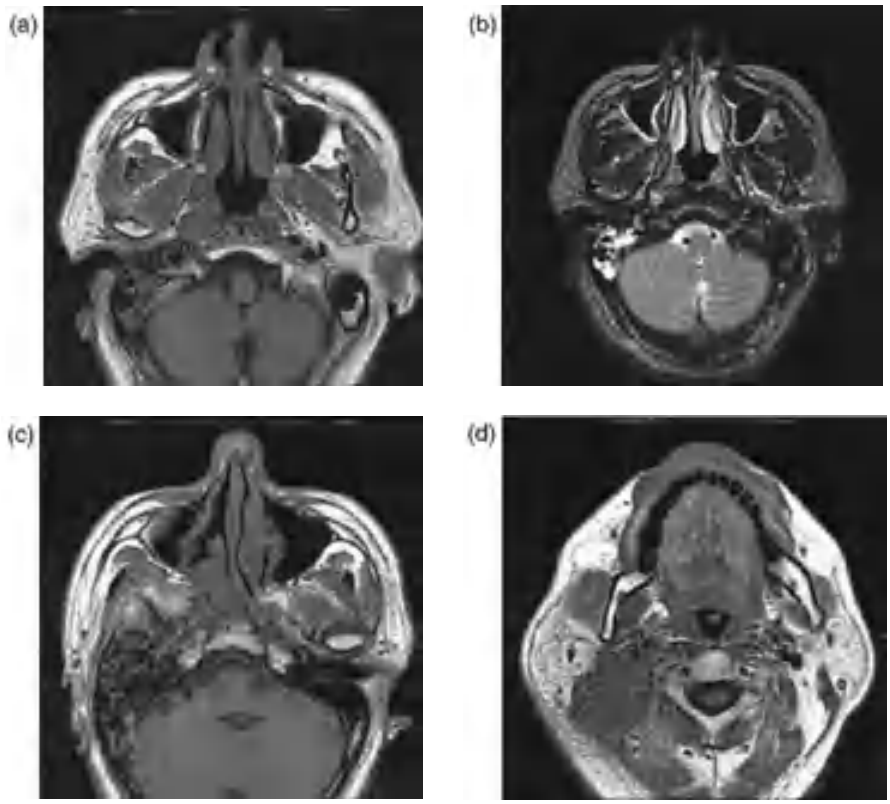

Figure 5 Nasopharynx carcinoma. This man presented with a neck mass. (a) T_1-weighted axial image through the nasopharynx shows a right sided fullness. (b) T_2-weighted image at the same level shows that the mass crosses the normal pharyngobasilar fascia and invades the parapharygeal space. (c) Higher axial T_1-weighted image shows the mass extending cephalad and involving the pterygopalatine fossa. (d) Axial T_1-weighted image shows the large [presenting] posterior triangle lymph node

appears as high signal fibrofatty tissue separating the two lateral halves of the tongue. If the tumor crosses this midline, the relationship of the tumor margin to the lingual artery and hypoglossal nerve should be accessed.

At least one hypoglossal nerve and one lingual artery must be retained in order to perform a hemiglossectomy. A total glossectomy is a much more involved procedure for selected patients, and ideally requires specialized preoperative planning. The lingual artery is easily visible between the genioglossus muscle and the interdigitation of the styloglossus and hyoglossus muscles. Disruption of the diaphragm of the floor of the mouth (the mylohyoid muscle) in a bilateral fashion clearly indicates a far advanced tumor. Adenoid cystic carcinomas almost invariably extend along perineural lymphatics. In this case, gadolinium enhanced MRI is helpful to demonstrate the enhancement of the involved nerve.

Carcinomas of the base of tongue (posterior to the foramen cecum) are particularly troublesome. Because of their relative inaccessibility, they are usually not discovered until relatively late. Of these tumors, 76% are reported to have metastases at the time of initial examination. Nodal disease is frequently bilateral because of the bilateral lymphatic drainage of the posterior third of the tongue. Tumors of the base of the tongue have a propensity to spread laterally into the glossopharyngeal sulcus and tonsillar bed regions and anteriorly into the vallecula and preepiglottic space.

Since the mucosal surface of the base of tongue varies and asymmetry does not necessary indicate the presence of tumor, the MRI finding which more strongly suggests the presence of an early base of tongue tumor is the disruption of the high signal intrinsic musculature. This is well visualized on axial and sagittal T_1-weighted images. Sagittal images are particularly helpful in showing tumor extension to the supraglottic larynx.

The remaining anterior lesions of the cheek, retromolar trigone, alveolar ridge, and lips are readily visible by inspection or available to the palpating finger, and imaging studies are seldom necessary, except for advanced cases that require the investigation of deep extension.

8 LARYNX AND HYPOPHARYNX

Rarely does any radiological imaging modality play a significant role in reaching a diagnosis of malignancy in the larynx. The larynx is so readily accessible to clinical examination that the combination of biopsy and visual inspection usually strongly indicates the diagnosis of cancer. The very small true cord cancer may not be detected by MRI. While laryngoscopy can show mucosal surfaces and masses involving the lumen, deep extensions are difficult to detect from clinical examination alone, yet, in several areas, these extensions have profound implications on the management of disease.[1,2,20–23] MRI to an even greater extent can define this important deep anatomy.

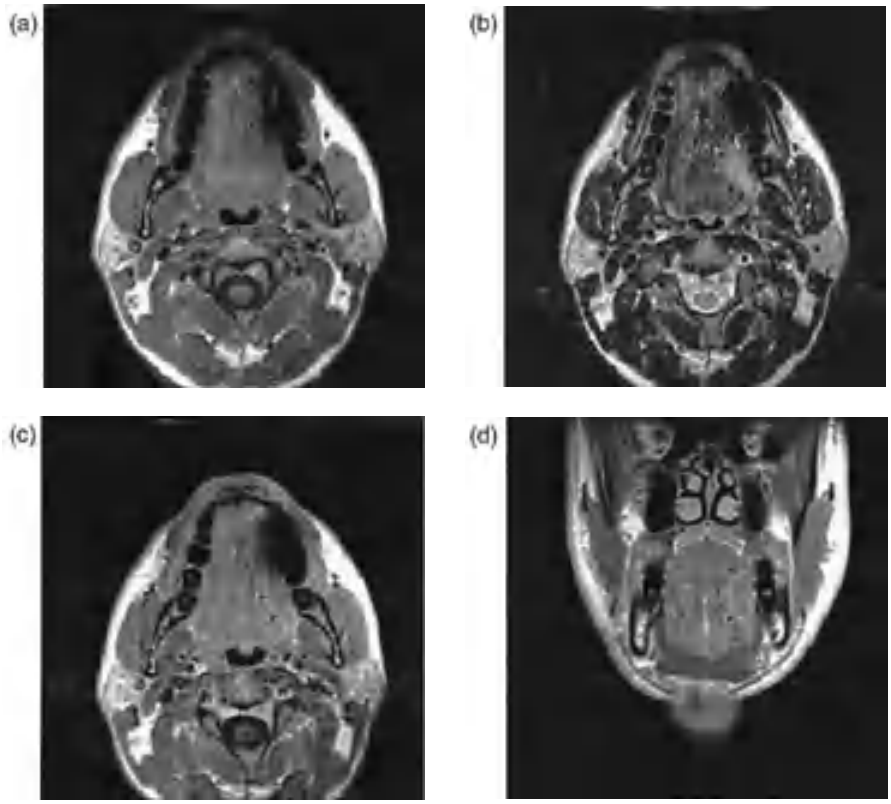

Figure 6 Tongue carcinoma. (a) Axial T_1-weighted image shows an artifact from ferromagnetic dental work. Conventional dental amalgam does not create an artifact. (b) Axial T_2-weighted image shows a small region of increased signal laterally which represents squamous carcinoma. It does not cross the midline nor invade the mandible. (c) Axial T_1-weighted image following contrast shows enhancement of the lesion. The information is similar to that in the T_2-weighted image. (d) Coronal T_1-weighted image following contrast administration again shows the lesion

T_1-weighted images with three scanning planes, axial, coronal, and sagittal, are ideal for the study of the larynx (Figure 7).[2,20] It is valuable to start with sagittal images which show the level of true vocal cords. Axial images are obtained parallel to the true cord which is readily visualized in the paramedian sagittal image. Then coronal images are acquired perpendicular to the true vocal cord. This will provide improved delineation of three important anatomical divisions—the glottic, subglottic and supraglottic regions. T_1-weighted sequences maximize contrast between the loose areolar tissue of the parapharyngeal and preepiglottic spaces, and most tumors. In addition, the laryngeal skeleton consists of several cartilages, which contain high signal marrow on T_1-weighted images. The level of the true vocal cord can be identified by the intrinsic vocalis muscle attached to the vocal process of arytenoid cartilage, which rests on top of the cricoid lamina.[24]

The supraglottic larynx consists of the laryngeal ventricle, the false cord, aryepiglottic folds, the epiglottis, and arytenoid cartilages. The supraglottic larynx is embryologically part of the buccopharyngeal anlage, and its lymphatic drainage is shared with the tongue, extending superiorly to the internal jugular chain. The preepiglottic space, anterior to the epiglottis, has a normal high signal which is displaced by low signal when tumors infiltrate this space.

The finding of the vertical spread of supraglottic tumors to the glottic region is even more important. Only advanced lesions spread down the inferior margin of the epiglottis to the anterior commissure or from superior to inferior in the paralaryngeal space. For the treatment of supraglottic tumors involving the tongue base, a partial glossectomy may have to be performed in addition to the primary surgery.[1] Coronal and sagittal MRI scans with T_1-weighted pulse sequences readily demonstrate these spreads. The true vocal cords and subglottic region act more like the trachea with the majority of the lymphatic drainage directed posteriorly and inferiorly.

Planning for any voice conservation laryngeal surgery depends on an accurate pre-operative knowledge of the precise extent of the disease within the larynx. Specifically, all techniques require an intact cricoid cartilage and at least one mobile arytenoid cartilage. MRI can provide this essential information. To plan this type of operation, the direct coronal and direct sagittal imaging capabilities of magnetic resonance far surpass axial CT images in the ability to define critical information regarding the cranial–caudal extent of the tumors. Compared to CT, MRI consistently shows superior soft tissue definition in cooperative patients. The use of direct coronal and sagittal scan planes allows the visualization of cranial–caudal tumor extension.

9 IMAGING GUIDED ASPIRATION CYTOLOGY

Imaging guided aspiration cytology has been applied to the nonpalpable deep sited head and neck lesion and has shown

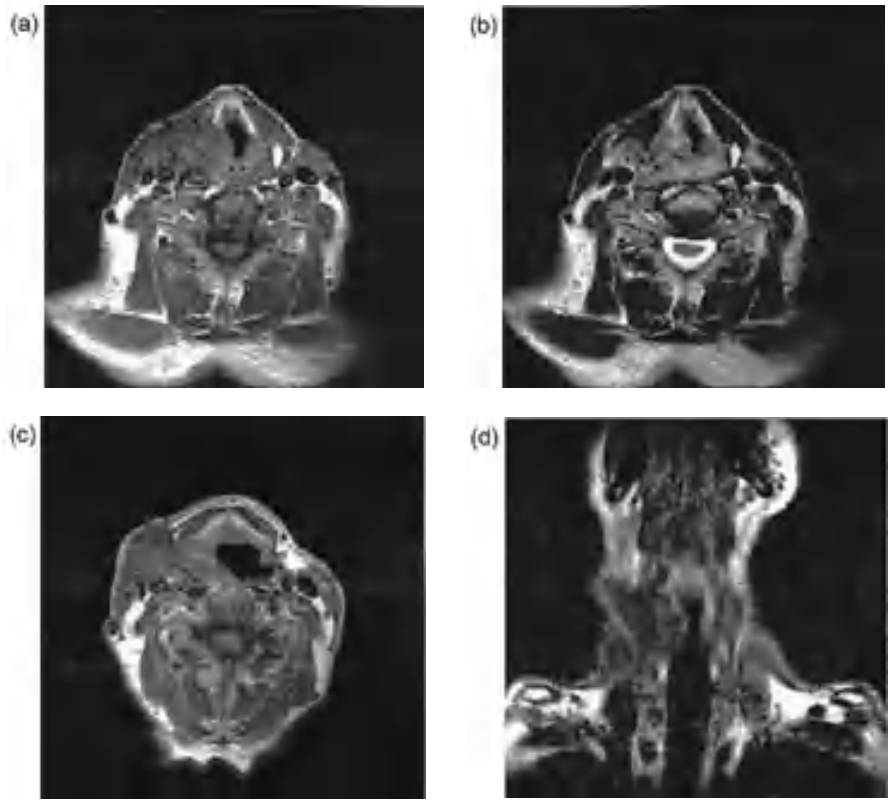

Figure 7 Supraglottic larynx carcinoma. (a) Axial T_1-weighted image shows a large right sided supraglottic mass. (b) The T_2-weighted image at the same level shows similar findings but improved muscle/tumor contrast. (c) More cephalad axial T_1-weighted image shows extralaryngeal spread to the adjacent neck. (d) Coronal T_1-weighted image shows that the mass does not involve the cricoid cartilage of subglottic region

promising results. This was initially performed under CT or ultrasound guidance. Imaging guided aspiration cytology is now a standard procedure in the evaluation of head and neck tumors that cannot be sampled by more blind approaches. Aspiration cytology is now possible with MRI guidance using specially developed MRI compatible needles (E-Z-EM Corporation, Westbury, New York).[25–28] The advantages of using MRI as an imaging guidance are lack of radiation, high soft tissue contrast allowing better delineation and detection of pathology, and multiplanar capability of showing the needle track in a single plane (see Figure 3).

10 RELATED ARTICLES

Eye, Orbit, Ear, Nose, and Throat Studies Using MRI; Gadolinium Chelate Contrast Agents in MRI: Clinical Applications; Multi Echo Acquisition Techniques Using Inverting Radiofrequency Pulses in MRI; Surface and Other Local Coils for In Vivo Studies; Temperomandibular Joint MRI; Whole Body Machines: NMR Phased Array Coil Systems.

11 REFERENCES

1. R. B. Lufkin, W. N. Hanafee, D. Wortham, and L. Hoover, *Radiology*, 1986, **158**, 747.
2. C. B. McArdle, B. J. Bailey, and E. G. Amparo, *Arch. Otolaryngol. Head Neck Surg.*, 1986, **112**, 616.
3. G. H. Zoarshi, J. R. Maskey, Y. Anzai, W. N. Hanafee, P. S. Melki, R. V. Mulkern, F. A. Jolesz, and R. B. Lughin, *Radiology*, 1993, **188**, 323.
4. J. D. Robinson, S. C. Crawford, M. Teresi, V. L. Schiller, R. B. Lufkin, H. R. Harnsberger, R. B. Dietrich, J. R. Grim, G. R. Duckwiler, and E. M. Spiekler, *Radiology*, 1989, **172**, 165.
5. J. Schwartz and H. Harnsberger, 'Imaging of the Temporal Bone', 2nd edn., Thieme, New York, 1992. pp. 192–246.
6. M. H. Han, B. A. Jabour, J. C. Andrews, R. F. Canelis, F. Chen, Y. Arzai, D. P. Becker, R. B. Lughin, and W. N. Hanafee, *Radiology*, 1991, **179**, 795.
7. R. W. Allen, H. R. Harnsberger, W. L. Davis, B. D. King, J. L. Parkin, and R. I. Affelbaum, *Radiology*, 1993, **189**(P), 141.
8. S. M. Mandelblatt, I. F. Brain, P. C. Davis, S. M. Fry, L. H. Jacobs, and J. Hoffman, Jr., *Radiology*, 1987, **163**, 411.
9. L. M. Teresi, E. Kolin, R. B. Lythin, and W. Hanafee, *Am. J. Neuroradiol.*, 1987, **148**, 995.
10. L. M. Teresi, D. Wortham, E. Abemayor, and W. Hanafee, *Radiology*, 1987, **163**, 405.
11. J. W. Casselman and A. A. Mancuso, *Radiology*, 1987, **165**, 183.
12. D. R. Mirich, C. B. McArelle, and M. V. Kulkarni, *J. Comput. Assist. Tomogr.*, 1987, **11**, 620.
13. D. H. Rice, *Arch. Otolaryngol. Head Neck Surg.*, 1987, **113**, 78.
14. M. P. Som, W. P. Dillon, G. D. Fullerton, R. A. Zimmeroner, B. Ragagopalan, and Z. Maron, *Radiology*, 1989, **172**, 515.
15. M. Shapiro and P. Som, *Radiol. Clin. N. Am.*, 1988, **27**, 447.
16. W. P. Dillon, C. M. Mills, B. Kjos, J. De Groot, and M. Brant-Zawalzki, *Radiology*, 1984, **152**, 731.

17. H. D. Curtin, *Radiology*, 1987, **163**, 195.
18. R. B. Lufkin, G. D. Wortham, R. B. Dietrich, A. L. Hoover, S. G. Larsson, H. Kangarloo, and W. N. Hanafee, *Radiology*, 1986, **161**, 69.
19. J. M. Unger, *Radiology*, 1985, **155**, 151.
20. R. B. Lufkin, S. G. Larsson, and W. N. Hanafee, *Radiology*, 1983, **148**, 173.
21. R. B. Lufkin and W. N. Hanafee, *Am. J. Neuroradiol.*, 1985, **145**, 483.
22. J. A. Castelijns, J. Doomber, B. Verbeeten, Jr., G. J. Vielroye, and J. L. Bloem, *J. Comput. Assist. Tomogr.*, 1985, **9**, 919.
23. H. D. Curtin, *Radiology*, 1989, **173**, 1.
24. C. R. Archer, S. S. Sagel, V. L. Yeager, S. Montin, and W. H. Friedman, *Am. J. Roentgenol.*, 1981, **136**, 571.
25. P. R. Mueller, D. D. Stark, J. F. Simeone, S. Saini, R. J. Butch, R. R. Edelmann, J. Wittenberg, and J. T. Ferrucci, Jr. *Radiology*, 1986, **161**, 605.
26. R. Lufkin and L. Layfield, *J. Comput. Assist. Tomogr.*, 1989, **13**, 1105.
27. R. Lufkin, L. Teresi, and W. Hanafee, *Am. J. Roentgenol.*, 1987, **149**, 380.
28. G. Duckwiler, R. B. Luphin, L. Jeresi, E. Spickler, J. Dion, F. Vinuela, J. Bentson, and W. N. Hanafee, *Radiology*, 1989, **170**, 519.

Hemorrhage in the Brain and Neck Observed by MRI

Robert I. Grossman

University of Pennsylvania Medical Center, Philadelphia, PA, USA

1 HISTORY

Any new imaging modality that purported to compete with computerized tomography, in the late 1970s and early 1980s, had to be capable of detecting hemorrhage reliably. The success of MRI was intimately related to its ability for characterizing all stages of hemorrhage. Initially, at low imaging field strengths (up to 0.3 T), demonstration of acute hemorrhage (within the first 24–48 hours) was problematic at best.[1] With the introduction of higher field (0.5–1.5 T) MRI scanners in approximately 1984, it was clear that MRI could reliably image all stages of hemorrhage from the acute stage (within the first 3 days or so after the acute event) to chronic hemorrhages (those that occurred months to years following the event). Both the ability to recognize older hemorrhages and localize them precisely were major factors enabling MRI to become the primary imaging modality for the vast majority of hemorrhagic conditions affecting the central nervous system.

It is interesting to note the magnetic properties of dried blood had been first studied by Faraday almost 150 years ago.[2] Pauling and Coryell in 1936 recognized that deoxyhemoglobin was paramagnetic and oxyhemoglobin was diamagnetic.[3] The T_1 relaxation mechanisms of solutions of methemoglobin were investigated by Davidson and Gold in 1957 and further elucidated by Koenig et al. in 1981.[4,5] These studies were based on the Bloembergen et al. theory (1948) of 'outer sphere' relaxation of protons by paramagnetic centers.[6]

Thulborn et al. in 1982 observed that, at Larmor frequencies from 80 to 469 MHz, deoxyhemoglobin inside intact red blood cells (RBCs) would cause significant heterogeneity of magnetic susceptibility resulting in selective T_2 shortening.[7] They also demonstrated that this phenomenon was proportional to the square of the magnetic field. De La Paz et al. attempted to characterize the MRI features of acute intracranial hemorrhage.[8] They appreciated that the relaxation times of hemorrhagic tissue could be related to several interacting factors including red cell integrity, oxygen saturation, and hemoglobin concentration. Bradley and Schmidt in 1984 modeled subarachnoid hemorrhage on a spectrometer operating at 20 MHz and concluded that methemoglobin may be at least partially responsible for the observed high intensity on some magnetic resonance images.[9] This was confirmed experimentally by Di Chiro et al. in an animal model of intraparenchymal hemorrhage.[10] Gomori et al. unequivocally showed on a 1.5 T MRI scanner that a variety of different stages in the evolution of hemorrhage could be detected.[11] The gradient echo technique was initially utilized clinically by Bydder and Young in 1985 and then applied by Edelman et al. to increase the sensitivity to susceptibility differences, thus improving the detectability of hemorrhage at all field strengths.[12,13]

This review begins with the biophysical principles relevant to hemorrhage. These include a brief discussion of paramagnetism and magnetic susceptibility followed by structure of hemoglobin, the effect of protein on MRI signal intensity, and the importance of heterogeneity of magnetic susceptibility in the appearance of hemorrhage. The benefits and limitations of common imaging pulse sequences is then described. Lastly, we shall apply those principles to understand and interpret the diverse, yet characteristic, findings produced by blood on MRI.

2 BIOPHYSICAL PRINCIPLES

2.1 Paramagnetism and Magnetic Susceptibility

The magnetic moment of an electron is the result of its momentum and electric charge. Electrons have very large magnetic moments because of their light mass (~1/2000th of the proton's mass). The term 'magnetic dipole' is applied to the electrons because of their north and south magnetic poles which are separated by a distance. Magnetic fields are induced by moving electric charges. Diamagnetic substances have paired electrons in their atomic and molecular orbitals. Paramagnetic molecules or atoms, on the other hand, contain unpaired orbital electrons. This produces a situation in which the magnetic moment of the unpaired electron is unopposed. Paramagnetic and diamagnetic molecules do not have magnetic fields of their own. In the absence of an external magnetic field, the electron dipoles of these substances randomly align, resulting in zero net magnetization. However, when placed in the magnetic field of an MRI scanner the electron dipoles of the paramagnetic substances line up in such a manner that the majority of the electrons point in the same direction as the external field. This results in augmentation of the external magnetic field. The ratio of the additional magnetic field strength to the strength of the applied magnetic field is termed the magnetic susceptibility of the paramagnetic substance. Magnetic susceptibility is thus a measure of how easily the substance may be magnetized.

Diamagnetic substances, which possess paired electrons, may still produce a magnetic field (when placed in an external magnetic field) by virtue of the fact that they are orbiting around the nucleus. This magnetic field is oriented to oppose the main magnetic field, and is called a Lenz field. It is far weaker than the field generated by the unpaired electron spins of paramagnetic substances. Paramagnetic substances, by virtue of having unpaired electrons, have the effect of magnetic susceptibility which augments the main magnetic field and also the much smaller effect of the Lenz field opposing the main magnetic field.

In the absence of unpaired electrons, protons relax (realign with the main magnetic field) by fluctuations in their magnetic fields caused by the motion of adjacent protons. Because of their large magnetic moments, unpaired electrons create fluctuations in local magnetic fields. These enable protons to realign faster with the external magnetic field producing a shortened T_1 relaxation time. This phenomenon is termed proton–electron dipole–dipole proton relaxation enhancement (PEDD PRE). In

order for this interaction to occur the water proton must come within 0.3 nm of the unpaired electron.

If a paramagnetic substance is nonuniformly distributed and the unpaired electrons are configured in a position such that water protons cannot come close (within 0.3 nm) to the unpaired electrons then the only interaction the water protons will appreciate is the locally increased magnetic field produced by the unpaired electrons (paramagnetic susceptibility). Protons will precess at a rate proportional to the local field strength which varies with the local susceptibility. The precession rate (Larmor frequency) is proportional to the local field strength. If a paramagnetic substance is heterogeneously distributed then the local field strength will vary throughout the region in which it is distributed. Protons, diffusing through these different areas of local field variation produced by susceptibility differences, will precess at different rates. Thus, protons sensing a slightly higher local field will precess more rapidly than those in a slightly lower magnetic field environment. The net effect is for the protons to develop phase differences with shortening of the apparent T_2 relaxation time (T_2 proton relaxation enhancement or T_2 PRE). The T_2 PRE occurs when there is a heterogeneous distribution of paramagnetic substances with diffusion of water protons.

In summary, paramagnetic substances enhance relaxation by two mechanisms, either PEDD PRE or T_2 PRE. The former requires the water protons to approach the unpaired electrons and produces shortening of both T_1 and T_2; however, the effect is predominantly noted as a T_1 effect. This relates to the fact that the T_1 relaxation rate ($1/T_1$) is much smaller than the T_2 relaxation rate ($1/T_2$). A paramagnetic relaxation effect added equally to either relaxation rate would contribute proportionally more to the much smaller term ($1/T_1$). Shortening of the T_1 relaxation time produces high intensity on the short *TR*/short *TE* (so-called T_1 weighted) images. The T_2 PRE produces low intensity on long *TR* images (so-called proton density and T_2 weighted images). Hypointensity from T_2 PRE can, at times, also be observed on T_1 weighted images. This is because there is a T_2 component to intensity even on a T_1-weighted image, and substances with a very short T_2 (heterogeneously paramagnetic) can produce hypointensity on a T_1-weighted image. The presence of susceptibility effects can be visualized by observing significant increases in hypointensity as the images become more T_2-weighted (i.e. as the *TE* is increased).

2.2 Structure of Hemoglobin

Hemoglobin, the primary oxygen carrier in the bloodstream, is composed of four protein subunits weighing approximately 16 000 Da apiece. Each subunit contains one heme molecule consisting of a porphyrin ring and an iron atom which provides the binding site for oxygen.[14] Binding of oxygen to the heme molecule of an individual subunit produces a conformational change in that subunit and adjacent subunits. The iron atom sits near the center of the porphyrin ring and is bound to one of the imidazole nitrogens of histidine-92. Molecular oxygen binds to the iron atom on the opposite side of the porphyrin ring.

In oxyhemoglobin, the oxidation state of the Fe is formally in the ferrous state which has six d orbital electrons. Molecular oxygen has two unpaired electrons. Oxyhemoglobin is diamagnetic, indicating that there must be pairing of the unpaired electrons of molecular oxygen and the d electrons of the heme iron atom. Suffice to say that theories have been proposed to conceptualize the electronic state of oxyhemoglobin which are beyond the scope of this discussion.[15,16]

There are four unpaired electrons in deoxyhemoglobin making it a paramagnetic molecule. When a hemoglobin subunit loses its oxygen molecule to form deoxyhemoglobin, the heme protein undergoes a small but significant change in its tertiary structure. The histidine ligand of the heme pulls the Fe^{2+} atom of deoxyhemoglobin out of the plane of the porphyrin ring and causes the porphyrin itself to dome. As a consequence, water molecules are unable to bind to the heme iron as they do in methemoglobin (see below), effectively preventing water from approaching close enough to the paramagnetic iron (<0.3 nm) to undergo PEDD PRE. However, deoxyhemoglobin can still produce local magnetic susceptibility changes (T_2 PRE).

Deoxyhemoglobin can be oxidized by one electron to methemoglobin by a number of different mechanisms. The Fe^{3+} is closer to the plane of the porphyrin ring in methemoglobin (in contrast to the Fe^{2+} atom of deoxyhemoglobin) so that water molecules can rapidly bind to the heme iron. Water must virtually bind to the heme iron in order to experience significant PEDD PRE. As the number of heme molecules is relatively small compared with the number of water molecules, this effect would be small except that the exchange rate of the water molecules is rapid relative to *TR*, allowing many water molecules to bind to the heme during the course of imaging. Normally an enzyme system within the RBCs rapidly reduces methemoglobin back to deoxyhemoglobin, but this process requires glucose and NADPH, which most likely are in short supply in sequestered hematomas.

2.3 The Effect of Protein

Hemorrhagic lesions generally contain significant concentrations of proteins. The effect of such protein is to slow the rotation of the water molecules. The much larger protein molecule has an intrinsically slower rate of rotation arising from Brownian motion due to its much larger mass. A strongly bound hydration shell of water molecules which surrounds the protein molecule with a zone of 'structured' water possesses slower rotational rates than the 'bulk' water molecules.[17,18] In hemorrhagic situations the concomitant increased protein results in a greater number of water molecules rotating more slowly, and associated T_1 shortening. A physical correlate of the change in rotational rate that occurs with increasing the protein concentration is the increased viscosity of solutions with high protein concentrations (i.e. acute and subacute intraparenchymal hematomas). The rotational correlation time is a measurement of the time it takes for this rotation to occur. The T_1 relaxation time is noted to decrease with increasing protein concentration. At very high concentrations, the T_1 shortening produced by the addition of protein molecules plateaus. Slowing of the rotational rate of the water molecules by the addition of protein also produces a decrease in T_2.

There are thus two major effects produced by the hemoglobin (deoxyhemoglobin or methemoglobin) molecule: (1) the paramagnetic effects secondary to the iron within the heme molecule and (2) the diamagnetic effects of the protein portion (apoprotein) of the hemoglobin molecule.

2.4 Heterogeneity of Hemorrhage

Heterogeneity of an RBC solution is proportional to Hct × (100 − Hct), where Hct is the hematocrit. Thus heterogeneity would be maximal at Hct = 50 and nil at Hct = 0 or Hct = 100. Since the Hct of clot is ~90, heterogeneity is present with a considerable susceptibility effect (36% of the maximal effect). Furthermore, retracted in vivo clot packs less efficiently and regularly than under experimental conditions. This further increases this predicted heterogeneity of magnetic susceptibility.

3 IMAGING PULSE SEQUENCES IN HEMORRHAGE

3.1 Spin Echo Imaging

The 90° rf pulse in a spin echo sequence rotates the protons into the transverse plane, and subsequently they precess at rates proportional to the field strength they sense. If there is heterogeneous distribution of paramagnetic molecules the protons will rapidly develop phase incoherence. This is because protons diffusing to different regions are experiencing varying magnetic strengths and precessing at slightly different rates. The 180° rf pulse in the spin echo sequence was designed to obviate local static magnetic inhomogeneities. The analogy is made to slow and fast runners that must reverse course half-way through a race so that all runners wind up at the finish line at precisely the same time. If, however, the protons diffuse randomly to different regions containing varying magnetic fields, then, the 180° rf pulse cannot rephase these diffusing protons to precisely the same location they had previously been at just prior to the pulse. This loss of coherence of the spins in the transverse plane results in the T_2 PRE and hypointensity on T_2-weighted images.

The longer the interecho interval (the time between 180° pulses) the shorter the T_2 in regions of heterogeneous distribution of paramagnetic molecules. This is because the protons have more time to diffuse through different regions of varying field strengths when the interecho times are increased. Protons will thus lose phase coherence faster and have a shorter T_2 under conditions of heterogeneity of magnetic susceptibility and long interecho times. The selective shortening of T_2 varies as the square of the magnitude of the applied magnetic field, and the square of the variation in the magnetic susceptibility.

3.2 Gradient Echo Imaging

Gradient refocused echo images are more sensitive to susceptibility changes because the resultant local field gradients superimpose upon the applied phasing and rephasing gradients. The presence of local field gradients from some blood products adds linearly to the phasing and rephasing gradients. This leads to rapid dephasing of the protons and signal loss on these T_2*-weighted images. This imaging technique is most sensitive for detection of heterogeneity of magnetic susceptibility but lacks some specificity with respect to particular hemorrhagic lesions. It is also problematic for routine imaging because of susceptibility differences at the skull base imposed by the air–tissue interfaces.

3.3 Fast Spin Echo Imaging

In the case of this pulse sequence there are up to 16 pulses of 180° per *TR* interval. This decreases the diffusion time of water protons and hence decreases the T_2 PRE. Susceptibility differences are decreased, and those elements of hemorrhage whose detection depends upon such differences (i.e. acute and chronic hemorrhage) become slightly more difficult to detect.[19]

4 CLINICAL SITUATIONS

4.1 Acute Hemorrhage

The biophysical effects just outlined sum to produce the appearance of acute hemorrhage as hypointensity on T_2-weighted images. In a simple intraparenchymal hemorrhage, blood is extravasated into the brain parenchyma. The RBCs are isolated from the circulation and cannot be reoxygenated. The RBCs which initially contain oxyhemoglobin become desaturated. Oxyhemoglobin has no unpaired electrons and is not paramagnetic. Imaging a hematoma containing only oxyhemoglobin will be iso- or slightly hypointense on short *TR* images and hyperintense on long *TR* images. This is related to the water content in the serum of the extravasated blood. Occasional images of hyperacute hematomas (within a few hours after an ictus) have noted a rim of hypointensity on long *TR*/long *TE* images. This rim has been postulated to be the result of early accumulation of iron or deoxyhemoglobin.[20]

Over hours the RBCs become desaturated. In addition, the inability of the isolated hematoma to rid itself easily of metabolic wastes with the possibility of increased lactic acid and CO_2 will to tend to shift the oxyhemoglobin dissociation curve to the right (Bohr effect) which at any pO_2 will result in less hemoglobin saturation and more deoxyhemoglobin. Such desaturation can usually be appreciated very early following an ictus (within a few hours). The high protein content of the clot, as evidenced by the hyperdensity noted on CT, shortens T_1 relative to cerebrospinal fluid causing the hematoma to be hyperintense relative to CSF and isointense to the brain parenchyma on the short *TR*/short *TE* images (T_1-weighted images). Since solvent water molecules are unable to approach close enough to the Fe^{2+} heme of deoxyhemoglobin, there is no additional T_1 shortening due to PEDD PRE interactions. On long *TR*/long *TE* images (T_2-weighted images), the protein also shortens T_2, rendering the clot hypointense relative to cerebrospinal fluid. Superimposed is a marked hypointensity secondary to susceptibility effects arising from the local field inhomogeneity produced by encapsulation of the paramagnetic deoxyhemoglobin within the RBCs. This effect is magnified on gradient refocused images, which as stated above are more sensitive to susceptibility effects. The end-result is the profound hypointensity of the acute hematoma on long *TR*/long *TE* and gradient refocused images (Figure 1). There is usually a penumbra of high intensity on long *TR* images surrounding the acute hematoma. This is a consequence of clot retraction with extrusion of serum into the surrounding normal brain and, later, the development of vasogenic edema (over days from the initial ictus). The high intensity of the surrounding edema and

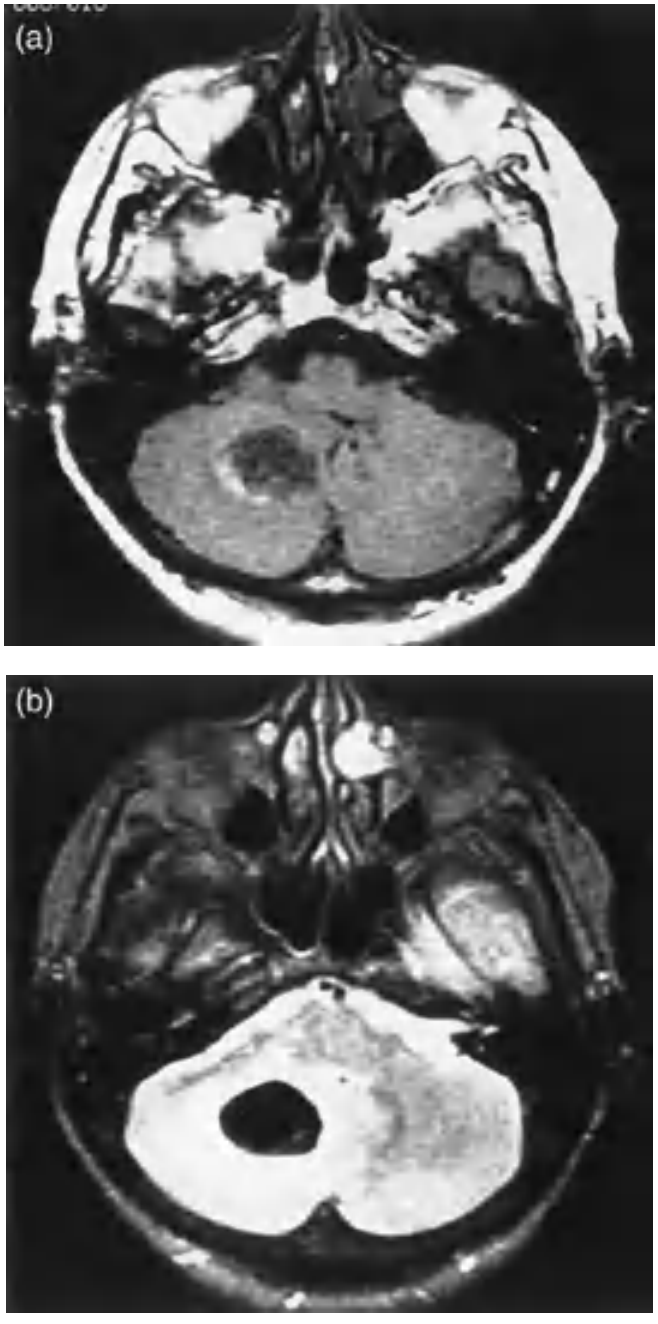

Figure 1 Acute hematoma. (a) Short *TR*/short *TE* image of right cerebellar hemorrhage. This image was performed approximately 72 hours after the ictus. Note the hypointensity of the hematoma compared with normal cerebellum. There is a slight rim of hyperintensity representing methemoglobin which is just beginning to form at the periphery of the hematoma. (b) Long *TR*/long *TE* image of (a). There is striking hypointensity of the hematoma which is the result of heterogeneity of magnetic susceptibility due to deoxyhemoglobin in intact RBCs. Surrounding the hematoma is a penumbra of high intensity from serum and/or vasogenic edema

the mass effect of the hemorrhage should disappear within 4–6 weeks. If persistent high intensity remains surrounding the hemorrhage, then one should be suspicious of an intratumoral hemorrhage.

4.2 Early Subacute Hemorrhage

Within 3–7 days there is oxidation of the deoxyhemoglobin to methemoglobin inside of the RBCs, occurring initially at the periphery of the clot. Unlike deoxyhemoglobin, water molecules are able to approach within 0.3 nm of the paramagnetic heme of methemoglobin, permitting PEDD PRE interactions which shorten T_1. It is this effect, in concert with the T_1 shortening from the high protein concentration, that gives methemoglobin its characteristic hyperintensity on T_1-weighted images. Because the paramagnetic methemoglobin remains encapsulated within the RBCs, marked hypointensity is also seen on the long *TR*/long *TE* and gradient refocused images due to the same susceptibility mechanism described above for deoxyhemoglobin. The PEDD PRE interaction also shortens T_2, but this effect is insignificant compared with the much larger susceptibility effects.

4.3 Mid Subacute Hemorrhage

The oxidation of deoxyhemoglobin proceeds centrally with time as evidenced by the development of hyperintensity within the center of the hematoma on the short *TR*/short *TE* images (Figure 2). Again the hematoma remains hypointense on the long *TR*, long *TE* and gradient refocused images due to susceptibility effects.[21]

4.4 Late Subacute Hemorrhage

Methemoglobin is less stable than deoxyhemoglobin, and the heme group can be lost spontaneously from the protein molecule. This free heme and/or other exogenous compounds (including peroxide and superoxide) can produce RBC lysis. Concomitantly there is protein breakdown and dilution of the remaining extracellular methemoglobin. Hyperintensity persists on the short *TR*/short *TE* images despite the decrease in the protein concentration due to the PEDD PRE of methemoglobin even at relatively low concentrations. The hematoma signal intensity increases on long *TR*/long *TE* images, approaching that of cerebrospinal fluid as there is loss of local field inhomogeneity upon RBC lysis as well as a decrease in the protein concentration. Also, the T_2 shortening effects of the paramagnetic heme due to PEDD PRE are rather small and unimportant except at the highest concentrations. Paralleling the breakdown of the methemoglobin is an accumulation of the iron molecules as hemosiderin and ferritin within macrophages at the periphery of the lesion which can be identified in the mid subacute stage of hemorrhage as well [Figure 2(b)].[22] The iron cores of hemosiderin and ferritin contain ~2000 iron molecules ferromagnetically coupled to produce a 'super paramagnetic' substance which exhibits a very large susceptibility effect. The result is a black ring surrounding the lesion visible on short *TR*/short *TE* images but increasingly prominent on long *TR*, long *TE* spin echo and gradient refocused images.

4.5 Chronic Hemorrhage

After months, there is near complete breakdown and resorption of the fluid and protein within the clot. The iron atoms

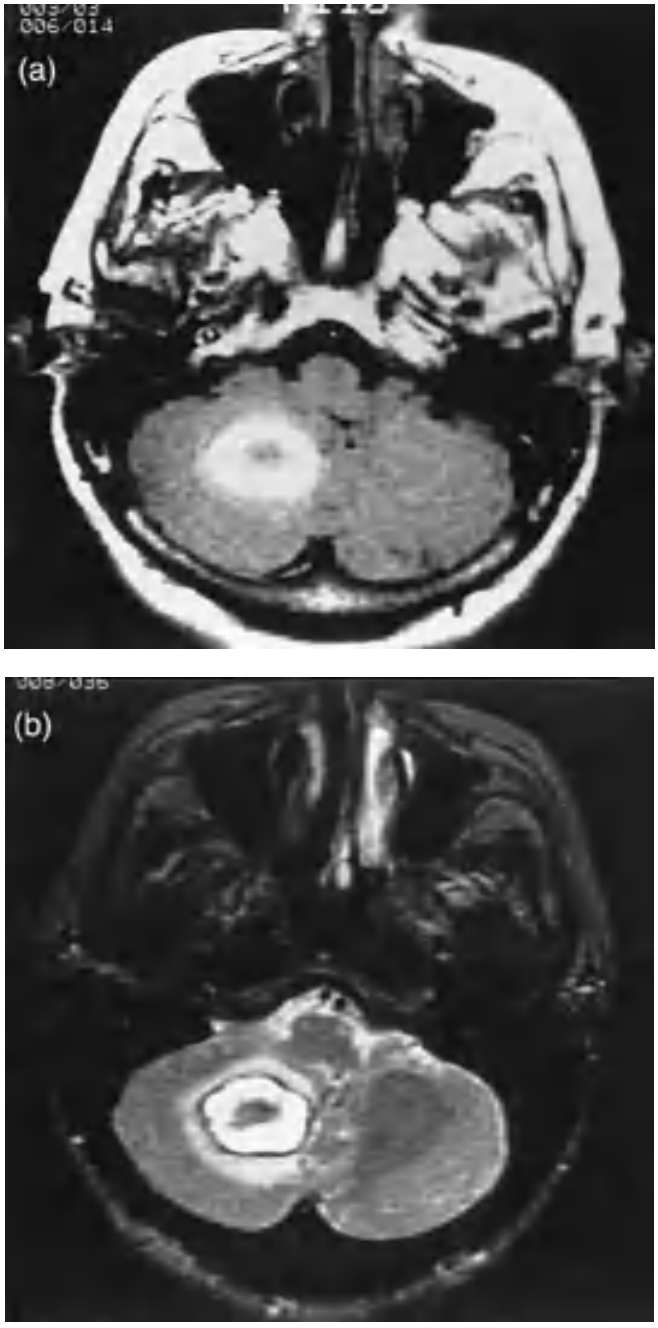

Figure 2 Subacute hematoma. Same patient as in Figure 1 except approximately 7 days after ictus. (a) Short *TR*/short *TE* image revealing ring of high intensity. This high intensity from the PEDD PRE of methemoglobin is the hallmark of the subacute stage of hemorrhage. (b) Long *TR*/long *TE* image demonstrates a rim of low intensity representing peripheral hemosiderin. Free methemoglobin is observed inside the hemosiderin rim. In the centermost portion of the hematoma is deoxyhemoglobin. There is edema surrounding the hemosiderin rim

from the metabolized hemoglobin molecules are deposited in hemosiderin and ferritin molecules unable to exit the brain parenchyma due to an intact blood–brain barrier. The susceptibility effects of the 'super paramagnetic' iron cores of hemosiderin produce hypointensity on all spin sequences but are most prominent on the long *TR*/long *TE* and gradient refocused images. There is no edema or mass effect associated with the hemorrhage. The methemoglobin (central high intensity) is gradually resorbed over months to years while the hemosiderin remains permanently in the brain. Very old hemorrhages often appear as slit-like cavities lined with hemosiderin and ferritin (Figure 3).

5 OTHER CLINICAL CONCEPTS

MRI is the technique of choice in virtually all hemorrhagic conditions of the head and neck. With its ability to detect hemorrhages of various ages, diagnosis of recurrent hemorrhagic events is facilitated. Conditions in which these situations are important include child abuse, siderosis of the central nervous system, and amyloid angiopathy.

It should be emphasized that the pO_2 of the hemorrhagic environs is important. Tumors are generally more hypoxic than normal brain so that an acute hemorrhage into a tumor may be more hypointense on long *TR* images because of increased amounts of deoxyhemoglobin. Conversely, in subarachnoid hemorrhage the red blood cells are bathed in the cerebrospinal fluid which has a pO_2 of approximately 43 mmHg. At this pO_2, 72% of the blood is in the oxyhemoglobin form, and 28% in the deoxyhemoglobin state. As the amount of T_2 shortening varies as the square of the concentration of the paramagnetic $(0.28)^2 \times 100\% = 7.8\%$ of the T_2 shortening would be expected in this case when compared with that from 100% deoxyhemoglobin.[23] Thus, acute subarachnoid hemor-

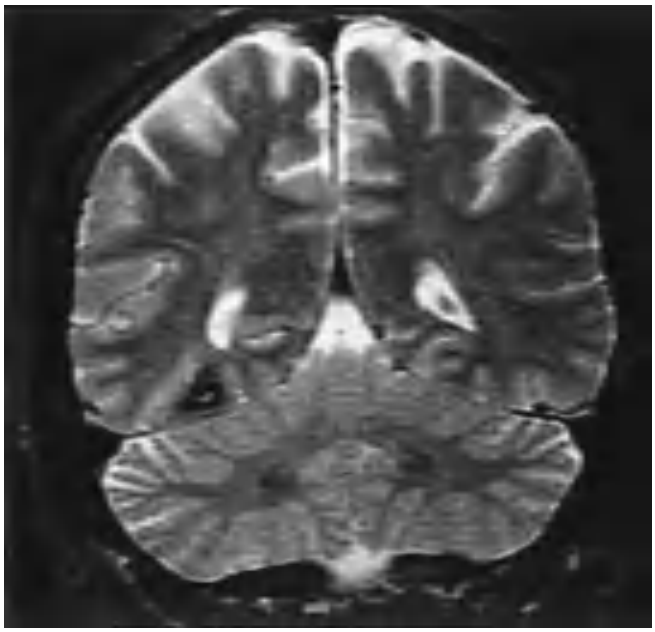

Figure 3 Chronic hemorrhage. Coronal long *TR*/long *TE* image of an old right occipital hemorrhagic cavity delineates the hypointensity of hemosiderin lining the walls of the collapsed hematoma cavity. Note that there is no mass effect or edema associated with this chronic hemorrhage

rhage is the lone condition in which MRI is not the imaging technique of choice.

In general the vast majority of hemorrhagic lesions follow the continuum of MRI changes that have just been described. This makes MRI an elegant probe for most hemorrhagic conditions including intraparenchymal hemorrhage, intratumoral hemorrhage, traumatic hemorrhage, hemorrhagic cortical infarction, vascular dissection, venous thrombosis, and cavernous hemangioma.

6 RELATED ARTICLES

Brain Neoplasms Studied by MRI; Contrast Agents in Magnetic Resonance: Operating Mechanisms; Contrast Agents in Whole Body Magnetic Resonance: An Overview; MRI in Clinical Medicine.

7 REFERENCES

1. J. T. Sipponen, R.E. Sepponen, and A. Sivula, *J. Comput. Assist. Tomogr.*, 1983, **7**, 954.
2. L Pauling and C. Coryell, *Proc. Natl. Acad. Sci. USA*, 1936, **22**, 210.
3. L Pauling and C. Coryell, *Proc. Natl. Acad. Sci. USA*, 1936, **22**, 159.
4. S. H. Koenig, R. D. Brown III, and T. R. Lindstrom, *Biophys. J*; 1981, **34**, 397.
5. N. Davidson and R. Gold, *Biochim. Biophys. Acta*, 1957, **26**, 370.
6. N. Bloembergen, E. M. Purcell, and R. V. Pound, *Phys. Rev.*, 1948, **73**, 679.
7. K. R. Thulborn, J. C. Waterton, P. M. Matthews, and G. K. Radda, *Biochim. Biophys. Acta*, 1982, **714**, 265.
8. R. L. De La Paz, P. F. J. New, F. S. Buonanno, J. P. Kistler, R. F. Oot, B. R. Rosen, J. M. Taveras, and T. J. Brady, *J Comput. Assist. Tomogr.*, 1984, **8**, 599.
9. W. G. Bradley Jr and P. G. Schmidt, *Radiology*, 1985, **156**, 99.
10. G. Di Chiro, R. A. Brooks, M. E. Girton, T. Caporale, D. C. Wright, A. J. Dwyer, and M. K. Harne, *Am. J. Neuroradiol.*, 1986, **7**, 193.
11. J. M. Gomori, R. I. Grossman, H. I. Goldberg, R. A. Zimmerman, and L. T. Bilaniuk, *Radiology*, 1985, **157**, 87.
12. G. M. Bydder and I. R. Young, *J. Comput. Assist. Tomogr.*, 1985, **9**, 1020.
13. R. R. Edelman, K. Johnson, R. Buxton, G. Shoukimas, B. R. Rosen, K. R. Davis, and T. J. Brady, *Am. J. Neuroradiol.*, 1986, **7**, 751.
14. R. Dickerson and I. Geis, 'Hemoglobin: Structure, Function, Evolution and Pathology', Benjamin/Cummings, Menlo Park, CA, 1983.
15. J. Weiss, *Nature*, 1964, **202**, 83.
16. W. A. Goddard and B. D. Olafson, *Proc. Natl. Acad. Sci. USA*, 1975, **72**, 1335.
17. S. Koenig, 'The Dynamics of Water-Protein Interactions', in ACS Symposium Series, No. 127, ed. S. P. Rowland, American Chemical Society, 1980, p. 157.
18. G. Fullerton, M. Finnie, K. Hunter, V. A. Ord, and I. L. Cameron, *Magn. Reson. Imaging*, 1987, **5**, 353.
19. K. M. Jones, R. V. Mulkern, M. T. Mantello, P. S. Melki, S. S. Ahn, P. D. Barnes, and F. A. Jolesz, *Radiology*, 1992, **182**, 53.
20. K. R. Thulborn and S. W. Atlas, in 'Magnetic Resonance Imaging of the Brain and Spine', ed. S. W. Atlas, Raven Press, New York, 1991, p. 175.
21. J. M. Gomori, R. I. Grossman, and D. B. Hackney, *Am. J. Neuroradiol.*, 1987, **8**, 1019.
22. K. R. Thulborn, A. G. Sorensen, N. W. Kowall, A. McKee, A. Lai, R. C. McKinsky, J. Moore, B. R. Rosen, and T. J. Brady, *Am. J. Neuroradiol.*, 1990, **11**, 291.
23. R. I. Grossman, S. S. Kemp, I. C. Yu, J. E. Fishman, J. M. Gomori, P. M. Joseph, and T. Asakura, *Acta Radiol.*, 1986; **369** (suppl), 56.

Biographical Sketch

Robert I. Grossman. *b* 1947. B.S., 1969, M.D., 1973 University of Pennsylvania School of Medicine, USA. Internship Beth Israel Hospital, Boston, USA, 1973–74. Neurosurgical Residency, University of Pennsylvania, USA, 1974–76. Radiology Residency, University of Pennsylvania, USA, 1976–79. Neuroradiology Fellowship, Massachusetts General Hospital, USA, 1979–81. Professor of Radiology, Neurosurgery, and Neurology, Associate Chairman of Radiology, Section Chief Neuroradiology, University of Pennsylvania Medical Center, 1981–present. Approx. 200 publications. Current research interests: white matter diseases, stroke, head trauma.

Intracranial Infections

Spyros K. Karampekios
University Hospital of Crete, Heraklion, Greece

and

John R. Hesselink
UCSD Medical Center, San Diego, CA, USA

1 INTRODUCTION

Despite the development of many effective antibiotic therapies and the evolution of new neurosurgical techniques, central nervous system (CNS) infections persist. Also the increasing, devastating effect of acquired immune deficiency syndrome (AIDS) has created a whole group of life-threatening opportunistic infectious diseases. CNS involvement usually occurs as a result of an infection from another organ system, or as a manifestation of a systemic disease. The brain, particularly, is well protected from invading agents by the calvarium, the meninges and the blood–brain barrier. However, different types of pathogens including bacteria, viruses, fungi, and parasites, can reach the brain by hematogenous spread (related to septicemia or endocarditis) and less likely by direct extension (bony erosion from an adjacent infected paranasal sinus, mastoid or middle ear). Other possible pathways for intracranial infections are via anastomotic veins from the face and scalp, along peripheral and cranial nerves (viruses) and after a penetrating head trauma.

Once in the intracranial cavity, pathogens can involve the parenchyma (cerebritis–abscess, encephalitis), the meninges (meningitis–ependymitis), and other extraaxial spaces (subdural and epidural empyemas). The brain's unique response to infection is due in part to the absence of draining lymphatics, the differentiation of vascular supply in gray and white matter, the presence of the blood–brain barrier, and the existence of perivascular cerebrospinal fluid (CSF) containing spaces (Virchow–Robin spaces). CSF assists in the dissemination of an infectious disease, acting as a perfect culture medium for microbial growth.

Magnetic resonance imaging (MRI) provides the most sensitive imaging modality to detect cerebral infection because of its optimal contrast resolution, the multiplanar imaging capability and the absence of signal from the surrounding bone. Intravenous contrast administration of gadolinium–diethylenetriaminepentaacetic acid (Gd-DTPA) increases the sensitivity of MRI and has allowed earlier detection of many infections compared to computed tomography (CT).[1] The only disadvantage of MRI is its poorer ability to detect calcifications, an important finding in some cerebral infections.

2 CEREBRITIS AND BRAIN ABSCESS

Cerebritis and abscess formation constitute a spectrum of the same process. Regardless of the pathogen, the brain tissue reacts in a predictable way to focal parenchymal infection, developing initially an area of focal cerebritis, which consists of vascular congestion, petechial hemorrhage, and brain edema. Progression from the cerebritis stage to an encapsulated abscess with a central area of liquefied, necrotic material requires 10–14 days, although the rapidity of this process depends on patient's immunocompetence and the organism.[2] In the late mature abscess stage, when the collagenous capsule is fully formed, the surrounding edema decreases, and surgical drainage is facilitated. A brain abscess is usually caused by direct extension from an adjacent infected sinus or mastoid, or by hematogenous spread from an extracerebral source. Rarely is an abscess secondary to meningitis. In up to 20% of cases the source of infection is not discovered. In children the majority of cerebral abscesses are associated with cyanotic congenital heart disease. Anaerobic bacteria are isolated most frequently in the brain abscesses, although a mixture of pathogens are often found. Overall, in otherwise immunocompetent individuals, the commonest cultured organisms are *Staphylococcus* and *Streptococcus* species.[3] Patients present usually in the late cerebritis–early abscess phase with nonspecific symptoms of headache, confusion, seizures or focal neurologic deficits. Fever and leukocytosis are common during the invasive phase of an abscess, but may resolve as it matures.

The MRI features of cerebritis–brain abscess depend on the stage of the infectious process at the time of imaging. In the early cerebritis stage MRI depicts the changes earlier than CT because of its superior sensitivity to alterations in water content. The area of cerebritis appears mildly hypointense on T_1-weighted images. On the same sequence the early, subtle mass effect is best demonstrated. The infectious focus depicts high signal on T_2-weighted images, both centrally from inflammation and peripherally from edema. As the infection matures, it increases in size due to an increase in edema and necrotic debris accumulates centrally, while the body attempts to isolate the infection by forming a capsule. The abscess capsule is thicker along the cortical surface because the vascularity of gray matter is much greater than that of white matter, resulting in increased local cortical reaction. The thinner portion of the capsule toward the white matter accounts for the predilection of abscesses to rupture into the ventricles producing ependymitis. At this stage of abscess formation, MRI demonstrates lengthening of T_1 and T_2 relaxation times in the core of the lesion. Peripherally there is moderate amount of vasogenic edema, which is mildly hypointense on T_1- and hyperintense on T_2-weighted images. On T_1-weighted images, against the hypointense areas of the necrotic center and the surrounding edema, the abscess capsule stands out as an iso- or slightly hyperintense ring. On T_2-weighted images the ring is markedly hypointense (Figure 1(a)). There is still discussion about the causes of capsular intensity. The hyperintensity on T_1-weighted images is attributed to capsular hemorrhage by some authors. More recently the signal properties of the abscess capsule have been attributed to paramagnetic hemoglobin degradation products, or free radicals within macrophages. Macrophages are abundant in the capsule, and their activity is highest at the late cerebritis–early abscess phase, exactly when the signal intensity of the capsule on the T_2-weighted images is particularly low.[4]

Contrast administration is very helpful in the evaluation of brain abscesses. Gd-DTPA produces mottled, heterogenous

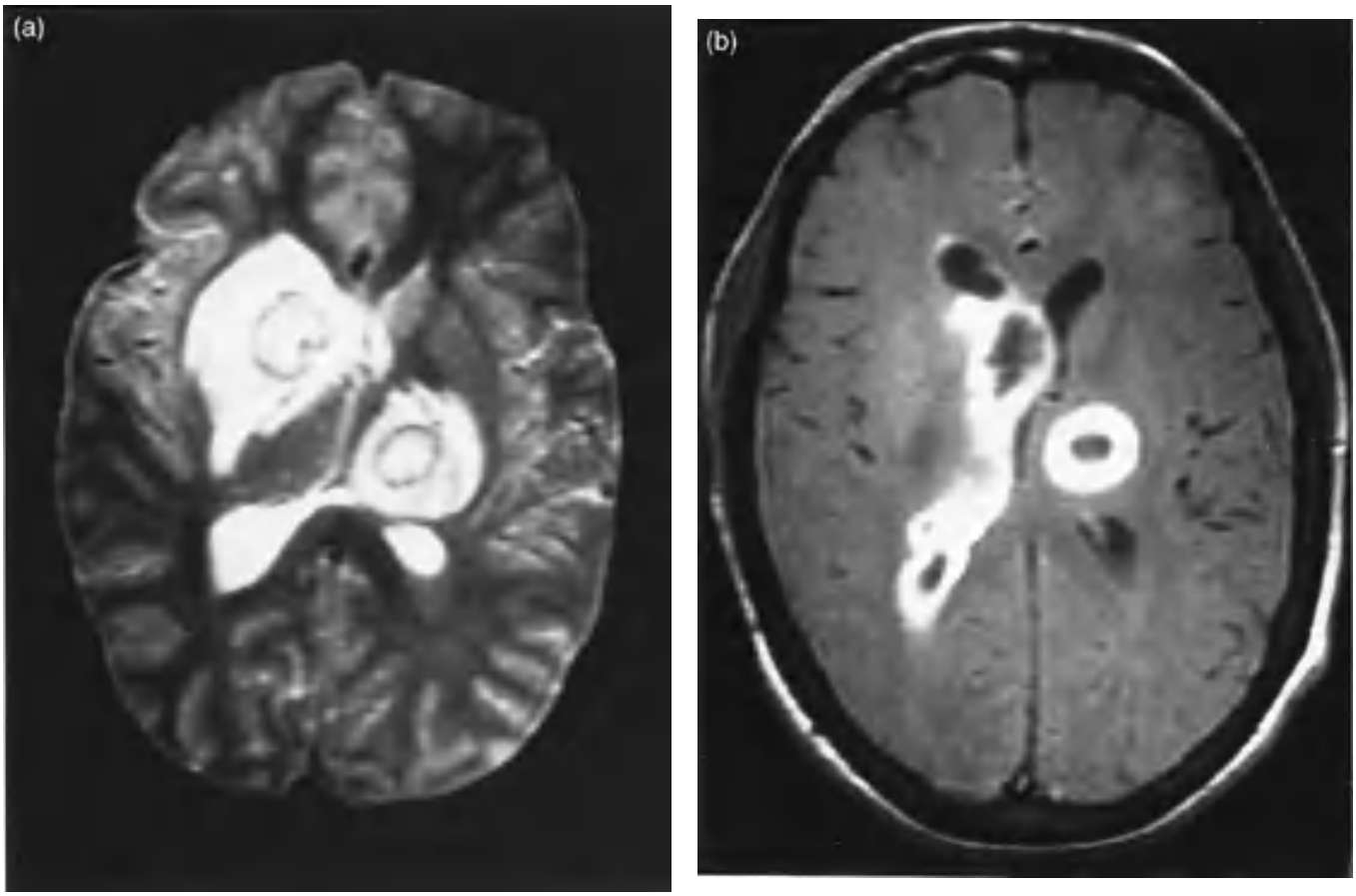

Figure 1 Streptococcal abscesses. (a) Axial, T_2-weighted (SE 2500/70) image shows the abscess capsules as hypointense rings surrounding the necrotic central core. There is also significant amount of peripheral edema. (b) Axial, postcontrast T_1-weighted (SE 800/20, Gd-DTPA) image one week later demonstrates intense ependymal enhancement of the right lateral ventricle from the resulting ependymitis secondary to rupture of an abscess into the ventricular system. (Reproduced by permission of W. B. Saunders from R. R. Edelman and J. R. Hesselink (eds), *Clinical MRI*, 1990, Chap. 19, p. 578)

areas of enhancement in the cerebritis stage, with an enhancing rim developing as the abscess matures. The ring-like enhancement reflects the damaged blood–brain barrier and is typically smooth, well defined and thin walled. The ring is thinnest at its medial margin and often points to the adjacent ventricle. If an abscess ruptures into a ventricle and secondary ependymitis develops, there is enhancement of the ventricular wall, suggesting a very poor prognosis [Figure 1(b)].

Brain abscesses produced by nonpyogenic organisms typically occur in immunocompromised patients; these will be discussed in the section of AIDS-related infections.

3 MENINGITIS

Meningitis is an acute or chronic inflammation of the pia-arachnoid (leptomeninges) and the adjacent CSF. Patients with meningitis present with fever, headache, neck stiffness, photophobia, and altered consciousness. Acute meningitis (purulent) is usually caused by bacteria. The most common pathogens are *Haemophilus influenza, Neisseria meningitidis*, and *Streptococcus pneumonia*. Significant morbidity and mortality occurs with meningitis. The overall mortality rate ranges from 5% to 15% and severe, persistent neurologic deficits may be seen in 10–25%.[5] In neonates and immunosuppressed patients Gram-negative meningitis is common, caused by *Escherichia coli, Pseudomonas aeruginosa* and *Klebsiella*. Viruses can also cause an acute meningitis (lymphocytic), particularly enteroviruses and the mumps virus. Viral meningitis is usually self-limited, with less significant symptoms and complications than those of bacterial origin.

Chronic meningitis is usually of tuberculous origin and presents as a long-standing, indolent process, in which vasculitis and cerebral infarctions from basal meningeal inflammation are more prevalent. In patients with an immunologic dysfunction, meningitis can be the result of fungal infection, with the main representatives being cryptococcosis, coccidiomycosis, and blastomycosis. Cryptococcal meningitis will be discussed in the section of AIDS-related infections. Finally, sarcoidosis is a noninfectious granulomatous disease that involves the CNS in 5% of patients, producing inflammation of the leptomeninges in the basal cisterns, the optic chiasma and the infundibulum. Other noninfectious processes which cause meningeal disease

and simulate infections are meningeal carcinomatosis, postoperative meningeal irritation, chemical meningitis, meningeal reaction adjacent to cerebral infarction, and subarachnoid hemorrhage.

Neuroimaging plays a limited role in the diagnosis of meningitis, which is made by history, physical examination and laboratory CSF findings. CT and MRI are mainly focused on the detection of associated complications, which include vascular thrombosis, infarctions, cerebritis–brain abscess, ventriculitis, hydrocephalus, empyemas of epidural and subdural space and subdural effusions. In case of uncomplicated acute meningitis, unenhanced MRI scans are usually unremarkable. More severe chronic cases may disclose hyperintense CSF on T_1-weighted and proton density (PD) images in the basal cisterns secondary to obliteration from the inflammatory exudate and meningeal hyperemia. Contrast administration is very helpful in the evaluation of suspected meningeal infection because the involved meninges enhance diffusely and intensely. In the majority of cases of acute bacterial or viral meningitis, the meningeal enhancement occurs predominantly over the cerebrum, especially involving the frontal and parietal lobes, and the interhemispheric and sylvian fissures. However, in cases of tuberculous, fungal and sarcoid meningitis, the meningeal enhancement is more prominent in the basal cisterns (Figure 2). Gd-DTPA enhanced MRI appears to be much more sensitive than postcontrast CT in the detection of the meningeal enhancement, particularly when it occurs near the convexity.[6] However, according to some authors, postcontrast MRI does not completely correlate with the extent of the inflammatory cell infiltration. Using animal models they have proved that above a threshold of inflammation, meningeal enhancement was visualized, but areas that exhibited mild meningitis histologically did not enhance.[7] While more sensitive, postcontrast MRI is no more specific, in that any process that causes meningeal irritation can also cause meningeal enhancement.

In untreated or more severe cases of meningitis significant complications may occur in the following days or weeks. The exposure of the blood vessels to the inflammatory exudate may result in vasculitis and thrombosis, a common complication in cases of tuberculous meningitis. Occlusion of small perforating arteries results in focal infarcts in the basal ganglia, while involvement of larger vessels can produce massive infarcts. Multiple hemorrhagic infarcts in the white matter are the result of cortical venous or dural sinus thrombosis.[8] Another severe complication of meningitis is cerebritis and brain abscess formation. Sometimes, rupture of a preexisting brain abscess into the CSF spaces can produce secondary meningitis. Ventriculitis and ependymitis can result from direct extension of an abscess, progression of meningitis, or from an infected intraventricular shunt. In cases of ependymitis, MRI exhibits increased periventricular signal on T_2- and PD-weighted images, that often has a nodular and irregular character to distinguish it from transependymal CSF flow associated with obstructive hydrocephalus. Also, on postcontrast scans ependymal enhancement outlines the ventricles. If purulent debris fills the ventricles, the CSF may give a higher signal than normal. It has been proved more accurate to compare the intraventricular CSF with the vitreous of the globe, since associated meningitis may prevent comparison with CSF of the basal cisterns.[9] Another frequent complication of meningitis is either obstructive, or communicating hydrocephalus, which occurs secondary

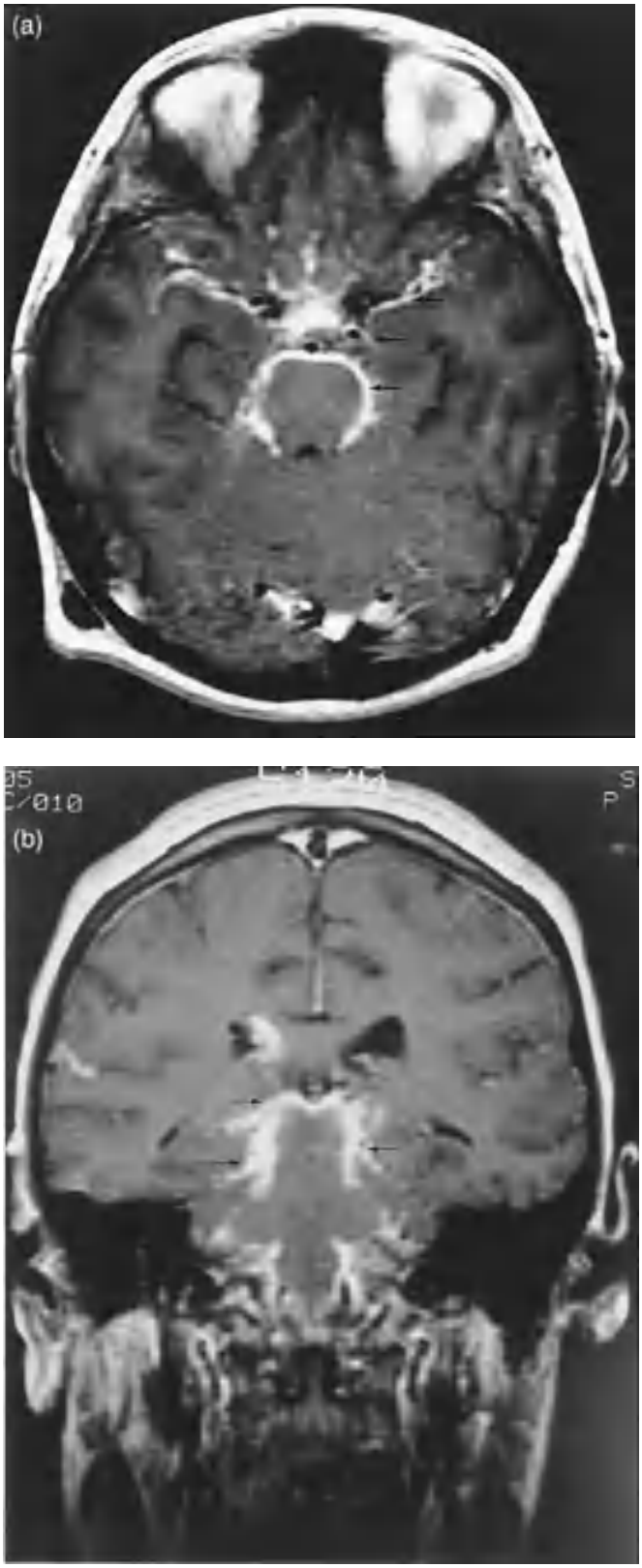

Figure 2 Coccidiomycosis meningitis. Contrast-enhanced T_1-weighted (SE 500/15, Gd-DTPA) axial (a) and coronal (b) scans demonstrate abnormal, extensive meningeal enhancement in the basal and ambient cisterns (arrows). (Reproduced by permission of the American Society of Neuroradiology from C. J. Wrobel, S. Meyer, R. H. Johnson, and J. R. Hesselink, *Am. J. Neuroradiol.*, 1992, **13**, 1243

to cellular debris obstructing the CSF pathways, or to arachnoid adhesions impairing extraventricular CSF flow and absorption. Ventricular dilatation may be the only abnormal finding in patients with meningitis and is adequately evaluated with both CT and MRI. Subdural collections can also complicate meningitis; these are discussed in the section on extraaxial empyemas.

4 ENCEPHALITIS

Encephalitis refers to a diffuse parenchymal inflammation of the brain caused primarily by viruses. Clinically, acute encephalitis should be suspected if the patient presents with convulsions, altered consciousness, delirium, aphasia, or ataxia. Particularly in herpetic encephalitis the symptoms reflect the propensity to involve the subfrontal and temporal lobes, with hallucinations, seizures, and personality changes. Viral encephalitis is usually acute, although it can occur from reactivation of a latent virus. The most common invading viruses are herpes simplex type 1 and type 2, herpes zoster, arbo- and enteroviruses, which produce almost the same reaction in brain tissue and appear similar on CT and MRI.[10] In patients with AIDS, viral encephalitis may be caused by the human immunodeficiency virus (HIV), the cytomegalovirus (CMV) and the papovavirus (PML); these are discussed in the section on AIDS-related infections. Acute disseminated encephalomyelitis (ADEM) represents an immune-mediated complication following an antecedent viral infection, especially measles, mumps, rubella, varicella, or a preceding vaccination. Various forms of viral encephalitis (slow virus) are described in association with Creutzfeldt–Jacob disease and subacute sclerosing panencephalitis (SSPE). Finally, neonatal encephalitis is caused frequently by the group of TORCH pathogens (from the initials of toxoplasma, rubella, cytomegalovirus, and herpes simplex type 2) and share some common features like microcephaly, brain atrophy, hydrocephalus, and cerebral calcifications.

Herpes simplex virus type 1 (HSV-1) accounts for 95% of herpetic encephalitis in adults. The mortality rate approaches 70% and most of the survivors exhibit severe, persistent neurologic impairment. The virus usually invades the brain after reactivation of a latent form, which is frequently located in the trigeminal (gasserian) ganglion. The marked predilection for temporal lobe involvement supports the proposed theory that the infection spreads intracranially from the trigeminal ganglion along the meningeal branches of the trigeminal nerve. The resulting necrotizing encephalitis rapidly disseminates in the brain, sparing the basal ganglia and producing mass effect and edema as well as small petechial hemorrhages. Early diagnosis is paramount in order to institute effective medical therapy (vidarabine or acyclovir) and avoid devastating and irreversible brain damage. Definitive diagnosis of HSV-1 encephalitis is done after isolation of the virus from brain biopsy. However, given the appropriate clinical presentation, with or without MRI confirmation, treatment should be instituted immediately. In the early course of the infection the characteristic distribution is almost pathognomonic for HSV-1 encephalitis. By MRI, the early edematous changes appear as ill-defined areas of low signal on T_1- and high signal on T_2-weighted images, usually beginning unilaterally but rapidly progressing to both hemispheres (Figure 3). Variable mass effect and gyral

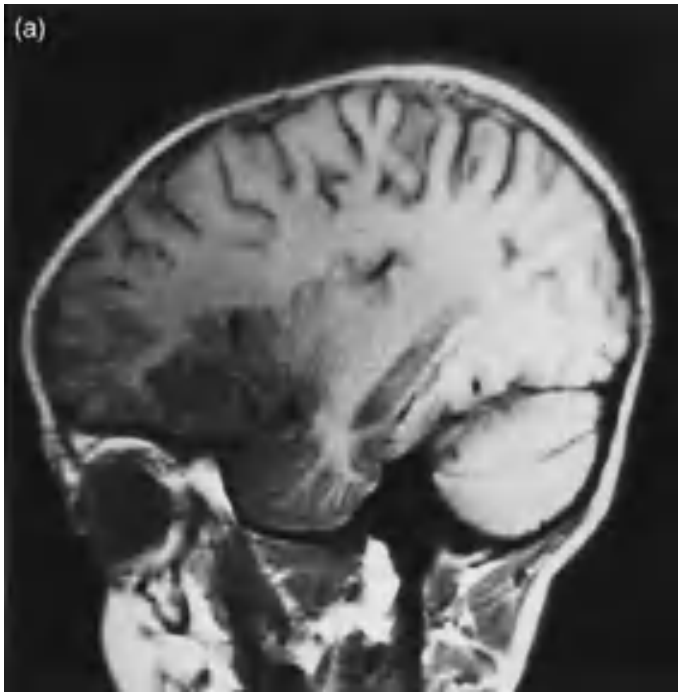

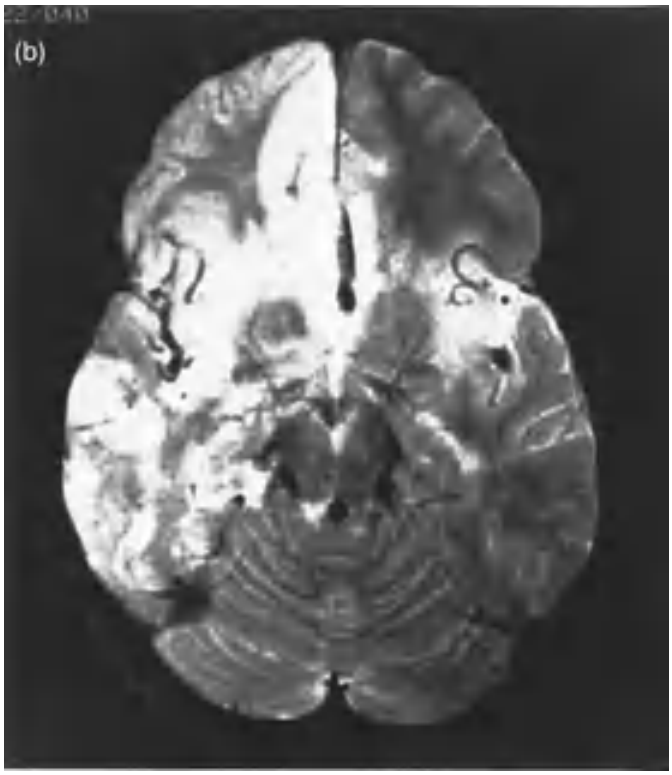

Figure 3 Herpes simplex encephalitis. (a) Sagittal, T_1-weighted (SE 800/20) image shows area of low signal intensity in the right temporal lobe and frontal operculum. (b) Axial, T_2-weighted (SE 2800/80) image demonstrates extensive hyperintense areas in the subfrontal and temporal lobes bilaterally, though more severe on the right hemisphere. (Reproduced by permission of W. B. Saunders from R. R. Edelman and J. R. Hesselink, (eds), *Clinical MRI*, 1990, Chap. 19, p. 584)

enhancement may also be present. Occasionally, foci of hemorrhage are visualized as areas of high intensity on both T_1- and T_2-weighted images.[11] Note that, unlike HSV-1, HSV-2 encephalitis, the most common neonatal viral encephalitis, is a panencephalitis without any predilection in the temporal lobes.

5 EXTRA-AXIAL EMPYEMAS

Accumulation of inflammatory debris may occur in the subdural or, less frequently, in the epidural space. Most of the extraaxial empyemas present acutely secondary to sinusitis or mastoiditis. Empyemas that occur secondary to an infected posttraumatic extra-axial hematoma or postcraniotomy cavity have a more prolonged and indolent course. Empyemas of the extra-axial compartments can also occur (particularly in infants) as complications of meningitis.

5.1 Subdural Empyemas

Pathogens may enter the subdural space via retrograde thrombophlebitis, via local dural erosion, or after contamination of a meningitis-induced subdural effusion. Most frequently, subdural empyemas are secondary to frontal sinusitis (40%).[12] Patients usually present with fever, seizures, focal neurologic deficit, or coma, and require urgent surgical and medical intervention. If completely or partially untreated, the empyema may be complicated with venous thrombosis, infarcts and parenchymal abscesses. The long *TR*, long *TE* sequence is the most sensitive in detecting small, crescentic fluid collections, especially when they are located near the inner table or along the falx. MRI can also distinguish subdural empyemas from subdural effusions or hematomas, depending on signal differences. T_1-weighted images demonstrate the purulent collections as areas with more signal than pure CSF, due to the increased content of proteins and inflammatory debris. Subdural hematomas (subacute) can be easily distinguished because the extracellular methemoglobin exhibits markedly hyperintense signal on both T_1- and T_2-weighted images. MRI can also evaluate mass effect on the adjacent brain or CSF spaces, as well as the underlying parenchymal abnormalities.

5.2 Epidural Empyemas

In the case of epidural empyema, the purulent collection tends to localize outside the inelastic and firm dura, which protects the underlying brain from undesirable concomitant abnormalities. Thus, patients usually have a more silent clinical course. As with subdurals, MRI is the most sensitive method for the evaluation of epidural disease. The signal characteristics of the lentiform extraaxial collections are similar to subdural empyemas on both T_1- and T_2-weighted images. Mass effect on the adjacent brain can also be seen, usually without any evidence of parenchymal changes. On postcontrast scans there is profound enhancement of the inflamed dura, often thicker than that observed in subdurals.

6 CYSTIC LESIONS

Parasitic infections of the brain can commonly produce focal, cystic areas. We review the imaging features of the most frequent parasitic diseases with emphasis on neurocysticercosis. Toxoplasmosis is included in the section on AIDS-related infections.

6.1 Cysticercosis

This is the most common parasitic infection of the CNS in immunocompetent individuals and is caused by the pork tapework *Taenia solium*. Humans ingest the eggs with food contaminated by human or pig feces. In the stomach the eggs release embryos (oncospheres) which enter the intestinal wall and spread hematogenously, invading any human tissue and developing the larvae (cysticerci). Skeletal muscles and CNS are more frequently affected by cysticercosis. CNS infection is reported in 70–90% of cases and constitutes the commonest cause of seizures in young patients in developing countries with poor hygiene. Neurocysticercosis may involve the brain parenchyma, the ventricles, or the subarachnoid space. In parenchymal cysticercosis as the larvae initially invade the brain, they produce a mild inflammatory reaction, which on MRI can be demonstrated as focal, nonenhancing area of edema. Typically, at this very early, active stage of the disease, CT findings are unremarkable. In the next stage (3–12 months after infection) cystic lesions with thin walls and clear fluid are formed. They are usually located at the gray-white matter junction and appear as 1–2 cm spherical cysts with signal intensity identical to CSF on all MRI sequences (Figure 4). There is no evidence of associated edema or contrast enhancement. At this stage, a mural nodule (scolex), which is pathognomonic for cysticercosis, can be seen as a small (1–2 mm) focal, mural projection, isointense to the brain parenchyma. Visualization of the scolex is much easier with magnetic resonance than CT, due to the superior contrast resolution of MRI. Later on, as the parasites degenerate and die, they induce an inflammatory response with associated thickened cystic walls, increased signal intensity from the cyst's content owing to protein accumulation, marked surrounding edema and ring-like enhancement around the cyst. Finally, at the end-stage of the disease process, the cysts are completely mineralized and only punctate foci of calcifications may be seen. Obviously CT is more effective than MRI in the detection of calcifications, although specific MR sequences (gradient echo) are relatively sensitive to calcified lesions.[13] Intraventricular cysticercosis occur in approximately 20% of cases. Cysts located near the aqueduct of sylvius or other CSF pathways can cause acute, obstructive hydrocephalus. The signal characteristics of the intraventricular cysts also follow CSF. Furthermore, on T_1- and PD-weighted images, the cystic wall and the scolex can be more apparent against the adjacent ventricular CSF, even though the cystic component is indistinguishable from CSF.[14] The unique feature in the ventricular variety of cysticercosis is that the degenerated cysticerci rarely calcify. In about 10%, cysticercosis may occur in the subarachnoid space, where the cysts have a racemose form and are larger, sterile, and usually without scoleces. Sometimes the only imaging finding is asymmetry of the CSF spaces. In the case of a profound inflammatory reaction, adja-

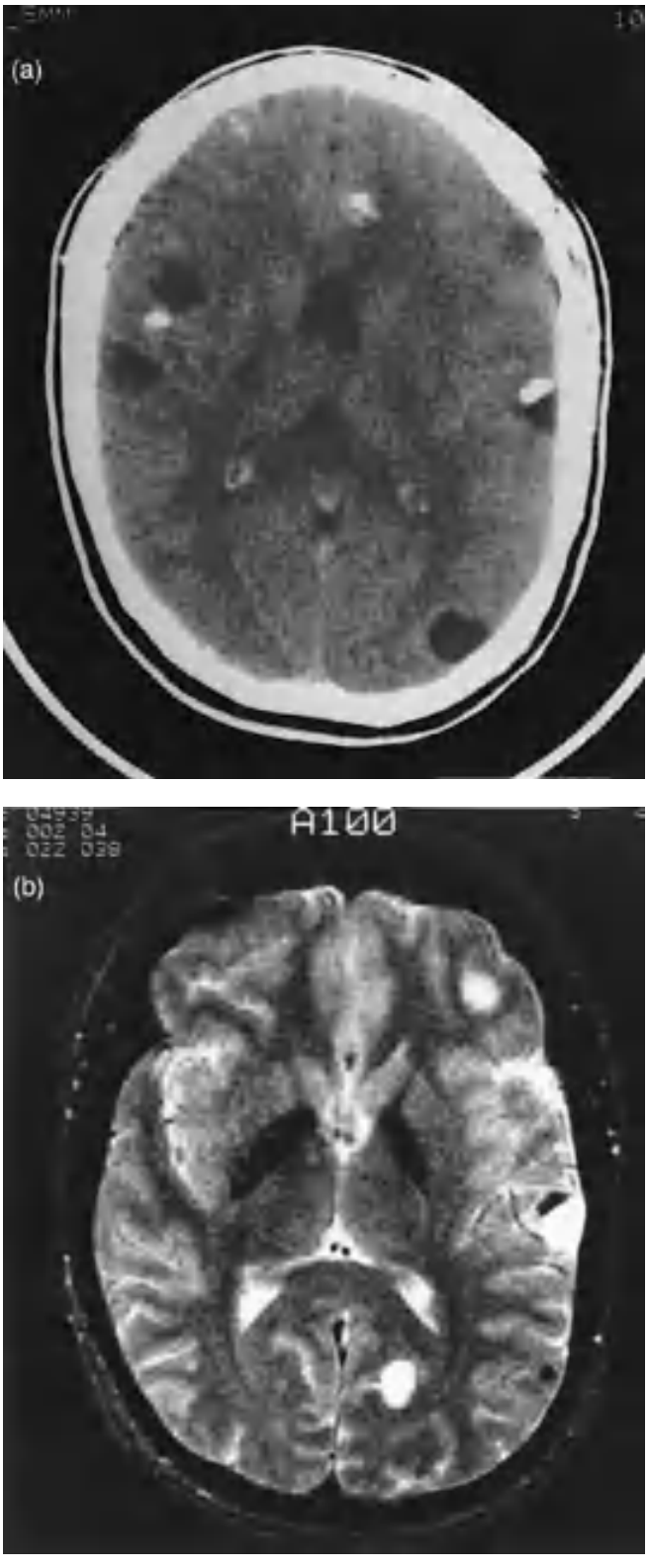

Figure 4 Parenchymal cysticercosis. (a) Noncontrast CT scan demonstrates multiple cysts in the brain parenchyma, several of which are calcified. (b) Axial, T_2-weighted (SE 2500/70) image at approximately the same level, reveals high signal intensity within the cysts. Small calcified foci are difficult to identify, although the larger calcifications exhibit markedly low signal intensity. (Reproduced by permission of W. B. Saunders from R. R. Edelman and J. R. Hesselink, (eds), *Clinical MRI*, 1990, Chap. 19, p. 580)

cent brain abnormalities such as edema, gliosis, or communicating hydrocephalus can be seen.

6.2 Hydatid Disease

This is a parasitic infection which results from the ingestion of contaminated dog feces, containing eggs of *Echinococcus granulosus*. After ingestion, the eggs release embryos (oncospheres) in the gastrointestinal tract that spread hematogenously via the portal circulation to other human tissues. The majority of the lesions affect the liver and the lungs, although some can reach the brain (2–5%), where the larvae develop into large, unilocular cysts. Either CT or MRI can demonstrate adequately the large, commonly solitary cerebral hydatid cyst as a spherical thin-walled structure containing clear, sterile fluid with CSF imaging characteristics. Calcification of the cystic wall may occasionally occur and is better shown by CT. Hydatid (echinococcal) cysts are not associated with edema or contrast enhancement, except in case of cystic rupture and leakage, when an extensive inflammatory reaction is created.[15]

7 AIDS-RELATED INFECTIONS

Patients with AIDS often develop neurologic complications. At least 10% of all AIDS patients present with problems related to the nervous system, and more than one-third of them will manifest a clinically apparent neurologic disorder during the course of the disease.[16] At autopsy it was revealed that 80–90% of patients with AIDS had neuropathologic abnormalities, and usually more than one disease process was present.[17] AIDS is due to the HIV, which on the one hand damages the nervous system by direct infection (HIV encephalitis), and on the other produces immune system dysfunction, especially of cell-mediated immunity. The resultant immunodeficiency leaves the person with AIDS vulnerable to many opportunistic CNS infections. The most important and the commonest of these will be further analyzed below.

7.1 Toxoplasmosis

Toxoplasmosis is the most frequent opportunistic brain infection in AIDS patients. It is caused by the parasite *Toxoplasma gondii* which is an obligate intracellular protozoan. Patients may present with clinical manifestations of focal mass effect such as seizures, focal neurologic deficits, or cranial nerve palsies, as well as more generalized symptoms like headache, confusion, lethargy, and declining mental status. MRI is the most sensitive imaging modality, demonstrating lesions in patients with normal CT scans, particularly lesions at an earlier stage or located in the posterior fossa. Postcontrast MRI scans show multiple ring or nodular enhancing lesions surrounded by vasogenic edema and an associated mass effect. Toxoplasma lesions are typically located at the corticomedullary junction and the basal ganglia. Hemorrhage is uncommon. On T_2-weighted images the lesions are either hyperintense or iso- to

hypointense to brain parenchyma.[18] The neuroimaging findings with both CT and MRI are not pathognomonic for toxoplasmosis and can also be seen in various infectious or noninfectious processes, such as brain metastases, intracerebral lymphoma, Kaposi's sarcoma, cryptococcoma, and tuberculoma. If the imaging studies are suggestive of toxoplasmosis and confirmatory toxoplasma titers are present, empiric antitoxoplasma medication is begun and the response of the treatment can be monitored with follow-up CT or MRI scans. If any or all of the lesions fail to respond to therapy by imaging criteria, toxoplasma may not be the causative infective agent, or there may be another, concurrent disease process present, and brain biopsy should be considered.[19]

7.2 Cryptococcosis

Cryptococcus neoformans causes the most common CNS fungal infection in AIDS patients, which in terms of relative frequency ranks third after HIV encephalitis and toxoplasmosis. It involves the CNS most commonly as a meningitis with minimal inflammatory response and extends mainly in the distribution of the perforating brain arteries and the perivascular (Virchow–Robin) spaces. On MRI there are four patterns: focal cryptococcomas; dilated Virchow–Robin spaces in the basal ganglia and midbrain; miliary enhancing nodules in the brain parenchyma and leptomeningeal-cisternal spaces; and a mixed pattern.[20]

7.3 Other Brain Abscesses

Brain abscesses caused by nonpyogenic organisms typically occur in immunocompromised patients and share almost the same characteristics as the bacterial ones. Some of their unique features have been attributed to the diminished host response. Thus, multiplicity and extraparenchymal spread are frequently encountered. Tuberculous brain abscesses usually spread hematogenously from the lungs. They contain encapsulated pus with viable tubercle bacilli and differ from the more common tuberculomas (granulomas) which are smaller and contain caseous debris. Other associated lesions such as basal meningitis, multiple granulomas, and deep cerebral infarctions are very helpful clues to the diagnosis of tuberculosis.[21] Another cause of nonbacterial brain abscess is fungal infections, which have recently increased substantially because of the large number of AIDS patients. The fungi may involve intracranial blood vessels, meninges, or the brain parenchyma (granulomas or abscesses). Fungal abscesses are caused primarily by *Aspergillus, Mucor* and *Candida* species, owing to their large hyphal forms which permit only limited access to the meningeal microcirculation. *Aspergillus* spreads to the brain hematogenously from the lung, gastrointestinal tract, or directly from the nasal cavity (paranasal sinuses). It readily invades vascular structures and causes hemorrhagic infarcts. In that case the resulting brain abscesses may mimic other hemorrhagic lesions such as metastases. CNS mucormycosis occurs in patients with compromised natural defense and uncontrolled diabetes and is spread by direct extension from adjacent facial compartments. Like *Aspergillus, Mucor* invades blood vessels and causes abscesses, more often at the inferior temporal and frontal lobes. Candidiasis may involve the brain parenchyma, producing multiple, scattered microabscesses.[22]

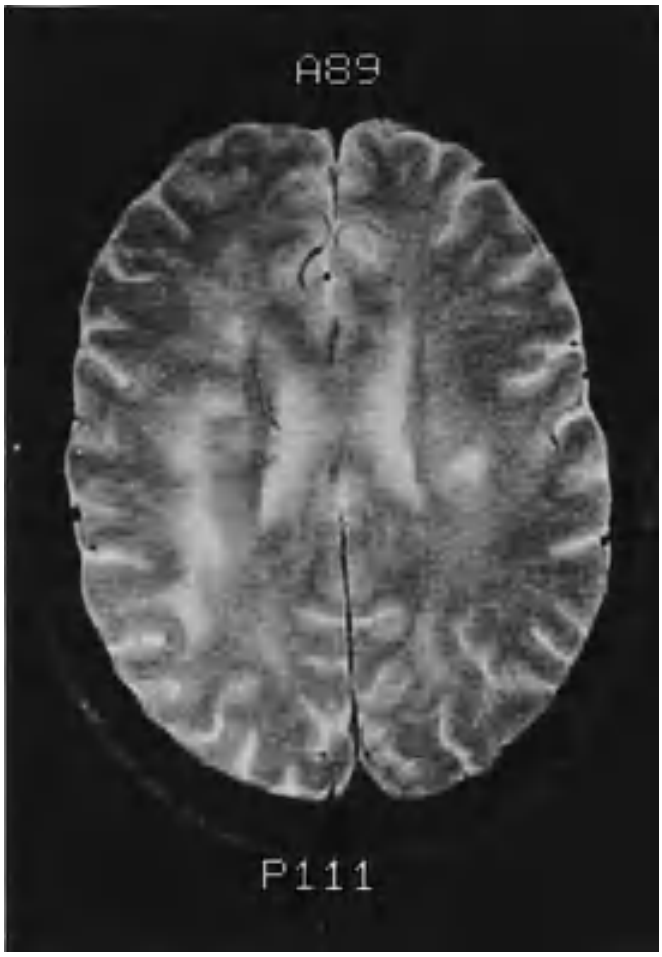

Figure 5 HIV encephalitis. The axial, T_2-weighted (SE 2500/70) image demonstrates multiple, ill-defined, hyperintense lesions in the periventricular white matter, becoming confluent in the right hemisphere. (Reproduced by permission of W. B. Saunders from R. R. Edelman and J. R. Hesselink (eds), *Clinical MRI*, 1990, Chap, 19, p. 590)

7.4 HIV Encephalitis

This is the most common CNS complication in AIDS patients, resulting in a progressive subcortical dementia with associated motor and behavioral abnormalities (AIDS dementia complex).[23] The hallmark of HIV encephalitis is the isolation of multinucleated giant cells and microglial nodules in the brain. Neither CT nor MRI are sensitive enough to detect those characteristic pathologic changes, showing only a nonspecific diffuse brain atrophy with a central predominance (ventricular enlargement). HIV leukoencephalopathy, which occurs in more severe cases of the encephalitis, is frequently located in the periventricular white matter and centrum semiovale. MRI depicts the white matter disease as extensive, nearly symmetric, ill-defined areas of high intensity on T_2-weighted images, without any evidence of mass effect or contrast enhancement[24] (Figure 5).

7.5 CMV Encephalitis

CMV is a herpes virus which can reactivate in the immunosuppressed host and produce a necrotizing encephalitis and ependymitis. CNS infection by CMV is found in more than one-third of autopsies of AIDS patients. Pathologically, there is necrosis of the periventricular parenchymal tissue, associated with accumulations of enlarged cells containing the typical inclusion bodies of CMV. However, the correlation between clinical diagnosis and postmortem results is very poor in cases of CMV encephalitis, for three reasons: firstly, the signs and symptoms of the encephalitis are subtle and nonspecific; secondly, there is no characteristic CSF profile; and, finally, the neuroimaging findings are usually absent or nonspecific. PD- and T_2-weighted magnetic resonance images may demonstrate a periventricular, thick, or nodular hyperintensity, which often involves the corpus callosum. CMV infection usually has a centrifugal spread from the ventricular ependyma involving diffusely the gray and white matter. On postcontrast scans there is diffuse subependymal enhancement around the lateral ventricles, representing the changes of ependymitis and making this an important differentiating point from HIV encephalitis or PML. The common simultaneous occurrence of both HIV and CMV viruses within the brain of AIDS patients supports the proposed theory that an interaction between them may play a role in the pathogenesis of encephalitis in patients with AIDS. There is also some evidence from recent studies that CMV by itself has immunosuppressive properties which may compromise a patient's natural defense against HIV or other opportunistic pathogens.[25,26]

7.6 Progressive Multifocal Leukoencephalopathy (PML)

PML is a progressive demyelinating disease of the brain, caused by reactivation of a latent papovavirus, and affecting 3–5% of all AIDS patients. The main target of PML is the oligodendrocyte which is the myelin-producing cell. The resulting demyelination develops a rapidly deteriorating clinical syndrome, with mental status changes, limb weakness, visual loss, or ataxia, and death usually ensues within 6 months. Initially, T_2-weighted images demonstrate focal, round, or oval areas of high intensity which become larger and confluent with time. These areas are predominantly located in the white matter of the parieto-occipital region. However, involvement of the cortical gray matter, as well as the basal ganglia, the cerebellum, or the brainstem, is not uncommon.[27] Generally the lesions in PML do not enhance and there is no evidence of significant edema or mass effect (Figure 6).

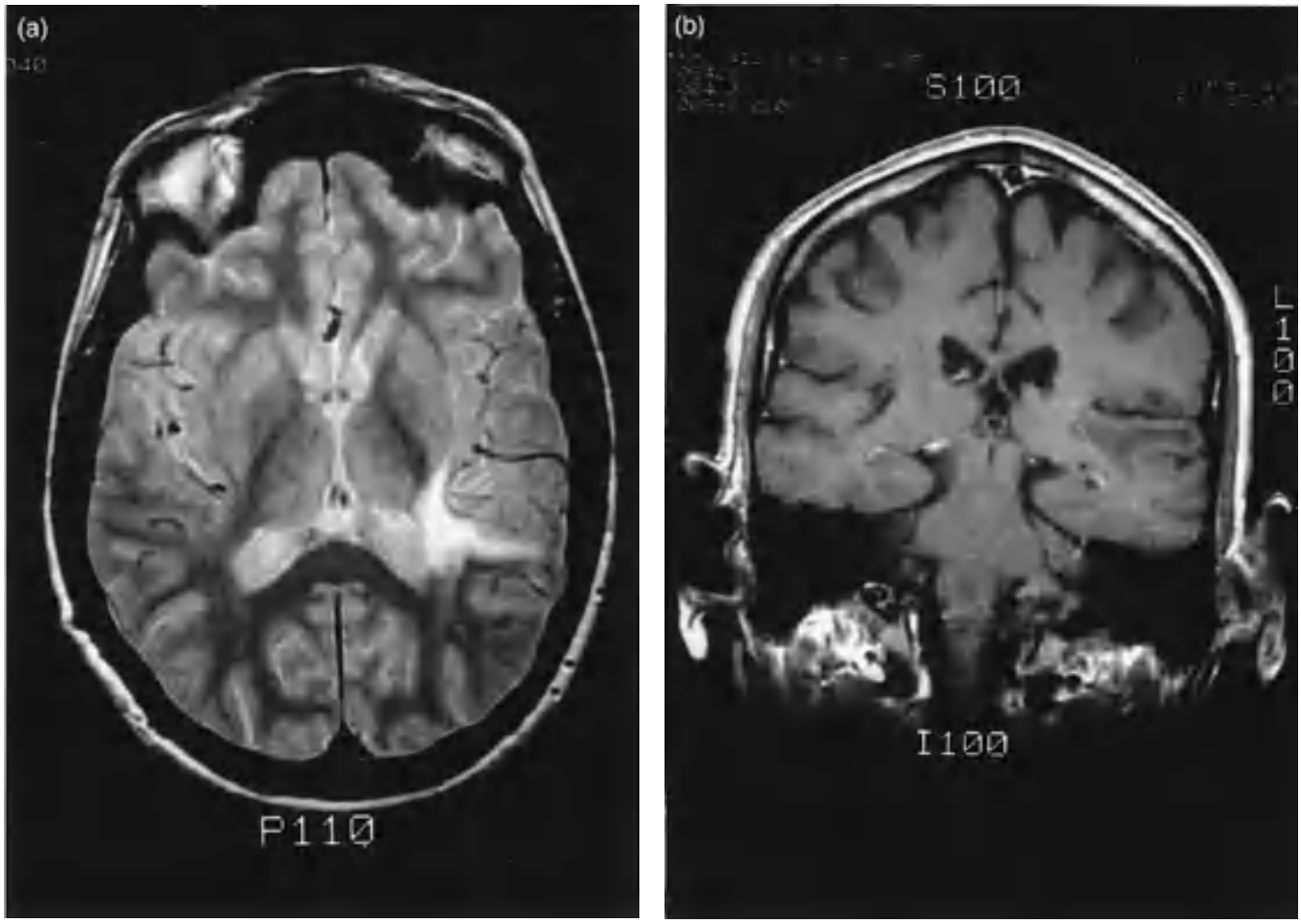

Figure 6 Progressive multifocal leukoencephalopathy. (a) Axial, proton density (Fast SE 3600/17) image demonstrates area of high signal intensity in the subcortical white matter of the left, posterior temporal lobe. (b) Postcontrast, T_1-weighted (SE 550/20, Gd-DTPA) coronal image discloses low signal intensity in the same region without any evidence of enhancement or mass effect

8 RELATED ARTICLES

Brain Neoplasms Studied by MRI; CSF Velocity Imaging; Gadolinium Chelate Contrast Agents in MRI: Clinical Applications; Hemorrhage in the Brain and Neck Observed by MRI; Magnetic Resonance Imaging of White Matter Disease; MRI in Clinical Medicine.

9 REFERENCES

1. G. Schroth, K. Kretzschmar, J. Gawehn, and K. Voigt, *Neuroradiology*, 1987, **29**, 120.
2. D. R. Enzmann, R. H. Britt, and R. Placone, *Radiology*, 1983, **146**, 703.
3. G. Sze and S. H. Lee, in 'Cranial MRI and CT', 3rd edn, eds. S. H. Lee, K. C. V. G. Rao, and R. A. Zimmerman, McGraw-Hill, New York, 1992, Chap. 13.
4. A. B. Haimes, R. D. Zimmerman, S. Morgello, K. Weingarten, R. D. Becker, R. Jennis, and M. D. F. Deck, *Am. J. Roentgenol.*, 1989, 152, 1073.
5. Z. A. McGee and J. R. Baringer, in 'Principles and Practice of Infectious Diseases', 3rd edn., eds. G. L. Mandell, R. G. Douglas, and J. E. Bennett, Churchill Livingstone, New York, 1990, Chap. 66.
6. K. H. Chang, M. H. Han, J. K. Roh, I. O. Kim, M. C. Han, and C. W. Kim, *Am. J. Neuroradiol.*, 1990, **11**, 69.
7. V. P. Mathews, M. A. Kuharik, M. K. Edwards, P. G. D'Amour, B. Azzarelli, and R. G. Dreesen, *Am. J. Neuroradiol.*, 1988, **9**, 1045.
8. G. Sze and R. D. Zimmerman, *Radiol. Clin. N. Am.*, 1988, **26**, 839.
9. T. J. Barloon, W. T. C. Yuh, L. E. Knepper, J. Biller, T. J. Ryals, and Y. Sato, *J. Comput. Assist. Tomogr.*, 1990, **14**, 272.
10. G. Sze, in 'Magnetic Resonance Imaging', 2nd edn., eds. W. G. Bradley and D. D. Stark, Mosby, 1992, Vol. 1, Chap. 22.
11. R. D. Tien, G. J. Felsberg, and A. K. Osumi, *Am. J. Roentgenol.*, 1993, **161**, 167.
12. K. Weingarten, R. D. Zimmerman, R. D. Becker, L. A. Heier, A. B. Haimes, and M. D. F. Deck, *Am. J. Roentgenol.*, 1989, **152**, 615.
13. H. R. Martinez, R. Rangel-Guerra, G. Elizondo, J. Gonzalez, L. E. Todd, J. Ancer, and S. S. Prakash, *Am. J. Neuroradiol.*, 1989, **10**, 1011.
14. G. P. Teitelbaum, R. J. Otto, M. Lin, A. T. Watanabe, M. A. Stull, H. J. Manz, and W. G. Bradley, *Am. J. Roentgenol.*, 1989, **153**, 857.
15. K. H. Chang, S. Y. Cho, J. R. Hesselink, M. H. Han, and M. C. Han, *Neuroimag. Clin. N. Am.*, 1991, **1**, 159.
16. R. M. Levy, D. E. Bredesen, and M. L. Rosenblum, *J. Neurosurg.*, 1985, **62**, 475.
17. P. L. Lantos, J. E. McLaughlin, C. L. Schoitz, C. L. Berry, and J. R. Tighe, *Lancet*, 1989, **i**, 309.
18. B. C. Bowen and M.J.D. Post, in 'MRI of the Brain and Spine', ed. S. W. Atlas, Raven, New York, 1991, Chap. 16.
19. J. A. Cohn, A. McMeeking, W. Cohen, J. Jacobs, and R. S. Holzman, *Am. J. Med.*, 1989, **86**, 521.
20. R. D. Tien, P. K. Chu, J. R. Hesselink, A. Duberg, and C. Wiley, *Am. J. Neuroradiol.*, 1991, **12**, 283.
21. C. Campi de Castro and J. R. Hesselink, *Neuroimag. Clin. N. Am.*, 1991, **1**, 119.
22. C. Bazan III, M. G. Rinaldi, R. R. Rauch, and J. R. Jinkins, *Neuroimag. Clin. N. Am.*, 1991, **1**, 57.
23. B. A. Navia, B. D. Jordan, and R. W. Price, *Ann. Neurol.*, 1986, **19**, 517.
24. H. S. Chrysikopoulos, G. A. Press, M. R. Grafe, J. R. Hesselink, and C. A. Wiley, *Radiology*, 1990, **175**, 185.
25. C. A. Wiley and J. A. Nelson, *Am. J. Pathol.*, 1988, **133**, 73.
26. R. L. Yarrish, in 'AIDS and other Manifestations of HIV Infection', 2nd edn, ed. G. P. Wormser, Raven, New York, 1992, Chap. 17.
27. A. S. Mark and S. W. Atlas, *Radiology*, 1989, **173**, 517.

Biographical Sketches

Spyros K. Karampekios. *b* 1959. M.D., 1984, M.D. Thesis, 1989, University of Athens, Greece, 1989. Faculty in the Department of Radiology, University Hospital of Crete, Greece, 1990–present. Currently lecturer in radiology, University of Crete, School of Medicine. Postdoctoral work as a research fellow in neuroradiology, University of California, San Diego. Approx. 15 publications. Research interests include MRI of central nervous system infections and magnetic resonance evaluation of spinal cord cavities.

John R. Hesselink. *b* 1945. M.D., University of Wisconsin, 1971. Neuroradiology fellowship, Massachusetts General Hospital, 1979. Assistant Professor of Radiology, Harvard Medical School, 1979–84. Professor of Radiology and Neurosciences, University of California, San Diego, 1984–present. Approx. 150 publications and coeditor of textbook with Robert Edelman entitled *Clinical MRI.* Research interests include MRI of infections in immune compromised patients, fat suppression imaging techniques, magnetic resonance angiography and functional magnetic resonance.

Ischemic Stroke

William T. C. Yuh and Toshihiro Ueda
The University of Iowa College of Medicine, Iowa City, IA, USA

and

J. Randy Jinkins and Ronald A. Rauch
University of Texas Health Science Center, San Antonio, TX, USA

1 INTRODUCTION

Stroke affects 750 000 people annually in the USA and is the third leading cause of death.[1] However, only a small percentage of patients die as a result of stroke, making this the leading cause of disability and the third most costly disease affecting adults in this country.[2] Because many diseases can mimic ischemic stroke symptoms (epilepsy, migraine, tumor, syncope, and psychiatric disorders), neuroimaging, particularly MRI with contrast injection, becomes essential for early diagnosis and prompt treatment.

2 ETIOLOGY OF STROKE

Ischemic stroke is the result of failure to perfuse and/or oxygenate the brain. This is usually caused by arterial occlusion. However, it may also be seen after systemic hypotension and/or hypoxia. The underlying pathophysiology during acute brain ischemia can be explained by the hypothetical ischemic models proposed by Virapongse et al.: complete ischemia (no perfusion) and incomplete ischemia (some perfusion).[3] The MRI appearance and clinical outcome are usually distinctly different in these two ischemic models (Figures 1–4).[4–6] Because of the paucity of collateral circulation, complete ischemia, caused by severe compromise of the arterial supply, generally involves most of the cerebral tissue supplied by the vessel and leads to complete infarction (Figures 1 and 2). Limited or no contrast agent can reach the ischemic tissue, thus early parenchymal enhancement is not expected. Incomplete ischemia, on the other hand, caused by a transient vascular

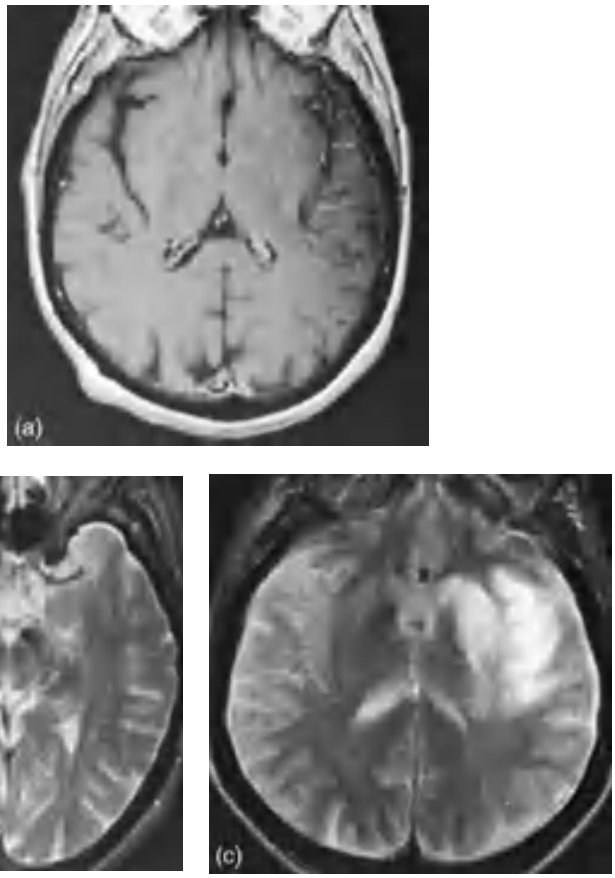

Figure 1 Complete ischemia in a 62-year-old man who presented with acute left hemispheric stroke symptoms. (a) Axial T_1-weighted contrast-enhanced image (SE700/20) obtained 3 hours after onset showing abnormal arterial enhancement (AE) in the distribution of the left middle cerebral artery. No abnormal parenchymal enhancement (PE) is noted (AE $\propto$ 1/PE). (b) The axial T_2-weighted image (SE2200/90) at the corresponding level shows no parenchymal T_2 signal changes ($T_2\Delta$ values) at this time. (c) Axial T_2-weighted image (SE2000/100) obtained 24 hours after (b) showing extensive T_2 signal changes consistent with ischemia of the left middle cerebral artery (AE $\propto$ $T_2\Delta$ $\propto$ 1/PE). (Reproduced by permission of the American Society of Neuroradiology from W. T. C. Yuh, M. R. Crain, D. J. Loes, G. M. Greene, T. J. Ryals, and Y. Sato, *Am. J. Neuroradiol.,* 1991, **12**, 565)

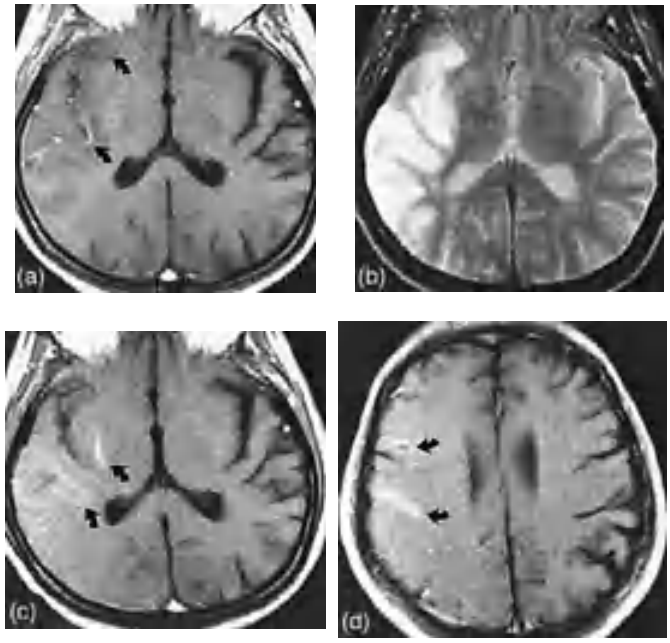

Figure 2 Complete ischemia with an inverse relationship between arterial enhancement (AE) and parenchymal enhancement (PE). (a) Axial T_1-weighted contrast-enhanced image (SE583/20) and (b) the corresponding T_2-weighted image (SE2000/100) obtained within the first 24 hours of ischemic symptoms. Arterial enhancement (arrowed) is demonstrated in the distribution of the right middle cerebral artery (a). An intense signal on T_2-weighted images ($T_2\Delta$ values) without parenchymal enhancement is present at this time (b). These findings are typical of complete ischemia expressed as $T_2\Delta \propto \text{AE} \propto 1/\text{PE}$. (c, d) Follow-up axial T_1-weighted contrast-enhanced images (SE583/20) obtained 7 days after the onset of acute ischemic symptoms when arterial enhancement (AE) has completely resolved and significant parenchymal gyriform enhancement (PE) has developed (PE $\propto$ 1/AE). (Reproduced by permission of the American Society of Neuroradiology from Crain et al.[6])

occlusion (complete or partial), tends to produce a less severe ischemic insult and may be associated with a potentially reversible or minimal neurological deficit (Figures 3 and 4). Contrast material may be able to reach the ischemic tissue, and therefore early parenchymal enhancement is possible.

Watershed infarction has a somewhat different pathophysiological basis from that of complete or incomplete ischemia.[4–6] This region is located at the edges of the vascular territory between major cerebral arteries (Figure 5). A decrease in perfusion pressure from either systemic hypotension or partial occlusion may therefore affect only the regions of the brain that have the most marginal blood supply. Watershed infarction is a hybrid of complete and incomplete ischemia in that collateral circulation and/or antegrade arterial supply are intact but inadequate. Despite the severe ischemic insult, contrast material can still be delivered to the ischemic tissue as in incomplete ischemia. The clinical outcome is less favorable, however, and is more characteristic of complete ischemic infarction.

3 ACUTE CEREBRAL ISCHEMIA

The MRI appearance of acute cerebral ischemia is dependent on several physiological factors (Table 1) that are often

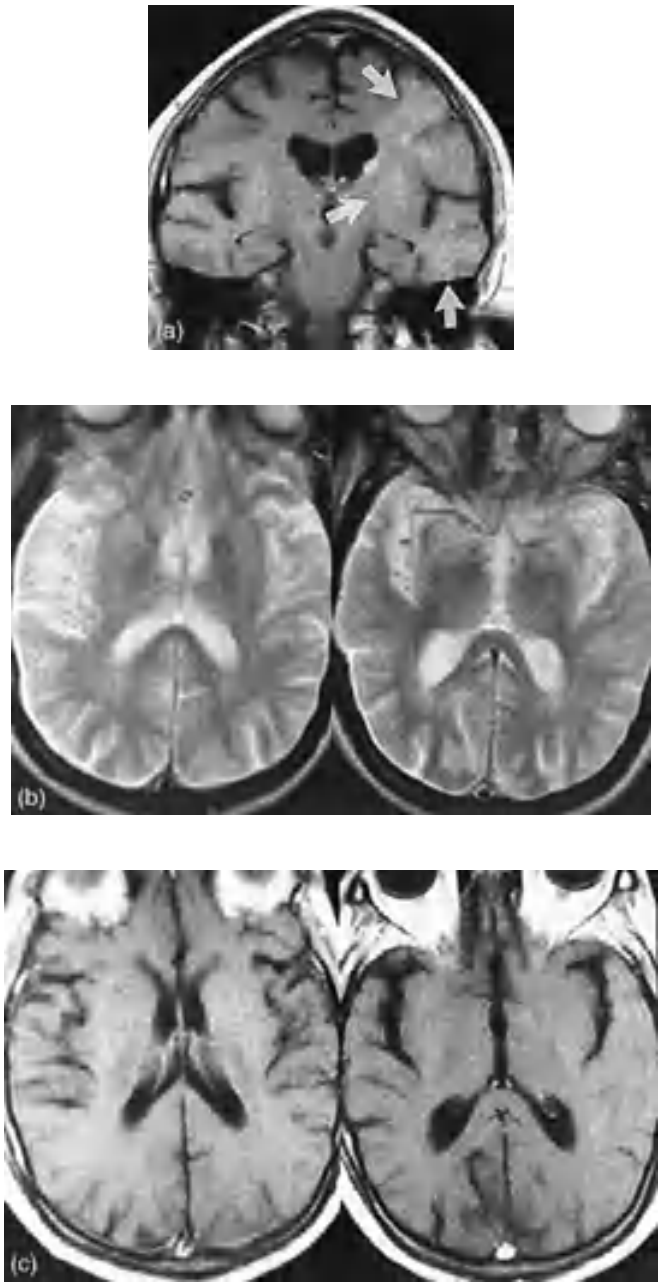

Figure 3 Incomplete ischemia in a patient with transient neurological symptoms and early parenchymal enhancement. This patient developed transient left hemispheric symptoms after 2 minutes of test balloon occlusion of the left internal carotid artery. (a) Coronal T_1-weighted contrast-enhanced image (SE538/20) obtained at 2 hours showing diffuse parenchymal enhancement (PE) (arrows) in the distribution of the left middle cerebral artery without arterial enhancement (AE) (PE $\propto$ 1/AE). Also noted is enhancement of the caudate nucleus. (b) The axial T_2-weighted images (SE2000/100) show no apparent signal change at this time. (c) Axial T_1-weighted contrast-enhanced images (SE583/20) at 24 hours show no evidence of parenchymal or arterial enhancement. The resolution of parenchymal enhancement by 24 hours parallels the rapid neurological improvement in this patient. (Reproduced by permission of the American Society of Neuroradiology from Crain et al.[6])

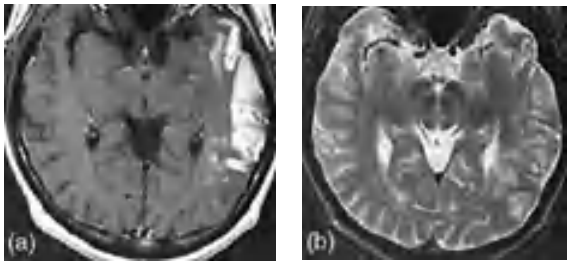

Figure 4 Incomplete ischemia with early, intense parenchymal enhancement (PE) in a patient who had a transient ischemic episode with right-sided weakness and aphasia that resolved almost completely in 2 hours. (a) Axial T_1-weighted contrast-enhanced image (SE700/20) showing diffuse, intense cortical enhancement in the distribution of the left middle cerebral artery without evidence of arterial enhancement (AE) (PE $\propto$ 1/AE). (b) The corresponding axial T_2-weighted image (SE2000/100) shows a much less extensive area ($T_2\Delta$ values) of signal abnormality (PE $\propto$ 1/AE $\propto$ $1/T_2\Delta$). (Reproduced by permission of the American Society of Neuroradiology from Crain et al.[6])

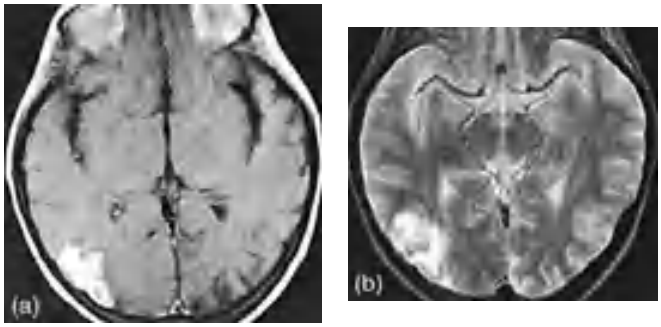

Figure 5 Watershed infarction in a patient with severe neurological sequelae and early, intense parenchymal enhancement. (a) Axial T_1-weighted contrast-enhanced image (SE516/20) showing early and intense parenchymal enhancement in the right posterior watershed zone without arterial enhancement. (b) Axial T_2-weighted image (SE2000/100) showing an area of signal abnormality approximating the area of enhancement in (a). (Reproduced by permission of the American Society of Neuroradiology from Crain et al.[6])

coexistent.[5] Four types of MRI abnormality occur soon after an acute cerebral insult: (1) alteration in arterial blood flow, (2) parenchymal swelling, (3) parenchymal signal change, and (4) abnormal parenchymal enhancement.[2,4,7–19]

Vascular flow abnormalities can be detected by MRI as an absence of flow void and/or abnormal arterial enhancement (Figures 1, 2, 6, and 7). Normal rapid flow in large arteries, such as the internal carotid or basilar arteries, typically produces a flow void on standard spin echo MRI, especially when studied with long *TE* pulse sequences. The loss of a flow void denotes thrombosis or abnormally slow flow (Figures 6 and 7).[5–9] Although angiography is necessary to discriminate slow flow from thrombosis, the loss of flow void on MRI suggests cerebral vascular disease.

In certain cases, contrast enhanced MRI can further accentuate the underlying vascular flow abnormalities. On T_1-weighted spin echo images ($TE \geqslant 20$ ms) obtained without flow compensation, arterial enhancement usually does not occur after the intravenous injection of paramagnetic contrast agents. In vessels where there is abnormally slow flow, caused either by a high degree of stenosis or by occlusion without significant collateral supply, enhancement of arterial structures may be evident (see Figures 1 and 2).[2,5,6,10,11] Although the absence of a flow void may represent either slow flow or thrombosis, arterial enhancement has been shown to correlate well with angiographic evidence of slow flow.[12] In cortical ischemia, patients with arterial enhancement typically have more severe clinical symptoms and a poorer outcome, whereas absent or minimal symptoms are usually seen in patients with evidence of cerebral ischemia without arterial enhancement. Although arterial enhancement occurs early, it generally lasts only about 1 week and seldom persists beyond 11 days (Figure 8).[6] This contrasts with absence of flow void, which can be permanent.[5,7–9] The disappearance of arterial enhancement probably indicates the reestablishment of rapid flow in the involved vessels and coincides with the 'luxury perfusion' demonstrated on computerized tomography or scintigraphy (occurring at 7–14 days). The early disappearance of arterial enhancement within 1 or 2 days has been seen in patients with transient ischemic attacks and coincides with the rapid resolution of the

Table 1 Pathophysiological Mechanisms for MRI Findings in Ischemia

Mechanism	MRI Findings	Possible causes	Estimated time (h)[a]
Flow kinetics	Absent flow void	Slow flow; occlusion	Immediately
	Arterial enhancement	Slow flow	Immediately
Biophysiological	T_1 morphological change (swelling)	Cytotoxic edema (free water)	2–4
	T_2 signal change	BBB breakdown; vasogenic edema; macromolecular binding	8
	T_1 signal change	BBB breakdown; vasogenic edema; macromolecular binding	16–24
Combination	Progressive parenchymal enhancement[b]	Impaired delivery of significant contrast agent	>120[c]
	Early exaggerated enhancement[d]	Intact delivery of contrast agent; focal hyperemia	2–4

BBB, blood–brain barrier.
[a]Time at which findings generally could first be detected by available MRI examinations; this does not necessarily imply the exact time of onset.
[b]Typical findings in completed cortical infarctions.
[c]Usually not detected before 5–7 days.
[d]Found in cases with transient or partial occlusions and in watershed infarctions.
(Reproduced by permission of the American Society of Neuroradiology from W. T. C. Yuh, M. R. Crain, D. J. Loes, G. M. Greene, T. J. Ryals, and Y. Sato, *Am. J. Neuroradiol.*, 1991, **12**, 621)

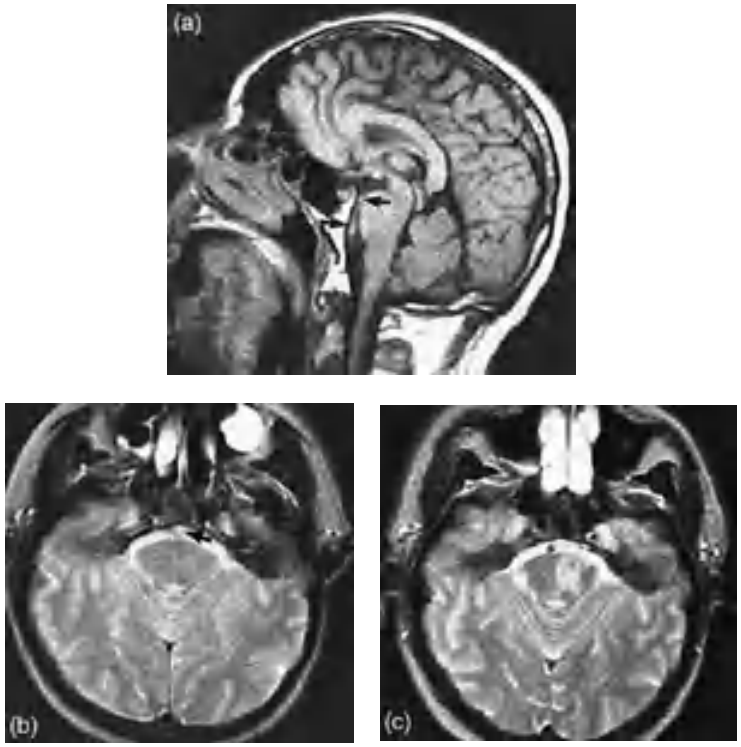

Figure 6 Arterial thrombosis in a 50-year-old man with symptoms of brain stem ischemia. (a) Parasagittal T_1-weighted image (SE350/26) obtained 4 hours after the onset showing a linear signal isointense to brain in the prepontine region (arrows) along the course of the basilar artery, suggesting an intraluminal clot. (b) Axial T_2-weighted image (SE2000/100) showing the absence of a flow void in the basilar artery (arrow). No apparent T_2 signal abnormality is detected within the pons at this time. (c) Repeat axial T_2-weighted image (SE2000/100) obtained 48 hours after (a) showing the interval development of ischemic changes in the pons. (Reproduced by permission of the American Society of Neuroradiology from W. T. C. Yuh, M. R. Crain, D. J. Loes, G. M. Greene, T. J. Ryals, and Y. Sato, *Am. J. Neuroradiol.,* 1991, **12**, 565)

underlying proximal vascular disorder.[6] Because watershed infarction usually has intact although insufficient blood flow, arterial enhancement is seen infrequently.

4 BRAIN SWELLING

Another early finding in ischemic stroke is brain swelling. Mass effect or brain swelling is probably caused by an abnormal accumulation of tissue water related to a complex combination of intra- and extracellular edema.[5] This swelling can be recognized by the distortion of normal brain anatomy, with sulcal obliteration being the first observable sign of cortical ischemia (see Figure 7). T_1-Weighted images offer the best definition of anatomy with minimal interference from cerebrospinal fluid and are generally superior for recognition of early swelling. Brain swelling often occurs as early as 2 hours before the onset of T_2 signal changes, presumably caused by cytotoxic edema (see Figures 3 and 7). This early (cytotoxic) edema primarily represents a shift of free water from the extracellular space into the intracellular space without an associated protein shift.

The swelling may then progress over several days, mostly caused by the development of vasogenic (interstitial) edema, and is associated with an abnormal signal on long *TE* sequences.[5,13–18] In the early phase of acute ischemia, the signal change due to vasogenic edema is generally not observed until 8 hours[5] (see Figures 1, 3, and 6), and is not fully developed until 24 hours after the infarction.[5,19] The fact that the signal change usually occurs after tissue swelling has begun supports the hypothesis of two phases of edema (cytotoxic and vasogenic). In transient ischemic attacks, swelling can be seen transiently on T_1-weighted images without the development of T_2 hyperintensity.[20] In fact, reversible ischemia seldom is associated with major T_2-weighted parenchymal signal changes. The absence of a T_2 signal change in cytotoxic edema is probably related not only to the small amount of free water shift (estimated at 3%) but also to the absence of a major change in the interactions between the water protons and the macromolecular proteins.[5,15] Vasogenic edema, by comparison, is readily detected on T_2-weighted images and usually becomes visible 8 hours after the onset of symptoms (see Figures 1, 2, and 6). It is associated with a significant amount of water and protein shift (exudate) from the intravascular space to the extracellular space. Because signal changes usually do not occur until 2 hours after the onset of the blood–brain barrier breakdown, appreciable signal changes detected by MRI may require a gradual accumulation of a sufficient amount of water in the extracellular space (the amount of water protons) as well as an alteration in the relaxation time of water molecules (the binding state of proton molecules). The maximal signal changes noted on T_2-weighted images usually occur in 24–48 hours (see Figures 1, 5, and 6).[5,21]

Signal changes are usually best seen on standard T_2-weighted images. Abnormalities in the cortex or near the ventricle may be difficult to separate from the normal hyperintensity of adjacent cerebrospinal fluid. For this reason, the abnormal tissue signal may be easier to recognize on the

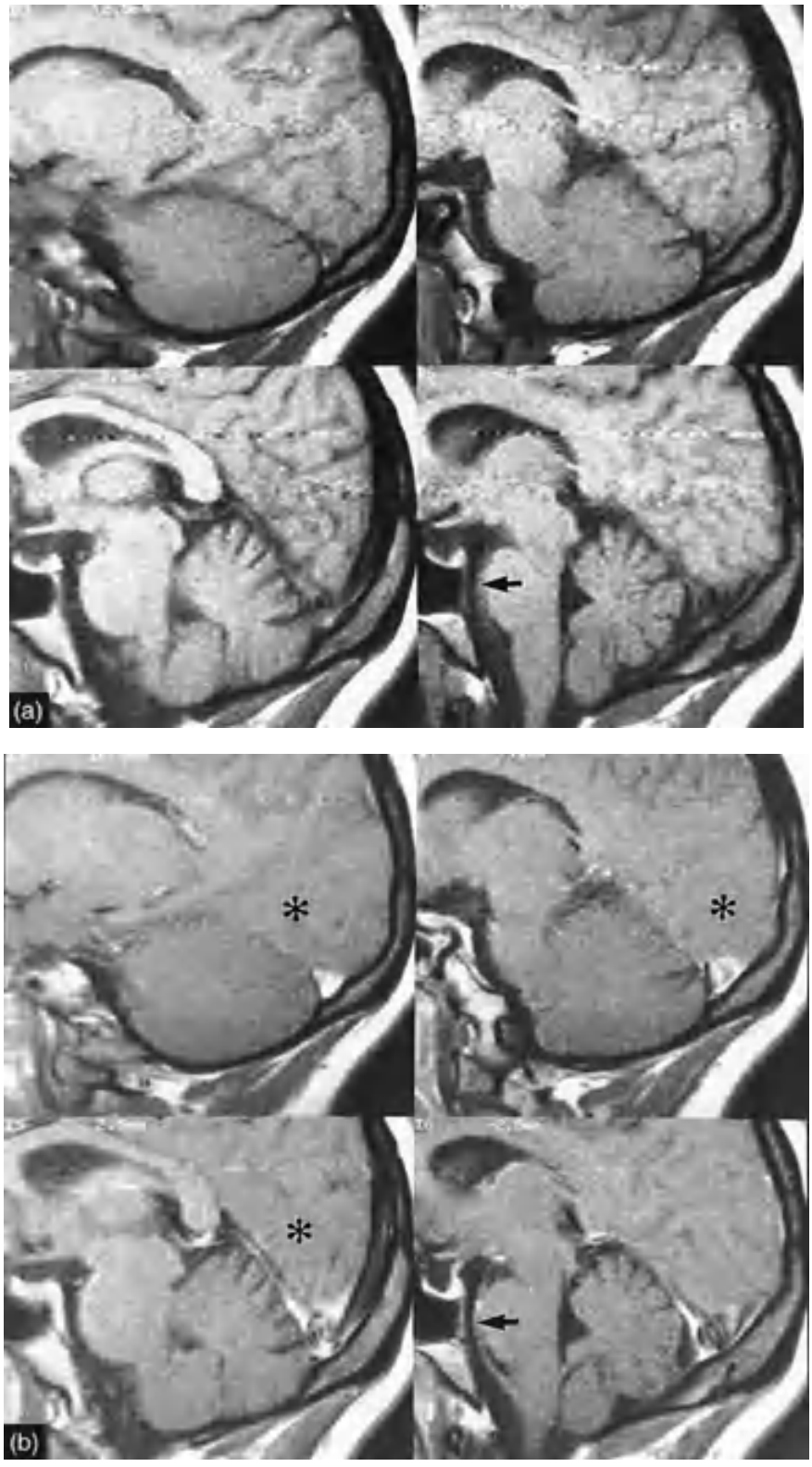

Figure 7 (a,b)

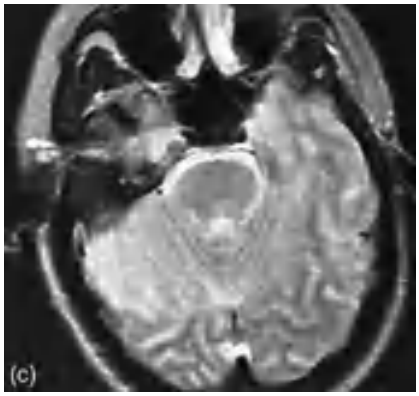

Figure 7 (c) Early development of brain swelling associated with complete ischemia in a 35-year-old woman. (a) Parasagittal T_1-weighted nonenhanced images (SE450/20) obtained 2.5 hours after the onset showing signals isointense to brain in the prepontine cistern (arrow). (b) Corresponding parasagittal T_1-weighted contrast enhanced images (SE450/20) obtained 40 minutes after (a) showing development of massive brain swelling in the occipital lobes (asterisk) and cerebellum and progression of a blood clot in the basilar artery (arrows). (Reproduced by permission of the American Society of Neuroradiology from W. T. C. Yuh, M. R. Crain, D. J. Loes, G. M. Greene, T. J. Ryals, and Y. Sato, *Am. J. Neuroradiol.,* 1991, **12**, 565)

first echo of a double-echo T_2-weighted study, also referred to as a proton density weighted image.

5 ABNORMAL ENHANCEMENT FOLLOWING ADMINISTRATION OF A CONTRAST AGENT

Abnormal enhancement of cerebral tissue with intravenously administered gadolinium after an ischemic insult is associated with a breakdown of the blood–brain barrier and/or a loss of arterial autoregulation.[4–6] Parenchymal enhancement usually occurs late in complete ischemia. During the acute phase of complete ischemia, severe arterial obstruction coupled with deficient collateral supply prevents both blood and contrast material from reaching the ischemic tissue (see Figures 1, 2, and 7). Therefore, no parenchymal enhancement is expected during the early phase of complete ischemia. By 5–7 days, the parenchymal enhancement will appear due to the reestablishment of the blood supply by recanalization of the occluded vessel and/or improved collateral circulation (see Figure 2). This reestablished blood supply will not only permit contrast material to reach the ischemic tissue, resulting in parenchymal enhancement, but also allow sufficiently rapid flow to cause the disappearance of arterial enhancement. This abnormal parenchymal enhancement will continue until the blood–brain barrier is reinstated with the maturation of the neovasculature, a process that normally takes several months after the infarction.[20]

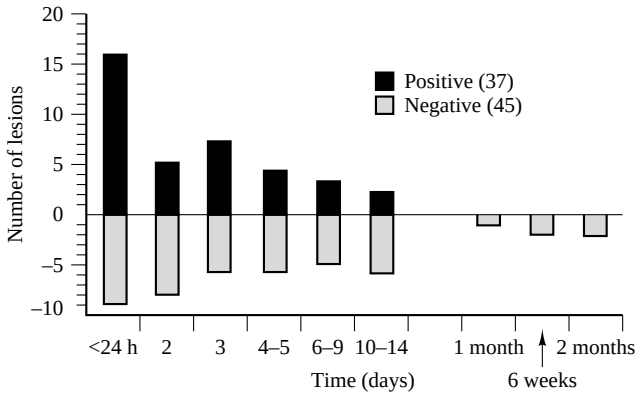

Figure 8 Graph depicting the number of lesions that demonstrated arterial enhancement at the time of the initial MRI examination. Arterial enhancement frequently was detected within the first 24 hours, rarely after 7 days, and not at all after 11 days, suggesting the reestablishment of the circulation or development of collateral circulation. (Reproduced by permission of the American Society of Neuroradiology from Crain et al.[6])

Early enhancement can be seen in either incomplete ischemia or watershed infarction (see Figures 3–5). In incomplete ischemia, the intact delivery of contrast material may allow for the possibility of early parenchymal enhancement (see Figure 2). We have seen parenchymal enhancement within a few hours after the onset of symptoms. Such enhancement is most likely caused by a loss of autoregulation or hyperemia and typically resolves on subsequent scans performed 24 hours later. Minimal or no T_2 signal abnormality develops. Similarly, in a watershed infarction (hypoperfusion with intact but inadequate blood supply), it is uncommon to see early parenchymal enhancement (see Figure 5). Unlike incomplete ischemia, however, the early enhancement observed in a watershed infarction does not indicate a favorable clinical outcome.

The complex relationship between the abnormal MRI findings, including extent of brain swelling (EBS), T_2 signal changes ($T_2\Delta$ values), arterial enhancement (AE), and parenchymal enhancement (PE), and clinical severity (CS) in acute ischemia generally can be expressed by the following formula:

$$\mathrm{CS} \propto T_2\Delta \propto \mathrm{AE} \propto \mathrm{EBS} \propto 1/\mathrm{PE} \qquad (1)$$

This formula expresses the direct relationship between clinical severity, signal changes, extent of brain swelling, and arterial enhancement, which in turn have an inverse relationship to parenchymal enhancement.

The two exceptions that do not apply to equation (1) are the relationship between clinical severity in a watershed infarction and arterial enhancement in a small noncortical infarction. In a watershed infarction there is intact delivery of the contrast agent as in incomplete ischemia; however, it is insufficient. Therefore, despite the fact that the MRI findings suggest incomplete ischemia by equation (1), the prognosis and clinical severity are more like those of complete ischemia. The other exception is the lack of arterial enhancement in noncortical ischemia. Because the blood vessels involved in these types of infarction tend to be small, arterial enhancement usually is not seen. Nevertheless, the clinical severity of such cases may be quite grave.

6 NEW MAGNETIC RESONANCE MODALITIES

6.1 Diffusion MRI

Recent advances in MRI techniques now provide new information directly related to the underlying pathophysiology at

the cellular and microscopic levels and may allow the diagnosis of acute ischemia and estimation of infarction size. Diffusion imaging reflects abnormal water movement in acute ischemic tissues caused by the failure of the high-energy Na^+–ATP pump and is sensitive to hyperacute ischemia within a few minutes after onset.[22] In both animal models and clinical cases, early ischemic changes have been reported on diffusion imaging when standard T_2-weighted imaging has shown no abnormalities.[22,23] The abnormality in diffusion imaging is shown as a high signal intensity area. This increase in signal demonstrates a region of diminished net diffusion, which is dark on the apparent diffusion coefficient (ADC) images. The ADC is obtained from an exponential fit of the signal intensities of a series of diffusion imaging as a function of b factor. Diffusion abnormality can be identified at high b values. ADC changes are a sensitive marker of ionic equilibrium because they show a function of intra–extracellular water homeostasis.

In animal studies, the signal abnormality in diffusion imaging appears a few minutes after occlusion of the middle cerebral artery and enlarges over the next 24 hours.[22,24] The abnormality in diffusion imaging is equivalent to that in T_2-weighted imaging by 24 hours after the onset of ischemia;[25] however, cytotoxic and vasogenic edema may cause an overestimation of lesion volume. Kohno et al. reported regional correspondence of hyperintensity in diffusion imaging with perfusion deficits at cerebral blood flow (CBF) thresholds of 34 ml/min per 100 g tissue after 30 minutes and 41 ml/min per 100 g tissue after 2 hours of a major coronary artery occlusion.[26] Their reports suggest that the threshold for ADC changes at a given CBF depending on the duration of ischemia.

In clinical studies, diffusion imaging has also been reported to have a high sensitivity and specificity for acute ischemia. Lövblad et al. reported that the sensitivity and specificity of diffusion imaging in acute ischemic patients within 24 hours of onset were 88% and 95%, respectively.[27] However, the pathophysiological changes in acute ischemia in humans are likely to be more heterogeneous than those found in animal models. Human subjects reportedly have two phases in the time course of ADC changes: a significant reduction for 96 hours from stroke onset and an increasing trend from reduction to pseudonormalization to elevation at later subacute to chronic time points (> 7 days).[28]

Previous reports do not conclude whether the diffusion imaging signal changes are indicative of reversibly or irreversibly injured tissue. The diffusion abnormality in global ischemia is reversible by early reperfusion within 12 minutes.[29] The regression of the diffusion abnormality was also reported in reperfusion models. Miyabe et al. indicated that if reperfusion occurred before ADC value decreased to approximately 70% or less of control values for 10–20 minutes, the ADC changes were usually reversible.[30] Ueda et al. suggested that diffusion imaging had the highest sensitivity but was not as specific as the regional cerebral blood volume (rCBV) map in predicting acute ischemic injury and tended to overestimate infarction size in patients studied within 72 hours of stroke onset.[31] In addition, 25% (4 out of 16 lesions) of ADC abnormalities were false positives or reversible ischemia. These results may support the suggestion that the diffusion abnormality indicates early changes of both reversible and irreversible ischemia.

6.2 Perfusion MRI

Perfusion imaging provides direct information related to a reduction in blood flow that reflects the primary underlying pathophysiology of acute ischemia. Compared with the conventional spin-echo pulse sequence, echo-planar imaging is more susceptible to field inhomogeneity and is more advantageous in the evaluation of the T_2* effect. The combination of dynamic echo-planar T_2*-weighted imaging and intravenous bolus injection of contrast material produces hemodynamic information such as mean transit time (MTT) and CBV. Although perfusion imaging cannot produce absolute values but only semiquantitative data in estimating MTT and CBV maps, it can be performed quickly and has proven essential in the emergent management of patients with acute ischemic stroke. Furthermore, higher temporal resolution and multisection images can be achieved by the echo-planar imaging techniques.

In an animal model, perfusion imaging demonstrated diminished perfusion within minutes of arterial occlusion.[32] Perfusion imaging shows a signal or a delay in peak signal loss in the vascular distribution when an artery is occluded. In clinical studies, perfusion imaging was reported to be superior to diffusion imaging in the assessment of hemodynamic changes of chronic cerebral hypoperfusion. Maeda et al. indicated that ischemic tissue with prolonged regional MTT (rMTT) and a marked decrease in rCBV tended to suffer irreversible damage.[33] A mild decrease in rCBV with prolonged rMTT may suggest an area of reversible ischemia. A marked increase in rCBV may show the state of luxury perfusion in subacute ischemia.

Combined diffusion and perfusion imaging can provide more important information in the management of patients with acute ischemic stroke. The volume of ischemic tissue demonstrated by both diffusion and perfusion MRI has been reported to have a high correlation with neurologic outcome as measured by the National Institutes of Health (NIH) stroke scale, and these imaging techniques, therefore, can play a useful prognostic role in acute ischemic stroke patients (Figure 9).[34]

Currently, the mismatch between diffusion and perfusion imaging in patients with acute ischemic stroke has been reported in several studies. Sorenson et al. studied patients within 10 hours of onset and showed that the abnormality in rMTT maps was larger than those in rCBV maps and diffusion imaging.[35] Rordorf et al. demonstrated that diffusion lesion volumes were smaller than the volumes of rCBV map abnormality in patients studied within 12 hours of onset, and the early CBV abnormality was slightly better than the diffusion abnormality as a predictor of final infarction size.[36] Röther et al. suggested that it was possible to differentiate between severely ischemic tissue and peri-infarct parenchyma by rCBV maps in hyperacute ischemia.[37] A recent report by Ueda et al. is similar to those reports in which the rMTT map overestimated the final infarction volume and the rCBV map provided the best estimation but differed in that their diffusion imaging underestimated final infarction volume.[31] The size of the abnormality in diffusion and perfusion imaging depends on the imaging time from the onset of symptoms. Quantitative assessment of ischemic tissue viability and/or reversibility requires further study.

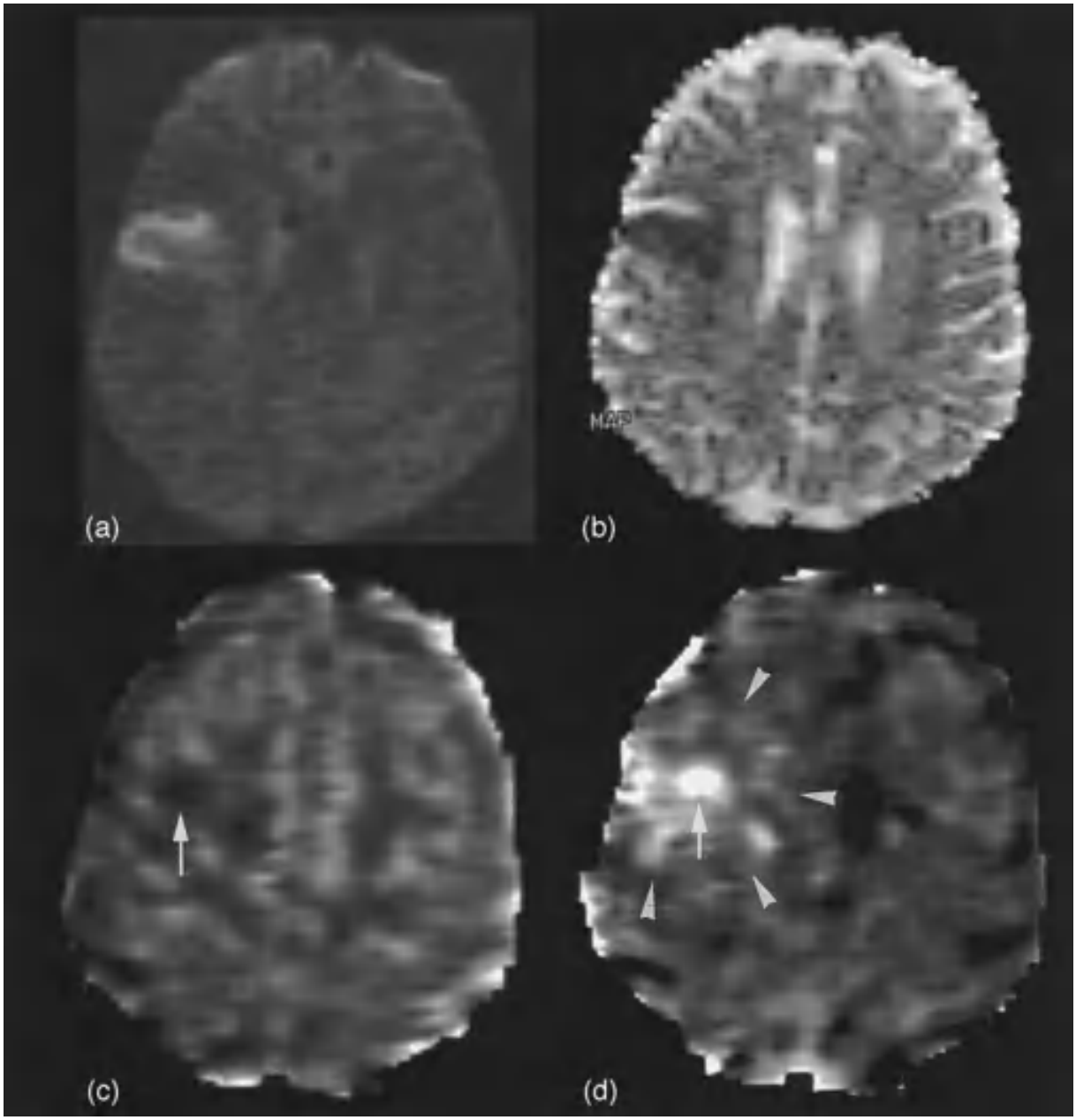

Figure 9 MRI within 12 hours in a 50-year-old male with acute onset of left hemiparesis. (a) Diffusion-weighted imaging; (b) apparent diffusion coefficient (ADC) map; (c) relative cerebral blood volume (rCBV); (d) relative mean transit time (rMTT) map. Both (a) and (b) demonstrate right hemisphere lesions in the middle cerebral artery distribution. The rMTT map (d) shows an area with hypoperfusion (arrow heads) that is much larger than that demonstrated by (a) and (b). The infarction core (arrow) may show the highest signal intensity (most severe hypoperfusion). In (c), the infarction core has a depletion of blood volume consistent with an inadequate collateral circulation (arrow)

6.3 MR Spectroscopy

Clinical application of MR spectroscopy (MRS) in the diagnosis and management of acute stroke has not been well established. There are several possible causes for the underutilization of spectroscopy in patients with strokes. (1) Most MR centers do not have sufficient scientific background and clinical expertise to facilitate such an application, and frequently avoid using such a technique. (2) The acquisition time for clinical MRS, which in the past has been long and not very reproducible, is not adequate for the management of acute stroke. (3) The diagnosis of acute stroke is usually quite straightforward by the conventional clinical examination and radiological means. Consequently, clinical MRS is usually only applied for diagnosis of problematic cases. The capability of MRS in the assessment of tissue viability/reversibility has not been well established, although it may have great potential if the acquisition times can be shortened with improved techniques.

MRS provides a means to assess the biochemical characteristics of brain disease through direct and noninvasive assay of cerebral metabolites.[38,39] Practically, phosphorus and protons are being measured in clinical applications for central nervous system disease. In ischemic brain tissue, MRS provides infor-

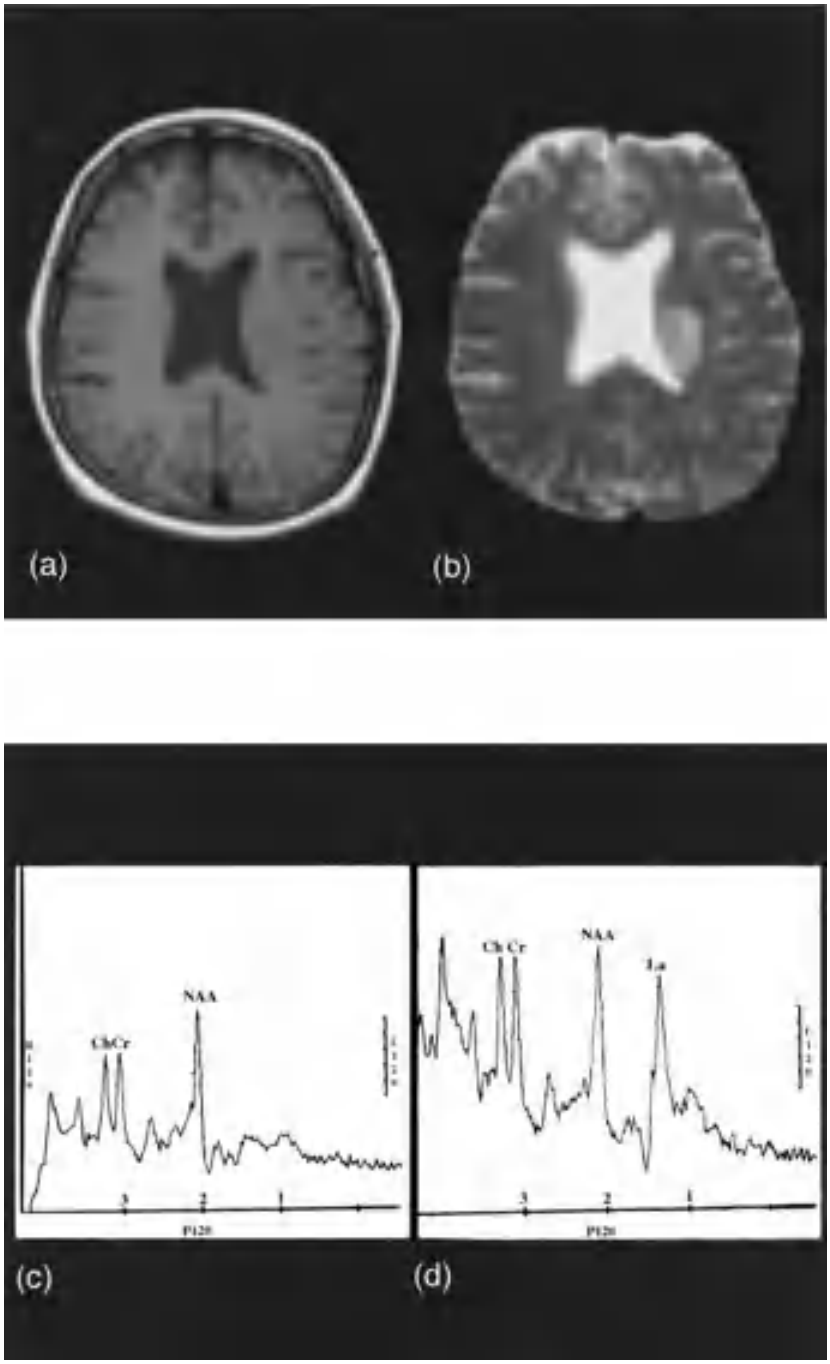

Figure 10 MRI examination of a 45-year-old patient with acute right side weakness: (a) T_1-weighted image; (b) T_2-weighted image. A rounded lesion at the left-periventricular region has hypointensity on the T_1-weighted image (a) and hyperintensity on the T_2-weighted image (b). This lesion does not demonstrate any contrast enhancement. Although the referring physician has high suspicion of acute stroke, the MR findings are not characteristic of acute stroke and are more consistent with a mass lesion. Proton spectra were obtained from normal parenchyma on the contralateral side (c) and from the lesion (d). This lesion shows a large lactate (La) peak and a diminished *N*-acetyl aspartate (NAA) peak at 1.3 and 2.0 ppm, respectively (d), compared with the normal tissue (c). (Ch, choline; Cr, creatine.) Follow-up MR examination obtained several months later demonstrated atrophy and gliosis at the same location, consistent with chronic infarction. In this particular patient, spectroscopy was valuable not only because it enabled surgical biopsy to be avoided, but also because it allowed a correct diagnosis for acute stroke

mation about energy status and oxidative metabolites related to the underlying pathophysiology (ischemia). Proton MRS is more effective because hydrogen atoms are more abundant than phosphorus in the brain parenchyma and proton MRS is easier to perform with the clinical unit.

There are two types of approach: localized and spectroscopic imaging (MRSI). Localized proton MRS methods can be separated into those with long and short echo times. Long *TE* (135 or 270 ms) acquisitions generally have proved easiest to use in clinical practice. Localization methods commonly

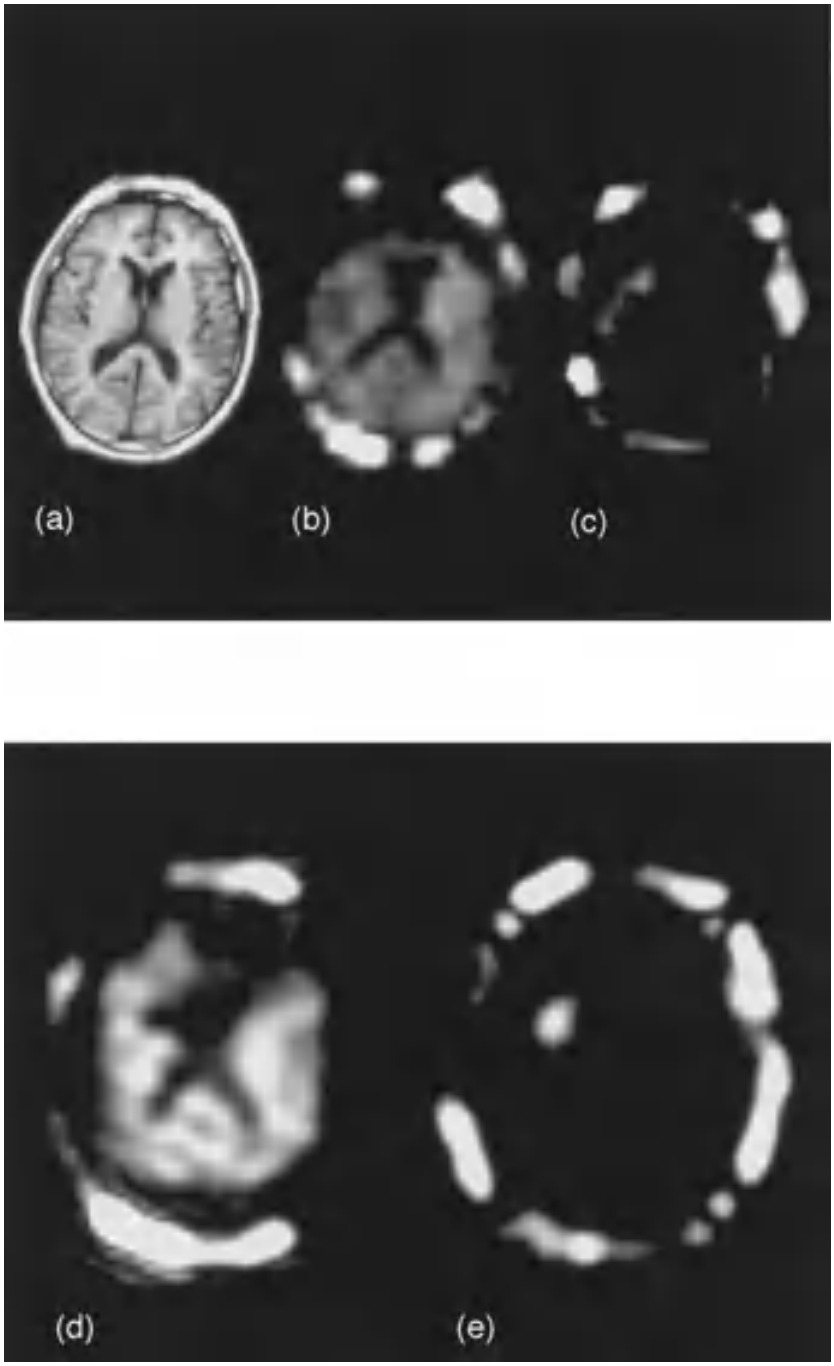

Figure 11 MRI examination 24 hours after a patient presented with acute stroke symptoms. (a) T_1-Weighted and T_2-weighted images were unremarkable. (b), Spectroscopic imaging of *N*-acetyl aspartate (NAA) did not demonstrate abnormality (area with decreased NAA). (c) Spectroscopy imaging of lactate showed an area of increased lactate in the right basal ganglia. (d) Follow-up spectroscopic imaging of NAA at 8 days demonstrated a focal area with decreased NAA at the right basal ganglia that was much smaller than the initial abnormalities demonstrated on the spectroscopy imaging of lactate (c) and was consistent with a focal infarction demonstrated on the T_2-weighted imaging obtained at the same day (not shown). (e) Spectroscopy imaging of lactate at the same time again showed persistent elevations of lactate in the infarcted tissue. (Courtesy of Dr Nick Bryan, Diagnostic Radiology Department, NIH)

used in clinical proton MRS include depth-resolved surface coil spectroscopy (DRESS), point-resolved surface coil spectroscopy (SPARS), and the stimulated-echo method (STEAM).[40–42] For practical purposes, STEAM allows for shorter echo times, thereby improving resolution of metabolites (e.g. myoinositol, glutamate, glutamine, and glycine).

Magnet designs have until recently favored the use of long *TE* sequences that are insensitive to eddy currents and can be easily implemented on the commercial scanner. Using long *TE*, the signal from most metabolites in the brain is lost except for that from four: choline, creatine, *N*-acetyl aspartate (NAA), and lactate. However, improvements in MRS techniques have

allowed short *TE* sequences taking 10–15 minutes; consequently these may realistically be incorporated into a routine imaging study without a significant time penalty.

The characteristic findings of a NAA and lactate peak can reflect the underlying pathophysiology of acute ischemia through a biochemical parameter. The NAA peak is attributable to its *N*-acetylmethyl group, which resonates at 2.0 ppm (Figure 10(c,d)). This peak also contains contributions from less-important *N*-acetyl groups. NAA is considered as a neuronal marker and is not present in tumors outside the central nervous system. Its concentration decreases with many diseases of the brain.[43] Similar to NAA, glutamate and *N*-acetylaspartyl glutamate are also localized in neurons. Glutamate is an excitatory neurotransmitter that plays a role in mitochondrial metabolism.[44] Glutamine plays a role in detoxification and regulation of neurotransmitter activities. These two metabolites resonate closely together and they are commonly represented by their sum as peaks located between 2.1 and 2.5 ppm. Breakdown of *N*-acetylaspartyl glutamate releases both NAA and glutamate, and subsequent breakdown of NAA leads to aspartate. The compounds are excitatory amino acids that increase with ischemia and cause 'toxic' effects, resulting in expanded tissue damage. Therefore, the concentrations of *N*-acetylaspartyl glutamate and glutamate may serve to monitor treatments designed to protect brain tissues by blocking excitatory amino acids.

The lactate peak has a special configuration and occurs at 1.32 ppm. It consists of two distinct, resonant peaks called a 'doublet' and is caused by the magnetic field interactions between adjacent protons (J coupling). Lactate levels of the normal brain parenchyma are low. The presence of lactate generally indicates that the normal cellular oxidative respiration mechanism is no longer in effect, and that carbohydrate catabolism is taking place.[45] Confirmation that a peak at 1.32 ppm corresponds to lactate may be obtained by altering the *TE*. At a *TE* of 272 ms, lactate projects above the baseline, whereas at a *TE* of 136 ms the lactate doublet is inverted below the baseline.

In humans, proton MRS performed within the first 24 hours after a stroke shows elevation of lactate, suggesting that anaerobic glycolysis is occurring as a result of ischemia (Figures 2 and 3).[46] Decreased NAA can be seen as early as 4 days after acute ischemia, suggesting neuronal loss (infarction) (Figures 10 and 11).[47] In chronic infarctions, there is a decrease in NAA, creatine, and choline, but no evidence of lactate.[48] Experimentally, an increase in lactate may be detected after only 2 to 3 minutes of cerebral ischemia.[49] In these animals, the lactate returned to normal when the underlying ischemia was reversed. In the evaluation of human hyperacute cerebral infarction, shortening of examination time as well as the better tolerance of the motion artifact will be needed in order to make spectroscopy a realistic tool in the management of the stroke patient.

The age-related white matter changes contain normal levels of NAA and creatine[50] but do not contain lactate. The increased choline levels are suggestive of an alteration of the white matter phospholipids.

7 CONCLUSIONS

An understanding of the spectrum of MRI findings in acute ischemia may facilitate a correct diagnosis of stroke, particularly in the hyperacute stage, and allow differentiation from other etiologies. Recent advances in diffusion and perfusion MRI indicate a potential for providing important information concerning factors that determine tissue viability and/or reversibility; this will assist clinical decisions in selecting the appropriate patients for thrombolytic therapy.

8 RELATED ARTICLES

Anisotropically Restricted Diffusion in MRI; Brain MRS of Human Subjects; Brain MRS of Infants and Children; Diffusion: Clinical Utility of MRI Studies; Hemorrhage in the Brain and Neck Observed by MRI; ; Magnetic Resonance Imaging of White Matter Disease.

9 REFERENCES

1. Stroke update, US Department of Public Health, HHS, National Institutes of Health, 1989, p. 3.
2. S. Imakita, T. Nishimura, H. Naito, N. Yamada, K. Yamamoto, M. Takamiya, Y. Yamada, Y. Sakashita, J. Minamikama, and H. Kikuohi, *Neuroradiology*, 1987, **29**, 422.
3. C. Virapongse, A. Mancuso, and R. Quisling, *Radiology*, 1986, **161**, 785.
4. W. T. C. Yuh and M. R. Crain, *Neuroimaging Clin. North Am.*, 1992, **2**, 421.
5. W. T. C. Yuh, M. R. Crain, D. J. Loes, G. M. Greene, T. J. Ryals, and Y. Sato, *Am. J. Neuroradiol.*, 1991, **12**, 621.
6. M. R. Crain, W. T. C. Yuh, G. M. Greene, D. J. Loes, T. J. Ryals, Y. Sato, and M. N. Hart, *Am. J. Neuroradiol.*, 1991, **12**, 631.
7. J. Biller, W. T. C. Yuh, G. W. Mitchell, A. Bruno, and H. P. Adams Jr., *Stroke*, 1988, **19**, 297.
8. A. Uchino, T. Mori, and M. Ohno, *Clin. Imaging*, 1991, **15**, 176.
9. J. I. Lane, A. E. Flanders, H. T. Doan, and R. D. Bell, *Am. J. Neuroradiol.*, 1991, **12**, 819.
10. A. D. Elster and D. M. Moody, *Radiology*, 1990, **177**, 627.
11. S. Imakita, T. Nishimura, N. Yamada, H. Naito, M. Takamiya, Y. Yamada, J. Minamikama, H. Kikuchi, M. Nakamura, and T. Swada, *Neuroradiology*, 1988, **30**, 372.
12. D. P. Mueller, W. T. C. Yuh, D. J. Fisher, K. B. Chandran, M. R. Crain, and Y.-H. Kim, *Am. J. Neuroradiol.*, 1993, **14**, 661.
13. M. Brant-Zawadzki, B. Pereira, P. Weinstein, S. Moore, W. Kucharczyk, T. Berry, M. McNamara, and N. Derugin, *Am. J. Neuroradiol.*, 1986, **7**, 7.
14. K. A. Hossmann and F. J. Schuier, *Stroke*, 1980, **11**, 583.
15. F. J. Schuier and K. A. Hossmann, *Stroke*, 1980, **11**, 593.
16. B. A. Bell, L. Symon, and N. M. Branston, *J. Neurosurg.*, 1985, **62**, 31.
17. O. Gotoh, T. Asano, T. Koide, and K. Takakura, *Stroke*, 1985, **16**, 101.
18. M. Brant-Zawadzki, P. Weinstein, H. Bartkowski, and M. Moseley, *Am. J. Neuroradiol.*, 1987, **8**, 39.
19. R. N. Bryan, *Radiology*, 1990, **177**, 615.
20. T. M. Simonson, T. J. Ryals, W. T. C. Yuh, G. P. Farrar, K. Rezai, and H. T. Hoffman, *Am. J. Roentgenol.*, 1992, **159**, 1063.
21. T. J. Masaryk, *Curr. Opin. Radiol.*, 1992, **4**, 79.
22. M. E. Moseley, Y. Cohen, J. Mintorovitch, L. Chileuitt, H. Shimizu, J. Kucharczyk, M. F. Wendland, and P. R. Weinstein, *Magn. Reson. Med.*, 1990, **14**, 330.
23. M. P. Marks, A. de Crespigny, D. Lentz, D. R. Enzmann, G. W. Albers, and M. E. Moseley, *Radiology*, 1996, **199**, 403.
24. R. A. Knight, M. O. Dereski, J. A. Helpern, R. J. Ordidge, and M. Chopp, *Stroke*, 1994, **25**, 1252.
25. I. Loubinoux, A. Volk, and J. Borredon, *Stroke*, 1997, **28**, 419.

26. K. Kohno, M. Hoehn-Berlage, G. Mies, T. Back, and K. A. Hossmann, *Magn. Reson. Imag.*, 1995, **13**, 73.
27. K. O. Lövblad, H. J. Laubach, A. E. Baird, F. Curtin, G. Schlaug, R. R. Edelman, and S. Warach, *Am. J. Neuroradiol.*, 1998, **19**, 1061.
28. G. Schlaug, B. Siewert, A. Benfield, R. R. Edelman, and S. Warach, *Neurology*, 1997, **49**, 113.
29. D. Davis, J. Ulatowski, S. Eleff, M. Izuta, S. Mori, D. Shungu, and P. C. M. van Zijl, *Magn. Reson. Med.*, 1994, **31**, 454.
30. M. Miyabe, S. Mori, P. C. M. van Zijl, J. R. Kirsch, S. M. Eleff, R. C. Koehler, and R. J. Traystman, *J. Cereb. Blood Flow Metab.*, 1996, **16**, 881.
31. T. Ueda, W. T. C. Yuh, J. E. Maley, J. P. Quets, P. Y. Hahn, and V. A. Magnotta, *Am. J. Neuroradiol.*, 1999, **20**, 983.
32. D. A. Finelli, A. L. Hopkins, W. R. Selman, R. C. Crumrine, S. U. Bhatti, and W. D. Lust, *Magn. Reson. Med.*, 1992, **27**, 189.
33. M. Maeda, W. T. C. Yuh, T. Ueda, J. E. Maley, D. L. Crosby, M. W. Zhu, and V. A. Magnotta, *Am. J. Neuroradiol.*, 1999, **20**, 43.
34. D. C. Tong, N. A. Yenari, G. W. Albers, M. O'Brien, M. P. Marks, and M. E. Moseley, *Neurology*, 1998, **50**, 864.
35. A. G. Sorensen, F. S. Buonanno, R. G. Gonzalez, L. H. Schwamm, M. H. Lev, F. E. Huang-Hellinger, T. G. Reese, R. M. Weisskoff, T. L. Davis, N. Suwanwela, U. Can, J. A. Moreira, W. A. Copen, R. B. Look, S. P. Finklestein, B. R. Rosen, and W. J. Koroshetz, *Radiology*, 1996, **199**, 391.
36. G. Rordorf, W. J. Koroshetz, W. A. Copen, S. C. Cramer, P. W. Schaefer, R. F. Budzik, L. H. Schwamm, F. Buonanno, A. G. Sorenson, and G. Gonzalez, *Stroke*, 1998, **29**, 939.
37. J. Röther, F. Gückel, W. Neff, A. Schwartz, and M. Hennerici, *Stroke*, 1996, **27**, 1088.
38. B. Ross and T. Michaelis, *Magn. Reson. Q.*, 1994, **10**, 191.
39. M. Castillo, L. Kwock, S. K. Mukherji, *Am. J. Neuroradiol.*, 1996, **17**, 1.
40. P. A. Bottomley, T. B. Foster, and R. B. Darrow, *J. Magn. Reson.*, 1984, **59**, 338.
41. P. R. Luyten, A. J. H. Marien, B. Systma, et al., *J. Magn. Reson.*, 1989, **9**, 126.
42. J. Frahm, H. Bruhn, M. L. Gyngell, K. D. Merboldt, W. Hanicke, and R. Sauter, *Magn. Reson. Med.*, 1989, **9**, 79.
43. B. L. Miller, *NMR Biomed.*, 1991, **4**, 46.
44. M. S. van der Knapp, B. Ross, and J. Valk, in 'Magnetic Resonance Neuroimaging', ed. J. Kucherarczyk, M. Mosely, A. J. Barkovich, CRC Press, Boca Raton, FL, 1994, pp. 245–318.
45. J. A. Sanders, in 'Functional Brain Imaging', ed. W. W. Orrison, J. D. Lewine, J. A. Sanders, M. F. Harthshorne, Mosby, St Louis, MO, 1995, pp. 419–467.
46. P. B. Barker, J. H. Gillard, P. C. M. van Zijl, B. J. Seher, D. F. Hanley, A. M. Agildere, S. M. Oppenheimer, and R. N. Bryan, *Radiology*, 1994, **192**, 723.
47. H. Bruhn, J. Frahm, M. L. Gyngell, K. D. Merboldt, W. Hanick, and R. Sauter, *Magn. Reson. Med.*, 1989, **9**, 126.
48. J. H. Duijn, G. B. Matson, A. A. Maudsley, J. W. Hugg, M. W. Weiner, *Radiology*, 1992, **183**, 711.
49. K. L. Behar, J. A. den Hollander, M. E. Stromski, T. Ogino, R. G. Shulman, O. A. Petroff and J. W. Prichard, *Proc. Natl. Acad. Sci. USA*, 1983, **80**, 4945.
50. Sappey-Marinier, G. Calabrese, H. P. Hetherington, S. N. Fisher, R. Deicken, C. Van Dyke, G. Fein, and M. W. Weiner, *Magn. Reson. Med.*, 1992, **26**, 313.

Biographical Sketches

William T. C. Yuh. *b* 1947. B.S., 1971, Chiao-tung University, Taiwan. M.S.E.E., 1974, Auburn University. M.D., 1980, University of Alabama-Birmingham, USA. Internship, Lloyd Noland Hospital. Radiology residency, UCLA Medical Center. Nuclear medicine fellowship, V. A. Wadsworth-UCLA. Magnetic resonance fellowship, UCLA Medical Center. Instructor and assistant professor, neuroradiology fellowship, associate professor, professor, Department of Radiology, The University of Iowa, 1994–present. Approx. 150 publications. Research specialties: magnetic resonance contrast agents, central nervous system ischemia.

Toshihiro Ueda. *b* 1960. M.D., 1987, Ehime University School of Medicine, Japan, Neurosurgery residency and fellowship at Ehime University School of Medicine, Ph.D., 1995, Postgraduate School of Ehime University School of Medicine. Associate (Staff Physician), Department of Neurosurgery, Ehime University School of Medicine, 1995–96. Research fellow, Department of Radiology, the University of Iowa, 1996–98. Visiting Assistant Professor, Department of Radiology, the University of Iowa, 1998–present. Approx. 40 publications. Research interests: cerebral ischemia, neurointervention, diffusion perfusion MRI, thrombolytic therapy.

J. Randy Jinkins. *b* 1949. B.A., 1971, Biology, University of Texas, Austin, USA. M.D., 1975, University of Texas, Galveston, USA. Radiology Residency, Emory University, Atlanta, USA. Neuroradiology Fellowship, Massachusetts General Hospital, Harvard Medical School, Boston, MA, USA. Currently Associate Professor of Radiology, University of Texas, San Antonio, USA. Approx. 125 publications. Current research specialty: pathophysiologic aspects of disease as they pertain to medical neuroradiologic imaging.

Ronald A. Rauch. *b* 1953. B.A. (Biochemistry), 1975, University of Kansas M.D., 1979, Baylor College of Medicine. Neurology Resident, Stanford, 1981–84. Radiology Resident, University of California, Irvine, 1985–88. Neuroradiology fellow, Long Beach Memorial, 1988–89, and UCLA, 1989–90. Currently assistant professor of radiology, University of Texas Health Science Center at San Antonio. Approx 20 publications. Current research interests: use of MRI to quantify corpus callosum morphology, MRI of white matter changes, especially those associated with dementia, and MRI of spondylolisthesis associated with spondylolysis.

Magnetic Resonance Imaging of White Matter Disease

Donald M. Hadley
Institute of Neurological Sciences, Glasgow, UK

1 INTRODUCTION

1.1 Characteristics

The white matter of the brain constitutes the core of the hemispheres, brainstem, and cerebellum. It is composed of axons, which transmit chemically mediated electrical signals, and glial supporting cells set in a mucopolysaccharide ground substance. The glial cells—oligodendrocytes, astrocytes, ependymal cells, and microglia—account for about half the brain's volume and 80–90% of its cells. The oligodendrocytes provide an insulating sheath of myelin by invagination, wrapping concentric layers of their cell membrane around the axons. Astrocytes are now known to influence and communicate through their long foot processes, which are in intimate contact with capillaries, neurones, synapses, and other astrocytes. The ependymal cells form the lining of the brain's internal cavities, while the microglia, normally relatively inconspicuous, are capable of enlarging and becoming active macrophages.

The white matter fibers are grouped into location-specific tracts, which can be divided into three main types:

(a) projection fibers that allow efferent and afferent communication between the cortex and target organ;
(b) long and short association fibers, which connect cortical regions in the same hemisphere; and
(c) commissural fibers, which connect similar cortical regions between hemispheres.

The formation and maturation of axons has been reviewed by Barkovich et al.[1] After development of the axons and their synapses, the final process of myelination occurs. This is crucial to the appearance on MRI.

1.2 Evolution and Imaging

The contrast obtained between gray and white matter is largely due to the myelination of the white matter tracts. Myelin is composed of a bilayer of lipids (phospholipids and glycolipids), cholesterol, and large proteins. In 1974, Parrish et al.[2] showed differences in the relaxation times of gray and white matter by spectroscopy before imaging was possible. These differences were later confirmed by MRI. In white matter, the myelin lipids themselves contain few mobile protons visible to routine MRI, but they are hydrophobic, and therefore, as myelination progresses, there is loss of brain water and a decrease in T_2 signal. Cholesterol tends to have a short T_1, and the increased protein also decreases the T_1 of water. This results in white matter having a reduced intensity on T_2-weighted images and increased intensity on T_1-weighted images compared with unmyelinated fibers or gray matter.

Myelination of the white matter is first noted in the cranial nerves during the fifth fetal month, and continues throughout life.[3] By birth, myelination is present in the medulla, dorsal midbrain, cerebellar peduncles, posterior limb of the internal capsule, and the ventrolateral thalamus. In general, myelination is completed from caudal to cephalad, from central to peripheral, and from dorsal to ventral. Key landmarks include the pre- and post-central gyri, which are myelinated at one month, with the motor tracts completed by three months. At this time, myelination is completed in the cerebellum, and progresses through the pons in the corticospinal tracts, cerebral peduncles, the posterior limb of the internal capsule, and up to the central portion of the centrum semiovale, to be completed by six months. The optic radiations and the anterior limb of the internal capsule are myelinated by three months. Myelination in the subcortical white matter is first noted in the occipital region at three months, and proceeds rostrally to the frontal lobes. This posterior-to-anterior maturation is noticeable in the corpus callosum, with the splenium first showing myelin at four months, progressing to the genu, where it is complete at six months.

This normal development is best visualized by MRI with age-related heavily T_1-weighted (e.g., inversion–recovery) sequences for the first six months, by which time the appearance is close to adult; after this, T_2-weighted sequences are most helpful, with all the major tracts assuming an adult appearance by 18 months. The cause of these differences is not fully understood, but is thought to be related to the initial hydrophilicity, with its associated increase in hydrogen bonding with water. Next, the T_2 shortening may be caused by the subsequent tightening of the myelin sheath, further redistributing the free water components. It has been shown that the very earliest changes of myelination are shown better by diffusion- or fluid-attenuated T_2-weighted sequences than by conventional T_1- or T_2-weighted sequences.[4,5] It must be noted, however, that some areas around the trigones of the lateral ventricles may not fully myelinate in normal children until they are 10 years old.

1.3 Classification of Abnormalities

There are a bewildering number of white matter diseases with multiple etiologies and pathological mechanisms. Although MRI is very sensitive to any white matter abnormality, it is rarely possible for the radiologist to make a specific diagnosis.[6] It is, however, useful to divide them into three main groups:

(a) a dysmyelinating group in which there is a biochemical defect in the production or maintenance of normal myelin; some of the individual enzyme deficiencies have been identified and will be discussed below;
(b) a demyelinating group in which myelin is formed normally but is later destroyed;
(c) a vascular group in which normally myelinated white matter is destroyed by a critical reduction in blood flow to a particular region; this may also involve the adjacent gray matter or a large segmental part of the brain, depending on

the extent and severity of the reduction in blood flow and the susceptibility of the cells involved.

In many of these conditions, the diagnosis is biochemical, but the radiologist has an important role in suggesting the diagnosis, and documenting progression, response to therapy, or complications.

2 DYSMYELINATION DISEASE

2.1 Leukodystrophies

These are diseases where dysmyelination occurs as a result of the production and maintenance of abnormal myelin. Becker[7] and Kendall[8] have produced excellent reviews of this subject.

2.1.1 Alexander's Disease (Fibrinoid Leukodystrophy)

This usually presents in the first few weeks of life with macrocephaly and failure to attain developmental milestones. There is progressive spastic quadriparesis and intellectual failure. Death ensues in infancy or early childhood, although cases have been reported in adolescents and adults. An enzyme defect has not yet been identified.

MRI shows increased T_1 and T_2 relaxation times, starting in the frontal lobes, and progressing to the parietal and capsular regions.[9,10] With the accumulation of Rosenthal fibers around blood vessels, there may be disruption of the blood–brain barrier, producing frontal periventricular enhancement. Frank cystic changes develop in the frontal lobes in the later stages, with atrophy of the corpus callosum.

2.1.2 Canavan's Disease (Spongiform Leukodystrophy)

This is a lethal autosomal recessive neurodegenerative disorder of Jewish infants caused by a deficiency of aspartoacylase. The disease progresses with marked hypotonia, macrocephaly, seizures, and failure to attain motor milestones in the first few months of life, although sometimes it starts as early as a few days, progressing to spasticity, intellectual failure, and optic atrophy. Death usually occurs in the second year of life. The radiological features may be seen before the full clinical picture has developed, but the diagnosis depends on the biochemical testing.

The demyelinated white matter shows increased T_1 and T_2 relaxation times, preferentially in the arcuate U fibers of the cerebral hemispheres. The occipital lobes are more involved than the frontal, parietal, and temporal lobes. Initially, it may spare the corpus callosum, deep white matter, and internal and external capsules, but, as it progresses, diffuse white matter involvement occurs, which leads to eventual cortical atrophy.[11]

2.1.3 Krabbe's Disease (Globoid Cell Leukodystrophy)

This is a rare, lethal, autosomal recessive leukodystrophy (locus now mapped to chromosome 14) due to a deficiency of the first of the two galactocerebroside β-galactosidases. This arrests the normal breakdown of cerebroside, disrupts the turnover of myelin, and results in the accumulation of galactosylsphingosine. This is toxic to oligodendrocytes, and causes a marked loss of myelin, although the minute amount of myelin remaining is normal. Changes become evident between one and six months old, although it is occasionally noted earlier, and leads to death within one to three years. The clinical diagnosis is based on an assay of β-galactosidase from leukocytes or skin fibroblasts.

Early in the disease process, MRI can be normal[12] and a spectrum of lesions then develops over several months. These are nonspecific symmetrical patchy changes in the periventricular white matter similar to many other demyelinating diseases such as multiple sclerosis, with increased T_1 and T_2 signals.[8,13] The thalami, central white matter, and cerebellar white matter may show decreased T_1 and normal or slightly decreased T_2 signals.[14] These changes are reflections of the increased attenuation sometimes seen on computerized tomography (CT), and are probably the result of paramagnetics such as crystalline calcification. In advanced disease, there is diffuse cerebral atrophy.[12]

2.1.4 Pelizaeus–Merzbacher Disease

This term has been used to cover the five subtypes of sudanophilic leukodystrophy,[15] but here it will be taken to mean the slowly progressive X-linked recessive leukodystrophy. The dysmyelination is now thought to be due to a point mutation in the PLP gene coding for the myelin–protein proteolipid protein. It presents in infancy, and runs a very chronic course leading to death in adolescence or early adulthood.

On MRI, there is a general lack of myelination without white matter destruction. The brain has the appearance of the newborn, with high signal intensity only appearing in the internal capsule, optic radiations, and proximal corona radiata on T_1-weighted images, and practically no low signal in the supratentorial region on T_2-weighted sequences.[16] A 'tigroid' pattern consisting of normal myelinated white matter within diffuse dysmyelination can be seen later on T_2-weighted sequences. When severe, there may be a complete absence of myelin. Cortical sulcal enlargement may be seen.

2.1.5 Metachromatic Leukodystrophy

The commonest of the sphingolipidoses is due to a deficiency in the activity of arylsulfatase A. This enzyme is responsible for normal metabolism of sulfatides, which are important constituents of the myelin sheath. The disease is subdivided into:

(a) neonatal, with a rapid downhill course leading to early death;
(b) infantile, presenting between one and four years with polyneuropathy, ataxia, progressive retardation, and spastic tetraparesis;
(c) juvenile, with dementia[17] and behavioral disorders progressing to spastic tetraparesis;
(d) the rare adult type, presenting at any age with dementia and spastic paraparesis.

The imaging findings are nonspecific, with symmetrical areas of increased T_1 and T_2 relaxation times in the centrum semiovale, representing progressive dysmyelination and gliosis within areas of normal myelination. The peripheral white matter, including the arcuate U fibers, is spared until late in the disease. As there is no inflammation, enhancement is not a feature. These appearances allow differentiation from the gross lack of myelination seen in Pelizaeus–Merzbacher disease. As

the disease progresses, brain atrophy becomes more prominent than the white matter signal changes. Proton MRS may have a clinical role in the diagnosis.[18]

2.1.6 *Adrenoleukodystrophy (Childhood Type: X-Linked)*

This is seen exclusively in males, and was thought to be due to a deficiency of acyl-CoA synthetase. Long-chain fatty acids are incorporated in cholesterol esters, replacing the normal nonesterified cholesterol. It usually presents between the ages of five and ten years, with a disturbance of gait and intellectual impairment, with fairly rapid progression and the development of hypotonia, seizures, visual impairment, and bulbar symptoms. Neurological complaints are classically preceded by adrenal insufficiency and skin pigmentation, which may be precipitated by an intercurrent infection; however, they sometimes may never appear.

Symmetrical long T_1 and T_2 signals are usually first seen in the peritrigonal regions extending into the splenium of the corpus callosum. Although typical, these may rarely be seen in other white matter diseases such as Krabbe's. These signal changes gradually extend to involve the occipital lobes and more anterior regions such as the medial and lateral geniculate bodies, thalami, and the inferior brachia. The pyramidal tracts and the occipito-temporo-parieto-pontine fibers show progressive alteration, with sparing of the fronto-pontine fibers in the medial part of the crus cerebri. The lateral lemnisci and the cerebellar white matter may also become involved. Although this is the usual pattern, atypical symmetrical or asymmetrical involvement of other lobes sometimes occurs[19] (Figure 1).

Three zones of abnormal long T_1 and T_2 signals can be recognized:

(a) a central region of gliosis with necrosis and cavitation, next to
(b) an intermediate region of active inflammatory demyelination that shows enhancement due to blood–brain barrier breakdown, surrounded by
(c) a peripheral less marked zone of demyelination without inflammatory reaction.

As the disease progresses, atrophy becomes the more dominant feature on MRI.[8]

2.1.7 *Adrenoleukodystrophy (Adrenomyeloneuropathy—Adult Type)*

This often presents in the same family as the childhood type, but occurs in adult life. It is caused by a similar enzyme defect. The abnormal myelination is most marked in the corticospinal and spinocerebellar tracts, but can extend into the brainstem, involving the pyramidal tracts running into the posterior limb of the internal capsules, and the frontopontine and occipito-temporo-parieto-pontine fibers. The cerebellar white matter is usually affected, with sparing of the cerebral white matter. MR changes usually appear late in the course of the disease.

2.1.8 *Adrenoleukodystrophy (Neonatal)*

Several disorders have been grouped under this heading, but with active research at present underway, the classification of the enzyme defects may change. Severe progressive neurological impairment occurs, with psychomotor retardation, dysmorphic facial features, hypotonia, seizures, and defective liver function. In contradistinction to the childhood type, these abnormalities are present from birth. The enzyme defect may be confined to fatty acyl-CoA oxidase resulting in defective very long chain fatty acid oxidation.

There is diffuse degeneration of cerebral white matter, causing atrophy at a very early age. Progressive MRI changes have

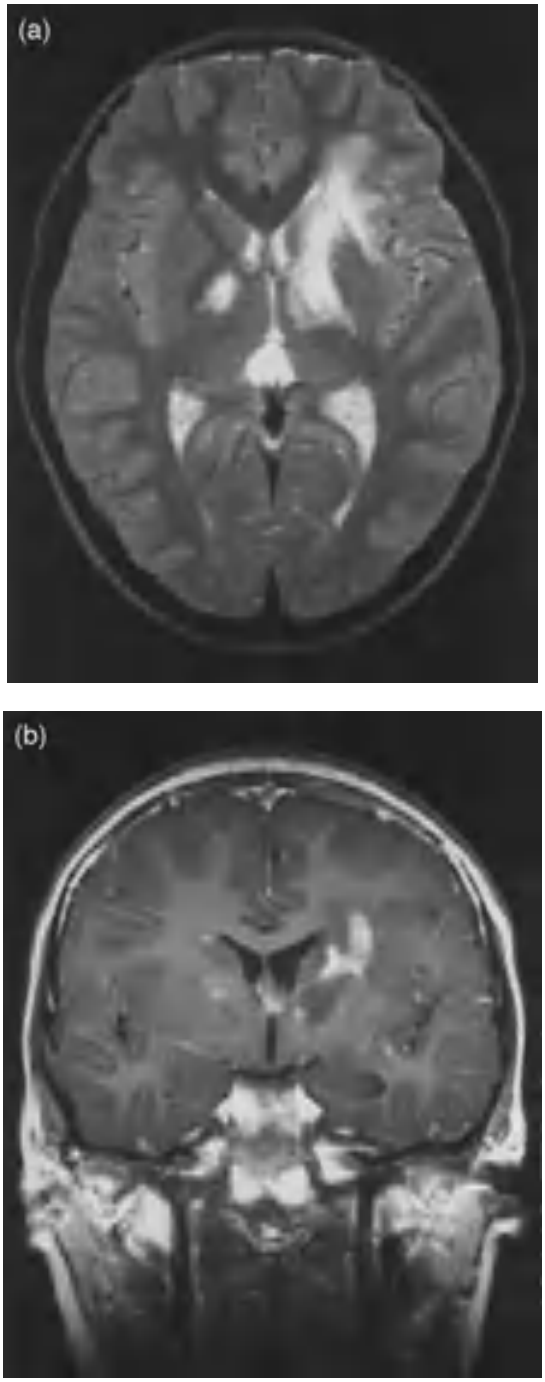

Figure 1 Adrenoleukodystrophy: (a) T_2-weighted and (*b*) gadolinium-enhanced T_1-weighted sections of a five-year-old boy showing bilateral focal areas of white matter abnormality with marginal enhancement (biopsy-proven)

been described[20] in a single case followed for three years, with delayed myelination followed by symmetrical demyelination of the corona radiata, optic radiations, and pyramidal tracts.

2.1.9 Phenylketonuria

This is an autosomal recessive metabolic encephalopathy due to a defect in phenylalanine hydroxylase conversion of phenylalanine to tyrosine, resulting in hyperphenylalaninemia. Strict dietary restrictions must be maintained from early infancy to prevent profound mental retardation. Other cofactor defect variants may result in lesser or greater degrees of encephalopathy.[21] When there is a defect of dihydropteridine reductase, there are severe neurological and cognitive abnormalities in spite of adequate dietary restrictions. Severe white matter changes have been noted,[22] with cystic degeneration and loss of parenchyma.

Subtle abnormalities of white matter have been shown by MRI in older children and adults who have classical phenylketonuria despite having maintained a degree of dietary restriction.[23,24] This possibly provides some evidence for continuing the restrictive diet and phenylalanine-free protein supplements and into adulthood.[25]

Varying degrees of periventricular white matter abnormality have been shown, with focal and diffuse lengthening of T_1 and T_2 relaxation times most easily seen on the T_2-weighted images (Figure 2). In some studies, these changes were found to correlate loosely with the adequacy of the reduction and maintenance of serum phenylalanine levels,[25,26] while other workers showed no clear relationship.[24]

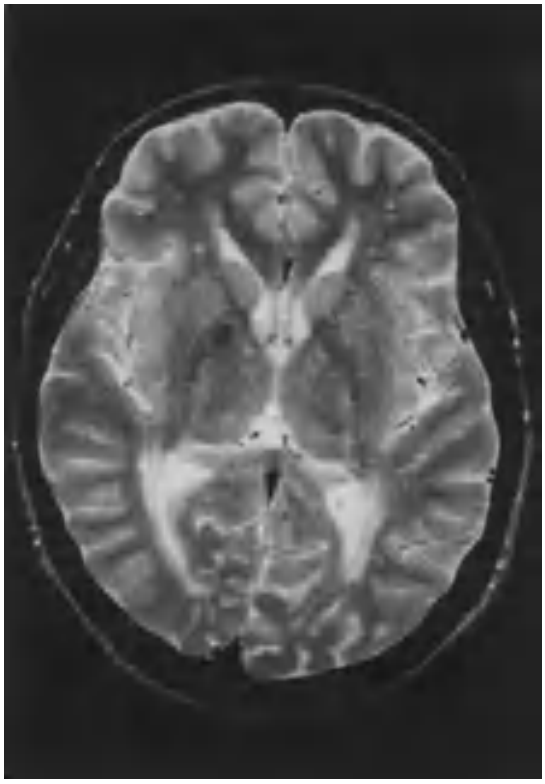

Figure 2 Phenylketonuria: T_2-weighted section showing subtle white matter hyperintensities in the optic radiations in spite of apparently adequate dietary control in a 13-year-old

2.2 Miscellaneous

Over 600 individual dysmyelination disorders that may affect MRI appearances have been identified in childhood alone. Continuing research is progressively isolating the individual enzyme or gene defects, which will in time allow more specific classification. Meanwhile, the following less well defined groups of disorders will be considered.

2.2.1 Neurodegenerative Disorders

These occur in a number of devastating developmental disorders of childhood, which are either congenital or acquired. Clinical findings are usually nonspecific, and laboratory tests have to be selected carefully. Imaging demonstrates the results of abnormal cellular function on parenchymal morphology. MRI is sensitive, but specificity is limited, and it must be integrated with the other clinical findings. Proton MRS may be able to detect abnormal metabolite levels and allow an earlier and more specific determination of neurodegeneration.[27]

2.2.2 Lysosomal Disorders

Several of these have been mentioned under specific enzyme defects above, such as metachromatic leukodystrophy and Krabbe's disease. All lack activity of a specific lysosome enzyme, which is inherited in an autosomal recessive manner except Hunter II, which is X-linked. Abnormal materials build up in the lysosomes. The CNS is affected directly or secondary to the metabolic abnormality in adjacent structures.

Dysmyelination is shown as an increase in T_1 and T_2 relaxation times in the white matter, with a variable degree of involvement of the arcuate U fibers. In Fabry's disease, involvement of the small arteries may cause multifocal small infarcts visible on MRI. The gangliosidosis in addition may show focal decreases of T_2 relaxation time in the thalami, possibly reflecting the calcification seen on CT.[7,8]

2.2.3 Peroxisomal Disorders

These relate to deficiencies in the activity of respiratory enzymes and organelles of most cells. In most of these diseases, the CNS is involved. Adrenoleukodystrophy has already been discussed above, but there are multiple other rarer diseases that belong to this classification. In general, they produce dysmyelination. Several also show disturbances of neuronal migration. In some, there is an additional inflammatory response.

2.2.4 Mitochondrial Encephalopathies

These group of disorders are characterized by functionally or structurally abnormal mitochondria in the CNS or muscle. They are transmitted by non-Mendelian maternal inheritance, resulting in slowly progressive multisystem diseases with a wide range of clinical presentations, usually appearing in childhood but showing considerable variability depending on their severity.

Imaging is nonspecific.[28] There is diffuse but variable white matter atrophy and lengthened T_1 and T_2 signals in the basal ganglia. Focal infarcts may also be seen (Figure 3). Abnormal metabolites, including lactate, have been shown by MRS in the brain lesions. This is thought to be due to impaired aerobic metabolism of pyruvate.[29,30]

In Leigh's disease, there may be spongy degeneration with astroglial and microglial reaction, with vascular proliferation

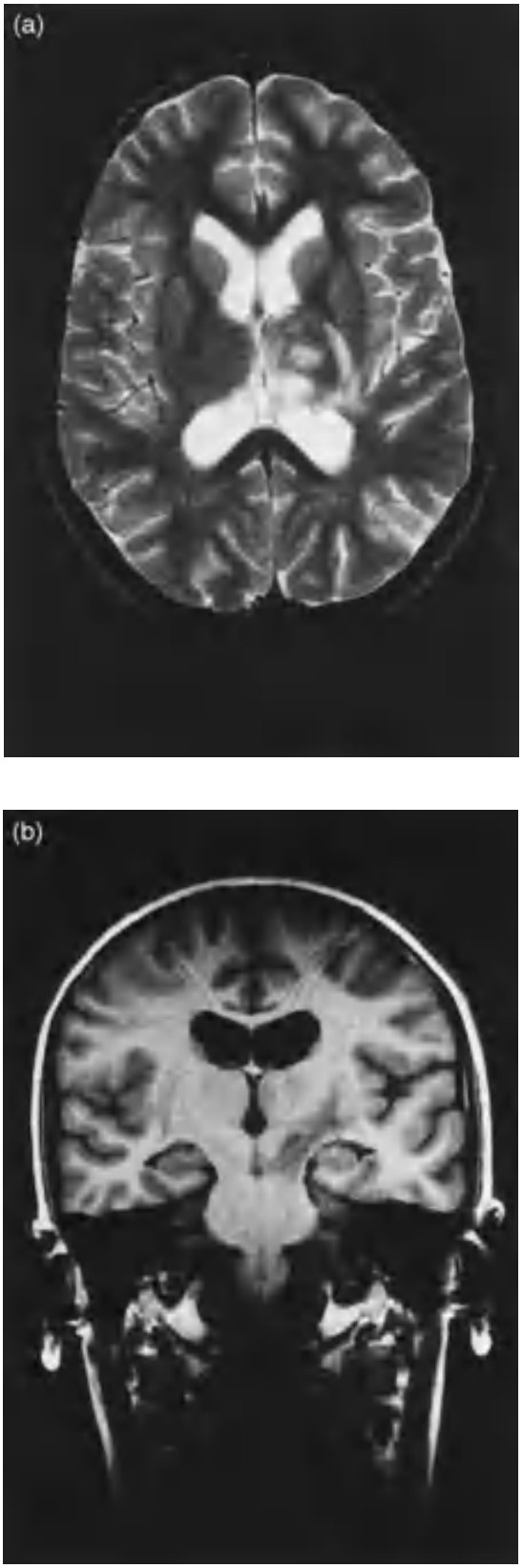

Figure 3 Mitochondrial encephalopathy: (a) T_2-weighted and (b) T_1-weighted sections in a nine-year-old boy showing increased T_1 and T_2 relaxation times representing focal infarction in the posterior limb of the left internal capsule and thalamus

affecting the basal ganglia, brainstem, and spinal cord. Cerebellar and cerebral white matter undergoes demyelination, with preservation of the nerve cells and axons resulting in hyperintensity and hypointensity on T_2- and T_1-weighted images, respectively.

3 DEMYELINATION DISEASE

3.1 Idiopathic

3.1.1 Multiple Sclerosis

Multiple sclerosis (MS) is an idiopathic inflammatory and demyelinating disorder of the central nervous system (CNS). The definitive clinical and pathological features of the disease were established by Charcot[31] as long ago as 1868. Since then, the disorder's characteristics have been refined, with improvements in imaging giving the most recent insights into its pathophysiology. It is now one of the commonest reasons given for requesting MRI in the northern latitudes of the Western world, and this diagnosis has huge social and economic consequences. It is therefore considered in some depth in the following paragraphs.

Clinically, MS usually follows a fluctuating course, with symptoms varying from paroxysmal and brief to slowly progressive and chronic. The lesions affect single or multiple sites simultaneously, usually involving long white matter tracts, but clinical–pathological correlation is often poor. The disorder leads to visual loss, numbness, tingling in the limbs, spastic weakness, and ataxia.[32] Diagnosis is allowed when a combination of signs and symptoms localize lesions in separate and distinct areas of the CNS disseminated in time and space.[33] Supportive laboratory and imaging data can now be defined for research studies, dividing the disease into clinically definite and probable MS, with or without laboratory support.[34,35]

Although some CT studies using high-dose iodine-enhanced delayed imaging have reported sensitivities as high as 72% when patients are in an acute relapse,[36] generally MRI has proved to have considerably greater sensitivity, and, by using intravenous gadolinium-based contrast agents, can separate acute from subacute and chronic lesions.[37]

Initially, MS lesions were shown at low field on T_1-weighted (inversion–recovery) sequences,[38] but within four years several rigorously controlled studies demonstrated the effectiveness of spin echo sequences where the T_2-dependent contrast can be organized to maximize the sensitivity between normal and abnormal tissue while minimizing partial volume effects between cerebrospinal fluid (CSF) and adjacent lesions.[39,40] Although no single sequence will detect all lesions, multifocal supratentorial white matter abnormalities have been shown on moderately T_2-weighted images in 96.5% of a group of 200 consecutive patients with clinically definite MS.[41] One or more periventricular lesions were seen in 98%, and lesions discrete from the ventricle in 92.5%, with cerebellar lesions in just over half of the group. Normal scans were found in 1.5% of patients. The majority of these lesions were clinically silent; therefore MRI can produce the extra information that helps to fulfill the criteria of dissemination in space (Figure 4). It can also exclude other causes of the patients' signs and symptoms, such as Arnold Chiari malformations and spinocerebellar degeneration. Serial studies with careful repositioning may also

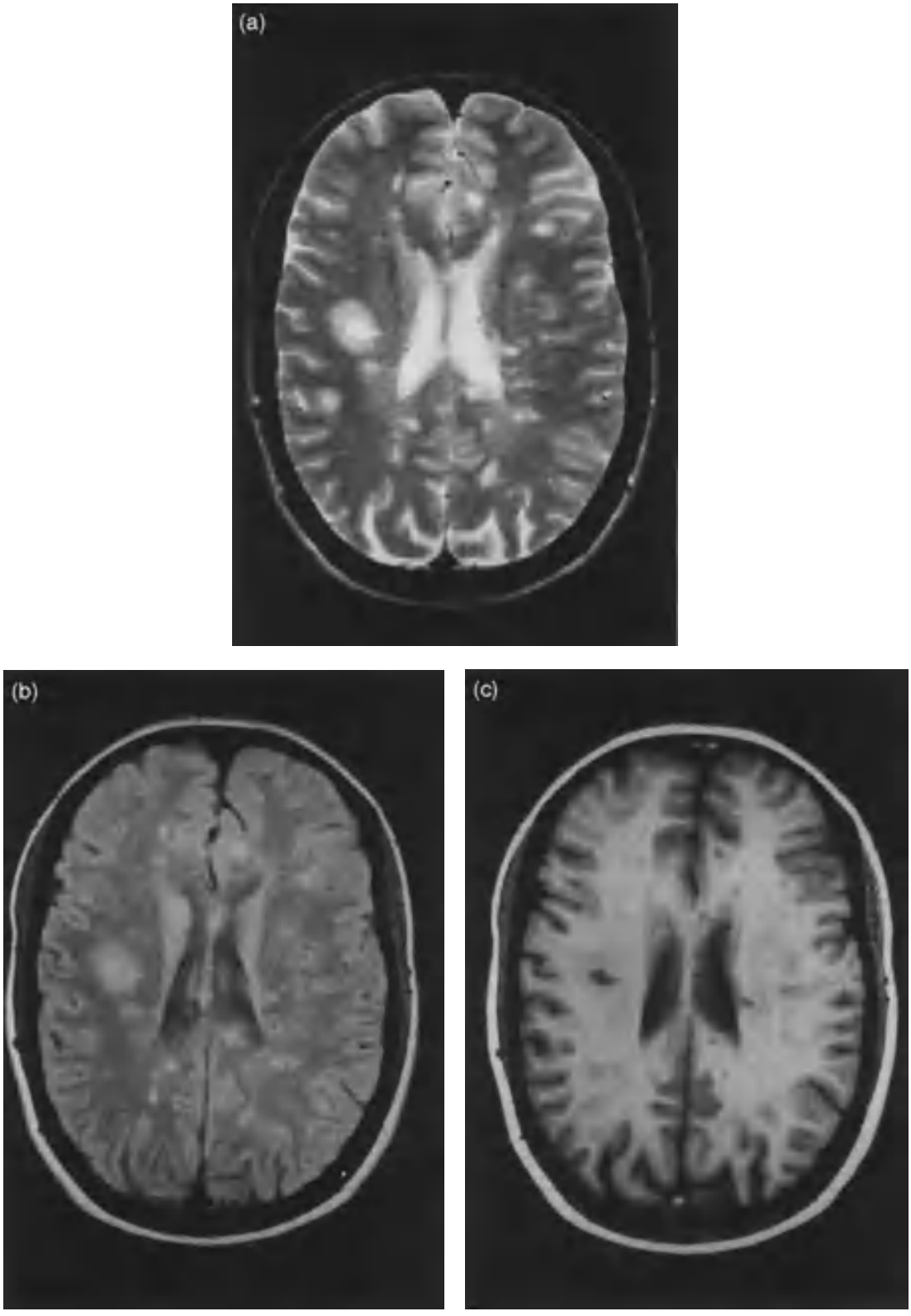

Figure 4 Multiple sclerosis: (a) T_2-weighted, (b) proton density, and (c) T_1-weighted sections showing the typical signal changes found in the multiple focal and coalescing acute and chronic plaques

fulfill the criterion of dissemination in time by showing new, often asymptomatic, lesions[42,43] This high sensitivity has now been confirmed by many workers.[36,42,44]

The T_1 of apparently normal white matter in patients with MS may be increased,[42,45] and an apparent increase in the iron content has been found in the thalamus and striatum at high

Table 1 Differential Diagnosis of Multifocal White Matter Lesions

Multiple sclerosis
Aging, small vessel vascular disease, lacunar infarcts
Infarction
Acquired immune deficiency syndrome
Encephalitis (ADEM), (SSPE)
Progressive multifocal leukoencephalopathy
Metastases
Trauma
Radiation damage
Granulomatous disease (e.g., sarcoid)
Inherited white matter disease
Normal (in healthy elderly, especially hypertensive)
Hydrocephalus with CSF interstitial edema

field.[46] Post-mortem studies have confirmed that the long T_2 lesions found correspond to MS plaques.[42] This sensitivity makes MRI the most appropriate modality for examining a patient with suspected MS.

Unfortunately, these multifocal white matter lesions may be indistinguishable from other conditions that produce demyelination, gliosis, or periventricular effusions[47] (Table 1), and between 5 and 30% of apparently normal controls older than 50 years have been shown to have white matter lesions, probably due to asymptomatic cerebrovascular disease. The patient's age and pattern of lesions can help to improve the specificity of the MRI examination.[48] Fazekas et al.[49,50] have shown that if at least three areas of increased T_2 signal intensity are present with two of the following features—abutting the body of the lateral ventricles, infratentorial location, and size greater than 5 mm—then the sensitivity is decreased to 88%, but the specificity increases to 96% in patients with clinically definite multiple sclerosis. Although the relaxation times of acute plaques have been found to be longer,[51] the range was wide, and the age of an individual lesion could not be determined by T_1 or T_2 measurement alone. It is important to be able to define new and active lesions to differentiate between multiphasic (MS) and monophasic (ADEM) disease and to determine whether there is evidence of continuing disease progression (e.g., in clinical therapeutic trials).

The areas of perivenular inflammation and edema associated with the acute MS plaque[52] cause a transient disruption of the blood–brain barrier[53,54] and allow leakage of intravascular contrast agents. This is shown as enhancement on T_1-weighted images (Figure 5), and is safer and more effective than high-dose delayed contrast-enhanced CT.[53] Correlation with the lesions seen on T_2-weighted sections is good. Only a small number of cortical or subcortical plaques were seen solely on enhanced T_1-weighted images. Enhancement is now considered a consistent feature of recognizably new lesions or new parts of existing plaques,[54] although occasionally blood–brain barrier breakdown develops in older previously nonenhancing plaques associated with no increase in their size. The inflammatory demyelination has been shown pathologically to begin in a perivenular distribution and spread centrifugally, corresponding with the ring enhancement noted in several studies[37,54] (Figure 5). Gadolinium enhancement is particularly useful in the clear delineation of lesions in the spinal cord and optic nerves, especially if T_1-weighted fat saturation chemical shift sequences are used to reduce the high signal from surrounding periorbital fat.[55,56]

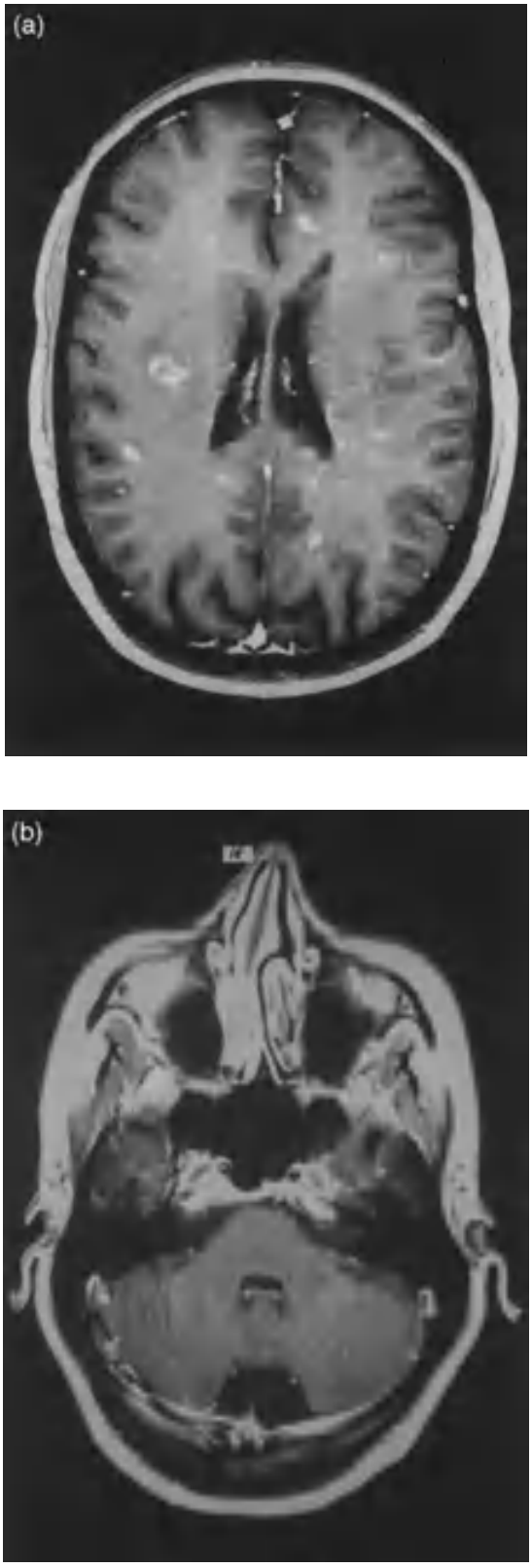

Figure 5 Multiple sclerosis: gadolinium-enhanced T_1-weighted sections showing (a) multiple enhancing acute lesions including a ring enhancing plaque and (b) a nonenhancing chronic cerebellar peduncular lesion

Differences in the enhancement pattern of primary and secondary progressive MS, the two major clinical patient groups, have been identified.[57] The secondary progressive group had more new lesions (18.2 lesions per patient per year), of which a larger proportion (87%) enhanced. In addition, there was enhancement at the edge of preexisting lesions. This compares with few new lesions (3.3 lesions per patient per year), of which only one enhanced in the primary progressive group at the time when there were no differences over six months in the rates of clinical deterioration between the two groups. This suggests a difference in the underlying dynamics of the inflammatory component of the disease. With improved imaging techniques, e.g., fast scanning methods, and particularly with real-time echo planar imaging,[58] the complex morphology of the initial phase of gadolinium enhancement after intravenous injection may be further elucidated and related to the lesions on the unenhanced scan. Correlation with lipid imaging may allow study of the relationship between demyelination and inflammation. Advances in the use of MRI and MRS have been reviewed by Paty et al.[59]

Now that new and biologically active lesions can be identified routinely in clinic patients by gadolinium-enhanced T_1-weighted scans, the association of blood–brain barrier leakage in some but not all of multiple plaques shown on T_2-weighted images indicates the presence of dissemination in time[60] and refines the diagnosis of MS. The method can be used to subdivide clinical groups, and will be useful in monitoring and possibly shortening the time required for therapeutic trials (e.g., with steroids[61] and interferon[62]) in MS.

3.1.2 Schilder's Disease (Myelinoclastic Diffuse Sclerosis)

This is a rare but distinctive acute demyelinating condition, which can be defined by biochemical, pathological, and electrophysiological criteria, yet remains faithful to Schilder's original description of 1912.[63] There is a severe selective inflammatory demyelination with sparing of the subcortical U fibers, and extensive attempts at remyelination.

MR white matter changes have been described,[64] with bilateral involvement of the anterior hemispheres, extensive fluctuating increased relaxation times, mass effect, and varying partial ring enhancement indicating changes in blood–brain barrier breakdown. Other leukodystrophies with a similar appearance such as adrenoleukodystrophy and Pelizaeus–Merzbacher disease must be excluded by biochemical testing.

3.2 Postinflammatory: Viral, Allergic, Immune-mediated Responses to Previous Infection

3.2.1 ADEM

Acute disseminated encephalomyelitis is a demyelinating disease that is thought to be an immune-mediated disorder secondary to a recent viral infection or more rarely to vaccination. It has an acute onset and a monophasic course, in contradistinction to MS. Most patients make a complete recovery, with no neurological sequelae. This makes it one of the most important differential diagnoses in the acute clinical situation.

Pathologically, there is a diffuse perivenous inflammatory process resulting in confluent areas of demyelination. These frequently occur at the corticomedullary junction, with gray matter much less often involved than white. Large areas of increased T_1 and T_2 relaxation time are found on MRI in both hemispheres, but the effects are usually asymmetrical.[65] Although in the acute stage, the demyelinating lesions may enhance, the blood–brain barrier quickly returns to normal. As with MS, MRI is much more sensitive than CT at demonstrating these lesions.

3.2.2 SSPE

Subacute sclerosing panencephalitis is a rare progressive demyelination resulting from reactivation of the measles virus due to a defect in immunity that allowed the virus to remain latent.[66] There is a variable rate of progression, with death between two months and several years after reactivation.

There is perivascular infiltration by inflammatory cells, cortical and subcortical gliosis, and white matter demyelination progressing from occipital to the frontal lobes and from the cerebellum to the brainstem and spinal cord. This is reflected in an increase in T_1 and T_2 relaxation times of the multifocal patchy white matter lesions.[67,68]

3.2.3 PML

Progressive multifocal leukoencephalopathy is a demyelinating disease probably caused by the papova viruses (e.g., JC and SV40-PML). These are universal childhood infections that are reactivated in the immunosuppressed patient. It is characterized by demyelination, with abnormalities of oligodendrocytes in the white matter. Initially, the lesions are widely disseminated, but later tend to become confluent, producing large lesions. It is now seen with increasing incidence in patients with AIDS[69] and those treated with immunosuppressive drugs. It most commonly involves the subcortical white matter of the posterior frontal and parietal lobes extending to the level of the trigones and occipital horns of the lateral ventricles (Figure 6). The lesions give an increased T_2 and slightly increased T_1 relaxation time, and because there is only occasional perivenular inflammation in the acute stage, they do not have mass effect and gadolinium enhancement is not usually a feature. These are useful differentiating features from lymphoma and toxoplasmosis.[70]

3.3 Posttherapy

3.3.1 Disseminated Necrotizing Leukoencephalopathy

When patients are treated with intrathecal antineoplastic agents such as methotrexate for disseminated lymphoma, leukemia, or carcinomatosis, a necrotizing leukoencephalopathy can occur despite the fact that the agent does not usually cross the blood–brain barrier.[71] Radiation therapy potentiates this neurotoxicity. There is endothelial injury, loss of oligodendroglial cells, coalescing foci of demyelination, and axonal swelling. The damaged endothelium responds by attempts at repair, resulting in hyalinization, fibrosis, and mineralization of the vessel walls. This causes a relative tissue ischemia, demyelination, and necrosis.

On MRI,[72] there is a diffuse increase in T_1 and T_2 relaxation times, with no mass effect and little or no gadolinium enhancement, reflecting only the edema and demyelination present.

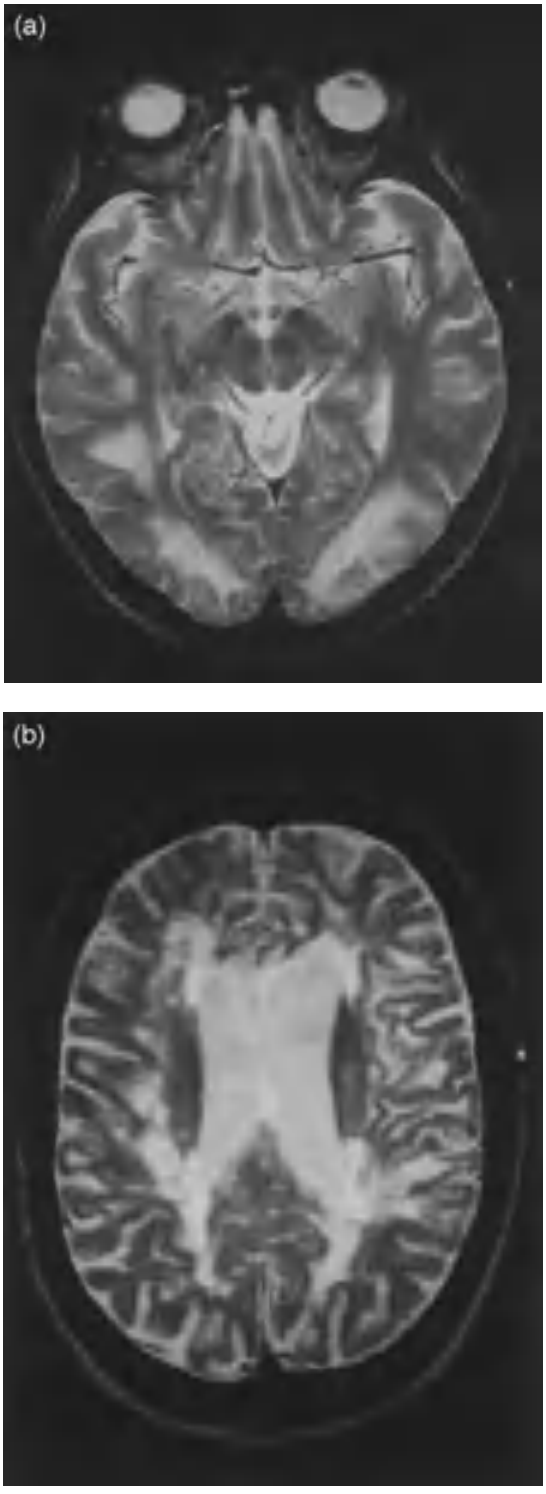

Figure 6 PML in AIDS: T_2-weighted images showing (a) extensive subcortical demyelination in the trigonal and occipital regions and, in a different patient, (b) gross loss of white matter substance with periventricular coalescing hyperintensities

The patterns of injury to the white matter from radiation therapy on its own are divided into three stages: (a) acute, (b) early, and (c) delayed. In the first days or weeks after therapy, vasogenic edema may be produced because of transient disruption of the blood–brain barrier, and some enhancement will occur. In the weeks or months following radiation, demyelination may occur. MRI may show focal or diffuse increases in T_1 and T_2 relaxation times in a patchy often periventricular distribution, which may be asymmetrical, affecting the white matter but generally sparing the corpus callosum, internal capsules, and basal ganglia.[73,74] The gray matter is only involved in severe cases. Delayed effects can occur months to years after therapeutic irradiation. These are less common, and develop later with hyperfractionated doses. There is endothelial hyperplasia, fibrinoid necrosis of perforating arterioles, and thrombosis. Cerebral necrosis supervenes, with blood–brain barrier disruption, edema, and mass effect. MRI at this stage shows mass effect, increased T_1 and T_2 relaxation times, and enhancement after intravenous gadolinium. Therefore this cannot be differentiated from recurrent tumor with MRI. There is some evidence that measures of the lesion's metabolism with ^{18}F-deoxyglucose positron emission tomography, ^{201}Tl or L-3-[^{123}I]iodo-α-methyltyrosine single photon emission computerized tomography will selectively differentiate the hypometabolic radiation necrosis from the hypermetabolic malignant tumor.[75,76]

A reversible acute cerebellar and cerebral syndrome has been reported[77] after systemic high-dose cytarabine therapy used for treatment of postremission and refractory leukemia treatment. Diffuse patchy areas of increased intensity on T_2-weighted images were shown in the deep white matter of the frontal, occipital, and parietal lobes. Punctate enhancement was observed in the occipital lobes. Over a month, the symptoms and white matter abnormalities resolved. At post-mortem later, there was no evidence of white matter disease.

3.4 Toxic and Degenerative Disease

3.4.1 Central Pontine Myelinolysis

In this condition, there is loss of myelin and oligodendroglia in the central pons, which may extend to the lateral thalamus and mesencephalon, sparing the ventrolateral longitudinal fibers.[78] It is usually associated with rapidly corrected hyponatremia, often in alcoholics.[79,80] When there is only a tiny lesion or the patient is in coma due to the underlying disease process, it may be asymptomatic, but usually there is tetraparesis with a pseudobulbar palsy or a 'locked-in' syndrome. Mild cases with full recovery have now been reported.[81]

The demyelination is depicted as T_1 and T_2 prolongation with no mass effect, and although there is a single report of ring enhancement, there is usually no blood–brain barrier breakdown.[82]

3.4.2 Marchiaflava–Bignami Disease

This is characterized by a toxic demyelination of the corpus callosum in alcoholics.[83,84] A rapidly fatal form and a more chronic form have been recognized. In the acute form, extensive lesions have been reported in the centrum semiovale and corpus callosum, while at the chronic stage only corpus callosum lesions are seen, and occasionally there is a favorable outcome.[85] MRI shows these as small areas of increased T_1 and T_2 relaxation times, with no mass effect. Enhancement has not been reported.

3.4.3 Carbon Monoxide Encephalopathy

As carbon monoxide binds to the hemoglobin molecule and displaces oxygen, it induces hypoxia and vulnerable cells are destroyed. Although the gray matter structures are damaged first, the white matter is also involved, especially when there is episodic or chronic exposure.

MRI shows areas of increased T_1 and T_2 relaxation time in the thalamus, basal ganglia, hippocampus, and centrum semiovale. These areas may show enhancement with gadolinium in the acute stage. The lesions are usually bilateral and symmetrical, but can be patchy. Laminar necrosis has been reported as high signal cortical foci on T_2-weighted images.[86]

3.4.4 Substance Abuse

Inhalation of organic solvents and black market drugs such as heroin vapors (pyrolysate) and cocaine produce a wide variety of acute and chronic neurological signs and symptoms. The effects on the white matter will depend largely on the chemical constituent involved.

Xiong et al.[87] have shown that in toluene (one of the constituents of paint sprays) abuse, there is generalized cerebral, cerebellar, and corpus callosum atrophy, with a loss of gray–white matter contrast associated with diffuse multifocal hyperintensity of the cerebral white matter on T_2-weighted sequences. Additionally, hypointensity of the thalami are also seen.

Adulterated and synthetically produced drugs can produce severe leukoencephalopathy. Tan et al.[88] reported on four patients who inhaled contaminated heroin vapor and developed extensive, symmetrical lesions of the white matter of the cerebrum, cerebellum, and midbrain. Selective involvement of the corticospinal tract and lemniscus medialis was also found.

These have to be differentiated from the effects of cocaine abuse, where there is generally neurovascular damage with vasculitis, vasospasm, and thrombosis. Eventually, cerebral atrophy can be seen.[89]

3.4.5 Hypoxic–Ischemic Encephalopathy

This generally refers to brain damage in the fetus and infant. It may be focal or diffuse. When focal, it may be the cause of territorial infarcts such as can occur in cyanotic congenital heart disease when emboli can bypass the filtering effect of the lungs. This will be discussed in Section 3.4.6. In asphyxia, there is diffuse hypoxia hypercarbia, acidosis, and loss of the brain's normal vascular autoregulation, resulting in pressure-passive flow and reduced perfusion. Capillary permeability is also altered. Sudden reperfusion of these weakened capillaries can result in rupture and intracerebral hemorrhage. The periventricular white matter is particularly susceptible, lying at the distal end of the supply zone of the long narrow centripetal arteries that run from the cerebral surface.[90]

When 100 high-risk neonates of different gestational ages were followed prospectively with MRI, CT, and ultrasound examinations,[91,92] it was found that lesions associated with hypoxic–ischemic encephalopathy such as coagulative necrosis and germinal matrix hemorrhage were best shown on MRI. In the analysis, ultrasound showed 80%, while CT only showed 40% of those lesions depicted on MRI.

This has raised interest in medico-legal circles, since the timing of the insult may be more clearly defined. The appearances of the brain damage on MRI can now give important clues as to the time and nature of the asphyxia. Barkovich and Truwit[93] found that when the asphyxia occurred before the 26th week of gestation, there was dilatation of the ventricles without any signal changes, whereas in older fetuses there was increasing periventricular gliosis. Both periventricular and more peripheral white matter gliosis with associated general atrophy were found in cases who had been partially asphyxiated, or where asphyxia had occurred near term or in postmature fetuses. Total asphyxia involves the deep gray matter nuclei and the brainstem, and presents a different pattern.

These MRI patterns may have prognostic value, with initial studies[94] reporting good correlations between imaging findings at 8 months and neurodevelopmental outcome at 18 months.

3.4.6 Trauma (Contusions–Shear Injuries)

In children, the effects of asphyxia and mechanical trauma, be they accidental or nonaccidental, may initially produce the same imaging appearance, with generalized cerebral swelling resulting in blurring of the clear distinction between the gray matter and white matter boundaries, ventricular compression, and loss of CSF from the sulci and cisterns. This is due to a combination of edema and a failure of autoregulation producing an increase in cerebral blood volume. This can result in watershed ischemia and infarction, with eventual loss of white matter producing ventricular and sulcal dilatation.

Focal cerebral contusions involve the gyral crests, and can extend into the subcortical and deeper white matter regions, depending on their severity. There is edema and petechial perivascular hemorrhage, but tissue integrity is largely preserved in small lesions. With more severe contusions, the petechial hemorrhages coalesce into focal hematomas, which have some space-occupying effect. These are well shown by MRI at all stages,[95,96] although, in practice, CT is easier to perform and gives clinically adequate information in the acute stage.

Blunt trauma resulting in sudden acceleration or deceleration of the skull, especially when this is rotational, sets up shear–strain deformation at the moment of impact in response to the inertial differences between tissues of different density and viscosity.[97] This can cause immediate and irreversible structural damage to axons, and has been termed diffuse axonal injury.[98–100]

Diffuse axonal injury is a pathological diagnosis, and imaging may only show a few apparently focal lesions in the lobar white matter. It is, however, very important to recognize these as the 'hallmark' of associated widespread microscopic axonal disruption. Although CT is the most commonly conducted examination in the acute situation, MRI is much more sensitive[95,101] and essential when the clinical state is not explained by the CT imaging appearances (Figure 7). In the acute situation, foci of edema that may or may not contain macroscopic hematomas can be seen on T_2-weighted MRI in the corpus callosum, the parasagittal frontal white matter close to the gray–white matter interface, the basal ganglial regions and the dorso-lateral quadrant of the rostral brainstem.[96] At the subacute stage, hemorrhage will be better depicted on T_1-weighted images, but both acutely and in the chronic phase T_2* gradient echo sequences are most sensitive to deoxyhemoglobin and hemosiderin respectively. MRI can rarely appear entirely normal[102] in severe diffuse axonal injury, and it is only on follow-up that the widespread white matter damage is reflected in atrophy with ventricular and cortical sulcal enlargement.[100,103,104]

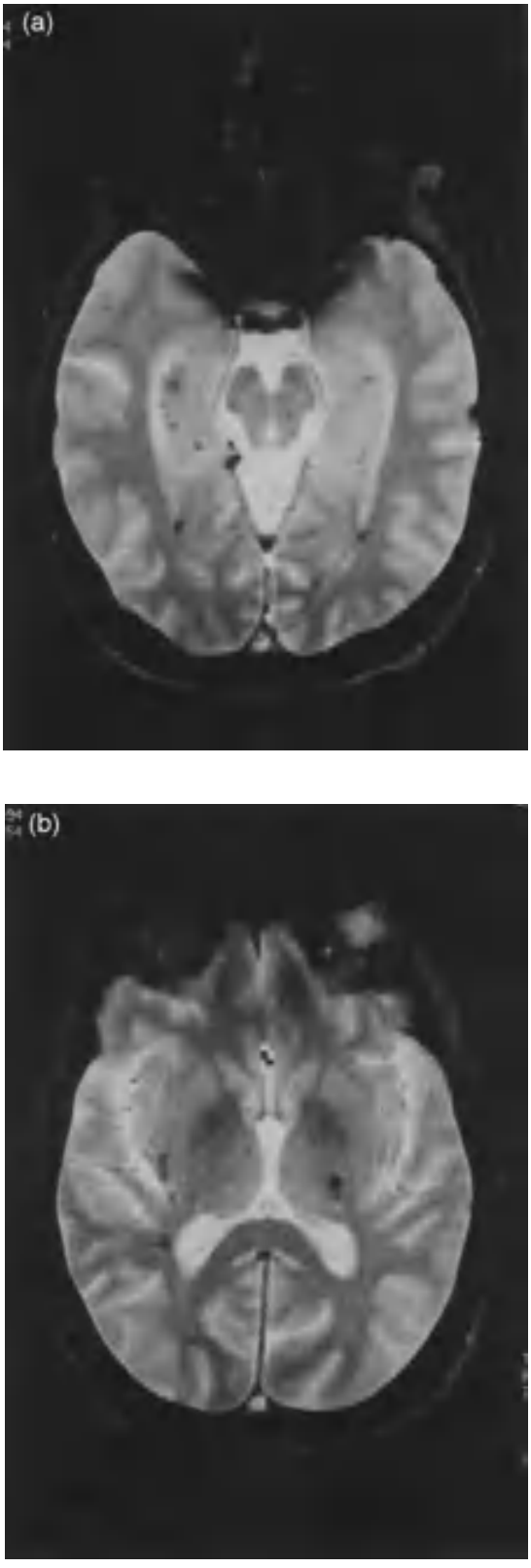

Figure 7 Head injury: T_2* gradient echo sections in an 25-year-old unconscious patient with a normal CT scan. Multiple focal hypointensities represent hemorrhage at white/gray matter interfaces—evidence of diffuse axonal injury

4 VASCULAR DISEASE

4.1 Infarction

Stroke remains one of the commonest causes of hospital admission in the developed world, has a high morbidity and mortality, and consumes more healthcare resources than any other single disease. Ninety percent of cases are due to ischemia (10% to cerebral hemorrhage) from thrombosis of a nutrient artery, with only a small number due to emboli from the heart or other vessels. Despite treatment advances, the mortality remains at around 50%. It is thought that only preventative public health measures and earlier thrombolytic therapy can improve this situation.[105] This requires the accurate early identification of patients with acute infarcts and those with transient ischemia at risk of completing their infarcts.

Routine unenhanced MRI can detect abnormalities within about 8 h of the onset of symptoms (although changes on MRI with a vessel occlusion stroke model were shown as early as 1–2 h without paramagnetic contrast),[106,107] whereas CT is normal for at least 14 h and if perfusion is not re-established remains 'bland' for several days. MRI initially shows subtle swelling and an increase in T_1 and T_2 signals due to failure of the 'sodium–potassium' pump and increasing intracellular water–cytotoxic edema. At this stage, function is lost but structure is maintained. It is only with continuing ischemia that blood–brain barrier breakdown occurs, structural integrity is lost, and vasogenic edema supervenes. Although there are anecdotal reports of MRI-defined cytotoxic edema being reversed on treatment of ischemia in humans,[108,109] and more rigorous demonstrations in cats using diffusion sequences,[107] it has not been established in routine clinical practice whether these MRI changes, unlike those on CT, are reversible.

Recent gadolinium-enhanced MRI studies[110–112] of the first 24–48 h after the ictus in the clinical population has shed light on this crucially important acute stage. Sato and colleagues[113] studied six patients within 8 h and a further two between 8 and 26 h. They showed areas of cerebral ischemia/infarction using gadolinium-enhanced T_1-weighted spin echo sequences. Abnormal curvilinear areas of enhancement thought to represent cortical arterial vessels with markedly slowed circulation were seen adjacent to affected brain. This tissue was shown to progress to frank infarction on follow-up CT and MRI. These features have been confirmed and extended by the Iowa group.[110,114] They demonstrated the vascular flow-related abnormalities with absence of normal flow voids and the presence of arterial enhancement detected within minutes of the onset of symptoms. Brain swelling on T_1-weighted images without signal changes on T_2-weighted images was detected within the first few hours. In contrast to the usual absence of parenchymal enhancement typically found in cortical infarctions in the first 24 h, a few lesions showed paradoxical early exaggerated enhancement. These were the transient or partial occlusions and isolated watershed infarcts. Longer term prospective observations through the first fortnight have defined the subacute appearances.[115] Three stages have been demonstrated:

(a) vascular enhancement—days 1–3, seen in 77% of cases;
(b) leptomeningeal enhancement—days 4–7, seen only in larger infarcts;
(c) brain parenchymal enhancement—days 7–14, seen in 100% of cases studied.

Enhancement is not noted after two to three months. These changing patterns of enhancement reflect the underlying pathophysiology, and may have prognostic significance; if this proves to be so then gadolinium enhancement will be crucial in the evaluation of early ischemia and its response to intervention.

Once the parenchymal long T_1 and T_2 signal changes are established, the differential diagnosis must be made in a similar way to conventional CT, following consideration of

(a) the site: vascular territory, watershed region, deep gray or white matter tracts;
(b) the shape: wedge, involving gray and white matter with subtle bowing of interfaces;
(c) the margins: sulcal effacement, blurring of the gray and white matter borders;
(d) the degree of edema;
(e) the sequence of resolution of mass effect over three to four weeks.[116]

Hypointensity on heavily T_2-weighted sequences and the use of gradient echoes or susceptibility mapping can often show petechial hemorrhage in the second week that is not seen on CT. While frank hemorrhage correlates with a worsening clinical state, fine interstitial bleeding mainly due to diapedesis relates neither to anticoagulation nor to a poorer clinical condition.[116]

The patency of the extracranial and major intracerebral arteries can be assessed on routine MRI sequences as a 'flow void' or with slower laminar flow even as echo rephasing. At present, projectional images produced by time-of-flight and phase contrast angiographic sequences are being evaluated, and may yet replace preoperative conventional cerebral angiography.[117,118]

Both diffusion imaging[119,120] and spectroscopy[121] are being used experimentally in clinical populations to try to gain an understanding of microscopic water shifts as the different types of edema develop and to give an insight into the progressive cycles of bioenergetic exchange as oxidative metabolism breaks down in the ischemic brain cells.

4.2 Ischemic White Matter Disease—Normal Aging

Focal and confluent white matter abnormalities seen on MRI do not necessarily represent actual necrosis and infarction, but can be due to a spectrum of chronic cerebrovascular insufficiency.[122] These merge with the changes found in as many as 30% of the normal aging population over 60 years of age who show no clinical cognitive deficit, but which are seen with increasing frequency in patients with hypertension, diabetes mellitus, and coronary artery disease (Table 1).[123]

Dilated perivascular spaces give a CSF signal, are usually smaller than lacunar infarcts, and occur in typical locations in the base, deep white matter, and cortex of the brain. Gliosis may become more confluent around these vessels as the vascular insufficiency progresses and produces an increased signal on proton density images in addition to the increased T_2 signal differentiating it from CSF. This has now been confirmed microscopically.

In a small post-mortem study,[124] histological examination showed that the larger lesions were characterized centrally by necrosis, axonal loss, and demyelination, and therefore represent true infarcts. Reactive astrocytes oriented along the degenerated axons were identified at distances of up to several centimeters from the central infarct. This isomorphic gliosis shows hyperintensity on T_2-weighted images, and increases the apparent size of the central lesion. Confirmation has been provided by Munoz et al.,[125] who investigated the pathological correlates of increased T_2 signal in the centrum ovale in an unselected series of 15 post-mortems. On the basis of size, greater than and less than 10 mm, two types of lesion were described, namely, extensive and punctate. The extensive areas of hyperintensity on T_2-weighted images were found to show myelin pallor that spared the subcortical U fibers. There was diffuse vacuolation and reduction in glial cell density. The punctate abnormalities were less well defined, and were found to be due to dilated Virchow–Robin spaces.

The white matter changes seen on MRI are therefore nonspecific, and although seen with increased frequency in ischemic brains, there is often little or no correlation with the clinical state in the elderly patient.

5 CONCLUSIONS

Over the last 15 years, MRI has become the main diagnostic tool in the investigation of white matter disease. In some conditions, its sensitivity is the key to selecting patients for further attention, while in others it identifies more specific features that in turn lead to further laboratory investigations leading to a final diagnosis. MRI can be used to select patients for treatment and to monitor the effects of this treatment. The implementation of new sequences, faster scanning techniques, and better patient–machine ergonomics will ensure the preemptive position of MRI for the investigation of white matter diseases for the foreseeable future.

6 RELATED ARTICLES

Brain MRS of Infants and Children; Brain Neoplasms Studied by MRI; Diffusion: Clinical Utility of MRI Studies; Echo-Planar Imaging; Gadolinium Chelate Contrast Agents in MRI: Clinical Applications; Hemorrhage in the Brain and Neck Observed by MRI; Intracranial Infections; Localization and Registration Issues Important for Serial MRS Studies of Focal Brain Lesions.

7 REFERENCES

1. A. J. Barkovich, G. Lyon, and P. Evrard, *Am. J.N.R.*, 1992, **13**, 447.
2. R. G. Parrish, J. R. Kurland, W. W. Janese, and L. Bakay, *Science (Washington, DC)*, 1974, **483**, 349.
3. A. J. Barkovich and T. V. Maroldo, *Top. Magn. Reson. Imaging*, 1993, **5**, 96.
4. Y. Nomura, H. Sakuma, K. Takeda, T. Tagami, Y. Okuda, and T. Nakasasa, *Am. J.N.R.*, 1994, **15**, 231.
5. A. Oatridge, J. V. Hajnal, F. M. Cowan, C. J. Baudouin, I. R. Young, and G. R. Bydder, *Clin. Radiol.*, 1993, **47**, 82.
6. B. E. Kendall, *J. Inherited Metab. Dis.*, 1993, **16**, 771.
7. L. E. Becker, *Am. J.N.R.*, 1992, **13**, 609.
8. B. E. Kendall, *Am. J.N.R.*, 1992, **13**, 621.
9. G. B. Bobele, A. Garnica, G. B. Schaefer, J. C. Leonard, D. Wilson, W. A. Marks, R. W. Leech, and R. A. Brumback, *J. Child. Neurol.*, 1990, **5**, 253.

10. T. Ichiyama, T. Hayashi, and T. Ukita, *Brain Dev.*, 1993, **15**, 153.
11. J. Brismar, G. Brismar, G. Gascon, and P. Ozand, *Am. J.N.R.*, 1990, **11**, 805.
12. D. A. Finelli, R. W. Tarr, R. N. Sawyer, and S. J. Horwitz, *Am. J.N.R.*, 1994, **15**, 167.
13. T. J. Farley, L. M. Ketonen, J. B. Bodensteiner, and D. D. Wang, *Pediatr. Neurol.*, 1992, **8**, 455.
14. S. Choi and D. R. Enzmann, *Am. J.N.R.*, 1993, **14**, 1164.
15. J. C. Koetsveld-Baart, I. E. Glaudemans-van-Gelderen, J. Valk, and P. G. Barth, *Ned. Tijdschr. Geneeskd.*, 1993, **137**, 2494.
16. M. Ishii, J. Takanashi, K. Sugita, A. Suzuki, M. Goto, Y. Tanabe, K. Tamai, and H. Niimi, *No To Hattatsu*, 1993, **25**, 9.
17. E. G. Shapiro, L. A. Lockman, D. Knopman, and W. Krivit, *Neurology*, 1994, **44**, 662.
18. B. Kruse, F. Hanefeld, H. J. Christen, H. Bruhn, T. Michaels, W. Hanicke, J. Frahm, *J. Neurol.*, 1993, **241**, 68.
19. P. J. Close, S. J. Sinnott, and K. T. Nolan, *Pediatr. Radiol.*, 1993, **23**, 400.
20. M. S. van der Knaap and J. Valk, *Neuroradiology*, 1991, **33**, 30.
21. J. Brismar, A. Aqeel, G. Gascon, and P. Ozand, *Am. J.N.R.*, 1990, **11**, 135.
22. R. Sugita, I. Takahashi, K. Ishii, K. Matsumoto, T. Ishibashi, K. Sakamoto, and K. Narisawa, *J. Comput. Assist. Tomogr.*, 1990, **14**, 699.
23. D. W. W. Shaw, K. R. Maravilla, E. Weinberger, J. Garretson, C. M. Trahms, and C. R. Scott, *Am. J.N.R.*, 1991, **12**, 403.
24. K. D. Pearsen, A. D. Gean-Marton, H. L. Levy, and K. R. Davis, *Radiology*, 1990, **177**, 437.
25. A. J. Thompson, I. Smith, D. Brenton, B. D. Youl, G. Rylame, D. C. Davidson, B. Kordall, and A. J. Lees, *Lancet*, 1990, **336**, 602.
26. A. J. Thompson, S. Tillotson, I. Smith, B. Kendall, S. G. Moore, and D. P. Brenton, *Brain*, 1993, **116**, 811.
27. A. A. Tzika, W. S. Ball Jr., D. B. Vigneron, R. S. Dunn, and D. R. Kirks, *Am. J.N.R.*, 1993, **14**, 1267.
28. A. J. Barkovich, W. V. Good, T. K. Koch, and B. O. Berg, *Am. J.N.R.*, 1993, **14**, 1119.
29. P. M. Matthews, F. Andermann, K. Silver, G. Karpati, and D. L. Arnold, *Neurology*, 1993, **43**, 2484.
30. B. Barbiroli, P. Montagna, P. Martinelli, R. Lodi, S. Lotti, P. Cortelli, R. Fanicello, and P. Zaniol, *J. Cereb. Blood Flow Metab.*, 1993, **13**, 469.
31. J. M. Charcot, *Gaz. des Hôp. Civ. Mil., Paris*, 1868, **41**, 554.
32. W. I. McDonald and D. H. Silberberg, 'Multiple Sclerosis', Butterworths, London, 1986.
33. G. A. Schumacher, G. Beebe, R. F. Kibler, L. T. Kurland, J. F. Kurtzke, F. McDowell, B. Nagler, W. A. Sibley, W. W. Tourtellotte, and T. L. Willmon, *Ann. NY Acad. Sci.*, 1965, **122**, 552.
34. C. M. Poser, D. W. Paty, L. Scheinberg, W. I. MacDonald, F. A. Davis, G. C. Ebers, K. P. Johnson, W. A. Sibley, D. H. Silberberg, and W. H. Tourtellote, *Ann. Neurol.*, 1983, **13**, 227.
35. A. K. Asbury, R. M. Herndon, H. F. McFarland, W. I. McDonald, W. J. McIlroy, D. W. Paty, J. W. Prineas, L. C. Scheinberg, and J. S. Wolinsky, *Neuroradiology*, 1987, **29**, 119.
36. D. W. Paty and D. K. B. Li, in 'Clinical Neuroimaging', ed. W. H. Theodore, Alan R. Liss, New York, 1988, Vol. 4, Chap. 10.
37. R. I. Grossman, B. H. Braffman, J. R. Brorson, H. I. Goldberg, D. H. Silberberg, and F. Gonzalez-Scarano, *Radiology*, 1988, **169**, 117.
38. I. R. Young, A. S. Hall, C. A. Pallis, N. J. Legg, G. M. Bydder, and R. E. Steiner, *Lancet*, 1981, **ii**, 1063.
39. S. A. Lukes, L. E. Crooks, M. J. Aminoff, L. Kaufman, H. S. Panitch, C. Mills, and D. Norman, *Ann. Neurol.*, 1983, **13**, 592.
40. I. E. C. Ormerod, G. H. du Boulay, and W. I. McDonald, in 'Multiple Sclerosis', ed. W. I. McDonald and D. H. Silberberg, Butterworths, London, 1986.
41. D. H. Miller, *MRI Decis.*, 1988, **2**, 17.
42. I. E. C. Ormerod, D. H. Miller, W. I. McDonald, E. P. G. H. du Boulay, P. Rudge, B. E. Kendall, I. F. Moseley, G. Johnson, P. S. Tofts, and A. N. Halliday, *Brain*, 1987, **110**, 1579.
43. D. W. Paty, *Can. J. Neurol. Sci.*, 1988, **15**, 266.
44. D. W. Paty, J. J. F. Oger, L. F. Kastrukoff, S. A. Hashimoto, J. P. Haage, A. A. Eisen, K. A. Eisen, S. T. Purves, M. D. Low, and V. Brandejs, *Neurology*, 1988, **38**, 180.
45. D. Lacomis, M. D. Osbakken, and G. Gross, *Magn. Reson. Med.*, 1986, **3**, 194.
46. B. P. Drayer, P. Burger, B. Hurwitz, D. Dawson, and J. Cain, *Am. J.N.R.*, 1987, **8**, 413.
47. D. H. Miller, I. E. C. Ormerod, A. Gibson, E. P. G. H. du Bouley, P. Rudge, and W. I. McDonald, *Neuroradiology*, 1987, **29**, 226.
48. F. Z. Yetkin, V. M. Haughton, R. A. Papke, M. E. Fischer, and S. M. Rao, *Radiology*, 1991, **178**, 447.
49. F. Fazekas, H. Offenbacher, S. Fuchs, R. Schmidt, K. Niederkorn, S. Horners, and H. Lechner, *Neurology*, 1988, **38**, 1822.
50. H. Offenbacher, F. Fazekas, R. Schmidt, W. Freidl, E. Floch, F. Payer, and H. Lechner, *Neurology*, 1993, **43**, 905.
51. I. E. C. Ormerod, A. Bronstein, P. Rudge, G. Johnson, D. G. P. MacManus, A. M. Halliday, H. Barratt, E. P. du Boulay, B. E. Kendall, and I. F. Moseley, *J. Neurol. Neurosurg. Psychiatry*, 1986, **49**, 737.
52. J. Prineas, *Hum. Pathol.*, 1975, **6**, 531.
53. R. I. Grossman, F. Gonzalez-Scarano, S. W. Atlas, S. Galetta, and D. H. Silberberg, *Radiology*, 1986, **161**, 721.
54. H. Miller, P. Rudge, B. Johnson, B. E. Kendall, D. G. MacManus, I. F. Moseley, D. Barnes, and W. I. McDonald, *Brain*, 1988, **111**, 927.
55. E.-M. Larsson, S. Holas, and O. Nilsson, *Am. J.N.R.*, 1989, **10**, 1071.
56. S. F. Merandi, B. T. Kudryk, F. R. Murtagh, and J. A. Arrington, *Am. J.N.R.*, 1991, **12**, 923.
57. A. J. Thompson, A. J. Kermode, D. Wicks, D. G. MacManus, B. E. Kendall, D. P. Kingley, and W. I. McDonald, *Ann. Neurol.*, 1991, **29**, 53.
58. M. K. Stehling, P. Bullock, J. L. Firth, A. M. Blamire, R. J. Ordidge, B. Coxon, P. Gibbs, and P. Mansfield, *Proc. VIIIth Ann Mtg. Soc. Magn. Reson. Med.*, Amsterdam, 1989, p. 358.
59. D. W. Paty, *Curr. Opin. Neurol. Neurosurg.*, 1993, **6**, 202.
60. R. Heun, L. Kappos, S. Bittkau, D. Staedt, E. Rohrbach, and B. Schuknecht, *Lancet*, 1988, **ii**, 1202.
61. M. J. Kupersmith, D. Kaufman, D. W. Paty, G. Ebers, M. McFarland, K. Johnson, J. Reingold, and J. Whitaker, *Neurology*, 1994, **44**, 1.
62. D. W. Paty and D. K. Li, *Neurology*, 1993, **43**, 662.
63. P. Schilder, *Z. Gesamte Neurol. Psychiatr.*, 1912, **10**, 1.
64. M. F. Mehler and L. Rabinowich, *Am. J.N.R.*, 1989, **10**, 176.
65. S. W. Atlas, R. I. Grossman, H. I. Goldberg, D. B. Hackney, L. T. Bilanuck, and R. A. Zimmerman, *J. Comput. Assist. Tomogr.*, 1986, **10**, 798.
66. A. J. Barkovich, 'Pediatric Neuroimaging', Raven Press, New York, 1996, p. 597.
67. R. Murata, H. Hattori, O. Matsuoka, T. Nakajima, and H. Shintaku, *Brain. Dev.*, 1992, **14**, 391.

68. S. Yagi, Y. Miura, S. Mizuta, A. Wakunami, N. Kataoka, T. Morita, K. Morita, S. Ono, and M. Fukunaga, *Brain. Dev.*, 1993, **15**, 141.
69. A. S. Mark and S. W. Atlas, *Radiology*, 1989, **173**, 517.
70. L. Ketonen and M. Tuite, *Semin. Neurol*, 1992, **12**, 57.
71. F. Ebner, G. Ranner, I. Slavc, C. Urban, R. Kleinert, H. Roulner, R. Ernspieler, and E. Justich, *Am. J.N.R.*, 1989, **10**, 959.
72. R. Asato, Y. Akiyama, M. Ito, M. Kubota, R. Okumura, Y. Miki, J. Konishi, H. Mikaua, *Cancer*, 1992, **70**, 1997.
73. J. T. Curnes, D. W. Laster, M. R. Ball, T. D. Koubek, D. M. Moody, and R. L. Witcofski, *Am. J.N.R.*, 1986, **7**, 389.
74. W. J. Curran, C. Hecht-Leavitt, L. Schut, R. A. Zimmerman, and D. F. Nelson, *Int. J. Radiat. Oncol. Biol. Phys.*, 1987, **13**, 1093.
75. R. B. Schwartz, P. A. Carvalho, E. Alexander III, J. S. Loeffler, R. Folkerth, and B. L. Holman, *Am. J.N.R.*, 1991, **12**, 1187.
76. Karl-J. Langen, H. H. Coenen, N. Roosen, P. Kling, O. Muzik, H. Herzog, T. Kuwort, G. Stocklin, and L. E. Femendegen, *J. Nucl. Med.*, 1990, **31**, 281.
77. D. J. Vaughn, J. G. Jarvik, D. Hackney, S. Peters, and E. A. Stadtmauer, *Am. J.N.R.*, 1993, **14**, 1014.
78. Y. Korogi, M. Takahashi, J. Shinzato, Y. Sakamoto, K. Mitsuzaki, T. Hirai, and K. Yoshizumi, *Am. J.N.R.*, 1993, **14**, 651.
79. M. Mascalchi, M. Cincotta, and M. Piazzini, *Clin. Radiol.*, 1993, **47**, 137.
80. R. D. Laitt, M. Thornton, and P. Goddard, *Clin. Radiol.*, 1993, **48**, 432.
81. V. B. Ho, C. R. Fitz, C. C. Yoder, and C. A. Geyer, *Am. J.N.R.*, 1993, **14**, 163.
82. K. J. Koch and R. R. Smith, *Am. J.N.R.*, 1989, **10**, S58.
83. M. E. Charness, *Alcohol Clin. Exp. Res.*, 1993, **17**, 2.
84. P. Tomasini, D. Guillot, P. Sabbah, C. Brosset, P. Salamand, and J. F. Briant, *Ann. Radiol. (Paris)*, 1993, **36**, 319.
85. S. Canaple, A. Rosa, and J. P. Mizon, *Rev. Neurol. (Paris)*, 1992, **148**, 638.
86. A. L. Horowitz, R. Kaplan, and G. Sarpel, *Radiology*, 1987, **162**, 787.
87. L. Xiong, J. D. Matthes, J. Li, and R. Jinkins, *Am. J.N.R.*, 1993, **14**, 1195.
88. T. P. Tan, P. R. Algra, J. Valk, and E. C. Wolters, *Am. J.N.R.*, 1994, **15**, 175.
89. E. Brown, J. Prager, H. Y. Lee, and R. G. Ramsey, *Am. J. Roentgenol.*, 1992, **159**, 137.
90. M. D. Nelson, I. Gonzalez-Gomez, and F. H. Gilles, *Am. J.N.R.*, 1991, **12**, 215.
91. S. E. Keeney, E. W. Adcock, and C. B. McArdle, *Pediatrics*, 1991, **87**, 421.
92. S. E. Keeney, E. W. Adcock, and C. B. McArdle, *Pediatrics*, 1991, **87**, 431.
93. A. J. Barkovich and C. L. Truwit, *Am. J.N.R.*, 1990, **11**, 1087.
94. P. Byrne, R. Welch, M. A. Johnson, J. Darrah, and M. Piper, *J. Pediatr.*, 1990, **117**, 694.
95. E. Teasdale and D. M. Hadley, in 'Handbook of Clinical Neurology, 2nd Series: Head Injury', ed. R. Braakman, Elsevier, Amsterdam, 1990, Vol. 13, Chap. 7.
96. D. M. Hadley, *Curr. Imaging*, 1991, **3**, 64.
97. A. H. S. Holbourn, *Lancet*, 1943, **ii**, 438.
98. J. H. Adams, D. I. Graham, L. S. Murray, and G. Scott, *Ann. Neurol.*, 1982, **12**, 557.
99. T. A. Gennarelli, G. M. Spielman, T. W. Langfitt, P. L. Gildenberg, T. Harrington, J. A. Jane, L. F. Marshall, J. D. Miller, and L. H. Pitts, *J. Neurosurg.*, 1982, **56**, 26.
100. A. D. Gean, 'Imaging of Head Trauma', Raven Press, New York, 1994.
101. A. Jenkins, G. M. Teasdale, D. M. Hadley, P. Macpherson, and J. O. Rowan, *Lancet*, 1986, **ii**, 445.
102. D. M. Hadley, P. Macpherson, D. A. Lang, and G. M. Teasdale, *Neuroradiology*, 1991, **33**, 86.
103. K. D. Wiedmann, J. T. L. Wilson, D. Wyper, D. M. Hadley, G. M. Teasdale, and D. N. Brooks, *Neuropsychology*, 1990, **3**, 267.
104. J. T. L. Wilson, K. D. Wiedmann, D. M. Hadley, B. Condon, G. M. Teasdale, and J. D. N. Brooks, *J. Neurol. Neurosurg. Psychiatry*, 1988, **51**, 391.
105. C. D. Forbes, *Scot. Med. J.*, 1991, **36**, 163.
106. M. Brant-Zawadzki, B. Pereira, P. Weinstein, S. Moore, W. Kusharczyk, I. Berry, M. McNamara, and N. Derugin, *Am. J.N.R.*, 1986, **7**, 7.
107. M. E. Moseley, Y. Cohen, J. Mintorovitch, L. Chileuitt, H. Shimizer, W. Kueharczyk, M. F. Wendland, and P. R. Weinstein, *Magn. Reson. Med.*, 1990, **14**, 330.
108. A. M. Aisen, T. O. Gabrielsen, and W. J. McCune, *Am. J.N.R.*, 1985, **6**, 197.
109. W. G. Bradley, *Neurol. Res.*, 1984, **6**, 91.
110. W. T. C. Yuh, M. R. Crain, D. J. Loes, G. M. Greene, T. J. Ryals, and Y. Sato, *Am. J.N.R.*, 1991, **12**, 621.
111. S. Warach, W. Li, M. Ronthal, and R. R. Edelman, *Radiology*, 1992, **182**, 41.
112. R. N. Bryan, L. M. Levy, W. D. Whitlow, J. M. Killian, T. J. Preziosi, and J. A. Rosario, *Am. J.N.R.*, 1991, **12**, 611.
113. A. Sato, S. Takahashi, Y. Soma, K. Ishii, T. Watanabe, and K. Sakamoto, *Radiology*, 1991, **178**, 433.
114. M. R. Crain, W. T. C. Yuh, G. M. Greene, D. J. Loes, T. J. Ryals, Y. Sato, and M. N. Hart, *Am. J.N.R.*, 1991, **12**, 631.
115. A. D. Elster and D. M. Moody, *Radiology*, 1990, **177**, 627.
116. W. G. Bradley, in 'MRI Atlas of the Brain', eds. W. G. Bradley and G. Bydder, Martin Dunitz, London, 1990, Chap. 5.
117. T. J. Masaryk, G. A. Laub, M. T. Modic, J. S. Ross, and E. M. Haacke, *Magn. Reson. Med.*, 1990, **14**, 308.
118. A. W. Litt, *Am. J.N.R.*, 1991, **12**, 1141.
119. M. Doran and G. M. Bydder, *Neuroradiology*, 1990, **32**, 392.
120. R. M. Henkelman, *Am. J.N.R.*, 1990, **11**, 932.
121. M. Brant-Zawadzki, P. R. Weinstein, H. Bartkowski, and M. Moseley, *Am. J. Roentgenol.*, 1987, **148**, 579.
122. M. L. Bots, J. C. van-Swieten, M. M. Breteler, P. T. de-Jong, J. Van Gijn, A. Hofman, and D. E. Grobbee, *Lancet*, 1993, **341**, 1232.
123. T. Horikoshi, S. Yagi, and A. Fukamachi, *Neuroradiology*, 1993, **35**, 151.
124. V. G. Marshall, W. G. Bradley, C. E. Marshall, T. Bhoopat, and R. H. Rhodes, *Radiology*, 1988, **167**, 517.
125. D. G. Munoz, S. M. Hastak, B. Harper, D. Lee, and V. C. Hachinski, *Arch. Neurol.*, 1993, **50**, 492.

Biographical Sketch

Donald M. Hadley. *b* 1950. M.B.Ch.B., 1974, Ph.D., 1980, D.M.R.D., 1981, Aberdeen University, Scotland; F.R.C.R., 1983, London, UK. Introduced to NMR by Professor John Mallard and Dr Francis Smith while carrying out postdoctoral work in the Department of Bio-medical Physics, University of Aberdeen 1981. MRC research fellow, Glasgow University 1984, consultant and director of Neuroradiology 1992, Institute of Neurological Sciences, Glasgow, UK. Approx. 200 publications. Current research interests: MRI and MRS investigation of acute trauma, epilepsy, metabolic white matter diseases and stroke.

MRI and MRS of Neuropsychiatry

Basant K. Puri

MRC Clinical Sciences Centre, Imperial College School of Medicine, London, UK

1 INTRODUCTION

MRI and MRS studies are becoming increasingly important in neuropsychiatry. In this chapter, the contributions will be considered of such studies to our understanding of schizophrenia, mood disorders, anxiety disorders, obsessive-compulsive disorder, eating disorders, attention deficit hyperactivity disorder (ADHD), psychoactive substance use, Alzheimer's disease, Lewy body disease and Binswanger's disease, Huntington's disease, autism, electroconvulsive therapy, dyslexia, brain changes following incomplete spinal injury in humans, and drug monitoring.

2 SCHIZOPHRENIA

Many studies using MRI have been carried out on patients with schizophrenia since 1983. In a well-researched critical review of these by Chua and McKenna,[1] it was found that the only well-established structural abnormality in schizophrenia is lateral ventricular enlargement; this is modest and overlaps with ventricular size in the normal population. The authors of the review came to the following conclusions: 'there is no consistent evidence from MRI studies for a global reduction in brain size in schizophrenia, and only a minority of studies have pointed to a focal reduction in the size of the frontal lobes. However, the numbers of positive and negative replications are approximately equal for the finding of reduced temporal lobe size, and when the hippocampus and amygdala (and perhaps also the parahippocampal gyrus) are specifically considered this turns into a slight majority in favour of reduced size. A reasonable conclusion might therefore be that, while not yet established beyond reasonable doubt, it is likely that any brain substance abnormality in schizophrenia will be found to be localised to the temporal lobe, where it will be predominantly subcortical and perhaps also predominantly left-sided.'

Recently developed techniques of subvoxel registration of high-resolution three-dimensional (3D) serial MR scans[2,3] and quantification of changes thereby discovered[4] have just started to be applied to various aspects of this disorder. For example, when first-episode schizophrenic patients were classified according to Gruzelier's syndromal model,[5,6] it was found that, compared with normal controls, over an 8-month period patients who were 'withdrawn' showed progressive ventricular enlargement, with an increase in ventricle-to-brain volume ratio. In contrast a group of 'active' patients showed a reduction in ventricle-to-brain volume ratio, with a change that was opposite in sign and smaller in magnitude.[7] These findings suggest that opposite patterns of functional hemispheric activation early in the course of schizophrenia may be associated with strikingly different structural cerebral changes. These techniques have also found application in testing specific predictions of Horrobin's neuronal membrane phospholipid model of schizophrenia.[8,9] In the first example of this, it has been found that in a patient with long-standing disease not being treated with conventional medication, sustained remission of positive and negative symptoms of schizophrenia associated with treatment with the omega-3 fatty acid eicosapentaenoic acid (EPA; Kirunal) was accompanied by a reversal of cerebral atrophy (Figure 1).[10]

Using ^{31}P MRS to study the prefrontal cortex in schizophrenia, a number of groups, including Pettegrew and colleagues[11] and Stanley and colleagues,[12] have reported changes in membrane phospholipid metabolism, irrespective of antipsychotic medication status, with reduced levels of phosphomonoesters (precursors of phospholipid biosynthesis) and increased levels of both phosphodiesters (phospholipid breakdown products) and intracellular magnesium ions. It has been suggested that these findings may be fundamentally related to the pathophysiology of schizophrenia,[11–13] with the reduced levels of phosphomonoesters being caused by reduced biosynthesis or altered degradation and the elevated levels of phosphodiesters being associated with increased activity of phospholipase A_2 or A_1, or perhaps decreased phosphodiesterase activity. An alternative explanation involves a putative disturbance of metabolic compartmentation of phosphatidylcholine biosynthesis.[14]

Many studies using proton MRS have demonstrated a reduction in the neuronal marker *N*-acetylaspartate, particularly in the left temporal lobe. In a recent study combining this technique with MRI, the volume of cortical gray matter was found to be reduced in patients with schizophrenia, while the *N*-acetylaspartate signal intensity from a comparable region was normal; by comparison, the volume of cortical white matter was normal while the *N*-acetylaspartate signal intensity from a comparable region was reduced.[15] The lack of reduction in gray matter *N*-acetylaspartate signal intensity suggests that the cortical gray matter deficit involved both neuronal and glial compartments, rather than a neurodegenerative process in which there is a decrease in the neuronal relative to the glial compartment. The reduced white matter *N*-acetylaspartate signal intensity without a white matter volume deficit may reflect abnormal axonal connections.[15]

3 MOOD DISORDERS

To date there have been relatively few MR studies of mood disorders and the findings are not consistent. For example, ventricular enlargement is an inconsistent finding in depression (using MRI or computed tomography (CT)); when it has been found it has sometimes been shown to be positively correlated with the length of illness. Neither first-episode bipolar disorder nor first-episode major depression appear to be associated with ventricular enlargement, however.[16] Another inconsistent finding is the possibility of an increased frequency of signal hyperintensities on T_2-weighted scans in elderly depressed patients, which may be associated with poor cognitive perform-

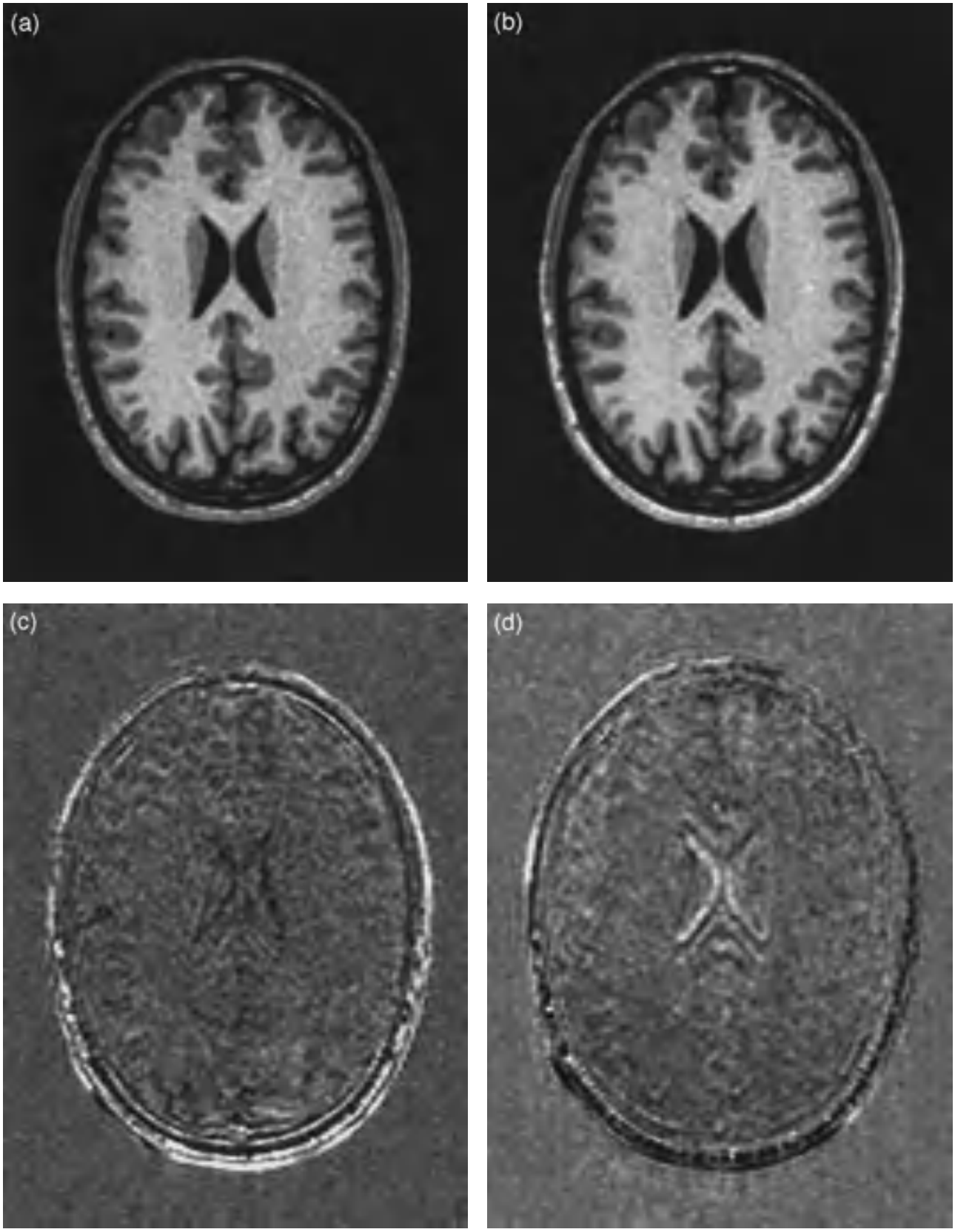

Figure 1 MRI in a patient with long-term schizophrenia. (a) Transverse image of the brain 12 months prior to commencing treatment with eicosapentaenoic acid (EPA). (b) Transverse image of the brain at baseline (0 months) with respect to EPA treatment. (c) Registered difference image of the baseline scan minus the scan at −12 months ((b) minus (a)). The dark lines around the ventricles are caused by a decrease in brain size. (d) Registered difference image of the scan at 6 months minus the scan at baseline (0 months). The white lines around the ventricles are caused by an increase in brain size. Changes are also seen in the cerebral cortex, with narrowing evident in some sulci and increased volume evident in some gyri

ance.[17,18] Although such hyperintensities may be a marker of underlying pathology, they are by no means specific to depression and indeed may also occur in older normal controls. It has been reported that the presence of such hyperintensities in both the basal ganglia and the pontine reticular formation in patients aged 65 years and over is associated with a poor response to antidepressant monotherapy.[19] It has also been suggested that treatment-resistant chronic unipolar depression is associated with reduced gray matter density in the left temporal cortex, including the hippocampus.[20] Studies using ^{31}P MRS and ^{1}H MRS have indicated possible abnormalities in membrane phospholipid metabolism, high-energy phosphate metabolism, and intracellular pH in mood disorders.[21]

4 ANXIETY DISORDERS

There have been very few MR studies of anxiety disorders, perhaps because anxiety and claustrophobic symptoms constitute a recognized cause of incomplete or cancelled MR examinations.[22] In one ^{31}P MRS study of the frontal lobes in panic disorder, no significant differences were found between patients and controls in ^{31}P metabolite levels, although a significant asymmetry (left greater than right) of phosphocreatine concentration was found in the patients; raised intracellular pH in 2 out of 18 of the patients may have resulted from respiratory alkalosis secondary to hyperventilation in the anxiety state.[23]

5 OBSESSIVE-COMPULSIVE DISORDER

Structural neuroimaging studies indicate that at least a subgroup of patients with obsessive-compulsive disorder may have abnormal basal ganglia development.[24] Although not all such studies demonstrate reduced volumes of these structures, it is noteworthy that a reduced level of the neuronal marker *N*-acetylaspartate has been found in either the left[25] or right[26] corpus striatum in obsessive-compulsive disorder using proton MRS, even when volumetric MRI studies of the same patients do not show reduced volumes.[25] Hence the inconsistent volumetric findings may reflect the relatively poorer sensitivity of MRI morphometry for detecting neuronal loss compared with proton MRS measurement of *N*-acetylaspartate.

6 EATING DISORDERS

The CT finding of cerebral atrophy in patients with eating disorders has been replicated using MRI.[27,28] Female patients with anorexia nervosa and bulimia nervosa have been reported to have smaller pituitary glands than matched controls.[29,30] In the absence of any other pituitary pathology, this atrophy is likely to be secondary to nutritional or endocrine alterations. Other reported structural abnormalities include enlarged lateral ventricles with dilated cortical and cerebellar sulci,[31] and subcortical signal hyperintensities on T_2-weighted scans.[32]

In a small cerebral ^{31}P MRS study of anorexia nervosa before treatment, increased levels of phosphodiesters were found compared with controls, while decreased phosphomonoesters were found that were associated with malnutrition reflected by endocrinological abnormalities.[33] These data suggest that severe malnutrition in patients with anorexia nervosa may result in an abnormality in membrane phospholipid metabolism, which might be related etiologically to the cerebral atrophy of anorexia nervosa. In another study of patients with anorexia nervosa recording proton MR spectra from parieto-occipital white matter immediately following an interval of excessive loss of body mass, higher signal intensity ratios of choline-containing compounds relative to total creatine and lower ratios of *N*-acetylaspartate relative to choline-containing compounds were found compared with controls,[34] suggesting that starvation may be associated with an abnormal neuronal membrane turnover in the white matter of the brain.

7 ATTENTION DEFICIT HYPERACTIVITY DISORDER

Recent MRI studies have shown that some regions of the frontal lobes (anterior superior and inferior) and basal ganglia (caudate nucleus and globus pallidus) are about 10% smaller in ADHD groups than in control groups of children,[35] with the right caudate nucleus being larger,[36] or left caudate being smaller,[37] in children with ADHD. These findings are consistent with theories implicating frontal-striatal circuit abnormalities in this disorder. Also in harmony with this theory is the fact that the corpus callosum has been found relatively consistently to be smaller in children with ADHD, particularly in the region of the genu and splenium.[38] Recently, the cerebellum has been systematically studied in this disorder; the vermal volume was found to be significantly smaller in a large sample of boys with ADHD than in matched controls.[39] This reduction involved mainly the posterior inferior lobe (lobules VIII to X) but not the posterior superior lobe (lobules VI to VII) and suggests that perhaps cerebello-thalamo-prefrontal circuit dysfunction may subserve the motor control, inhibition, and executive function deficits seen in this disorder.

Advances in genetic studies of ADHD have occurred while these advances in structural neuroimaging have been taking place. An important example of how both of these investigative techniques can complement each other relates to polymorphisms of the D_4 dopamine receptor (DRD4). One allele with seven tandem repeats in exon 3 (*DRD4*7R*) has been associated with ADHD, and when this putative association was investigated by Castellanos and colleagues, it was found that cerebral MRI measures, previously found to discriminate ADHD patients from controls, did not differ significantly between subjects having and those lacking a *DRD4*7R* allele.[40] Hence the MRI results did not support the reported association between *DRD4*7R* and the behavioral or brain morphometric phenotype associated with ADHD.

8 PSYCHOACTIVE SUBSTANCE ABUSE

Chronic alcoholism is associated with MRI-detectable atrophic changes in many regions of the brain, including the cerebral cortex, cerebellum,[41] and corpus callosum.[42] Hippocampal volume reduction is proportional to the reduction in volume of the brain as a whole.[43] It has been found that over a 5-year period brain volume shrinkage is exaggerated in the pre-

frontal cortex in normal aging but with additional loss occurring in the anterior superior temporal cortex in alcoholism.[44] This association of cortical gray matter volume reduction with alcohol consumption over time suggests that continued alcohol abuse results in progressive cerebral tissue volume shrinkage.

MRI, but not CT, has been shown to be useful in confirming the diagnosis of acute Wernicke's encephalopathy. In one recent study, increased T_2 signal of the paraventricular regions of the thalamus and the mesencephalic periaqueductal regions was observed in patients with Wernicke's encephalopathy compared with both controls and asymptomatic chronic alcohol abusers, with the sensitivity of MRI in revealing evidence of this disease being 53% and the specificity 93%.[45] It should be borne in mind, however, that the absence of abnormalities on MRI does not exclude this diagnosis.

With MRI, widespread cerebral atrophy is seen in alcoholic Korsakoff patients;[46] this is largely subcortical and does not develop independently of the diencephalic pathology. It should be noted that while chronic alcohol abuse is associated with mammillary body and cerebellar tissue volume loss, these markers do not distinguish accurately between amnesic and nonamnesic patients; mammillary body atrophy that is detectable on MRI is not necessary for the development of amnesia in alcoholic patients.[47]

It has recently been shown that cerebral MRI may be of use clinically in the differential diagnosis of chronic alcohol abuse and schizophrenia.[48] In this study, patients with both disorders showed widespread cortical gray matter volume deficits compared with controls, but only those with chronic alcoholism showed white matter volume deficits. The patients with schizophrenia had significantly greater volume deficits in prefrontal and anterior superior temporal gray matter than in more posterior cortical regions. By contrast, the deficits in the patients with alcoholism were relatively homogeneous across the cortex. For white matter, the deficits in the patients with alcoholism were greatest in the prefrontal and temporoparietal regions. Although both patient groups had abnormally larger cortical sulci and lateral and third ventricles than the controls, the patients with alcoholism had significantly larger sulcal volumes in the frontal, anterior, and posterior parieto-occipital regions than those with schizophrenia.

Reduced levels of *N*-acetylaspartate and choline have been found using cerebral proton MRS in chronic alcoholism.[49] The reduction of *N*-acetylaspartate is consistent with neuronal loss while the reduction in choline may be related to neuronal membrane lipid changes.

In a recent large MRI and proton MRS study comparing asymptomatic abstinent cocaine users with matched controls, it was found that while the ventricle-to-brain ratio and level of white matter lesions did not differ significantly between the two groups, elevated creatine and *myo*-inositol in the white matter were associated with cocaine use.[50] The *N*-acetylaspartate level was normal in the cocaine users, suggesting that there was no neuronal loss or damage in the brain regions examined. It was, therefore, concluded that the neurochemical abnormalities observed might result from alterations in nonneuronal brain tissue.

MRI changes associated with chronic toluene abuse include cerebral atrophy, cerebral and cerebellar white matter T_2 hyperintensity, T_2 hyperintensity involving the middle cerebellar peduncle and the posterior limb of the internal capsule, and T_2 hypointensity involving the basal ganglia and thalamus.[51,52] Chronic solvent abusers who have white matter MRI changes have been found have a lower performance intelligence quotient, as measured by the Weschler Adult Intelligence Scale – Revised, with a particularly low score on the digit symbol subtest.[53]

In polysubstance abusers, there is MRI evidence of reduced volume of the prefrontal cortex (both left and right) consistent with either atrophy or hypoplasia.[54] Ventriculomegaly has not been found to be a feature.[55] Abnormal cerebral metabolism has been found using ^{31}P MRS in male polysubstance abusers during early withdrawal: increased phosphomonoesters and decreased β-nucleotide trisphosphates were found in the abusers compared with controls, indicating that cerebral high-energy phosphate and phospholipid metabolite changes result from long-term drug abuse and/or withdrawal.[56]

9 ALZHEIMER'S DISEASE, LEWY BODY DISEASE, AND BINSWANGER'S DISEASE

The first part of this section considers recent studies focusing on the use of MRI in differentiating Alzheimer's disease from both normal aging and other causes of dementia.

While the finding of cortical or subcortical atrophy on MRI or CT is not pathognomonic of Alzheimer's disease, hippocampal atrophy provides a useful early marker of the disorder, although further longitudinal and neuropathological study is required.[57] CT- and MRI-based measurements of hippocampal atrophy may provide useful diagnostic information for differentiating patients with probable Alzheimer's disease from normal elderly individuals.

A recent pilot study has indicated that MRI may have a role in assisting with the clinical differentiation between dementia with Lewy bodies and Alzheimer's disease.[58] Subjects with known or probable Alzheimer's disease were found to have significantly smaller left temporal lobes and parahippocampal gyri than those with known or probable Lewy body disease. Medial temporal atrophy was present in 9 out of 11 patients with Alzheimer's disease and absent in six out of nine patients with Lewy body disease. While two patients with neuropathologically confirmed Lewy body disease had severe medial temporal atrophy, in both concurrent Alzheimer's disease-type pathology was present in the temporal lobe. Therefore, this pilot study supports the hypothesis that a greater burden of pathology centers on the temporal lobes in Alzheimer's disease compared with Lewy body disease, unless Lewy body disease occurs with concurrent Alzheimer pathology.

Another recent study has suggested that diffusion-weighted MRI may be useful in the differential diagnosis of subcortical arteriosclerotic encephalopathy (vascular dementia of the Binswanger type) and Alzheimer's disease with white matter lesions.[59] Apparent diffusion coefficients in the anterior and posterior white matter and the genu and splenium of the corpus callosum were significantly higher in patients with both these disorders compared with age-matched controls, with apparent diffusion coefficient values in the groups with Binswanger's disease and those with Alzheimer's disease being almost the same. Apparent diffusion coefficient ratios, defined as diffusion-restricted perpendicular to the direction of nerve fibers, were also significantly higher in both groups of patients than in the

controls. However, there were regional differences in these ratios in the two disorders, with ratios in Binswanger's disease being higher in the anterior portions of the white matter while ratios in Alzheimer's disease were higher in the posterior portions.

In vitro and in vivo ^{31}P MRS studies of the brain in Alzheimer's disease show alterations in membrane phospholipid metabolism and high-energy phosphate metabolism: compared with control subjects, mildly demented patients with Alzheimer's disease have increased levels of phosphomonoesters, decreased levels of phosphocreatine and probably adenosine diphosphate, and an increased oxidative metabolic rate; as the dementia worsens, levels of phosphomonoesters decrease and levels of phosphocreatine and adenosine diphosphate increase.[60] The changes in oxidative metabolic rate suggest that the brain in Alzheimer's disease is under energetic stress while the phosphomonoester findings implicate basic defects in membrane metabolism in the brain.[60] Thus, in addition to aiding with diagnosis, ^{31}P MRS may provide a noninvasive tool to follow both the progression of this disorder and any response to putative therapeutic interventions.

Proton MRS studies of occipital gray matter show that reduced levels of *N*-acetylaspartate (presumably reflecting neuronal loss) and increased levels of *myo*-inositol characterize Alzheimer's disease.[61,62] Studies using proton MRS to measure cerebral amino acids have tended to demonstrate increased glutamate levels and sometimes reduced γ-aminobutyric acid (GABA); following neuronal loss, the remaining neurons might be exposed to excess glutamate and relatively low levels of GABA, an imbalance that might be neurotoxic.[63,64]

10 HUNTINGTON'S DISEASE

Initially, structural neuroimaging studies showed atrophy of the caudate and loss of definition between the caudate and the adjacent ventricle as Huntington's disease progresses; however more recent studies have also shown cortical atrophy, particularly in the frontal lobes.[65]

Using proton MRS, Jenkins and colleagues found that lactate concentrations were increased in the occipital cortex of patients with symptomatic Huntington's disease compared with normal controls, with the lactate level correlating with duration of illness.[66] Several patients in the same study also showed highly elevated lactate levels in the basal ganglia, while basal ganglia levels of *N*-acetylaspartate were lowered and choline dramatically elevated, relative to creatine, reflecting neuronal loss and gliosis in this brain region. The authors of this study suggested that these findings are consistent with a possible defect in energy metabolism in Huntington's disease, which could contribute to the pathogenesis of the disease, and that the presence of elevated lactate might provide a simple marker that could be followed over time noninvasively and repeatedly to aid in devising and monitoring possible therapies.

A more recent proton MRS study by Taylor-Robinson and colleagues found an elevated ratio of glutamine and glutamate relative to creatine in the striatum compared with healthy controls, suggesting disordered striatal glutamate metabolism and possibly supporting the theory of glutamate excitotoxicity in Huntington's disease.[67]

Huntington's disease is now known to result from expanded CAG repeats in a gene on chromosome 4, a possible consequence of which might be progressive impairment of energy metabolism. Jenkins and colleagues have recently extended their previous studies to examine correlations between proton MRS changes and CAG repeat number.[68] The spectra in three presymptomatic gene-positive patients were found to be identical to normal control subjects in cortical regions, but three in eight showed elevated lactate in the striatum. Similar to recently reported increases in task-related activation of the striatum in the dominant hemisphere, they found that striatal lactate levels in patients with Huntington's disease were markedly asymmetric (left greater than right). Markers of neuronal degeneration, decreased *N*-acetylaspartate to creatine and increased choline to creatine ratios, were symmetric. Both decreased *N*-acetylaspartate and increased lactate in the striatum significantly correlated with duration of symptoms. When divided by the patient's age, an individual's striatal *N*-acetylaspartate loss and lactate increase were found to correlate with the subject's CAG repeat number, with correlation coefficients of 0.8 and 0.7, respectively. Similar correlations were noted between postmortem cell loss and age versus CAG repeat length. Together, these data provide further evidence for an interaction between neuronal activation and a defect in energy metabolism in Huntington's disease that may extend to presymptomatic subjects.[68]

11 AUTISM

MRI studies of individuals with autism have variously and inconsistently shown evidence of hypoplasia of the cerebellum and brainstem with increased size of the fourth ventricle, increased brain volume (though with relative hypofrontality), and smaller size of the body and posterior subregions of the corpus callosum; in addition, previous pneumoencephalographic and CT studies have described lateral ventricular enlargement while MRI studies in general have failed to show abnormality in limbic structures.[69] The degree of cerebellar hypoplasia is significantly correlated with the degree of slowed attentional orienting to visual cues in both children and adults with autism.[70] It should be noted that even in the absence of abnormal MRI findings, autism may be associated with focal areas of decreased perfusion.[71]

The finding that autism is not necessarily associated with MRI abnormalities is consistent with the results of a recent cerebral proton MRS study comparing 28 patients with autism with both 28 age-matched patients with unclassified mental retardation and 25 age-matched healthy children. The ratio of *N*-acetylaspartate to choline was lower in the nonautistic patients with mental retardation than in the patients with autism and the controls, and, interestingly, there were no significant differences in this ratio between patients with autism and controls.[72]

A ^{31}P MRS study of the dorsal prefrontal cortex of 11 high-functioning autistic adolescent and young adult men and 11 matched normal controls found that the autistic group had decreased levels of phosphocreatine, α-ATP, α-ADP, dinucleotides, and diphosphosugars compared with the controls.[73] When the metabolite levels were compared within each subject group with psychological and language test scores, a common pattern of correlations was observed across measures in the

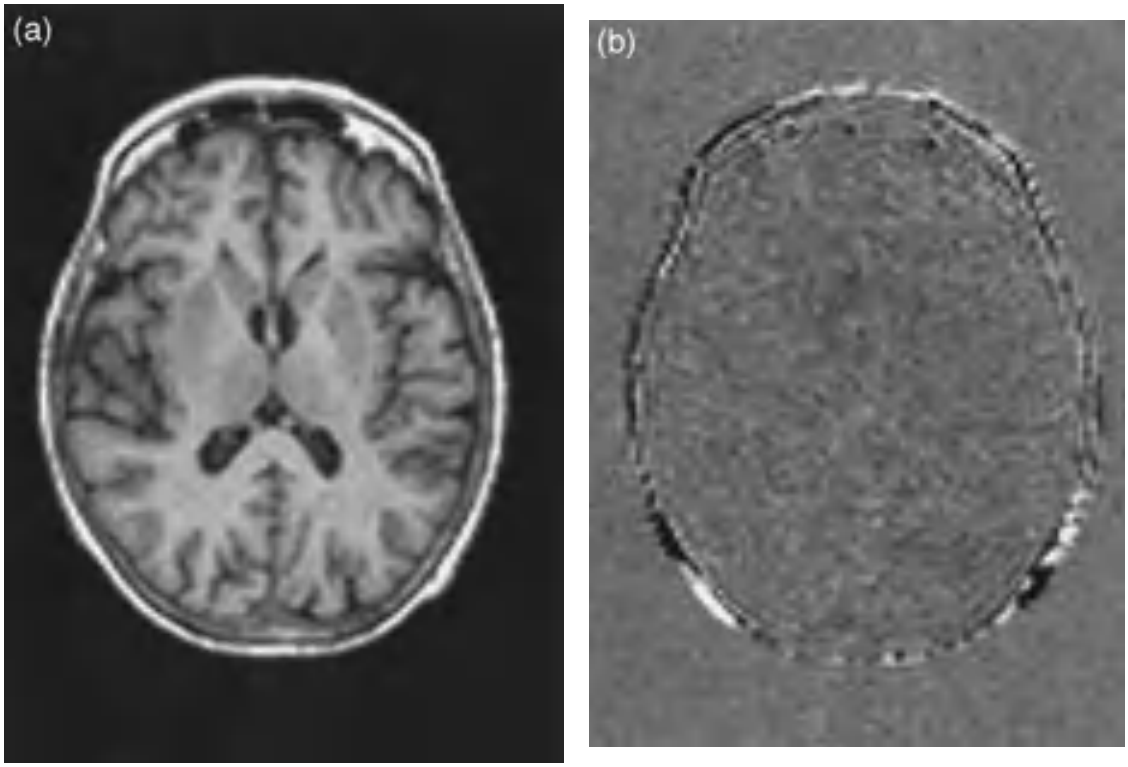

Figure 2 MRI in patients receiving electroconvulsive therapy. (a) Transverse T_1-weighted MR baseline scan showing the anatomy. (b) Difference image obtained by subtracting the baseline scan from the registered follow-up scan showing no evidence of acute structural changes in the brain following electroconvulsive therapy

autistic group, but not in the control group. As test performance declined in the autistic subjects, levels of the most labile high-energy phosphate compound and of membrane-building blocks decreased, and levels of membrane breakdown products increased. No significant correlations were present with age in either group or with IQ in the control group, suggesting that these findings were not the consequence of age or IQ effects. This study provides some evidence of alterations in brain energy and phospholipid metabolism in autism that correlate with psychological and language deficits.

12 ELECTROCONVULSIVE THERAPY

For many years clinicians have been concerned that electroconvulsive therapy may result in acute cerebral structural changes. Indeed, some retrospective imaging studies using MRI and CT have reported an association between a history of electroconvulsive therapy and cerebral change, particularly affecting the lateral ventricles and/or cerebral cortex. However, recently, a prospective MRI study of four electroconvulsive therapy-naïve depressed patients in which they underwent scanning 1 week prior to their first treatment with electroconvulsive therapy and then again following this treatment showed that, using accurate subvoxel registration and subtraction of serial MR images,[2,3] there was no significant difference in cerebral structure following electroconvulsive therapy, either within 24 h or after 6 weeks (Figure 2).[74]

A proton and ^{31}P MRS study of three patients found no evidence of changes in lactate or in cerebral energy metabolism following electroconvulsive therapy.[75] However, Woods and Chiu have found, using proton MRS, that electroconvulsive therapy reliably induces an elevation in the lipid signal that resonates at approximately 1.2 ppm and observed a similar increase in brain lipids in a patient with temporal lobe epilepsy temporarily off medication, the signal disappearing following restarting medication.[76] This is of interest given that elevations of brain concentrations of arachidonic acid and other free fatty acids have been demonstrated to occur after seizures induced in animals. Large shifts of potassium ions from the intra- to the extracellular space occur during seizure activity, and free fatty acids have a direct effect on membrane potassium ion conductance, suggesting that free fatty acids may play a primary role in seizure evolution in brain tissue.[76]

13 DYSLEXIA

MRI studies have inconsistently shown reversed or diminished asymmetry, compared with normal, in the brain in children with dyslexia, including loss of the usual left greater than right asymmetry of the lateral ventricles and right greater than left asymmetry of the temporal lobes; loss of the normal left greater than right asymmetry of the planum temporale in adolescents, which correlates with the degree of phonological decoding deficits; reversal of the normal left greater than right asymmetry of the angular gyrus in familial dyslexia; and loss

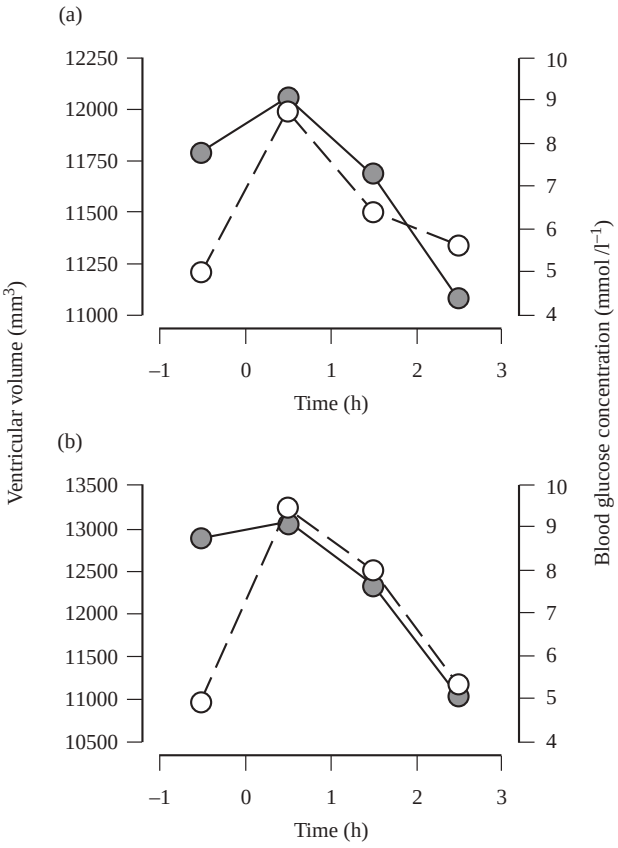

Figure 3 Volume changes in lateral ventricles following oral glucose loading. Blood glucose concentrations (○) and lateral ventricular volumes (●) for two human subjects (a and b) who each ingested 53.7 g glucose at time zero. (After Puri et al.[85])

of normal right greater than left asymmetry of the frontal cortices and bilaterally smaller size of the frontal cortices. Inconsistent corpus callosum changes have also been reported.[77]

In the first ^{31}P MRS study of dyslexia, Richardson and colleagues found elevated phosphomonoesters in the brain in dyslexia compared with that in controls.[78] This finding is consistent with the hypothesis that neuronal membrane phospholipid metabolism is abnormal in dyslexia, with reduced incorporation of phospholipids into neuronal membranes occurring.[79]

The first proton MRS study of dyslexia showed lateral differences in the ratios of choline to *N*-acetylaspartate and of creatine to *N*-acetylaspartate in the temporo-parietal region and the cerebellum in dyslexic subjects but not in controls.[80]

14 SPINAL INJURY

The first proton MRS study of the human motor cortex following incomplete spinal cord injury showed elevation of *N*-acetylaspartate in this part of the brain compared with normal controls.[81] The authors suggested that this might reflect neuronal adaptation to injury, the finding being consistent with the hypothesis that dendritic sprouting occurs in the motor cortex following recovery from incomplete spinal injury in humans. Clinically, this finding also suggests that MRS might provide a noninvasive method for monitoring such patients.

15 DRUG MONITORING

It is possible to use ^{7}Li MRS directly to measure the cerebral concentration of lithium while ^{19}F MRS can be used to measure the cerebral concentrations of psychotropic drugs containing fluorine, for example the selective serotonin reuptake inhibitor fluoxetine and the antipsychotics trifluoperazine and fluphenazine.[82]

16 FUTURE DIRECTIONS

As mentioned above, the recently developed MRI techniques of subvoxel registration of high-resolution 3D serial MR scans[2,3] and quantification of the changes thereby discovered[4] are only just starting to be applied in neuroimaging studies. The sensitivity and accuracy of these techniques hold great promise for neuroimaging applications and the discovery of important new facts concerning the central nervous system.[83,84] For example, they have been used recently to show that volumetric change takes place in the lateral ventricles in the human brain following oral glucose loading (Figure 3).[85]

Cerebral MRS is currently used primarily as a research tool in neuropsychiatry; in due course it is likely to become more widely used diagnostically and prognostically.

It seems probable that MRI and MRS will interface more often with other disciplines (for instance molecular genetics, as in ADHD) and other investigative tools (such as transcranial magnetic stimulation).

In summary, MRI and MRS are proving to be extremely useful in neuroscientific and neuropsychiatric research. These powerful noninvasive tools are likely to continue to grow in importance in these fields and to gain ever more important clinical applications.

17 RELATED ARTICLES

Brain Infection and Degenerative Disease Studied by Proton MRS; Brain MRS of Human Subjects; Brain Neoplasms in Humans Studied by Phosphorus-31 NMR Spectroscopy; Brain Neoplasms Studied by MRI; Brain Parenchyma Motion Observed by MRI; Hemodynamic Changes owing to Sensory Activation of the Brain Monitored by Echo-Planar Imaging; Central Nervous System Degenerative Disease Observed by MRI; Chemical Shift Imaging; CSF Velocity Imaging; Intracranial Infections; Localization and Registration Issues Important for Serial MRS Studies of Focal Brain Lesions; Magnetic Resonance Imaging of White Matter Disease; Structural and Functional MR in Epilepsy.

18 REFERENCES

1. S. E. Chua and P. J. McKenna, *Br. J. Psychiatry*, 1995, **166**, 563.

2. J. V. Hajnal, N. Saeed, E. J. Soar, A. Oatridge, I. R. Young, and G. M. Bydder, *J. Comput. Assist. Tomogr.*, 1995, **19**, 289.
3. J. V. Hajnal, N. Saeed, A. Oatridge, E. J. Williams, I. R. Young, and G. M. Bydder, *J. Comput. Assist. Tomogr.*, 1995, **19**, 677.
4. N. Saeed, B. K. Puri, A. Oatridge, J. V. Hajnal, and I. R. Young, *Magn. Reson. Med.*, 1998, **16**, 1237.
5. J. H. Gruzelier and R. Manchanda, *Br. J. Psychiatry*, 1982, **141**, 488.
6. J. H. Gruzelier 'Handbook of Schizophrenia', Vol. 5, ed. S. R. Steinhauer, J. H. Gruzelier, and J. Zubin, Elsevier, London, 1991, p. 599.
7. B. K. Puri, N. Saeed, A. J. Richardson, A. Oatridge, S. B. Hutton, J. V. Hajnal, and G. M. Bydder, *Schizophr. Res.*, 1999.
8. D. F. Horrobin, *Lancet*, 1977, **i**, 936.
9. D. F. Horrobin, A. I. M. Glen, and K. Vaddadi, *Schizophr. Res.*, 1994, **13**, 195.
10. B. K. Puri, A. J. Richardson, T. Easton, N. Saeed, A. Oatridge, J. V. Hajnal, D. F. Horrobin, and G. M. Bydder, *Schizophr. Res.*, 1999, **36**, 312.
11. J. W. Pettegrew, M. S. Keshavan, K. Panchalingam, S. Strychor, D. B. Kaplan, M. G. Tretta, and M. Allen, *Arch. Gen. Psychiatry*, 1991, **48**, 563.
12. J. A. Stanley, P. C. Williamson, D. J. Drost, T. J. Carr, R. J. Rylett, A. Malla, and R. T. Thompson, *Arch. Gen. Psychiatry*, 1995, **52**, 399.
13. D. F. Horrobin, *Prostaglandins Leukot. Essent. Fatty Acids*, 1996, **55**, 3.
14. T. P. George and M. W. Spence, *Arch. Gen. Psychiatry*, 1996, **53**, 1065.
15. K. O. Lim, E. Adalsteinsson, D. Spielman, E. V. Sullivan, M. J. Rosenbloom, and A. Pfefferbaum, *Arch. Gen. Psychiatry*, 1998, **55**, 346.
16. W. G. Iacono, G. N. Smith, M. Moreau, M. Beiser, J. A. Fleming, T. Y. Lin, and B. Flak, *Am. J. Psychiatry*, 1988, **145**, 820.
17. C. E. Coffey, G. S. Figiel, W. T. Djang, W. B. Saunders, and R. D. Weiner, *J. Neuropsychiatry Clin. Neurosci.*, 1989, **1**, 135.
18. E. Kramer-Ginsberg, B. S. Greenwald, K. R. Krishnan, B. Christiansen, J. Hu, M. Ashtari, M. Patel, and S. Pollack, *Am. J. Psychiatry*, 1999, **156**, 438.
19. S. Simpson, R. C. Baldwin, A. Jackson, and A. S. Burns, *Psychol. Med.*, 1998, **28**, 1015.
20. P. J. Shah, K. P. Ebmeier, M. F. Glabus, and G. M. Goodwin, *Br. J. Psychiatry*, 1998, **172**, 527.
21. T. Kato, T. Inubushi and N. Kato, *J. Neuropsychiatry Clin. Neurosci.*, 1998, **10**, 133.
22. S. A. Sarji, B. J. Abdullah, G. Kumar, A. H. Tan, and P. Narayanan, *Australas. Radiol.*, 1998, **42**, 293.
23. T. Shioiri, T. Kato, J. Murashita, H. Hamakawa, T. Inubushi, and S. Takahashi, *Biol. Psychiatry*, 1996, **40**, 785.
24. S. Saxena, A. L. Brody, J. M. Schwartz, and L. R. Baxter, *Br. J. Psychiatry*, 1998, **35 (Suppl.)**, 26.
25. R. Bartha, M. B. Stein, P. C. Williamson, D. J. Drost, R. W. Neufeld, T. J. Carr, G. Canaran, M. Densmore, G. Anderson, and A. R. Siddiqui, *Am. J. Psychiatry*, 1998, **155**, 1584.
26. D. Ebert, O. Speck, A. Konig, M. Berger, J. Hennig, and F. Hohagen, *Psychiatry Res.*, 1997, **74**, 173.
27. G. W. Hoffman Jr, E. H. Ellinwood Jr, W. J. Rockwell, R. J. Herfkens, J. K. Nishita, and L. F. Guthrie, *Biol. Psychiatry*, 1989, **25**, 894.
28. G. W. Hoffman Jr, E. H. Ellinwood Jr, W. J. Rockwell, R. J. Herfkens, J. K. Nishita, and L. F. Guthrie, *Biol. Psychiatry*, 1989, **26**, 321.
29. P. M. Doraiswamy, K. R. Krishnan, G. S. Figiel, M. M. Husain, O. B. Boyko, W. J. Rockwell, and E. H. Ellinwood Jr, *Biol. Psychiatry*, 1990, **28**, 110.
30. P. M. Doraiswamy, K. R. Krishnan, O. B. Boyko, et al., *Prog. Neuropsychopharmacol. Biol. Psychiatry*, 1991, **15**, 351.
31. K. Kingston, G. Szmukler, D. Andrewes, B. Tress, and P. Desmond, *Psychol. Med.*, 1996, **26**, 15.
32. K. G. Sieg, M. S. Hidler, M. A. Graham, R. L. Steele, and L. R. Kugler, *Int. J. Eat. Disord.*, 1997, **21**, 391.
33. T. Kato, T. Shioiri, J. Murashita, and T. Inubushi, *Prog. Neuropsychopharmacol. Biol. Psychiatry*, 1997, **21**, 719.
34. H. P. Schlemmer, R. Mockel, A. Marcus, F. Hentschel, C. Gopel, G. Becker, J. Kopke, F. Guckel, M. H. Schmidt, and M. Georgi, *Psychiatry Res.*, 1998, **82**, 171.
35. J. Swanson, F. X. Castellanos, M. Murias, G. LaHoste, and J. Kennedy, *Curr. Opin. Neurobiol.*, 1998, **8**, 263.
36. M. Mataro, C. Garcia-Sanchez, C. Junque, A. Estevez-Gonzalez, and J. Pujol, *Arch. Neurol.*, 1997, **54**, 963.
37. P. A. Filipek, M. Semrud-Clikeman, R. J. Steingard, P. F. Renshaw, D. N. Kennedy, and J. Biederman, *Neurology*, 1997, **48**, 589.
38. G. W. Hynd, M. Semrud-Clikeman, A. R. Lorys, E. S. Novey, D. Eliopulos, and H. Lyytinen, *J. Learn. Disabil.*, 1991, **24**, 141.
39. P. C. Berquin, J. N. Giedd, L. K. Jacobsen, S. D. Hamburger, A. L. Krain, J. L. Rapoport, and F. X. Castellanos, *Neurology*, 1998, **50**, 1087.
40. F. X. Castellanos, E. Lau, N. Tayebi, P. Lee, R. E. Long, J. N. Giedd, W. Sharp, W. L. Marsh, J. M. Walter, S. D. Hamburger, E. I. Ginns, J. L. Rapoport, and E. Sidransky, *Mol. Psychiatry*, 1998, **3**, 431.
41. K. Hayakawa, H. Kumagai, Y. Suzuki, N. Furusawa, T. Haga, T. Hoshi, Y. Fujiwara, and K. Yamaguchi, *Acta Radiol.*, 1992, **33**, 201.
42. R. Estruch, J. M. Nicolas, M. Salamero, C. Aragon, E. Sacanella, J. Fernandez-Sola, and a Urbano-Marquez, *J. Neurol. Sci.*, 1997, **146**, 145.
43. I. Agartz, R. Momenan, R. R. Rawlings, M. J. Kerich, and D. W. Hommer, *Arch. Gen. Psychiatry*, 1999, **56**, 356.
44. A Pfefferbaum, E. V. Sullivan, M. J. Rosenbloom, D. H. Mathalon, and K. O. Lim, *Arch. Gen. Psychiatry*, 1998, **55**, 905.
45. E. Antunez, R. Estruch, C. Cardenal, J. M. Nicolas, J. Fernandez-Sola, and A. Urbano-Marquez, *Am. J. Roentgenol.*, 1998, **171**, 1131.
46. R. Emsley, R. Smith, M. Roberts, S. Kapnias, H. Pieters, and S. Maritz, *Alcohol Alcohol.*, 1996, **31**, 479.
47. P. K. Shear, E. V. Sullivan, B. Lane, and A. Pfefferbaum, *Alcohol. Clin. Exp. Res.*, 1996, **20**, 1489.
48. E. V. Sullivan, D. H. Mathalon, K. O. Lim, L. Marsh, and A. Pfefferbaum, *Biol. Psychiatry*, 1998, **43**, 118.
49. N. R. Jagannathan, N. G. Desai, and P. Raghunathan, *Magn. Reson. Imag.*, 1996, **14**, 553.
50. L. Chang, C. M. Mehringer, T. Ernst, R. Melchor, H. Myers, D. Forney, and P. Satz, *Biol. Psychiatry*, 1997, **42**, 1105.
51. S. Kojima, K. Hirayama, H. Furumoto, T. Fukutake, and T. Hattori, *Rinsho Shinkeigaku*, 1993, **33**, 477.
52. K. S. Caldemeyer, S. W. Armstrong, K. K. George, C. C. Moran, and R. M. Pascuzzi, *J. Neuroimaging*, 1996, **6**, 167.
53. N. Yamanouchi, S. Okada, K. Kodama, T. Sakamoto, H. Sekine, S. Hirai, A. Murakami, N. Komatsu, and T. Sato, *Acta Neurol. Scand.*, 1997, **96**, 34.
54. X. Liu, J. A. Matochik, J. L. Cadet, and E. D. London, *Neuropsychopharmacology*, 1998, **18**, 243.
55. X. Liu, R. L. Phillips, S. M. Resnick, V. L. Villemagne, D. F. Wong, J. M. Stapleton, and E. D. London, *Acta Neurol. Scand.*, 1995, **92**, 83.
56. J. D. Christensen, M. J. Kaufman, J. M. Levin, J. H. Mendelson, B. L. Holman, B. M. Cohen, and P. F. Renshaw, *Magn. Reson. Med.*, 1996, **35**, 658.
57. P. Scheltens, *J. Neurol.*, 1999, **246**, 16.
58. G. T. Harvey, J. Hughes, I. G. McKeith, R. Briel, C. Ballard, A. Gholkar, P. Scheltens, R. H. Perry, P. Ince, and J. T. O'Brien, *Psychol. Med.*, 1999, **29**, 181.

59. H. Hanyu, Y. Imon, H. Sakurai, T. Iwamoto, M. Takasaki, H. Shindo, D. Kakizaki, and K. Abe, *Eur. J. Neurol.*, 1999, **6**, 195.
60. J. W. Pettegrew, W. E. Klunk, K. Panchalingam, R. J. McClure, and J. A. Stanley, *Ann. N. Y. Acad. Sci.*, 1997, **826**, 282.
61. R. A. Moats, T. Ernst, T. K. Shonk, and B. D. Ross, *Magn. Reson. Med.*, 1994, **32**, 110.
62. T. K. Shonk, R. A. Moats, P. Gifford, T. Michaelis, J. C. Mandigo, J. Izumi, and B. D. Ross, *Radiology*, 1995, **195**, 65.
63. W. E. Klunk, K. Panchalingam, J. Moossy, R. J. McClure, and J. W. Pettegrew, *Neurology*, 1992, **42**, 1578.
64. R. J. McClure, J. N. Kanfer, K. Panchalingam, W. E. Klunk, and J. W. Pettegrew, *Neuroimaging Clin. N. Am.*, 1995, **5**, 69.
65. J. M. Hoffman 'Brain Imaging in Clinical Psychiatry', ed. K. R. R. Krishnan and P. M. Doraiswamy, Marcel Dekker, New York, 1997, p. 544.
66. B. G. Jenkins, W. J. Koroshetz, M. F. Beal, and B. R. Rosen, *Neurology*, 1993, **43**, 2689.
67. S. D. Taylor-Robinson, R. A. Weeks, D. J. Bryant, J. Sargentoni, C. D. Marcus, A. E. Harding, and D. J. Brooks, *Mov. Disord.*, 1996, **11**, 167.
68. B. G. Jenkins, H. D. Rosas, Y. C. Chen, T. Makabe, R. Myers, M. MacDonald, B. R. Rosen, M. F. Beal, and W. J. Koroshetz, *Neurology*, 1998, **50**, 1357.
69. S. Deb and B. Thompson, *Br. J. Psychiatry*, 1998, **173**, 299.
70. N. S. Harris, E. Courchesne, J. Townsend, R. A. Carper, and C. Lord, *Brain Res. Cogn. Brain Res.*, 1999, **8**, 61.
71. Y. H. Ryu, J. D. Lee, P. H. Yoon, D. I. Kim, H. B. Lee, and Y. J. Shin, *Eur. J. Nucl. Med.*, 1999, **26**, 253.
72. T. Hashimoto, M. Tayama, M. Miyazaki, Y. Yoneda, T. Yoshimoto, M. Harada, H. Miyoshi, M. Tanouchi, and Y. Kuroda, *J. Child Neurol.*, 1997, **12**, 91.
73. N. J. Minshew, G. Goldstein, S. M. Dombrowski, K. Panchalingam, and J. W. Pettegrew, *Biol. Psychiatry*, 1993, **33**, 762.
74. B. K. Puri, A. Oatridge, N. Saeed, J. E. Ging, H. M. McKee, S. K. Lekh, and J. V. Hajnal, *Br. J. Psychiatry*, 1998, **173**, 267.
75. S. R. Felber, R. Pycha, M. Hummer, F. T. Aichner, and W. W. Fleischhacker, *Biol. Psychiatry*, 1993, **33**, 651.
76. B. T. Woods and T. M. Chiu, *Adv. Exp. Med. Biol.*, 1992, **318**, 267.
77. J. N. Giedd and F. X. Castellanos, 'Brain Imaging in Clinical Psychiatry', ed K. R. R. Krishnan and P. M. Doraiswamy, Marcel Dekker, New York, 1997, p. 126.
78. A. J. Richardson, I. J. Cox, J. Sargentoni, and B. K. Puri, *NMR Biomed.*, 1997, **10**, 309.
79. D. F. Horrobin, A. I. M. Glen, and C. J. Hudson, *Med. Hypotheses*, 1995, **45**, 605.
80. C. Rae, M. A. Lee, R. M. Dixon, A. M. Balmire, C. H. Thompson, P. Styles, J. Talcott, A. J. Richardson, and J. F. Stein, *Lancet*, 1998, **351**, 1849.
81. B. K. Puri, H. C. Smith, I. J. Cox, J. Sargentoni, G. Savic, D. W. Maskill, H. L. Frankel, P. H. Ellaway, and N. J. Davey, *J. Neurol. Neurosurg. Psychiatry*, 1998, **65**, 748.
82. H. C. Charles, T. B. Snyderman, and E. Ahearn, 'Brain Imaging in Clinical Psychiatry', ed. K. R. R. Krishnan and P. M. Doraiswamy, Marcel Dekker, New York, 1997, p. 20.
83. G. M. Bydder and J. V. Hajnal, 'Advanced MR Imaging Techniques', ed. W. G. Bradley and G. M. Bydder, Martin Dunitz, London, 1997, p. 239.
84. G. M. Bydder and J. V. Hajnal, 'Advanced MR Imaging Techniques', ed. W. G. Bradley and G. M. Bydder, Martin Dunitz, London, 1997, p. 259.
85. B. K. Puri, H. J. Lewis, N. Saeed, and N. J. Davey, *Exp. Physiol.*, 1999, **84**, 223.

Biographical Sketch

Basant K. Puri. *b* 1961. B.A. 1982, B.Chir. 1984, M.B. 1985, M.A. 1986, University of Cambridge; M.R.C. Psych. 1989; Dip. Math. 2000. Residency in psychiatry, Addenbrooke's Hospital, Cambridge 1986–88. Research fellow in molecular genetics, MRC Molecular Neurobiology Unit, Cambridge and Peterhouse, Cambridge University 1988–89. Residency in psychiatry, Charing Cross & Westminster Medical School, London 1990–96. Senior Lecturer and Consultant Psychiatrist, MRI Unit, MRC Clinical Sciences Centre, Imperial College School of Medicine, Hammersmith Hospital, London University, and Honorary Consultant, Department of Radiology, Hammersmith Hospital, London 1997–present. Approx. 13 books (psychiatry, neuroscience, statistics) and 60 papers. Research interests: central nervous system MRI and MRS.

Pediatric Brain MRI: Applications in Neonates and Infants

Jacqueline M. Pennock

Royal Postgraduate Medical School, Hammersmith Hospital, London, UK

1 INTRODUCTION

The ability of magnetic resonance imaging (MRI) to provide physiological, anatomical and functional information without posing any biological hazard makes it particularly suitable for studying the central nervous system of children where repeated examinations may be critical for diagnosis.

Clinical MRI systems are almost always designed for adults and sequences are optimized to maximize contrast in adults. The first task in examining infants is often to modify the equipment to optimize it for small infants and to develop imaging patterns which provide equivalent contrast to that seen in adults. This article covers particular techniques used to examine preterm babies and infants, the normal appearances of the developing brain, and clinical conditions encountered in infants and children.

2 PATIENT PREPARATION

For a successful examination, both the child and the parent must be considered. We actively encourage parents to accompany their infants to the imaging unit so that they do not feel excluded and can see that their child is asleep and comfortable. If it is their wish, we invite the parents to watch us putting their baby into the machine, bearing in mind that for many parents seeing their sleeping child enclosed in a head coil and being slid into the machine may be a stressful experience. With older children, parents are asked to stay with them during the examination, although talking is limited to the time between scans.

2.1 Sedation

Diagnostic images can only be obtained in a quiet, immobile child, so if possible appointments are made to coincide with the natural sleeping pattern of the child. Children come to a children's day ward where they are seen by a pediatrician who goes through the metal check with the parent and ensures that there are no contraindications to sedation. This is given to children under 2 years of age 20–30 min before the scan time. The child stays on the ward with the supervision of a nurse until she or he is asleep and is then brought to the scanning unit. Once the scan is over, the child returns to the ward until she or he is fully recovered.

Preterm infants and neonates are fed prior to the examination and scanned during natural sleep. However, in the irritable stable neonate, oral chloral hydrate via a nasal gastric tube or per rectum (50–80 mg kg^{-1}) is used. For infants aged 6 weeks and over, oral chloral hydrate (70–100 mg kg^{-1}) is given. This dose is successful in most children up to the age of 3 years or about 15 kg. Once the child is asleep, further immobilization is achieved by partly surrounding the head with a plastic globe filled with tiny polystyrene balls which is then evacuated. This minimizes motion, helps to keep the baby warm and provides insulation from sound. Swaddling the infant also prevents movement and provides extra security and warmth. Neonates usually sleep better on their sides, and this position also reduces the risk of inhalation of regurgitated milk or vomit.

MRI of the critically ill intubated infant is feasible as long as the imaging unit has the appropriate facilities to offer the same care for the child as does the neonatal intensive care unit (NICU). These include suitably trained staff, gases and suction, and pediatric-sized resuscitation equipment.

In our hospital the baby is brought from the NICU in a standard Vickers transport incubator. The incubator is parked and locked in a corner of the room well beyond the 5 G (5×10^{-4} T) line and, as an extra precaution, attached to a wall by a plastic chain. Infants are ventilated from the Vicker neovent unit via long extension tubes from the incubator to the baby, with appropriate adjustment of the inspiratory and expiratory pressure to take account of the large dead space.

2.2 Monitoring

Monitoring of the sedated and naturally sleeping infant is mandatory. A variety of magnetic resonance (MR) compatible physiological monitoring devices is available for monitoring blood pressure, heart rate, respiration, and blood oxygen saturation. We use electrocardiogram (ECG) monitoring with fiber optic leads and infant-sized MR-compatible electrodes, as well as pulse oximetry with neonatal probes attached to the infant's foot to display blood oxygen saturation and pulse rate. Further details and information on the sedation and anesthesia of the critically ill infant is available in the radiological literature.[1–3]

2.3 General Safety

Baby clothing with metal poppers should be removed. Although the fastenings are not ferromagnetic they may conduct eddy currents which can lead to artifacted images. An infant is almost always accompanied by medical staff and parents unaccustomed to an MR unit, and constant care has to be taken to check for loose metal objects on persons in a magnetic field. Pacemakers and aneurysm clips are usually associated with an older population; however, young mothers may also have aneurysm clips. A strict routine and protocol for access is necessary.

Scheduling of sedated infants and sleeping children is difficult and requires considerable flexibility. It is much easier to have exclusively pediatric sessions and not to try to mix sedated and sleeping children with ambulant adults. Prior knowledge of the clinical condition with a presumptive diagnosis is essential so that suitable protocols can be set up before each scan. Protocols which we have found useful in neonatal imaging are given in Table 1.

Table 1 Suggested Protocol for Imaging Neonates at 1.0 T

	First scan (all ages, short *TR*/*TE* SE)	Inversion recovery	T_2-weighted spin echo
Slice orientation	Transverse	Transverse	Transverse
Phase-encoding axis	Left–right	Left–right	Left–right
Number of slices	24	18	24
Echo time (*TE*)	20	30	200–120[a]
Inversion time (*TI*)	–	1500–700[a]	–
Repeat time (*TR*)	860	6000–3500	3500
Field-of-view	22–25	22–25[a]	22–25
Phase resolution	192	128	128
Frequency encode resolution	256	256	256
Number of signals (average)	2	1 or 2	1 or 2
Slice thickness (mm)	4	5–6	5
Slice gap	0	0	0
Receive coil	Small diameter	Small diameter	Small diameter
Flip angle (degrees)	90	90	90
Estimated time of scan	4 min	Variable	Variable

[a]Choice will depend on age of infant (see Table 2).

3 TECHNICAL CONSIDERATIONS

The signal-to-noise ratio is an important factor in producing high quality diagnostic images at all field strengths. Image quality can be improved by using the smallest diameter coil available. Adult knee coils with an internal diameter of approximately 19 cm have proved useful for imaging premature infants (head circumference approximately 30 cm) as well as infants up to 45 weeks gestational age. For children up to 18 months of age we use a receiver coil with an internal diameter of 24 cm. This coil is made in two halves of clear Perspex, making positioning and observation of the baby easier.

4 PULSE SEQUENCES

The neonatal brain contains a higher proportion of water (92–95%) than the adult brain (82–85%) and this is associated with a marked increase in T_1 and T_2.[4] The amount of water in the brain falls with increasing age, and by 2 years of age it has almost reached adult levels.[5]

A brief description of the standard pulse sequences and useful variations for imaging neonates and children are given below. The major pulse sequences and their specific variations for neonatal practice are shown in Table 2.

4.1 The Inversion–Recovery (IR) Sequence

The short inversion time (*TI*) inversion–recovery (STIR) sequence is of value in demonstrating myelination and pathological periventricular changes where the cerebrospinal fluid (CSF) signal can be kept less than that of brain.[6] This sequence has many features in common with the T_2-weighted spin echo sequence, but gives greater gray–white matter contrast (Figure 1).

The medium *TI* version of the IR sequence provides excellent gray–white matter contrast and displays white matter with high signal intensity and gray matter with a lower signal intensity. This sequence is particularly useful for scan-

Table 2 Inversion Recovery and Spin Echo (SE) sequences at 1.0 T

Age	Type	*TR* (ms)	*TE* (ms)	*TI* (ms)
Inversion–recovery sequences				
29–34 weeks	IR medium *TI*	7000	30	1500
35–39 weeks		6500	30	1200
40 weeks to 3 months		3800	30	950
>3 months to 2 years		3500	30	800
>2 years		3200	30	700
<3 months	FLAIR long *TI*	6000	240	2100
>3 months		6000	160	2100
All ages	STIR short *TI*	3800	30	130–150
Spin echo sequences				
All ages	T_1-weighted	860	20	
$\leqslant$2 years	T_2-weighted	3500	120	
>2 years	T_2-weighted	2500	20/80	

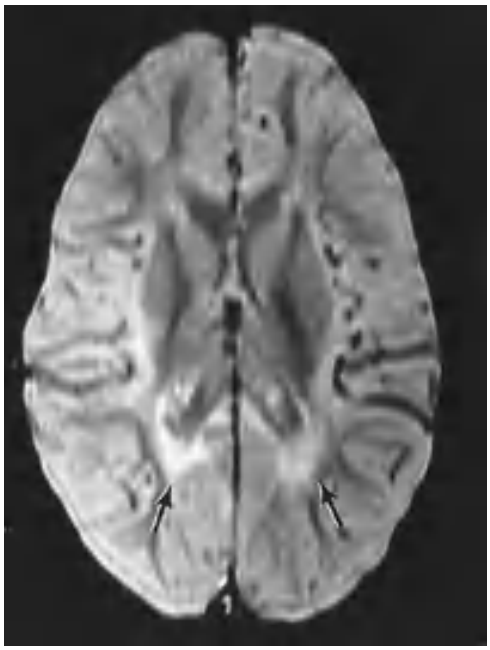

Figure 1 Female infant aged 9 months. Short *TI* inversion recovery (STIR) sequence (IR 3000/30/125). Pathological white matter adjacent to the posterior horns of the lateral ventricles is seen (arrows). The CSF is displayed as moderate signal intensity and the myelin as low signal intensity

ning the developing brain, especially for assessment of myelination, but the *TI* requires adjustment to accommodate the changing water content of the brain with age (see Figure 4 and Section 5).

The long *TI*, long *TE* version of this sequence is designed to display the CSF with low signal intensity and heavy T_2-weighting. The acronym for this sequence is FLAIR (fluid attenuated inversion–recovery sequence) and it provides better lesion conspicuity than conventional T_2 spin echo sequences (Figure 2).[7] It is not always helpful in the immature brain, but in older children we have found it of great help for lesions with a periventricular distribution.

4.2 The Spin Echo Sequence

The short *TR TE* T_1-weighted spin echo sequence has less gray–white matter contrast than the medium *TI* inversion recovery sequence. However, the former sequence is quicker and is recommended for use as the first sequence in all studies on sedated infants under 2 years of age. It is extremely useful for the assessment of brain swelling, hemorrhage, cystic change, and contrast enhancement with gadopentetate dimeglumine.

With the T_2-weighted spin echo sequence it is necessary to increase the *TE* to 120–200 ms in order to identify long T_2 lesions against the background of the long T_2 of the immature brain.[8] However, the extended *TE* results in high signal inten-

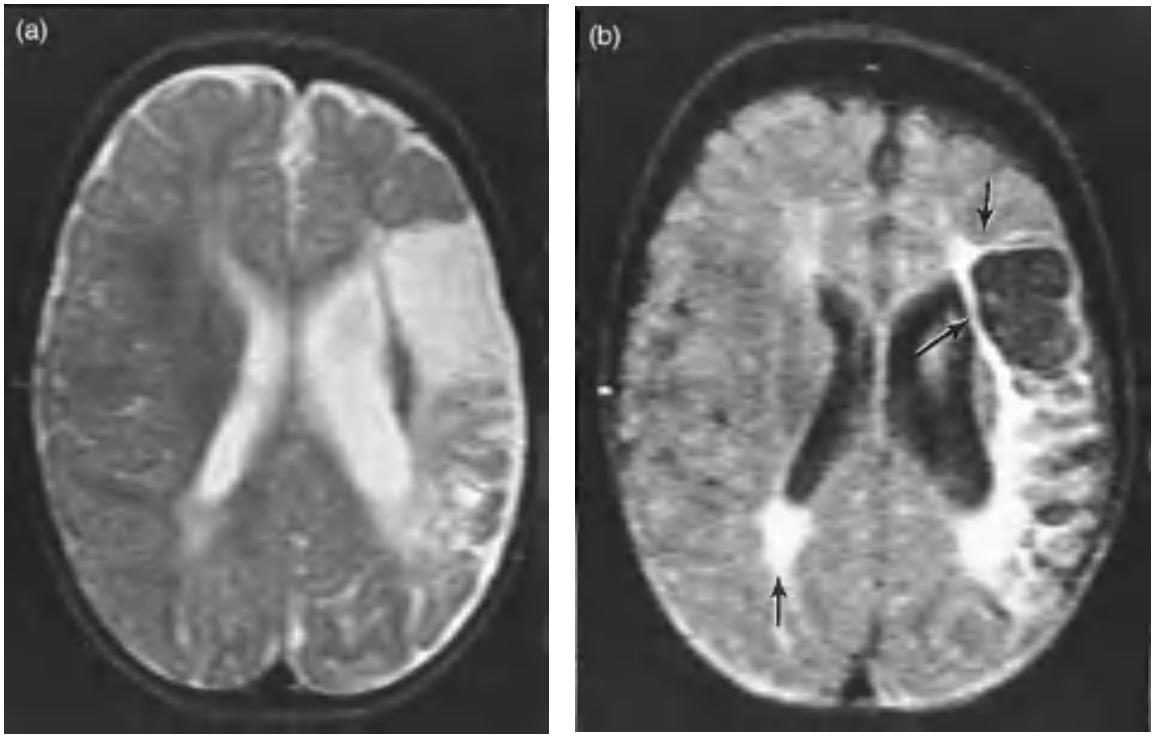

Figure 2 Male infant aged 1 year. (a) T_2-weighted spin echo (SE 2700/120) and (b) FLAIR (IR 7203/240/2100) sequences. A porencephalic cyst is seen in both images in the left hemisphere. Gliosis is shown as high signal intensity in both sequences; however, it appears more extensive and is seen with greater conspicuity in (b) (arrows). Note the low signal intensity of CSF within the porencephalic cyst with the FLAIR sequence

sity of CSF, which makes it difficult to detect lesions in a periventricular distribution.

4.3 Diffusion Weighted Imaging

Image contrast in diffusion weighted sequences depends on the molecular motion of water. These sequences are particularly useful for demonstrating early myelination before it can be seen with conventional sequences.[9] It also shows regions of focal infarction and diffuse ischemic anoxic brain injury which are not visible on spin echo and inversion–recovery images in the early phase (see Section 9).

4.4 Magnetization Transfer Techniques

These sequences have proved useful for improving lesion contrast both for short and long T_1 lesions[10] and in newborn infants the conspicuity of some cystic lesions is improved. It is also a useful technique for demonstrating myelination.

4.5 MR Angiography

MR angiography (MRA) is a noninvasive method of examining cerebral blood flow, although its use in pediatric practice has so far been limited. Cerebral blood flow is slow in infants and the blood vessels are smaller than in adults. A recent innovation in this technique has been the implementation of magnetization transfer MRA which involves the application of a specialized frequency-selective pulse followed by the desired MRA sequence. This results in a darkening of the background static tissue with an increase in contrast with the flowing blood. Our initial studies using two- and three-dimensional time-of-flight angiography have been of value in showing the internal carotid and basilar arteries and the proximal regions of the anterior, middle, and posterior cerebral arteries in the term infant (Figure 3). Large veins are also well shown.

Figure 3 Three-dimensional time-of-flight (*TR* 44, *TE* 8) angiogram: an 18-month-old male infant with known infarction of the left middle cerebral artery. The anterior, posterior, and middle cerebral arteries are seen, but there is a paucity of vessels on the left in the anterior branches from the middle cerebral artery (arrows)

4.6 The Gradient Echo (GE) and Partial Saturation (PS) Sequences

The gradient echo and partial saturation sequences have a specific role in pediatric practice, especially in the detection of neonatal hemorrhage. Low signal regions in and around hematomas are seen with higher sensitivity with partial saturation sequences than with spin echo sequences, indicating a significant contribution from susceptibility effects.[11] Phase maps can be derived from two partial saturation sequences with different values of *TE*, and are particularly useful for looking at the susceptibility effects of intracerebral hemorrhage.[12]

The use of these sequences in fast imaging techniques increases the speed of MR examinations, which is of particular interest when scanning infants; however, high signal from CSF remains a problem.[13] A GE sequence with a *TE* of 29 ms and a flip angle that corresponds to the choice of *TR* is recommended at 1.5 T to optimize the detection of calcification in the brain.[14]

4.7 Volume Imaging

This may be of particular value in infants and children because reconstruction and reslicing of images can provide a precise correction for differences in registration of follow-up examinations so that subtle differences in growth and development can be recognized.

5 NORMAL DEVELOPMENT AND MRI APPEARANCES

During the first 2 years of life the pediatric brain changes rapidly as physiological myelination takes place. This continues at a slower rate into the second decade. The process of myelination begins in utero and is first seen in the cerebellum and brainstem and then spreads from the posterior limb of the internal capsule to the postcentral gyrus. After birth, white matter develops in a predictable manner with sensory tracts myelinating before motor tracts from dorsal to ventral and from central to the peripheral areas of the brain.[15,16] Several descriptions of this process with MRI using a variety of sequences are available in the literature.[2,3,17–20] The pattern of development from 29 weeks gestational age to 1 year of age is shown by IR sequences in Figure 4.

5.1 Delays or Deficits in Myelination

Delays or deficits in myelination are difficult to recognize before 3–6 months of age, since relatively little myelin is present. Conversely, after 2 years of age there is time for cases of delayed myelination to 'catch up'. As a result, delays or defi-

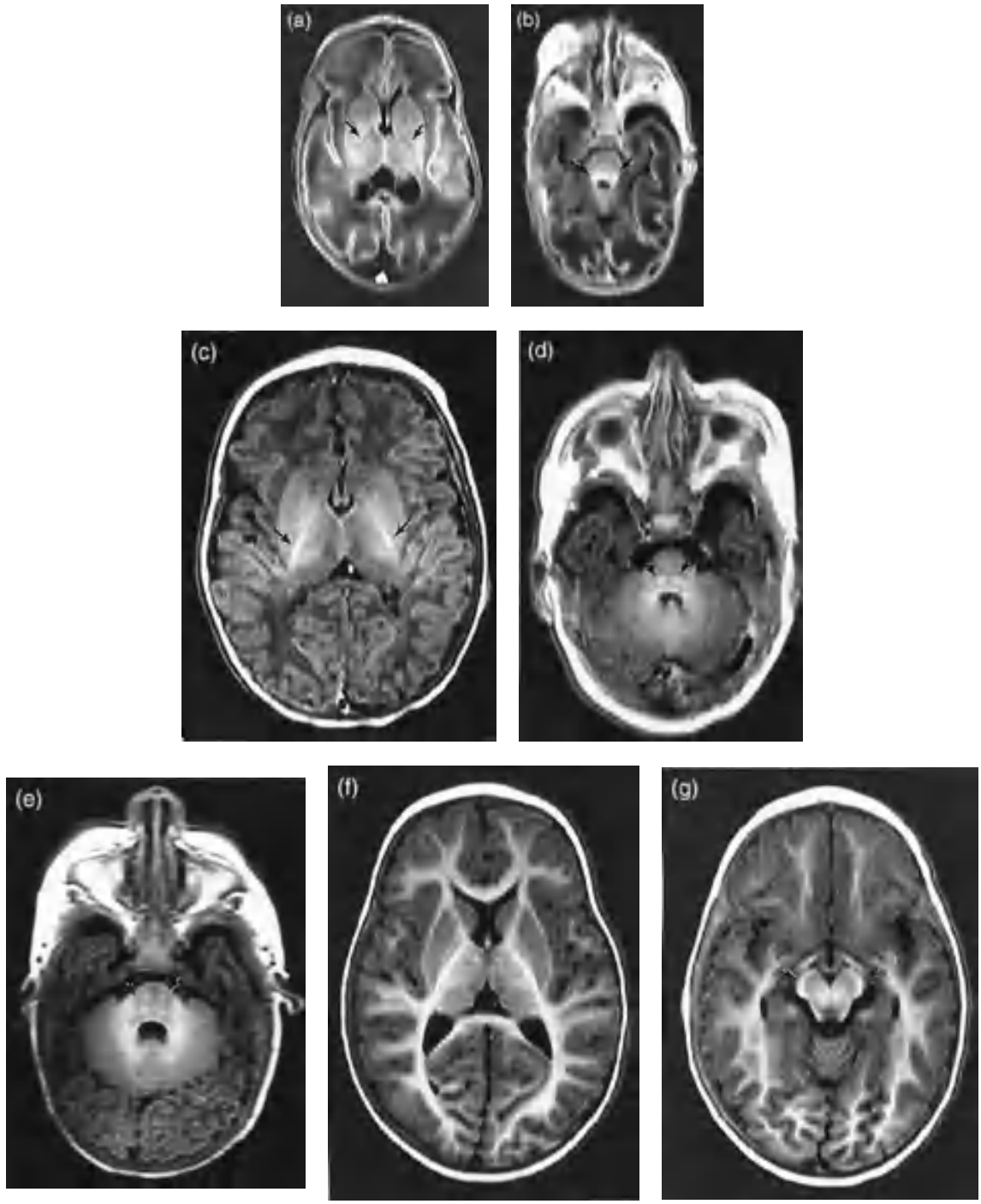

Figure 4 Infant born at 29 weeks gestational age and examined at 31 weeks gestational age (IR 7096/30/1500). At the level of the diencephalon (a) no myelin is seen; however, the posterior limb of the internal capsule is seen as low signal intensity (arrows), the remaining white matter is featureless. The cortex is of high signal intensity and the gyral pattern is underdeveloped. At the level of the pons (b) the corticospinal tracts are of low signal intensity (SI); however, myelin is seen in the medial longitudinal fasciculus and the inferior cerebellar peduncle (arrows). Term infant (IR 3500/30/950) (c–d). At the level of the diencephalon (c) the cortex remains of higher SI than unmyelinated white matter, but more structure is seen than in (a). Myelination is present in the ventrolateral nuclei in the thalami and in the posterior limb of the internal capsule (arrows). The lentiform nuclei have relatively high signal compared to the caudate nuclei and the thalami. At the level of the pons (d) myelin is seen in the medial lemnisci (arrows). At the age of 2 months at the level of the pons (e) myelin is present in the corticospinal tracts (arrows) anterior to the medial leminisci and further myelination is seen in the cerebellum. (f, g) Infant aged 12 months (IR 3200/30/800). At the level of the diencephalon (f) myelination is now seen throughout the internal and external capsule, along the occipitothalamic pathways and the corpus callosum. At the level of the mesencephalon (g) myelin is seen in the crus cerebri (arrows)

cits are most obvious from 6 to 24 months of age. With only limited information about the normal range we have preferred to use age-matched controls and diagnose delays only in the absence of or marked reduction in myelination of named tracts or commissures relative to controls, with both examinations performed using the same technique.

Delays or deficits in myelination have been recognized following probable intrauterine rubella infection, in posthemorrhagic hydrocephalus, after hypoxic ischemic encephalopathy, infarction, periventricular cystic leukomalacia, and metabolic disease.

6 INTRACRANIAL HEMORRHAGE

Intraventricular/periventricular hemorrhage (IVH/PVH) is the most important and most common type of hemorrhage in infants of less than 32 weeks gestation, with 90% of the hemorrhage occurring in the germinal matrix adjacent to the heads of the caudate nuclei.[21,22]

The basal ganglia are the most vulnerable site for hemorrhagic lesions in term infants suffering from severe birth asphyxia.[22] Ultrasound is used to detect and monitor the progression of IVH/PVH in the early stages in infants too sick to transport to the MR unit. However, MR is useful in the stable neonate[23] and for long-term follow-up. The MR appearance of hemorrhage parallels that seen in adults; however, in neonates hemorrhage occurs against a background of long normal values of brain T_1 and T_2, so that the T_2 of hematoma may appear distinctly shorter than that of the surrounding brain (Figure 5).

The signal characteristics of subdural and extradural hematomas are similar to those seen in adults. Subarachnoid blood, especially along the Rolandic fissure, is a common finding in the newborn term infant (Figure 6).

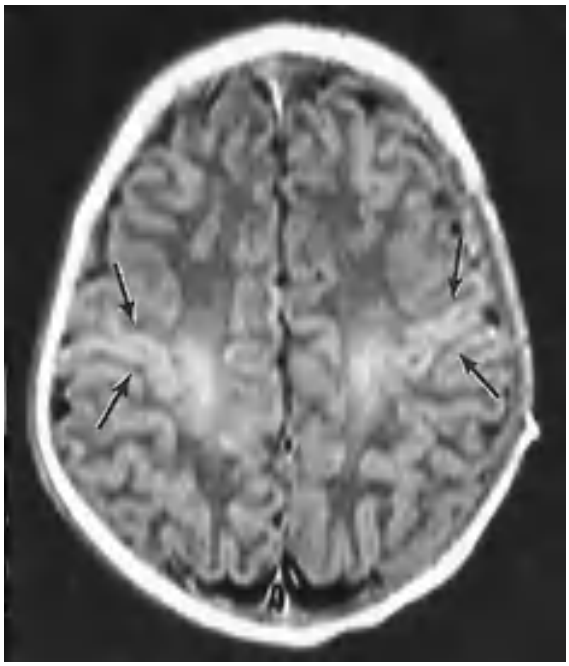

Figure 6 Normal term infant examined at 24 hours of age (IR 3800/30/950). Note the high signal intensity of the subarachnoid blood along the Rolandic fissure (arrows)

The ability to demonstrate methemaglobin and hemosiderin by a shortening of T_2* and susceptibility effects provides a high degree of sensitivity, and may function as a marker of early hemorrhage years after the event.[24] The late sequelae of intracranial hemorrhage may have important consequences such as hydrocephalus.

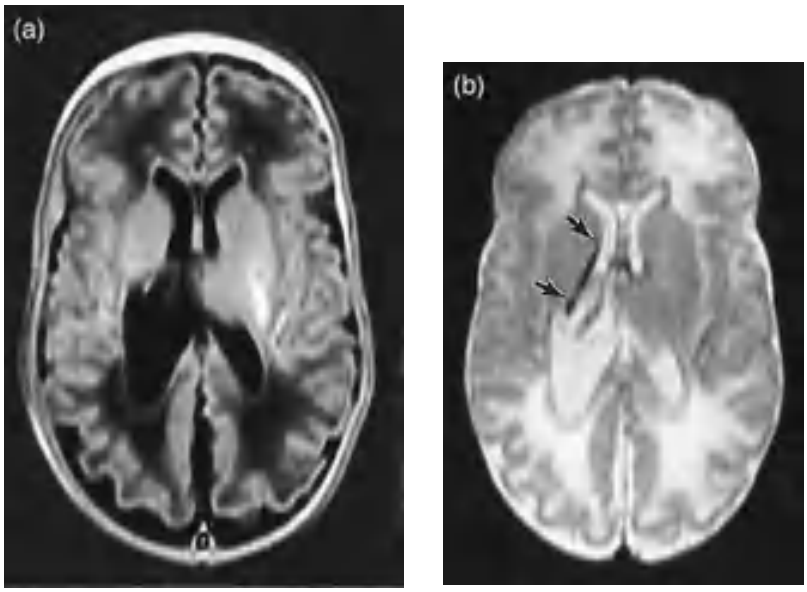

Figure 5 Female infant with IVH/PVH born at 26 weeks gestational age and examined at 40 weeks gestational age. (a) Inversion–recovery (IR 6000/30/1200) and (b) T_2-weighted spin echo (SE 2700/120) sequences. Hemorrhage is seen as high signal intensity on the IR image (a), but is seen more clearly on (b) as low signal intensity (arrows). Myelin in the posterior limb of the internal capsule is better seen in (a) than in (b)

7 PERIVENTRICULAR LEUKOMALACIA

The second most frequent condition to afflict premature infants is periventricular leukomalacia (PVL),[21,22] which occurs in a characteristic distribution in white matter around the lateral ventricles. Ultrasound scanning is generally used to make the diagnosis of leukomalacia; however, periventricular cysts and subcortical cysts are clearly seen with MRI in the early neonatal period and the changes can be quite extreme. Sometimes the cysts coalesce and become continuous with the adjacent ventricles producing hydrocephalus. The presence of severe or moderately severe cysts in infancy is frequently associated with a delay or deficit in myelination (Figure 7).

The MRI features are closely correlated with clinical outcome.[25] For example, infants with mild periventricular change on MRI have a mild spastic diplegia and normal intellectual development, whereas infants with subcortical cysts, diminution of white matter and microcephaly are severely mentally retarded with quadriplegia and seizures. In older children PVL is seen, with a T_2-weighted spin echo sequence, as an increased signal intensity usually in white matter in the centrum semiovale and adjacent to the anterior and/or the posterior horns of the lateral ventricles. We have found greater conspicuity of the lesions with the FLAIR and the short *TI* inversion–recovery sequences. To date, MRI has been most useful for studying the late stages of cystic leukomalacia.[26] MRI also permits retrospective diagnosis of the condition in infants who were not scanned either during the neonatal period or were scanned at a stage of evolution when the cysts were not apparent.

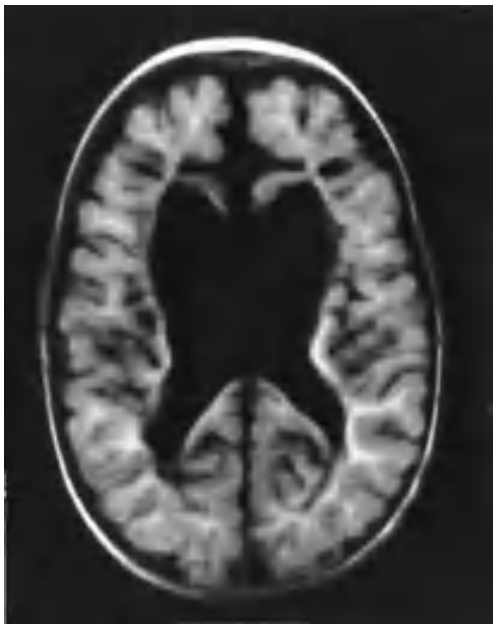

Figure 7 Male infant with severe cystic periventricular leukomalacia born at 33 weeks and examined aged 11 months (IR 1800/44/600). There is a severe delay in myelination compared with that seen in Figure 4(f)

8 INFARCTION

Cerebral infarction is most commonly seen in term infants and appears as a region of increased T_1 and T_2 which may be difficult to distinguish from areas of unmyelinated white matter normally present in the brain. There may be a loss of gray–white matter contrast and loss of the normal gyral pattern in a focal area, with or without a slight increase in T_1. The use of diffusion weighted imaging, where contrast is mainly determined by differences in the molecular motion of water (and not T_1 and T_2), may show the extent of the lesion within hours of the onset of injury (Figure 8).[27]

However, 1–4 days after the onset of symptoms, changes in T_1 and T_2 occur and the region of infarction may become visible with standard imaging techniques. With increasing age there is some apparent shrinking of the lesion and a porencephalic cyst may develop. Some porencephalic cysts decrease in size, some remain the same size, and others appear smaller due to increasing head size (Figure 9). Associated hydrocephalus with porencephalic cysts communicating with the ventricles may produce an apparent increase in the size of cysts. Wallerian degeneration within the corticospinal tracts can be seen as early as 7 days after the insult in newborn infants, with atrophy of the brainstem occurring by 3 months of age. These findings occur much earlier in children than in adults.[28,29]

9 HYPOXIC ISCHEMIC ENCEPHALOPATHY

Hypoxic ischemic encephalopathy (HIE) is most frequently seen in term infants[22] and the pattern of damage and its evolution is very variable even in children who appear to be seriously affected immediately after birth. Specific early MR features include brain swelling and increased signal intensity on the inversion–recovery sequence in the cortex which is usually the most marked around the Rolandic fissure with decreased signal intensity on the T_2-weighted spin echo sequence. Loss of the normal signal intensity in the posterior limb of the internal capsules as well as focal hemorrhagic lesions in the basal ganglia, which are most commonly located in the lentiform nuclei, are also seen (Figure 10).

Brain swelling is not seen after the first 4 days and the evolution of the early MR findings may include breakdown of white matter into subcortical cysts within the first 2 weeks of life, with diminution of white matter and a severe delay in myelination by 3 months of age. The basal ganglia lesions become less obvious with time and may regress completely. Development of myelination in the posterior limbs of the internal capsules may occur by 3 months of age. Alternatively, the lesions in the basal ganglia and thalami become cystic and this may occur as early as 17 days of age with atrophy of the basal ganglia by 6 weeks of age. The degree of cortical highlighting is also variable and diminishes with time; however, in our experience it may still be present up to 6 months of age.

Early diffusion weighted imaging is important in these children (Figure 11) and correctly predicts the sites of injury which become more obvious on standard imaging at a later stage. These striking early MR findings closely correlate with the location of the selective neuronal necrosis[21,22] seen at post mortem in asphyxiated infants.

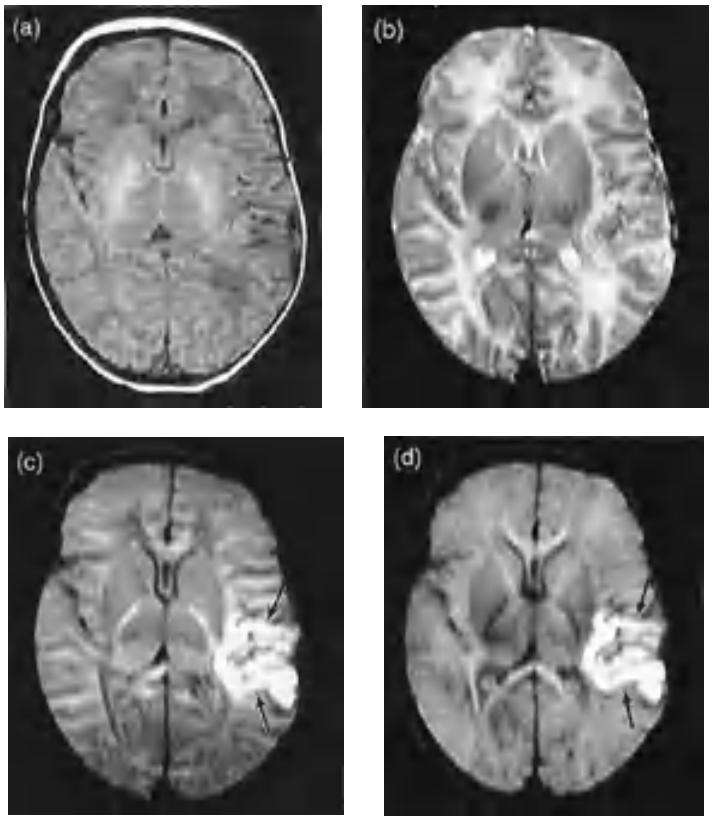

Figure 8 Cerebral infarction in a male infant born at 40 weeks gestational age. (a) Transverse T_1-weighted spin echo (SE 720/20), (b) T_2-weighted spin echo (SE 3000/120), (c) diffusion weighted (SE pulse interval/200 ms, A-P sensitization, b = 600 s mm^{-2}), and (d) diffusion weighted (SE pulse interval/200 ms through plane sensitization, b = 600 s mm^{-2}) images. The infarction is difficult to recognize on (a) or (b) but is readily apparent as a high signal region on (c) and (d) (arrows)

The prognosis for infants with global hypoxia can be devastating. However, new cerebroprotective drugs are at present undergoing investigation in stroke models, but these therapies are only effective in the first few hours after birth before the onset of secondary energy failure.[30] It is hoped that these MR findings may be used to monitor such treatment in the future.

10 HYDROCEPHALUS

Hydrocephalus can arise in a number of circumstances in children.[31] The ventricular size can be readily assessed, and MRI has obvious advantages in the long-term follow-up of children with shunts. It is also possible to recognize periventricular edema both with spin echo and inversion–recovery sequences; this condition may regress following satisfactory ventricular shunting. The periventricular changes are displayed as increased signal intensity in the periventricular regions in some cases of hydrocephalus, probably indicating transependymal spread of fluid. We have found the STIR sequence (CSF displayed as moderate signal intensity) and the FLAIR sequence (CSF displayed as low signal intensity) are better than the conventional spin echo sequence for looking at periventricular change in children with hydrocephalus (Figure 12). However, similar changes may be seen in other diseases such as periventricular leukomalacia, and the changes are not specific. It is not always possible to distinguish between acute and chronic hydrocephalus.

Hydrocephalus caused by aqueduct stenosis and other obstructive lesions is generally well displayed with MRI and the ability to scan in more than one plane is very useful in these conditions.

11 CONGENITAL MALFORMATIONS

Brain development follows a well defined sequence. A disturbance at any particular time may affect one or more stages and result in a developmental anomaly.[2,3,32–34] Dorsal induction occurs during week 3–4 of gestation when the nasal plate folds to form the nasal tube. Failure to close caudally results in myelomeningocoele, and failure to close at the cephalad end may result in anencephaly encephalocele, etc. In the next stage the mesencephalon divides to form the telencephalon. Failure at this stage produces prosencephaly. Normal proliferation then follows in which the germinal matrix forms the neurons that form the cortex. Neurons may fail to form the normal cortical layers, or stop along their path resulting in multiple cortical abnormalities including heterotopia.

Neurofibromatosis, tuberous sclerosis, and Sturge–Weber disease are the common neurocutaneous diseases occurring in children.[35] However, the MRI features may be difficult to define in the neonate, before some degree of myelination has

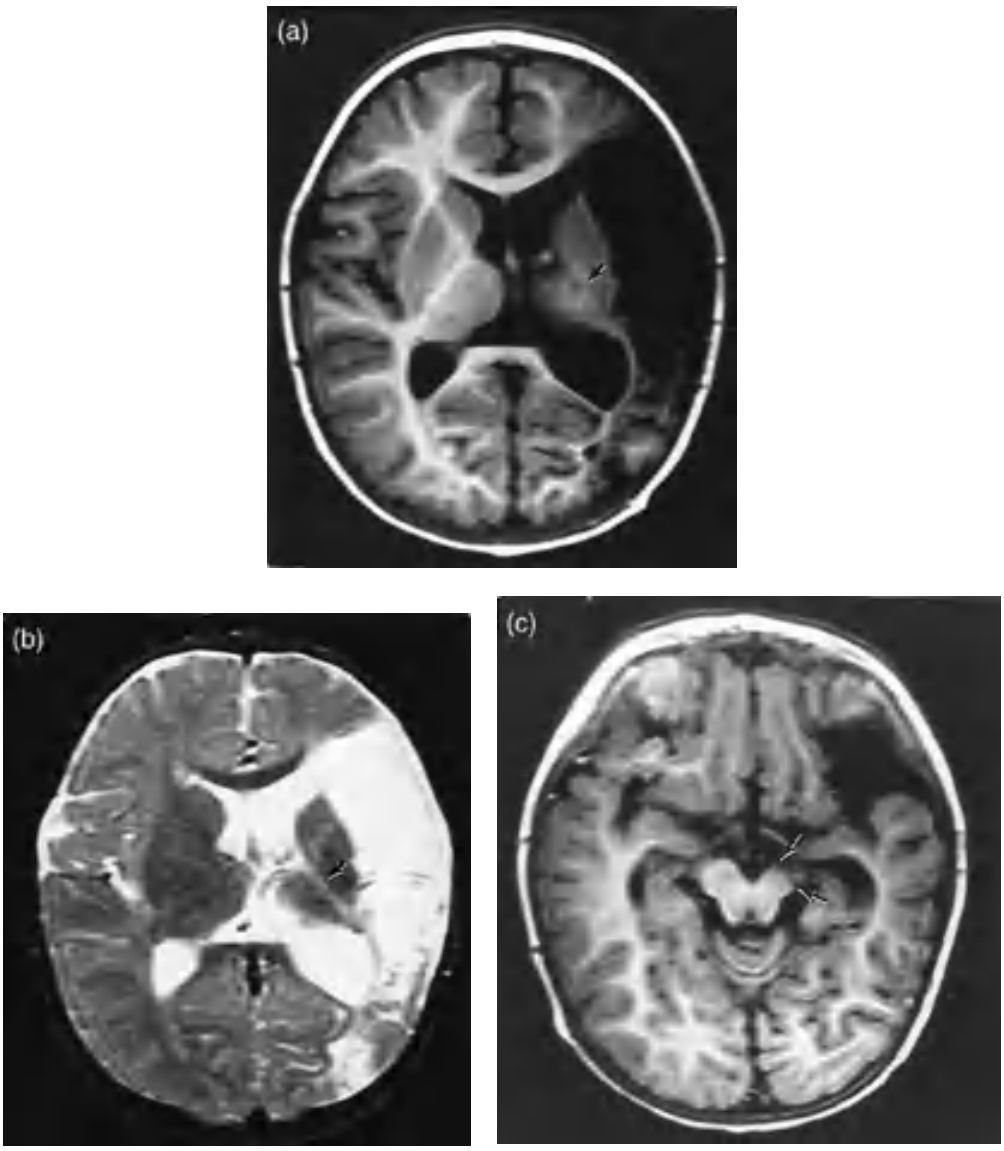

Figure 9 Infant aged 9 months with a left middle cerebral infarct. (a, c) Inversion–recovery (IR 3400/30/800) and (b) T_2-weighted spin echo (SE 2700/120) images. A large porencephalic cyst is seen in the left hemisphere. Increased signal intensity is seen along the length of the posterior limb of the internal capsule in (b) and low signal intensity is seen in (a) (arrows). The mesencephalon on the left is smaller than on the right (c) (arrows). Less myelin is seen on the left hemisphere than on the right

taken place. MRI is of considerable value in demonstrating tumors associated with the phakomatoses as well as MRI regions of gliosis, hematomas, and cerebral atrophy.[36] Calcification in tuberous sclerosis is poorly shown, but may be seen.[37] Computed tomography (CT) or plain skull X-rays may be more useful in this situation.

Obvious anatomical deformations are readily shown, e.g. anencephalopathy, holoprosencephaly, and Dandy–Walker syndrome. The sagittal plane lends itself to demonstration of many of these conditions including, for example, agenesis of the corpus callosum.

12 WHITE MATTER DISEASE

The most common white matter disease to affect infants is periventricular leukomalacia (see Section 7). Recognition of other white matter disease is difficult in early life because of the lack of myelin present at birth and in the first 6 months of life. Once myelin has been laid down it can disappear in two principal ways, namely demyelination and dysmyelination.[38] In demyelination the breakdown of myelin is caused by extrinsic factors (e.g. infection, trauma, chemotherapy), and in dysmyeli-

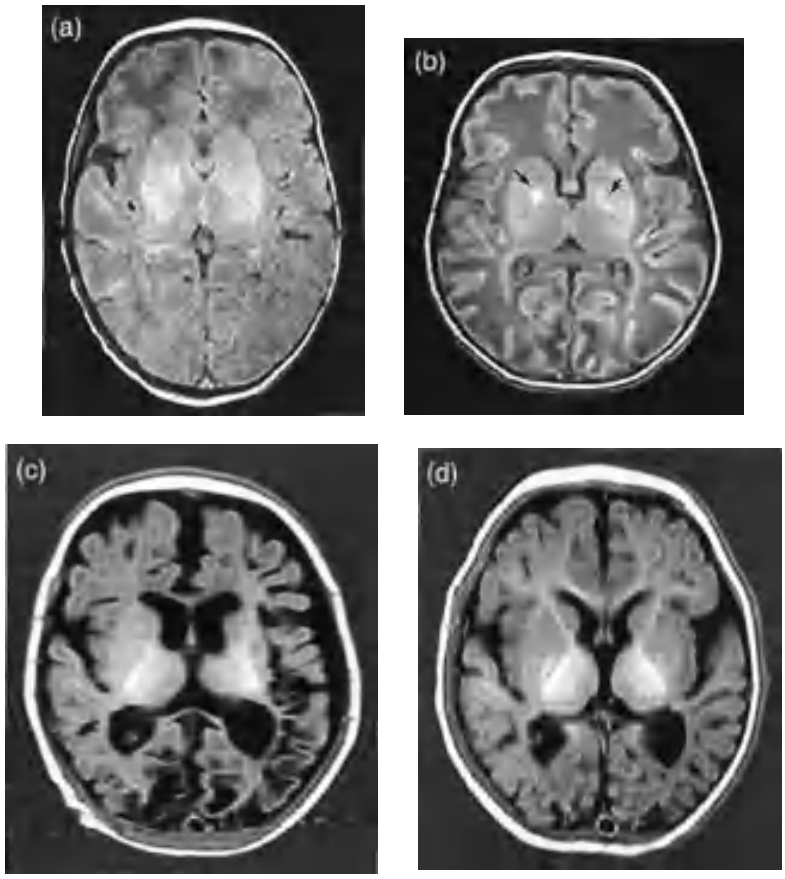

Figure 10 Male infant born at 40 weeks with severe birth asphyxia: T_1-weighted spin echo (SE 860/20). Images at age 2 days (a) and 10 days (b); (c) inversion–recovery (IR 3797/30/95) image at age 5 weeks; (d) IR 3405/30/800 at age 6 months. At age 2 days brain swelling is present and there is a loss of sulcal patterns and gray–white matter contrast. The ventricles and the interhemispheric fissure are small (a). At 10 days, the brain swelling is no longer present. High signal intensity is seen throughout the cortex and the white matter is featureless. Hemorrhagic lesions are seen with the globus pallidus (arrows). There has been loss of the normal increased signal intensity in the posterior limb of the internal capsule (b). At 5 weeks (c) there has been a diminution in white matter and cystic change is noted in the posterior lobes. Myelin is now present in the posterior limb of the internal capsule. At 6 months (d), there has been further loss of white matter relative to normal. Abnormal signal intensity is seen in the thalami and globus pallidus. Further myelination has taken place

nation there is a genetic disorder of myelin formation which is a feature of metabolic disorders such as the leukodystrophies. Diffuse abnormalities are seen within white matter in leukodystrophy. The changes are usually extensive and not confined to the periventricular region. In other forms of white matter disease, such as Alexander's disease, changes may be confined to the frontal lobes. A variety of other abnormalities have been described in different forms of leukodystrophy.[2,38] We have also seen periventricular abnormalities associated with intrathecal methotrexate therapy in leukemia. Along with delays in myelination, both demyelination and dysmyelination are readily recognized on MRI in children.[2,38,39]

13 INFECTION

Excellent reviews on inflammatory diseases of the brain in childhood are available in the literature.[2,40] Cerebral abscess displays an increase in T_1 and T_2. Edema is well displayed but the exact margins of the abscess may be difficult to define.[40] However, ring enhancement after the intravenous injection of gadolinium diethylenetriaminepentaacetic acid (Gd-DTPA) may help in the differential diagnosis of cerebral abscess. Calcification associated with abscess is poorly demonstrated in comparison with CT.

In two cases of brainstem encephalitis, changes have been seen with very little associated mass effect. This has been the main distinction between tumors at the initial examination and on regression on follow-up examination. It provides strong support for the diagnosis, although a certain amount of caution is necessary as patients are frequently treated with steroids which may result in some regression of edema associated with a tumor. In a case of cytomegalovirus, marked white matter change has been observed in a child of 2 years without any overt clinical signs (Figure 13). In neonatal meningitis, contrast enhancement may be seen in the meninges (Figure 14).

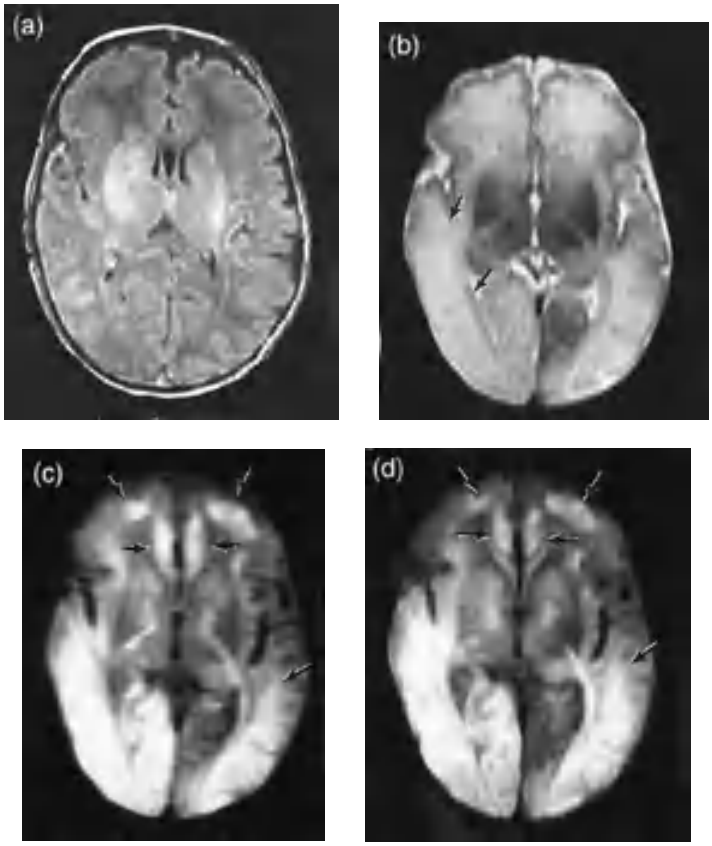

Figure 11 Hypoxic ischemic encephalopathy on day 1: (a) transverse T_1-weighted spin echo (SE 720/20), (b) T_2-weighted spin echo (SE 3000/120) (c) diffusion weighted (SE pulse interval/200 ms, left–right sensitization, b = 600 s mm^{-2}), and (d) diffusion weighted (SE pulse interval/200 ms, through-plane sensitization, b = 600 s mm^{-2}) images. High intensity signal is only seen in the medial right occipital lobe in (b) (arrows), suggesting the diagnosis of infarction; much more extensive abnormalities are seen bilaterally in the frontal, temporal, and occipital lobes using diffusion weighted imaging (c and d) (arrows showing some of the high intensity signal areas)

14 TUMORS

In general, the features of tumors in children parallel those in adults; however, there is a higher incidence of tumors in the posterior fossa, and embryological tumors are more common.[2] The high incidence of midline tumors lends itself to sagittal imaging, and the clarity with which the posterior fossa is seen is also an advantage.

Most tumors display an increased T_1 and T_2 providing high contrast with long *TE* long *TR* spin echo sequences, although distinction between tumor and edema may be difficult. Differentiation between brainstem and cerebellar sites is reasonably easy. Craniopharyngiomas and various other lipid-containing tumors may show characteristic features. Hamartomas may not display a significant change in T_1 and T_2 and may then need to be recognized by their indirect signs. Hypothalamic tumors which may be poorly seen with CT are well recognized with MR.

15 OTHER DISEASE

Certain other conditions are worth reviewing, although they are quite rare. Delays or deficits in myelination have been recognized in Hurler's disease, and these may be reversed following successful bone marrow transplantation.[41]

Hallervorden–Spatz disease is of particular theoretical interest as a condition in which there is abnormal iron deposition in the brain, and in one case abnormalities have been seen in the basal ganglia.

In Wilson's disease abnormalities are seen in the lentiform nucleus and within the thalamus;[42] however, the findings are not specific as similar changes are seen in children with Leigh's disease.[2]

16 FOLLOW-UP EXAMINATIONS

This is an important aspect of pediatric practice. The normal appearances including the value of T_1 and T_2, the presence of periventricular long T_1 areas, the degree of myelination, as well as the size and the shape of the brain, all change. Pathological changes must be assessed against this changing background.

The lack of known hazard is a strong incentive for pediatric MRI. Follow-up examinations in conditions in which long-term survival is expected without accumulating significant X-ray dosage is important. Nevertheless, there are problems in achieving MRI scans at the same level and angulation as in the

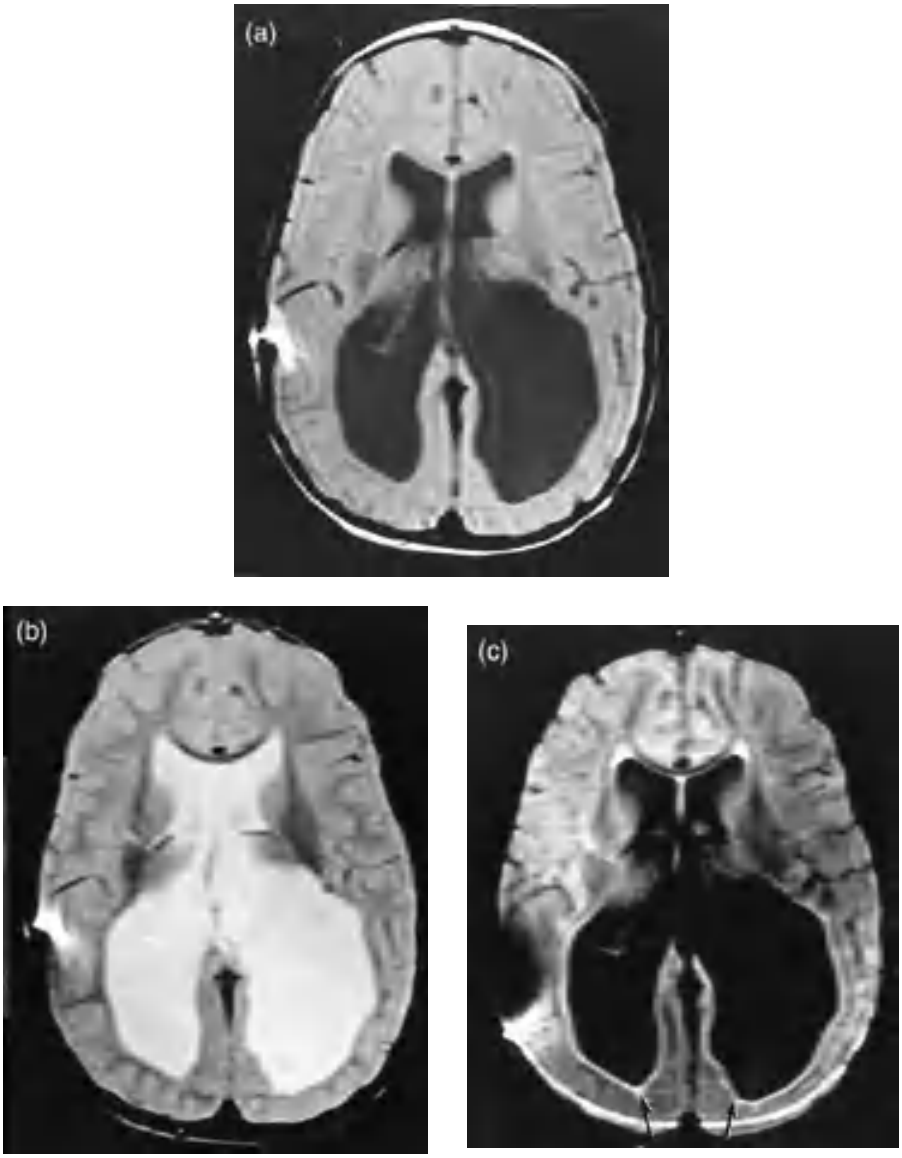

Figure 12 Male infant aged 2 years with posthemorrhagic hydrocephalus: (a) mildly T_2-weighted (SE 2500/20) and (b) moderately T_2-weighted (SE 2500/80) spin echo sequences; (c) fluid attenuated inversion–recovery sequence (FLAIR 6500/160/2100). A shunt artifact is seen. There is an increase in signal intensity around the lateral ventricles in (a), which is less well seen in (b) and best seen in (c) (arrows)

initial studies. There is also a theoretical problem in using age-adjusted sequences since the machine parameters are different. Genuine advances in technique can also make comparison difficult.

17 CONCLUSIONS

Developments in pediatric MRI lag behind those of adults, but it is possible to extrapolate findings in adults to children. Clinical correlation has been progressing, but the correlation is not precise and some children may have very large lesions with relatively small clinical deficits. Large unsuspected lesions have been found where the clinical signs are quite subtle. The capacity for repeated examination without cumulative radiation dosage problems has been of value in studying the natural history of a variety of neonatal insults.

The versatility of MRI with its basic image parameters ρ, T_1, T_2, chemical shift, flow, susceptibility, and diffusion effects provides a wide variety of options for the various problems encountered in clinical practice. Only a small number of these options has yet been employed in pediatric practice, and a growing role for MRI in this area is certain. The application of MR may be greatly expanded by the installation of suitable

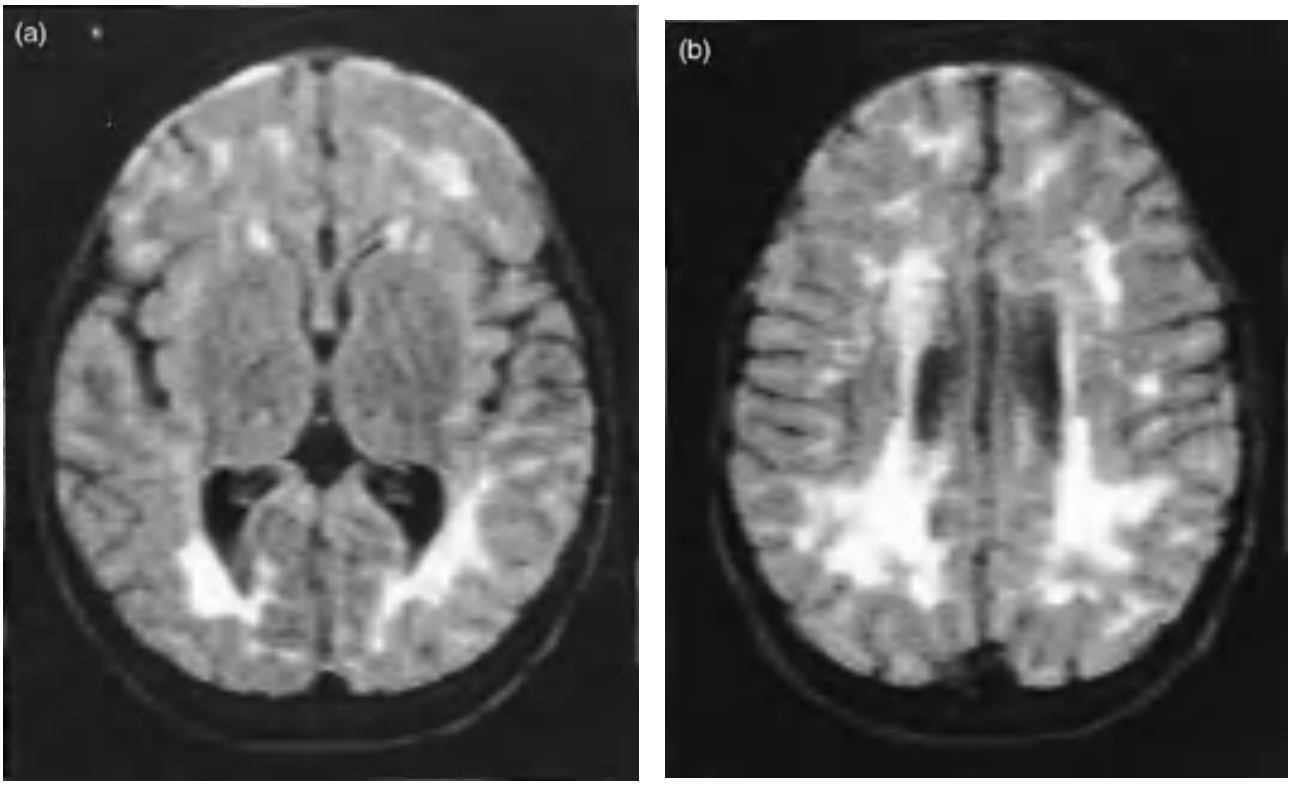

Figure 13 Female infant aged 2 years with cytomegalovirus; fluid attenuated inversion–recovery (FLAIR 6500/160/2100) sequences. Areas of long T_2 are seen throughout the white matter

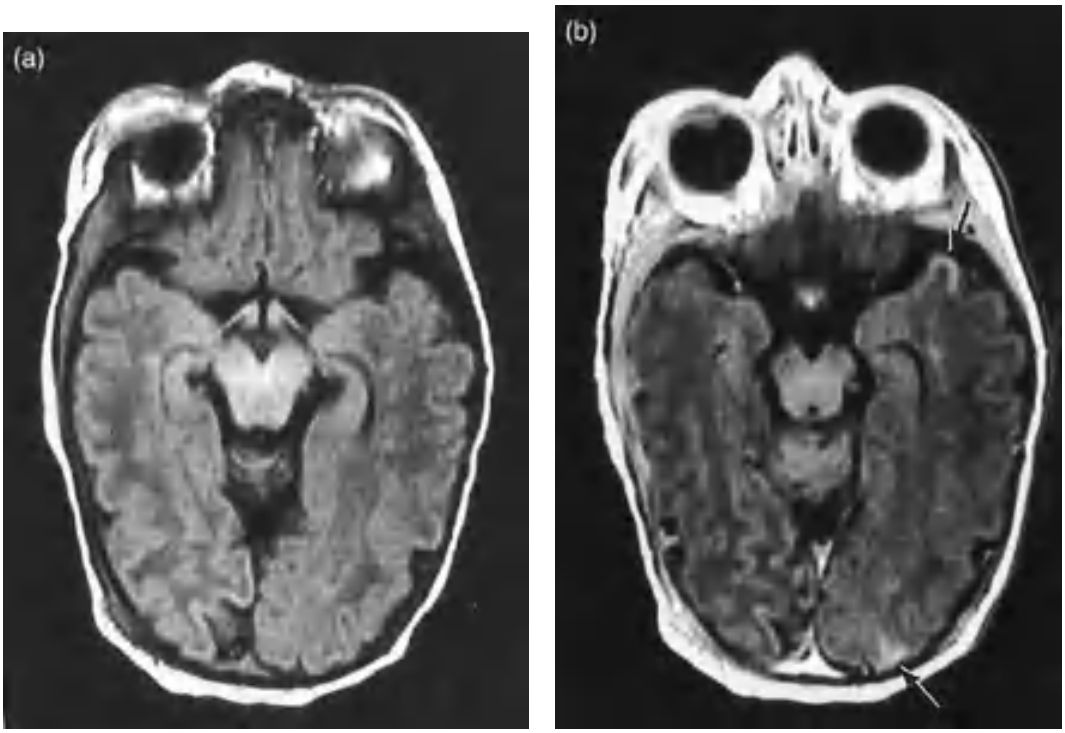

Figure 14 Male infant aged 6 weeks with meningitis. T_1-weighted spin echo (SE 720/20) sequence before (a) and after intravenous injection of Gd-DTPA (b). Meningeal enhancement is seen in (b) (arrows)

systems in neonatal intensive care units. To date only relatively large and stable infants have been examined, but the impact of MRI on the management of the critically ill and very premature infants may be much expanded in the future.

18 RELATED ARTICLES

Brain MRS of Infants and Children; Diffusion: Clinical Utility of MRI Studies; Intracranial Infections; MRI in Clinical Medicine.

19 REFERENCES

1. R. S. Boyer, *Am. J. Neuroradiol.*, 1992, **13**, 777.
2. A. J. Barkovich, in 'Contemporary Neuroimaging', ed. D. Norman, Raven, New York, 1990, Vol. 1.
3. M. D. Cohen and M. K. Edwards (eds), 'Magnetic Resonance Imaging of Children', B. C. Decker, Philadelphia, 1990.
4. M. A. Johnson, J. M. Pennock, G. M. Bydder, R. E. Steiner, D. J. Thomas, R. Hayward, D. J. Bryant, J. A. Payne, M. I. Levene, A. Whitelaw, L. M. S. Dubowitz, and V. Dubowitz, *Am. J. Roentgenol.*, 1983, **141**, 1005; *Am. J. Neuroradiol.*, 1983, **4**, 1013.
5. J. Dobbing and J. Sands, *Arch. Dis. Child.*, 1973, **48**, 757.
6. L. S. de Vries, L. M. S. Dubowitz, V. Dubowitz, and J. M. Pennock, 'Colour Atlas of Brain Disorders in the Newborn', Wolfe Medical, Chicago, 1990.
7. B. De Coene, J. V. Hajnal, P. Gatehouse, D. B. Longmore, S. J. White, A. Oatridge, J. M. Pennock, I. R. Young, and G. M. Bydder, *Am. J. Neuroradiol.*, 1992, **13**, 1555.
8. M. A. Nowell, D. B. Hackney, R. A. Zimmerman, L. T. Bilaniuk, R. I. Grossman, and H. I. Goldberg, *Radiology*, 1987, **162**, 272.
9. M. A. Rutherford, F. M. Cowan, A. Y. Manzur, L. M. S. Dubowitz, J. M. Pennock, J. V. Hajnal, I. R. Young, and G. M. Bydder, *J. Comput. Assist. Tomogr.*, 1991, **15**, 188.
10. J. V. Hajnal, C. J. Baudouin, A. Oatridge, I. R. Young, and G. M. Bydder, *J. Comput. Assist. Tomogr.*, 1992, **16**, 7.
11. R. R. Edelman, K. E. Johnson, R. Buxton, G. Shoukimos, B. R. Rosen, K. R. Davis, and T. J. Brady, *Am. J. Neuroradiol.*, 1986, **7**, 751.
12. I. R. Young, S. Khenia, D. G. T. Thomas, C. H. Davis, D. G. Gadian, I. J. Cox, B. D. Ross, and G. M. Bydder, *J. Comput. Assist. Tomogr.*, 1987, **11**, 2.
13. F. W. Wehrli, 'Fast-Scan Magnetic Resonance: Principles and Applications', Raven, New York, 1991.
14. R. M. Henkelman and W. Kucharczyk, *Am. J. Neuroradiol.*, 1994, **15**, 465.
15. A. Feess-Higgins and J.-C. Larroche, 'Le Developpement du Cerveau Foetal Humain: Atlas Anatomique', Masson, Paris, 1987.
16. P. I. Yakovlev and A. R. Lecours, in 'Regional Development of the Brain in Early Life', ed. A. Minkowski, Blackwell Scientific, Oxford, 1967, p. 3.
17. C. B. McArdle, C. J. Richardson, D. A. Nicholas, M. Mirfakhraee, C. F. Hayden, and E. G. Amporo, *Radiology*, 1987, **162**, 223.
18. A. J. Barkovitch and C. L. Truwit, 'Practical MRI Atlas of Neonatal Brain Development', Raven, New York, 1990.
19. E. C. Prenger, W. W. Beckett., S. S. Koleias, and W. S. Ball, *JMRI*, 1994, 179.
20. S. M. Wolpert and T. D. Barnes, 'MRI in Pediatric Neuroradiology', Mosby, St Louis, 1992.
21. K. E. Pape and J. S. Wigglesworth, 'Hemorrhage, Ischemia and the Perinatal Brain', Lippincott, Philadelphia, 1979.
22. J. J. Volpe, 'Neurology of the Newborn', Saunders, Philadelphia, 1987.
23. C. B. McArdle, C. J. Richardson, C. K. Hayden, D. A. Nicholas, M. J. Crofford, and E. G. Amparo, *Radiology*, 1987, **163**, 387.
24. J. M. Gomori, R. I. Grossman, H. I. Goldberg, D. B. Hackney, R. A. Zimmerman, and L. T. Bilaniuk, *Neuroradiology*, 1987, **29**, 339.
25. L. S. de Vries, L. M. S. Dubowitz, J. M. Pennock, and G. M. Bydder, *Clin. Radiol.*, 1989, **40**, 158.
26. L. L. Baker, D. K. Stevenson, and D. R. Enzmann, *Radiology*, 1988, **168**, 809.
27. F. M. Cowan, J. M. Pennock, D. D. Hanrahan, K. Manji, J. D. Hanrahan, and A. D. Edwards, *Neuropediatrics*, 1994, **25**, 172.
28. J. M. Pennock, M. A. Rutherford, F. M. Cowan, and G. M. Bydder, *Clin. Radiol.*, 1993, **47**, 311.
29. M. J. Kuhn, D. J. Mikulis, D. M. Ayoub, B. E. Kosofsky, K. R. Davis, and J. M. Taveras, *Radiology*, 1989, **172**, 179.
30. D. Azzopardi, J. S. Wyatt, E. B. Cady, D. T. Delby, T. Boudin, A. L. Stewart, P. L. Hope, P. A. Hamilton, and E. O. Reynolds, *Pediatr. Res.*, 1989, **25**, 445.
31. C. R. Kitz, *Semin. US, CT MR*, 1988, **9**, 216.
32. S. E. Byrd, R. E. Osborn, M. A. Radkorvoski, C. B. McArdle, E. C. Prengen, and T. P. Naidich, *Semin. US, CT MR*, 1988, **9**, 201.
33. S. R. Pollei, R. S. Boyer, S. Crawford, H. R. Harnsberger, and A. J. Barkovich, *Semin. US, CT MR*, 1988, **9**, 231.
34. M. S. Van der Knaap, and J. Valk, *Am. J. Neuroradiol.*, 1988, **9**, 315.
35. S. C. Crawford, R. S. Boyer, H. R. Harnsberger, S. R. Pollei, W. R. T. Smoker, and A. G. Osborn, *Semin. US, CT MR*, 1988, **9**, 247.
36. J. G. Smirniotopoulos and F. M. Murphy, *Am. J. Neuroradiol.*, 1992, **13**, 725.
37. B. H. Braffman, L. T. Bilaniuk, and R. A. Zimmerman, *Radiol. Clin. North Am.*, 1988, **26**, 773.
38. J. Valk, 'MRI of the Brain, Head, Neck and Spine: A Teaching Atlas of Clinical Application', Martinus Nijhoff, Dordrecht, 1987.
39. M. A. Nowell, R. I. Grossman, D. B. Hackney, R. A. Zimmerman, H. I. Goldberg, and L. T. Bilaniuk, *Am. J. Roentgenol.*, 1988, **151**, 359.
40. C. R. Fitz, *Am. J. Neuroradiol.*, 1992, **13**, 551.
41. M. A. Johnson, S. Desai, K. Hugh-Jones, and F. Starer, *Am. J. Neuroradiol.*, 1984, **5**, 816.
42. G. A. Lawler, J. M. Pennock, R. E. Steiner, W. J. Jenkins, S. Sherlock, and I. R. Young, *J. Comput. Assist. Tomogr.*, 1983, **7**, 1.

Biographical Sketch

Jacqueline M. Pennock. *b* 1940. M.Phil., 1976. Department of Diagnostic Radiology, Hammersmith Hospital, London 1963–present. Currently, senior scientific officer. Approx. 80 publications. Metabolic and endocrine disease (with Professor Frank Doyle). Current research interests: pediatric magnetic resonance, specifically related to normal development and critically ill preterm and term infants (with Frances Cowan, Mary Rutherford, Lilly Dubowitz and Graeme Bydder).

Pituitary Gland and Parasellar Region Studied by MRI

Richard Farb and Walter Kucharczyk
University of Toronto, Toronto, ON, Canada

1 ANATOMY AND THE MRI TECHNIQUE

The pituitary gland is a small but important organ situated in a small bony depression in the skull base called the sella turcica. Although the average weight of the pituitary gland in the adult is only 0.5 g, it is responsible for the regulation of many of the body's most critical endocrine functions. The gland enlarges slowly with maturation reaching a peak height of no more than 9–10 mm in early adulthood. There are two periods when the gland may transiently enlarge beyond its normal dimensions, those being adolescence and pregnancy. This is principally due to physiological hypertrophy of prolactin-secreting cells.

The pituitary gland is made up of three distinct lobes: anterior, intermediate, and posterior. The intermediate lobe is a vestigial remnant in humans and serves no function; however, it may be the site of an incidental cyst. The anterior lobe, or adenohypophysis, is a true endocrine organ responsible for synthesizing many hormones. Its function is regulated by stimulatory and inhibitory hormones arising from the hypothalamus. The posterior lobe of the pituitary gland, also called the neurohypophysis, is actually a downward extension of the hypothalamus. The hormones of the posterior pituitary gland, vasopressin and oxytocin, are synthesized within the hypothalamus and axonally transported to the posterior pituitary gland where they are stored and from which they are ultimately released.

The anterior and posterior lobes of the pituitary gland are therefore two functionally distinct entities, although they reside in very close association within the sella turcica. The posterior lobe is much smaller than the anterior lobe and takes up only 10–20% of the sella turcica. The anterior lobe of the pituitary gland generally takes up the anterior, central, and lateral aspects of the sella turcica. The posterior lobe resides centrally in the midline just anterior to the dorsum sella. The lateral wings of the adenohypophysis usually extend laterally around the posterior pituitary gland.

The anterior and posterior lobes of the pituitary gland are easily distinguishable on MRI. The anterior lobe of the pituitary gland is normally isointense with cerebral white matter on all pulse sequences, whereas the posterior lobe of the pituitary gland is easily distinguishable by its characteristic hyperintense signal on T_1-weighted images. Following the administration of intravenous contrast material the anterior and posterior lobes, as well as the pituitary stalk, enhance intensely.

The pituitary gland is enclosed within the sella turcica by a dural diaphragm (the diaphragma sella), the center of which has a defect in it allowing for passage of the pituitary stalk. The superior surface of the diaphragma sella is lined with arachnoid, and the suprasellar cistern lies above the diaphragma sella. The suprasellar cistern contains all the vascular structures of the circle of Willis. The optic chiasm is immediately anterior to the pituitary stalk (infundibulum) within the suprasellar cistern.

On either side of the sella turcica lie the cavernous sinuses. These are complex dural venous sinuses passing from the anteromedial aspect of the posterior fossa (Meckel's cave) anteriorly to the superior orbital fissure, transmitting cranial nerves III, IV, V1, and V2 within the lateral walls of the cavernous sinus. Cranial nerve VI is the only cranial nerve that actually passes within the cavernous sinus. The appearance of the cavernous sinuses on MRI is somewhat variable in signal intensity; however they are usually symmetric in dimensions. Following contrast administration the cavernous sinuses enhance intensely. The normal MRI anatomy is illustrated in Figure 1.

Imaging of the pituitary gland and sella turcica for possible structural abnormalities is a frequent indication for MRI. Exact specifications of the technique are not provided here because the constantly improving capabilities of modern scanners require that technique be continually revised. However high spatial detail is very important in this area and should be achieved through the use of thin slices, a fine matrix size, and a relatively small field-of-view. Requirements for spatial detail must be balanced against the need for adequate signal-to-noise ratio as well as imaging time.

The pulse sequence for best tissue contrast is still a matter of opinion. Several groups have shown that short *TR*, short *TE* spin echo images (i.e. T_1-weighted) generate very good contrast for visualizing pituitary pathology.[1,2,3] Because fast spin echo (FSE) methods are now readily available, and do not incur the time penalty of conventional T_2-weighted spin echo sequences, coronal T_2-weighted FSE imaging is being utilized with increasing frequency as a supplementary sequence for investigation of pituitary adenomas. Several other pulse sequences have been implemented for parasellar imaging and have met with varying degrees of success.[4]

Paramagnetic contrast-enhanced images are widely used and are very useful. Although most adenomas are visible without the injection of intravenous contrast, several studies have shown that small adenomas may become visible only after contrast injection.[5,6] To take better advantage of the differential rates of contrast enhancement between adenomas and normal pituitary gland, dynamic pituitary scanning immediately after bolus contrast injection is also useful.[7]

2 CONGENITAL ABNORMALITIES

2.1 Pituitary Gland Hypoplasia

Congenital abnormalities of the pituitary gland and hypothalamus are usually present in association with anomalies of other midline cranial, orbital, and facial structures. Pituitary gland hypoplasia is usually accompanied by a small sella turcica, and is commonly clinically associated with growth failure and other endocrine abnormalities. A curious form of pituitary hypoplasia has recently been recognized to occur with a

Figure 1 *Normal MR anatomy of the pituitary region*. T_1-weighted sagittal (a), and coronal (b), images. A. Anterior pituitary gland, B. optic chiasm, C. cavernous sinus, D. pituitary stalk, E. right internal carotid artery (supraclinoid portion), F. left internal carotid artery (cavernous portion), G. medial temporal lobe, H. sphenoid sinus, I. hypothalamus, J. trigeminal nerve, K. pterygoid canal, L. sylvian fissure, M. mammillary body, N. frontal lobe, O. midbrain, P. pons, Q. medulla, R. interpeduncular cistern, S. genu of corpus callosum, T. tuber cinereum, U. cerebral aqueduct, V. third ventricle, W. posterior pituitary gland

slightly higher frequency in patients with a history of breech deliveries.[8–10] These patients have short stature and growth hormone deficiency, as well as the MRI findings of pituitary hypoplasia, hypoplasia of the distal pituitary stalk, and absence of the normal hyperintensity within the posterior pituitary gland.

2.2 Ectopic Posterior Pituitary Tissue

Occasionally, the normal hyperintensity on T_1-weighted images within the posterior pituitary gland and in the posterior aspect of the sella turcica is not visualized. Instead there is a small area of hyperintensity seen along the course of the pituitary stalk. This may be associated with discontinuity of the pituitary stalk. These patients may present with hormonal abnormalities, particularly of the anterior pituitary gland, due to transection of the hypothalamo-pituitary portal anastomosis. It is rare for these patients to present with posterior pituitary gland hormonal deficiencies.

'Ectopic posterior pituitary tissue' is thought to occur by one of two mechanisms, either incomplete embryologic descent of hypothalamic neurons, or possibly due to traumatic transection of the pituitary stalk above the diaphragma sella. In either case, the neurosecretory granules descending down toward the posterior pituitary gland from the hypothalamus accumulate within the proximal stump of the amputated pituitary stalk. This simply becomes the new site or location of posterior pituitary tissue thus accounting for the increased signal intensity on T_1-weighted images as well as the normal hormonal profile of the posterior pituitary gland.

2.3 The Empty Sella Turcica

The terms 'empty sella syndrome' or 'empty sella turcica' refer to the roentgenographic, pneumoencephalographic, or computed tomographic appearance of the sella turcica, which is filled predominantly with cerebrospinal fluid (CSF), with the normal posterior pituitary gland and stalk being crowded posteriorly and inferiorly within the sella turcica. The cause of this displacement is the presence of a large defect in the diaphragma sella allowing the arachnoid membrane to herniate through the diaphragma sella adjacent to the stalk and thus allowing CSF pulsations to enter the sella turcica and result in the eventual displacement of the pituitary gland and stalk posteriorly. It is actually quite rare for patients with an 'empty sella' to have symptoms referable to the area of the sella turcica. 'The empty sella' is most commonly seen as an incidental finding of little or no clinical significance.

2.4 Cephaloceles

Cephaloceles are herniations of the meninges (meningocele) or of the meninges and the brain (meningoencephalocele) through a congenital cranial defect. Cephaloceles in the sellar

region (transphenoidal encephaloceles) are very rare. Most of these are associated with other midline anomalies, particularly agenesis of the corpus callosum.

3 TUMORS AND TUMOR-LIKE CONDITIONS

3.1 Pituitary Adenoma

The most common tumors affecting the pituitary gland are pituitary adenomas. These are benign, slow growing, epithelial adenomas originating in the adenohypophysis. Pituitary adenomas are usually well demarcated lesions that are separated from the normal pituitary gland by a pseudocapsule of compressed tissue. Pituitary adenomas are commonly classified based on size and hormonal activity. Adenomas measuring greater than 1 cm in diameter are referred to as **macro**adenomas; those less than 10 mm are **micro**adenomas. Those adenomas that are hormonally active may also be referred to by the hormone that they secrete. For example, the most common hormonally active adenoma is the 'prolactin-secreting microadenoma', or simply prolactinoma. The various hormonal types of adenomas are indistinguishable from one another by MRI imaging.

On MRI, pituitary microadenomas are usually small, focal hypointensities within the pituitary gland on T_1-weighted images. On T_2-weighted images the corresponding lesion is seen as hyperintense to the surrounding pituitary tissue.[3] Approximately 80–95% of pituitary adenomas present with these characteristic signal intensities (Figure 2). Intratumoral hemorrhage occurs in 20–30% of adenomas. These are usually macroadenomas (Figure 3). The incidence of intratumoral bleeding is higher in patients receiving bromocryptine therapy.[11] We have found that tumors that are hyperintense on T_1-weighted images are always cystic with the cyst containing elements of previous hemorrhage.

Tissue contrast represented by a differential signal intensity between the tumor and normal pituitary gland is the most sensitive and reliable indicator of the presence of a microadenoma (Figure 2). Indirect signs previously utilized for computed tomography imaging of the pituitary gland such as tilt of the pituitary gland, contour of the superior aspect of the pituitary gland, and deviation of the pituitary stalk, all appear to be quite insensitive to the presence of microadenomas and indeed may be misleading (Figure 2).

It is difficult to determine the accuracy of MRI for the diagnosis of pituitary microadenomas. It is estimated that about 90% of microadenomas are detected and accurately localized with MRI.[3] The detection rate of macroadenomas approaches 100%. Their signal intensities are qualitatively similar to their smaller counterparts; however they more commonly demonstrate cystic degeneration or hemorrhage.

An area of continued difficulty in pituitary and parasellar imaging is that of the postoperative examination in search of residual or recurrent pituitary adenoma. In these cases, it may be very difficult to distinguish postoperative scarring, or graft material, from the normal gland or adenomatous tissue. This is especially true in the first 6 months after surgery. In these cases, progressive growth of a soft tissue mass on sequential postoperative MR scans is the best imaging sign of recurrent tumor. This must also be interpreted in conjunction with endocrinologic markers.

3.2 Craniopharyngioma

Craniopharyngiomas are epithelial-derived neoplasms thought to arise from remnants of Rathke's cleft in the region of the pars tuberalis. They account for 3% of all intracranial tumors and show equal incidence in males and females. Tumors can vary greatly in size from several millimeters to several centimeters in diameter with the epicenter of the tumour usually located in the suprasellar cistern. Craniopharyngiomas typically have both solid and cystic components (Figure 4). Calcification is commonly seen in the solid portion of the tumor. The cystic contents of the tumour can vary in color and viscosity.

On MRI craniopharyngiomas are typically lobulated with heterogeneous signal intensities on T_1- and T_2-weighted images.[12] The cystic component of the tumor is uniform and commonly hyperintense on both T_1- and T_2-weighted images, and contains fluid that has been likened to 'machine oil'.

3.3 Rathke's Cleft Cyst

Rathke's cleft cysts share a common origin with craniopharyngiomas in that they originate from remnants of squamous epithelium of Rathke's cleft. The cysts are common incidental findings at autopsy; however the larger cysts can be symptomatic. The contents of the cysts are typically mucoid. Less commonly they are filled with serous or desquamated cellular debris.[13] The mucoid-containing cysts can be hyperintense on T_1 and T_2-weighted images; the serous-containing cysts have signal intensities that closely match CSF (Figure 5). Rathke's cleft cysts do not enhance following contrast injection, except for perhaps marginal enhancement around the cyst wall. If nodular enhancement or calcification is seen, craniopharyngioma should be suspected.

3.4 Meningioma

Approximately 10% of meningiomas occur in the parasellar region. These tumors arise from a variety of locations around the sella including the tuberculum sella, clinoid processes, medial sphenoid wing, and cavernous sinus. Meningiomas are most frequently isointense relative to gray matter on unenhanced T_1-weighted images. Approximately 50% remain isointense on T_2-weighted images.[14,15] Meningiomas, as well as other extraaxial tumors, can demonstrate a typical CSF cleft between the tumor and the adjacent brain parenchyma. Also, meningiomas have been noted to demonstrate a peripheral black rim around their margins, thought to represent veins surrounding the tumor.

Meningiomas commonly encase arteries of the parasellar region, particularly the cavernous and supraclinoid portions of the internal carotid artery. Meningiomas will typically narrow the vessels they encase (Figure 6). Adenomas, though they commonly encase vessels, usually do not narrow these vessels. Other distinguishing features of meningiomas include intense enhancement with intravenous contrast, tumor calcification, and hyperostosis of adjacent bone.

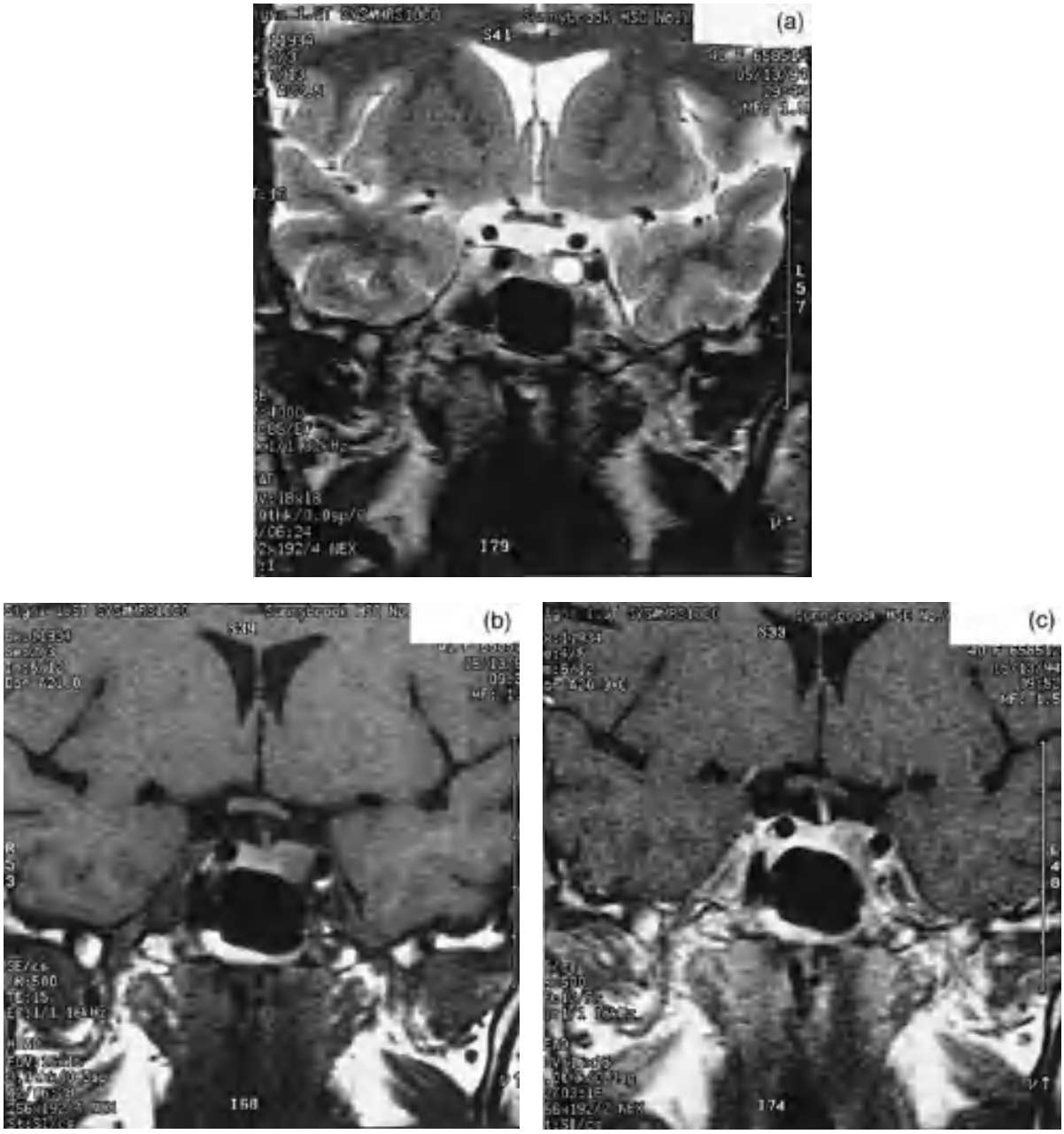

Figure 2 *Pituitary microadenoma*. (a) T_2-weighted, (b) T_1-weighted, and (c) enhanced T_1-weighted images. This 40-year-old female was noted to have marked elevation of cortisol in the blood and urine due to this hormonally active tumor secreting adrenocorticotropic hormone. This tumor demonstrates the typical features of a microadenoma including hyperintensity on T_2-weighted images and hypointensity on T_1-weighted images. Note the differential signal intensity between the intensely enhancing normal, anterior pituitary gland and the less enhancing tumor. Note also how the pituitary stalk deviates toward the tumor, thus stressing the unreliability of contralateral stalk deviation as a lateralizing sign of tumor

3.5 Germinoma and Teratoma

Germinomas account for less than 2% of primary intracranial tumors. Most of these tumors occur in the pineal region. However, approximately 20% of these tumors occur in the suprasellar cistern or pituitary fossa. Suprasellar germinomas occur either as metastatic deposits from a pineal region tumor or arise primarily in the suprasellar cistern. Most patients present between 5 and 25 years of age. Although pineal region germinomas are most commonly seen in males, there is no sex predilection for the primary suprasellar germinoma. Other tumors of germ cell origin occurring in this region, albeit rarely, include yolk sac tumors, choriocarcinoma, embryonal cell carcinoma, and teratoma. Suprasellar germinomas are usually large midline tumors with a propensity to infiltrate and spread by the CSF pathways. In contrast to craniopharyngiomas, germinomas are homogeneous and only rarely have cystic components. Germinomas are mildly hypointense on T_1-weighted images and hyperintense on T_2-weighted images. Marked uniform contrast enhancement is the rule (Figure 7).

Figure 3 *Pituitary macroadenoma*. Nonenhanced T_1-weighted image demonstrating a large, lobulated tumor occupying the sella and extending superiorly into the suprasellar cistern displacing the optic chiasm (A) superiorly. A focal area of increased signal intensity represents a small hemorrhage within the tumor. The tumor only abuts and does not clearly invade the cavernous sinus regions bilaterally

Teratomas have mixed heterogeneous signal intensities, often demonstrating evidence of fat or calcification.

3.6 Epidermoid and Dermoid

Epidermoids and dermoids are benign, slow-growing 'inclusion tumors' that can occur intracranially or intraspinally resulting from inclusions of epithelium during the time of neural tube closure. Dermoids are approximately one-fifth as common as epidermoids. Epidermoids account for approximately 1% of all intracranial neoplasms. The cerebellopontine angle is the most frequent site for epidermoids with the parasellar region being the second most common site.

Epidermoids are generally cystic tumors with the walls composed of simple, stratified, squamous epithelium resting on a layer of connective tissue. The interior of the cyst is composed of desquamated keratin products of the cyst wall. These tumors are benign and grow slowly with expansile characteristics. They also typically insinuate within and around structures, or conform to the space within which they are situated. Rarely the cyst can rupture producing a chemical granulomatous meningitis. Epidermoids are typically only slightly hyperintense to CSF on T_1- and T_2-weighted images, making the proton density image the most valuable sequence for identification of the epidermoid tumor. Epidermoids are characteristically hyperintense to brain and CSF on the proton density sequence.[16] Unfortunately epidermoids can also retain signal intensities identical to CSF making them nearly indistinguishable from arachnoid cysts. Enhancement, if it occurs, occurs only along the periphery of the tumor. Dermoids are more heterogeneous. Most dermoid tumors show evidence of fatty component as well as small areas of calcification.

3.7 Metastases

Metastases to the pituitary gland are a common autopsy finding but only about 1–2% of cancer patients have symptomatic metastases to the pituitary gland. These are usually metastases from breast or bronchogenic carcinoma.

3.8 Chordoma

Chordomas are rare neoplasms arising from remnants of the primitive notochord. Most cranial chordomas are found in the midline in relation to the clivus. Chordomas are locally invasive and destructive and commonly result in large, lobulated, destructive lesions extending in an extradural fashion. Portions of the sella and the parasellar regions are commonly involved. Chordomas are characteristically isointense or hypointense on T_1-weighted images and hyperintense on T_2-weighted images[17] with moderate enhancement following intravenous contrast administration.

Figure 4 *Craniopharyngioma*. T_1-weighted, enhanced, midline sagittal image of the parasellar region in this 3-year-old male demonstrating the typical findings of a craniopharyngioma. Note the enhancing solid tumor A, and the large cystic portion of the tumor B, extending supero-posteriorly, draping over the dorsum sella into the posterior fossa displacing the pons, C

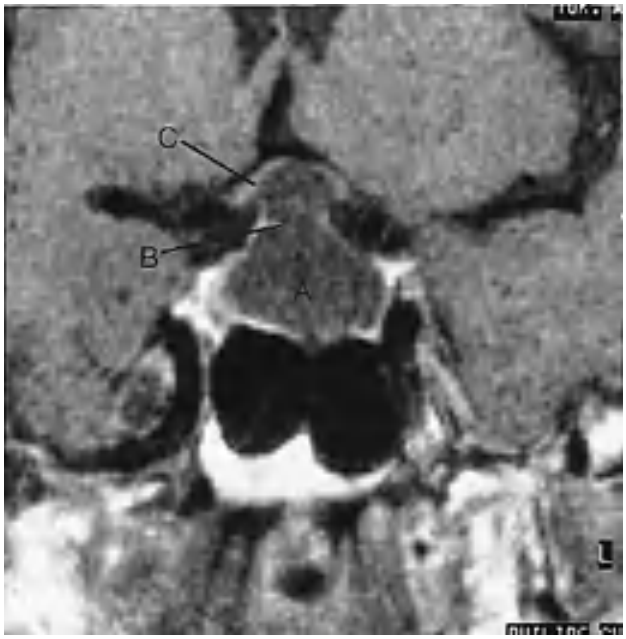

Figure 5 *Rathke's cleft cyst*. T_1-weighted, enhanced coronal image of the sella region demonstrating a somewhat bilobed cystic mass **A**, extending from the sella into the suprasellar cistern through the diaphragma sella **B**, displacing the optic chiasm superiorly **C**. This 28-year-old male presented with bitemporal hemianopsia and normal pituitary function. This typical appearance of the Rathke's cleft cyst has been likened to the appearance of a snowman

3.9 Arachnoid Cysts

Approximately 15% of arachnoid cysts occur in the juxtasellar region.[18] Suprasellar arachnoid cysts are thought to be developmental in origin and arise from an imperforate membrane of Liliequist. They have MRI characteristics identical to normal CSF.

3.10 Hamartoma of the Tuber Cinereum

Hamartomas of the tuber cinereum are sessile or pedunculated masses extending inferiorly from the hypothalamus into the suprasellar cistern between the pituitary stalk and mammillary bodies. Histologically they resemble cerebral cortex with little histologic similarity to the normal hypothalamus. Hamartomas of the tuber cinereum can be associated with precocious puberty. On MRI hamartomas are isointense to gray matter on all imaging sequences and should not enhance with contrast material (Figure 8).[19]

3.11 Eosinophilic Granulomatosis (Histiocytosis X, Langerhan's Cell Granulomatosis)

Histiocytosis can involve the pituitary gland, pituitary stalk, or hypothalamus. Twenty-five per cent of cases develop the classical clinical triad of diabetes insipidus, exophthalmos, and lytic bone lesions (the Hand–Schuller–Christian syndrome). In these cases granulomas can be found in the hypothalamus or the pituitary stalk. With MRI there is thickening of the pituitary stalk, hyperintensity on T_2-weighted images, and intense enhancement following contrast administration.[20,21]

4 INFECTIONS AND INFLAMMATORY CONDITIONS

4.1 Infections

Infections of the pituitary gland are a rare occurrence. Previous viral infection has been proposed as an etiology for diabetes insipidus. Leptomeningeal tuberculosis at the base of the brain can involve the pituitary gland. Bacterial infection of the pituitary gland is usually unnoticed until it manifests as a pituitary abscess, an entity which is also exceedingly rare. Pituitary abscesses are most frequently seen in association with preexisting conditions such as craniopharyngioma or pituitary adenoma. Transphenoidal surgery is rarely complicated by infection.

Infection of the parasellar regions, in particular the cavernous sinus is also very rare. Cavernous sinus thrombophlebitis is thought to be secondary to venous spread of a septic embolus from a periorbital or perinasal source.

4.2 Lymphocytic Hypophysitis

Lymphocytic hypophysitis is characterized by diffuse infiltration of the adenohypophysis by lymphocytes. It is most

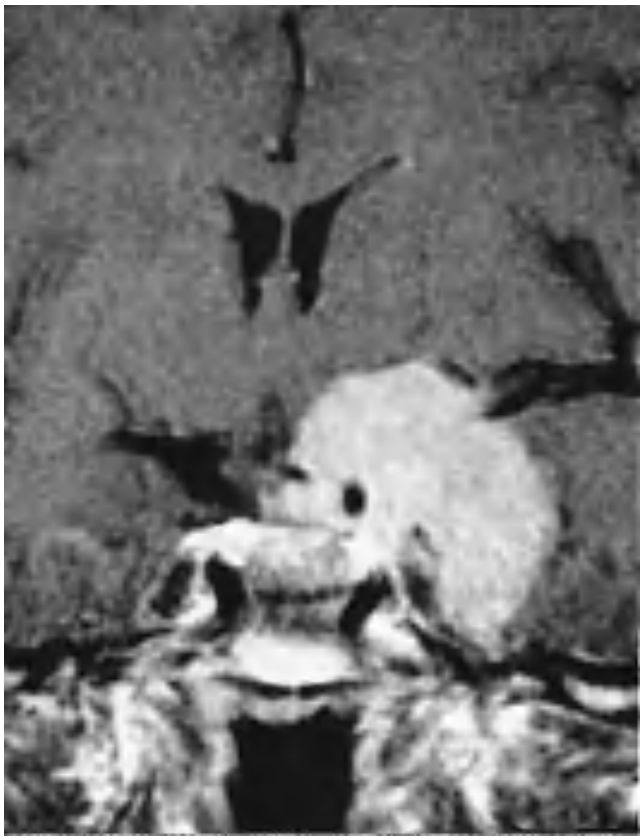

Figure 6 *Meningioma*. This T_1-weighted, enhanced coronal image demonstrates a homogeneously enhancing meningioma arising from the left anterior clinoid. Note the encasement of the left supraclinoid internal carotid artery, which is slightly narrowed when compared with the cavernous portion of the artery

Figure 7 *Germinoma*. T_1-weighted, midline, sagittal, enhanced image demonstrating homogeneously enhancing masses within the pineal region A, and suprasellar region B. The presence of tumors in both the pineal and suprasellar regions is highly characteristic of germinoma

commonly seen in late pregnancy or the postpartum period, and has been associated with other autoimmune disorders such as Hashimoto's thyroiditis. Clinically the woman complains of headache, visual loss, and failure to resume normal menstrual cycle. MRI demonstrates diffuse enlargement of the anterior pituitary gland without focal abnormality.

Figure 8 *Hamartoma of the tuber cinereum*. T_1-weighted, enhanced, midline sagittal image demonstrating a homogeneous mass located posterior to the pituitary stalk and anterior to the mammillary bodies, extending from the region of the tuber cinereum into the posterior aspect of the suprasellar cistern. This mass did not enhance and remained isointense to gray matter on all sequences, demonstrating the typical findings of hamartoma of the tuber cinereum

4.3 Sarcoidosis

Sarcoidosis most commonly occurs in an intrathoracic location. Any part of the central nervous system however can also be involved and 5% of patients with sarcoidosis will have neurologic complaints. The most typical findings for neurosarcoidosis include a basal meningitis with an abnormal, thick, enhancement pattern involving particularly the leptomeninges at the base of the brain characteristically in the midline. Abnormal parenchymal lesions are also noted within the brain. Neurosarcoidosis can be indistinguishable from other causes of leptomeningeal disease, in particular tuberculosis and leptomeningeal carcinomatosis.

4.4 Tolosa–Hunt Syndrome

This syndrome consists of painful ophthalmoplegia associated with a lesion within the cavernous sinus which is responsive to steroid therapy. Pathologically the lesion is similar to orbital pseudotumor.

5 VASCULAR LESIONS AND INFARCTION

5.1 Aneurysms

The large arteries in the suprasellar region are a common site of aneurysms. Aneurysms are for obvious reasons extremely important lesions to identify correctly. Fortunately their MRI appearance is distinctive and easily appreciated.[22,23] Aneurysms centrally contain signal void created by rapidly flowing blood. This flowing blood may also cause a substantial ghosting artifact in the phase-encoding direction, which is a useful diagnostic sign. Thrombus within the aneurysm is laid down against the wall in a sequential fashion over a long period of time and results in a typical laminated appearance. Hemosiderin staining of the adjacent brain can also be seen. If confusion persists regarding the diagnosis, conventional angiography remains the gold standard for diagnosis of intracranial aneurysms.

5.2 Carotid Cavernous Fistulas

Carotid cavernous fistulas (direct or indirect type) can be spontaneous, posttraumatic, or atherosclerotic. Dural arteriovenous malformations of the cavernous sinus are another form of abnormal venous communication in this region. On MRI, dilatation of the venous structures, in particular the ophthalmic vein and cavernous sinus, is usually clearly visible. The carotid artery can also be somewhat dilated.

5.3 Postpartum Pituitary Necrosis

During pregnancy the pituitary gland increases in size thus making it vulnerable to circulatory disturbances. Postpartum ischemic necrosis of the pituitary gland is a well-known entity, which can follow complicated deliveries associated with hemorrhage and shock.

6 MISCELLANEOUS CONDITIONS

6.1 Diabetes Insipidus

Diabetes insipidus results from the lack of appropriate release of antidiuretic hormone (vasopressin) from the posterior pituitary gland. This results in the inability to concentrate urine and causes polydipsia and polyuria. The inability to release vasopressin in response to normal stimuli can have several possible etiologies: (1) primary failure to synthesize the hormone in the periventricular nuclei of the hypothalamus, (2) destruction of these nuclei or proximal transport pathways in the hypothalamus and proximal pituitary stalk, (3) dysfunction of hypothalamic osmoreceptors such that despite adequate vasopressin reserves, the hormone is not released appropriately. The causes of diabetes insipidus include neoplasms, infiltrative disorders, surgery, and head trauma. Approximately 30% of cases are idiopathic. MRI is valuable in demonstrating not only the causative lesions, but also the status of the posterior pituitary gland, the storage site for the neurosecretory vesicles containing vasopressin. It is a unique feature of this gland that it is hyperintense on T_1-weighted images and regardless of the etiology this signal disappears in cases of diabetes insipidus.

6.2 Hemochromatosis

Hemochromatosis is a metabolic disorder in which excess iron is deposited throughout the body particularly in the solid abdominal viscera. For unknown reasons the pituitary gland is frequently involved. There is relative preferential deposition of iron within the gonadotrophic cells of the adenohypophysis. Dysfunction commonly manifests as loss of libido and hypogonadism. The characteristic finding on MRI is marked hypointensity emanating from the anterior pituitary gland on T_2-weighted images. This is due to the high levels of iron deposited within the region resulting in susceptibility effects and loss of signal.[24]

7 RELATED ARTICLES

Cranial Nerves Investigated by MRI; Eye, Orbit, Ear, Nose, and Throat Studies Using MRI; Head and Neck Investigations by MRI; Intracranial Infections; Temperomandibular Joint MRI.

8 REFERENCES

1. D. W. Chakeres, A. Curtin, and G. Ford, *Radiol. Clin. North Am.*, 1989, **27**, 265.
2. W. W. Peck, W. P. Dillon, D. Norman, T. H. Newton, and C. B. Wilson, *Am. J. Neuroradiol.*, 1988, **9**, 1085.
3. W. Kucharczyk, D. O. Davis, W. M. Kelly, G. Sze, D. Norman, and T. H. Newton, *Radiology*, 1986, **161**, 761.
4. T. Stadnik, A. Stevenaert, A. Beckers, R. Luypaert, T. Buisseret, and M. Osteaux, *Radiology*, 1990, **176**, 419.
5. J. L. Doppman, J. A. Frank, A. J. Dwyer, E. H. Oldfield, D. L. Millor, L. R. Nieman, G. P. Chrousos, G. B. Cutler, Jr., and D. L. Loriaux. *J. Comput. Assist. Tomogr.*, 1988, **12**, 728.
6. D. R. Newton, W. P. Dillon, D. Norman, T. H. Newton, and C. B. Wilson. *Am. J. Neuroradiol.*, 1989, **10**(5), 949.
7. W. Kucharczyk, J. E. Bishop, D. B. Plewes, M. A. Keller, and S. George. *Am. J. Roentgenol.*, 1994, **163**, 671.
8. W. M. Kelly, W. Kucharczyk, J. Kucharczyk, B. Kjos, W. W. Peck, D. Norman, and T. H. Newton. *Am. J. Neuroradiol.* 1988, **9**, 453.
9. I. Fujisawa, K. Kikuchi, K. Nishimura, K. Togashi, K. Itoh, S. Noma, S. Minami, T. Sagoh, T. Hiraoka, and T. Nomaoi, *Radiology*, 1987, **165**, 487.
10. M. Maghnie, F. Triulzi, D. Larizza, G. Scotti, G. Beluffi, A. Cecchini, and F. Severi. *Pediatr. Radiol.*, 1990, **20**, 229.
11. D. M. Yousem, J. A. Arrington, S. J. Zinreich, A. J. Kumar, and R. N. Bryan, *Radiology*, 1989, **170**, 239.
12. E. Pusey, K. E. Kortman, B. D. Flannigan, J. Tsuruda, and W. G. Bradley, *Am. J. Neuroradiol.*, 1987, **8**, 439.
13. W. Kucharczyk, W. W. Peck, W. M. Kelly, D. Norman, and T. H. Newton, *Radiology*, 1987, **165**, 491.
14. M. Castillo, P. C. Davis, W. K. Ross, and J. C. Hoffman, Jr., *J. Comput. Assist. Tomogr.*, 1989, **13**, 679.
15. J. W. Yeakley, M. V. Kulkarni, C. B. McArdle, F. L. Hoar, and R. A. Tang, *Am. J. Neuroradiol.*, 1988, **9**, 279.
16. D. Tampieri, D. Melanson, and R. Ethier, *Am. J. Neuroradiol.*, 1989, **10**, 351.
17. G. Sze, L. S. Uichanco, M. N. Brant-Zawadzki, R. L. Davis, P. M. Gutin, C. B. Wilson, D. Norman, and T. H. Newton, *Radiology*, 1988, **166**, 187.
18. S. N. Wiener, A. E. Pearlstein, and A. Eiber, *J. Comput. Assist. Tomogr.*, 1987, **11**, 236.
19. E. M. Burton, W. S. Ball, Jr., K. Crane, and L. M. Dolan, *Am. J. Neuroradiol.*, 1989, **10**, 497.
20. J. B. Moore, R. Kulkarn, D. C. Crutcher, and S. Bhimani, *Am. J. Pediatr. Hematol. Oncol.*, 1989, **11**, 174.
21. R. D. Tien, T. H. Newton, M. W. McDermott, W. P. Dillon, and J. Kucharczyk, *Am. J. Neuroradiol.*, 1990, **11**, 703.
22. S. W. Atlas, A. S. Mark, E. K. Fram, and R. Grossman, *Radiology*, 1988, **169**, 455.
23. A. Biondi, G. Scialfa, and G. Scotti, *Neuroradiology*, 1988, **30**, 214.
24. I. Fujisawa, M. Morikawa, Y. Nakano, and J. Konishi, *Radiology*, 1988, **168**, 213.

Biographical Sketches

Richard I. Farb. *b* 1959. B.Sc., 1981, University of Toronto. MD, 1985, University of Toronto, Canada. Radiology residency, Wayne State University Medical Center, Michigan 1991. Certification by examination by the Royal College of Physicians (Canada) and the American Board of Radiology 1991. Two year Neuroradiology Fellowship at University of Toronto completed 1993. Currently staff neuroradiologist at Sunnybrook Health Science Centre and lecturer at University of Toronto.

Walter Kucharczyk. *b* 1955. MD, 1979, University of Toronto, Canada. Radiology residency, University of Toronto, completing in 1983. Certified by examination as a Fellow of the Royal College of Physicians (Canada) in 1983, followed by two years of Neuroradiology MRI post residency training at UCSF and University of Toronto. Successively, visiting assistant professor (UCSF), assistant professor, full professor (University of Toronto). Currently Professor and Chair of the Department of Medical Imaging at the University of Toronto. Main interests: MRI of pituitary gland and parasellar area, tissue characterization using MR techniques, interventional methods with MRI.

Sodium-23 Magnetic Resonance of Human Subjects

Peter M. Joseph

Hospital of the University of Pennsylvania, Philadelphia, PA, USA

1 INTRODUCTION

Sodium-23 is a nucleus with spin quantum number $\frac{3}{2}$ whose gyromagnetic ratio, γ, corresponds to a frequency of 11.262 MHz tesla^{-1}, which is approximately one-quarter that of protons. It is widely but inhomogeneously distributed in body tissues. It is present in highest concentrations in extracellular water in a concentration of about 150 mM. Hence in vivo sodium NMR signals are less than one-thousandth those of hydrogen so that sodium MR images can never hope to compete with proton images in quality. Only little preliminary research effort has been directed toward the clinical utility of sodium MRI.

However, Na MRI may be able to contribute unique medical/physiological information that is not available in proton MRI. Intracellular Na is typically at the level of about 10–20 mM in most healthy cells. The enormous difference between intracellular (IC) and extracellular (EC) concentrations is maintained by the Na–K pump which actively transports the two kinds of ions across the cell membrane. Certain pathologies alter the function of that pump resulting in a significant rise in IC Na. There is evidence from in vitro experiments that this occurs in certain disease states, especially ischemia, infarction, and cancer. Thus one aim of Na MRI is to demonstrate a rise in the IC sodium concentrations. While there is still debate as to whether that goal has been achieved with in vivo MRI, it is one of the factors driving research interest in this field. There are various subtle aspects of the Na NMR signal that are thought to differ in the IC and EC environments, and much research has been directed toward clarifying this question.

2 BIOPHYSICS OF ^{23}Na NMR

The major difference between Na and ^{1}H NMR is that Na has spin quantum number $I = \frac{3}{2}$. This means there will be four energy levels, corresponding to the quantum numbers $m = I_z = -\frac{3}{2}, -\frac{1}{2}, \frac{1}{2}$, and $\frac{3}{2}$. Since normal NMR excitation and radiation permits only transitions whose m values differ by 1, there will in general be three possible Larmor frequencies; these are classified as 'inner', meaning $\frac{1}{2}$ to $-\frac{1}{2}$, and 'outer', meaning either $\frac{3}{2}$ to $\frac{1}{2}$ or $-\frac{1}{2}$ to $-\frac{3}{2}$. If there are no other interactions in the system, the energy levels are equally spaced and the three Larmor frequencies are equal.

However, the Na nucleus also has an electric quadrupole moment, denoted by eQ.[1] (e = electron charge.) This implies that the energy of the nucleus will be influenced by the presence of an electric field gradient, which is described by a second-rank tensor of strength eq. In this case there is another energy term in the Hamiltonian given by

$$\hat{\mathcal{H}}_Q = \frac{e^2qQ[3m^2 - I(I+1)][3\cos^2(\theta) - 1]}{8I(2I-1)} \quad (1)$$

where θ is the angle between the major axis of the quadrupolar tensor and the z axis. From this Hamiltonian comes a quadrupolar energy E_Q and frequency $\omega_Q = 2\pi E_Q/h$ depending on the quantum state.

Equation (1) has important consequences for the energy levels of the nuclei, the relaxation rates, and signal strength. First, we see that $\hat{\mathcal{H}}_Q$ depends quadratically on m; this changes the energy level differences of the outer levels but not the inner. Hence the quadrupolar interaction does not change the Larmor frequency corresponding to the inner transition. Both the magnitude and the sign of the energy level shift of the external transitions depend on the angle θ. If the local environment is isotropic, then averaging over angles gives zero average energy displacement. However, in situations of exceptional order (such as liquid crystals) the orientations are not random and a net shifting of the energy levels can occur. The resulting spectrum will show three lines as illustrated in Figure 1. Note that whereas the central line, corresponding to the inner transition, is narrow, the external spectral lines may be broadened by an amount dependent on the details of the microscopic electrostatic environment.

In this situation, quantum theory predicts that only 40% of the total radiated energy will lie in the unshifted inner line, while the remaining 60% may be distributed over the broad outer lines.[2] Depending on the experimental conditions, it is possible that the outer transitions will be so broadened as to be virtually undetectable with most NMR spectrometers. This leads to the widely discussed phenomenon of 'NMR invisibility' of sodium; i.e. several experiments have suggested that the observed Na NMR signal strength is less than what should be observed based on measured Na concentration levels. For example, Shporer and Civan proposed that this would explain previously reported discrepancies between the strength of the Na NMR signal observed and that expected from tissue measurements.[3] In particular, they demonstrated this effect for the relatively simple system of sodium linoleate in water.

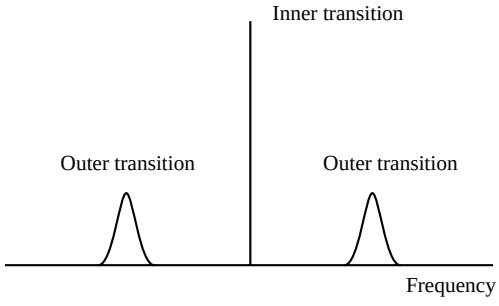

Figure 1 Schematic diagram of the spectrum from ^{23}Na in an ordered environment with electric quadrupolar interaction in a first-order approximation. The width of the outer transition lines depends on the strength and correlation time of the quadrupolar interaction. The inner transition carries 40% of the total signal

Joseph and Summers[4] noted that if the loss of Na NMR visibility were in fact due to a nonoverlapping displacement of the energy levels, then quantum theory predicts that the rate of nutation of the inner (unshifted) spectral component is *twice* that predicted by the usual classical vector model of the NMR excitation. In other words, if an NMR spectrometer is adjusted on a homogeneous phantom (such as aqueous NaCl) so that a particular radiofrequency pulse gives 90° of spin flip, then the same pulse applied to the split Na system will rotate the unsplit component by 180°. They demonstrated the vanishing of the sodium linoleate signal under conditions in which a NaCl phantom gave optimal signal.[4] This suggests that this 'flip angle effect' could be used to test for the presence of quadrupolar splitting in vivo without the need actually to detect the invisible Na spectral lines. To date, however, no one has demonstrated this effect using realistic in vivo biological material.

The more common interpretation of the quadrupolar interaction is that the orientation angle is isotropically distributed and is rapidly changing with a correlation time, τ_c, on the order of microseconds or less. In this situation the effect of $\hat{\mathcal{H}}_Q$ is not to induce energy level splitting but to broaden the lines, i.e., to induce relaxation. The physics of this situation is rather complex.[2,5,6] The result depends both on the whether the product $\omega_0\tau_c$ is large or small compared with unity as well as the product $\omega_Q\tau_c$. If $\omega_0\tau_c << 1$, the signal will show only one spectral line. If $\omega_0\tau_c > 1$ (but with $\omega_Q\tau_c << 1$) this line may have two distinct decay rates (i.e., two rates for T_1 and two for T_2). The inner and outer transitions give the same spectral frequency but differ in their relaxation rates. The outer transitions produce 60% of the signal and the inner 40%. This phenomenon of biexponential relaxation (BR) is widely observed in nature. For example, most biological tissue shows a short T_2 on the order of a few milliseconds and a longer one on the order of 20–30 ms. These results are interpreted in terms of a correlation time on the order of microseconds. In contrast, the relaxation times of NaCl–water are usually 50 ms or less for both T_1 and T_2 (at 2 tesla); this is due to a very short τ_c on the order of 10^{-11} s.

The phenomenon of BR is related to the question of Na visibility, i.e., if $T_{2f} << TE$ then the fast component will have died out before the signal is detected in a spin echo experiment. Obviously, this definition of 'invisibility' is highly dependent on the NMR equipment, and especially the shortest *TE* used. The use of a pulse spectrometer with very short *TE* is equivalent to being able to detect a very broad spectral component with a CW spectrometer. Most recent experiments have reported high visibility in biological materials. Joseph and Summers[4] found essentially 100% visibility in excised cat brain and porcine skeletal muscle. Kohler et al.[7] found only 80% visibility for Na in the vitreous humor of enucleated eyes, but it increased to 100% after digestion with collagenase.

The actual environment of biological Na ions is considerably more complex than that of a simple solution. Even in the EC space there is always a multitude of proteins, fatty acids, sugars, and other hydrophilic molecules with which the Na ions can interact. One expects short-term 'bonding' and exchange of the Na ions among the various bound and free pools. Such exchange processes are known also to influence the relaxation rates.[6,8] It is often assumed that the degree of IC Na bonding is much greater than the EC, so that IC Na will have a shorter T_2 than EC. This conclusion is subject to considerable doubt however, since even homogeneous solutions can produce BR very similar to that seen in vivo. For example, the relatively simple system consisting of NaCl ions in 4% agarose gel shows T_2 values of 5.5 and 23 ms.[4]

Since one motivation for doing Na MRI is the hope of imaging IC versus EC Na, we will review what is currently known about the scientific basis for this. All of this work relies on the use of a hyperfine shift reagent (SR),[9] such as dysprosium tripolyphosphate (Dy-TPP), which shifts the Larmor frequency of the EC Na only; this means that IC and EC Na have separate spectral lines. Such experiments show that IC Na often displays BR. Shinar and Navon[10] observed BR in red blood cells (RBC) with T_2 values of about 6.6 and 23.6 ms. However, the precision with which one can measure two T_2 components is limited and somewhat dependent on the assumptions made in modeling the decay. For example, Shinar and Navon *assumed* a 40/60 distribution between the slow and fast components (T_{2s}/T_{2f}) as predicted by theory for a single population of spins with BR. From their data one can probably not rule out a somewhat shorter T_{2f} with a different short/fast distribution ratio. Later work by Shinar and Navon[11] in the nuclei of chicken RBCs showed T_{2f} values in the 2–8 ms range, where the decay rate had a strong dependence on the IC concentration of DNA.

The BR of the IC Na is only one-half of the question, however. One wants to know if the BR phenomenon is found *only* in the IC Na. In 1986, Shinar and Navon[12] found that none of blood plasma, serum nor various solutions of proteins in water gave BR. This would suggest that the BR phenomenon is limited to IC Na. However, from a detailed analysis of the T_1 and T_2 decay rates they concluded that there was a significant contribution to quadrupolar relaxation from a pool of bound Na even in this noncellular environment. That is, one assumed that the physics of BR was operative but the effect was too weak to be resolvable into two distinct T_2 values. This experiment was done without the use of shift reagents.

Since blood is a relatively small fraction of the fluid in most tissues, one wonders whether the results on blood plasma can be applied to interstitial Na in living tissues. A very careful study of this question was conducted by Foy and Burstein[13] using Na spectroscopy of perfused hearts in both frog and rat models. They eliminated the contribution of blood by a selective inversion–recovery technique. In part of their experiment they used a shift reagent to distinguish IC from EC Na, with the result that 85% of the signal was EC in this model. They analyzed the transverse decay of the parenchymal signal (i.e., both IC and EC but excluding the blood) without SR and found BR with $T_{2s} \approx 25$ ms and $T_{2f} \approx 2$ ms in both models. Since the fast component was about 40% of the total signal it could not have come solely from the IC compartment. This is clearly a counter example to the hypothesis that short T_2 components are found *only* in the IC compartment of living tissues. However, it is still possible that the *average* IC T_2 could be less than that in the EC space.

Pekar et al. proposed using double quantum (DQ) filtration to distinguish IC from EC sodium.[14] The main point is that DQ, and in general multiple quantum (MQ), signals can emerge only if the physical parameters (strength of the quadrupolar constant and correlation time) are such that BR occurs. Pekar et al. used a SR and found the DQ sodium signal to be

limited to the IC space. This encouraged the hope that IC could be distinguished from EC solely by the physical characteristics of the NMR signal. However, subsequent work by Jelicks and Gupta[15] demonstrated that the presence of the SR in the EC would itself quench an MQ NMR signal. This means that the absence of EC MQ signal as observed by Pekar et al. did not contradict the finding of Foy and Burstein that BR does occur in the EC space. However, by detecting an MQ signal in the presence of SR it does provide an alternative method for obtaining a pure IC signal.[16,17]

3 IMAGING TECHNIQUES

The principles of imaging sodium do not differ from those used to image protons; basically, in addition to exciting the Na spins and reading out the signal, some means must be provided for spatial encoding.[18] The main differences are due to the characteristics of the Na signal already discussed, namely, the low S/N and the short values of T_1 and T_2. Short T_1, on the order of 50 ms in tissue, is an advantage since it implies rapid recovery of longitudinal magnetization after excitation so that short *TR* values can be used with little loss of signal. The low S/N forces one to employ techniques with relatively poor spatial resolution and long imaging times; typical values are 3 $\times$ 3 mm in-plane resolution and 10 mm slice thickness. Imaging times are usually a large fraction of 1 h.

The most important aspect of Na imaging is the need to achieve short echo times. One wants quantitation of the short versus long T_2 components, and the goal of imaging is to demonstrate these differences anatomically. A common technique is to use gradient echo (GE), which is equivalent to imaging the free induction decay (FID). The fact that GE is more sensitive than spin echo (SE) to background field gradients is rarely of importance for sodium, partly because the low γ implies less sensitivity of phase shift to the background fields and partly because the *TE* values achieved are usually less than 3 ms.

There are several ways in which spatial encoding can be applied. The single slice two-dimensional Fourier transform (2DFT) technique widely used in proton images can be used. More commonly, however, for multislice imaging, three-dimensional Fourier transform (3DFT) is used (Figure 2). The initial excitation may be a hard, nonselective pulse or a 'slab' which consists of a set of slices to be imaged. The slice definition is obtained by phase encoding the z axis. To reduce aliasing one can saturate spins outside of the desired region.[19] As shown in Figure 2, it is possible to obtain both a FID and SE signals. Some workers have employed a prephasing G_x pulse during the phase-encoding interval so that the $k_x = 0$ echo is delayed; this is called a GE. The advantage of the GE is that both positive and negative k_x values are obtained in the same data acquisition (DA), which leads to fewer imaging artifacts due to background gradients, eddy currents, etc. However, the resulting delay in the minimum echo time is disadvantageous for detecting the short T_2 component.

Both of the FT techniques require the use of phase-encoding gradient pulses applied after excitation and before signal read out. This is a major disadvantage because they delay the time at which signal acquisition can begin and will therefore severely attenuate the short T_2 component. A technique that avoids that delay is projection–reconstruction imaging (PRI). PRI works by reconstructing an object from measurements of its projections along many lines or planes over a wide range of angles. The two dimensional (2D) form of PRI is the basis of all clinical X-ray computerized tomography (CT) scanners, and was also the first technique used for MRI.[20] Shepp[21] showed how the 2D PRI method could be generalized to three dimensions. In this method, whose pulse sequence is illustrated in Figure 3, each excitation is completely nonselective and is followed immediately by readout of signal in the presence of all three gradients. The signal $S(t)$ will be the Fourier transform of the spin density along the direction defined by the gradient vector, $\boldsymbol{g}$:

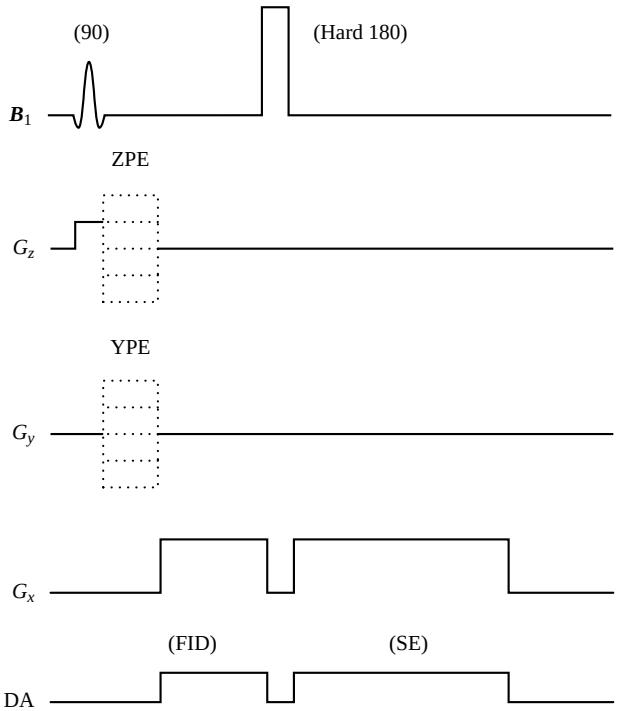

Figure 2 Pulse sequence diagram for 3DFT with both a FID and a spin echo (SE) detected. The 90° pulse is meant to excite a slab of slices in the z direction. The dotted lines on the G_z and G_y pulses indicate phase encoding which varies from one excitation to another (ZPE, z phase encoding; YPE, y phase encoding)

$$S(t) = \iiint M(x,\ y,\ z) \exp(\mathrm{i}\gamma\, \boldsymbol{g} \cdot \boldsymbol{r}t)\ \mathrm{d}x\, \mathrm{d}y\, \mathrm{d}z \tag{2}$$

where $\boldsymbol{r} = (x, y, z)$ is the position vector and $M(x, y, z)$ is the spin density at point $\boldsymbol{r}$, weighted by the relevant relaxation factor. If we can neglect T_2 decay during the readout period, Fourier transform of the signal yields a frequency distribution $S_{\mathrm{f}}(\omega)$ given by

$$S_{\mathrm{f}}(\omega) = \int S(t) \exp(-\mathrm{i} * \omega t)\ \mathrm{d}t = \iiint M(x, y, z)\ \delta(\omega - \gamma \boldsymbol{g} \cdot \boldsymbol{r})\ \mathrm{d}x\, \mathrm{d}y\, \mathrm{d}z \tag{3}$$

where $\delta()$ is the Dirac delta function. Equation (3) indicates that the signal corresponding to any given frequency ω comes from a *plane* perpendicular to the $\boldsymbol{g}$ vector and displaced by

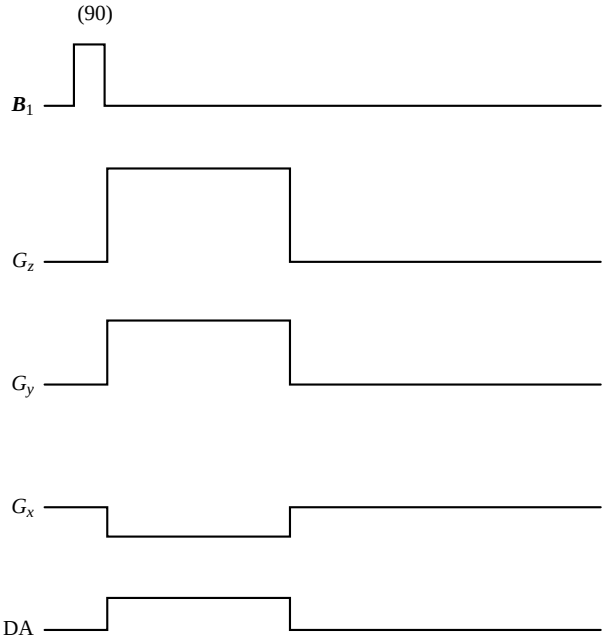

Figure 3 Pulse sequence diagram for 3D PRI. The 90° pulse is hard. The relative magnitudes of the G_x, G_y, and G_z pulses are varied from pulse to pulse such that the gradient vector sweeps over a spherical surface in $\boldsymbol{k}$-space

distance $\omega/(\gamma g)$ from the origin. To reconstruct the density $M(x, y, z)$ it is necessary to collect a set of signals in which the gradient vector ranges, more or less uniformly, over the full range of the 4π solid angle of a sphere.[22] In the language of $\boldsymbol{k}$-space, each gradient vector defines a vector in three-dimensional (3D) $\boldsymbol{k}$-space, which varies with time t as

$$\boldsymbol{k}(t) = \int \gamma \boldsymbol{g}\, \mathrm{d}t = \gamma t \boldsymbol{g} \qquad (\text{for } \boldsymbol{g} = \text{const}) \tag{4}$$

Hence, the 3D PRI method essentially scans $\boldsymbol{k}$-space along a series of spokes starting from the origin and extending out to some maximum value. To reconstruct the function $M(x, y, z)$ the data in $\boldsymbol{k}$-space are first multiplied by the factor k^2 then Fourier transformed back to the image domain to yield a set of modified planar data.[23] These planar ('filtered') data are then directly projected onto the 3D image matrix. The method is easily generalized to include multiple spin echoes.[24]

The major advantage of 3D PRI for Na MRI is that data acquisition can begin immediately after excitation, without the need to wait for gradient pulses to play out. This is especially advantageous when eddy currents and gradient amplifier limitations add ≈ 1 ms to the nominal time duration of gradient pulses. The method is intrinsically three dimensional, so one is committed to a rather large number of pulses to sample $\boldsymbol{k}$-space adequately. However, like 3DFT, the method is very efficient for signal to noise ratio (S/N) because each excitation includes the entire volume imaged. However, the method is sensitive to frequency offset and $\boldsymbol{B}_0$ inhomogeneity errors, but for Na MRI these are rarely a significant problem.

This method has no dephasing gradient prior to signal readout; this means that on any excitation only one-half of the k region is covered; i.e. $k > 0$ on one excitation and $k < 0$ on another. This technique is called 'half echo', and results in the earliest possible time for the $k = 0$ part of phase space. However, if $T_{2\mathrm{f}}$ is much less than the DA time window, high k values will be attenuated and the image will suffer loss of spatial resolution. This is a consequence of imaging objects with very short T_2 using frequency encoding.

An interesting variant of this technique combines Fourier encoding in the slice direction with PRI in the transverse plane; a Hahn SE time of 3.6 ms has been obtained on a clinical MRI machine.[25]

Another approach to the problem of achieving rapid data acquisition after excitation is to use gradients in the rf $\boldsymbol{B}_1$ field. This method has been applied to Na MRI, but the image quality obtained was less than that obtained by workers using the more conventional $\boldsymbol{B}_0$ gradient methods.[26]

When shift reagents are used, it is necessary somehow to image separately the two spectral lines produced. This can be done using various methods well known from proton chemical shift imaging.[27] For example, Kohler et al.[28] used a 2D phase-encoding technique equivalent to that originally proposed by Brown et al.[29] This technique uses a standard spatially selective excitation produced by the application of the z gradient, followed by phase encoding in both the x and y planes. The signal is read out in the absence of a gradient, so that Fourier transform will yield the spectrum. This sequence commits the experimenter to a relatively large number of excitations ($Nx \cdot Ny$). However, for Na imaging this is not a problem since one is usually forced to use a long scan time to achieve acceptable S/N. This technique can be generalized to use multiple echoes (on the long T_2 component) and a matched filter can be used to optimize S/N.[30]

The previous techniques are classed as single quantum (SQ). There is interest in obtaining MQ signals and using them for imaging. Wimperis and co-workers have investigated this, and the details are discussed elsewhere.[31] Triple quantum (TQ) is a better choice than DQ for this purpose. The minimum pulse sequence to generate MQ coherence consists of three rf pulses: α_1-t_1-α_2-t_2-α_3-t_3-DA, where the optimal values for the flip angles α_i depend on the type of experiment, and the optimal interpulse time intervals t_i depend on the relaxation properties of the Na. This pulse sequence gives a mixture of coherence orders, and it is necessary to 'filter' the signal to obtain the desired coherence. This is done by cycling the phase (ϕ in Figure 4) of the last rf pulse; the choice of flip angle = 109° maximizes the TQ signal component for this sequence.[32]

The simplest technique for MQ MRI is simply to append one of the previous SQ imaging pulse sequences to the previous MQ preparation sequence. However, a more ingenious imaging pulse sequence has been suggested by Wimperis and Wood[31] which uses the unique properties of the TQ coherence to select the TQ signal without phase cycling. The pulse sequence is shown in Figure 4. The first 90-180-90 set of pulses refocuses dephasing due to $\boldsymbol{B}_0$ inhomogeneity and/or chemical shift effects. During time interval t_2 there is TQ coherence. This implies that the phases of the relevant matrix elements evolve at three times the SQ Larmor frequency. Thus, the gradient pulses applied during that time need only be one-third as strong (or long) as in SQ techniques. This is an advantage in systems whose gradients are designed for proton imaging and in which it is difficult to achieve the factor of four increase needed to obtain high-resolution Na images. Furthermore, the TQ signal decays during that time at a rate

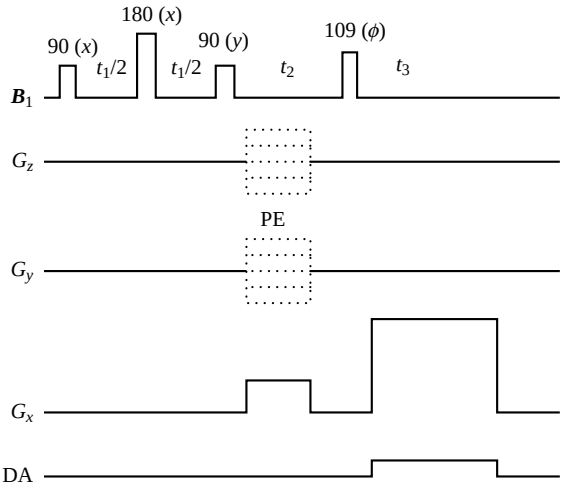

Figure 4 Pulse sequence diagram for triple quantum Na imaging. The dotted lines for the G_z and G_y pulses indicate phase encoding (PE). The x axis is frequency encoded during the data acquisition period (DA)

comparable to T_{2s}, so there is less need to minimize the time duration.[31] Application of the frequency-encoding prephasing pulse (on G_x) during this time sets up a typical echo during the readout time as shown. However, in this case the area under the prephase pulse needs to be only one-third that of the readout gradient pulse; this unusual condition acts to select only the TQ desired coherence component so that phase cycling is in principle not necessary. (However, in practice the SQ signals are so strongly excited that phase cycling is recommended.) The strength of the TQ signal developed, S, depends on both t_1 and t_3 according to the function

$$S(t_1,\ t_3) \propto f(t_1) f(t_3) \tag{5}$$

where

$$f(t) = \exp(-t/T_{2s}) - \exp(-t/T_{2f}) \tag{6}$$

When $T_{2s} >> T_{2f}$, $f(t)$ starts at zero, builds to a maximum in time $\approx T_{2f}$, and decays with time constant T_{2s}. Hence it is not necessary to achieve ultrashort echo or DA times with this sequence.

The drawback to MQ imaging is the reduction in signal amplitude relative to SQ.[15] In particular, the use of gradients to filter the MQ coherence reduces signal by a factor of two.[32] Wimperis et al.[33] have modified the technique in an attempt to increase S/N. However, they demonstrated only modest image quality in a phantom of 200 mM Na, which is 10 times the amount present IC. Keltner et al.[34] have used a technique similar to Figure 4 to image a phantom containing 12 mM Na, obtaining an excellent S/N in voxels of 1.5 × 1.5 × 1.5 cm size. To date, no one has published in vivo MQ images of Na with an image quality acceptable for biological application.

4 BIOLOGICAL APPLICATIONS

To date, most applications of Na MRI to biomedical problems have been experimental. These applications can be roughly categorized as concerning edema, infarction, and neoplasia.

4.1 Imaging Studies of Edema

Edema means the pathological increase in water content of tissues. When the edema is due to leaking blood vessels, the excess water is EC and its Na content should be about 150 mM, i.e., much greater than the IC level. This will result in increased Na signal. Furthermore, since the IC [Na] is so low, the amount of signal increase will largely reflect the increase in the size of the EC space. However, these same factors lead to increased signal in conventional T_2-weighted proton images, so Na MRI has not found widespread use as a clinical tool for this purpose.

One application of this principle was described by Lancaster et al.[35] who imaged experimental lung edema in rats. Proton MRI is especially problematic in this case because of severe suppression of signal due to the inhomogeneous magnetic susceptibility of normal lung tissue. Sodium MRI is less sensitive to this effect because of its reduced γ. They demonstrated much more dramatic increases in Na signal than proton signal in their model of permeability edema. They also attempted to isolate the vascular component of Na by using an iron oxide superparamagnetic particle suspension to suppress the vascular Na.

4.2 Imaging of Stroke and Infarction

The rationale for this application is that if a cell dies, its Na–K pump will shut down and the IC [Na] will increase. However, to demonstrate the effect experimentally sometimes involves reperfusing the organ following vascular occlusion in order to provide a source of the excess Na. Working with such a dog heart model, Cannon et al.[36] demonstrated increased Na signals in regions of ischemic damage. Some early work by Hilal et al.[37] demonstrated increased Na signal in MRI of the brain in one patient; both an old and a recent (2 h) stroke were shown. However, visualization of old strokes is easily accomplished with T_2-weighted proton MRI. The demonstration of early stroke would be very valuable clinically if it could be accomplished in a rapid and routine fashion. There has been little subsequent work in this area, and current research on MRI of stroke is more focused on the possible utility of diffusion-weighted proton MRI.

4.3 Imaging Studies of Cancer

There is much work in the area of distinguishing IC Na levels in normal and malignant cells. For example, Liebling and Gupta[38] found that IC Na of a benign uterine leiomyoma was relatively depressed at only 5.1 mM, while a malignant leiomyosarcoma had the elevated value of 34.6 mM. There have been many in vitro nonimaging studies of tumors in animal models which will not be reviewed here. Imaging is useful when it is desirable to see the spatial distribution of Na in more detail. Summers et al.[39] used Na MRI to study the development of necrosis in an animal model of human neuroblastoma; they found that the total Na signal (not distinguishing IC from EC) tended to rise with increasing tumor necrosis. Lin et al.[40] used Na MRI to distinguish two different

grades of tumor in a rat prostate tumor model; they found the two differed in the magnitude of T_{2s} in a way that could not be seen using proton MRI.

Several groups have demonstrated increased Na signal in human brain cancer. However, since most tumors are visualized using proton MRI, the interest is whether Na MRI can make more specific diagnoses. In some cases, the technique uses a relatively short gradient echo as well as several spin echoes with longer *TE*. In the normal brain, if $TE > 10$ ms the only structures visible are those containing cerebrospinal fluid and the vitreous humor of the eye. Looking only at echo times greater than 13 ms, Turski et al.[41] found that a brain stem glioma showed less enhancement than an astrocytoma in the pons. Hashimoto et al.[42] used a short *TE* (1.9 ms) gradient echo as well as longer spin echoes. However, they reported that the most useful differences between the Na and proton images of a meningioma were derived from the long *TE* images; the short *TE* images were obviously blurred. Schuierer et al.[43] looked at a variety of supratentorial lesions with Na MRI at 4.0 tesla using only a $TE = 11$ ms echo; they found that Na MRI did not contribute any information that was not provided by proton MRI or X-ray CT.

Hilal and co-workers[44] have energetically applied Na MRI to brain cancer. Skirting the recognized difficulties in differentiating IC from EC Na, they derive an image of 'putative intracellular' Na from a gradient echo starting at $TE = 0.2$ ms and two spin echoes ($TE = 12$ and 24 ms). The long T_2 signal, assumed to be purely EC, is used to estimate the EC volume fraction by comparison with the vitreous humor. The short T_2 component is computed by subtracting the value of the EC signal extrapolated to $TE = 0$ (equivalent to what is called 'curve stripping'). From these numbers an estimate of the putative IC *concentration* {[Na]/(IC volume)} is obtained for each pixel in the image. From their preliminary sample of 23 patients, they found a correlation between the IC [Na] and the histological grade of gliomas and astrocytomas. Like Hashimoto et al., they also found that Na MRI often reveals a larger tumor than proton MRI.

Thus, there is ample evidence that Na levels are increased in various types of tumor. However, whether this is due to increases in the IC or EC space is a complex question, and the answer probably will depend on the type of tumor and which organ it is in. In particular, many tumors have a loosely organized cellular system and so have a relatively large EC space compared with normal tissues. In these cases, the increase in EC Na would probably correlate with the signal increase seen in proton MRI.

5 RELATED ARTICLES

Chemical Shift Imaging; Image Formation Methods; Projection–Reconstruction in MRI.

6 REFERENCES

1. C. P. Slichter, 'Principles of Magnetic Resonance', 3rd edn., Springer-Verlag, New York, 1990, pp. 494–500.
2. W. D. Rooney and C. S. Springer, *NMR Biomed.*, 1991, **4**, 209.
3. M. Shporer and M. M. Civan, *Biophys. J.*, 1972, **12**, 114.
4. P. M. Joseph and R. M. Summers, *Magn. Reson. Med.*, 1987, **4**, 67.
5. T. E. Bull, *J. Magn. Reson.*, 1972, **8**, 344.
6. S. Forsen and B. Lindman, *Methods Biochem. Anal.*, 1981, **27**, 289.
7. S. J. Kohler, N. H. Kolodny, D. J. D'Amico, S. Balasubramanian, P. Mainardi, and E. Gragoudas, *J. Magn. Reson.*, 1989, **82**, 505.
8. U. Eliav and G. Navon, *J. Magn. Reson.*, 1990, **88**, 223.
9. M. S. Albert, W. Huang, J. H. Lee, J. A. Balschi, and C. S. Springer, *NMR Biomed.*, 1993, **6**, 7.
10. H. Shinar and G. Navon, *Biophys. Chem.*, 1984, **20**, 275.
11. H. Shinar and G. Navon, *Biophys. J.*, 1991, **59**, 203.
12. H. Shinar and G. Navon, *Magn. Reson. Med.*, 1986, **3**, 927.
13. B. D. Foy and D. Burstein, *Biophys. J.*, 1990, **58**, 127.
14. J. Pekar, P. F. Renshaw, and J. S. Leigh, *J. Magn. Reson.*, 1987, **72**, 159.
15. L. A. Jelicks and R. K. Gupta, *J. Magn. Reson.*, 1989, **83**, 146.
16. J. L. Allis, A. M. L. Seymour, and G. K. Radda, *J. Magn. Reson.*, 1991, **93**, 71.
17. H. Shinar, T. Knubovets, U. Eliav, and G. Navon, *Biophys. J.*, 1993, **64**, 1273.
18. S. J. Kohler and N. H. Kolodny, *Prog. NMR Spectrosc.*, 1992, **24**, 411.
19. W. H. Perman, D. M. Thomasson, M. A. Bernstein, and P. A. Turski, *Magn. Reson. Med.*, 1989, **9**, 153.
20. P. C. Lauterbur, *Nature (London)*, 1973, **242**, 190.
21. L. A. Shepp, *J. Comput. Assist. Tomogr.*, 1980, **4**, 94.
22. A. K. Louis, *J. Comput. Assist. Tomogr.*, 1982, **6**, 334.
23. O. Nacioglu and Z. H. Cho, *IEEE Trans. Nucl. Sci.*, 1984, **31**, 553.
24. J. B. Ra, S. K. Hilal, and C. H. Oh, *J. Comput. Assist. Tomogr.*, 1989, **13**, 302.
25. J. B. Ra, S. K. Hilal, and Z. H. Cho, *Magn. Reson. Med.*, 1986, **3**, 296.
26. J. P. Boehmer, K. R. Metz, J. Mao, and R. W. Briggs, *Magn. Reson. Med.*, 1990, **16**, 335.
27. D. Burstein and M. Mattingly, *J. Magn. Reson.*, 1989, **83**, 197.
28. S. J. Kohler, E. K. Smith, and N. H. Kolodny, *J. Magn. Reson.*, 1989, **83**, 423.
29. T. R. Brown, B. M. Kincaid, and K. Ugurbil, *Proc. Natl. Acad. Sci. U.S.A.*, 1982, **79**, 3523.
30. D. Lu and P. M. Joseph, *Magn. Reson. Imaging*, 1995, **13**, in press.
31. S. Wimperis and B. Wood, *J. Magn. Reson.*, 1991, **95**, 428.
32. J. W. C. VanderVeen, S. Slegt, J. H. N. Creyghton, A. F. Mehlkopf, and W. M. M. J. Bovee, *J. Magn. Reson., Ser. B*, 1993, **101**, 87.
33. S. Wimperis, P. Cole, and P. Styles, *J. Magn. Reson.*, 1992, **98**, 628.
34. J. R. Keltner, S. T. S. Wong, and M. S. Roos, *J. Magn. Reson., Ser. B*, 1994, **104**, 219.
35. L. Lancaster, A. R. Bogdan, H. L. Kundel, and B. McAffee, *Magn. Reson. Med.*, 1991, **19**, 96.
36. P. J. Cannon, A. A. Maudsley, S. K. Hilal, H. E. Simon, and F. Cassidy, *J. Am. Coll. Cardiol.*, 1986, **7**, 573.
37. S. K. Hilal, A. A. Maudsley, J. B. Ra, H. E. Simon, P. Roschmann, S. Wittekoek, Z. H. Cho, and S. K. Mun, *J. Comput. Assist. Tomogr.*, 1985, **9**, 1.
38. M. S. Liebling, R. K. Gupta, and H. L. Kundel, *Ann. N.Y. Acad. Sci.*, 1987, **508**, 149.
39. R. M. Summers, P. M. Joseph, and H. L. Kundel, *Invest. Radiol.*, 1991, **26**, 233.
40. R. Lin, A. R. Bogdan, L. Lancaster, K. Meyer, H. L. Kundel, E. Kassab, V. Liuolsi, M. Salscheider, and P. M. Joseph, *Proc. IXth Ann Mtg. Soc. Magn. Reson. Med.*, New York, 1990, Vol. 1, p. 722.

41. P. A. Turski, L. W. Houston, W. H. Perman, J. K. Hald, D. Turski, C. M. Strother, and J. F. Sackett, *Radiology*, 1987, **163**, 245.
42. T. Hashimoto, H. Ikehira, H. Fukuda, A. Yamaura, O. Watanabe, Y. Tateno, R. Tanaka, and H. E. Simon, *Am. J. Physiol. Imaging*, 1991, **6**, 74.
43. G. Schuierer, R. Ladebeck, H. Barfuss, D. Hentschel, and W. J. Huk, *Magn. Reson. Med.*, 1991, **22**, 1.
44. S. K. Hilal, C. H. Oh, I. K. Mun, and A. J. Silver, in 'Magnetic Resonance Imaging' eds. D. Stark and W. Bradley, Mosby Year Book, St. Louis, MO, 1992, pp. 1091–1112.

Biographical Sketch

Peter M. Joseph. *b* 1939. B.S., 1959, Ph.D., 1967, physics, Harvard University, USA; assistant professor of high energy physics, Carnegie Mellon University, 1970–72. NIH postdoctoral fellow in medical physics, Memorial Sloan Kettering Inst., New York, 1972–73. Instructor and assistant professor of clinical radiology, Columbia-Presbyterian Medical Center, New York, 1973–80. Associate Professor of Diagnostic Imaging Physics, University of Maryland, Baltimore, 1980–82. Associate and full professor, University of Pennsylvania, 1983. Approx. 120 publications in high energy physics, X-ray and computerized tomography scanning, and MRI. Current research specialty: electron beam tomography, sodium and fluorine MRI.

Structural and Functional MR in Epilepsy

Graeme D. Jackson

Brain Imaging Research Institute, Austin and Repatriation Medical Centre, Heidelberg, West Australia and Howard Florey Institute, University of Melbourne, Australia

and

Alan Connelly

Institute of Child Health and Great Ormond Street Hospital for Children, NHS Trust, London, UK

1 SUMMARY

Recently, developments in magnetic resonance imaging (MRI), magnetic resonance spectroscopy (MRS), and functional magnetic resonance imaging (fMRI) have opened up new opportunities for the noninvasive investigation of the brain. In epilepsy, these noninvasive techniques play a major role in the clinical investigation of patients with epilepsy.

MRI can noninvasively detect virtually all foreign tissue lesions (tumors) such as hamartomas, gliomas, oligodentrocytomas, dysembryoplastic neuroepithelial tumors and other developmental lesions. It has been able to define these lesions with a great deal of anatomical accuracy. This in itself is a tremendous advance which can now easily be taken for granted. Perhaps even more impressive has been the ability of optimized structural imaging techniques to detect smaller abnormalities of gray matter, in particular lesions like subtle cortical dysplasias, minor abnormalities of gray matter, and especially hippocampal sclerosis. In the important lesion of hippocampal sclerosis, quantitative measures of both the abnormal morphology (volume) and abnormal signal (T_2 relaxation measurement) have allowed this diagnosis to be made objectively. The clinical impact of this noninvasive information cannot be overstated. A major challenge now is to be able to reliably detect subtle areas of dysgenesis in the cortical gray matter.

MR spectroscopy provides information about brain metabolites that appears to provide objective information about regional damage in the temporal lobe which is not readily apparent with conventional imaging. Both these methods have enabled the detection of bilateral temporal lobe abnormalities, and the consequences of this bilateral damage on cognitive and seizure outcome is being explored. These techniques show fixed brain pathology. With the development of functional MRI it is possible to see signal change associated with activated neurons. As well as detecting normal activation (such as hand movement), it has been possible to image seizures. This gives information about both the spatial and the temporal location of signal changes during seizures. It appears that interictal activations may also be detectable.

This abundance of new MR techniques that allows so many aspects of brain structure, function and biochemistry to be investigated in the clinical setting has revolutionized the ability to detect brain abnormalities which underlie the epilepsy condition. In surgical programs for the treatment of epilepsy, MR has become at least as important as the EEG. The information from MR will have a major impact on the classification and understanding of epilepsy syndromes.

2 EPILEPSY, THE CLINICAL PROBLEM

Epilepsy is a common problem occurring in up to 1% of the population.[1,2] Intractable epilepsy which is a debilitating disorder may occur in up to 0.25% of the population. It is an extremely important neurological condition because there are severe social and medical consequences of the disorder[3,4] (up to 1% of patients die per year and many more are severely affected). Individuals otherwise often have the capacity to live normal lives, and complete cure is possible in a large number of these if a seizure focus exists, can be identified, and can be surgically removed.

Epilepsy is a disorder predominantly of the gray matter. This includes a wide variety of pathologies such as tumors (some of which may be small), subtle lesions such as cortical dysplasia, and often minor abnormalities of development of subtle degrees of brain injury such as hippocampal sclerosis or cortical gliosis. The predominant abnormality in these patients varies from the macroscopic to the cellular level, and may be characterized by predominantly biochemical or metabolic abnormalities.

3 CLASSIFICATION OF EPILEPSY CONDITIONS

In general terms epilepsy can be divided into two main groups: generalized and partial epilepsy.[5] In generalized epilepsy the seizure arises almost simultaneously in all parts of the brain. In partial epilepsy, by comparison, the seizure begins in one distinct part of the brain, and may then spread to other parts of the brain. There is an implication that generalized epilepsy involves an abnormality in multiple, or all, parts of the brain, while partial epilepsy implies that the abnormality is confined to a limited portion of the brain. The international classification which is most widely accepted[6] further divides the epilepsy conditions into those that are 'symptomatic' (that is have a defined pathological cause such as a tumor) and those that are 'idiopathic' (have no defined lesional cause). The recent development of MR tools for the investigation of brain structure, biochemistry, and function have had a major impact on the thinking in clinical epilepsy. The ability to define lesions (such as hippocampal sclerosis and cortical dysplasia), which were previously 'cryptogenic' and only detectable when pathological studies had been performed, means that the classification and principles upon which clinical epilepsy is based are undergoing major revision at the present time as a direct consequence of the information provided by MR studies.

4 THE CHALLENGE FOR MR STUDIES: THE INFORMATION THAT IS SOUGHT IN EPILEPSY PATIENTS

The problem of epilepsy necessitates understanding of brain structure, function, and biochemistry in normal and pathological states. The central problems in the understanding and management of intractable epilepsy are as follows.

1. To determine whether the epilepsy syndrome is generalized (no defined site of seizure onset, i.e. onset almost simultaneous in all or many parts of the brain) or partial (focal or localized seizure onset, with or without subsequent generalized spread).
2. To define whether a structural abnormality of the brain exists which may give rise to the epilepsy disorder (if so, known as symptomatic epilepsy; if not, then defined as idiopathic epilepsy).
3. If partial, to define the location, and extent, of the region (or regions) responsible for the generation of the seizures, and how functional events relate to underlying structural abnormality.
4. To understand which lesions are epileptogenic, and what abnormalities of structure and function define such areas.
5. To determine the effects of seizures on the brain. Do seizures cause damage (e.g. cellular damage, neuronal loss, hippocampal sclerosis) or is it the disease or condition that gives rise to the epilepsy disorder which causes all of the damage to the brain?
6. To identify important functional areas of cortex (movement, speech, memory) which must be preserved if a neurosurgical procedure is to be performed for treatment of intractable seizures.

Therefore, noninvasive investigations contribute to the solution of these problems by identifying gray matter lesions such as hippocampal sclerosis, replacing the use of invasive methods used to localize the site of seizure origin, defining the nature and extent of the structural, functional and metabolic abnormalities of the seizure focus, and determining preoperatively factors which influence the likely seizure and functional outcome from surgical treatment.

5 STRUCTURAL ABNORMALITIES SHOWN BY MR IMAGING

5.1 Tumors

Approximately 20% of all patients with intractable epilepsy will have a relatively large lesion (tumor) as the basis of their epilepsy. Before MRI only about 50% of these lesions were detected preoperatively (with CT) when located in the temporal lobes.[7] As these patients generally have an excellent outcome after surgery it is essential to identify them. Many series have now established that MR detects virtually all tumors, including dysembryoblastic lesions, hamartomas, and gliomas.

5.2 Hippocampal Sclerosis

Hippocampal sclerosis is one of the most common lesions found in the brains of patients with intractable epilepsy.[8–10] It is important for several reasons. It is a highly epileptogenic lesion. The side of the most affected hippocampus is almost always the side from which the majority of temporal lobe seizures originate. The detection of hippocampal sclerosis by MRI may obviate the need for invasive EEG monitoring with its attendant morbidity in patients being considered for surgery. Until new MR techniques arose, hippocampal sclerosis was considered as nonlesional epilepsy: the reliable detection of hippocampal sclerosis changes the clinical perspective of these patients.

The first reports of the MR detection of hippocampal sclerosis were rather confusing with encouraging results reported in some small studies, confusion with artifacts in others, and inadequate pathological verification in many. There were even studies that failed to detect any abnormality. In 1987, Kuzniecky and colleagues, from the Montreal Neurologic Institute, published the first major series of papers in which hippocampal sclerosis was detected in a systematic way, and shown to be related to pathological findings.[11] This study relied almost entirely on T_2-weighted signal changes. Using optimally oriented imaging planes, and heavily T_1-weighted inversion recovery sequences in addition to T_2-weighted sequences, hippocampal sclerosis was shown to be reliably detected by visual inspection of images acquired at 0.3 tesla using the criteria of hippocampal atrophy and T_2-weighted signal change in hippocampal gray matter.[7,12] Since then optimized imaging at 1.5 tesla has shown that there are four main features of hippocampal sclerosis visible in MRI[13,14] (Table 1).

The criteria for assessing these optimized images include both morphological and signal intensity changes. The morphological features are atrophy and disruption of internal hippocampal structure. Abnormal signal in the hippocampus can be seen on both inversion–recovery (T_1) and T_2-weighted imaging. The imaging of the fine anatomical structure of the hippocampus, to a level of detail previously possible only with microscopic examination (Figure 1 shows details of this) may become an even more important method of detecting hippocampal sclerosis with improvements in imaging resolution.

Table 1 Features of hippocampal sclerosis

MRI feature of hippocampal sclerosis	Suggested histopathological correlate of the MR imaging abnormality
• Unilateral atrophy (right cf. left)	• hippocampal atrophy
• Loss of internal morphological structure on IR images	• loss of neurones in CA1, CA2, and CA4 and replacement gliosis [Figure 6(d)]
• Increased signal on T_2-weighted images	• gliosis
• Decreased signal on T_1-weighted images (IR)	• gliosis

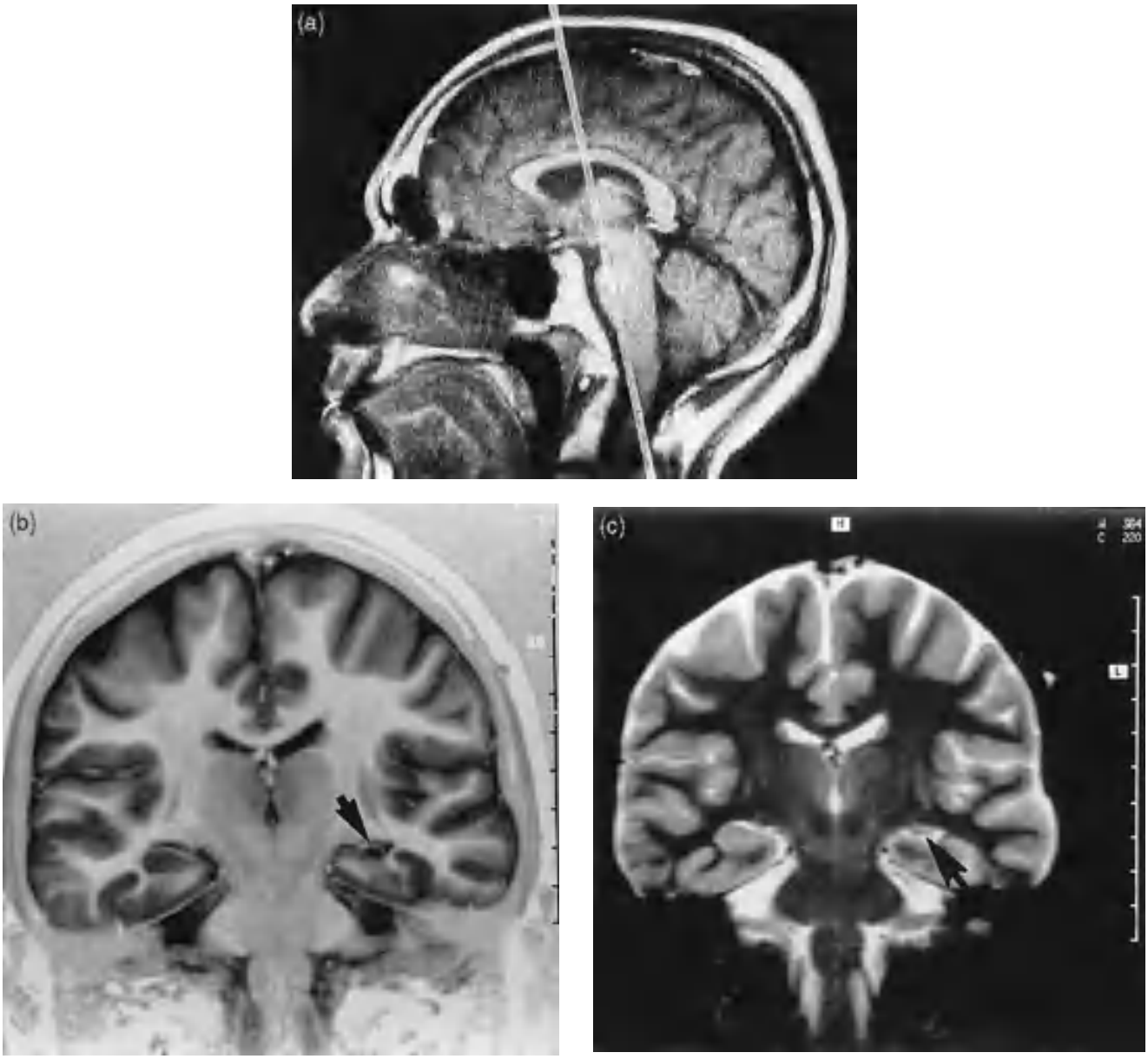

Figure 1 The features of hippocampal sclerosis on optimized imaging are shown here in the imaging plane which transects the hippocampus at right angles (a). These images show atrophy, and reduced T_1 signal (b) and increased T_2 signal (c)

5.3 Visual Analysis of the Hippocampus

The visual diagnosis of hippocampal sclerosis can be highly subjective, and even experienced neuroradiologists may have difficulty detecting this subtle lesion. It must be emphasized that not all features are seen in all cases. Unequivocal signal change (as long as the hippocampus is not enlarged) or atrophy may be accepted as diagnostic of hippocampal sclerosis, with the certainty increased if both are present. The addition of internal structure loss can be very helpful if the abnormality is subtle. Several series which compare blinded visual reports to pathological material have shown beyond doubt that hippocampal sclerosis can be reliably diagnosed by visual analysis. In experienced hands, and with optimized images, high sensitivity and specificity can be achieved. In order to do this optimized images must be performed[13] and all features of hippocampal sclerosis must be appreciated and searched for. It is our experience that no single feature (such as atrophy) on its own is sensitive enough for reliable routine visual diagnosis, although some expert centers achieve an accurate diagnosis in about 80% of cases.[15,16]

5.3.1 Atrophy

The assessment of the cross-sectional size of the hippocampus must be made in images obtained in the modified (tilted) coronal axis that transects the hippocampus at right

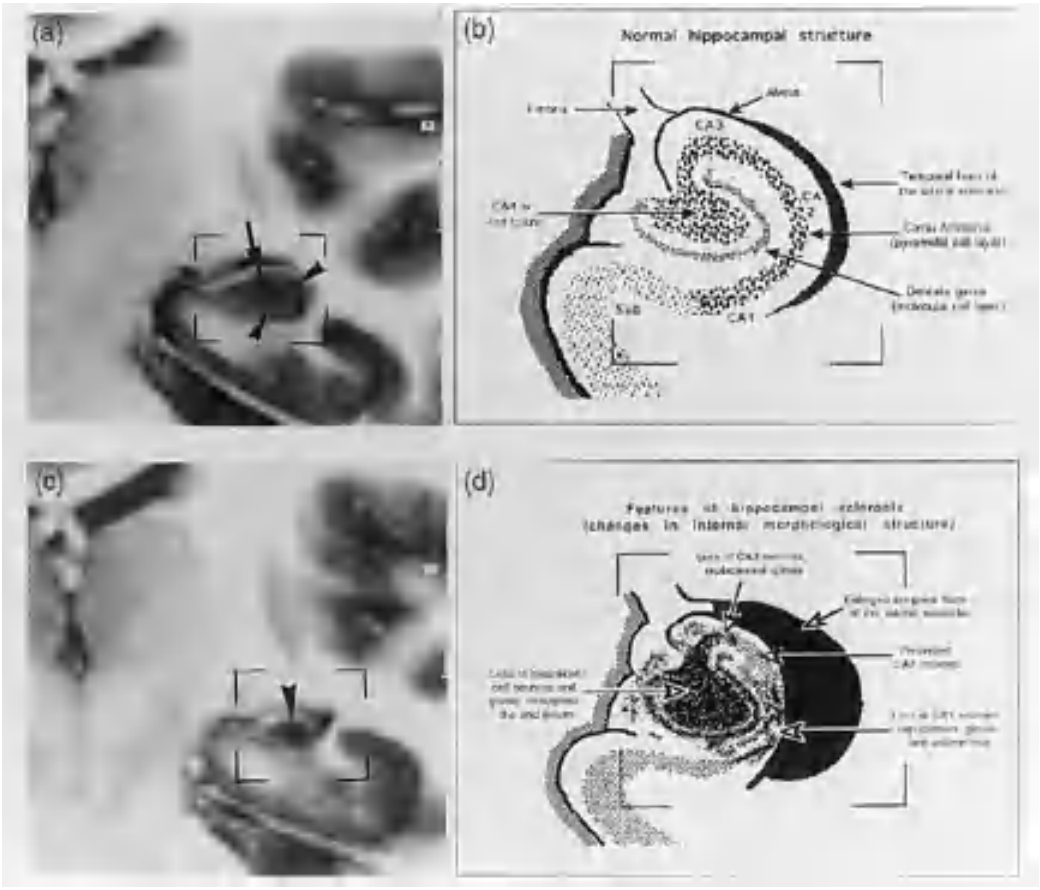

Figure 2 Internal structure of the hippocampus as seen on optimized MR images [normal (a),(b), hippocampal sclerosis(c),(d)]

angles. A smaller hippocampus as detected in this plane either qualitatively, or by quantitative methods, reliably predicts the side of the epileptogenic focus in the case of temporal lobe epilepsy but absolute measures of hippocampal size must be interpreted with caution.[17] Quantitation of atrophy (hippocampal volume measurement) is slightly more sensitive than visual assessment of hippocampal size. But with the addition of other visual features of hippocampal sclerosis this difference is less marked, or even reversed.

5.3.2 *Loss of the Normal Internal Morphological Structure of the Hippocampus*

Normal internal morphological structure of the hippocampus is produced by the alveus, the molecular cell layer of the dentate gyrus, and the pyramidal cell layer of the cornu ammonis, and can be seen on optimized coronal MR images [Figure 2(a) and (b)]. In hippocampal sclerosis, the loss of this normal internal structure is a consequence of neuronal cell loss and replacement of normal anatomical layers with gliotic tissue [Figure 2(c) and (d)]. This feature of hippocampal sclerosis is potentially very important as, with increasing spatial resolution, thinning of the CA1 region of the cornu ammonis may prove to be the most sensitive and specific means of diagnosing hippocampal sclerosis. Attempts have been made to define this with specially designed coils; however, increased resolution which will routinely show this microanatomy is becoming possible using standard equipment.

5.3.3 *Signal Hyperintensity on T_2-Weighted Images*

Increased T_2-weighted signal when localized imprecisely to the 'mesial temporal region' may be due to foreign tissue such as a glioma or hamartoma, to gliotic tissue in the hippocampus, to increased cerebrospinal fluid in the atrophied region, to flow artifacts and occasionally from a developmental cyst in the hippocampal head stemming from failure of closure of the lateral aspect of the hippocampal fissure. Careful determination of the exact location of this signal change by detailed examination of the anatomical features enables the correct diagnosis to be made. It is important to have sufficient knowledge of both the hippocampal anatomy and the easily recognizable artifacts that can occur in this region so that artifacts are not confused with significant signal abnormalities in the hippocampal gray matter.

5.3.4 *Signal Hypointensity on T_1-Weighted IR Images*

At 1.5 tesla, using a *TR* of 3500 and a *TI* of 300 ms, a sclerotic hippocampus appears small and dark, and the internal features are obscured (Figure 1). The presence of three features in a single coronal image makes the visual diagnosis of hippo-

Table 2 340 Patients, pathological verification of MRI diagnosis in 149

MRI diagnosis	%	Number/location
Hippocampal sclerosis	57	194
Foreign tissue lesion (glioma, astrocytoma or dysembryoplastic tumor)	13.5	46 (36 temporal, 10 extratemporal)
Cortical dysplasia	10.5	35 (12 temporal, 23 extratemporal)
Vascular malformations (12 cavernous hemangiomas, two high flow lesions)	4	14 (6 temporal, 8 extratemporal)
Cystic lesions	1.5	5 (4 temporal, 1 extratemporal)
Miscellaneous	5	17 (5 trauma, 1 tuberous sclerosis, 2 epidermoid, 4 extensive white matter lesions, 1 cerebellar atrophy, 4 uncertain)
No lesion demonstrated	8.5	29
Total	100	340

campal sclerosis much easier, and makes it possible to detect mild degrees of abnormality.

An abnormal signal on T_1- or T_2-weighted images arising from an atrophic hippocampus almost always represents hippocampal sclerosis. An abnormal signal arising from an apparently enlarged hippocampus may represent a hamartoma or glioma. If one relied only on a single feature such as atrophy, then these cases of the larger hippocampus being abnormal would be incorrectly lateralized.

5.4 Visual Analysis: Findings Other than Hippocampal Sclerosis

Detailed analysis of MRI images reveals a high percentage of abnormalities which can be detected in the brains of patients with intractable partial epilepsy. As MR techniques improve, it is becoming clear that most patients with intractable epilepsy have detectable imaging abnormalities. Table 2 shows the range of abnormalities which were detected in a combined series of patients from several centers. While often, in the past, no cause could be identified for many cases of intractable partial epilepsy, it is now becoming clear that most adults and children with partial epilepsy will have defined brain abnormalities visualized on appropriate optimized imaging.[7,13,16,18–26]

6 QUANTITATIVE DIAGNOSIS OF HIPPOCAMPAL SCLEROSIS

There has been a widespread problem in achieving the best results using visual analysis (and routine reporting of MR studies) in the clinical environment. It is clear that the results of visual inspection can be replicated in different centers, and that the findings are specific and sensitive when optimized images are interpreted in expert hands. It is equally clear that this expertise is hard to come by. This is probably because the lesion of hippocampal sclerosis differs from a normal hippocampus by a degree that might have previously been attributed to artifact or normal variation. Therefore considerable experience is required to gain expertise in this diagnosis. For this reason, for research purposes, and for the detection of abnormalities beyond the sensitivity of the eye, quantitative diagnosis of hippocampal abnormalities has been essential. The features of hippocampal sclerosis are the same as when assessed visually. Much initial attention has been given to the quantitation of hippocampal atrophy but quantitation of signal characteristics is also possible.

6.1 Volumetric Analysis

In 1990 Jack and co-workers[17,27,28] published their method of quantifying hippocampal atrophy which for the first time enabled an objective measurement of hippocampal pathology. The use of volumetric measurement to assess hippocampal size had been successfully adopted (and adapted) by many centers.[7,13,16,22–26,29–33] Despite different protocols, this has proven to be a reliable means of determining the lateralization of hippocampal pathology in up to 90% of cases with hippocampal sclerosis. It is our impression that visual analysis in the most expert centers detects virtually all cases that are detected by volumetric analysis, although volume techniques are more sensitive than visual analysis for the detection of the single feature of hippocampal atrophy. There are some cases, because features in addition to atrophy are considered, which can be detected by visual analysis and not by volumetric analysis.[34] Because of the range of normal variation, and measurement error, the most reliable use of the volume measurement technique (and indeed visual analysis) has been in lateralization. It has not been easy to determine bilateral hippocampal abnormalities or to determine abnormality without comparison between sides. The strength of the volumetric technique is that the anterior–posterior distribution of the atrophy can be determined[35] and the quantitative analysis removes the sometimes subjective nature of the analysis. The greatest weakness is that the only well verified and reliable technique (because of normal variation) is the use of side to side ratios. This means that bilateral disease is not usually detectable.

6.2 T_2 Relaxometry

As well as quantifying the hippocampal atrophy, one can quantify the T_2 signal in the hippocampus by measuring the T_2 relaxation time in the hippocampal gray matter (Figure 3).[36] The T_2 relaxation time can be measured quantitatively by measuring the decay in signal intensity at different echo times in a series of T_2-weighted images acquired in the same slice.

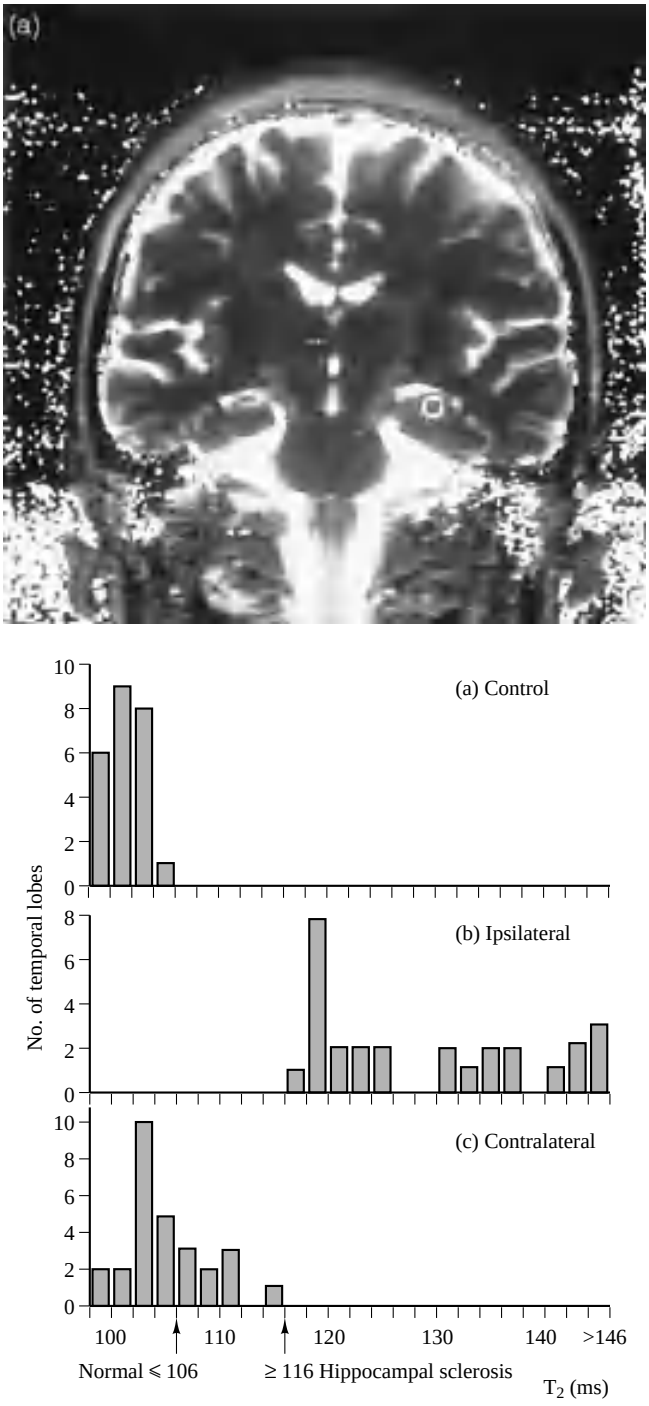

Figure 3 The T_2 map (a) is constructed from the T_2 relaxation times measured for each pixel. The relaxation time is presented as intensity, and can be measured directly for any region of interest (shown for the hippocampus). The histogram (b) shows the distribution of measured T_2 relaxation times in those patients with hippocampal sclerosis (labeled ipsilateral and contralateral to the side of seizure onset) and controls

Each pixel of the resulting T_2 map is derived from the intensity in each of 16 images in that same slice.

This objective measurement has a small range of values in normal subjects. The T_2 relaxation time appears to be very precise in normal tissue. This enables the detection of pathology without requiring comparison between two hippocampi. Therefore, as well as being sensitive, it permits the detection of pathology in the contralateral hippocampus.

In our experience, the T_2 relaxation time within the hippocampus is a robust and reliable objective measurement of hippocampal pathology, providing a means of assessing the hippocampus which is as good as our most skilled visual interpretation of hippocampal abnormality in optimized scans. In contrast to both visual interpretation and volumetric analysis of hippocampal atrophy, the definition of a normal hippocampal T_2 relaxation time is very precise. Therefore, T_2 quantification has the ability to detect very mild, bilateral and progressive hippocampal abnormalities. Moreover, T_2 values can be interpreted in terms of hippocampal pathology even when the other hippocampus is incomplete or distorted, such as when a lesion is present or following temporal lobe surgery. In these difficult cases, pathology of the residual ipsilateral hippocampus and the contralateral hippocampus may still be diagnosed. It has recently been shown that there is a very close correlation between hippocampal atrophy, hippocampal T_2 abnormality and pathological findings. Therefore, findings from hippocampal volume studies (such as outcome, and pathology correlations) should apply to T_2 abnormalities, while the latter has the advantage of detecting bilateral disease.

7 MR SPECTROSCOPY

As discussed elsewhere in this volume, several lines of evidence suggest that almost all the *N*-acetylaspartate (NAA) within the brain is neuronal,[37–40] and so a reduction in the NAA signal is commonly interpreted in terms of neuronal loss or damage. Such a case is shown for the temporal lobe in Figure 4. Here the NAA signal is reduced and the signals from choline containing compounds (Cho) and creatine + phosphocreatine (Cr) are increased. While interest focuses on the NAA signal as a marker of neuronal damage or loss, it is often impractical to quantitate this as an absolute quantity. Usually a marker of abnormality is being sought, so the ratio of NAA to Cho or Cr is often used as such a marker. In the temporal lobe it may often be difficult to resolve the Cho and Cr signals unequivocally, therefore we recommend that the ratio NAA/(Cho + Cr) is an appropriate marker of pathology for clinical use.

MR spectroscopy studies have shown overall abnormalities in the NAA, Cr and Cho signals in the temporal lobes of patients with well localized intractable temporal lobe epilepsy.[41,42] In comparison with controls, the temporal lobes ipsilateral to the seizure focus show a 22% reduction in NAA signal intensity, a 15% increase in the Cr signal, and a 25% increase in the Cho signal. The NAA change is interpreted in terms of neuronal loss (or damage). The interpretation of the increase in Cho and Cr signals is not yet clearly defined. However, studies of neural cells show that the concentrations of choline-containing compounds and of creatine + phosphocreatine are much higher in astrocyte and oligodendrocyte preparations than in cerebellar granule neurons.[37] Thus, increases in Cr and Cho may reflect reactive astrocytosis suggesting that both neuronal loss and astrocytosis may be identified by the noninvasive measurement of metabolites by MRS.[37,43–45]

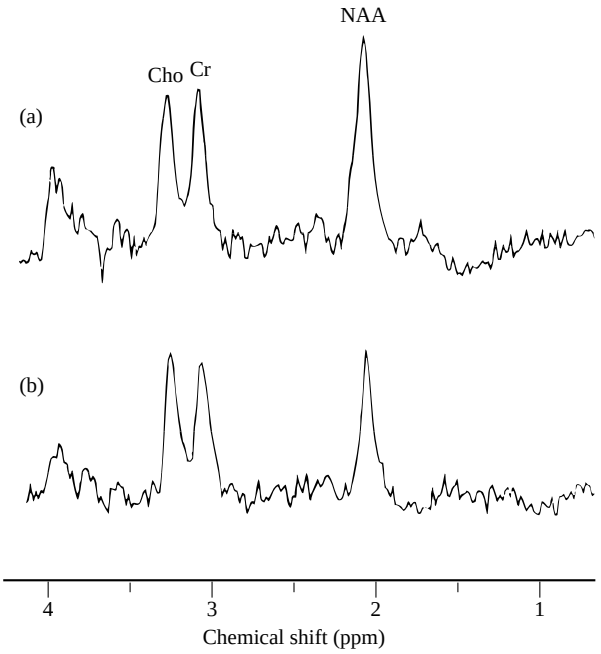

Figure 4 Spectra from (a) the temporal lobe contralateral to the seizure focus in a patient with temporal lobe epilepsy and (b) from the ipsilateral temporal lobe. Note the decrease in NAA in the ipsilateral temporal lobe

Using the ratio NAA/(Cho + Cr), MRS has been used to lateralize up to 70 patients with intractable temporal lobe epilepsy. In about 40 of these cases the abnormality was bilateral, and like T_2 relaxation time measurements could be used to detect bilateral abnormalities. MRS is sensitive to bilateral and diffuse pathology and it is an objective measure of metabolite abnormalities which cannot be visualized directly with MR imaging. We view these MR spectroscopic abnormalities as a marker of regional abnormalities of the temporal lobe in these patients. We do not believe that it is a marker simply of hippocampal sclerosis, but it provides additional information about pathology of the temporal lobes which is not available by other MR methods.

Chemical shift imaging (CSI) or magnetic resonance spectroscopic imaging has the advantages of being able to determine the regional distribution of metabolites and to identify areas of maximal abnormality. In a study of ten patients with temporal lobe epilepsy and five controls the left–right asymmetry of NAA/Cr ratios was found to be significantly different from controls in all cases.[46] The use of such an asymmetry index alone precludes the detection of bilateral abnormalities. However, comparison of NAA/Cr ratios in patients and controls indicated that two patients had bilateral reduction in the NAA/Cr ratio in the posterior temporal region, and the greatest reduction was ipsilateral to the maximum EEG disturbance. A further CSI study, using a 2T Philips system with a 4 mL effective voxel size, was performed on eight patients with unilateral complex partial seizures and eight controls.[47] Significant asymmetry in the intensity of the NAA signal was found in all patients. In each case the lower NAA corresponded to the side of seizure focus as determined by EEG. No significant changes in Cho or Cr were observed.

It is apparent that CSI has distinct advantages over single voxel techniques in terms of coverage of the brain, and it is becoming the method of choice in a number of centers for the study of epilepsy. However, it is technically more demanding than single voxel MRS, particularly with respect to magnetic field homogeneity (shimming), water suppression, and infiltration of subcutaneous fat signal into voxels other than just those adjacent to the scalp. Cendes et al.[46] noted that anterior temporal lobe structures were more accessible to single voxel methods, and reported only posterior and midtemporal results from their CSI study and Xue et al.[48] have reported problems with suboptimal shimming when performing CSI in a large

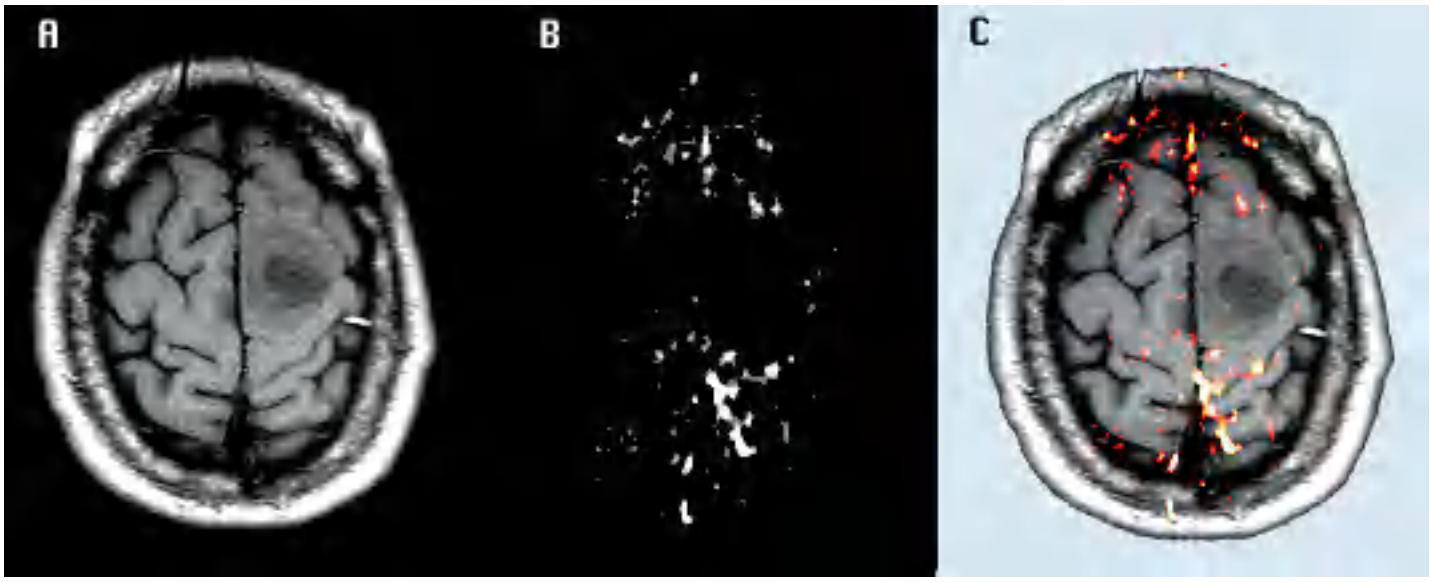

Figure 5 Functional MR image showing the area of increased signal associated with leg movement near a tumor thought to involve the motor strip: (a) baseline image; (b) activation image; (c) superimposition image

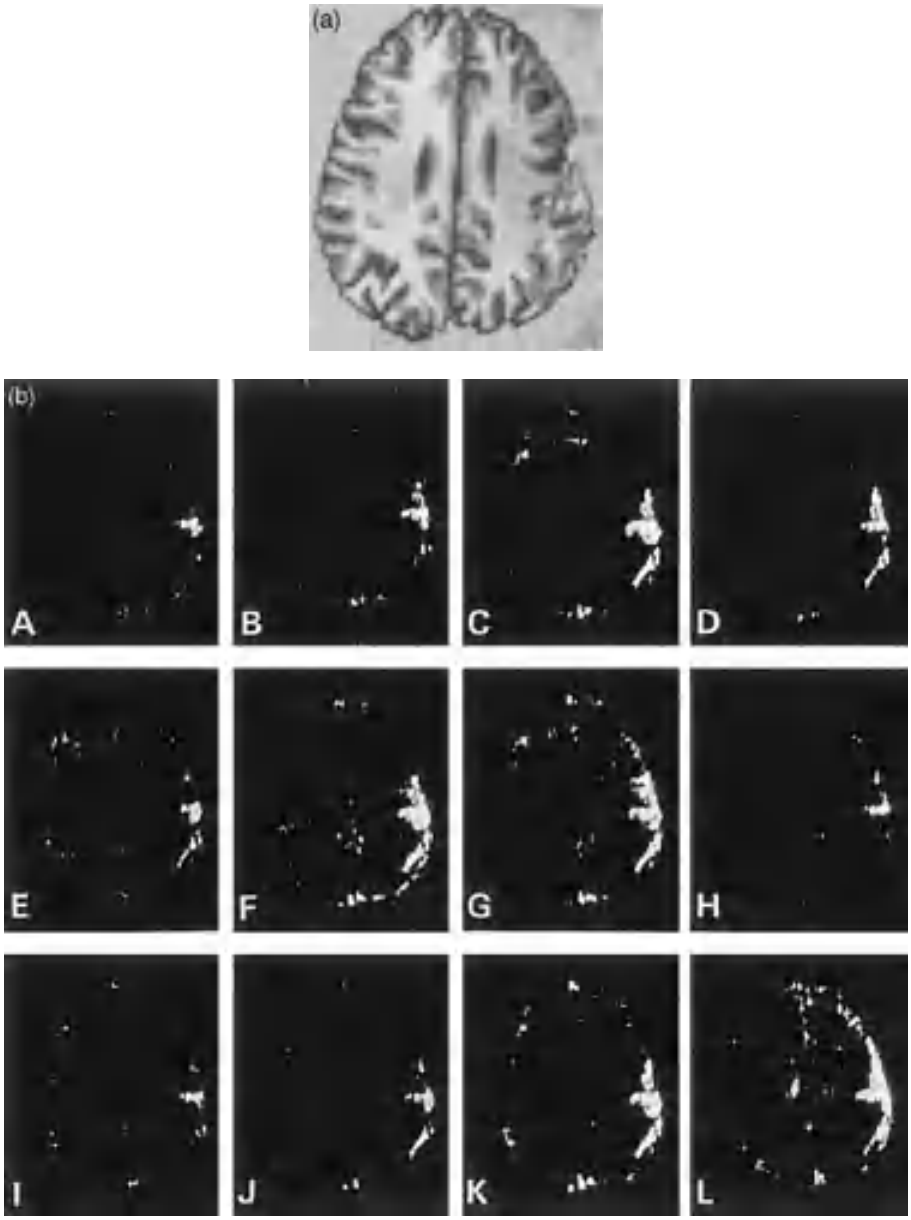

Figure 6 (a) Signal change associated with the onset of a focal motor seizure in the same region in a 4 year old boy with intractable epilepsy. This activation was seen 20 s before the onset of the seizure. (b) The upper two rows (A–D and E–H) show activation seen using fMRI during two clinical seizures. After activity is first seen, images 20, 60 and 100 s later are shown (all rows). In the first row a clinical motor seizure began at the time of the third image. The lower row is a period of activation not associated with a seizure. The surface EEG suggested seizure onset in this region, and ictal single photon emission computed tomography (SPECT) localized it to this same region. The base anatomy image is the same for all these figures

region including both temporal lobes. They have therefore adopted the strategy of acquiring CSI volumes from each temporal lobe separately.

8 FUNCTIONAL MRI (fMRI)

The clinical potential of fMRI is enormous and will be dealt with in many other sections of this Encyclopedia. For clinical epilepsy the following are major applications.

8.1 Mapping of Eloquent Areas of Cortex

Epilepsy surgery entails resection of abnormal areas of cortex in order to relieve the epilepsy condition. In many cases it is important to determine the location of important functions which must not be affected by this surgery such as movement, speech, and memory. The ability of fMRI to demonstrate this eloquent cortex helps in the preoperative assessment of these patients. At present this is largely limited to the motor strip[49] (Figure 5), but demonstration of speech areas will also be important.

At the moment, many groups have produced images of signal changes during 'speech activation'. While some of these are compeling, the problem of speech activation and localization is complex, and a great deal of validation and careful interpretation of these signal changes will be required before they assume their potential importance in clinical practice.

8.2 Functional Imaging of Seizures

Functional MRI can detect cortical activation which occurs during partial motor seizures.[50] Activation can be seen in the region which is activated during seizures even when no clinical seizure occurs. Also, quite remarkably, activation could first be seen up to 1 min before the onset of clinical or EEG changes during similar seizures [Figure 6(a) and (b)]. The implication of these observations is that the vascular and oxygenation changes may precede, or at least be detectable earlier than, the EEG or clinical events which are associated with seizures. It also provides compeling evidence that subclinical activation can be identified using fMRI, and this may enable precise localization of the seizure focus in some cases. These observations allow structural and dynamic functional information to be obtained in a single, integrated, totally noninvasive, MR examination, and point the way to the future role of MR as a means of imaging neurophysiology.

9 CONCLUSION

The impact of MR and its application to clinical epilepsy is akin to the impact of the EEG in the 1940s. It is enabling abnormalities of the brain to be demonstrated by noninvasive techniques in many of these patients with epilepsy. The impact has been great in the field of epilepsy surgery where, already, patients who had previously required invasive depth electrodes, are now able to go to resective surgery directly based on noninvasive studies which include noninvasive EEG, routine clinical evaluation, and these new MR techniques. In the broader field of clinical epilepsy problems, MR findings are beginning to have a large impact on the view of epilepsy, and of the syndromes that can be defined in individual patients. This will ultimately affect the classification of epilepsy, with new syndromes such as temporal lobe epilepsy with hippocampal sclerosis being defined. The consequence of these new MR techniques will be to benefit those who are most affected by this disease: patients with epilepsy.

10 RELATED ARTICLES

Brain MRS of Human Subjects; Brain Neoplasms in Humans Studied by Phosphorus-31 NMR Spectroscopy; Localization and Registration Issues Important for Serial MRS Studies of Focal Brain Lesions.

11 REFERENCES

1. W. A. Hauser, J. F. Annegers, and L. T. Kurland, *Epilepsia*, 1991, **32**, 429.
2. W. A. Hauser, 'Epilepsy Surgery'; ed. H. A. Luders, Raven Press, New York, 1992, pp. 133–141.
3. P. Klenerman, J. W. Sander, and S. D. Shorvon, *J. Neurol. Neurosurg. Psychiatry* 1993, **56**, 149.
4. D. C. Taylor 'Surgical treatment of the epilepsies', ed. J. Engel, Jr. 2nd edn., Raven Press, New York, 1993.
5. J. J. Engel 'Seizures and epilepsy' Contemporary Neurology series, Davis, Philadelphia, 1989.
6. Commission on classification and terminology of the international league against epilepsy, *Epilepsia*, 1989, **30**, 389.
7. G. D. Jackson, S. F. Berkovic, B. M. Tress, R. M. Kalnins, G. Fabinyi, and P. F. Bladin, *Neurology*, 1990, **40**(12), 1869.
8. J. H. Margerison and J. A. N. Corsellis, *Brain*, 1966, **89**, 499.
9. M. A. Falconer, E. A. Serafetinides, and J. A. N. Corsellis, *Arch. Neurol.*, 1964, **10**, 233.
10. M. A. Falconer, *Lancet*, 1974, **2**, 767.
11. R. Kuzniecky, V. De La Sayette, R. Ethier, D. Melanson, F. Andermann, S. Berkovic, Y. Robitaille, A. Olivier, T. Peters, and W. Feinder, *Ann. Neurol.*, 1987, **22**(3), 341.
12. S. F. Berkovic, F. Andermann, A. Olivier, R. Ethier, D. Melanson, Y. Robitaille, R. Kuzniecky, T. Peters, and W. Feindel, *Ann. Neurol.*, 1991, **29**, 175.
13. G. D. Jackson, S. F. Berkovic, J. S. Duncan, and A. Connelly, *Am. J. Neurorad.*, 1993, **14**, 753.
14. R. Kuzniecky, E. Faught, and R. Morawetz, *Epilepsia*, 1993, **34**(6), 141.
15. C. R. J. Jack, F. W. Sharbrough, G. D. Cascino, K. A. Hirschorn, P. C. O'Brien, and W. R. Marsh, *Ann. Neurol.*, 1992, **31**(2), 138.
16. G. D. Cascino, C. R. Jack, Jr., K. A. Hirschorn, and F. W. Sharbrough, *Epilepsy Res.*, 1992, (suppl. 5), 95.
17. C. J. Jack, M. D. Bentley, C. K. Twomey, and A. R. Zinsmeister, *Radiology*, 1990, **176**(1), 205.
18. J. H. Cross, G. D. Jackson, B. G. R. Neville, A. Connelly, F. J. Kirkham, S. G. Boyd, M. C. Pitt, and D. G. Gadian, *Arch. Dis. Child.*, 1993, **69**, 104.
19. G. D. Cascino, C. R. Jack, Jr., J. E. Parisi, W. R. Marsh, P. J. Kelly, F. W. Sharbrough, K. A. Hirschorn, and M. R. Trenerty, *Epilepsy Res.*, 1992, **11**(1), 51.
20 R. Duncan, J. Patterson, D. M. Hadley, P. Macpherson, M. J. Brodie, I. Bone, A. P. McGeorge, and D. J. Wyper, *J. Neurol. Neurosurg. Psychiatry*, 1990, **53**(1), 11.
21. P. Gulati, A. Jena, R. P. Tripathi, and A. K. Gupta, *Indian Pediatr.*, 1991, **28**(7), 761.
22. B. Jabbari, A. D. Huott, G. DiChiro, A. N. Martins, and S. B. Coker, *Surg. Neurol.*, 1978, **10**, 319.
23. R. Kuzniecky, A. Murro, D. King, R. Morawetz, J. Smith, K. Powers, F. Yaghmai, E. Faught, B. Gallagher, and O. C. Snead, *Neurology*, 1993, **43**, 681.
24. C. J. Kilpatrick, B. M. Tress, C. O'Donnell, S. C. Rossiter, and J. L. Hopper, *Epilepsia* 1991, **32**(3), 358.
25. K. Miura, M. Kito, F. Hayakawa, M. Maehara, T. Negoro, and K. Watanabe, *J. Jpn. Epilepsy Soc.*, 1990, **8**(2), 159.
26. S. S. Spencer, G. McCarthy, and D. D. Spencer, *Neurology*, 1993.
27. C. J. Jack, C. K. Twomey, A. R. Zinsmeister, F. W. Sharbrough, R. C. Petersen, and G. D. Cascino, *Radiology*, 1989, **172**(2), 549.
28. C. J. Jack, F. W. Sharbrough, C. K. Twomey, G. D. Cascino, K. A. Hirschorn, W. R. Marsh, A. R. Zinsmeister, and B. Scheithauer, *Radiology* 1990, **175**(2), 423.
29. M. Ashtari, W. B. Barr, N. Schaul, and B. Bogerts, *Am. J. Neurorad.*, 1991, **12**, 941.
30. M. Baulac, O. Granat, X. Gao, and D. Laplane, *Epilepsia*, 1991, **3**(2), 2.
31. G. Castorina and D. L. McRae, *Acta Radiol.*, 1963, **1**, 541.
32. T. Lencz, G. McCarthy, R. A. Bronen, T. M. Scott, J. A. Inserni, K. J. Sars, R. A. Novelly, J. H. Kim, and D. D. Spencer, *Ann. Neurol.*, 1992, **31**(6), 629.

33. K. Matsuda, K. Yagi, T. Mihara, T. Tottori, Y. Watanabe, and M. Seino, *Jpn. J. Psychiatry Neurol.*, 1989, **43**(3), 393.
34. G. D. Jackson, R. I. Kuzniecky, and G. D. Cascino, *Neurology*, 1994, **44**, 42.
35. M. J. Cook, D. R. Fish, S. D. Shorvon, K. Straughan, and J. M. Stevens, *Brain*, 1992, **115**, 1001.
36. G. D. Jackson, A. Connelly, J. S. Duncan, R. A. Grünewald, and D. G. Gadian, *Neurology*, 1993, **43**, 1793.
37. J. Urenjak, S. R. Williams, D. G. Gadian, and M. Noble, *J. Neurochem.*, 1992, **59**, 55.
38. J. Urenjak, S. R. Williams, D. G. Gadian, and M. Noble, *Neurosci.*, 1993, **13**, 981.
39. J. W. Hugg, K. D. Laxer, G. B. Matson, A. A. Maudsley, C. A. Husted, and M. W. Weiner, *Neurology*, 1992, **42**, 2011.
40. J. K. Joller, R. Zaczek, and J. T. Coyle, *J. Neurochem.*, 1984, **43**, 1136.
41. J. W. Hugg, K. D. Laxer, G. B. Matson, A. A. Maudsley, and M. W. Weiner, *Proc. XIth Ann Mtg. Soc. Magn. Reson. Med.*, Berlin, 1992, 1913.
42. J. Peeling, G. Sutherland, *Neurology*, 1993, **43**, 589.
43. D. G. Gadian, A. Connelly, J. S. Duncan, J. M. Cross, F. J. Kirkham, C. L. Johnson, F. Vargha-Khadom, B. G. Nevik, and G. D. Jackson, *Acta Neurol. Scand.*, 1994, suppl. 152, 116.
44. D. G. Gadian, A. Connelly, J. H. Cross, G. D. Jackson, F. J. Kirkham, J. V. Leonard, B. G. R. Neville and F. Vargha-Khadom, 'New Trends in Pediatric Neurology', eds. N. Fejerman and N.A. Chamoles, Amsterdam 1993, pp. 23-32.
45. A. Connelly, D. G. Gadian, D. G. Jackson, J. H. Cross, M. D. King, J. S. Duncan, and F. J. Kirkham, 'Proton Spectroscopy in the Investigation of Intractable Temporal Lobe Epilepsy', *Proc. XIth Ann Mtg. Soc. Magn. Reson. Med.*, Berlin, 1992, p. 234.
46. F. Cendes, F. Andermann, P. C. Preul, and D. L. Arnold, *Ann. Neurol.*, 1994, **35**, 211.
47. J. W. Hugg, K. D. Laxer, G. B. Matson, G. B. Maudsley, and M. W. Weiner, *Ann. Neurol.*, 1993, **34**, 788.
48. M. Xue, T. C. Ng, M. Modic, Y. Comair, and H. Kolem, *Proc. XIIth Ann Mtg. Soc. Magn. Reson. Med.*, New York, 1993, 435.
49. C. R. Jack, R. M. Thompson, R. C. Botts, R. R. Butts, F. W. Sharbrough, P. J. Kelly, D. P. Hanson, S. J. Rieslerer, R. L. Ehman, N. J. Hangrandrean, and G. D. Cascino, *Radiology*, 1994, **190**(1), 85.
50. G. D. Jackson, A. Connelly, J. H. Cross, I. Gordon, and D. G. Gadian, *Neurology*, 1994, **44**, 850.

Acknowledgements

Dr Jackson was supported, in part, by grants from the Wellcome Trust and Action Research. We would like to thank David Gadian, Cheryl Johnson, Brian Neville, John Duncan, Richard Grünewald, Wim Van Paeschen, and Simon Robinson.

Biographical Sketches

Graeme D. Jackson. *b* 1956. B.Sc. (Hons) Psychology, 1977; MB.BS. Monash University, Melbourne, Australia, 1982.; FRACP (Neurology), 1992; M.D. thesis 'Magnetic Resonance in Intractable Epilepsy', Monash University, 1995. Introduced to epileptology by Drs. Peter Bladin and Sam Berkovic, Austin Hospital, Melbourne, 1988–90. Then a research registrar, National Hospital for Neurology and Neurosurgery, 1990–92. Subsequently lecturer then senior lecturer and Honorary Consultant in Paediatric Neurology at the Institute of Child Health, and Great Ormond Street Hospital and NHS Trust, London, 1992–1996. Director of the Brain Imaging Research Institute, Austin and Repatriation Medical Centre, Heidelberg, West Australia 1996–current. Howard Florey Institute, University of Melbourne 1998–current. Current research specialities: MR applications in epilepsy, neurotoxicity.

Alan Connelly. *b* 1955. B.Sc. (Hons) Chemistry, University of Glasgow, Scotland, 1977; Ph.D., University of East Anglia, Norwich, UK. Ph.D. in high resolution NMR under the supervision of Prof. Robin Harris. Began work on in vivo spectroscopy and imaging as NMR development scientist at Oxford Research Systems, UK, 1983–88. Subsequently lecturer (1988–93) then senior lecturer (1993–present) at the Institute of Child Health, London, UK. Current research specialties: imaging and spectroscopy applications in stroke and epilepsy.

Systemically Induced Encephalopathies: Newer Clinical Applications of MRS

Brian D. Ross, Stefan Bluml, Kay J. Seymour, Jeannie Tan, Jong-Hee Hwang and Alexander Lin

Huntington Medical Research Institutes, Pasadena, CA, USA

1 SYSTEMICALLY INDUCED ENCEPHALOPATHIES

1.1 Background: Biochemistry of Coma

Metabolic disturbances of liver, kidney, endocrine or other systems have remote effects; those on the brain result in a variety of well-defined encephalopathies. When severe, these disorders present as coma. Posner and Plum published a comprehensive account of human coma.[1,2] Many were the result of presumed metabolic events with normal brain anatomy, setting the stage for noninvasive elucidation by means of biochemically based techniques. Among these are MRA, diffusion imaging, positron emission tomography (PET), single-photon emission tomography (SPECT), and multinuclear magnetic resonance spectroscopy (MRS). MRS has increasingly been used to identify specific biochemical changes in the brain, from which information on diagnosis and pathogenesis of these poorly understood disorders is beginning to emerge.

As a model for this group of disorders, we discuss hepatic encephalopathy, with additional remarks about diabetic, hyperosmolar, and hypoxia-induced encephalopathies. Renewed interest in the use of MRS for differential diagnosis of focal brain pathologies is reflected in studies of stroke and adrenoleukodystrophy.

1.2 Neurochemical Pathology of Hepatic Encephalopathy

Hepatic encephalopathy (HE) is an excellent example of metabolic encephalopathy,[3] with identifiable neurotoxins originating in a systemic disease. In animal studies, several distinct neurotoxins have been identified. The earliest of these was ammonia;[4,5] ammonia is normally fully removed from portal blood by hepatic urea synthesis.[6,7] The combination of the loss of biosynthetic liver function and the diversion of nondetoxified blood to the brain by so-called portal systemic shunts (PSSs) accounts for the frequently demonstrated excess of cerebral and cerebrospinal fluid glutamine[8] [Equation (1)].

$$\mathrm{NH_4^+} + \text{glutamate} \underset{\text{glutaminase}}{\overset{\text{GS}}{\rightleftharpoons}} \text{glutamine} \qquad (1)$$

The enzyme glutamine synthetase (GS) responsible for this reaction is located exclusively in astrocytes.[9] Resynthesis of glutamate and of γ-aminobutyrate (GABA) from glutamine (both vital neurotransmitter amino acids) occurs principally in neurons.[10]

Lest it be thought that ammonia 'toxicity' accounts for all of the clinical syndromes covered by the term HE, the interested reader is referred to Butterworth[11] for an extensive review of several other well-documented alternatives. Metabolic theories abound: failure of oxidative energy metabolism (a corollary of glutamate and 2-oxoglutarate depletion from the Krebs cycle), tryptophan and serotonin (5-hydroxytryptamine) accumulation, branched-chain amino acid deficits, endogenous benzodiazepine agonists which modify access of GABA to its inhibitory receptors, and neurotoxic fatty acids, octanoate in particular, have been proposed.

An attractive unifying theory proposed by Zieve[12] is that multiple neurotoxins derived from liver, blood, or from the diet, gain access via PSSs to a previously 'sensitized' brain. No mechanism of sensitization is known, but with the advent of MRS, a candidate has been proposed in the form of cerebral *myo*-inositol (mI) depletion.[13]

1.3 Animal Studies in Hepatic Encephalopathy Using Multinuclear MRS

Three groups[14–16] independently perfected methods for the noninvasive determination of cerebral glutamine (including a variable contribution from glutamate in each assay) with ^{1}H MRS and confirmed the elevation of this metabolite in a variety of animal models of acute liver 'failure' with HE. One of these groups[14] also demonstrated a hitherto unrecognized abnormality, the significant reduction of choline (Cho; cerebral choline-containing compounds) in the ^{1}H spectra of rats with acute HE.

More recently, ^{15}N NMR[17–19] and ^{1}H–^{15}N heteronuclear multiple quantum coherence (HMQC)[20,21] identified cerebral glutamine unequivocally in vivo in HE produced by ammonia infusion in the normal and portocaval shunted rat, respectively.

The glutamine protons coupled to amide nitrogen (termed H_Z and H_E) provide additional information regarding the compartmentalized pH adaptation during severe ammonia-induced coma in rats.[22] Alkalinization of the astrocyte (glial) cell cytoplasm can be inferred from alterations in ^{1}H–^{15}N HMQC spectral line-widths in vivo, whereas whole brain pH, determined from chemical shift of inorganic phosphate (^{31}P MRS, ***pH Measurement In Vivo in Whole Body Systems***) is apparently unaltered.[23]

In extracts of portacaval shunt rat brain, high-performance liquid chromatography (HPLC) confirms the accumulation of glutamine and the depletion of glycerophosphorylcholine (GPC). The latter has also been demonstrated in human subjects using a technique of quantitative proton-decoupled ^{31}P MRS.[24] It partly explains the reduced Cho in the prior ^{1}H NMR study as well as demonstrating the expected depletion by 50% or more of the cerebral mI and *scyllo*-inositol (sI) content.[25] This result in rats confirmed the observations that first emerged from human studies with short-echo time ^{1}H MRS[13,26,27] and establishes the validity of the portacaval shunt rat for future experimental studies.

1.4 Pathogenesis, Diagnosis, and Therapeutic Management of Hepatic Encephalopathy in Humans: The Emerging Role of Proton MRS

Studies using stimulated echo acquisition mode (STEAM) localized, short echo time ^{1}H MRS defined the changes in 10 patients with clinically confirmed chronic HE. The average increase in cerebral glutamine was estimated as +50%, Cho decreased 14% and mI decreased by 45%[21] (Figure 1). Very similar findings have now been reported at 2 T by Bruhn (Figure 2)[26,29] and by McConnell[30] using PRESS at short or long echo times. An early study which used long echo time PRESS-localized ^{1}H MRS failed to identify the depletion of mI but was the first clearly to show 'Cho' depletion in human brain.[31]

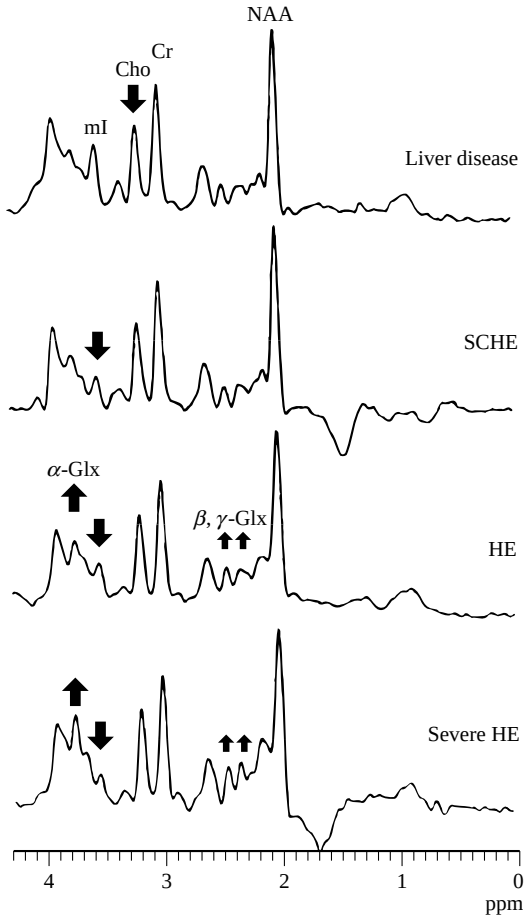

Figure 1 Development of hepatic encephalopathy in human subjects (1.5 T spectra). A series of spectra of parietal cortex (white matter) acquired under closely similar conditions (GE Signa 1.5 T, STEAM localization *TR* 1.5 s, *TE* 30 ms, NEX 128) from different patients is presented. A normal spectrum for comparison is that in Figure 7(b). In liver disease (top) there is a relatively normal spectrum with a slight decrease in choline (Cho). In subclinical hepatic encephalopathy (SCHE) there is a definite decrease in *myo*-inositol (mI) with a minor increase in the glutamine (Gln) regions (glutamine plus glutamate, Glx). There is a very significant increase in the Glx regions in HE (grade 1) and mI is further depleted. The spectrum of grade 3 HE shows more severe changes in the biochemical markers of this disease, most notably glutamine. Cr, creatine

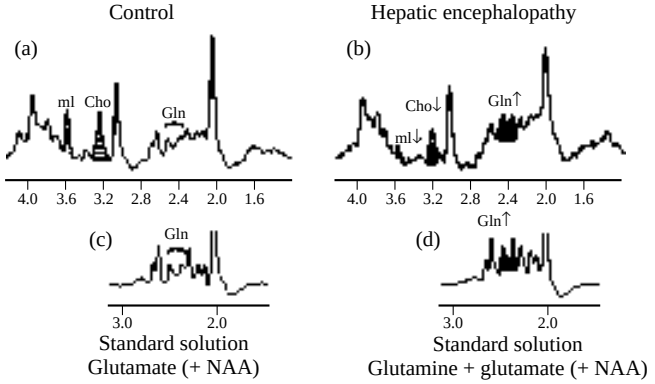

Figure 2 Identification of glutamine in the proton spectra at 2.0 T. A 51-year-old patient with HE resulting from surgical portacaval shunt (b) is compared with a normal control (a). Spectra were obtained from an occipital gray matter location and show the expected changes of HE: increased glutamine, decreased Cho/Cr and mI/Cr. With the improved resolution at 2 T, separate analysis of glutamine and glutamate is possible. Inset are spectra from model solutions (c) 5 mM glutamate + 5 mM *N*-acetylaspartate (NAA); (d) 5 mM glutamine + 5 mM glutamate + 5 mM NAA, indicating that in this patient the increase in glutamine occurs without obvious depletion of cerebral glutamate. Spectra were acquired on a Siemens 2.0 T clinical spectrometer, with STEAM localization; *TR* 3 s, *TE* 20 ms. Abbreviations as in Figure 1. (Modified from Bruhn et al.,[26] with permission from J. Frahm, T. Michaelis and colleagues)

This information considerably alters our understanding of the pathogenesis of HE, emphasizing an underlying defect in cerebral osmoregulation in addition to the clear relationship to ammonia toxicity and glutamine accumulation by the cerebral astrocytes. Proton-decoupled ^{31}P MRS revealed additional osmotic and metabolic disturbances in patients with HE.[24] Quantitative analyses in 16 patients with liver disease, ten with and six without chronic hepatic encephalopathy, in four patients with hyponatremia, and in 20 age-matched normal subjects were reported (Figure 3). Patients with HE were distinguished from controls by significant reduction in cerebral nucleoside triphosphate (NTP = ATP) (2.45 ± 0.20 versus 2.91 ± 0.21 mmol kg^{-1} brain; $P < 0.0003$), inorganic phosphate ($P < 0.03$) and phosphocreatine ($P < 0.04$).

In addition to increased cerebral levels of glutamate plus glutamine (Glx) and decreased concentrations of mI, patients with HE showed reduction of total visible Cho (in ^{1}H MRS), GPC (0.67 ± 0.13 versus 0.92 ± 0.20 mmol kg^{-1} brain in controls; $P<0.005$), and glycerophosphorylethanolamine (GPE) (0.40 ± 0.12 versus 0.68 ± 0.12 mmol kg^{-1} brain in controls; $P < 0.0003$) (in proton-decoupled ^{31}P MRS). Of the reduction of 'total Cho', 61% was accounted for by GPC, a cerebral osmolyte. Similar metabolic abnormalities were seen in hyponatremic patients.

The results are consistent with disturbances of cerebral osmoregulation and energy metabolism in patients with chronic HE.[24]

1.5 Energetics of the Human Brain in Hepatic Encephalopathy

The predicted cerebral energy deficit (reduction in [ATP]) has previously only been convincingly shown in mice and tree

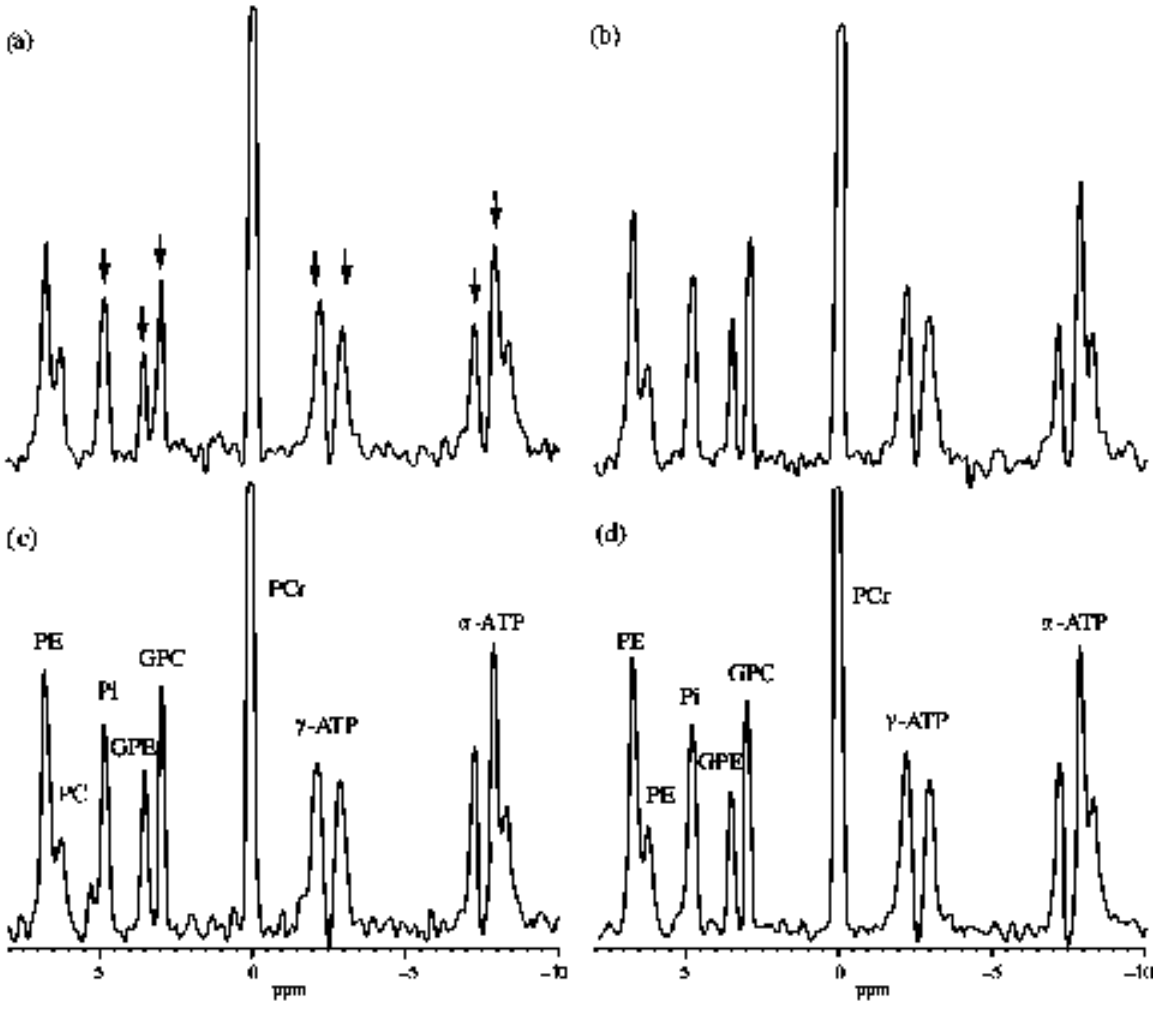

Figure 3 Osmotic and metabolic disturbances in hepatic encephalopathy (HE). Averaged proton-decoupled ^{31}P MRS from patients with (a) HE, (b) liver disease without HE, (c) elderly controls and (d) young controls. The averaged spectra calculated from all patients with HE can readily be distinguished from averaged spectra obtained from liver-diseased patients without HE and controls by reduced concentrations of phosphoethanolamine (PE), inorganic phosphate (Pi), glycerophosphorylethanolamine (GPE), glycerophosphorylcholine (GPC), and ATP. Furthermore, phosphocreatine (PCr) content (not obvious here owing to the expanded scale) was significantly decreased in HE. Phosphorylcholine (PC) remained normal

shrews.[32] Phosphorus-31 MRS should be the easiest tool with which to establish any energy deficit in HE (as predicted) but Ross,[33] Tropp,[34] Chamuleau,[35] Barbiroli,[36] and Morgan[37] have obtained conflicting and hence unconvincing data with ^{31}P MRS on such effects in humans. Using quantitative ^{1}H MRS, however, Geissler and colleagues showed a small but significant increase in cerebral creatine concentration [Cr] following liver transplantation in humans.[38] Since [Cr] is the sum of phosphocreatine (PCr) and creatine, this may indicate that patients with HE have an 'energy deficit'. A 10% reduction of PCr and a 16% reduction of NTP (of which perhaps up to 80% of the ^{31}P signal arises from ATP) is reported by Bluml et al. in patients with HE[24] and is hypothesized to be a contributing factor in the complex pathogenesis of the disorder. Because ATP depletion occurred without a marked increase in glutamine accumulation, the depletion of TCA cycle intermediates, hypothesized to limit energy metabolism,[5] is deemed an unlikely explanation. Instead, the hypothesis proposed is that ATP depletion may occur in the astrocytes as part of a failure of astrocyte volume regulation, which is reflected in reduced concentrations of several cerebral osmolytes. In the astrocyte, a possible rate-limiting role of ATP as a co-factor for GS would be most relevant. The difficulty which has been confronted in demonstrating such an effect by ^{31}P MRS, where sensitivity is 10% that of ^{1}H MRS, becomes obvious. Since reduced cerebral oxygen consumption and blood flow are recognized abnormalities in HE, the ^{13}C NMR techniques pioneered by Shulman may be best suited to demonstrate the anticipated reduction in the overall rate of the Krebs cycle.[39]

From these clinical studies, it appears that ^{1}H MRS, particularly if applied with effective water suppression to reveal mI, is currently most efficient for the elucidation of pathogenesis of

HE, and also, as will be shown, for its early clinical diagnosis. Direct measurement of mI by ^{13}C NMR may become a valuable adjunct.[40–42]

2 SUBCLINICAL HEPATIC ENCEPHALOPATHY

As indicated, HE is a group of diseases presumed to have identical etiology but presenting a great variety of distinct clinical pictures. Underlying all of them is believed to be the entity of 'subclinical HE' (SCHE), although it is by no means clear that the HE and coma of fulminant (very acute) liver failure, goes through any truly 'subclinical' phase.

Proton MRS accurately reflects the entity of SCHE,[43,44] and in preliminary studies also appears to mirror the progressive and increasingly severe syndromes of overt HE defined by Parsons-Smith as grades 1–4 (Figure 1). Elevation of glutamine is rather more obvious at 2 T (Figure 3) but presents little difficulty at 1.5 T.

Figure 1 should not be taken as proof, however, that in the individual patient such orderly progression of neurochemical dysfunction occurs. Longitudinal studies have not been performed in sufficient numbers to be certain of this. Nevertheless, it is tempting to suggest, as Figure 1 appears to indicate, that in the brain exposed to liver 'toxins', Cho depletion (principally GPC) precedes the loss of mI and sI, with later accumulation of glutamine. If this sequence is correct, then perhaps 'sensitization' of the brain is the result of mI or Cho depletion, or both. In keeping with the theory of many years standing, increasing cerebral glutamine underlies the neurological syndromes of grades 1–4, severe, overt chronic HE, as well as, perhaps, that of acute, fulminant HE and coma. Figure 4 shows the similar but more severe neurochemical changes of Reye's syndrome, giving an effective indication of what may be seen in acute HE.[45] Unfortunately, published spectra from patients with fulminant HE are limited and difficult to interpret.[46]

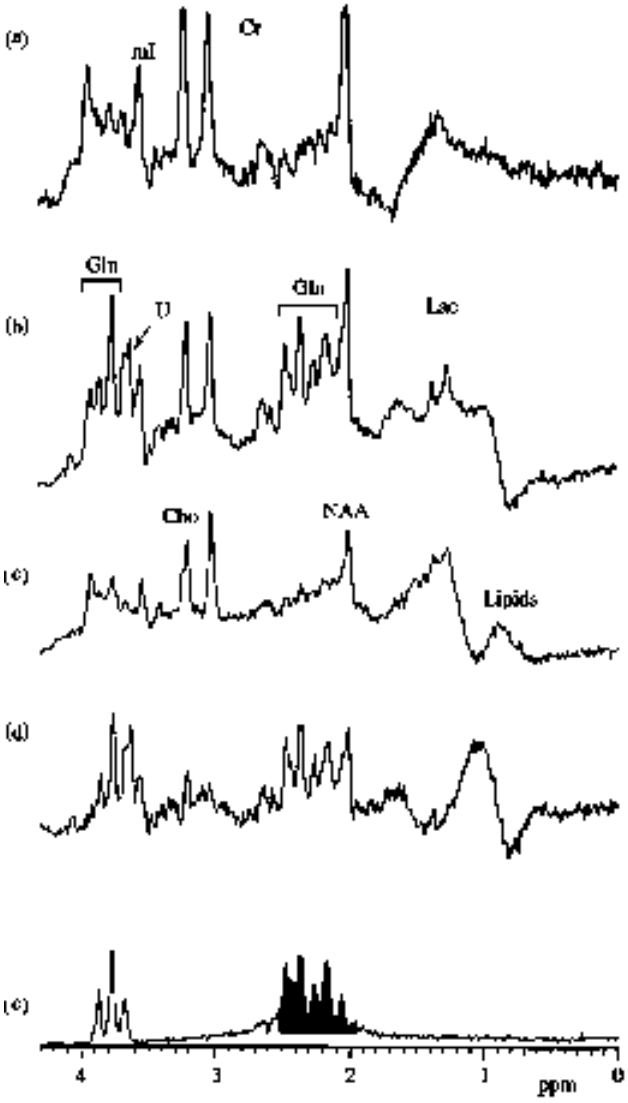

Figure 4 Proton MRS in acute hepatic encephalopathy caused by Reye's syndrome. In vivo proton MRS spectra acquired from a parietal white matter region in infant brain from: (a) 10-month-old normal subject; (b) patient, day 2 after admission; (c) patient, day 8 after admission; (d) difference (b) − (c) between days 2 and 8 in patient; (e) solution with 15 mM glutamine. All spectra are scaled. Spectral assignments: Lac, lactate (1.3 ppm); NAA, *N*-acetylaspartate (2.02 ppm); Gln, glutamine (2.10–2.50 ppm, and 3.65–3.90 ppm); Cr + PCr, creatine + phosphocreatine (3.03 ppm); Cho, choline-containing compounds (3.23 ppm); mI, *myo*-inositol (3.56 ppm). U, Unassigned (3.62 ppm). Notable abnormalities concern a huge accumulation of cerebral Gln, reduced Cho, and, later, reduced mI, all of which reflect liver failure. In addition there is a decrease in NAA and [Cr] and appearance of the unassigned peak. Reye's syndrome, a toxic viral disease associated with aspirin intake, is known to produce severe neuronal damage, and may not, therefore, completely correspond to the picture of acute liver failure. An occipital gray matter region gave almost identical results. (Reproduced with permission from Ernst et al.)[45]

2.1 Depletion of *myo*-Inositol and the Induction of Hepatic Encephalopathy

A human 'experiment' which goes some way towards verifying this sequence is the new interventional procedure known as TIPS (transjugular intrahepatic portal systemic shunt), which is used as a life-saving procedure in cirrhosis-induced hematemesis. Not surprisingly, TIPS induces clinical HE in up to 90% of survivors.[47–49] Proton MRS performed both before and after TIPS in 10 patients showed a universal increase in mean intracerebral glutamine following the procedure. More importantly, in a small number of individuals in whom mI was normal prior to TIPS (these patients often show SCHE), a progressive reduction in mI/Cr and development of subclinical and clinical HE follows the introduction of the shunt (Figure 5).

2.2 Restoration of Cerebral *myo*-Inositol and Choline Accompanies Reversal of Hepatic Encephalopathy

Yet another common human 'experiment', that of orthotopic liver transplantation, allows the reverse process to be unequivocally demonstrated, thereby establishing a firm, albeit circumstantial link between mI depletion and the syndromes of SCHE and overt HE (Figure 6). There was also a recovery in Glx and Cho also recovered. Indeed, an overshoot of cerebral Cho is consistently observed, perhaps linking the earlier Cho

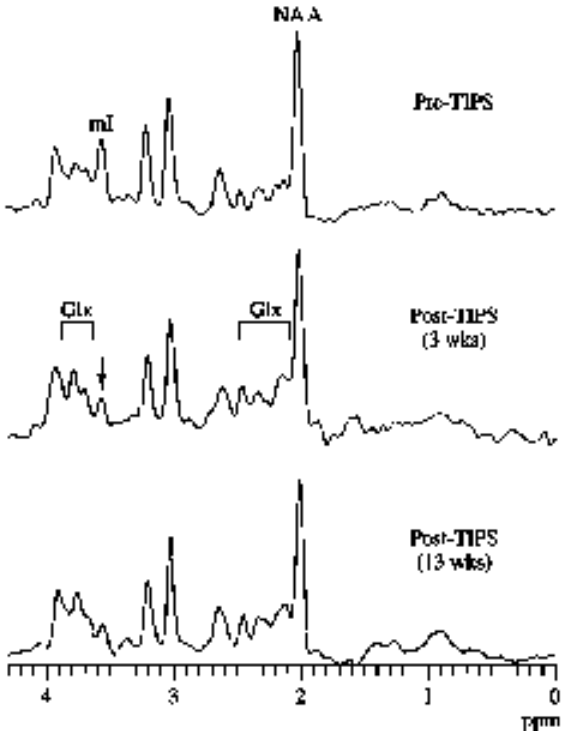

Figure 5 Effect of a transjugular intrahepatic portal systemic shunt (TIPS) on the proton MR spectrum. Spectra are from a 30-year-old female, 5 days after a hematemesis caused by esophageal varices and chronic alcoholic liver disease. Spectra acquired from a parietal white matter location (GE Signa 1.5 T, volume 12.5 cm^3, STEAM *TR* 1.5 s *TE* 30 ms, NEX 128) before a TIPS procedure shows no abnormalities apart from a small but significant reduction in Cho/Cr, attributable to liver disease (top). Three weeks after TIPS, changes are seen in the Glx and mI regions and a further reduction on Cho/Cr (middle). The bottom spectrum shows the progression of changes seen (13 weeks post-TIPS); Glx is markedly increased and mI is significantly reduced. Abbreviations as in Figure 1. (With permission from Shonk et al.[48])

depletion with deficient hepatic biosynthesis of some relevant precursor of GPC.

2.3 Ornithine Transcarbamylase Deficiency

A description of MRS in HE would be incomplete without consideration of a rare but informative inborn error of hepatic urea synthesis, ornithine transcarbamylase (OTC) deficiency. The single known biochemical consequence is hyperammonemia. Gadian and colleagues[50] demonstrated the inevitable elevation of cerebral glutamine in two such patients, while Ross[51] showed the extraordinary parallel with HE, in depletion of cerebral mI (Figure 7).

3 CONTRIBUTION OF NMR TO ASSESSMENT OF CLINICAL HEPATIC ENCEPHALOPATHY

3.1 Pathogenesis

Both experimentally and clinically, NMR (particularly ^{1}H MRS) supports the classical concept of HE as a disorder of cerebral ammonia metabolism, be it by ammonia toxicity or glutamine synthesis (as a newer variant of the theory would have it).[52] The concept of an underlying brain 'sensitization' receives substantial new impetus deserving of further research in animal models. Either Cho (GPC) depletion, caused perhaps by failure of hepatic synthesis of a necessary precursor, or cerebral mI depletion could fulfill the role of 'sensitizer'. In neither case is there a precedent; as a result basic research is urgently required. It is likely that NMR will play a crucial role in such investigations, and the portacaval shunt rat is a convenient model. Carbon-13 NMR is the only method of unequivocally determining mI as distinct from the lower concentrations of inositol-1-phosphate (Inos-1-P) and glycine with which mI coresonates in the ^{1}H MR spectrum.

3.2 Osmoregulation in Human Hepatic Encephalopathy

A new concept in HE can justifiably be attributed to these endeavors with in vivo MRS. This is related to cell-volume regulation in the brain and is conveniently termed osmolyte disorder.

GPC was first identified as an osmolyte in the kidney, while mI, GPC and taurine (in rats) were proposed for that role in brain,[53] Haussinger et al.[54] first used the term hypo-osmolarity to link mI with HE. The importance of the concept may lie in the hitherto obscure connection between hepatic coma (in fulminant liver failure), a disease treated as an emergency because of the massive edema that occurs (dysregulation of cerebral

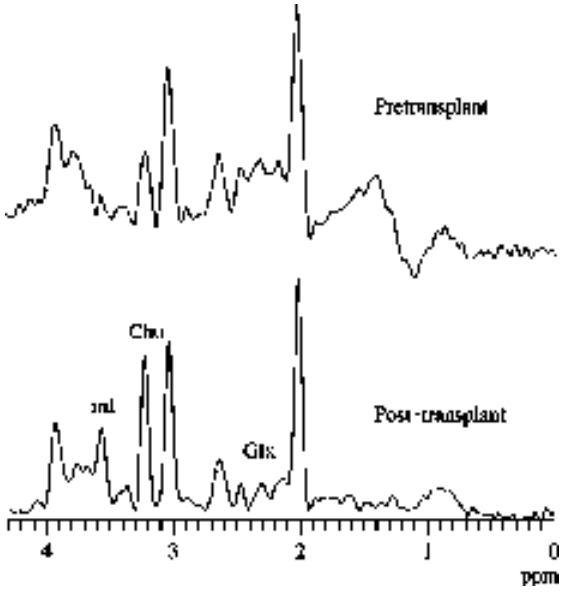

Figure 6 Restoration of biochemical abnormalities post-liver transplant. The patient is a 30-year-old male with acute-on-chronic hepatic encephalopathy secondary to hepatitis, and subsequently successfully treated by liver transplantation. Spectra were acquired 6 months apart from the same parietal white matter location, (15.0 cm^3 STEAM *TR* 1.5 s, *TR* 30 ms, NEX 128) and scaled to the same Cr intensity for comparison. The obvious abnormalities before liver transplantation, increased α-, β-, and γ-glutamine, reduced Cho/Cr and mI/Cr (upper spectrum) were completely reversed 3 months after transplantation, and Cho/Cr exceeded normal (lower spectrum). Abbreviations as in Figure 1

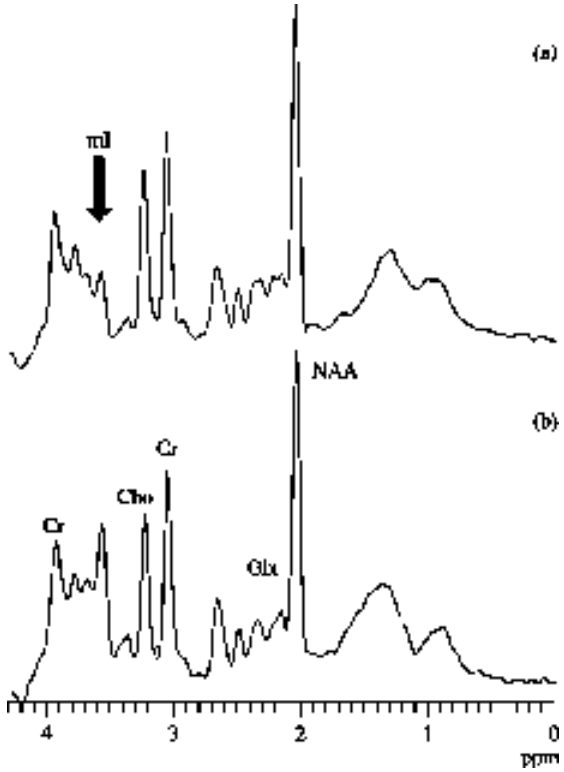

Figure 7 Treated ornithine transcarbamylase (OTC) deficiency versus healthy age-matched subject. Both spectra were acquired from a similar location in parietal white matter (STEAM *TR* 1.5 s, *TE* 30 ms, NEX 128) and processed as described in the literature.[47] Single-enzyme defects in the urea cycle result in severe hyperammonemia and 'hepatic encephalopathy'. Because the patient was receiving treatment with sodium benzoate, no excess of cerebral glutamine is present. However, as anticipated by studies in the commoner condition of hepatic encephalopathy caused by portosystemic shunting, a decrease in mI was noted in the proton spectrum of a 14-year-old with OTC deficiency (a) when compared with a normal age-matched control (b). NAA, *N*-acetylaspartate; other abbreviations as in Figure 1

osmolytes perhaps?), and the more mundane and relatively slow-evolving biochemical disturbance outlined above as chronic HE and SCHE.

3.3 Proton MRS for Diagnosis

Early in these investigations, it became apparent that mI depletion and Glx accumulation occurred when clinical HE was absent. Other systemic or metabolic diseases (apart from OTC deficiency already discussed) did not result in mI depletion; consequently ^{1}H MRS offers an unique opportunity for early, specific diagnosis of this still perplexing condition. Paradoxically, there is at present little enthusiasm for this, most probably because prevention (with lactulose or neomycin) and treatment (by liver transplantation) of overt or severe HE is relatively straightforward (albeit rather costly in the case of orthotopic liver transplantation (OLT) at \$150 000–200 000 per patient in USA). If a ready medical means of restoring cerebral mI were to be discovered, the value of ^{1}H MRS in diagnosis might increase. This point is covered in a recent report in which treatment with lactulose for 7 days in overt HE significantly increased mI/Cr.[55,56]

3.4 Unanswered Questions in Neurology of Hepatic Encephalopathy

Wilson's disease, caused by excess copper deposition, is believed to result in an encephalopathy analogous to HE. However, the ^{1}H MRS findings are not surprisingly rather different, lacking either mI depletion or glutamine accumulation (unpublished study from this laboratory).

Myelopathy is an unusual form of chronic HE. It presents with paraplegia. Athough neurological considerations would suggest cord involvement, the ^{1}H MRS findings in the parietal cortex are typical of other patients with the more classical clinical presentation (see Fig. 4 in Ross et al.).[51]

Often noted in MRI, the basal ganglia may be 'bright' in inversion recovery (IR) images of patients with known HE. There is no consistent relationship with ^{1}H MRS findings, and increasingly this MRI finding is recognized as nonspecific. Nevertheless, the extrapyramidal signs, the changes on postmortem, and these albeit inconsistent MRI findings continue to suggest that there may be as yet unrecognized underlying neurochemical changes in the basal ganglia in HE.

4 OTHER SYSTEMIC ENCEPHALOPATHIES

4.1 Diabetes Mellitus and Ketogenesis

Like HE, diabetic encephalopathy is common and obviously 'metabolic' in origin. Three principal syndromes are recognized: diabetic ketoacidosis, lactacidosis, and nonketotic hyperosmolar coma.

Elevated cerebral glucose,[57] significant excess of mI, a reversible accumulation of 'Cho', and the presence of ketone bodies have been detected in various patients with varying severity of diabetic encephalopathy.[58] The hyperosmolar state, which is discussed in more detail below, is well known in diabetes mellitus as so-called nonketotic hyperglycemia (NKH). NKH is responsible for coma and neurological symptoms more frequently even than diabetic ketoacidosis. MRS findings in a young adult with NKH-induced coma[59] are consistent with many years of experimental work in demonstrating altered cerebral osmolytes, Cho, mI and even *N*-acetylaspartate (NAA) (Figure 8).

The most surprising finding of proton MRS, which requires further study, is the identification of acetone (rather than the more widely anticipated β-hydroxybutyrate and acetoacetate) as the ketone of human diabetic ketoacidotic encephalopathy (Figure 9).[58]

A therapeutic idea dating from the 1920s has reemerged in the use of a so-called 'ketogenic diet' to provide excellent control of seizures in drug-resistant patients with epilepsy. Perhaps not surprisingly, the cerebral ketone body that accumulates in these patients is also acetone, rather than acetoacetate or β-hydroxybutyrate (Figure 10).[60] In epilepsy, we suggest that this finding is more than of academic importance and may ultimately lead to more focused dietary or pharmacological treatments. At the very minimum, ^{1}H MRS should be considered for clinical monitoring in iatrogenic ketosis.

Long-term neurological and cerebral 'complications' of diabetes contribute to the much increased mortality. The biochemical basis of these conditions may lie in those changes

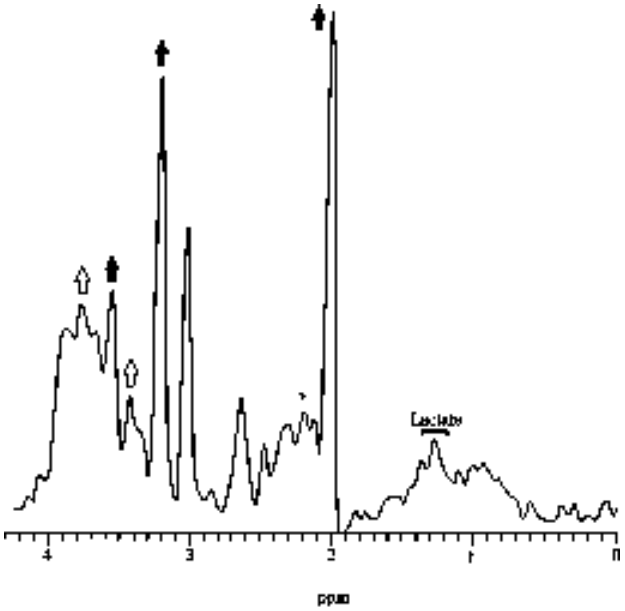

Figure 8 Proton MRS of occipital gray matter in recovering nonketotic hyperglycemia. Excess Cho/Cr, NAA/Cr, mI/Cr (⬆) as well as abnormal intensities for glucose (⇧), lactate and (possibly) acetone (*) are indicated. Abbreviations as in Figure 1

in Cho, NAA, mI, ketones, and glucose, now recognized by ^{13}C and ^{1}H MRS to be present in the acutely and chronically diabetic brain.

4.2 The Hyperosmolar State: Identification of Idiogenic Organic Osmolytes by Proton MRS

Lien et al. first used ^{1}H MRS to investigate a 'new' family of cerebral metabolites collectively known as organic osmolytes because of their believed role in the maintenance of cerebral osmotic equilibrium.[61] Such molecules were also first thoroughly researched in the papilla of the kidney with the help of in vitro NMR.[62]

First in sporadic cases of diabetic hyperosmolar coma[58] and in a patient after closed head injury,[63,64] and then most convincingly in a single infant with holoprosencephaly and deficient thirst mechanisms, these concepts were confirmed as contributing to human encephalopathy by the use of ^{1}H MRS (Figure 11). mI was three times normal, and other resonances, also markedly affected, returned toward normal with treatment. Difference spectroscopy is particularly helpful in identifying these changes.[65,66] The converse, or hypoosmolar state of hyponatremia has been identified by ^{1}H MRS in significant numbers of patients.[67]

4.3 The Hypoosmolar State: Hyponatremia and Pituitary Failure

Hyponatremia is so common that its impact on the human brain spectrum needs to be included in all discussion of clinical MRS interpretations. The characteristic features are reduction of mI/Cr and Cho/Cr in the ^{1}H MRS examination[67] and reduced GPE and GPC in the proton-decoupled ^{31}P spectrum.[24] Similarities to the findings in HE have already been discussed. Unexpected reduction of mI/Cr or Cho/Cr, in, for example, screening MRS examinations for dementia might be an indicator of hyponatremia.[59]

Central pontine myelinolysis (CPM) is a rare clinical disorder believed to follow inappropriate corrections of severe hyponatremia in patients. This link led Lien and colleagues to investigate the value of in vitro MRS of the newly discovered cerebral osmolytes in rats.[68]

The correction of cerebral osmolytes disturbed by hyponatremia is even more striking than the initial discovery of their depletion because of its relevance to clinical management. Slow restoration of plasma sodium is advocated and is accompanied by even slower restoration of cerebral osmolytes. In one human study, a mean interval of 10.5 weeks elapsed before cerebral osmolyte correction in three of four patients.[67] Now we have identified the MRS pattern of CPM in a patient in whom hyponatremia was not apparent, and in whom cerebral osmolytes were normal (Figure 12). An illuminating study of

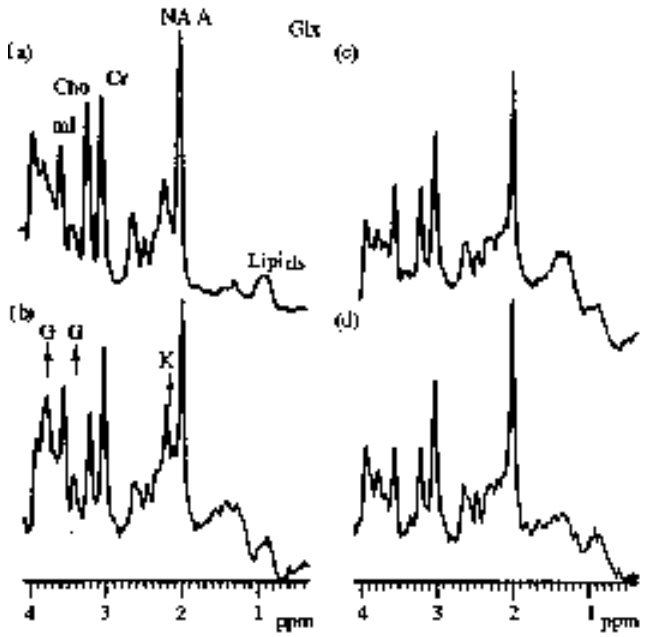

Figure 9 Diabetic ketoacidosis (DKA): cerebral ^{1}H spectra during two DKA episodes and recovery. (a) Episode 1, acquired 3 days after admission to hospital, at a time when the patient had supposedly totally recovered and was ready to be discharged. A peak characteristic for the presence of ketone (K) bodies was noted at 2.22 ppm, obtained from an 18 cm^3 volume in the left parietal lobe. The patient relapsed into DKA 2 days later. (b) Episode 2, acquired 5 months later from an occipital gray matter location (10.3 cm^3) during a second episode of DKA. In addition to the ketone peak, peaks for glucose (G) were seen. (c) Recovery, 6 days after episode 2 (from the same occipital location), when no more ketone bodies were detected in the urine. (d) Occipital cortex of an age- and sex-matched healthy subject. Acquisition conditions: GE Signa 1.5 T, 4X software; STEAM *TR* 1.5 s, *TE* 30 ms, NEX 128. More detailed analysis of peak K indicates the resonance frequency to be that of acetone, rather than acetoacetate, the ketone body more commonly identified in blood and urine of diabetics in coma. Abbreviations as in Figure 1. (Reproduced by permission of the Radiological Society of North America from R. Kreis and B. D. Ross, *Radiology*, 1992, **184**, 123)

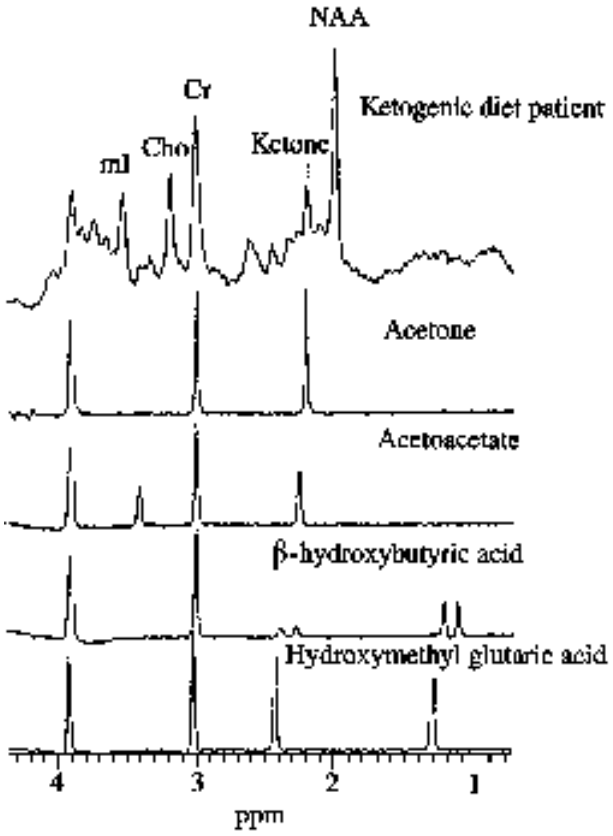

Figure 10 Identification of the ketone body observed in patients on the ketogenic diet. Top trace is the summed ^{1}H MRS of three examinations of a patient on ketogenic diet. Lower four traces show ^{1}H MRS of model solutions containing 5 mmol l^{-1} of acetone, β-hydroxybutyric acid and hydroxymethyl glutaric acid, and 10 mmol l^{-1} acetoacetate. Each model solution also contained 10 mmol l^{-1} creatine as a chemical shift reference at 3.02 and 3.94. Abbreviations as in Figure 1. (Reproduced with permission from Seymour et al.)[60]

hyponatremia secondary to pituitary failure suggests that some cerebral osmolytes may also be markers of hormone activity. A clearer understanding of the neuroendocrine axis may emerge from systematic use of MRS (either ^{1}H or ^{1}H–^{31}P) in these very common disorders (Figure 13).

5 HYPOXIC ENCEPHALOPATHY AND 'BRAIN ATTACK'

The prime example of a systemically induced encephalopathy is that resulting from insufficient oxygenation of blood, with resultant failure of cerebral oxygen delivery. Hypoxic encephalopathy is best understood in the context of energy failure and altered redox state through all cerebral metabolic pathways. Loss of ATP and PCr, accumulation of ADP, AMP, inorganic phosphate, and Cr are obvious consequences; H^{+} accumulates, both from failure to remove CO_2 and from formation of lactate. Reduced partners of the equilibrium enzymes lactate and glutamate dehydrogenase accumulate. In practice, glutamate is probably equally rapidly converted to glutamine. Innumerable animal studies, using principally ^{31}P NMR, but also ^{1}H NMR, confirm these principles and document other previously unsuspected changes, notably the loss of the neuronal marker NAA.

The very common occurrence of hypoxic encephalopathy in humans has given ample opportunity for verification of these events in the human brain. 'Recovery' from nonlethal hypoxic encephalopathy gives yet another view of the metabolic process. From ^{31}P MRS in neonates,[69] the expected changes emerged.

More recently, ^{1}H MRS has been used to quantify and plot the time course of changes which occur after oxygen deprivation, applying the information to defining the degree of irreversible hypoxic neuronal damage—and hence prognosis. 'Near-drowning' is the term applied when virtually total oxygen deprivation occurs owing to submersion in water. It must be presumed that all ATP and PCr is lost, and all glucose converts to lactate in this period of anoxia. Yet at the first clinical examinations, 24 hours after rescue and artificial life support,

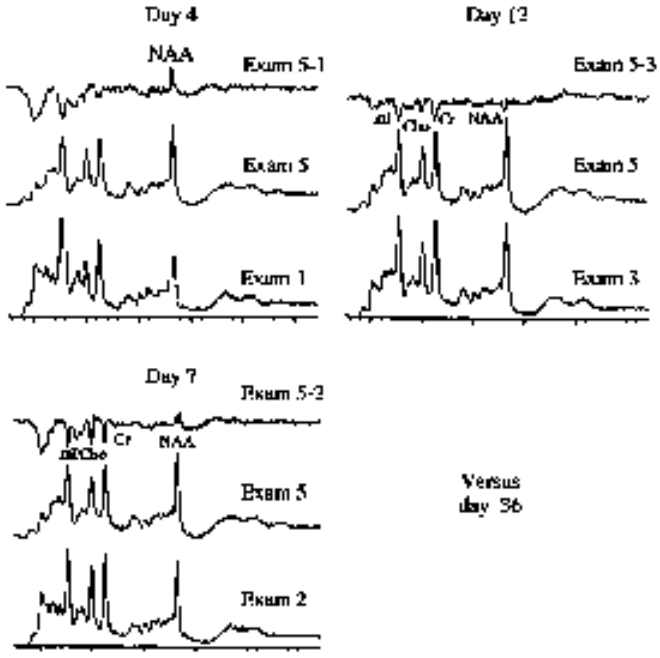

Figure 11 Time course of changes in principal cerebral organic osmolytes during correction of severe dehydration. A series of spectra were obtained from the same (occipital gray matter) brain location, in a 14-month-old child, recovering from severe dehydration and hypernatremia (plasma sodium 195 mmol l^{-1}; normal range 135–142 mmol l^{-1}) using identical acquisition conditions. Spectra were processed and scaled identically to permit subtraction of sequential spectra (difference spectroscopy). The day of examination refers to interval since admission to hospital. Examinations are numbered sequentially, from the first (Exam. 1) to last (Exam. 5) on day 36. Compared with a relevant normal [spectrum (b), Figure 7], the principal abnormality appears to be a reversal of the intensities of *N*-acetylaspartate (NAA) (reduced) and mI (increased); as a result mI dominates the spectrum. These changes slowly reverse to be nearly normal on day 36. The resultant difference spectra more clearly identify the progressively falling concentrations of several metabolites, with a possible elevation in the resonance peak assigned to the neuronal marker NAA. Quantitative MRS defines the principal abnormality as a threefold increase in the concentration of the cerebral osmolyte mI. Abbreviations as in Figure 1

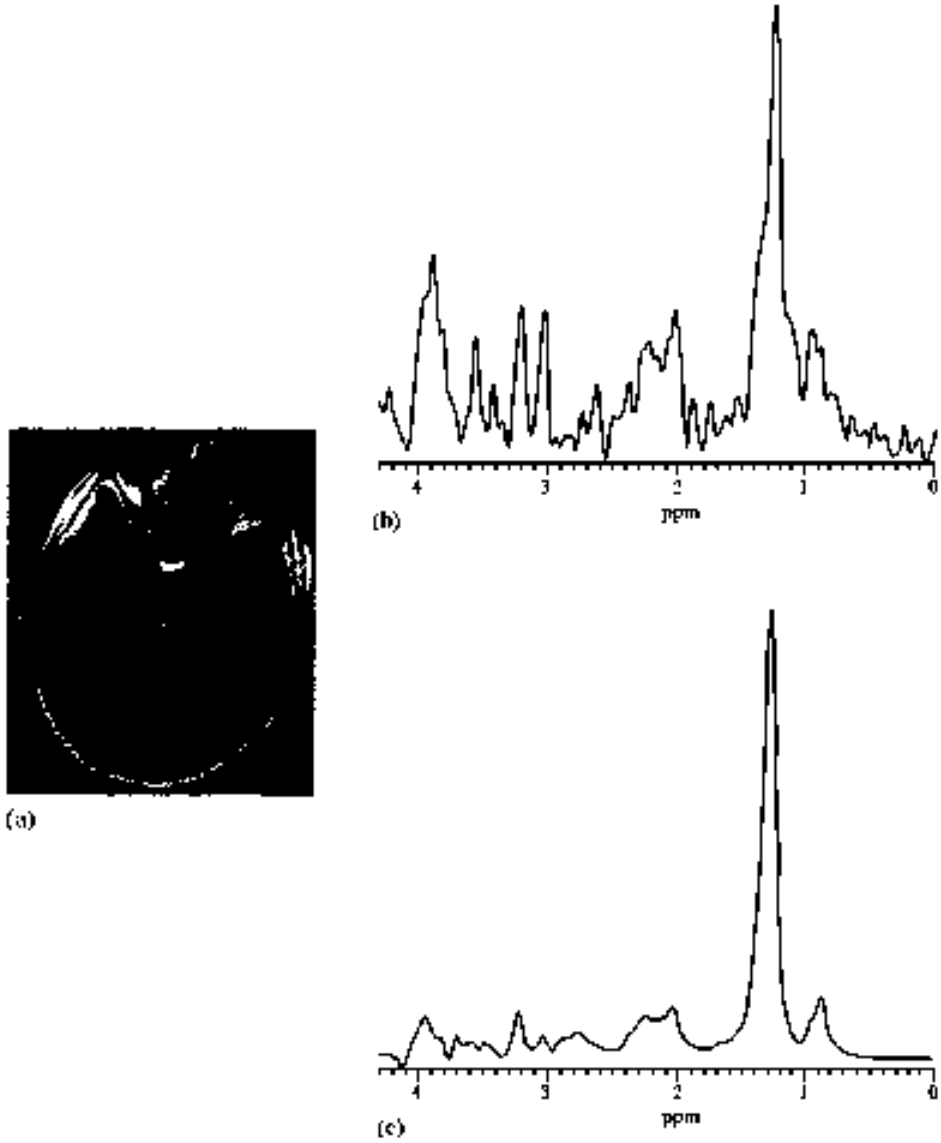

Figure 12 Proton MRS of the pons in central pontine myelinolysis (CPM). (a) A 29-year-old female with characteristic MRI changes that developed in the absence of hyponatremia. The spectra [9 weeks post-insult (b); 1 month later (c)] shows marked elevation in lipid, which appropriately reflects the histology of this lesion in autopsy-proven cases of CPM. (Illustration courtesy of David Dubowitz M.D.)

MRS demonstrates more often than not the absence of lactate, normal Cr (plus PCr), and NAA at nearly full concentration. Only subsequently do NAA and total Cr fall and lactate appears. The severity of the changes gives a fairly good guide to outcome.[70]

The classic events of anoxia described by Lowry[71] are probably reversible, but secondary damage results in progressive cell death, the consequences of which are loss of NAA (in the case of dying neurons), loss of PCr and oxidative function and reaccumulation of lactate. It is unclear why the large accumulations of glutamine occur (Figure 14). A systematic analysis of the MRS changes and their impact on outcome after global hypoxia[72] should go some way to clarifying the MRS literature in focal ischemia of the human brain in stroke and provide much needed noninvasive guidance in treatment of hypoxic encephalopathy. This includes tissue plasminogen activator (TPA), neuroprotectives and other innovations in human 'brain attack'.

5.1 Chemical Shift Imaging in Acute Stroke

Most clinical questions can be quickly answered using single-voxel technique discussed in the previous section, particularly since the arrival of complete automation of voxel selection, localization, shimming, water suppression, data acquisition, phasing and semiquantitative print-out of the salient metabolite ratios.[73] Nevertheless, chemical shift imaging (CSI), a much more efficient use of MR signal,[74] is re-emerging for clinical questions in which multivoxel information is essential. In our opinion, only stroke (in adults) and adrenoleukodystrophy (ALD) in children completely fulfill this criterion. In

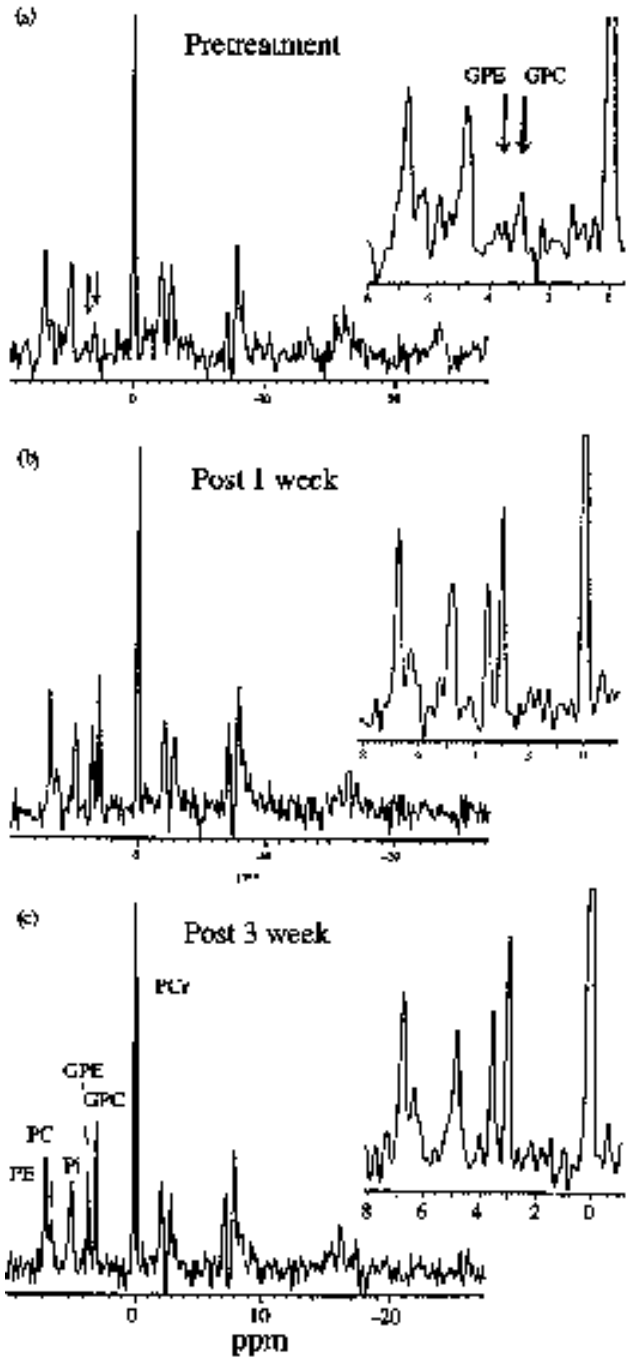

Figure 13 Endocrine-responsive hyponatremia. Proton-decoupled ^{31}P MRS shows almost complete depletion of GPE and GPC [(a) pretreatment] that recovered rapidly after initiation of pituitary replacement therapy [after 1(b) and 3(c) weeks of treatment]. Inset are expanded portions of the spectra. Abbreviations as in Figure 3. (Adapted from J. Tan et al., unpublished work in this laboratory)

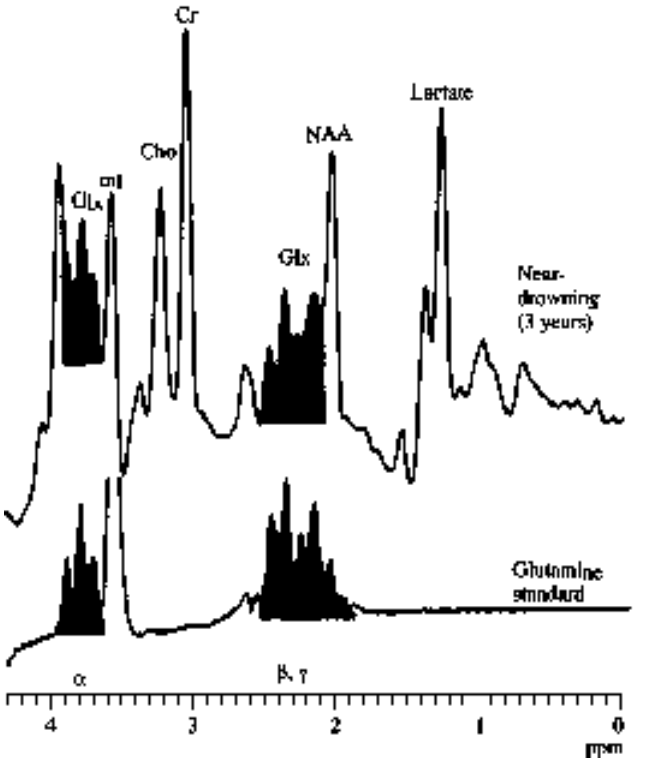

Figure 14 Near-drowning with fatal outcome. Brain spectrum from occipital cortex of a severe near-drowning victim (3 years old), examined 48 hours post-immersion (top), and the glutamine standard (bottom). The patient died on the 5th day post-injury. The ^{1}H spectrum was acquired from a volume of 12 cm^3 (STEAM *TR* 3.0 s, *TE* 30 ms, data processing including correction for residual water, line fitting, and quantification as described by Kreis et al.).[63] The spectrum of the glutamine standard (10 mmol l^{-1}) was acquired in the same way and scaled appropriately. Notable abnormalities in the patient spectrum are the very much reduced *N*-acetylaspartate (NAA) concentration and NAA/Cr ratio, excess of lactate (doublet at 1.3 ppm), and of the strongly coupled resonances of α, β, and γ glutamine protons. A 25% reduction in [Cr] was apparent on quantitative examination. Abbreviations as in Figure 1. (Thanks to R. Kreis, T. Ernst, and E. Arcinue)

tumor MRS, for example, single voxel[75] matches CSI with 96–97% sensitivity for diagnosis,[76] making it generally unnecessary to use the more time-consuming CSI.

The MRS changes in chronic stroke are well documented. More recent interest in reversal therapies for acute stroke has emphasized the need for very early differentiation of penumbra, infarcts and transient ischemic attacks. When cerebral artery flow falls below 100 ml min^{-1} (normal ~130 ml min^{-1}), lactate was observed in the symptomatic cerebral cortex with increasing frequency.[77] This single-voxel study was excellent in determining differences between the affected and unaffected hemisphere and in distinguishing borderzone infarcts, territory infarcts and no infarct.[77] However, obvious regional heterogeneity could not be determined. The power of a multivoxel (single-slice) ^{1}H MRS acquisition in distinguishing three degrees of neurochemistry after stroke is illustrated with spectra obtained for a patient who had suffered two strokes 7 days apart (Figure 15). These are seen in T_2 MRI and in diffusion-weighted images (DWI) as bright areas. While it was readily apparent which of the two infarcts occurred first, DWI could not immediately separate the acute from the subacute lesion.

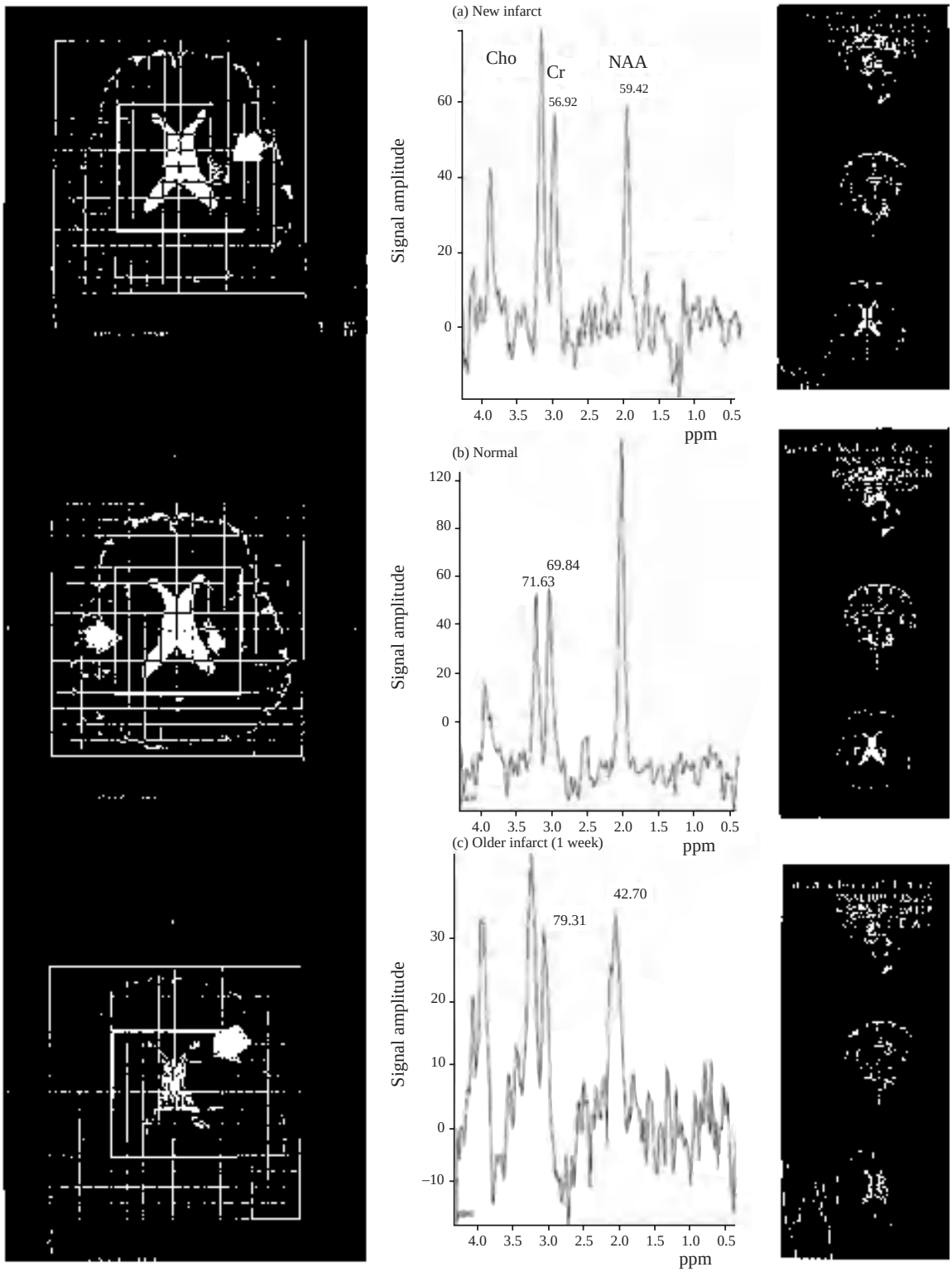

Figure 15 Chemical shift image (CSI) of acute stroke. The patient suffered a series of focal infarcts in the left internal capsule, seen in diffusion-weighted images (DWI) in left of figure. Three representative spectra (CSI, STEAM *TE* 135 ms) illustrates a new infarct (a), normal contralateral brain region (b) and a slightly older infarct, possibly 1 week earlier (c). Note that reduced *N*-acetylaspartate (NAA) and increased choline (Cho) are present in the early and later stages of evolving stroke. However, lactate (inverted doublet at 1.33 ppm) was present only in the more recent stroke. In this case, DWI and CSI give similar information. (Reproduced with kind permission of Stephen Holmes M.D., Queens Medical Center, Honolulu, HI)

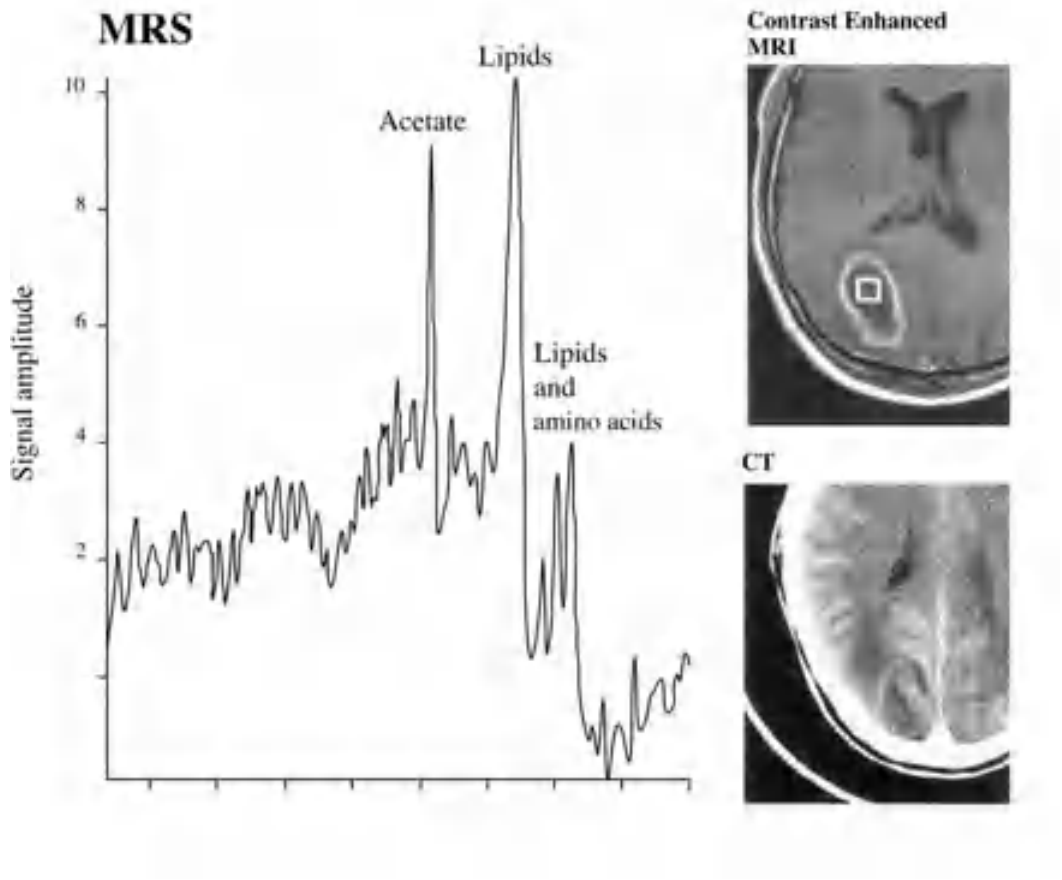

Figure 16 Diagnostic ^{1}H MRS of brain abscess. Computed tomographic scan (CT) was misleadingly diagnosed as malignant tumor in a young man. MRI and ^{1}H MRS confirms the presence of an abscess, based upon high concentrations of bacterial breakdown products within a ring-enhancing cyst. (Reproduced with kind permission of Else R. Danielsen, University of Copenhagen, Copenhagen, Denmark)

The synchronous acquisition of spectra from each shows subtle differences between them, and from normal as determined in the unaffected hemisphere. Intuitively, it is attractive to consider lactate (present as an inverted doublet at 1.3 ppm only in the more recent 'infarct') to be the much needed marker of viable tissue. This example is merely a pilot to the much larger studies now in progress in which CSI will be performed rapidly and as part of a broader MRI protocol of DWI, MRS and perfusion imaging.

5.2 Adrenoleukodystrophy

The most common of a very rare group of inherited brain disorders of white matter, the peroxisomal disease adrenoleukodystrophy, has now been studied exhaustively with single-voxel MRS. MRS is consistently more sensitive than MRI in detection of neurologic abnormality,[78] which leads to the next question. If MRI is normal in a leukodystrophy, where is the single voxel to be sited to achieve reliable preclinical diagnosis in this disorder? Currently we use the posterior horn of the lateral ventricle as a landmark to future disease. It would be safer to apply a robust multivoxel technique.[79]

6 OTHER FOCAL BRAIN DISORDERS

There is now a huge published database on which to found the clinical practice of MRS (neurospectroscopy). In papers where original data are provided (i.e. actual spectra with details of the processing applied after acquisition), this can be reliably assumed to be transferable from one instrument to another, and even across field-strength (1.0–4.02).[59] In the USA, a CPT code (76390) signals release of MRS into the day-to-day clinical environment by virtue of its efficacy in a number of common diagnoses. Limited use has been made of the discov-

Figure 17 MRI and ^{1}H MRS in human neurotransplantation. MRI and MRS of an individual patient with Huntington's disease showing CNS immune response to resuming immunosuppression after halting for 6 months. Significant decrease of *N*-acetylaspartate (NAA/Cr) ratio and presence of lactate strongly suggests deterioration of graft growth without immunosuppression (middle). Abbreviations as in Figure 1

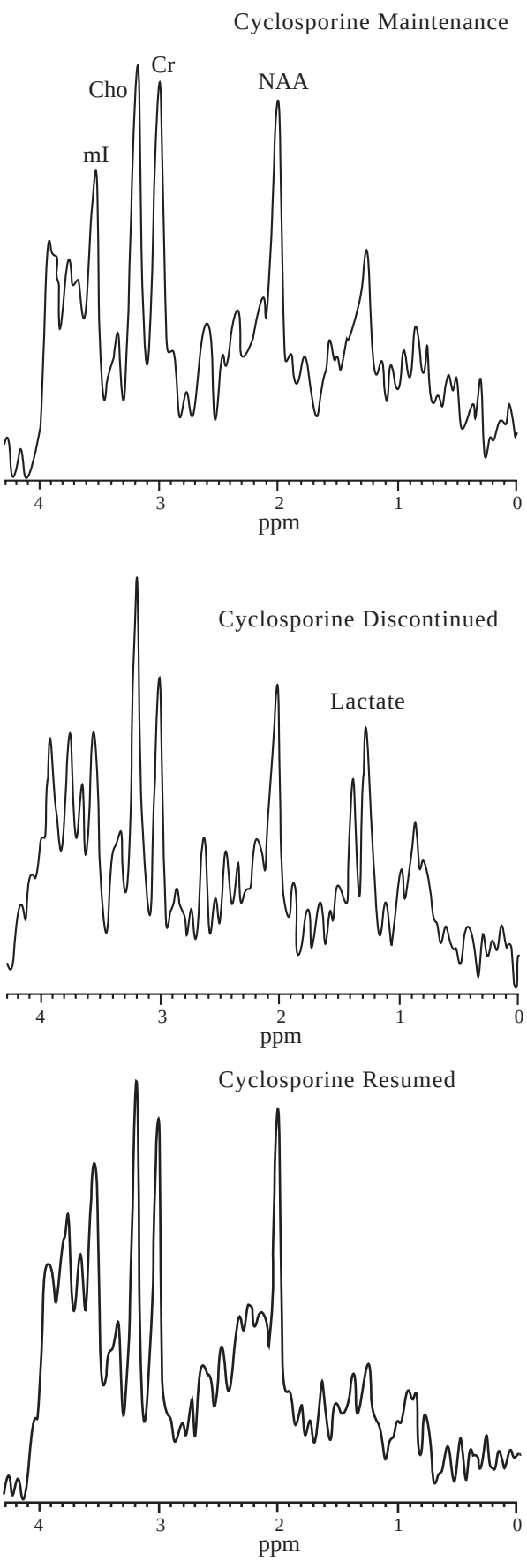
Cyclosporine Maintenance
Cho
Cr
NAA
mI
4
3
2
1
0
ppm
Cyclosporine Discontinued
Lactate
4
3
2
1
0
ppm
Cyclosporine Resumed
4
3
2
1
0
ppm

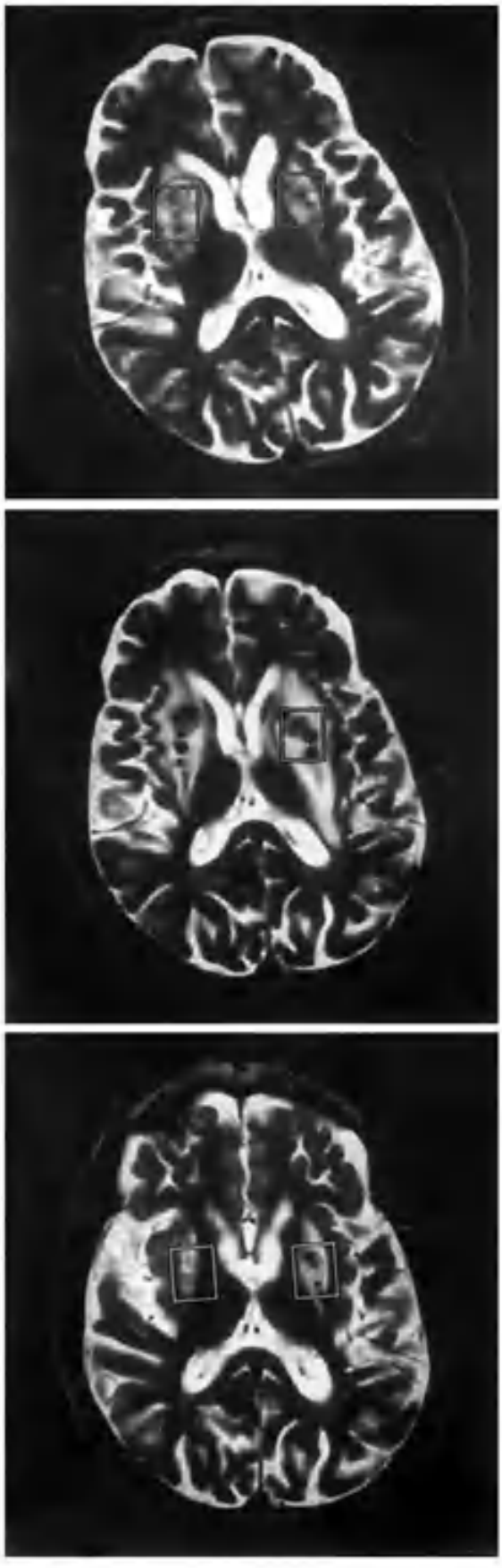

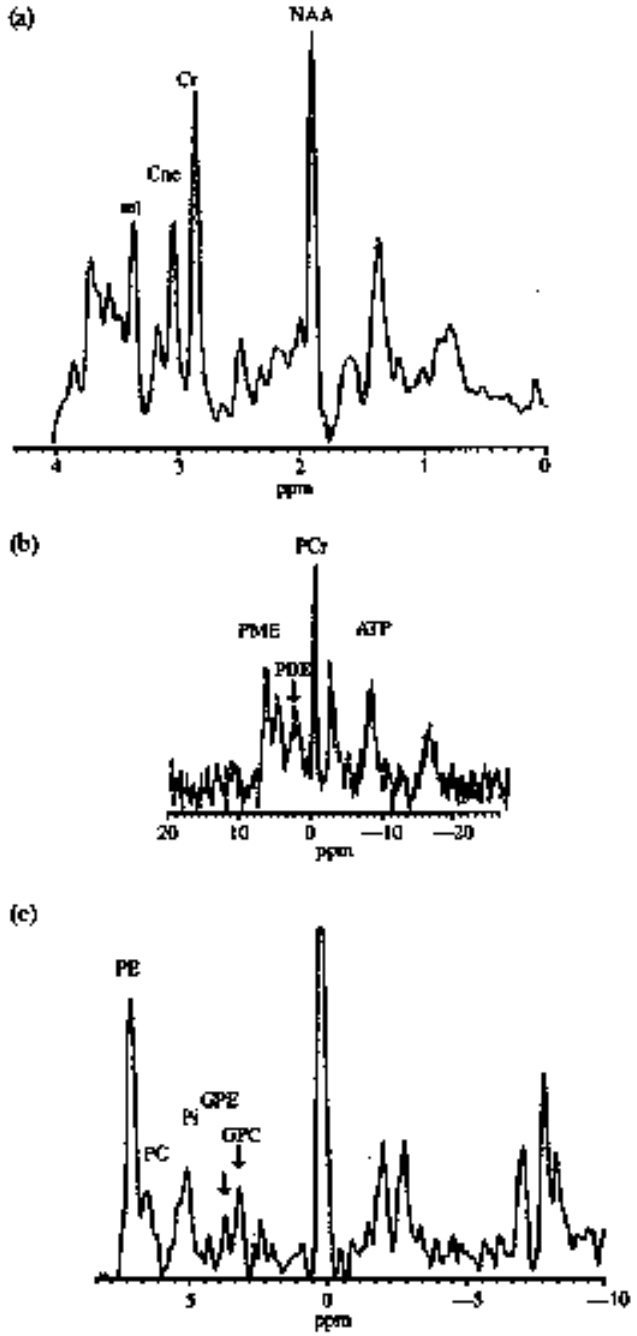

Figure 18 Identification of abnormal or delayed myelination with proton-decoupled ^{31}P MRS. MRS of a child with an unidentified dysmyelination syndrome who appears to lack significant amounts of white matter. (a) ^{1}H MRS of parietal 'white matter' shows significant reduction of Cho. An unidentified peak at 1.4 ppm is possibly lipid. (b) ^{31}P MRS with low–normal phosphodiester (PDE) for age. (c) Proton-decoupled ^{31}P MRS is markedly abnormal for a 2-year-old. GPE and GPC are reduced to the neonatal MRS level. PE and PC, however, are normal for age. Abbreviations as in Figures 1 and 3

eries reviewed in Sections 1–4, perhaps because MRI is often entirely normal! By and large, radiologists have used MRS to add detail in the differential diagnosis of lesions identified first by MRI: tumor recurrence versus necrosis, primary versus secondary tumor, stroke versus venous infarction, tumor versus stroke, abcess versus tumor in the immunocompromised patient.[80]

Single-voxel ^{1}H MRS readily distinguishes between lymphoma, toxoplasmosis, progressive multifocal leukoencephalopathy and coccidiomycosis in patients with AIDS.[81] Bacterial abcesses can no longer be confused with tumor, stroke, or multiple sclerosis plaque, since ^{1}H MRS identifies the abcess from its unique bacterial metabolic products (E. R. Danielsen, personal communication; Figure 16).

6.1 Central Pontine Myelenolysis

A rare focal lesion known pathologically to consist of lipid-filled macrophages similarly yields an unmistakable ^{1}H MR spectrum of triglyceride (see Figure 12). Lipid pathologies in the brain can be reliably studied only with short echo times. One example of a useful clinical MRS examination, prognosis after non accidental trauma (shaken-baby syndrome) hinges on identification of increasing concentrations of free lipid or 'macromolecules'[82] in ^{1}H MRS.[83,84]

6.2 Neurotransplantation in Humans

Among the neurodegenerative diseases regularly examined by ^{1}H MRS, only Alzheimer disease appears to have a diagnostic pattern;[85–87] Parkinson's disease and Huntington's disease do not. In particular, earlier demonstrations of lactate in brain spectra of patients with Huntington's disease, or of excess glutamate in basal ganglia of patients with Parkinson's disease, have not been confirmed.[88]

A recent study of patients who had received fetal cell transplants into the diseased putamen and caudate demonstrates a new clinical role of ^{1}H MRS in focal 'lesions'. The maturation, viability, partial rejection and subsequent recovery of the grafts can all be tracked in repeated ^{1}H MRS examinations (Figure 17).

7 ADVANCES IN MULTINUCLEAR CLINICAL NEUROSPECTROSCOPY

Human brain research with ^{31}P MRS and ^{13}C MRS are dealt with elsewhere in this series (***MRI and MRS of Neuropsychiatry***; ***Localization and Registration Issues Important for Serial MRS Studies of Focal Brain Lesions***; ***Central Nervous System Degenerative Disease Observed by MRI***; ***Brain Neoplasms in Humans Studied by Phosphorus-31 NMR Spectroscopy***; ***Brain Infection and Degenerative Disease Studied by Proton MRS*** and ***Brain MRS of Human Subjects***). In the purely clinical setting, ^{31}P MRS remains disappointing. With the exception of the discovery of a new syndrome characterized by absence of PCr from the brain spectrum[89] and the characterization of brain death as spectra lacking both PCr and ATP, few diagnostic ^{31}P MR brain spectra have been identified.

However, proton-decoupling of ^{31}P spectra has brought significant clinical advantages and several diagnostic uses to this modality. In particular, proton-decoupled ^{31}P MRS now permits accurate evaluation of the state of myelination in the

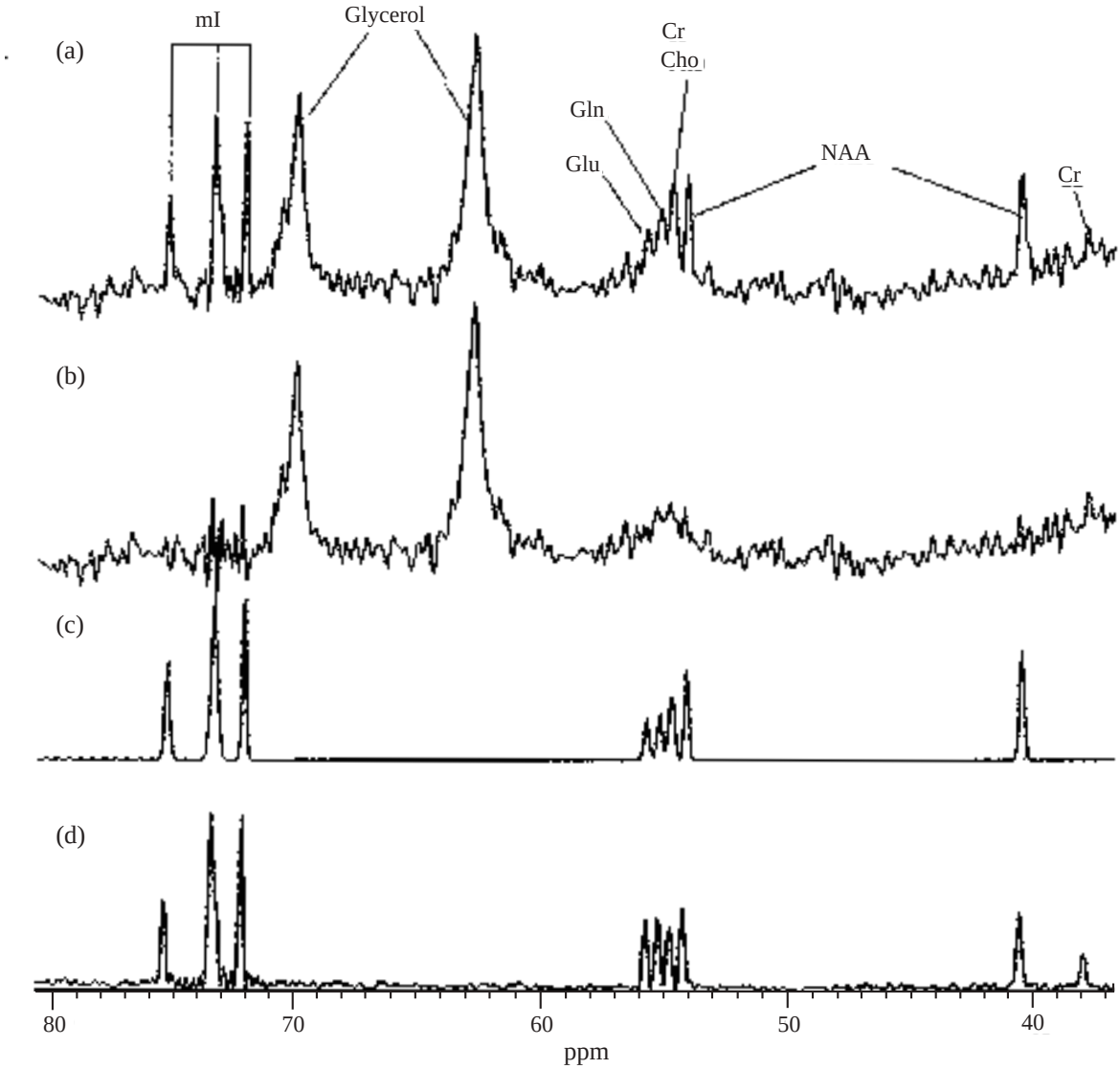

Figure 19 Clinical neurospectroscopy with ^{13}C MRS. (a) A ^{1}H–^{13}C spectrum acquired in Canavan disease. Metabolite peak areas were fitted and subtracted from the spectrum (b). From the fitted curves (c) the peak ratios of Glu, Gln, and *N*-acetylaspartate (NAA) relative to mI were calculated and compared with the peak ratios obtained from a model solution containing equal concentrations of NAA, Cr, mI, glutamate, and glutamine (d). Absolute concentrations in mmol per kilogram brain tissue were calculated using [mI] quantified with ^{1}H MRS in the occipital region of the brain as an internal reference. Abbreviations as in Figure 1

normally developing and dysmyelinating infant brain (Figure 18).[90]

The identification of other membrane or myelin disorders in adults is also gaining some specificity through the application of proton-decoupled ^{31}P MRS, since GPC, GPE, phosphorylcholine (PC) and phosphoethanolamine apparently vary almost independently in different pathological settings.[91] New insights into osmolyte disturbances of hepatic encephalopathy and hyponatremia were discussed above.

From being a research tool in the 1980s, natural abundance ^{13}C MRS has achieved clinical status through identification of mI, glutamate and several other useful neurometabolites in individual patients (Figure 19).[41]

FDA-IND approval of [1-^{13}C]-glucose (FDA 56,510; Figure 20)[91] infusion allows exploration in a clinical setting of the very promising techniques developed in the 1980s at Yale.[92] This is a dynamic technique, with many parallels to functional MRI. Carbon-13 MRS has particular relevance to the diagnosis and elucidation of the encephalopathies discussed at the beginning of this article.[93–95]

8 CONCLUSIONS

Diffuse metabolic changes in brain biochemistry are the result of complex interactions of disordered biochemistry in

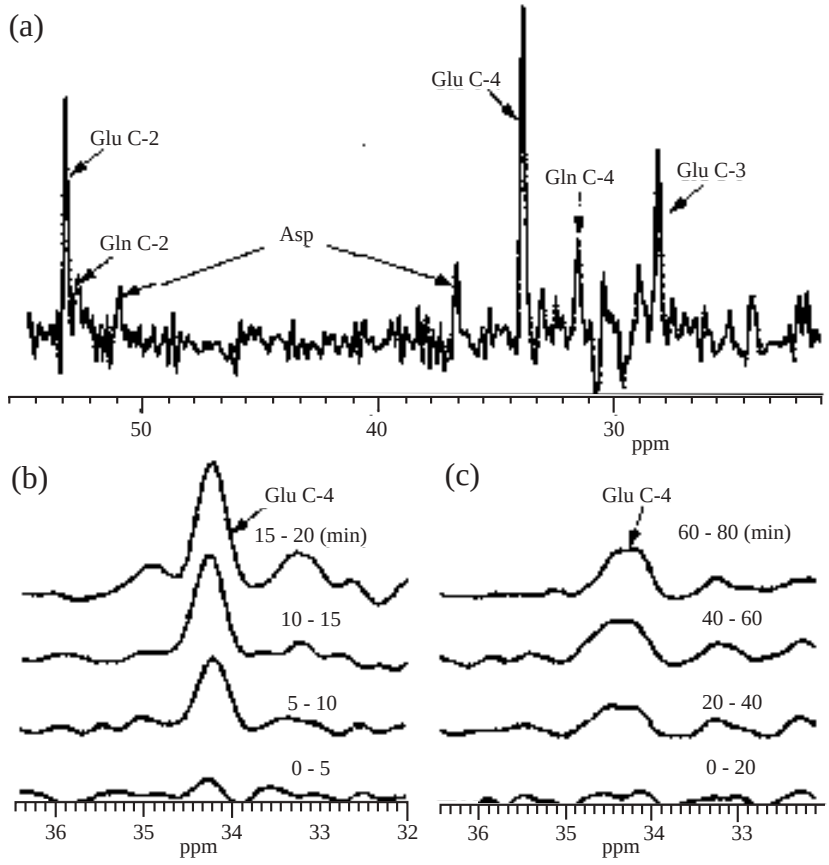

Figure 20 Dynamic ^{13}C MRS after [1-^{13}C]-glucose infusion. Using intravenous ^{13}C glucose infusion to enrich cerebral metabolite pools several fold higher than the 1% natural abundance (illustrated in Figure 19) provides a measure of glutamate (Glu) synthesis and metabolism. (a) Difference spectrum from a fed adult acquired 50–70 min after infusion start. Incorporation of the ^{13}C label into Glu C-4 in fasted mature (b) and immature brain (c) is clearly different and has diagnostic value in the premature infant (S. Bluml, J.-H. Wang, and B. D. Ross[91])

many other organs and tissues. Hepatic encephalopathies, diabetic coma, hypo- and hyperosmolar states, endocrine and hypoxic encephalopathy are examples of such conditions in which accurate application of quantitative NMR spectroscopy sheds new light. A thorough knowledge of the clinical MRS of coma will almost certainly be of crucial importance to health care in these difficult cases. Clinical uses of ^{1}H MRS has focused on lesions already identified by MRI, but its uses are likely to expand. Routine clinical MRI scanners can now provide excellent informative proton-decoupled ^{31}P spectroscopy and ^{13}C brain spectra; consequently these tools too are now entering clinical use.

9 RELATED ARTICLES

Animal Methods in MRS; Brain MRS of Human Subjects; In Vivo Hepatic MRS of Humans; Single Voxel Localized Proton NMR Spectroscopy of Human Brain In Vivo; Water Suppression in Proton MRS of Humans and Animals.

10 REFERENCES

1. F. Plum and J. B. Posner, 'The Diagnosis of Stupor and Coma', Davis, Philadelphia, 1986.
2. G. B. Young, A. H. Ropper, and C. F. Bolton, 'Coma and Impaired Consciousness', McGraw-Hill, New York, 1998.
3. S. Sherlock, W. H. J. Summerskill, L. P. White, and E. A. Phear, *Lancet*, 1954, **2**, 453.
4. S. Bessman and A. Bessman, *J. Clin. Invest.*, 1955, **34**, 622.
5. S Bessman and N. Pal, in 'The Urea Cycle', eds. S. Grisolia, R. Baguena, and F. Mayor, Wiley, Chichester, 1976, p. 83.
6. H. A. Krebs and K. Henseleit, *Hoppe-Seyler's Z. Physiol. Chem.*, 1932, **210**, 33.
7. A. Geissler, K. Kanamori, and B. D. Ross, *Biochem. J.*, 1992, **287**, 813.
8. B. T. Hourani, E. M. Hamlin, and T. B. Reynolds, *Arch. Intern. Med.*, 1971, **127**, 1033.
9. M. D. Norenberg and A. Martinez-Hernandez, *Brain Res.*, 1979, **161**, 303.
10. J-C Reubi, C. van den Berg, and M. Cuenod, *Neurosci. Lett.*, 1978, **10**, 171.
11. R. F. Butterworth and G. P. Layrargues, 'Hepatic Encephalopathy: Pathophysiology and Treatment', Humana Press, Clifton, 1989.

12. L. Zieve, in 'Diseases of the Liver', eds. L. Schiff and E. R. Schiff, Lippincott, Philadelphia, 1987, p. 925.
13. R. Kreis, N. A Farrow, and B. D. Ross, *Lancet*, 1990, **336**, 635.
14. N. E. P. Deutz, A. A. de Graaf, J. B. de Haan, W. M. M. J. Bovee and R. A. F. M. Chamuleau, *J. Hepatol.*, 1987, **4**(1), S13.
15. T. E. Bates, S. R. Williams, R. A. Kauppinen, and D. G. Gadian, *J. Neurochem.*, 1989, **53**, 102.
16. S. M. Fitzpatrick, H. P. Hetherington, K. L. Behar, and R. G. Shulman, *J. Cereb. Blood Flow Metab.*, 1990, **10**, 170.
17. K. Kanamori and B. D. Ross, *Biochem. J.*, 1993, **293**, 461.
18. K. Kanamori, F. Parivar, and B. D. Ross, *NMR Biomed.*, 1993, **6**, 21.
19. J. Shen, N. R. Sibson, G. Cline, K. L. Behar, D. L. Rothman, and R. G. Shulman, *Devel. Neurosci.*, 1998, **20**, 434.
20. K. Kanamori, B. D. Ross, and E. L. Kuo, *Biochem. J.*, 1995, **311**, 681.
21. K. Kanamori, B. D. Ross, and J. Tropp, *J. Magn. Reson. B*, 1995, **107**, 107.
22. K. Kanamori and B. D. Ross, *J. Neurochem.*, 1997, **68**, 1209.
23. S. H. Fitzpatrick, H. P. Hetherington, K. L. Behar, and R. G. Shulman, *J. Neurochem.*, 1989, **52**, 741.
24. S. Bluml, E. Zuckerman, J. Tan, and B. D. Ross, *J. Neurochem.*, 1998, **71**, 1564.
25. R. A. Moats, Y-H. H. Lien, D. Filippi, and B. D. Ross, *Biochem. J.*, 1993, **295**, 15.
26. H. Bruhn, J. Frahm, T. Michaelis, K.-D Merboldt, W. Hänicke, M. L. Gyngell, P. Brunner, J. Frohlich, D. Haussinger, P. Schauder, and B.D. Ross, *Hepatology*, 1991, **14**, 121.
27. R. Kreis, N. A. Farrow, and B. D. Ross, *NMR Biomed.*, 1991, **4**, 109.
28. R. Kreis, B. D. Ross, N. A. Farrow, and Z. Ackerman, *Radiology*, 1992, **182**, 19.
29. H. Bruhn, K.-D. Merboldt, T. Michaelis, M. L. Gyngell, W. Hanicke, J. Frahm, P. Schauder, K. Held, G. Brunner, J. Frolich, D. Haussinger, and B. D. Ross, *Proc. Xth Annu. Mtg Soc. Magn. Reson. Med.*, San Francisco, 1991, p. 400.
30. J. R. McConnell, C. S. Ong, W. K. Chu, M. F. Sorrell, B. W. Shaw, and R. K. Zetterman, *Proc. XIth Annu. Mtg Soc. Magn. Reson. Med.*, Berlin, 1992, p. 1957.
31. R. A. F. M. Chamuleau, D. K. Bosman, W. M. M. J. Bovee, P. R. Luyten, and J.A. den Hollander, *NMR Biomed.*, 1991, **4**, 103.
32. S. Schenker, K. J. Breen, and A. M. Hoyumpa, *Gastroenterology*, 1974, **66** 121.
33. B. D. Ross, M. R. Morgan, I. J. Cox, K. E. Hawley, and I. R. Young, *J. Cereb. Blood Flow Metab.*, 1987, **7**, 5396.
34. B. D. Ross, J. P. Roberts, J. Tropp, K. Derby, N. Bass, and C. Hawryszko, *Magn. Reson. Imag.*, 1989, **7**, 82.
35. P. R. Luyten, J. A. den Hollander, W. M. M. J. Bovée, B. D. Ross, D. K. Bosman, and R. A. F. M. Chamuleau, *Proc. VIIIth Annu. Mtg Soc. Magn. Reson. Med.*, Amsterdam, 1989, p. 375.
36. L. Barbara, B. Barbiroli, S. Gaiani, L. Bolondi, S. Sofia, G. Zironi, R. Lodi, S. Iotti, P. Zaniol, C. Sama, and S. Brillanti. *Eur. J. Hepatol.*, 1993, **2**, 60.
37. S. Taylor-Robinson, R. J. Mallalieu, J. Sargentoni, J. D. Bell, D. J. Bryant, G. A. Coutts, and M. Y. Morgan, *Proc. XIIth Annu. Mtg Soc. Magn. Reson. Med.*, New York, 1993, p. 89.
38. A. Geissler, N. Farrow, F. Villamil, L. Makowka, T. Ernst, R. Kreis, and B. Ross, *Proc. XIth Annu. Mtg Soc. Magn. Reson. Med.*, Berlin, 1992, p. 647.
39. R. Gruetter, E. J. Novotny, S. D. Boulware, G. F. Mason, D. L. Rothman, G. I. Shulman, J. W. Prichard, and R. G. Shulman, *J. Neurochem.*, 1994, **63**, 1377.
40. R. Gruetter, D. L. Rothman, E. J. Novotny, and R. G. Shulman, *Magn. Reson. Med.*, 1992, **25**, 204.
41. S. Bluml, *J. Magn. Reson.*, 1999, **136**, 219.
42. S. Bluml and B. D. Ross, in 'Impact of Molecular Biology and New Technical Developments in Diagnostic Imaging', eds. W. Semmler and M. Schwaiger, Springer-Verlag, Heidelberg, 1998, p. 43.
43. B. D. Ross, S. Jacobson, F. G. Villamil, R. A. Moats, T. Shonk, and J. Draguesku, *Hepatology*, 1993, **18**, 105A.
44. B. D. Ross, S. Jacobson, F. Villamil, J. Korula, R. Kreis, T. Ernst, T. Shonk, and R.A. Moats, *Radiology*, 1994, **193**, 457.
45. T. Ernst, B. D. Ross, and R. Flores, *Lancet*, 1992, **340**, 486.
46. R. K Gupta, V. A Saraswat, H. Poptani, R. K. Dhiman, A. Kohli, R. B Gujral, and S. R. Naik, *Am. J. Gastroenterol.*, 1993, **88**, 670.
47. B. D. Ross, T. Shonk, R. A. Moats, S. Jacobson, J. Draguesku, T. Ernst, J. H. Lee, and R. Kreis, *Proc. XIIth Annu. Mtg Soc. Magn. Reson. Med.*, New York, 1993, p. 131.
48. T. Shonk, R. Moats, J. H. Lee, J. Korula, T. Ernst, R. Kreis, J. Draguesku, and B. D. Ross, *Gastroenterology*, 1993, **104**, A-449, 1793
49. J. Korula, D. Kravetz, M. Katz, T. Shonk, S. Hanks, and B. D. Ross, *Hepatology*, 1993, **18**, 282A, 903.
50. D. G. Gadian, A. Connelly, J. H. Cross, S. Burns, R. A Iles, and J. V. Leonard, *Proc. Xth Annu. Mtg Soc. Magn. Reson. Med.*, San Francisco, 1991, p. 193.
51. B. D. Ross, R. Kreis, and T. Ernst, *Eur. J. Radiol.*, 1992, **14**, 128.
52. R. A. Hawkins, J. Jessy, A. M. Mans, and M. R. De Joseph, *J. Neurochem.*, 1993, **60**, 1000.
53. B. D. Ross and S. Bluml, *NMR Biomed.*, 1996, **9**, 279.
54. D. Haussinger, J. Laubenberger, S. V. Dahl, T. Ernst, S. Bayer, M. Langer, W. Gerok, and J. Hennig, *Gastroenterology*, 1994, **107**, 1475.
55. L. J. Haseler, W. L. Sibbit Jr, H. N. Mojtahedzadeh, S. Reddy, V. P. Agarwal, and D. M. McCarthy, *Am. J. Neuroradiol*, 1998, **19**, 1681.
56. R. N. Bryan and P. Barker, *Am. J. Neuroradiology*, 1998, **19**, 1593.
57. H. Bruhn, T. Michaelis, K-D. Merboldt, W. Hanicke, M. L. Gyngell, and J. Frahm, *Lancet*, 1991, **337**, 745.
58. R. Kreis, and B. D. Ross, *Radiology*, 1992, **184**, 123.
59. E. R. Danielsen and B. D. Ross, 'Magnetic Resonance Spectroscopy Diagnosis of Neurological Diseases', Marcel Dekker, New York, 1999.
60. K. J. Seymour, S. Bluml, J. Sutherling, W. Sutherling, and B. D. Ross, *MAGMA*, 1999, **8**, 33.
61. Y-H. H. Lien, J. I. Shapiro, and L. Chan, *J. Clin. Invest.*, 1990, **85**, 1427.
62. G. G. Wong D.Phil. Thesis, University of Oxford, 1981.
63. R. Kreis, T. Ernst, and B. D. Ross, *J. Magn. Reson.*, 1993, **102**, 9.
64. B. D. Ross, T. Ernst, R. Kreis, L. J. Haseler, S. Bayer, E. Danielsen, S. Bluml, T. K. Shonk, J. C. Mandigo, W. Caton, C. Clark, S. Jensen, N. Lehman, E. Arcinue, R. Pudenz, and C. H. Shelden, *JMRI*, 1998, **8**, 829.
65. J. H. Lee and B. D. Ross, *Proc. XIIth Annu. Mtg Soc. Magn. Reson. Med.*, New York, 1993, p. 1553.
66. J. H. Lee, E. Arcinue, and B. D. Ross, *N. Engl. J. Med.*, 1994, **331**, 439.
67. J. S. Videen, T. Michaelis, P. Pinto, and B. D. Ross, *J. Clin. Invest.*, 1995, **95**, 788.
68. Y.-H. H. Lien, J. I. Shapiro, and L. Chan, *J. Clin. Invest.*, 1991, **88**, 303.
69. P. L. Hope, E. B. Cady, P. S. Tofts, P. A. Hamilton, A. M. de Costello, D. T. Delpy, A. Chu, E. O. R. Reynolds, and D. R. Wilkie, *Lancet*, 1984, 366.
70. R. Kreis, T. Ernst, E. Arcinue, R. Flores, and B. D. Ross, *Proc. XIth Annu. Mtg Soc. Magn. Reson. Med.*, Berlin, 1992, p. 237.
71. O. H. Lowry in 'Neurology of the Newborn,' ed. J. J. Volpe, Saunders, Philadelphia, 1987, p. 33.

72. R. Kreis, E. Arcinue, T. Ernst, T. Shonk, R. Flores and B. D. Ross, *J. Clin. Invest.*, 1996, **97**, 1.
73. G. A. Webb (ed.), 'Annual Reports on NMR Spectroscopy', Vol. 25, Academic Press, London, 1993, p. 480.
74. D. R. Bailes, D. J. Bryant, H. A. Case, A. G. Collins, I. J. Cox, A. S. Hall, R. R. Harman, S. Khenia, P. McArthur, B. D. Ross, and I. R. Young, *J. Magn. Reson.*, 1988, **77**, 460.
75. A. Lin, S. Bluml, W. Caton, C. Duma, A. Mamelak, R. Rand, S. Wiseman, and B. D. Ross, *Proc. VIIth Annu. Mtg (Int.) Soc. Magn. Reson. Med.*, Philadelphia, 1999, p. 1394.
76. M. C. Preul, Z. Caramanos, D. L. Collins, J.-G. Villemure, R. Leblanc, A. Olivier, R. Pokrupa, and D. L. Arnold, *Nature Med.*, 1996, **2**, 323.
77. J. van der Grond, K. J. van Everdingen, B. C. Eikelboom, J. Kenez, and W. P. T. M. Mali, *JMRI*, 1999, **9**, 1.
78. P. Dechent, P. J. W. Pouwels, F. Hanefield, and J. Frahm, *Proc. VIth Annu. Mtg Soc. Magn. Reson. Med.*, Sydney, 1998, **3**, p. 1754.
79. B. Kruse, P. B. Barker, P. C. M. van Zigl, J. H. Duyn, C. T. W. Moonen, and H. W. Moser, *Ann. Neurol.*, 1994, **36**, 595.
80. M. Castillo (ed.), 'Proton MR Spectroscopy of the Brain', Vol. 8, Saunders, Philadelphia, PA, 1998, p. 926.
81. L. Chang, B. L. Miller, D. McBride, M. Cornford, G. Oropilla, S. Buchthal, F. Chiang, H. Aronow, and T. Ernst, *Radiology*, 1995, **197**, 525.
82. K. L. Behar and T. Ogino, *Magn. Reson. Med.*, 1993, **30**, 38.
83. L. J. Haseler, E. Arcinue, E. R. Danielsen, S. Bluml, and B. D. Ross, *Pediatrics*, 1997, **99**, 4.
84. T. Chen, N. Farrow, S. Bluml, C. Huang, and B. D. Ross, *Proc. VIth Annu. Mtg (Int.) Soc. Magn. Reson. Med.*, Sydney, 1998, **1**, 537.
85. B. L. Miller, R. Moats, T. Shonk, T. Ernst, S. Woolley, and B. D. Ross, *Radiology*, 1993, **187**, 433.
86. R. A. Moats and T. Shonk, *Am. J. Neuroradiol.*, 1995, **16**, 1779.
87. T. K. Shonk, R. A. Moats, P. Gifford, T. Michaelis, J. C. Mandigo, J. Izumi, and B. D. Ross, *Radiology*, 1995, **195**, 65.
88. T. Hoang, D. Dubowitz, S. Bluml, O. V. Kopyov, D. Jacques, and B. D. Ross, *Proc. 27th Meeting of the Society for Neuroscience*, New Orleans, FL, 1997, **23**(2), 1682.
89. S. Stockler, F. Hanefeld, and J. Frahm, *Lancet*, 1996, **348**, 789.
90. K. Seymour, S. Bluml, G. McComb, and B. D. Ross, *Proc. VIth Annu. Mtg (Int.) Soc. Magn. Reson. Med.*, Sydney, 1998, **3**, p. 1807.
91. S. Bluml, J. H. Hwang, and B. D. Ross, *Proc. VIIth Annu. Mtg (Int.) Soc. Magn. Reson. Med.*, Philadelphia, 1999, p. 335.
92. G. F. Mason, R. Gruetter, D. L. Rothman, K. L. Behar, R. G. Shulman, and E. J. Novotny, *J. Cereb. Blood Flow Metab.*, 1995, **15**, 12.
93. S. Bluml, *J. Magn. Reson.*, in press.
94. S. Bluml, J. H. Wang, A. Moreno, L. Lim, J. Tam, and B. D. Ross, *Radiology*, 1999, **213**, 330P.
95. S. Bluml, A. Moreno, and B. D. Ross, *Lancet* submitted.

Acknowledgements

Work reported was largely funded by the Rudi Schulte Research Institute, Santa Barbara, the Jameson Foundation and by funds from the HMRI MRS Program. BDR is grateful to the following colleagues: K. Kanamori, E. Rubaek-Danielsen, J.D. Roberts, N. Kumar, M. Linsey and C. Sharp.

Biographical Sketch

Brian D. Ross. *b* 1938; B.Sc., 1958, University College, London. D.Phil., 1966, University of Oxford. M.B., 1961, University College Hospital, London. F.R.C.S., 1973, Royal College of Surgeons, London. M.R.C.Path., 1976, Royal College of Pathologists, London. 1989, F.R.C.Path. University of Oxford lecturer, Metabolic Medicine. Director, Renal Metabolism Unit and Consultant Chemical Pathologist, Radcliffe Infirmary, Oxford, 1976–84. Director of Clinical Spectroscopy Programs at Radcliffe Infirmary, Oxford, 1981–84, Hammersmith Hospital, London, 1986–88, and Huntington Medical Research Institutes, Pasadena, CA, 1986–present. Visiting Associate, California Institute of Technology, 1986–present.

Temporomandibular Joint MRI

Steven E. Harms
Baylor University Medical Center, Dallas, TX, USA

1 INTRODUCTION

The value of medical imaging is determined by its ability to define treatment decisions. If those decisions are separated by treatments that greatly differ in cost or morbidity, the value of the diagnostic test is high. On the other hand, if the treatment is safe and inexpensive, then it may be more cost-effective to treat without diagnosis. As the treatment of temporomandibular joint (TMJ) disease evolves, the role of MR imaging as a determinant for clinical management decisions becomes better defined. In this chapter, the MR imaging of the TMJ is reviewed with its relationship to the current concepts for clinical management of TMJ disorders.

2 ANATOMY AND PHYSIOLOGY

The TMJ is a compound joint with the three components being the temporal bone, the mandibular condyle, and the articular disk (Figure 1). There are two joint spaces: the superior joint space lying between the disk and the temporal bone and the inferior joint space lying between the disk and the mandibular condyle.[1,2]

The articular disk is a lens-shaped structure divided into three parts: the posterior band, the anterior band, and the thin zone. In the young asymptomatic population without previous orthodontic manipulation, the posterior band normally lies between 11 o'clock and 1 o'clock relative to the superior aspect of the mandibular condyle. As opposed to what was originally thought, the disk can be quite variable in location without producing symptoms.[3]

The articular disk of the TMJ is held in place by the discal ligaments which extend from the medial and the lateral poles of the condyle to the medial and lateral margins of the disk. As a result of the strong attachment to the condyle by the diskal ligaments, the disk and condyle move together as a unit called the disk–condyle complex. The posterior band of the disk is connected to the posterior aspect of the temporal fossa by elastic tissues called the retrodiskal attachments. Since the retrodiskal attachment is composed of two major elastic structures, this area is sometimes called the bilaminar zone. The anterior band of the disk is attached to the superior belly of the lateral pterygoid muscle.[1,2]

There are two movements that occur with opening: translation and rotation. The first movement is rotation which is the swinging of the condyle relative to the disk. The next movement is the translation of disk–condyle complex anteriorly from the articular fossa to a position beneath the articular eminence.[1,2]

The disk position is primarily determined by weight bearing, with the thin zone being the point of maximum load. During mastication, weight bearing is transferred to the food between the teeth and the TMJ is unloaded. Without weight bearing to hold the thin zone in position, there is a tendency for the elastic retrodiskal tissues to pull the disk posteriorly. This force is opposed by a contraction of the anterior belly of the lateral pterygoid muscle. Disk displacement is most commonly anterior due to laxity or disruption of the elastic retrodiskal tissues that hold the disk posteriorly.[1,2]

3 TREATMENT

Currently, most treatment teams accept the goal of TMJ treatment as relief of pain and/or restoration of function. This philosophy is a departure from the early years of TMJ treatment when restoration of normal anatomical relationships was thought to be the treatment goal. This distinction is important since relief of symptoms may be achieved in the face of abnormal anatomical relationships.

Conservative TMJ therapy may consist of approaches such as: biofeedback, nonsteroidal antiinflammatory agents, muscle relaxers, bedtime sedatives, splints, and/or any combination of these approaches. Conservative therapy generally refers to the fact these treatments are generally noninvasive and reversible. In terms of cost, however, some conservative therapy may be more expensive than surgery. It is generally accepted that a trial of some form of conservative therapy should be attempted before invasive therapy is considered. Since the decision for conservative therapy approach is based upon the symptoms and clinical settings, MRI is not typically indicated in this management decision.[4,5]

If conservative therapy fails, then surgery may be required to relieve pain and/or restore function. There are a number of possible surgical treatments that are designed to address a particular physical defect. Joint adhesions may be treated by therapies as simple as joint lavage or as complex as arthro-

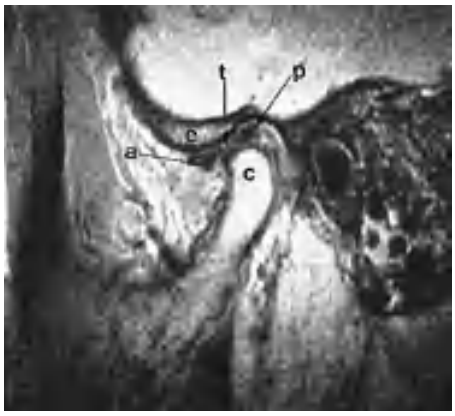

Figure 1 Normal temporomandibular joint. The bone landmarks are clearly visible on the oblique sagittal SE 15/2000 image of the temporomandibular joint. The mandibular condyle, c, and eminence, e, are labeled. Normal disk architecture is demonstrated with good demonstration of the anterior band, a, posterior band, p, and the thin zone, t

scopy.[6] Although attempts to correct disk displacement are made by TMJ arthroscopists, it is generally recognized that the major treatment effect of arthroscopy is the lysis of joint adhesions.[7] The lysis of adhesions is often highly effective in relieving joint symptomology without any correction in disk displacement. This discovery is a significant change from the original concept of TMJ disorders which attributed TMJ pain and dysfunction to disk displacement alone. The success of adhesion lysis therapy has made the imaging diagnosis of adhesions an important part of the MR evaluation.

Internal derangements of the articular disk can be approached with a variety of conventional surgical procedures. If the disk architecture is relatively well preserved, then disk plication may be used. The plication procedure pulls the usually anteriorly displaced disk back into position over the condyle and repairs the posterior attachment. Disk plication was once the most common surgical procedure but has fallen out of favor with many surgeons due to the common complication of adhesions in the postoperative period. In addition, abnormal disk architecture is often seen in association with displacement. Repositioning of a torn or otherwise deformed disk by plication is not possible. Diskectomy is often accompanied by replacement with a dermal graft, elastic cartilage graft, or alloplastic material.[8] The common complication of giant cell foreign body reaction to Proplast TMJ implants has greatly reduced the use of alloplastic disk replacements.[9,10] The poor outcome experienced with alloplastic implants has increased the popularity of autologous tissues as disk replacements. Postoperative adhesions remain a problem and despite attempts the ideal replacement material for severely degenerated or deformed disks has not yet been found.

For end-stage TMJ disorders where degeneration changes in the condyle and temporal bone predominate, the surgical treatment is often total joint replacement. A variety of appliances have been designed for total TMJ replacement. All of the devices comprise some form of artificial fossa and condyle. Because metallic components are used, MRI evaluations of the TMJ in postoperative total joint patients is not possible. As with total joint replacement in other joints, the long-term durability of the appliance is a problem. As a result, surgeons tend to restrict this approach to older individuals or to patients with severe degenerative change.[11]

Avascular necrosis of the mandibular condyle has been described by some workers as a common cause of TMJ disorders.[12,13] These workers favor corrections of the problem by condylar decompression or replacement. This diagnosis and treatment is highly controversial. Many in the TMJ treatment field refute this theory.

4 TECHNIQUE

The TMJ examination should consist of the following components:

1. static sagittal high-resolution images in the closed mouth position;
2. static coronal views in the closed mouth position;
3. kinematic or real time images during opening;
4. at least one sagittal T_2-weighted series.

A dedicated TMJ surface coil is now considered an essential feature for adequate TMJ imaging. The coil may be as simple as a single 3-inch-diameter loop.[14] Both sides must be evaluated simultaneously in order to demonstrate asymmetry. About 80% of TMJ disorders are bilateral. These coils can be combined either with a special combiner box or with signals separately acquired with phased array coils and receivers.[15,16] The phased array approach will result in a theoretical square root of 2 S/N improvement but the technology is considerably more costly.

The anatomical diagnosis of most TMJ disorders is made from the high-resolution sagittal images.[14,17–23] A short *TE* proton density or T_1-weighted pulse sequence, similar to the technique used for knee imaging, is required for optimal S/N and resolution. Because volume averaging effects are an important cause of image degradation, the slice thickness should be around 3 mm. An oblique image plane is performed using the angle of the mandibular body and condyle as determined on axial scout views as a reference. The short echo anatomical images are most important in TMJ diagnosis. As a result, traditional spin echo (SE) pulse sequences are preferred over fast SE or RARE sequences due to the blurring of short, effective *TE* echo images.

T_2 weighting can be achieved in both a dual echo SE sequence and a separate, long, effective *TE* fast SE (FSE) sequence. The FSE will result in improved image resolution but the fat signal will be more intense. The fat signal can be addressed with the addition of a fat saturation prepulse which lengthens the *TR*. Since the objective of T_2 weighting is the identification of fluid and not anatomical definition, there is little advantage in the use of FSE over a dual echo traditional SE.[14,17–23]

Coronal T_1-weighted imaging is used to localize the disk in the medial-lateral direction. A faster sequence with diminished resolution compared with the sagittal images will usually be satisfactory.[24,25]

Kinematic or real-time motion images are needed to demonstrate TMJ physiology (Figure 2). A fast T_1-weighted SE is usually satisfactory. Gradient echo sequences may be employed if the timing parameters are adjusted to demonstrate good diskal anatomy. Often gradient echo images for cine TMJ imaging are inadequate to demonstrate this anatomy and are not the favored method for this reason. Because multiple slices are needed, there is no time saving associated with the use of gradient echo sequences. Scan time on the order of one minute per view are satisfactory. At least two slices per side should be performed in case the disk moves medially or laterally out of the view of one slice. Since the condyle is the reference for disk reduction, the slices are oriented sagittally, not oblique sagittally, as in the anatomical images. The condyle is a rigid structure that must travel in a straight line in the sagittal plane. The disk, however, will tend to move anteromedially. If oblique images are performed, the late opening images will display a disk and no condyle for reference. The determination of disk reduction will require the identification of the disk relative to the condyle. For kinematic imaging, the TMJ will need to be incrementally opened at predetermined intervals. We prefer to open in 3 mm increments until the patient can no longer proceed either due to pain or inability to open. One of several commercially available patient-controlled positioning imaging devices may be employed for establishing consistent incremen-

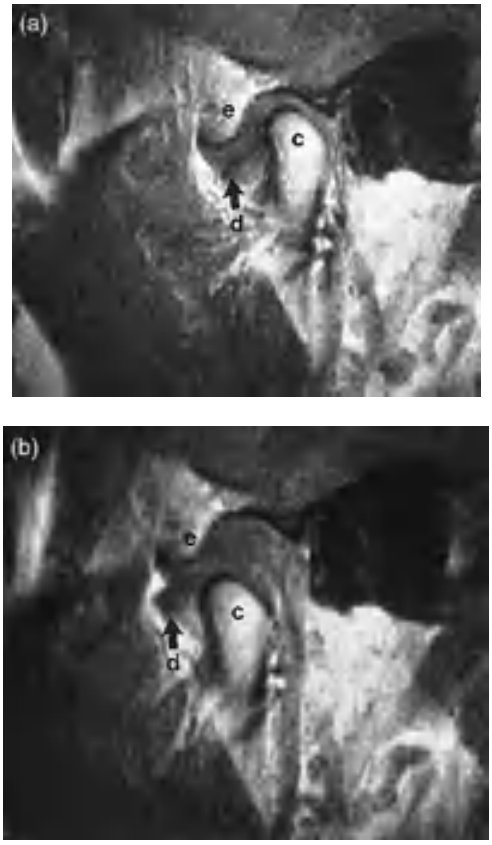

Figure 2 Kinematic imaging. Two images from a kinematic display are shown: the closed mouth (a) and the maximum open mouth (b) views. The closed mouth view demonstrates an anteriorly displaced disk, d, relative to the mandibular condyle, c. With opening, there is poor translation of the condyle which only translates to mid-eminence, e. The disk remains anteriorly displaced throughout opening

tation. A reliable device is needed in order to quantitate the interincisor opening at the time of disk reduction.[26–29]

Most commercially available instruments have this kinematic display capability. Unfortunately, some manufacturers offer this capability only at additional cost. The lack of kinematic display will greatly limit the ability to make clinically significant TMJ diagnoses.

A more sophisticated and more physiologic approach is the gating of the MR imaging acquisition. Gating similar to cardiac gating is used during repetitive opening of the TMJ. It remains to be seen if this approach provides a clinically significant improvement in examination quality.

Echo planar methods may be used in the future for real-time TMJ imaging. Some believe that this approach would be more physiologic. Imaging during mastication would be possible with echo planar imaging.

5 ELEMENTS OF A TMJ INTERPRETATION

5.1 Bone

The landmarks for TMJ anatomy are the mandibular condyle and temporal bone. These structures should themselves be evaluated for anatomic defects. Osteophytes and beaking of the mandibular condyle are common. A steep articular eminence is associated with an increased incidence of TMJ disorders. Displacement of the condyle in the fossa may be a clue as to more subtle soft tissue defects. Hypointensity of the condylar marrow may indicate avascular necrosis.[12,13]

End-stage TMJ disorders result in severe degenerative changes. Erosions and large osteophytes are common. The eminence and condyle may be flattened. The joint space may be almost totally obliterated. If these findings are detected, a total joint replacement may be indicated.

In patients with a history of alloplastic implants, destruction of bone should be recognized as an effect associated with giant-cell foreign-body reaction. If large erosions are seen in these patients, look for an associated soft tissue mass that is hypointense on T_2-weighted images which is the hallmark of giant-cell reaction. Fragments of implant material that are hypointense on all sequences may be identified. Giant-cell foreign-body reactions may be very severe and on occasion can penetrate through the temporal bone into the middle cranial fossa.[8–10]

5.2 Disk Position and Morphology

The common method for recording disk position in the closed mouth sagittal views is the relationship to the condyle. Imagine the round mandibular condyle as a clock face and then locate the posterior band of the disk. The posterior band will usually be the thickest part of the posterior aspect of the disk. Sometimes the posterior band will be flattened or the disk may be deformed with an unidentifiable posterior band. In these cases record position as the posterior aspect of the disk rather than the posterior band. The normal posterior band position is 11 o'clock to 1 o'clock; anything else is displaced. If the disk is displaced greater than the length of the disk from the fossa, then this severe displacement should be noted. Anterior displacements are the most common. Posterior displacements are rare.[3–5]

The position of the disk in the medial-lateral direction is demonstrated on the coronal views. If the disk is difficult to identify on the sagittal view, look on the coronal view where a pure medial or lateral displacement may be seen. Antero-medial displacements are common. Antero-lateral displacements are less commonly seen.[24,25]

Disk morphology should be described. Are the anterior band, posterior band, and thin zone well demonstrated? If not, the disk morphology is abnormal. The disk may be thickened or distorted. A thin posterior band is a common finding in early TMJ disease.

End-stage TMJ disease results in fragmentation and degeneration. The disk may not be identifiable. Fragments of disk-like intensity may be seen. These areas commonly represent a combination of disk fragments, fibrosis, and metaplasia of the retrodiscal tissues.

Tears or perforations are findings described in TMJ arthrography as a communication of contrast from one joint space to another. Most of these perforations actually involve the retrodiscal tissues, not the disk itself. Perforations of the disk itself are rare and are almost always associated with other, more significant, abnormalities. Temporomandibular joint perforations are difficult to diagnose with MRI. With more experience, MR

imaging has demonstrated more detail of the defects that better define appropriate treatment requirements.[17]

5.3 Hyperintense Signal on T_2-Weighted Images

Fluid in either the superior or interior joint spaces is best seen on the T_2-weighted images. As with other joints, fluid in the TMJ is a nonspecific sign of inflammation. Fluid may also be seen around the pterygoid muscle as a sign of possible myofascial disease.

Edema in the retrodiskal area indicates possible retrodiskitis. Retrodiskitis is acutely painful and often difficult to separate from an internal derangement on physical examination. The MR diagnosis of retrodiskitis is important since this disorder may be effectively treated with antiinflammatory agents. Hyperintensity in retrodiskitis begins at the posterior margin of the disk and extends posteriorly in the fossa. Often the condyle is displaced antero-inferior by the soft tissue mass. This appearance should be distinguished from normal retrodiskal veins that are hyperintense on T_2-weighted images. These veins can be distinguished by their location, posterior and inferior compared with retrodiskitis. In contrast to retrodiskitis which is confluent, retrodiskal veins are seen as multiple, small spots typical of vessels in cross-section.[17]

5.4 Kinematic Evaluation

Kinematic imaging is needed to describe accurately abnormalities in joint function. Disk rotation and disk–condyle complex translation should be observed. The right and left sides should be compared side-by-side using a kinematic display.[26–29]

What is the relationship of the disk to the condyle during the opening cycle? If the disk is displaced in the closed mouth view, does it reduce upon opening? When does it reduce? Early or late? By knowing the interincisor distance associated with each step, the extent of opening at the point of disk reduction can be determined.

Kinematic imaging is used for the diagnosis of joint adhesions. Adhesions between the disk and the condyle are demonstrated by fixation of the disk to the condyle during the entire opening cycle. Adhesions to the eminence are shown as lack of separation between the disk and eminence as well as fixation to the eminence during opening. Asymmetric translation is indirect evidence of adhesions.

Very poor translation on physical examination is often called a closed locked joint. The classic description of closed locked physiology is an anteriorly displaced disk without reduction. Theoretically the displaced disk impairs condylar translation and locks the joint in the closed mouth position. MR studies, however, reveal that an anteriorly displaced disk, without reduction on opening, uncommonly produces locking. Other causes for a closed locked joint on physical examination should be considered. Severe adhesions can more commonly cause the clinical picture of a locked joint. When these adhesions totally encompass the condyle and prevent any translation, the condition is called fibrous ankylosis. Previous surgery with dislocated or adhesed implant is another common cause of poor translation in the postoperative patient. As mentioned previously, adhesions can be managed with arthroscopy, whereas a closed locked joint, due to disk displacement, usually requires surgery (an open surgical procedure).[26–29]

6 SUMMARY

There is a multifaceted spectrum of causes for TMJ-associated pain and dysfunction. As the understanding of TMJ disorders increases, the methods for treatment become more focused and more effective. Accurate diagnosis of these entities is essential in designing treatment protocol that is appropriate for a particular patient. Modern MRI methods can make the most of the diagnostic determinations needed for these treatment decisions.

7 RELATED ARTICLES

Cardiac Gating Practice; Eye, Orbit, Ear, Nose, and Throat Studies Using MRI; Surface and Other Local Coils for In Vivo Studies; Whole Body Machines: NMR Phased Array Coil Systems.

8 REFERENCES

1. J. P. Okeson, 'Fundamentals of Occlusion and Temporomandibular Disorders', Mosby Year Book, St. Louis, MO, 1985.
2. W. E. Bell, 'Temporomandibular Disorders: Classification, Diagnosis, Management', 2nd edn., Mosby Year Book, Chicago, 1986.
3. L. T. Kircos, D. A. Ortendahl, A. S. Mark, and M. Arakawa, *J. Oral Maxillofac. Surg.*, 1987, **45**, 852.
4. F. M. Bush, J. H. Butler, and D. M. Abbott, in 'Advances in Occlusion: Diagnosis and Treatment', eds. H. C. Lundeen and C. H. Gibbs, Publishing Sciences Group, Littleton, MA, 1982.
5. M. F. Dolwick, in 'Internal Derangements of the Temporomandibular Joints,' eds. C. A. Helms, R. W. Katzberg, and M. F. Dolwick, Radiology Research and Education Foundation, San Francisco, 1983.
6. J. J. Moses, D. Sartoris, R. Glass, T. Tanaka, and I. Toker, *J. Oral Maxillofac. Surg.*, 1989, **47**, 674.
7. M. T. Montgomery, J. E. Van Sickels, S. E. Harms, and W. J. Thrash, *J. Oral Maxillofac. Surg.*, 1989, **47**, 1263.
8. D. P. Timmis, S. B. Aragon, J. E. Van Sickels, and T. B. Aufdemorte, *J. Oral Maxillofac. Surg.*, 1986, **44**, 541.
9. P. A. Kaplan, J. D. Ruskin, H. K. Tu, and M. A. Knibbe, *Am. J. Roentgenol.*, 1988, **151**, 337.
10. K. P. Schellhas, C. H. Wilkes, M. el Deeb, L. B. Lagrotteria, and M. R. Omlie, *Am. J. Roentgenol.*, 1988, **151**, 731.
11. R. W. Bessette, R. Katzberg, J. R. Natrella, and M. J. Rose, *Plast. Reconstr. Surg.*, 1985, **75**, 192.
12. K. P. Schellhas, C. H. Wilkes, H. M. Fritts, M. R. Omlie, and L. B. Lagrotteria, *Am. J. Roentgenol.*, 1989, **152**, 551.
13. C. H. Wilkes, *Arch. Otolaryngol. Head Neck Surg.*, 1989, **115**, 469.
14. S. E. Harms and R. W. Wilk, *Radiographics*, 1987, **7**, 521.
15. C. J. Hardy, R. W. Katzberg, R. L. Frey, J. Szumouski, S. Totterman, and O. M. Mueller, *Radiology*, 1988, **167**, 835.
16. J. S. Hyde, A. Jesmanowicz, W. Froncisz, J. B. Kneeland, T. M. Grist, and N. F. Campagna, *J. Magn. Reson.*, 1986, **70**, 512.
17. S. E. Harms, R. M. Wilk, L. M. Wolford, D. G. Chiles, and S. B. Milan, *Radiology*, 1985, **157**, 133.
18. C. A. Helms, L. B. Kaban, C. McNeill, and, T. Dodson, *Radiology*, 1989, **172**, 817.

19. C. A. Helms, T. Gillespy III, R. E. Sims, and M. L. Richardson, *Radiol. Clin. North Am.*, 1986, **24**, 189.
20. T. L. Miller, R. W. Katzberg, R. H. Tallents, R. W. Bessette, and K. Hayakawa, *Radiology*, 1985, **154**, 121.
21. R. W. Katzberg, R. W. Bessette, R. H. Tallents, D. B. Plewes, and J. V. Manzione, *Radiology*, 1986, **158**, 183.
22. R. W. Katzberg, *Radiology*, 1989, **170**, 297.
23. M. T. Cirbus, M. S. Smilack, J. Beltran, and D. C. Simon, *J. Prosthet. Dent.*, 1987, **57**, 488.
24. R. W. Katzberg, P.-L. Westesson, R. H. Tallents, R. Anderson, K. Kurita, J. V. Manzione Jr., and S. Totterman, *Radiology*, 1988, **169**, 741.
25. M. B. Khoury and E. Dolan, *American Journal of Neuroroentgenography*, 1986, **7**, 869.
26. K. R. Burnett, C. L. Davis, and J. Read, *Am. J. Roentgenol.*, 1987, **149**, 959.
27. W. F. Conway, C. W. Hayes, and R. L. Campbell, *J. Oral Maxillofac. Surg.*, 1988, **46**, 930.
28. W. F. Conway, C. W. Hayes, R. L. Campbell, and D. M. Laskin, *Radiology*, 1989, **172**, 821.
29. J. M. Fulmer and S. E. Harms, *Top. Magn. Reson. Imag.*, 1989, **1**, 75.

Biographical Sketch

Steven E. Harms. M.D., 1978, University of Arkansas for Medical Sciences. Postdoctoral research associate, physical chemistry, Stony Brook, 1977–78; assistant radiologist, Depts. of Diagnostic Radiology and Biophysics; M.D., Anderson Cancer Center, Houston, 1982–83 TX. Director of Magnetic Resonance, Dept. of Radiology, Baylor University Medical Center, Dallas, 1983–present. Approx. 80 papers. Current research interests: three-dimensional imaging applications, development of new fast scanning sequence, and musculoskeletal, temperomandibular joint, breast, body, and ophthalmological applications of MRI.

Applications of ^{19}F-NMR to Oncology

Paul M. J. McSheehy

St George's Hospital Medical School, London, UK

Laurent P. Lemaire

Laboratoire de Biophysique Médicale Faculté de Médecine, Angers, France

and

John R. Griffiths

St George's Hospital Medical School, London, UK

1 INTRODUCTION

The first reported ^{19}F MRS experiments that applied directly to chemotherapy date from 1984, in which the metabolism of an anticancer fluoropyrimidine, 5-fluorouracil (5FU), was studied in mouse liver and a subcutaneous mouse tumor.[1] Subsequently, most preclinical ^{19}F MRS studies have indeed been concerned with 5FU and its metabolism in liver, and a variety of tumors in different animal models. This work, and other applications of ^{19}F MRS, have been extensively reviewed since the late 1980s.[2–5] The most recent review[6] demonstrates that ^{19}F MRS is of increasing use in the clinic and could, in the future, be used to individualize and optimize chemotherapy.

This review will briefly describe the rationale for the development of fluoropyrimidines as anticancer drugs, the key ^{19}F MRS experiments that have led to the exciting developments in the clinic, and the future mechanistic research required to realize fully the potential of this technique. Reference will also be made to other types of fluorinated compound which have been studied by ^{19}F MRS to investigate tumor hypoxia, blood flow and pH, and drug pharmacokinetics in animal models. These other studies show how ^{19}F MRS can be used at an earlier stage in drug development as a research tool.

2 5-FLUOROPYRIMIDINES: ANIMAL MODELS AND CLINICAL APPLICATIONS

The 5-fluoropyrimidine (FP) 5FU was synthesized in 1957, and is an example of rational synthesis in which the substitution of a fluorine atom for hydrogen in position 5 of the pyrimidine uracil was intended to lead to misincorporation of the drug into RNA, and inhibition of DNA synthesis.[7] Anticancer activity is now known to be mediated via conversion to cytotoxic 5-fluoronucleotides (Fnuct) (see Figure 1). Specifically, FdUMP inhibits the key DNA synthesis enzyme thymidylate synthase (TS), FdUTP becomes misincorporated into DNA, and misincorporation of FUTP interferes with RNA maturation.[8] Effective prodrugs of 5FU have also been synthesized which first require conversion to 5FU in the liver, or tumor, and can have a better therapeutic ratio. These prodrugs include capecitabine and the FPs, Flox (5-fluorouridine), Tegafur (tetrahydro-2-furanyl-5-fluorouracil), and Doxfluoridine (5-deoxy-5-fluorouridine)[9]; however, 5FU remains the FP of choice, predominantly for the treatment of breast, head and neck, and gastrointestinal tumors. Despite problems with toxicity, 5FU remains the only drug with significant activity against colorectal adenocarcinoma, which is a tumor frequently metastasizing to the liver. At least 50% of 5FU is catabolized in the liver, i.e. deactivated, with probably small contributions from some types of tumors (Figure 1).[10,11] The metabolism of 5FU can be modulated to increase cytotoxicity, e.g. by increasing Fnuct formation using methotrexate, interferon, or *N*-(phosphonacetyl)-L-aspartate (*N*-PALA), or by increasing binding of FdUMP to TS using leucovorin, or decreasing catabolism by coadministration of thymidine. Because of the relatively wide chemical shift range of ^{19}F MRS, many of the metabolites of 5FU can be resolved, especially in vitro, where pH-dependent differences in chemical shift can be exploited. It is this property, along with a relatively high sensitivity (~80% of ^{1}H), and the absence of a background signal, that makes ^{19}F MRS ideally suited to monitoring the pharmacokinetics of 5FU and other fluorine-containing drugs. That said, in models in vivo, and especially in the clinic, where fields of only 1.5 T are employed, the 5-fluoronucleosides (Fnucs) and Fnuct, and the fluorocatabolites (Fcat) of fluoro-β-ureidoproprionic acid (FUPA) and α-fluoro-β-alanine(FBal) are not easily distinguishable. Nevertheless, 5FU, Fcat, and often Fnuct, can be detected in both liver and tumor in vivo at doses near or equivalent to those in clinical use, and this has allowed real-time pharmacokinetics to be used, which in some cases can predict tumor response. Figure 2 shows these signals, in this case those observed in a rat mammary tumor following treatment with 5FU.

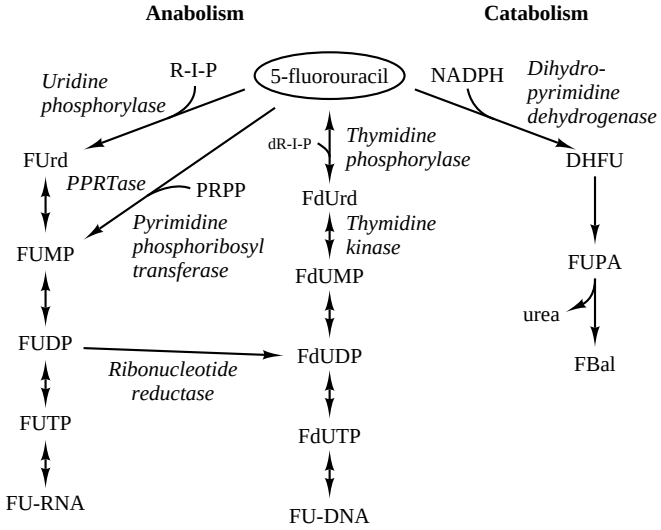

Figure 1 Anabolic and catabolic pathways of 5FU. DHFU, dihydrofluorouracil; FUPA, fluoro-β-ureidopropionic acid; FBal, α-fluoro-β-alanine; FUrd, 5-fluorouridine; FUMP, 5-fluorouridine monophosphate; FUDP, 5-fluorouridine diphosphate; FUTP, 5-fluorouridine triphosphate; FdUrd, 5-fluorodeoxyuridine; FdUMP, 5-fluorodeoxyuridine monophosphate; FdUDP, 5-fluorodeoxyuridine diphosphate; FdUTP, 5-fluorodeoxyuridine triphosphate; pyrimidine phosphoribosyl transferase

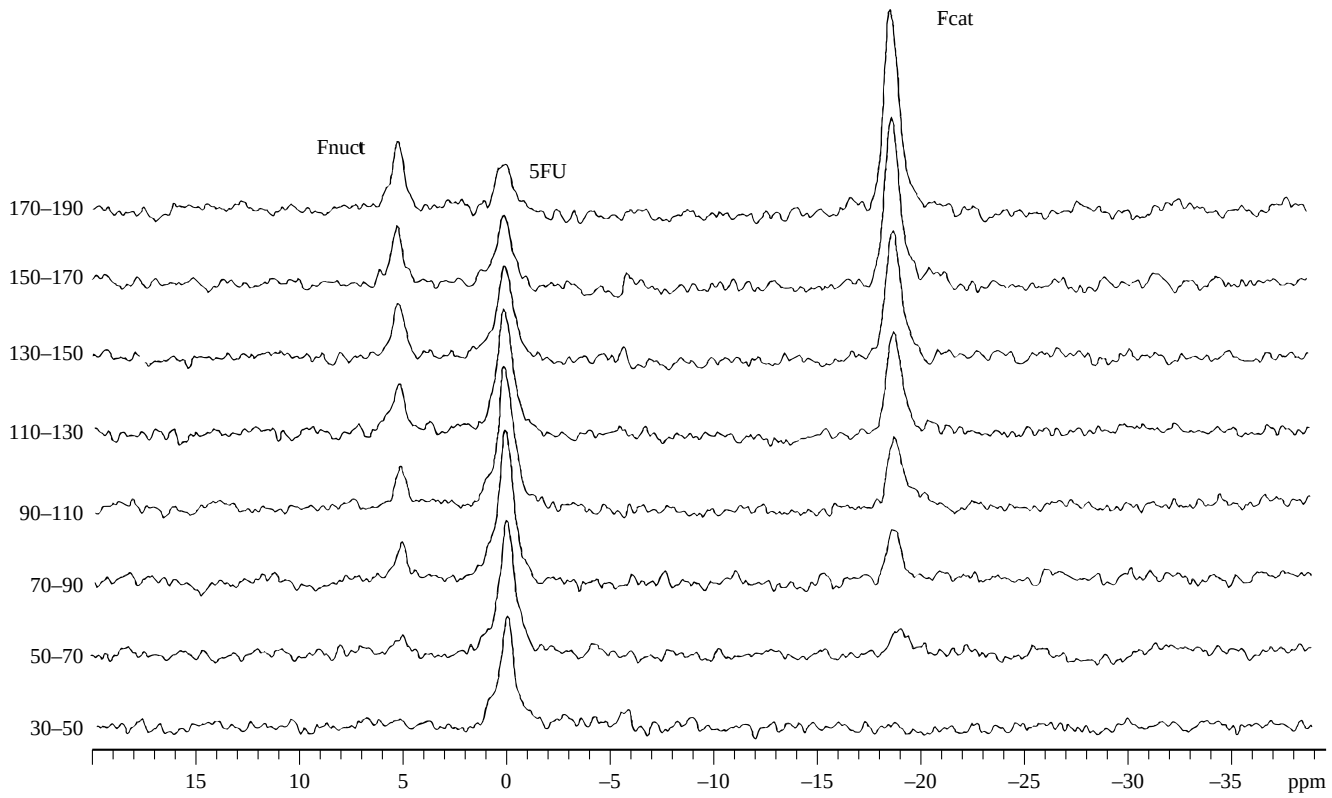

Figure 2 Fluorine-19 MRS spectra of 5FU metabolism by a chemically induced primary rat mammary tumor. Spectra (20 min blocks) were acquired at 4.7 T using a one-turn surface coil on a 5 g tumor following injection of 5FU (150 mg kg^{-1} intraperitoneally)

After the demonstration that ^{19}F MRS could detect 5FU and metabolites in vivo,[1] research was initiated to relate the amount of signal to tumor response. Decreasing doses of 5FU administered as an intravenous bolus (120, 50, and 25 mg kg^{-1}) to rats bearing the Walker carcinosarcoma led to decreased 5FU signal and Fnuct formed in the tumors. Tumors showed a significant response to the 50 mg kg^{-1} dose, but not to the 25 mg kg^{-1} dose.[12] Other studies[13,14] showed a significant correlation between shrinkage of mouse (RIF-1) tumors with the amount of Fnuct formed in the tumor. Furthermore, there was a negative correlation between Fcat in the mouse liver and Fnuct formed in the tumor, indicating liver deactivation and tumor activation of 5FU were competing processes. This latter observation was important for clinical studies, where the tumor signal-to-noise ratio (S/N) may be very low, but analysis of liver signals may still be of value for prognosis. However, in these animal studies the correlation between 5FU retention in the tumor and response to treatment was weaker or not significant.[13–15] Detection of increased Fnuct formation by ^{19}F NMS, signifying increased cytotoxicity, has also been recorded in ascites tumor cells.[16]

Modulation of 5FU metabolism by a range of substances, including allopurinol,[12] methotrexate,[17–20] interferon[20,21], *N*-PALA and leucovorin,[20] and thymidine,[21,22] has been observed in animal tumor models. In some cases this has been shown to lead to a change in the halflife ($t_{1/2}$) for 5FU clearance,[12,13,18,21,22] and, more significantly, to an increase in the rate[18,19] and final amount of Fnuct formed;[17–19,21,22] results that have also been confirmed in extracts.[12,18–21] In general, the biochemical basis for these modulations is fairly well established. Fluorine-19 MRS demonstrated this could be observed in situ, noninvasively, and in real time, providing additional data on the rate of elimination of 5FU from the tumor, which normally can only be obtained by biopsy, indirectly via blood or urine samples, or by sacrifice of many animals. Furthermore, in some cases, increased Fnuct formation was also correlated with tumor response.[19,22]

Besides biochemical modulation of 5FU metabolism, the tumor environment can be transiently altered to favor increased drug uptake, an approach with potentially important applications in the clinic where effective drug delivery to solid tumors can be a major problem. For example, breathing of carbogen gas by rodents can lead to increased tumor blood flow and oxygenation,[23,24,25] and in RIF-1 tumors this led to increased 5FU uptake and FNuct formation, with a corresponding increase in tumor growth inhibition.[14]

In the clinic, the SNR is lower, predominantly because of the lower field strengths employed: 1.5–2 T. This means that in contrast to the experimental tumors in animals, generally only the 5FU and Fcat signals are observed, and rarely the cytotoxic species Fnuct. However, results accumulating in the clinic have shown correlations between 5FU retention in the tumor and patient response, whether partial, or complete.[26–29] In three independent studies,[26–28] 5FU signals have been observed in 78–100% of responders, but in only 8–23% of nonresponders. Furthermore, there is clearly a slower clearance of 5FU from tumors ($t_{1/2}$ of 20–60 min) compared with blood (8–20 min). This phenonomon is known as 'tumor trapping', and its signifi-

cance is described below. Some studies on the modulation of 5FU metabolism have also begun in the clinic, and changes have been detected using methotrexate, leucovorin, and interferon.[6] Previously undetected, or more intense and prolonged, 5FU signals were observed, and, furthermore, when using combination chemotherapy, Fnuct signals were also detected. The clinical utility of this type of information would be the detection of nonresponders during the early phases of treatment, and the optimization of scheduling for others.

A number of preclinical studies have been performed to identify the mechanism(s) for the trapping of 5FU that is observed clinically. It is already clear that the tumor energy status is likely to play a major role, since a high-energy status (high NTP/Pi ratio) would enable a more effective activation of 5FU to FNuct and would be likely to reflect a well-vascularized tumor, making 5FU access to the tumor easier. In two multinuclear MRS studies,[15,30] there were significant correlations between the pretreatment tumor Pi, PCr, or NTP, the final amount of FNuct formed, and the response of the RIF-1[15] or primary rat[30] tumors to 5FU treatment. Consistent with these observations, treatment with hydralazine (a vasodilator that deenergizes tumors[31]) favored the conversion of FNuct to 5FU.[6] In contrast, in both the mouse[15] and rat model,[30] no significant correlation was observed between the pretreatment pH measured by MRS (i.e. intracellular pH, pH_i) and treatment response. However, in a rat fibrosarcoma model, a 2.5-fold increase in the 5FU $t_{1/2}$ (increased 5FU trapping) was observed when the pH_i was reduced by increased tumor glycolysis,[32] suggesting tumor pH could have a role in tumor retention of 5FU. What may be of significance is the low extracellular pH (pH_e) of solid tumors,[33] which in combination with a neutral pH_i leads to a reverse, or negative, pH gradient across the tumor plasma membrane (i.e. $-\Delta pH$).[34] One study using isolated tumor cells showed that 5FU uptake was increased when the $-\Delta pH$ was increased;[35] a similar relationship was observed in vivo.[21] An explanation of these apparently conflicting different studies is that in the rat fibrosarcoma model, the induced decrease in pH_i probably casued a larger decrease in pH_e,[35] thereby increasing the $-\Delta pH$. Consequently, it may be that pH_e and/or $-\Delta pH$ measurements in vivo will correlate with 5FU trapping. These observations on tumor pH and energy status provide a clear direction for further studies that could lead to protocols with a potentially improved therapuetic index for 5FU.

For chemotherapy, it is also beneficial to study the pharmacology of a drug in other tissues besides tumor. With respect to the FPs, this normally involves liver studies to determine the rate of drug detoxification and/or liver damage.[11,36,37] Measurement of the rate of drug disappearance in the liver, formation or destruction of 5FU, and the appearance of catabolites, with or without rescue schedules, have been performed. In principle, these studies may also relate to tumor cytotoxicity.[13] Similar studies have been performed clinically, the first in 1987 by Wolf et al.,[38] and most recently to provide parameters such as the maximal velocity of metabolic conversion, using only the proportional peak areas of the signals from 5FU and its metabolites.[39]

The relatively high doses of 5FU used (0.6–1 g m^{-2} d^{-1} over 5 days) can also lead to a number of adverse clinical reactions including myelosuppression, diarrhea, and mucositis. The cardiotoxicity of 5FU was first reported in 1975,[40] and incidences of about 8% have been reported.[41] Various hypotheses were proposed to explain the cardiotoxicity of this drug, including ischemia secondary to coronary artery spasms, interaction of 5FU with the coagulation system, immunoallergic phenomena, and direct toxicity of 5FU on the myocardium.[42] The precise biochemical mechanism underlying this cardiotoxicity was unclear. It has been suggested that the major catabolite of 5FU, Fbal, might be transformed into fluoroacetate (FAC), a highly cardiotoxic and neurotoxic poison.[43] Fluorine-19 MRS demonstrated, using an isolated perfused rat liver model, that although Fbal is indeed metabolized into FAC, commercial solutions of 5FU also contain 'impurities'. Degradation compounds are gradually formed in the basic medium, which is indispensable to the solubilization of 5FU. Two cardiotoxic compounds were identified: fluoroacetaldehyde, and fluorosemialdehyde malonic acid, the former being metabolized into FAC, a violent cardiotoxic compound.[44,45]

3 OTHER FLUORINATED COMPOUNDS

Apart from the FP work described that has led directly to similar clinical studies, ^{19}F MRS has been applied to other fluorinated compounds as a research tool to investigate tumor hypoxia and pH and the pharmacokinetics of drugs in development.

The useful clinical activity of 5FU as a TS inhibitor encouraged the development of other TS inhibitors, such as the antifolate CB 3717. This drug had clinical anticancer activity against breast and hepatoma, but dose-limiting nephrotoxicity. Animal studies revealed renal and hepatic toxicity that was partly due to long-term retention of the drug. A fluorinated version of the drug, CB 3988, was synthesized to determine tissue distribution and concentration by NMR. Pharmacokinetics were studied in vivo in the mouse and rat using both surface and solenoid coils for fluorine imaging and spectroscopy.[46] These studies demonstrated, noninvasively, both hepatic and renal clearance and, ultimately, localization of the drug to the abdominal cavity. The $t_{1/2}$ values determined were similar to those measured by high-performance liquid chromatography of body fluids. Recently, another fluorinated TS inhibitor, ZD9331, has been developed and is currently in phase II/III clinical trials. Attempts to study a fluorinated alkylating agent, β,β-difluorochlorambucil, were limited because of binding of the drug to proteins in blood plasma and tumors and excessive toxicity.[47] A difluorinated nucleoside analog, gemcitabine, developed in the 1980s is now showing considerable success in the clinic against a range of solid tumors. The high doses that are used (approximately 1.5 g m^{-2}) have permitted ^{19}F-imaging in rat tumors;[48] ^{19}F MRS showed increased uptake in gemcitabine-sensitive murine human xenografts compared with less sensitive xenografts.[49]

The energy state of a tumor is critical in determining chemo- and radiosensitivity, and a major regulator of this is the blood flow to the tumor. A number of methods have been applied to measure directly or indirectly tumor hypoxia, or blood supply. A number of studies have been performed using ^{19}F-labeled nitromidazoles, such as fluoromisonidazole, Ro-070741,[47] and SR-4554.[50] These are bioreductive agents that in hypoxic conditions undergo nitroreduction to reactive intermediates such as hydroxylamines, which bind to

macromolecules. Selective retention was seen in tumor compared with normal tissue, and increased retention was seen in mouse tumors that were known to have a greater hypoxic fraction.[14,47,50] Perfluorocarbons (PFCs) are fluorinated organic molecules which provide a high S/N for ^{19}F MRS studies. The ^{19}F spin–lattice relaxation rates of the PFC resonances are sensitive to the oxygen tension (PO_2), and this has been exploited to measure tumor oxygenation. The principle has been reviewed,[4] and new methods,[51] and PFC types,[25,52] including one with 12 equivalent fluorine atoms,[53] are continually developed. One group has used a PFC to demonstrate potential chemotherapeutic applications.[24,54] A PFC emulsion was injected intraperitoneally, and 3 days later ^{19}F MRS was performed prior to and immediately following administration of the radiosensitizer nicotinamide. Highly significant increases in PO_2 were recorded in the mouse RIF-1 tumor with the maximum effect at 60–70 min posttreatment.[54]

Tumor pH is another important determinant of chemotherapeutic response, as described for 5FU. Although in vivo pH is generally measured by ^{31}P MRS, a number of specific fluorinated probes have been developed by Deutsch and colleagues to measure intracellular pH.[55,56] While these studies provided useful information on cell function, there is some doubt about their applicability to studying tumors in vivo; other probes, while confirming ^{31}P measurements of pH, have suffered from poor solubility.[57] The Fnuct formed from FPs is an unequivocal intracellular pH marker,[12,15] although the S/N is generally low, and the composite nature of the peak (many Fnucs each with a slightly different pK_a) precludes absolute pH measurements. Nevertheless, dynamic 5FU-induced increases in tumor pH_i were recorded using FNuct in RIF-1 tumors.[14] Recently, new pH probes have been described that are sufficiently soluble and sensitive to allow studies in vivo.[58,59] One, ZK 150471, is a difluorinated extracellular probe that has been shown to give comparable measurements of tumor pH_e when compared with a ^{31}P-pH probe.[60] The other, F6POL, is a monofluorinated probe that has been shown to measure both pH_i and pH_e in perfused rat heart[59] and may permit measurements in situ of tumors.

Finally, the fluorinated 2-deoxyglucose analog 2-fluoro-2-deoxyglucose (FDG) has been used to study glucose uptake in ascites tumors.[61,62] Contrary to dogma, FDG metabolism does not cease with phosphorylation to FDG 6-phosphate. By ^{19}F MRS, it has been shown that FDG 6-phosphate may be epimerized to the mannose 6-phosphate derivative; this undergoes further conversions by ascites cells as well as in brain, heart, and muscle to a number of FDG metabolites.[62] Significantly, one of these metabolites, NDP-FDM, persists for 24–48 h in ascites cells at sufficiently high concentrations to permit ^{19}F imaging, allowing the possibility of using ^{19}F imaging of FDG metabolites for the detection of tumors in the body.

4 SUMMARY

The high sensitivity of fluorine, absence of a background signal, and wide chemical shift range make the fluorine atom ideal for noninvasive measurements of drug pharmacokinetics. In some cases the fluorine is already an integral part of the drug, which allows direct applications of animal models to the clinic, with the increasingly realizable potential of optimizing drug schedules. Other fluorinated compounds can be used as probes of tumor glycolysis, pH, and hypoxia, which are important determinants of chemo- and radiosensitivity.

5 RELATED ARTICLES

Brain Neoplasms in Humans Studied by Phosphorus-31 NMR Spectroscopy; In Vivo Hepatic MRS of Humans; Localization and Registration Issues Important for Serial MRS Studies of Focal Brain Lesions; Spectroscopic Studies of Animal Tumor Models.

6 REFERENCES

1. A. N. Stevens, P. G. Morris, R. A. Iles, P. W. Sheldon, and J. R. Griffiths, *Br. J. Cancer*, 1984, **50**, 113.
2. P. M. J. McSheehy and J. R. Griffiths, *NMR Biomed.*, 1989, **2**, 133.
3. M. C. Malet-Martino, R. Martino, and J. P. Armand, *Bull. Cancer Paris*, 1990, **77**, 1223.
4. M. J. W. Prior, R. J. Maxwell, and J. R. Griffiths, in 'NMR Basic Principles and Progress', ed. Springer-Verlag, Berlin, 1992, Vol. 28, Chap. 3
5. R. J. Maxwell, *Cancer Surv.*, 1993, **17**, 415.
6. M. P. N. Findlay and M. O. Leach, *Anticancer Drugs*, 1994, **5**, 260.
7. C. Heidelberger, P. V. Danenberg, and R. G. Moran, *Adv. Enzymol.*, 1983, **54**, 57.
8. H. M. Pinedo, and G. F. J. Peters, *J. Clin. Oncol.*, 1988, **6**, 1653.
9. Y. O. Rustum, A. Harstrick, S. Cao, U. Vanhoefer, M.-B. Yin, H. Wilke, and S. Seeber, *J. Clin. Oncol.*, 1997, **15**, 389.
10. F. N. M. Naguib, M. H. el Kouni, and S. Cha, *Cancer Res.*, 1985, **45**, 5405.
11. M. J. W. Prior, R. J. Maxwell, and J. R. Griffiths, *Biochem. Pharm.*, 1990, **39**, 857.
12. P. M. J. McSheehy, M. J. W. Prior, and J. R. Griffiths, *Br. J. Cancer*, 1989, **60**, 303.
13. P. E. Sijens, Y. Huang, N. J. Baldwin, and T. C. Ng, *Cancer Res.*, 1991, **51**, 1384.
14. P. M. J. McSheehy, S. P. Robinson, A. S. E. Ojugo, E. O. Aboagye, M. B. Cannell, M. O. Leach, I. R. Judson, and J. R. Griffiths, *Cancer Res.*, 1998, **58**, 1185.
15. P. E. Sijens, N. J. Baldwin, and T. C. Ng, *Magn. Reson. Med.*, 1991, **19**, 373.
16. P. M. J. McSheehy, R. J. Maxwell, and J. R. Griffiths, *NMR Biomed.*, 1991, **4**, 274.
17. J. A. Koutcher, R. C. Sawyer, A. B. Kornblith, R. L. Stolfi, D. S. Martin, M. L. Devitt, D. Cowburn, and C. W. Young, *Magn. Reson. Med.*, 1991, **19**, 113.
18. A. El-Tahtawy and W. Wolf, *Cancer Res.*, 1991, **51**, 5806.
19. P. M. J. McSheehy, M. J. W. Prior, and J. R. Griffiths, *Br. J. Cancer*, 1992, **65**, 309.
20. Y. J. L. Kamm, I. M. C. M. Rietjens, J. Vervoort, A. Heerachap, G. Rosenbusch, H. Hofs, and D. J. T. Wagner, *Cancer Res.*, 1994, **54**, 4321.
21. P. M. J. McSheehy, M. T. Seymour, A. S. E. Ojugo, L. M. Rodrigues, M. O. Leach, I. R. Judson, and J. R. Griffiths, *Eur. J. Cancer*, 1997, **33**, 2418.
22. P. E. Sijens and T. C. Ng, *Magn. Reson. Imaging*, 1992, **10**, 385.
23. S. P. Robinson, L. M. Rodrigues, A. S. E. Ojugo, P. M. J. McSheehy, F. A. Howe, and J. R. Griffiths, *Br. J. Cancer*, 1997, **75**, 1000.
24. K. G. Helmer, S. Han, and C. H. Sotak, *NMR Biomed.*, 1998, **11**, 120.

25. S. Hunjan, R. P. Mason, A. Constantinescu, P. Peschke, E. W. Hahn, and P. P. Antich, *Int. J. Radiat. Oncol. Biol. Phys.*, 1998, **41**, 161.
26. C. A. Presant, W. Wolf, M. J. Albright, K. L. Servis, R. Ring, D. Atkinson, R. L. Ong, C. Wiseman, M. King, D. Blayney, P. Kennedy, A. El-Tahtawy, M. Singh, and J. Shani, *J. Clin. Oncol.*, 1990, **8**, 1868.
27. M. P. N. Findlay, M. O. Leach, D. Cunningham, D. J. Collins, G. S. Payne, J. Glaholm, J. L. Mansi, and V. R. McCready, *Ann. Oncol.*, 1993, **4**, 597.
28. C. A. Presant, W. Wolf, V. Waluch, C. Wiseman, P. Kennedy, D. Blayney, and R. R. Brechner, *The Lancet*, 1994, **343**, 1184.
29. H.-P. Schlemmer, P. Bachert, W. Semmler, P. Hohenberger, P. Schlag, W. J. Lorenz, and G. Van Kaick, *Magn. Reson. Imaging*, 1994, **12**, 497.
30. L. P. Lemaire, P. M. J. McSheehy, and J. R. Griffiths, *Cancer Chemother. Pharmacol.*, 1998, **42**, 201.
31. G. M. Tozer, R. J. Maxwell, J. R. Griffiths, and P. Pham, *Br. J. Cancer*, 1990, **62**, 553.
32. J.-L. Guerquin-Kern, F. Leteurtre, A. Croisy, and J.-M. Lhoste, *Cancer Res.*, 1991, **51**, 5770.
33. J. R. Griffiths, *Br. J. Cancer*, 1991, **64**, 425.
34. M. Stubbs, L. M. Rodrigues, F. A. Howe, J. Wang, K. S. Jeong, R. L. Veech, and J. R. Griffiths, *Cancer Res.*, 1994, **54**, 4011.
35. A. S. E. Ojugo, P. M. J. McSheehy, M. Stubbs, G. Alder, R. J. Maxwell, C. L. Bashford, M. O. Leach, I. R. Judson, and J. R. Griffiths, *Br. J. Cancer*, 1998, **77**, 873.
36. M. Harada, K. Koga, I. Miura, and H. Nishitani, *Magn. Reson. Med.*, 1991, **22**, 499.
37. Y. Kanazawa, S. Kuragi, S. Shinahara, Y. Noda, and K. Masuda, *Chem. Pharm. Bull.*, 1994, **42**, 774.
38. W. Wolf, M. J. Albright, M. S. Silver, H. Weber, U. Reichardt, and R. Sauer, *Magn. Reson. Imaging*, 1987, **5**, 165.
39. R. E. Port, H.-P. Schlemmer, and P. Bachert, *Eur. J. Clin. Pharmacol.*, 1994, **47**, 187.
40. R. G. Dent and I. McColl, *The Lancet*, 1975, **1**, 347.
41. W. J. Gradishar and E. E. Vokes, *Ann. Oncol.*, 1990, **1**, 409.
42. N. J. Freeman and M. E. Costanza, *Cancer*, 1988, **61**, 36.
43. I. Matsubara, J. Kamiya, and S. Imai, *Jpn. J. Pharmacol.*, 1980, **30**, 871.
44. L. Lemaire, M. C. Malet-Martino, M. de Forni, R. Martino, and B. Lasserre, *Br. J. Cancer*, 1992, **66**, 119.
45. L. Lemaire, M. C. Malet-Martino, M. de Forni, R. Martino, and B. Lasserre, *Oncol. Rep.*, 1994, **1**, 173.
46. D. R. Newell, R. J. Maxwell, and B. T. Golding, *NMR Biomed.*, 1992, **5**, 273.
47. P. Workman, R. J. Maxwell, and J. R. Griffiths, *NMR Biomed.*, 1992, **5**, 270.
48. M. E. Belleman, G. Brix, U. Haberkorn, J. Blatter, L. Gerlach, F. Oberdorfer, and W. J. Lorenz, *Proc. 3rd Ann Mtg. Int. Soc. Magn. Reson. Med.*, Nice, 1995, **3**, 1685.
49. P. E. G. Kristjansen, B. Quistorff, M. Spang-Thomsen, and H. H. Hansen, *Ann. Oncol.*, 1993, **4**, 157.
50. E. O. Aboagye, R. J. Maxwell, A. D. Lewis, P. Workman, M. Tracey, and J. R. Griffiths, *Br. J. Cancer*, 1998, **77**, 65.
51. R. P. Mason, H. Shukla, and P. P. Antich, *Magn. Reson. Med.*, 1993, **29**, 296.
52. B. J. Dardzinski and C. H. Sotak, *Magn. Reson. Med.*, 1994, **32**, 88.
53. C. H. Sotak, P. S. Hees, H. N. Huang, M. H. Hung, C. G. Krespan, and S. Raynolds, *Magn. Reson. Med.*, 1993, **29**, 188.
54. P. S. Hees and C. H. Sotak, *Magn. Reson. Med.*, 1993, **29**, 303.
55. C. J. Deutsch and J. S. Taylor, *Biophys. J.*, 1989, **55**, 799.
56. M. Bental and C. J. Deutsch, *Am. J. Physiol.*, 1994, **266**, C541.
57. J. S. Beech and R. A. Iles, *Magn. Reson. Med.*, 1991, **19**, 386.
58. T. Frenzel, S. Kossler, H. Bauer, U. Niedballa, and H. J. Wienmann, *Invest. Radiol.*, 1994, **29**, S220.
59. S. Hunjan, R. P. Mason, V. D. Mehta, V. Padmakar, P. V. Kulkarni, V. Arora, and P. P. Antich, *Mag. Res. Med.*, 1998, **39**, 551.
60. A. S. E. Ojugo, P. M. J. McSheehy, D. J. O. McIntyre, C. McCoy, M. Stubbs, M. O. Leach, I. R. Judson, and J. R. Griffiths, *NMR Biomed.*, 1999, **12**, 000.
61. M. Kojima, S. Kuribayashi, Y. Kanazawa, T. Hardahira, Y. Maehara, and H. Endo, *Chem. Pharm. Bull.*, 1988, **36**, 1194.
62. Y. Kanazawa, K. Umayahara, T. Shimmura, and T. Yamashita, *NMR Biomed.*, 1997, **10**, 35.

Biographical Sketches

Paul M. J. McSheehy. *b* 1959. B.Sc.(Hons), 1980, Biochemistry, University of Sussex, Ph.D., 1984, Biochemistry, University of London, UK. Introduced to in vivo MRI by Professor J. R. Griffiths in 1986. Bone endocrinologist, currently Research Fellow at St. George's Hospital Medical School UK, studying the action mechanisms, and pharmacokinetics of chemotherapeutic drugs.

Laurent P. Lemaire. *b* 1968. B.S. 1989, Biochemistry–Biophysics, Ph.D., 1993, Pharmacology, University of Toulouse, France. Introduced to NMR by P. Cozzone in 1989. Current research speciality: metabolism of anticancer drugs by NMR.

John R. Griffiths. *b* 1945. M.B. B.S., 1969, London, D. Phil., 1974, Biochemistry, Oxford, Studied ESR with George Radda, 1970–74 and (with David Gadian and Richard Isles) ^{31}P MRS of livers, 1979–80. Approx. 100 publications. Including (with E. R. Andrews et al.,) 'Clinical Magnetic Resonance: Imaging and Spectroscopy', publ. Wiley, Chichester, 1990. Since 1980 research interests have been in MRS as applied to cancer, latterly also MRI of nerves.

Brain Neoplasms in Humans Studied by Phosphorus-31 NMR Spectroscopy

Wolfhard Semmler

Institut für Diagnostikforschung (IDF) an der Freien Universität, D-14050 Berlin, Germany

and

Peter Bachert

Forschungsschwerpunkt Radiologische Diagnostik und Therapie, Deutsches Krebsforschungszentrum (DKFZ), D-69120 Heidelberg, Germany

1 INTRODUCTION

1.1 Value of ^{31}P NMR Spectroscopy for Studies of the Human Brain

In vivo ^{31}P NMR spectroscopy in humans was first applied in studies of muscle diseases and soft tissue tumors. Subsequently, metabolic, ischemic, and neoplastic disorders of the human brain have been studied by means of this technique. In vivo ^{31}P NMR spectroscopy offers a window to study high-energy phosphate and membrane phospholipid turnover in human neurometabolism. It also permits the noninvasive measurement of the intracellular pH in the tissue.

1.2 Problems of Tumor Diagnosis

The major diagnostic problems in oncology are: (i) early tumor detection, (ii) tumor grading, and (iii) tumor staging. After diagnosis of a malignant tumorous disease and selection of an adequate therapy, monitoring is important for the optimization of the treatment and for the prediction of the response to treatment.

The value of ^{31}P NMR spectroscopy for solving these clinical problems is not yet established, although animal experiments could clearly demonstrate the high potential of this noninvasive technique for monitoring tumor biochemistry and the response of tumors to radiation therapy and chemotherapy.[1–6]

1.3 Heterogeneity of Neoplastic Tissue

Tumor tissue is heterogeneous on both macroscopic and microscopic scales. Vital and hypoxic tissue as well as necrotic cell masses and hemorrhage may coexist in tumors, reflecting regional differences in oxygen supply, vascularization, and nutrition of the cells.[1,5] Because of the poor spatial resolution, ^{31}P NMR spectroscopy can provide only an overall picture of the metabolic state of the tumor, being completely insensitive to tissue heterogeneity below the centimeter range.

This is a particular problem when high-grade gliomas are examined in vivo by ^{31}P NMR spectroscopy. Histopathological studies show heterogeneities in these tumors, but often they are also heterogeneous macroscopically as can be detected by MR imaging. ^{31}P NMR spectra will therefore comprise different signal contributions from vital, hypoxic, and necrotic tissue within the selected voxel rather than give a metabolic fingerprint of this tumor entity. The problem is less serious in the case of the relatively homogeneous meningioma and pituitary adenoma. In any case, however, MR imaging is mandatory before each NMR spectroscopic examination in order to detect gross inhomogeneities within the tumor mass.

1.4 NMR Spectroscopic Techniques

Adequate performance of the method requires the acquisition of localized NMR spectra with high signal-to-noise ratio (SNR) and high frequency resolution. A variety of localization techniques has been developed for ^{31}P NMR spectroscopy in humans. Localization means that NMR signals are obtained from a volume of interest (VOI) in the examined organ, while signal contributions of regions outside the VOI are suppressed. Single-voxel localization methods, e.g. ISIS,[7] and STEAM,[8] are available that employ selective rf pulses in the presence of orthogonal magnetic field gradients. A frequently used localization technique for in vivo ^{31}P NMR spectroscopy studies of the human brain is chemical shift imaging (CSI), also called spectroscopic or metabolic imaging, which employs phase-encoding gradients in two or three spatial directions to generate a 2D or 3D array of localized spectra in one measurement process.[9–14] These techniques permit the selective acquisition of ^{31}P NMR signals from regions with volumes >30 cm^3 within the human brain.

Frequency resolution and SNR of ^{31}P NMR spectra can be improved significantly using ^{31}P-{^{1}H} double resonance. By this means multiplet splittings resulting from scalar ^{31}P–^{1}H spin–spin couplings are removed (proton-decoupling[15]) and ^{31}P NMR signal intensities are enhanced owing to dipolar relaxation of phosphorus nuclei interacting with close protons (^{31}P–{^{1}H} NOE[16,17]).

Luyten and co-workers obtained localized (ISIS with 200 cm^3 voxel) proton-decoupled ^{31}P–{^{1}H} NMR spectra with resolved phosphomonoester (PME) and phosphodiester (PDE) resonance bands from the human brain.[18] The 2D ^{31}P CSI combined with ^{1}H irradiation to induce NOE signal enhancements yields in vivo brain spectra of good quality from 8×8 voxels with 3 cm × 3 cm × 4 cm volume each in a measurement time of 19 min.[19]

In general, comparison of in vivo NMR spectra without quantitative analysis is of limited value. Quantification must include the fit of the signals in the time or frequency domain to obtain chemical shifts, line widths, and a measure of signal intensity. Determination of absolute metabolite concentrations in tissue from in vivo ^{31}P NMR data would be of great value. However, this is a complicated problem and, therefore, ratios of integrated peak areas are often used for data analysis.

2 ASSESSMENT OF NEOPLASTIC BRAIN DISEASE WITH THE USE OF ^{31}P NMR SPECTROSCOPY

2.1 Detection and Differentiation of Brain Tumors

Tumor diagnosis was one of the primary issues to which ^{31}P NMR spectroscopy has been directed. The central diagnostic problem is the detection, localization, and differentiation of a tumor in its *early* stage when the neoplastic tissue mass is still very small. Because of its poor spatial resolution, ^{31}P NMR can hardly contribute to the solution of this problem. To our knowledge there is no case reported which clearly demonstrates the value of ^{31}P NMR spectroscopy for early cancer detection and where this modality was indispensable for clinical decisions.

On the other hand, the potential of ^{31}P NMR spectroscopy for tumor grading[19] is believed to be high, because changes of signal intensities and linewidths of the various resonances, and of the inorganic phosphate (Pi) chemical shift (a measure of intracellular pH) are observed in tumor spectra in comparison to spectra from normal brain tissue. These effects reflect metabolic differences of tumor and surrounding unaffected tissue as well as physiological conditions related to tumor oxygenation, perfusion, microcirculation, and angiogenic activity.[1,5,20,21]

Spectral differences are also expected when human brain tumors are examined at different growth stages. Animal experiments show strong changes of ^{31}P NMR spectra during growth (Figure 1). A progressive decrease of high-energy phosphate levels is attributed to an increase of the fraction of hypoxic cells,[22] while an increase of PME and P_i intensities may result from the emergence of necrotic cells.[1] The frequently observed alkalinic shift of pH in tumor tissue[20] is explained by necrosis.[5]

For tumor characterization, the presence of an NMR-visible compound unique to a specific type of tumor cells or tumor species would be highly important. In fact, no tumor-specific resonance has been found in in vivo ^{31}P NMR spectra of all tumors studied so far. Neuroepithelial and mesodermal tumors and cerebral metastases, for example, show the same resonances as spectra obtained from healthy brain tissue.[23–25]

The ^{31}P NMR spectrum of a glioblastoma, a neuroepithelial tumor, shows a reduction of PME, Pi, PDE, and PCr relative to nucleoside 5′-triphosphate (NTP) signals [Figure 2(c)]. Heiss et al. found a similar spectral pattern in their ^{31}P NMR study of glioblastomas except for a cystic glioblastoma which produced only poor spectral SNR.[23] In contrast, Arnold et al. observed enhanced PME and barely reduced PDE levels in glioblastomas[23,26] (Figure 3(e)). Resonance intensities from high- and low-grade astrocytomas, which were also examined in this study, did not differ significantly. In pituitary adenomas, reduced PDE and exceedingly high PME signals were found (Figure 3(b)). Segebarth et al. observed elevated PME and reduced PCr intensities in the ^{31}P NMR spectrum of a prolactinoma[27] (Figure 4(a)) in comparison to the spectrum from the unaffected brain region of the same patient (Figure 4(b)). Hwang et al. found reduced PDE/NTP and PCr/NTP signal intensity ratios and elevated pH values in high-grade gliomas and in a meningioma.[28] Similar findings were reported from other studies.[29,30] The localized in vivo ^{31}P NMR spectra in Figure 2 show increased PME and decreased PDE and PCr signal intensities for the meningioma (Figure 2(b)),[24] a mesodermal tumor that originates from meningial tissue, compared with the spectrum from healthy brain tissue (Figure 2(a)).

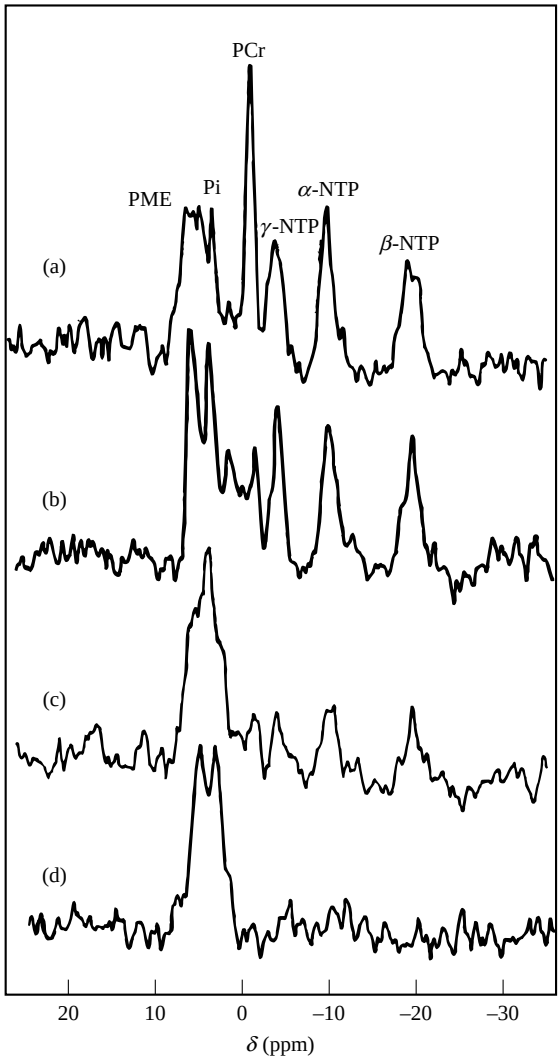

Figure 1 Metabolic changes during tumor growth reflected in in vivo ^{31}P NMR spectra, showing progressive decline of high-energy phosphate signals (NTP, nucleoside 5′-triphosphate, mainly ATP, adenosine 5′-triphosphate; PCr, phosphocreatine) and an increase of inorganic phosphate (Pi) signals. The concentration of phosphomonoesters (PME), which are attributed to precursors of major membrane phospholipids, is elevated. (a) Base line spectrum and subsequent spectra recorded at (b) day 3, (c) day 7, and (d) day 11. The pH value of the tumor tissue dropped from 7.1 for (a) to 6.6 for (c). Experimental tumor: subcutaneously implanted MOPC 104E myeloma (modified from Evanochko et al.[2])

Negendank reviewed in vivo NMR data of human tumors.[31] His evaluation shows that about 80% of all examined high-grade glioma (Kernohan III–IV) showed reduced PDE and about 50% reduced PCr signal intensities. In 96% of all examined meningioma, low PDE and low PCr signals were observed. Intracellular pH values were higher in high-grade glioma and meningioma than in normal brain tissue.

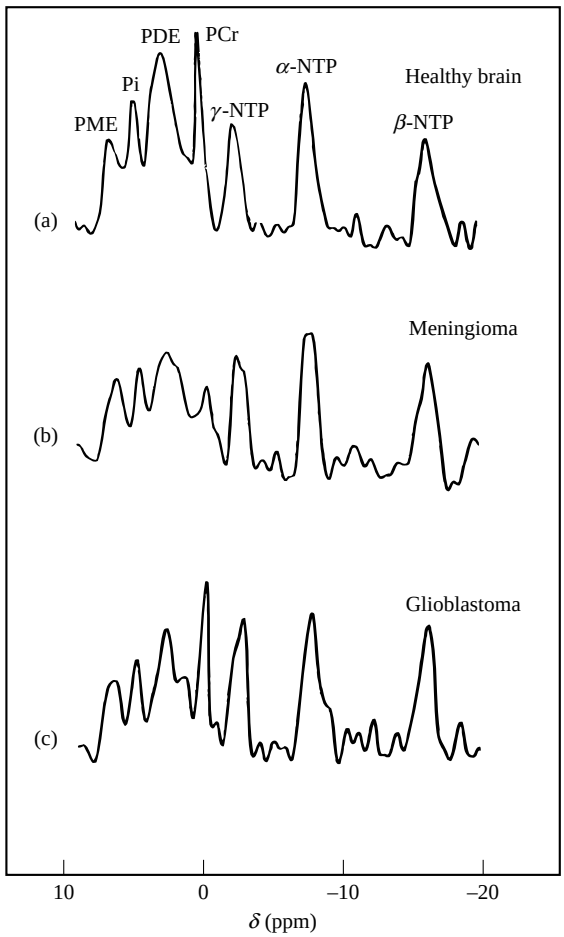

Figure 2 Localized ^{31}P NMR spectra of (a) healthy human brain tissue, (b) meningioma, and (c) glioblastoma obtained with the ISIS localization technique (modified from Heindel et al.[24])

Benign pituitary adenomas showed reduced PDE levels in 75% and high PME and low PCr levels in all patients examined.[31] In all cases the observed pH was comparable to the value measured in normal brain tissue. Low PDE/NTP signal intensity ratios and elevated pH values were found in ependymoma.

In vivo ^{31}P NMR spectra from neuroepithelial tumors (glioma) and mesodermal tumors (meningioma) are similar, so this technique does not allow the differentiation between these two entities. On the other hand, the pH, which was found in the normal range for low-grade and elevated in high-grade glial tumors, may help to grade gliomas. However, discrepant pH values have also been reported.[23,25] High pH values in post-therapy stages of soft tissue sarcomas were found to be related to necrosis.[5,32]

In a recent study, Rutter et al. employed 1D ^{31}P CSI in vivo and detected statistically significant differences in NMR parameters of brain hemispheres of patients with untreated brain tumors (astrocytomas, glioblastomas, meningiomas).[33] PME/NTP and PDE/NTP signal intensity ratios were higher in glioblastomas and astrocytomas than in healthy brain tissue. The P_i/NTP and PCr/NTP ratios of astrocytomas were higher compared with glioblastomas and normal brain.

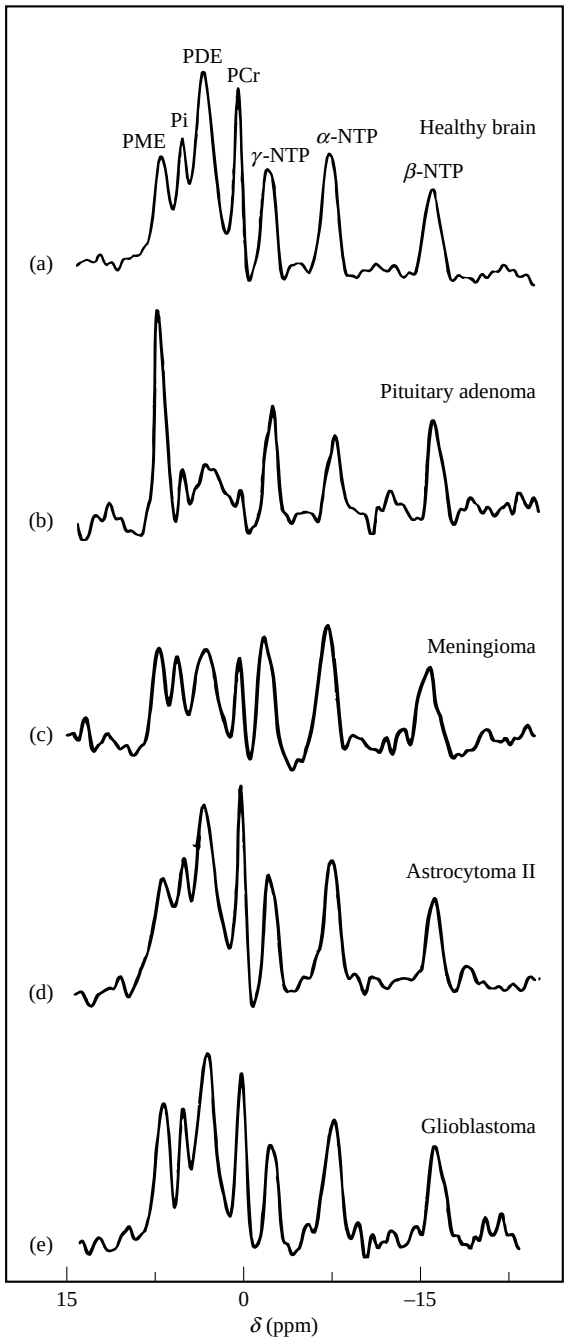

Figure 3 Localized ^{31}P NMR spectra in vivo of (a) normal human brain tissue and different tumors of the brain: (b) pituitary adenoma, (c) meningioma, (d) grade II astrocytoma, and (e) glioblastoma. Spectra were obtained by means of the ISIS localization technique with voxel sizes of 41–220 cm^3 (modified from Arnold et al.[26])

2.2 Therapy Monitoring of Brain Tumors by Means of ^{31}P NMR

Studies of experimental tumors in animals by means of in vivo ^{31}P NMR spectroscopy showed significant changes of levels of phosphorus-containing metabolites during the course

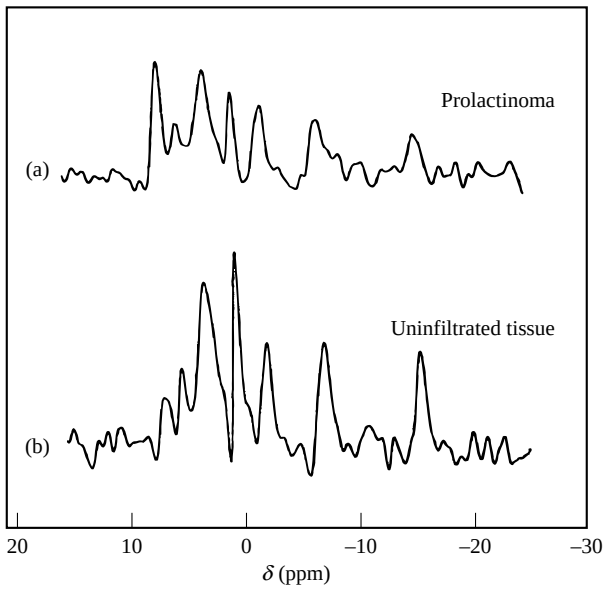

Figure 4 Localized ^{31}P NMR spectra in vivo of (a) a prolactinoma and (b) the unaffected brain tissue in the same patient (modified from Segebarth et al.[27])

of radiation therapy and chemotherapy.[2,3] A common feature is the decrease of high-energy phosphate signals (PCr, NTP) and of pH and the increase of Pi, PME, and PDE resonances; however, the opposite effects have also been observed.[2,3,6] A strong increase in the Pi resonance is often accompanied by a collapse of high-energy phosphate signals, as demonstrated in animal studies (Figure 5). This effect has also been observed in a clinical study monitoring the hyperthermic regional perfusion therapy of the recurrence of a malignant melanoma.[34]

The majority of studies on therapy monitoring by means of in vivo ^{31}P NMR spectroscopy have been performed in soft tissue tumors[32,34–41] (for reviews, see Steen[21] and Negendank[31]). Only a few studies focused on monitoring treatment of brain tumors, among them monitoring of radiation therapy and/or chemotherapy,[23,24,26,27,29,42] immunotherapy,[43] and embolization.[18]

One of the first reports in this field was published in 1987 by Segebarth et al.[27] Figure 6 shows the ^{31}P NMR spectra obtained in a patient with invasive prolactinoma before and one and five weeks after pharmacotherapy with bromocriptine [the same patient as in Figure 4(a)]. Upon therapy the patient improved clinically while no morphological changes of the tumor were found by MR imaging. After five weeks, a small decrease of the NTP level was detected, but no pH change. Elevated pH values were observed in the tumor tissue before and one and five weeks after therapy when compared with the pH of the unaffected brain tissue.

More pronounced ^{31}P spectral effects were found after two weeks of radiation therapy in a patient with an intracranial lymphoma. The enhanced PME and the reduced PCr resonances before treatment changed to the intensities of normal tissue after a radiation dose of 24.2 Gy (Figure 7). The pH of the tumor tissue did not change. The patient improved clinically during therapy. Similar results were obtained in the examination of a patient with a grade II astrocytoma treated with radiation therapy of 60 Gy total dose after subtotal surgical removal of the tumor.

In their ^{31}P NMR follow-up study of tumor radiation therapy, Heindel et al. examined patients with meningiomas, glioblastomas, astrocytomas, and other cerebral tumors.[24] NMR signal intensity changes similar to those in Figure 7, in particular a PME signal reduction, were observed in the spectra of grade II astrocytoma upon radiation therapy (Figure 8).

Arnold et al. examined four patients with malignant gliomas after intraarterial (Figure 9) and three patients after intravenous 1,3-bis(2-chloroethyl)-1-nitrosourea (BCNU) therapy.[44,45] They found statistically significant differences of pH values upon evaluation of ^{31}P NMR spectra acquired before and after chemotherapy: i.v. application of BCNU resulted in a transient acidosis and i.a. administration of the same drug in an alkalosis in the tumor tissue. These pH changes were detected before

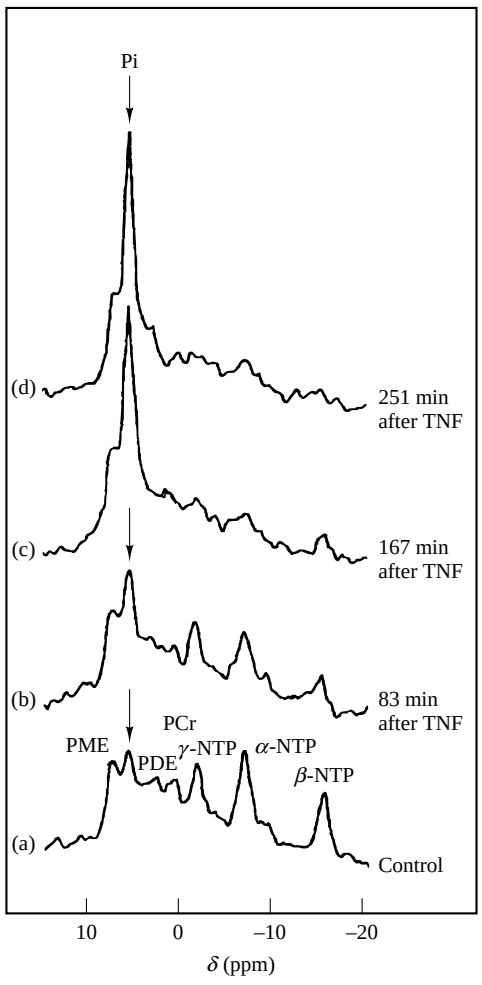

Figure 5 Changes of in vivo ^{31}P NMR spectra of an experimental tumor (murine methylcholanthrene-induced [Meth-A] sarcoma) upon application of recombinant human tumor necrosis factor α (rHuTNF-α). The series of spectra shows a progressive decline of high-energy phosphate signals (NTP, PCr) and a strong increase in the inorganic phosphate (Pi) level (modified from Shine et al.[6])

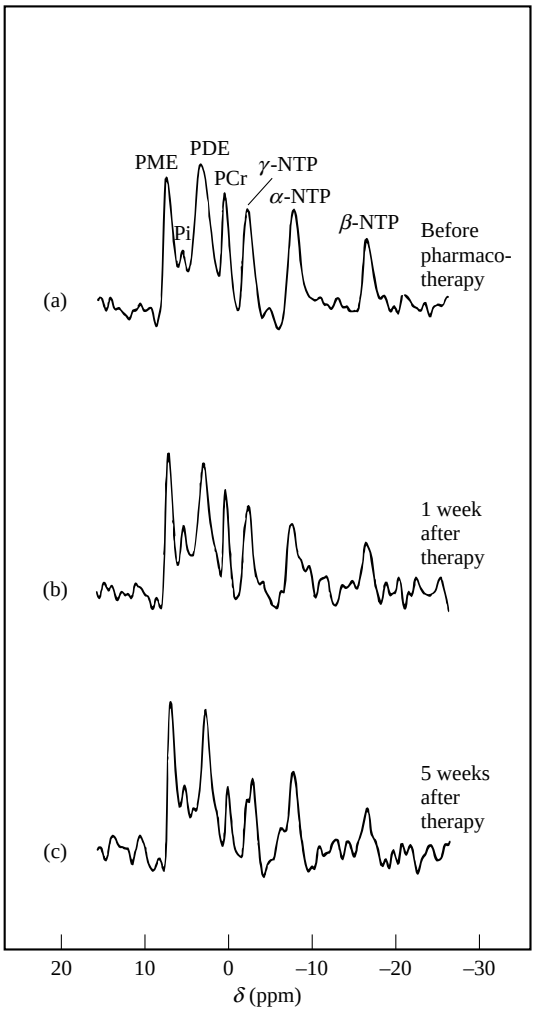

Figure 6 Localized ^{31}P NMR spectra of prolactinoma obtained in a patient before and one and five weeks after the beginning of bromocriptine pharmacotherapy. The spectra were rescaled to take into account differences of measured voxel sizes (modified from Segebarth et al.[27])

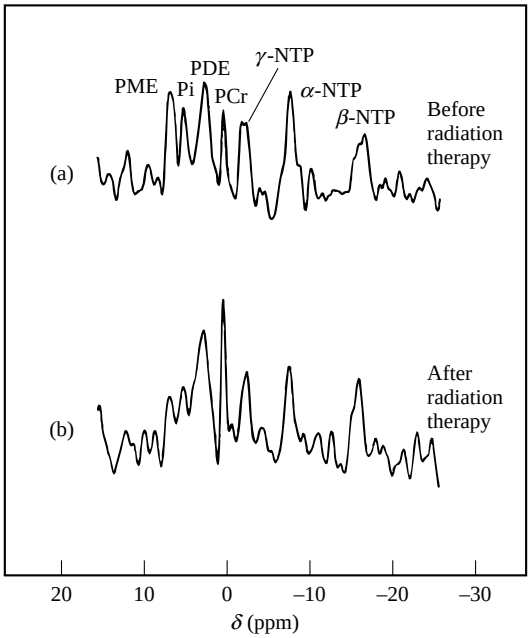

Figure 7 Localized ^{31}P NMR spectra in vivo of intracranial lymphoma obtained (a) before and (b) after radiation therapy with a dose of 24.2 Gy (modified from Segebarth et al.[27])

any effects were seen by imaging modalities. The authors discuss the alkalosis after i.a. administration as being a result of cell membrane damage due to the high local drug concentration in this route of application. In soft tissue sarcomas, alkalosis was found to be associated with necrosis[32] which may also be true for brain tumors.

Superselective catheter embolization of meningiomas with poly(vinyl alcohol) particles is performed to minimize bleeding during subsequent neurosurgery. This treatment form is suitable to validate ^{31}P NMR spectroscopy for clinical application. Since the spectra reflect the strong ischemia caused by the embolization, in vivo NMR spectroscopy should help to assess response to therapy. Employing two-dimensional CSI, increased P_i/β-NTP signal intensity ratio was detected in meningioma the day following embolization.[18] A complete depletion of the NTP pool was not observed (Figure 10).

In studies of therapy monitoring of human brain tumors by means of ^{31}P NMR spectroscopy, different tumor entities have been examined and also different treatment protocols applied. The comparability of results of independent studies can be compromised when different measurement techniques are used. Besides further progress in experimental techniques and quantification, a generally applicable examination protocol must be established. Notwithstanding these current limitations, the clinical studies presented on cerebral neoplasms demonstrate the potential of ^{31}P NMR spectroscopy for monitoring tumor therapy response in patients.

3 CONCLUSIONS

At present, clinical ^{31}P NMR spectroscopy of human brain tumors can be rated as follows:

1. The method allows an assessment noninvasively of bioenergetic status, levels of intermediates of phospholipid metabolism, intracellular pH, and the extent of necrosis within macroscopic regions of proliferating tissue in the brain.
2. Limitations in spatial localization, sensitivity, and spectral resolution prevent differential diagnosis of human brain tumors by means of ^{31}P NMR spectroscopy.
3. Tumor therapy monitoring is feasible with the use of ^{31}P NMR due to the observation of cellular energy status and membrane turnover rate, and the quantitative comparison with spectral data obtained before the beginning of therapy and from unaffected tissue.

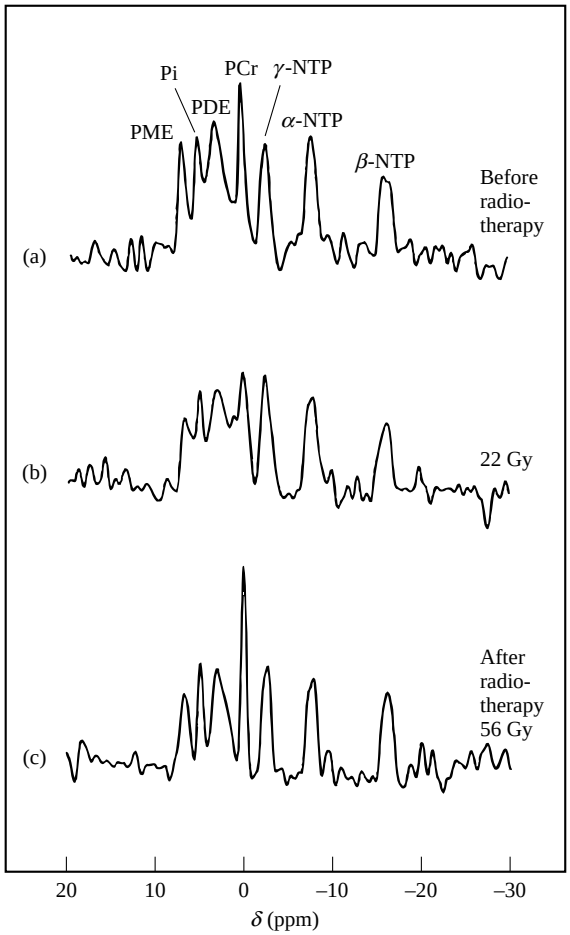

Figure 8 Follow-up study in a patient with grade II astrocytoma. Localized ^{31}P NMR spectra obtained (a) before, (b) after 22 Gy, and (c) after completion of the radiation therapy (56 Gy) show intensity changes of phosphomonoester (PME) and phosphocreatine (PCr) resonances (modified from Heindel et al.[24])

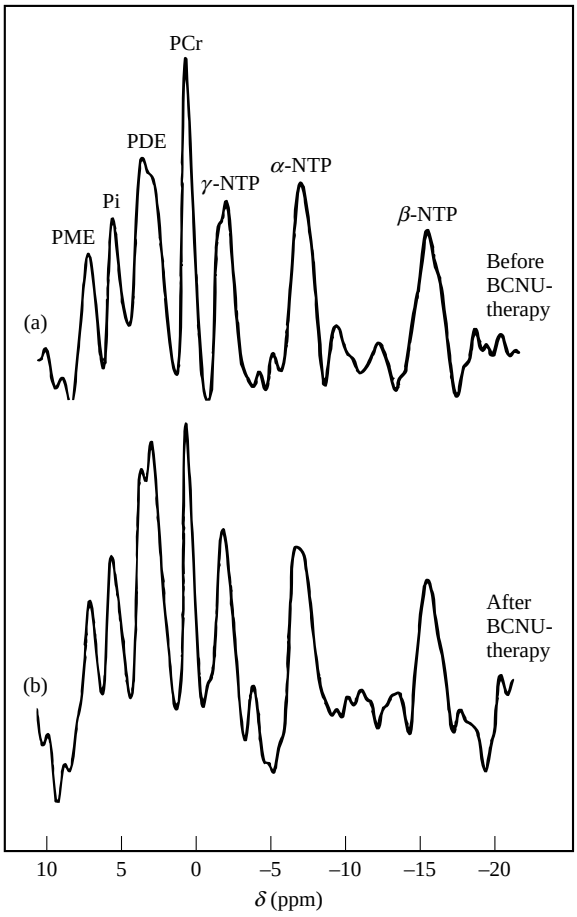

Figure 9 Localized ^{31}P NMR spectra of a glioblastoma in a patient (a) before and (b) after superselective intraarterial infusion of 1,3-bis(2-chloroethyl)-1-nitrosourea (BCNU) over 3 h (modified from Arnold et al.[45])

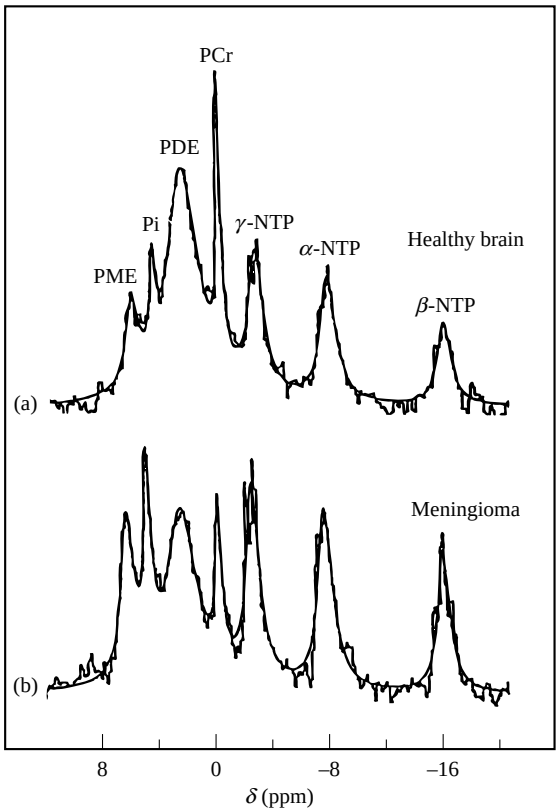

Figure 10 ^{31}P spectroscopic imaging of the brain of a patient with meningioma after presurgical superselective catheter embolization. Localized spectra (voxel size 3 cm × 3 cm × 3 cm) from (a) unaffected hemisphere and (b) meningioma. For quantitative evaluation, Lorentzian line-fits are superimposed on the measured spectra (modified from Knopp et al.[18])

4 ABBREVIATIONS

CSI chemical shift imaging
ISIS image-selected in vivo spectroscopy
NOE nuclear Overhauser effect
NTP nucleoside 5′-triphosphate
PCr phosphocreatine
PDE phosphodiester
P_i inorganic phosphate
PME phosphomonoester
SNR signal-to-noise ratio
STEAM stimulated echo acquisition mode
VOI volume of interest

5 RELATED ARTICLES

Chemical Shift Imaging; Localization and Registration Issues Important for Serial MRS Studies of Focal Brain Lesions; Proton Decoupling During In Vivo Whole Body Phosphorus MRS; Single Voxel Localized Proton NMR Spectroscopy of Human Brain In Vivo; Single Voxel Whole Body Phosphorus MRS; Whole Body Studies: Impact of MRS.

6 REFERENCES

1. T. C. Ng, W. T. Evanochko, R. N. Hiramoto, V. K. Ganta, M. B. Lilly, A. J. Lawson, T. H. Corbett, J. R. Durant, and J. D. Glickson, *J. Magn. Reson.*, 1982, **49**, 271.
2. W. T. Evanochko, T. C. Ng, and J. D. Glickson, *Magn. Reson. Med.*, 1984, **1**, 508.
3. S. Naruse, K. Hirakawa, Y. Horikawa, C. Tanaka, T. Higuchi, S. Ueda, H. Nishikawa, and H. Watari, *Cancer Res.*, 1985, **45**, 2429.
4. P. F. Daly, R. C. Lyon, P. J. Faustino, and J. S. Cohen, *J. Biol. Chem.*, 1987, **262**, 14875.
5. P. Vaupel, F. Kallinowski, and P. Okunieff, *Cancer Res.*, 1989, **49**, 6449.
6. N. Shine, M. A. Palladino, J. S. Patton, A. Deisseroth, G. S. Karczmar, G. B. Matson, and M. W. Weiner, *Cancer Res.*, 1989, **49**, 2123.
7. R. J. Ordidge, A. Connelly, and J. A. B. Lohman, *J. Magn. Reson.*, 1986, **66**, 283.
8. K. D. Merboldt, D. Chien, W. Hänicke, M. L. Gyngell, H. Bruhn, and J. Frahm, *J. Magn. Reson.*, 1990, **89**, 343.
9. P. C. Lauterbur, D. M. Kramer, W. V. House, and C.-N. Chen, *J. Am. Chem. Soc.*, 1975, **97**, 6866.
10. T. R. Brown, B. M. Kincaid, and K. Ugurbil, *Proc. Natl. Acad. Sci. USA*, 1982, **79**, 3523.
11. A. A. Maudsley, S. K. Hilal, W. H. Perman, and H. E. Simon, *J. Magn. Reson.*, 1983, **51**, 147.
12. A. A. Maudsley, S. K. Hilal, H. E. Simon, and S. Wittekoek, *Radiology*, 1984, **153**, 745.
13. D. B. Vigneron, S. J. Nelson, J. Murphy-Boesch, D. A. Kelly, H. B. Kessler, T. R. Brown, and J. S. Taylor, *Radiology*, 1990, **177**, 643.
14. J. W. Hugg, G. B. Matson, D. B. Twieg, A. A. Maudsley, D. Sappey-Marinier, and M. W. Weiner, *Magn. Reson. Imaging*, 1992, **10**, 227.
15. P. R. Luyten, G. Bruntink, F. M. Sloff, J. W. A. H. Vermeulen, J. I. van der Heijden, J. A. den Hollander, and A. Heerschap, *NMR Biomed.*, 1989, **1**, 177.
16. P. Bachert-Baumann, F. Ermark, H.-J. Zabel, R. Sauter, W. Semmler, and W. J. Lorenz, *Magn. Reson. Med.*, 1990, **15**, 165.
17. P. Bachert and M. E. Bellemann, *J. Magn. Reson.*, 1992, **100**, 146.
18. M. V. Knopp, P. Bachert, G. Ende, M. Blankenhorn, H. Kolem, W. Semmler, T. Hess, M. Forsting, K. Sartor, W. J. Lorenz, and G. van Kaick, *Proc. 11th Ann Mtg. Soc. Magn. Reson. Med.*, Berlin, 1992, p. 1954.
19. D. L. Arnold, E. A. Shoubridge, J. G. Villemure, and W. Feindel, *NMR Biomed.*, 1990, **3**, 184.
20. R. D. Oberhänsli, D. Hilton-Jones, P. J. Bore, L. J. Hands, R. P. Rampling, and G. K. Radda, *Lancet*, 1986, **ii**, 8.
21. R. G. Steen, *Cancer Res.*, 1989, **49**, 4075.
22. W. T. Evanochko, T. C. Ng, M. B. Lilly, A. J. Lawson, T. H. Corbett, J. R. Durant, and J. D. Glickson, *Proc. Natl. Acad. Sci. USA*, 1983, **80**, 334.
23. D. L. Arnold, E. A. Shoubridge, J. G. Villemure, and W. Feindel, *Proc. 7th Ann Mtg. Soc. Magn. Reson. Med.*, San Francisco, 1988, p. 333.
24. W. Heindel, J. Bunke, S. Glathe, W. Steinbrich, and L. Mollevanger, *J. Comput. Assist. Tomogr.*, 1989, **12**, 907.
25. W. D. Heiss, W. Heindel, K. Herholz, J. Rudolf, J. Bunke, J. Jeske, and G. Friedmann, *J. Nucl. Med.*, 1990, **31**, 302.
26. D. L. Arnold, J. Emrich, E. A. Shoubridge, J.-G. Villemure, and W. Feindel, *J. Neurosurg.*, 1991, **74**, 447.
27. C. M. Segebarth, D. F. Balériaux, D. L. Arnold, P. R. Luyten, and J. A. den Hollander, *Radiology*, 1987, **165**, 215.
28. Y. C. Hwang, J. Mantil, M. D. Boska, D.-R. Hwang, W. Banks, M. Jacobs, and C. Peterson, *Proc. 11th Ann Mtg. Soc. Magn. Reson. Med.*, Berlin, 1992, p. 3610.

29. B. Hubesch, D. Sappey-Marinier, K. Roth, D. J. Meyerhoff, G. B. Matson, and M. W. Weiner, *Radiology*, 1990, **174**, 401.
30. T. A. D. Cadoux-Hudson, M. J. Blackledge, B. Rajagopalan, D. J. Taylor, and G. K. Radda, *Br. J. Cancer*, 1989, **60**, 430.
31. W. Negendank, *NMR Biomed.*, 1992, **5**, 303.
32. D. Sostman, M. Dewhirst, C. Charles, K. Leopold, D. Moore, R. Burn, A. Tucker, J. Harrelson, and J. Oleson, *Proc. 9th Ann Mtg. Soc. Magn. Reson. Med.*, New York, 1990, p. 319.
33. A. Rutter, H. Hugenholtz, J. K. Saunders, and I. C. Smith, *Invest. Radiol.*, 1995, **30**, 359.
34. W. Semmler, G. Gademann, P. Schlag, P. Bachert-Baumann, H.-J. Zabel, W. J. Lorenz, and G. van Kaick, *Magn. Reson, Imaging*, 1988, **6**, 335.
35. J. M. Maris, A. E. Evans, A. D. McLaughlin, G. J. D'Angio, L. Bolinger, H. Manos, and B. Chance, *N. Engl. J. Med.*, 1985, **312**, 1500.
36. T. C. Ng, S. Vijayakumar, A. W. Majors, F. J. Thomas, T. F. Meaney, and N. J. Baldwin, *Int. J. Radiat. Oncol. Biol. Phys.*, 1987, **13**, 1545.
37. B. D. Ross, J. T. Helper, I. J. Cox, I. R. Young, R. Kempf, A. Makepeace, and J. Pennock, *Arch. Surg.*, 1987, **122**, 1464.
38. W. Semmler, G. Gademann, P. Bachert-Baumann, H. J. Zabel, W. J. Lorenz, and G. van Kaick, *Radiology*, 1988, **166**, 533.
39. O. M. Redmond, J. Stack, M. Scully, P. Dervan, D. Carney, and J. T. Ennis, *Proc. 7th Ann Mtg. Soc. Magn. Reson. Med.*, San Francisco, 1988, p. 432.
40. G. S. Karczmar, D. J. Meyerhoff, M. D. Boska, B. Hubesch, J. Poole, G. B. Matson, F. Valone, and M. W. Weiner, *Radiology*, 1991, **179**, 149.
41. O. M. Redmond, J. P. Stack, N. G. O'Connor, D. N. Carney, P. A. Dervan, B. J. Hurson, and J. T. Ennis, *Magn. Reson. Med.*, 1992, **25**, 30.
42. S. Naruse, Y. Horikawa, C. Tanaka, T. Higuchi, H. Sekimoto, S. Ueda, and K. Hirakawa, *Radiology*, 1986, **160**, 827.
43. B. D. Ross, J. Tropp, K. A. Derby, S. Sugiura, C. Hawryszko, D. B. Jacques, and M. Ingram, *J. Comput. Assist. Tomogr.*, 1989, **13**, 189.
44. D. L. Arnold, E. A. Shoubridge, W. Feindel, and J.-G. Villemure, *Can. J. Neurol. Sci.*, 1987, **14**, 570.
45. D. L. Arnold, E. A. Shoubridge, J. Emrich, W. Feindel, and J.-G. Villemure, *Invest. Radiol.*, 1989, **24**, 958.

Biographical Sketches

Wolfhard Semmler. *b* 1944. M.Sc. (Dipl.-Phys.), 1972, Ph.D. (Dr. rer. nat.), 1976, Free University of Berlin, M.D. (Dr. med.), 1990, University of Heidelberg. University of Aarhus (Denmark), 1976; Rutgers University and Bell Laboratories, New Jersey, USA, 1977–79; Hahn–Meitner-Institute, Berlin, 1979–83; Department of Radiology, Free University of Berlin, 1983–85; German Cancer Research Center (DKFZ), Heidelberg, 1985–91; Director, Institute of Diagnostic Research, Free University of Berlin, 1992–present. Approx. 120 publications. Research specialties: MR imaging and spectroscopy, development of contrast media for MRI, basic principles of contrast media for imaging modalities.

Peter Bachert. *b* 1954. M.Sc., 1979, Ph.D. (Dr. rer. nat), 1983, University of Heidelberg. Introduced to NMR by K. H. Hausser and U. Haeberlen. Application scientist, Siemens, 1984–86; German Cancer Research Center (DKFZ), Heidelberg, 1986–present. Approx. 40 publications. Research specialties: applications of NMR to problems in biophysics and biomedicine.

Brain Neoplasms Studied by MRI

Andrew P. Kelly and Michael N. Brant-Zawadzki
Hoag Memorial Hospital Presbyterian, Newport Beach, CA, USA

1 INTRODUCTION

Magnetic resonance imaging (MRI) has become the imaging modality of choice for the evaluation of brain neoplasms. There are two main reasons why MRI has supplanted computerized axial tomography (CT) scanning at many institutions in the USA. First and foremost is the superior sensitivity that MRI possesses in detecting alterations in brain tissue caused by neoplasms. As location of an intracranial neoplasm is a factor with important diagnostic as well as prognostic implications, the ability of MRI to image in multiple planes is the second reason. This advantage helps to determine whether a lesion is intraaxial (of parenchymal origin, such as a glioma) versus extraaxial (of dural origin, for example, such as a meningioma).

A short article on MRI of brain neoplasms leaves important areas uncovered. For more extensive discussion of the topic, the reader is referred to the excellent recent reviews on brain neoplasms in the books edited by Stark and Bradley[1] and Atlas.[2–4] Also, cross references to pertinent related subjects discussed elsewhere in this volume are given at the end of this article. The initial part of this article focuses on the general features exhibited by many brain neoplasms and why MRI is sensitive to these changes. Technical considerations behind deciding appropriate imaging pulse sequences are also discussed. The second section discusses some of the most common brain neoplasms and their characteristics, as displayed by MRI.

2 GENERAL NEOPLASM FEATURES SEEN ON MRI

MRI of the brain and its pathology takes advantage of the exponential time constants, T_1 and T_2, exhibited by normal brain tissue, and alterations in these values caused by brain neoplasms. The reader is referred to other chapters in this volume for discussions on the complex basis of signal intensity and magnetic relaxation characteristics of normal brain and brain pathology. Essentially, calculated T_1 and T_2 values of brain tumors, such as astrocytomas, are longer than normal gray and white matter, but widespread differences exist even within single histological classifications, and attempts at histologic stratification of brain neoplasms by quantitative T_1 and T_2 relaxation analysis have proven futile.[5] The presence of edema, hemorrhage, necrosis, cyst development, and even calcification can help characterize neoplasms in the brain.

Standard MRI sequences employed by most institutions include a sagittal short *TR*, short *TE* (T_1-weighted) localizing sequence, axial long *TR*, long *TE* (T_2-weighted) sequences, and axial T_1-weighted sequences, usually obtained after administration of a paramagnetic contrast agent such as gadolinium-DTPA. Gradient recalled sequences are sometimes added to help characterize lesions in regards to foci of hemorrhage or calcification, as these sequences optimize magnetic susceptibility effects. Additional planes are included when deemed necessary for further information on tumor location and extension. Because T_2-weighted spin echo (SE) MRI sequences have the disadvantage of long acquisition times resulting in degradation of image quality secondary to patient motion, many scans are now performed using fast spin echo (FSE) techniques. The usefulness of FSE sequences already has been demonstrated in the imaging of pathologic intracranial conditions.[6,7] Utilizing these techniques, a routine entire brain scan can now be completed in under 15 min.

By analyzing tumor signal intensity on different pulse sequences, some insight can be gained as to the nature of the cells making up the tumor. For example, neoplasms containing a high nuclear/cytoplasm ratio, such as lymphoma and meningioma, may display this lack of water content as low signal intensity on T_2-weighted sequences.

3 SPECIFIC TUMOR FEATURES SEEN ON MRI

3.1 Location, Mass Effect, Infiltration and Hydrocephalus

The multiplanar capability of MRI allows the determination of the location of a tumor, i.e., intra-axial versus extraaxial, and thus helps to identify the potential cell of origin. The multiplanar capability of MRI aids in defining the extent of certain tumors that can be infiltrative, such as gliomas and primary lymphomas, which can extend via white matter tracts such as the corpus callosum. By assessing ventricular size and shape as well as gray and white matter interfaces, the presence or absence of mass effect and hydrocephalus can be determined. Recently, mass effect and necrosis, as displayed by and graded on MRI, were found to be statistically significant characteristics for grading astrocytic series gliomas, as compared with biopsy findings, which sometimes can be subject to sampling error.[8]

3.2 Edema

One of the major diagnostic advantages of MRI over CT is in the detection of brain edema, which is one of the most striking features associated with tumors. Termed 'vasogenic' edema, it is probably secondary to neovascularity devoid of the usual blood–brain barrier or stretching of normal vessels secondary to mass effect.[9] Edema, by increasing bulk water, causes prolongation of T_1 and T_2, as most tumors do; thus, changes detected on T_2-weighted images actually represent tumor in addition to edema. MRI is highly sensitive to these changes, but specifically defining areas representing actual tumor versus edema is difficult if using T_2-weighted images alone.

3.3 Necrosis and Cyst Formation

In most cases, intratumoral necrosis is considered to be a sign of a more aggressive lesion, and necrosis is well demonstrated by MRI. Necrosis can be cystic or noncystic; therefore, a varied appearance can be seen on MRI. Cystic necrosis with increased bulk water content will prolong T_1 and T_2 relaxation

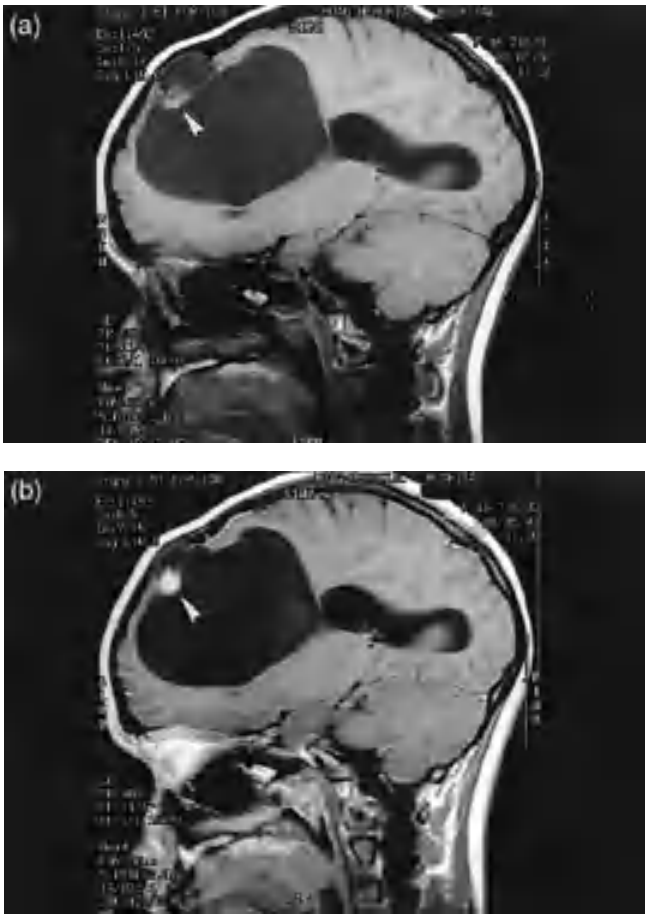

Figure 1 A 16-year-old female with a large juvenile pilocytic astrocytoma occupying much of the right frontal lobe. (a) Before gadolinium-DTPA T_1-weighted sagittal image obtained on a 1.5-T GE Signa magnet shows the large cystic tumor with a mural nodule (white arrowhead). (b) Note the dense enhancement of the mural nodule after contrast administration

times, while nonnecrotic cysts can show shortened T_1 and T_2 relaxation times due to hemorrhage and accumulation of proteinaceous debris, leading to high signal intensity on T_1-weighted images.[2]

Benign or malignant lesions may have cystic components. Benign lesions, such as arachnoid cysts, will exhibit the behavior of 'true' cysts, following CSF signal intensity on all pulse sequences. Other benign cysts, such as colloid cysts or craniopharyngiomas, show greater variability in cyst components which determine signal changes on MRI. Malignant lesions may contain cystic components for a number of reasons, ranging from true tumoral cysts, to hemorrhage into solid lesions with subsequent clot lysis, and other causes of necrosis. Certain tumors may present as mural nodules in the cyst wall, particularly childhood astrocytomas and juvenile pilocytic astrocytomas, the latter having a very low malignant potential (Figure 1).

3.4 Hemorrhage in Brain Neoplasms

Many primary brain neoplasms may initially be discovered secondary to symptoms related to intratumoral hemorrhage, which, when accompanied by vasogenic edema, can cause a confusing picture on MRI. The physics behind the appearance of blood on MRI is beyond the scope of this article, but the evolution of blood breakdown products from oxyhemoglobin through paramagnetic methemoglobin to hemosiderin is followed well by MRI and affords the potential for timing the event.[4] Certain tumors, especially metastases from melanoma, lung and renal cell carcinoma, have a propensity to bleed, as do a small percentage of gliomas. Hemorrhage itself should not be considered specific for tumor, since most cerebral bleeds have other causes.

3.5 Use of Paramagnetic Contrast Agents and Enhancement

A highly regulated and consistent internal milieu must be maintained for optimal brain and spinal cord function. Specialized capillaries, with endothelial tight junctions, provide this 'blood–brain barrier' in the normal state, aided by foot processes from nearby astrocytes. By administration of paramagnetic contrast agents such as gadolinium-DTPA, areas of breakdown in the blood–brain barrier caused by tumor can be detected. This is most helpful in determining to a close approximation the extent of neoplasm versus edema by comparing post-gadolinium T_1-weighted images with T_2-weighted images. By enhancing the relaxation of nearby water protons, contrast agents can decrease T_1 values in areas where a breakdown in the blood–brain barrier has occurred. The vast majority of glioblastoma multiforme tumors will enhance in a heterogeneous, thick, irregular pattern, but it is important to note that degree of enhancement does not correlate with aggressiveness of tumor.[10] Metastases also enhance in almost all instances. Contrast is most useful in detecting lesions that are isointense on T_1-weighted images, show little edema on T_2-weighted images, but which strongly enhance. This is seen in such tumors as meningiomas and acoustic neuromas. Postoperatively, contrast agents can help detect areas of suspected tumor recurrence or residual tumor, but these changes can be nonspecific, as discussed, below.

3.6 Postoperative Changes and Radiation

MRI with gadolinium is indicated following surgery, radiation or chemotherapy to follow tumor size, but recurrent tumor is not all that enhances. Local enhancement secondary to leptomeningeal scarring may persist for years after surgery, and only a size increase on sequential studies in a region of enhancement is likely to be definitive evidence of recurrent tumor.[10]

Many intracranial neoplasms now undergo radiotherapy as a mainstay for treatment, and most high-grade astrocytomas are now treated by gross resection followed by high energy local radiotherapy (radiation implants or radiosurgery). Sites of radiation necrosis can enhance and show edema, simulating tumor.[11]

3.7 Tumoral Calcification

Certain neoplasms, such as oligodendrogliomas and craniopharyngiomas, have a tendency to display areas of calcification, but identification of tumoral calcification in itself seldom causes one to favor a particular neoplasm over another.

Secondary to the low resonant proton density of calcified tissue, calcium may be missed on MRI; when seen, it is generally noted to appear hypo- or isointense on T_1- and T_2-weighted spin echo sequences, and with gradient echo sequences signal loss is more profound due to the sensitivity of this method to the heterogeneous magnetic susceptibility found in calcified tissue. Recent articles have described occasional calcified brain lesion as appearing bright on T_1-weighted images due to shortening of T_1 relaxation times by a surface relaxation mechanism.[12]

4 SPECIFIC NEOPLASMS AND CHARACTERISTICS DISPLAYED ON MRI

Since location as well as histologic subtype are important features that help determine the clinical presentation and prognosis of most brain neoplasms, an attempt has been made to categorize the most common neoplasms according to site of origin, with subcategorization according to cell of origin.

4.1 Intra-axial Lesions

4.1.1 Gliomas and Tumor of Glial Cell Origin

Almost 50% of primary brain tumors are gliomas, and three major tumor types are recognized, corresponding to types of glial cell: astrocytes, oligodendrocytes and ependymal cells. Since neoplastically transformed astrocytes give rise to 75–95% of all gliomas, the discussion here will center on astrocytomas.[11]

The classification system providing the greatest prognostic validity is a three-level system where: grade I refers to low grade benign astrocytomas, such as the juvenile pilocytic astrocytoma; grade II indicates anaplastic astrocytoma with intermediate grade of malignancy; and grade III refers to the highly malignant astrocytomas and glioblastoma multiforme.

MRI features suggesting a more benign variety include absence of necrosis, well-defined margins, minimal edema and little mass effect. The hallmark of the glioblastoma multiforme, on the other hand, is necrosis, marked edema and mass effect, with prominent enhancement (Figure 2). Wide variability exists, however, since highly malignant and infiltrative tumors may not show edema or demonstrate significant enhancement.

The reader is referred to other texts on brain neoplasms for discussions of oligodendrogliomas and ependymomas.[1,2]

4.1.2 Nonglial-Cell Intra-axial Tumors

Once considered rare, the frequency of primary intracranial lymphoma is increasing due to its occurrence in patients with immunodeficiencies, particularly patients with the acquired immune deficiency syndrome (AIDS). Because of this and its fairly characteristic MRI appearance, lymphoma deserves mention. More than 50% of cases are multifocal, and can exist in supratentorial and infratentorial locations. Lymphomas can infiltrate and cross the corpus callosum, a property shared with gliomas. Dense hypercellularity causes this tumor to appear isointense to hypointense on T_2-weighted images. Most lymphomas enhance densely and homogeneously after contrast is administered, and tend to show less edema than gliomas of the same size, although wide variability in enhancement patterns and edema can exist (Figure 3).

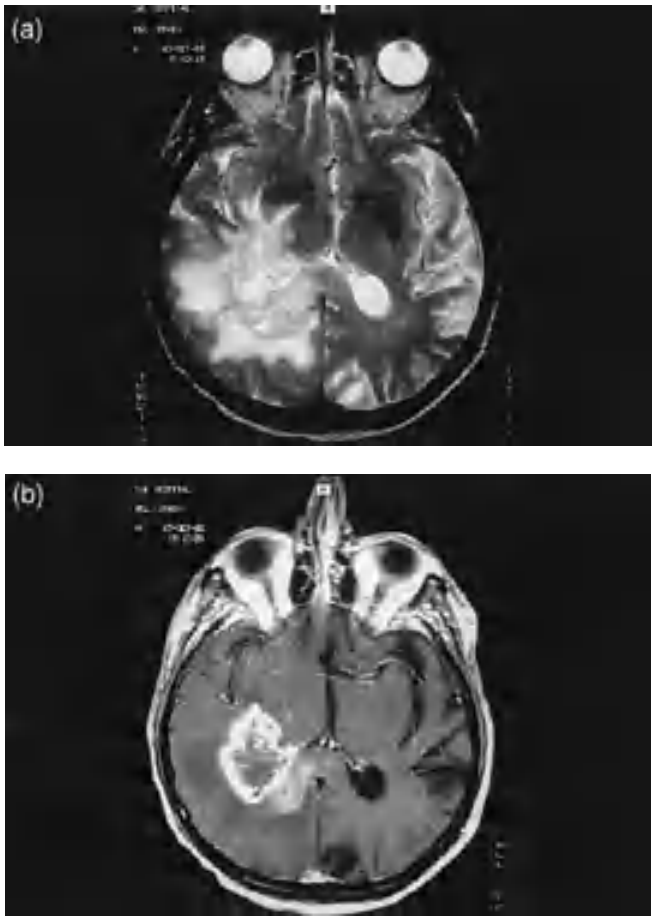

Figure 2 A 69-year-old man with a high-grade astrocytoma. (a) T_2-weighted axial image obtained on a 1.5-T Siemens Magneton magnet demonstrates a large necrotic tumor with extensive surrounding edema in the right temporal and parietal lobes. (b) Postgadolinium T_1-weighted image shows the ring-enhancing mass lesion, but the edema is not as evident on this sequence

Medulloblastoma, a common primary intracranial neoplasm in children, is one of several tumors occurring more commonly in an infratentorial location. Other tumors commonly seen in this location include cerebellar astrocytomas, juvenile pilocytic astrocytomas, hemangioblastomas, and fourth ventricular ependymomas. Because of its usually cerebellar location, multiplanar MRI is important in diagnosis. Tending to be hypercellular like lymphoma, medulloblastoma enhances diffusely and is usually isointense to hypointense on T_2-weighted images.[13]

An important use of MRI is in diagnosis of CSF dissemination of tumor. Termed leptomeningeal spread, this is a common pathway for this malignancy to metastasize or recur. Gadolinium-enhanced views of the brain and spinal cord are used to evaluate for CSF seeding.[11]

In searching for *intracranial metastatic spread* from extracranial primary tumors such as breast, lung, and colon carcinomas and melanoma, MRI with gadolinium is the opti-

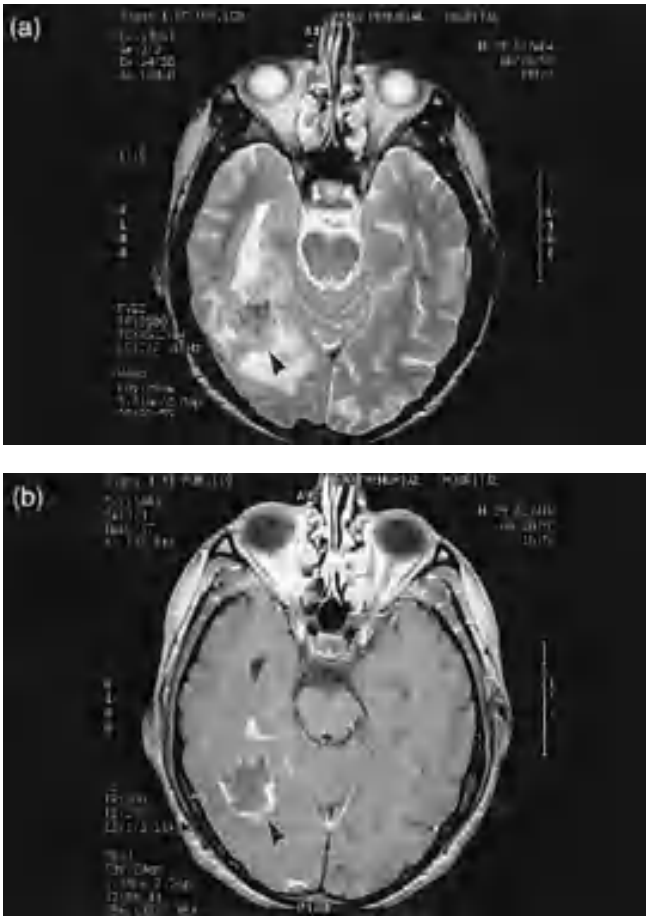

Figure 3 A 29-year-old male with AIDS and primary intracranial lymphoma. (a) Note the low signal intensity (black arrowhead) on this T_2-weighted axial sequence obtained on a 1.5-T GE Signa magnet. (b) Post-gadolinium T_1-weighted axial image shows little enhancement in this case

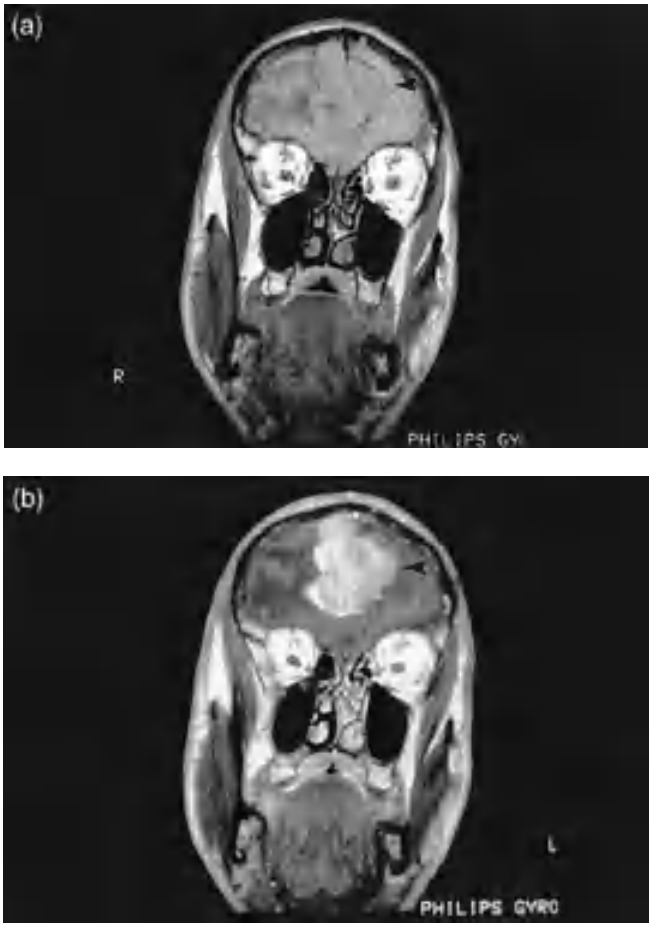

Figure 4 A 60-year-old male with a meningioma originating from the falx. (a) On this coronal T_1-weighted precontrast image, the signal intensity of the tumor is similar to the brain parenchyma (black arrowhead). The images were obtained on a 1.5-T Siemens Magneton magnet. (b) After gadolinium administration, the borders of this densely enhancing meningioma are easily defined

mal screening test.[14] Metastases incite greater edema as compared with primary tumors. The presence of multiple lesions strongly favors metastic disease over a primary tumor such as glioma, although a small percentage of gliomas are multicentric.

4.2 Extra-axial Tumors

4.2.1 Meningiomas

Comprising 10–20% of intracranial tumors, meningiomas are the most common extra-axial tumor, with an autopsy prevalence of 1–2%.[3] Common sites of occurrence include the cerebral convexities, the falx, and the sphenoid wing. Meningiomas originate from the dural layer covering the brain parenchyma.

Because most meningiomas show only a slight increase in T_1 over white matter and a T_2 within normal range for brain, they may appear mildly hypointense on T_1-weighted images and isointense to hyperintense on T_2-weighted images. Heterogeneous signal intensity, especially on T_2-weighted images, may be seen secondary to vascular flow voids, calcification, and cystic foci. Usually little mass effect or significant edema is seen, though these tumors can be quite large. A hallmark is intense enhancement after contrast administration, and a tapered extension of enhancement along the tumor base, called a 'dural tail', may be present, (Figure 4).

4.2.2 Acoustic Neuroma: a Cerebellopontine Angle Tumor

Being a relatively common site of tumor occurrence, the cerebellopontine angle (CPA) is well imaged by MRI. The prototype tumor occurring in this location is the acoustic neuroma arising from the eighth cranial nerve. On precontrast images, enlargement of the seventh and eighth cranial nerve complex is seen, and intense enhancement is demonstrated with contrast. Extension into the internal auditory canal highly suggests this tumor type.

4.2.3 Pituitary Gland Tumors

MRI has become the primary modality for diagnosis of hormone-secreting pituitary microadenomas as well as other tumors that may occur in the sella or suprasellar locations,

such as craniopharyngiomas. Coronal and sagittal pre- and post-gadolinium images are usually employed. Timing of the imaging with the administration of contrast agent is important, as enhancement of a microadenoma will be delayed compared with the normal enhancement of the rest of the gland. Larger pituitary tumors, such as macroadenomas, may displace the carotid artery or invade the cavernous sinus, both features being depicted well by MRI.

4.2.4 Other Extra-axial Tumors

Tumors may originate in the bones comprising the base of the skull, chordomas and chondrosarcoma being two such examples. A difficult area to image by CT, MRI demonstrates skull base masses well and may depict infiltrative changes in the marrow-containing portions of the skull base, as can be seen with metastatic involvement of the clivus. A number of tumors may originate in the pineal gland, and multiplanar imaging is important in identifying the pineal gland as the origin. Ependymoma, a tumor which originates in the ependymal lining cells of the ventricular system, is the most common intraventricular brain neoplasm and can cause expansion of the ventricle at the site of origin.[15] Extrusion through various ventricular foramina, such as the foramen of Magendie or Luschka, highly suggest this tumor type when it originates in the fourth ventricle.

5 SUMMARY

MRI has proven its usefulness in the diagnosis and follow-up of brain neoplasms. As discussed, its major limitations are in the diagnosis of tumor recurrence after surgical excision and in distinguishing tumor recurrence from radiation necrosis. Recent developments in magnetic resonance spectroscopy (MRS) and positron emission tomography (PET) offer further help in such cases. Experimental work with proton MRS, for example, has shown that increased levels of lactate, choline and lipids may be associated with certain malignancies.[16] In the future, the noninvasive assessment of brain neoplasm histology will probably combine the efforts of MRI, MRS and PET as the two latter technologies are further developed.

6 RELATED ARTICLES

Brain MRS of Infants and Children; Brain Neoplasms in Humans Studied by Phosphorus-31 NMR Spectroscopy; Cranial Nerves Investigated by MRI; Gadolinium Chelate Contrast Agents in MRI: Clinical Applications; Gadolinium Chelates: Chemistry, Safety, and Behavior; Hemorrhage in the Brain and Neck Observed by MRI; MRI in Clinical Medicine; Relaxation Measurements in Imaging Studies.

7 REFERENCES

1. A. N. Hasso, K. E. Kortman, and W. G. Bradley, in 'Magnetic Resonance Imaging', 2nd edn., eds. D. D. Stark and W. G. Bradley, Mosby Year Book, St. Louis, 1992, Chap. 25.
2. S. W. Atlas, in 'Magnetic Resonance Imaging of the Brain and Spine', ed. S. W. Atlas, Raven, New York, 1991, Chap. 10.
3. H. I. Goldberg, in 'Magnetic Resonance Imaging of the Brain and Spine', ed. S. W. Atlas, Raven, New York, 1991, Chap. 11.
4. K. R. Thulborn and S. W. Atlas, in 'Magnetic Resonance Imaging of the Brain and Spine', ed. S. W. Atlas, Raven, New York, 1991, Chap. 9.
5. M. Just and M. Thelen, *Radiology*, 1988, **169**, 779.
6. S. W. Atlas, D. B. Hackney, D. M. Yousem, and J. Listerud, *Radiology*, 1991, **181**, 165.
7. G. H. Zoarski, J. K. Maskey, Y. Anzai, W. N. Hanafee, P. S. Melki, R. V. Mulkern, F. A. Jolesz and R. B. Lufkin, *Radiology*, 1993 **188**, 323.
8. B. L. Dean, B. P. Drayer, C. R. Bird, R. A. Flom, et al., *Radiology*, 1990, **174**, 411.
9. W. M. Kelly and M. Brant-Zawadzki, in 'Radiology, Diagnosis, Imaging, Intervention', eds. J. M. Taveras and J. T. Ferrucci, J. B. Lippincott, Philadelphia, 1989, Chap. 53.
10. W. G. Bradley, Jr., W. T. C. Yuh, and G. M. Bydder, *J. Magn. Reson. Imaging*, 1993, **3**, 199.
11. R. B. Schwartz and M. T. Mantello, *Semin. Ultrasound CT MR*, 1992, **13**, 449.
12. R. M. Henkelman, J. F. Watts, and W. Kucharczyk, *Radiology*, 1991, **179**, 199.
13. S. P. Meyers, S. S. Kemp, and R. W. Tarr, *Am. J. Roentgenol.*, 1992, **158**, 859.
14. J. H. Bisese, *Semin. Ultrasound CT MR*, 1992, **13**, 473.
15. J. Jelinek, J. G. Smirniotopoulos, J. E. Parisi, and M. Kanzer, *Am. J. Roentgenol.*, 1990, **155**, 365.
16. P. R. Luyten, J. H. Marien, and W. Heindel, P. M. van Gerwen, K. Herholz, J. A. den Hollander, G. Friedmann, and W. D. Heiss, *Radiology*, 1990, **176**, 791.

Biographical Sketches

Andrew P. Kelly. *b*. 1960. B.A. Chemistry, 1983, California State University, Fullerton; M.D., 1988, University of California, Davis. Fellow in MRI, Hoag Memorial Hospital Presbyterian, Newport Beach, CA, 1993–present.

Michael Brant-Zawadzki. Approx. 150 articles, including the textbook 'Magnetic Resonance Imaging of the Central Nervous System'. A frequent lecturer on MR imaging applications and contrast agents.

Body Fat Metabolism: Observation by MR Imaging and Spectroscopy

E. Louise Thomas and Jimmy D. Bell

Imperial College School of Medicine, Hammersmith Hospital, London, UK

1 INTRODUCTION

The importance of lipids in both health and disease is increasingly recognized. The major causes of morbidity and mortality in the western world include cancer, coronary heart disease (CHD), diabetes mellitus, and obesity. Lipids appear to have a major role in both treatment and prevention.[1,2] There is, therefore, a growing need for in vivo methods for studying human lipid metabolism and investigating lipid depots in the body. The development and use of nuclear magnetic resonance (NMR) techniques of imaging (MRI) and spectroscopy (MRS) for lipid studies is a major recent advance.

Since the late 1980s, interest has increased in the use of both in vivo and in vitro NMR for investigation of human and animal metabolism. Researchers are taking advantage of the nondestructive and noninvasive nature of the technique. These characteristics are particularly important for widespread, population-based studies, which often require serial examinations.

The initial applications of in vivo NMR to the study of lipids were principally concerned with development of the NMR methodology, rather than focusing on specific biochemical problems.[3,4] However, even at this early stage, the potential of MRI and MRS when applied to lipid metabolism could be envisaged. In this chapter, we will review the recent use of these techniques both in vivo and in vitro for investigation of human lipid metabolism and body fat composition and deposition.

2 USEFUL NUCLEI FOR NMR STUDIES OF LIPIDS

MRS with ^{1}H, ^{2}H, ^{13}C, and ^{31}P nuclei has been applied to the study of lipid metabolism in animals and humans.[3–9] The ^{1}H nucleus has the highest natural abundance in biological tissues and is the highest sensitivity in NMR compared with other useful nuclei. In the past, the application of in vivo ^{1}H MRS to the study of lipids was not considered to be a useful technique. Problems arising from the intrinsically small chemical shift range resulted in severe signal overlap, which had limited its use. Recently, however, ^{1}H NMR has been shown to be an extremely powerful noninvasive method to determine intramuscular lipid content.[7,8]

MRS using ^{13}C in vivo has been successfully applied to studies of lipid metabolism and adipose tissue composition.[3,4,9] Compared with studies using ^{1}H, ^{13}C MRS is relatively insensitive because of the low gyromagnetic ratio and low natural abundance (1.1%) of the ^{13}C nucleus. Its relative sensitivity is further reduced by the ^{1}H–^{13}C coupling, which splits the ^{13}C signal, effectively reducing intensity. These problems are partially offset by the short relaxation times of most ^{13}C resonances, the high adipose tissue content of ^{13}C-containing compounds, and the use of decoupling techniques. Moreover, the very fact that ^{13}C has 1.1% natural abundance has been exploited by using ^{13}C-enriched metabolites in turnover studies, similar to classical ^{14}C-tracer studies.

MRS with ^{2}H has only had limited use in in vivo metabolic studies. The deuterium nucleus is quadrupolar ($I=1$). It has both a low gyromagnetic ratio and natural abundance (0.015%), which leads to a very low sensitivity relative to proton spectroscopy (1.45×10^{-6}). These unfavorable properties are offset by its short relaxation times and high body content (12 mmol/l), allowing its detection by natural abundance in vivo MRS. Furthermore, the tissue content can be readily increased by use of deuterated water (D_2O), a fact that Brereton et al. have utilized to great effect in lipid turnover studies.[5]

Limited information can be obtained from in vivo ^{31}P MRS of lipids because ^{31}P NMR detects only phosphate-containing compounds. Consequently, ^{31}P MRS has principally been applied to lipid studies in vitro.[10–12] One area of research where in vivo ^{31}P MRS has been applied is to the study of membrane phospholipids. However, as the signals from the bound phospholipids tend to be very broad, the useful resonances come principally from phospholipid precursors (phosphocholine and phosphoethanolamine) or breakdown (glycerophosphocholine and glycerophosphoethanolamine) products and, therefore, will not be discussed further in this chapter.

3 MRI OF BODY FAT CONTENT AND DISTRIBUTION

The accurate determination of total body fat content and measurement of regional fat depots has become an important issue as the contribution of body fat to diseases such as non-insulin-dependent diabetes mellitus and CHD has become clearer. There are many techniques that have long been used to give estimates of total and peripheral body fat content with varying degrees of accuracy. However, until the development of techniques such as X-ray computed tomography (CT) and MRI, it was not possible to differentiate between subcutaneous and internal fat depots (Figure 1).

Internal fat depots, in particular visceral fat, may be a key factor in disease development. CT gives an accurate direct measurement of visceral fat depots, though exposure to ionizing radiation makes whole body fat measurements, especially for serial studies, impractical; consequently only single slices tend to be acquired.

Initial studies using MRI to study body fat have focused on the validation of the technique. MRI has been validated in phantoms, animals, and human cadavers and has been shown to measure both muscle and adipose tissue in vivo accurately, showing good agreement with values produced by dissection and chemical analysis.[13–17] MRI has also been compared with other techniques such as underwater weighing, anthropometry, body water dilution, impedance, and dual-energy X-ray absorptiometry (DEXA).[18–24] Generally there is good degree of

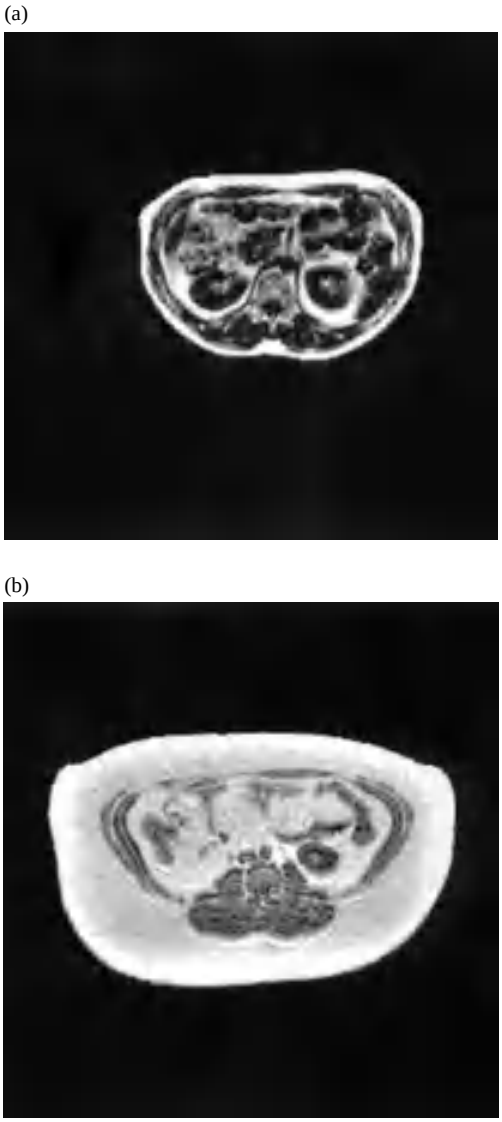

Figure 1 Typical abdominal transverse MR images showing distribution of internal and subcutaneous fat in a lean (a) and an obese (b) volunteer. Images were acquired using a rapid T_1-weighted spin echo sequence

correlation between the different methods, though agreement between methods for individuals can be quite variable.[24]

A wide variety of methodologies have been used in the application of MRI to the study of body fat. Different parameters and methods of data collection ranging from extrapolation of single-slice or multiple-slice acquisitions over selected regions of the body to whole body fat measurements have been used. Many studies have been published with single-slice MR data from the abdomen, generally at the level of L4/L5; however, there are significant drawbacks with this approach.

For an accurate measurement of body fat content, it is important that sufficient data be collected from the whole region of interest so that subtle changes are not missed or overinterpreted. A change or lack of change reported using single-slice CT or MRI scans from a selected region of the abdomen might not reflect the effect of the intervention on the entire adipose tissue depot. Indeed, it has previously been shown that a single CT scan obtained at the level of the umbilicus contains a substantial amount of retroperitoneal fat, which is less metabolically active than other visceral fat depots. It has been suggested that changes occurring in the entire visceral fat depot may be 'diluted out' by the presence of the less-active retroperitoneal fat in the single slice. Factors such as this can have a profound effect on the final results and their interpretation. It is, therefore, more appropriate to collect sufficient data from the entire depot to be studied. One approach is to obtain multislice data from the whole body, as shown in Figure 2.

The main applications of MRI to the measurement of body fat depots in human subjects have been following interventions such as diet and exercise.[25–27] Ross et al., using whole body MRI, have shown significant reductions in total and regional body fat content in obese subjects following a combination of diet and exercise (resistance or aerobic) and diet alone.[25,26] They found similar changes in body composition in response

Figure 2 Transverse MR images showing distribution of internal and subcutaneous fat from a whole body MRI data set from a healthy female volunteer age 21 years, basal metabolic index 27.9 kg/m^{-2}, waist to hips girth ratio 0.81, subcutaneous fat 29.6 l, and visceral fat 2.25 l. Images were acquired using a rapid T_1-weighted spin echo sequence from the volunteer's fingertips to her toes by acquiring 10 mm thick transverse images with 30 mm gaps between the slices

to diet combined with resistance exercise and diet combined with aerobic exercise.[26] Furthermore, significantly more subcutaneous fat was lost from the abdomen compared with the lower body and there was a greater loss of visceral fat from the upper than from the lower abdomen. The combination of diet and exercise resulted in a greater fat loss than occurred with diet alone.[25] Thomas et al., also using whole body MRI, have suggested that there is a preferential loss of visceral fat in lean women following moderate aerobic exercise without dietary restriction.[27] Interestingly, the change in body composition was only detected using MRI; weight and body fat content measured by impedance and anthropometry were not significantly different following exercise.

A preferential loss of visceral fat has also been reported in obese individuals following dietary restriction and treatment with dexfenfluramine.[28–31] However, these studies evaluated regional body fat distribution by measuring the area on a single MRI scan, which, as discussed above, could give misleading results.

4 IN VIVO MRS

4.1 Proton MRS

The application of in vivo proton MRS to the study of lipids has until recently been rather limited because of the small chemical shift range of ^{1}H resonances and the intense water signal. However, a number of researchers have shown that in vivo ^{1}H MRS can be used to determine noninvasively the triglyceride content within muscle cells known as intramyocellular lipids (IMCL). This is particularly important as there is evidence to suggest that these 'muscle triglycerides' may be implicated in the pathogenesis of insulin resistance. Schick et al., using ^{1}H MRS to detect signals from human skeletal muscle, reported that the methyl and methylene lipid signals each consisted of two well-resolved peaks (Figure 3).[7] They suggested that the two pairs of peaks corresponded to IMCL and triacylglycerols in adipocytes between muscle fibers (extramyocellular lipids, EMCL).

Evidence in support of this interpretation has come from other groups.[32,33] Boesch et al. compared measurement of IMCL by in vivo ^{1}H MRS with morphometry and chemical analysis of human biopsy samples and suggested that measurement of IMCL by ^{1}H MRS had the best correlation with the estimation of the 'true' level of IMCL.[32] Szczepaniak et al., in a very elegant study of subjects with congenital lipodystrophy, a condition associated with almost complete absence of EMCL, showed that the in vivo ^{1}H NMR spectra revealed only single methylene and methyl resonances, corresponding to IMCL.[33]

Using ^{1}H MRS, Rico-Sanz et al. have shown diversity in the level of IMCL (as well as other muscle metabolites) in human skeletal muscle.[34] Levels of IMCL were significantly lower in the tibialis muscle than in the soleus and gastrocnemius muscles, possibly resulting from differences in fiber type composition and deposition of metabolites owing to adaptation of the muscles for locomotion.

To date, most studies have concentrated on looking at the effects of exercise on IMCL. Boesch et al. reported a significant decrease (about 40%) in IMCL in tibialis anterior muscle following 3 h of intensive cycling.[8] However, it appears that the nature and intensity of the exercise may also be important, as Rico-Sanz et al. showed no changes in IMCL levels in the tibialis, gastrocnemius, or soleus muscles following two different 90 min moderate exercise protocols.[35]

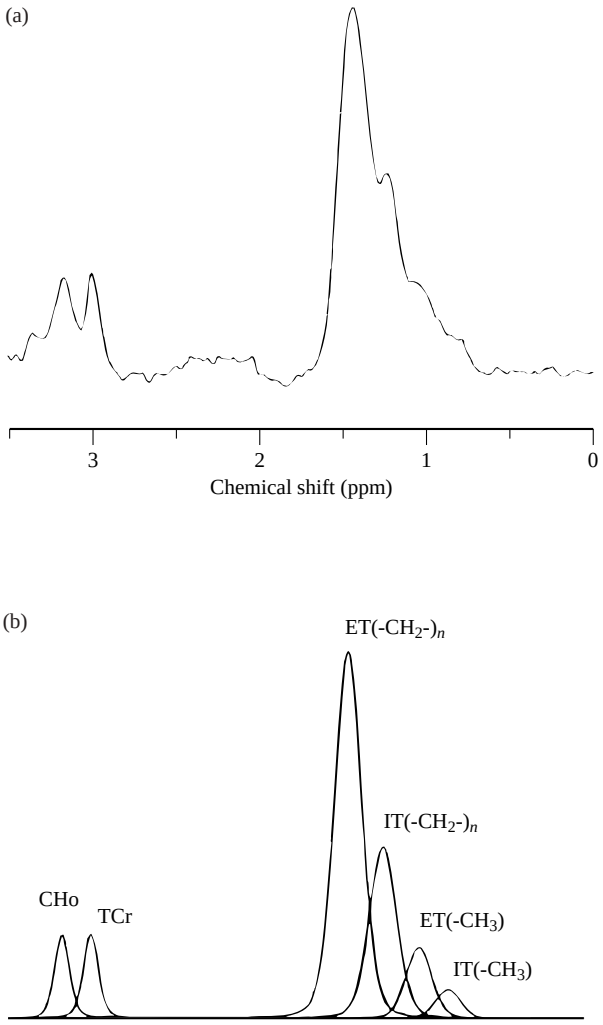

Figure 3 In vivo ^{1}H MR spectrum from the soleus muscle of a healthy volunteer before (a) and after (b) line fitting. Cho, choline and carnitine; TCr, creatine and phosphocreatine; ET($-CH_2-)_n$, extracellular muscle triglycerides methylene; IT($-CH_2-)_n$, intracellular muscle triglycerides methylene; ET($-CH_3)_n$, extracellular muscle triglycerides methyl; IT($-CH_3)_n$ intracellular muscle triglycerides methyl

Interestingly, there have been several reports in abstract form demonstrating that IMCL content assessed by ^{1}H MRS is elevated in insulin-resistant individuals.[36,37] However, this relationship was not found in subjects from all ethnic groups.[37]

NMR images of the leg also tend to be acquired during the spectroscopy examination. These provide additional information from which it is possible to measure subcutaneous fat, bone marrow, bone, and levels of EMCL. The role of EMCL in muscle metabolism is not fully understood, but it is thought that EMCL and IMCL may have different roles. The combination of MRI and ^{1}H MRS will be excellent tools for increasing our knowledge of the metabolism of these two lipid depots.

4.2 Carbon-13 MRS

High-resolution ^{13}C MRS has found widespread use in the study of lipids in vitro.[38,39] In particular, the clear distinction of multiple, different fatty acid groups allows this technique to be used, often quantitatively, in studies of dietary oils.[40–43] This degree of resolution cannot be achieved in vivo, which limits the utility of this technique in noninvasive human research. However, major lipid groups can be distinguished and, within these constraints, important clinical and biochemical work has been carried out using proton-coupled ^{13}C and proton-decoupled $\{^1H\}$ ^{13}C MRS. A typical ^{13}C NMR spectrum of human adipose tissue is shown in Figure 4.

Canioni et al. first showed that in vivo ^{13}C $\{^1H\}$ MRS could detect differences in the lipid composition of adipose tissue and liver in rats fed a diet high in polyunsaturated fatty acids.[3] Further work by Sillerud et al. examined $^{13}C\{^1H\}$ NMR of triacylglycerols in rat adipocytes in vitro and advanced our knowledge particularly of signal assignment in biological systems.[44] Moonen et al. developed in vivo $^{13}C\{^1H\}$ NMR to characterize adipose tissue in human subjects.[4] They confirmed that linoleic acid ($C_{18:2n-6}$), usually the principal polyunsaturated fatty acid present in human adipose tissue, dominated the polyunsaturated fatty acid carbon signal observed in vivo, allowing estimation of this stored essential fatty acid.

In vivo ^{13}C MRS has been used to study the fatty acid composition of adipose tissue in rats fed diets based on significantly different fatty acid mixtures.[3,45,46] In animals fed fats with different fatty acid content (butter/lard, olive oil, sunflower oil, fish oil), clear differences were found in the in vivo spectra, consistent with a significant effect of dietary fatty acid intake on the tissue fatty acid profile. Progressively increasing total unsaturated and polyunsaturated fatty acid content in the diet was reflected in the adipose tissue composition. However, data from both groups appeared to show discrepancy in the results obtained by ^{13}C MRS compared with GLC, which worsened in adipose tissue from animals on a diet high in complex polyunsaturated fat, a finding later confirmed in human subjects.[47]

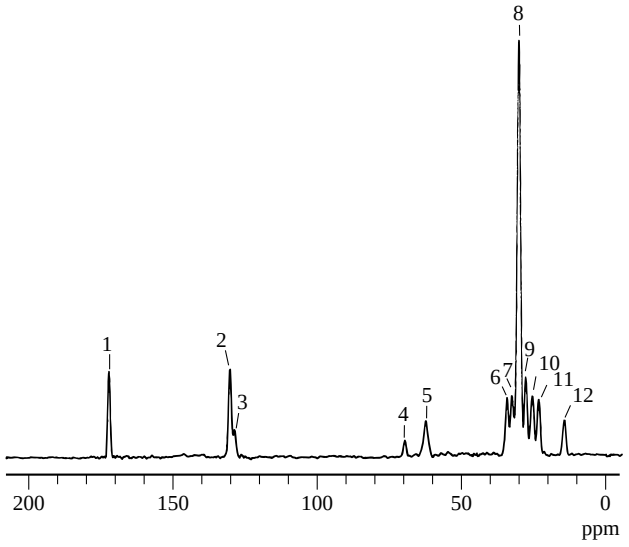

Figure 4 Natural abundance in vivo $^{13}C\{^1H\}$ NMR spectrum of human adipose tissue, dominated by signal from triglycerides. Peak assignment (referenced to $-\mathbf{C}H_3$): 1. **C**=O (171.79 ppm); 2. $-\mathbf{C}H=\mathbf{C}H-$ (monounsaturated) and $-\mathbf{C}H=CH-CH_2-CH=\mathbf{C}H-$ (polyunsaturated) (129.83 ppm); 3. $-CH=\mathbf{C}H-CH_2-\mathbf{C}H=CH-$ (polyunsaturated) (128.13 ppm); 4. **C**2 glycerol (69.21 ppm); 5. **C**1, **C**3 glycerol (62.05 ppm); 6. $-CH_2\mathbf{C}H_2-CO-O-R$ (33.93 ppm); 7. $-\mathbf{C}H_2-CH_2-CH_3$ (32.14 ppm); 8. $-(\mathbf{C}H_2)_n-$ (29.69 ppm); 9. $-\mathbf{C}H_2-CH=CH-$ (27.39 ppm); 10. $-\mathbf{C}H_2-CH_2-CO-O-R$ (25.04 ppm); 11. $-CH_2-\mathbf{C}H_2-CH_3$ (22.94 ppm); 12. $-CH_2-\mathbf{C}H_3$ (14.1 ppm)

In humans, the turnover of fatty acids in adipose tissue is slow (half-life 600 days).[48] The fatty acid profile of human subcutaneous fat, therefore, provides an index of the habitual dietary fatty acid intake over the previous 2 to 3 years.[49] This information is important for long-term epidemiological surveys but has previously been limited by the need for repeat tissue biopsies for fatty acid estimation. The application of in vivo ^{13}C MRS to the noninvasive analysis of adipose tissue composition is, therefore, of particular value for human nutritional studies.

Beckmann et al. have used in vivo ^{13}C MRS to show a significant change in human adipose tissue fatty acid composition following a fat-reduced diet, with a correlation between diet and tissue monounsaturated fatty acids.[9] No difference was found in the degree of polyunsaturation, and this may reflect the limited period (6 months) of dietary change. Thomas et al. studied vegan subjects as a defined population, with an established long-term diet high in polyunsaturated fatty acids.[50] A significantly increased adipose tissue total unsaturated and mono- and polyunsaturated fatty acid carbon content was shown in the ^{13}C spectra from the vegan group compared with omnivore controls (Figure 5). Interestingly they found no significant differences in adipose tissue composition between vegetarian subjects and the omnivore controls.

MRS with ^{13}C has also been used to investigate the influence of maternal diet on infant adipose tissue composition. Thomas et al. compared the adipose tissue composition of breast-fed infants of women who maintained either an omnivore or a vegan diet.[51] The adipose tissue composition of infants directly reflects that of their mothers, with the vegan infants having 70% more polyunsaturated fatty acid carbons than the omnivore infants. Although the consequences of essential fatty acid deficiency in formula-fed infants are well documented, less is known about the effects of very high levels of long-chain polyunsaturated fatty acids in the infant diet. The long-term effects for vegan infants having such high levels of polyunsaturated fatty acids in their diet and adipose tissue are unknown. In the same study, Thomas et al. studied the adipose tissue composition of term and pre-term infants at birth, 6 weeks, and 6 months and compared them with their mothers. They found an increase in unsaturated fatty acids with increasing gestational age and maturity (Figure 6).

The complex interactions between lipids in plasma and those in the body tissues are not fully defined and are becoming an area for NMR-based, dynamic studies of nutrition and lipid metabolism.

In vivo ^{13}C MRS has also been used in combination with GLC to study the adipose tissue composition in malnourished patients with cirrhosis of the liver.[52] No significant differences were found in overall adipose tissue composition in the patients compared with healthy volunteers by either technique, although

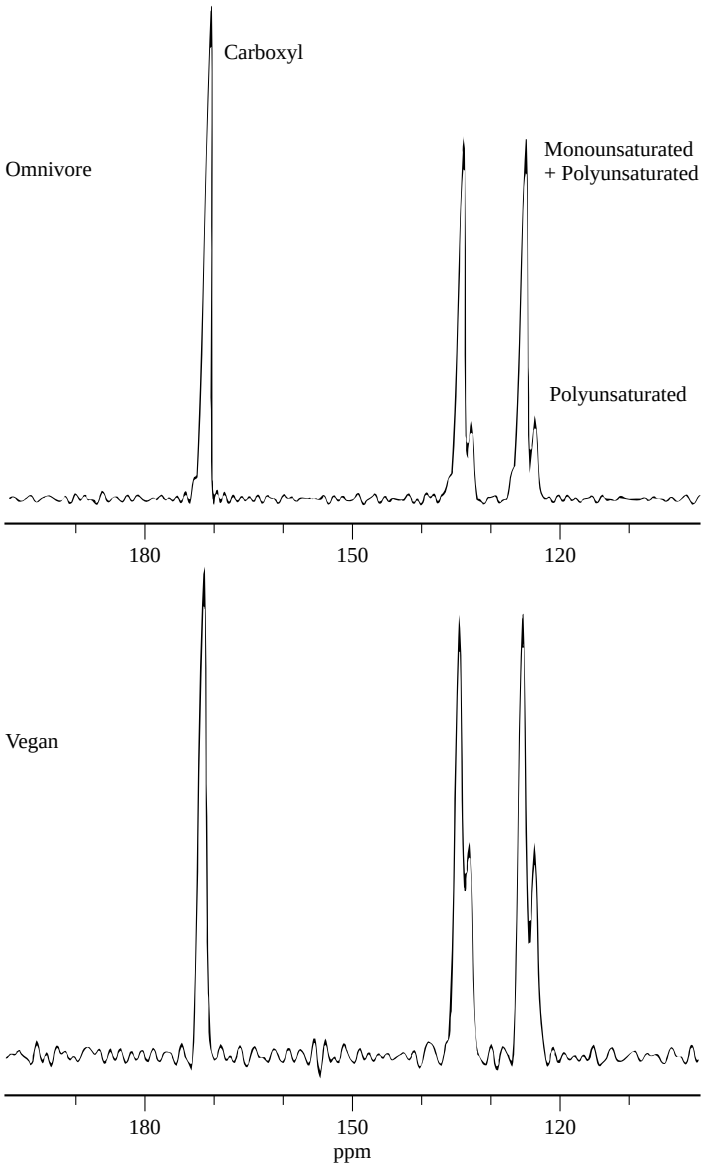

Figure 5 Alkene region from natural abundance in vivo coupled ^{13}C NMR spectra of human thigh adipose tissue in vegan and omnivore subjects. Spectra are scaled to the carboxyl signal. The vegan subjects, compared with omnivores, have an increased adipose tissue content of both total unsaturated and polyunsaturated fatty acid carbons (polyunsaturated: 3.45±0.87% versus 2.39±0.55% of total fatty acid carbons, $p < 0.05$). This reflects at least 3 years' adherence to the vegan diet, which, in the absence of all animal products, is high in polyunsaturated fats (polyunsaturates 33.13±7.4% versus 25.2±8.5% total dietary fat polyunsaturated, $p < 0.05$)

GLC did reveal significant differences in individual fatty acids. Following liver transplantation and subsequent recovery, the patients were re-scanned by ^{13}C MRS. The resulting increase in body fat mass was accompanied by a preferential increase in saturated fatty acids.[52] This may be a dietary effect, as high levels of saturated fatty acids in patients' diets following liver transplantation would result in the deposition of saturated fatty acids in the adipose tissue. Alternatively, this may be secondary to a general repletion of membrane polyunsaturated fatty acids or the use of essential fatty acids (polyunsaturated) for biosynthesis of eicosanoids in the postoperative period.

Dimand et al. have shown that the composition of human adipose tissue may also be a useful marker of fatty acid status in diseases such as cystic fibrosis.[53] They found levels of polyunsaturated fatty acids to be reduced and monounsaturated fatty acids elevated in patients compared with healthy controls.

Several studies have investigated the influence of exercise on adipose tissue composition.[27,54] Intensive exercise was shown to have a significant independent effect on adipose tissue composition, with a significant decrease in polyunsaturated fatty acids following 10 weeks of basic military training.[54] Interestingly, no changes were found in adipose tissue composition following more moderate exercise.[27]

The use of in vivo ^{13}C MRS in humans and animals has not solely been applied to adipose tissue. Barnard et al. used in vivo $^{13}C\{^{1}H\}$ NMR spectroscopy to examine the hepatic fatty acid profile in rats fed fats with different fatty acid patterns.[55] The liver has a pivotal role in lipid metabolism. Hepatic receptor-mediated low-density lipoprotein (LDL) clearance is a major process controlling plasma LDL concentrations. Dietary saturated fat may increase plasma LDL by suppression of hepatic LDL-receptor activity, whereas dietary substitution with polyunsaturated fatty acids may increase hepatic LDL clearance and lower plasma LDL, possibly by increasing membrane fluidity.[56] A significant dietary effect was shown with an increasing hepatic content of unsaturated fatty acids and an increasing degree of polyunsaturation as these fatty acids increased in the diet.

Investigation of the metabolism of specific fatty acids is largely unexplored and a possible future application of ^{13}C MRS. The use of ^{13}C-labeled fatty acids to trace metabolic pathways and kinetic rates is an exciting prospect. These studies may be restricted by the limited availability of labeled fatty acids, their oxidation after administration, and the sensitivity of the system, given the pre-existing strong lipid signals. However, preliminary work has been performed by Cunnane et al. and this demonstrated the ability of in vitro $^{13}C\{^{1}H\}$ NMR to detect carbon-specific incorporation of injected [U-^{13}C]-eicosapentaenoic acid in extracted rat liver lipids.[57]

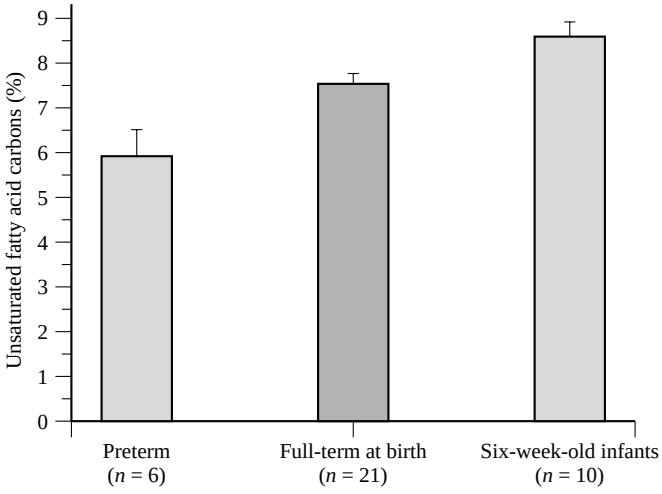

Figure 6 Fatty acid composition of adipose tissue from preterm infants and full-term infants at birth and after 6 weeks of development

4.3 Deuterium Spectroscopy

There is considerable interest in monitoring lipid turnover in both health and disease. A novel approach to the study of dynamic in vivo tissue lipid metabolism was developed by Brereton et al.[5] They investigated the use of in vivo ^{2}H MRS in mice. Administration of D_2O (10% v/v) in the drinking water for 3–4 days allowed the detection of deuterium-enriched tissue lipid resonances in spectra acquired in less than 2 min, as shown in Figure 7a. The spectra consist of resonances from deuterated water (HOD) and the CHD-group of the tissue lipids. Removal of D_2O from the drinking water led to clear changes in the intensity of both signals (Figure 7b). The loss of ^{2}H from the water signal was significantly faster than from tissue lipids. The loss of ^{2}H from the lipid resonance was, therefore, proposed as a noninvasive measure of the rate of fat utilization. This method has since been applied to the study of fat utilization in obesity.

Obesity is one of the most common medical disorders and is characterized by excess adipose tissue and elevated plasma nonesterified fatty acids. Furthermore, obesity is known to lead to glucose intolerance and insulin resistance. Fat turnover, as reflected by the levels of plasma nonesterified fatty acids, may be implicated in this process. However, the lack of in vivo techniques for measuring fat utilization has greatly hampered progress in this area. Body fat turnover in mouse models of obesity and diabetes mellitus have been studied in vivo using the ^{2}H NMR technique.[58] Brereton et al. showed that the rates of fat utilization in obese mice were significantly lower than the rates for nonobese mice; the induction of diabetes did not affect utilization of fat as a metabolic fuel.[58] These studies clearly suggest that ^{2}H MRS will provide researchers with a powerful method for noninvasive assessment of fat turnover rates.

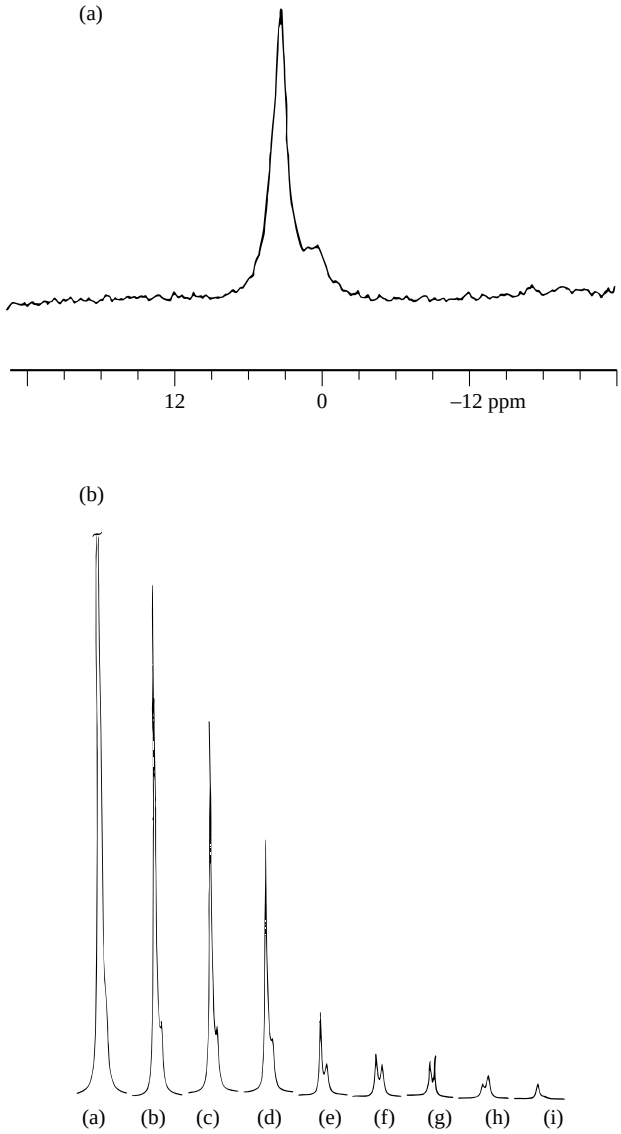

Figure 7 In vivo ^{2}H MRS in mice. (a) Natural abundance spectrum of a mouse. The resonance linked to the CHD-group of lipids is to high field at 1 ppm. Chemical shifts were reference to the deuterated water (HOD) resonance assigned to 4.8 ppm. (b) Spectra of a mouse following the removal of 10% (v/v) D_2O from its drinking water. The spectra were recorded at 1, 4, 5, 8, 11, 15, 16 and 21 days after the resumption of normal drinking water, indicated by (a) to (h), respectively. Spectrum (i) was recorded prior to the administration of D_2O to drinking water. (Adapted with permission of Heyden & Son Ltd from I. M. Brereton, D. M. Doddrell, S. M. Oakenfull, D. Moss, and M. G. Irving, *NMR Biomed*., 1989, **2**, 55.)

5 IN VITRO MRS

Plasma concentrations of LDL and high-density lipoproteins (HDL) are well-established markers for CHD risk assessment. Standard methods for quantification and compositional analysis of plasma lipoproteins require laborious and time-consuming physical separation based on particle size, density, or apolipoprotein content. Bell et al. have shown that MRS can be readily applied to distinguish lipoprotein fractions as well as to study alterations in plasma lipoproteins associated with dietary manipulation, both in intact plasma and in the isolated lipoprotein classes.[11,12] For example, sophisticated computer deconvolution methods (line-fitting analysis) are being developed to identify and quantify lipoprotein fractions in the ^{1}H NMR spectra of intact plasma samples (500 μl) within minutes.[59,60]

The effects of dietary manipulation on the ^{1}H NMR profile of lipoproteins are illustrated in Figure 8. Changes in composition following fish oil supplementation are shown by the presence of a new lipid resonance (peak 2A) arising from fish oil *n*-3/ω-3 fatty acids incorporated into plasma lipoproteins, while the methylene ($-(C\mathbf{H}_2)_n-$) signal (peak 3) is markedly reduced. Furthermore, T_2 analysis of the lipid resonances showed that these changes in lipid composition of the LDL particles are accompanied by alteration in the structural characteristics of these particles.[11]

6 SUMMARY

In this chapter, we have reviewed the current state of in vivo MRS as applied to the study of lipids. It is clear that this is a relatively new area of NMR research. However, it offers

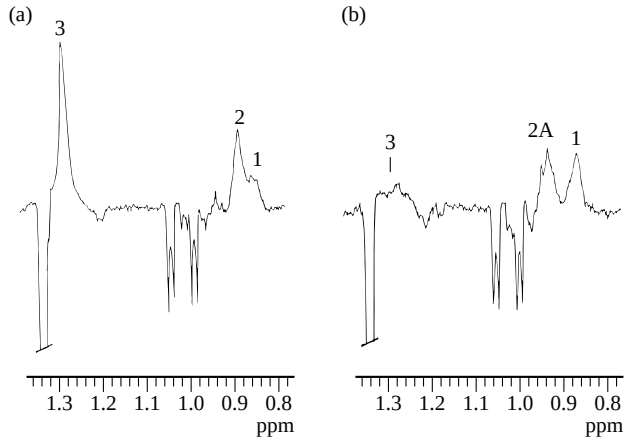

Figure 8 Expansions of spin echo ^{1}H NMR spectra of intact human plasma (a) before and (b) after 7 days of fish oil supplementation. Peaks 1, 2: terminal $-C\mathbf{H}_3$ group from LDL/HDL and very-low-density lipoprotein (VLDL), respectively; peak 3: $-(C\mathbf{H}_2)_n-$ of VLDL. Peak 2A arises from *n*-3/ω-3 fatty acids incorporated into plasma lipoproteins

many exciting prospects for future research into human lipid metabolism and body composition.

7 RELATED ARTICLES

Brain MRS of Human Subjects; Imaging and Spectroscopy of Muscle; Whole Body Studies: Impact of MRS.

8 REFERENCES

1. J. E. Kinsella, B. Lokesh, and R. A. Stone, *Am. J. Clin. Nutr.*, 1990, **52**, 1.
2. R. A. DeFronzo and E. Ferrannini, *Diabetes Care*, 1991, **14**, 173.
3. P. Canioni, J. R. Alger, and R. G. Shulman, *Biochemistry*, 1983, **22**, 4974.
4. C. T. W. Moonen, R. J. Dimand, and K. L. Cox, *Magn. Reson. Med.*, 1988, **6**, 140.
5. I. M. Brereton, M. G. Irving. J. Field, and D. M. Doddrell, *Biochem. Biophys. Res. Commun.*, 1986, **137**, 579.
6. P. C. Dagnelie, J. D. Bell, S. C. R. Williams, I. J. Cox, D. K. Menon, J. Sargentoni, and G. A. Coutts, *NMR Biomed.*, 1993, **6**, 2.
7. F. Schick, B. Eismann, W. I. Jung, H. Bongers, M. Bunse, and O. Lutz, *Magn. Reson. Med.*, 1993, **29**, 158.
8. C. Boesch, J. Slotboom, H. Hoppeler, and R. Kreis, *Magn. Reson. Med.*, 1997, **37**, 484.
9. N. Beckmann, J. J. Brocard, U. Keller, and J. Seelig, *Magn. Reson. Med.*, 1992, **27**, 97.
10. J. D. Bell, O. Lavender, V. C. Morris, and P. J. Sadler, *Magn. Reson. Med.*, 1991, **17**, 414.
11. J. D. Bell, J. C. C. Brown, R. E. Norman, and P. J. Sadler, *NMR Biomed.*, 1988, **1**, 90.
12. J. D. Bell, M. L. Barnard, H. G. Parkes, E. L. Thomas, C. H. Brennan, S. C. Cunnane, and P. C. Dagnelie, *J. Lipid Res.*, 1996, **37**, 1664.
13. R. Ross, L. Léger, R. Guardo, J. de Guise, and B. G. Pike, *J. Appl. Physiol.*, 1991, **70**, 2164.
14. P. A. Fowler, M. F. Fuller, C. A. Glasbey, G. G. Cameron, and M. A. Foster, *Am. J. Clin. Nutr.*, 1992, **56**, 7.
15. N. Abate, A. Garg, R. Coleman, S. M. Grundy, and R. M. Peshock, *Am. J. Clin. Nutr.*, 1997, **65**, 403.
16. M. L. Barnard, J. V. Hajnal, J. E. Schwieso, E. L. Thomas, J. D. Bell, N. Saeed, G. Frost, and S. R. Bloom, *NMR Biomed.*, 1996, **9**, 156.
17. N. Mitsiopoulos, R. N. Baumgartner, S. B. Heymsfield, W. Lyons, D. Gallagher, and R. Ross, *J. Appl. Physiol.*, 1998, **85**, 115.
18. P. Tothill, T. S. Han, A. Avenell, G. McNeill, and D. M. Reid, *Eur. J. Clin. Nutr.*, 1996, **50**, 747.
19. A. Sohlström, L. O. Wahlund, and E. Forsum, *Am. J. Clin. Nutr.*, 1993, **58**, 830.
20. M. A. Staten, W. G. Totty, and W. M. Kohrt, *Invest. Radiol.*, 1989, **24**, 345.
21. R. Ross, L. Léger, D. Morris, J. de Guise, and R. Guardo, *J. Appl. Physiol.*, 1992, **72**, 787.
22. P. A. Fowler, M. F. Fuller, C. A. Glasbey, M. A. Foster, G. G. Cameron, G. McNeill, and R. J. Maughan, *Am. J. Clin. Nutr.*, 1991, **54**, 18.
23. R. Ross, D. S. Kimberley, Y. Martel, J. de Guise, and L. Avruch, *Am. J. Clin. Nutr.*, 1993, **57**, 470.
24. E. L. Thomas, N. Saeed, J. V. Hajnal, A. E. Brynes, A.P. Goldstone, G. Frost, and J. D. Bell, *J. Appl. Physiol.*, 1998, **85**, 1778.
25. R. Ross, H. Pedwell, and J. Rissanen, *Am. J. Clin. Nutr.*, 1995, **61**, 1179.
26. R. Ross and J. Rissanen, *Am. J. Clin. Nutr.*, 1994, **60**, 695.
27. E. L. Thomas, A. Byrnes, J. V. Hajnal, N. Saeed, G. Frost, and J. D. Bell, *Proc. VIth Ann Mtg. (Int) Soc. Magn. Reson. Med.*, Sydney, 1998, (Vol. 3), p. 1812.
28. D. S. Gray, K. Fujioka, P. M. Colletti, H. Kim, W. Devine, T. Cuyegkeng, and T. Pappas, *Am. J. Clin. Nutr.*, 1991, **54**, 623.
29. R. Leenen, K. van der Kooy, P. Deurenberg, J. C. Seidell, J. A. Weststrate, F. J. Schouten, and J. G. Hautvast, *Am. J. Physiol.*, 1992, **263**, E913.
30. K. van der Kooy, R. Leenen, J. C. Seidell, P. Deurenberg, and J. G. Hautvast, *Am. J. Clin. Nutr.*, 1993, **58**, 853.
31. S. J. Marks, N. R. Moore, M. L. Clark, B. J. Strauss, and T. D. Hockaday, *Obes. Res.*, 1996, **4**, 1.
32. C. Boesch, R. Kreis, H. Howald, S. Matter, R. Billeter, B. Essen-Gustavsson, and H. Hoppeler, *Proc. VIth Ann Mtg. (Int) Soc. Magn. Reson. Med.*, Sydney, 1998, (Vol. 3), p. 1785.
33. L. S. Szczepaniak, D. T. Stein, F. Schick, A. Garg, and J. D. McGarry, *Proc. Vth Ann Mtg. (Int) Soc. Magn. Reson. Med.*, Vancouver, 1997, (Vol. 2), p. 1334.
34. J. Rico-Sanz, E. L. Thomas, G. Jenkinson, S. Mierisova, R. Iles, and J. D. Bell, *J. Appl. Physiol*, 1999, **87** (in press).
35. J. Rico-Sanz, J. V. Hajnal, E. L. Thomas, S. Mierisova, M. Ala-Korpela, and J. D. Bell, *J. Physiol.*, 1998, **510**, 615.
36. D. T. Stein, R. Dobbins, L. Szczepaniak, C. Malloy, and J. D. McGarry, *Diabetes*, 1997, **46**, (Suppl 1), 23A.
37. N. G. Forouhi, G. Jenkinson, S. Mullick, E. L. Thomas, U. Bhonsle, P. M. McKeigue, and J. D. Bell, *Proc. Br. Diabetic Assoc.*, 1998, S36.
38. J. G. Batchelor, R. J. Cushley, and J. H. Prestegard, *J. Org. Chem.*, 1974, **39**, 1698.
39. J. Bus, I. Sies, and M. S. F. Lie Ken Jie, *Chem. Phys. Lipids*, 1976, **17**, 501.
40. F. D. Gunstone, M. R. Pollard, C. M. Scrimgeour, and L. Vedanayagam, *Chem. Phys. Lipids*, 1977, **18**, 115.
41. J. N. Shoolery, *Prog. NMR Spect.*, 1977, **11**, 79.
42. N. G. Soon, *Lipids*, 1985, **20**, 778.
43. F. D. Gunstone, *Chem. Phys. Lipids*, 1991, **59**, 83.
44. L. O. Sillerud, C. H. Han, M. W. Bitensky, and A. A. Francendese, *J. Biol. Chem.*, 1986, **261**, 4380.
45. M. L. Barnard, J. D. Bell, S. C. R. Williams, T. A. B. Sanders, H. G. Parkes, K. K. Changani, J. S. Beech, M. L. Jackson, and S. R. Bloom, *Proc. XIth Ann Mtg. Soc. Magn. Reson. Med.*, Berlin, 1992, p. 3339.

46. T. W. Fan, A. J. Clifford, and R. M. Higashi, *J. Lipid Res.*, 1994, **35**, 678.
47. E. L. Thomas, S. C. Cunnane, and J. D. Bell, *NMR Biomed.*, 1998, **11**, 290.
48. J. Hirsch, J. W. Farquhar, E. H. Ahrens, M. L. Peterson, and W. Stoffel, *Am. J. Clin. Nutr.*, 1960, **8**, 499.
49. A. C. Beynen, R. J. J. Hermus, and J. G. A. J. Hautvast, *Am. J. Clin. Nutr.*, 1980, **33**, 81.
50. E. L. Thomas, G. Frost, M. L. Barnard, D. J. Bryant, J. Simbrunner, S. D. Taylor-Robinson, G. A. Coutts, M. Burl, S. R. Bloom, K. D. Sales, and J. D. Bell, *Lipids*, 1996, **31**, 145.
51. E. L. Thomas, J. D. Hanrahan, M. Ala-Korpela, G. Jenkinson, D. Azzopardi, R. A. Iles, and J. D. Bell, *Lipids*, 1997, **32**, 645.
52. E. L. Thomas, S. D. Taylor-Robinson, M. L. Barnard, G. Frost, J. Sargentoni, B. R. Davidson, S. C. Cunnane, and J. D. Bell, *Hepatology*, 1997, **25**, 178.
53. R. J. Dimand, C. T. W. Moonen, S. Chu, E. M. Bradbury, G. Kurland, and K. L. Cox, *Pediatr. Res.*, 1988, **24**, 243.
54. E. L. Thomas, A. Byrnes, G. Jenkinson, M. Jubb, G. Frost, and J. D. Bell, *J. Magn. Reson. Anal.* 1999, in press.
55. M. L. Barnard, J. D. Bell, S. C. R. Williams, T. A. B. Sanders, and S. R. Bloom, *Proc. XIIth Ann Mtg. Soc. Magn. Reson. Med.*, New York, 1993, p. 92.
56. J. Loscalzo, J. Freedman, A. Rudd, I. Barsky-Vasserman, and D. E. Vaughan, *Arteriosclerosis*, 1987, **7**, 450.
57. S. C. Cunnane, R. J. McDonagh, S. Narayan, and D. J. Kyle, *Lipids*, 1993, **28**, 273.
58. I. M. Brereton, D. M. Doddrell, S. M. Okenfull, D. Moss, and M. G. Irving, *NMR Biomed.*, 1989, **2**, 55.
59. M. Ala-Korpela, Y. Hiltunen, J. Jokisaari, S. Eskelinen, K. Kiviniitty, M. Savolainen, and Y. A. Kesaniemi, *NMR Biomed.*, 1993, **6**, 225.
60. J. D. Otvos, E. J. Jeyarajah, D. W. Bennett, and R. M. Krauss, *Clin. Chem.*, 1993, **38**, 1632.

Biographical Sketches

E. Louise Thomas. *b* 1970; B.Sc. Biochemistry University of London, 1992; Ph.D. London, 1996. Ph.D. thesis on in vivo ^{13}C NMR spectroscopy under the supervision of J. D. Bell and K. D. Sales. Currently a Senior Research Fellow at Imperial College School of Medicine. Over 20 publications. Research interests include application of MRI/MRS to the study of human fat and muscle metabolism.

Jimmy D. Bell. *b* 1958; B.Sc. Biochemistry University of Warwick, 1982; Ph.D. London, 1987. Lecturer Hammersmith Hospital 1989–94. Senior lecturer Royal Postgraduate Medical School 1994–97. Senior lecturer at MRC Clinical Sciences Centre, Imperial College 1997–present. Approximately 90 publications. Research interests include application of MRI/MRS in clinical research, and MRS to the chemistry of tissue and body fluids.

Dietary Changes Studied by MRS

Maria L. Barnard and Jimmy D. Bell
Royal Postgraduate Medical School, Hammersmith Hospital, London, UK

1	Introduction	1
2	Useful Nuclei for Dietary Studies	1
3	In Vivo NMR Spectroscopy	1
4	High-Resolution NMR Spectroscopy	4
5	Related Articles	5
6	References	5

1 INTRODUCTION

The importance of diet in both the preservation of health and treatment of disease is increasingly recognized. The major causes of morbidity and mortality in the Western world include cancer, coronary heart disease, diabetes mellitus, and obesity. Nutrition appears to have a major role both in their treatment and prevention.[1,2] There is therefore a growing need for the application of current scientific techniques to nutritional studies, to delineate the response of human metabolism to dietary alterations. The development and use of spectroscopy for nutritional studies is a major recent advance.

The last decade has seen increasing interest in the use of both in vivo and in vitro NMR spectroscopy for investigation of human and animal metabolism. Researchers are taking advantage of the nondestructive and noninvasive nature of the technique. These characteristics are particularly important for widespread, population-based studies of human nutrition, which often require serial examinations.

The initial applications of NMR to dietary studies were principally concerned with development of the NMR methodology, rather than focusing on specific nutritional and biochemical problems.[3,4] However, even at this early stage the potential of NMR spectroscopy when applied to lipid and glycogen metabolism could be envisaged. In this article we will review the recent use of in vivo and in vitro NMR spectroscopy for the investigation of the metabolic effects of diet.

2 USEFUL NUCLEI FOR DIETARY STUDIES

Carbon-13, ^{2}H, ^{1}H and ^{31}P NMR techniques have all been applied to study the effects of dietary manipulation in animals and humans.[3–9] Limited information can be obtained with in vivo ^{31}P and ^{1}H NMR spectroscopy as applied to nutrition. Phosphorus-31 NMR detects only phosphate-containing compounds; ^{1}H NMR suffers from a small chemical shift range, resulting in severe signal overlap and signals near the water resonance which cannot be readily detected. This has meant that ^{1}H and ^{31}P NMR techniques have principally been applied to dietary studies in vitro.[10–12] However, ^{2}H and ^{13}C NMR methods have been used in elegant in vivo metabolic studies.

The deuterium nucleus is quadrupolar ($I = 1$). It has both a low gyromagnetic ratio and natural abundance (0.015%), which leads to a very low sensitivity relative to proton spectroscopy (1.45×10^{-6}). These unfavourable properties are offset by its short relaxation times and high body content (12 mM), allowing its detection by natural abundance in vivo NMR spectroscopy. Furthermore, the tissue content can be readily increased by the use of deuterated water (D_2O), a fact that Brereton et al.[5] have utilized to great effect in lipid turnover studies.

Carbon-13 NMR spectroscopy in vivo has also been successfully applied in dietary studies.[3,4,8,9] Compared with ^{1}H NMR, ^{13}C NMR spectroscopy is very insensitive due to the low gyromagnetic ratio and low natural abundance (1.1%) of the ^{13}C nucleus. Its relative sensitivity is further reduced by the $^{1}H–^{13}C$ coupling which splits the ^{13}C signal, effectively reducing intensity. These problems are partially offset by the short relaxation times of most ^{13}C resonances, the use of decoupling techniques, and the high tissue content of important dietary-related, ^{13}C-containing compounds, including lipids and glycogen. Moreover, the very fact that ^{13}C has 1.1% natural abundance has been exploited by using ^{13}C-enriched metabolites in turnover studies, similar to classical ^{14}C tracer studies.

3 IN VIVO NMR SPECTROSCOPY

3.1 Lipid Metabolism

3.1.1 Carbon-13 NMR Spectroscopy

High-resolution ^{13}C NMR spectroscopy has found widespread use in the study of lipids in vitro.[13,14] In particular, the clear distinction of multiple different fatty acid groups allows this technique to be used, often quantitatively, in studies of dietary oils.[15–18] This degree of resolution cannot be achieved in vivo, which limits the utility of this technique in noninvasive human research. However, major lipid groups can be distinguished and, within these constraints, important clinical and biochemical work has been carried out using proton-coupled ^{13}C and proton-decoupled $^{13}C\{^{1}H\}$ NMR spectroscopy.

Canioni et al.[3] first showed that in vivo $^{13}C\{^{1}H\}$ NMR spectroscopy could detect differences in the lipid composition of adipose tissue and liver in rats fed a diet high in polyunsaturated fatty acids. Further work by Sillerud et al.[19] examined $^{13}C\{^{1}H\}$ NMR of triacylglycerols in rat adipocytes in vivo, advancing our knowledge particularly of signal assignment in biological systems. Moonen et al.[4] developed in vivo $^{13}C\{^{1}H\}$ NMR to characterize adipose tissue in human subjects. They confirmed that linoleic acid ($C_{18:2n-6}$), usually the principal polyunsaturated fatty acid present in human adipose tissue, dominated the polyunsaturated fatty acid carbon signal observed in vivo, allowing estimation of this stored essential fatty acid. A typical ^{13}C NMR spectrum of human adipose tissue is shown in Figure 1.

Barnard et al.[9] demonstrated the capability of in vivo $^{13}C\{^{1}H\}$ NMR spectroscopy to monitor the effect of diet on

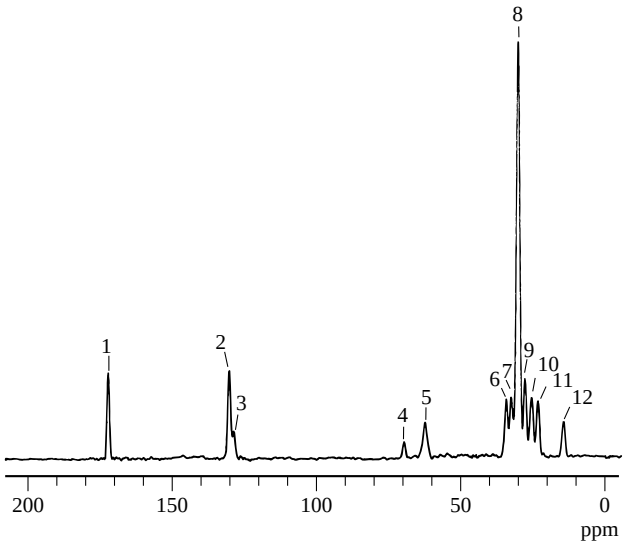

Figure 1 Natural abundance in vivo $^{13}C\{^1H\}$ NMR spectrum of human adipose tissue, dominated by signals from triacylglycerols. Peak assignment (referenced to $-\mathbf{C}H_3$): 1, **C**=O (171.79 ppm); 2, $-\mathbf{C}H{=}\mathbf{C}H-$(monounsaturated) and $-\mathbf{C}H{=}CHCH_2CH{=}\mathbf{C}H-$(polyunsaturated) (129.83 ppm); 3, $-CH{=}\mathbf{C}HCH_2\mathbf{C}H{=}CH-$(polyunsaturated) (128.13 ppm); 4, **C**-2 glycerol (69.21 ppm); 5, **C**-1, **C**-3 glycerol (62.05 ppm); 6, $-CH_2\mathbf{C}H_2CO_2R$ (33.93 ppm); 7, $-\mathbf{C}H_2CH_2CH_3$ (32.14 ppm); 8, $-(\mathbf{C}H_2)_n-$(29.69 ppm); 9, $-\mathbf{C}H_2CH{=}CH-$(27.39 ppm); 10, $-\mathbf{C}H_2CH_2CO_2R$ (25.04 ppm); 11, $-CH_2\mathbf{C}H_2CH_3$ (22.94 ppm); 12, $-CH_2\mathbf{C}H_3$ (14.1 ppm)

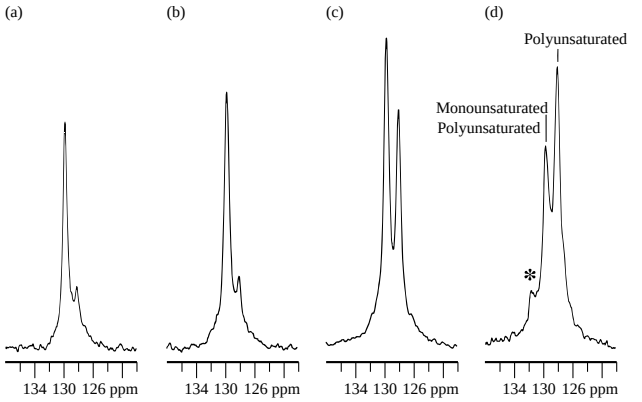

Figure 2 Olefinic region of natural abundance in vivo $^{13}C\{^1H\}$ NMR spectra of epididymal fat pad in rats fed fats high in different fatty acids. Unsaturated fatty acid carbon resonances appear in this region: monounsaturated ($-\mathbf{C}H{=}\mathbf{C}H-$) and polyunsaturated ($-\mathbf{C}H{=}CHCH_2CH{=}\mathbf{C}H-$) at 129.8 ppm; polyunsaturated ($-CH{=}\mathbf{C}H-CH_2\mathbf{C}H{=}CH-$) at 128.2 ppm. (a) Butter/lard diet–saturated fatty acids; (b) olive oil diet–monounsaturated fatty acids [oleic acid ($C_{18:1n-9}$)]; (c) sunflower oil–polyunsaturated fatty acids [linoleic acid ($C_{18:2n-6}$)]; (d) fish oil–($n-3$) polyunsaturated fatty acids [($C_{20:5n-3}$) and ($C_{22:6n-3}$)]. In these rats, adipose tissue lipid composition measured by NMR correlates to dietary content. Increasing dietary unsaturated and polyunsaturated fatty acid content produces similar changes in the adipose tissue, shown by an increasing total signal from **C**=**C** carbons and an increasing signal from polyunsaturated carbons at 128.2 ppm. Further, there appears to be a novel peak (*) at 132 ppm from unsaturated carbons at the $n-3$ position ($-CH{=}*\mathbf{C}HCH_2CH_3$), a double bond particularly found in the $n-3$ fatty acids of fish oil

adipose tissue in rats. In animals fed fats with different fatty acid patterns (butter/lard, olive oil, sunflower oil, fish oil), clear differences were found in the in vivo spectra, consistent with a significant effect of dietary fatty acid intake on the tissue fatty acid profile. Progressively increasing the total unsaturated and polyunsaturated fatty acid content in the diet was reflected in the adipose tissue composition (Figure 2), and results were correlated with in vitro spectroscopy and gas chromatography analyses. In humans, the turnover of fatty acids in adipose tissue is slow ($T_{\frac{1}{2}}$ = 600 d). The fatty acid profile of human subcutaneous fat therefore provides an index of the habitual dietary fatty acid intake over the previous 2–3 years.[20] This is of importance in long-term epidemiological surveys, but has previously been limited by the need for repeat tissue biopsies for fatty acid estimation. The application of in vivo ^{13}C NMR spectroscopy to the noninvasive analysis of adipose tissue composition is therefore of particular value for human nutritional studies.

Beckmann et al.[8] have used in vivo ^{13}C NMR to show a significant change in human adipose tissue fatty acid composition following a fat-reduced diet, with a correlation between diet and tissue monounsaturated fatty acids. No difference was found in the degree of polyunsaturation, and this may reflect the limited 6 month period of dietary change. Bryant et al.[21] chose to study vegan subjects as a defined population, with an established long-term diet, high in polyunsaturated fatty acids. A significantly increased adipose tissue total unsaturated and mono- and polyunsaturated fatty acid carbon content was shown in the ^{13}C spectra from the vegan group compared with omnivore controls (Figure 3). In addition, this was associated with a significant reduction in plasma concentrations of total cholesterol (4.55 ± 1.30 versus 5.39 ± 1.42 mmol l^{-1}, $p < 0.05$) and low-density lipoprotein (LDL) cholesterol (2.72 ± 1.06 versus 3.37 ± 1.34 mmol l^{-1}, $p < 0.05$) in the vegan subjects. The complex interactions between lipids in plasma and the body tissues are not fully defined, but are likely to be the subject of future NMR-based, dynamic studies of nutrition and lipid metabolism.

The interaction between diet and tissue lipids has been further studied by NMR in the liver. The liver has a pivotal role in lipid metabolism. Hepatic receptor-mediated LDL clearance is a major process controlling plasma LDL concentrations, and dietary saturated fat may increase plasma LDL levels by suppression of hepatic LDL receptor activity. The mechanisms underlying this effect are unclear, but it has been suggested that enrichment of hepatic membrane lipids with saturated fatty acids interferes with LDL receptor function.[22] Dietary substitution with polyunsaturated fatty acids may then increase hepatic LDL clearance and lower plasma LDL levels, possibly by increasing membrane fluidity.[23] Barnard et al.[24] used in vivo $^{13}C\{^1H\}$ NMR to examine the hepatic fatty acid profile in rats fed fats with different fatty acid patterns (butter/lard, sunflower oil, fish oil). The resolution of hepatic ^{13}C spectra is limited. The authors therefore used analysis by integration of signals across chemical shift ranges, and suggested expressing results by calculation of unsaturation and polyunsaturation indices (Table 1). A significant dietary effect was shown, with an increasing hepatic content of unsaturated fatty acids and an increasing degree of polyunsaturation as these fatty acids increased in the diet. However, in vitro $^{13}C\{^1H\}$ NMR studies of the liver lipid extracts showed a complex relationship,

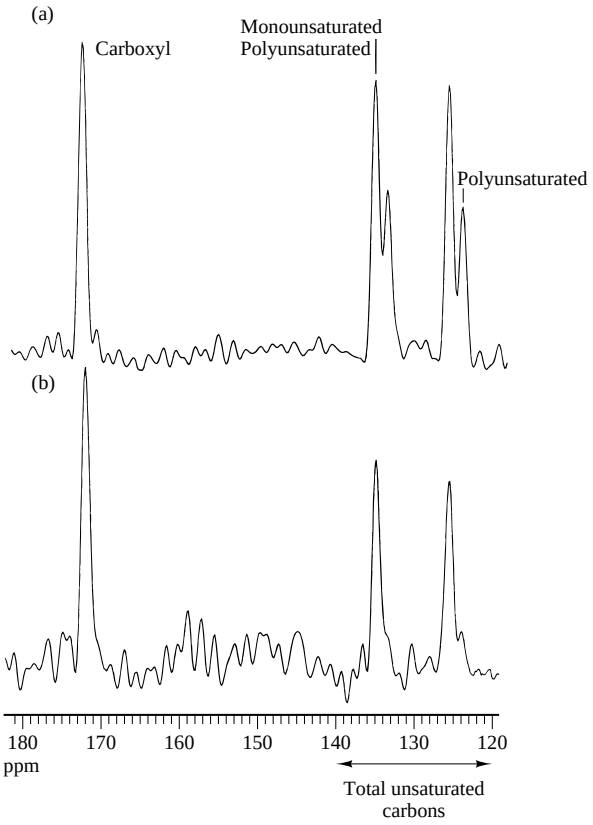

Figure 3 Olefinic region from natural abundance in vivo coupled ^{13}C NMR spectra of human thigh adipose tissue in (a) vegan and (b) omnivore subjects. Spectra are scaled to the carboxyl signal. The vegan subjects, compared to omnivores, have an increased adipose tissue content of both total unsaturated and polyunsaturated fatty acid carbons (polyunsaturated: 3.45 ± 0.87 versus 2.39 ± 0.55% of total fatty acid carbons, $p < 0.05$). This reflects at least 3 years' adherence to the vegan diet, which, in the absence of all animal products, is high in polyunsaturated fats (polyunsaturated: 33.13 ± 7.4 versus 25.2 ± 8.5% of total dietary fatty acids, $p < 0.05$)

with evidence of hepatic metabolism of the dietary fatty acids. Indeed, the liver is a major site of fatty acid uptake, desaturation, synthesis, storage, and secretion.

Investigation of the metabolism of specific dietary fatty acids is a largely unexplored possible future application of ^{13}C NMR spectroscopy. The use of ^{13}C-labeled fatty acids to trace metabolic pathways and kinetic rates is an exciting prospect. These studies may be restricted by the limited availability of labeled fatty acids, their oxidation after administration, and the sensitivity of the system, given the preexisting strong lipid signals. However, preliminary work has been performed by Cunnane et al.[25] and this demonstrated the ability of in vitro $^{13}C\{^1H\}$ NMR to detect carbon-specific incorporation of injected [U-^{13}C] eicosapentaenoic acid in extracted rat liver lipids.

3.1.2 Deuterium Spectroscopy

There is considerable interest in monitoring lipid turnover in both health and disease. A novel approach to the study of dynamic in vivo tissue lipid metabolism was developed by Brereton et al.[5] They investigated the use of in vivo ^2H NMR spectroscopy in mice. Administration of D_2O (10% v/v) in the drinking water for 3–4 d allowed the detection of deuterium-enriched tissue lipid resonances in spectra acquired in less than 2 min, as shown in Figure 4(a). The spectra consist of resonances from deuterated water (HOD) and the CHD groups of tissue lipids. Removal of D_2O from the drinking water led to clear changes in the intensity of both signals [Figure 4(b)]. The loss of deuterium from the water signal was significantly faster than from tissue lipids. The loss of deuterium from the lipid resonance was therefore proposed as a noninvasive measure of the rate of fat utilization. This method has since been applied to the study of fat utilization in obesity.

Obesity is one of the most common dietary disorders. It is characterized by excess adipose tissue and elevated levels of plasma nonesterified fatty acids. Furthermore, obesity is known to lead to glucose intolerance and insulin resistance. Fat turnover, as reflected by the levels of plasma nonesterified fatty acids, has been suggested as being implicated in this process. However, the lack of in vivo techniques for measuring fat utilization has greatly hampered progress in this area. Body fat turnover in mouse models of obesity and diabetes mellitus have been studied in vivo using the ^2H NMR technique.[26] Brereton et al.[26] showed that the rates of fat utilization in obese mice were significantly lower than the rates for nonobese mice (Figure 5) and the induction of diabetes did not affect utilization of fat as a metabolic fuel.

These studies clearly suggest that deuterium NMR spectroscopy provides researchers with a powerful method for noninvasively assessing fat turnover rates.

3.1.3 Proton Spectroscopy

The application of in vivo proton NMR spectroscopy to dietary studies has been rather limited. Indeed, many of the

Table 1 Hepatic Fatty Acid Profile by In Vivo $^{13}C\{^1H\}$ NMR Spectroscopy of Rats Fed Different Fats

Dietary Fat	Unsaturation Index[a]	Polyunsaturation Index[b]	Methylene–Methyl/%[c]	Olefinic/%[c]
Butter/lard	0.19 ± 0.04	0.90 ± 0.04	84.1 ± 0.91	15.9 ± 0.91
Sunflower oil	0.24 ± 0.01	1.04 ± 0.04	80.9 ± 0.31	19.1 ± 0.31
Fish oil	0.27 ± 0.01	1.32 ± 0.03	78.9 ± 0.79	21.1 ± 0.79

$p < 0.05$ for all differences between dietary groups.

[a]Unsaturation index = olefinic/methylene–methyl signal integration (measures the ratio of unsaturated to saturated fatty acid carbons).

[b]Polyunsaturation index = signal intensity at 128.2 ppm (=C–C–C=)/129.8 ppm (–C=C–) (measures the ratio of polyunsaturated to monounsaturated + polyunsaturated carbons).

[c]Olefinic and methylene–methyl signal area as the percentage of the total fatty acid signal integration (measures the percentage of fatty acid carbons that are unsaturated or saturated, respectively).

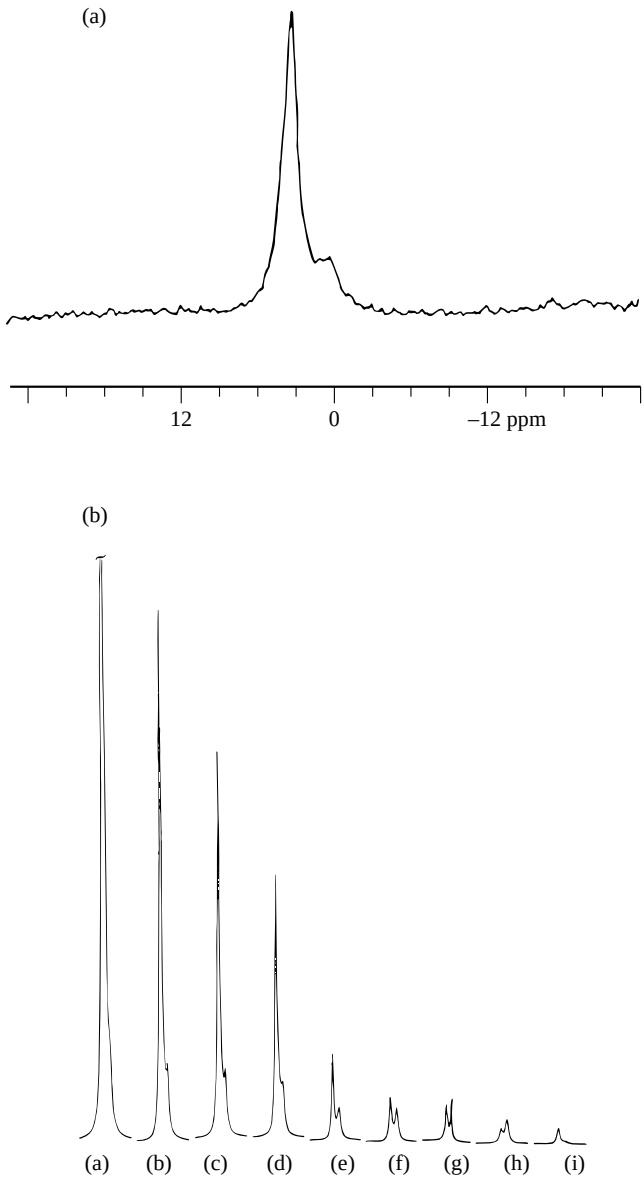

Figure 4 (a) Natural abundance ^{2}H NMR spectrum of a mouse. The CHD resonance is to high field at 1 ppm. Chemical shifts were referenced to the HOD resonance assigned to 4.8 ppm. (b) Deuterium NMR spectra of a mouse following the removal of 10% (v/v) of D_2O from its drinking water. The spectra were recorded (a) 1, (b) 4, (c) 5, (d) 8, (e) 11, (f) 15, (g) 16 and (h) 21 days after the resumption of normal drinking water. Spectrum (i) was recorded prior to the administration of D_2O to the drinking water (Adapted with permission of Heyden & Son Limited from I. M. Brereton, D. M. Doddrell, S. M. Oakenfull, D. Moss, and M. G. Irving, *NMR in Biomed.*, 1989, **2**, 55)

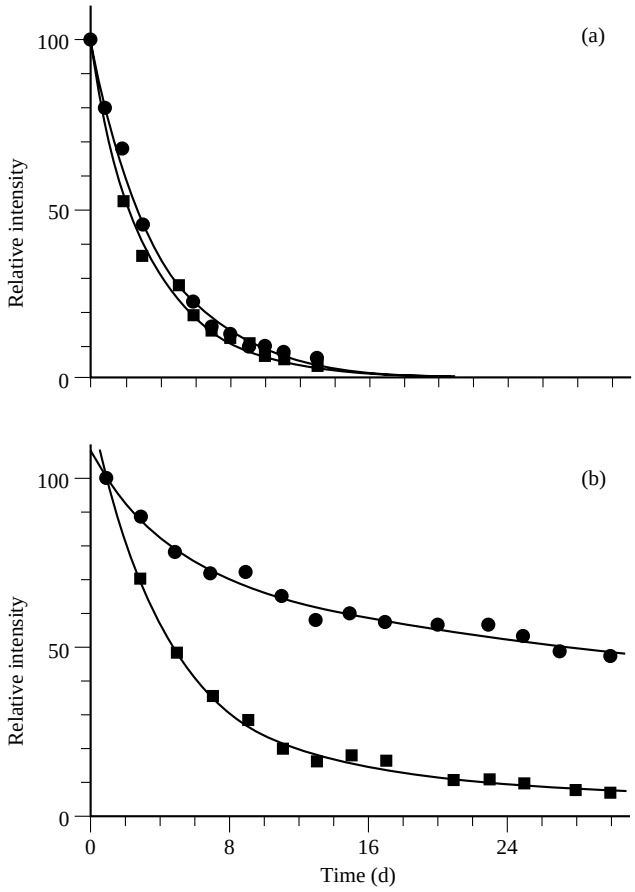

Figure 5 Plots of ^{2}H NMR signal intensity as a function of time showing (a) best fit single exponential decay curves for HOD and (b) best fit biexponential function for CHD intensities. The experimental data for control (solid square) and obese (solid circle) mice were used to calculate the body water and fat utilization rates. (Reproduced by permission of Heyden & Son Limited from I. M. Brereton, D. M. Doddrell, S. M. Oakenfull, D. Moss, and M. G. Irving, *NMR in Biomed.*, 1989, **2**, 55)

metabolites observed by ^{1}H NMR spectroscopy do not appear to be affected by diet, with the exception of lipids.[7] However, due to the small chemical shift range of ^{1}H resonances and the intense water signal, in vivo ^{1}H lipid studies have also been restricted. A potentially important alternative application of ^{1}H NMR is the use of fat imaging to determine quantitative fat distribution in human subjects.[27] Regional fat distribution has been correlated to serum lipids and coronary heart disease. Existing methods for measurement of body fat distribution are limited, and fat imaging may in future become the modality of choice in nutritional and metabolic studies evaluating the risk of coronary heart disease.

3.2 Glycogen Studies

Tissue glycogen values may be a marker of carbohydrate intake and could therefore be of value in dietary studies. Shulman and co-workers[28] have developed a ^{13}C NMR technique to provide a direct noninvasive method to measure liver and muscle glycogen concentration in humans. The time course of liver glycogen concentration, following standard test meals, has been carried out by ^{13}C NMR spectroscopy. This opens the possibility of following quantitative changes in glycogen storage with varying diets.[29,30]

4 HIGH-RESOLUTION NMR SPECTROSCOPY

The unique exploratory capability of NMR spectroscopy has been utilized to investigate the effects of diet on the metabolic profile of body fluids.[31] The ^{1}H NMR spectra of urine from

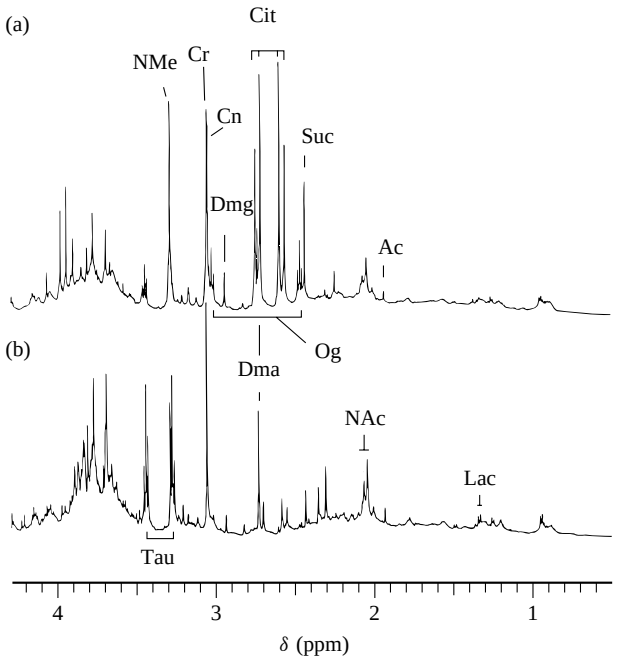

Figure 6 Proton NMR spectra at 500 MHz (aliphatic regions) of urine from 1-month-old rats fed either (a) chow or (b) casein diets. Assignments: Lac, lactate; Ac, acetate; NAc, *N*-acetyl groups of glycoproteins; Suc, succinate; Og, 2-oxoglutarate; Cit, citrate; Dma; dimethylamine; Dmg, dimethylglycine; Cr, creatinine; Cn, creatine; Tau, taurine; NMe, betaine plus trimethylamine *N*-oxide. (Reproduced by permission of Academic Press, Inc. from J. D. Bell, O. Lavender, V. C. Morris, and P. J. Sadler., *Magn. Reson. Med.* 1991, **17**, 414)

rats fed different diets are shown in Figure 6. Clear changes in the metabolic profile of the urine can be observed.[10] Rats fed casein diets for 1 month postweaning did not excrete 2-oxoglutarate, and excreted lower levels of hippurate, succinate, and citrate compared with age/sex-matched rats fed standard chow diets. The acquisition of these spectra took ∼2 min. This suggests that high-resolution NMR of urine or other body fluids could be utilized as a fast, multicomponent technique in human studies, for example to screen rapidly for multiple metabolic effects or to check dietary compliance.

Plasma concentrations of LDLs and high-density lipoproteins (HDLs) are well established markers for coronary heart disease risk assessment. Standard methods for quantification and compositional analysis of plasma lipoproteins require laborious and time-consuming physical separation based on particle size, density, or apolipoprotein content. Bell et al. have shown that NMR spectroscopy can be readily applied to study alterations in plasma lipoproteins associated with dietary manipulation, both in intact plasma or in the separated lipoprotein classes.[11,12] The effects of fish oil supplementation on the ^{1}H NMR profile of lipoproteins in intact plasma are illustrated in Figure 7. Changes in composition are shown by a new lipid resonance (peak 2A) arising from fish oil $n - 3/\omega - 3$ fatty acids incorporated into plasma lipoproteins, while the methylene $[-(C\mathbf{H}_2)_n-]$ signal (peak 3) is markedly reduced. Furthermore, T_2 analysis of the lipid resonances showed that these changes in lipid composition of the LDL particles are accompanied by alteration in the structural characteristics of these particles.

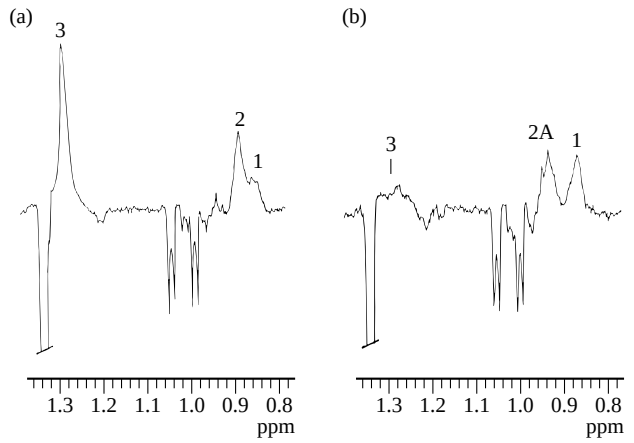

Figure 7 Expansions of spin echo ^{1}H NMR spectra of intact human plasma (a) before and (b) after 7 d of fish oil supplementation. Assignments: peaks 1 and 2, terminal $-C\mathbf{H}_3$ group from LDLs/HDLs and very low-density lipoproteins (VLDLs), respectively; peak 3, $-(C\mathbf{H}_2)_n-$of VLDLs. Peak 2A arises from $n - 3/\omega - 3$ fatty acids incorporated into plasma lipoproteins. (Reproduced by permission of Birkhauser Verlag from P. C. Dagnelie, J. D. Bell, M. L. Barnard, and S. C. R. Williams, in 'Omega-3 Fatty Acids: Metabolism and Biological Effects' ed. C. A. Drevon, I. Baksaas, and H. E. Krokan, Birkhauser Verlag, Basel/Switzerland, 1993, p. 27–34)

At present, sophisticated computer deconvolution methods (line-fitting analysis) are being developed to identify and quantify lipoprotein fractions in the ^{1}H NMR spectra of intact plasma samples (500 μl) within minutes.[32,33]

In this article we have reviewed the current state of NMR spectroscopy as applied to dietary studies. It is clear that this is a relatively new area of NMR research. However, it offers many exciting prospects for future research into diet and nutrition in humans.

5 RELATED ARTICLES

Analysis of High-Resolution Solution State Spectra; Brain Neoplasms Studied by MRI; Body Fluids; Chemical Shifts in Biochemical Systems; High-Field Whole Body Systems; Lipoproteins; Whole Body Studies: Impact of MRS.

6 REFERENCES

1. J. E. Kinsella, B. Lokesh, and R. A. Stone, *Am. J. Clin. Nutr.*, 1990, **52**, 1.
2. R. A. DeFronzo and E. Ferrannini, *Diabetes Care.*, 1991, **14**, 173.
3. P. Canioni, J. R. Alger, and R. G. Shulman, *Biochemistry*, 1983, **22**, 4974.
4. C. T. W. Moonen, R. J. Dimand, and K. L. Cox, *Magn. Reson. Med.*, 1988, **6**, 140.
5. I. M. Brereton, M. G. Irving, J. Field J, and D. M. Doddrell, *Biochem. Biophys. Res. Commun.*, 1986, **137**, 579.
6. P. C. Dagnelie, J. D. Bell, S. C. R. Williams, I. J. Cox, D. K. Menon, J. Sargentoni, and G. A. Coutts, *NMR Biomed.*, 1993, **6**, 2.

7. F. Schick, B. Eismann, W. I. Jung, H. Bongers, M. Bunse, and O. Lutz, *Magn. Reson. Med.*, 1993, **29**, 158.
8. N. Beckmann, J. J. Brocard, U. Keller, and J. Seelig, *Magn. Reson. Med.*, 1992, **27**, 97.
9. M. L. Barnard, J. D. Bell, S. C. R. Williams, T. A. B. Sanders, H. G. Parkes, K. K. Changani, J. S. Beech, M. L. Jackson, and S. R. Bloom, *Proceedings of the 11th Annual Meeting of the Society of Magnetic Resonance in Medicine, 1992*, p. 3339.
10. J. D. Bell, O. Lavender, V. C. Morris, and P. J. Sadler., *Magn. Reson. Med.*, 1991, **17**, 414.
11. J. D. Bell, J. C. C. Brown, R. E. Norman, P. J. Sadler, and D. R. Newell, *NMR Biomed.*, 1988, **1**, 90.
12. P. C. Dagnelie, J. D. Bell, M. L. Barnard, and S. C. R. William, in *Omega-3 Fatty Acids: Metabolism and Biological Effects*, ed. C. A. Drevon, I. Baksaas, and H. E. Krokan, Birkhauser Verlag, Basel, 1993, p. 27.
13. J. G. Batchelor, R. J. Cushley, and J. H. Prestegard, *J. Org. Chem.*, 1974, **39**, 1698.
14. J. Bus, I. Sies, and M. S. F. Lie Ken Jie, *Chem. Phys. Lipids*, 1976, **18**, 130.
15. F. D. Gunstone, M. R. Pollard, C. M. Scrimgeour, and H. S. Vedanayagam, *Chem. Phys. Lipids*, 1977, **18**, 115.
16. J. N. Shoolery, *Prog. NMR Spectrosc.*, 1977, **11**, 79.
17. N. G. Soon, *Lipids*, 1985, **20**, 778.
18. F. D. Gunstone, *Chem. Phys. Lipids*, 1991, **59**, 83.
19. L. O. Sillerud, C. H. Han, M. W. Bitensky, and A. A. Francendese, *J. Biol. Chem.*, 1986, **261**, 4380.
20. A. C. Beynen, R. J. J. Hermus, and J. G. A. J. Hautvast, *Am. J. Clin. Nutr.*, 1980, **33**, 81.
21. D. J. Bryant, J. D. Bell, E. L. Thomas, S. D. Taylor-Robinson, J. Simbrunner, J. Sargentoni, M. Burl, G. A. Coutts, G. Frost, M. L. Barnard, S. Cunnane, and R. A. Iles, *Proceedings of the 12th Annual Meeting of the Society of Magnetic Resonance in Medicine, 1993*, P. 1048.
22. S. M. Grundy, and M. A. Denke, *J. Lipid Res.*, 1990, **31**, 1149.
23. J. Loscalzo, J. Freedman, A. Rudd, I. Barsky-Vasserman, and D. E. Vaughan, *Arteriosclerosis*, 1987, **7**, 450.
24. M. L. Barnard, J. D. Bell, S. C. R. Williams, T. A. B. Sanders, and S. R. Bloom, *Proceedings of the 12th Annual Meeting of the Society of Magnetic Resonance in Medicine, 1993*, p. 92.
25. S. C. Cunnane, R. J. McDonagh, S. Narayan, and D. J. Kyle, *Lipids*, 1993, **28**, 273.
26. I. M. Brereton, D. M. Doddrell, S. M. Oakenfull, D. Moss, and M. G. Irving, *NMR Biomed.*, 1989, **2** 55.
27. R. Ross, L. Leger, D. Morris, J. De Guise, and R. Guardo, *J. Appl. Physiol.*, 1992, **72**, 787.
28. M. J. Avisoz, D. L. Rothman, E. Nadel, and R. G. Shulman. *Proc. Natl. Acad. Sci. USA*, 1988, **85**, 1634.
29. T. Jue, D. L. Rothman, B. A. Tavitian, and R. G. Shulman. *Proc. Natl. Acad. Sci. USA*, 1989, **86**, 1439.
30. M. Ishihara, H. Ikehira, S. Nishikawa, T. Hashimoto, K. Yamada, F. Shishido, T. Ogino, K. Cho, S. Kobayashi, M. Kawana, T. Matumoto, T. A. Iinuma, N. Arimizu, and Y. Tateno, *Am. J. Phys. Imag.*, 1992, **7**, 32.
31. J. D. Bell, J. C. C. Brown, and P. J. Sadler, *NMR Biomed.*, 1989, **2**, 246.
32. M. Ala-Korpela, Y. Hiltunen, J. Jokisaari, S. Eskelinen, K. Kiviniity, M. J. Savolainen, and Y. A. Kesaniemi. *NMR Biomed.*, 1993, **6**, 225.
33. J. D. Otvos, E. J. Jeyarajah, D. W. Bennett, and R. M. Krauss. *Clin. Chem.*, 1993, **38**, 1632.

Biographical Sketches

Maria L. Barnard. *b* 1960. B.Sc., 1981, M.B., Ch.B., 1984, University of Bristol, UK. Introduced to NMR by Graeme M. Bydder and Jimmy D. Bell, MRI Unit, Hammersmith Hospital during Medical Research Council (MRC) UK Training Fellowship with Stephen R. Bloom, Division of Endocrinology and Metabolism, Hammersmith Hospital, UK 1989–93. MRC (UK) Travelling Fellow to R.G. Shulman, Yale University, USA, 1992–93. Approx. 23 publications. Research interests: application of NMR spectroscopy to metabolic and nutritional studies.

Jimmy D. Bell. *b* 1958. B.Sc. Biochemistry 1982, University of Warwick. Ph.D. (supervisor P. J. Sadler), 1987, London. Senior NMR research fellow (with I. Young and D. G. Gadian), Hammersmith Hospital, 1989–93. Faculty in Biochemistry, Royal Postgraduate Medical School, 1993–present. Approx. 60 publications. Research interests include application of MRI/MRS in clinical research, and NMR spectroscopy to the chemistry of tissues and body fluids

Hepatic and Other Systemically Induced Encephalopathies: Applications of MRS

Brian D. Ross

Huntington Medical Research Institutes, Pasadena, CA, USA

1	Background: Biochemistry of Coma	1
2	Neurochemical Pathology of Hepatic Encephalopathy	1
3	Animal Studies in HE using Multinuclear MR Spectroscopy	1
4	Pathogenesis, Diagnosis, and Therapeutic Management of HE in Man: The Emerging Role of Proton MRS	1
5	Energetics of the Human Brain in HE	2
6	Subclinical HE	2
7	mI Depletion and the Induction of HE	3
8	Restoration of Cerebral mI and Cho Accompanies Reversal of HE	4
9	Ornithine Transcarbamylase (OTC) Deficiency	4
10	Contribution of NMR to Clinical HE	4
11	Other Systemic Encephalopathies	5
12	Conclusions	7
13	Related Articles	7
14	References	7

1 BACKGROUND: BIOCHEMISTRY OF COMA

Metabolic disturbances of liver, kidney, endocrine or other systems have remote effects; those on the brain result in a variety of well defined encephalopathies. When severe, these disorders present as coma. Posner and Plum published a comprehensive account of human coma.[1] Many were the result of presumed metabolic events with normal brain anatomy, setting the stage for noninvasive elucidation by means of biochemically based techniques. Among these are MRA, diffusion imaging, positron emission tomography (PET), single-photon emission tomography (SPECT), and multinuclear magnetic resonance spectroscopy (MRS). MRS has increasingly been used to identify specific biochemical changes in the brain, from which information on diagnosis and pathogenesis of these poorly understood disorders is beginning to emerge.

As a model for this group of disorders, we discuss hepatic encephalopathy, with additional remarks about diabetic, hyperosmolar, and hypoxia-induced encephalopathies.

2 NEUROCHEMICAL PATHOLOGY OF HEPATIC ENCEPHALOPATHY

Hepatic encephalopathy (HE) is an excellent example of metabolic encephalopathy,[2] with identifiable neurotoxins originating in a systemic disease. In animal studies, several distinct neurotoxins have been identified. The earliest of these was ammonia;[3,4] ammonia is normally fully removed from portal blood by hepatic urea synthesis.[5,6] The combination of the loss of biosynthetic liver function and the diversion of nondetoxified blood to the brain by so-called portal systemic shunts (PSSs) accounts for the frequently demonstrated excess of cerebral and cerebrospinal fluid glutamine[7] [equation (1)].

$$\mathrm{NH_{4+}} + \text{glutamate} \underset{\text{glutaminase}}{\overset{\text{GS}}{\rightleftharpoons}} \text{glutamine} \qquad (1)$$

The enzyme glutamine synthetase (GS) responsible for this reaction is located exclusively in astrocytes.[8] Resynthesis of glutamate and of γ-aminobutyrate (GABA) from glutamine (both vital neurotransmitter amino acids) occurs principally in neurons.[9]

Lest it be thought that ammonia 'toxicity' accounts for all of the clinical syndromes covered by the term HE, the interested reader is referred to Butterworth[10] for an extensive review of several other well-documented alternatives. Metabolic theories abound: failure of oxidative energy metabolism (a corollary of glutamate and 2-oxoglutarate depletion from the Krebs cycle), tryptophan and serotonin (5-hydroxytryptamine) accumulation, branched-chain amino acid deficits, endogenous benzodiazepine agonists which modify access of GABA to its inhibitory receptors, and neurotoxic fatty acids, octanoate in particular, have been proposed.

An attractive unifying theory proposed by Zieve[11] is that multiple neurotoxins derived from liver, blood, or from the diet, gain access via PSSs to a previously 'sensitized' brain. No mechanism of sensitization is known, but with the advent of MRS, a candidate has been proposed in the form of cerebral *myo*-inositol depletion.[12]

3 ANIMAL STUDIES IN HE USING MULTINUCLEAR MR SPECTROSCOPY

Three groups[13–15] independently perfected methods for the noninvasive determination of cerebral glutamine (including a variable contribution from glutamate in each assay) with ^{1}H NMR spectroscopy (now referred to as MRS) and confirmed the elevation of this metabolite in a variety of animal models of acute liver 'failure' with HE. One of these groups[13] also demonstrated a hitherto unrecognized abnormality, the significant reduction of choline (Cho; cerebral choline-containing compounds) in the ^{1}H spectra of rats with acute HE. More recently, ^{15}N NMR[16,17] and ^{1}H–^{15}N HMQC (unpublished work from this laboratory) identified cerebral glutamine unequivocally in vivo in HE produced by ammonia infusion in the normal and portocaval shunted rat, respectively.

Finally, in extracts of portacaval shunt (PCS) rat brain, high-performance liquid chromatography confirms the accumulation of glutamine and the depletion of glycerophosphoryl choline (GPC, which is therefore the explanation for the reduced 'Cho' in the previous ^{1}H NMR study), as well as demonstrating the expected depletion by 50% or more, of the cerebral *myo*-inositol (mI) and *scyllo*-inositol (sI) content.[18] This result in rats confirmed the observations which first emerged from human studies with short echo time ^{1}H MRS,[12,19,20] and establishes the validity of the portacaval shunt rat for future experimental studies.

4 PATHOGENESIS, DIAGNOSIS, AND THERAPEUTIC MANAGEMENT OF HE IN MAN: THE EMERGING ROLE OF PROTON MRS

Studies using STEAM localized, short echo time ^{1}H MRS defined the changes in 10 patients with clinically confirmed chronic HE. The average increase in cerebral glutamine was estimated as +50%, Cho decreased 14% and mI decreased by 45%[21] (Figure 1). Very similar findings have now been reported at 2T by Bruhn;[19,22] and by McConnell[23] using PRESS at short or long echo times. An early study which used long echo time PRESS-localized ^{1}H MRS failed to identify the depletion of mI, but was the first clearly to show 'Cho' depletion in human brain.[24]

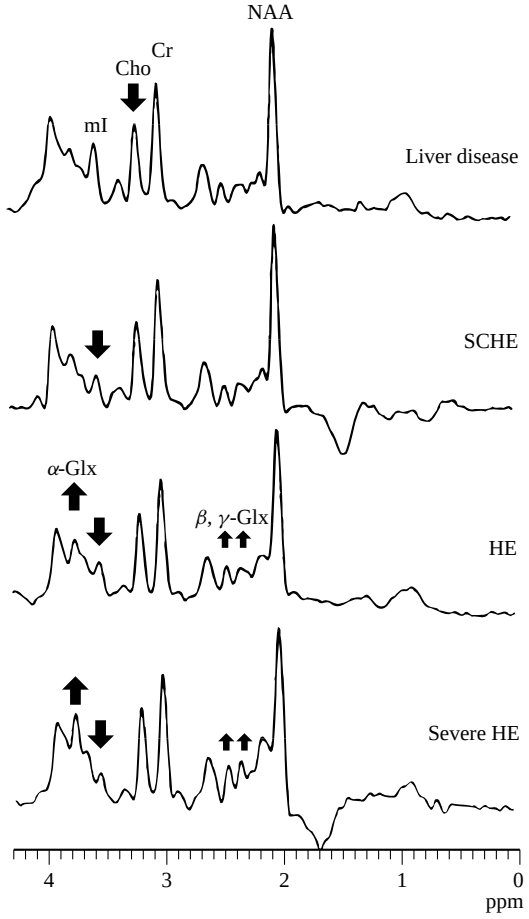

Figure 1 Development of hepatic encephalopathy in human subjects (1.5 T spectra). A series of spectra of parietal cortex (white matter) acquired under closely similar conditions (GE Signa 1.5 T, STEAM localization *TR* 1.5 s, *TE* 30 ms, NEX 128) from different patients is presented. A normal spectrum for comparison is that in Figure 6(b). In liver disease (top) there is a relatively normal spectrum with a slight decrease in choline. In subclinical hepatic encephalopathy (SCHE) there is a definite decrease in *myo*-inositol (mI) with a minor increase in the glutamine regions (glutamine plus glutamate = Glx). There is a very significant increase in the Glx regions in HE (grade 1) and mI is further depleted. The spectrum of grade 3 HE shows more severe changes in the biochemical markers of this disease, most notably glutamine

5 ENERGETICS OF THE HUMAN BRAIN IN HE

The predicted cerebral energy deficit (reduction in [ATP]) has convincingly only been shown in mice and tree shrews.[25] Phosphorus-31 MRS should be the easiest tool with which to establish any energy deficit in HE (as predicted). Ross,[26] Tropp,[27] Chamuleau,[28] Barbiroli,[29] and Morgan[30] have obtained conflicting and hence unconvincing data with ^{31}P MRS on such effects in man. Using quantitative ^{1}H MRS, however, Geissler and colleagues showed a small but significant increase in cerebral creatine concentration [Cr] following liver transplantation in man.[31] Since [Cr] is the sum of phosphocreatine (PCr) and creatine, this may indicate that patients with HE have an 'energy deficit'. The difficulty which has been confronted in demonstrating such an effect by ^{31}P MRS, where sensitivity is 10% that of ^{1}H MRS, becomes obvious. Since reduced cerebral oxygen consumption and blood flow are recognized abnormalities in HE, the ^{13}C NMR techniques pioneered by Shulman may be best suited to demonstrate the anticipated reduction in the overall rate of the Krebs cycle.[32]

From these clinical studies, it appears that ^{1}H MRS, particularly if applied with effective water suppression to reveal mI, is currently most efficient for the elucidation of pathogenesis of HE, and also, as will be shown, for its early clinical diagnosis. Direct measurement of mI by ^{13}C NMR may become a valuable adjunct.[33]

6 SUBCLINICAL HE

As indicated, HE is a group of diseases presumed to have identical etiology, but presenting a great variety of distinct clinical pictures. Underlying all of them is believed to be the entity of 'subclinical HE', although it is by no means clear

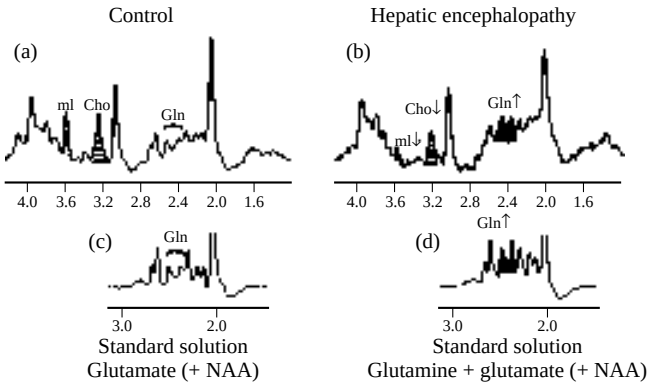

Figure 2 Identification of glutamine in the proton spectra at 2.0 T. A 51-year-old patient with HE due to surgical portacaval shunt (b) is compared with a normal control (a). Spectra were obtained from an occipital GM location and show the expected changes of HE: increased glutamine, decreased Cho/Cr and mI/Cr. With the improved resolution at 2 T, separate analysis of glutamine and glutamate is possible. Inset are spectra from model solutions (c) 5 mM glutamate + 5 mM NAA; (d) 5 mM glutamine + 5 mM glutamate + 5 mM NAA, indicating that in this patient the increase in glutamine occurs without obvious depletion of cerebral glutamate. Spectra were acquired on a Siemens 2.0 T clinical spectrometer, with STEAM localization; *TR* 3 s, *TE* 20 ms. (Modified from Bruhn et al.)[22]

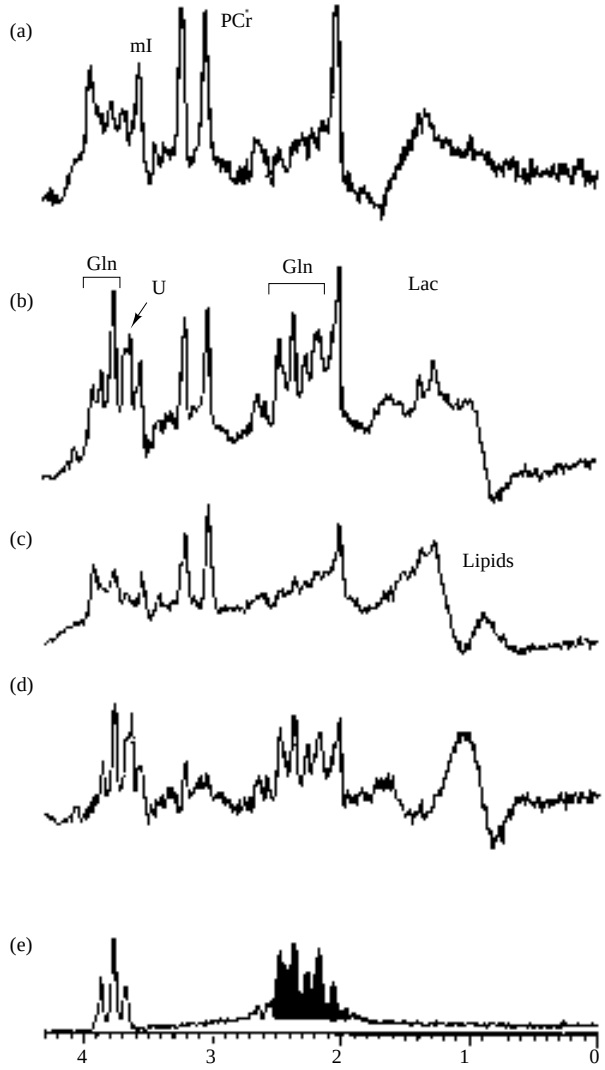

Figure 3 Proton MRS in acute hepatic encephalopathy due to Reye's syndrome. In vivo proton MRS spectra acquired from a parietal white matter region in infant brain from: (a) 10-month-old normal subject; (b) patient, day 2 after admission; (c) patient, day 8 after admission; (d) difference (b)–(c) between days 2 and 8 in patient; (e) solution with 15 mM glutamine. All spectra are scaled. Spectral assignments: Lac, lactate (1.3 ppm); NAA, *N*-acetylaspartate (2.02 ppm); Gln, glutamine (2.10–2.50 ppm, and 3.65–3.90 ppm); Cr + PCr, creatine + phosphocreatine (3.03 ppm); Cho, choline containing compounds (3.23 ppm); mI, *myo*-inositol (3.56 ppm). U, Unassigned (3.62 ppm). Notable abnormalities concern a huge accumulation of cerebral glutamine, reduced Cho, and, later, reduced mI, all of which reflect liver failure. In addition there is a decrease in NAA and [Cr] and appearance of the unassigned peak. Reye's syndrome, a toxic viral disease associated with aspirin intake is known to produce severe neuronal damage, and may not therefore completely correspond to the picture of acute liver failure. An occipital grey matter region gave almost identical results. (Reproduced with permission from Ernst et al.)[36]

that the HE and coma of fulminant (very acute) liver failure, goes through any truly 'subclinical' phase.

Proton MRS accurately reflects the entity of SCHE,[34,35] and in preliminary studies also appears to mirror the progressive and increasingly severe syndromes of overt HE defined by Parsons-Smith as grades 1–4 (Figure 1). Elevation of glutamine is rather more obvious at 2 T (Figure 2), but presents little difficulty at 1.5 T.

Figure 1 should not be taken as proof, however, that in the individual patient such orderly progression of neurochemical dysfunction occurs. Longitudinal studies have not been performed in sufficient numbers to be certain of this. Nevertheless, it is tempting to suggest, as Figure 1 appears to indicate, that in the brain exposed to liver 'toxins', Cho depletion (possibly GPC) precedes the loss of mI and sI, with later accumulation of glutamine. If this sequence is correct, then perhaps 'sensitization' of the brain is the result of mI or Cho depletion, or both. In keeping with the theory of many years standing, increasing cerebral glutamine underlies the neurological syndromes of grades 1–4, severe, overt chronic HE, as well as, perhaps, that of acute, fulminant HE and coma. Figure 3 shows the similar but more severe neurochemical changes of Reye's syndrome, giving an effective indication of what may be seen in acute HE.[36] Unfortunately, published spectra from patients with fulminant HE are limited and difficult to interpret.[37]

7 mI DEPLETION AND THE INDUCTION OF HE

A human 'experiment' which goes some way towards verifying this sequence is the new interventional procedure known as

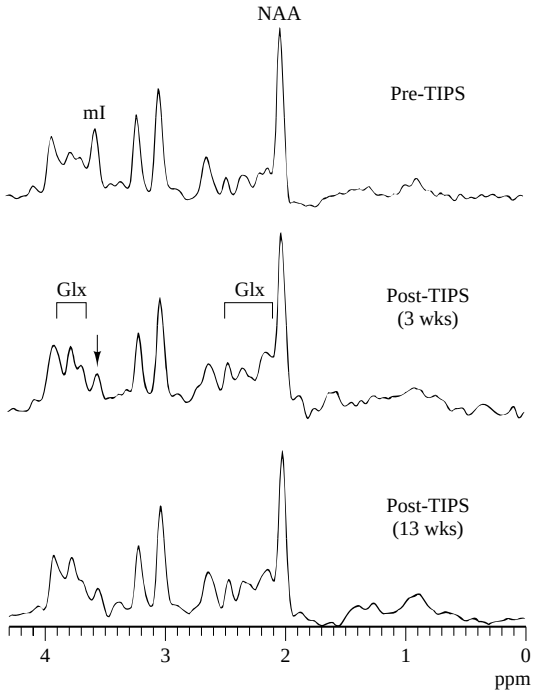

Figure 4 Effect of TIPS on the proton MR spectrum. Spectra are from a 30-year-old female, 5 days after a hematemesis due to esophageal varices and chronic alcoholic liver disease. Spectra acquired from a parietal WM location (GE Signa 1.5 T, volume 12.5 cm^3, STEAM *TR* 1.5 s *TE* 30 ms, NEX 128) before a TIPS procedure shows no abnormalities apart from a small but significant reduction in Cho/Cr, attributable to liver disease (top). Three weeks after TIPS, changes are seen in the Glx and mI regions and a further reduction on Cho/Cr (middle). The bottom spectrum shows the progression of changes seen (13 weeks post-TIPS); Glx is markedly increased and mI is significantly reduced

TIPS (transjugular intrahepatic portal systemic shunt), which is used as a life-saving procedure in cirrhosis-induced hematemesis. Not surprisingly, TIPS induces clinical HE in up to 90% of survivors.[38,39] Proton MRS performed both before and after TIPS in 10 patients showed a universal increase in mean intracerebral glutamine following the procedure. More importantly, in a small number of individuals in whom mI was normal prior to TIPS (these patients often show subclinical HE), a progressive reduction in mI/Cr and development of subclinical and clinical HE follows the introduction of the shunt (Figure 4).

8 RESTORATION OF CEREBRAL mI AND CHO ACCOMPANIES REVERSAL OF HE

Yet another common human 'experiment', that of orthotopic liver transplantation, allows the reverse process to be unequivocally demonstrated, thereby establishing a firm, albeit circumstantial link between mI depletion and the syndromes of subclinical and overt HE (Figure 5). Glutamine plus glutamate and Cho also recovered. Indeed, an overshoot of cerebral Cho is consistently observed, perhaps linking the earlier Cho depletion with deficient hepatic biosynthesis of some relevant precursor of GPC.

9 ORNITHINE TRANSCARBAMYLASE (OTC) DEFICIENCY

A description of MRS in HE would be incomplete without consideration of a rare but informative inborn error

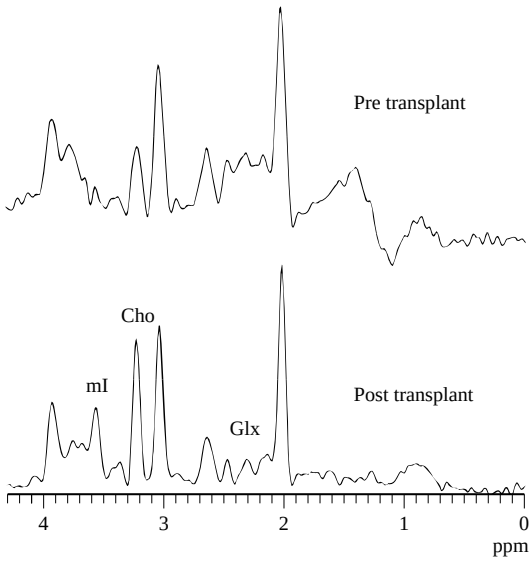

Figure 5 Restoration of biochemical abnormalities post-liver transplant. The patient is a 30-year-old male with acute-on-chronic hepatic encephalopathy secondary to hepatitis, and subsequently successfully treated by liver transplantation. Spectra were acquired 6 months apart from the same parietal WM location, (15.0 cm^3 STEAM *TR* 1.5 s, *TR* 30 ms, NEX 128) and scaled to the same Cr intensity for comparison. The obvious abnormalities before liver transplantation, increased α, β, and γ glutamine, reduced Cho/Cr and mI/Cr (upper spectrum) were completely reversed 3 months after transplantation, and Cho/Cr exceeded normal (lower spectrum)

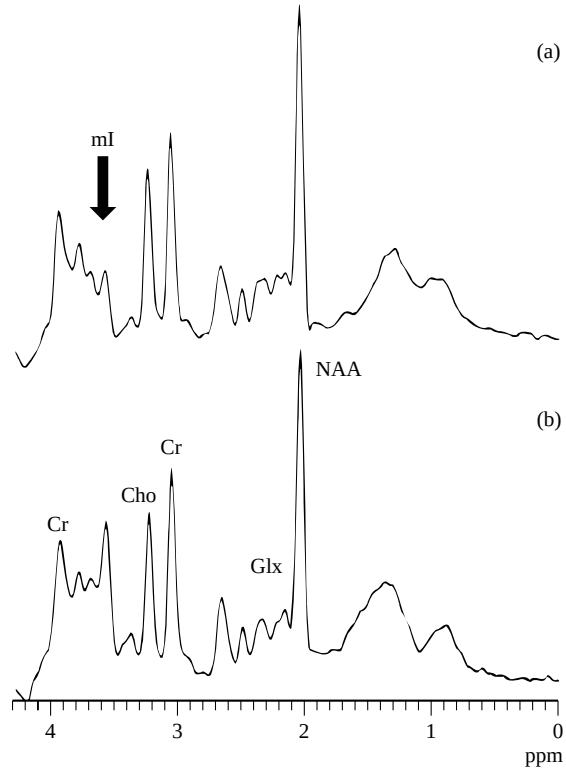

Figure 6 Treated OTC deficiency versus healthy age-matched subject. Both spectra were acquired from a similar location in parietal WM (STEAM *TR* 1.5 s, *TE* 30 ms, NEX 128) and processed as described in the literature[46]. Single-enzyme defects in the urea cycle result in severe hyperammonemia and 'hepatic encephalopathy'. Because the patient was receiving treatment with sodium benzoate, no excess of cerebral glutamine is present. However, as anticipated by studies in the commoner condition of hepatic encephalopathy due to portosystemic shunting, a decrease in mI was noted in the proton spectrum of a 14 year-old with OTC deficiency (a) when compared with a normal age-matched control (b)

of hepatic urea synthesis, ornithine transcarbamylase (OTC) deficiency. The single known biochemical consequence is hyperammonemia. Gadian and colleagues[??] demonstrated the inevitable elevation of cerebral glutamine in two such patients, while Ross[40] showed the extraordinary parallel with HE, in depletion of cerebral mI (Figure 6).

10 CONTRIBUTION OF NMR TO CLINICAL HE

10.1 Pathogenesis of HE

Both experimentally and clinically, NMR (particularly ^1H MRS) supports the classical concept of HE as a disorder of cerebral ammonia metabolism, be it by ammonia toxicity or glutamine synthesis (as a newer variant of the theory would have it).[41] The concept of an underlying brain 'sensitization' receives substantial new impetus deserving of further research in animal models. Either 'Cho' (GPC) depletion, due perhaps to failure of hepatic synthesis of a necessary precursor, or cerebral mI depletion could fulfill the role of 'sensitizer'. In neither case is there a precedent, so that basic research is

urgently required. It is likely that NMR will play a crucial role in such investigations, and the PCS rat is a convenient model. Carbon-13 NMR is the only method of unequivocally determining mI as distinct from the lower concentrations of inositol-1-phosphate (Inos-1-P) and glycine with which mI coresonates in the ^{1}H MR spectrum.

10.2 Proton MRS for Diagnosis

Early in these investigations, it became apparent that mI depletion and Glx accumulation occurred when clinical HE was absent. Other systemic or metabolic diseases (apart from OTC deficiency already discussed) did not result in mI depletion, so that ^{1}H MRS offers an unique opportunity for early, specific diagnosis of this still perplexing condition. Paradoxically, there is at present little enthusiasm for this, most probably because prevention (with lactulose or neomycin) and treatment (by liver transplantation) of overt or severe HE is relatively straightforward (albeit rather costly in the case of orthotopic liver transplantation (OLT) at $150 000–200 000 per patient in USA). If a ready medical means of restoring cerebral mI were to be discovered, the value of ^{1}H MRS in diagnosis might increase.

10.3 Unanswered Questions in Neurology of HE

Wilson's disease, caused by excess copper deposition, is believed to result in an encephalopathy analogous to HE. However, the ^{1}H MRS findings are not surprisingly rather different, lacking either mI depletion or glutamine accumulation (unpublished study from this laboratory).

Myelopathy is an unusual form of chronic HE. It presents with myelopathy and paraplegia. Athough neurological considerations would suggest cord involvement, the ^{1}H MRS findings in the parietal cortex are typical of other patients with the more classical clinical presentation (see Fig. 4 in Ross et al.).[40]

Often noted in MRI, the basal ganglia may be 'bright' in inversion recovery (IR) images of patients with known HE. There is no consistent relationship with ^{1}H MRS findings, and increasingly this MRS finding is recognized as nonspecific. Nevertheless, the extrapyramidal signs, the changes on postmortem, and these albeit inconsistent MRI findings continue to suggest that there may be as yet unrecognized underlying neurochemical changes in the basal ganglia in HE.

11 OTHER SYSTEMIC ENCEPHALOPATHIES

11.1 Diabetes Mellitus

Like HE, diabetic encephalopathy is common and obviously 'metabolic' in origin. Three principal syndromes are recognized: diabetic ketoacidosis, lactacidosis, and nonketotic hyperosmolar coma.

Elevated cerebral glucose,[42] significant excess of mI, a reversible accumulation of 'Cho', and the presence of ketone bodies have been detected in various patients with varying severity of diabetic encephalopathy.[43]

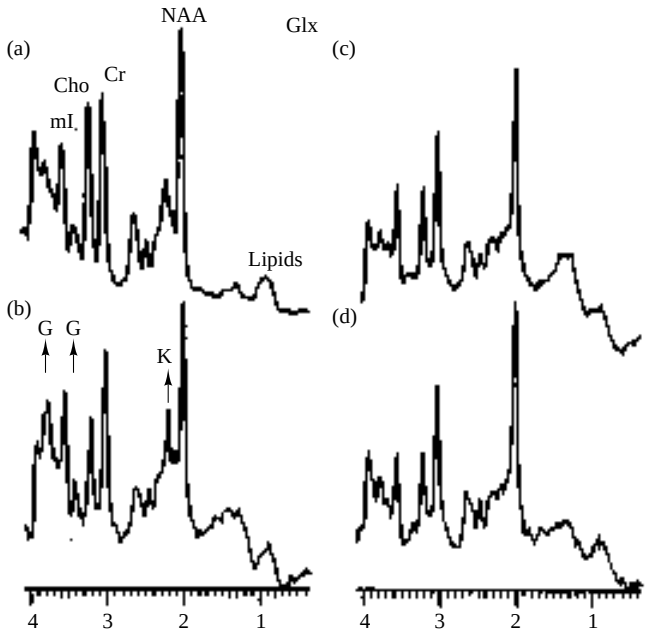

Figure 7 Diabetic ketoacidosis (DKA): cerebral ^{1}H spectra during two DKA episodes and recovery. (a) Episode 1, acquired 3 days after admission to hospital, at a time when the patient had supposedly totally recovered and was ready to be discharged. A peak characteristic for the presence of ketone (K) bodies was noted at 2.22 ppm, obtained from an 18 cm^3 volume in the left parietal lobe. The patient relapsed into DKA 2 days later. (b) Episode 2, acquired 5 months later from an occipital gray matter location (10.3 cm^3) during a second episode of DKA. In addition to the ketone peak, peaks for glucose (G) were seen. (c) Recovery, 6 days after episode 2 (from the same occipital location), when no more ketone bodies were detected in the urine. (d) Occipital cortex of an age- and sex-matched healthy subject. Acquisition conditions: GE Signa 1.5 T, 4X software; STEAM *TR* 1.5 s, *TE* 30 ms, NEX 128. More detailed analysis of peak K indicates the resonance frequency to be that of acetone, rather than acetoacetate, the ketone body more commonly identified in blood and urine of diabetics in coma. (Reproduced by permission of the Radiological Society of North America from Kreis and Ross)[43]

The most surprising finding of proton MRS which requires further study is the identification of acetone (rather than the more widely anticipated β-hydroxybutyrate and acetoacetate) as the ketone of human diabetic ketoacidotic encephalopathy[43] (Figure 7).

Long-term neurological and cerebral 'complications' of diabetes contribute to the much increased mortality. The biochemical basis of these conditions may lie in those changes in Cho, *N*-acetylaspartate (NAA), mI, ketones, and glucose, now recognized by ^{13}C and ^{1}H MRS, to be present in the acutely and chronically diabetic brain.

11.2 The Hyperosmolar State: Identification of Idiogenic Organic Osmolytes by Proton MRS

Lien et al. first used ^{1}H MRS to investigate a 'new' family of cerebral metabolites collectively known as organic osmolytes, because of their believed role in the maintenance of cerebral osmotic equilibrium.[44] Such molecules were also first thoroughly researched in the papilla of the kidney with the help of in vitro NMR.[45]

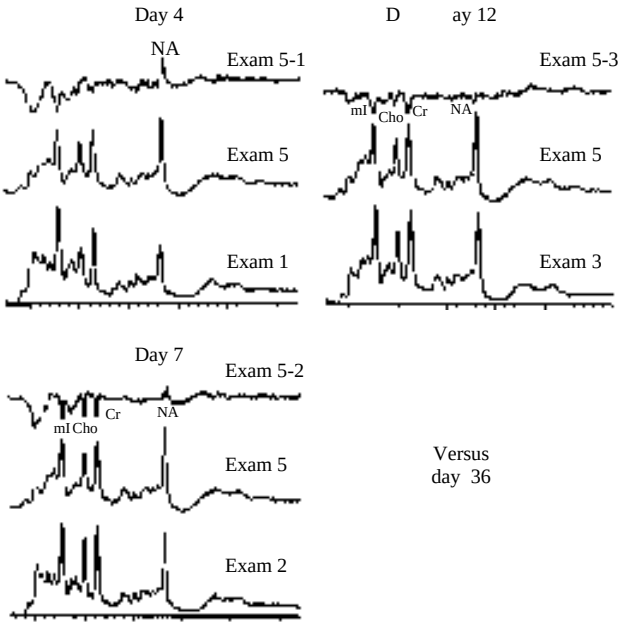

Figure 8 Time course of changes in principal cerebral organic osmolytes during correction of severe dehydration. A series of spectra were obtained from the same (occipital gray matter) brain location, in a 14-month-old child, recovering from severe dehydration and hypernatremia (plasma sodium 195 mEq l^{-1}; normal range 135–142 mEq l^{-1}) using identical acquisition conditions. Spectra were processed and scaled identically to permit subtraction of sequential spectra (difference spectroscopy). The day of examination refers to interval since admission to hospital. Examinations are numbered sequentially, from the first (Exam. 1) to last (Exam. 5) on day 36. Compared with a relevant normal [spectrum (b), Figure 6], the principal abnormality appears to be a reversal of the intensities of NAA (reduced) and mI (increased), so that mI dominates the spectrum. These changes slowly reverse to be nearly normal on day 36. The resultant difference spectra more clearly identify the progressively falling concentrations of several metabolites, with a possible elevation in the resonance peak assigned to the neuronal marker NAA. Quantitative MRS defines the principal abnormality as a threefold increase in the concentration of the cerebral osmolyte

First in sporadic cases of diabetic hyperosmolar coma[43] and in a patient after closed head injury,[46] and then most convincingly in a single infant with holoprosencephally and deficient thirst mechanisms, these concepts were confirmed as contributing to human encephalopathy by the use of ^{1}H MRS (Figure 8). mI was three times normal, and other resonances, also markedly affected, returned toward normal with treatment. Difference spectroscopy is particularly helpful in identifying these changes.[47,48] The converse, or hypoosmolar state of hyponatremia has been identified by ^{1}H MRS in significant numbers of patients.[49]

11.3 Hypoxic Encephalopathy

The prime example of a systemically induced encephalopathy is that due to insufficient oxygenation of blood, with resultant failure of cerebral oxygen delivery. Hypoxic encephalopathy is best understood in the context of energy failure and altered redox state through all cerebral metabolic pathways. Loss of ATP and PCr, accumulation of ADP, AMP, inorganic phosphate, and Cr are obvious consequences; H^+ accumulates, both due to failure of removal of CO_2 and formation of lactate. Reduced partners of the equilibrium enzymes, lactate and glutamate dehydrogenase, accumulate. In practice, glutamate is probably equally rapidly converted to glutamine. Innumerable animal studies, using principally ^{31}P NMR, but also ^{1}H NMR, confirm these principles and document other previously unsuspected changes, notably the loss of NAA.

The very common occurrence of hypoxic encephalopathy in humans has given ample opportunity for verification of these events in the human brain. ‘Recovery’ from nonlethal hypoxic encephalopathy gives yet another view of the metabolic process. From ^{31}P MRS in neonates,[50] the expected changes emerged.

More recently, ^{1}H MRS has been used to quantify and plot the time course of changes which occur after oxygen deprivation, applying the information to defining the degree of irreversible hypoxic neuronal damage—and hence prognosis. ‘Near-drowning’ is the term applied when virtually total oxygen deprivation occurs, due to submersion in water. It must be presumed that all ATP and PCr is lost, and all glucose

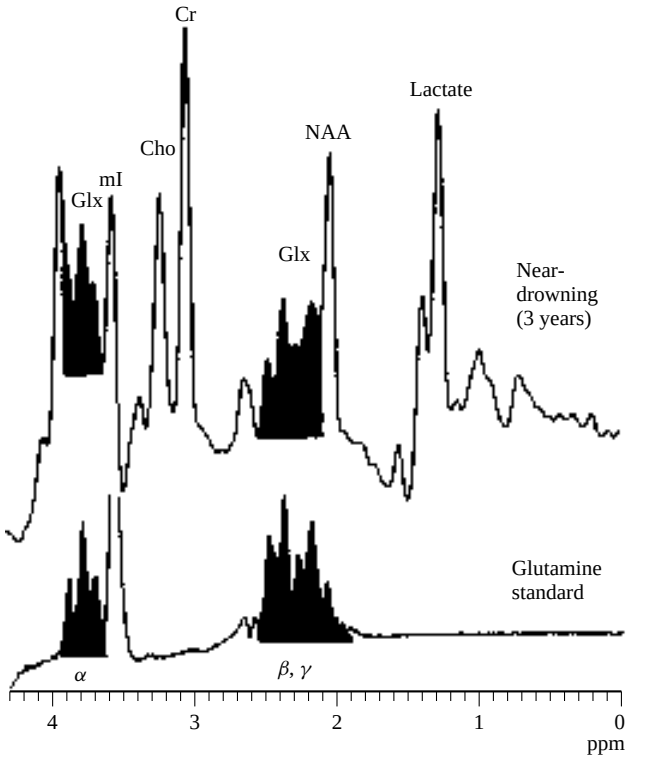

Figure 9 Near-drowning with fatal outcome. Brain spectrum from occipital cortex of a severe near-drowning victim (3 years old), examined 48 hours post-immersion (top), and the glutamine standard (bottom). The patient died on the 5th day post-injury. The ^{1}H spectrum was acquired from a volume of 12 cm^3 (STEAM *TR* 3.0 s, *TE* 30 ms, data processing including correction for residual water, line fitting, and quantification as described by Kreis et al.).[46] The spectrum of the glutamine standard (10 mM) was acquired in the same way, and scaled appropriately. Notable abnormalities in the patient spectrum are the very much reduced NAA/Cr ratio (and [NAA] concentration), excess of lactate (doublet at 1.3 ppm), and of the strongly coupled resonances of α, β, and γ glutamine protons. A 25% reduction in [Cr] was apparent on quantitative examination. (Thanks to Dr. Roland Kreis, Thomas Ernst, and Edgardo Arcinue MD)

converts to lactate in this period of anoxia. Yet at the first clinical examinations, 24 hours after rescue and artificial life support, MRS demonstrates more often than not the absence of lactate, normal Cr (plus PCr), and NAA at nearly full concentration. Only subsequently do NAA and total Cr fall and lactate appear. The severity of the changes gives a fairly good guide to outcome.[51]

The classic events of anoxia described by Lowry[52] are probably reversible, but secondary damage results in progressive cell death, the consequences of which are loss of NAA (in the case of dying neurons), loss of PCr and oxidative function and reaccumulation of lactate. It is unclear why the large accumulations of glutamine occur, or what the consequences are for survival (Figure 9).

12 CONCLUSIONS

Diffuse metabolic changes in brain biochemistry are the result of complex interactions of disordered biochemistry in many other organs and tissues. Hepatic encephalopathies, diabetic coma and hyperosmolar states and hypoxic encephalopathy are examples of such conditions in which accurate application of quantitative NMR spectroscopy sheds new light. Diagnostic utility of MRS in metabolic encephalopathies will increase as new therapeutic options are developed.

13 RELATED ARTICLES

Animal Methods in MRS; Brain MRS of Human Subjects; In Vivo Hepatic MRS of Humans; Single Voxel Localized Proton NMR Spectroscopy of Human Brain In Vivo; Water Suppression in Proton MRS of Humans and Animals.

14 REFERENCES

1. F. Plum and J. B. Posner, *The Diagnosis of Stupor and Coma*, Davis, Philadelphia, 1986.
2. S. Sherlock, W. H. J. Summerskill, L. P. White, and E. A. Phear, *Lancet*, 1954, **2**, 453.
3. S. Bessman and A. Bessman, *J. Clin. Invest.*, 1955, **34**, 622.
4. S Bessman and N. Pal, in *The Urea Cycle*, eds. S. Grisolia, R. Baguena, and F. Mayor, Wiley, Chichester, 1976, p. 83.
5. H. A. Krebs and K. Henseleit, *Hoppe-Seyler's Z. Physiol. Chem.*, 1932, **210**, 33.
6. A. Geissler, K. Kanamori, and B. D. Ross, *Biochem. J.*, 1992, **287**, 813.
7. B. T. Hourani, E. M. Hamlin, and T. B. Reynolds, *Arch. Intern. Med.*, 1971, **127**, 1033.
8. M. D. Norenberg and A. Martinez-Hernandez, *Brain Res.*, 1979, **161**, 303.
9. J-C Reubi, C. van den Berg, and M. Cuenod, *Neurosci. Lett.*, 1978, **10**, 171.
10. R. F. Butterworth and G. P. Layrargues, *Hepatic Encephalopathy: Pathophysiology and Treatment*, Humana Press, Clifton, 1989.
11. L. Zieve in *Diseases of the Liver*, eds. L. Schiff and E. R. Schiff, Lippincott, Philadelphia, 1987, p. 925.
12. R. Kreis, N. A Farrow, and B. D. Ross, *Lancet*, 1990, **336**, 635.
13. N. E. P. Deutz, A. A. de Graaf, J. B. de Haan, W. M. M. J. Bovee and R. A. F. M. Chamuleau, *J. Hepatol.*, 1987, **4**(1), S13.
14. T. E. Bates, S. R. Williams, R. A. Kauppinen, and D. G. Gadian, *J. Neurochem.*, 1989, **53**, 102.
15. S. M. Fitzpatrick, H. P. Hetherington, K. L. Behar, and R. G. Shulman, *J. Cereb. Blood Flow Metab.*, 1990, **10**, 170.
16. K. Kanamori, F. Parivar, and B. D. Ross, *NMR Biomed.*, 1993, **6**, 21.
17. K. Kanamori and B. D. Ross, *Biochem. J.*, 1993, **293**, 461.
18. R. A. Moats, Y-H. H. Lien, D. Filippi, and B. D. Ross, *Biochem. J.*, 1993, **295**, 15.
19. H. Bruhn, J. Frahm, T. Michaelis, K.-D Merboldt, W. Hänicke, M. L. Gyngell, P. Brunner, J. Frohlich, D. Haussinger, P. Schauder, and B.D. Ross, *Hepatology*, 1991, **14**, 121.
20. R. Kreis, N. A. Farrow, and B. D. Ross, *NMR Biomed.*, 1991, **4**, 109.
21. R. Kreis, B. D. Ross, N. A. Farrow, and Z. Ackerman, *Radiology*, 1992, **182**, 19.
22. H. Bruhn, K.-D. Merboldt, T. Michaelis, M. L. Gyngell, W. Hanicke, J. Frahm, P. Schauder, K. Held, G. Brunner, J. Frolich, D. Haussinger, and B. D. Ross. *Soc. Magn. Reson. Med.*, 1991, **10**, 400.
23. J. R. McConnell, C. S. Ong, W. K. Chu, M. F. Sorrell, B. W. Shaw, and R. K. Zetterman, *'11th Annual Meeting of the Society of Magnetic Resonance in Medicine', Berlin, WIP, 1992* , p. 1957.
24. R. A. F. M. Chamuleau, D. K. Bosman, W. M. M. J. Bovee, P. R. Luyten, and J.A. den Hollander, *NMR Biomed.*, 1991, **4**, 103.
25. S. Schenker, K. J. Breen, and A. M. Hoyumpa, *Gastroenterology*, 1974, **66** 121.
26. B. D. Ross, M. R. Morgan, I. J. Cox, K. E. Hawley, and I. R. Young, *J. Cereb. Blood Flow Metab.*, 1987, **7**, 5396.
27. B. D. Ross, J. P. Roberts, J. Tropp, K. Derby, N. Bass, and C. Hawryszko, *Magn. Reson. Imag.*, 1989, **7**, 82.
28. P. R. Luyten, J. A. den Hollander, W. M. M. J. Bovée, B. D. Ross, D. K. Bosman, and R. A. F. M. Chamuleau, *Proceedings, Society of Magnetic Resonance in Medicine, Amsterdam, 1989* , 8, 375.
29. L. Barbara, B. Barbiroli, S. Gaiani, L. Bolondi, S. Sofia, G. Zironi, R. Lodi, S. Iotti, P. Zaniol, C. Sama, and S. Brillanti. *Eur. J. Hepatol., 1993* , **2**, 60.
30. S. Taylor-Robinson, R. J. Mallalieu, J. Sargentoni, J. D. Bell, D. J. Bryant, G. A. Coutts, and M. Y. Morgan, *Proceedings, Society of Magnetic Resonance in Medicine, New York, 1993* , 12, 89.
31. A. Geissler, N. Farrow, F. Villamil, L. Makowka, T. Ernst, R. Kreis, and B. Ross, *Annual Meeting of Society of Magnetic Resonance in Medicine, Berlin, 1992* , 11, 647.
32. G. F. Mason, R. Gruetter, D. L. Rothman, K. L. Behar, R. G. Shulman, and E. J. Novotny *J. Neurochem.*, 1994, in press.
33. R. Gruetter, D. L. Rothman, E. J. Novotny, and R. G. Shulman, *Magn. Reson. Med.*, 1992, **25**, 204.
34. B. D. Ross, S. Jacobson, F. G. Villamil, R. A. Moats, T. Shonk, and J. Draguesku, *Hepatology*, 1993, **18**, 105A.
35. B. D. Ross, S. Jacobson, F. Villamil, J. Korula, R. Kreis, T. Ernst, T. Shonk, and R.A. Moats, *Radiology*, 1994, **193**, 457.
36. T. Ernst, B. D. Ross, and R. Flores, *Lancet*, 1992, **340**, 486.
37. R. K Gupta, V. A Saraswat, H. Poptani, R. K. Dhiman, A. Kohli, R. B Gujral, and S. R. Naik, *Am. J. Gastroent.*, 1993, **88**, 670.
38. B. D. Ross, T. Shonk, R. A. Moats, S. Jacobson, J. Draguesku, T. Ernst, J. H. Lee, and R. Kreis *Proceedings, Society of Magnetic Resonance in Medicine, New York, 1993* , 12, 131.
39. T. Shonk, R. Moats, J. H. Lee, J. Korula, T. Ernst, R. Kreis, J. Draguesku, and B. D. Ross, *Gastroenterology*, 1993, **104**, A-449, 1793.

39a. J. Korula, D. Kravetz, M. Katz, T. Shonk, S. Hanks, and B. D. Ross, *Hepatology*, 1993, **18**, 282A, 903.
40. D. G. Gadian, A. Connelly, J. H. Cross, S. Burns, R. A Iles, and J. V. Leonard, *Annual Meeting of the Society of Magnetic Resonance in Medicine, San Francisco, 1991*, 10, 193.
41. B. D Ross, R. Kreis, and T. Ernst, *Eur. J. Radiol.*, 1992, **14**, 128.
42. R. A. Hawkins, J. Jessy, A. M. Mans, and M. R. De Joseph, *J. Neurochem.*, 1993, **60**, 1000.
43. H. Bruhn, T. Michaelis, K-D. Merboldt, W. Hanicke, M. L. Gyngell, and J. Frahm, *Lancet*, 1991, **337**, 745.
44. R. Kreis, and B. D. Ross, *Radiology*, 1992, **184**, 123.
45. Y-H. H. Lien, J. I. Shapiro, and L. Chan, *J. Clin. Invest.*, 1990, **85**, 1427.
46. G. G. Wong D.Phil. Thesis, University of Oxford, 1981.
47. R. Kreis, T. Ernst, and B. D. Ross, *J. Magn. Reson.*, 1993, **102**, 9.
48. J. H. Lee and B. D. Ross, *Proceedings, Society of Magnetic Resonance in Medicine, New York, 1993*, 12, 1553.
49. J. H. Lee, E. Arcinue, and B. D. Ross, *N. Eng. J. Med.*, 1994, **331**, 439.
50. J. S. Videen, T. Michaelis, P. Pinto, and B. D. Ross, *J. Clin. Invest.*, 1995, **95**, 788.
51. P. L. Hope, E. B. Cady, P. S. Tofts, P. A. Hamilton, A. M. de Costello, D. T. Delpy, A. Chu, E. O. R. Reynolds, and D. R. Wilkie, *Lancet*, 1984, 366.
52. R. Kreis, T. Ernst, E. Arcinue, R. Flores, and B. D. Ross, *Society of Magnetic Resonance in Medicine, Berlin, 1992*, 11, 237.
53. O. H. Lowry in *Neurology of the Newborn*, ed. J. J. Volpe, Saunders, Philadelphia, 1987, p 33.

Acknowledgments

Work reported was largely funded by the L.K. Whittier Foundation of California, the Norris Foundation, the Richard M. Lucas Cancer Foundation (1, 2, 3 and 13) and by funds from the HMRI MRS Program. BDR is grateful to the following colleagues: T. Ernst, N. Farrow, A. Geissler, K. Kanamori, R. Kreis, J. Mandigo-Bellinger, T. Michaelis, R.A. Moats, E. Rubaek-Danielsen, T. Shonk, J. Videen, and J.D. Roberts.

Biographical Sketch

Brian D. Ross. *b* 1938; B.Sc., 1958, University College, London. D.Phil., 1966, University of Oxford. M.B., 1961, University College Hospital, London. F.R.C.S., 1973, Royal College of Surgeons, London. M.R.C.Path., 1976, Royal College of Pathologists, London. 1989, F.R.C.Path. University of Oxford lecturer, Metabolic Medicine. Director, Renal Metabolism Unit and Consultant Chemical Pathologist, Radcliffe Infirmary, Oxford, 1976–84. Director of Clinical Spectroscopy Programs at Radcliffe Infirmary, Oxford, 1981–84, Hammersmith Hospital, London, 1986–88, and Huntington Medical Research Institutes, Pasadena, CA, 1986–present. Visiting Associate, California Institute of Technology, 1986–present.

In Vivo Hepatic MRS of Humans

Isobel Jane Cox
Imperial College School of Medicine, London, UK

1 INTRODUCTION

The liver is the largest organ in the human body. By virtue of its anatomical position, the liver is readily suited to study by in vivo magnetic resonance spectroscopy (MRS) (***Whole Body Studies: Impact of MRS***). The liver is the principal homoeostatic organ in the body, being responsible for the metabolism of carbohydrates, fats, and circulating proteins and the detoxification of the body's waste products. It is the most important site for the metabolism of drugs and alcohol. Bile is produced in the liver, which is important for the digestion of fats in the gut and which also acts as a transport medium for the excretion of bilirubin and certain drugs. Information about a number of these processes can be obtained by multinuclear MRS study. For example, the phosphorus spectrum provides an assessment of hepatic energy state, membrane turnover, levels of endoplasmic reticulum and glycolytic/gluconeogenic intermediates. Signals from glycogen and lipids can be measured using natural abundance ^{13}C MRS. Fluorine-19 MRS can be used to detect metabolites of fluorinated drugs. Proton MRS provides a measure of hepatic water and fat content, but it has proved very difficult to obtain a metabolite spectrum because of the effects of respiratory motion. Clinical hepatic MRS builds on experience from the study of cell lines (see ***Cells and Cell Systems MRS***) and animal models (see ***Animal Methods in MRS***). The majority of human applications to date have used ^{31}P MRS as this is technically the easiest, and the data obtained have been used to aid diagnoses, monitor treatment effects, and to study hepatic biochemistry.

2 THE NORMAL LIVER SPECTRUM

2.1 Phosphorus-31 MRS

The phosphorus liver spectrum from a healthy adult volunteer comprises six major peaks, assigned to phosphomonoesters (PMEs), inorganic phosphate (Pi), phosphodiesters (PDEs) and the three phosphate groups (α, β, and γ) in nucleotide triphosphates (NTPs) (Figure 1). Notably absent from this spectrum are signals from membrane phospholipids such as phosphatidylcholine. The phosphorus nuclei in such large molecules have reduced mobility and the signals are NMR invisible. Similarly, the signal from adenosine diphosphate (ADP) bound to proteins is not detectable using NMR methods, and therefore the small ADP signal observed only represents free ADP.

2.1.1 The Phosphomonoester Resonance

The peak assigned to phosphomonoesters (PMEs) contains at least 10 components,[1] including: glucose 6-phosphate (G6P), glycerol 3-phosphate (G3P), glycerol 1-phosphate (αPG), and ribose 5-phosphate, which are intermediates in carbohydrate metabolism; coenzyme A, which is important in the metabolism of fatty acyl moieties; phosphoethanolamine (PE) and phosphocholine (PCh), which are metabolites on the pathway of membrane synthesis; adenosine monophosphate (AMP), which is an intermediate of adenosine triphosphate (ATP) and ADP turnover; and 2,3-diphosphoglycerate (2,3-DPG) which is present in blood, although it is unclear how much 2,3-DPG in circulating blood contributes to the in vivo spectrum.

2.1.2 The Inorganic Phosphate Resonance

The Pi signal is thought to represent about 40% of intracellular levels of Pi.[2] It is unclear why the remainder is invisible, but may be bound in the mitochondria. Pi, together with ATP and ADP, play a key role in energy metabolism, and changes in hepatic energy state may therefore be reflected by an alteration in the ATP/Pi ratio. The chemical shift of Pi in liver cells is dependent on pH, and cytosolic pH has been measured to be 7.18 ± 0.03 in perfused rat liver using microelectrodes.[3] In humans, the pH has been found to be consistent with this, and examples of values from healthy adult volunteers are: 7.18 ± 0.08,[4] 7.32 ± 0.02,[5] 7.36 ± 0.23,[6] and 7.23 ± 0.14.[7]

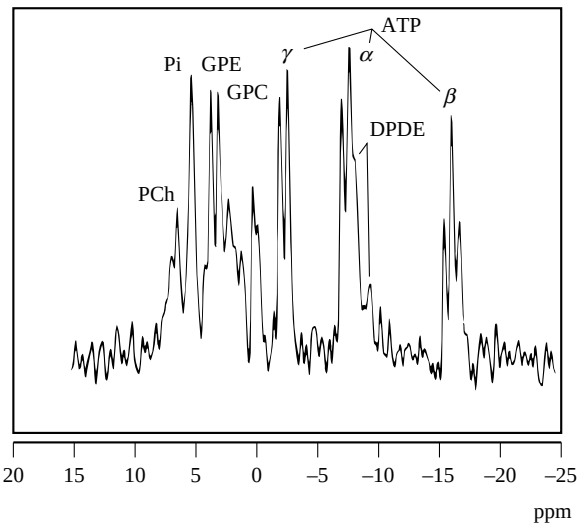

Figure 1 Proton decoupled localized ^{31}P NMR spectrum of the human liver, obtained at 1.5 T, using a 14 cm diameter surface coil. The localization scheme was ISIS with frequency modulated inversion and excitation pulses. The spectrum was obtained in 280 scans with 3 s repetition time. Proton decoupling has improved resolution in the phosphodiester, phosphomonoester, and diphosphodiester regions. Well-resolved resonances are observed for glycerophosphoethanolamine (GPE), glycerophosphocholine (GPC), and phosphocholine (PCh). DPDE, diphosphodiester. (Reproduced by permission of Heydon & Son from P. R. Luyten, G. Bruntink, F. M. Sloff, J. W. A. H. Vermeulen, J. I. van der Heijden, J. A. den Hollander, and A. Heerschap, *NMR Biomed.*, 1989, **4**, 177)

2.1.3 The Phosphodiester Resonance

The phosphodiester (PDE) signal contains contributions from at least three water-soluble metabolites,[1] including glycerophosphoethanolamine (GPE) and glycerophosphocholine (GPC). GPE and GPC are intermediates in phospholipid catabolism. At the field strengths used for clinical studies, a broad, field-dependent signal has also been identified, which has been assigned to phospholipid bilayer, including endoplasmic reticulum, with a small contribution from motionally averaged macromolecules.[8,9] In addition, phosphoenolpyruvate (PEP), although not a PDE, resonates in this region.

2.1.4 The Nucleotide Triphosphate Resonances

The dominant contribution to the nucleotide triphosphate (NTP) peaks are from ATP, but 10–20% of the peak area may be due to guanosine triphosphate (GTP) and uridine triphosphate (UTP). Further signals can be identified, overlapping with peaks from the three phosphate groups. For example, the αNTP resonance overlaps with signals from αADP and nicotinamide adenosine dinucleotide (NAD) or its reduced form (NADH). The γNTP signal overlaps with signals from βADP. It is interesting that the majority of ADP is NMR invisible, as discussed above. NAD and NADH play a pivotal role in electron transport in redox reactions, but it remains unclear what proportion is bound to proteins and is therefore not detected by in vivo MRS.

Binding to magnesium affects the chemical shifts of ATP, and therefore ^{31}P MRS provides information about the ratio of free ATP to magnesium-bound ATP.[4] This, in turn, reflects the intracellular concentration of free magnesium.[10] Oberhaensli et al.[4] measured the separation of βATP and γATP to be 13.70 ± 0.07 ppm, and estimated that 86% of the cytosolic ATP pool was magnesium bound, corresponding to a free cytosolic magnesium concentration of approximately 300 μmol L^{-1}. This result is consistent with the estimated free magnesium concentration of 450 μmol L^{-1} in the perfused rat liver.[11]

2.1.5 Age-Related Changes

The hepatic phosphorus spectrum from neonates and infants differs from the adult liver, in that the signal assigned to PMEs is elevated compared with that for ATP, and that for PDE/ATP is reduced.[12] The chemical shift of the PME signal is 6.8 ± 0.1 ppm, suggesting that PE is a major component. This would be consistent with the findings from neonatal brain, in which an elevated PME level has been attributed to PE.

2.2 ^{1}H MRS

The ^{1}H spectrum is dominated by signals from water and lipid. While this spectrum can be used to evaluate the degree of fatty infiltration, for example, both resonances need to be suppressed in order to observe metabolite signals. There has been one early paper describing high-resolution in vivo hepatic MRS, tentatively assigning the minor peaks to carnitine, taurine, glutamate, and glutamine.[13] Further in vivo studies have not been forthcoming, because of the problems of effective water and lipid suppression. However, the potential of ^{1}H MRS is illustrated by in vitro MRS studies of human tissue,[1] in which resonances from choline-containing groups, creatine, acetate, glutamine/glutamate, and glycogen have been assigned to the main resonances in the aliphatic region. Less intense signals from threonine, succinate, alanine, citrate, glycine, aspartate, and taurine have also been observed. The aromatic region shows resonances from a number of metabolites including NTP, nucleotide diphosphate (NDP), AMP, NAD and NADH.

2.3 ^{13}C MRS

The natural abundance of ^{13}C is only 1.1%. Therefore the only endogenous metabolites detectable in the liver by natural abundance ^{13}C MRS are storage compounds, such as triglycerides and glycogen, which can achieve high intracellular concentrations.

Fats are insoluble in water and are transported in the plasma as protein–lipid complexes (lipoproteins). The liver plays a major role in the metabolism of lipoproteins, synthesizing very low density proteins (VLDLs) and high density lipoproteins (HDLs). The liver and kidney are the major sites of HDL catabolism; low density lipoproteins (LDLs) are degraded by the liver after uptake by specific cell receptors. Triglycerides may be of dietary origin, but are also formed in the liver from circulating free fatty acids and glycerol and incorporated into VLDLs. There have been no studies to date interpreting the liver lipid profile with different diet or in disease. This reflects the fact that the concentrations of bulk triglycerides do not change sufficiently rapidly with time for short-term studies of fat metabolism to be carried out by this means.

On the other hand, glucose homeostasis and the maintenance of the blood sugar is an important function of the liver. In the fasting state, blood glucose is maintained either by glucose released from the breakdown of glycogen (glycogenolysis) or by newly synthesized glucose (gluconeogenesis). The relative contributions of these processes to glucose production have been difficult to quantify in humans, and therefore a noninvasive measurement at multiple time points of hepatic glycogen levels using ^{13}C MRS is of considerable importance.

The chemical shift range of the ^{13}C spectrum is 200 ppm, and the hepatic spectrum is dominated by resonances from saturated groups (–*CH_3 and –*CH_2–) from the fatty acyl chain at 15–35 ppm, unsaturated groups (–H*C=CH–) from the fatty acyl chain at 128–131 ppm, and carbonyl groups (–*CO–) from the fatty acyl chain at 172 ppm.[14] The signal from C-1 of glycogen resonates at 100.5 ppm, away from other resonances, and is therefore the most easily detected peak from glycogen. Smaller resonances from ethanolamine, choline, glucose, and carbonyl groups in proteins and phospholipids are observed in high-resolution spectra of rat liver.[14] While signals from triacylglycerides dominate the in vivo spectrum, often obliterating signals from other compounds resonating nearby, the majority of applications of hepatic ^{13}C MRS have concentrated on the detection and quantitation of glycogen levels.[15–19]

The relaxation times of glycogen are short; the T_1 is 240 ms and the T_2 is 30 ms,[20] so that rapid repetition times can be used. The sensitivity of measurement of the glycogen signal can be improved by proton decoupling[21] or polarization transfer techniques.[22] Signals from superficial lipids may need to be suppressed, for example by using shaped rf pulses, incorporation of an inversion pulse parallel to the coil axis at the sample surface,[17] or by exploiting the characteristics of the surface transmitter–receiver coil.[19]

2.4 ^{19}F MRS

The body does not naturally contain ^{19}F and therefore there are no signals in the hepatic ^{19}F MRS spectrum of the normal liver. However, signals from ^{19}F-containing drugs or their metabolites can be detected, for example 5-fluorouracil (5FU), enabling information about the time course and metabolic pathways of the drugs to be obtained.[23]

3 METHODOLOGY AND QUANTIFICATION

3.1 Field Strength

The majority of studies have been undertaken at field strengths of around 1.5 T. Boska et al. have formally compared the quality of hepatic ^{31}P MRS spectra at 1.5 T and 2.0 T.[24] The signal-to-noise ratio (S/N) of a localized hepatic ^{31}P MRS spectrum improved by 32 ± 10%, which is comparable with the improvement by 33 ± 13% in the S/N of a spectrum from a loading phantom.

Hepatic spectra have been reported by two groups using 4 T systems, with the aim of illustrating the increased sensitivity and spectral dispersion obtained at higher field strengths.[25,26] The hepatic ^{31}P MRS spectrum showed that resonances from PME, Pi, and PDE were well resolved, the two peaks from GPC and GPE in the PDE region could be distinguished, and resonances from nicotinamide adenine dinucleotide (NAD) and its phosphate (NADP) were seen as a shoulder on the αNTP/NDP peak.[26] The C-1 resonance from glycogen was detected at 4 T with an acceptable S/N in an acquisition time of 12–15[25] or 20 min.[26]

3.2 Localization

In the majority of studies, localization to the liver has been achieved by a suitable choice of rf coils combined with localization techniques. By virtue of the position of the liver, a surface receiver coil has almost always been used. The transmitter coil has been the same or another surface coil (producing a nonuniform $\boldsymbol{B}_1$ field)[4,6] or a saddle-shaped transmit coil (producing a uniform $\boldsymbol{B}_1$ field).[7] Additional localization has generally been achieved using single volume methods, such as ISIS, or multivoxel techniques such as chemical shift imaging or rotating frame zeugmatography.[27] Choice of technique will depend to some extent on the clinical problem and on the timescale of spectral acquisition.

3.3 Quantification (see *Quantitation in In Vivo MRS*)

It is difficult to realize the full potential of the technique because a number of factors limit the accuracy with which absolute quantitation can be achieved in hepatic MRS. Nevertheless, the majority of centers have provided some measure of absolute quantitation in both hepatic ^{31}P and ^{13}C MRS.[6,17,28,29] Factors to be borne in mind include the effect of respiratory motion, which causes ghosting of signals and degrades spectral resolution[30] and is a problem common to all nuclei. The presence of paramagnetics broadens the water linewidth, for example, compared with the linewidth in the brain and muscle. However, reasonable linewidths can be achieved in the hepatic phosphorus spectrum, and linewidths of 11 Hz have been measured at 1.6 T for Pi.[31] Another problem is the varying contribution of signals from overlying tissues, for example, subcutaneous lipid and posterior and anterior muscle. In ^{31}P MRS the contributions from muscle can be separated from the liver spectrum using the phosphocreatine signal as a marker for muscle. In both ^{13}C and ^{1}H MRS, contributions from subcutaneous lipid may be a serious problem, particularly if a surface coil is used, since these lipid signals are relatively intense and can mask the very much weaker metabolite signals.

Other factors need to be considered for hepatic ^{31}P MRS. Many of the signals are multicomponent, and the limited chemical shift dispersion of in vivo ^{31}P MRS spectra is a major cause of poor spectral resolution. Interpretation of a change in signal intensity to a specific metabolite or metabolites is often difficult without recourse to animal models or biopsy studies. The spectral resolution in the ^{31}P spectrum can be improved by ^{31}P–^{1}H decoupling,[5] since the three-bond coupling constant in, for example, PE, GPC, 2,3-DPG, and NAD, may become a dominant factor in determining the residual linewidth of these signals (see ***Proton Decoupling During In Vivo Whole Body Phosphorus MRS***). Finally, the relaxation times T_1 and T_2 are difficult to characterize for each individual study because the T_1 values can be long and there is limited time available for a clinical examination. The overall T_1 of the multicomponent signals does vary in some pathologies,[32] so it is not always possible to extrapolate from values obtained from healthy control subjects.

3.4 Relaxation Parameters in Hepatic ^{31}P MRS

A number of studies have specifically addressed the issue of T_1 measurement in healthy subjects. For example, Blackledge et al.[33] used an inversion–recovery depth-selection sequence based on rotating frame zeugmatography methods to measure T_1 values of the liver. They measured the T_1 of γATP to be 0.33 ± 0.05 s, that of PME as 0.74 ± 0.10 s, and that of Pi as 0.44 ± 0.06 s. The PDE peak appeared to exhibit heterogeneity in T_1, with a fast component (T_1 < 200 ms) and a slowly recovering component (T_1 > 1 s). Due to off-resonance effects, Blackledge et al. could not quote values for other peaks.

Buchthal et al.[34] used progressive saturation techniques, in combination with a surface coil and one-dimensional phase encoding. A uniform 90° pulse was achieved by using an adiabatic half passage pulse that compensated for the spatially nonuniform rf field of the surface coil. The mean T_1 values from seven individuals were: Pi, 0.41 ± 0.1 s; PDE, 1.4 ± 0.13 s; and γATP, 0.68 ± 0.09 s.

Meyerhoff et al.[6] used a fast inversion–recovery sequence, combined with ISIS, to measure T_1 relaxation values from four healthy volunteers. The results were: PME, 0.84 ± 0.26 s; Pi, 0.97 ± 0.25 s; PDE, 1.36 ± 0.37 s; γATP, 0.35 ± 0.06 s; αATP, 0.46 ± 0.09 s; and βATP, 0.35 ± 0.05 s.

Cox et al.[32] estimated T_1 values, from a comparison of signal intensities at *TR* 0.5 and 5 s, to be: PME, up to 3 s; PDE, 3–6 s; Pi, 1 s; and βATP, 0.7 s.

4 MRS STUDIES IN PROTEIN, CARBOHYDRATE, AND LIPID METABOLISM IN THE NORMAL LIVER

The complex interrelationships between protein, carbohydrate and fat metabolism are illustrated in Figure 2. Different aspects of these pathways can be probed measuring spectral changes after a metabolic challenge.

The formation of glycogen has been followed under different conditions, for example after a long fast,[17] an intravenous infusion of [1-^{13}C]glucose under hyperglycemic and hyperinsulinemic clamp conditions[19] and an oral intake of glucose in the form of bolus,[18,19] Rothman et al.[17] serially measured hepatic glycogen concentrations using ^{13}C MRS at 3–12 h intervals during a 68 h fast. The liver volume was determined by MRI. Net hepatic glycogenolysis was calculated by multiplying the rate of glycogen breakdown by the liver volume. The net rate of gluconeogenesis was calculated by subtracting the rate of net hepatic glycogeneolysis from the rate of glucose production in the whole body measured with tritiated glucose. Even in the first 22 h of fast they found that gluconeogenesis accounted for a substantial fraction of total glucose production (64 ± 5%) and this increased to 82 ± 5% (22–46 h of fasting) and 96 ± 1% (46–64 h of fasting). These important results suggest that hepatic gluconeogenesis is always operating at an appreciable rate in humans.

Ishihara et al.[18] measured glycogen and glucose resonances in one subject, after a bolus of glucose (100 g) following a 20 h fast, and also after administration of ^{13}C enriched (99%) [1-^{13}C]D-glucose (1 g) mixed with 75 g glucose.

Beckmann et al.[19] followed the formation of glycogen in the liver of normal volunteers after an intravenous infusion of [1-^{13}C]glucose under hyperglycemic and hyperinsulinemic clamp conditions and an oral intake of glucose in the form of bolus. They found that changes in the glycogen signal correlated well with the time course of insulin and glucagon during the spectral measurement. They showed that liver glycogen formation in man can be followed using nonlabeled glucose or [1-^{13}C]glucose with a low level of enrichment (16.6%). The use of nonlabeled glucose has the advantage that quantitation of net liver glycogen synthesis is simplified because label dilution through the various metabolic pathways of glucose is avoided. Measurements of glucose uptake, estimated from the increase in the glycogen signal, was consistent with findings from more complex and invasive studies of glucose uptake in the liver. The average liver glycogen concentration after a 12 h overnight fast in 18 volunteers without any dietary preparation was estimated to be 229 ± 34 mM.

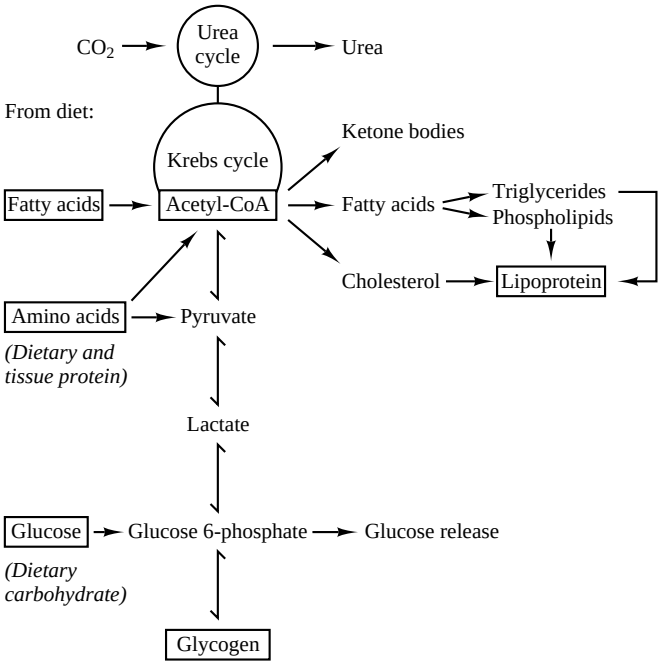

Figure 2 Interrelationships of protein, carbohydrate and lipid metabolism in the liver. (Reprinted by permission of Baillière Tindall from P. J. Kumar and M. L. Clark, (eds) 'Clinical Medicine', 1987, p. 212)

Of the physiological precursors for hepatic gluconeogenesis, the amino acid L-alanine is of special importance since it is a key protein-derived gluconeogenic precursor. It is cleared rapidly by the liver and has a half-life of only 30 min in the plasma of healthy subjects. After an overnight fast the plasma concentration of glucose falls and glycolysis in the liver is inhibited while gluconeogenesis is stimulated. Infusion of L-alanine induces rapid and consistent changes in ^{31}P MRS spectra (Figure 3).[35] A marked change with a clear dose–response relationship was observed for PME/ATP (maximal change +98%) and Pi/ATP (−33%), while smaller changes were demonstrated for PDE/ATP (+24%) which were independent of the alanine dose. Levels of ATP did not change, suggesting there was no change in phosphorylation status. In vitro MRS spectra obtained from animal models after alanine infusion showed marked increases in the gluconeogenic intermediates, 3-phosphoglycerate (PME region) and phosphoenolpyruvate (PDE region). Since the plasma glucose concentrations in humans were unaltered following the alanine infusion, MRS spectral changes have been interpreted as suggesting increased flux through the gluconeogenic pathway, possibly with glucagon rather than glucose as the endpoint. Therefore this metabolic stress test constitutes a useful tool for use in studies of gluconeogenesis.

Conventional liver function tests measure plasma clearance of the compounds metabolized by the liver, but these can be influenced by extrahepatic factors such as renal excretion. Therefore a direct measure of liver function would be of value. One example studied in detail has been a measure of hepatic sugar metabolism following a rapid intravenous bolus injection of fructose,[4,36,37] and the dose–response curves have been established.[36] Fructose is a major source of carbohydrate in the Western diet and is metabolized mainly in the liver. It is rapidly metabolized to fructose 1-phosphate by fructokinase in the liver, causing a rapid decrease in ATP and Pi. Thus, following intravenous infusion of fructose (bolus injection of 200–250 mg kg^{-1}) findings using hepatic ^{31}P MRS showed there was an approximately threefold increase in PME, predominantly fructose 1-phosphate, by 10 min and a return to basal values by 20–30 min. The hepatic concentration of Pi decreased by more than 80% immediately after fructose infusion, while the plasma Pi concentration dropped by only 20%. Pi levels rebounded and hepatic Pi concentration was increased to about three times the preinfusion values by 15 min. Thereafter, hepatic Pi levels gradually decreased, while plasma Pi

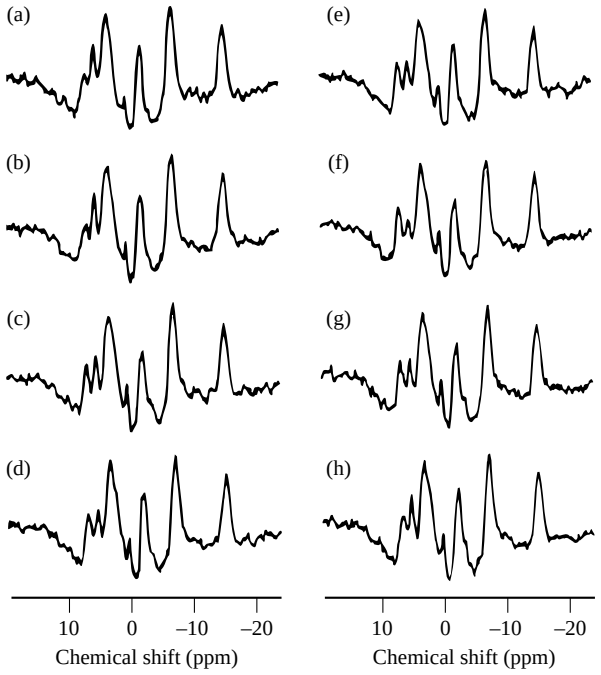

Figure 3 Representative ^{31}P NMR spectra of normal human liver before and after a bolus infusion of L-alanine 2.80 mmol kg^{-1} body weight. ^{31}P NMR data were acquired using a two-dimensional pulse sequence with a repetition time of 1 s and a pulse angle of 45° (256 signal averages). Spectra shown are plotted on the same absolute scale (referenced to the highest ATP peak of the whole set of spectra), so that absolute peak areas of all spectra are comparable. Two baseline spectra were obtained (a and b). Time after start of L-alanine infusion (i.e. midtime-point of data collection referenced to start of infusion) for spectra (c–h): (c) 8, (d) 13, (e) 26, (f) 39, (g) 67, and (h) 103 min. (Reproduced by permission of the Biochemical Society and Portland Press from P. C. Dagnelie, D. K. Menon, I. J. Cox, J. D. Bell, J. Sargentoni, G. A. Coutts, J. Urenjak, and R. A. Iles, *Clin. Sci.*, 1992, **83**, 183)

increased. The changes in Pi were several times greater in liver cells than in blood plasma, suggesting that large concentration gradients had been generated across the liver cell membrane. Hepatic ATP levels showed a transient decrease by 60% after infusion of fructose, but after 60 min the ATP pool was still reduced by about 40%, and this was attributed to the breakdown of ATP to inosine monophosphate and, ultimately, to uric acid. These changes in PME, Pi, and ATP showed a linear dose dependence.[36]

5 DIFFUSE LIVER DISEASE

5.1 Diabetes

Alterations in glucose–glycogen metabolism are important consequences for a number of diseases. For example, type II diabetes mellitus is characterized by fasting hyperglycemia and an excessive, prolonged rise in the plasma glucose concentration after glucose or meal ingestion. Magnusson et al.[38] measured glycogenolysis and gluconeogenesis in seven type II diabetic subjects and five control subjects during 23 h of fasting. They found that increased gluconeogenesis was responsible for the increased whole body glucose production in type II diabetes mellitus after an overnight fast. In detail, 4 h after a meal liver glycogen concentration was lower in diabetics than in controls, 131 ± 20 versus 282 ± 60 mmol L^{-1} liver ($p < 0.05$) (Figure 4). Net hepatic glycogenolysis was decreased in the diabetics, 1.3 ± 0.2 versus 2.8 ± 0.7 μmol per (kg body wt × min), $p < 0.05$. Whole body glucose production was increased in the diabetics, 11.1 ± 0.6 versus 8.9 ± 0.5 μmol per (kg body wt × min), $p < 0.05$. Gluconeogenesis was consequently increased in the diabetics, 9.8 ± 0.7 versus 6.1 ± 0.5 μmol per (kg body wt × min), $p < 0.01$, and accounted for 88 ± 2% of total glucose production compared with 70 ± 6% in controls, $p < 0.05$.

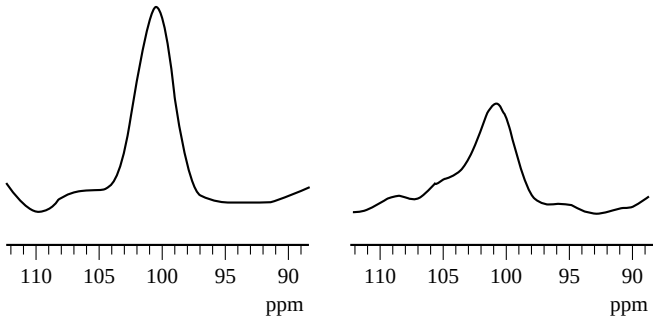

Figure 4 Typical ^{13}C NMR spectrum of the C-1 position of liver glycogen from one control subject (left panel) and one type II diabetic patient (right panel) 4 h after the liquid meal. (Reproduced by permission of The American Society for Clinical Investigation, Inc., from I. Magnusson, D. L. Rothman, L. D. Katz, R. G. Shulman, and G. I. Shulman, *J. Clin. Invest.*, 1992, **90**, 1323)

5.2 Hereditary Fructose Intolerance

Hereditary fructose intolerance (HFI) is a rare autosomal recessive disorder. The effect of fructose on liver metabolism in patients with HFI and in heterozygotes for HFI has been studied by hepatic ^{31}P MRS.[39] In five patients with HFI small amounts of fructose (1.5 g) were followed by an increase in sugar phosphates and a decrease in Pi, and it was suggested that hepatic ^{31}P MRS could be used to diagnose fructose intolerance and to monitor patients' compliance with a fructose-restricted diet. In eight heterozygotes, ingestion of much larger amounts of fructose (50 g) led to an accumulation of sugar phosphates, a reduction of Pi, and a larger increase in plasma urate compared with control subjects. The effects were most pronounced in heterozygotes with gout, and it was suggested that heterozygosity for HFI may predispose to hyperuricemia.

5.3 Familial Gout

The hyperuricemia responsible for the development of gouty arthritis results from a wide range of environmental factors and, less commonly, from inborn errors of metabolism. As a continuation from the studies on homozygous and heterozygous patients with HFI, 11 volunteers with familial gout were examined with hepatic ^{31}P MRS following a 50 g load of oral fructose.[40] Spectral changes in response to the fructose load similar in magnitude to those observed in earlier studies of

obligate heterozygotes for HFI were found in 2 of the 11 patients with familial gout. In one family the index patient's three brothers and his mother all showed the fructose-induced abnormality of metabolism, in agreement with the maternal inheritance of the gout in this family group. The test dose of fructose used produced a significantly larger increment in the concentration of serum urate in the patients showing changes on hepatic ^{31}P MRS. The biochemical basis for the fructose-induced increase in purine metabolism was discussed, and it was suggested that a lower activity of aldolase B prevailed in the two patients with hereditary gout who showed fructose-induced abnormality of metabolism. It was suggested that in these two subjects the causal role for generating gout is the aberrant fructose metabolism, and indeed that a restriction of fructose ingestion is a possible approach to the clinical management of patients with this disorder.

5.4 Cirrhosis

The clinical spectrum of cirrhosis varies widely, and adequate characterization of the functional state is therefore essential for making management decisions in these patients. At present, characterization usually depends on the assessment of indirect clinical and laboratory measurements of hepatic function. These parameters provide some measure of the functional grade of cirrhosis, but are subject to extrahepatic influences that may reduce their value as markers of liver function. Quantitative estimates of liver function may also be obtained from various clearance studies, but individual tests may not provide a good picture of overall liver function.

Several groups of workers have used hepatic ^{31}P MRS to study subjects with alcoholic cirrhosis and chronic liver disease of other etiologies,[28,29,41–45] and two studies have addressed hepatic ^{31}P MRS in the context of varying functional severity of liver disease.[43,45] The results from different centers are not consistent, reflecting differences in the acquisition parameters (and, therefore, the degree of quantitation) and also differences in clinical state of the patients.

Patients with alcoholic liver disease were studied using image-guided hepatic ^{31}P MRS methods, to yield an estimate of absolute molar concentrations of phosphorus metabolites in a 64–120 cm^3 volume within the liver.[41] The patient group included nine patients with alcoholic cirrhosis of varying severity. The pH value was more acidotic in the cirrhotic patient group (7.26 ± 0.2) compared with controls (7.44 ± 0.2) (p = 0.04). The chemical shifts of the other peaks were not significantly different between the cirrhotic and control group. The metabolite ratios were similar in the control and cirrhotic group. However, absolute concentrations of metabolites were decreased by 13–50%. Except for the decrease in PME of 13%, all the decreases from values obtained in normal liver were significant ($p < 0.05$). There was no significant difference between the absolute values for cirrhotics and hepatitics.

In a study of patients with alcohol liver disease, including five patients with cirrhosis, Angus et al.[42] found no change in any of the metabolite ratios in the patients with cirrhosis. There was no change in Pi/ATP, suggesting no evidence of impaired cellular energetics. The hepatic pH was also similar in patients with cirrhosis and in controls. This patient group had previously been found to have established cirrhosis, and had been abstinent from alcohol for at least 6 months.

Absolute concentrations were measured using one-dimensional chemical shift imaging (CSI) techniques in five healthy volunteers and five patients with alcoholic cirrhosis.[29] Absolute metabolite levels were calculated with reference to an external standard. Metabolite ratios were not altered in cirrhosis compared with controls, although absolute concentrations of all hepatic metabolites tended to be lower. However, only the reduction in βATP, of 31%, was significant. Histological evidence suggested that the reduction in ATP levels reflected fewer functioning liver cells per volume of liver, since functional cells had been destroyed and replaced by fibrosis. The amount of ATP per liver parenchymal cell was thought to be unchanged. The authors suggested that metabolite ratios were of limited diagnostic value in the assessment of alcoholic cirrhosis, if they were unsupported by quantitative analysis.

Fourteen patients with liver cirrhosis of differing severity were examined using one-dimensional CSI methods.[43] Patients were divided into two groups according to the severity of their liver disease using Child's classification and the aminopyrine breath (AB) test. The PME/total phosphorus ratio was significantly higher in patients with mild and severe cirrhosis. There was no change in the PME T_1 value in cirrhotics. There was a significant negative linear correlation of PME with percentage dose of $^{14}CO_2$ excreted over 2 h in the AB test. The pH values were significantly elevated in mild cirrhosis (pH 7.45), but not in severe cirrhosis (pH 7.36), compared with controls (pH 7.29). This was the first paper highlighting the clinical potential of hepatic ^{31}P MRS as a noninvasive means of assessing the severity of liver cirrhosis.

In a study of a group of 86 patients with histologically proven cirrhosis of varying etiology and functional grade (Menon et al.[45]), patients with liver disease showed a significantly higher median PME/ATP ($p < 0.0001$), PME/PDE ($p < 0.0001$), PME signal height ratio (SHR) ($p < 0.0001$), and Pi SHR ($p < 0.02$), and a lower median PDE/ATP ($p < 0.001$) and PDE SHR ($p < 0.001$) (the SHR was obtained by dividing the peak height at *TR* 5 s by that at *TR* 0.5 s to yield a T_1-related SHR). The magnitude of these changes significantly and progressively increased with worsening functional state (Figure 5).

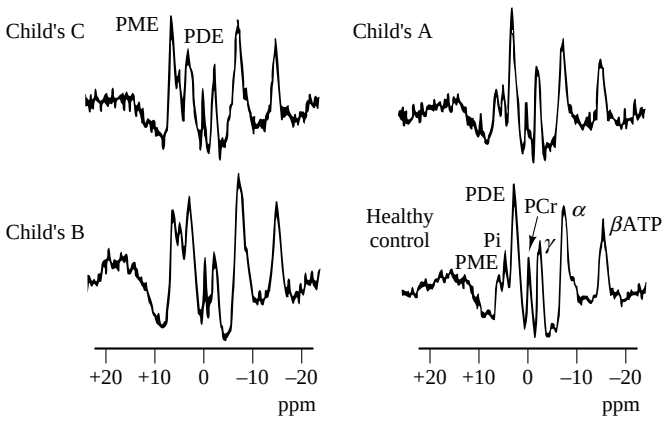

Figure 5 Hepatic ^{31}P MR spectra collected using a two-dimensional CSI sequence with *TR* T_p-5 s, pulse angle 45° from a healthy volunteer, and patients with Child's A, B and C functional grades of alcoholic cirrhosis

Etiological differences were noted in patients with compensated cirrhosis. Spectra from patient with cirrhosis secondary to viral hepatitis showed a significantly higher PME/ATP, Pi/ATP, and PME/PDE, and those with cirrhosis secondary to primary sclerosing cholangitis showed a significantly lower Pi/ATP than did other etiological groups.[45] However, spectral appearances did not vary with etiology of cirrhosis in decompensated patients. In vitro ^{31}P MRS of perchloric extracts of biopsy samples of liver tissue obtained from 10 patients with cirrhosis at transplant hepatectomy showed increases in levels of PE and PC, and a reduction in levels of GPE and GPC. These changes suggest regenerative activity in cirrhotic livers. The reduction in soluble PDE in the aqueous extracts did not quantitatively account for the reduced PDE resonance seen in vivo, and the changes seen in vivo may therefore be partly due to reduction in contributions from hepatic endoplasmic reticulum, resulting from replacement of hepatocytes by fibrous tissue.

In order to determine the feasibility and utility of dynamic hepatic ^{31}P MRS, Dufour et al. studied six healthy subjects and nine patients with nonalcoholic cirrhosis after an intravenous infusion of a fructose load (250 mg kg^{-1}).[44] The basal spectra between the healthy and cirrhotic subjects had comparable metabolite areas, except that the contribution of PDE was significantly smaller in cirrhotic patients than in healthy subjects (33 ± 5% versus 38 ± 5%; $p < 0.05$). In both groups, the relative PME peak increased and then returned to basal values, Pi decreased then rapidly increased and overshot basal values and slowly returned to basal values, and βATP decreased and slowly returned to basal values. However, in the cirrhotic group the magnitude of these changes were reduced; PME increased to 9 ± 5% versus 20 ± 8% in controls, Pi decreased by 5 ± 4% versus 11 ± 3% of total area ($p < 0.005$). These measurements correlated with the severity of the impairment of liver function measured by galactose-elimination capacity.

5.5 Alcoholic Hepatitis

As with studies on alcoholic cirrhosis the hepatic MRS findings varied according to the MRS technique used, the degree of quantitation achieved and the clinical state of the patient. Meyerhoff et al.[41] found that in 10 patients absolute concentrations of metabolites were decreased by 25–44%, but there was no change in metabolite ratios. Also, intracellular pH was more alkaline in the patient group compared with controls.

Angus et al.[42] measured the metabolite ratios to be abnormal in 16 patients with hepatitis, none of whom had consumed alcohol within the previous 72 h. PME/Pi and PME/ATP were elevated, and the PME level showed a significant positive correlation with the severity of alcoholic hepatitis, assessed by histology. Pi/ATP and pH were similar to control values. These data were similar to findings from four other patients previously studied by the same group.[28]

5.6 Viral Hepatitis

A number of patients with viral hepatitis have been studied, generally as a subgroup of a study of a heterogeneous patient group. Elevated PME/ATP has been reported in five patients with acute viral hepatitis,[28] three patients with viral hepatitis B,[41] and one patient with non-A non-B hepatitis.[7] Oberhaensli et al. found that the high phosphomonoesters returned to normal as liver function became normal, suggesting they were probably associated with liver regeneration 1–2 weeks after the onset of jaundice when the investigations were performed.[28]

5.7 Chronic Hepatitis

Serial changes in phosphorus metabolites were monitored after fructose infusion in five patients with chronic hepatitis.[46] Following 0.5 g kg^{-1} fructose the increase in PME at 15–20 min (151 ± 49% of the preadministration value) was significantly less than in healthy volunteers ($p < 0.05$). Also, the rebound of Pi at 35–40 min (126 ± 42%) was significantly less than that in healthy volunteers ($p < 0.05$). These findings were interpreted as suggesting that reduced fructose utilization is caused by impaired fructose transport into liver cells, thus indicating that this is a promising method in the functional evaluation of certain diffuse liver diseases.

5.8 Glycogen Storage Disease

Over 10 forms of glycogen storage disease resulting from inherited enzyme defects have been characterized. The different diseases are characterized by a storage of glycogen in abnormal quantities and/or synthesis of glycogen with an abnormal structure.

Beckmann et al.[47] obtained hepatic ^{13}C MRS spectra from one patient with type IIIA glycogen storage disease, which is characterized by an increased glycogen concentration of abnormal structure in liver and muscle, due to inactivation of the amylo-1,6-glucosidase debrancher enzyme. They found glycogen levels, measured from the C-1 resonance, to be increased by a factor of 2–3 compared with well-trained athletic normals.

A hepatic ^{31}P MRS study of two patients with glucose 6-phosphatase deficiency (glycogen storage disease type 1A) showed that, after an overnight fast, PME was increased and Pi was low–normal (Pi/PME was markedly reduced).[48] The increase in PME was attributed to accumulation of sugar phosphates (mainly glycolytic intermediates), on the basis of chemical shift measurements. After 1 g kg^{-1} oral glucose, hepatic sugar phosphates decreased by 40–64% and reached normal levels, whereas Pi increased by 40–130%. Liver Pi levels remained elevated in both patients 30 min after ingestion of glucose. Liver PME and Pi levels did not change in four control subjects after a glucose load. These high levels of PME were interpreted as suggesting that the activity of residual glucose 6-phosphatase may be enhanced, thus increasing hepatic glucose production and reducing the degree of hypoglycemia during fasting. The finding of large fluctuation in hepatic Pi levels may be directly related to the increase in uric acid production typically seen in these patients.

5.9 Galactose Intolerance

Galactosemia is an autosomal recessive disorder caused by a deficiency of the enzyme UDPglucose:α-D-galactose-1-phosphate uridyltransferase (EC 1.7.7.12). Liver damage is thought to be caused by accumulation of metabolites of galactose, although the exact mechanism is unclear. In a study of two galactosemic patients,[49] an oral load of 20 mg kg^{-1} produced significant changes in the hepatic ^{31}P MRS spectrum of one of

the patients. The peak at 5.2 ppm increased on two occasions to about twice its original size 60 min after galactose administration. In vitro animal studies showed this increase was largely due to galactose 1-phosphate.

5.10 Miscellaneous

Hypothyroidism is known to affect nearly every organ and organ system in the body. However, in seven patients with severe hypothyroidism there were no differences in the hepatic ^{31}P MRS spectra compared with controls, either before or after treatment with thyroid hormone substitution therapy.[50]

In a study of seven patients with iron overload[28] (ferritin levels 600 to >3000 mg mL^{-1}), the hepatic ^{31}P MRS resonances were all broadened, resulting in part from susceptibility effects of Fe^{3+}, which is stored as ferritin and hemosiderin in liver lysosomes. The line broadening correlated with the degree of iron overload.

6 FOCAL LIVER DISEASE

The majority of applications of NMR to focal liver disease have involved tumors, and these have recently been reviewed by Negendank.[51] Ideally, the tumor spectrum should be compared with the normal spectrum of cells from which the neoplasm arises, which is possible for primary liver cancers, but not for secondary liver tumors. A further problem arises because the normal liver spectrum has prominent PME and PDE signals, and as these are signals that are abnormal in tumors it can be difficult to define the tumor spectrum.

The ^{31}P MRS characteristics of hepatic tumors in adults are summarized in Table 1 and Figure 6. A number of technical points must be noted: in the majority of studies peak intensities were reported as relative ratios of areas, and molar quantitation was only attempted in two studies; most spectra were reported to be contaminated with signals from background tissue, but few authors provided estimates of the extent of contamination; and data were partially saturated, so that the effect of any difference in T_1 was not taken into account when comparing cancer and normal hepatic spectra. Despite these comments, a number of points can be made. The most obvious and most consistent abnormality is an elevation of PME. The change in PDE is less consistent, with some groups reporting an elevation and others reporting a reduction. Changes in the Pi signal showed no obvious pattern. The pH in tumors was either similar or slightly higher than that of normal tissue. Furthermore there were no obvious differences between different types of tumor, either between primary and secondary tumors or between secondary tumors from different sites. It is interesting that there appears to be no obvious compromise of energy metabolism, and effects of ischemia or hypoxia do not dominate the tumor spectrum.

Thus, in distinguishing neoplasms from normal tissue, only PME can be considered a diagnostic discriminant. Since proton decoupling during acquisition of the ^{31}P MRS data has not been performed in human tumor studies, there is no direct information on individual components in vivo. However, high-resolution MRS of perchloric acid extracts of tissue obtained at the time of surgery show that phosphoethanolamine and phosphocholine were elevated in four hepatocellular carcinomas and four secondary tumors.[1,56]

It is hoped that MRS will provide a marker of treatment response, particularly in the early stages of therapy. For example, hepatic embolization combined with intraarterial administration of cytostatic changes (chemoembolization) may be used to treat primary and metastatic cancers to the liver. As an acute response to chemoembolization in three patients, ATP, PME, and/or PDE concentrations diminished, whereas Pi concentrations increased or stayed relatively constant.[52] Long-term follow-up after chemoembolization showed elevated PME/ATP and increased ATP concentrations in the absence of changes by conventional imaging techniques.[52] In another study of 10 patients with liver metastases from colorectal carcinoma and two patients with hepatocellular carcinoma a marked increase in Pi and a decrease in ATP were observed during the first few hours after local chemotherapy of chemoembolization and later, PME increased and PDE decreased.[55] In a study of two

Table 1 ^{31}P MRS Spectral Parameters for Patients with Hepatic Malignancy ($n \geqslant 2$)

Diagnosis	n	MRS findings[a]
Primary malignancy		
Hepatocellular carcinoma[52]	2	PME/ATP ↑
Hepatocellular carcinoma[53]	7	PME/ATP ↑, if tumor occupied more than 50% of VOI
Hepatocellular carcinoma[54]	3	PME/Pi ↑, PME/ATP ↑
Hepatocellular carcinoma[55]	2	PME ↑
Various[56]	3	PME/PDE ↑
Secondary malignancy		
Lymphoma[57]	22	PME/ATP ↑, PME/Pi ↑
Adenocarcinoma[56]	11	PME/PDE ↑
Carcinoid[56]	14	PME/PDE ↑
Various[52]	3	PME/ATP ↑, ATP ↓, Pi ↓
Various[28,59]	3	PME ↑
Breast carcinoma[54]	2	PME/ATP ↑, PME/Pi ↑, PDE/Pi ↑, pH ↑
Various[58]	19	PME/ATP ↑, PDE/ATP ↑, Pi/ATP ↑
Colorectal carcinoma[55]	10	PME ↑
Various[53]	30	PME/ATP ↑, if tumor occupied more than 50% of VOI

[a]VOI, volume of interest.

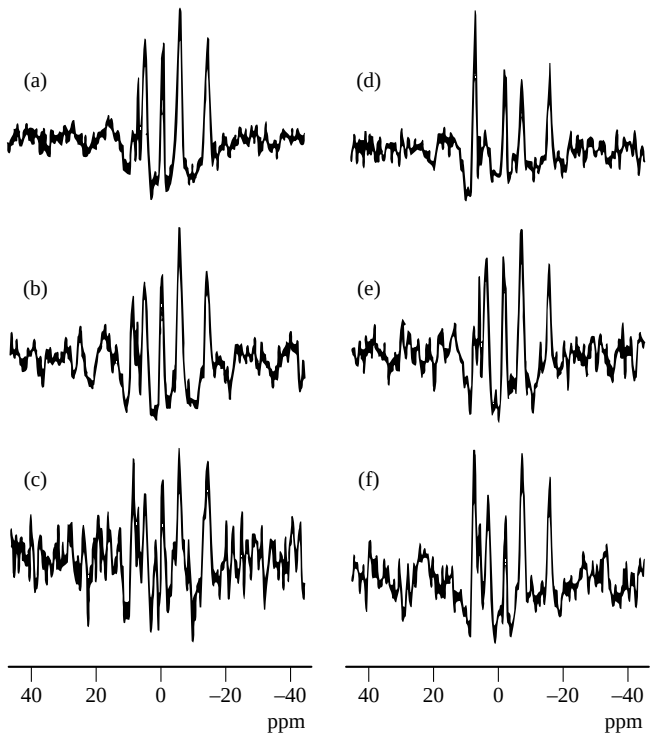

Figure 6 Representative ^{31}P hepatic MRS spectra obtained from a healthy adult volunteer and patients with hepatic malignancies of varying histology using CSI techniques, *TR*-1 s, pulse angle 45°. (a) Spectrum from a healthy 22-year-old female acquired using two-dimensional CSI; nominal planar resolution, 30 mm; total number of data collections, 256. (b) Spectrum from a 61-year-old man with squamous cell carcinoma obtained from a voxel containing tumor acquired using four-dimensional CSI; nominal resolution, 30 mm × 30 mm × 30 mm; total number of data collections 2048. (c) Spectrum from a 59-year-old man with carcinoid liver metastases obtained from a voxel containing tumor acquired using four-dimensional CSI; nominal resolution, 20 mm × 20 mm × 20 mm; total number of data collections 2048. (d) Spectrum from a 56-year-old man with carcinoid liver metastases obtained from a voxel containing tumor acquired using four-dimensional CSI; nominal resolution, 30 mm × 30 mm × 30 mm; total number of data collections 2048. (e) Spectrum from a 79-year-old man with carcinoid liver metastases obtained from a voxel containing tumor acquired using four-dimensional CSI; nominal resolution, 30 mm × 30 mm × 30 mm; total number of data collections 2048. (f) Spectrum from a 53-year-old man with hepatocellular carcinoma obtained from a voxel containing tumor acquired using four-dimensional CSI; nominal resolution, 30 mm × 30 mm × 30 mm; total number of data collections 2048. (Reproduced by permission of Heydon & Son from I. J. Cox, J. D. Bell, C. J. Peden, R. A. Iles, C. S. Foster, P. Watanapa, and R. C. N. Williamson, *NMR Biomed.*, 1992, **5**, 114)

patients with carcinoid syndrome, successful arterial embolization was accompanied by a decrease in PME/PDE and an increase in Pi/ATP, whereas in a patient in whom the tumor blood supply was not effectively interrupted there was little change in metabolite ratios.[7]

In a study of 22 patients with lymphoma, 11 were re-examined after chemotherapy treatment.[57] Before treatment, PME/ATP and PME/Pi were elevated and approximately related to clinical stage, although there were some notable discrepancies. Liver phosphomonoester levels decreased following chemotherapy in all but one of the patients who had abnormally high ratios in their initial spectra; this decrease was seen as early as 1 day and as late as 2 weeks after commencing treatment. In patients with initially normal PME levels, treatment did not produce a fall in PMEs. These findings suggest that detection of falling PME levels indicates that the drugs are reaching the target cells and affecting tumor cell metabolism, which may be of considerable clinical importance.

A study of two children with neuroblastoma[60] examined on a number of occasions from the ages of 1–9 months, showed the hepatic ^{31}P MRS spectrum from the region of pathology to be abnormal with elevated PME levels in the initial spectroscopic examinations. Further treatment showed a reduction in PME levels, and the spectra finally became similar to the normal subject (aged 3 months).

A small number of other focal liver lesions have been studied.[54,58] The metabolite ratios from two patients with cavernous hemangiomas were apparently normal, although the S/N was reduced.[54] The in vitro high-resolution MRS spectra from a multiloculated cyst showed elevated PME and reduced PDE, and this was similar to data from extracts of tumor tissue.[1]

7 DRUGS AND THE LIVER

The liver is the major site of drug metabolism. Lipid-soluble drugs are converted to more water-soluble forms by a group of hepatic mixed-function enzymes, including cytochrome P450. These processes facilitate excretion of the drugs in urine or bile. Drug metabolism firstly involves oxidation, reduction, or demethylation of the drug, followed by conjugation of the derivatives produced with glucrudine, sulfate, or glutathione. These conjugates are excreted in the urine and bile as they cannot be reabsorbed by renal tubular or bile ductular cells. A number of factors affect drug metabolism, including the microsomal enzyme system (which will influence the speed of metabolism), the route of administration, the liver blood flow, and competitive inhibition.

The majority of studies involving alcohol abuse have reported the spectral characteristics of resultant liver damage, rather than the effects of alcohol per se.[28,29,41–45] However, it may be important to distinguish between the two effects, particularly as the metabolic consequences of an alcohol load may persist for a few hours to a few weeks and may depend on the degree of liver injury.

In a study of three healthy volunteers, acute alcohol ingestion (0.5–1.0 g kg^{-1} alcohol) was associated with a transient but significant elevation in PME/ATP.[61] In 14 patients with minimal liver injury, active drinking was associated with elevation in mean PME/ATP ($p = 0.12$) and in mean PDE/ATP ($p < 0.0001$); abstinence from alcohol was associated with a prompt (3–7 day) reduction in PME/ATP and with a reduction in PDE/ATP over a longer timescale (3–28 days). In eight patients with alcoholic cirrhosis, active drinking was associated with elevation in mean PME/ATP ($p < 0.05$) and mean PDE/ATP ($p = 0.4$); abstinence from alcohol had no effect on the mean PME/ATP, although the mean PDE/ATP fell to within or below the reference range. The reversible elevation in PME/ATP in healthy volunteers given an alcohol load and in chronic

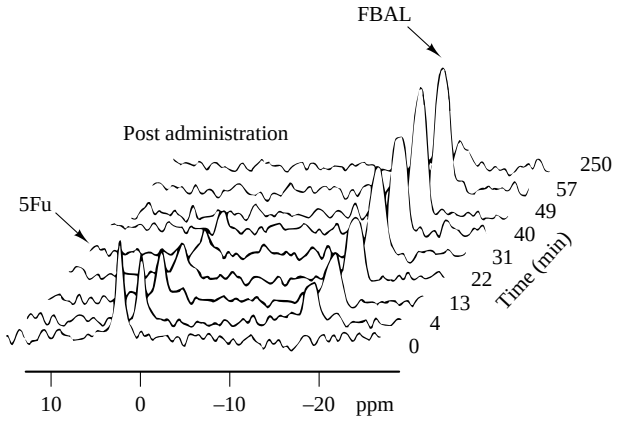

Figure 7 Serial ^{19}F spectra acquired with a surface coil over the liver of a patient (66 year old male) in a 1.5 T MRI system, operating at 59.8 MHz for ^{19}F. Each spectrum is the result of 128 FIDs using a 250 μs, 90° pulse with 512 complex points collected over a period of 8.5 min. Actual spectral width was 29 to −54 ppm. A shifted sine-bell squared apodization was used for S/N enhancement. (Reproduced by permission of Pergamon Journals Ltd. from W. Wolf, M. J. Albright, M. S. Silver, H. Weber, U. Reichardt, and R. Sauer, *Magn. Reson. Imag.*, 1987, **5**, 165)

alcohol abusers while actively drinking was interpreted as reflecting changes in hepatic redox potential as a result of obligatory alcohol metabolism. The irreversible elevation in PME/ATP, observed in patients with cirrhosis, probably reflects changes associated with hepatocyte regeneration. The reversible elevation in PDE/ATP observed in chronic alcohol abusers while actively drinking most likely reflects induction of hepatocyte endoplasmic reticulum.

Self-poisoning with acetaminophen accounts for many emergency hospital admissions. Overdoses cause cell damage through increased oxidation of the drug as the conjugation pathways are saturated. Early prediction of outcome in patients with acetaminophen overdose is difficult; for example, aspartate aminotransferase levels peak late after the ingestion of the drug and correlate poorly with prognosis. While the prothrombin time gives some indication of synthetic ability, methods for directly assessing cell viability are sought. Dixon and colleagues[62] studied 18 patients with acetaminophen poisoning and found that the concentrations of all metabolites fell in parallel with a decrease in the synthetic ability of the liver. ATP and PDE fell to about 20% of their normal concentrations in severely affected patients. The reduction in PDE was interpreted as a reduction in endoplasmic reticulum.

The direct observation of 5FU and its metabolites in the human liver was first reported in 1987.[63] Signals from 5FU and one of its catabolites, α-fluoro-β-alanine (FBAL), were observed in the human liver in patients undergoing cancer chemotherapy (Figure 7). The pharmacokinetics of 5FU in the tumors of 11 patients with carcinoma at various sites were studied, including three patients with tumor located in the liver.[64] A long liver tumor pool of 5FU was observed in six of 11 tumors, including one of three patients with carcinoma in the liver. The halflife of this 'trapped' pool was 0.33–1.3 h, considerably longer than the halflife of 5FU in blood (5–15 min). Neither the anabolites or catabolites of 5FU were detected by ^{19}F MRS. Patient response to chemotherapy appeared to correlate with the extent of trapping of free 5FU in tumors.

Semmler et al.[65] reported hepatic ^{19}F MRS data from eight patients with liver tumors, receiving intra-arterial 5FU. Contributions from liver and tumor could not be distinguished in the spectrum. The time constants for the kinetics of 5FU ranged from 8 to 75 min, whereas the time constants for FBAL were either approximately 15 or 50 min. A broad peak comprising nucleoside and nucleotide anabolites was detected in one patient.

More recently, Findlay et al.[66] studied hepatic ^{19}F MRS in 26 colorectal cancer patients treated with a continuous low dose intravenous infusion of 5FU, until the point of refractory disease, at which time interferon-α was added with the objective of modulating 5FU activity. In patients observed by MRS during the first 8 weeks of 5FU treatment, those with a visible 5FU signal were likely to respond to treatment ($p = 0.017$). At the time of interferon-α addition, MRS showed that seven patients developed new or increased 5FU signals, and four patients showed a signal from the active metabolites of 5FU. The patients who exhibited a new or increased 5FU signal were more likely to show further response to interferon-α ($p = 0.007$).

The in vivo pharmacokinetics of a model drug, fleroxacin, was studied in healthy human subjects.[67] After oral administration a signal was detected in the hepatic ^{19}F MRS spectrum, and also muscle, and monitored over a period of 24 h. Pharmacokinetic data for the liver were obtained, combining MRS results with high-performance liquid chromatography (HPLC) analysis of plasma: $t_{max} = 1.4$ h; $C_{max} = 53$ μmol L^{-1}; $t_{1/2} = 4.4$ h (fast phase) and 10.8 h (slow phase).

8 FUTURE APPLICATIONS

Hepatic MRS can provide a direct measure of hepatic function, for example from the baseline spectrum or following a metabolic challenge. Since the indirect clinical and laboratory measures of hepatic function may be subject to extrahepatic influences, direct noninvasive measurement is of importance. A range of studies have been made, as described above, and these can be extended, for example, specifically to study gluconeogenesis in diabetics and tumor-bearing patients using ^{13}C or ^{31}P MRS combined with an alanine stress test. In addition, the interpretation that metabolite changes in end-stage liver disease can provide an index of hepatocyte regeneration, rather than reflecting production of fibrous tissue or inflammatory cell activity, suggests that hepatic ^{31}P MRS may provide a specific marker which could be used to guide management decisions and as a prognostic assessment in patients with liver disease. Further studies correlating functional grades and etiology to absolute metabolite levels are appropriate.

The clinical management of a range of pathologies relies on the interpretation of histological results from liver biopsy. Since liver biopsy has a defined risk, a noninvasive technique of providing the same information would be of value, particularly when serial liver biopsies are required, for example in patients undergoing liver transplantation. In such patients hepatic MRS may be used to provide a guide to optimal timing of transplantation, to indicate good or poor liver metabolic status for noninvasive assessment of donor livers prior to transplan-

tation[68] and also to provide a useful early marker of rejection after transplantation.

For patients with hepatic malignancy, ^{31}P MRS may provide an early marker of response to treatment, and ^{19}F MRS can be used to measure the pharmacokinetics of specific anticancer drugs and their metabolites. Other areas of study include the metabolism of the liver in patients with tumor at distant sites. Hepatic MRS may provide insights into the mechanisms responsible for cachexia.

Many of the clinical and biochemical applications of hepatic MRS to date have relied on the interpretation of changes in metabolite ratios, rather than absolute metabolite concentrations. However, in a number of pathologies, metabolite ratios alone do not adequately reflect the underlying metabolic changes, particularly if there is an alteration in ATP levels. Recourse to absolute metabolite concentrations is therefore required. This may be difficult to achieve within the confines of a clinical examination because the low S/N of hepatic spectra means it is time consuming to measure the NMR characteristics of individual resonances. Improvements in sensitivity and/or spectral resolution may be achieved using proton decoupling techniques, higher field strengths, and more efficient rf coil arrangements. However, detailed interpretation of clinical data will continue to rely on results from animal models. A wide range of metabolite resonances can be detected using ^{1}H MRS,[1] and, if the technical problems in acquiring hepatic ^{1}H MRS spectra can be overcome, hepatic ^{1}H MRS will provide additional and new information.

In conclusion, hepatic MRS can provide a noninvasive measure of hepatic function, which has a range of clinical and biochemical applications in diagnosis, prognosis, and assessment of treatment efficacy in liver disease.

9 RELATED ARTICLES

Animal Methods in MRS; Applications of ^{19}F-NMR to Oncology; Cells and Cell Systems MRS; Chemical Shift Imaging; High-Field Whole Body Systems; pH Measurement In Vivo in Whole Body Systems; Proton Decoupling During In Vivo Whole Body Phosphorus MRS; Quantitation in In Vivo MRS; Single Voxel Whole Body Phosphorus MRS; Spatial Localization Techniques for Human MRS; Spectroscopic Studies of Animal Tumor Models; Susceptibility Effects in Whole Body Experiments; Tissue and Cell Extracts MRS; Tissue Behavior Measurements Using Phosphorus-31 NMR; Whole Body Studies: Impact of MRS.

10 REFERENCES

1. J. D. Bell, I. J. Cox, J. Sargentoni, C. J. Peden, D. K. Menon, C. S. Foster, P. Watanapa, R. A. Iles, and J. Urenjak, *Biochim. Biophys. Acta*, 1993, **1225**, 71.
2. R. A. Iles, A. N. Stevens, and J. R. Griffiths, *Prog. NMR Spectrosc.*, 1982, **15**, 49.
3. R. D. Cohen, R. M. Henderson, R. A. Iles, J. P. Monson, and J. A. Smith, 'Metabolic Acidosis', Ciba Foundation Symposium 84, Pitman, London, 1982, p. 20.
4. R. D. Oberhaensli, G. J. Galloway, D. J. Tayor, P. J. Bore, and G. K. Radda, *Br. J. Radiol.*, 1986, **59**, 695.
5. P. R. Luyten, G. Bruntink, F. M. Sloff, J. W. A. H. Vermeulen, J. I. van der Heijden, J. A. den Hollander, and A. Heerschap, *NMR Biomed.*, 1989, **4**, 177.
6. D. J. Meyerhoff, G. S. Karczmar, G. B. Matson, M. D. Boska, and M. W. Weiner, *NMR Biomed.*, 1990, **3**, 17.
7. I. J. Cox, D. K. Menon, J. Sargentoni, D. J. Bryant, A. G. Collins, G. A. Coutts, R. A. Iles, J. D. Bell, I. S. Benjamin, S. Gilbey, H. J. F. Hodgson, and M. Y. Morgan, *J. Hepatol.*, 1992, **14**, 265.
8. E. J. Murphy, B. Rajagopalan, K. M. Brindle, and G. K. Radda, *Magn. Reson. Med.*, 1989, **12**, 282.
9. T. E. Bates, S. R. Williams, and D. G. Gadian, *Magn. Reson. Med.*, 1989, **12**, 145.
10. R. K. Gupta and R. D. Moore, *J. Biol. Chem.*, 1980, **255**, 3987.
11. S. M. Cohen, *J. Biol. Chem.*, 1983, **258**, 14 294.
12. R. A. Iles, I. J. Cox, J. D. Bell, L. M. Dubowitz, F. Cowan, and D. J. Bryant, *NMR Biomed.*, 1990, **3**, 90.
13. M. Barany, D. G. Spigos, E. Mok, P. N. Venkatasubramanian, A. C. Wilbur, and B. G. Langer, *Magn. Reson. Imaging*, 1987, **5**, 393.
14. P. Canioni, J. Alger, and R. G. Shulman, *Biochemistry*, 1983, **22**, 4974.
15. T. Jue, J. A. B. Lohman, R. J. Ordidge, and R. G. Shulman, *Magn. Reson. Med.*, 1987, **5**, 377.
16. T. Jue, D. L. Rothman, B. A. Tavitian, and R. G. Shulman, *Proc. Natl. Acad. Sci. USA*, 1989, **86**, 1439.
17. D. L. Rothman, I. Magnusson, L. D. Katz, R. G. Shulman, and G. I. Shulman, *Science*, 1991, **254**, 573.
18. M. Ishihara, H. Ikehira, S. Nishikawa, T. Hashimoto, K. Yamada, J. Shishido, T. Ogino, K. Cho, S. Kobayashi, M. Kawana, T. Matumoto, T. A. Iinuma, N. Arimizu, and Y. Tateno, *Am. J. Physiol. Imaging*, 1992, **7**, 32.
19. N. Beckmann, R. Fried, I. Turkalj, J. Seelig, U. Keller, and G. Stalder, *Magn. Reson. Med.*, 1993, **29**, 583.
20. J. Alger, K. Behar, D. L. Rothman, and R. G. Shulman, *J. Magn. Reson.*, 1984, **56**, 334.
21. A. Heerschap, P. R. Luyten, J. I. van der Heyden, L. J. M. P. Oosterwaal, and J. A. den Hollander, *NMR Biomed.*, 1989, **2**, 124.
22. M. Saner, G. McKinnon, and P. Boesiger, *Magn. Reson. Med.*, 1992, **28**, 65.
23. J. L. Evelhoch, *Invest. New Drugs*, 1989, **7**, 5.
24. M. D. Boska, B. Hubesch, D. J. Meyerhoff, D. B. Tweig, G. S. Karczmar, G. B. Matson, and M. W. Weiner, *Magn. Reson. Med.*, 1990, **13**, 228.
25. H. Bomsdorf, T. Helzel, D. Kunz, P. Roschmann, O. Tschendel, and J. Wieland, *NMR Biomed.*, 1988, **1**, 151.
26. H. Barfuss, H. Fischer, D. Hentschel, R. Ladebeck, A. Oppelt, R. Wittig, W. Duerr, and R. Oppelt, *NMR Biomed.*, 1990, **3**, 31.
27. W. P. Aue, *Rev. Magn. Reson. Med.*, 1986, **1**, 21.
28. R. Oberhaensli, B. Rajagopalan, G. J. Galloway, D. J. Taylor, and G. K. Radda, *Gut*, 1990, **31**, 463.
29. V. Rajanayagam, R. R. Lee, Z. Ackerman, W. G. Bradley, and B. D. Ross, *J. Magn. Reson. Imaging*, 1992, **2**, 183.
30. I. R. Young, I. J. Cox, G. A. Coutts, and G. M. Bydder, *NMR Biomed.*, 1989, **2**, 329.
31. I. J. Cox, D. J. Bryant, B. D. Ross, I. R. Young, D. G. Gadian, G. M. Bydder, S. R. Williams, A. L. Busza, and T. E. Bates, *Magn. Reson. Med.*, 1987, **5**, 186.
32. I. J. Cox, G. A. Coutts, D. G. Gadian, P. Ghosh, J. Sargentoni, and I. R. Young, *Magn. Reson. Med.*, 1991, **17**, 53.
33. M. J. Blackledge, R. D. Oberhaensli, P. Styles, and G. K. Radda, *J. Magn. Reson.*, 1987, **71**, 331.
34. S. D. Buchhal, W. J. Thoma, J. S. Taylor, S. J. Nelson, and T. R. Brown, *NMR Biomed.*, 1989, **2**, 298.
35. P. C. Dagnelie, D. K. Menon, I. J. Cox, J. D. Bell, J. Sargentoni, G. A. Coutts, J. Urenjak, and R. A. Iles, *Clin. Sci.*, 1992, **83**, 183.

36. F. Terrier, P. Vock, J. Cotting, R. Ladebeck, J. Reichen, and D. Hentschel, *Radiology*, 1989, **171**, 557.
37. C. Segebarth, A. R. Grivegnee, R. Longo, P. R. Luyten, and J. A. den Hollander, *Biochemie*, 1991, **73**, 105.
38. I. Magnusson, D. L. Rothman, L. D. Katz, R. G. Shulman, and G. I. Shulman, *J. Clin. Invest.*, 1992, **90**, 1323.
39. R. D. Oberhaensli, B. Rajagopalan, D. J. Taylor, G. K. Radda, J. E. Collins, J. V. Leonard, H. Schwarz, and N. Herschkowitz, *Lancet*, 1987, **ii**, 931.
40. J. E. Seegmiller, R. M. Dixon, G. J. Kemp, P. W. Angus, T. E. McAlindon, P. Dieppe, B. Rajagopalan, and G. K. Radda, *Proc. Natl. Acad. Sci. USA*, 1990, **87**, 8326.
41. D. J. Meyerhoff, M. D. Boska, A. M. Thomas, and M. W. Weiner, *Radiology*, 1989, **173**, 393.
42. P. W. Angus, R. M. Dixon, B. Rajagopalan, N. G. Ryley, K. J. Simpson, T. J. Peters, D. P. Jewell, and G. K. Radda, *Clin. Sci.*, 1990, **78**, 33.
43. T. Munakata, R. D. Griffiths, P. A. Martin, S. A. Jenkins, R. Shields, and R. H. T. Edwards, *NMR Biomed.*, 1993, **6**, 168.
44. J.-F. Dufour, C. Stoupis, F. Lazeyras, P. Vock, F. Terrier, and J. Reichen, *Hepatology*, 1992, **15**, 835.
45. D. K. Menon, J. Sargentoni, S. D. Taylor-Robinson, J. D. Bell, I. J. Cox, D. J. Bryant, G. A. Coutts, K. Rolles, A. K. Burroughs, and M. Y. Morgan, *Hepatology*, 1995, **21**, 417.
46. H. Sakuma, K. Itabashi, K. Takeda, T. Hirano, Y. Kinosada, T. Nakagawa, M. Yamada, and T. Nakano, *J. Magn. Reson. Imaging*, 1991, **1**, 701.
47. N. Beckmann, J. Seelig, and H. Wick, *Magn. Reson. Med.*, 1990, **16**, 150.
48. R. D. Oberhaensli, B. Rajagopalan, D. J. Taylor, G. K. Radda, J. E. Collins, and J. V. Leonard, *Pediatr. Res.*, 1988, **23**, 375.
49. B. Kalderon, R. M. Dixon, B. Rajagopalan, P. W. Angus, R. D. Oberhaensli, J. E. Collins, J. V. Leonard, and G. K. Radda, *Pediatr. Res.*, 1992, **32**, 39.
50. K. D. Hagspiel, C. von Weymarn, G. McKinnon, R. Haldemann, B. Marincek, and G. K. von Schulthess, *J. Magn. Reson. Imaging*, 1992, **2**, 527.
51. W. Negendank, *NMR Biomed.*, 1992, **5**, 303.
52. D. J. Meyerhoff, G. S. Karczmar, F. Valone, A. Venook, G. B. Matson, and M. W. Weiner, *Invest. Radiol.*, 1992, **27**, 456.
53. I. R. Francis, T. L. Chenevert, B. Gubin, L. Collomb, W. Ensminger, S. Walker-Andrews, and G. M. Glazer, *Radiology*, 1991, **180**, 341.
54. G. M. Glazer, S. R. Smith, T. L. Chenevert, P. A. Martin, A. N. Stevens, and R. H. Edwards, *NMR Biomed.*, 1989, **1**, 184.
55. A. Schilling, B. Gewiese, G. Berger, J. Boese-Landgraf, F. Fobbe, D. Stiller, U. Gallkowski, and K. J. Wolf, *Radiology*, 1992, **182**, 887.
56. I. J. Cox, J. D. Bell, C. J. Peden, R. A. Iles, C. S. Foster, P. Watanapa, and R. C. N. Williamson, *NMR Biomed.*, 1992, **5**, 114.
57. R. M. Dixon, P. W. Angus, B. Rajagopalan, and G. K. Radda, *Br. J. Cancer*, 1991, **63**, 953.
58. G. Brinkmann, and U. H. Melchert, *Magn. Reson. Imaging*, 1992, **10**, 949.
59. R. D. Oberhaensli, D. Hilton-Jones, P. J. Bore, L. J. Hands, R. P. Rampling, and G. K. Radda, *Science*, 1986, **2**, 8.
60. J. M. Maris, A. E. Evans, A. C. Mclaughlin, G. J. D'Angio, L. Bolinger, H. Manos, and B. Chance, *New Engl. J. Med.*, 1985, **312**, 1500.
61. D. K. Menon, M. Harris, J. Sargentoni, S. Taylor-Robinson, I. J. Cox, and M. Y. Morgan, *Gastroenterology*, 1995, **108**, 776.
62. R. M. Dixon, P. W. Angus, B. Rajagopalan, and G. K. Radda, *Hepatology*, 1992, **16**, 943.
63. W. Wolf, M. J. Albright, M. S. Silver, H. Weber, U. Reichardt, and R. Sauer, *Magn. Reson. Imaging*, 1987, **5**, 165.
64. C. A. Presant, W. Wolf, M. J. Albright, K. L. Servis, R. Ring, D. Atkinson, R. L. Ong, C. Wiseman, M. King, D. Blayney, P. Kennedy, A. El-Tahtawy, M. Singh, and J. Shani, *J. Clin Oncol*, 1990, **8**, 1868.
65. W. Semmler, P. Bachert-Baumann, F. Guckel, F. Ermark, P. Schlag, W. J. Lorenz, and G. van Kaick, *Radiology*, 1990, **174**, 141.
66. M. P. Findlay, M. O. Leach, D. Cunningham, D. J. Collins, G. S. Payne, J. Glaholm, J. L. Mansi, and V. R. McCready, *Ann. Oncol.*, 1993, **4**, 597.
67. P. Jynge, T. Skjetne, I. Gribbestad, C. H. Kleinbloesem, H. F. Hoogkamer, O. Antonsen, J., Krane, O. E. Bakoy, K. M. Furuheim, and O. G. Nilsen, *Clin. Parmacol. Ther.*, 1990, **48**, 481.
68. R. F. Wolf, R. L. Kamman, E. L. Mooyaart, E. B. Haagsma, R. P. Bleichrodt, and M. J. Slooff, *Transplantation*, 1993, **55**, 949.

Biographical Sketch

Isobel Jane Cox. *b* 1959. B.A. (Nat. Sci.), 1981, University of Cambridge, UK; M.Sc., 1982, Ph.D., 1984 (supervisors Peter S. Belton and Robin K. Harris), University of East Anglia, UK. Introduced to clinical MRS on joining I.R. Young's team at GEC Hirst Research Centre. Lecturer in Diagnostic Radiology, RPMS, 1986–present. Approx. 50 publications. Current research speciality: development and applications of liver and brain MRS.

Kidney, Prostate, Testicle, and Uterus of Subjects Studied by MRS

Michael W. Weiner

University of California, San Francisco, CA, USA

1 KIDNEY

1.1 Proton MRS of Kidney

Shah et al.[1] reported a technique for using the stimulated echo amplitude mode (STEAM) sequence for ^{1}H MRS of the human kidney. The results demonstrated the presence of trimethylamines (TMAs). A prominent peak observed at 5.8 ppm was from urea. Avision et al.[2] used volume localized ^{1}H MRS to detect and measure changes in medullary trimethylamines in the human kidney (Figure 1). Proton magnetic resonance spectra were obtained from the human renal medulla using a stimulated echo localization sequence.

In addition to residual water and lipid, TMAs were identified at 3.25 ppm. In normal volunteers, overnight dehydration led to a significant increase of urine osmolality, and an increase in medullary TMAs (Figure 2). Water loading caused a water diuresis and a significant reduction in medullary TMAs within 4 hours. These results are consistent with the view that TMAs may play an osmoregulatory role in the medulla of the normal human kidney.

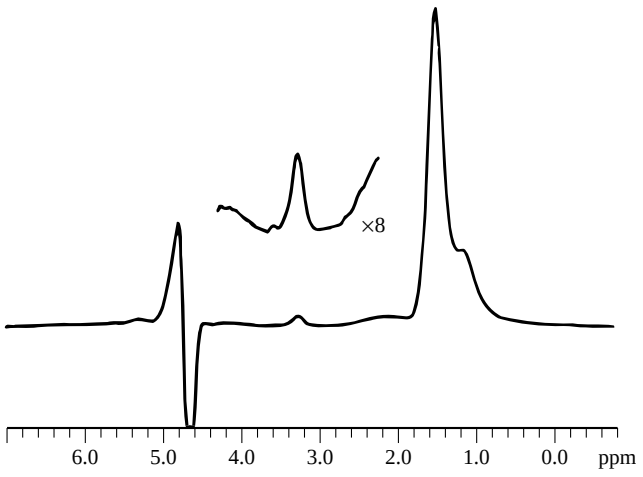

Figure 1 Water suppressed, volume localized ^{1}H spectrum from kidney. Water suppression consisted of a Silver–Hoult phase swept adiabatic fast passage pulse for selective water inversion followed by an inversion–recovery time of 0.8 second to allow the water Z magnetization to null. This sequence was delivered at the start of the volume localized stimulated echo sequence. TE = 68 ms, TM = 44 ms, TR = 3 s. Number of scans = 128. Filtering was 5 Hz of exponential line broadening. The resonances are water (4.75 ppm), lipids (0.9–1.4 ppm), and TMA (3.25 ppm)—which is shown expanded (×8) above the main spectrum. (Reproduced by permission of the National Academy of Sciences from Avison et al.[2])

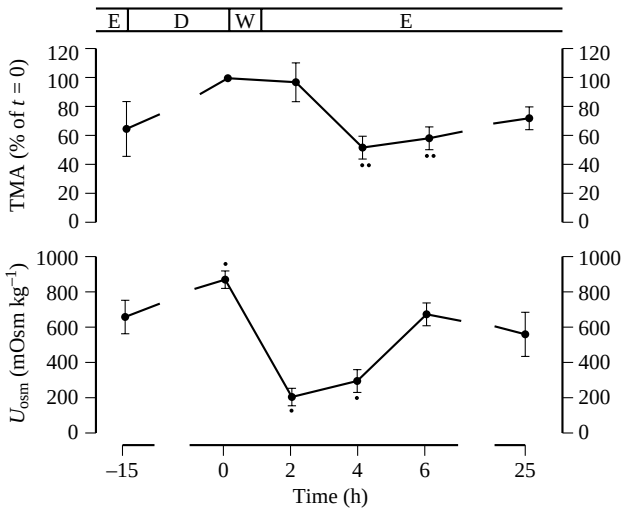

Figure 2 Time-course of changes in medullary TMA levels and U_{osm} in the four volunteers studied. TMA levels are expressed as the TMA area (%) at the point of maximal dehydration (i.e. t = 0). Error bars are ± SEM. $*p < 0.05$ versus t = 0 value for the TMA time-course. $**p < 0.05$ versus $t = -15$ for the U_{osm} time-course. E, euvolemic; D, dehydration; W, water load. (Reproduced by permission of the National Academy of Sciences from Avison et al.[2])

1.2 Phosphorus-31 MRS of Kidney

Jue et al.[3] demonstrated that ^{31}P MRS signals can be obtained from the normal human kidney. Matson et al.[4] also demonstrated the feasibility of obtaining ^{31}P magnetic resonance spectra from human kidneys using the image selected in vivo spectroscopy (ISIS) localization technique. Boska et al.[5] obtained spatially localized ^{31}P magnetic resonance spectra from healthy normal human kidneys and from well functioning renal allographs (Figure 3). Little or no phosphocreatine (PCr) in all spectra verified the absence of muscle contamination and was consistent with proper volume localization. The PME/ATP ratio (PME, phosphomonoester) was slightly elevated in transplanted kidneys (1.1) compared with normal healthy kidneys (0.8). Despite the practical problems produced by organ depth, respiratory movement, and tissue heterogeneity, these results demonstrate the feasibility of obtaining ^{31}P magnetic resonance spectra from human kidneys.

Bretan et al.[6,7] reported their clinical experience with pretransplant assessment of renal viability using ^{31}P MRS to study 40 renal transplant recipient patients (Figure 4). The purpose of their study was to develop and investigate the use of MRS in the clinical transplant setting by correlation of pretransplant MRS parameters with subsequent renal function. Kidneys were studied during simple hypothermic storage within their sterile containers using an external ^{31}P MRS surface coil. Mean storage times were about 38 hours. Cold storage times did not correlate with subsequent clinical renal function. However,

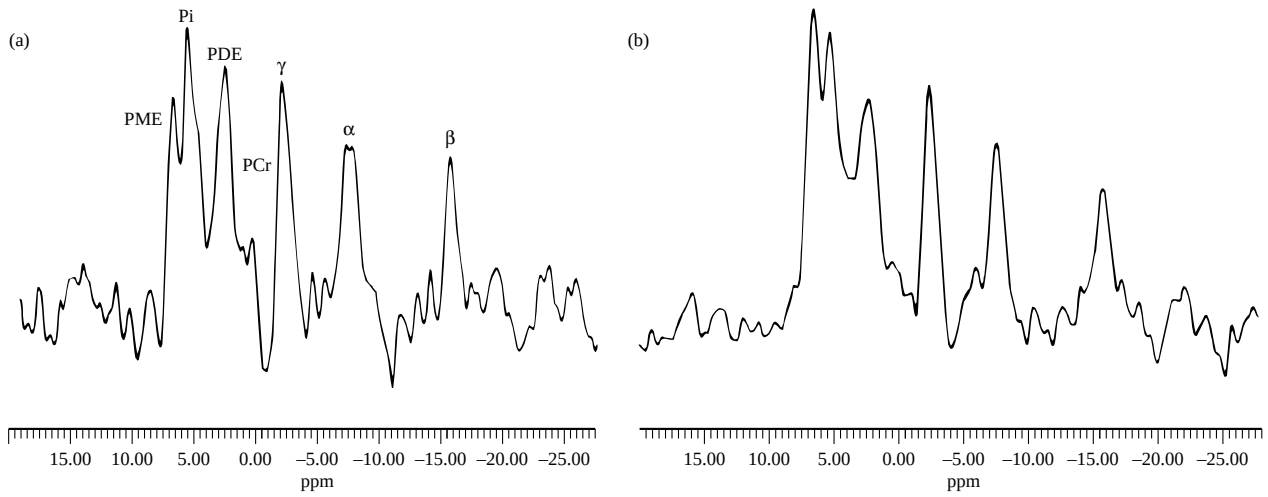

Figure 3 Phosphorus-31 ISIS spectra of (a) the healthy normal kidney and (b) of the well functioning kidney transplant. Acquisition parameters: *TR* = 2.0 seconds, acquisition time = 1 hour, 90° pulse set for the region of interest, distance of the center of the volume of interest (VOI) from the 14 cm surface coil = 70 mm for normal kidney and 42 mm for transplanted kidney, size of the VOI is 25 × 45 × 55 mm = 62 ml for normal kidney and 25 × 50 × 54 mm = 68 ml for transplanted kidney. (Reproduced by permission of Springer-Verlag from Boska et al.[5])

selected ^{31}P MRS data did. ATP was present in 11 kidneys and was associated with the best subsequent renal function. Only 36% of these patients required dialysis, compared with 71 patients without detectable ATP who required a posttransplant dialysis. Kidneys with ATP had the highest PME/Pi (Pi, inorganic phosphate) ratios; in general, the higher the PME/Pi ratio, the better the renal function posttransplant. The intracellular pH did not correlate with subsequent renal function. The authors suggested that MRS provided a better correlation with renal function after transplantation than existing methods.

Grist et al.[8] used ^{31}P MRS to investigate the effects of rejection on renal transplants (Figures 5 and 6). The PDE/PME (PDE, phosphodiester) and Pi/ATP ratios in the transplants with rejection differed significantly from the corresponding metabolite ratios of patients without rejection. A PDE/PME ratio exceeding 0.8 had a sensitivity of 100% and a specificity of 86% for predicting rejection. A Pi/ATP ratio greater that 0.6 had a sensitivity of 72% and a specificity of 86% for predicting rejection. The authors concluded that ^{31}P MRS may be useful as a noninvasive method for evaluating renal metabolism during episodes of transplant rejection.

2 PROSTATE

2.1 Proton MRS of Prostate

Normal prostate has a very high concentration of citrate, a unique feature of this tissue related to the function of prostate cells to secrete citrate into the semen. Most of the MRS of prostate has focused on investigating changes of citrate associated with benign prostatic hypertrophy (BPH) and prostatic carcinoma. Schick et al.[9] investigated the signal characteristics of citrate at low field strengths at 1.5 T using spatially selected spectroscopy and theoretical methods. In vivo localized spectroscopy of small volume elements (2 ml) using a double spin echo method within the prostate gland provided citrate signals. Volume selected proton spectra with different echo times were recorded.

Thomas et al.[10] performed ^{1}H MRS of normal and malignant human prostates in vivo (Figures 7 and 8). The results demonstrated that water-suppressed ^{1}H MRS spectra could be obtained from the prostate. Normal healthy prostate showed a large resonance from citrate. The spectrum from a malignant human prostate showed a much lower level of citrate. The results also suggested that the low concentration of citrate might be useful for the identification of prostate cancer.

Schnall et al.[11] performed localized ^{1}H MRS of the human prostate in vivo using an endorectal surface coil. High levels of citrate were observed in all regions of normal prostate and benign prostatic hypertrophy. The citrate levels in regions containing tumor were variable. The presence of high citrate levels in one case of prostate cancer was confirmed from extracts.

Schiebler et al.[12] reported high-resolution ^{1}H MRS of human prostate perchloric acid extracts (Figure 9). The citrate peak area was higher in benign prostatic hyperplasia than in adenocarcinoma. However, citrate peak areas from the normal peripheral zones were not significantly different from those found in adenocarcinomas. A sharp peak at 2.05 ppm that was seen in four out of thirteen adenocarcinoma samples and only one out of thirteen in the BPH samples was assigned to *N*-acetylneuraminic acid. Fowler et al.[13] also obtained ^{1}H NMR spectra from perchloric extracts of tissue samples from human prostate. Statistically significant differences between the normals, the benign prostratic hypertrophy, and the cancer groups occurred for metabolite ratios of creatine, citrate, and phosphorylcholine. None of the ratios correlated with the Gleason grade of the cancer samples. Different sections of large tumors often yielded substantially different ratios.

Yacoe et al.[14] reported in vitro ^{1}H MRS of normal and abnormal prostate cells (Figure 10).

Proton MRS was used to determine if cell strains derived from prostatic cancers could be distinguished from normal prostate. Prostatic cancer cells had lower concentrations of

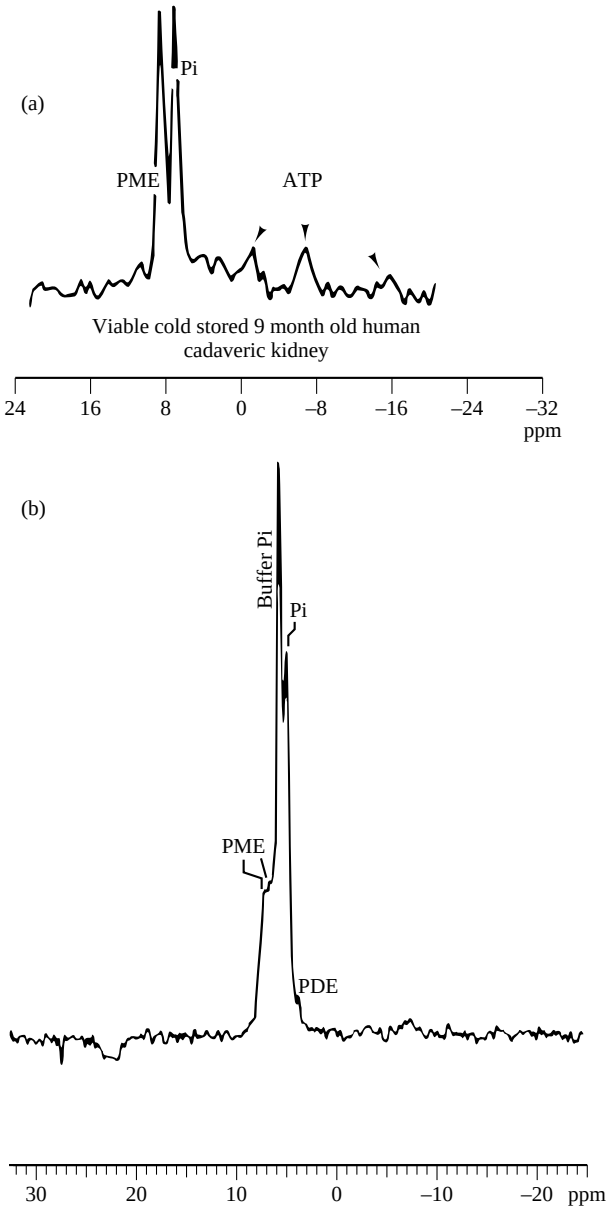

Figure 4 Ex situ in vivo magnetic resonance spectrum of (a) a viable pediatric and (b) an adult kidney. PME, Pi, PDS (phosphodiester), and ATP (adenosine triphosphate) peaks are defined. (Reproduced by permission of Williams & Wilkins from Bretan et al.[6])

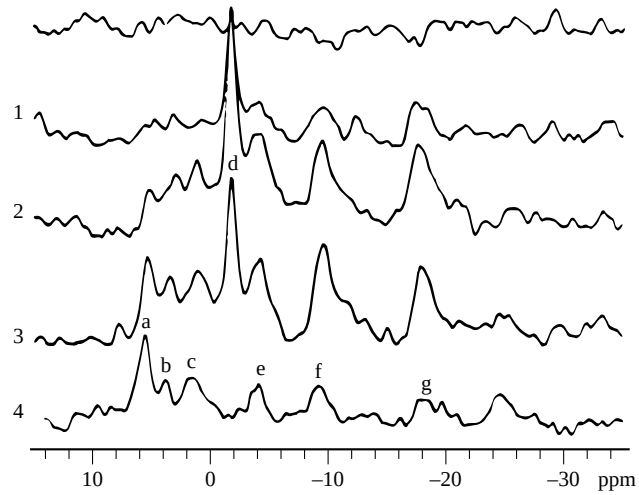

Figure 5 Contiguous ^{31}P magnetic resonance spectra obtained from slices of kidney. Note the presence of significant PCr at the surface, consistent with muscle tissue. The deepest slice shows a large PME peak and little PCr, consistent with renal tissue. Peaks from left to right correspond to PMEs (a), Pi (b), PDEs (c), PCr (d) and γ- (e), α- (f), and β- (g) phosphates of ATP. (Reproduced by permission of Williams & Wilkins from Grist et al.[8])

In the past several years Kurhanewicz, Vigneron and their colleagues have published a series of reports using ^{1}H MRSI of the prostate in a clinical setting. They have used an endorectal coil[16] and a high spatial resolution technique.[17] This

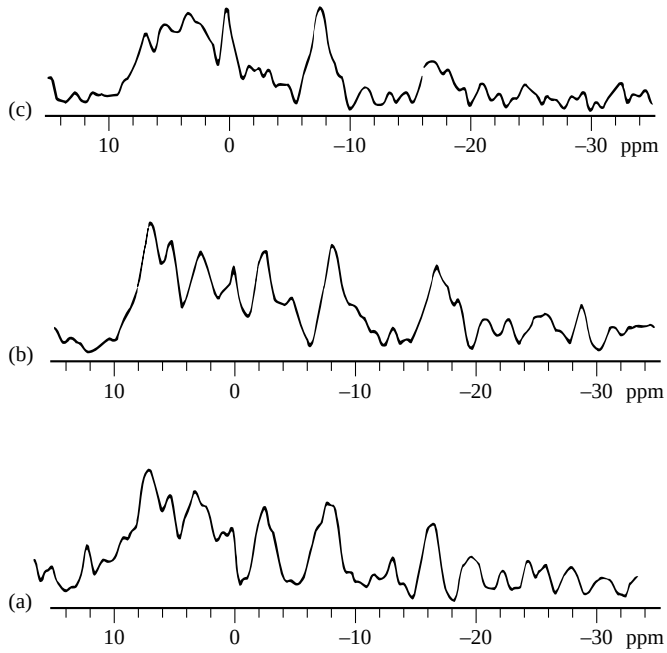

Figure 6 Phosphorus-31 magnetic resonance spectra from a patient with (a) a normally functioning renal allograft, (b) a patient with cyclosporine nephrotoxicity, and (c) a patient with moderate cellular rejection. Note the increase in Pi and PDE in the patient with rejection compared with the normal control subject or the patient with cyclosporine toxicity. PCr is a contaminant from extrarenal tissue. (Reproduced by permission of Williams & Wilkins from Grist et al.[8])

citrate compared with normal prostate epithelium, but the differences were small and not statistically significant. However, both the cancer and normal prostate cells were washed, which may have removed diffusable citrate.

Kurhanewicz et al.[15] performed ^{1}H MRS and enzymatic assays of human prostate adenocarcinomas and prostate DU145 xenographs grown in nude mice. The results showed that citrate concentrations in primary human adenocarcinomas were significantly lower than those observed for normal benign hyperplastic prostatic tissue. There was a 10-fold reduction of citrate associated with DU145 xenographs compared with primary prostate cancer. These findings support the hypothesis that citrate concentrations are low in prostate cancer.

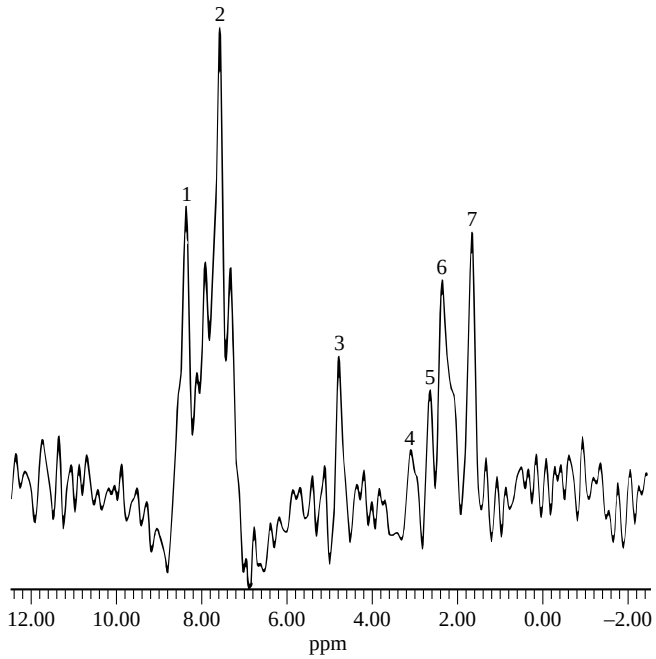

Figure 7 Proton magnetic resonance spectrum prostate in a healthy 26-year-old subject with *TE* = 40 ms. The total acquisition time was 1.5 minutes. Resonance assignments: 1, 2, water and MDPA from the external standard, situated in the plane of the surface coil; 3, residual water; 4, spermine/creatine/PCr; 5, 6, the methylene protons of citrate; 7, methylene protons of spermine and lipids. (Reproduced by permission of the Society for Magnetic Resonance Imaging from Thomas et al.[10])

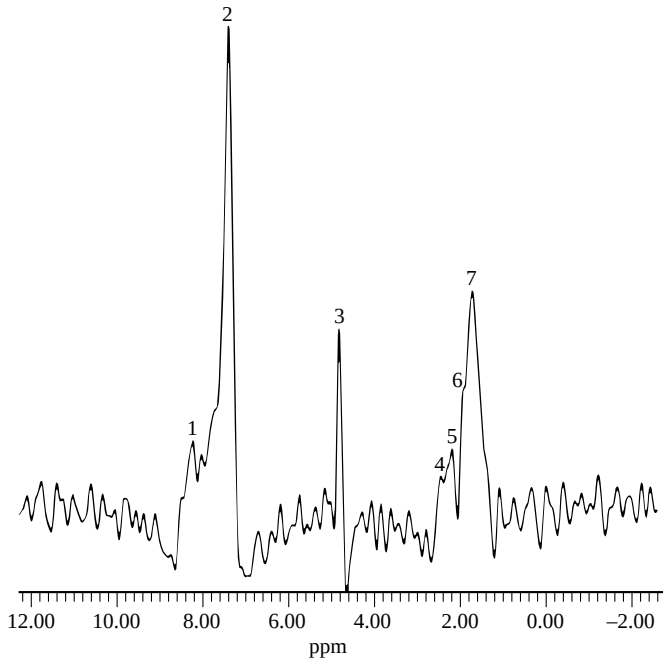

Figure 8 Proton magnetic resonance spectrum of a malignant human prostate with binomial water suppression. Number of scans = 16; repetition time, 5 seconds; *TE* = 80 ms; total acquisition time = 80 seconds. The residual water and the resonances from the external standard were identified at 4.8 and 7.8 ppm, respectively. A 16-step phase cycling was used. Resonance assignments: 1, 2, external standard; 3, residual water; 4, 5, C-2 and C-5 protons of the citrate molecule; 6, 7, methylene protons of spermine and lipids. (Reproduced by permission of the Society for Magnetic Resonance Imaging from Thomas et al.[10])

approach has been used to study the effects of hormone ablation[18] and cryosurgery,[19] and for the detection of local recurrence.[20,21]

2.2 Phosphorus-31 MRS of Prostate

Kurhanewicz et al.[22] reported the use of a ^{31}P MRS transrectal probe for studies of the human prostate (Figures 11–13). The preliminary results indicated that transrectal ^{31}P MRS may characterize ^{31}P metabolites in normal prostates, benign prostatic hyperplastia, and malignant prostates. The preliminary results suggested that malignant prostates are characterized by significantly decreased levels of PCr and increased levels of PME compared to healthy prostates. Thomas et al. evaluated some of the problems encountered with transrectal ^{31}P MRS of human prostate to determine the optimal conditions for these studies.[23] The authors investigated the reproducibility of ^{31}P MRS, regional differences of ^{31}P metabolites, the T_1 relaxation times, and metabolic alterations associated with disease. The PME/ATP ratio was highest in the upper region and lowest in the lower region. Similarly, the PDE/ATP ratio was highest in the upper region and lowest in the lower region. In contrast, the PCr/ATP was lowest in the upper region but was increased in the lower region.

The PME/ATP ratio of normal subjects (0.09 ± 0.1) was increased in the patients with BPH (1.5 ± 0.1) and significantly increased in patients with cancer (1.7 ± 0.2). The PCr/ATP ratio in normal subjects (1.5 ± 0.2) was not significantly reduced in BPH, but it was reduced to 0.9 in prostatic cancer. The PME/PCr ratio in normal subjects was 0.7, was not significantly increased in BPH to 1.4 but was significantly increased in prostate cancer to 2.2.

Hering and Muller reported ^{31}P MRS and ^{1}H MRI of the human prostate with a transrectal probe.[24] Fourteen patients were evaluated with ^{1}H MRI and seven patients with ^{31}P MRS. The PME/ATP ratio was higher in patients with prostatic cancer.

Narayan et al. investigated the ability of ^{31}P MRS to characterize normal human prostate as well as prostate with benign and prosthetic hypertrophy and malignant neoplasms (Figure 14).[25] Normal prostate had PCr/ATP, PME/ATP, and PME/PCr ratios of 1.2, 1.1, and 0.9, respectively. Malignant prostates had PCr/ATP ratios that were lower than normal prostates. Malignant prostates had PME/ATP ratios that were higher than normal prostates.

Using the PME/PCr ratio it was possible to differentiate metabolically malignant prostates from normal prostates with no overlap of individual ratios.

2.3 Carbon-13 MRS of Prostate

Halliday et al. obtained high-quality, high-resolution proton decoupled natural abundance ^{13}C NMR spectra from various human tumors, including prostate (Figure 15).[26]

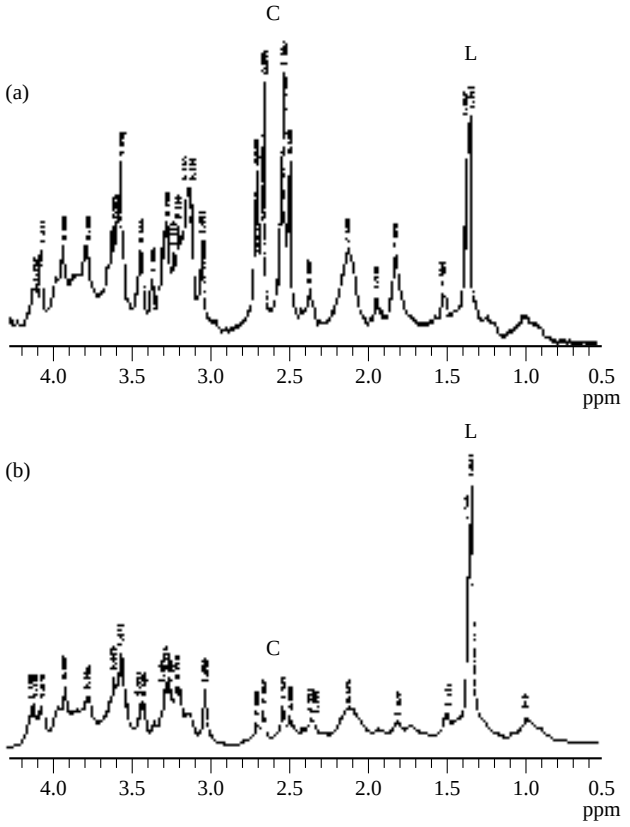

Figure 9 (a) In vitro ^{1}H NMR spectra at 360 MHz, demonstrating a normal pattern with a large citrate peak seen in a sample of benign prostatic hyperplasia with a glandular predominance (C, citrate; L, lactate). Standard not shown. (b) In vitro ^{1}H NMR spectra at 360 MHz for adenocarcinoma showing the expected low citrate peak. Standard not shown. (Reproduced by permission of Williams & Wilkins from Schiebler et al.[12])

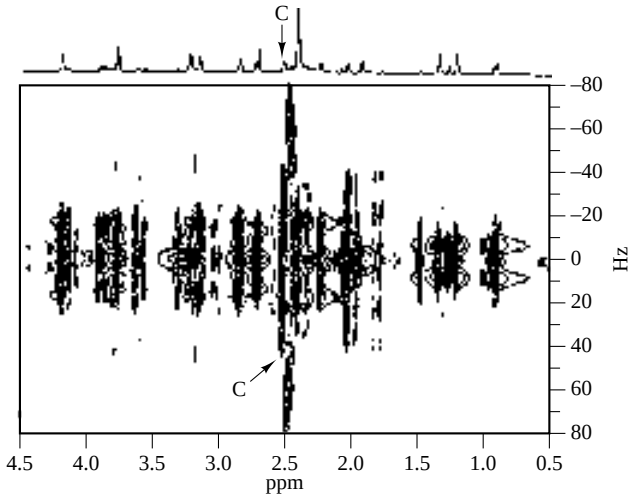

Figure 10 Two-dimensional *J* resolved spectrum of an $HClO_4$ extract of a normal peripheral zone epithelial cell strain, obtained at 500 MHz. The chemical shift is resolved in the horizontal axis and the *J* coupling constant of complex peaks is resolved in the vertical axis. The complex peaks assigned to citrate (C) are pointed out. A one-dimensional projection in the chemical shift dimension is plotted at the top. (Reproduced by permission of Williams & Wilkins from Yacoe et al.[14])

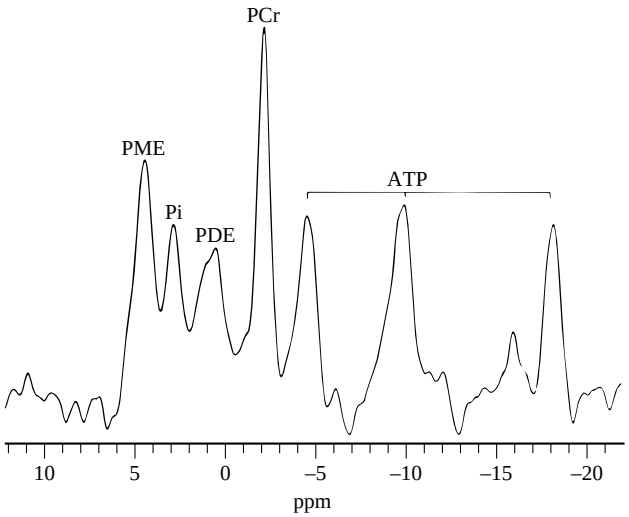

Figure 11 Phosphorus-31 magnetic resonance spectrum of a normal prostate from a normal subject (26 years old), *TR* = 20 seconds; NS = 100. (Reproduced by permission of the Society for Magnetic Resonance Imaging from Thomas et al.[23])

When prostatic adenocarcinoma was compared with adjacent hyperplastic tissue, the tumors were found to contain larger amounts of triacylglycerols, smaller amounts of citrate, and acid mucins. The citrate-to-lipid ratio appeared to differentiate malignant from nonmalignant prostates.[26] Halliday et al. obtained ^{13}C NMR spectra from prostate tumor cell lines.[27] The results showed that the amount of taurine was increased, and tyrosine was decreased in androgen sensitive rat prostatic tumors in comparison to androgen responsive malignant or normal tissue. The authors concluded that the amount of these

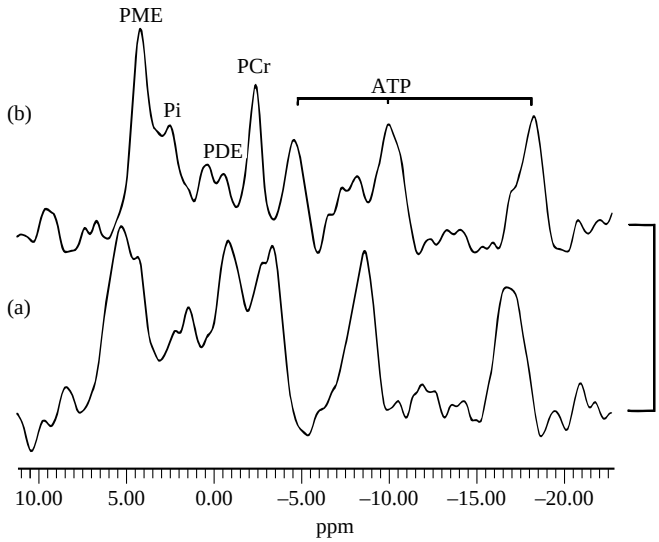

Figure 12 Phosphorus-31 magnetic resonance spectra from human prostates in patients with (a) BPH and (b) prostatic cancer. (Reproduced by permission of the Society for Magnetic Resonance Imaging from Thomas et al.[23])

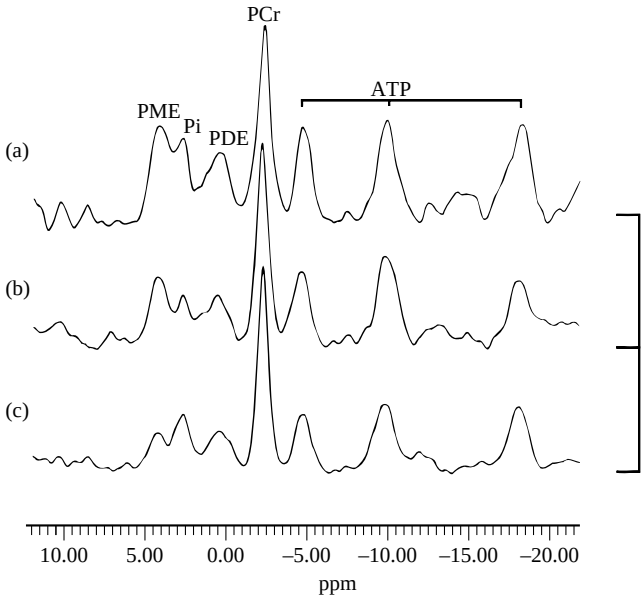

Figure 13 Phosphorus-31 magnetic resonance spectra from (a) upper, (b) middle, and (c) lower regions of the prostate. (Reproduced by permission of the Society for Magnetic Resonance Imaging from Thomas et al.[23])

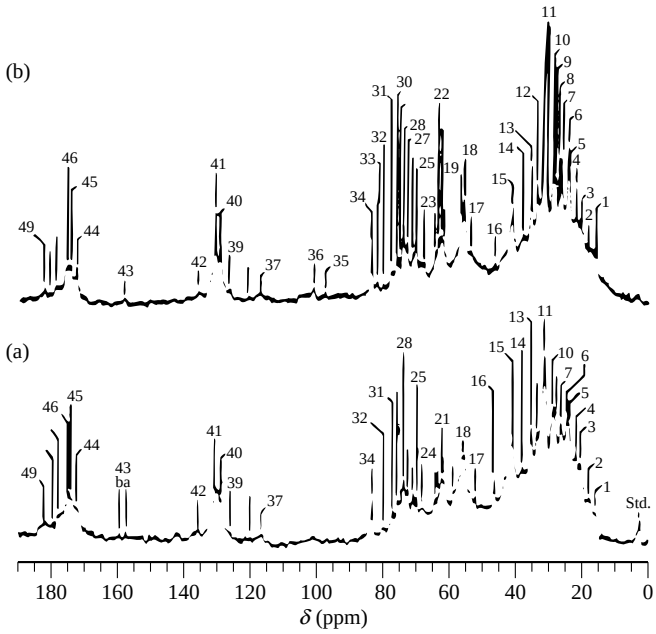

Figure 15 Natural abundance proton decoupled 100.6 MHz ^{13}C NMR spectrum of (a) human prostate with benign prostatic hypertrophy. This proton decoupled spectrum was taken from 2.24 g of tissue, at a temperature of 310 K, with a total of 17 271 scans. (b) A spectrum of poorly differentiated adenocarcinoma of human prostate from the same individual as (a), taken from 3.51 g of tissue with the same parameters, except for the use of 11 241 scans in total. It should be noted that peak 11 is truncated. Assignments for the numbered resonances are given elsewhere.[26] These spectra are representative of seven hyperplastic prostates, three of which contained adenocarcinoma, plus a fourth sample of adenocarcinoma, with the following exception: lactate was increased relative to the control tissue only in the depicted case and resonances from acidic mucins were not present in all of the tumors. (Reproduced by permission of Williams & Wilkins from Halliday et al.[26])

amino acids discriminates androgen-sensitive from insensitive rat prostatic tissues. Sillerud et al. followed this up with an in vivo ^{13}C NMR study of human prostate (Figure 16).[28]

High levels of citrate were measured in the human prostate in vivo as well as the tissue samples of human and rat prostate in vitro.

3 TESTICLE

3.1 Phosphorus-31 MRS of Testicle

Chew et al. investigated the clinical feasibility of ^{31}P MRS to assess the metabolic integrity of the human testicle (Figures 17 and 18).[29] The PME/ATP ratio was greatly reduced in the abnormal testicle; furthermore, the PME/PDE ratio was also reduced in patients with primary testicular failure.

In patients with azoospermia, there were significant differences in the same peak area ratios between patients with primary testicular failure and those with chronic tubular

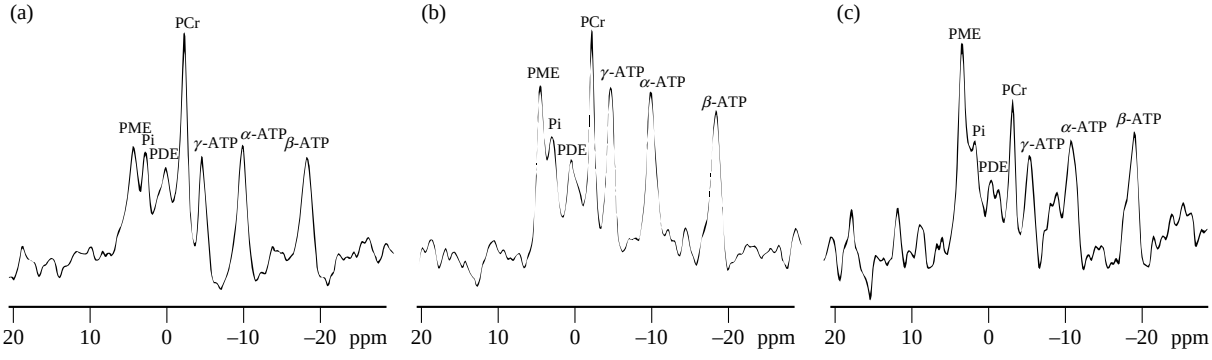

Figure 14 In vivo ^{31}P magnetic resonance prostate spectra. (a) Normal volunteer, (b) patient with BPH, and (c) patient with prostatic cancer. (Reproduced by permission of Williams & Wilkins from Narayan et al.[25])

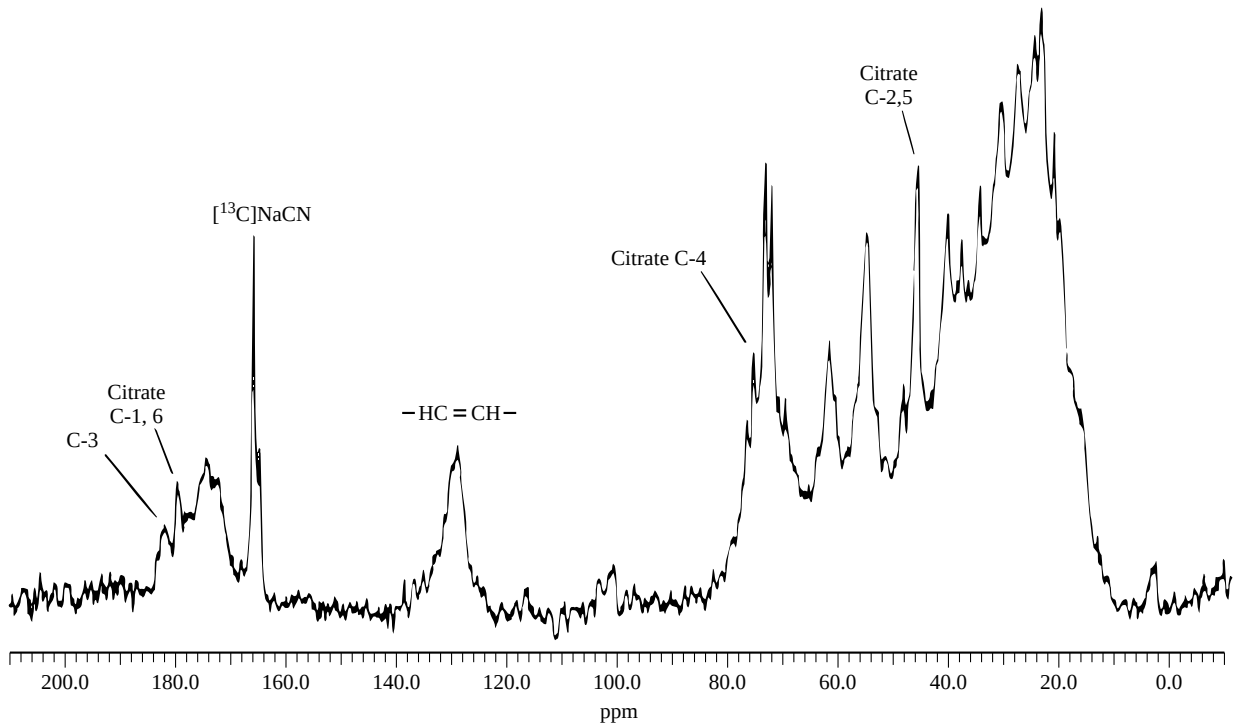

Figure 16 Proton decoupled, natural abundance 100.614 MHz ^{13}C NMR in vitro spectrum from 3.88 g of human benign hypertrophic prostate tissue sample. This spectrum is the average of 13 600 scans at a temperature of 283 K. The signal at 165 ppm is from 15 μl of a 0.15 M [^{13}C]sodium cyanide standard. (Reproduced by permission of Williams & Wilkins from Sillerud et al.[28])

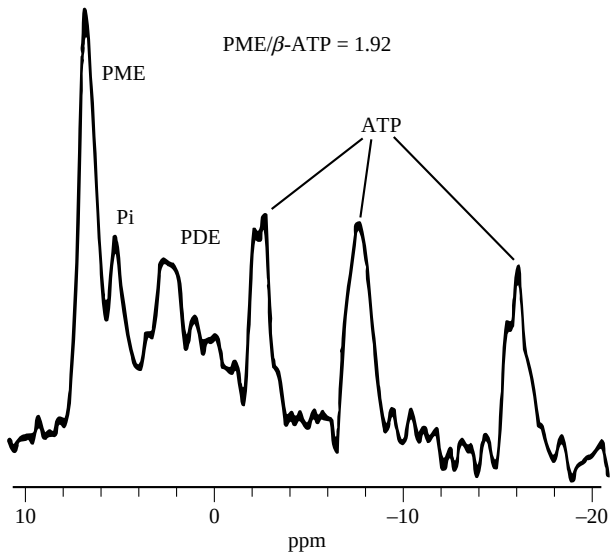

Figure 17 Characteristic ^{31}P magnetic resonance spectrum from the in vivo normal human testicle. Present are the three peaks due to ATP, small signals from PDE and Pi, and a large contribution from the PME peak. This spectrum was acquired with 400 signals averaged in 13.5 minutes. (Reproduced by permission of the Radiological Society of North America from Chew et al.[29])

obstruction. Bretan et al. compared ^{31}P MRS of human testicle with conventional semen analysis.[30] The glycerophosphorylcholine (GPC)/total phosphate ratio in azoospermic men after vasectomy significantly differed from the control GPC/total phosphate ratio, which appropriately reflected complete vasal occlusion. The results suggested that a significant portion of seminal GPC is derived from epidymal secretion and that ^{31}P MRS is useful for monitoring GPC/total phosphate levels when assessing epidymal function in male infertility.

4 UTERUS

High-resolution ^{1}H MRS was used as an adjunct to conventional and histological diagnosis of cervical neoplasia.[31] Cervical biopsy specimens were examined with ^{1}H MRS and the results compared with histology. A high-resolution lipid spectrum was observed in 39 of 40 invasive carcinomas whereas 119 preinvasive samples showed little or no lipids but were characterized by a strong unresolved peak between 3.8 and 4.2 ppm. Peak ratios of the methylene/methyl and the unresolved/methylene resonances allowed accurate distinction between invasive and preinvasive malignancy.

5 RELATED ARTICLES

In Vivo Hepatic MRS of Humans; NMR Spectroscopy of the Human Heart; Proton Decoupling During In Vivo Whole Body Phosphorus MRS; Proton Decoupling in Whole Body Carbon-13 MRS; Quantitation in In Vivo MRS; Whole Body Studies: Impact of MRS.

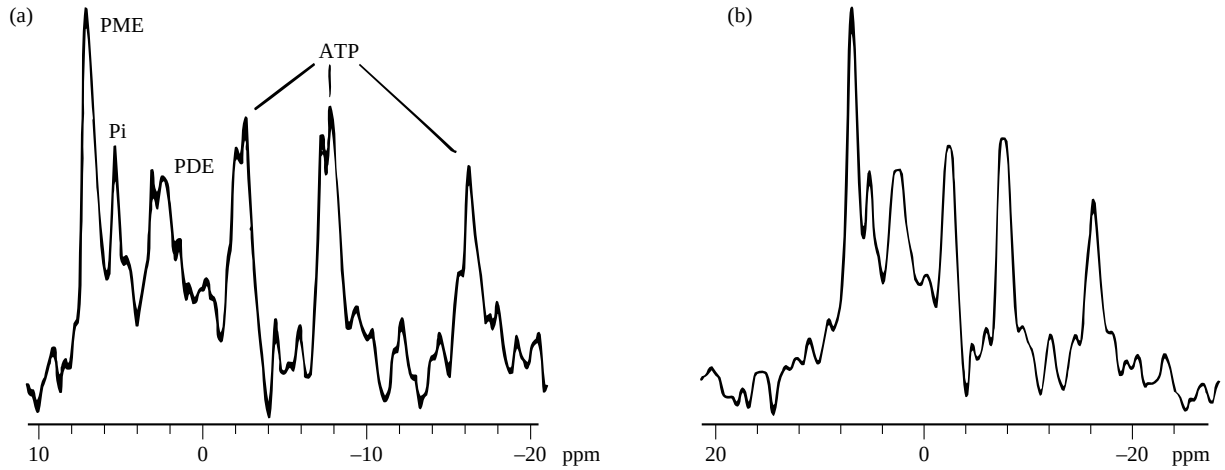

Figure 18 (a) Phosphorus-31 magnetic resonance spectrum from an azoospermic testicle due to primary testicular failure. It is characterized by the same peaks found in the normal spectrum, but the PME/β-ATP peak area ratio is substantially lower (1.32 in this case). (b) Phosphorus-31 magnetic resonance spectrum from an azoospermic testicle due to chronic ductal obstruction. It is characterized by the same peaks found in the normal spectrum, but the PME/β-ATP peak area ratio is lower than normal (1.51 in this case). (Reproduced by permission of the Radiological Society of North America from Chew et al.[29])

6 REFERENCES

1. N. J. Shah, T. A. Carpenter, I. D. Wilkinson, L. D. Hall, A. K. Dixon, C. E. L. Freer, K. Prosser, and D. B. Evans, *Magn. Reson. Med.*, 1991, **20**, 292.
2. M. J. Avison, D. L. Rothman, T. W. Nixon, W. S. Long, and N. J. Siegel, *Proc. Natl. Acad. Sci. USA*, 1991, **88**, 6053.
3. T. Jue, D. L. Rothman, J. A. B. Lohman, E. W. Hughes, C. C. Hanstock, and R. G. Shulman, *Proc. Natl. Acad. Sci. USA*, 1988, **85**, 971.
4. G. B. Matson, D. B. Twieg, G. S. Karczmar, T. J. Lawry, J. R. Gober, M. Valenza, M. D. Boska, and M. W. Weiner, *Radiology*, 1988, **169**, 541.
5. M. D. Boska, D. J. Meyerhoff, D. B. Twieg, G. S. Karczmar, G. B. Matson, and M. W. Weiner, *Kidney Int.*, 1990, **38**, 294.
6. P. N. Bretan, N. Baldwin, A. C. Novick, A. Majors, K. Easley, T. Ng, N. Stowe, P. Rehm, S. B. Streem, and D. R. Steinmuller, *Transplantation*, 1989, **48**, 48.
7. P. N. Bretan, N. Baldwin, A. C. Novick, A. Majors, K. Easley, T. C. Ng, N. Stowe, S. Streem, D. Steinmuller, P. Rehm, and R. Go, *Transplant. Proc.*, 1989, **21**, 1266.
8. T. M. Grist, H. C. Charles, and H. D. Sostman, *Am. J. Roentgenol.*, 1991, **156**, 105.
9. F. Schick, H. Bongers, S. Kurz, W. I. Jung, M. Pfeffer, and O. Lutz, *Magn. Reson. Med.*, 1993, **29**, 38.
10. M. A. Thomas, P. Narayan, J. Kurhanewicz, P. Jajodia, and M. W. Weiner, *J. Magn. Reson.*, 1990, **87**, 610.
11. M. D. Schnall, R. Lenkinski, B. Milestone, and H. Y. Kressel, *Proc. 9th Ann Mtg. Soc. Magn. Reson. Med.*, New York, 1990, p. 288.
12. M. L. Schiebler, K. K. Miyamoto, M. White, S. J. Maygarden, and J. L. Mohler, *Magn. Reson. Med.*, 1993, **29**, 285.
13. A. H. Fowler, A. A. Pappas, J. C. Holder, A. E. Finkbeiner, G. V. Dalrymple, M. S. Mullins, J. R. Sprigg, and R. A. Komoroski, *Magn. Reson. Med.*, 1992, **25**, 140.
14. M. E. Yacoe, G. Sommer, and D. Peehl, *Magn. Reson. Med.*, 1991, **19**, 429.
15. J. Kurhanewicz, R. Dahiya, J. M. Macdonald, L. H. Chang, T. L. James, and P. Narayan, *Magn. Reson. Med.*, 1993, **29**, 149.
16. H. Hricak, S. White, D. Vigneron, J. Kurhanewicz, A. Kosco, D. Levin, J, Weiss, P. Narayan, and P. Carroll, *Radiology*, 1994, **193**, 703.
17. J. Kurhanewicz, D. Vigneron, H. Hricak, P. Carroll, P. Narayan, and S. Nelson, *Radiology*, 1996, **198**, 795.
18. H. Chen, H. Hricak, C. L. Kalbhen, J. Kurhanewicz, D. Vigneron, J. Weiss, and P. Carroll, *Am. J. Roentgenol.*, **166**, 1157.
19. J. Kurhanewicz, H. Hricak, D. B. Vigneron, S. Nelson, F. Parivar, K. Shinohara, and P. R. Carroll, *Radiology*, 1996, **200**, 489.
20. F. Parivar, H. Hricak, J. Kurhanewicz, K. Shinohara, D. B. Vigneron, S. J. Nelson, and P. R. Carroll, *Urology*, 1996, **48**, 594.
21. F. Parivar and J. Kurhanewicz, *Curr. Opin. Urol.*, 1998, **8**, 83.
22. J. Kurhanewicz, A. Thomas, P. Jajodia, M. W. Weiner, T. L. James, D. B. Vigneron, and P. Narayan, *Magn. Reson. Med.*, 1991, **22**, 404.
23. M. A. Thomas, P. Narayan, J. Kurhanewicz, P. Jajodia, T. L. James, and M. W. Weiner, *J. Magn. Reson.*, 1992, **99**, 377.
24. F. Hering and S. Muller, *Urolog. Res.*, 1991, **19**, 349.
25. P. Narayan, P. Jajodia, J. Kurhanewicz, A. Thomas, J. MacDonald, B. Hubesch, M. Hedgcock, C. M. Anderson, T. L. James, E. A. Tanagho, and M. Weiner, *J. Urol.*, 1991, **146**, 66.
26. K. R. Halliday, C. Fenoglio-Preiser, and L. O. Sillerud, *Magn. Reson. Med.*, 1988, **7**, 384.
27. K. R. Halliday, L. O. Sillerud, and D. Mickey, *Proc. 11th Ann Mtg. Soc. Magn. Reson. Med.*, Berlin, 1992, p. 492.
28. L. O. Sillerud, K. R. Halliday, R. H. Griffey, C. Fenoglio-Preiser, and S. Sheppard, *Magn. Reson. Med.*, 1988, **8**, 224.
29. W. M. Chew, H. Hricak, R. D. McClure, and M. F. Wendland, *Radiology*, 1990, **177**, 743.
30. P. N. Bretan, D. B. Vigneron, R. D. McClure, H. Hricak, R. A. Tom, M. Moseley, E. A. Tanagho, and T. L. James, *Urology*, 1989, **33**, 116.
31. E. J. Delikatny, P. Russell, J. C. Hunter, R. Hancock, K. H. Atkinson, C. van Haaften-Day, and C. E. Mountford, *Radiology*, 1993, **188**, 791.

Acknowledgements

Supported by NIH grant R01AG10897 and the DVA Medical Research Service.

Biographical Sketch

Michael W. Weiner. *b* 1940. B.S., 1961, Johns Hopkins. M.D., 1965, SUNY Upstate Medical Center. Intern and Resident, Mount Sinai Hospital 1965–67. Resident and Fellow in Metabolism, Yale University, 1967–70. Fellow in Biochemistry Institute for Enzyme Research, University of Wisconsin, 1970–72. Faculty at University of Wisconsin, 1971–74, Stanford University, 1974–80, University of California San Francisco, 1980–present. Director, Magnetic Resonance Department, Veterans Affairs Medical Center. Professor of Medicine and Radiology, University of California San Francisco. Research interests include application of MRI to investigation of human metabolism and diagnosis of disease.

Liver, Pancreas, Spleen, and Kidney MRI

David Stark and Ashley Davidoff
University of Massachusetts, MA, USA

1 INTRODUCTION

The upper abdomen presents unique diagnostic challenges. Numerous organs with diverse physiological functions are in close proximity with each other, abut the cardiopulmonary system through a thin diaphragm, and have open contact with the dependent organs of the pelvis. Thus, tumors, inflammatory disease, and other pathology of the upper abdomen may present clinically with symptoms attributable to an organ involved only secondarily, or they may appear to arise from the thorax or pelvis, leading the clinician away from the primary problem. Imaging of the abdomen is confounded by its large anatomic area, the mobility of the organs and their fluids, and the presence of tissues of varying imaging characteristics.

This article briefly introduces the advantages and limitations of magnetic resonance imaging (MRI) methods as applied to the evaluation of abdominal cancer. After the technical introduction, which provides an understanding of the philosophy of probing the abdomen for known or unsuspected disease, the remainder of the discussion reviews the MRI characteristics of the major upper abdominal neoplasms.

Virtually all diagnostic medicine, and certainly diagnostic imaging, is guided by three hierarchical objectives:

1. detection of disease;
2. characterization of disease; and
3. staging of disease.

Detection itself is the most important challenge, as it begins with the patients themselves deciding whether a symptom is sufficiently abnormal to warrant a visit to the doctor. After several clinical steps, imaging is most commonly used to determine whether an anatomic area (head, neck, chest, abdomen, pelvis, or musculoskeletal system) or physiologic organ system (e.g. hepatobiliary system) is normal or abnormal. This simple, binary decision is critical in selecting patients for more intensive investigation at considerable expense and no small risk of iatrogenic complications.

Characterization of disease commences once an abnormality is found. In the abdomen, nearly all patients develop benign masses if they live long enough (e.g. renal cyst or nodular hyperplasia of the prostate). Where imaging for other reasons results in detection of these benign masses, imaging must also solve the diagnostic dilemma it created and, at low cost, identify these lesions as benign and of no clinical significance.

Staging is essential to determining prognosis and therapy once treatable disease has been characterized. In many ways, staging is a subset of detection as it is the process by which multiple lesions are discriminated from a single abnormality, and the extent of disease within an organ or spread to adjacent areas is measured. Since staging often involves monitoring of treatment, it presents unique problems because the background normal structures may be altered by surgery, radiation, or progression of the disease itself. As society raises ethical and economic questions concerning the merit of treating various conditions, imaging becomes more important as a noninvasive low-cost method of determining which treatments are appropriate and effective.

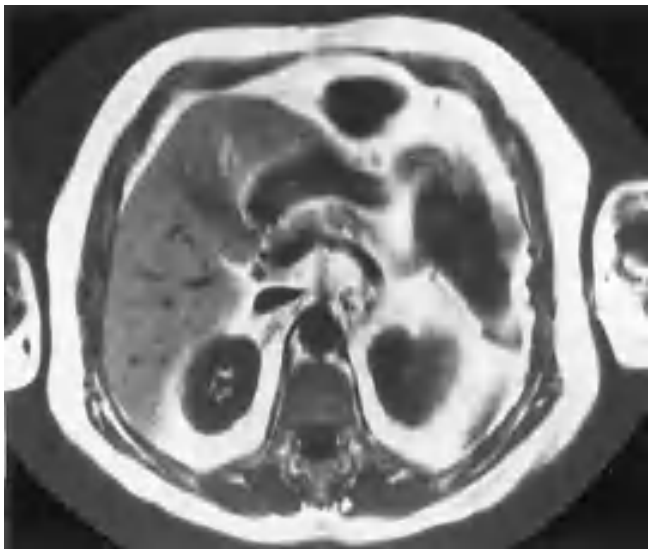

Figure 1 Normal abdomen. T_1-weighted spin echo image at the level of the pancreatic head shows a normal common bile duct, gall bladder, hepatic artery, and confluence of the splenic and portal veins. The absence of a motion artifact and the low signal intensity of kidneys relative to that of the liver are clues that this is a short *TE* sequence

2 IMAGING TECHNIQUES

MRI is similar to computerized tomography (CT) in providing a full field of view of the abdomen, and a permanent record of the entire examination, to a comparable level of anatomic detail (spatial resolution). MRI has the further advantage of allowing selection of sagittal, coronal, or oblique planes of section. However, in the abdomen virtually all imaging is performed in the transverse plane (see Figure 1).

MRI in the 1990s, like CT in the 1970s, is getting faster, with the expectation that speed will solve the problem of motion. Debate rages concerning the optimal methods for obtaining T_1 or T_2 contrast and the best signal-to-noise ratio (S/N) per unit time. These technical details are addressed elsewhere in this volume.

3 IMAGE QUALITY

Specific magnetic resonance (MR) pulse sequences and their user-selectable timing parameters are of utmost importance for lesion–liver contrast and image quality. MR image quality can be quantified by calculating the lesion–liver contrast-to-noise ratio (CNR) and the liver S/N.[1] Motion artifacts contribute

most to (systematic) noise in abdominal imaging. Vascular ghost artifacts arising from the aorta and inferior vena cava may obscure focal hepatic abnormalities, especially in the left lobe. Changing the phase-encoding direction results in artifacts projected outside the region of interest.[2,3] Signal averaging or implementation of presaturation pulses are highly effective methods of motion artifact reduction in the upper abdomen.

The CNR is an effective parameter for quantitating pulse sequence performance with respect to lesion detection. A useful rule is that spleen–liver CNR will, on average, match cancer–liver CNR. This rule holds for all pulse sequences, on all machines, and at all field strengths, since, on average, cancer and spleen have the same proton density, T_1 and T_2.

Thus, the spleen can serve as a reference signal intensity, and the spleen–liver CNR will be predictive of pulse sequence performance for liver cancer detection.

4 PULSE SEQUENCE PERFORMANCE

Theoretical calculations suggest that the optimal pulse sequence for hepatic tumor detection varies with field strength. However, clinical results have not confirmed any significant field strength differences. Performance variations due to gradients, other hardware, and software appear to be more substantial. The dominant factor appears to be the level of commitment of the practicing radiologist who implements and maintains quality imaging protocols tailored to the specific machine and its generation (upgrade level). In an area such as the abdomen, of which relatively few MRI examinations are conducted, the necessary expertise and attention to detail is too often lacking.

Properly performed T_1- or T_2-weighted sequences yield comparable CNR values and hence efficacy at liver cancer detection. Cancer or lymphoma of the spleen is poorly detected by any method, since cancer and spleen have the same proton density, T_1, and T_2, on average. T_1-weighted sequences generally offer greater S/N per unit time than do T_2-weighted sequences. This fact, combined with excellent fat–tissue T_1 contrast, leads to the choice of short TE T_1-weighted sequences for imaging the pancreas, kidneys, adrenal glands, and the remainder of the retroperitoneum and mesentery.

While T_1-weighted images offer superior anatomic resolution and are generally superior for detection of abdominal pathology, it is well established that T_2-weighted sequences are preferred for tissue characterization, especially in the liver and adrenal glands. Less is known about the kidney, where both benign (solid or cystic) and malignant lesions are also common.

4.1 Contrast Media

Parenchymal tissue contrast is enhanced by intravenous or arterial administration of magnetopharmaceuticals. Commonly gadolinium diethylenetriaminetetraacetic acid, Gd-DTPA, (Magnevist) or the newer nonionic contrast agents, such as Gd-DTPA-BMA (Omniscan) or GdDO3A (ProHance) are given by the intravenous route. These agents are designed for rapid excretion and do not significantly interact with body physiology. Binding to blood proteins or cells is negligible. Excretion is by passive glomerular filtration. Thus, these agents, introduced to the blood stream, will penetrate capillaries in the body and have an extracellular distribution, although in the brain they are limited to the vascular space by the blood–brain barrier. It is the molecular weight of these agents (less than 1000 Da) that determines their diffusion into the extracellular space of the abdominal organs.

Intravenous contrast agents are concentrated in the renal tubules, distinguishing functioning renal tissue from all but the most vascular kidney tumors. Unfortunately, in the liver, spleen, and pancreas, the blood supply, capillary permeability, and capacity of the extracellular space of tumors is quite variable. The kinetics and degree of enhancement of the tumors is often described in general terms such as 'hypovascular' or 'hypervascular'. Unfortunately, enormous biological variation exists, and tumors of a common cell type (e.g. colon adenocarcinoma) show wide variations in enhancement characteristics.

Efforts to enhance selectively liver parenchyma and improve the contrast between normal liver and cancer include rapid ('dynamic-bolus') intravenous infusion to exploit the dual (portal venous and hepatic arterial) vascular supply of normal liver as opposed to cancers, which are typically supplied by arteries and may have fewer vessels than normal liver. Dissatisfaction with intravenous techniques has stimulated attempts to administer contrast agents at angiography via selective cannulation of the hepatic artery or via the superior mesenteric artery, looking at the portal venous phase of contrast circulation. This latter approach may improve tumor–liver image contrast, and some authors have claimed improved sensitivity for detecting liver lesions. However, due to variations in the portal venous perfusion of the liver, nonneoplastic perfusion inhomogeneities create numerous false-positive diagnoses of cancer, lowering specificity and limiting the value of this technique for planning therapy.

For more than a decade, investigators have attempted to adapt cholegraphic agents, taken up by hepatocytes and excreted into the biliary system, for use in the detection of liver cancer.[4] Similarly, colloidal or particulate magnetopharmaceuticals have been used to target the normal hepatic Kupffer cells in an attempt to contrast liver against cancer, which does not show phagocytic uptake of magnetic particles. Unfortunately, attempts to target particulate agents in bulk to normal liver have been complicated by toxic side effects. Newer superparamagnetic iron oxide agents under development may show improved safety profiles.[5]

5 THE LIVER

5.1 Metastases

The liver is the most common organ in the body to which cancer spreads from primary disease elsewhere. Gastrointestinal neoplasms, including those in the pancreas, nearly always involve the liver before metastasizing to other organs. In addition, breast, lung, renal, and ovarian and other common malignancies spread hematogenously, lymphatically or transperitoneally to the liver. Indeed, liver failure is one of the most common causes of death in cancer patients, and liver metastases serve as a basis for determining prognosis and monitoring therapy.

Serologic studies of liver function, including enzymes leaked into the blood stream when the liver is injured [serum

glutamic oxaloacetate transaminase, (SGOT), serum glutamic pyruvic transaminase (SGPT), and alkaline phosphatase], have such poor sensitivity and specificity that they cannot be justified for use as an independent diagnostic test. When metastatic cancer to the liver is suspected or a reasonable risk exists, imaging must be performed. Unfortunately, imaging also has its limitations and pitfalls.

Metastatic spread of cancer is thought to begin as a single cell or a small cluster of cells, well below the resolution limit of imaging. Indeed, imaging cannot reliably detect liver lesions smaller than 5 mm in size. As a metastasis grows exponentially it is therefore submillimeter in size for the vast majority of its 'life cycle' before it enlarges to the point of causing symptoms and ultimately killing the patient. Therefore, it is obvious that the majority of metastases present in an individual, or speaking epidemiologically, the majority of metastases present in a population, are below the threshold size for detection by any means.

5.2 Imaging: Detection

Liver cancer detection does offer clinically useful information because most patients with metastatic cancer have multiple lesions, some of which are sufficiently large (>1 cm diameter) to be detected reliably. The accuracy of imaging for detecting liver metastases is the subject of endless disputes and revision of the radiological literature. The major problem with the literature is the lack of suitable 'gold standards'. It is simply impossible to collect a large series of patients for whom autopsy and histologic confirmation of imaging findings are available. Thus, radiologists frequently resort to comparative studies where one modality is compared to another, and a third technique (such as surgery) or a third imaging modality is used as the arbiter of 'truth'. Such comparative studies consistently overestimate the accuracy of detection of liver lesions.[6–9]

It is now generally accepted that MRI is the best test, followed by CT, ultrasonography, and then angiography. CT angioportography (CTAP) techniques are equal to or slightly better than MRI; however, the angiographic CT methods are generally not available and are nearly 10 times more expensive. Therefore, when the clinician is able to focus the diagnostic question of the detection of liver metastases, MRI is now the preferred technique. Unfortunately, clinicians often have mixed objectives and request inspection of the adrenal glands, retroperitoneum, and other abdominal organs. As a practical matter, in such unfocused clinical situations, ultrasonography or CT are preferred, despite their inaccuracy, as widely available, cheap, and, arguably, acceptable (i.e. 'cost-effective') compared to MRI.

In summary, for patients at risk of metastatic cancer it is an economic and public policy issue whether the best test (MRI) is made available. Given the cost of misdirected cancer therapy in patients with undiagnosed metastases (in societies where cancer treatment is available), it is likely that diagnostic imaging pays for itself. Unfortunately, neither MRI nor CT is available to many patients. For a variety of nonscientific reasons, doctors often accept ultrasonography as the primary screening test, notwithstanding the hidden costs of false-negative and false-positive examinations.

The dominant worldwide use of ultrasonography for liver imaging may in fact be cost-effective, as this rapid and inexpensive method does reliably identify the majority of patients having metastatic cancer. Since the treatments available have such a poor outcome, is it any wonder that misdiagnosis and inappropriate therapy combined do not noticeably alter this miserable outcome? Despite government pressure to sacrifice health and life that is not measurable or statistically cost-effective, medical ethics dictates that in those cases having a solitary or questionable liver lesion at ultrasonography, CT should be made available. Setting aside economic issues, state-of-the-art oncologic practice requires use of either CT or MRI to screen for liver metastases in the abdomen.

Table 1 Relaxation Times for Liver, Hemangioma, Metastases, and Hepatocellular Carcinoma at 0.6 T[a]

Tissue	T_1	T_2
Normal liver	499 ± 140	48 ± 11
Hemangioma	1010 ± 497	143 ± 51
Metastases	691 ± 100	71 ± 21
Hepatocellular carcinoma	569 ± 133	87 ± 17

[a]Values are the mean ± SD calculated from four or more spin echo measurements.

5.3 Lesion Characterization

MRI is more likely than CT to demonstrate internal nodular structure, rings and hemorrhage. In particular, T_2-weighted MR images are useful as they show edema at the border of active lesions which may be manifested as rings or as geographic zones of increased signal intensity. T_1-weighted images are less sensitive to edema; as a result, metastases are virtually always the same size or larger on T_2-weighted images.

5.4 Staging

Staging of hepatic neoplasms principally involves identifying the lobe and segment of disease. Patients with larger tumor burdens and receiving chemotherapy can be monitored by scan-to-scan comparison of tumor diameters or estimates of tumor volume. Some idea about the extent of differentiation that is possible is given by Table 1.

Surgical approaches to hepatic metastases depend primarily on confidence that all of the tumors have been identified. If there is reason to believe that a solitary metastasis exists or that a cohort of a few similar sized lesions represent the only disease in the liver, then the question of resection depends upon the functional hepatic reserve and the technical ability to remove the lesions. Lesions invading an adjacent structure, such as the diaphragm or inferior vena cava, or lesions in difficult areas, such as the porta hepatis, make surgery challenging and risky. Undoubtedly, the greatest risk to resective therapy is undiagnosed residual disease.

6 HEPATOCELLULAR CARCINOMA

Also known as 'hepatoma', primary malignancy of hepatocytes [i.e. hepatocellular carcinoma (HCC)] comprises 1% of all cancers in the USA. Worldwide, variation in nutritional fac-

tors and the incidence of viral hepatitis[10,11] account for major differences in the incidence and nature of HCC. It is far more common in Japan, the rest of Asia, and sub-Saharan Africa in association with chronic viral hepatitis. Articles can be found in the literature citing a wide range of sensitivity, specificity, and overall accuracy for ultrasonography, CT and MRI.[13,14,15] It is evident that HCC is more difficult to detect with any of the imaging methods than is metastatic cancer. The principal reason for this difficulty is that HCC most often occurs against a background of chronic hepatitis, fatty liver and cirrhosis.[11–14]

Fatty change within malignant hepatocytes serves to decrease tumor–liver contrast on conventional MR images, although the presence of fat can be exploited to increase contrast if chemical shift selective techniques are used.

Ongoing regeneration and areas of nodular hyperplasia serve to mask or mimic hepatoma. Bands of scar tissue in the liver have increased water content, and the long T_1/T_2 signal intensity characteristics are very similar to hepatoma.

6.1 Lesion Characterization

Characterization of hepatoma and discrimination from metastatic cancer or benign hepatic masses is rarely possible with ultrasonography, CT, or scintigraphy. MRI, however, has the ability to detect three features characteristic of hepatoma. Each of these features is present in approximately 30% of hepatomas, and therefore one or more features can be found in a majority of cases.

First, a capsule of compressed liver or scar tissue may create a sharp boundary with adjacent liver tissue. The capsule has long T_1/long T_2 signal intensity characteristics, and is usually best seen on T_1-weighted images. The capsule must be distinguished from low signal intensity blood vessels on T_1-weighted spin echo images. Hepatic adenoma may also show peripheral capsules indistinguishable from those of hepatoma. However, hepatic adenoma is an unusual tumor with different demographics. Tumor and capsules can be distinguished from the rings of metastases, as the latter are better seen on T_2-weighted images and are not well seen at all on T_1-weighted images. Images from a hepatic adenoma study are shown in Figure 2.

Second, hepatomas accumulate intracellular triglyceride. Fatty accumulation can be detected using a variety of chemical shift methods such as phase contrast frequency-selective imaging. Although fatty accumulation may occur in injured hepatocytes in other conditions, including adenoma, focal nodular hyperplasia, hepatitis, and dietary disturbances, it is usually possible to distinguish focal fatty infiltration from fat within a mass, as the latter displaces normal blood vessels, while focal fat infiltration usually does not.

Third, hepatoma has a propensity to grow into hepatic and portal veins, and MRI is able to demonstrate this morphology to advantage. Certainly ultrasonography also has this capability; however, the ability of ultrasonography to distinguish the solid tumor from adjacent liver makes it more difficult to follow the tumor into vessels.[17]

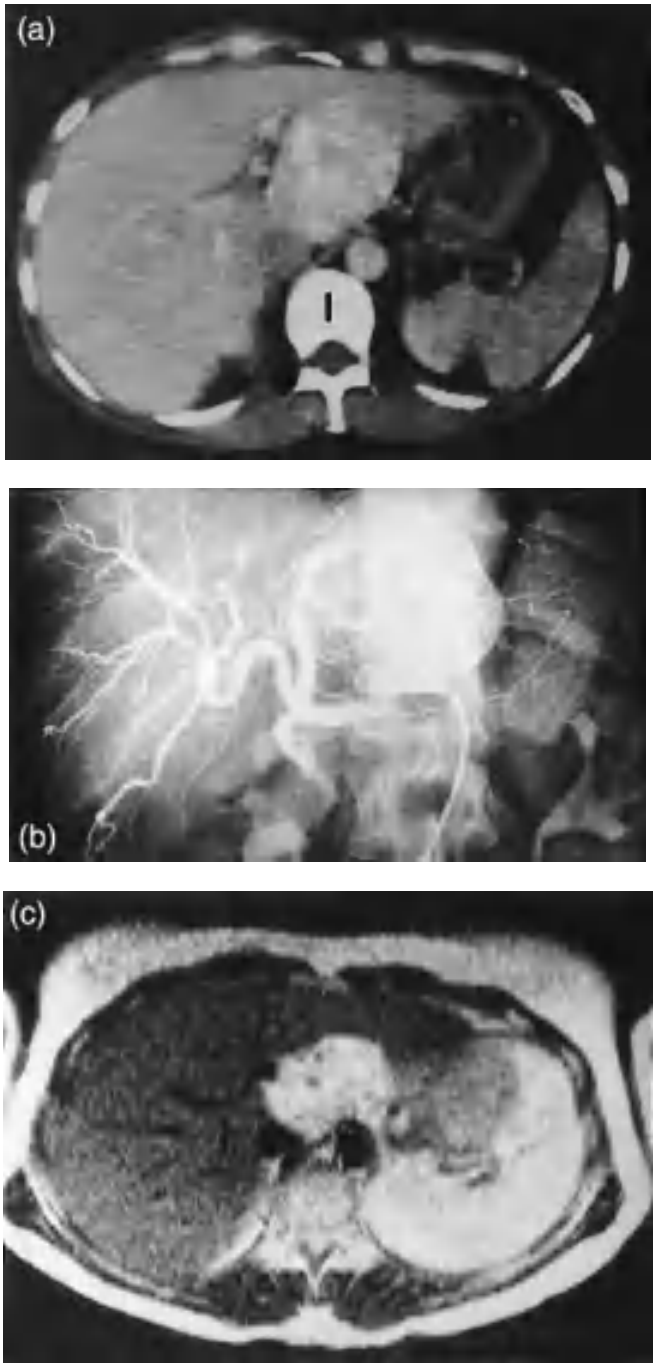

Figure 2 Hepatic adenoma. (a) A CT scan enhanced with bolus infusion of iodinated contrast media shows a large enhancing lesion in the left hepatic lobe. This finding is nonspecific and resembles cancer or any other solid neoplasm. (b) A catheter angiogram suggests a benign solid tumor, most likely hepatic adenoma. (c) MRI (SE 1500/100) shows a heterogenous mass that is isointense with the spleen, consistent with any solid neoplasm; surgery confirmed the diagnosis

7 BENIGN DISEASE: CAVERNOUS HEMANGIOMA

Hemangioma is a vascular malformation characterized by a cavernous collection of blood spaces (Figure 3). Blood flow is very slow and virtually undetectable, except for the occasional peripheral site of venous entry. Hemangioma is exceedingly common in both sexes and all races around the world. Approximately 15–20% of the adult population has such a lesion.[8]

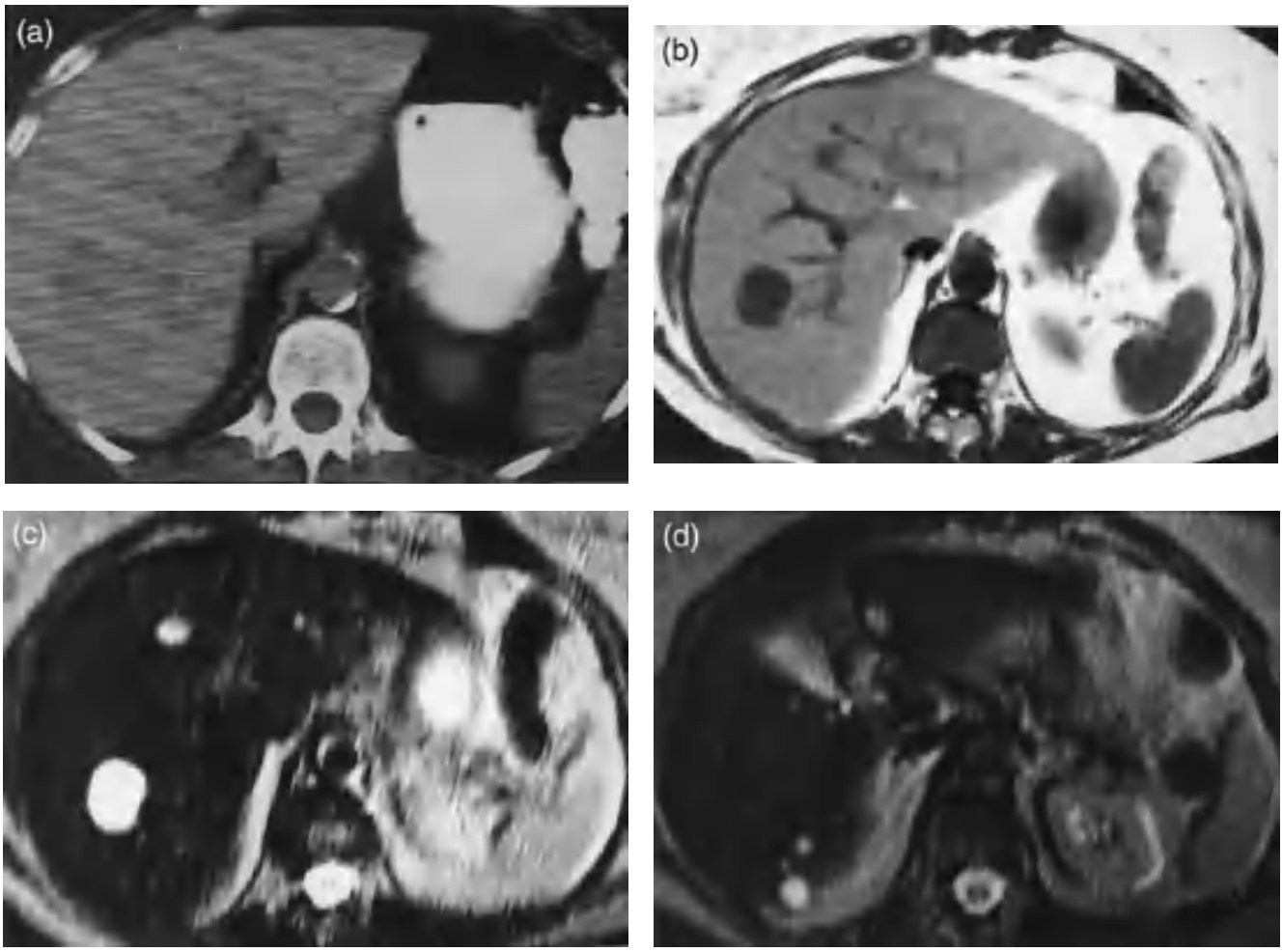

Figure 3 Cavernous hemangioma of the liver. (a) A CT scan shows a 3 cm lesion in the posterior segment, right hepatic lobe, with a hypodense appearance identical to cancer. (b) MRI (SE 300/15) shows the lesion to have a low intensity, similar to cancer (very slightly darker than the spleen). Note a second, 1 cm lesion in the anterior segment not seen on the CT scan. (c) MRI (SE 2400/180) shows the lesions to be hyperintense relative to spleen, and nearly isointense with cerebrospinal fluid; this is consistent with blood in cavernous hemangiomas. (d) Lesions as small as 3 mm diameter can be characterized by MRI

7.1 Lesion Characterization

MRI has been remarkably successful in identifying the fluid content of cavernous hemangiomas by its long T_2 relaxation time (Table 1).[15,16] Long *TE* spin echo images, which reduce the signal intensity of solid tissue relative to fluid, show cavernous hemangiomas, cerebrospinal fluid, bile, and gastric contents as extremely bright structures. Properly performed, with *TE* in excess of 120 ms and successful suppression of motion artifact, cavernous hemangiomas are homogeneous and sharply circumscribed on the MR image. Tumors, on the other hand, are ill-defined, heterogeneous, and lower in signal intensity due to their gelatinous (solid) make-up.

Contrast-enhanced blood-pool studies provide an alternative method of identifying hemangiomas and other vascular lesions. CT uses iodine based diagnostic pharmaceuticals; scintigraphy uses technetium-labeled red blood cells, and MRI uses the paramagnetic agent Gd-DTPA. In addition, iron oxide particles and other magnetic contrast media have been shown to be effective blood-pool markers. The concept behind these studies depends principally on the kinetics and distribution of the vascular agents. Cavernous hemangiomas tend to enhance uniformly over 5–30 min and may retain contrast longer than the circulating blood pool. Solid tumors show more rapid wash-in and wash-out of the contrast agent and usually show less peak enhancement than do cavernous hemangiomas. As these findings depend upon the cardiac output, circulation time, timing of contrast administration, and the specifics of the perfusion pattern of the vascular malformation, contrast-enhanced studies are less predictable than plain T_2-weighted MRI. Nevertheless, MRI can be used in both methods.

Controlled studies have shown that MRI can discriminate cavernous hemangioma from solid neoplasm with an overall accuracy of 90%. If, in addition to this T_2-weighted technique, a contrast study is done, the accuracy increases further. With MRI one can perform both an unenhanced and enhanced scan within a single 1-h examination.

8 THE PANCREAS

Adenocarcinoma is a malignant mucinous neoplasm of the pancreas that arises from the ductal epithelium. It is the fourth most common cause of death from cancer in the USA and accounts for 3% of all cancers. Adenocarcinoma represents 75% of nonendocrine pancreatic malignancies. The disease usually affects people over the age of 70 years, with a male/female ratio of 1.5:1.0. Proposed etiologic factors include cigarette smoking and coffee consumption, alcohol consumption and dietary intake of fat, protein and a high number of calories.[7,18,19]

Disease states of the pancreas that are reportedly associated with the development of pancreatic carcinoma include diabetes mellitus and familial pancreatitis. The etiologic association with chronic pancreatitis is not clear.

Because the pancreas is not encased by a capsule, early spread into the surrounding retroperitoneal fat is common. Local structures then become involved, including the portal vein, superior mesenteric vein, splenic vein, gastroduodenal artery, bile duct and duodenum. Local lymph-node involvement and hematogenous spread to the liver via the portal vein are also seen.

8.1 Imaging: Detection

Lesions in the head of the pancreas are generally visualized by both ultrasonography and CT. The former is limited by surrounding bowel gas or obesity in about 30% of patients. Maneuvers such as altering respiration, filling the stomach with water, placing the patient in the upright position and repeat scanning are helpful. Lesions in the tail of the pancreas are difficult to detect by ultrasonography, but visualization can be improved by using the spleen as a window. With CT, tail and body lesions are sometimes obscured by a partial volume artifact from a bowel not filled with contrast. Intraoperative ultrasound scanning is very sensitive to small and impalpable tumors, particularly for small, functioning tumors such as insulinomas.

MRI has little or no role at the present time due to inferior anatomic resolution and no better contrast than ultrasonography or CT.

8.2 Characterization

Ultrasonography, CT, and MRI are equally nonspecific in distinguishing pancreatic cancer from benign masses. Pancreatitis is the most important differential diagnosis. In most cases, radiologically guided fine-needle aspiration biopsy (FNAB) is necessary for diagnosis.

9 THE SPLEEN

The spleen rarely causes clincial symptoms and is most often imaged as a bystander to a study directed at another abdominal organ. Trauma and suspected rupture is the most frequent indication for imaging the spleen itself. While MRI would be preferred, CT is usually selected because of its availability and resistance to motion artifacts.

Oncologic disease within the spleen is infrequently identified, even though more than half of patients with widespread malignancy may have splenic involvement at autopsy. Melanoma probably accounts for most of the metastases found in the spleen, although various studies have described the origin of metastases, in decreasing order of frequency, as lung, prostate, colon, stomach, melanoma, ovary, and pancreas.

9.1 Lymphoma

Imaging of lymphoma has traditionally been insensitive to splenic involvement. Splenic size is unreliable, as one-third of patients with splenomegaly do not have lymphomatous involvement, and one-third of patients without splenomegaly have such an involvement. In patients with aggressive disease, such as the poorly differentiated nodular type, involvement becomes probable, but not necessarily visible.[20]

Ultrasonography, CT, and scintigraphy have unsatisfactory accuracy rates, ranging between 54% and 75%. MRI is beginning to show some promise. When the water content of lymphoma is high, such as in the large lesions of histiocytic lymphoma, they become detectable on T_2-weighted sequences. MRI using superparamagnetic iron oxide is showing promise in demonstrating splenic involvement, but these research findings need further clinical verification.[21]

10 THE KIDNEY

Renal disease, like diseases of the liver and pancreas, can be divided between diffuse and focal processes. Most diffuse disease is inflammatory or metabolic in nature.

Solid renal masses are cancers until proven otherwise, usually at the expense of nephrectomy given the habit of urologists to avoid referral of patients for FNAB, a less expensive alternative practice by radiologists. Since the aging population at risk of cancer has a high prevalence of benign simple cysts, it has been a challenge to identify benign lesions noninvasively, in order to save good kidneys from the knife. Unfortunately, features demonstrable by ultrasonography, CT, and MRI add little to the low pretest probability of malignancy. The few cancers picked up as cystic structures with nodular irregularities or septations by ultrasonography, calcifications or density changes on CT, or hemorrhage on MRI are outnumbered by similar findings in nonmalignant cysts falsely diagnosed as positive for malignancy.

While the identification of renal cysts by MRI should be as straightforward as identification of hepatic hemangioma, comparable research has not been performed to establish quantitative or qualitative criteria. Furthermore, renal cell carcinoma is more difficult than other cancers to distinguish from cysts because of its hypervascularity, tendency for necrosis, and the resultant long T_1/T_2, approaching that of cysts.

MRI studies in the kidney have largely consisted of anatomic descriptions recapitulating the findings known from CT, albeit less clearly. The sole application of MRI to the diagnosis and management of renal disease is inspection of the draining veins for extension of tumor. For all other questions, ultrasonography and CT are preferred. As a result, very little renal MRI is practiced.

11 SUMMARY

Abdominal imaging is historically anatomic, based on the delineation of high contrast fatty tissue boundaries. Ultrasonography and CT are widely available, familiar to clinicians, competitive in diagnostic quality, and cheap. MRI of the abdomen is best established in the liver for detection and differential diagnosis of focal masses.

12 RELATED ARTICLES

In Vivo Hepatic MRS of Humans; Kidney, Prostate, Testicle, and Uterus of Subjects Studied by MRS; Lung and Mediastinum MRI; Male Pelvis Studies Using MRI; MRI of the Female Pelvis.

13 REFERENCES

1. R. E. Hendrick, T. R. Nelson, and W. R. Hendee, *Magn. Reson. Imag.*, 1984, **2**, 193.
2. G. M. Bydder, J. M. Pennock, R. E. Steiner, S. Khenia, J. A. Payne, and I. R. Young, *Magn. Reson. Imag.*, 1985, **3**, 251.
3. D. R. Bailes, D. J. Gilderdale, G. M. Bydder, A. G. Collins, and D. M. Firmin, *J. Comput. Assist. Tomogr.*, 1985, **9**: 835.
4. Y. M. Tsang, M. Chen, and G. Elizondo, in 'Sixth Annual Meeting, Society for Magnetic Resonance Imaging, Boston, MA, 1988', 6 (S1), 124.
5. D. D. Stark, R. Weissleder, G. Elizondo, P. F. Hahn, S. Sains, L. E. Todel, G. J. Wittenberg, and J. T. Ferrucci, *Radiology*, 1988, **168**, 297.
6. D. D. Stark, J. Wittenberg, R. J. Butch, and J. T. Ferrucci, *Radiology* 1987, **165**, 399.
7. D. G. Mitchell and D. D. Stark, 'Hepatobiliary MRI', Mosby, St Louis, 1992.
8. K. Okuda, K. G. Ishak, 'Neoplasms of the Liver', Springer, Berlin, 1987.
9. J. P. Heiken, P. J. Weyman, J. K. Lee, D. M. Balfe, D. Picus, E. M. Brunt, and M. W. Flyte, *Radiology*, 1989, **171**, 47.
10. P. F. Hahn, D. D. Stark, S. Saini, E. Rummeny, G. Elizonilo, R. Weissleder, J. Wittenberg, and J. T. Ferrucci, *Am. J. Roentgenol.*, 1990, **154**, 287.
11. M. Ebara, M. Ohto, Y. Watanabe, K. Kimura, H. Saisho, Y. Tsuchiya, K. Ohuda, N. Arimuzu, F. Konilo, and H. Ikcheva, *Radiology*, 1986, **159**, 371.
12. P. R. Ros, B. J. Murphy, J. E. Buck, G. Olmedilla, and Z. Goodman, *Gastrointest. Radiol.*, 1990, **15**, 233.
13. H. Yoshida, Y. Itai, K. Ohtomo, T. Kohubo, M. Minami, and N. Yashiro, *Radiology*, 1989, **171**, 339.
14. E. Rummeny, R. Weissleder, D. D. Stark, S. Saini, C. C. Compton, W. Bennett, P. F. Hohn, J. Wittenburg, R. A. Malt, and J. T. Ferruci, *Am. J. Roentgenol.*, 1989, **152**, 63.
15. Y. Itai, K. Ohtomo, S. Furui, T. Yamauchi, M. Minomi, and N. Yashiro, *Am. J. Roentgenol.*, 1985, **145**, 1195.
16. D. D. Stark, R. C. Felder, J. Wittenberg, S. Saini, R. J. Butch, M. E. White, R. R. Edelman, P. R. Mueller, J. F. Simeone, and A. M. Cohen, *Am. J. Roentgenol.*, 1985, **145**, 213.
17. D. D. Stark, P. F. Hahn, C. Trey, M. E. Clouse, and J. T. Ferrucci, *Am. J. Roentgenol.*, 1986, **146**, 1141.
18. A. L. Cubilla and P. J. Fitzgerald, *Clin. Bull.*, 1978, **8**, 143.
19. R. E. Schultz and N. J. Finkler, *Mt. Sinai J. Med.*, 1980, **47**, 622.
20. M. Federle and A. A. Moss, *CRC Crit. Rev. Diagn. Imaging*, 1983, **10**, 1.
21. R. Weissleder, G. Elizondo, D. D. Stark, P. F. Hahn, J. Margel, J. F. Gonzalez, F. Saini, W. E. Todel, and J. T. Farruci, *Am. J. Roentgenol.*, 1989, **152**, 175.

Biographical Sketch

David D. Stark. *b* 1952. B.A., 1974, M.D., 1978, Harvard University, USA. Postdoctoral work, University of California, San Francisco. Successively, instructor, assistant professor and associate professor of radiology, Harvard Medical School, Massachusetts General Hospital. Currently Professor of Radiology, University of Massachusetts Medical Center, USA. Approx. 200 publications. Current research specialties: contrast media, clinical applications of MRI, quantitation of tissue iron.

Male Pelvis Studies Using MRI

Hedvig Hricak
Memorial Sloan-Kettering Cancer Center, New York, NY, USA

and

William T. Okuno
University of California, San Francisco, CA, USA

1 INTRODUCTION

Superb soft tissue contrast resolution and multiplanar imaging capability have placed MR imaging in an eminent position in the evaluation of pelvic anatomy and pathology. In the male pelvis, much work has been performed in studying the prostate gland, seminal vesicles, testes, penis, and urethra. While the results of MR imaging in these areas were promising from the very beginning, these applications are still wrapped in controversy, and the indications are not generally accepted by many clinicians. As MR techniques keep evolving and overall image resolution is improved, MRI is gaining recognition and converting many skeptics into ardent advocates.

2 PROSTATE GLAND

2.1 Anatomy

The mature prostate is composed of both glandular and nonglandular tissue. The glandular portion is differentiated into three major zones: peripheral (70%); central (25%); and transition (5%) zones.[1] A small amount of glandular tissue is also present in the periurethral glands. Zonal differentiation is clinically significant because most (68%) prostate carcinomas arise in the peripheral zone whereas benign prostatic hyperplasia (BPH) usually originates in the transition zone.[2] Nonglandular tissue within the prostate includes the urethra and anterior fibromuscular stroma.

The normal prostate gland demonstrates a homogeneous intermediate signal intensity on T_1-weighted images, regardless of patient age or magnetic field strength; T_2-weighted images are necessary to delineate the zonal anatomy of the prostate (Figure 1).[3] The peripheral zone is of high signal intensity, equal to or greater than that of the adjacent periprostatic fat. In contrast, the central zone has a lower signal intensity than the surrounding peripheral zone.[3] These differences in signal characteristics are thought to be related to the presence of striated muscle and fewer glandular elements in the central zone.[3] The transition zone also has a lower signal intensity than the peripheral zone. The signal intensities of the central and transition zones are similar at all imaging parameters, and the two can be differentiated only by knowledge of their respective anatomic locations.[3] On Gd chelate-enhanced T_1-weighted images, the zonal anatomy of the gland is depicted but not as consistently as on T_2-weighted images.[4]

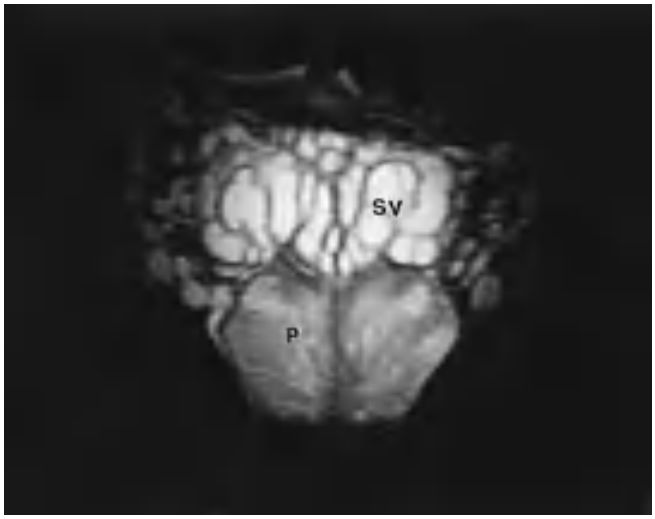

Figure 1 Prostate gland, normal anatomy: T_2-weighted image, endorectal coil, coronal plane of section. The peripheral zone (P) of the prostate gland demonstrates homogeneous high signal intensity. Seminal vesicles (SV) are seen cephalad to the prostate gland. They are convoluted in Nature and have a grape-like appearance

2.2 Pathology

2.2.1 Congenital Anomalies

Agenesis and hypoplasia of the prostate are frequently encountered with other congenital anomalies of the genitourinary tract. While MRI can establish the diagnosis, this frequently is an associated finding and not the clinical reason for the study.

Congenital cysts of the prostate are the most common anomalies of this gland. Prostatic utricle and Müllerian duct cysts are midline structures that arise at the level of the verumontanum and extend cephalad (Figure 2). Their signal intensity is nonspecific and depends on the nature of their content, ranging from serous to proteinaceous and hemorrhagic fluid.[5]

2.2.2 Inflammatory Disease

MR imaging does not play a role in the diagnosis of prostatic inflammatory disease. When discovered incidentally, acute prostatitis will demonstrate diffuse glandular enlargement and the peripheral zone sometimes exhibits a low signal intensity on the T_2-weighted image.[6] Thus far, there is only limited experience in MR imaging of prostate abscess. If this diagnosis is clinically suspected, transrectal ultrasound (TRUS) or CT should be the modalities of choice.

2.2.3 Benign Prostatic Hyperplasia

Benign prostatic hyperplasia (BPH) is a glandular and/or stromal proliferation in the transition zone and periurethral glands. The prostate gland is enlarged, and often the hyperplastic tissue is separated from the compressed peripheral zone

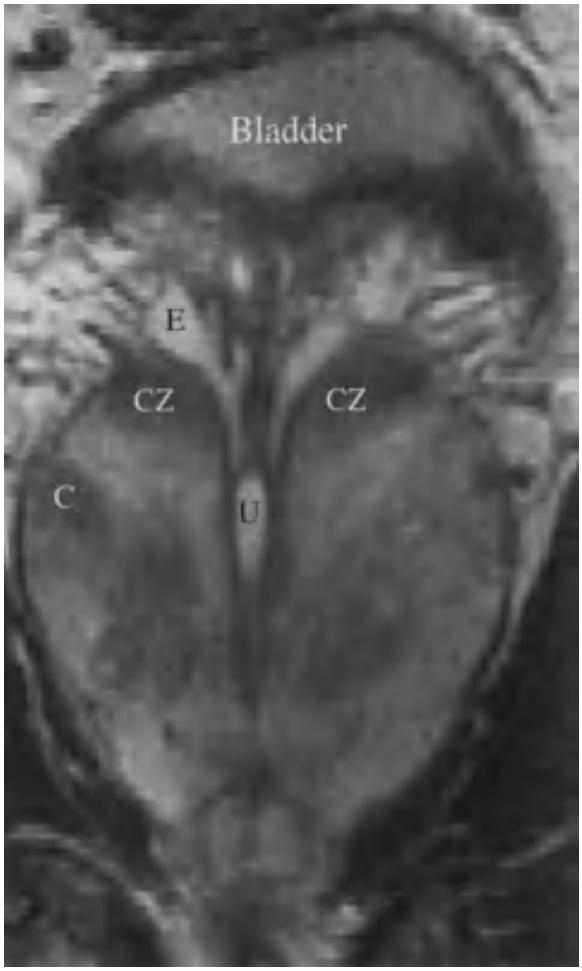

Figure 2 Prostatic utricle: T_2-weighted image, coronal plane of section. The utricle (U) is seen as a midline cyst of high signal intensity extending superior to the verumontanum. In the right peripheral zone, the low signal intensity region is a focus of prostate cancer (C). E, right ejaculatory duct; CZ, central gland

tissue by the surgical pseudocapsule (Figure 3). MR imaging of BPH includes a spectrum of findings, based on the varying histologic composition and depending on the imaging sequence utilized.[7] Although MRI provides excellent morphologic definition of BPH, it is not possible to differentiate benign from malignant disease of the prostate.

The multiplanar imaging capability of MRI allows accurate volumetric measurement of the hyperplastic prostate gland and is especially useful in glands greater than 100 g, where ultrasound is limited in accuracy.[8] Because of its accuracy in volumetric measurement and depiction of zonal anatomy, MR imaging has been used in the follow-up of patients on androgen deprivation therapy in order to monitor the changes in gland size and in differential volume reduction in zones of the gland.[9]

2.2.4 *Prostate Carcinoma*

Cancer of the prostate is the most common cancer in men and ranks as the second most common cause of cancer death

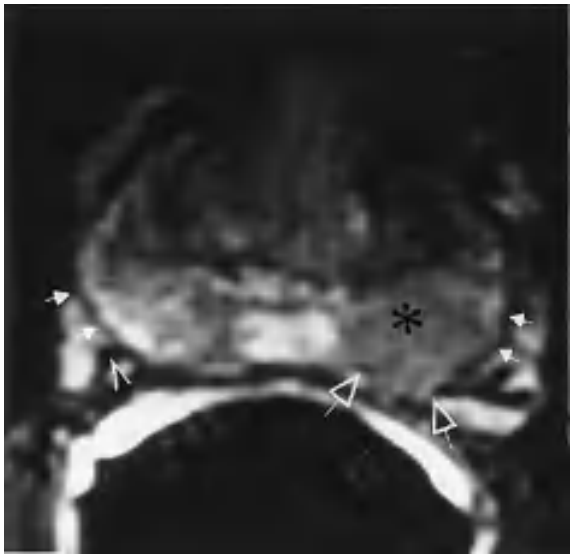

Figure 3 Benign nodular hyperplasia: T_2-weighted image, coronal plane of section. The prostate gland is enlarged. The heterogeneous signal intensity is secondary to benign nodular hyperplasia. A large hyperplastic nodule (*) protrudes into the urinary bladder (B)

in American men.[2,10] MR imaging is not applicable for the detection of prostate carcinoma. The strength of MRI is in the staging of biopsy-proven prostate cancer, although this application continues to be controversial and is a subject of numerous ongoing investigations. On T_2-weighted MR images, prostatic carcinoma (PCa) is most commonly shown as a decreased signal intensity area within the high-signal-intensity normal peripheral zone. The detection of PCa on MRI is applicable only to the tumors located in the peripheral zone. The normal low or heterogeneous signal intensity of the transition and central zones precludes tumor detection.[11] Even in the peripheral zone, tumor detection may be hampered by postbiopsy changes (Figure 4).[11] Depending on the time interval between biopsy and MRI scan, the biopsy changes may cause either under- or overstaging of tumor presence and extent. Recent studies have demonstrated that MRI should not be performed for at least 2 weeks after biopsy.[12] The finding of low signal intensity within the peripheral zone is not specific for prostate cancer.[13] A number of other etiologies such as chronic prostatitis, dystrophic changes, scar, previous trauma, postbiopsy hemorrhage, radiation, and hormonal changes can all cause low signal intensity within the peripheral zone.[13]

Recently, *in vivo* MR spectroscopic imaging of the prostate gland has been developed to increase the specificity of cancer detection in the peripheral zone. This three-dimensional proton spectroscopic technique allows the simultaneous acquisition of multiple spectra from the prostate gland with a tissue voxel resolution down to 0.24 ml.[14,15] Since the metabolic changes of prostate cancer cause an increase in choline and a decrease in citrate levels, the ratio of the area under the choline spectroscopic peak to that under the citrate peak is increased in areas of cancer. The increased choline/citrate ratio in areas of prostate cancer enables the differentiation of cancer from the other causes of low T_2 signal in the peripheral zone listed above (Figure 5).[16] In addition, the ability to

Figure 4 Postbiopsy hemorrhage: T_1-weighted image, transaxial plane of section. In this patient, hemorrhage after a prostate biopsy is seen as increased signal intensity diffusely in the peripheral zone (PZ) and more focally in the right central gland (CZ). Normally on T_1-weighted images, the entire prostate shows homogeneous intermediate signal intensity

estimate the spatial extent of prostate cancer has important implications for assessing the efficacy of various cancer treatments.[17]

Prostate cancer, particularly the mucinous type, can demonstrate high signal intensity indistinguishable from the surrounding peripheral zone.[18] While prostate cancer detection rates as high as 92% have been reported,[11] the results of large multicenter studies are disappointingly low, with only 60% of lesions greater than 5 mm in any one dimension being detected on MRI scans.[19] Attempts have also been made to measure tumor volume by MRI. As with ultrasound, the results are inaccurate, and smaller lesions are overestimated in 44% of patients and larger lesions underestimated in 55% of patients.[19]

Prostate cancer staging can follow either the TNM or Jewitt classification.[20] The TNM stage 1 or Jewitt stage A are tumors not applicable to MRI detection. Most of those cancers are within the transition zone, the area where MRI can neither depict nor stage the disease. TNM stage 2–Jewitt B disease in-

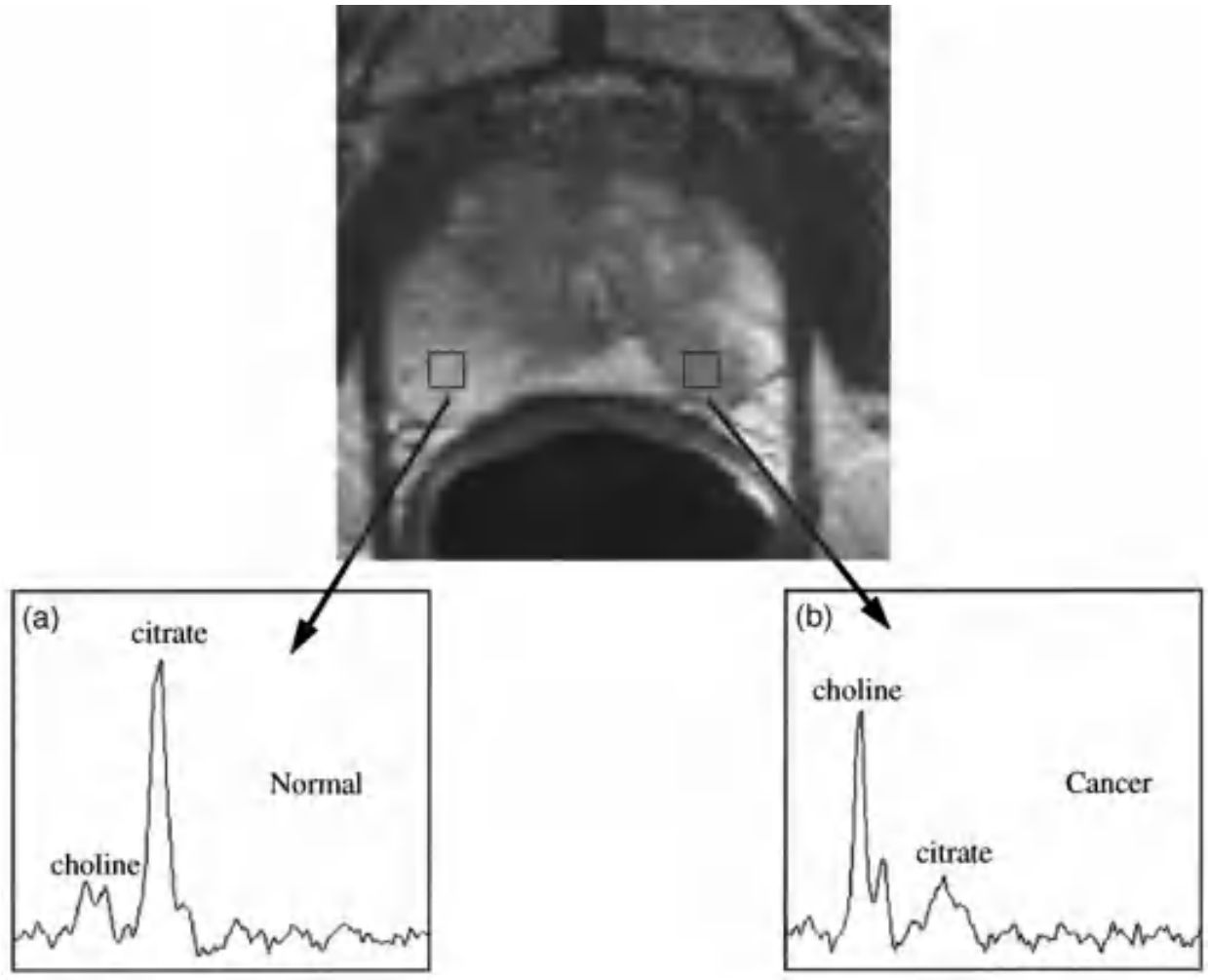

Figure 5 MR spectroscopic imaging of the prostate gland: transaxial T_2-weighted image and MR spectra. The spectrum from the normal peripheral zone (a) shows the normal relationship between the choline and citrate peaks. The spectrum from the prostate cancer (b) shows increased choline and reduced citrate levels

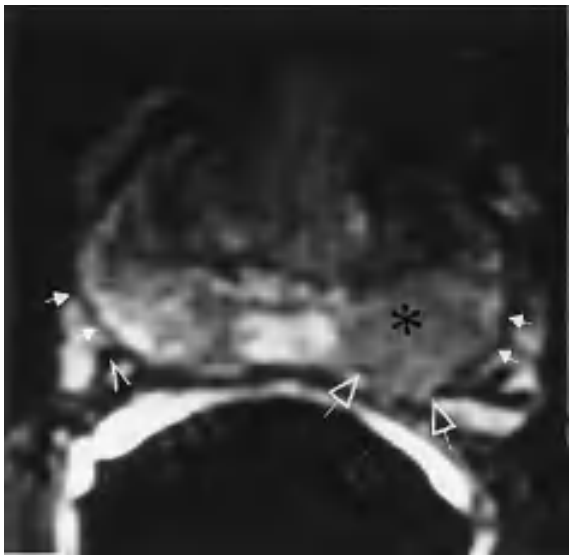

Figure 6 Prostate carcinoma with extracapsular extension on the left: T_2-weighted image, transaxial plane of section. Carcinoma (*) demonstrates low signal intensity. Prostate capsule (white solid arrows). There is a breach of the capsule (open white arrows) with direct cancer invasion to the neurovascular bundle. Normal neurovascular bundle on the right side (black and white arrowhead)

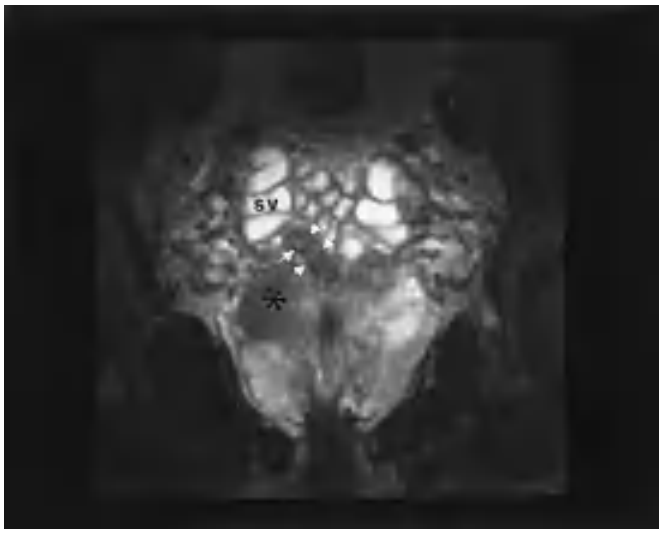

Figure 7 Prostate carcinoma with extracapsular and seminal vesicle extension: T_2-weighted image, coronal plane of section. Prostate cancer (*) is seen at the base of the prostate gland on the right. Irregular outer margin indicates extracapsular invasion. There is also evidence of direct tumor invasion (white arrows) into the right seminal vesicle (SV)

dicates tumor confined to the prostate gland. The low-signal-intensity tumor is seen within the peripheral zone, and while the lateral margin can bulge, the bulge is smooth in contour.[21,22] With the endorectal coil, direct visualization of the prostate capsule increases the confidence level in the evaluation of TNM stage 2. In TNM stage 3 and Jewitt C disease, the findings of importance are extracapsular extension and seminal vesicle invasion.

MRI findings of extracapsular extension on endorectal coil include (a) bulge of the prostate gland with an irregular margin, (b) contour deformity with step-off or angulated margin, (c) breech of the capsule with direct tumor extension, (d) obliteration of the fat in the rectoprostatic angle, and (e) asymmetry, of the neurovascular bundles (Figure 6).[12,21,22] Seminal vesicle invasion is diagnosed when there is (a) demonstration of contiguous low-signal-intensity tumor extension into and around the seminal vesicles, and/or (b) tumor extension along the ejaculatory duct resulting in nonvisualization of the ejaculatory duct, decreased signal intensity of seminal vesicles, and loss of seminal vesicle wall on T_2-weighted images (Figure 7).

While transaxial planes of section are essential in the evaluation of extracapsular extension, the invasion of the seminal vesicles is facilitated by the evaluation of transaxial and coronal planes of section.[12,23–25] In recently reported studies using the Jewitt classification and endorectal coil, the accuracy for extracapsular extension was 82% and accuracy for seminal vesicle invasion 97%.[12] These reports are in accordance with previously published results by Schnall et al.,[24] although they are higher than the latest publications by Chelsky et al.[25] In the evaluation of lymph node metastases, reports in the literature testify to the superiority of MRI over CT. However, none of the studies has sufficiently high numbers of positive nodes for statistically meaningful analysis. The accuracy of staging of cancer of the prostate depends on the type of coil used and appears to be most accurate when the combination of endorectal and surface multicoil system is used.[11,19–26] Contrast-enhanced images do not contribute to either tumor detection or staging except in rare instances when they help in the detection of seminal vesicle invasion.[4]

3 SEMINAL VESICLES

3.1 Anatomy

The seminal vesicles are paired, androgen-dependent accessory sex glands. On T_1-weighted images, normal seminal vesicles demonstrate homogeneous medium signal intensity similar to that of the adjacent pelvic muscle. On T_2-weighted images, seminal vesicles demonstrate a grape-like configuration with the high-signal-intensity fluid differentiated from the low signal intensity of the inner convolutions and outer wall (Figure 1).[27] The size and the signal intensity of the seminal vesicles depends on patient's hormonal status and will decrease with patient's age, hormonal replacement therapy, radiation therapy, or severe alcoholism.[27] On contrast-enhanced T_1-weighted images, the internal architecture of the seminal vesicles is depicted with the convolutions and wall demonstrating enhancement while the vesicular fluid remains of low signal intensity.[4,6] Although great variation in the size of normal seminal vesicles can occur in adult men of the same age, there is a tendency for a decrease in size with advancing years. Seminal vesicles are usually symmetric in size, but asymmetry has been reported in up to 10% of patients.[6]

3.2 Pathology

3.2.1 Congenital Anomalies

Congenital anomalies of the seminal vesicles include the absence of the seminal vesicles and more commonly seminal vesicle cysts. In diagnosing the absence of seminal vesicles, T_1-weighted transaxial images are most useful.[27] In the evaluation of seminal vesicle cysts, MRI provides precise anatomical localization but the signal intensity depends on its fluid composition.[5] Blood is often present within the cyst with its signal intensity depending on the age of the hemorrhage.

3.2.2 Inflammatory Disease

Inflammation of the seminal vesicles is usually associated with epididymitis and the associated ascending spread of infection through the prostate gland. The MRI appearance varies with the stage of inflammation. Seminal vesicles are often enlarged in the acute stage and small in the chronic phase. Hemorrhage within the seminal vesicles is common in subacute infection.[27] Chronic inflammation results in small atrophic seminal vesicles often of lower than normal signal intensity on T_2-weighted images.[6]

3.2.3 Tumors

The benign tumors of seminal vesicles (leiomyomas predominate) are more common than primary malignant neoplasms which are usually adenocarcinomas. The vast majority of malignant tumors of the seminal vesicles are secondary usually from prostate carcinoma, but extension from cancer of the bladder or rectum can be seen as well. The differentiation between benign and malignant tumors is usually based on the morphologic findings.[28] Benign tumors appear as smooth, well-marginated masses while malignant invasion of the seminal vesicles usually results in masses of low signal intensity and are irregular in configuration.[28] Loss of normal adjacent tissue planes also suggests secondary involvement of the seminal vesicles (Figure 7). Tumor extension into the seminal vesicles is best seen on T_2-weighted images, in the sagittal and coronal planes.[6,28]

4 PENIS/URETHRA

4.1 Anatomy

The penis is composed of three erectile bodies: the two lateral corpora cavernosa and the ventromedial corpus spongiosum (Figure 8).[29] Each of the three erectile bodies is enveloped by a fibrous sheath—the tunica albuginea. Buck's fascia—a common fibrous sheath—divides the penis into its dorsal compartment by enclosing the two corpora cavernosa and the ventral compartment by enclosing the corpus spongiosum. The male urethra extends from the bladder neck to the fossa navicularis in the glans penis. It is divided into the prostatic, membranous, and penile portions of the urethra. On T_1-weighted images, the three erectile bodies demonstrate medium signal intensity, and they all increase in signal intensity on T_2-weighted images (Figure 8). While the corpus spongiosum demonstrates homogeneous high signal intensity, the normal corpora cavernosa can be either homogeneous or heterogeneous in signal intensity depending on the blood volume within the erectile tissue.[29] The tunica albuginea and Buck's fascia appear as a low-signal-intensity stripe surrounding the corporeal bodies on T_2-weighted images and provide excellent contrast with the high-signal-intensity corpora.[29] The use of contrast enhancement allows demonstration of the penile anatomy on T_1-weighted images.[6]

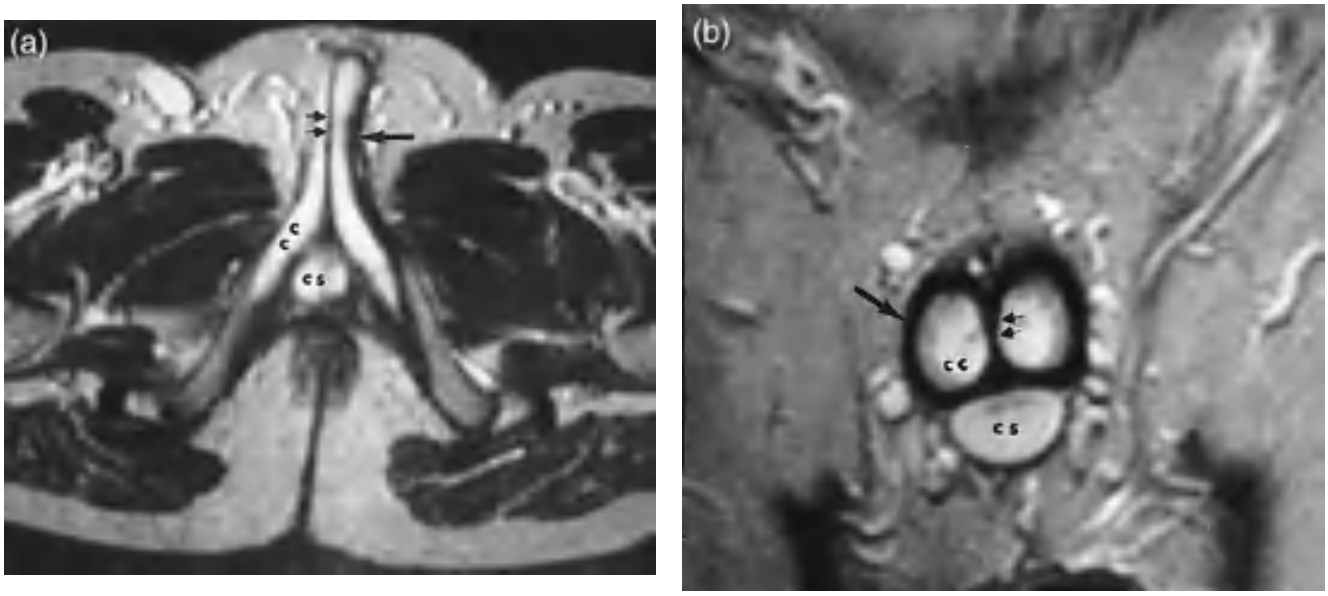

Figure 8 Normal anatomy of the penis. (a) Transaxial and (b) coronal plane of section: T_2-weighted images. Corpora cavernosa (cc), corpus spongiosum (cs), tunica albuginea (short arrows), and Buck's fascia (long black arrow)

4.2 Pathology

4.2.1 Congenital Anomalies

Epispadia, hypospadia, or duplication of the penis (penis diphallus) are the three groups of most commonly encountered congenital anomalies of the penis. The ability of MRI to delineate each of the corpora allows precise definition of the type of anomaly and provides depiction of associated anomalies involving the perineum and the remaining genitourinary tract.[29] The clinical indications, however, are rare, the most common being evaluation of penis diphallus.

4.2.2 Inflammatory Disease

Peyronie's disease is an inflammatory condition of unknown etiology characterized by the development of fibrous plaque involving the tunica albuginea and extending into the corpora cavernosa. On T_2-weighted MR images, the lower-signal-intensity plaque can be depicted in contrast to the higher-signal-intensity corpora cavernosa.[30,31] MRI is not the primary method for diagnosing this condition. MRI, however, can provide information about the location and size of the plaque as well as the degree of cavernosal involvement. Furthermore, MRI can differentiate between the acute and chronic form of Peyronie's disease, especially when contrast media are used.

4.2.3 Trauma

Penile trauma usually results from direct blunt injury to the erect penis causing fracture of the penis or rupture of the corpora cavernosa. On T_2-weighted MR images, the diagnosis of penile fracture is based on the finding of interruption of the normal low-signal-intensity tunica albuginea. Peripenile hematoma is often detected.[29,32]

MRI is valuable in the presurgical evaluation of urethral trauma (grade 3) associated with complex pelvic injury. Separation between the prostatic apex, membranous, and bulbous urethra can occur in superior anteroposterior or lateral direction. Misalignment of greater than 2 cm in the superior direction and greater than 1 cm in the lateral direction necessitates a different surgical approach (perineal versus suprapubic with removal of the symphysis pubis).[33,34] MRI can greatly assist in planning the surgical approach but thin-section T_2-weighted images in all three orthogonal planes are essential for the assessment of this complicated problem.[34]

4.2.4 Tumors

Penile carcinoma accounts for only about 1% of all male cancers, and carcinoma of the male urethra is even more rare.[35] When cancers are located in the glans penis or in the penile shaft, the locoregional tumor extent can usually be determined by physical examination. However, when the tumor involves the root of the penis or bulbomembranous urethra, the clinical evaluation is limited and MRI has a role in local staging of disease.[29] On MRI, penile and urethral carcinomas are usually not distinguishable as most lesions requiring radiologic assessment are advanced and have spread to involve adjacent structures. The use of T_2-weighted images demonstrates the tumor of different signal intensity (usually lower) as compared with the adjacent normal high-signal-intensity erectile bodies (Figure 9). MRI, however, is not specific for cancer detection and cannot be distinguished from inflammatory disease.[6,29] This is especially true for smaller lesions of the urethra. However, MRI can be of great help in locoregional tumor staging, and in therapy planning—surgery versus radiation therapy.[29] Metastasis to the penis can also be well evaluated by MRI. Metastasis demonstrates diffuse low signal intensity infiltrating the erectile bodies on T_2-weighted images. Differentiation between primary and metastatic lesions is not possible.[29]

5 TESTIS

5.1 Anatomy

On T_1-weighted images, the testis demonstrates intermediate signal intensity, similar to that of the corpora cavernosa or corpus spongiosum and lower than that of subcutaneous fat. On T_2-weighted images, the testis demonstrates high signal intensity in contrast to the lower-signal-intensity tunica albuginea (a dense fibrous connective tissue capsule) covering the testis (Figure 10).[36] The mediastinum testis has signal characteristics similar to tunica albuginea and is seen as a low-signal-intensity stripe invaginating into the high-signal-intensity testicular parenchyma (Figure 10).[36] The parietal and visceral layers of the tunica vaginalis are often separated by a small amount of normal serous fluid. As in a hydrocele, this normal fluid surrounds the testis completely except for the posteromedial bare area. The signal intensity of the epididymis is similar to the testis on T_1-weighted images and much lower than the testis on T_2-weighted images.[36]

5.2 Pathology

5.2.1 Undescended Testis

An undescended testis is defined as a testis located outside the scrotum. MR diagnosis of undescended testes relies on the finding of an elliptical mass demonstrated along the expected path of testicular descent.[37] However, it has recently been reported that dynamic gadolinium-enhanced MR angiography improves the detection of atrophic undescended testes by showing enhancement of the pampinform plexus.[38] When the undescended testis is in the inguinal canal, it is usually oval in shape while the intraabdominal testis assumes a more rounded configuration. The large field of view and multiplanar image capability of MRI allows precise identification of the undescended testis as being either high scrotal, intracanalicular, or intraabdominal in location. When the intraabdominal testis is located close to the internal inguinal ring, it is easily depicted by MRI. However, high abdominal testis is difficult to demonstrate with MRI and CT is the procedure of choice. MR imaging allows differentiation between the undescended testis, gubernaculum, and lymph nodes.[37] Lymph nodes lie outside the expected descent of the testis. The differentiation between the gubernaculum and the testis relies on their respective differences in signal intensity. The gubernaculum characteristically demonstrates very low signal intensity on both T_1- and T_2-weighted images as its predominant histologic composition is fibrous tissue. The signal intensity of the testis varies depending on the degree of atrophy but is never as low as a fibrous cord.

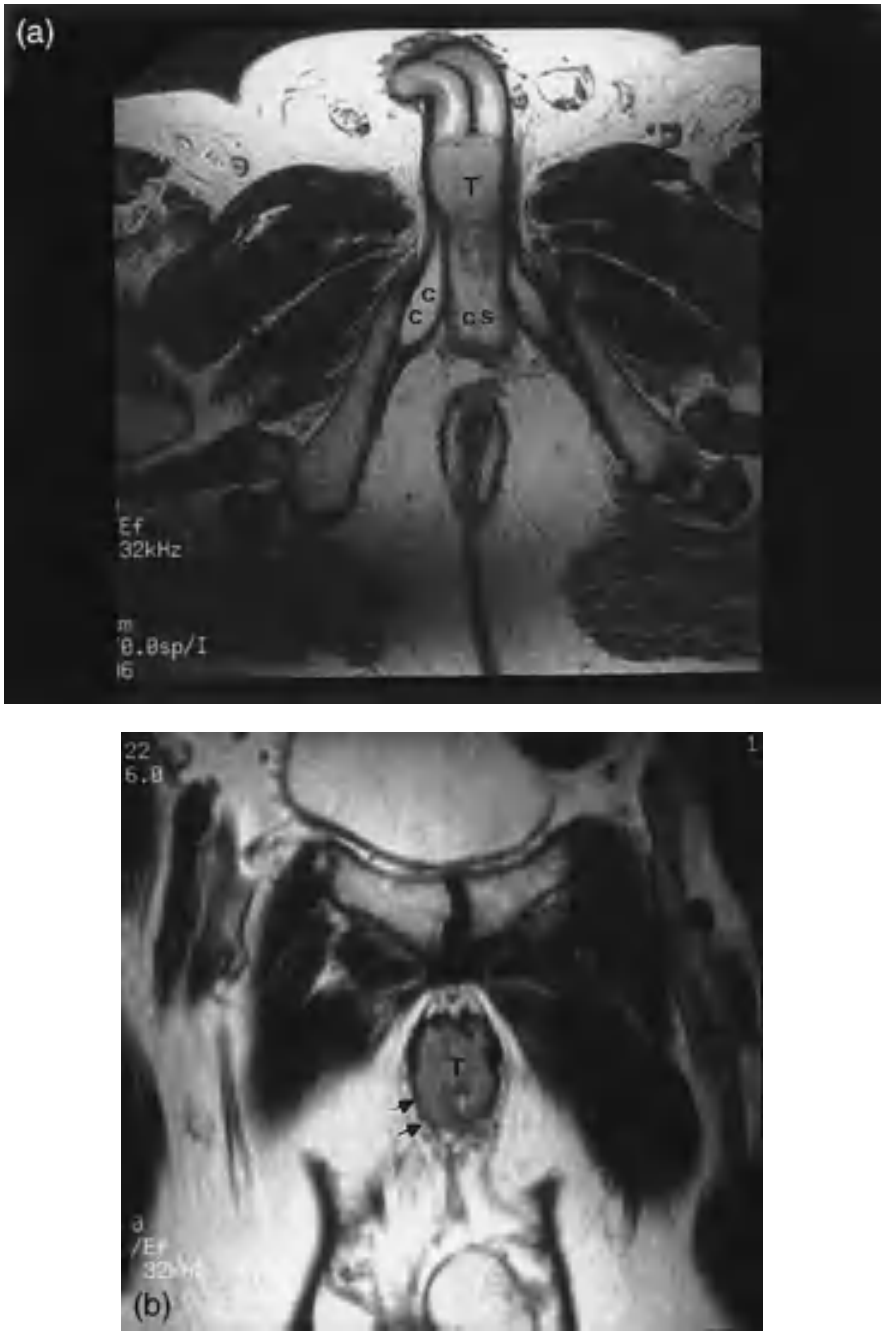

Figure 9 Cancer of the penis. (a) Transaxial and (b) coronal plane of section: T_2-weighted images. Tumor (T) is seen invading both corpora cavernosa (cc), spectum corpora cavernosa as well as corpus spongiosum (cs). In the coronal plane of section, the zonal anatomy of the penis is not visualized, and there is demonstration of tumor extension through the tunica albuginea (small black arrows)

5.2.2 Testicular Tumors

Testicular tumor is the most common malignancy among men of 15 to 34 years of age although it accounts for only 1% of all cancers in males.[35] The majority (90–95%) of testicular tumors are malignant germ cell tumors. The homogeneous high signal intensity of the normal testicular tissue serves as an excellent background for the depiction of intratesticular pathology.[36,39,40] On T_2-weighted images, testicular tumors usually demonstrate a lower signal intensity than the adjacent normal testicular tissue (Figure 11). Although MR imaging has a high sensitivity rate for the detection of testicular tumors, its findings are variable and are not specific for tumor histology. While on T_2-weighted images testicular tumors are mostly hypointense to the testis, they may demonstrate a signal intensity similar or even higher than testicular tissue. Tumors can be homogeneous or heterogeneous in signal pattern. While seminomas are typically homogeneous and hypointense, the

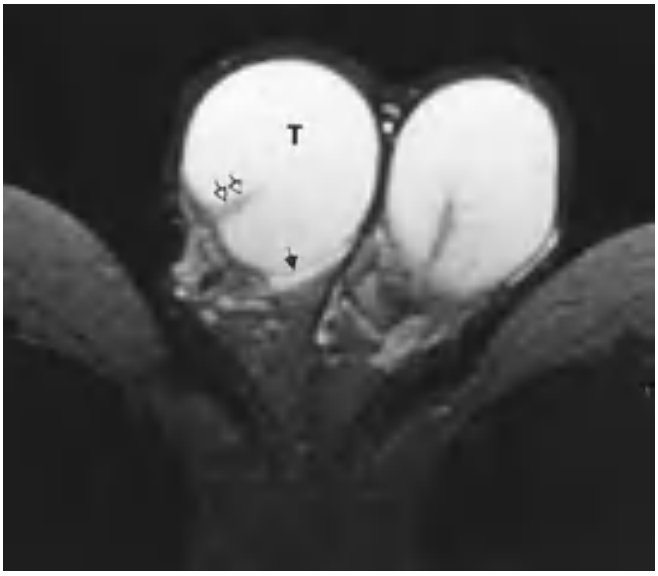

Figure 10 Normal testis, transaxial plane of section: T_2-weighted image. Testis (T) demonstrates homogeneous high signal intensity. Tunica albuginea (solid arrow) is seen as a low-signal-intensity stripe. Mediastinum testis (open arrows)

nonseminomatous tumors are often heterogeneous and exhibit various signal intensities.[40] However, exceptions to the rule can be encountered.[36] Furthermore, differentiation between primary and secondary testicular tumors is not possible, and the MR appearance of benign tumors is similar to testicular cancer.[41]

Testicular cysts can usually be differentiated from testicular tumors especially when contrast media are used. They appear as sharper marginated lesions with fluid signal intensity characteristics.[36]

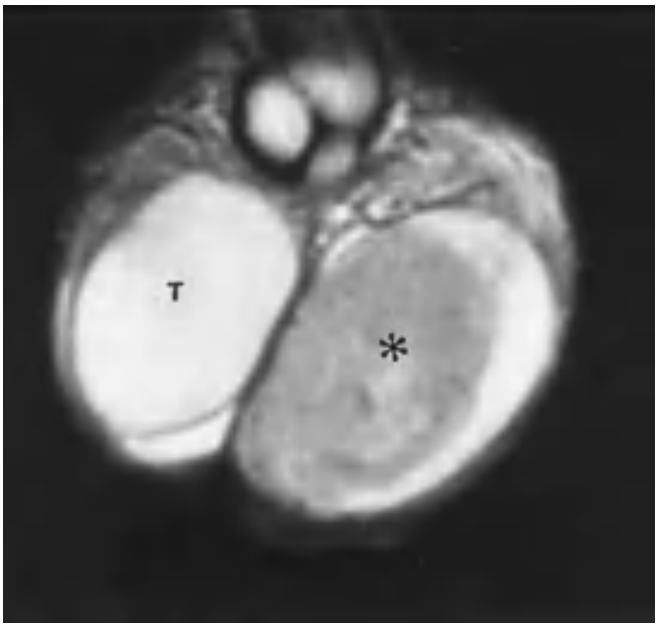

Figure 11 Seminoma of the left testis. Testicular tumor (*) demonstrates low signal intensity as compared with the adjacent remaining higher signal intensity testicular tissue. Normal right testis (T)

5.2.3 Inflammatory Disease

Acute epididymitis is the most common inflammatory lesion in the scrotum. In acute epididymitis, the epididymis is enlarged and demonstrates heterogeneous and often higher signal intensity than normal. Hemorrhage may complicate acute epididymitis producing signal intensity commensurate with its age. Reactive hydrocele is often present. In chronic epididymitis, the signal intensity of the epididymis is reduced, a finding best appreciated on T_2-weighted images.[39] Associated orchitis, when present, appears as a homogeneous or heterogeneous hypointense lesion within the normal sized or enlarged testis. The signal intensity change is most commonly present in the mediastinum region. Fibrotic thickening of the tunica albuginea can occur following epididymitis, and the thickening may sometimes be difficult to differentiate from small testicular cancer, thus the term 'pseudotumor of the tunica albuginea' has been introduced.[42]

5.2.4 Spermatic Cord Torsion

Torsion is considered a surgical emergency since delaying intervention may result in irreversible damage to the testis. MRI plays no role and is not a primary imaging modality in diagnosing testicular torsion. Reports on MRI findings in acute torsion in humans are sporadic and not well documented. The testis may be normal or enlarged and of heterogeneous signal intensity. With testicular torsion, the spermatic cord can enlarge, exhibiting a high signal intensity due to edema. A twisted cord can be seen as multiple low-intensity curvilinear structures rotating in a 'whirlpool' pattern which is best seen in a plane perpendicular to its axis.[43] Torsion of the testicular or epididymal appendices can be identified with MRI by their typical location and the signal characteristics of hemorrhage.[43]

5.2.5 Fluid Collection and Benign Scrotal Masses

Fluid collections whether hydrocele, hematocele, or pyocele all indicate abnormal fluid located between the parietal and visceral layers of the tunica vaginalis. The signal of hydrocele is typical for fluid (low signal intensity on T_1-weighted image and high intensity on T_2-weighted image).[36,39] The signal intensity of hematocele varies with the age of the hemorrhagic fluid, and the proteinaceous component of pyocele usually makes the fluid signal intensity on T_1-weighted images higher than that of hydrocele. Spermatocele is a retention cyst of small tubules which connect the rete testis to the head of epididymis. On MRI scan, the diagnosis of spermatocele can be made by its typical location (usually in the head of the epididymis) and its cystic nature.[6]

In scrotal pathology, MRI serves as a problem-solving modality when ultrasound findings are equivocal, technically inadequate, or there is a discrepancy between the physical examination and ultrasound findings. Recent studies have shown that when ultrasound and physical examination of the scrotum are inconclusive, MRI can improve patient management and reduce treatment costs.[37–46]

6 RELATED ARTICLES

Coils for Insertion into the Human Body; MRI of the Female Pelvis.

7 REFERENCES

1. J. E. McNeal, *Monogr. Urol.*, 1983, **4**, 5.
2. T. A. Stamey, J. E. McNeal, F. S. Freiha, and E. A. Redwine, *J. Urol.*, 1988, **139**, 1235.
3. H. Hricak, G. C. Dooms, J. E. McNeal, A. S. Monk, M. Marotti, A. Avalloro, M. Pelzer, E. C. Proctor, and E. A. Tanagho, *Am. J. Roentgenol.*, 1987, **148**, 51.
4. S. A. Mirowitz, J. J. Brown, and J. P. Heiken, *Radiology*, 1993, **186**, 153.
5. S. Thurnher, H. Hricak, P. R. Carroll, R. S. Pobiel, and R. A. Frilly, *Radiology*, 1988, **167**, 631.
6. H. Hricak, in 'MRI of the Pelvis. A Text Atlas', eds. H. Hricak and B. M. Carrington, Martin Dunitz, London, 1991, p. 313.
7. W. G. Way, Jr., J. J. Brown, J. K. Lee, E. Gutierrez, and G. L. Andriole, *Magn. Reson. Imag.*, 1992, **10**, 341.
8. A. Rahmouni, A. Yang, C. M. Tempany, T. Frenkel, J. Epstein, P. Walsh, P. K. Leichner, C. Ricci, and E. Zerhouni, *J. Comput. Assist. Tomogr.*, 1992, **16**, 935.
9. C. M. Tempany, A. W. Partin, E. A. Zerhouni, S. J. Zinreich, and P. C. Walsh, *Prostate*, 1993, **22**, 39.
10. S. H. Landis, T. Murray, S. Bolden, and P. A. Wingo, *CA Cancer J. Clin.*, 1999, **49**, 8.
11. M. D. Schnall, R. E. Lenkinski, H. M. Pollack, Y. Imai, and H. Y. Kressel, *Radiology*, 1989, **172**, 570.
12. S. F. Quinn, D. A. Franzini, T. A. Demlow, D. R. Rosencrantz, J. Kim, R. M. Hanna, and J. Szumowski, *Radiology*, 1994, **190**, 323.
13. K. Lovett, M. D. Rifkin, P. A. McCue, and H. Choi, *JMRI*, 1992, **2**, 35.
14. J. Kurhanewicz, D. B. Vigneron, S. J. Nelson, H. Hricak, J. M. MacDonald, B. Konety, and P. Narayan, *Urology*, 1995, **45**, 459.
15. J. Kurhanewicz, D. B. Vigneron, H. Hricak, P.Narayan, P. Carroll, and S. J. Nelson, *Radiology*, 1996, **198**, 795.
16. Y. Kaji, J. Kurhanewicz, H. Hricak, D. L. Sokolov, L. R. Huang, S. J. Nelson, and D. B. Vigneron, *Radiology*, 1998, **206**, 785.
17. J. Kurhanewicz, D. B. Vigneron, H. Hricak, F. Parivar, S. J. Nelson, K. Shinohara, and P. Carroll, *Radiology*, 1996, **200**, 489.
18. E. Outwater, M. L. Schiebler, J. E. Tomaszewski, M. D. Schnall, and H. Y. Kressel, *JMRI*, 1992, **2**, 597.
19. M. D. Rifkin, E. A. Zerhouni, C. A. Gatsonis, L. E. Quint, D. M. Paushter, J. I. Epstein, W. Hamper, P. C. Walsh, and B. J. McNeil, *N. Engl. J. Med.*, 1990, **323**, 621.
20. M. Graf, P. Hermanek, R. V. P. Hutter, L. H. Sobin, G. Wagner, and C. Wittekind (eds.), 'TNM Atlas: Illustrated Guide to the TNM/pTNM-Classification of Malignant Tumors, 4th edn', Springer-Verlag, Berlin, 1997.
21. E. K. Outwater, R. O. Petersen, E. S. Siegelman, L. G. Gomella, C. E. Chernesky, and D. G. Mitchell, *Radiology*, 1994, **193**, 333.
22. K. K. Yu, H. Hricak, R. Alagappan, D. M. Chernoff, P. Bacchetti, and C. J. Zaloudek, *Radiology*, 1997, **202**, 697.
23. H. Hricak, G. C. Dooms, R. B. Jeffrey, A. Arallone, D. Jacobs, W. K. Benton, P. Narayan, and E. A. Tanagho, *Radiology*, 1987, **162**, 331.
24. M. D. Schnall, Y. Imai, J. Tomaszewski, H. M. Pollack, R. Lenkinski, and H. Y. Kressel, *Radiology*, 1991, **178**, 797.
25. M. D. Schnall, R. E. Lenkinski, H. M. Pollack, Y. Imai, and H. Y. Kressel, *Radiology*, 1989, **172**, 570.
26. M. J. Chelsky, M. D. Schnall, E. J. Seidmon, and H. M. Pollack, *J. Urol.*, 1993, **150**, 391.
27. E. Secaf, R. N. Nuruddin, H. Hricak, R. D. McClure, and B. Demas, *Am. J. Roentgenol.*, 1991, **156**, 989.
28. R. D. McClure and H. Hricak, *Urology*, 1986, **27**, 91.
29. H. Hricak, M. Marotti, T. J. Gilbert, T. F. Lue, L. H. Wetzel, J. W. McAninch, and E. A. Tanagho, *Radiology*, 1988, **169**, 683.
30. G. Helweg, W. Judmaier, W. Buchberger, K. Wicke, H. Oberhauser, R. Knapp, O. Ennemoser, and D. Zur Nedden, *Am. J. Roentgenol.*, 1992, **158**, 1261.
31. R. Vosshenrich, I. Schroeder-Printzen, W. Weidner, U, Fischer, M. Funke, and R. H. Ringert, *J. Urol.*, 1995, **153**, 1122.
32. M. Fedel, S. Venz, R. Andreessen, F. Sudhoff, and S. A. Loening, *J. Urol.*, 1996, **155**, 1924.
33. C. M. Dixon, H. Hricak, and J. W. McAninch, *J. Urol.*, 1992, **148**, 1162.
34. Y. Narumi, H. Hricak, N. A. Armenakas, C. M. Dixon, and J. W. McAninch, *Radiology*, 1993, **188**, 439.
35. D. M. Parkin, P. Pisani, and J. Ferley, *CA Cancer J. Clin.*, 1999, **49**, 33.
36. S. Thurnher, H. Hricak, P. R. Carroll, R. Pobiel, and R. A. Frilly, *Radiology*, 1988, **167**, 631.
37. P. J. Fritzsche, H. Hricak, B. A. Kogan, M. L. Winkler, and E. A. Tanagho, *Radiology*, 1987, **164**, 169.
38. W. W. Lam, P. K. Tam, V. H. Ai, K. L. Chan, W. Cheng, F. L. Chan, and L. Leong, *J. Pediatr. Surg.*, 1998, **33**, 123.
39. L. L. Baker, P. C. Hajek, T. K. Burkhard, L. Dicepua, H. M. Landa, G. R. Leopold, J. R. Hesselink, and R. F. Mattrey, *Radiology*, 1987, **163**, 93.
40. J. O. Johnson, R. F. Mattrey, and J. Phillipson, *Am. J. Roentgenol.*, 1990, **154**, 539.
41. F. V. Coakley, H. Hricak, and J. C. Presti Jr, *Urol. Clin. North Am.* 1998, **25**, 375.
42. R. B. Poster, B. A. Spirt, A. Tamsen, and B. V. Surya, *Radiology*, 1989, **173**, 561.
43. M. A. Trambert, R. F. Mattrey, D. Levine, and D. P. Merthoty, *Radiology*, 1990, **175**, 53.
44. H. Derouet, H. U. Braedel, G. Brill, K. Hinkeldey, J. Steffens, and M. Ziegler, *Urol. Ausg.*, 1993, **32**, 327.
45. B. M. Cramer, E. A. Schlegel, and J. W. Thueroff, *Radiographics*, 1991, **11**, 9.
46. A. D. Serra, H. Hricak, F. V. Coakley, B. Kim, A. Dudley, A. Morey, B. Tschumper, and P. R. Carroll, *Urology*, 1998, **51**, 1018.

Biographical Sketches

Hedvig Hricak. *b* 1946. M.D., 1970, University of Zagreb, Croatia; Ph.D., 1992, Karolinska Institute, Stockholm, Sweden. University of California, San Francisco, Faculty in Radiology, 1982–99; Faculty in Urology, 1986–present; Faculty in Radiation Oncology, 1991–99. Department of Radiology, Sloan-Kettering Cancer Center, New York, 2000–present. Involved in clinical MR imaging of gynecologic and urologic diseases since the introduction of this technique. Over 150 papers on MR imaging in peer-reviewed journals and co-author of four major textbooks on the subject. Member of numerous editorial boards of prestigious journals in radiology and radiation oncology and serves on national and international committees of prestigious professional organizations.

William T. Okuno. *b* 1967. M.D., 1993, University of Illinois, USA. Radiology Residency, Massachusetts General Hospital, 1994–1998; Abdominal Imaging Fellowship, University of California, San Francisco, 1998–1999; Lutheran General Hospital, Park Ridge, Illinois, 1999–present. Special interests: abdominal imaging.

MRI of the Female Pelvis

Robert C. Smith, Michael J. Varanelli, Leslie M. Scoutt, and Shirley McCarthy

Yale University School of Medicine, New Haven, CT, USA

1 INTRODUCTION

The article will describe the clinical applications and technical considerations of MRI of the female pelvis. Due to its improved tissue contrast capability (compared with computerized tomography and ultrasound), MRI is the technique of choice for depicting normal uterine and cervical anatomy as well as a variety of benign and malignant conditions affecting these structures. MRI is also capable of delineating a number of nongynecological abnormalities of the pelvis.

Recent technical advances have dramatically improved the resolution that can be obtained when imaging the female pelvis. At the same time, these technical improvements have greatly reduced the imaging time. Both of these factors should improve the accuracy of MRI not only for detecting abnormalities but in the staging of gynecological malignancies. Cost–benefit analyses have shown MRI of the female pelvis to be cost-effective.

2 MRI TECHNIQUE

Imaging of the female pelvis requires both T_1- and T_2-weighted images.[1] T_1-weighted images are useful for lymph node detection and to characterize regions which contain blood products and/or fat. T_2-weighted images are necessary to depict the internal anatomy of the gynecological organs, characterize masses and other abnormalities, and determine the origin of a mass as uterine or ovarian.

T_1-weighted images are typically acquired in the axial plane from the level of the aortic bifurcation through the pubic symphysis. The *TR* (repetition time) used is between 500 and 600 ms, and the minimum possible *TE* (echo time) is used (usually 10–15 ms). Superior and inferior saturation pulses are routinely used to diminish the intravascular signal and therefore help decrease pulsation artifacts and distinguish lymph nodes from vascular structures. In some cases, use of a longer *TE* (up to 20 ms) will help diminish intravascular signal. Respiratory compensation is always utilized to diminish ghost artifacts from the high-signal subcutaneous fat.[2]

Other typical parameters would include a field of view (FOV) of 24–30 cm, section thickness of 5 mm, intersection spacing of 2.0–2.5 mm, a frequency matrix size of 256, a phase matrix size of 128 or 192, and one or two signal averages. If there is a large amount of bowel within the pelvis, glucagon can be administered to help diminish artifacts from bowel peristalsis. In the majority of cases, glucagon is not necessary.

T_2-weighted images should be acquired through the uterus and ovaries in at least two orthogonal planes. The main purpose of sagittal images is to depict the uterine and cervical zonal anatomy. Depending upon the orientation of the uterus, the axial or coronal plane can be chosen to image the uterus in a plane perpendicular to its long axis. Both the axial and coronal planes will usually depict the ovaries to good advantage. The T_2-weighted images should be acquired using fast spin echo (FSE) or turbo spin echo (TSE) pulse sequences.[3,4] Using these, high-resolution T_2-weighted images can be acquired through the entire pelvis in less than 5 min.

3 FSE IMAGING

When FSE T_2-weighted images are acquired in a body coil, typical imaging parameters would include a *TR* of 4500–6000 ms, a *TE* of 100–130 ms, a 5 mm section thickness, a 2.0–2.5 mm intersection spacing, a minimum phase matrix size of 192, a FOV of 24–28 cm, and two to four signal averages. If a small FOV is used with a phase matrix size of 256, this usually necessitates use of four signal averages to maintain the signal-to-noise ratio (S/N) at an acceptable level.

In addition to the above parameters, the echo train length (ETL) and the echo spacing (ESP) must also be specified when using FSE sequences. With conventional spin echo sequences, a single phase-encoding step is acquired during each *TR* interval. Even if multiple echoes are measured (as with proton density and T_2-weighted images), each is acquired with the same phase-encoding step. The multiple echoes are used to generate multiple images (of different *TE*) at each imaging location. In order to reconstruct an image, the number of phase-encoding steps must equal the size of the phase matrix. It is this fact which makes the imaging time of conventional spin echo sequences so long.

FSE sequences acquire multiple phase-encoding steps during each *TR* interval. This is achieved by applying multiple 180° pulses after each 90° pulse and separately phase encoding the resulting spin echoes. The ETL is equal to the number of separately phase-encoded echoes acquired following each 90° pulse. The maximum value of the ETL is usually 16 or 32. Recent development of 'single-shot' techniques using a half-Fourier reconstruction allows an ETL of 128 or 192 and acquisition of each image in about 1 s. Once all of the separately phase-encoded echoes have been acquired in one section, data are then acquired in the next section. The spacing between the separate phase-encoded echoes is the ESP. The minimum value of ESP is usually 6–8 ms and depends on the bandwidth. In almost all circumstances the minimum value of ESP should be used.

Regardless of the imaging technique, each phase-encoding step uses a different strength phase-encoding gradient. Echoes acquired with the weak phase-encoding gradients provide most of the signal (and hence contrast) of an image, and echoes acquired with the strong phase-encoding gradients provide most of the spatial resolution of an image. With the fast spin echo technique, multiple separately phase-encoded echoes are used to generate a single image at each location. The overall contrast of such images is determined by the echo times at which the weak phase-encoding steps are acquired.[5–7] If the weak phase-encoding steps are used for the early echoes, the image will appear as either proton density or T_1 weighted (depending on the *TR*). If the weak phase-encoding steps are used for the late echoes, the image will appear as T_2 weighted.

For this reason, the echo time of an FSE image is usually referred to as an effective *TE*. When the user selects an effective *TE*, the phase-encoding steps are assigned to the appropriate echoes of each multiecho train following each 90° pulse. Severe artifacts can result from this technique. Late echoes have diminished signal due to T_2 decay. If the strong phase-encoding gradients are applied to the late echoes (as with proton density- and T_1-weighted FSE images), there may be no useful signal left. Since the strong phase-encoding gradients provide the spatial resolution of an image, without these phase-encoding steps there will be a loss of spatial resolution. This is manifest as image blurring, which can be severe.

Image blurring is minimized by using a shorter ETL (usually 4 or 6) when acquiring proton density- or T_1-weighted FSE images. T_2-weighted FSE images never suffer from this blurring effect since the strong phase-encoding gradients are always applied to the early echoes. Early echoes suffer minimal signal loss due to T_2 decay. Therefore, T_2-weighted FSE images can usually be acquired with the maximum possible value of ETL.

The imaging time of a conventional spin echo sequence is given by *TR* × (phase matrix size) × (number of signal averages). The imaging time of an FSE sequence is this same product divided by ETL. However, when using FSE sequences, the number of sections that can be acquired for a given *TR* will be diminished. This results from the fact that many more echoes must be measured in each section before moving on to the next section. Depending on the choice of ETL, this will usually necessitate the use of a longer *TR* with FSE sequences.

The shorter the ETL, the more sections that can be acquired per *TR* interval. For example, using a *TR* of 3000 and an ETL of 8 will give approximately the same number of sections as using a *TR* of 6000 and an ETL of 16. The imaging times will be the same. The advantage of using a longer *TR* is that it gives a true T_2-weighted image. The trade-off is that use of a shorter ETL will improve the S/N since fewer late echoes are acquired. One must always keep in mind that the maximum value of *TE* that can be achieved is equal to ETL × ESP. Therefore, use of a shorter ETL will limit the maximal value of *TE*.

When imaging the pelvis in a body coil with FSE sequences, one can use either an ETL of 8 (with a *TR* of 3000–4000 ms) or an ETL of 16 (with a *TR* of 6000–8000 ms). It is recommended that a 192 or 256 phase matrix is used. There is usually a significant relative image degradation when a 128 phase matrix size is used with FSE images.

4 MULTICOIL IMAGING

When imaging with a single surface coil there is a marked improvement in the S/N, but the FOV that can be achieved is severely limited (roughly of the order of the diameter of the coil). In addition, the relative phase of the signal will depend upon the orientation of the surface coil within the magnet. If multiple surface coils are used together and their signals are combined into a circuit, there can be signal loss due to phase differences between the two signals. This can be minimized by careful orientation of the coils.

A multicoil (also called a phased-array coil) consists of multiple surface coils which act independently in a receive-only mode. Each separate coil of the multicoil inputs its signal into separate receiver channels. The signals from the individual coils are then used to reconstruct an individual image for each coil. These separate images are then recombined into a single composite image. In this case the relative phases of the individual signals is irrelevant, as the signals are only combined after magnitude reconstruction. By using a multicoil one gets the improved S/N of a surface coil, and the FOV that can be achieved is comparable to a body coil.[8–10] The only disadvantage of a multicoil is that four separate receiver channels must be used, which is expensive. All pelvic imaging should now be performed using a multicoil and FSE pulse sequences.

When using a multicoil, the signal from subcutaneous fat immediately adjacent to the coils will be markedly increased and can result in significant ghost artifacts. This can be eliminated by the placement of saturation pulses (within the field of view) through the subcutaneous fat both anteriorly and posteriorly.

5 NORMAL ANATOMY

On T_1-weighted images the uterus has a homogeneous low signal intensity. The appearance is similar to that of the uterus on computed tomography images, as no internal architecture is visible. On T_2-weighted images, a zonal architecture of the uterus is readily identified. The appearance of the zonal anatomy depends upon whether the patient is pre- or postmenopausal and the phase of the menstrual cycle.[11–13]

In virtually all premenopausal patients, three distinct zones of signal intensity can be seen in the uterine corpus (Figure 1).[12] An inner zone of high signal corresponds to the endometrium. An adjacent zone of low signal intensity corresponds to the so-called junctional zone. Histological studies have shown this zone to represent an inner layer of myometrium which has an increased nuclear area.[14] The remainder of the myometrium has intermediate signal intensity but can be quite variable, depending on the hormonal milieu of the patient.

Previous studies have shown that the inner bright zone progressively increases in thickness during the menstrual cycle with a peak thickness occurring late in the secretory phase. The thickness may vary from 4 mm early in the proliferative phase to 13 mm late in the secretory phase. The junctional zone shows no significant change in thickness during the menstrual cycle. In patients taking oral contraceptives (combined estrogen and progestin), endometrial thickness is markedly reduced after several months. In addition, the outer myometrium of these patients shows relatively increased signal intensity compared with those not using oral contraceptives.

Ultrasound studies have been performed in an attempt to determine an approximate upper limit of normal for endometrial stripe thickness in postmenopausal patients.[15,16] Regardless of hormonal replacement therapy, an upper limit of 8 mm has been suggested. No similar large series have as yet been performed with MRI. However, a comparative study of ultrasound and MRI has shown that the MRI measurement of endometrial thickness is almost always smaller than the corresponding ultrasound measurement.[17]

The cervix also has a unique zonal anatomy on T_2-weighted MRI (Figure 1). Four distinct zones of signal intensity have been described:[4,18] a thin inner bright zone which corresponds

Figure 1 Sagittal FSE multicoil image demonstrating the zonal anatomy of the uterus. The endometrium is the central bright stripe (curved arrow). Note the surrounding low-signal junctional zone and intermediate-signal outer myometrium. Within the cervix, the central high signal represents the canal (straight arrow) and contained mucus. The next layer is the intermediate-intensity signal of the cervical mucosa which is surrounded by the low-intensity signal of the fibrous stroma. Finally, the outer cervical stroma has an intermediate signal intensity and is continuous with the myometrium

to the endocervical canal; an adjacent thin zone of intermediate signal intensity corresponding to the cervical mucosa; a thicker zone of very low signal intensity thought to correspond to the predominantly fibrous portion of the wall of the cervix; and an outer zone which is continuous with the myometrium and is isointense with the myometrial signal.

Previous studies have shown little variation in the appearance of the cervix during the course of the menstrual cycle.[13] In addition, there is no apparent difference in the appearance of cervical zonal anatomy between premenopausal and postmenopausal women, or between those using and not using oral contraceptives.

The normal MRI appearance of the vagina is less complex. The vaginal wall typically shows low signal intensity, and the vaginal canal typically appears as a bright stripe of high signal intensity corresponding to vaginal secretions. The vagina is surrounded by the high signal intensity perivaginal venous plexus.

The ovaries appear homogeneously hypointense on T_1-weighted images. Follicles appear as small, round, homogeneous areas of high signal intensity on T_2-weighted images. The ovarian stroma is of low to intermediate signal intensity on T_2-weighted images. With high-resolution imaging, it is almost always possible to identify the ovaries in premenopausal patients, and most of the time in postmenopausal patients.

6 BENIGN DISEASES OF THE UTERUS AND CERVIX

The most common benign mass of the uterus is the leiomyoma, also commonly referred to as a fibroid. These masses are sharply circumscribed, usually spherical in shape, and typically have low signal intensity on all pulse sequences. When fibroids become large, they can undergo degeneration, which is usually manifest as central increased signal intensity on T_2-weighted images.

MRI is uniquely able to determine the intrauterine location of these masses. Fibroids are usually described as being submucosal, intramural, or subserosal in location. Submucosal fibroids are commonly associated with abnormal menstrual bleeding (Figure 2). Intramural fibroids are not usually associated with abnormal menstrual bleeding but are a common cause of uterine enlargement (Figure 3). Subserosal fibroids can be on a stalk and therefore can undergo torsion. Subserosal fibroids can also be confused with an adnexal mass on physical examination and on other imaging modalities.

When fibroids cause significant clinical symptoms and surgery is contemplated, the surgical approach is dependent upon the precise location of the fibroids. Some submucosal fibroids can be removed hysteroscopically. Intramural and subserosal fibroids can only be removed using a transabdominal approach. In addition to their location, another important surgical consideration is the size and increased vascularity of these lesions. Hormonal therapy is sometimes used to decrease their size and vascularity prior to possible surgery. MRI can be used to follow precisely the size and vascularity during such therapy.

Adenomyosis is defined as the presence of endometrial tissue within the myometrium. This tissue is usually not functional. The appearance of adenomyosis on MRI scans is rather characteristic.[19] It appears as focal or diffuse ill-defined thickening of the junctional zone (Figure 4). It has low signal

Figure 2 Sagittal FSE multicoil image demonstrating a submucosal fibroid (arrow)

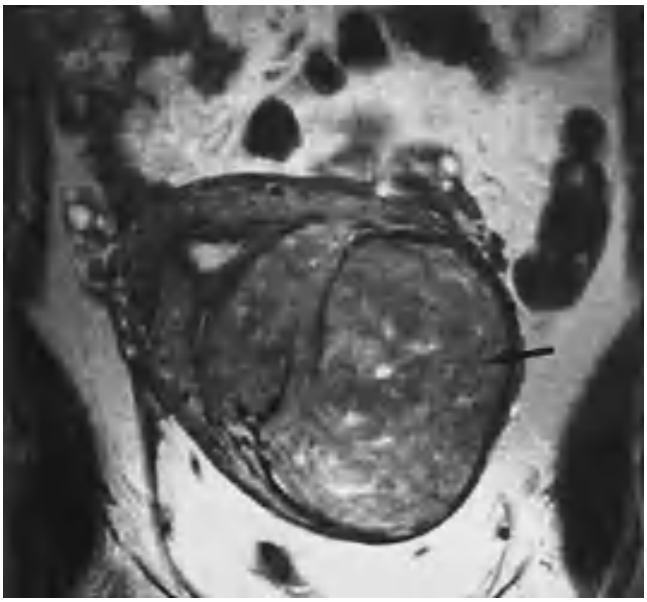

Figure 3 Coronal FSE multicoil image demonstrating a large intramural fibroid (arrow) displacing the endometrial stripe

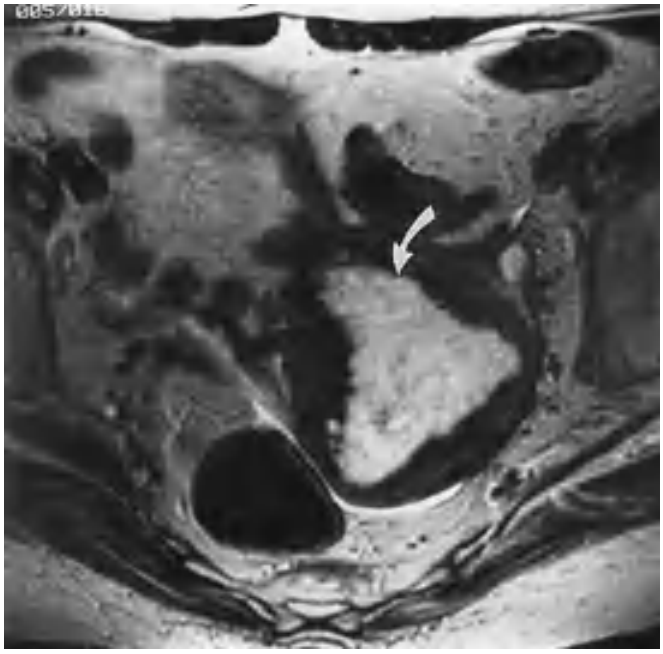

Figure 5 Axial FSE multicoil image demonstrating diffuse thickening of the endometrium (arrow) consistent with endometrial hyperplasia

intensity on T_2-weighted images, being isointense with the junctional zone. In some cases, adenomyosis can appear as small foci of high signal intensity within the myometrium on T_2-weighted images. Adenomyosis can result in uterine enlargement and abnormal menstrual bleeding. It is therefore important to differentiate this condition from fibroids. MRI is particularly useful in making this distinction.

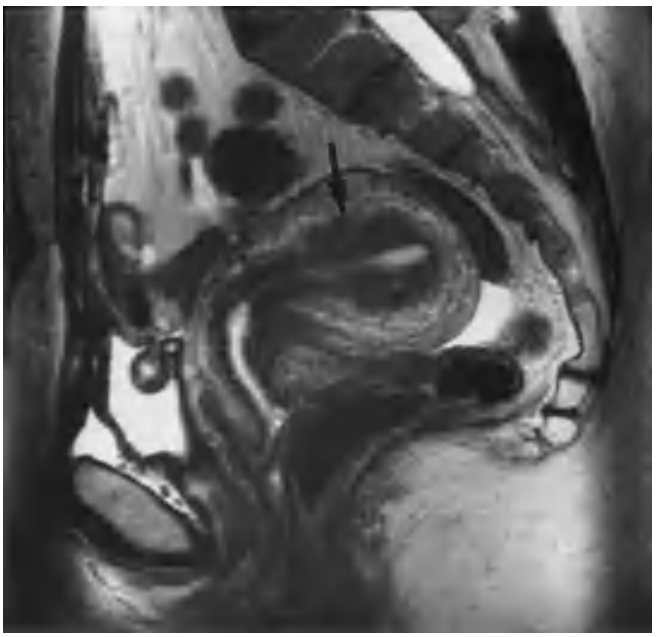

Figure 4 Sagittal FSE multicoil image demonstrating adenomyosis (arrow). Note the diffuse irregular thickening of the junctional zone with tiny areas of hyperintensity characteristic of the disease

Endometrial hyperplasia is thought to represent a physiological response of the endometrium to unopposed estrogenic stimulation. Some forms of endometrial hyperplasia are known to be precursors of endometrial carcinoma. On MRI, endometrial hyperplasia appears as thickening of the high-signal endometrium on T_2-weighted images (Figure 5).[1] However, MRI cannot distinguish between hyperplasia and early carcinoma.

Endometrial polyps can be sessile or pedunculated masses projecting into the endometrial cavity. They can be associated with abnormal uterine bleeding. However, endometrial carcinoma can sometimes have a polypoid configuration and cannot be reliably distinguished from simple polyps. On T_2-weighted images, polyps may appear as intermediate-signal masses (with respect to the low-signal junctional zone and the high-signal endometrium) but can also be isointense with the endometrium. Gadolinium-enhanced T_1-weighted images may be useful in detecting endometrial polyps. The enhancing polyp can be outlined by nonenhancing fluid within the endometrial cavity.

Pedunculated submucosal fibroids can also appear as polypoid filling defects within the endometrial cavity on MRI. Their signal intensity is usually significantly lower than that of endometrial polyps, which helps in their distinction.

The two most common uterine anomalies that need to be differentiated are the septate uterus and the bicornuate uterus.[20] In the septate uterus, the external contour of the uterus is normal (Figure 6). In the bicornuate uterus (Figure 7), there are two separate horns of the endometrial cavity, and the external contour of the uterus is significantly indented at the fundus (as there is no uterine tissue in the space between the two horns).

By imaging through the fundus along the long axis of the uterus, these two entities can be reliably distinguished. The signal characteristics of the septum may reflect myometrial or fibrous tissue, and hence signal behavior is not useful in classi-

Figure 6 Axial FSE multicoil image of a septate uterus. The contour of the uterine fundus is normal, and a large myometrial septum (arrow) is present

Figure 7 Axial FSE multicoil image of a bicornuate uterus. The contour of the uterine fundus is abnormal, with a large indentation separating the two endometrial cavities. There is a large low-signal intensity leiomyoma in the right horn

fying anomalies. The septate uterus is more commonly associated with infertility, and can be treated surgically through a hysteroscopic approach.

There are only a few benign lesions of the cervix commonly seen on MRI. Nabothian cysts represent dilated cervical glands usually seen following inflammation. These are very commonly visualized on MRI as homogeneous, round, sharply circumscribed areas of very high signal intensity on T_2-weighted images. Rarely, fibroids can be seen originating from the cervix. These are otherwise identical to those originating within the uterus.

7 MALIGNANT DISEASE OF THE UTERUS

Endometrial carcinoma is the most common invasive malignancy of the female genital tract. Unlike cervical carcinoma, there is not a well documented progression from precursor lesions to invasive carcinoma. Known risk factors for the development of endometrial carcinoma include obesity, nulliparity, late menopause, diabetes mellitus, hypertension, polycystic ovarian syndrome, estrogen-producing tumors, and unopposed exogenous estrogen supplementation.

MRI has been shown to be useful in evaluating patients with known endometrial carcinoma. The vast majority of patients with endometrial carcinoma (up to 75%) will have stage I disease at the time of diagnosis. Tumor grade and depth of myometrial invasion are the two important prognostic factors which can affect therapy in these patients.[21–23] Tumor grade will be known based upon histological findings. However, depth of myometrial invasion can only be determined preoperatively with the use of imaging studies.

On T_1-weighted images, most endometrial carcinomas are isointense with the uterus unless they contain hemorrhagic areas. On T_2-weighted images, most endometrial carcinomas (large enough to be detected as distinct masses) have a signal intensity intermediate between normal endometrium (higher signal intensity) and normal myometrium (lower signal intensity).

Multiple studies have been performed evaluating the ability of MRI to depict accurately the depth of myometrial invasion.[24–31] Using T_2-weighted images and/or gadolinium-enhanced T_1-weighted images, these studies have shown an accuracy of 75–95% in distinguishing superficial from deep myometrial invasion (Figure 8). More importantly, these studies have shown that an intact junctional zone has a 100%

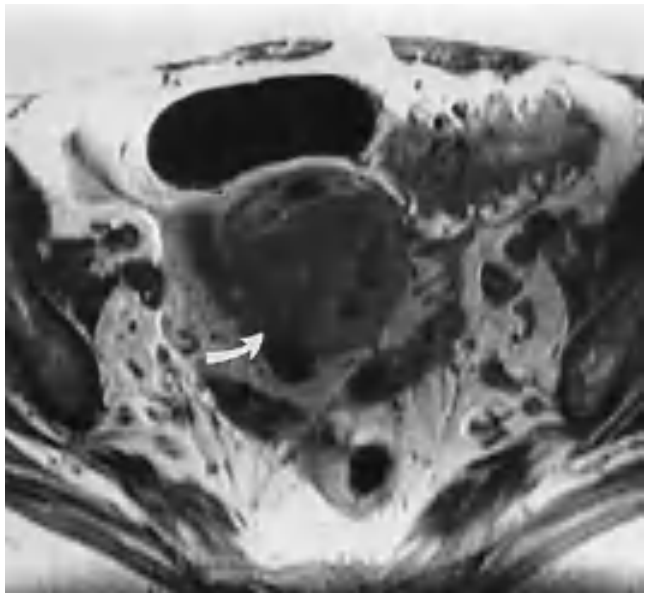

Figure 8 Axial multicoil image acquired following gadolinium administration demonstrates a large tumor extending beyond the uterus (arrow)

negative predictive value (NPV) in excluding myometrial invasion, and that segmental disruption of an otherwise intact junctional zone has a 100% positive predictive value (PPV) in detecting at least superficial myometrial invasion.

Unfortunately, most patients with endometrial carcinoma are postmenopausal, and uterine zonal anatomy may not be as conspicuous as that seen in premenopausal patients. Thus, these data are based on a small number of patients. In addition, patients with large intraluminal polypoid tumors can have significant expansion of the endometrial cavity with resultant distortion of zonal anatomy. Accurate assessment of myometrial invasion can be impossible in such cases.[32]

In patients without visible zonal anatomy, the presence of myometrial invasion must be presumed, based upon the appearance of the endometrial/myometrial interface. If this interface is irregular, invasion is presumed to be present, and if this interface is smooth, invasion is presumed to be absent. However, these findings do not have a high PPV or NPV, and this limits their usefulness.

All patients with clinically suspected stage I endometrial carcinoma must have evaluation of the cervix for possible tumor involvement. Endocervical curettage can be unreliable in this assessment. A few studies indicate an NPV of nearly 100% for MRI detection of cervical involvement.[25,29] The positive data regarding MRI evaluation of cervical involvement in patients with endometrial carcinoma are more limited. This is because only a small number of patients will have cervical involvement, since the vast majority have stage I disease at the time of presentation. In addition, some patients may have distention of the cervical canal by clot or debris, which can give a false-positive diagnosis of cervical involvement.

Uterine sarcomas are relatively rare tumors accounting for only 3–5% of all uterine cancers.[33] The three most common histological variants are malignant mullerian mixed tumor (MMMT), leiomyosarcoma (LMS), and endometrial stromal sarcoma (ESS). MMMT and LMS each account for about 40% of all uterine sarcomas, while ESS accounts for 10–15%. The staging system for uterine sarcomas is the same as that used for endometrial carcinoma.

The incidence of sarcomatous change in preexisting uterine leiomyomas is reported to be between 0.1 and 0.8%.[33] A small percentage (4%) of these patients will have a history of prior pelvic radiotherapy. The presenting clinical symptoms include vaginal bleeding, pelvic pain, and pelvic mass. The diagnosis should be suspected if rapid uterine growth occurs, especially in a postmenopausal patient.

MMMTs are histologically composed of a mixture of sarcoma and carcinoma. Almost all of these tumors occur after menopause. A history of prior pelvic radiotherapy can be elicited in up to 35% of cases.[33] Postmenopausal bleeding is the most common presentation. The tumor usually grows as a large polypoid mass with areas of necrosis and hemorrhage. It spreads in a manner identical to endometrial carcinoma but tends to be more aggressive with significant myometrial invasion in almost all cases.

Endometrial stromal tumors are rare tumors composed of cells resembling normal endometrial stroma. They can be divided into three types based upon mitotic activity, vascular invasion, and prognosis.[33] The endometrial stromal nodule is a benign lesion confined to the uterus. Endolymphatic stromal myosis infiltrates the myometrium, may extend beyond the uterus, and can metastasize. ESS, the third type of stromal tumor, is differentiated from stromal myosis mainly on the basis of mitotic activity and its much more aggressive course. Stromal tumors usually occur in perimenopausal patients. The MRI appearance of LMS and endometrial stromal tumors is not well known. The MRI findings in a series of seven patients with surgically proven MMMT showed this tumor to have an appearance similar to endometrial carcinoma.[34] The only feature that might suggest the diagnosis is that these tumors are usually very large and show deep myometrial invasion. However, when detected early, these tumors have an appearance identical to early endometrial carcinoma.

Trophoblastic tissue can give rise to a variety of tumors.[35] Complete hydatidiform mole, partial hydatidiform mole, invasive mole, and choriocarcinoma arise from villous trophoblastic tissue, while placental site trophoblastic tumor arises from nonvillous trophoblastic tissue.

Complete hydatidiform mole has been shown to be the result of a purely paternal conceptus. This genetic abnormality results in trophoblastic differentiation and proliferation without development of an embryo. Partial hydatidiform mole is seen almost exclusively in triploid conceptuses, with two paternal chromosomal complements and one maternal chromosomal complement. Often a malformed fetus is found in association with a partial mole. The partial mole itself usually arises from only a portion (or part) of the placenta. Clinical presentation of these entities can be abnormal uterine enlargement, vaginal bleeding, elevated human chorionic gonadotropin levels, or the absence of fetal heart sounds.

Invasive moles are thought to develop in previously existing complete moles. They are most commonly seen in the early months following evacuation of a complete hydatidiform mole. The hallmark of this entity is myometrial invasion. Choriocarcinoma is a malignant neoplasm which most commonly occurs after a molar pregnancy (sometimes remotely) but can be seen after a normal pregnancy, abortion, ectopic pregnancy, and possibly de novo.

Placental site trophoblastic tumor arises from the nonvillous trophoblast which infiltrates the placental site in normal pregnancy. It is considered an atypical form of choriocarcinoma. The importance of recognizing this tumor type pathologically lies in its less aggressive behavior compared with choriocarcinoma. This behavior makes this tumor amenable to surgery but often resistant to chemotherapy.

There are few data regarding the role of MRI in the evaluation and management of patients with trophoblastic tumors.[36,37] MRI is usually performed in patients with a known diagnosis of persistent mole following therapy or patients developing invasive mole or choriocarcinoma. A few studies have shown that prior to therapy most tumors show heterogeneous signal intensity on T_2-weighted images and distort or obliterate the normal zonal anatomy. These tumors only rarely appear as endometrial masses. Many tumors show markedly increased vascularity as evidenced by visualization of tortuous, dilated vessels within the tumor and/or the adjacent myometrium.

Previous studies have also shown that in patients responding to chemotherapy there was a progressive decrease in uterine size, tumor size, tumor vascularity, and a progressive improvement in visualization of normal zonal anatomy. All patients completely responding to therapy will show normal uterine

size, normal zonal anatomy and no evidence of tumor following completion of chemotherapy.

8 MALIGNANT DISEASE OF THE CERVIX

Invasive cervical cancer is thought to develop over time from noninvasive precursor lesions.[38] These precursor lesions are referred to as cervical intraepithelial neoplasia (CIN). CIN is divided pathologically into three grades: CIN 1 (minor dysplasia), CIN 2 (moderate dysplasia), and CIN 3 (severe dysplasia). CIN 3 is synonymous with carcinoma-in-situ. Available evidence indicates that up to 40% of CIN 3 lesions and a lesser proportion of CIN 1 and CIN 2 lesions would progress to invasive cancer if untreated. Imaging studies play no role in the detection of cervical carcinoma or its precursor lesions.

On T_1-weighted images, cervical carcinoma is of intermediate signal intensity and usually isointense with the uterine corpus and cervix. On T_2-weighted images, cervical carcinoma is usually of intermediate signal intensity relative to the low-signal fibrous cervical stroma and high-signal cervical and endometrial canals. It is the sharp contrast with the fibrous stroma that makes T_2-weighted imaging so crucial in depicting the tumor and its depth of invasion.

Most patients with CIN or microinvasion will have a normal appearance on MRI.[39] However, some patients with early invasive disease can also have a normal appearance on MRI. Prior studies have shown that the detection of a macroscopic lesion on MRI had a 100% PPV in determining the presence of at least invasive disease. A normal appearance on MRI has a less than 100% NPV in excluding the presence of invasive disease. Thus, a normal MRI requires further investigation to exclude early invasive disease. It is important to note that there are few studies in the literature evaluating this point, and few studies have been performed with high-resolution imaging.

The therapy of cervical carcinoma is dependent upon the stage of the disease at the time of diagnosis. The most crucial determination is the presence or absence of tumor invasion into the parametrium. Patients without parametrial invasion will usually be treated surgically. The presence of parametrial invasion precludes surgical therapy.

A number of MRI studies have shown that the finding of a completely intact ring of low-signal intensity cervical stroma has a 100% NPV in excluding parametrial invasion (Figure 9).[39–42] Unfortunately, focal areas of disruption of the stromal ring or full-thickness involvement of the fibrous stroma by tumor have a significantly lower than 100% PPV in determining parametrial invasion

The ability of MR imaging to accurately determine vaginal, pelvic sidewall, bladder, and rectal involvement in patients with cervical carcinoma has been evaluated in only a limited number of studies. The NPV of MR in excluding involvement of these structures is probably close to 100%. The PPV is difficult to assess because of the small number of positive cases.

There is little if any role for gadolinium-enhanced MR imaging in the staging of cervical carcinoma.[24,27,43] Several studies have indicated that gadolinium-enhanced images consistently overestimate the depth of cervical invasion. In addition, there is overestimation of involvement of the parametrium, bladder, and vagina with gadolinium-enhanced images.

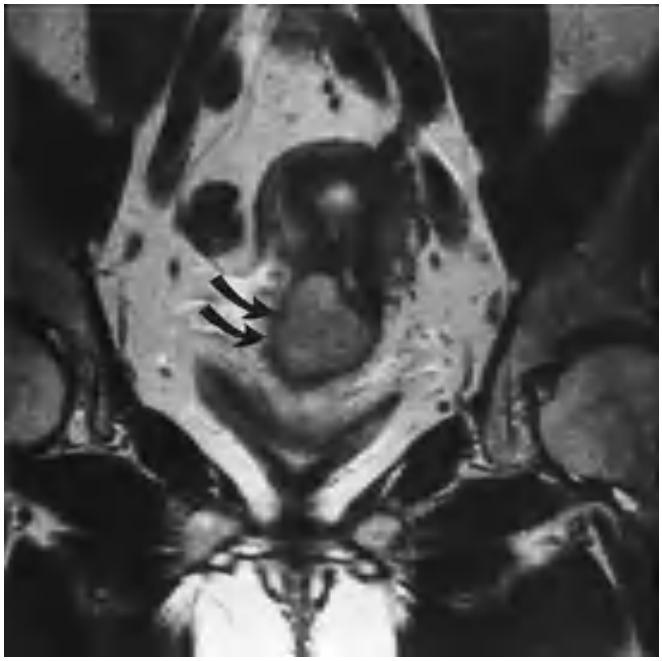

Figure 9 Coronal FSE multicoil image demonstrating a large tumor in the right cervix. The thin rim of intact fibrous stroma (curved arrows) indicates that parametrial invasion is absent

9 BENIGN DISEASE OF THE OVARIES

In premenopausal patients the normal ovaries almost always contain multiple small follicles (Figure 10). These appear as round, unilocular, sharply circumscribed high-signal areas on T_2-weighted images. They are usually less than 1.0 cm across but can attain a size of 2.5 cm and still be considered normal follicles. A corpus luteum cyst or follicular cyst can have an identical appearance to normal follicles other than their slightly larger size. They can sometimes contain hemorrhage, which will be seen as a high signal on T_1-weighted images. Theca lutein cysts can be seen in association with excessive levels of hCG, generally associated with trophoblastic disease. These cysts are usually multilocular, bilateral, and very large.

It is well known that even postmenopausal patients may have simple cysts within their ovaries.[44] Studies in the ultrasound literature have shown that if a cyst is simple, less than 3.0 cm in size, and shows no abnormal flow on Doppler evaluation, it is most probably benign. There are no similar studies in the MRI literature.

An infrequently seen benign disorder of the ovaries is polycystic ovarian disease. This is thought to result from unopposed estrogenic stimulation and chronic anovulation. This disorder is commonly associated with obesity, hirsutism, and oligomenorrhea. On MRI, the ovaries in these patients usually appear mildly enlarged, and contain multiple small cysts in the periphery with an abundant central stroma.

A common cystic lesion of the adnexal region is the paratubal cyst. These cysts develop from wolffian duct remnants within the broad ligament, separate from the ovary. These are almost always benign in nature. Their appearance is indistinguishable from simple ovarian cysts, other than their

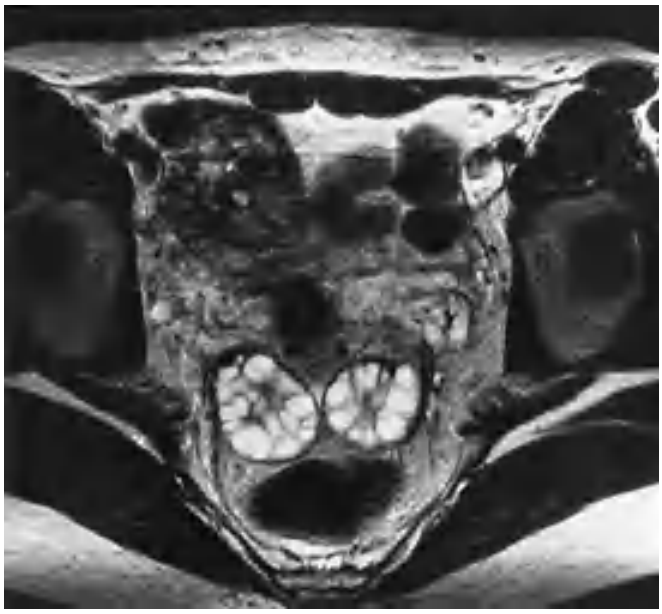

Figure 10 Axial FSE multicoil image demonstrating multiple follicles within the ovaries. The appearance suggests polycystic ovarian disease

extraovarian origin. It is this latter point that is key to their diagnosis. Although there is a paucity of published data, paratubal cysts usually displace an otherwise normal appearing ovary and therefore appear as a separate structure.[45]

Another cystic adnexal lesion is the Gartner's duct cyst.[45] This develops in a remnant of the müllerian duct. Their signal characteristics are identical to other cystic lesions. They can be diagnosed by their paravaginal location (separate from the ovaries) and usually tubular configuration. They are usually well demonstrated on high-resolution MRI. These patients commonly present with dyspareunia.

Figure 11 Sagittal conventional spin echo image of a mucinous cystadenoma (curved arrow). Note the thin septations and lack of solid elements. The signal behavior of the mass is identical to urine in the bladder (straight arrow) on all sequences

Benign epithelial tumors of the ovary include serous and mucinous cystadenomas (Figure 11). The appearance of these tumors at MR imaging is variable, and can be indistinguishable from their malignant counterparts. Benign cystadenomas can appear as simple cystic intraovarian masses. The presence of internal septations, solid components, or papillary projections makes malignancy more likely. Intravenous gadolinium can sometimes be helpful in detecting solid components, papillary projections or even septations.[46]

Ovarian fibromas, fibrothecomas, and Brenner tumors are solid ovarian masses that can contain fibrous tissue, and, therefore, may show diffuse or focal areas of low signal intensity on all pulse sequences. Fibromas are typically extremely low signal intensity, while fibrothecomas typically contain multiple high-signal foci. One must be careful to distinguish these masses from pedunculated subserosal fibroids. The only way to do so definitively is to identify them as intraovarian.

Two ovarian lesions which can occasionally be difficult to distinguish are the ovarian dermoid and an ovarian endometrioma.[47] The dermoid tumor is the most common form of benign teratoma, and can be definitively characterized by its fat content. Endometriosis is a disease characterized by rests of normal functional endometrium in abnormal locations. The most common location of endometriosis is the ovary. This can occur as a large mass, referred to as an endometrioma, which can be characterized by its blood content.

On MRI, a dermoid and an endometrioma can have identical signal characteristics on both T_1- and T_2-weighted images. The most definitive way to distinguish these lesions is by using sequences which selectively suppress the signal from fat- or water-containing structures.[47] The fat in dermoids is of high signal on T_1-weighted images obtained with and without water suppression, and is of low signal on T_1-weighted images obtained with fat suppression (Figure 12). Endometriomas appear as a high signal on T_1-weighted images obtained with and without fat suppression, and appear as a low signal on T_1-weighted images obtained with water suppression.

Unfortunately, endometriomas are indistinguishable from other hemorrhagic cysts. Multiple such cysts make the diagnosis of endometriosis more likely (Figure 13). Sometimes hemosiderin can be visualized within and on the surface of the ovaries. Hemosiderin appears as tiny foci of low signal, most conspicuous on T_2-weighted images. MRI is insensitive in detecting small implants of endometriosis involving bowel, the bladder, or other peritoneal surfaces.

10 MALIGNANT DISEASE OF THE OVARIES

The most common malignant neoplasms of the ovary are of epithelial origin, particularly serous and mucinous cystadenocarcinomas (Figure 14). These tumors often appear primarily cystic in nature. On MRI, the cystic portions will appear as very high-signal areas on T_2-weighted images. They also, however, commonly contain internal septations and solid elements.

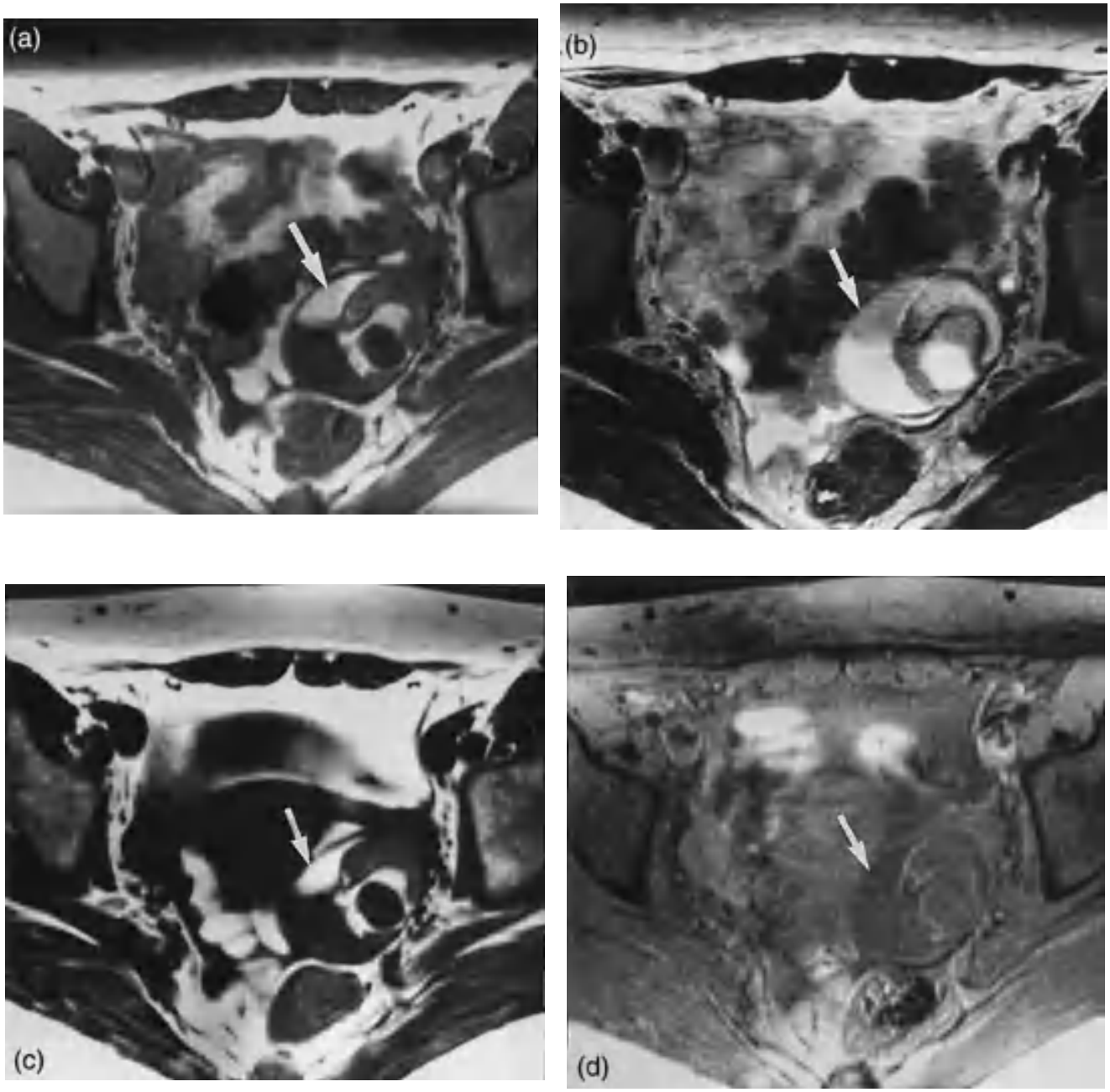

Figure 12 Complex dermoid containing both fluid and fat elements. Note that the fat (arrow) is isointense with pelvic fat on the (a) T_1-weighted and (b) T_2-weighted images. On the (c) water suppression and (d) fat suppression images, the fat (arrows) suppresses on the latter sequence

The solid components are of lower signal on the T_2-weighted images, and often show enhancement following intravenous administration of gadolinium.[46] However, these tumors can sometimes appear indistinguishable from simple cysts. In general, even when purely cystic in appearance, these masses will be larger in size than other simple benign cysts. A variety of other malignant neoplasms that are primarily solid or mixed can involve the ovaries.

Ovarian malignancies usually spread from the surface of the ovaries into the peritoneal cavity. Most commonly, metastases involve the omentum, mesentery, and peritoneal surface of solid viscera. Due to artifacts from the bowel, MRI is not as sensitive as computerized tomography in detecting these metastases. Intravenous gadolinium is essential if one attempts to detect these metastases on MRI.

11 RELATED ARTICLES

Male Pelvis Studies Using MRI; Multi Echo Acquisition Techniques Using Inverting Radiofrequency Pulses in MRI; Whole Body Machines: NMR Phased Array Coil Systems.

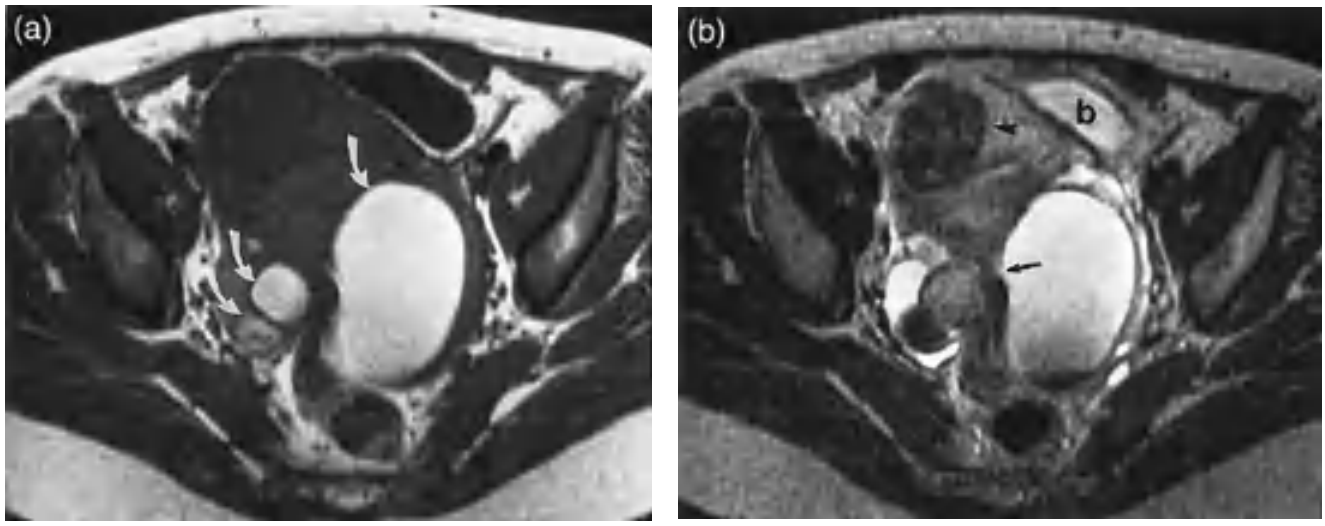

Figure 13 Axial conventional spin echo images demonstrating endometriosis. Note on (a) the intermediate weighted sequence, multiple hyperintense lesions (arrows) are seen. On (b) the T_2-weighted image, some of these lesions become hypointense whereas others remain hyperintense consistent with blood of various ages. Also note tethering of the rectum (arrow) secondary to adhesions, an intramural fibroid (arrowhead) and the bladder (b) pushed anteriorly

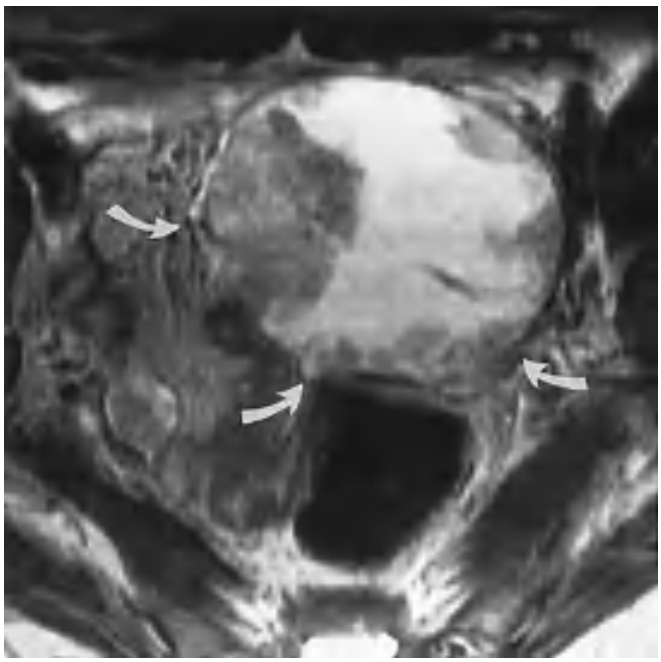

Figure 14 Axial FSE multicoil image of a clear cell adenocarcinoma of the ovary (arrows). Note both solid and cystic elements indicative of a malignancy

12 REFERENCES

1. R. C. Smith and S. M. McCarthy, *Radiol. Clin. N. Am.*, 1994, **32**, 109.
2. M. L. Wood and R. M. Henkelman, *Med. Phys.*, 1986, **13**, 794.
3. R. C. Smith, C. Reinhold, R. C. Lange, T. R. McCauley, R. Kier, and S. McCarthy, *Radiology*, 1992, **184**, 665.
4. R. C. Smith, C. Reinhold, T. R. McCauley, R. C. Lange, R. T. Constable, R. Kier, and S. M. McCarthy, *Radiology*, 1992, **184**, 671.
5. J. Hennig, A. Nauerth, and H. Friedburg, *Magn. Reson. Med.*, 1986, **3**, 823.
6. J. Hennig and H. Friedburg, *Magn. Reson. Imag.*, 1988, **6**, 391.
7. R. V. Mulkern, P. S. Melki, P. Jakab, N. Higuchi, and F. A. Jolesz, *Med. Phys.*, 1991, **18**, 1032.
8. C. E. Hayes, and P. B. Roemer, *Magn. Reson. Med.*, 1990, **16**, 181.
9. C. E. Hayes, N. Hattes, and P. B. Roemer, *Magn. Reson. Med.*, 1991, **18**, 309.
10. P. B. Roemer, W. A. Edelstein, C. E. Hayes, S. P. Souza, and O. M. Mueller, *Magn. Reson. Med.*, 1990, **16**, 192.
11. C. L. Janus, H. P. Wiczyk, and N. Laufer, *Magn. Reson. Imag.*, 1988, **6**, 669.
12. A. R. Lupetin, in 'Magnetic Resonance Imaging', ed. D. D. Stark and W. G. Bradley, C. V. Mosby, St Louis, 1988, p. 1270.
13. S. McCarthy, C. Tauber, and J. Gore, *Radiology*, 1986, **160**, 119.
14. L. M. Scoutt, S. D. Flynn, D. J. Luthringer, T. R. McCauley, and S. M. McCarthy, *Radiology*, 1991, **179**, 403.
15. M. C. Lin, B. B. Gosink, S. I. Wolf, M. R. Feldesman, C. A. Stuenkel, P. S. Braly, and D. H. Pretorius, *Radiology*, 1991, **180**, 427.
16. T. J. Dubinsky, H. R. Parvey and N. Maklad, *Am. J. Roentgenol.*, 1997, **169**, 145.
17. D. G. Mitchell, L. Schonholz, P. L. Hilpert, R. G. Pennell, L. Blum, and M. D. Rifkin, *Radiology*, 1990, **174**, 827.
18. T. R. McCauley, L. M. Scoutt, and S. B. Flynn, *JMRI*, 1991, **1**, 319.
19. D. G. Mitchell, *Radiol. Clin. N. Am.*, 1992, **30**(4), 777.
20. J. S. Pellerito, S. M. McCarthy, M. B. Doyle, M. G. Glickman, and A. H. Decherney, *Radiology*, 1992, **183**, 795.
21. W. T. Creasman, C. P. Morrow, B. N. Bundy, M. D. Homesley, J. E. Graham, and P. B. Heller, *Cancer*, 1987, **60**, 2035.
22. W. T. Creasman and J. C. Weed in 'Gynecologic Oncology', 2nd edn, ed. M. Coppleson, Churchill Livingstone, London, 1992, p. 780.
23. M. H. Lutz, P. B. Underwood, A. Kreutner, and M. C. Miller, *Gynecol. Oncol.*, 1978, **6**, 83.

24. Y. Hirano, K. Kubo, Y. Hirai, S. Okada, K. Yamada, S. Sawano, T. Yamashita, and Y. Hiramatsu, *RadioGraphics*, 1992, **12**, 243.
25. H. Hricak, J. L. Stern, M. R. Fisher, L. G. Shapeero, M. L. Winkler, and C. G. Lacey, *Radiology*, 1987, **162**, 297.
26. H. Hricak, L. V. Rubinstein, G. M. Gherman, and N. Karstaedt, *Radiology*, 1991, **179**, 829.
27. H. Hricak, B. Hamm, R. C. Semelka, C. E. Cann, T. Nauert, E. Secaf, J. L. Stern, and K. J. Wolf, *Radiology*, 1991, **181**, 95.
28. H. H. Lien, V. Blomlie, C. Trope, J. Kaern, and V. M. Abeler, *Am. J. Roentgenol.*, 1991, **157**, 1221.
29. H. V. Posniak, M. C. Olson, C. M. Dudiak, M. J. Castelli, J. Dolan, R. A. Wisniewski, J. H. Isaacs, S. K. Sharma, and V. Bychkov, *RadioGraphics*, 1990, **10**, 15.
30. S. Sironi, G. Taccagni, P. Garancini, C. Belloni, and A. DelMaschio, *Am. J. Roentgenol.*, 1992, **158**, 565.
31. S. Sironi, E. Colombo, G. Villa, G. Taccagni, C. Belloni, P. Garancini, and A. DelMaschio, *Radiology*, 1992, **185**, 207.
32. L. M. Scoutt, S. M. McCarthy, S. D. Flynn, R. C. Lange, F. Long, R. C. Smith, S. K. Chambers, E. I. Kohorn, P. Schwartz and J. T. Chambers, *Radiology*, 1995, **194**, 567.
33. J. R. Lurain and M. S. Piver in 'Gynecologic Oncology', 2nd edn, ed. M. Coppleson, Churchill Livingstone, London, 1992, p. 827.
34. L. G. Shapeero and H. Hricak, *Am. J. Roentgenol.*, 1989, **153**, 317.
35. F. J. Paradinas, in 'Gynecologic Oncology', 2nd edn, ed. M. Coppleson, Churchill Livingstone, London, 1992, p. 1013.
36. J. W. Barton, S. M. McCarthy, E. I. Kohorn, L. M. Scoutt, and R. C. Lange, *Radiology*, 1993, **186**, 163.
37. H. Hricak, B. E. Demas, C. A. Braga, M. R. Fisher, and M. L. Winkler, *Radiology*, 1986, **161**, 11.
38. M. Coppleson, K. H. Atkinson, and F. C. Dalrymple, in 'Gynecologic Oncology', 2nd edn, ed. M. Coppleson, Churchill Livingstone, London, 1992, p. 571.
39. K. Togashi, K. Nishimura, T. Sagoh, S. Minami, S. Noma, I. Fujisawa, Y. Nakano, J. Konishi, H. Ozasa, I. Konishi, and T. Mori, *Radiology*, 1989, **171**, 245.
40. H. Hricak, C. G. Lacey, L. G. Sandles, Y. C. F. Chang, M. L. Winkler, and J. L. Stern, *Radiology*, 1988, **166**, 623.
41. S. H. Kim, B. I. Choi, H. P. Lee, S. B. Kang, Y. M. Choi, M. C. Han, and C. W. Kim, *Radiology*, 1990, **175**, 45.
42. S. Sironi, C. Belloni, G. L. Taccagni, and A. DelMaschio, *Am. J. Roentgenol.*, 1991, **156**, 753.
43. Y. Yamashita, M. Takahashi, T. Sawada, K. Miyazaki, and H. Okamura, *Radiology*, 1992, **182**, 643.
44. D. Levine, B. B. Gosink, S. I. Wolf, M. R. Feldesman, and D. H. Pretorius, *Radiology*, 1992, **184**, 653.
45. R. Kier, *Am. J. Roentgenol.*, 1992, **158**, 1265.
46. S. K. Stevens, H. Hricak, and J. L. Stern, *Radiology*, 1991, **181**, 481.
47. R. Kier, R. C. Smith, and S. M. McCarthy, *Am. J. Roentgenol.*, 1992, **158**, 321.

Biographical Sketches

Robert Smith. *b* 1960. B.A. (Mathematics), 1981, Johns Hopkins University, M.D., 1985, Yale University. Radiology Resident and MR Fellow, Yale University, 1986–91. Assistant Professor, Yale University, 1991–96. Associate Professor, and Director of MRI, Yale University, 1996–97. Research interests: fast spin echo MRI, clinical applications of multicoil arrays, basic MRI physics.

Michael J. Varanelli. *b* 1970. B.Sc. (Biology), Bucknell University, 1992. M.D., University of Pittsburgh, 1996. Radiology Resident, Yale University, 1997–present.

Leslie M. Scoutt, *b* 1952. B.A. (Biology), Wesleyan University, 1974, M.D., University of Rochester, 1978. Radiology Resident, Beth Israel Hospital, Boston, MA, 1982–85. Cross-Sectional Imaging Fellow, Yale University, 1985–87. Assistant Professor, Yale University, 1987–94. Associate Professor, Yale University, 1994–present. Research interests: MRI and ultrasound of the female pelvis, breast and vascular ultrasound.

Shirley McCarthy. *b* 1949. B.A. (Biological Sciences), 1971, State University of New York, Albany Ph.D. (Mammalian Physiology), 1975, Cornell University, M.D., 1975, Yale University School of Medicine. Associate Professor, Yale University, 1989–present. Chief of MRI, Yale University, 1987–present. Research interests: gynecological imaging, cost-effective analyses of MRI use.

Pediatric Body MRI

Rosalind B. Dietrich and Gerald M. Roth
University of California, Irvine, Orange, CA, USA

1 INTRODUCTION

Although initially slow to become established, magnetic resonance imaging (MRI) now plays a vital role in the diagnostic imaging evaluation of many pediatric diseases and disorders. The ability to produce multiplanar images in a noninvasive manner without the use of ionizing radiation and with only minimal patient preparation has made MRI a useful complement to other cross-sectional modalities such as ultrasound and computerized tomography (CT). The most frequent indications for an MRI study in the pediatric population include the evaluation of congenital anomalies and the characterization of tumors and other mass lesions.

2 CONGENITAL ANOMALIES

MRI plays an important role in evaluating both complex congenital anomalies, where ultrasound is inadequate, and simple congenital anomalies, where sonography is not possible, is incomplete or is suboptimal. Congenital anomalies are well visualized with MRI due to its provision of excellent anatomical detail and its multiplanar capabilities. The majority of lesions are adequately assessed using multiplanar T_1- and T_2-weighted spin echo imaging. Occasionally, additional sequences are required, especially if the presence of fat or flowing blood is to be determined.

The ability of MRI to differentiate vessels containing flowing blood from other mediastinal structures without the use of bolus injection of contrast material makes it an ideal choice for evaluating anomalies of the great vessels.[1,2] Preoperative mapping may alleviate the need for angiography in selected patients. In addition, in such lesions as the double aortic arch and the right aortic arch with an aberrant left subclavian artery and a left ligamentum arteriosum, MRI can evaluate for the presence of esophageal and/or tracheal compression that may be associated with these lesions. In the entity known as the 'pulmonary sling', where the left pulmonary artery arises from the right pulmonary artery and passes between the trachea and the esophagus, the presence of tracheal compression may be similarly assessed. Other, more rare, symptomatic abnormalities, as well as the asymptomatic great vessel anomalies can also be evaluated. In patients with a right aortic arch, MRI can determine the presence or absence of mirror image branching and can demonstrate any associated cardiac anomalies. Cardiac gated T_1-weighted images in the axial and coronal planes can often provide sufficient information for these diagnoses to be made, although sometimes images parallel to the course of the aorta are very useful.

The most common congenital pediatric abnormalities involving the lung include congenital lobar emphysema, cystic adenomatoid malformation, and sequestration. The first two entities can be evaluated using MRI, although plain film radiography and/or CT examination are usually sufficient. MRI, however, can be very useful in cases of sequestration, as it may be able to demonstrate the anomalous feeding vessels and draining veins.[3] The corresponding lung tissue may appear solid or aerated on MRI, depending on its connection, if any, with the bronchial tree.

Abnormalities of the diaphragm, such as diaphragmatic hernias and eventrations, can also be evaluated by MRI. Coronal and/or sagittal T_1-weighted images are useful in determining the presence or absence of a portion of the diaphragm, as well as identifying which, if any, of the normal abdominal components are in the chest.[4] In patients with anterior abdominal wall defects, such as gastroschisis and omphalocele, MRI can be used to determine which abdominal organs have protruded through the defect and define their position (Figure 1).

In the abdomen, congenital anomalies of the hepatobiliary system such as choledochal cysts, biliary atresia, and polycystic liver disease can all be evaluated using MRI, but are more commonly diagnosed using ultrasound. MRI plays a more important role in the visualization of abnormal vascular anatomy in such anomalies as the Budd–Chiari malformation and discontinuity of the inferior vena cava. In the Budd–Chiari malformation, MRI may identify obliteration of the hepatic veins and may help determine if a congenital web or a thrombus is responsible for the condition.

In the retroperitoneum, abnormalities in renal position and development are readily seen with MRI. Renal ectopia, whether high (intrathoracic) or low (pelvic) can be differentiated from renal agenesis more easily with MRI than with ultrasound, since visualization of the abdominopelvic cavity by MRI is not limited by the presence of bowel gas or bone, as it is with ultrasound. Fusion anomalies, such as crossed fused ectopia and horseshoe kidney are also well demonstrated by MRI.[5–7] Crossed fused ectopia, like most congenital renal anomalies, is best imaged using coronal T_1-weighted images, and is diagnosed when an abnormally positioned fused kidney is visualized on one side and there is no identifiable renal tissue on the contralateral side. Horseshoe kidneys, on the other hand, are easier to diagnose on axial T_1-weighted images, as the fusion of the lower poles is often more apparent in this plane. In children with renal agenesis, the ipsilateral adrenal gland develops a discoid rather than a chevron-shaped appearance, and can be seen as an elongated linear structure on coronal magnetic resonance (MR) images.[4]

Although all of the renal cystic diseases can be demonstrated using MRI, ultrasound remains the primary imaging modality for this class of diseases. MRI is most useful in clarifying confusing cases and in demonstrating complications such as hemorrhage. Simple renal cysts appear as homogeneous, well-defined masses on the MR image and are of low signal intensity on T_1-weighted sequences and of very high signal intensity on T_2-weighted sequences. The cyst wall and the fluid in the cyst may be indistinguishable. If hemorrhage into the cyst occurs, or if the cyst has a high protein concentration for another reason, inhomogeneous high signal intensity can be demonstrated on both T_1- and T_2-weighted sequences. Despite these guidelines, there is a wide range of variability in the appearance of hemorrhagic cysts, and in some cases it is not

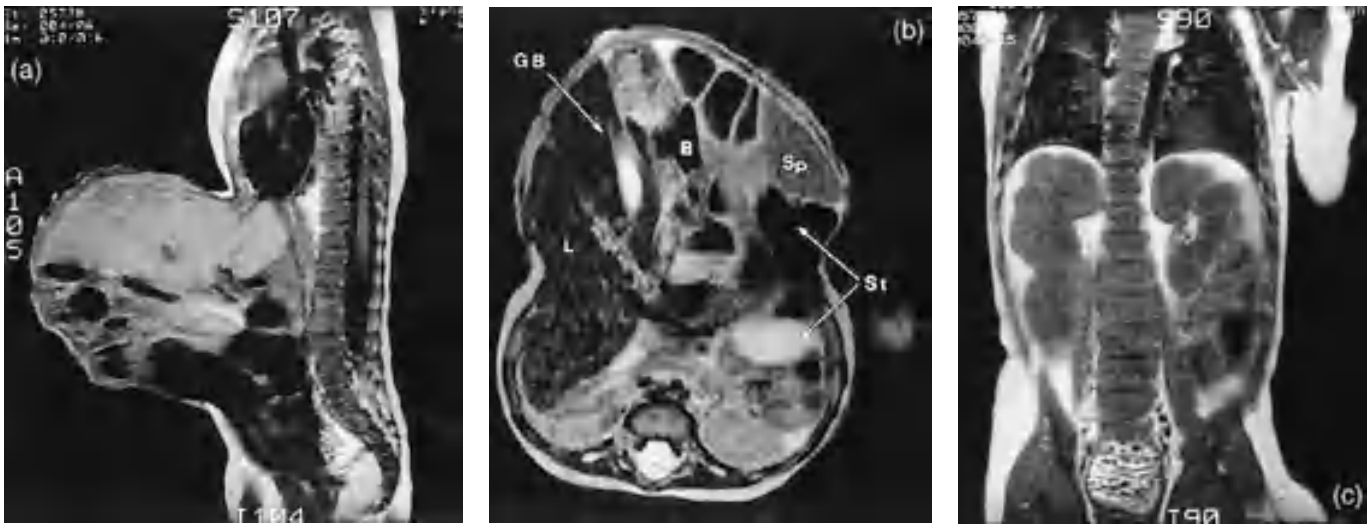

Figure 1 Omphalocele. (a) Sagittal view (SE 350/11): multiple loops of bowel and a large volume of the liver have herniated into the omphalocele sac. (b) Axial view (FSE 4000/102Ef): liver (L), gall bladder (GB), bowel (B), spleen (Sp) and stomach (St) are identified in the omphalocele sac. (c) Coronal view (SE 350/12): both kidneys are abnormally superior in position, lying just below the diaphragm

always possible to distinguish a hemorrhagic cyst from an infected cyst or even from a neoplasm.

MRI is an excellent modality for the evaluation of congenital anomalies of the genital tract. In disorders of sexual differentiation, MRI can clearly show the absence of, or abnormal location of, pelvic organs in children with ambiguous genitalia or genetic abnormalities.[7–9] Imaging in both the axial and sagittal planes, and with both T_1- and T_2-weighted sequences is often necessary in these patients with Turner syndrome, testicular feminization, hermaphrodism, or one of the various forms of pseudohermaphrodism.

MRI can also evaluate the spectrum of Müllerian duct anomalies, ranging from uterus didelphys (two uteri, two cervices, and two vaginas) through bicornuate uterus (two uteri, single vagina, and cervix) to uterus septus (single uterus, cervix, and vagina with a uterine septum).[10–12] The distinction between the last two entities is crucial if surgical intervention is planned. MRI can often make this distinction in postpubertal girls. On T_2-weighted images in a plane axial to the body of the uterus, the bicornuate uterus will demonstrate a medium signal intensity strip of myometrium separating the two low signal intensity junctional zones that the septate uterus will not. MRI can also evaluate the urinary anomalies, such as renal agenesis or renal malposition, which are often associated with Müllerian duct anomalies.

Renal anomalies can also occur in patients with the Mayer–Rokitansky–Kuster–Hauser syndrome.[13] In this syndrome, which is characterized by aplasia of both the uterus and upper vagina, the spectrum of renal anomalies includes unilateral agenesis, unilateral or bilateral ectopia, horseshoe kidney, malrotation, and collecting system abnormalities. Vertebral anomalies have also been reported. Because MRI can be used to evaluate the vagina noninvasively, it is the modality of choice for patients with this disorder, as well as for patients with isolated vaginal atresia.

In patients with hematometrocolpos, T_1- and T_2-weighted images can demonstrate a high signal intensity collection within a markedly dilated upper vagina and uterine cavity[14–16] (Figure 2). These dilated structures may compress the adjacent bladder or rectum. The fluid collection may extend into the fallopian tube, leading to a dilated tortuous fallopian tube visualized extending into the abdomen.

MRI has also proved useful in identifying undescended testes in male children prior to surgery. Ultrasound is performed initially and, if it is unsuccessful, MRI is then performed.[17,18] The undescended testis is usually in the inguinal canal, but if it is in the abdomen or pelvis, the testis can be adjacent to the lateral bladder wall, the psoas muscle, the iliac vessels or in the retroperitoneum or the superficial inguinal pouch. On T_1-weighted images, the testis is of medium signal intensity and can frequently be identified if it is surrounded by fat, which is of high signal intensity. On T_2-weighted images, the central portion of the testis is of high signal intensity with a surrounding rim of medium signal intensity, and therefore can be easily distinguished from muscles and lymphadenopathy.

Anorectal anomalies, such as imperforate anus and ectopic anus, are also well visualized using MRI. Both these disorders are due to failure of descent of the hindgut. In imperforate anus, the rectum terminates in a blind pouch, whereas in ectopic anus, the more common of the two entities, there is a fistulous connection between the pouch and another structure, such as the perineum, vestibule, vagina, urethra, bladder, or cloaca. Plain film radiography, contrast examination, and ultrasonography have all been helpful in the preoperative evaluation of these patients. MRI, however, can noninvasively give a multiplanar view of the hindgut, puborectalis sling and adjacent structures, defining the anatomy to better advantage.[19–22] In this regard, axial and coronal T_1-weighted images can demonstrate the anatomy of the puborectalis sling, determine whether

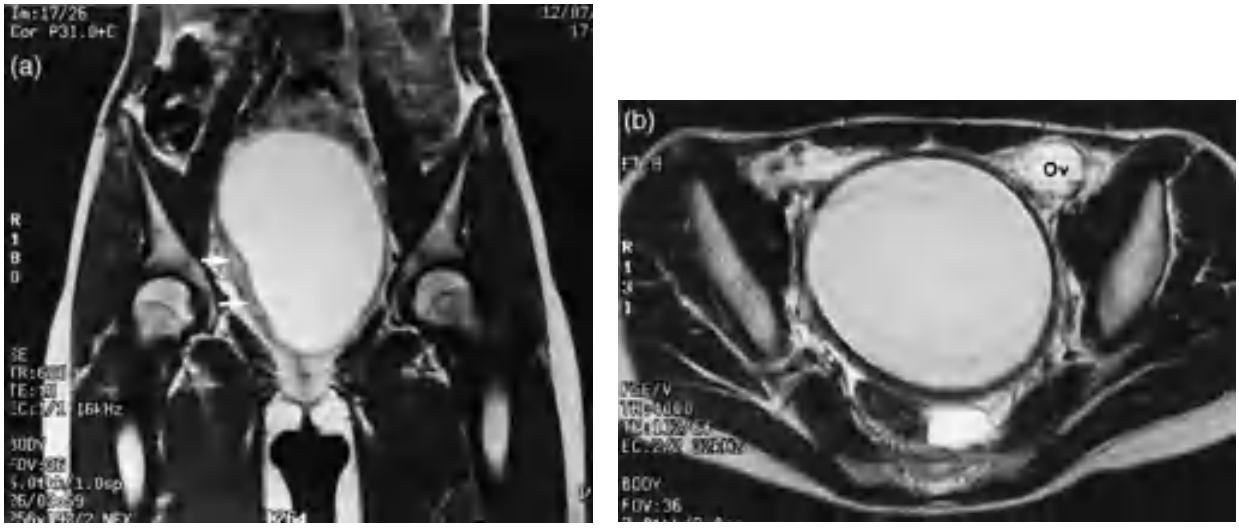

Figure 2 Hematometros involving one side of a uterus didelphys. (a) Coronal view (SE 600/18): high signal intensity blood products are identified in a markedly distended uterine cavity; a second uterine cavity (arrows) with an endometrial stripe is identified compressed on the right. (b) Axial view (FSE 4000/102Ef): the distended left uterine cavity occupies most of the volume of the pelvis, displacing the left ovary (Ov) anteriorly

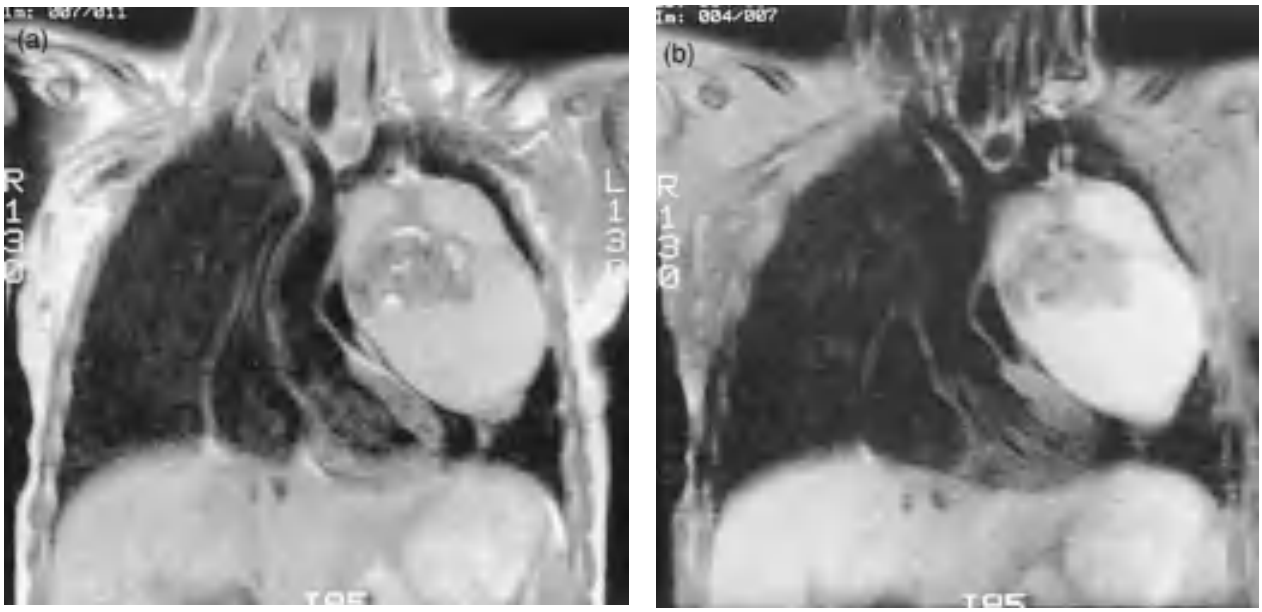

Figure 3 Mediastinal teratoma. (a) Coronal view (SE 625/11): a mediastinal mass is identified with locules of differing signal intensity; a few small foci of bright signal intensity are noted within the mass. (b) Coronal view (SE 625/11, chemical lipid presaturation): using a lipid-selective presaturation pulse, the formerly bright areas in the lesion become dark, verifying that they represent fat; the presence of fat in the lesion histologically characterizes it as a teratoma

or not it is hypoplastic, and define its relationship to the hindgut.

3 TUMORS AND OTHER MASS LESIONS

Due to its multiplanar capability, its ability to distinguish vessels with flowing blood from other structures, without the need for bolus injection of contrast material, and its superior contrast resolution compared with that of CT, MRI is an extremely useful tool in the evaluation of mass lesions.[4] Once a lesion has been discovered on a chest radiograph or on an abdominal or pelvic ultrasound, MRI can help to characterize the lesion, identify the organ of origin, define its extent, clarify its relationship to adjacent vessels, and evaluate for distant metastasis. MRI can classify a lesion as either cystic, solid, or mixed. Although some solid lesions such as teratomas, lipomas, and hemorrhagic lesions may demonstrate characteristic MR appearances, the majority of solid lesions are impossible to differentiate using signal intensity alone. Most such solid lesions are of medium signal intensity on T_1-weighted images and of high signal intensity on T_2-weighted images. However, when the signal characteristics of a lesion are combined with information about its organ of origin, its relationship to adja-

cent vessels and/or its sites of metastasis, a definitive diagnosis can often be made. MRI can be used before treatment, to plan a surgical approach or a radiation port, as well as after treatment, to assess for residual or recurrent tumor after surgery, chemotherapy and/or radiation therapy.

Gadolinium chelate contrast agents may be useful in characterizing vascular masses and in evaluating renal and perirenal lesions.[23] In these instances, T_1-weighted images obtained dynamically during, and/or immediately after, intravenous contrast administration may more clearly define the borders of the lesion, characterize its internal architecture, accentuate surrounding adenopathy, and/or uniquely define the histology of the lesion.

In the thorax, MRI is particularly useful in the evaluation of masses arising in the posterior mediastinum, as it may noninvasively demonstrate the presence or absence of intraspinal extension.[24,25] These posterior mediastinal masses are most frequently of neurogenic origin and include such entities as neuroblastoma, ganglioneuroma, and neurofibroma. They are all of medium signal intensity on T_1-weighted images and of high signal intensity on T_2-weighted images. Coronal and axial images are useful in demonstrating intraspinal extension, if any, and in clarifying the relationship of the lesion to adjacent vasculature.

MRI can also demonstrate lesions in the anterior and middle compartments of the mediastinum, and may even have a slight edge over CT in selected cases.[26] For example, coronal and/or sagittal images may help define the extent of neck masses that secondarily involve the mediastinum or lung apices. These lesions include cystic hygroma, hemangioma, and fibromatosis. Fat selective sequences may also be helpful in distinguishing mediastinal teratomas from other mass lesions (Figure 3). Additionally, as with posterior compartment masses, MRI may help clarify the relationship of the lesion to adjacent vessels and other structures, due to its multiplanar capability, its ability to distinguish vessels with flowing blood from other structures, without the need for bolus injection of contrast material, and its superior contrast resolution.

In the abdomen and pelvis, MRI is an excellent modality with which to differentiate masses arising from the liver, kidney, adrenal gland, and paraspinal regions. Some of the more common lesions arising from these areas warrant discussion.

In children with hemangioendotheliomas, MRI can often demonstrate the mass in the liver and may be able to map the feeding and draining vessels. An abrupt caliber decrease in the abdominal aorta distal to the origin of the celiac axis may also be observed.[4] Serial imaging after gadolinium chelate administration can often uniquely identify the hepatic lesion as a hemangioendothelioma due to its distinctive temporal pattern of peripheral to central enhancement.

The most common malignant tumors of the liver, hepatoblastomas and hepatocellular carcinomas, can also be evaluated using MRI. Both lesions demonstrate variable signal intensity on both T_1- and T_2-weighted images (Figure 4). Because MRI can usually identify the portal and hepatic veins, it can assess for vascular invasion by the tumor and can also define the extent of the tumor with respect to the segmental anatomy of the liver, thus aiding in determining resectability of the lesion.

Wilms' tumor is the most common solid abdominal mass and the most common primary renal neoplasm in children, with a peak incidence between the ages of 1 and 3 years. An increased incidence of Wilms' tumor is noted in children with aniridia, hemihypertrophy, neurofibromatosis, genitourinary abnormalities, and the Beckwith–Wiedemann syndrome. The tumor presents most often as a unilateral abdominal mass, although the lesion is bilateral in 5–10% of cases. The initial diagnosis is usually made by ultrasound, which demonstrates a solid renal mass. MRI, however, may be superior to both ultrasound and CT in diagnosing and defining the extent of Wilms' tumor.[27,28] In this area of the body, coronal T_1-weighted images can often define the organ of origin of a lesion extremely well, separating renal lesions from those arising in the adjacent liver or adrenal gland. With a combination of coronal and axial planes, and T_1- and T_2-weighting, a study can define the full extent of the lesion, its possible invasion of adjacent organs or vessels, as well as assess for the presence of associated lymphadenopathy. In selected cases, intravenous administration of a gadolinium chelate and/or use of MR angiographic techniques may be necessary.[23]

Neuroblastoma is the most common extracranial solid malignant tumor in children. Neuroblastoma and its more differentiated forms, ganglioneuroblastoma and ganglioneuroma, arise from primitive sympathetic neuroblasts and therefore may

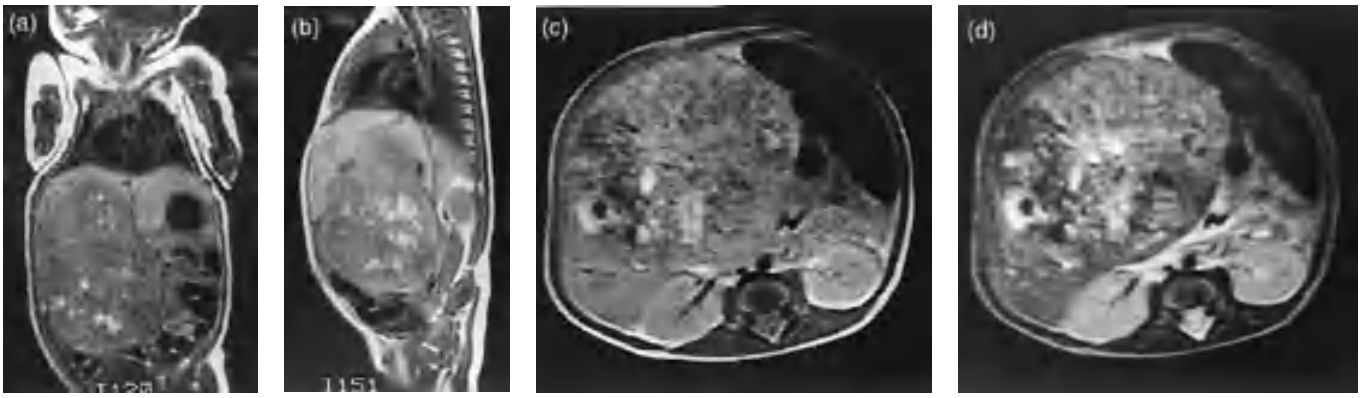

Figure 4 Hepatoblastoma. (a) Coronal and (b) sagittal (SE 300/20) views: a large mass, hetereogeneous in signal intensity, projects inferiorly from the liver and invades the portal vein; the speckled high signal intensity areas probably represent hemorrhage. (c, d) Axial views (SE 2500/30,80): although markedly heterogeneous, the lesion is predominantly low in signal intensity

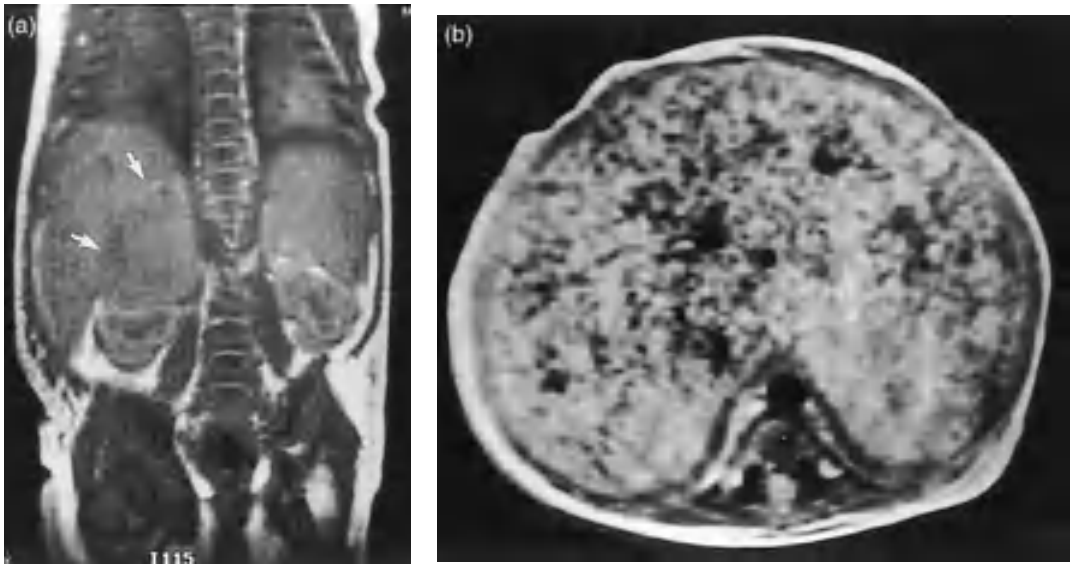

Figure 5 Neuroblastoma. (a) Coronal view (SE 300/16): an enlarged right adrenal gland (arrows) displaces the right kidney inferiorly. (b) Axial view (FSE 2500/17Ef): the liver is also enlarged and filled with metastases, leading to a salt and pepper heterogeneity to its signal intensity

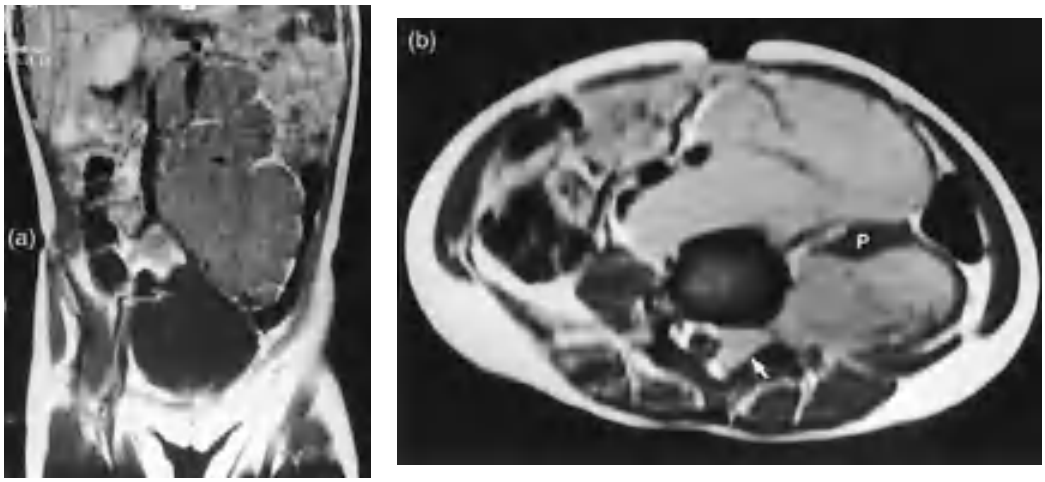

Figure 6 Neuroblastoma. (a) Coronal view (SE 616/15): a large multilobulated medium signal intensity mass surrounds the aorta, displacing it and the inferior vena cava to the right and anteriorly. (b) Axial view (SE 2128/15): a portion of the mass is seen extending into the bony spinal canal (arrow); the left psoas muscle (P) is elevated and displaced to the left by this high signal intensity tumor

arise from the adrenal gland (most commonly) or from anywhere else along the sympathetic chain from the nasopharynx to the presacral region. Children with neuroblastoma may present with a palpable abdominal mass or with symptoms referable to metastases, such as bone pain. The staging of neuroblastoma is based on both local extent as well as on the presence or absence of metastases. Clinically, however, it is more important to determine resectability of the lesion, as surgery remains the treatment of choice. On MRI, neuroblastoma is usually of medium signal intensity on T_1-weighted images and of high signal intensity on T_2-weighted images. It is less well defined than Wilms' tumor and if it arises from the adrenal gland it can displace the kidney inferiorly and/or laterally (Figure 5). As with Wilms' tumor, MRI can play a role in defining the full extent of a lesion, identifying its organ of origin, assessing for possible invasion of adjacent organs or vessels, and demonstrating the presence or absence of metastases.[29–31] Evidence of tumor extending into the spinal canal or encasing the retroperitoneal vessels can classify the neuroblastoma as unresectable (Figure 6).

Neonatal adrenal hemorrhage is another entity that may present as an asymptomatic abdominal mass. Differentiation of neonatal adrenal hemorrhage from neuroblastoma is crucial, and can usually be done using ultrasound or MRI. On ultrasonography, neonatal adrenal hemorrhage is usually anechoic and avascular, in contradistinction to neuroblastoma, which is usually echogenic and vascular. In some instances, adrenal hemorrhage does not appear cystic on ultrasonography and MRI may be extremely useful in helping to make this distinction. On MR images neonatal adrenal hemorrhage behaves similarly to hematomas elsewhere in the body, with a changing MR appearance as the hematoma evolves (Figure 7). More

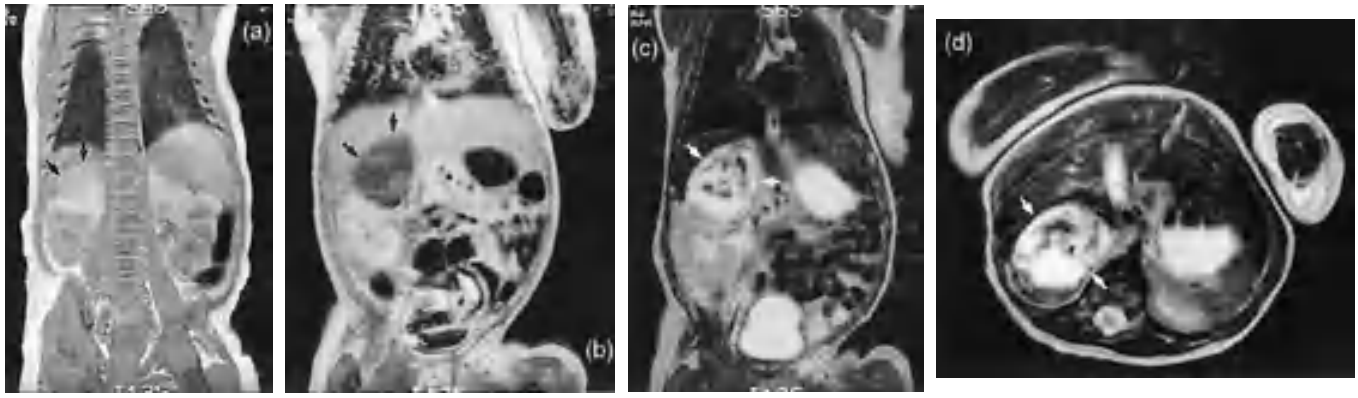

Figure 7 Neonatal adrenal hemorrhage. (a, b) Coronal views (SE 450/11): an enlarged right adrenal gland (arrows) is identified (a) that does not demonstrate enhancement after gadolinium administration (b). (c) Coronal view (FSE 4000/102Ef) and (d) axial view (FSE 3500/102Ef): blood products in varying stages of oxidation are identified in the enlarged right adrenal gland (arrows)

Figure 8 Presacral teratoma. (a) Sagittal view (SE 800/23): a presacral mass is identified with components that are hypointense, isointense, and hyperintense to muscle. (b) Sagittal view (SE 800/16, chemical lipid presaturation): using a lipid-selective presaturation pulse, the formerly hyperintense component is suppressed to the same degree as the adjacent subcutaneous fat; the presence of fat in the lesion histologically characterizes it as a teratoma. (c) Sagittal view (FSE 3000/102Ef): the presence of chemical shift spatial misregistration can also be used to verify the presence of fat in this lesion (arrows); when this artifact is present, lipid-selective presaturation pulses are not necessary to characterize the lesion

specifically, on T_1-weighted images acute hematomas are isointense to muscle, whereas subacute hematomas are hyperintense to muscle. Neuroblastoma usually demonstrates homogeneous medium signal intensity on T_1-weighted images. On T_2-weighted images, neonatal adrenal hemorrhage may be of high signal intensity or of low signal intensity, depending on the chemical state of the blood products. In rare cases of cystic neuroblastoma with hemorrhage, however, the distinction may be difficult. In these cases, evaluation of the liver for the presence of metastasis (low signal intensity on T_1-weighted images and high signal intensity on T_2-weighted images) may help make the diagnosis of neuroblastoma.

Rhabdomyosarcoma is the most common pediatric soft tissue sarcoma and can occur in almost any primary site except the brain. In children, it is most frequently found in the pelvis and genitourinary tract or in the head and neck. In the genitourinary tract, the tumor most frequently arises in the bladder; other common sites are the urethra, prostate, and vagina. Bladder lesions most commonly arise from the submucosa of the trigone or the bladder base and then infiltrate the bladder wall and adjacent structures including the urethra, prostate, vagina, and uterus. Because of the propensity for local invasion, it can be difficult to determine if the primary site was the bladder or the prostate in males or the bladder or the vagina in females. The multiplanar capabilities of MRI make it well suited for demonstrating bladder wall thickening, demarcating the inferior, lateral and posterior extent of the tumor, and detecting distant metastases.[6,24]

Sacrococcygeal teratomas are the most common tumors of the caudal region in children. These lesions are derived from all three germinal cell layers and have a characteristic MR appearance. Specifically, on T_1- and T_2-weighted images a large presacral mass is identified that contains rounded, well-defined areas of different signal intensity. Often one of these locules will contain fat, which can be demonstrated using a lipid-selective presaturation pulse or by simply looking for chemical shift misregistration. (Figure 8). Since these lesions displace the rectum anteriorly, as do all lesions in the presacral space, they can be distinguished from lesions arising in the pelvic cavity. The differential diagnosis for presacral masses in infants also includes anterior meningocele, rectal duplication, neuroblastoma, lymphoma, and lipoma.

4 SUMMARY

During the relatively short time that MRI has been applied to the evaluation of pediatric diseases and disorders, it has proven to be a useful tool in the diagnostic evaluation of a variety of entities, many of which we have touched upon in this article. More detailed information about some of these diseases and disorders can be found in the references given at the end of this article, and it is the authors' hope that the reader will learn from these references and, perhaps in time, add to them.

5 RELATED ARTICLES

Abdominal MRA; Brain MRS of Infants and Children; Lung and Mediastinum MRI; Male Pelvis Studies Using MRI; MRI of the Female Pelvis; Liver, Pancreas, Spleen, and Kidney MRI.

6 REFERENCES

1. B. D. Fletcher and M. D. Jacobstein, *Am. J. Roentgenol.*, 1986, **146**, 941.
2. G. S. Bisset III, J. L. Strife, D. R. Kirks, and W. W. Bailey, *Am. J. Roentgenol.*, 1987, **149**, 251.
3. M. L. Pessar, R. L. Soulen, J. S. Kan, S. Kadir, and E. A. Zerhouni, *Pediatr. Radiol.*, 1988, **18**, 229.
4. R. B. Dietrich, in 'Magnetic Resonance Imaging', 2nd edn, ed. D. D. Stark and W. G. Bradley, Jr, Mosby-Year Book, St Louis, 1992, Vol. 2, Chap. 59.
5. R. B. Dietrich and H. Kangarloo, *Radiology*, 1986, **159**, 215.
6. R. B. Dietrich, in 'Magnetic Resonance Imaging of Children', ed. M. D. Cohen and M. K. Edwards, B. C. Decker, Philadelphia, 1990, Chap. 21.
7. A. Daneman and D. J. Alton, *Radiol. Clin. North Am.*, 1991, **29**, 351.
8. J. Gambino, B. Caldwell, R. B. Dietrich, I. Walot, and H. Kangarloo, *Am. J. Roentgenol.*, 1992, **158**, 383.
9. E. Secaf, H. Hricak, and C. A. Gooding, *Pediatr. Radiol.*, 1994, **24**, 291.
10. H. Hricak and M. J. Popovich, in 'Magnetic Resonance Imaging of the Body', 2nd edn, ed. C. B. Higgins, H. Hricak, and C. A. Helms, Raven, New York, 1992, Chap. 31.
11. M. C. Mintz, D. I. Thickman, D. Gussman, and H. Y. Kressel, *Am. J. Roentgenol.*, 1987, **148**, 287.
12. B. M. Carrington, H. Hricak, R. N. Nuruddin, E. Secaf, R. K. Laros Jr, and E. C. Hill, *Radiology*, 1990, **176**, 715.
13. H. Hricak, Y. C. F. Chang, and S. Thurnher, *Radiology*, 1988, **169**, 169.
14. K. Togashi, K. Nishimura, K. Itoh, I. Fujisawa, Y. Nakano, K. Torizuka, H. Ozasa, and M. Oshima, *Radiology*, 1987, **162**, 675.
15. C. Hugosson, H. Jorulf, and Y. Bakri, *Pediatr. Radiol.*, 1991, **21**, 281.
16. R. B. Dietrich and H. Kangarloo, *Radiology*, 1987, **163**, 367.
17. P. J. Fritzsche, H. Hricak, B. A. Kogan, M. L. Winkler, and E. A. Tanagho, *Radiology*, 1987, **164**, 169.
18. A. H. Troughton, J. Waring, and A. Longstaff, *Clin. Radiol.*, 1990, **41**, 178.
19. S. J. Pomeranz, N. Altman, J. J. Sheldon, T. A. Tobias, K. P. Soila, L. J. Jakus, and M. Viamonte, *Magn. Reson. Imag.*, 1986, **4**, 69.
20. Y. Sato, K. C. Pringle, R. A. Bergman, W. T. C. Yuh, W. L. Smitt, R. T. Soper, and E. A. Franken, *Radiology*, 1988, **168**, 157.
21. K. McHugh, N. E. Dudley, and P. Tarr, *Pediatr. Radiol.*, 1998, **25**, 33.
22. A. Vade, H. Reyes, and A. Wilbur, *Pediatr. Radiol.*, 1989, **19**, 179.
23. D. D. Kidney, R. B. Dietrich, and A. K. Goyal, *Pediatr. Radiol.*, 1998, **28**, 322.
24. R. B. Dietrich and H. Kangarloo, *Am. J. Roentgenol.*, 1986, **146**, 251.
25. M. J. Siegel, G. A. Jamroz, H. S. Glazer, and C. L. Abramson, *J. Comput. Assist. Tomogr.*, 1986, **10**, 593.
26. M. J. Siegel and G. D. Luker, *MRI Clin. North Am.*, 1996, **4**, 599.
27. T. G. Belt, M. D. Cohen, J. A. Smith, D. A. Cory, S. McKenna, and R. Weetman, *Am. J. Roentgenol.*, 1986, **146**, 955.
28. H. Kangarloo, R. B. Dietrich, R. M. Ehrlich, M. I. Boechat, and S. A. Feig, *Urology*, 1986, **28**, 203.
29. B. D. Fletcher, S. Y. Kopiwoda, S. E. Strandjord, A. D. Nelson, and S. P. Pickering, *Radiology*, 1985, **155**, 699.

30. M. D. Cohen, R. M. Weetman, A. J. Provisor, W. McGuire, S. McKenna, B. Case, A. Siddiqui, D. Mirksh, and I. Seo, *Am. J. Roentgenol.*, 1984, **143**, 1241.
31. B. D. Fletcher and S. C. Kaste, *Urol. Radiol.*, 1992, **14**, 263.

Biographical Sketches

Rosalind B. Dietrich. *b* 1953. M.B., Ch.B, 1976, University of Manchester School of Medicine, UK. Internship and radiology residency, Cedars-Sinai Medical Center, Los Angeles, CA, USA, 1979–84. Successively, fellow and Assistant Professor of Pediatric Radiology, University of California, Los Angeles, CA, USA, 1984–1990. Professor of Radiology and Director of MRI, University of California, Irvine, Orange, CA, USA, 1990–1995. Director of Research 1996–present. Approx. 65 publications. Research specialties: applications of MRI in the evaluation of the pediatric brain and body; MRI of brain maturation and white matter diseases.

Gerald M. Roth. *b* 1962. A.B. (biochemical sciences), 1984, Harvard University, USA; M.D., 1988, Columbia University College of Physicians and Surgeons, USA. Internship, Cedars-Sinai Medical Center, Los Angeles, CA, USA. Radiology residency, Hospital of the University of Pennsylvania, Philadelphia, PE, USA, 1989–1993. Successively, MRI Fellow, Faculty, Department of Radiological Sciences, University of California at Irvine, 1993–present. Approx. 5 publications. Research interests: applications of MRI in the chest, abdomen and pelvis; optimization of MR scan protocols.

Tissue Behavior Measurements Using Phosphorus-31 NMR

Simon D. Taylor-Robinson
Hammersmith Hospital, London, UK

and

Claude D. Marcus
Hôpital Robert Debré, Reims, France

1 INTRODUCTION

Phosphorus-31 MRS provides a noninvasive method of assessment of mobile phosphorus-containing compounds. A typical in vivo ^{31}P MR spectrum contains seven resonances (Figure 1). Phospholipid cell membrane precursors, adenosine monophosphate (AMP) and glycolytic intermediates (sugar phosphates) contribute to the phosphomonoester (PME) peak. Phospholipid cell membrane degradation products and endoplasmic reticulum contribute to the phosphodiester (PDE) peak. Information on tissue bioenergetics can be obtained from inorganic phosphate (Pi), phosphocreatine (PCr) and the three nucleoside triphosphate resonances. A measurement of intracellular pH (pHi) can be calculated from the chemical shift of the Pi peak.

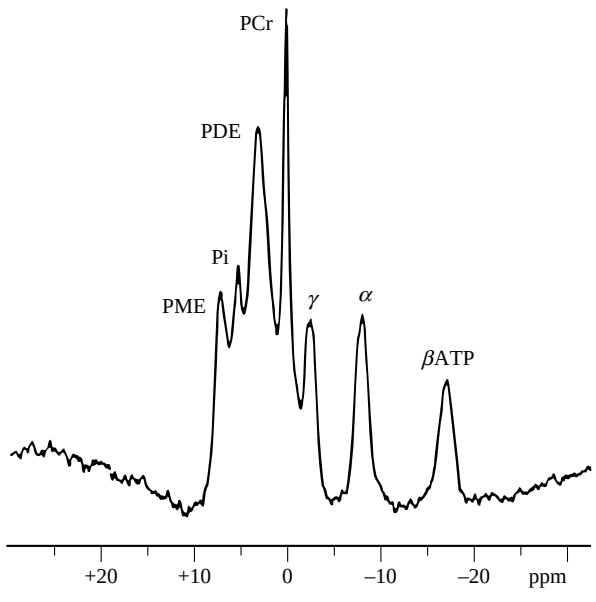

Figure 1 An unlocalized ^{31}P MR spectrum from the head of a healthy adult volunteer. There are seven resonances. PME, phosphomonoester; Pi, inorganic phosphate; PDE, phosphodiester; PCr, phosphocreatine; ATP, adenosine triphosphate

Pathological processes involving hypoxia and ischemia are particularly amenable to ^{31}P MRS assessment using absolute or relative quantitation of the PCr and Pi peaks. The PCr/Pi ratio has been the most commonly used marker of tissue energy reserve under these conditions. Phosphorus-31 MRS may also provide an indication of the viability of isolated donor organs prior to transplantation.

In this article, we discuss the role of in vivo ^{31}P MRS in the examination of tissue bioenergetics in human studies.

2 ^{31}P MRS AND CELLULAR ENERGY STATUS

The energy metabolism of each cell is dependent on the synthesis and utilization of compounds which contain high-energy phosphate bonds such as ATP and PCr.[1] ATP is present in all cells, but PCr is limited to those tissues containing creatine and the enzyme creatine kinase (CK), such as skeletal muscle and brain. ATP has a pivotal role in cellular bioenergetics. The demand for ATP is usually reasonably constant under normal resting conditions. The hydrolysis of ATP to ADP (adenosine 5′-diphosphate) and Pi releases potential energy from high-energy phosphate bonds for all activities involved in maintaining intracellular homeostasis and the specialized functions which may be unique to each cell type. Phosphocreatine acts as an energy reservoir in tissues such as muscle and brain. The enzyme CK splits PCr to provide an energy source for ATP resynthesis (Figure 2). Oxidative phosphorylation, which involves an electron transport chain in the mitochondrial membrane, is the process which provides most of the ATP for each cell under conditions of adequate oxygen supply. In a range of situations the requirements for ATP cannot be met by oxidative phosphorylation in the mitochondria. For example, oxidative phosphorylation is impaired in hypoxia and may be inadequate in normal exercising muscle. The shortfall in ATP production is met by glycolysis in the cytoplasm. Lactic acid may accumulate as a consequence of this process. Phosphocreatine is utilized under these conditions and as PCr falls, Pi increases, but any reduction in ATP is minimized because of the buffering effect of CK. Only when the PCr pool is completely consumed do the tissue ATP levels fall appreciably, leading to a rise in both ADP and Pi.

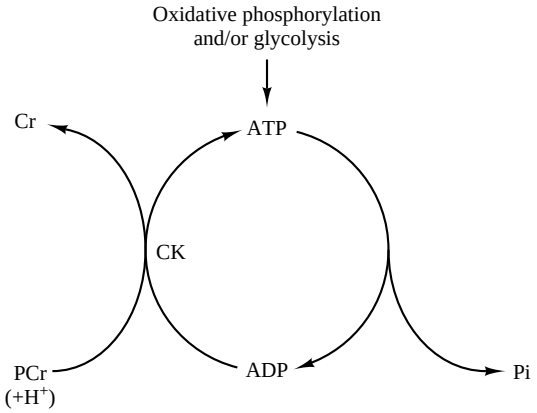

Figure 2 The interrelationship between ATP and PCr. Cr, creatine; CK, creatine kinase; ADP, adenosine diphosphate

Mitochondrial oxidative metabolism may also be affected by changes in pHi,[2] but the rate of ATP biosynthesis remains constant under normal conditions. The concentration of ADP is a major factor in the rate of ATP production.[2,3] The majority of ADP is not directly detectable using NMR methods because of tissue binding. The ability of a particular tissue to synthesize ATP may be calculated from the phosphorylation potential, given by equation (1)

$$[\mathrm{ATP}]/[\mathrm{ADP}][\mathrm{Pi}] \quad (1)$$

A further indication of cellular energy status is given by equation (2):

$$[\mathrm{PCr}]/[\mathrm{Cr}][\mathrm{Pi}] \quad (2)$$

Absolute or relative concentrations of tissue PCr, Pi, and ATP can be obtained using ^{31}P MRS. The rate of ATP biosynthesis, the phosphorylation potential, ADP concentrations, and the kinetics of CK may be calculated from ^{31}P MRS measurements.[2,3] The PCr/Pi and PCr/ATP ratios are commonly used MR indices of cellular energy status or 'bioenergetic reserve', as they reflect equations (1) and (2).

The oxidative phosphorylation pathway can be assessed using the PCr/Pi ratio. Glycolytic intermediates contribute to the PME peak and therefore an indirect assessment of glycolysis may be obtained from quantitation of this resonance. This is of particular importance in assessment of glycolytic disorders in muscle and in dynamic studies of liver metabolism.

3 ^{31}P MRS AND INTRACELLULAR pH

Phosphorus-31 MRS can be used to measure intracellular pH from the chemical shift of the Pi peak with reference to the PCr resonance in tissues such as brain and muscle where PCr is present. In tissues such as liver where PCr is absent the reference used is αATP. The MR signal from Pi is thought not to represent the total intracellular levels of Pi. It is unclear why the remainder is not detected, but it may be bound in the mitochondria. It is not known whether there are pH differences between the cytoplasm and the mitochondria. Split Pi resonances representing intracellular compartmentation have not been observed in human ^{31}P MRS in vivo.

Different body tissues are more susceptible to ischemia and hypoxia than others. In normal exercising muscle, anaerobic glycolysis may take place with the accumulation of lactic acid as a normal sequence of events. The large PCr reservoir in muscle ensures an energy source for these anaerobic reactions. The accumulation of lactate in the brain is more likely to be of pathological consequence because cerebral function is particularly sensitive to hypoxic insults. The measurement of intracellular acidosis may be used as a marker of hypoxia–ischemia and cellular dysfunction in conditions such as stroke or birth asphyxia. Under these circumstances, the PCr/Pi ratio is reduced. Lactate accumulation leads to a reduction in pHi and a change in the chemical shift of Pi. Intracellular pH may change with time: for example, an intracellular alkalosis can develop in ischemic brain tissue of stroke patients over an extended time period.[4] The underlying mechanisms behind such pH changes are not known. However, the MR measurement of pHi may be used to discriminate between diseased and healthy tissue in combination with indices of bioenergetic reserve such as PCr/Pi.

4 ^{31}P MRS AND PHOSPHOLIPID METABOLISM

The PME and PDE peaks are multicomponent. Phosphoethanolamine (PE) and phosphocholine are cell membrane precursors and contribute to the PME peak with signal from glycolytic intermediates and AMP. Glycerophosphorylethanolamine (GPE) and glycerophosphorylcholine (GPC), which are cell membrane degradation products, contribute to the PDE resonance. Phosphoenolpyruvate and endoplasmic reticulum form other contributory factors. The relative contributions of these compounds to the PME and PDE peaks may change with disease. In situations where there is rapid cell turnover, the PME resonance may be elevated due to an increase in PE and phosphocholine. Similarly, under conditions of rapid cell death, after tumor embolization or chemotherapy, for example, an increased contribution of GPE and GPC to the PDE peak may be expected. Phosphorus–proton decoupling can be used to resolve further these resonances in vivo.

5 ^{31}P MRS AND TRANSPLANT ORGAN VIABILITY

Organ transplantation is a steadily expanding surgical field. Increased patient survival rates have been achieved because of improved operative techniques, anti-rejection chemotherapy, and methods for harvesting and preserving donor organs.

The success of any transplant procedure is dependent on the quality of the donor graft and this is a reflection of organ storage methods. The use of more physiological preservation fluids has led to increased storage times, allowing donor organs to be transported between transplant centers. Despite these advances, tissue damage, caused by cold preservation, is an important factor in patient morbidity and mortality. Phosphorus MRS provides a noninvasive assessment of the viability of the isolated donor organ prior to transplantion. The standard indices of bioenergy reserve such as PCr/ATP and PCr/Pi ratios may be appropriate markers in heart transplantation, but the ^{31}P MR spectra from healthy liver and kidney contain no appreciable PCr. Therefore, other indices such as the PME/Pi ratio have to be employed. Adenosine 5′-triphosphate begins to degenerate to ADP and Pi immediately each organ has been harvested. With time, ADP further degenerates to AMP which contributes to the PME peak. The PME/Pi ratio may reflect the ability of the isolated organ to rephosphorylate AMP to ATP on transplantation. Specific transplant studies are considered later in this chapter.

6 CLINICAL APPLICATIONS

The development of whole body magnets has allowed clinical ^{31}P MRS studies to be undertaken in patients with a variety of pathological processes, facilitating comparisons with healthy volunteers and offering the possibility of disease monitoring in response to treatment. MR measurements of bioenergetic reserve such as the PCr/Pi ratio have been proposed as predictors of outcome in hypoxic and/or

ischemic conditions such as birth asphyxia. A review of the role of ^{31}P MRS in some of the major disease processes follows.

6.1 ^{31}P MRS and the Adult Brain

6.1.1 Stroke

Stroke is the most common adult neurological condition and is a prominent cause of mortality in developed countries. Early diagnosis of ischemia facilitates more appropriate treatment, and delay may result in an irreversible loss of neuronal function. Ischemia and the consequent tissue hypoxia result in a depletion in PCr, ATP levels being maintained initially. The acute stages of stroke are characterized by a decreased PCr/Pi ratio in the ^{31}P MR spectrum and an intracellular acidosis.[5] These changes may be detectable before MRI changes become evident.[5] A combination of ^{31}P MRS and MRI may aid early diagnosis, and help to monitor the brain's response to treatment.

Persistent cerebral ischemia results in irreversible cell damage and neuronal death. A reduction in phosphorus signal has been seen in patients with chronic stroke, consistent with a reduction in viable cells in the area of infarction.[4] The pHi has been noted to change with time, resulting in a rebound intracellular alkalosis which may persist.[4] The reasons underlying this change remain unclear.

6.1.2 Transient Ischemia

A transient ischemic attack is defined as a reversible neurological deficit that lasts for 24 h or less. The diagnosis is therefore retrospective and treatment is aimed at preventing recurrence. One study of two patients suggested that the total phosphorus signal was reduced in the absence of MRI changes.[4] This may be due to ischemia, but remains difficult to explain.

6.1.3 Epilepsy

Temporal lobe epilepsy may be unresponsive to standard antiepileptic therapy and a small number of patients require surgical resection of the epileptogenic focus. The definition of the pathological area needs careful preoperative planning. MRI studies have been used to obtain hippocampal volumes[6] but the role of ^{31}P MRS has been limited. A reduced PME, probably as a result of underlying hippocampal sclerosis, has been noted in some studies. An increased Pi and an unexplained intracellular alkalosis have been noted in most studies,[4,7] all of which have involved relatively small numbers of patients.

6.1.4 Alzheimer's Disease

The results of ^{31}P MRS studies have been disappointing. Bottomley and colleagues[8] found no changes in either metabolite ratios or absolute concentrations of metabolites.

6.1.5 Multiple Sclerosis

This condition is common in temperate climates and is characterized by episodes of focal neurological deficit which relapse and remit over a period of many years. The classic histological lesions are plaques of demyelination. MRI has revolutionized the diagnosis of this condition, but the results of ^{31}P MRS studies are less clear-cut. In one study[9] there was a decrease in the PCr/ATP ratio in some patients with active disease, whereas in another study[10] there was an increase in the PCr/ATP ratio with disease activity.

6.1.6 Other Cerebral Conditions

Decreased PCr/Pi has been observed in the cerebral ^{31}P MR spectra from patients with migraine and mitochondrial cytopathies. This suggests an alteration in bioenergetic reserve.

Chronic hepatic encephalopathy is defined as the neuropsychiatric impairment observed in patients with cirrhosis of the liver. The results of some ^{31}P MRS studies have suggested altered brain energy metabolism in these patients (see also ***Systemically Induced Encephalopathies: Newer Clinical Applications of MRS***).

6.2 ^{31}P MRS and Pediatric Brain Studies

The normal ^{31}P MR spectrum from a healthy neonatal brain is significantly different from adult spectra. The PME signal is much larger in the neonate and this varies with gestational age. Azzopardi and colleagues[11] found that the PME is smaller and the PDE larger in the healthy full-term infant than the healthy preterm infant, related most probably to the changes in membrane lipids with myelin formation. The PCr/Pi ratio increases with gestational age, indicating an increased phosphorylation potential with brain development. The measured intracellular pH appears not to vary with the gestational age of healthy newborn infants.

6.2.1 Hypoxic–Ischemic Encephalopathy

Birth asphyxia of the newborn infant has been extensively investigated using ^{31}P MRS. This condition is almost unique because there are well-defined MR indices of prognosis. Reduced PCr/Pi ratio has been correlated with outcome.[12] Spectra obtained in the initial 24 h after birth may be normal, but a fall in PCr and a rise in Pi (reduced PCr/Pi ratio) may develop over the ensuing hours and days (Figure 3). This reflects defective oxidative phosphorylation as a result of birth trauma. Intracellular pH tends to rise in a delayed response to the hypoxic–ischemic insult and there may also be a reduction in ATP levels. The metabolite ratios tend to return to normal within 2 weeks in neonates who recover. The reduction in PCr/Pi ratio is proportional to the degree of subsequent neurodevelopmental impairment and to reduced cranial growth in the first year of life.[12] In the severest cases, where the neonates subsequently die, the PCr and ATP may be almost undetectable. The Pi often rises out of proportion to the reduction in PCr. This delayed or secondary response to ischemic injury is poorly understood, but may be partly due to the toxic effects of neurotransmitters such as glutamate, which may induce mitochondrial membrane disruption through the generation of free radicals.[13] Phosphorus-31 MR spectroscopy may be utilized to monitor the effectiveness of treatment designed to prevent this secondary energy failure. The development of suitable therapeutic regimens is an area of current and future research. However, the PCr/Pi ratio is already being used as a predictor of patient outcome and may give the pediatrician insight into planning future management decisions.

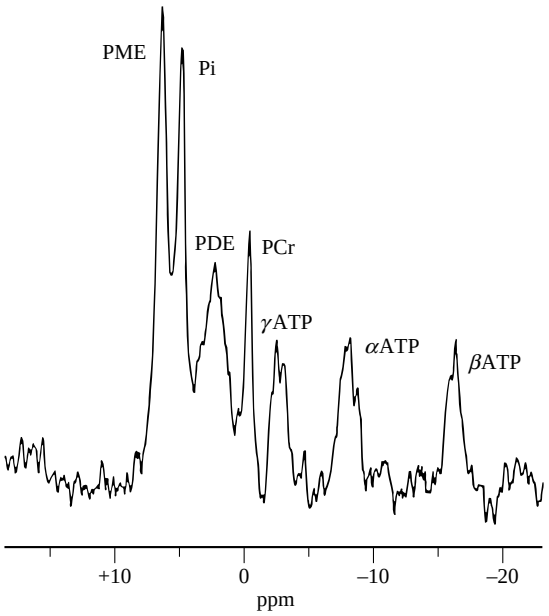

Figure 3 An unlocalized ^{31}P MR spectrum from the head of a birth asphyxiated neonate. The PCr peak is reduced and the Pi peak is elevated

6.3 Myocardial Metabolism

Heart muscle is well supplied with oxygen and mitochondria. It relies on glycolysis to a much smaller extent than skeletal muscle, which has a higher concentration of glycolytic enzyme and fewer mitochondria. The regulation of cardiac metabolism and its relation to mechanical function has been widely studied in animals and humans[14,15] (see also ***Cardiovascular NMR to Study Function*** and ***NMR Spectroscopy of the Human Heart***).

6.3.1 Measurements in Normal Myocardium

Some of the major problems encountered in cardiac studies are related to signal contamination of the myocardium from the chest wall and from blood circulating through the cardiac chambers. The chest wall contains about four times more PCr than the normal myocardium. Signal from blood usually includes appreciable amounts of ATP and PDE, and an intense 2,3-diphosphoglycerate (2,3-DPG) resonance, which may obscure the Pi and PME resonances. Under such circumstances the pHi and the PCr/Pi ratio cannot be measured.[16]

Inorganic phosphate and pHi measurements still remain difficult in humans. Localization techniques may be used to minimize signal contamination from chest wall or blood. Correction for residual blood contamination and saturation effects may also be made.

The PCr/ATP ratio is the most frequently used index of bioenergy reserve in cardiac studies. Results from human and animal studies are comparable.[17] This ratio remains relatively constant during the cardiac cycle and in exercise. It is also highly reproducible. The PDE/ATP ratio is difficult to measure accurately because of interference from the 2,3-DPG signal. The available data show considerable biological variation in human studies. Different examination techniques may complicate this matter. The pHi of normal human myocardium is pH 7.15 ± 0.03.[18]

6.3.2 Measurements in Myocardial Diseases

Spectral abnormalities in human myocardium mainly reflect ischemic conditions.[19] The PCr/ATP ratio decreases significantly during hand grip exercise[20] in patients with a high degree of coronary artery stenosis. This ratio is also reduced in advanced stages of heart failure, in left ventricular hypertrophy, or dilated cardiomyopathy.[21] An increase in normal PCr/ATP ratio has been shown during treatment for heart failure.[17] Apart from blood contamination, an increased PDE/ATP ratio might reflect an accumulation of cell membrane degradation products in patients with a decreased left ventricular ejection fraction.[22]

6.3.3 Cardiac Transplantation

Advances in operative technique and in antirejection therapy have led to cardiac transplantation being used as a viable treatment for patients with end-stage heart disease. Endomyocardial biopsies with histological grading are the gold standard for detection of rejection. No reliable noninvasive alternative is available at present. Phosphorus-31 MRS has been studied in this context.

Animal models of cardiac transplantation have demonstrated an early decrease in PCr/ATP and PCr/Pi ratios.[23] A parallel rise in PDE/ATP was found in two studies which preceded the onset of histologically detectable rejection by 1 or 2 days.[23,24] The increase in the PDE peak measurements may be due to immunological or reperfusion injury. The abnormalities of high-energy phosphate during acute, severe rejection are reversible with antirejection therapy.[25]

In human studies no correlation was found between the decrease in the PCr/ATP ratio measurements and the biopsy grading. Severe rejection may therefore not be distinguishable from mild or moderate rejection by ^{31}P MRS alone.[26] The discrepancy between animal and human studies may be explained by the different time courses for MRS examinations and the rather more heterogeneous human population and study conditions.

6.4 ^{31}P MRS and the Kidney

Spectral localization is required because there are considerable regional differences in renal function and metabolism. The cortex is dependent on oxidative phosphorylation and the inner medulla is more reliant on glycolysis for energy requirements. Localization has proved difficult owing to the anatomical position and the displacement on respiratory excursion. No large-scale studies have been undertaken in the renal failure patients, but transplanted kidneys are positioned in a relatively superficial, static position in the anterior pelvis and are therefore much more amenable to MRS examination.

The normal ^{31}P MR spectrum does not contain a large PCr signal arising from the kidney. There is a relatively large PME peak compared with liver and muscle. Urinary Pi may contribute to the PDE resonance, but this only becomes significant when the collecting ducts are distended through obstructive disease.[27]

6.4.1 The Isolated Donor Kidney

Phosphorus-31 MRS can be used to assess the viability of isolated donor organs, kept in physiological preservation fluid, prior to transplantation. An alternative index of tissue energy reserve has to be used because the renal PCr pool is small. Adenosine 5′-triphosphate degrades to ADP and Pi fairly rapidly, but provided there is sufficient cellular AMP, rephosphorylation to ATP should be possible. Adenosine monophosphate resonates in the PME region of the spectrum and therefore the PME/Pi ratio has been used as an indicator of viability. Human studies have positively correlated the PME/Pi ratio with subsequent postoperative renal function.[28] The best renal function was observed in kidneys where ATP was seen in the donor organ spectra.

6.4.2 The Transplanted Kidney

Phosphorus-31 MRS may be used to investigate renal failure, graft rejection, or organ viability postoperatively. The PME/ATP ratio may be slightly higher in the transplanted kidney than in healthy volunteers. Animal studies have shown an elevated Pi/ATP ratio with renal failure or ischemia due to poor graft viability. Organ rejection or renal dysfunction due to cyclosporin toxicity may produce a similar picture.[27] Such changes are nonspecific, but perhaps may be used to monitor the effectiveness of antirejection chemotherapy.

6.5 ^{31}P MRS and Liver

The position of the liver renders it much more amenable to MRS investigation. The MR spectrum contains no PCr signal arising from the liver itself. Most studies have concentrated on changes in PME/ATP and PDE/ATP ratios with disease, reflecting changes in hepatic phospholipid and carbohydrate metabolism. The Pi/ATP ratio remains relatively constant. Clinical interest has focused on spectral changes under conditions such as alcoholic liver disease, cirrhosis, primary and secondary liver tumors, and the dynamic changes in metabolites following infusions of fructose, alanine, and alcohol. This subject is discussed in detail in another article (see ***In Vivo Hepatic MRS of Humans***). Tissue behavior measurements have been used to measure the effectiveness of chemoembolization therapy for hepatic cancers. The resulting ischemia can be assessed using PME/Pi or PME/ATP ratios, both of which fall after successful treatment.[29]

The PME/Pi ratio has been used to assess the viability of isolated donor organs prior to transplantation in a similar fashion to the renal studies already mentioned.[30]

6.6 ^{31}P MRS in Tumors

The difficulty with reporting metabolic changes in tumors, as reflected by ^{31}P MRS, is that the results are variable, depending on the size, location, and precise histology. In human tumors, the typical metabolite characteristics include lower PCr and higher PME and PDE levels.[31] Variations in the PME and PDE levels may reflect different rates of membrane synthesis, catabolism, or metabolic turnover. (See also ***Spectroscopic Studies of Animal Tumor Models***; ***In Vivo Hepatic MRS of Humans***; and ***Brain Neoplasms in Humans Studied by Phosphorus-31 NMR Spectroscopy***).

The PCr/Pi ratio is reduced in most high-grade tumors of the brain, reflecting an increased demand for ATP in rapid growth. The measured pHi is often found to be alkaline under these circumstances.[32] The reasons for this intracellular alkalinization remain unclear.

Treatment such as radiotherapy or chemotherapy may induce hypoxia, ischemia, or necrosis in tumors. These changes may lead to an increase in Pi[33] and acidosis.[34] The early decrease in PME seems to be a sensitive indicator of changes in the phospholipid metabolism of the cell membrane.[31] However, because of the wide interindividual variability, changes should be related to initial measurements performed in patients before the start of therapy.

6.7 ^{31}P MRS and Muscle

Phosphorus-31 MRS allows investigation of muscle bioenergetics at rest, during exercise, and during the recovery period. Normal muscle has a low metabolic rate and a high energy capacity at rest, reflected in a high PCr/Pi ratio. During exercise the ATP levels are maintained at the expense of the PCr pool. Anaerobic glycolysis results in lactate accumulation and a reduced pHi. In the recovery phase PCr regenerates and the PCr/Pi ratio rises to preexercise levels. The observed pHi also returns to normal, because oxidative phosphorylation then provides the bulk of the energy requirements. Phosphorus-31 MRS may be utilized as a screening test in patients with exercise intolerance. The various muscle pathologies are discussed in a separate article (see ***Peripheral Muscle Metabolism Studied by MRS***). We briefly consider some of the major conditions where tissue behavior measurements are important.

6.7.1 Mitochondrial Myopathies

Mitochondrial myopathies, where there is defective oxidative phosphorylation, are characterized by a reduced resting energy state and a decreased PCr/Pi ratio, which falls rapidly to very low levels on exercise.[35] The capacity for exercise is reduced and the resynthesis of PCr after exercise is impaired, because this is dependent on mitochondrial function. Therefore there is a prolonged recovery phase before the PCr/Pi ratio reaches resting levels. Intracellular acidosis is often observed, which may become marked on exercise.

6.7.2 Glycolytic Disorders

Specific enzyme deficiencies in the glycolytic pathway block the production of lactic acid and therefore the pHi does not fall in anaerobic exercise as it does in normal muscle. This failure of intracellular acidification is characteristic.[35] During exercise an accumulation of glycolytic intermediates can be measured indirectly from the ^{31}P MR spectrum, because sugar phosphates contribute to the PME resonance.

7 CONCLUSIONS

In vivo ^{31}P MRS provides a noninvasive assessment of tissue bioenergetics and phospholipid metabolism. Comparisons may be made between healthy and diseased tissue. Measurements of the PCr/Pi ratio and pHi may provide insights into

pathogenic mechanisms and in the future, the efficacy of therapeutic intervention in cardiac and cerebral hypoxic–ischemic states. Energy reserves at rest and during exercise may be monitored in muscle disease, and the PME/Pi ratio is a noninvasive indicator of viability in isolated donor organs prior to transplantation. In vivo ^{31}P MRS remains predominantly a research tool, but it has proved to be clinically useful in birth-asphyxiated babies and in studies of muscle disease.

8 RELATED ARTICLES

Brain MRS of Human Subjects; Brain Neoplasms in Humans Studied by Phosphorus-31 NMR Spectroscopy; Cardiovascular NMR to Study Function; In Vivo Hepatic MRS of Humans; Localization and Registration Issues Important for Serial MRS Studies of Focal Brain Lesions; NMR Spectroscopy of the Human Heart; Peripheral Muscle Metabolism Studied by MRS; Quantitation in In Vivo MRS; Spectroscopic Studies of Animal Tumor Models; Systemically Induced Encephalopathies: Newer Clinical Applications of MRS; Whole Body Studies: Impact of MRS.

9 REFERENCES

1. E. E. Conn, P. K. Stumpf, G. Bruening, and R. H. Doi, 'Outlines of Biochemistry', 5th edn., Wiley, New York, 1987.
2. S. Nioka, B. Chance, M. Hilberman, H. V. Subramanian, J. S. Leigh, Jr., R. L. Veech, and R. E. Forster, *J. Appl. Physiol.*, 1987, **62**, 2094.
3. B. Chance, J. S. Leigh, Jr., J. Kent, K. McCully, S. Nioka, B. J. Clark, J. M. Maris, and T. Graham, *Proc. Natl. Acad. Sci., U.S.A.*, 1986, **83**, 9458.
4. J. W. Hugg, G. B. Matson, D. B. Twieg, A. A. Maudsley, D. Sappey-Marinier, and M. W. Weiner, *Magn. Reson. Imaging*, 1992, **10**, 227.
5. J. Kucharczyk, M. Moseley, J. Kurhanewicz, and D. Norman. *Invest. Radiol.*, 1989, **24**, 951.
6. C. R. Jack, F. W. Sharbrough, C. K. Twomey, G. D. Cascino, K. A. Hirschorn, W. R. Marsh, A. R. Zinsmeister, and B. Scheithauer. *Radiology*, 1990, **175**, 423.
7. J. W. Hugg, K. D. Laxxer, G. B. Matson, A. A. Maudsley, C. A. Husted, and M. W. Weiner. *Neurology*, 1992, **42**, 2011.
8. D. G. M. Murphy, P. A. Bottomley, J. A. Salerno, C. DeCarli, M. J. Mentis, C. L. Grady, D. Teichberg, K. R. Giacometti, J. M. Rosenberg, C. J. Hardy, M. B. Schapiro, S. I. Rapoport, J. R. Alger, and B. Horwitz. *Arch. Gen. Psychiatry*, 1993, **50**, 341.
9. T. A. D. Cadoux-Hudson, A. Kermode, B. Rajagopalan, D. Taylor, A. J. Thompson, I. E. C. Ormerod, W. I. McDonald, and G. K. Radda. *J. Neurol. Neurosurg. Psychiatry*, 1991, **54**, 1004.
10. J. M. Minderhoud, E. L. Mooyaart, R. L. Kamman, A. W. Teelken, M. C. Hoogstraten, L. M. Vencken, E. J's. Gravenmade, and W. van den Burg. *Arch. Neurol.*, 1992, **49**, 161.
11. D. Azzopardi, J. S. Wyatt, P. A. Hamilton, E. B. Cady, D. T. Delpy, P. L. Hope, and E. O. R. Reynolds. *Pediatr. Res.*, 1989, **25**, 440.
12. D. Azzopardi, J. S. Wyatt, E. B. Cady, D. T. Delpy, J. Baudin, A. L. Stewart, P. L. Hope, P. A. Hamilton, and E. O. R. Reynolds. *Pediatr. Res.*, 1989, **25**, 445.
13. J. S. Wyatt, A. D. Edwards, D. Azzopardi, and E. O. R. Reynolds. *Arch. Dis. Child.*, 1989, **64**, 953.
14. C. B. Higgins, M. Saeed, M. Wendland, and W. M. Chew. *Invest. Radiol.*, 1989, **24**, 962.
15. S. Schaefer. *Am. J. Cardiol.*, 1990, **66**, 45F.
16. A. de Roos, J. Doornbos, S. Rebergen, P. van Rugge, P. Pattynama, and E. E. van der Wall. *J. Radiol.*, 1992, **14**, 97.
17. S. Neubauer, T. Krahe, R. Schindler, M. Horn, H. Hillenbrand, C. Entzeroth, H. Mader, E. P. Kromer, G. A. J. Riegger, K. Lackner, and G. Ertl. *Circulation*, 1992, **86**, 1810.
18. A. de Roos, J. Doornbos, P. R. Luyten, L. J. M. P. Oosterwaal, E. E. van der Wall and J. A. den Hollander. *J. Magn. Reson. Imaging*, 1992, **2**, 711.
19. S. Schaefer, G. G. Schwartz, J. R. Gober, B. Massie, and M. W. Weiner. *Invest. Radiol.*, 1989, **24**, 969.
20. R. G. Weiss, P. A. Bottomley, C. J. Hardy, and G. Gerstenblith. *N. Engl. J. Med.*, 1990, **323**, 1593.
21. H. Sakuma, K. Takeda, T. Tagami, T. Nakagawa, S. Okamoto, T. Konishi, and T. Nakano. *Am. Heart J.*, 1993, **125**, 1323.
22. W. Auffermann, W. M. Chew, C. L. Wolfe, N. J. Tavares, W. W. Parmley, R. C. Semelka, T. Donnelly, K. Chatterjee, and C. B. Higgins. *Radiology*, 1991, **179**, 253.
23. R. C. Canby, W. T. Evanochko, L. V. Barrett, J. K. Kirklin, D. C. McGiffin, T. T. Sakai, M. E. Brown, R. E. Foster, R. C. Reeves, and G. M. Pohost. *J. Am. Coll. Cardiol.*, 1987, **9**, 1067.
24. C. D. Fraser, Jr., V. P. Chacko, W. E. Jacobus, R. L. Soulen, G. M. Hutchins, B. A. Reitz, and W. A. Baumgartner. *Transplantation*, 1988, **46**, 346.
25. P. McNally, N. Mistry, J. Idle, J. Walls, and J. Freehally. *Transplantation*, 1989, **48**, 1068.
26. P. A. Bottomley, R. G. Weiss, C. J. Hardy, and W. A. Baumgartner. *Radiology*, 1991, **181**, 67.
27. M. D. Boska, D. J. Meyerhoff, D. B. Twieg, G. S. Karczmar, G. B. Matson, and M. W. Weiner. *Kidney Int.*, 1990, **38**, 294.
28. P. N. Bretan, Jr., N. Baldwin, A. C. Novick, A. Majors, K. Easley, T. Ng, N. Stowe, P. Rehm, S. B. Streem, and D. R. Steinmuller. *Transplantation*, 1989, **48**, 48.
29. D. J. Meyerhoff, G. S. Karczmar, F. Valone, A. Venook, G. B. Matson and M. W. Weiner. *Invest. Radiol.*, 1992, **27**, 456.
30. R. F. E. Wolf, R. L. Kamman, E. L. Mooyaart, E. B. Haagsma, R. P. Bleichrodt, and M. J. H. Slooff. *Transplantation*, 1993, **55**, 949.
31. W. Negendank. *NMR Biomed.*, 1992, **5**, 303.
32. W.-D. Weiss, W. Heindel, K. Herholz, J. Rudolf, J. Burke, J. Jeske, and G. Friedman. *J. Nucl. Med.*, 1990, **31**, 302.
33. A. Schilling, B. Gewiese, G. Berger, J. Boese-Landgraf, F. Fobbe, D. Stiller, V. Gallkowski, and K. J. Wolf. *Radiology*, 1992, **182**, 887.
34. M. W. Dewhirst, H. D. Sostman, K. A. Leopold, H. C. Charles, D. Moore, R. A. Burn, J. A. Tucker, J. M. Harrelson, and J. R. Oleson. *Radiology*, 1990, **174**, 847.
35. Z. Argov and W. J. Bank. *Ann. Neurol.*, 1991, **30**, 90.

Biographical Sketches

Simon. D. Taylor-Robinson. *b* 1960. M.B., B.S., 1984, London; M.R.C.P., 1989, (UK) M.D., 1996, London. Introduced to NMR by G. M. Bydder. Honorary lecturer, medicine, Royal Free Hospital and School of Medicine, London, 1992–94. Research fellow and Honorary Senior Registrar at NMR Unit, Royal Postgraduate Medical School, Hammersmith Hospital, London, 1992–94. Senior Registrar, Division of Gastroenterology, Department of Medicine, Royal Postgraduate Medical School, Hammersmith Hospital, London, 1994–1996. Senior Lecturer and Honorary Consultant Physician, Department of Medicine, Imperial College Medical School, Hammersmith Hospital, London 1996–present. Approx. 60 publications. Research interests include clinical application of NMR to liver disease and transplant organ viability.

Claude D. Marcus. *b* 1957. M.D., 1986, Reims, France. Chef de clinique assistant des hopitaux, 1986–1990; praticien hospitalier temps plein centre hospitalier universitaire de Reims, France, 1990–present. Introduced to NMR by Professor D. Doyon (CHU Kremlin-Bicetre, France). Titulaire du Diplome d'Université d'imagerie par resonance magnétique, 1988. Research interests include clinical applications of NMR to brain and breast diseases.

Imaging and Spectroscopy of Muscle

Chris Boesch and Roland Kreis
University of Bern, Switzerland

1 INTRODUCTION

Examinations of extremities and skeletal muscle have been among the first applications of NMR in the human body. At the advent of in vivo NMR, magnets were available with sufficiently high field strength for magnetic resonance spectroscopy (MRS) but their limited bore size allowed only small animals or human extremities to be examined. The development of surface coils (see ***Spatial Localization Techniques for Human MRS***) allowed localized acquisition of NMR signals—a technique that was mainly used for ^{31}P MRS and to a lesser extent for ^{13}C MRS. For a while, classical ^{31}P MRS experiments (see ***Peripheral Muscle Metabolism Studied by MRS***, ***Tissue Behavior Measurements Using Phosphorus-31 NMR***) were the major application of MRS and led to a substantial contribution to knowledge in muscle physiology. In the following years, the development of whole-body magnets introduced NMR applications to clinical medicine (see ***Whole Body Studies: Impact of MRS***). MRI of extremities, muscle tissue, and joints became a routine diagnostic tool (see ***ESR Probes as Field Detectors in MRI***, ***MRI of Musculoskeletal Neoplasms***, ***Skeletal Muscle Evaluated by MRI***). The combination of MRI and MRS in whole-body magnets led not only to improved anatomical localization defined by gradients but also to better description of the sensitive volume by MRI in the same magnet. The wider bore of these systems allowed for examinations of larger muscle groups, for example those of the thigh. Gradient-based volume selection and improved localization sequences particularly promoted the development of ^{1}H MRS methods.

The number of NMR applications in perfused muscles and animals is huge but will not be covered in this chapter, which focuses on human skeletal muscle. At present, publications on ^{31}P MRS in small-bore and whole-body systems still represent a considerable portion of the physiological applications of MR (see also ***Peripheral Muscle Metabolism Studied by MRS***). An increasing number of new applications, however, combine and use other MR techniques and other nuclei. Some of these applications will be described in this chapter.

2 STRUCTURAL ORDER AND COMPARTMENTATION IN MUSCLE TISSUE

Skeletal muscle is a biological structure that is highly organized at different spatial levels. (a) Skeletal muscles are composed of various types of muscle fiber with inherently different composition and metabolism. (b) Bulk fat along fasciae around muscles forms macroscopic plates that run almost parallel with the axes of extremities. (c) Muscle fibers may extend parallel to the muscle ('fusiform' arrangement) or with a certain 'pennation' angle between muscle and fibers ('unipennate' with one major direction or 'bipennate' if two different types of fiber orientation exist that are attached to one tendon). (d) Myofibrils form the well-known striated structures (sarcomeres) including actin and myosin molecules, which are spatially organized on the microscopic level. (e) Membranes and cell organelles such as mitochondria separate a specific metabolite from the same metabolite in the cytoplasm, leading to different pools and transport processes.

Structural order and compartmentation in biological tissue can influence MR signals such that measurable parameters or artifacts are generated, depending on the way the experiment and observer are using or neglecting that information. Several effects, which will be discussed below, can be attributed to structure or compartmentation.

1. the relaxation times of muscle, tendons, and cartilage, depend on fiber orientation and type;[1–3]
2. the muscle- or subject-specific metabolite content, energy kinetics, and recruitment pattern based on distributions of fiber types;[3–7]
3. the isotropic and ordered compartments, as distinguished by ^{23}Na double quantum filtered (DQF) MR spectra;[8,9]
4. susceptibility effects, which are different for extramyocellular (bulk) (EMCL) fat and for intramyocellular lipids (spherical droplets) (IMCL);[10,11]
5. magnetization transfer (MT) of the invisible fixed pool of molecules to the moving and visible pool;[1]
6. restricted diffusion measurable by specialized MRI and MRS sequences;[12–16]
7. the dipolar coupling effects of creatine (Cr) and/or phosphocreatine (PCr) resonances owing to anisotropic motional averaging;[17,18]
8. differences in the NMR visibility of Cr/PCr and other metabolites as a result of compartmentation and/or limited motional freedom.[19–21]

MR is a unique tool with which to investigate order and compartmentation in biological tissues. Even if these are not the major target of a specific examination, their effects should always be kept in mind when interpreting images and spectra.

3 USE OF MRI FOR HUMAN MUSCLE PHYSIOLOGY

3.1 MRI for Volume Localization

The combination of MRI and MRS improves the anatomical localization of spectra considerably. MRS examinations in small-bore systems often have to rely on palpation and approximate positioning of the surface coil. With appropriate imaging sequences, it was possible to show that palpation incorrectly identified flexor muscle margins by more than 15 mm in 50% of attempts.[22] In principle, MRI makes it possible to place the region of interest with an accuracy of about 1 mm. Even if images are acquired prior to MRS, it may not be feasible to place the sensitive volume of a surface coil with the same precision. However, the subsequent use of gradient-based localization schemes and a proper fixation of the examined extremity allow for a volume selection within adequate

accuracy. Since the fiber orientation, composition, and activation are muscle specific and can vary even within one muscle,[23] combined MRI/MRS systems are, therefore, necessary to obtain MR parameters from one specific muscle type, as shown in several examples below.

3.2 Activity-dependent MRI

The amount and distribution of water in skeletal muscle is changed by muscular activity.[2,23–27] Subsequent variations in relaxation times make MR signal intensity highly sensitive to changes in the water distribution, oxygenation, pH, and other factors. Fleckenstein et al.[28] suggested imaging parameters with which it was possible to detect and document muscular activity (see also ***Skeletal Muscle Evaluated by MRI***). This technique can be used to study intersubject variations of normal anatomy and muscular activation. Ergometers to be used in an MR system have to be redesigned to fit into the restricted space of the patient bore. The technique described can help to document the activity imposed by such an ergometer. While it is clear that activity-dependent MRI is a valuable and practical tool to investigate muscular activity, it is not so clear which changes in MR parameters lead to this effect. It seems that water inflow and pH changes contribute only partially to the observed increase in T_2 relaxation.[25,27]

3.3 Muscle Volume Determination using MRI

Muscle mass is a variable parameter and is dependent on training, ageing, temporary immobilization, disease, and other factors. Knowing muscle mass is, therefore, crucial for an estimation of training effects and also for calculations of total body content of metabolites and components of the muscular cell. Many localized observations of physiological parameters, such as biopsies, need additional data on the absolute volume of the muscle, since changes in concentration could be a result of increased muscle mass (i.e. simple dilution with unchanged total content) or an effective increase in total content.

It is obvious that MRI with its excellent soft tissue contrast is predestined to be used for in vivo morphometric measurements.[4,29–33] However, all approaches have specific advantages and disadvantages, for example three-dimensional versus multislice techniques, nonlinearity of the spatial representation, different ways of image analysis, and partial volume effects.

The image acquisition can be done either by three-dimensional sequences or using sequential two-dimensional data (i.e. multislice techniques) (Figure 1). As long as discrete slices are evaluated, the so-called Cavalieri principle needs to be respected.[31] It states that the starting point of a series of slices should be arbitrarily set such that every position has equal probability. This avoids systematic over- or underestimation of a volume through specific sampling of the structure.

In principle, images can be measured in one acquisition as long as the muscle does not exceed the homogeneous volume of the magnet, which is typically about 50 cm in diameter. However, the linearity of the gradients within the homogeneous volume and subsequently the accuracy of the mapping is significantly reduced in the outer portions of the volume because of the nonlinearity of the gradients. Therefore, imaging of larger muscles may be more appropriate in multiple steps. The imperfect spatial accuracy of MR systems is usually improved by retrospective image-correction algorithms, which use the known spatial characteristics of the gradients. This procedure is acceptable for diagnostic images where the relative positions are much more important than the absolute dimensions. For quantitative measurements, however, a continuous monitoring of these effects is necessary, especially if variations over longer time periods are investigated, such as training effects on muscular volume.

The cross-sectional area and actual volume can be determined by several methods:[29,31–33] simple threshold, voxel counting within operator-defined borders, elaborated tissue segmentation algorithms, or point counting. Simple threshold methods need a homogeneous rf sensitivity of the coil since substantial inhomogeneities in signal intensity will lead to wrong assignment of voxels. Computed tissue segmentation, often based on different MRI scans, uses several steps to distinguish between tissues, in many cases with human interaction. Image intensity threshold can be followed by boundary tracing, edge detection filters, morphological erosion, seed-growing algorithms,[29,30] etc. Point counting[31] is an interactive method very popular in morphometry, for example to analyze electron micrographs. Grids are placed over the region of interest (Figure 1) and crosses that hit the structure of interest are counted. The probability for a hit is proportional to the area covered by the structure. If large enough numbers are counted (typically over 100 hits per structure), variations resulting from the counting procedure are negligible and the number of hits represents the desired area almost perfectly. Point counting is a very robust method but is very time consuming and, to a certain extent, operator dependent.

All digitization methods are somewhat susceptible to partial volume effects: the misinterpretation of voxels that contain more than one type of tissue. If a T_1-weighted MR sequence is used that leads to a strong signal of fat, voxels that are only half filled with adipose tissue will produce sufficient signal to be counted as fat. Since this happens in all voxels at the border of fat and muscle tissue, fat content will be systematically overestimated. Optimized imaging sequences and appropriate windowing of the signal intensity may help to reduce this problem.

3.4 Use of MRI for Determination of Muscle Fiber Orientation and Composition

In addition to assessment of gross morphology, histological characterization of muscle tissue by means of MR is desirable. So far, fiber orientations in muscle and the 'pennation angle' between muscle fibers and axis of the muscle have been measured by ultrasound. It has been proposed that MR images would show sufficient morphological detail to see striations generated by fat, which runs parallel and between the muscle fascicles, and that this would allow for an assessment of the fascicle pennation.[4,33] One interesting finding of such a three-dimensional analysis was a considerable variation of pennation angles within one muscle;[4] for example a range of 5 to 50° was observed in the vastus medialis. This noninvasively obtained information helps to evaluate muscle mechanics. Further suggestions have been made to use the effect of

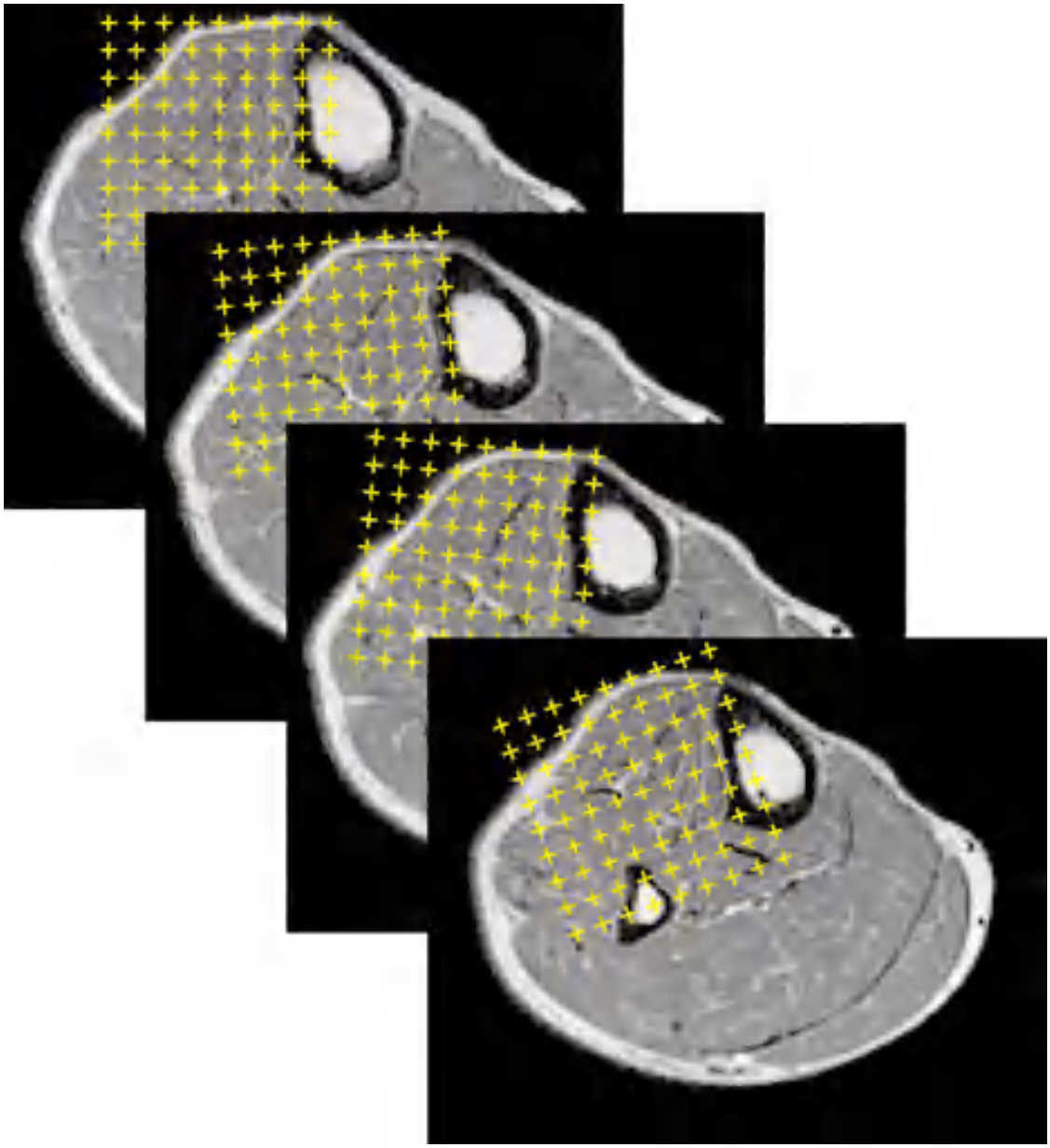

Figure 1 Selected axial slices of the lower leg with an illustration of morphometry based on the point counting method. A grid is placed arbitrarily over the anatomical structure to be measured—here the tibialis anterior muscle—and points lying within the structure of interest are counted. The number of counted points is proportional to the volume of the structure when a series of slices is evaluated. The error introduced by the placement of the grid and the counting becomes negligible if more than 100 points are counted overall

anisotropic diffusion[1,14,16] within heart or skeletal muscle tissue to visualize fiber orientation in MR images.[13,15]

So far, fiber composition has mainly been assessed by ^{31}P MRS using differences in PCr content and pH (see ***Peripheral Muscle Metabolism Studied by MRS***). The method requires relatively large sensitive volumes and, therefore, it is inherently susceptible to partial volume effects: a mixture of signals from different muscles that are partially activated and resting. Activity-dependent MR images and gradient-based volume selection may improve these observations in future.

The determination of fiber composition by MRI is based on differences in relaxation times of water.[3] Using the effect of gadolinium diethylenetriamine pentaacetic acid (DTPA) on MR images of rabbit muscle, larger extracellular space has been observed in slow-twitch (red) muscle (see ***Skeletal Muscle Evaluated by MRI***).[7]

4 USE OF MRS FOR HUMAN MUSCLE PHYSIOLOGY

4.1 The Use of Different Nuclei to Observe Muscular Metabolism

The high-energy phosphates visible in the ^{31}P MR spectrum and the pH titration of the inorganic phosphate (Pi) relative to

PCr made ^{31}P MRS the favorite tool for biochemists and physiologists interested in muscular metabolism (see ***Peripheral Muscle Metabolism Studied by MRS***).

The application of ^{13}C MRS for examinations of muscular metabolism attracted the attention of physiologists because glycogen is 100% visible in the ^{13}C MR spectrum despite the very large molecular weight of this molecule. However, the technical requirements for ^{1}H-decoupled ^{13}C MRS are considerably higher than those usually provided in a standard clinical scanner.

Until recently, there had only been some exploratory studies using ^{1}H MRS. This is particularly remarkable since ^{1}H is the most frequently used nucleus in brain examinations. Originally, the reasons for this obvious disinterest were of a technical nature (water suppression, eddy currents for short echo times), but later the sparse attention to ^{1}H MRS of muscle may have resulted from a general feeling that its information content would be rather low. It will be shown below that this impression was wrong.

Other nuclei such as ^{23}Na have only rarely been used to study muscle metabolism.[8,9] However, we expect that studies of order on the molecular level will benefit from the potential of less popular nuclei in the future.

Some very elegant examinations of muscular metabolism use combinations of different nuclei, for example ^{13}C with ^{31}P MRS:[34–37] the ^{13}C studies follow the depletion and recovery of glycogen while ^{31}P is used to monitor phosphorylation. Combinations of different nuclei and the fusion of MRS and MRI in the same session will be vital approaches in the future development of MR of human muscle metabolism and will prove the enormous versatility of MR.

4.2 Classical ^{31}P MRS of Human Muscle

Many of the classical studies of human muscle using ^{31}P MRS are covered in other monographs in these volumes and these provide a wide range of references to work in this area (see ***Peripheral Muscle Metabolism Studied by MRS***, ***Phosphorus-31 Magnetization Transfer Studies In Vivo***, ***Proton Decoupling During In Vivo Whole Body Phosphorus MRS***, ***Single Voxel Whole Body Phosphorus MRS***, ***Tissue Behavior Measurements Using Phosphorus-31 NMR***, ***Whole Body Studies: Impact of MRS***, ***pH Measurement In Vivo in Whole Body Systems***). The first report on a muscular disease documented by ^{31}P MRS—McArdle disease—promoted the application of MRS in vivo. However, widespread distribution of ^{31}P MRS in clinical routine and the use of this modality in all-day diagnostics did not occur as expected and it remained an excellent, but somewhat specialized, tool for research in physiology and pathology.

Beside the well-known observation of high-energy phosphates by ^{31}P MRS and the determination of intracellular pH, MT experiments have also examined the creatine kinase reaction (see also ***Phosphorus-31 Magnetization Transfer Studies In Vivo***). The very recent development of genetically manipulated mice (e.g. creatine kinase knock-out mice) may help in the understanding of many aspects of ^{31}P MRS.

Proton decoupling during acquisition of phosphorus spectra (see ***Proton Decoupling During In Vivo Whole Body Phosphorus MRS***) allows signals such as those from glycerophosphorylcholine and glycerophosphorylethanolamine to be distinguished, which may help to improve understanding of membrane metabolism.

Diffusion-weighted ^{31}P MRS of PCr and Pi—together with MT techniques—may provide more information on the creatine kinase reaction and the role and nature of Cr/PCr as energy shuttle, reservoir, or buffer in the myocyte.

4.3 Application of ^{13}C MRS in Human Muscle

The main application of ^{13}C MRS in human muscle has been the observation of glycogen depletion and repletion, with and without labeling of blood glucose at the C1 position by ^{13}C, and in some experiments controlled by clamp techniques.[38–40] Specific labeling of other compounds and subsequent isotopomer analysis has been very successful in whole animals and isolated organs but has hardly been used in humans. Despite the fact that ^{13}C MRS is extremely useful and elegant, only a few groups worldwide are using this method in studies of human metabolism. This can be explained by the technical requirements (broadband acquisition, ^{1}H decoupling) and by the low signal-to-noise ratio (SNR), which would benefit from field strengths higher than those available in routine scanners. Studies with substrates labeled with ^{13}C are expensive and clamp studies require additional experience. The increasing number of MR systems at field strengths of 3–4.7 T will hopefully overcome the technical limitations and prove the value of ^{13}C MRS studies.

Four main factors characterize ^{13}C MRS: (a) the low gyromagnetic ratio, which is about 25% of that of ^{1}H; (b) the low natural abundance of ^{13}C (most carbons are NMR invisible in the form of ^{12}C); (c) the large chemical shift dispersion of about 250 ppm compared with about 10 ppm for ^{1}H; and (d) the direct chemical bonds to ^{1}H of most ^{13}C atoms. All these factors have methodological consequences. The low gyromagnetic ratio leads not only to a lower resonance frequency but also to an inherently low sensitivity of ^{13}C, which is about 0.016 compared with ^{1}H. The natural abundance of 1.1% for ^{13}C further reduces signal intensity. However, the low natural abundance does not only have negative consequences; it also allows for the use of ^{13}C-labeled substrates as tracers, which is obviously not feasible for ^{1}H or ^{31}P. The large chemical shift dispersion per se is advantageous since the separation of different resonances increases. This makes an unspoiled observation of a specific metabolite much easier than in the much more crowded ^{1}H MR spectrum. However, the large chemical shift dispersion leads to a spatial misregistration that may be intolerable when popular gradient-based volume localization methods are used directly. The fact that gradients have not been widely used for localization of ^{13}C MR spectra is also a consequence of the very short T_2 of glycogen; the signals would have decayed at echo times that are typically used in point-resolved spectroscopy (PRESS) or stimulated echo acquisition (STEAM) sequences. (For additional information on localization sequences see ***Spatial Localization Techniques for Human MRS***). The use of image-selected in vivo spectroscopy (ISIS) overcame the problem of fast transverse relaxation since the magnetization is kept in the longitudinal direction during the localization procedure.[41] Localization of ^{13}C nuclei can also be accomplished indirectly via the coupled ^{1}H nuclei and subsequent polarization transfer.[42–46] Because of very short ^{1}H T_2, these methods are not useful for localization of glycogen. Most

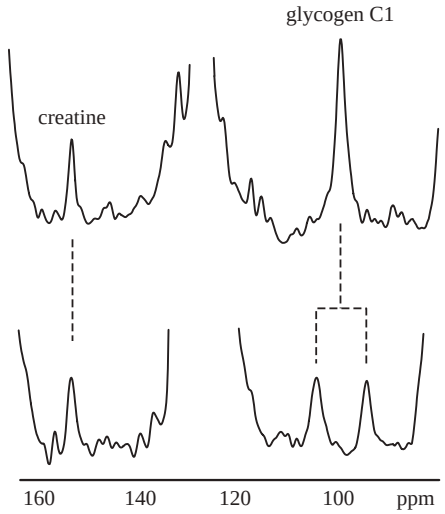

Figure 2 Carbon-13 MR spectrum of the thigh at 1.5 T (GE SIGNA, Milwaukee, WI), without (lower trace) and with (upper trace) continuous wave decoupling of the protons (decoupler S.M.I.S., UK). The decoupling and NOE build up of the doublet of glycogen C1 leads to an improved signal-to-noise ratio that allows a reduction of measurement time (lower trace 10 000 scans, upper trace 4000 scans)

applications, therefore, apply surface coils for localized transmission and reception of the signals, using pulse-and-acquire sequences. Nevertheless, volume localization of ^{13}C MR spectra is often a critical issue for several reasons: (a) adjacent muscle groups may have differences in metabolite levels but usually contribute to an overall signal; (b) huge signals from subcutaneous fat may mask the tiny resonances from metabolites (e.g., signal contributions from muscular glycogen in the abdominal wall may not be separable from liver glycogen); (c) sensitivity profiles of surface coils are complicated and make absolute quantification much more difficult than methods with a rectangular shape of the selected region. Some methods use bottles filled with known solutions that replace the human body to calibrate the metabolite levels;[47] others use Cr as an internal standard.[48] The chemical bonds between carbon atoms and adjacent ^{1}H lead to substantial heteronuclear spin–spin coupling and to splitting of the resonance lines, which further reduce the amplitudes. With ^{1}H decoupling by irradiation on a second rf channel, it is possible to cancel the coupling effect, restoring the full resonance amplitude (Figure 2). In addition, irradiation on the ^{1}H frequency prior to acquisition leads to the so-called nuclear Overhauser enhancement (NOE), which results in an additional 50–90% in signal intensity[49] under in vivo conditions (Figure 2).

Glycogen is a large molecule with a molecular weight of 10^7 to 10^9. Since macromolecules are usually not visible by MRS because of their very short T_2 relaxation, it was surprising that glycogen turned out to be 100% visible.[50,51] It seems that the internal molecular mobility leads to effective decoupling from fast relaxation processes. The observation of glycogen in human muscle (and liver) is meanwhile one of the 'workhorse' applications of in vivo MRS. NOE effect and short repetition times guarantee a reasonable SNR within approximately 10 min even at 1.5 T. Higher field strengths, however, are desirable to increase SNR and/or temporal resolution.

Studies of noninsulin-dependent diabetes mellitus (NIDDM) patients[36] showed a slower glycogen repletion compared with healthy volunteers. Combination with ^{31}P MRS was then used to identify the limiting step in glycogen synthesis more closely (see below). Patients suffering from glycogen storage diseases[48,52] were found to have higher levels of glycogen in muscle and liver. Studies on normal subjects[37,43,47,53,54] revealed important physiological information on glycogen as an energy reserve for the human muscle, for example changing with different diets, with different exercise intensity, and as a function of the insulin-dependent and independent control mechanisms.

Studies of lipid metabolism using ^{13}C MRS would be very attractive since the degree of saturation and chain length could be evaluated.[55–57] However, the difficulties in separating signals from subcutaneous adipose tissue and muscular lipids (IMCL, see below) restrict this method to studies of bulk fat so far.

Since ^{13}C has a very low natural abundance, substrates can be enriched at specific positions in the molecule. This can either be used to distinguish between 'old' and 'new' fractions of a metabolite pool, e.g., to identify glycogen that is newly built in the muscle, or it can be used to distinguish between several potential biochemical pathways. One of the most popular applications is labeling of glucose at the C1 position and the follow-up by ^{13}C MRS during its incorporation into muscular glycogen in clamp studies.[36,50]

Most ^{13}C labeling experiments with subsequent isotopomer analysis (i.e., analysis of the coupling patterns of mixtures of the same compound with different degrees of labeling), have been done in animals, perfused organs, or plasma samples.[58–63] An example in skeletal muscle is the observation of [1-^{13}C]-glucose incorporation into intramuscular [1-^{13}C]-glycogen, [3-^{13}C]-lactate, and [3-^{13}C]-alanine.[59] Carbon-13 MRS requires much higher enrichment of the ^{13}C isotope than does mass spectrometry; it does, however, have the advantage of organ selectivity (e.g., compared with analysis of breathing air) and chemical specificity.

4.4 Application of ^{1}H MRS in Human Muscle

4.4.1 General Features

Proton MR spectra of skeletal muscle were believed to be swamped by the large signal from fat, which would render all other metabolites invisible. Recent work has shown that the spectrum is indeed very complex, but it is rich in information and reflects several aspects of the physiology of exercise.

A typical ^{1}H MR spectrum of human muscle tissue acquired by a PRESS sequence (see ***Spatial Localization Techniques for Human MRS***) is shown in Figure 3. Based on high-resolution spectra of muscle extracts and in vivo rat and frog muscle, the peaks visible in spectra of human muscle in vivo have been assigned early on[5,64–68] to the following compounds: lipids (methyl protons 0.9 ppm, aliphatic chain methylene protons 1.3 ppm, aliphatic protons near double bonds and carboxyl group at 1.7–2.5 ppm and protons of unsaturated carbons at 5.4 ppm); Cr/PCr (methyl at 3.03 ppm (Cr3), methylene at 3.93 ppm (Cr2)); trimethylammonium group-containing metabolites (TMA), such as choline, phosphocholine, glycerophosphocholine, and carnitine at 3.2 ppm; a line that has been tentatively assigned to taurine at approximately 3.4 ppm, depending on the orientation of the muscle; and two his-

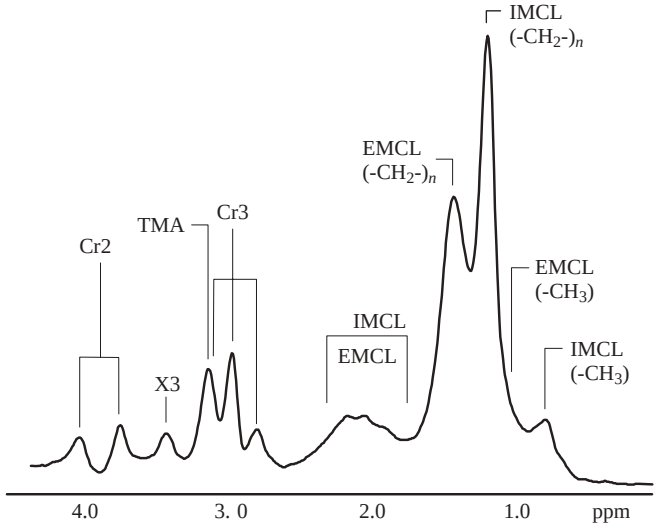

Figure 3 PRESS-localized ^{1}H MR spectrum of the human tibialis anterior muscle. The orientation of the fibers in this muscle parallel to the magnetic field leads to the separation of the signals from intra- (IMCL) and extramyocellular lipids (EMCL), and the splitting of the creatine (methylene Cr2, methyl Cr3) resonances. Trimethylammonium (TMA) covers one part of the Cr3 triplet and the coupling partner of resonance X3, which can be tentatively assigned to taurine. Acetylcarnitine at 2.13 ppm is not visible at rest; while lactate at 1.3 ppm is only visible with editing techniques and during workload/ischemia

tidine protons of the dipeptide carnosine at 7.0 and 8.0 ppm (anserine in some species). A peak at the unusual position of 78 ppm (Figure 4), which is invisible under the experimental conditions used for Figure 3, could be detected and assigned to deoxymyoglobin.[69,70] Lactate at 1.3 ppm can also be observed only under specific experimental conditions.[6,21,68,71–73]

As seen above, skeletal muscle is highly organized at different spatial levels and many aspects of order influence ^{1}H MR spectra. These aspects are summarized in a previous paragraph and for the different metabolites separately below.

4.4.2 Lactate

The signal of the methyl group of lactate is overlaid by the much larger signals from lipids in human muscle. However, using the hetero- or homonuclear spin–spin interaction and editing techniques by inversion and decoupling,[68] zero- or double-quantum filters[6,21,71–73] are able to observe the lactate signal without the huge overlapping resonances. Promoted by the physiological importance of this metabolite, observations of lactate have been among the first applications of ^{1}H MRS in human muscle.

4.4.3 pH

A second important parameter for the description of muscular metabolism is the intracellular pH, usually determined by

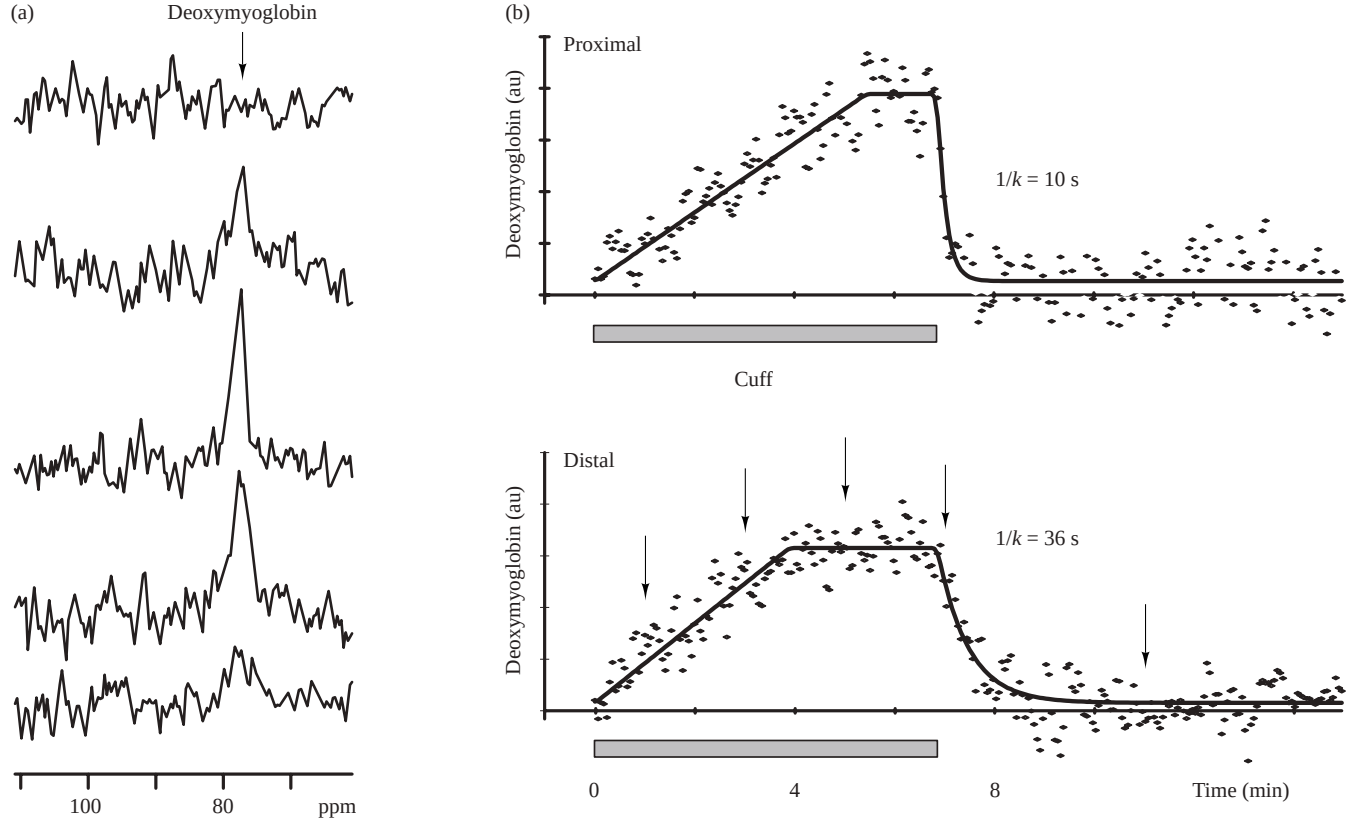

Figure 4 (a) Spectra showing the resonance of deoxymyoglobin from the lower leg in a patient with peripheral arterial disease. (b) Signal development during ischemia and recovery proximal and distal to the lesion (au, arbitary units). Arrows indicate time points when the spectra shown on the left were acquired. The time resolution in the graphs is 3.5 s, one spectrum represents a 16 s acquisition (30 Hz apodization). The time constant for recovery is 10 s proximal and 36 s distal from the lesion (unpublished data; clinical support by Dr I. Baumgartner is greatly appreciated)

the frequency difference between Pi and PCr in the ^{31}P MR spectrum. Proton MRS provides the same information, since the aromatic signals of histidine in the carnosine molecule are titrating and can, therefore, be used to determine intracellular pH. A comparison between titration observed in ^{31}P and ^{1}H MR spectra[68] showed the accuracy of ^{1}H MRS. Because of the fairly low concentrations of carnosine, the ^{1}H MRS measurement may be less sensitive than ^{31}P MRS during exercise. However, ^{1}H MRS has the advantage of identical sensitivity independent of exercise scheme, while the undershoot of Pi after exercise and the low Pi content in resting muscle can make pH measurements with ^{31}P MRS impossible in some instances.

4.4.4 *Myoglobin*

Proton ^{1}H MRS can also be used during exercise or ischemia to estimate the degree of intracellular oxygenation by measuring deoxymyoglobin resonances. The signals from oxymyoglobin are in the normal frequency range of an ^{1}H MR spectrum and, therefore, are overlapped by many other resonances at 1.5 T. Only at 7 T, the resonance of the γ-methyl group of Val-E11 at -2.8 ppm can be observed separately under oxygenated conditions.[74] However, while this resonance disappears with deoxygenation, the F8 proximal histidyl N-δ proton shifts to 78 ppm,[69,70,75] and becomes visible also at moderate field strength. This histidine resonance has dramatically shortened T_2 relaxation times and is, therefore, very broad, but the chemical shift separation from the large resonances between 0 and 10 ppm is sufficient to detect it reliably. Figure 4 shows the increase of deoxymyoglobin during ischemia in human skeletal muscle, observed at 1.5 T.

4.4.5 *Acetylcarnitine*

After heavy workload, a peak at 2.13 ppm can be detected in localized spectra of human muscle,[76] while spectra from resting muscle do not feature a sharp singlet at this position in general. Based on its chemical shift, its singlet nature, its approximate concentration, and physiological behavior, the peak was tentatively assigned to the acetyl group of acetylcarnitine.[76] Carnitine has long been known for its vital role in the transportation of fatty acids into mitochondria for β-oxidation. More recently, it was recognized that carnitine is equally important as a buffering system for a potential surplus of acetyl groups.[77] The export of acetyl groups in the form of acetylcarnitine out of the mitochondria helps to keep the acetyl CoA/coenzyme A ratio balanced such that the nonacetylated form of the co-factor can play its roles in the TCA cycle and in pyruvate dehydrogenation.

4.4.6 *Creatine*

Considering the concentration and chemical shift differences of Cr and PCr in muscle tissue, one could expect that the resulting signals would be well above the noise level and would represent the sum of both, i.e., total Cr, since these species would not be separable at 1.5 T. A detailed analysis of Cr in ^{1}H MR spectra, however, showed several unexpected features[17–20,78] such as an orientation-dependent dipolar splitting for several compounds that were not assigned at the very beginning.[17] In a subsequent Cr-loading study,[78] one of these metabolites has been identified as Cr and/or PCr. The methylene group of Cr/PCr appears as a prominent dipolar doublet and the methyl group as a less well-defined triplet (see Figure 5). This finding was unexpected since in vivo MRS had been seen as spectroscopy of metabolite solutions where dipolar coupling is averaged out and dipolar effects are restricted to relaxation processes. Using more elaborate methods such as one-dimensional zero- and double-quantum filtering, two-dimensional *J*-resolved spectroscopy, two-dimensional constant time COSY, and longitudinal order separation spectroscopy,[18] it was possible to prove unequivocally that peaks of Cr methylene result from a pair of dipolar coupled protons.[78] Most other resonance peaks, including the methyl group of Cr, were also found to be—at least partially—dependent on the angle between muscle fibers and magnetic field. The form of the orientation dependence and the approximate size of the coupling have been confirmed at a higher field in rat muscle.[19] One can now speculate about the mechanisms behind the observed effects. Irrespective of the chemical nature of the metabolites involved, there are three main explanations to account for incomplete temporal averaging of dipolar couplings. First of all, the observed molecules may be hindered from isotropic tumbling by being constrained into small elongated spaces between the actin/myosin chains. Second, they might be temporarily bound to macromolecules that themselves are strictly ordered within the muscle cells. Finally, dipolar-coupled peaks might originate from large molecules that are permanently bound to ordered structures in muscle but have enough side-chain mobility to be observable and partially average dipolar couplings. The most likely explanation of the three is that PCr and/or free Cr together with their hydration spheres are large enough to be hindered from isotropic tumbling in the elongated

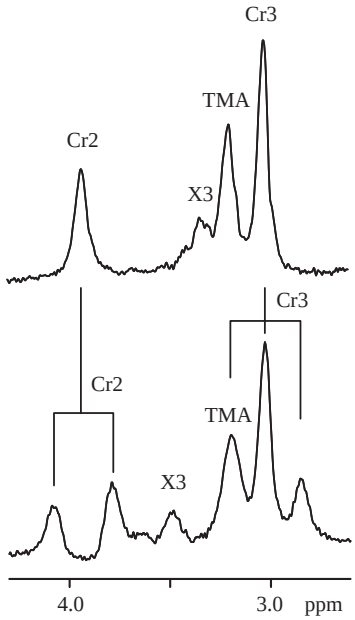

Figure 5 Spectra from the same voxel in the tibialis anterior muscle show the effect of orientation upon creatine Cr2 (methylene) and Cr3 (methyl). The lower spectrum has been acquired with the leg parallel to the magnetic field, the upper spectrum at the magic angle (54° between muscle and field). At the magic angle, splitting owing to dipolar coupling vanishes. TMA, trimethylammonium; X3 tentatively assigned to taurine

spaces between actin/myosin chains. Because of charge distributions on these molecules, specific or unspecific coupling to the actin/myosin complexes may exacerbate the ordering. It has been postulated previously that some of this space is inaccessible to PCr. Since Cr and PCr are involved in the creatine kinase equilibrium and may serve not only as a short-term energy storage but also for some forms of energy transportation, a motional restriction as observed in these experiments would be of crucial importance since the overall reaction could be limited in vivo by transport processes.

Additional experiments lead to further questions about the exact nature of the Cr resonances: (a) in a postmortem study of rat muscle, the doublet of Cr methylene was shown to disappear from the MR spectrum on a time scale similar to the disappearance of PCr;[19] and (b) in human skeletal muscle, Cr/PCr during and after heavy exercise showed decrease and recovery similar to PCr in the ^{31}P MR spectrum.[20] It is surprising that depletion and recovery appear to be related to the PCr content of human muscle, since the Cr signals in ^{1}H MRS have hitherto always been associated with total Cr, not PCr. This finding is, however, in agreement with the signal behavior observed in rat muscle postmortem.[19] A straightforward but still questionable explanation for that observation would be that only the protons from PCr are detected by ^{1}H MRS while free Cr is invisible. The reduced visibility of Cr may or may not have similar roots to the incomplete dipolar averaging, MT effects, restricted diffusion, anisotropy of relaxation times, and the questioned visibility of lactate. The calculation of ADP concentrations based on ATP, free Cr, pH, and the creatine kinase reaction constant would be questionable if reduced visibility of Cr was an indication for reduced availability of this substrate. Therefore, findings on reduced visibility of creatine would have a serious effect on the modeled phosphorylation kinetics derived from ^{31}P MRS.

Diffusion-weighted spectroscopy may be another tool to identify restricted motion of specific metabolites. An excellent overview of diffusion effects in human muscle can be found in Nicolay et al.[12] This study shows restricted motion of PCr compared with water in rat hindleg muscle.

4.4.7 Intramyocellular Lipids

IMCL are stored in droplets in the cytoplasm of muscle cells and are a form of stored energy readily accessed during long-term exercise. When Schick et al.[11] compared the lipid resonances in calf muscle and fat tissue, they observed two compartments of triglycerides with a resonance frequency shift of 0.2 ppm. They assigned the resonance at 1.5 ppm to lipids in fat cells and hypothesized that the resonance at 1.3 ppm could be attributed to lipids located inside muscle cells (i.e., in their cytoplasm) experiencing different bulk susceptibility (see Figure 3). This assignment was verified by Boesch et al.[10] who demonstrated that IMCL signals scale linearly with voxel size, water and Cr signals, while EMCL signals do not. Furthermore the resonance frequency shift of EMCL and the orientation dependence of their spectral pattern could be attributed to the spatial arrangement of these lipids (plate-like structures for EMCL versus spheroid droplets for IMCL). Experimental data agree very well with theoretical estimations of susceptibility effects. Inter- and intraindividual reproducibility studies indicate that the error of the method is about 6% and that IMCL levels differ significantly between identical muscles in different subjects, different muscles in the same subject, as well as intraindividually in the same muscle when measured at 1 week intervals. The accuracy of IMCL determination by ^{1}H MRS is sufficient to follow IMCL depletion and recovery after exercise in single individuals (Figure 6). Dietary modulation of IMCL levels has been investigated by biopsy studies, with the well-known advantages and disadvantages of this invasive method. A consequence of the invasiveness is the scarcity of results and follow-up measurements. With ^{1}H MRS it is now feasible to follow IMCL depletion and repletion more or less continuously and in different muscle groups.

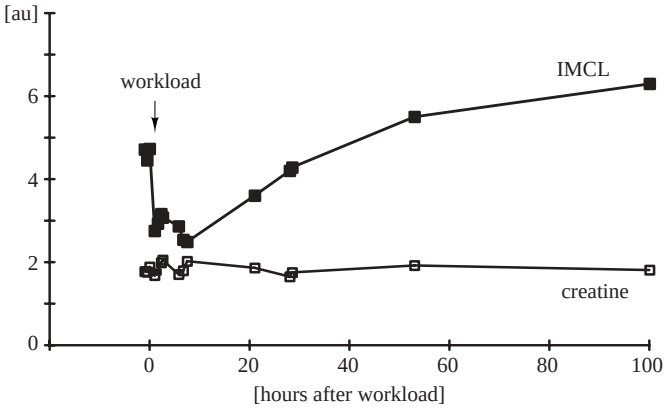

Figure 6 Depletion and repletion of intramyocellular lipids (IMCL) in tibialis anterior muscle after strenuous exercise (3 h bicycle training). In this example, the recovery phase of IMCL can be characterized by an exponential fit with a time constant of about 40 h. Further experiments have shown that recovery is strongly dependent on the diet. Creatine levels stay constant within the experimental accuracy (au, arbitary units; graph adapted from Boesch et al.[10])

A correlation of increased IMCL levels and insulin sensitivity has been shown by ^{1}H MRS in diabetic patients.[79,80] Since it is not trivial to separate EMCL and IMCL, the comparison of measurements in obese patients with normal weight volunteers could be prone to systematic errors. Comparing cohorts of patients with volunteers, weight and muscular fat infiltration should be matched between the groups to avoid systematic differences between the resulting EMCL contaminations of the spectra.

5 CONCLUSIONS

MRI and MRS of muscular physiology has occurred in distinct separate centers with different equipment for a considerable time. A combination of the two complementary modalities is now developing while classical pulse and acquire ^{31}P MRS has become less prominent. Multinuclear MRS in whole-body systems using combinations of MRI and MRS with elaborate MR techniques such as diffusion weighting, editing, and MT seem to lead the way to future MR studies of muscle physiology. Less popular nuclei such as ^{23}Na have the potential to elucidate order in biological tissues further. Decoupling of ^{31}P and ^{13}C spectra, and the use of whole-body magnets at higher field, have already promoted the application

of MRS in humans. This use will increase as soon as a larger number of versatile, high-field MR systems is installed.

Recent results obtained with localized ^{1}H MRS in skeletal muscle have shown that it is a very attractive tool to study muscle physiology both at rest and during exercise. It now appears that with ^{1}H MRS alone one can, in principle, determine pH, oxygenation, lactate levels, substrate use (IMCL, potentially also glycogen in addition to ^{13}C MRS), acetyl group buffering, and possibly PCr levels. It has also become thoroughly evident that the molecular basics of muscle tissue leads to most interesting NMR findings that can by no means be modeled by a single isotropic compartment consisting of an aqueous solution. Incompletely averaged dipolar couplings, reduced visibility of Cr, MT effects on Cr, the postulated compartmentation of lactate, and the susceptibility induced separation between IMCL and EMCL are all reflections of the complex and partly oriented architecture of muscle tissues, where (partial) compartmentation, chemical exchange, varying susceptibility, structural anisotropy, and protein interactions are essential ingredients.

6 RELATED ARTICLES

ESR Probes as Field Detectors in MRI; MRI of Musculoskeletal Neoplasms; Peripheral Muscle Metabolism Studied by MRS; pH Measurement In Vivo in Whole Body Systems; Phosphorus-31 Magnetization Transfer Studies In Vivo; Proton Decoupling During In Vivo Whole Body Phosphorus MRS; Proton Decoupling in Whole Body Carbon-13 MRS; Quantitation in In Vivo MRS; Single Voxel Localized Proton NMR Spectroscopy of Human Brain In Vivo; Single Voxel Whole Body Phosphorus MRS; Skeletal Muscle Evaluated by MRI; Spatial Localization Techniques for Human MRS; Tissue Behavior Measurements Using Phosphorus-31 NMR; Whole Body Studies: Impact of MRS.

7 REFERENCES

1. R. M. Henkelman, G. J. Stanisz, J. K. Kim, and M. J. Bronskill, *Magn. Reson. Med.*, 1994, **32**, 592.
2. W. C. Cole, A. D. LeBlanc, and S. G. Jhingran, *Magn. Reson. Med.*, 1993, **29**, 19.
3. J. M. Bonny, M. Zanca, O. Boespflug-Tanguy, V. Dedieu, S. Joandel, and J. P. Renou, *Magn. Reson. Imag.*, 1998, **16**, 167.
4. S. H. Scott, C. M. Engstrom, and G. E. Loeb, *J. Anat.*, 1993, **182**, 249.
5. J. Hu, M. R. Willcott, and G. J. Moore, *J. Magn. Reson.*, 1997, **126**, 187.
6. J. A. Kmiecik, C. D. Gregory, Z. P. Liang, D. E. Hrad, P. C. Lauterbur, and M. J. Dawson, *Magn. Reson. Med.*, 1997, **37**, 840.
7. I. K. Adzamli, F. A. Jolesz, A. R. Bleiler, R. V. Mulkern, and T. Sandor, *Magn. Reson. Med.*, 1989, **11**, 172.
8. R. Reddy, L. Bolinger, M. Shinnar, E. Noyszewski, and J. S. Leigh, *Magn. Reson. Med.*, 1995, **33**, 134.
9. T. Kushnir, T. Knubovets, Y. Itzchak, U. Eliav, M. Sadeh, L. Rapoport, E. Kott, and G. Navon, *Magn. Reson. Med.*, 1997, **37**, 192.
10. C. Boesch, H. Slotboom, H. Hoppeler, and R. Kreis, *Magn. Reson. Med.*, 1997, **37**, 484.
11. F. Schick, B. Eismann, W. I. Jung, H. Bongers, M. Bunse, and O. Lutz, *Magn. Reson. Med.*, 1993, **29**, 158.
12. K. Nicolay, A van der Toorn, and R. M. Dijkhuizen, *NMR Biomed.*, 1995, **8**, 365.
13. A. van Doorn, P. H. Bovendeerd, K. Nicolay, M. R. Drost, and J. D. Janssen, *Eur. J. Morphol.*, 1996, **34**, 5.
14. P. J. Basser, *NMR Biomed.*, 1995, **8**, 333.
15. T. G. Reese, R. M. Weisskoff, R. N. Smith, B. R. Rosen, R. E. Dinsmore, and V. J. Wedeen, *Magn. Reson. Med.*, 1995, **34**, 786.
16. E. W. Hsu and S. Mori, *Magn. Reson. Med.*, 1995, **34**, 194.
17. R. Kreis and C. Boesch, *J. Magn. Reson. Series B*, 1994, **104**, 189.
18. R. Kreis and C. Boesch, *J. Magn. Reson. Series B*, 1996, **113**, 103.
19. V. Ntziachristos, R. Kreis, C. Boesch, and B. Quistorff, *Magn. Reson. Med.*, 1997, **38**, 33.
20. R. Kreis, B. Jung, J. Slotboom, J. Felblinger, and C. Boesch, *J. Magn. Reson.*, 1999, **137**, 350.
21. L. Jouvensal, P. G. Carlier, and G. Bloch, *Magn. Reson. Med.*, 1997, **38**, 706.
22. J. L. Fleckenstein, L. A. Bertocci, R. L. Nunnally, R. W. Parkey, and R. M. Peshock, *Am. J. Roentgenol.*, 1989, **153**, 693.
23. E. R. Weidman, H. C. Charles, R. Negro-Vilar, M. J. Sullivan, and J. R. MacFall, *Invest. Radiol.*, 1991, **26**, 309.
24. T. Ogino, H. Ikehira, N. Arimizu, H. Moriya, K. Wakimoto, S. Nishikawa, H. Shiratsuchi, H. Kato, F. Shishido, and Y. Tateno, *Ann. Nucl. Med.*, 1994, **8**, 219.
25. L. L. Ploutz-Snyder, S. Nyren, T. G. Cooper, E. J. Potchen, and R. A. Meyer, *Magn. Reson. Med.*, 1997, **37**, 676.
26. G. Yue, A. L. Alexander, D. H. Laidlaw, A. F. Gmitro, E. C. Unger, and R. M. Enoka, *J. Appl. Physiol.*, 1994, **77**, 84.
27. H. A. Cheng, R. A. Robergs, J. P. Letellier, A. Caprihan, M. Icenogle, and L. J. Haseler, *J. Appl. Physiol.*, 1995, **79**, 1370.
28. J. L. Fleckenstein, R. C. Canby, R. W. Parkey, and R. M. Peshock, *Am. J. Roentgenol.*, 1988, **151**, 231.
29. M. A. Elliott, G. A. Walter, H. Gulish, A. S. Sadi, D. D. Lawson, W. Jaffe, E. K. Insko, J. S. Leigh, and K. Vandenborne, *MAGMA*, 1997, **5**, 93.
30. N. Mitsiopoulos, R. N. Baumgartner, S. B. Heymsfield, W. Lyons, D. Gallagher, and R. Ross, *J. Appl. Physiol.*, 1998, **85**, 115.
31. N. Roberts, L. M. Cruz-Orive, N. M. K. Reid, D. A. Brodie, M. Bourne, and R. H. T. Edwards, *J. Microsc.*, 1993, **171**, 239.
32. T. Fukunaga, R. R. Roy, F. G. Shellock, J. A. Hodgson, M. K. Day, P. L. Lee, H. Kwong-Fu, and V. R. Edgerton, *J. Orthop. Res.*, 1992, **10**, 926.
33. M. V. Narici, L. Landoni, and A. E. Minetti, *Eur. J. Appl. Physiol.*, 1992, **65**, 438.
34. K. F. Petersen, R. Hendler, T. Price, G. Perseghin, D. L. Rothman, N. Held, J. M. Amatruda, and G. I. Shulman, *Diabetes*, 1998, **47**, 381.
35. D. L. Rothman, R. G. Shulman, and G. I. Shulman, *J. Clin. Invest.*, 1992, **89**, 1069.
36. G. I. Shulman, D. L. Rothman, T. Jue, P. Stein, R. A. DeFronzo, and R. G. Shulman, *N. Engl. J. Med.*, 1990, **332**, 223.
37. R. Roussel, P. G. Carlier, J. J. Robert, G. Velho, and G. Bloch, *Proc. Natl. Acad. Sci. USA*, 1998, **95**, 1313.
38. N. Beckman, in 'Carbon-13 NMR spectroscopy of biological systems', ed. N. Beckmann, Academic Press, New York, 1995, p. 269.
39. J. Seelig and A. P. Burlina, *Clin. Chim. Acta*, 1992, **206**, 125.
40. R. Badar-Goffer and H. Bachelard, *Essays Biochem.*, 1991, **26**, 105.
41. R. Gruetter, E. J. Novotny, S. D. Boulware, D. L. Rothman, G. F. Mason, G. I. Shulman, R. G. Shulman, and W. V. Tamborlane, *Proc. Natl. Acad. Sci. USA*, 1992, **89**, 1109.
42. R. Gruetter, G. Adriany, H. Merkle, and P. M. Andersen, *Magn. Reson. Med.*, 1996, **36**, 659.
43. M. Saner, G. McKinnon, and P. Boesiger, *Magn. Reson. Med.*, 1992, **28**, 65.

44. R. Kreis, J. Slotboom, J. Felblinger, and C. Boesch, *Proc. Vth Ann Mtg. (Int.) Soc. Magn. Reson. Med.*, Vancouver, 1997, p. 1438.
45. H. Watanabe, Y. Ishihara, K. Okamoto, K. Oshio, T. Kanamatsu, and Y. Tsukada, *J. Magn. Reson.*, 1998, **134**, 214.
46. A. J. van den Bergh, H. J. van den Boogert, and A. Heerschap, *J. Magn. Reson.*, 1998, **135**, 93.
47. R. Taylor, T. B. Price, L. D. Katz, R. G. Shulman, and G. I. Shulman, *Am. J. Physiol.*, 1993, **265**, E224.
48. P. Jehenson, D. Duboc, G. Bloch, M. Fardeau, and A. Syrota, *Neuromuscul. Disord.*, 1991, **1**, 99.
49. G. Ende and P. Bachert, *Magn. Reson. Med.*, 1993, **30**, 415.
50. R. Roussel, P. G. Carlier, C. Wary, G. Velho, and G. Bloch, *Magn. Reson. Med.*, 1997, **37**, 821.
51. R. Taylor, T. B. Price, D. L. Rothman, R. G. Shulman, and G. I. Shulman, *Magn. Reson. Med.*, 1992, **27**, 13.
52. N. Beckman, J. Seelig, and H. Wick, *Magn. Reson. Med.*, 1990, **16**, 150.
53. A. van den Bergh, S. Houtman, A. Heerschap, N. J. Rehrer, H. J. van den Boogert, B. Oeseburg, and M. T. E. Hopman, *J. Appl. Physiol.*, 1996, **81**, 1495.
54. T. B. Price D. L. Rothman, R. Taylor M. J. Avison, G. I. Shulman, and R. G. Shulman, *J. Appl. Physiol.*, 1994, **76**, 104.
55. C. Wary, G. Bloch, P. Jehenson, and P. G. Carlier, *Anticancer Res.*, 1996, **16**, 1479.
56. C. T. Moonen, R. J. Dimand, and K. L. Cox, *Magn. Reson. Med.*, 1988, **6**, 140.
57. E. L. Thomas, S. C. Cunnane, and J. D. Bell, *NMR Biomed.*, 1998, **11**, 290.
58. J. G. Jones, M. A Solomon, A. D. Sherry, F. M. H. Jeffrey, and C. R. Malloy, *Am. J. Physiol.*, 1998, **275**, E843.
59. B. M. Jucker, A. J. Rennings, G. W. Cline, K. F. Petersen, and G. I. Shulman, *Am. J. Physiol.*, 1997, **273**, E139.
60. E. D. Lewandowski, C. Doumen, L. T. White, K. F. LaNoue, L. A. Damico, and X. Yu, *Magn. Reson. Med.*, 1996, **35**, 149.
61. A. D. Sherry, P. Zhao, A. Wiethoff, and C. R. Malloy, *Magn. Reson. Med.*, 1994, **31**, 374.
62. L. A. Bertocci, J. G. Jones, C. R. Malloy, R. G. Victor, and G. D. Thomas, *J. Appl. Physiol.*, 1997, **83**, 32.
63. H. Bachelard, *Dev. Neurosci.*, 1998, **20**, 277.
64. S. R. Williams, D. G. Gadian, E. Proctor, D. B. Sprague, D. F. Talbot, I. R. Young, and F. F. Brown, *J. Magn. Reson.*, 1985, **63**, 406.
65. P. A. Narayana, J. D. Hazle, E. F. Jackson, L. K. Fotedar, and M. V. Kulkarni, *Magn. Reson. Imag*, 1988, **6**, 481.
66. M. Barany and P. N. Venkatasubramanian, *NMR Biomed.*, 1989, **2**, 7.
67. H. Bruhn, J. Frahm, M. L. Gyngell, K. D. Merboldt, W. Haenicke, and R. Sauter, *Magn. Reson. Med.*, 1991, **17**, 82.
68. J. W. Pan, J. R. Hamm, H. P. Hetherington, D. L. Rothman, and R. G. Shulman, *Magn. Reson. Med.*, 1991, **20**, 57.
69. Z. Wang, E. A. Noyszewski, and J. S. Leigh, *Magn. Reson. Med.*, 1990, **14**, 562.
70. C. Brillault-Salvat, E. Giacomini, L. Jouvensal, C. Wary, G. Bloch, and P. G. Carlier, *NMR Biomed.*, 1997, **10**, 315.
71. J. E. van Dijk, D. K. Bosman, R. A. F. M. Chamuleau, and W. M. M. J. Bovee, *Magn. Reson. Med.*, 1991, **22**, 493.
72. R. E. Hurd and D. Freeman, *NMR Biomed.*, 1991, **4**, 73.
73. G. Bloch, L. Jouvensal, and P. G. Carlier, *Magn. Reson. Med.*, 1995, **34**, 353.
74. U. Kreutzer, D. S. Wang, and T. Jue, *Proc. Natl. Acad. Sci. USA*, 1992, **89**, 4731.
75. E. A. Noyszewski, E. L. Chen, R. Reddy, Z. Wang, and J. S. Leigh, *Magn. Reson. Med.*, 1997, **38**, 788.
76. R. Kreis, B. Jung, S. Rotman, J. Slotboom, J. Felblinger, and C. Boesch, *Proc. Vth Ann Mtg. (Int.) Soc. Magn. Reson. Med.*, Vancouver, 1997, p. 162.
77. E. P. Brass and W. R. Hiatt, *Life Sci.*, 1994, **54**, 1383.
78. R. Kreis, M. Koster, M. Kamber, H. Hoppeler, and C. Boesch, *Magn. Reson. Med.*, 1997, **37**, 159.
79. J. Machann, F. Schick, S. Jacob, O. Lutz, H. U. Häring, and C. D. Claussen, *MAGMA*, 1998, p. 220.
80. D. T. Stein, L. S. Szczepaniak, R. L. Dobbins, P. Snell, and J. D. McGarry, *Proc. VIth Ann Mtg. Soc. (Int.) Magn. Reson. Med.*, Sydney, 1998, p. 388.

Biographical Sketch

Chris Boesch. *b* 1951. M.S. (Physics diploma) ETH Zurich (Swiss Federal Institute of Technology) Switzerland, 1976; Ph.D. ETH Zurich, 1979 (High-resolution NMR studies of polypeptide conformation, supervisor K. Wüthrich); Studies in Medicine, 1977–86; M.D. University Zurich 1986. Research assistant at the University Children's Hospital in Zurich, Switzerland: Installation of a 2.35T/40 cm MR system in a clinical setting, patient-monitoring systems for pediatric and intensive care patients, MRI and MRS studies of brain development, 1985–90; Professor and Director of MR Spectroscopy and Methodology at the University of Bern, Switzerland, 1991–present. Current research specialties: in vivo spectroscopy (^{1}H, ^{31}P, and ^{13}C) of brain, muscle, and liver; methodology of in vivo NMR: patient monitoring.

Roland Kreis. *b* 1958. M.S. (diploma in chemistry) ETH (Federal Institute of Technology) Zurich, Switzerland, 1983; Ph.D. ETH Zurich, 1989 (Zero-field NMR, supervisor R. R. Ernst). Boswell Fellow at Caltech and Huntington Medical Research Institutes, Pasadena, CA, USA, 1989–91; Assistant Professor at Department for Clinical Research (MR Spectroscopy and Methodology) University of Bern, Switzerland, 1991–present. Research interests: quantitative clinical spectroscopy using methods for optimized data acquisition and pro-Breakcessing while studying cerebral, musculoskeletal and cardiac (patho) physiology.

Imaging of Trabecular Bone

Felix W. Wehrli

University of Pennsylvania Medical School, Philadelphia, PA, USA

1 INTRODUCTION

Bone is a composite material consisting of an inorganic phase—calcium apatite, $Ca_{10}(PO_4)_6(OH)_2$, corresponding to about 65% of total volume—and an organic phase—essentially collagen—accounting for most of the remaining 35%. From an architectural point of view, bone can be subdivided into cortical and trabecular, the latter providing most of the strength of the axial skeleton (e.g., the vertebral column) and the portions of the appendicular skeleton near the joints. Trabecular bone is made up of a three-dimensional network of struts and plates, the trabeculae, which are on the order of 100–150 μm in width and spaced 300–1000 μm apart.

Like engineering materials, trabecular bone derives its mechanical strength from its inherent elastic properties, its volume density, and its structural arrangement. Bone is constantly renewed through a process called 'bone remodeling', a term referring to a dynamic equilibrium between bone formation and bone resorption, controlled by two essential types of cells: the osteoblasts—bone-forming cells—and the osteoclasts—bone-resorbing cells. During bone formation, osteoblasts eventually become imbedded in bone, turning into osteocytes, which presumably act as piezoelectric sensors transmitting signals to the osteoblasts to induce bone formation. Since the seminal work of Wolff,[1] it has been known that bone grows in response to the forces to which it is subjected (see, for example, Roesler[2]). Therefore, weightlessness and physical inactivity are well-known factors inducing bone loss.

The most common pathologic process leading to bone loss is osteoporosis.[3] Among the various etiologies, postmenopausal osteoporosis, which results from increased osteoclast activity, is the most frequent form of the disease, afflicting a substantial fraction of the elderly female population and, increasingly, the male population. The most common clinical manifestations are fractures of the hip and vertebrae. If detected early, calcium supplements and estrogen replacement are effective forms of therapeutic intervention. Further, the development of drugs inhibiting osteoclastic activity is in progress.

Bone mineral density is the most widely invoked criterion for fracture risk assessment, typically measured by dual energy X-ray absorptiometry (DEXA), which is based on the measurement of the attenuation coefficient in a quantitative radiographic procedure, or by quantitative computed tomography (QCT). Whereas both methods measure bone mineral density with sufficient precision, neither provides information on the properties or structural arrangement of the bone. NMR, however, has the potential to probe structure as well as chemical composition of bone, both relevant to biomechanical competence.

2 DIRECT DETECTION OF BONE MINERAL BY ^{31}P NMR

The difficulties of detecting phosphorus in the solid state in vivo are considerable but do not seem insurmountable. The problems are symptomatic of high-resolution NMR in the solid state in general: a combination of long T_1 (on the order of minutes) and short T_2 (on the order of 100 μs), as well as additional line broadening by anisotropic chemical shift and dipolar coupling.

Brown et al. first demonstrated the feasibility of quantitative analysis by solid state ^{31}P spectroscopy in human limbs as a means of measuring bone mineral density noninvasively.[4] Imaging adds an additional level of complexity, since the short lifetime of the signal demands short gradient duration, a requirement that can only be reconciled with gradients of high amplitude and large slew rates, which are both difficult to achieve in large sample volumes. Ackerman et al. produced one-dimensional spin echo images at 7.4 T with echo times on the order of 1 ms and flip-back 180° rf pulses as a means to restore the longitudinal magnetization, inverted by the phase reversal pulse.[5] The same group of workers reported two-dimensional images of chicken bone at 6 T by means of a combination of back-projection and ^{1}H–^{31}P cross polarization for sensitivity enhancement, with echo times as short as 200 μs.[5] In the cross-polarization technique, the ^{31}P magnetization is derived from that of dipolar-coupled protons, which have shorter T_1 and thus permit shorter pulse sequence recycling times. Making use of the dependence of the cross-polarization rate on the proton–phosphorus dipolar coupling, the same workers showed that different phosphate species can be distinguished, demonstrating the presence of a minor HPO_4^{2-} species in immature chicken bone.[7] Very recently, Wu et al. have measured three-dimensional mineral density of hydroxyapatite phantoms and specimens of bone ex vivo.[8] While this work is at an early stage, it clearly has unique potential for nondestructive assaying of the chemical composition and its age-related changes of bone parameters that might in part explain the increased fragility of bone in older individuals.

3 IMPLICATIONS OF BONE DIAMAGNETISM ON NMR LINE BROADENING

Another approach toward assessing the properties of trabecular bone—specifically, as its architectural arrangement is concerned—exploits the diamagnetic properties of bone mineral. By virtue of the higher atomic number of its elemental composition (i.e., calcium and phosphorus), mineralized bone is more diamagnetic than marrow constituents in the trabecular marrow cavities, which consist mainly of water and lipids (i.e., oxygen, carbon, and hydrogen).

Note that in this article, the following definitions and notation will be used for the contribution from magnetic field inhomogeneity to the total dephasing rate $R_2^* \equiv 1/T_2^*$, irrespective of the notation in the original literature: $1/T_2' \equiv R_2' \approx \frac{1}{2}\gamma\,\Delta H_z = 1/T_2^* - 1/T_2$, with ΔH_z representing the full width at half maximum of the magnetic field histogram in the sampling volume such as the imaging voxel and R_2' the effective transverse relaxation rate.

It is well known that near the interface of two materials of different magnetic susceptibility, and depending on the geometry of the interface, the magnetic field is inhomogeneous. Among the first to investigate these effects systematically were Glasel and Lee, who studied deuteron relaxation of beads of different size and susceptibility, suspended in ^2H_2O.[9] Specifically, they showed that the linewidth $1/\pi T_2^*$ scaled with $\Delta\chi$, the difference in volume susceptibility between the beads and deuterium oxide. The transverse relaxation rate $1/T_2$ was found to increase linearly with reciprocal bead size, an observation that could be reconciled with diffusion in the induced magnetic field gradients. Similar phenomena were reported by Davis et al., who measured proton NMR linewidths at 5.9 T in powdered bone suspended in various solvents and found T_2^* to decrease with decreasing grain size and thus increased surface-to-volume ratio.[10] Rosenthal et al. measured R_2' in specimens from human vertebrae following marrow removal and immersion in water at 0.6 T, reporting a value of 6.1 s^{-1}, more than an order of magnitude smaller than that found for powdered bone at 5.9 T.[11] Wehrli et al. first reported a gradient-echo-based method for measuring the line width in vivo in humans in vertebral trabecular bone marrow and found R_2^* in the vertebrae to be increased by a factor of two to three relative to those in the intervertebral discs.[12]

One of the earliest studied magnetically heterogeneous systems in biology is lung tissue, where the local magnetic field distortions are caused by air in the alveoli, and some of the concepts described here have parallels in imaging pulmonary parenchyma.[13] Transverse relaxation enhancement from diffusion in intrinsic microscopic gradients has received increased attention in conjunction with the blood oxygenation level-dependent (BOLD) contrast phenomenon, resulting from physiologic variations of deoxyhemoglobin in capillary vessels during functional activation.[14,15] However, since trabeculae are considerably larger than the venules of the capillary bed (100–200 μm versus 10–20 μm), and diffusion of the protons in the marrow spaces is small (on the order of 10^{-5} cm^2 s^{-1}), diffusion-induced shortening of T_2 is expected to be negligible. Consequently, the effect of the susceptibility-induced inhomogeneous field is essentially line broadening.

Suppose there is a distribution $\Delta B(x,y,z)$ across the sample volume, such as an imaging voxel of dimension $\Delta x\,\Delta y\,\Delta z$; then the transverse magnetization $M_{xy}(t)$ can be written as

$$M_{x,y}(t) = \frac{M_0}{\Delta x\,\Delta y\,\Delta z} e^{-t/T_2} \times \int_{\Delta x}\int_{\Delta y}\int_{\Delta z} e^{i\gamma\Delta B(x,y,z)t}\,dx\,dy\,dz \quad (1)$$

For a Lorentzian field distribution, the integral in Equation (1) can be described as an additional damping term, yielding

$$M_{x,y}(t) = M_0 e^{-t/T_2} e^{-t/T_2'} \quad (2)$$

T_2' is, therefore, the time constant for inhomogeneity-induced spin dephasing. While the line broadening, in general, of course, is not Lorentzian, it will be seen subsequently that the assumption of a single exponential time constant is often a valid approximation.

3.1 Susceptibility of Bone

Although there is plenty of evidence for the susceptibility hypothesis, a quantitative determination of the volume magnetic susceptibility of bone has not been reported until recently. In preliminary experiments the author determined the susceptibility of bone using a susceptibility matching technique.[16] For this purpose, powdered bone from bovine femoral head was suspended in a cylindrical sample tube with a coaxial capillary containing water and serving as a reference, both aligned along the axis of a superconducting magnet. Potassium ferricyanide, $K_4Fe(CN)_6$, which is highly diamagnetic, was then added incrementally to the suspension. This operation resulted in a decrease in linewidth and an increase in the bulk magnetic susceptibility (BMS) shift. For concentric cylinders, the BMS shift is given as[17]

$$\Delta\nu = \frac{\gamma B_0}{2\pi}\frac{|\chi_d - \chi_w|}{3} \quad (3)$$

with χ_w and χ_d being the volume susceptibilities of water and ferricyanide solution, respectively. Whereas the critical concentration at which the solution matched the susceptibility of bone could not be attained owing to limited solubility of $K_4Fe(CN)_6$, the matching concentration was determined by extrapolation of the line broadening–concentration curve, from which a BMS shift of -0.95 ± 0.13 ppm was obtained (corresponding to $\chi_d - \chi_w = -2.85$ ppm). Hence, bone is considerably less diamagnetic than calcium hydroxyapatite.

Based on these earlier experimental approaches, Hopkins and Wehrli conducted a more rigorous study to determine the absolute susceptibility of bone, with potassium chloride as the diamagnetic additive.[18] Specifically, they showed that the susceptibility of the suspension, χ_{susp}, is related to the line broadening $\Gamma - \Gamma_0$ [difference between the line width in the presence (subscript p) and absence (subscript 0) of bone powder], as follows:

$$\chi_{susp} = \chi_p - \frac{1 - f_p}{f_p k H_0}(\Gamma - \Gamma_0) \quad (4)$$

where f_p represents the volume fraction of the bone powder and k is an empirical proportionality constant, which is a function of particle size, shape, orientation, diffusion, and so forth. Therefore, extrapolation of the straight line defined by equation (4) to $\Gamma - \Gamma_0 = 0$ directly provides the susceptibility of the powder. The concentration-dependent decrease in line width and increase in BMS shift is shown in Figure 1. The susceptibility of bovine rib bone was found to be -11.3 $(\pm 0.25) \times 10^{-6}$ (S.I.), indicating bone to be about 2.3 ppm more diamagnetic than water, which is somewhat less than the earlier experiments suggested.

3.2 Theoretical Considerations and Computer Modeling

Consider two adjoining materials of susceptibilities χ_m and χ_b. The induced magnetic surface charge density σ at some location on the interface between the two materials is then given as

$$\sigma = \Delta\chi \boldsymbol{H}_0 \cdot \boldsymbol{n} \quad (5)$$

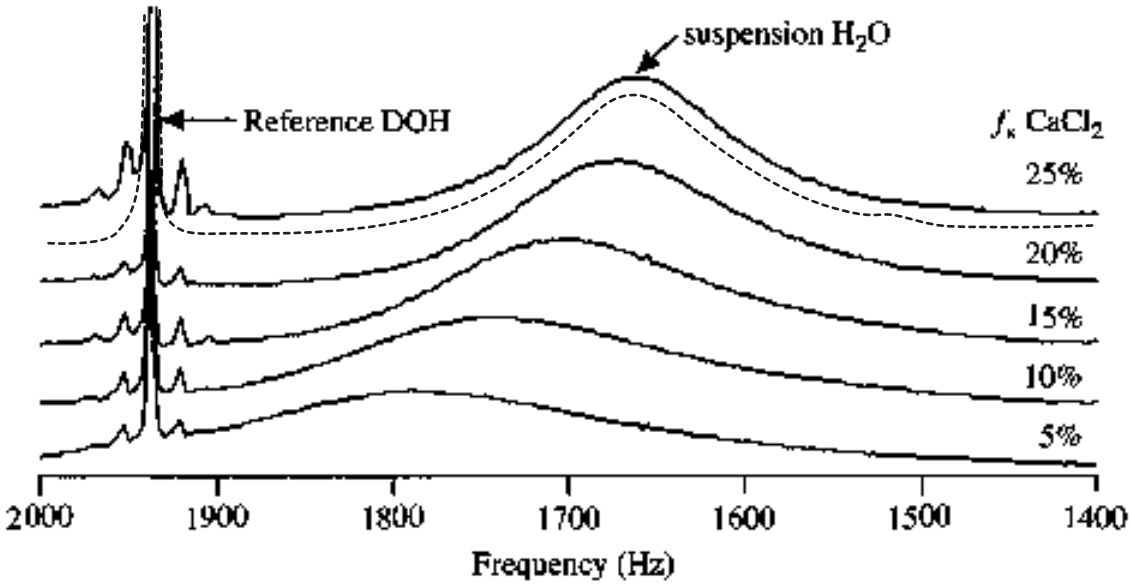

Figure 1 Spectra of ^1H at 400 MHz from suspensions of bovine rib bone in $CaCl_2$ solutions of increasing volume fraction of salt, ranging from 5 to 25% (bottom to top). The dotted line spectrum offset from the top spectrum is the best fit Lorentzian line used to estimate the spectral parameters. Small symmetric resonances about the DOH reference line are spinning sidebands. (With permission from Hopkins and Wehrli[18])

where $\boldsymbol{n}$ is the unit vector normal to the interface and $\Delta\chi = \chi_m - \chi_b$. The additional field $\boldsymbol{H}_i(\boldsymbol{r})$ resulting from the magnetic charges at the phase boundary can be estimated from the Coulomb integral[19]

$$\boldsymbol{H}_i(\boldsymbol{r}) = \int \sigma(\boldsymbol{r}') \frac{\boldsymbol{r} - \boldsymbol{r}'}{|\boldsymbol{r} - \boldsymbol{r}'|^3} \, dS' \tag{6}$$

where the integration is over the surface S of the interface, with $\boldsymbol{r}'$ and $\boldsymbol{r}$ representing the locations of the source and field points, respectively.

The induced field is thus proportional to the difference in susceptibility of the two adjoining materials, the strength of the applied field, and the inverse square of the distance between source and field location. For an array of trabeculae, the field should be highly inhomogeneous, and a relationship is expected to exist between the magnetic field distribution within the volume of interest and the number density, thickness, and orientation of trabeculae.

Ford et al.[20] developed a three-dimensional model that resembles strut-like trabecular bone as found in the vertebrae[21] to predict the line broadening behavior of protons in the marrow spaces, as a means to investigate the structural dependence of R_2'. The model consists of a tetragonal lattice of interconnected parallelepipeds ('struts') of square cross-section, differing in susceptibility from the medium by $\Delta\chi$. When oriented so that the two parallel faces of each transverse strut are normal to the direction of the applied field $\boldsymbol{H}_0$ then, according to Equation (5), these two faces will have uniform charge density $\sigma = \pm\Delta\chi \boldsymbol{H}_0$. The other faces of the transverse (and longitudinal) struts will have $\sigma = 0$, and so do not contribute to $\boldsymbol{H}_i(\boldsymbol{r})$. If the field is oriented arbitrarily relative to the lattice, all faces will be uniformly polarized, with a charge density $\sigma = \Delta\chi \boldsymbol{H}_0 \cos\alpha$ where α is the angle between $\boldsymbol{H}_0$ and the unit vector normal to any given polarized surface. An analytical expression exists for the induced field given by the integral of Equation (6) for a rectangular lamina; consequently, the total field at any one point in space can be calculated as a sum of contributions from all charge-bearing faces. In this manner, a histogram of the field for the unit cell of this lattice was obtained by randomly placing field points within the unit cell, and R_2' was calculated by fitting the Fourier transform of the field histogram to a decaying exponential. The model predicts nearly exponential decay within the experimentally practical range of echo times (about 10–50 ms). Further, R_2' is predicted to increase with both the number density of transverse struts and their thickness. Since the latter two quantities scale with material density, this finding appears unremarkable, since it would imply that R_2' merely measures bone mineral density. However, if both strut thickness and number density are varied in an opposite manner (so as to keep the material density constant), the model indicates that R_2' will increase as strut thickness decreases and number density increases. These predictions, which have been confirmed in analogous physical models,[22] underscore the importance of the distribution of the material, and suggest that different etiologies of bone loss (e.g., trabecular thinning as opposed to loss of trabecular elements) might be distinguishable.

Extending the numerical approaches described above, Hwang and Wehrli computed the magnetic field distribution in trabecular bone of human and bovine origin on the basis of a surface model derived from isotropic high-resolution three-dimensional NMR images.[23] Surfaces were modeled with triangular elements of constant magnetic surface charge density, which allows the induced field to be computed from the charged surfaces. The method was applied to computing histograms of the induced fields in specimens of trabecular bone. The width of the induced field distributions was found to be narrowest when the polarizing field was parallel to the preferred orientation of the trabeculae, confirming previous experimental findings,[24] which provides further support for the

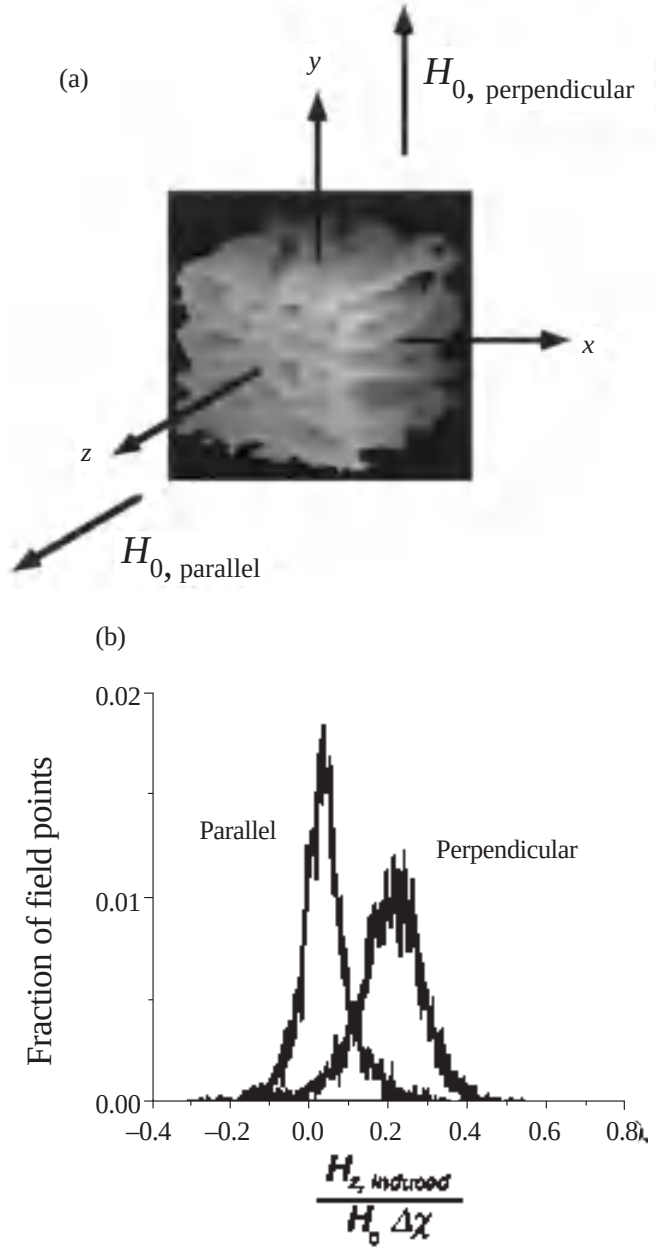

Figure 2 Induced magnetic field in trabecular bone from bovine tibia. (a) Shaded three-dimensional surface display derived from three-dimensional NMR micrograms. (b) Histogram of the induced magnetic field resulting from the bone's diamagnetism with respect to the marrow constituents

anisotropic nature of the effect. Figure 2 shows a histogram of the induced magnetic field, derived from three-dimensional MR micrograms of bovine tibia with the magnetic field oriented along two orthogonal directions, together with a projection image of the specimen.

The dependence of the induced field, expressed in terms of the reversible contribution to R_2', was also investigated by Yablonskiy and Haacke, who derived an analytical expression for R_2' in a model of trabecular bone consisting of a distribution of mutually orthogonal cylindrical columns and struts.[25] They showed that beyond a critical time within which signal decay is Gaussian, signal evolution can be described by a single exponential time constant:

$$R_2' \propto \Delta\chi H_0 \left[\varsigma_h + \left(\varsigma_v - \frac{1}{2}\varsigma_h \right) \sin^2 \vartheta \right] \qquad (7)$$

where $\Delta\chi$ is the susceptibility difference between bone and marrow, ς_h and ς_v are the densities of the struts and columns, and ϑ is the angle between the magnetic field $\boldsymbol{B}_0$ and the columns. Yablonskiy et al. demonstrated the angular dependence of R_2' in a simple trabecular bone phantom composed of parallel polyethylene filaments and found their experimental findings to agree well with their theory.[26] Similar findings were reported by Selby et al. in microphantoms consisting of cylindrical Pyrex rods.[27] Previously, Chung et al. had demonstrated the anisotropic behavior of R_2^*, in vivo in the distal radius where trabeculae are highly ordered, following the anatomic axis.[24] This observation was confirmed by Yablonskiy et al., who found R_2' in the radius to be twice as large with the axis of the wrist perpendicular compared with parallel to the direction of the field.[26]

4 RELATIONSHIP BETWEEN TRABECULAR ARCHITECTURE, LINE BROADENING, AND MECHANICAL COMPETENCE

Trabecular bone is well known to be anisotropic, with the orientation of the trabeculae following the major stress lines. In the vertebrae, for example, the preferred orientation of the trabeculae is along the body axis, in response to the compressive forces acting in this direction. The role of the horizontal trabeculae is to act as cross ties preventing failure by buckling. It has also been shown that, during aging, horizontal trabeculae are lost preferentially.[28]

If the static magnetic field is applied parallel to the inferior–superior axis of the vertebrae, the horizontal trabeculae (i.e., those orthogonal to the field) are polarized and, therefore, are expected to be the principal cause of the susceptibility-induced line broadening. Chung et al. measured the mean spacing of horizontal trabeculae (i.e., the reciprocal of horizontal trabecular number density) in cadaver specimens of human lumbar trabecular bone after bone marrow removal and suspension of the bone in water, using NMR microscopy and digital image processing.[29] They found a positive correlation between water proton R_2', measured at 1.5 T, and mean number density of the horizontal trabeculae ($r = 0.74$, $p < 0.0001$).

The critical role of the horizontal trabeculae in the vertebrae in conferring compressive strength is illustrated with the correlation between R_2' measured with the polarizing field parallel to the body axis and Young's modulus of elasticity (stiffness) for compressive loading. Figure 3(a) shows the relationship between anatomic axis, trabecular orientation, the orientation of the applied magnetic field, and the direction of compressive loading. A strong association between stiffness and R_2' exists over a wide range of values ($r = 0.90$), corresponding to trabecular bone of very different morphologic composition

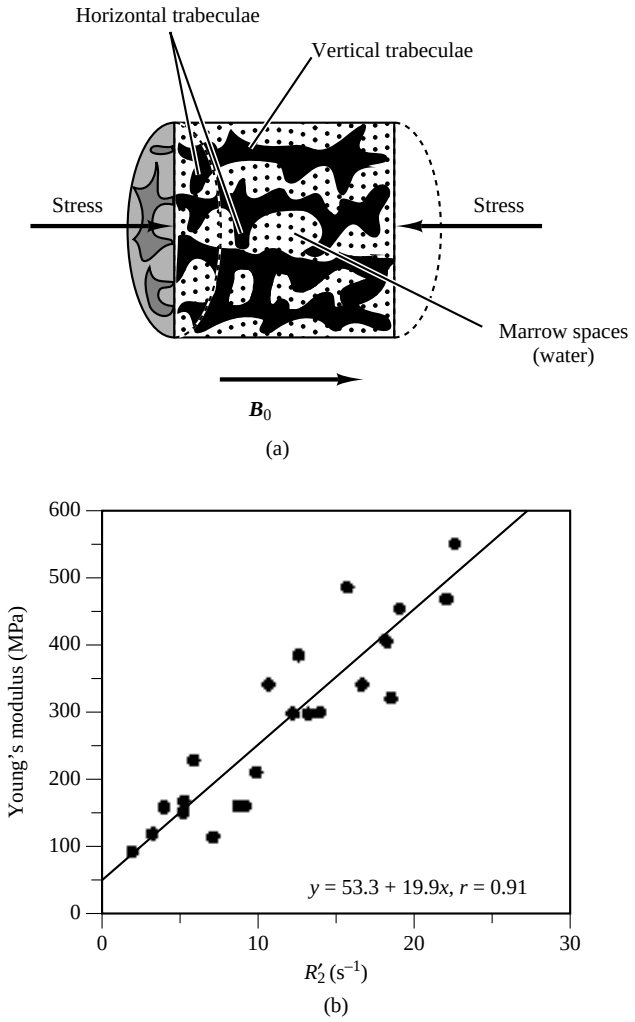

Figure 3 (a) Cross-section through a cylindrical trabecular bone specimen (schematic) used for R_2', structural, and stress analysis. The cylinder axis is parallel to the anatomic inferior–superior axis, aligned with the external field polarizing predominantly horizontal trabeculae, which cause line broadening of the proton resonances in the marrow spaces. Compressive loading is applied along the cylinder axis. (b) Young's modulus of elasticity obtained from compression tests in 22 cylindrical specimens from the lumbar vertebral bodies of 16 human subjects aged 24–86 years, plotted as a function of R_2' for the water protons in the intertrabecular spaces ($r = 0.91$, $p < 0.0001$). (Modified from Chung et al.[29])

Figure 3(b). From these data, it is inferred that a global measurement of R_2' in trabecular bone is able to predict the compressive strength of this highly complicated structure. Subsequently, Jergas et al. evaluated the ability of R_2^* to predict the elastic modulus for uniaxial loading in specimens of the human proximal tibia.[30] They found correlations ranging from 0.87 to 0.95 in specimens in which the marrow was removed, but much weaker associations in another set of specimens where the measurements were conducted with the bone marrow intact.

5 IN VIVO QUANTITATIVE NMR OF TRABECULAR BONE

5.1 Measurement and Data Analysis

Bone marrow has cellular (hematopoietic) and fatty components, with the relative fractions varying widely, depending on anatomical site and age. The major chemical constituents of the two types of marrow are water and fatty acid triglycerides. This chemical heterogeneity of bone marrow complicates in vivo measurement of T_2^*. A linewidth measurement by means of image-guided localized spectroscopy has the advantage of providing T_2^* for each spectral component.[31,32] Schick, in an excellent review on bone marrow NMR in vivo, described the potential of localized spectroscopy as a means to probe osteoporosis in the calcaneus, showing dramatic reductions in the linewidth of the CH_2 lipid resonance in response to trabecular bone loss.[32]

Image-based (nonspectrally resolved) techniques, typically conducted by means of gradient echo[33] or asymmetric spin echo techniques,[34] have the advantage of providing information at multiple skeletal locations rapidly, allowing generation of maps of R_2^*[35] or R_2'.[36] By collecting an array of images with incrementally stepped time for inhomogeneity dephasing (gradient echo delay or echo offset), the pixel amplitudes can be fitted to some model for signal decay. These methods are less sensitive to magnetic field inhomogeneity arising from effects unrelated to susceptibility-induced gradients, since the field across an imaging voxel of a few cubic millimeters is, in general, quite homogeneous.

The presence of multiple chemically shifted constituents causes an amplitude modulation that has the characteristics of an interferogram. The latter can be expressed as the modulus of the vector sum of the individual phase-modulated spectral components:[33,37]

$$I(t) = \left| \sum_{i=1}^{n} \boldsymbol{I}_i \right| = \left[\sum_{i=1}^{n} \sum_{j=1}^{n} I_{0i} e^{-t/T_{2i}^*} I_{0j} e^{-t/T_{2j}^*} \cos(\Delta\omega_{ij} t) \right]^{1/2} \quad (8)$$

where I_{0i} is the initial amplitude of the ith chemically shifted constituent, $\Delta\omega_{ij}$ is the chemical shift difference in rad s^{-1} between nuclei i and j, t is the dephasing time (e.g., the echo time TE in a gradient echo), and the summation is over all spectral components n. Typically, the most abundant spectral components are those of the CH_2 protons of fatty acids and of water, which are separated by chemical shift (δ) = 3.35 ppm. It has been shown that $I(t)$ can be fitted to a two-component interferogram with T_2^* and fat and water signal amplitudes as adjustable parameters and assuming $T_{2,\text{fat}}^* \approx T_{2,\text{water}}^*$.[33]

Multiparameter curve fits are hampered by the difficulty of locating the global minimum, and require a relatively large number of images. One alternative is to suppress one spectral component,[35] which sacrifices some of the signal-to-noise ratio and is relatively sensitive to global magnetic field inhomogeneity, demanding that the field across the sample volume vary less than the chemical shift. Another approach to suppress the modulation is to sample the interferogram at the modulation frequency, ideally in such a manner that the two components are in phase with one another.[38] This condition is satisfied for sampling at multiples of the modulation period $T = 2\pi/\gamma\delta\boldsymbol{H}_0$, which is 4.65 ms at 1.5 T field strength.

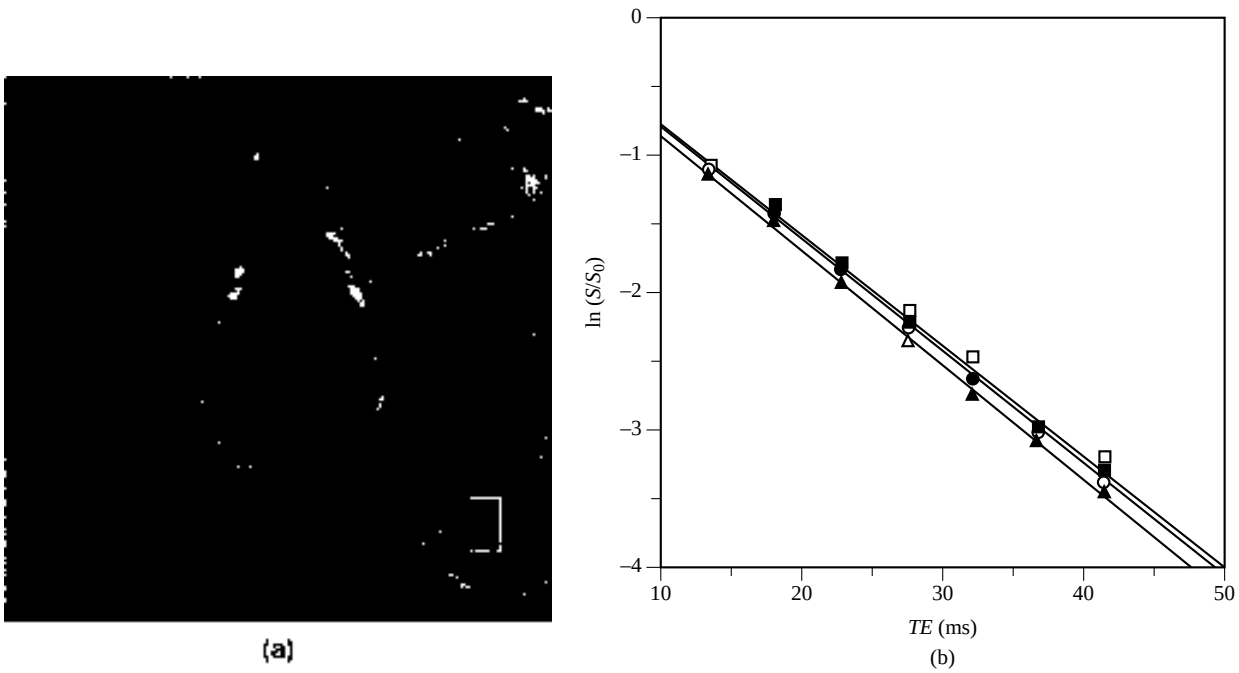

Figure 4 (a) First of a series of eight coronal gradient echo images for simultaneous measurement of T_2^* in the hip and lumbar spine, obtained by collecting 128 data samples every 4.65 ms, from a single gradient echo train so as effectively to demodulate the signal (see text for details). (b) Plot of signal measured in the trochanter [see region indicated in (a)] versus echo time, obtained from five successive scans. Solid lines are linear least-square fits, affording $T_2^* = 12.55 \pm 0.38$ ms

Another approach consists of deconvolving the amplitude-modulated signal with a reference signal.[39] If the marrow composition is known (e.g., all fatty, such as in most of the appendicular skeleton), the reference signal could be derived from subcutaneous fat or marrow in the diaphysis, locations where no line broadening occurs. In the time domain, deconvolution can be achieved by simple division of the marrow signal at the location of interest (trabecular bone marrow) by the reference signal, resulting in a demodulated signal that fits to a decaying exponential of rate constant R_2'. Difficulties of this approach lie in the uncertainties of the marrow composition and large-scale static field inhomogeneities, which may differ at the region of interest and the reference region.

Rather than computing T_2^* by fitting the mean signal from a two-dimensional array of pixels (often called the 'region of interest'), it is desirable to perform this calculation pixel by pixel for the generation of T_2^* maps. This, however, requires that misregistration be minimal between acquisitions, which may, for example, be achieved with a multiple echo pulse sequence that collects gradient echoes of the same polarity at multiples of the chemical shift modulation period. The precision achievable in vivo with this technique is illustrated with the data obtained from five separate scans in the same test subject in Figure 4. The data also show that chemical shift modulation is completely suppressed and that the decay is exponential to a high degree (Figure 4b). Excellent precision was also reported by Funke et al., who used a 16-echo gradient echo pulse sequence to give a coefficient of variation of 2.5% from 11 successive scans, which included repositioning following each scan.[40]

Since variations in R_2 (for example from variations in marrow composition) could mask effects resulting from changes in trabecular architecture or density, a direct measurement of R_2' would be preferable. The asymmetric echo technique[34,35] measures R_2' but is inherently inefficient as it requires separate image acquisitions for each time increment. Recently, Ma and Wehrli reported a new multislice pulse sequence capable of measuring both R_2' and R_2 in a single scan.[36] The method, termed GESFIDE (gradient echo sampling of FID and echo), is based on sampling the descending and ascending portion of a Hahn echo with a train of gradient echoes. The transient signal before and after the phase-reversal rf pulse decays with rate constants $R_2^* = R_2 + R_2'$ and $R_2^- = R_2 - R_2'$, respectively. If, further, the time interval between successive gradient echoes is set equal to the fat–water chemical shift modulation period (see above), R_2^* and R_2^- can be determined by curve fitting and R_2 and R_2' determined algebraically. Salient features of the method are its insensitivity to rf pulse imperfections, as well as its high precision and efficiency. Figure 5 shows the evolution of the GESFIDE signal in a region where $R_2' > R_2$, along with a computed R_2' parameter image.

5.2 Dependence of R_2^* and R_2' on Image Voxel Size and Field Strength

For a perturber that is smaller than the imaging voxel but much larger than the molecular scale (also referred to as 'mesoscopic' scale[41]) the susceptibility-induced line broadening should be independent of image voxel size. However, if the

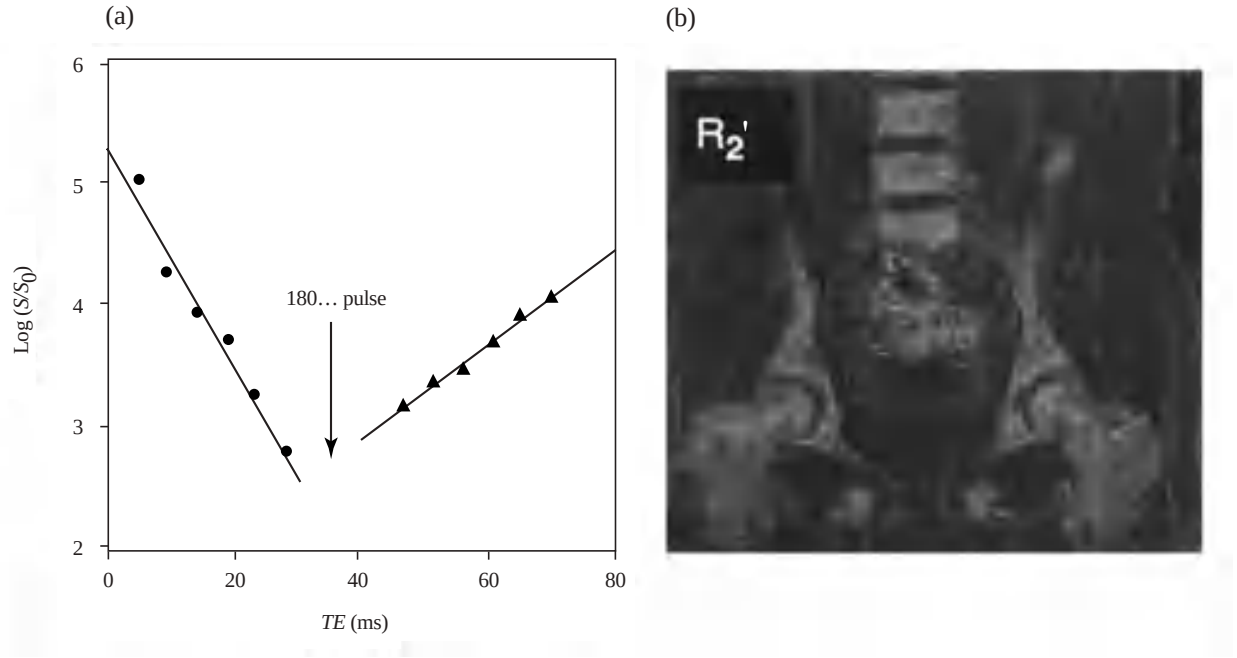

Figure 5 The GESFIDE method. (a) Evolution of the gradient echo signal from the region of interest in the greater trochanter before and after the phase-reversal rf pulse (S, signal; points obtained from five successive scans). Prior to the phase-reversal pulse, the signal evolves with a time constant $R_2^* = R_2 + R_2'$, subsequently with $R_2^- = R_2 + R_2'$. The change in the sign of the slope indicates that $R_2' >> R_2$. (b) Computed R_2' map. Note the high intensity for structures pertaining to trabecular bone, consistent with enhanced R_2' as a result of susceptibility-induced line broadening. (Modified from Ma and Wehrli[36])

voxel size decreases below the typical range of gradients induced by the field pertubing trabeculae, then the likelihood of this voxel falling in a region sufficiently removed from the field gradients induced by trabeculae increases. As a consequence, the mean T_2' is expected to increase with decreasing pixel size. Majumdar and Genant studied this effect in trabecular bone of various densities.[35] They found that the T_2' histogram becomes wider and more asymmetric with decreasing pixel size. However, if the voxel size is large relative to the range of the gradients, the value of T_2' becomes independent of voxel size, which is the case for pixels on the order of 1.5–2 mm. The distribution of T_2' as a function of image resolution is shown in Figure 6.

The induced magnetic field is proportional to the polarizing static field. In the absence of diffusion (static dephasing regime) one would, therefore, expect a linear relationship between trabecular bone marrow R_2' and field strength. Parizel et al. reported the field strength dependence of R_2^* from measurement of the gradient echo signal decay at 1.5, 1.0, and 0.2 T in vertebral bone marrow in a single volunteer[42] and found R_2^* to increase with field strength. More recently, Song et al. performed a detailed study of the field strength dependence of R_2 and R_2' in the calcaneus at 1.5 and 4 T by means of the GESFIDE technique.[43] They found R_2' to scale nearly proportionally with field strength while R_2 was almost field-strength invariant. The data, which show that at 4 T R_2' accounts for nearly 90% of the total relaxation rate ($R_2^* = R_2 + R_2'$), are summarized in Table 1.

5.3 Clinical Studies in Patients with Osteoporosis

The most likely association involving R_2^* is with bone marrow density (BMD). In fact, the theory developed by

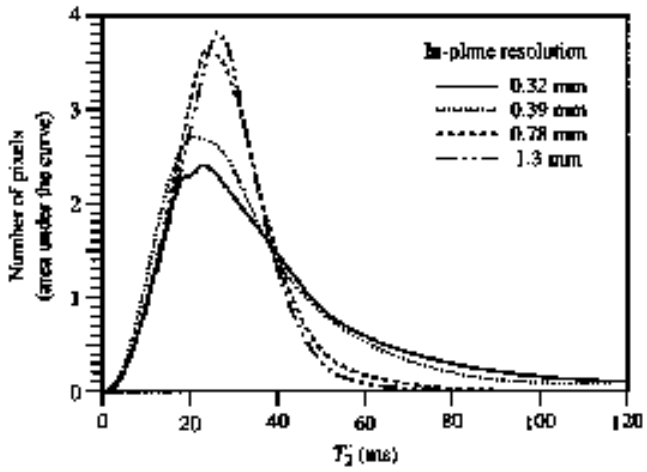

Figure 6 Smoothed T_2' histograms obtained from T_2' maps computed from axial images in the epiphysis of the distal femur, a site of dense trabeculation. As image resolution increases (smaller pixel size), the histogram broadens and becomes skewed. Means are found to vary between 41.7 ms at 0.32 mm pixels size and 25.7 ms at 1.25 mm pixel size. (Modified, with permission, from Majumdar and Genant[35])

Table 1 Field dependence of cancellous bone marrow relaxation rates

Field (T)	Relaxation rate ±SD (s^{-1})[a] R_2	R_2'
1.5	16.4 ± 1.6	65.4 ± 11.2
4.0	19.2 ± 3.4	178.4 ± 37.6

[a]SD, standard deviation from values for five subjects. R_2' (at 4 T)/R_2' (at 1.5 T) = 2.73. Source: Song et al.[43]

Yablonskiy and Haacke predicts a linear relationship between R_2' and the volume fraction of the perturber.[25] A possible relationship between these parameters was suggested by the observed T_2^* shortening in the distal femur from the diaphysis (lowest trabeculation) toward the metaphysis and epiphysis of the bone (highest trabeculation).[31] Majumdar et al. determined R_2' in intact specimens of human vertebral trabecular bone after bone marrow removal and suspending the bone in saline.[44] The measurements afforded a linear correlation between R_2' and BMD (in $mg\,cm^{-3}$), obtained from QCT, with a slope of 0.20 ± $0.02\,s^{-1}\,mg^{-1}\,cm^3$ (r = 0.92). The same group extended these studies in vivo in normal volunteers to the distal radius and proximal tibia.[35] Confirming earlier work, they found both BMD and R_2' to depend on the anatomical site of measurement. In excellent agreement with in vitro data, they measured 0.20 ± $0.01\,s^{-1}\,mg^{-1}\,cm^3$ (r = 0.88) for the combined data from both anatomic sites.

Since inception of the T_2^* method, several groups have evaluated its potential for assessing osteoporosis and have compared it with other modalities, notably DEXA and QCT.[33,40,45–47]

An early pilot study on a small group of patients with clinically established osteoporosis of the spine (n = 12) and an equal number of control subjects showed the former to have significantly prolonged bone marrow T_2^* in lumbar vertebra L5.[33] A larger follow-up study was designed to explore whether image-based measurements of T_2^* could provide an index of the integrity of trabecular bone as a possible criterion for predicting fracture risk. The value of R_2^* was measured in 146 non-black women at 1.5 T field strength by means of five successive gradient echoes, spaced 4.6 ms apart to minimize fat–water chemical shift modulation. Data were fitted to an exponential model and data sets with $p > 0.05$ for the Pearson correlation rejected. The control population ($n = 77$, mean age 46.6 ± 14.9 years) consisted of women with mean spinal BMD >0.9 g cm^{-2} (DEXA) or >90 mg cm^{-3} (QCT), and no vertebral deformities. The patient population ($n = 59$; mean age 59.7 ± 10.2 years) was made up of women with osteoporosis of the spine, exhibiting at least one radiographic deformity of the thoracic vertebrae and/or BMD below the cutoff for controls. The extent of deformity was determined as a mean deformity index, DI_{av}. The value of R_2^* was significantly lower in osteoporosis for all L vertebrae ($p < 0.001$), except for L1. The best discriminator was the average of L3–L5 ($R_{2\,av}^*$) for which means and standard errors obtained were 64.8 ± 1.2 s^{-1} and 53.4 ± 1.2 s^{-1} in controls and osteoporotics, respectively ($p < 0.0001$). Both R_2^* and BMD correlated with DI_{av}, the correlation with R_2^* being slightly stronger ($r = 0.40$; $p < 0.0005$, versus $r = 0.36$; $p < 0.001$). Finally, $R_{2\,av}^*$ was significantly correlated with mean BMD ($r = 0.54$; $p < 0.0001$, slope = 31.4 s^{-1} g cm^{-2}, $p < 0.0001$).

Overall, these findings corroborate the results of the prior study in that subjects with osteoporosis have lower R_2^* values of their vertebral marrow and show that MR may have the potential to distinguish patients with fractures from those without this condition. Nevertheless, the results fell short of demonstrating MRI's superiority over bone densitometry.

A more recent study from the same laboratory, undertaken with more advanced methodology, involving measurements of R_2' (rather than R_2^*) at multiple skeletal sites, indicates the complementary nature of this parameter to BMD.[48] In this work, the rate constants R_2' and R_2 and the marrow fat fraction were measured in the lumbar vertebrae and proximal femur by the GESFIDE method.[36] Sixteen gradient echoes were collected, eight each before and after the phase-reversal pulse, at *TE* 4.6, 6.9, 9.2, 11.5, 13.8, 18.4, 23.0, and 27.6 ms at 57.0, 61.6, 66.2, 70.8, 73.1, 75.4, 77.7, and 80 ms, the latter being an rf echo. Fat and water signal amplitudes were computed from echoes 1–3 by three-point Dixon processing,[49] and from these, the volume fractions of the two constituents. The value of R_2' was moderately (positively) correlated with BMD at all sites ($r = 0.46$–0.69; $p < 0.0001$), albeit with different slopes, indicative of the different trabecular orientation relative to the static field at the various anatomical locations. For example, in the femoral neck, the slope was twice that found for the average R_2' from lumbar vertebrae 2–4 (38.0 s^{-1} g cm^{-2} versus 19.2 s^{-1} g cm^{-2}). The value of R_2' classified the subjects well at all sites, but the strength of the discrimination was greater at the femoral sites, a finding that agrees with a small patient study by Machann et al.,[50] and suggests that skeletal sites rich in yellow marrow (such as the calcaneus) are better predictors of osteoporosis than measurements in the vertebrae. This observation can be understood when the different susceptibilities of fat (i.e., yellow marrow) and water (i.e., hematopoietic marrow) are considered. It is well known that fat is less diamagnetic than water (see, for example, Hopkins and Wehrli[18]) thus resulting in a greater absolute susceptibility difference $\Delta\chi$ between bone and bone marrow, which increases the sensitivity of R_2' to variations in bone volume fraction [Equation (7)]. In fact, when the spine R_2' values are normalized by correcting for varying bone marrow composition, achieved by computing R_2' as it would be observed for an all yellow marrow composition, the slope of the R_2' versus BMD correlation increased from 19.2 to 28.4 s^{-1} g cm^{-2}.

Finally, the value of R_2' in this study was found to be predictive of vertebral fracture status. The latter was defined by measuring vertebral deformities in the thoracic and lumbar spine in terms of standard deviations from normalcy and by selecting a threshold beyond which a fracture was considered present. When only a single parameter was included in the logistic regression, DEXA BMD was found to predict fracture status better than R_2', with Ward's triangle exhibiting the strongest correlation ($r^2 = 0.48$). Further, the femoral sites were more predictive than the lumbar spine, a finding that applies to both R_2' and BMD. However, combining MR and BMD significantly improved prediction. The strongest association was found for the combination of R_2' measured in the greater trochanter and BMD at the Ward's triangle, affording a 30% increase in the strength of the correlation relative to BMD alone ($r^2 = 0.62$). By contrast, the combination of multiple

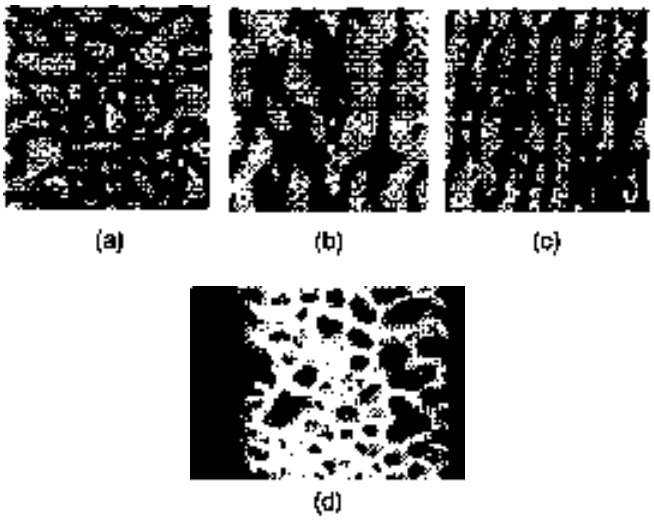

Figure 7 Images at microscopic dimension showing trabecular structure: (a)–(c) orthogonal views obtained from a 64^3 array of 3D spin echo array of images acquired at 9.4 T on a specimen of trabecular bone from bovine tibia (114 μm × 114 μm × 139 μm voxel size); (a) transverse and (b), (c) longitudinal sections. Note the preferential orientation of the trabeculae along the inferior–superior direction. (d) Shaded surface display of the same array of data, resolution-enhanced by means of a subvoxel tissue classification technique using Bayesian segmentation[60]

BMD sites did not yield stronger associations. These data are promising in that they underscore the complementary nature of R_2' and the potential role of structure in affecting the trabecular bone's mechanical competence.

6 HIGH-RESOLUTION IMAGING OF TRABECULAR BONE STRUCTURE

6.1 In Vitro Cancellous Bone NMR Microscopy

Whereas the measurement of the induced magnetic field inhomogeneity provides structural information indirectly, high-resolution MRI at microscopic dimensions has the potential for nondestructive mapping of three-dimensional trabecular morphology, as an alternative to conventional microscopy from sections[51] or tomographic X-ray microscopy.[52–54] Bone is well suited for imaging by NMR since it appears with background intensity and, therefore, provides excellent contrast with marrow, which has high signal intensity. Ideally, the image voxel size is smaller than a typical structural element (i.e., a trabecula), in which case partial volume blurring is minimal and the resulting histogram is bimodal, allowing segmentation (generation of a binary image) by setting the intensity threshold midway between the marrow peak and background. Clearly, the voxel size needed to satisfy this requirement depends on the trabecular width, which is species dependent. Bovine trabeculae are 200–300 μm thick, those in humans between 100 and 200 μm, whereas the trabecular thickness in rats is only 50–70 μm, consequently demanding considerably higher resolution.

Most of the work reported so far has been conducted on small-bore microimaging systems at 300 or 400 MHz proton resonance in human cadaver or biopsy specimens[55–58] or animals, at resolutions ranging from 25 to 120 μm. Ex vivo, the quality of the images is optimized by substituting the marrow with gadolinium-doped water as a means to optimize the signal-to-noise ratio. The background gradients from the susceptibility-induced fields can cause artifacts in the form of signal loss from intravoxel phase dispersion [Equation (1)]. Since these phase losses are recoverable—assuming diffusion to be negligible—spin echo detection is advantageous. Alternatively, the dephasing time should be minimal; this can, for example, be achieved with projection–reconstruction techniques, as applied in microimaging of lung parenchyma.[59]

At marginal resolution the accuracy of the 3D structures derived from NMR images can be improved with such techniques as subvoxel tissue classification.[60] Based on a statistical model for the noise and partial volume averaging, the number of subvoxels containing marrow can be determined and the most likely spatial arrangement ascertained using probabilistic arguments for the interaction between adjacent subvoxels. Chung et al. developed algorithms for the measurement of the structural parameters of interest (bone volume fraction, mean trabecular thickness, and mean trabecular plate separation[55] based on two-dimensional images. These techniques, however, are merely the digital imaging adaptations of stereology, the methodology practiced by the histomorphometrist who performs measurements on anatomic sections which are then extrapolated to the third dimension.[61] However, trabecular bone is inherently three-dimensional and anisotropic. Figure 7 shows three orthogonal images from bovine trabecular bone illustrating the bone's anisotropic structure, along with a surface projection image enhanced by subvoxel classification.[60]

6.2 Relationship between Architecture and Strength

Knowledge of the three-dimensional architecture of cancellous bone allows one of the key questions to be addressed, i.e., whether structure is predictive of the bone's strength. While still controversial, it is known that apparent density (essentially bone volume fraction, i.e., the amount of bone present per unit volume) predicts anywhere from 40–80% of Young's modulus (and thus ultimate strength); the remainder is generally attributed to architecture.[62]

To investigate whether architecture is predictive of the modulus of elasticity for compressive loading, Hwang et al. acquired three-dimensional images at 78 μm isotropic resolution of cadaver specimens cored from the ultradistal radius, after the cores were tested nondestructively in compression along the bone's anatomic axis. Rather than segmenting the images, bone volume fraction (BVF) images were generated by fitting the histogram to a two-peaked noiseless histogram convolved with Rician noise, using maximum likelihood methods. In this manner the true BVF can be found for each pixel as the probability of finding bone at that location. This idea was then extended to two-point probabilities, for example the probability of finding bone at two neighboring locations x_i and x_{i+n} along a row of voxels, $P(x_i, x_{i+n}) = \mathrm{BVF}(x_1)\mathrm{BVF}(x_{i+n})$. Averaging the two-point probabilities over all locations yields the spatial autocorrelation function (AFC). Because of the quasiregular nature of the trabecular lattice, the AFC has a maximum at the average spacing between trabeculae along that direction. This concept can be extended and other parameters characterizing

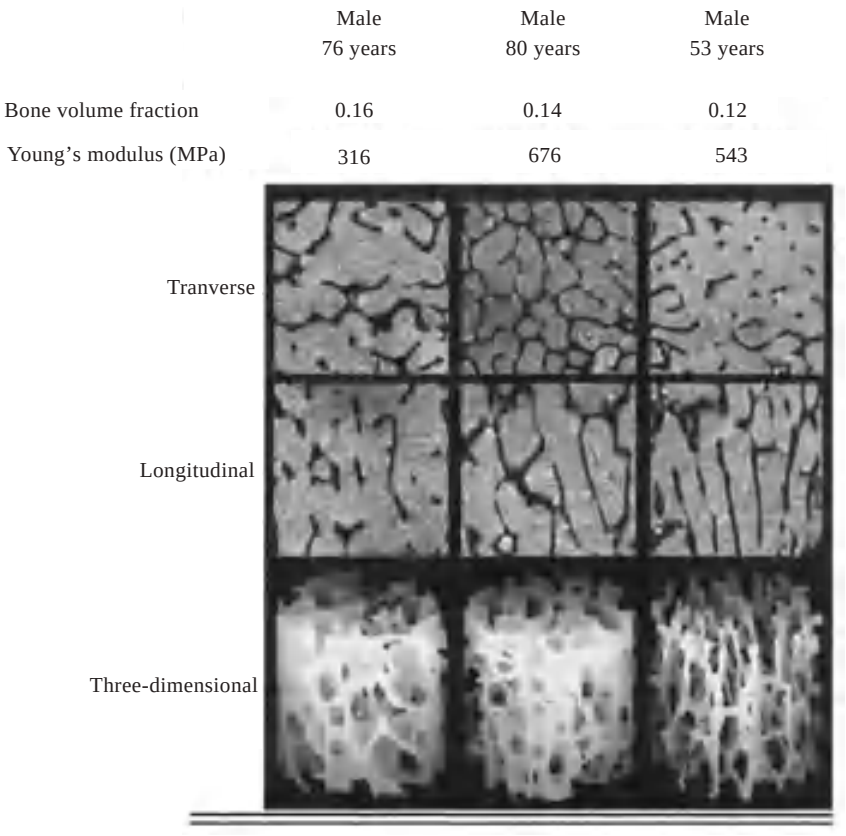

Figure 8 NMR images of three samples of trabecular bone illustrating its structural variability. Note that the sample from the 76-year-old man has the lowest modulus in spite of having the highest bone volume fraction. However, the bone of the 80- and 50-year-old donors is considerably more tubular, which explains their greater Young's modulus.

the trabecular network defined. One useful parameter is tubularity, which quantifies how 'tubular' the bone is along its anatomic axis, which is the direction along the radius (z). Tubularity is given as $AFC_z(1)/AFC(0)$, where $AFC_z(1)$ is the average of the product of BVF in corresponding voxels of successive slices. The significance of this parameter in determining cancellous bone strength is illustrated with Figure 8 showing cross-sectional and projection images of three radius specimens of varying BVF. It is noteworthy that the specimen with the highest BVF is only half as strong as the two other specimens that are both more tubular. A detailed analysis on specimens from 23 cadavers of widely varying BVF, tubularity, and longitudinal spacing (spacing between trabeculae orthogonal to the direction of loading) jointly best predicted Young's modulus, accounting for over 90% of its variance (as opposed to BVF, which explained only 50%). Clearly, a perfectly tubular structure could not fail by loading in the direction of these trabeculae. However, as the deviation from such an ideal geometry decreases, the transverse trabeculae, acting as cross-ties, become increasingly important.

6.3 In Vivo Microimaging

In vivo imaging of the microarchitecture of cancellous bone at voxel sizes sufficient to resolve individual trabeculae is considerably more challenging than measurements on small specimens in vitro. The main difficulty is to achieve sufficient signal to noise ratio in scan times tolerated by the patient, typically on the order of 10 min. A second problem is subject movement, which, even on a minute scale on the order of a pixel (100–200 μm), can cause blurring and artifacts, precluding derivation of accurate structural parameters. Restraining the portion of the body being scanned is usually not sufficient to prevent motional blurring. However, the incorporation of navigator echoes into the pulse sequence proves to be effective.[63] Additional echoes, which are not phase-encoded, generate projections of the object from which the displacement can be measured and a commensurate phase correction applied to the k-space data. The effect of alternate navigator echoes incorporated into a three-dimensional spin echo sequence was found to eliminate motion degradation effectively (Figure 9).[43]

The third problem is the considerably lower resolution achievable in vivo, which, while sufficient to visualize the trabecular architecture, demands more sophisticated methods for image restoration and analysis. In spite of these difficulties, a growing body of literature has accumulated during the past few years, highlights the potential of in vivo micro-MRI to probe bone structure.[64–68]

The image voxel sizes reported for cancellous bone imaging in humans range from 2×10^{-5} mm^3 in the distal phalanx of the middle finger[69] to 2×10^{-2} mm^3 in the calcaneus.[68] At these resolutions, the histogram is monomodal (instead of

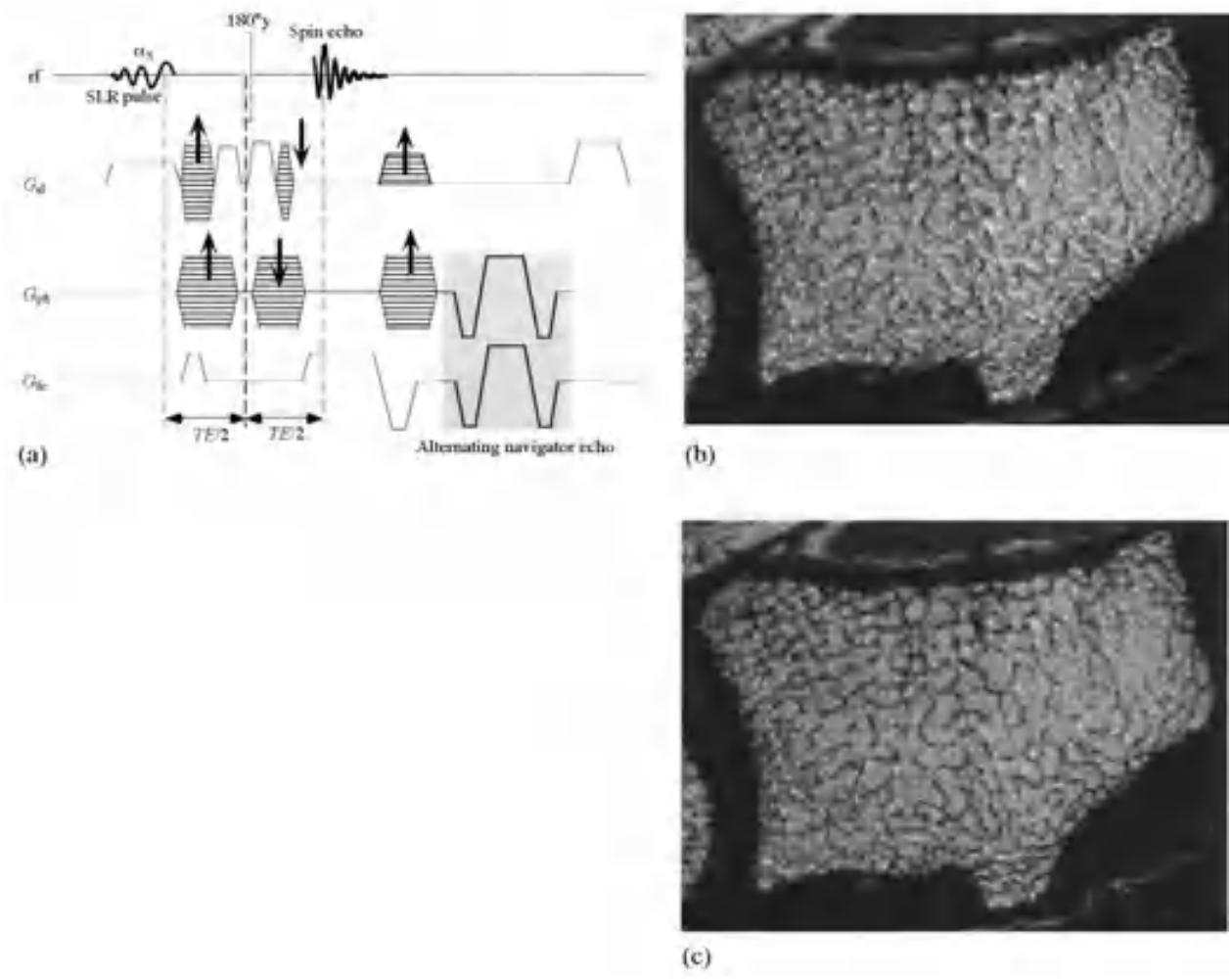

Figure 9 (a) FLASE (fast large-angle spin echo) sequence with navigator echoes alternating between frequency and phase-encoding axes (137 $\mu m^3 \times 137$ $\mu m^3 \times 350$ μm^3 voxel size). The zeroeth moment of all three gradients are nulled before the navigators are acquired. Also, to maintain steady state, the navigator gradients are refocused after collecting motion data. (b) Image of the distal radius from a 56-year-old female at this voxel size, before motion correction. (c) Image after motion correction. (With permission from Song et al.[43])

bimodal as it is at higher resolution) and, therefore, does not provide simple criteria for segmenting the images into bone and bone marrow. The limitations imposed by marginal resolution to segment the images and derive structural parameters by image processing has been addressed in various ways. Majumdar et al. set the threshold at half the peak maximum (observed for cortical bone) in the grayscale-inverted histogram.[65] In recent work on the calcaneus, Link et al. compared structural measures in postmenopausal subjects who had suffered hip fractures with those in age-matched controls.[68] They found that both apparent trabecular bone volume and apparent trabecular separation were stronger predictors of hip fracture than BMD of the proximal femur. Gordon et al. applied an adaptive threshold to eliminate errors from intensity variations caused by the inhomogeneous reception profile of the surface coil, by thresholding the image against the low-pass filtered version of itself, followed by a second threshold at 50% of the maximum.[66] From the threshold and subsequent skeleton images they determined hole size and a connectivity index and found these parameters to be correlated with subject age (positively and negatively).

Whereas the above methods cannot retrieve the true BVF, they, nevertheless, can provide parameters that can effectively characterize the trabecular network and provide clinically relevant information. True BVF images have been obtained in vivo in the distal radius by means of a histogram deconvolution technique.[70] In brief, a model histogram is convolved with Rician noise (the type of noise encountered in magnitude NMR images[71]) and the result compared with the observed histogram. The resulting error then serves as input to improve the noiseless histogram, and the process is repeated until the error falls below a predetermined level. Finally, the actual noiseless image is computed using both intensity and connectivity arguments. Wehrli et al. obtained BVF images in this manner in the distal radius of a small cohort of patients with and without vertebral fractures.[67] The parameters that proved to be successful in predicting the elastic modulus in vitro were also evaluated to explore whether architecture is associated with the

degree of vertebral deformities, measured in terms of a fracture index, D_{fract}. Whereas none of the individual structural measures was found to correlate with the D_{fract}, a highly significant relationship ($R = 0.78$; $p = 0.0016$) was found between D_{fract} and a function of tubularity and longitudinal spacing. These data further emphasize the role of architecture in determining trabecular bone's resistance to fracture, and highlight the prospects of in vitro micro-MRI as a noninvasive modality to assess trabecular microstructure.

7 RELATED ARTICLES

Lung and Mediastinum: A Discussion of the Relevant NMR Physics; Susceptibility and Diffusion Effects in NMR Microscopy; Susceptibility Effects in Whole Body Experiments.

8 REFERENCES

1. J. Wolff, 'Das Gesetz der Transformation der Knochen', A. Hirschwald, Berlin, 1892.
2. H. Roesler, *J. Biomech.*, 1987, **20**, 1025.
3. B. Riggs and L. Melton, 'Osteoporosis', Raven Press, New York, 1988.
4. C. E. Brown, J. R. Allaway, K. L. Brown, and H. Battocletti, *Clin. Chem.*, 1987, **33**, 227.
5. J. L. Ackerman, D. P. Raleigh, and M. J. Glimcher, *Magn. Reson. Med.*, 1992, **25**, 1.
6. J. Moore, L. Garrido, and J. Ackerman, *Magn. Reson. Med.*, 1995, **33**, 293.
7. Y. Wu, M. Glimcher, C. Rey, and J. Ackerman, *J. Mol. Biol.*, 1994, **244**, 423.
8. Y. Wu, J. L. Ackerman, D. A. Chesler, J. Li, R. M. Neer, J. Wang, and M. J. Glimcher, *Calcif. Tissue Int.*, 1998, **62**, 512.
9. J. Glasel and K. Lee, *J. Am. Chem. Soc.*, 1974, **96**, 970.
10. C. A. Davis, H. K. Genant, and J. S. Dunham, *Invest. Radiol.*, 1986, **21**, 472.
11. H. Rosenthal, K. R. Thulborn, D. I. Rosenthal, S. H. Kim, and B. R. Rosen, *Invest. Radiol.*, 1990, **25**, 173.
12. F. W. Wehrli, J. C. Ford, D. A. Gusnard, and J. Listerud, *Proc. VIIIth Annu. Mtg Soc. Magn. Reson. Med.*, Amsterdam, 1989, **1**, 217.
13. D. C. Ailion, T. A. Case, D. Blatter, A. H. Morris, A. Cutillo, C. H. Durney, and S. A. Johnson, *Bull. Magn. Reson.*, 1984, **6**, 130.
14. K. K. Kwong, J. W. Belliveau, D. A. Chesler, I. Goldberg, R. Weisskoff, B. Poncelet, D. N. Kennedy, B. Hoppel, M. Cohen, R. Turner, H. Cheng, T. Brady, and B. Rosen, *Proc. Natl. Acad. Sci. USA*, 1992, **89**, 5675.
15. S. Ogawa, D. W. Tank, R. Menon, J. M. Ellerman, S. G. Kim, H. Merkle, and K. Ugurbil, *Proc. Natl. Acad. Sci. USA*, 1992, **89**, 5951.
16. P. C. Lauterbur, B. V. Kaufman, and M. K. Crawford, in 'Biomolecular Structure and Function', ed. P. F. Agris. Academic Press, New York, 1978, p. 343.
17. S. Chu, Y. Xu, J. Balschi, and C. Springer, *Magn. Reson. Med.*, 1990, **13**, 239.
18. J. A. Hopkins and F. W. Wehrli, *Magn. Reson. Med.*, 1997, **37**, 494.
19. A. Morrish, 'The Physical Principles of Magnetism', Robert E. Krieger, Malabar, FL, 1983.
20. J. C. Ford, F. W. Wehrli, and H. W. Chung, *Magn. Reson. Med.*, 1993, **30**, 373.
21. L. J. Gibson, *J. Biomech.*, 1985, **18**, 317.
22. K. Engelke, S. Majumdar, and H. K. Genant, *Magn. Reson. Med.*, 1994, **31**, 380.
23. S. Hwang and F. Wehrli, *J. Magn. Reson. B*, 1995, **109**, 126.
24. H. Chung and F. W. Wehrli, *Proc. XIIth Annu. Mtg Soc. Magn. Reson. Med.*, New York, 1993, **1**, 138.
25. D. A. Yablonskiy and E. M. Haacke, *Magn. Reson. Med.*, 1994, **32**, 749.
26. D. A. Yablonskiy, W. R. Reinus, E. M. Haacke, and H. Stark, *Magn. Reson. Med.*, 1996, **37**, 214.
27. K. Selby, S. Majumdar, D. C. Newitt, and H. K. Genant, *J. Magn. Reson. Imaging*, 1996, **6**, 549.
28. L. Mosekilde, *Bone*, 1990, **11**, 67.
29. H. Chung, F. W. Wehrli, J. L. Williams, and S. D. Kugelmass, *Proc. Natl. Acad. Sci. USA*, 1993, **90**, 10 250.
30. M. Jergas, S. Majumdar, J. Keyak, I. Lee, D. Newitt, S. Grampp, H. Skinner, and H. Genant, *J. Comput. Assist. Tomogr.*, 1995, **19**, 472.
31. J. C. Ford and F. W. Wehrli, *Magn. Reson. Med.*, 1991, **17**, 543.
32. F. Schick, *Prog. Nucl. Magn. Reson. Spect.*, 1996, **29**, 169.
33. F. W. Wehrli, J. C. Ford, M. Attie, H. Y. Kressel, and F. S. Kaplan, *Radiology*, 1991, **179**, 615.
34. G. L. Wismer, R. B. Buxton, B. R. Rosen, C. Fisel, R. Oot, T. Brady, and K. Davis, *J. Comput. Assist. Tomogr.*, 1988, **12**, 259.
35. S. Majumdar and H. K. Genant, *JMRI*, 1992, **2**, 209.
36. J. Ma and F. W. Wehrli, *J. Magn. Reson. B*, 1996, **111**, 61.
37. F. W. Wehrli, T. G. Perkins, A. Shimakawa, and F. Roberts, *Magn. Reson. Imag.*, 1987, **5**, 157.
38. J. C. Ford and F. W. Wehrli, *JMRI*, 1992, **2**(P), 103.
39. F. W. Wehrli, J. Ma, J. A. Hopkins, and H. K. Song, *J. Magn. Reson.*, 1998, **131**, 61.
40. M. Funke, H. Bruhn, R. Vosshenrich, O. Rudolph, and E. Grabbe, *Fortschr. Geb. Rontgen. (Neuen Bildgeb Verfahr)*, 1994, **161**, 58.
41. D. A. Yablonskiy, *Magn. Reson. Med.*, 1997, **39**, 417.
42. P. M. Parizel, B. van Riet, B. A. van Hasselt, J. W. Van Goethem, L. van den Hauwe, H. A. Dijkstra, P. J. van Wiechem, and A. M. De Schepper, *J. Comput. Assist. Tomogr.*, 1995, **19**, 465.
43. H. K. Song, F. W. Wehrli, and J. Ma, *JMRI*, 1997, **7**, 382.
44. S. Majumdar, D. Thomasson, A. Shimakawa, and H. K. Genant, *Magn. Reson. Med.*, 1991, **22**, 111.
45. H. Sugimoto, T. Kimura, and T. Ohsawa, *Invest. Radiol.*, 1993, **28**, 208.
46. F. W. Wehrli, J. C. Ford, and J. G. Haddad, *Radiology*, 1995, **196**, 631.
47. S. Grampp, S. Majumdar, M. Jergas, D. Newitt, P. Lang, and H. K. Genant, *Radiology*, 1996, **198**, 213.
48. F. W. Wehrli, J. A. Hopkins, H. K. Song, S. N. Hwang, J. D. Haddad, and P. J. Snyder, *Proc. VIth Annu. Mtg (Int.) Soc. Magn. Reson. Med.*, Sydney, 1998, p. 456.
49. G. H. Glover and E. Schneider, *Magn. Reson. Med.*, 1991, **18**, 371.
50. J. Machann, F. Schick, D. Seitz, et al, *Proc. IVth Annu. Mtg (Int.) Soc. Magn. Reson. Med.*, New York, 1996, **2**, 1093.
51. A. Odgaard, K. Andersen, F. Melsen, and H. J. Gundersen, *J. Microsc.*, 1990, **159**, 335.
52. L. A. Feldkamp. S. A. Goldstein, A. M. Parfitt, G. Jesion, and M. Kleerekoper, *J. Bone Miner. Res.*, 1989, **4**, 3.
53. J. H. Kinney, N. E. Lane, and D. L. Haupt, *J. Bone Miner. Res.*, 1995, **10**, 264.
54. P. Rüegsegger, B. Koller, and R. Muller, *Calcif. Tissue Int.*, 1996, **58**, 24.
55. H. W. Chung, F. W. Wehrli, J. L. Williams, S. D. Kugelmass, and S. L. Wehrli, *Proc. Natl. Acad. Sci. USA*, 1995, **10**, 803.
56. H. W. Chung, F. W. Wehrli, J. L. Williams, and S. L. Wehrli, *J. Bone Miner. Res.*, 1995, **10**, 1452.

57. S. N. Hwang, F. W. Wehrli, and J. L. Williams, *Med. Phys.*, 1997, **24**, 1255.
58. M. Wessels, R. P. Mason, P. P. Antich, J. E. Zerwekh, and C. Y. Pak, *Med. Phys.*, 1997, **24**, 1409.
59. S. L. Gewalt, G. H. Glover, L. W. Hedlund, G. P. Cofer, J. R. MacFall, and G. A. Johnson, *Magn. Reson. Med.*, 1993, **29**, 99.
60. Z. Wu, H. Chung, and F. W. Wehrli, *Magn. Reson. Med.*, 1994, **31**, 302.
61. A. M. Parfitt, in 'Bone Histomorphometry: Techniques and Interpretation', ed. R. R. Recker, CRC Press, Boca Raton, FL, 1981, p. 53.
62. M. J. Ciarelli, S. A. Goldstein, J. L. Kuhn, D. D. Cody, and M. B. Brown, *J. Orthop. Res.*, 1991, **9**, 674.
63. R. L. Ehman and J. P. Felmlee, *Radiology*, 1989, **173**, 255.
64. S. Majumdar, D. Newitt, M. Jergas, A. Gies, E. Chiu, D. Osman, J. Keltner, J. Keyak, and H. Genant, *Bone*, 1995, **17**, 417.
65. S. Majumdar, H. K. Genant, S. Grampp, D. C. Newitt, V.-H. Truong, J. C. Lin, and A. Mathur, *J. Bone Miner. Res.*, 1997, **12**, 111.
66. C. L. Gordon, C. E. Webber, N. Christoforou, and C. Nahmias, *Med. Phys.*, 1997, **24**, 585.
67. F. W. Wehrli, S. N. Hwang, J. Ma, H. K. Song, J. C. Ford, and J. G. Haddad, *Radiology*, 1998, **207**, 833; erratum in *Radiology*, 1998, **206**, 347.
68. T. M. Link, S. Majumdar, P. Augat, J. C. Lin, D. Newitt, Y. Lu, N. E. Lane, and H. K. Genant, *J. Bone Miner. Res.*, 1998, **13**, 1175.
69. H. Jara, F. W. Wehrli, H. Chung, and J. C. Ford, *Magn. Reson. Med.*, 1993, **29**, 528.
70. S. N. Hwang and F. W. Wehrli, *Int. J. Imaging Syst. Technol.*, 1999, **10**, 186.
71. H. Gubdjartsson and S. Patz, *Magn. Reson. Med.*, 1995, **34**, 910.

Biographical Sketch

Felix W. Wehrli. *b* 1941. M.S., 1967, Ph.D., 1970, chemistry, Swiss Federal Institute of Technology, Switzerland. NMR application scientist, Varian AG, 1970–79; Executive Vice President, Bruker Instruments, Billerica, 1979–82; NMR Application Manager, General Electric Medical Systems, Milwaukee, 1982–88. Currently Professor of Radiologic Science and Biophysics, University of Pennsylvania Medical School. Editor-in-Chief of *Magnetic Resonance in Medicine* 1991–present. Over 100 publications. Current research specialty: NMR imaging of connective tissues, biomaterials, specifically trabecular bone.

MRI of Musculoskeletal Neoplasms

Johan L. Bloem
Leiden University Medical Center, The Netherlands

1 INTRODUCTION

Staging of disease is the single most important reason for performing MRI in patients with musculoskeletal tumors. Other indications for MRI in these patients are detection, specific diagnosis, chemotherapy monitoring, and detection of recurrence. The last two indications are becoming increasingly important. After a short discussion about technique, this article deals with clinical applications of MRI in patients with primary musculoskeletal tumors, tumor-like lesions and metastases.

2 TECHNIQUE

When a bone lesion is potentially malignant, imaging studies (to allow local staging) and biopsy are needed. Imaging studies are performed prior to histologic biopsy, because they can be used to plan the biopsy procedure. Furthermore, biopsy induces reactive changes (edema, hemorrhage), which interfere with accuracy of staging. Cytologic biopsy is a minimally invasive procedure that can be useful in soft tissue tumors, prior to MRI, to differentiate between broad categories such as lymphoma or sarcoma metastasis. Conventional radiographs have to be present when MRI is planned and executed. This should be a golden rule and will avoid both major disasters and silly mistakes.

High- or low-frequency (low or high field) magnetic resonance (MR) systems can be used for imaging musculoskeletal tumors. It is possible to stage bone tumors accurately at 0.5 T. Whenever possible, dedicated coils should be used in order to increase spatial resolution. It is important to use both T_1- and T_2-weighted sequences.

T_1-weighted sequences are used for intramedullary staging and T_2-weighted sequences are used for defining soft tissue extension and cortical involvement. A large number of pulse sequences, such as STIR (short τ inversion–recovery), gradient echo (GE) imaging, fast or turbo spin echo (TSE), chemical shift imaging, magnetization transfer contrast added to various pulse sequences, etc., are available. For imaging of musculoskeletal tumors, conventional spin echo or TSE sequences are best used to obtain T_1-weighted images. For T_2-weighting conventional spin echo sequences, or preferably TSE sequences, are used. Contrast between tumor and normal tissue, especially fat containing tissue, is greatly enhanced by combining TSE with fat selective presaturation. It is important to make sure that enough T_2 weighting is achieved. At 0.5 T, a TSE sequence with a *TR* of 3000–4000 ms and an effective *TE* of 150 ms has proven to be as good as the conventional T_2-weighted spin echo sequences in our practice. When fat suppression is used, the TE should be shortened. Contrast between tumor and muscle on T_2-weighted SE or TSE images is superior to that on native T_2^*-proton density weighted, or enhanced GE images. STIR–TSE sequences are very sensitive, but the specificity and low signal-to-noise ratio are low. When T_1 or T_2-weighted images are mentioned in this article, I refer to both conventional spin echo and TSE sequences.

Routinely, multiple imaging planes are used: the transverse plane (T_2-weighted) for soft tissue extension, and sagittal or coronal planes (T_1-weighted) for intraosseous extension (Figure 1). The sagittal and coronal planes can be angulated to be parallel to the long bones. Additional planes are used when necessary, for instance the transverse plane for intraosseous staging to rule out partial volume effects of cortical bone which may occur in the sagittal and coronal plane in thin tubular bones in children. Slice thickness varies between 2 and 10 mm and the number of excitations will be 1–4, depending on various parameters such as slice thickness, *TR*, *TE*, type of coil, and field strength used. Echo train length will vary between 3 and 8.

Gadolinium enhanced studies are performed following intravenous injection of 0.1–0.2 mmol Gd chelate/kg body weight with a T_1 spin echo or TSE technique and dynamic magnetization prepared GE imaging. The T_1-weighted sequences are combined with fat selective presaturation. It is not advisable to combine STIR sequences with gadolinium, since suppression of signal from enhancing tissue is possible. Out-of-phase GE images may further enhance contrast as compared with in-phase GE images.

Gadolinium can be used in patients with poor renal function, and can be removed from the body with dialysis.

3 MRI CHARACTERISTICS

Bone marrow and fat exhibit a high signal intensity (white) on T_1-weighted sequences, whereas cortex, fibrous cartilage, and ligaments are seen as signal void (black) structures. Hyaline cartilage and muscle have an intermediate signal intensity (gray). Relative signal intensities of muscle, fat, and bone marrow decrease somewhat on T_2-weighted spin echo sequences. This is in contrast to the increase of signal intensity of structures containing a large amount of water, such as hyaline cartilage. Fat displays a high signal intensity on TSE images.

Distribution of areas with abnormal signal intensity is important, not only for differentiating tumors and tumor-like lesions, but also in identifying normal variants. The low to intermediate signal intensity areas of red bone marrow in the axial skeleton and femur diaphysis in adults and also in the periphery of the skeleton in adolescents and children on T_1-weighted images may be confusing.[1] On STIR sequences, the high signal intensity of red marrow is easily differentiated from the absence of signal from the nulled yellow marrow. Low signal intensity areas within bone marrow on GE images are due to susceptibility effects secondary to the presence of bone trabeculae and cortex, and iron in red bone marrow.

Like most pathologic tissues, musculoskeletal tumors usually have prolonged T_1 and T_2 relaxation times (Figure 1). Therefore, osteolytic tumors have a relatively high signal intensity on T_2-weighted images and a relatively low signal intensity on T_1-weighted images. Because of their low spin

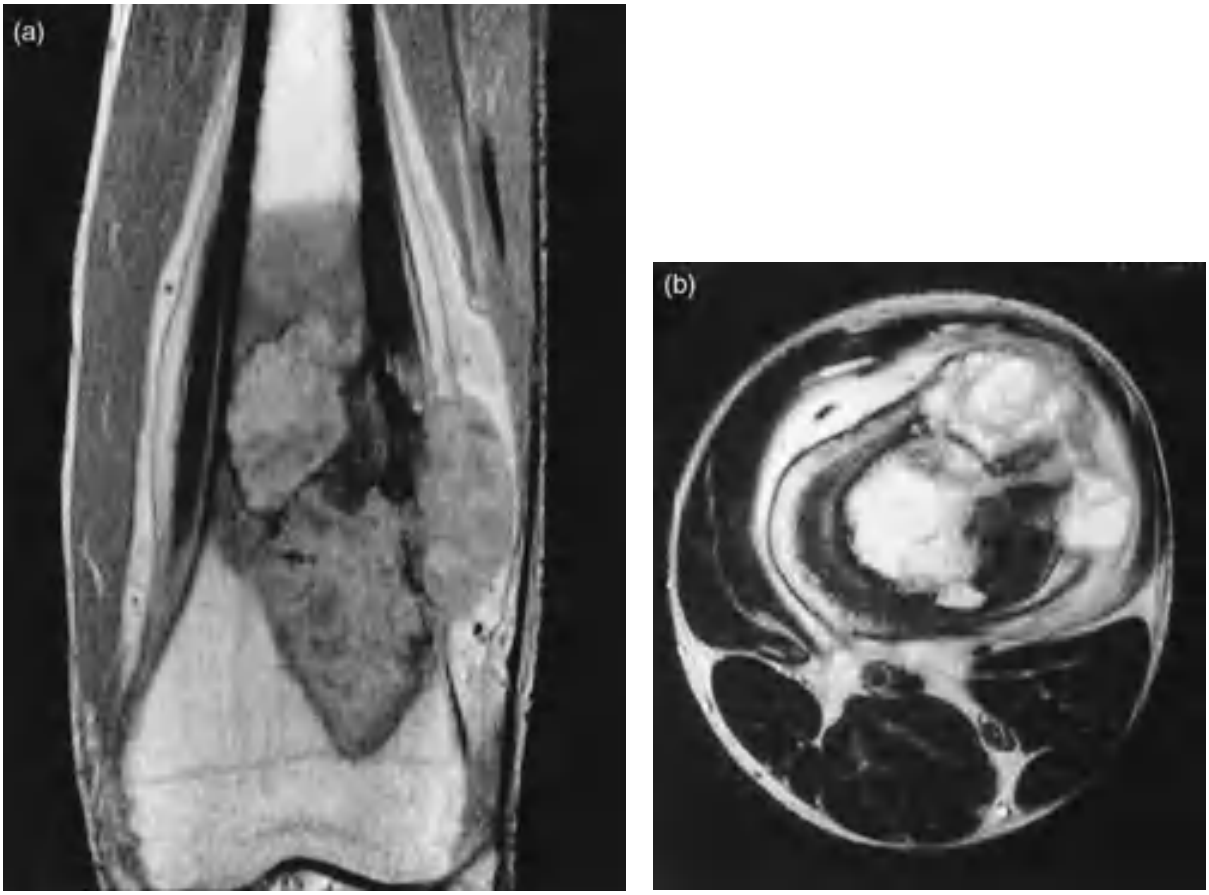

Figure 1 Osteosarcoma in an 18-year-old male imaged with a 0.5 T MRI system. (a) Coronal T_1-weighted (600/20) MR image displays the intraosseous tumor margins very well. Medial soft tissue extension and periosteal reaction are also depicted. The tumor has an inhomogeneous low to intermediate signal intensity. (b) Axial T_2-weighted TSE (3570/150) MR image. Contrast between the high signal intensity of viable tumor and the low signal intensity of muscle is excellent. However, both tumor and fat have a similar high signal intensity. Ossified periosteal reaction and ossified tumor display a signal void

density and short T_2 relaxation time, osteosclerotic components or calcifications within the tumor have a low signal intensity on both T_1- and T_2-weighted images. Small calcifications detected by plain radiographs or computerized tomography (CT) often cannot be detected by MRI. Liquefaction or lacunae caused by necrosis within a tumor can often be identified because the T_1 and T_2 relaxation times are even longer than those of viable tumor.

Cortical bone and periosteal reaction can be evaluated not only with CT, but also with MRI. Normal cortical bone is represented as a signal void area, whereas intracortical lesions almost invariably show areas of increased signal intensity relative to cortex, on T_1-weighted, gadolinium enhanced and T_2-weighted images. Likewise, mineralized periosteal reaction is seen as a solid or layered signal void area, whereas the nonmineralized cellular cambium layer of the periosteum has a high signal intensity on T_2-weighted images.

Only in selected cases does MRI allow a specific diagnosis to be made. The inhomogeneity of the tumor consisting of viable tumor with different histologic components, necrosis, hemorrhage, and reactive changes make it impossible to differentiate histologic types by relaxation times. MRI increases specificity only when unusual features such as high signal intensity on T_1-weighted images, low signal intensity on T_2-weighted images, or specific morphology or enhancement patterns are observed. Examples of lesions with a high signal intensity on T_1-weighted sequences are fat and subacute (one week to several months old) hematoma. The signal intensity of hematoma depends on the sequential degradation of hemoglobin, cell lysis, and field strength of the MR system.[2] The high signal intensity representing methemoglobin is initially seen in the periphery, and subsequently extends towards the center of the hematoma. Interstitial hemorrhage is more diffuse than hematoma and is accompanied by edema resulting in aspecific prolonged T_1 and T_2 relaxation times, irrespective of age.

Although hemorrhage and hematoma may occur in any tumor or hemophiliac pseudotumor, telangiectatic osteosarcoma and aneurysmal bone cyst are the lesions to consider when hemorrhage is found.[3] Telangiectatic osteosarcoma will display malignant features such as indistinct margins and inhomogeneity, whereas aneurysmal bone cyst often contains multiple compartments and displays well-defined margins. Layering or a fluid level, as can be demonstrated with MRI, is more often

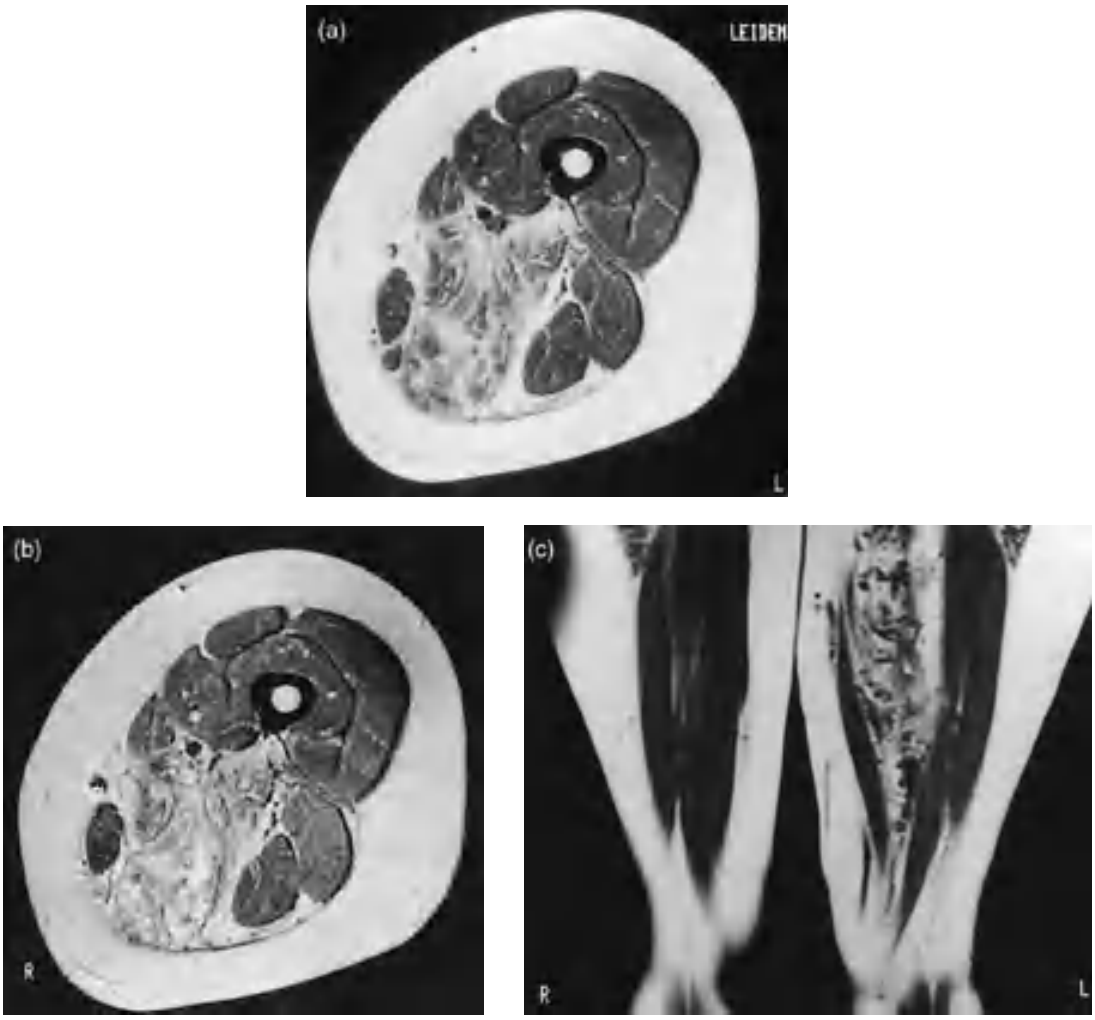

Figure 2 Hemangioma in the adductor compartment of the left thigh imaged with a 1.5 T MRI system. (a) The high signal intensity and morphology on this axial T_1-weighted (600/20) spin echo image are typical of hemangioma. A soft tissue sarcoma would occupy more space. (b) After intravenous administration of 0.1 mmol Gd-DTPA/kg body weight, diffuse enhancement resulting in an increase in signal intensity is appreciated. This is consistent with the presence of well-vascularized cellular tissue. (c) On the coronal T_1-weighted (600/20) spin echo image, the same features are visualized. The signal void of rapid flow within the hemangioma is shown to best advantage

seen in aneurysmal bone cyst than in telangiectatic osteosarcoma. These fluid levels may also be encountered in chondroblastoma, giant cell tumor, especially when a secondary aneurysmal bone cyst is present, and occasionally in other tumors as well.[3] Another reason for hematoma is surgical intervention. Since hematoma and edema may be quite extensive following histological needle or open biopsy, imaging studies are preferably performed prior to invasive procedures.

High signal intensity may also be encountered in lipoma. On T_2-weighted images the signal intensity will remain identical to that of subcutaneous fat. Liposarcomas may contain areas consisting of well-differentiated fat; these areas have the same appearance on MRI as benign lipomas. Liposarcomas, however, invariably contain large areas (myxoid liposarcoma) or some areas (lipoblastic liposarcoma) of poorly differentiated fat and mesenchymal tissue, which have the same MRI characteristics as other high-grade malignancies.

The signal intensity of hemangioma and arteriovenous malformations is variable. The signal intensity may be high on T_1-weighted sequences due to adipose tissue within the lesion and due to slow flow through dilated sinuses and vessels (Figure 2). Because of slow flow, the serpiginous vascular channels typically display a high signal intensity on T_2-weighted images. Signal void represents high flow in vascular channels. Fat predominates in asymptomatic vertebral hemangiomas. Vascularity is often more pronounced in symptomatic hemangiomas.[4]

A low signal intensity on T_2-weighted sequences, secondary to a low spin density and/or short T_2 relaxation time, may indicate the presence of calcification, osteoid, collagen, fibrosis, hemosiderin, or bone cement. Low signal intensity areas on T_2-weighted images may be present in pigmented villonodular synovitis, giant cell tumor of tendon sheath, elastofibroma, fibromatoses, fibrous dysplasia, neuroma (Morton neuroma), etc.[3] The signal intensity reflects the amount of collagen and

fibrous tissue present. Cellular areas will be seen as high signal intensity areas on T_2-weighted images, whereas the paucicellular areas will exhibit a low signal intensity on all pulse sequences.

Low signal intensity masses located within ligaments (Achilles tendon) representing xanthomas may be encountered in patients suffering from familial hypercholesterolemia. This is caused by deposition of cholesterol in combination with dense collagen fibers.

The flow void phenomenon, representing rapid flow in vascular channels, such as found in arteriovenous malformations, may also be a cause for low signal intensity on T_2-weighted images. This is in contrast to the characteristics of cavernous or capillary hemangioma.

The morphology, distribution, and localization of disorders can also be used in MRI to characterize a lesion. Indistinct margins, a soft tissue lesion with size larger than 3 cm, and heterogeneity indicate malignancy, whereas well-defined margins and homogeneity are more indicative of a benign lesion.[3,5] Of course there are exceptions to these general statements. Aggressive fibromatosis is a benign lesion characterized by infiltrative growth and a very high recurrence rate. Other benign lesions such as active eosinophilic granuloma may also present with indistinct margins, just as malignant lesions may present with well-defined margins.

Edema, characterized by an increased signal intensity on T_2-weighted images, a decreased signal intensity on T_1-weighted images, and indistinct margins, is a poor indicator of malignancy. Extensive soft tissue and bone marrow edema is frequently encountered in osteoid osteoma, osteoblastoma, and chondroblastoma. Edema in these benign entities is often more pronounced than in malignant tumors. Peritumoral high signal intensity in the soft tissue of patients with primary malignant tumors may represent only edema or a reactive zone also containing tumor. Edema is found in and around many lesions, including eosinophilic granuloma, fracture, bone bruise, necrosis, and transient osteoporosis.[3]

Neurofibroma is easily recognized on both CT and MRI when it presents as the classic dumb-bell tumor of the vertebral canal. Plexiform neurofibromatosis extends along neural bundles in a lobulated fashion, and is thus also easily recognized. When located in the retroperitoneum or pelvis, these plexiform neurofibromas may be quite extensive. The signal intensity of neurofibroma is determined by its prolonged T_1 and T_2 relaxation times, low to intermediate signal intensity on T_1-weighted images, and a very high signal intensity on T_2-weighted images. When present, collagen and fibrous tissue decrease the signal intensity (usually centrally).

The distribution of areas with abnormal signal intensity is important, not only for differentiating between tumors and tumor-like lesions, but also for identifying normal variants. The low to intermediate signal intensity areas of red bone marrow in the axial skeleton and femur diaphysis in adults and also in the periphery of the skeleton in adolescents and children on T_1-weighted images may be confusing.

When reviewing an MR examination, clinical data and radiographs are of paramount importance. Many tumor-like lesions, such as those due to Paget's disease, pseudoaneurysms, polymyositis, osteomyelitis, and stress fractures, can be identified in the proper clinical setting.

Osteomyelitis will, in contrast to Ewing's sarcoma, usually display only reactive changes in the surrounding soft tissue. However, a soft tissue abscess may be encountered.

Stress fractures present as irregular or band-like (perpendicular to cortical bone) areas of low signal intensity on T_1-weighted images. The high signal intensity seen on T_2-weighted or STIR sequences represents edema.

4 GADOLINIUM ENHANCED MRI

The pharmokinetics of gadolinium chelates are similar to iodinated contrast agents. This paramagnetic contrast agent acts indirectly by facilitating T_1 and T_2 relaxation processes through an alteration of the local magnetic environment. Shortening of both relaxation times is a function of the concentration of the gadolinium complex. Initially, an increase in the gadolinium complex concentration results in a predominantly shortened T_1 relaxation time and an ensuing increased signal intensity on T_1-weighted images (Figure 2). With an increasing concentration of the gadolinium complex, the signal intensity drops because of the dominant effect on the T_2* relaxation time (dephasing). With the concentrations used in clinical practice (0.1–0.2 mmol/kg body weight for intravenous administration), the shortening of T_1 relaxation time supervenes. Only in areas where a high concentration is reached, such as in the urinary bladder or early in a dynamic sequence during bolus administration in an artery, can a signal void occur.

Well perfused, often cellular, tumor components are able to accumulate a high concentration of gadolinium, which results, through shortening of the T_1 relaxation time, in a high signal intensity on short *TR/TE* (600/20) images, as opposed to some tumor components, such as sclerosis, old fibrosis and liquefaction, which are not well perfused and therefore do not show a high signal intensity on the postcontrast images. In general, the presence or absence of late enhancement is not a very good indicator of malignancy. Still, gadolinium may increase tissue characterization.

Although the intravenous administration of Gd-DTPA (DTPA, diethylenetriaminepentaacetic acid) may assist in differentiating viable tumor from liquefaction and edema, neovascularity in necrotic areas may also be enhanced. Differentiation between viable and necrotic tumor is, as a consequence, not always possible. Dynamic MRI may assist in differentiating tumor from reactive tissue, since viable tumor usually enhances faster than reactive tissue. Dynamic sequences, obtained during gadolinium complex administration, with a temporal resolution of at least 3 s can be used to help to differentiate benign from malignant soft tissue tumors. Peripheral enhancement starting within 6 s after arterial enhancement without further increase in enhancement suggests malignancy.[6]

Static short *TR/TE* spin echo images may suggest a specific diagnosis in selected cases. Well-differentiated cartilaginous tumors containing large paucicellular cartilage fields or cartilage fields with mucoid degeneration demonstrate no or only slight enhancement. Only the margin and cellular septae in the periphery and within the tumor enhance. Because of the lobulated gross anatomy of enchondroma and low grade (grade I and II) chondrosarcoma, the postcontrast MRI scans of these tumors exhibit a septal-like or curvilineair (serpengineous) enhancement pattern[7] (Figure 3). Mature enchondromas do not

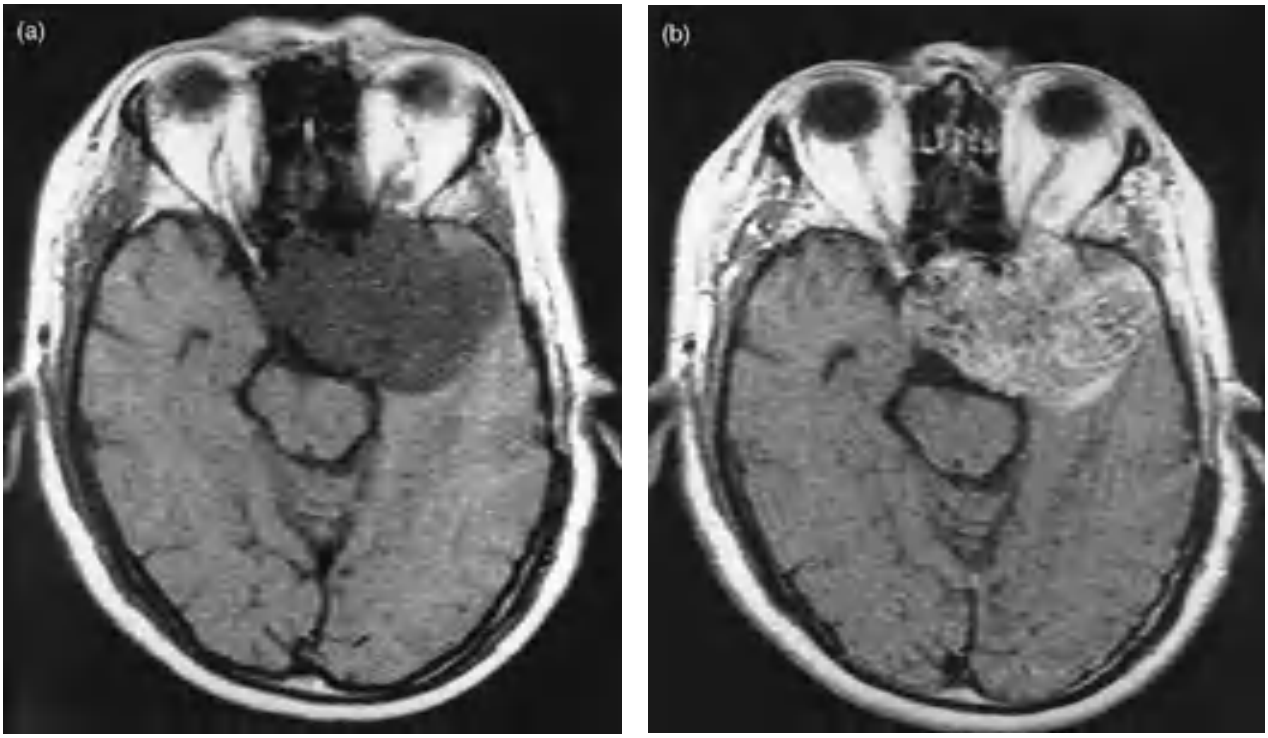

Figure 3 Chondrosarcoma grade II imaged with a 1.5 T MRI system. (a) The tumor originating from the petrous bone has an atypical low signal intensity on this axial T_1-weighted (550/20) spin echo image. (b) The same sequence is repeated 5 min after intravenous administration of 0.1 mmol Gd-DTPA. A serpentiginous enhancement pattern consistent with the presence of fibrovascular septations of well-differentiated chondrosarcoma is visualized. Compression on the temporal lobe and the brainstem is present

enhance. Enchondromas and osteochondromas may, however, enhance in the adult population 10 s or later after arrival of contrast agent in the artery. Central or peripheral chondrosarcoma grade 1 typically enhances within 10 s of arterial enhancement. Benign cartilaginous lesions in children or in association with sursae (mechanical stress) may also enhance early. Only high-grade cartilaginous tumors such as chondrosarcoma grade III and mesenchymal chondrosarcoma exhibit the aspecific homogeneous or inhomogeneous enhancement displayed by most tumors.

Other cartilage containing tumors such as chondroid osteosarcoma may also show areas with curvilineair enhancement. Usually other criteria such as morphology will assist in differentiating these lesions. A chondroid osteosarcoma is less homogeneous than a well-differentiated cartilaginous tumor and often contains large areas with osteoid, which can be recognized.

The curvilinear enhancement of well-differentiated cartilaginous tumors must be differentiated from thin peripheral enhancement of the pseudocapsule of lesions such as eosinophilic granuloma and solitary bone cyst.

5 LOCAL TUMOR STAGING

Adequate, wide or radical surgery has been a prerequisite for proper treatment of patients with primary malignant musculoskeletal tumors. The choice of therapy depends on a number of factors such as the grade of malignancy, the response to neoadjuvant therapy, local tumor extension, and the presence or absence of regional or distant metastases. The surgical staging system developed by Enneking takes all these factors, with the exception of the response to neoadjuvant therapy, into account.

The biologic aggressiveness, indicated by the grade, is the key factor in the selection of the surgical margin required to achieve control. Four different surgical procedures, which imply four different margins, are recognized: intralesional, marginal, wide, and radical. The exact anatomic location of tumor is the key factor in selecting how a required tumor-free margin can be accomplished.

5.1 Bone Marrow Involvement

For extremities, a plane through the long axis of a long bone is chosen, i.e. sagittal or coronal. MRI is superior to technetium bone scanning because tumor related hyperemic osteoporosis is not depicted on MRI and is therefore not a source of false-positive readings. MRI has an almost perfect correlation ($r = 0.99$) with pathologic/morphologic examination; CT has a less substantial correlation ($r = 0.93$); ^{99m}Tc methylene diphosphonate (MDP) scintigraphy has a weak correlation ($r = 0.69$).[3,8]

The osseous tumor margin may be obscured by the presence of intraosseous edema. Often a double margin can be visualized. The margin nearest to the center of the tumor represents the true tumor margin, whereas the outer margin represents the margin of the edematous reactive zone towards normal bone

marrow. Differentiation can be facilitated by using gadolinium. Tumor and the edematous reactive zones display different enhancement patterns: a well-vascularized tumor will enhance more rapidly than the reactive zone, but usually (for instance in osteosarcoma) the intraosseous reactive zone will enhance more than the tumor itself on images taken 5 min after contrast injection. Furthermore, enhancement of the edematous reactive zone is, as a rule, more homogeneous than that of tumor. The intraosseous reactive zone is usually not a clinical problem, because it disappears after one or two cycles of chemotherapy. The true tumor margin is then easily identified.

Caution is needed in the diagnosis of skip metastases. Skip metastases, as may be encountered in patients with osteosarcoma and Ewings's sarcoma, are detected with bone scintigraphy unless the size is below the detection threshold. Skip lesions of less than 5 mm may thus pose a diagnostic problem. Imaging of the entire bone on T_1-weighted images by using a large field of view may be of help.

5.2 Cortical Involvement

Destruction of cortical bone is not a diagnostic problem since it can be evaluated on plain radiographs and, if necessary, with tomography or CT. MR images are also able to visualize the status of cortex. Invasion of cortex by tumor is best shown on T_2-weighted images as a disruption of the cortical line and replacement of cortex by the high signal intensity of tumor. The sensitivity and specificity of MRI (92% and 99% respectively) were not found to be significantly higher than the sensitivity and specificity (91% and 98% respectively) of CT.[3,8] MRI is superior to CT in visualizing sclerotic osteosarcomas, because the signal intensity of osteosclerotic tumor is still slightly higher than the low signal intensity of normal cortex. The high density of osteosclerotic tumor and cortex may be indistinguishable on CT.

5.3 Involvement of Muscular Compartments

MRI is significantly superior (sensitivity 97%, specificity 99%) to CT in identifying muscle compartments containing tumor.[3,8] The superior performance of MRI is based on the display of tumor relative to muscular compartments with, compared to CT, superior contrast in the ideal imaging plane. The presence of peritumoral edema is, as a rule, easily identified because of its slightly different signal intensity compared to that of tumor, and especially because of the fading margins of edema as opposed to the distinct margin of the (pseudo)capsule of the tumor. However, accurate delineation of the tumor–edema interface can be rather difficult. Differences in signal intensity on multiple echoes and enhancement following administration of gadolinium may be used to differentiate tumor from edema.

5.4 Vascular Involvement

Vessels are more often displaced than encased by tumor. The relationship between tumor and neurovascular bundle is easily evaluated on T_2-weighted images because normal flow in a vessel results in low or absent signal intensity, the so-called 'flow void phenomenon.' The lumen of the vessel may have a higher signal intensity due to paradoxal enhancement, even-echo rephasing, or slow flow caused by compression. CT (sensitivity 36%, specificity 94%) and MRI (sensitivity 92%, specificity 98%) provide more information than angiography (sensitivity 75%, specificity 71%) because large vessels are, especially with MRI, well visualized in relation to the tumor.[3,8]

5.5 Joint Involvement

CT (sensitivity 94%, specificity 90%) and MRI (sensitivity 95%, specificity 98%) are both able to demonstrate joint involvement with high accuracy.[3,8] Joint involvement is sometimes more accurately demonstrated on MR images than on CT, because the articular surfaces may be parallel to the transverse CT plane. Cartilage is an effective barrier that is not easily crossed by tumor. Osteosarcoma and giant cell tumor are the tumors that are able to cross cartilage. When assessing possible joint involvement, the number of false-positive readings is much higher than the number of false-negative readings. When in doubt, the joint usually is not affected. Joint effusion with or without hemorrhage, often but not always a secondary sign of a contaminated joint, is easily identified on CT and MRI.

6 RECURRENCE

Detection of recurrent or residual tumor following initial treatment is a challenging problem for diagnostic imaging. A large recurrent tumor mass may be detected at clinical examination, with radiographs or by CT. Small recurrent tumors are difficult to define in relation to posttherapy changes caused by surgery, radiation therapy, and chemotherapy. The matter is further complicated when fixation devices have been used in reconstructive surgical procedures. These devices cause susceptibility artifacts on MRI. Even when no hardware is used, susceptibility artifacts, caused by metallic particles left behind after instrumentation, can degrade the MR images.

Despite these drawbacks, MRI can be used to detect recurrence (Figure 4). A recurrence is very likely (sensitivity 96–100%) when, following surgery, with or without chemotherapy, a mass is seen on MRI which is characterized by a high signal intensity of Gd-DTPA enhanced or T_2-weighted images.[9] Cystic masses without tumor have a high signal intensity on T_2-weighted images, but do not enhance after intravenous administration of Gd-DTPA. A tumor recurrence is very unlikely when, following surgery, no enhancement or a low signal intensity on T_2-weighted images is found. However, knowledge of the signal intensity of the primary tumor prior to therapy is crucial, especially when the primary tumor was characterized by a low signal intensity on T_2-weighted images.

When an equivocal lesion is detected, follow-up studies, biopsy or other imaging studies such as radiographs or ultrasound may be helpful. Radiation therapy adds to the confusion because it may induce inflammatory, reactive changes that may be indistinguishable from tumor recurrence. These reactive

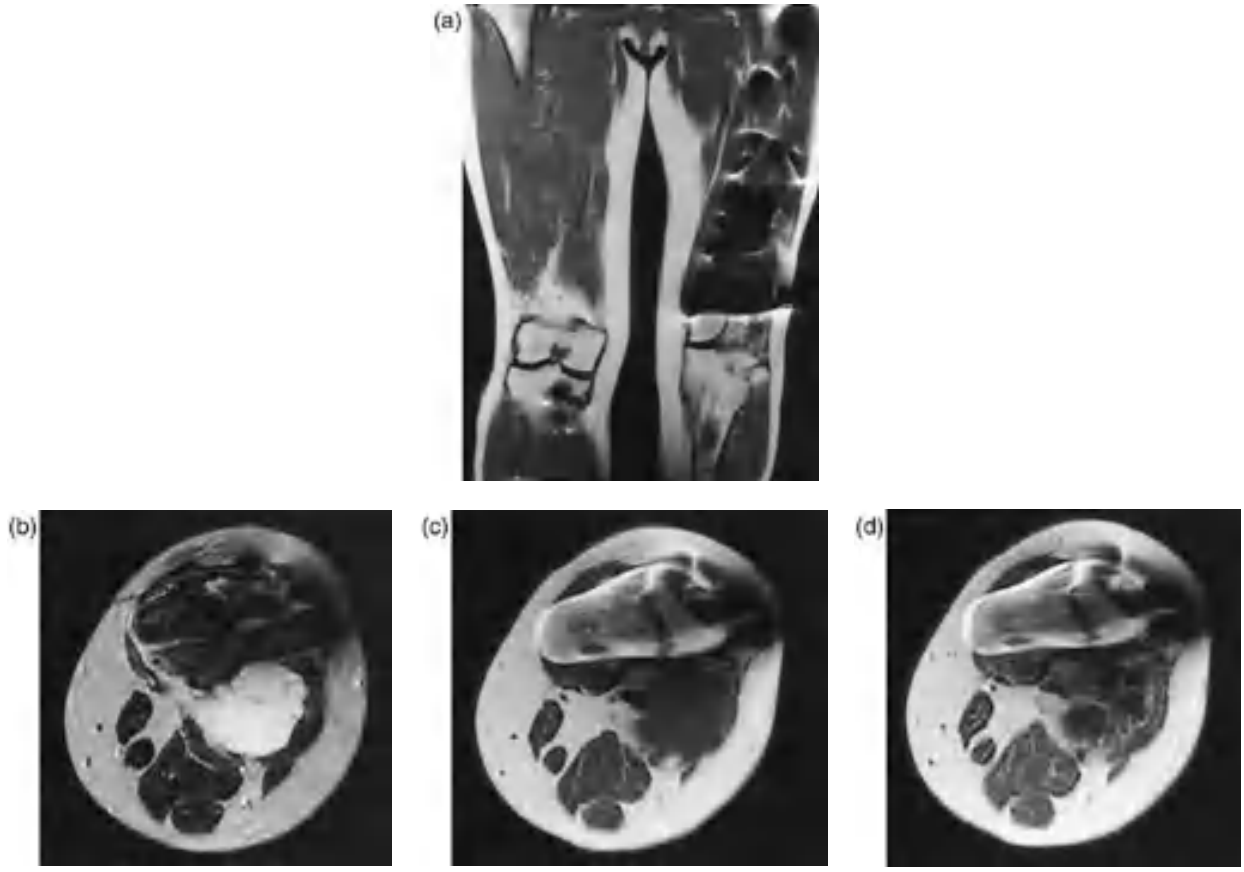

Figure 4 MRI images obtained with a 1.5 T imager of a patient with enchondromatosis and recurrent chondrosarcoma after resection and reconstructive surgery. (a) Coronal large field of view, T_1-weighted (600/20) spin echo images show cartilaginous tumors in both proximal tibias. Marked susceptibility artifacts, secondary to metallic hardware left by the orthopedic surgeon, are seen in the left femur and proximal right tibia. (b) Axial T_2-weighted (2000/100) spin echo images show a lobulated soft tissue recurrence posterior to the artifacts within the femur. (c) The soft tissue mass has an atypical low signal intensity on this T_1-weighted (600/20) image. (d) After injection of Gd-DTPA the serpentiginous enhancement pattern indicative of recurrent well-differentiated chondrosarcoma is easily appreciated, despite the marked susceptibility artifacts

changes are characterized by a high signal intensity on static Gd-DTPA enhanced and T_2-weighted images, and may persist for more than a year. However, reactive lesions usually confine themselves to the space available and, unlike tumor recurrence, do not present themselves as space occupying expansile masses. Dynamic MRI can be used to differentiate reactive tissue from viable tumor. Viable tumor typically enhances 6 s after arrival of gadolinium complex in the artery. When detection of early recurrence is of vital importance, or when there is a high risk of recurrence, a baseline study obtained 3–6 months after surgery may be of help.

7 MONITORING CHEMOTHERAPY

Preoperative (neoadjuvant) chemotherapy of bone sarcomas has increased the feasibility of limb salvage procedures. As a consequence of chemotherapy, a soft tissue tumor mass may shrink and, in combination with encapsulation of the residual extramedullary tumor mass, improve surgical conditions (down staging). However, identification of good and poor respondents is a challenging and controversial exercise.[10] Assessment of viable and necrotic tumor at histology is the gold standard. Spontaneous necrosis of up to 50% is not uncommon in high-grade malignancies. Therefore a histologic good response is defined as the presence of 10% or less viable tumor tissue. A change of tumor volume and signal intensity in osteosarcomas and Ewing sarcoma may correlate with response to chemotherapy. Despite major limitations, several qualitative and quantitative MR parameters contribute to the differentiation of good and poor respondents during and after preoperative chemotherapy.

Increase in tumor volume without hemorrhage and increase of signal intensity on T_2-weighted images in patients with osteosarcoma, even after the first cycle of chemotherapy, indicates poor response.[11] At present there are no reliable criteria for identifying good respondents on native MRI.

Reduction of tumor volume in Ewing sarcoma is characteristically seen in all patients with Ewing sarcoma after successful, or unsuccessful, chemotherapy.[10] A 75% decrease in tumor volume, or complete absence of a residual soft tissue mass after chemotherapy, are consistent with good response. Resolution of the soft tissue mass in Ewing sarcoma is frequently accompanied by reactive subperiosteal bone formation, which may result in the development of an inhomogeneous cuff of tissue encircling the original cortex.

Progressive ossification of the periosteal mass may reflect healing of these tumors, but the presence of minimal residual disease in this peripheral area cannot be excluded with any imaging modality.

A well-defined rim of low signal intensity forming a margin for the extramedullary tumor compartment represents a fibrous pseudocapsule continuous with the periosteum; however, there is no correlation with the percentage of tumor necrosis.[10,11] Although this qualitative sign cannot be used as a differentiating criterion between good and poor respondents, the improved tumor demarcation can facilitate the surgical resection.[10,11]

Following chemotherapy, the amount of viable residual tumor can be assessed by dynamic gadolinium-enhanced images. Viable tumor enhances within 6 s after arterial enhancement. Non-viable tumor components enhance later or not at all.[12]

8 BONE METASTASES

Bone metastases primarily occur in the red bone marrow of the axial skeleton. We therefore focus here on the vertebral column. Conventional radiographs have a very low yield in depicting skeletal metastases when these are still located in the bone marrow. The origin of metastatic deposits is within the bone marrow of the vertebral body. Metastatic tumor may fill the marrow and leave cortical bone intact. Detection of metastatic disease can occur at a much earlier stage when destruction of cortical bone is present. The contours of collapsed vertebral bodies can suggest the nature of the underlying disease, but conventional radiography alone is unreliable in differentiating between benign and malignant causes of vertebral body collapse.

MRI can be performed using several pulse sequences; spin echo, TSE, STIR, GE, and out-of-phase chemical shift imaging. Each pulse sequence has its own imaging features and will exhibit normal bone marrow and pathology in a characteristic manner. The signal intensities reflect the histology of the tissue. Typically, metastases display a low signal intensity on T_1-weighted sequences and a high signal intensity on T_2-weighted sequences. There are exceptions, such as in sclerotic metastases which exhibit a low signal intensity on all pulse sequences, and lipoblastic metastases which have a relatively high signal intensity on T_1-weighted images.

In the STIR pulse sequence, yellow marrow signal is nulled, such that bone marrow appears black. T_1 and T_2 values other than those for fat are additive. Lytic metastases, because of their high water content, produce an increase in both T_1 and T_2 relaxation times. This will enhance the contrast between lytic metastases and bone marrow. Often lytic metastases are better depicted on STIR images than on T_1-weighted spin echo images. Early edema (10–14 days) after radiation therapy can typically be seen earlier on STIR images than on T_1- or T_2-weighted spin echo images.

Contrast between normal bone marrow and tumor can also be increased by using the difference in resonance frequency between aliphatic and water protons. Out-of-phase images will increase image contrast in the case of lytic bone marrow metastases. Fat suppression with presaturation pulses may further increase contrast on T_2-weighted sequences. Fat presaturation may be used in combination with opposed-phase imaging.

Gadolinium will further increase sensitivity when used in combination with fat suppression. It may also increase the specificity of MRI, as metastatic deposits in vertebral bodies will exhibit diffuse enhancement of signal intensity on T_1-weighted images, whereas osteoporotic collapsed vertebral bodies will show band-like enhancement. Some authors, however, have found that the use of Gd-DTPA can be disappointing in the differential diagnosis of malignant and benign tissues.

T_1- and T_2-weighted (STIR or fat suppression) images will constitute a sufficient routine imaging protocol. Additional imaging in orthogonal planes will render valuable information in the case of soft tissue involvement. Gadolinium should be reserved for selected cases such as differential diagnosis between malignant and benign collapsed vertebrae and where there is suspected leptomeningeal tumor spread.

MRI is more sensitive in the detection of vertebral metastases than is bone scintigraphy.[13] This is not surprising since MRI visualizes bone marrow directly rather than depending on secondary signs such as new bone formation.

Although the MR characteristics of metastatic disease do not always allow reliable differentiation between benign and malignant disease, MRI is still more specific than bone scintigraphy in distinguishing between benign and malignant disease. For instance, by means of MR examination it is usually possible to make a reliable distinction between degenerative bone disease in the vertebral column and malignant infiltration. Morphologic characteristics of the lesion and adjacent disk must be taken into account. Loss of height of the intervertebral disk can be seen in degenerative disease and in diskitis, whereas the shape and height of the disk is usually preserved in metastatic diseases. In diffuse bone marrow lesions, the intervertebral disk may show a high signal intensity relative to the decreased signal intensity of abnormal bone marrow on T_1-weighted SE images.

The morphology of vertebral bodies and the signal intensity changes of bone marrow, particularly in relation to the vertebral endplates, may assist in differentiating between benign and malignant compression fractures. In old osteoporotic compression fractures the signal intensity is typically normal (fat), whereas in malignant compression fractures an abnormal signal intensity due to replacement of bone marrow is seen. In the (sub)acute phase, an inhomogeneous increase in signal intensity on STIR or T_2-weighted images, or a sharply delineated isointense vertical band of preserved normal (fatty) bone marrow along the dorsal aspect of the compressed body, indicates a benign fracture. The abnormal signal intensity in benign fractures may have the shape of a horizontal band. Fractures at multiple levels with preservation of normal bone marrow, vertebral body fragmentation, and disk rupture also indicate benign disease. Signs in favor of malignancy are: homogeneous signal intensity changes; convex anterior, and especially posterior, contour; cortical destruction; multiple levels with abnormal signal intensity, but without fracture; and abnormal signal intensity in posterior elements. Paraspinal masses are more conspicuous in malignant disease, but can be seen in both traumatic and malignant cases. Care must be taken in interpreting MR examinations in recently collapsed vertebral

bodies as they can show signal intensities indistinguishable from metastatic disease.

Currently, bone scintigraphy remains the screening procedure of choice because it is readily available, and it allows imaging of the entire skeleton in a time effective way. However, secondary to increased sensitivity, specificity, and faster pulse sequences, the role of MRI is increasing. MRI can visualize metastatic disease when bone scintigraphy is falsely negative. Thus MRI is currently indicated when a strong clinical suspicion is combined with a negative bone scan.

MRI may also elucidate the true nature of hot spots in the vertebral column in cancer patients, as it can often assist in making a distinction between malignant and benign disease. MRI can also be helpful in the guidance of biopsies.

In order to rule out compressive myelopathy or to establish soft tissue extension of tumor tissue, multiplanar MRI offers unique imaging features. The use of MRI is helpful in determining the local extent of metastatic disease when planning palliative surgery or radiation therapy.

9 RELATED ARTICLES

Imaging of Trabecular Bone; Skeletal Muscle Evaluated by MRI.

10 REFERENCES

1. S. G. Moore and K. L. Dawson, *Radiology*, 1990, **175**, 219.
2. J. M. Gomori and R. I. Grossman, *RadioGraphics*, 1988, **8**, 427.
3. J. L. Bloem, H. C. Holscher, and A. H. M. Taminiau, in 'MRI and CT of the Musculoskeletal System', ed. J. L. Bloem and D. J. Sartoris, Williams & Wilkins, Baltimore, 1992, Chap. 15.
4. J. D. Laredo, E. Assouline, F. Gelbert, M. Wybier, J. J. Merland, and J. M. Tubiana, *Radiology*, 1990, **177**, 467.
5. M. J. Kransdorf, J. S. Jelinek, and R. P. Moser, *Radiol. Clin. North Am.*, 1993, **31**, 359.
6. H. D. van der Woude, K. L. Verstraete, P. C. W. Hogendoorn, A. H. M. Taminiau, J. Hermans, and J. L. Bloem, *Radiology*, 1998, **208**, 821.
7. M. J. A. Geirnaerdt, J. L. Bloem, F. Eulderink, P. C. W. Hogendoorn, and A. H. M. Taminiau, *Radiology*, 1993, **186**, 813.
8. J. L. Bloem, A. H. M. Taminiau, F. Eulderink, J. Hermans, and E. K. J. Pauwels, *Radiology*, 1988, **169**, 805.
9. D. Vanel, L. G. Shapeero, T. de Baere, R. Gilles, A. Tardivon, J. Genin, and J. M. Guinebretiere, *Radiology*, 1994, **190**, 263.
10. H. D. van der Woude, J. L. Bloem, and P. C. W. Hogendoorn, *Skeletal Radiol.*, 1998, **27**, 145.
11. H. C. Holscher, J. L. Bloem, D. Vanel, J. Hermans, M. A. Nooy, A. H. Taminian, and M. Henry-Anar, *Radiology*, 1992, **182**, 839.
12. H. D. van der Woude, J. L. Bloem, K. L. Verstraete, A. H. M. Taminiau, M. A. Nooy, and P. C. W. Hogendoorn, *Radiology*, 1995, **165**, 593.
13. P. R. Algra and J. L. Bloem, in 'MRI and CT of the Musculoskeletal Systems', ed. J. L. Bloem and D. J. Sartoris, Williams & Wilkins, Baltimore, 1992, Chap. 16.

Acknowledgements

The contributions of M. Geirnaerdt, H. C. Holscher, H. J. van der Woude, A. H. M. Taminiau, P. Hogendoorn, F. Eulderink, M. A. Nooy, and H. M. Kroon, are gratefully acknowledged.

Biographical Sketch

Johan L. (Hans) Bloem. *b* 1954. M.D., 1979, Ph.D., 1988, Leiden University, The Netherlands. Visiting professor, Charles Gairdner Hospital, Perth; Thomas Jefferson University, Philadelphia. NMR program at Leiden University, 1983–present. Currently, Professor and Chairman of Radiology at Leiden University. Approx. 100 publications; editor of *MRI and CT of the Musculoskeletal System*. Research interest: MRI of the musculoskeletal system.

Peripheral Joint Magnetic Resonance Imaging

Paul S. Hsieh
Kaiser Permanente Medical Center, San Diego, CA, USA

and

John V. Crues III
RadNet Management, Inc., Los Angeles, CA, USA

1 INTRODUCTION

MRI is an important tool in the radiological evaluation of peripheral joint disease. Previously available noninvasive imaging techniques include X-ray and ultrasound imaging. X-ray techniques (plain radiographs and computerized tomography) are able to image cortical bone but are not sensitive in imaging medullary bone disease or intra-articular soft tissues.[1,2] Ultrasound can evaluate soft tissue structures but is limited in its ability to visualize internal structures in joints and detect some soft tissue diseases.[3] Nuclear medicine bone scintigraphy has also been used to detect articular pathology, but is not commonly used because of its lack of specificity and poor spatial resolution.[4,5] MRI is capable of demonstrating the anatomy of the various components of peripheral joints in exquisite detail, including muscles, tendons, ligaments, nerves, blood vessels, fat, and osseous structures.[6,7] In addition to its high spatial resolution, MRI displays excellent contrast between musculoskeletal soft tissues because differences in chemical structures lead to different T_1 and T_2 values. These differences in relaxation times can be exploited to generate images with striking contrast between normal tissues and between normal and pathologic tissues. Intra-articular injection of contrast material (arthrography) allows X-ray techniques to visualize the surfaces of intra-articular structures, but X-ray arthrography is both invasive and insensitive to numerous pathologic conditions that do not manifest with surface irregularities.[8] MR arthrography is now widely used for the evaluation of specific articular pathology because it combines the sensitivity of arthrography for surface abnormalities with high soft-tissue contrast.[9–11] For these reasons, many consider MRI to be the modality of choice for noninvasive imaging of peripheral joint disease.

2 BASIC TECHNIQUES

Most MRI of peripheral joints is performed with two-dimensional spin echo pulse sequences.[6] This is a basic (90–180°) sequence, with the time between successive 90° pulses denoted *TR* and that between 90° pulse and the signal acquisition denoted *TE*. A slice selection gradient is applied during each rf pulse to limit the excitation to the desired anatomic plane of interest. Perpendicular gradients are also used to provide frequency and phase encoding. The basic pulse sequence is repeated 128, 192, or 256 times, each time with a different phase-encoding gradient. The signals or echoes from each acquisition are collected and processed using a two-dimensional Fourier transform to generate the final medical image. Many varieties of the basic scheme are now in clinical use.[12]

By adjusting the *TR* and *TE*, the signal can be manipulated to have lesser or greater degrees of T_1 or T_2 contrast. Hence, an image acquired with a sequence with a short *TR* (~600 ms) and short *TE* (~15 ms) is referred to as a T_1-weighted image. Similarly, if the *TR* is long (~2000–4000 ms) and the *TE* is long (~80 ms), this is referred to as a T_2-weighted image. If the *TR* is long but the *TE* is short, then many refer to this as a proton density-weighted image.

Most structures in peripheral joints have fairly characteristic T_1 and T_2 values that make them easy to distinguish on the spin echo images. For instance, fat has a short T_1, so it has bright signal intensity on T_1-weighted images. Ligaments, tendons, and bone cortex have a paucity of mobile protons and therefore demonstrate low signal intensity on all pulse sequences. Muscle tissue also has a fairly long T_1 and therefore looks dark on a T_1-weighted image, although not as dark as tendon or ligament. Bone marrow can have intermediate to bright intensity on T_1-weighted images depending on the fat content (nonhematopoietic or 'yellow' marrow has more fat than hematopoietic or 'red' marrow). Fluid within joints has a long T_1 and a long T_2; hence it will appear dark on T_1-weighted images and bright on T_2-weighted images.

Most pathologic tissues have increased edema compared with their normal counterparts. This increased water content causes prolongation of their T_1 and T_2 values. Hence, on T_1-weighted images, abnormal tissues tend to look dark, whereas on T_2-weighted images, these tissues generally look abnormally bright. Most lesions are fairly obvious on T_2-weighted images. However, the presence of bright signal on a T_2-weighted image is a nonspecific finding: many disease processes (i.e., tumor, infection, trauma, etc.) can cause this appearance and other clues (such as lesion morphology and location) must be sought in order to make a more specific diagnosis.

In particular, abnormalities within ligamentous, tendinous, and other fibrocartilaginous structures (such as the menisci in the knee and the labra in the shoulder) manifest themselves as foci of abnormally increased signal within a usually homogeneously dark structure.[4,13] Normally, there are few mobile water molecules within these structures capable of generating any significant signal. The water that does exist within them is bound to the large macromolecules such as cartilage and is incapable of free translation and rotation.[14] The protons within these bound water molecules have very short T_2 values and therefore do not generate any detectable signal. However, if the collagen matrix undergoes degeneration with microscopic tears, then small amounts of water can be trapped in the interstices. These water molecules are more mobile and therefore have slightly longer T_2 values, which can be detected on short *TE* images (i.e., T_1-weighted and proton density-weighted images). The T_2 values are still too short to generate signal on longer *TE* images (i.e. true T_2-weighted images). There may also be a secondary T_1 shortening effect that might contribute signal on T_1-weighted images. With degenerative disruption of macromolecules, water protons may be exposed to protons deep in the macromolecules. This close proximity between the two sets of protons allows for some magnetization exchange to occur,

Figure 1 A sagittal proton density-weighted image of a knee (*TR* 2000, *TE* 25) demonstrating tear within the lateral meniscus. These are visualized as increased signal (white arrowhead) within the normal low signal of the menisci. A larger area of bulk fluid is seen anteriorly (white arrow) representing an intrameniscal cyst

with resulting shortening of the T_1 time.[14] The hallmark of this type of pathologic process is increased signal on the proton density-weighted images but *not* on the T_2-weighted images.[13]

In the presence of more significant trauma, macroscopic amounts of free fluid can be present. Clinical examples would include complete rotator cuff tears and large meniscal tears with development of intrameniscal cysts.[4,13] In these settings, the abnormal area would show increased signal on *both* the proton density- and T_2-weighted images (see Figures 1 and 2).

Figure 2 A sagittal T_2-weighted image (*TR* 2000, *TE* 80) of the same knee as in Figure 1 clearly showing the bulk fluid (white arrow) of the intrameniscal cyst. The T_2 of the bulk fluid is prolonged, making this fluid visible. However, the meniscal tears (white arrowhead) are considerably less apparent because their T_2 values are not as prolonged

Another commonly used pulse sequence is the STIR or *s*hort *t*au *i*nversion *r*ecovery sequence. This pulse sequence consists of (180°–τ–90°–180°), where τ is the delay time between the initial 180° inversion pulse and the 90° pulse. In a STIR sequence, τ is set to the null point of fat, i.e. the length of time it takes for the fat to recover to a point of zero longitudinal magnetization after an initial inversion. At a typical field strength of 1.5 T, the appropriate value of τ is approximately 160 ms.

In a STIR sequence, the signal intensity of the tissue is directly related to its T_1 and T_2 values. Tissues with short T_1 and T_2 values such as fat show little or no signal, whereas tissues with long T_1 and T_2 values have bright signal. Because most pathologic tissues have prolonged T_1 and T_2 relaxation times they are bright on STIR images even more so than on T_2-weighted images. This is especially valuable when imaging at mid and low magnetic fields (0.2–0.5 *T*). However, as with a T_2-weighted image, bright signal is not specific for any one disease process and other information (such as morphology and location of the lesion) must be considered to make a more specific diagnosis.

Another set of pulse sequences commonly used in musculoskeletal MRI is the RARE sequence,[15] which is also known as *f*ast *s*pin *e*cho (FSE) or *t*urbo *s*pin *e*cho.[16] In this pulse sequence, an initial 90° pulse is followed by a rapid succession of 180° pulses to generate a series of echoes known as an echo train. Typically 4, 8, or 16 echoes are generated per excitation, each preceded by a different phase-encoding gradient. Hence, several lines of *k*-space are acquired per excitation, resulting in a considerable saving in scanner time. However, the *TE* values are not uniform within the image: some of the echoes making up the image will have shorter *TE*s, whereas others will have longer *TE*s. This can result in a variety of image artifacts including blurring and loss of resolution and changes in image contrast.[17] Also, because some pathological processes (such as meniscal tears in knees) demonstrate increased signal on short *TE* sequences but not on long *TE* sequences, it is possible that the mix of long and short *TE*s in a FSE image might make it less sensitive to subtle lesions than a standard spin echo image.[18] For this reason, at our institution the following compromise is used: for the key anatomic plane of a joint (which is the sagittal plane for knees and the oblique coronal plane for shoulders), a slower standard spin echo pulse sequence is used to generate proton density and T_2-weighted images. For the other anatomic planes, FSE is used. In this way, a reasonable balance between scanning time and diagnostic accuracy is maintained. However, as interpreters get more experience with the vagaries of these sequences on individual scanners, more sequences are being converted to the faster techniques. Spectral fat saturation is often advocated with the use of FSE imaging in the musculoskeletal system to eliminate increased signal from fat on FSE T_2-weighted images.[19]

Gradient echo pulse sequences are only infrequently used in MRI of peripheral joints. They are fairly sensitive for the same pathological processes that are detected by short *TE* spin echo sequences. However, the soft tissue contrast is worse with gradient echo sequences than with spin echo sequences. This is because the contrast in gradient echo sequences is dependent on differences in T_2* rather than in T_2.[20] In clinical MR imaging, most of the T_2* effect is caused by field inhomogeneities and other factors not dependent on the biomedical make-up of

the tissue. Hence, the signal from the tissues undergoes T_2 decay before the differences in the true tissue T_2s can manifest themselves. For this reason, most soft tissues have very similar appearances and signal intensities on gradient echo images, regardless of the tissue type or the degree of involvement by pathology. Nevertheless, some investigators use gradient echo sequences because the short *TR*s allow 3-dimensional Fourier transform acquisitions in a reasonable time period for isotropic high-resolution imaging. This may be valuable in imaging the labrum and articular cartilage.[13,21]

In certain settings, intravenous or intraarticular gadolinium may prove useful for diagnosis. Gadolinium is a paramagnetic metal which can be bound to an organic chelating agent such as diethylenetriaminepentaacetic acid (DTPA). In the doses used in clinical practice, the main effect of intravenous gadolinium is to shorten the T_1 relaxation times of the perfused tissues. This causes them to appear brighter on T_1-weighted images. Some investigators have found this useful in evaluating possible recurrences of soft-tissue neoplasms following surgical resection.[22,23] Intravenous gadolinium can also be useful in determining if a soft-tissue mass with long T_1 and long T_2 is cystic or solid. A cystic lesion would not show any signal enhancement following contrast administration whereas a solid lesion would. Similarly, in the setting of a soft-tissue infection, it can be very difficult to tell the difference between an area of phlegmonous and inflamed solid tissue and a drainable fluid collection. On a postgadolinium image, the phlegmon should enhance, whereas the fluid collection should not enhance.[24,25]

Gadolinium can also be injected into a joint space in the form of a dilute mixture of saline and gadolinium-DTPA.[9,10] This forms a positive contrast on T_1-weighted images that distends the joint capsule and helps delineate adjacent structures. This type of MR arthrography has proven particularly useful in the shoulder, where subtle abnormalities in the cartilaginous labra can be better appreciated following contrast injection.[26] However, this converts the MR study from a noninvasive procedure to an invasive procedure, with resultant discomfort and potential risk to the patient. (Some radiologists also inject saline without gadolinium, which produces a similar arthrographic effect on T_2-weighted images).[26] MR knee anthrography is helpful in some patients who have had previous meniscal repair.[27]

3 DISEASE ENTITIES

3.1 Trauma

MR has proven to be a valuable tool in the evaluation of acute trauma to peripheral joints as well as in evaluation of chronic trauma and degeneration. For instance, within the knee joint (the most commonly imaged peripheral joint), MR can be used to detect partial and complete tears of key anatomic structures including the medial and lateral collateral ligaments, the anterior and posterior cruciate ligaments, and the medial and lateral menisci.[6] Injuries to these structures can be detected by identifying abnormally increased signal within these normally low-signal structures. Other important radiographic signs include alterations in the contour and morphology of these structures, and the presence of edema in the surrounding soft tissues (manifested as high signal intensity on T_2-weighted images). These principles apply to evaluation of ligamentous and tendinous, and muscular structures at all joints, including the rotator cuff of the shoulder and the achilles tendon in the ankle (see Figures 1–3).[13,28,29]

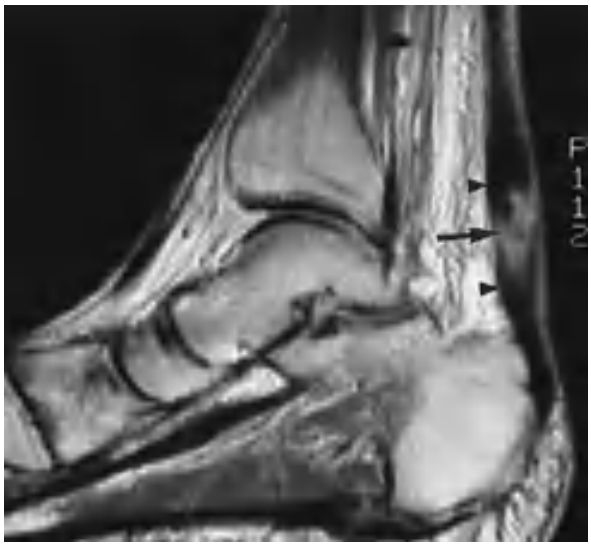

Figure 3 A sagittal proton density-weighted image (*TR* 2200, *TE* 20) of the ankle showing a tear of the achilles tendon. The tear is the area of increased signal (arrow) within the normally dark substance of the tendon (arrowheads). Notice the focal thickening of the tendon at the site of the tear

MRI has also proven to be sensitive in the detection of radiographically occult fractures.[28,30] Often these fractures produce a characteristic linear pattern of bone marrow edema, which can be visualized as a region of low signal intensity within the marrow on T_1-weighted images and high signal intensity within the marrow on T_2-weighted images. Detection of these fractures can have important therapeutic implications, so MRI should be strongly considered in the setting of a patient with clinical findings suspicious for fracture with normal radiographs. Many investigators feel that MR is at least as sensitive for detection of such fractures as the other major technique, bone scinitigraphy, and is more specific (see Figure 4).[31,32]

Traumatic lesions of the articular cartilage and subchondral bone can also be detected with MRI. In an acute setting, these are known as osteochondral fractures, whereas in the setting of chronic repetitive microtrauma, these lesions are referred to as osteochondritis dissecans. Pertinent MR findings which may be seen include disruption or thinning of the articular cartilage, alterations of the contour of low-signal subchondral bony plate (which may be accompanied by abnormal high signal within the normal low signal of cortical bone), and edema in the adjacent bone marrow.[33]

3.2 Infection

Another common use of MRI is in the evaluation of suspected infections of peripheral joints.[24,34] MR can detect the presence of abnormal fluid within a joint space, but cannot determine if the fluid is sterile or infected (i.e., if the patient has a bland joint effusion or a septic arthritis). MR is also useful in the evaluation of osteomyelitis. The principal finding in

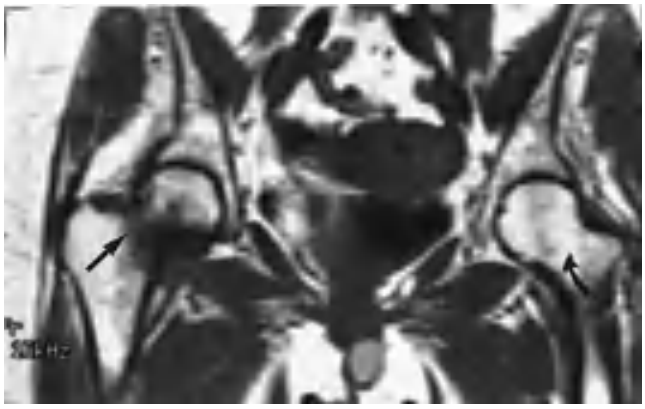

Figure 4 A coronal T_1-weighted image (*TR* 600, *TE* 15) of the hips showing a fracture of the right femoral neck (straight arrow). The abnormal low signal in the marrow is caused by edema. For comparison, the marrow signal in the left femoral neck is normal (curved arrow)

osteomyelitis is bone marrow edema (manifested by the usual low signal intensity in the marrow on the T_1-weighted images and high signal intensity on the T_2-weighted image). Osteomyelitis is also often accompanied by inflammatory changes in the adjacent soft tissues. If an area of soft tissue edema is identified, then MR with intravenous gadolinium administration can help to determine if there is a component of drainable fluid within the inflamed phlegmonous region.[24,25] This is extremely valuable in the evaluation of the diabetic foot.[34] As discussed above, a fluid collection should not enhance, whereas the phlegmonous component should (see Figure 5).

3.3 Arthritis

The role of MRI in evaluation of arthritis patients is fairly limited. MR can detect the findings seen in osteoarthritis,

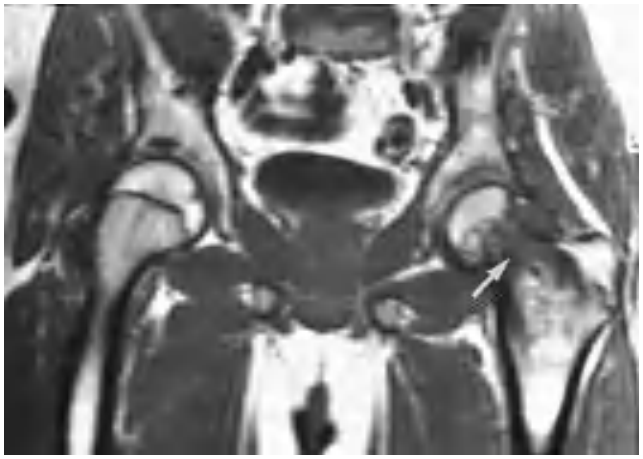

Figure 5 A coronal T_1-weighted image (*TR* 800, *TE* 20) of the hips showing marrow edema caused by osteomyelitis in the left femoral neck (white arrow). The signal intensity is similar to that of the edema caused by the fracture in Figure 4, but the abnormal area is more extensive and ill-defined. This is more compatible with an infectious process. Edema is a nonspecific finding; clinical history and morphologic clues are often necessary to distinguish between various disease entities

Figure 6 A coronal T_1-weighted image (*TR* 500, *TE* 21) of the wrist showing avascular necrosis of the proximal pole of the scaphoid bone (straight arrow), with abnormally low signal intensity within the marrow. The distal pole of the scaphoid bone has relatively normal signal intensity within the marrow (curved arrow)

including the cartilage loss, subchondral sclerosis and cyst formation, and osteophytes.[35] In rheumatoid arthritis, MR may be helpful in delineating the exact extent of the inflammed pannus tissue. On standard MR images, the pannus can look similar to joint fluid, but after the administration of intravenous gadolinium, the pannus should enhance intensely. MR is also sensitive for early detection of erosions, which may also be helpful in patients with rheumatoid arthritis or other erosive arthritides.[36]

3.4 Ischemic Disease

MR is sensitive in the evaluation of ischemic bone disease including avascular necrosis and bone infarcts.[37,38] The devascularized portion of bone becomes edematous initially. Later, as fibrovascular tissue replaces granulation tissue the T_2 relaxation time shortens (Figure 6).

Some investigators have found that dynamic gadolinium enhancement studies are useful in assessing the prognosis of involved bone.[39,40] For instance, with avascular necrosis of the femoral head and scaphoid fractures, patients with lesions which enhanced following intravenous gadolinium administration may have an improved prognosis over patients whose lesions did not enhance. Further work remains to be done to see if this is true in other areas of the body.

3.5 Neoplasms

MR has proven valuable in staging of osseous and soft tissue neoplasms.[22,41–45] With MRI, one can evaluate the anatomic extent of the tumor and the integrity of adjacent neurovascular bundles. MR is helpful in determining whether a tumor of soft tissue origin involves adjacent bone and if a tumor of bony origin involves adjacent soft tissue structures. The extent of the bone marrow involvement can also be evaluated with MRI. Most neoplasms have prolonged T_1 and T_2

values, resulting in the typical dark appearance on T_1-weighted images and bright on T_2-weighted images. The contrast between the tumor and bone marrow or subcutaneous fat is most marked on T_1-weighted or STIR images because fat has such a short T_1 in contrast with the long T_1 of the tumor. On the other hand, T_2-weighted images are better at demonstrating the difference between the tumor and normal muscle or normal neurovascular structures.

These tumors are often surrounded by a halo of edema, which also has similar signal characteristics to the main tumor. In this case, the area of signal abnormality on the images is larger than the size of the actual tumor. In this setting, evaluation with intravenous contrast and fat-saturated T_1-weighted images may be valuable.[46,47]

MRI is not very specific for most tumor cell types. The only major exceptions are lipomas, which are nearly entirely composed of fat.[48] These can be identified by the characteristic signal intensity equal to normal fat on all pulse sequences, as well as by secondary signs such as chemical shift artifact. If a fat suppression pulse sequence is used (where rf energy is applied to the fat peak prior to image acquisition), or a STIR series is acquired, the signal from lipomas should disappear. If a tumor demonstrates all of these signal characteristics, and does not contain any significant amounts of nonfatty tissue, then the diagnosis of benign lipoma can be confidently made.

Most soft tissue tumors have a nonspecific appearance, and the main role of MR is to evaluate for anatomic extent. This is useful in planning biopsies, surgical resections, and/or radiation therapy. MRI is also helpful in the evaluation of suspected recurrence following resection. In this setting, some investigators have found that intravenous gadolinium is helpful in distinguishing recurrent tumor from normal postoperative reaction.[29,49,50] Examples of bone and soft tissue tumors are shown in Figures 7–10.

Figure 7 A coronal T_1-weighted image (*TR* 800, *TE* 20) showing a large destructive mass in the lateral femoral condyle (arrow), caused by metastatic renal cell carcinoma

4 FUTURE DIRECTIONS

There are several technical advances that may have promising applications in musculoskeletal MRI. One of these is MR microscopy. With current clinical MRI, the spatial resolution is on the order of 0.5–1.0 mm per pixel. With specialized gradients and other MR microscopy techniques, this can be improved by a factor of approximately 10. If this is done, then it becomes possible to evaluate structures such as articular cartilage in much greater detail. Instead of appearing as a thin stripe of signal, 2 or 3 pixels thick, the articular cartilage will be a broad band, 20 or 30 pixels thick. (See Figure 11). It may then be possible to evaluate subtle pathology within the various sublayers of articular cartilage.[51–53] Any technique that can determine the presence or absence of early changes in rheumatological disease is also helpful, particularly for evaluating the efficacy of various treatments.

Other potentially important advances are the various diffusion and perfusion imaging techniques. The musculoskeletal system is well suited for application of these techniques because these body parts can be kept fairly immobile during scanning, which is a requirement for successful use of these techniques. Although this has not yet been proven, it is possible that some pathological processes may manifest themselves as alterations in either local perfusion or alterations in the local diffusion coefficients before one sees evidence of gross edema and prolongation of T_1 and T_2 relaxation times.[54]

Magnetization transfer contrast is another technique that may prove useful in musculoskeletal application, particularly in

Figure 8 A transaxial T_2-weighted image (*TR* 2117, *TE* 80) of the same lesion shown in Figure 7, showing increased signal intensity within the mass (arrow) caused by T_2 prolongation

Figure 9 A coronal T_1-weighted image (*TR* 600, *TE* 20) of the right thigh showing a round mass in the medial soft tissues (white arrow). The mass (a malignant fibrous histiocytoma) is difficult to identify because it has similar signal intensity to normal muscle on this sequence

Figure 10 A coronal STIR image (*TR* 2200, *TE* 35, τ 160) showing the same lesion as that shown in Figure 9 (arrow). The mass is much more conspicuous on the STIR image

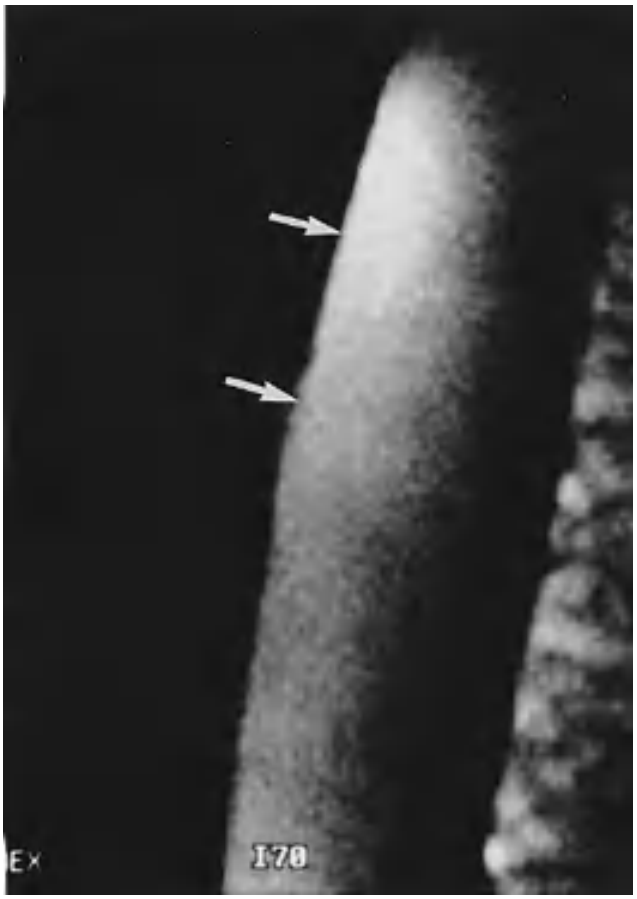

Figure 11 A T_1-weighted MR microscopy image showing the articular cartilage as a thick band of intermediate signal intensity (arrows)

articular cartilage. Some investigators have demonstrated a large magetization transfer effect due to the high degree of interaction between water and collagen macromolecules in articular cartilage. Specifically, it has been shown that the majority of the magnetization transfer effect is caused by interactions between water and the collagen matrix, and not between water and the proteoglycan component of cartilage.[55] This finding may prove useful in evaluation of subtle cartilaginous pathology, perhaps in conjuction with MR microscopy.

MR spectroscopy has existed for many years. Some work has been done using spectroscopy to evaluate metabolic diseases of muscles, but none of these techniques is in routine clinical use as yet. In recent years several manufacturers have developed smaller, relatively inexpensive scanners designed to scan extremity joints. These scanners are often 50 to 80% less expensive than traditional whole-body scanners and can be installed in standard clinic examining rooms (e.g. Esaote, Genoa, Italy). Though these scanners typically operate at low magnetic fields (0.2 T) and produce relatively noisy images, the price, convenience, and comfort is highly attractive to many patients. These devices are currently the fastest growing segment of the MR market.

5 CONCLUSIONS

In summary, MRI is a powerful tool in noninvasive evaluation of abnormalities of peripheral joints. The combination of high spatial resolution and sensitivity to local alterations in water content and T_1 and T_2 relaxation times makes it ideal for demonstrating pathological processes. MR has a role in the evaluation of many disease processes including trauma, infection, vascular compromise, and neoplasm. Additional techniques that may prove clinically useful in the future include MR microscopy, diffusion and perfusion imaging, magnetization transfer contrast, MR spectroscopy, and speciality scanners.

6 RELATED ARTICLES

Gadolinium Chelate Contrast Agents in MRI: Clinical Applications; Gadolinium Chelates: Chemistry, Safety, and Behavior; MRI of Musculoskeletal Neoplasms; Skeletal Muscle Evaluated by MRI.

7 REFERENCES

1. J. Tehranzadeh, W. Mnaymneh, C. Ghavam, G. Morillo, and B. J. Murphy, *J. Comput. Assist. Tomogr.*, 1989, **13**, 466.
2. W. P. Chan, P. Lang, M. P. Stevens, K. Sack, S. Majumdar, D. W. Stoller, C. Basch, and H. K. Genant, *Am. J. Roentgenol.*, 1991, **157**, 799.
3. P. Dragorot and C. Claussen, *ROFO*, 1980, **133**, 185.
4. J. V. Crues and D. W. Stoller, in 'Magnetic Resonance Imaging of the Knee', 2nd edn., eds., J. Mink, M. Reicher, J. V. Crues, and A. Deutsch, Raven Press, New York, 1993, pp. 91–140.
5. I. P. C. Murray, J. Dixon, and L. Kohan, *Clin. Nucl. Med.*, 1990, **15**, 828.
6. J. H. Mink, M. A. Reicher, J. V. I. Crues, and A. L. Deutsch, 'Magnetic Resonance Imaging of the Knee', 2nd edn. eds. J. Mink, M. Reicher, J. V. Crues, and A. Deutsch, Raven Press, New York, 1993, p. 474.
7. D. W. Stoller, 'Magnetic Resonance Imaging in Orthopedic and Sports Medicine', Lippincott, Philadelphia, PA, 1993, 1127.
8. D. Resnick and M. Niwayama, eds. 'Diagnosis of Bone and Joint Disorders', 2nd edn. W. B. Saunders, Philadelphia, PA, 1988, Vol. 2, 4174+.
9. B. Flannigan, S. Kursunoglu-Brahme, S. Snyder, R. Karzel, W. Del Pizzo and D. Resnick, *Am. J. Roentgenol.*, 1990, **155**, 829.
10. J. Hodler, S. Kursunoglu-Brahme, S. J. Snyder, V. Cervilla, R. P. Karzel, M. E. Schweitzer, B. D. Flannigan, and D. Resnick, *Radiology*, 1992, **182**, 4316.
11. J. W. Helgason, V. P. Chandnani, and J. S. Yu, *Am. J. Roentgenol.*, 1997, **168**, 1473.
12. J. V. I. Crues, in 'MRI of the Knee', eds. J. H. Mink et al., Raven Press, New York, 1993, p. 1.
13. J. V. Crues and R. Ryu, in 'Magnetic Resonance Imaging', eds. D. Stark and W. G. Bradley, Mosby, St. Louis, MO, 1992, Vol. 2, pp. 2424–2458.
14. S. Koenig, R. D. Brown III, and R. Ugolini, *Magn. Reson. Med.*, 1993, **29**, 77.
15. J. Hennig and H. Friedburg, *Magn. Reson. Imaging*, 1988, **6**, 391.
16. J. Listerud, S. Einstein, E. Outwater, H. Y. Kressel, *Magn. Reson. Q.*, 1992, **8**, 199.
17. R. T. Constable and J. C. Gore, *Magn. Reson. Med.*, 1992, **28**, 9.
18. D. A. Rubin, J. B. Kneeland, J. Listerud, S. J. Underberg-Davis, and M. K. Dalinka, *Am. J. Roentgenol.*, 1994, **162**, 1131.
19. J. A. Carrino, T. R. McCauley, L. D. Katz, R. C. Smith, and R. C. Lange, *Radiology*, 1997, **202**, 533.
20. E. M. Haacke and J. A. Tkach, *Am. J. Roentgenol.*, 1990, **155**, 951.
21. M. P. Recht, G. A. Piraino, J. P. Schils, and G. H. Belhobek, *Radiology*, 1996, **198**, 209.
22. M. J. Geirnaerdt, J. L. Bloem, F. Eulderink, P. C. Hogendoorn, and A. H. Taminiau, *Radiology*, 1993, **186**, 813.
23. K. Herrlin et al., *Acta Radiol.*, 1990, **31**, 233.
24. B. C. Dangman, F. A. Hoffer, F. F. Rand, and E. J. O'Rourke, *Radiology*, 1992, **182**, 743.
25. M. F. Reiser and M. Naegele, *J. Magn. Reson. Imaging*, 1993, **3**, 307.
26. P. F. J. Tirman, A. E. Stauffer, J. V. Crues III, R. M. Turner, W. M. Nottage, W. E. Schobert, B. D. Rubin, D. L. Janzen, and R. C. Linares, *Arthroscopy*, 1993, **9**, 550.
27. A. L. Deutsch, J. H. Mink, J. M. Fox, M. J. Friedman, and S. M. Howell, *Magn. Res. Q.*, 1992, **8**, 23.
28. A. L. Deutsch, J. H. Mink, and R. Kerr, 'MRI of the Foot and Ankle'. New York, Raven Press, 1992, p. 378.
29. J. H. Mink, in 'MRI of the Foot and Ankle', eds. A. L. Deutsch, J. H. Mink, and R. Kerr, Raven Press, New York, 1992.
30. T. C. Lynch, J. V. Crues III, F. W. Morgan, W. E. Sheehan, L. P. Harter, and R. Ryu, *Radiology*, 1989, **171**, 761.
31. G. A. Bogost, E. K. Lizerbram, and J. V. Crues III, *Radiology*, 1995, **197**, 263.
32. A. Vellet, P. Marks, P. Fowler, and T. Munro, *Radiology*, 1991, **178**, 271.
33. G. M. Blum, P. F. J. Tirman, and J. V. Crues III, in 'MRI of the Knee', 2nd. edn., eds. J. H. Mink, M. A. Reicher, J. V. Crues III, and A. L. Deutsch, Raven Press, New York, 1993, pp. 295–332.
34. A. Wang, D. Weinstein, L. Greenfield, L. Chiu, R. Chambers, C. Stewart, G. Hung, F. Diaz, and T. Ellis, *Magn. Reson. Imaging*, 1990, **8**, 675.
35. C. P. Sabiston, M. E. Adams, and D. K. Li, *J. Orthop. Res.*, 1987, **5**, 164.
36. M. O. Senac, Jr., D. Deutsch, B. H. Bernstein, P. Stanley, J. V. Crues III, D. W. Stoller, and J. Mink, *Am. J. Roentgenol.*, 1988, **150**, 873.
37. H. J. Mankin, *N. Engl. J. Med.*, 1992, **326**, 1473.
38. D. G. Mitchell, M. E. Steinberg, M. K. Dalinka, V. M. Rao, M. Fallon, and H. Y. Kressel, *Clin. Orthop.*, 1989, **244**, 60.
39. H. Tsukamoto, Y. S. Kang, L. C. Jones, M. Cova, C. J. Herold, E. McVeigh, D. S. Hungerford, and E. A. Zerhouni, *Invest. Radiol.*, 1992, **4**, 275.
40. M. Cova, Y. S. Kang, H. Tsukamoto, L. C. Jones, E. McVeigh, B. L. Neff, C. J. Herold, J. Scott, D. S. Hungerford, and E. A. Zerhouni, *Radiology*, 1991, **179**, 535.
41. M. J. A. Geirnaerdt, J. Hermans, J. L. Bloem, H. M. Kroon, T. L. Pope, A. H. M. Taminiau, and P. C. W. Hogendoorn, *Am. J. Roentgenol.*, 1997, **169**, 1097.
42. J. S. Jelinek, M. J. Kransdorf, B. M. Shmookler, A. J. Aboulafia, and M. M. Malawer, *Radiology*, 1993, **186**, 455.
43. J. S. Jelinek, M. J. Kransdorf, B. M. Shmookler, A. A. Aboulafia, and M. M. Malawer, *Am. J. Roentgenol.*, 1994, **162** 919.
44. J. S. Jelinek, M. D. Murphey, M. J. Kransdorf, B. M. Shmookler, M. M. Malawer, and R. C. Hur, *Radiology*, 1996, **201**, 837.
45. D. G. Varma, A. G. Ayala, S. Q. Guo, L. A. Moulopoulos, E. E. Kim, and C. Charnsangavej, *J. Comput. Assist. Tomogr.*, 1993, **17**, 414.
46. S. L. Hanna, B. D. Fletcher, D. M. Parham, and M. F. Bugg, *J. Magn. Reson. Imaging*, 1991, **1**, 441.
47. P. Lang, G. Honda, T. Roberts, *et al.*, *Radiology*, 1995, **197**, 83.

48. T. H. Berquist, R. L. Ehman, B. F. King, C. G. Hodgman, and D. M. Iistrup, *Am. J. Roentgenol.*, 1990, **155**, 1251.
49. R. Erlemann, J. Sciuk, A. Bosse, J. Ritter, C. R. Kusnierz-Glaz, P. E. Peters, and P. Wuisman, *Radiology*, 1990, **175**, 791.
50. R. Erlemann, M. Reiser, P. Peters, P. Vasallo, B. Nommensen, C. R. Kusnierz-Glaz, J. Ritter, and A. Roessner, *Radiology*, 1989, **171**, 767.
51. J. Rubenstein, M. Recht, D. G. Disler, J. Kim, and R. M. Henkelman, *Radiology*, 1997, **204**, 15.
52. J. D. Rubenstein, J. G. Li, S. Majumdar, and R. M. Henkelman, *Am. J. Roentgenol.*, 1997, **169**, 1089.
53. K. B. Lehner, H. P. Rechl, J. K. Gmeinwieser, A. F. Heuck, H. P. Lukas, and H. P. Kohl, *Radiology*, 1989, **170**, 495.
54. D. Le Bihan, *Radiology*, 1998, **207**, 305.
55. D. K. Kim, T. L. Ceckler, V. C. Hascall, A. Calabro, and R. S. Balaban, *Magn. Reson. Med.*, 1993, **29**, 211.

Biographical Sketches

Paul S. Hsieh. *b* 1962. B.S. (Mathematics), MIT, 1984; M.D. University of Michigan, 1989; residency in Diagnostic Radiology, Mallinckrodt Institute of Radiology, 1993; MRI training with John V. Crues, 1994; Faculty in Musculoskeletal Radiology at the Mallinckrodt Institute of Radiology 1994–1997. Currently staff radiologist, Kaiser Permanente, San Diego, CA. Research interests: musculoskeletal MRI.

John V. Crues, III. *b* 1949. A.B., 1972, Harvard; M.S., 1975, physics, with Charles Slichter, University of Illinois; M.D., 1979 Harvard Medical School, residency in Internal Medicine 1982 and Radiology 1985 at Cedars-Sinai Medical Center. Currently Director of Magnetic Resonance at Cedars-Sinai Medical Center. Former President of the International Society for Magnetic Resonance in Medicine. Currently Medical Director of RadNet Management, Inc. and President, ProNet Imaging in Los Angeles, CA. Approx. 200 publications. Current research specialty: musculoskeletal MRI, picture archiving and communication systems.

Peripheral Muscle Metabolism Studied by MRS

Peter A. Martin, Henry Gibson, and Richard H. T. Edwards

Magnetic Resonance Research Centre and Muscle Research Centre, The University of Liverpool, Liverpool, UK

1 INTRODUCTION

Muscle is a unique biological machine providing the main method of generating motive force, work, and power: it constitutes some 40% of total body cell mass in normal man. It is easily accessible for study and capable of great versatility in performance from a delicate touch to a powerful punch or from running a sprint to a marathon. Muscle metabolic rates can rapidly increase by over 100-fold. The body has nearly 600 muscles divided into three groups, skeletal (striated), visceral (non-striated), and cardiac; cardiac muscle is dealt with elsewhere (see ***NMR Spectroscopy of the Human Heart***). Here we are only concerned with the muscles of the limbs, i.e., 'peripheral' skeletal muscle, which was one of the first tissues to be studied by magnetic resonance spectroscopy (MRS). Diseases of muscle (myopathies) are rare and often chronic and disabling, largely due to wasting of muscle tissue, which may be progressively replaced by fat or fibrous tissue, such as in the inherited X-linked muscular dystrophies. This creates a problem in trying to monitor muscle biochemistry because of serious partial volume effects, i.e., any volume of muscle under study contains an abnormally high proportion of fat or fibrous tissue as is readily seen on muscle biopsy. Quite different are the specific cellular enzyme and membrane defects of muscle, where this fat replacement is absent or less evident. They represent 'Nature's experiments' where the impairment is due to interference with some essential metabolic pathway. They constitute an interesting group of disorders which are particularly amenable to study by in vivo MRS. Magnetic resonance imaging (MRI) has been confined largely to the study of anatomy and gross pathology (see ***Skeletal Muscle Evaluated by MRI***), whereas MRS has mostly been confined to metabolic studies of phosphorus (^{31}P)-containing compounds, although some work has been done using hydrogen (^{1}H)[1,2] and carbon-13 (^{13}C).[3] Fortunately, the phosphorus-containing compounds visible by MRS—phosphocreatine (PCr), adenosine triphosphate (ATP) and inorganic phosphate (Pi)—are of great interest since they are involved in the energy metabolism of the muscle cells enabling MRS to be used to study muscle energetics noninvasively.

2 MUSCLE STRUCTURE AND FUNCTION

Human muscle comprises at least two populations of fibers with different functional and metabolic characteristics. In health, the distribution of fibers in particular muscles reflects the physiological function of the muscle, whether for postural control (e.g. soleus) or for rapid movement (e.g. biceps). Muscles are organized in bundles (fascicles) and form into groups with a particular gross structure characteristic of that muscle (e.g. pennation angle, which can be determined by MRI[4]).

Muscles work together as 'agonists' and 'antagonists' to achieve a particular force or movement. The protein chemistry and fine structural features responsible for force generation in muscle are beyond the resolution of whole body MR systems, and are, thus, not covered here.

The muscle fibers (cells) have an outer membrane, the sarcolemma, filled with a fluid, sarcoplasm, containing the endoplasmic reticulum, mitochondria, and the many peripherally located nuclei. The myofibrils, which constitute a large component of the cell, consist of a matrix of interdigitating actin and myosin protein chains. Muscle performance is achieved by the action of actin and myosin chains sliding over each other, shortening the length of the sarcomere and thus the muscle. Muscles contract in response to a nerve impulse and each muscle cell must therefore have a neuronal connection. However a single neurone will have from a few to several hundred branches, each connecting with muscle cells that all contract together. This group forms a motor unit and the recruitment of an increasing number of motor units is one of the main factors governing the control and precision of any force generated.

Initiation of a contraction depends on a nerve signal being transmitted to the muscle via a chemical messenger acetylcholine. This causes an 'action potential' to be produced in the form of a region of electrical depolarization on the sarcolemmal membrane. The action potential rapidly travels the length of the muscle cell releasing calcium from the lateral cisternae of the endoplasmic reticulum. The calcium release activates actomyosin ATPase and triggers myofibrillar cross bridge interaction and thus force generation. A single action potential produces a single twitch involving the *entire* muscle fiber. Gradation of strength depends on changing the number of muscle fibers that are active. For a prolonged contraction of greater force, multiple stimuli are used, and if the frequency of stimulation is high enough the individual twitches fuse together to produce a smoothly sustained *tetanic* contraction, which lasts longer and is several-fold stronger than a single twitch. The two basic types of skeletal muscle fibers contract at different speeds; the 'red', slow-twitch (or type I) fibers are best suited to prolonged aerobic exercise, whereas the 'white' fast-twitch (or type II) fibers are best adapted to high intensity exercise that is largely anaerobic; intermediate fiber types also occur, and their prevalence depends on the activity history of the muscle (see Table 1). The importance of the recognition of two main fiber type populations in human muscles is that regional metabolic inhomogeneity can develop within the muscle as a consequence of particular forms of muscular activity in which individual populations of muscle become fatigued to different extents, resulting in their discrete appearance in the spectra. [e.g. split inorganic phosphate (Pi) peak]. Another consideration which can confuse this interpretation is that the sensitive volume of tissue studied may include more than one agonist muscle group, of which only one may be active.

Table 1 Summary of broad characteristics of main fiber types in human skeletal muscle

Characteristic	Slow twitch, Type I	Fast twitch, Type II
Contraction time	Long	Short
Relaxation time	Long	Short
Myosin ATPase activity	Low	High
Fatigability	Low	High
Phosphocreatine content	Low	High
Oxidative enzyme activity	High	Low
Capillary density	High	Low
Mitochondria	Numerous	Few
Glycogen content	No difference	No difference
Fat content	High	Low
Myoglobin content	High	Low

3 MUSCLE AS A BIOLOGICAL MACHINE

When considering muscle function it is important to recognize the relationships between energy, force, work, and power. In the human body energy, measured in joules (J), is available for muscle metabolism via either the long- or the short-term energy supply processes. The maximum force, measured in newtons (N), that a muscle can generate (its strength), depends on the cross-sectional area of active muscle fibers. Comparison of working muscles requires that they are doing the same amount of work, i.e. force $\times$ distance, or generating the same power output (force $\times$ distance/time) which is measured in watts (W). The work done by the muscle will equal the energy expended only if the muscle is 100% efficient. Most muscular activity is about 20% efficient, the remainder of the energy being dissipated as heat. The maximum power output of the muscle depends on its maximum force *and* its velocity of shortening. During isometric exercise, when the muscle contracts without altering its length, external power output is zero; however the force–time integral can be used as an indicator of muscular activity.[5]

4 PRACTICAL ASPECTS OF ERGOMETRY

Of vital importance in the study of any particular muscle is the need to be able to measure accurately and objectively its force, work, and power output. In the body, muscles in vivo form part of a complex machine, with their diverse attachments to bones and the agonist/antagonist arrangement by which they work together or against each other respectively. Sensible force measurement depends on the careful design of the ergometers used. The 'man–machine interface' thus becomes of paramount importance to provide an objective work standard against which NMR measurements may be correlated. Exercise can be dynamic such as running or walking or isometric (static) as in holding various body postures or a heavy weight. Although much human activity consists of dynamic exercise the constraints of space within the magnet system mean that isometric exercise is more easily studied. Although many ergometers are available, their use in conjunction with MR systems is limited, not least because human muscle studies by MRS carried out in the 1.5–2 T horizontal bore, whole body magnet systems, necessitate that the subject should lie down in the magnet. MR systems have magnets that are designed to have good homogeneity, but they also produce strong fringe fields. Commercially available ergometers are made of ferromagnetic materials or involve electrical motors or dynamos, which means that they will not work properly in the close proximity of strong magnetic fields of the MR system; such ergometers will in turn destroy the homogeneity of the magnetic field.

In the future, we may expect both these problems to be resolved as new magnet designs are becoming available that will enable the subject to stand up within the magnet system and carry out exercise routines such as running or cycling, which are more in keeping with normal human activity. Secondly, improved magnetic shielding is reducing the stray field of the magnet systems to such an extent that conventional ergometers can be used within 1 m or so of the MR magnet. However it is unlikely that the need for specially designed nonmagnetic ergometers will disappear; indeed the opportunities opened up by this new field will require new and more sophisticated designs.

Figure 1 shows an example of an apparatus that has been used for the study of isometric exercise in the quadriceps muscle during both voluntary and electrically stimulated exercise studies.[6] The subject lies supine with the knees bent and resting at an angle of 120° over a polystyrene foam block. The ankle is restrained by a strap which is attached to a force transducer while a wide belt across the waist prevents subjects from using their back and abdominal muscles to aid in the exercise. Stimulation electrodes strapped on with crepe bandages are applied both superior and inferior of the quadriceps to allow electrical stimulation of the muscle. The electrodes are connected via screened leads and a radiofrequency filter to a

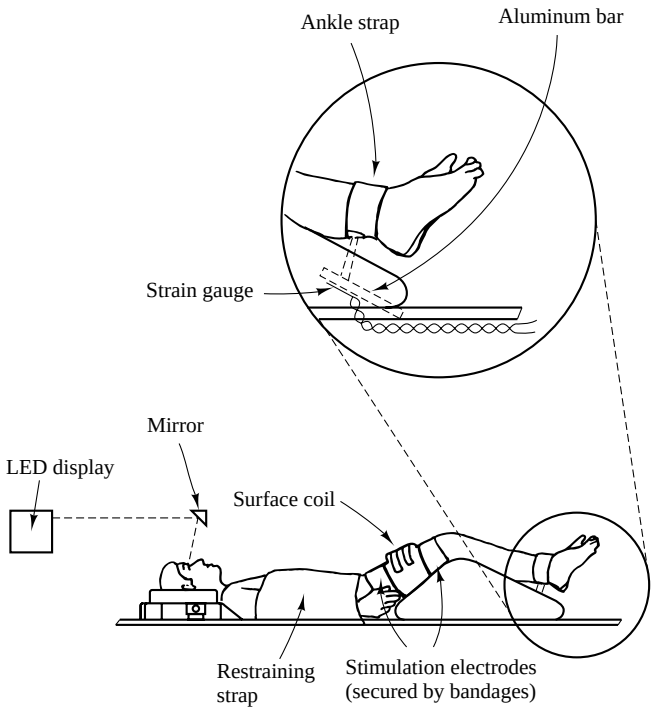

Figure 1 Apparatus for the study of the quadriceps muscles

commercial stimulator and consist of 2 cm^2 of copper over a conducting gel pad, 5 cm × 10 cm, cut from a commercial defibrillator pad. The force transducer consists of an aluminum bar and strain gauge connected to a preamplifier, the output of which passes out of the scan room via a radiofrequency filter. Visual and audio feedback of the measured force are provided to the subject from a LED bar graph and tone generator to enable the subject to make voluntary contractions to prescribed target forces. Red, yellow and green LEDs under control from the spectrometer's computer are used to tell the subject when to exercise and to provide warning of forthcoming electrical stimulation. The limb may be made ischemic (blood supply stopped) by simply inflating a thigh sphygmomanometer cuff to 100 mmHg above systolic blood pressure, thereby providing a closed system trapping metabolites and preventing oxidative recovery processes. Measurement of myographic activity is also possible without deterioration of the magnetic homogeneity.[7]

5 MRS TECHNIQUES FOR MUSCLE STUDIES

The spectacular improvement in MRI has not been matched by a comparable improvement in in vivo MRS over the 15 or so years since the introduction of the first small-bore in vivo spectroscopy systems. Clinical applications of spectroscopy have been slow to appear, and it is still not a routine diagnostic tool. An illustration of the range and quality of spectra that can be obtained is shown in Figure 2. This shows a set of spectra from the forearm of a normal boy and a dystrophic boy with Duchenne muscular dystrophy.[8] The ^{1}H spectrum for the dystrophic forearm shows a decrease in the water peak and an increase in the fat peak. The ^{13}C spectrum shows a lot more peaks, but at the resolution achievable with the 1.5–2.3 T of most in vivo systems, this is difficult to interpret with many overlapping peaks. The peaks due to CH_3 and CH_2 groups are clearly visible, however, and the dystrophic forearm shows a general increase in the ^{13}C signal, which is most obvious in fat signals in the CH_2 region. The phosphorus spectrum shows a large peak due to PCr and three peaks due to ATP, as well as a small peak due to Pi. The dystrophic ^{31}P spectrum shows a decrease in the total signal of phosphorus metabolites as the fat displaces the muscle. The utility of MRS for muscle studies depends primarily on the quality of the spectra that can be obtained. Quantitative analysis requires as good a signal-to-noise ratio (S/N) as possible for all the peaks of interest. Qualitative studies can tolerate a poorer S/N but here extra care needs to be taken in the interpretation of results. Many factors interact to influence the spectral quality, e.g. the field strength and homogeneity of the magnet, the size and location of the muscle to be studied, the magnetic sensitivity of the nucleus, e.g. ^{31}P, ^{13}C, ^{1}H, the type of radiofrequency coil to be used, the MR localization technique, and the type of muscular activity to be studied.

The first localization technique used in muscle studies was 'surface coil localization'.[9] This is suitable for all nuclei and relies entirely on the localized but inherently nonuniform response of a simple loop antenna (the surface coil) to restrict the region from which signals would be obtained (see ***Surface Coil NMR: Detection with Inhomogeneous Radiofrequency Field Antennas***); when both transmitter and receiver surface

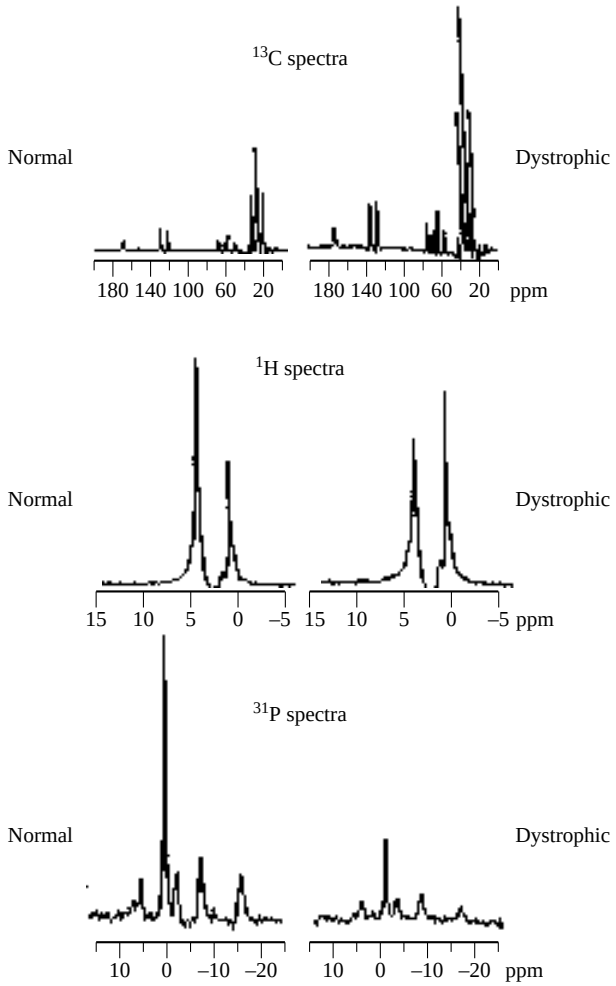

Figure 2 Resting ^{13}C, ^{1}H, and ^{31}P NMR spectra of the forearm. The spectra on the right are from a 9-year-old with Duchenne's dystrophy, and on the left are from an age-matched control with similar skin thickness

coils are used they have a sensitive volume which forms a hemisphere penetrating to a depth of roughly one coil radius. This was later supplemented by the use of magnetic field localization techniques of which the most widely used for muscle studies has been the topical magnetic resonance (TMR) method.[10] This used a static, high order ($Z4$) gradient to spoil deliberately the magnet homogeneity over all but the chosen small diameter, central region of the magnet; any signals coming from this uniform central volume would be sharp peaks, whereas any signals coming from outside this volume would appear as a broad hump in the baseline, which could be removed from the final spectra via a convolution difference technique.

Topical magnetic resonance had the big advantage that good localization (superior to that of a surface coil alone) can be obtained from a single acquisition, making it suitable for studies requiring time resolution of the order of 1 or 2 s. It had the disadvantage of relying on static magnetic field gradients, which could not be switched rapidly on and off, and which only produced a uniform field at the center of the magnet, requiring the muscle of interest to be located there. This put

Table 2 ^{31}P relaxation times in human skeletal muscle

	Field (T)	α-ATP	β-ATP	γ-ATP	PCr	Pi	Ref.
T_1(s)	1.5	3.603	4.310	4.755	5.517	4.017	[16]
T_2(ms)	1.5	22.2[a]	8.1[a]	16.1[a]	424.3	204.7	[14]

[a]These measured values are probably lower than the true in vivo values due to the effects of *J* coupling which were not taken into account in this study[17]

physical and anatomical constraints on what could be studied. Thus, the TMR method rapidly fell out of favor once magnets with switched gradients became available holding the promise of combining imaging and spectroscopy in studies and pulsed gradient localization techniques, allowing localization of any volume within the (larger) homogenous region in the center of the magnet. An alternative localization strategy that has been used by some groups is to use one-dimensional, 'Rotating Frame' chemical shift imaging;[11] this has not been widely adopted, however, largely because of the T_2 distortion to which it is susceptible. This shows itself primarily as a decrease in the area of the β-ATP peak which is a particular disadvantage since this peak is often used as an internal reference for quantitation.

Of the many gradient localization techniques that have been introduced over the last 10 years, few of them have found practical application in muscle studies. This is because most muscle studies have used ^{31}P spectroscopy. Carbon-13 spectroscopy has been done at natural abundance,[12,13] but generally the most useful results are obtained with the introduction of ^{13}C labeled compounds, but with greatly increased cost. Water-suppressed ^{1}H spectroscopy has not yet been widely applied to muscle and for the most part unsuppressed ^{1}H spectra are only of limited value. Compared with protons, phosphorus nuclei tend to have short T_2 relaxation times,[14] which makes them unsuitable for any localization technique that relies on long echo time, spin, or stimulated echoes, e.g. Pixel-RESolved Spectrocopy (PRESS) and the STimulated Echo Acquisition Method (STEAM). One simple localization technique which has found some application in muscle spectroscopy is Depth-REsolved Surface coil Spectroscopy (DRESS). This consists of a conventional slice selection followed by collection of an FID signal, though the loss of some signal, particularly from β-ATP, is a disadvantage, and baseline distortions caused by the long delays between excitation and data acquisition make subsequent processing and any attempts at accurate quantitation difficult.[15] The best true volume localization technique for ^{31}P spectroscopy is the Image-Selected In vivo Spectroscopy technique (ISIS). This has the advantage that it does not use spin echoes and thus is capable of giving good, undistorted spectra suitable for quantitation, but ISIS suffers from the serious disadvantage that it is a differencing technique requiring a minimum of eight signals for full volume localization. This makes it highly susceptible to motion artifacts and thus completely unsuitable for exercise studies. The quality of localization is affected by T_1 effects and thus, for muscle studies, it should ideally be run at repetition times (*TR*) of 15 s, making it unsuitable for short-duration time course studies.

Because of the problems associated with volume localization techniques most muscle studies still use surface coil localization alone. This presents some difficulties for quantitation since the nonuniform response of the coil results in a variation of the flip angle throughout the sensitive volume causing variation in signal strength due to T_1 and T_2 effects (see Table 2). This has been ameliorated a little with the introduction of specially designed rf pulses designed to give uniform flip angles over a larger proportion of the coil's sensitive volume (see ***Surface Coil NMR: Detection with Inhomogeneous Radiofrequency Field Antennas***).

Table 3 Energy sources for muscular activity

Short-term (anaerobic) energy sources

ATP hydrolysis:

$$\text{Adenosine triphosphate (ATP)} + H_2O \xrightarrow{\text{myosin-ATPase}} \text{adenosine diphosphate (ADP) + inorganic phosphate (Pi) + energy}$$

Creatine kinase reaction:

$$\text{Phosphocreatine} + \text{ADP} + 0.9\ H^+ \xrightarrow{\text{creatine kinase}} \text{creatine} + \text{ATP}$$

Anaerobic glycolysis:

$$\text{Glycogen (glycosyl unit)} + 3\ \text{Pi} + 3\ \text{ADP} \longrightarrow 2\ \text{lactate} + 3\ \text{ATP}$$

Long-term (aerobic) sources

Oxidative phosphorylation:

$$\text{Glycogen/Glucose/Free fatty acids/Free amino acids} \longrightarrow \text{NADH}$$

$$\text{NADH} + 1.5\ H^+ + 0.5O_2 + 3\text{ADP} + 3\text{Pi} \longrightarrow H_2O + NAD^+ + 3\text{ATP}$$

In vivo spectroscopy is currently only capable of 'seeing' narrow lines produced from long T_2 metabolites, i.e. those in solution in the cytoplasm. These metabolites become MR invisible or only give broad lines, which appear as a hump in the baseline, when in a viscous medium or when bound to the mitochondrial matrix. This is an advantage in that only the cytoplasmic metabolites are important in assessing the muscle energy metabolism during exercise.

In vivo quantification has always been difficult. As a result, many muscle studies report their results in terms of ratios of peak areas. An approximation to quantitation can then be made if appropriate assumptions are made, e.g., the total MRS visible phosphorus concentration or the ATP concentration. This enables estimates to be made of the ^{31}P-containing metabolite concentrations. A common reference method is by comparison with β-ATP concentration. Improved quantitation can be obtained if some form of external or internal standard is used. Internal standards have to be inherent in the muscle under study and thus one method is to collect a ^{1}H spectrum and to use the water peak as a reference. One problem with this is that the water content of muscle varies, especially during exercise. Assumptions about the water concentration cannot therefore be used. To overcome this, several water spectra at different *TR*s must be obtained and the true H_2O concentration calculated, but again this is not suitable for exercise studies. An acceptable method is to use an external phantom, often attached to the coil as a reference, and the ^{31}P concentration in vivo is determined by comparison with that from a series of different concentration phosphate solutions external to the limb studied or suitably substituted for the limb after the study.

6 METABOLIC PATHWAYS

Most MRS studies of muscle concern the biochemical pathways (see Table 3) for the supply and utilization of energy. The first reaction to be considered is the hydrolysis of ATP to ADP, catalyzed by myosin ATPase, which produces the energy-driving muscular contraction. Normal muscle only contains a small amount of cytosolic ATP and so can only sustain contractile activity for a very short period of time before fresh supplies of ATP must be made available. These supplies are obtained not from stores of ATP itself but via a reservoir of energy in the form of PCr which is used in the cytosol by the creatine kinase reaction to recycle ADP rapidly back to ATP again. The resulting creatine (Cr) is transported to the mitochondria of the cell where the reverse reaction occurs catalyzed by creatine kinase and Cr is converted back to PCr at the expense of mitochondrial ATP; this is the oxidative phosphorylation reaction or mitochondrial respiration.

Under aerobic conditions, i.e. when the O_2 supply from the blood is maintained, mitochondrial respiration supplies most of the muscles' energy requirements in the form of ATP. This results in production of one-tenth of a mole of H^+, from carbonic acid, per mole of ATP. When the energy demand exceeds the mitochondrial capacity or when anaerobic (ischemic) conditions exist, only PCr and glycogenolysis can supply the ATP for contraction. When anaerobic metabolism takes place, large amounts of lactate are therefore produced from glycogenolysis, giving two-thirds of a mole of H^+ per mole of ATP leading to a large decrease in intracellular pH.[18] This fall in pH may have profound effects on pH-sensitive metabolic processes (see e.g., Table 1). Phosphocreatine hydrolysis consumes protons whereas PCr synthesis produces protons. Fortunately it is easy to measure pH by ^{31}P MRS, and after taking into account the effects of buffering and proton efflux, i.e. loss of protons from the cell, the rate of proton production can be calculated. Thus the effect of pH on ATP fluxes can be allowed for. Furthermore, it is believed that pH affects cross bridge kinetics[19] leading to a reduction in force generation, i.e. fatigue.

7 THE STUDY OF MUSCLE USING ^{31}P MRS

7.1 Estimation of pH

Inorganic phosphate (Pi) in vivo has a pK_a of about 6.75 at physiological pH and exists in an equilibrium between two forms $H_2PO_4^-$ and HPO_4^{2-}. These give rise to two separate phosphate resonances, 2.3 ppm apart, which undergo rapid chemical exchange (10^9–10^{10} s^{-1}), resulting in a spectrum containing a single resonance whose frequency depends on the relative amounts of the two moieties. Since the equilibrium between the two forms of Pi is pH-dependent, the chemical shift of the Pi peak can be used as an indicator of pH by measuring its chemical shift either relative to an external standard such as methylenediphosphonate or relative to internal standards such as the pH-insensitive resonances due to the phosphorus PCr peak or the proton water signal. In the normal, resting, human forearm muscle of Figure 2, the chemical shift of Pi from PCr is 5.00 ppm corresponding to a pH of 7.15, whereas during exercise the chemical shift of Pi falls to 4.66 ppm corresponding to a pH of 6.88, due to the presence of lactate. The pH may be calculated from the equation.

$$\mathrm{pH} = 6.75 + \log[(\delta - 3.27)/(5.69 - \delta)] \quad (1)$$

where δ is the chemical shift difference, in ppm, between the Pi and PCr peaks.

7.2 The Buffering Capacity of Muscle

A knowledge of the buffering capacity is necessary for determination of ATP fluxes since the H^+ ions are involved in the equilibria (see Table 3). During the initial part of aerobic exercise the assumption can be made that the proton efflux can be neglected, enabling the glycogenolytic rate to be estimated in the same way as for ischemic exercise. This assumption falls down when the buffering capacity has been exhausted and the pH starts to fall. The cytosolic buffering capacity of skeletal muscle depends on Pi (pK = 6.57), bicarbonate (pK = 6.1), and other buffers, largely imidazole groups in histidine residues. It has been shown[20] that in a closed system where the total CO_2 is constant (e.g. during ischemia) the buffer capacity β is given by:

For Pi:

$$\beta = 2.3\,[\mathrm{Pi}]/\{[1 + 10^{(\mathrm{pH} - 6.75)}]\,[1 + 10^{(6.75 - \mathrm{pH})}]\} \quad (2)$$

where β is measured in slykes (i.e. mmol L^{-1} per pH unit).

For bicarbonate:

$$\beta = 2.3\, S\, pCO_2\, 10^{(pH-6.1)} / \{[1 + 10^{(pH-6.1)}]\,[1 + 10^{(6.1-pH)}]\} \quad (3)$$

where S is the solubility of CO_2. Taking pCO_2 as 5 kPa and S as 0.3 mmol L^{-1} kPa^{-1} then at its resting pH in closed muscle β is less than 5 slykes.

For other buffers: $\beta = 20$–30 slykes; inferred by analysis of ^{31}P MRS data and from measurements in muscle homogenates.[20]

7.3 Muscle at Rest

Many studies have been performed on resting muscle but these have frequently been hampered by the wide range of physiological states of the muscle under study, largely due to the intrinsic variations in the level of training in the populations under study. One of the first and most important findings from studies of resting muscle has been the observation that the concentration of PCr is consistently higher when measured by ^{31}P MRS than when measured by freeze-clamped needle biopsy.[8] This is almost certainly due to the rapid hydrolysis of PCr to Pi during the freeze-clamping process and this interpretation can be supported by the observation that the total phosphorus concentration [PCr + Pi] obtained by both methods is approximately the same. No such discrepancies between the techniques have been observed with ATP, possibly due to equilibration of the creatine kinase reaction during the extraction procedures. Most quantitative ^{31}P MRS studies on resting muscle have relied not on true quantitation, but on the assumption that the ATP levels are reasonably constant. This assumption requires care as there is evidence that changes in the resting levels of metabolites depend on the prior history of the muscle. If the muscle has been involved in exercise involving lengthening contractions,[21] the PCr/Pi ratio is significantly reduced up to 1 h after exercise; the reduction continues with the ratio reaching a minimum at 1 day postexercise and remaining low for between 3 and 10 days postexercise. Similarly, abnormal spectra have been reported for up to 2–3 days after short-term exercise, even when no muscle fiber damage is thought to have occurred. Much evidence is now accumulating to show that type I and type II fibers have different PCr/Pi ratios, with type II fibers having elevated PCr and ATP compared with type I. The resting ratios and changes discussed above may be related to the different fiber-type ratios found in normal subjects.[22]

7.4 Exercise and Fatigue

While much information about muscle energy status can be obtained at rest, it is during exercise that the most dramatic changes are seen owing to the high metabolic exchanges associated with muscular activity. Particular interest lies in the study of individuals with defects of metabolism, which can give information about metabolic processes not normally accessible. This is discussed further in Section 8. Metabolic requirements may be determined at various workloads and metabolic processes may be related to physiological changes in function. Muscle fatigue, the decline in force or power output with prolonged activity, has received much attention in this respect, but is complicated by the type of muscular activity undertaken and the many cellular physiological factors that appear to be interrelated with the chemical changes taking place. For this reason, and the importance of maintaining and improving muscle performance in sports and disease, the various known mechanisms contributing to fatigue are described below.

The central contribution to fatigue can be measured by comparing force output between alternate periods of voluntary contractions with that produced from electrical stimulation of a peripheral nerve. If the voluntary force output falls more than the stimulated force output the difference is due to fatigue of central motor control mechanisms rather than of the muscle itself.[23]

Except in the rare neuromuscular disease myasthenia gravis, fatigue due to failure of the neuromuscular transmission is rare. Much of the research of the last half century in this field has been directed toward gaining an understanding of the extent to which impaired energy supply or electromechanical coupling failure is the dominant problem in a particular form of muscular activity.[24,25] Fatigue of the muscle itself can be classified according to the response to different frequencies of electrical stimulation. Fatigue that is produced more with high-frequency electrical stimulation (HFF) occurs in myasthenia gravis. Low-frequency fatigue (LFF), in which there is selective impairment of force generation at low frequency, i.e., reduced 20:50 Hz force ratio, can occur for a long time after ischemia[26] or an eccentric muscular contraction[27] when force generation at high frequency has recovered.

From the energetics point of view HFF and LFF can be distinguished by the fact (from needle biopsy and MR studies early in recovery from severe ischemic exercise) that with HFF, recovery of force may occur before full recovery of PCr/β-ATP (or Pi/PCr), due to rapid recovery of membrane excitation (compound muscle action potential; CMAP). With LFF, force is still reduced 1 h after exercise when CMAP and PCr/β-ATP have recovered.[28]

7.4.1 ATP Turnover in Ischemic Exercise

In ischemic (anaerobic) exercise (i.e. when the blood supply to the muscle has been occluded), ATP is produced from two sources, the hydrolysis of PCr catalyzed by creatine kinase (= PCr depletion) and glycogenolysis, the breakdown of glycogen to lactic acid.[29] Knowledge of [PCr] and pH can be used to estimate the rate of ATP synthesis. Since decay of the PCr peak can be measured directly, the rate of ATP synthesis from the hydrolysis of PCr (D) can also be measured directly:

$$D = -\delta[PCr]/\delta t \quad (4)$$

Hydrolytic ATP synthesis also results in a net proton consumption at the rate:

$$\text{net proton consumption} = D/[1 + 10^{(pH-6.75)}] \quad (5)$$

The production of ATP via glycogenolysis (L) can be estimated from the effect of lactic acid production on pH. Since during ischemic exercise protons cannot escape from the system, glycogenolysis (from glycosyl units) produces 2 mol of lactic acid thereby releasing 3 mol of ATP.[29] Thus:

$$L = (3/2)\{D/[1 + 10^{(\mathrm{pH}-6.75)}] - \beta\delta\mathrm{pH}/\delta t\} \quad (6)$$

where β is the cytosolic buffering capacity of the muscle (derived as above). Since the total rate of ATP synthesis (F) is:

$$F = D + L \quad (7)$$

the total turnover of ATP is:

$$F = D + (3/2)\{D/[1 + 10^{(\mathrm{pH}-6.75)}] - \beta\delta\mathrm{pH}/\delta t\} \quad (8)$$

7.4.2 ATP Turnover in Aerobic Exercise

In aerobic (oxidative) exercise ATP is produced from PCr and the oxidative synthesis of ATP in the mitochondria. As before, the rate of depletion of PCr and thus the rate of hydrolytic ATP production is readily accessible by MRS. However the presence of oxidative ATP synthesis and the fact that the system is no longer closed, i.e. there is a net efflux of protons from the cells, complicates the assessment of total ATP production. One strategy has been to compare aerobic with ischemic exercise, making use of the power output relationships derived from graded ischemic exercise to provide the 'missing data' from aerobic exercise studies at the same power output.

At the start of aerobic exercise, proton efflux can be neglected and the glycogenolytic rate estimated as for ischemic exercise. At the end of ischemic exercise, when the pH is falling, estimates of glycogenolytic ATP synthesis rates must be corrected for the large proton efflux from the system. This can be done by assuming the proton efflux rate has a linear relationship to pH and [PCr] and thus can be inferred from the initial phase of recovery from exercise.

7.5 Recovery

The study of postexercise recovery provides an opportunity of studying the kinetics of recovery of muscle metabolites, and in particular it can be used to provide information on the pH-dependence of proton efflux, which can also be applied as a correction during the analysis of aerobic exercise.[30] After the completion of exercise, the accumulated ADP continues to stimulate mitochondrial respiration to resynthesize ATP; as a consequence, the cytoplasmic PCr pool is replenished through the creatine kinase equilibrium. The PCr replenishment during recovery from exercise has been shown to depend entirely on mitochondrial respiration by the absence of any metabolic recovery when the muscle is made ischemic after exercise by rapid inflation of a sphygmomanometer cuff.[31] Thus, we can consider the rate of PCr resynthesis to be a good index of mitochondrial function.[32]

The recovery of PCr after exercise appears to follow an exponential time course and experimentally is usually treated as such although it has been shown to be biphasic,[33] showing an initial rapid rise followed by a much slower rate of recovery back to resting level. The rate of PCr resynthesis is dependent on the extent of intracellular acidosis, which in turn depends on the work rate during exercise. The final rate of PCr recovery is dependent on the rate of pH recovery and a direct linear relationship has been shown between the value of intracellular pH at the end of exercise and the rate of PCr recovery.[34]

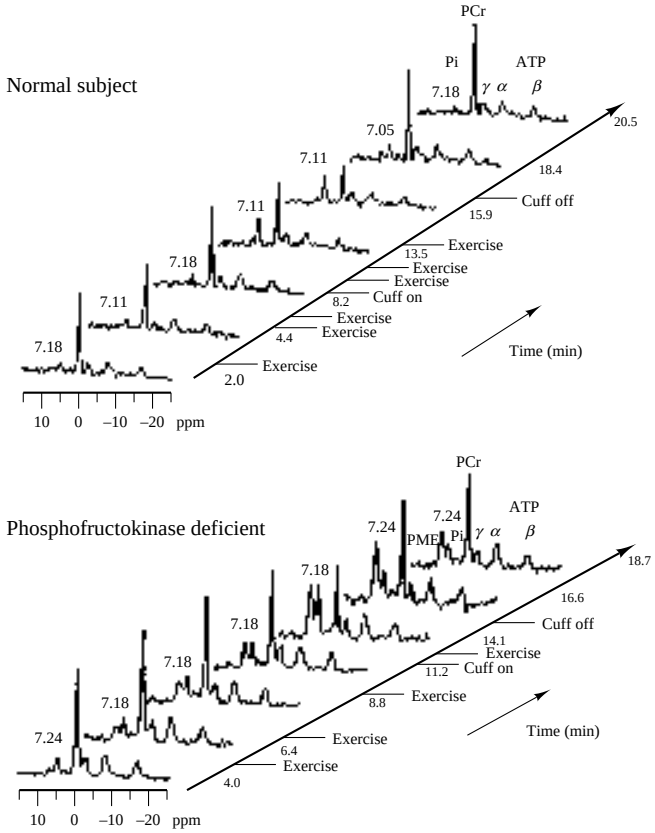

Figure 3 A comparative ^{31}P NMR exercise study of a patient with phosphofructokinase deficiency and a normal subject

At the end of exercise, intracellular pH continues to fall until a minimum which, depending on the work rate during the exercise, occurs approximately 1 min after the end of the exercise period. The higher the work rate the later pH recovery begins (see Figure 3). The mechanisms that control intracellular pH are not well known though it is likely that active transport mechanisms are involved.[35]

During recovery [Pi] generally mirrors [PCr]. The Pi accumulated during exercise is transported into the mitochondria where it is used in the phosphorylation of ADP. Like PCr, Pi recovery is biphasic.[36] After the end of exercise and during the period in which pH is still falling Pi recovery is fast. Subsequently, as the pH recovers, Pi recovery slows down, and [Pi] decreases to undetectable levels for several minutes before it again reappears and recovers to resting levels. During this time a temporary decrease in the total [PCr + Pi] occurs, which otherwise remains constant throughout exercise. When exhaustive exercise has been carried out, such as to show a reduction of [ATP], e.g. strenuous aerobic exercise, then all recovery processes are substantially impaired.[37]

8 STUDIES OF MUSCLE DISEASE

Much of what is known about muscle energy metabolism in disease has come from needle biopsy studies. MRS affords a noninvasive approach to the study of metabolism in disease, but the diagnostic value of MRS in muscle is still yet to be

Table 4 Diseases studied by MRS of skeletal muscle (after Barbiroli[39])

Disease	Nucleus	Cause or defect	Conclusions from MRS	Ref.
Congenital heart disease	^{31}P	Impaired O_2 cyanosis	Resting pH and Pi elevated; abnormal PCr depletion and acidification during exercise; prolonged recovery times	40
Duchenne/Becker dystrophy	^{31}P, ^{1}H	Inherited lack of dystrophin	Progressive replacement of muscle tissue by fat; high resting Pi/PCr ratio and slightly alkaline pH; PDE peak increases with age; altered energy metabolism in carriers	41–43
Mitochondrial myopathy	^{31}P	Various enzyme defects	Abnormal transfer function: slow recovery of PCr after exercise	44,45
Encephalomyopathy	^{31}P	Mitochondrial enzyme defects	Abnormal transfer function and slow recovery of PCr and pH; abnormal brain energy metabolism	46,47
Glycogenosis	^{31}P	Phosphofructokinase deficiency	Limited acidosis, abnormal build up of PME peak during exercise	48,49
		Phosphoglycerate mutase	Limited acidosis and abnormally raised PME peak during exercise	50
McArdle's disease	^{31}P	Myophosphorylase deficiency	Lack of acidosis during sustained aerobic or ischemic exercise	51,48
Sickle cell anemia	^{31}P	Muscle ischemia	Reduced total ^{31}P compared with normals	52
Malignant hyperthermia	^{31}P	Anesthetic-induced hyperthermia	High resting Pi/PCr ratio; slow post-exercise recovery of PCr/Pi ratio	53
Peripheral vascular disease	^{31}P	Relative ischemia	Acid shift and a fall in PCr/Pi with exercise	54

shown. The advantage of MRS here is in continually providing information of metabolic levels during exercise (whereas repeated biopsy samples were previously required), although resting spectra can provide valuable metabolic information in certain myopathies such as in dystrophy[38] and muscle injury.[21] The question of whether metabolic abnormalities are secondary to other disease processes is becoming of increasing interest clinically in view of the consequences of disease with respect to muscle pain, performance, and fatigue. Some examples are shown in Table 4. A further application has been to study the effects of therapy, for example, in altering muscle energetics, where enzyme defects have limited the energy supply for contraction, such as glucose infusion in McArdle's disease (myophosphorylase deficiency in which glycolysis is impaired),[55] drug trials in Duchenne dystrophy,[38] and the consequences of insulin infusion on phosphate metabolism.[56]

The early applications of MRS in disease, in particular to patients with clear metabolic defects, provided a novel means to study the normal physiological mechanisms limiting exercise. Such patients can be considered to represent 'Nature's experiments' allowing examination of metabolic processes under conditions that would normally not be possible in human muscle. McArdle's disease[57] represents an example where a defect in metabolism may manifest itself as a failure of membrane excitation, highlighting the importance of glycolysis for the maintenance of membrane excitability. No lactate is produced in these individuals and hence no acidic shift in the Pi peak occurs, making it possible to measure initial rates of PCr resynthesis and K_m for ADP control of oxidative phosphorylation.[51] Figure 3 illustrates the metabolic changes seen during exercise in a patient with phosphofructokinase deficiency,[58] which is arguably a more significant metabolic defect than McArdle's disease, in that oxidation of blood-borne glucose is not possible. Accumulation of fructose 6-phosphate traps Pi resulting in a relatively small rise in Pi, and again no change in pH occurs. In these patients fatigue occurs rapidly, but this cannot be attributed to Pi or H^+.

Another group of the metabolic myopathies is represented by the mitochondrial abnormalities. Those patients affected show abnormalities in oxidative phosphorylation and consequently a high Pi and low PCr,[59] and slow PCr resynthesis.[60,61] A number of these patients have been studied with various defects in mitochondrial function, with slowed PCr and ADP recovery, although the most reliable indication comes from the resting spectrum.

Abnormalities in MRS parameters in Duchenne muscular dystrophy have been discussed earlier (see Section 5). The question of whether there is a reduction in energy state of the dystrophic tissue has been difficult to answer owing to the increasing proportion of muscle tissue replaced with fat and connective tissues as the disease progresses,[38] and highlights an inherent problem in acquiring a signal from an inhomogenous tissue. Attempts to correct the acquired phosphorus signal by dilution effects from noncontractile tissue have been made from biopsy samples and indeed several studies have shown a reduced PCr/ATP ratio in dystrophic muscle. Moreover, a reduction in PCr/Pi ratio suggests impairment of mitochondrial function[62] which is likely to be secondary to the dystrophic process, probably owing to disuse of the muscle, rather than contributing to the damage process, as greater changes are seen in patients with enzyme defects in whom histological evidence of damage is not apparent. Indeed, ^{31}P MRS has been reported to be sufficiently sensitive to show abnormalities in metabolism in patients with minimal or no muscle weakness.[39]

The most marked changes in muscle metabolism demonstrated in disease are probably secondary in origin, particularly where impairment of blood flow is evident. Examples include peripheral vascular disease,[54] sickle cell anemia,[52] and congenital heart disease.[40] It is likely that many more disease states where some degree of fatigue or muscle impairment occurs may also demonstrate abnormalities in metabolism of muscle.

Although MRS has found application in the study of muscle disease for purely scientific purposes, it has yet to find any great application as a routine diagnostic test for muscle disease. This is primarily due to the specialized nature of the MRS examination and the great expense involved when many less expensive procedures are available, e.g. needle biopsy, followed by chemical and genetic analysis. Furthermore, these other procedures are capable of providing information on a greater range of metabolites or gene products than is currently possible by MRS. There is little doubt however that MRS will continue to provide a useful tool for the scientific elucidation of muscle biochemistry in the future, particularly when combined with the use of labeled compounds such as ^{13}C-labeled glucose as tracers.

9 RELATED ARTICLES

Animal Methods in MRS; Body Fat Metabolism: Observation by MR Imaging and Spectroscopy; MRI in Clinical Medicine; MRI of Musculoskeletal Neoplasms; NMR Spectroscopy of the Human Heart; Proton Decoupling in Whole Body Carbon-13 MRS; Quantitation in In Vivo MRS; Skeletal Muscle Evaluated by MRI; Surface Coil NMR: Detection with Inhomogeneous Radiofrequency Field Antennas; Tissue and Cell Extracts MRS; Tissue Behavior Measurements Using Phosphorus-31 NMR; Whole Body Studies: Impact of MRS.

10 REFERENCES

1. J. W. Pan, J. R. Hamm, D. L. Rothman, and R. G. Shulman, *Proc. Natl. Acad. Sci. U.S.A.*, 1988, **85**, 7836.
2. J. W. Pan, J. R. Hamm, H. P. Hetherington, D. L. Rothman, and R. G. Shulman, *Magn. Reson. Med.*, 1991, **20**, 57.
3. R. Taylor, T. B. Price, D. L. Rothman, R. G. Shulman, and G. I. Shulman, *Magn. Reson. Med.*, 1993, **27**, 13.
4. M. V. Narici, L. Landoni, and A. E. Minetti, *Eur. J. Appl. Physiol.*, 1992, **65**, 438.
5. M. Boska, *NMR Biomed.*, 1991, **4**, 173.
6. P. A. Martin, H. Gibson, S. Hughes, and R. H. T. Edwards, *Proc. Xth Ann Mtg. Soc. Magn. Reson. Med.*, San Francisco, 1991, p. 547.
7. P. Vestergaard-Poulsen, C. Thomsen, T. Sinkjaer, M. Stubgaard, A. Rosenfalck, and O. Henriksen, *Electroencephalogr. Clin. Neurophysiol.*, 1992, **85**, 402.
8. R. H. T. Edwards, M. J. Dawson, D. R. Wilkie, R. E. Gordon, and D. Shaw, *Lancet*, 1982, 725.
9. D. I. Hoult, S. J. W. Busby, D. G. Gadian, G. K. Radda, R. E. Richards, and R. J. Seeley, *Nature (London)*, 1974, **252**, 285.
10. R. E. Gordon, P. E. Hanley, and D. Shaw, *Prog. Nucl. Magn. Reson. Spectrosc.*, 1981, **15**, 1.
11. J. F. Dunn, G. K. Kemp, and G. K. Radda, *NMR Biomed.*, 1992, **5**, 154.
12. T. B. Price, D. L. Rothman, M. J. Avison, P. Buonamico, and R. G. Shulman, *J. Appl. Physiol.*, 1991, **70**, 1836.
13. R. Taylor, T. B. Price, L. D. Katz, R. G. Shulman, and G. I. Shulman, *Am. J. Physiol.*, 1993, **265**, 224.
14. C. Thomsen, K. E. Jensen, and O. Henriksen, *Magn. Reson. Imag.*, 1989, **7**, 557.
15. P. A. Bottomley, T. B. Foster, and R. D. Darrow, *JMRI*, 1984, **59**, 338.
16. C. Thomsen, K. E. Jensen, and O. Henriksen, *Magn. Reson. Imag.*, 1989, **7**, 231.
17. W. I. Jung, K. Straubinger, M. Bunse, S. Widmaier, F. Schick, K. Kuper, G. Dietze, and O. Lutz, *Proc. XIIth Ann Mtg. Soc. Magn. Reson. Med.*, New York, 1993, **30**, 138.
18. K. Sahlin, *Acta Physiol. Scand., Suppl.*, 1978, **455**, 1.
19. A. Fabiato and F. Fabiato, *J. Physiol. London*, 1978, **276**, 233.
20. G. K. Kemp, D. J. Taylor, P. Styles, and G. K. Radda, *NMR Biomed.*, 1993, **6**, 73.
21. K. McCully, Z. Argov, B. P. Boden, R. L. Brown, W. J. Bank, and B. Chance, *Muscle Nerve*, 1988, **11**, 212.
22. M. J. Kushmerick, T. M. Moerland, and R. W. Wiseman, *Proc. Natl. Acad. Sci. U.S.A.*, 1992, **89**, 7521.
23. B. Bigland-Ritchie, D. A. Jones, G. P. Hosking, and R. H. T. Edwards, *Clin. Sci.*, 1978, **54**, 609.
24. 'Human Muscle Fatigue: Physiological Mechanisms', eds. R. Porter and J. Whelan, Ciba Foundation Symposium 82, Pitman Medical, London, 1981.
25. 'Neuromuscular Fatigue', eds. A. J. Sargeant and D. Kernell, R. Neth. Acad. Arts & Sci., Amsterdam, 1993.
26. R. H. T. Edwards, D. K. Hill, D. A. Jones, and P. A. Merton, *J. Physiol. London*, 1977, **272**, 769.
27. D. J. Newham, K. R. Mills, B. M. Quigley, and R. H. T. Edwards, *Clin. Sci.*, 1983, **64**, 55.
28. R. G. Miller, D. Giannini, H. S. Milner-Brown, R. B. Layzer, A. P. Koretsky, D. Hooper, and M. W. Weiner, *Muscle Nerve*, 1987, **10**, 810.
29. G. K. Kemp, C. H. Thompson, P. R. Barnes, and G. K. Radda, *Proc. Ist Ann Mtg. Int. Soc. Magn. Reson. Med.*, Dallas, 1994, **31**, 248.
30. G. K. Kemp, D. J. Taylor, and G. K. Radda, *NMR Biomed.*, 1993, **6**, 66.
31. D. J. Taylor, P. J. Bore, P. Styles, D. G. Gadian, and G. K. Radda, *Mol. Biol. Med.*, 1983, **1**, 77.
32. G. K. Kemp, D. J. Taylor, C. H. Thompson, P. Styles, L. J. Hands, B. Rajagopalan, and G. K. Radda, *NMR Biomed.*, 1993, **6**, 302.

33. D. L. Arnold, P. M. Matthews, and G. K. Radda, *Proc. IIIrd Ann Mtg. Soc. Magn. Reson. Med.*, New York, 1984, **1**, 307.
34. D. Bendahan, S. Confort-Gouny, G. Kozak-Reiss, and P. J. Cozzone, *FEBS Lett.*, 1990, **272**, 155.
35. I. H. Nadshus. *Biochem. J.*, 1988, **250**, 1.
36. S. Iotti, R. Funicello, P. Zaniol, and B. Barbiroli, *Biochem. Biophys. Res. Commun.*, 1991, **176**, 1204.
37. D. J. Taylor, P. Styles P. M. Matthews, D. L. Arnold, D. G. Gadian, P. J. Bore, and G. K. Radda, *Proc. Vth Ann Mtg. Soc. Magn. Reson. Med.*, Montreal, 1986, **3**, 44.
38. R. D. Griffiths, E. B. Cady, R. H. T. Edwards, and D. R. Wilkie, *Muscle Nerve*, 1985, **8**, 760.
39. B. Barbiroli, *Magn. Reson. Spectrosc. Biol. Med.*, 1992, **20**, 369.
40. I. Adatia, G. J. Kemp, D. J. Taylor, G. K. Radda, B. Rajagopalan, and S. G. Haworth, *Clin. Sci.*, 1993, **85**, 105.
41. R. J. Newman, P. J. Bore, L. Chan, D. L. Gadian, P. Styles, D. Taylor, and G. K. Radda, *Br. Med. J.*, 1982, **284**, 1072.
42. D. Younkin, P. Berman, J. Sladky, C. Chee, W. Bank, and B. Chance, *Neurology*, 1987, **37**, 165.
43. B. Barbiroli, R. Funicello, A. Ferlini, P. Montagna, and P. Zaniol, *Muscle Nerve*, 1992, **15**, 344.
44. D. L. Arnold, D. J. Taylor, and G. K. Radda, *Ann. Neurol.*, 1985, **18**, 189.
45. Z. Argov, W. J. Bank, J. Maris, P. Peterson, and B. Chance, *Neurology*, 1987, **37**, 257.
46. D. J. Hayes, D. Hilton-Jones, D. L. Arnold, G. Galloway, P. Styles, J. Duncan, and G. K. Radda, *J. Neurol. Sci.*, 1985, **71**, 105.
47. B. Barbiroli, P. Montagna, P. Cortelli, P. Martinelli, T. Sacquegna, P. Zaniol, and E. Lugaresi, *Cephalalgia*, 1990, **10**, 263.
48. D. Duboc, P. Jehenson, S. Tran Dinh, C. Marsac, A. Syrota, and M. Fardeu, *Neurology*, 1987, **37**, 663.
49. Z. Argov, W. J. Bank, J. Maris, J. S. Leigh, Jr., and B. Chance, *Ann. Neurol.*, 1987, **22**, 46.
50. Z. Argov, W. J. Bank, B. Boden, Y. I. Ro, and B. Chance, *Arch. Neurol.*, 1987, **44**, 614.
51. G. K. Radda, *Biochem. Soc. Trans.*, 1986, **14**, 517.
52. S. L. Norris, J. R. Gober, L. J. Haywood, J. Halls, W. Boswell, P. Colletti, and M. Terk, *Magn. Reson. Imag.*, 1993, **11**, 119.
53. J. Olgin, H. Rosenberg, G. Allen, R. Seestedt, and B. Chance, *Anesth. Analg. (Cleveland)*, 1991, **72**, 36.
54. M. A. Zatina, H. D. Berkowitz, G. M. Gross, J. M. Maris, and B. Chance, *J. Vasc. Surg.*, 1986, **3**, 411.
55. S. F. Lewis, R. G. Haller, J. D. Cook, and R. L. Nunnally, *J. Appl. Physiol.*, 1985, **59**, 1991.
56. D. J. Taylor, S. W. Coppack, T. A. D. Cadoux-Hudson, G. J. Kemp, G. K. Radda, K. N. Frayn, and L. L. Ng, *Clin. Sci.*, 1991, **81**, 123.
57. B. McArdle, *Clin. Sci.*, 1951, **10**, 13.
58. R. H. T. Edwards, *Muscle Nerve.*, 1984, **7**, 599.
59. D. G. Gadian, G. K. Radda, B. D. Ross, J. Hockaday, P. Bore, D. Taylor, and P. Styles, *Lancet ii*, 1981, 774.
60. G. K. Radda, P. J. Bore, D. G. Gadian, B. D. Ross, P. Styles, D. J. Taylor, and J. Morgan-Hughes, *Nature, (London)*, 1982, **295**, 608.
61. R. H. T. Edwards, R. D. Griffiths, and E. B. Cady, *Clin. Physiol.*, 1985, **5**, 93.
62. B. Chance, S. Eleff, J. S. Leigh, Jr., D. Sokolow, and A. Sapega, *Proc. Natl. Acad. Sci. U.S.A.*, 1981, **78**, 6714.

Biographical Sketches

Peter A. Martin. *b* 1954. B.Sc. (Loughborough), Ph.D. (Dunelm). Applications scientist at Oxford Research Systems Limited, 1980–85. Operations manager of Liverpool University's Magnetic Resonance Research Centre 1986–present. Research interests include the applications of neural networks to spectral analysis, proton spectroscopy of the brain, and the quantitation of muscle physiology via MRI and MRS.

Henry Gibson. *b* 1961. B.Sc. (Liverpool), M.Sc. (King's College, London), Ph.D. (Liverpool). Honorary nonclinical lecturer in medicine, Research interests; quantification of muscle physiology via MRI and MRS and ultrasonography of muscle.

Richard H. T. Edwards. *b* 1939. B.Sc., M.B., B.S., Ph.D. (London), F.R.C.P., Codirector of the Jerry Lewis Muscle Research Centre, Royal Postgraduate Medical School. Honorary Consultant Respiratory Physician, Hammersmith Hospital; Professor of Human Metabolism, Hospital Medical School and Head of Department of Medicine, University College, London; Professor and Head of Department of Medicine, University of Liverpool, 1984–present. Director, Magnetic Resonance Research Centre, 1986–present.

Skeletal Muscle Evaluated by MRI

James L. Fleckenstein

University of Texas Southwestern Medical Center, Dallas, TX, USA

1 INTRODUCTION

Clinical evaluation of skeletal muscle has long been hampered by difficulty in assessing the morphology and functional integrity of skeletal muscles. Proton magnetic resonance imaging (MRI) represents a major advance in the diagnosis and management of patients with muscle disease by probing beyond the relatively bland surface of skin to identify focal muscle structural lesions, to determine their extent, and to characterize their composition, and guide invasive procedures and monitor therapies. The purpose of this chapter is to review advances made by MRI in understanding the quality of muscle in health and disease.

2 MR TECHNIQUES

MRI is used to examine patients' muscular anatomy noninvasively and determine which muscles are abnormal in size and shape. MRI further characterizes the quality of muscle by discriminating between the mesenchymal alterations of muscle fat and edema, depending on the pulse sequences used.[1–4] Fat is detected on T_1-weighted images (short *TR*, short *TE*) by high signal intensity due to its short T_1 time constant. Because fat has a long T_2 time constant, it also manifests high signal intensity on T_2-weighted (long *TR*, long *TE*) sequences.

Increased tissue water leads to increased spin density and elevated T_1 and T_2 relaxation times; hence, muscle edema is detectable using MRI.[1,2] The long T_1 can be manifested by decreased signal intensity on heavily T_1-weighted spin echo images. However, in cases in which the sequence is also sensitive to changes in proton density and T_2, the change in T_1 is frequently not sufficient to result in a net change in signal intensity.[2]

Using conventional T_1-weighted and T_2-weighted spin echo sequences, difficulty is sometimes encountered in differentiating intramuscular fat from edema, especially when they coexist. This is because both edema and fat are hyperintense to muscle on long *TR*/long *TE* sequences. This accounts in part for why fat-suppression techniques improve detection of muscle edema.

Multiple fat suppression sequences have been developed that improve detection of muscle edema.[1–3] One of these employs an inversion pulse that nulls signal from tissue having a T_1 time equal to that of fat [short inversion time inversion recovery (STIR)]. STIR has the additional advantage of producing heightened lesion conspicuity due to additive effects to signal intensity caused by edema-associated increases in lesion spin density and T_1 and T_2 times.[3] Other sequences employ frequency selective pulses to null the fat signal. These techniques generally require a longer *TE* to achieve the same degree of lesion conspicuity as STIR sequences at the same *TR*. Important from a financial perspective, a variety of fat-suppression sequences can be incorporated into fast scan techniques, so that high sensitivity to muscle edema can be realized with short scan times. This makes muscle imaging an economically viable, as well as informative, application of MRI.

3 NORMAL MUSCLE ANATOMY AND PHYSIOLOGY

Like computerized tomography and ultrasound, MRI aids physiological studies of muscle size by providing quantitative morphological data regarding the mass of muscle performing work. While cross-sectional area (CSA) has most frequently been used for this purpose, the safety and high spatial resolution of MRI allow for accurate determinations of muscle volume, eliminating errors inherent in modeling volume estimates from single CSA measurements. Incorporation of the muscle fiber pennation angle into estimates of size has further defined morphological determinants of muscle strength.[5] The ability of MRI to accurately define muscle fascicle architecture also enhances MRI assessment of muscle morphology.[6] A variety of these techniques has been used to monitor changes in muscle volume during training[7] and detraining.[8]

Compositional alterations of muscle that can potentially be quantitated with MRI include fiber type, water content and compartmentation, and fat content.[9–25] MRI of muscle fiber type has been studied in both animals and humans, although with conflicting results. In rat soleus muscle, which is nearly all type I (slow twitch, oxidative) fibers, T_1 and T_2 relaxation times are longer than in gastrocnemius muscle, which has a greater proportion of type II (fast twitch, glycolytic) fibers. This difference correlates with a greater extracellular water content in the soleus muscle.[9] Muscles having such markedly disparate fiber type proportions can easily be differentiated from other muscles on MRI (Figure 1).[2] Although human muscle has much less variability in fiber type proportion than does animal muscle, a study in humans indicated that the percentage of type II fibers positively correlated with T_2 times.[10] This result is the opposite of what would be predicted from the animal data and so additional studies are needed to determine the accuracy and validity of this MRI application.

MRI measurement of muscle water content can be applied not only to studies of fiber typing, but also to changes that occur as a result of muscular contraction,[11–22] diuresis,[11] and denervation atrophy.[23,24] As an example, the effects of exercise on the MRI appearance of exercise muscle will be examined in detail. During low-intensity muscular contractions, increases of muscle water primarily occur in the extracellular space; during maximal intensity exercise small increases also occur in the intracellular water space.[26] These changes in muscle water content/compartmentation are associated with transient increases in muscle spin density and T_2 times, while T_1 times are relatively less affected.[12] Interestingly, postexercise hyperemia is neither required[12,13] nor sufficient[14] for the effect to be observed (Figure 1). Animal studies suggest that increases in muscle extracellular water content underlie an increase in the

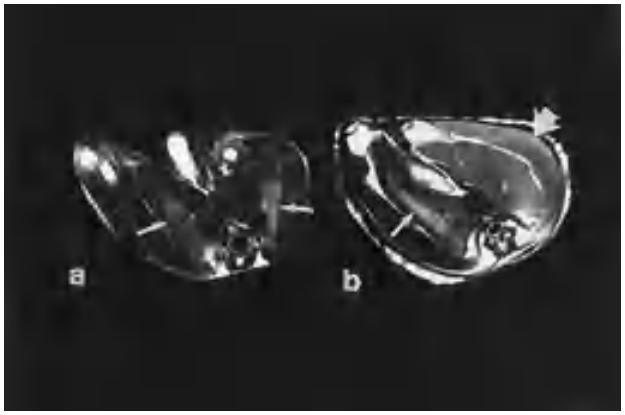

Figure 1 Effects of fiber type heterogeneity and ischemic muscle contraction visible by MRI. Coronal 2000/60 images of rabbit thighs before (a) and after (b) ischemic muscle stimulation. Note on the prestimulation image that a single muscle (semitendinosus, arrows) has a higher signal intensity than nearby muscles. This is a normal finding in this breed of rabbit and reflects a high proportion of oxidative fibers. After stimulation of the left sciatic nerve, signal intensity increases markedly within the left lateral thigh muscles (arrowhead). Because aortic ligation and death preceded the stimulation, blood flow could not have contributed to signal intensity changes in the stimulated muscles, supporting data in humans that blood flow is not critical in mediating transient MRI changes of signal intensity due to exercise. (Reproduced by permission of the Radiological Society of N. America from J. L. Fleckenstein, R. G. Haller, L. A. Bertocci, R. W. Parkey, and R. M. Peshock, *Radiology*, 1992, **183**, 25)

number of proton spins having long T_2 decay times.[9,11] This has led some investigators to propose that an increase in this water space is the primary determinant of the changes visible on MRI.[12,13,15] A role for changes in intracellular water content has also been proposed[16] and debated.[12] These MRI-visible alterations in muscle water are speculated to result from increased muscle osmolality due to accumulation of lactate and other ions which cause osmotic shifts of water between intracellular and extracellular water compartments. This conclusion is supported by absence of the normal postexercise muscle T_2 variations in patients in whom muscle lactate accumulation is absent due to defective muscle phosphorylase (glycogenosis V, McArdle's disease)[14] and by a high correlation between the magnitude of T_2 change and fall in pH in healthy volunteers.[17]

Magnetization transfer contrast techniques, exploiting selective saturation of a pool of 'bound' water protons, were applied in two studies to improve the understanding of water compartmentation during MRI of exercise in humans.[15,18] However, the studies provided conflicting results and conclusions. Another area of apparent controversy regards changes in the T_2 time as a function of work performed. While some studies suggested that T_2 increases in direct proportion to work intensity, the linearity of this relationship has been questioned.[19] Taking these data together it is likely that T_2 varies linearly with work in some regimens but not in others. Recognition that a limit exists in the magnitude of T_2 response (~30%)[19] suggests the existence of a limit to the amount of water that muscle can imbibe from the vasculature during exertion and/or to the magnitude of changes of muscle water compartmentation/binding that can occur during exercise.

Figure 2 Finger-specific components of the flexor digitorum superficialis. Four discrete parts of this muscle can be demonstrated by selective exercise of individual fingers. From left to right are the index, long, ring, and small components of the flexor digitorum superficialis at the mid-forearm. The bones are the radius and ulna. (Reproduced by permission of Raven Press from J. L. Fleckenstein et al.[2])

Although the precise mechanism(s) involved in exercise-induced changes in muscle relaxation times during exercise remains unknown, the changes in image contrast between strongly recruited muscle and less active muscle have been exploited in a number of interesting practical applications: diagnosis of disorders of muscle energy metabolism;[14] chronic exertional compartment syndromes;[20] identification of muscle recruitment patterns relevant to MR spectroscopy studies of exercise (Figure 2);[21,22] assessment of manufacturers' claims of muscle recruitment patterns using commercially available exercise equipment (Figure 3).

4 MRI OF MUSCLE PATHOLOGY

MRI has been applied to the evaluation of a broad range of neuromuscular and orthopedic muscle disorders. One of the critical issues that faces a clinician evaluating a patient with neuromuscular disease is determining whether the disease is primarily neurogenic or muscular in origin. This is of particular importance in pediatrics because patients with spinal muscular atrophies (SMA) may present with similar clinical findings to patients with muscular dystrophies, particularly of the Duchenne type (DMD). Early attempts to differentiate SMA from DMD employed ultrasound of the extremities and reported that in SMA the overall volume of muscle was decreased, compared with that of subcutaneous fat.[27,28] As an additional diagnostic clue, MRI has disclosed selective sparing of specific muscles in DMD, particularly of the gracilis, semimembranosus, and sartorius.[25,29] A more recent study sought to distinguish SMA of the Kugelberg–Welander type (KW) from DMD.[30] It was reported that in KW, muscle deterioration tended to be more diffuse than in DMD and the previous finding of generalized muscle atrophy in SMA was corroborated. A tendency toward relatively selective involvement of type II muscles in DMD was also observed. While more work needs

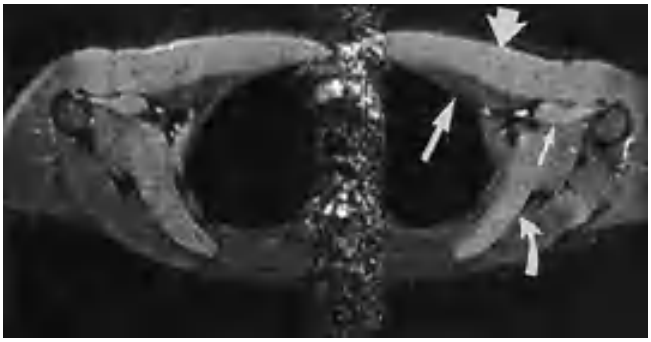

Figure 3 MRI of 'fly' exercise. Using a commercially available exercise device this healthy subject performed arm abduction against resistance within 1 min of scan acquisition. Note that the pectoralis major (arrowhead), subscapularis (curved arrow), and coracobrachialis (small arrow) are strongly stressed while the pectoralis minor is relatively unstressed (arrow). Therefore, the device does not stress the pectoralis group homogeneously, despite claims of the manufacturer to the contrary

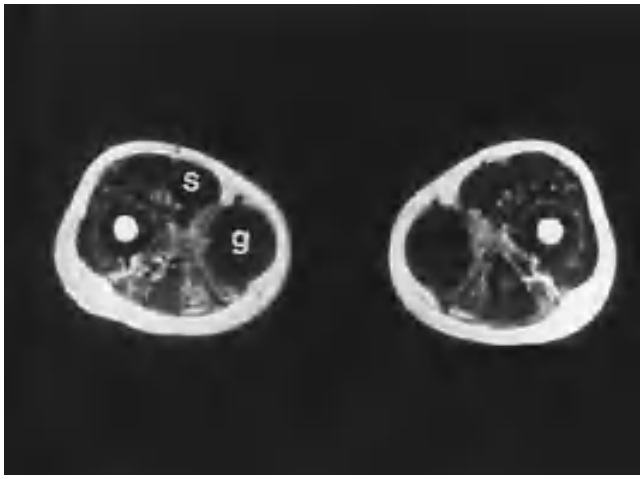

Figure 5 Muscle atrophy and hypertrophy in muscular dystrophy. Symmetric, proximal diminution in muscle volume is evident on a 500/30 sequence. Note sparing of the gracilis (g) and sartorius (s). (Reproduced by permission of Raven Press from J. L. Fleckenstein et al.[2])

to be performed to assess the capability of MRI to distinguish between neurogenic and primary muscle diseases, results to date indicate that MRI may be helpful in this distinction.

Muscle dysfunction that results from peripheral neuropathy has also been evaluated with MRI.[24] MRI was found able to detect edema-like changes in muscles affected by traumatic or compressive peripheral nerve lesions (Figure 4). These changes were anticipated based on results from an animal study in which proton relaxation times were shown to be prolonged in denervated muscle due to fiber atrophy and a resultant increase in the extracellular water space.[23] Like electromyography, MRI was limited in its ability to detect muscle abnormalities in the first few weeks of denervation. On the other hand, denervation was readily visible on edema-sensitive sequences when denervation had occurred prior to 1 month before the MRI scan. While edema-like change dominated the appearance of muscle in the first year of denervation, fatty change of the muscle was observed in more long-standing denervation. Muscle hypertrophy is a relatively rare result of denervation, and while the finding may be prominent in patients with a remote history of poliomyelitis, it may also be observed relatively early after insult to peripheral nerves.[2]

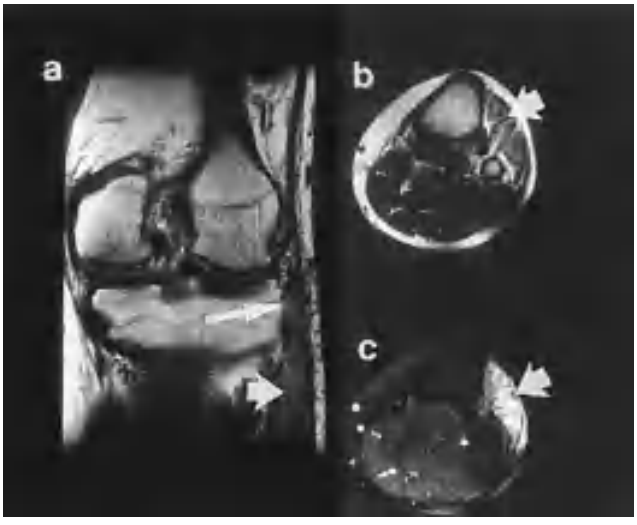

Figure 4 MRI of subacute leg muscle denervation: edema-like change. Lateral collateral ligament injury (arrow, 500/40) (a) and subsequent scar formation resulted in compression of common peroneal nerve (not shown). Note that signal intensity of denervated anterior leg muscles mimics edema, being normal on coronal T_1-weighted image (arrowhead) (a), and increased on axial T_2-weighted image (arrowhead, 2000/60) (b) and STIR (arrowhead, 1500/30/100) (c)

Unlike disease of nerve and muscle, neuromuscular junction dysfunction, such as seen in myasthenia gravis, has yet to be reported to have an abnormal appearance on MRI, or any other imaging modality. On the other hand, primary myopathies, including dystrophies, idiopathic inflammatory myopathies, metabolic myopathies, and congenital myopathies, display various muscle abnormalities on MRI.[25,29,31,32] These findings, including edema-like change and fatty infiltration of muscles, tend to be nonspecific in terms of distribution. For example, selective sparing of the sartorius and gracilis is a feature not only of DMD (Figure 5), but also of polymyositis (Figure 6), congenital myopathies,[29] and metabolic myopathies (Figure 7). Selective involvement of the same muscles is a feature of some mitochondrial myopathies[2] but may be seen in centronuclear myopathy. The character of the imaging abnormality is also nonspecific, in that edema-like change on MRI may be seen in denervation, necrosis, and inflammation.[2] While not pathognomonic for specific disease processes, the MRI abnormalities are useful in directing invasive procedures, such as biopsy.[31,32] The objective nature of imaging abnormalities can also be used to monitor response to therapy, which is otherwise limited by the subjective aspects of the patients' sense of well being and by limitations in assessing muscular strength.

In the field of orthopedics, muscle injuries are extremely common and include muscle strains and contusions, delayed onset muscle soreness, and chronic overuse syndromes.[33–37] Associated injuries and sequelae of injuries are important determinants of the prognosis of muscle injuries. Because MRI is

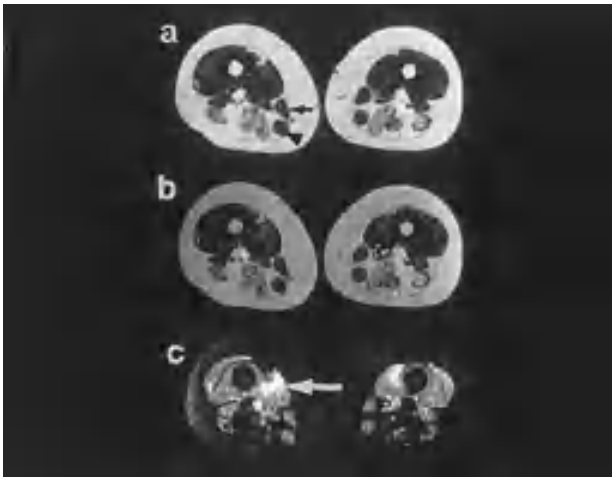

Figure 6 Chronic polymyositis. The extensive high signal intensity throughout the thigh muscles on 500/30 (a), and 2000/60 (b), images implies fatty change. STIR suppresses signal intensity from fat, while high signal intensity identifies regions of coexistent muscle edema (arrow) (c). Note that muscle edema is easy to identify only with fat suppression. Such edematous areas are of particular interest during biopsy when inflammatory myopathy is suspected. Note sparing of multiple muscles, including sartorius (arrow) (a) and gracilis (arrowhead) (a)

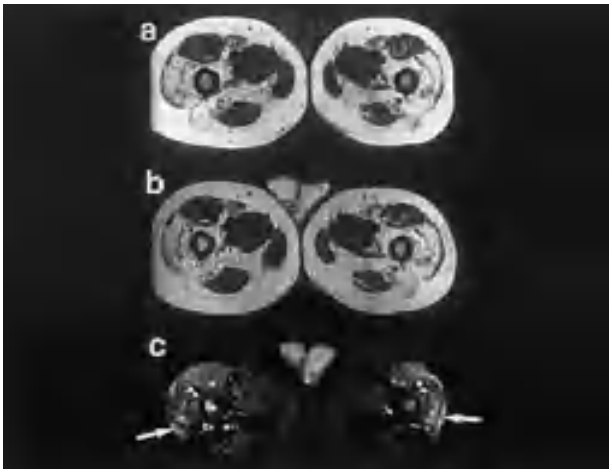

Figure 7 Glycogenosis: T1W (500/30) (a) and T2W (2000/60) (b) images of the thighs in a patient with phosphofructokinase deficiency demonstrate marked replacement of most thigh muscles by high signal intensity fat. STIR (c) suppresses signal intensity from fat, while areas of high signal intensity identify regions of coexistent muscle edema in the vastus lateralis (arrows). Such edematous areas should be avoided during biopsy when glycogenoses are considered because muscle necrosis may produce a small amount of fetal myophosphorylase in patients who usually lack the adult form of that enzyme (McArdle's disease, Glycogenosis V)

sensitive to both muscle trauma and associated abnormalities, it has been aggressively applied to these orthopedic issues.

Muscle strain is defined as an indirect injury to muscle caused by excessive stretch. Although various clinical schemes of grading severity of muscle strains have been advanced, it is acknowledged that clinical evaluation of muscle strains is difficult, even more so than injuries of tendons or bones. MRI aids in assessing integrity of muscles, myotendinous junctions, fascia, and the tendoosseous unit. MRI identifies edema within and/or around injured muscles, depending on the stage of healing.[33,34]

The myotendinous junction is frequently the point of rupture and the extent of associated fascial or tendinous tear can be addressed by MRI (Figures 8–10). When a fascial or tendinous tear is small (Figure 8), the injury can safely be managed conservatively. However, when a rupture is complete, or nearly complete (Figures 9 and 10), early surgery may be indicated; a lapse of even a short time may cause an inferior functional result, due to muscle fibrosis and retraction. Fluid collections also frequently accompany strains. These can themselves be a cause of swelling and weakness in the absence of fascial tear. The use of MRI to distinguish focal hematomas from swollen, edematous muscles can guide clinical management; the former may benefit from drainage while the latter are often treated with wrapping procedures for compression and support of the injured area.[4]

Since recurrent muscle strains can devastate elite athletes, it is noteworthy that MRI in muscle injuries can provide information regarding the prognosis of muscle strain. Two studies have reported on MRI findings that are associated with poor outcome. These studies indicated that the occurrence of focal fluid collections (Figure 10), relatively large volume of abnormality (Figure 11) and fibrosis (Figure 12), correlate with either recurrence of muscle strain, delayed convalescent interval, or both.[35,36] It is interesting that MRI alterations of strained muscles typically persist for longer than any other clinical evidence of injury.[33,34] One could speculate that reinstitution of exercise in this setting might be harmful to the healing muscle, but this has not yet been studied. A more immediately practical implication of the delayed disappearance of edema from muscle after injurious exercise is that one may detect evidence of previous muscle injury on MRI after the patient forgets the inciting event. This suggests a potential

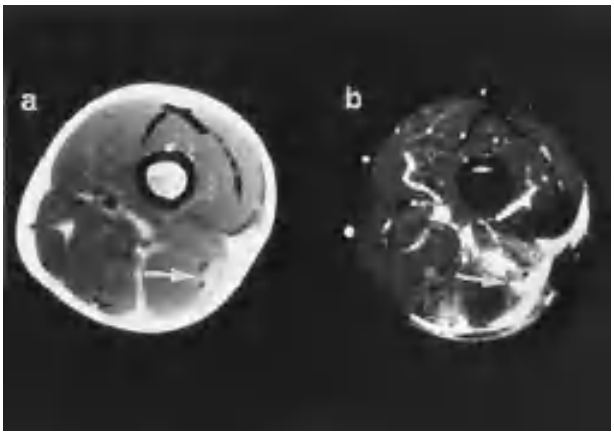

Figure 8 Important MRI findings in muscle injury: partial tendon tear. Associated injuries to fasciae and tendons are important to quantitate since small fibrous tears may require no operative intervention. Note partial biceps femoris tendon tear (arrow, 600/20) (a) and STIR (b), and the superior delineation of perifascial fluid using STIR. The lesion was conservatively managed. (Reproduced by permission of Raven Press from J. L. Fleckenstein et al.[2])

Figure 9 Important MRI findings in muscle injury: complete avulsion. When muscle tearing is complete, myotendinous avulsion occurs. Complete myotendinous avulsion of a juvenile football player's gluteus medius is easily appreciated on the coronal spin density-weighted image (arrow, 2000/30). The patient was treated by immobilization in a body cast for 12 weeks. (Reproduced by permission of Raven Press from J. L. Fleckenstein et al.[2])

Figure 11 Important MRI findings in muscle injury: large volume edema. Factors that suggest a longer convalescent period after injury include a large volume of muscle edema, such as in an axial STIR image of an acutely strained rectus femoris muscle (arrow). (Courtesy of S. C. Schultz, Fort Worth, TX)

source of serendipitously observed MRI abnormalities. On the other hand, this radiographic finding may be the only clue to the true origin of the patient's musculoskeletal complaints.[4]

Other sequelae of muscle injury detectable by MRI include muscle calcification and ossification. Calcific myonecrosis is a delayed complication of muscle injury in which progressive calcification of an injured muscle is associated with slow development of a mass lesion of the extremities. This condition is a rare complication but its radiology is well described, allowing for a confident preoperative diagnosis.[37] Muscle ossification (myositis ossificans) is also detectable by MRI but its appearance is nonspecific early in its development, mimicking neoplastic disease. As it matures, ossified muscle may be identified by peripheral low signal intensity, corresponding to the outer zone of ossification (see ***MRI of Musculoskeletal Neoplasms***).

5 CONCLUSION

MRI circumvents traditional obstacles in the clinical evaluation of muscle physiology and pathology. MRI detection of muscle size, fiber composition and orientation, and water shifts are promising research arenas in the field of exercise physiology. The high sensitivity of MRI in detecting muscle edema

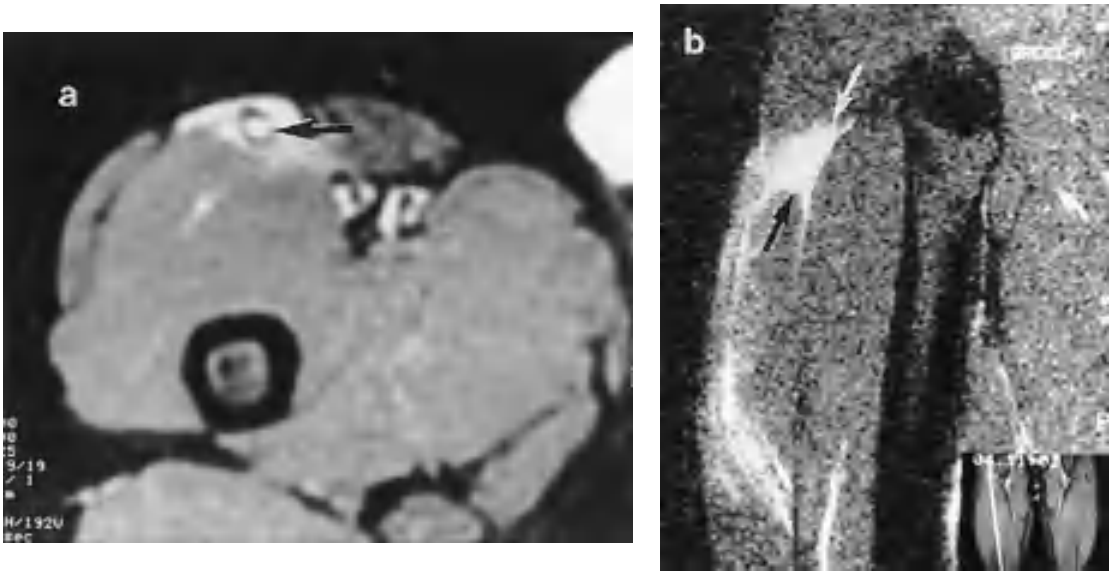

Figure 10 Important MRI findings in muscle injury: fluid collection. Rupture and retraction of the posterior head of the rectus femoris in an elite kicker with recurrent muscle strain reveals a 'ganglion-like' fluid collection within a portion of the rectus femoris on axial STIR image (arrow) (a), corresponding to fluid collecting between the retracted posterior head of the rectus femoris and its origin (arrows, sagittal STIR) (b). This injury was treated by resection of the avulsed muscle head

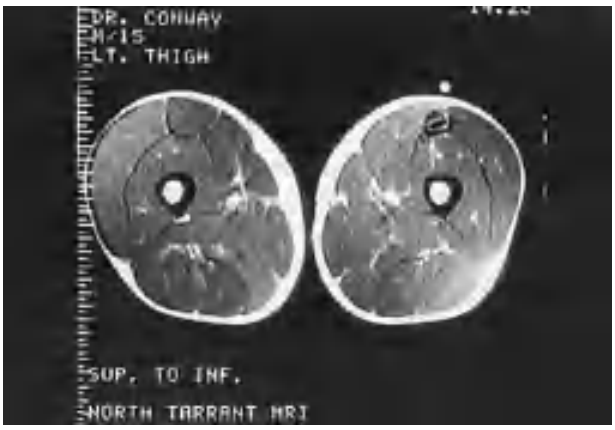

Figure 12 Important MRI findings in muscle injury: scar. MRI-visible scar formation in myotendinous tears is associated with recurrence of strains. Scar is characterized by excessive deposition of signal poor tissue and muscle atrophy (arrow). (Courtesy of S. C. Schultz, Fort Worth, TX)

and fat allows improved delineation of the distribution and composition of neuromuscular and orthopedic disorders. This sensitivity can be used to substantiate muscle as the source of musculoskeletal pain, weakness, or stiffness in a broad range of patients and on the basis of positive, objective findings rather than by exclusion.

6 RELATED ARTICLES

Inversion–Recovery Pulse Sequence in MRI; Magnetization Transfer Contrast: Clinical Applications; MRI of Musculoskeletal Neoplasms; Peripheral Joint Magnetic Resonance Imaging; Peripheral Muscle Metabolism Studied by MRS.

7 REFERENCES

1. J. L. Fleckenstein, B. T. Archer, B. A. Barker, J. T. Vaughn, R. W. Parkey, and R. M. Peshock, *Radiology*, 1991, **179**, 499.
2. J. L. Fleckenstein, P. T. Weatherall, L. A. Bertocci, M. Ezaki, R. G. Haller, R. Greenlee, W. W. Bryan, and R. M. Peshock, *Magn. Reson. Q.*, 1991, **7**, 79.
3. A. J. Dwyer, J. A. Frank, V. J. Sank, J. W. Reinig, A. M. Hickey, and J. L. Doppman, *Radiology*, 1988, **168**, 827.
4. J. L. Fleckenstein and F. G. Shellock, *Top. Magn. Reson. Imaging*, 1991, **3**, 50.
5. T. Fukunaga, R. R. Roy, F. G. Shellock, J. A. Hodgson, M. K. Day, P. L. Lee, H. Kwong-Fu, and V. R. Edgerton, *J. Orthop. Res.*, 1992, **10**, 928.
6. S. H. Scott, C. M. Engstrom, and G. E. Loeb, *J. Anat.*, 1993, **182**, 249.
7. W. J. Roman, J. L. Fleckenstein, J. Stray-Gundersen, S. E. Alway, R. Peshock, and W. J. Gonyea, *J. Appl. Physiol.*, 1993, **74**, 750.
8. T. Fukunaga, K. Day, J. H. Mink, and V. R. Edgerton, *Med. Sci. Sports Med.*, 1991, **23**, 5110.
9. J. F. Polak, F. A. Jolesz, and D. F. Adams, *Invest. Radiol.*, 1988, **23**, 107.
10. S. Kuno, S. Katsuta, T. Inouye, I. Anno, K. Matsumoto, and M. Akisada, *Radiology*, 1988, **169**, 567.
11. E. Le Rumeur, J. de Certaines, P. Toulouse, and P. Rochcongar, *Mag. Reson. Imaging*, 1987, **5**, 267.
12. B. Archer, J. L. Fleckenstein, L. A. Bertocci, R. G. Haller, B. Barker, R. W. Parkey, and R. M. Peshock, *J. Magn. Reson. Imaging*, 1992, **2**, 407.
13. J. L. Fleckenstein, R. C. Canby, R. W. Parkey, and R. M. Peshock, *Am. J. Roentgenol.*, 1988, **151**, 231.
14. J. L. Fleckenstein, R. G. Haller, S. F. Lewis, B. T. Archer, B. R. Banker, J. Payne, R. W. Parkey, and R. M. Peshock, *J. Appl. Physiol.*, 1991, **71**, 961.
15. X. P. Zhu, S. Zhao, and I. Isherwood, *Br. J. Radiol.*, 1992, **65**, 39.
16. F. G. Shellock, T. Fukunaga, J. H. Mink, and V. R. Edgerton, *Am. J. Roentgenol.*, 1991, **156**, 765.
17. E. R. Weidman, H. C. Charles, R. Negro-Vilar, M. J. Sullivan, and J. R. MacFall, *Invest. Radiol.*, 1991, **26**, 309.
18. K. T. Mattila, M. E. Komu, S. K. Koskinen, and P. T. Niemi, *Acta Radiol.*, 1993, **34**, 559.
19. J. L. Fleckenstein, D. Watumull, D. D. McIntire, L. A. Bertocci, D. P. Chason, and R. M. Peshock, *J. Appl. Physiol.*, 1993, **74**, 2855.
20. A. Amendola, C. H. Rorabeck, D. Vellett, W. Vezina, B. Rutt, and L. Nott, *Am. J. Sports Med.*, 1990, **18**, 29.
21. J. L. Fleckenstein, L. A. Bertocci, R. L. Nunnally, R. W. Parkey, and R. M. Peshock, *Am. J. Roentgenol.*, 1989, **153**, 693.
22. J. L. Fleckenstein, D. Watumull, L. A. Bertocci, R. W. Parkey, and R. M. Peshock, *J. Appl. Physiol.*, 1992, **72**, 1974.
23. J. F. Polak, F. A. Jolesz, and D. F. Adams, *Invest. Radiol.*, 1988, **23**, 365.
24. J. L. Fleckenstein, D. Watumull, K. E. Conner, M. Ezaki, R. G. Greenlee, Jr., W. W. Bryan, D. P. Chason, R. W. Parkey, R. M. Peshock, and P. D. Purdy, *Radiology*, 1993, **187**, 213.
25. W. A. Murphy, W. G. Totty, and J. E. Carroll, *Am. J. Roentgenol.*, 1986, **146**, 565.
26. G. Sjogaard, R. P. Adams, and B. Saltin, *Am. J. Physiol.*, 1985, **248**, R190.
27. J. Z. Heckmatt, N. Pier, and V. Dubowitz, *J. Clin. Ultrasound*, 1988, **16**, 171.
28. A. Lamminen, J. Jaaskelainen, J. Rapola, and I. Suramo, *J. Ultrasound Med.*, 1988, **7**, 505.
29. A. E. Lamminen, *Br. J. Radiol.*, 1990, **63**, 946.
30. D. Suput, A. Zupan, A. Sepe, and F. Demsar, *Acta Neurol. Scand.*, 1993, **87**, 118.
31. A. Pitt, J. L. Fleckenstein, R. G. Greenlee, D. K. Burns, W. W. Bryan, and R. G. Haller, *Mag. Res. Imaging*, 1993, **11**, 1093.
32. J. H. Park, S. J. Gibbs, R. R. Price, C. L. Partain, and A. E. James, Jr., *Radiology*, 1991, **179**, 343.
33. J. L. Fleckenstein, P. T. Weatherall, R. W. Parkey, J. A. Payne, and R. M. Peshock, *Radiology*, 1989, **172**, 793.
34. F. G. Shellock, T. Fukunaga, J. H. Mink, and V. R. Edgerton, *Am. J. Roentgenol.*, 1991, **156**, 765.
35. S. J. Pomeranz and R. S. Heidt, Jr., *Radiology*, 1993, **189**, 897.
36. A. Greco, M. T. McNamara, R. M. B. Escher, G. Trifilio, and J. Parienti, *J. Comput. Assist. Tomogr.*, 1991, **15**, 994.
37. D. L. Janzen, D. G. Connell, and B. J. Vaisler, *Am. J. Roentgenol.*, 1993, **160**, 1072.

Biographical Sketch

James L. Fleckenstein. *b* 1957. B.S. 1979, M.D. 1984, University of Washington. Medical internship, 1984–1985, University of Texas. Radiology residency 1985–1989, University of Texas. Assistant instructor, Radiology, University of Texas, 1989–1990. Director of Neuro MRI, Division of Neuroradiology, and Associate Professor of Radiology at University of Texas Southwestern Medical Center, 1991–present. Approx. 200 publications. Research specialties: MRI of muscle in health and disease.

High-Field Whole Body Systems

Hoby P. Hetherington
Brookhaven National Laboratory, Upton, NY, USA

and

Gerald M. Pohost
University of Alabama at Birmingham, AL, USA

1 INTRODUCTION

Throughout the history of nuclear magnetic resonance research there has been a push toward the use of higher field magnets for their advantages in signal-to-noise ratio (SNR), spectral resolution, and simplification of the complex multiplet structures present in *J*-coupled spin systems. Although the advantages of high field systems have been demonstrated for use in analytical work and structural determinations, their application to in vivo spectroscopy in humans has been limited by technical demands. Additionally, because of field-dependent changes in the relaxation properties of the molecules being studied, significant methodological limitations have occurred when lower field (1.5 T) approaches have been applied at high field. Recently, the development of new hardware and alternative methodological approaches has enabled these obstacles to be overcome and many of the advantages of in vivo high-field spectroscopy and imaging to be realized.

In this section we will provide a brief summary of the hardware and methodological advances that have led to the realization of the benefits of high field in vivo spectroscopy in humans, and present several examples of their application. The first section will deal with some of the limitations of conventional rf coil design and an alternative approach for the design of large highly homogeneous rf coils. The second section will describe some of the advantages and the limitations of spectroscopy at high field. The final section will summarize the advantages of both anatomical and functional imaging and how performing these measurements at high field when coupled with the correct methodology yields improvements in both contrast, resolution and sensitivity to physiological alterations.

2 HARDWARE LIMITATIONS

Although homogeneous volume rf coils and efficient surface coils for low-field human studies or high-field small animal research are widely available, the performance of these coils becomes very limited as their dimensions approach the wavelength of the rf being applied. For volume coils of the 'birdcage design', self-resonance for head coils may occur substantially before reaching the desired field strength. Because of the propagation velocity in the conductors used in these coils and the length of the current-carrying elements (as a fraction of the wavelength), phase changes along the conductors can occur that degrade the homogeneity and sensitivity of the rf coil. Although using distributed lumped element approaches can reduce some of these effects, an alternative approach using transmission line segments and a resonant cavity has seen substantial success.

The utility of transmission lines for high-frequency NMR probes has been recognized since the mid 1970s by Schneider and Dullenkopf.[1] As the first 4 T systems became available Barfuss[2] used capacitively shortened half wave slotted tubes to construct a 170 MHz body coil. Roschmann[3] improved on the high-field design by replacing the unshielded lumped element slotted tubes with half wave coaxial transmission line segments. This design minimized the electric field losses, thereby improving the sensitivity and efficiency of the coil. However, these initial coils had no provision for tuning or matching on each subject, thereby prohibiting maximum performance to be achieved under all conditions. Vaughan[4] has overcome these limitations by providing a capacitively coupled matching network and a tuning mechanism to adjust the capacitance of all of the transmission line segments, permitting in situ tuning and matching.

Initial theoretical predictions of the homogeneity of high-field rf coils suggested that enhanced skin depth effects would cause an attenuation of the rf field resulting in severe inhomogeneities. However, Vaughan[4] has shown that the effects of dielectric resonance tend to offset these skin depth effects to provide a highly homogeneous rf field within the human head at 4 T. An additional concern is the perturbation of the rf field by the geometry of the head and the differing electrical properties of the layers surrounding the brain. In most cases these effects can be minimized for a typical head by calculating the $\boldsymbol{B}_1$ field distribution and/or mapping it, and then adjusting the capacitance and inductance of the coil elements to compensate for the inhomogeneity induced by the cranial geometry and electrical properties. Excellent homogeneity is obtained throughout the slice. The high sensitivity of the coil supports 512×512 resolution for this 3 mm slice, yielding an inplane resolution of 0.47 mm (Figure 1).[5] Recently, using the same design with multiple drive points, a highly homogeneous 8 T head coil has been constructed.[6]

With the improvement in SNR afforded by higher field strengths, there has been renewed interest in performing spectroscopy studies of lower gyromagnetic ratio nuclei, such as ^{31}P and ^{13}C. For purposes of spatial co-registration, ^{1}H decoupling and or heteronuclear acquisition methods, special multiply tuned coil systems have been developed. Vaughan has extended the single-tuned cavity resonator design to a double-tuned coil. Specifically, the ^{1}H and X nuclei are driven 90° out of phase to each other, using alternate elements around the coil.[7] This design achieves high homogeneity, high SNR, and (because of the high degree of isolation between the ^{1}H and X nucleus elements) heteronuclear decoupling is readily achieved without SNR loss. Alternatively, for studies investigating peripheral regions, Adrianny has described a combined surface coil with orthogonal quadrature decoupling coils.[8] Isolation between the surface coil and quadrature decoupling is achieved through manipulation of the geometry between the two coils. When applied to the occipital lobe, the ^{1}H quadrature decoupling coils provide excellent visualization of the posterior

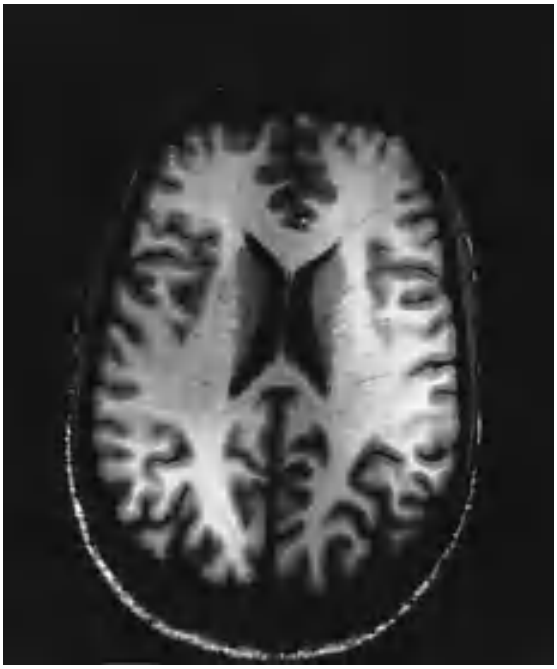

Figure 1 Axial image (3 mm) of the human brain acquired at 4.1 T using a cavity resonator. The field-of-view is 240 × 240 mm using a resolution of 512 × 512 pixels

portion of the head, with relatively homogeneous decoupling throughout the sensitive volume of the surface coil.

3 SPECTROSCOPY

Perhaps the most obvious advantage of performing spectroscopy at high field is the predicted theoretical linear improvement in the SNR with field. This improvement (a factor of 2.7 from 1.5 to 4.1 T) translates into a linear increase in accuracy of the measurement of metabolites, or a reduction in necessary volume size to achieve the same SNR by 2.7 or, alternatively, a factor of 7.3 increase in speed of acquisition for an equivalent volume and SNR. However, reductions in volume size, especially for spectroscopic imaging, provide special challenges with respect to volume misregistration arising from the increased spectral bandwidth and limited rf amplifier power and gradient strength. To achieve these gains, the alterations in relaxation properties (significantly shorter T_2 values of metabolites) must also be addressed in the methods used in data collection. Finally, changes in the J coupling of ^{1}H metabolites must also be added before improvements in spectral resolution and spectral simplification can be realized.

3.1 Improvements in SNR and Spatial Resolution at High Field

Hoult has previously predicted that the SNR improvement under sample noise dominant conditions should be linear with increasing field.[9] This improvement has been documented for ^{1}H spectroscopy where the increase in the SNR for *N*-acetylaspartate (NAA) was found to be increased by a factor of 2.62–3.44 at 4.1 T over that of 1.5 T after corrections for pulse sequence efficiencies, volume sizes, scans and differential relaxation properties.[10] This improvement in the SNR has allowed high-resolution spectroscopic images of human cerebral NAA to be created with an SNR of 32.5 : 1 from voxel sizes of 0.5 ml (Figure 2), a factor of two smaller than that typically used at 1.5 T. Despite the small spatial extent of the gray matter about the intrahemispheric fissure, the 0.5 ml voxel allows resolution of the alterations in metabolite ratios and content in gray and white matter. Specifically, the elevated total creatine (Cr)/NAA ratio reported in autopsy results[11] for gray matter to white matter is easily visualized in the spectra from parietal white and gray matter (Figure 2). The ratio NAA/Cr has been extensively used as a marker for neuronal loss, such that the resolution of these differences has important applications in resolving true neuronal loss from partial volume effects resulting from inclusion of a mixture of gray and white matter. By optimizing the repetition time, echo time, and using frequency selective suppression of the lipid resonances, ultra-high-resolution spectroscopic images can be obtained. Proton spectroscopic images employing volumes as small as 175 μl have been acquired using a homogeneous volume head coil and are presented in Figure 3. In these images, the 2–3 mM difference in Cr content between gray and white matter is easily visualized in the Cr spectroscopic image.

Perhaps more significantly, the improved SNR can also be used to improve the spatial resolution of low sensitivity nuclei such as ^{31}P and ^{13}C. Typically, ^{31}P spectra of the human heart are acquired with voxel resolutions of 20 to 80 ml using single voxel localization methods or, more recently, one-dimensional chemical shift imaging.[12–14] Because of the large voxels acquired in these studies, significant contamination from the myocardial blood pool occurs. Owing to this contamination, corrections for the adenosine triphosphate (ATP) content of the blood pool, based on the 2,3-diphosphoglycerate (2,3-DPG) content are required, before correct myocardial PCr/ATP ratios can be calculated. At 4 T, Menon has demonstrated, using a one-dimensional chemical shift imaging method, that voxels of 8–25 ml can be collected from the human heart that are free of blood pool contamination.[15] Using the increased SNR available at 4.1 T, complete three-dimensional chemical shift images of the myocardial PCr content can be acquired using three-dimensional spectroscopic imaging methods. Displayed in Figure 4 are representative spectra of human heart acquired with a spectroscopic imaging sequence using 8 ml voxels.[16] Evaluation of spectra acquired from the apex, septum, and left ventricular free wall shows that they have minimal contributions from 2,3-DPG (Figure 4). Therefore, quantitative measurements of the regional levels of high-energy myocardial phosphates are possible. Gruetter has used the enhanced sensitivity at 4 T to acquire ^{13}C spectra of human brain from volumes of 72 ml using a 72 min acquisition.[17]

3.2 Relaxation Properties at High Field

Many ^{1}H localization methods have relied heavily on long spin echo sequences (TE = 136–272 ms) to achieve good water and lipid suppression. These methods have been highly successful and provide good sensitivity through the long T_2 values of many cerebral metabolites at 1.5 T. Frahm has measured the

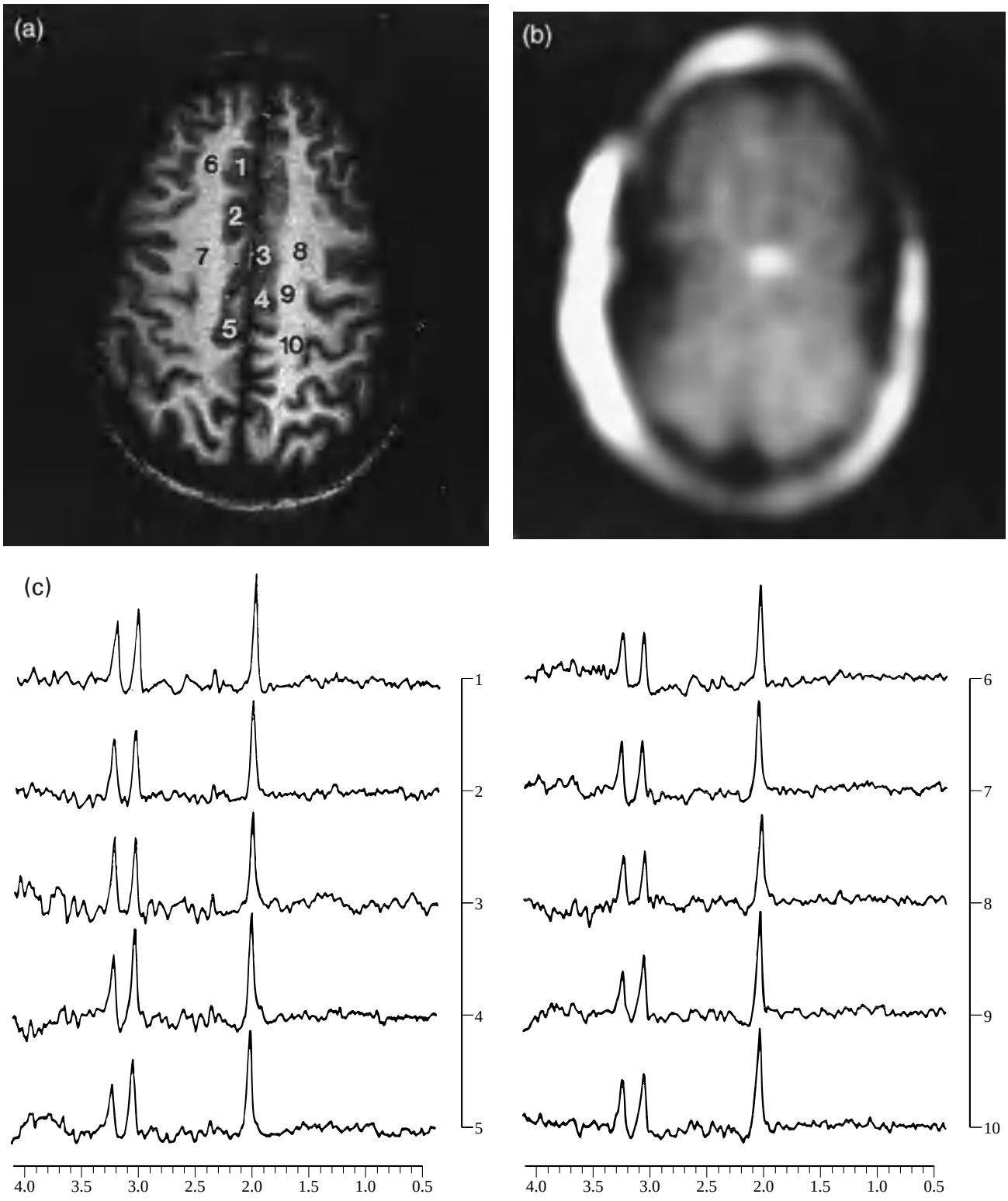

Figure 2 (a) Proton scout image of the human brain and (b) the corresponding NAA image. The NAA image is acquired from a FOV of 240 × 240 mm using 32 × 32 encodes. The echo time (*TE*) of the spectroscopic image is 50 ms. (c) The numbered locations (1–10) on the scout image correspond to the numbered spectra. The resolved resonances are NAA 2.02 ppm, creatine 3.02 ppm, and choline 3.19 ppm. (Reproduced from Hetherington et al.[10])

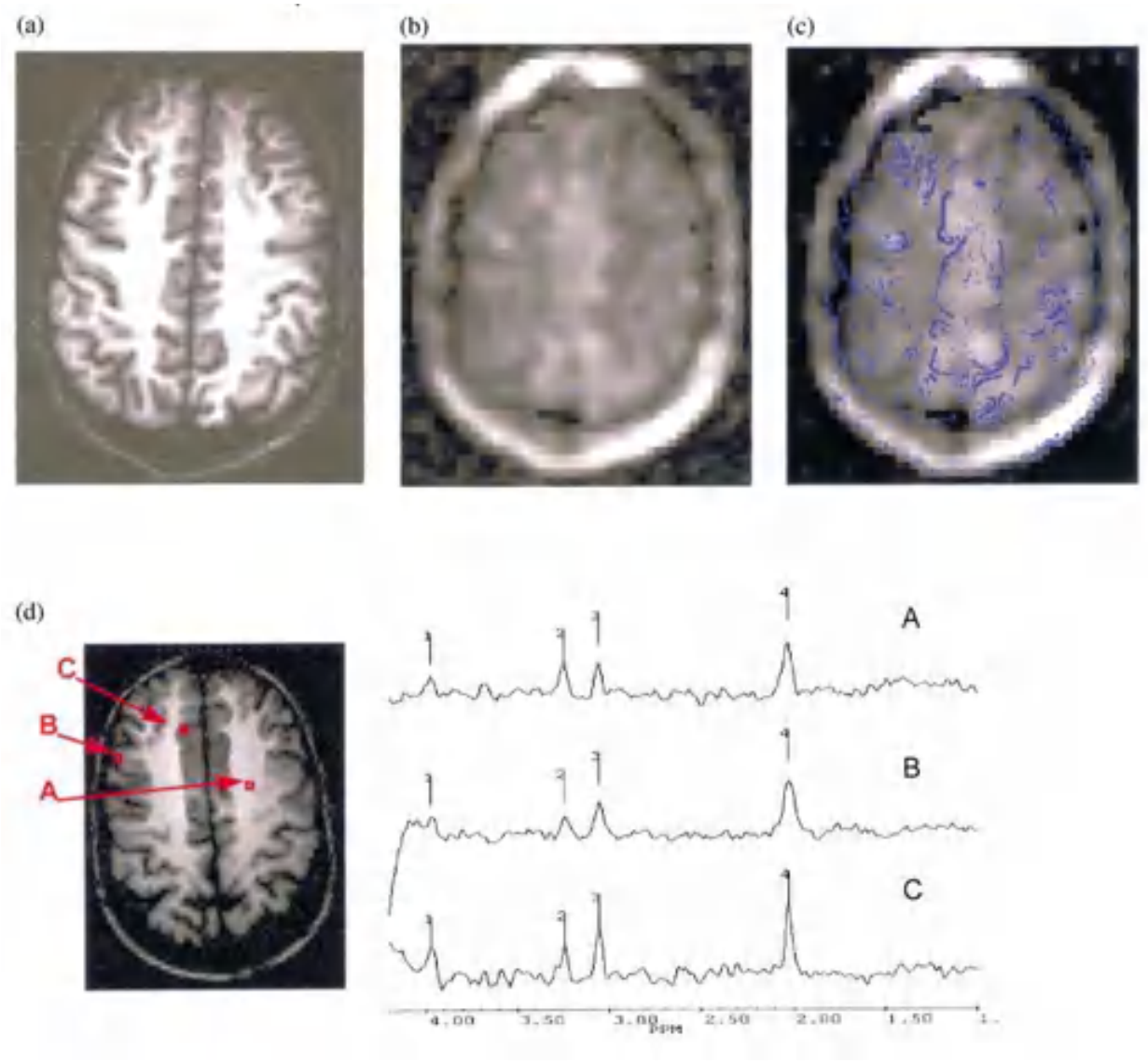

Figure 3 A scout image (a), a spectroscopic image of the distribution of creatine (CR) in the selected slice (b), and an overlay image (c), where the blue contours indicate the edges between gray and white matter. (d) An image and three representative spectra (175 μl nominal volume) and the corresponding locations on the scout image

T_2 values of NAA, Cr, and choline to be 450, 240, and 330 ms, respectively.[18] At 4.1 T the T_2 values of these metabolites become significantly shorter, decreasing by nearly a factor of two to 220, 140, and 190 ms, respectively.[10] Similar values have also been reported by Posse and co-workers.[19] Therefore, significant losses occur at high field when long echo times are used. This necessitates the use of short-echo localization methods such as stimulated echo acquisition (STEAM)[20] and/or simple spin echo methods.[21]

Unlike T_2 relaxation, T_1 relaxation times for ^{1}H metabolites are relatively unchanged. Posse has reported T_1 times of 1.6, 1.6, and 1.2 s for NAA, Cr, and choline, respectively, at 4 T. These values compare well with the T_1 values of 1.45, 1.55, and 1.15 s, respectively, measured at 1.5 T. Therefore, no additional sequence modifications are required for T_1-based selection or discrimination methods.

Myocardial ^{31}P metabolites show increases in their T_1 values. Menon et al. have measured myocardial T_1 values of ATP and PCr to be 2.7 and 5.4 s, respectively. Therefore, the lengthening of the T_1 at 4 T for ^{31}P metabolites will tend somewhat to offset the SNR gains for equivalent repetition times by causing greater saturation effects. To take full advantage of the SNR gains possible in ^{31}P spectroscopy, methods utilizing partial tip adiabatic excitations[22] and/or combinations of homogeneous transmit and surface coil receivers[23] will be of significant benefit.

3.3 Spectral Resolution

One advantage of high-field spectroscopy is the improvement in spectral resolution achievable for *J*-coupled

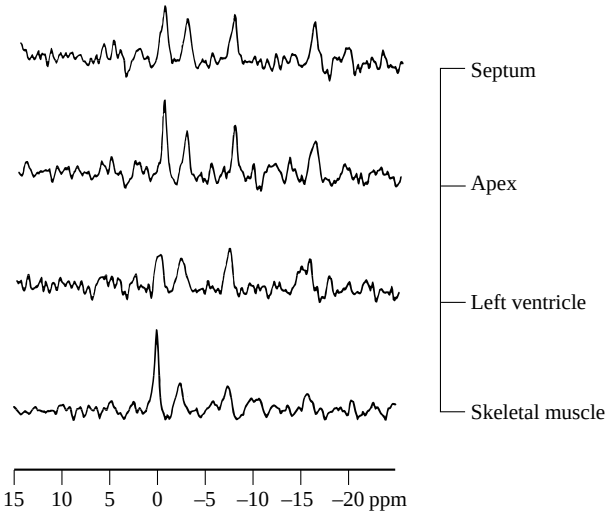

Figure 4 Voxels (8 ml) acquired from a three-dimensional spectroscopic imaging sequence applied to the human heart. The resolved resonances are for PCr, (0 ppm), α-, γ-, and β-ATP (-2 to -18 ppm) and inorganic phosphate (Pi) + 2,3-DPG (5–10 ppm) (Reproduced from H. P. Hetherington, D. J. E. Luney, and J. T. Vaughan, *Magn. Reson. Med.*, 1995, **33**, 427.)

resonances. This effect stems from two factors, the increase in spectral dispersion (in hertz) from the increased field in the presence of a field invariant coupling constant and a simplification of strong coupling for homonuclear coupled ^{1}H resonances. The advantage of the increased spectral resolution is most easily seen in the ^{1}H spectra of human brain. For ^{1}H spectroscopy, the most dramatic improvement is in the resolution of the C-3 and C-4 resonances of amino acids such as glutamate and glutamine. At 1.5 T, the C-3 and C-4 resonances of glutamate are strongly coupled such that they appear as a broad complex multiplet (Figure 5). However at 4.1 T the C-3 and C-4 resonances experience much weaker coupling such that they resolve into two clearly distinct multiplets. This improved resolution also permits the individual C-4 resonances of glutamate and glutamine to be resolved from each other. Specifically the two most downfield lines of the glutamine triplet are resolved from the two most upfield lines of the glutamate triplet (Figure 6). Therefore, unlike measurements at 1.5 T, where the strongly coupled resonances of glutamate and glutamine show substantial overlap, the individual contributions of these resonances can be clearly determined at 4 T.[24] However, as the nature of the coupling changes, so do the amplitudes of the multiplets as a function of echo time. Although echo times of 20–30 ms can be used for detection of amino acids at 1.5–2.0 T,[25,26] an echo time of 20 ms results in substantial loss in sensitivity at 4.0 T.[24] However, Pan has demonstrated that SNR losses in amino acids can be avoided at moderate echo times when using a *J*-refocused acquisition.[27] In this sequence, the effects of *J*-modulation for coupled spins is reversed by transferring magnetization through a multiple quantum evolution period. Figure 7 shows spectra acquired with a 40 ms *TE* using the *J*-refocused sequence from human brain at 4 T.

In addition to the improvement in spectral resolution of amino acids, the increased separation between coupled reson-

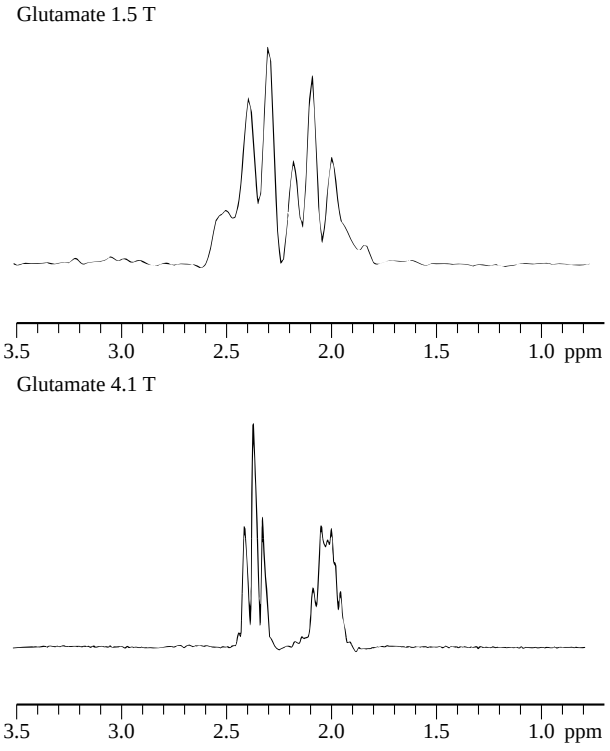

Figure 5 Spectra of a solution of glutamate acquired at 1.5 and 4.1 T

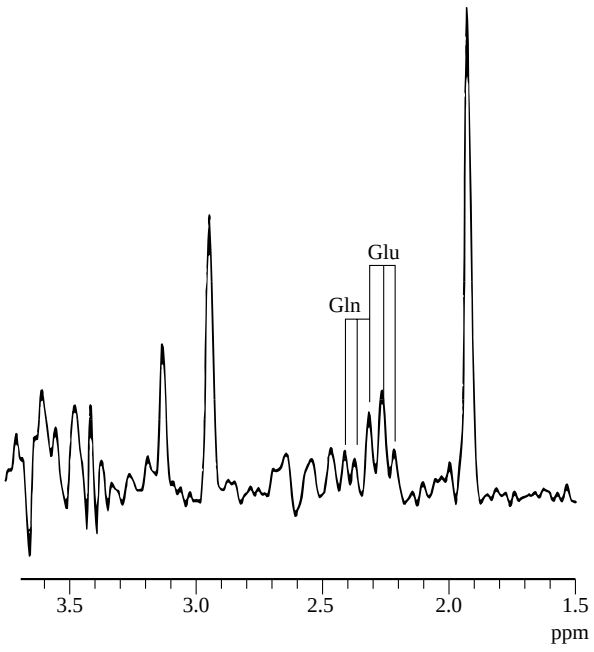

Figure 6 Spectrum acquired for a 2.25 ml voxel from human brain at 4.1 T as part of a spectroscopic imaging study using a *TE* of 15 ms. The two most upfield lines of glutamate (Glu) are resolved from the two most downfield lines of glutamine (Gln). The data set was acquired using 16 $\times$ 16 phase encodes with four phase cycles and a *TR* of 2000 ms

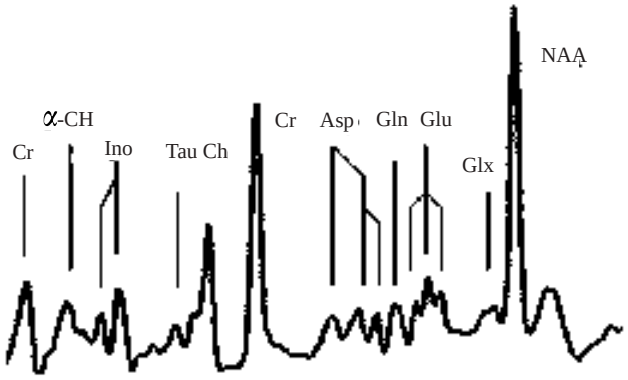

Figure 7 The *J*-refocused spectroscopic imaging sequence used to acquire a 1 ml spectrum from the occiptal lobe. NAA, *N*-acetylaspartate; Glx, glutamate and glutamine C-3; Glu, glutamate C-4; Gln, glutamine C-4; Asp, aspartate; CR, creatine; Ch, choline; Tau, taurine; Ino, inositol; α-CH, the alpha amino proton resonance of a variety of amino acids

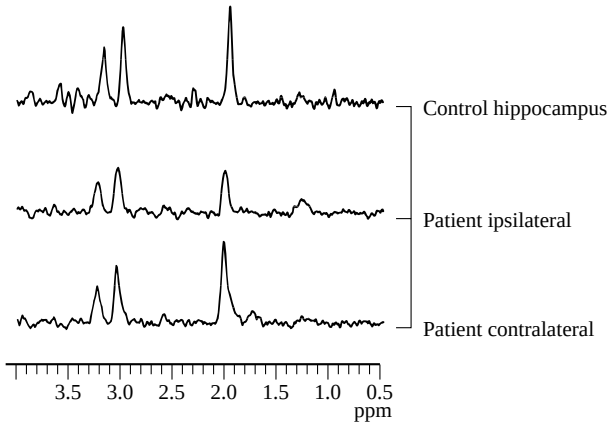

Figure 9 Spectra acquired from the hippocampi of a patient with temporal lobe epilepsy and a normal volunteer as part of a spectroscopic imaging at 4.1 T. The data were acquired using a *TE* of 50 ms and a *TR* of 2000 ms. The 240 × 240 field-of-view was acquired using 32 × 32 phase encodes with a single acquisition per encode

ances at 4 T affords significant advantages for spectral editing sequences. Rothman has demonstrated at 2.1 T that gamma-aminobutyric acid (GABA), the primary inhibitory neurotransmitter in mammalian brain, can be detected using spectral editing sequences.[28] However, because of the proximity of a macromolecule resonance and similarity in chemical structure, substantial overlap (60%) between the two resonances occurs in the edited spectrum. At 4 T, as a result of the additional separation in hertz between the coupled resonances of the macromolecule (1.7 ppm) and C-3 GABA resonance (1.9 ppm), this overlap can be reduced to 24% when highly selective inversion pulses are used.[29] Use of even more highly selective pulses can reduce this overlap to less than 10%. Use of these methods has permitted the measurement of acute elevations of brain GABA levels in response to novel antiepileptic drugs in normal controls (Figure 8).[30]

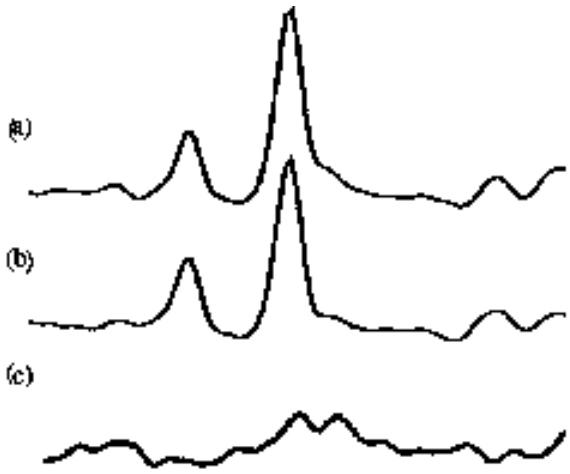

Figure 8 Spectra acquired from a 13.5 ml volume in the occipital lobe employing a 4.26 min acquisition. Spectrum acquired without (a) and with (b) a selective inversion pulse applied to the 1.9 ppm gamma-aminobutyric acid (GABA) C-3 resonance. (c) The difference spectrum of (a) and (b) displays the characteristic doublet GABA-edited spectrum (outer two lines of the GABA triplet)

3.4 Clinical Applications

The impact of the ability to acquire small voxels can be appreciated in the use of ^{1}H spectroscopic imaging in the diagnosis of temporal lobe epilepsy in patients with intractable seizures. It has been demonstrated by a number of laboratories that ^{1}H spectroscopy at 1.5–2.0 T provides a sensitive measure of neuronal loss as expressed in NAA content or NAA/Cr ratio measures.[31–33] However, the small size of the hippocampus (1.5 ml × 1 ml × 3 ml) and the complex anatomy surrounding the hippocampus, cerebellar vermis, temporal gray and white matter, and midbrain, with their varying Cr/NAA ratios (0.5–1.33, normal gray matter is 0.7) can obscure measurement of neuronal loss. False positives and negatives can occur when significant amounts of the cerebellar vermis or temporal white matter are included.[34] However, the small voxels afforded at 4 T (0.5 ml nominal volume) permit separation of these regions and improve the sensitivity of the detection of epileptic foci. Figure 9 shows typical spectra from the ipsilateral and contralateral hippocampi of an epilepsy patient and a healthy volunteer. The affected hippocampus is identified by the marked increase in the ratio of Cr/NAA.

4 ANATOMICAL AND FUNCTIONAL IMAGING

Previously it has been expected that anatomical images at high field would be degraded by the effects of an increased skin depth effect and the loss in intrinsic contrast by decreasing differences in the T_1 values of gray matter, white matter and cerebrospinal fluid. Ugurbil and colleagues first demonstrated that excellent gray/white contrast could be achieved in the human brain at 4 T using a modified driven equilibrium sequence exchanging the SNR for contrast.[35] The sequence uti-

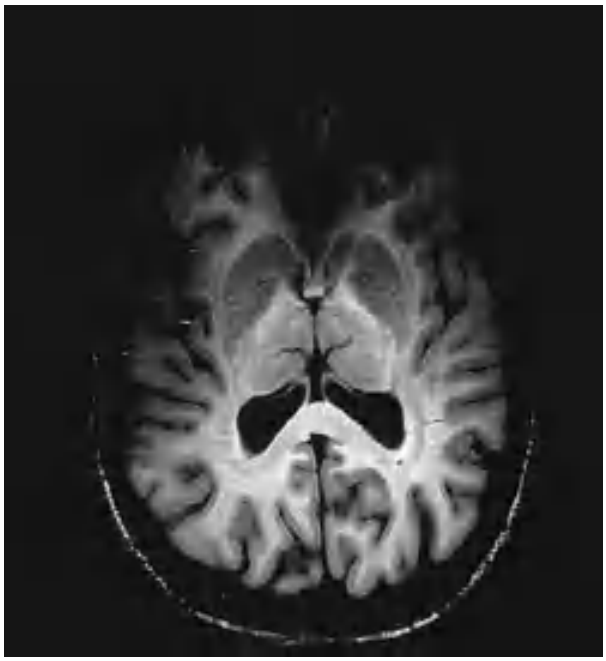

Figure 10 High resolution 3 mm image of the human brain acquired at 4.1 T. The field-of-view is 240 × 240 using a resolution of 512 × 512. The data were acquired with 3 mm slice thickness as part of an eight slice study using an inversion–recovery time of 1000 ms, a *TR* of 2500 ms, and a *TE* of 17.5 ms

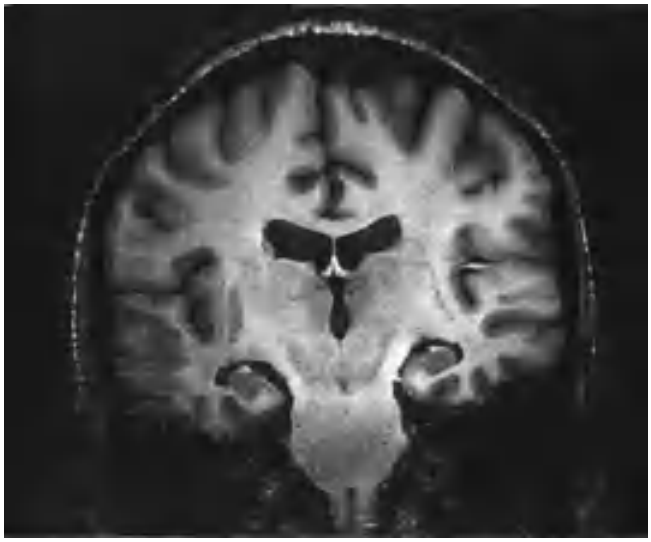

Figure 11 High-resolution 3 mm image of the human brain acquired at 4.1 T. The field-of-view is 240 × 240 using a resolution of 512 × 512. The data were acquired with a 3 mm slice thickness as part of an eight slice study using an inversion–recovery time of 1000 ms, a *TR* of 2500 ms, and a *TE* of 17.5 ms. The data were acquired with a coronal orientation through the hippocampi

lized a 90–180–90 sequence to provide an approximate quadratic dependence on T_1.

More recently it has been demonstrated that excellent contrast can be achieved using a simple inversion–recovery sequence with a gradient echo readout.[5] Displayed in Figure 10 is a 3 mm 512 × 512 gradient echo image of a human brain acquired at 4.1 T. Such images display excellent resolution of a number of cerebral anatomical features (caudate head, globus pallidus and putamen). The internal capsule is resolved through the high gray/white matter contrast. Resolution of these subcortical structures is important since they are frequently the site of small strokes less than 10 mm in diameter (lacuneae). The major groups of the thalami are resolved and correspond to the medial and lateral thalamic nuclear masses. The high spatial resolution and contrast are critical for visualizing the thalamic masses given that the internal medullary lamina, the intervening structure, is approximately 1 mm thick.

Because of the arterial blood flow originating from the posterior aspect of the circle of Willis medial to the temporal lobe, the highest quality coronal images of the temporal lobes are obtained by gating the acquisition to the cardiac cycle. Owing to the strong susceptibility differences in the regions around the temporal lobes and the relatively long echo time used, some degradation of image quality is experienced in the temporal lobe. This can be compensated for in part by using a shorter gradient echo time in the acquisition sequence. Regardless, excellent resolution and detail is observed in the visualization of the hippocampus (Figure 11). Specifically, the parahippocampal gyrus, Ammon's horn with the alveus extending into the fornix, the subiculum, and the overlying superficial medullary stratum are well defined. The reliability of lateralizing the focus in temporal lobe epilepsy by MRI will be improved with this level of resolution. Such high-resolution images may also aid in the further study and diagnosis of Alzheimer's disease.

Perhaps the most striking qualitative difference between 4.1 T high-resolution images and those acquired on widely available lower field clinical systems is the visualization of small cerebral vessels in all axial images (Figure 12). With finer slice separation it should be possible to define the majority of the deep cerebral veins. The fine radiation of vessels has not previously been seen routinely in vivo. Visualization of such vessels is most demanding of resolution and contrast available at high field. The contrast is most likely related to the deoxygenated hemoglobin present in veins, decreasing the signal against a background of high signal intensity from white matter.

In summary, imaging at 4.1 T depicts the brain with very high resolution, which should allow detection of disease states not heretofore imaged noninvasively. This approach could potentially obviate the need for angiography or biopsy.

The best advantage of high-field imaging is that of the enhanced sensitivity to changes in deoxyhemoglobin, which forms the mechanism for blood oxygenation-dependent (BOLD) contrast in functional imaging.[35] The enhancement of field strength is believed to range from linear to quadratic in strength. Thus the small changes that are seen in functional imaging studies (1–5%) can be measured with the highest sensitivity only at high field. This effect has been used by a number of investigators at 4 T to investigate the effects of various paradigms of brain activity on oxygen consumption and delivery and the localization of those effects. The results suggest that valuable insights into brain physiology and psychiatric and various pathological states are on the horizon. The utility of functional imaging at high field will provide a primary driving force for the proliferation of high field systems.

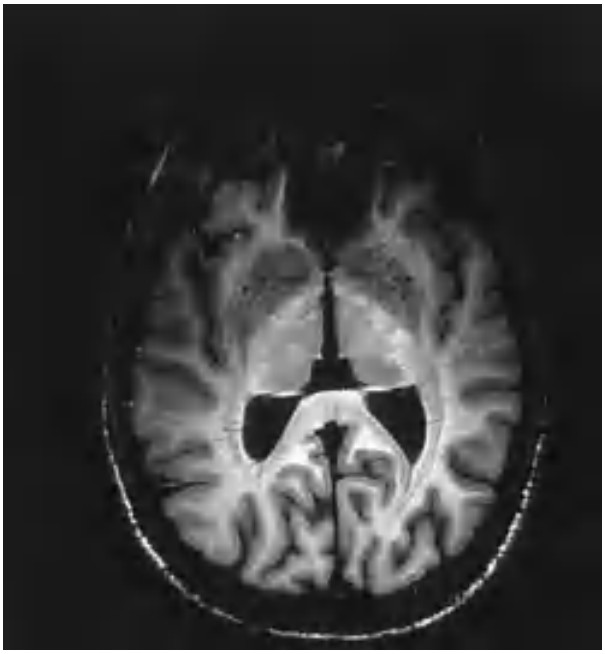

Figure 12 High-resolution 3 mm image of the human brain acquired at 4.1 T. The field-of-view is 240 × 240 using a resolution of 512 × 512. The data were acquired with a 3 mm slice thickness as part of an eight slice study using an inversion–recovery time of 1000 ms, a *TR* of 2500 ms, and a *TE* of 17.5 ms. Note the fine detail showing deep cerebral veins about the ventricles

5 RELATED ARTICLES

Birdcage Resonators: Highly Homogeneous Radiofrequency Coils for Magnetic Resonance; Low-Field Whole Body Systems; MRI at Midfield Strength; Structural and Functional MR in Epilepsy; Whole Body Studies: Impact of MRS.

6 REFERENCES

1. H. J. Schneider and P. Dullenkopf, *Rev. Sci. Instrum.*, 1977, **48**, 68.
2. H. Barfuss, H. Fischer, D. Hentschel, R. Ladebeck, A. Oppelt, R. Wittig, W. Duerr, and R. Opelt, *NMR Biomed.*, 1990, **3**, 31.
3. P. K. Roeschmann, US Patent 4 746 866, 1988.
4. J. T. Vaughan, H. P. Hetherington, J. O. Otu, J. W. Pan, and G. M. Pohost, *Magn. Reson. Med.*, 1994, **32**, 206.
5. J. W. Pan, J. T. Vaughan, R. I. Kuzniecky, G. M. Pohost, and H. P. Hetherington, *Magn. Reson. Imag.*, 1995, **13**, 915.
6. N. Zhang, M. S. Roos, J. T. Vaughan, S. T. S. Wong, and T. F. Budinger, *Proc. IVth Annu. Mtg (Int.) Soc. Magn. Reson. Med.*, New York, 1996, p. 252.
7. J. T. Vaughan, H. P. Hetherington, and G. M. Pohost, *Proc. IInd Annu. Mtg (Int.) Soc. Magn. Reson. Med.*, San Francisco, 1994, p. 1119.
8. G. Adrianny, J. T. Vaughan, P. Andersen, H. Merkle, M. Garwood, and K. Ugurbil, *Proc. IInd Annu. Mtg (Int.) Soc. Magn. Reson. Med.*, Nice, 1995, p. 921.
9. D. I. Hoult, and P. C. Lauterbur, *J. Magn. Reson.*, 1979, **34**, 425.
10. H. P. Hetherington, G. F. Mason, J. W. Pan, S. L. Ponder, J. T. Vaughan, D. B. Twieg, and G. M. Pohost, *J. Magn. Reson.*, 1994, **32**, 565.
11. O. A. C. Petroff, D. D. Spencer, J. R. Alger, and J. W. Prichard, *Neurology*, 1989, **39**, 1197.
12. P. A. Bottomley, R. J. Herfkens, L. S. Smith, and T. M. Bashore, *Radiology*, 1987, **165**, 703.
13. P. R. Luyten, A. de Roos, L. J. M. J. Oosterwaal, K. Doornbos, and J. A. den Hollander, *Proc. XIth Annu. Mtg Soc. Magn. Reson. Med.*, Berlin, 1992, p. 74.
14. R. G. Weiss, P. A. Bottomley, C. J. Hardy, and G. Gerstenblith, *N. Engl. J. Med.*, 1990, **323**, 1593.
15. R. S. Menon, K. Hendrich, X. Hu, and K. Ugurbil, *Magn. Reson. Med.*, 1992, **26**, 368.
16. H. P. Hetherington, D. J. E. Luney, J. T. Vaughan, J. W. Pan, S. L. Ponder, O. Tschendel, D. B. Twieg, and G. M. Pohost, *Magn. Reson. Med.*, 1995, **33**, 427.
17. R. Gruetter, G. Adriany, H. Merkle, and P. M. Andersen, *Magn. Reson. Med.*, 1996, **36**, 659.
18. J. Frahm, H. Bruhn, M. L. Gyngell, K. D. Merboldt, W. Hanicke, and R. Sauter, *Magn. Reson. Med.*, 1989, **11**, 47.
19. S. Posse, C. A. Cuenod, R. Risinger, D. Le Bihan, and R. S. Balaban, *Magn. Reson. Med.*, 1995, **33**, 246.
20. J. Frahm, K. D. Merboldt, and W. Hanicke, *J. Magn. Reson.*, 1987, **72**, 502.
21. H. P. Hetherington, J. W. Pan, G. F. Mason, S. L. Ponder, D. B. Twieg, G. Deutsch, J. Mountz, and G. M. Pohost, *Magn. Reson. Med.*, 1994, **32**, 530.
22. M. Garwood and K. Ugurbil, *NMR Basic Princ. Progr.*, 1992, 110.
23. P. A. Bottomley, C. J. Hardy, and R. G. Weiss, *J. Magn. Reson.*, 1991, **95**, 341.
24. G. F. Mason, J. W. Pan, S. L. Ponder, D. B. Twieg, G. M. Pohost, and H. P. Hetherington, *Magn. Reson. Med.*, 1994, **32**, 145.
25. T. Michaelis, K. D. Merboldt, W. Hanicke, M. L. Gyngell, H. Bruhn, and J. Frahm, *NMR Biomed.*, 1991, **4**, 90.
26. R. Kreis and B. D. Ross, *Radiology*, 1992, **184**, 123.
27. J. W. Pan, G. F. Mason, G. M. Pohost, and H. P. Hetherington, *Magn. Reson. Med.*, 1996, **36**, 7.
28. D. L. Rothman, O. A. C. Petroff, K. L. Behar, and R. H. Matson, *Proc. Natl. Acad. Sci. USA*, 1993, **90**, 5662.
29. H. P. Hetherington, B. R. Newcomer, and J. W. Pan, *Magn. Reson. Med.*, 1998, **39**, 6.
30. R. I. Kuzniecky, R. H. P. Hetherington, S. Ho, J. W. Pan, R. Martin, F. Gilliam, and E. Faught, *Neurology*, 1998, **51**, 627.
31. D. G. Gadian, A. Connelly, J. S. Duncan, J. H. Cross, F. J. Kirkham, C. L. Johnson, F. Vargha-Khadem, B. G. R. Neville, and G. D. Jackson, *Acta Neurol. Scand.*, 1994, **152**, 116.
32. F. Cendes, F. Andermann, P. C. Preul, and D. L. Arnold, *Neurology*, 1993, **43**, 223.
33. J. W. Hugg, K. D. Laxer, G. B. Matson, A. A. Maudsley, and M. W. Weiner, *Ann. Neurol.*, 1993, **34**, 788.
34. H. P. Hetherington, R. I. Kuzniecky, J. W. Pan, G. F. Mason, J. T. Vaughan, C. Harris, H. Morawetz, and G. M. Pohost, *Ann. Neurol.*, 1995, **38**, 396.
35. K. Ugurbil, M. Garwood, J. Ellerman, K. Hendrich, R. Hinkle, X. Hu, S. G. Kim, R. Menon, H. Merkle, S. Ogawa, and R. Salmi. *Magn. Reson. Q.*, 1993, **9**, 259.

Low-Field Whole Body Systems

Leon Kaufman, David Kramer, Joseph Carlson and Mitsuaki Arakawa

UCSF-RIL, San Francisco, CA, USA

1 INTRODUCTION

MRI is a medical diagnostic modality. As such, it is of value only if it is available to the people who can benefit from its use. Because for most subjects MRI use is not limited by risk–benefit considerations, cost–benefit analysis is becoming the major determinant of use. In cases like this, as the cost of a study decreases, the utilization (and presumably the benefit) increases. Decreasing the costs of MRI requires careful attention to the physics and engineering of the discipline. The major determinant of cost is field strength. By reducing the field strength it becomes possible to use nonsuperconducting magnets. Low-field systems can be sited in smaller rooms, and this further reduces initial and ongoing costs. Other components where significant savings are achieved include rf transmitters and, in some cases, gradient coils. Once the cylindrical magnet configuration can be avoided, the range of suitable low-field magnets includes some that are open. These, in turn, offer opportunities in terms of interventional studies (where low fields have some other practical advantages), and in dealing with difficult or ill patients.

2 PHYSICS OF LOW FIELD STRENGTH OPERATION

As field strength decreases, so does the strength of the NMR signal emitted by the body. Nevertheless, imaging is a complex process that involves many factors. With decreasing field strength, noise from the body also decreases. Chemical shift and susceptibility artifacts decrease, permitting narrower bandwidths and consequent reductions in noise. T_1 shortens[1,2] and T_2 lengthens,[2] this increasing signal level during imaging. Motion artifacts decrease, so that the fraction of study time spent on motion reduction can be used for data acquisition, and rf power deposition decreases dramatically. Radiofrequency pulses can be tailored to improve section profiles and, more importantly, the hazard from rf heating is all but eliminated. At lower field, absolute magnetic field inhomogeneities get smaller (for imaging, a magnet with a 30 ppm homogeneity specification at 500 G is equivalent to one with a 1 ppm specification at 1.5 T). This, and decreased susceptibility effects, permit the use of gradient echo techniques where spin echoes may need to be used at higher fields.[3] The shortened T_1 values favor the use of three-dimensional FT techniques, which can be designed to provide a wide range of contrast capabilities with good signal-to-noise ratios.[4,5] Furthermore, for water-elevating lesions, for the same sequence, contrast will typically be higher at the lower field. This is due to two factors: the shortened T_1 of tissues permits contrast from T_2 and proton density N(H) changes to become visible at shorter *TR* values;[6] and the change in T_1 and T_2 with water content is larger the lower the field.[1,2] The impact of these effects will depend on the type of study being performed, but, in general, for the same volume resolution and coverage, and for equivalent contrast, there will be a signal-to-noise ratio difference of 2–3 over a range of field strength of a factor of 25.

3 MAGNETS FOR LOW-FIELD MRI

Various choices of magnet are available for low-field development. Resistive magnets were the early choices, but with the advent of practical permanent magnet designs the latter have become incorporated into the more recent commercially available products. Magnet technology involves two basic components: the driver and the core of the magnet. The driver provides the motive force that establishes the magnetic field. Three types of driving technology are available in the marketplace: resistive, permanent, and superconducting. The Earth's magnetic field is a fourth source that has been discussed in the literature but has not become commercially available. The core is the medium upon which the driver acts. Because a patient has to be able to be located in the magnet (a prerequisite for reimbursement), all magnets have at least a portion of their field in air. Air-core magnets are those where all of the core is air. These may have a return path (the region outside of the core where the magnetic field lines close) that is either air or iron. Iron-core magnets have, except for the patient volume, iron paths both for the drivers to act on and as return paths. The relative merits of these approaches to magnet design are discussed below.

3.1 Drivers

3.1.1 Resistive Drivers

In a resistive driver, a current is established on a good conducting material, typically copper or aluminum (during the Manhattan Project silver from the US reserves was used for huge magnets for uranium separation, since copper and aluminum were needed for armaments). The conductor is at or near room temperature, so it offers resistance to the flow of current. This resistance has two effects: power has to be used to maintain the current flow and attendant magnetic field, and heat is generated in the conductor through resistive losses. Consequently, water needs to be used to extract this heat. In addition, the stability of the field depends on power-supply stability, stability coming at a price.

The advantages of the resistive driver is that the technology is well known and understood, and the entry is easy, since a great deal of expertise exists or is easily acquired by a company. The disadvantages are high power consumption, large cooling demand, a large conductor mass, and its consequent weight. When an iron core is used, the larger mass of conduc-

tor forces an increase in the physical size of the core, which then results in further weight increases.

3.1.2 Permanent Drivers

In a permanent magnet, the field originates in blocks of permanently magnetized material. Currently available are ferrite magnets for low-field operation and Neomax (a rare earth alloy) for higher fields. The attractive aspect of permanent magnet drivers is that they are totally passive, requiring no added services such as electricity, cryogens, or cooling. The disadvantages are that there is a very steep cost/field curve, especially when rare-earth materials are needed for higher fields; in addition, the weight of the permanent magnet material adds to the weight of an iron core.

For the higher field units, a potential problem is that the magnet cannot be discharged in an emergency.

3.1.3 Superconducting Drivers

There are materials, generically known as superconductors, that if kept at a sufficiently low temperature lose all resistance to current flow. In typical magnets for MRI, this temperature has to be well below 10 K, that is, under 10°C above absolute zero. A convenient way to achieve this is by the use of liquid helium, which has a temperature of near 4 K. The liquid boils away through heat leaking into the magnet from room temperature. Because of cost, it is desirable to minimize the boil-off of the helium. One method used in the early years of commercial MRI was to use a surrounding container with liquid nitrogen, which has a temperature of 77 K, intermediate between the helium and room temperatures. This, of course, adds liquid nitrogen consumption to the services needed for magnet operation. Later, electrical shield coolers were added to magnets to replace the liquid nitrogen 'shield'; these coolers usually reached temperatures well below 77 K, thus improving the shielding effect. Also, recirculating coolers that reliquefied the vented helium gas were added to some magnets, even though in the USA this was not usually economic because of the relatively low cost of liquid helium.

More recently, electrical coolers that reach 4 K have become commercially available. This opens the way to cryogenless superconducting magnets with low power consumption. It is worth noting that the high-temperature superconducting materials that a few years ago were promoted as permitting magnets cooled by liquid nitrogen have yet to provide the performance required by MRI magnets; however, they have found use as superconducting leads, which bring current from the outside to the main windings during magnet charging and discharging.

The advantage of superconductors for MRI is the achievement of relatively higher fields compared with the other technologies, with low weight and modest power consumption. The disadvantage is the need for cryogens (or, more recently, cryocoolers that can replace cryogens) and the technical complexity of these systems compared with other drivers, this making entry more difficult. In terms of cost, at a certain field strength crossover point superconductors become cheaper than other drives. Once the midfield range is reached, they have definite advantages in this respect.

3.2 Magnet Core

The driver can be shaped to obtain the desired imaging field and field return path without the aid of significant amounts of iron; this is known as an air-core magnet. Alternatively, the iron can be used for shaping the imaging field and providing a return path; this is an iron-core magnet. Some air-core magnets have an iron return path or shield.

The advantage of air-core magnets is low weight. The disadvantages are inefficient use of conductor, demands on the conductor configuration and manufacturing tolerances (since the homogeneity depends on the conductor), and large fringe fields that require active or passive shielding. All of this, of course, results in increased costs.

Iron-core magnets make more efficient use of the driver, since the iron provides a medium that offers less 'resistance' to the flow of the magnetic field lines. In iron-core magnets fringe fields are relatively small, and homogeneity is determined by the shape of the iron. This places fewer demands on the driver's configuration and tolerances. The main unavoidable disadvantage of these cores is weight.

3.3 Other Factors

There are obviously other nuances about the different drivers and cores that need to be taken into account when designing an MRI system, but the characteristics described above are of a reasonably general nature and not amenable to significant manipulation. Commercially, we have seen the following driver–core combinations become available at one time or another in the lifetime of clinical MRI: (a) resistive, superconducting, and permanent driver air cores, the first two sometimes with iron shielding; and (b) resistive, permanent, and superconducting driver iron core. Iron cores can be 1-(C), 2-, and 4-post designs. Recent magnet assembly technology results in elimination of eddy currents without the need for active gradient coil shielding. The design of these magnets involves tradeoffs among cost, size, weight, gap, homogeneity, fringe field and field strength. Typically, larger gaps, higher homogeneities, smaller fringe fields, and higher field strengths require larger, heavier magnets of higher cost.

4 SEQUENCING FOR LOW-FIELD IMAGING

Sequence development for low-field imaging needs to take into account, and take advantage of, the short T_1 value of solid tissues. Also of importance are reduced chemical shift and susceptibility artifacts. One example involves strategies for the detection of lesions where water content is increased. This is a typical effect seen in tumors, edema, and infarcts. Considering the case where there is no blood, for these lesions N(H), T_1, and T_2 are all elevated.[6] In a spin echo sequence the elevation of N(H) and T_2 increases signal, while the elevation of T_1 decreases signal. Thus N(H) and T_2 effects are diluted by T_1 effects. To obtain a lesion that is brighter than the background it is necessary to increase TR to the point that T_1 effects become unimportant. This results in what is misnomered a 'T_2-weighted' image. In fact, a more accurate measure would be 'not T_1-weighted'. To achieve this condition reliably, it is

necessary to operate with a *TR* of at least $2T_1$, preferably 2.5–$3T_1$. Since T_1 increases with field strength, this means that it is necessary to operate with a longer *TR* at the higher field. For instance, for brain tissue the increase between 0.064 T and 1.5 T is approximately a factor of 4, from 250 ms to about 1 s for white matter, and from 300 ms to 1.2 s for gray matter. Thus, for a spin echo sequence, the desired lesion contrast is easier to achieve, and is more reliably achieved, at the lower field. This has significant consequences in terms of the signal-to-noise ratio, since shorter *TR* values can lead to a larger number of data averages for fixed imaging time.

For 'watery' lesions, the ability to use short *TR* values opens an avenue for imaging with three-dimensional FT sequences. The *TR* that can be achieved in three-dimensional FT imaging is limited by practical considerations of time, since this time increases linearly with the number of slices obtained. If gradient echo instead of spin echo imaging is used, a flip angle smaller than 90° results in a decrease of T_1 effects. Lowering the angle at fixed *TR* has the same effect as lengthening *TR* for a 90° angle. Unfortunately, this cannot be carried to extremes, but this process is more effective the larger the TR/T_1 ratio. Thus, from a practical point of view, it is only achievable for short T_1 values, where it is highly effective. Furthermore, to obtain the desired contrast level it is desirable to operate with a relatively long *TE*, to take advantage of T_2 effects.

Gradient echo imaging (used in conjunction with partial flip angles) is highly sensitive to susceptibility and inhomogeneity effects, this sensitivity increasing with *TE* and with field strength. At low field the gradient echo technique shows no noticeable artifacts from susceptibility, chemical shift or inhomogeneity artifacts, permitting a late echo (*TE* = 53 ms) with a long sampling window. A relatively long *TR* value (110–145 ms in our case), combined with a flip angle of 12–20°, at 640 G, reduces T_1 effects so that the elevated T_2 and N(H) of lesions makes them appear bright, with cerebrospinal fluid (CSF) still being of low intensity[4] (Figure 1). Thus, the combination of short T_1 and the low inhomogeneity and susceptibility effects that accompany low-field operation permit for this application the use of gradient echo three-dimensional FT imaging, which under these conditions results in signal-to-noise ratios at low fields comparable to those of mid- and high-field systems when taking into account the imaging time and the number of sections obtained.[4] At this field strength three-dimensional FT imaging is the preferred method for obtaining images of thin sections.[5] Figures 2 and 3 show a pituitary with section thicknesses of 4.5 and 2.25 mm, respectively.

A hybrid technique consisting of a multislab two-dimensional FT sequence with two-slice encodings within a slab, coupled with partial flip angle gradient echo imaging, has permitted us to develop a sequence that takes advantage of low field operation characteristics and doubles the signal-to-noise ratio over that of conventional spin echo.[3] The multislice double echo spin echo imaging technique introduced by Crooks[7] quickly became the 'gold standard' of lesion detection.[8] At low field it is possible to increase its efficiency dramatically by the following steps:

1. Take advantage of short T_1 values by using a short *TR* and slice doubling[9] to maintain high coverage. The shortened *TR* is traded off against increased data averaging to increase the signal-to-noise ratio.
2. Lengthen the echo window.
3. Use gradient reversal instead of rf refocused echoes to reduce dead time in the sequence. This permits the number of slices obtained to be high, even though the windows are long.

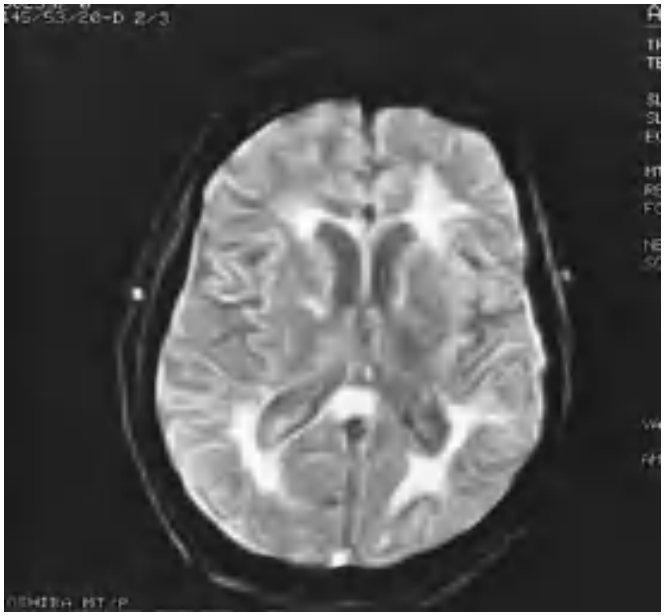

Figure 1 Transaxial view of a patient with multiple sclerosis lesions, obtained at 640 G. Lesions are brightest, and, in descending order of intensity, gray matter, white matter and CSF. Three-dimensional FT gradient echo with *TR* = 145 ms, *TE* = 53 ms, and flip angle = 20°

Figure 2 Three-dimensional FT gradient echo imaging with *TR* = 68 ms, *TE* = 24 ms, and flip angle = 60°, at 640 G. Section thickness 4.5 mm

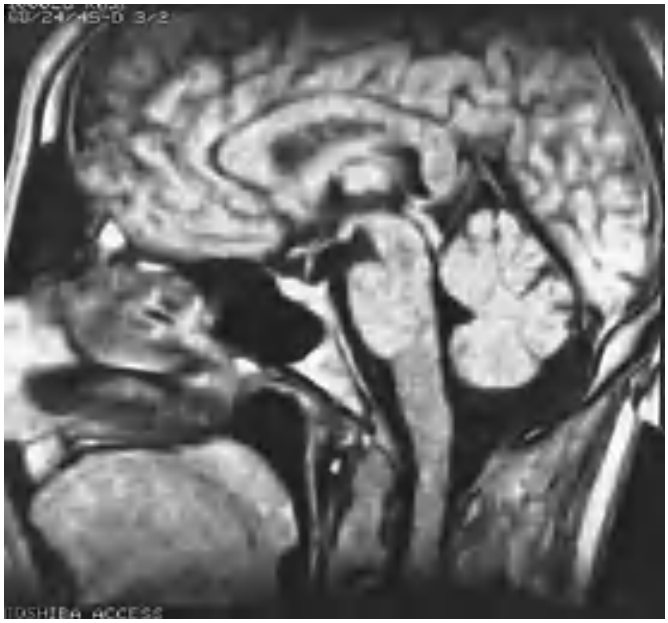

Figure 3 As Figure 2, but with a flip angle of 45° and a section thickness of 2.25 mm

4. Take advantage of the gradient reversal echo to use partial flip angle excitations, in order to maximize further the signal-to-noise ratio and the contrast.

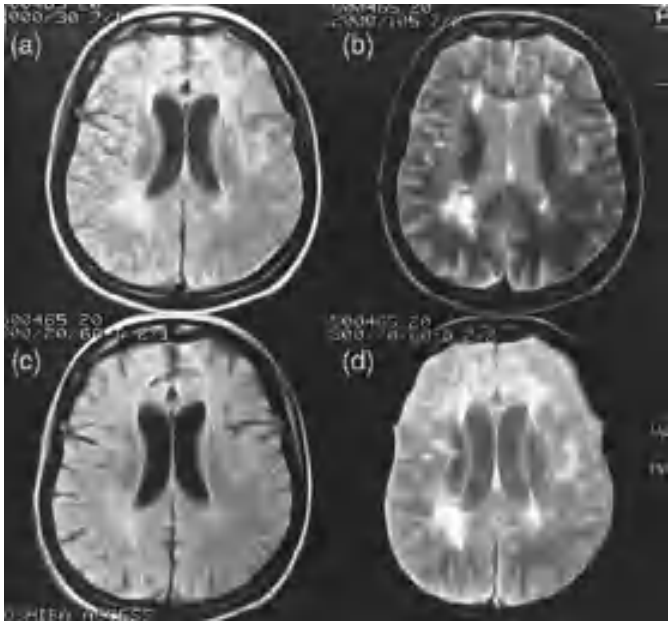

Figure 4 (a, b) Spin echo imaging 640 G in a patient with multiple sclerosis; *TR* = 2 s, and *TE* = 30 and 105 ms in (a) and (b), respectively. (c, d) Gradient echo images; flip angle = 60°, *TR* = 0.8 s, and *TE* = 20 and 70 ms in (c) and (d), respectively. The spatial resolution and number of sections are the same for both sequences. The earlier *TE* values of the set (c, d) reduce contrast, but the display system can be set to display any *TE* in a real-time basis. Comparing (a, b) and (c, d), the signal-to-noise ratio has essentially doubled, in the latter

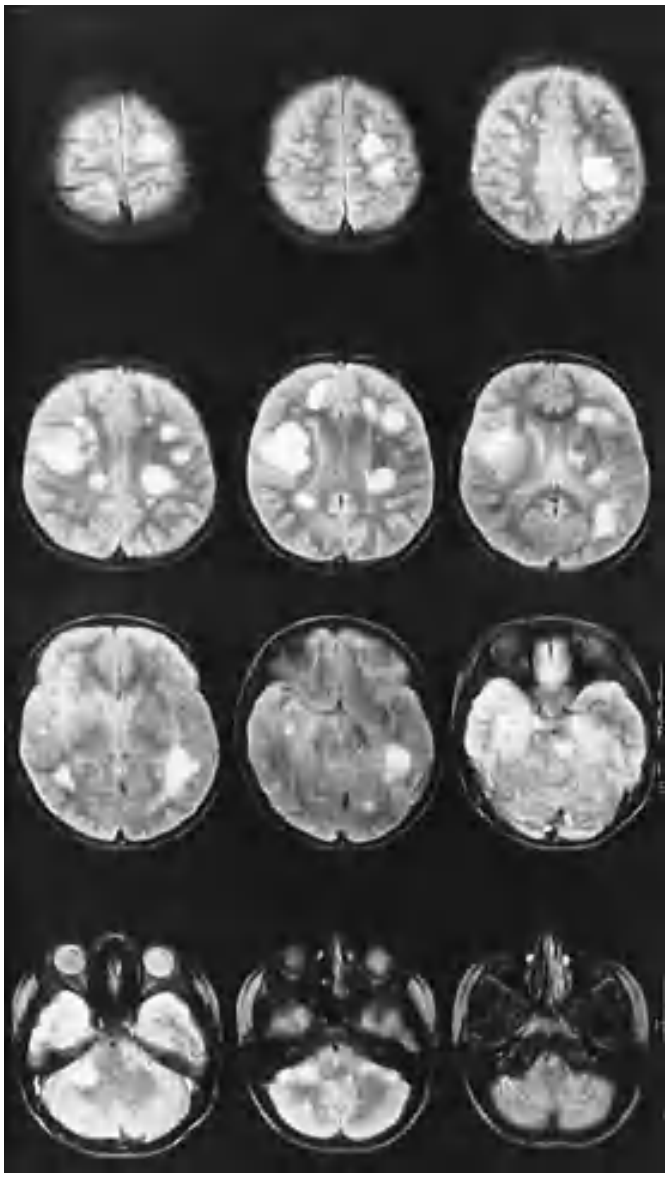

Figure 5 Two-dimensional FT, multislice gradient echo images through the head of a subject with white matter lesions. Note the low level of susceptibility artifacts at 640 G

Compared with a spin echo sequence, for equal imaging time and number of slices, this sequence has comparable contrast and twice the signal-to-noise ratio[3] (Figures 4 and 5).

A significant benefit is derived in low-field operation from the fact that, while at low field solid tissues have shorter T_1 values, CSF has a T_1 that is constant with field. Consequently, at the short *TR* where lesion contrast is achieved, the signal from CSF is small. At high field, because *TR* has to be long, the CSF signal is large, obscuring lesions that may be contiguous with CSF spaces. To summarize, low field strengths offer many advantages for the detection of water-elevating lesions, including increased sensitivity to water changes, the ability to operate with relatively short *TR* values, and the avoidance of confusing effects from bright CSF.

Figure 6 MRA at 640 G, using phase contrast imaging

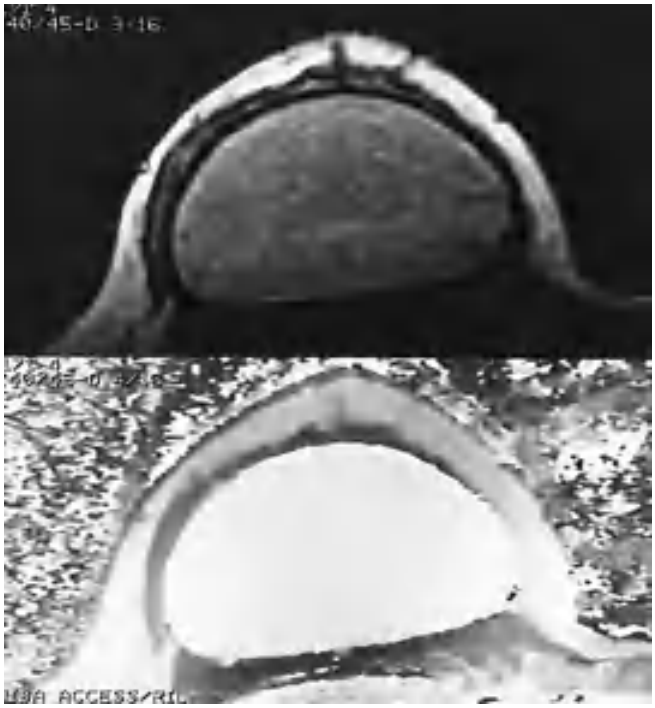

Figure 7 Subject with silicone breast implants. Top row: TR = 110 ms, TE = 40 ms, flip angle = 45°, magnitude image. Bottom row: phase image from the same data set. At 640 G, silicone and water are nearly out of phase (silicone, bright; water, dark) and fat is intermediate

Another example of low-field sequencing involves magnetic resonance angiography (MRA). In MRA the clinically most successful techniques take advantage of wash-in effects.[10] The blood entering the volume has not been excited previously and thus produces a great deal of signal following the first one or two excitations.[11] Meanwhile, it is desirable to saturate the signal from stationary tissues by the same repeated excitations that produce signal from blood. This saturation is more effective the longer the T_1, since recovery time is longer. Because high-field operation entails long T_1 values, high contrast between blood and nonmoving tissues is easier to obtain. This permits more flexibility in trading vessel contrast for depth of penetration (field of view) than at low field, where T_1 values are short. For low-field systems, phase contrast angiography becomes an extremely attractive alternative. Figure 6 shows an example.

Imaging of chemical shift is also accessible at low field for protons in water, fat, and silicone, by reconstruction of phase images for three-dimensional FT sequences. We have found this method particularly powerful in searching for extracapsular silicone in breast implant patients.[12] The chemical shift images have the same resolution and signal-to-noise ratio and do not require additional imaging time (Figure 7).

5 SEQUENCES FOR MID-FIELD IMAGING

MRI started as a mid-field technique. Many of the sequences that are currently considered 'routine' were originally developed at mid-field, so contrast characteristics are more familiar. The contrast characteristics of mid-field MRI are closer to low than to high field. For instance, brain lesions are bright while CSF remains of lower intensity; consequently, fluid attenuation inversion recovery techniques (FLAIR) are not needed to highlight periventricular lesions (Figure 8). Fat signal gains in relative intensity compared with low field, but inversion recovery and multipoint Dixon techniques make it easier to suppress fat (Figure 9). In gradient echo imaging, water and fat are out of phase at a convenient TE of 10 or 30 ms and in phase at TE of 20 ms. The former results in fast sequences for screening for bone marrow abnormalities (Figure 10). The T_1 of blood lengthens enough to make time-of-flight MRA techniques attractive (Figure 11). Also, CSF is easier to highlight (Figure 12). Single-shot fast spin echo imaging results in effective imaging of long T_2 tissues, principally CSF. Double-contrast fast spin echo imaging adds to the flexibility with which contrast can be varied (Figure 13). Asymmetric spin echo sequences[13] can be used to highlight T_2* effects (Figure 14).

A crossover occurs between the efficacy of two- and three-dimensional imaging [14] so either is effective. Particularly effective are three-dimensional spin echo techniques, which provide fine anatomic detail (Figure 15).

6 SIGNAL-TO-NOISE RATIO AND FIELD STRENGTH

A perception exists that the signal-to-noise (S/N) ratio increases linearly with field strength. The physics of MRI shows that signal increases as the square of the field, and measurements and theoretical considerations (based on certain assumptions about the body) support a linear increase in noise with field, although the latter assumption should be considered

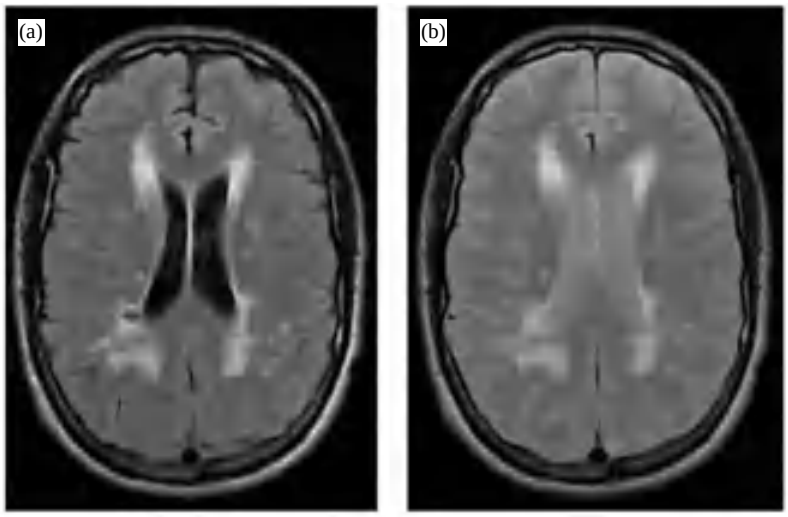

Figure 8 FSE imaging in a subject with multiple sclerosis. At high field, when a *TR* is long enough to make lesions bright, CSF is also very bright. Consequently, inversion recovery (IR) techniques are used to suppress CSF (FLAIR). The cost is in the inefficiency of IR imaging. FLAIR techniques can also be used at mid-field (a) ($TR = 8$ s, $TE = 120$ ms, $T_1 = 1.9$ s) but are not necessary, as shown in (b) ($TR = 2000$ ms, $TE = 60$ ms). Both images were obtained at 0.35 T. The mid-field image (a) requires $TR = 267$ ms per slice, while without the IR pulse (b) *TR* is 91 ms

with caution. Based on these two factors, the 'intrinsic' S/N ratio should increase linearly with field. This simplistic view depends on disregarding all the factors that are important in imaging, all of which result in a much smaller increase than presumed.

In addition to the 'intrinsic' factor, the S/N ratio depends on the imaging conditions. Of interest is the S/N ratio per unit time for fixed voxel dimensions and imaged volume, as well as constant number of slices. For a 90° flip angle the relative S/N ratio will be proportional to

$$\{\exp(-TE/T_2)[1-\exp(TR/T_1)]\sqrt{\text{window length}}\sqrt{\text{slices}}/\sqrt{TR}\} \quad (1)$$

for two-dimensional FT imaging. The reasons for the $\sqrt{\text{slices}}$ term is that if sequence A yields 10 slices and sequence B yields 20 slices with one excitation, then to cover the same volume sequence A has to be run twice, while sequence B in the same time could be run once with two excitations and a gain of $\sqrt{2}$ in the S/N ratio. Similarly, the $\sqrt{TR}$ term comes in because, if two sequences provide the same coverage for one excitation, then the sequence with the shorter *TR* can be run with more excitations and increase the S/N ratio accordingly. For three-dimensional FT there is an additional $\sqrt{\text{slices}}$ term. For a discussion of the relative merits of two- and three-dimensional FT imaging the reader is directed to the paper by Carl-

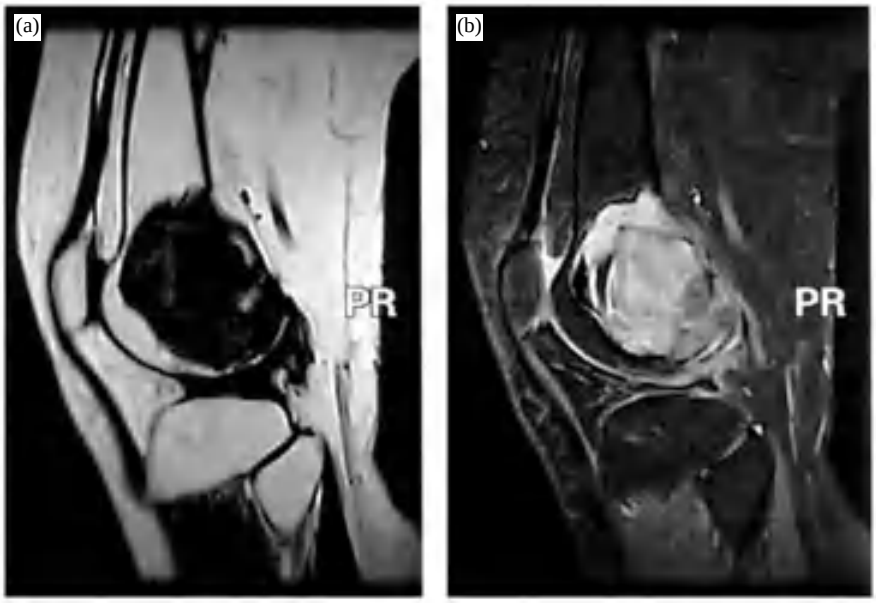

Figure 9 Knee imaging in a subject with a bone marrow tumor. (a) Single-shot image for water. (b) Single-shot image of fat.

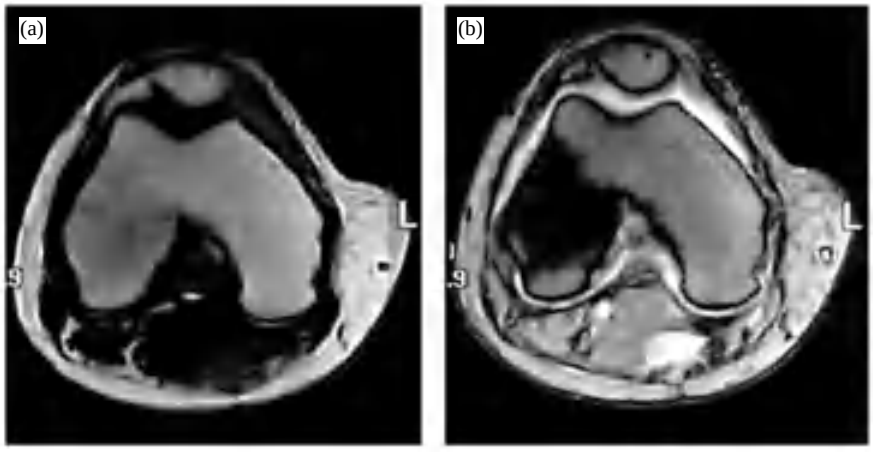

Figure 10 Gradient echo images of the knee in a subject with a vascular necrosis. (a) Water and fat in phase ($TE = 20$ ms at 0.35 T). (b) Water and fat out of phase ($TE = 30$ ms)

son et al.[15] Based on imaging considerations we can analyze how the S/N ratio will behave.

6.1 T_1

As field strength increases, so does T_1.[1,2] A longer T_1 means smaller signals. For discussion purposes, consider T_1 varying as the square root of field strength. For a short *TR* sequence the signal will decrease linearly with T_1, or as the square root of the field. For a long *TR* sequence the signal will not change much, but for a fixed *TR* the contrast will be lower, or for fixed contrast *TR* will be longer (longer imaging time). In this case the equivalent loss in S/N ratio will be smaller, approximately as the fourth root of field strength. Thus, for longer *TR* values, T_1 effects result in a loss in signal that increases as the fourth root to the square root of the field.

6.2 T_2

There is clear evidence that T_2 drops with field strength.[2] Between 0.063 and 3 T the T_2 of brain drops from about 80 to 58 ms, for muscle from 37 to 30 ms, and for liver from 49 to 25 ms. For a *TE* of 30 ms, this results in signal drops from 16% to 50%, corresponding to a 1/20 to 1/6 power of field for the loss in S/N ratio due to T_2. The loss will be smaller for shorter *TE* and bigger for longer *TE* values.

6.3 Window Length

Chemical shift, susceptibility, and inhomogeneity limit window lengths. As discussed above, the artifacts depend linearly on field strength and window length. A shorter window reduces the artifacts, but also decreases the S/N ratio as the square root of window length. The net effect is that at a constant artifactual level there is a square root of field strength term available in the S/N ratio, favoring low field operation. In some sequences

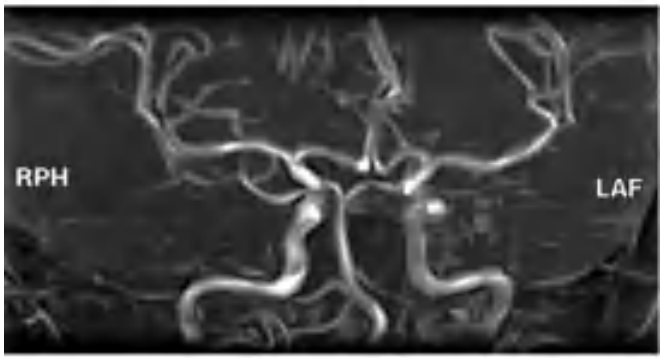

Figure 11 Three-dimensional time-of-flight MRA at 0.35 T, acquisition time of 13.5 min

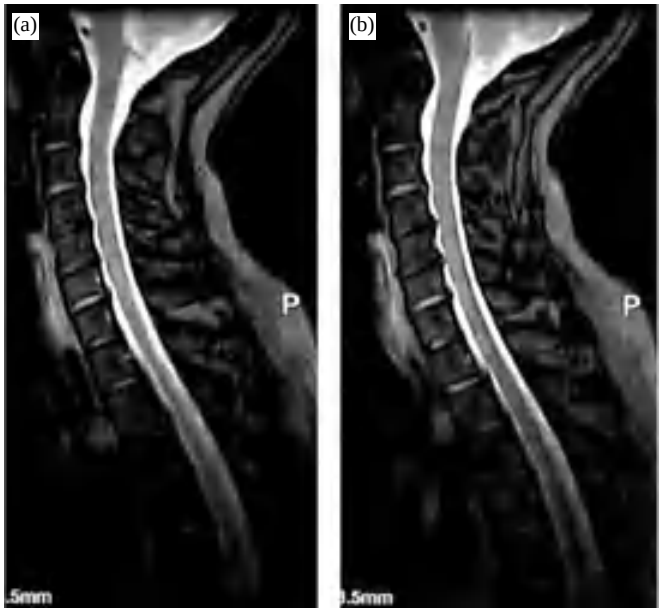

Figure 12 Sagittal C-spine images obtained with gradient echo imaging ($TR = 360$ ms, $TE = 30$ ms, flip angle = 15°)

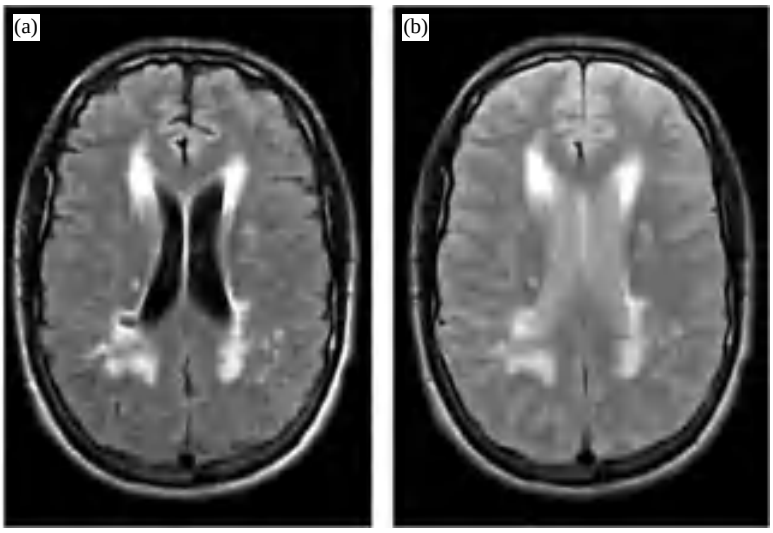

Figure 13 Double-contrast fast spin echo (FSE) imaging in a subject with multiple sclerosis, using half-Fourier techniques. ($TR = 2$ s, $TE = 20/120$ ms, with 24 slices in 6.75 min)

this term is not usable, (for instance where *TE* is very short), and in others it is not fully usable, but in general it provides relative advantages of factors of 2–3 in S/N ratio for low-field operation.

6.4 Radiofrequency Power

As discussed above, high-field systems compromise slice profile in the interest of savings in peak and average rf power. At mid- and low-fields these conditions are not important, and square profiles can be obtained.[16] For a system where a gap of 50% is needed to avoid interslice cross-talk, the loss in the S/N ratio for the slice itself may amount to 20%, and the gap can be considered as an unused potential source of 50% more signal.[17] Thus, the full S/N ratio is not being achieved if the slice profile is poor. The loss in two-dimensional FT imaging is sequence dependent. For three-dimensional FT imaging there is no difference.

6.5 Artifact Reduction

As discussed above, artifact reduction schemes take time away from data collection, either by reducing the echo window length or the number of sections, or by lengthening *TE*, and

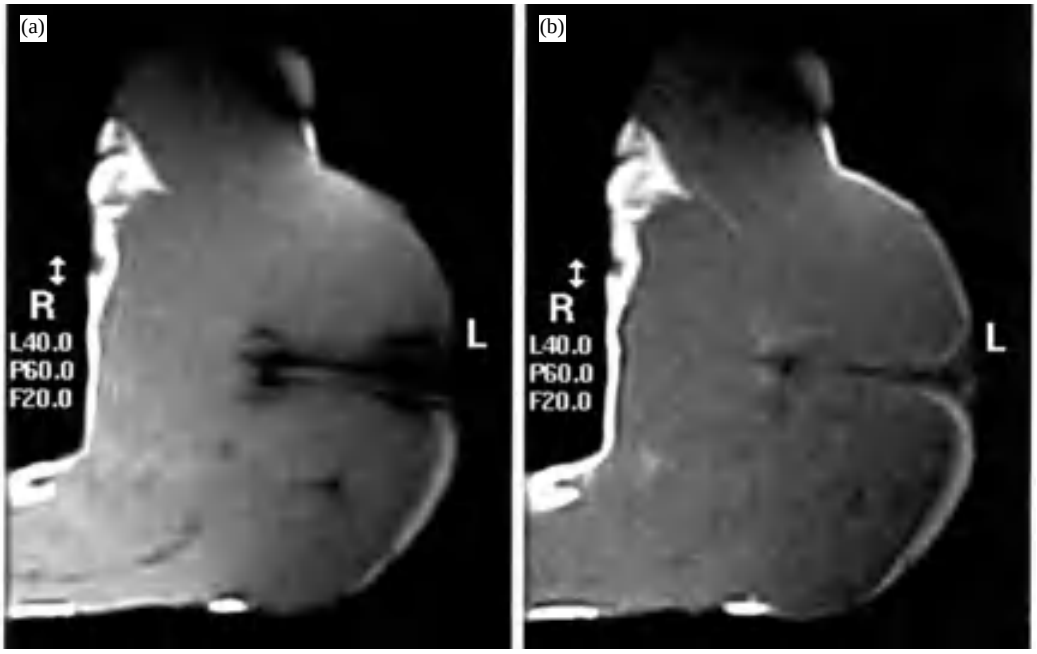

Figure 14 Asymmetric spin echo sequence ($TE = 15$ms). An MRI-compatible biopsy needle inserted in beef is imaged with 5 ms offset (a) and zero offset (b). By varying the offset, the visibility of the needle can be altered during an interventional procedure

Figure 15 High-resolution head imaging using three-dimensional FSE (3 mm thickness, 0.5 mm resolution, 32 slices in 9.5 min)

may result in penalties in the S/N ratio per unit time. This loss depends on the particular sequence and can be as small as zero where artifact reduction is not needed, and as big as 50% in some extreme cases such as presaturation in multislice imaging.

6.6 Net S/N Ratio Change

From the above considerations it can be seen that the S/N ratio changes with field in a complex manner, which depends on the clinical purpose of the sequence, the type of sequence used and tissue imaged, on coverage (including gaps) and on artifacts. For a sequence such as MRA, a major part of the 'theoretical' S/N ratio available from increasing field strength can be obtained. For other sequences the gain is small. An approximate rule is that in many situations the S/N ratio increases as the third to fourth root of field strength, so that for a 20-fold increase in field, the S/N ratio is doubled or tripled.

7 DISCUSSION

In the excitement of academic work, commercial competition, and a desire to share by publication, we tend to forget that MRI, outside a relatively few research institutions, is nothing more than a diagnostic tool. Its value is based on diagnostic accuracy and noninvasiveness. The lower the cost at which the service can be delivered, the more the people with need can have access to it. Very few studies have rigorously compared diagnostic efficacy at different field strengths. One study, commissioned by the Australian Government, was a broad based evaluation of five units at 0.3, 1.0, and 1.5 T.[18] Another study was limited to head imaging, comparing 0.064 and 1.5 T units,[19] and a ROC study of MS and knee imaging was recently published.[20] The earliest such study compared field strengths of 0.5, 1 and 1.5 T.[21] None of these studies showed a statistically significant difference in efficacy. At the end of the 1990s, approximately 50% of the market in the USA is for open (low- and mid-field) MRI systems.

8 RELATED ARTICLES

High-Field Whole Body Systems.

9 REFERENCES

1. S. H. Koenig, R. D. Brown, D. Adams, D. Emerson, and C. G. Harrison, *Invest. Radiol.*, 1984, **19**, 76.
2. J.-H. Chen, H. Avram, L. E. Crooks, M. Arakawa, L. Kaufman, and A. C. Brito, *Radiology*, 1992, **184**, 1.
3. D. M. Kramer, A. Li, L. Kaufman, and K. Hake, *J. Neuroimaging*, 1992, **2**, 195.
4. P. A. Rothschild, M. Schulz, D. M. Kramer, and L. Kaufman, *J. Neuroimaging*, 1991, **1**, 79.
5. D. M. Kramer, R. J. Guzman, J. W. Carlson, L. E. Crooks, and L. Kaufman, *Radiology*, 1989, **173**, 541.
6. D. A. Ortendahl, N. M. Hylton, L. Kaufman, J. C. Watts, L. E. Crooks, C. M. Mills, and D. Stark, *Radiology*, 1984, **153**, 479.
7. L. E. Crooks, M. Arakawa, J. C. Hoenninger, J. C. Watts, R. W. McRee, L. Kaufman, P. L. Davis, and A. R. Margulis, *Radiology*, 1982, **143**, 169.
8. M. Brant-Zawadzki, D. Norman, T. H. Newton, W. M. Kelly, B. Kjos, C. M. Mills, W. Dillon, D. Sobel, and L. E. Crooks, *Radiology*, 1984, **152**, 71.
9. A. A. Maudsley, *J. Magn. Reson.*, 1980, **41**, 112.
10. D. D. Blatter, D. L. Parker, S. S. Ahn, A. L. Bahr, R. O. Robison, R. B. Schwartz, F. A. Jolesz, and R. S. Boyer, *Radiology*, 1992, **183**, 379.
11. L. Kaufman, L. E. Crooks, P. E. Sheldon, W. Rowan, and T. Miller, *Invest. Radiol.*, 1982, **17**, 554.
12. K. A. Derby, S. D. Frankel, L. Kaufman, D. M. Kramer, J. W. Carlson, M. I. Mineyev, K. A. Occhipinti, and R. Friedenthal, *Radiology*, 1993, **189**, 617.
13. W. T. Dixon, *Radiology*, 1984, **153**, 189.
14. D. M. Kramer, L. Kaufman, P. Rothschild, J. Hale, J. Wummer, and K. K. Hake, *IEEE Trans. Med. Imag.*, 1991, **10**, 382.
15. J. C. Carlson, L. E. Crooks, D. A. Ortendahl, D. M. Kramer, and L. Kaufman, *Radiology*, 1988, **166**, 266.
16. D. A. Feinberg, L. E. Crooks, J. C. Hoenninger, J. C. Watts, M. Arakawa, H. Cheng, and L. Kaufman, *Radiology*, 1986, **158**, 811.
17. J. B. Kneeland, A. Shimakawa, and F. Wehrli, *Radiology*, 1986, **158**, 819.
18. MRI Technical Committee of the National Health Technology Advisory Panel, 'MRI Assessment Program Final Report', Australian Institute of Health, Canberra, August 1990.
19. W. W. Orrison, G. K. Stimac, E. A. Stevens, D. K. LaMasters, M. C. Espinosa, L. Cobb, and F. A. Mettler, *Radiology*, 1991, **181**, 121.
20. B. K. Rutt and D. H. Lee, *JMRI*, 1996, **6**, 57.
21. US Food and Drug Administration, 'Summary of Safety and Effectiveness Data, Premarket Approval Application No. P830074', submitted to the US Food and Drug Administration by the General Electric Company, 1989, p. 11.

Biographical Sketches

Leon Kaufman. *b* 1942. B.S., 1964, (engineering), Ph.D., 1967, (physics), University of California, Berkeley. University of California, San Francisco, 1970–present. Introduced to NMR in a junior modern physics class; started NMR imaging project at UCSF in 1975. Currently, Professor of Physics and Director, UCSF-RIL. Approx. 400 publications. Research interests include image formation and interpretation, and socioeconomic aspects of the technology.

David M. Kramer. *b* 1952. B.A., 1973, (chemistry), Ph.D., 1978, (chemistry), State University of New York at Stony Brook. Worked on development of instrumentation and methods for applications of NMR in medicine. Previously employed by Technicare, 1981–86. Currently, Associate Adjunct Professor of Physics at the University of California at San Francisco, Radiologic Imaging Laboratory and a development scientist for Toshiba America MRI.

Joseph W. Carlson. *b* 1957. A.B. 1979, (physics) Princeton University, Ph.D. 1985, (physics), University of California, Berkeley. Presently on faculty in radiology, University of California, San Francisco. Research interests are centered on the development of medical MRI technology, with emphasis on the physics of MRI, design and analysis of electromagnetic components of magnetic resonance imagers and data analysis.

Mitsuaki Arakawa. *b* 1943. B.S., 1966, (physics), Seoul University. Introduced to NMR at Japan Electron Optics Laboratory, 1970, and by Lawrence Crooks and Leon Kaufman. University of California, San Francisco, 1977–present. Approx. 60 publications, including a chapter in the book *NMR in Medicine–Its Basic and Clinical Application* (in Japanese). Holds 18 US patents. Research and engineering interests include MRI detectors, and their interface and general instrumentation.

Magnetic Resonance Imaging: A Historical Overview

E. Raymond Andrew
University of Florida, Gainesville, FL, USA

1 INTRODUCTION

MRI has become a most powerful modality of radiological imaging and is now found in all major hospitals throughout the world. It is a technique which provides the physician with clear pictures of the interior of the human body from any angle without using hazardous radiations. In the future it promises to provide interventional images to guide operations in progress. It is already giving valuable insights into the detailed functioning of the brain. Physicians sometimes express surprise that the basic phenomenon on which MRI is based was discovered 50 years ago. In this historical overview of MRI we therefore begin with a brief account of the origins of NMR and its applications in physics and chemistry and then go on to describe in more detail its applications in biology and medicine, with particular reference to MRI.[1,2]

2 DISCOVERY

The first successful demonstrations of NMR in bulk matter were published in 1946. Two independent groups, unknown to each other, working in physics laboratories on opposite coasts of the USA, discovered NMR almost simultaneously. Bloch, Hansen, and Packard,[3] working at Stanford University, and Purcell, Torrey, and Pound,[4] working at Harvard University, published their results in consecutive issues of *Physical Review*. The impact of their work was immediate, and applications of NMR have widened steadily from physics and chemistry to a broad range of disciplines from archeology to medicine. The importance of the discovery was recognized by the joint award of the 1952 Nobel Prize for Physics to the two leaders, Bloch and Purcell. Professor Bloch died in 1983; Professor Purcell died in 1997.

These early experiments were described by their discoverers in quite different physical terms, and it was only after discussion between the two groups that it was realized that their discoveries were essentially identical. At Harvard University the emphasis was on transitions of magnetic nuclei between quantized states in a magnetic field and on resonant absorption of radiofrequency energy. At Stanford University the description was of the precession of nuclear magnetization in a magnetic field, inducing an electromotive force (EMF) in the surrounding radiofrequency coil. The first description led to the name 'nuclear magnetic resonance' for the phenomenon, and the second to the name 'nuclear induction'. These two descriptions, which can be shown to be quantitatively equivalent,[5] still provide complementary views of the basic phenomenon, which are mutually illuminating. Today everyone uses the name 'nuclear magnetic resonance', but the alternative 'nuclear induction' is still often used by physicists and particularly survives in the term 'free induction decay' (FID) for the NMR signal following an exciting pulse.

Although NMR was first discovered and experimentally demonstrated in ordinary materials in 1945, the subject did have a prehistory. In 1936 Gorter[6] looked for the resonance of ^{7}Li nuclei in crystalline lithium fluoride and of protons in crystalline potassium alum, but without success. The failure of these early experiments and of some later attempts[7] was attributed to the use of unfavorable materials.[8] Meantime, NMR was first demonstrated in molecular beams by Rabi and co-workers[9] at Columbia University in the USA in 1939. Although the fundamental principles are closely similar, applications of NMR to atomic and molecular beams represent a separate subject from NMR in ordinary materials with which we are concerned here.

Now that hospitals are spending vast sums on NMR clinical equipment it is sobering to recall that the first NMR experiments were done at almost no cost at all. The Harvard University group borrowed a large electromagnet previously used in cosmic ray experiments, which in turn had been converted from a discarded generator from the Boston elevated railway. At Stanford University an electromagnet was borrowed from the physics lecture theater, and only a few hundred dollars were spent, mainly on an oscilloscope.

3 PHYSICS

Many physicists joined this exciting new field of research over the next few years, and NMR was detected for almost all magnetic nuclei in the Periodic Table. NMR was detected in solids, liquids, and gases, in insulators, semiconductors, and metals, in polymers, membranes, and adsorbed and occluded phases, indeed in matter in all its forms. Resonances in liquids and gases were remarkably sharp, those from solids somewhat broader. Exploiting the sharpness of the resonances from fluids, extremely precise measurements were made of nuclear magnetic moments; nuclear spins were determined or confirmed and other nuclear parameters obtained.

Since the NMR frequency is directly proportional to the magnetic field strength, NMR presented the physicist with an excellent magnetometer for measurement of unknown magnetic fields in the laboratory. The method was readily extended to the Earth's magnetic field, and became useful in civil engineering projects, in archeological surveys for buried magnetic materials, for aerial geomagnetic surveys, for oceanographic surveys, and for measurements in space. The high precision of magnetic field measurement enabled more precise measurements to be made of some of the fundamental constants of physics.[5]

From the very beginning, the importance of relaxation times in NMR had been realized. At Stanford University the proton NMR was first found in water, and a paramagnetic salt was dissolved in the water in some experiments with a view to shortening the relaxation time.[3] At Harvard University the pro-

ton NMR was first found in solid paraffin,[4] and great pains were taken to use an extremely low radiofrequency power level to avoid saturation. The relaxation times T_1 and T_2 were introduced at the outset, and the foundations for understanding these basic quantities were laid in famous pioneering papers by Bloch,[10,11] Purcell,[12] and their colleagues; to all NMR practitioners interested in relaxation processes this last paper[12] is known simply as 'BPP' (Bloembergen, Purcell, and Pound). Fundamental studies of relaxation behavior in solids and liquids have given great insight into molecular dynamics in a wide range of materials, including cellular systems and living tissues.

In the early years NMR was detected using a steady source of resonant radiofrequency radiation, often referred to as continuous wave (CW) detection. The spectacular discovery of spin echoes by Hahn[13] stimulated the widespread use of pulsed NMR. The NMR spectrum could be obtained by Fourier transformation of the free induction decay with tremendous savings of time, and relaxation times could be determined with greater simplicity.

In the first decade of its activity, NMR was largely the province of the physicist and the physical chemist. By 1954 some 400 papers had been published, and the first book on NMR[5] was able to make reference to all of them. Two later books[14,15] devoted to the fundamental physical principles of NMR have become landmarks in the development of the subject.

4 CHEMISTRY

Quite early it had been noted by several workers[16–18] that the NMR frequency of a given nucleus was to a small degree dependent on the chemical form in which the element was present. The molecular electrons slightly shielded the nucleus and shifted the resonance; the effect was appropriately called the chemical shift. Consequently, a molecule with nuclei in several environments generated a spectrum with several distinct NMR responses, and the subject of NMR spectroscopy had begun.[19] Spin multiplets provided finer features in the NMR spectrum.[20,21] The NMR spectrum was thus a fingerprint of the chemical compound and enabled NMR spectroscopy to become one of the chemist's most valuable structural and analytical tools.

The NMR spectral lines are narrow and close together; consequently the development of high-resolution NMR spectroscopy called for very uniform magnetic fields, uniform to 1 part in 10^8 or better over a 1 mL sample. Varian Associates in California can be credited fairly with opening up this field to chemists generally in the late 1950s by responding to the challenge posed by small proton chemical shift differences and providing NMR spectrometers with magnets having the requisite uniformity of field. In the quest for improved resolution and sensitivity the proton NMR frequency was steadily advanced from 30 to 60 to 100 MHz, this last frequency corresponding to a magnetic field of 2.3 T. Many other nuclei, especially ^{13}C, ^{19}F, and ^{31}P, were exploited under high-resolution conditions. Pulse methods replaced CW, and a dedicated computer became an integral part of the spectrometer system, controlling the pulse sequences, gathering the data, performing the Fourier transforms, and displaying the spectra.

The pursuit of still higher resolution and sensitivity called for still higher magnetic fields, which in turn required a change of magnet technology from the iron electromagnets used hitherto. Using superconducting magnets, proton NMR spectra are now recorded at frequencies up to 1 GHz in fields up to 20 T. Designs are in hand at the US National High Magnetic Field Laboratory in Florida for high-resolution proton NMR spectroscopy at 900 MHz and eventually at 1 GHz, which will require a high-resolution superconducting magnet with a field of 23.5 T.

The investigation of larger molecules including peptides, proteins, enzymes, and nucleic acids yielded spectra with a forest of fine lines difficult to resolve and assign. The advent of 2D NMR spectroscopy,[22] spreading out the spectra in two dimensions with detailed connectivity, gave great spectral clarity and renewed impetus. This has been extended to three dimensions and beyond.

Nowadays no chemistry research laboratory is properly equipped without its high-resolution NMR spectrometer. The widespread use of NMR spectrometers in chemical laboratories has led to the growth of a substantial NMR instrument industry. The principles and practice of NMR are now a feature of chemistry courses at quite elementary levels. Most science students and medical students today will have heard of NMR before going to university. The use of high-resolution NMR spectroscopy has spread from chemistry to biochemistry, microbiology, pharmacy, agricultural chemistry, polymer science, and, as we shall see, biology and medicine.

We note in passing that specimens investigated by chemists and physicists are usually homogeneous and rather less than 1 ml in volume. Consequently, the bore of a superconducting NMR magnet for such work is usually about 5 cm in diameter. This provides just sufficient access for the specimen, its surrounding radiofrequency probe, and other accessories.

5 BIOLOGY

The earliest biological NMR experiments take us back to the inventors of the subject. Soon after the first successful NMR experiments at Stanford University,[3] Bloch obtained a strong proton NMR signal when he inserted his finger in the radiofrequency coil of his spectrometer. In 1948, Purcell and Ramsey in turn inserted their heads into the 2 T field of the Harvard University cyclotron; around their heads was a coil connected to a powerful radiofrequency generator tuned to the proton NMR frequency. The only sensation recorded was that of EMFs generated in the metal fillings of their teeth as their heads were moved into and out of the magnet and detected by their tongues. Fifty years later there is no evidence of any damage arising from this magnetic adventure.

Occasional NMR experiments were subsequently reported on materials of biological interest.[23,24] A pioneering series of investigations was carried out by Odeblad and his colleagues in Stockholm on tissues and fluids from animals and humans starting in 1955 and continuing over the next decade. These studies included blood cells,[25,26] cervical mucus,[27] tissues and fluids of the eye[28] and the eye lens,[29] saliva,[30] and muscle.[31] However, substantial advances in the application of NMR in biology awaited the development of high-field, high-resolution, Fourier transform spectrometers in the late 1960s. As men-

tioned in the previous section, these technical advances enabled high-resolution NMR spectra in one and two dimensions to be obtained, and yielded structural and dynamic information of importance in biochemistry and molecular biology.

At the same time, high-resolution NMR spectroscopy began to be applied to living systems. First Moon and Richards[32] reported high-resolution ^{31}P NMR studies of intact red blood cells in which they could assign lines to individual metabolites. This was followed the next year by recordings of ^{31}P spectra from an intact freshly excised muscle from the leg of a rat by Hoult et al.[33] It was found possible to maintain muscles in good physiological condition in the spectrometer and to record the effects of electrical stimulation. The 5 cm diameter bore of a conventional NMR superconducting magnet was nevertheless a severe restriction. Soon magnets with a 10 cm diameter bore were provided, and a wide range of studies on perfused animal hearts, kidneys, livers, and other organs were pursued, using mainly ^{31}P NMR but also ^{1}H and ^{13}C NMR spectroscopy.

It was then a natural step to examine whole intact living organisms from bacteria to mice, rats, and rabbits. With animals it was of course important to know from what anatomical part or organ the NMR spectrum originates. In some cases this could be achieved by winding the radiofrequency coil around the part concerned; in other cases a radiofrequency coil was placed on the surface of the animal to record the NMR signal from the region immediately below.

From animals it was just a further step to the in vivo NMR spectroscopy of humans and its applications in medicine. Spatial localization continued to be an important challenge, and other more sophisticated methods were introduced such as ISIS and spectroscopic imaging. However, in this article we shall not follow this trail further. Instead we follow the parallel trail of MRI in the next section. Further information on magnetic resonance spectroscopy (MRS) may be found in books by Gadian,[34] Andrew et al.,[35] Gillies[36] and in other articles in these volumes.

6 MAGNETIC RESONANCE IMAGING

In contrast to the steady onward march of NMR spectroscopy from physics through chemistry and biology to medicine, NMR imaging represents a distinctly different approach which appeared rather suddenly on the scene in 1973.

In 1973, Lauterbur[37] published the first NMR 2D image of a heterogeneous structured object: two tubes of water. He pointed out the simple fact that if a field gradient is applied to a structured object each nucleus responds with its own NMR frequency determined by its position; the NMR spectrum is the 1D projection of nuclear density along the gradient direction. Applying the gradient in a series of directions and so obtaining a series of projections, he devised an algorithm to generate a 2D proton NMR image of the object from its projections, in just the same way as it is done in X ray computed tomography (CT) scanning. This first image is reproduced in Figure 1.

The impact of this first image and of the work that followed has been tremendous. Within a decade of its publication, manufacturers worldwide were producing NMR scanners that generated high quality images of all parts of the human body, challenging traditional modalities of radiological imaging in clinical practice. After two decades all major hospitals are now equipped with NMR whole body scanners—over 10000 systems worldwide—and the total expenditure for this equipment overshadows that for all previous uses of NMR. Moreover, it

Figure 1 The first 2D NMR image (Lauterbur[37])

has brought NMR to the notice of the man and woman in the street, and NMR has entered our everyday vocabulary. In the interests of simplicity and the happiness of patients the adjective 'nuclear' has been dropped in the context of medicine, and the subject is now just 'magnetic resonance imaging' or MRI. Other names, such as Zeugmatography, introduced by Lauterbur,[37] have now largely dropped out of use.

Just as in NMR itself there was a prehistory before the final discovery (see above), so in NMR imaging there was a prehistory in the use of magnetic field gradients. NMR 1D projections in a magnetic field gradient were investigated quite early in 1951–52 with simple glass and liquid structures by Gabillard[38–40] in France. The dynamic NMR response is given by the Fourier transform of the distribution function of nuclei in the gradient applied to the structure, and it follows conversely that a 1D projection is obtained from the Fourier transform of the free induction decay.

Magnetic field gradients are a basic feature in the study of molecular diffusion in liquids by the NMR spin echo method. The diffusion of molecules from their original locations in a liquid sample in a field gradient reduces their contribution to the echo, and this enables the diffusion constant of the liquid to be determined.[13,41]

In 1956, Walters and Fairbank[42] studied the distribution of ^{3}He in liquid ^{3}He–^{4}He solutions in three vertically arranged connected containers by applying a field gradient from top to bottom. A separate ^{3}He NMR signal was recorded from each container. In this way phase separations below 0.8 K were determined. In this experiment the field gradient was being used to provide a 1D NMR image of the ^{3}He density in the containers.

Magnetic field gradients are a feature of NMR methods of information storage.[43,44] In one method,[44] information is stored in a 3D cellular structure and refreshed frequently to avoid loss by relaxation. The information is then retrieved by application of gradients which enable the specific location of the desired piece of information in the store to be excited. Reading the information from such an information store was in fact an early NMR imaging procedure, which could be used in one, two, or three dimensions.

In 1972, Damadian[45,46] filed a prophetic patent in which he proposed without detail a method for scanning the human body (Figure 2) by NMR and detecting pathological deviations, for example cancer, through differences in the relaxation times T_1 and T_2. This proposal was based on his pioneering observations[47] that the relaxation times T_1 and T_2 were significantly higher in cancerous rat tissue than in the corresponding normal tissue.

In 1973, Mansfield and Grannell[48] introduced the concept of NMR diffraction in solids. Multiple pulse line narrowing sequences sharpened the NMR response, and a magnetic field gradient provided spatial resolution. A model 1D lattice of several plates of camphor was used to generate the 1D images shown in Figure 3. While technical difficulties might prevent application to crystallographic structures, it was suggested that the method would be useful in the study of biophysical systems with regular or approximately regular macroscopic structures such as cell membranes and filamentary or fibrous structures. In 1975 in an amplification and extension of this work[49] the authors discuss the application of these ideas to more general nonperiodic structures, including microstructures.

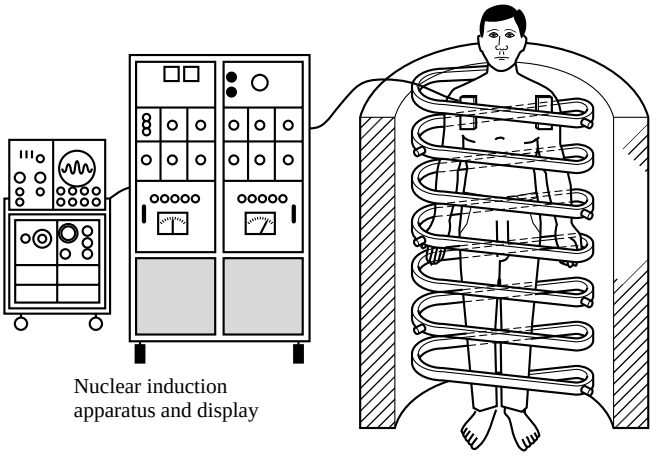

Figure 2 An early schematic diagram for human NMR imaging (Damadian[45,46])

A magnetic resonance image is a 2D representation of the NMR signal from the resonant nuclei in a particular thin slice of the object of interest. We may imagine the slice divided up into an array of $n \times n$ elements. If we are able to measure the NMR signal from all n^2 elements in the slice, we can construct a picture or image consisting of these $n \times n$ picture elements (pixels). The larger the value of n, the finer is the detail in the

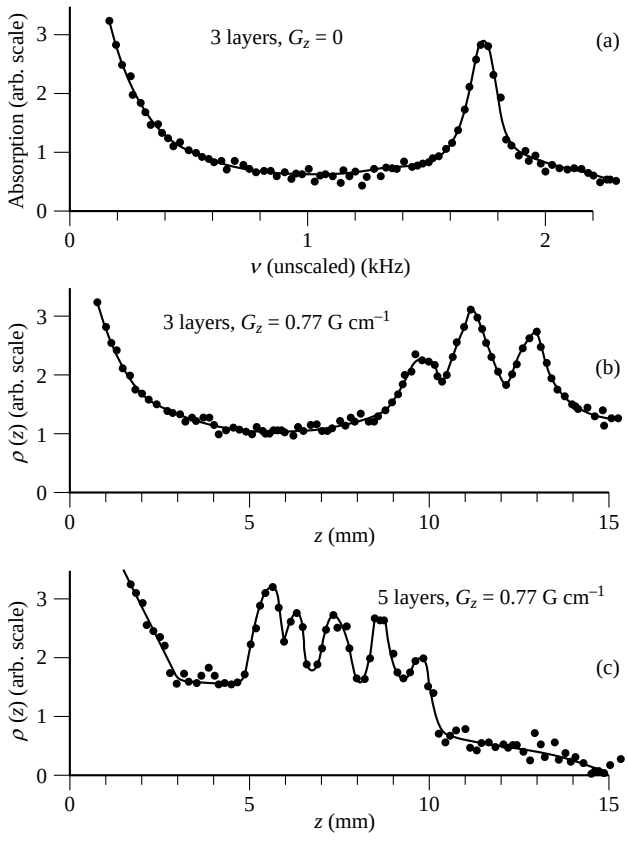

Figure 3 1D NMR images of (a) one, (b) three, and (c) five layers of camphor (Mansfield and Grannell[48])

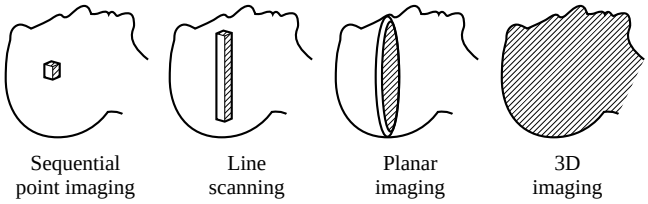

Figure 4 A classification of imaging methods[35]

image. However, if we were to double the value of n in order to improve the resolution, we should have to measure four times as many pixels, each containing only a quarter the number of nuclei from which to generate their NMR signals. In practice, n is usually 256 or 512; computers are happy with numbers that are powers of 2.

A field gradient is an essentially 1D probe, and many different methods have been advanced for manipulating the gradient to secure 2D or 3D information. A basic classification of methods is illustrated in Figure 4. First we might arrange to isolate a small volume and collect the NMR signals from it. This elemental volume may then be traversed through a plane in the object of interest, enabling us to build a magnetic resonance image of a plane, point by point. This is the sequential point method, and it is inevitably slow. Next we might arrange to gather the NMR signal from a whole line or column of n elements simultaneously by a Fourier transform procedure, which is n times faster. If n is 256, this represents a substantial gain. This is line scanning. We can then scan the line through the plane of interest to build an image.

Then we might gather the NMR signal from a whole plane of n^2 pixels simultaneously and process the data in such a way that we get an image of the plane. This is planar imaging. It may not necessarily be faster than line scanning, but since NMR signals are being gathered from the whole plane all the time it will certainly give a much better quality image. Finally, we might gather the NMR signal from the whole 3D object simultaneously and process the data in such a way as to characterize all $n \times n \times n = n^3$ volume elements (voxels). This is 3D imaging. An image of any desired slice can then be displayed.

The first two methods (sequential point and line scanning) were important in the early days of MRI,[50–53] but have now been superseded by the third (planar imaging). 3D imaging is available on many instruments but takes longer and gives more information than is generally needed. Planar imaging may be achieved by the projection-reconstruction method[37] or more usually by the 2D Fourier imaging method devised by Kumar, Welti, and Ernst,[54] which is readily extensible to three dimensions. A careful assessment of the relative performance of the various imaging methods was carried out by Brunner and Ernst.[55]

In order to do planar imaging it is of course necessary to define the slice to be imaged. This is usually achieved by the selective excitation method of Garroway, Grannell, and Mansfield.[56] Implementation of the 2D Fourier imaging method usually makes use of the spin warp technique developed by Edelstein, Hutchison, Johnson, and Redpath.[57]

The first MRI experiments were carried out in physics and chemistry laboratories using modified NMR spectrometers with magnets which had limited access. The imaging subjects were therefore necessarily small. Over the period 1974–78, NMR images were published from the fruit and vegetable kingdom: pecan,[58] onion,[51] lemon[59,60] (see Figure 5), pepper,[61] and okra.[62] Images were also published from the animal kingdom: clam,[58] chicken wing,[51] turkey leg,[63] mouse,[58,64–66] rat,[67–69] and rabbit[70] (see Figure 6). These pictures showed that geometrically faithful NMR images could be obtained of the interior of biological structures, with contrast arising from differences in tissue density, mobility and relaxation. The stage was set for applications of MRI to the human body.

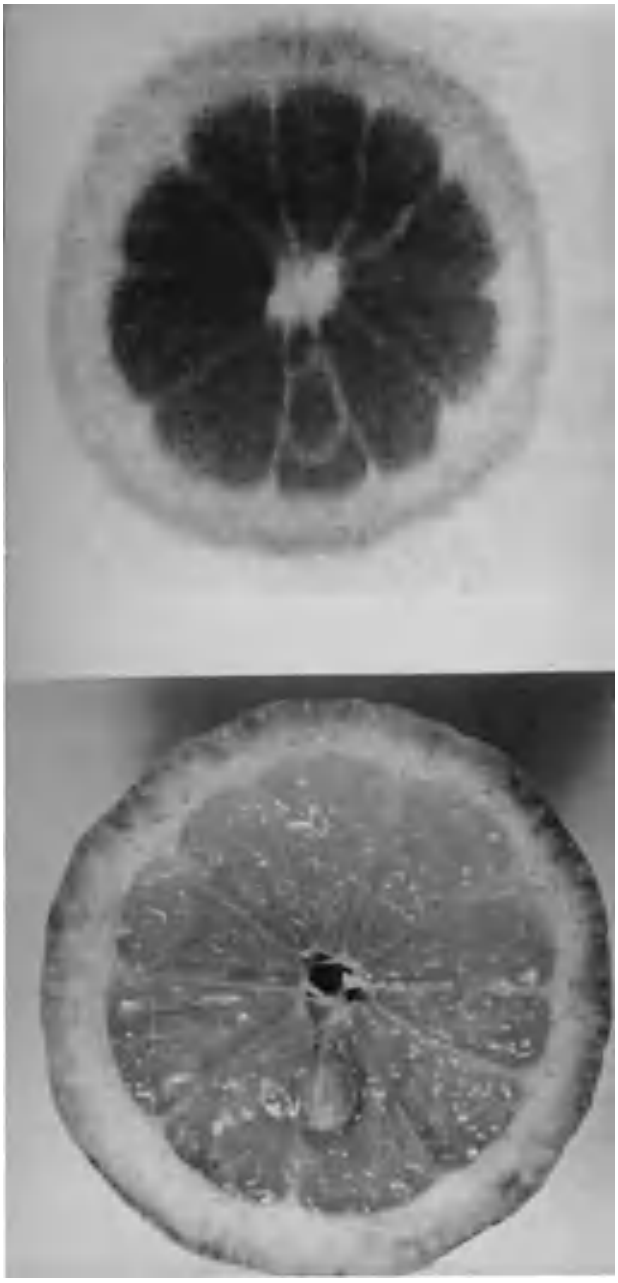

Figure 5 (a) Thin transverse section proton NMR image of an intact lemon and (b) a photograph of the actual section cut subsequently (Andrew et al.[59] and Andrew[60])

Figure 6 Thin coronal section proton NMR image through the orbits of the head of a rabbit (Hinshaw et al.[70])

7 HUMAN MRI

The first human NMR image, reported in 1976 by Mansfield and Maudsley,[71,72] was of a live human finger (Figure 7). The finger could be inserted into the 5 cm gap of a conventional iron NMR electromagnet. Using a magnet with a 12 cm gap, NMR images were obtained of a live human hand,[67] wrist[73,74] (Figure 8), and forearm[75] by Hinshaw, Andrew, Bottomley, and their co-workers. The anatomical detail and tissue contrast

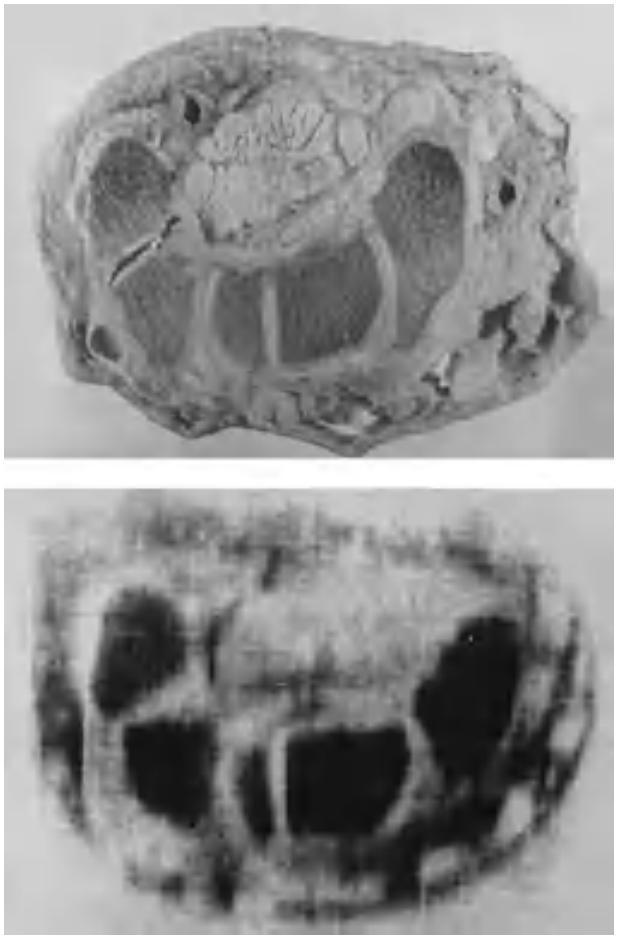

Figure 8 Thin proton NMR image of a live human wrist (bottom). For comparison, a cross section of an actual wrist is also shown (top) (Hinshaw et al.[73,74])

Figure 7 Cross-section proton NMR image of a live human finger (Mansfield and Maudsley[71,72])

Figure 9 Whole body NMR imaging magnet at Nottingham University, 1978

Figure 10 Commercial whole body NMR imaging magnet at the University of Florida, 1983

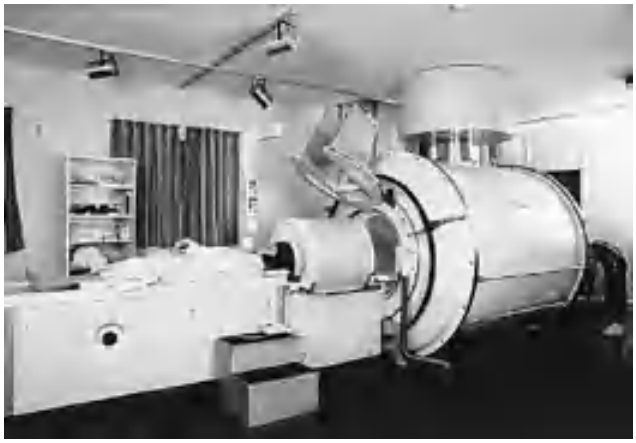

Figure 11 The first superconducting whole body magnet for regular clinical use, installed at Hammersmith Hospital, London, 1981

were good and gave optimism for successful NMR imaging of the whole human body, head, chest, and abdomen.

An essential requirement of human MRI was a magnet capable of accepting the whole human body and generating a magnetic field uniform and stable to at least 1 part in 10^5 over a central sphere about 30 cm in diameter. Early whole body magnets were air cored resistive solenoids producing fields up to 0.15 T, with an aperture of about 80 cm in diameter. An

Figure 12 Transverse NMR image of a normal human thorax (Damadian et al.[52,77])

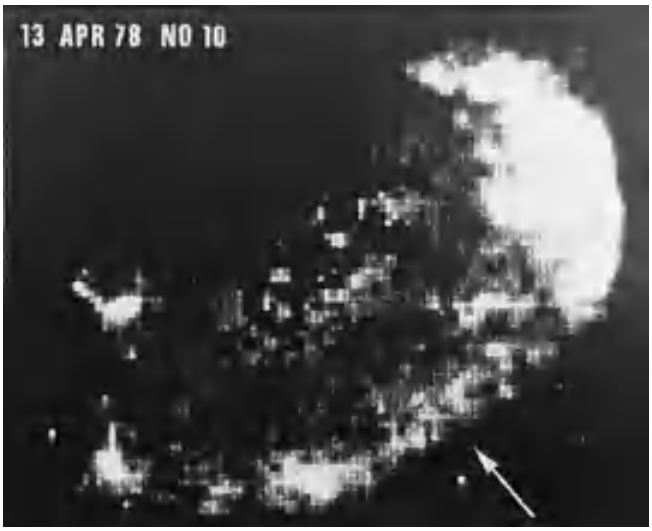

Figure 13 Transverse NMR image of a normal human abdomen (Mansfield et al.[79])

example used in the University of Nottingham in 1978 is shown in Figure 9; a commercial version in clinical use in 1983 in the University of Florida is shown in Figure 10. A similar magnet but with a vertical axis was used in Aberdeen.[66] For higher field strengths superconducting solenoids are generally used, although at least one system uses a large permanent magnet and another uses an iron electromagnet. The development of high-field whole body superconducting magnets has played a crucial role in opening up clinical MRI; Oxford Instruments in the UK in particular were pioneers in this development. The first superconducting whole body magnet for clinical use was installed at Hammersmith Hospital, London in 1981 (Figure 11).

Biological tissues are moderate electrical conductors, and we might therefore expect some attenuation of the electromagnetic radiation at the NMR frequency as it penetrates the body. Calculations by Bottomley and Andrew[76] suggested that significant attenuation and phase distortion might be encountered above 40 MHz, corresponding to 1 T for proton NMR. Actually the calculations were based on a homogeneous cylinder 20 cm in radius, which was somewhat pessimistic since the human body contains many cavities. In practice little attenuation is seen at 2 T (85 MHz for protons), but has been noticed at 4 T.

The first human whole body MR image was an image of the human thorax by Damadian, Goldsmith, and Minkoff[52,77] in 1977 (Figure 12). This was closely followed in 1978 by the first magnetic resonance image of the human head, by Clow and Young,[78] and the first image of the human abdomen, by Mansfield, Pykett, Morris, and Coupland[79] (Figure 13). In computerized X-ray tomography the slice imaged was usually transverse. Such a restriction does not apply in MRI, and this was clearly demonstrated with the publication in 1980 of the first coronal and sagittal images of the human head by Holland, Hawkes, and Moore[80] (Figure 14).

These early human images were all of normal healthy volunteers. Soon afterwards in 1980 the first images of human pathology began to appear. Hawkes, Holland, Moore, and Worthington[81] demonstrated a wide range of intracranial pathological behavior by MRI. This included examples of

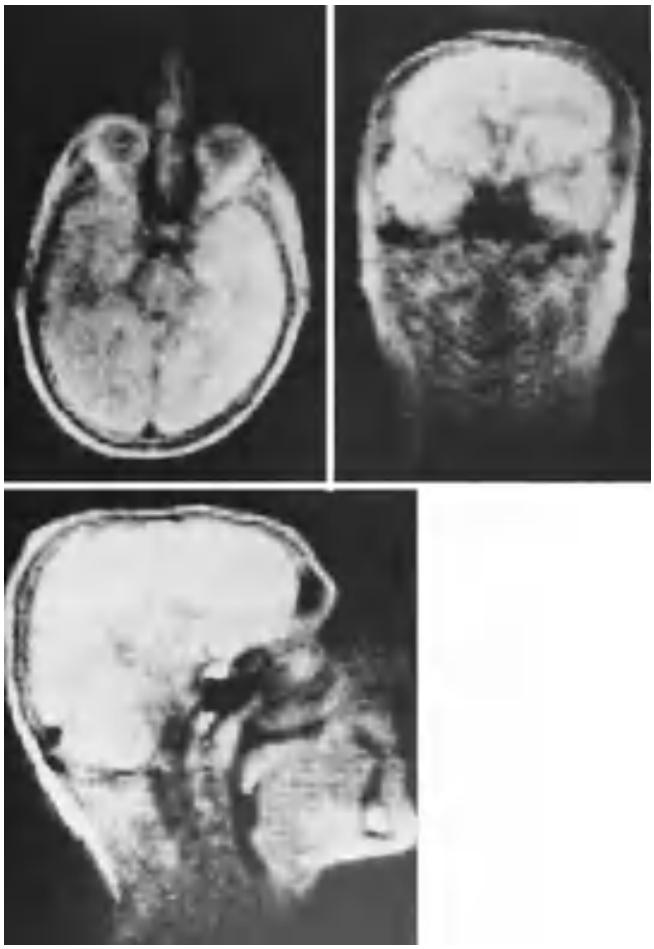

Figure 14 Transverse and first coronal and sagittal NMR images of a normal human head (Holland et al.[80])

hydrocephalus, a variety of tumors, aneurysms, arteriovenous malformations, and chronic sinus infection. Damadian[46] demonstrated a number of cases of carcinoma of the chest.

We should notice that when imaging the human body, the proton is by far the most commonly used nucleus. After all, hydrogen is the most abundant chemical element in the body, ^{1}H is isotopically almost 100% abundant, and it has the highest magnetic moment among stable nuclei. The next most abundant chemical element, oxygen, has no convenient magnetic isotope. For carbon, the isotope ^{13}C is only 1.1% abundant and it has a low magnetic moment. The principal isotope of nitrogen is ^{14}N, which has a low magnetic moment and other complications, while ^{15}N has a low abundance. Phosphorus is an element of considerable interest on account of the important metabolites that contain it. The isotope ^{31}P is 100% abundant and it has a reasonable magnetic moment. However, concentrations of phosphorus are very low in living systems. So summarizing, protons (hydrogen nuclei) are by far the best nuclei for human MRI. Nevertheless there has been some MRI interest in ^{2}D, ^{7}Li, ^{14}N, ^{19}F, ^{23}Na, and ^{31}P. Some early work has also been done on MRI of unpaired electrons.[82]

Since the first successful human magnetic resonance images of healthy volunteers and patients there has been a rapid development of technique and a great improvement in the quality of the images. By 1983 the first commercial MRI systems were being installed in hospitals, yielding images in 4 min with 1 mm resolution. No longer do physicists and chemists and others make their own MRI systems. Images of the author taken in March 1984 using the 0.15 T magnet of Figure 10 are shown in Figure 15, illustrating the performance reached at that time. With the availability of higher fields to 2 T images have improved steadily since then. Magnets with fields of 3, 4, and 5 T have been built for human imaging but are not yet in general use.

Over the past decade, MRI has become an accepted modality of clinical radiology. We may note some of the advantages which recommend it. First it does not use ionizing radiation and is intrinsically safer than modalities using X-rays, γ rays, positrons, or heavy ions. In contrast with ultrasound the radiation penetrates bony structures. Besides giving morphological information, MRI gives additional diagnostic insights and improved contrast through relaxation parameters, susceptibility, and diffusion, not available from other modalities. In contrast with CT, MRI provides direct images in transverse, coronal, or sagittal slices, or slices of arbitrary orientation. Flow can be measured. Contrast may be improved by injection of paramagnetic agents.

Conventional magnetic resonance images take several minutes to acquire whereas CT images take several seconds only. However, it is possible to acquire simultaneously magnetic resonance images from typically 10 parallel slices and four T_2-weighted images of each, a total of 40 images in the time of one, making an average acquisition time of only a few seconds. Further, using new techniques such as FLASH[83] a single magnetic resonance image can be acquired in a few seconds. Still faster magnetic resonance images may be obtained using a sequence proposed by Mansfield[84] back in 1977, and demonstrated the following year,[62] called echo planar imaging. A complete image could be obtained in less than 0.1 s, enabling real time movie magnetic resonance images to be recorded.[85]

8 CONCLUDING REMARKS

The rapid expansion of interest in NMR of living systems led to the organization of special conferences to discuss these topics. In March 1979 the Royal Society held a Discussion Meeting in London entitled 'Nuclear magnetic resonance in intact biological systems', which reviewed achievements to date in both MRI and MRS. The papers given at this meeting were published as a special issue of *Philosophical Transactions of the Royal Society*, (1980, Vol. 289, no. 1037), and constitute a historic landmark in the development of the subject. In October 1981 another significant meeting devoted solely to MRI was held in Winston-Salem, North Carolina. With the widespread deployment of commercial MRI systems in all major hospitals it was clear that annual meetings were needed, and the Society of Magnetic Resonance in Medicine was formed, holding its first meeting in Boston, Massachusetts, in August 1982 with an attendance of 800 participants. Since then the Society has met annually in August either in North America or in Europe; by 1993 attendance had trebled. In 1983 the Society started a new journal *Magnetic Resonance in Medicine*, edited by E. Ray-

Figure 15 Magnetic resonance images of the author taken in March 1984, using the magnet of Figure 8: (a) head, transverse; (b) head, sagittal; (c) spine, sagittal; (d) abdomen, transverse

mond Andrew, and since 1991 by Felix Wehrli. Other societies and journals began at this time in various parts of the world.

This historical overview covers the period up to 1983. The reader can now go on to embrace the multitude of detailed applications of MRI to every branch and corner of medicine, to microimaging, spectroscopic imaging, functional brain imaging, interventional MRI, to the solid state, and much more. Many of these developments are covered in recent books such as that by Morris[86] for the mathematically inclined reader or that by Andrew et al.,[35] which is addressed particularly to physicians; it has no mathematics and covers both MRI and MRS. More detailed information on very many topics relating to MRI will found elsewhere in these volumes.

9 RELATED ARTICLES

Image Formation Methods; MRI in Clinical Medicine; Outcome and Efficacy–Analysis of Healthcare Models.

10 REFERENCES

1. E. R. Andrew, *Br. Med. Bull.*, 1984, **40**, 115.
2. E. R. Andrew, in 'Magnetic Resonance Imaging', ed. C. L. Partain, A. E. James, F. D. Rollo, and R. R. Price, Saunders, Philadelphia, 1988, Chap. 1, p. 3.
3. F. Bloch, W. W. Hansen, and M. E. Packard, *Phys. Rev.*, 1946, **69**, 127.
4. E. M. Purcell, H. C. Torrey, and R. V. Pound, *Phys. Rev.*, 1946, **69**, 37.
5. E. R. Andrew, 'Nuclear Magnetic Resonance', Cambridge University Press, Cambridge, 1955, Chaps. 2 and 4.
6. C. J. Gorter, *Physica*, 1936, **3**, 995.
7. C. J. Gorter and L. F. J. Broer, *Physica*, 1942, **9**, 591.
8. C. J. Gorter, *Physica*, 1951, **17** 169.
9. I. I. Rabi, S. Millman, P. Kusch, and J. R. Zacharias, *Phys. Rev.*, 1939, **55**, 526.
10. F. Bloch, *Phys. Rev.*, 1946, **70**, 460.
11. F. Bloch, W. W. Hansen, and M. E. Packard, *Phys. Rev.*, 1946, **70**, 474.
12. N. Bloembergen, E. M. Purcell, and R. V. Pound, *Phys. Rev.* 1948, **73**, 679.

13. E. L. Hahn, *Phys. Rev.*, 1950, **80**, 580.
14. A. Abragam, 'The Principles of Nuclear Magnetism', Clarendon Press, Oxford, 1961.
15. C. P. Slichter, 'Principles of Magnetic Resonance', 3rd edn., Springer-Verlag, Berlin, 1990.
16. W. D. Knight, *Phys. Rev.*, 1949, **76**, 1259.
17. W. C. Dickinson, *Phys. Rev.*, 1950, **77**, 736.
18. W. G. Proctor and F. C. Yu, *Phys. Rev.*, 1950, **77**, 717.
19. J. T. Arnold, S. S. Dharmatti, and M. E. Packard, *J. Chem. Phys.*, 1951, **19**, 507.
20. H. S. Gutowsky, D. W. McCall, and C. P. Slichter, *Phys. Rev.*, 1951, **84**, 589.
21. E. L. Hahn and D. E. Maxwell, *Phys. Rev.*, 1951, **84**, 1246.
22. W. P. Aue, E. Bartoldi, and R. R. Ernst, *J. Chem. Phys.*, 1976, **64**, 2229.
23. T. M. Shaw and R. L. Elsken, *J. Chem. Phys.*, 1950, **18**, 1113.
24. B. Jacobsen, W. A. Anderson, and J. T. Arnold, *Nature*, 1954, **173**, 772.
25. E. Odeblad and G. Lindstrom, *Acta Radiol.*, 1955, **43**, 469.
26. E. Odeblad, B. N. Bhar, and G. Lindstrom, *Acta Biochem. Biophys.*, 1956, **63**, 221.
27. E. Odeblad and V. Bryhu, *Acta Radiol.*, 1957, **47**, 315.
28. A. Huggert and E. Odeblad, *Acta Radiol.*, 1959, **51**, 385.
29. A. Huggert and E. Odeblad, *Acta Opthalmol.*, 1959, **37**, 26.
30. E. Odeblad and E. Soremark, *Acta Odontol. Scand.*, 1962, **20**, 23.
31. E. Odeblad and A. Ingelman-Sundberg, *Acta Obstet. Gynecol. Scand.*, 1965, **44**, 117.
32. R. B. Moon and J. H. Richards, *J. Biol. Chem.*, 1973, **248**, 7276.
33. D. I. Hoult, S. J. W. Busby, D. G. Gadian, G. K. Radda, R. E. Richards, and P. J. Seeley, *Nature*, 1974, **252**, 285.
34. D. G. Gadian, 'Nuclear Magnetic Resonance and Its Application to Living Systems', Clarendon Press, Oxford, 1980.
35. E. R. Andrew, G. Bydder, J. Griffiths, R. Iles, and P. Styles, 'Clinical Magnetic Resonance: Imaging and Spectroscopy', Wiley, Chichester, 1990.
36. R. J. Gillies, 'NMR in Physiological and Biomedicine', Academic Press, San Diego, 1994.
37. P. C. Lauterbur, *Nature*, 1973, **242**, 190.
38. R. Gabillard, *C. R. Acad. Sci. Paris*, 1951, **232**, 1551.
39. R. Gabillard, *Phys. Rev.*, 1952, **85**, 694.
40. E. R. Andrew, 'Nuclear Magnetic Resonance', Cambridge University Press, Cambridge, 1955, p. 134.
41. H. Y. Carr and E. M. Purcell, *Phys. Rev.*, 1954, **96**, 630.
42. G. K. Walters and W. M. Fairbank, *Phys. Rev.*, 1956, **103**, 262.
43. A. G. Anderson, R. L. Garvin, E. L. Hahn, J. W. Horton, G. L. Tucker, and R. M. Walker, *Phys. Rev.*, 1955, **26**, 1324.
44. E. R. Andrew, A. Finney, and P. Mansfield, Royal Radar Establishment Research Report, 1970, PD/24/026/AT.
45. R. Damadian, US Patent 3 789 832 filed 17 March 1972.
46. R. Damadian, *Philos. Trans. R. Soc. London, Ser. B*, 1980, **289**, 489.
47. R. Damadian, *Science*, 1971, **171**, 1151.
48. P. Mansfield and P. K. Grannell, *J. Phys. C: Solid State Phys.*, 1973, **6**, L422.
49. P. Mansfield and P. K. Grannell, *Phys. Rev. B*, 1975, **12**, 3618.
50. W. S. Hinshaw, *Phys. Lett.*, 1974, **48A**, 87.
51. W. S. Hinshaw, *J. Appl. Phys.*, 1976, **47**, 3709.
52. R. Damadian, M. Goldsmith, and L. Minkoff, *Physiol. Chem. Phys.*, 1977, **9**, 97.
53. P. Mansfield, A. A. Maudsley, and T. Baines, *J. Phys. E: Sci. Instrum.*, 1976, **9**, 271.
54. A. Kumar, D. Welti, and R. R. Ernst, *J. Magn. Reson.*, 1975, **18**, 69.
55. P. Brunner and R. R. Ernst, *J. Magn. Reson.*, 1979, **33**, 83.
56. A. N. Garroway, P. K. Grannell, and P. Mansfield, *J. Phys. C: Solid State Phys.*, 1974, **7**, L457.
57. W. A. Edelstein, J. M. S. Hutchison, G. Johnson, and T. W. Redpath, *Phys. Med. Biol.*, 1980, **25**, 751.
58. P. C. Lauterbur, *Pure Appl. Chem.*, 1974, **40**, 149.
59. E. R. Andrew, P. A. Bottomley, W. S. Hinshaw, G. N. Holland, and W. S. Moore, *Nature*, 1977, **270**, No. 5638 front cover.
60. E. R. Andrew, *Philos. Trans. R. Soc. London, Ser. B*, 1980, **289**, 471.
61. P. C. Lauterbur, in 'NMR in Biology', ed. R. A. Dwek, Academic Press, Orlando, 1977.
62. P. Mansfield and I. L. Pykett, *J. Magn. Reson.*, 1978, **29**, 355.
63. P. Mansfield and A. A. Maudsley, *Phys. Med. Biol.*, 1976, **21**, 847.
64. J. M. S. Hutchinson, J. R. Mallard, and C. C. Goll, in 'Magnetic Resonance and Related Phenomena', ed. P. S. Allen, E. R. Andrew, and C. A. Bates, North-Holland, Amsterdam, 1975, p. 283.
65. R. Damadian, L. Minkoff, M. Goldsmith, M. Stanford, and J. Koutcher, *Science*, 1976, **194**, 1430.
66. J. Mallard, J. M. S. Hutchison, W. A. Edelstein C. R. Ling, M. A. Foster, and G. Johnson, *Philos. Trans. R. Soc. London, Ser. B*, 1980, **289**, 519.
67. E. R. Andrew, P. A. Bottomley, W. S. Hinshaw, G. N. Holland, W. S. Moore, and C. Simaroj, *Phys. Med. Biol.*, 1977, **22**, 971, errata 1291.
68. L. E. Crooks, T. P. Grover, L. Kaufman, and J. R. Singer, *Invest. Radiol.*, 1978, **13**, 63.
69. I. L. Pykett and P. Mansfield, *Phys. Med. Biol.*, 1978, **23**, 961.
70. W. S. Hinshaw, E. R. Andrew, P. A. Bottomley, G. N. Holland, and W. S. Moore, *Br. J. Radiol.*, 1978, **51**, 273.
71. P. Mansfield and A. A. Maudsley, Proc. 19th Congress Ampere, Heidelberg, 1976, 247.
72. P. Mansfield and A. A. Maudsley, *Br. J. Radiol.*, 1977, **50**, 188.
73. W. S. Hinshaw, P. A. Bottomley, and G. N. Holland, *Nature*, 1977, **270**, 722.
74. W. S. Hinshaw, E. R. Andrew, P. A. Bottomley, G. N. Holland, W. S. Moore, and B. S. Worthington, *Neuroradiology*, 1978, **16**, 607.
75. W. S. Hinshaw, E. R. Andrew, P. A. Bottomley, G. N. Holland, W. S. Moore, and B. S. Worthington, *Br. J. Radiol.*, 1979, **52**, 36.
76. P. A. Bottomley and E. R. Andrew, *Phys. Med. Biol.*, 1978, **23**, 630.
77. R. Damadian, L. Minkoff, M. Goldsmith, and J. A. Koutcher, *Naturwissenschaften*, 1978, **65**, 250.
78. H. Clow and I. R. Young, *New Sci.*, 1978, **80**, 588.
79. P. Mansfield, I. L. Pykett, and P. G. Morris, *Br. J. Radiol.*, 1978, **51**, 921.
80. G. N. Holland, R. C. Hawkes, and W. S. Moore, *J. Comput. Assist. Tomogr.*, 1980, **4**, 429.
81. R. C. Hawkes, G. N. Holland, W. S. Moore, and B. S. Worthington, *J. Comput. Assist. Tomogr.*, 1980, **4**, 577.
82. M. J. R. Hoch and A. R. Day, *Solid State Commun.*, 1979, **30**, 211.
83. A. Haase, J. Frahm, D. Matthaei, W. Hanicke, and J. Merboldt, *J. Magn. Reson.*, 1986, **67**, 258.
84. P. Mansfield, *J. Phys. C: Solid State Phys.*, 1977, **10**, L55.
85. R. Rzedzian, B. Chapman, P. Mansfield, R. E. Coupland, M. Doyle, A. Chrispin, D. Guilfoyle, and P. Small, *Lancet*, 1983, **ii**, 1281.
86. P. G. Morris, 'Nuclear Magnetic Resonance Imaging in Medicine and Biology', Clarendon Press, Oxford, 1986.

Biographical Sketch

E. Raymond Andrew. *b* 1921. B.A. (Physics), M.A. Ph.D., Sc.D., Cambridge University, UK, Hon. D.Sc. Turku, Poznan, Leipzig and Wales, FRSE and FRS. Postdoctoral Fellow, Harvard with E. M. Purcell. Lecturer, St. Andrews University, Scotland. Professor of

Physics, University of Wales, Bangor. Professor and Dean of Science, Nottingham University, England. Currently Research Professor, University of Florida, USA. President, Groupement AMPERE, 1974–80. President, ISMAR, 1983–86. Editor, Magnetic Resonance in Medicine, 1983–91. Four books: Nuclear Magnetic Resonance, Magnetic Resonance and Related Phenomena (jtly), Clinical Magnetic Resonance (jtly), NMR in High Magnetic Fields (jtly), 400 publications. Research interests: NMR in condensed matter, NMR imaging, MRI in medicine.

MRI at Midfield Strength

Jane M. Hawnaur and Ian Isherwood
Department of Diagnostic Radiology, University of Manchester, UK

1 INTRODUCTION

Whole body magnetic resonance imaging (MRI) was initially performed in the early 1980s using magnetic resonance (MR) scanners based on resistive electromagnets. In the decade that followed, superconducting MR scanners became the most popular scanners for both research and clinical purposes. The superior signal-to-noise ratio (S/N), field homogeneity and field stability, particularly for high field (1.5 T) systems, proved to be major factors in this selective process. An initial emphasis on brain and spine imaging during the early development of MRI served to reinforce the concept that a high field strength was necessary for good quality images, a view encouraged by some of the systems manufacturers.

Since then, manufacturers have expended significant research and development effort on their midfield range of systems, many of which now offer the same capabilities (apart from spectroscopy) as higher field MRI systems. As diagnostic applications for MRI have expanded outside the central nervous system into the musculoskeletal and cardiovascular systems, abdomen, and pelvis, some of the disadvantages of high-field MRI have become more apparent. Chemical shift, susceptibility effects and movement artifacts cause greater interference during body imaging than cranial or spinal imaging. In addition, the practical and economic difficulties associated with the installation and running of high-field systems in some hospital settings have prompted reassessment of the value of low and midfield systems as a necessary compromise between S/N, versatility and cost. Of 719 MRI systems installed in Japan by 1990, 72 were low-field (less than 0.2 T), 488 were midfield (0.2–1.0 T), and 159 were 1.5 T superconducting systems.[1] A similar trend away from high-field systems was apparent worldwide; sales of midfield MRI scanners worldwide exceed sales of high-field systems by a factor of 2–3, and the single most popular model in Europe is a 1.0 T superconducting MR scanner.

2 TYPES OF SCANNER AT MIDFIELD (0.2–1.0 T)

Most of the components of MRI scanners for use at mid and high field are identical apart from the magnet itself. There are three types of magnet design capable of operating in the midfield range.

2.1 Superconducting Magnets

2.1.1 Design

MRI scanners using a superconducting magnet offer a wide range of field strengths from 0.2 T upwards and are the most popular choice for clinical whole body systems operating at 0.5 or 1.0 T. The field-generating coil is constructed from a superconducting alloy of niobium/titanium (NbTi) filaments in a copper matrix through which an electric current is passed. To remove electrical resistance, the system is cooled to 4 K. Once the superconducting state has been achieved, minimal electrical energy is required to maintain the magnetic field. The conducting NbTi wires are suspended in liquid helium, which evaporates as it absorbs heat conducted away from the wires. In older systems, the cooling system required several layers of vacuum insulation, liquid nitrogen and insulating materials around the helium cryostat, and was relatively inefficient. The helium boil-off rate was of the order of 1 L h^{-1} and the inconvenience and cost of weekly or monthly cryogen refills was a major disadvantage of superconducting systems. In modern midfield scanners, however, efficient refrigeration is achieved without liquid nitrogen, and systems are designed to minimize cryogen costs. Helium boil-off rates vary between manufacturers, but are of the order of 0.04–0.2 L h^{-1}. Refill rates have consequently fallen, with recently introduced models offering refill intervals of up to 7 years.

2.1.2 Field Homogeneity and Shielding

Superconducting magnets produce a stable and homogeneous magnetic field; their solenoidal design produces a main magnetic field $\boldsymbol{B}_0$ oriented along the length of the patient. Homogeneity is of the order of ±2–5 ppm on a 40 cm diameter spherical volume (DSV). Early designs reduced the fringe field passively by means of bolt-on steel shielding around the magnet, resulting in a combined weight of up to 40 ton. Active shielding, with an integral shielding coil built around the primary coil, is more efficient and less costly, reducing the weight of the scanner to around 5 ton for a 1.0 T magnet. Actively shielded magnets are thus more compact and lightweight, but there is a small reduction in magnetic field homogeneity and less protection from variation in external rf fields. Typical 5 G contours for a 0.5 T passively shielded superconducting MR system are 3.7 m axial by 2.5 m radial. Many manufacturers offer compact midfield systems with integral passive shielding, also resulting in a small fringe field.

2.1.3 Specifications

Many midfield superconducting magnets have been adapted from high-field systems in the same manufacturer's range, and offer similar facilities (Table 1).

2.1.4 Installation and Running Costs

A superconducting MR scanner in the midfield range weighs about 5 ton, including the enclosure, helium and gradient coils. This compares with a weight of 5–15 ton for a similar system operating at 1.5 T. Most current midfield MR scanners are designed for installation in an existing room within the imaging department. Minimum space requirements are typically 6.0 m×5.0 m with a 2.65 m ceiling height. Additional space is required for computers and console area, generally less than 10 m^2 each. The capital cost of superconducting MR equipment is relatively high and installation may involve the expense of fringe field shielding, rf shielding, and ventilation to enable effective operation of the system.

Table 1 Selected Specifications for MR Systems from the Same Manufacturer Operating at 0.5 T and 1.5 T (Phillips) 1998

	0.5 T	1.5 T
Magnet homogeneity	±1 ppm (40 cm DSV)	±1 ppm (40 cm DSV)
Weight (similar dimensions) (kg)	2600	3100
Fringe field (5 G)	2.9 m × 2.1 m	3.9 m × 2.5 m
Helium consumption (L h^{-1})	0.004	0.004
Gradient:		
Strength (mT m^{-1})	15	15 (standad), 23 (upgrade)
Slew rate (mT ms^{-1})	17	17 (standard), 53 or 105 (upgrade)
Capabilities		
Spectroscopy	No	Yes
Diffusion imaging	Yes	Yes
Functional brain MRI	No	Yes
Angiography	Yes	Yes
Receiver coils		
Surface coils	Yes	Yes
Flexible torso surface coil	Yes	No
Multiple phased-array torso coil	No	Yes
Endoluminal coil	Yes	Yes
Siting:		
Magnet room	6 m×5 m	6 m×5 m
Technical room	2 m×3.2 m	2 m×3.2 m

DSV, diameter spherical volume

2.2 Resistive Magnets

2.2.1 Design

The static field from a resistive magnet is produced by electric current passing through coils or sheets of resistive wire wound around a central iron core. For example, a resistive magnet with a bore of about 1 m and a field strength of 0.15 T requires approximately 1500 turns of wire through which around 200 A of current is passed.

Resistive magnets usually have a solenoidal configuration with $\boldsymbol{B}_0$ oriented along the long axis of the patient, but their relatively light weight enables them to be built with a vertical configuration which facilitates the use of rf receiver coils to generate a field perpendicular to $\boldsymbol{B}_0$. This design also increases access to the magnet bore for claustrophobic patients, interventional procedures, or for supervision of high-dependency patients. Magnetic field strength is limited by power consumption, the amount of heat produced, and the weight of magnet required to support a large number of turns of wire. Power is dissipated in the coil windings as heat is removed by air/water cooling, necessitating the delivery of large volumes of deionized water. A stable, continuous supply of electricity is required, and power consumption is high compared with permanent or superconducting magnets. A typical power requirement for a resistive magnet is of the order of 50 kW for a 0.15 T field, the power requirement increasing with increasing field strength. The fields of commercially available resistive MR systems range from 0.02 to 0.4 T. Air cored designs are also available.

2.2.2 Field Homogeneity and Shielding

A typical main field homogeneity in a shimmed resistive magnet over a 40 cm FOV is 20–200 ppm, i.e. less than for most superconducting magnets. Any problems in maintaining a constant power supply can result in temporal instability of the magnetic field. Stability will also be affected by temperature variations if cooling and heat exchange systems malfunction. However, the magnetic field can be switched off easily to allow removal of metallic objects attached to the bore of the magnet.

2.2.3 Specifications

The weight and installation requirements for a 0.2 T resistive magnet are similar to those of 0.5 T superconducting scanners, and the imaging capabilities are broadly similar (Table 2).

2.2.4 Installation and Running Costs

Resistive MRI scanners are cheaper to buy than superconducting types, and cost less to install. Despite the relatively high electricity costs, running costs overall are less than those of superconducting magnets.

2.3 Permanent Magnets

2.3.1 Design

The magnetic field is generated by units of permanently magnetized material arranged to construct a magnet with north and south poles separated by an air gap of sufficient size for imaging. Permanent magnets usually have a horseshoe or bipolar shape, with the patient lying perpendicular to $\boldsymbol{B}_0$. Containment of the magnetic flux lines to produce a uniform field between the poles of the magnet requires a large mass of iron, with the result that a permanent MRI scanner is heavier than types using superconducting magnets. Modern systems weigh approximately 10 ton but lighter permanent magnets using rare earth alloys such as neodymium alloy are also available. MRI systems based on a permanent magnet have a limited field strength of up to 0.2–0.3 T. The extent of the

Table 2 Comparison of Representative Specifications of MR Systems available in mid-1990s

Field strength/type	Homogeneity	Installation area (m^2)	Fringe field, axial × vertical (m)	Weight (kg)
0.2 T Permanent	±20 ppm 1810 cm DSV	25	1.7 × 2.2	8900
0.2 T Resistive	±5 ppm 40 cm DSV	30	2.6 × 2.4	12 000
Superconducting:				
0.5 T	±5 ppm 40 cm DSV	23	3.7 × 2.5, passive shield	7000
0.5 T	±5 ppm 40 cm DSV	25	3.5 × 2.5, active shield	2800
1.0 T	±7.5 ppm 50 cm DSV	40	2.4 × 4.3, active shield	4900
1.5 T	±5 ppm 50 cm DSV	65	3.1 × 5.0, active shield	13 100

DSV, diameter spherical volume

stray field is usually less than for wire-wound open-core magnets, but magnetic field intensity often rises sharply near the bore of the magnet and the 'missile effect' may be greater than for wire-wound magnets.[2] Systems are available with an open configuration, which reduces claustrophobia and improves access to high-dependency patients or for MR-guided interventional procedures. Solenoidal rf coils can be used to improve the S/N.

2.3.2 Field Homogeneity and Stability

Magnetic field homogeneity is of the order of 40 ppm on a 36 cm DSV, compared with 20 ppm on a 45 cm DSV for a 0.5 T actively shielded superconducting magnet. Variations in the temperature of the iron core will affect field strength, and field homogeneity can be ruined by damage to the magnet surface.

2.3.3 Specifications

The limited field strength is associated with an increase in examination time of 5–15% depending on the area being examined. A vertical field orientation is said to produce image quality similar to that of a 0.5 T system, and models are available with a three-dimensional imaging capability. Fast scan and MR angiography packages are available.

2.3.4 Installation and Running Costs

Permanent magnets are becoming more popular as alternatives to superconducting or resistive MR scanners in budget-conscious markets. Installation does not require magnetic shielding, a separate computer room, or special air conditioning. Running costs are about one-tenth of those for a superconducting magnet system, since permanent magnets use little electrical power and no cooling water or cryogens. The latter consideration is particularly important in Japan and Italy, where cryogens are expensive. Operational costs are also reduced by a low downtime of around 5%. Installation requires a space of 25 m^2, similar to that for a computerized tomography (CT) scanner, and can be completed in 10 days.

3 ADVANTAGES OF MIDFIELD MRI

The specification of commercially available MRI scanners in the midfield range has improved in recent years, while the purchase price, installation, and running costs have fallen. Manufacturers have concentrated on reducing site costs whilst upgrading capabilities. Efficient refrigeration with low cryogen consumption helps to reduce running costs at midfield. Operating costs for midfield MR systems can be covered with an average daily patient volume of 6–7 patients, while up to 10 patients are required to cover costs on a high-field system, assuming similar reimbursement rates. The cost of a maintenance agreement for a representative 1.5 T MR scanner can be 30% greater than for a midfield system. The Guidelines published by the Medical Devices Directorate of the UK Department of Health (1993)[2] recommend that MR equipment is contained within a designated controlled area, encompassing the 5 G magnetic field contour. Selfshielded, lightweight magnets with tight fringe fields enable easy siting without major structural modification to existing rooms. The compact fringe field also enables magnetic-field-sensitive devices such as monitoring equipment to be taken into the magnet room, thus allowing MRI of high dependency patients. Compact fringe fields also help to limit staff exposure, which should not exceed 0.2 T to the whole body including the hands and limbs as an 8 h time-weighted-average exposure.

Intravascular devices exhibiting ferromagnetism display greater torque and magnetic susceptibility artifacts at 1.5 T than at 0.35 T.[3]

Acoustic noise levels in the magnet bore do not correlate as might be expected with magnetic field strength, averaging 82–93 dB on a range of MR instruments operating from 0.35 to

1.5 T.[4] The level of noise depends more on the efficiency of damping of the gradient coil vibration in different manufacturers' systems and will always tend to be greater when using fast gradient recalled echo (GRE) sequences with short *TR* and *TE* times and thin sections. Ear protection should be worn when the level of acoustic noise exceeds 85 dB.

4 EFFECT OF FIELD STRENGTH ON IMAGING PARAMETERS AND OPTIONS

4.1 General Specifications

Advances in hardware and software first introduced for high-field systems are now available at midfield. Software packages for cardiac imaging and angiography, and software for reducing acquisition times are all available for midfield systems. The rf components of 0.5, 1.0, and 1.5 T systems available from the same manufacturer are in many cases identical, and 0.5 T systems are now available with 15 mT m^{-1} gradients. While systems with a wide variety of field strengths are capable of producing images of diagnostic quality, high-field systems can normally produce esthetically pleasing images more rapidly. The introduction of quadrature coils to midfield systems and the use of powerful computers to facilitate multiple system operations and improve patient throughput have reduced this differential. Endoluminal coils are becoming more available on midfield systems.

4.2 Signal-to-Noise Ratio

The S/N increases as the field strength. This advantage of high field strength MRI has to be weighed against the concomitant potential for greater image artifacts due to increased eddy currents, chemical shift, and susceptibility, as well as the potential risk of excessive rf power deposition or heating (see below). At any field strength, image quality is improved by using a surface receiver coil to improve the S/N.

4.3 Contrast

The ability to detect a structure on an MR image and differentiate it from neighboring tissues depends on spatial resolution and signal intensity differences. The latter can be partly manipulated by selection of appropriate pulse sequences but is largely determined by the T_1 and T_2 relaxation times of the tissues. The resonant frequency and T_1 relaxation time of protons increase with increasing magnetic field strength. T_1 values increase by approximately 400–500 ms T^{-1}, the values for normal and pathological tissue tending to converge and the T_1-dependent contrast to decrease as field strength increases. T_2 contrast does not show the same degree of field dependence, most tissues having a T_2 value in the range 50–150 ms. Taking the effect of noise on image quality into consideration, however, there is a trend for the tissue contrast-to-noise ratio to increase with field up to 1.5 T.[5]

Tissue components exhibiting susceptibility effects, e.g. iron in liver or basal ganglia, may result in an overall reduction in T_2 relaxation time at higher field strength.

4.4 Fat Suppression

Chemical shift imaging depends on the difference in resonant frequency between water and fat hydrogen protons, which allows selective excitation of one or other species. The amount of chemical shift (3.3 ppm) is independent of field strength, but the difference in frequency is proportional to field strength. Separation of fat and water resonant frequencies is less pronounced at midfield (70 Hz at 0.5 T) than at high field (200 Hz at 1.5 T). Magnetic field homogeneity will also tend to be less at midfield than at high field, with the variation in resonant frequencies due to field inhomogeneity causing imperfect selective excitation. The effect of field inhomogeneity will be least when using small fields of view near the magnet center. When using a binomial pulse to achieve selective saturation, the interpulse spacing must be longer at lower field strengths to achieve the same chemical shift effect as at high field, thus limiting the minimum *TE*.[6]

The *TE* times at which fat and water protons are out of phase are inversely proportional to the field strength, i.e., are longer at midfield than at high field.

4.5 Magnetization Transfer Contrast

Magnetization transfer contrast (MTC) using saturation transfer techniques reflects cross relaxation between free water and water bound to macromolecules. The reduction of the net available magnetization and of T_1 in the 'free' pool by application of a saturating off-resonance rf pulse to the 'bound' protons is a field dependent phenomenon. Magnetization transfer rate decreases with increasing field strength, for example the magnetization transfer rate constant for white matter is 2.27 s^{-1} at 0.5 T and 1.42 s^{-1} at 1.5 T.[7] Although the degree of MTC in a given tissue would be expected to diminish as the T_1 relaxation time shortens with decreasing field strength, satisfactory MTC images have been obtained at low and midfield strengths. Selective saturation is possible at midfield using off-resonance rf irradiation of short duration. Power deposition in the subject from the rf dose generated by the preirradiation pulse is also less of a limiting factor at midfield strength. The safety guidelines for exposure to rf energy in MRI currently recommend a limit of 1 W kg^{-1} body weight.[8]

4.6 Fast/High-Resolution Scanning

The ability to achieve sequences with short *TR* and *TE* times and low flip angles (fast scanning) and small field of view (FOV)/thin slice imaging (high-resolution) scanning is dependent on gradient strength and rise time rather than field strength. New systems of any field strength typically offer gradient strengths of 15–23 mT m^{-1} and a rise time of less than 1 ms. Image contrast and S/N may be compromised in fast/high resolution sequences, and image quality is more difficult to maintain at midfield than high field, when the amount of tissue signal at midfield is intrinsically less.

4.7 Magnetic Resonance Angiography

Magnetic resonance angiography (MRA) is not usually limited by S/N and does depend on contrast between flowing

blood and background tissues and adequate spatial resolution. Intravoxel phase dispersion, which is an important cause of loss of contrast in MRA, is reduced by minimizing field inhomogeneity and by using the minimum voxel size and shortest *TE* time possible. Systems with excellent magnetic field homogeneity, high gradient strengths and slew rates, and good S/N characteristics are required, these properties generally being associated with high-field MRI systems. However, satisfactory MR angiograms have been obtained on midfield superconducting MR scanners and on systems employing a permanent magnet with a field strength of 0.2 T.[9,10] Permanent magnets suffer less from eddy current artifacts during gradient switching, thereby preserving field homogeneity and thus improving background suppression in MR angiograms. At low and midfield, T_1 relaxation times are relatively short, so that with time-of-flight (TOF) techniques based on flow-related enhancement, signal from flowing blood will tend to be greater at midfield than high field because of the reduction in saturation due to the more rapid T_1 recovery. Conversely, saturation of stationary tissue is more difficult for the same reason, so that relatively larger flip angles and shorter *TE* times have to be employed at midfield than at high field to achieve an adequate degree of background suppression. For example, at 0.5 T the flip angle used for two-dimensional TOF is typically 85°, whilst at 1.5 T a similar sequence would employ a flip angle of about 60°. The degree of artifactual loss of flow signal from local field inhomogeneities caused by metallic surgical clips adjacent to vessels is less at midfield than high field.

4.8 Echo Planar Imaging

Peripheral nerve stimulation has been experienced by volunteers undergoing echo planar imaging (EPI) on a 1.5 T MR system modified by the addition of high-performance gradient sets. Subjective twitches were felt when EPI was being performed near peak gradient operating levels of around 60 T s^{-1}.[11] US Food and Drug Administration guidelines recommend that the gradient operating levels are kept below 20 T s^{-1} or one-third of the observed threshold for peripheral nerve stimulation. On 0.5 T EPI scanners (Mansfield, Nottingham), gradient operating levels are one-sixth of that inducing peripheral nerve stimulation. An inversion–recovery (IR) preparation pulse combined with EPI at 0.5 T produces T_1-weighted images in which tissue contrast can be optimized, with potential applications in dynamic contrast-enhanced studies.[12] Gradient strengths and switching rates are very similar for snapshot FLASH techniques and EPI.

4.9 MR Spectroscopy

^{31}P MR spectroscopy (MRS) requires a minimum field strength of 1.5 T, but ^{1}H MR spectroscopy is feasible at lower field strengths. Stimulated echo acquisition mode ^{1}H MRS at 1.0 T demonstrates cerebral metabolites such as *N*-acetylaspartate and creatinine without significant loss of relative spectral resolution, compared with higher fields.[13]

5 ARTIFACTS

5.1 Motion

Ghost artifacts due to physiological motion during image acquisition occur in the phase-encoding direction and are most conspicuous when the moving tissue has a bright signal, e.g. fat in the abdominal wall or flowing blood on gradient echo sequences. Breathing artifacts are more apparent at high field strength than at low to midfield strength, due to the greater S/N (and fewer averages used) and higher fat–muscle contrast on the image.[14]

5.2 Chemical Shift

Chemical shift misregistration causes displacement of fat–water interfaces along the frequency-encoding direction due to the difference in the resonant frequencies of fat and water protons. This phenomenon is an important cause of error in the evaluation of tissue interfaces, particularly in areas containing abundant fat–soft tissue interfaces such as the orbit, extracranial head and neck, abdominal and pelvic cavities, and the musculoskeletal system. The amount of chemical shift increases with increasing field strength, despite the larger imaging gradients that are often integral to high-field systems.[15] Many manufacturers of midfield systems offer the option of variable bandwidth, narrowing the bandwidth when an increase in S/N is desirable, or using a wider bandwidth to minimize chemical shift.

5.3 Susceptibility

The magnetic susceptibility of a material describes its ability to become magnetized in an external magnetic field. Susceptibility artifacts occur at the interface between materials having different susceptibilities and result in local field inhomogeneities and image distortion in the frequency-encoding direction. Artifactual image degradation is greater at high field than at mid or low field and when using GRE sequences rather than spin echo (SE) sequences, particularly T_2*-weighted GRE sequences.

6 CLINICAL APPLICATIONS OF MIDFIELD VERSUS HIGH-FIELD MRI

6.1 Diagnostic Accuracy

Images obtained at both 0.5 and 1.5 T using similar protocols have been reviewed in a blind study of patients with various craniospinal, abdominal, and joint conditions. receiver-operated characteristic (ROC) analysis of interpretation by expert radiologists at 0.5 and 1.5 T suggested that the differences in field strength are not significant for diagnostic accuracy.[16] The S/N increases linearly with field strength, conferring an advantage on high-field systems, particularly when imaging small structures using a high-resolution matrix and thin slices. Advantages of midfield systems include superior T_1-dependent contrast, fewer problems with chemical shift, susceptibility effects, and certain motion artifacts. Narrowing the

Table 3 Imaging of Intracranial Hemorrhage on Midfield MRI.[18,19]

Stage	Composition[a]	Signal intensity and optimal sequences[b]
Hyperacute (<24 h)	Fresh blood	Hyperintense + on T_1 WIs Hyperintense +++ on STIR, > T_2* WIs > T_2 WIs
Acute (1–3 days)	DeoxyHb in intact RBCs	Hypointense + on T_1 WIs, Hypointense +++ on T_2 WIs, GRE > SE
Subacute (4–7 days)	DeoxyHb in lysed RBCs	Hyperintense +++ on T_1 WIs Hypo- to hyperintense on T_2 WIs
Chronic (1–3 weeks)	MetHb	Hyperintense on T_1 WIs Hyperintense on T_2 WIs, GRE > SE

[a]DeoxyHb, deoxyhemoglobin; MetHb, methemoglobin; RBCs, red blood cells.
[b]WIs, weighted images; IR, inversion–recovery; SE, spin echo; +, mild; +++, marked.

bandwidth at midfield increases the S/N and is a strategy used to improve image quality towards that of high-field systems where the concomitant increase in chemical shift is tolerable. The theoretical reduction in rf power deposition at midfield will become of practical interest with the use of MTC imaging and fast spin echo techniques.

6.2 Craniospinal MRI

When systems with hardware and software specifications that are virtually identical apart from field strength are compared, image S/N is greater at 1.5 T than at 0.5 T, but there is no significant change in diagnostic accuracy for head and spine imaging between the two field strengths.[17] Most conditions, such as cerebrovascular disease and tumors, have similar signal intensity characteristics at mid and high field. A notable exception is the appearance of intracranial hemorrhage, which depends on the stage of evolution of the hematoma as well as the field strength of the MR scanner used (Table 3).[18,19]

Twelve to 24 h after an intracranial bleed, acute hematoma containing oxyhemoglobin is most readily detected on midfield MRI using T_2*-weighted GRE sequences or a short τ inversion–recovery (STIR) sequence which takes advantage of the combination of high proton density and relatively long T_1 relaxation time of fresh blood. Subsequent T_2 shortening due to deoxyhemoglobin formation is more easily demonstrated on T_2*-weighted GRE than T_2-weighted SE sequences at midfield strength. As deoxyhemoglobin converts to methemoglobin, paramagnetic T_1 shortening results in hyperintensity on T_1-weighted sequences. Visibility of low signal intensity due to T_2 shortening is maximized on T_2*-weighted sequences. When hemolysis occurs after about 7 days, hematoma becomes hyperintense on all sequences.

Comparative studies have demonstrated that midfield MR is more sensitive than CT in detecting both hemorrhagic and non-hemorrhagic lesions resulting from closed head trauma, with the exception of subarachnoid hemorrhage.[20] The greater sensitivity of high-field MRI to magnetic susceptibility confers a theoretical advantage for demonstrating acute hemorrhage. In practice, selection of appropriate pulse sequences at midfield strength, i.e. heavily T_2-weighted SE or T_2*-weighted GRE sequences to maximize differences in susceptibility, compensates for field strength differences. Similarly, acute hemorrhagic contusion of the spinal cord can be demonstrated at midfield, using T_2*-weighted GRE sequences to detect the susceptibility effects of deoxyhemoglobin. In a clinical setting, imaging of high dependency patients requiring ventilation or close monitoring is more easily achieved at midfield than high field. Specific circumstances where high field strength may be advantageous in craniospinal MRI include high resolution imaging, for example of the pituitary gland, and demonstration of brain iron.

6.3 Extracranial Head and Neck MRI

Many studies evaluating MRI for the demonstration and staging of tumors in the maxillofacial region and anterior neck have been performed at midfield strength. MRI of small structures such as the parathyroid glands has been successful at both mid and high field. The need to obtain thin slices with high spatial resolution confers some advantage on high field MRI, but images of diagnostic quality are achievable at field strengths of 0.35–0.5 T. The use of surface receiver coils specifically designed for anterior neck imaging overcomes the handicap of reduced S/N at midfield strength, and image quality is high due to relatively little motion or chemical shift artifacts.

6.4 Cardiovascular MRI

Much of the early experience of cardiovascular MRI was at midfield strength, typically employing T_1-weighted SE sequences gated to the cardiac cycle to provide anatomic information in congenital and acquired cardiovascular disease. Cardiac gated fast SE sequences are now also available at midfield strength; uses include the demonstration of cardiac and paracardiac masses, myocardial disease, and anomalies of the great vessels such as aneurysms and stenosis. Phase contrast sequences providing flow information are also readily available at midfield strength, providing semiquantitative flow information in conditions such as valvular heart disease and coarctation of the aorta. High-field MRI scanners offer increased S/N in the body coil and very fast sequences, thus effectively freezing cardiac motion and enabling 'real-time' stu-

dies of cardiac motion to be performed. Monitoring equipment may be more difficult to use in the proximity of a high field strength magnet however, and cardiac-gated acquisitions may be more difficult to set up than at midfield strength. Chemical shift artifacts mimicking intraluminal disease, e.g. dissection flaps, are more troublesome at high field strength, as are susceptibility artifacts in the postoperative patient. MR angiography of the coronary arteries is more successful at high field strength where the ability to reduce voxel size while maintaining the S/N is crucial. Routine display of larger visceral and peripheral vessels, however, is possible using commercially available software and receiver coils on midfield MR scanners.

6.5 Musculoskeletal MRI

There is no important advantage of high-field MRI over midfield MRI when evaluating bone and soft tissue tumors, trauma, or inflammation. Indeed, the greater degree of chemical shift and susceptibility effects may be deleterious to image quality. The availability of specific surface receiver coils for imaging joints and small peripheral body parts usually overcomes the potential problem of inadequate signal at midfield strength. The exception may be high-resolution imaging of small structures; studies have demonstrated a significant increase in accuracy for imaging the medial meniscus at 1.5 T compared with imaging at 0.35 T ($p < 0.0002$).[21] No significant difference was demonstrated between field strengths for imaging the lateral meniscus or cruciate ligaments. More recent studies however, have shown no clinically significant field strength dependent difference between 0.5 T and 1.5 T systems for diagnosis of internal derangements of the knee.[22]

6.6 Abdominal MRI

The convergence of T_1 relaxation times for normal liver parenchyma and neoplasm with increasing field strength renders T_1-weighted SE imaging at high field strength less sensitive to focal liver pathology than low or midfield MRI. Hepatic tumors are also demonstrated using heavily T_1-weighted inversion–recovery (IR) sequences or T_2-weighted sequences. Using these sequences, there is no significant difference in the ability of 0.5 and 1.5 T MRI systems to detect focal hepatic lesions.[23,24]

Measured relaxation times for normal and pathological tissues vary between mid- and high-field MRI systems. Magnetic susceptibility effects tend to increase as the square of the field strength, resulting in relative shortening of the observed T_2 relaxation time at high field. Variability will also be introduced by individual and lesional differences, the specific MRI system and pulse sequences used, and the method of calculation. However, statistically significant differences in calculated T_2 values have been demonstrated between normal liver and tumor, and between hepatocellular carcinoma and cavernous hemangioma imaged at both 0.35 and 1.5 T.[25] No significant differences in focal liver lesion detection can be demonstrated between 0.2 and 1.5 T systems when using T_2-weighted sequences enhanced by intravenous superparamagnetic iron oxide contrast medium.[26]

In abdominal MRI, conventional SE sequences are often degraded by movement artifacts. Very fast GRE sequences allowing breath-hold imaging of abdominal structures, which effectively freeze respiratory motion, are available on midfield systems. Although motion artifact is reduced, contrast on the fast sequences is relatively poor, and such dynamic MRI sequences are usually acquired in conjunction with a bolus of intravenous paramagnetic contrast agent. Maximum intensity pixel (MIP) reconstructions from this type of acquisition produce an elegant display of portal venous anatomy. The combination of very fast GRE sequences with steady state precession allows MIP projections of the main bile ducts and peripheral biliary tree.

In pancreatic imaging the lack of a reliable gastrointestinal contrast agent limits the ability of MRI to delineate the margins of the gland distinctly from adjacent small bowel. Contrast between pancreas and retroperitoneal fat may be poor, particularly when fatty involution of the gland is present. Solid pancreatic masses can be very similar in signal intensity to normal parenchyma on both T_1- and T_2-weighted sequences, and the inability of MRI to identify calcification is a disadvantage when attempting to characterize pancreatic masses. Spatial resolution is also currently less than is possible with CT. MR image degradation from motion artifacts due to respiration, peristalsis, and vascular pulsation are less of a problem at midfield than high field. Breath-hold sequences can overcome some motion artifacts, but the intrinsically poor soft tissue contrast of the GRE sequence on which they are based does not improve detection of small pancreatic masses, unless gadolinium enhancement with fat suppression is used. The results of studies assessing the ability of midfield MRI to identify pancreatic tumors and inflammation have been encouraging. Solid pancreatic carcinomas are demonstrated as an area of low signal intensity on T_1-weighted and medium signal intensity on T_2-weighted SE sequences at 0.5 T, whereas a very high signal intensity is seen on T_2-weighted sequences of cystadenocarcinomas.[27] Islet cell tumors less than 2.5 cm in diameter can be successfully localized using T_1- and T_2-weighted sequences.[28] In severe acute pancreatitis, contrast-enhanced fast GRE MRI at 1.0 T is equivalent to CT in determining pancreatic viability.[29]

MRI has a limited role in demonstrating renal masses, and the potential for characterizing renal tumors and differentiating between small benign and malignant lesions has not yet been realized at midfield strength. Results have been more encouraging using higher field strength systems, breath-hold imaging, dynamic contrast enhancement, and fat suppression. Studies of the adrenal glands performed at midfield strength (0.35–0.5 T) have analyzed signal intensity ratios of adrenal masses, and claim the ability to separate a proportion of benign and malignant adrenal masses on the basis of their signal intensities or calculated relaxation times. No consistent difference in the signal intensity of adrenal adenomas and malignant adrenal tumors has been demonstrated with T_1- or T_2-weighted sequences at 1.5 T (using fat or liver tissue as the internal reference). Calculated T_2 values may be more helpful, a calculated T_2 value of 65 ms or greater being associated with malignancy.[30]

6.7 Pelvic MRI

Staging of pelvic malignancy is useful in carcinoma of the body of the uterus, the uterine cervix, bladder, and rectum. It may also help to differentiate between recurrent pelvic tumor

and the effects of previous surgery or radiotherapy. Good results have been achieved using MRI, both at midfield and high field strengths. The S/N at all field strengths is improved by the use of a pelvic surface coil, e.g. of Helmholtz design, or by using multiple phased array coils. Motion artifacts due to respiration are less of a problem in the pelvis than in the upper abdomen, but the effects of peristalsis, vascular pulsation, chemical shift, and susceptibility are important causes of reduced image quality, their effects being greater at high field than at midfield. Endoluminal MRI is available at the end of the 1990s at both midfield and high field and offers the prospect of improved accuracy of prostate cancer staging over body coil imaging.

7 SUMMARY

There is little objective evidence of a substantial difference in diagnostic accuracy between MR images obtained at midfield or high field. Image quality depends more on using a modern scanner which is maintained to specification by means of a routine quality assurance program, and the use of appropriate pulse sequences by experienced personnel. Studies of machines of different field strength using test objects have shown wide variability in performance between machines of the same field strength and of individual systems at different times due to variable quality assurance. For certain diagnostic applications, the relatively good tissue contrast and easier operation of midfield systems may be preferable to the higher S/N and spatial resolution of high-field systems. Very fast GRE sequences obtained at 1.5 T are available at 1.0 T but do not necessarily reduce the overall examination time, which includes the time necessary to prepare the patient for scanning.

8 RELATED ARTICLES

Cryogenic Magnets for Whole Body Magnetic Resonance Systems; High-Field Whole Body Systems; Low-Field Whole Body Systems; MRI in Clinical Medicine; Resistive and Permanent Magnets for Whole Body MRI.

9 REFERENCES

1. Japan Municipal Hospital Association data provided by Hitachi for Diagnostic Imaging International 1991, Jan./Feb., 32–38.
2. Department of Health Medical Devices Directorate, 'Guidelines for Magnetic Resonance Diagnostic Equipment in Clinical Use', HMSO, London, 1993.
3. G. P. Teitelbaum, W. G. Bradley, Jr., and B. D. Klein, *Radiology*, 1988, **166**, 657.
4. R. Hurwitz, S. R. Lane, R. A. Bell, and M. N. Brant-Zawadski, *Radiology*, 1989, **173**, 545.
5. H. R. Hart, Jr., P. A. Bottomley, W. A. Edelstein, S. G. Karr, W. M. Leue, O. Mueller, R. W. Redington, J. F. Schenck, L. S. Smith, and D. Vatis, *Am. J. Roentgenol.*, 1983, **141**, 1195.
6. C. J. Baudouin, D. J. Bryant, and I. R. Young, *Br. J. Radiol.*, 1992, **65**, 132.
7. R. P. Gullapalli, P. Margosian, and L. Kasuboski, in *Proc. XIIth Ann Mtg. Soc. Magn. Reson. Med.*, New York, 1993, Vol. **3**, p. 1292.
8. National Radiation Protection Board, *Br. J. Radiol.*, 1983, **56**, 974.
9. P. Pavone, L. Marsili, C. Catalano, G. A. Petroni, E. Aytan, G. P. Cardone, and R. Passariello, *Radiology*, 1992, **184**, 401.
10. C. B. Grandin, P. Mathurin, T. Duprez, G. Stroobandt, F. Hammer, P. Goffette, and G. Cosnard, *Am. J. Neuroradiol.*, 1998, **19**, 245.
11. M. S. Cohen, R. M. Weisskoff, R. R. Rzedzian, and H. L. Kantor. *Magn. Reson. Med.*, 1990, **14**, 409.
12. M. K. Stehling, R. J. Ordidge, R. Coxon, and P. Mansfield, *Magn. Reson. Med.*, 1990, **13**, 514.
13. R. Sauter, W. Loeffler, H. Bruhn, and J. Frahm, *Radiology*, 1990, **176**, 221.
14. M. L. Wood and R. M. Henkelman, *Magn. Reson. Imag.*, 1986, **4**, 387.
15. R. Lufkin, M. Anselmo, J. Crues, W. Smoker, and W. Hanafee, *Comput. Med. Imaging Graphics*, 1988, **12**, 89.
16. D. Vellet, D. Lee, M. Eliasziw, P. Munk, W. Romano, C. Romano, R. Farb, R. Sevick, and L. Vidito, in *Proc. XIIth Ann Mtg. Soc. Magn. Reson. Med.*, New York, 1993, Vol. 3, p. 1480.
17. C. R. Jack, Jr., T. H. Berquist, G. M. Miller, G. S. Forbes, J. E. Gray, R. L. Morin, and D. M. Ilstrup, *J. Comput. Assist. Tomogr.*, 1990, **14**, 505.
18. R. D. Zimmerman, L. A. Heier, R. B. Snow, D. P. C. Liu, A. B. Kelly, and M. D. F. Deck, *Am. J. Roentgenol.*, 1988, **150**, 651.
19. R. A. Brooks, G. Di Chiro, and N. Patronas, *J. Comput. Assist. Tomogr.*, 1989, **13**, 194.
20. L. R. Gentry, J. C. Godersky, B. Thompson, and V. D. Dunn, *Am. J. Roentgenol.*, 1988, **150**, 673.
21. S. P. Fischer, J. M. Fox, W. Del Pizzo, M. J. Friedman, S. J. Snyder, and R. D. Ferkel, *J. Bone Joint Surg.*, 1991, **73A**, 2.
22. M. J. Barnett. *Am. J. Roentgenol.*, 1993, **161**, 115.
23. J. W. Reinig, A. J. Dwyer, D. L. Miller, J. A. Frank, G. W. Adams, and A. E. Chang, *Radiology*, 1989, **170**, 149.
24. H. V. Steinberg, J. J. Alarcon, and M. E. Bernardino, *Radiology*, 1990, **174**, 153.
25. K. Ohtomo, Y. Itai, K. Yoshikawa, T. Kokubo, and M. Iio, *Radiology*, 1988, **168**, 621.
26. F. Deckers, B. Corthouts, Y. Nackaerts, O. Ozsarlak, P. M. Parizel, and A. M. de Schepper, *Eur. Radiol.*, 1997, **7**, 887.
27. P. Pavone, R. Occhiato, O. Michelini, S. Guiliani, G. Cardone, G. A. Petroni, N. De Stafano, E. Aytan, and R. Passariello, *Eur. Radiol.*, 1991, **1**, 124.
28. P. Pavone, D. G. Mitchell, F. Leonetti, M. Di Girolamo, G. Cardone, C. Catalano, G. Tamburrano, and R. Passariello, *J. Comput. Assist. Tomogr.*, 1993, **17**, 403.
29. A. Saifuddin, J. Ward, J. Ridgway, and A. G. Chalmers, *Clin. Radiol.*, 1993, **48**, 111.
30. R. Kier and S. McCarthy, *Radiology*, 1989, **171**, 671.

Biographical Sketches

Jane M. Hawnaur. *b* 1957. MBChB, 1981, MRCP, 1984, DRMD, 1987, FRCR, 1987. Senior lecturer in Radiology, University of Manchester, 1991–present, and Honorary Consultant Radiologist, Central Manchester Healthcare Trust. Clinical radiologist, with research interest in MRI in oncology.

Ian Isherwood. *b* 1931. MBChB, 1954, DMRD, 1957, FFR, 1960, FRCR, 1975, FFR RCSI (Hon.), 1980, FRCP, 1986, Honorary MD, University of Zaragoza, 1986, CBE 1996. Emeritus Professor of Radiology, University of Manchester.

MRI in Clinical Medicine

Fergus V. Coakley and Alexander R. Margulis
University of California, San Francisco, CA, USA

Magnetic resonance imaging (MRI) is the third and most recently developed of the major cross-sectional imaging techniques. MRI entered clinical usage in 1980, well after ultrasonography and computed X-ray tomography. MRI has revolutionized radiology by greatly extending the soft tissue contrast resolution of conventional imaging techniques. Clinical MRI was introduced in Nottingham and Aberdeen, and this was followed in 1981 by high-quality images from the Hammersmith Hospital, the Cleveland Clinic, the Massachusetts General Hospital, and the University of California, San Francisco.[1–10] At that time, ultrasound was the most common and most readily available cross-sectional modality, while computed tomography (CT) was regarded as the pre-eminent imaging technique: CT sections of the body were obtainable with an acquisition time of 5–6 s each. Despite these established alternative imaging modalities, the diagnostic advantages of MRI were apparent from the very beginning. Starting in 1981, all meetings where MRI reports were presented attracted overflowing audiences.

What particularly captured the interest of the physicians in these audiences was the soft tissue contrast resolution of MRI, the ability to image in any plane, the wide field of view, the rapidly improving quality of the images, the ability to visualize blood vessels because of the effects of flow, and, above all, the dependence of the method on many variable physical parameters offering a never-ending number and variation of sequences and coil improvements. All of these advantages provided for better lesion detection and characterization and greater speed of imaging. In addition, sequences could be manipulated to suppress many artifacts, such as those owing to respiratory motion, cardiac and arterial pulsatility, eddy currents and chemical shift.[11–14] An important later advance was the development of intravenously administered MR contrast media which are even safer than the iodinated intravascular contrast media used in conventional radiography and CT. The versatility of the method is manifested by the vast array of instruments that have been available since the early stages of clinical MRI. Images of acceptable quality can be generated from permanent, resistive or superconducting magnets, with field strengths varying from 0.03 to 1.5 T. Higher field strength scanners of up to 3–4 T are available for investigational and animal studies. Because of its many advantages, MRI rapidly became a popular and widely accepted imaging tool in developed countries, particularly the United States and Japan, and later in western Europe. The number of MRI scanners in the United States in 1997 was 3670, or 13.85 per million population. Differences in the availability of MRI scanners is largely a consequence of government and state control over the proliferation of high-cost procedures and technology and does not relate to the desires of either physicians or patients. For example, the number of MRI scanners in California in 1997 was 55 per million population, while in Massachusetts, a state that requires certificates of need, the number was 13 per million population. In the United States, most of the MRI scanners have a field strength of 1.5 T. In the rest of the industrialized world, notably Japan and western Europe, 0.5 to 1 T instruments predominate. In 1997, MRI had a 21% share of all global medical imaging expenditure. By comparison, conventional rediography had a 34% share. CT and nuclear medicine had a comparatively minor share of the global imaging expenditures.[15–18]

Until the late 1980s, the main clinical applications of MRI were in the brain and spine. In these anatomic regions, MRI was superior to other imaging modalities mainly because of the relative lack of motion. As the number of MRI scanners increased, and with the development of motion suppression, faster sequences, and fat suppression, other anatomic regions started to be imaged routinely. A further contributory factor to the growth in interest in non-neurological applications of MRI was the emergence of a cadre of body-imaging radiologists who were adequately trained in the performance and interpretation of MRI. These factors resulted in a spectacular increase in the application of MRI to areas other than the brain and spine in the United States. For example, between 1991 and 1997, the total increase in the use of MRI was a startling 81%. When examined by system, chest imaging rose 88%, brain imaging rose 78%, spinal imaging rose 61%, and general abdominal imaging rose 57%. However, pelvic imaging decreased by 19%. Despite the disproportionately greater rise in non-neurological applications, the absolute number of studies remained higher for neurological examinations. For example, in 1997, the number of brain and spinal MRI studies performed in the United States was 8 032 000, compared with 199 000 abdominal studies, and 109 000 chest studies. The number of pelvic MRI was a relatively modest 130 000.

By the 1990s, MR had become the primary imaging technique for diseases of the brain, head and neck, major blood vessels, spine, musculoskeletal system, and pelvis, including the male and female reproductive organs.

MRI with intravenously administered Gd-DTPA has essentially replaced contrast-enhanced CT in the diagnostic evaluation of brain tumors, stroke, and multiple sclerosis (Figures 1 and 2).[19–21] MRI has not yet been able to demonstrate specific diagnostic findings in Alzheimer's disease, and it is often unable to identify accurately the source of focal epileptic seizures.

In the head and neck,[22] MRI is outstanding in showing parathyroid and thyroid neoplasms, tumors of salivary glands, enlarged lymph nodes, and tumors of the upper air passages.[13,14] It is also valuable in diagnosing brachial plexus injuries. In the musculoskeletal system, MRI is the optimal modality for studying degenerative, inflammatory and trauma induced changes in the spine[22–24] and major joints: the knee, hip, shoulder.[25–27] As experience increases, smaller joints in hand and foot are being examined with MRI and the findings guide therapy. MRI is also the best method for the evaluation of bone and soft tissue tumors. With newer techniques, it is very promising in the evaluation of different types of arthritis (Figure 3).

In the male pelvis, MRI is used predominantly for staging cancer of the prostate (Figure 4) and the evaluation of major trauma prior to definitive surgical repair. MRI of the prostate is

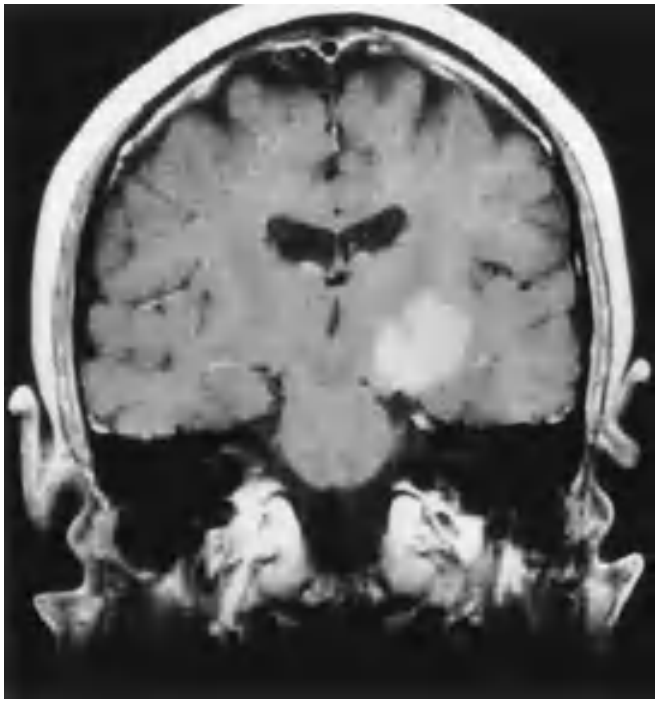

Figure 1 Spin-echo T_1-weighted coronal MR image of the brain, showing marked enhancement of a left lateral geniculate glioma

generally not used for cancer diagnosis but rather for local and regional staging of biopsy-proven cancer. Assessment of extracapsular extension, seminal vesicle invasion, and lymphadenopathy are critical observations in staging prostate cancer and can all be assessed with relatively high accuracy by MRI. The addition of magnetic resonance spectroscopy to routine clinical MRI of the prostate can also help in tumor evaluation.[28–31]

In the female pelvis, MRI is used for the staging of tumors of the endometrium (Figure 5), cervix uteri, ovaries, and vagina. Intravenous Gd-DTPA is helpful in staging most gynecologic malignancies, with the exception of cervical cancer.[31] The use of Gd-DTPA is usually only helpful in cervical cancer when there is suspected invasion of adjacent organs, tumor necrosis, or post-radiation change.

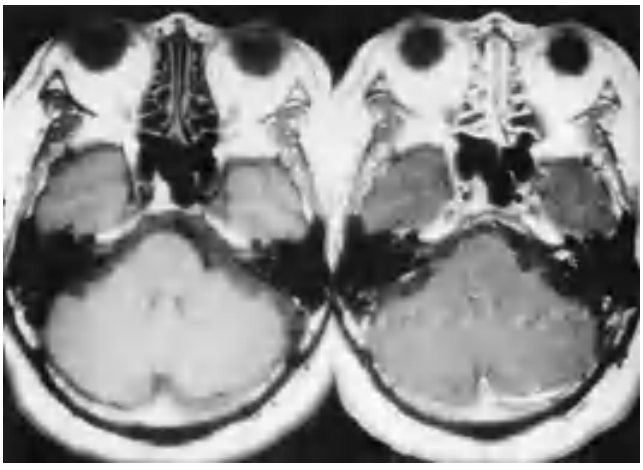

Figure 2 Spin-echo T_1-weighted axial MR image of the posterior fossa, before (left) and after (right) intravenous administration of Gd–DTPA. An enhancing small left acoustic neuroma (arrow) is evident. The use of Gd–DTPA helps in lesion detection

Figure 3 Saturation-transfer subtraction axial MRI section of the knee of a patient with nonspecific synovitis. The image was generated by subtracting T_2-weighted steady-state gradient-echo images without an on-resonance pulsed saturation transfer from the same sequence obtained with a pulsed saturation transfer. Patellar cartilage can be clearly distinguished from adjacent joint fluid and subchondral bone. Hypertropic synovial tissue is sharply delineated, without the use of intravenous gadolinium-containing contrast media. The patient subsequently underwent surgical synovectomy.

In the heart, MRI can diagnose and evaluate various types of congenital and valvular heart disease.[32–35] However, cardiac applications of MRI remain relatively limited because of a lack of enthusiasm for the technique among most cardiologists and

Figure 4 Fast spin-echo T_2-weighted axial MR image of the prostate, obtained using an endorectal coil. Invasion of the right seminal vesicle (arrow) by carcinoma of the prostate is seen

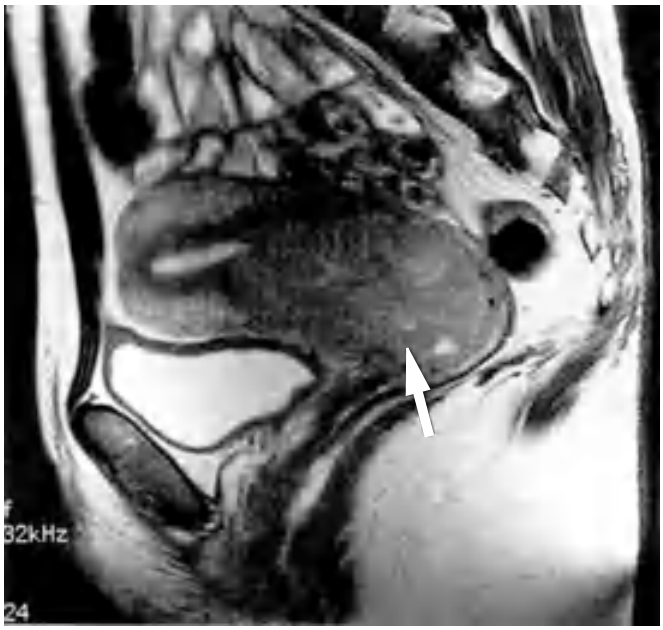

Figure 5 Fast spin-echo T_2-weighted sagittal MR image of the uterus, showing a large cervical carcinoma (arrow) with deep cervical stromal invasion and extension above the internal os into the uterine body

because of the relatively small number of cardiac radiologist-investigators. Major breakthroughs in the area of cardiac MRI are likely in the coming years, as ultrafast sequences and strategies to overcome image degradation by cardiac motion continue to evolve.

Although CT is still the principal imaging method for demonstrating renal abnormalities, MR with Gd–DTPA is becoming at least as accurate.[36] MRI may be preferable in patients with an elevated creatinine or a history of previous reactions to iodinated contrast. MRI may also be helpful in assessing vascular invasion in renal cell carcinoma.

MRI is extremely useful in the detection and characterization of focal liver lesions (Figure 6). Initially, dynamic Gd-DTPA-enhanced MRI appeared inferior to CT arterioportography, but more recent results with improved technology suggest that the two techniques are of comparable overall accuracy. MRI may be slightly less sensitive but more specific than CT arterioportography, when intraoperative exploration and ultrasound are used as the standard of reference. Newer specific contrast media such as Mn-DPDP and superparamagnetic iron oxide particles have recently become available. These agents may help in lesion detection and characterization, although a definite advantage over the standard use Gd-DTPA has not been demonstrated.[37–41] In the future, optimized use of such newer contrast agents is likely to be more rewarding. A relatively recent application of MRI in the liver is the use of ultrafast T_2-weighted sequences to image the fluid in the biliary and pancreatic ducts. This technique of MR cholangiopancreatography appears set to replace diagnostic endoscopic retrograde cholangiopancreatography in the next few years (Figure 7).

MRI has established at least an equality with other imaging techniques in the examination of the heart, mediastinum, retroperitoneum, and for focal lesions of the spleen.[11–14] MRI is still inferior to CT in the evaluation of the gastrointestinal tract and its mesentery.[42,43] This may change very shortly with shorter sequences and the use of antiperistaltic agents such as glucagon.[44] Interesting advances are also being made in the examination of the lung, particularly in the evaluation of pulmonary edema, embolism, and fibrosis.[45–47] More recently, there has been considerable interest in the use of inhaled hyperpolarized ^{3}He or ^{129}Xe to produce images of lung ventilation.[48] Currently, MRI is as limited as CT in the evaluation of tumor involvement of lymph nodes, although it is very likely that with new contrast media this difficulty may be overcome.

Recently, MRI of the breast combined with the intravenous use of Gd–DTPA has shown great promise by being more sensitive in discovering cancer in dense breasts than conventional X-ray mammography. Dramatic progress has been made since MR mammography was first described in the early 1980s, although many questions remain unanswered. The development of better and more specific contrast agents is likely to be the

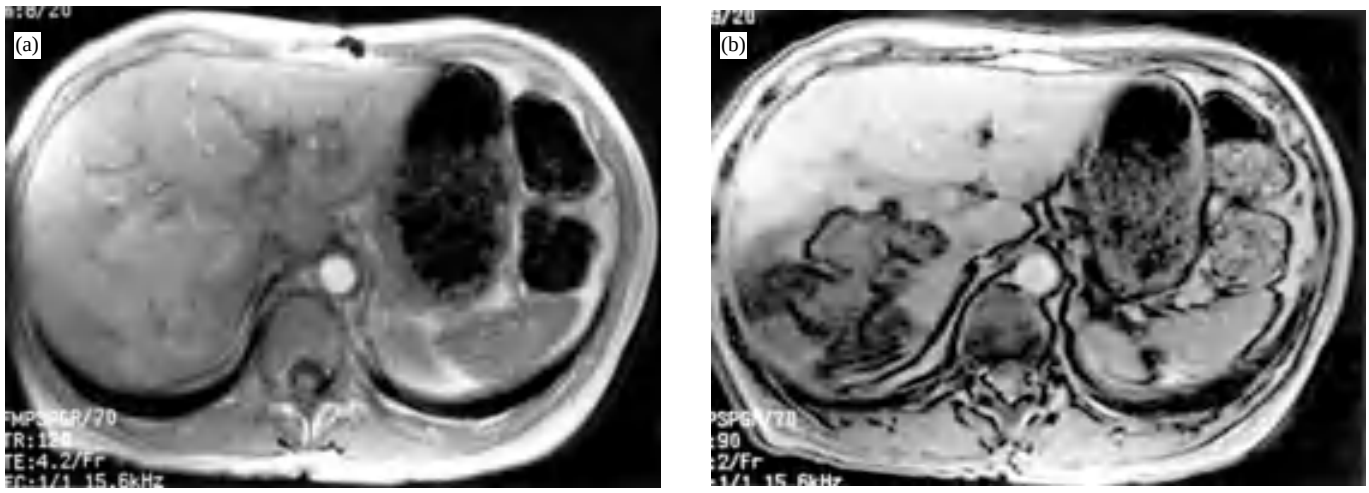

Figure 6 In phase (a) and out of phase (b) fast spoiled gradient-echo T_1-weighted axial MR image of the liver, showing a large irregular lesion in the right hepatic lobe. The lesion has markedly reduced signal intensity on the out of phase image (b), confirming the presence of fat and establishing the diagnosis of focal fatty infiltration. A prior CT image had been interpreted as suggestive of malignancy

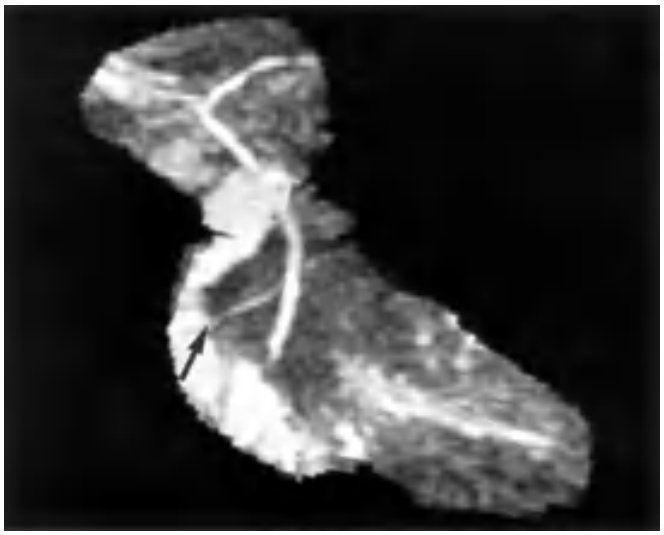

Figure 7 Single-shot fast spin-echo T_2-weighted coronal MR cholangiopancreatography in a patient with pancreas divisum. The main pancreatic duct is seen draining to the minor papilla (arrow) at a level superior to the entry of the common bile duct to the major papilla. The image was generated as a maximum-intensity projection of a slab of multiple contiguous thin coronal sections through the pancreaticobiliary tree

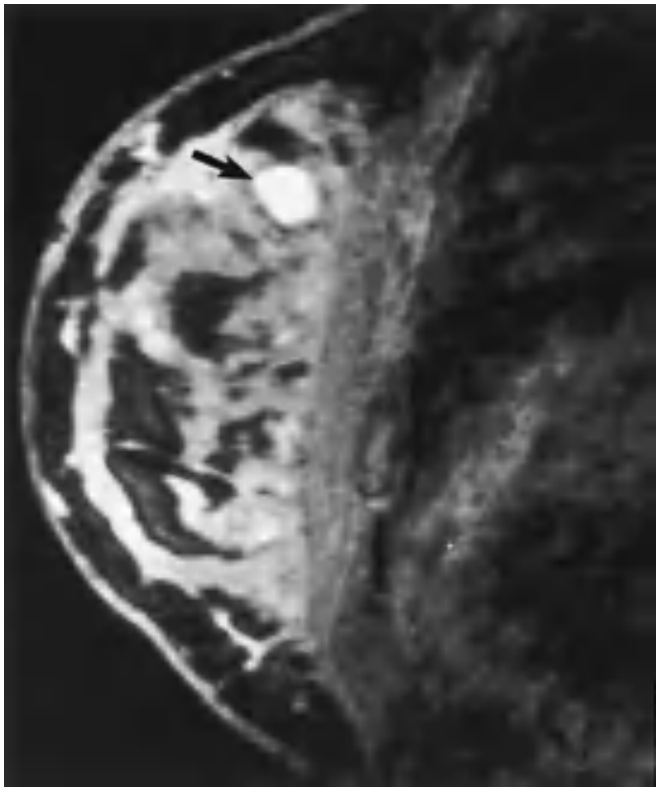

Figure 8 Gradient-echo T_1-weighted sagittal MR image of the breast after the intravenous administration of Gd-DTPA, with fat suppression. This MR mammogram shows a small enhancing carcinoma (arrow). The lesion was not detected using conventional radiographic mammography

next major advance. A practical system of MRI-guided breast biopsy is also essential, especially for those lesions that are seen only on MRI and not evident on conventional radiographic mammography or ultrasound (Figure 8). Better coils and low-cost dedicated equipment are also required.[49–52]

MRI of the fetus has been slow to develop, because of image degradation by fetal motion and the need for high spatial resolution. The recent development of ultrafast spin-echo based T_2-weighted sequences has been a major advance, and fetal imaging is emerging as one of the more exciting new clinical applications of MRI. The use of fetal MRI remains confined to those cases where antenatal ultrasound is indeterminate or inconclusive, since in most cases ultrasound is an adequate study. In difficult situations, MRI can provide significant incremental information (Figure 9) and impacts on management in a substantial proportion of patients.[53,54]

The field of MRI has also advanced with the construction and application of a multitude of surface coils, single or assembled in phased arrays, sometimes in conjunction with

Figure 9 Single-shot fast spin-echo T_2-weighted MR image of a fetus with suspected laryngeal atresia from a prior sonograph, in an oblique longitudinal plane relative to the fetus. The constellation of diaphragmatic eversion (white arrows), a large volume of fetal ascites (asterisk), marked subcutaneous edema (black arrow), and a blind-ending fluid-filled upper airway (curved white arrow) is diagnostic of laryngeal atresia. The fetus was successfully treated by in utero tracheostomy

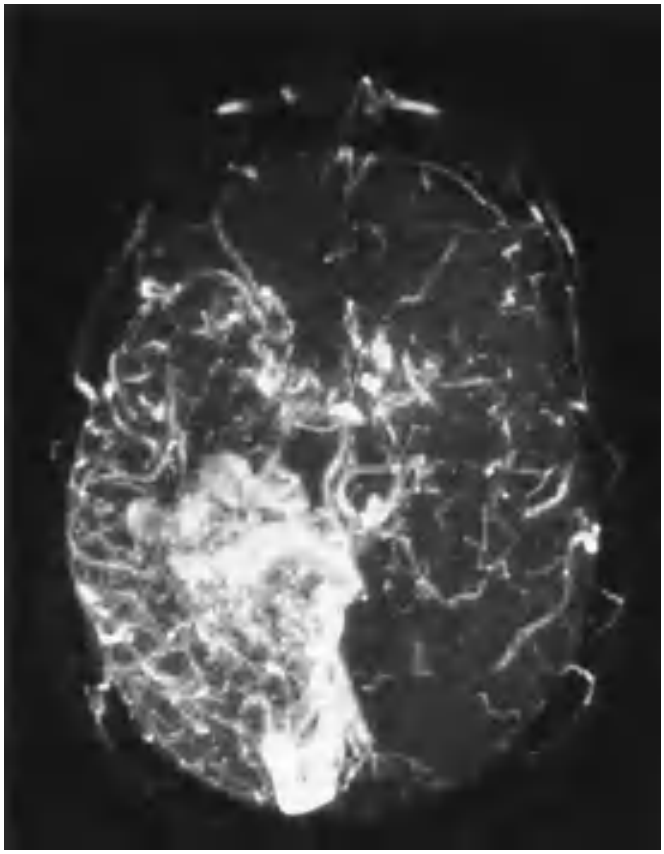

Figure 10 Gradient-echo flow-sensitive axial MR time-of-flight angiogram in a patient with a large arteriovenous malformation. The image was generated as a maximum-intensity projection of a slab of multiple contiguous thin axial sections through the circle of Willis

endoluminal coils such as with the endorectal coil used for examination of the prostate (Figure 4).[30]

MR angiography has rapidly advanced since it was first introduced in the late 1980s. Initially, MR angiography was limited by relatively long acquisition times and low spatial resolution. These problems have been largely overcome by improvements in hardware, pulse sequence design, and sequencing strategies. MR angiography is increasingly used in the evaluation of arterial and venous disease throughout the body, especially in patients who have contraindications to conventional angiography, such as renal impairment, iodinated contrast allergy, and coagulopathy. MR angiographic techniques may be based on time of flight (Figure 10), phase contrast, black blood, or contrast enhancement. Magnetization transfer can be used to suppress signal from stationary tissue approaches. Recently, first-pass gadolinium-enhanced MR angiography has received considerable attention. In the future, the emergence of blood pool contrast agents is likely to contribute further to the development of MR angiography. This technique, with its noninvasive nature and ease of performance, is already a clinical procedure in the evaluation of major vessels in the brain, neck, body, and extremities.[55–58] Imaging of the coronary arteries with a resolution equivalent to conventional angiography remains a crucial goal that has not yet been achieved. Coronary MR angiography poses unique challenges because of rapid motion and the small size of the vessels. Coronary MR angiography is the 'holy grail' of clinical MRI, but despite the technical problems is likely to become clinically available in the first decade of the 21st century. Techniques for the evaluation of the proximal segments of the major coronary arteries already exist. Clinical acceptance requires the procedure to produce diagnostic images in a cost-effective manner. Improved contrast agents may be needed.[35]

Interventional MRI units are being feverishly developed. These interventional units vary greatly in design and cost. Permanent magnets with wide separation allowing manipulation, a resistive magnet with four ports to provide good field homogeneity and allow ample access, and a unit with two separated tunnels (the separation to permit space for the surgeon to work), are all at various stages of completion. These units will significantly differ in cost. The quality of the image, the speed of acquiring the image, the size and weight of the units, and shielding requirements will all play a significant role in clinical acceptance. Interventional MRI requires MR-compatible instruments and anesthesia equipment. Better techniques for MRI tracking of guidewires and catheters are also needed. Initially, interventional MRI is likely to be most useful in the evaluation of interstitial therapies such as laser treatment, radiofrequency ablation, and cryosurgery.[59] It remains to be seen how the roles

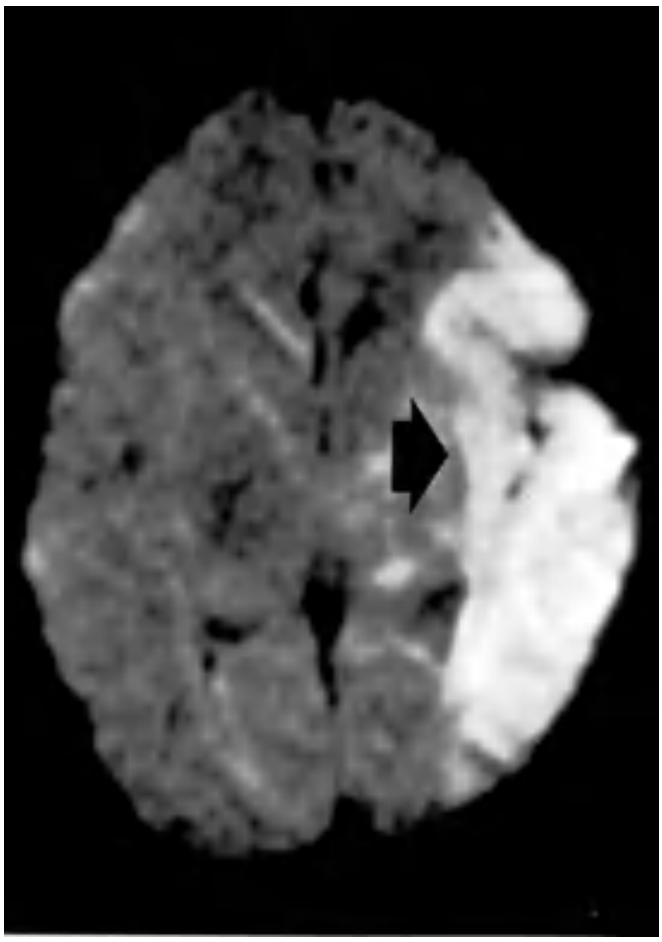

Figure 11 Diffusion-weighted axial MR image in a patient with an acute right hemiparesis. Increased signal (arrow) in the distribution of the left middle cerebral artery territory confirms the diagnosis of cerebral infarction

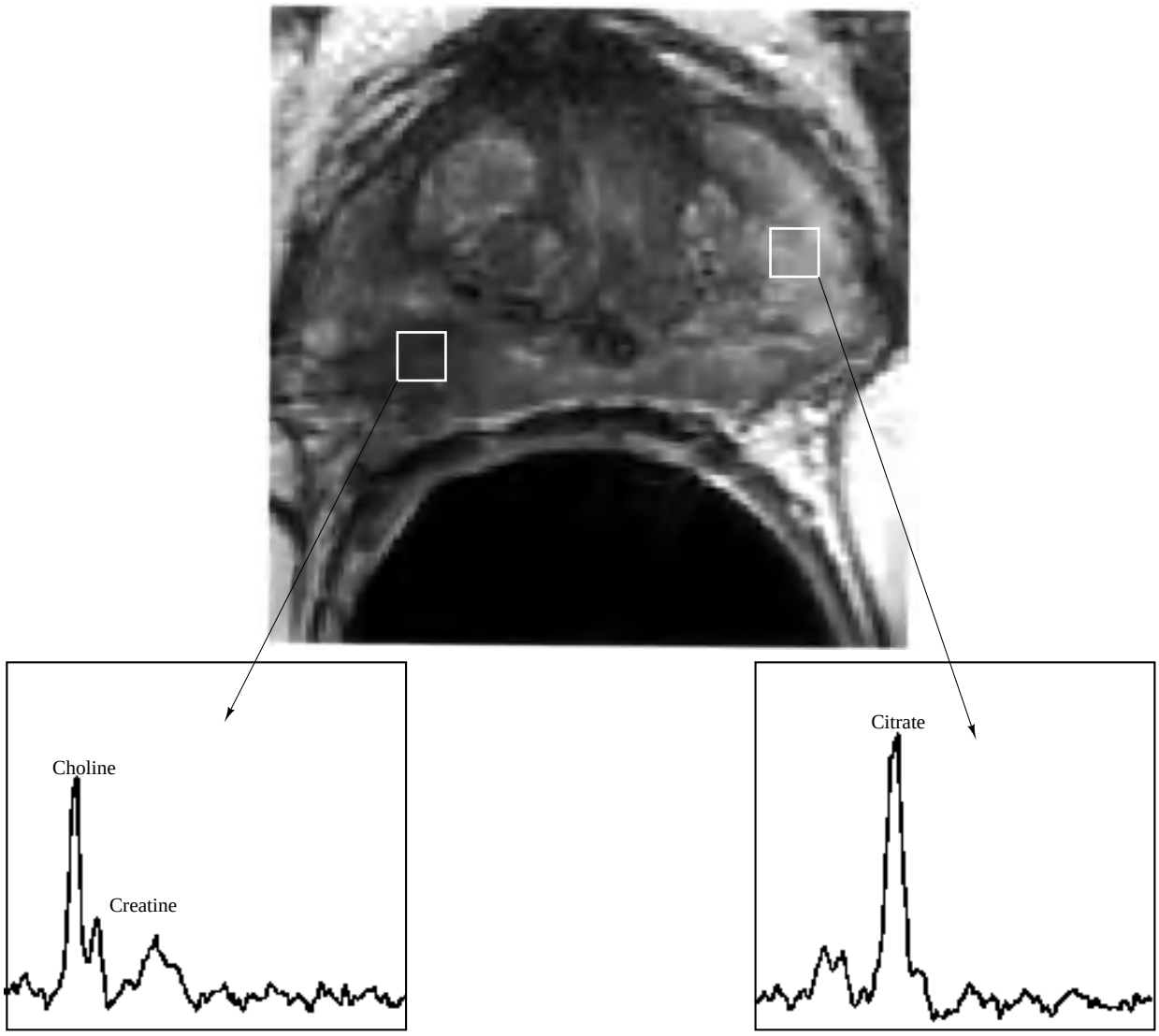

Figure 12 MR spectroscopy performed in a patient with prostate cancer. The T_2-weighted fast spin-echo axial image of the prostate shows an area of reduced signal intensity in the right peripheral zone. The corresponding MR spectra demonstrate elevation of choline and reduction of citrate in this area, confirming the presence of malignancy. Normal data, obtained from the healthy part of the gland, are shown for comparison and demonstrate a high level of citrate and no detectable choline

of radiologists, surgeons, anesthesiologists, and other health care professionals will develop in this complex field.

Advances in the basic sciences and continued improvements in hardware and software have resulted in an increasing array of MRI techniques capable of evaluating physiological rather than anatomical information. Such techniques include diffusion MRI, perfusion MRI, functional MRI, MR spectroscopy, MR thermography, and MR elastography.[11–14] Diffusion MRI has been used mainly in the assessment of brain disease, because disruption in the regular three-dimensional configuration of nerve fibers results in marked alterations in the local pattern of molecular diffusion. Diffusion MRI has become clinically useful in the diagnosis of stroke, because diffusion abnormalities can be detected in the earliest stages of a cerebral infarct (Figure 11) at a time when other imaging techniques are often nondiagnostic and when thrombolytic therapy still has the potential to improve outcome.[60] Diffusion MRI may also be helpful in locating epileptogenic foci prior to neurosurgical treatment.[61] Perfusion MRI utilizes exogenous or endogenous contrast to measure blood flow at the capillary level and in the future may have clinical applications in the brain, heart, and kidneys.[62] Functional MRI utilizes focal changes in blood volume, flow, or oxygenation to produce images that reflect local organ function. Functional MRI has been used predominantly to map the spatial and temporal distribution of neuronal activity in the brain during specific cognitive, motor, or sensory tasks.[63] MR spectroscopy utilizes the slight differences in Larmor frequency between protons in different molecules to assess the level of different proton-containing tissue metabolites. Clinical applications are emerging in tumors of the breast, prostate (Figure 12), and brain.[30,64,65]

Many of the current and future developments in MRI will be accompanied and augmented by the introduction of new MR contrast media. Such new contrast media are likely to

Figure 13 A resistive 0.5-T MR imager transported through a narrow doorway and later assembled in room, making siting much more economical

evolve along the following lines.[66–70] (a) High-molecular-weight contrast media will be useful for perfusion and blood-pool MRI techniques, since these remain in the circulation. (b) Tissue-specific contrast agents, which enhance only a single organ or tissue type, will increase the ability to detect and characterize lesions. Such contrast media are already available, for example the manganese-based contrast media that are picked up and excreted by hepatocytes and the ferumoxides that are taken up by reticuloendothelial cells. (c) Contrast media that exit the capillaries and enter the lymphatic system to be picked up by lymph nodes will increase the ability to detect and characterize lymph node abnormalities. (d) Contrast media enveloped in liposomes can be designed for uptake by different targeted organ systems, for example the bone marrow. (e) Contrast media incorporated with monoclonal antibodies may provide the ultimate 'magic bullet' for imaging of targeted abnormal cells, for example cancer cells.

Cost remains a major hurdle to the greater availability and use of clinical MRI in much of the world. As competition between companies grows and the marketplace becomes increasingly global, a vast array of scanner types is emerging. Scanner technology now includes permanent magnets, resistive magnets (Figure 13), and various types of superconductive magnet. These different machines allow considerable choice in the degree of sophistication and cost, so that small dedicated scanners are available to purchasers who do not have the resources to acquire an expensive high-field-strength multipurpose scanner. This wide choice helps make MRI more widely available. Almost all scanners have the potential to be upgraded. The size of scanners and extent of fringe fields is being reduced, making siting less expensive. As governments realize that MRI is cost effective, the clinical use of MRI will be expanded and encouraged. However, strict regulation of reimbursement for MRI studies will undoubtedly become universal.[18] Such regulations already exist in many parts of the industrialized world.

MRI offers an unparalleled choice of techniques for the imaging of normal and abnormal anatomy and pathology. Current and future developments in MR contrast media are likely to expand the clinical utility of MRI still further. The complexity of MRI and the necessity to be familiar with anatomy in all planes and all body parts makes MRI a more difficult diagnostic modality to master than any other imaging technique. As a result, for optimal MRI performance and interpretation, clinical expertise and technical proficiency are essential. The radiological community must continue to maintain a strong influence over clinical standards in MRI.

1 RELATED ARTICLES

Contrast Agents in Whole Body Magnetic Resonance: An Overview; High-Field Whole Body Systems; Low-Field Whole Body Systems; MRI at Midfield Strength; Outcome and Efficacy–Analysis of Healthcare Models.

2 REFERENCES

1. R. C. Hawkes, G. N. Holland, and W. S. Moore, *J. Comput. Assist. Tomogr.*, 1980, **4**, 429.
2. R. C. Hawkes, G. N. Holland, W. S. Moore, E. J. Roebuck, and B. S. Worthington, *J. Comput. Assist. Tomogr.*, 1981, **5**, 605.
3. R. C. Hawkes, G. N. Holland, W. S. Moore, E. J. Roebuck, and B. S. Worthington, *J. Comput. Assist. Tomogr.*, 1981, **5**, 613.
4. F. H. Doyle, J. C. Gore, J. M. Pennock, G. M. Bydder, J. S. Orr, R. E. Steiner, M. Burl, M. Clow, D. J. Goldisdale, D. R. Bailes and P. E. Walton, *Lancet*, 1981, **2**, 53.
5. G. M. Bydder, R. E. Steiner, I. R. Young, A. S. Hall, D. J. Thomas, J. Marshall, C. A. Pallis, and N. J. Legg, *Am. J. Nucl. Reson.*, 1982, **3**, 459.
6. R. J. Alfidi, J. R. Haaga, S. J. El Yousef, P. J. Bryan, B. D. Fletcher, J. P. Li Puma, S. C. Morrison, B. Kaufman, J. B. Richey, W. S. Hinshaw, D. M. Kramer, H. N. Yeung, A. M. Cohen, H. E. Butler, A. E. Ament, and J. M. Lieberman, *Radiology*, 1982, **143**, 175.
7. I. R. Young, D. R. Bailes, M. Burl, A. G. Collins, D. T. Smith, M. J. McDonnell, J. S. Orr, L. M. Banks, G. M. Bydder, R. H. Greenspan, and R. E. Steiner, *J. Comput. Assist. Tomogr.*, 1982, **6**, 1.
8. L. Crooks, M. Arakawa, J. Hoenninger, J. Watts, R. McRee, L. Kaufman, P. L. Davis, A. R. Margulis, and J. DeGroot, *Radiology*, 1982, **143**, 169.
9. T. J. Brady, M. C. Gebhardt, I. L. Pykett, F. S. Buonanno, J. H. Newhouse, C. T. Burt, R. J. Smith, H. J. Mankin, J.P, Kistler, M. R. Goldman, W. S. Hinshaw, and G. M. Pohost, *Radiology*, 1982, **144**, 549.

10. A. R. Margulis, C. B. Higgins, L. Kaufman, and L. E. Crooks, 'Clinical Magnetic Resonance Imaging', Radiology Research and Education Foundation, San Francisco, CA, 1983.
11. R. R. Edelman and J. R. Hesselink, 'Clinical Magnetic Resonance Imaging', Saunders, Philadelphia, PA, 1990.
12. V. M. Runge, 'Clinical Magnetic Resonance Imaging', Lippincott, Philadelphia, PA, 1990.
13. C. B. Higgins, H. Hricak, and C. A. Helms, 'Magnetic Resonance Imaging of the Body', 3rd edn., Raven Press, New York, 1997.
14. D. Stark and W. G. Bradley, Jr., 'Magnetic Resonance Imaging', 3rd edn., Mosby Year Book, St Louis, MO, 1998.
15. G. J. Schieber, J. P. Poullier, and L. M. Greenwald, *Health Care Financ. Rev.*, 1992, **1**, 87.
16. G. E. Medical Systems data, 1999.
17. American College of Radiology data, 1999.
18. R. L. Arenson, C. A. Gooding, and A. R. Margulis, *Invest. Radiol.*, 1993, **28**, Suppl. 3.
19. J. A. Barkovich, 'Pediatric Neuroimaging', 2nd edn., Raven Press, New York, 1995.
20. J. Kucharczyk, M. Moseley, and J. A. Barkovich, 'Magnetic Resonance Neuroimaging', CRC Press, Boca Raton, FL, 1994.
21. S. W. Atlas, 'Magnetic Resonance Imaging of the Brain and Spine', 2nd edn, Lippincott-Raven Press, New York, 1996.
22. R. B. Lufkin and W. N. Hanafee, 'Pocket Atlas of Head and Neck MRI Anatomy', Raven Press, New York, 1989.
23. R. Kricun and M. E. Kricun, 'MRI and CT of the Spine', Raven Press, New York, 1994.
24. M. T. Modic, T. J. Masaryk, and J. S. Ross, 'Magnetic Resonance Imaging of the Spine', Mosby Year Book, St Louis, MO, 1993.
25. D. Resnick, 'Bone and Joint Imaging', Saunders, Philadelphia, PA, 1989.
26. W. P. Chan, P. Lang, and H. K. Genant, 'MRI of the Musculoskeletal System', Saunders, Philadelphia, PA, 1994.
27. D. W. Stoller, 'Magnetic Resonance Imaging in Orthopaedics and Sports Medicine', Lippincott, Philadelphia, PA, 1993.
28. C. Langlotz, M. Schnall, and H. Pollack, *Radiology*, 1995, **194**, 645.
29. E. K. Outwater, R. O. Petersen, E. S. Siegelman, L. G. Gomella, C. E. Chernesky, and D. G. Mitchell, *Radiology*, 1994, **193**, 333.
30. J. Kurhanewicz, D. B. Vigneron, H. Hricak, P. Naraan, P. R. Carroll, and S. J. Nelson, *Radiology*, 1996, **198**, 795.
31. H. Hricak and B. M. Carrington, 'MRI of the Pelvis: A Text Atlas', Martin Dunitz, London, 1991.
32. A. M. Hubbard, K. E. Fellows, P. M. Weinberg, and M. A. Fogel, *Semin. Roent.*, 1998, **23**, 218.
33. J. L. Boxerman, T. J. Mosher, E. R. McVeigh, E. Atalar, J. A. C. Limar, and D. A. Bluemke, *RadioGraphics*, 1998, **18**, 543.
34. C. B. Higgins, 'Essentials of Cardiac Radiology and Imaging', Lippincott, Philadelphia, PA, 1992.
35. T. F. Budinger, A. Berson, E. R. McVeigh, R. J. Pettigrew, G. M. Pohost, J. T. Watson, and S. A. Wickline, *Radiology*, 1998, **208**, 573
36. R. A. Huch Boni, J. F. Debatin, and G. P. Prestin, *MRI Clinics North Am.*, 1996, **4**, 101.
37. P. Soyer, S. C. deGivry, C. Gueye, S. Lenormand, E. Somveille, and A. Scherrer, *Am. J. Roentgenol.*, 1996, **166**, 1115.
38. A. D. P. Lang, and R. N. Gibson, *JMRI*, 1998, **8**, 337.
39. J. P. Heiken, P. J. Weyman, J. K. T. Lee, et al., *Radiology*, 1989, **171**, 47.
40. P. Soyer, M. Levesque, C. Caudron, D. Elias, G. Zeitoun, and A. Roche, *J. Comput. Assist. Tomogr.*, 1993, **17**, 67.
41. R. C. Semelka, R. F. Schlund, P. L. Molina, et al., *JMRI*, 1996, **1**, 39.
42. R. M. Gore, I. Laufer, and M. Levine, 'Gastrointestinal Radiology', Saunders, Philadelphia, PA, 1994.
43. P. C. Freeny and G. W. Stevenson, 'Alimentary Tract Radiology', Mosby Year Book, St Louis, MO, 1994.
44. J. K. T. Lee, H. B. Marcos, and R. C. Semelco, *Am. J. Roentgenol.*, 1998, **170**, 1457.
45. E. A. Zerhouni, 'CT and MRI of the Thorax', Churchill Livingstone, New York, 1990
46. D. P. Naidich, E. A. Zerhouni, S. S. Siegelman, and J. P. Kuhn, 'Computed Tomography and Magnetic Resonance of the Thorax', Raven Press, New York, 1991.
47. J. F. Meaney, J. G. Wegg, T. L. Chenevert, D. Stafford-Johnson, B. H. Hamilton, and M. R. Prince, *N. Engl. J. Med.*, 1997, **336**, 1422.
48. J. P. Mugler III, B. Driehuys, J. R. Brookeman, et al., *Magn. Reson. Med.*, 1997, **37**, 809.
49. M. B. Williams, E. D. Pisano, M. D. Schnall, and L. L. Fajardo, *Radiology*, 1998, **206**, 297.
50. W. A. Kaiser, 'MR Mammography (MRM)', Springer-Verlag, Berlin, 1993.
51. S. G. Orel, M. D. Schnall, R. N. Newman, C. M. Powell, M. H. Torosian, and E. F. Rosato, *Radiology*, 1994, **193**, 97.
52. C. K. Kuhl, A. Elevett, C. C. Leutner, J. Gieseke, E. Pakos, and H. H. Schild, *Radiology*, 1997, **204**, 667.
53. D. Levine, P. D. Barnes, S. Sher, R. C. Semelka, W. Li, C. R. McCardle, S. Worawattanakul, and R. R. Edelman, *Radiology*, 1998, **206**, 549.
54. F. V. Coakley, H. Hricak, R. A. Filly, A. J. Barkovich, and M. R. Harrison, *Radiology*, 1998, **209**(P), 189.
55. D. B. Stafford-Johnson, M. R. Prince, and T. L. Chenevert, *Acad. Radiol.*, 1998, **5**, 289.
56. M. R. Prince, *MRI Clin. North Am.*, 1998, **6**, 257.
57. E. A. Knopp, *Neuroimag. Clin. North Am.*, 1996, **6**, 769.
58. Y. Anzai, M. R. Prince, T. L. Chenevert, J. H. Maki, F. Londy, M. London, and S. J. McLachlan, *JMRI*, 1997, **7**, 209.
59. K. D. Hagspiel, K. Kandarpa, and F. A. Jolesz, *JVIR*, 1997, **8**, 745.
60. N. J. Beauchamp Jr, A. M. Ulug, T. J. Passe, and P. C. M. van Zijl, *RadioGraphics*, 1998, **18**, 1269.
61. K. L. Weiss, R. E. Figueroa, and J. Allison, *MRI Clin. North Am.*, 1998, **6**, 95.
62. P. Jezzard, *Radiology*, 1998, **208**, 296.
63. B. R. Buchbinder and G. R. Cosgrove, *MRI Clin. North Am.*, 1998, **6**, 67.
64. J. R. Roebuck, K. M. Cecil, M. D. Schnall, and R. E. Lenkinski, *Radiology*, 1998, **209**, 269.
65. M. Castillo, L. Kwock, and S. K. Mukherji, *Am. J. Neuroradiol*, 1996, **17**, 1.
66. W. Schima, A. Mukerjee, and S. Saini, *Clin. Radiol.*, 1996, **51**, 235.
67. H. Niendorf, J. Dinger, J. Haustein, I. Cornelius, A. Alhassan, and W. Clauss, *Eur. J. Radiol.*, 1991, **13**, 15.
68. R. C. Brasch, *Radiology*, 1992, **183**, 1.
69. V. Runge, 'Contrast Media in Magnetic Resonance Imaging: A Clinical Approach', Lippincott, New York, 1992.
70. R. Brasch, 'MRI Contrast Enhancement in the Central Nervous System: A Case Study Approach', Raven Press, New York, 1993.

Biographical Sketches

Fergus V. Coakley. *b* 1964. M.B. B.Ch., University College, Cork, Ireland, 1988. Intern, Mercy Hospital, Cork, 1988–89. Resident, Medicine, Mater and St Vincent's Hospitals, Dublin, 1989–91. M.R.C.P.Irel., 1990. Resident, Radiology, Leicester Royal Infirmary, Leicester, 1991–96. F.R.C.R., 1994. Fellow, Body Imaging, Memorial Sloan-Kettering Cancer Center, New York, 1996–97. Visiting Assistant Professor, University of California, San Francisco, 1997–98. Visiting Associate Professor, 1998–present. Over 50 publications. Research specialties: abdominopelvic MRI, including MR cholangiopancreatography, prostate MRI, and fetal MRI.

Alexander R. Margulis. *b* 1921. M.D., Harvard Medical School, 1951, residency in radiology, University of Michigan, Ann Arbor, American Board of Radiology, 1951–54. Assistant Professor, University of Minnesota, Minneapolis, 1959–1963; Assistant, Associate, and Full Professor, Washington University, St. Louis, MO, 1963; Professor & Chairman, Department of Radiology, University of California, San Francisco, 1963–89; Professor of Radiology, Associate Chancellor of Special Projects & Director, Magnetic Resonance Center, 1989–93; Special Consultant to Vice Chancellor & Professor of Radiology, 1993–present. Over 250 publications. Research specialties: gastrointestinal radiology, magnetic resonance imaging in magnetic resonance spectroscopy, and radiologic and health policy issues.

Sensitivity of Whole Body MRI Experiments

David I. Hoult

Institute for Biodiagnostics, National Research Council Canada, Winnipeg, MB, Canada

1 INTRODUCTION

Surprisingly, the signal-to-noise ratio of a routine, clinical proton NMR image is governed by parameters that are somewhat subjective, and therefore difficult to assess. Concomitantly, optimizing the amount of diagnostic information that can be extracted by NMR imaging in a given time is fraught with difficulty and uncertainty. The subjectivity arises from the juggling of a number of often ill-defined variables, and from the fact that the end product of the experiment is not a spectrum, as in conventional NMR spectroscopy, but a picture. Both the variables and the picture are manipulated and interpreted in the light of substantial experience and with all the extra information that such experience brings to bear. Thus, for example, imaging parameters that produce 'perfectly acceptable' images from one patient may produce 'images with artifacts' from other, and the removal of these artifacts, at the whim (in the eyes of an untutored observer) of the viewer, may entail a reduction of image signal-to-noise ratio, but an increase of information. In the light of difficulties such as these, and the huge impact that magnetic resonance has had upon the discipline of radiology, the subject of imaging sensitivity is here treated separately from the more general topic of ***Sensitivity of the NMR Experiment***. However, the present discussion builds upon the foundations laid in that article, with its relatively 'firm' conclusions, which the reader is therefore encouraged to read before becoming immersed in the complexities of the present analysis—notwithstanding its being only a brief overview aimed at routine imaging with 90° and 180° pulses at field strengths of 1.5 T or less.

To summarize the conclusions of ***Sensitivity of the NMR Experiment***, it was shown that, following a 90° rf pulse, the voltage induced in a receiving coil by a small volume's precessing nuclear magnetic moment could easily be calculated, provided the magnetic field that would be created at that volume by unit receiving coil current was known. Thus the signal (the free induction decay or FID) from a volume element (a 'voxel') in an imaging experiment can usually be found without difficulty. However, it was also shown that the random voltages ('noise') present in the receiving coil were somewhat more difficult to calculate, being associated with the resistance of the coil conductor and the electrical conductivity of the sample. As human tissues exhibit a range of conductivities, we shall be particularly interested in the latter type of noise, for the Brownian motion of electrolytes in the body induces random voltages in the receiving coil that usually predominate over the voltages associated with Brownian motion of the coil's electrons. Finally, it was also shown that once an NMR protocol was run repeatedly, the accumulated signal became a function of the longitudinal relaxation time T_1 of the sample. Thus, our aim in the present article is to extend these results to estimate the sensitivity of the whole body imaging experiment, particularly as a function of magnetic field strength, while introducing those additional factors, such as spatial resolution and power deposition, that are unique to the imaging experiment.

Underlying all the arguments to be presented is an analytical technique based upon the principle of superposition. The end result of most imaging experiments is the production of one or more large matrices of data (typically 256 × 256), where the row and column positions correspond to grid coordinates (u,v) within the sample plane or 'slice'. Now such a matrix is most fruitfully examined (at least, by a human) not by scrutiny of its individual numbers (which are functions of amount of hydrogen, relaxation times, etc. at the corresponding spatial position), but rather by causing the numbers to modulate, according to a given law, the brightness of a video display. Once again, the matrix row and column positions correspond to grid coordinates—in this instance on the video screen. Thus, via the intermediary of the data matrix, there is a direct correspondence between position on the screen and position in the sample—there is an image, which is much easier to appreciate than a large matrix. Now the content of each matrix element is a measure of the signal emanating from the corresponding spatial position, and, ideally, each signal would come just from a cuboidal volume, the voxel, associated with that position. (In practice, the voxel is not so well defined—it is fuzzy round the edges, and overlaps its neighbors a little.) The process of spatial selectivity that allows the multitude of signals from different parts of a person to be sorted into their volumes of origin, is, of course, the essence of the imaging experiment (see ***Image Formation Methods***). However, because the latter is a linear process, we may take the stunning liberty, right from the beginning of our analysis, of ignoring the vast majority of the signals and concentrating our attention upon the signal from a particular voxel of interest! We may then follow that signal, through all the indignities to which the imaging experiment subjects it, to find the final matrix element associated with the voxel. We may also find how the indignities affect the noise, and thus arrive for our voxel at a measure of its signal-to-noise ratio in the image. This then will be our course, with various digressions and comments as necessary.

2 FREE INDUCTION DECAY SIGNAL AND NOISE

With the above philosophy in mind, consider first a free induction decay signal (maybe in the form of an echo) received by a coil wrapped around a portion of the human body, for example, the head.[1,2] The signal is from a voxel of volume $\mathrm{d}V$ subject to a 90° pulse, at a spatial position defined by Cartesian coordinates (u,v,w). Let the proton magnetic moment in the voxel be initially $\mathrm{d}\boldsymbol{m} = M_0\,\mathrm{d}V\boldsymbol{z}$ where $\boldsymbol{z}$ is the unit vector in the z direction, and M_0 is the spatially averaged equilibrium magnetization $\langle M_0(u,v,w)\rangle$ of the voxel. Using the principle of reciprocity, it may be shown [see equation (5) of ***Sensitivity of the NMR Experiment***] that, following the pulse, the precessing magnetic moment $\mathrm{d}\boldsymbol{m}$ induces in the receiving coil a voltage $\mathrm{d}\xi$ given by

$$\mathrm{d}\xi = 2\pi\nu_0(\tilde{B}_{1xy}M_0\,\mathrm{d}V)\exp(-t/T_2)\cos(2\pi\nu_0 t+\phi) \qquad (1)$$

where ν_0 is the Larmor frequency, $_{1xy}$ is the field at the voxel, parallel to the (x,y) plane, that *would* be produced *if* a current of 1 A at the Larmor frequency were passed through the receiving coil, T_2 is the transverse relaxation time of the elementary volume, and ϕ is a phase determined by the imaging protocol. As M_0 is proportional to the main field strength B_0 [see equation (1) of ***Sensitivity of the NMR Experiment***], the amplitude of the FID is proportional to the square of B_0, via the Larmor relationship $2\pi\nu_0 = \gamma B_0$. At the risk of stating the obvious, we emphasize that the signal from a voxel is directly proportional to the volume of the voxel, and therefore proportional to the cube of voxel side, or spatial resolution. This strong dependence is easily forgotten when one is deep in the intricacies of imaging, but can return to haunt one. That little factor-of-2 improvement in spatial resolution can lead to an order-of-magnitude loss of sensitivity!

As was shown in ***Sensitivity of the NMR Experiment***, the noise induced in the receiving coil by a conducting sample may also be estimated with the aid of the principle of reciprocity.[1,3] Experience shows that with a well-designed head coil, this noise dominates the noise associated with the coil's resistance at frequencies above about 8 MHz, while with a good body coil, the same is true above approximately 4 MHz.[4] (Hence, there is little point at the frequencies usually used in imaging, 20–70 MHz, to attempt to cool head or body coils, for the improvement in performance will be negligible.) Some idea of the magnitude of the induced noise may be obtained by finding the power that would be deposited in a sphere of the tissue under consideration, by a homogeneous, on-resonance, radiofrequency transmitting field parallel to the (x,y) plane. Assuming this $\boldsymbol{B}_1$ field is produced by an RMS current I in the receiving coil, the power deposited when the wavelength within the sphere is considerably greater than the latter's radius is[1,3]

$$W = I^2R_\mathrm{m} = \tfrac{8}{15}\pi^3\nu_0^2I^2\tilde{B}_{1xy}^2b^5\sigma(\nu_0) \equiv \frac{64\pi^5\nu_0^2\nu_1^2b^5\sigma(\nu_0)}{15\gamma^2} \qquad (2)$$

where R_m is the equivalent resistance in series with the receiving coil, b is the sphere's radius, γ is the gyromagnetic ratio, ν_1 is the nutational frequency of the rf field, and $\sigma(\nu_0)$ is the tissue conductivity. (Note the explicit inclusion of the conductivity's frequency dependence; σ is usually of the order of $0.4\,\mathrm{S\,m^{-1}}$ in the NMR frequency range, but can vary considerably.[5]) The noise in bandwidth $\Delta\nu$ is now easily found [see equation (9) of ***Sensitivity of the NMR Experiment***] from the effective resistance R_m, and when we use it to find the signal-to-noise ratio (S/N) of the FID, we obtain from equations (1) and (2)

$$\mathrm{d}\Psi_\mathrm{FID} = \left\{M_0(\nu_0)\,\mathrm{d}V\left[\frac{15}{8\pi b^5\sigma(\nu_0)k_\mathrm{B}T\Delta\nu}\right]^{1/2}\right\} \times \exp\left(-\frac{t}{T_2}\right)\cos(2\pi\nu_0 t+\phi) \qquad (3)$$

where k_B is Boltzmann's constant and T is the sample temperature (310 K). This is a remarkable equation in that all dependence upon the field $\tilde{\boldsymbol{B}}_{1xy}$ has vanished. The sample determines its own 'intrinsic' signal-to-noise ratio by its effective size (radius b) and composition [$\sigma(\nu_0)$ and $M_0(\nu_0)$]. Thus, while in no way can a sphere of tissue be considered a good approximation to the human head or torso, we would expect the S/N associated with a voxel in the head to be considerably better than that for a voxel in the torso (say, by a factor of approximately $1.5^{\frac{5}{2}} = 2.75$), while a body scan of a pregnant patient would have relatively poor sensitivity. We might also expect the direction of the $\tilde{\boldsymbol{B}}_1$ field to influence the S/N when the sample is asymmetric, for the effective value of b then depends on orientation. Further, the advantages and limitations of using a surface coil, with its very small effective value of b, have been discussed in ***Sensitivity of the NMR Experiment***. Thus, in a set of experiments aimed at determining the validity of equation (3) and the magnitude of the term in braces,[4] it has been shown that for water in a human head, with a typical receiving coil and a 90° pulse, over the range 5–80 MHz, the intrinsic S/N ratio is

$$\mathrm{d}\Psi_\mathrm{FIDhead} \approx \left[440\frac{\nu_0\,\mathrm{d}V}{(\Delta\nu)^{1/2}} \pm 10\%\right] \times \exp\left(-\frac{t}{T_2}\right)\cos(2\pi\nu_0 t+\phi) \qquad (4)$$

while for the torso, with the $\boldsymbol{B}_1$ field from a typical coil running laterally,

$$\mathrm{d}\Psi_\mathrm{FIDtorso} \approx \left[2100\frac{\nu_0^{0.8}\,\mathrm{d}V}{(\Delta\nu)^{1/2}} \pm 60\%\right] \times \exp\left(-\frac{t}{T_2}\right)\cos(2\pi\nu_0 t+\phi) \qquad (5)$$

Note that ν_0 is in hertz and $\mathrm{d}V$ in cubic meters. On the other hand, with an anterior–posterior $\boldsymbol{B}_1$ field, it was found that the amplitude of equation (5) was roughly halved, bearing out the assertions concerning the shape of the sample. At first sight, it might appear odd that the coefficient in equation (4) is less than that in equation (5)—until it is remembered that the equations are only valid in the range 5–80 MHz. However, the interesting facet of equations (4) and (5) is their differing frequency dependences, attributable directly to the conductivity frequency dependences of the various tissues subject to the probe $\tilde{\boldsymbol{B}}_1$ field. Note too the large percentage range allowed in the values: not error in the measurements, but rather the range of values likely to be encountered, given the great variety of the human form.

An offshoot of these measurements was an estimate of the power W [equation (2)] needed to produce a given transmitting $\boldsymbol{B}_1$ field for the pulses. The power is deposited overwhelmingly in the patient in the form of heat from rf eddy currents, and general agreement with equation (2) was found. Thus, for the head,

$$W \approx 4.8\times10^{-20}\nu_0^2\nu_1^2 \qquad (6)$$

while for the torso with an anterior–posterior field,

$$W \approx 3\times10^{-21}\nu_0^{2.4}\nu_1^2 \qquad (7)$$

We shall encounter the rf power deposited again later in the article, but the reader is correct in assuming that this power is potentially dangerous. It is the only known hazard associated

with routine imaging. (See ***Health and Safety Aspects of Human MR Studies***).

3 THE FOURIER TRANSFORM

The expectation aroused by the confirmation of theory contained in equations (4) and (5) is that the S/N of a brain image should improve linearly with field strength. Concomitantly,[3] we expect the power absorbed in the head of a patient to increase as the square of the field strength for a given nutational frequency (i.e., pulse width and strength). For the torso, we might expect the sensitivity to increase somewhat more modestly, and the power deposited to increase more dramatically. An image's information content, however, is dependent not just upon intrinsic S/N, but on other factors too—primarily the resolution, the chemical shift range δ_H, and the relaxation times T_1 and T_2, which are functions of frequency. We must therefore consider how FIDs [and, in particular, the FID from our chosen voxel at position (u, v, w)] are utilized in an imaging experiment involving these factors, and it is at this juncture that uncertainty clouds the analysis.

With most imaging techniques, each FID or echo in an imaging protocol suffers Fourier transformation as described in ***Sensitivity of the NMR Experiment***, as the first stage in image formation. Now the essence of any imaging experiment (see ***Image Formation Methods***) is a linear correspondence between Larmor frequency ν_0 and spatial position u during data acquisition:

$$2\pi\nu_0 = \gamma(B_0 + G_u u) \tag{8}$$

This correspondence is imposed by the user by impressing a known field gradient G_u (the 'read gradient') on the main (homogeneous) field B_0. From the value of ν_0, as determined from the 'spectrum' (the Fourier transform of the FID), the position u of our voxel is easily determined. However, suppose there is a small, additional field dB present, caused, for example, by nuclear shielding (a 'chemical shift'). From equation (8) we then have

$$u = \frac{2\pi\nu_0/\gamma - B_0 - dB}{G_u} \tag{9}$$

and there is a positional error of $du = -dB/G_u$ in the determined value of u and hence in the position of our signal in the final matrix of data, the image. If that error is more than a fraction of the image's 'spatial resolution' in u (i.e., the distance Δu equivalent to a shift of one picture element, a voxel side, or a jump of one matrix column—they are all approximately equivalent), it is potentially serious, for it represents a visible and possibly misleading misregistration of a portion of the image. However, to assess the potential for damage, we need to know both the range of any chemical shifts in the portion of the human body being imaged, and also the desired spatial resolution.

Now the hydrogen NMR spectrum of a region within a human, though complicated, is sometimes utterly dominated by only a single line—that of water, an ideal situation. Sometimes, however, it is dominated by a spectral structure, associated with both fat and water, covering a chemical shift range of roughly $\delta_H = 3.5$ ppm. (Thus, $dB = \delta_H B_0 \approx 3.5 \times 10^{-6} B_0$.) It follows that, since we require the error $du << \Delta u$, the gradient must obey the inequality

$$\Delta u G_u \gg \delta_H B_0 = 3.5 \times 10^{-6} B_0 \tag{10}$$

In other words, if both water and fat are present in the portion of the body being imaged, the stronger the static field B_0, the greater the read gradient G_u must be if we wish to render 'chemical shift artifacts' negligible. If this condition is disobeyed, water and fat signals *from the same spatial location* will appear at different locations in the image, while water and fat from *different* spatial locations may appear in the same image location. Thus, voids and overlaps are seen, with the potential for confusion and misdiagnosis, particularly if the viewer is inexperienced. If the only consequence of obeying equation (10) were an increase in engineering difficulty, it would be worthy of only passing consideration: we should note that extra expense was incurred, while a cynic might suppose that a salesman would therefore make sure his sale pitch would show only images that resulted from water alone. However, the employed gradient strength bears a direct relation to the 'acquisition window' (the time for which the FID is collected), to the resolution, and to the available S/N. To understand this statement, recall that in Section 4 of ***Sensitivity of the NMR Experiment***, the S/N following Fourier transformation was optimized by collecting the FID for an optimum time $1.26T_2$, or, even better, by imposition of an exponential filter of time constant T_2 prior to transformation. Other filters, beyond the scope of this article, may also be advantageously imposed in imaging experiments, but no matter what method is employed to shape and define the data collection period, there is an 'uncertainty relation' linking the characteristic duration Δt of the time-domain data with the width $\Delta\nu$ of the ensuing spectral 'line'. ('Protuberance' might be a better appellation than 'line', since the latter implies smoothness and symmetry.) This relation is of the form

$$\Delta\nu\Delta t \sim 1 \tag{11}$$

(A well-known example, wherein the duration Δt is naturally limited, is $\Delta\nu = 1/\pi T_2$ for a Lorentzian line.) Now the frequency width of the spectral 'line' that results from transformation of the FID of our voxel of interest determines the *spectral* resolution—how close in frequency two 'lines' can be while still being distinguishable. (This is the Rayleigh criterion from the theory of optics.) However, because of the synonymy of frequency and distance, courtesy of the imposed gradient G_u, spectral resolution is directly linked to spatial resolution. Thus,

$$2\pi\Delta\nu = \gamma\Delta u G_u \tag{12}$$

and

$$\Delta t \sim \frac{1}{\Delta\nu} = \frac{2\pi}{\gamma\Delta u G_u} \tag{13}$$

Hence, from equation (10),

$$\Delta t \ll \frac{2\pi}{\gamma\delta_H B_0} = \frac{1}{\delta_H \nu_0} = \frac{2.86 \times 10^5}{\nu_0} \tag{14}$$

In other words, if chemical shift artifacts are to be avoided, not only must the read gradient increase with field strength, but the effective data acquisition window Δt must also become shorter and shorter. Once Δt becomes much less than T_2, the S/N of the Fourier transform data begins to diminish rapidly—we are throwing away most of the FID signal and just using its beginning. With a typical value of T_2 for water in tissue of 50 ms, this transition occurs above approximately 6 MHz. Thus, for example, when imaging with a 1.5 T machine (ν_0 = 64 MHz), equation (14) states that the data acquisition window Δt should be much less than 4.5 ms. Not surprisingly, the interpretation of 'much less than' can range from the pedantic to the flagrantly false, depending on the importance—commercial, diagnostic or scientific—placed upon the image sensitivity and chemical shift artifacts. Concomitantly, Δt is a variable of some importance that is frequently overlooked. However, once $\Delta t << T_2$, from equation (3) and (14), and from equation (15) and (16) of ***Sensitivity of the NMR Experiment***, the S/N of the frequency-domain signal becomes

$$\begin{aligned} \mathrm{d}\Psi_{\mathrm{SP}} &= M_0(\nu_0)\,\mathrm{d}V\left[\frac{15\Delta t}{8\pi b^5\sigma(\nu_0)k_{\mathrm{B}}T}\right]^{1/2} \\ &<< M_0(\nu_0)\,\mathrm{d}V\left[\frac{15}{8\pi\delta_{\mathrm{H}}\nu_0 b^5\sigma(\nu_0)k_{\mathrm{B}}T}\right]^{1/2} \end{aligned} \tag{15}$$

while the resolution in the image becomes independent of variations in T_2: a redeeming feature of the condition.

To summarize, we may conclude that for a head experiment, following a single 90° pulse, if chemical shift artifacts are to be avoided, the S/N ratio following Fourier transformation is

$$\begin{aligned} \mathrm{d}\Psi_{\mathrm{SPhead}} &= 440\nu_0\,\mathrm{d}V(\Delta t)^{1/2} \pm 10\% \\ &<< 440\,\mathrm{d}V\left(\frac{\nu_0}{\delta_{\mathrm{H}}}\right)^{1/2} \pm 10\% \\ &= 2.4\times 10^5\,\mathrm{d}V\,\nu_0^{1/2} \pm 10\% \end{aligned} \tag{16}$$

Thus, the price paid for restricting the acquisition window to render negligible the chemical shift artifact, is that the sensitivity increases only as the square root of field strength. For the torso, the rate of increase is even less, being approximately as $\nu_0^{0.4}$.

To recoup this loss and fulfil our initial expectations, Hahn echo formation, using a number of 180° pulses, is needed. Images formed from each echo of a Carr–Purcell sequence may then be coadded [with weighting as $\exp(-t/T_2)$] to recover the lost sensitivity, and, as an added bonus, T_2 information may also be obtained. However, as we shall see, the power deposition in the patient is then substantially increased, and, further, the use of the sequence in a multislice experiment is not trivial. Other possible strategies include the use of chemical shift imaging techniques to give separate fat and water images (see ***Chemical Shift Imaging***), or presaturation of either water or fat magnetization to remove its influence. However, chemical shift methods at least double the time taken to get an image, while presaturation demands excellent $\boldsymbol{B}_0$ field homogeneity.

4 FROM TRANSFORM TO IMAGE

4.1 Signal-to-Noise Ratio

One FID does not an image make, and, with the exception of certain fast imaging methods (see ***Echo-Planar Imaging***), data must usually be garnered from a prescribed number of FID's or echoes. Typically, that number is related to one of the dimensions of the image matrix (e.g., 256), but we need not inquire too closely into the details—the important point for our analysis is that a minimum number of repetitions is required. (The protocol may then be repeated, and images effectively coadded if better S/N is wanted.) This subject had been examined in some detail in ***Sensitivity of the NMR Experiment***, and Figure 5 of that article shows a contour plot of relative sensitivity versus flip angle and repetition rate. (For convenience, the plot is included in Figure 1 of the present article.) However, 90° pulses are mostly used in imaging protocols, and it may be seen that with a repetition period of $1.26T_1$, only about a 10% loss in sensitivity is suffered thereby. However, if T_1 changes, the length of time taken to collect the 256 FIDs must also change if we wish to maintain sensitivity. In short, the T_1 of the region of interest in the patient is the gold standard by which the repetition period *TR* must be judged. It follows that if we are to further our examination of signal-to-noise ratio, we must know how T_1 varies with tissue type and frequency. There are two reviews of the pertinent literature,[6,7] and each shows that in the frequency range 1–100 MHz, T_1 for most tissues can be modeled in the form

$$T_1 \approx \zeta\nu_0^{\eta} \tag{17}$$

where the constants ζ and η are contained in brief summary in Table 1. An inescapable conclusion, then, is that as we increase the field strength, the minimum time taken to build an image increases as per equation (17) unless the imaging protocol is changed for some reason. The gains reaped as this increase in imaging time is suffered are that (i) the expected increase in S/N as $\nu_0^{1/2}$ (or as ν_0 if chemical shift artifacts are ignored or multiple echoes are used) is realized, and (ii) as the ratio $T_1/\Delta t$ increases with increasing field, so multiple slice methods gain in their ability to produce more cuts. (This improved ability is usually only of consequence at the lowest fields, and we do not consider it further.) However, in all fairness, we must ask how much the S/N of a low-field image could be improved if we were to allow for its acquisition the same time taken, perforce, at high fields. For example, if the minimum time $T_{\min}$ we are forced to take to acquire a scan at

Table 1 Tissue Longitudinal Relaxation Times T_1 ($\approx \zeta\,\nu_0^{\eta}$)[a]

Tissue	ζ	η
Adipose	0.012	0.17
Kidney	0.007 3	0.25
Gray matter	0.003 6	0.31
White matter	0.001 5	0.35
Heart muscle	0.001 3	0.36
Liver	0.000 52	0.38
Skeletal Muscle	0.000 45	0.42

[a]Derived from Bottomley et al.;[6] T_1 in s and ν_0 in Hz.

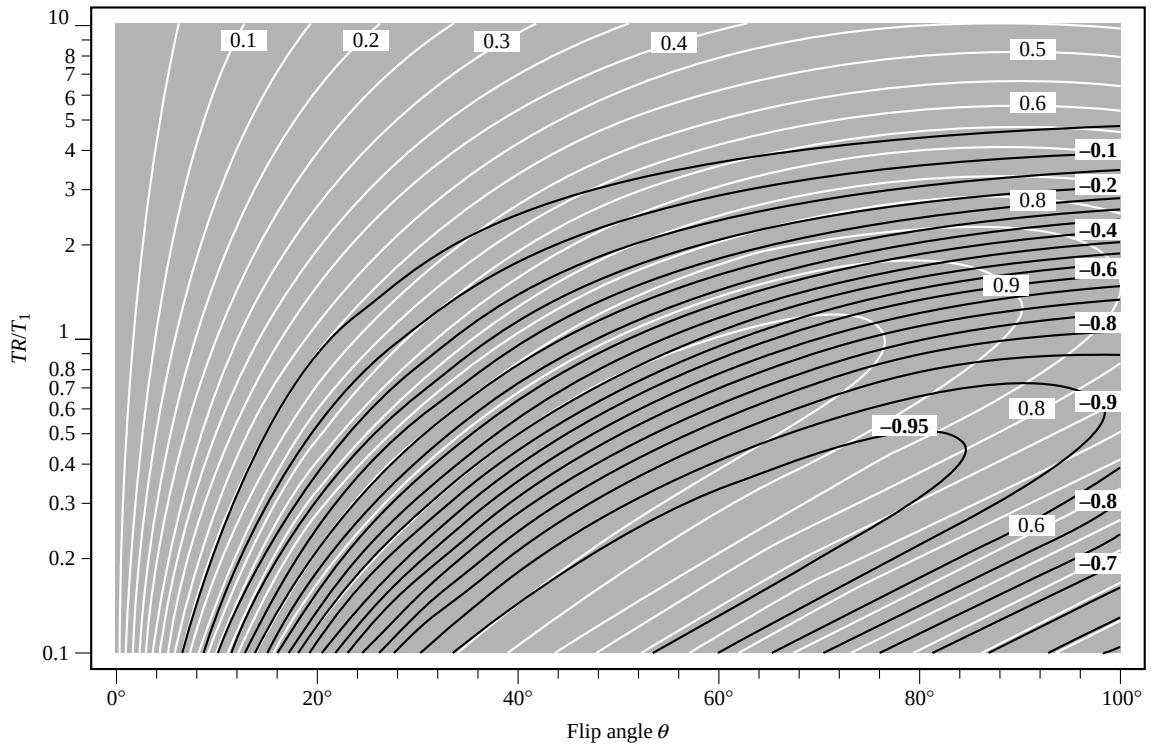

Figure 1 Normalized signal-to-noise ratio Ψ and relaxational contrast-to-noise ratio $\partial\Psi/\partial T_1$ in a repeated FID image as functions of effective flip angle θ and repetition period TR. The effects of any pulse used to produce an echo are neglected, and the plot is for a constant imaging time rather than a constant number of pulses. The C/N contours are the black lines, with values in bold print; the S/N contours are white lines, with values in plain print. The topologies of the two functions are similar, and it is possible to obtain simultaneous high absolute values. However, the plots are for constant hydrogen concentration, and therefore must be employed with care when there is a correlation between concentration (water content) and relaxation time T_1: $\partial\Psi/\partial M_0$ and $\partial\Psi/\partial T_1$ have opposite signs and tend to cancel

80 MHz is four times longer (thanks to the frequency dependence of T_1) than that taken to acquire an equivalent image at 5 MHz then, by coadding four 5 MHz images (thereby also taking time $T_{\min}$), the S/N of the 5 MHz picture could be doubled. In short, a factor of $T_1^{1/2}$ has to be included in any assessment of image signal-to-noise ratios. Thus in a simple, S/N-optimized, 90° pulse, repeated FID imaging experiment (sometimes inaccurately termed a 'saturation–recovery' experiment) that avoids chemical shift artifacts and does not employ a Carr–Purcell multiple echo sequence, the head image S/N varies for fixed imaging time T as

$$\begin{aligned} \mathrm{d}\Psi_{\mathrm{Ihead}} &\approx 350\nu_0\,\mathrm{d}V\left(\frac{T\Delta t}{T_1}\right)^{1/2} \pm 10\% \\ &<< 350\,\mathrm{d}V\left(\frac{T\nu_0^{(1-\eta)}}{\delta_{\mathrm{H}}\zeta}\right)^{1/2} \pm 10\% \end{aligned} \tag{18}$$

Thus, taking gray matter with 80% water as an example,

$$\mathrm{d}\Psi_{\mathrm{Igray}} << 2.5\times 10^6\,\mathrm{d}V\,\nu_0^{0.35}T^{1/2} \pm 10\% \tag{19}$$

and in 4 min at 64 MHz, an image with an S/N of 40:1 can have a voxel size of about 5 μl, or in other words a resolution of about 1 mm in a 5 mm thick slice.

Summarizing, we have established the credentials of NMR imaging—resolutions of the order of 1 mm in 5 mm thick slices in times of the order of a minute or two. However, lest other credentials be sought ('Why not 1 μm in 30 s?'), the relationships in equations (18) and (19) are worthy of note.

1. We remarked earlier that the linear resolution Δu in an image, if all three dimensions are similarly scaled, is proportional to the cube root of the volume. Thus the time taken to attain a given S/N (whatever may be needed—normally in the range 16:1–64:1) is proportional to the inverse *sixth* power of the linear resolution Δu. It follows that if the S/N in an image is marginal, any idea of increasing resolution by imaging for longer should be promptly abandoned: the return is almost worthless. Keeping the resolution constant and imaging for longer (effectively coadding images) to improve the sensitivity is a reasonable course (improvement as the square root of time), but the overwhelming temptation must be to suffer the chemical shift artifacts and increase the data acquisition window!
2. The relationship between spatial resolution and field strength for constant S/N and imaging time is also weak, since $\Delta u \propto \nu_0^{(\eta\,-\,1)/6}$. For example, for gray matter, a 10-fold increase in field strength affords only a 25% improvement in linear resolution, unless one can be absolutely certain that only water is being observed.
3. Looking at the relationship between field and time for constant S/N and resolution, we see that $T \propto \nu_0^{(\eta\,-\,1)}$, and as the field is increased, so the time needed to gather and coadd multiple images decreases fairly rapidly—fewer additions are needed. However, once only a few additions are

needed, the use of imaging time T in the above arguments and equations is, in truth, a little artificial, since T must be granular—corresponding to say 128, 256, 2048, etc. FIDs, depending on the desired resolution and number of repetitions. Thus, as the field strength is increased and T diminishes, there will come a point at which one run of the imaging sequence, with its fixed number of FIDs, suffices. Thereafter, further increase in field strength serves to *increase* the time to collect that fixed number (thanks to the frequency dependence of T_1) while admittedly improving S/N.

Perhaps the overriding message of equations (18) and (19) is that the richest dividends come from innovative and minute attention to every detail of rf design. For example, a change of preamplifier from one with a noise figure of 4 dB to one with a noise figure of 1 dB, coupled with a switch to quadrature receiving coils, can improve linear resolution by 25%. It is perhaps for this reason that the literature is full of special coil designs for every conceivable part of the human body, even though there are, for the most part, no new design principles enunciated. Finally, there are those who would image other nuclei. The overwhelming obstacle to this desire is the paucity of elements other than hydrogen in the body. (Carbon-12 and oxygen-16 have no nuclear magnetic moments.) For example, the magnetization of metabolic phosphorus is less than 10^{-4} that of the body's hydrogen, leading *very* roughly from equation (19), to a voxel size in the head of the order of 30 ml at 64 MHz (3.7 T). Such a size is incompatible with the formation of a recognizable image.

4.2 Contrast-to-Noise Ratio

A common aspect of imaging is the desire to impart to the data a strong dependence on either relaxation time T_1 or T_2, so that tissues with similar water content but different relaxation behavior can easily be distinguished. In this context, we draw a sharp distinction between absolute and relative contrast. The former relates to the *difference* in signal strength between two regions of differing relaxation, and is here our main concern. One's ability to distinguish that difference depends on its size relative to that of the noise in the image. However, it may be difficult to view the difference adequately in the context of the full image, since careful 'windowing' may be needed—the image brightness must go from dark black to full white over a small range of signal strengths, thereby blacking- or whiting-out detail in the rest of the picture. The *relative* contrast is simply the ratio of two signals, without consideration of the noise. If the *relative* contrast is large and the S/N is reasonable, there are no windowing problems, but only gross changes in relaxation behavior can be viewed.

We begin by considering absolute T_1 contrast, a measure of which for repeated FID imaging can be obtained by differentiation of equation (18) with respect to T_1. Figure 1 is a normalized contour plot of absolute T_1 contrast-to-noise ratio (C/N) $\partial\Psi/\partial T_1$ versus flip angle and repetition period *for a fixed imaging time T*. Note that the contrast is negative, since a longer T_1 implies a greater degree of saturation and therefore a *reduction* in signal. It may be seen that for a 90° pulse, the point of maximum contrast (at $TR = 0.50\ T_1$) is somewhat removed from that of maximum sensitivity at $TR = 1.26\ T_1$. The relative values of sensitivity and C/N at these two repetition periods are shown in Table 2, and it may be seen that at the compromise value of $TR = 0.81T_1$, 87% of both the maximum possible S/N and C/N are obtained. This percentage is only a few points less then the maximum possible with a 90° pulse. As when considering sensitivity, the overall best T_1 contrast is obtained when repeating as fast as possible, albeit with a small flip angle θ obeying the equations

$$\exp(TR/T_1) = \frac{2+\cos\theta}{1+2\cos\theta}, \quad \cos\theta = \frac{2\exp(-TR/T_1)-1}{2-\exp(-TR/T_1)} \qquad (20)$$

While normal imaging methods employ 90° and 180° pulses, fast imaging techniques can take advantage of such low-flip-angle pulses.

When the C/N in an image is so good that multiple runs of the imaging protocol are not required, the optimum conditions are somewhat different. With a 90° pulse, the best T_1 contrast, as shown in Table 2, is obtained with $TR = T_1$, but then only 63% of the maximum sensitivity is garnered. A reasonable compromise is $TR = 1.75T_1$. An unfortunate aspect of imparting T_1 contrast by partial saturation is that there is often a correlation between tissue water content and T_1: the more water, the longer is T_1. The two variables then work in opposition, the greater saturation of the longer lived species tending to reduce its larger signal, thereby *reducing* contrast by the tendency to equate signal strengths. In these circumstances, an 'inversion–recovery' pulse sequence (see ***Image Formation Methods***) is often employed, but, as shown in Figure 2, a considerable price is paid in both C/N and S/N. The lure of the inversion–recovery method is that the relative contrast (the ratio of the signal strengths of two species) can be very large, and thus the image is easily viewed. However, since both positive and negative signals can exist, a magnitude image can often not be used, and this can be both a considerable inconvenience and a trap for the unwary.

If we wish to determine how the contrast varies with field strength, we must have excellent knowledge of the frequency dependence of each T_1 of interest, and such data may be unavailable. Using the values for brain gray and white matter in

Table 2 Normalized Maximum and Compromise Signal-to-Noise and Contrast-to-Noise Ratios in a Repeated FID Image[a]

Experiment	TR/T_1	S/N	C/N
'Low-field'[b]	0.5	0.78	−0.92*
	0.81	0.87	−0.87
	1.26	0.90*	−0.50
'High-field'[c]	1	0.63	−1*
	1.75	0.83	−0.83
	∞	1*	0

[a]For a 90° pulse. 'Low-field' values are normalized to the maxima of the absolute values obtainable with a variable flip angle pulse. Contrast is negative because *increasing* T_1 results in *decreasing* signal.
[b]Imaging for a constant time, by adjustment of the number of repetitions of the imaging protocol. Usually applicable at fields of about 0.1 T.
[c]Imaging for a constant number of pulses, regardless of the time taken. Usually applicable at fields of about 1.5 T.
*Maxima of absolute values.

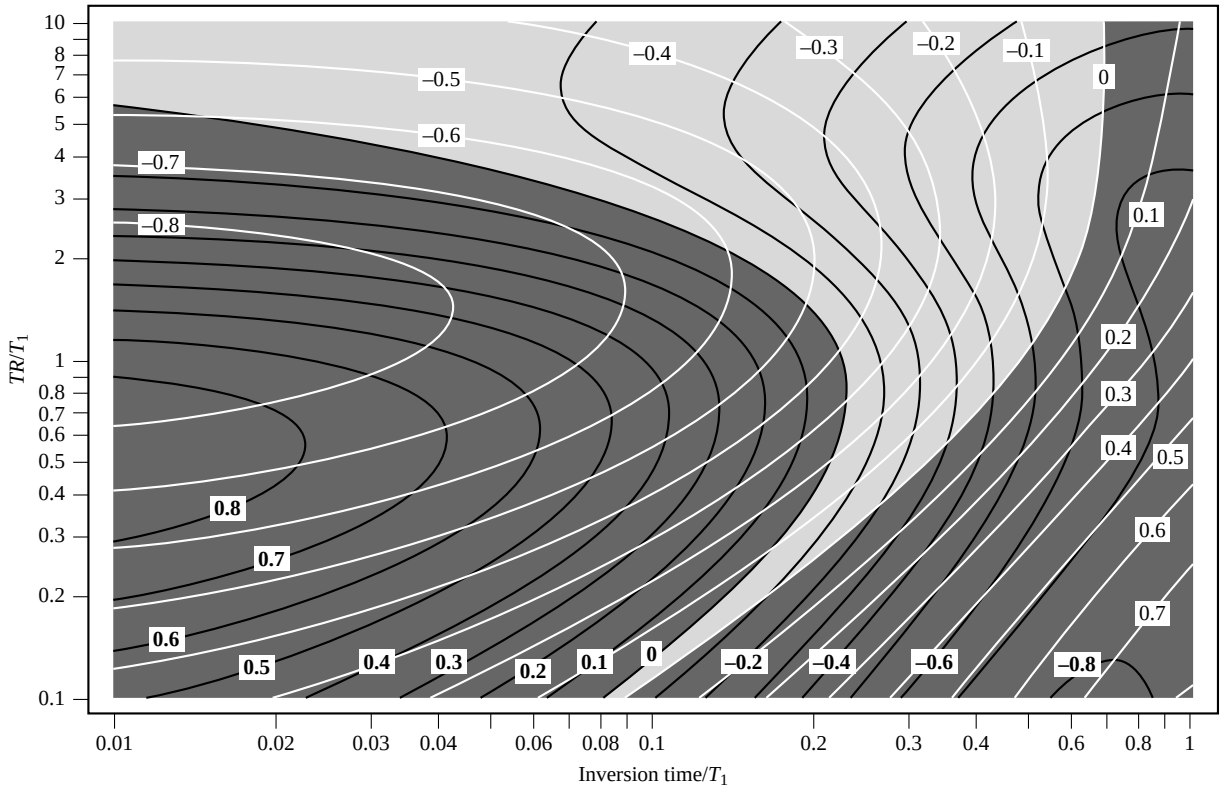

Figure 2 Normalized signal-to-noise ratio Ψ and relaxational contrast-to-noise ratio $\partial\Psi/\partial T_1$ in an inversion–recovery image as a function of inversion time (the time between the inverting 180° pulse and the following, signal-generating 90° pulse) and of recovery time *TR* (the time between the 90° pulse and the next 180° inverting pulse). The functions are normalized to the maximum values attainable under the conditions pertinent to Figure 1, the effects of any pulse used to produce an echo are neglected, and the plot is for a constant imaging time rather than a constant number of pulses. The C/N contours are the black lines, with values in bold print; the S/N contours are white lines, with values in plain print. The area with the lighter shading is where a positive correlation between hydrogen content and longitudinal relaxation time enhances T_1 contrast. It may be noted that the maximum absolute contrast in this area is obtained where the signal is weakest. Thus, the *relative* contrast of the inversion–recovery method can be very large. However, there is a considerable price to be paid, as may be seen from the values of the contours

Table 1, the absolute C/N is easily calculated at any frequency, but it is found that in going from 21 to 64 MHz (0.5 to 1.5 T), the increase in absolute contrast is only 12%. Again, it is stressed that this result is for the same imaging time at the two field strengths, and that chemical shift artifacts have been suppressed by an appropriate choice of data acquisition window.

Turning to T_2 contrast, dependence is easily imparted by generating an echo from the FID; indeed, most modern imaging methods use an echo anyway, since it helps to deal with a number of phasing problems. If we assume, as is usually the case, that $T_1 >> T_2$, the repetition rate has almost no bearing on T_2 contrast. It may then be shown that to excellent accuracy for $\Delta t \leqslant 1.5\ T_2$, the maximum absolute contrast is obtained when the acquisition window Δt is centered on echo time $TE = T_2$. However, this positioning can entail a loss of up to 63% in image sensitivity when $\Delta t << T_2$. On the other hand, the maximum *relative* contrast is obtained when the echo time is as long as possible, and the S/N in the image is then very poor indeed. The frequency dependence of T_2 (which is normally quite small) has little effect on the calculation once $\Delta t << T_2$. However, if multiple echoes are accumulated with an optimum filter, or if chemical shift artifacts are neglected, what little dependence there is, is reflected directly in the image sensitivity and contrast.

5 POWER DEPOSITION

In the preceding paragraphs, the discussion of the frequency dependence of an image's sensitivity and contrast has been dominated by the possible effects of chemical shift artifacts and the changing longitudinal relaxation time. However, there is an additional aspect to imaging that we dare not ignore, and that is the power deposited in the patient by the rf pulses. While a healthy individual can safely absorb 1 kW of infrared radiation for many minutes, our concern must be with a patient who may have cardiovascular or thermoregulatory problems. Further, it is obvious that the eddy currents induced in the body by the transmitter's $\boldsymbol{B}_1$ field may be forced, at certain parts of the body (e.g., the shoulder blades), to flow through relatively thin layers of tissue, thereby generating so-called 'hot spots'. How the body handles such insults is not clear, but, in the context of this article, it is clear that there has to be a limit—and indeed, government agencies advise on the issue.[8,9]

To attempt an assessment of the issue's seriousness, we must look at the factors that govern the rf pulses used in imaging. It is obvious that they must have a duration that is much less than T_2, but they must also be powerful enough to cover the required bandwidth. While there may be problems with

main field inhomogeneity that require an increase in pulse bandwidth, such difficulties can usually be solved by the application of money—no amount of money can change the fundamental limit that is determined by the chemical shift range δ_H. If a composite image of water and fat is to be obtained, the exciting field must obey the inequality

$$\nu_1 \gg \delta_H \nu_0 \tag{21}$$

where ν_1 is once again the nutational frequency and ν_0 is the Larmor frequency. Needless to say, the meaning of 'very much greater than' is open to a wide variety of interpretations, and is also dependent on the type of pulse used. However, substitution into equations (6) and (7) to find the instantaneous power needed to produce the necessary field in the human body gives

$$W_{\text{head}} \gg 4.8 \times 10^{-20} \delta_H^2 \nu_0^4, \quad W_{\text{body}} \gg 3 \times 10^{-21} \delta_H^2 \nu_0^{4.4} \tag{22}$$

As usual, it is helpful to insert numbers, since with them we obtain the power specifications of the transmitter. Setting $\delta_H = 3.5 \times 10^{-6}$, we have at 10 MHz, $W_{\text{head}} >> 6$ mW and $W_{\text{body}} >> 230$ mW, whereas at 64 MHz, $W_{\text{head}} >> 10$ W and $W_{\text{body}} >> 820$ W. The very rapid increase with Larmor frequency demonstrated in these numbers, and in equation (22), shows that rf engineering problems become immense and expensive at fields not much larger than 1.5 T if composite imaging of water and fat is still to be entertained. Indeed, a typical specification for a transmitter at 64 MHz is already 10 kW.

Turning to the energy absorbed by the human body, we have already mentioned that 180° pulses are commonly used in imaging protocols. It is usually these pulses, rather than 90° pulses, that deposit the most energy in the patient. Now, with a rectangular envelope, the duration of such a pulse is $(2\nu_1)^{-1}$, and so the energy absorbed from each pulse is

$$E_{\text{head}} = 2.4 \times 10^{-20} \varepsilon \delta_H \nu_0^3, \quad E_{\text{body}} = 1.5 \times 10^{-21} \varepsilon \delta_H \nu_0^{3.4} \tag{23}$$

where ε (>> 1) is a factor that takes account of the inequality in equation (21). In practice, pulses are often selective, which increases the energy a little, but this minor uncertainty is lost amid the greater uncertainty surrounding the factor ε, the size of the patient, etc. Now the recommendations of most governments concerning absorbed power P are related, among other factors, to the resting human metabolic rate (of order 100 W). (There are also recommendations concerning localized power deposition—the so-called 'specific absorption rate', SAR.) It follows from equation (23) that the number of 180° pulses per second that may be safely applied is

$$R_{180\text{head}} = \frac{4.2 \times 10^{19} P}{\varepsilon \delta_H \nu_0^3}, \quad R_{180\text{body}} = \frac{6.7 \times 10^{20} P}{\varepsilon \delta_H \nu_0^{3.4}} \tag{24}$$

For example, consider imaging at 80 MHz on the torso. Let $P = 30$ W, $\varepsilon = 3$, and $\delta_H = 3.5 \times 10^{-6}$. Then $R_{180\text{body}} = 2.6$, which is highly restrictive. Such a value would prohibit, for example, a single echo, multislice experiment. We may manipulate the factor ε in equation (24) or justify to ourselves a little more power, but the overwhelming dependence in the equation is upon Larmor frequency. A small lowering of frequency makes a large difference to the flexibility and versatility of the equipment. Turning this statement about, even if our estimates of power deposition are considerably in error or we manage to invent a pulse where ε can be honestly as low as 1, it will make little difference to the maximum frequency to which we can aspire. Put plainly, 'high-field' imaging with large-angle pulses presents serious problems for any method that aims to excite the whole chemical shift range encountered in the human body.

6 CONCLUSIONS

In any attempt to assess the imaging experiment, and in particular, the composite imaging of fat and water, which is the mainstay of clinical imaging practice, some objective criterion of usefulness is needed—a commodity hard to come by, for signal-to-noise ratio alone does not suffice. One possible approach to this dilemma is to realize that, with each 180° pulse used for echo formation, there is, in general, an associated and useful image. Thus, the 'information' potentially available to the radiologist can, to some degree, be measured by the number of 180° pulses that can be gainfully applied. We have already encountered an upper limit on that number as field strength increases, equation (24), caused by power deposition problems. However, there is another limit, as field *decreases*, caused by the fact that we presumably do not wish to apply 180° pulses more frequently than one every data acquisition period Δt. Thus, from equation (14), the maximum average rate at which they are likely to be applied is

$$R_{180\,\max} = \lambda \delta_H \nu_0 \tag{25}$$

where the factor λ (< 1) allows for slower running, to accommodate the phase-encoding period, for example. To gather data at the maximum rate, a multislice, multiecho experiment would almost certainly be required. However, we note that the limits implied by equation (24) and (25) intersect at a frequency given by

$$\begin{aligned} \nu_{0\text{head}} &= 8.1 \times 10^4 \left(\frac{P}{\varepsilon \lambda \delta_H^2} \right)^{0.25} \\ \nu_{0\text{body}} &= 5.4 \times 10^4 \left(\frac{P}{\varepsilon \lambda \delta_H^2} \right)^{0.227} \end{aligned} \tag{26}$$

Below these frequencies, the rate of application of 180° pulses is limited by the long data acquisition window; and above, by the allowable power deposition. For example, with $P = 30$ W, $\varepsilon = 3$, and $\delta_H = 3.5 \times 10^{-6}$, as previously, and with $\lambda = 0.5$, we have for the torso an intersection frequency of 32 MHz, allowing about fifty-six 180° pulses per second. These pulses could be used, for example, to obtain eight-slice, seven-echo images (if a slice repetition rate of one per second were used), thereby giving full T_2 information for each slice, and by weighted, coaddition of images, the full S/N unhampered by chemical shift artifacts. On the other hand, at both lower and higher frequencies, the maximum rate of application would be less.

The crux of the argument being presented here is that as field strength is increased *in a single slice experiment*, so a point slowly arrives at which resolution and S/N are those desired (without any need for repetition of the imaging protocol), and further field increases give little in return while

consuming some extra time. However, *for a multislice experiment* (and even more so for multislice, multiecho techniques), there comes a point at which power dissipation problems rapidly impose severe constraints, and versatility and flexibility are quickly hampered. It is a little like taking a walk over a gentle hill and suddenly finding a precipice on the other side! The reason for this behavior is clearly contained in equation (26): the frequency at which it occurs can be influenced but little by changing the allowable power deposition P, or by fudging one's notions of what are acceptable chemical shift artifacts, for these factors are raised to a small power—about 0.25. The numerical constants in the equations totally dominate, and they in their turn are dominated by the effective radius and conductivity of the sample. Thus, for the head, it may well be that a frequency of 70 MHz might maximize the information available; while for the torso, about 30 MHz might be best.

As the novelty of NMR imaging has worn off, and it has become a routine clinical tool, it has become clear that the bulk of the market has, in fact, settled for machines in the frequency range mentioned. Neuroradiologists tend to prefer the higher field strengths, for example, 1.5 T (64 MHz); many average radiology departments have settled for a strength of 0.5 T (21 MHz). The technology is reasonably mature, and its limits of resolution and sensitivity are understood, and have been, for the most part, reached. Having said this, the application of the technique is, at the time of writing, still expanding. However, it is salutary to think that if the amount of electrolytes in the body were considerably greater (thereby greatly increasing conductivity), or if hydrogen, like oxygen and carbon, had no nuclear spin, NMR imaging would have remained a curiosity.

7 RELATED ARTICLES

Chemical Shift Imaging; Image Formation Methods; Echo-Planar Imaging; Health and Safety Aspects of Human MR Studies; Sensitivity of the NMR Experiment.

8 REFERENCES

1. C.-N. Chen and D. I. Hoult, 'Biomedical Magnetic Resonance Technology', Adam Hilger, Bristol, 1989.
2. D. I. Hoult and R. E. Richards, *J. Magn. Reson.*, 1976, **24**, 71.
3. D. I. Hoult and P. C. Lauterbur, *J. Magn. Reson.*, 1979, **34**, 425.
4. C-N. Chen, V. J. Sank, S. M. Cohen, and D. I. Hoult, *Magn. Reson. Med.*, 1986, **3**, 722.
5. C. H. Durney, C. C. Johnson, P. W. Barber, H. Massoudi, M. F. Iskander, J. L. Lords, O. K. Ryser, S. J. Allen, and J. C. Mitchell, 'Radiofrequency Radiation Dosimetry Handbook', 2nd edn., USAF School of Aerospace Medicine, Brooks Air Force Base, TX, 1978.
6. P. A. Bottomley, T. H. Foster, R. E. Argersinger, and L. M. Pfeifer, *Med. Phys.*, 1984, **11**, 425.
7. P. T. Beall, S. R. Amtey, and S. R. Kasturi, 'NMR Handbook for Biomedical Applications', Pergamon Press, New York, 1984.
8. National Radiological Protection Board, *Br. J. Radiol.*, 1983, **56**, 974.
9. Office of Radiological Health, 'Guidelines for Evaluating Electromagnetic Risk for Trials of Clinical NMR Systems', US Food and Drug Administration, Rockville, MD, Communications of February 25 and December 28, 1982.

Acknowledgements

The author gratefully acknowledges the hospitality of the In Vivo NMR Center, University of Utrecht.

Biographical Sketch

David I. Hoult *b.* 1945; B.A. (Physics) 1968. D.Phil. (supervisor Sir Rex Richards F.R.S.) 1974, both University of Oxford, UK. Biochemistry Department, Oxford University, 1974–1977. National Institutes of Health, Bethesda, MD, 1977–1982. Head, NMR Instrumentation Group, NIH, Bethesda, MD, 1982–1991. University of Utrecht, The Netherlands, 1991–1994. Institute for Biodiagnostics, NRC, Winnipeg, 1994–present. Approx. 70 publications, and with C-N Chen, the book 'Biomedical Magnetic Resonance Technology'. 7 awards including Gold Medal, Society of Magnetic Resonance in Medicine, 1985. Research interests: all aspects of instrumentation (mainly NMR), mostly in the biological and medical fields.

Whole Body MRI: Strategies Designed to Improve Patient Throughput

Felix W. Wehrli

University of Pennsylvania Medical School, Philadelphia, PA, USA

1	Introduction	1
2	***k***-Space Formalism	1
3	Classification of Imaging Techniques	2
4	Various Embodiments of Spin Warp Imaging	2
5	Multiline Scanning Techniques	5
6	Other Methods of Scanning ***k***-Space	7
7	Related Articles	7
8	References	8

1 INTRODUCTION

Since the inception of clinical MRI at the beginning of the 1980s, the rate at which a subject can be scanned—often denoted 'patient throughput'—has been reduced by nearly an order of magnitude. Some of the improved scan efficiency is unrelated to a shortening of the actual data acquisition time, and can be accounted for by improvements in some of the ancillary procedures such as patient set-up, rf coil placement, scan parameter entry, prescan (MRI jargon for rf carrier selection and adjustment of transmit and receive gain), and advances in digital system architecture (shortening in reconstruction times, concurrence of data acquisition and reconstruction, etc.). The focus of this article, however, will be on techniques for reducing scan time, since it is this that determines patient tolerance. Scan times in excess of 5–10 min typically lead to image degradation from subject motion. Another strong motivation for shortening scan time is physiologic motion such as cardiac pulsation, respiration, and peristalsis. Clearly, if the data acquisition time could be lowered below the period of physiologic motion, the effect of motion unsharpness in the image data could effectively be suppressed. Many of the new applications, such as the assessment of organ function by monitoring the passage of a bolus of contrast agent[1] or the study of brain function by recording the response to stimuli,[2–4] demand temporal resolution on the order of 0.1–1 s (see also ***Contrast Agents in Whole Body Magnetic Resonance: An Overview***).

While many of the ideas for improved scan efficiency have been in existence for a decade or longer, they have become practical only recently, owing to engineering advances such as digital transceiver electronics (see also ***Whole Body Magnetic Resonance Spectrometers: All-Digital Transmit/Receive Systems***) and gradient technology (see ***Gradient Coil Systems***). A case in point is echo planar imaging (EPI), which was first conceived in 1977,[5] but has only recently become practical.[6] Finally, an increased data sampling rate typically exacts an unavoidable penalty in signal-to-noise ratio (S/N). Since the minimum tolerable S/N is usually dictated by diagnostic criteria such as lesion detectability, increases in temporal resolution will usually have to be traded against spatial resolution.

This article briefly reviews the concepts underlying the most important classes of rapid imaging techniques, each of which is discussed in more detail in other articles in this Encyclopedia, referenced later. For a simple introduction to rapid MRI imaging techniques, the reader is referred to Wehrli.[7]

2 *k*-SPACE FORMALISM

We shall in the following resort to the classical ***k***-space formalism[8] (see also ***Image Formation Methods***). In brief, data sampling occurs in reciprocal space, referred to as '***k***-space' or the 'spatial frequency domain'. For an object of spin density $\rho(\boldsymbol{r})$, ignoring relaxation, the spatial frequency signal $\rho'(\boldsymbol{k})$ is given by

$$\rho'(\boldsymbol{k}) = \int_{\boldsymbol{r}_1}^{\boldsymbol{r}_2} \rho(\boldsymbol{r}) \mathrm{e}^{-\mathrm{i}\boldsymbol{k}(t)\cdot\boldsymbol{r}}\, \mathrm{d}^3 r \tag{1}$$

Here $\boldsymbol{k}(t)$ is the spatial frequency vector, expressed in units of rad cm^{-1}:

$$\boldsymbol{k}(t) = \gamma \int_0^t \boldsymbol{G}(t')\, \mathrm{d}t' \tag{2}$$

where $\boldsymbol{G}(t')$ is the time-dependent spatial encoding gradient in vector format. Pictorially, the spatial frequency may be regarded as the phase rotation per unit length of the object experienced by the magnetization after being exposed to a gradient $\boldsymbol{G}(t')$ for some period t.

We further recognize from equation (1) that $\rho'(\boldsymbol{k})$ and $\rho(\boldsymbol{r})$ form a Fourier transform pair, and so

$$\rho(\boldsymbol{r}) = \int_{\boldsymbol{k}_1}^{\boldsymbol{k}_2} \rho'(\boldsymbol{k}) \mathrm{e}^{\mathrm{i}\boldsymbol{k}(t)\cdot\boldsymbol{r}}\, \mathrm{d}^3 k \tag{3}$$

The path of the spatial frequency vector during execution of the pulse sequence is determined by the time-dependent gradient waveforms.

Since ***k***-space is sampled discretely, sampling needs to satisfy the Nyquist criterion

$$\tfrac{1}{2} L_i k_{i,\max} = \tfrac{1}{2} N_i \pi \tag{4}$$

where $k_{i,\max}$ is the highest spatial frequency, L_i and N_i represent the field-of-view and number of data samples, respectively, and $i = x, y, z$. We can then write for the sampling interval Δk_i

$$\Delta k_i = \frac{k_{i\max}}{\frac{1}{2}N_i} = \frac{2\pi}{L_i} = \frac{2\pi}{N_i \Delta L_i} \tag{5}$$

with ΔL_i representing the pixel size. The factor of 2 in equation (5) arises because we collect N_i samples from $-k_{\max}$ to $+k_{\max}$ or $\frac{1}{2}N_i$ samples from 0 to $k_{\max}$.

Since the data sampling time increases with the number of data samples, one obvious approach toward shortening the sampling time is to reduce N_i. It is readily seen from equation (5) that this can be achieved in two different ways. If we wish to maintain the pixel size, this will result in a reduction in the

field-of-view and thus an increase in Δk_i. Conversely, we may want to maintain the field-of-view, in which case Δk_i remains invariant but $k_{\max}$ is lowered, and thus pixel size is increased. In the latter case, we trade spatial resolution for a reduction in sampling time.

Further, since $\Delta k \approx \gamma \Delta t\, G$, the sampling interval Δt scales inversely with the amplitude of the spatial encoding gradients. Therefore, the duration of the spatial encoding process is governed significantly by the achievable gradient amplitudes. At a given resolution, the latter essentially determine what fraction of ***k***-space can be covered following a single excitation (since the signal decays with time constant T_2). Therefore, the properties of the gradients, notably their amplitudes, and for many imaging sequences also their slew rates, are paramount in determining ultimate imaging speed.

3 CLASSIFICATION OF IMAGING TECHNIQUES

Most of the currently used imaging techniques use rectilinear ***k***-space sampling, and as such may be regarded as descendants of the spin warp technique of Edelstein et al.,[9] which itself is an outgrowth of Fourier zeugmatography, pioneered by Kumar, Welti, and Ernst.[10] Since the latter is an embodiment of two-dimensional NMR spectroscopy,[11] conceptionally all rectilinear sampling techniques may be regarded as originating from 2D NMR. By contrast, projection–reconstruction imaging[12–14] or imaging with nonperiodic time-varying gradients[15] such as spiral scanning[16,17] are not rectilinear sampling techniques, since the ***k***-space path is non-Cartesian.

Common to all rectilinear ***k***-space sampling techniques are two distinct phases of spatial encoding, a first period during which a gradient G_y is applied whose time integral determines k_y and during which no sampling occurs, followed by a second period during which a gradient G_x is applied while the free precession signal is sampled, resulting in a line k_x. The former is typically called 'phase encoding' and the latter 'frequency encoding'. In this manner, a 2D ***k***-space grid is sampled by incrementally stepping the amplitude of the phase-encoding gradient. The concept can be extended to a third dimension by phase encoding along a second spatial coordinate to afford k_z, in which case ***k***-space is three-dimensional. In both back-projection and spiral scanning, two or all three spatial encoding gradients are simultaneously active while data are sampled. A generic 3D spin warp pulse sequence and ***k***-space map are shown in Figure 1.

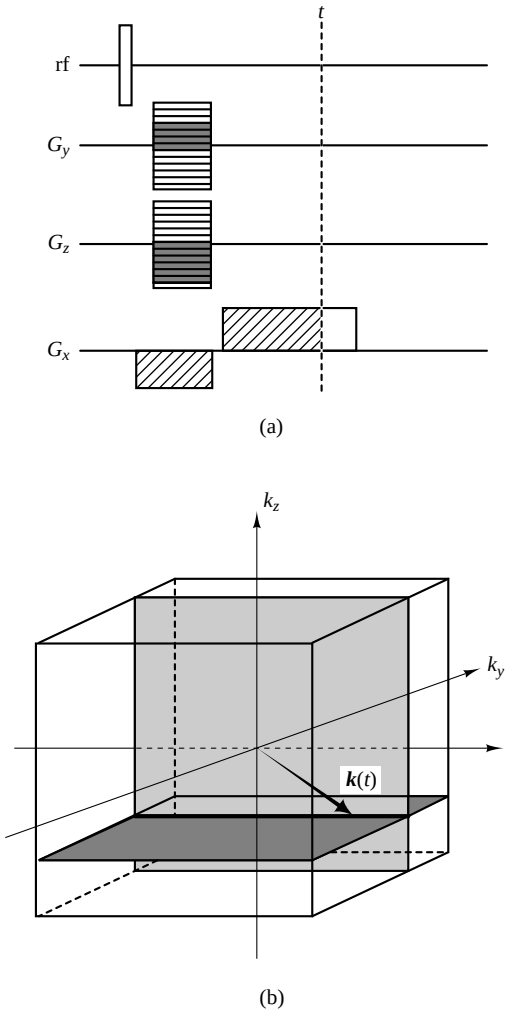

Figure 1 (a) Generic 3D spin warp imaging with phase encoding on the x and y axes and frequency encoding on z. Hatched areas indicate the spatial frequency vector at time t (b). Amplitudes of phase-encoding gradients are arbitrary. During readout, a line k_x is scanned corresponding to intersection between the (k_x,k_y) and (k_x,k_z) planes (shaded areas)

4 VARIOUS EMBODIMENTS OF SPIN WARP IMAGING

4.1 Scan Time, Signal-to-Noise Ratio and Spatial Resolution

Except in those situations where ***k***-space can be scanned in a period on the order of T_2, such as in EPI[5] or multiple pulse techniques,[18] resulting in a series of consecutive echoes that can be individually encoded, only a fraction of ***k***-space is typically scanned upon creating transverse magnetization, and the process repeated several times, each cycle affording another ***k***-space segment. Longitudinal magnetization builds up in a recurrent fashion between cycles of period *TR* (also called 'pulse repetition time'). The data acquisition time T_{ac} thus scales with *TR* and the number of pulse sequence cycles, the latter being a function of the number of spatial encoding steps or ***k***-space samples. It is customary to denote the frequency-encoding axis by x and the phase-encoding axis by y (or y and z, respectively, if phase encoding in an additional dimension is effected), with N_i $(i = x, y, z)$ representing the number of data samples. Assuming further that during a frequency-encoding period a single line $k_{x,i=1,\ldots Nx}$ is sampled, T_{ac} to sample ***k***-space is given by

$$T_{\text{ac}} = N_y N_z n T R \tag{6}$$

where n represents the number of sequence repetitions (also called 'number of excitations' in imaging jargon) at given values of ***k***. At typical sampling rates, the sampling time for frequency encoding is on the order of 10 ms or less, and so does not appear in equation (6). It will, however, become critical in high-speed gradient echo imaging[19,20] and EPI and its derivatives.[21–23]

The scan time scales with the number of phase encodings (N_y in 2D, and N_y and N_z in 3D spin warp imaging), and thus a reduction in the number of phase-encoding samples entails a concomitant reduction in scan time. As previously pointed out, this can be achieved in two different ways: either by lowering $k_{\max}$ or decreasing sampling density $1/\Delta k$. The former lowers resolution, the latter leads to reduced field-of-view while preserving resolution [cf. equation (4) and (5)]. Thus, the term 'matrix size' is ambiguous, though in common parlance a change in matrix implicitly implies fixed field-of-view. The two different situations, each lowering data acquisition time of a 3D image acquisition by a factor of 4, are illustrated in Figure 2.

Let us now examine the S/N implications of the two different operations. The signal amplitude S scales with voxel size, i.e.,

$$S \propto \Delta x\, \Delta y\, \Delta z = \frac{L_x L_y L_z}{N_x N_y N_z} \tag{7}$$

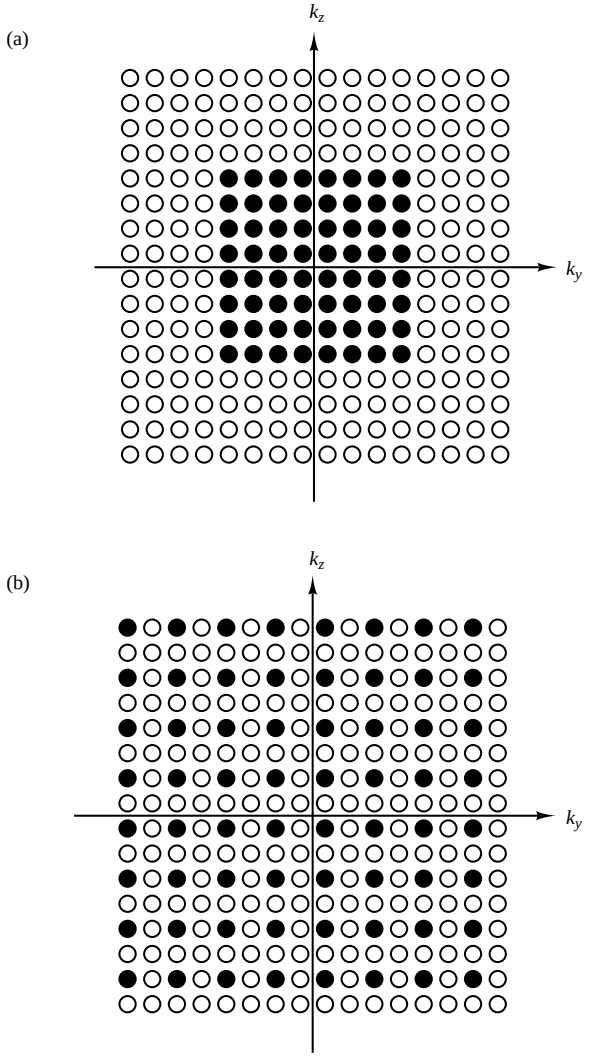

Figure 2 Halving the number of phase and slice encodings (N_y, N_z) in a 3D spin warp acquisition can be achieved by reducing either the ***k***-space area (a) or the sampling density (b), leading to lower resolution (a) or reduced field-of-view (b). Open circles represent skipped data samples

where the product $\Delta x\ \Delta y\ \Delta z$ expresses the voxel volume, the remaining parameters have previously been defined. Further, the noise-reducing effect of sampling leads to

$$\text{S/N} \propto \sqrt{N_x N_y N_z n} \tag{8}$$

and thus

$$\text{S/N} \propto \frac{L_x L_y L_z \sqrt{n}}{\sqrt{N_x N_y N_z}} \tag{9}$$

From equation (9), we conclude that halving the number of data samples N_y and N_z by halving $k_{y,\max}$ and $k_{z,\max}$, increases S/N by a factor of 2 (Figure 2a). Skipping alternate data samples, on the other hand, penalizes S/N by a factor of 8 since this operation halves the field of view for both L_y and L_z [equation (5); Figure 2b].

4.2 Slice Multiplexing and Multiecho Acquisition

In most embodiments of 2D spin warp imaging, the period comprising slice selection, phase encoding, and frequency encoding accounts for only a fraction of the *TR* interval. Therefore, minimizing the dead time by shortening the pulse recycle time seems to be a straightforward means of optimizing scan time. However, *TR* is typically dictated by contrast requirements. Shortening of *TR* leads to progressive saturation, and thus, in spin echo imaging at least, is incompatible with proton density and T_2-weighted contrast A solution to this problem was first conceived by Crooks et al.,[24] who introduced what is commonly called '2D multislice imaging'. By making the rf pulses slice-selective, only the spins in the slice of interest are stimulated. Adjacent slices are then excited in sequence without perturbing the steady state. The gain in efficiency achieved in this manner depends on *TR*, the echo time *TE*, and the time required for applying the spatial encoding gradients, and typically ranges from about 10 to 50. The second important innovation was the incorporation of Carr–Purcell echoes into spin warp imaging. In this manner, images with different contrast[25] can be derived from a single acquisition. It is obvious that adding echoes reduces the number of slices that can be interrogated in a given *TR* period. Both 2D multislice and multiecho spin warp imaging, perhaps appearing trivial in hindsight, are, in historic perspective, among the most significant milestones in the quest for imaging efficiency.

4.3 Conjugate Synthesis

A salient property of ***k***-space with implications for imaging speed is its conjugate symmetry, i.e.,

$$\rho(\boldsymbol{k}) = \rho(-\boldsymbol{k}) \tag{10}$$

This implies that two data samples corresponding to spatial frequencies $\boldsymbol{k}$ and $-\boldsymbol{k}$ are identical. In principle, therefore, it suffices to acquire only half of ***k***-space. In reality, however, the conjugate symmetry is often not perfect. Causes of deviations are phase shifts from magnetic field inhomogeneity and motion, which require appropriate correction of the raw

data before Fourier reconstruction[26] (see also ***Partial Fourier Acquisition in MRI***).

As already pointed out, sampling in the k_y and k_z directions is much slower than sampling in the k_x direction. Therefore, by exploiting the redundancy in phase-encoding lines, scan time is halved. Halving imaging time by conjugation was described by Margosian et al.[27] and also by Feinberg et al.[28] Because the phase correction requires sampling of a small number of data lines on the conjugate half, the time saving is usually somewhat less than 50%.

4.4 Variable Flip Angle Imaging

In their seminal work on pulse Fourier transform spectroscopy Ernst and Anderson[29] showed that for a train of equidistant rf pulses, the extent of saturation can be controlled by adjusting the rf pulse flip angle α and further that the signal peaks for the condition

$$\alpha_{\text{opt}} = \cos^{-1} \exp(-TR/T_1) \tag{11}$$

where α_{opt} is the optimum pulse flip angle (also called the 'Ernst angle'), which is valid provided that $TR \gg T_2$. It is readily recognized that flip angles $\alpha < 90^\circ$ are not compatible with the simple Hahn or Carr–Purcell imaging pulse sequence, since inversion of the residual longitudinal magnetization by the subsequent phase reversal pulse would lead to a steady state of very low magnetization. Haase et al.[30] modified the original spin warp technique in which a gradient echo is sampled and showed that in this manner TR could be reduced at least 10-fold relative to corresponding spin echo implementations, which may have prompted the authors to the acronym 'FLASH' (*f*ast *l*ow *a*ngle *sh*ot). Other solutions to the problem involve the idea to restore the longitudinal magnetization with a second 180° pulse.[31] An alternative solution is to select a flip angle so that $90^\circ < \alpha < 180^\circ$, followed by the usual phase-reversal 180° pulse.[32,33] In contrast to FLASH, the latter techniques provide true spin echo images in which the signal is attenuated as $\exp(-TE/T_2)$ rather than $\exp(-TE/T_2{*})$ as in FLASH.

The FLASH signal can readily be calculated from the Bloch equations to yield

$$S(TR, \alpha, TE) \propto \frac{1 - \exp(-TR/T_1)}{1 - \cos\alpha \exp(-TR/T_1)} \sin\alpha \times \exp(-TE/T_2^*) \tag{12}$$

For $\alpha = \alpha_{\text{opt}}$, equation (12) simplifies to

$$S_{\alpha_{\text{opt}}}(TE) \propto \tan(\tfrac{1}{2}\alpha) \exp(-TE/T_2^*) \tag{13}$$

In Figure 3(a), the relative S/N is plotted as a function of TR/T_1 for $\alpha = 90^\circ$ and $\alpha = \alpha_E$, equation (12). In either case, a shortened data acquisition time exacts an S/N penalty, which, however, is less severe if the flip angle is optimized. At typical imaging field strengths (1 ± 0.5 T), mammalian tissue T_1 relaxation times span a range of about one order of magnitude (from about 0.3 s for fat to about 3–4 s for extracellular fluids). Hence, a compromise setting will have to be chosen for α. Figure 3(b) shows a series of images for which the flip angle was gradually increased, demonstrating the effect of increasing saturation and the progression from proton density to T_1-weighting. Low flip angles emphasize structures with long T_1, such as cerebrospinal fluid in the ventricles. It is noteworthy, however, that the flip angle for optimum contrast between two tissues of differing T_1 is greater than α_{opt}.[34]

The assumption implicit in equation (12), i.e., $TR \gg T_2$ between successive rf pulses, may be invalid at high pulse repetition rates. As first described by Carr,[35] a steady-state situation arises for spins subjected to a train of rf pulses in inhomogeneous magnetic fields, with magnetization building up in a recurrent fashion from cycle to cycle. A similar situation applies in imaging, at least as long as the

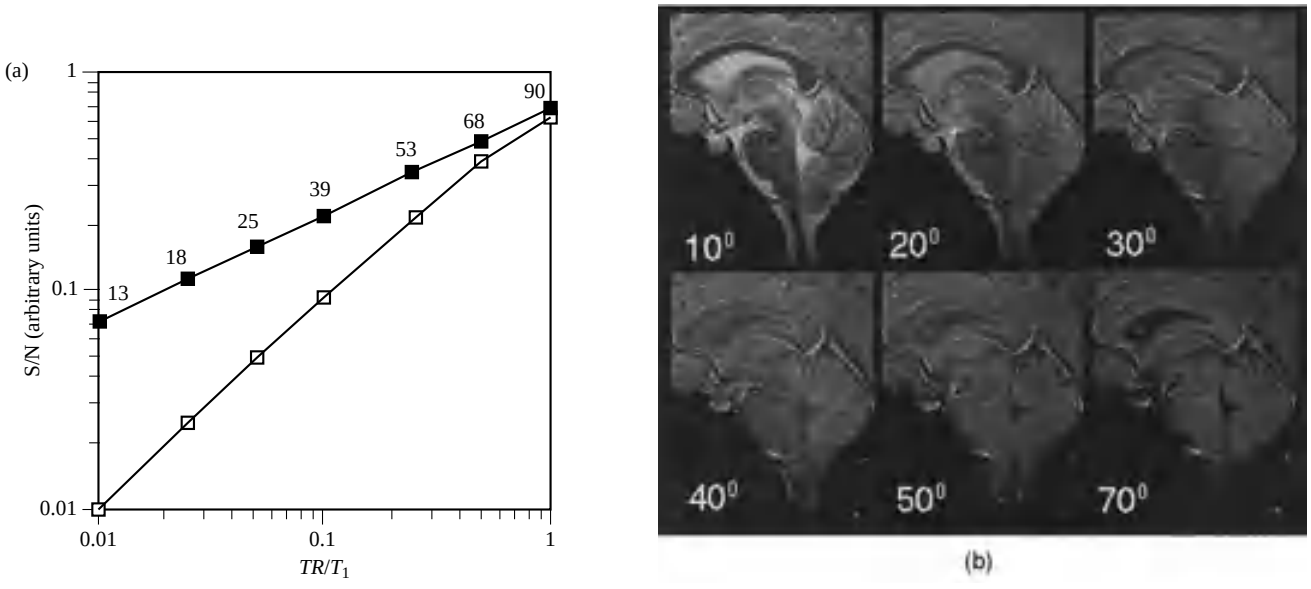

Figure 3 (a) Signal amplitude as a function of TR/T_1 for repetitive pulses after attaining steady state: α=α_{opt} (upper curve, with optimum flip angle indicated), and $\alpha = 90^\circ$ (lower curve), assuming negligible residual transverse magnetization. (b) Effect of increasing pulse flip angle in 2D gradient echo images (TR = 0.3 s), showing effect of gradual differential saturation

gradient moments are constant during successive cycles. In spin warp imaging, however, this latter condition is not satisfied, since the phase-encoding gradient is stepped in an incremental fashion. The ensuing cycle-dependent phase shifts cause intensity artifacts that have a positional dependence, since the phase depends on the spins' location on the phase-encoding axis.[36] If, on the other hand, the phase imparted by the phase-encoding gradient is unwound by a gradient of opposite moment prior to the next-following rf pulse,[36,37] the spatial dependence of the steady state vanishes. Common acronyms for this modification to the generic FLASH pulse sequence are 'GRASS' (*g*radient *r*ecalled *a*cquisition in the *s*teady *s*tate) and 'FISP' (*f*ast *i*maging with *s*teady state *p*recession).

From a tissue contrast point of view, it is often desirable to suppress transverse coherences. Application of spoiler gradients of varying amplitude has been found to be relatively ineffective for this purpose,[38] though schemes were later reported that provide some spoiling efficiency.[39] Nevertheless, a more effective means of eliminating the carry-over of transverse magnetization from previous cycles is to step the rf transmit and receive phase in constant increments from cycle to cycle. Although predicted by Crawley et al.[38] rf-spoiled gradient echo imaging was developed by Matt Bernstein and his colleagues in 1989, but, unfortunately, never published. The contrast characteristics of the two embodiments of FLASH are substantially different. In the high-flip-angle regime, GRASS affords images in which the signal scales as $T_2/(T_2 + T_1)$, hence favoring fluids, where $T_2 \approx T_1$ (as opposed to tissues, where $T_1 \gg T_2$). By contrast, with spoiling, the signal obeys equation (12).

4.5 High-Speed Gradient Echo Techniques

Combination of increased sampling frequency bandwidth and fractional echo sampling with partial Fourier processing,[40] reduction in the number of frequency-encoding samples, and other strategies such as truncated rf pulses permit shortening of pulse repetition times to 5 ms or less.[19,20] The impact of reduced pulse repetition time on S/N is illustrated in Figure 3(a). These methods therefore need to be assessed in terms of the benefits and trade-offs they entail. Besides S/N, contrast is perhaps the single most important criterion for clinical utility. The typically unsatisfactory contrast inherent in high-speed steady-state techniques can be enhanced by means of magnetization preparation,[19] discussed in more detail in ***Whole Body Magnetic Resonance: Fast Low-Angle Acquisition Methods***. The underlying idea is to create a nonequilibrium situation by preceding the train of low angle rf pulses by an inversion pulse for T_1-dependent contrast[41–43] or driven-equilibrium pulses to achieve T_2-weighted contrast.[44] Since, in this case, the magnetization evolves during scanning of ***k***-space, effectively filtering the data in a manner determined by the spin dynamics, the usual sequential scanning from $-k_{max}$ to $+k_{max}$ is not optimal. Remembering that the signal components pertaining to $k \approx 0$ contribute most to contrast, it is necessary to acquire these data at the desired time point during magnetization evolution (e.g., when the signal from a particular tissue is nulled). These requirements can, for example, be reconciled with a ***k***-space ordering scheme that has been called 'centric phase encoding',[42] in which data collection starts at ***k***-space center and proceeds outward.

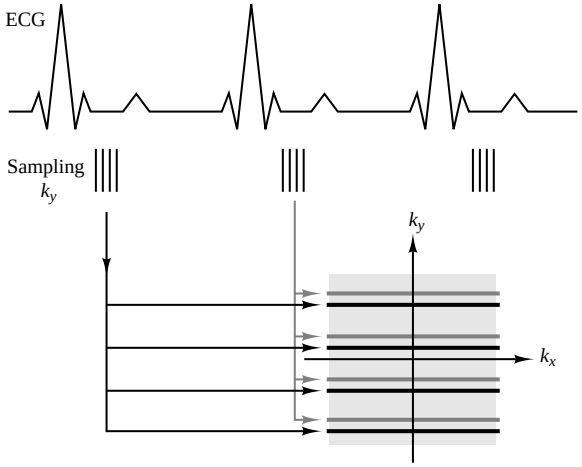

Figure 4 Principle of segmented ***k***-space acquisition in cardiac cine imaging. The RR interval is divided into time periods ('segments') of short duration, during which several lines k_y are encoded. The process is repeated during subsequent cycles until all lines are scanned

Finally, real-time implementations of fast gradient echo scanning are possible by confining images to a single spatial dimension. In this manner, projections can be displayed in real time at a frame rate of 100 s^{-1} as a scrolling bar, analogous to M-mode ultrasound, with possible applications in cardiology.[45] Another interesting idea based on fast gradient echo imaging is a method designed to track interventional devices. It consists of the consecutive generation of three orthogonal projections from a small pointlike object, followed by computation and display of its coordinates in a real-time mode.[46]

A comprehensive review of short-*TR* imaging techniques has been given by Haacke et al.[47]

4.6 Cardiac Gated Techniques

Except when the entire ***k***-space can be covered in a small fraction of the cardiac cycle, such as in EPI,[48] data acquisition in cardiac imaging needs to be synchronized to the cardiac cycle. Therefore, it appears that the minimum scan time in 2D spin warp imaging of the heart is given as $N_y T_c$, with N_y and T_c being the number of phase-encoding samples and cardiac period, respectively. The inherent speed of the gradient echo then can be exploited to subdividing the cardiac period by collecting data at multiple cardiac phases, resulting in a series of temporally resolved images that can be played back in a movie loop, a technique that has been called 'cardiac cine' imaging.[49,50] The minimum scan time can be considerably shortened (albeit at some cost in temporal resolution) if, instead of a single line k_y, multiple lines are scanned per cardiac phase, as illustrated in Figure 4. This modification, also termed 'segmented ***k***-space acquisition'[43] permits shortening of the data acquisition time in cardiac cine imaging to 16–24 heartbeats,[51] which is within the range of a breath-hold period, thus considerably improving cardiac image quality.

5 MULTILINE SCANNING TECHNIQUES

All previously discussed embodiments of spin warp imaging have in common that within one pulse sequence cycle, a single

data line is sampled. Additional echoes are merely a replication of the procedure affording images of increasing T_2-weighting. An inherently more efficient approach makes use of the idea to exploit a plurality of echoes in such a manner that each echo affords a separate k_y line.

5.1 Echo Planar Imaging

In 1977, Mansfield first proposed what he termed 'echo planar imaging' (EPI), in which the entire 2D encoding process could be completed during a single FID. The fundamental principle underlying the technique is to oscillate the read gradient G_x in the presence of a constant gradient G_y.[5] It is readily seen that in this manner, half of ***k***-space is traversed in a zig–zag trajectory. The difficulties in reconstructing images from only half the data and nonorthogonal sampling grids were remedied with the introduction of pre-encoding gradients and discontinuous phase encoding.[22,23] In this manner, entire images of 64 × 128 data samples could be obtained in as little as 50 ms at 2 T field strength.[23,48] For an overview of the subject, the reader is referred to a review by Cohen and Weisskoff[6] (see also ***Echo-Planar Imaging***).

An interesting corollary of single shot EPI is that the pulse repetition time loses its meaning, since the data are collected in single sequence cycle. However, concatenation of individual acquisitions for the purpose of generating movies, for example, underlies the same restrictions as the conventional FLASH method, demanding adjustment of the rf flip angle to control saturation. Cohen and Weisskoff[6] showed 16-frame cardiac movies obtained by acquiring complete images every 67 ms within a single heart beat. Unlike gated techniques, where each image data set, or fraction thereof, is collected during consecutive heart beats, the method is insensitive to variations in heart rate. In contrast to the high-speed FLASH-type methods, however, echo planar imaging puts far more stringent demands on instrumentation, in particular to amplitudes and slew rates of the gradients, which explains its currently limited diffusion. Some of these conditions are relaxed if only a fraction of ***k***-space is scanned from a single echo train. For a detailed discussion of the subject, see ***Echo-Planar Imaging***.

Finally, one wonders what S/N penalty this extraordinary scan speed exacts. At a given resolution, three parameters contribute to S/N:

1. sampling time (S/N $\propto \sqrt{t_s}$);
2. transverse relaxation losses (S/N $\propto \exp(-TE/T_2)$);
3. the fraction of magnetization available for signal creation (determined by saturation) (S/N $\propto f(TR, T_1, \alpha)$.

The following comparison may be instructive. Suppose a typical tissue such as neural white matter is scanned at 1.5 T field strength ($T_1 \approx 700$ ms, $T_2 \approx 75$ ms). Then consider a high-speed gradient echo acquisition with 128 phase encodings and 2 ms readout time, $TR = 5$ ms, $TE \approx 0$, operated at the optimum flip angle, which is 6.8°, and compare it with a single shot EPI with 50 ms total sampling time, performed such that $k_y = 0$ is sampled at $TE = 30$ ms. The results are summarized in Table 1. They imply a net advantage of about a factor of 5 in favor of EPI, defeating the common notion that shortened scan time inevitably exacts a S/N penalty.

Similar arguments in favor of EPI have been put forward by Cohen and Weisskoff.[6] Such a comparison, however, does not withstand more rigorous scrutiny. Suppose we were to repeat the EPI scan every 640 ms, i.e., the equivalent of the FLASH data acquisition time. This would mean that the longitudinal magnetization has only incompletely recovered, therefore requiring operation at the Ernst angle, which is 65°. Doing so reduces the transverse magnetization following the rf pulse to 0.64 [from equation (13)], thus lowering the relative S/N advantage of EPI to (a still substantial) factor of 3.

Table 1 Comparison of S/N in Single Shot EPI and High-Speed FLASH; For Assumptions, See Text

	EPI	FLASH	$(S/N)_{EPI}/(S/N)_{FLASH}$
Sampling time (ms)	50	256	0.44
Magnetization	1	0.06	16.7
exp ($-TE/T_2$)	0.67	1	0.67
Net gain			4.9

5.2 RARE

In 1986, Hennig introduced the spin echo counterpart of EPI,[52,53] initiating a development with significant impact on clinical efficiency. Surprisingly, this work did initially not elicit broad interest. The perception that the images emphasized structures with long T_2, thereby producing significantly T_2-weighted images, prompted Hennig to dub his technique 'RARE', short for *r*apid *a*cquisition with *r*elaxation *e*nhancement. While obviously highly efficient, the extreme T_2 weighting appeared to limit the method to specialized applications such as imaging of cerebrospinal fluid.

Besides scan time reduction by up to an order of magnitude, the current widespread clinical use of the method owes its popularity to its spin echo nature, i.e., being insensitive to magnetic field inhomogeneities. Equally important, however, is the almost unlimited latitude in image contrast RARE provides if implemented in a hybrid mode with only a fraction of ***k***-space covered per echo train. It is interesting that the possibilities for contrast manipulation of the RARE sequence were already recognized by Hennig in his 1986 paper.[52] By ***k***-space weighting the echoes appropriately, Melki et al.[54] showed that virtually any arbitrary contrast is possible. For this purpose, they devised an algorithm for phase-encoding ordering while minimizing adverse effects from discontinuous sampling of k_y-space. For example, assigning early echoes to low spatial frequencies de-emphasizes T_2 weighting. The convolution of the data with the relaxation function, of course, may result in point spread function blurring, since high-k signals are attenuated.[55]

Since each of the n echoes generates n lines k_y, the minimum data acquisition time is lowered n-fold. Nevertheless, when assessing the method's efficiency in terms of scan time per image, one has to consider that the prolonged echo train reduces the number of slice locations that can be interleaved during the dead time following data collection. For example, at an echo train length of 250 ms consisting of 16 echoes, a $TR = 3$ s acquisition provides for fewer than 12 slice locations, rather than about 30 as for a conventional dual echo scan with a second echo time of 100 ms. Finally, Hennig showed that the per-unit-time S/N can be up to a factor of 100 higher in single shot RARE, which again emphasizes what we have seen for EPI, i.e., that increased scan speed does not inevitably penalize S/N. Therefore, the greatly improved efficiency can be traded

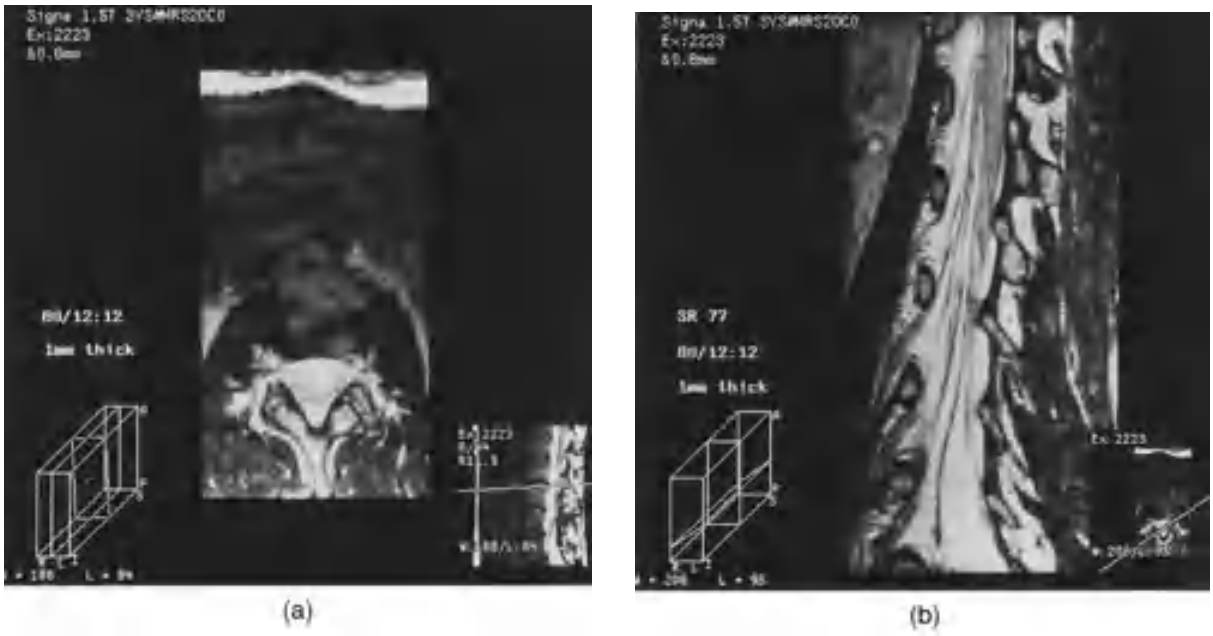

Figure 5 Three-dimensional RARE images of the lumbar spine: (a) axial section; (b) oblique reformation showing nerve roots

for improved resolution (by a factor of four in linear resolution) without adversely affecting S/N when compared with single line spin echo imaging. Further, it enables 3D imaging with all its benefits such as retrospective data rearrangement with image display in secondary planes, which was hitherto impractical in spin echo imaging because of excessive scan time. Examples of 3D RARE images are given in Figure 5. Finally, it has also been shown that RARE and EPI principles can be combined in such a manner that gradient echoes are interweaved into a spin echo train,[56,57] and thus the efficiency is further augmented. (See also ***Multi Echo Acquisition Techniques Using Inverting Radiofrequency Pulses in MRI***.)

6 OTHER METHODS OF SCANNING *k*-SPACE

An alternative ***k***-space scanning technique that, like EPI, uses oscillating gradients is spiral scanning. As implied by the term, the ***k***-space trajectory in this case is a spiral originating at the ***k***-space center. Ahn et al.,[16] who published the first spiral scan images, used a back-projection algorithm for reconstruction. Most of the more recent work is based on constant-velocity interleaved ***k***-space spirals (as opposed to constant angular frequency), an embodiment that is credited to Macovski's laboratory[17] (see ***Spiral Scanning Imaging Techniques***). This scanning mode has the advantage that ***k***-space is covered more uniformly and that the amplitude of the oscillating gradients is constant. Compared with EPI, the gradient amplitude and slew rate requirements are less demanding, and the technique has been found to be tolerant to flow-related dephasing, an observation that was attributed to the low gradient moments near the ***k***-space center and the periodic simultaneous return to zero of all moments.[17]

Spiral scans require different reconstruction algorithms. Fourier transformation along the radial coordinate affords a series of projections, from which the image is obtained by filtered back-projection.[16] Alternatively, the data can be rearranged into a rectilinear grid by interpolation, thus allowing Fourier reconstruction[17] (see also ***Spiral Scanning Imaging Techniques***).

Another nonrectilinear sampling technique suited for high-speed imaging is projection imaging, where ***k***-space is sampled radially in two or three dimensions by simultaneous application of two or three constant-amplitude gradients that are proportional to the sine and cosine of the projection angle. In this manner, a radial path is traced, starting at the center of ***k***-space.[13,14] ***k***-space is covered by stepping the gradient amplitudes by incrementing the projection angle in successive sequence cycles. By selecting shallow rf pulses, the pulse sequence can be run at rates comparable to gradient echo spin warp imaging. Since sampling can start almost immediately following excitation, the technique is particularly suited for imaging short-T_2 tissues such as lung parenchyma[58] or imaging of nuclei with inherently short T_2 such as ^{11}B.[59] (See also ***Projection–Reconstruction in MRI***.)

In summary, during the past two decades since its inception, MRI has revealed a wide spectrum of technical approaches for covering data space. Scan speed is a continuum ranging from milliseconds to minutes, with trade-offs between temporal resolution, S/N and spatial resolution. The rate at which ***k***-space can be scanned is determined significantly by the imager's hardware, in particular the achievable amplitudes of the spatial encoding gradients and their switching rates, and the receiver's bandwidth. Besides intrinsic S/N, the ultimate scan speed may be limited by adverse bioeffects, notably peripheral nerve stimulation caused at increased dB/dt of the switched gradients.

7 RELATED ARTICLES

Echo-Planar Imaging; Gradient Coil Systems; Image Formation Methods; Multi Echo Acquisition Techniques Using Inverting Radiofrequency Pulses in MRI; Partial Fourier

Acquisition in MRI; Projection–Reconstruction in MRI; Spiral Scanning Imaging Techniques; Whole Body Magnetic Resonance: Fast Low-Angle Acquisition Methods; Whole Body Magnetic Resonance Spectrometers: All-Digital Transmit/Receive Systems.

8 REFERENCES

1. A. Villringer, B. R. Rosen, J. W. Belliveau, J. L. Ackerman, R. B. Lauffer, R. B. Buxton, Y. S. Chao, V. J. Wedeen, and T. J. Brady, *Magn. Reson. Med.*, 1988, **6**, 164.
2. J. W. Belliveau, D. N. Kennedy, R. C. McKinstry, B. R. Buchbinder, R. M. Weisskoff, M. S. Cohen, J. M. Vevea, T. J. Brady, and B. R. Rosen, *Science (Washington, DC)*, 1991, 716.
3. K. K. Kwong, J. W. Belliveau, D. A. Chesler, I. E. Goldberg, R. M. Weisskoff, B. Poncelet, D. N. Kennedy, B. E. Hoppel, M. S. Cohen, R. Turner, H. Cheng, T. Brady, and B. Rosen, *Proc. Natl. Acad. Sci. USA*, 1992, **89**, 5675.
4. S. Ogawa, D. W. Tank, R. Menon, J. M. Ellerman, S. G. Kim, H. Merkle, and K. Ugurbil, *Proc. Natl. Acad. Sci. USA*, 1992, **89**, 5951.
5. P. Mansfield, *J. Phys. C*, 1977, **10**, L55.
6. M. S. Cohen and R. M. Weisskoff, *Magn. Reson. Imaging*, 1991, **9**, 1.
7. F. W. Wehrli, *Fast-Scan Magnetic Resonance: Principles and Applications*, Raven Press, New York, 1991, p. 1.
8. S. Ljunggren, *J. Magn. Reson.*, 1983, **54**, 338.
9. W. A. Edelstein, J. M. S. Hutchison, G. Johnson, and T. Redpath, *Phys. Med. Biol.*, 1980, **25**, 751.
10. A. Kumar, D. Welti, and R. Ernst, *J. Magn. Reson.*, 1975, **18**, 69.
11. W. Aue, E. Bartholdi, and R. Ernst, *J. Chem. Phys.*, 1976, **64**, 2229.
12. P. C. Lauterbur, *Nature (London)*, 1973, **243**, 190.
13. C.-M. Lai and P. C. Lauterbur, *Phys. Med. Biol.*, 1981, **26**, 851.
14. I. R. Young, D. R. Bailes, M. Burl, A. G. Collins, D. T. Smith, M. J. McDonnell, J. S. Orr, M. L. Banks, G. M. Bydder, R. H. Greenspan, and R. E. Steiner, *J. Comput. Assist. Tomogr.*, 1982, **6**, 1.
15. A. Macovski, *Magn. Reson. Med.*, 1985, **2**, 29.
16. C. Ahn, J. Kim, and Z. Cho, *IEEE Trans. Med. Imaging*, 1986, **5**, 2.
17. C. H. Meyer, B. S. Hu, D. G. Nishimura, and A. Macovski, *Magn. Reson. Med.*, 1992, **28**, 202.
18. O. Heid, M. Deimling, and W. Huk, *Magn. Reson. Med.*, 1993, **29**, 280.
19. A. Haase, *Magn. Reson. Med.*, 1990, **13**, 77.
20. J. Frahm, K. D. Merboldt, H. Bruhn, M. L. Gyngell, W. Hänicke, and D. Chien, *Magn. Reson. Med.*, 1990, **13**, 150.
21. R. Rzedzian, B. Chapman, P. Mansfield, R. E. Coupland, M. Doyle, A. Crispin, D. Guilfoyle, and P. Small, *Lancet*, 1983, **2**, 1281.
22. B. Chapman, R. Turner, R. Ordidge, M. Doyle, M. Cawley, R. Coxon, P. Glover, and P. Mansfield, *Magn. Reson. Med.*, 1987, **5**, 246.
23. I. L. Pykett and R. R. Rzedzian, *Magn. Reson. Med.*, 1987, **5**, 563.
24. L. Crooks, M. Arakawa, J. Hoenninger, J. Watts, R. McRee, L. Kaufman, P. L. Davis, A. R. Margulis, and J. DeGroot, *Radiology*, 1982, **143**, 169.
25. L. E. Crooks, D. A. Ortendahl, L. Kaufman, J. Hoenninger, M. Arakawa, J. Watts, E. R. Cannon, M. Brant-Zawadzki, P. L. Davis, and A. R. Margulis, *Radiology*, 1983, **146**, 123.
26. J. R. MacFall, N. J. Pelc, and R. M. Vavrek, *Magn. Reson. Imaging*, 1988, **6**, 143.
27. P. Margosian, F. Schmitt, and D. Purdy, *Health Care Instrum.*, 1986, **1**, 195.
28. D. A. Feinberg, J. D. Hale, J. C. Watts, L. Kaufman, and A. Mark, *Radiology*, 1986, **161**, 527.
29. R. R. Ernst and W. A. Anderson, *Rev. Sci. Instrum.*, 1966, **37**, 93.
30. A. Haase, J. Frahm, and D. Matthaei, *J. Magn. Reson.*, 1986, **67**, 258.
31. J. A. Tkach and E. M. Haacke, *Magn. Reson. Imaging*, 1988, **6**, 373.
32. A. R. Bogdan and P. M. Joseph, *Magn. Reson. Imaging*, 1990, **8**, 13.
33. H. Jara, F. W. Wehrli, H. Chung, and J. C. Ford, *Magn. Reson. Med.*, 1993, **29**, 528.
34. N. J. Pelc, *Magn. Reson. Med.*, 1993, **29**, 695.
35. H. Carr, *Phys. Rev.*, 1958, **112**, 1693.
36. J. Frahm, K. D. Merboldt, and W. Hanicke, *J. Magn. Reson.*, 1987, **27**, 307.
37. K. Sekihara, *IEEE Trans. Med. Imaging*, 1987, **6**, 157.
38. A. P. Crawley, M. L. Wood, and R. M. Henkelman, *Magn. Reson. Med.*, 1988, **8**, 248.
39. H. Z. Wang and S. J. Riederer, *Magn. Reson. Med.*, 1990, **15**, 175.
40. T. K. Foo, F. G. Shellock, C. E. Hayes, J. F. Schenck, and B. E. Slayman, *Radiology*, 1992, **183**, 277.
41. J. P. Mugler III and J. R. Brookeman, *Magn. Reson. Med.*, 1990, **15**, 152.
42. A. E. Holsinger and S. J. Riederer, *Magn. Reson. Med.*, 1990, **16**, 481.
43. R. R. Edelman, B. Wallner, A. Singer, D. J. Atkinson, and S. Saini, *Radiology*, 1990, **177**, 515.
44. J. P. Mugler, III, T. A. Spraggins, and J. R. Brookeman, *J. Magn. Reson. Imaging*, 1991, **1**, 731.
45. J. D. Pearlman, C. J. Hardy, and H. E. Cline, *Radiology*, 1990, **175**, 369.
46. C. L. Dumoulin, S. P. Souza, and R. D. Darrow, *Magn. Reson. Med.*, 1993, **29**, 411.
47. E. M. Haacke, P. A. Wielopolski, and J. A. Tkach, *Rev. Magn. Reson. Med.*, 1991, **3**, 53.
48. R. R. Rzedzian and I. L. Pykett, *Am. J. Roentgenol.*, 1987, **149**, 245.
49. G. Nayler, D. N. Firmin, and D. B. Longmore, *J. Comput. Assist. Tomogr.*, 1986, **10**, 715.
50. G. H. Glover and N. J. Pelc, in *Magnetic Resonance Annual*, ed. H. Y. Kressel, Raven Press, New York, 1988, p. 299.
51. R. R. Edelman, W. J. Manning, D. Burstein, and S. Paulin, *Radiology*, 1991, **181**, 641.
52. J. Hennig, A. Nauerth, and H. Friedburg, *Magn. Reson. Med.*, 1986, **3**, 823.
53. J. Hennig, H. Friedburg, and D. Ott, *Magn. Reson. Med.*, 1987, **5**, 380.
54. P. S. Melki, R. V. Mulkern, L. P. Panych, and F. A. Jolesz, *Magn. Reson. Imaging*, 1991, **1**, 319.
55. P. S. Melki, F. A. Jolesz, and R. V. Mulkern, *Magn. Reson. Med.*, 1992, **26**, 328.
56. K. Oshio and D. A. Feinberg, *Magn. Reson. Med.*, 1991, **20**, 344.
57. D. A. Feinberg and K. Oshio, *Radiology*, 1991, **181**, 597.
58. C. J. Bergin, G. H. Glover, and J. M. Pauly, *Radiology*, 1991, **180**, 845.
59. G. H. Glover, J. M. Pauly, and K. M. Bradshaw, *J. Magn. Reson. Imaging*, 1992, **2**, 47.

Biographical Sketch

Felix W. Wehrli. *b* 1941. M.S., 1967, Ph.D., 1970, chemistry, Swiss Federal Institute of Technology, Switzerland. NMR application scientist, Varian AG, 1970–79; Executive Vice President, Bruker Instruments, Billerica, 1979–82; NMR Application Manager, General Electric Medical Systems, Milwaukee, 1982–88. Currently Professor of Radiologic Science and Biophysics, University of Pennsylvania Medical School. Approximately 95 publications. Current research specialty: NMR imaging of biomaterials, specifically trabecular bone.

Whole Body Studies: Impact of MRS

George K. Radda

University of Oxford and The John Radcliffe Hospital, Oxford, UK

1 INTRODUCTION

It is common to refer to MRS studies of humans as 'whole body' MRS, or, as indicated in the title of this article, 'whole body studies'. This is a misnomer, since much effort is expended in obtaining MR spectra from a defined organ or even a defined part of the given organ and not from the whole body. The term arose because generally, though not exclusively, this kind of measurement is taken in magnets that can accommodate the human body. In the study of limbs and the head, this is not always necessary, and much human MRS has been done using magnets that only accommodate part of the body. This article is therefore about the impact of MRS in human investigations, but excludes discussion of work in which MRS is used to study samples from biopsies or body fluids of humans. Much of the human data is inevitably backed up, extended, or elucidated by parallel animal investigations. Although such studies have played an essential role in the development and evaluation of human MRS, they are not included in this article for organizational rather than conceptual reasons.

1.1 The Varying Aims of Human MRS

Following from the success of MRI as a radiological tool in clinical diagnosis, it is not uncommon to view MRS as just another extension of the technique for the characterization and description of pathology. Thus one aim is to find clinical applications that can contribute to diagnosis in a routine examination. It will be shown below that this aim is far from having been achieved, and it will be argued that, given the nature and cost of the technique, the major justification for using MRS rests elsewhere. The second main aim of MRS is to investigate the dynamics of normal human biochemical processes. It is necessary to ask, however, why it is important to study fundamental biochemical processes in humans when the same cellular mechanisms are likely to be operative in all mammalian species. Significant special aspects of human biology, among others, include the wide range of polymorphism that results in the biochemical heterogeneity, the nature of the immune system, the advanced central nervous system, and the ease by which the effects of training, adaptation and environmental factors can be studied in humans. In addition, developmental processes at the structural and biochemical level require direct human investigations. The most important of the goals in MRS research is the study of the biochemical basis of human disease. Many human diseases have no useful animal models; the response to pharmacological interventions is often species-specific, and human morphology and anatomy has a unique influence on the expression and development of disease.

1.2 Approaches to Clinical MRS

A successful clinical study by MRS has several basic requirements:

(a) to obtain well-resolved spectra from defined regions of human organs and tissues in a time acceptable to patients;
(b) to obtain as much information as possible, and to assign and interpret the biochemical meaning of the spectra;
(c) to use the biochemical information derived to advance clinical understanding or management.

(a) Localization strategies fall into two major categories: single volume selection and spectroscopic images obtained in the form of one-dimensional slices or with lower frequency as two- or three-dimensional data acquisition. The choice of the method used is often limited by the instrumentation provided by the manufacturer (different manufacturers emphasize their own preferred options). It would be desirable if the localization could be tailored to the nature of the clinical condition to be studied. This is likely to become increasingly the case. Since the majority of current human spectrometers are based primarily on advanced MRI systems, image guided localization is the common practice.

(b) There are instances where a single spectroscopic measurement provides valuable clinical data. In most instances, however, the information content of the study is considerably increased by the measurement of reaction rates either directly, or more generally, in response to some intervention or stress test. For example, almost all the investigations of muscle metabolism and energetics in disease rely on following changes in the concentrations of high- and low-energy phosphates and in the pH values in response to exercise (dynamic or isometric), and during the recovery phase after exercise. In organs such as the liver, stress might be induced by the infusion or oral administration of substrates (glucose, fructose, etc.), while the intervention of most interest in tumors could well be the therapeutic method that is being used.

In the human brain, sensory stimulation may be used in some measurements (e.g., glucose uptake[1]) to provide regional activation. It is also possible that metabolic changes may be detected in responses to the administration of drugs that interfere with neurotransmitter release or function. Cardiac work can be increased by exercise (dynamic leg exercise or isometric hand grip) or by infusion of dobutamine.

The assignment of peaks in the spectra observed in vivo and their biochemical interpretation are largely based on extensive studies of cells, isolated organs, and animals. Spectral resolution and quantification often remain a problem, but progress is being made to replace measurements of metabolite ratios with derivation of absolute amounts or intracellular concentrations.

(c) Increasingly, the understanding of mechanisms of human disease should lead to the design and evaluation of new therapies. MRS, in the first instance, contributes to this process in a general sense. There are, at present, only a handful of specific

For References see p. 9

cases where a spectroscopic evaluation altered the management of a particular patient. Indeed, the view has been advanced by the present author that the success of MRS will be measured by how readily the expensive and technically demanding MRS study can be replaced by a relatively simple but perhaps less informative and more empirical test for following the clinical status of a patient. This view is based on the belief that if we can define the nature and extent of the disease from MRS studies, it should be possible to design tests that can be correlated.

1.3 What Nuclei?

The nuclei that have been used so far in human investigations are ^{31}P, ^{1}H, ^{13}C, ^{19}F, ^{23}Na, and ^{7}Li. This choice is often governed by the technology, i.e., relative sensitivities, ease of detection, resolution, and quantification. Since we now know that high-resolution spectra can be obtained from all these nuclei in human organs (with the exception of ^{23}Na, where only total, largely extracellular, Na^+ is measured), it is essential that their choice should be governed by the biomedical problems we wish to solve.

1.3.1 ^{31}P MRS

This is widely used to investigate cellular bioenergetics in vivo.[2] Essentially, the following parameters that relate to the energetics are measured: the relative and, more seldom, absolute concentrations of ATP, PCr, Pi, and hexose phosphate, and the value of intracellular pH, which is often equated with the production of lactic acid. The concentration of ADP is often calculated assuming that creatine kinase is at equilibrium. Following changes in these values with stress (e.g., exercise in skeletal muscle and heart), substrate infusion, or administration (e.g., fructose, galactose, and glucose) yields direct or indirect measures of specific enzyme activities or of rates of transport of substrates or ions (e.g., Na^+/H^+ exchange rates). Additionally, magnetization transfer has been used to measure the activities of creatine kinase in human muscle,[3] brain,[4] and heart,[5] and in principle the activity of ATP synthase, so far only achieved in animal studies in vivo.[6]

In addition to the study of energetics, ^{31}P MRS can be used to follow pathways associated with the synthesis and degradation of phospholipids. Key molecules often detected include phosphoethanolamine and phosphocholine, which are intermediates in the Kennedy pathway of phospholipid biosynthesis, but may also be generated by specific phospholipase C catalyzed degradation of membrane phospholipids, perhaps involved in signaling pathways during cell proliferation. Other degradation products observed are glycerophosphorylcholine and glycerophosphorylethanolamine. In vivo, the resonances of these small metabolites may be obscured by the much larger and broader phosphodiester (PDE) signal arising from the phospholipids in the bilayers of membranes.[7]

1.3.2 ^{13}C MRS

This provides an extremely powerful approach, since, through the use of ^{13}C-enriched substrates, it can lead to measurements of individual reaction rates or fluxes through specific pathways.[8] The formation and breakdown of muscle and liver glycogen can be studied in this way.[9] The sensitivity of ^{13}C detection is considerably enhanced by the proton observe carbon edit (POCE) method. This allows detection of the ^{13}C label in the ^{1}H spectrum with heteronuclear editing, thus obtaining the information in the ^{13}C spectra with the sensitivity of ^{1}H MRS. This technique, as well as direct ^{13}C measurements, has been used to observe the flow from [1-^{13}C]glucose into the C-4 of glutamate via the tricarboxylic acid cycle in human brain.[10]

1.3.3 ^{1}H MRS

This is now widely used in clinical and physiological investigations, particularly of the human brain. Special techniques are required to suppress the water resonance, and in addition it is sometimes necessary to edit the spectra if specific components (e.g., lactate) are to be observed. The major metabolites that can be detected include *N*-acetylaspartate, glutamate and glutamine, creatine + phosphocreatine, and, under some conditions, lactate.[11] Additional signals are obtained from the so-called 'choline-containing compounds' (likely to represent a mixture of several substances), taurine and inositol phosphates.

Unlike the metabolites that are detected in the ^{31}P MR spectra, the components seen in ^{1}H NMR are not directly linked through major pathways, or in several instances have no established functional role. The lactate signal, however, represents a sensitive handle on anaerobic glycolysis. Knowledge of total creatine (from creatine and phosphocreatine) provides useful data when combined with measurements of phosphocreatine by ^{31}P MRS. *N*-acetylaspartate has been used empirically as a 'neuronal marker', though this remains to be established.

1.3.4 ^{19}F MRS

This is used for the measurement of the tissue concentration and metabolism of fluorinated drugs (e.g., the antidepressant fluoxetine in the brain)[12] or fluorinated agents like halothane.

1.3.5 ^{7}Li MRS

The unique use of lithium therapy in psychiatric patients is beginning to be studied by this technique, allowing the determination of brain concentrations and pharmacokinetics.[13]

In the discussion below, studies will not be classified according to the nuclei observed, but rather will be presented in relation to the investigation of physiological and pathological problems.

2 NORMAL HUMAN BIOCHEMISTRY

The distinguished Harvard physiologist Walter B. Cannon (1871–1945) coined the term 'homeostasis' to describe the coordinated physiological processes that maintain most of the steady state in an organism. The structural and functional features of the components of the organism are optimized to provide adjustments to the required performance of the system (input/output balance). Ultimately, cellular biochemical regulatory processes perform this function. In addition to short-term molecular control, the long-term response to chronically increased needs involves adjustments in the design properties of the system. Weibel[14] introduced the principle of symmorphosis

and defined it 'as a state of structural design commensurate to functional needs resulting from regulated morphogenesis'.

MRS in vivo provides a unique way of studying control, development and adaptation, since it provides quantitative data about 'molecular integrative physiology' through the measurement of dynamics, structure and interactions within any part of the whole organism. While traditionally medicine is 'organ-oriented' and MRS is used to examine organs, the exciting aspect of the method is that it is particularly suited for the observation of coordinated bodily functions at the molecular level.

2.1 Control of Bioenergetics In Vivo

2.1.1 Skeletal Muscle

One of the fundamental questions in the understanding of bioenergetics in vivo is how the demand for ATP utilization is linked to increased supply of energy via oxidative metabolism and therefore to increased rate of oxygen delivery to the tissue. Oxygen delivery to the mitochondrion within the intact cells has four components:

1. the oxygen-carrying capacity of blood, i.e., the nature and amount of hemoglobin present;
2. the rate of flow of blood through major blood vessels;
3. capillary density and diffusion from the capillary to the mitochondrion;
4. the ability of oxyhemoglobin to release its oxygen, i.e., the dissociation of curve for oxyhemoglobin.

^{1}H NMR has been used to observe the ratio of oxy/deoxymyoglobin, since the chemical shifts of the proximal histidine resonance of the two forms are different.[15] Indirectly, blood oxygenation can be measured through the effect of paramagnetic deoxyhemoglobin on the T_2 relaxation time of blood,[16] although this effect has not yet been explored in studies of human muscle. It is believed to be partly responsible for the changes seen in the brain during sensory stimulation.[1]

It is possible to link NMR studies to measurement of tissue oxygenation using infrared detection of oxy/deoxymyoglobin and hemoglobin. During exercise, the decrease in the oxy forms can be related to oxygenation, and the rate of recovery is a measure of the oxidative capacity of the system.[17]

While the various pathways involved in the energetics of skeletal and cardiac muscle are well mapped out, the way in which they are controlled in the intact cell is less well understood. NMR studies in vivo have contributed a great deal to our understanding of some of the control functions, particularly in skeletal and cardiac muscle.

In skeletal muscle, mitochondrial oxidation in vivo was shown to depend, in a hyperbolic manner, on the concentration of ADP, with a K_m of about 30 μM. This value is very close to that reported by Chance and Williams for isolated mitochondria. Three types of experiments have been performed to arrive at this conclusion.

1. Chance and his colleagues have shown that in a graded exercise protocol in which the work is measured with an ergometer, during performance going from rest (state 4) to exercise (state 3), the transfer function, as defined in Chance et al.,[18] approximates a rectangular hyperbola (i.e., the plot of work against Pi/PCr is hyperbolic), giving a K_m for ADP of 28 μM. This follows from the fact that if there are no pH changes, as is the case in the relatively submaximal protocol used, the Pi/PCr ratio is proportional to the concentration of ADP.[18]
2. It was shown that the ADP concentration reached at the end of exercise and the initial rate of phosphocreatine resynthesis during recovery in human arm muscle also follow the same relationship, giving a K_m value of 27 mM and a V_{max} for the ATP synthesis rate of 43 mM min^{-1}.[19]
3. Measurements of the flux between ATP and Pi during steady state isometric muscle contraction using magnetization transfer in animal muscle give a direct indication of the relationship between ADP and mitochondrial oxidative phosphorylation.[6]

Recovery from exercise is a function of mitochondrial ATP synthesis.[20] It can therefore be thought of as an aerobic work jump, in which the rate constant of PCr recovery is a function of V_{max} for ATP synthesis, with the complication that the pH may also be recovering from a low value. As no work is done, the absolute rate of PCr resynthesis is an estimate of the oxidative ATP synthesis rate minus a small component of basal ATP turnover. The hyperbolic relationship between oxidation rate and [ADP] can be used to estimate apparent V_{max} and mitochondrial K_m in the same way as in oxidative exercise.

The apparent V_{max} is a function of the density and capacity of working mitochondria and the supply of substrate and oxygen and is independent of muscle mass. A preliminary calculation for human forearm muscle suggests that the V_{max} calculated from PCr recovery kinetics is 60–70% of that predicted from the intrinsic activity and muscle content of mitochondria. A reduction in apparent V_{max} can be caused by an intrinsic mitochondrial defect or a reduction in mitochondrial density (e.g., heart failure) in arterial oxygen carrying capacity or arterial pO_2 or in muscle blood flow.[21]

The quantitative analysis of the energetic processes during exercise is more complex, since both oxidative and anaerobic glycolytic processes contribute to ATP synthesis while the ATP used against the work done depends on muscle mass and other parameters. In a detailed analysis of exercise performed at three levels of mechanical power output under ischemic and aerobic conditions, it was suggested that oxidative ATP synthesis was negligible during the first half-minute of aerobic exercise, and increased with a half-time of around 0.75 min, although the mitochondrial controller [ADP] increased much more rapidly.[22] Initial PCr resynthesis after exercise appeared to be an adequate estimate of oxidative synthesis at the end of aerobic exercise. The pH dependence of proton efflux inferred from analysis of recovery could be used to estimate ATP synthesis by glycogenolysis/glycolysis to lactic acid during aerobic exercise. Measurement of lactic acid production by ^{1}H NMR, which has been demonstrated as a possibility,[23] might be used to confirm these conclusions. The quantitative interpretation of ^{31}P MRS data from human skeletal muscle, which has many applications to the study of physiology and pathophysiology, and of muscle bioenergetics and proton handling, has been analyzed in detail.[20]

^{31}P NMR is particularly suited for the examination of the relationship between work output and energetics in vivo. This has been achieved in animal models using, preferentially, sciatic nerve stimulation inducing tetani at different frequencies and with different time intervals. In humans, a variety of experimental protocols have been worked out. Some studies have used the steady state or graded work rate from a constant load

For References see p. 9

or a Cybex ergometer, while others have used force produced in an isometric contraction. Chance and co-workers have examined the relationship between reaction velocities (e.g., ATP utilization) and tissue work rates to the concentration of regulatory molecules in skeletal muscle.[18] They examined the forearm muscle and measured values of Pi/PCr and the work by an ergometer in a graded metabolic load situation. They expressed the relationship between work and velocities as a 'transfer function', showing the hyperbolic relationship between velocity and Pi/PCr. The form of this transfer function varies between normal individuals and well-trained athletes, and can be used as an indication of exercise performance. Boska studied the ATP cost of force production in the human *gastrocnemius* muscle using ^{31}P NMR and an exercise protocol of isometric maximum voluntary contraction, and estimated the contributions to ATP production from three different processes.[24] The rate of change of PCr was used to estimate ATP production rates from creatine kinase rates during exercise and from oxidative phosphorylation during the first 10 s of recovery. The anaerobic glycolysis was estimated from the rate of change of pH, from an assumed buffering capacity and hydrogen ion production stoichiometry. The results showed that by the end of 30 s of exercise, the total ATP production and ATP cost of force production had stabilized and remained constant until the end of a 2 min period. It was also shown that the ATP cost of force production is lower in the first second than at any time, or possibly that ATP production is underestimated at later time points.

2.1.2 ^{13}C NMR and Glycogen

A major new approach to the study of substrate utilization in bioenergetics is provided by the use of ^{13}C NMR and in particular in the use of ^{13}C-enriched substrates, which can lead to measurements of individual reaction rates or fluxes through specific pathways (for a recent review of ^{13}C NMR, see Cerdan and Seelig[25]).

An important new observation for muscle investigations was that, in spite of its high molecular weight, glycogen is fully visible by ^{13}C NMR in organs and tissues.[26] Thus the synthesis and breakdown of glycogen during muscle exercise can now be followed for the first time noninvasively in human muscles. There are many opportunities to study fundamental questions of the regulation of carbohydrate metabolism under a variety of conditions. One example of this was the pioneering study in which the rate of human muscle glycogen formation was measured in normal and diabetic subjects, using infused, isotopically labeled [1-^{13}C]glucose and ^{13}C NMR.[27] The important conclusions from these measurements were that

(i) synthesis of muscle glycogen accounted for most of the total body glucose uptake and all of the nonoxidative glucose metabolism;
(ii) in subjects with non-insulin-dependent diabetes, the rate of glycogen formation was decreased by 60% compared with the rate in normal controls.

2.1.3 Human Heart

Many of the same parameters can, in principle, be measured in heart muscle, and have indeed been studied in isolated and in vivo animal hearts. So far, only the PCr/ATP ratio as an index of energetics has been quantitatively measured in the human heart, using special localization or spectroscopic imaging techniques (for a review see Conway and Radda[28]). In normal subjects, the PCr/ATP ratio remained constant when the heart was stressed, either by an isometric hand grip exercise[29] or by a dynamic leg exercise performed in the prone position.[28] Thus, in the normal situation, the heart can adequately regulate its phosphates over a range of workloads. The results show that free ADP is not the primary regulator of increased ATP synthesis in the normal heart in these situations.

2.1.4 Brain Metabolism

Glucose is the main, and generally the sole, energy source for the brain. Thus measurement of the regional cerebral rate of glucose consumption together with that of oxygen consumption and regional blood flow has been used to describe brain energetics. Using radiolabeled compounds, in humans [2-^{11}F]fluorodeoxyglucose accumulation and ^{17}O uptake are followed by positron emission tomography.

Recently, largely as a result of work by Shulman and colleagues (for a review, see Shulman et al.[1]) NMR spectroscopic methods have been developed for measuring regional metabolic parameters.

The kinetics of glucose transport in the human brain has been determined by measuring brain glucose concentration by ^{13}C NMR at steady state as a function of plasma glucose concentration. Using a model for facilitated transport, values of K_m = 4.9 mM and V_{max} = 1.1 μmol g^{-1} min^{-1} were derived from the transporter. The maximal glucose influx was 3.6 times the normal glycolytic rate, showing that increases in energy demand can be accommodated by glucose transport. In addition, the concentration of glucose in the brain (about 1.2 mM) is well above the K_m for hexokinase, so that changes in plasma glucose will not change the hexokinase flux except at very low concentrations. The turnover rate of the brain glutamate pool can be measured by following the incorporation of ^{13}C isotope from [1-^{13}C]glucose into C-4 of glutamate on the first timing of the tricarboxylic acid (TCA) cycle. The isotopic flux has been measured directly by ^{13}C NMR and by the proton observe carbon edit method. By fitting the results to a metabolic model, the rates of the TCA cycle can be determined, which gives a measure for the O_2 consumption rates. For the human occipital lobe/visual cortex, this was found to be 1.5 μmol O_2 g^{-1} min^{-1}, a value close to that reported from PET studies.[1]

Visual stimulation results in observable metabolic changes in the visual cortex that include increased lactate production (observed by ^{1}H NMR),[1] decreased brain glucose concentration,[30] and a change in the PCr/ATP ratio[31] as seen from ^{31}P NMR.

2.1.5 Magnetization Transfer and Reaction Fluxes

One of the many advantages of NMR in cellular studies is that it can provide dynamic information about intracellular events, and give a measure of reaction fluxes catalyzed by enzymes, whether in the steady state or at equilibrium. The role of creatine kinase in skeletal muscle, heart, and brain has been debated for some years, and has been studied in these organs (in animal preparations) by magnetization transfer techniques.[2] In humans, creatine kinase fluxes have been measured in skeletal muscle, where it was shown that the PCr → ATP

flux decreases during exercise,[3] and in the brain, where the activity was shown to be twice as high in gray as in white matter.[4] These kinds of measurements as well as studies of ATP-synthase activities have not yet been explored further in human investigations, largely because of the time required for obtaining reliable data.

3 HUMAN DISEASE

In broad terms, human diseases that have been studied using MRS can be conveniently divided into four major categories (Sections 3.1–3.4 below).

3.1 Impaired Oxygen and Substrate Delivery

Oxygen delivery to tissues and organs depends on three factors: blood flow, hemoglobin concentration in the blood, and oxyhemoglobin dissociation characteristics. Alterations in any one of these parameters may impair oxidative phosphorylation, with a concomitant increase in anaerobic glycolysis leading to the production of lactic acid.

3.1.1 Muscle

Stenosis in limb arteries produces cramp and pain in patients, with intermittent claudication. ^{31}P MRS has been used by several groups to investigate the metabolic consequences and severity of peripheral vascular disease. While at rest changes in metabolites and intracellular pH (pH_i) were observed in severe claudicants (the pH being significantly alkali), the most characteristic and specific changes were detected during exercise and during the following recovery phase. During exercise, PCr utilization and intracellular acidosis were enhanced, indicating a greater dependence on glycolytic mechanisms for energy production. The reduced rate of PCr resynthesis is consistent with abnormal mitochondrial oxidation, and the slow pH recovery is indicative of substantially reduced blood flow and hence a decreased oxygen delivery (for a review, see Radda et al.[32]).

The hyperbolic relationship between cytosolic [ADP] and rate of PCr resynthesis after exercise has been used to estimate the apparent maximum rate of oxidative ATP synthesis (Q_{max}) in several human diseases in which mitochondrial oxidation may be impaired (see Table 1).[21]

Muscle responds to impaired oxidation by stimulating anaerobic ATP synthesis and/or by increasing [ADP], the stimulus to the mitochondrion. However, these responses interact: [ADP] depends on pH and [PCr], and lactic acid production tends to lower [ADP] (by lowering pH), while proton efflux has the opposite effect. Four patterns were identified:

(d) in mitochondrial myopathy, apparent Q_{max} is reduced and [ADP] is appropriately increased, because increased proton efflux reduces the pH change in exercise despite increased lactic acid production;
(e) in some conditions (e.g., cyanotic congenital heart disease), apparent Q_{max} is reduced, but there is no compensatory rise in [ADP], probably because anaerobic ATP synthesis during exercise is increased without increase in proton efflux;
(f) in other conditions (e.g., myotonic dystrophy) [ADP] is increased during exercise, but apparent Q_{max} is normal, suggesting either an increase in proton efflux and/or decrease in anaerobic ATP synthesis during exercise;
(g) there are also conditions (e.g., respiratory failure) where, despite impaired oxygen supply, both apparent Q_{max} and end-exercise [ADP] are normal.

Patients with heart failure might have been expected to have reduced muscle blood flow and, perhaps, reduced oxygen delivery due to arterial hypoxemia. Several groups, however, found no blood flow changes,[32] but demonstrated reduced mitochondrial content and activity and increased glycolytic ca-

Table 1 Conditions with Probable or Possible Defects of Mitochondrial ATP Synthesis

Mechanism	Examples analyzed
Intrinsic mitochondrial defects	Mitochondrial myopathy Iron deficiency Cardiac failure Uremia
Impaired blood flow	Peripheral vascular disease
Reduced blood oxygen tension	Chronic respiratory failure Cyanotic congenital heart disease
Reduced blood oxygen content	Iron-deficient anemia Myelodysplastic anemia
Increased Hb oxygen affinity	Treatment with 12C79[a]
Other conditions with increased [ADP] in exercise	Hypertension Duchenne dystrophy carriers Myotonic dystrophy

[a]12C79 is an experimental 'left-shifter' drug, 5-(2-formyl-3-hydroxyphenoxy)pentanoic acid.

For References see p. 9

pacity in the muscles of such patients, the pattern of response falling largely in group (b) above.

3.1.2 Heart

The elucidation of the metabolic abnormalities in ischemic heart disease has been a major objective of MR spectroscopists for some time. Recently Weiss et al.[29] have demonstrated a decrease in the PCr-to-ATP ratio during hand grip exercise in patients with coronary heart disease and ischemia, reflecting a transient imbalance between O_2 supply and demand in the myocardium with compromised blood flow. Exercise testing in five of these patients after revascularization showed no changes in high-energy phosphates, as was also observed in normal subjects and in nine patients with nonischemic heart disease. The possibility that an exercise-linked spectroscopic test may markedly improve the recognition and evaluation of myocardial ischemia is certainly of great interest.

3.1.3 Brain

Several important clinical problems arising out of impaired O_2 delivery have been investigated by both ^{31}P and ^{1}H MRS.

Perinatal asphyxia is the commonest cause of neurological handicap in full-term infants. Reynolds and colleagues[33] have studied infants with birth asphyxia from birth onwards. ^{31}P NMR spectra from neonatal brain differ from those from the adult brain in that a large monoester peak, identified as phosphoethanolamine, is present and the ratios PCr/ATP are lower. These workers found that birth asphyxia caused significant changes in the ratio PCr/Pi, the magnitude of which was helpful in prognosis. These changes occurred early, and the ratios returned to normal within a few days.

Several ^{1}H MRS studies have reported that the *N*-acetylaspartate (NAA) signal in neurologically abnormal infants was lower than in normal controls (for a review, see Howe et al.[34]).

Cerebrovascular disease and stroke are among the major causes of death in the adult population in the Western world. Numerous ^{1}H MRS studies in patients with stroke have suggested that NAA may be a marker for neuronal loss. Serial measurements of NAA following stroke demonstrated recovery of the NAA peak with neurological improvement.[34] Elevation of brain lactate during acute ischemia could be detected, but surprisingly lactate was also found within the infarcted area months after the event. The metabolic turnover of this lactate pool was demonstrated by the appearance of [^{13}C]lactate, following infusion of [1-^{13}C]glucose.[35] It has been suggested that brain macrophages, which begin to appear three days after infarction and gradually disappear over several months, could be a major source of elevated lactate signals that persists for months after stroke.[36] Levine et al. investigated early human focal ischemia with ^{31}P MRS to characterize the temporal evolution and relationship of brain pH and phosphate energy metabolism.[37] Serial ischemic brain pH levels indicated a progression from early acidosis to subacute alkalosis. When acidosis was present, there was a significant elevation in the relative signal intensity of inorganic phosphate and significant reductions in signal intensities of ATP compared with those of control subjects. Ischemic brain pH values correlated directly with the relative signal intensity of PCr and the PCr index, and correlated inversely with the signal intensity of Pi. There was a general lack of correlation between either ischemic brain pH or phosphate energy metabolism and the initial clinical stroke severity. The data suggested a link between high-energy phosphate metabolism and brain pH, especially during the period of ischemic brain acidosis, and the authors proposed that effective acute stroke therapy should be instituted during this period.

Subarachnoid hemorrhage may be complicated by cerebral ischemia, which, though reversible initially, can progress to an irreversible neurological deficit. ^{31}P MRS studies of 10 patients on 30 occasions at various times after hemorrhage showed in some of the patients ($n = 5$) focal areas of intracellular acidosis (pH < 6.8), which in most cases returned towards normal.[38] The recovery of pH_i to normal paralleled an improvement in clinical conditions in each case. These areas of acidosis probably affect ischemia, which is potentially reversible. The MRS measurement provides an opportunity for assessing methods of treatment.

3.2 Genetic and Metabolic Diseases

MRS is particularly valuable in the study of metabolic diseases and genetic conditions.

3.2.1 Mitochondrial Disease

Abnormal mitochondria are increasingly recognized as being responsible for muscle and brain disorders. In primary mitochondrial diseases, there are mutations in the nuclear or mitochondrial genes necessary for the synthesis of the components of the electron transport chain. The functional bioenergetic consequences of these abnormalities can be studied by ^{31}P MRS.[39] At rest, in both skeletal muscle and the brain, PCr/Pi and PCr/ATP are decreased, while the Pi/ATP ratio is often increased. This means that the phosphorylation potential, a measure of the available cellular energy, is decreased.

In skeletal muscle, oxidative ATP synthesis is impaired, and this often results in slow PCr resynthesis during recovery. As already pointed out (see Table 1), the reduction in mitochondrial Q_{max} is partly compensated for by an increase in free ADP during exercise and recovery, which stimulates the ATP synthesis rate. This arises from an apparent adaptation in the muscle to chronic mitochondrial insufficiency in which the rate of H^+ removal from the cell by the Na^+/H^+ exchange mechanism is enhanced. This provides a protection to the cell against low pH that would arise out of excess lactate production, and also results in an increase in ADP through the creatine kinase equilibrium.

3.2.2 Diseases in Carbohydrate Metabolism

Defects of glycogenolysis and glycolysis are inborn errors of metabolism mainly of muscle or liver. As in the mitochondrial myopathies, the biochemical defects result in impaired production of ATP and in reduced (or absent) amounts of pyruvate for mitochondrial oxidation. Not only are the MRS findings in this group of disorders quite distinct from the oxidative disorders, but glycogenolytic defects are distinguishable from glycolytic defects.[32]

Among several metabolic liver disorders, abnormal metabolism of fructose was studied in livers of patients with

hereditary fructose intolerance.[40] In this autosomal recessive disease, aldolase B activity is greatly reduced in liver, kidney, and small intestine. Homozygotes were easily detectable by MRS. Heterozygotes for this disorder cannot be identified by conventional tolerance tests, but in the MRS investigations they showed impaired tolerance to fructose compared with control subjects. In the heterozygotes, the rise in plasma urate after fructose (attributed to the activation of AMP deaminase by the low Pi concentration) correlated significantly with the decrease in liver Pi. The drop in liver Pi after fructose was very marked in those heterozygotes who also suffered from gout, suggesting that some patients suffering from gouty attacks might benefit from a low-fructose diet. Indeed, subsequent studies on a group of patients with a family history of gout show that in some families this resulted from being carriers of hereditary fructose intolerance, and a fructose-free diet improved their condition.[41]

^{1}H MRS has been used to detect specific signals in metabolic brain diseases. For example, high lactate concentrations were found in the brains of patients with Leigh's disease, and *N*-acetylaspartate was consistently increased in Canavan's disease, an inborn error of *N*-acetylaspartate metabolism.[34]

3.2.3 Dystrophy

^{31}P MRS studies of skeletal muscle bioenergetics in patients with muscular dystrophies have given new clues as to the functional consequences of the genetic lesion. For example, in patients with Duchenne (DMD) and Becker (BMD) muscular dystrophy, there is an increase in intracellular Pi and decrease in PCr. Intracellular pH was raised substantially in DMD, moderately in BMD, and slightly but significantly in carriers of the disease.[2,42] Investigations on the mouse equivalent of DMD (the mdx mouse) have shown that the raised pH_i is linked to increased intracellular Na^+ and Ca^{2+}, suggesting that the absence of dystrophin in the muscle leads to a series of ionic abnormalities. Measurements of these biochemical parameters in vivo may provide a way of following the success of therapies such as might be achieved by gene replacement.

Dystrophin is also known to be absent in the brain (neuronal cells) of patients with DMD, and it is known that about 30% of such patients are mentally retarded. It is of interest, therefore, that abnormal Pi/PCr ratios are also observed in the brains of children with DMD and in the brain of the mdx mouse. Neuropsychological studies on such children have shown a relationship between full-scale IQ and the Pi/PCr in the brain.[43]

3.3 Abnormal Control and Disease

The control and coordination of metabolic processes require an intricate network of input functions. Some of these have been emphasized in Section 2, while others include the role of specific ions, general ionic environment, potentials across intra- and extracellular membranes, concentrations of substrates, and hormonal input.

We may consider diseases arising out of a 'control lesion' as being primary intracellular or extracellular, i.e., systemic in origin.

3.3.1 Intracellular Control

There are several examples where MRS has led to the identification of defects that affect intracellular control. These include a patient with abnormal intracellular substrate transport in skeletal muscle (malate aspartate shuttle defect) and the recognition of a sarcoplasmic reticulum Ca^{2+}-ATPase defect.[32]

As already mentioned, perturbations in the ionic balance occur in Duchenne and Becker muscular dystrophy. There are other conditions where the rates of ion-exchange processes (Na^+/H^+ antiport/Na^+/K^+-ATPase) are significantly increased. For example, in essential hypertension, skeletal and heart muscle as well as vascular smooth muscle are affected in this way, as are other peripheral cells (white cells and erythrocytes). It is not known in this case to what extent these changes are secondary or whether they are related to the fundamental mechanism of the disease.[2]

3.3.2 Extracellular Control

The relationships between the extracellular environment (blood biochemistry) and intracellular processes is central to our understanding of physiological regulation.

3.3.2.1 Acid/Base Regulation In Vivo. This is an important physiological problem, with profound clinical implications. Intracellular pH regulation in individual organs and its dependence on the physiological acid/base balance can be examined very well by ^{31}P MRS,[44] and many studies have been carried out on this problem in animal models and humans. Some illustrative examples are given below. Hood et al.[45] examined the effect of systemic pH on pH_i using ^{31}P MRS by measuring lactic acid generation in the forearm muscle of a group of volunteers who performed exhaustive arm exercise with arterial blood flow occluded. On ingestion of NH_4Cl (acidosis), blood pH decreased to 7.30 from 7.39 (control), whereas muscle pH_i did not change. During alkalosis induced by $NaHCO_3$ ingestion, blood pH increased, while pH_i was again well controlled. Systemic acidosis inhibited and alkalosis stimulated lactic acid output (during exercise), which suggests that systemic pH regulates cellular acid production, protecting muscle pH at the expense of energy availability. In contrast, in severe respiratory acidosis produced by CO_2 breathing, muscle pH is significantly reduced.[45] The adult mammalian brain is protected from oscillations in arterial blood pH by a different mechanism, namely the blood–brain barrier, but it is not protected from changes in arterial partial pressure of CO_2 that have been shown to produce changes in the pH of cerebrospinal fluid. ^{31}P MRS was used to measure intracellular pH in different parts of the human brain while the subject was breathing air, and during hypercapnea. The white matter responded with a greater decrease in pH_i than gray matter.[46] The response of liver to acidosis was examined in rats.[47] Varying severity of acidosis was induced by HCl infusion, NH_4Cl ingestion, or induction of experimental diabetic ketoacidosis. Whereas at the more severe degrees of systemic acidosis a marked decrease in hepatic pH_i was observed, there was little change in ketoacidosis. This explained why, in the latter condition, gluconeogenesis from lactate is not inhibited, despite evidence in vitro of inhibition of glyconeogenesis by systemic acidosis.

3.3.2.2 Cellular Inorganic Phosphate (Pi) Concentration and

For References see p. 9

Total Intracellular Phosphate. These are dependent on blood Pi homeostasis, which in turn is linked to renal Pi clearance and whole body phosphate incorporation and regulation in bones. The relationship between extracellular and intracellular concentrations of Pi was studied in the muscles and erythrocytes of patients with vitamin-D-resistant rickets and patients with Paget's disease of bone before and after they had been made hyperphosphatemic by treatment with the drug ethylidene-1-hydroxy-1,1-biphosphonate. Even though the plasma Pi concentration in these patients spanned a fourfold range (0.5–2.0 mmol L^{-1}), the corresponding intramuscular Pi concentration increased by only 70%.[32]

Patients in renal failure also have elevated blood phosphate, and again this is accompanied by a proportional but smaller increase in muscle Pi. In spite of this, in this condition, the resting phosphorylation potential remains unaltered, implying that cellular levels of ADP and ATP are adjusted to compensate for increase in Pi.

3.3.2.3 Hormonal Regulation of Metabolism. This has long been recognized, and MRS has been used in many investigations of patients with abnormal hormonal levels on hormonal control. The study of diabetes using ^{13}C MRS has already been mentioned in Section 2.1.2. An extension of this work to insulin resistance is of some interest, since the latter may precede the diabetic condition.

Thyroid hormones affect metabolism in many tissues. Skeletal muscle metabolism has been examined in patients with both hypo- and hyperthyroid conditions.[2] The abnormalities found are totally reversible with treatment, and MRS is therefore particularly useful in the evaluation of the relationship between clinical symptoms (e.g., decreased exercise capacity in hypothyroidism) and the underlying metabolic abnormalities.

3.3.3 Tumor Biochemistry

Uncontrolled cellular growth and proliferation represent an extreme case of disease where normal molecular homeostasis is not observed. The study of tumor biochemistry by MRS represents a major area of clinical research, and advances in the field have been regularly reviewed since the 1980s and more recently examined in some detail.[34,48]

In the majority of studies, ^{31}P or ^{1}H MRS have been used but there are reports using ^{13}C, ^{19}F, and ^{23}Na as the nuclei of interest. Several specific developments have arisen out of the ^{31}P MRS measurements.

1. The fact that the majority of human tumors were shown to have alkaline intracellular pH values—and not acidic as was expected—focused attention on the role of ionic control in relation to cellular proliferation.
2. The observation that many tumors had prominent signals in the phosphomonoester (PME) region, which were mostly associated with increased phosphoethanolamine and phosphocholine, brought into the forefront research on phospholipid metabolism in tumors. While it is still not known whether such changes are the result of alterations in the biosynthetic pathways or are associated with phospholipid degeneration and cellular signaling, the possibility that they can be used as an index of cellular proliferation rates has generated much interest.
3. Some researchers hoped that the bioenergetic status of the tumour as reflected in the ^{31}P MR spectrum might be characteristic of tumor types. Others argued[32] that such measures of the metabolic state are more likely to provide an indication of the physiological state of a particular tumor in its specific location. The latter property could then be used to guide the choice of therapies that would utilize the state of oxygenation and activity of a given tumor at a defined stage of its development.
4. There is considerable evidence that response to therapy, particularly chemotherapy, might well be measurable by quantification of the phospholipid components.[48]

Recently, there has been a rapid expansion in the use of ^{1}H MRS in clinical investigations of tumors.[34] Given that in most ^{1}H MRS experiments, only four peaks are measured, namely those assigned to *N*-acetylaspartate, total creatine, choline-containing molecules, and lactate, much emphasis has been placed on empirical correlations with other measurements (histology, PET, etc.) or on pattern recognition methods.[34] It is perceived that multicenter clinical trials might clarify the applicability of such approaches to the grading and possible diagnosis of human tumors.

3.4 Disease and Foreign Invasion

Biochemical changes associated with the administration of toxic substances, viral infections, inflammation, and autoimmune disorders are readily observed by MRS. Alcoholic liver disease, the hepatic consequences of paracetamol poisoning, and viral hepatitis are just some of the conditions that have been studied by ^{31}P MRS.[49] Both the extent of damage and the liver regeneration process can be assessed from the MR measurements.

Acute liver failure can result in hepatic encephalopathy, possibly through the action of toxic substances like ammonia, mercaptans, and amino acids. Several ^{1}H MRS studies demonstrated an elevation of glutamine levels and the parallel decrease in brain myoinositol.[34,50] Liver transplantation completely reversed the ^{1}H MRS changes. Other forms of treatment (e.g., by neomycin or lactulose) were also examined by Kreis et al.[50]

4 CONCLUSIONS AND FUTURE PROSPECTS

This article has been written from the point of view of the author with emphasis on the biochemical aspects of human MRS. There can be no doubt that we have already learned a great deal from MRS about biochemical aspects of human diseases and control and fluxes in normal situations. The method is thus established as a truly new approach in clinical research. In some areas, such as muscle investigations and possibly the empirical uses of brain ^{1}H spectroscopy, it could be considered as part of clinical examination aimed at evaluation of the nature and severity of the disease. As the capability of obtaining spectra in a relatively routine manner becomes available on standard diagnostic imaging instruments, such examinations will become more common, though probably restricted to specialist centers. The author's bias remains, however, that, being a quantitative biochemical technique, the strength of MRS will remain in bringing new understanding about disease mechanisms. Once such understanding is derived from careful and focused studies

on specific conditions, we should attempt to devise simpler, cheaper, and generally more readily available tests, probably with a less precise information content, that can be adopted in daily clinical use.

5 RELATED ARTICLES

Applications of ^{19}F-NMR to Oncology; Brain Infection and Degenerative Disease Studied by Proton MRS; Brain MRS of Human Subjects; Brain Neoplasms in Humans Studied by Phosphorus-31 NMR Spectroscopy; Fluorine-19 MRS: General Overview and Anesthesia; In Vivo Hepatic MRS of Humans; Localization and Registration Issues Important for Serial MRS Studies of Focal Brain Lesions; NMR Spectroscopy of the Human Heart; Peripheral Muscle Metabolism Studied by MRS.

6 REFERENCES

1. R. G. Shulman, A. M. Blamire, D. L. Rothman, and G. McCarthy, *Proc. Natl. Acad. Sci. USA*, 1993, **90**, 3127.
2. G. K. Radda and D. J. Taylor, in 'Molecular Mechanisms in Bioenergetics', ed. L. Ernster, Elsevier, Amsterdam, 1992, Chap. 19, p. 463.
3. D. Rees, M. B. Smith, J. Harley, and G. K. Radda, *Magn. Reson. Med.*, 1988, **9**, 39.
4. T. A. D. Cadoux-Hudson, M. J. Blackledge, and G. K. Radda, *FASEB J.*, 1989, **3**, 2660.
5. P. A. Bottomley and C. Hardy, *J. Magn. Reson.*, 1992, **99**, 443.
6. K. M. Brindle, M. J. Blackledge, R. A. J. Challis, and G. K. Radda, *Biochemistry*, 1989, **28**, 4887.
7. P. M. Kilby, J. L. Allis and G. K. Radda, *FEBS Lett.*, 1990, **272**, 163.
8. R. G. Shulman, *Ann. NY Acad. Sci.*, 1987, **508**, 10.
9. T. Jue, D. L. Rothman, B. A. Tavitian, and R. G. Shulman, *Proc. Natl. Acad. Sci. USA*, 1989, **86**, 1439.
10. D. L. Rothman, E. J. Novotny, G. I. Shulman, A. M. Howseman, O. A. C. Petroff, G. Mason, T. Nixon, C. C. Hanstock, J. W. Pritchard, and R. G. Shulman, *Proc. Natl. Acad. Sci. USA*, 1992, **89**, 9603.
11. J. Frahm, T. Michaelis, K. D. Merboldt, W. Hanicke, M. L. Gyngell, D. Chien, and H. Bruhn, *NMR Biomed.*, 1989, **2**, 188.
12. P. F. Renshaw, A. R. Guimares, M. Fava, J. F. Rosenbaum, J. D. Pearlman, J. G. Flood, P. R. Puopolo, K. Clancy, and R. G. Gonzale, *Am. J. Psychiatry*, 1992, **149**, 1592.
13. R. A. Komorski, J. E. Newton, J. R. Sprigg, D. Cardwell, P. Mohanakrishnan, and C. N. Karson, *Psychiatry Res.*, 1993, **50**, 67.
14. E. R. Weibel, 'The Pathway of Oxygen', Harvard University Press, Cambridge, MA, 1984.
15. Z. Wang, E. A. Noyszewski, and J. S. Leigh Jr., *Magn. Reson. Med.*, 1990, **14**, 562.
16. K. R. Thulborn, J. C. Waterton, P. M. Matthews, and G. K. Radda, *Biochim. Biophys. Acta*, 1982, **714**, 265.
17. W. J. Bank, G. Tino and B. Chance, *Neurology*, 1992, **42**, 146.
18. B. Chance, B. J. Clark, S. Nioka, H. Subramanian, J. M. Maris, Z. Argov, and H. Bodle, *Circulation*, 1985, **72**, 103.
19. G. K. Radda, *Phil. Trans. R. Soc. Lond. Ser. A.*, 1990, **333**, 515.
20. G. J. Kemp and G. K. Radda, *Magn. Reson. Quart.*, 1994, **10**, 43.
21. G. J. Kemp, D. J. Taylor, C. H. Thompson, L. J. Hands, B. Rajagopalan, P. Styles, and G. K. Radda, *NMR Biomed.*, 1993, **6**, 302.
22. G. J. Kemp, C. H. Thompson, P. R. J. Barnes, and G. K. Radda, *Magn. Reson. Med.* 1994, **31**, 248.
23. H. P. Hetherington, J. R. Hamm, J. W. Pan, D. L. Rothman, and R. G. Shulman, *J. Magn. Reson.*, 1989, **82**, 86.
24. M. Boska, *NMR Biomed.*, 1991, **4**, 173.
25. S. Cerdan and J. Seelig, *Annu. Rev. Biophys. Chem.*, 1990, **19**, 43.
26. J. R. Alger, L. O. Sillerud, K. L. Behar, R. J. Gillies, R. G. Shulman, R. E. Gordon, D. Shaw, and P. E. Hanley, *Science*, 1981, **214**, 660.
27. G. I. Shulman, D. L. Rothman, T. Jue, P. Stein, R. A. De Fronzo, and R. G. Shulman *N. Engl. J. Med.*, 1990, **322**, 223.
28. M. A. Conway and G. K. Radda, *Trends Cardiovasc. Med.*, 1991, **1**, 300.
29. R. G. Weiss, P. A. Bottomley, C. J. Hardy, and G. Gerstenblith, *N. Engl. J. Med.*, 1990, **323**, 1593.
30. K.-D. Merboldt, H. Bruhn, W. Hanicke, T. Michaelis, and J. Frahm, *Magn. Reson. Med.*, 1992, **25**, 187.
31. D. Sappey-Marinier, G. Calabrese, G. Fein, J. W. Hugg, C. Biggins, and M. W. Weiner *J. Cereb. Blood Flow Metab.*, 1992, **12**, 584.
32. G. K. Radda, B. Rajagopalan, and D. J. Taylor, *Magn. Reson. Quart.*, 1989, **5**, 122.
33. P. L. Hope, A. M. Costello, E. B. Cady, D. T. Delpy, P. S. Tofts, A. Chu, P. A. Hamilton, E. O. R. Reynolds, and D. R. Wilkie, *Lancet*, 1984, **2**, 366.
34. F. A. Howe, R. J. Maxwell, D. E. Saunders, M. M. Brown, and J. R. Griffiths, *Magn. Reson. Quart.*, 1993, **9**, 31.
35. D. L. Rothman, A. M. Howseman, G. D. Graham, O. A. C. Petroff, G. Lantos, P. B. Fayad, L. M. Brass, G. I. Shulman, R. G. Shulman, and J. W. Pritchard, *Magn. Reson. Med.*, 1991, **21**, 302.
36. O. A. Petroff, G. D. Graham, A. M. Blamire, M. al-Rayess, D. L. Rothman, P. B. Fayad, L. M. Brass, R. G. Shulman, and J. W. Pritchard, *Neurology*, 1992, **42**, 1349.
37. S. R. Levine, J. A. Helpern, K. M. Welch, A. M. Vande-Linde, K. L. Sawaya, E. E. Brown, N. M. Ramadan, R. K. Deveshwar, and R. J. Ordidge, *Radiology*, 1992, **185**, 537.
38. N. S. R. Brooke, R. Ouwerkerk, C. B. T. Adams, G. K. Radda, J. G. G. Ledingham and B. Rajagopalan, *Proc. Natl. Acad. Sci. USA*, 1994, **91**, 1903.
39. D. J. Taylor and G. K. Radda, in 'Current Topics in Bioenergetics', ed. C. P. Lee, Academic Press, San Diego, 1994, Vol. 17, p 99.
40. R. D. Oberhaensli, B. Rajagopalan, D. J. Taylor, G. K. Radda, J. E. Collins, J. V. Leonard, H. Schwarz, and N. Herschkowitz, *Lancet*, 1987, **24**, 931.
41. J. E. Seegmiller, R. M. Dixon, G. J. Kemp. P. W. Angus, T. E. McAlindon, P. Dieppe, B. Rajagopalan, and G. K. Radda, *Proc. Natl. Acad. Sci. USA*, 1990, **87**, 8326.
42. G. J. Kemp, D. J. Taylor, J. F. Dunn, S. P. Frostick and G. K. Radda, *J. Neurol. Sci.*, 1993, **116**, 201.
43. I. Tracey, R. Scott, C. H. Thompson, J. F. Dunn, P. R. J. Barnes, P. Styles, G. J. Kemp, C. D. Rae, M. Pike, and G. K. Radda, in *Proc. IInd Ann Mtg. (Int.) Soc. Magn. Reson. Med.*, San Francisco, 1994, p. 345.
44. G. K. Radda, *FASEB J.*, 1992, **6**, 3032.
45. V. L. Hood, C. Schubert, U. Keller, and S. Muller, *Am. J. Physiol.*, 1988, **255**, 479.
46. T. A. D. Cadoux-Hudson, B. Rajagopalan, J. G. G. Ledingham, and G. K. Radda, *Clin. Sci.*, 1990, **79**, 1.
47. J. S. Beech, S. R. Williams, R. D. Cohen, and R. A. Iles, *Biochem. J.*, 1989, **263**, 737.
48. W. Negendank, *NMR Biomed.*, 1992, **5**, 303.
49. G. K. Radda, R. M. Dixon, P. W. Angus, and B. Rajagopalan, in 'Regulation of Hepatic Function (Alfred Benzon Symposium 30)', eds. N. Grunnet and B. Quistorff, Munksgaard, Copenhagen, 1990, p. 433.
50. R. Kreis, N. Farrow, and B. D. Ross, *Lancet*, 1990, **336**, 635.

For References see p. 9

Biographical Sketch

George K. Radda. *b* 1936. B.A. 1960, chemistry, M.A., D. Phil., 1962, University of Oxford, UK. Introduced to NMR by Rex Richards. Successively junior research fellow, lecturer (biochemistry), and Professor (Molecular Cardiology), University of Oxford, 1962–present. Approx. 650 publications. Research specialties: in vivo NMR, clinical spectroscopy, control of bioenergetics.

Gastroscopy and Colonoscopy

Nandita M. deSouza
Imperial College School of Medicine, London, UK

Glyn A. Coutts and David J. Larkman
Marconi Medical Systems, UK

and

David J. Gilderdale
Engineering Consultant, UK

1 INTRODUCTION

Since the 1960s, endoscopy has revolutionized the diagnosis and treatment of both upper and lower gastrointestinal (GI) disease and has become the gold standard in management. However, detection of disease is limited to visualization of the surface mucosa. The extent of invasion beneath the surface may be shown with biopsy, but lesions with no superficial component or those with infiltration remote from the biopsy site may be missed.[1] Ultrasound probes have been used in conjunction with endoscopy to address this problem, and transducers that can be passed down flexible gastroscopes[2] or bronchoscopes[3] have been used in order to locate lesions and demonstrate their vascularity. However, low soft-tissue contrast limits the application of this technique.

MRI provides a valuable method for visualizing soft tissue; however, with conventional external whole-body or phased array receiver coils, image resolution of small areas of interest is generally low. Dedicated surface receiver coils can greatly improve image resolution of adjacent structures, and intracavitary coils have been used in the rectum and vagina for imaging the adjacent prostate and cervix.[4,5] It is possible to use coils of this type in conjunction with a nonferromagnetic endoscope for MRI of lesions of the upper and lower GI tract.

2 MR-COMPATIBLE ENDOSCOPE DESIGN

Ferromagnetic materials are normally used in the construction of endoscopes. These not only produce an unacceptable degree of artefact but may be subject to movement forces when placed within the magnetic field. It is now possible to produce endoscopes from MR-compatible components. We have developed a MR-compatible gastroscope and colonoscope that contains no ferromagnetic materials (Endoscan Ltd, Burgess Hill, UK). The general handling attributes are similar to those of conventional instruments. An alloy of chrome is used as a substitute for the normal stainless steel guide wires. The conventional steel shroud, which provides integral strength, is replaced by copper braid. Each of the substitute materials is tested to ensure there is no significant MR artefact. The whole assembly is encased in a heat-shrink sleeve that seals the instrument in an acceptable fashion.

The tip of the instrument is associated with the MR receiver coil and must be modified accordingly. In early versions of the endoscope, the coil was separated from the endoscope but used in conjunction with it. The coil could, therefore, be advanced away from the tip itself so that artefacts associated with components in the tip were not critical. The tip endpiece in this instrument is configured from an amalgam for the viewing lens, irrigation, and biopsy channels. Although polymers would be preferable, forming an impervious seal to the optics proved impossible and alloys of gold-plated copper were used instead. A newer version of the endoscope uses a coil design integral to the tip itself, which means that the tip must be artefact free and the tip design has to be appropriately modified to accommodate the coil circuitry.

The finished instrument incorporates conventional steering controls, an eyepiece, a light guide with an illumination source (Olympus CLE-3 with 150 W dichroic bulb), and a biopsy channel 2.8 mm in internal diameter (Figure 1). The length of the upper GI endoscope from eyepiece to tip is 1 m with a diameter of 12.5 mm, which equals that of a therapeutic gastroscope. The colonoscope is 1.7 m in length and 14 mm in diameter.

3 RECEIVER COIL DESIGN

The simplest design uses a solid coil that is separate from the endoscope itself but can be used in conjunction with it. The outer diameter of a rigid coil cannot be larger than that of the endoscope itself. Such a coil may be advanced some distance from the endoscopic viewing lens or pulled back up to it. It is maintained in the latter position during intubation of the pharynx. Advantages of its rigidity are not only ease of maintenance but also that it does not require tuning on every occasion. We have used a single turn saddle geometry receiver coil 25 mm in length and 10 mm in diameter wound on an acetyl homopolymer (Delrin) former. The conductor is of 18 swg varnish insulated copper and the on-board electronics contain no ferro- or paramagnetic materials. The receiver coil is connected to the external electronics by a specially constructed 50 ohm coaxial cable 2.1 mm in external diameter in a low-friction polytetrafluoroethylene (PTFE) jacket purpose built with MR-compatible components. The cable is accommodated within the biopsy channel of the endoscope.

The addition of an immobilization device to the coil, such as an inflatable balloon or suction cup, would greatly improve image quality. Inflatable balloon devices are currently in use with gastroscopic[2] and bronchoscopic[3] transducers. However, inflatable designs require individual tuning and matching and are subject to distortion while the endoscope is being maneuvered.

Using the receiver soil separately from the tip itself has several disadvantages: it reduces maneuverability of the instrument, compromises optical field-of-view, and decreases suction (because its cable is fed through the biopsy channel). The incorporation of the receiver coil into the wall of the endoscope itself improves maneuverability and optical viewing. However, it is more challenging to construct and has important implications for housing and repair to the electronics. In particular,

Figure 1 MR-compatible endoscope and receiver coil (arrow). The appearance and handling of the endoscope are identical to a standard instrument. The receiver coil is the same diameter as the endoscope itself

immersion of the electronics during sterilization of the endoscope must be considered. In addition, the tip of the endoscope must be completely MR compatible in order to avoid unacceptable artefact on the images.

In our design, the coil incorporates an electronic switch that renders the coil electrically invisible during the transmit phase of the MR sequence. Computer controlled switching of rf is used to achieve this. Diodes are selected for their optimal rf switching characteristics while avoiding the ferromagnetic materials that are routinely found in conventional diodes. The small inductors used to form part of the rf switch have minimal detrimental effect on coil performance. A further circuit is provided to transform the impedance of the coil to match that of the transmission cable, thereby minimizing signal degradation within the cable. The capacitors used for both coil tuning and impedance transformation are selected for their high quality factor (Q), while avoiding the ferromagnetic nickel barrier terminations that are often preferred for capacitors in a mass-production environment. The board required to accommodate the additional coil control circuitry is typically 11.5 mm$\times$10 mm and is placed immediately behind the coil.

The signal-to-noise ratio (SNR) figures for coil performance are often misleading. When compared with the standard pelvic phased array coil, the gastroscope coil performs significantly better at distances up to 2 cm from the coil surface. A clinically acceptable field-of-view for diagnostic purposes is obtained up to 2.5 cm from the coil surface. However, coil orientation relative to the fixed magnetic flux density field, $\boldsymbol{B}_0$, also has a significant effect on the local field-of-view. For a single coil, the regions in which the flux is parallel to $\boldsymbol{B}_0$ produce no useful signal. Employing two or more coils each with a different orientation such that the blind spot of one is compensated for by the other may overcome this problem. Such coil arrays are crucial in imaging a tortuous structure such as the gut, where coil orientation is extremely variable.

4 SCANNER DESIGN

Modern short-bore magnet designs can be usefully adapted to perform MR endoscopy. Our experience has been with a short-bore design Picker Asset, where the distance from the magnet face to center is 60 cm and an operator can reach at arm's length into the center of the bore (Figure 2). Traditional MR scanner designs in which the patient is at a distance down the long magnet bore do not provide sufficient patient access and are unsuitable. The newer 'interventional' MR scanners (C-arm, double doughnut) specifically address the issues of patient accessibility, and their open-plan features are designed to cater for endoscopic procedures.

4.1 Pulse Sequences

Imaging strategies for use with the gastroscopic receiver coil seek a balance between two major considerations. On the one hand the coil gives a large gain in sensitivity over a limited region that can be exploited to reduce patient scan times as well as to provide high-resolution images of immediately adjacent tissue. In particular, image wrap around is not an issue

Figure 2 MR endoscopic procedure being performed

when choosing small fields-of-view. On the other hand, it is important to avoid image degradation associated with motion. The exact sources of motion artefact depend on the positioning of the coil. Major contributions arise from the pulsatile motion of the heart and great vessels in the thorax and from respiratory motion, as well as from patient movement if scan times are too long. If no immobilization is provided for the receiver coil, the sensitivity profile is such that smearing of the very high signal from regions immediately adjacent to the coil occurs and can swamp signal from regions of interest a few centimeters from the coil.

There are many well-known strategies for dealing with motion artefact in MR imaging. In the upper GI tract, cardiac gating is useful. Typically a standard gated spin echo sequence will have a repetition time (*TR*) of 700–800 ms, so T_1-weighted images, which provide useful anatomic landmarks, may be obtained. These sequences do not have a high gradient demand; consequently, with normal imaging gradients (10 mT m^{-1} with a rise time of 1 ms), 3 mm slice thicknesses and 10 cm fields-of-view can be easily achieved. A small reduction in the achievable resolution and the number of slices that can be scanned (although still more than enough to cover the extent of the coil) allows the use of gated fast-spin echo sequences, which significantly reduce the scan times. With longer pseudo-echo times, these sequences give more T_2-weighted images.

Although gating greatly improves image quality, images collected in this way are still subject to extensive motion artefact. In these sedated patient examinations, breath-hold techniques are impractical while the requirement for high resolution means that single-shot techniques that have proved useful for body imaging, such as HASTE (half-Fourier acquisition single-shot turbo spin echo),[6] require gradient performances well above those that are generally available. Single-slice, fast-scanning techniques may be used to further reduce artefact by 'freezing' motion. An alternative technique is to use gated fast gradient echo sequences with segmented ***k***-space acquisition.[7,8] At a *TR* of 15 ms, 32 lines or more of data can be collected per R–R interval and scan times of a few seconds are possible. Collection of the full image data can be divided over a few heartbeats. Optimization of the SNR depends on further refinements of the sequences, such as varying the flip angle through each cycle of data acquisition.[9] Preparation pulses can be used before the data collection in each cardiac cycle in order to achieve the required image contrast. In combination with this, centrally ordered phase encoding seeks to collect views from the center of ***k***-space early in each cycle of data collection.

In the colon, cardiac motion is not an issue; however residual bowel air reduces contact between the receiver coil and the bowel wall and facilitates movement of the coil within a distended lumen. Modified gradient optimized gradient echo sequences with a *TR* of 8–15 ms and *TE* of 3.7–6.1 ms can achieve a 1–25 s acquisition. In addition, versions of this sequence may be used with an inversion prepulse of 300–700 ms to maximize contrast between bowel wall layers.

Finally navigator echoes for line-by-line quantification of motion, together with postcorrection or phase encode re-ordering techniques, have been used in, for instance, cardiac imaging.[10,11] For the application here, the limited field-of-view of the imaging coil means that navigator echoes are impractical. We have investigated exploiting similar techniques by adding an additional small receiver coil (internal diameter ~3 mm) within the tip of the endoscope, attached to a separate receiver channel and containing a small MR-visible fiducial marker (~1 mm diameter).[12] Motion of the endoscope tip can then be monitored by application of four gradient projections,[13] acquired in 60 ms, before each line of data acquisition, from which the current position of the fiducial can be measured. In situations where fast scan times are not necessary for patient tolerance, this method allows full exploitation of the coil sensitivity for high-resolution imaging within the gradient performance of clinical scanners, as well as permitting the full range of diagnostic image contrast.

5 EX VIVO IMAGING

From inner to outer, four layers are seen in normal bowel (Figure 3). First, a layer of high signal intensity on both T_1 and T_2-weighted images that represents the mucosa. Second, there is a layer of low signal intensity on T_1-weighted imaging that represents the muscularis mucosa. This layer is intermediate in signal intensity on T_2-weighted imaging and, therefore, indistinguishable from the adjacent outer layer. Third, a layer of

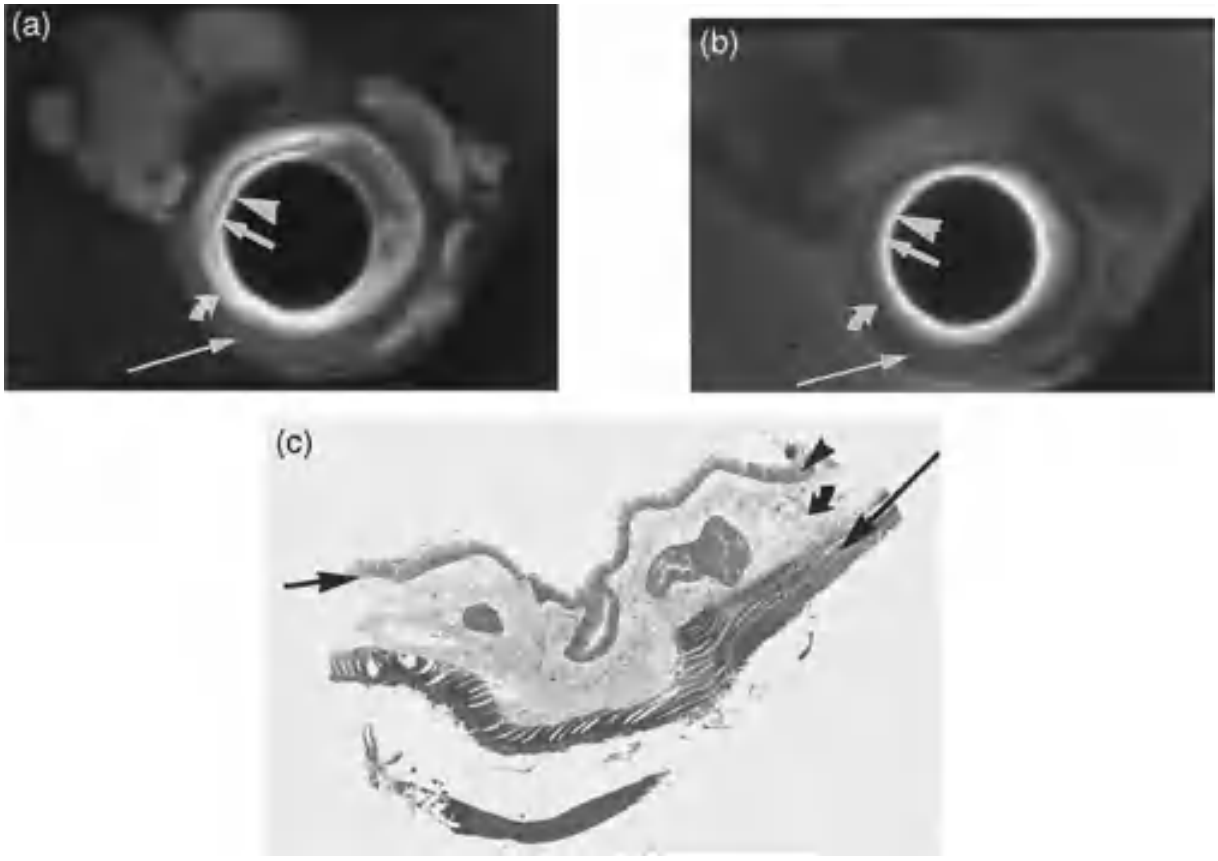

Figure 3 The normal colon ex vivo showing normal colonic layers. (a) Transverse spin echo T_1-weighted image [repetition time (*TR*) 355 ms; echo time (*TE*) 20 ms]; (b) T_2-weighted image (*TR* 2500 ms; *TE* 80 ms); (c) histologic section. The innermost ring of high signal intensity represents mucosal epithelium (arrowhead). The next thin layer of low signal intensity represents the muscularis mucosa (short arrow). The submucosa is seen as a band of high signal intensity in (a) and as an inner ring of intermediate signal intensity and an outer ring of low signal intensity in (b) (curved arrow). The muscularis propria is a thick band of low signal intensity in both (a) and (b) (long arrows). This correlates with the appearance on histologic section

high signal intensity on T_1-weighted imaging is seen that has two counterparts on the T_2-weighted images: an inner layer of intermediate signal intensity and an outer rim of lower signal intensity. These correspond to the submucosa. Finally, a homogeneous thick outer layer has low signal intensity on both T_1- and T_2-weighted imaging; this represents the muscularis propria.

6 IN VIVO STUDIES

6.1 Upper Gastrointestinal Tract

The procedure initially follows standard endoscopy practices. Following local anesthesia to the back of the pharynx, the patient's esophagus is intubated with the coil in advance of the tip of the endoscope. After visual inspection of the upper GI tract, the coil is placed adjacent to a lesion or region of interest under direct vision and the patient positioned with the region to be imaged in the center of the magnetic field.[14]

Use of a short-bore scanner (0.5 T, 60 cm from magnet face to center) allows access to the patient's mouth. Imaging strategies described in Section 4 are then used to study normal anatomy (Figure 4), the extent of tumors (Figure 5), varices not detectable on visual inspection (Figure 6), and post-surgical appearances at the gastroesophageal junction.

6.2 Lower Gastrointestinal Tract

Patient preparation is identical to that used for a standard colonoscopy. During visual inspection of the colon, note is taken of areas where imaging may be of interest. On completion of inspection, the receiver coil is placed adjacent to these areas and images obtained. As in the ex vivo studies, three layers of bowel wall can be identified: mucosa, submucosa, and muscularis propria (Figure 7).

7 SAFETY ISSUES

7.1 Technical Factors

An alternating magnetic field gives rise to an electric field in a plane normal to the magnetic field. This statement of Faraday's law may be made more concisely as

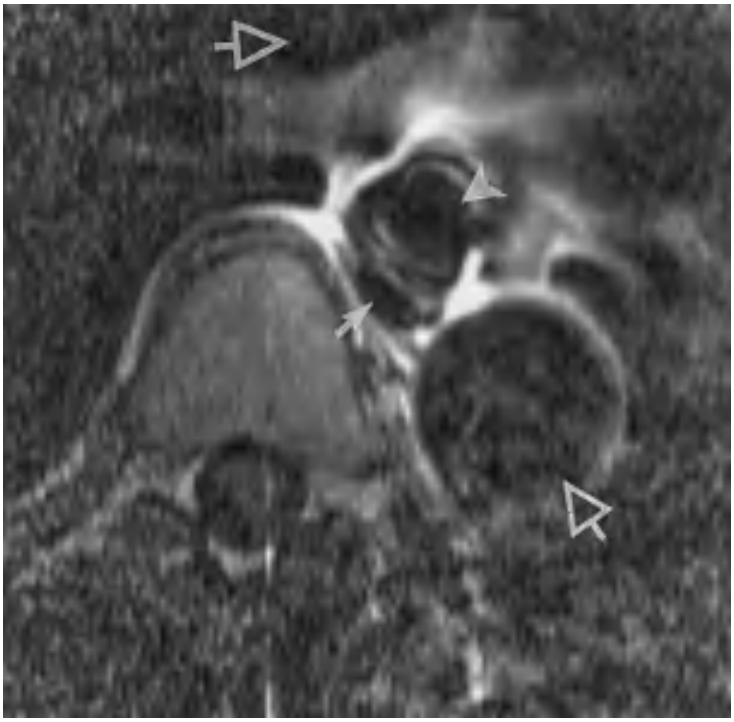

Figure 4 The normal mid-esophagus. Spin echo T_1-weighted transverse image (repetition time 660 ms; echo time 20 ms) showing normal esophagus (arrowhead), ascending and descending aorta (open arrows), and azygos vein (short arrow)

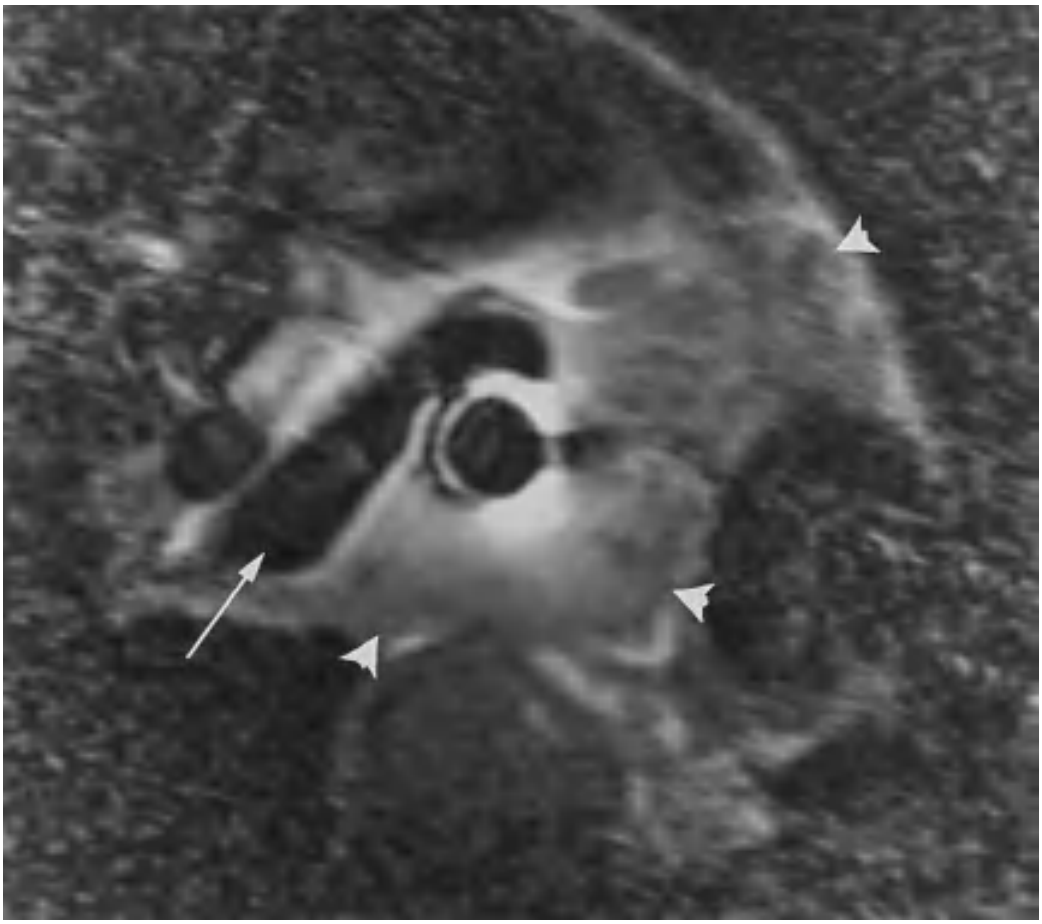

Figure 5 Carcinoma of the esophagus. Spin echo T_1-weighted transverse image (repetition time 660 ms; echo time 20 ms) through the mid-esophagus showing a large mass of intermediate signal intensity in the mediastinum (arrowheads) surrounding the esophagus. A pulmonary vessel is seen passing through it (arrow)

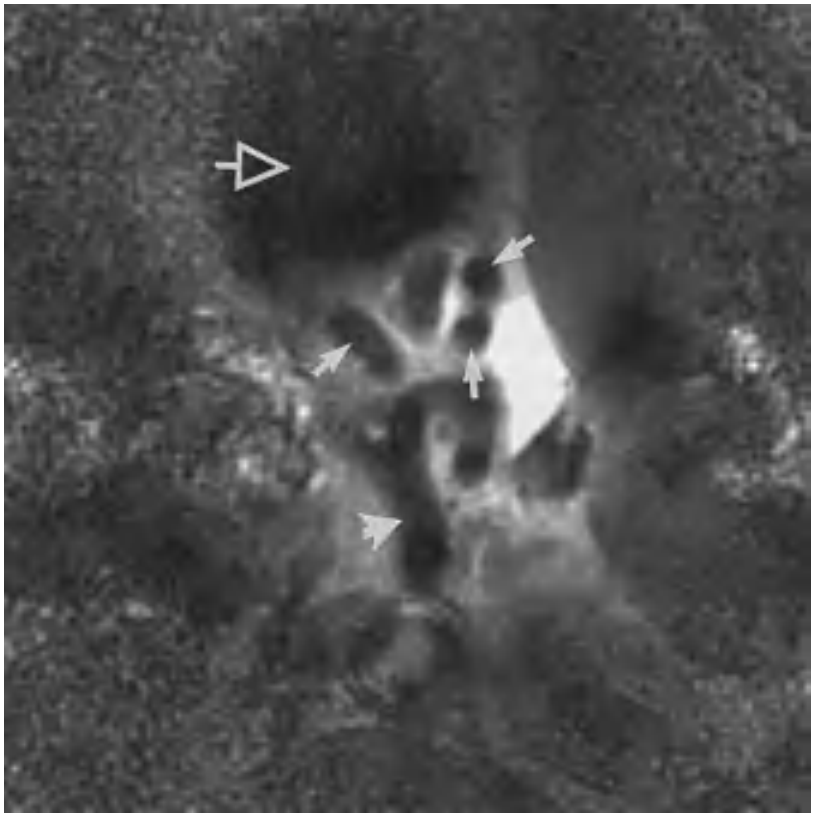

Figure 6 Gastric varices. Electrocardiograph-gated spin echo T_1-weighted transverse image (repetition time 660 ms; echo time 20 ms) at the level of the gastric fundus (open arrow) and coeliac axis (arrowhead). Numerous signal voids (arrows) at the splenic hilum represent recurrence of varices in the left gastric territory

Figure 7 Normal colon. In vivo spin echo T_1-weighted transverse image (repetition time 660 ms; echo time 20 ms) through the sigmoid colon showing a trilaminar wall structure of mucosa (intermediate signal intensity; short arrow), submucosa (high signal intensity; curved arrow), and muscularis propria (low signal intensity; long arrow)

$$\oint \boldsymbol{E}\mathrm{d}l = \frac{-\mathrm{d}}{\mathrm{d}t}\int \boldsymbol{B}\mathrm{d}A$$

where $\boldsymbol{E}$ is the induced electric field strength along a path of length dl, t is time, and $\boldsymbol{B}$ is the inducing magnetic flux density over an area dA, all variables being vector qualities.

If we take the relatively simple case of a closed circuit path of radius r in free space in a plane normal to the magnetic flux, then $\oint \boldsymbol{E}\mathrm{d}l = \boldsymbol{E}.2\pi r$. The corresponding rate of flux change is:

$$-\int \frac{\mathrm{d}\boldsymbol{B}}{\mathrm{d}t}\mathrm{d}A$$

which will have magnitude

$$\left|\frac{\mathrm{d}\boldsymbol{B}}{\mathrm{d}t}\right|\pi r^2.$$

Then

$$\boldsymbol{E}.2\pi r = \frac{\mathrm{d}\boldsymbol{B}}{\mathrm{d}t}\pi r^2$$

and

$$\boldsymbol{E} = \frac{\mathrm{d}\boldsymbol{B}}{\mathrm{d}t}\frac{r}{2}$$

Consequently, the induced electric field increases linearly with the enclosed loop radius.

If part of this circular path is replaced by a conducting medium, a copper wire for example, the resulting electric field within the wire will be zero and the electric field around this loop will be concentrated into the lower conductivity portion of the loop outside the wire. Since, for a given diameter, the total loop electromotive force ($\boldsymbol{E}.2\pi r$) is fixed, increasing the length of the wire portion of the loop to create a smaller gap will increase the electric field in the gap proportionately. Should this gap be now filled with a nonmetallic medium capable of supporting electric currents (e.g., human tissue), this relatively high electric field could give rise to currents sufficiently high to produce significant tissue heating and a potential safety hazard.

Such a situation can exist within a MR scanner if suitable precautions are not taken. The $\boldsymbol{B}_1$ magnetic field, alternating at the Larmor frequency, typically irradiates the whole body. Under normal operating conditions, the induced electric fields and their associated currents are small enough that the resultant tissue heating is well within safety guidelines. However, the introduction of a conductor, for example an electrocardiograph lead positioned so as to form a large loop, can result in a large electric field between the ends of the loop. If this high-field region is adjacent to the body surface, the local electric current can produce tissue heating that far exceeds the safety guidelines, resulting, in extreme cases, in localized tissue burning. This conducting-loop problem could equally apply to a colonoscope, for example as it performs loops within the abdomen. This hazard is minimized by providing a sufficiently thick layer of insulating material of high dielectric strength between conductive material within the colonoscope and the external tissue, so ensuring that electric fields are confined largely within these layers and that their levels are kept within reasonable limits.

The coil is coated in an epoxy-based adhesive commonly used in medical devices. It is biologically inert and nontoxic, meeting US pharmacopeia biocompatibility standards, thus avoiding allergic reactions and long-term toxic effects. In addition, it is chemical and water resistant, which allows sterilization of the coil by soaking it in a solution of glutaraldehyde.

7.2 Clinical Factors

Upper GI endoscopy carries a significant morbidity and mortality.[15] In a large prospective audit across 36 hospitals to include over 14 000 examinations, the death rate was 1 in 2000 and the morbidity rate 1 in 200; cardiorespiratory problems were most prominent and there was a strong relationship between the lack of monitoring and the use of high-dose benzodiazepines and adverse outcomes. A lack of recovery area and poor staffing exacerbates this problem. No complications have been experienced in our unit so far, but as the procedure is considerably longer than a standard upper GI endoscopy and often requires an additional dose of sedative, an increase in the morbidity and mortality must be anticipated. Also although the patient is accessible, this is less than achieved in a standard procedure and all monitoring requires increased vigilance. Continuous oxygen and close observation of the sedated patient during the entire period of imaging must be maintained.

Performing endoscopy in the MR environment, therefore, requires additional considerations. The MR suite must be equipped with full resuscitation facilities nearby. This includes oxygen available to the patient in the scanner and a MR-compatible trolley to transfer a patient in an emergency to a space outside the scanner room where normal resuscitation procedure may be carried out. Finally, all staff must be trained in metal safety and in resuscitation practice peculiar to the MR environment.

8 FUTURE APPLICATIONS

MR endoscopy will provide a useful means of staging neoplastic masses in the upper and lower GI tract. It may also be used as a way of monitoring or guiding therapeutic interventions administered endoscopically. For example, injection or banding esophageal varices may benefit from being performed with simultaneous cross-sectional images so that the completeness and efficacy of the procedure can be monitored in realtime. Laser treatments for the palliative recanalization of esophageal carcinoma may also be monitored in this way, thus reducing the risks of perforation or inadequate treatment and optimizing treatment outcome.

9 CONCLUDING REMARKS

MR imaging using a surface coil placed within the GI tract during an endoscopic procedure enables visualization of mural and extramural lesion extension and may provide a useful adjunct to diagnostic upper and lower GI endoscopy. Formal evaluation of this technique and comparison with ultrasound, computed tomography, and surgical findings is warranted.

10 RELATED ARTICLES

Coils for Insertion into the Human Body; Design and Use of Internal Receiver Coils for MRI.

11 REFERENCES

1. T. W. Rice, G. A. Boyce, and M. V. Sivak, *J. Thorac. Cardiovasc. Surg.*, 1991, **101**, 536.
2. M. D. Rifkin, S. J. Gordon, and B. B. Goldberg, *Radiology*, 1984, **151**, 175.
3. B. B. Goldberg, R. M. Steiner, J. B. Liu, D. A. Merton, G. Articolo, J. R. Cohn, J. Gottlieb, B. L. McCombe, and P. W. Spirn, *Radiology*, 1994, **190**, 233.
4. B. N. Milestone, M. D. Schnall, R. E. Lenkinski, and H. Y. Kressel, *Radiology*, 1991, **180**, 91.

5. N. M. deSouza, I. C. Hawley, J. E. Schwieso, D. J. Gilderdale, and W. P. Soutter, *Am. J. Roentgenol.*, 1994, **163**, 607.
6. T. Miyazaki, Y. Yamashita, T. Tsuchigame, H. Yamamoto, J. Urata, and M. Takahashi, *Am. J. Roentgenol.*, 1996, **166**, 1297.
7. A. Haase, J. Frahm, and K. D. Matthaei, *J. Magn. Reson.*, 1986, **67**, 258.
8. A. Haase, *Magn. Reson. Med.*, 1990, **12**, 77.
9. M. K. Stehling, *Magn. Reson. Imag.*, 1992, **10**, 165.
10. Y. Wang, R. C. Grimm, J. P. Felmlee, S. J. Riederer, and R. L. Ehman, *Magn. Reson. Med.*, 1996, **36**, 117.
11. A. M. Taylor, P. Jhooti, D. N. Firmin, and D. J. Pennell, *JMRI*, 1999, **9**, 395.
12. G. A. Coutts, D. J. Gilderdale, K. M. Chui, L. Kasuboski, and N. M. deSouza, *Magn. Reson. Med.*, 1998, **40**, 908.
13. C. L. Dumoulin, S. P. Souza, and R. D. Darrow, *Magn. Reson. Med.*, 1993, **29**, 411.
14. N. M. deSouza, A. H. Gibbons, G. A. Coutts, A. S. Hall, R. Puni, J. Calam, and I. R. Young, *Minim. Invas. Ther.*, 1995, **4**, 277.
15. A. M. Thompson, K. G. Park, F. Kerr, and A. Munro, *Br. J. Surg.*, 1992, **79**, 1046.

Acknowledgements

We gratefully acknowledge the help we received in undertaking the work described here from Picker International Inc., Cleveland, OH, and Endoscan Ltd, Burgess Hill, UK.

The work was supported by MedLINK grant P37.

Biographical Sketches

Nandita M. deSouza. *b* 1957. B.Sc. Hons (Physiology) 1978, MBBS, 1983, University of Newcastle upon Tyne, UK, M.R.C.P. 1986, F.R.C.P. 1991, M.D. 1996. House Surgeon and Physician and Senior House Physician, Newcastle upon Tyne 1983–85. Registrar in internal medicine 1986–87. Registrar and Senior Registrar in Diagnostic Radiology, Guy's Hospital, London 1987–92. Senior Research Fellow in MR Imaging, Royal Postgraduate Medical School, Hammersmith Hospital, 1993–97. Senior Lecturer 1997–present. Research Interests: internal receiver coils, interventional MRI.

Glyn A. Coutts. *b* 1959. B.A. (Physics) University of Oxford, UK, 1980; D.Phil, University of Oxford 1985. Senior Research Associate at Picker Research UK, 1987–99. Marconi Medical Systems, UK, 1999–present. Approximately 30 publications in the field of MRI and MRS. Current interest: interventional MRI.

David J. Larkman. *b* 1969. 1993, Ph.D. Physics, Manchester University, 1997, BSc (Hons) Physics, Liverpool John Moores University, Research Scientist at the Robert Steiner MRI Unit, Hammersmith Hospital, London, UK, 1997–99. Marconi Medical Systems, UK, 1999–present. Publications as conference and journal papers on small-coil MR, fast imaging using multicoil techniques, and artefact control in MR images.

David J. Gilderdale. *b* 1947. B.Sc. telecommunications, Ph.D. computer simulation as an aid to lighting design. Research Assistant, Plymouth Polytechnic, 1974–78. Electronic Engineer, Central Research Laboratories, Thorn-EMI Ltd, 1978–81. Senior Scientist, GEC Hirst Research Centre, 1981–84. Senior Lecturer, Department of Electrical Engineering, Plymouth Polytechnic, 1981–88. Engineering Consultant, 1988–present.

Interventional MRI: Specialist Facilities and Techniques

Glynn A. Coutts and Nandita M. deSouza
Royal Postgraduate Medical School, Hammersmith Hospital, London, UK

1	Introduction	1
2	MR-Guided Diagnostic Procedures	1
3	MR-Guided Therapeutic Procedures	7
4	Conclusions	9
5	Related Article	9
6	References	9

1 INTRODUCTION

The excellent anatomical detail and high level of soft tissue contrast provided by magnetic resonance imaging (MRI) are potentially of enormous value in guiding both diagnostic and therapeutic procedures. However, the use of MRI has been limited because of the poor access to the patient provided by most scanners and the practical difficulties of working within a magnetic field. Both these problems are now being addressed. Newer more open-plan magnet configurations provide greatly improved access to the patient, and manufacturers are now producing a wide range of MR-compatible equipment.

The indications for MR-guided diagnostic procedures include lesions visualized only with MRI, e.g. focal lesions in the breast where MR-guided biopsy may be carried out using MR-compatible needles. The technical aspects of such procedures may also be simpler under MR guidance when particular access routes are preferred because of the oblique planes and 3D acquisition facility offered by MRI. In addition, MR-guided diagnostic procedures may be performed via endoscopes and facilitated by the use of specially designed insertable coils. These dedicated surface coils inserted through body orifices or into blood vessels and placed adjacent to localized areas of interest, e.g. cervix, prostate, oesophagus, and inner ear, provide remarkably high resolution images.

MR-guided therapeutic procedures are largely performed through flexible fiber-optic endoscopes, and may embrace a wide clinical spectrum of applications including treatment of very common conditions such as benign prostatic hypertrophy and prolapsed intervertebral disks.

2 MR-GUIDED DIAGNOSTIC PROCEDURES

2.1 Breast Biopsy

Over a decade has elapsed since the first clinical trials predicted an important role for MRI in breast cancer diagnosis.[1–3] Use of gadopentate dimeglumine as a contrast agent in the 1980s showed that malignant breast tumors enhanced reliably and predictably,[4–6] and thus lack of enhancement excludes malignancy. However, other lesions such as atypical hyperplasia and areas of fibrocystic change also enhance, so that the specificity of MRI for malignancy is low.[7] More detailed studies demonstrated that cancers enhanced early, and were best discriminated from benign lesions in the first 2 min after injection of contrast agent.[5] The rise time for the enhancement of benign lesions, such as sclerosing adenosis and fibroadenomas, is generally slower than for neoplastic lesions,[7] but there is overlap in individual cases, which makes it difficult to exclude a definitive diagnosis of malignancy with the necessary high level of certainty.

These difficulties in interpretation are compounded following treatment with surgery and/or radiation therapy. Post-treatment changes mimic malignancy clinically, mammographically, and on ultrasound.[8–11] Mammographic evaluation of such breasts is frequently impaired by decreased compressibility, generalized or locally increased density, architectural distortion, skin thickening, mass-like areas of fibrosis or fat necrosis, and indeterminate microcalcification. Furthermore, different radiation protocols as well as individual differences in tissue response may affect the timing of this enhancement seen on MRI. As a result, histology is frequently necessary not only for the diagnosis of the primary lesion but also for the diagnosis of disease recurrence in treated patients.

MR-guided biopsy can therefore provide histological diagnosis of primary lesions not visible on mammography, secondary foci and nonspecific areas of contrast enhancement, and lesions visible in mammographically uninterpretable cases, e.g. dense and treated breasts. It provides a means for identifying multifocal disease where mastectomy rather than lumpectomy may be indicated. MRI may also be used for evaluating and biopsying focal clinical abnormalities during pregnancy when mammography and radiation exposure are undesirable.

2.1.1 Techniques

Several schemes for MR-guided breast biopsy have so far emerged. One method uses the patient in the prone position with the breast under gentle compression in a multicoil array. Following the diagnostic study the lesion is reimaged using an interventional device consisting of a perforated lateral plate incorporating a single coil and a medial plate incorporating two coils.[12] Intravenous gadolinium contrast agent is administered for lesion identification, and fiducials are used to calculate the coordinates of the entry site.

Stereotactic MR-compatible biopsy equipment is now becoming commercially available, and may be used to place needles with 1 mm accuracy. The first step is the acquisition of the 3D data set, which is equivalent to obtaining the scout views for stereotactic mammographic biopsy. The coordinates of the lesion are then calculated from the reconstructed images, and entered into the unit which aligns the gun and needle along the proper trajectory. In comparison with conventional stereotactic mammography, use of the 3D data set reduces the errors associated with estimation of tip position and makes it possible to visualize the lesion and the needle trajectory in three planes.

In patients who have had surgery and radiotherapy to the axilla, elevation of the arm is difficult and sometimes painful, making the prone position unacceptable. In these patients the

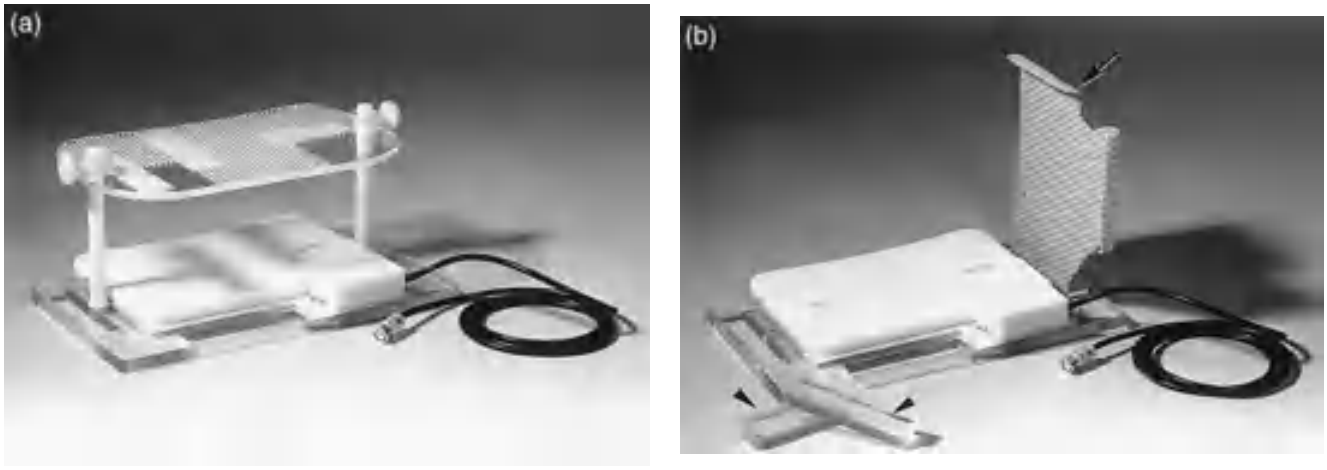

Figure 1 Breast biopsy device comprising baseplate with integral surface coil and (a) upper compression plate with holes for needle access and (b) shaped thermoplastic material. This is immobilized on three sides to the modified baseplate using Plexiglas blocks

breast may be immobilized in the lateral decubitus position. This provides the added advantage of an easy medial or lateral needle approach that automatically runs parallel to the chest wall. This is essential in the distorted scarred breast, where the lesion is often retracted toward the chest wall. Also, in the lateral decubitus position, good access is provided to lateral lesions of the uppermost breast and medial lesions of the lowermost breast. Our biopsy device consists of a rectangular receiver coil coupled to a mechanism for immobilization (Figure 1). The receiver coil is a 180 × 80 mm rectangle of copper foil. The coil is mounted at a distance of 2 mm from a double split radiofrequency screen to minimize electric field effects.[13] The whole assembly is mounted 10 mm behind the breast support plate.

Immobilization is achieved by using two flat compression plates with one edge contoured to the chest wall. The lower plate incorporates the rectangular receiver coil mounted on its outer surface. The upper plate contains a 250 × 140 mm area of holes approximately 5 mm apart. The plates are connected by two posts: the position of the upper plate can be adjusted, and it is locked in place when breast compression is adequate (Figure 1(a)).

Adequate immobilization with a greater degree of comfort may be achieved using a nonshrinking thermoplastic that is commercially available for use as a radiation therapy mask (Figure 1(b)). It is a thermoplastic that is rendered deformable by heating in a water bath at 70–80 °C for 30–60 s. It can then be stretched and molded around the breast to be biopsied. Hardening occurs in 60 s, after which it forms a rigid exoskeleton. It is fixed to the baseplate on three sides and fastened around the chest wall using tapes. Two MR-visible scales provide the X- and Y-coordinates of the lesion to be biopsied, and the depth is calibrated from the images in a perpendicular plane using an electronic caliper.

Another approach is to use MRI guidance without having to perform the biopsy within the bore of the scanner. This can be achieved by using frameless stereotaxy with an ultrasonic localizer. It is based on a localizing tip with a handle onto which two ultrasound emitters are mounted (the 'wand'). Ultrasound detectors on a board placed nearby can locate the position of the tip in three dimensions to an accuracy of 2 mm (Figure 2). A 3D data set is then acquired with the breast immobilized, and the data are transferred to a workstation. MR-visible fiducials placed on the breast and imaged at the same time are then registered in relation to the images of the breast using the 'wand'. The image of the lesion and the position of the biopsy needle mounted on the localizing 'wand' can be displayed simultaneously on the screen so that the entry point and the needle trajectory can be planned.

2.1.2 Needles

A variety of MR-compatible hollow needles suitable for fine-needle aspiration cytology of the breast are currently commercially available in 22G, 20G, and 18G diameters and in 5, 10, and 15 cm lengths. The tip designs include straight short bevels (Lufkin needle, E-Z-M, New York, U.S.A.; Chiba needle, William Cook, Europe), a serrated edge (Franseen needle, William Cook, Europe), and a spiral cutting edge (Tip Cut needle, William Cook, Europe). With the serrated or spiral bevel needles, a 360° quick rotation of the needle prior to withdrawal may yield small fragments of tissue for histology. However, fine-needle aspiration has a failure rate due to insufficient tissue as high as 37%, and reported false-negative rates as high as 31%.[14] The technical failure rate is higher in the treated breast, where sampling from an enhancing scar can produce a very acellular aspirate. In this situation, a two-piece cutting-edge core needle is usually necessary.

Even with MR-compatible alloys a small susceptibility effect may be seen around the needle. This may arise from the metal itself or the air within. Seen in cross-section, this artifact appears as a triangular central signal void with bright edges (Figure 3). It varies with magnetic field strength, alloy, and diameter of needle. Operators should be familiar with the type and amount of artifacts produced by the needles they are using at their particular operating frequencies in order to avoid errors in locating the needle.

2.1.3 Image Localization and Marking of Lesions Prior to Surgery

Needle marking for localization of breast lesions based on imaging immediately prior to surgery was developed

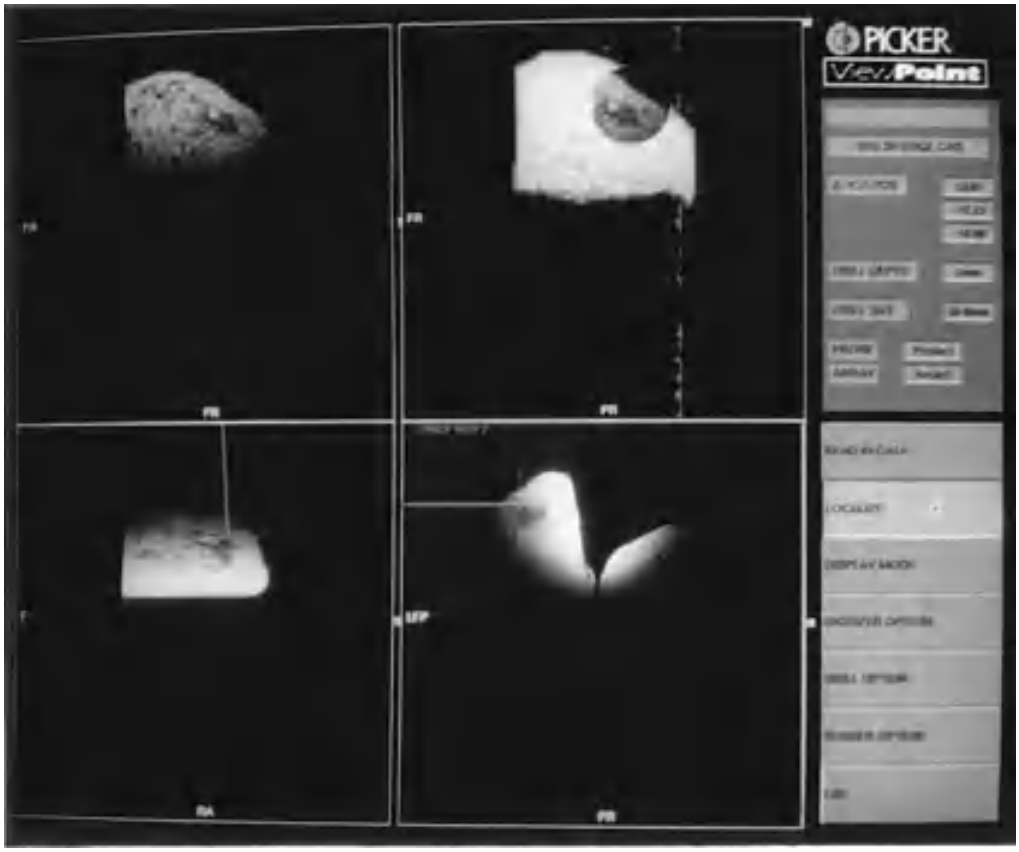

Figure 2 Targeting a breast lesion using a 3D data set. The needle trajectory is projected in three planes in relation to the lesion and the surface entry point

to reduce the amount of tissue excised during biopsy.[15–18] The original technique involved the freehand placement of a needle in the breast as a marker to guide the surgeon.[15] Although needle localization is more accurate than the external localization alone, there are significant problems due to needle displacement before or during surgery. Localization wires with hooked ends have been developed to secure the tip of the marker wire in place within the breast,[19–21] but with mammography these may become displaced because patient and breast movement may occur when altering the position of the compression plates in order to obtain an image in a perpendicular plane.

MRI not only provides 2D imaging in multiple planes without moving the patient, but a volume acquisition allows reconstruction in multiple planes. MR-compatible marker wires are now commercially available (Kopans wire, William Cook, Europe), and, using a technique similar to that for MR-guided breast biopsy, it is possible to place a hooked wire in a lesion and confirm its positioning using a 3D imaging data set. With faster scanning methods it will also be possible to use real-time guidance to advance and steer the wire into the center of the lesion.

2.2 Upper Gastrointestinal Endoscopy

Upper gastrointestinal endoscopy is limited to visualizing lesions on the surface mucosa, and though the extent of invasion beneath the surface may be shown with biopsy, lesions with no surface component or those with infiltration remote from the biopsy site remain a problem in diagnosis. MRI provides a means of visualizing the full submucosal and intramural extent of a lesion deep to the surface, and thus complements existing techniques.

Endoscopes require detailed reengineering to be acceptable for use in an MR scanner. Because many of the component parts of a standard endoscope such as the steel tension steering wires have a detrimental effect on the uniformity of the static magnetic field (B_0), it is necessary to replace them with MR-compatible alloys. In other respects the appearance and function of such an instrument [Figure 4(a)] are identical to those of a standard endoscope.[22]

A small coil positioned just ahead of the endoscope and inserted with it may be placed in the upper gastrointestinal tract adjacent to surface lesions or suspected sites of pathology. A coil 50 mm in length with a diameter identical to that of the endoscope is optimal for ease of insertion whilst retaining a useful field of view for imaging. We have developed such a coil which incorporates a hybrid circuit to satisfy tune and match as well as decoupling requirements [Figure 4(b)]. The cable to the coil is fed through the biopsy channel of the endoscope. The procedure is performed under sedation in the center of the magnetic field. This can easily be managed in an open-plan or even a short-bore magnet such as the Picker Asset (70 cm magnet face to center plane) whilst maintaining full monitoring with pulse oximetry and electrocardiography, as well as providing pharyngeal suction as necessary.

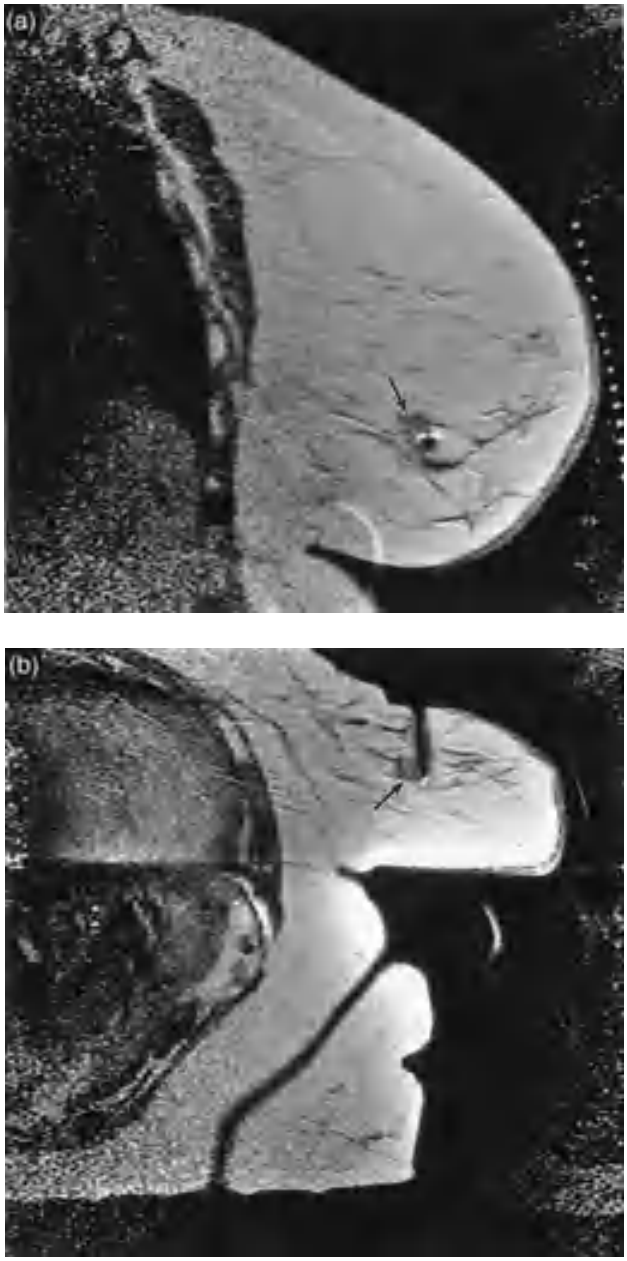

Figure 3 T_1-weighted SE (660/20) (a) sagittal and (b) axial scans with an MR-compatible needle in situ during a biopsy procedure. The needle tip lies at the periphery of enhancing scar tissue (arrow)

Imaging in the esophagus with the coil in position necessitates the use of cardiac gating or fast imaging techniques to reduce motion artifacts from the heart and great vessels. High-resolution images of the esophagus and adjacent mediastinum (Figure 5) may be obtained.[22] Initial experience with this technique is promising for visualizing intramural changes (for example, mural thickening may be seen at the level of a stricture in reflux esophagitis).

2.3 Insertable Coils

These have been developed for endovaginal use in order to image the cervix, for endorectal use to image the prostate, for endoanal use to image the anal sphincter, and for use in the external auditory meatus to image the cochlea.

2.3.1 Cervix

In early cervical neoplasia, conventional MRI is of limited value in detecting invasion of the cervix when this is only of the order of a few millimeters.[23] There are also difficulties in demonstrating extension of disease into the urinary bladder,[24] as well as involvement of adjacent parametrial lymph nodes. Endorectal coils have therefore been used to increase the resolution of cervical images,[25] but while this helps to visualize the posterior lip of the cervix, the drop off of signal anteriorly makes demonstration of the anterior lip of the cervix and the fascial planes between the cervix and bladder difficult.

We have developed a solenoidal receiver coil mounted on an acetal homopolymer (Delrin) former (internal diameter, 37 mm) for endovaginal placement around the uterine cervix which provides high-resolution images of this structure.[26] The coil is attached to a 20 cm tubular Delrin handle (Figure 6). Although designs with an angle of 45° between the coil and handle have been used, in most cases a design with no angle between the coil and handle suffices. A 10–15 cm field of view is optimal, as good parametrial detail is seen up to 6 cm from the center of the coil. With this technique (pixel size, 0.6 mm^2), details of the endocervical mucosa are easily distinguished, as well as the inner and outer zones of cervical stroma [Figure 7(a)]. The mucosa shows a smooth and regular outline in the nulliparous cervix and a more irregular and indented outline in the parous cervix. In addition, dilated glands filled with secretions are sometimes seen in the latter group. This detail is rarely provided by standard body coil or even phased-array coil images. The stromal zones are readily distinguished, and no obvious differences are seen in women taking the oral contraceptive pill or between the follicular and luteal phases of the menstrual cycle.

On administration of 0.1 mmol kg^{-1} of gadopenetate dimeglumine, brisk mucosal enhancement is seen at 30 s, which peaks at about 120 s after injection. The inner and outer stroma enhance more slowly, with the outer zone showing more prominent enhancement, and zonal differentiation being maximal at about 90 s.[26]

In Stage I carcinoma, use of an internal coil provides accurate delineation of neoplastic lesions [Figure 7(b)], including the precise position and extent of stromal invasion as well as of extension of the tumor into the parametrium, bladder base, rectum, and locoregional lymph nodes.[27]

2.3.2 Endorectal Coil

Carcinoma of the prostate is the second leading cause of cancer death in males. For younger patients, surgical excision offers the best chance of survival. MRI using an endorectal coil helps distinguish whether the disease is confined to the capsule and is therefore suitable for treatment by radical prostatectomy.

The first prototype endorectal coil was developed in 1988, and a 3.5 × 8 cm inflatable version is now commercially available with a tune and match box (Medrad, Pittsburgh, USA). It provides a two- to fourfold increase in the signal-to-noise ratio, and allows thin slices (3.0 mm) and small fields of view (10 cm) to be used. It is flexible, and may be inserted with a minimum of discomfort. As the device requires inflation of

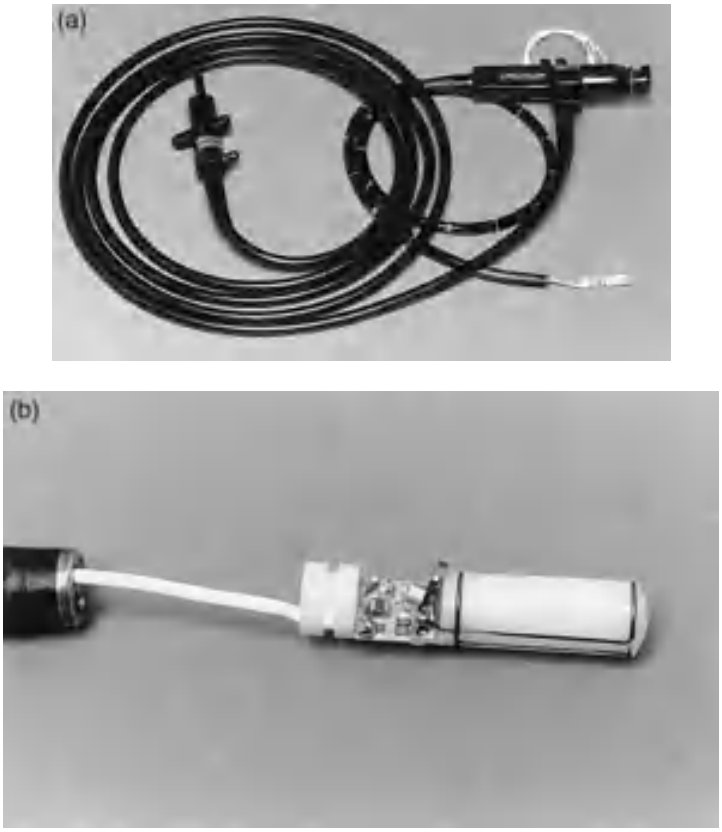

Figure 4 (a) MR compatible gastroscope. The internal receiver coil cable is passed through the biopsy channel. (b) Internal receiver coil with integral electronics for an endoscope. The diameter of the coil is the same as that of the endoscope

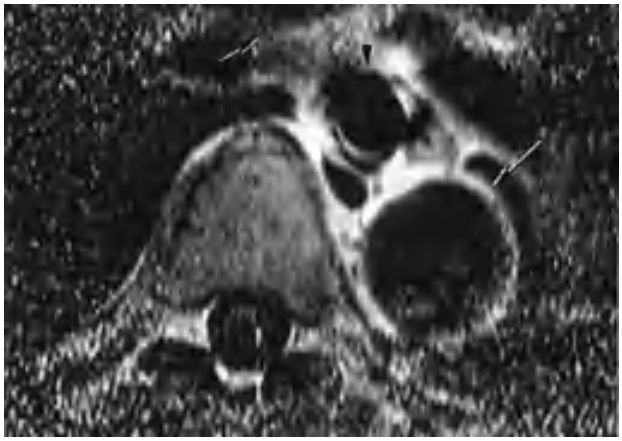

Figure 5 T_1-weighted SE (600/20) transverse image through the midoesophagus of a normal volunteer showing the trachea (short arrow), aorta (long arrow), and signal void from a coil in the oesophagus (arrowhead)

Figure 6 Intravaginal coil with a clamp stand for immobilizing it in situ. The height, angle, and tilt can be adjusted at both universal joints (arrows)

a balloon in the rectum, potential contraindications to its use are radiation strictures, rectal fistulas, and obstructing rectal masses.

Maximal contrast between the central and peripheral zones of the prostate is obtained on the T_2-weighted images, where the central zone appears of low signal intensity and the peripheral zone, which is more prominent posteriorly, is of intermediate signal intensity [see Figure 12(a)]. With increasing age the central zone enlarges and may become adenomatous (benign prostatic hypertrophy). Nodular components within such an adenoma are often mucus-containing, and are seen as high signals on the T_2-weighted scans (Figure 8).

Carcinomas tend to occur in the peripheral zone often adjacent to the capsule, and are usually seen as low signal intensity nodules. The use of fat suppression techniques either with an inversion recovery approach[28] or with chemical saturation using either frequency selective chemical saturation

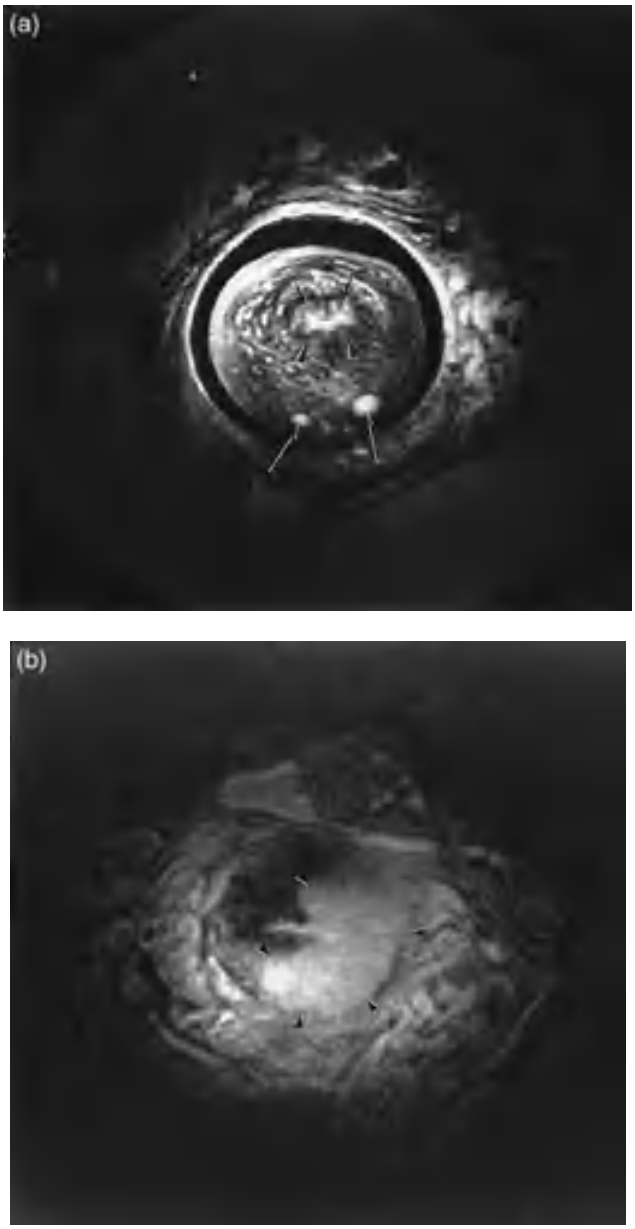

Figure 7 T_2-weighted SE (2500/80) transverse images obtained with a cervical coil in the normal nulliparous cervix show (a) a regular mucosal outline (small arrows) and a low signal intensity inner stromal zone (arrowheads). Nabothian follicles are clearly seen (long arrows). (b) In Stage I cancer the inner stromal zone is displaced by the central tumor (arrowheads)

or a three-point Dixon technique[29] has been reported to improve the detection of the capsular penetration. Experience with gadopentate dimeglumine in the preoperative assessment of carcinoma of the prostate has proved it to be of marginal use, with no improvement in the detection of malignant nodules over the T_2-weighted images.[30]

Use of an endorectal coil improves the overall staging efficacy of MR over body coil images.[31] Minor extracapsular invasion may be identified as an irregular bulge or asymmetry of the neurovascular bundle due to retraction. Tumor infiltration of the normally fluid-filled seminal vesicles is seen as low signal intensity foci within them on the T_2-weighted

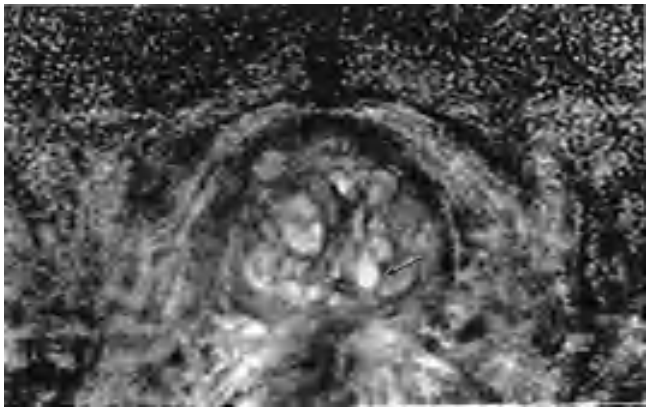

Figure 8 T_2-weighted SE (1000/130) transverse image through the mid-prostate in benign prostatic hypertrophy. The central zone of the gland is nodular and massively enlarged. Mucus-containing nodules with long T_2 components (arrow) are prominent

images.[32] However, low-signal areas in the seminal vesicles may also result from calculi or adenomatous nodules of benign prostatic hypertrophy protruding posteriorly. Understaging of prostatic carcinoma despite the use of an endorectal coil is common, and may occur because sheets of infiltrating neoplastic cells grow around glandular structures without causing displacement or distortion. Moreover, microscopic extension into the walls of the seminal vesicles is frequent and often cannot be demonstrated even with the increased resolution afforded by the endorectal coil technique.

2.3.3 Anal Coil

Disruption of the function of the anal sphincter is a common and distressing problem in which preoperative imaging is of considerable value. At present, transrectal sonography is the 'gold standard' for this purpose, but differentiation of the muscle layers (particularly anteriorly in females) is not always possible.[33] MRI of the anal sphincter with a dedicated coil provides very high-resolution images of the muscle layers.

We have developed a coil consisting of a simple saddle geometry on a 9 mm diameter Delrin former.[34] The length of the coil is 50 mm, and it is designed to image the anal sphincter from the subcutaneous external component to the lower rectum. The coil is encased in an outer sheath, and molded in shape so that it is anatomically acceptable. It incorporates a hybrid circuit to satisfy tune and match as well as $\boldsymbol{B}_1$ decoupling requirements. To reduce coil motion during imaging, we immobilize it in an external clamp which is mounted on a baseplate under the patient's thighs. Universal bossheads allow adjustment of the angle and tilt of the coil (Figure 9).

Good differentiation is obtained between the external sphincter, longitudinal muscle of the rectum, and the internal sphincter[34] (Figure 10). The internal sphincter is of high signal intensity on both T_1- and T_2-weighting, and enhances very briskly on administration of intravenous gadopentate dimeglumine.

2.3.4 Ear Coil

An 8×10 mm coil angled at 55° to mimic anatomically the plane of the tympanic membrane may be inserted under direct

Figure 9 Insertable anal coil with integral electronics for imaging the sphincter. The coil may be immobilized in a clamp stand during imaging

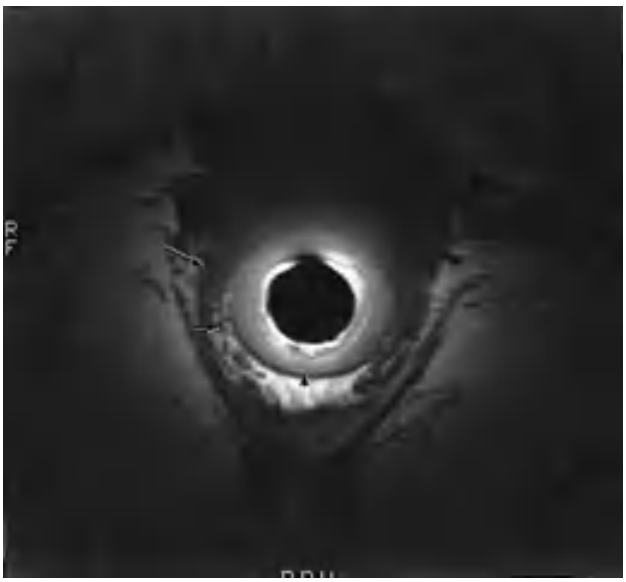

Figure 10 T_1-weighted SE (720/20) transverse image through the normal anal sphincter showing the internal sphincter (arrowhead), the longitudinal muscle of the rectum (short arrow), and the external sphincter (long arrow)

vision into the external auditory meatus in order to obtain high-resolution images of the cochlea and semicircular canals (Figure 11).

Placement of such a coil is best performed with an operating microscope, and may also require local anesthesia of the tympanic membrane.

3 MR-GUIDED THERAPEUTIC PROCEDURES

3.1 Laser Thermotherapy Techniques

Tissue damage can be produced for therapeutic purposes using lasers. The extent depends on the distribution of the laser light, the optical properties of the target tissue and the wavelength of the light used. The most important effects are

Figure 11 T_2-weighted SE (2500/80) coronal images through the petrous temporal bone in a cadaver specimen using a dedicated ear coil in the external auditory canal. High-resolution images of the cochlea (arrow) and semicircular canals (arrowhead) are obtained

thermal, as a result of the laser energy being dissipated in the target tissue as heat. The neodymium:yttrium aluminum garnet (Nd:YAG) laser with its near-infrared beam penetrates tissues for several millimeters, and may be transmitted via flexible optical fibers. These fibers can be passed down hollow needles into solid organs in order to carbonize tissue at low power (2–5 W),[35] or may be passed down endoscopes into hollow organs and be used at much higher powers (50–70 W) to recannalize them, e.g. in the esophagus, and urethra.[36] Such treatments achieve in situ necrosis of tissue, but the dose of laser energy is often empirical, and the depth of penetration and extent of tissue damage is frequently unknown. The use of MR to image tissue changes during the delivery of laser energy helps visualize the degree and extent of the changes, so that the dose of laser energy may be matched to the tissue response.

Previous animal studies have correlated laser-induced acute tissue damage with pathological findings.[37–39] During application of laser energy to rabbit muscle with a direct contact fiber at 2000 J, three layers were seen with T_2-weighted MR scans: a central cavity with a high signal rim corresponding to carbonized tissue, a broad low signal intensity layer corresponding to denatured tissue with a zone of coagulative necrosis, and a high signal zone corresponding to a layer of edema.[39] Similar therapy in patients with liver tumors using a diffusing fiber tip implanted directly in the lesion and 4320 J of laser energy demonstrated an area of hyperintensity on T_1-weighted scans at 2 min.[40] This may have been due to the formation of methemoglobin in the heated tissue, as has been shown in vitro.[41]

The noncontact mode and a side-firing technique at 40–60 W may be used in hollow organs such as the prostate to achieve maximal coagulation and minimal evaporation of tissue.[42] With this technique, improvement in symptoms may occur due to sloughing of tissue over a period of months. However, this may also cause obstructive and/or irritative symptoms for variable periods of time.[43,44] The technique

was perfected on a canine prostate model,[43] which, unlike the human prostate, is very acinar and has little stroma.[45] It therefore undergoes more dramatic sloughing of tissue when laser coagulation is performed.

3.1.1 Laser Prostatectomy

Endoscopic laser ablation (ELAP) is challenging the position of transurethral prostatectomy (TURP) in the management of benign prostatic hyperplasia because it offers major advantages over TURP such as reduced blood loss and greatly reduced hospital stay.[36] However, unlike TURP, the subjective and objective benefits associated with ELAP are usually not apparent for several weeks after treatment, and the resulting cavitation in the prostate is much less. As a result there may be much less long-term benefit from the procedure.[46] MR-monitored ELAP provides a method of imaging during treatment, allowing the operator to match tissue changes to the size and shape of the prostate in order to improve the long-term clinical outcome.

The procedure may be performed in the MR suite under general or regional (spinal or epidural) anesthesia. After establishing anesthesia the patient is transferred to the scanning table, and preoperative images are obtained using an endorectal receiver coil. A suprapubic catheter is inserted to maintain adequate irrigation throughout the laser therapy. In a short-bore design magnet, the patient's head lies outside the magnet whilst imaging the pelvis, thus facilitating continuous anesthetic monitoring.[47]

Using a Nd:YAG laser (Cardiolase 4000 Triamedyne Inc., USA) with a side-firing fiber (Bard, USA), a standard four-quadrant ablation of 40 W in each quadrant for 90 s (14 400 J) in our group of patients produced a striking increase in glandular size (approximately 34%) on the immediate postoperative images.[47] This swelling was accompanied by a loss of the nodular architecture of the gland. An area of T_1 shortening was seen in some cases. On the T_2W scans, development of a periurethral band of low signal was seen in the immediate postoperative period [Figure 12(a) and (b)].

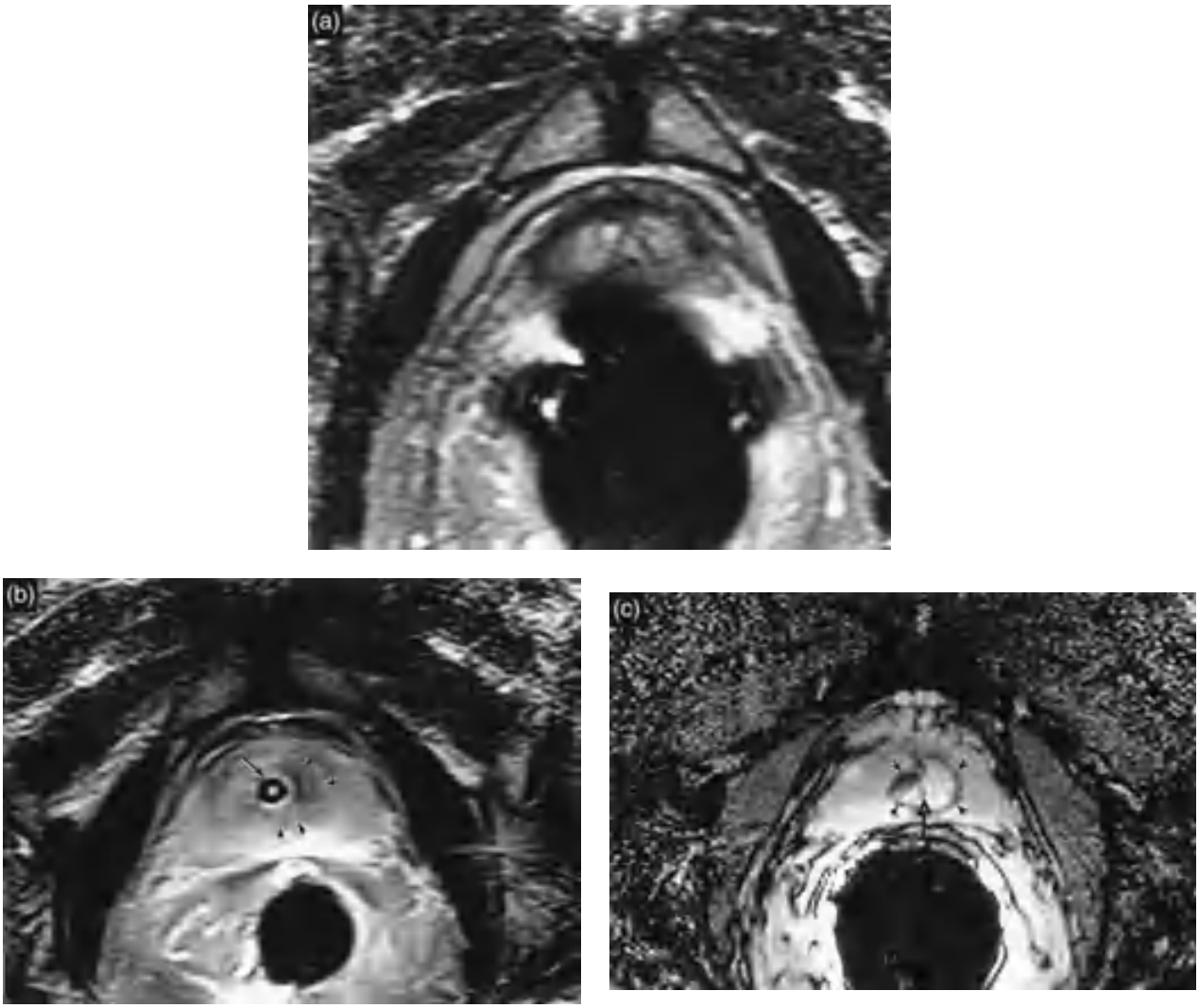

Figure 12 T_2-weighted SE (2500/80) transverse images through the prostate (a) before, (b) immediately after, and (c) 3 months following laser prostatectomy. In addition to glandular swelling and loss of nodular architecture, in image (b) there is a high-signal central region immediately adjacent to the catheter and probably related to it. Outside of this area there is a diffuse low-signal region within the prostate (arrows). (c) At 3 months there is a well-demarcated low-signal ring (arrowheads) several millimeters from the urethra (open arrow), but no evidence of cavitation

Glandular swelling was markedly reduced 1 week later, and resolved 3 months postoperatively. At this time a well-demarcated low-signal ring was seen several millimeters away from the urethra [Figure 12(c)]. The appearance of the gland was otherwise unchanged from the preoperative appearance, and there was no significant reduction in prostatic size or evidence of periurethral cavity formation.

3.1.2 Laser Discectomy

It has been possible to place hollow needles within the nerve root foraminae using real-time MRI, and pass microendoscopes down these in order to visualize fragments of prolapsed disk material and the adjacent nerve root prior to laser discectomy under direct vision.[48]

3.2 Cryoablation, Radiofrequency Ablation, and Focused Ultrasound

These modalities produce useful tissue ablation and have all been used to a limited extent under MR guidance.[49–52] The equipment necessary is cumbersome, and not only must it be rendered MR compatible but it must be easy to manipulate if access to the patient is limited. The issue of radiofrequency shielding of such equipment whilst in use during scanning also requires consideration. Cryotherapy has the particular advantage of freezing the mobile protons and creating a 'black hole' effect in the treated area, thus sharply demarcating treated from normal tissue.[51] Technical advances and the trend toward image-guided minimally invasive intervention are making these techniques more popular.

4 CONCLUSIONS

MRI offers unique advantages of good soft tissue contrast as well as multiplanar cross-sectional imaging. Its potential for monitoring and guiding radiological and surgical interventional procedures is now beginning to be expanded. It should enable many procedures to be optimized whilst reducing their complications, thus making minimally invasive therapy safer and more cost-effective.

5 RELATED ARTICLES

Coils for Insertion into the Human Body.

6 REFERENCES

1. S. J. El Yousef, R. J. Alfidi, R. H. Duchesneau, C. A. Hubay, J. R. Haaga, P. J. Bryan, J. P. LiPuma, and A. E. Ament, *J. Comput. Assist. Tomogr.*, 1983, **7**, 215.
2. S. J. El Yousef, R. H. Duchesneau, R. J. Alfidi, J. R. Haaga, P. J. Bryan, and J. P. LiPuma, etc. *Radiology*, 1984, **150**, 761.
3. C. B. Sterling, P. C. Wang, A. Lieber, S. S. Mattingley, W. O. Griffen, and D. E. Powell, *Radiology*, 1985, **154**, 457.
4. W. A. Kaiser and E. Zeitler, *Radiology*, 1989, **170**, 681.
5. S. H. Heywang, A. Wolf, E. Pruss, T. Hilbertz, W. Eiermann, and W. Permanetter, *Radiology*, 1989, **171**, 95.
6. J. P. Stack, O. M. Redmond, M. B. Codd, P. A. Dervan, and J. T. Ennis, *Radiology*, 1990, **174**, 491.
7. S. E. Harms, D. P. Flamig, K. L. Hesley, M. D. Meiches, R. A. Jensen, W. P. Evans, D. A. Savino, and R. V. Wells, *Radiology*, 1994, **187**, 493.
8. P. C. Stomper, A. Recht, A. L. Berenberg, M. S. Jochelson, and J. R. Harris, *Am. J. Radiol.*, 1987, **148**, 39.
9. M. Rebner, D. R. Pennes, D. D. Adler, M. A. Helvie, and A. S. Lichter, *Radiology*, 1989, **170**, 691.
10. C. Balu-Maestro, J. N. Bruneton, A. Geoffray, C. Chauvel, A. Rogopoulus, and O. Bittman, *J. Ultrasound Med.*, 1991, **10**, 1.
11. E. B. Mendelson, *Semin. Ultrasound, CT, MR*, 1989, **10**, 154.
12. M. D. Schnall, R. Newman, and S. Orel, Abstracts, *Society of Magnetic Resonance*, 1993, p. 163.
13. N. M. deSouza, G. A. Coutts, J. E. Schweiso, A. S. Hall, M. Burl, T. Krausz, and C. Vernon, Abstracts, *Society of Magnetic Resonance*, 1994, p. 1582.
14. G. S. Grant, J. R. Goellner, J. S. Welch, and J. K. Martin, *Mayo Clin. Proc.*, 1986, **61**, 377.
15. G. D. Dodd, K. Fry, and W. Delaney, In *Management of Patients with Cancer*, ed. T. F. Neaton, Saunders, Philadelphia, 1965, pp. 88–113.
16. S. A. Feig, *Radiol. Clin. North Am.*, 1983, **21**, 155.
17. H. A. Frank, F. M. Hall, and M. L. Steer, *N. Engl. J. Med.*, 1976, **295**, 259.
18. B. Threatt, H. Apelman, R. Dow, and T. O'Rourke, *Am. J. Roentgenol. Radium Ther. Nucl. Med.*, 1974, **121**, 839.
19. J. E. Myer, D. B. Kopans, P. C. Stomper, and K. K. Lindfors, *Radiology*, 1984, **150**, 335.
20. E. J. Urrutia, M. C. Hawkins, B. G. Steinbach, M. A. Meacham, K. I. Bland, E. M. Copeland, and I. F. Hawkins, *Radiology*, 1988, **169**, 845.
21. M. J. Homer, *Radiology*, 1985, **157**, 259.
22. A. S. Hall, D. J. Bryant, M. Burl, and N. M. deSouza, Abstracts, *Society of Magnetic Resonance*, 1994, p. 1581.
23. D. Rubeno, J. R. Thornbury, C. Angel, M. H. Stoler, S. L. Weiss, R. M. Lerner, and J. Beecham, *Am. J. Radiol.*, 1988, **150**, 135.
24. H. Hricak, C. G. Lacey, L. G. Sandles, Y. C. Chang, M. L. Winkler, and J. L. Stern, *Radiology*, 1988, **166**, 623.
25. B. N. Milestone, M. D. Schnall, R. E. Lenkinski, and H. Y. Kressel, *Radiology*, 1991, **180**, 91.
26. N. M. deSouza, I. C. Hawley, J. E. Schwieso, D. J. Gilderdale, and W. P. Soutter, *Am. J. Radiol.*, 1994, **163**, 607.
27. N. M. deSouza, D. Scoones, J. Schwieso, D. J. Gilderdale, and W. P. Soutter, Abstracts, *Society of Magnetic Resonance*, 1994, p. 1542.
28. F. Parivar, V. Rajanavagam, V. Waluch, R. T. Eto, L. W. Jones, and B. D. Ross, *J. Magn. Reson. Imaging*, 1991, **1**, 657.
29. B. Tamlet, F. G. Sommer, G. H. Glover, and E. Schneider, *Radiology*, 1991, **179**, 43.
30. S. A. Mirowitz, J. J. Brown, and J. P. Heiken, *Radiology*, 1993, **186**, 153.
31. M. D. Schnall, Y. Imai, J. Tomaszewshi, H. M. Pollack, R. E. Lenkinski, and H. Y. Kressel, *Radiology*, 1991, **178**, 797.
32. M. L. Schiebler, J. E. Tomaszewski, M. Bezzi, H. M. Pollack, H. Y. Kressel, E. K. Cohen, H. G. Altman, W. B. Gefter, A. J. Wein, and L. Axel, *Radiology*, 1989, **172**, 131.
33. A. H. Sultan, M. A. Kamm, C. N. Hudson, J. R. Nicholls, and C. I. Bartram, *Clin. Rad.*, 1994, **49**, 368.

34. R. Puni, A. S. Hall, G. A. Coutts, and N. deSouza, *Proceedings of Progress in Magnetic Resonance*, British Institute of Radiology, London, 1994.
35. A. Masters, A. C. Steger, W. R. Lees, K. M. Walmsley, and S. G. Bown, *Br. J. Cancer*, 1992, **66**, 518.
36. A. J. Costello, W. G. Bowsher, D. M. Bolton, K. G. Braslis, and J. Burt, *Br. J. Urol.*, 1992, **69**, 603.
37. Y. Anzai, R. B. Lufkin, S. Hirschowitz, K. Farahani, and D. J. Castro, *J. Magn. Reson. Imaging*, 1992, **2**, 671.
38. K. Anson, K. Seenivasagam, R. Miller, and G. Watson., *Br. J. Urol.*, 1994, **73**, 225.
39. Y. Anzai, R. B. Lufkin, D. J. Castro, K. Farahani, B. A. Jabour, L. J. Layfield, R. Udkoff, and W. N. Hanafee, *J. Magn. Reson. Imaging*, 1991, **1**, 553.
40. B. Gewiese, J. Benthan, F. Fobbe, D. Stiller, G. Muller, J. Bose-Landgraf, K. Wolf, and M. Deimling, *Invest. Radiol.*, 1994, **29**, 345.
41. K. Farahani, H. C. Yoon, J. Kumiyoshi, R. E. Saxton, S. Sinha, Y. Anzai, A. A. F. DeSalles, K. L. Black, and R. B. Lufkin, Abstracts, *Society of Magnetic Resonance*, 1994, p. 576.
42. J. N. Kabalin, *J. Urol.*, 1993, **150**, 95.
43. D. G. Assimos, D. L. McCullough, R. D. Woodruff, L. H. Harrison, L. J. Hart, and W. J. Li, *J. Endourol.*, 1991, **5**, 145.
44. D. L. McCullough, *J. Urol.*, 1991, **146**, 1126.
45. G. Bartch, G. Daxenbichler, and H. P. Rohr, *J. Steroid Biochem.*, 1983, **19**, 147.
46. P. Narayan, G. Fournier, R. Indukara, R. Leidich, K. Shinohara, and A. Ingerman, *Urology*, 1994, **43**(6), 813.
47. N. M. deSouza, R. Flynn, G. A. Coutts, D. J. Gilderdale, A. S. Hall, R. Puni, M. Chui, D. N. F. Harris, and E. A. Kiely, *Am. J. Radiol.*, 1995, in press.
48. R. Seibel and D. Groenmeyer, *Abstracts, Symposium on Interventional MRI, Los Angeles, 1994*, pp. 135–136.
49. K. Farahani, *Abstracts, Symposium on Interventional MRI, Los Angeles, 1994*, p. 39.
50. K. L. Black, *Abstract, Symposium on Interventional MRI, Los Angeles, 1994*, pp. 72–74.
51. J. Gilbert, *Abstracts, Symposium on Interventional MRI, Los Angeles, 1994*, pp. 20–30.
52. K. Hynyen, *Abstracts, Symposium on Interventional MRI, Los Angeles, 1994*, pp. 40–44.

Biographical Sketches

G. A. Coutts. *b* 1959. B.A. Physics, 1980, D.Phil. 1985, University of Oxford, UK. Research associate at GEC Hirst Research Centre in laboratory headed by Ian R. Young, 1987–present. Approx. 30 publications in the field of MRI and MRS. Current research specialty: interventional MRI.

Nandita M. deSouza. *b* 1957. B.Sc. (Hons.) (Physiology), 1978, MBBS, 1983, University of Newcastle upon Tyne, UK. M.R.C.P., 1986, F.R.C.R., 1991, House Surgeon and Physician and Senior House Physician, Newcastle upon Tyne, 1983–85. Registrar in Internal Medicine, 1986–87. Registrar and Senior Registrar in Diagnostic Radiology, Guys Hospital, UK, 1987–1992. Senior research fellow in MR Imaging, Royal Postgraduate Medical School, Hammersmith Hospital, UK, 1993–present. Research specialty: interventional MRI.

MR-Guided Biopsy, Aspiration, and Cyst Drainage

Jonathan S. Lewin

University Hospitals of Cleveland and Case Western Reserve University, Cleveland, OH, USA

1 INTRODUCTION

As the practice of radiology has evolved since the late 1980s, there has been increasing emphasis on intervention. Recent trends in minimally invasive methods for diagnosis and treatments have created a burgeoning interest in the use of MRI for guidance of radiological procedures.

Historically, the relatively long imaging times and the difficulty in patient access resulting from closed-bore superconducting cylindrical system designs have combined to make MR an unlikely guidance modality for radiological procedures. More recently, many of these disadvantages have been overcome with the advent of system hardware and pulse sequence improvements that have allowed the development of rapid imaging on open systems. This chapter discusses the hardware and software improvements that have made interventional MRI a reality and the use of this technology for guidance of biopsy, aspirations, and cyst drainage.

2 IMAGING SYSTEM DEVELOPMENT

Recent advances in magnet and system design have accelerated progress in MR-guided intervention. Many different MR system configurations have been used to guide percutaneous procedures. Each of these systems has advantages and disadvantages, with a constant tradeoff between signal-to-noise ratio, (SNR) access to the patient, useable field of view, and expense.

The use of MRI for interventional procedure guidance includes its use by radiologists during manipulation of needles, electrodes, catheters, or laser fibers. This form of intervention requires a significant departure from conventional diagnostic concepts and traditional imaging systems.

The factors contributing to high image quality in diagnostic MR include system field strength and the homogeneity and stability of the static and gradient magnetic fields. These factors are best obtainable by decreasing the 'openness' of an imaging system. The optimal design of a magnet with regard to field homogeneity would be a complete sphere, without opening.[1] In contrast, the environment best suited to radiological intervention is one with maximum access to the patient, allowing complete freedom in interventional approach and maintaining close proximity of monitoring and therapeutic devices. These attributes are in direct opposition to those facilitating image quality.[1] The use of MRI for guidance of interventional procedures has required a compromise between these opposing forces; this balance has been achieved through a number of different concepts and solutions.

Some of the first interventional procedures under MRI guidance were performed on conventional cylindrical systems, simplifying imaging but significantly compromising the access to the patient that is necessary for performance of the procedure and monitoring of patient discomfort and safety. Biopsy and aspiration procedures have been and can be performed using these cylindrical superconducting systems, but the patient must be withdrawn from the magnet in order to reposition the needle between scans.[2] This results in relatively long procedure times and contributed to the sparse use of MRI for biopsy and aspiration during the late 1980s. In particular, when the lesion in question was visible and accessible for biopsy by computed tomography (CT) or ultrasound, these more conventional methods for procedure guidance were clearly better suited modalities.

These disadvantages were overcome, in part, through the access to the patient provided by permanent or resistive 'open' magnet imaging systems.[3–6] Unfortunately, the open low-field imaging systems available in the late 1980s often required significant imaging time to obtain a sufficiently high SNR to allow needle insertion under MRI guidance. However, the access to the patient provided by these systems led to an increased number of reports of its use, primarily for biopsy in the head and neck region.[7–9]

Since then, many magnet, gradient, and receiver chain design improvements have occurred and have led to a number of approaches for interventional imaging. A brief description of the most commonly used current designs for intervention follows. Each system has benefits and limitations for interventional procedure guidance, as each has chosen a different balance between the spatial constraints necessary for high-quality imaging and the freedom necessary for surgical or radiological intervention.

2.1 Cylindrical Superconducting Systems

From an image quality viewpoint, cylindrical superconducting systems enjoy many significant advantages relative to static magnetic field strength and homogeneity, and the adoption of this system design as the standard for image quality in the diagnostic arena is not a chance occurrence. The limited patient access for procedure performance and direct visual observation is a compromise that still allows certain procedures.

One more recent approach to the use of cylindrical superconducting systems for interventional procedures has been the siting of a superconducting system in an interventional or surgical environment. With the rapid fall-off of the static magnetic field achieved by actively shielded magnet designs, it is possible to site a superconducting system in near proximity to a surgical work space. This design has been adopted in a system constructed by Philips Medical systems (Eindhoven, the Netherlands) in which a procedure suite including a fluoroscopy system has been constructed just outside of the fringe field of a superconducting short-bore 1.5 T imaging system. Fluoroscopic or angiographic procedures can be performed in a conventional manner. However, when desired, intermittent images can be obtained by sliding the patient into the cylindrical imaging system. The imaging system allows all of the standard capabilities of a high-field system, including functional imaging, with high

image quality. Although there are very few compromises to either the fluoroscopic or MRI portions of this environment, this configuration does not allow interactive MR guidance of the intervention, as access to the patient is markedly limited. Therefore, needle placement under MR guidance must still be performed in an 'in and out' manner, which can be time consuming for difficult needle placements. Once a needle is placed, the access to fluoroscopy can greatly facilitate guidewire and catheter placement during drainage procedures.

The use of cylindrical magnets has also been successfully applied for guidance of stereotactic biopsy for breast lesions.[10] This type of stereotactic procedure lends itself well to the immobilized breast but is less applicable to most other areas in which motion is more of an issue.

2.2 'Double Donut' Configuration

A novel approach to obtaining access to a patient in a cylindrical system is exemplified in the 'double donut' configuration of the General Electric Medical Systems Signa SP system (Milwaukee, WI), designed specifically for interventional applications.[11–13] This design has taken the central segment out of a cylindrical system, allowing access to the patient from the sides and top at the isocenter of the imaging system. This product design has been directed toward siting in a surgical environment and allows enough room in the gaps between the halves (54 cm) for two physicians or nurses, one on either side of the patient.[1] This system provides a marked improvement in access to the patient relative to a closed-bore cylindrical system, although the technology is expensive. This concept represents the first system designed and constructed specifically for interventional guidance. This magnet design has been used both to guide and to monitor a large number of surgical procedures, in addition to an early published series of biopsies and aspirations.[12,14,15] However, the marked improvement in access to the patient is achieved at the expense of a decrease in field strength at the imaging isocenter (0.5 T imaging field strength) compared with the field generated by each individual superconducting half, and it compromises magnetic field homogeneity.[1] The unobstructed side and vertical access to the patient also complicates the engineering of the radiofrequency coil, requiring a local transmit–receive coil with a somewhat limited field of view.

2.3 Biplanar Magnet Designs

Another approach that has found widespread application for diagnostic MRI in the burgeoning 'open MRI' market has been the use of a biplanar magnet design. With these magnets, the patient is positioned between flat magnetic poles, leaving access from a range of side approaches. These systems typically utilize lower-field permanent or resistive magnets, with field strengths ranging from 0.064 to 0.3 T, although superconducting mid-field models of this design have also been introduced. The degree of access around the circumference of the biplanar magnet depends upon the number and position of supports separating the two magnetic poles.

A large degree of access around the circumference is afforded by the 'C-arm' design, produced by Siemens Medical Systems (Erlangen, Germany) and Picker International (Highland Heights, OH). In this design, a single column on one side of the patient supports the upper pole, allowing access from the contralateral side, head, and foot end of the magnet (Figure 1). Several manufacturers produce biplanar systems with two supporting posts, resulting in slightly more restricted access to the patient. These include systems produced by Fonar Corporation (Melville, New York), Hitachi Medical Corporation of America (Twinsburg, OH), and General Electric Medical Systems. There are also designs with four support posts from Toshiba America Medical Systems (San Francisco, CA) and Fonar Corporation. The biplanar concept has the advantage of a fairly homogeneous static magnetic field but is limited to lower field strengths than available with the cylindrical superconducting designs. The side access provided by these systems is analogous to that of C-arm fluoroscopy and is amenable to needle or catheter-directed procedures. However, anterior or posterior interventional approaches require decubitus or oblique positioning of the patient, which may not be possible with large patients because of relatively limited space between the poles of the biplane magnet. A true direct vertical approach to the patient is only possible when the patient table is brought outside of the magnet, essentially excluding simultaneous vertical intervention and imaging.

Figure 1 The C-arm system for percutaneous intervention. Intervention MR suite set up for radiological intervention demonstrates two-camera video sensor array (curved black arrow), which detects the location and orientation of a hand-held probe or needle guide (straight white arrow). The system automatically acquires continuous MR images based on the probe position and automatically updates display of four images on a shielded LCD monitor adjacent to the scanner (straight black arrow). A computer mouse on the LCD console (curved white arrow) and foot pedals (not shown) allow the scanner to be fully operated by the radiologist throughout the procedure

2.4 Other Systems

Other concepts for intervention have also been evaluated, although these systems are still in earlier stages of development. A biplanar design with a very large interpole distance approaching a 'flat bed' scanner was also recently described by Fonar Corporation, but this is still in development. Most likely,

different system designs will be advocated for different interventional applications. The choice of interventional system will depend upon each institution's optimal balance between the types of procedure to be performed, required image quality, and financial constraints.

2.5 Supplemental Technical Developments

There are several recent technical developments that are common to many of the magnet and system designs discussed above and that have facilitated the guidance phase of interventional procedures in a time-efficient manner. First, the construction of higher-quality low-noise receiver chains has allowed lower field systems to be constructed, providing relatively high SNR images and greatly improving image quality compared with earlier attempts at low-field MRI. These systems now provide image quality sufficient for the procedure-guidance phases of minimally invasive procedures. Image acquisition times of 1–3 s per image, or less, provide the necessary temporal resolution.

The second development that has impacted on the use of MR methods for procedure guidance has been the modification and development of rapid gradient echo pulse sequences for use in interactive guidance during device placement. Rapid gradient echo sequences have been developed to allow a wide range of tissue contrast in a time frame sufficient for device tracking (0.3–7 s per image) even at low field strength and with the suboptimal coil position sometimes required to access the puncture site (Figure 2).[16–19] Because the area of interest to the interventionalist is often limited to a small portion of the entire image acquired, a number of strategies have been proposed to decrease the imaging time for these methods further. These strategies include alternative reconstruction techniques such as Keyhole imaging, singular value decomposition, and wavelet encoding.[20–32] The use of these rapid gradient echo techniques for guidance of interventional procedures also takes advantage of the reduced needle artifact at lower fields compared with that at 1.5 T, allowing a wider choice of materials for device construction and still allowing high spatial accuracy despite the increased metallic artifact encountered with gradient echo techniques.[33,34]

The third innovation of significant benefit for MR-guided intervention has been the development of an interface between an optically-linked 3D digitizer and the measurement control software of the MR imager. Previously, frameless stereotactic systems had been used primarily for surgical guidance based on historical imaging data sets. The ability to acquire MR images rapidly and interactively in an arbitrary plane determined by a hand-held, sterilizable probe, or other interventional device, allows rapid planning and confirmation of complex trajectories for rigid instruments. This type of interactive image-guidance system was first described as a component of the 'double donut' system and subsequently has been applied for guidance of image acquisition on C-arm systems (Figure 1).[12,18]

An additional technical factor facilitating near-real-time procedure guidance has been the ability to view images in the magnetic field through the development of in-room high-resolution rf-shielded monitors.[12,18,35] In combination with the patient access allowed by open-imaging systems, the ability to view images at scanner side allows the entire procedure to be performed with the operator sitting next to the patient, with no need to remove the operator's hand from the interventional device at any time (Figure 1). This manner of intervention, analogous to an angiographic or sonographically guided procedure, is well-suited to the skill set developed by radiologists during more conventional types of image-guided intervention.

3 MR-SPECIFIC ISSUES FOR INSTRUMENT GUIDANCE AND VISUALIZATION

Unlike guidance by X-ray-based techniques such as fluoroscopy and CT, there are a number of user-defined imaging parameters and needle trajectory decisions that can markedly alter needle visibility and, therefore, accuracy and safety of MR-guided procedures.[33] The primary factors affecting needle visibility in clinical application can most simply be divided into those dependent upon the pulse sequence and those dependent upon the needle.

The most important pulse-sequence issue with regard to needle visibility is the sensitivity of the sequence to magnetic susceptibility effects.[33] At our institution, as in other recent reports,[12,18,35–37] near-real-time imaging for primary needle guidance is performed with gradient echo pulse sequences, taking advantage of the rapid scan time and high SNR of this sequence design. Use of these sequences has the primary advantage of rapid temporal resolution and is extremely useful for guiding needles into lesions 1 cm or greater in size that are not immediately adjacent to major neurovascular structures. At 0.2 T, the apparent width of the biopsy needle under gradient echo image guidance generally ranges from approximately 4 mm for smaller needles to 9 mm for larger needles.[33] Although this degree of artifactual widening is acceptable for larger lesions in areas of low neurovascular density, such as the abdomen and extremities, it is clearly unacceptable for head and neck lesions adjacent to major vessels. The degree of artifactual widening can be reduced by approximately a factor of two through use of a turbo spin echo pulse sequence or higher sampling bandwidth.[33] The use of turbo spin echo pulse sequences should be routinely performed prior to cutting needle biopsy to exclude smaller vessels at the level of the cutting edge of the needle; it will be rarely used as the primary mode of image guidance for lesions immediately adjacent to the carotid or vertebral artery, or for spinal lesions for which precise needle visualization is mandatory (Figures 2–4). Spin echo pulse sequences can also be applied to reduce the artifactual needle widening by a similar factor,[33] but are less useful during procedures because of the longer imaging time necessary to obtain a sufficiently high SNR. Therefore, the use of turbo spin echo imaging for position confirmation or primary guidance should be strongly considered when needle placement within 5 mm of major neurovascular structures is contemplated (Figure 3), rather than relying on the more rapid gradient echo sequences for guidance of the entire procedure.[18]

The second sequence-related parameter that can be easily varied to adjust the degree of artifactual widening is less intuitively obvious but has had significant clinical utility in our experience. This variable is the direction of frequency encoding relative to the needle shaft. The presence of a needle within tissue creates a local nonuniform spatial distortion in the magnetic field and, therefore, a variation in the local resonant

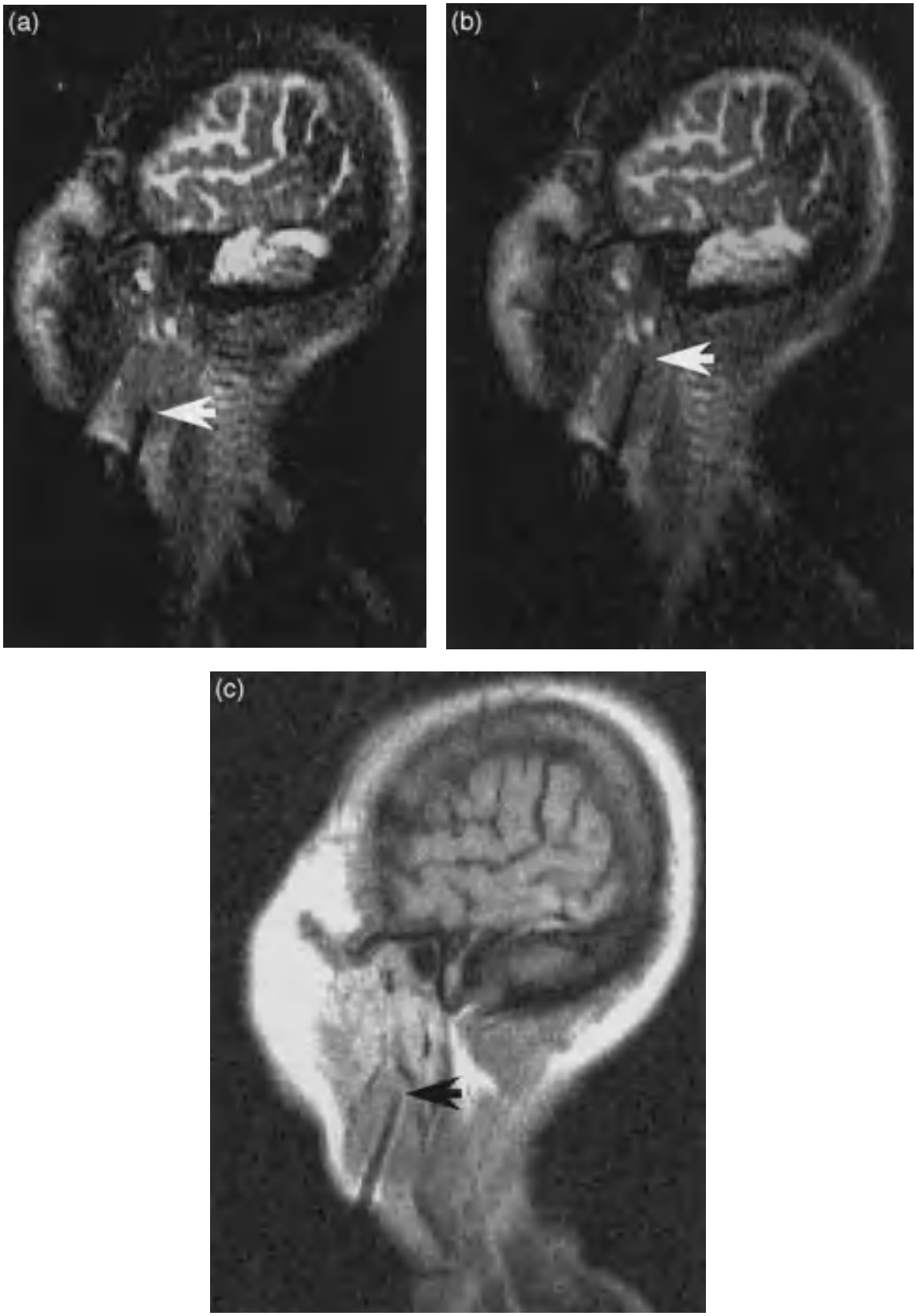

Figure 2 An 89-year-old woman with Warthin's tumor of the parotid gland. The inferior approach to the parotid tail lesion in this patient allowed this 18-gauge side-notch cutting needle to be placed in the lesion without traversing normal parotid gland and without risk to the facial nerve and its branches. (a,b) Two images from true fast imaging with steady-state precession (FISP) sequence (11.7/5.9/1/90° *TR*/*TE*/number of signal averages/flip angle) frames obtained at approximately 1 image per second during advancement of the inner stylet of this core biopsy needle (arrows). (c) A higher resolution turbo spin echo T_1-weighted image (500/24/1 *TR*/*TE*/number of signal averages, 70 s scan time) was obtained to confirm the needle (arrow) position prior to obtaining the core biopsy. (Reproduced with permission from Lewin et al.[18])

Figure 3 A 50-year-old subject with recurrent squamous cell carcinoma of the oropharynx. Turbo spin echo T_1-weighted image (500/24/1 *TR*/*TE*/number of signal averages) clearly documents needle position (arrow) and cutting notch location, particularly important when biopsy is performed near the internal carotid artery (arrowhead) or the larger branches of the external carotid artery. The external carotid artery in this patient had been previously occluded with Gianturco coils to control oropharyngeal bleeding. The coils did not result in significant image distortion and did not preclude biopsy

frequency. For imaging, a spatially linear gradient is used to encode location in the frequency-encoded direction, imparting a linear one-to-one mapping between frequency and position. The local field distortion resulting from the needle disrupts this linear relationship and leads to image artifact along this axis.

Figure 4 Needle position confirmation in a 43-year-old man with leukemic infiltration (chloroma) of scalene muscle. Coronal turbo spin echo T_1-weighted image (680/24/1 *TR*/*TE*/number of signal averages) demonstrates 18-gauge side-notch cutting needle (arrowheads) with stylet extended into the patient's right thoracic inlet paraspinal mass. (Reproduced with permission from Lewin et al.[18])

When frequency encoding is perpendicular to the needle, this results in artifactual widening. When parallel to the needle, this results in less obvious artifact at the tip and hub of the needle. Depending upon needle composition and orientation, swapping the frequency and phase-encoding axes relative to the needle shaft can reduce or increase the apparent width of the needle by a factor of 0.33 to 2.5 for turbo spin echo sequences.[33] This effect can be used to decrease the apparent needle width when the needle artifact obscures adjacent anatomic structures by setting the frequency-encoding axis of the image parallel to the needle shaft.[18] In the presence of even mild respiratory motion, the needle tip for thinner (e.g., 22 gauge) needles can be difficult to visualize in tissue with certainty. Therefore, this effect is more commonly useful, in our experience, to identify the needle tip location more confidently on turbo spin echo images by maximizing the needle artifact through frequency encoding the image in a direction perpendicular to the needle shaft. This ability to alter the appearance of the needle significantly is used on a daily basis in a variety of clinical settings.

Several other important factors are related more to the needle and its trajectory rather than to the pulse sequence and imaging parameters. The dependence of visualization for safe and accurate biopsy on needle composition is obvious and has been well described in many reports since the inception of MR-guided procedures.[2,3,33] The optimal material for needle fabrication will vary with MR system field strength. Relatively less-expensive materials such as high-nickel, high-chromium stainless steel may be adequate at 0.2 T but may give rise to unacceptable artifact at 1.5 T.[33,34] Conversely, small-caliber needles constructed from low-artifact materials such as titanium may be difficult to identify in certain clinical settings at low field.

Another issue that may have significant impact on needle localization may be somewhat less obvious: the angle between the needle shaft and the static magnetic field of the MR imager. The apparent needle diameter diminishes markedly from a decrease in artifact as the needle shaft approaches the axis of the static magnetic field.[2,33,34] Artifacts resulting from field distortion arise most significantly where the field enters and exits objects of differing magnetic susceptibility, such as the needle and surrounding tissue. When the needle is parallel to the field, distortion of the field (and, therefore, image artifact) occurs mostly at the tip and hub, and to a lesser extent along the shaft. The field is increased within the needle shaft. However, because there are no protons to image within the needle, no image distortion occurs. The field is also distorted slightly adjacent to the shaft. At low fields, the distortion adjacent to the shaft is much less than the effect of the applied imaging gradients, and, therefore, little mismapping occurs, with artifact along the shaft primarily related to mild signal loss caused by decreased T_2* relaxation.

When the needle is perpendicular to the main magnetic field, the field enters and exits throughout the length of the shaft. Local field distortion and, therefore, more prominent artifact can be observed along the entire needle. Although the apparent needle width decreases as the needle is positioned parallel to the static magnetic field (vertically for most biplanar magnets and along the long axis of cylindrical or 'double donut' systems), artifact at the device tip blooms and obscures the true tip position. Steep needle trajectories may be more familiar or appear advantageous in some anatomic locations

but may be prohibited because of this poor needle conspicuity and loss of tip position information. Safe clinical application of MR-guided techniques requires careful consideration of these factors during procedure planning and execution.

4 CLINICAL APPLICATION FOR BIOPSY AND ASPIRATION

Biopsy, aspiration, and cyst drainage represent some of the most straightforward interventional applications for a cross-sectional imaging modality. The tissue contrast, spatial resolution, and multiplanar capabilities of MR have obvious benefits for guidance of biopsy and aspiration applications, and this application was the first reported use of MRI to guide intervention. As noted above, a number of investigators have described the use of MRI for guidance of biopsy and aspiration since the late 1980s.[3,7–9,18,35,38]

MR guidance for head and neck biopsies has represented a large part of this early literature, owing at least in part to the striking advantages that MR guidance provides for interventional procedures performed in areas of complex anatomy. The benefits of multiplanar image acquisition were quickly discovered by Lufkin and colleagues, who first reported the advantages derived from going beyond the single imaging plane, usually axial, available in CT-guided procedures.[7] The elimination of beam-hardening artifact, inherent in CT, has also supported the use of MRI for guidance of skull base procedures.[9,18] Furthermore, the high vascular conspicuity resulting from flow-related enhancement effects inherent in 2D gradient echo imaging is an additional benefit of MR guidance for lesions in regions of complex vascular anatomy.

In our experience, the use of MRI for guidance of biopsy and aspiration has been of most advantage in sampling lesions of the suprahyoid neck, including high cervical spine lesions (Figure 5). The major benefit of MR guidance in this region is the ability to visualize the internal carotid, vertebral, and major branches of the external carotid artery continuously during the entire needle insertion (Figure 6). Masses at the base of the neck, in particular those encroaching upon the brachial plexus, have also presented an excellent application, exploiting the multiplanar capabilities, tissue contrast, and spatial resolution of MRI to allow confident tissue sampling adjacent to the neurovascular structures of the thoracic inlet (Figure 4).[18,39] The ability to guide needle insertion with continuous imaging has also been helpful for biopsies of laryngeal and pharyngeal submucosal lesions, which are often difficult to define on CT and may be hidden by normal overlying mucosa on endoscopic examination (Figure 7). The T_2-weighted techniques can also be used to increase diagnostic tissue yield by allowing sampling of non-necrotic regions of complex masses. Rapid gradient echo T_2-weighted images are also helpful for biopsies and drainages within the spinal canal, in which a clear distinction between cerebrospinal fluid or cyst contents and the adjacent spinal cord is essential (Figure 8).

Other lesions that are particularly well suited to MR guidance are musculoskeletal tumors, for which CT and ultrasound often lack sufficient tissue contrast between pathological and normal muscle. MR-guided needle insertion is also time efficient for contrast injection prior to MR arthrograms.[40]

The use of MR guidance may be less useful for biopsy of abdominal lesions where ultrasound and CT are well suited. In our practice, we restrict the use of MR for abdominal procedures to lesions that are high under the hemidiaphragm,[35] liver tumors in which ultrasound and CT fail to provide adequate tissue contrast, and for patients in whom prior ultrasound- or CT-guided procedures have been unsuccessful (Figure 9).

Depending upon the radiologist's preference, biopsies under MR guidance can be performed using free-hand methods, needle holders, or with real-time guidance from optically linked systems, as described above.[7,12,18,35] Currently, most biopsies at our institution are performed with free-hand techniques, with optically linked frameless guidance reserved for particularly complex procedures. Using the free-hand technique,[18] most biopsies can be performed in less than 1 h of MR table time. For many of these procedures, the rapid frame-rate and high visibility of nearby vessels provided by 2D gradient echo MR techniques allow needle placement in less time than required with CT guidance (less than 8 min per needle pass for both aspiration and core cutting-needle biopsy).[18]

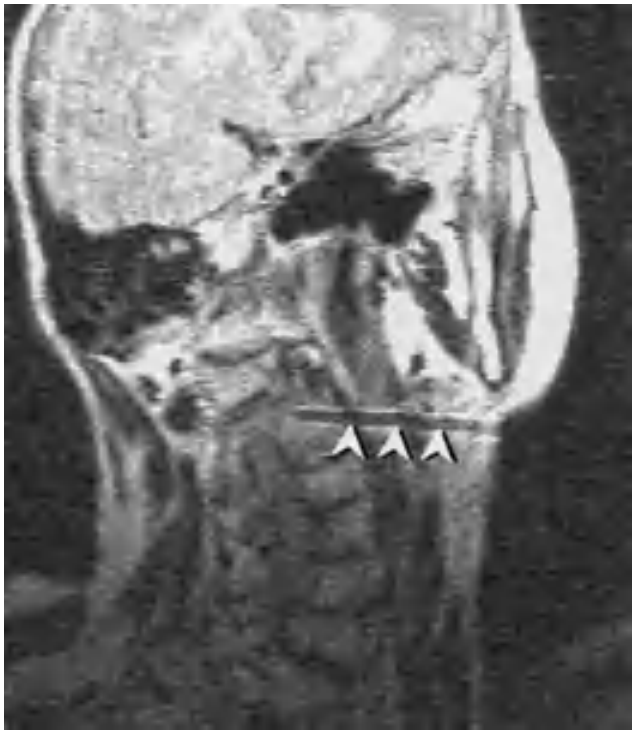

Figure 5 A 77-year-old woman with neck pain showing a C2 vertebral body lesion on MRI. The capability to guide biopsy with oblique imaging plane also allows the needle to be angled around the internal carotid and vertebral arteries for biopsy of high cervical spine lesions. Turbo spin echo T_2-weighted image (2000/105/3/17 *TR/TE/* number of signal averages echo train length, 51 s scan time) image obtained prior to sampling with 18-gauge Menghini-type needle. Frequency encoding must be performed perpendicular to the needle shaft with turbo spin echo or spin echo images to maximize needle visualization. Histological diagnosis was plasmacytoma, and the patient subsequently developed multiple myeloma. (Reproduced with permission from Lewin[39])

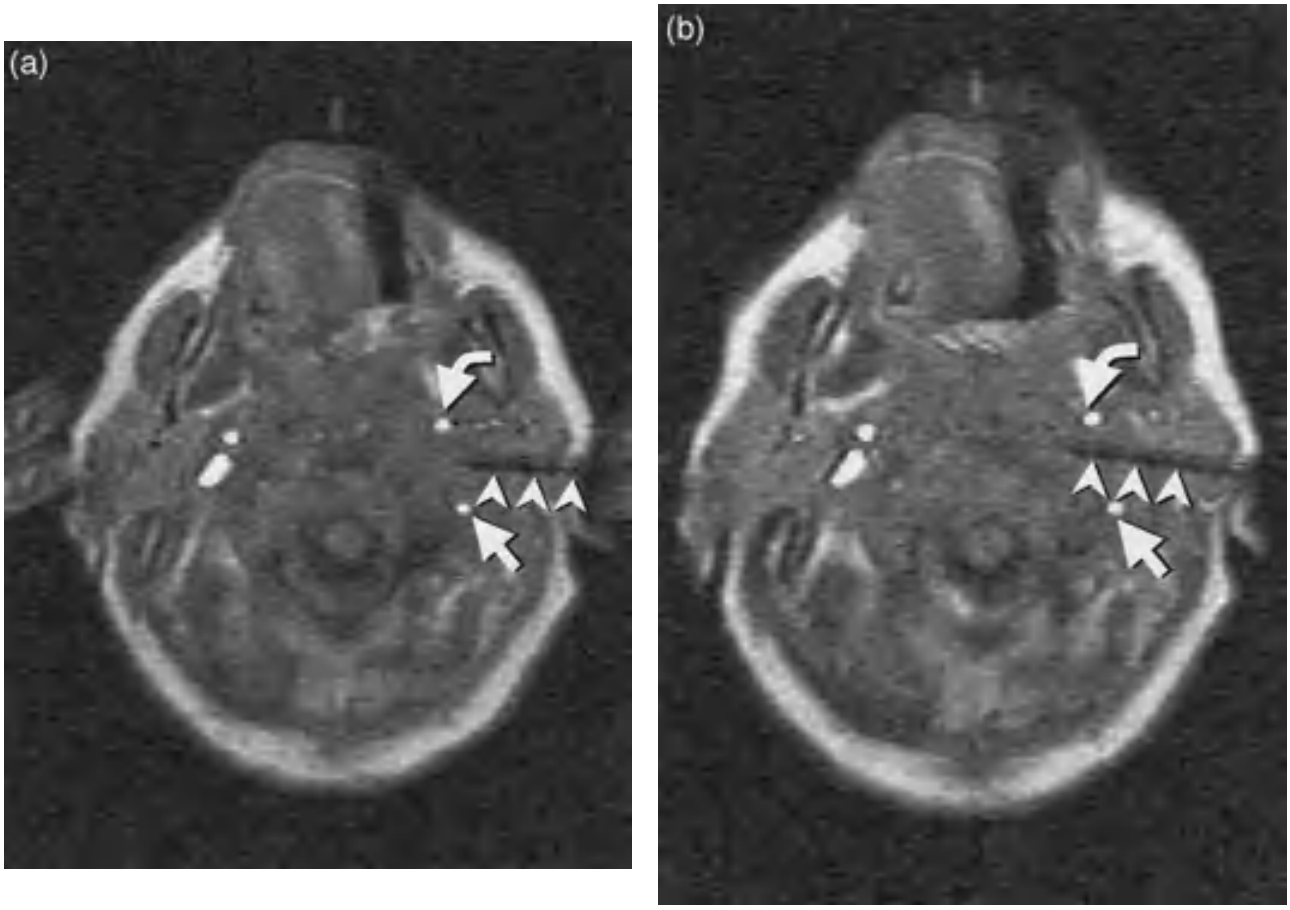

Figure 6 Images from a continuous series obtained at 7 s image with fast imaging with steady-state precession (FISP) sequence (18/7/4/90° *TR*/*TE*/number of signal averages/flip angle) obtained during guidance of needle insertion in a 68-year-old man with C1–2 vertebral and prevertebral mass. Previous attempt at surgical transoral biopsy had been unsuccessful. (a) Image early during insertion demonstrates needle tip passing through the left parotid space. An ill-defined mass can be seen in the prevertebral space. High vascular conspicuity resulting from 2D Fourier transform technique allows ready visualization of flow-related enhancement within the internal carotid (curved arrow) and vertebral (straight arrow) arteries. The needle tip (arrowheads) can be interactively directed to avoid these major vascular structures. (b) Mid-insertion, the needle (arrowheads) is interactively redirected more anteriorly once safely beyond the internal carotid artery. Histology demonstrated chronic osteomyelitis and cellulitis and the offending organism was successfully isolated

An additional use of the interventional MRI techniques that form the basis for biopsy guidance is their application for the guidance and monitoring of direct intralesional drug injection, including injection for sclerotherapy of vascular malformations. The same rapid image updates used for interactive needle placement can be used to monitor the injection of sclerosing agents for the treatment of low-flow vascular malformations.[41] The multiplanar cross-sectional images obtained with MR allow the injection of alcohol or other sclerosing agents to be monitored during administration, to ensure filling of the entire targeted portion of the malformation and to exclude extravasation or dissipation of the agent through venous egress.

5 UTILIZATION AND ECONOMIC CONSIDERATIONS

In addition to the many engineering challenges related to MR procedure guidance, the development of appropriate utilization guidelines to optimize cost-effectiveness of these interventions also represents a difficult task. When compared with current ultrasound- and CT-guided procedures, MR-guided procedures are slightly more expensive (charges for an MR-guided procedure are currently approximately 10–15% more than for a similar procedure under CT guidance at our institution). Therefore, when less-expensive CT or ultrasound guidance is suitable, their use is warranted as the most cost-effective choice. There are a number of procedures in which other imaging modalities lack the tissue contrast or vascular conspicuity to provide safe routes for biopsy or aspiration.[18] It is the procedures for which other imaging modalities are limited or open surgical biopsy is the primary alternative that provide the best area for application of MR-guided techniques.

The most formidable barrier to widespread dissemination of these techniques has been the economic issues related to interventional MRI. The financial resources necessary for an institution to acquire interventional MRI capabilities are often initially considered an insurmountable problem outside of the academic setting. The cost of an interventional system and associated siting depends on several factors, including field strength and system fringe field; the more novel the interventional design, the more expensive it is to acquire. The least-

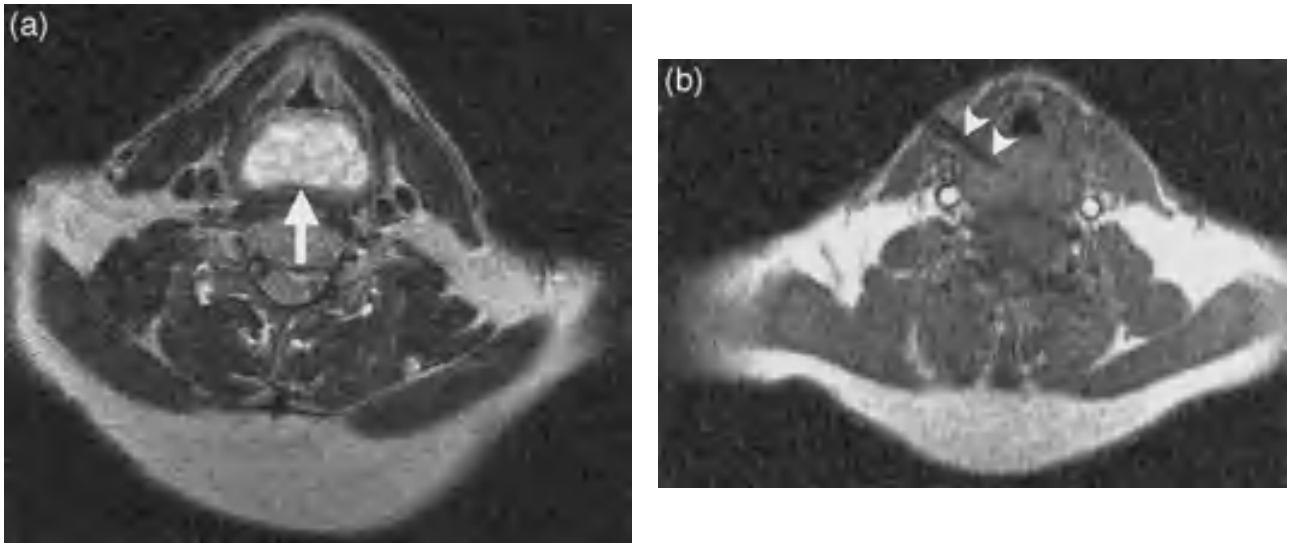

Figure 7 Chondrosarcoma of cricoid cartilage in a 65-year-old man. (a) A T_2-weighted image obtained before biopsy shows large cricoid cartilage mass (arrow), stretching the cricopharyngeous muscle posteriorly. (b) Fast imaging with steady-state precession (FISP) (18/7/1/90° *TR/TE/* number of signal averages/flip angle) shows coaxial placement of 22-gauge aspiration needle (arrowheads) through 18-gauge introducer needle. MR guidance allowed avoidance of both large and small external carotid artery branches. (Reproduced with permission from Lewin et al.[18])

expensive approach for percutaneous procedures is to add the necessary supplemental equipment for MR-guided procedures to an existing diagnostic MR system. Several vendors offer interventional accessories at prices below US $160 000, making the variable cost required to perform percutaneous MR-guided procedures relatively low for those sites with pre-existing open MR scanners. Purchase and siting of a low-field system specifically outfitted for intervention, a 1.5 T superconducting short-bore system or the 'double donut' system are each progressively more expensive. As the speed at which procedures can be performed further increases with improvements in MR-guidance techniques, the contribution to fixed cost compared with that of CT-guided techniques should continue to decrease.

Finally, even with the current level of technology and expense, appropriate utilization of interventional MRI can potentially result in a tremendous reduction in the costs associated with treating certain patients. In particular, there has been a marked decrease in cost at our institution for patients for whom the application of MR-guided biopsy or sclerotherapy has avoided an open surgical procedure. This has resulted from a decrease in cost of the procedure itself, relative to surgery, along with equal or more pronounced savings through avoidance of intensive-care unit and routine care hospitalization. This is in addition to the benefit to the patient that results from the reduction in morbidity, mortality, postprocedure discomfort, and time required for recovery when open surgical procedures can be avoided. These potential advantages of interventional MRI have provided the rationale for an increased interest in these techniques, with a growing number of centers and radiology practices developing interventional or intraoperative MRI capabilities. The overall success for this developing field within interventional radiology will require the careful application of these techniques to ensure appropriate utilization. Intraoperative and minimally invasive MR-guided techniques hold tremendous potential, but much effort remains necessary to define their appropriate role in the delivery of cost-effective medical care.

6 RELATED ARTICLES

Design and Use of Internal Receiver Coils for MRI; Gastroscopy and Colonoscopy; Head and Neck Investigations by MRI; Thermal Therapies in the Body Monitored by MRI.

7 REFERENCES

1. R. S. Hinks, M. J. Bronskill, W. Kucharczyk, M. Bernstein, B. D. Collick, and R. M. Henkelman, *JMRI*, 1998, **8**, 19.
2. P. R. Mueller, D. D. Stark, J. F. Simeone, S. Saini, R. J. Butch, R. R. Edelman, J. Wittenberg, and J. T. J. Ferrucci, *Radiology*, 1986, **161**, 605.
3. R. Lufkin, L. Teresi, and W. Hanafee, *Am. J. Roentgenol.*, 1987, **149**, 380.
4. R. Lufkin, G. Duckwiler, E. Spickler, L. Teresi, M. Chang, and G. Onik, *J. Comput. Assist. Tomogr.*, 1988, **12**, 1088.
5. L. Kaufman, M. Arakawa, J. Hale, P. Rothschild, J. Carlson, K. Hake, D. Kramer, W. Lu, and H. J. Van, *Magn. Reson. Q.*, 1989, **5**, 283.
6. D. H. Gronemeyer, L. Kaufman, P. Rothschild, and R. M. Seibel, *Radiol. Diagn.* (Berlin), 1989, **30**, 519.
7. R. Lufkin, L. Teresi, L. Chiu, and W. Hanafee, *Am. J. Roentgenol.*, 1988, **151**, 193.
8. G. Duckwiler, R. B. Lufkin, L. Teresi, E. Spickler, J. Dion, F. Vinuela, J. Bentson, and W. Hanafee, *Radiology*, 1989, **170**, 519.
9. R. Wenokur, J. C. Andrews, E. Abemayor, J. Bailet, L. Layfield, R. F. Canalis, B. Jabour, and R. Lufkin, *Skull Base Surgery*, 1992, **2**, 167.
10. S. G. Orel, M. D. Schnall, R. W. Newman, C. M. Powell, M. H. Torosian, and E. F. Rosato, *Radiology*, 1994, **193**, 97.

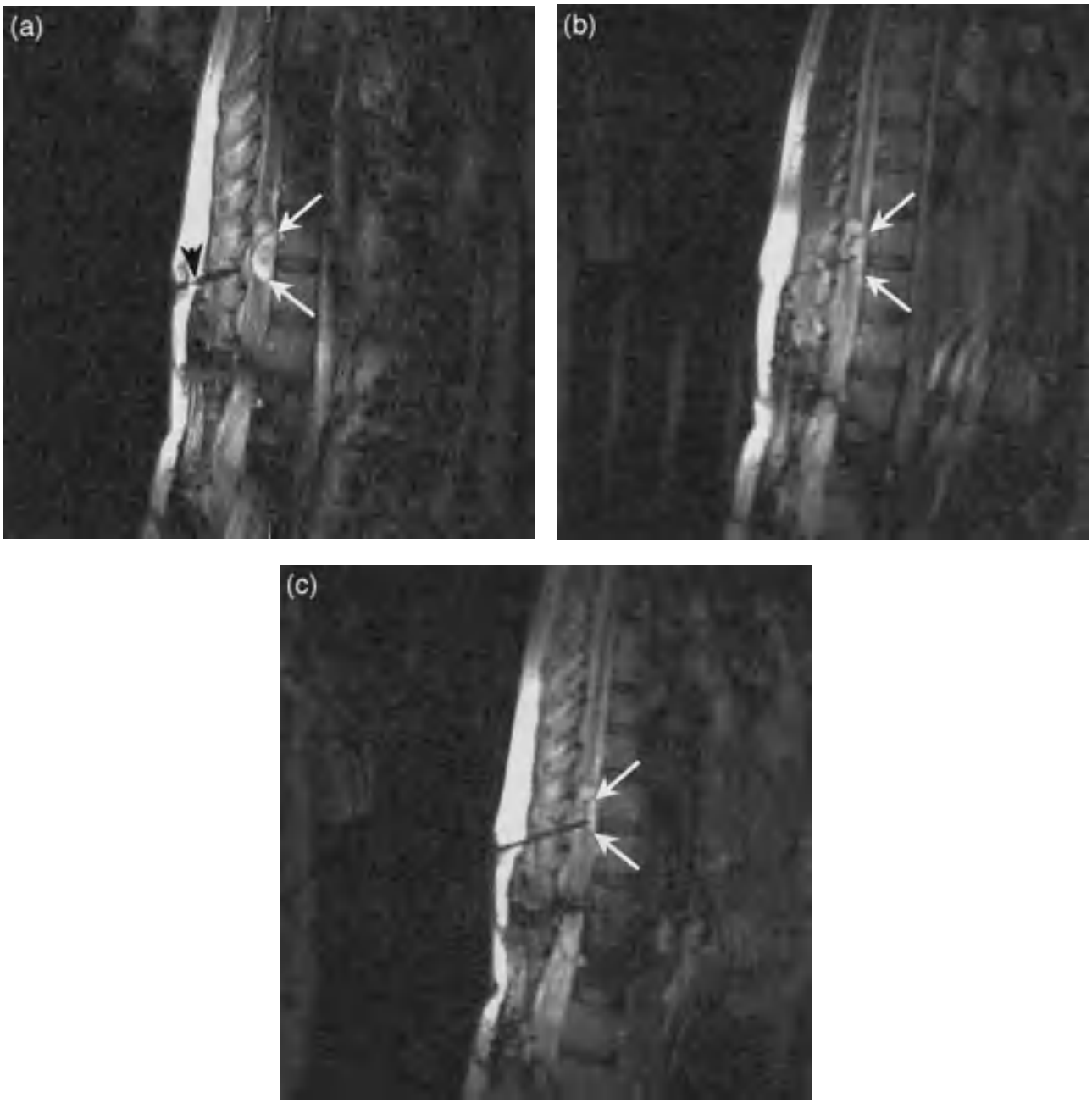

Figure 8 A 36-year-old woman with paraparesis and pain after a motor vehicle accident with recent worsening of symptoms. (a) A sagittal image from true fast imaging with steady-state precession (FISP) sequence (11.7/5.9 *TR*/*TE*) during posterior interlaminar 22-gauge needle placement (arrowhead) into large post-traumatic subarachnoid cyst (white arrows). A posterior approach was used with the patient in the decubitus position. The procedure was performed to see if cyst decompression would be beneficial prior to definitive open surgical repair. (b) True FISP (11.7/5.9 *TR*/*TE*) sagittal image after needle placement and partial aspiration of cyst (arrows). A smaller cyst can also be seen immediately superior as the larger cyst is decompressed. (c) True FISP (11.7/5.9/3/90° *TR*/*TE*/number of signal averages/flip angle) sagittal image at the end of the aspiration procedure demonstrates small residual cyst (arrows) with re-expansion of the thoracic spinal cord. (Reproduced with permission from Lewin et al.[18])

Figure 9 A 38-year-old man with pancreatic carcinoma and liver mass with a previous unsuccessful CT-guided biopsy attempt. Liver masses, in particular, are typically very difficult to visualize without T_2-weighted images. Guidance of a 22-gauge needle (arrow) was provided in this case with a true fast imaging with steady-state precession imaging sequence (11.7/5.9/1/90° *TR*/*TE*/number of signal averages/flip angle, 1 s per frame scan), with a series of 9–12 images obtained with continuous update during each breath-hold. Pathological diagnosis was simple hepatic cyst. (Reproduced with permission from Lewin et al.[18])

11. J. F. Schenck, F. A. Jolesz, P. B. Roemer, H. E. Cline, W. E. Lorensen, R. Kikinis, S. G. Silverman, C. J. Hardy, W. D. Barber, and E. T. Laskaris, *Radiology*, 1995, **195**, 805.
12. S. G. Silverman, B. D. Collick, M. R. Figueira, R. Khorasani, D. F. Adams, R. W. Newman, G. P. Topulos, and F. A. Jolesz, *Radiology*, 1995, **197**, 175.
13. S. G. Silverman, F. A. Jolesz, R. W. Newman, P. R. Morrison, A. R. Kanan, R. Kikinis, R. B. Schwartz, L. Hsu, S. J. Koran, and G. P. Topulos, *Am. J. Roentgenol.*, 1997, **168**, 1465.
14. P. M. Black, T. Moriarty, E. Alexander, P. Stieg, E. J. Woodard, P. L. Gleason, C. H. Martin, R. Kikinis, R. B. Schwartz, and F. A. Jolesz, *Neurosurgery*, 1997, **41**, 831.
15. E. Alexander, T. M. Moriarty, R. Kikinis, P. Black, and F. M. Jolesz, *Stereotact. Funct. Neurosurg.*, 1997, **68**, 10.
16. A. E. Mahfouz, A. Rahmouni, C. Zylbersztejn, and D. Mathieu, *Am. J. Roentgenol.*, 1996, **167**, 167.
17. J. L. Duerk, J. S. Lewin, M. Wendt, and C. Petersilge, *JMRI*, 1998, **8**, 203.
18. J. S. Lewin, C. A. Petersilge, S. F. Hatem, J. L. Duerk, G. Lenz, M. E. Clampitt, M. L. Williams, K. R. Kaczynski, C. F. Lanzieri, A. L. Wise, and J. R. Haaga, *Am. J. Roentgenol.*, 1998, **170**, 1593.
19. Y. C. Chung, E. M. Merkle, J. S. Lewin, J. R. Shonk, and J. L. Duerk, *Magn. Reson. Med.*, 1999, **42**, 335.
20. M. Busch, A. Bornstedt, M. Wendt, J. L. Duerk, J. S. Lewin, and D. Groenemeyer, *JMRI*, 1998, **8**, 944.
21. J. L. Duerk, J. S. Lewin, and D. H. Wu, *JMRI*, 1996, **6**, 918.
22. L. P. Panych, C. Oesterle, G. P. Zientara, and J. Hennig, *Magn. Reson. Med.*, 1996, **35**, 554.
23. Y. Cao and D. N. Levin, *Magn. Reson. Med.*, 1995, **33**, 140.
24. J. L. Duerk, D. H. Wu, Y. C. Chung, Z. P. Liang, and J. S. Lewin, *JMRI*, 1996, **6**, 957.
25. G. P. Zientara, L. P. Panych, and F. A. Jolesz, *Magn. Reson. Med.*, 1994, **32**, 268.
26. N. Gelman and M. L. Wood, *Magn. Reson. Med.*, 1998, **39**, 383.
27. L. P. Panych, P. D. Jakab, and F. A. Jolesz, *JMRI*, 1993, **3**, 649.
28. L. P. Panych and F. A. Jolesz, *Magn. Reson. Med.*, 1994, **32**, 738.
29. L. P. Panych, R. V. Mulkern, P. Saiviroonporn, G. P. Zientara, and F. A. Jolesz, *Magn. Reson. Med.*, 1997, **38**, 964.
30. R. D. Peters and M. L. Wood, *JMRI*, 1996, **6**, 529.
31. J. B. Weaver, Y. Xu, D. M. Healy, and J. R. Driscoll, *Magn. Reson. Med.*, 1992, **24**, 275.
32. M. Wendt, M. Busch, G. Lenz, J. L. Duerk, J. S. Lewin, R. M. Seibel, and D. Groenemeyer, *IEEE Trans. Med. Imag.*, 1998, **17**, 803.
33. J. S. Lewin, J. L. Duerk, V. R. Jain, C. A. Petersilge, C. P. Chao, and J. R. Haaga, *Am. J. Roentgenol.*, 1996, **166**, 1337.
34. C. Frahm, H. B. Gehl, U. H. Melchert, and H. D. Weiss, *Cardiovasc. Intervent. Radiol.*, 1996, **19**, 335.
35. H. B. Gehl, C. Frahm, H. Schimmelpenning, and H. D. Weiss, *Rofo. Fortschr. Geb. Rontgenstr. Neuen. Bildgeb. Verfahr.*, 1996, **165**, 70.
36. C. Frahm, H. B. Gehl, H. D. Weiss, and W. A. Rossberg, *Rofo. Fortschr. Geb. Rontgenstr. Neuen. Bildgeb. Verfahr.*, 1996, **164**, 62.
37. D. S. Lu, H. Lee, K. Farahani, S. Sinha, and R. Lufkin, *Am. J. Roentgenol.*, 1997, **168**, 737.
38. G. Hathout, R. B. Lufkin, B. Jabour, J. Andrews, and D. Castro, *JMRI*, 1992, **2**, 93.
39. J. S. Lewin, *Am. J. Neuroradiol.*, 1999, **20**, 211.
40. C. A. Petersilge, J. S. Lewin, J. L. Duerk, and S. F. Hatem, *Am. J. Roentgenol.*, 1997, **169**, 1453.
41. J. S. Lewin, E. M. Merkle, J. L. Duerk, R. W. Tarr, *Radiology*, 1999, **211**, 566.

Acknowledgements

The author would like to acknowledge the members of the Interventional MR Imaging Research Program at University Hospitals of Cleveland and Case Western Reserve University for their ongoing commitment to the development of interventional MRI techniques; in particular, Drs Andrik Aschoff, Elmar Merkle, Michael Wendt, and Jeffrey Duerk of the Department of Radiology. In addition, I would like to thank Elena DuPont and Rayna Lipscomb for their invaluable help with manuscript preparation.

The University Hospitals of Cleveland/Case Western Reserve University Interventional MR Program is supported in part through research collaborations with Siemens Medical Systems, Radionics, and Minrad, Inc. This project was also supported through grants from the Whitaker Foundation, American Cancer Society, Mary Ann S. Swetland Fund, and the M. E. and F. J. Callahan Foundation.

Biographical Sketch

Jonathan S. Lewin. *b* 1959. B.A. 1981 Brown University, MD 1985 Yale. Residency in Diagnostic Radiology University Hospitals Cleveland 1985–89, MRI Research Fellowship Siemens Erlangen, Germany 1989–90, Fellowships in Neuroradiology at Cleveland Clinic Foundation 1991–93. Associate Professor and Vice Chairman for Research and Academics in Department of Radiology, Case Western Reserve University and Director MRI at University Hospitals, Cleveland 1993–present. Approx. 105 publications. Current interests: basic science and clinical aspects of interventional MRI, functional MRI, and the imaging of acute stroke.

MR-Guided Therapy in the Brain

Volker Tronnier
University of Heidelberg, Germany

Antonio A. F. De Salles
University of California at Los Angeles, CA, USA

Yoshimi Anzai
University of Michigan, USA

Keith L. Black
University of California at Los Angeles, CA, USA

and

Robert B. Lufkin
University of California at Los Angeles, CA, USA

1 INTRODUCTION

Through the technological and clinical advances of the 1990s, MRI has become one of the most powerful noninvasive diagnostic tools in the evaluation of the brain. The superior soft-tissue contrast, the oblique and multiplanar imaging capability, and the absence of ionizing radiation have made MRI the imaging modality of choice for most diagnostic applications of the brain.

These advantages also make MRI an ideal guide for invasive and interventional procedures in the brain. The high sensitivity of MRI to flow enables the delineation of blood vessels without the use of contrast agents. The absence of beam-hardening artifacts from bone and metal devices allows complex instrumentation approaches to anatomic regions that may be difficult or impossible to reach under conventional computed tomography (CT) guidance. Nearly a decade of experience with MR-guided stereotaxis has proven MRI to be an effective and reliable means to visualize and localize neurosurgical targets and a valuable aid in optimizing surgical approaches.[1–4]

Recently, MRI has been applied to treatment monitoring procedures in the brain, such as interstitial therapy and even open surgery.[5] New developments in MR imaging techniques and MR-compatible instrumentation and the availability of open magnet designs are revolutionalizing the role of MRI in guiding and monitoring interventional procedures.

2 MR-GUIDED STEREOTAXIS

Since the mid 1980s, MRI stereotaxis has been successfully employed in neurosurgery to guide biopsies, in tumor resection, deep electroencephalographic (EEG) electrode placement, functional target development and resection, and other interventional procedures.[6–14] The noninvasive visualization and localization provided by MRI greatly reduce the surgical invasion necessary to access the target and significantly lower patient morbidity. Several stereotactic systems with localizer frames designed for MRI localization are commercially available: the BRW and CRW (Radionics, Burlington, MA), Leksell (Elekta Instruments Inc., Atlanta, GA), Laitinen (Sandström Trade & Technology Inc., Welland, Ontario, Canada), and others.

Since MRI is more prone to geometric distortion than CT, the accuracy of MRI stereotaxis must be evaluated. The maximum localization error reported in the literature ranges from 1 to 5 mm.[15–18] The variation in the maximum error may be accounted for partly by the use of different stereotactic systems and different reference imaging modalities (CT, ventriculography, etc.) with which MRI is compared. The spatial accuracy of MRI depends on the linearity and calibration of magnetic field gradients and on magnetic susceptibility artifacts, which manifest as spatial distortions. Meticulous quality control should decrease errors in magnetic field linearity and calibration. MRI sequences should use high bandwidth signal acquisition to reduce spatial distortion from susceptibility effects. Several researchers have proposed practical correction algorithms to improve the spatial accuracy of MRI further.[19,20]

Although accurate and reliable, conventional stereotactic systems require the fixation of a frame to the patient's skull. Recent developments in frameless stereotactic systems will improve patient comfort, localization efficiency, and surgical access in open procedures.[21–23] Projects are underway to develop MR-compatible navigational systems that use an arm-based three-dimensional digitizer or light-emitting diode (LED)-based optical digitizers registered to the coordinate system of the interventional MR scanner for interactive scan plane control and near-realtime MRI monitoring of the interventional procedure (Figure 1).

3 MR-GUIDED BIOPSY

One of the earliest applications of intracranial interventional MR was to obtain biopsy specimens for tissue diagnosis. As with biopsies elsewhere in the body, the approach utilized for accessing an intracranial lesion is chosen to limit the risk of injury to surrounding vital structures. Either fine needle aspirates or core biopsies can be obtained by utilizing various gauge MR-compatible needles. Also, either frame-based or frameless stereotaxis may be used to guide the approach, depending on the location and size of the target lesion. The primary goal of an intervention within the MR scanner, however, will be a frameless procedure with on-line imaging control of the needle trajectory. The point of entry is determined with an optical tracking device, a gadolinium-filled wand, or simply with the surgeon's finger. Fast image sequences (e.g., two-dimensional fast imaging, with steady-state precession, FISP) allow a near realtime image while advancing the biopsy needle to the desired target. An obvious advantage compared with intraoperative CT is the possibility of taking specimens from different tumor areas best displayed by MRI under direct visual control (Figure 2).

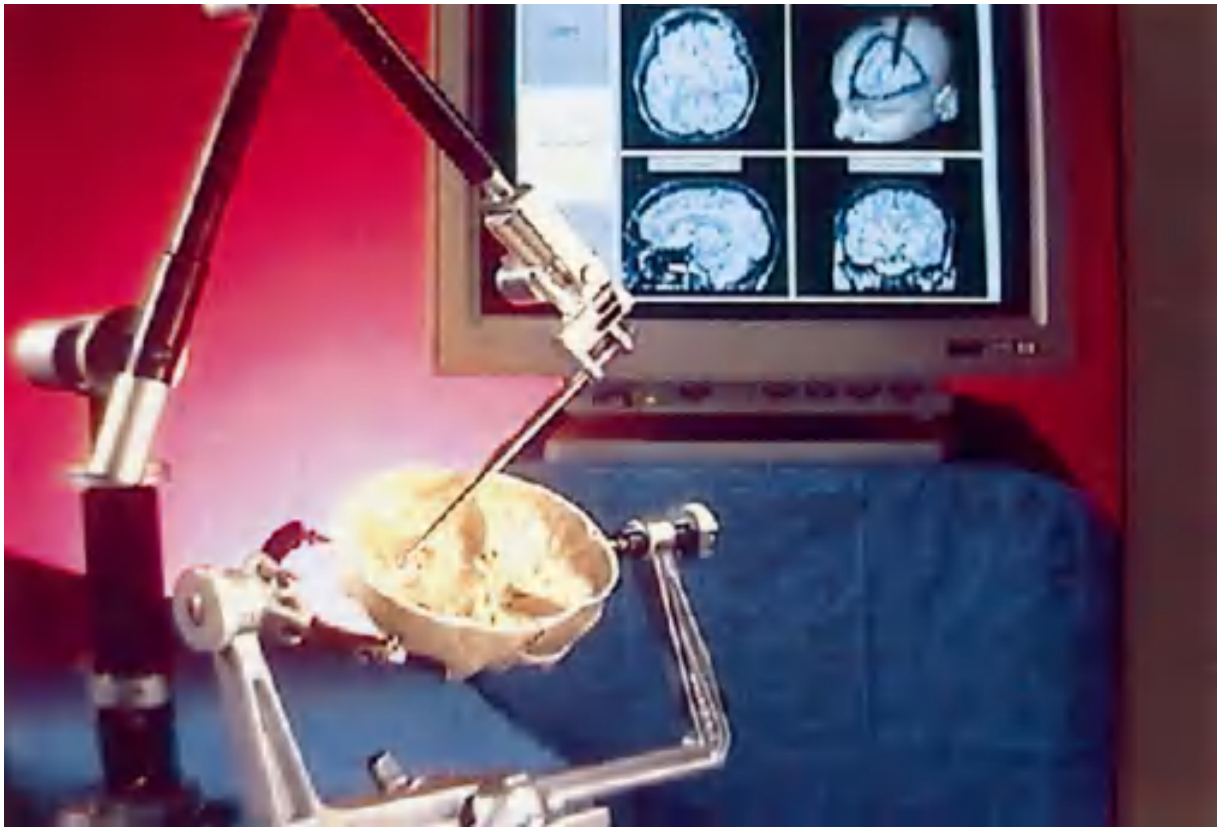

Figure 1 Mechanical articulated arm systems (Operating Arm System Radionics Software Applications, Inc., Burlington, MA) provides intraoperative neuronavigation using a previously acquired three-dimensional CT or MR data set

4 MR-GUIDED ELECTRODE PLACEMENT

Another application of interventional MR is to assist in the placement and in post-placement evaluation of intracerebral depth electrodes.[24–27] Intracerebral depth electrodes are used to localize the seizure focus in those patients who are refractory to medical therapy. Prior to the development of this technique, such electrodes were placed by inferring their position relative to previously acquired imaging studies. Postplacement examination of electrode placement could not be accurately performed because of the extensive beam-hardening artifact produced in CT by the stainless steel composition of the electrodes. Previously, MR imaging was not feasible because of the ferromagnetic properties of stainless steel and concern for heat and torque production, which could result in local brain injury. With the manufacture of electrodes with different metal compositions, such as platinum alloys, MR imaging guidance can be employed during electrode placement to confirm position without risk of brain injury. Sufficient anatomic detail is obtained to evaluate electrode placement adequately and to avoid possible procedural complications (Figure 3). This should result in improved anatomic–physiologic correlation and surgical outcome for these patients. Intraoperative documentation of long-term implanted depth electrode placed for treatment of chronic pain or movement disorders is another indication in which the anatomical position can be correlated with intraoperative neurophysiological target determination.

5 MR-GUIDED CLOSED MINIMALLY INVASIVE THERAPEUTIC PROCEDURES

In the effort to reduce patient morbidity, hospitalization length, and recovery time associated with conventional craniotomy, several researchers are pioneering new, minimally invasive therapeutic techniques that may achieve results comparable to surgical resection or serve as effective palliative measures. In these minimally invasive procedures, it is particularly appealing to employ MRI beyond mere stereotactic localization and begin to use MRI to monitor treatment administration directly. The sensitivity of MRI to temperature change and other acute tissue effects (e.g. edema) enables the physician to adjust treatment parameters interactively to maximize the destruction of pathologic tissue and minimize undesirable injury to normal tissue.[28–30]

5.1 Cryoblation

Freezing has been explored as a minimally invasive technique for tissue ablation in the brain. Postoperative MRI of patients who underwent cryothalamotomy demonstrated excellent depiction of the lesions created (Figure 4).[31] Intraoperative MRI guidance and monitoring of the cryoablation procedure awaits the development of practical MR-compatible freezing devices.

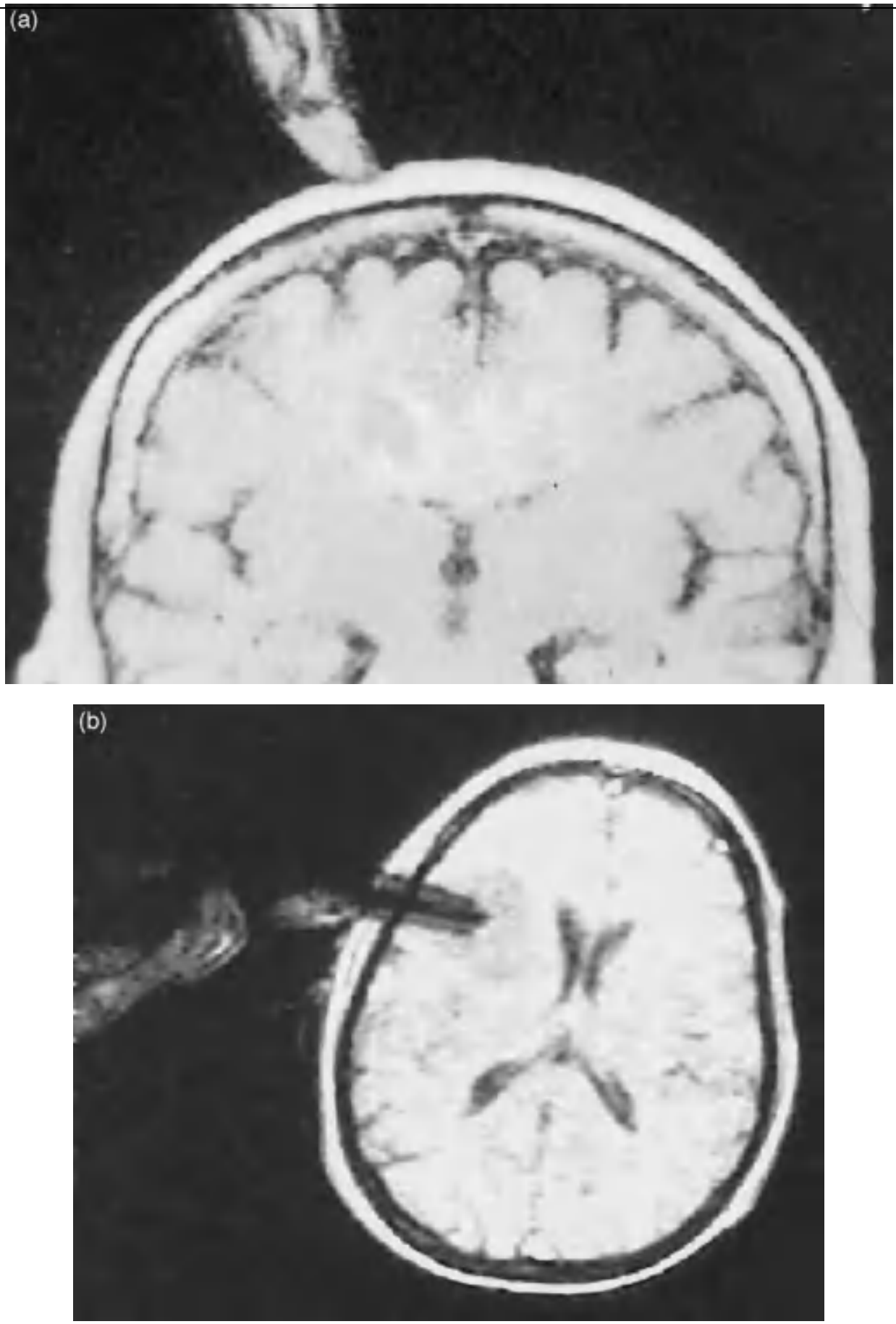

Figure 2 MR-guided biopsy. (a) Direct imaging allows rapid localization of a glioma. (b) MR-guided approach for a deeper lesion

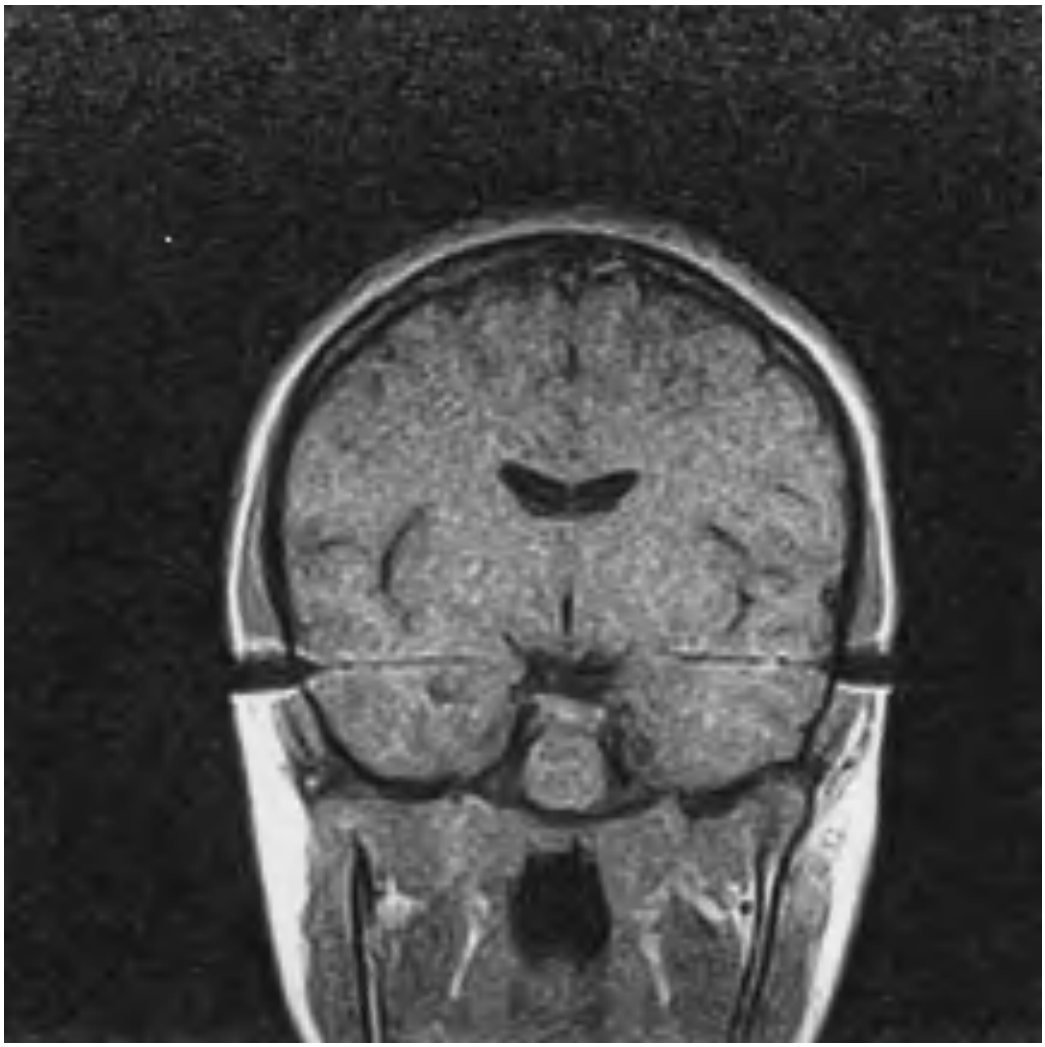

Figure 3 Deep electroencephalographic electrode implantation for patients with medically refractory partial complex seizures who are being considered for possible temporal lobectomy. Coronal MRI was obtained with MR-compatible electrodes in satisfactory position in the hippocampal region

5.2 Ablation by Interstitial Laser Photocoagulation

Traditionally, the use of lasers in neurosurgery has been limited to applications in which direct visualization was possible. Now, MRI guidance allows stereotactic placement of an interstitial laser probe into a deep tumor through a small burr hole in the skull. Laser energy travels through the optic fiber directly into the tumor and produces heat-induced protein denaturation and coagulation necrosis. However, since the penetration and absorption of laser energy are complex functions of tissue characteristics, it is difficult to predict a priori the extent of tissue damage as a function of dose. Therefore, a monitoring technique is required to follow the destructive process in tissue as laser energy is applied. Although CT can show laser-induced tissue changes, these are relatively late findings. Early tissue reaction to laser is missed by CT because of its low soft-tissue contrast.[32] Fortunately, many researchers have demonstrated the ability of MRI to detect acute tissue changes secondary to the application of laser energy.[33–37]

Animal studies have characterized the acute and chronic tissue effects of the Nd:YAG (neodymium:yttrium–aluminum–garnet) laser and correlated the histopathologic findings with their MRI appearance.[33,35,38] It has been shown that T_2-weighted images are particularly sensitive to tissue changes and can clearly demonstrate concentric rings of central cavitation, coagulation necrosis, and edema around the point of laser application. Higuchi et al. detected similar patterns in T_2-weighted images 5 min after laser irradiation in the live rabbit brain.[33]

Since the primary tissue effect of Nd:YAG laser irradiation is thermal damage,[39,40] the thermal sensitivity of MRI can also be exploited to monitor the progress of the laser therapy. The dependence of T_1-time, diffusion coefficient, water proton chemical shift, and other MR parameters on temperature is well known and has been utilized for noninvasive thermal mapping during the application of laser and other thermal ablation techniques.[28–30,41–43] Knowledge of the temperature distribution in the treatment area will allow the surgeon to confirm

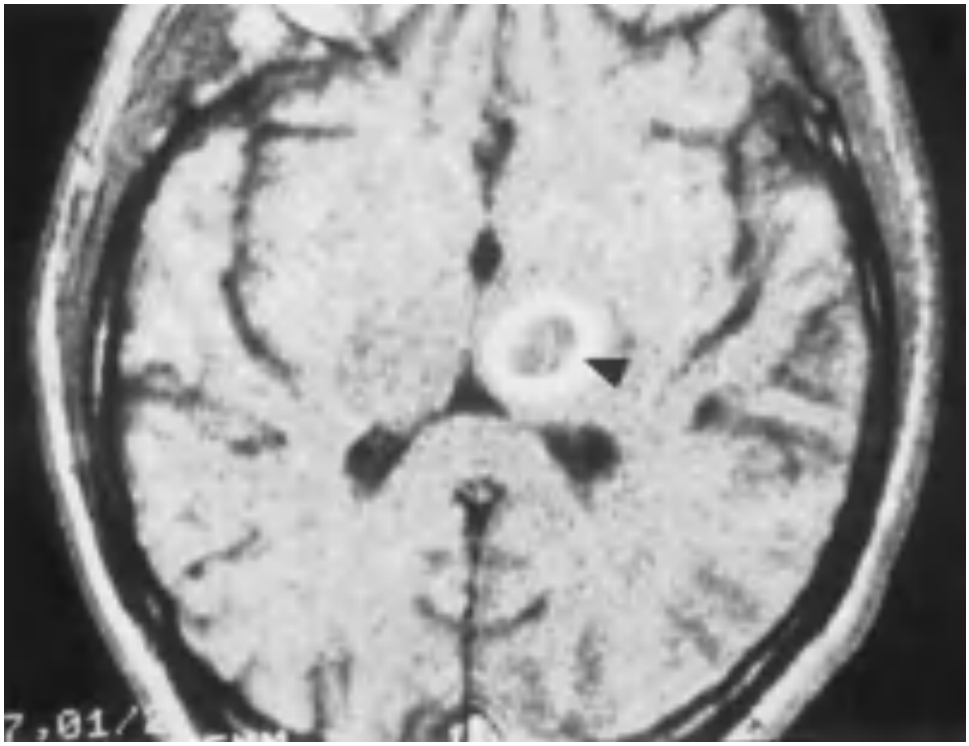

Figure 4 A T_1-weighted image obtained several days after stereotactic cryothalamotomy shows the lesion well circumscribed by a hyperintense ring (arrowhead)

the destruction of the target unambiguously while avoiding irreversible thermal damage to vital structures.

Interstitial laser therapy is particularly well suited for intraoperative MRI guidance because the laser-delivering optic fiber is intrinsically MR compatible and because the application of laser energy does not interfere with MR signal acquisition. Initial clinical experience with MR-guided interstitial laser therapy has yielded promising results in the treatment of brain tumors.[24] This procedure can be executed under local anesthesia, which allows the neurologic status of the patient to be monitored continuously. MR guidance enables the physician to minimize damage to normal brain tissue, while the absence of systemic toxicity permits repetition of the procedure as necessary.

The Dusseldorf group performed a clinical pilot study of MR-guided Nd:YAG laser ablation on 31 patients with brain tumors. Three-dimensional turbo fast low angle shot (FLASH) sequences were used to determine the position of light guide. The time of irradiation varied from 10 to 20 min. Phase-sensitive two-dimensional FLASH and echo-shifted turbo FLASH were used to generate a color-coded heat map. The result is summarized in Table 1. The study shows that MRI is well suited to monitor laser-induced thermotherapy. A typical laser lesion has a central and peripheral zone that make up the total lesion, and it is circumscribed by an enhancing rim demarcating the outer border of the irreversible damaged lesion (Figure 5).

5.3 Radiofrequency-induced Thermal Ablation

Thermal ablation induced by rf is a technique of tissue destruction by resistive heating using rf (~500 kHz) electrical current. A probe with a conductive tip is inserted into the target, and rf current is then delivered from the tip to cause focal heating; this results in protein denaturation and coagulation necrosis. Over three decades of extensive neurosurgical experience with rf has established the efficacy and safety of this ablation technique.[26,27,44–52] Ablation with rf has been used primarily for functional neurosurgical procedures including thalamotomy and pallidotomy for parkinsonism and other

Table 1 Results of a Clinical Pilot Study of MR-guided Laser Ablation of Brain Tumors: the Dusseldorf Study

	No.
Study population	31
Neurologic deterioration during ablation	2
Transient deficit after ablation (vasogenic edema)	4
Persistent deficit after ablation	1
Patients with astrocytoma WHO II	24
Neurologic status unchanged after ablation	6
Neurologic status improved after ablation	18

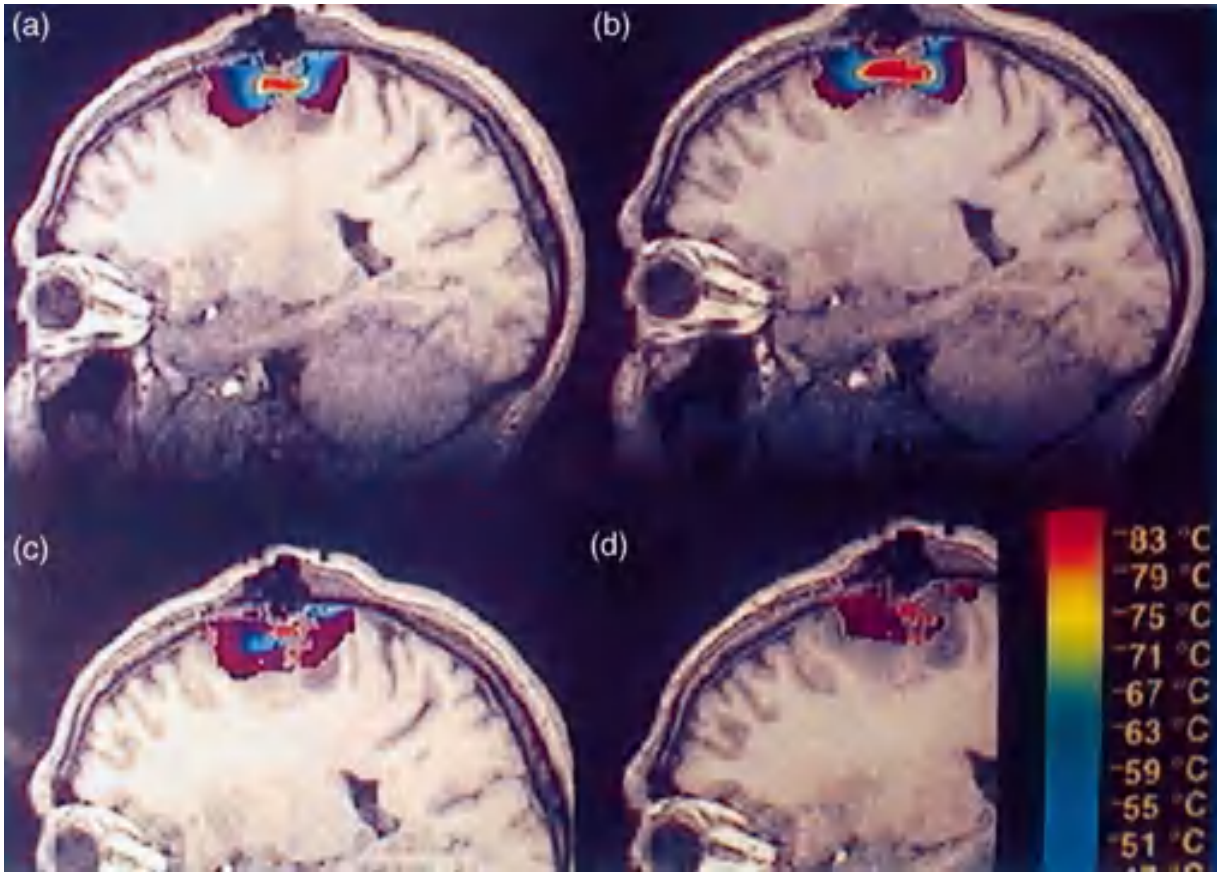

Figure 5 Post-processed phase-sensitive two-dimensional fast low angle shot images acquired and displayed during and after laser-induced thermotherapy (LITT). The calculated temperatures are color-coded (bottom right), gradually increasing the heat-affected zone with increasing maximum temperatures. Images acquired during treatment; (a) 1; (b) 4; (c); 8; and (d) 10 min after starting the laser therapy. (Courtesy of T. Kahn. In R. Lufkin: 'Interventional MRI', St Louis, 1999, Mosby)

movement disorders, leucotomy for intractable pain, and rhizotomy for trigeminal neuralgia. Postoperative MRI has demonstrated excellent depiction of lesion details in patients who underwent rf thalamotomy.[44,53,54]

One group has recently completed an initial study of MR-guided rf ablation of primary and metastatic brain tumors.[5,55] The procedure used MR-guided stereotaxis to place an rf probe (Radionics, Burlington, MA) into the tumor through a 2 mm twist-drill hole in the skull (Figure 6). The rf power was then applied to achieve an intratumoral temperature of 80 °C for 1 min. Depending on the shape and size of the tumor, the probe position was adjusted and additional doses were administered. The entire procedure was performed under light sedation and local anesthesia, which allowed the surgeon to monitor the neurologic status of the patient throughout.

Pretreatment T_1- and T_2-weighted MR images provided clear depiction of tumor morphology and anatomic relationships with surrounding vital structures and proved critical in planning the best trajectory for the rf probe. MR angiography with two-dimensional time-of-flight sequences also proved useful to visualize vascular structures surrounding the planned trajectory of the rf probe. The rf lesion was detected in post-treatment MRI as a region of low signal on T_1-weighted images and as a region of high signal on T_2-weighted images within 20 to 30 min of the rf ablation. Gadolinium-enhanced T_1-weighted images demonstrate a rim of enhancement that outlines the zone of tissue necrosis. A total of 15 tumors were treated in 11 patients. During the 2-year follow-up period, seven tumors were controlled by treatment while eight tumors recurred. Five tumors had a durable response to treatment (11.9–23.8 months of follow up; median 15.1 month) (Figure 7). Neurologic complications were few and transient except for one patient, who still had mild expressive speech difficulty at 10 weeks after treatment.

MR-guided rf thermal ablation promises to be a safe, minimally invasive treatment of brain tumors. This technique may become an effective palliative measure and may serve as an adjuvant to radiation therapy. However, unlike radiation therapy, which is contraindicated by accumulative toxicity, rf ablation can be repeated as many times as necessary to treat recurrences. Greater efficacy is anticipated as improved MR-compatible rf generator and therapy probes are developed to allow real-time artifact-free MR imaging of the ablation procedure. As with interstitial laser therapy, the heating effects of the rf ablation can be monitored by temperature-mapping MRI sequences during the application of rf power to confirm the destruction of target tissue before physiologic changes become apparent.

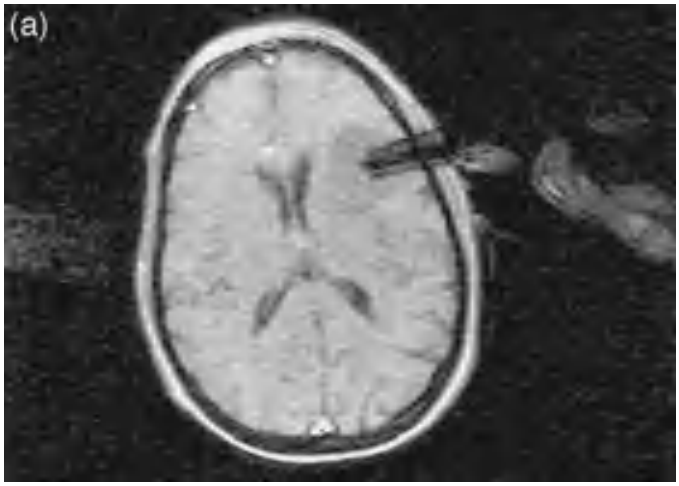

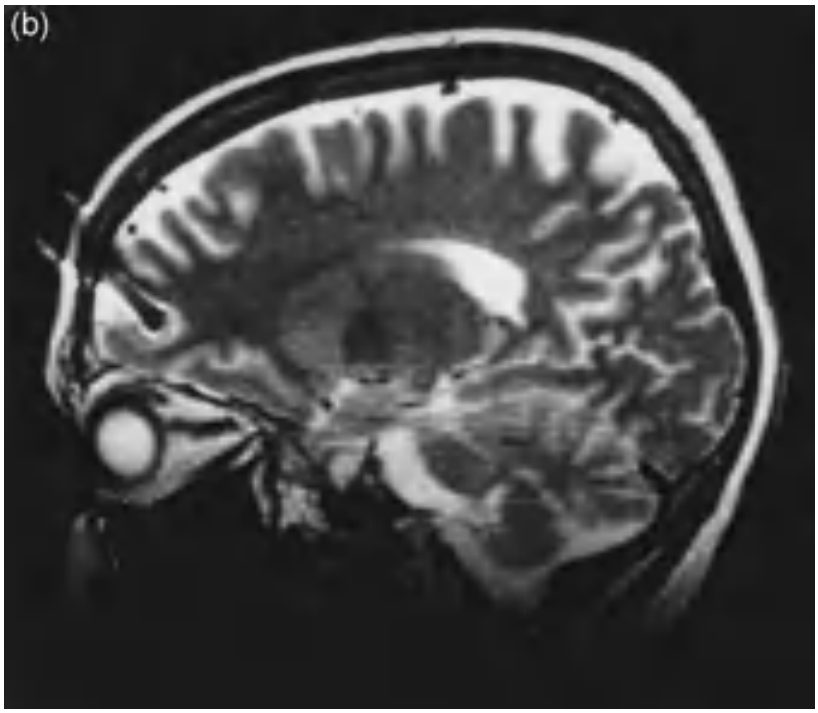

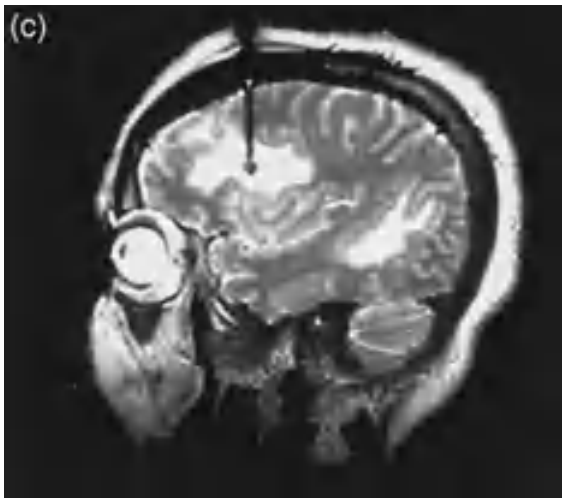

Figure 6 MR-guided rf ablation. (a) The therapy probe is placed into the patient's brain through a 2 mm twist-drill hole using MR-guided stereotaxis. The entire procedure is done under light sedation and local anesthesia in the MR suite. (b,c) Images from two other patients treated in the same way

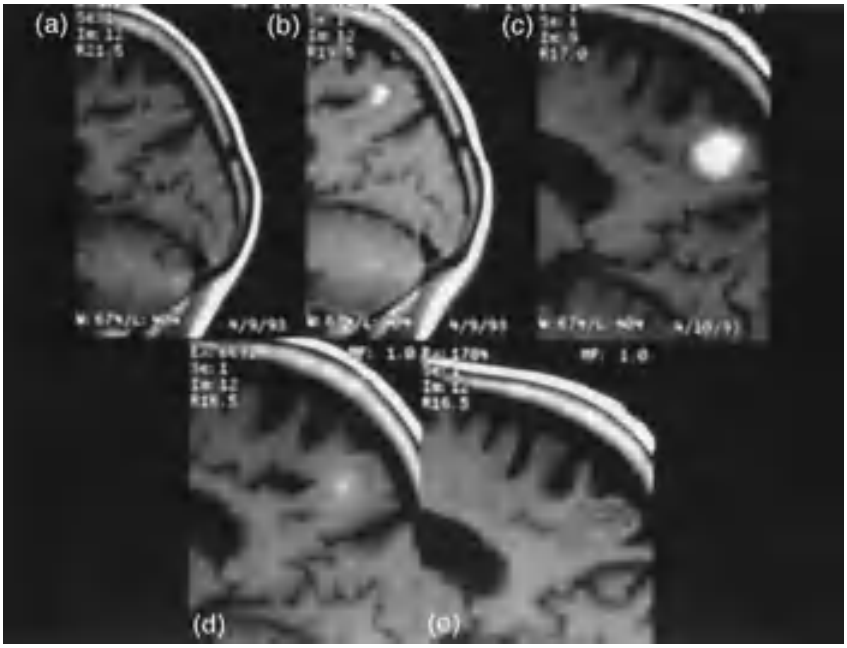

Figure 7 Contrast-enhanced MR images of a patient who underwent MR-guided rf ablation of a metastatic adenocarcinoma. (a) Image before treatment and (b) immediately after rf ablation. Further images were obtained at (c) 1 week, (d) 5 months, and (e) 1 year after treatment

5.4 High-intensity Focused Ultrasound Ablation

High-intensity focused ultrasound (HIFU) is a new technique of thermal ablation by remote heating. An extracorporeal ultrasound transducer focuses vibrational energy to a point inside the patient's body so that only the tissue within a small focal zone is heated to lethal temperatures (60 °C or above for thermal coagulation and protein denaturation) while the surrounding tissue experiences only a slight temperature increase. HIFU ablation under ultrasound imaging guidance has been used in clinical trials to treat glaucoma, benign prostatic hyperplasia, tumors of the brain, the breast, the liver, the kidney, and the bladder.[56–60] The greatest advantage of HIFU over other thermal ablation techniques is that no surgical invasion is required to access the target provided there is a sonic path clear of bone and air. However, noninvasive methods to measure the temperature of the focal heating zone must be developed to provide adequate control.

By combining the high soft-tissue contrast and the temperature sensitivity of MRI with HIFU ablation, a powerful minimally invasive therapy technique can be developed. Several researchers have demonstrated the feasibility of using MRI to guide and monitor HIFU ablation procedures.[41,43,61,62] Fast T_1-weighted gradient echo sequences can be used to track in realtime the high-temperature focal zone, which appears as a hypointense region, to guide the positioning of the ultrasound transducer. Tissue changes secondary to HIFU heating can be detected easily on T_2-weighted images, as with interstitial laser therapy. Although practical application of HIFU to the intracranial region necessitates the removal of a skull bone flap to expose the dura, surgical invasion of the brain parenchyma can be avoided and the potential for infection and other complications greatly reduced. Clinical application of HIFU in neurosurgery awaits the further development of MRI-compatible HIFU therapy systems and MRI temperature-mapping techniques.

6 CONCLUSION

MRI has traditionally been criticized as an expensive diagnostic technology. However, when compared with more costly open surgical procedures and the associated higher patient morbidity, hospitalization costs, and lost time from work, MRI-guided minimally invasive interventions can potentially lower the final cost of medical care in selected patients. More work is clearly warranted in this exciting field to determine its ultimate areas of application in neurosurgery.

7 RELATED ARTICLES

MR-Guided Biopsy, Aspiration, and Cyst Drainage; Temperature Measurement Using In Vivo NMR; Thermal Therapies in the Body Monitored by MRI.

8 REFERENCES

1. P. Mueller, D. Stark, J. Simeone, et al. *Radiology*, 1986, **161**, 605.
2. R. Lufkin, L. Teresi, and W. Hanafee, *Am. J. Roentgenol.*, 1987, **149**, 380.
3. R. Lufkin, and L. Layfield, *J. Comput. Assist. Tomogr.*, 1998, **13**, 1105.
4. S. To, R. Lufkin, and L. Chiu, *Comput. Med. Imaging Graph.*, 1989, **13**, 469.

5. Y. Anzai, K. Black, A. DeSalles, et al. *Am. J. Neuroradiol.*, 1999, in press.
6. G. Kratimenos, and D. Thomas, *Br. J. Neurosurg.*, 1993, **7**, 155.
7. D. Wen, W. Hall, D. Miller, et al. *Neurosurgery*, 1993, **32**, 407.
8. P. Kelly, *Adv. Tech. Stand. Neurosurg.*, 1990, **17**, 77.
9. R. Lufkin, S. Jordan, P. Lylyck, et al. *Am. J. Neuroradiol.*, 1988, **9**, 953.
10. L. Lunsford, *Neurosurgery*, 1988, **23**, 363.
11. P. Kelly, F. Sharbrough, K. Ball, et al. *Mayo. Clin. Proc.*, 1987, **62**, 103.
12. S. Uematsu, A. Rosenbaum, M. Delong, et al. *Acta Neurochir. Suppl.*, 1987, **39**, 21.
13. L. Lunsford, A. Martinez, and R. Latchaw, *J. Neurosurg.*, 1986, **64**, 872.
14. L. Leksell, D. Leksell, and J. Schwebel, *J. Neurol. Neurosurg. Psychiatry*, 1985, **48**, 14.
15. K. Burchiel, *Clin. Neurosurg.*, 1992, **39**, 314.
16. D. Kondziolka, P. Dempsey, L. Lunsford, et al. *Neurosurgery*, 1992, **30**, 402.
17. C. Derosier, G. Delegue, T. Munier, et al. *J. Radiol.*, 1991, **72**, 349.
18. J. Villemure, E. Marchand, T. Peters, et al. *Appl. Neurophysiol.*, 1987, **50**, 57.
19. C. Bakker, M. Moerland, R. Bhagwandien, et al. *Magn. Reson. Imag.*, 1992, **10**, 597.
20. J. Fitzpatrick, H. Chang, M. Willcott, et al. *Proc. IXth Annu. Mtg. Soc. Magn. Reson. Med.*, New York, 1990, p. 426.
21. T. Takizawa, *Stereotact. Funct. Neurosurg.*, 1993, **60**, 175.
22. R. Maciunas, R. J. Galloway, J. Fitzpatrick, et al. *Stereotact. Funct. Neurosurg.*, 1992, **58**, 108.
23. A. Kato, T. Yoshimine, T. Hayakawa, et al. *J. Neurosurg.*, 1991, **74**, 845.
24. P. Ascher, E. Justich, and O. Schrottner, *Acta Neurochir.*, 1991, **52**, 78.
25. T. H. Khan, et al. *JMRI*, 1998, **8**, 160.
26. S. Blond, D. Caparros-Lefebvre, and F. Parker, et al. *Neurosurg.*, 1992, **77**, 62.
27. L. Laitinen, M. Harriz, and T. Bergenheim, *J. Neurosurg.*, 1992, **76**, 53.
28. D. LeBihan, J. Delannoy, and R. L. Levin, *Radiology*, 1989, **161**, 401.
29. R. Dickinson, A. Hall, A. Hind, et al. *J. Comput. Assist. Tomogr.*, 1986, **10**, 468.
30. D. Parker, *IEEE Trans. Biomed. Eng.*, 1984, **31**, 161.
31. E. Vining, G. Duckwiler, R. Udkoff, et al. *J. Neuroimag.*, 1991, **1**, 146.
32. R. A. Gatenby, W. H. Hartz, P. F. Engstrom, et al. *Radiology*, 1987, **163**, 172.
33. N. Higuchi, A. Bleier, F. Jolesz, et al. *Invest. Radiol.*, 1992, **27**, 814.
34. J. Robinson, R. Lufkin, D. Castro, et al. *Eur. Radiology*, 1992, **2**, 24.
35. Y. Anzai, R. Lufkin, D. Castro, et al. *JMRI*, 1991, **1**, 553.
36. D. J. Castro, R. E. Saxton, L. J. Layfield, et al. *Laryngoscope*, 1990, **100**, 541.
37. F. A. Jolesz, A. R. Bleier, P. Jokab, et al. *Radiology*, 1988, **168**, 249.
38. Y. Anzai, R. Lufkin, S. Hirschowitz, et al. *JMRI*, 1992, **1**, 671.
39. F. Jolesz, G. Moore, R. Mulkern, et al. *Invest. Radiol.*, 1989, **24**, 1024.
40. K. Matthewson, P. Coleridge-Smith, J. P. O'Sullivan, et al. *Gastroenterology*, 1987, **93**, 550.
41. R. Matsumoto, R. Mulkern, S. Hushek, et al. *JMRI*, 1994, **4**, 65.
42. R. Stollberger, M. Fan, E. Ebner, et al., *Proc. XIIth Annu. Mtg. Soc. Magn. Reson. Med.*, New York, 1993, p. 156.
43. H. Cline, J. Schenck, K. Hynynen, et al. *J. Comput. Assist. Tomogr.*, 1992, **16**, 956.
44. F. Tomlinson, C. Jack, and P. Kelly, *J. Neurosurg.*, 1991, **74**, 579.
45. S. Hassenbusch and P. Pillary, *Neurosurgery*, 1990, **27**, 220.
46. K. Matsumoto, F. Shichijo, and T. Fukami, *J. Neurosurg.*, 1984, **60**, 1033.
47. P. Kelly and F. Gillingham, *J. Neurosurg.*, 1980, **53**, 322.
48. J. Siegfried, *Surg. Neurol.*, 1977, **8**, 126.
49. L. Organ, *Appl. Neurophysiol.*, 1976, **39**, 69.
50. H. Rosomoff, C. Brown, and P. Sheptak, *J. Neurosurg.*, 1965, **23**, 639.
51. S. Aronow, *J. Neurosurg.*, 1960, **17**, 431.
52. W. Sweet, V. Mark, and H. Hamlin, *J. Neurosurg.*, 1960, **17**, 213.
53. Y. Anzai, A. Desalles, K. Black, et al. *Radiographics*, 1993, **13**, 897.
54. S. Matsumoto, F. Shima, K. Hasuo, et al. *Nippon Igaku Hoshasen Gakkai Zasshi*, 1992, **52**, 1559.
55. K. Black, A. DeSalles, Y. Anzai, et al. *J. Clin. Oncol.*, 1999, in press.
56. R. Foster, R. Bihrle, N. Sanghvi, et al. *Eur. Urol.*, 1993, **23**(Suppl. 1), 29.
57. G. Vallancien, M. Harouni, B. Veillon, et al. *J. Endourol.*, 1992, **6**, 173.
58. R. Silverman, B. Vogelsang, M. Rondeau, et al. *Am. J. Ophthalmol.*, 1991, **111**, 327.
59. F. Fry, and L. Johnson, *Ultrasound Med. Biol.*, 1978, **4**, 337.
60. A. Burov, *Dokl. Akad. Nauk. SSSR*, 1956, **106**, 239.
61. H. Cline, K. Hynynen, C. Hardy, et al. *Magn. Reson. Med.*, 1994, **31**, 628.

Neurosurgical Procedures Monitored by Intraoperative MRI

Terence Z. Wong
Duke University, Durham, NC, USA

and

Richard B. Schwartz, Arya Nabavi, Richard S. Pergolizzi Jr, Peter M. Black, Eben Alexander III, Claudia H. Martin, and Ferenc A. Jolesz
Brigham and Women's Hospital, Boston, MA, USA

1 INTRODUCTION

Image guidance has historically been an integral part of neurosurgery. The introduction of the operating microscope was a major development that enabled the surgeon to decrease the size of the craniotomy and provided superior surface visualization through magnification and perfect illumination. Nonetheless, its advantages for surgical navigation were confined to the visible surface, and the distance to underlying structures had to be estimated. Subsequently, interactive stereotactic image-guided systems were introduced to yield information on the subsurface structures. This allowed the position of the surgeon's tools or visual field to be interactively correlated anatomically with preoperative computed tomographic (CT) or MR images.[1–8] However, image-guided systems that are based on preoperative imaging cannot account for tissue shifts that occur during the course of surgery.[9] This has ultimately led to the development of intraoperative imaging techniques. One modality that can be used is ultrasound. Although the image quality of intraoperative ultrasound has improved in recent years, it is still inadequate as the sole means for guiding neurosurgical procedures.

Intraoperative MRI would appear to be an ideal imaging modality for guiding neurosurgical procedures. The inherent multiplanar capability of MRI facilitates interactive selection of imaging planes in near-realtime. Conventional T_1- and T_2-weighted images provide exquisite sensitivity for identifying abnormalities within the brain. In addition, specialized imaging sequences are available. These include MR angiographic techniques for mapping blood vessels, dynamic gadolinium-enhanced imaging, functional imaging to map cortical activity, and optimized gradient-echo sequences for early identification of blood products.[10,11]

The design of new open-configuration MRI systems combined with the development of MR-compatible surgical instrumentation, anesthesia equipment, and monitoring devices has made intraoperative MRI-guided neurosurgery a reality. At Brigham and Women's Hospital, over 400 neurosurgical procedures have been performed using intraoperative MRI guidance. Design and operational features of the intraoperative MRI system will be described, and our clinical experience with neurosurgical procedures summarized.

2 INTERVENTIONAL MRI DESIGN

Several magnet configurations are currently used for MRI-guided procedures. These include modification of the conventional long-bore configuration, a short-bore design, a horizontal gap open configuration, and a vertical gap open configuration. While the conventional closed long-bore configuration will provide the highest image quality, it offers the least patient access. However, noninvasive energy sources such as high-energy focused ultrasound can be integrated into long-bore MRI systems; the imaging capabilities of the 1.5 T magnet allow prelocalization with subtherapeutic temperatures prior to high-energy ablation.[12,13] The closed short-bore configuration with flanged bore openings provides improved patient access and maintains the high image quality of a high-field system; however it is not easily amenable for perioperative applications. The open-configuration horizontal gap MRI design allows access to the patient from the sides, permitting most radiologic percutaneous procedures to be performed. The low field minimizes the need for shielding of equipment but also potentially limits imaging capability. Currently, the overlying magnet structure precludes open surgical procedures while the patient is within the imaging field.

Both conventional closed-bore and horizontal open configuration MRI designs can be used intraoperatively by performing surgery outside of the magnet and physically moving the patient into the imaging field for scanning. This must be accomplished while maintaining sterility and is further complicated by the presence of equipment for anesthesia and monitoring the patient. In 1998, Hall et al. reported on perioperative MRI using a conventional 1.5 T system for guiding pediatric neurosurgery.[14] Although the patient had to be repositioned in the magnet for each set of images, these authors point out that the use of the high-field imager allowed state-of-the-art pulse sequences to be used and enabled images of the highest quality to be obtained. In 1997, Tronnier et al. reported on the use of a 0.2 T horizontal-gap open-configuration magnet for intraoperative neurosurgical guidance on 27 patients.[15] The advantages of direct MRI visualization during biopsies, cyst aspiration, and catheter placement procedures were realized. For open craniotomy procedures, however, the patient had to be transferred into the magnet for each imaging set. Newer horizontal-gap MRI units are being designed with improved access, which may permit intraoperative imaging without moving the patient.

In 1993, a vertical gap mid-field strength MRI system was developed as a collaborative effort by General Electric (Signa SP, Milwaukee, WI, USA) and Brigham and Women's Hospital (Figure 1). By allowing vertical access to the patient, this is currently the only interventional MRI design that permits imaging during surgical procedures without moving the patient. The MRI system has been previously described in detail,[11,16–22] and consists of two vertically oriented superconducting coils (55 cm inner bore diameter) in a modified Helmholtz configuration separated by a 56 cm gap. This spacing permits access to the patient from both sides and allows the surgeon and assistant to work simultaneously in the operating field. Other design

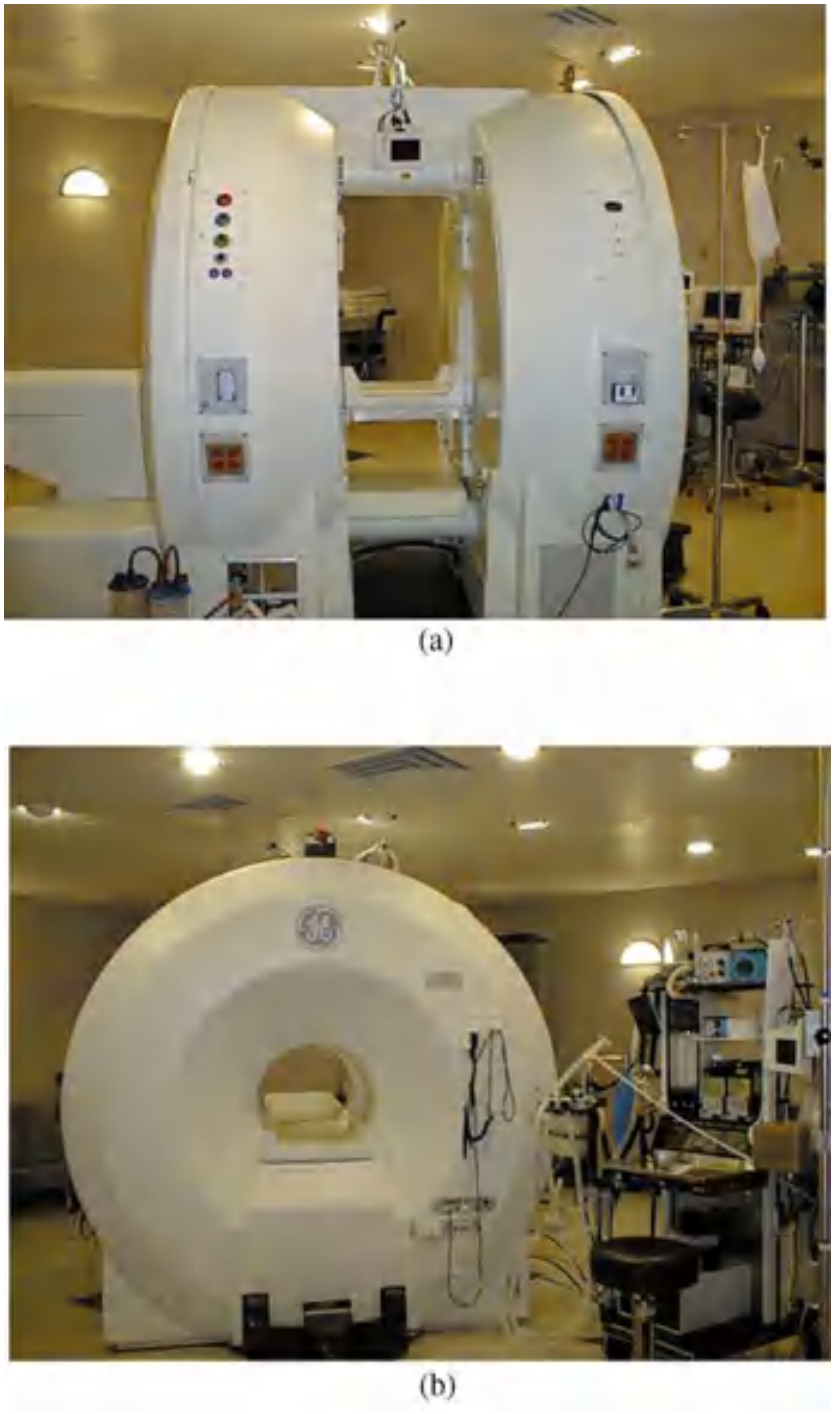

Figure 1 Interventional/intraoperative MRI system (GE Signa SP) features a vertical gap for surgical access, and is sited within an operating room. (a) Side view: liquid crystal display monitors mounted at eye level on either side of the magnet allow interactive visualization of the MR images. Connections for headlights, suction, navigation, and other instrumentation can be seen on the side of the magnet structure. (b) End-on view: MRI-compatible anesthesia and patient monitoring equipment are shown to the right

features included the use of niobium tin as the superconducting material, which has a higher transition temperature and allows the static field to be maintained without a liquid helium bath, thus permitting a wider gap for patient access. The design results in an imaging volume having a 0.5 T static field defined by a 30 cm sphere in the center of the open magnet bore. Flexible transmit/receive coils have been designed to be placed on the patient in close proximity to the imaging volume, while simultaneously allowing surgical and interventional access. The MRI system is maintained in an operating room environment, with adjacent clean and scrub areas. Disposable sterile drapes have been designed to fit within the surgical space of the mag-

net (Baxter, Deerfield, IL, USA). The design considerations for the intraoperative MRI interventional suite have been previously reported in detail.[20] Considerations for safety and imaging compatibility in the MRI environment have been reviewed,[20,23] and appropriate materials are available that have low magnetic susceptibility and minimal effect on local MRI.[24] Anesthesia equipment, surgical instruments, patient monitors, and electrocautery devices have already been modified by the manufacturers to be MRI compatible. Specialized devices such as the neurosurgical head holder (Mayfield; Ohio Medical Instrument Co., Cincinnatti, OH, USA), flexible Bookwalter arm (Codman Inc., Burlington, MA, USA), pneumatic neurosurgical drill (Midas Rex, Ft Worth, TX, USA), ultrasonic aspirator for neurosurgical resection (Selector; Elekta, Atlanta, GA, USA), and MR-compatible microscope (Studor Medical Engineering, Rhenfaal, Switzerland) have also been developed and are used routinely at our institution.[16]

The environment of the MRI system permits it to be used for both *interventional* and *intraoperative* applications.[20] Although open surgery is by definition not a minimally invasive procedure, image guidance can, with accurate targeting and presurgical planning, minimize the damage to healthy tissue and maximize removal of the abnormality; this reduces the invasiveness of the surgical intervention. We summarize below our experience with MRI-guided interventional and intraoperative intracranial procedures using the vertical gap 0.5 T MRI system. To date, approximately 300 tumor resection procedures and 100 intracranial biopsies have been performed by our group with intraoperative MRI guidance. Other procedures have included evaluation of cystic lesions by injection of dilute gadopentetate dimeglumine,[25] laser ablation of intracranial tumors,[26] and endoscopic sinus surgery.[27,28]

2.1 Interactive Image Guidance

During the MRI-guided neurosurgical procedures, the patient's head is immobilized with a head frame and maintained in the same position throughout the procedure. This provides several important advantages for image guidance. First, patient movement is minimized during imaging. Second, identical slice positions can be obtained and compared during the procedure. Finally, other three-dimensional imaging data sets, such as preoperative MRI, SPECT (single photon emission computed tomography), or PET (positron emission tomography) scans can be co-registered with the MR images and utilized for planning approach and therapy.[29–35] It should be emphasized, however, that although the skull is fixed in position, we have observed that spatial shifts and deformations occur within the brain during the course of surgery, and anatomic co-registration to preoperative imaging studies alone can be subject to significant errors. This problem of tissue shifts may be minimized if access for biopsy or therapeutic probes is limited to small burr holes. In addition, computer models are under development to account for this problem.[36,37]

2.2 Interactive Imaging Tools

Optical, acoustic, and rf techniques have been used to establish the location of biopsy needles or interventional probes in three-dimensional space, and this technology is commonly applied to frameless stereotactic surgery where target coordinates are defined based on preoperative imaging.[1–8]. The intraoperative MRI unit features built-in optical (Flashpoint; Image Guided Technologies Inc., Boulder, CO, USA) and rf (CRD; GE Medical Systems, Inc., Schenectady, NY, USA) tracking capabilities.

Tracking by rf can be implemented using miniature coils mounted on the surgical device.[38,39] Unlike optical or acoustic tracking, intervening tissues are not a problem with rf localization, and this technique is ideal for endoscopic or intravascular procedures.

Currently, the optical tracking system is used for most procedures at Brigham and Women's Hospital. Three charge-coupled device (CCD) cameras are mounted over the imaging field in the MRI unit. These detect infrared light-emitting diodes (LEDs) that are, in turn, attached to the interventional probe. Since the spatial relationship between the LEDs and interventional probe is fixed, the position of the LEDs can be used to define an imaging plane either containing or perpendicular to the probe. Knowledge of the length of the probe allows localization of the probe tip or its projected location. Coordinates of the probe are determined through an interactive workstation (Sun Microsystems, Mountain View, CA, USA), which, in turn, is used to prescribe imaging planes to the SP scanner. Images are subsequently acquired and displayed to the surgeon or interventionalist on liquid crystal display (LCD) monitors which are mounted at eye level on either side of the work area for the MRI (Figure 1). Images are updated every few seconds, reflecting adjustments in probe position and providing visual feedback in near-realtime. For *interactive imaging*, the interventionalist or surgeon uses the interactive probe to navigate through the region of interest, in a manner similar to that utilizing ultrasonography. This technique is particularly useful for establishing the relationship between surface landmarks and underlying structures, and for planning the approach for biopsy or surgical exposure. For needle biopsies or placement of therapeutic probes, the *targeting* mode is particularly useful. Annotation is added to the acquired images in the form of a 'virtual needle', which enables the operator to view the proposed needle path and tip. The trajectory and target can then be verified by imaging in three orthogonal planes, and the operator is provided with near-realtime visual feedback. When the desired trajectory and target point has been established, the interventional probe can be advanced in a stepwise fashion and observed on the MR images as they are acquired in near-realtime; this is termed the *tracking* mode and confirms satisfactory positioning of the biopsy needle or therapeutic probe.

Two optical tracking handpieces are available for attachment to interventional probes (Figure 2): one has three localization LEDs in a triangular configuration that form a plane perpendicular to the probe. This device can be fixed to the surgical table with the Bookwalter clamp and is the handpiece of choice for intracranial biopsies. One of the three LEDs is offset relative to the other two, and this LED along with the biopsy needle defines a reference imaging plane that contains the needle trajectory. Other planes containing the needle can be selected by physically rotating the handpiece and/or by specifying a relative rotation through the interactive navigation software. This is done at the workstation under the direction of the radiologist and MR technologist. In addition, the software allows the plane perpendicular to the needle to be imaged at

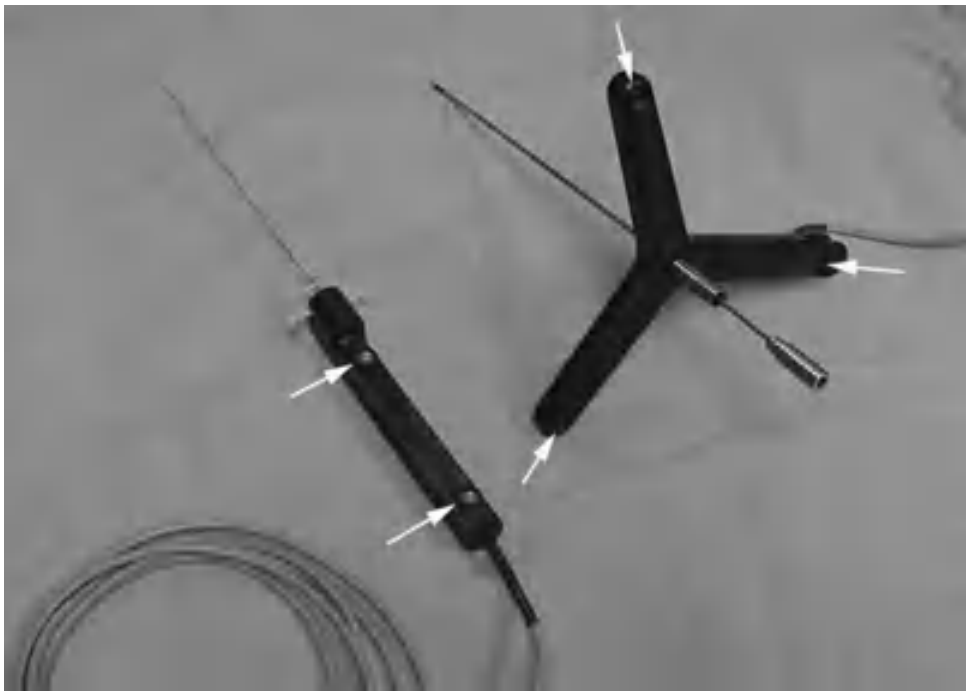

Figure 2 Navigational tools feature either two or three LEDs (white arrows) for optical tracking by three cameras mounted overhead in the MRI unit. The two-LED device (left) is used to establish the trajectory of a biopsy needle attached to the end of the handle and is generally used for interventions involving the abdomen, pelvis, or extremities. In the three-LED handpiece (right), the probe is positioned perpendicular to the handle and is typically immobilized using a Bookwalter clamp during neurosurgical procedures. Near-realtime annotation is used to establish the needle trajectory (Figure 3), after which the biopsy needle is advanced under MRI observation

any desired depth relative to the needle tip. The needle length is specified, and software annotation provides a projected tract, or 'virtual needle' that can be interactively directed to the target lesion by positioning the handpiece.

The second handpiece for optical navigation (Figure 2, left) features two LEDs mounted on a handle that defines the trajectory of the interventional probe. This device is used most frequently for non-neurosurgical applications, such as interventions in the abdomen, pelvis, or soft tissues.[19] With the two-LED handpiece, the reference imaging plane is defined to be the plane containing the interventional probe and perpendicular to the ground. Other planes can be selected through interactive software prescription.[19]

Although used routinely for biopsy procedures, the optical navigation system can be similarly utilized to position other catheters or needles (e.g. for cyst evaluation or drainage[25]) or to place thermal ablation probes.[26]

3 MRI-GUIDED BIOPSY PROCEDURES

Interactive MRI guidance offers several advantages over conventional stereotactic biopsy techniques. Conventional stereotactic procedures require the placement of a head frame on the patient followed by a set of preprocedure CT or MR images to define target coordinates. A significant advantage of interactive guidance is that it eliminates the need for this two-step process. The MRI sequence best defining the target tissue can be selected for image guidance; gadolinium contrast can be injected prior to biopsy; this is usually done after the burr hole or craniotomy has been made and the dura exposed. Perhaps the most important advantage of interactive MRI guidance is that the actual path of the biopsy needle can be followed as it is advanced toward the lesion, and small compensatory changes can be made until the sampling port is positioned within the target. Imaging can then confirm in all three dimensions that the biopsy site lies within the tissue having the abnormal MR signal. The ability to make realtime adjustments of the biopsy needle, along with confirmation of biopsy location, may significantly reduce sampling error, as well as decrease the number of needle passes. This can lead to higher diagnostic yield with reduced morbidity.

Of the nearly 100 MRI-guided intracranial biopsies performed to date at Brigham and Women's Hospital, approximately two thirds were performed under general anesthesia with the remaining one third performed using monitored conscious sedation. Average procedure time was less than 2 h if general anesthesia was used, and approximately 1.5 h when conscious sedation was utilized. For navigational MRI, sequences were selected to define the target best. For enhancing lesions, 10–20 ml intravenous gadopentetate dimeglumine was injected, and T_1-weighted fast spin-echo (FSE) images used (updated every 14 s). For nonenhancing lesions, T_2-weighted FSE imaging was usually used (updated every 15–30 s). More recently, a SSFSE (single-shot fast spin-echo) protocol has been developed that allows T_2-weighted images to be acquired every 4 s. An example of a biopsy performed using

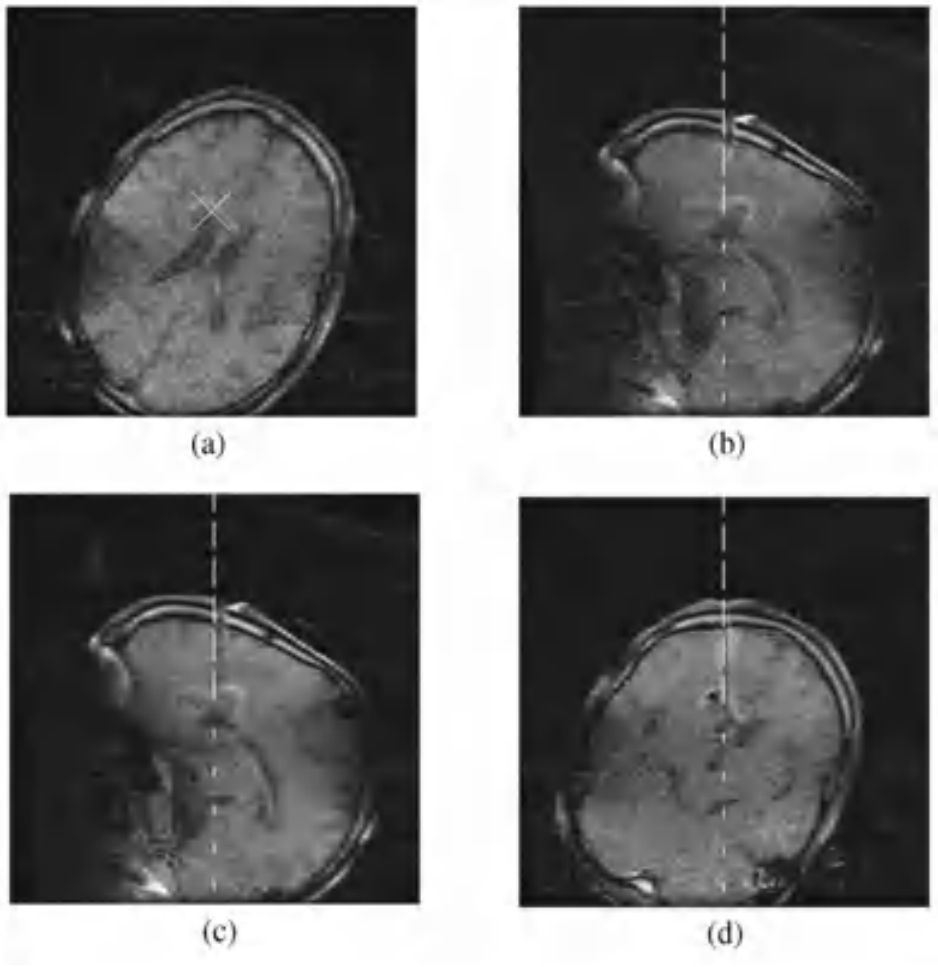

Figure 3 Interactive MRI for biopsy of a right frontal lesion using the 3-LED handpiece and T_1-weighted images following intravenous gadolinium enhancement. (a) Para-axial image perpendicular to needle in the plane of the biopsy port allows targeting of enhancing margin. (b) Para-sagittal image in the plane of the needle shows the 'virtual needle' depicted as dashed lines directed at the target. Note the small signal void at the cortical surface from the biopsy needle tip prior to insertion. (c) As the titanium needle is advanced, near-realtime imaging allows observation of the needle tract along the virtual needle annotation. This allows fine adjustments to be made accordingly and enables the position of the actual biopsy needle to be confirmed prior to sampling. (d) Actual needle tract is confirmed in the perpendicular para-coronal plane. The tip of the virtual needle corresponds to the level of the sampling port of the biopsy needle; as a result the actual needle tip extends a few millimeters beyond the dashed annotation. Note focal signal void within the enhancing rim from biopsy sample

MRI-based navigation is illustrated in Figure 3. In this case, contrast-enhanced T_1-weighted imaging was used for guidance. After the patient has been positioned in the headholder on the MRI operating table, the handpiece may be used in the interactive imaging mode to plan the incision location and biopsy trajectory. Prior to inserting the biopsy needle, the targeting mode is utilized, with annotation used to define a virtual needle. The target position can be confirmed in three orthogonal planes (Figure 3). With the handpiece immobilized with the Bookwalter arm, the titanium biopsy needle is advanced in a stepwise manner as MR images are acquired. The needle is observed as a signal void overlying the virtual needle annotation (Figure 3c,d). It should be noted that the tip of the virtual needle is set to correspond to the location of the sideport of the biopsy needle; therefore, the actual needle tip extends several millimeters beyond the virtual needle annotation. This confirms that the biopsy needle is traveling along the expected trajectory and to the desired target depth. If necessary, the annotation can be removed to allow the actual needle location to be seen more clearly and reconfirmed in all three planes. The ability to confirm that the biopsy specimen was obtained within the MR-defined abnormality minimizes sampling error and potentially reduces the number of needle passes and associated complications.

4 MRI GUIDANCE FOR OPEN CRANIOTOMIES

Since 1996, approximately 270 open craniotomies have been performed at Brigham and Women's Hospital for MRI-guided tumor resection. Patient selection, demographics, and preliminary clinical results have been previously reported.[11,16,18,22] In preparation for surgery, the patient's head is

positioned in the MRI with the head holder to allow the best surgical access. As a result, the patient's anatomic frame of reference no longer corresponds to conventional MRI planes. To overcome this problem, a new frame of reference is established to allow true axial, sagittal, and coronal images to be obtained. This can be easily accomplished using the navigational tools previously described; interactive imaging is used to define an appropriate reference imaging plane from which conventional axial, sagittal, or coronal images can be prescribed. Since the patient is immobilized, the reference imaging procedure need only be performed once and is typically done immediately after the patient has been positioned within the intraoperative MRI. The use of conventional imaging planes facilitates accurate localization and identification of critical anatomic structures as the surgery progresses. During the procedure, the radiologist prescribes the appropriate imaging planes and sequences that will best address specific questions of the surgeon as the surgery progresses. For example, for initial identification of tumor boundaries, either conventional spin-echo gadolinium-enhanced T_1-weighted images or T_2-weighted images may be most useful. Other specialized imaging sequences have been developed, including SSFSE for rapid T_2-weighted imaging, dynamic contrast-enhanced imaging, susceptibility sensitive sequences to evaluate early hemorrhage,[10,11] and rapid volumetric image acquisition techniques.

In patients who have been previously treated with high-dose radiotherapy (stereotactic radiosurgery), it is not possible to distinguish active tumor recurrence from postradiation necrosis on conventional delayed gadolinium-enhanced images. Dual-isotope ^{201}T1/^{99m}Tc-HMPAO (hexamethylpropyleneamine oxime) SPECT scanning has been found to be useful for making this important distinction,[33,34] and these images can be co-registered with intraoperative MR images. Alternatively, a dynamic contrast-enhanced MR study can be performed. These techniques have been useful for estimating tumor grade as well as for distinguishing recurrent tumor from post-treatment change.[40–42] Our intraoperative technique is to obtain two-dimensional fast spoiled gradient-echo images through the tumor volume, with each slice sampled every 11–15 s for 2–3 min following rapid bolus contrast injection. Tumor recurrence, with associated neovascularily, will tend to enhance early, while post-treatment necrosis, related primarily to blood–brain barrier breakdown, will tend to show delayed enhancement. Distinguishing active recurrence from radionecrosis is valuable both for selecting appropriate biopsy sites and for planning the surgical resection. This has been very useful in the intraoperative setting. In an evaluation of a series of 24 patients with intraoperative dynamic MRI,[43]14 of 15 lesions demonstrating early enhancement had recurrent tumor by pathology; out of the nine lesions that did not show early enhancement, eight had only reactive post-treatment changes. In this study, early enhancement was determined visually when the appearance of contrast within the lesion occurred at the same time as in vascular structures or the choroid plexus.

For all intraoperative MR, an initial baseline set of two-dimensional slices is obtained through the volume of interest. Imaging is repeated at intervals during the surgery to verify the present location in relation to the remaining tumor to be excised. Additionally, the location of the surgical resection cavity relative to adjacent eloquent cortical pathways is always of major importance. Once the most appropriate imaging sequence and imaging plane have been preloaded into the MR console, identical image slices can be acquired simply by rescanning. This allows direct serial comparison in the same imaging plane. Acquisition time for each imaging data set varies depending on the imaging sequence but takes approximately 1–2 min. Prior to imaging, electrical equipment and metallic instruments are removed from the surgical field. Although these devices are MRI-compatible they can produce significant imaging artifacts if they are left in place. Imaging is possible, however, with the operating microscope in position. In our experience, intraoperative MRI guidance enables the surgeon to verify his or her planned approach and surgical procedure and also allows him or her to change the strategy during the procedure according to the newly acquired information.

Figure 4 illustrates an MRI-guided tumor resection. In this case, T_2-weighted images were used for surgical guidance. Serial images from a single axial slice are shown in this example. Early in the procedure, the resection site was defined by a locator. The tissue anterior to this (white arrow, Figure 4(a)) was felt to represent non-neoplastic changes after previous surgery, and this was confirmed by intraoperative histopathology. The remaining tumor was represented by a high T_2 signal posterior to the pointer and just anterior to the motor strip. Stepwise resection of the tumor is illustrated in Figure 4b,c, with complete resection shown in Figure 4d. Prior to closing, the cavity was irrigated with saline (Figure 4e), and multi-echo gradient-echo images were obtained to evaluate for significant hemorrhage. The MRI characteristics of hyperacute intracranial hemorrhage have been recently described.[25] In our experience, T_2-weighted images (FSE, *TR*/*TE*=4000/100 ms; Figure 4e) in combination with gradient-echo sequences (30° flip angle, *TR*=600 ms) is sensitive for identifying hyperacute hemorrhage and for distinguishing this from postsurgical fluid. Figure 4f,g shows postsurgical gradient-echo images with *TE* of 9 and 60 ms, respectively. A typical postoperative appearance is illustrated here, with irrigation saline (bright T_2) within the resection cavity, and a thin rim of low signal bordering the resection cavity on the short *TE* image (Figure 4f) that 'blooms' on the second echo (*TE*=60 ms; Figure 4g). This rim is felt to represent deoxyhemoglobin content within acute blood products at the resection border. No hematoma, mass effect, or extra-axial collection was noted in this patient. Hematomas tend to have a nonfluid central area (lower T_2 signal), with a rim of susceptibility that also blooms on gradient-recalled echo imaging.

Intraoperative MRI-guided tumor resection provides several advantages over conventional techniques. Image guidance is interactive. Specific sequences and imaging planes can be applied during the procedure to optimize selection of involved tissue. For example, dynamic or steady-state contrast-enhanced images can be used to delineate active tumor, and T_2-weighted images can be used to identify nonenhancing tumor. Neoplastic tissue having abnormal MR signal characteristics but normal appearance visually can be identified and resected. Tissue shifts during surgery have been observed and are easily compensated for with intraoperative imaging. Critical anatomical and functional structures can be identified during resection and, at crucial points in the procedure, images can be obtained more frequently in multiple planes if necessary to refine the resection margin. Finally, imaging capability allows early detection of

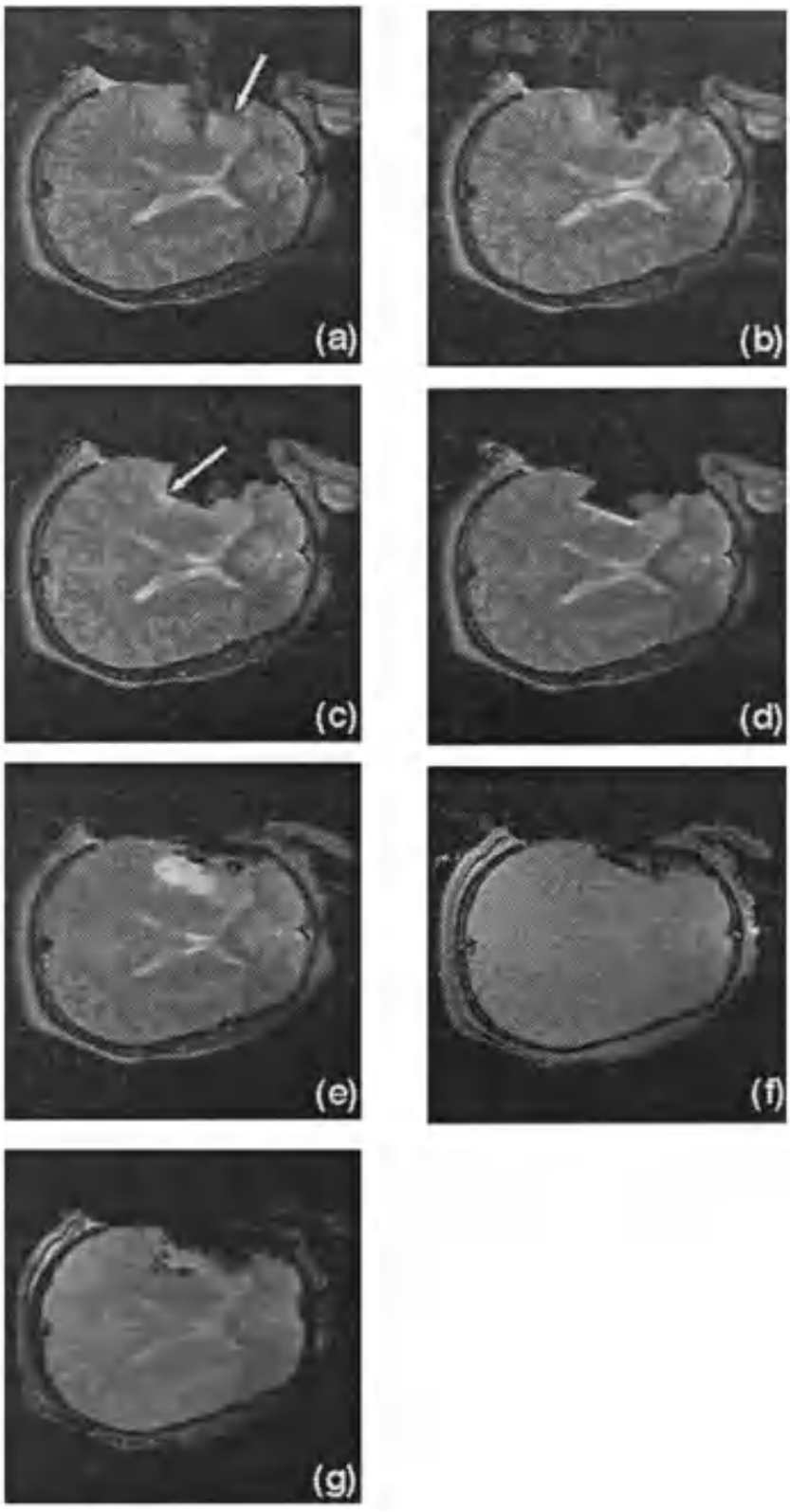

Figure 4 Intraoperative imaging during neurosurgical resection: serial T_2-weighted axial images. (a) Early in the surgery, the neoplastic tissue is posterior to the surgeon's finger. Anterior tissue (arrow) represents postoperative change from previous surgery and was present on prior MR study (b,c) Serial resection, (d) complete resection of the T_2-abnormal tissue. Some tissue shift is evident. (e) Following resection, the cavity is filled with saline. (f,g) Postsurgical gradient-echo images allow evaluation of hyperacute hemorrhage. These show typical postsurgical changes. (Reprinted with permission from Wong et al.[22])

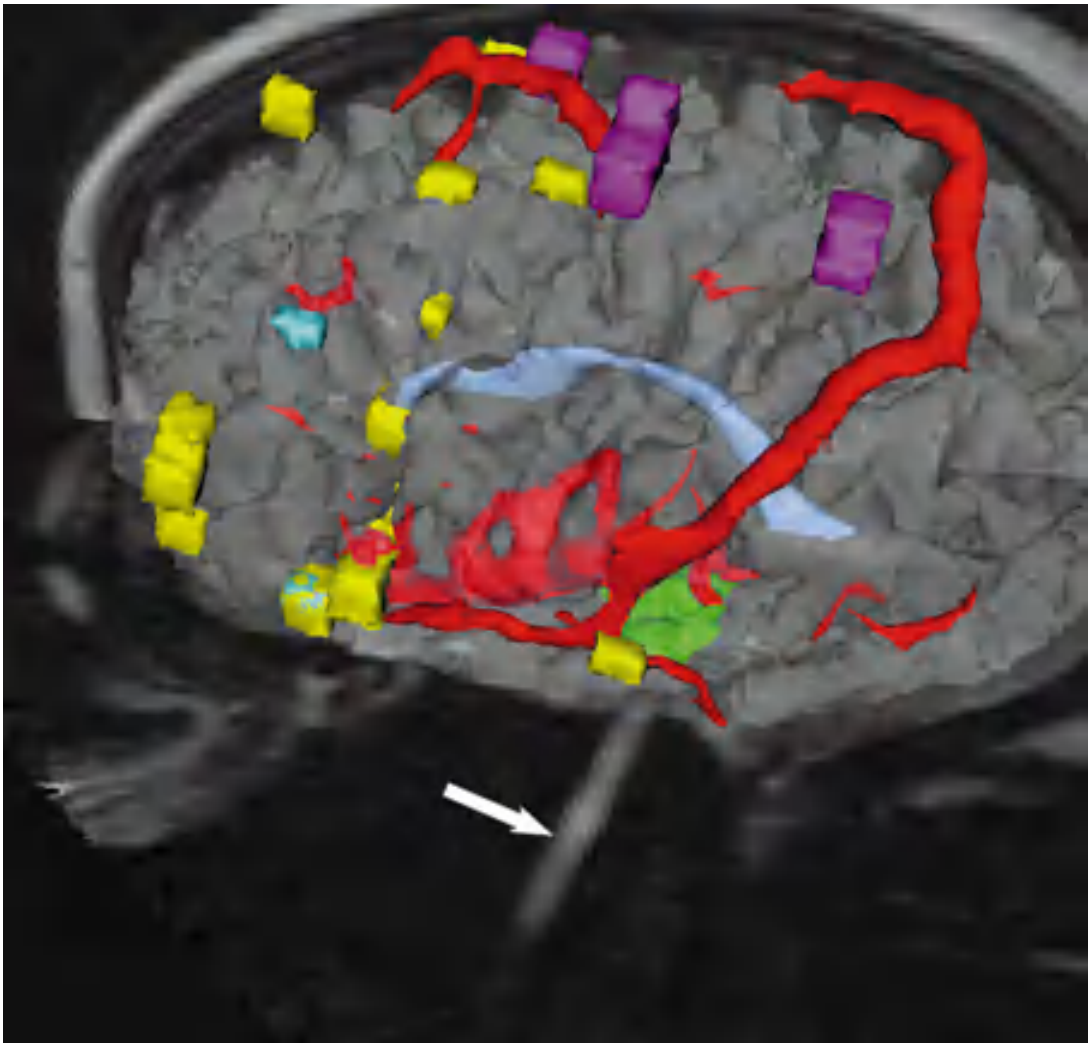

Figure 5 Intraoperative parasagittal image (note intraoperative pointer, white arrow) co-registered with the patient's preoperative three-dimensional brain model. Operative skin flap in the lower portion of the image on the left. The preoperative model includes conventional MRI with segmentation of tumor (green) and ventricles (light blue). In addition, MR angiography was performed to display large vessels (red). Functional MRI was used to identify cortical activation during complex speech tasks (turquoise and yellow) and motor tasks (magenta)

any unexpected complication, such as hemorrhage. Out of some 400 neurosurgical procedures, postsurgical hematomas were observed in four patients. In all cases, imaging permitted immediate identification, and facilitated removal in three patients. In the fourth patient, serial MR images were used to confirm stability of a small hematoma, and removal was unnecessary. In one patient, a hematoma was noted in the hemisphere contralateral to the surgery and was felt to represent a spontaneous hematoma, possibly from blood pressure instability. This would not have been identified without immediate postoperative imaging; a second craniotomy was performed using MRI guidance to evacuate it.

5 FUTURE PERSPECTIVES

Specialized MRI sequences are available on higher-field MRI units that are not yet available on the intraoperative MRI system, and sophisticated interactive methods have been developed for preoperative surgical planning.[44] In addition, other three-dimensional imaging modalities can provide important information not available by MR techniques. Therefore, we have developed co-registration software to integrate preoperatively acquired multimodality information with the intraoperative imaging. Examples of specialized studies that can be performed prior to surgery include MR angiography, PET, SPECT, and functional MRI. MR angiography can define the relationship of the tumor to major vascular structures during the surgical procedure. PET imaging with [^{18}F]-fluorodeoxyglucose reflects metabolic activity of gliomas, and areas of higher uptake correlate with higher tumor grade and poorer prognosis.[29–31] Dual-isotope ^{201}T1/^{99m}Tc-HMPAO SPECT is useful for distinguishing tumor recurrence from radiation necrosis,[33] and findings also correlate with histopathological findings and survival.[34] Image registration of MRI with PET or SPECT images can, therefore, be useful for directing biopsy to regions most repre-

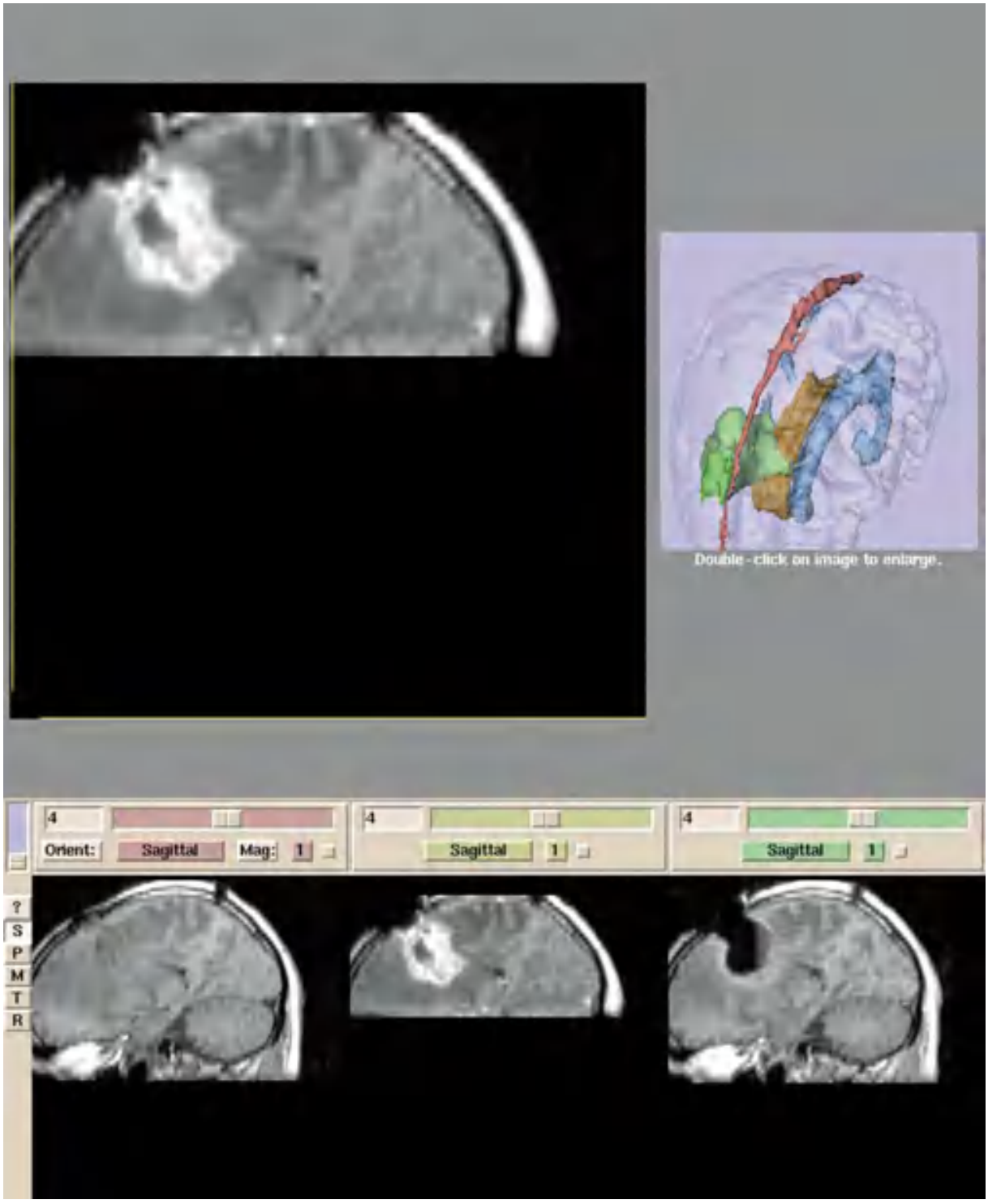

Figure 6 Surgical planning computer display. Preoperative three-dimensional model (right, upper frame) demonstrating tumor (green) and anatomic relationship to superior sagittal sinus (red), corpus callosum (brown), and ventricle (blue). The bottom row displays three intraoperative sagittal images in the same imaging plane. On the left is the unenhanced T_1-weighted image prior to craniotomy. The middle image demonstrates enhancing tumor prior to resection and is reproduced in the large upper left frame. The image on the bottom right demonstrates the surgical resection cavity following tumor removal

sentative of tumor behavior; this may reduce sampling error. For image-guided tumor resection, the addition of PET or SPECT data can help the neurosurgeon to select most aggressive portions of tumor for resection. Functional MRI can be used to map areas of cortical activation during motor tasks, enabling critical sensorimotor areas to be identified and allowing the neurosurgeon to avoid eloquent areas during tumor resection.[45]

The preoperatively acquired information is combined with the intraoperative imaging data set using registration algorithms, thus maximizing the information available during surgery. The grayscale images and three-dimensional models of specific structures are displayed to the surgeon and correspond spatially to the actual patient as positioned in the intraoperative MRI (Figure 5). The combination of the preoperative information and the intraoperative renewal of the grayscale information allows updated neuronavigation. With progress of the surgical intervention and increasing brain deformation, the validity of the preoperative information decreases. We are currently evaluating the definition of a deformation field from the intraoperatively acquired grayscale images to align the three-dimensional models and their preoperative information to the updated situation. Other models to account for brain deformation are being developed.[36,37] The combination of pre- and intraoperative information, their alignment and the tracking of instruments in this defined space comprise the capabilities of this system for realtime interactive image-guided surgery (Figure 6).

6 CONCLUSIONS

Intraoperative MRI-guided neurosurgical procedures are a collaborative effort, involving neurosurgeons, neuroradiologists, anesthesiologists, MR technologists, nurses, and engineers. MRI provides excellent contrast between abnormal and healthy brain tissue, and intraoperative imaging permits these areas to be defined relative to the surgeon's field of view. This improves the accuracy of intracranial biopsies and surgical resection of tumors. Early identification of unexpected complications is another benefit. To date, MRI guidance has been utilized in selected complex cases or repeat surgery. Based on our current experience, there is little question that MRI guidance for neurosurgical procedures augments the technical capability of the neurosurgeon to remove neoplastic tissue selectively. However, evaluation of cost effectiveness and clinical outcomes relative to conventional neurosurgical procedures will require a prospective, randomized clinical trial.

In the future, technological developments will continue to reduce the degree of invasiveness required for tumor resection. Definition of the tissue targeted for resection and its relationship to critical functional structures will continue to be improved through multimodality presurgical planning. Improvements to MRI will include faster acquisition times and refinement of imaging sequences for neurosurgical guidance. Currently available 'near-realtime' imaging will become closer to realtime. Image processing will continue to become faster, and techniques to compensate for intraoperative tissue shifts and removal are under development. Surgical image guidance will ultimately be a synthesis of anatomical/functional preoperative images with updated co-registered intraoperative imaging.

Image guidance will allow neurosurgeons to treat benign and malignant lesions using minimally invasive tools. Thermal ablation techniques using laser, rf, ultrasound, and microwave energy sources are currently being investigated, as is cryotherapy. Central to the success of these minimally invasive therapies is image guidance to position the ablation probes and monitor the thermal therapy. The navigational tools available for MRI-guided biopsies described above can be used to position thermal ablation probes accurately. In addition, MRI is uniquely suited to reveal subtherapeutic as well as irreversible thermal effects, and development of improved, faster imaging sequences to monitor these tissue effects will parallel the refinement of energy sources to deliver controlled, directed thermal ablation.

7 RELATED ARTICLES

ESR Probes as Field Detectors in MRI; MR-Guided Biopsy, Aspiration, and Cyst Drainage; MR-Guided Therapy in the Brain; Thermal Therapies in the Body Monitored by MRI.

8 REFERENCES

1. D. W. Roberts, J. W. Strohbehn, J. F. Hatch, W. Murray, and H. A. Kettenberger, *J. Neurosurg.*, 1986, **65**, 545.
2. R. J. Maciunas, M. S. Berger, B. Copeland, M. R. Mayberg, R. Selker, and G. S. Allen, *Neurosurg. Clin. North Am.*, 1996, **7**, 245.
3. D. Kondziolka and L. D. Lunsford, Intraoperative navigation during resection of brain metastases, *Neurosurg. Clin. North Am.*, 1996, **7**, 267.
4. P. K. Doshi, L. Lemmieux, D. R. Fish, S. D. Shorvon, W. H. Harkness, and D. G. Thomas, *Acta Neurochir. Suppl. (Wien)*, 1995, **64**, 49.
5. C. R. Maurer Jr, J. M. Fitzpatrick, M. Y. Wang, R. L. Galloway Jr, R. J. Maciunas, and G. S. Allen, *IEEE Trans. Med. Imag.*, 1997, **16**, 447.
6. D. G. Thomas, P. Doshi, A. Colchester, D. J. Hawkes, D. L. Hill, J. Zhao, N. Maitland, A. J. Strong, and R. I. Evans, *Sterotact. Funct. Neurosurg.*, 1996, **66**, 81.
7. E. Watanabe, Y. Mayanagi, Y. Kosugi, S. Manaka, and K. Takakura, *Neurosurgery*, 1991, **28**, 792.
8. C. Schaller, B. Meyer, D. van Roost, and J. Schramm, *Comput. Aided Surg.*, 1997, **2**, 162.
9. C. R. Maurer Jr, D. L. Hill, A. J. Martin, H. Liu, M. McCue, D. Rueckert, D. Lloret, W. A. Hall, R. E. Maxwell, D. J. Hawkes, and C. L. Truwit, *IEEE Trans. Med. Imag.*, 1998, **17**, 817.
10. S. W. Atlas and K. R. Thulborn, *Am. J. Neuroradiol.*, 1998, **19**, 1471.
11. R. B. Schwartz, L. Hsu, T. Z. Wong, D. F. Kacher, A. A. Zamani, P. M. Black, E. Alexander, P. E. Stieg, T. M. Moriarty, C. A. Martin, R. Kikinis, and F. A. Jolesz, *Radiology*, 1999, **211**, 477.
12. K. Hynynen, N. I. Vykhodtseva, A. H. Chung, V. Sorrentino, V. Colucci, and F. A. Jolesz, *Radiology*, 1997, **204**, 247.
13. K. Hynynen, W. R. Freund, H. Cline, A. H. Chung, R. D. Watkins, J. P. Vetro, and F. A. Jolesz, *Radiographics*, 1996, **16**, 185.
14. W. A. Hall, A. J. Martin, H. Liu, C. H. Pozza, S. O. Casey, E. Michel, E. S. Nussbaum, R. E. Maxwell, and C. L. Truwit, *Pediatr. Neurosurg.*, 1998, **29**, 253.
15. V. M. Tronnier, C. R. Wirtz, M. Knauth, G. Lenz, O. Pastyr, M. M. Bonsanto, F. K. Albert, R. Kuth, A. Staubert, W. Schlegel, K. Sartor, and S. Kunze, *Neurosurgery*, 1997, **40**, 891.
16. P. M. Black, T. Moriarty, E. A. Alexander III, P. Stieg, E. J. Woodard, P. L. Gleason, C. H. Martin, R. Kikinis, R. B. Schwartz, and F. A. Jolesz, *Neurosurgery*, 1997, **41**, 831.
17. J. F. Schenck, F. A. Jolesz, P. B. Roemer et al., *Radiology*, 1995, **195**, 805.
18. T. M. Moriarty, R. Kikinis, F. A. Jolesz, P. M. Black, and E. Alexander III, *Neurosurg. Clin. North Am.*, 1996, **7**, 323.

19. S. G. Silverman, B. D. Collick, M. R. Figueira, R. Khorasani, D. F. Adams, R. W. Newman, G. P. Topulos, and F. A. Jolesz, *Radiology*, 1995, **197**, 175.
20. S. G. Silverman, F. A. Jolesz, R. W. Newman, P. R. Morrison, A. R. Kanan, R. Kikinis, R. B. Schwartz, L. Hsu, S. J. Koran, and G. P. Topulos, *Am. J. Roentgenol.*, 1997, **168**, 1465.
21. F. A. Jolesz, *Radiology*, 1997, **204**, 601.
22. T. Z. Wong, R. B. Schwartz, PMcL Black, E. Alexander III, and F. A. Jolesz, *Semin. Intervent. Radiol.*, 1999, **16**, 23.
23. J. F. Schenck, *Med. Phys.*, 1996, **23**, 815.
24. F. A. Jolesz, P. R. Morrison, S. J. Koran, R. J. Kelley, S. G. Hushek, R. W. Newman, M. P. Fried, A. Melzer, R. M. Seibel, and H. Jalahej, *JMRI*, 1998, **8**, 8.
25. R. B. Schwartz, L. Hsu, P. M. Black, *JMRI*, 1998, **8**, 807.
26. J. Kettenbach, S. G. Silverman, N. Hata, K. Kuroda, P. Saiviroonporn, G. P. Zientara, P. R. Morrison, S. G. Hushek, P. M. Black, R. Kikinis, and F. A. Jolesz, *JMRI*, 1998, **8**, 933.
27. M. P. Fried, G. Topulos, L. Hsu, H. Jalahej, H. Gopal, A. Lauretano, P. R. Morrison, and F. A. Jolesz, *Otolaryngol. Head Neck Surg.*, 1998, **119**, 374.
28. L. Hsu, M. P. Fried, and F. A. Jolesz, *Am. J. Neuroradiol.*, 1998, **19**, 1235.
29. M. W. Hanson, M. J. Glantz, J. M. Hoffman, A. H. Friedman, P. C. Burger, S. C. Schold, and R. E. Coleman, *J. Comput. Assist. Tomogr.*, 1991, **15**, 796.
30. J. B. Alavi, A. Alavi, J. Chawluk, M. Kushner, J. Powe, W. Hickey, and M. Reivich, *Cancer*, 1988, **62**, 1074.
31. M. Levivier, S. Goldman, B. Pirotte, J. Brucher, D. Baleriaux, A. Luxen, J. Hildebrand, and J. Brotchi, *J. Neurosurg.*, 1995, **82**, 445.
32. T. G. Turkington, R. J. Jaszczak, C. A. Pelizzari, C. C. Harris, J. R. MacFall, J. M. Hoffman, and R. E. Coleman, *J. Nucl. Med.*, 1993, **34**, 1587.
33. R. B. Schwartz, P. A. Carvalho, E. A. Alexander III, J. S. Loeffler, R. Folkerth, and B. L. Holman, *Am. J. Neuroradiol.*, 1991, **12**, 1187.
34. R. B. Schwartz, B. L. Holman, J. F. Polak, B. M. Garada, M. S. Schwartz, R. Folkerth, P. A. Carvalho, J. S. Loeffler, D. C. Shrieve, P. M. Black, and E. Alexander III, *J. Neurosurg.*, 1998, **89**, 60.
35. B. L. Holman, R. E. Zimmerman, K. A. Johnson, P. A. Carvalho, R. B. Schwartz, J. S. Loeffler, E. Alexander, C. A. Pelizzari, and G. T. Chen, *J. Nucl. Med.*, 1991, **32**, 1478.
36. P. J. Edwards, D. L. Hill, J. A. Little, and D. J. Hawkes, *Med. Image Anal.*, 1998, **2**, 355.
37. K. D. Paulsen, M. I. Miga, F. E. Kennedy, P. J. Hoopes, A. Hartov, and D. W. Roberts, *IEEE Trans. Biomed. Eng.*, 1999, **46**, 213.
38. D. A. Leung, J. F. Debatin, S. Wildermuth, N. Heske, C. L. Dumoulin, R. D. Darrow, M. Hauser, C. P. Davis, and G. K. Schulthess, *Radiology*, 1995, **197**, 485.
39. S. Wildermuth, J. F. Debatin, D. A. Leung, C. L. Dumoulin, R. D. Darrow, G. Uhlschmid, E. Hoffman, J. Thyregod, and G. K. von Schulthess, *Radiology*, 1997, **202**, 578.
40. H. J. Aronen, I. E. Gazit, and D. N. Louis et al., *Radiology*, 1994, **191**, 41.
41. H. F. Aronen, J. Glass, F. S. Pardo et al., *Acta Radiol.*, 1995, **36**, 520.
42. J. D. Hazle, E. F. Jackson, D. F. Schomer, and N. E. Leeds, *JMRI*, 1997, **7**, 1084.
43. R. B. Schwartz, L. Hsu, D. F. Kacher et al., *JMRI*, 1998, **8**, 1085.
44. R. Kikinis, P. L. Gleason, T. M. Moriarty, M. R. Moore, E. Alexander III, P. E. Stieg, M. Matsumae, W. E. Lorensen, H. E. Cline, P. M. Black, and F. A. Jolesz, *Neurosurgery*, 1996, **38**, 640.
45. M. F. Nitschke, U. H. Melchert, C. Hahn, V. Otto, H. Arnold, H. D. Herrmann, G. Nowak, M. Westphal, and K. Wessel, *Acta Neurochir. (Wien)*, 1998, **140**, 1223.

Biographical Sketches

Terence Z. Wong. *b* 1955. B.S.E. biomedical engineering, 1977, Duke University, M.D. and Ph.D., 1990, Dartmouth College and Dartmouth Medical School. Residency in Diagnostic Radiology, Deaconess Hospital, Harvard Medical School, 1992–96, Fellowship in Nuclear Medicine, Deaconess Hospital 1995–96, Fellowship in Cross-sectional Imaging, Beth Israel Deaconess Medical Center 1996–97, Fellowship in Interventional MRI, Brigham and Women's Hospital 1997–98. Assistant Professor of Radiology, Assistant Professor of Radiation Oncology, and Assistant Professor of Biomedical Engineering, Duke University Medical Center 1998–present. Current research interests: image-guided therapy, multimodality metabolic and functional imaging, selective oncologic imaging and therapy, thermal therapy.

Richard B. Schwartz. *b* 1956. B.S., 1978, M.D., 1982, Ph.D., 1985, Neuroanatomy, University of Pennsylvania, USA. Neuropathology internship, Tufts-New England Medical Center, Boston MA, 1984–85. Radiology residency, Brigham and Women's Hospital, Boston MA, 1985–89. Neuroradiology fellowship, Brigham and Women's Hospital, Boston MA, 1989. Certificate of Additional Qualification, 1996. Instructor, assistant professor, and associate professor of radiology, Harvard University, 1989–present. Assistant Director of the Neuroradiology division, Brigham and Women's Hospital, Boston MA, 1992–present. Director of Functional and Navigational Neuroimaging, 1999. Approx. 80 publications in CT, MR and SPECT scanning of the brain. Current research interests: intracranial intervention under MR guidance, acute hypertensive disorders of the brain, neurovascular applications of spiral CT, and functional imaging of brain tumors using MR and SPECT.

Arya Nabavi. *b* 1966, M.D. University of Kiel/Germany. Neurosurgeon, Research Fellow at the Department of Neurosurgery, Brigham and Women's Hospital, Harvard Medical School. Current research interests: application of MR in neurosurgery, image-guided surgery, intraoperative brain deformations.

Richard S. Pergolizzi Jr. *b* 1964. B.Sc. Chemistry, 1987, The State University of New York at Stony Brook, M.D. 1993, Northeastern Ohio Universities College of Medicine. Residency in Diagnostic Radiology at University of Cincinnati, University Hospital 1993–97, Fellowship in Neuroradiology, University Hospital Health Science Center, Syracuse NY 1997–98, Fellow in Neurointerventional Radiology, Brigham and Women's Hospital and Massachusetts General Hospital, Harvard University, 1998–present. Current research interests: clinical applications for MR image-guided therapy.

Peter M. Black. *b* 1944, A.B., 1966, Harvard College, M.D. 1970 McGill University, Montreal, Canada, Ph.D., 1978, Georgetown University, USA. Research fellow in Neuro-oncology, Massachusetts General Hospital, 1976, Asst. Professor of Surgery, Harvard Medical School, 1980–84, Associate Professor of Surgery, Harvard Medical School, 1984–86. Franc D. Ingraham Professor of Neurosurgery, Harvard Medical School, 1987–present. Neurosurgeon-in-Chief, Brigham and Women's and Children's Hospitals, 1987–present. Chief of Neurosurgical Oncology, Dana Farber Cancer Institute, 1987–present. Chairman of the Board, Brain Tumor Center, BWH, CH, DFCI, 1988–present. Chairman, Department of Surgery, CH, 1994–98. More than 40 visiting professorships and lectureships. Approx. 155 original articles, 7 books, 150 reviews and book chapters, and several clinical communications. Current major research interests: advanced imaging techniques for surgery including the intraoperative MRI and brain mapping, and in the laboratory, molecular biology of brain tumors, specifically the relation between glial development and glioma formation, and hormonal influences on meningioma progression.

Eben Alexander III. *b* 1953. A.B., 1975, Chemistry, University of North Carolina, Chapel Hill. M.D., 1980, Duke University School of Medicine, Durham, North Carolina, Intern in General Surgery, Duke University Medical Center, 1980–81. Resident, Neurological Surgery,

Duke University Medical Center, 1981–83. Research Fellow in Neurosurgery, Massachusetts General Hospital, Harvard Medical School, 1983–84. Acting Resident in Neurology, Massachusetts General Hospital, Boston, Massachusetts, 1985. Resident in Neurological Surgery, Duke University Medical Center, 1985–87. Senior Registrar and Cerebrovascular Fellow, Neurosurgical Service, Newcastle General Hospital, Newcastle-Upon-Tyne, England, U.K., 1987. Instructor in Surgery, Brigham and Women's Hospital, Harvard Medical School, Boston, Massachusetts 1988–90. Assistant Professor of Surgery (Neurosurgery), 1990–94, and Radiation Oncology, Harvard Medical School, 1990–99. Associate Professor of Surgery (Neurosurgery), Harvard Medical School, 1994–99. Director of the Stereostatic and Functional Neurosurgery Program, Brigham and Women's Hospital. Approx. 150 publications in neurosurgery, especially radiosurgery and image-guided surgery. Current research speciality: development of advanced synergistic radiation and surgical techniques through image-guidance.

Claudia H. Martin. *b* 1959. B.Mus., 1984, M.D., 1988, McGill University, Canada: Surgical Internship. Yale University, New Haven, 1989–90, NIH postdoctoral fellow in neurosurgery, Bethesda, Maryland, 1990–91, Neurosurgery resident, Yale University, New Haven, 1991–95, Neurosurgery clinical fellow, Brigham and Women's Hospital, Harvard University, Boston, 1996–99. Chief resident Brigham and Women's Hospital, Boston, 1999–2000. Approximately 10 publications in image guided neurosurgery.

Ferenc A. Jolesz. *b* 1946. M.D., 1971, Semmelweis Medical School, Hungary. Resident in Neurosurgery, Medical School Pecs, Hungary, 1971–72. Research Fellow, Biomedical Engineering Computer Sciences, K. Kando College, Hungary, 1972–73. Resident in Neurosurgery, Institute of Neurosurgery, Hungary, 1975–79, Research Fellow, Neurology, Massachusetts General Hospital, Boston, MA, 1979–80, Milton Research Fellow, Physiology, Harvard Medical School, Boston, MA, 1980, Research Fellow, Physiology, Harvard Medical School, Boston, MA, 1980–81, Research Associate, Physiology, Harvard Medical School, Boston, MA, 1981–82, Resident, Radiology, Brigham and Women's Hospital, Boston, MA, 1982–85, Assistant Professor, Radiology, Harvard Medical School, Boston, MA, Director, Neuro MR Imaging Section, Brigham and Women's Hospital, Boston MA, 1987–88, Director, Division of Magnetic Resonance Imaging, Brigham and Women's Hospital, Boston, MA, 1988, Associate Professor of Radiology, Harvard Medical School, Boston, MA, 1989–96, Director, Image-guided Therapy Program, Brigham and Women's Hospital, Boston, MA, 1993–present. Professor of Radiology, Harvard Medical School, Boston, MA, 1996. B. Leonard Holman Professor of Radiology, Harvard Medical School, Boston, MA, 1998. Member of the Institute of Medicine, National Academy of Sciences. Approx. 200 publications. Current research speciality: interventional and intraoperative MRI, quantitative neuroimaging, focused ultrasound surgery.

Temperature Measurement In Vivo Using NMR

Ian R. Young
The Robert Steiner MRI Unit, Hammersmith Hospital, London, UK

1 INTRODUCTION

Philosophically, the desirability of using imaging to monitor therapy as it happens seems indisputable, with the potential this offers for reducing any uncertainty in treatment and for permitting adjustment of treatment as it proceeds to optimize outcome. Allied to the advantages of minimally invasive therapy – reduced patient trauma, shorter duration in hospital – the case for imaging in conjunction with the ablative therapies has seemed excellent. In this respect, because MR has so many potentially useful temperature dependencies, which might allow quantitative measurement of what is happening, it has seemed the modality of choice, and significant research effort has been expended in efforts to convert that perception to reality.

Most of this work has gone into attempts to exploit the thermal dependencies of T_1 and the chemical shift of water; a much smaller resource has been applied to the temperature sensitivity of the diffusion coefficient. Attempts to use T_1 changes have included studies of the relaxation behavior of other nuclei than hydrogen; while chemical shift strategies have employed spectroscopy as well as imaging techniques. All of these approaches will be reviewed in the article. Each method will be covered in a brief section that will include a description of attempts made to use it.

2 TARGETS OF PERFORMANCE FOR IN VIVO TEMPERATURE MEASUREMENT

A prime concern in thermal ablations is to control the extent of any unwanted damage to normal tissue around the lesion being treated. While the temperature in the target region for the ablation may well exceed 60°C, and there is little need to measure its actual level with great accuracy, it is important that temperatures of up to perhaps 45°C be observed with some precision. If precedents from low-temperature rf hyperthermia are applied (in which considerable care was exercised to avoid collateral damage) then the targets for measurement are:[1] temperature accuracy of ±0.5°C, volume of interest 5 mm^3, and temporal resolution of 30 s.

Temporal resolution is desirably substantially better in therapies such as focused ultrasound, where significant quantities of energy can be deposited in a small volume very quickly, with consequently swift changes in temperature. Spatial resolution cannot be allowed to deteriorate significantly as tissue can support quite considerable temperature gradients (certainly in the range of 5°C cm^{-1} or more).

3 TEMPERATURE DEPENDENCE OF T_1

Theory predicts a relationship between temperature and T_1 of the general form:

$$\frac{1}{T_1}\alpha\frac{\eta}{T} \tag{1}$$

where η is the macroscopic viscosity, and T the absolute temperature.

Over the limited temperature excursions of tissue temperature for which real accuracy is important (see above), there is effectively a linear relationship between T_1 and T. Energy level considerations predict a temperature coefficient of around 1.3% $°C^{-1}$ for sensitivity of the measurement of T_1 for water;[2] because this approach to the measurement has been perceived as being the simplest of those that are available, it was the first approach to be investigated.[3,4]

The usual approach that has been adopted[4] is to acquire a short *TE* spin echo, or gradient recalled echo, image with long *TR* for use as a reference (data set A), then follow this with short *TR* data acquisitions using the same *TE* as before whenever needed (data set B). From this T_1 is calculated using the relationship:

$$\frac{S_B}{S_A}=\frac{1-\exp(-TR_B/T_{1B})}{1-\exp(-TR_A/T_{1A})} \tag{2}$$

when S_A and S_B are the respective signals from the two data sets; T_{1A} and T_{1B} are the T_1 values at the times of the A and B acquisitions; and TR_A and TR_B are the respective *TR* values. The methods has been successfully evaluated many times in phantoms and in vitro.[5–7]

However, it is clear that the relationship in Equation (2) is defective in at least one respect – it assumes that the intrinsic signal is independent of temperature, which, via the Curie relationship, it is not:[8]

$$M=\frac{N\gamma^2\hbar^2 I(I+1)}{3kT}H_o=\chi_o H_o \tag{3}$$

where M is the magnetization arising from an applied field H_o, χ_o is the nuclear susceptibility, N Avogadro's number; γ, $\hbar$ and k are, respectively, the gyromagnetic ratio, Planck and Boltzman constants; I is the spin quantum number.

More exactly, Equation (2) should include an extra ratio on its right-hand side (M_B/M_A) where M_A and M_B are the respective tissue magnetizations; this effectively reduces to (T_B/T_A) using Equation (3), and allowing for the possibility that T_2 is also temperature sensitive, though it seems to be only weakly so in near-normal tissue;[9] consequently, the ratio in Equation (2) becomes

$$\frac{S_A}{S_B}=\frac{T_A}{T_B}\frac{(1-\exp(-TR_{1B}/T_{1B}))\exp(-TE/T_{2B})}{(1-\exp(-TR_{1A}/T_{1A}))\exp(-TE/T_{2A})}. \tag{4}$$

The problems of obtaining an accurate measurement are compounded by other changes that are likely to take place during actual therapy. For example, when tissue is cooled[10] or heated during thermal ablation,[11] it can swell, and this can affect the measurements still further. As noted by Young et

al.,[12] the type of relationship that can be required to describe the changes with real precision (even if a two-component system (*p*, *r* subscripts) only is used) can become very complex, as illustrated by Equation (5).

$$\frac{S_{\mathrm{B}}}{S_{\mathrm{A}}} = T_{\mathrm{A}}/T_{\mathrm{B}} \frac{\left\{x_{\mathrm{B}}\left(1-\exp\left(\frac{-TR_{\mathrm{B}}}{T_{1\mathrm{B}p}}\right)\right)\exp\left(-\frac{TE}{T_{2\mathrm{B}p}}\right) - (1-x_{\mathrm{B}})\left(1-\exp\left(-\frac{TR_{\mathrm{B}}}{T_{1\mathrm{B}r}}\right)\right)\exp\left(-\frac{TE}{T_{2\mathrm{B}r}}\right)\right\}}{\left\{x_{\mathrm{A}}\left(1-\exp\left(\frac{-TR_{\mathrm{A}}}{T_{1\mathrm{A}p}}\right)\exp\left(-\frac{TE}{T_{2\mathrm{A}p}}\right) - (1-x_{\mathrm{A}})\left(1-\exp\left(-\frac{TR_{\mathrm{A}}}{T_{a\mathrm{A}r}}\right)\right)\exp\left(-\frac{TE}{T_{2\mathrm{A}r}}\right)\right\}} \tag{5}$$

where x is the effective NMR visible fraction of component p present – which is, of course, temperature sensitive itself. Note that x is, using this definition, not, in general, the actual physical fraction of p that is present and so cannot be assessed by purely analytical methods. The potential impact of temperature changes on the fraction of the hydrogen nuclei in a component that actually contribute usefully to the NMR signal is another matter altogether.

Clearly such relationships contain so many variables that can only be known with low, if any, precision at all that T_1 cannot provide an accurate temperature scale within the requirements noted in Section 2.

Figure 1 gives some measure of the impact of these complexities on the measurement temperature in human calf muscle, in an experiment in which the tissue was cooled using water circulated through bags on either side of the leg.[12] The curve $T_{1(\mathrm{R})}$ was plotted from the data set assuming the relationship in Equation (2) was valid, and that the reference measurement (A) was made initially and not checked thereafter. The resultant coefficient of T_1 versus temperature is rather larger (at about 1.6% $^{\circ}\mathrm{C}^{-1}$) than would be expected. The second T_1 set of data ($T_{1(\mathrm{N})}$) was plotted using Equation (2) again, but, using long and short *TR* data taken at the same temperature; consequently, to an adequate extent T_{A}=T_{B}, and the relationship (ignoring the possibility of there being other components) is tractable. The third curve (proton density) reveals what is happening. It is a plot obtained from the long *TR* data only, which shows that this is changing at around 1% $^{\circ}\mathrm{C}^{-1}$, indicating the possible formation of edema and/or increased tissue perfusion. Equation (2) does not then reflect what is happening, and the very low coefficient of T_1 dependence on temperature obtained using it (and plotted as $T_{1(\mathrm{N})}$) is not a true value. The value of T_2 was assumed to be unaffected by temperature in this work.

Nevertheless, the changes associated with variation in T_1 are easy to demonstrate using TurboFLASH or similar sequences,[5,6] which are available on most scanners. These are probably capable, for example with methods in which the local temperature can be changed very rapidly, such as focal ultrasound,[13] of a measurement accuracy in the range 3–5°C. As such, they may well not be capable of providing useful data to help to avoid collateral damage, though it will be possible to use them to make sure the temperature of a target region has exceeded a lethal level for cells present there.

4 TEMPERATURE DEPENDENCE OF T_2

The possibility of T_2 being the basis of a temperature scale has been previously noted, through largely discounted. It does not seem to have a useful dependence in vivo in near normal tissue[9] and has been little investigated as such. There is, however, one circumstance when it could be very significant. This

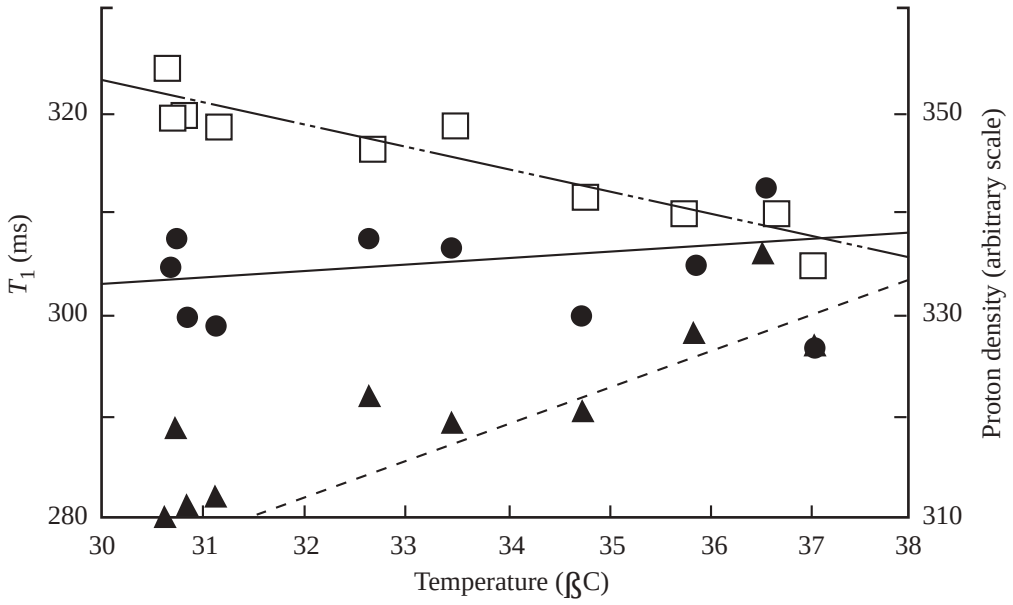

Figure 1 Temperature and proton density from a region of calf muscle undergoing temperature stress in a volunteer. The curves fitted to the points are $T_{1(\mathrm{R})}$ (▲), $T_{1(\mathrm{N})}$ (●) (both left-hand scale), and proton density curve (□). (Reproduced with permission from Young et al., *Magn. Reson. Med.*, 1994, **32**, 366.)

is in cryoblation, where its application has been extensively studied.[14] The problem with this approach is that it is not sufficient just to freeze the tissue in order to damage it; the temperature must be reduced substantially below 0°C. Conventionally, it would be assumed that once the tissue had solidified no further useful MRI signals would be obtained, and any attempts at tracking further temperature changes would need to be done by computer modeling.[15] However Daniel et al. showed how it is possible to use variations in T_2 of the unfrozen water fraction in the tissue as a means of monitoring temperature.[14]

5 TEMPERATURE DEPENDENCE OF THE DIFFUSION COEFFICIENT

Le Bihan et al. were the first to propose the temperature dependence of the diffusion coefficient as a viable in vivo scale, pointing out that its theoretical sensitivity is usefully larger (at 2.2% $^{\circ}C^{-1}$) than that of T_1.[2] The relationships they exploited are simple. Data from the sequences (A and B) with differing degrees of diffusion weighting (b) are used. If, as before, the signals for these are S_A and S_B respectively, and the diffusion weightings are, respectively, b_A and b_B then, in more complete form:

$$\frac{S_B}{S_A} = \frac{M_B}{M_A} \frac{\left(1 - \exp\left(-\frac{TR}{T_{1B}}\right)\right)\exp\left(-\frac{TE}{T_{2B}} - b_B D(T_B)\right)}{\left(1 - \exp\left(-\frac{TR}{T_{1A}}\right)\right)\exp\left(-\frac{TE}{T_{2A}} - b_A D(T_B)\right)} \quad (6)$$

where $D(T)$ is the diffusion coefficient at the temperature at which the measurements were acquired. From this, b is given by:

$$b = \gamma^2 G^2 \delta^2 \left(\frac{\Delta}{3} - \delta\right) \quad (7)$$

where γ is the gyromagnetic ratio, G is the gradient strength in each of two identical pulses of effective duration δ and having their leading edges Δ apart in time, using the classic pulsed gradient spin echo (PGSE) experiment of Stejskal and Tanner.[16] If both data acquisitions are made at substantially the same temperature (as described in Cline et al.[13]) then Equation (6) can be simplified to:

$$\frac{S_B}{S_A} = \exp(D(T)(b_A - b_B)) \quad (8)$$

In vivo applications of the use of diffusion weighting to monitor temperature are few and far between,[9,17] though the implementation now of echo planar imaging (EPI)[18] in many machines may change that. Diffusion experiments are notoriously vulnerable to motion artifact, and rapid acquisition of data is highly desirable. As with T_1, phantom and in vitro data yield very good calibrations of D versus T.

Unfortunately, it is probable that some of the problems noted in connection with T_1 measurement will also affect diffusion-weighted studies. Diffusion in tissue is anisotropic;[19] as a result, the changes in edema and/or perfusion already noted will cause variations in the observed value of D that are not necessarily related to temperature at all. It is possible that calculating the full diffusion tensor[20] may allow variations caused by temperature change to be sorted out from those resulting from tissue structure alterations, but this has yet to be demonstrated, and, at best, will require more images (12, in two sets of 6 at least) to be obtained at each temperature.

6 TEMPERATURE DEPENDENCE OF THE CHEMICAL SHIFT OF WATER

Hindman first demonstrated, and characterized, the chemical shift of water as a means of measuring its temperature.[21] He suggested that the small effect he observed (of the order of -0.0108 ppm $^{\circ}C^{-1}$) was the result of temperature dependence of the shielding constant of the electrons in the water molecule. He based his analysis on the relationship:

$$\sigma_i = \sigma_o + \sigma_d + \sigma_a + \sigma_F \quad (9)$$

where σ_i is the total shielding constant, σ_o is the intramolecular shielding constant for an atom in an isolated molecule, σ_d is the bulk diamagnetic susceptibility component, σ_a is shielding caused by anisotropy in the susceptibility of neighboring molecules, and σ_F is the contribution to the shielding by local electric field effects. Some of these component contributions are temperature sensitive.[21]

This phenomenon was ignored in human MR terms until Ishihara et al. revived interest in it.[22] Since then it has been exploited in two quite different ways: through imaging and through spectroscopy. These will be discussed separately below.

6.1 Approaches Using MRI to Exploit the Temperature Dependence of the Chemical Shift of Water

The method Ishirara et al. proposed involved observing the phase differences in the image data as the temperature varied.[22] The experiment is a gradient recalled echo (GRE) system in which TE (the echo time) is extended to obtain the necessary sensitivity for the desired temperature scale. If $\omega(T)$ is the temperature-dependent resonant frequency of the water, the phase difference developed between the signals at two different temperatures, ($\Delta\varphi_T$), assuming nothing else is changed, is:

$$\Delta\varphi_T = (\omega T_B - T_A)TE = k(T_B - T_A) \quad (10)$$

where k is the phase coefficient of temperature for the sequence and field used.

If the aim is a measurement accuracy of 0.5°C, then the desirable phase shift sensitivity should be no less than perhaps 30°C per 360° of phase if the phase noise is in the range 3–4°. Even in a 1.5 T magnet (remembering that $\omega=\gamma B_o$) this means that TE has to be around 48 ms. The practicality of the method has been demonstrated at a variety of fields, including as low as 0.2 T,[23] but it is, at the least, a technique that makes substantial demands on machine performance.

A major issue is the possibility of susceptibility effects, which can arise from the tissue itself or as artifacts from neighboring objects.[24] A very small susceptibility difference indeed is sufficient to cause substantial errors. If $\Delta\psi$ is an effective susceptibility change that develops, then the phase error caused by it is:

$$\Delta\varphi_s = \gamma\Delta\psi B_o TE \tag{11}$$

De Poorter et al. were concerned about the nature of possible chemical shift-like changes in lipid-rich tissue as well as in water-based ones,[25] but, in practice, effects in fatty tissues seem to be minimal and, indeed, as will be described in the next section, can even be used as a reference.

Since the effects sought are so small, correction for various machine drifts is normally essential.[26] This can be done by a variety of methods but involves at least one means of monitoring any drift in the B_o field. This can be done by phantoms, the temperature of which is controlled, or, in principle, by other methods.

Figure 2 is a phase map typical of those obtained during temperature measurement experiments. The image shows a volunteer's calf muscle during cooling by water pads, which can be seen on either side of the leg. These appear black since, in the image, calculated from an initial data set obtained prior to cooling and one taken as the leg temperature was dropped, the temperature of the water in the pads is much lower than it was at the start of the experiment. The phantoms used to enable corrections for field drift to be made are apparent round the leg. They are insulated from the cooling pads, and the temperatures of two of them were monitored. The fat in the tissue retains the mid-gray color indicative of no phase change, while the muscle near the pads inside it is colder than it was at the start.

The data in Figure 2 were generated using a protocol involving stabilization of the leg temperature at around 37°C for 30–40 min followed by a rapid reduction in the temperature demand for the water in the pads to 5°C. This command was followed by the water temperature with some delay; consequently when the temperature was reset to 37°C again, typically after 1 h, it had reached a minimum temperature of perhaps 10°C. After resetting, the leg was monitored for a further 40 min. Optical probes on the phantom, on the surface of the skin, and implanted in the muscle under the pads to a depth of 15 mm were used to monitor temperature (Luxtron 3000, Luxtron Inc., Santa Clara, CA, USA).

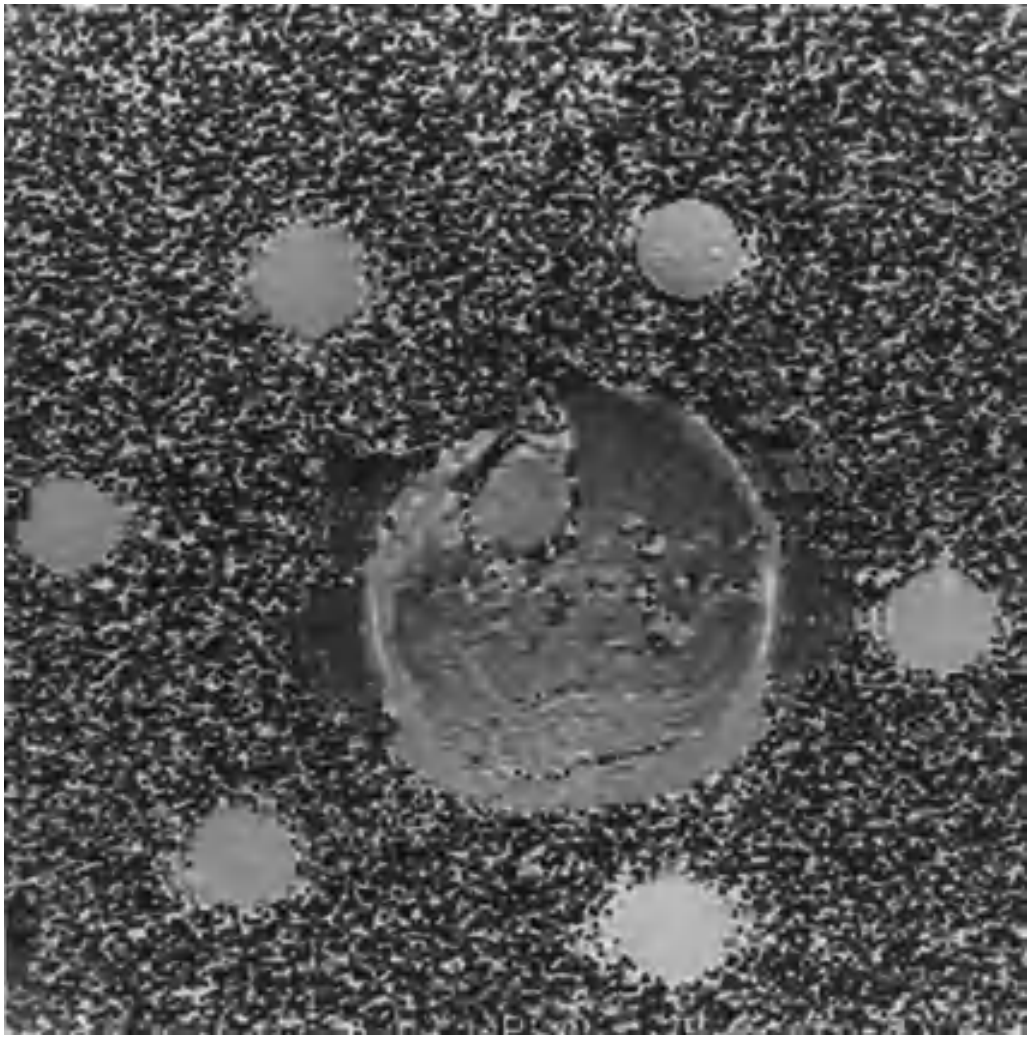

Figure 2 Image of a phase map of a leg of a volunteer during cooling. The phantoms and fat retain the mid-gray tone indicative of a very small change in phase, while the water pads (seen outside the leg) are very black, as the water is very cold. The muscle temperature has been reduced to some degree. (Reproduced with permission from Young et al., *Magn. Reson. Med.*, 1994, **36**, 369.)

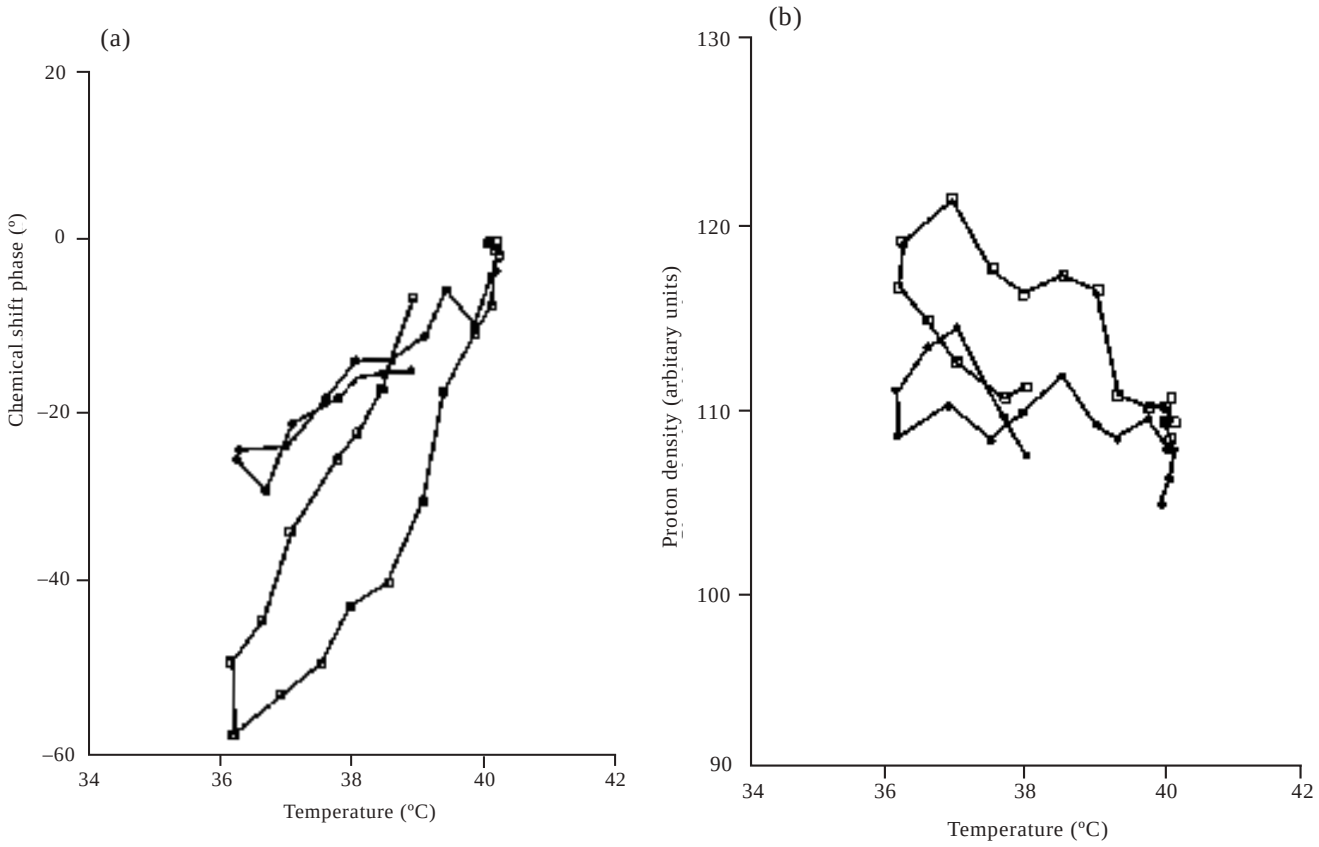

Figure 3 The effect of temperature cycling in a volunteer's calf muscle. Data were obtained from directly under a cooling pad, in the muscle (□) and at the top of the leg in muscle but not directly cooled (●). (a) Chemical shift of water versus temperature; note the hysteresis observable in these data. (b) Proton density values at changing temperature. (Reproduced with permission from Young et al., *Magn. Reson. Med.*, 1994, **36**, 372.)

This temperature cycling produced results of which those shown in Figure 3 are typical. Data from two points are shown: one under one of the pads, and the other at the top of the leg away from any direct cooling. Two pairs of curves are shown, those in Figure 3a being the chemical shift data, while Figure 3b shows proton density data analogous to that shown in Figure 1. It is apparent that the data from the point under the pads both show an unexpectedly large change in phase (as the likely expected change at 1 T with a *TE* of 60 ms was about 9.3° phase $^{\circ}C^{-1}$) and also reveals marked hysteresis. The proton density data from the same region also shows substantial changes, and hysteresis. Both sets of data from the other point are much more convincing. Because of suspicions about possible changes in the blood content of the tissue as the body responded to the cooling, it was thought that such changes could have been caused by susceptibility differences,[26] though later data (see below) suggests this may well not be correct. The hysteresis effects in the chemical shift phase data are not easy to explain if this factor is excluded; however it seems likely that it will involve changes in the lipid content of the voxels owing to physical movements and composition changes arising as the tissue swells. Since the chemical shift of lipids is around 3.5 ppm relative to water, first sight suggests that small alterations only are needed to explain errors in a measurement where the scale is -0.0108 ppm $^{\circ}C^{-1}$.

However, though the scale differences are dramatic, the worst case occurs when the lipid and water components are out of phase by 90 or 270°C, and the many Hertz differences between the two resonant frequencies cannot cause larger errors than those angular differences allow.

If the fraction of lipid components in a voxel is initially δ_A and ultimately δ_B at the same time as the temperature changed from T_A to T_B, at which values the observed phase differences (relative to a starting reference value) were φ_A and φ_B and *TE* was such that the lipid component was initially 90° out of phase with the water signal, then

$$\varphi_A - \varphi_B = \frac{(1-\delta_B)\sin kT_B + \delta_B \sin\alpha}{(1-\delta_B)\cos kT_A + \delta_B \sin\alpha} - \frac{(1-\delta_A)\sin kT_A + \delta_A \sin\alpha}{(1-\delta_A)\cos kT_A + \delta_A \sin\alpha} \qquad (12)$$

which simplifies to:

$$\varphi_A - \varphi_B = (k(T_B - T_A) + \frac{\delta_B - \delta_A}{(1-\delta_B)(1-\delta_A)} \qquad (13)$$

if it is assumed that kT_A and the δ values are small; α is the phase angle difference between the two components determined by the sequence.

Equation (13) suggests that the involvement of lipid changes cannot be the only, or even, it is likely, the dominant cause of the calibration errors observed. The fractional change in the

value of δ would need to be too large for this, for example a 1% change in δ (from 4 to 5%) would result in a change of perhaps 0.6° of phase. At this time, the phenomena seen in Figure 3a have no convincing explanation.

While the true accuracy of the chemical shift method in vivo may not be as good as the many phantom experiments using it have suggested, nevertheless it is a reliable indicator of larger temperature changes and is being studied by a number of groups to this end.[27,28]

6.2 Chemical Shift Temperature Measurements Using MRS

Cady et al. were the first to suggest using the chemical shift of water to measure temperature in vivo using spectroscopic rather than imaging methods.[29] They exploited earlier in vitro data which showed that many metabolites other than water had no temperature coefficient of chemical shift;[30] as a result, their signals could be used as internal references in human studies. If there was to be susceptibility, or small main field alterations, this would affect the reference moieties as well as the water, and any differences in the chemical shift of the latter could be readily assigned to temperature changes.

While Cady et al. were interested in measuring the temperature of the neonatal brain during hypothermia to stabilize infants who had been seriously brain damaged at birth,[29] the data to be described here were obtained from volunteer calf muscle using the same kind of protocol as described previously.[31]

Typical examples of the data obtained from the spectroscopic studies are shown in Figure 4. Figure 4a shows a typical spectrum and illustrates some of the problems with the method. Since the water peak is essential for the measurement and since its phase and chemical shift are key issues, it cannot be suppressed, and *TE* has to be long enough to allow it to be very substantially attenuated relative to the signals of any long T_2 moieties that might act as a reference (or source of comparison). This attenuation has to be sufficient for the dynamic range of the data to be les than that of the receiver system in the spectrometer, with inevitable attenuation of other signals and a relatively poor signal-to-noise ratio. In spite of these problems, performance is good enough for the results shown in Figure 4b to be obtained. This shows data from several other moieties, creatine, choline and lipid (a number of partly resolved peaks treated as a single entity), as well as water. Analysis by Young et al. shows that these components are really very stable, suggesting that susceptibility changes were not a factor in this instance and that the impact of tissue swelling, which occurred as usual in the experiment from which these data were obtained, was minimal using this strategy.[31]

The data shown in Figure 4 were derived from a voxel 15 mm^3 in size, with a temporal resolution of 7–8 min. In both these respects, it fails the criteria discussed in Section 2. Detailed analysis of imaging data overlapping the spectroscopic region of interest showed the same type of pattern that is illustrated in Figure 3.

Spectroscopy appears, on the basis of relatively skimpy data,[29,31,32] to have robustness for use as a thermal scale that is lacking in the imaging data. At least partly this is because of the large voxel (with the much greater spatial averaging inherent in its use). It is interesting to speculate on how, and if, the two approaches can be used to support each other to produce data that both are accurate and have adequate temporal and spatial resolutions.

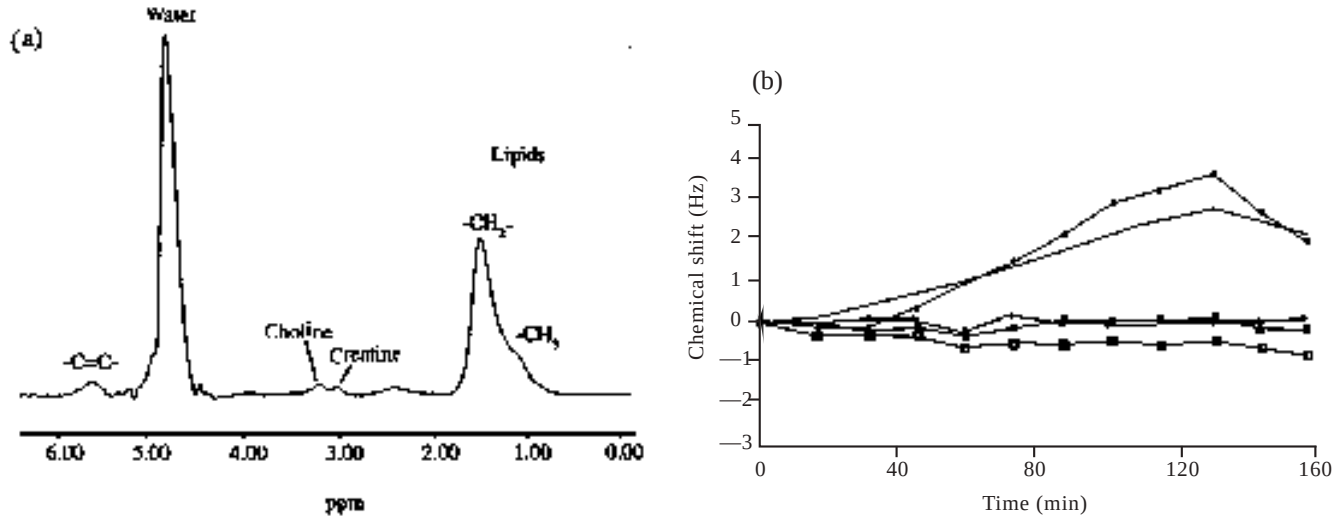

Figure 4 Magnetic resonance spectroscopy of temperature changes in a volunteer's calf muscle. (a) Spectrum obtained in the study. The small amplitude of the creatine and choline peaks relative to the water and lipid one is very obvious. (b) Plots of the chemical shift of a number of moieties against temperature. The continuous line is the chemical shift that might be expected from modeling the temperatures to be expected in the tissue using the thermoheat Equation (15), then assuming that the temperature coefficient of chemical shift of muscle is the same as that of water. The chemical shift change for water (●) is derived from the data. The minimal chemical shift of the creatine (■), choline (□) and lipid (▶) peaks versus temperature is very apparent. (Reproduced with permission from Young et al., *JMRI*, 1998, **8**, 1116, 1117.)

7 VARIATIONS IN T_1 OF NUCLEI OTHER THAN HYDROGEN

Many components, such as the chemical shift of methyl groups in complex molecules including paramagnetic nuclei, vary with temperature, and suggestions have been made as to their utility for temperature measurement.[33,34] The fluorocarbons also have properties that can be exploited,[35] though, in this case, the T_1s of the fluorocarbon lines are also pH sensitive. The relationship between the various quantities is of the form:

$$1/T_1 = A + B(pH) + CT + D(pH)T \qquad (14)$$

where A, B, C, and D are constants for any one spectral line; T is the absolute temperature, and (pH) is the tissue pH. As described by Mason et al., from a spectroscopy experiment, the behavior of the multiple lines can allow the solution of a set of simultaneous equations and resolve the differences between changes caused by temperature and pH.[35]

As yet none of the methods suggested has been used in vivo.

8 IMAGE PROCESSING

A problem with temperature measurement in vivo, which distinguishes it from any phantom experiment, is that tissue is mobile and responds to thermal stress by a range of potential changes. Without identifying its source, cooling the leg, for example, results in swelling of the tissue. Then, if no action is taken, the tissue content of a region of interest in a voxel determined by the machine gradients, and not adjusted in any way, will change continuously. It is not surprising, therefore, that content variations can result in substantial errors in small voxels, with relatively low signal-to-noise ratio, and be less apparent in the much larger voxels used in spectroscopy.

The extent of the effects is demonstrated in Table 1 (line 1) and the results of the efforts to improve the situation using registration are described by Hajnal et al.,[36] while data correction using other strategies is described by Saeed et al.[37] The latter includes attempts to track the mean intensity of the voxel by selecting a closest local match to the standard deviation of the original gray-scale voxel. Another variant combined that approach with a best match to distances from a number of landmarks surrounding it.

All the data in Table 1 are from a T_1 experiment, and it is clear that though substantial image processing can improve matters, it does not transform the situation completely.

9 CONCLUSION

Temperature measurement in vivo using MRI and MRS has become a matter of considerable interest to the scientific community, particularly since the usefulness of interventional MRI has come to be appreciated. It seems unlikely that it will reach the performance target suggested in Section 2 of this article. However, if the temperature target were to be reduced so that the accuracy were to be ±3°C, then it is likely that MRI will become of real value as a temperature measurement. This will not allow as much appreciation of the risks, and extent, of collateral damage to normal tissue round a target lesion as is desirable. If this is acceptable clinically, then we can look forward to the increasingly widespread application of direct temperature measurement in interventional MRI.

10 RELATED ARTICLES

Relaxation Measurements in Whole Body MRI: Clinical Utility; Thermal Therapies in the Body Monitored by MRI.

11 REFERENCES

1. International Collaborative Hyperthermia Group, *Int. J. Radiat. Oncol. Biol. Phys.*, 1996, **35**, 731.
2. D. LeBihan, J. Delannoy, and R. L. Levin, *Radiology*, 1989, **171**, 853.
3. D. L. Parker, V. Smith, P. Sheldon, L. E. Crooks, and L. Fusell, *Med. Phys.*, 1983, **10**, 321.
4. R. J. Dickinson, A. S. Hall, A. J. Hind, and I. R. Young, *J. Comput. Assist. Tomogr.*, 1986, **10**, 468.
5. D. L. Parker, *IEEE Trans. Biomed. Eng.*, 1984, **BME-31**, 161.
6. C. J. Hardy, H. E. Cline, and R. D. Watkins, *J. Comput. Assist. Tomgr.*, 1994, **18**, 476.
7. K. Hynynen, A. Darzazanli, E. C. Unger, and J. F. Schenck, *Med. Phys.*, 1993, **20**, 107.
8. A. Abragam, 'The Principles of Nuclear Magnetism', Clarendon Press, Oxford, 1961, pp. 2–53, 289–305, 566–569.
9. A. S. Hall, M. V. Prior, J. W. Hand, I. R. Young, and R. J. Dickinson, *J. Comput. Assist. Tomogr.*, 1990, **14**, 430.
10. I. R. Young, J. W. Hand, A. Oatridge, M. V. Prior, N. Saeed, and G. R. Forse, *Magn. Reson. Med.*, 1994, **31**, 342.

Table 1 Changes in tissues as a result of thermal stress: the level of areas in temperature measurement that is observed in a typical in vivo measurement of T_1 using the temperature protocol described in the text and in Hajnal et al.[36]

Tracking/registration method	Region of interest number[a]					
	A	B	C	D	E	F
No tracking at all	20.0	1.7	13.5	4.8	9.3	10.6
Using registration	6.9	2.8	6.7	5.2	4.6	4.3
Using gray scale matching only	5.6	11.7	16.6	5.1	4.6	6.4
Using gray and landmark tracking	5.6	5.5	16.6	4.2	2.7	6.1

[a]Values for typical regions of interest for the equivalent temperature spread using a temperature coefficient of 1.3% $°C^{-1}$. The maximum true excursion of the temperature was less than 5°C.

11. N. M. deSouza, R. Flynn, G. A. Coutts, D. J. Gilderdale, A. S. Hall, R. Puni, M. Chui, D. N. F. Harris, and E. A. Keily, *Am. J. Roentgenol.*, 1995, **164**, 1429.
12. I. R. Young, J. W. Hand, A. Oatridge, and M. V. Prior, *Magn. Reson. Med.*, 1994, **32**, 358.
13. H. E. Cline, J. F. Schenck, R. D. Watkins, K. Hynynen, and F. A. Jolesz, *Magn. Reson. Med.*, 1993, **30**, 98.
14. B. L. Daniel, K. Butts, and W. F. Block, *Proc. VIth Annu. Mtg. (Int.) Soc. Magn. Reson. Med.*, Sydney, 1998, p. 353.
15. H. H. Pennes, *J. Appl. Physiol.*, 1948, **1**, 93.
16. E. O. Stejskal and J. E. Tanner, *J. Chem. Phys.*, 1965, **42**, 288.
17. D. Morvan, A. Leroy-Willig, A. Malgouyres, C. A. Ceunod, and P. Jehenson, *Magn. Reson. Med.*, 1993, **29**, 371.
18. P. Mansfield, *J. Phys. C., Solid State Phys.*, 1977, **10**, L55.
19. M. E. Moseley, J. Kucharczyk, H. S. Asgari, and D. Norman, *Magn. Reson. Med.*, 1991, **19**, 321.
20. S. Mori and P. C. M. van Zijl, *Magn. Reson. Med.*, 1995, **33**, 41.
21. J. D. Hindman, *J. Chem. Phys.*, 1966, **44**, 4582.
22. Y. Ishihara, A. Calderon, H. Watanabe, K. Okamoto, Y. Suzuki, K. Kuroda, and Y. Suzuke, *Magn. Reson. Med.*, 1995, **34**, 814.
23. S. Sinha, T. Oshiro, U. Sinha, and R. Lufkin, *JMRI*, 1997, **7**, 918.
24. J. de Poorter *Proc. IInd Annu. Mkg. (Int.) Soc. Magn. Reson. Med.*, San Francisco, 1994, p. 426.
25. J. de Poorter, C. de Wagter, Y. de Deene, C. Thomsen, F. Ståhlberg, and E. Achten, *Magn. Reson. Med.*, 1995, **33**, 74.
26. I. R. Young, J. V. Hajnal, I. G. Roberts, J. X. Ling, R. J. Hill-Cottingham, A. Oatridge, and J. A. Wilson, *Magn. Reson. Med.*, 1996, **36**, 366.
27. H. E. Cline, K. Hynynen, E. Schneider, C. J. Hardy, S. E. Maier, R. D. Watkins, and F. A. Jolesz, *Magn. Reson. Med.*, 1996, **35**, 309.
28. T. Harth, T. Kahn, M. Rassek, B. Schwabe, H.-J. Schwarzmaier, J. S. Lewin, and U. Mödder, *Magn. Reson. Med.*, 1998, **38**, 238.
29. E. B. Cady, P. C. D'Souza, J. Penrice, and A. Lorek, *Magn. Reson. Med.*, 1995, **33**, 862.
30. G. Aras, Y.-C. Chang, and M. Barany, *J. Magn. Reson.*, 1985, **63**, 369.
31. I. R. Young, J. D. Bell, J. V. Hajnal, G. Jenkinson, and J. Ling, *JMRI*, 1998, **8**, 1114.
32. R. J. T. Corbett, A. R. Laptook, and P. Weatherall, *Proc. Vth Annu. Mtg. (Int.) Soc. Magn. Reson. Med.*, Vancouver, 1997, p. 403.
33. T. Frenzel, K. Roth, S. Kossler, B. Raduchel, H. Bauer, J. Platzek, and H. J. Weinmann, *Magn. Reson. Med.*, 1996, **35**, 364.
34. S. Aime, M. Botta, M. Fasano, E. Terreno, P. Kinschesh, L. Calabi, and L. Paleari, *Magn. Reson. Med.*, 1996, **35**, 648.
35. R. P. Mason, F. M. Jeffrey, C. R. Malloy, E. E. Babcock, and P. P. Antich, *Magn. Reson. Med.*, 1992, **27**, 310.
36. J. V. Hajnal, N. Saeed, A. Oatridge, E. J. Soar, I. R. Young, and G. M. Bydder, *J. Comput. Assist. Tomogr.*, 1995, **19**, 289.
37. N. Saeed, J. V. Hajnal, A. Oatridge, and I. R. Young, *JMRI*, 1998, **8**, 182.

Acknowledgements

The author would like to acknowledge the help and support of his colleagues and the Robert Steiner MRI Unit, Imperial College School of Medicine, Hammersmith Hospital, London, in the work which comprises the basis of much of the material discussed in this article.

Biographical Sketch

Ian R. Young. *b* 1932. B.Sc., 1954, Ph.D., 1988, Aberdeen. No involvement with NMR until joining EMI in 1976, where charged with leading the engineering group developing first a resistive, then a cryogenic machine. This was installed at Hammersmith Hospital in 1980–1. Approx. 150 papers and 30 patents in whole body NMR and related aspects. Research interests are in obtaining better images and spectra in vivo.

Therapy Monitoring by MRI

D. R. Hamilton, Y. Anzai, K. L. Black, K. Farahani and R. B. Lufkin

UCL School of Medicine, Los Angeles, CA, USA

1	Introduction	1
2	Basic Principles of MR Therapy Monitoring	1
3	Therapeutic Techniques and Clinical Applications	3
4	Specialized Equipment	4
5	Future Directions	5
6	Related Articles	6
7	References	6

1 INTRODUCTION

In its short history, MRI has been championed over X-ray techniques as a noninvasive, noninterventional, diagnostic tool that provides exquisite anatomical detail and soft tissue contrast. Ironically, many of the advantages contributing to the diagnostic success of MRI are now being used to expand the role of MRI into the interventional or therapeutic arena (Figure 1).

1.1 Visualization

Much of surgical technique has been developed to provide exposure or visualization of the surgical field. The actual treatment is often a small portion of the entire procedure compared with the surgical steps necessary for visualization.

MRI has the ability to acquire high-contrast, submillimeter resolution detail in two or three dimensions in any orientation. This feature has been used since the mid 1980s to locate and guide biopsies of deep target tissues with limited accessibility. Stereotactic frames with MR visible markers have traditionally been used to register the target location on the MR images with an external reference. The MR image not only provides an accurate location of the target but also demonstrates the relationship of the target to surrounding vital structures including nerves and vessels using MRA techniques. This information is essential to planning the least invasive trajectory for a biopsy or therapeutic device. Although large-scale clinical acceptance of MR-guided biopsy has been slow due to the high cost and inaccessibility of conventional MR units, the reported clinical applications are growing and now include head and neck, brain, prostate, liver, and mediastinum.[1–7] One new area that is expected to become a large application for MR-guided procedures is the evaluation of breast lesions detected by MR that are invisible on mammography.

Ultrasound and computerized tomography (CT) have been used in the past to guide biopsy procedures. MR provides soft tissue detail superior to CT and higher spatial resolution than ultrasound. The impact of MR guidance on surgical procedures is to reduce both the time required for visualization and the potential for related complications, ultimately improving patient management.

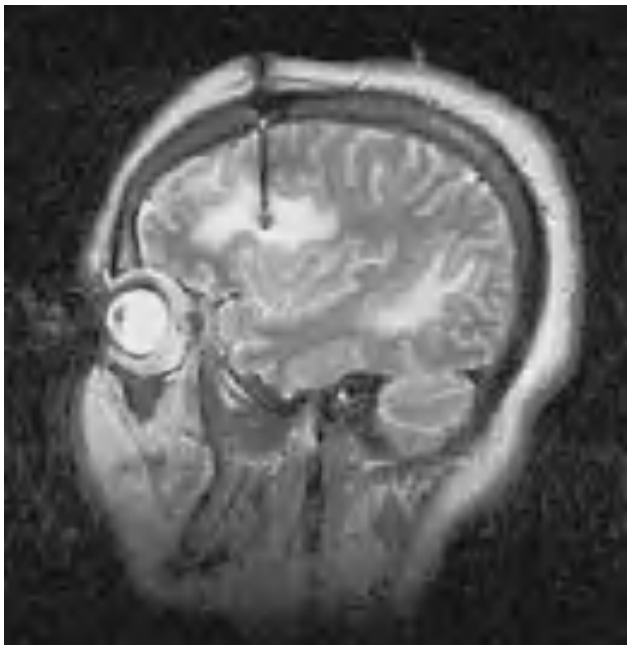

Figure 1 T_2-weighted fast spin echo image demonstrating MR-compatible rf therapy probe placed on target in patient with metastatic brain tumor

1.2 Therapy Monitoring

While facilitated visualization is a key aspect of improving an interventional procedure, MR is uniquely qualified to participate in the therapeutic process itself. Once the probe has been placed on target and the therapy administered, MR imaging can demonstrate thermal changes as well as tissue characteristics secondary to the treatment. Sequential MR acquisition, coupled with image subtraction and display in the examination room, provide an environment in which the therapy session becomes an iterative process. Projects are currently underway to develop accurate and reproducible methods of thermal dosimetry using MR, providing the physician with feedback on therapeutic effect during the procedure.[8]

2 BASIC PRINCIPLES OF MR THERAPY MONITORING

Any imaging technique, by definition, makes use of physical differences between neighboring tissues to create a visual map of tissue interfaces (e.g. density in CT, acoustic impedance in ultrasound, uptake of radioisotope in nuclear medicine, etc.). The MRI signal depends on the structure and dynamics of water–macromolecular interactions. Since these interactions are affected by energy absorption, the MRI technique provides a means of visualizing therapeutic administration.

2.1 T_1 Temperature Monitoring

As a tissue is heated, the distribution and mobility of water and lipid molecules change. These changes alter the tissue relaxation times, T_1 and T_2. T_1 dependence on temperature can be exploited to detect temperature changes during and after therapy using MRI[9] (Figures 2 and 3).

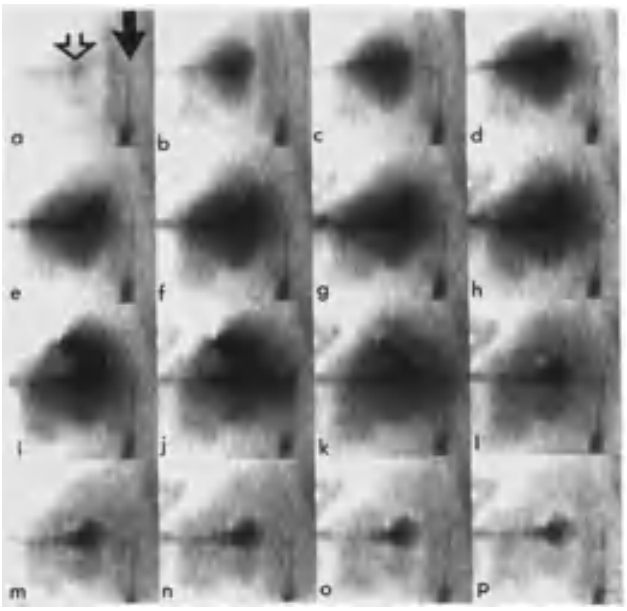

Figure 2 Series of time-lapsed T_1-weighted MR images acquired before (a), every 25 s during (b)–(j), and after (k)–(p) laser irradiation of sheep brain in vitro. Open arrow designates tip of laser fiber optic and bold arrow shows temperature probe 1.5 cm from laser

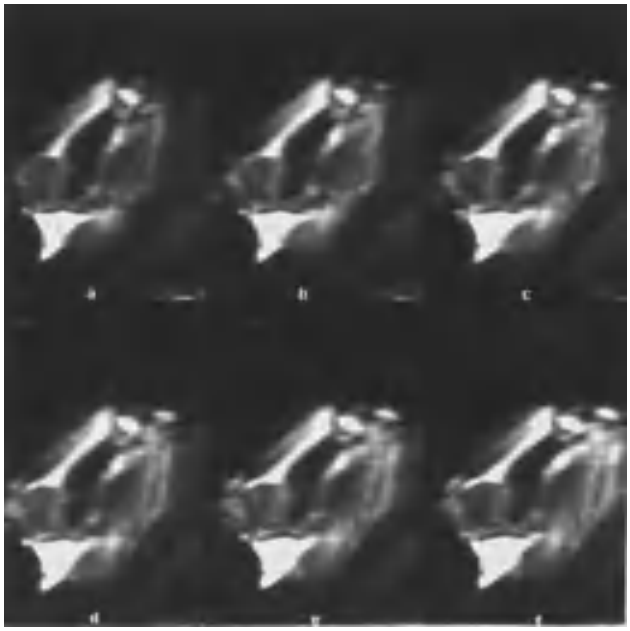

Figure 4 T_2-weighted images of a laser-induced lesion in an animal model immediately after laser exposure (a) and up to 40 min later (f). Note the expansion of the lesion (arrow)

2.2 T_2 Edema Monitoring

In a typical thermal ablation procedure, the tissue temperature is raised to 60–80 °C in order to produce protein denaturation and coagulation necrosis. Tissue changes associated with these processes are detectable using T_2-weighted MRI. Basic animal studies have characterized the acute tissue effects of laser heating, for example, and their MR appearances.[10] In addition to a high sensitivity to edema, T_2-weighted images reveal a clear-cut MR appearance of thermal-induced lesions: concentric rings which closely reflect the actual pathologic changes of central cavitation, coagulation necrosis, and tissue edema (Figures 4 and 5).

Although the regions of cavitation and coagulation necrosis clearly represent irreversible cell damage and death, the ultimate disposition of the edema layer is important in the quantification of the tissue damage. Preliminary data from chronic studies in animal models suggest that the area of cell death may expand up to 44% into the edema region depending on a number of factors as the healing process occurs.[11]

2.3 Position Monitoring

While most of the new developments in interventional MR involve therapy monitoring, there is also a need for

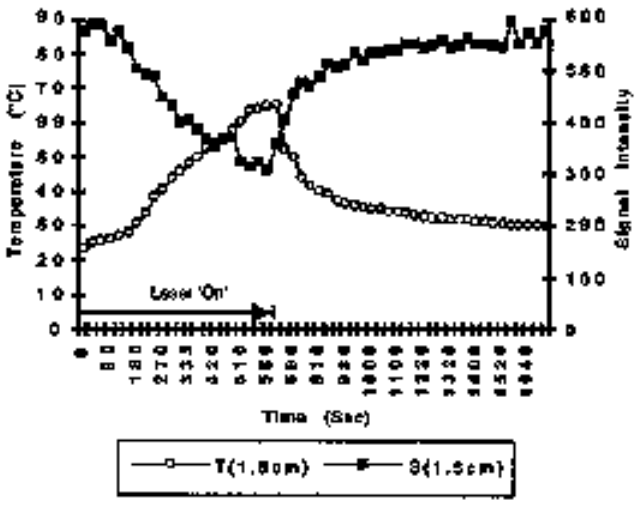

Figure 3 Relationship between temperature (T) and T_1 signal intensity (S) during and after laser irradiation

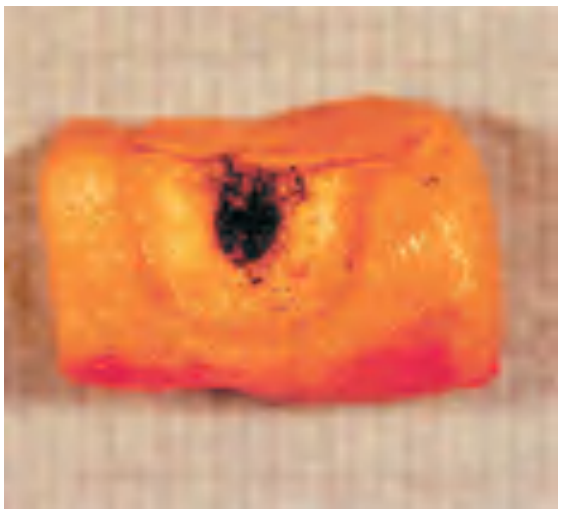

Figure 5 Gross pathology of the laser-induced lesion showing concentric regions of cavity, coagulation necrosis, and edema

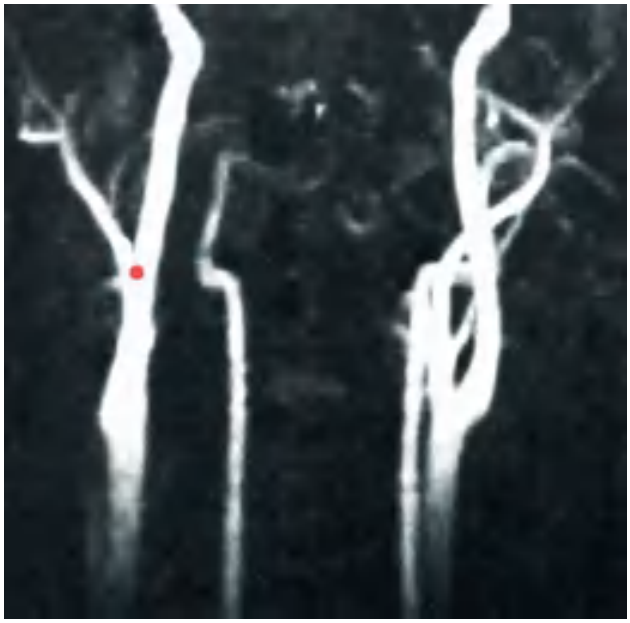

Figure 6 Simulation of real-time position tracking of catheter using an MR angiography road-map, real-time MR scanning and an rf-based tracking system

real-time position tracking of therapeutic instruments. Techniques are under development that will allow tracking of invasive devices (e.g. catheter) in real time using magnetic resonance.[12] By incorporating one or more small rf coils into a device, MR signals will be detected only from excited tissue in the immediate vicinity of the device. An MR pulse sequence using only read-out gradient pulses can localize the position of the receiver coil in the direction of the applied gradient. Repeating this technique in three orthogonal directions permits localization of the rf coil in three dimensions. Such a sequence can be repeated rapidly to provide position information in real time. This position information can be superimposed on a prospectively acquired anatomical 'road-map' (Figure 6). This technology may prove instrumental in making a field such as interventional MR angiography a reality.

3 THERAPEUTIC TECHNIQUES AND CLINICAL APPLICATIONS

Techniques of interstitial therapy can be separated into two mechanistic categories: chemical and thermal.

3.1 Chemoablation

Various strategies for chemoablation under imaging guidance have been used for years in angiography and other areas of classical (endovascular) interventional radiology. Many of these approaches will have applications interstitially as well. For example, injection of ethanol into tissues in sufficiently high concentration will result in local dehydration necrosis. Animal studies confirm the ability of MR to demonstrate lesion size and shape.[13] Initial human studies have been reported in liver applications.[14]

3.2 Thermal Ablation

Manipulation of temperature can cause tissue destruction either by freezing and cell lysis at low temperature or protein denaturation at high temperature. Hyperthermia, tissue heating to temperatures in the range of 43–45 °C, can sustain sublethal injury that becomes irreversible after extended exposure, depending on the type of tissue and experimental or therapeutic conditions.

Thermal ablation at higher temperatures (60–90 °C) is more useful for MR-guided therapeutic purposes because it is quicker to deliver. Unlike alcohol injection, which follows fascial planes, thermal ablation results in an ellipsoidal area of tissue destruction, depending on local thermal conductivity. Neighboring vessels, for example, can act as heat sinks, decreasing the heating effect on surrounding tissues.

There are two main techniques currently being used clinically for administering thermal interstitial therapy: laser ablation and radiofrequency ablation. In addition, a new technique using focused ultrasound is currently under investigation.

3.2.1 Laser Ablation

This technique involves a fiber-optic-laser delivery system such as a neodymium–yttrium-aluminum-garnet (Nd:YAG) laser placed interstitially. The technique has been used in the past for treatment of hepatic tumors and head and neck lesions.[15,16] Since the absorption coefficient of laser energy is variable, depending on the tissue characteristics, the prediction of tissue volume that will be coagulated with a given power output or exposure time setting is difficult in the clinical setting without a monitoring technique such as MRI. Laser therapy is well suited for MR guidance since fiber optic probes are MR-compatible.

Laser-induced lesions show the characteristic zonal segmentation described earlier: cavitation, coagulative necrosis, and edema. In a study of laser lesions in muscle tissue of an animal model, the area of coagulative necrosis resulting from laser irradiation increased in size up to 7 days posttreatment. Progressive resolution resulted in absorption of injured tissue and subsequent replacement with fibrous scar tissue.[11] MRI findings correlated well with pathologic findings in this chronic model.

3.2.2 Radiofrequency Ablation

A radiofrequency probe may also be used to produce tissue destruction by means of remote heating. Applications of this technique using MR monitoring were made possible with the development of MR-compatible rf-generating systems and probes.[17]

By defining rf dose based on temperature exposure in seconds (e.g. 80 °C for 60 s), lesions created using radiofrequency ablation can be more accurately controlled. Using a thermocouple to monitor tissue temperature adjacent to the rf probe during ablation, MR images are acquired to assess acute tissue changes secondary to rf therapy.

A clinical series involving treatment of primary and metastatic brain tumors using MR-guided rf ablation is currently underway with a 12 month follow-up completed[18,19] (Figure 7). Patients are treated under MR guidance with local anesthetic, accessing the brain through a 2 mm-twist drill hole

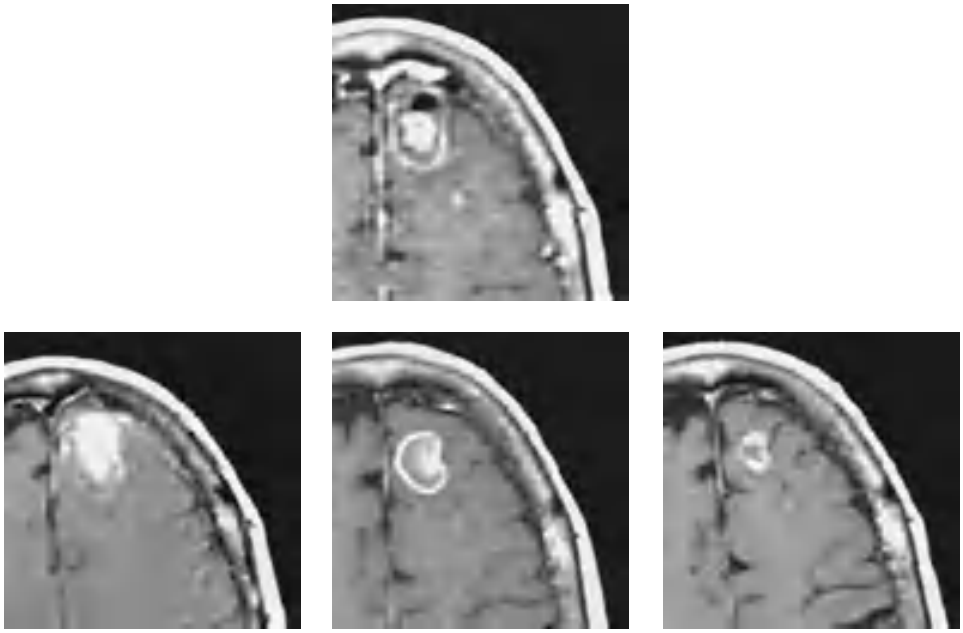

Figure 7 Serial postcontrast MR images of a patient treated with MR-guided rf ablation of a metastatic adenocarcinoma to the brain. The images were acquired (a) immediately following rf ablation, (b) 1 week, (c) 1 month, and (d) 5 months posttreatment

instead of an open craniotomy (Figure 1). Since the patients are awake and communicating with the physician, neurological symptoms can be monitored during the entire procedure, a significant advantage over open craniotomy procedures requiring general anesthesia. The procedure may be done as part of a biopsy procedure and can be used in previously fully radiated patients and/or in instances of recurrence. These types of interventional MR procedures are ideal for patients who are elderly and/or have systemic diseases that preclude the option of general surgery.

3.2.3 Focused Ultrasound Ablation

New techniques in which focused high-power ultrasound beams are used to create tissue necrosis under MRI guidance are being investigated.[20,21] This technique is capable of creating focal lesions in deep tissues which are clearly depicted by MRI, particularly using T_2-weighted sequences (Figure 8). Although this approach has the distinct advantage of not requiring a needle, catheter, or any direct skin violation, it does require an ultrasonic path to the lesion (i.e. a path free of air and bone). Projects are underway to develop an MR-compatible, focused, ultrasound hyperthermia system to improve the clinical utility of this technique.

Figure 8 Focused ultrasound ablation. T_2 fast spin echo image showing lesions (arrows) induced in rabbit thigh muscle. These lesions were produced with the rabbit in the MR imager. (Courtesy of K. Hynynen et al., University of Arizona Health Sciences Center)

4 SPECIALIZED EQUIPMENT

4.1 MR-Compatible Instruments

The first step toward practical interventional MRI was the development of satisfactory instruments that could be used in the high magnetic field necessary for clinical MRI. Even 'low'-field MRI systems produce significant untoward effects on many standard interventional instruments.

Instruments made from ferromagnetic metals result in geometric distortions of the image causing large artifacts. A more dangerous effect of many of these metals is the tendency for them to experience torque and be accelerated in the magnetic field, thus risking damage to patients and imaging team personnel. By substituting high nickel content stainless steel or other nonferrous materials, researchers have developed new MRI-compatible instruments at reasonable costs.[1,17] These devices are safer for the patient and imaging

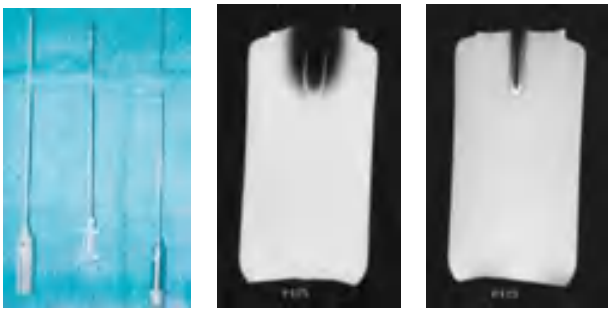

Figure 9 (a) MR-compatible rf therapy probes (Radionics, Inc.), (b) susceptibility artifact caused by stainless steel biopsy needle, (c) reduced artifact from MR-compatible needle (E-Z-EM, Inc)

team personnel and result in reduced artifacts relative to standard instruments (Figure 9).

4.2 Open MR Systems

In 1993, the first of a new generation of MR scanners specifically designed for MR-guided interventional procedures was introduced (Figure 10). An interventional magnet must have open patient access, flexible patient positioning, and open rf coil designs that provide sufficient image quality for MR therapy monitoring without impeding therapeutic access.

4.3 Advanced Localization and Display Systems

Although very accurate and reliable, frame-base stereotactic techniques are uncomfortable and invasive. The development of powerful new frameless localization systems using articulated arms and optic sensors are enhancing the impact of MR guidance on minimally invasive surgical procedures, improving efficiency and patient acceptance (Figure 11). These devices obviate the need for stereotactic frames that fit inside rf coils, opening up more applications of interventional MR.

The MRI scanning paradigm used over the last decade in which the technologist stands outside the scanner room and obtains images on a console is currently being rethought with interventional MR. Rapid three-dimensional segmentation and rendering of patient image information is necessary for treatment planning and monitoring during the procedure. Image subtraction, dosimetry modeling, and calculation routines are necessary for proper treatment administration and should be displayed in the MR scan room. In addition, the need for interactive scan plan definition and sequence selection is required in the MR scan room to improve efficiency of the therapeutic procedure. New interventional MR workstations with powerful graphics capabilities are currently under development to address these issues.

Figure 10 An example of one of a new generation of MR instruments specifically designed for interventional procedures. This system is from Siemens and operates at 0.2 T

Figure 11 Operating Arm System^{TM} (Radionics/RSA, Inc.) allows registration of the surgical field to three-dimensional MR data. Ultimately, the physician will be able to define scan plane orientation and initiate acquisition interactively during the interventional procedure

5 FUTURE DIRECTIONS

Interventional MR is clearly in its early stages of development. With dedicated interventional MR units now available and sophisticated workstations under development, the next step is to identify clear-cut clinical indications and begin large clinical trials to define the ultimate value of interventional MR.

Even with current technology, it is possible to imagine dedicated MR therapy units for combined radiological and surgical approaches in what may be the archetype for operating rooms of the 21st century.

6 RELATED ARTICLES

Resistive and Permanent Magnets for Whole Body MRI; Temperature Measurement In Vivo Using NMR.

7 REFERENCES

1. R. B. Lufkin, L. Teresi, and W. Hanafee, *Am. J. R.*, 1987, **149**, 380.
2. G. Duckwiler, R. B. Lufkin, L. E. Teresi, E. Shukler, J. Dion, F. Vinuela, J. Benrson, and W. Hanafee, *Radiology*, 1989, **170**, 519.
3. A. A. Saltiel, T. A. S. Matalon, and D. A. Turner, *J. Interventional Radiol.*, 1990, **5** 165.
4. S. D. Herman, A. C. Friedman, P. D. Radecki, and D. F. Caroline, *Am. J. R.*, 1986, **146**, 351.
5. D. G. Thomas, C. H. Davis, S. Ingram, J. S. Olney, G. M. Bydder, and I. R. Young, *Am. J. N. R.*, 1986, **7**, 161.
6. G. Duckwiler, R. B. Lufkin, and W. N. Hanafee, *Radiol. Clin. North Am.*, 1989, **27**, 255.
7. T. Trapp, R. B. Lufkin, E. Abemeyer, L. Layfield, W. Hanafee, and P. Ward, *Laryngoscope.*, 1989, **99**, 105.
8. Y. Anzai, R. B. Lufkin, D. Castro, R. E. Saxton, H. Fettermen, K. Farahani, L. J. Layfield, F. C. Jdesz, W. N. Hanafee, and D. J. Castro, *Laryngoscope*, 1991, **101**, 755.
9. K. Farahani, Doctoral dissertation, UCLA Department of Radiological Sciences, 1992.
10. Y. Anzai, R. B. Lufkin, D. J. Castro, K. Farahani, B. A. Jabour, L. J. Layfield, R. Udkoff, and W. N. Hanafee, *J. Magn. Reson. Imaging*, 1991, **1**, 553.
11. Y. Anzai, R. B. Lufkin, S. Hirschowitz, K. Farahani, and D. J. Castro, *J. Magn. Reson. Imaging*, 1992, **2**, 671.
12. C. L. Dumoulin, S. P. Souza, and R. D. Darrow, *J. Magn. Reson. Med.*, 1993, **29**, 411.
13. Y. Anzai, R. B. Lufkin, D. J. Castro, et al. *J. Comp. Radiol.*, (in press).
14. Y. Kubota, T. Nakano, T. Seki, S. Kitagawa, T. Rizuno, Y. Sameshima, T. Katoh, and Y. Tanara, *Hepatogastroenterology*, 1989, **36**, 262.
15. D. Hashimoto, M. Takami, and Y. Idezuki, *Gastroenterology*, 1985, **88**, 1663.
16. D. J. Castro, R. B. Lufkin, R. E. Saxton, A. Nyerges, J. Soudant, L. J. Layfield, B. A. Jabour, P. H. Ward, and H. Kangarloo, *Laryngoscope*, 1992, **102**, 26.
17. S. Sinha, J. Parker, Y. Anzai, et al. MR compatible RF system: initial experience (abstr)., *Soc. Magn. Reson. Imaging*, 1993.
18. Y. Anzai, K. L. Black, A. A. F. DeSalles, D. R. Hamilton, K. Farahani, and R. B. Lufkin, *Am. J. N. R.*, (in press).
19. K. L. Black, A. A. F. DeSalles, Y. Anzai, G. Nelson, E. Behnke, K. Farahani, S. Sinha, D. P. Becker, and R. B. Lufkin, *J. Clin. Oncology*, (in press).
20. K. Hynynen, A. Darkazanli, E. Unger, and J. F. Schenck, *Med. Phys.*, 1993, **20**(1), 107.
21. H. E. Cline, J. F. Schenck, R. D. Watkins, K. Hynynen, and F. A. Jolesz, *Magn. Reson. Med.*, 1993, **30**, 98.

Thermal Therapies in the Body Monitored by MRI

Margaret A. Hall-Craggs, S. Smart, and A. Gillams
The Middlesex Hospital, UCLH, London, UK

1 INTRODUCTION

The purpose of minimally invasive therapy (MIT) is to deliver effective treatment with the minimum disruption and damage to normal surrounding tissue. Consequently the morbidity of the procedure may be reduced compared with an open operation. Measures of this may be such factors as reduced scarring and deformity (as in the breast), more rapid postprocedural recovery, and reduced hospital stay (as in intra-abdominal procedures). In some cases, therapy may be used where there is no other treatment option, as in tumor metastases to multiple lobes in the liver.

Treatment using MIT is fundamentally different in benign and malignant disease. In benign disease, total eradication of the target tissue may not be necessary and size reduction may be adequate. This is the case with breast fibroadenomata and also in uterine fibroid disease where amelioration of menorrhagia or infertility is the treatment aim. With malignant disease, surgical principles preside; in general, tumor resection/destruction with an adequate margin is the treatment aim. Further MIT must not impose additional risks such as increasing the rate of local recurrence or distant disease spread, or reducing disease survival.

A host of MIT techniques have been developed since the mid-1970s; these include the thermal ablative techniques to be discussed in this chapter. Other are percutaneous excision, photodynamic therapy, interstitial radiotherapy/brachytherapy, chemical ablations, laparoscopic surgery, lithotripsy, and intraluminal/intravascular procedures such as stenting, embolization, dilatation, etc.

2 METHODS OF THERMAL ABLATION

There are four principal methods of thermal ablation. Three of these involve heating of the sample—interstitial laser photocoagulation (ILP), radiofrequency (rf)-induced coagulation (RFC) and focused ultrasound (FUS)—while the fourth, cryoblation, uses cooling.

2.1 Interstitial Laser Photocoagulation

For ILP, fiber optic cables that emit light only from their tips are placed into the target region. These are coupled to a laser source and the light is turned on for the duration of the treatment. Theoretically the frequency of the light has to match an absorption band of some (unspecified) chromophore within the target region so the light energy can be converted into heat. There have been a number of approaches to improving the coupling of light to the tissue and these include the use of a focusing lens at the fiber tip and diffuser tip fibers. However it appears that laser energy deposition is primarily a thermal process. Pre-charring the optical fiber causes the fiber to behave as a point heat source (paradoxically reducing light transmission) and increases the size of the laser burn.[1] The use of low laser powers (<5W) allows the slow and controlled development of lesions over extended periods (300–1000s).

In our practice, we have used the semiconductor diode laser as it offers a number of advantages. It is small, compact, and easily transportable; it does not require a cooling system and operates from a conventional phase electrical source.

2.2 Radiofrequency

RFC uses rf alternating current source applied through needles tipped with rf electrodes. Frictional heating is induced via ionic agitation arising from the impedance of the tissue to alternating currents. The rf source typically operates at up to 500 kHz and will often interfere with the MR acquisition at all field strengths. Such interference with the MR measurement can be reduced or eliminated with an appropriate choice of electronic filters, or by gating the rf source off during MR signal reception. This latter approach can easily be performed by simple modification of pulse sequence code. To complete the electric circuit for the applied AC, grounding pads must be applied to the patient. Care must be taken with these to prevent the possibility of local skin burns at the site of the pads. RFC can form lesions faster than ILP; however, because the deposition of the heat depends upon the electrical characteristics of the tissue, the formation of the lesion may be inhomogeneous, especially in regions of tissue boundaries.

2.3 Focused Ultrasound

FUS uses an array of ultrasound sources, typically operating at 1.5 MHz, the energy of which converges at a focus within the body. In this region, a significant amount of acoustic energy is converted into heat. The volume of the hyperthermia is very well defined for FUS; as a result, a sharp boundary may be observed between normothermic regions and those bound for necrosis. The duration of the treatment depends upon the ultrasound parameters but is typically in the region of tens of minutes. Lesions as small as 1 mm^3 can be created; consequently, high-resolution imaging techniques, such as MRI, are necessary for their accurate detection and monitoring.

2.4 Cryotherapy

Cryosurgery will typically involve the use of a needle that is continuously cooled by liquid nitrogen and which is insulated along the length of its shaft except for at the tip. The tip of the needle acts as a heat sink for the tissue and so acts as a point source for cooling. Thermal conduction increases the volume of cooled tissue. There are a variety of mechanisms responsible for the subsequent necrosis, and these depend upon the organ undergoing the cryosurgery. As for FUS, there is a well-defined boundary between normal and treated tissues.

3 ROLE OF IMAGING IN THERMAL ABLATION

The principal roles of imaging in ablative treatments are to define the extent of disease, to guide instruments, to monitor treatment during the therapeutic procedure, and to show the effect of therapy. In practice, a combination of imaging modalities are used to achieve these aims, including computed tomography (CT), ultrasound, and MR. However, there are a number of specific properties that have made MR the subject of much research interest. The exploitation of temperature-sensitive sequences can potentially be used to map areas of tissue damage during an ablative procedure, and this may facilitate treatment modification at the time of delivery to improve efficacy. Other advantages include multiplanar imaging, which facilitates the guidance and accurate placement of tools. The lack of ionizing radiation is of importance to both the patient and the operator with lengthy therapeutic procedures.

4 MAGNET AND EQUIPMENT CONSIDERATIONS

Interventional procedures have been described both in conventional tubular high-field systems and in lower-field magnets designed to have more open access. In open systems, the tissue of interest can be located within the 'active volume' of the magnet for MRI, and the surgeon may have access to this volume from several sides. The use of the more conventional tubular high-field magnets is hindered by limited bore diameter, which limits the size of interventional devices, and by the restricted access owing to the magnet length, which prevents realtime MR-monitored adjustments of interventional tool position. On open access systems, rapidly and dynamically acquired MRI scans can assist with the positioning of interventional devices. Fast MRI may also allow near realtime visualization of physical changes within the tissue during interventional procedures. Typical procedures include MR-guided biopsies, tissue excisions, and thermal ablations. In this article we shall describe aspects of thermal ablation treatment in the human body as monitored by MRI.

All interventional devices located within the region of treatment must be made of MR-compatible materials. Such tools are available and are usually made of alloys or ceramics that present a low magnetic susceptibility difference to the body. However residual susceptibility artifacts, dependent upon the applied magnetic field strength and on the orientation of $\boldsymbol{B}_0$ relative to the interventional device, persist and may compromise image quality in their locale, especially when using gradient echo methods. The materials used in the manufacture of these MR-compatible devices are often soft, too flexible, and are difficult to tool to sharp and cutting tips. They are also expensive.

For ILP therapy it is possible to use MR-compatible needles to position the optical fibers and then to withdraw the needles leaving the fiber in place; this eliminates the susceptibility problem. For RFC and cryotherapy, the needles must remain in place; consequently susceptibility artifacts are unavoidable. This is not necessarily a severe problem for FUS as the sonic transducers are positioned around the body not within the target region of tissue.

5 MR METHODOLOGY

Fast imaging methods are required for interventional therapies to facilitate tool guidance and to monitor therapy. Long scan times are also precluded by gross patient motion arising from respiration or peristalsis. The use of navigator echoes may allow the correction of some but not all of these motions. Prospective ordering of the phase-encode steps (e.g., respiratory ordered phase encoding, ROPE) can reduce the degree of motion artifact but requires good calibration and is sensitive to any respiratory irregularity. The use of breath-holding, especially when controlled under general anesthesia, allows imaging free of motion artifacts for scan times of up to about 30 s.

Open-access scanners tend to operate at lower field strengths than those used for routine clinical imaging and this reduces the possible signal-to-noise ratio (SNR). The rf and gradient hardware of the open-access scanner also tends to be of lower specification than that of a high-field research-grade scanner. Some fast imaging protocols, e.g., echo planar imaging, may, therefore, not be available. Further the inherently low SNR realistically achievable with low-field scanners and the persistence of susceptibility artifacts, arising from interventional tools, may make echo planar imaging impractical for some of these applications.

Rapid image reconstruction and display is necessary for realtime monitoring. This may be achieved more quickly by by-passing the scanner and using custom built hardware and software. Methods such as keyhole imaging and local-look scanning have also been used to enhance image update rates.

5.1 Sources of Contrast for Monitoring Thermal Ablations

Successful monitoring of hyperthermic ablations requires a temperature-dependent source of contrast for the heated region. It is important that any contrast seen is a direct consequence of the heating effect rather than resulting from a subsequent effect such as coagulation. Most successful studies demonstrating realtime monitoring of the effects of temperature in thermal ablations have, to date, been performed in model systems and generally using high-field systems. Currently favored mechanisms of temperature-dependent contrasts are T_1 based, where a focal change in the signal amplitude is seen when running under conditions of partial saturation, and proton resonance frequency, where changes in the signal phase with temperature are seen. The proton resonance frequency method is essentially a chemical shift effect and so is most successful at high field. Molecular diffusion has also been proposed as a method for introducing temperature-dependent contrast. However, this method has not been used widely as it is extremely sensitive to bulk patient motion, and because of the potential for anisotropic diffusion to introduce orientation-dependent contrast.

For cryogenic ablations, rapid and accurate monitoring of the region of treatment is possible. As the tissue water solidifies, its T_2 time is greatly reduced; as a result, no echo signal can be measured using conventional MRI hardware. The border of frozen and unfrozen tissues is extremely well defined and for situations where multiple cooling probes are used, any pockets of normothermy can be readily identified allowing repositioning of probes to encompass a given volume of interest. However, direct and unequivocal MR thermometry is

precluded, at all field strengths, by the absence of signal from those regions that are frozen.

6 MR-MONITORED THERMAL ABLATION PROCEDURES

6.1 Interstitial Laser Photocoagulation in Breast Disease

Most work has been performed using the semiconductor diode laser (805 nm) and Nd:Yag (1064 nm) pulse lasers.[2–5] Studies have shown that a power of 2–2.5 W applied for about 500 s will generate lesions of up to 10 mm. Lesion size and reproducibility can be improved by pre-charring the fiber. Larger burns (of up to 40 mm) can be generated by using multiple fibers or pull-back techniques. In a dose escalation study, Akimov has shown that at higher power (over 3 W), tumor vaporization can lead to tissue explosions.[4]

In most studies, patients are treated with local anesthesia and sedation alone; general anesthesia is unnecessary.

6.1.1 Benign Breast Tumors

In our institution we have treated just under 50 benign fibroadenomas of the breast with ILP. Diagnosis is made before treatment by triple assessment and either cytology (C2) or core biopsy. Lesions of up to 4 cm diameter have been treated with between one and four fibers at 2–2.5 W (1000–4000 J). Follow-up for at least 1 year by clinical and ultrasound examination is available in 14 of these patients; in each case the mass has become impalpable by 1 year. In 13 patients, the tumor could not be seen on ultrasound by 12 months' follow-up and in the remainder a 9 mm remnant persisted.[6]

MR has a very limited role to play in the monitoring of ILP therapy to benign tumors. Fibroadenomas have variable enhancement characteristics; some enhance very intensely and others not at all. Consequently contrast-enhanced MR is not of consistent value. Those lesions that do enhance before treatment show areas of devascularization after treatment, but this is not of any clear clinical value. Ultrasound is a quick method of localizing needles within lesions and the treatment parameters are relatively standard. Unlike malignant disease, the treatment of margins is not critical; therefore, accurate monitoring of therapy is not essential.

6.1.2 Breast Cancer

All studies have reported that ILP can cause cell necrosis in breast cancers.[3–5] Treatment of small relatively spherical tumors can be complete. Treatment of larger lesions is more challenging as modeling the treatment area to conform with irregular large masses and ensuring treated margins is much more difficult.

Most studies have examined ILP where treatment has been followed by early surgical excision of the tumor and there are very few long-term follow-up data. There are small numbers reported where ILP has been the sole method of treatment. Akimov treated seven women with ILP alone. Two of these died of other causes and without tumor recurrence; a third had disease-free survival of over 5 years. In our own recent experience in a cohort of selected elderly women who are undergoing ILP and delayed excision at 3 months, we have been able to show complete tumor ablation sustained over the 3-month period in small numbers.

Complete tumor ablation and treatment of an adequate margin is essential in the management of breast cancer. The surgical literature has shown that incomplete tumor excision is a major risk factor for local tumor recurrence. Yet it is the margins that are most difficult to treat with ILP because, when the fiber is placed in the center of a lesion, the periphery does not reach as high a temperature as the center of the tumor. In one patient treated with ILP alone, Akimov has shown peripheral tumor recurrence. We have found that when there is inadequate tumor ablation, viable cells are invariably found around the periphery of the mass. Unless margins can be reliably and consistently treated, ILP cannot be accepted as a reasonable form of primary therapy in breast cancer.

Contrast-enhanced MR imaging has an essential role to play before therapy to map accurately the extent of the tumor and thus facilitate appropriate case selection. Treatment changes can be seen at high field during ILP using T_1-weighting sequences. Areas of low signal develop around the fiber tip within a minute of treatment starting and these areas broadly correlate with the histologic extent of tumor necrosis.[3,5] Consequently, MR does appear to have the potential to monitor treatment in close to realtime. Ideally, areas of signal change should be matched to the tumor. This is not easy in practice as the majority of tumors are only visible on contrast-enhanced scans. Repeated use of contrast causes enhancement of normal breast parenchyma and the loss of contrast between normal and abnormal breast tissue.

Following treatment, delayed contrast-enhanced MR can be used to show the effects of treatment. Areas of devascularization (nonenhancement) occur within the treated area. Occasionally rim enhancement may occur around an adequately treated lesion as a result of peripheral inflammation.

The only significant complications of ILP reported are collateral burns to skin and muscle. The former can be avoided by irrigating the skin with chilled saline during treatment. Burns to the pectoralis muscle can be avoided by accurate placement of the fiber tip.

6.2 Radiofrequency, Cryotherapy, and Focused Ultrasound in Breast Disease

Experience using these thermal treatments in breast disease is very limited. Preliminary reports of the use of rf in vivo[7] and in vitro[8] have shown that histologically confirmed areas of cell necrosis occur. MR monitoring of rf therapy during treatment is limited by the need to have the metallic probe in position during the procedure. There are limited reports of the use of FUS in breast tumors.[9,10] Prolonged treatment times reduce patient acceptance of the procedure, and patient movement compromises treatment. Cryotherapy has been shown to produce tissue necrosis in breast cancers[11] but no significant clinical studies have been reported.

6.3 Bone and Soft Tissue Tumors

There are limited reports of the application of MIT to bone and soft tissue tumors. ILP and rf are being used routinely in the ablation of benign osteoid osteomas. As the tumors are best

seen on CT and treatment parameters are standard, MRI has no role.

There has been some preliminary experience with the treatment of bone metastases with MIT, but it is difficult to justify these experimental therapies when local radiotherapy is effective, widely available, and well tolerated.

We have limited experience treating soft tissue metastases from soft tissue and bone sarcomas with PDT, rf, and ILP. In these patients (with chemo- and radio-insensitive tumors who have all undergone multiple previous operations), we have had variable results ranging from complete tumor ablation in patients with small volume disease to no effect in patients with massive recurrence.

MR has been useful in these patients to stage local disease and for showing post-treatment changes. For complex tumors, needle placement is facilitated by MR as frequently the tissue/tumor contrast is not sufficient to enable accurate tumor localization with CT guidance.

6.4 Fibroid Disease

ILP and rf have been used to treat uterine fibroids (leiomyomata) percutaneously, endoluminally, and at laparoscopy. The advantage of the last approach is that the peritoneum, which is very susceptible to thermal damage, can be directly visualized. The main role described for MR is in the monitoring of treatment response: fibroids frequently exhibit an iceberg effect and the extent of local damage cannot be accurately assessed by direct visualization. There is no published experience of per-procedural MR guidance to our knowledge.

6.5 MR-Guided Ablation of Liver Tumors

The four principal techniques used to achieve percutaneous hepatic tumor ablation are ILP, RFC, cryotherapy, and percutaneous ethanol injection.

A number of centers including our own are now routinely using rf and ILP to ablate hepatic metastases. In our own center most procedures are performed under local anesthesia and conscious sedation, with approximately 15–20% requiring general anesthesia. The 0.2 T Siemens Viva open-interventional MR system provides good access for either a subcostal or intercostal approach to the right lobe of the liver, or an anterior oblique approach to left lobe lesions with the patient in the supine position. A body flex coil provides adequate coverage of the area of interest and good access for needle positioning. Initial breath-hold T_1-weighted gradient echo images (repetition time (*TR*); echo time (*TE*) 152 ms, 9 ms; flip angle 70°) scans are performed to locate the tumor. If tumor visualization is not adequate on baseline images, then liver-specific contrast agents are given (Figure 1). Either super-paramagnetic iron oxide particles (Ferumoxide, 15 mmol kg^{-1}, Guerbet) or T_1-shortening manganese-based agents (Mangafodipir trisodium Teslascan, 0.5 ml kg^{-1}, Nycomed Amersham) will provide a long period of enhancement, facilitating tumor visualization. Needle placement can be performed entirely using MR guidance or by using a combination of ultrasound and MR. Generally we have favored the use of ultrasound for speed of needle placement, reserving MR for tumors not easily visualized by ultrasound and for confirmation or finessing of the final needle position. If ultrasound guidance is used, the patient is positioned within the coil on the MR table, and then the table is undocked and moved across the 5 G line, approximately 2 m from the magnet, to the ultrasound machine.

Figure 1 Coronal section through the liver following Endorem during interstitial laser photocoagulation therapy to a colorectal metastasis. The large tumor is seen as a relatively bright mass in the low signal liver. Two 19 gauge MR-compatible needles are shown positioned within the mass

6.5.1 Needle Visualization

Needle positioning is confirmed using multiplanar, often double-oblique T_1 or T_2 gradient echo images (Figure 1). As needle visualization is reduced when it is aligned with the $\boldsymbol{B}_0$ field, a direct vertical puncture is best avoided. Other mechanisms for increasing needle visualization include swapping the phase- and frequency-encoding directions. Greater magnetic susceptibility and, therefore, better needle positioning can be achieved with the frequency encode perpendicular to the needle direction. Other techniques include increasing the number of averages of using breath-hold imaging. In practice breath-hold imaging is very difficult to achieve in sedated patients and if general anesthesia is being performed will require the addition of muscle paralysis and intubation.

For laser therapy, up to eight bare-tip fibers are used inserted through 19 G hollow, MR-compatible needles (Cook, Europe). For RFC, MR-compatible single rf electrodes are inserted directly. Where electrode clusters are required, guide needles are used as MR-compatible electrode arrays are still in development.

6.5.2 Monitoring the Treatment

We use a T_1-weighted fast inversion–recovery sequence (*TR*, 1068 ms; *TE* 48 ms; time to inversion, 80 ms; number of signals averaged, 1 in 59 s; collimation, 10 mm; matrix, 182×256) to monitor the changes produced by thermal ablation (Figure 2). On this sequence, untreated tumor is seen as high signal intensity against lower signal intensity liver. Over time, an area of reduced signal intensity develops at the treatment site and becomes progressively lower in signal intensity and larger in size. Around the area of low signal intensity, a high

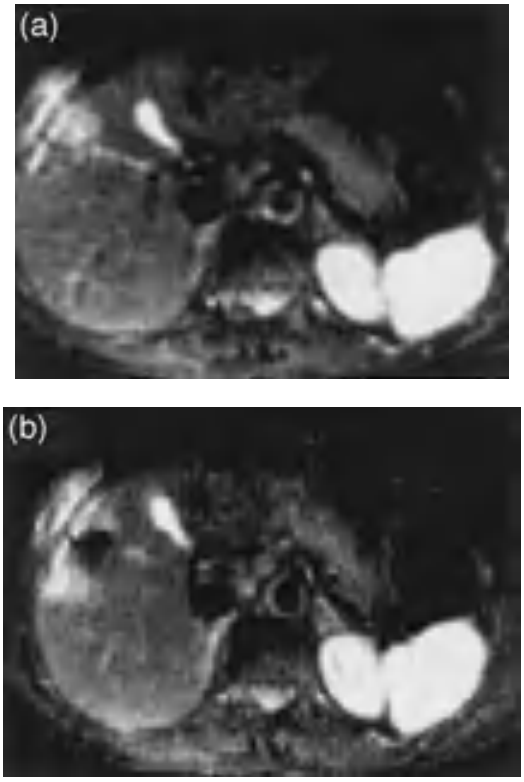

Figure 2 Transverse short tau inversion recovery images through the liver before (a) and after (b) interstitial laser photocoagulation (ILP) to a hepatic metastasis, showing treatment effect. The high-signal peripheral metastasis shows a low-signal focus within the center of the tumor following 8-fiber ILP to the mass. These changes confirmed a treatment effect but underestimated the changes seen on follow-up contrast-enhanced computed tomography

signal intensity ring of edema is also visualized. Although the area of low signal intensity correlates with the final area of thermal ablation on contrast-enhanced CT at 18 h, in general the MR image underestimates the final extent of necrosis. We perform monitoring scans at 10-min intervals throughout the treatment.

Treatment-sensitive sequences could theoretically provide more accurate monitoring information but are difficult to implement in the liver in vivo. Minimal signal intensity changes requiring image registration and subtraction are inaccurate. The shape of the liver is not constant but changes on respiration. A 13% error in liver registration in the craniocaudal direction has been reported.[12] Further thermal injury itself produces a change in the liver shape and contour. Motion artifact becomes increasingly problematic during treatment when the patient is sedated and unable to breath-hold. Therefore, although ex vivo and animal experimentation suggest that both T_1 contrast and phase frequency shift will provide accurate temperature information[13–15] both Kettenbach and Vogl report difficulties with susceptibility and motion in vivo.[16,17] Vogl uses phase frequency shift at 1.5 T with the relatively simple indicator of a 50% reduction in signal to terminate treatment; and this is considered sufficient for tumor ablation by this group.[17]

The use of rf suffers from the additional problem of interference with MR image acquisition; as a result, monitoring sequences are performed at breaks in the treatment cycle. Steiner et al. found good correlation between phase frequency shift imaging at 0.5 T immediately at treatment end and final ablation volume.[15] However, liver cooling is rapid (of the order of 50 s) and, therefore, there is only limited opportunity to acquire the necessary information.

For cryotherapy, MR-compatible cryoprobes have been developed. The iceball is well visualized but tends to underestimate the final lesion size.[18,19]

Percutaneous ethanol injection, unlike the other ablation techniques, is reserved for the treatment of hepatocellular carcinoma. Although ex vivo experiments have suggested the use of water-suppressed T_2 fast-spin echo images for monitoring the actual injection and animal experiments have suggested that ethanol produces low signal on all sequences, in practice a range of signal intensity changes are produced and MR assessment relies on the absence enhancement during arterial phase imaging to indicate complete ablation.[20–23]

6.5.3 Long-term Follow-up

Most groups prefer CT for long-term follow-up because of cost and availability.

6.5.4 Conclusions

MR guidance offers improved multiplanar imaging compared with other imaging techniques; although quantitative temperature measurement is not yet a reality, MR does provide some monitoring information.

6.6 MR-Guided Ablation in the Prostate

Failure of traditional treatments and the associated morbidity has driven a multifaceted search for alternative therapies for prostate treatment. There are now a number of image-guided treatment options under evaluation for localized prostate cancer, including cryotherapy, brachytherapy, and photodynamic therapy. Laser therapy has been used in benign prostatic hypertrophy. Fluoroscopy, CT and transrectal ultrasound have all been used to guide prostatic interventions. Of these, CT and fluoroscopy provide no information about the internal architecture of the prostate and are unidimensional; transrectal ultrasound offers significant detail of the internal prostatic architecture but does not show the needle trajectory from perineum to prostate. In addition, the presence of the probe in the rectum holds the rectal wall against the prostate gland. MR offers multiplanar imaging, any plane, any obliquity, good prostate detail, and images of the full needle trajectory and of neighboring structures without distortion of the anatomy.

6.6.1 Photodynamic Therapy in the Prostate

We have used interventional MR to guide needle placement for photodynamic therapy in the prostate. Necrosis is produced by the interaction of light of a particular wavelength with a photosensitizing agent. The exact mechanism is unknown but a popular theory is that short-lived oxygen radicals are produced and these cause cell death. Necrosis does not occur immediately and the oxygen radicals are MR occult; therefore, MR does not have a monitoring role during the treatment. However, MR is excellent in guiding needle placement (Figures 3 and 4). As many as eight, 19 G hollow needles are introduced trans-

Figure 3 Coronal two-dimensional gradient echo image during photodynamic therapy to the prostate. Two 19 G MR-compatible needles are inserted within the gland and MR is used to confirm the position of the needles

perineally into the peripheral zone of the prostate gland. Multiplanar T_1-weighted gradient echo images are obtained to confirm needle position and spacing. Laser fibers are introduced through the needles and the tissue is illuminated with red light. Approximately a 16 mm sphere of necrosis is produced around each laser fiber. Treatment is targeted to areas containing tumor on mapping biopsy and away from the urethra, neurovascular bundles, and external sphincter. Imaging assessment of the extent of necrosis is performed using gadolinium-enhanced T_1-weighted sequences at high field (1.5 T).

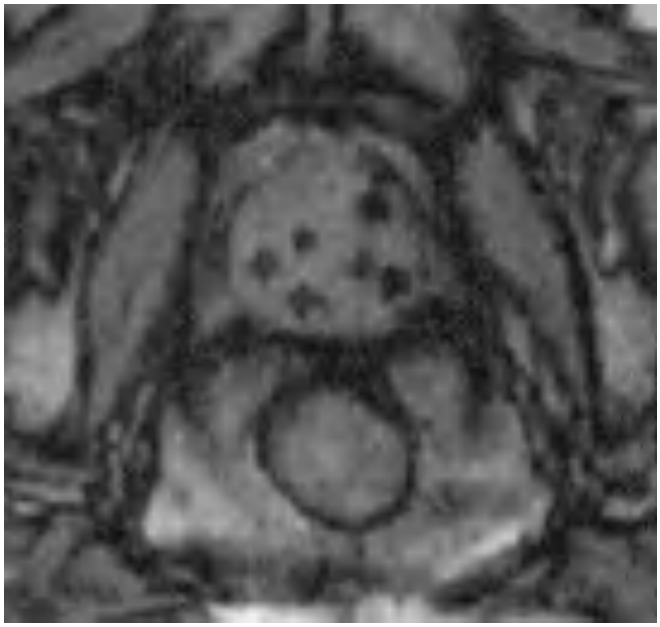

Figure 4 Transverse two-dimensional gradient echo image through the prostate during multifiber photodynamic therapy to the gland. Multiple needles are positioned within the tumor in posterior and left-sided lobes of the gland

Necrosis is appreciated as an area of nonenhancement at the treatment site (Figure 5). In comparison, CT demonstrates limited tissue contrast and both gray scale and Doppler ultrasound do not show any specific features.

6.6.2 Brachytherapy

MR guidance of seed insertion has been reported in nine patients at 0.5 T.[24] MR allowed confirmation of seed position in three planes. Both T_1-weighted fast gradient echo and proton density fast spin echo sequences have been used satisfactorily.[25,26]

6.6.3 Cryotherapy

During cryotherapy, the iceball can be well visualized, although actual temperature measurement is not available. MR has also been used in the follow-up of cryotherapy-induced changes. Contrast-enhanced T_1-weighted images show necrosis as areas of nonenhancement. Expected changes on follow-up include a reduction in prostatic volume of 30–52%, loss of zonal architecture in 81–100%, and soft tissue thickening of the rectal wall (47%) or around the capsule and neurovascular bundles in the majority (89%).[27–29]

6.6.4 Laser-induced Thermotherapy in Benign Prostatic Hypertrophy

MR has been used for monitoring of thermal ablation in benign prostatic hypertrophy and for follow-up assessment. On-line monitoring is feasible using phase-frequency shift[30] providing an accurate prediction of final lesion size in ten of 13 patients in one study.[31] Follow-up MR showed lack of gadolinium enhancement in necrotic areas and volume reduction.[32]

Figure 5 Transverse contrast-enhanced T_1-weighted image through the prostate 5 days after photodynamic therapy (PDT). A lobulated region of nonenhancement is seen within the gland that corresponds to the region of devascularization after PDT. Similar changes are seen after cryotherapy

6.6.5 Conclusion

MR guidance and follow-up is preferable to other techniques in prostate ablation; for cryotherapy and thermal techniques there is the added advantage of treatment monitoring.

7 NAVIGATIONAL DEVICE

As indicated above, accurate placement of tools is essential for thermal therapies to ensure that lesions are accurately localized and damage to collateral tissue is avoided. Although freehand placement is usually adequate where lesions are superficial and large, the same is not true for deep and small lesions. In these cases, tool placement may be facilitated by navigational devices. There are a number of systems being developed currently. We are investigating the use of a passive navigation device for interactive definition of the slice selection plane. The device can potentially increase the speed with which needles are positioned as it is possible to define the image slice automatically, during needle insertion, according to the orientation of the needle itself. The biopsy needle within its holder is attached to the passive navigation probe (Figure 6). The reference point for image slice selection can be set relative to the tip of the needle. The stereoscopic camera detects the position and rotation of the probe so as to define the slice selection axis. In situations where multiple needles require accurate positioning, the device reduces any ambiguity in identifying needles and so increases the safety of the procedure.

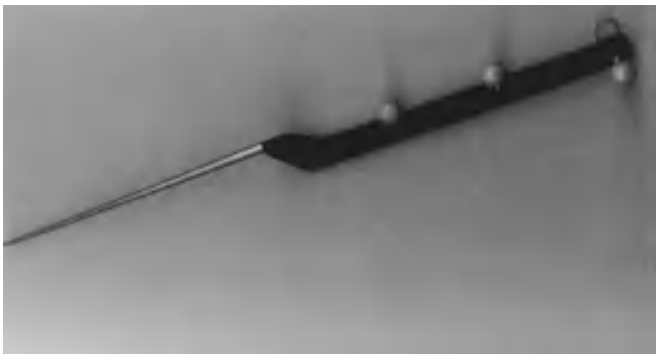

Figure 6 Navigational pointing device. A number of highly reflective balls are mounted on the handle of the pointing device, the light being detected by the stereoscopic camera. Tools may be mounted onto the device to facilitate accurate placement within the target

8 SUMMARY

Temperature-sensitive MRI can be achieved for the monitoring of thermal treatments in the body within a realistic scan time. Low-field open-access scanners offer good surgical access to the patient. However, the image quality is poor compared with that expected from high-field closed-bore magnet systems. Several of the temperature-dependent mechanisms of contrast are field strength dependent; consequently, for these, high-field magnets should be preferable for the monitoring of thermal interventions in the body. The development of shorter and wider bore high-field magnets should also assist in the promotion and acceptance of MRI monitoring of thermal interventions in the body, head, and extremities.

9 RELATED ARTICLES

MR-Guided Biopsy, Aspiration, and Cyst Drainage; Temperature Measurement Using In Vivo NMR.

10 REFERENCES

1. S. A. Harries, Z. Amin, M. E. F. Smith, W. R. Lees, J. Cooke, M. G. Cook, J. H. Scurr, M. W. Kissin, and S. G. Bown, *Br. J. Surg.*, 1994, **81**, 1617.

2. H. Mumtaz, M. A. Hall-Craggs, G. Buonnacorssi, M. Kissin, and S. Bown, *Radiology*, 1996, **201**(P), 177.
3. H. Mumtaz, M. A. Hall-Craggs, A. Wotherspoon, M. Paley, G. Buonaccorsi, Z. Amin, I. Wilkinson, M. Kissin, T. Davidson, I. Taylor, and S. Bown, *Radiology*, 1996, **200**, 651.
4. A. B. Akimov, V. E. Seregin, K. V. Rusanov, E. G. Tyurina, T. A. Glushko, V. P. Nevzorov, O. J. Nevzorova, and E. V. Akimova, *Lasers Surg. Med.*, 1998, **22**, 257.
5. S. E. Harms, H. Mumtaz, V. S. Klimberg, C. L. Cowan, S. Korourian, and W. B. Hyslop, *Radiology*, 1998, **209**(P), 468.
6. L. M. Lai, M. A. Hall-Craggs, H. Mumtaz, P. M. Ripley, M. Kissin, T. I. Davidson, C. Saunders, I. Taylor, and S. G. Bown, *Breast*, 1999, **8**, 89.
7. R. L. Birdwell, S. S. Jeffrey, E. L. Kermit, D. M. Ikeda, and K. W. Nowels, *Radiology*, 1998, **209**(P), 198.
8. T. Boehm, I. Hilger, W. Mueller, J. R. Reichenbach, M. Fleck, and W. A. Kaiser, *Radiology*, 1998, **209**(P), 198.
9. H. E. Cline, J. F. Schenck, R. D. Watkins, K. Hynynen, and F. A. Jolesz, *Magn. Reson. Med.*, 1993, **30**, 98.
10. J. W. Hand, C. C. Vernon, and M. V. Prior, *Int. J. Hypertherm.*, 1992, **8**, 587.
11. R. W. Rand, R. P. Rand, F. Eggerding, L. DenBesten, and W. King, *Surg. Gynecol. Obstet.*, 1987, **165**, 392.
12. D. L. Wilson, A. Carrillo, and L. Zheng, *JMRI*, 1998, **8**, 77.
13. T. Kahn, T. Harth, B. Schwabe, H. J. Schwarzmaier, and U. Modder, *Roto. Fortschr. Geb. Rontgenstr. Neuen. Bildgeb. Verfahr.*, 1997, **167**, 187.
14. J. Olsrud, R. Wirestam, S. Brockstedt, A. M. Nilsson, K. G. Tranberg, F. Stahlberg, and B. R. Persson, *Phys. Med. Biol.*, 1998, **43**, 2597.
15. P. Steiner, R. Botnar, B. Dubno, G. G. Zimmermann, G. S. Gazelle, and J. F. Debatin, *Radiology*, 1998, **206**, 803.
16. J. Kettenbach, S. G. Silverman, N. Hata, K. Kuroda, P. Saiviroonporn, G. P. Zientara, P. R. Morrison, S. G., Hushek, P. M. Black, R. Kikinis, and F. A. Jolesz, *JMRI*, 1998, **8**, 933.
17. T. J. Vogl, M. G. Mack, A. Roggan, R. Straub, K. C. Eichler, P. K. Muller, V. Knappe, and R. Felix, *Radiology*, 1998, **209**, 381.
18. J. Tacke, G. Adam, and R. Speetzen, *Magn. Reson. Med.*, 1998, **39**, 354.
19. H. P. Klotz, R. Flury, A. Schonenberger, J. F. Debatin, G. Uhlschmid, and F. Largiader, *Comput. Aided Surg.*, 1997, **6**, 340.
20. D. S. Lu, S. Sinha, J. Lucas, K. Farahani, R. Lufkin and K. Lewin, *JMRI*, 1997, **7**, 303.
21. H. Shinmoto, R. V. Mulkern, K. Oshio, S. G. Silverman, V. M. Colucci, and F. A. Jolesz, *J. Comput. Assist. Tomogr.*, 1997, **21**, 82.
22. T. Fujita, L. Honjo, K. Ito, K. Takano, S. Koike, H. Okazaki, T. Matsumoto, and N. Matsunaga, *J. Comput. Assist. Tomogr.*, 1998, **22**, 379.
23. C. D. Becker, M. Grossholz, G. Mentha, A. Roth, E. Giostra, P. A. Schneider, and F. Terrier, *Cardiovasc. Intervent. Radiol.*, 1997, **20**, 204.
24. A. V. D'Amico, R. Cormack, C. M. Tempany, S. Kumar, G. Topulos, H. M. Kooy, and C. N. Coleman, *Int. J. Radiat. Oncol. Biol. Phys.*, 1998, **42**, 507.
25. D. F. Dubois, B. R. Prestidge, L. A. Hotchkiss, W. S. Bice, Jr, and J. J. Prete, *Int. J. Radiat. Oncol. Biol. Phys.*, 1997, **39**, 1037.
26. M. A. Moerlaand, H. K. Wijrdeman, R. Beersma, C. J. Bakker, and J. J. Battermann, *Int. J. Radiat. Oncol. Biol. Phys.*, 1997, **37**, 927.
27. C. L. Kalbhen, H. Hrciack, K. Shinohara, M. Chen, F. Parivar, J. Kurhanewicz, D. B. Vigneron, and P. R. Carroll, *Radiology*, 1996, **198**, 807.
28. H. Howighorst, J. Dorsam, M. V. Knopp, W. Jugowski, S. O. Schoenberg, M. Wiesel, M. Essig, and G. Van-Kaick, *Roto. Fortschr. Geb. Rontgenstr. Neuen. Bildgeb. Verfahr.*, 1998, **168**, 44.
29. A. D. Vellet, J. Saliken, B. Donnelly, E. Raber, R. F. McLaughlin, D. Wiseman, and N. H. Ali-Ridha, *Radiology*, 1997, **203**, 653.
30. U. G. Mueller Lisse, A. F. Heuck, M. Thoma, R. Muschter, P. Schneede, E. Weninger, S. Faber, A. Hofstetter, and M. F. Reiser, *JMRI*, 1998, **8**, 31.
31. R. A. Boni, T. Sulser, W. Jochum, B. Romanowski, J. F. Debatin, and G. P. Krestin, *Radiology*, 1997, **202**, 232.
32. U. G. Mueller Lisse, A. Heuck, P. Schneede, R. Muschter, J. Scheidler, A. G. Hofstetter, and M. F. Reiser, *J. Comput. Assist. Tomogr.*, 1996, **20**, 273.

Dynamic Nuclear Polarization and High-Resolution NMR of Solids

Robert A. Wind

Battelle/Pacific Northwest Laboratories, Richland, WA, USA

1	Introduction	1
2	Theory	1
3	Applications of DNP NMR	4
4	Summary, Conclusions, and Perspectives	8
5	Related Articles	9
6	References	9

1 INTRODUCTION

In solids containing both magnetic nuclei and unpaired electrons, polarization transfer can be obtained between the electron and nuclear spin systems by irradiating at or near the electron Larmor frequency. The result is an enhanced nuclear polarization and, henceforth, an enhanced NMR signal. This effect is called dynamic nuclear polarization (DNP).

Several mechanisms can be responsible for the DNP phenomenon. In 1953, Overhauser predicted that in metals the NMR signal could be enlarged by saturating the resonance line of the conducting electrons: the Overhauser effect.[1] Carver and Slichter[2] showed experimentally in metallic lithium that Overhauser's revolutionary concept was correct.

Later on, Abragam and Proctor[3] and, independently, Jeffries[4] and Erb et al.[5] found the occurrence of a DNP effect in solids containing fixed, mutually more or less isolated, unpaired electrons: the solid state effect. Finally, a third DNP effect has also been observed: the thermal mixing effect, which is present when the concentration of (fixed) unpaired electrons is so high that the mutual dipolar interactions between the electrons become comparable to the other interactions between the electrons and their surroundings. Provotorov[6] showed that in that case the electron spin system can be characterized by two polarizations: one associated with the population distribution over the Zeeman levels and one associated with the population distribution over the internal local magnetic fields which the electrons are experiencing. These polarizations may change if off-resonance irradiation is applied. Abragam and Borghini[7] used the results of Provotorov and showed that when the polarization associated with the local fields is changed, the nuclear polarization changes as well, due to a coupling between these two polarizations induced by the irradiating microwave field: the indirect thermal mixing effect. Goldman[8] remarked that this coupling could be present also in the absence of microwave irradiation, and its significance for DNP was shown by Buishvili:[9] the direct thermal mixing effect. The thermal mixing effects become especially important when the nuclear Larmor frequency is comparable to or smaller than the ESR line width.

In principle large NMR signal enhancements can be obtained via DNP, maximal of the order of the ratio of the gyromagnetic ratios of the electrons and the nuclei. For example, for protons this would result in an enhancement factor of 660, and for ^{13}C nuclei this factor would be as large as 2600. In the earlier days of DNP this aspect was mainly used and applied for the production of polarized targets used in high-energy physics or to study magnetic ordering in the μK region. However, during the past 15 years new applications have emerged as well. This has been achieved by combining DNP with modern solid state NMR techniques such as cross polarization (CP), magic angle spinning (MAS), and two-dimensional NMR spectroscopy. As a result, more detailed information about structures and dynamics of materials amenable to DNP NMR could be obtained than would have been possible without DNP.

DNP NMR spectroscopy can be applied successfully in a large variety of solid materials such as those in which the unpaired electrons occur naturally, e.g., in the form of dangling bonds, materials in which bond ruptures have occurred, e.g., resulting from pyrolysis or ionizing radiation, materials containing paramagnetic impurities, and materials doped with a suitable paramagnetic agent. In this paper several applications of DNP NMR spectroscopy in solid materials research will be given following a brief description of the DNP phenomenon. Finally, some future aspects of the technique will be discussed.

2 THEORY

Extensive reviews of the different DNP effects have been given elsewhere.[10–14] Here we shall confine ourselves to a short treatment of the main features of DNP. We shall restrict ourselves to discussing only the Overhauser and the solid state effects. Hence we shall neglect the thermal mixing effects The main reasons for this omission are that in many cases the Overhauser and solid state effects dominate, and that the overall features of the thermal mixing effects are not much different from that of the solid state effect. Moreover, the thermal mixing effects require a rather lengthy derivation, which is beyond the scope of this article.

As is necessary in the description of any NMR experiment, we have to start with the Hamiltonian. For an electron–nuclear spin system the relevant Hamiltonian is given by

$$\hat{\mathcal{H}} = -\omega_e \hat{S}_z - \omega_n \hat{I}_z + \hat{\mathcal{H}}_{ee} + \hat{\mathcal{H}}_{en} + \hat{\mathcal{H}}_{nn} \qquad (1)$$

The first two terms are the Zeeman interactions of the electrons and nuclei, respectively, where $\hat{S}_z = \sum_{j=1}^{N_e} \hat{S}_z^j$ are the electron spin operators and $\hat{I}_z = \sum_{i=1}^{N_n} \hat{I}_z^i$ are the nuclear spin operators. The term N_e is the number of unpaired electrons and N_n is the number of nuclei. Furthermore, in equation (1), $\omega_e = \gamma_e B_0$ and $\omega_n = \gamma_n B_0$, where γ_e and γ_n are the magnetogyric ratios of the electrons and nuclei, respectively, and B_0 is the external magnetic field strength. Finally, $\hat{\mathcal{H}}_{ee}$, $\hat{\mathcal{H}}_{en}$, and $\hat{\mathcal{H}}_{nn}$ denote the spin–spin interactions between the electrons, between the electrons and the nuclei, and between the nuclei, respectively. For DNP, the most

important term in equation (1) is the so-called hyperfine interaction term $\hat{\mathcal{H}}_{\mathrm{en}}$. In general, this term consists of two parts, the scalar interaction term $\hat{\mathcal{H}}^{\mathrm{s}}_{\mathrm{en}}$ and the dipolar term $\hat{\mathcal{H}}^{\mathrm{d}}_{\mathrm{en}}$. The scalar interaction arises from a finite electron spin density at the nuclear sites, either directly from the unpaired electron itself or mediated by bonding electrons polarized by the unpaired electrons.

Before describing the DNP phenomenon we first consider the energy level scheme of electron–nuclear spin pairs. For simplicity we restrict ourselves to nuclear spin-$\frac{1}{2}$ systems, with positive γ_{n} values. The result is then the simple four-energy-level scheme given in Figure 1. Also given are the nuclear and electron quantum numbers, m_{n} and m_{e}, respectively (for the electrons the highest energy state corresponds to $m_{\mathrm{e}} = +\frac{1}{2}$, because γ_{e} is negative), and as usual we denote a state in which, for example, $m_{\mathrm{n}} = +\frac{1}{2}$ and $m_{\mathrm{e}} = -\frac{1}{2}$ by the notation $|+-\rangle$. Finally, the amount of nuclei in each state is denoted by $N_{\mathrm{n}1}, N_{\mathrm{n}2}$, etc. Then, defining $N_{\mathrm{n}}^{+} = N_{\mathrm{n}2} + N_{\mathrm{n}4}$ and $N_{\mathrm{n}}^{-} = N_{\mathrm{n}1} + N_{\mathrm{n}3}$ as the total amounts of nuclei in the + and − states, respectively, we can define the nuclear polarization, P_{n}, as

$$P_{\mathrm{n}} = \frac{N_{\mathrm{n}}^{+} - N_{\mathrm{n}}^{-}}{N_{\mathrm{n}}^{+} + N_{\mathrm{n}}^{-}} = \frac{N_{\mathrm{n}}^{+} - N_{\mathrm{n}}^{-}}{N_{\mathrm{n}}} = \frac{\Delta N_{12} + \Delta N_{34}}{N_{\mathrm{n}}} \qquad (2)$$

In Figure 1 the situation of thermal equilibrium is depicted, where the population distribution is governed by the Boltzmann distribution corresponding to the lattice temperature. Then P_{n} is defined as P_{n}^{0}. Similar expressions can be given for the electron polarization, P_{e}, and its thermal equilibrium value, P_{e}^{0}. It can easily be derived that in the high-temperature approximation, where $h\omega_{\mathrm{e}}/kT_{\mathrm{L}}$, $h\omega_{\mathrm{n}}/kT_{\mathrm{L}} \ll 1$, P_{n}^{0} and P_{e}^{0} are given by

$$P_{\mathrm{n}}^{0} = \frac{1}{2}\,\omega_{\mathrm{n}}\hbar(kT_{\mathrm{L}})^{-1} \quad \text{and} \quad P_{\mathrm{e}}^{0} = \frac{1}{2}\omega_{\mathrm{e}}\hbar(kT_{\mathrm{L}})^{-1} \qquad (3)$$

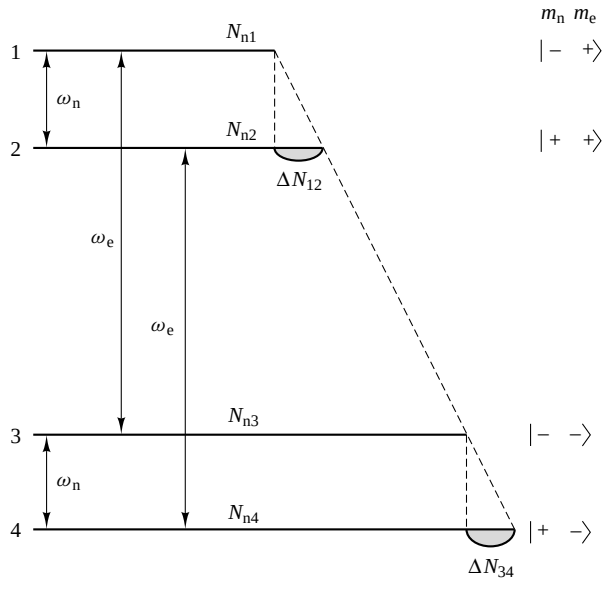

Figure 1 The Zeeman energy level scheme of electron–nuclear spin pairs. The population distribution over the energy levels depicts the thermal equilibrium situation

where T_{L} is the lattice temperature. It follows from equation (3) that the thermal equilibrium polarization of the electrons is a factor $\gamma_{\mathrm{e}}/\gamma_{\mathrm{n}}$ larger than that of the nuclei. It is this difference in polarization that is used in DNP, which we shall now consider.

2.1 The Overhauser Effect

The Overhauser effect occurs when $\hat{\mathcal{H}}_{\mathrm{en}}$ is time-dependent on a timescale of the order ω_{e}^{-1}. Then $\hat{\mathcal{H}}_{\mathrm{en}}(t)$ causes relaxation transitions between the various levels depicted in Figure 1, which, when combined with an irradiation at the electron Larmor frequency, results in a change in the nuclear polarization.

In order to illustrate this, we assume that the scalar interaction term, $\hat{\mathcal{H}}^{\mathrm{s}}_{\mathrm{en}}$, dominates. It can be shown that $\hat{\mathcal{H}}^{\mathrm{s}}_{\mathrm{en}}$ causes a relaxation transition between the $|+-\rangle$ and $|-+\rangle$ states of the electron–nuclear system, hence between the levels 1 and 4 in Figure 1. We shall call this relaxation rate W^{s}_{14}, which is given by $W^{\mathrm{s}}_{14} = \frac{1}{2}\overline{a_{ij}^{2}}\,\boldsymbol{J}(\omega_{\mathrm{e}} + \omega_{\mathrm{n}}, \tau_{\mathrm{c}})$; $\boldsymbol{J}(\omega, \tau_{\mathrm{c}})$ is the spectral density function characterizing the time dependence, $\overline{a_{ij}^{2}}$ is the time-averaged value of a_{ij}^{2}, where a_{ij} denotes the strength of the scalar interaction. As with all relaxation transitions, after some population distortion $W_{14}{}^{\mathrm{s}}$ restores the Boltzmann distribution between the energy levels connected by W^{s}_{14}, hence between levels 1 and 4. Now suppose that we are irradiating with a microwave field of amplitude B_1 and a frequency ω close to ω_{e}. This means that we are irradiating between the electron Zeeman levels 1 and 3 respectively 2 and 4 with an induced transition probability $W/2 = (\pi/2)\gamma_{\mathrm{e}}^{2}B_1^{2}g(\omega - \omega_{\mathrm{e}})$, where $g(\omega)$ is the normalized lineshape function of the ESR line.

Suppose also that W is large enough to saturate the ESR line completely. Then in the stationary situation, the population distribution over the various levels becomes as given in Figure 2. Due to the saturating irradiation the population of level 1 becomes equal to that of level 3, and the population of level 2 becomes equal to that of level 4. Due to the relaxation transition, W^{s}_{14}, the Boltzmann distribution exists between the levels 1 and 4. As a result, the population differences between the nuclear Zeeman levels 1 and 2 respectively 3 and 4 is increased: the nuclear polarization is (positively) enhanced. The enhancement curve, which is the Overhauser enhancement factor as a function of the irradiation frequency ω, reflects the (saturated) ESR line, and is symmetrical about ω_{e} for symmetrical ESR lines. The enhancement becomes maximal for $\omega = \omega_{\mathrm{e}}$. An Overhauser effect also occurs when the (time-dependent) dipolar electron–nuclear interactions, $\hat{\mathcal{H}}^{\mathrm{d}}_{\mathrm{en}}$, dominate. It can be shown that $\hat{\mathcal{H}}^{\mathrm{d}}_{\mathrm{en}}$ causes relaxation transitions between all four energy levels, so that the result becomes more complicated. However, it can be shown that often the relaxation transition between the levels 2 and 3 dominates, and the reader can easily convince himself that in this situation the nuclear polarization enhancement becomes negative.

The question arises under which circumstances we can expect to observe an Overhauser effect. As already stated above, a time-dependence in $\hat{\mathcal{H}}_{\mathrm{en}}$ is needed with a correlation time of the order of $(\omega_{\mathrm{e}} \pm \omega_{\mathrm{n}})^{-1} \simeq \omega_{\mathrm{e}}{}^{-1}$, which in practice means that τ_{c} has to be of the order 10^{-11} to 10^{-12} s. In

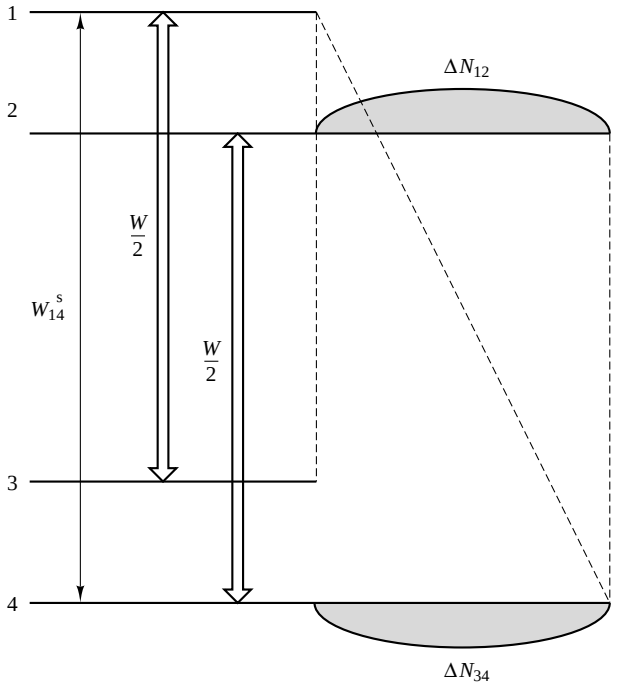

Figure 2 The Overhauser effect due to the scalar electron–nuclear interactions. The population distribution over the energy levels depicts the stationary situation

solids, the molecular motions are almost never that fast, so that an Overhauser effect due to this type of motion is highly unlikely. However, other processes may occur in solids that do provide the required time dependence: (1) in conductors or semiconductors, the conducting electrons move very rapidly through the lattice, rendering the spatial coordinates in $\hat{\mathcal{H}}_{\text{en}}$ time-dependent on a fast scale (this explains the success of observing an Overhauser effect in metals[2]); (2) in solids with large amounts of unpaired electrons and/or with electrons with a delocalized electron density distribution, strong electron–electron spin exchange interaction may occur.[15] These interactions, which arise from electrostatic Coulomb interactions, cause a time-dependence in the electron spin operator $\hat{S}$ occurring in $\hat{\mathcal{H}}_{\text{en}}$, and hence in $\hat{\mathcal{H}}_{\text{en}}$ itself. Also this time-dependence can be fast enough to fulfill the requirements for the Overhauser effect.[10] An example is the Overhauser effect observed in graphite and other solids containing large aromatic clusters.

2.2 The Solid State Effect

The solid state effect occurs in solids with fixed paramagnetic centers and with electron–nuclear interactions that are time-independent or only slowly time-dependent, with correlation times typically larger than about 10^{-5} s. The presence of $\hat{\mathcal{H}}_{\text{en}}$ means that there exist, beside the external B_0 field, static local magnetic fields in the sample, partly oriented perpendicular to B_0. It is well known from second-order perturbation theory that the result of such interactions is that the electron–nuclear states can no longer be described by the pure product functions given in Figure 1, but become mixed with other states. The admixture coefficient depends on the energy

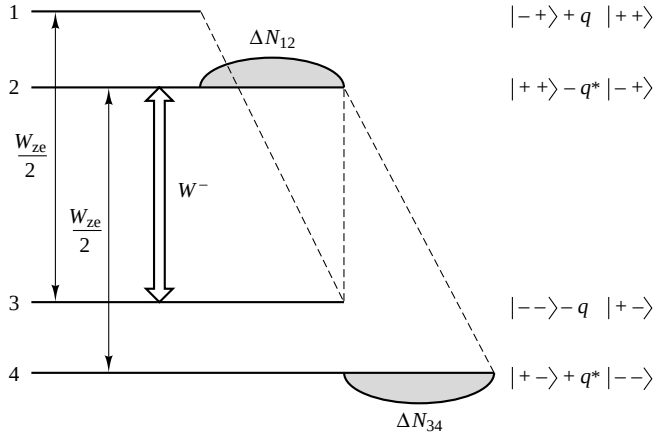

Figure 3 The solid state effect due to the forbidden transition W^-. The population distribution over the energy levels depicts the stationary situation

difference between the levels corresponding to the states and increases with decreasing energy differences. Hence, in highest order, the mixture occurs between the states corresponding to the levels 1 and 2 respectively 3 and 4. The result is given in Figure 3, where q (and its complex conjugate q^*) denotes the admixture coefficient. It should be emphasized that q is small, typically of the order 10^{-3} to 10^{-4}. Nevertheless, these small admixtures have as an important consequence that irradiation with a frequency $\omega_e - \omega_n$ or $\omega_e + \omega_n$ leads to a nonzero transition probability between the levels 2 and 3 respectively 1 and 4.

In order to understand this we consider the effect of irradiating with a frequency $\omega_e - \omega_n$. If the eigenstates were not mixed nothing would happen, because the matrix element $\langle -- |\hat{\mathcal{H}}_{\text{rf}}| ++\rangle$ is zero as the Hamiltonian $\hat{\mathcal{H}}_{\text{rf}}$ representing the rf irradiation is proportional to single spin operators. However, if the eigenstates are mixed, a small but nonzero transition probability is obtained because now nonzero matrix elements such as $-q\langle +- |\hat{\mathcal{H}}_{\text{rf}}| ++\rangle$ occur. This is called the 'forbidden' transition, W^-. Similar results are obtained for irradiation at $\omega_e + \omega_n$, giving rise to a 'forbidden' transition W^+. The quantities W^+ and W^- are given by

$$W^{\pm} = 2|q|^2 \pi \gamma_e^2 \boldsymbol{B}_1^2 g(\omega_e - \omega \pm \omega_n) \qquad (4)$$

The effect of irradiating at $\omega_e - \omega_n$ on the nuclear polarization is depicted in Figure 3. Here we have also incorporated the effect of the electron Zeeman relaxation rate, W_{Ze}. Then, in the stationary situation, W_{Ze} maintains the Boltzmann distribution between the electron Zeeman levels 1 and 3 with respect to 2 and 4, whereas W^- equalizes the populations of levels 2 and 3. The result is a positive enhancement of the nuclear polarization P_n: the solid state effect. In a similar way it can be shown that irradiation at $\omega_e + \omega_n$ leads to a negative enhancement of P_n. For symmetrical ESR lines the solid state enhancement curve, which is the enhancement factor as a function of the irradiation frequency ω, is antisymmetrical about ω_e. The enhancement becomes maximal for $\omega = \omega_e \pm \omega_n$.

In Figure 4 examples are given of enhancement curves due to the various DNP effects, including the effects of thermal mixing. As mentioned before we will not treat thermal mixing in any detail. Here we confine ourselves to remarking that,

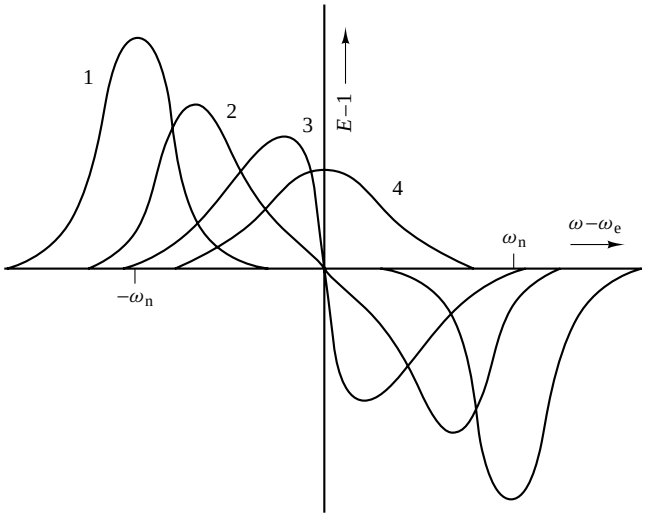

Figure 4 The enhancement curves of the various DNP effects: curve 1, solid state effect; curve 2, indirect thermal mixing effect; curve 3, direct thermal mixing effect; curve 4, Overhauser effect. Reproduced by permission of Marcel Dekker, Inc., from R. A. Wind, in 'Modern NMR Techniques and Their Application in Chemistry', eds. A. I. Popov and K. Hallenga, 1991, p. 125

like the enhancement curve due to the solid state effect, the thermal mixing enhancement curves are antisymmetrical about ω_e for symmetrical ESR lines. The direct effect of thermal mixing becomes maximal when the offset frequency, $\omega - \omega_e$, is comparable to the ESR linewidth, whereas indirect thermal mixing gives a maximal enhancement for offset frequencies between those for which the direct thermal effect and the solid state effect become maximal.

2.3 Enhancement Factors

As already mentioned in the Introduction, in theory large DNP enhancement factors can be expected, of the order of γ_e/γ_n. However, in practice, several factors can limit the magnitude of the enhancement factor which is actually obtained. We shall illustrate this for enhancements by the Overhauser and solid state DNP effects (for a more general treatment the reader is referred elsewhere[13,14,16,17]). For the Overhauser effect, we have already remarked that DNP enhancement can be positive or negative, depending on whether the scalar or the dipolar electron–nuclear interactions dominate. As a consequence, as in general both types of interactions are present, the enhancement is reduced and can become almost zero in unfavorable cases.

In the solid state effect, irradiation with a frequency ω can lead simultaneously to both forbidden transition probabilities W^- and W^+. This is especially the case when the ESR linewidth is comparable to the ω_n, see Figure 5 (in fact, as is shown in the figure, irradiation can result in both the allowed transition probability, W, and the forbidden transition probabilities W^- and W^+). As W^- and W^+ result in enhancements of opposite sign, the result is a decreased solid state enhancement, the so-called unresolved solid state effect. This can occur especially for low γ_n nuclei, for which ω_n is small. (However, it can be shown[13,14] that in these cases the enhancements due to thermal mixing increase, so that

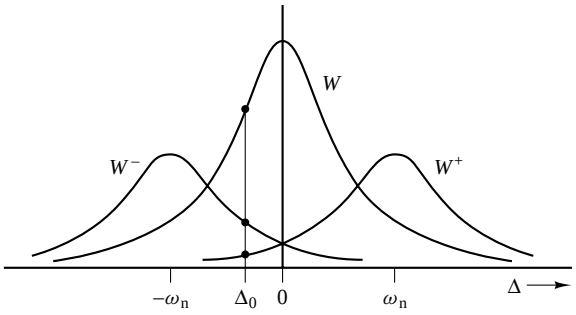

Figure 5 The allowed and forbidden transition probabilities as a function of the offset frequency $\Delta = \omega - \omega_e$. Irradiation at Δ_0 simultaneously leads to W, W^-, and W^+

the overall enhancement can still be large.) Other parameters that determine the enhancements are the amount of unpaired electrons, N_e, which has to be relatively large; the ESR linewidth, which should be small; the electron spin–lattice relaxation rate, W_{ze}, which should be large; the amplitude of the microwave field, B_1, which should be large; the external magnetic field, B_0, which should be small in order to obtain appreciable forbidden transition rates (this is only important for the solid state effect); the nuclear Zeeman relaxation rate, which should be small; and the correlation time τ_c characterizing the time dependence in $\hat{\mathcal{H}}_{en}$. As has already been mentioned, if $\tau_c \approx \omega_e \approx 10^{-11}$ to 10^{-12} s, the Overhauser effect dominates, whereas the solid state effect is observed when $\tau_c \geq 10^{-5}$ s. For τ_c values between these limits, both effects are small; if electron–nuclear interactions exist with different time constants, both effects might be present. We shall encounter this situation later.

The author and others[14,16,17] have given expressions for the different enhancement factors, from which the enhancements can be calculated if the various parameters mentioned above are known. For instance, for abundant-spin systems with large γ_n values and fixed paramagnetic centers, appreciable solid state enhancement factors (a factor 10 or more) can be expected under the following conditions: $N_e \geq 10^{24}\,m^{-3}$; ESR linewidth ≤ 1 mT; ${W_{ze}}^{-1}$ of the order of μ s; $B_1 \geq 0.03$ mT; $B_0 = 1.4$ T; nuclear Zeeman relaxation time ≥ 1 s. For rare-spin systems with small γ_n values, the enhancement factors are often at least an order of magnitude larger, which is mainly due to larger Zeeman relaxation times and an increased importance of the direct thermal mixing effect.[14]

It should be kept in mind, however, that these parameters are not independent of each other, and that large enhancements have been observed under completely different conditions. For instance, in natural diamonds a large ^{13}C enhancement factor of 200 is observed[14] despite the small value of N_e ($\simeq 10^{22}\,m^{-3}$). The reason is the large carbon Zeeman relaxation time ($\simeq 2000$ s) occurring in this material.

3 APPLICATIONS OF DNP NMR

Both the DNP enhancement curves and the DNP-enhanced NMR spectra can be used to obtain detailed and often unique information about the chemical and physical properties of solid materials, and representative illustrations of such applications will be given in this section. All experiments that will be

described have been performed in an external field of 1.4 T, corresponding to an electron Larmor frequency of 40 GHz and nuclear Larmor frequencies of 60 MHz for protons, 15 MHz for ^{13}C nuclei, and 12 MHz for ^{29}Si nuclei. Elaborate descriptions of the experimental setups, including the probes have been given.[18,19] All measurements were performed at room temperature.

3.1 The DNP Enhancement Curves

The symmetrical or antisymmetrical character of the DNP curve makes it possible to determine whether the electron–nuclear interactions are time-dependent, time-independent, or whether both types of interactions are present. This is illustrated in Figure 6, where are given the enhancement curves for ^{1}H and ^{13}C using DNP for a low-volatile bituminous coal. The ^{1}H DNP curve, Figure 6(a), contains both a symmetric and antisymmetric contribution, presumably because part of the electrons undergo rapid spin-exchange interactions whereas other electrons behave as fixed paramagnetic centers. The ^{13}C curve, Figure 6(b), is antisymmetric within experimental error, probably due to the much larger enhancements resulting from the static electron–carbon interactions, which overshadow the relatively small Overhauser enhancement. The occurrence of both the Overhauser and solid state effect in the ^{1}H DNP curves has been observed in a large variety of coals of different rank,[20] as well as in cellulose heat-treated in the temperature range 250–1000 °C.[21] It was found that for heating temperatures above 275 °C unpaired electrons were formed as a result of band ruptures and a DNP effect was observed. In the lower temperature range, up to ca. 450 °C, the solid state and thermal mixing effects dominate, whereas, between 450 °C and 700 °C, it is mainly an Overhauser effect which is observed (above 700 °C no DNP effect may be measured because the ESR line becomes very broad). However, the DNP enhancement curves indicate that an Overhauser effect also exists in the low temperature range, and that the solid state and thermal mixing effects are present for heating temperatures up to 500 °C. This is attributed to the small amounts of unpaired electrons undergoing rapid spin-exchange interactions at low temperatures, and behaving as fixed centers at the higher temperatures, respectively. In fact, it could be shown that the DNP curves could be used to detect fractions of electrons smaller than 1% either behaving as fixed centers or submitted to exchange interactions.

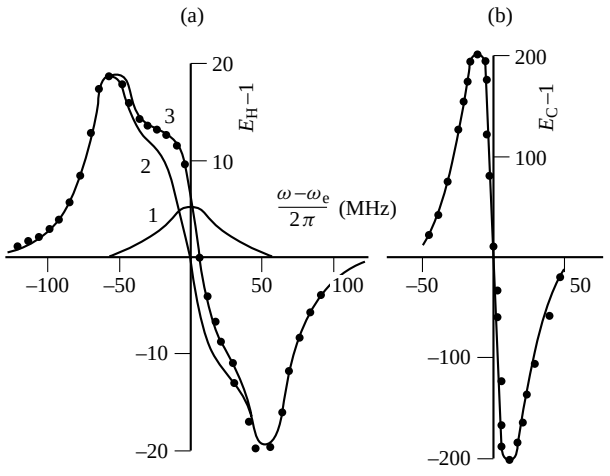

Figure 6 DNP enhancement curves obtained in a low-volatile bituminous coal. (a) ^{1}H DNP curves: curve 1, symmetric part; curve 2, antisymmetric part; curve 3, overall enhancement; dots, experimental. (b) ^{13}C DNP curve. Reproduced by permission of the American Chemical Society from R. A. Wind, R. H. Lewis, H. Lock, and G. E. Maciel, in 'Magnetic Resonance in Carbonaceous Solids', eds. R. E. Botto and Y. Sanada, ACS Ser. No. 229, 1993, p. 45

3.2 DNP and High-Resolution NMR in Solids

The increase in the NMR signal due to DNP can be used to reduce measuring times or to measure relatively small amounts of compounds. This ability is especially important for NMR spectroscopy on rare-spin species where, in the absence of DNP, long measuring times, several hours or more, are required in order to obtain an acceptable signal-to-noise ratio. In this section we shall give examples of such DNP NMR experiments.

In solids containing, besides unpaired electrons, both abundant spins and rare spins, the rare-spin polarization can be enhanced via DNP in two ways. (1) *Indirectly*, by first enhancing the abundant-spin polarization followed by a polarization exchange between the abundant and rare spins via cross polarization (CP). This is called the DNP CP (or DNP CP MAS when magic angle spinning is applied as well) experiment. In those cases where both the abundant spins and the electrons are homogeneously distributed in the sample, the spin diffusion among the abundant nuclei is generally strong enough to establish a single, average, polarization enhancement for all abundant nuclei, resulting, after CP, in an enhanced, undistorted, NMR spectrum of the rare nuclear spins. (In compounds where the electrons and/or the abundant nuclei are not homogeneously distributed, a distribution in DNP enhancements may also occur. As we shall see later, this effect can be used selectively to study interfaces and surfaces.) (2) The rare-spin polarization can also be enhanced *directly* via a polarization exchange between the electrons and the rare nuclei. This experiment, in which the rare-spin NMR signal is observed via a standard 90° rf pulse, will be called the DNP SP (MAS) experiment (SP = single pulse). Of course, in materials such as ceramics and diamonds, which do not contain abundant spins, DNP SP is the only possible technique. As the spin diffusion between rare spins is small, a distribution of enhancement factors often exists in the DNP SP experiment with larger enhancements for the nuclei in the vicinity of the unpaired electrons.[14] This has the disadvantage that distortions can occur in the DNP SP NMR spectra, but has the (potentially powerful) advantage that this experiment makes it possible selectively to probe structures and dynamics near the unpaired electrons.

It should be noted that in solids containing both rare and abundant nuclear spins, even in a DNP SP experiment the rare spin polarization can also be enhanced indirectly via a polarization exchange with the abundant spins. This has been called the three-spin effect.[22] This phenomenon is observed in cases that the rare-spin Zeeman relaxation is dominated by the interactions between the rare and abundant nuclear spins. Hence this effect is more likely to occur for rare nuclei remote from the unpaired electrons, where the electron–nuclear

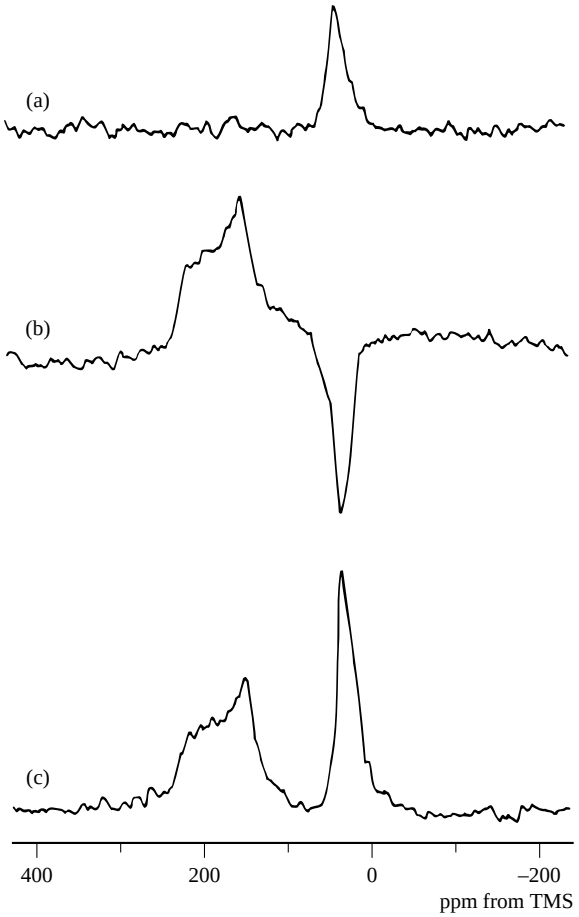

Figure 7 ^{13}C NMR spectra of a composite of *trans*-polyacetylene and polyethylene. (a): Result of an SP experiment; (b) and (c): Results of a DNP SP experiment without (b) and with (c) proton saturation. Reproduced by permission of the Academic Press from G. G. Maresch, R. D. Kendrick, C. S. Yannoni, and M. E. Galvin, *J. Magn. Reson.*, 1989, **82**, 41

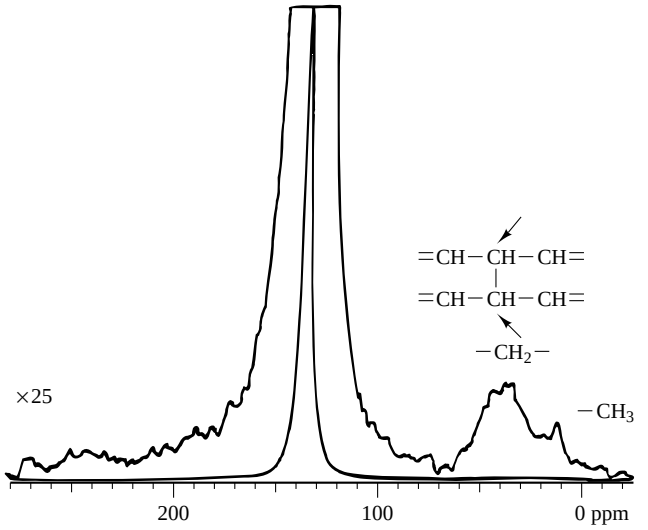

Figure 8 ^{13}C spectrum of *trans*-polyacetylene, obtained via ^{1}H–^{13}C DNP CP MAS NMR. The main line at 135 ppm is due to the ^{13}C nuclei inside the $(CH)_x$ chains; structural defects responsible for the other lines are indicated in the figure

interactions become weak. The three-spin effect arises from the nuclear Overhauser effect (NOE). This is similar to the Overhauser effect described in Section 2. The only differences are that NOE is caused by nuclear–nuclear interactions instead of electron–nuclear interactions, and that NOE is due to dipolar interactions only. It follows from Section 2 that NOE leads to a positive polarization enhancement of the rare-spin polarization if the abundant spin polarization is decreased via saturation (assuming that the gyromagnetic ratio of the nuclei is positive). However, if the abundant spin polarization is, for example, positively enlarged via DNP, the NOE enhancement of the rare spins becomes negative. Consequently, in a rare-spin DNP SP experiment, a positive direct enhancement from the electrons can be counteracted by a negative NOE enhancement. The three-spin effect is illustrated in Figure 7 where ^{13}C spectra are shown of a polymer consisting of small islands of *trans*-polyacetylene (PA) embedded in a matrix of polyethylene (PE). In *trans*-polyacetylene, $(CH)_x$, unpaired electrons (the so-called solitons) are present, presumably arising from bond-alternation domain walls.[23] These solitons move rapidly over the chains at least part of the time, giving rise to an Overhauser effect.[14,24] It follows that for the ^{13}C line around 20 ppm, which is due to the PE carbons which are for the major part remote from the solitons in the PA chains, the NOE effect leads to a negative enhancement in a DNP SP experiment without proton saturation. However, the ^{13}C line around 200 ppm is due to the carbons in the PA chains. Here the soliton–carbon interactions are so strong that the NOE effect is not observed. The three-spin effect can be avoided by partially saturating the abundant-spin polarization to such an extent that the polarization remains at its thermal equilibrium value.

We shall now consider applications of the DNP CP MAS and DNP SP MAS experiments.

3.2.1 Increase in Sensitivity

The increase in sensitivity due to DNP can result in dramatic decreases in the measuring time of an experiment. This can be used, for instance, for a fast (of the order of minutes) characterization of coal,[20] ceramics,[25] and diamonds,[14] to perform two-dimensional experiments in a relatively short time[24] (in this latter case, a two-dimensional experiment is reported for PA which would have required a measuring time of 165 years without DNP!), or to detect small amounts of molecules. An example of the latter application is shown in Figure 8 where the (natural abundance) ^{13}C DNP CP MAS spectrum of *trans*-polyacetylene is shown. Despite the fact that the amount of material was small (8 mg), the ^{1}H enhancement was so large (27-times in this experiment), that a ^{13}C spectrum with an excellent signal-to-noise ratio was obtained in a relatively short time.[26] In fact, it can be determined that the small narrow line at 13 ppm, which is due to the methyl end groups of the polyacetylene chains, represents only 0.5% of the total amount of carbons, or 3×10^{16} ^{13}C nuclei.

3.2.2 Structures and Dynamics Near the Unpaired Electrons

An example of the type of local information that can be obtained via DNP is shown in Figure 9. In this figure, ^{13}C spectra are shown of *trans*-polyacetylene obtained after a few

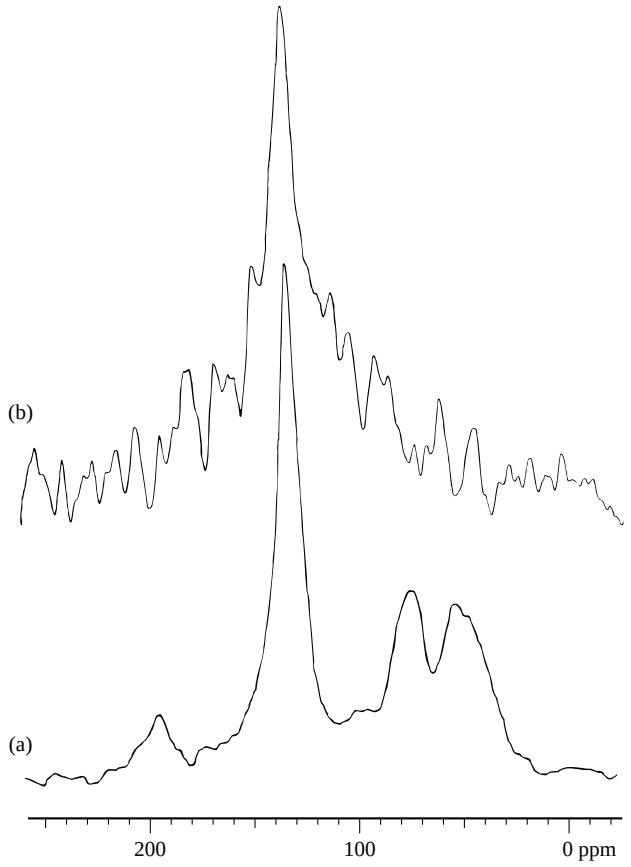

Figure 9 ^{13}C spectra of *trans*-polyacetylene, exposed to air for 4 months, obtained via (a) DNP CP MAS NMR and (b) DNP SP MAS NMR

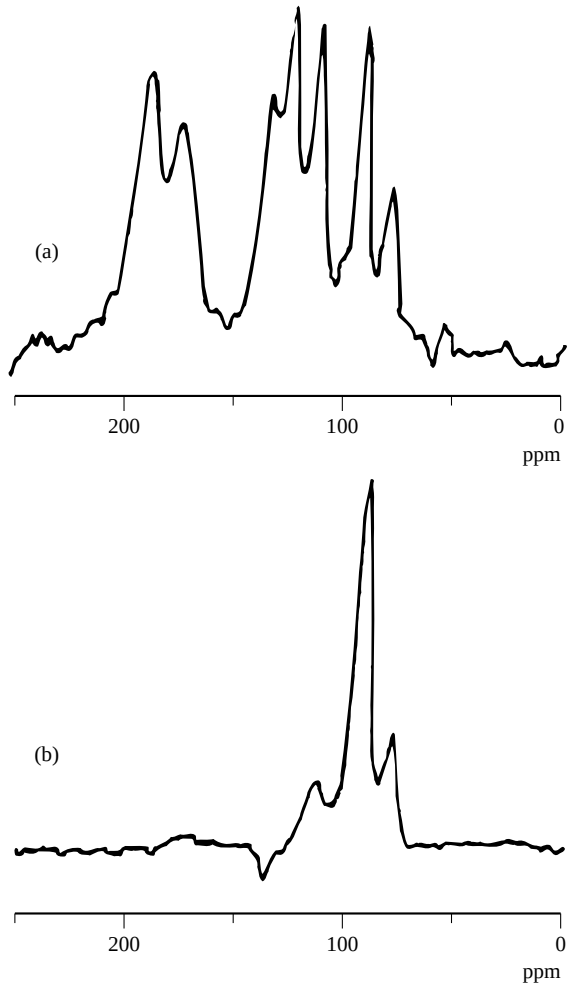

Figure 10 ^{13}C spectra of (fluoranthenyl)$_2PF_6$, obtained via (a) DNP CP MAS NMR and (b) DNP SP MAS NMR. Reproduced by permission of Marcel Dekker, Inc., from R. A. Wind, in 'Modern NMR Techniques and Their Application in Chemistry', eds. A. I. Popov and K. Hallenga, 1991, p. 125

months of exposure of the sample to air. Figure 9(a) shows the result of a DNP CP MAS experiment on ^{13}C. Compared with Figure 8, it follows that extra lines are observed due to the formation of ethene oxide groups, oxygen bridges, hydroxyl groups, and carbonyl groups.[27] Figure 9(b) shows the spectrum obtained via a ^{13}C DNP SP MAS experiment. We observe here that only the carbons in the $(CH)_x$ chains are detected. Hence in the latter experiment mainly the carbons in the chains below the surface are observed. These are not affected by exposure to the air.

Another type of local information that can be obtained via DNP SP MAS is the spin-density distribution of the unpaired electrons over the molecules.[26] An example of this possibility is the organic conductor (fluoranthenyl)$_2PF_6$. At room temperature this material behaves as a one-dimensional metal where the conduction electrons move more or less freely along paths parallel to the molecular stacks.[28] The electron mobility is so large that only an Overhauser effect is observed in this sample.[29] The average enhancement for ^1H is positive. This means that the dominating electron–proton hyperfine interaction is scalar. As a consequence, the overall enhancement of the DNP CP MAS spectrum of ^{13}C is positive as well, and Figure 10(a) shows the result of such an experiment. However, completely different results are obtained in the DNP SP MAS experiment on ^{13}C, shown in Figure 10(b). Here some lines are enhanced positively, indicative of a dominant electron–carbon scalar interaction, and one line is enhanced negatively due to a dominating electron–carbon dipolar interaction, whereas for the other lines the two DNP effects eliminate one another, resulting in a negligibly small enhancement. This phenomenon is due to the distribution of the electron density over the fluoranthenyl molecules, which is different at the different sites of the carbons, resulting in different ratios of the electron–carbon scalar and dipolar interactions. Hence, experiments utilizing DNP SP MAS can be used to determine the electron density distribution over the sites of the chemically different carbons.

Another application of DNP NMR in conductors is the determination of Knight shifts.[29] The Knight shift is proportional to the polarization of the conducting electrons. Hence, by saturating the ESR line, not only a signal enhancement due to DNP is obtained, but the Knight shift is suppressed as well. It has been shown[29] that for (fluoranthenyl)$_2PF_6$ the Knight shifts in the various carbon lines could be separated from the 'ordinary' chemical shift.

3.2.3 Interfaces and Surfaces

An example of an interfacial study with DNP NMR is an investigation of an immiscible mixture of polycarbonate

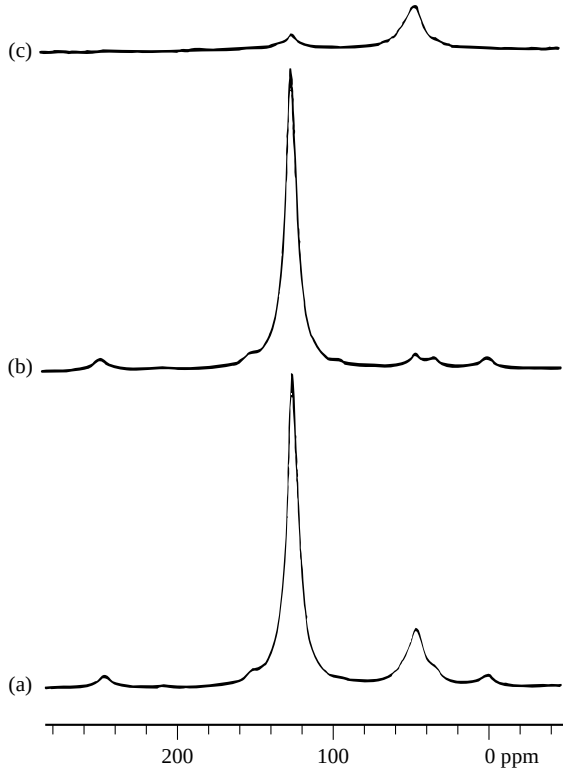

Figure 11 ^{13}C CP MAS NMR spectra of polycarbonate/polystyrene blends (a) with and (b) without ^{1}H DNP. The difference spectrum (c) has two features: the intensity around 40 ppm is due to the sp^3-hybridized carbons in PS whereas the intensity around 120 ppm arises from the carbons in the PC chains at the interface. Reproduced by permission of the American Society from M. Afeworki, R. A. McKay, and J. Schaefer, *Macromolecules*, 1992, **25**, 4084

(PC) and polystyrene (PS).[19,30] The samples consisted of thin film blends in which the polystyrene was doped with the stable radical BDPA [1,3-bis(diphenylene)-2-phenylallyl]. The interfacial region of PC could then be studied by measuring the DNP enhancement of protons via $^{1}H-^{13}C$ DNP CP MAS NMR. Figure 11 shows the results of such a measurement, carried out on a blend consisting of PC, which is labeled at the 3 and 3′ ring positions with 99 atom% ^{13}C, and PS, which is ^{13}C-depleted in all phenyl ring carbons. In this way, interferences between the NMR resonances of the aromatic carbons of the two polymers, which are partially overlapping, were avoided, and the peak observed at 120 ppm was almost exclusively due to the ^{13}C-labeled sites in PC. As the unpaired electrons in BDPA behave as fixed paramagnetic centers, the DNP enhancement of ^{1}H is mainly due to the solid state effect. Figure 11(a) and (b) show the $^{1}H-^{13}C$ CP MAS spectra obtained with and without ^{1}H DNP, respectively. It follows that the protons in PS, which are close to the unpaired electrons, are enhanced to the greatest extent (a factor of 20) and that there is also a small but noticeable enhancement for the protons in PC. This can be seen more clearly in Figure 11(c) where the differential spectrum is given. It has been shown[30a] that the proton polarization in PC is enhanced due to direct polarization transfer from these protons to the electrons, and that the signal of ^{13}C in PC observed in the differential spectrum arises from a 60 Å region from the PC/PS boundary which is 2% of the PC film thickness. Moreover, the

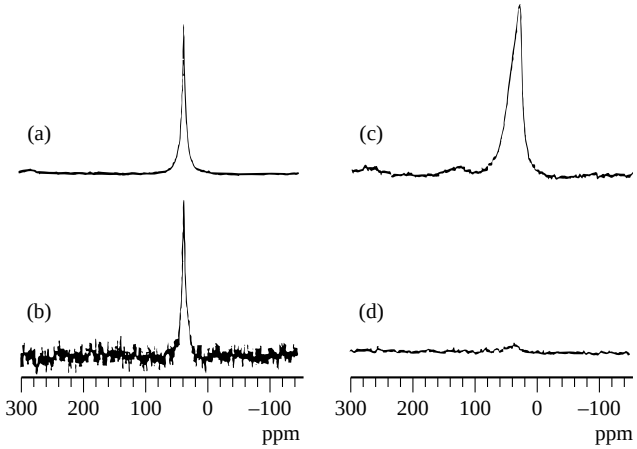

Figure 12 ^{13}C spectra of a 14% ^{13}C-enriched CVD diamond film, obtained via (a) DNP SP MAS NMR, (b) SP MAS NMR, (c) $^{1}H-^{13}C$ DNP CP MAS NMR, and (d) $^{1}H-^{13}C$ CP MAS NMR. Reproduced by permission of the American Institute of Physics from H. Lock, R. A. Wind, and G. E. Maciel, *J. Chem. Phys.*, 1993, **99**, 3363

authors were able to show that the interfacial aromatic carbons in PC have less motion than that of the bulk-PC aromatic carbons. This was attributed to restricted interchain motions resulting from a more dense packing for the PC chains near the PS barrier.

An example of a surface that can be studied via DNP NMR is provided by an investigation of chemical vapor deposited (CVD) diamond films.[31] Figure 12 shows ^{13}C spectra of a 14% ^{13}C enriched diamond film prepared by microwave-plasma-assisted CVD, using CH_4 and H_2 as feed gases.[31b] During the formation of the diamond films, unpaired electrons occur in the form of dangling bonds, which can be used for DNP measurements. Figure 12(a) and (b) show the results of ^{13}C DNP SP MAS NMR and SP MAS NMR, respectively, illustrating the increase in sensitivity due to DNP (the ^{13}C DNP enhancement factor is 50). Figure 12(c) and (d) show ^{13}C spectra obtained via $^{1}H-^{13}C$ DNP CP MAS and CP MAS NMR. A small percentage of protons (<0.1 atom %) is present at the intergrain boundaries of the diamond, and DNP can be used to enhance the proton signal (the enhancement factor is 25). It follows from Figure 12(c) that the hydrogenated diamond surfaces give rise to new resonances in the carbon spectrum (it was shown that the broad resonance at around 45 ppm actually consists of two lines), and the chemical shifts corresponding to these lines have been used to investigate the possibilities of different ‘diamondoids’, hydrogen-bearing carbon structures, occurring at the surfaces.[31b]

4 SUMMARY, CONCLUSIONS, AND PERSPECTIVES

High-resolution NMR combined with microwave-induced DNP has resulted in new areas of rare-spin NMR studies in solids. In many materials large DNP enhancement factors have been observed, which made possible NMR experiments which could not have been performed without DNP. The maximum proton enhancement that has been measured in a probe capable of MAS was 60, carbon enhancements of a few hundred were no exception, and in a ceramic fiber a silicon

enhancement factor 1000 was reported.[25] Although the DNP enhancements were not so large in some other materials, it should be kept in mind that even smaller enhancements can be very useful as they cause a reduction in the measuring time proportional to the square of the enhancement. Besides increasing the NMR sensitivity, DNP can also be used for other purposes such as the study of the structures and dynamics near the unpaired electrons, the detection of small amounts of electrons undergoing strong exchange interactions or behaving as fixed centers, the determination of the mobility and the spin-density distribution of conducting electrons, the study of surfaces and interfaces, the determination of Knight shifts, and DNP-enhanced imaging.[32] Finally, DNP NMR has been applied in a large variety of solid materials, such as doped polymers, coal, pyrolyzed materials, amorphous silica, organic conductors, semiconductors, natural and artificial diamonds, polymer composites, and ceramics.

However, it should be noted that many other possibilities for utilizing DNP NMR still remain to be explored:

1. Other types of radicals such as ions, nitroxide radicals, or radicals resulting from ionizing radiation.
2. Other materials; for example, experiments have already been started to explore the potential of DNP in zeolites, catalysts, and biomaterials.
3. High-resolution DNP NMR on quadrupolar nuclei.
4. High-resolution DNP NMR at different temperatures.
5. High-resolution DNP NMR at different pressures.
6. Combination of DNP with other high-resolution solid NMR techniques such as CRAMPS, fast MAS, DAS, DOR.
7. Combination of high-resolution NMR with different DNP techniques, which have been developed to increase the DNP enhancement factors and to improve the polarization transfer rates. Examples of these new techniques are the NOVEL (Nuclear spin Orientation Via Electron spin Locking) experiment,[33] which is an electron–nuclear analog of the CP experiment, and which provides fast polarization transfer (μs); the integrated solid effect (ISE),[34] where DNP is combined with adiabatic rapid passage through the ESR line, resulting in increased enhancement factors; DNP in the nuclear rotating frame,[35] which reduces the polarization transfer time by several orders of magnitude and which can be used to avoid distortion in the CP spectra resulting from rotating frame relaxation effects; DNP in higher external magnetic fields,[36] which might improve the resolution of the NMR spectra, and nuclear polarization enhancement using light irradiation. Examples of the latter techniques are microwave-induced optical nuclear polarization (MIONP),[37] optically polarized xenon and other rare gases, which can be used to study surfaces[38] and optical nuclear polarization (ONP).[39] Large enhancements have been obtained; for example, by applying the ISE technique in a naphthalene crystal doped with pentacene, in which the triplet state is highly polarized by photo-excitation, a DNP enhancement factor of the naphthalene protons of 5500 has been found.[40]

It can be expected that this and the other new methodologies and applications will further enhance the applicability of solid state NMR, and that many exciting new results will emerge in the near future.

5 RELATED ARTICLES

Cross Polarization in Rotating Solids: Spin-1/2 Nuclei; Cross Polarization in Solids; Electron–Nuclear Hyperfine Interactions; Electron–Nuclear Multiple Resonance Spectroscopy; Magic Angle Spinning; Nuclear Overhauser Effect; Optically Enhanced Magnetic Resonance.

6 REFERENCES

1. A. W. Overhauser, *Phys. Rev.*, 1953, **92**, 411.
2. T. R. Carver and C. P. Slichter, *Phys. Rev.*, 1953, **92**, 212.
3. A. Abragam and W. G. Proctor, *C. R. Acad. Sci.*, 1958, **246**, 2253.
4. C. D. Jeffries, *Phys. Rev.*, 1957, **106**, 164.
5. E. Erb, J. L. Motchane, and J. Uebersfeld, *C. R. Acad. Sci.*, 1958, **246**, 2121.
6. B. N. Provotorov, *Sov. Phys. JETP*, 1962, **14**, 1126.
7. A. Abragam and M. Borghini, in *Progress in Low Temperature Physics*, ed. C. J. Gorter, North-Holland Publishing Co., Amsterdam, 1964, Vol. 4, Chap. 8
8. M. Goldman, *Phys. Rev.*, 1965, **138**, A1675.
9. L. L. Buishvili, *Sov. Phys. JETP*, 1966, **22**, 1277.
10. A. Abragam, *The Principles of Nuclear Magnetism*, Clarendon Press, Oxford, 1961.
11. K. H. Hausser and D. Stehlik, in *Advances in Magnetic Resonance*, ed. J. S. Waugh, Academic Press, New York, 1968, Vol. 3, p. 79.
12. M. Goldman, *Spin Temperature and NMR in Solids*, Clarendon Press, Oxford, 1970.
13. A. Abragam and M. Goldman, *Nuclear Magnetism: Order and Disorder*, Clarendon Press, Oxford, 1982.
14. R. A. Wind, M. J. Duijvestijn, C. van der Lugt, A. Manenschijn, and J. Vriend, *Prog. NMR Spectrosc.*, 1985, **17**, 33.
15. N. W. Ashcroft and N. D. Mermin, *Solid State Physics*, Saunders College, Philadelphia, PA, 1976, Chap. 32
16. M. J. Duijvestijn, R. A. Wind, and J. Smidt, *Physica*, 1986, **138B**, 147.
17. R. A. Wind, R. H. Lewis, H. Lock, and G. E. Maciel, in *Magnetic Resonance of Carbonaceous Solids*, eds. R. E. Botto and Y. Sanada, *ACS Ser. No. 229*, 1993, 45.
18. R. A. Wind, F. E. Anthonio, M. J. Duijvestijn, J. Smidt, J. Trommel, and G. M. C. de Vette, *J. Magn. Reson.*, 1983, **52**, 424.
19. M. Afeworki, R. A. McKay, and J. Schaefer, *Macromolecules*, 1992, **25**, 4084.
20. R. A. Wind, M. J. Duijvestijn, C. van der Lugt, J. Smidt, and H. Vriend, *Fuel*, 1987, **66**, 876.
21. R. A. Wind, L. Li, G. E. Maciel, and J. B. Wooten, *Appl. Magn. Reson.*, 1993, **54**, 161.
22. G. G. Maresch, R. D. Kendrick, C. S. Yannoni, and M. E. Galvin, *J. Magn. Reson.*, 1989, **82**, 41.
23. W. P. Su, J. R. Schrieffer, and A. J. Heeger, *Phys. Rev. Lett.*, 1978, **42**, 1698.
24. M. J. Duijvestijn, A. Manenschijn, J. Smidt, and R. A. Wind, *J. Magn. Reson.*, 1985, **64**, 461.
25. R. H. Lewis, R. A. Wind, and G. E. Maciel, *J. Mater. Res.*, 1993, **8**, 649.
26. R. A. Wind, in *Modern NMR Techniques and Their Application in Chemistry*, eds. A. I. Popov and K. Hallenga, Marcel Dekker, Inc., New York, 1991, p. 125.
27. R. A. Wind, M. J. Duijvestijn, and J. Vriend, *Solid State Commun.*, 1985, **56**, 713.

28. M. Mehring and J. Spengler, *Phys Rev. Lett.*, 1984, **53**, 2441.
29. (a) W. Stocklein, C. S. Yannoni, H. Seidel, and D. Singel, *Chem. Phys. Lett.*, 1987, **141**, 277; (b) R. A. Wind, H. Lock, and M. Mehring, *Chem. Phys. Lett.*, 1987, **141**, 283.
30. (a) M. Afeworki and J. Schaefer, *Macromolecules*, 1992, **25**, 4092; (b) M. Afeworki and J. Schaefer, *Macromolecules*, 1992, **25**, 4097; (c) M. Afeworki, S. Vega, and J. Schaefer, *Macromolecules*, 1992, **25**, 4100.
31. (a) H. Lock, G. E. Maciel, and C. E. Johnson, *J. Mater. Res.*, 1992, **7**, 2791; (b) H. Lock, R. A. Wind, and G. E. Maciel, *J. Chem. Phys.*, 1993, **99**, 3363.
32. G. E. Maciel and M. F. Davis, *J. Magn. Reson.*, 1985, **64**, 356.
33. A. Henstra, P. Dirksen, J. Schmidt, and W. Th. Wenckebach, *J. Magn. Reson.*, 1988, **77**, 389.
34. A. Henstra, P. Dirksen and W. Th. Wenckebach, *Phys. Lett. A*, 1988, **134**, 134.
35. R. A. Wind and H. Lock, *Adv. Magn. and Opt. Reson.*, 1990, **15**, 51.
36. S. Un, T. Prisner, R. T. Weber, M. J. Seaman, K. W. Fishbein, A. E. Dermott, D. J. Singel, and R. G. Griffin, *Chem. Phys. Lett.*, 1992, **189**, 54.
37. (a) H. Brunner, R. H. Fritsch, and K. H. Hausser, *Z. Naturforsch.*, 1987, **42a**, 1456; (b) P. Dirksen, A. Henstra, and W. Th. Wenckebach, *J. Magn. Reson.*, 1990, **86**, 549.
38. (a) Z. Wu, W. Happer, M. Kitano, and J. Daniels, *Phys. Rev. A*, 1990, **42**, 2774; (b) D. Raftery, L. Reven, H. Long, A. Pines, P. Tang, and J. A. Reimer, *J. Phys. Chem.*, 1993, **97**, 1649.
39. (a) D. Stehlik and H.-M. Vieth, in *Pulsed Magnetic Resonance: NMR, ESR and Optics*, ed. D. M. S. Bagguley, Clarendon Press, Oxford, UK, 1992, p. 446; (b) S. K. Buratto, D. N. Shykind, and D. P. Weitekamp, *Phys. Rev. B*, 1991, **44**, 9035.
40. A. Henstra, T.-S. Lin, J. Schmidt, and W. Th. Wenckebach, *Chem. Phys. Lett.*, 1990, **165**, 6.

Biographical Sketch

R. A. Wind. *b* 1942. B.S., 1966, Ph.D., 1972, Delft, The Netherlands Introduced to NMR by J. Smidt. Faculty in Delft University of Technology, 1972–85; Senior research scientist, Colorado State University, 1985–90; Director of Research and Development, Chemagnetics/Otsuka Electronics, 1990–93; Senior staff scientist, Battelle/PNL, 1993–present. Approx. 90 publications. Current research specialties: NMR/DNP NMR and its applications in liquids and solids chemistry.

Electron–Nuclear Hyperfine Interactions

Karl H. Hausser and Hermann Brunner
Max-Planck-Institut, Heidelberg, Germany

1	Introduction	1
2	Principle	1
3	^{1}H NMR	2
4	NMR with Other Nuclei	3
5	NMR of Radical Ions	4
6	Related Articles	5
7	References	5

1 INTRODUCTION

The literature on electron–nuclear hyperfine coupling as measured by NMR is so large that a comprehensive survey would by far exceed the scope of this article. Hence we concentrate on the principles which determine the applicability and the limitations of this method. The selection of the few examples given is necessarily subjective; for reasons discussed below, we have restricted ourselves to free radicals in solution.

The electron–nuclear hyperfine interaction between a nuclear spin and an unpaired electronic spin causes a splitting of the resonance absorption lines of electron paramagnetic resonance (EPR) which is termed 'hyperfine splitting' (HFS). The splitting is usually described in terms of a coupling constant a_i for the ith nucleus given either in tesla or in hertz; it was measured in the first 20 years of NMR by analyzing the splitting in the EPR spectrum. While the obtainable resolution of NMR depends mainly on the homogeneity of the external magnetic field $\boldsymbol{B}_0$, the resolution of EPR depends on the relaxation phenomena of the unpaired electrons which contribute to the transverse relaxation time T_2 of the electronic spin and hence to the linewidth. It would be outside the scope of this paper to discuss the various mechanisms which contribute to the linewidth—in particular the spin–orbit interaction can broaden the line in metal complexes beyond the resolvability of HFS. It turns out that free radicals in solution are the most suitable systems for studying hyperfine interactions.

The HFS can frequently not be resolved, even in solutions of free radicals consisting of first row elements in low viscosity liquids where the spin–orbit interaction and dipolar broadening are negligible. This is often due to the interaction of the unpaired spins of the electrons with the paramagnetic oxygen O_2 present in most solvents in contact with air. Therefore, the linewidth can be drastically decreased and the resolution correspondingly increased by carefully removing O_2 from the solvent.[1] This is illustrated by the example given in Figure 1, the EPR spectrum of 2,4,6-triphenylphenoxyl in benzene.[2]

However, even without oxygen the HFS in EPR spectra cannot be resolved in many cases. This is due to the large number of lines in an EPR spectrum because the total number of HFS components equals the product of the number of lines

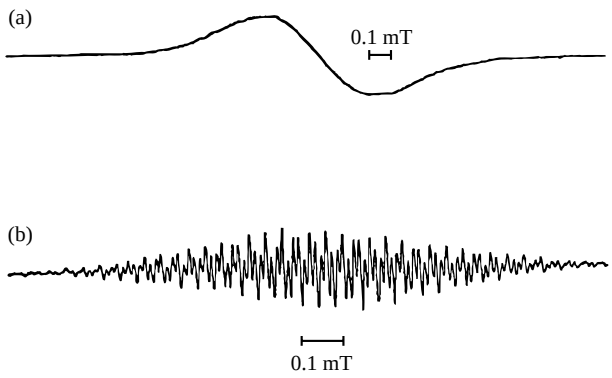

Figure 1 EPR spectra of 2,4,6-triphenylphenoxyl in benzene (concentration 5×10^{-4} mol l^{-1}): (a) saturated with air, (b) after the exclusion of oxygen

originating from nonequivalent nuclei (nuclei with identical HFS coupling constants are termed 'equivalent'). If a free radical contains three types of equivalent protons, namely l_i protons with coupling constant a_i, m_j with coupling constant a_j, and n_k with coupling constant a_k, the total number of HFS lines is $(l + 1)(m + 1)(n + 1)$, which easily leads to several hundreds and even thousands of HFS components. If this large number of HFS lines cannot be resolved, the coupling constants can be measured in many cases by means of electron–nuclear double resonance (ENDOR) or electron–nuclear triple resonance.[3–5] For the example given above, one expects six ENDOR absorption lines, two for each type of equivalent protons. One drawback of ENDOR is that the number of equivalent nuclei that cause an ENDOR transition can usually not be deduced from an ENDOR spectrum, since the intensity of the lines is not proportional to the number of equivalent nuclei, but depends in a complicated manner on the relaxation processes within the sample; we shall not discuss this further here since it is not the topic of this paper, but it is dealt with in another article in this Encyclopedia (see ***Electron–Nuclear Multiple Resonance Spectroscopy***).

Although ENDOR may help by very drastically reducing the number of absorption lines in cases where the coupling constants cannot be measured by high-resolution ESR because the number of HFS components is too high, both methods fail in the case of small coupling constants.

2 PRINCIPLE

The interaction of a nucleus with spin $I = \frac{1}{2}$ and a magnetogyric ratio γ_I and an unpaired electron with spin $S = \frac{1}{2}$ and a magnetogyric ratio γ_S in an external magnetic field $\boldsymbol{B}_0$ can be described by the Hamiltonian

$$\hat{\mathcal{H}} = \gamma_S \hbar(\hat{\boldsymbol{S}} \cdot \boldsymbol{B}_0) + \gamma_I \hbar(\hat{\boldsymbol{I}} \cdot \boldsymbol{B}_0) + \gamma_S \gamma_I \hbar^2 \times \left[\tfrac{8}{3}\pi |\Psi_{(0)}|^2 (\hat{\boldsymbol{I}} \cdot \hat{\boldsymbol{S}}) + \frac{3(\hat{\boldsymbol{I}} \cdot \boldsymbol{r})(\hat{\boldsymbol{S}} \cdot \boldsymbol{r})}{\boldsymbol{r}^5} - \frac{(\hat{\boldsymbol{I}} \cdot \hat{\boldsymbol{S}})}{\boldsymbol{r}^3} \right] \quad (1)$$

The first two terms are the electronic and nuclear Zeeman term; the third term is the scalar Fermi contact term which causes the hyperfine splitting.

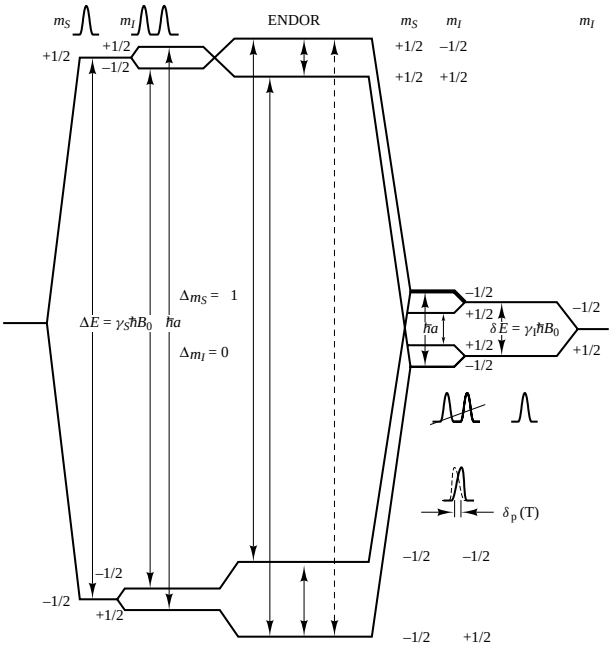

Figure 2 Energy levels and transitions in a coupled two-spin system of one electronic spin $S = \frac{1}{2}$ and one nuclear spin $I = \frac{1}{2}$

The fourth term, (the dipolar term) depends explicitly on the angle Θ between the vector $\boldsymbol{r}$ connecting $\boldsymbol{S}$ and $\boldsymbol{I}$ and the magnetic field $\boldsymbol{B}_0$. The term is averaged out to zero by the molecular motion in low viscosity liquids and hence does not contribute to the time-independent interaction, i.e. the energy levels, but it must be taken into account for the time-dependent interactions, such as relaxation and dynamic nuclear polarization (DNP).

It is instructive to consider the energy levels and possible transitions given by the first three time-independent terms of this two-spin system (Figure 2) the method is easily extended to more nuclei as are present in most practical cases, but the simple example shown in Figure 2 is suitable for understanding the principle. On the left, we recognize the four energy levels originating from the secular parts (the z components) of the first and third terms in the Hamiltonian [equation (1)] and the corresponding EPR transitions. When considering ENDOR, the second term in equation (1), the nuclear Zeeman term, must be taken into account. This leads to the energy levels and the corresponding ENDOR transitions shown in the center of Figure 2.

In principle, the energy levels of the NMR shown on the right in Figure 2 should also be split into two lines with the same splitting constant a. However, this splitting cannot be observed because the NMR lines are broadened by at least two types of time-dependent phenomena associated with the unpaired electrons; first, electronic spin–lattice relaxation with the time constant $T_{1,S}$ and second, electronic exchange with the time constant τ_{ex}. In general, these time constants are sufficiently short to satisfy the following condition

$$T_{1,S} \ll \frac{1}{2\pi a} \quad \text{and/or} \quad \tau_{ex} \ll \frac{1}{2\pi a} \tag{2}$$

Hence one obtains in this case, instead of a splitting, a paramagnetic shift $\Delta B = B_d - B_p$ or $\Delta\nu = \nu_p - \nu_d$.[6,7] In this paper we use frequency units rather than magnetic field units since they give a direct measure of the energy differences and since the coupling constant a is identical whether it is measured by EPR or by NMR, while in magnetic field units the ratio of the magnetogyric ratios of the electron and the nucleus must be taken into account.

A paramagnetic shift δ_p termed the isotropic hyperfine contact interaction shift was defined[6] in analogy to the diamagnetic chemical shift but with the opposite sign, i.e. with a positive sign for a downfield shift and a negative sign for an upfield shift. Since the magnitude of δ_p depends on the Boltzmann factor of the electronic Zeeman energy levels, it is temperature dependent. Its magnitude measured in ppm is given by

$$\delta_p(T) = \frac{B_d - B_p}{B_d} = \frac{a'\hbar\gamma_S^2}{4kT\gamma_I} \tag{3a}$$

$$\delta_p(T) = \frac{\nu_p - \nu_d}{\nu_d} = \frac{ah\gamma_S}{4kT\gamma_I} \tag{3b}$$

where the coupling constant a' is measured in tesla and a is in hertz. For protons at room temperature the result is

$$\delta_p(295\,\text{K}) = a \cdot 26.8\,\text{ppm MHz}^{-1} \tag{3c}$$

Note that with this definition the paramagnetic shift is not measured with respect to any standard, but is measured with respect to the same nucleus in a diamagnetic molecule as similar as possible to the radical.

As $\delta_p(T)$ is proportional to the coupling constant a, the latter can be determined by measuring $\delta_p(T)$ using NMR as well as from the HFS of EPR. At room temperature the coupling constant a_i of the ith nucleus is given by

$$a_i = \frac{4kT\gamma_I}{h\gamma_S}\delta_p(295\,\text{K})\,\text{MHz} \tag{4a}$$

Inserting the constants, one obtains for protons

$$a_i = 3.73 \times 10^{-2}\delta_p(295\,\text{K})\,\text{MHz} \tag{4b}$$

Measuring the coupling constant a by NMR has one additional advantage: while EPR renders only the absolute value of a, $\delta_p(T)$ gives the sign as well. This is particularly valuable for small coupling constants. While in the case of medium or large coupling constants the sign can usually be calculated theoretically with high certainty, this is not so for small coupling constants, the measurement of which is the main domain of NMR.

3 ^{1}H NMR

The first NMR spectrum of a free radical, namely di-*t*-butyl nitroxide (DBNO), which is a liquid at room temperature, is shown (with TMS as an internal standard) in Figure 3.[6] The linewidth is found to be $\Delta\nu = 230$ Hz and the shift δ_p (295 K) $= -8.0$ ppm which, following equation (4), give a coupling constant $a_i = -0.298$ MHz. Note that in this case $\delta_p(T)$ was

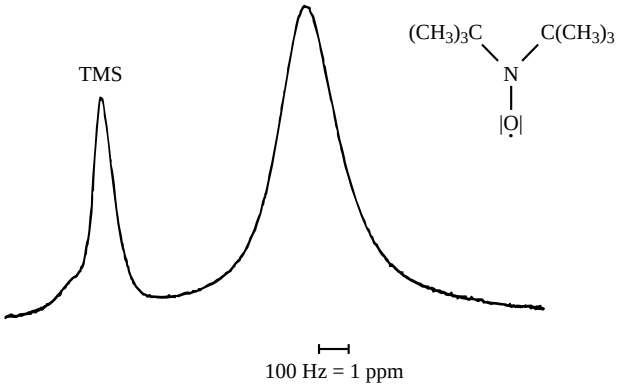

Figure 3 ^{1}H NMR spectrum of the liquid free radical di-*t*-butyl nitroxide with TMS as internal standard

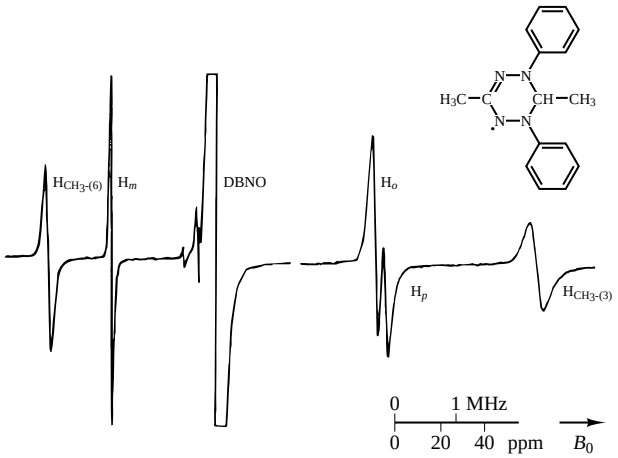

Figure 4 ^{1}H NMR spectrum of 3,6-dimethyl-1,5-diphenylverdazyl in DBNO

measured with respect to the internal standard TMS because no diamagnetic molecule of similar structure was available; since the ^{1}H nuclei in TMS are also in methyl groups, the deviation can be assumed to be rather small. It has been pointed out[8] that to obtain the correct paramagnetic shift $\delta_p(T)$ for neutral radicals its dependence on the concentration of the paramagnetic species must be measured and extrapolated to zero, because otherwise the varying magnetic susceptibility falsifies the result. This is certainly true when using an external standard. However, when using an internal standard, either a general standard like TMS for ^{1}H nuclei or an atom in a molecule that is as similar as possible, this effect is compensated for by the fact that the standard is in a medium with the same bulk susceptibility as the radical. In this case, the error when measuring the different concentrations up to a neat liquid radical stays usually below 10%, i.e. it does not exceed the typical solvent effect.

It is obvious that the critical quantity in NMR measurements of paramagnetic species is the linewidth, since this determines both the possible resolution and the sensitivity. For nuclei with spin $I = \frac{1}{2}$ in paramagnetic compounds the linewidth $\Delta\nu$ is proportional to the square of the interaction between the nucleus and the unpaired electron. The two main types of interaction are the scalar contact interaction discussed above and the dipolar interaction. For larger coupling constants a_i, the scalar interaction dominates, but for small a_i values the two can become comparable.

Since the linewidth $\Delta\nu \propto a_i^2$, medium and large values of a_i lead in general to very broad, unobservable NMR absorption lines. However, this broadening effect can be averaged out by sufficiently short time constants. The condition for obtaining narrow lines is much more limiting than equation (2), namely

$$T_{1,S} \ll \frac{1}{2\pi\nu_S} \tag{5}$$

$$\tau_{ex} \ll \frac{1}{2\pi\nu_S} \tag{6}$$

where ν_S is the Larmor frequency of the electron. Equation (5) and/or equation (6) may be satisfied in favorable cases of certain metal chelate compounds for which very narrow lines have been obtained.

Several attempts can be made to reduce the linewidth to come closer to the condition given in equation (6). One possibility is to use the liquid free radical DBNO as solvent.[9] Figure 4 shows as an example the NMR spectrum of 3,6-dimethyl-1,5-diphenylverdazyl in DBNO at a resonance frequency of 90 MHz.[7] The linewidth varies from about 0.09 MHz to 0.3 MHz, and the different NMR absorption lines are well resolved. The paramagnetic shifts δ_p(295 K) with respect to the corresponding ^{1}H resonances of the diamagnetic leucoverdazyl vary between −148 and +63.5 ppm. As expected, the linewidth increases with the coupling constant, but even the absorption line of the ^{1}H atoms in the methyl group in the R^3 position in the central ring, with a linewidth of about 250 kHz, is easily seen although it has a coupling constant as large as $a_i = -5.52$ MHz. One problem with DBNO is that some absorption lines may be hidden below the broad absorption line of DBNO, in this example the line due to the H atom at the C atom in the central ring. In general, the gain in resolution when using DBNO as a solvent is one order of magnitude for larger coupling constants, but much lower for absorption lines of nuclei with small coupling constants.

4 NMR WITH OTHER NUCLEI

Another approach to increasing the resolution is to use ^{2}H NMR instead of ^{1}H NMR. The paramagnetic shift of the deuterons (in ppm) is, of course, identical to the shift of the protons. Because of the much smaller magnetogyric ratio of the deuterons one expects a reduction of the shift measured in hertz by a factor of γ_P/γ_D, but a reduction of the linewidth by the square of this quantity $(\gamma_P/\gamma_D)^2$. Hence the net increase in resolution when using deuterons instead of protons should be proportional to $\gamma_P/\gamma_D \approx 6.5$.

The ^{2}H NMR spectrum of 3-*t*-butyl-1,5-bis(pentadeuterophenyl)verdazyl in DBNO is reproduced as an example in Figure 5.[7] The gain in resolution when using ^{2}H NMR instead of ^{1}H NMR is found to be about a factor of 2 to 3, but not 6 as expected from theory, considering the Fermi contact interaction only. It follows that the best possible resolution can be obtained using ^{2}H NMR in DBNO; the maximum gain in resolution $\Delta\nu/\nu$ which is obtained in practice is a factor of about 20.

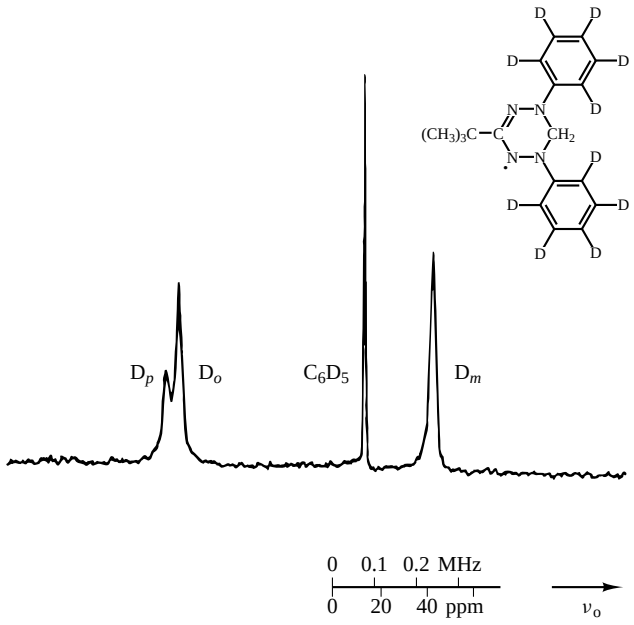

Figure 5 ^{2}H NMR spectrum of 3-*t*-butyl-1,5-bis(pentadeuterophenyl)verdazyl in DBNO

The measurement of the coupling constant a_i was extended to ^{13}C NMR.[10] In cases where a_i could be measured by ESR as well, good agreement was found in general. Differences are of the same order (about 10%) as found with ESR in different solvents; the concentration dependence mentioned above also plays a role, since the NMR is usually measured at high concentration (>2 M), while the concentration with the ESR measurements was mostly about 10^{-3}–10^{-4} M.[11] While the coupling constant a_i of the ^{1}H nucleus is generally mainly determined by the spin density at the atom to which the ^{1}H is bound (with some geometrical effects), ^{13}C NMR measurements of a series of nitroxide radicals showed that the coupling constants a_i depend in a more complex manner on the polarization of the electrons in the nitrogen–carbon bond and on the carbon–carbon bonds, as well as on geometrical effects.[11] The situation is even more complicated with aromatic fluoro compounds where the spin polarization between the 2p orbital of the fluorine and the spin in the 2p orbital of the adjacent carbon atom has to be considered. In favorable cases the sign and magnitude of the fluorine coupling could be obtained.[12]

5 NMR OF RADICAL IONS

A somewhat different situation is encountered when measuring the NMR of radical ions in solution. In general, in the solution both neutral molecules M and the corresponding negative radical ions M^- will be present. In this case there is an electron transfer reaction between these two species, which may be symbolized by[13]

$$M + M^- \rightleftharpoons M^- + M \tag{7}$$

Here the paramagnetic shift $\delta_p(T)$ of a nucleus in the molecule is not given directly by equation (3), but the fraction f_p of paramagnetic radicals in the solution must be taken into account; this is given by

$$f_p = M^-/(M + M^-) \tag{8}$$

Hence the paramagnetic shift $\delta'_p(T)$ becomes

$$\delta'_p(T) = f_p \delta_p(T) \tag{9}$$

Since the measured quantity in this case is $\delta'_p(T)$, in equation (4), $\delta_p(T)$ must be replaced by $\delta_p(T)/f_p$ in order to obtain the coupling constant a_i. The fraction f_p can be determined from the solvent shift due to the change in the susceptibility of the solution as a function of the reduction of the molecule M.[13]

It was stated above that measurement of the coupling constant a_i of a nucleus within a neutral free radical by NMR is usually restricted to small coupling constants. However, in the case of radical ions the chemical exchange with the time constant τ_{ex}^{ch} can be so fast that it approaches the much stricter conditions of equations (5) and (6); it was estimated to be of the order of $\tau_{ex}^{ch} \simeq 10^{-11}$.[14] This is illustrated by the example of biphenyl in diglyme.

Figure 6 shows the ^{1}H NMR spectrum of biphenyl in diglyme. The ^{1}H NMR line of the *meta* protons is much sharper and shifted downfield, as would be expected from the negative spin density at the *meta* carbon atom in biphenyl, as opposed to the much broader lines of the *ortho*- and *para*-^{1}H atoms. The paramagnetic shift $\delta_p(T)$ of the *ortho*- and *meta*-^{1}H atoms is plotted in Figure 7[14] as a function of the solvent shift $\delta_S(T)$ in diglyme when the biphenyl is gradually reduced with sodium.

Over the past 20 years the coupling constants between ^{1}H and ^{2}H nuclei and the unpaired electron spins have been measured in many such chemical exchange systems. In the case of ion radicals, even the coupling between the negative ion radicals and the alkali metal counterions (^{6}Li, ^{23}Na, ^{39}K, etc.) could be measured from the NMR of the alkali metals and the solvent, temperature and concentration dependence could be studied.[15] For more information on hyperfine interaction in NMR, the reader is referred to a series of review articles on the subject which cover the period from 1972 until 1990.[16]

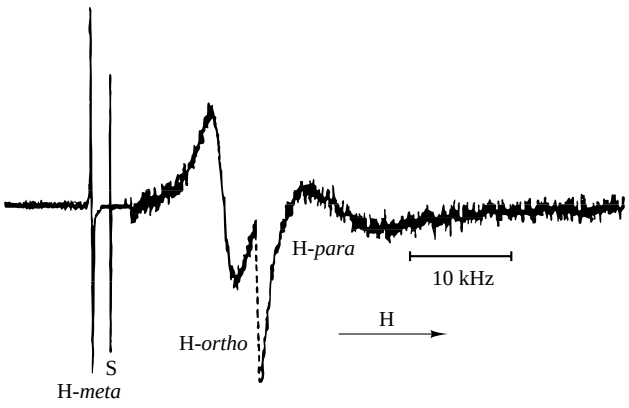

Figure 6 ^{1}H NMR spectrum at room temperature of a completely reduced 1 M solution of biphenyl in diglyme, with sodium as the reducing agent. S, solvent peak. All the peaks were measured with different rf power, gain, and modulation

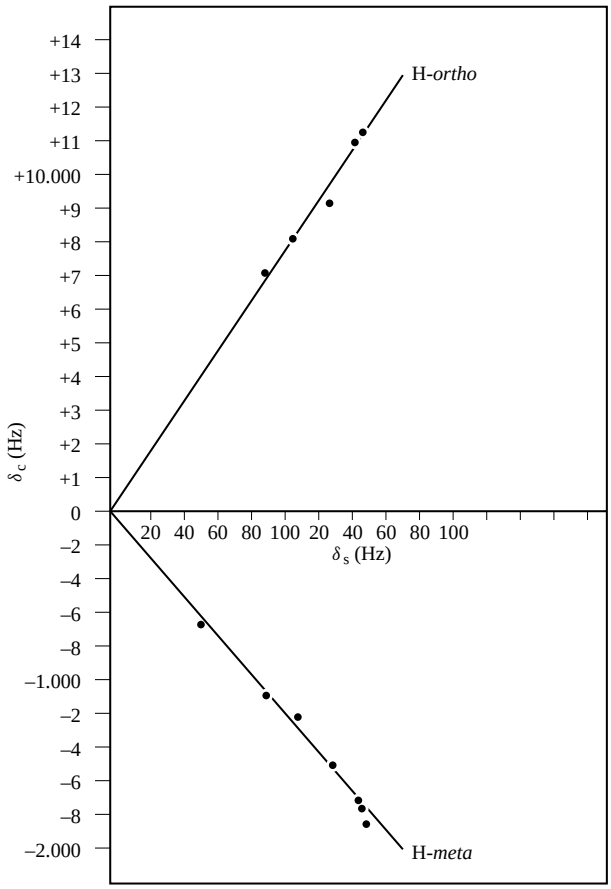

Figure 7 Contact shift δ_c at room temperature of *ortho*-^{1}H and *meta*-^{1}H of biphenyl as a function of the solvent shift δ_s for a solution of diglyme (concentration 1 M) gradually reduced with sodium

6 RELATED ARTICLES

Chemical Exchange Effects on Spectra; Electron–Nuclear Multiple Resonance Spectroscopy.

7 REFERENCES

1. K. H. Hausser, *Naturwissenschaften*, 1960, **47**, 251.
2. K. H. Hausser, C. R. 9^e Coll. Ampère, Pisa, 1960.
3. G. Feher, *Phys. Rev.*, 1956, **103**, 834.
4. J. S. Hyde and A. H. Maki, *J. Chem. Phys.*, 1964, **40**, 3117.
5. K. P. Dinse, R. Biehl, and K. Möbius, *J. Chem. Phys.*, 1974, **61**, 4335.
6. K. H. Hausser, H. Brunner, and J. C. Jochims, *Mol. Phys.*, 1966, **10**, 253.
7. H. Brunner, K. H. Hausser, and F. A. Neugebauer, *Tetrahedron*, 1971, **27**, 3611.
8. P. A. Petillo, J. De Felippis, and S. F. Nelsen, *J. Org. Chem.*, 1991, **56**, 6496.
9. R. W. Kreilick, *Mol. Phys.*, 1968, **14**, 495.
10. G. F. Hatch and R. Kreilick, *Chem. Phys. Lett.*, 1971, **10**, 490.
11. G. F. Hatch and R. W. Kreilick, *J. Chem. Phys.*, 1972, **57**, 3696.
12. W. G. Espersen and R. W. Kreilick, *Mol. Phys.*, 1969, **16**, 577.
13. E. de Boer and C. MacLean, *Mol. Phys.*, 1965, **9**, 191; *J. Chem. Phys.*, 1966, **44**, 1334.
14. G. W. Canters and E. de Boer, *Mol. Phys.*, 1967, **13**, 395.
15. G. N. La Mar, W. DeW. Horrocks, Jr, and R. H. Holm, *NMR of Paramagnetic Molecules. Principles and Applications*, Academic, New York, 1973.
16. G. A. Webb, *Nuclear Magnetic Resonance*, Royal Society of Chemistry, London, 1972–90, Vols 1–19.

Biographical Sketches

Karl H. Hausser. *b* 1919. Ph.D., Tübingen University, 1950. Visiting scientist, Physics Department, University of Chicago (Prof. Mulliken), 1956–57. Scientific member of the Max-Planck-Gesellschaft and Director of Department of Molecular Physics at Max-Planck-Institut für Medizinische Forschung, Heidelberg, 1966–87. Emeritus since 1987. More than one hundred publications. Research specialties: electron paramagnetic resonance, nuclear magnetic resonance and relaxation, dynamic nuclear polarization.

Hermann Brunner. *b* 1931. Diploma, 1959; Ph.D. 1964, Physics, Heidelberg University/Max-Planck-Institut für Medizinische Forschung, Heidelberg–present. Approx. 25 publications. Research fields: EPR in free radicals and organic conductors, optical nuclear polarization, and organic superconductors.

Electron–Nuclear Interactions

Timothy E. Machonkin and John L. Markley

Department of Biochemistry and National Magnetic Resonance Facility at Madison, University of Wisconsin, Madison, WI, USA

1 Introduction 1
2 Electron–Nuclear Interactions in Mononuclear Systems 1
3 Exchange Coupling and its Influence on Electron–Nuclear Interactions 5
4 Concluding Remarks 14
5 References 15

1 INTRODUCTION

NMR has proven to be of great utility in the study of paramagnetic proteins. Although the presence of the paramagnetic center creates inherent difficulties in obtaining structural information from nearby residues, numerous solution structures now exist for certain classes of paramagnetic proteins.[1–3] In addition, the interactions between the unpaired electron and surrounding nuclei create new effects that provide sensitive probes of the electronic and geometric structure of the paramagnetic center. Traditionally, it has been very difficult to obtain quantitative information from these electron–nuclear interactions, but with the advent of reliable, high-level computational techniques and the development of new NMR methodologies, this has begun to change. In coupled systems, a vector coupling model has been of great utility in providing a qualitative picture. In this review, we focus exclusively on FeS proteins, which have been extensively studied by NMR, and although they pose some of the greatest challenges, they have yielded some of the most satisfying agreement between theory and experiment.

2 ELECTRON–NUCLEAR INTERACTIONS IN MONONUCLEAR SYSTEMS

Paramagnetic proteins containing a single transition metal site represent the simplest case for the study of electron–nuclear interactions. Even in these systems, however, the analysis of the resulting effects can be quite complex.

2.1 Theory

We discuss here three types of electron–nuclear interactions: hyperfine shifts,[4,5] paramagnetic relaxation,[4–6] and residual dipolar couplings.[7,8] Electron–nuclear interactions provide an additional contribution to the chemical shift, called the hyperfine shift. This frequently results in peaks appearing far outside the region typical for diamagnetic shifts. Electron–nuclear interactions also give rise to additional NMR relaxation mechanisms that can broaden peaks and make them inaccessible to detection by traditional multidimensional NMR approaches. Residual dipolar couplings appear when a molecule becomes partially ordered with respect to the external magnetic field of the NMR experiment. A protein with an anisotropic magnetic susceptibility tensor will become ordered in a strong magnetic field; and this ordering will show up as changes in couplings between the nuclei of nearby magnetically active atoms. All three effects, hyperfine shifts, paramagnetic relaxation, and residual dipolar couplings, can be rich sources of information about protein structure and the properties of the metal site.

Hyperfine shifts arise from the sum of two distinct interactions: the Fermi contact shift, δ_{con}, and the electron–nuclear dipolar or pseudocontact shift, δ_{pc}. The observed chemical shift, δ_{tot}, is the sum of these two plus the diamagnetic chemical shift, δ_{dia}:

$$\delta_{\text{tot}} = \delta_{\text{con}} + \delta_{\text{pc}} + \delta_{\text{dia}} \tag{1}$$

The Fermi contact shift arises from delocalization of unpaired electron density onto ligand orbitals. Only unpaired spin density at the nucleus contributes to the Fermi contact coupling. The equation for the Fermi contact shift in ppm is:

$$\delta_{\text{con}} = 10^6 \left(\frac{\Delta\nu}{\nu_0}\right)^{\text{con}} = -10^6 \frac{A}{\hbar\gamma_N B_0}\langle S_z\rangle \tag{2}$$

where A is the isotropic hyperfine constant in Joules and $\langle S_z\rangle$ is the expectation value of S_z. (Note that hyperfine coupling is usually reported as $A/\hbar$, which has units of hertz.) In the absence of first-order orbital angular momentum or zero-field splitting (ZFS), this simplifies to:

$$\delta_{\text{con}} = 10^6 \left(\frac{\Delta\nu}{\nu_0}\right)^{\text{con}} = 10^6 \left(\frac{A}{\hbar}\right) \frac{g\mu_B S(S+1)}{3\gamma_N kT} \tag{3}$$

where g is the average molecular electron g-value (frequently assumed to be $\sim g_e$, the free electron g-value). This isotropic hyperfine coupling constant can in turn be related to the unpaired spin density at the nucleus:

$$A = \frac{\mu_0}{3S}\hbar\gamma_N g\mu_B \sum_i [|\psi_i^-(0)|^2 - |\psi_i^+(0)|^2] \tag{4}$$

where $|\psi_i^-(0)|^2$ and $|\psi_i^+(0)|^2$ are the negative and positive spin density at the nucleus of the ith molecular orbital.

The pseudocontact shift is the other contribution to the hyperfine shift. The electron magnetic moment is anisotropic as a result of coupling with the orbital angular momentum, and thus it does not average to zero with molecular tumbling. This yields an isotropic shift that is dependent upon the electron–nuclear distance. The 'point-dipole' approximation is usually invoked, in which all of the unpaired electron density is localized at the metal center. This yields:

$$\delta_{\text{pc}} = 10^6 \left(\frac{\Delta\nu}{\nu_0}\right)^{\text{pc}} = 10^6 \frac{1}{8\pi r^3} \Bigg[(3\cos^2\theta - 1) \times \left(\frac{2}{3}\chi_{zz} - \frac{1}{3}\chi_{xx} - \frac{1}{3}\chi_{yy}\right) + \sin^2\theta \cos 2\phi (\chi_{xx} - \chi_{yy}) \Bigg] \tag{5}$$

where r is the electron–nuclear distance, χ_{zz}, χ_{xx}, and χ_{yy} are the principle components of the magnetic susceptibility tensor, and θ and ϕ are the angles formed by r and the molecular z axis and the projection of r in the xy plane with the molecular x axis. Again, assuming no ZFS, this simplifies to:

$$\delta_{\text{pc}} = 10^6 \left(\frac{\Delta\nu}{\nu_0}\right)^{\text{pc}} = 10^6 \frac{\mu_0}{4\pi} \frac{\mu_B^2 S(S+1)}{18kTr^3} \times \{[2g_{zz}^2 - (g_{xx}^2 + g_{yy}^2)](3\cos^2\theta - 1) + 3(g_{xx}^2 - g_{yy}^2)\sin^2\theta\cos 2\phi\} \quad (6)$$

In analyzing hyperfine shifts, a first step is the separation of the Fermi contact and pseudocontact contributions. As seen in equation (5), the pseudocontact shift is related to the magnetic susceptibility anisotropy. In FeS systems at room temperature, this is small, and for nuclei that are only a few bonds away from the Fe, the Fermi contact term will overwhelmingly dominate. For nuclei close in space but many bonds away from the Fe, the pseudocontact shift will dominate, and can in principle provide useful distance information.

As in the case of hyperfine shifts, the paramagnetic contribution to the nuclear T_1 and T_2 relaxation rates arise from several different contributions: electron–nuclear dipolar, contact, and Curie spin. The equations for these are

$$T_{1_{\text{dip}}}^{-1} = \frac{2}{15}\left(\frac{\mu_0}{4\pi}\right)^2 \frac{\gamma_N^2 g^2 \mu_B^2 S(S+1)}{r^6} \times \left[\frac{\tau_c}{1+(\omega_I-\omega_S)^2\tau_c^2} + \frac{3\tau_c}{1+\omega_I^2\tau_c^2} + \frac{6\tau_c}{1+(\omega_I+\omega_S)^2\tau_c^2}\right] \quad (7)$$

$$T_{1_{\text{con}}}^{-1} = \frac{2}{3}\left(\frac{A}{\hbar}\right)^2 S(S+1)\frac{\tau_e}{1+(\omega_I-\omega_S)^2\tau_e^2} \quad (8)$$

$$T_{2_{\text{dip}}}^{-1} = \frac{1}{15}\left(\frac{\mu_0}{4\pi}\right)^2 \frac{\gamma_N^2 g^2 \mu_B^2 S(S+1)}{r^6} \times \left[4\tau_c + \frac{\tau_c}{1+(\omega_I-\omega_S)^2\tau_c^2} + \frac{3\tau_c}{1+\omega_I^2\tau_c^2} + \frac{6\tau_c}{1+(\omega_I+\omega_S)^2\tau_c^2} + \frac{6\tau_c}{1+\omega_S^2\tau_c^2}\right] \quad (9)$$

$$T_{2_{\text{con}}}^{-1} = \frac{1}{3}\left(\frac{A}{\hbar}\right)^2 S(S+1)\left[\tau_e + \frac{\tau_e}{1+(\omega_I-\omega_S)^2\tau_e^2}\right] \quad (10)$$

$$T_{2_{\text{Curie}}}^{-1} = \frac{1}{5}\left(\frac{\mu_0}{4\pi}\right)^2 \frac{\omega_I^2 g^4 \mu_B^4 S^2(S+1)^2}{(3kT)^2 r^6}\left[4\tau_r + \frac{3\tau_r}{1+\omega_I\tau_r^2}\right] \quad (11)$$

where ω_I and ω_S are the nuclear and electron Larmor precession frequencies, τ_r is the rotational correlation time, τ_e is the electronic relaxation rate, and τ_c is the total correlation time, given as:

$$\tau_c^{-1} = \tau_r^{-1} + \tau_e^{-1} \quad (12)$$

In these equations, several simplifying assumptions have again been made: the point-dipole approximation holds, g is isotropic, and ZFS is negligible. More complex equations have been derived that include g anisotropy and ZFS.[6] Of these simplifications, the point-dipole approximation generally is the one that fails in a quantitative analysis of relaxation rates. This is especially the case in Fe–S proteins, where the Fe is highly covalent and the electron density is delocalized significantly out onto the ligands. This is sometimes referred to as the 'ligand-centered' dipolar contribution to the relaxation rate, and attempts have been made to account for it.[9] In the high-temperature limit, the electronic transverse and longitudinal relaxation rates (T_{1e}, T_{2e}) are essentially equal, and this can be taken as the value of τ_e. The contributions to τ_e are numerous, and in general, prevent its independent determination. Nonetheless, τ_e is assumed to be $\sim 10^{-10}$–10^{-11} s for mononuclear high-spin (h.s.) Fe^{3+} and $\sim 10^{-11}$–10^{-12} s for mononuclear h.s. Fe^{2+}.[6] Curie spin relaxation, which arises from the interaction of the nuclear magnetic moment with the large static magnetic moment provided by the unpaired electrons of the metal center, can be by far the dominant contribution to T_2, especially at high fields, for proteins with a high-spin metal site (e.g., h.s. Fe^{3+}) and/or high molecular weight. The Curie spin contribution to T_1 is very small and can be ignored. Because of the strong dependence of the relaxation rate on the nuclear magnetogyric ratio, γ, hyperfine signals from nuclei with a low γ (e.g., ^{15}N and ^{2}H) are more readily observed than signals from nuclei with high γ (^{1}H). Thus, one strategy for the study of paramagnetic systems is to collect 1D ^{15}N and ^{2}H NMR data on isotopically labeled samples. Note that the chemical shifts of ^{1}H and ^{2}H are essentially equivalent.

The third type of electron–nuclear interaction is residual dipolar coupling. In solution-state NMR, rapid molecular tumbling normally averages out dipolar couplings. However, in a system with a sufficiently anisotropic magnetic susceptibility tensor, a high magnetic field can lead to partial ordering of the molecules. Because the effect is proportional to the square of the magnetic field, the dipolar couplings can be extracted from analysis of one-bond ^{1}H–X couplings at two different fields. The magnitude of $^{1}D_{\text{HX}}$ is related to the magnetic susceptibility anisotropy:

$${}^{1}D_{\text{HX}} = \frac{-\gamma_{\text{X}}\gamma_{\text{H}}B_o^2}{40kT\pi^2 r^3}\left[(3\cos^2\theta - 1)\left(\chi_{zz} - \frac{1}{2}\chi_{xx} - \frac{1}{2}\chi_{yy}\right) + \frac{3}{2}\sin^2\theta\cos 2\phi(\chi_{xx} - \chi_{yy})\right] \quad (13)$$

Note that the form of this equation is very similar to that for the pseudocontact shift (equation 5); however, residual dipolar couplings can be measured directly, whereas pseudocontact shifts must be deconvoluted from the Fermi contact and diamagnetic components of the observed chemical shift.

2.2 Applications to Fe(Cys)$_4$ Proteins

The most extensive study of hyperfine shifts in Fe(Cys)$_4$ proteins is for *Clostridium pasteruianum* rubredoxin (CpRd). Extensive and definitive assignments were obtained for the H and N atoms of the ligating Cys residues and eight nearby amide N atoms in both oxidation states through the use of selective ^{2}H and ^{15}N labeling, including chirally deuterated Cys and single-site labeling (Figure 1(a)–(f), Table 1).[10–13] Also, the Cys C^{β} resonances from reduced CpRd were identified by selective labeling (Figure 1(g), Table 1).[12]

For CpRd, Fermi contact shifts were calculated with hybrid density functional theory (HDFT) using 104-atom models[14] derived from three published crystal structures of oxidized CpRd at 1.1–1.2 Å resolution.[15–17] Extremely good agreement was obtained between the calculated Fermi contact shifts and all of the observed ^{2}H and ^{15}N hyperfine shifts for all three models (in one model, a correction to the placement of the amide H atoms was required). The pseudocontact shift was small enough that it could safely be ignored. The agreement between calculated and experimental hyperfine shifts was excellent. All assignments achieved by selective labeling were confirmed in the calculations, and the calculations allowed definitive sequence-specific assignments for nearly all the remaining hyperfine-shifted ^{2}H and ^{15}N signals. These results validate the approach and indicate that HDFT calculations are a powerful tool for obtaining a quantitative understanding of hyperfine shifts and electronic structure of metalloproteins.

In the case of CpRd, this approach demonstrated the importance of hydrogen bonding to the ligating Cys S^{γ} atoms. In CpRd, six backbone amides donate H-bonds to the Cys S^{γ} atoms: residues Val8, Cys9, Tyr11, Leu41, Cys42, and Val44. In particular, the N atoms of Tyr11 and Val44 exhibit large hyperfine shifts but are eight covalent bonds from the Fe. The conclusion, corroborated by the HDFT calculations, is that H-bonds are capable of delocalizing spin density, a feature that may be important in the electron transfer function of these systems. The calculations further showed an inverse correlation between the magnitude of the hyperfine shift and $H\cdots S^{\gamma}$ distance. (Signals from the ^{15}N atoms of the ligating Cys residues have a separate intercept because they also derive appreciable unpaired spin density through covalent bonds.) Another effect of spin delocalization through H-bonds is the large ($\geq$8 ppm) negative one-bond $^{1}H/^{2}H$ isotope effects on the chemical shifts of the Val8, Tyr11, Leu41, and Val44 N atoms (Table 1).[13] Again, HDFT calculations were able to quantitatively account for this isotope effect.[13] Recent ^{15}N NMR data[18] on a mutant of CpRd with a very different N–S^{γ} length for one of the H-bonds as determined by X-ray crystallography[19] are consistent with the correlation between H-bond length, spin density, and in turn, hyperfine shift. The calculations also helped interpret the ^{2}H, ^{15}N, and ^{13}C chemical shifts for reduced CpRb.[14] Since only coordinates for oxidized CpRd were available, the correlation between the experimental and calculated chemical shifts were not as good, and therefore the residue-specific assignments are only preliminary. Subsequent calculations based on the recently

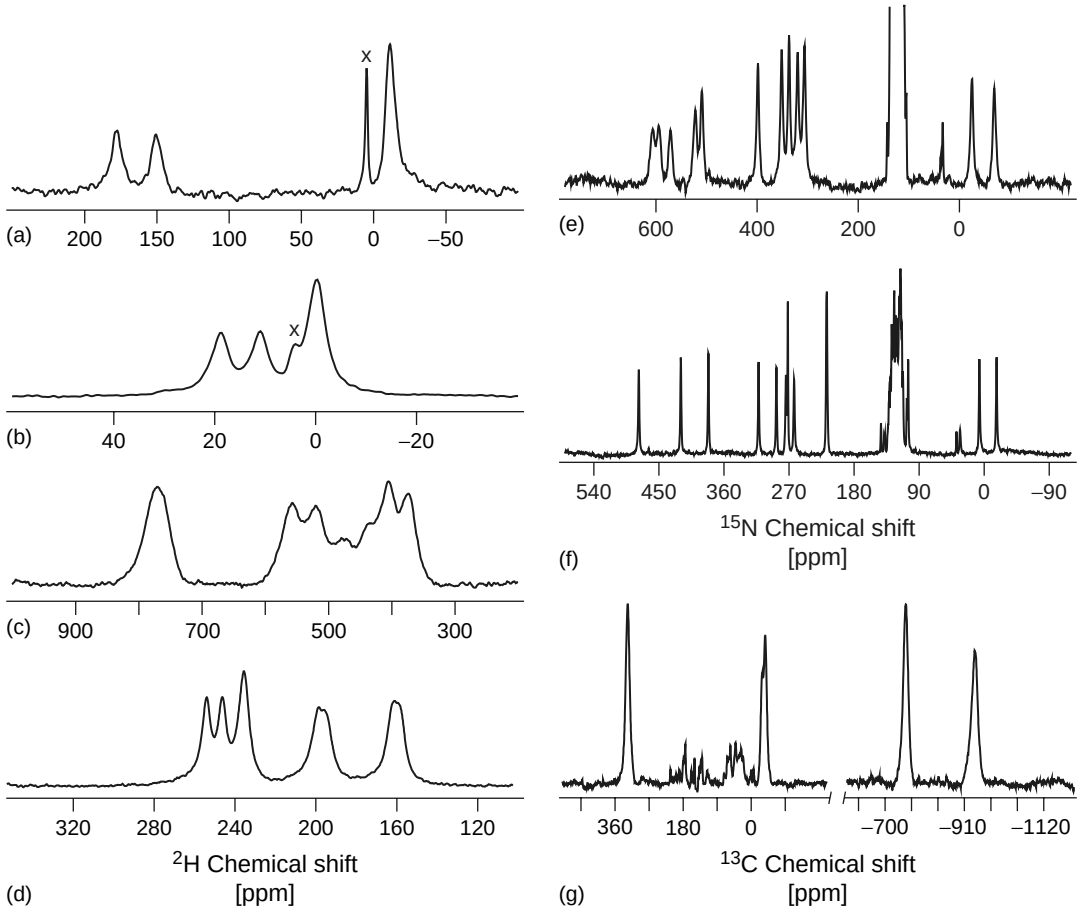

Figure 1 NMR spectra of ^{2}H-, ^{15}N-, and ^{13}C-labeled CpRd at 35 °C. (a) ^{2}H NMR spectrum of oxidized [$^{2}H^{\alpha}$]Cys-labeled CpRd. The peak labeled 'x' arises from $^{1}H^{2}HO$. (b) ^{2}H NMR spectrum of reduced [$^{2}H^{\alpha}$]Cys-labeled CpRd. The peak labeled 'x' arises from $^{1}H^{2}HO$. (c) ^{2}H NMR spectrum of oxidized [$^{2}H^{\beta}$]Cys-labeled CpRd. (d) ^{2}H NMR spectrum of reduced [$^{2}H^{\beta}$]Cys-labeled CpRd. (e) ^{15}N NMR spectrum of oxidized [U–^{15}N]-labeled CpRd. (f) ^{15}N NMR spectrum of reduced [U–^{15}N]-labeled CpRd. (g) ^{13}C NMR spectrum of reduced [$^{13}C^{\beta}$]Cys-labeled CpRd. Parts (a–d) reproduced with permission from Ref.[10] Copyright 1995 American Chemical Society. Parts (e) and (f) adapted from Ref.[13]

Table 1 Experimental chemical shifts of hyperfine resonances in the rubredoxin from *Clostridium pasteruianum* (CpRd)

Assignment	Chemical shifts (ppm)	
	Oxidized	Reduced
Cys6 $H^{\beta 3}$	478.5	196.0
Cys6 $H^{\beta 2}$	406.7	157.0/158.6
Cys9 $H^{\beta 3}$	520.6	233.0
Cys9 $H^{\beta 2}$	771.7	243.7
Cys39 $H^{\beta 3}$	437.0	193.4
Cys39 $H^{\beta 2}$	376.9	158.6/157.0
Cys42 $H^{\beta 3}$	557.4	233.0
Cys42 $H^{\beta 2}$	771.7	251.3
Cys6 H^{α}	−11.5	10.9/18.6
Cys9 H^{α}	150.4/177.3	−0.4
Cys39 H^{α}	−11.5	18.6/10.9
Cys42 H^{α}	177.3/150.4	−0.4
Cys6 C^{β}	nd	327
Cys9 C^{β}	nd	−939
Cys39 C^{β}	nd	−36
Cys42 C^{β}	nd	−755
Cys6 N	571.1	287.4/311.9
Cys9 N	−25.1/−68.8	−17.3/6.5
Cys39 N	594.4	311.9/287.4
Cys42 N	−68.8/−25.1	6.5/−17.3
Thr7 N	351.0	274.1
Val8 N	508.9 (494.5)[a]	477.7 (465.2)
Gly10 N	319.5/305.9	217.5
Tyr11 N	606.0 (588.3)	381.6 (372.8)
Pro40 N	398.2	271.4
Leu41 N	521.3 (507.5)	419.6 (408.6)
Gly43 N	305.9/319.5	217.5
Val44 N	336.6 (328.4)	262.8 (256.4)

[a]Chemical shifts in parentheses are for CpRd in D_2O; four resonances shift to higher frequency owing to a one-bond $^1H/^2H$ isotope effect (see text for details).

published X-ray structure for reduced CpRd[20] are yielding improved agreement with experiment and hence more insight into the electronic structure.[21]

HDFT calculations were extended to a obtain a quantitative understanding of the ^{15}N T_1 relaxation rates in oxidized CpRd.[22] In this system, the contact contribution is small even for the most strongly hyperfine-shifted resonances and the T_1 rates are dominated by electron–nuclear dipolar relaxation. However, given that the unpaired spin density in this system is known to be highly delocalized, the point-dipole approximation is a poor model. This was accounted for by replacing the r^{-6} distance dependence in equation (7) with an effective reciprocal distance, r_{eff}^{-6}:

$$r_{\text{eff}}^{-6} = \frac{1}{4}\left[\frac{1}{3}(\langle q_{xx}\rangle_{\text{spin}} - \langle q_{yy}\rangle_{\text{spin}})^2 + \langle q_{xx}\rangle_{\text{spin}}^2 + \frac{4}{3}(\langle q_{xy}\rangle_{\text{spin}}^2 + \langle q_{xz}\rangle_{\text{spin}}^2 + \langle q_{yz}\rangle_{\text{spin}}^2)\right] \quad (14)$$

In equation (14), the $\langle q_{\alpha\beta}\rangle_{\text{spin}}$ terms are the matrix elements of the spin-differential field gradient tensor:

$$\langle q_{\alpha\beta}\rangle_{\text{spin}} = \sum_{st} D_{st}\langle s|\hat{q}|t\rangle \quad (15)$$

where D_{st} is the normalized, spin-only density matrix and $q_{\alpha\beta}$ is the electric field gradient operator:

$$\hat{q}_{\alpha\beta} = \frac{3r_\alpha r_\beta - \delta_{\alpha\beta}r^2}{r^5} \quad (16)$$

This approach provided excellent agreement between experimental and calculated ^{15}N T_1 rates, whereas the point-dipole model failed for nuclei closer than 7 Å. A comparison of r_{eff} with the crystallographic distance demonstrates this (Figure 2). These calculations yielded a τ_c of $\sim 4 \times 10^{-10}$ s. In this system, $\tau_c \approx \tau_e$, and this value for τ_e is typical for Fe^{3+}.

The magnetic field-dependence of one-bond ^1H–^{15}N and $^1H^{\alpha}$–$^{13}C^{\alpha}$ couplings were measured in order to determine the residual dipolar couplings in oxidized and reduced CpRd.[8] These, in combination with the crystallographic data, were used to obtain the magnitude and orientation of the magnetic susceptibility anisotropy, $\Delta\chi_{\text{ax}}$ and $\Delta\chi_{\text{rh}}$ (Figure 3). By subtracting the calculated diamagnetic contribution from the protein, $\Delta\chi_{\text{ax}}$ and $\Delta\chi_{\text{rh}}$ for the metal center can be determined: 7.93×10^{-28} and 3.24×10^{-28} cm^3 molecule^{-1} for oxidized and 22.3×10^{-28} and 10.5×10^{-28} cm^3 molecule^{-1} for reduced CpRd, respectively (Table 2).

These values, in turn, can be compared with ZFS parameters and g-values previously obtained by other methods for rubredoxins and $Fe(SR)_4$ model complexes. Since the magnetic susceptibility anisotropies were measured at 10 °C, the values are very sensitive to small differences in both the **D**-

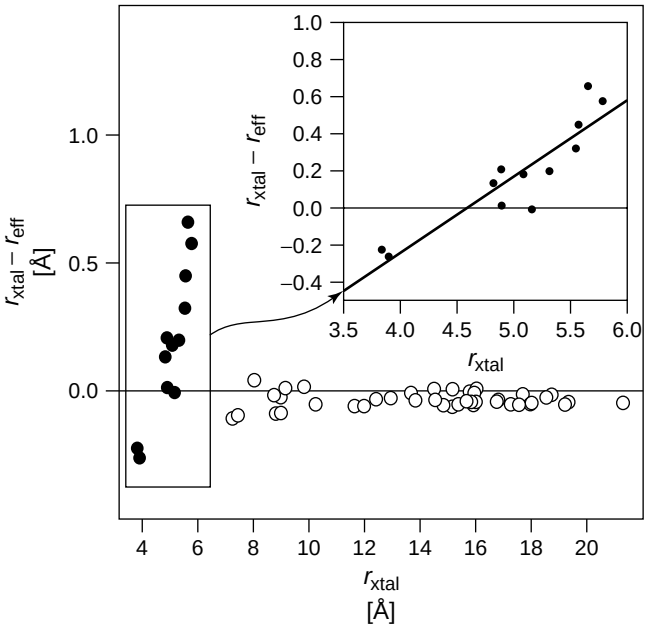

Figure 2 Plot of $r_{\text{xtal}} - r_{\text{eff}}$ versus r_{xtal}, where r_{xtal} is the measured distance between individual ^{15}N nuclei and the Fe atom in the 4RXN crystal structure and where r_{eff} is the effective distance calculated from the wave function using the spin-differential field gradient tensor method. Black circles represent ^{15}N nuclei that give rise to hyperfine-shifted resonances and open circles represent the 'diamagnetic' ^{15}N nuclei. The horizontal line is drawn at the zero of the abscissa. The inset plot shows an expansion of the ordinate for nuclei that are close to the metal center. Reproduced with permission from Ref.[22] Copyright 1998 American Chemical Society

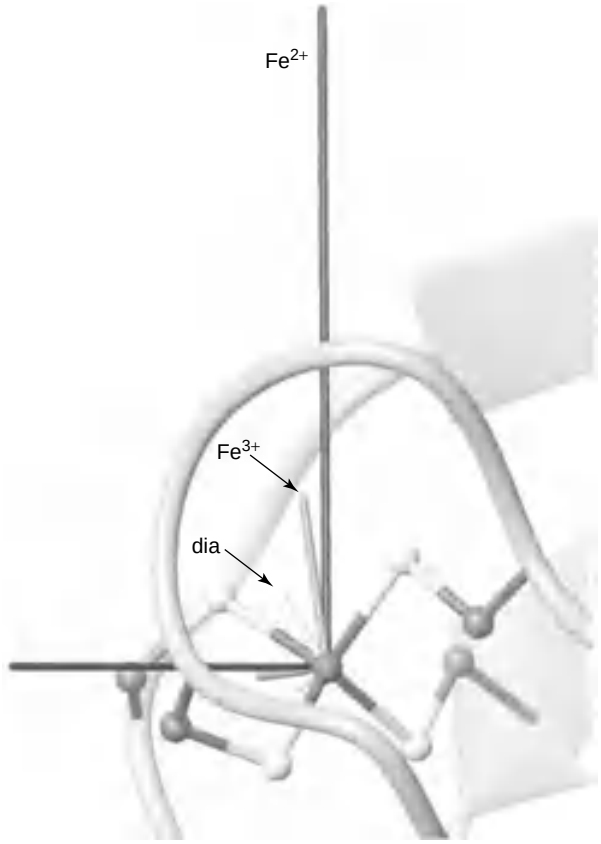

Figure 3 Structural representation of magnetic susceptibility anisotropies. A ribbon diagram of the structure of CpRd is shown, including the atoms of the $Fe(Cys)_4$ center. Vectors originating at the Fe indicate the magnitudes and show the orientations of the $\Delta\chi_{ax}$ and $\Delta\chi_{rh}$ terms obtained from fits to the 5RXN structure of dipolar splittings from oxidized and reduced CpRd. The diamagnetic $\Delta\chi_{ax}$ and $\Delta\chi_{rh}$ values calculated for 5RXN are also shown. Reproduced with permission from Ref.[8] Copyright 1998 American Chemical Society

and **g**-tensors and their relative orientation; thus, they can only be compared to the previous data in general terms.

ZFS parameters have been obtained for oxidized CpRd from Mössbauer spectroscopy[23,24] and for oxidized *Pseudomonas oleovorans* rubredoxin from variable-temperature X-band EPR spectroscopy[25] (Table 2). Both approaches yielded a D that is small and positive, consistent with an approximately D_{2d} geometry; in these calculations, g was assumed to be isotropic and ∼2.0. The values of D, E, and g obtained from EPR can be used to calculate $\Delta\chi_{ax}$ and $\Delta\chi_{rh}$, which yields the qualitatively consistent values of 7.27×10^{-28} and $4.15 \times 10^{-28}\,cm^3\,molecule^{-1}$, respectively. Agreement with the NMR-derived values can be improved substantially by assuming a g-anisotropy of 0.004; this small value is reasonable on the basis of data for a $Fe^{3+}(SR)_4$ model complex.[26]

ZFS parameters have been obtained for reduced CpRd from Mössbauer spectroscopy (Table 2)[23] and for a model complex, $[Fe(SPh)_4]^{2-}$, from Mössbauer,[27] high-frequency EPR (HFEPR),[28] and far-infrared (FIR) absorption spectroscopies.[29] In the latter system, the ZFS parameters obtained from HFEPR and FIR were in agreement and significantly smaller than from those obtained from Mössbauer. Results from the model system were used to derive ZFS parameters for CpRd (Table 2).[28] In all cases, g-values were inferred from expressions derived from second-order perturbation theory (Table 2).[30] $\Delta\chi_{ax}$ and $\Delta\chi_{rh}$ values calculated from Mössbauer-derived values of D, E, and g are approximately twice the experimental values determined by NMR, whereas those derived from HFEPR (22.5×10^{-28} and $13.4 \times 10^{-28}\,cm^3\,molecule^{-1}$, respectively) are in good agreement. Again, small changes in the g-anisotropy would account for the remaining difference.

Once the magnitude and orientation of the magnetic susceptibility anisotropy were determined for oxidized and reduced CpRd, these data could be used to estimate the pseudocontact shifts for nuclei >11 Å from the Fe center. From this it was found that pseudocontact shifts entirely accounted for the observed chemical shift differences between the oxidized and reduced states for the diamagnetic resonances. This, in turn, indicated that the structure of the protein 7 Å or more from the Fe remains the same in the two redox states.

3 EXCHANGE COUPLING AND ITS INFLUENCE ON ELECTRON–NUCLEAR INTERACTIONS

Electron–nuclear interactions in exchange coupled multinuclear systems are considerably more complicated than those in simple single-metal site systems. As with simpler systems, NMR data can be used to evaluate theoretical models describing the paramagnetic center. In particular, the nature of exchange coupling in the mixed-valence states of these clusters has been a topic of great interest. The types of exchange-coupled FeS clusters that have been studied by NMR spectroscopy and their different formal redox states are listed in Table 3. An extensive list of NMR results on different FeS proteins is provided in Table 4.

In this section, we present the theory of how exchange coupling impacts hyperfine shifts and paramagnetic relaxation. We then show how the vector coupling model of hyperfine shifts has been applied to representative FeS clusters and the insight this has provided.

3.1 Theory

In a coupled system, the exchange coupling can be described by the phenomenological spin Hamiltonian:

$$\mathcal{H} = \sum_{i<j} -2J_{ij}\mathbf{S}_i \cdot \mathbf{S}_j \qquad (17)$$

where J is the isotropic or Heisenberg exchange coupling constant and $\mathbf{S}_i$ and $\mathbf{S}_j$ are the local spin operators for each metal site. For a system with two metal centers, such $[2Fe–2S]^{2+}$, this yields a set of levels or "spin ladder" for the total spin S, in which S ranges from $|S_1 + S_2|$ to $|S_1 - S_2|$, the relative energies of which are given by:

$$E(S) = -JS(S+1) \qquad (18)$$

J can be positive (ferromagnetic coupling) or negative (antiferromagnetic coupling). In FeS clusters J is always negative. In mixed-valence systems, such as $[2Fe–2S]^{+}$, the extra electron can be on either Fe; this doubles the number of total spin states. Consideration of this effect, called double

Table 2 Comparison of the magnetic susceptibility anisotropy of oxidized and reduced rubredoxin obtained from NMR with the ZFS parameters and g-values obtained from Mössbauer and EPR and the magnetic susceptibility anisotropy calculated from these

		Oxidized rubredoxin	Reduced rubredoxin
Magnetic susceptibility anisotropy from NMR:	$\Delta\chi_{ax}$ (10^{-28} cm^3 molecule^{-1})	7.93	22.3
	$\Delta\chi_{rh}$	3.24	10.5
ZFS parameters and g-values from Mössbauer:	D (cm^{-1})	1.74[a]	7.58[b]
	E	0.30	2.1
	g_z	2.0	2.00
	g_x	2.0	2.11
	g_y	2.0	2.19
ZFS parameters and g-values from EPR:	D (cm^{-1})	1.76[c]	5.3[d]
	E	0.495	1.5
	g_z	2.0	2.01
	g_x	2.0	2.06
	g_y	2.0	2.10
Calculated magnetic susceptibility anisotropy:	$\Delta\chi_{ax}$ (10^{-28} cm^3 molecule^{-1})	7.27[e]	22.5[e]
	$\Delta\chi_{rh}$	4.15	13.4

[a]Fit included a fourth-order fine structure term, which is not listed here and was not included in the calculation of the magnetic susceptibility anisotropy.[24]
[b]g-values were inferred based upon second-order perturbation theory expressions.
[c]*Pseudomonas oleovorans* rubredoxin.[25]
[d]ZFS parameters were estimated from HFEPR results for the model complex $[Fe(SPh)_4]^{2-}$; g-values were inferred from analysis based on second-order perturbation theory.[28]
[e]Calculated based upon the ZFS parameters and g-values obtained from EPR.

Table 3 Formal redox states in Fe–S clusters

Cluster and protein type	Oxidized state		Reduced state	
[2Fe-2S] clusters	$[2Fe\text{-}2S]^{2+}$	$2Fe^{3+}$	$[2Fe\text{-}2S]^{+}$	Fe^{3+}, Fe^{2+}
[3Fe-4S] clusters	$[3Fe\text{-}4S]^{+}$	$3Fe^{3+}$	$[3Fe\text{-}4S]^{0}$	2 Fe^{3+}, 1 Fe^{2+}
[4Fe-4S] HiPIPs	$[4Fe\text{-}4S]^{3+}$	$3Fe^{3+}$, 1 Fe^{2+}	$[4Fe\text{-}4S]^{2+}$	2 Fe^{3+}, 2 Fe^{2+}
[4Fe-4S] clusters in Fds and other systems	$[4Fe\text{-}4S]^{2+}$	2 Fe^{3+}, 2 Fe^{2+}	$[4Fe\text{-}4S]^{+}$	1 Fe^{3+}, 3 Fe^{2+}

exchange or spin-dependent delocalization, yields the following equation for the energies of the total spin states are now defined by:

$$E(S) = -JS(S+1) \pm B\left(S + \frac{1}{2}\right) \tag{19}$$

where B is the double exchange term. The interplay between J and B determines the ground state (g.s.) of the system. Two additional effects must be considered: static and dynamic asymmetry. Static asymmetry arises from differences in the coordination geometry, H-bonding, and protein electrostatics at the two Fe sites that cause the extra electron to be preferentially localized on one side. Dynamic asymmetry, or vibronic coupling, arises from the change in geometry upon transferring the extra electron from one side to the other. The magnitude of this nuclear distortion defines the height of the barrier to electron transfer between the two sides. Thus, in the limit of large B and small vibronic coupling, there is no barrier to intersite electron transfer and the system is said to be completely valence-delocalized. For example, a valence-delocalized $[2Fe–2S]^{+}$ cluster would be described as $2Fe^{2.5+}$. Together, static asymmetry and vibronic coupling counteract the effect of double exchange. In the limit where these effects are large relative to B, the system is valence-localized and can be described by equations (17) and (18), where J is replaced by a J_{eff}, which is the Heisenberg J plus a correction factor to account for B, static asymmetry, and vibronic coupling. For systems of higher nuclearity, the exchange coupling can be described by decomposing the system into subunits and first considering the coupling within the subunits, and then the coupling between the subunits. For a more detailed account of exchange coupling, see Ref.[31] and references therein.

In an exchange coupled system, the Fermi contact shift can still be described by equation (2), but now one must calculate the Fermi contact shift for each total spin state, each of which will have a different isotropic hyperfine coupling constant, A_i, and sum over the Boltzmann population of the total spin states. The difficulty lies in determining each A_i; however, this can be accomplished readily because the hyperfine coupling constant for each total spin state S, in turn, can be related to the intrinsic hyperfine coupling constant for each metal site, A_j. Thus, equation (2) may be rewritten as:[32]

$$\delta_{con} = 10^6\left(\frac{\Delta\nu}{\nu_0}\right)^{con} = -10^6\frac{1}{\hbar\gamma_N B_0}\sum_i\sum_j A_j C_{ji}\langle S_z\rangle_i \tag{20}$$

where C_{ji} are spin projection coefficients for each metal site j for each total spin state i. These are derived from the

Wigner–Eckart theorem and vector coupling.[33] For a binuclear system, C_1 is given by[31–34]

$$C_1 = \frac{S(S+1) + S_1(S_1+1) - S_2(S_2+1)}{2S(S+1)} \tag{21}$$

where S is the total spin and S_1 and S_2 are the spin states of each metal site. C_2 is given by simply reversing the indices in equation (21). This can be easily extended to systems of higher nuclearity by use of a chain rule.[34] Consider a tetranuclear system that can be divided into two subunits of spin S_p and S_q. From equation (21), spin projection coefficients C_1^p and C_2^p can be calculated by replacing S with S_p and C_p by replacing S_1 and S_2 with S_p and S_q. Coefficients projecting out the spin onto the total spin state are then:

$$C_1 = C_1^p C_p \tag{22}$$

Note also that the spin projection coefficients for each total spin state always sum to one. Considering an explicit expression for the spin expectation value in equation (20) yields:

$$\delta_{\text{con}} = 10^6 \left(\frac{\Delta\nu}{\nu_0}\right)^{\text{con}} = -10^6 \frac{g\beta}{\hbar\gamma_N 3kT} \times \sum_j \frac{A_j \sum_i C_{ji} S(S+1)(2S+1)\exp(-E_S/kT)}{\sum_i (2S+1)\exp(-E_S/kT)} \tag{23}$$

Application of equation (23) is still difficult, and as shown below, has only been attempted qualitatively.

Paramagnetic relaxation can be analyzed by a treatment similar to equations (20) and (23). For example, the point-dipole approximation of the electron–nuclear dipolar contribution to T_1 may be written as:[32]

$$T_{1j}^{-1} = \frac{2}{15}\left(\frac{\mu_0}{4\pi}\right)^2 \frac{\gamma_N^2 g^2 \beta^2}{r_j^2} \frac{\sum_i C_{ji}^2 S(S+1)(2S+1)\exp(-E_S/kT)}{\sum_i (2S+1)\exp(-E_S/kT)} \times \left[\frac{\tau_c}{1+(\omega_I-\omega_S)^2\tau_c^2} + \frac{3\tau_c}{1+\omega_I^2\tau_c^2} + \frac{6\tau_c}{1+(\omega_I+\omega_S)^2\tau_c^2}\right] \tag{24}$$

where T_{1j} is the dipolar relaxation from metal site j, r_j is the distance to that metal site, and τ_c is given as in equation (12). This is then summed over all metal sites. Similar equations may be derived for the other types of paramagnetic relaxation. The issue arises as to what value to use for the electronic relaxation rate. In the limit of strong exchange coupling, where the coupling frequency is large relative to the electronic relaxation rates for the uncoupled spins (τ_{ej}) but small relative to the electronic correlation time (τ_{vj}) the electronic relaxation rate is the same for all metal sites.[35]

$$\frac{|J|}{\hbar} \gg \tau_{ej}^{-1} \tag{25}$$

Table 4 NMR data available on different FeS proteins

Protein type	Oxidized	Reduced
2Fe ferredoxins		
Anabaena PCC7120 vegetative	**43, 44**	**43, 44, 51**
Spinach	**32**	**32**
Porphyra umbicalis,	**32, 52**	**32, 52**
Spirulina platensis	**52, 121**	**52, 121**
Azotobacter vinelandii	**122**	**122**
Phytolacca americana	**121**	**121**
Halobacterium halobium	**121**	**121**
Human	**42, 44**	**42, 44**
Pseudomonas putida	**123–127**	**123–126**
Rieske proteins		
Alkene monooxygenase of *Xanthobacter* strain Py2	**128**	**128**
bc_1 complex of *Paracoccus denitrificans*	**129**	**129**
Toluene-4 monooxygenase of *Pseudomonas mendocina*	**60**	**60**
3Fe ferredoxins		
Bacillus stearothermophilus	**121**	**121**
Bacillus thermoproteolyticus	**121**	**121**
Desulfovibrio gigas	**61, 67**	
Thermococcus litoralis	**66, 71**	
Pyrococcus furiosus	**66, 79**	
4Fe ferredoxins		
Bacillus polymyxa	**121, 130**	**121, 130**
Bacillus stearothermophilus	**121**	**121**
Bacillus thermoproteolyticus	**121**	**121**
Desulfovibrio gigas	**61, 121**	**61, 121**
Desulfovibrio africanus	**131, 132**	
Thermococcus litoralis	**71, 133**	**71**
Thermotoga maritima	**134**	
Pyrococcus furiosus	**115–117**	**115–117**
Desulfovibrio desulfuricans	**135**	

Table 4 (*continued*)

Protein type	Oxidized	Reduced
7Fe ferredoxins		
Thermus thermophilus	**74**	**74**
Mycobacterium smagmatis	**74**	**74**
Pseudomonas ovalis	**74**	**74**
Azotobacter vinelandii	**121**	**121**
Pseudomonas putida	**75, 76**	
Rhodopseudomonas palustris	**70, 77**	**70, 77**
Desulfurolobus ambivalens	**68**	**68**
Bacillus schlegleii	**69, 80**	**69, 80**
Pseudomonas nautica	**78**	
Sulfolobus sp. Strain 7	**72**	
Sulfolobus acidocaldarius	**73**	**73**
Desulfovibrio africanus	**73, 136**	**73**
8Fe ferredoxins		
Clostridium pasteurianum	**102, 107, 108, 137–142**	**102, 107, 108**
Clostridium acidi-urici	**102, 137**	**102**
Clostridium perfringens	**137**	
Peptococcus aerogenes	**137**	
Chromatium vinosum	**105, 143**	**105, 143**
High-potential iron proteins		
Chromatium vinosum	**96, 144–147**	**96, 144, 145, 147–149**
Rhodocyclus gelatinosus	**144, 150, 151**	**144, 150, 151**
Ectothiorhodospira halophila iso I	**38, 83–85**	**38, 85, 152**
Ectothiorhodospira halophila iso II	**85–87**	**85**
Ectothiorhodospira vacuolata iso I	**85, 153**	**85, 153**
Ectothiorhodospira vacuolata iso II	**85, 99**	**85**
Chromatium gracile	**154**	**154**
Rhodospirillum tenue	**155**	**155**
Rhodopseudomonas globiformis	**100**	**100**
Rhodoferax fermentans	**101**	**101**
Nitrogenase Fe protein		
Clostridium pasteurianum		**156**
Azotobacter vinelandii		**120**
PsaC subunit of photosystem I		
Synechococcus elongatus	**157**	**157**
Synechococcus PCC7002	**158**	**158**

$$\frac{|J|}{\hbar} \ll \tau_{vj}^{-1} \tag{26}$$

This case holds for FeS clusters. See[6] and[35] for more details. Although detailed analyses of nuclear and electronic relaxation in coupled systems are few, equation (24) has been of great utility in providing distance constraints for solution structure determination.[36–39]

3.2 Applications to Fe–S Cluster Proteins

3.2.1 [2Fe–2S] Clusters

[2Fe–2S] proteins can be divided into two classes: 2Fe ferredoxins (Fds), in which each Fe is ligated by two Cys residues, and Rieske proteins, in which one Fe is ligated by two Cys and the other by two His.[40,41] The 2Fe Fds can be subdivided further into several types, two of which have been studied by NMR: plant-type and hydroxylase-type. In the oxidized state of both types, the ^{1}H hyperfine-shifted resonances are extremely broad and unresolved. The Cys H^{β} and H^{α} protons have been assigned by selective labeling, as have the Cys C^{β} and N resonances (Table 5).[42–44] All the hyperfine resonances move to higher frequency with increasing temperature or exhibit little temperature-dependence.

The electronic structure of the reduced state is very highly conserved among plant-type 2Fe Fds, based upon EPR, Mössbauer, and other studies.[45–48] Similar studies on reduced hydroxylase-type 2Fe Fds indicate that they, too, have a very highly conserved spectral signature that differs considerably from that of plant-type Fds,[45–48] despite their very similar geometries in the oxidized state (cf., e.g.,[49] and[50]). In the plant-type Fds, the hyperfine resonances are far narrower in the reduced state than in the oxidized state, thus facilitating their assignment. In reduced *Anabaena* PCC7120 vegetative Fd, extensive assignments were obtained for the Cys H^{β}, H^{α}, C^{β}, and N resonances through selective labeling, 2D NOESY (tailored for fast-relaxing resonances), 2D ^{1}H{^{13}C} HSQC, and 1D heteronuclear decoupling experiments (Table 5).[43,44,51] The ^{1}H NMR spectrum is shown in Figure 4(a).

One very important conclusion from these studies is that the $[2Fe–2S]^+$ cluster is valence trapped even at room temperature on the NMR timescale and that the electron resides entirely on the Fe ligated to Cys 41 and 46.[52] This is consistent with, although not necessarily predicted by, the large negative

value of J_{eff} that has been measured by magnetic susceptibility and temperature-dependent EPR. Less work has been done on reduced hydroxylase-type Fds. Partial assignments derived from selective ^{2}H labeling are available for human Fd: H^{β} resonances occur at 103, 80, −10, and −15 ppm, and H^{α} resonances at 37 and 13 ppm.[44] As in the case of plant-type Fds, these data indicate valence-trapping.

A theoretical model was developed by Dunham[53] and later extended by Banci and Bertini[32,54] by use of equation (23) to explain the sign, magnitude, and temperature dependence of the chemical shifts of the ^{1}H hyperfine resonances in reduced Fds. In this model, the intrinsic hyperfine coupling constants for Cys H^{β} and H^{α} protons were assumed to be 1.0 and 0.1 MHz, respectively, and to be only coupled to the closer of the two Fe sites; thus, J_{eff} becomes the only scalable parameter. From magnetic susceptibility and temperature-dependent EPR, J_{eff} is approximately $-100\,\text{cm}^{-1}$ in plant-type Fds[46,55–59] and $-250\,\text{cm}^{-1}$ in hydroxylase Fds.[45,46,59] Remarkably good agreement with this model is obtained for the ^{1}H hyperfine data on plant-type Fds, but only if J_{eff} is assumed to be half the experimental value (Figure 5(b)).

In this case, at room temperature, the H^{β} and H^{α} protons on the Fe^{3+} side are predicted to be at 123 and 17 ppm, respectively, and to shift to lower frequency with increasing

Table 5 Chemical shifts and temperature dependencies of the hyperfine resonances in representative oxidized and reduced [2Fe-2S] and [3Fe-4S] clusters

Oxidized				Reduced			
Peak label	Assignment	Chemical shift (ppm)	Temperature increases, peak moves…	Peak label	Assignment	Chemical shift (ppm)	Temperature increases, peak moves…
			Anabaena PCC7120 2Fe Ferredoxin (at 298 K)				
	Cys H^{β}	25–50	←	A	Cys49/79 $H^{\beta 2}$	134.6	→
			←	B	Cys49/79 $H^{\beta 3}$	125	→
			←	C	Cys79/49 $H^{\beta 2}$	104.2	→
				D	Cys79/49 $H^{\beta 3}$	98	→
				F	Cys41 $H^{\beta 2}$	24.4	←
				G	Cys41 $H^{\beta 3}$	24.4	←
				H	Cys46 $H^{\beta 2}$	19.7	←
				I	Cys46 $H^{\beta 3}$	16.7	←
	Cys H^{α}	15	←	E	Cys49 H^{α}	43.5	→
	Cys H^{α}	9	←	J	Cys79 H^{α}	16.7	→
					Cys46 H^{α}	5.05	nd
					Cys41 H^{α}	3.2	nd
	Cys C^{β}	89.3	←		Cys79 C^{β}	150.2	→
	Cys C^{β}	89.3	←		Cys49 C^{β}	123.4	←
	Cys C^{β}	62.7	←		Cys46 C^{β}	63.1	→
	Cys C^{β}	56.9	←		Cys41 C^{β}	−32.7	→
	Cys49/79 N	155.0	←		Cys49/79 N	362.1	→
	Cys79/49 N	152.9	←		Cys79/49 N	324.5	→
	Cys46 N	131.3	∼0		Cys46 N	155.6	→
	Cys41 N	113.7	∼0		Cys41 N	61.9	→
			Toluene 4-monooxygenase Rieske protein from *P. mendocina* (at 293 K)				
	Cys H^{β}	20–30	←	A	Cys H^{β}	82.7	→
				B	Cys H^{β}	76.7	→
				C	Cys H^{β}	61.1	→
				D	Cys H^{β}	52.6	→
				E	His $H^{\varepsilon 1}$	25.2	→
	Cys45/64 N	143.5	←		Cys45/64 N	201.8	→
	Cys64/45 N	142.1	←		Cys64/45 N	200.6	→
	His47/67 $N^{\varepsilon 2}$	233.8	←		His47/67 $N^{\varepsilon 2}$	119.7	nd
	His67/47 $N^{\varepsilon 2}$	231.5	←		His67/47 $N^{\varepsilon 2}$	116.3	nd
	His47/67 N	158.7	←		His47/67 N	304.2	→
	His67/47 N	122.6	←		His67/47 N	270.3	→
		D. gigas 3 Fe Fd (303 K)				*P. Schlegii* 7 Fe Fd (297 K)	
A	Cys50 H^{β}	29.1	→		Cys H^{β}	190	→
B	Cys50 H^{β}	24.4	→		Cys H^{β}	190	→
C	Cys8 H^{β}	18.1	←		Cys H^{β}	−192	←
D	Cys14 H^{β}	15.3	←		Cys H^{β}	−290	←
Y	Cys14 H^{β}	8.5	nd				
	Cys8 H^{β}	3.5	nd				
E	Cys14 H^{α}	9.9	←				
	Cys8 H^{α}	1.5	nd				

temperature, and the H^{β} and H^{α} protons on the Fe^{2+} side are predicted to be at 26 and 7 ppm, respectively, and to shift to higher frequency with increasing temperature. Qualitative agreement is found for the hydroxylase-type Fds using the experimental value for J_{eff}: the H^{β} and H^{α} protons on the Fe^{3+} side are predicted to be at 67 and 11 ppm, respectively, and to shift to lower frequency with increasing temperature, and the H^{β} and H^{α} protons on the Fe^{2+} side are predicted to be at -29 and 1.5 ppm, respectively, and to shift to higher frequency with increasing temperature (Figure 5(b)). The model breaks down when comparing temperature dependence of the ^{15}N and ^{13}C hyperfine shifts, where there is not a clear pattern of two resonances shifting to higher frequency and two to lower frequency. A similar approach can be used for understanding the hyperfine shifts in $[2Fe–2S]^{2+}$ clusters. Since in this case the g.s. is $S = 0$, only thermal population of paramagnetic excited states yields hyperfine shifts. Here J is large ($-175\,cm^{-1}$),[46] so all of the resonances shift to higher frequency with increasing temperature as the population of paramagnetic excited states increases (Figure 5(a), solid lines).[54] Overall, the success of the vector coupling model in qualitatively explaining hyperfine shifts in [2Fe–2S] clusters justifies its use in more complex systems.

Among the Rieske proteins, the one from the toluene-4 monooxygenase system of *P. mendocina* (TMOC) is the best characterized by NMR. In the reduced state, the ^{1}H spectrum exhibits five resonances at high frequency (Figure 4(b), Table 5) that have been assigned as Cys H^{β} and His $H^{\varepsilon 1}$ protons based upon selective ^{2}H labeling.[60] This study also provided a thorough examination of the ^{15}N hyperfine shifts of H-bonded N nuclei.[60] In both the redox states, six amide and two His $H^{\varepsilon 2}$ N nuclei were found to exhibit paramagnetic shifts and were assigned by selective ^{15}N-labeling. Four of these are H-bonded to the [2Fe–2S] cluster in the crystal structure of a homologous Rieske protein. The crystal structure also showed a fifth amide that was H-bonded to the cluster, but the homologous residue in this system did not exhibit any

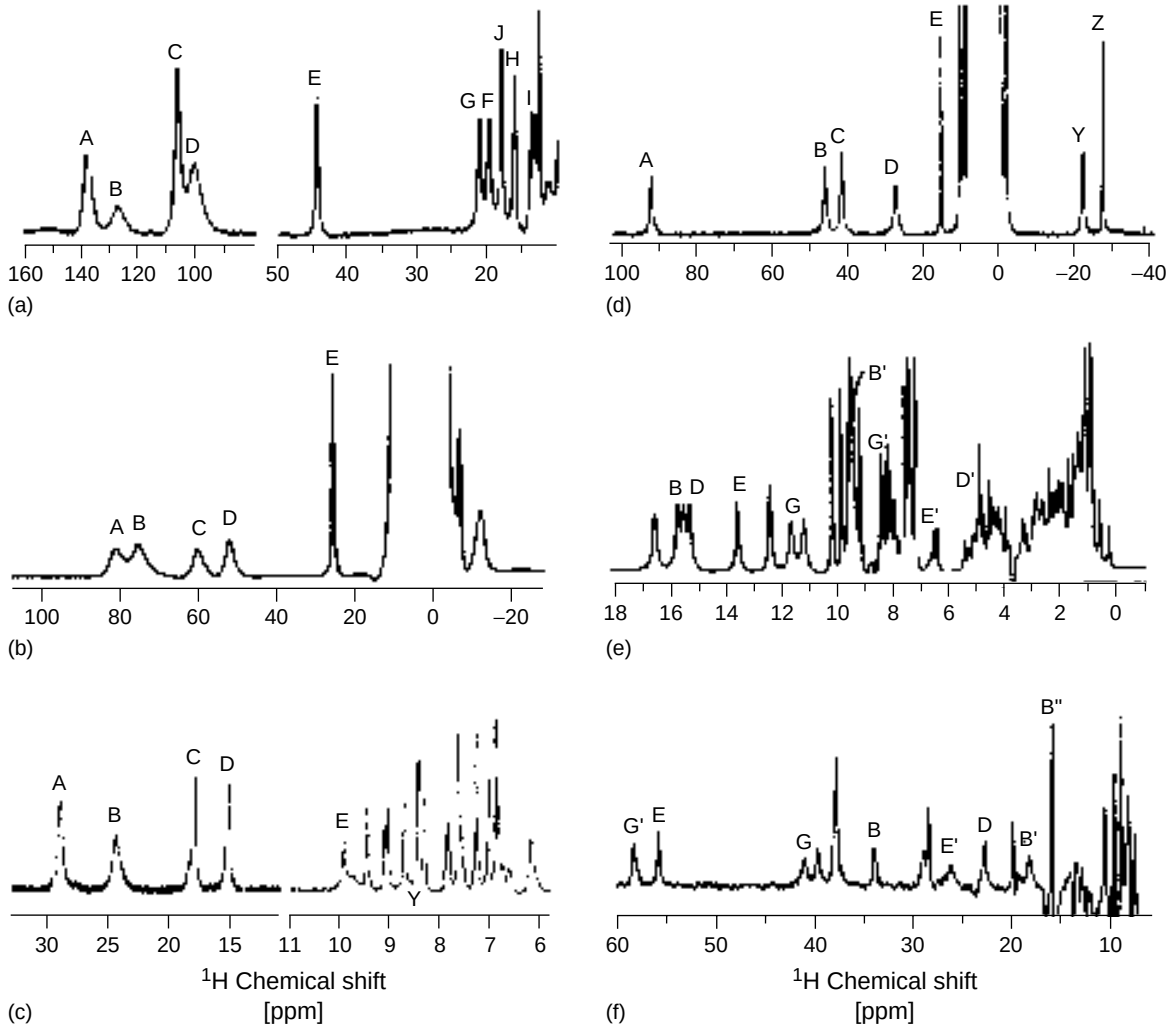

Figure 4 ^{1}H NMR spectra of various FeS Clusters. Peak labels correspond to those listed in Tables 5 and 6. (a) Reduced *Anabaena* PCC7120 2Fe Fd at 283 K. Left-hand panel is scaled up arbitrarily. Adapted from Ref.[43] (b) Reduced toluene 4-monooxygenase Rieske protein from *P. mendocina* at 303 K. Adapted from Ref.[60] (c) Oxidized *D. gigas* 3Fe Fd at 303 K. Left-hand panel is scaled up arbitrarily. Adapted from Ref.[61] (d) Oxidized *E. halophila* HiPIP I at 288 K. Adapted from Ref.[83] (e) Oxidized *C. acidi-urici* at 298 K. Left-hand panel is scaled up arbitrarily. Adapted from Ref.[102] (f) Reduced *C. acidi-urici* at 298 K. Adapted from Ref.[102]

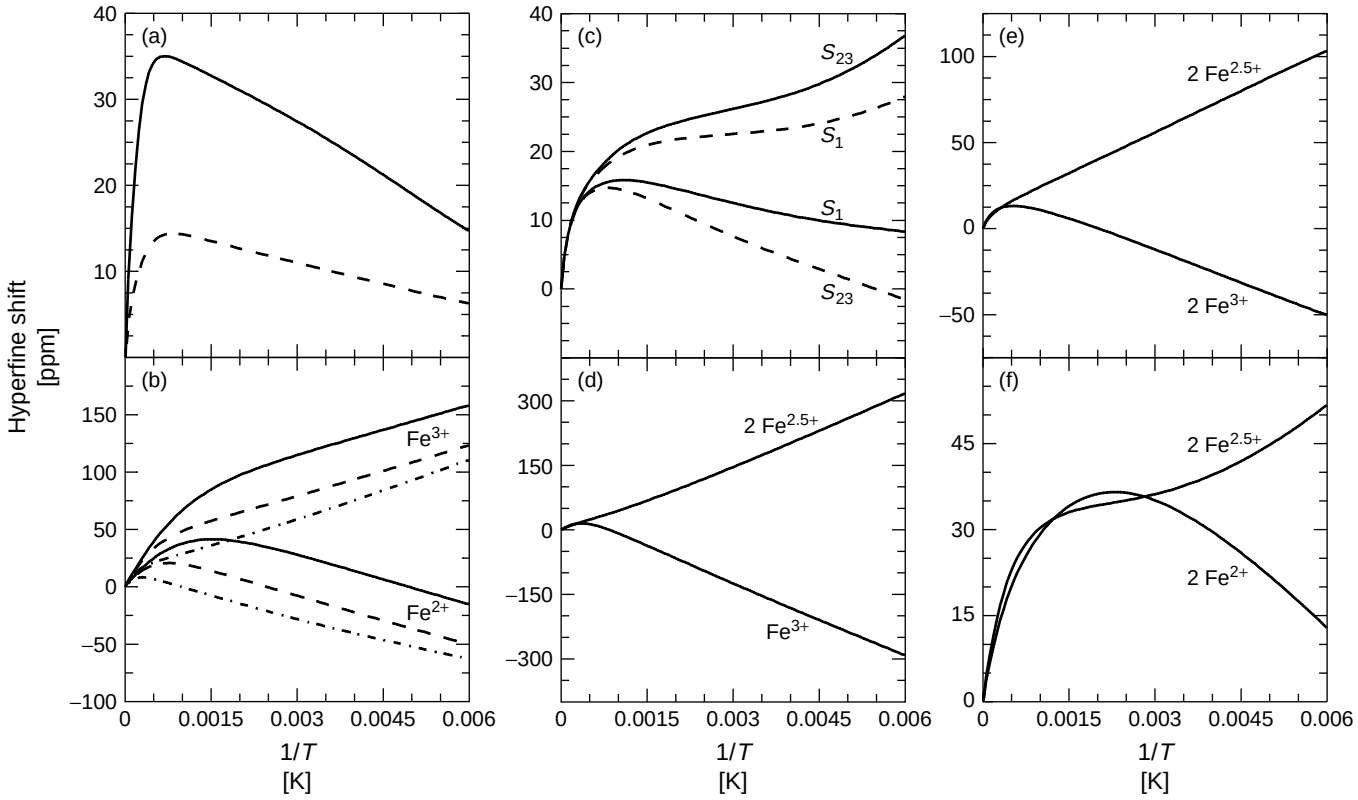

Figure 5 Plots of the temperature dependence of the hyperfine shift of Cys H^{β} resonances versus $1/T$ for different FeS clusters. $A/h = 1$ MHz except where noted. (a) $[2Fe\text{-}2S]^{2+}$, $J = -175\,cm^{-1}$, $A/h = 1.8$ MHz (solid line). $[4Fe\text{-}4S]^{2+}$, $J = -150\,cm^{-1}$, $B = 400\,cm^{-1}$ (dashed line). (b) $[2Fe\text{-}2S]^{+}$, $J = -50\,cm^{-1}$ (solid line), $J = -100\,cm^{-1}$ (dashed line), $J = -250\,cm^{-1}$ (dot-dash line). (c) $[3Fe\text{-}4S]^{+}$, $J_{12} = J_{13} = -185\,cm^{-1}$, $J_{23} = -192\,cm^{-1}$ (solid line). $J_{12} = J_{13} = -185\,cm^{-1}$, $J_{23} = -178\,cm^{-1}$ (dashed line) (d) $[3Fe\text{-}4S]^{0}$, $J = -125\,cm^{-1}$, B= $650\,cm^{-1}$. (e) $[4Fe\text{-}4S]^{3+}$, $J = -130\,cm^{-1}$, $\Delta J_{12} - 32\,cm^{-1}$, $B_{34} = 250\,cm^{-1}$. (f) $[4Fe\text{-}4S]^{+}$, J= $-62\,cm^{-1}$, $\Delta J_{12} = 28\,cm^{-1}$, $B_{34} = 75\,cm^{-1}$

hyperfine shift. The origin of the hyperfine shifts in Rieske proteins has not yet been analyzed in detail.

3.2.2 [3Fe–4S] Clusters

The [3Fe–4S] clusters that have been studied by NMR are found in two types of proteins: 3Fe Fds and 7Fe Fds. The 3Fe Fds are formed from Fds that contain one [4Fe–4S] cluster in which one Fe is labile and is readily removed to yield a stable [3Fe–4S] cluster. The 7Fe Fds contain one $[3Fe–4S]^{+}$ cluster and one $[4Fe–4S]^{2+}$ cluster, in which only the former can be readily reduced. The hyperfine-shifted ^{1}H resonances in $[3Fe–4S]^{+}$ clusters have substantially narrower linewidths than in $[2Fe–2S]^{2+/+}$ clusters. Hyperfine-shifted signals from $[3Fe–4S]^{+}$ clusters have been extensively assigned by 1D NOEs, 2D NOESY, 2D magnitude COSY, and 2D TOCSY. In all cases, the Cys H^{β} resonances are found in the 35 to -1 ppm range; some shift to higher frequency with increasing temperature and some to lower frequency. A representative example is *D. gigas* 3Fe Fd (Figure 4(c), Table 5).[61]

The chemical shifts and temperature dependencies of the hyperfine-shifted resonances are readily understood using the vector coupling model outlined above. The pattern of hyperfine-shifted resonances depends upon the relative values of the three exchange coupling parameters, J_{12}, J_{13}, and J_{23}. From Mössbauer[62] and temperature-dependent EPR,[63,64] all J-values are close in magnitude but not equal. From magnetic susceptibility, J is large and negative ($|J| > 100\,cm^{-1}$).[65] S_2 and S_3 are coupled to yield spin S_{23}, which ranges from 0 to 10, and S_{23} is coupled with S_1 to yield states of the form $|S_{23}, S\rangle$.[62] One can consider three cases.[66–70] (1) If $|J_{12}| = |J_{13}| < |J_{23}|$, then $|2, 1/2\rangle$ is the g.s., and one expects one pair of Cys H^{β} protons to exhibit large high-frequency shifts that decrease in frequency with increasing temperature since they are coupled to the larger spin ($S_1 = 5/2$), and the other two pairs of Cys H^{β} protons exhibit smaller high-frequency shifts that increase in frequency with increasing temperature (Figure 5(c), solid lines). (2) If $|J_{12}| = |J_{13}| > |J_{23}|$, then $|3, 1/2\rangle$ is the g.s., and two pairs of Cys H^{β} protons are expected to exhibit large high-frequency shifts that decrease in frequency with increasing temperature, since they area coupled to the larger spin ($S_{23} = 3$), and the third pair of Cys H^{β} protons to exhibit low-frequency shifts that increase in frequency with increasing temperature (Figure 5(c), dashed lines). (3) In the intermediate case, $|J_{12}| > |J_{13}| > |J_{23}|$, the g.s. is a mixture of $|2, 1/2\rangle$ and $|3, 1/2\rangle$, and one pair of Cys H^{β} protons will have high-frequency shifts that decrease with temperature, one will have minor hyperfine shifts that increase in frequency with temperature, and the third will be slightly shifted to higher frequency and weakly temperature-dependent, with the direction dependent on the exact strength of the coupling.[66–70] Indeed, this range of behavior has been observed. The 3Fe Fds of

D. gigas[61,67] and *T. litoralis*[66,71] and the 7Fe Fds from *D. ambivalens*,[68] *Sulfolobus* sp. Strain 7,[72] and *S. acidocaldarius*[73] are examples of the first case. Most of the other 7Fe Fds exhibit behavior of the third type[69,70,74–78] *Pyrococcus furiosus* 3Fe Fd is somewhat different in that the two Cys H^{β} protons that shift to lower frequency with temperature are at slightly lower frequency than in other [3Fe–4S] clusters and have a much larger chemical shift difference between them (23.6 and 11.8 ppm).[66,79] This was originally ascribed to magnetic coupling of the first type, but with the $S_1 = 5/2$ Fe ligated to Cys11 (equivalent to Cys8 in *D. gigas*) rather than Cys56 (equivalent to Cys50) as is found in other 3Fe Fds;[79] however, this interpretation has recently been challenged.[70,73] In *Desulfovibrio africanus* 7Fe Fd, four resonances were found at high frequency that moved to lower frequency with increasing temperature. This would appear to be an example of the case where $|J_{12}| \approx |J_{13}| > |J_{23}|$; however, detailed assignments were not reported, and no signals were found at frequencies below the diamagnetic region as expected from the above model. Thus, in the $[3Fe–4S]^{+}$ clusters, the vector coupling model has provided a firm basis for beginning to understand how differences among proteins modulate electronic structure.

For many years, there were essentially no reports on the hyperfine-shifted resonances in $[3Fe–4S]^{0}$ clusters, despite an attempt to selectively ^{2}H-label the Cys residues[80] and exploit the slower relaxation rate expected for ^{2}H, as had been done for CpRd.[10] $[3Fe–4S]^{0}$ clusters are a case where double exchange must be considered, and it was revealed by Mössbauer that the coupling could be viewed as mixed-valent iron pair in which double exchange exceeds the effects of isotropic exchange, vibronic coupling, and static asymmetry to yield a valence-delocalized (i.e., $2Fe^{2.5+}$)$S_{23} = 9/2$ state that is in turn coupled to the remaining Fe^{3+}.[81] In the simplest model (all J-values are equal), the Hamiltonian describing this is:

$$\mathcal{H} = -2J \sum_{i<j=1-3} \mathbf{S}_i \cdot \mathbf{S}_j \pm B\left(S_{23} + \frac{1}{2}\right) \tag{27}$$

yielding energies for the total spin states of

$$E(S) = -JS(S+1) \pm B\left(S_{23} + \frac{1}{2}\right) \tag{28}$$

From Mössbauer, the g.s. is $|9/2, 2\rangle$ which indicates that $B > 4|J|$.[81] It is likely that the location of the valence-delocalized $Fe^{2.5+}$ pair can exchange among the three irons, and such an exchange, with a rate constant of $\sim 10^{5}–10^{6}\,s^{-1}$, was invoked as the reason the hyperfine-shift Cys resonances were not observed.[82] Indeed, a new signal appears in the Mössbauer spectrum at higher temperatures (150 K) that indicates that all Fe sites are equivalent as a result of complete delocalization of the extra electron.[81] Reduction of the $[3Fe–4S]^{+}$ cluster at neutral pH is believed to involve protonation of the μ-sulfido bridges. Thus, chemical exchange resulting from dynamic protonation/deprotonation of the sulfides could provide the mechanism for signal broadening. Consistent with this view is the observation of very broad hyperfine-shifted NMR signals at high pH, where the protonation/deprotonation mechanism should be minimal. These signals, shifted both to higher and lower frequencies by 100–300 ppm have been preliminarily assigned to Cys H^{β} protons (Table 5).[82]

3.2.3 [4Fe–4S] Clusters

[4Fe–4S] clusters have been extensively studied by NMR, much more so than all of the other classes of FeS proteins, in part because their relatively narrow hyperfine-shifted signals greatly aid in sequence-specific assignment. As listed in Table 3, they can exist in three different redox states. The $[4Fe–4S]^{3+}$ state is found in the oxidized HiPIPs. In most of these, the protons of the ligating Cys residues have been extensively assigned by 1D NOEs, 2D NOESY, 2D magnitude COSY, 2D TOCSY, 1D saturation-transfer, and 2D EXSY. Representative ^{1}H NMR data from *E. halophila* HiPIP I is given in Figure 4(d) and Table 6; the latter also lists ^{13}C and ^{15}N data obtained from 2D experiments.[38,83,84]

In the oxidized HiPIPs, the Cys H^{β} resonances are found throughout the 150 to −70 ppm range and vary significantly among different HiPIPs, despite their close structural homology. In all cases, however, four Cys H^{β} resonances shift to lower frequency with increasing temperature, and four to higher frequency. To understand this behavior it is necessary to first consider the case of *E. halophila* HiPIP II. This is the only HiPIP that exhibits four Cys H^{β} resonances at high field (95–45 ppm) that shift to lower frequency with increasing temperature and four at low field (−10 to −25 ppm) with the opposite temperature-dependence.[85–87] From Mössbauer, the oxidized HiPIPs consist of a Fe^{3+} pair and a valance-delocalized $Fe^{2.5+}$ pair that are coupled to yield a net $S = 1/2$ g.s.,[88–90] as also shown by EPR.[54,90,91] Noodleman explained this behavior based upon the following Hamiltonian:

$$\mathcal{H} = \sum_{i<j=1-4} -2J_{ij}\mathbf{S}_i \cdot \mathbf{S}_j \pm B_{34}\left(S_{34} + \frac{1}{2}\right) \tag{29}$$

where S_1 and S_2 are the spins of the Fe^{3+} pair and S_3 and S_4 are the spins of the $Fe^{2.5+}$ pair ($S_1 = S_2 = 5/2$ and $S_3, S_4 = 5/2, 2$).[34,92,93] Since J_{12} is the Heisenberg exchange coupling parameter for the Fe^{3+} pair, it is assumed to be the largest. B_{34} is the double exchange term for the valance-delocalized $Fe^{2.5+}$ pair. This then yields the following for the energies of the total spin states:

$$E(S) = -JS(S+1) - \Delta J_{12}S_{12}(S_{12}+1) \pm B_{34}\left(S_{34} + \frac{1}{2}\right) \tag{30}$$

where $J = J_{13} = J_{14} = J_{23} = J_{24} = J_{34}$ and $\Delta J_{12} = J_{12} - J$. There are multiple states with total spin $S = 1/2$. Based upon single-crystal X-band ENDOR data on a $[4Fe–4S]^{3+}$ model complex with very similar Mössbauer and EPR spectral properties, the correct g.s. is $|7/2, 3, 1/2\rangle$ (nomenclature is $|S_{34}, S_{12}, S\rangle$).[94] With $J_{12} > J$, this requires $6 < B_{34}/\Delta J_{12} < 8$.[95] With the same vector coupling model (see below), $J = -130\,cm^{-1}$, $J_{12} = -162\,cm^{-1}$, and $B_{34} = 250\,cm^{-1}$ yields qualitatively correct agreement with the behavior of the Cys H^{β} resonances of *E. halophila* HiPIP II (Figure 5(d)).[32,86,96,97] In a slightly more sophisticated model in which $J_{34} \neq J$, B_{34} and J_{34} are covariant, and hence it currently is not possible to determine any of the parameters independently. This has led to considerable debate as to the exact values to use for the Heisenberg and double exchange parameters.[95,98] Regardless, the picture remains the same: signals of the Cys ligated to the $Fe^{2.5+}$ pair will be shifted to higher frequency and those ligated

Table 6 Chemical shifts and temperature dependencies of the hyperfine resonances in representative [4Fe-4S] clusters

Oxidized				Reduced			
Peak label	Assignment	Chemical shift (ppm)	Temperature increases, peak moves	Peak label	Assignment	Chemical shift (ppm)	Temperature increases, peak moves
			E. halophila HiPIP I (at 288 K)				
A	Cys50 $H^{\beta 3}$	92.0	→		Cys33 $H^{\beta 3}$	16.5	←
B	Cys36 $H^{\beta 2}$	47.0	→		Cys50 $H^{\beta 3}$	14.3	←
C	Cys36 $H^{\beta 3}$	42.4	→		Cys66 $H^{\beta 2}$	10.8	←
D	Cys50 $H^{\beta 2}$	27.8	→		Cys36 $H^{\beta 2}$	9.06	nd
	Cys66 $H^{\beta 2}$	6.26	←		Cys36 $H^{\beta 3}$	7.5	nd
	Cys66 $H^{\beta 3}$	2.59	←		Cys33 $H^{\beta 3}$	7.5	←
Y	Cys33 $H^{\beta 2}$	−21.58	←		Cys66 $H^{\beta 3}$	5.81	←
Z	Cys33 $H^{\beta 3}$	−26.7	←		Cys50 $H^{\beta 2}$	4.7	nd
	Cys66 H^{α}	16.2	←		Cys66 H^{α}	7.74	←
	Cys50 H^{α}	6.48	nd		Cys50 H^{α}	4.16	←
	Cys36 H^{α}	0.62	nd		Cys36 H^{α}	3.81	nd
	Cys33 H	9.75[a,b]	nd		Cys33 H	9.28[a]	nd
	Cys36 H	7.60[a,b]	nd		Cys50 H	8.88[a]	nd
	Cys50 C^{β}	440	→		Cys50 C^{β}	112.4	nd
	Cys36 C^{β}	390	→		Cys36 C^{β}	103.7	nd
	Cys66 C^{β}	59.3	nd		Cys33 C^{β}	102.3	nd
	Cys33 C^{β}	41.1	←		Cys66 C^{β}	88.7	nd
	Cys50 C^{α}	152.2	nd		Cys50 C^{α}	89.0	nd
	Cys66 C^{α}	129.0	←		Cys33 C^{α}	86.7	nd
	Cys33 C^{α}	54.7	nd		Cys66 C^{α}	85.8	nd
	Cys36 C^{α}	28.6	nd		Cys36 C^{α}	78.2	nd
	Cys36 N	150[a,b]	nd		Cys50N	137.27[a]	nd
	Cys33 N	127.5[a,b]	nd		Cys33 N	128.93[a]	nd
			Cluster I of *C. acidi-urici* (at 293 K)				
B	Cys11 $H^{\beta 3}$	15.4	←	G'	Cys8 $H^{\beta 3}$	56.5	→
D	Cys14 $H^{\beta 2}$	15.0	←	E	Cys47 $H^{\beta 3}$	55.9	←
E	Cys47 $H^{\beta 3}$	13.4	←	G	Cys8 $H^{\beta 2}$	41.5	→
G	Cys8 $H^{\beta 2}$	11.4	←	B	Cys11 $H^{\beta 3}$	32.7	←
B'	Cys11 $H^{\beta 2}$	9.2	←	E'	Cys47 $H^{\beta 2}$	26.0	←
G'	Cys8 $H^{\beta 3}$	8.2	←	D	Cys14 $H^{\beta 3}$	23.9	→
E'	Cys47 $H^{\beta 2}$	6.5	←	B'	Cys11 $H^{\beta 2}$	18.5	←
D'	Cys14 $H^{\beta 3}$	4.8	←				
	Cys11 H^{α}	10.0	←		Cys40 H^{α}	15.7	nd
	Cys14 H^{α}	7.4	←	B"	Cys11 H^{α}	15.5	nd
	Cys47 H^{α}	4.7	←				
	Cys8 H^{α}	3.5	←				
	Cys14 C^{β}	121	nd				
	Cys47 C^{β}	109	nd				
	Cys11 C^{β}	97	nd				
	Cys8 C^{β}	91	nd				
	Cys14 C^{α}	92	nd				
	Cys11 C^{α}	81	nd				

[a]298 K.
[b]These values were not reported in tabulated form, but were read off the published spectrum[84] and are therefore approximate.

to the Fe^{3+} pair will be shifted to lower frequency. ^1H hyperfine data of the other HiPIPs, in which only two resonances are at lower frequency than the diamagnetic region, have been explained by invoking a spin equilibrium mechanism, in which the location of the delocalized $Fe^{2.5+}$ pair alternates between two different sets of Fe atoms with the exchange rapid on the NMR timescale.[99] Based upon the *E. halophila* HiPIP I sequence, Cys 33, 36, 50 and 66 are designated I, II, III, and IV, respectively. In *E. halophila* HiPIP II, Cys I and IV ligated to the Fe^{3+} pair and Cys II and III are ligated to the delocalized $Fe^{2.5+}$ pair. All other HiPIPs exist in equilibrium between this arrangement and a second one, in which Cys I and II are ligated to the Fe^{3+} pair and Cys III and IV are ligated to the delocalized $Fe^{2.5+}$ pair. Thus, in *E. halophila* HiPIP I, Cys II experiences ∼20% Fe^{3+} character, and Cys IV ∼20% $Fe^{2.5+}$ character. The degree in which the delocalized $Fe^{2.5+}$ pair is found ligated to Cys III and IV increases in the order *E. halophila* iso I, *R. globiformis*, *E. vacuolata* iso I, *E. vacuolata* iso II, *C. vinosum*, *R. gelatinosus*, and *R. fermentans*. In the last two HiPIPs, Cys II experiences ∼70% Fe^{3+} character, and Cys IV ∼70% $Fe^{2.5+}$ character.[100,101] This spin equilibrium model also explains the noticeable deviation in linearity in the temperature dependencies of the Cys H^{β} protons in *E. vacuolata* HiPIP II, behavior that is not readily accounted for

by other models.[99] In addition, the EPR spectra of oxidized HiPIPs exhibit a mixture of $S = 1/2$ species in all cases except *E. halophila* iso II. These results have been described in terms of the same model as given above, where now the two species are either frozen out or are exchanging on a timescale slower than the EPR experiment.[99] The vector coupling picture and the spin equilibrium model provide a remarkably reliable basis for understanding a range of features seen among the oxidized HiPIPs. The exception again is the failure of the simple vector coupling picture to explain the hyperfine shifts of ^{13}C nuclei, in particular the Cys C^{α} resonances.[38]

The $[4Fe{-}4S]^{2+}$ state is found among all [4Fe–4S] proteins: HiPIPs, the 4Fe, 7Fe, and 8Fe ferredoxins (which in the oxidized state contain 2 $[4Fe{-}4S]^{2+}$ clusters), and two other systems that have been examined by NMR, the nitrogenase Fe-protein and the PsaC subunit of photosystem I. The Cys protons are found in the 22–0 ppm range and always increase in frequency with increasing temperature. In a number of systems, they have been sequence-specifically assigned by the usual assortment of 1D and 2D NMR experiments. Representative data from cluster I of the *C. acidi-urici* 8Fe Fd is given in Figure 5(e) and Table 6.[102] The $[4Fe{-}4S]^{2+}$ cluster consists of two nearly identical $Fe^{2.5+}$ pairs that are antiferromagnetically coupled to yield a net $S = 0$ g.s., as shown by Mössbauer spectroscopy on reduced HiPIPs,[88,89] oxidized 8Fe and 4Fe Fds,[103–105] and oxidized nitrogenase Fe-protein.[106] Thus, as in the case of the $[2Fe{-}2S]^{2+}$ clusters, the hyperfine shifts arise solely from thermal population of paramagnetic excited states. This behavior can be readily fit by using a Hamiltonian of the sort in equation (29) and adding another $B_{12}(S_{12} + 1/2)$ term to account for double exchange in the second valence-delocalized $Fe^{2.5+}$ pair.[34,93,96,97,107] In the simplest possible model all J-values are equal, yielding the following for the energy of the total spin states:

$$E(S) = -JS(S+1) \pm B_{12}\left(S_{12} + \frac{1}{2}\right) \pm B_{34}\left(S_{34} + \frac{1}{2}\right) \qquad (31)$$

This readily accounts for the observed hyperfine shifts of the Cys H^{β} resonances (Figure 5(a), dashed lines).[96,97,107]

The $[4Fe{-}4S]^{+}$ state occurs in the reduced 4Fe and 8Fe ferredoxins, nitrogenase Fe-protein, and PsaC subunit of photosystem I. The Cys protons are found in the 65 to −5 ppm range and exhibit a mixture of temperature-dependent behavior: some shift to higher frequency and some to lower frequency with increasing temperature. Representative data from cluster I of the *C. acidi-urici* 8Fe Fd is given in Figure 5(f) and Table 6.[102] In this system and a number of others, the Cys protons have been sequence-specifically assigned by 1D and 2D NMR experiments and in particular, with the use of 2D EXSY and existing assignments of the oxidized form.[102,108] In reduced *C. acidi-urici* 8Fe Fds and in most other cases, the H^{β} resonances of two Cys residues shift to higher frequency with increasing temperature, and the other two to lower frequency, and all occur in roughly the same chemical shift range.[102,108] Mössbauer spectroscopy indicates that the $[4Fe{-}4S]^{+}$ cluster consists of a Fe^{2+} pair and a valance-delocalized $Fe^{2.5+}$ pair.[103–106,109] In general, the g.s. is $S = 1/2$, although there are notable exceptions, discussed below.[47] The exchange coupling in the $[4Fe{-}4S]^{+}$ cluster is significantly more complex than in other FeS clusters. The decrease in the average valence of the four Fe atoms leads to a decrease in the magnitude of J, which in turns means that B has a proportionally greater influence and that the total spin states are closer in energy.[34,93,110–113] Nonetheless, some insight may be gained by the same simple model as used in equations (29) and (30), where now S_1 and S_2 are the spins of the Fe^{2+} pair and S_3 and S_4 are the spins of the $Fe^{2.5+}$ pair ($S_1 = S_2 = 2$ and $S_3, S_4 = 5/2, 2$). With reasonable estimates for J and B_{34} one obtains the qualitatively correct behavior of the Cys H^{β} resonances: those ligated to the $Fe^{2.5+}$ pair shift to lower frequency with increasing temperature and those ligated to the Fe^{2+} pair shift to higher frequency, and all of them will be higher frequency than the diamagnetic region (Figure 5(f)).

P. furiosus 4Fe Fd is an unusual case. First, one of the ligands to the cluster is an Asp instead of a Cys. Second, the g.s. is a physical mixture of $S = 3/2$ and $S = 1/2$ species based upon EPR.[114] The temperature dependencies of the hyperfine-shifted resonances in the reduced state are complex and very unusual; for example, the H^{β} protons of Cys17 exhibit *opposite* temperature dependence.[115–117] In contrast, the D14C mutant exhibits hyperfine behavior extremely similar to those of other 4Fe and 8Fe Fds; specifically, the H^{β} protons of Cys11 and 17 shift to lower frequency with increasing temperature and are assigned to the $Fe^{2.5+}$ pair, and Cys14 and 56 shift to higher frequency and are assigned to the Fe^{2+} pair.[116] Similarly, from EPR, the g.s. is purely $S = 1/2$.[118] The unusual hyperfine temperature-dependent behavior observed in the wild-type was explained by invoking a spin-equilibrium model similar to that for the oxidized HiPIPs. In one arrangement, Cys 14 and 56 ligate the $Fe^{2.5+}$ pair and Cys 11 and 17 the Fe^{2+} pair, and in the other, Cys 14 and 17 ligate the $Fe^{2.5+}$ pair and Cys 11 and 56 the Fe^{2+} pair, indicating that Asp stabilizes the mixed-valence $Fe^{2.5+}$ pair.[116] Notably, the hyperfine shifts and relaxation rates of the ligand protons in the wild-type protein are not significantly different from other $[4Fe\text{-}4S]^{+}$ clusters, leading to the conclusion that the presence of $S = 3/2$ species in the EPR spectrum is an artifact of freezing and that in solution the g.s. is purely $S = 1/2$.[115] A similar picture exists for the nitrogenase Fe-protein, which also exists as a mixture of $S = 3/2$ and $S = 1/2$ species based upon EPR and Mössbauer.[106,109] Addition of urea increases the fraction of the $S = 3/2$, and addition of ethylene glycol decreases it.[106] Again, the NMR spectra are not significantly different from those of other $[4Fe{-}4S]^{+}$ clusters.[119,120] Indeed, the addition of urea or ethylene glycol had little effect, leading to the conclusion that in solution the g.s. is purely $S = 1/2$.

4 CONCLUDING REMARKS

The last decade has seen a dramatic increase in our understanding of electron–nuclear interactions. We have progressed from merely noting the different sorts of the hyperfine-shifted resonances in paramagnetic proteins to being able to accurately calculate them. Relaxation rates are now often used as distance constraints in solution structure determination. The use of residual dipolar couplings holds similar promise. The vector coupling model has been enormously successful in explaining the ^{1}H hyperfine data in FeS clusters and has contributed greatly to our understanding of the exchange coupling in these complex systems. Further refinement of this model to help better explain ^{13}C and ^{15}N hyperfine data is needed and may lead

to further insights. With these tools in hand, NMR will be capable of answering detailed questions regarding how H-bonds and other aspects of the protein matrix tune the properties of metal active sites and thus their function. Thus, while paramagnetic NMR already is acknowledged as one of the most powerful spectroscopic methods available for investigating the biophysics of metalloproteins, it is now poised to assume similar importance for studies of metalloprotein biochemistry.

5 REFERENCES

1. I. Bertini, C. Luchinat, and A. Rosato, *Prog. Biophys. Mol. Biol.*, 1996, **66**, 43–80.
2. B. J. Goodfellow and A. L. Macedo, *Annu. Rep. NMR Spectrosc.*, 1999, **37**, 119–177.
3. I. Bertini, C. Luchinat, and A. Rosato, *Adv. Inorg. Chem.*, 1999, **47**, 251–282.
4. I. Bertini and C. Luchinat, 'NMR of Paramagnetic Molecules in Biological System', Benjamin/Cummings: Menlo Park, CA, 1986.
5. I. Bertini and A. J. Vila, *Chem. Rev.*, 1993, **93**, 2833–2932.
6. L. Banci, I. Bertini, and C. Luchinat, 'Nuclear and Electron Relaxation', VCH: Weinheim: Germany, 1991.
7. A. A. Bothner-By, P. J. Domaille, and C. Gayathri, *J. Am. Chem. Soc.*, 1981, **103**, 5602–5603.
8. B. F. Volkman, S. J. Wilkens, A. L. Lee, B. Xia, W. W. Westler, R. Beger, and J. L. Markley, *J. Am. Chem. Soc.*, 1999, **120**, 4677–4683.
9. L. Banci, I. Bertini, C. Luchinat, and A. Scozzafava, *J. Am. Chem. Soc.*, 1987, **109**, 2328–2334.
10. B. Xia, W. M. Westler, H. Cheng, J. Meyer, J.-M. Moulis, and J. L. Markley, *J. Am. Chem. Soc.*, 1995, **117**, 5347–5350.
11. B. Xia, Thesis, University of Wisconsin, 1996.
12. B. Xia, B. F. Volkman, D. S. King, D. Jenk, D. M. LeMaster, W. M. Westler, S. J. Wilkens, and J. L. Markley, unpublished data.
13. B. Xia, S. J. Wilkens, W. W. Westler, and J. L. Markley, *J. Am. Chem. Soc.*, 1998, **120**, 4893–4894.
14. S. J. Wilkens, B. Xia, F. Weinhold, J. L. Markley, and W. M. Westler, *J. Am. Chem. Soc.*, 1998, **120**, 4806–4814.
15. K. D. Watenpaugh, L. C. Sieker, and L. H. Jensen, *J. Mol. Biol.*, 1979, **131**, 509–522.
16. K. D. Watenpaugh, L. C. Sieker, and L. H. Jensen, *J. Mol. Biol.*, 1980, **138**, 615–633.
17. Z. Dauter, K. S. Wilson, L. C. Sieker, J. M. Moulis, and J. Meyer, *Proc. Natl. Acad. Sci. USA*, 1996, **93**, 8836–8840.
18. J. Lin, E. Gebel, W. M. Westler, and J. L. Markley, unpublished data.
19. Z. Xiao, M. J. Maher, M. Cross, C. S. Bond, J. M. Guss, and A. G. Wedd, *J. Biol. Inorg. Chem.*, 200, **5**, 75–84.
20. T. Min, C. E. Ergenekan, M. K. Eidsness, T. Ichiye, and C. Kang, *Protein Sci.*, 2001, **10**, 613–621.
21. W. M. Westler and J. L. Markley, unpublished results.
22. S. J. Wilkens, B. Xia, B. F. Volkman, F. Weinhold, J. L. Markley, and W. M. Westler, *J. Phys. Chem. B*, 1998, **102**, 8500–8505.
23. C. Schulz and P. G. Debrunner, *J. Physique*, 1976, **37**, C6-153–C6-158.
24. P. G. Debrunner, E. Münck, L. Que, and C. E. Schulz, in 'Iron-Sulfur Proteins', Vol. III, ed W. Lovenberg, Academic Press: New York, 1977, pp. 381–417.
25. J. Peisach, W. E. Blumberg, E. T. Lode, and M. J. Coon, *J. Biol. Chem.*, 1971, **256**, 5877–5881.
26. M. S. Gebhard, J. C. Deaton, S. A. Koch, M. Millar, and E. I. Solomon, *J. Am. Chem. Soc.*, 1990, **112**, 2217–2231.
27. V. Petrouleas, A. Simopoulos, A. Kostikas, and D. Coucouvanis, *J. Physique*, 1976, **37**, C6-159–C6-164.
28. M. J. Knapp, J. Krzystek, L.-C. Brunel, and D. N. Hendrickson, *Inorg. Chem.*, 2000, **39**, 281–288.
29. P. M. Champion and A. J. Sievers, *J. Chem. Phys.*, 1977, **66**, 1819–1825.
30. A. Abragam and B. Bleaney, 'Electron Paramagnetic Resonance of Transition Ions', Dover: New York, 1970.
31. O. Kahn, 'Molecular Magnetism', Wiley-VCH: New York, 1993.
32. L. Banci, I. Bertini, and C. Luchinat, *Struct. Bonding*, 1990, **72**, 113–136.
33. R. P. Scaringe, D. J. Hodgson, and W. E. Hatfield, *Mol. Phys.*, 1978, **35**, 701–713.
34. L. Noodleman, C. Y. Peng, D. A. Case, and J.-M. Mouesca, *Coord. Chem. Rev.*, 1995, **144**, 199–244.
35. I. Bertini, O. Galas, C. Luchinat, G. Parigi, and G. Spina, *J. Magn. Reson.*, 1998, **130**, 33–44.
36. I. Bertini, M. M. J. Couture, A. Donaire, L. D. Eltis, I. C. Felli, C. Luchinat, M. Piccioli, and A. Rosato, *Eur. J. Biochem.*, 1996, **241**, 440–452.
37. J. G. Huber, J.-M. Moulis, and J. Gaillard, *Biochemistry*, 1996, **35**, 12 705–12 711.
38. I. Bertini, A. Donaire, I. C. Felli, C. Luchinat, and A. Rosato, *Inorg. Chem.*, 1997, **36**, 4798–4803.
39. I. Bertini, A. Donaire, C. Luchinat, and A. Rosato, *Proteins: Struct. Funct. Genet.*, 1997, **29**, 348–358.
40. R. Cammack, *Adv. Inorg. Chem.*, 1992, **38**, 281–322.
41. H. Matsubara and K. Saeki, *Adv. Inorg. Chem.*, 1992, **38**, 223–280.
42. L. Skjeldal, J. L. Markley, V. M. Coghlan, and L. E. Vickery, *Biochemistry*, 1991, **30**, 9078–9083.
43. H. Cheng, W. M. Westler, B. Xia, B.-H. Oh, and J. L. Markley, *Arch. Biochem. Biophys.*, 1995, **316**, 619–634.
44. B. Xia, D. Jenk, D. M. LeMaster, W. M. Westler, and J. L. Markley, *Arch. Biochem. Biophys.*, 2000, **373**, 328–334.
45. P. Bertrand and J.-P. Gayda, *Biochim. Biophys. Acta*, 1979, **579**, 107–121.
46. R. H. Sands and W. R. Dunham, *Q. Rev. Biophys.*, 1975, **7**, 443–504.
47. B. Guigliarelli and P. Bertrand, *Adv. Inorg. Chem.*, 1999, **47**, 421–497.
48. W. Fu, P. M. Drozdzewski, M. D. Davies, S. G. Sligar, and M. K. Johnson, *J. Biol. Chem.*, 1992, **267**, 15 502–15 510.
49. R. Morales, M.-H. Chron, G. Hudry-Clergeon, Y. Pétillot, S. Norager, M. Medina, and M. Frey, *Biochemistry*, 1999, **38**, 15 764–15 773.
50. A. Müller, J. J. Müller, Y. A. Muller, H. Uhlmann, R. Bernhardt, and U. Heinemann, *Structure*, 1998, **6**, 269–280.
51. L. Skjeldal, W. M. Westler, B.-H. Oh, A. M. Krezel, H. M. Holden, B. L. Jacobson, I. Rayment, and J. L. Markley, *Biochemistry*, 1991, **30**, 7363–7368.
52. L. B. Dugad, G. N. La Mar, L. Banci, and I. Bertini, *Biochemistry*, 1990, **29**, 2263–2271.
53. W. R. Dunham, G. Palmer, R. H. Sands, and A. J. Bearden, *Biochim. Biophys. Acta*, 1971, **253**, 373–384.
54. I. Bertini, S. Ciurli, and C. Luchinat, *Struct. Bonding*, 1995, **83**, 1–53.
55. G. Palmer, W. R. Dunham, J. A. Fee, R. H. Sands, T. Ikuza, and T. Yonetani, *Biochim. Biophys. Acta*, 1971, **245**, 201–207.
56. J.-P. Gayda, J. F. Gibson, R. Cammack, D. O. Hall, and R. Mullinger, *Biochim. Biophys. Acta*, 1976, **434**, 154–163.
57. R. E. Anderson, W. R. Dunham, R. H. Sands, A. J. Bearden, and H. L. Crespi, *Biochim. Biophys. Acta*, 1975, **408**, 306–318.
58. S. G. Lloyd, R. Franco, J. J. G. Moura, I. Moura, G. C. Ferreira, and B. H. Huynh, *J. Am. Chem. Soc.*, 1996, **118**, 9892–9900.
59. J. C. Salerno, T. Ohnishi, H. Blum, and J. S. Leigh, *Biochim. Biophys. Acta*, 1977, **494**, 191–197.

60. B. Xia, J. D. Pikus, W. Xia, K. McClay, R. J. Steffan, Y. K. Chae, W. M. Westler, J. L. Markley, and B. G. Fox, *Biochemistry*, 1999, **38**, 727–739.
61. A. L. Macedo, P. N. Palma, I. Moura, J. LeGall, V. Wray, and J. J. G. Moura, *Magn. Reson. Chem.*, 1993, **31**, S59–S67.
62. T. A. Kent, B. H. Huynh, and E. Münck, *Proc. Natl. Acad. Sci. USA*, 1980, **77**, 6574–6576.
63. J.-P. Gayda, P. Bertrand, and F.-X. Theodule, *J. Chem. Phys.*, 1982, **77**, 3387–3391.
64. J. Telser, H.-I. Lee, and B. M. Hoffman, *J. Biol. Inorg. Chem.*, 2000, **5**, 369–380.
65. E. P. Day, J. Peterson, J. J. Bonvoisin, I. Moura, and J. J. G. Moura, *J. Biol. Chem.*, 1988, **263**.
66. S. C. Busse, G. La Mar, L. P. Yu, J. B. Howard, E. T. Smith, Z. H. Zhou, and M. W. W. Adams, *Biochemistry*, 1992, **31**, 11 952–11 962.
67. A. L. Macedo, I. Moura, J. J. G. Moura, J. LeGall, and B. H. Huynh, *Inorg. Chem.*, 1993, **32**, 1101–1105.
68. D. Bentrop, I. Bertini, C. Luchinat, J. Mendes, M. Piccioli, and M. Teixeira, *Eur. J. Biochem.*, 1996, **236**, 92–99.
69. S. Aono, I. Bertini, J. A. Cowan, C. Luchinat, A. Rosato, and M. S. Viezzoli, *J. Biol. Inorg. Chem.*, 1996, **1**, 523–528.
70. I. Bertini, A. Dikiy, C. Luchinat, R. Macinai, M. S. Viezzoli, and M. Vincenzini, *Biochemistry*, 1997, **36**, 3570–3579.
71. A. Donaire, C. M. Gorst, Z. H. Zhou, M. W. W. Adams, and G. La Mar, *J. Am. Chem. Soc.*, 1994, **116**, 6841–6849.
72. T. Iwasaki, E. Watanabe, D. Ohmori, T. Imai, A. Urushiyama, M. Akiyama, Y. Hayashi-Iwasaki, N. J. Cosper, and R. A. Scott, *J. Biol. Inorg. Chem.*, 2000, **276**, 25 391–25 401.
73. J. P. Hannan, J. L. H. Busch, J. Breton, R. James, A. J. Thompson, G. R. Moore, and S. L. Davy, *J. Biol. Inorg. Chem.*, 2000, **5**, 432–447.
74. K. Nagayama, D. Ohmori, T. Imai, and T. Oshima, *FEBS Lett.*, 1983, **158**, 208–212.
75. H. Cheng, K. Grohmann, and W. Sweeney, *J. Biol. Chem.*, 1990, **265**, 12 388–12 392.
76. H. Cheng, K. Grohmann, and W. Sweeney, *J. Biol. Chem.*, 1992, **267**, 8073–8080.
77. G. Battistuzzi, M. Borsari, S. Ferretti, C. Luchinat, and M. Sola, *Arch. Biochem. Biophys.*, 1995, **320**, 149–154.
78. A. L. Macedo, S. Besson, C. Moreno, G. Fauque, J. J. Moura, and I. Mouara, *Biochem. Biophys. Res. Commun.*, 1996, **229**, 524–530.
79. C. M. Gorst, Y.-H. Yeh, Q. Teng, L. Calzolai, Z.-H. Zhou, M. W. W. Adams, and G. La Mar, *Biochemistry*, 1995, **34**, 600–610.
80. I. Bertini, C. Luchinat, G. Mincione, and A. Soriano, *Inorg. Chem.*, 1998, **37**, 969–972.
81. V. Papaefthymiou, J.-J. Girerd, I. Moura, J. J. G. Moura, and E. Münck, *J. Am. Chem. Soc.*, 1987, **109**, 4703–4710.
82. D. Bentrop, I. Bertini, M. Borsari, G. Cosenza, C. Luchinat, and Y. Niikura, *Angew. Chem. Int. Ed.*, 2000, **29**, 3620–3622.
83. I. Bertini, F. Capozzi, L. D. Eltis, I. C. Felli, C. Luchinat, and M. Piccioli, *Inorg. Chem.*, 1995, **34**, 2516–2523.
84. I. Bertini, L. D. Eltis, I. C. Felli, D. H. W. Kasrau, C. Luchinat, and M. Piccioli, *Chem. Eur. J.*, 1995, **1**, 698–607.
85. R. Krishnamoorthi, J. L. Markley, M. A. Cusanovich, C. T. Przysiecki, and T. E. Meyer, *Biochemistry*, 1986, **25**, 60–67.
86. L. Banci, I. Bertini, F. Briganti, A. Scozzafava, M. Vincens-Oliver, and C. Luchinat, *Inorg. Chim. Acta*, 1991, **180**, 171–175.
87. L. Banci, I. Bertini, F. Capozzi, P. Carloni, S. Ciurli, C. Luchinat, and M. Piccioli, *J. Am. Chem. Soc.*, 1993, **115**, 3431–3440.
88. D. P. E. Dickson, C. E. Johnson, R. Cammack, M. C. W. Evans, D. O. Hall, and K. K. Rao, *Biochem. J.*, 1974, **139**, 105–108.
89. P. Middleton, D. P. E. Dickson, C. E. Johnson, and J. D. Rush, *Eur. J. Biochem.*, 1980, **104**, 289–296.
90. I. Bertini, A. P. Campos, C. Luchinat, and M. Teixeira, *J. Inorg. Biochem.*, 1993, **52**, 227–234.
91. B. C. Antanaitis and T. H. Moss, *Biochim. Biophys. Acta*, 1975, **405**, 262–279.
92. L. Noodleman, *Inorg. Chem.*, 1988, **27**, 3677–3679.
93. L. Noodleman and D. A. Case, *Adv. Inorg. Chem.*, 1992, **38**, 423–470.
94. J.-M. Mouesca, G. Ruis, and B. Lamotte, *J. Am. Chem. Soc.*, 1993, **115**, 4714–4731.
95. L. Noodleman, D. A. Case, J.-M. Mouesca, and B. Lamotte, *J. Biol. Inorg. Chem.*, 1996, **1**, 177–182.
96. I. Bertini, F. Briganti, C. Luchinat, A. Scozzafava, and M. Sola, *J. Am. Chem. Soc.*, 1991, **113**, 1237–1245.
97. I. Bertini, F. Briganti, C. Luchinat, A. Scozzafava, and M. Sola, *J. Am. Chem. Soc.*, 1991, **113**, 7084.
98. M. Belinskiy, I. Bertini, O. Galas, and C. Luchinat, *Inorg. Chim. Acta*, 1996, **243**, 91–99.
99. L. Banci, I. Bertini, S. Ciurli, S. Ferretti, C. Luchinat, and M. Piccioli, *Biochemistry*, 1993, **32**, 9387–9397.
100. I. Bertini, F. Capozzi, C. Luchinat, and M. Piccioli, *Eur. J. Biochem.*, 1993, **212**, 69–78.
101. S. Ciurli, M. A. Cremonini, P. Kofod, and C. Luchinat, *Eur. J. Biochem.*, 1996, **236**, 405–411.
102. I. Bertini, F. Capozzi, C. Luchinat, M. Piccioli, and A. Vila, *J. Am. Chem. Soc.*, 1994, **116**, 651–660.
103. C. L. Thompson, C. E. Johnson, D. P. E. Dickson, R. Cammack, D. O. Hall, U. Weser, and K. K. Rao, *Biochem. J.*, 1974, **139**, 97–103.
104. P. Middleton, D. P. E. Dickson, C. E. Johnson, and J. D. Rush, *Eur. J. Biochem.*, 1978, **88**, 135–141.
105. P. Kyritsis, R. Kümmerle, J. G. Huber, J. Gaillard, B. Guigliarelli, C. Popescu, E. Münck, and J.-M. Moulis, *Biochemistry*, 1999, **38**, 6335–6345.
106. P. A. Lindahl, E. P. Day, K. Thomas A., W. H. Orme-Johnson, and E. Münck, *J. Biol. Chem.*, 1985, **260**, 11 160–11 173.
107. I. Bertini, F. Briganti, C. Luchinat, and A. Scozzafava, *Inorg. Chem.*, 1990, **29**, 1874–1880.
108. I. Bertini, F. Briganti, C. Luchinat, L. Messori, R. Monnanni, and A. Scozzafava, *Eur. J. Biochem.*, 1992, **204**, 831–839.
109. P. A. Lindahl, N. J. Gorelick, E. Münck, and W. H. Orme-Johnson, *J. Biol. Chem.*, 1987, **262**, 14 945–14 953.
110. L. Noodleman, *Inorg. Chem.*, 1991, **30**, 246–256.
111. L. Noodleman, *Inorg. Chem.*, 1991, **30**, 256–264.
112. J.-M. Mouesca, L. Noodleman, D. A. Case, and B. Lamotte, *Inorg. Chem.*, 1995, **34**, 4347–4359.
113. F. Moriaud, S. Gambarelli, B. Lamotte, and J.-M. Mouesca, *J. Phys. Chem. B*, 2001, **105**, 9631–9642.
114. R. C. Conover, A. T. Kowal, W. Fu, J.-B. Park, S. Aono, M. W. W. Adams, and M. K. Johnson, *J. Biol. Chem.*, 1990, **265**, 8533–8541.
115. L. Calzolai, C. M. Gorst, Z.-H. Zhao, Q. Teng, M. W. W. Adams, and G. La Mar, *Biochemistry*, 1995, **34**, 11 373–11 384.
116. L. Calzolai, C. M. Gorst, K. L. Bren, Z.-H. Zhou, M. W. W. Adams, and G. N. La Mar, *J. Am. Chem. Soc.*, 1997, **119**, 9341–9350.
117. C. M. Gorst, Z. H. Zhou, K. Ma, Q. Teng, J. B. Howard, M. W. W. Adams, and G. La Mar, *Biochemistry*, 1995, **34**, 8788–8795.
118. Z. H. Zhou and M. W. W. Adams, *Biochemistry*, 1997, **36**, 10 892–10 900.
119. J. Meyer, J. Gaillard, and J.-M. Moulis, *Biochemistry*, 1988, **27**, 6150–6156.
120. W. N. Lanzilotta, R. C. Holz, and L. C. Seefeldt, *Biochemistry*, 1995, **34**, 15 646–15 653.
121. K. Nagayama, Y. Ozaki, Y. Kyogoku, T. Hase, and H. Matsubara, *J. Biochem. (Tokyo)*, 1983, **94**, 893–902.
122. J. Lou, F. Moshiri, M. K. Johnson, M. E. Lafferty, D. L. Sorkin, A.-F. Miller, and R. J. Maier, *Biochemistry*, 1999, **38**, 5563–5571.

123. G. Ratnaswamy and T. C. Pochapsky, *Magn. Reson. Chem.*, 1993, **31**, S73–S77.
124. B. Coxon, N. Sari, M. J. Hoden, and V. L. Vilker, *Magn. Reson. Chem.*, 1997, **35**, 743–751.
125. N. Sari, M. J. Holden, M. P. Mayhew, V. L. Vilker, and B. Coxon, *Biochem. Biophys. Res. Commun.*, 1998, **249**, 773–780.
126. N. U. Jain and T. C. Pochapsky, *J. Am. Chem. Soc.*, 1998, **120**, 12 984–12 985.
127. N. U. Jain and T. C. Pochapsky, *Biochem. Biophys. Res. Commun.*, 1999, **258**, 54–59.
128. R. C. Holz, F. J. Small, and S. A. Ensign, *Biochemistry*, 1997, **36**, 14 690–14 696.
129. S. DeVries, A. Cherepanov, A. Berg, and G. W. Canters, *Inorg. Chim. Acta*, 1998, **275/276**, 493–499.
130. W. D. Phillips, C. C. McDonald, N. A. Stombaugh, and W. H. Orme-Johnson, *Proc. Natl. Acad. Sci. USA*, 1974, **71**, 140–143.
131. S. L. Davy, J. Breton, M. J. Osborne, A. J. Thomson, A. P. Thurgood, L.-Y. Lian, Y. Pétillot, C. Hatchikian, and G. R. Moore, *Biochim. Biophys. Acta*, 1994, **1209**, 33–39.
132. S. L. Davy, M. J. Osborne, J. Breton, G. R. Moore, A. J. Thompson, I. Bertini, and C. Luchinat, *FEBS Lett.*, 1995, **363**, 199–204.
133. A. Donaire, Z.-H. Zhou, M. W. W. Adams, and G. La Mar, *J. Biomol. NMR*, 1996, **7**, 35–47.
134. G. Wildegger, D. Bentrop, A. Ejchart, M. Alber, A. Hage, R. Sterner, and P. Rösch, *Eur. J. Biochem.*, 1995, **229**, 658–668.
135. E. Lebrun, C. Simenel, F. Guerlesquin, and M. Delepierre, *Magn. Reson. Chem.*, 1996, **34**, 873–880.
136. J. L. H. Busch, J. L. Breton, S. L. Davy, R. James, G. R. Moore, F. A. Armstrong, and A. J. Thomson, *Biochem. J.*, 2000, **346**, 375–384.
137. E. L. Packer, W. V. Sweeney, J. C. Rabinowitz, H. Sterlicht, and E. N. Shaw, *J. Biol. Chem.*, 1977, **252**, 2245–2253.
138. I. Bertini, F. Briganti, C. Luchinat, L. Messori, R. Monnanni, A. Scozzafava, and G. Vallini, *FEBS Lett.*, 1991, **289**, 253–256.
139. S. C. Busse, G. La Mar, and J. B. Howard, *J. Biol. Chem.*, 1991, **266**, 23 714–23 723.
140. S. D. B. Scrofani, P. S. Brereton, A. M. Hamer, M. J. Lavery, S. G. McDowall, G. A. Vincent, R. T. C. Brownlee, N. J. Hoogenraad, M. Sadek, and A. G. Wedd, *Biochemistry*, 1994, **33**, 14 486–14 495.
141. S. D. B. Scrofani, R. T. C. Brownlee, M. Sadek, and A. G. Wedd, *Inorg. Chem.*, 1995, **34**, 3942–3952.
142. I. Bertini, A. Donaire, B. A. Feinberg, C. Luchinat, M. Piccioli, and H. Yuan, *Eur. J. Biochem.*, 1995, **232**, 192–205.
143. J. G. Huber, J. Gaillard, and J.-M. Moulis, *Biochemistry*, 1995, **34**, 194–205.
144. D. G. Nettesheim, T. E. Meyer, B. A. Feinberg, and J. D. Otvos, *J. Biol. Chem.*, 1983, **258**, 8235–8239.
145. J. A. Cowan and M. Sola, *Biochemistry*, 1990, **29**, 5633–5637.
146. D. G. Nettesheim, S. R. Harder, B. A. Feinberg, and J. D. Otvos, *Biochemistry*, 1992, **31**, 1234–1244.
147. I. Bertini, F. Capozzi, S. Ciurli, C. Luchinat, L. Messori, and M. Piccioli, *J. Am. Chem. Soc.*, 1992, **114**, 3332–3340.
148. J. Gaillard, J.-P. Albrand, J.-M. Moulis, and D. E. Wemmer, *Biochemistry*, 1992, **31**, 5632–5639.
149. L. Banci, I. Bertini, A. Dikiy, D. H. W. Kastrau, C. Luchinat, and P. Sompornpisut, *Biochemistry*, 1995, **34**, 206–219.
150. L. Banci, I. Bertini, F. Briganti, C. Luchinat, A. Scozzafava, and M. Vincens-Oliver, *Inorg. Chem.*, 1991, **30**, 4517–4524.
151. I. Bertini, F. Capozzi, C. Luchinat, M. Piccioli, and M. Vincens-Oliver, *Inorg. Chim. Acta*, 1992, **198–200**, 483–491.
152. I. Bertini, I. C. Felli, D. H. W. Kastrau, C. Luchinat, M. Piccioli, and M. S. Viezzoli, *Eur. J. Biochem.*, 1994, **225**, 703–714.
153. I. Bertini, A. Gaudemer, C. Luchinat, and M. Piccioli, *Biochemistry*, 1993, **32**, 12 887–12 893.
154. M. Sola, J. A. Cowan, and H. B. Gray, *Biochemistry*, 1989, **28**, 5261–5268.
155. R. Krishnamoorthi, M. A. Cusanovich, T. E. Meyer, and C. T. Przysiecki, *Eur. J. Biochem.*, 1989, **181**, 81–85.
156. J. Meyer, J. Fujinaga, J. Gaillard, and M. Lutz, *Biochemistry*, 1994, **33**, 13 642–13 650.
157. D. Bentrop, I. Bertini, C. Luchinat, W. Nitschke, and U. Mühlenhoff, *Biochemistry*, 1997, **36**, 13 629–13 637.
158. M. L. Antonkine, D. Bentrop, I. Bertini, C. Luchinat, G. Shen, D. A. Bryant, D. Stehlik, and J. H. Golbeck, *J. Biol. Inorg. Chem.*, 2000, **5**, 381–392.

Biographical Sketches

Timothy E. Machonkin, *b* 1971, B.S. Chemistry, 1993, Ph.D., 2000, Stanford University. Dr. Machonkin has been working in the area of bioinorganic chemistry since an undergraduate. In the laboratory of Prof. Edward Solomon at Stanford, he was involved in spectroscopic studies of metalloproteins and model systems, and in particular, EPR and magnetic susceptibility of Cu-containing systems. Since joining the laboratory of Prof. Markley, he has worked on NMR of FeS systems and the development of new methods to study paramagnetic systems with slow electronic relaxation rates by NMR.

John L. Markley, *b* 1941, B.A. Chemistry, 1963, Ph.D., 1969, Harvard University. Dr. Markley is Steenbock Professor of Biomolecular Structure in the Department of Biochemistry at the University of Wisconsin-Madison. He is Head of the National Magnetic Resonance Facility at Madison and the BioMagResBank, the international repository for biomolecular NMR data. Recently, he became Director of the Center for Eukaryotic Structural Genomics at the University of Wisconsin-Madison.

Electron–Nuclear Multiple Resonance Spectroscopy

Hans Thomann and Marcelino Bernardo

Exxon Research and Engineering Company, Annandale, NJ, USA

1	Introduction	1
2	Basic Principles	2
3	Experimental Techniques with Selected Applications	6
4	Concluding Remarks	15
5	Related Articles	15
6	References	16

1 INTRODUCTION

The term 'pulsed electron–nuclear multiple resonance' (PE NMR) spectroscopy refers to a broad range of experimental methods in which pulsed NMR techniques are combined with pulsed electron paramagnetic resonance (EPR) techniques. This combination provides the capability to measure the spectra and spin dynamics of nuclei which are magnetically coupled to unpaired electrons by the hyperfine interaction. Related experimental techniques for measuring the interactions of nuclei coupled to unpaired electrons are paramagnetically shifted NMR, dynamic nuclear polarization (DNP), electron spin resonance (ESR), the pulsed ESR technique of electron spin echo envelope modulation (ESEEM), and continuous wave (CW) electron–nuclear double resonance (ENDOR). These techniques are complementary rather than competing methods for measuring different aspects of the magnetic interactions of the coupled electron–nucleus spin system. Each technique offers certain advantages as well as certain limitations. The most appropriate experimental approach for a given problem also depends on the type of information desired.

The PE NMR techniques discussed in this article are best suited for measuring the magnetic interactions of nuclei in the local coordination structure of a paramagnetic electron. A distinguishing characteristic of nuclei which are detected in PE NMR experiments is that the NMR transition frequencies are shifted by very large values when compared with NMR spectra of diamagnetic samples. These large shifts arise from the large local magnetic fields originating from the unpaired electron spins. Consequently, the resonance frequency is described by the hyperfine coupling and is measured in units of kilohertz or megahertz as opposed to a resonance frequency shift of parts per million referenced to the nuclear Larmor frequency of a standard.

Nuclei which experience large local magnetic fields originating from unpaired electrons are encountered in a wide spectrum of research areas, including chemistry, materials science, polymer science, environmental science, and the biological sciences. Specific examples include: organic and inorganic radical molecules;[1–3] fossil fuels;[4,5] organic conductors, semiconductors and electroactive polymers; organometallic transition metal complexes;[6,7] dopants and other localized states in semiconductors;[8] surfaces such as on oxides and semiconductors; at the internal interfaces of semiconductors, superlattice structures, polymers, and composite materials; catalysis; transition metal ions in zeolites; and at the active sites for electron transfer or substrate binding in metalloproteins and metalloenzymes.[9]

If the unpaired electron spins can be treated as independent (or only weakly coupled) dipoles, their magnetic susceptibility is described by paramagnetism. Nuclei which sustain a hyperfine coupling with such electrons are therefore also referred to as paramagnetically coupled nuclei. Under certain conditions the NMR spectrum of paramagnetically coupled nuclei can be observed directly in the NMR spectrum as a paramagnetic shift. This is usually identified by the magnitude of the frequency shift and its temperature dependence. The local magnetic field originating from the unpaired electron spin shifts the NMR frequency and broadens the linewidth for those nuclei which sustain a hyperfine interaction. Both the magnitude of the frequency shift and the linewidth depend on the magnitude of the hyperfine coupling and on the details of the spin dynamics, specifically on the spin relaxation rates of the electron and nuclei. Well-resolved NMR lines can be observed if the electron spin–lattice relaxation time T_{1e}, or electron spin correlation time τ_e, which describes the time dependence of the local magnetic field, is short enough to assure that the orientation dependence of the local field is time averaged to its isotropic value. The paramagnetic shift is then determined by the isotropic hyperfine coupling arising from the unpaired spin density on the nucleus. Several texts have been written which describe the theory and applications of NMR to paramagnetic molecules including proteins and enzymes with paramagnetic transition metal ions.[10–12]

The short electron spin relaxation time required to observe paramagnetically shifted nuclei directly in NMR spectra also typically result in very broad ESR linewidths. In fact, as a rough guide, paramagnetically shifted NMR transitions are usually only observed in cases where the ESR spectrum is too broad to be observed. However, very broad ESR linewidths can also originate from inhomogeneous line broadening, even if the electron spin relaxation times are very long. In either case, if an ESR spectrum is observed, several experimental approaches are potentially applicable for the measurement of the magnetic interactions of the hyperfine coupled nuclei in these cases. These include DNP, ESR, ESEEM, ENDOR, and the extension of the latter to PE NMR.

In DNP spectroscopy the hyperfine coupling is used as a mechanism to enhance the nuclear polarization. The details of the mechanism for this enhancement and the magnitude of the enhancement depend on the details of the hyperfine interaction, particularly on the time dependence of the hyperfine coupling, and on the details of the ESR spectrum, such as the ESR linewidth and relaxation time. The theory and applications of DNP spectroscopy have been discussed in several texts and review articles.[13–18] (See ***Dynamic Nuclear Polarization and High-Resolution NMR of Solids***.) Here we discuss only those aspects of DNP spectroscopy that are relevant for comparison and contrast with the related techniques mentioned above.

In DNP spectroscopy the NMR signal is detected directly. The ESR transition is used only as a source for achieving enhanced nuclear polarization. Theoretically a maximum enhancement of the NMR signal of the order of ω_e/ω_n can be achieved, but in practice significantly lower values are

usually observed. Direct detection of the NMR signal has the advantage that the high resolution of NMR spectroscopy is maintained. At the same time, this excludes from detection those nuclei which have large hyperfine couplings. This is a result of the combination of low sensitivity and the large shift in transition frequencies. DNP spectroscopy has been applied most successfully in cases where the ESR spectrum consists of a narrow line which is easily saturated. Examples include studies of fossil fuels[19] and polymer interfaces.[20–22]

Paramagnetically coupled nuclei may be observed directly as hyperfine splittings in the ESR spectrum. Such splittings are often observed in ESR spectra of organic radical molecules in liquids (see ***Electron–Nuclear Hyperfine Interactions***). However, if the spin dynamics are not in the fast motion limit, hyperfine splittings are generally not resolved because of inhomogeneous line broadening.

Two different general approaches are available for measuring the magnetic couplings of nuclei which are not resolved in the ESR spectra. One approach is ESEEM.[23–26] In this technique both the allowed and the semiforbidden ESR transitions are coherently excited using two or more short, intense microwave pulses. The nuclear hyperfine and quadrupole interactions (in the case of nuclei with spin multiplicity $I \geq 1$) are observed as a periodic modulation of the envelope of the primary spin echo or stimulated echo intensity. Fourier transformation of this modulation pattern yields a spectrum of frequencies corresponding to the hyperfine (and quadrupolar for $I \geq 1$) frequencies.

One of the advantages of the ESEEM experiment is its high sensitivity, which is roughly comparable with that obtained in an ESR experiment. Furthermore, by selecting the appropriate microwave excitation frequency and applied magnetic field conditions, it is possible to measure the pure nuclear quadrupolar resonance frequencies for nuclei with $I \geq 1$.[27,28] This is possible despite the fact that the experiment is performed at finite magnetic field and the only spin transitions that are excited are the ESR transitions. One limitation of this type of experiment is that nuclear modulation can only be observed if the hyperfine interaction has finite anisotropic coupling components. The second criteron for modulation to be observed is that the microwave pulses must be able to excite both allowed and semiforbidden ESR transitions. This places constraints on the nature of the hyperfine interaction which will yield observable modulation. The theory, techniques, and applications of ESEEM spectroscopy have been reviewed in several texts and review articles.[23–27,29]

The second approach for measuring the magnetic couplings of nuclei which are not resolved in the ESR spectra is directly to excite both the NMR and ESR transitions with rf and microwave excitation. The first double resonance experiment of this type, known as an 'electron–nuclear double resonance', or simply ENDOR, experiment was reported by Feher in 1956.[30] The continuous wave (CW) ENDOR experiment is performed by applying a strong microwave field which is selected to irradiate continuously an EPR transition while simultaneously applying a strong rf field. The rf field is swept through the range of frequencies that encompass the NMR spectrum while continuously observing the intensity of the EPR transition. The intensity of the latter changes whenever the rf frequency matches an NMR transition frequency. The intensity of the EPR transition plotted as a function of the rf frequency generates the ENDOR spectrum. Thus, the ENDOR spectrum is a spectrum of the NMR transitions detected indirectly via the EPR transition. This is in contrast to the ESEEM experiment where the nuclear spin flip is a consequence of exciting a semiforbidden ESR transition. As a result, anisotropic hyperfine interactions are not necessary to observe hyperfine frequencies in the ENDOR experiment.

The ENDOR technique and applications have been documented in several texts and review articles.[1,8,9,31–36] In the case of one electron coupled to a spin-$\frac{1}{2}$ nucleus, and considering for simplicity that the hyperfine interaction is isotropic, the ENDOR spectrum comprises two transitions corresponding to one NMR transition for each of the two electron spin states. There exists a one-to-one correspondence between the number of coupled inequivalent nuclei and the number of ENDOR transitions observed. This can be contrasted to the number of transitions observed in the EPR spectrum where the number of transitions observed is a multiplicative function of the number of inequivalent nuclei coupled to the unpaired electron spin. The reduced number of transitions results in spectral simplification and, consequently, in enhanced spectral resolution.

While the success of the CW ENDOR experiment has been well documented, certain inherent problems in the technique have also limited its applicability. One well-documented limitation of the CW ENDOR experiment is the constraints on the relationship between NMR and ESR relaxation rates that must be satisfied in order to observe an ENDOR signal.[31,32,37–41] These constraints are changed (although not removed) with pulsed excitation techniques. This was recognized by W. B. Mims who reported the first pulsed ENDOR experiment in 1965, roughly a decade after Feher's initial report of the CW ENDOR experiment. Since then the advantages and applications of employing pulsed excitation techniques for both the ESR and NMR transitions have been demonstrated in publications from several laboratories.[37,38,41–46]

A second significant advantage of employing pulsed excitation techniques for both the ESR and NMR transitions is the potential for extending the type of experiments which can be performed. This is in many respects analogous to the extension of the experimental capabilities which become possible using pulsed excitation techniques in NMR spectroscopy. There are, however, distinct differences that must be kept in mind when using the analogy to pulsed NMR. These will be discussed in more detail in the next section. Furthermore, since multiple irradiation frequencies may be used to excite both the NMR and EPR transitions, the modern combined pulsed NMR and pulsed EPR experiments will be referred to as 'pulsed electron NMR' (PE NMR) spectroscopy. In this article, we describe the basic principles of these techniques, their implementation, including the pulse schemes and specific examples of experimental techniques, and illustrate the type of information that can be derived with examples in selected applications.

2 BASIC PRINCIPLES

In this section the magnetic interactions that determine the frequencies and amplitudes in pulsed ENDOR spectra are briefly reviewed. More comprehensive treatments can be found in several texts.[2,6,31,32,47,48] The analysis of the pulsed ENDOR spectrum provides the starting point for understanding the extensions of the basic pulsed ENDOR technique. After

the properties of the pulsed ENDOR spectrum have been presented, the general approach for the PE NMR techniques will be introduced. This is followed by specific experimental techniques with examples of applications.

2.1 Nuclear Spin Interactions and the Spectrum

2.1.1 Transition Frequencies

For spin-$\frac{1}{2}$ nuclei, the NMR spectrum of the paramagnetically coupled nuclei is dominated by the local magnetic field generated by the unpaired electron spin and by the applied magnetic field. The magnitude and orientation of this local field depends on whether the electron spin is aligned along or opposed to the direction of the external magnetic field. The effect of the combined local field and applied field on the nuclear spin is described by the nuclear spin Hamiltonian (expressed in units of frequency)

$$\hat{\mathcal{H}}_n = \sum_{i=1}^{3} (\hat{\boldsymbol{S}}' \cdot \boldsymbol{A} - g_n \beta_n B_0 b_i) \hat{I}_i \tag{1}$$

where the subscript i = 1, 2, 3 on $\hat{I}_i$ refers to the x, y, z components of the nuclear spin operator $\hat{\boldsymbol{I}}$. The prime on the electron spin operator $\hat{\boldsymbol{S}}'$ indicates that a coordinate system is selected in which the $\boldsymbol{g}$ tensor is diagonal. The b_i are the unit vectors of the applied magnetic field expressed in spherical polar coordinates:

$$(b_1, b_2, b_3) = (\cos\phi \sin\theta, \sin\phi \sin\theta, \cos\phi) \tag{2}$$

In most pulsed EPR experiments, particularly on transition metal ions, the microwave pulses excite only a small region of the spectrum centered about the magnetic field for resonance. This magnetic field position selects a subset of molecular orientations defined by the resonance condition, $h\nu = g\beta B_0$, where the orientation dependence of the electronic g factor is expressed by

$$g(\theta, \phi) = \left[\sum_{i=1}^{3} (g_i b_i)^2 \right]^{1/2} \tag{3}$$

The number of molecular orientations which contribute to the ENDOR spectrum is minimum for values of (θ,ϕ) that correspond to the principal axes of the $\boldsymbol{g}$ tensor. This phenomenon is referred to as g-factor orientation selectivity.[49] Since a lower number of molecular orientations contribute, higher spectral resolution can be observed in ENDOR spectra recorded at magnetic field values corresponding to those values of (θ,ϕ) which correspond to these principal axes.

The local field is described by the term $\hat{\boldsymbol{S}}' \cdot \boldsymbol{A}$, where $\boldsymbol{A}$ is the hyperfine interaction tensor. The magnitude of the local field depends on the distance between the electron and the nucleus and on the nature of the chemical bonding that pertains to the electron and nucleus, i.e. on the electronic state in which the electron resides. The distance separating the electron and nucleus determines a classical dipolar interaction. Since the gyromagnetic ratio of the electron is very large, this local magnetic field can be very large. The classical dipolar field will only provide a valid description of the distance between the electron and nucleus if the electron can be treated as a point dipole. Contributions to the hyperfine anisotropy also depend on the nature of the electronic wavefunction. The latter also determines whether the nucleus has a finite unpaired electron spin density at the nucleus. A finite unpaired spin density at the nucleus can only occur if the molecular orbital that describes the unpaired electron has some atomic s-orbital contribution in the wavefunction. The nonclassical contribution to the hyperfine anisotropy is sometimes referred to as 'pseudodipolar coupling'.

The orientation dependence of the local field can be expressed by an orientation-dependent hyperfine coupling $A(\theta, \phi)$. The NMR transition frequencies are then given by

$$\nu_{\pm} = \nu_n \pm \tfrac{1}{2}|A(\theta, \phi)| \tag{4a}$$

$$\nu_{\pm} = \tfrac{1}{2}|A(\theta, \phi)| \pm \nu_n \tag{4b}$$

where the first expression applies if $2\nu_n > |A|$ and the second expression applies if $2\nu_n < |A|$, while in both cases it is assumed that $I = \frac{1}{2}$.

The two limiting expressions [equations (4a) and (4b)] for the NMR frequencies are a recognition of the fact that the local magnetic field described by the hyperfine interaction can be comparable to or larger than the applied magnetic field. This is especially the case at the low applied field strengths, typically 0.35 T, at which many ENDOR and PE NMR experiments are performed. If the local field is greater than the applied field, then the local field is the dominant term that defines the nuclear quantization axis and the applied field is a perturbation. In either case, equations (4a) and (4b) indicate that for a nucleus with $I = \frac{1}{2}$, two NMR transitions will be observed in the ENDOR spectrum, with one transition originating from each of the two electron spin manifolds defined by the eigenvalue, $m_{S'}$, of $\hat{\boldsymbol{S}}'$. These NMR transitions will either be centered on the nuclear Larmor frequency if $2\nu_n > |A|$ or on one-half of the hyperfine coupling if $2\nu_n < |A|$.

In the case of organic radicals, the anisotropy of the g factor can be ignored in the first order analysis of the paramagnetically shifted NMR transitions. The NMR transition frequencies $\nu_{\pm}$ are then given by[50]

$$\begin{aligned} \nu_{\pm} = [&(S_z A_{xx} - \nu_n)^2 \sin^2\theta \cos^2\phi \\ &+ (S_z A_{yy} - \nu_n)^2 \sin^2\theta \sin^2\phi \\ &+ (S_z A_{zz} - \nu_n)^2 \cos^2\theta]^{1/2} \end{aligned} \tag{5}$$

where θ and ϕ are the spherical polar angles relating the applied static field $\boldsymbol{H}_0$ to the principal axis of the hyperfine tensor (A_{xx}, A_{yy}, A_{zz}). Equation (5) assumes that the high-field approximation is valid where the electron and nuclear spin operators $\hat{\boldsymbol{S}}$ and $\hat{\boldsymbol{I}}$ are completely decoupled from the molecular framework and quantized along the applied magnetic field direction. An energy level structure corresponding to an arbitrary selected set of (θ, ϕ) values is shown in Figure 1.

In general, the g factor for the electron will not be isotropic as assumed in the expressions described by equations (4a), (4b) and (5). Anisotropy of the electron g factor is usually

significant in ESR spectra of transition metal ions.[6,7] If the g factor is anisotropic, the NMR frequencies and lineshape will depend on the magnetic field position and microwave frequency selected.[6,48,51,52] In a noncrystalline solid, a single pair of NMR transitions will only be observed if the principal axes of the $\boldsymbol{g}$ and $\boldsymbol{A}$ matrices are collinear. Otherwise a powder pattern lineshape will be observed because of the angular dependence of the $\boldsymbol{g}$ and $\boldsymbol{A}$ matrices.

The NMR frequencies described in equation (5) do not account for the second-order frequency shifts of the ENDOR lines observed for large hyperfine couplings. Since these second-order frequency shifts are proportional to $A^2/4\nu_e$, they can usually be ignored under most experimental conditions. However, even for relatively small hyperfine coupling values, these second-order effects, arising from the spin Hamiltonian terms $\hat{S}_x\hat{I}_x$ and $\hat{S}_y\hat{I}_y$ must be included to calculate correct wave functions that reproduce the rf frequency dependence of the ENDOR amplitudes. These spin coupling terms lead to an enhancement, known as the 'hyperfine enhancement', of the rf field seen by the nucleus. Note that the enhancement can also be negative, i.e. a decrease in the rf field at the nucleus, depending on the eigenvalue m'_S of $\hat{\boldsymbol{S}}'$.

The simple four-level system with isotropic hyperfine coupling described by the spin Hamiltonian:

$$h^{-1}\hat{\mathcal{H}}_0 = \nu_e\hat{S}_z - \nu_n\hat{I}_z + aS_z\hat{I}_z \tag{6}$$

is usually adequate for describing the basic concepts for the sublevel polarization transfer experiments as well as several other PE NMR experiments described later in this article. In the high temperature limit, i.e. $g_e\beta_eB_0/kT \ll 1$, the spin eigenvalues, $h^{-1}E_0(M_S,M_I)$, are given by:

$$h^{-1}E_0(M_S, M_I) = \nu_eM_S - \nu_nM_I + aM_SM_S \tag{7}$$

The energy levels in Figure 1 also describe these eigenstates which arise from the coupling of an $S = I = \frac{1}{2}$ system with isotropic hyperfine coupling. With this level of simplification it is possible to gain considerable insight into the spin dynamics of PE NMR experiments using the spin operator formalism[42] frequently used in NMR spectroscopy.[53]

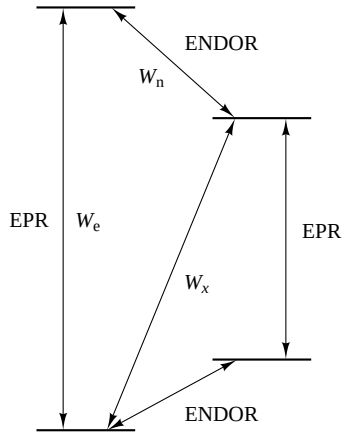

Figure 1 Energy level structure corresponding to the spin Hamiltonian of a four-level system. EPR, ENDOR, and relaxation transitions are identified

In the literature on pulsed ENDOR and PE NMR spectroscopy, the hyperfine splitting of the electron spin eigenstates are referred to as 'hyperfine sublevels' or simply as 'sublevels'. The EPR, NMR, and spin relaxation transitions relevant in the discussion of the ENDOR experiment are identified in Figure 1. The ENDOR transitions indicated in the figure are NMR transitions detected indirectly by the ESR transition. The electron and nuclear relaxation transition probabilities W_e and W_n correspond to effective T_{1e}^{-1} and T_n^{-1} rates; these are also identified in Figure 1. In the analysis of signal amplitudes in the CW ENDOR experiment, the effective rates are the intrinsic rates enhanced by the application of the microwave or rf excitation fields.

If the nuclear spin multiplicity $I \geq 1$, the quadrupolar interaction will result in additional splittings of the hyperfine sublevels. The quadrupolar interaction is described by adding the nuclear self-coupling term, $\hat{\boldsymbol{I}} \cdot \boldsymbol{P} \cdot \hat{\boldsymbol{I}}$ to the spin Hamiltonians of either equation (1) or equation (6). If the principal axes of the $\boldsymbol{g} \cdot \boldsymbol{A} \cdot \boldsymbol{P}$ are collinear and the magnetic field $\boldsymbol{B}_0$ is oriented parallel to one of these principal axes, the first-order ENDOR frequencies are given by[2,6,48]

$$\nu_{ENDOR} = \left| \frac{A_i}{2} \pm \nu_n \pm \frac{3}{2}|P_i|(2m_i + 1) \right| \tag{8}$$

where A_i and P_i denote the principal values of the $\boldsymbol{A}$ and $\boldsymbol{P}$ tensors along the i axis. The nuclear transitions in equation (8) are assumed to increase in the nuclear spin quantum number, i.e. $m_I \rightarrow m_I + 1$. It has also been assumed that ($|A| > 2\nu_n > 3|P_i|$). The principal values of the quadrupolar tensor $\boldsymbol{P}$ are defined as $|P_{zz}| > |P_{yy}| > |P_{xx}|$. These principal values are related to the magnitude of the quadrupolar coupling constant χ and asymmetry parameter η by

$$\chi = 2I(2I - 1)P_zz \tag{9a}$$

$$\eta = \frac{P_xx - P_yy}{P_zz} \tag{9b}$$

According to equation (8), four ENDOR transitions are expected for a nucleus with $I = 1$. However, not all ENDOR transitions may be observed when exciting an ESR transition at a given magnetic field value, since it is possible that each m_I state may be selectively excited. For example, a two-line ENDOR spectrum will be observed if the ESR transition connects the $m_I = 1$ to $m_I = 1$ sublevels of the $m_S = +\frac{1}{2}$ and $m_S = -\frac{1}{2}$ electron spin manifolds.

2.1.2 ENDOR Amplitudes

ENDOR signal amplitudes are proportional to the change in the EPR signal intensity, ΔE, induced by an NMR transition. Since the EPR signal intensity E is proportional to the electron spin susceptibility χ_e, a relative ENDOR susceptibility can be defined by

$$\frac{\Delta\chi_e}{\chi_e} = \frac{\Delta E}{E} \tag{10}$$

The transition frequencies and amplitudes that are described by the time-independent terms in the spin Hamiltonian are independent of the method of exciting and detecting the transitions. However, the dynamic terms of the total spin Hamiltonian that describe the spin system have different effects on the amplitudes in the CW and pulsed experiment. In the CW experiment, the ENDOR signal amplitude depends on the rate at which the ESR and NMR transitions are excited by the applied microwave and rf magnetic fields compared with the rate of intrinsic relaxation pathways that will compete to restore the spin system to thermal equilibrium. Once the spin eigenstates and relaxation rates that connect the eigenstates have been defined, coupled rate equations can be used to model the ENDOR signal amplitude. In contrast, the pulsed ENDOR or ENMR experiment is performed on a timescale which is short compared with the intrinsic spin relaxation rates. The amplitudes can therefore be analyzed without resorting to coupled rate equations.

In the CW experiment, the interplay between the transition intensity induced by the applied magnetic fields and the intrinsic spin relaxation rates is further complicated by the effect of the hyperfine enhancement on the ENDOR amplitudes.[31,32,50,54] For intense rf fields, the ENDOR amplitudes can be independent of the rf frequency. For very weak rf fields, the ENDOR amplitudes increase with the square of the rf frequency. For intermediate values, the ENDOR amplitudes can be a complex function of the transition moments and relaxation parameters, especially since both the transition moments and the relaxation rates can be orientation dependent.

In pulsed ENDOR experiments, the analysis of the hyperfine enhancement and the effects of the spin relaxation on the ENDOR amplitudes is less complex. The pulsed ENDOR experiment is usually performed on a timescale which is short compared with the electron, nuclear, and the electron–nucleus cross-relaxation rates. In this case the relaxation rates do not influence the relative ENDOR amplitudes. The loss of electron spin polarization by T_{1e} processes during the mixing period (described in Section 2.2) results in a uniform decrease in the signal amplitudes, $\Delta\chi_e/\chi_e$, across the ENDOR spectrum. The hyperfine enhancement of the NMR transition moment is then simply observed as a change in the sublevel nutation angle as a function of rf frequency. The sublevel nutation angle θ_R is given by $\theta_R = \gamma_n \epsilon B_2 t_{rf}$, where ϵ is the hyperfine enhancement factor. If the hyperfine interaction is isotropic, the hyperfine enhancement factor is given by $\epsilon = |1 + m_s a/\nu_n|$. The hyperfine enhancement can be observed directly in EPR detected sublevel transient nutation experiments.[43,55]

As described in the next section, the pulsed ENDOR experiment can be divided into pulse periods. The ENDOR amplitude is a function of the microwave pulses in the preparation period and detection period as well as of the nutation angle of the sublevel polarization in the mixing period. The latter can be expressed by

$$EA(\nu_{rf}) = \tfrac{1}{2}(1 - \cos(\theta_{R\pm})) \qquad (11)$$

In the limit of small nutation angles, the cosine term can be expanded in a power series:

$$EA(\nu_{rf}) \approx \frac{(\theta_{R\pm})^2}{4} = \frac{(m_s A)^2}{(2\nu_n)^2} = \frac{(m_s)^2}{(2\nu_n)^2}(\nu_\pm - \nu_n)^2 \qquad (12)$$

Equation (12) explicitly indicates that the Fermi golden rule result for the rf frequency dependence of the transition probability is obtained in the limit of small nutation angle. If the nutation angle is adjusted to correspond to a π pulse at each ENDOR frequency, the ENDOR amplitudes should be independent of the hyperfine enhancement factor. It is straightforward, although time consuming, to measure the sublevel nutation frequency at each ENDOR frequency in the ENDOR spectrum for a quantitative analysis of the ENDOR amplitudes. Additional contributions to the ENDOR amplitudes arise from the effect of hyperfine contrast selectivity in the preparation period and from possible electron–nucleus coherence effects in the detection period.[37,38] These effects are discussed in more detail in Section 3. Contributions originating from the hyperfine anisotropy[6,48] and g-factor orientation selectivity[6,48] will also affect the amplitudes in both the CW and pulsed ENDOR experiments.

2.2 Pulse Schemes

Many of the PE NMR experimental techniques can be understood by analogy to heteronuclear NMR experiments. However, in making this comparison between PE NMR and heteronuclear NMR experiments, some important differences must be recognized. These originate from the fundamental properties of the unpaired electron compared with a nucleus. The two most significant differences are the γ values of the electron and nucleus and the differences between the nature of the wave functions that describe the electron and the nucleus.

The larger γ for the electron compared with any nucleus has two important consequences. The first is the practical consequence for the type of instrumentation required for PE NMR experiments compared with heteronuclear NMR experiments. The heteronuclear NMR experiment requires a transmitter, probe, and receiver capable of handling two (or more) different rf frequencies. In contrast, for the double resonance experiment between the electron and nucleus, the hardware must be capable of handling both rf and microwave frequency components.

A second consequence of the larger γ of the electron is that the local magnetic field generated by the electron is much larger than is generated by any nucleus. This has several consequences on the properties of the spectra observed for nuclei that are coupled to this local field and also has implications on the types of experiments which can be performed. In most cases, PE NMR experiments must be analyzed within the so-called ‘soft pulse limit’, i.e. the bandwidth of the excitation pulses for both the ESR and NMR transitions are much smaller than the spectral bandwidth. In other words, both the ESR and NMR pulses are generally selective excitation pulses. The broad linewidths also exclude certain techniques such as cross polarization in the rotating frame and magic angle spinning which have had such an important impact on NMR of solids from being directly adapted to PE NMR experiments.

The second important difference to bear in mind when comparing PE NMR spectroscopy with pulsed heteronuclear NMR is the difference in the nature of the total wavefunction associated with the electron compared with the nucleus. The electron is generally in an eigenstate, such as an atomic or

molecular orbital, which has a much greater spatial extent than the localized eigenstate which describes the nucleus. This has the consequence that the electron spin is delocalized so that the electron is generally coupled to many more nuclei than would be the case if the electron were represented by a point dipole. The delocalization of the electron spin density in molecular orbitals that have well defined spatial extents can also contribute large anisotropic components to the local (i.e. hyperfine) field. The anisotropy of the hyperfine interaction also assures that the quantization axis for the nucleus does not point in the same direction in the two electron spin eigenstates. This anisotropy in the hyperfine interaction is therefore responsible for the broad spectral widths observed for the NMR transitions and also affects the transitions which are observed, since formally forbidden transitions become 'semiforbidden' transitions.

Another consequence of the nature of the electronic states that host the unpaired electron is that spin coupling mechanisms such as the spin–orbit coupling are effective in broadening the ESR linewidth and in enhancing the spin relaxation rate. Both the broad lines and the shorter relaxation times have implications on the types of PE NMR experiments that can be performed.

The pulse sequences employed in PE NMR experiments can be conveniently divided into pulse periods in direct analogy to NMR spectroscopy. With the above-mentioned caveats in mind, the pulse periods can be analyzed by analogy to a pulsed heteronuclear NMR solids experiment within the soft pulse limit, wherein selective excitation is considered in the analysis. The most basic experiment consists of a preparation, mixing, and detection period. The purpose of the preparation period is to create an initial state perturbed from the equilibrium spin polarization established by the conditions of the temperature and external field (as well as by the level structure of the electron–nuclear coupled spin system). In all PE NMR experiments reported to date, one or two microwave pulses are applied to excite ESR transitions in the preparation period.

Two basically different types of PE NMR experiments will be performed depending on whether the microwave preparation pulses have created sublevel nuclear spin polarization or electron spin coherence at the end of the preparation period. The former are the starting points for ESR detected sublevel polarization transfer experiments and for ESR detected nuclear coherence experiments. The latter is the starting point for coherence transfer ENDOR experiments. In this experiment, a single microwave pulse, ideally a $\pi/2$ pulse, creates electron spin coherence in the preparation period.

In the mixing period, one or more rf pulses are applied to manipulate the sublevel polarization or sublevel coherence. The nature of the perturbation determines the type of experiment performed. The mixing period may include an evolution period, again depending on the type of experiment performed. If sublevel nuclear coherence has been created and is to be indirectly observed via the ESR transition intensity, the mixing period must end with a $\pi/2$ rf pulse that converts the sublevel coherence to sublevel polarization.

In the detection period one or more microwave pulses are applied to create electron spin coherence which is detected in the PE NMR experiment. The electron spin transverse magnetization provides a readout of the electron–nucleus longitudinal order. The transverse magnetization can be detected by a primary spin echo,[56] a stimulated echo,[57] or as a free induction signal.[58] It is also possible to use CW irradiation to detect the transverse electron magnetization[42] or to detect the longitudinal electron magnetization directly.[29]

3 EXPERIMENTAL TECHNIQUES WITH SELECTED APPLICATIONS

3.1 ESR Detected Sublevel Polarization Transfer

It is possible to envisage many pulse sequences which create sublevel nuclear spin polarization. The most common methods, shown in Figure 2, are a single microwave pulse which selectively excites one ESR transition or two microwave pulses. The former was first proposed by Davies[56] and is the starting point for what has become known as the Davies ENDOR experiment. The latter was first proposed by Mims[57] and is the preparation pulse sequence for the experiment now known as Mims ENDOR.

Referring to Figure 3, the selective excitation of one of the two allowed ESR transitions converts the electron spin polarization, represented by the boxes, into electron–nucleus two-spin longitudinal order. The spin polarization from the nuclear Zeeman and hyperfine interactions is negligible compared with the electron spin polarization and can be ignored. The two spin order refers to the fact that the nuclear spins in both NMR transitions are polarized.

Two spin electron–nucleus longitudinal order can also be created using two selective microwave pulses or two nonselective microwave excitation pulses if an evolution time separates the two pulses.[42] Sublevel polarization is created from the transverse components of the magnetization that evolves following the first pulse in the local field of the hyperfine interaction. The second pulse converts the transverse magnetization to two-spin longitudinal order. This suggests that the two pulses should be $\pi/2$ pulses for maximum efficiency in creating sublevel polarization. After the second

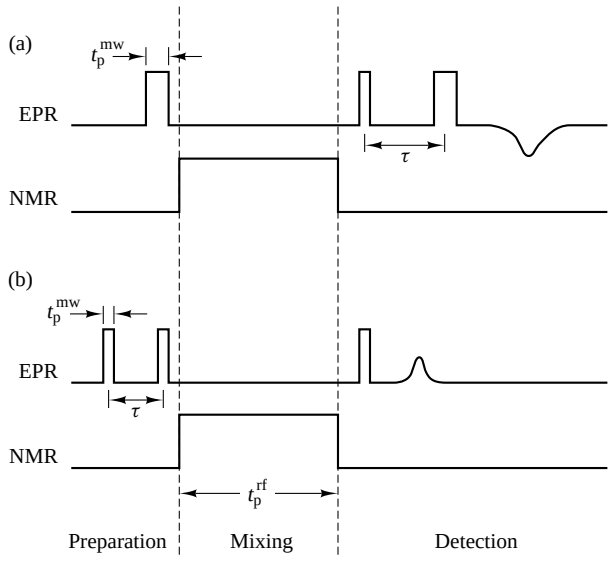

Figure 2 Davies ENDOR (a) and Mims ENDOR (b) pulse sequences

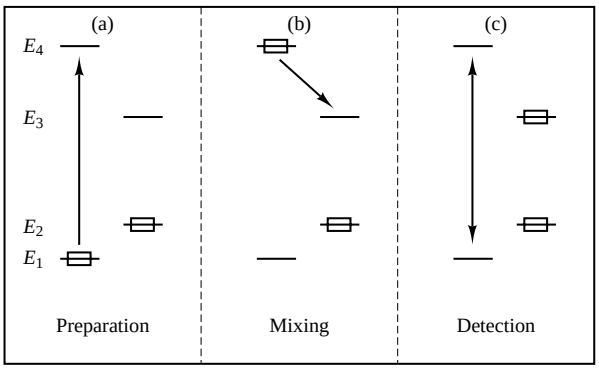

Figure 3 The transfer of spin polarization during the preparation (a), mixing (b) and detection (c) periods of the Davies ENDOR sequence for the four level system shown in Figure 1

pulse, the net sublevel polarization is approximately $\sin(a\tau/2)$ $\sin(\Omega_S\tau)$, where a is the hyperfine coupling in equation (6) and Ω_S is a resonance offset. Note that no sublevel polarization exists for values $a\tau/2 = n\pi$, where n is an integer. These are known as blind spots in the Mims ENDOR experiment.

For an ESR lineshape which is inhomogeneously broadened, the sublevel polarization created by the microwave pulses in the preparation period burn a hole into the envelope of the ESR absorption lineshape as shown in Figure 4(a). The width of the hole is determined by the excitation bandwidth of the preparation pulse. In the case of two pulse excitation, a serrated pattern of magnetization is superimposed on the hole, as shown in Figure 4(b).

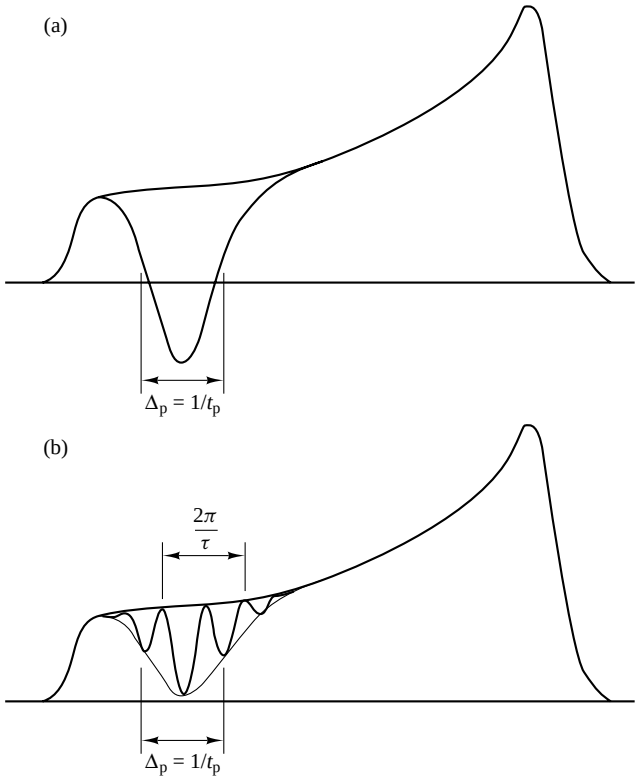

Figure 4 EPR spectra of an inhomogeneously broadened line after the preparation period in the Davies ENDOR (a) and Mims ENDOR (b) pulse sequences. (Reproduced by permission of Academic Press from H. Thomann and M. Bernardo, in 'Methods in Enzymology', eds. J. F. Riordan and B. L. Vallee, 1993, Vol. 227, Chap. 6)

3.1.1 Davies and Mims ENDOR

The pulse sequences for the two most commonly used experiments for the ESR detection of sublevel polarization transfer are shown in Figure 2. The hole-burning effect created by the preparation pulses on an inhomogeneously broadened ESR absorption envelope is shown in Figure 4. The effect of a selective ESR excitation on the electron spin polarization in a four level system described by equation (7) is shown in Figure 3(a). The electron spin polarization associated with these two energy levels will be inverted if the selective microwave pulse is a π pulse. Note that the sublevel longitudinal polarization of both the upper and lower NMR sublevels are not at equilibrium at the end of the preparation period.

In the next step of the pulse sequence, an rf pulse transfers and thereby 'mixes' the electron spin polarization between the sublevels. This is shown in Figure 3(b) for an rf pulse on resonance with the upper sublevel. In the hole-burning picture shown in Figure 4, the sublevel polarization transfer corresponds to the transfer of polarization from within the hole to a frequency offset by the value of the hyperfine coupling. This sublevel polarization transfer occurs at frequencies corresponding to the NMR frequency shifted by the hyperfine interaction (see Section 2.1.1).

The sublevel polarization transfer could, in principle, be detected directly as an NMR signal. Indeed, this would correspond to a pulsed DNP experiment. Note, however, that the sublevel polarization transfer has also changed the electron longitudinal polarization of the two ESR transitions. The sublevel polarization transfer can therefore be detected by measuring the change in the ESR transition intensity. This can be accomplished using a variety of techniques, as discussed in Section 2.2. In the Davies and Mims ENDOR pulse sequences the change in electron longitudinal polarization is detected by observing the change in intensity of a primary or stimulated spin echo. This electron spin coherence is indicated by the double arrow in Figure 3(c).

The spectrum of NMR transition frequencies shifted by the hyperfine coupling, i.e. the ENDOR spectrum, usually far exceeds the excitation bandwidth of the rf pulses. The complete spectrum must therefore be recorded by incrementing stepwise the rf frequency on successive iterations of the pulse sequences shown in Figure 2. The limit of resolution in the spectrum is determined by the excitation bandwidth of the rf pulse.

The Davies ENDOR spectrum of a single crystal of malonic acid which has been irradiated by X-rays to generate carbon π radicals[59] is shown in Figure 5. The transitions at approximately 5 and 30 MHz are the two sublevel transitions associated with the α proton of the CH fragment of the $\dot{C}H(COOH)_2$ radical molecule. The other proton lines originate from the carboxylic protons, from coupling to protons on neighboring malonic molecules, and from overlapping ESR signals from different malonic acid radical molecules.[59] The increase in spectral resolution obtained by decreasing the excitation bandwidth of the rf mixing pulse is shown in the inset of the figure.

The relative amplitudes of the ENDOR transitions are determined by the spin Hamiltonian (as discussed in

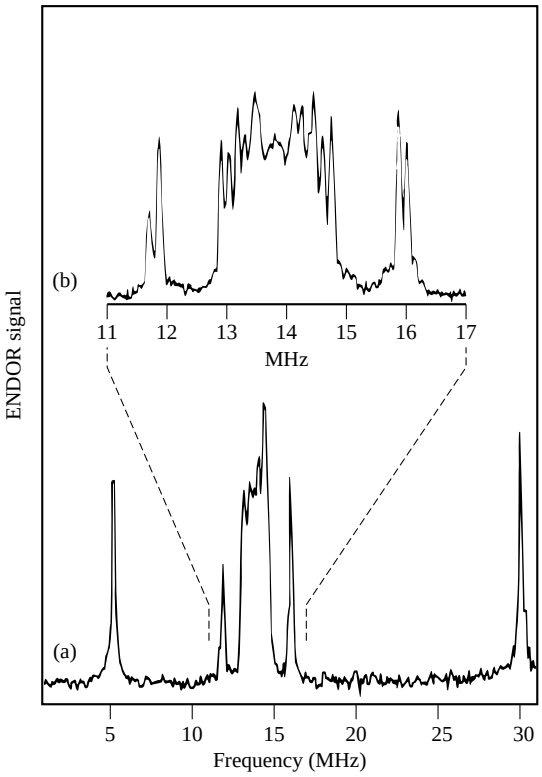

Figure 5 Davies ENDOR spectrum of an X-ray irradiated crystal of malonic acid with rf pulse widths of 5 μs (a) and 10 μs (b). (Reproduced by permission of the American Chemical Society from H. Thomann and M. Bernardo, in 'Advances in Chemistry Series 229: Magnetic Resonance of Carbonaceous Solids', eds. R. E. Botto and Y. Sanada, Washington, DC, 1993, Chap. 4)

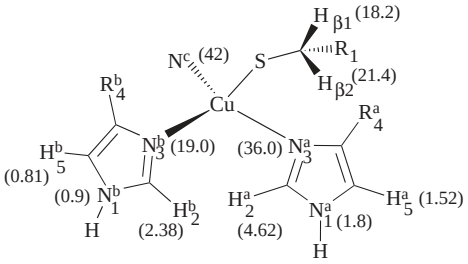

Figure 6 Spectroscopic model for the copper coordination structure in the high pH form of stellacyanin showing the hyperfine couplings (in MHz). (Reproduced by permission of Academic Press from H. Thomann and M. Bernardo, in 'Methods in Enzymology', eds. J. F. Riordan and B. L. Vallee, London, 1993, Vol. 227, Chap. 6)

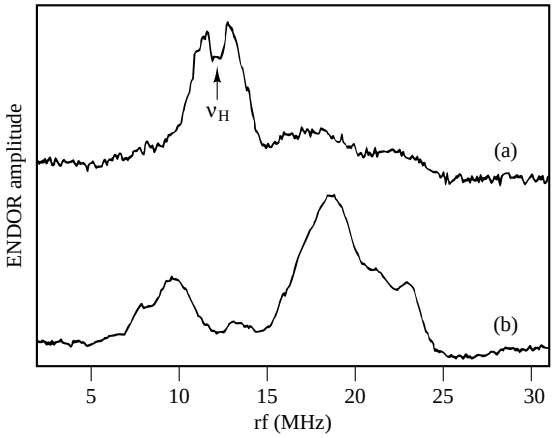

Figure 7 Davies ENDOR spectra of stellacyanin using microwave inversion and detection pulse widths t_{mw} of 0.40, 0.20, 0.40 μs (a) and 0.04, 0.02, 0.04 μs (b). (Reproduced by permission of Academic Press from H. Thomann and M. Bernardo, in 'Methods in Enzymology', eds. J. F. Riordan and B. L. Vallee, 1993, London, Vol. 227, Chap. 6)

Section 2.1.2) but also by the excitation bandwidth, Δ_p of the preparation pulse. In order for a sublevel polarization transfer signal to be detected indirectly using the Davies ENDOR pulse sequence [Figure 2(a)], the condition that $\Delta_p > a$, where a is the hyperfine coupling, must be satisfied.[56] If $\Delta_p > a$, the transfer of polarization remains within the hole burned into the absorption envelope. In this case the change in electron polarization is reduced, resulting in a weaker ENDOR signal. This relationship between Δ_p and a has been referred to as 'hyperfine contrast selectivity',[37–39] as a 'spin alignment hole',[41] and as a 'self-ELDOR effect'.[42] The relationship between Δ_p and a can be used to eliminate or reduce the overlap of ENDOR signals originating from nuclei with different hyperfine couplings.[37–39,60]

Davies ENDOR spectra on a blue copper protein, stellacyanin,[61] will serve to illustrate the application of pulsed ENDOR (and PE NMR) spectroscopy. Transition metal ions and ion clusters are found at the active site for electron transfer in metalloproteins and at the active site for substrate conversion in metalloenzymes. The electron spin echo detected ESR (ED ESR) absorption envelope recorded by plotting the intensity of the primary electron spin echo as a function of magnetic field is shown in the inset of Figure 9. A spectroscopic model for the ligand coordination structure of the Cu^{2+} ion for the high-pH form of the protein is shown in Figure 6. The hyperfine coupling frequencies for each nucleus on the copper ligands are indicated in Figure 6. The NMR transitions for nuclei in the primary ligand coordination structure of the Cu^{2+} ion would be difficult to measure by any other spectroscopic technique.

The hyperfine contrast selectivity mechanism for eliminating the overlap of ENDOR lines is illustrated in Figure 7, where two Davies ENDOR spectra of stellacyanin[61] are shown. When a preparation pulse with narrow excitation bandwidth is used [Figure 7(a)], the proton ENDOR lines which have small hyperfine coupling values that originate from protons on the two imidazole ligands overlap the nitrogen ENDOR lines, particularly the nitrogen line centered at roughly 8 MHz. When a larger excitation bandwidth is used [Figure 7(b)] the amplitudes for these proton ENDOR lines are significantly attenuated. The 1 : 2 relative intensities of the two ^{14}N ENDOR lines centered at 8 and 18 MHz in Figure 7(b) are in agreement with the expected intensity difference due to the hyperfine enhancement factor.[37,38]

The proton ENDOR signals from protons with small hyperfine couplings can also be observed using preparation pulses with large excitation bandwidths with the Mims ENDOR pulse sequence. A comparison of the Davies and Mims ENDOR spectra for the stellacyanin protein is shown in Figure 8. The arrows in the Mims ENDOR spectrum indicate the positions of the 'blind spots' where no ENDOR signal is observed. The position of these blind spots in the spectrum

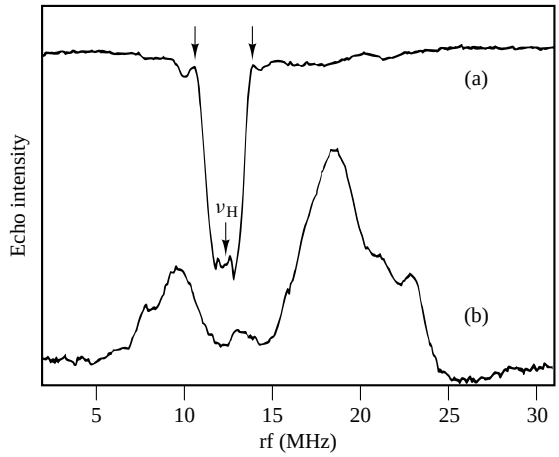

Figure 8 Comparison of the Davies and Mims ENDOR spectra for the stellacyanin protein. (Reproduced by permission of Academic Press from H. Thomann and M. Bernardo, in 'Methods in Enzymology', eds. J. F. Riordan and B. L. Vallee, London, 1993, Vol. 227, Chap. 6)

can be selected by the value of τ chosen in the Mims ENDOR pulse sequence. Note that the ENDOR signal for the protons with small hyperfine couplings is significantly enhanced in the Mims ENDOR spectrum. This is a consequence of the fact that a larger fraction of the electron magnetization can be sampled without suppressing the ENDOR signals from the nuclei with small hyperfine couplings.

An example of the advantage of the increased sensitivity achieved by the indirect detection scheme of the pulsed ENDOR experiment is shown in Figure 9, where the ENDOR signals from the central metal Cu^{2+} ion as well as those from all the (NMR active) ligand nuclei on the metal ligands are observed. The position in the ED ESR spectrum at which this Davies ENDOR spectrum was recorded is shown in the inset of the figure. Although the hyperfine splitting of the Cu^{2+} ion can be observed at the high-field end of the ESR spectrum, the hyperfine splittings are not resolved in the low-field region of the ESR spectrum. Note also that the pulsed ENDOR spectrum reveals the quadrupolar splitting of the Cu^{2+} nucleus. It is not possible to measure these quadrupolar interactions in the ESR spectrum.

3.1.2 Transient Nuclear Nutations

The sublevel nuclear transient nutations can be detected indirectly with the pulse sequences in Figure 2 by incrementing stepwise the rf pulse length on successive pulse sequence iterations. An example is shown for the malonic acid radical in Figure 10. The effect of the time dependence of the signal from the electron spin–lattice relaxation during the mixing time can be eliminated by choosing a fixed, long mixing time before detection or by subtracting the signal recorded without the rf pulse applied (or with the rf frequency set to an off-resonance position in the ENDOR spectrum). The electron spin echo amplitude in the detection period oscillates with a periodicity proportional to $\cos \theta_2$ where θ_2 is the sublevel nutation angle (see Section 2.1.2). These oscillations are sometimes referred to as Rabi oscillations. The influence of the hyperfine enhancement factor on the nutation angle is evident in Figure 10.

The sublevel nutation experiment provides a method for setting the rf mixing pulse conditions to the selected nutation angle. For ESR detected sublevel polarization transfer experiments, the optimum pulse is a π pulse. For the ESR detection of sublevel coherence, the rf mixing pulse would be set for a $\pi/2$ pulse. For samples which are not single crystals and that exhibit hyperfine anisotropy, the Rabi oscillations are rapidly damped after the first period.[37,38] Consequently, the effect on the ENDOR amplitudes due to the hyperfine enhancement can be reduced by selecting a long rf pulse length. However, this produces power broadened lines, and therefore a lower resolution in the spectrum. When two or more magnetically equivalent nuclei are coupled to the electron, harmonics may be observed in the sublevel nutation pattern.[42] An example is shown in Figure 11. Analysis of these

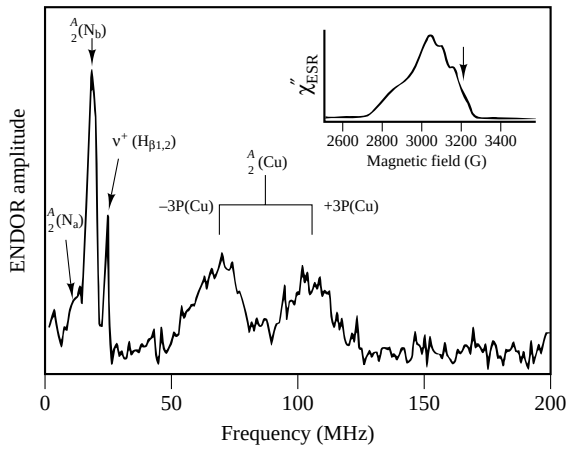

Figure 9 Davies ENDOR spectra of stellacyanin showing the Cu, N, and H resonances. Inset shows the position in the ED ESR spectra where the ENDOR spectra was recorded. (Reproduced by permission of Plenum Press from H. Thomann and M. Bernardo, in 'Biological Magnetic Resonance', eds. L. J. Berliner and J. Reuben, New York, 1993, Vol. 13, Chap. 7)

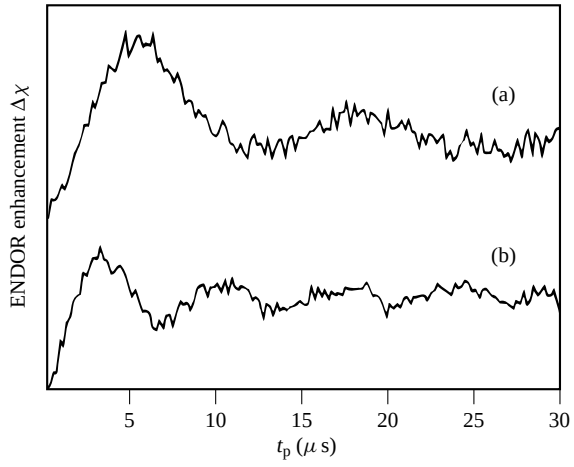

Figure 10 Sublevel nuclear transient nutations detected for the irradiated malonic acid radical at an rf of (a) 7.32 and (b) 21.29 MHz. (Reproduced by permission of the American Chemical Society from H. Thomann and M. Bernardo, in 'Advances in Chemistry Series 229: Magnetic Resonance of Carbonaceous Solids', eds. R. E. Botto and Y. Sanada, Washington, DC, 1993, Chap. 4)

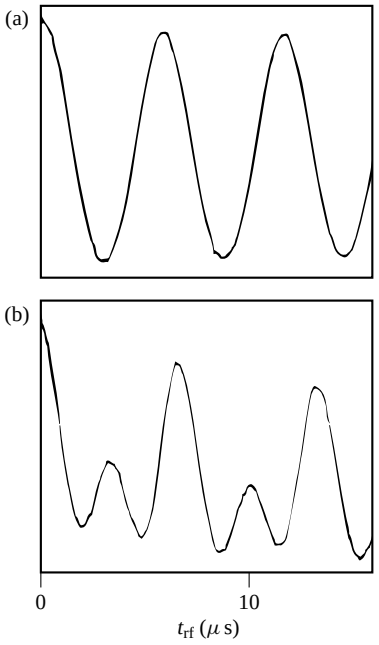

Figure 11 Sublevel nuclear transient nutation patterns of protons in VO(IV)- and Cu(II)-doped $Mg(NH_4)_2(SO_4)_2{\cdot}6H_2O$ single crystals: (a) one proton in $VO(H_2O)_5^{2+}$ and (b) two magnetically equivalent protons in $Cu(H_2O)_6^{2+}$. (Reproduced by permission of the American Chemical Society from C. Gemperle and A. Schweiger, *Chem. Rev.*, 1991, **91**, 1481)

harmonics provides a method for determining the number of equivalent nuclei coupled to the electron.

3.1.3 Optimized Davies and Mims ENDOR

The Davies or Mims ENDOR pulse sequences produce a maximum ENDOR enhancement of $\Delta\chi_e/\chi_e = 1$. A pulse scheme for theoretically increasing this efficiency to $\Delta\chi_e/\chi_e = 2$ has been proposed and demonstrated.[42] This is accomplished by inserting a microwave π pulse and a second rf π pulse following the first rf π pulse in the mixing period. This pulse sequence is the pulsed analog of the Special TRIPLE resonance technique which was also introduced to improve the efficiency in the CW ENDOR experiment.[34,62,63] In practice, the improvement in efficiency of the Davies or Mims ENDOR signal intensity is much smaller than theoretically possible, primarily because of pulse imperfections. Nevertheless, a gain in ENDOR enhancement is observed, as shown in the example given in Figure 12. Nonideal nutation angles due to pulse imperfections are particularly problematic for noncrystalline samples where the ENDOR lines are significantly overlapped.

3.1.4 Electron–Nucleus Coherence Effects

Electron–nucleus coherence effects can be observed in the Davies ENDOR experiment if the microwave pulses in the detection period excite both allowed and semiforbidden ESR transitions.[38,37] These coherence effects generate a nuclear modulation on the envelope of the primary electron spin echo in the detection period analogous to the ESEEM experiment. An example of this phenomenon is shown in Figure 13 where two Davies ENDOR spectra for the blue copper protein,

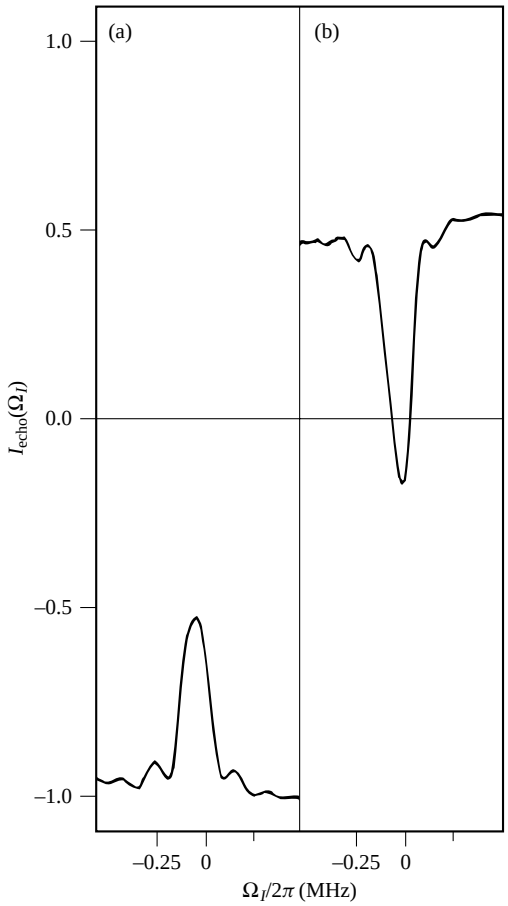

Figure 12 Mims-ENDOR spectra (a) of Cu(II)-doped TGS single crystal around the proton transition at $\omega_p/2\pi = 10.15$ MHz and the optimized spectra obtained using the pulse sequence described in the text. (Reproduced by permission of Academic Press from C. Gemperle et al., *J. Magn. Reson.*, 1990, **87**, 502)

stellacyanin, are shown recorded for two different values of the spin echo delay time τ in the detection period. The values of τ used in the detection period are indicated on the echo envelope waveform shown in the inset. These coherence effects can have important consequences for the analysis of the ENDOR spectrum. Note that the relative amplitudes of the ENDOR intensities depend on the value of τ in the detection period. This effect can be used as a spectral editing technique.[38,37]

3.1.5 Electron–Nucleus–Nucleus Triple Resonance

The Double ENDOR was originally introduced as a CW ENDOR technique to establish the connectivity of hyperfine sublevels and to determine the relative signs of the hyperfine interaction for nonequivalent nuclei.[63,64] The pulsed implementation of the Double ENDOR experiment is shown in Figure 14.[41] The experiment is analogous to the Davies ENDOR experiment, except that a second rf π pulse is inserted in the mixing period to irradiate a preselected ENDOR transition. The Double ENDOR difference spectrum, obtained from the difference between the ENDOR and Double ENDOR spectrum, identifies any changes in intensities of the ENDOR transitions induced by pumping at the second rf frequency. A peak in the Double ENDOR difference spectrum will only be

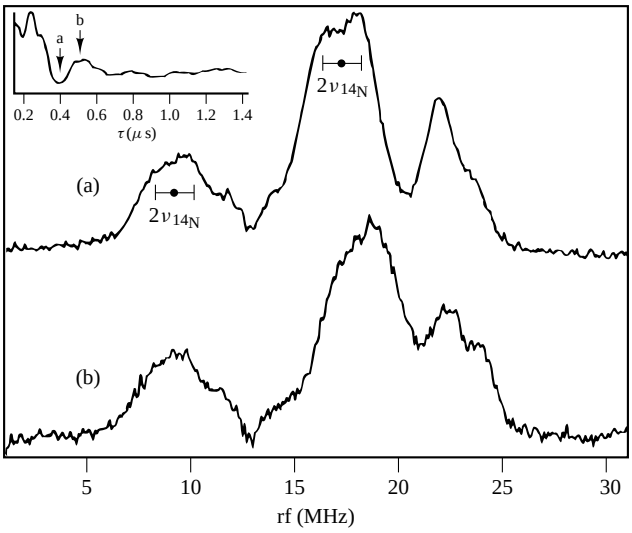

Figure 13 Davies ENDOR spectra of stellacyanin at the two pulse modulation minimum at τ = 0.40 μs (a) and at the maximum at τ = 0.51 μs (b). (Reproduced by permission of Academic Press from H. Thomann and M. Bernardo, in *Methods in Enzymology*, eds. J. F. Riordan and B. L. Vallee, London 1993, Vol. **227**, Chap. 6)

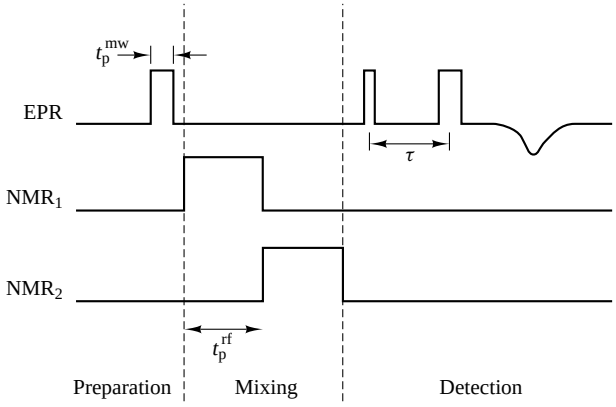

Figure 14 Pulsed implementation of double ENDOR. (Reproduced by permission of Academic Press from H. Thomann and M. Bernardo, in 'Methods in Enzymology', eds. J. F. Riordan and B. L. Vallee, London 1993, Vol. 227, Chap. 6)

observed if the two sublevels each have a level in common with the ESR transition.

An example of the pulsed Double ENDOR and Double ENDOR difference spectrum recorded for the radical in the conjugated conducting polymer, polyacetylene, is shown in Figure 15.[41] The Double ENDOR difference spectra indicate that the unpaired electron is coupled to protons with both positive and negative hyperfine interactions. In this case, similar conclusions were obtained using the CW Double ENDOR experiment and the results were used to determine an electron–electron correlation energy using a Hartree–Fock molecular orbital calculation.[65] However, the CW Double ENDOR experiment was only successful over a restricted temperature range, which is not the case for the pulsed version of the experiment. The pulsed Double ENDOR experiment has also been applied to studies of the irradiated malonic acid radical molecule[45,43] and to studies of the coordination

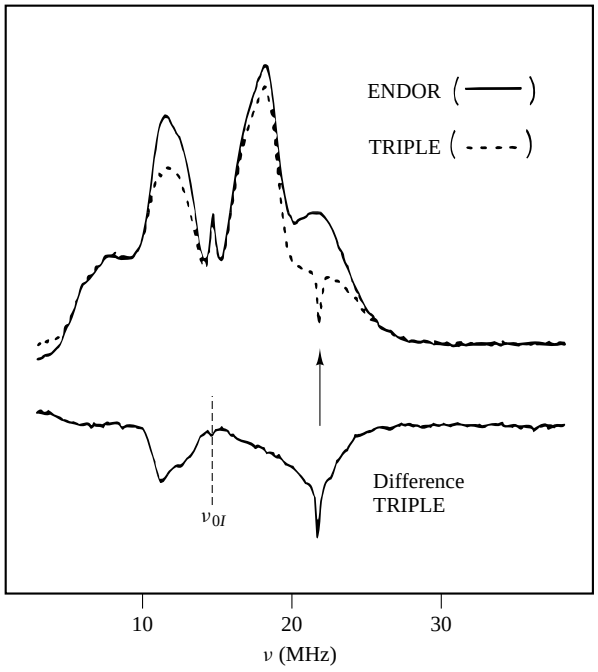

Figure 15 Pulsed Double and Double ENDOR difference spectrum of the polyacetylene radical. (Reproduced by permission of John Wiley & Sons from A. Grupp and M. Mehring in 'Modern Pulsed and Continuous Wave Electron Spin Resonance', eds. L. Kevan and M. K. Bowman, Chichester, 1979, Chap. 4)

structure of transition metal ions and metal clusters in metalloenzymes.[38]

3.1.6 Electron–Nucleus–Electron Triple Resonance

Another variation of a pulsed triple resonance experiment is shown in Figure 16.[38,37] This experiment is related to the Davies ENDOR experiment, except that the frequency of the detection pulses are offset by a frequency Δ from the frequency of the preparation pulse. This is shown schematically in Figure 17 by the magnetic positions at which the preparation, indicated by B_p, and detection, indicated by B_d, irradiation pulses are applied within the ESR absorption envelope. Sublevel polarization transfer that connects the positions B_p and B_d must originate from rf driven sublevel NMR transitions. Polarization transfer by mechanisms other than rf driven nuclear spin flips, such as by spin diffusion, are ineffective because of the short time interval between the preparation and detection period. The value of Δ therefore preselects nuclei with the hyperfine coupling $A = \Delta$. For this reason, the ENDOR spectrum generated for $\Delta = A$ is referred to as a hyperfine selective (HS) ENDOR spectrum. An HS ENDOR spectrum can also be generated by jumping the applied magnetic field.[42]

The HS ENDOR technique is illustrated in Figure 18. The Davies ENDOR spectra for the blue copper protein, stellacyanin, recorded for the native pH 7 form of the protein and for the high-pH (pH 11) perturbed blue form of the protein are shown in Figures 18(a) and 18(b), respectively. The spectra are identical except for the intensity of a transition at 21 MHz observed in the spectrum of the high-pH form. The assignment of this peak is facilitated using the HS ENDOR experiment, as

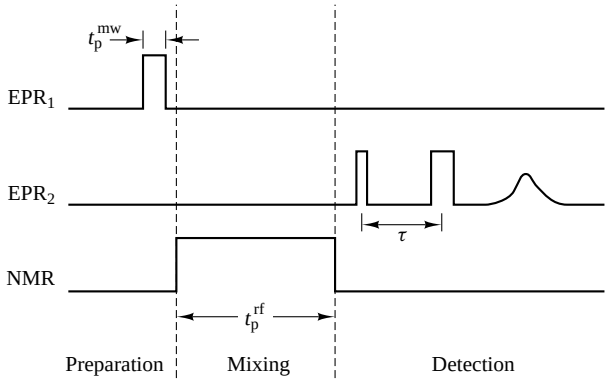

Figure 16 Pulsed electron–nucleus–electron triple resonance pulse sequence. (Reproduced by permission of Academic Press from H. Thomann and M. Bernardo, in 'Methods in Enzymology', eds. J. F. Riordan and B. L. Vallee, London 1993, Vol. 227, Chap. 6)

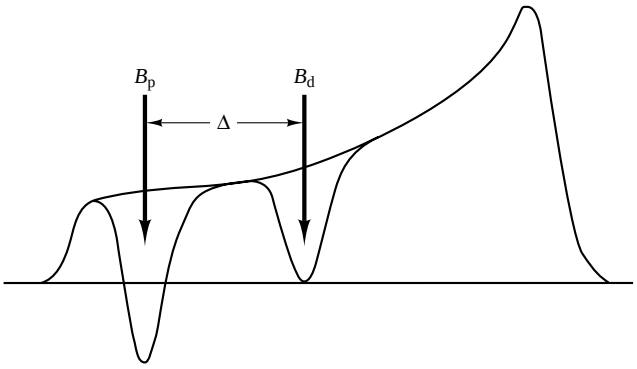

Figure 17 EPR spectra of an inhomogeneously broadened line showing the inversion 'hole' at B_p after the preparation period and the position B_d of the detection pulses. (Reproduced by permission of Academic Press from H. Thomann and M. Bernardo, in 'Methods in Enzymology', eds. J. F. Riordan and B. L. Vallee, London, 1993, Vol. 227, Chap. 6)

illustrated by the three HS ENDOR spectra recorded for values of Δ = 19, 42, and 36 MHz, which are shown in Figures 18(c), 18(d) and 18(e) respectively.

3.2 EPR Detected Sublevel Nuclear Coherence

Sublevel coherence can be created by a $\pi/2$ rf pulse applied at the end of the preparation period. Once created, this sublevel coherence can be manipulated in analogy to many other solid state NMR experiments. Specific examples of these type of experiments are described in this section.

3.2.1 Nuclear Free Induction

The evolution of the sublevel coherence under free precession in the local field can be detected indirectly using the pulse sequence shown in Figure 19.[41,43] The frequency of the rf pulses are set to excite a transition in the ENDOR spectrum. The sublevel coherence evolving during the evolution time t_1 is converted back to electron spin longitudinal polarization by a second rf $\pi/2$ pulse. The sublevel coherence signal at evolution time t_1 is then detected indirectly from the intensity

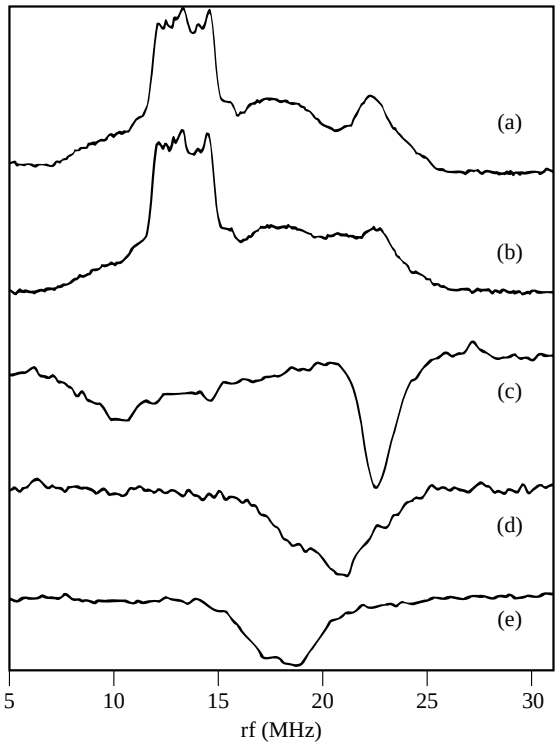

Figure 18 Davies ENDOR spectra of the native (pH 7) form (a) and the high-pH (pH 11) form (b) of stellacyanin. HS ENDOR spectra of the high pH form with Δ = 19.0 (c), 42.0 (d), and 36 (e) MHz were used to assign the feature at 21 MHz to nitrogen. (Reproduced by permission of Academic Press from H. Thomann and M. Bernardo, in 'Methods in Enzymology', eds. J. F. Riordan and B. L. Vallee, London, 1993, Vol. 227, Chap. 6)

modulation of the primary electron spin echo in the detection period. The sublevel free induction signal is then detected point by point by incrementing t_1 on successive pulse sequence iterations. Both the in-phase and phase-quadrature sublevel free precession signals can be detected by phase shifting the relative phase of the two rf pulses by $\pi/2$. Additional phase cycling by π can be used to cancel the effects of electron spin–lattice magnetization recovery during the t_1 evolution period. The rf pulse excitation bandwidth is usually much smaller than the spectral spread of the ENDOR spectrum. In order to record the entire ENDOR spectrum, the pulse sequence shown in Figure 19 must be repeated with the rf frequency incremented on successive experiments. A spectral slice of the overall ENDOR spectrum, determined by the bandwidth of the rf excitation pulse, is recorded for each selected rf. The whole ENDOR spectrum is reconstructed by adding the slices of the limited spectral regions recorded in each experiment.

The ESR detected sublevel free precession experiment is illustrated in Figure 20. These data are collected for a crystal of irradiated malonic acid. In the Davies ENDOR spectrum, a transition that shows no evidence of fine structure is observed at 14.42 MHz. The in-phase and phase-quadrature sublevel free precession signals recorded using the pulse sequence in Figure 19 and the procedure described above are shown in Figure 20(a). The complex Fourier transform of these waveforms is shown in Figure 20(b). This spectrum indicates that the ENDOR line is composed of three overlapping

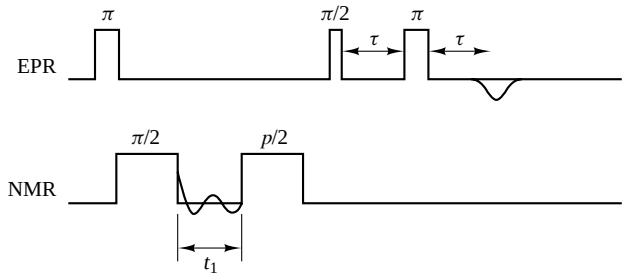

Figure 19 Pulse sequence for EPR detection of sublevel FID. (Reproduced by permission of the American Chemical Society from H. Thomann and M. Bernardo, in 'Advances in Chemistry Series 229: Magnetic Resonance of Carbonaceous Solids', eds. R. E. Botto and Y. Sanada, Washington, DC, 1993, Chap. 4)

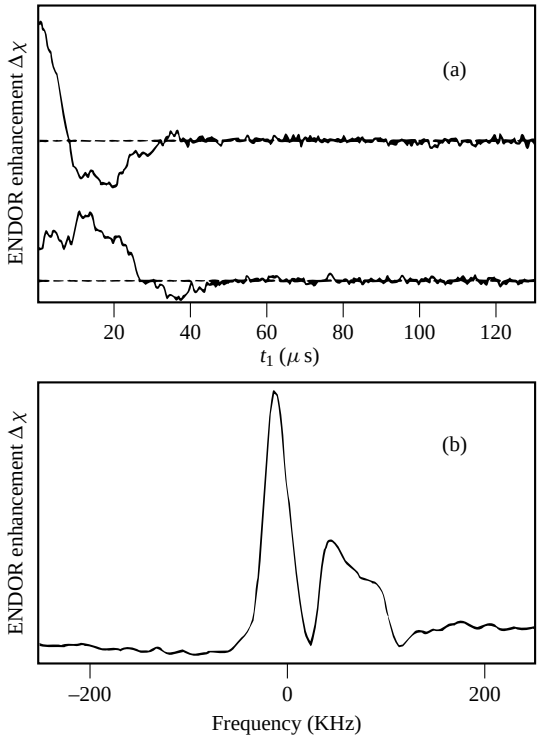

Figure 20 Quadrature sublevel FID signals of malonic acid with ν_{rf} = 14.42 MHz (a) and corresponding complex FT spectrum (b). (Reproduced by permission of the American Chemical Society from H. Thomann and M. Bernardo, in 'Advances in Chemistry Series 229: Magnetic Resonance of Carbonaceous Solids', eds. R. E. Botto and Y. Sanada, Washington, DC, 1993, Chap. 4)

transitions which are not resolved in the Davies ENDOR spectrum.

3.2.2 Multiple Quantum Electron–Nucleus Coherence

The coupling of two or more nuclei with equivalent hyperfine couplings can be detected indirectly using the pulse sequences shown in Figure 21.[41,66] The sublevel polarization can be created using either the inversion–recovery technique with primary spin echo detection (i.e. as in the Davies ENDOR pulse sequence) or by the two pulse excitation in the preparation period with a single pulse in the detection

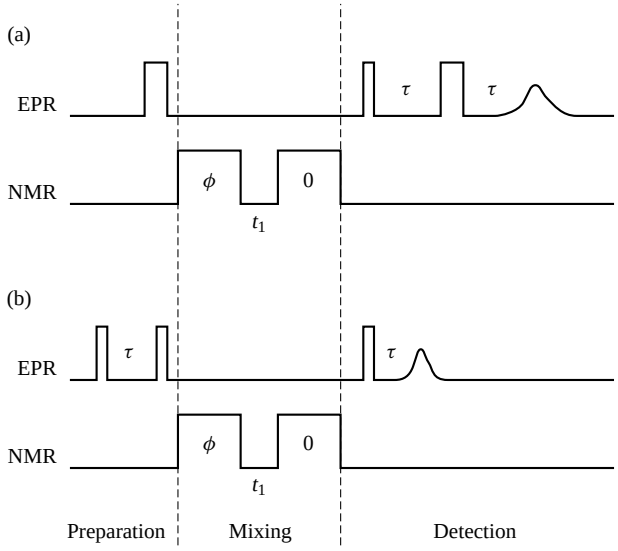

Figure 21 Multiple quantum (MQ) ENDOR pulse sequences: Davies MQ ENDOR (a) and Mims MQ ENDOR (b). (Reproduced by permission of Laser Pages Publishing from H. Thomann and M. Bernardo, *Isr. J. Chem.*, 1992, **32**, 323)

period to create a stimulated echo (i.e. as in the Mims ENDOR pulse sequence). An n-quantum sublevel coherence is detected using the phase incrementation technique in analogy to the NMR experiment.[53,67] An n-quantum coherence accumulates a phase $\theta_n = n\omega_{ENDOR}t_{evol}$ where t_{evol} is an evolution time and ω_{ENDOR} is the sublevel transition frequency.

In the present experiments the phase accumulation occurs during the nutation of the sublevel polarization so that $t_{evol} = t_p^{rf}$. This phase accumulation can be detected by incrementing the phase of the rf mixing pulse in the middle of the mixing period. Theoretically, the optimum ENDOR signal is obtained by applying two $\pi/2$ rf pulses. Each point on the plot of the phase interferogram is collected by incrementing the phase of the second rf pulse on successive pulse sequence iterations.

An example of a multiple quantum spectrum recorded using the pulse sequence in Figure 21(a) for the malonic acid radical molecule is shown in Figure 22.[66] Multiple quantum coherences up to n = 3 are observed for an ENDOR transition at 14.42 MHz recorded for the malonic acid radical molecule in a crystal at an arbitrary orientation. This is consistent with the three lines observed in the ESR detected sublevel FID spectra recorded under identical conditions [Figure 20(b)]. Multiple quantum spectra recorded for several evolution times for free precession are also shown in Figure 22. The oscillation for each order of coherence originates from the free precession of transverse sublevel magnetization in the presence of the local field.

3.2.3 Nuclear Spin Echoes

Hyperfine sublevel spin echoes can be created and detected indirectly by inserting a refocusing rf pulse in the evolution period of the mixing period for the pulse sequence shown in Figure 20. The pulse sequence for this indirect detection of sublevel spin echoes is shown in Figure 23.[40,41] The first rf pulse in the mixing period creates sublevel coherence. This coherence evolves under free precession for time τ_n and is

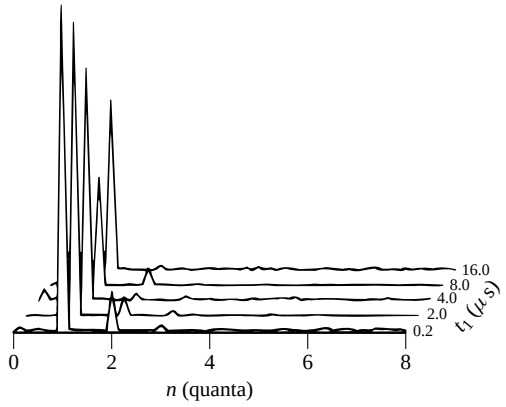

Figure 22 Davies multiple quantum ENDOR spectra of the malonic acid radical for various evolution times. (Reproduced by permission of Laser Pages Publishing from H. Thomann and M. Bernardo, *Isr. J. Chem.*, 1992, **32**, 323)

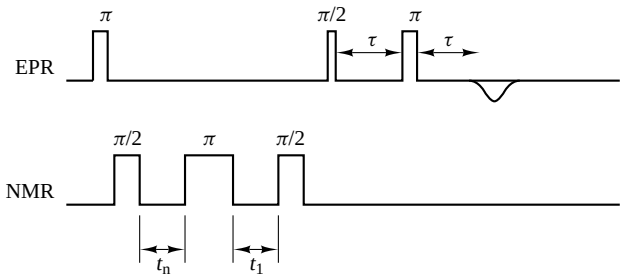

Figure 23 Pulse sequence for EPR detection of sublevel spin echo. (Reproduced by permission of the American Chemical Society from H. Thomann and M. Bernardo, in 'Advances in Chemistry Series 229: Magnetic Resonance of Carbonaceous Solids', eds. R. E. Botto and Y. Sanada, Washington, DC, 1993, Chap. 4)

then refocused by the rf π pulse. The sublevel spin echo formed at time τ_n after the refocusing pulse can be detected by incrementing the time t_1 of the third rf mixing pulse. The third rf pulse transforms the sublevel coherence into two spin electron–nucleus longitudinal order. This is transformed to electron spin coherence for detection of the electron spin polarization by the microwave pulses in the detection period.

The sublevel echo can be detected point by point by incrementing the value of t_1 from $t_1 < \tau_n$ to $t_1 > \tau_n$ on successive pulse sequence iterations. In each pulse sequence iteration the sublevel coherence is detected by the change in intensity of the electron spin echo in the detection period. An example of sublevel spin echoes detected by this procedure for an X-ray irradiated malonic acid crystal are shown in the inset of Figure 24. The two sublevel spin echoes shown were recorded for τ_n values of 5 and 20 μs.

The circles shown in the inset of Figure 24 indicate the echo envelope intensities recorded for several values of $t_1 = \tau_n$. The full sublevel spin echo decay envelope along with a fit to a single exponential and the residuals for the fit are also shown in Figure 24. These sublevel echoes and envelope decay were recorded for the ν_+ = 30.19 MHz ENDOR transition. This corresponds to the proton NMR transition for the α proton of the $\cdot CH(COOH)_2$ radical molecule which is shifted to the high-frequency side of the proton Larmor frequency. The sublevel T_{2n} decay time obtained from the single exponential fit shown

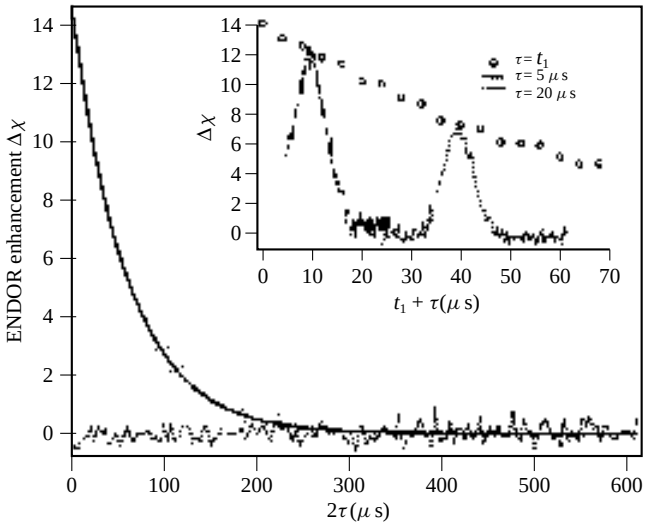

Figure 24 The sublevel spin echo decay recorded with $t_1 = \tau_n$ along with the fit to a single exponential and the residuals of the fit. (Reproduced by permission of the American Chemical Society from H. Thomann and M. Bernardo, in 'Advances in Chemistry Series 229: Magnetic Resonance of Carbonaceous Solids', eds. R. E. Botto and Y. Sanada, Washington, DC, 1993, Chap. 4)

in Figure 24 is 60 μs. The proton T_{2n} values measured for $\nu_{rf} = \nu_n$ are shorter than the values measured at frequencies shifted away from the proton Larmor frequency.

Similar results have been obtained in sublevel nuclear T_{2n} studies of protons in coal samples.[46] In these coal studies, the ESR detected sublevel T_{2n} values measured at $\nu_{rf} = \nu_n$ were similar to the value measured directly by NMR.[68] The ESR detected sublevel T_{2n} values increased for NMR transitions shifted further away from the proton Larmor frequency. Apparently the time-dependent local magnetic field from the hyperfine interaction is not an effective sublevel T_{2n} relaxation mechanism. The T_{2n} value measured directly by NMR is determined by the proton homonuclear dipolar coupling. The equivalence of the value measured in the ESR detected sublevel T_{2n} experiment for $\nu_{rf} = \nu_n$ suggests that the T_{2n} value is also determined by the proton dipolar interaction with the hyperfine coupling serving only as a mechanism for detecting the sublevel coherence signal. Quite different results can be expected if the time dependence of the local field is an effective T_{2n} mechanism. In this case the T_{2n} values would be expected to decrease as the NMR transition frequency is shifted away from the proton Larmor frequency.

3.3 Coherence Transfer ENDOR

In analogy to the coherence transfer experiments known in NMR spectroscopy, it is also possible to detect the hyperfine sublevel transitions by an electron–nuclear double resonance coherence transfer experiment.[41,43,69] Three different pulse sequences for coherence transfer ENDOR experiments are shown in Figure 25. The basic principle in all three types of experiment is similar. The rf pulses applied during the period of free precession of the electron spin coherence created by a $\pi/2$ microwave pulse interfere with the refocusing of this electron coherence following the microwave π pulse.

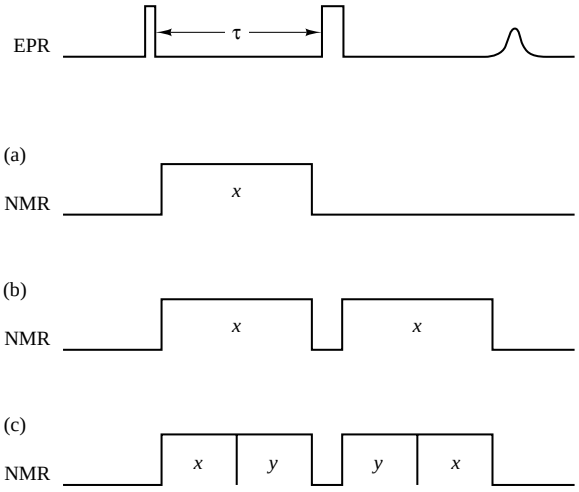

Figure 25 Pulse sequences for coherence transfer ENDOR

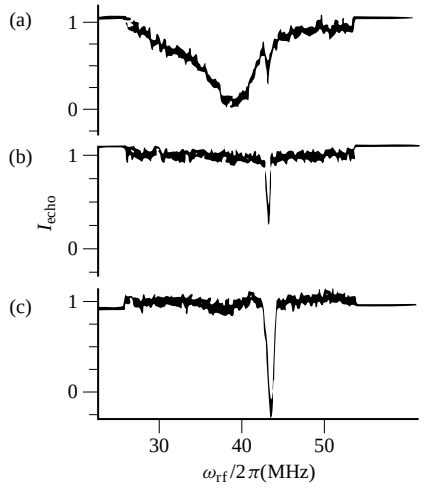

Figure 26 Coherence transfer single crystal ENDOR spectra of the malonic acid radical recorded with corresponding pulse sequences shown in Figure 25. (Reproduced by permission of the American Chemical Society from C. Gemperle and A. Schweiger, *Chem. Rev.*, 1991, **91**, 1481)

This occurs if the rf pulse is on resonance with an NMR transition that has a sublevel in common with the electron spin eigenlevel that belongs to the states from which the electron spin coherence was created. In this case, the sublevel NMR transition shifts the phase of the electron spin coherence which is detected as an attenuation of the electron spin echo. If the rf pulse is a π pulse the electron spin echo intensity is reduced to zero resulting in $\Delta\chi_e/\chi_e = 1$. If the rf pulse is a 2π pulse, the echo intensity changes sign resulting in $\Delta\chi_e/\chi_e = 2$. If a 4π pulse is applied, the electron spin echo intensity returns to its original intensity. This response of the electron spin echo intensity to the rotational symmetry of the sublevel nutation angle is called the 'spinor property' and is a property of wavefunctions for spin-$\frac{1}{2}$ particles.

The ENDOR spectrum recorded using the pulse sequence shown in Figure 25(a) is sufficient to observe the coherence transfer ENDOR effect. However, the application of a single rf pulse also produces a large Bloch–Siegert (BS) frequency shift $\omega_{BS} = -\gamma_e(B_2^2/B_0)$, which results in a phase shift of $\omega_{BS}t_p^{rf}$. Since the rf magnetic field strength is not constant as a function of frequency across the ENDOR spectrum, the Bloch–Siegert phase shift is observed as a broad feature, as shown in Figure 26(a), which can mask the ENDOR transitions. The Bloch–Siegert phase shift can be refocused by applying a second rf pulse, as shown in Figure 25(b), which is symmetrically displaced about the microwave refocusing pulse. This eliminates the broad feature in the ENDOR spectrum as shown in Figure 26(b). The maximum ENDOR effect of $\Delta\chi_e/\chi_e = 1$ is observed when the two rf pulses are π pulses. The efficiency of the ENDOR effect can theoretically be increased to $\Delta\chi_e/\chi_e = 2$ if the two rf pulses are 2π pulses but with a 90° shift introduced, as shown in Figure 25(c).[41,43] The enhancement in the ENDOR signal intensity is shown in Figure 26(c). In practice, the ENDOR efficiency is improved for this phase shifted spinor ENDOR pulse sequence, but because of technical limitations (primarily pulse imperfections) the increase in efficiency is much smaller than theoretically expected. Another limitation of coherence transfer ENDOR experiments is that the ENDOR lines are usually power broadened because of the short electron phase memory time encountered for most samples. It is rare that phase memory times are longer than a few microseconds, even at liquid helium temperatures. Nevertheless, the coherence transfer ENDOR experiment has revealed fundamentally interesting properties of the spin dynamics of the electron–nucleus spin system.

4 CONCLUDING REMARKS

ENDOR and the extension to PE NMR spectroscopy are presently tools of the specialist. They are very powerful techniques in specific cases where the spectra and/or spin dynamics for the nuclei of interest are strongly influenced by the large local magnetic fields originating from the hyperfine coupling with unpaired electron spins. In such cases the NMR transition frequencies are shifted by very large values when compared with NMR spectra of diamagnetic samples. When these circumstances do apply, ENDOR and PE NMR spectroscopy are often the only techniques which can provide the desired information. In this review we have included examples of applications in organic solids, metallobiochemistry, and organometallic chemistry. With the introduction of pulsed excitation techniques, extension to multiple irradiation frequencies, and the introduction of commercially available pulsed instrumentation, continued development of the methodology and an increasing range of applications can be expected for these techniques in the near future. Recent developments in high-frequency ESR,[70] including the extension to high-frequency ENDOR,[71] will also likely expand the range of research applications. The combination of pulsed ESR and pulsed NMR should continue to be a vibrant area of research as new technology becomes available and as new methodologies and applications are developed.

5 RELATED ARTICLES

Chemically Induced Dynamic Nuclear Polarization; Cobalt(II)- and Nickel(II)-Substituted Proteins; Contrast

Agents in MRI: Superparamagnetic Iron Oxide; Contrast Agents in Whole Body Magnetic Resonance: An Overview; Contrast Agents in Magnetic Resonance: Operating Mechanisms; Copper Proteins; Dynamic Nuclear Polarization and High-Resolution NMR of Solids; Electron–Nuclear Hyperfine Interactions; EPR and In Vivo EPR: Roles for Experimental and Clinical NMR Studies; Heme Peroxidases; Iron—Sulfur Proteins; EPR and In Vivo EPR: Roles for Experimental and Clinical NMR Studies.

6 REFERENCES

1. H. Kurreck, B. Kirste, and W. Lubtiz, *ENDOR Spectroscopy of Radicals in Solution*, VCH, New York, 1988.
2. J. E. Wertz and J. R. Bolton, *Electron Spin Resonance: Elementary Theory and Practical Applications*, Chapman & Hall, London, 1986.
3. J. A. Weil (ed.), *Electronic Magnetic Resonance of the Solid State*, Canadian Society for Chemistry, Ottawa, 1987.
4. L. Petrakis and J. R. Fraissard (eds), *Magnetic Resonance. Introduction to Advanced Topics and Applications to Fossil Energy* (*NATO ASI Series C, Vol. 124*), Reidel, Dordrecht, 1984.
5. R. E. Botto and Y. Sanada (eds), *Advances in Chemistry Series: Magnetic Resonance of Carbonaceous Solids*, American Chemical Society, Washington, DC, 1993.
6. A. Abragam and B. Bleaney, *Electron Paramagnetic Resonance of Transition Ions*, (*International Series of Monographs on Physics*), Oxford University Press, Oxford, 1970.
7. J. R. Pilbrow, *EPR of Transition Metal Ions* (*International Series of Monographs on Physics*), Clarendon, Oxford, 1991.
8. J.-M. Spaeth, J. R. Niklas, and R. H. Bartram, *Structural Analysis of Point Defects in Solids*, Springer, New York, 1992.
9. L. J. Berliner and J. Reuben (eds), *EMR of Paramagnetic Molecules* (*Biological Magnetic Resonance, Vol. 13*), Plenum, New York, 1993.
10. L. J. Berliner and J. Reuben (eds), *NMR of Paramagnetic Molecules* (*Biological Magnetic Resonance, Vol. 12*), Plenum, New York, 1993.
11. I. Bertini and C. Luchinat, *NMR of Paramagnetic Molecules in Biological Systems*, Benjamin Cummings, Menlo Park, CA, 1986.
12. G. N. LaMar (ed.), *NMR of Paramagnetic Molecules*, Academic, New York, 1973.
13. A. Abragam, *The Principles of Nuclear Magnetism* (*International Series of Monographs on Physics*), Oxford University Press, Oxford, 1961.
14. C. D. Jeffries, *Dynamic Nuclear Orientation*, Wiley, New York, 1963.
15. M. Goldman, *Spin Temperature and Nuclear Magnetism in Solids* (*International Series of Monographs on Physics*), Oxford University Press, Oxford, 1970.
16. A. Abragam and M. Goldman, *Nuclear Magnetism: Order and Disorder* (*International Series of Monographs on Physics*), Oxford University Press, Oxford, 1982.
17. R. A. Wind, M. J. Duijvestijn, C. van der Lugt, A. Manenschijn, and J. Vriend, *Prog. NMR Spectrosc.*, 1985, **17**, 33.
18. R. D. Bates, Jr, *Magn. Reson. Rev.*, 1993, **16**, 237.
19. R. A. Wind, R. Lewis, H. Lock, and G. E. Maciel, in *Advances in Chemistry Series: Magnetic Resonance of Carbonaceous Solids*, ed. R. E. Botto and Y. Sanada, American Chemical Society, Washington, DC, 1993, Vol. 229, Chap. 3, p. 45.
20. M. Afeworki, R. McKay, and J. Schaefer, *Macromolecules*, 1992, **25**, 4084.
21. G. G. Maresch, R. D. Kendrick, C. S. Yannoni, and M. E. Galvin, *J. Magn. Reson.*, 1989, **82**, 41.
22. R. A. Wind, in *Modern NMR Techniques and their Applications in Chemistry*, eds. A. I. Popov and A. I. Hallenga, Marcel Dekker, New York, 1991.
23. W. B. Mims, in *Electron Paramagnetic Resonance*, ed. S. Geschwind, Plenum, New York, 1973.
24. S. A. Dikanov and Yu. D. Tsvetkov, *Electron Spin Echo Envelope Modulation (ESEEM) Spectroscopy*, CRC, Boca Raton, FL, 1992.
25. L. Kevan and R. N. Schwartz (eds.), *Time Domain Electron Spin Resonance*, Wiley, New York, 1979.
26. L. Kevan and M. K. Bowman (eds.), *Modern Pulsed and Continuous Wave Electron Spin Resonance*, Wiley, New York, 1990.
27. W. B. Mims and J. Peisach, in *Biological Magnetic Resonance*, Plenum, New York, 1981, Vol. 3, p. 213.
28. D. J. Singel, in *Advanced EPR: Applications in Biology and Biochemistry*, ed. A. J. Hoff, Elsevier, Amsterdam, 1989.
29. A. Schweiger, *Angew. Chem., Int. Ed. Engl.*, 1991, **30**, 265.
30. G. Feher, *Phys. Rev.*, 1956, **103**, 834.
31. L. Kevan and L. D. Kispert, *Electron Spin Double Resonance Spectroscopy*, Wiley, New York, 1976.
32. M. M. Dorio and J. Freed (eds.), *Multiple Electron Resonance Spectroscopy*, Plenum, New York, 1979.
33. B. M. Hoffman, *Acc. Chem. Res.*, 1992, **24**, 164.
34. K. Moebius, M. Plato, and W. Lubitz, *Phys. Rep.*, 1982, **87**, 171.
35. A. J. Hoff (ed.), *Advanced EPR: Applications in Biology and Biochemistry*, Elsevier, Amsterdam, 1989.
36. A. Schweiger, in *Structure & Bonding*, Springer, Berlin, 1982, Vol. 51, p. 1.
37. H. Thomann and Marcelino Bernardo, in *Biological Magnetic Resonance*, eds. L. J. Berliner and J. Reuben, Plenum, New York, 1993, Vol. 13, Chap. 7, p. 275.
38. H. Thomann and M. Bernardo, in *Methods in Enzymology*, eds. J. F. Riordan and B. L. Vallee, Academic, San Diego, 1993, Vol. 227, Chap. 6, p. 118.
39. H. Thomann and W. B. Mims, in *Pulsed Magnetic Resonance: NMR, ESR, and Optics*, ed. D. M. S. Bagguley, Clarendon, Oxford, 1992, p. 362.
40. P. Hoefer, A. Grupp, and M. Mehring, in *Electronic Magnetic Resonance of the Solid State*, ed. J. A. Weil, Canadian Society for Chemistry, Ottawa, 1987.
41. A. Grupp and M. Mehring, in *Modern Pulsed and Continuous Wave Electron Spin Resonance*, eds. L. Kevan and M. K. Bowman, Wiley, New York, 1979, Chap. 4, p. 195.
42. C. Gemperle and A. Schweiger, *Chem. Rev.*, 1991, **91**, 1481.
43. M. Mehring, P. Hoefer, and A. Grupp, *Ber. Bunsenges. Phys. Chem.*, 1987, **91**, 1132.
44. W. A. J. A. van der Poel, D. J. Singel, J. Schmidt, and J. H. van der Waals, *Mol. Phys.*, 1983, **49**, 1017.
45. H. Thomann and M. Bernardo, in *Magnetic Resonance of Carbonaceous Solids* (*Advances in Chemistry Series, Vol. 229*), ed. R. E. Botto and Y. Sanada, American Chemical Society, Washington, DC, 1993, Chap. 4, p. 65.
46. H. Thomann, M. Bernardo, and B. G. Silbernagel, in *Magnetic Resonance of Carbonaceous Solids*, (*Advances in Chemistry Series, Vol. 229*), eds. R. E. Botto and Y. Sanada, American Chemical Society, Washington, DC, 1993, Chap. 30, p. 561.
47. C. P. Slichter, *Principles of Magnetic Resonance* (*Springer Series in Solid State Sciences*), 3rd edn., Springer, New York, 1990.

48. N. M. Atherton, *Principles of Electron Spin Resonance*, Ellis Horwood, Chichester, 1993.
49. G. H. Rist and J. H. Hyde, *J. Chem. Phys.*, 1970, **52**, 4633.
50. L. R. Dalton and A. L. Kwiram, *J. Chem. Phys.*, 1972, **57**, 1132.
51. G. C. Hurst, T. A. Henderson, and R. W. Kreilick, *J. Am. Chem. Soc.*, 1985, **107**, 7294.
52. B. M. Hoffman, J. Martinsen, and R. A. Venters, *J. Magn. Reson.*, 1984, **59**, 110.
53. R. R. Ernst, G. Bodenhausen, and A. Wokaun, *Principles of Nuclear Magnetic Resonance in One and Two Dimensions*, Clarendon, Oxford, 1987.
54. V. L. Hochmann, V. Ya. Zevin, and B. D. Shanina, *Sov. Phys. Solid State*, 1968, **10**, 269.
55. C. Gemperle, A. Schweiger, and R. R. Ernst, *Chem. Phys. Lett.*, 1988, **1**, 145.
56. E. R. Davies, *Phys. Lett. Ser. A*, 1974, **47**, 1.
57. W. B. Mims, *Proc. R. Soc. London*, 1965, **283**, 452.
58. T. Wacker, G. A. Sierra, and A. Schweiger, *Isr. J. Chem.*, 1992, **32**, 305.
59. R. C. McCalley and A. L. Kwiram, *J. Phys. Chem.*, 1993, **97**, 2888.
60. P. E. Doan, C. Fan, C. E. Davoust, and B. M. Hoffman, *J. Magn. Reson.*, 1991, **95**, 169.
61. J. Peisach, W. G. Levine, and W. E. Blumberg, *J. Biol. Chem.*, 1967, **242**, 2847.
62. K. Moebius, W. Lubitz, and M. Plato, in *Advanced EPR: Applications in Biology and Biochemistry*, ed. A. J. Hoff, Elsevier, Amsterdam, 1989, p. 441.
63. K. Moebius, in *Multiple Electron Resonance Spectroscopy*, eds. M. M. Dorio and J. Freed, Plenum, New York, 1979.
64. R. J. Cook and D. H. Whiffen, *Proc. R. Soc. London*, 1964, **84**, 845.
65. H. Thomann and L. R. Dalton, in *Handbook of Conducting Polymers*, ed. T. A. Skotheim, Marcel Dekker, New York, 1986, p. 1157.
66. H. Thomann and M. Bernardo, *Isr. J. Chem.*, 1992, **32**, 323.
67. J. Baum, M. Munowitz, A. N. Garroway, and A. Pines, *J. Chem. Phys.*, 1985, **83**, 2015.
68. B. C. Gerstein, C. Chow, R. G. Pembleton, and R. C. Wilson, *J. Phys. Chem.*, 1977, **81**, 565.
69. I. M. Brown, D. J. Sloop, and D. P. Ames, *Phys. Rev. Lett.*, 1969, **22**, 324.
70. S. S. Eaton and G. R. Eaton, *Magn. Reson. Rev.*, 1993, **16**, 157.
71. O. Burghaus, A. Kischkat-Toth, R. Klette, and K. Mobius, *J. Magn. Reson.*, 1988, **80**, 383.

Biographical Sketches

Hans Thomann. *b* 1954. B.S., 1976, Ph.D., 1982, Chemistry, State University of New York at Stony Brook, USA. Research interests: development of pulsed electron NMR techniques and their application to problems in catalysis, metallobiochemistry, and molecular solids; spin relaxation and molecular motion of fluids in porous media.

Marcelino Bernardo. *b* 1957. B.S., 1979, Rochester Institute of Technology, NY, USA. Research interests: development of pulsed electron NMR techniques and their application to problems in catalysis, metallobiochemistry, and molecular solids; MRI.

EPR and In Vivo EPR: Roles for Experimental and Clinical NMR Studies

Harold M. Swartz and Goran Bačíc
Dartmouth Medical School, Hanover, NH, USA

1 INTRODUCTION

1.1 Scope and Rationale of Coverage

The use of electron paramagnetic resonance (EPR or, completely equivalently, electron spin resonance) in biomedicine is a vast and still developing subject, with many areas of direct or indirect relevance to the subject of this volume (related articles are listed at the end of the text). We will not, however, attempt to cover all of these topics but instead will restrict our discussion to four topics that are especially important to the use of MRI and MRS in vivo for experimental and clinical purposes:

1. measurement of the concentration of oxygen, especially in tissues in vivo;
2. measures of redox metabolism and/or distribution of drugs;
3. measurement of the viability of cells;
4. measurement of the concentration and distribution of contrast agents, especially in vivo.

These topics were chosen because they are areas of great importance for the use of NMR in biomedicine and are measurements for which EPR techniques can provide critically needed information that cannot be obtained as easily and/or as well by other techniques, including NMR. Our coverage of these topics will focus on overviews of the current status and the likely future developments; we will not attempt to provide extensive reviews of the rapidly expanding literature on these subjects (see[1–5] for recent reviews).

The measurement of the concentration of oxygen in cells and tissues, with an emphasis on the determination of hypoxia, seems especially important. Many of the uses of NMR, especially spectroscopy, really are aimed at making such measurements, and/or studying phenomena that are very dependent on the concentration of oxygen. This is certainly the case for most phosphorus NMR studies, which usually are aimed at measurements of the redox sensitive concentrations of phosphorus metabolites. Similarly much of proton NMR spectroscopy is aimed at measurements of intermediates such as lactic acid which reflect the concentration of oxygen in the tissues and, indeed, in many cases these measurements are used to provide indirect measures of the extent of hypoxia because more direct measurements are not available. As we will see EPR can make very sensitive and accurate measurements of the concentration of oxygen in tissues but it cannot, as yet, achieve the depth of penetration and the spatial resolution of NMR imaging. As a consequence, there is a great potential for the combined use of EPR and NMR in which the EPR techniques provide the needed determinations of the relationships between NMR spectroscopic measurements and the actual concentrations of oxygen. Such data will then make it much more feasible to use NMR techniques to obtain accurate insights into the state of oxygen dependent metabolism and therefore better address the diagnosis and therapy of diseases in which hypoxia plays a significant role (e.g. cancer, ischemia, and inflammation).

From the preceding discussion it seems evident that to the extent that EPR can provide additional measures of metabolism, beyond the direct measurement of the concentration of oxygen, EPR will further complement NMR measurements significantly. The metabolism of nitroxides appears to provide such a measure. EPR also can be used to follow the distribution and metabolism of some drugs, which can provide additional information on redox metabolism as well as pharmacokinetics. These studies are feasible through the use of metabolizable paramagnetic spin labels which are either the objects of interest themselves or attached to drugs, etc. as labels which then can be followed selectively by EPR.

The measurement of the viability of cells by EPR, while still at an early stage of development, provides an essentially unique capability that is very complementary to NMR studies. At the present time the results of this approach are available only in aggregates of cells (spheroids) and isolated cells. In the former they provide perhaps the most advanced and effective applications of EPR imaging (EPRI) in a biological system.

The use of EPR to study NMR contrast agents in many ways is very straightforward and logical, although it has not been applied as widely as would seem desirable. Virtually all NMR contrast agents are active because they have unpaired electrons and therefore they are directly observable by EPR. This is so because EPR sensitively and exclusively responds to electronic magnetic moments; usually those associated with unpaired electrons. While this approach has been very productive for the study of some NMR contrast agents such as the nitroxides, there are some significant limitations in the application of this technique in vivo to many of the metal ion based contrast agents due to unfavorably short relaxation times and/or spectral features. (The metal ion contrast agents, of course, can be studied very effectively by EPR in vitro.)

1.2 Brief Summary of the Principles of EPR Applied to the Study of In Vivo Systems

Although there are few fundamental differences between the principles of electron and nuclear magnetic resonance, differences in physical and chemical properties of the resonant species (unpaired electrons vs. nuclei with net spin) lead to profound differences in the techniques that are used to record spectra. Perhaps the greatest differences arise because the gyromagnetic ratio of an unpaired electron is ~700 times larger than that of a proton, so the resonance frequency/magnetic field ratio for the electron is 28 GHz T^{-1}, vs. 42.5 MHz T^{-1} for the proton. Consequently, standard EPR spectrometers operate at much higher frequencies and lower fields than conventional NMR spectrometers. While EPR spectroscopy is now performed using a wide range of frequencies from rf to far-infrared, most standard, commercial EPR spectrometers operate

at 9.5 and 35 GHz (*X*- and *Q*-band). At these frequencies nonresonant absorption of the electromagnetic radiation by the liquid water in biological systems presents a serious problem, thus limiting the sample size to a thickness of less than 1 mm. Larger aqueous samples or animals can be studied only by reducing the operating frequency to 1 GHz or less, but, of course, this results in reduced sensitivity. To date most of the published successful applications of in vivo EPR techniques to actual biomedical problems have used spectroscopy rather than imaging and have been done at 1 GHz (*L*-band). Several groups are investigating the feasibility of extending these approaches to imaging and/or lower frequencies, but sensitivity may be a limiting factor. The use of lower frequencies (e.g. 300–500 MHz) would be especially attractive because this would extend the sensitive depth from about 10 mm to about 70 mm.

The lack of sufficient amounts of naturally occurring paramagnetic materials is another potential source of problems. Both direct observations and theoretical calculations show that endogenous paramagnetic species such as paramagnetic metal ions and free radicals are present in insufficient concentrations to be detected directly by EPR in vivo.[4] (The only naturally occurring exception is the polymer, melanin.[4]) This presents an obvious problem since the paramagnetic substance has to be introduced, which can cause problems with regard to sensitivity and, potentially, toxicity. However, this has some beneficial aspects, since the only paramagnetic species that will be observed in vivo will be those introduced by the experimenter. The absence of background signals is particularly convenient for in vivo EPR spectroscopy (e.g. in contrast to proton spectroscopy where water suppression is required). With the addition of appropriate paramagnetic species the sensitivity of EPR, on a molar basis, is 700 times greater than for NMR. Paramagnetic species which are very stable and have appropriate lineshapes have been developed recently and these have been a significant factor in the successful development of in vivo EPR techniques.[4]

The short relaxation times of most paramagnetic species can be an additional potential source of problems. The timescale of electron spin relaxation of most paramagnetic species is nanoseconds (in contrast to NMR where the relaxation times typically are milliseconds); consequently, essentially all in vivo studies have been done using CW-EPR and have not been able to utilize most of the pulse techniques developed for NMR in biological systems. At the same time, the large widths of EPR resonance lines necessitate the use of high magnetic field gradient strengths for imaging that are at least one order of magnitude greater than those used in NMR imaging. Additional problems for EPRI arise from the fact that the EPR spectra of most paramagnetic species have multiple lines and multiple lineshapes; these spectral features, however, can be very valuable for EPR spectroscopy because they can provide very sensitive parameters of the environment in which the paramagnetic species are located.

As a consequence of the above factors the development of in vivo EPR techniques, especially imaging, has not occurred as rapidly as with NMR. Recently, however, there has been a significant increase of productivity in these areas, especially with in vivo spectroscopy. The emphasis on spectroscopy vs. imaging has not turned out to be a very significant limitation because the most useful applications of EPR in vivo can probably be achieved best by localized spectroscopy.

To date almost all of the in vivo EPR studies have been done with small animals and there are only two reports of human studies. It appears very likely, however, that rapid progress will occur in the next few years, because of the very promising data which have been obtained recently, especially in regard to oximetry.

1.3 Experimental Considerations

The first EPR experiment conducted by Zavoisky in 1944[6] was performed at 133 MHz. With the development of commercial EPR spectrometers the usual frequency was raised by 2–3 orders of magnitude to increase sensitivity, but this simultaneously reduced the size of nonfrozen aqueous samples that could be studied by standard cylindrical or rectangular EPR cavities to less than 1 mm, due to an increase in the nonresonant absorption of microwave by aqueous samples, thus considerably limiting applications of EPR to biological systems. In the first in vivo EPR study performed in 1975 at 9 GHz (*X*-band) these limitations were avoided by implanting a helix antenna into the rat liver,[7] and more recently in vivo EPR studies in small animals have been carried out at 9 GHz by inserting the tail into the cavity. The obvious constraints of such approaches eventually led to the development of low-frequency EPR instruments, thus increasing the ability to penetrate deeper into biological tissues; however, it took almost 10 years before the next studies aimed at in vivo EPR were performed.[8,9] Subsequently developments have occurred at an ever-increasing rate and have led to a number of very productive applications of in vivo EPR techniques. The key technical advances occurred in four areas: development of low-frequency EPR spectrometers suitable for use with living objects,[10–14] development of detectors suitable for in vivo studies,[15,16] recognition and development of paramagnetic species with properties suited for particular applications (especially the measurement of pO_2),[17] and improved methods for data acquisition and analysis.[18–21] Limitations of space prevent us from describing these developments in detail here, but they are illustrated in the following descriptions of applications and further details are available in the references that are cited.

While these developments have greatly expanded the use of EPR in living subjects, some fundamental limitations remain and therefore the application of EPR techniques to clinical medicine is unlikely to reach the extent of NMR techniques. Probably the key factors are a combination of depth of penetration and sensitivity. These are, of course, related because in order to achieve greater depth of penetration of the microwaves one must decrease the frequency and this inevitably leads to decreased sensitivity. Many of the principal uses of EPR in vivo are likely to occur with the use of frequencies around 1 GHz. At 1 GHz there is relatively high sensitivity but the practical limit for depth is about 10 mm. This can be partially overcome by the use of catheters, etc. to insert the detector deeper into the body. If the frequency is reduced to 300–500 MHz the practical limits on depth increase by a factor of up to 10 but there is a concomitant decrease in sensitivity. Very useful data have already been obtained in experimental animals with in vivo EPR at both ends of these frequency ranges, and feasibility studies have been successful in human subjects, so it

is therefore clear that EPR will be quite useful in vivo. The extent of the usefulness of in vivo EPR seems certain to be extended by combining it with complementary approaches such as NMR.

2 MEASUREMENT OF THE CONCENTRATION OF OXYGEN, ESPECIALLY IN TISSUES IN VIVO, BY EPR OXIMETRY

One of the most effective and rapidly developing uses of EPR in biological systems is the measurement of pO_2. The importance to NMR of these measurements rests on (a) the profound role of oxygen in many physiological and pathophysiological processes (ischemic diseases, reperfusion injury, response of tumors to therapy, etc.); (b) the lack of an adequate alternative methodology to make accurate in vivo measurements under biologically pertinent conditions (these conditions include making the measurements directly in the tissues, at the relatively low concentrations of oxygen which occur in tissues in vivo); and (c) the suitability of NMR techniques, especially spectroscopy, to measure metabolites whose concentrations and importance are linked closely to pO_2.

The term EPR oximetry encompasses a number of distinct experimental techniques; however, most of these methods rely on the paramagnetic properties of molecular oxygen. The ground state of oxygen has two unpaired electrons and a very rapid relaxation rate, which via Heisenberg spin exchange between oxygen and other paramagnetic species provides an efficient relaxation mechanism for the latter. As a consequence, the presence of oxygen has an effect on both T_1 and T_2 of spectra and these effects can be followed quantitatively by a variety of spectral parameters (e.g. linewidth, resolution of superhyperfine structure, and microwave power saturation). An NMR counterpart of this type of oximetry uses the effect of oxygen on the spin–lattice relaxation time of ^{19}F in tissues preloaded with fluorine compounds.

The use of EPR to measure the concentration of oxygen in biological samples was introduced more than 20 years ago and while it has been a useful technique for many studies of model systems and cells, it is only recently that it has been applied successfully in vivo. The latter applications have been very successful because of the development of new techniques and new oxygen sensitive paramagnetic materials. Some of the latter appear to have properties that are virtually ideal for the measurement of the concentration of oxygen in tissues in vivo, including a high degree of chemical and physical stability, essentially complete inertness in tissues, an apparent lack of toxicity, high sensitivity to the concentration of oxygen, and retention of their response to oxygen for periods of years or longer.[22]

There are two principal types of oxygen sensitive materials which are now available for the direct measurement of pO_2 in biological systems: soluble, stable free radicals (especially nitroxides and their derivatives), and stable paramagnetic particles with oxygen sensitive spectra (especially fusinite coal, lithium phthalocyanine, India ink, and chars of carbohydrates). Each of these has properties that may be especially useful for particular applications and, in aggregate, they provide a versatile and effective set of approaches to measure the concentration of oxygen under most or all conditions that are likely to occur experimentally and clinically.

The use of particulate materials has already led to some very useful data on pO_2 in vivo.[22–26] These materials share several very desirable properties for such studies including:

1. relative noninvasiveness and repeatability (after an initial placement of the paramagnetic materials, measurements can be made noninvasively as frequently as desired over a period of a year or more);
2. sensitivity (measurements can, at low pO_2, resolve differences of the order of 0.1 torr);
3. accuracy (repeated measurements have a small variability and correlate closely with measurements of pO_2 by other methods);
4. provide localized measurements (the spatial resolution is the same as the size of the paramagnetic particles, which can be as small as a single particle of less than 0.2 mm in diameter. At the same time, accurate localization of the probe can be achieved using MR imaging);[24]
5. capability of making several measurements simultaneously (this is accomplished by inserting multiple discrete solid particles and applying a magnetic field gradient such that sites less than 1 mm apart can be resolved);[25]
6. little or no effects of chemical and physical conditions likely to be encountered in viable biological systems (changes in pH or the presence of oxidants, reductants, or other paramagnetic materials do not affect measurements of pO_2);
7. little or no toxicity (the paramagnetic materials are very inert in biological systems as assayed in both cell culture and in vivo);
8. capability of following changes in pO_2 with a time resolution of seconds or less;
9. response to pO_2 (in contrast to nitroxides and other oxygen sensitive materials which may respond to the concentration of oxygen or a product of concentration and the rate of diffusion).

The organs that have been studied by this approach include brain, heart (both in situ and as isolated perfused systems, especially the Langendorf preparation), lung, liver, kidney, skeletal muscle, and joints. These approaches have also been applied to the study of several important pathological and physiological conditions including tumors, ischemia, inflammation, and anesthesia.

The capabilities of these approaches are indicated in Figure 1 which shows the change in pO_2 in tumors as a function of time and therapeutic irradiation. The ability to resolve small changes in pO_2 (less than 0.2 torr) in unanesthetized animals provides a powerful tool for understanding and interpreting NMR spectroscopic studies of this type of system.

While it appears that many studies in the future will utilize the oxygen-sensitive particulate paramagnetic materials, there also are a number of very effective uses of the nitroxides in measuring pO_2 (in general the nitroxides actually measure the product of the concentration of oxygen and the rate of diffusion but this measurement can usually be converted directly to pO_2 under most experimental conditions). EPR oximetry with nitroxides can utilize both the physical and the physiological effects of oxygen, and its application to cellular systems has been extensively reviewed and will not be considered further here.

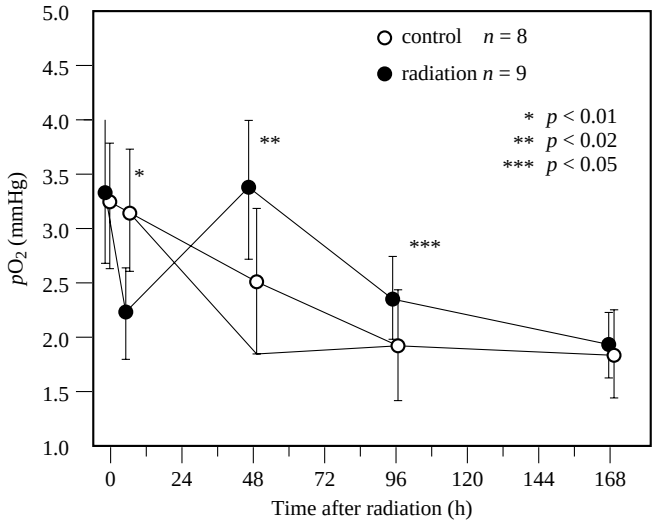

Figure 1 In vivo EPR measurements of changes of pO_2 as measured by India ink in a mouse tumor (mammary adenocarcinoma) after a single dose of radiation (20 Gy)

The nitroxides have also been used for oximetry in larger systems, including intact animals. The results of these studies, while very promising, have not yet been applied to the direct study of pathological processes, although they have produced some very exciting data on pO_2 in perfused hearts and some promising data on in vivo systems.[11,27–29] The advantages of nitroxides for such studies includes their versatility (nitroxides can be synthesized with virtually any chemical and physical properties) and that they are usually available as soluble materials that can diffuse throughout the system. Their potential disadvantages include a tendency to undergo bioreduction and their relatively weaker response to changes in pO_2 (it seems unlikely that they will be able to resolve changes of less than 5 torr in vivo).

Nitroxides have also been used in extended systems where EPR imaging or in vivo EPR spectroscopy were used to study the concentration, distribution, and diffusion of oxygen in macroscopic biological samples. Several experiments have been performed on small samples with higher frequency EPR (9 GHz) using one-dimensional (1D) and two-dimensional (2D) EPR. 1D EPR imaging is based on the use of conventional EPR spectroscopy in the presence of a unidirectional linear magnetic field gradient. The obvious restriction is that the sample has to possess a high degree of symmetry and/or isotropic properties; however, 1D EPR allows rapid accumulation (e.g. 2 s per spectrum) and is particularly suitable for studying fast diffusion processes such as diffusion of oxygen. Interaction of oxygen with nitroxides shortens relaxation times; hence the diffusion of oxygen can be measured in samples preloaded with oxygen sensitive paramagnetic species. To illustrate this approach, fast 1D EPRI has been used to follow oxygen diffusion in aqueous media[30] and the results agree well with the value of the oxygen diffusion coefficient measured by classical methods.

A few 2D EPRI experiments have been reported, including studies to examine the feasibility of visualizing the distribution of oxygen in model and biological samples and the basic mechanisms for the contrast enhancement.[31,32] The effects of oxygen on the relaxation times of nitroxides (analogous to the action of paramagnetic agents on proton relaxation) were utilized for contrast enhancement. Shortening of T_2 of the nitroxides causes line broadening and a concomitant decrease of line height, while shortening of T_1 induces differences in microwave power saturation. Using proper selection of EPR imaging parameters, both effects can be utilized to produce either positively or negatively enhanced oxygen dependent images.[31] Other properties such as differential solubility of oxygen in lipophilic and hydrophilic environments also can be used to distinguish different regions of the tissue. This was demonstrated on a tissue slice containing fat and muscle regions, all of them containing the same amount of nitroxide, but they have different intensities in the image due to the higher concentration of oxygen in fat-rich areas.[32]

Although EPR imaging can give insights on the distribution of oxygen it is probably not suitable for precise and direct measurements of pO_2. Such measurements will probably require a form of spectral-spatial imaging, where the EPR spectrum can be displayed as a function of spatial localization.[18,19,33] This considerably increases the time required for the measurement. The feasibility of doing spectral spatial oximetry has been explored in model systems.[33] It is not clear whether sufficient sensitivity can be achieved to apply this technique to animals, but it does appear to be very promising for the study of detailed distribution of pO_2 in systems amenable to study at higher frequencies, especially the tumor model, spheroids, at 9 GHz.

3 MEASURES OF REDOX METABOLISM AND/OR DISTRIBUTION OF DRUGS BY EPR

There are several interrelated approaches, based on nitroxides (although in principle other metabolizable, stable free radicals could also be used), that provide data on redox metabolism and the distribution of drugs which should be very complementary for NMR studies.

The oxygen dependent metabolism of nitroxides has been advocated as an approach to the measurement of pO_2 and redox metabolism.[34] Functional biological systems can reversibly reduce the nitroxides to the nonparamagnetic hydroxylamines.[35] While this effect was originally considered only to be a drawback, subsequently it has been demonstrated to be a potentially powerful tool for following redox metabolism. In principle this effect could be followed both by direct EPR studies and by NMR (the latter by using the change in contrast from the change in local concentrations of the nitroxides). Extensive studies of the reduction of nitroxides and its reverse, the oxidation of hydroxylamines back to nitroxides by various cellular systems, have shown that these metabolic rates can be very sensitive indicators of the presence of profound hypoxia, with the principal changes in the rate of metabolism occurring at $pO_2 < 1$ torr.[36] This approach is similar to NMR measurements of phosphorus metabolites (e.g. Pi/ATP ratio) and lactic acid production, both of which appear to change especially when the pO_2 becomes very low. To date, however, data are lacking on the correlation between these changes as followed by NMR and the actual concentration of oxygen.

The nonoxygen dependent metabolism of nitroxides should also be a very useful parameter for evaluating redox metabolism in vivo. The reduction of the nitroxides to the hydroxylamines occurs primarily through reduction by the mitochondria, with the reducing equivalents coming from approximately the level of ubiquinone. Therefore the rate of reduction of nitroxides can provide a useful measure of this activity that may not be obtainable by other means in vivo. Redox processes at different sites can be followed selectively by the use of nitroxides whose physical or chemical properties (e.g. solubility, charge, reactivity of side groups) result in their selective localization.

Recent studies illustrate the potential for using the metabolism of nitroxides as a means of investigating redox metabolism in vivo. These uses may be extended to the study of other biophysical parameters which can be reflected in the EPR spectra of nitroxides. There are many regions of interest such as tumors which fall within the sensitive depth for 1 GHz EPR and there are also some techniques in which an insertable probe can be used to probe depths up to several cm with this frequency.[4] These approaches may be especially useful in studies of the skin since the depth of penetration of microwaves is sufficient to cover the region of interest using a surface probe. We describe some of these studies in skin as an indication of what might be obtained in other systems as well.

Nitroxides have been applied topically and their diffusion into skin and their metabolism deduced from temporal changes of 1D EPR spectra in the presence of a field gradient orthogonal to the skin surface. Both the rate and spatial distribution of the physiological processes involved in the metabolism of nitroxides or nitroxide-labeled compounds can be studied. Fuchs et al.[37] studied diffusion of several nitroxides into skin biopsies of hairless mice and found that penetration of lipophilic nitroxides is much faster than penetration of more hydrophilic nitroxides. They also studied percutaneous absorption and distribution of a nitroxide-labeled drug (estradiol) and a local anesthetic (procaine) finding that the former readily penetrates into deep skin layers while the latter does not, even in the presence of a penetration enhancer, such as dimethyl sulfoxide. Using spectral spatial imaging and analysis of spectral features, the same authors showed spatially resolved (surface, epidermis, dermis) partitioning of the nitroxide di-*t*-butyl nitroxide (DTNB) between polar and apolar regions (Figure 2), as well as the spatial distribution of thiol groups by studying the diffusion of proxylmaleimide, which chemically reacts with thiol groups.

The study of Gabrijelcic et al.[38] illustrates the capability of studying potential applications of liposomes as drug carriers for topical treatment of skin disorders. They found that entrapment in liposomes promotes the penetration of otherwise impenetrable, charged nitroxides into pig skin and that the size and phospholipid composition of liposomes significantly influences their efficiency. Combining these results with the study of reduction of free nitroxides, the loss of integrity of liposomes in different layers of the skin was assessed.[39] The physiological information obtained by EPR in these studies cannot be obtained by other imaging modalities (MRI, ultrasound), with the same spatial resolution (well below 100 μm). Although these experiments were performed at 9 GHz and used tissue slices, there are no apparent obstacles for the use of these techniques in living animals (or humans) using lower frequency spectrometers.

Another area of overlapping interest for both EPR and MRI is the study of redox metabolism of ischemia/reperfusion injury of the heart. Free radicals derived from oxygen are believed to be involved in reperfusion injury of cardiac tissue, but current techniques do not permit their direct observation. However, generation of free radicals and underlying molecular mechanisms can be studied indirectly by spin-trapping, and the potential of this approach has been investigated in isolated perfused hearts[40] using nitroxides which resemble the molecular structure of the most commonly used spin-trapping molecules. Zweier & Kuppusamy[11,28] studied the kinetics of nitroxide uptake from perfusate and their subsequent reduction upon induction of ischemia. The average oxygen concentration was simultaneously determined from measurements of linewidth. By including spectral spatial imaging in the experimental protocol and synchronizing acquisition with the heart beat these experiments could provide valuable data.

There is also a wide range of biophysical parameters that can be studied by EPR since nitroxide spectra are sensitive, in addition to pO_2, to viscosity, polarity, membrane order and fluidity, pH, redox processes, and other metabolic properties. Some of these parameters are not amenable to study by other means and could be very useful for understanding changes detected by NMR techniques.

4 MEASUREMENT OF THE VIABILITY OF CELLS, ESPECIALLY BY EPR MICROSCOPY

EPR has the capability of measuring the viability of cells in an accurate, nonperturbing, and repeatable manner, under appropriate circumstances.[41] This essentially unique capability is based on the use of nitroxides in combination with the presence of significant concentrations of charged, paramagnetic metal ions. Under these circumstances the EPR signal from the nitroxides is observable only where the nitroxide is not in close proximity to the metal ion. This occurs inside viable cells; when the cells lose their viability the EPR signal from those cells is suppressed. This measure of viability, which reflects the function of the membrane, appears to correlate well with other measures of viability.[41]

This approach is most suitable at higher frequencies (e.g. 9 GHz) where there is maximum sensitivity; at such frequencies this approach can be used for microscopic imaging with resolution of the order of cell dimensions or less.

This approach has been used successfully in spheroids, which are an important and frequently used in vitro model of solid tumors.[42] The authors have demonstrated that noninvasive assessment of spatial distribution of viable and necrotic regions of spheroids can be done using 2D EPRI microscopy (Figure 3). They used a water soluble, cell permeable nitroxide (^{15}N substituted, perdeuterated Tempone) and a paramagnetic broadening agent (chromium oxalate), which is excluded from viable cells, but enters dead cells thus leaving observable only nitroxide signals from living cells. Using a magnetic field gradient of 1 T m^{-1}, a linear resolution of 10–20 μm was obtained; this is quite comparable to that obtained in a similar MRI study.[43] The method was used to resolve microscopic areas of necrosis in spheroids at different stages of their growth. The same approach has also been used to study the cytotoxicity of an antitumor drug (Adriamycin). The advantages of this approach

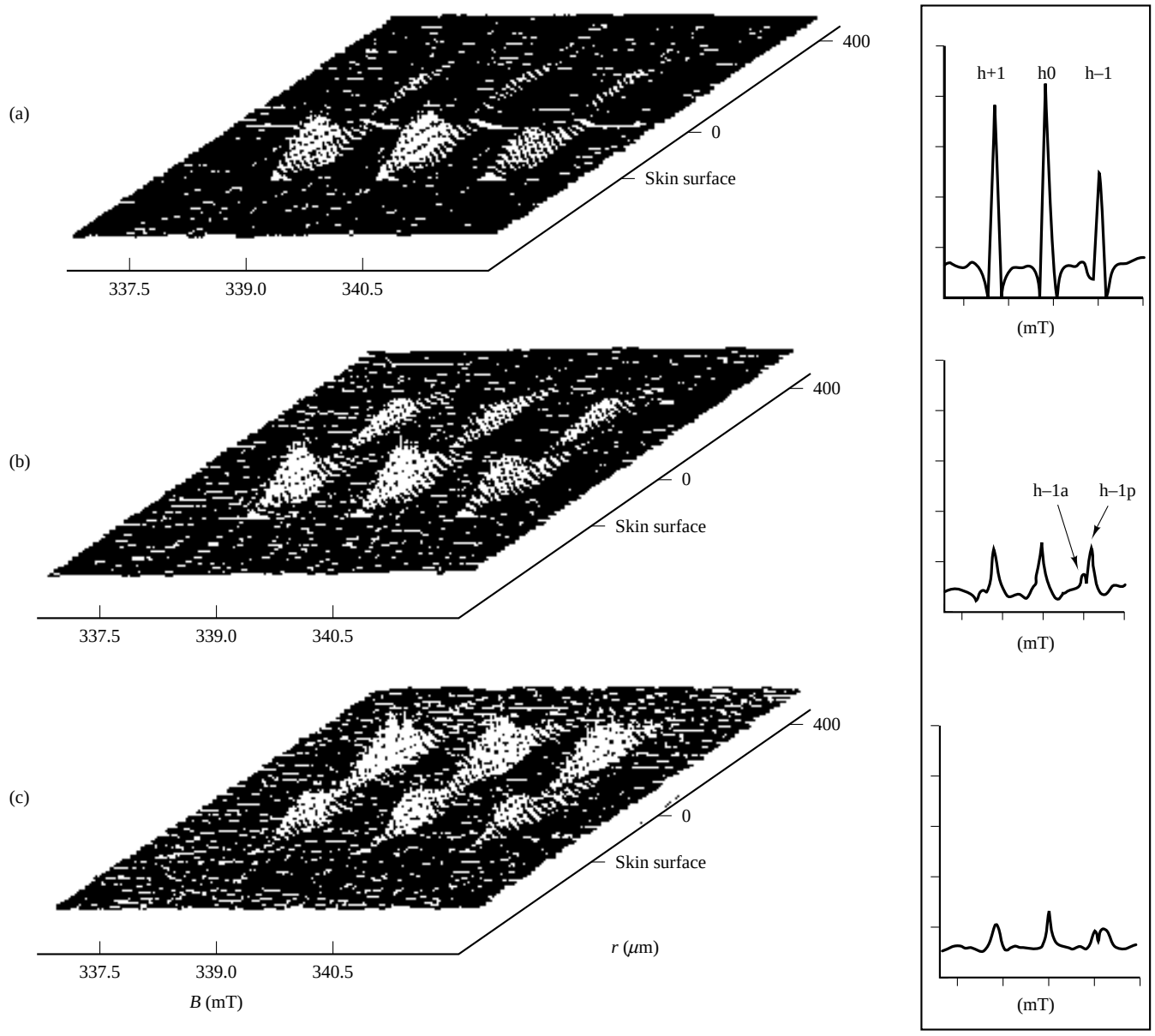

Figure 2 Penetration of DNTB into mouse skin as monitored by EPR imaging at 9 GHz. Punch biopsy samples were pretreated with *N*-ethylmaleimide prior to topical application of DNTB. Left: 2D spectral spatial images of the time dependent changes of the distribution of DNTB: (a), 5 min; (b) 15 min; (c) 45 min. Right: EPR spectra of DNTB (2nd harmonics) in different layers of the skin: (a) epidermal surface; (b) epidermis; (c) dermis. A splitting of the high-field resonance line, h-1, into two peaks indicates distribution of DNTB between apolar (h-1a) and polar (h-1p) microenvironments within the epidermis and dermis. (Reproduced by permission of Elsevier Science from J. Fuchs, N. Groth, T. Herrling, R. Milbradt, G. Zimmer, and L. Packer, *J. Invest. Dermatol.*, 1992, **98**, 713)

include that it can be applied to single spheroids and that the same spheroid can be studied repeatedly over periods of several weeks.[41]

This technique could potentially be used in vivo, although this would necessarily involve lower resolution because of the lower frequency that is needed for in vivo EPR, and a method would need to be developed for achieving locally high concentrations of a suitable paramagnetic metal ion.

Another potential approach to the use of EPR to measure viability in vivo was demonstrated by Berliner et al.[44] in the first reported EPR image of a living animal. Using an EPR spectrometer operating at 1.5 GHz and a loop-gap resonator they obtained images of a melanoma which was implanted into the tail of a mouse, using serial intravenous (i.v.) injections of a nitroxide (CTPO; 3-carbamoyl-2,2,5,5-tetramethyl- pyroline-1-oxyl) as the imaging agent. Although reconstructed from only four projections, the resulting 2D image of the tumor showed distinguishable necrotic and viable areas. Additional studies are needed to determine if the distribution plus metabolism of nitroxides can provide a reproducible means of distinguishing between viable and nonviable regions. If so, the resolution obtainable when imaging at 1 GHz may be sufficient to provide

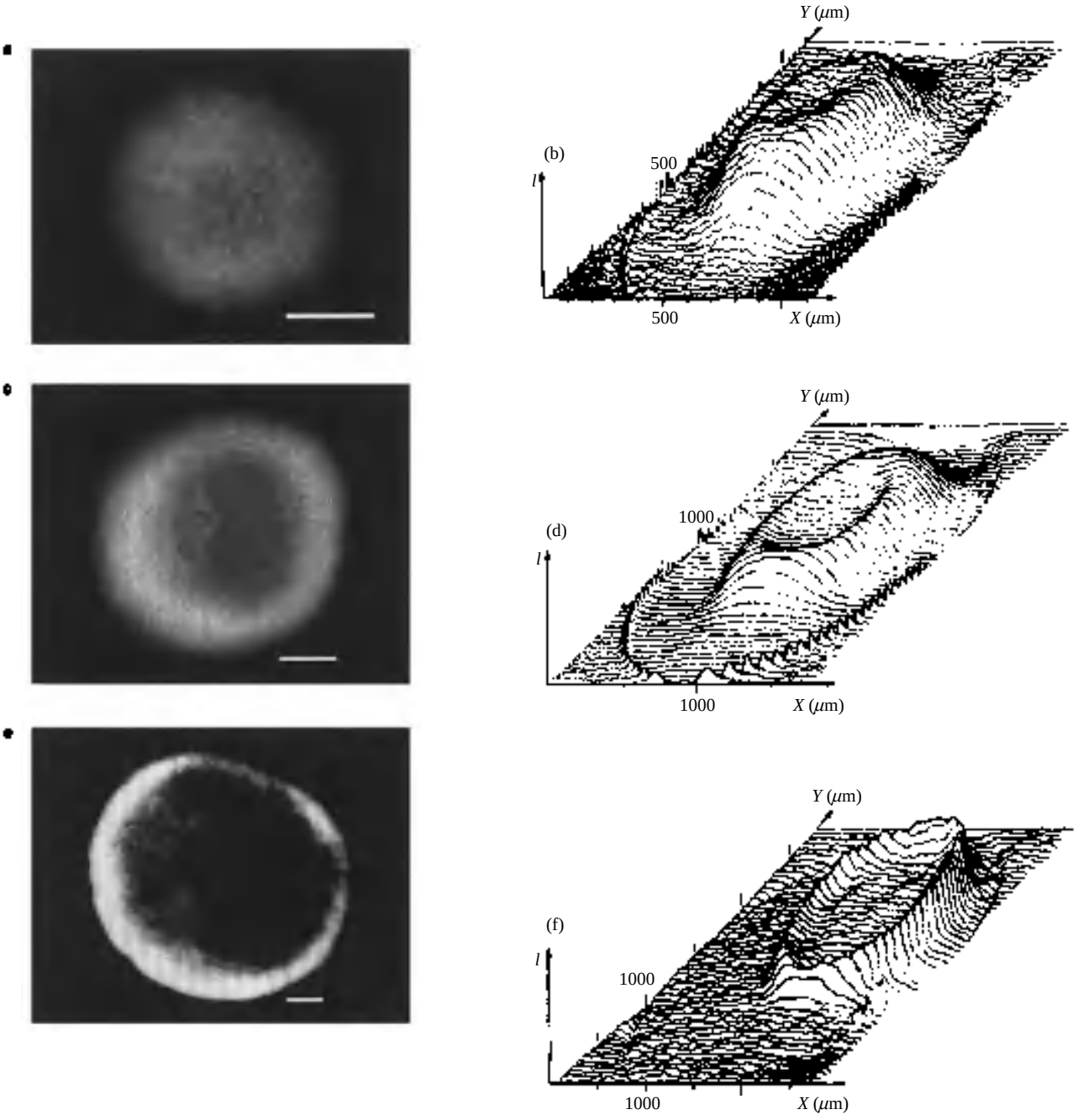

Figure 3 Two-dimensional EPRI microscopy (gray scale and surface plots) of cell viability in spheroids at different stages of growth: (a) and (b) = 12 days; (c) and (d) = 3 weeks; (e) and (f) = 5 weeks, or diameter of 0.58, 0.99 and 1.49 mm. The intensity of the image corresponds to the amount of viable cells in different regions. Note that the thickness of the viable rim remains the same regardless of the size of the spheroid (bars are approximately 0.2 mm). For each image 64 projections were collected with a magnetic field gradient of 0.9 T m^{-1}. (Reproduced by permission of Macmillan Press from J. W. Dobrucki, F. Demsar, T. Walczak, R. K. Woods, G. Bacic, and H. M. Swartz, *Br. J. Cancer*, 1990, **61**, 221)

very useful information, especially in connection with studies of metabolism by NMR spectroscopy.

5 MEASUREMENT OF THE CONCENTRATION AND DISTRIBUTION OF CONTRAST AGENTS, ESPECIALLY IN VIVO

5.1 Nitroxides

The main interest in studying nitroxides as potential MRI contrast agents arises from the concept of metabolically responsive contrast agents.[34,45] Namely, if the administered paramagnetic contrast agent can undergo reduction or oxidation to a nonparamagnetic product, then it may be possible to obtain a set of images where the contrast reflects regions with different redox metabolism. The productive use of nitroxides as metabolically responsive contrast agents for MRI requires knowledge of at least three elements: their metabolic responsiveness; their effectiveness as relaxation enhancers; and their pharmacological properties.

5.1.1 Metabolic Responsiveness of Nitroxides

In vitro EPR studies of mammalian cells in suspensions[46] showed that virtually all nitroxides undergo metabolism to a nonparamagnetic state under appropriate conditions and that the rate of reduction is primarily affected by the concentration of oxygen. Susceptibility to reduction varies by a factor of more than 100 between different nitroxides, with the principal factors being whether the nitroxide readily enters the cells and the structure of the ring to which the nitroxide group is attached (nitroxides based on five membered rings are generally more resistant to reduction than nitroxides based on the six-membered piperidine ring). The mechanism of metabolic reduction in vivo has been studied only to a limited extent[29,47–49] but it seems that the relationship between the structure of the nitroxides and their susceptibility to bioreduction is similar to that observed in vitro systems. It has also been shown that cells can oxidize hydroxylamines back to paramagnetic nitroxides,[50] which raises the possibility of administering hydroxylamines and obtaining differential amounts of contrast in direct proportion to the tissue pO_2.

5.1.2 Relaxivity of Nitroxides

The ability of nitroxides to affect the relaxation times of protons (i.e. relaxivity) is an order of magnitude lower than that of metal ions. The nitroxides are spin-$\frac{1}{2}$ systems with a single unpaired electron, which is a disadvantage when compared with metal ions (e.g. Mn or Gd) that have several unpaired electrons. A second disadvantage is that nitroxides do not bind water tightly, in contrast to the metal ions and their complexes, so that relaxation occurs via relatively inefficient outer sphere mechanisms.[51] However, the relaxivity of nitroxides can be improved by binding them to macromolecules which changes their rotational mobility and the correlation times of the interaction of the unpaired electron and the proton. In order to optimize such an approach, two major points should be considered: the possibility of binding multiple nitroxides to macromolecules and the degree of the immobilization of the nitroxide groups. EPR plays a key role in designing such types of contrast agents since both the number of nitroxides per macromolecule and their molecular dynamics can be determined directly from EPR spectra. Several nitroxide–macromolecule (serum albumin, polysaccharide, fatty acids) complexes have been investigated by EPR, and their relaxivity and in vivo distribution have been determined by NMR.[51–55] In addition to increasing relaxivity, binding of nitroxides to certain vector molecules such as arabinogalactans, which are specifically taken up by hepatocytes, increases organ selective delivery while retaining metabolic responsiveness.[55]

5.1.3 Pharmacological Studies of Nitroxides

The nitroxide groups themselves appear to play a relatively minor role in the distribution of the nitroxides, which is usually determined by the other parts of the molecule based on the usual factors such as size, charge, and lipophilicity. The in vivo kinetics appear to be highly complex, depending upon the type of nitroxide, amount of reduction that can occur in the blood, specific accumulation in particular organs, cellular uptake and intracellular reduction rates, and clearance mechanisms. Figure 4(a) and (b) illustrate an in vivo EPR spectroscopy experiment in which patterns of distribution and reduction of three nitroxides were followed.[47] A surface detector was placed over the region of interest to localize the spectra. The different behavior of the three nitroxides [Figure 4(a)] reflects differences in the rate of membrane permeation and bioreduction and is consistent with results from in vitro studies. These experiments also demonstrated the presence of ascorbate in the bladder. Reduction by ascorbate in the bladder caused the decay of the EPR signal of Cat_1 [Figure 4(b)]. Subsequent in vivo EPR spectroscopic studies further analyzed the pharmacology of nitroxides in these and other organs such as brain and lungs.[29,48,49] Although these experiments were designed to study nitroxide metabolism and their potential use as a metabolically sensitive contrast agent for MRI or EPR imaging, the same technique, combined with the use of spin-labeled analogs of drugs, could also be used for detailed pharmacokinetic studies of a wide range of drugs taking advantage of the high specificity and sensitivity of EPR spectroscopy.

Low-frequency EPRI (operating frequencies 1.2 GHz to 280 MHz) has also been used in pharmacological studies.[56,57] While demonstrating that potentially both whole body distribution and pharmacokinetics can be simultaneously studied, these papers also outlined some of the principal problems facing in vivo EPRI. As already mentioned, the major problem arises from the fact that the imaging substance (nitroxide) has to be introduced externally. Toxicity considerations limit the maximum amount to be administered and although in vivo EPR spectrometers can in principle detect very low concentrations of nitroxides (1–10 μmol kg^{-1}), imaging requires at least 100-fold higher concentrations and even then the resulting image may have a rather poor signal/noise ratio. The inability of in vivo EPRI to utilize pulsed, slice selected imaging procedures results in a long imaging time and/or a small number of projections. The acquisition time for 2D images is 2–10 min which is acceptable, but results in superposition of different planes so that it can be difficult to interpret images on an ana-

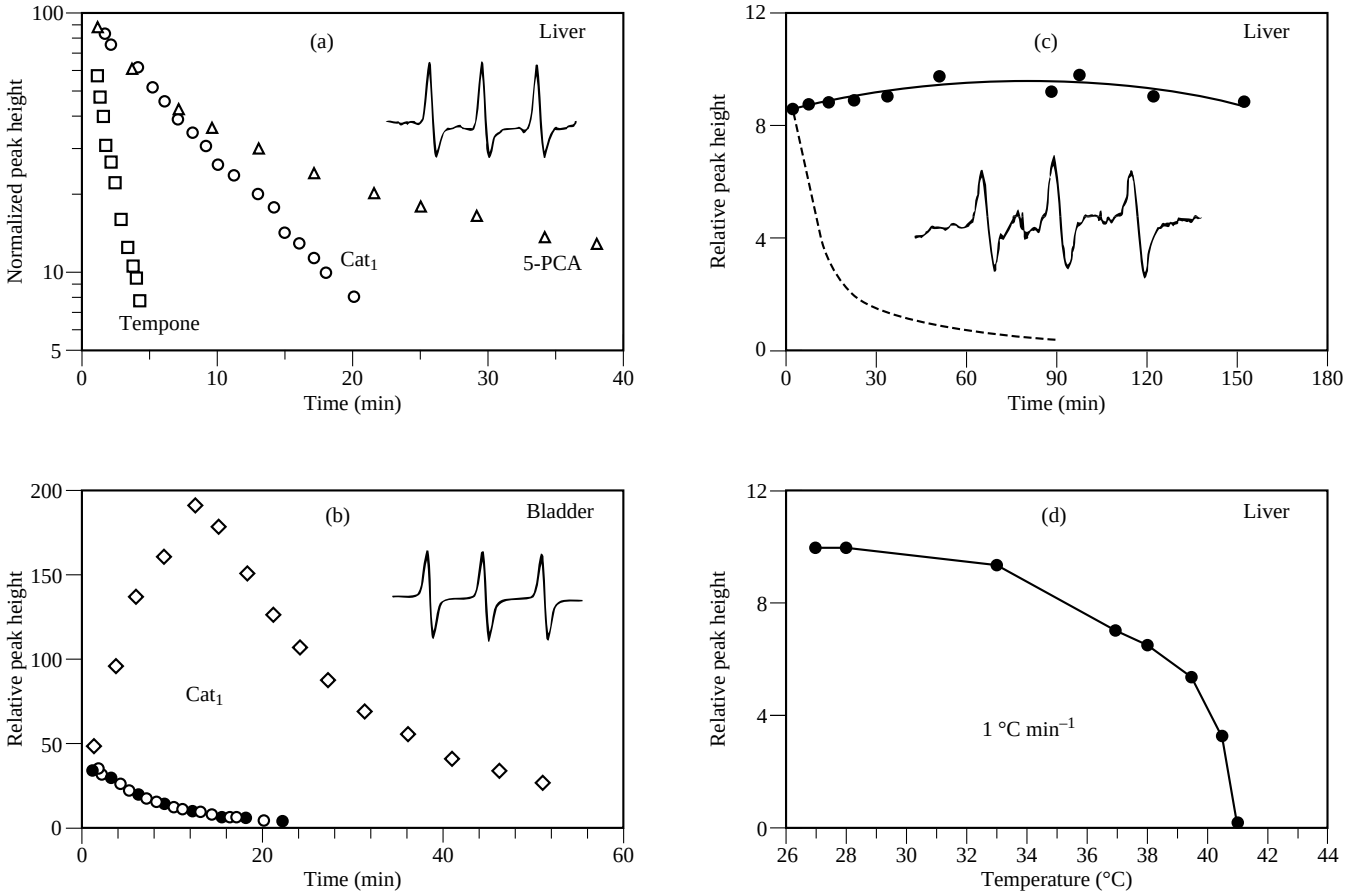

Figure 4 In vivo EPR spectroscopy. (a) and (b) Pharmacokinetics of nitroxides. (a) Decrease of the intensities of the EPR signals of nitroxides from the liver region of mice following the i.v. injection of three different nitroxides: Tempone (4-oxo-2,2,6,6-tetramethylpiperidine-1-oxyl), Cat_1 (4-trimethylammonium-2,2,6,6-tetramethylpiperidine-1-oxyl), and PCA (3-carboxy-2,2,5,5-tetramethylpyrroline-1-oxyl) at doses 0.10–0.15 mmol kg^{-1} body wt. The signals of all nitroxides are normalized to the signal intensity at the termination of injection. The temperature of the mice was maintained at 37 °C. The inset shows the in vivo spectrum of PCA obtained 5 min after injection. (b) The EPR intensities of Cat_1 from the bladder region under the same experimental conditions. The decrease of the signal from the vascular pool, measured by the placement of the surface probe over regions without localized uptake, is also shown (solid and open circles indicate points from two different experiments). (c) and (d) Studies of the status of liposomes. Changes of the intensity of the EPR signal of a nitroxide from the liver region of a mouse following the i.v. injection of Cat_1 encapsulated in dipalmitoyl phosphatidylcholine/DPPG liposomes. The injected dose was 0.03 mmol kg^{-1}. (c) Changes of the signal intensity vs. time after injection. The temperature of the mouse was maintained at 30 °C, i.e. below the phase transition point of liposomes. The inset is a typical spectrum obtained 30 min after injection. The broken line shows a typical blood clearance curve for these liposomes. (d) Changes of the signal intensity vs. temperature of the mouse. Heating of the mouse by flowing warm air (1 °C min^{-1}) was started 30 min after injection of the liposomes. (Reproduced by permission of Academic Press from G. Bacic, M. J. Nilges, R. L. Magin, T. Walczak, and H. M. Swartz, *Magn. Reson. Med.*, 1989, **10**, 266)

tomical basis. True zeugmatographic 3D images require 20–80 min, during which a concentration of nitroxide in a selected region has to be maintained as constant. Reported inplane resolution for rat head at 780 MHz was 0.5 mm with an effective slice thickness of 1.5 mm. Resolution can be improved by using larger field gradients, but this would, besides being technically demanding, further reduce the S/N ratio of the image. In addition, all resonators currently used have a nonhomogeneous rf field distribution, particularly along the axial direction, which further complicates accurate image reconstruction. Use of larger resonators can alleviate this problem, but at the expense of a further reduction in sensitivity. A potential solution for many of the above mentioned problems is the development of pulsed EPRI techniques. The frequency ranges of in vivo EPRI machines nowadays overlap with high-field MRI machines, which should make development of pulsed EPRI easier. Until then, it seems that much more reliable images of spin-labels in animals can be obtained using standard MRI[55] or proton electron double resonance imaging (see ***Overhauser Effect Imaging of Free Radicals***).

5.2 Other Contrast Agents

Metal ion (e.g. Mn, Gd) complexes or aggregates (iron particles) are paramagnetic species and it would appear that their pharmacology can be directly studied using in vivo EPR in the same manner as for nitroxides. However, at the low fields,

required for in vivo EPR, their EPR spectra have some unfavorable characteristics that effectively prevent their detection in vivo. For example, the spectrum of Gd-DTPA at 9.5 GHz contains one broad line spanning 60 mT and measurements of physiological concentrations of species with such broad resonant lines are well below the sensitivity of *L*-band EPR spectrometers. Despite these limitations, a few studies demonstrate that properly designed EPR studies can substantially add to our understanding of the pharmacology of MRI contrast agents. For example, liposomes have been extensively studied as an alternative means for targeted delivery of contrast agents. Encapsulation of contrast agents within liposomes increases selective delivery, but restricts the accessibility of the tissue water to the relaxation center. It has been found that a liposome encapsulated contrast agent (Mn^{2+}) delivered to the liver remains MRI silent as long as it is confined within liposomes or Kupffer cells due to the limited exchange of water.[58] Consequently, measurements of the rates of liposome breakdown and subsequent redistribution of contrast agents are important steps in evaluating the usefulness of liposomes as carriers of contrast agents. MRI detects these processes indirectly via changes in water relaxation and the results are often difficult to interpret, but EPR can be used effectively for these measurements as illustrated in Figure 4(c) and (d).[47] The experiment took advantage of the rapid bioreduction of the nitroxide, Cat_1, to follow the integrity of the liposomes in the liver, because intact liposomes protect encapsulated Cat_1 from bioreduction. When liposomes were heated to near their transition temperature, their contents began to leak out and the EPR signal decreased as the Cat_1 became reduced. The clearance from the blood of the intact liposomes could also be followed by this technique.[58] Besides the localization within the tissue, the state of the contrast agent (bound/free) also has a profound effect on relaxation enhancement. Again MRI measures this indirectly, but EPR can measure free and bound fractions directly. In an experiment similar to the one in Figure 4(c) and (d) liposomes were loaded with Mn^{2+} and liver samples at different time points were analyzed by EPR and NMR. It was determined that as long as manganese is within the Kupffer cells and is predominantly an aquoion, no substantial changes in the relaxation of the protons of water in the liver were observed. Subsequent release of manganese from Kupffer cells resulted in binding of Mn^{2+}, as detected by EPR, yielding a pronounced increase in relaxation enhancement.[58]

6 CONCLUSIONS

EPR spectroscopy has capabilities which are quite complementary to those of NMR, especially for studies in vivo which involve contrast agents, and for measurements related to pO_2 and/or redox metabolism. The appropriate use of EPR in such studies can significantly enhance the value of the NMR studies. It is already quite clear that for *experimental* studies EPR provides data that are widely applicable and useful for NMR studies, especially the capability of measuring pO_2 in tissues in vivo. It is unlikely that EPR will become a widespread *clinical* tool with the very important exception that it is quite possible that in the near future it will become the method of choice for measuring pO_2 in tissues in vivo.

7 RELATED ARTICLES

Cells and Cell Systems MRS; Contrast Agents in Magnetic Resonance: Operating Mechanisms; Contrast Agents in Whole Body Magnetic Resonance: An Overview; Overhauser Effect Imaging of Free Radicals; Spectroscopic Studies of Animal Tumor Models; Surface and Other Local Coils for In Vivo Studies.

8 REFERENCES

1. G. R. Eaton, S. S. Eaton, and K. Ohno, eds. 'EPR Imaging and in vivo EPR', CRC Press, Boca Raton, FL, 1991.
2. K. Ohno and N. Tsuchihashi, *Trends Phys. Chem.*, 1991, **2**, 79.
3. S. Colacicchi, M. Ferrari, and A. Sotgiu, *Int. J. Biochem.*, 1992, **24**, 205.
4. H. M. Swartz and T. Walczak, *Phys. Med.*, 1993, **9**, 41.
5. J. H. Freed, *J. Chem. Soc., Faraday Trans.*, 1990, **86**, 3173.
6. E. Zavoisky, *J. Phys. (Moscow)*, 1945, **9**, 211.
7. A. Feldman, E. Wildman, G. Bartolini, and L. H. Piette, *Phys. Med. Biol.*, 1975, **20**, 602.
8. S. J. Lukiewicz and S. G. Lukiewicz, *Magn. Reson. Med.*, 1984, **1**, 297.
9. L. J. Berliner and H. Fujii, *Science*, 1985, **227**, 517.
10. M. J. Nilges, T. Walczak, and H. M. Swartz, *Phys. Med.*, 1989, **5**, 195.
11. J. L. Zweier and P. Kuppusamy, *Proc. Natl. Acad. Sci. U.S.A.*, 1988, **85**, 5703.
12. H. J. Halpern, D. P. Spencer, J. van Polen, M. K. Bowman, A. C. Nelson, E. M. Dowey, and B. A. Teicher, *Rev. Sci. Instrum.*, 1989, **60**, 1040.
13. M. Alecci, S. Della Penna, A. Sotgiu, L. Testa, and I. Vannucci, *Rev. Sci. Instrum.*, 1992, **63**, 4263.
14. J. A. Brivati, A. D. Stevens, and M. C. R. Symons, *J. Magn. Reson.*, 1991, **92**, 480.
15. W. Froncisz and J. S. Hyde, *J. Magn. Reson.*, 1982, **47**, 515.
16. A. Sotgiu, *J. Magn. Reson.*, 1985, **65**, 206.
17. J. F. Glockner and H. M. Swartz, in 'Oxygen Transport to Tissue', eds. W. Erdmann and D. F. Bruley, Plenum, New York, 1993, Vol. 14.
18. U. Ewert and T. Herrling, *Chem. Phys. Lett.*, 1986, **129**, 516.
19. M. M. Maltempo, S. S. Eaton, and G. R. Eaton, *J. Magn. Reson.*, 1987, **72**, 449.
20. K. Ohno, *Spectrosc. Rev.*, 1986, **22**, 1.
21. R. K. Woods, G. Bačíc, P. C. Lauterbur, and H. M. Swartz, *J. Magn. Reson.*, 1989, **84**, 247.
22. N. Vahidi, R. B. Clarkson, K. J. Liu, S. W. Norby, M. Wu, and H. M. Swartz, *Magn. Reson. Med.*, 1994, **31**, 139.
23. K. J. Liu, P. Gast, M. Moussavi, S. W. Norby, N. Vahidi, T. Walczak, M. Wu, and H. M. Swartz, *Proc. Natl. Acad. Sci. U.S.A.*, 1993, **90**, 5438.
24. G. Bačíc, K. J. Liu, J. A. O'Hara, R. D. Harris, K. Szybinski, F. Goda, and H. Swartz, *Magn. Reson. Med.*, 1993, **30**, 568.
25. A. I. Smirnov, S. W. Norby, R. B. Clarkson, T. Walczak and H. M. Swartz, *Magn. Reson. Med.*, 1993, **30**, 213.
26. H. M. Swartz, K. J. Liu, F. Goda, and T. Walczak, *Magn. Reson. Med.*, 1994, **31**, 229.
27. W. K. Subczynski, S. Lukiewicz, and J. S. Hyde, *Magn. Reson. Med.*, 1986, **3**, 747.
28. J. L. Zweier and P. Kuppusamy, *J. Bioenerg. Biomembr.*, 1991, **23**, 855.
29. M. Ferrari, S. Colacicchi, G. Gualtieri, M. T. Santini, and A. Sotgiu, *Biochem. Biophys. Res. Commun.*, 1990, **166**, 168.
30. F. Demsar, T. Walczak, P. D. Morse II, G. Bačíc, Z. Zolnai, and H. M. Swartz, *J. Magn. Reson.*, 1988, **76**, 224.

31. G. Bačíc, F. Demsar, Z. Zolnai, and H. M. Swartz, *Magn. Reson. Med. Biol.*, 1988, **1**, 55.
32. G. Bačíc, T. Walczak, F. Demsar, and H. M. Swartz, *Magn. Reson. Med.*, 1988, **8**, 209.
33. R. K. Woods, W. B. Hyslop, and H. M. Swartz, *Phys. Med.*, 1989, **5**, 121.
34. H. M. Swartz, in 'Advances in Magnetic Resonance Imaging', ed. E. Feig, Ablex Publishing, Norwood, NJ, 1989, Chapt. 2.
35. K. Chen and H. M. Swartz, *Biochim. Biophys. Acta*, 1989, **992**, 131.
36. K. Chen, J. F. Glockner, P. D. Morse II, and H. M. Swartz, *Biochemistry*, 1989, **28**, 2496.
37. J. Fuchs, N. Groth, T. Herrling, R. Milbradt, G. Zimmer, and L. Packer, *J. Invest. Dermatol.*, 1992, **98**, 713.
38. V. Gabrijelcic, M. Sentjurc and J. Kristl, *Int. J. Pharm.*, 1990, **62**, 75.
39. V. Gabrijelcic, M. Sentjurc, and M. Schara, *Period. Biol.*, 1991, **93**, 245.
40. G. M. Rosen, H. J. Halpern, L. A. Brunsting, D. P. Spencer, K. E. Strauss, M. K. Bowman, and A. S. Wechsler, *Proc. Natl. Acad. Sci. U.S.A.*, 1988, **85**, 7772.
41. J. W. Dobrucki, R. M. Sutherland, and H. M. Swartz, *Magn. Reson. Med.*, 1991, **19**, 42.
42. J. W. Dobrucki, F. Demsar, T. Walczak, R. K. Woods, G. Bačíc, and H. M. Swartz, *Br. J. Cancer*, 1990, **61**, 221.
43. L. O. Sillerud, J. P. Freyer, M. Neema, and M. A. Mattingly, *Magn. Reson. Med.*, 1990, **16**, 380.
44. L. J. Berliner, H. Fujii, X. Wan, and S. J. Lukiewicz, *Magn. Reson. Med.*, 1987, **4**, 380.
45. R. C. Brasch, *Radiology*, 1983, **147**, 781.
46. H. M. Swartz, M. Sentjurc, and P. D. Morse II, *Biochim. Biophys. Acta*, 1986, **888**, 82.
47. G. Bačíc, M. J. Nilges, R. L. Magin, T. Walczak, and H. M. Swartz, *Magn. Reson. Med.*, 1989, **10**, 266.
48. F. Gomi, H. Utsumi, A. Hamada, and M. Matsuo, *Life Sci.*, 1993, **52**, 2027.
49. K. Takeshita, H. Utsumi, and A. Hamada, *Biochem. Biophys. Res. Commun.*, 1991, **177**, 874.
50. K. Chen and H. M. Swartz, *Biochim. Biophys. Acta.*, 1988, **970**, 270.
51. H. F. Bennett, R. D. Brown III, S. H. Koenig, and H. M. Swartz, *Magn. Reson. Med.*, 1987, **4**, 93.
52. G. Sosnovsky, N. U. M. Rao, J. Lukszo, and R. C. Brasch, *Z. Naturforsch. Teil B.*, 1986, **41**, 1170.
53. H.-C. Chan, K. Sun, R. L. Magin, and H. M. Swartz, *Bioconjugate Chem.*, 1990, **1**, 32.
54. B. Gallez, R. Debuyst, R. Demeure, F. Dejehet, C. Grandin, B. Van Beers, H. Taper, J. Pringot, and P. Dumont, *Magn. Reson. Med.*, 1993, **30**, 592.
55. B. Gallez, V. Lacour, R. Demeure, R. Debuyst, F. Dejehet, J.-L. De Keyser, and P. Dumont, *Magn. Reson. Imag.*, 1994, **12**, 61.
56. V. Quaresima, M. Alecci, M. Ferrari, and A. Sotgiu, *Biochem. Biophys. Res. Commun.*, 1992, **183**, 829.
57. S.-I. Ishida, S. Matsumoto, H. Yokoyama, N. Mori, H. Kumashiro, N. Tsuchihashi, T. Ogata, M. Yamada, M. Ono, T. Kitajima, H. Kamada, and E. Yoshida, *Magn. Reson. Imag.*, 1992, **10**, 109.
58. G. Bačíc, M. R. Niesman, R. L. Magin, and H. M. Swartz, *Magn. Reson. Med.*, 1990, **13**, 44.

Biographical Sketches

Harold M. Swartz. *b* 1935. M.D., 1959, University of Illinois, Ph.D., 1969, Biophysics, Georgetown University. Professor of Radiology and Biochemistry, Medical College of Wisconsin, Milwaukee, WI, USA, 1970–1979; Professor of Physiology & Biophysics, Medicine, and Bioengineering, University of Illinois, Urbana-Champaign, IL, USA, 1980–1991; Professor of Radiology, Physiology, and Bioengineering Dartmouth, Hanover, NH, USA, 1991–present. Approx. 225 publications in applications of magnetic resonance to biology and medicine, measurements of pO_2 in cells and in vivo, structure and function of melanins, radiation biology, free radicals in biology and medicine, contrast agents for MRI and MRS.

Goran Bačíc. *b* 1951. B.S., 1976, M.S., 1980, Ph.D., 1985, Physical Chemistry, University of Belgrade, YU. Postdoctoral work at University of Illinois, USA (with H.M. Swartz). Successively research associate and assistant professor at University of Belgrade. Currently visiting research professor at Dartmouth College, NH, USA. Approx. 50 publications. Research specialties: in vivo EPR and EPR imaging, proton NMR relaxation, MRI contrast agents.

In Vivo ESR Imaging of Animals

Graham R. Cherryman, Andrew D. Stevens, and Colin M. Smith

University of Leicester, Leicester, UK

1 INTRODUCTION

The first successful electron spin resonance (ESR) experiment was reported in 1945 by Zavoisky.[1] ESR spectroscopy rapidly developed into an essential tool for the analytical chemist. It is only since the mid 1960s that its value to the biologist has been established. ESR is a technique that can detect and characterize molecules (or fragments of molecules) with an unpaired electron without destroying the molecule.

The existence of radical species with unpaired electrons was first proposed in the early 1900s. The importance of radicals in biology was first recognized in the 1930s by Leonor Michaelis (1875–1949) with his work on quinones and semiquinones. Today radical species are perceived to be important in understanding the pathogenesis of common and important diseases such as cancer and ischemia/reperfusion injury in stroke and myocardial infarction. Knowing the importance of radicals in initiating tissue damage also makes them targets for therapy with appropriate antioxidant therapies aimed at reducing tissue damage resulting from the overproduction of radicals. Medical scientists are now interested in the possibility of obtaining real-time in vivo ESR data on intact animal and human subjects.

When a paramagnetic substance is placed in a magnetic field, the degeneracy of the energy states for the unpaired electron is lifted. Upper and lower energy states are produced and transitions occur as a result of the absorption or emission of electromagnetic (em) energy at the resonant frequency. An ESR signal is obtained as a result of the net absorption of em energy which results from the slightly greater population of the lower energy level under nonsaturating conditions. The type of radical present determines the em frequency and magnetic field strength where this absorption occurs (g-factor). For technical reasons the absorption spectrum is usually plotted as a first derivative. The influence of magnetic nuclei within the molecule will split the ESR signal into several components (hyperfine splitting), which in turn will help characterize the radical species present. The linewidth of the ESR spectrum is also influenced by variations in the local paramagnetic environment. ESR signals are specific for the presence of unpaired electrons and can be obtained even when the majority of molecules present are nonradicals.

Biological ESR experiments are typically conducted at microwave frequencies, on tiny body fluid and tissue samples. Specimens are often frozen to 77 K to slow down the rapid bioreduction of short-lived natural radical species. Under these conditions ESR signals can be obtained from almost all tissues. The validity and usefulness of many of these observations remains to be determined.

In order to obtain adequate signal from larger aqueous samples and animals, ESR experiments must be conducted at a lower frequency than currently used in the laboratory so as to achieve sufficient tissue penetration or depth. Existing spectrometers may be modified to experiment on small animals or parts of an animal, e.g. a rat tail can be imaged at low microwave L-band frequencies, but for serious animal work and eventual human studies the ideal em frequency will lie in the radiofrequency region.

The present challenge is to develop radiofrequency ESR spectrometer design to a point where spectra and images can be obtained with suitable sensitivity on large biological specimens and to develop satisfactory methods of image creation and processing.

2 RADIOFREQUENCY ESR SPECTROMETERS AND IMAGERS

These are still at an early stage of development.[2,3] The essential components are (i) an rf bridge with transmitter and receiver circuitry, (ii) a resonator or surface coil, (iii) a magnet assembly and power supply for producing $\boldsymbol{B}_0$, (iv) magnets and power supplies for producing G_x, G_y and G_z, and (v) a host computer(s) for control, data accumulation and image processing.

Continuous wave (CW) irradiation is normally used, in contrast to the pulse techniques used in MRI, because T_2 values are normally very short (about 10^{-9}–10^{-7} s) and the bandwidth is very broad (about 90 MHz for nitroxides). The frequency must be low enough to give complete tissue penetration without a prohibitive loss of sensitivity. The best compromise between these factors is difficult to predict. Models for tissue absorption have to be adapted to account for resonator geometry and the precise relationship between sensitivity and frequency is still a matter for conjecture. For human studies, 250 MHz is probably the upper limit.[4] Our 250 MHz and 300 MHz rf bridges use phase-locked crystal oscillator sources which have better spectral purity than the voltage controlled oscillators normally used.[5,6] Various systems can be incorporated into the transmitter and receiver circuitry to reduce instrumental and motional artifacts and we have designed automatic rf coupling, resonator tuning and rf phase controls for this.[5,7]

Resonators with moderately good quality factors (Q), the most advantageous B-field characteristics and the least disadvantageous E-field geometries have to be used. Loop-gaps appear to be the most suitable. We have constructed a range of multigap, single loop and multiloop, multigap resonators up to 0.4 m in diameter.[8] Figure 1 shows a section through a double split-ring type loop-gap which we use for whole body studies of rats and which can also be used as a surface coil for larger specimens.

$\boldsymbol{B}_0$ is usually produced using air-cored Helmholtz coils, and is swept through the resonance position. A field of only 8.9 mT is required at 250 MHz for resonance at 'free spin' (g = 2.0023). The field is modulated using additional coils. Subsequent phase-sensitive detection at the modulation frequency

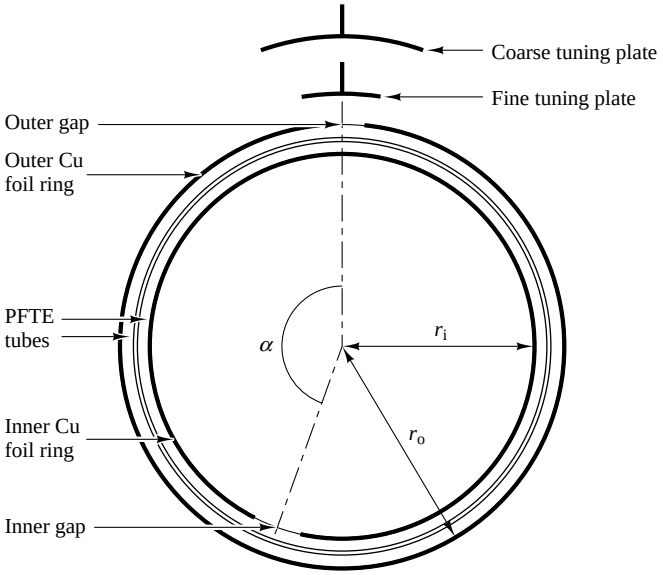

Figure 1 Schematic cross section of the 250 MHz double split-ring resonator. The inner radius (r_0) is 27.5 mm. The resonator is tuned by rotating the inner split ring (changing α) and by use of the servo driven tuning plates

produces a first derivative signal. Because of the large signal bandwidth, much larger field gradients than used for MRI are necessary, which can present an engineering problem with large samples. G_z is normally produced by an oil or water cooled Maxwell pair, G_x and G_y by Anderson coils or variants.[9] Figure 2 shows the coil arrangement for our 250 MHz imager, which can produce continuous gradients of up to 15 mT m^{-1}, sufficient to give a resolution of about 5 mm using nitroxides. A multipole magnet for producing field gradients of up to 150 mT m^{-1} has also been described.[10]

A spectrometer for FT ESR spectroscopy and imaging at 300 MHz has recently been constructed, but is only suitable for spectroscopy using lithium phthalocyanine crystals in vacuo, for which the FID lasts about 4 μs,[11] and imaging phantom systems comprising solvated electrons, for which the FID lasts about 9 μs. At present the signal-to-noise ratio does not appear to be better than can be obtained using CW EPR, but this is bound to improve as the technology is developed. In addition, biologically useful spin probes suited to this technique will undoubtedly be produced.

3 IMAGE RECONSTRUCTION FROM ESR SPECTRA

An ESR lineshape of a chemical species with unpaired electrons (free radical), is a function, $z(B)$, which relates ESR activity (a measure of spin density) to magnetic field and is independent of spatial position. If a constant field gradient is applied in the spectrometer, then the local magnetic field experienced in a spatial distribution of free radicals will depend upon their positions, and the measured ESR spectrum will be the mathematical convolution of the ESR lineshape of the system (the spectrum when no field gradient is applied) and the projection $p(r,\theta)$ of the spatial distribution function $F(x,y)$[12,13] (here we show results for the two-dimensional case) along the ray at angle θ defining the field gradient. In other words, the spatial extent of the free radicals causes ESR spectra to be broadened in the presence of a field gradient. If the spatial distribution is approximated on a finite grid by an array F_{ij}, then:

$$p(r,\theta) = \sum_{ij} F_{ij}\delta_{r,(x_i\cos\theta + y_j\sin\theta)} \quad (1)$$

where $\delta_{i,j}$ = 1 only if i=j and 0 otherwise. If units are chosen so that the field gradient has unit magnitude and the spatial origin corresponds to the middle of the magnetic field scan

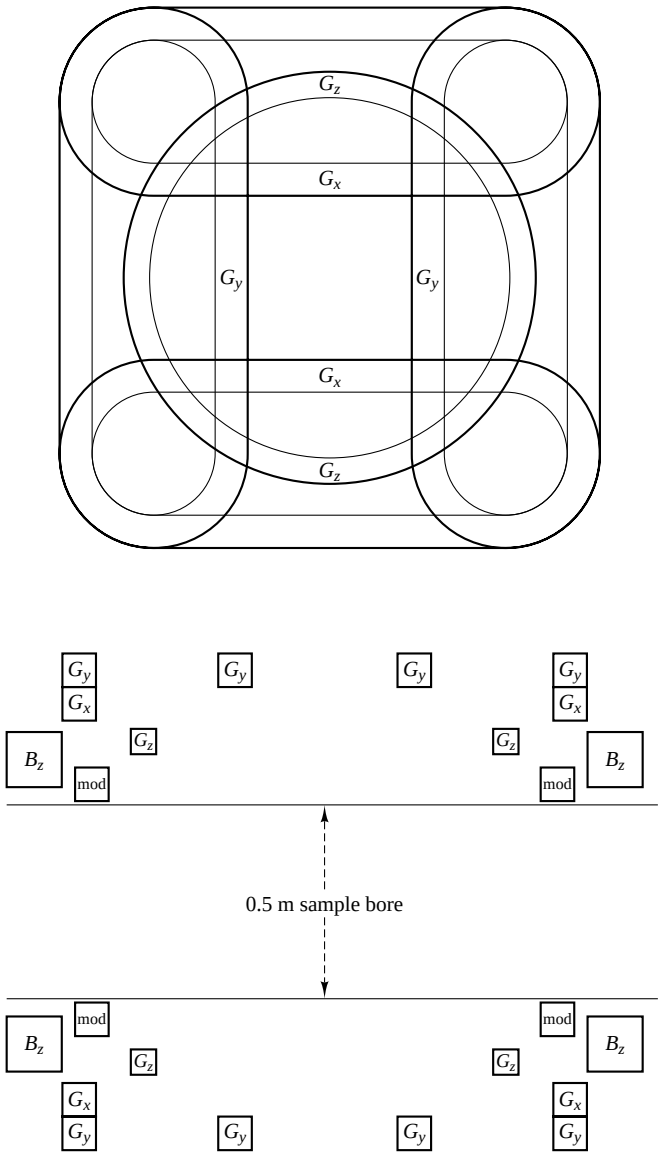

Figure 2 The arrangement of magnet coils in the 250 MHz imager, viewed from above and also from the side along the y axis. The $\boldsymbol{B}_0$ and modulation coils (mod) are not shown in the top view for the sake of clarity

range, the ESR spectrum measured for nonzero field gradient is:

$$\begin{aligned} d(B,\theta) &= \sum_i p(r_i,\theta) z(B - r_i) \\ &= \sum_i \left[\sum_{kl} F_{kl} \delta_{r_i (x_k \cos\theta + y_l \sin\theta)} \right] z(B - r_i) \\ &= \sum_{kl} F_{kl} z(B - x_k \cos\theta - y_l \sin\theta) \end{aligned} \quad (2)$$

We actually measure the first derivative spectra and integrate to form the functions $z(B)$ and $d(B,\theta)$. The first derivative spectra may be used directly but better results are obtained using $z(B)$ and $d(B,\theta)$.

In principle, the projection of the spatial distribution may be recovered exactly by deconvolution, i.e. dividing the Fourier transform of the ESR spectrum with nonzero field gradient by that of the lineshape, entry by entry, and inverse Fourier transforming the result. With a complete (infinite) set of projections, the free radical spatial distribution may be found using the convoluted back-projection formula for the inverse Radon transform and an acceptable reconstruction may be found using a large, finite set.[12] The field gradients are chosen to have the same magnitude along uniformly distributed projection angles θ between 0 and 180°. Although some workers use the Fourier reconstruction formula for the inverse of the Radon transform because it is much quicker computationally, we prefer the convoluted back-projection formula because it gives clearer reconstructions.

In practice, deconvolution is numerically unstable and a filter must be used to neglect or modify[14] the Fourier coefficients that are polluted by noise. Also, having a small number of projections introduces ripple artifacts into the reconstruction whose magnitude depends inversely on the projection number. With in vivo experiments time considerations dictate that our spectra are very noisy and sometimes we must be satisfied with only 16 projections. We have therefore developed an indirect reconstruction method that avoids the numerical instability and which does not admit ripples.[15] From a given spatial distribution of free radicals, one may calculate a set of ESR spectra. Starting from a simple guess and iterating, the spatial distribution, whose projections broaden the lineshape to the ESR spectra measured in a field gradient, can be found by minimizing the mean squared error between observed and calculated spectra. If the observed spectrum at angle θ is denoted $d(B,\theta)$ we define the mean squared error as:

$$S^2 = \frac{1}{n} \sum_{ij} \left[\sum_{kl} F_{kl} z(B_i - x_k \cos\theta_j - y_l \sin\theta_j) - d(B_i, \theta_j) \right]^2 \quad (3)$$

where n is the total number of measured data points. S^2 is minimized initially using a simple steepest descent update, which is chosen to ensure that F_{ij} are all nonnegative, using exact first derivatives and then following with a maximum entropy[16] algorithm to give a reconstruction that is closely consistent with the real data without fitting the random noise. This method is much slower than the convoluted back-projection reconstruction, but it does avoid the numerical instability and does not produce the ripple artifacts. Figure 3 shows a maximum entropy reconstructed image from 16 projections of a rat using our ESR spectrometer.

4 ESR IMAGING EXPERIMENTS

In 1971 Hutchison and Mallard reported endogenous ESR signals from a live mouse using a 100 MHz ESR spectrometer.[17] In 1987 Berliner et al.[18] demonstrated ESR signals arising from a melanoma tumor implanted into a mouse tail and imaged at *L*-band, following the intravenous injection of the nitroxide spin label CTPO (2,2,5,5-tetramethyl-1-oxyl-pyrrolidine-3-carboxamide). Four projections were used to construct a low resolution, filtered, back-projection image, which appeared to show central necrosis within the tumor. Subsequent serial studies showed dynamic differences in spin density between different regions of the tumor.

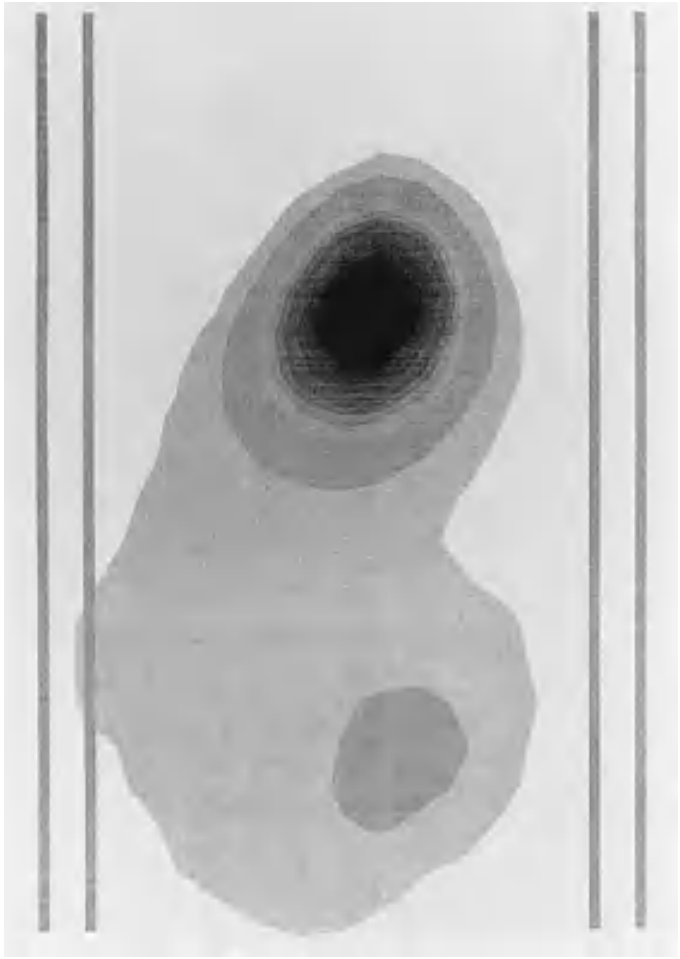

Figure 3 Sagittal maximum entropy reconstructed 250 MHz ESR image of a rat after injection of ^{15}N PCA (2,2,5,5-tetramethyl-1-oxyl-[1-^{15}N]pyrrolidine-d_{15}-3-carboxylic acid) (1 mL, 16 mM). Field gradients of 15 mT m^{-1} and a power level of 80 mW were used. Data were accumulated in 7 min and corrected for signal decay due to metabolism. The resonator split rings are shown for reference. The animal was positioned with the head toward the bottom of the resonator. A variation in spin density is seen with the highest concentration in the bladder. An area of increased spin density in the abdomen is most probably due to the concentration of the spin probe in the kidneys

The same group[19] then followed the in vivo pharmacokinetics of the same intravenous nitroxide (CTPO) by serial ESR spectra obtained from a rat tail inserted into a cavity resonator again operating at *L*-band. They observed that bioreduction of the nitroxide to the corresponding hydroxylamine in the plasma accounted for the bulk of signal loss rather than urinary or biliary excretion of the tracer.

A method of three-dimensional (3D) reconstruction was first proposed by Colacicchi et al. in 1988,[20] followed in 1989 by reports on spatial localization of signal and oximetry in mice.[21] In 1990 Alecci et al.[22] published a 3D reconstruction of the injected spin label 3-carbamoyl-2,2,5,5-tetramethyl-3-pyrrolidin-1-yloxy in the tail vein of a 300 g anesthetized rat. The solution (1 mL, 50×10^{-3} M) was injected into the caudal vein and spectra collected over the following 18 min. The images were calculated by Fourier interpolation from 32×8 field gradient orientations. The experiment was performed at 1.2 GHz. The same group published their experience with free radical pharmacokinetics in vivo.[23] In Japan, spin labeled images of a rat head were obtained at *L*-band.[24]

With the success of *L*-band ESR imaging the move to radiofrequency became inevitable. A new generation of ESR equipment was required. Fortunately CW ESR imagers could be constructed at relatively low cost. The Leicester (UK) group published their description of a small bore 300 MHz machine.[5]

In vivo radiofrequency ESR experiments have now been published from several groups including some from Italy[2,25] and Leicester, UK. In Leicester a much larger 250 MHz ESR imager has been built and used for in vivo imaging in the rat.[6,7,15,26,27] A surface coil has been constructed for use with larger animal and human subjects.[26]

5 THE FUTURE

There is sufficient evidence to suggest that in vivo spin label ESR spectroscopy and imaging at radiofrequency using nitroxide tracers works. We should expect to see in the next few years rapid development of the technique as a method of investigating intra and extracellular redox status.[28] Nitroxides constitute an extensive and diverse area of organic chemistry. There are already nitroxide analogs of many molecules of interest in medicine. Nitroxides with variable side chains can be used to localize within specific body compartments. When considering the development of nitroxide compounds for human use as ESR spin labels it is reassuring to note that some nitroxides, including PCA, which at one time were under development as possible paramagnetic contrast agents for MRI, showed remarkably little toxicity.[29–31]

Other ESR spin labels will also emerge. To develop ESR imaging there is also a need to develop single line spin labels with longer T_1 and T_2 relaxation times than found at present with nitroxide compounds. This will allow the development of 'pulse' ESR equipment capable of working in a similar fashion to FT MRI. In the laboratory experiments on lithium phthalocyanine and compounds based on carbon, semiquinones and the $Ph_3C^{\bullet}$ radical have shown some of the necessary characteristics.

Swartz and colleagues have pioneered the use of spin labels to measure tissue oxygenation in vivo.[32] Promising compounds include lithium phthalocyanine and fusinite,[33] nitroxide–liposome systems,[34] carbohydrate chars[35] and India ink.[36]

Will we ever be able directly to image endogenous free radicals of medical interest? This seems unlikely due to their low concentrations and ultrashort half-lives. It is possible that suitable, safe, spin traps with identifiable spin adducts will evolve and provide some useful information about the turnover of the highly reactive radicals found in the body.[37] These same spin trap compounds may have a therapeutic effect through trapping the reactive radicals. This possibility is likely to act as a stimulus to the development of effective spin traps.

Animal experimentation is crucial to the development of human ESR imaging. It is only by demonstrating the ability of in vivo ESR imaging to answer important clinical questions that suitable, safe, spin labels and spin traps will be developed for human use.

6 RELATED ARTICLES

EPR and In Vivo EPR: Roles for Experimental and Clinical NMR Studies; Projection–Reconstruction in MRI; Relaxometry of Tissue.

7 REFERENCES

1. E. Zavoisky, *J. Phys.*, 1945, **9**, 211.
2. S. Colacicchi, M. Ferrari, and A. Sotgiu, *Int. J. Biochem.*, 1992, **24**, 205.
3. eds. G. R. Eaton, S. S. Eaton, and K. Ohno 'EPR Imaging and In-Vivo EPR', CRC Press, Boca Raton, FL, 1991.
4. H. J. Halpern and M. K. Bowman, in 'EPR Imaging and In-Vivo EPR', eds. G. R. Eaton, S. S. Eaton, and K. Ohno, CRC Press, Boca Raton, FL, 1991, pp. 45–61.
5. J. A. Brivati, A. D. Stevens, and M. C. R. Symons, *J. Magn. Reson.*, 1991, **92**, 480.
6. A. D. Stevens, *Br. J. Radiol.*, 1994, **67**, 1243.
7. A. D. Stevens and J. A. Brivati, *Meas. Sci. Technol.*, 1994, **5**, 793.
8. A. D. Stevens, J. A. Brivati, M. C. R. Symons and C. M. Smith, 'A 250 MHz EPR Spectrometer for the In Vivo Imaging of Large Specimens', *Proc. XIth Ann Mtg. Soc. Magn. Reson. Med.*, Berlin, 1992, 4111.
9. R. W. Quine, G. R. Eaton, K. Ohno, and S. S. Eaton, in 'EPR Imaging and In-Vivo EPR', eds. G. R. Eaton, S. S. Eaton, and K. Ohno, CRC Press, Boca Raton, FL, 1991, pp. 15–24.
10. M. Alecci, G. Gualtieri, A. Sotgiu, L. Testa, and A. Varoli, *Meas. Sci. Technol.*, 1991, **2**, 32.
11. J. Bourg, M. C. Krishna, J. B. Mitchell, R. G. Tschudin, T. J. Pohida, W. S. Friauf, P. D. Smith, J. Metcalfe, F. Harrington, and S. Subramanian, *J. Magn. Reson.*, 1993, **102**, 112.
12. G. T. Herman, 'Image Reconstruction from Projections. Computer Science and Applied Mathematics', Academic Press, London, 1980.
13. R. K. Woods, W. B. Hyslop, R. B. Marr, and P. C. Lauterbur, in 'ESR Imaging and In Vivo EPR', eds. G. R. Eaton, S. S. Eaton, and K. Ohno, CRC Press, Boca Raton, FL, 1991.
14. F. Momo, S. Colacicchi, and A. Sotgui, *Meas. Sci. Technol.*, 1993, **4**, 60.
15. C. M. Smith and A. D. Stevens, *Br. J. Radiol.*, 1994, **67**, 1186.
16. J. Skilling and R. K. Bryan, *Mon. Not. R. Astron. Soc.*, 1984, **211**, 111.
17. J. M. S. Hutchison and J. R. Mallard, *J. Phys. E*, 1971, **4**, 237.
18. L. J. Berliner, H. Fujii, X. M. Wan, and S. J. Lukiewicz, *Magn. Reson. Med.*, 1987, **4**, 380.

19. L. J. Berliner and X. M. Wan, *Magn. Reson. Med.*, 1989, **9**, 430.
20. S. Colacicchi, P. L. Indovina, F. Momo, and A. Sotgiu, *J. Phys. E*, 1988, **21**, 910.
21. S. Colacicchi, M. Ferrari, G. Gaultieri, M. T. Santini, and A. Sotgiu, *Phys. Med. Biol.*, 1989, **5**, 297.
22. M. Alecci, S. Colacicchi, P. L. Indovina, F. Momo, P. Pavone, and A. Sotgiu, *Magn. Reson. Imaging*, 1990, **8**, 59.
23. M. Ferrari, S. Colacicchi, G. Gaultieri, M. T. Santini, and A. Sotgiu, *Biochem. Biophys. Res. Commun.*, 1990, **166**, 168.
24. S. I. Ishida, S. Matsumoto, H. Yokoyama, N. Mori, H. Kumashiro, N. Tsuchihashi, T. Ogata, M. Yamada, M. Ono, T. Kitajima, H. Kamada, and E. Yoshida, *Magn. Reson. Imaging*, 1992, **10**, 109.
25. V. Quaresima, M. Alecci, M. Ferrari, and A. Sotgiu, *Biochem. Biophys. Res. Commun.*, 1992, **183**, 829.
26. A. D. Stevens, C. M. Smith, J. A. Brivati, A. R. Moody, G. R. Cherryman, and M. C. R. Symons 'Radiofrequency EPR Imaging Using a Surface Coil', *Proc. XIIth Ann Mtg. Soc. Magn. Reson. Med.*, New York, 1993, Vol. 2, p. 948.
27. A. D. Stevens, C. M. Smith, and G. R. Cherryman, *Br. J. Radiol.*, 1994, **67** (Congress Supplement), 106.
28. H. M. Swartz and T. Walczak, *Phys. Med. Biol.*, 1993, **9**, 41.
29. V. Afzal, R. C. Brasch, D. E. Nitecki, and S. Wolff, *Invest. Radiol.*, 1984, **19**, 549.
30. W. R. Couet, U. G. Eriksson, R. C. Brasch, and T. N. Tozer, *Pharmacol. Res.*, 1985, **2**, 69.
31. L. K. Griffeth, G. M. Rosen, E. J. Rauckman, and B. P. Drayer, *Invest. Radiol.*, 1984, **19**, 553.
32. H. M. Swartz, K. Chen, M. Pals, M Sentjung, and P. D. Morse, *Magn. Reson. Med.*, 1986, **3**, 169.
33. H. M. Swartz, S. Boyer, P. Gast, J. F. Glockner, H. Hu, K. J. Liu, M. Moussavi, S. W. Norby, N. Vahidi, T. Walczak, M. Wu, and R. B. Clarkson, *Magn. Reson. Med.*, 1991, **20**, 333.
34. J. F. Glockner, H. C. Chan, and H. M. Swartz, *Magn. Reson. Med.*, 1991, **20**, 123.
35. S. W. Norby, A. I. Smirnov, S. Boyer, H. M. Swartz, and R. B. Clarkson, 'Measurement of [O2] In Vivo Utilizing Synthetic Carbohydrate Char and EPR', *Proc. XIth Ann Mtg. Soc. Magn. Reson. Med.*, Berlin, 1992, 4107.
36. H. M. Swartz, K. J. Liu, F. Goda, and T. Walczak, *Magn. Reson. Med.*, 1994, **31**, 229.
37. H. M. Swartz, *Free Radical Res. Commun.*, 1990, **9**, 399.

Biographical Sketches

Graham R. Cherryman. *b* 1952. M.B., Ch.B., Cape Town, 1975, F.R.C.R., London, 1981. Introduced to NMR by J. R. Mallard and F. W. Smith, University of Aberdeen, 1983 and ESR by M. C. R. Symons and co-workers, University of Leicester, 1991. Approx. 60 publications on imaging and MR. Research interests include the application of radiofrequency ESRI to imaging, fast MRI of heart and brain and the assessment of new health technologies.

Andrew D. Stevens. *b* 1957. B.Sc., Chemistry, Nottingham University, 1978, Ph.D., Leicester University, 1985. Introduced to ESR in 1981 by M. C. R. Symons at Leicester and R. S. Eachus at Eastman Kodak, New York. Approx. 15 publications on ESR including five on radiofrequency ESRI. Research interests include the use of ESR to investigate the physics of the photographic process and high-temperature superconductors and the design and construction of equipment for low frequency ESRI.

Colin M. Smith. *b* 1955. B.Sc., Mathematics, Exeter University, 1977, Ph.D., Nottingham University, 1981. Spent 10 years studying applications of optimization in quantum chemistry, in England and Japan. Introduced to ESR imaging in 1992 by A. D. Stevens. Approx. 15 publications including four on imaging. Current research interests: nonlinear minimization image reconstruction.

Accuracy Limitations on Internuclear Distances Measured by REDOR

Akira Naito

Yokohama National University, Yokohama, Japan

&

Hazime Saitô

Himeji Institute of Technology, Kamigori, Japan

1	Introduction	1
2	Theoretical Background of the REDOR Experiment	1
3	Rotational Echo Amplitude Calculated by the Density Operator Approach	2
4	Separation of S–I Distances from a S_m–I_n Multiple Spin System	2
5	Tips for Obtaining Accurate Interatomic Distances by REDOR Experiment	4
6	Natural Abundance ^{13}C REDOR Experiment	5
7	Accuracy Limit for REDOR Structure of Peptide and Proteins	6
8	Conclusions	8
9	Related Articles in Volumes 1–8	9
10	References	9

1 INTRODUCTION

In principle, accurate interatomic distances can be evaluated from careful analysis of specific dipolar interactions that were normally sacrificed under the condition of high power decoupling and magic angle spinning (MAS) techniques. A number of methods to recouple a single pair of dipolar interaction among homo and hetero nuclear spin pairs under the magic angle spinning condition have been proposed for determining the interatomic distances.[1–10] These distances have been used as constraints to determine the three-dimensional (3D) structure of peptides and proteins.[11–16] Rotational Echo DOuble Resonance (REDOR) was explored to recouple the relatively weak heteronuclear dipolar interactions under the MAS condition by applying a π pulse synchronously with the rotor period.[8,9] Consequently, the transverse magnetization cannot be refocused completely at the end of the rotor cycle, leading to a reduction of the echo amplitude. The extent of the reduction of the echo amplitude as a function of the number of rotor periods depends on the strength of the heteronuclear dipolar interaction. This method is extensively used to determine the relatively remote interatomic distance of 2–8 Å. When a number of isolated pairs are involved in a REDOR dephasing, the REDOR transformation could be useful in determining interatomic distances because it yields single peaks against distance axis for each heteronuclear coupling strength.[17,18] This approach is, however, not applicable for the case where the observed nuclei in REDOR are coupled with multiple nuclei.

It turned out that determination of accurate interatomic distances ($\pm$0.1 Å) is a prerequisite to arrive at a unique 3D structure of peptides and proteins.[15,16] It is emphasized that the distance measurement by REDOR is the only available means to satisfy this condition among the many kinds of proposed procedures mentioned above in view of the achieved accuracy and precision. Nevertheless, it is important to bear in mind that every possible effort to achieve the distance measurement with ultimate accuracy is essential to any possible applications. This is because any measurement based on the peak-intensity is susceptible to unexpected errors, which are not easy to check. After brief survey, tips to avoid this problem will be discussed in detail.

2 THEORETICAL BACKGROUND OF THE REDOR EXPERIMENT[8]

Transverse magnetization that precesses about the static magnetic field due to the dipolar interaction under the MAS condition moves back to the same direction at every rotor period because the integration of ω_D over one rotor period is zero. Consequently, the rotational echo signals are refocused at every rotor period. When a π pulse is applied to the I nucleus (Figure 1), which is coupled with the S nucleus, in one rotor period, this pulse plays a role to invert the precession direction of the magnetization of the observed S nucleus. Consequently, the magnetization vector of the S nucleus cannot move back to the same direction after one rotor period. Therefore the amplitude of the echo intensity decreases.

The extent of the reduction of the rotational echo amplitude yields the interatomic distances. To evaluate the REDOR echo amplitude theoretically, one has to consider the average precession frequency in the presence of the π pulse at the center of the rotor period over one rotor cycle as follows:

$$\overline{\omega_D(\alpha,\beta)} = \pm\frac{1}{Tr}\left[\int_0^{Tr/2}\omega_D dt - \int_{Tr/2}^{Tr}\omega_D dt\right] = \pm\frac{D}{\pi}\sqrt{2}\sin 2\beta\sin\alpha \quad (1)$$

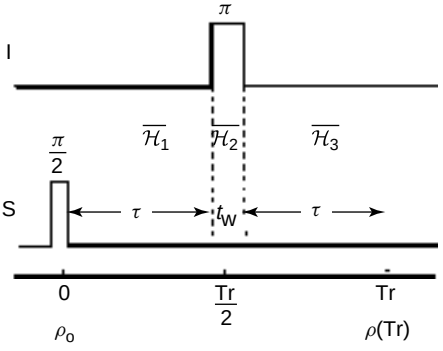

Figure 1 Pulse sequence and timing chart of REDOR experiment

where α is the azimuthal angle and β is the polar angle defined by the internuclear vector with respect to the rotor axis. Therefore, the phase angle, $\Delta\Phi(\alpha, \beta)$ for the Nc rotor cycle can be given by

$$\Delta\Phi(\alpha, \beta) = \overline{\omega_{\mathrm{D}}(\alpha, \beta)}\mathrm{NcTr} \tag{2}$$

where Tr is the rotor period. Finally, the echo amplitude can be obtained by averaging over every orientations as follows

$$S_{\mathrm{f}} = \frac{1}{4\pi}\int_{\alpha}\int_{\beta} cos[\Delta\varphi(\alpha, \beta)]\,\mathrm{d}\alpha \sin\beta\,\mathrm{d}\beta \tag{3}$$

Therefore, the normalized echo difference, $\Delta S/S_{\mathrm{o}}$, can be given by

$$\frac{\Delta S}{S_{\mathrm{o}}} = \frac{S_{\mathrm{o}} - S_{\mathrm{f}}}{S_{\mathrm{o}}} = 1 - S_{\mathrm{f}} \tag{4}$$

Experimentally, REDOR and full echo spectra are acquired for a variety of NcTr values and the respective REDOR (S_{f}) and full echo (S_{o}) amplitudes are evaluated.

3 ROTATIONAL ECHO AMPLITUDE CALCULATED BY THE DENSITY OPERATOR APPROACH[15]

The REDOR echo amplitude can be evaluated more rigorously by using density matrix operators and for the REDOR experiment. The time evolution of density operator, ρ_{o}, under the heteronuclear dipolar interaction during one rotor period, can be considered by taking the pulse length into account. The average Hamiltonian in the rotating frame over one rotor period can be given by

$$\begin{aligned}
\overline{\mathcal{H}} &= \frac{1}{\mathrm{Tr}}\left[\overline{\mathcal{H}_1(t)}\tau + \overline{\mathcal{H}_2(t)}\tau + \overline{\mathcal{H}_3(t)}\tau\right] \\
&= \frac{\mathrm{D}}{4\pi}\Big\{\sin^2\beta[\sin(2\alpha + \omega_{\mathrm{r}}t_{\mathrm{w}}) + \sin(2\alpha - \omega_{\mathrm{r}}t_{\mathrm{w}}) - 2\sin 2\alpha] \\
&\quad - 2\sqrt{2}\sin 2\beta\left[\sin\left(\alpha + \frac{1}{2}\omega_{\mathrm{r}}t_{\mathrm{w}}\right) + \sin\left(\alpha - \frac{1}{2}\omega_{\mathrm{r}}t_{\mathrm{w}}\right) + 2\sin 2\alpha\right] \\
&\quad - \sin^2\beta\,[\sin(2\alpha + \omega_{\mathrm{r}}t_{\mathrm{w}}) + \sin(2\alpha - \omega_{\mathrm{r}}t_{\mathrm{w}})]\,\frac{4\omega_{\mathrm{r}}^2 t_{\mathrm{w}}^2}{4\omega_{\mathrm{r}}^2 t_{\mathrm{w}}^2 - \pi^2} \\
&\quad + \sqrt{2}\sin 2\beta\left[\sin\left(\alpha + \frac{1}{2}\omega_{\mathrm{r}}t_{\mathrm{w}}\right) + \sin\left(\alpha - \frac{1}{2}\omega_{\mathrm{r}}t_{\mathrm{w}}\right)\right] \\
&\quad \times \frac{2\omega_{\mathrm{r}}^2 t_{\mathrm{w}}^2}{\omega_{\mathrm{r}}^2 t_{\mathrm{w}}^2 - \pi^2}\Big\}\hat{I}_Z\hat{S}_Z \\
&\quad + \frac{\mathrm{D}}{4\pi}\Big\{\sin^2\beta[\cos(2\alpha + \omega_{\mathrm{r}}t_{\mathrm{w}}) + \cos(2\alpha - \omega_{\mathrm{r}}t_{\mathrm{w}})] \\
&\quad \times \frac{2\pi\omega_{\mathrm{r}}t_{\mathrm{w}}}{4\omega_{\mathrm{r}}^2 t_{\mathrm{w}}^2 - \pi^2} \\
&\quad - \sqrt{2}\sin 2\beta\left[\cos\left(\alpha + \frac{1}{2}\omega_{\mathrm{r}}t_{\mathrm{w}}\right) + \cos\left(\alpha - \frac{1}{2}\omega_{\mathrm{r}}t_{\mathrm{w}}\right)\right] \\
&\quad \times \frac{2\pi\omega_{\mathrm{r}}t_{\mathrm{w}}}{\omega_{\mathrm{r}}^2 t_{\mathrm{w}}^2 - \pi^2}\Big\}\hat{I}_Z\hat{S}_Y \\
&= a\hat{I}_Z\hat{S}_Z + b\hat{I}_Z\hat{S}_Y
\end{aligned} \tag{5}$$

where ω_{r} is the angular velocity of the rotor and t_{w} is the duration of π pulse. $\overline{\mathcal{H}_1(t)}$, $\overline{\mathcal{H}_2(t)}$, and $\overline{\mathcal{H}_3(t)}$ are the average Hamiltonians corresponding to the period shown in Figure 1. Pulse length, t_{w}, is also considered in the calculations for the analysis of the REDOR results. The density operator, ρ (Tr), at Tr after evolution under the average Hamiltonian can be calculated as

$$\rho(\mathrm{Tr}) = \exp(-i\overline{\mathcal{H}}\mathrm{Tr})\rho_{\mathrm{o}}\exp(i\overline{\mathcal{H}}\mathrm{Tr}) \tag{6}$$

where ρ_{o} is considered to be $\hat{I}y$ after the contact pulse. Then finally the transverse magnetization at Tr can be given by

$$\begin{aligned}
\langle\hat{I}y(\mathrm{Tr})\rangle &= \mathrm{Tr}\{\rho(\mathrm{Tr})\hat{I}y\} \\
&= \cos\left(\frac{1}{2}\sqrt{a^2 + b^2}\mathrm{Tr}\right)
\end{aligned} \tag{7}$$

Echo amplitude in the powder sample can be calculated by averaging over every orientation as follows

$$S_{\mathrm{f}} = \frac{1}{4\pi}\int_{\alpha}\int_{\beta}\langle\hat{I}y(\mathrm{Tr})\rangle\sin\beta\,\mathrm{d}\beta\,\mathrm{d}\alpha \tag{8}$$

Therefore, the normalized echo difference, $\Delta S/S_{\mathrm{o}}$, can be given by equation (4). When the length of t_{w} is zero, equation (7) can be simplified as follows:

$$\langle\hat{I}y(\mathrm{Tr})\rangle = \cos\left(\frac{D}{\pi}\sqrt{2}\sin 2\beta\sin\alpha\mathrm{Tr}\right) \tag{9}$$

In this case, equation (8) is equivalent to equation (3) in the case of $\mathrm{Nc} = 1$.

4 SEPARATION OF S–I DISTANCES FROM A S_m–I_n MULTIPLE SPIN SYSTEM

It should be taken into account that a spin system for a doubly labeled sample should be generally treated as a multiple spin system (S–I_n system) as shown in Figure 2(a) in which S^* is the observed nuclei and the recoupling pulse is applied to the I^* nuclei. The ideal S–I system is available only when the doubly labeled preparation is infinitely diluted with unlabeled preparation. In contrast, uniformly and singly labeled preparations are treated as S_m–I_n and S–I_n systems, respectively (Figure 2b,c), although S^* in the latter is S nuclei of natural abundance. For this reason, it is advisable to utilize a variety of isotopically doubly labeled samples in order to obtain respective interatomic distances, although it is too laborious to make so many kinds of preparations. In fact, we made six kinds of doubly labeled preparations to determine the 3D structure of the pentapeptide, Leu-enkephalin.[16] In addition, it is essential to make certain that all such preparations take the same polymorphic structure, because crystalline peptides or proteins under consideration may take different kinds of polymorphs depending on condition for crystallization, pH, temperature, etc.[15,16] The most convenient way to check this problem is to use the conformation-dependent ^{13}C chemical shifts,

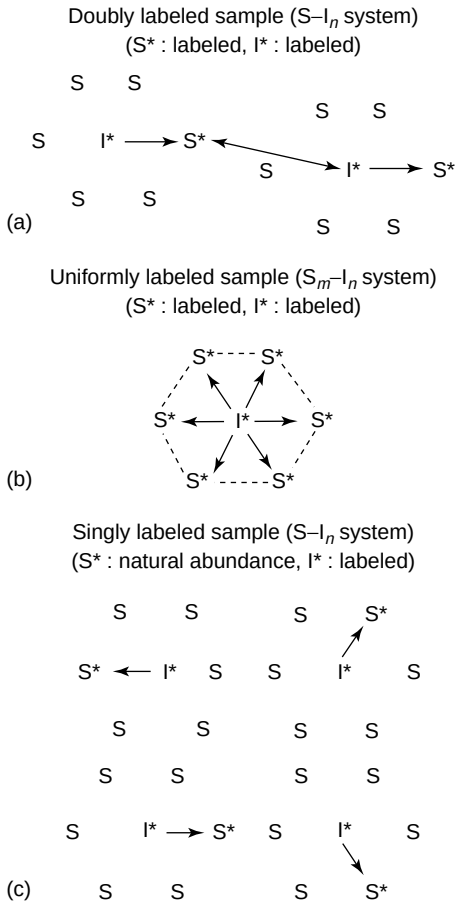

Figure 2 Schematic representation of multiple spin systems for (a) doubly labeled, (b) uniformly labeled and (c) singly labeled samples

which are very sensitive to the presence of such polymorphic structure.[15,16,19]

In this connection, use of a uniformly labeled sample seems to be more attractive both for the sample preparation and also to avoid the problem of polymorphs.[20] This view turned out to be not always true, however, because separation of a particular S–I interaction from S$_m$–I$_n$ spin systems, consisting of many homo- and heteronuclear dipolar and scalar interactions, is not always as straightforward as anticipated. In practice, all of the following conditions should be taken into account to determine the accurate interatomic distances of a particular spin pair from the uniformly labeled samples. First, J coupling among the observed S nuclei should be removed to reduce the phase twist due to the coherent evolution by J coupling, when its magnitude is comparable to the dipolar coupling, as illustrated for uniformly [^{15}N, ^{13}C]-labeled ammonium L-glutamate monohydrate at NcTr = 8 ms (Figure 3).[21,28] This phase twist can be removed by using a shaped pulse as a Z-filter instead of a π pulse at the center position of the REDOR evolution period.[21] Second, the linewidths of individual signals might be broadened due to strong homonuclear dipolar interaction with neighboring S nuclei, which should be eliminated by homonuclear decoupling pulses.[22] Thus, in the case of a uniformly labeled sample, combination of both homonuclear dipolar and scalar decoupling is required to simplify the S$_m$–I$_n$ to S–I$_n$ spin system. Third, relatively shortened transverse relaxation times (T_2), due to residual dipolar interactions, reduce the

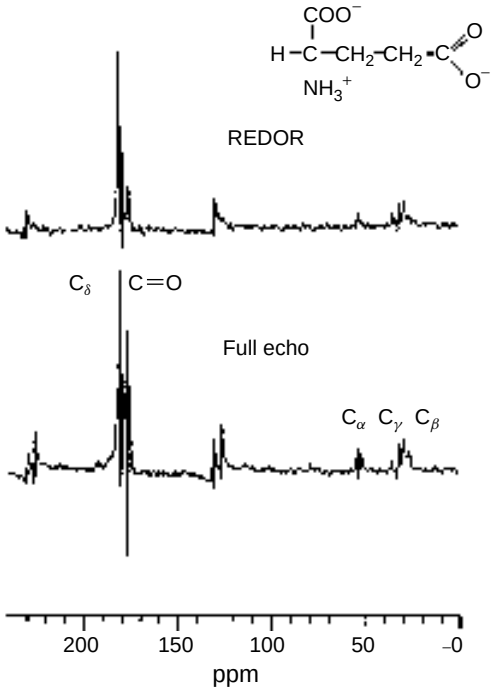

Figure 3 ^{13}C-REDOR and full echo spectra at NcTr = 8 ms for crystalline uniformly labeled ammonium [^{15}N]L-glutamate monohydrate

transverse magnetization during the dipolar recoupling period in REDOR experiments. This makes it difficult to observe the REDOR effect for the nuclei with relatively long internuclear distances, because it is required to measure relatively long evolution times to observe slow dephasing of the REDOR signals. Fourth, REDOR factors against the dipolar evolution time should be analyzed using multiply coupled S–I$_n$ spin systems rather than an isolated two-spin system under the condition of homonuclear decoupling.[23–26] Accordingly, the four kinds of obstacles mentioned above should be removed to determine a set of accurate interatomic distances simultaneously for a uniformly labeled sample.

Gullion et al.[27] proposed a θ-REDOR as an approach to determine the individual interatomic distance in a uniformly labeled sample by dividing S–I$_n$ spin system into 'n' number of isolated S–I two-spin systems. This makes the REDOR analysis simple and allows one to use the REDOR transformation to obtain the dipolar coupling frequencies of individual S–I spin couplings, although this method is not always easy to apply for measurement of a relatively long interatomic distance. Alternatively, homonuclear and scalar interactions are completely removed when natural abundant ^{13}C REDOR experiments were performed.[28] This approach provides an excellent means to determine the interatomic distances for a number of isolated spin pairs simultaneously under condition of high resolution (Figure 2c). Further, it is emphasized that this approach is free from the problem of the above-mentioned shortened T_2 values due to homonuclear ^{13}C spin interactions. However, a multiple coupled spin system, ^{13}C–^{15}N$_n$, has still to be explicitly considered, because the intermolecular dipolar interactions cannot be neglected for a small molecule. In practice, we have recently demonstrated that accurate interatomic distances can be determined by analyzing intramolecular and

intermolecular dipolar contributions based on root mean square deviation (RMSD) between the theoretically and experimentally obtained REDOR factors.[28]

5 TIPS FOR OBTAINING ACCURATE INTERATOMIC DISTANCES BY REDOR EXPERIMENT

It is emphasized that determination of interatomic distances accurate to 0.1 Å is a prerequisite to arrive at a unique solution of the three-dimensional structure of peptides, proteins, etc. A careful evaluation of the following points are the most important steps to obtain reliable interatomic distances by the REDOR experiment, although they have not always been seriously taken into account in a number of papers so far published.

5.1 The Finite Pulse Length and Fluctuation of RF Power

This effect is experimentally observed and calculated using equation (8) as shown in Figure 4. The REDOR parameter, $\Delta S/S_o$, as measured for 20% [1 − ^{13}C, ^{15}N]Gly($r_{CN} = 2.48$ Å) is plotted for the lengths of the ^{15}N π pulse of 13.0 μs for the experiment and 24.6 μs (chosen to satisfy 10% rotor cycle) as a function of NcTr with the calculated lines using the π pulse

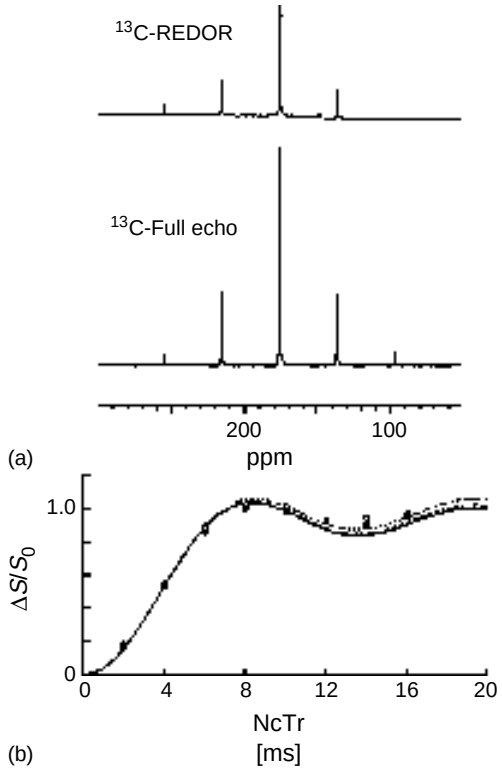

Figure 4 ^{13}C REDOR and full echo spectra of [1-^{13}C, ^{15}N]glycine as recorded by the rotor frequency of 4000 Hz and NcTr of 4 ms (a) and plots of the $\Delta S/S_o$ vs. NcTr (b). Solid and open circles denote the experimental points recorded using a ^{15}N π-pulse of 13.0 and 24.6 μs, respectively. Solid, broken and dotted lines are calculated using the π-pulses of δ, 13.0 and 24.6 μs, respectively, together with the C–N interatomic distance of 2.48 Å[15]

length and finite lengths (13.0 and 24.6 μs) of the π pulse. It turns out, however, that the finite length of the ^{15}N π pulse does not significantly affect the REDOR effect provided that the pulse length is less than 10% of the rotor cycle at the rotor frequency of 4000 Hz. This effect, however, should be seriously taken into account if fast MAS, e.g., 40 kHz is used.

For most spectrometers, it is difficult to be free from fluctuations of RF power during the acquisition of REDOR experiments. It is, therefore, critical that RF power be stabilized. If not, the π pulse will vary in length. Consequently, the REDOR factor is greatly decreased to yield relatively longer interatomic distances. Compensation of instability of such RF power, e.g., by approximate pulse sequence is, therefore, necessary to be free from long term fluctuations of amplifiers. xy-4 and xy-8 pulse sequences have been developed for this purpose. The xy-8 pulse is known to be the best sequence to compensate for the fluctuation of the RF power.[29]

5.2 Contribution from Natural Abundance Nuclei

Since the early stages of the REDOR experiment, contributions from natural abundance nuclei have been seriously considered as a major source of error in the distance measurement.[30] It appears that the observed dipolar interaction can be modified by the presence of such neighboring naturally abundant nuclei. This effect was originally taken into account by simply calculating the $\Delta S/S_o$ value for two isolated pairs and adding proportionally to the natural abundant fraction.[30] Careful analysis of the three-spin system, however, indicates that this sort of simple addition of the fraction of the two-spin system may result in a serious overestimate of the natural abundance effect, to yield shorter distances.[23] The most accurate way to consider the natural abundance effect is, therefore, to treat the whole spin system as a three-spin system by taking into account the neighboring carbons in addition to the labeled pair. In practice, contributions from naturally abundant nuclei can be ignored for ^{13}C REDOR but not for ^{15}N REDOR, because the proportion of naturally abundant ^{13}C nuclei is much higher than that of the ^{15}N nuclei.[23]

5.3 Sample Dilution

^{13}C, ^{15}N-doubly labeled samples are usually used in the REDOR experiment to determine the interatomic distances between the labeled nuclei. More importantly, the dipolar interaction with the labeled ^{15}N nuclei for the neighboring molecules should be taken into account as an additional factor to contribute to the dipolar interaction of the observed pair under consideration. This contribution could be serious when the observed distance is quite remote, because there are many contributions from nearby nuclei. This effect can be completely removed by diluting the labeled sample with a sample of naturally abundant molecules.[23] The sensitivity of the signals, however, has to be sacrificed if one wants to remove the effect completely as the sample must be diluted to 1/49 so that the signal intensity is reduced by a factor roughly 0.02.[11] Instead, it is advised to evaluate the REDOR factors at the infinitely diluted condition by extrapolating the data by stepwise dilution of the sample (i.e., 60%, 30%, etc.) without losing sensitivity, because a linear relationship between the REDOR factor and the dilution is ascertained by a theoretical consideration.[23] Alternatively, the observed plots of $\Delta S/S_o$ values against the

corresponding NcTr values for the sample without dilution can be fitted by a theoretical curve obtained from the dipolar interactions among three-spin systems, although the accuracy is not always improved to the level of the dilution experiment.

5.4 T_2 Effect

The transverse magnetization of the REDOR experiment decays as a function of the ^{1}H decoupling field.[31,32] Under appropriate conditions, molecular motion may interfere with dipolar decoupling. This occurs when molecular motion, if any, exists when the motional frequency is of the same order of magnitude as the decoupling field, and hence the transverse relaxation times (T_2) are significantly shortened. In fact, it was found that the T_2 values of the carbonyl carbons in crystalline Leu-enkephalin are relatively short because of the presence of backbone motion.[33] This is a serious problem for the REDOR experiment, especially for the long distance pairs, because the S/N ratio is significantly deteriorated. In this case, it is required to measure the ^{13}C REDOR signal under a sufficiently strong decoupling field to elongate the transverse relaxation times. It is also useful to perform measurements at low temperature so as to reduce the motional frequency. Note, however, that crystalline phase transitions might be associated together with the freezing of the solvent molecules. This effect has been observed in a variety of enkephalin samples.[34,35]

5.5 RF Inhomogeneity and Confinement of the Sample within RF Coil

In the commercial spectrometer, the rotor is designed to allow the sample volume to be as large as possible in order to gain better sensitivity. Obviously, this arrangement causes H_1 inhomogeneity, which results in a broad distribution of the lengths of the 90° pulses. This problem is serious for the REDOR experiment in which a number of π pulses are applied. As a result, the pulse error can accumulate during the acquisition to give serious error in the measurements of internuclear distances. Particularly, the samples located at the top or bottom part of the sample rotor feel quite a weak RF field. This causes a great reduction of the REDOR factor for a sample that is filled all the way along the sample rotor.[15] This effect should be seriously taken into account prior to experiments with a commercial spectrometer. It is, therefore, strongly recommended to fill the sample only in the central part of the coil just like a multiple pulse experiment to be able to acquire as accurate interatomic distances as possible in the REDOR experiment.

5.6 Standard Sample

All of the considerations mentioned above are essential to achieve accurate interatomic distances. Nevertheless, it is also possible that accuracy may deteriorate even if one of the conditions is not satisfied for every possible measurement. It is therefore advisable to determine the interatomic distances from a standard sample, in order to check that all the conditions are satisfied. More preferentially, use of two standard samples for short and long distances is recommended. In practice, it is recommended to use [1-^{13}C, ^{15}N]glycine as the former standard sample whose C–N interatomic distance is determined as 2.48 Å by a neutron diffraction study, and to check that all the instrumental conditions of a given spectrometer are satisfied prior to every new experiment. As a second standard sample for long distance, it is recommended to use [^{13}C, ^{15}N]*N*-acetyl-Pro-Gly-Phe (Table 1). This crystalline peptide is very stable with relatively long T_2 values, because it does not contain solvent molecules, and the presence of two polymorphic structures is well characterized.[15]

6 NATURAL ABUNDANCE ^{13}C REDOR EXPERIMENT[28]

As mentioned already, it is impossible to obtain meaningful interatomic distances from a uniformly labeled sample as far as the standard REDOR procedure is concerned. Instead, the natural abundance REDOR experiment is more preferable as a means free from both homonuclear dipolar and scalar interactions (Figure 3). This approach provides the interatomic distances for a number of isolated spin pairs simultaneously under high resolution conditions. Further, this approach is free from the problem of the shortened T_2 values due to homonuclear ^{13}C spin interactions. Figure 5 shows the REDOR and full echo spectra of natural abundance ^{13}C nuclei of singly ^{15}N labeled crystalline ammonium [^{15}N]L-glutamate monohydrate (I) at NcTr = 8 ms, in contrast to the twisted spectra from the same sample uniformly labeled (Figure 3). The assignment of peaks to the C_β, $C\gamma$, C_α, C=O and C_δ carbon nuclei, from high to low field, is also shown in Figure 5. The C=O (176.6 ppm) peak was distinguished from the C_δ (179.5 ppm) peak as a peak yielding a stronger REDOR effect as shown in Figure 5. Similarly, the peak at 56.0 ppm was assigned to the C_α carbon nucleus that give the strongest REDOR effect among the three aliphatic ^{13}C peaks. In a similar manner, the peak at 30.5 ppm showed a stronger REDOR effect compared

Table 1 C–N interatomic distances (Å) determined from REDOR experiments as compared with those by X-ray diffraction and MD[15]

Labeled peptides	Experimental			Calculated		
	REDOR	X-Ray		Energy-minimized[a]	MD	
	Orthorhombic	Orthorhombic	Monoclinic[b]		Orthorhombic	Monoclinic
I	3.24 ± 0.05 (3.43 ± 0.05)[c]	3.19	3.76	3.17	3.22 ± 0.10	3.63 ± 0.10
II	3.43 ± 0.05 (3.66 ± 0.05)	3.35	3.21	3.57	3.32 ± 0.10	3.33 ± 0.10
III	4.07 ± 0.05 (4.45 ± 0.05)	3.99	3.91	4.17	3.92 ± 0.10	3.83 ± 0.10

[a]Energy-minimized structure based on REDOR data.
[b]Ref.[36]
[c]Data from Ref.[23] based on fully packed 7.5 mm rotor systems.

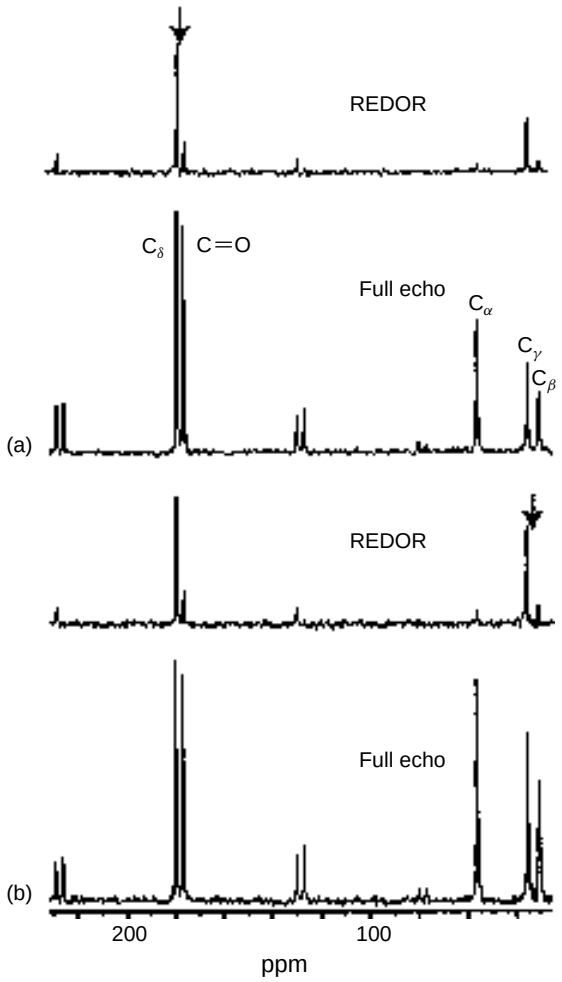

Figure 5 Naturally abundant ^{13}C-REDOR and full echo spectra at NcTr = 8 ms with two different carrier frequencies for crystalline ammonium [^{15}N]L-glutamate monohydrate. Arrows indicate carrier frequency positions at the center of (a) C=O and C_δ resonances; and (b) Cβ and C_γ resonances

with that at 35.2 ppm. Thus, the peaks at 35.2 and 30.5 ppm were assigned to the C_γ and C_β carbon nuclei, respectively.

The interatomic C–N distances between ^{15}N and ^{13}C=O, $^{13}C_\alpha$, $^{13}C_\beta$, $^{13}C_\gamma$, and $^{13}C_\delta$ carbon nuclei were determined with accuracy of 0.15 Å, after experimental conditions were carefully optimized. ^{13}C-REDOR factors for a three-spin system, $(\Delta S/S_o)_{CN1N2}$, and the sum of two isolated two-spin systems, $(\Delta S/S_o)^* = (\Delta S/S_o)_{CN1} + (\Delta S/S_o)_{CN2}$, were further evaluated by the REDOR measurements on isotopically diluted I in a controlled manner. Subsequently, the intramolecular and intermolecular C–N distances were separated by searching the minimum in the contour map of the root mean square deviation (RMSD) between the theoretically and experimentally obtained $(\Delta S/S_o)^*$ values against two interatomic distances, r_{C-N1} and r_{C-N2}. When the intramolecular C–N distance (r_{C-N1}) of the particular carbon nucleus is substantially shorter than the intermolecular distance (r_{C-N2}), C–N distances between the molecule in question and the nearest neighboring molecules can also be obtained, although accuracy is inevitably deteriorated. On the other hand, it was difficult to determine the interatomic distances in the same molecule when the intermolecular dipolar contribution is larger than the intramolecular one as in the case of the C_δ carbon nucleus.

7 ACCURACY LIMIT FOR REDOR STRUCTURE OF PEPTIDE AND PROTEINS

Naito et al.[15] systematically applied this technique to elucidate the three-dimensional structure of *N*-acetyl-Pro-Gly-Phe. They proposed that the carbonyl carbon of the (i-1)th residue and the amino nitrogen of the (i+1)th residue should be labeled with ^{13}C and ^{15}N, respectively. Namely, [1-^{13}C]*N*-acetyl-Pro-[^{15}N]Gly-Phe(I), *N*-acetyl-[1-^{13}C]Pro-Gly-[^{15}N]Phe(II) and [1-^{13}C]*N*-acetyl-Pro-Gly-[^{15}N]Phe(III) were synthesized and the resulting distances were determined to be 3.24 ± 0.05, 3.43 ± 0.05, and 4.07 ± 0.05 Å respectively, utilizing the REDOR factor obtained for the infinitely diluted state to prevent errors from the contributions of the neighboring labeled nuclei. No correction from the contribution of the naturally abundant nuclei turned out to be necessary. Surprisingly, these distances do not agree well with the values obtained from an X-ray diffraction study available when the initial part of this experiment was performed, showing the maximum discrepancy between them to be 0.5 Å.[36] This value seems to be much larger than the expected error as estimated from the precision of the REDOR experiment (±0.05 Å). The reason why the discrepancy is unexpectedly larger was explained by the fact that the crystal (orthorhombic) used for the REDOR experiments is different from that used in the X-ray diffraction study (monoclinic). To check the accuracy of the REDOR experiment, an X-ray diffraction study was performed on the same crystals used for the REDOR experiment. It was found that the distances from the new crystalline polymorph (orthorhombic) agree well between REDOR and X-ray diffraction, within an accuracy of 0.05 Å as shown in Table 1.

Conformational maps based on the possible combinations of the torsion angles of the Pro and Gly residues are calculated on the basis of the distance constraints thus obtained. Further, the difference of the chemical shifts between the C_β and C_γ carbons of the Pro residues $\Delta\beta\gamma$ was used as a constraint to determine the ψ value (−13°).[37] The φ angle of the Pro residue is in many instances restricted to −75° which shows the minimum energy in the residue. Therefore, the torsion angles of the Pro residue are uniquely determined to be (−75°, −28°). Using these torsion angles, conformational maps were again calculated. Finally two pairs of torsion angles were selected as (−112°, 48°) and (−112°, −48°). Minimization by a molecular mechanics calculation yielded the structure of the β-turn I structure, as shown in Figure 6(a). It is found that the three-dimensional structure of this peptide is well reproduced by a molecular dynamics simulation by taking into account all of the intermolecular interactions in the crystals, although a molecular dynamics calculation treating *single* molecular system does not always yield a correct picture as illustrated in Figure 6(b), unless otherwise all the molecules in a unit cell are correctly taken into account.[15,38]

Elucidation of the three dimensional structure of an opioid peptide Leu-enkephalin crystal, Tyr-Gly-Gly-Phe-Leu grown from MeOH/H_2O mixed solvent was performed by the REDOR method alone.[16] This seems to be an additional challenge for this technique to reveal the three-dimensional structure of more complicated systems. Six differently labeled

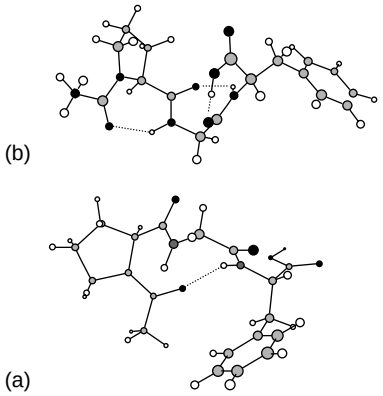

Figure 6 Optimized conformation of *N*-acetyl-Pro-Gly-Phe as obtained by the minimization of energy from the initial form as deduced from the REDOR experiment (a) and a snapshot of the conformation deduced by MD simulation in vacuo (at 100 K) (b)[15]

Leu-enkephaline molecules were synthesized and the resulting interatomic distances (Figure 7a) are accurately determined. It turns out, however, that an extremely careful experiment is required to avoid unexpected crystalline conversion among polymorphs either by dehydration from a tightly sealed rotor or a phase transition occurring at ambient temperature. In principle, pressure under MAS may shift a temperature of phase transition to some extent, because centrifugal force is proportional to the square of the spinning frequency. No significant effect, however, has been noted so far as a sample is spun at relatively low frequency such as 2−4 kHz but care might be taken when rotor is spun at a frequency one order of magnitude high as in 40 kHz.

This may be the reason why final refinement of X-ray diffraction data was abandoned in spite of the pioneering X-ray diffraction data as to the similarity of the tertiary structure between this opioid peptide and morphine.[39] Therefore, it is necessary to check whether the six differently labeled samples are all in the same crystalline polymorph by means of the ^{13}C chemical shifts. Otherwise, meaningless data can be obtained without this precaution. When the distance data are converted to yield the necessary numbers of torsion angles, a unique combination of torsion angles in the corresponding conformational map is determined sequentially as shown in Figure 7(b). It is emphasized that accuracy within 0.1 Å is essential to select unique torsion angles for each amino acid residue. Namely, if the error is larger than 0.41 Å, torsion angles can no longer be selected as shown in Figure 8.

It is also important to point out that the chemical shift data can be used as additional constraints. A three dimensional structure was thus determined as shown in Figure 9. However, this structure is not the same as that previously determined

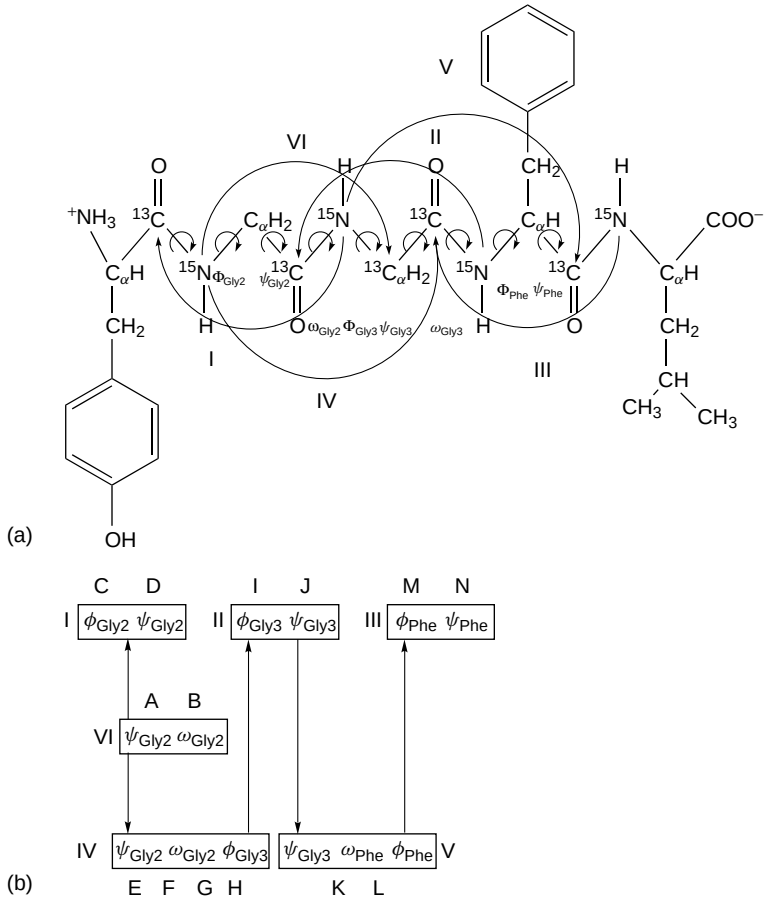

Figure 7 (a) Schematic representation between the sites of a variety of [^{13}C, ^{15}N]-doubly-labeled Leu-enkephalin dehydrates and their related torsion angles. (b) Block diagram to show how respective torsion angles are uniquely determined by the combined examinations of the conformation maps based on the distances of four-bonds apart (I, II, III and VI) and five-bonds apart (IV and V)[16]

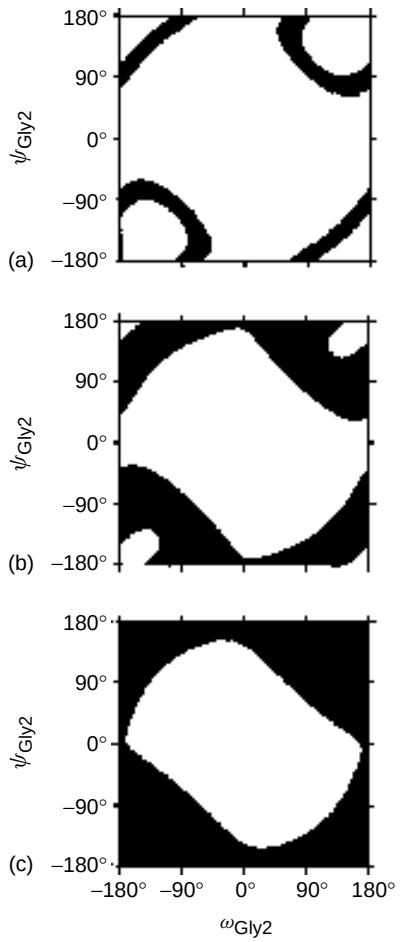

Figure 8 Conformation maps for (Ψ_{Gly2}, ω_{Gly2}) based on the interatomic distance of 4.55 Å with increased experimental errors: (a) ±0.10 Å, (b) ±0.20 Å, and (c) ±0.41 Å[16]

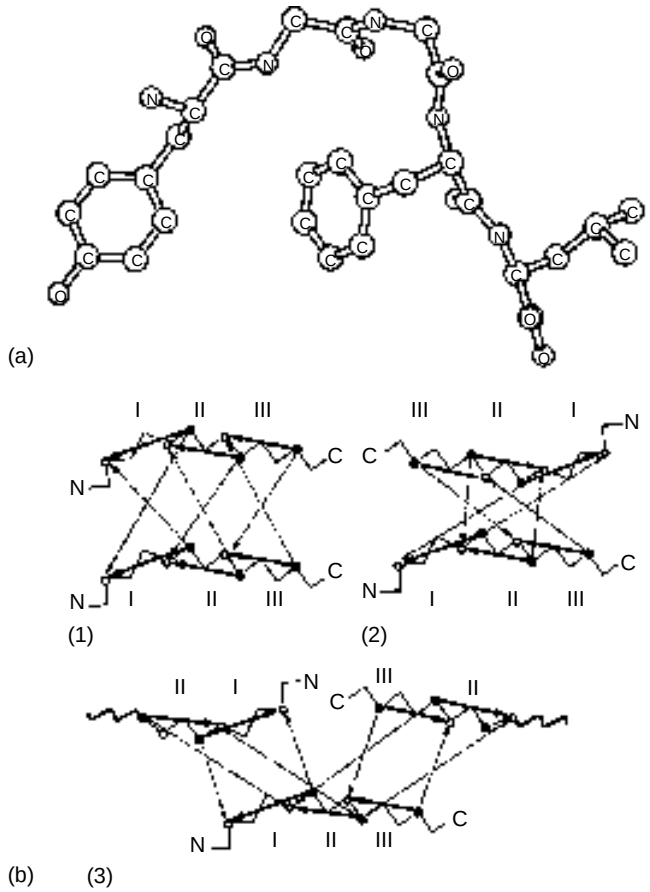

Figure 9 (a) Three-dimensional structure of Leu-enkephalin dihydrate determined uniquely by the successive application of the conformation maps as well as additional constraints of the conformation-dependent ^{13}C chemical shifts. (b) Three kinds of models for putative intermolecular packing as illustrated in the cartoons: (1) interaction through parallel β-sheet form; (2) interaction through an antiparallel β-sheet; and (3) interaction through interaction of three molecules. Solid and dotted arrows correspond with the dipolar interactions between intramolecular and intermolecular $^{13}C-^{15}N$ pairs, respectively[16]

by X-ray diffraction because one is dealing with a crystalline polymorph that is not fully explored. It is possible to figure out the molecular packing in the crystals by looking at the intermolecular dipolar contribution. Since the intermolecular dipolar contributions in I and III are larger than that of II, a β-sheet is formed as one peptide interacts with two peptides as an antiparallel β-sheet as shown in Figure 9(b).

Finally, it should be pointed out that, in order to isolate an S–I spin pair, it is essential to avoid any unnecessary errors from dipolar contributions of neighboring molecules from the overall $S-I_n$ spin system. This is generally encountered for a variety of peptides and the aforementioned dilution procedure turned out to be not required in the case of α-helical polypeptides as far as the measurement of the interatomic distance for $^{15}NH(i)\cdots O = {}^{13}C(i+4)$ is concerned.[40] This is because the interhelical dipolar contribution is found to be negligible in view of the mutual packing of α-helical chains or random mutual orientation between isotopically labeled atoms. Further, it was found that in helical peptides, due to the manner of chain packing, this kind of measurement is feasible to yield 4.5 ± 0.1 Å, without any assumptions, for a variety of transmembrane α-helical peptides in lipid bilayers to mimic a biomembrane at a temperature below liquid crystalline-gel phase transition at which rotation of such peptides about the α-helical axis turns out to be frozen, in spite of the presence of rotational motions of lipid molecules, as viewed from the observation of three principal components of ^{13}C and ^{31}P chemical shift tensors.[41] As is shown in this example, it is essential to ensure that molecular motion is reasonably ceased.

8 CONCLUSIONS

REDOR is one of the most powerful methods to determine accurate interatomic distances after taking into account a number of points in applying the method to a practical sample. Simultaneous measurement of interatomic distances using uniformly labeled samples can only be achieved by removing the homonuclear dipolar and scalar interactions. Alternatively, natural abundance ^{13}C REDOR measurements provide interatomic distances simultaneously free from homonuclear dipolar and scalar interactions. These accurate interatomic distances obtained from REDOR experiments can provide important information on structure and molecular packing of solid peptides and proteins.

9 RELATED ARTICLES IN VOLUMES 1–8

REDOR & TEDOR, Volume 6.

10 REFERENCES

1. D. P. Raleigh, M. H. Levitt, and R. G. Griffin, *Chem. Phys. Lett.*, 1988, **146**, 71.
2. M. H. Levitt, D. P. Raleigh, F. Creuzet, and R. G. Griffin, *J. Chem. Phys.*, 1990, **92**, 6347.
3. R. Tycko and G. Dabbagh, *Chem. Phys. Lett.*, 1990, **173**, 461.
4. B. -Q. Sun, P. R. Costa, D. Kocisko, P. T. Lansbury Jr., and R. G. Griffin, *J. Chem. Phys.*, 1995, **102**, 702.
5. T. Gullion and S. Vega, *Chem. Phys. Lett.*, 1992, **194**, 423.
6. A. E. Bennett, J. H. Ok, R. G. Griffin, and S. Vega, *J. Chem. Phys.*, 1992, **96**, 8624.
7. D. M. Gregory, D. J. Mitchell, J. A. Stringer, S. Kiihne, J. C. Shiels, J. Callahan, M. A. Mehta, and G. P. Drobny, *Chem. Phys. Lett.*, 1995, **246**, 654.
8. T. Gullion and J. Schaefer, *Adv. Magn. Reson.*, 1989, **13**, 57.
9. T. Gullion and J. Schaefer, *J. Magn. Reson.*, 1989, **81**, 196.
10. A. W. Hing, S. Vega, and J. Schaefer, *J. Magn. Reson.*, 1992, **96**, 205.
11. J. R. Garbow and C. A. McWherter, *J. Am. Chem. Soc.*, 1993, **115**, 238.
12. J. R. Garbow, M. Breslav, O. Antohi, and F. Naider, *Biochemistry*, 1994, **33**, 10 094.
13. A. W. Hing, N. Tjandra, P. F. Cottam, J. Schaefer, and C. Ho, *Biochemistry*, 1994, **33**, 8651.
14. R. C. Anderson, T. Gullion, J. M. Joers, M. Shapiro, E. B. Villhauer, and H. P. Weber, *J. Am. Chem. Soc.*, 1995, **117**, 10 546.
15. A. Naito, K. Nishimura, S. Kimura, S. Tuzi, M. Aida, N. Yasuoka, and H. Saitô, *J. Phys. Chem.*, 1996, **100**, 14 995.
16. K. Nishimura, A. Naito, S. Tuzi, H. Saitô, C. Hashimoto, and M. Aida, *J. Phys. Chem. B*, 1998, **102**, 7476.
17. K. T. Mueller, T. P. Jarvie, D. J. Aurentz, and B. W. Roberts, *Chem. Phys. Lett.*, 1995, **242**, 535.
18. T. P. Jarvie, G. T. Went, and K. T. Mueller, *J. Am. Chem. Soc.*, 1996, **118**, 5330.
19. H. Saitô, S. Tuzi, and A. Naito, *Annu. Rep. NMR Spectrosc.*, 1998, **38**, 79.
20. C. A. Michal and L. W. Jelinski, *J. Am Chem. Soc.*, 1997, **119**, 9059.
21. C. P. Jaroniec, B. A. Tounge, C. M. Rienstra, J. Herzfeld, and R. G. Griffin, *J. Am. Chem. Soc.*, 1999, **121**, 100–237.
22. J. Schaefer, *J. Magn. Reson.*, 1999, **137**, 272.
23. A. Naito, K. Nishimura, S. Tuzi, and H. Saitô, *Chem. Phys. Lett.*, 1994, **229**, 506.
24. K. Nishimura, A. Naito, S. Tuzi, and H. Saitô, *J. Phys. Chem. B*, 1999, **103**, 8398.
25. L. M. McDowell, C. A. Klug, D. D. Beusen, and J. Shaefer, *Biochemistry*, 1996, **35**, 5395.
26. J. M. Goetz and J. Schaefer, *J. Magn. Reson.*, 1997, **127**, 147.
27. T. Gullion and C. H. Pennington, *Chem. Phys. Lett.*, 1998, **290**, 88.
28. K. Nishimura, K. Ebisawa, E. Suzuki, H. Saito, and A. Naito, *J. Mol. Struct.*, 2001, **560**, 29.
29. T. Gullion and J. Schaefer, *J. Magn. Reson.*, 1991, **92**, 439.
30. Y. Pan, T. Gullion, and J. Schaefer, *J. Magn. Reson.*, 1990, **90**, 330.
31. D. Suwelack, W. P. Rothwell, and J. S. Waugh, *J. Chem. Phys.*, 1980, **73**, 2559.
32. W. P. Rothwell and J. S. Waugh, *J. Chem. Phys.*, 1981, **74**, 2721.
33. A. Naito, A. Fukutani, M. Uitdehaag, S. Tuzi, and H. Saitô, *J. Mol. Struct.*, 1998, **441**, 231.
34. M. Kamihira, A. Naito, K. Nishimura, S. Tuzi, and H. Saitô, *J. Phys. Chem. A*, 1998, **102**, 2826.
35. M. Kamihira, A. Naito, S. Tuzi, and H. Saitô, *J. Phys. Chem.*, 1999, **103**, 3356.
36. S. K. Brahmachari, T. N. Bhat, V. Sudhakar, M. Vijayan, R. S. Rapaka, R. S. Bhatnagar, and V. S. Aranthanarayanan, *J. Am. Chem. Soc.*, 1981, **103**, 1703.
37. von I. Z. Siemion, T. Wieland, and K. -H. Pook, *Angew. Chem.*, 1975, **87**, 712.
38. M. Aida, A. Naito, and H. Saitô, *J. Mol. Struct. Theochem.*, 1996, **388**, 187.
39. G. D. Smith and T. Blundel, *Science*, 1978, **199**, 1214.
40. S. Kimura, A. Naito, H. Saitô, K. Ogawa, and A. Shoji, *J. Mol. Struct.*, 2001, **157**, 562.
41. S. Kimura, A. Naito, S. Tuzi, and H. Saitô, *J. Mol. Struct.*, 2002, **125**, 602–603.

Biographical Sketches

Akira Naito, *b* 1949. B.Eng., 1973, Nagoya Institute of Technology. Ph.D., 1978, Kyoto University. Post Doctoral Fellow, University of British Columbia, 1978–1984. Assistant Professor, Kyoto University, 1984–1990. Associate Professor, Himeji Institute of Technology, 1990–2001. Professor, Yokohama National University, 2001–present. Approx. 110 publications. Current research specialty: development of solid-state NMR technique and its application to biological systems.

Hazime Saitô, *b* 1937. B.Sc., 1961, Ph.D., 1968, Kyoto University. Research Scientist, Basic Research Laboratories, Toray Industries, Inc., 1963–1975, Section head, Biophysics Division, National Cancer Center Research Institute, Tokyo, 1975–1990. Professor, Himeji Institute of Technology, 1990–present. Approx. 250 publications. Current research specialty: solid state NMR and its application to structural biology with emphasis on membrane proteins.

Dipolar and Indirect Coupling Tensors in Solids

Roderick E. Wasylishen

Dalhousie University, Halifax, Nova Scotia, Canada

1	Introduction	1
2	Direct Dipolar Coupling	2
3	Indirect Spin–Spin Coupling	4
4	Summary	10
5	Related Articles	10
6	References	10

1 INTRODUCTION

Nuclei which possess the property of spin also have an associated nuclear magnetic moment. It is the interaction between these nuclear magnetic moments and a strong applied magnetic field $\boldsymbol{B}_0$ which forms the basis of the NMR experiment. This interaction, known as the Zeeman interaction, is always the most important spin interaction for spin-$\frac{1}{2}$ nuclei. In addition to the externally applied magnetic field, nuclei may also experience much smaller internal magnetic fields. For example, the field-induced motion of electrons generates small magnetic fields which modify the applied magnetic field and result in the phenomenon known as nuclear magnetic shielding or chemical shielding. In addition, neighboring nuclear spins may also create small magnetic fields which modify the applied magnetic field. There are two fundamental mechanisms by which one nuclear magnetic moment may interact with another: the *direct* magnetic dipole–dipole interaction and the *indirect* spin–spin interaction. The magnitude of the direct dipolar interaction is directly proportional to the inverse cube of the separation between two spins, while the indirect interaction does not depend on distance in any simple way since it is a two-stage process mediated by the intervening electrons. Because the mechanism of indirect spin–spin coupling involves electrons, this parameter depends on the detailed electronic structure of a molecule. Both the direct and indirect coupling interactions are bilinear in the nuclear spin operators (see below). In principle, the direct dipolar and indirect spin–spin interactions couple every spin of the sample with all others.

Most early NMR investigations were ^{1}H NMR studies, because of the relatively large magnetic moment of ^{1}H (hence its high inherent sensitivity to NMR detection), its large natural abundance (99.985%), and its ubiquitous presence in chemical compounds. The direct dipolar interaction has special significance in these studies since proton–proton direct dipolar interactions are largely responsible for the general appearance of ^{1}H NMR spectra of solid materials. Furthermore, the ^{1}H–^{1}H dipolar interaction provided the first important application of NMR in chemistry. Specifically, Pake[1] used the ^{1}H–^{1}H direct dipolar interaction to determine the H–H separation of water molecules in gypsum ($CaSO_4.2H_2O$): $r_{H-H} = 0.158$ nm.

The indirect spin–spin coupling interaction was first observed as magnetic field-independent splittings in the NMR spectra of solution samples.[2–4] In solution, the direct dipolar interaction averages to zero because of the rapid random tumbling motion of molecules. The first indirect spin–spin coupling constant J was reported by Proctor and Yu in 1951.[2] It involved the indirect spin–spin coupling between the antimony and fluorine nuclei of the SbF_6 anion in an aqueous solution of $NaSbF_6$; $J(^{121}Sb, ^{19}F)$ = 1.9 kHz. Shortly after this report, Gutowsky and co-workers reported the observation of $J(^{31}P, ^{19}F)$ in $P(O)Cl_2F$ (1.2 kHz), $P(O)ClF_2$ (1.1 kHz), and $CH_3(O)PF_2$ (1.3 kHz).[3] The first ^{1}H–^{1}H electron-mediated spin–spin couplings were reported in the same year by Hahn and Maxwell.[4] They studied the frequency modulation of ^{1}H NMR spin echoes arising from molecules with chemically nonequivalent hydrogen nuclei. For dichloroacetaldehyde ($CHCl_2CHO$), two distinct modulation frequencies were observed on the ^{1}H spin echo envelope: one corresponding to the difference in ^{1}H chemical shifts, and a second, much smaller frequency J which was independent of the applied magnetic field [$^3J(^1H, ^1H) = 0.7$ Hz]. On the basis of their measurements, Hahn and Maxwell proposed that the Hamiltonian describing electron coupled spin interactions in isotropic fluids should be of the form $J_{N,N'}\boldsymbol{I}_N \cdot \boldsymbol{I}_{N'}$. However, for a pair of coupled spins residing in a molecule which is not rapidly tumbling in an isotropic fluid, Ramsey[5] later pointed out that the energy of interaction $E_{N,N'}$ depends on the orientation of the spin pair in the applied magnetic field. In general, the energy of interaction is given by

$$E_{N,N'} = h\boldsymbol{I}_N \cdot \boldsymbol{J}_{N,N'} \cdot \boldsymbol{I}_{N'} + hJ_{N,N'}\boldsymbol{I}_N \cdot \boldsymbol{I}_{N'} \qquad (1)$$

where $\boldsymbol{J}_{N,N'}$ is a second rank tensor whose trace is zero and $J_{N,N'}$ is the isotropic indirect spin–spin coupling constant.

In solid samples, splittings arising from indirect spin–spin coupling were not observed until 1967.[6] In the solid state, the magnitude of direct dipolar interactions among magnetically abundant spins, such as ^{1}H or ^{19}F, precluded the measurement of much smaller indirect spin–spin interactions. However, by spinning samples rapidly about an axis inclined at 54° 44′ with respect to the applied magnetic field, broadening due to anisotropic chemical shielding and direct dipolar interactions can be largely removed. Using this technique, known as magic angle spinning (MAS), Andrew et al.[6] observed splittings due to $J(^{75}As, ^{19}F)$ of 905 Hz, and $J(^{121}Sb, ^{19}F)$ of 1820 Hz in the ^{19}F NMR spectra of solid $KAsF_6$ and $KSbF_6$, respectively. From the ^{19}F NMR linewidths observed in nonspinning samples of these salts, the authors were able to conclude that the hexafluoroarsenate and hexafluoroantimonate anions are dynamically disordered. Rapid jumps of the MF_6 octahedra about their symmetry axes average *intra*molecular dipolar interactions to zero. Subsequently, VanderHart et al.[7] studied the ^{19}F and ^{31}P NMR lineshapes of static samples of polycrystalline $BaFPO_3$ where the directly bonded ^{19}F and ^{31}P nuclei are coupled by both the direct dipolar and the indirect spin–spin coupling interactions. The authors indicated that with an accurate value of the ^{19}F–^{31}P separation r_{FP}, one could calculate the contribution that the direct dipolar interaction makes to the overall ^{19}F or ^{31}P NMR lineshape and, in principle, determine the anisotropy in the indirect spin–spin coupling, a parameter which is usually inaccessible.

The objective of this article is to present an introductory discussion of how spin–spin coupling interactions are described

and how they manifest themselves in the NMR spectra of diamagnetic systems, particularly in NMR studies of solids. The discussion will focus on the indirect spin–spin coupling tensor $\boldsymbol{J}$, since detailed discussions of the direct dipolar interaction can be found in several textbooks on NMR.[8–11] For pedagogical reasons, it is most convenient to focus the discussion on simple two-spin systems.

2 DIRECT DIPOLAR COUPLING

A nucleus with nonzero total spin angular momentum $\hbar\boldsymbol{I}$ also possesses a magnetic moment $\boldsymbol{\mu}$. The magnetic moment and angular momentum vectors are related by the magnetogyric ratio γ, a unique constant for any given isotope:

$$\boldsymbol{\mu} = \gamma\hbar\boldsymbol{I} \tag{2}$$

It is useful to consider the total static magnetic field emanating from a magnetic dipole. At a point P, the static field depends on the distance r and the angle θ between the magnetic dipole and P; the z component of the local field is $\gamma r^{-3}\hbar\,(3\cos^2\theta - 1)\,(\mu_0/4\pi)$. With $\theta = 0^\circ$, the local field 0.1 nm from a proton is 5.64 mT, several orders of magnitude less than the magnitude of typical external fields employed in NMR experiments.

From classical electrodynamics, the energy of interaction E between two magnetic dipoles, $\boldsymbol{\mu}_1$ and $\boldsymbol{\mu}_2$, separated by a distance r may be written as

$$E = [(\boldsymbol{\mu}_1 \cdot \boldsymbol{\mu}_2)r^{-3} - 3(\boldsymbol{\mu}_1 \cdot \boldsymbol{r})(\boldsymbol{\mu}_2 \cdot \boldsymbol{r})r^{-5}](\mu_0/4\pi) \tag{3}$$

where μ_0 is the permeability constant, $\mu_0 = 4\pi \times 10^{-7}$ kg m s^{-2} A^{-2}. If the two dipoles $\boldsymbol{\mu}_1$ and $\boldsymbol{\mu}_2$ have the same orientation with respect to $\boldsymbol{r}$ then equation (3)becomes:

$$E = (\boldsymbol{\mu}_1 \cdot \boldsymbol{\mu}_2)r^{-3}(1 - 3\cos^2\theta)(\mu_0/4\pi) \tag{4}$$

where θ is the angle between the direction of the two magnetic dipoles and the vector $\boldsymbol{r}$ which separates them.

In NMR studies, one is generally concerned with nuclear magnetic moments. Consider two nuclei (1 and 2) separated by a distance r in a magnetic field (Figure 1). The quantum mechanical Hamiltonian describing the direct dipolar interaction, $\hat{\mathcal{H}}_{\mathrm{DD}}$, is constructed by replacing the vectors $\boldsymbol{\mu}_1$ and $\boldsymbol{\mu}_2$ in equation (3) by their corresponding operators, $\gamma_1\hbar\hat{\boldsymbol{I}}_1$ and $\gamma_2\hbar\hat{\boldsymbol{I}}_2$:

$$\hat{\mathcal{H}}_{\mathrm{DD}} = \gamma_1\gamma_2\hbar^2[(\hat{\boldsymbol{I}}_1 \cdot \hat{\boldsymbol{I}}_2)r^{-3} - 3(\hat{\boldsymbol{I}}_1 \cdot \boldsymbol{r})(\hat{\boldsymbol{I}}_2 \cdot \boldsymbol{r})r^{-5}](\mu_0/4\pi) \tag{5}$$

where γ_i is the magnetogyric ratio of nucleus i (in rad s^{-1} T^{-1}), $\hat{\boldsymbol{I}}_i$ is the nuclear spin angular momentum operator, and $\boldsymbol{r}$ is the internuclear vector. In an NMR experiment, the direction of the magnetic moments is defined by the direction of the applied magnetic field $\boldsymbol{B}_0$.

If one expands the scalar products in equation (5),

$$\hat{\boldsymbol{I}}_1 \cdot \hat{\boldsymbol{I}}_2 = \hat{I}_{1x}\hat{I}_{2x} + \hat{I}_{1y}\hat{I}_{2y} + \hat{I}_{1z}\hat{I}_{2z} \tag{6}$$

$$\hat{\boldsymbol{I}}_1 \cdot \boldsymbol{r} = \hat{I}_{1x}x + \hat{I}_{1y}y + \hat{I}_{1z}z \tag{7}$$

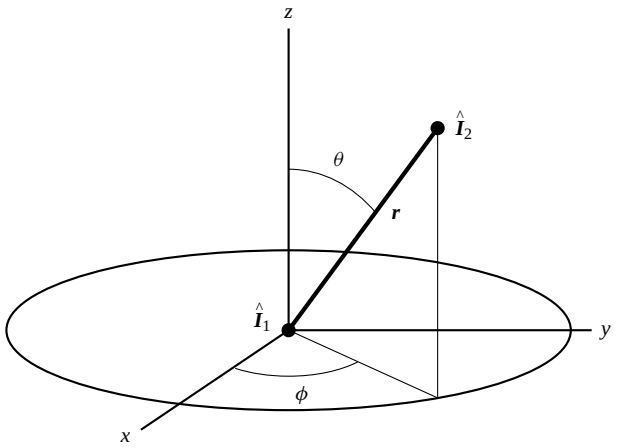

Figure 1 Coordinate system used to describe the coupling of two spins $\hat{\boldsymbol{I}}_1$ and $\hat{\boldsymbol{I}}_2$ separated by a distance r. A strong applied magnetic field lies along the z axis

$$\hat{\boldsymbol{I}}_2 \cdot \boldsymbol{r} = \hat{I}_{2x}x + \hat{I}_{2y}y + \hat{I}_{2z}z \tag{8}$$

the direct dipolar Hamiltonian may be expanded and rewritten as

$$\begin{aligned}\hat{\mathcal{H}}_{\mathrm{DD}} = \gamma_1\gamma_2\hbar^2 r^{-5}[&\hat{I}_{1x}\hat{I}_{2x}(r^2 - 3x^2) + \hat{I}_{1y}\hat{I}_{2y}(r^2 - 3y^2)\\ &+\hat{I}_{1z}\hat{I}_{2z}(r^2 - 3z^2) - (\hat{I}_{1x}\hat{I}_{2y} + \hat{I}_{1y}\hat{I}_{2x})3xy\\ &-(\hat{I}_{1y}\hat{I}_{2z} + \hat{I}_{1z}\hat{I}_{2y})3yz - (\hat{I}_{1z}\hat{I}_{2x} + \hat{I}_{1x}\hat{I}_{2z})3zx]\\ &\times(\mu_0/4\pi)\end{aligned} \tag{9}$$

This equation can be expressed in matrix form:

$$\hat{\mathcal{H}}_{\mathrm{DD}} = hR\left\{[\hat{I}_{1x} \quad \hat{I}_{1y} \quad \hat{I}_{1z}]\right.$$
$$\left.\begin{bmatrix} (r^2 - 3x^2)/r^2 & -3xy/r^2 & -3xz/r^2 \\ -3xy/r^2 & (r^2 - 3y^2)/r^2 & -3yz/r^2 \\ -3xz/r^2 & -3yz/r^2 & (r^2 - 3z^2)/r^2 \end{bmatrix} \begin{bmatrix} \hat{I}_{2x} \\ \hat{I}_{2y} \\ \hat{I}_{2z} \end{bmatrix}\right\} \tag{10}$$

where R is defined as the direct dipolar coupling constant,

$$R = \gamma_1\gamma_2 r^{-3}(\hbar/2\pi)(\mu_0/4\pi) \tag{11}$$

Equation (10) can be abbreviated as

$$\hat{\mathcal{H}}_{\mathrm{DD}} = hR(\hat{\boldsymbol{I}}_1 \cdot \boldsymbol{D} \cdot \hat{\boldsymbol{I}}_2) \tag{12}$$

where $\boldsymbol{D}$; is the direct dipolar tensor.

It is easy to see that if the internuclear vector $\boldsymbol{r}$, lies along the z axis, then the dipolar tensor becomes diagonal:

$$\boldsymbol{D} = \begin{bmatrix} 1 & 0 & 0 \\ 0 & 1 & 0 \\ 0 & 0 & -2 \end{bmatrix} \tag{13}$$

This is the so-called principal axis system (PAS) of the dipolar tensor. Note that the principal components of the dipolar tensor

are axially symmetric, i.e. $D_{11} = D_{22}$. From equation (10) it is also obvious that the dipolar tensor is symmetric (i.e. $D_{\alpha\beta} = D_{\beta\alpha}$). Finally, it is also clear that the trace of the dipolar tensor is zero. This result indicates that the direct dipolar interaction does not influence the positions of peaks in liquid phase NMR spectra. It can also be shown that for isolated spin pairs in solid samples the time averaged expectation value of $\hat{\mathcal{H}}_{\mathrm{DD}}$ is zero under conditions of MAS.[12] The sample must be spun rapidly with respect to the direct dipolar coupling constant R.

In order to discuss the NMR spectrum of two dipolar coupled spins in the solid state, it is convenient to transform equation (5) from Cartesian coordinates to spherical polar coordinates. This is readily accomplished by setting: $x = r \sin\theta \cos\phi$, $y = r \sin\theta \sin\phi$, $z = r \cos\theta$ and expressing $\hat{I}_x$ and $\hat{I}_y$ in terms of the raising and lowering operators $\hat{I}^+$ and $\hat{I}^-$, respectively:

$$\hat{\boldsymbol{I}}^+ = \hat{I}_x + \mathrm{i}\hat{I}_y, \quad \hat{\boldsymbol{I}}^- = \hat{I}_x - i, \hat{I}_y \tag{14}$$

Spin functions used to describe a nuclear spin state are eigenfunctions of the Zeeman Hamiltonian; they are often denoted by $|\, I,\, m\rangle$, where I is the nuclear spin quantum number and m is the z component of the spin angular momentum in units of $\hbar$ (i.e. $\hat{I}_z \mid I,\, m\rangle = m|I,\, m\rangle$). The spin quantum number m may take on values of $-I, -I+1, \ldots, +I$. Thus, for spin-$\frac{1}{2}$ nuclei there are only two states $|\, \frac{1}{2}, \frac{1}{2}\rangle$ and $|\, \frac{1}{2}, -\frac{1}{2}\rangle$, which are generally denoted by $|\, \alpha\rangle$ and $|\, \beta\rangle$, respectively: $\hat{I}_z \mid \alpha\rangle = \frac{1}{2}|\alpha\rangle$ and $\hat{I}_z|\beta\rangle = -\frac{1}{2}|\beta\rangle$, while $\hat{I}^+|\alpha\rangle = 0$, $\hat{I}^+|\beta\rangle = |\alpha\rangle$, $\hat{I}^-|\alpha\rangle = |\beta\rangle$ and $\hat{I}^-|\beta\rangle = 0$. Further details concerning the quantum mechanics of angular momentum can be found elsewhere.[8–11,13,14]

In spherical polar coordinates, the dipolar Hamiltonian can be expressed in terms of the so-called dipolar alphabet:

$$\hat{\mathcal{H}}_{\mathrm{DD}} = hR(\hat{A} + \hat{B} + \hat{C} + \hat{D} + \hat{E} + \hat{F}) \tag{15}$$

Each of the terms $\hat{A}$ to $\hat{F}$ contains spin operators and a spatial term generally involving both θ and ϕ. Each term alters the spin functions used to describe a spin pair in a characteristic way. Explicit expressions for the terms $\hat{A}$ to $\hat{F}$ are given in several NMR textbooks.[8–11]

To describe the NMR spectrum of a pair of equivalent homonuclear spins in a strong magnetic field, it is only necessary to consider the terms $\hat{A}$ and $\hat{F}$:

$$\hat{A} = -\hat{I}_{1z}\hat{I}_{2z}(3\cos^2\theta - 1) \tag{16}$$

$$\hat{B} = \tfrac{1}{4}[\hat{\boldsymbol{I}}_1^+ \cdot \hat{\boldsymbol{I}}_2^- + \hat{\boldsymbol{I}}_1^- \cdot \hat{\boldsymbol{I}}_2^+](3\cos^2\theta - 1) \tag{17}$$

Clearly, the $\hat{A}$ term does not alter the simple product spin functions $|\, \alpha\alpha\rangle$, $|\, \alpha\beta\rangle$, $|\, \beta\alpha\rangle$, and $|\, \beta\beta\rangle$ (e.g. $\hat{I}_{1z}\hat{I}_{2z}|\alpha\beta\rangle = (\frac{1}{2})(-\frac{1}{2})|\alpha\beta\rangle$). On the other hand, the $\hat{B}$ term contains the 'flip-flop' operator $\hat{I}_1^+\hat{I}_2^- + \hat{I}_1^-\hat{I}_2^+$, which alters the spin functions $|\, \alpha\beta\rangle$ to $|\, \beta\alpha\rangle$, and vice versa. For a pair of magnetically equivalent spins which are dipolar coupled in a strong applied magnetic field $\boldsymbol{B}_0$, the appropriate Hamiltonian operator is

$$\hat{\mathcal{H}} = \hat{\mathcal{H}}_{\mathrm{Z}} + \hat{\mathcal{H}}_{\mathrm{DD}} \tag{18}$$

where $\hat{\mathcal{H}}_{\mathrm{Z}} = -\nu_0 h(\hat{I}_{1z} + \hat{I}_{2z}$, and $\nu_0 = \gamma B_0/2\pi$. To describe such a spin system, it is convenient to use the following basis functions:

$$|t_1\rangle = |\alpha\alpha\rangle \tag{19a}$$

$$|t_0\rangle = 2^{-1/2}(|\alpha\beta\rangle + |\beta\alpha\rangle)$$

$$|s\rangle = 2^{-1/2}(|\alpha\beta\rangle - |\beta\alpha\rangle) \tag{19b}$$

$$|t_{-1}\rangle = |\beta\beta\rangle \tag{19c}$$

Using these basis functions, the total matrix of the truncated dipolar Hamiltonian operator is diagonal. The resulting eigenvalues of $\hat{\mathcal{H}}$ (in frequency units) are:

$$|t_1\rangle: \quad -\nu_0 - \tfrac{1}{4}R(3\cos^2\theta - 1) \tag{20a}$$

$$|t_0\rangle: \quad \tfrac{1}{2}R(3\cos^2\theta - 1) \tag{20b}$$

$$|t_{-1}\rangle: \quad \nu_0 - \tfrac{1}{4}R(3\cos^2\theta - 1) \tag{20c}$$

$$|s\rangle: \quad 0 \tag{20d}$$

where θ is the angle between the dipolar vector and the applied magnetic field $\boldsymbol{B}_0$. Transitions involving the antisymmetric $|\, s\rangle$ level are symmetry-forbidden; therefore only two transitions, $\nu_0 \pm \frac{3}{4}R(3\cos^2\theta - 1)$, are allowed.

For any general orientation of a spin pair in an applied magnetic field, the two peaks are separated by $(\frac{3}{2})R(3\cos^2\theta - 1)$. Spectra from an isolated homonuclear spin pair in a hypothetical single crystal and powder sample are shown in Figure 2. The powder spectrum, known as a Pake powder pattern, is obtained by considering all orientations of the dipolar vector in $\boldsymbol{B}_0$ ($0^\circ \le \theta \le 180^\circ$; $0^\circ \le \phi \le 360^\circ$). The separation between the discontinuities, $(\frac{3}{2})R$, corresponds to $\theta = 90^\circ$ while the shoulders are separated by $3R$, which corresponds to the $\theta = 0^\circ$ orientation.

For a pair of unlike spins A and X, where the two spins have different magnetogyric ratios but both are spin $\frac{1}{2}$, it is only necessary to consider the A term of $\hat{\mathcal{H}}_{\mathrm{DD}}$ since this is the only term in the dipolar alphabet which commutes with $\hat{\mathcal{H}}_{\mathrm{Z}}$. The A-spin NMR spectrum consists of two peaks at $\nu_{\mathrm{A}} \pm (\frac{1}{2})R(3\cos^2\theta - 1)$, where $\nu_{\mathrm{A}} = \gamma_{\mathrm{A}}B_0/2\pi$; the X-spin spectrum will be identical, except for the fact that it is centered about ν_{X} instead of ν_{A}. For unlike spins, the separation between the discontinuities in the A-spin or X-spin Pake powder pattern is R. If the X spin is a quadrupolar nucleus, calculation of the A-spin NMR spectrum may be more difficult, particularly if the high-field approximation is not applicable [i.e. $\hat{\mathcal{H}}_{\mathrm{Z}}(X) \approx \hat{\mathcal{H}}_{\mathrm{Q}}(X)$]. An instructive example of this problem was provided by Stoll et al.[15] who discussed the ^{13}C NMR spectra of the $^{13}\mathrm{C} - {}^{14}\mathrm{N}$ spin pair in a single crystal of $K_2Pt(CN)_4Br_{0.3}{\cdot}3H_2O$.

In practice, the chemical shielding interaction is orientation dependent, and thus it will also influence the detailed NMR lineshape. For protons, anisotropic chemical shielding generally causes a minor perturbation on the Pake doublet powder pattern, since it will be several orders of magnitude smaller than the direct dipolar interaction. However, for most other nuclei, the anisotropic chemical shielding (in frequency units) may be comparable to or greater than the dipolar interactions with adjacent nuclei. Under such conditions the

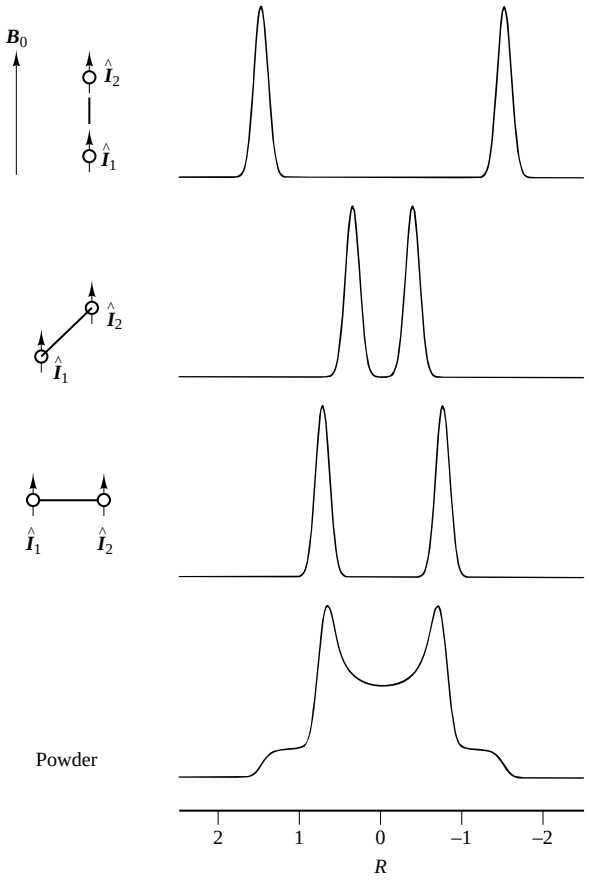

Figure 2 Calculated NMR spectra for two equivalent spins $\hat{\boldsymbol{I}}_1$ and $\hat{\boldsymbol{I}}_2$ which interact with one another by the direct dipolar interaction. From top to bottom: calculated spectra for three orientations of the internuclear vector in the applied magnetic field $\boldsymbol{B}_0$, θ = 0°, 45°, 90°, respectively. The bottom spectrum is the Pake powder pattern which results from a sum of spectra of individual crystallites which are randomly distributed in the sample. The calculated spectra have been convoluted with a Gaussian function to simulate weak dipolar interactions with more remote nuclei

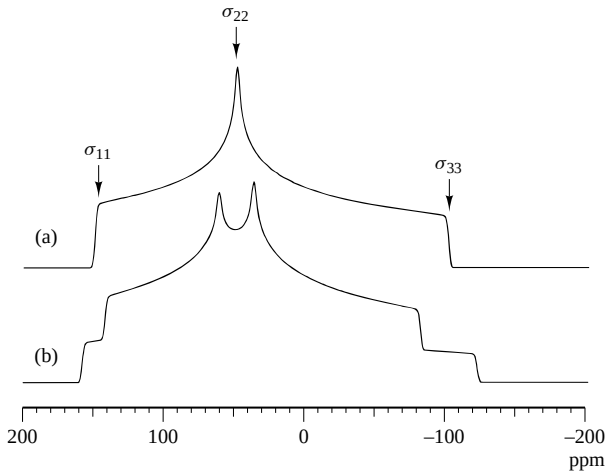

Figure 3 (a) A typical spin-$\frac{1}{2}$ NMR powder pattern of an isolated spin with anisotropic chemical shielding. The principal components of the chemical shielding tensor are easily identified from the powder pattern by the shoulders at σ_{11} and at σ_{33} and the discontinuity at σ_{22}. (b) Same as (a), but the influence of direct dipolar coupling with an adjacent spin-$\frac{1}{2}$ nucleus is illustrated. The direct dipolar interaction causes an apparent splitting of the chemical shielding powder pattern

Table 1 Typical Direct and Indirect Spin–Spin Coupling Constants Involving Carbon

X	Compound	R [a](Hz)	$J(\mathrm{M},^{13}\mathrm{C})_{\mathrm{iso}}$ (Hz)	$K(\mathrm{M,C})_{\mathrm{iso}}$ [b]
^{13}C	$C(CH_3)_4$ [c]	2080	37	4.9
^{29}Si	$Si(CH_3)_4$ [c]	−920	−50	8.4
^{73}Ge	$Ge(CH_3)_4$ [c]	−140	−19	17.7
^{119}Sn	$Sn(CH_3)_4$ [c]	−1090	−340	30.1
^{207}Pb	$Pb(CH_3)_4$ [c]	590	250	39.9
^{113}Cd	$Cd(CH_3)_2$ [d]	−740	−513	76.3
^{199}Hg	$Hg(CH_3)_2$ [e]	660	690	127
^{199}Hg	$Hg(CH_3)(NO_3)$ [e]	660	1800	331

[a]Approximate values. [b]$K_{\mathrm{N,N'}} = 4\pi^2 J_{\mathrm{N,N'}}/h\gamma_{\mathrm{N}}\gamma_{\mathrm{N'}}$ (units 10^{20} N A^{-2} m^{-3}). [c]Dalling and Gutowsky.[57] [d]Dreeskamp and Hildenbrand.[58] [e]Jokisaari et al.[59]

'A'-spin NMR spectrum of an AX-spin system in a static powder sample will consist of $2I$ + 1 overlapping powder patterns, where I is the spin quantum number of X (Figure 3). One can often obtain valuable information concerning the orientation of chemical shielding tensors by analyzing dipolar chemical shift NMR spectra.[14,16–18]

Typical values of the direct dipolar coupling constant involving directly bonded spin pairs range from a few hundred hertz to several kilohertz. For example, for the directly bonded ^{13}C–^{15}N spin pair in the amide fragment of a peptide, $R \approx 1.3$ kHz; for the directly bonded ^{13}C–^{1}H spin pair in a typical organic compound, $R \approx 23$ kHz. Further examples of direct dipolar coupling constants involving carbon are given in Table 1.

Much recent research is being focused on recoupling of dipolar interactions in high-resolution MAS experiments, e.g. the rotational resonance and rotational echo double resonance (REDOR) techniques.[19–21] The objective of these experiments is to determine internuclear separations from small dipolar coupling constants. In fact, as will be outlined in Section 3.2, these experiments yield only an effective dipolar coupling constant which is dependent on the anisotropy in the indirect coupling as well as the direct dipolar coupling constant R.

As an aside, it is important to indicate that anisotropic molecular vibrations can result in a subtle vibrationally induced asymmetry of the dipolar coupling tensor; this will be most important when the direct dipolar coupling involves a hydrogen nucleus.[22,23]

The discussion presented here can be extended to more complex spin systems. For example, Van Hecke et al.[24] studied the ^{1}H and ^{19}F NMR spectra of the bifluoride ion in a single crystal of KHF_2. In addition, systems containing the $^{13}CH_2$ fragment have attracted considerable attention.[25–27]

3 INDIRECT SPIN–SPIN COUPLING

As mentioned in Section 1, indirect spin–spin coupling is a two-stage process. One can imagine the spin at one nucleus perturbing the electrons in its vicinity. The resulting

perturbation is transferred via the electronic framework of the molecule to electrons in the vicinity of the second nucleus. The distinctive ways in which a nuclear moment perturbs the surrounding electrons is known as a mechanism for indirect spin–spin coupling (see below). The total indirect spin–spin coupling constant J is a sum of the contributions arising from each mechanism. Clearly, the contribution that each coupling mechanism makes to J is directly proportional to the product of the nuclear magnetic moments of the two coupled nuclei. The sign of indirect spin–spin coupling constants can be either positive or negative. If the indirect spin–spin coupling interaction stabilizes the antiparallel arrangement of the nuclear spins, then the indirect spin–spin coupling is positive. The magnitudes of isotropic indirect spin–spin coupling constants are readily measured in solution NMR studies. Values as small as 0.10 Hz are routinely measured. Isotropic values rarely exceed 30 kHz; however, a ^{199}Hg,^{199}Hg indirect spin–spin coupling constant of 139.6 kHz has been reported for the Hg_3^{2+} ion.[28] Typical values of one-bond indirect spin–spin coupling constants involving carbon, $^1J(\mathrm{M},^{13}\mathrm{C})_{\mathrm{iso}}$, are given in Table 1. The literature on isotropic indirect spin–spin coupling constants is extensive.[29] Over the past 45 years many important relationships between spin–spin coupling constants J_{iso} and molecular structure have been established. On the other hand $\boldsymbol{J}$ tensors are difficult to characterize experimentally. Furthermore, reliable quantum mechanical calculations of $\boldsymbol{J}$ tensors or their corresponding isotropic values are a challenge.[30] Here, the properties of the $\boldsymbol{J}$ tensor are outlined. This is followed by a discussion of how the $\boldsymbol{J}$ tensor can be experimentally characterized from solid state NMR measurements.

3.1 Nature of $\boldsymbol{J}$ Coupling Tensors

The Hamiltonian describing the indirect spin–spin coupling of two spins, $\boldsymbol{I}_1$ and $\boldsymbol{I}_2$, may be expressed as

$$\hat{\mathcal{H}}_J = h\hat{\boldsymbol{I}}_1 \cdot \boldsymbol{J} \cdot \hat{\boldsymbol{I}}_2 \tag{21}$$

where $\boldsymbol{J}$ is the indirect spin–spin coupling tensor. The $\boldsymbol{J}$ tensor is a second rank tensor which is described by nine matrix elements in a Cartesian coordinate system. For example, in a particular molecular fixed axis system, the $\boldsymbol{J}$ tensor might be represented by the matrix:

$$\boldsymbol{J} = \begin{bmatrix} J_{aa} & J_{ab} & J_{ac} \\ J_{ba} & J_{bb} & J_{bc} \\ J_{ca} & J_{cb} & J_{cc} \end{bmatrix} \tag{22}$$

In contrast to the direct dipolar tensor, the $\boldsymbol{J}$ tensor has a nonvanishing trace.

A general second-rank tensor can be decomposed into a sum of irreducible tensors of rank l = 0, 1, 2.[31,32] Thus the indirect spin–spin coupling tensor can be written as

$$\boldsymbol{J} = \boldsymbol{J}^{(0)} + \boldsymbol{J}^{(1)} + \boldsymbol{J}^{(2)} \tag{23}$$

In equation (23) the l = 0 tensor is the isotropic part of the tensor,

$$\boldsymbol{J}^{(0)} = (\tfrac{1}{3}\ \mathrm{Tr}\ \boldsymbol{J})\boldsymbol{1} = J_{\mathrm{iso}}\boldsymbol{1} \tag{24}$$

where $\mathrm{Tr}\ \boldsymbol{J} = (J_{aa} + J_{bb} + J_{cc})$ and $\boldsymbol{1}$ is the unit tensor with diagonal components equal to 1 and all off-diagonal elements zero. The second term in equation (23), l = 1, is the antisymmetric part of the tensor,

$$\boldsymbol{J}^{(1)} = \tfrac{1}{2}(\boldsymbol{J} - \boldsymbol{J}^{\mathrm{t}}) \tag{25}$$

where $\boldsymbol{J}^{\mathrm{t}}$ is the transpose of $\boldsymbol{J}$. The transpose of a 3 × 3 matrix is obtained by replacing the first column by the first row, the second column by the second row, and the third column by the third row. Since the diagonal elements of $\boldsymbol{J}$ and $\boldsymbol{J}^{\mathrm{t}}$ are identical, the diagonal elements of the antisymmetric tensor are zero. The third term in equation (23), l = 2, is the symmetric part of the tensor, defined as

$$\boldsymbol{J}^{(2)} = \tfrac{1}{2}(\boldsymbol{J} + \boldsymbol{J}^{\mathrm{t}}) - J_{\mathrm{iso}}\boldsymbol{1} \tag{26}$$

Although the trace of the symmetric part is zero, the diagonal elements are, in general, not zero.

To a very good approximation, only tensors with l = 0 and l = 2 affect the general appearance of an NMR spectrum.[32] That is, even though the antisymmetric components of a particular $\boldsymbol{J}$ tensor may be non zero, these components do not perturb the observed spectrum in first order. In fact, the existence of antisymmetric components in any indirect spin–spin coupling tensor has never been demonstrated experimentally.[33]

For each symmetric $\boldsymbol{J}$ tensor ($\boldsymbol{J}^{(0)} + \boldsymbol{J}^{(2)}$), there exists a principal axis system for which the matrix $\boldsymbol{J}^{(2)}$ is diagonal. The diagonal elements, denoted by J_{xx}, J_{yy}, and J_{zz}, are called the principal elements, with the convention:

$$|J_{zz}| \geq |J_{xx}| \geq |J_{yy}| \tag{27}$$

The principal axis system of the $\boldsymbol{J}$ tensor is often fixed by the molecular symmetry. For a linear molecule there are only two components, $J_{\parallel}$ and $J_{\perp}$, describing the coupling of the nuclear spin components parallel and perpendicular to the internuclear axis, respectively. Similarly, there are only two non-zero components of the symmetric $\boldsymbol{J}$ tensor for a pair of nuclei sitting on the highest order symmetry axis of molecules in the point groups D_{nd}, D_{nh}, C_{nh}, C_{nv}, and S_n, with $n \geq 3$. The number of independent components in the $\boldsymbol{J}$ tensor for other group symmetries has been tabulated by Buckingham et al.[33] and by Robert and Wiesenfeld.[34]

In describing the orientation dependence of NMR parameters, it is often useful to define the anisotropy of the parameter. This provides a measure of the maximum orientation dependence of that particular parameter. The anisotropy of the indirect spin–spin coupling tensor is usually defined as

$$\Delta J = J_{zz} - \tfrac{1}{2}(J_{xx} + J_{yy}) \equiv \tfrac{3}{2}(J_{zz} - J_{\mathrm{iso}}) \tag{28}$$

In the case of axial symmetry, equation (28) simplifies to

$$\Delta J = J_{\parallel} - J_{\perp} \tag{29}$$

In such cases it is straightforward to show that

$$\boldsymbol{J} = \begin{bmatrix} J_{\perp} & 0 & 0 \\ 0 & J_{\perp} & 0 \\ 0 & 0 & J_{\parallel} \end{bmatrix} = J_{\mathrm{iso}}\boldsymbol{1} + \begin{bmatrix} -\Delta J/3 & 0 & 0 \\ 0 & -\Delta J/3 & 0 \\ 0 & 0 & 2\Delta J/3 \end{bmatrix} \tag{30}$$

Under these conditions the Hamiltonian equation (21), becomes

$$\hat{\mathcal{H}}_{\boldsymbol{J}} = hJ_{\rm iso}\hat{\boldsymbol{I}}_1 \cdot \hat{\boldsymbol{I}}_2 + h\hat{\boldsymbol{I}}_1 \cdot \boldsymbol{J}' \cdot \hat{\boldsymbol{I}}_2 \tag{31}$$

where $\boldsymbol{J}'$ is the traceless '$\Delta\boldsymbol{J}$' tensor which is of the same form as the dipolar tensor [equation (13)]. Since the trace of $\boldsymbol{J}'$ is zero, it is clear that the anisotropy in the principal components of $\boldsymbol{J}$ has no influence on the NMR spectra of isotropic fluids. In principle, ΔJ could provide a mechanism for spin–lattice relaxation, but this mechanism has never been identified as being important.[35]

Ramsey's theory[5] serves as the basis for most theoretical discussions of indirect spin–spin coupling tensors. Following Ramsey, the nonrelativistic Hamiltonian describing nuclear spin, electron spin interactions can be represented by

$$\hat{\mathcal{H}} = \hat{\mathcal{H}}^{(1a)} + \hat{\mathcal{H}}^{(1b)} + \hat{\mathcal{H}}^{(2)} + \hat{\mathcal{H}}^{(3)} \tag{32}$$

The first two terms are the so-called orbital diamagnetic (OD) and orbital paramagnetic (OP) terms which account for the interaction between the nuclear magnetic moments and the orbital motion of the electrons. The third term, $\hat{\mathcal{H}}^{(2)}$, accounts for the spin-dipolar (SD) interactions between the nuclear and electronic magnetic moments. The last term, $\hat{\mathcal{H}}^{(3)}$, accounts for the interaction of the nucleus and the electron spin at the nucleus; this interaction is known as the Fermi contact (FC) interaction. Using these interactions, various approaches, generally based on second-order perturbation theory, are used to calculate indirect nuclear spin–spin coupling tensors. Five separate terms contribute to the overall $\boldsymbol{J}$ tensor:

$$\boldsymbol{J} = \boldsymbol{J}^{(1a)} + \boldsymbol{J}^{(1b)} + \boldsymbol{J}^{(2)} + \boldsymbol{J}^{(3)} + \boldsymbol{J}^{(4)} \tag{33}$$

The orbital diamagnetic contribution $\boldsymbol{J}^{(1a)}$ involves only the ground electronic state of the system. The other four terms involve the following combination of interactions: OP–OP, SD–SD, FC–FC, and FC–SD. The OP term has matrix elements between the ground state and excited singlet states while the SD and FC interactions have matrix elements between the ground state and excited triplet states. The FC–FC contribution to the $\boldsymbol{J}$ tensor is completely isotropic. In contrast, the FC–SD cross term does not contribute to the isotropic value of the spin–spin coupling tensor, but only to its anisotropy, thus the trace of the tensor arising from this term is zero. The other two terms contribute to both the isotropic and anisotropic portion of the total $\boldsymbol{J}$ tensor.

Explicit expressions for each of the five terms in equation (33) are given in several standard NMR texts and review articles.[29,36] It should be mentioned that the theory of Ramsey is a nonrelativistic theory which assumes that orbital and spin angular momenta are L–S coupled. Pyykkö[37] has developed a relativistic analogue of Ramsey's theory based on j–j coupling. Undoubtedly, relativistic effects will be important for indirect spin–spin coupling constants involving nuclei beyond the second row. Furthermore, it has been found that consideration of relativistic effects in extended Hückel calculations tends to increase the calculated anisotropy of spin–spin coupling tensors.[38]

In equation (33), each term is of the form $\gamma_N\gamma_{N'}h\boldsymbol{K}_{N,N'}/4\pi^2$, where $\boldsymbol{K}_{N,N'}$ is called the reduced indirect spin–spin coupling tensor involving nuclei N and N'. The reduced coupling tensor is independent of the magnitude of the nuclear magnetic moments and, therefore, it is useful in comparing indirect spin–spin coupling tensors involving different spin pairs. Note that $\boldsymbol{J}_{N,N'}$ has units of Hz (s^{-1}) and $\boldsymbol{K}_{N,N'}$ has units of N A^{-2} m^{-3} (or, equivalently, T^2 J^{-1}).[39] The isotropic indirect spin–spin coupling constants involving carbon in Table 1 have also been expressed as reduced coupling constants. As one descends the group 14 elements, M, of the Periodic Table in the series $M(CH_3)_4$, $\boldsymbol{K}$(M,C) increases with atomic number Z_M. Similarly, in the series X_3MPR_3, where M is a group 13 element, $\boldsymbol{K}$(M,P) increases as follows: $\approx 10 \times 10^{20}$ N A^{-2} m^{-3} (M = B), $\approx 20 \times 10^{20}$ (Al), $\approx 65 \times 10^{20}$ (M = Ga), and $\approx 100 \times 10^{20}$ (M = In).[40] Qualitatively, these trends can be rationalized by considering only the Fermi contact mechanism; however, there is evidence that the tensor, $\boldsymbol{K}$(In,P), in $Br_3InP[4\text{-}(CH_3O)\text{-}C_6H_4]_3$ is anisotropic, implying that mechanisms other than the Fermi contact contribute to this particular $\boldsymbol{J}$ tensor.[40]

3.2 Measurement of $\boldsymbol{J}$ Coupling Tensors

Using NMR spectroscopy, $\boldsymbol{J}$ tensors can be characterized by studying the spectra of single crystals,[41–43] solid powder samples,[44–47] or samples oriented in liquid crystalline solvents.[48,49] In isotropic fluids, only the isotropic indirect spin–spin coupling constant (a scalar) is measured. For simple molecules in the gas phase ΔJ can, in principle, be measured using molecular beam magnetic resonance techniques.[50] So far, the latter technique has only been successfully applied to thallium fluoride.[51] In this case, $J(^{205}\text{Tl}, {}^{19}\text{F})_{\rm iso} = -13.3 \pm 0.7$ kHz and $\Delta J(^{205}\text{Tl}, {}^{19}\text{F}) = 11.1 \pm 0.7$ kHz. Below, the NMR spectra of a simple heteronuclear two-spin system residing in a rigid solid will be discussed. Particular emphasis is placed on describing how the NMR spectra depend on ΔJ.

Consider a pair of heteronuclear spins A and X, also denoted by '1' and '2', respectively, which are coupled to one another via direct and indirect spin–spin interactions in a strong applied magnetic field. Furthermore, if the $\boldsymbol{J}$ tensor is axially symmetric and coincident with the direct dipolar tensor, $J_\parallel$ and $J_\perp$ correspond to orientations where the internuclear vector is parallel and perpendicular, respectively, to the applied magnetic field. Under these conditions the appropriate nuclear spin Hamiltonian for the A spin is:

$$\hat{\mathcal{H}} = \hat{\mathcal{H}}_{\rm Z} + \hat{\mathcal{H}}_{\rm CS} + \hat{\mathcal{H}}_{\rm DD} + \hat{\mathcal{H}}_J \tag{34}$$

where $\hat{\mathcal{H}}_{\rm CS}$ accounts for the anisotropic chemical shielding. For now it is assumed that the chemical shielding is independent of the orientation of the molecule in the applied magnetic field. Both $\hat{\mathcal{H}}_{\rm DD}$ and $\hat{\mathcal{H}}_J$ are of the same form. As already indicated

$$\hat{\mathcal{H}}_{\rm DD} = hR\hat{\boldsymbol{I}}_1 \cdot \boldsymbol{D} \cdot \hat{\boldsymbol{I}}_2 = -hR\hat{I}_{1z}\hat{I}_{2z}(3\cos^2\theta - 1) \tag{35}$$

Similarly, equation (31) becomes

$$\hat{\mathcal{H}}_J = h\hat{\boldsymbol{I}}_1 \cdot \boldsymbol{J} \cdot \hat{\boldsymbol{I}}_2 = hJ_{\rm iso}\hat{I}_{1z}\hat{I}_{2z} + h(\Delta J/3)\hat{I}_{1z}\hat{I}_{2z} \times (3\cos^2\theta - 1) \tag{36}$$

Using the basic product functions for an AX spin system consisting of two spin-$\frac{1}{2}$ nuclei, it is straightforward to calculate the four energy levels. The A spectrum results from two allowed transitions at:

$$\nu = \nu_A - m_X J_{iso} + m_X[R - (\Delta J/3)](3\cos^2\theta - 1) \quad (37)$$

where $m_X = +\frac{1}{2}$ or $-\frac{1}{2}$. The two A peaks are separated by

$$\Delta\nu = J_{iso} - [R - (\Delta J/3)](3\cos^2\theta - 1) \quad (38)$$

Often, the term $R - (\Delta J/3)$ in equations (37) and (38) is called the effective dipolar coupling constant R_{eff}; thus,

$$\Delta\nu = J_{iso} - R_{eff}(3\cos^2\theta - 1) \quad (39)$$

The splittings, $\Delta\nu$, that would be observed as the A–X bond axis, $\boldsymbol{r}_{AX}$, in a single crystal is rotated about an axis perpendicular to $\boldsymbol{B}_0$ are shown in Figure 4. Several important points emerge from equations (37)–(39) and Figure 4:

1. For a single crystal sample, equation (39) also applies if the chemical shielding is anisotropic.
2. From Figure 4 it is apparent that the maximum *variation* in the splitting of the A peaks is $3R_{eff}$. Experimentally, one cannot separately determine R and ΔJ; only R_{eff} can be measured. If a value for the internuclear separation r_{AX} can be determined independently by diffraction techniques, R can be calculated from equation (11), and ΔJ can be obtained from the experimental value of R_{eff}.
3. The relative sign of J_{iso} and R_{eff} can be deduced from single crystal measurements. If J_{iso} and R_{eff} have the same sign, the maximum splitting will be $|J_{iso}| + |R_{eff}|$, while the minimum splitting will be $|J_{iso}| - 2|R_{eff}|$. On the other hand, if J_{iso} and R_{eff} have opposite signs, the maximum splitting will be $|J_{iso}| + 2|R_{eff}|$ and the minimum splitting will be $|J_{iso}| - |R_{eff}|$.

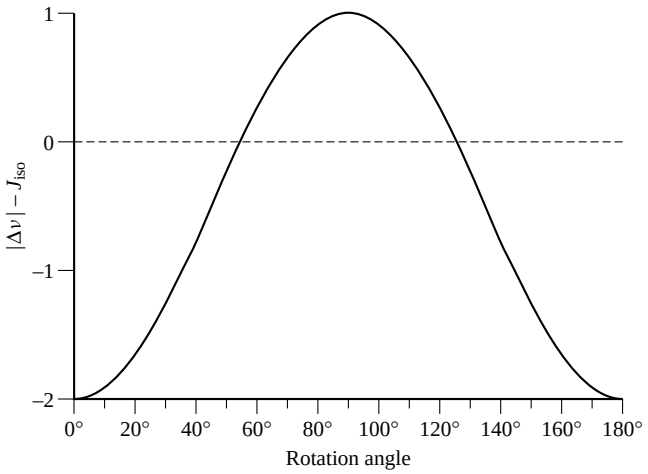

Figure 4 Separation between the two allowed A spin transitions for an AX spin system in a single crystal as a function of the orientation in the applied magnetic field $\boldsymbol{B}_0$. Splittings are given in units of R_{eff}. The rotation axis is perpendicular to $\boldsymbol{B}_0$ and the rotation angle θ is defined as the angle between $\boldsymbol{r}_{AX}$ and $\boldsymbol{B}_0$

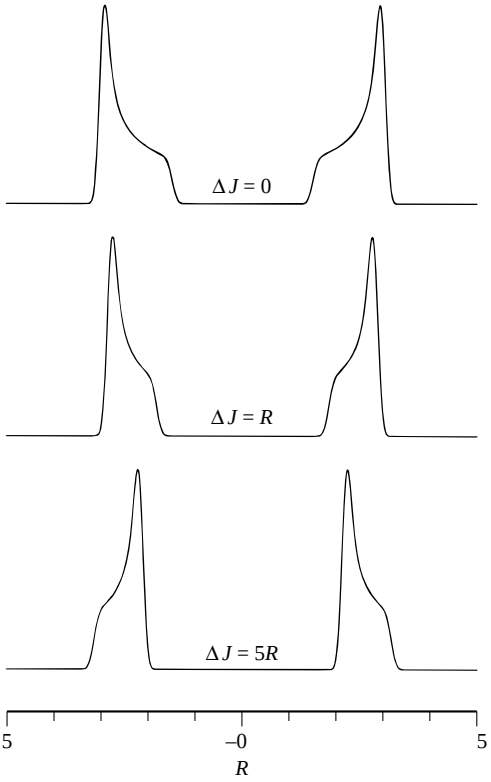

Figure 5 The effect of ΔJ on the A-spin NMR spectrum of a powder sample containing a heteronuclear AX spin pair. In each case $J_{iso} = 5R$. With $\Delta J = 3R$, each subspectrum collapses into an isotropic peak

In the case of a powder sample, the A spectrum consists of two subspectra corresponding to $m_X = +\frac{1}{2}$ and $m_X = -\frac{1}{2}$. Each subspectrum is one-half of a conventional Pake powder pattern (Figure 5). The isotropic frequencies of the two subspectra are separated by J_{iso}. (Note that if $J_{iso} = 0$, conventional Pake powder patterns would be observed except for the case where $\Delta J = 3R$.)

In calculating the spectra shown in Figure 5, the chemical shielding is assumed to be isotropic (i.e. independent of orientation). In order to calculate the A-spin NMR powder lineshape, allowing for the possibility of anisotropic chemical shielding, it is convenient to define the orientation of the internuclear vector in the PAS of the chemical shielding tensor (Figure 6). In this case one can show that the frequency of the A-spin transitions are given by:

$$\nu_m(\theta,\phi) = \nu_L - \nu_{CS} - m_X\nu_D - m_X J_{iso} \quad (40)$$

$$\nu_L = \gamma_A B_0/2\pi \quad (41)$$

$$\nu_{CS} = \left(\frac{\gamma_A B_0}{2\pi}\right)(\sigma_{11}\sin^2\theta\cos^2\phi + \sigma_{22}\sin^2\theta\sin^2\phi + \sigma_{33}\cos^2\theta) \quad (42)$$

$$\nu_D = R_{eff}\{1 - 3[\sin\beta\sin\theta\cos(\phi - \alpha) + \cos\beta\cos\theta]^2\} \quad (43)$$

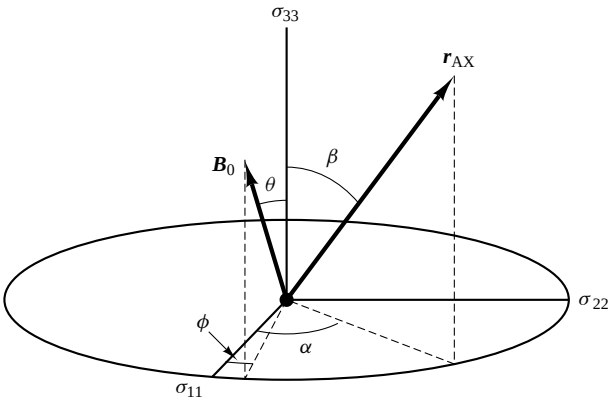

Figure 6 The orientation of an internuclear vector $\boldsymbol{r}_{AX}$ in the principal axis system (PAS) of the A-spin shielding tensor. The angles θ and ϕ define the orientation of $\boldsymbol{B}_0$ in the PAS of the shielding tensor

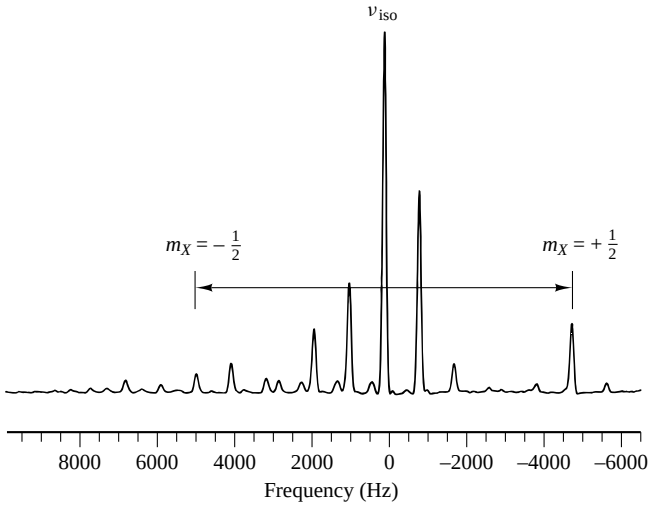

Figure 7 The ^{31}P NMR spectrum of a powder sample of [HgP(*o*-tolyl)$_3$(NO$_3$)$_2$]$_2$ obtained with relatively slow magic angle sample spinning (ν_r = 892 Hz). The spectrum was obtained with high-power ^{1}H decoupling and cross polarization in an applied magnetic field of 4.7 T, corresponding to a ^{31}P NMR Larmor frequency of 81.0 MHz. Frequencies are given with respect to the isotropic ^{31}P NMR peak of solid $NH_4H_2PO_4$. The horizontal arrow indicates the separation between the isotropic peak positions of the ^{199}Hg satellite peaks (J_{iso} = 9660 Hz). Note that the spinning sidebands of the high-frequency satellite peak, $m_{Hg-199} = -\frac{1}{2}$, extend over a much larger range than do those of the low-frequency satellite corresponding to $m_{Hg-199} = \frac{1}{2}$

where the principal components of the chemical shielding tensor σ_{11}, σ_{22}, and σ_{33} are defined such that $\sigma_{11} \leq \sigma_{22} \leq \sigma_{33}$. All angles are defined in Figure 6. In deriving equations (40)–(43), it is assumed that the $\boldsymbol{J}$ tensor is axially symmetric and that the $\boldsymbol{J}$ and $\boldsymbol{D}$ tensors are coincident. Even with these assumptions, the A-spin NMR powder spectrum may prove difficult to analyze.[18]

From the above discussion, it should be clear that if one is interested in characterizing a particular $\boldsymbol{J}$ tensor using solid state NMR techniques, single crystal NMR studies are desirable. Unfortunately, few studies have been reported to date.[41–43] Such studies are generally tedious, require relatively large single crystals (e.g. sides of 1 mm or greater), and the results of an X-ray or neutron diffraction investigation. In some cases, values of ΔJ can be obtained from the analysis of NMR powder spectra which arise from isolated spin pairs.[44–47] For example, for a series of mercury phosphine complexes values of $\Delta J(^{199}\text{Hg}, ^{31}\text{P})$ of the order of 5 kHz have been estimated from the analysis of static ^{31}P NMR spectra.[46,47] Below, the general procedure used to analyze such spectra is outlined.

The ^{31}P CP MAS spectrum of one of these complexes, [HgP(*o*-tolyl)$_3$(NO$_3$)$_2$]$_2$, is shown in Figure 7. The natural abundance of ^{199}Hg is 16.84% ($I = \frac{1}{2}$), therefore the ^{31}P NMR spectrum of the molecules containing the ^{199}Hg–^{31}P spin pair is a doublet with separation $J(^{199}\text{Hg},^{31}\text{P})_{iso}$ = 9660 Hz. The sign of this indirect spin–spin coupling constant is assumed to be positive on the basis of double resonance NMR experiments carried out on related molecules in solution. The only other naturally occurring isotope of mercury with nonzero spin is ^{201}Hg ($I = \frac{3}{2}$; natural abundance 13.22%), but the ^{31}P NMR spectrum of the ^{201}Hg–^{31}P spin pair is very broad and difficult to observe at room temperature. Molecules containing other naturally occurring isotopes of mercury give rise to a single isotropic peak, since the mercury nuclei of these isotopes have $I = 0$. In order to obtain R_{eff}, it is most advantageous to obtain a ^{31}P NMR spectrum of a static powder sample (Figure 8). Again, the intense central feature in the ^{31}P NMR spectrum corresponds to molecules where mercury nuclei have a spin $I = 0$.

Analysis of this central lineshape provides the principal components of the phosphorus shielding tensor, information required to analyze the subspectra arising from the ^{199}Hg–^{31}P spin pairs. In this case, the phosphorus shielding tensor is

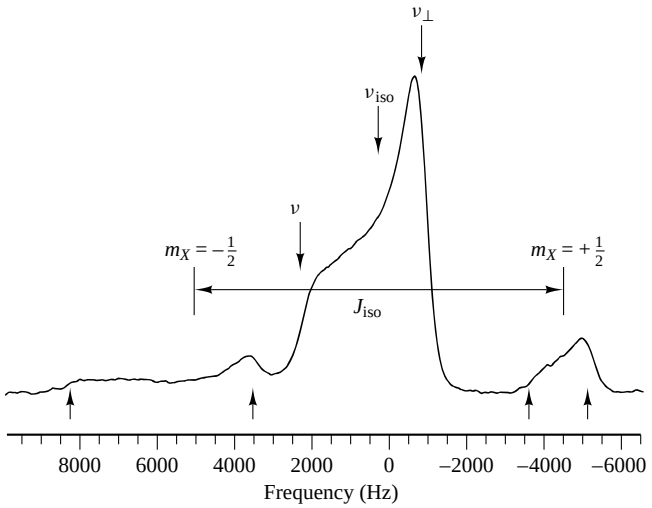

Figure 8 The ^{31}P NMR spectrum of a static powder sample of [HgP(*o*-tolyl)$_3$(NO$_3$)$_2$]$_2$ obtained at 81.0 MHz

approximately axially symmetric with the unique component along the Hg–P bond axis. Inspection of the spectrum shown in Figure 8 indicates that the high-frequency subspectrum corresponding to $m_{Hg-199} = -\frac{1}{2}$ is stretched (breadth ≈4.75 kHz), while the low-frequency subspectrum corresponding to $m_{Hg-199} = \frac{1}{2}$ is squeezed (breadth ≈1.45 kHz) relative to the intense central powder pattern [$(\nu_\parallel - \nu_\perp) \approx 3.10$ kHz]. In this particular case it is straightforward to show that the

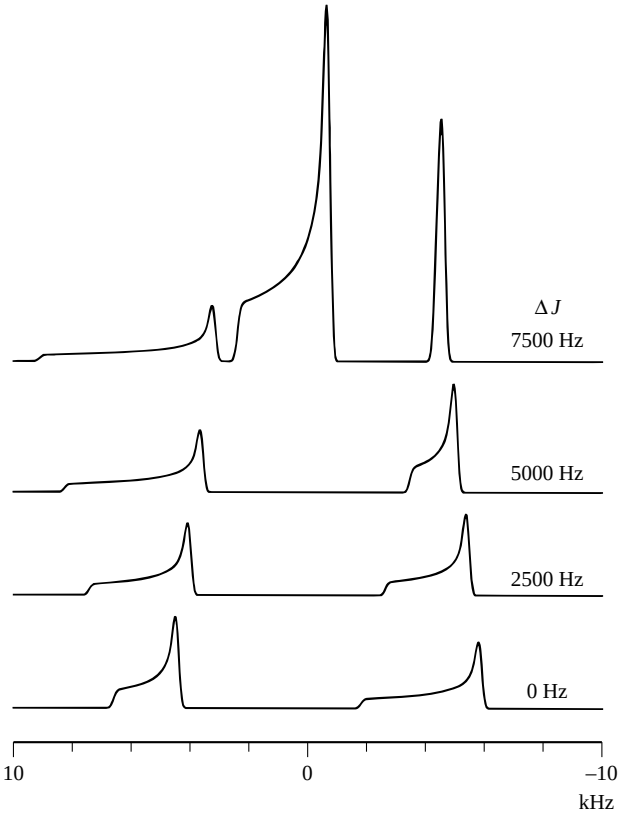

Figure 9 Calculated ^{31}P NMR powder spectra of [HgP(*o*-tolyl)$_3$(NO$_3$)$_2$]$_2$ as a function of ΔJ. The direct dipolar coupling constant, R = 0.64 kHz, and ($\nu_{\parallel} - \nu_{\perp}$) $\approx$ 3.10 kHz were held constant in each calculation. The central uncoupled ^{31}P NMR spectrum is only shown in the top spectrum; its intensity has been suppressed to emphasize the variations in the satellite subspectra as a function of ΔJ

breadth of each subspectrum is given by

$$\Delta\nu_{\pm m(Hg-199)} = (\nu_{\parallel} - \nu_{\perp}) \pm 3m_{Hg-199}R_{eff} \qquad (44)$$

Solving equation (44), one obtains R_{eff} = −1.10 kHz. From the known values of r_{Hg-P} in closely related compounds, R = 0.64 kHz; thus (ΔJ/3) = 1.74 kHz and ΔJ = 5.2 kHz. Note that if the relative signs of R_{eff} and J_{iso} were not known, another acceptable solution would be R_{eff} = + 1.10 kHz, hence ΔJ = −1.38 kHz. The sensitivity of the ^{31}P NMR spectrum of [HgP(*o*-tolyl)$_3$(NO$_3$)$_2$]$_2$ to ΔJ is illustrated in Figure 9. A complete single crystal ^{31}P NMR study of a closely related compound, HgP(cyclohexyl)$_3$(NO$_3$)$_2$, has recently been completed.[52] A typical rotation pattern is shown in Figure 10. Analysis indicates that R_{eff} = −1.07 kHz, leading to comparable values of ΔJ(^{199}Hg,^{31}P).[52] The results of these studies are significant in that they indicate that mechanisms other than the Fermi contact contribute to the $\boldsymbol{J}$(^{199}Hg, ^{31}P) tensor.

For AX spin systems in powder samples, one can also obtain R_{eff} from slow spinning MAS or variable angle spinning NMR studies; however, the errors tend to be large. Therefore, unless R_{eff} is significantly different than R, any estimate of ΔJ may be meaningless.

If a spin-$\frac{1}{2}$ nucleus is coupled to a neighboring quadrupolar nucleus, the spin-$\frac{1}{2}$ MAS NMR lineshape will often exhibit

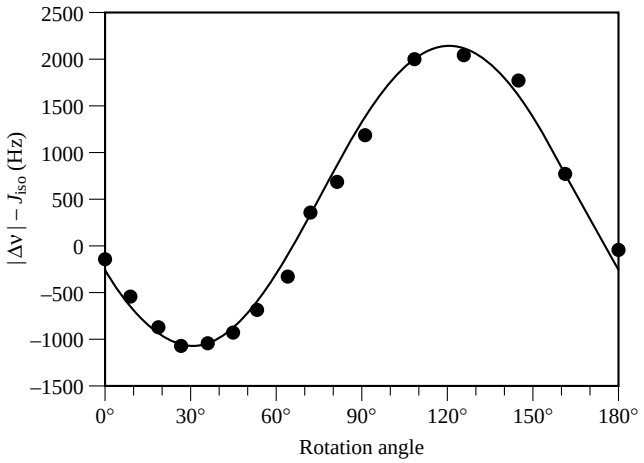

Figure 10 Plot of $\Delta\nu - J$(^{199}Hg,^{31}P)$_{iso}$ versus the rotation angle for a single crystal of HgP(cyclohexyl)$_3$(NO$_3$)$_2$. In this case the rotation axis is approximately perpendicular to the vector $\boldsymbol{r}_{Hg-P}$ so that the maximum observed variation in frequency (3.21 kHz) is approximately $3R_{eff}$

residual 'dipolar splittings' due to coupling with the quadrupolar nucleus.[53] In such cases the magic angle is no longer 'magic' because of the breakdown of the high-field approximation. Qualitatively, the Zeeman states of the quadrupolar nuclei are perturbed by the quadrupolar interaction. Thus, the detailed spin-$\frac{1}{2}$ MAS NMR lineshape depends on R_{eff}, $\boldsymbol{B}_0$, the nuclear quadrupolar coupling constant, and the orientation of the EFG tensor at the quadrupolar nucleus with respect to R_{AX}. Unless information concerning the EFG tensor at the quadrupolar nucleus is available from independent NMR or NQR studies, analysis of the spin-$\frac{1}{2}$ MAS NMR spectrum will be problematic.

Information concerning ΔJ is also available from NMR studies of solute molecules partially ordered in liquid crystalline solvents; however, again one can only determine $\boldsymbol{R}_{AX}$. In fact, from such experiments one measures a parameter which is related to $-S_{zz}[R - (\Delta J/3)]$, where S_{zz} is an order parameter, typically of the order of 0.1. In addition, it is necessary to make vibrational corrections and consider solute–liquid crystal solvent interactions. In spite of these problems, reliable values of ΔJ appear to be available for several compounds. For example, for methyl fluoride, ΔJ(^{19}F,^{13}C) = 404 ± 31 Hz, and thus ΔJ(^{19}F,^{13}C)/J(^{19}F,^{13}C)$_{iso}$ = −2.5 ± 0.2;[54] for dimethylmercury, ΔJ(^{199}Hg,^{13}C) = 855 ± 14 Hz, and thus ΔJ(^{199}Hg,^{13}C)/ J(^{199}Hg,^{13}C)$_{iso}$ = 1.25 ± 0.02.[55]

As mentioned in Section 2, several NMR experiments have been developed to recouple the direct dipolar interaction under conditions of MAS. Although such experiments actually measure R_{eff}, and not R, it is probably reasonable to assume that (ΔJ/3) $\ll R$, if the coupled nuclei are both first row elements (e.g. ^{13}C and ^{15}N), where J_{iso} is probably at least an order of magnitude less than R. Clearly, reliable theoretical calculations could be of value in assessing the validity of this assumption for any given spin pair.

Finally, it is of interest to mention that, several years ago, Andrew and Farnell[56] investigated the effect of magic angle sample spinning on each of the irreducible tensors which describe the indirect spin–spin coupling tensor [equation (23)]. Of course, MAS does not influence the term $J\mathbf{1}$; also, the traceless symmetric components do not influence

the MAS spectrum. However, for a homonuclear spin pair, they found that MAS will not necessarily result in a complete averaging of the antisymmetric components of the **J** tensor [i.e. components of $\boldsymbol{J}^{(1)}$ in equation (23)]. The contribution of the antisymmetric components was predicted to be most important when the chemical shift difference between the two coupled spins was very small. Further discussions of the possibility of measuring antisymmetric components of the **J** tensor are given in the excellent review by Robert and Wiesenfeld.[34] As already mentioned, the antisymmetric components of any indirect spin–spin coupling tensor have not been experimentally characterized.

4 SUMMARY

From the experimental point of view, it is clear that the mathematical properties of the anisotropic indirect **J** tensor are analogous to those of the direct dipolar tensor. As a result, it is impossible to measure separately the anisotropic **J** tensor and the direct dipolar tensor. Fortunately, for isolated spin pairs in rigid solid samples, the direct dipolar tensor can always be calculated if structural data are available. The most reliable procedure for characterizing **J** tensors in the solid state involves single crystal NMR experiments. For solid powder samples the determination of ΔJ is often problematic. The reliability of a powder analysis will always be greatest when: (i) the spin pair of interest lies along a symmetry axis, (ii) J_{iso} is large enough so that the individual subspectra are well resolved, and (iii) R is small or at least comparable to $\Delta J/3$. With the availability of higher sensitivity NMR hardware and advanced single crystal NMR experiments one can hope that more reliable experimental data will become available. In the future, one can also anticipate significant advances in computational techniques, particularly for relatively small molecules involving atoms of the first two rows of the Periodic Table. Unfortunately, these are the systems where it is most difficult to obtain reliable experimental data concerning the anisotropy in the **J** tensor. In any case, it is clear that in order to formulate meaningful models relating J couplings to molecular structure, a better understanding of the **J** tensor is essential. Obviously, any information that indicates which mechanisms are or are not operative is critically important in leading to a better understanding of J coupling phenomena.

5 RELATED ARTICLES

Anisotropy of Shielding and Coupling in Liquid Crystalline Solutions; CRAMPS; Electron–Nuclear Multiple Resonance Spectroscopy; Indirect Coupling: Semiempirical Calculations; Indirect Coupling: Theory and Applications in Organic Chemistry; Internal Spin Interactions and Rotations in Solids; Magic Angle Spinning; REDOR and TEDOR; Rotating Solids.

6 REFERENCES

1. G. E. Pake, *J. Chem. Phys.*, 1948, **16**, 327.
2. W. G. Proctor and F. C. Yu, *Phys. Rev.*, 1951, **81**, 20.
3. H. S. Gutowsky and D. W. McCall, *Phys. Rev.*, 1951, **82**, 748.
4. E. L. Hahn and D. E. Maxwell, *Phys. Rev.*, 1951, **84**, 1246.
5. N. F. Ramsey, *Phys. Rev.*, 1953, **91**, 303.
6. E. R. Andrew, L. F. Farnell, and T. D. Gledhill, *Phys. Rev. Lett.*, 1967, **19**, 6.
7. D. L. VanderHart, H. S. Gutowsky, and T. C. Farrar, *J. Chem. Phys.*, 1969, **50**, 1058.
8. M. Mehring, *High Resolution NMR in Solids*, 2nd edn, Springer, Berlin, 1983.
9. B. C. Gerstein and C. R. Dybowski, *Transient Techniques in NMR of Solids*, Academic, Orlando, Fl., 1985.
10. R. K. Harris, *Nuclear Magnetic Resonance Spectroscopy*, Longman, Burnt Mill, 1986.
11. C. P. Slichter, *Principles of Magnetic Resonance*, 3rd edn, Springer, Berlin, 1989.
12. E. R. Andrew, *Progr. NMR Spectrosc.*, 1971, **8**, 1.
13. P. L. Corio, *Structure of High-Resolution NMR Spectra*, Academic, New York, 1966.
14. M. Munowitz, *Coherence and NMR*, Wiley, New York, 1988.
15. M. E. Stoll, R. W. Vaughan, R. B. Saillant, and T. Cole, *J. Chem. Phys.*, 1974, **61**, 2896.
16. K. W. Zilm and D. M. Grant, *J. Am. Chem. Soc.*, 1981, **103**, 2913.
17. R. K. Harris, K. J. Packer, and A. M. Thayer, *J. Magn. Reson.*, 1985, **62**, 284.
18. K. Eichele and R. E. Wasylishen, *J. Magn. Reson., Ser A*, 1994, **106**, 46, and references therein.
19. M. H. Levitt, D. P. Raleigh, F. Creuzet, and R. G. Griffin, *J. Chem. Phys.*, 1990, **92**, 6347.
20. T. Gullion and J. Schaefer, *Adv. Magn. Reson.*, 1989, **13**, 57.
21. J. M. Griffiths and R. G. Griffin, *Anal. Chim. Acta*, 1993, **283**, 1081.
22. T. Nakai, J. Ashida, and T. Terao, *Mol. Phys.*, 1989, **67**, 839.
23. J. M. Millar, A. M. Thayer, D. B. Zax, and A. Pines, *J. Am. Chem. Soc.*, 1986, **108**, 5113.
24. P. Van Hecke, H. W. Spiess, U. Haeberlen, and S. Haussühl, *J. Magn. Reson.*, 1976, **22**, 93 (see also p. 103).
25. T. Terao, H. Miura, and A. Saika, *J. Chem. Phys.*, 1986, **85**, 3816.
26. A. J. Kim, M. I. Altbach, and L. G. Butler, *J. Am. Chem. Soc.*, 1991, **113**, 4831.
27. K. Schmidt-Rohr, M. Wihelm, A. Johansson, and H. W. Spiess, *Magn. Reson. Chem.*, 1993, **31**, 352.
28. R. J. Gillespie, P. Granger, K. R. Morgan, and G. J. Schrobilgen, *Inorg. Chem.*, 1984, **23**, 887.
29. C. J. Jameson, in *Multinuclear NMR*, ed. J. Mason, Plenum, New York, 1987, Chap. 4, pp. 89–131.
30. R. H. Contreras and J. C. Facelli, *Ann. Rep. NMR Spectrosc.*, 1993, **27**, 255.
31. R. F. Schneider, *J. Chem. Phys.*, 1968, **48**, 4905.
32. H. W. Spiess, *NMR, Basic Principles Prog.*, 1978, **15**, 55.
33. A. D. Buckingham, P. Pyykkö, J. B. Robert, and L. Wiesenfeld, *Mol. Phys.*, 1982, **46**, 177.
34. J. B. Robert and L. Wiesenfeld, *Phys. Rep.*, 1982, **86**, 363.
35. J. S. Blicharski, *Z. Naturforsch., Teil a*, 1972, **27**, 1355.
36. J. Kowalewski and A. Laaksonen, in *Theoretical Models in Chemical Bonding*, Part 3, ed. Z. B. Maksić, Springer, Berlin, 1991, p. 387.
37. P. Pyykkö, *Chem. Phys.*, 1977, **22**, 289.
38. A. Viste, M. Hotokka, L. Laaksonen, and P. Pyykkö, *Chem. Phys.*, 1982, **72**, 225.

39. W. T. Raynes, *Magn. Reson. Chem.*, 1992, **30**, 686.
40. R. E. Wasylishen, K. C. Wright, K. Eichele, and T. S. Cameron, *Inorg. Chem.*, 1994, **33**, 407.
41. A. Nolle, *Z. Phys. B*, 1979, **34**, 175.
42. P. N. Tutunjian and J. S. Waugh, *J. Chem. Phys.*, 1982, **76**, 1223; *J. Magn. Reson.*, 1982, **49**, 155.
43. K. Eichele, G. Wu, R. E. Wasylishen, and J. F. Britten, *J. Phys. Chem.*, 1995, **99**, 1030.
44. D. L. VanderHart and H. S. Gutowsky, *J. Chem. Phys.*, 1968, **49**, 261.
45. U. Haubenreisser, U. Sternberg, and A.-R. Grimmer, *Mol. Phys.*, 1987, **60**, 151.
46. G. H. Penner, W. P. Power, and R. E. Wasylishen, *Can. J. Chem.*, 1988, **66**, 1821.
47. W. P. Power, M. D. Lumsden, and R. E. Wasylishen, *J. Am. Chem. Soc.* 1991, **113**, 8257.
48. J. W. Emsley and J. C. Lindon, *NMR Spectroscopy Using Liquid Crystal Solvents*, Pergamon, Oxford, 1975.
49. J. Lounila and J. Jokisaari, *Prog. NMR Spectrosc.*, 1982, **15**, 249.
50. N. F. Ramsey, *Molecular Beams*, Oxford University Press, Oxford, 1956.
51. R. von Boeckh, G. Gräff, and R. Ley, *Z. Phys.*, 1964, **179**, 285.
52. M. D. Lumsden, K. Eichele, R. E. Wasylishen, T. S. Cameron, and J. F. Britten, *J. Am. Chem. Soc.*, 1994, **116**; 11129.
53. R. K. Harris and A. C. Olivieri, *Prog. NMR Spectrosc.*, 1992, **24**, 435.
54. J. Jokisaari, Y. Hiltunen, and J. Lounila, *J. Chem. Phys.*, 1986, **85**, 3198.
55. A. Pulkkinen, Y. Hiltunen, and J. Jokisaari, *Liq. Cryst.*, 1988, **3**, 737.
56. E. R. Andrew and L. F. Farnell, *Mol. Phys.*, 1968, **15**, 157.
57. D. K. Dalling and H. S. Gutowsky, *J. Chem. Phys.*, 1971, **55**, 4959.
58. H. Dreeskamp and K. Hildenbrand, *Z. Naturforsch., Teil a*, 1968, **23**, 940.
59. J. Jokisaari, K. Räisänen, J. Kuonanoja, P. Pyykkö, and L. Lajunen, *Mol. Phys.*, 1980, **39**, 715.

Acknowledgments

I wish to thank Dr. Klaus Eichele and Michael D. Lumsden for their assistance in preparing the figures for this contribution. Also, I wish to thank Klaus, Mike, Gang Wu, and Professor Aatto Laaksonen for many helpful comments. Our research has been generously supported by NSERC of Canada.

Biographical Sketch

Roderick Wasylishen. *b* 1944. B.Sc., 1968, Waterloo, Ph.D., 1972, Manitoba. Introduced to NMR by Terry Gough at the University of Waterloo and Ted Schaefer at the University of Manitoba. NRC of Canada PDF at the National Institutes of Health, Bethesda, Maryland with Ted Becker. 1972–74. Department of Chemistry, University of Winnipeg, 1974–82; Dalhousie University, 1982–present. Approx. 180 publications. Current research specialty: NMR studies of solids, chemical shielding, spin–spin coupling, EFG tensors, NMR lineshapes, NMR relaxation.

Distance Geometry

Timothy F. Havel
Harvard Medical School, Boston, MA, USA

1	Introduction	1
2	Geometric Reasoning with Distance Information	1
3	Distance Geometry Algorithms	4
4	The Contributions of Distance Geometry to NMR	8
5	Related Articles	9
6	References	9

1 INTRODUCTION

Distance geometry is a general methodology which formulates conformational problems in terms of distance and chirality constraints.[1] It has been applied to such diverse problems as the conversion of two-dimensional chemical diagrams into three-dimensional structures, the systematic enumeration of all possible stereoisomers and conformers of small molecules, the docking of ligands to their receptors, and the construction of protein models by homology. It also plays a central role in present-day methods for determining the solution structures of proteins and other biological macromolecules from NMR data. There are several reasons for this. First, NMR spectroscopy, particularly the NOESY experiment, provides a wealth of data that are readily interpreted in terms of distance constraints. Second, although the problem of finding atomic coordinates consistent with distance constraints is a highly nonlinear one, unlike the problem of locating the global energy minimum it can nevertheless be solved quite reliably. Third, since the global minima of the functions that are minimized in distance geometry should have the value zero, the distance geometry formulation of the structure determination problem makes it relatively straightforward to find errors in the interpretation of the data.

2 GEOMETRIC REASONING WITH DISTANCE INFORMATION

Newcomers to distance geometry should be careful not to confuse it with the least-squares fits that are widely used in crystallography. Instead of seeking a *single* 'best fit' to the data as in the least-squares method, the goal of distance geometry is to understand better the set of all conformations consistent with the data as a whole. This is done by deriving new geometric facts about the molecule from those that are available experimentally, in a process known more generally as *geometric reasoning*. There are several ways of going about this, as described below.

2.1 Describing Molecular Conformation

A *distance geometry description* defines the set of possible conformations of a nonrigid molecule by means of lower and upper bounds on its interatomic distances, together with the chiralities of its rigid tetrahedra of atoms. The set of conformations consistent with these constraints itself is called *conformation space*. Such a description is usually not chemically complete, meaning that there may be conformations in the space that do not exist in appreciable concentration under the conditions of interest. It may also contain noncritical constraints, i.e. constraints that could be tightened without reducing the conformation space consistent with them, or it may contain redundant constraints, i.e. constraints that could be loosened or eliminated without enlarging the space.

The distance constraints may come from many sources. Clearly, the molecular formula (bond arrangement) is one of them, since both covalent bond lengths as well as the geminal distances which define the bond angles are determined essentially exactly by this information. Many other distances can also be fixed within larger rigid groups of atoms, e.g. aromatic ring systems. In addition, the distance between all pairs of atoms separated by four or more bonds may be assumed to be at least the sum of suitable hard sphere atomic radii, and other noncovalent interactions, e.g. hydrogen bonds, can also be modeled by means of distance constraints. Finally, distance constraints are available from many kinds of experiment, including optical fluorescence transfer, various noncrystallographic diffraction experiments and, of course, NMR spectroscopy. As a general rule, one should collect as many constraints as possible, since even redundant constraints are useful in distance geometry calculations.

The most obvious case in which chirality constraints are needed is at asymmetric carbon atoms, since the distances between their neighboring atoms cannot be used to distinguish enantiomers. It turns out that chirality constraints are also useful in many other cases. For example, prochiral centers should usually be constrained in distance geometry calculations, against the possibility that stereospecific assignments may be available, and chirality constraints among α-carbon atoms can be used to enforce the handedness of α-helices. Planarity can also be viewed as a sort of chirality constraint (neither left- nor right-handed), which is applicable to most double bonds. Finally, although the absolute value of a torsion angle about the 2,3-bond in a chain of four atoms can be determined by specifying the 1,4-distance, its sign can only be fixed by also constraining the chirality of the tetrahedron the vertices of which are these four atoms.

In solution, by far the richest source of distance constraints is the two-dimensional NMR experiment NOESY. Since the nuclear Overhauser effect (NOE) that this experiment measures is due to dipole–dipole interactions, the intensity of a cross peak in a NOESY spectrum is roughly proportional to the average inverse sixth power of the distance between a pair of protons in the molecule. This means that (provided a short enough mixing time is used to eliminate the possibility of indirect NOEs) the mere presence of such a cross peak implies that the maximum distance between the protons is quite small, 0.50 nm at the most. Because the NOE is also proportional to a factor that depends on the unknown average

rate at which the interproton vector reorients (and may, in addition, be influenced by many other sources of relaxation), a more quantitative interpretation of the cross-peak intensities is difficult. Fortunately, as discussed in the last section of this article, in the important special case of globular proteins a reasonably precise and well-defined structure can often be obtained without quantifying most of the NOESY cross-peak intensities.

2.2 Inconsistent Distance Constraints

The task of collecting, processing, and interpreting NMR data, particularly on large molecules such as proteins in solution, is a complex one which is susceptible to many sources of systematic as well as random error. The distance geometry approach attempts to distinguish between these two types of error by interpreting the data geometrically in terms of constraints that are intended to encompass the *full range* consistent with the intrinsic uncertainty of the measurements due to thermal noise, intramolecular motion, and similar phenomena. Assuming (as is often the case) that the data are sufficiently complete and precise to determine a nearly unique conformation, any serious errors in the interpretation of some of the data will usually cause the constraints as a whole to become mutually *inconsistent*. This means that it is impossible to satisfy the constraints by any single conformation, which in turn implies that one or more of the assumptions made in interpreting the data must be false. Although the inconsistencies can be arbitrarily complex, in most cases it is possible to isolate them to relatively small subsets of atoms, meaning that the constraints among those atoms are by themselves inconsistent with any three-dimensional structure.

Any method of detecting inconsistencies in the constraints also makes it possible to falsify structural hypotheses, and thereby opens up one possible route towards geometric reasoning. Certain relatively simple 'patterns' of inconsistent constraints can not only be detected, but also isolated, by a process known as 'bound smoothing' (see below). More often, however, inconsistency can only be detected by repeatedly trying to calculate a conformation consistent with the constraints, and failing. Since the currently available algorithms for doing this are quite reliable, this situation strongly implies that the constraints are inconsistent. Unfortunately, the minimization procedures commonly used to calculate conformations result in a compromise between violations of the correct as well as the incorrect constraints, which makes it relatively difficult to isolate inconsistency by this approach, although there is a significant correlation between the frequency and severity of constraint violations and the correctness of the constraints.

2.3 Bound Smoothing and Distance Limits

An important class of distance geometry algorithms are designed to perform *bound smoothing*. These play a central role in the so-called EMBED algorithm (see Section 3.4), but the distance limits that bound smoothing algorithms compute are of much broader interest, and hence are described here. A more complete description, together with a detailed presentation of the algorithms themselves, is available.[1]

The three-dimensional *distance limits* associated with any set of distance bounds are simply the minimum and maximum value that each distance can assume in any spatial structure the other distances of which all lie within their given bounds. Since the distance bounds available from NMR spectroscopy are necessarily imprecise and very sparse, computing the corresponding distance limits can reveal a great many consequences of the NMR data that are not obvious from direct inspection, thus providing another approach to geometric reasoning. The distance limits also enable one to detect redundant and critical distance constraints, since by definition the distance limits for redundant bounds are tighter than those bounds, while the distance limits for critical bounds are looser. Finally, the distance bounds as a whole are inconsistent if and only if the limits implied by the bounds among some subset of atoms violate the bounds, i.e. a lower bound exceeds its upper limit, or vice versa.

Unfortunately, the computation of the true three-dimensional distance limits is a difficult and unsolved problem, and only loose approximations are readily available. These are the limits implied by the bounds among subsets of three or four atoms at a time, which are known as the *triangle inequality and tetrangle inequality limits*, respectively (Figure 1). These can be computed in time proportional to at most the cube, and at least the fourth power, of the number of atoms, respectively. Although much weaker than the true three-dimensional limits, particularly with regard to the lower limits, they are capable of revealing considerable redundancy in many sets of distance constraints, and they often succeed in catching typographical errors committed during data entry that otherwise could be located only after careful proofreading or long calculation.

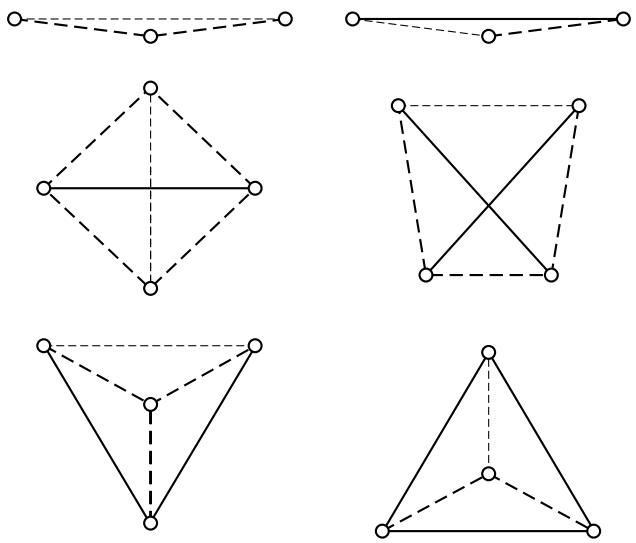

Figure 1 Schematic drawing of the triangle (top) and tetrangle (middle and bottom) limits; the upper limits are shown on the left half and the lower limits on the right. In these diagrams, solid lines indicate distances at their lower bounds, thick dotted lines indicate distances at their upper bounds, and thin dotted lines indicate the limit determined by this combination of bounds. Thus, for example, the upper left diagram indicates that the upper triangle inequality limit on the distance between the endpoints is obtained when the two distances to the midpoint are stretched to their upper bounds. The complete set of triangle or tetrangle limits may be obtained by iteratively replacing the bounds by the corresponding limits whenever these are tighter, until no further changes occur

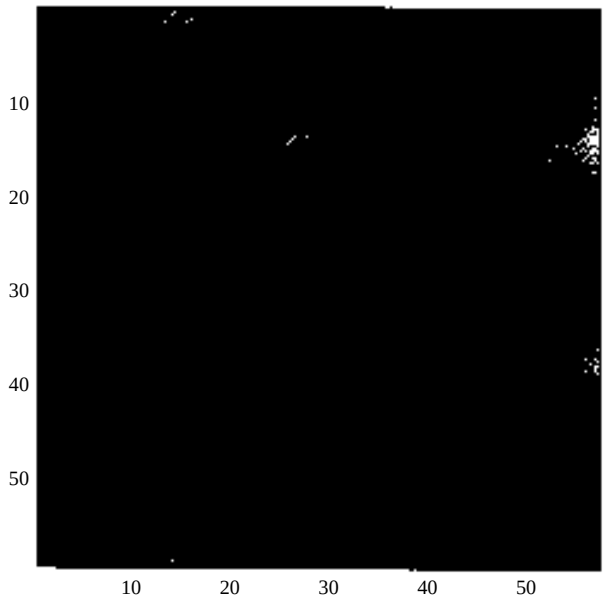

Figure 2 The triangle inequality limits among the α-carbon atoms of the 58 residue protein BPTI (above the diagonal), together with the distance matrix obtained from its crystal structure (below the diagonal). The rows and columns of this combined matrix are ordered in the same way as the corresponding residues in the BPTI sequence, and the cells are shaded according to the value of the corresponding limit or distance. The correlation between the upper limits and the distances is obvious

Another important use of the triangle (or tetrangle) limits is as a means of predicting various structural features prior actually to calculating any structures. Although this can, in principle, be done with any sort of molecule, we shall concentrate here on the important case of globular proteins subject to NOESY distance constraints. Contoured plots of the distances among the α-carbon atoms have long been used as a visual aid to recognizing the secondary structure 'topology' of globular proteins. Moreover, there exists a strong positive correlation between the upper triangle limits and the actual distances (even when only a few NOESY constraints per residue are available).[2] Therefore, contoured plots of the upper limits can serve much the same purpose as distance matrices, and it is possible to determine the chain fold and other basic features of a protein from NMR data at a very early stage in the analysis. This in turn should facilitate that analysis. Figure 2 shows an example of such a contour plot for the protein basic pancreatic trypsin inhibitor (BPTI), along with its distance matrix.

2.4 The Ensemble Approach

Bound smoothing constitutes an example of *deductive* geometric reasoning. Another, in some ways even more important approach may be called *inductive* geometric reasoning. Here, one computes an *ensemble* of conformations which satisfy the constraints, but are otherwise 'random'. Then, provided that this conformational ensemble is sufficiently large (meaning, for most purposes, 10 to 20 conformations), any geometric features that are uniformly present in all its members may safely be assumed to be necessary consequences of the constraints. The geometric features of interest are not limited to distances, but may include angles, chiralities, and far more subtle things such as the radius of gyration, surface accessibility or chain 'topology'. They may also include properties of the ensemble as a whole, such as the average or maximum 'difference' between any two conformations.

In structure determination by NMR spectroscopy, the most widely used measure of the difference between two conformations is the root mean square coordinate deviation (RMSD). This is simply the root mean square difference in their coordinate vectors (or equivalently, the root mean square distance between corresponding pairs of atoms) minimized over all translations and rotations of one conformation with respect to the other. This quantity may be computed among all the atoms, or among any desired subset (e.g. the α-carbons atoms of a protein). The average of the RMSD over all pairs of conformations in the ensemble is often used as a measure of the overall precision of an NMR structure determination, with 0.10 nm generally regarded as good, 0.20 nm as fair and 0.30 nm or more as poor. One should nevertheless be careful not to read too much into this single number. It is far more important to determine exactly how the conformations in the ensemble differ from one another than it is to determine by how much they differ on average. Fortunately, the translation and rotation which gives the RMSD also allows one to

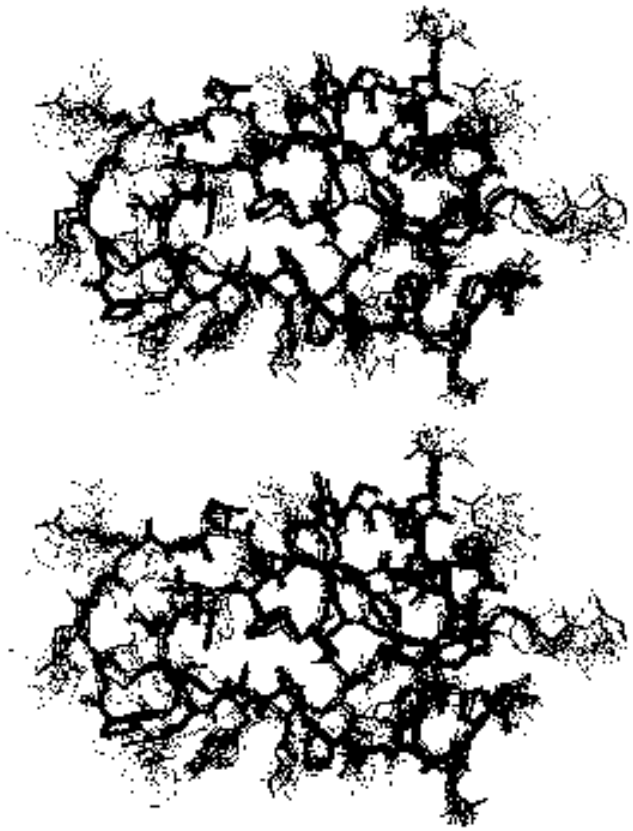

Figure 3 Stereoview of an ensemble of 25 BPTI conformations computed from a set of simulated NMR distance constraints using the program DGII.[4] These conformations (thin gray lines) have been superimposed on the crystal structure from which the constraints were derived (heavy black line) so as to minimize the RMSD to its α-carbon atoms, for an average RMSD of 0.085 nm

superimpose the structures so as to visualize easily their detailed differences by computer graphics (Figure 3).

Another commonly studied geometric feature is the torsion angles about single bonds. The precision of such cyclic parameters is best quantitated by means of an average value and 'order parameter', which is defined as follows. Given a single bond in the molecule, one puts a unit vector down in the plane for each conformation in the ensemble, whose angle with the x axis is equal to the value of the corresponding torsion angle in that conformation. On summing these unit vectors and dividing by the size of the ensemble, one obtains an average vector whose angle with the x axis is the average of the torsion angle, and whose length is the corresponding order parameter. This angular order parameter is unity only if the angle has exactly the same value in all conformations, and approaches zero as the angle becomes random.

3 DISTANCE GEOMETRY ALGORITHMS

Here the term 'distance geometry algorithm' is used somewhat loosely for any procedure that helps us to perform computer-aided geometric reasoning with distance and chirality constraints (including torsion angle constraints). Because of their utility in NMR studies of solution conformation, we concentrate here on algorithms for computing conformational ensembles. Several, rather different approaches have been taken to this problem, each of which has its advantages and disadvantages, but all of which have been successfully applied to large molecules. Rather than attempting an exhaustive survey, the discussion is limited to those algorithms which have been most widely used by NMR spectroscopists to date, or which appear particularly promising.

3.1 Restraints and Error Functions

A common feature of all these algorithms is that they rely on minimization of an error function, which measures the violations of the constraints.[1,3,4] As such, an error function is always non-negative, and zero if, and only if, all the constraints are fully satisfied. The construction of an error function involves translating the constraints into *restraints*, that is, into functions of a single geometric parameter that force that parameter to satisfy its constraint when they are minimized. The error function is then obtained as the sum over all restraints.

A simple example of such a function is

$$E(\boldsymbol{p}_1, \ldots, \boldsymbol{p}_N) = \sum \left[\max\left(0, \frac{d_{ij}^2}{u_{ij}^2} - 1\right) \right]^2 + \sum \left[\max\left(0, 1 - \frac{d_{ij}^2}{l_{ij}^2}\right) \right]^2 + \sum C_{ijkl}^2(\boldsymbol{p}_1, \ldots, \boldsymbol{p}_N) \qquad (1)$$

where u_{ij} and l_{ij} denote the upper and lower distance bounds, and $C_{ijkl}^2(\boldsymbol{p}_1, \ldots, \boldsymbol{p}_N)$ is a chirality restraint, which is described below. Squaring the distance restraints ensures that the function has continuous first derivatives, as required by many minimization algorithms, while scaling them by the inverse-squared bounds ensures that the various restraints receive roughly equal weight, which tends to make minimization of the error function somewhat easier. Ideally, however, the results should be independent of the assumed weights.

The chirality restraints, which are ordinarily needed only when Cartesian coordinates are used as the variables (see below), are usually defined as

$$C_{ijkl}^2(\boldsymbol{p}_1, \ldots, \boldsymbol{p}_N) = [\mathrm{vol}(\boldsymbol{p}_i, \boldsymbol{p}_j, \boldsymbol{p}_k, \boldsymbol{p}_l) - v_{ijkl}]^2 \qquad (2)$$

Here

$$\mathrm{vol}(\boldsymbol{p}_i, \boldsymbol{p}_j, \boldsymbol{p}_k, \boldsymbol{p}_l) = (\boldsymbol{p}_i - \boldsymbol{p}_l) \cdot [(\boldsymbol{p}_j - \boldsymbol{p}_l) \times (\boldsymbol{p}_k - \boldsymbol{p}_l)] \qquad (3)$$

is the oriented volume of the four atoms whose Cartesian coordinates are $\{\boldsymbol{p}_i, \boldsymbol{p}_j, \boldsymbol{p}_k, \boldsymbol{p}_l\}$, and v_{ijkl} is its target value. The well-known properties of the vector triple product imply that the oriented volume has absolute value equal to six times the volume of the tetrahedron spanned by the four atoms, and that its sign is positive for one chirality of this tetrahedron, negative for its mirror image, and zero whenever the atoms are coplanar.

There are two distinct ways of parameterizing the space of atomic configurations over which the minimizations must be carried out. The first uses three independent Cartesian coordinates for each atom, while the second uses the torsion angles about single bonds as the variables. The latter has the advantage of reducing the number of variables by about a factor of 10, which greatly improves the performance of many minimization algorithms. It also enables one to impose torsion angle constraints simply and directly, and maintains the covalent geometry automatically without the use of constraints on the bonded and geminal distances. As a consequence, however, it is not possible to correct violations of these constraints, which limits the methods that can be used to derive good starting structures for the minimizations. In addition, torsion angle optimizations are relatively complicated to implement, particularly if flexible rings are present in the molecules of interest. Both parameterizations are widely used in computational chemistry.

3.2 The Variable Target Function Algorithm

The variable target function algorithm was developed by Braun and Go̅[5] specifically for the purpose of computing the structures of proteins using distance constraints derived from NMR spectroscopy. By repeating the calculation many times, each time starting from a different set of randomly chosen torsion angles, one obtains the desired conformational ensemble. The method has been under continuous development since its introduction, and has become an effective tool for determining protein structures using distance and torsion angle constraints derived from NMR data. A survey of the early structures solved by this method is available.[6]

3.2.1 Avoiding Local Minima by Variable Target Functions

Even though torsion-based optimizations are quite efficient at converging to local minima, when used to solve distance geometry problems it is essential to find a global minimum of the error function. With large molecules such as proteins, the number of local minima is so large that this is highly unlikely to be achieved in any given run starting from a random conformation. The essential idea behind the variable target function approach is to avoid becoming trapped in local minima by initially minimizing a target (i.e. error!) function that restrains only the torsion angles together with the 'short-range' distances between neighboring amino acid residues, and gradually adding on longer and longer range restraints. In this way the 'short-range' or secondary structure is formed first, after which the secondary structural elements are docked together to form the tertiary structure, in a fashion that is analogous to the way in which proteins are widely believed to fold in solution. Although this heuristic method does not guarantee that a global minimum will be attained in any given run, it does increase the convergence ratio enough essentially to ensure that, with a little persistence, a global minimum with zero error will be found if one exists.

Because they require memory that grows only linearly with the size of the molecule, first-derivative based minimization methods such as conjugate gradients are generally used with the variable target function algorithm. The number of minimization iterations performed at each stage (restraint range) must be determined largely by trial and error, but does not seem to vary greatly from one protein to another. As a rule, it has been found more efficient to increase the range of the upper distance restraints obtained from NMR more rapidly than the lower distance restraints obtained as the sum of the hard-sphere radii (or, roughly equivalently, to weight the NMR restraints more strongly than the hard-sphere restraints in the initial stages), probably because the NMR restraints are far more effective at determining the tertiary structure than are the hard-sphere restraints. The method is particularly effective at determining the structures of proteins whose secondary structure consists primarily of α-helices, where the convergence ratio may approach 100%. With β-sheets or irregular structures, the convergence ratio can drop below 10%. This effectively lowers the efficiency of the method by a factor of 10, since nonconverging structures must be discarded and the minimization repeated until the desired number of conformations has been obtained.

3.2.2 Further Improvements in Speed and Reliability

The time required for each function/gradient evaluation is generally dominated by the time required to find all the hard-sphere overlaps, especially in the final stages of the variable target function algorithm when most of the hard-sphere restraints are considered. This can be greatly alleviated by using either grid-based or list-based methods to avoid checking most pairs of atoms for overlap. The hard-sphere overlap check, as well as much of the rest of the algorithm, has also been efficiently vectorized, so that each run can be performed very rapidly on a supercomputer.[7] The convergence ratio can be improved by choosing the torsion angles of the starting structure for the minimization from within their allowed ranges, rather than completely at random. These ranges can be reduced, and stereospecific assignments elucidated, by grid search methods which find those combinations of angles in each single residue that are consistent with the intraresidue distance constraints.[8] More recently, it has been suggested that the throughput can be greatly improved by imposing the ranges of angles observed in converged segments of nonconverged structures as constraints in subsequent calculations.[9] Finally, a minimization procedure has been proposed which, though apparently less efficient than conjugate gradients, yields error bounds on the torsion angles in the final conformations.[10]

3.3 Simulated Annealing and Related Methods

A second class of methods rely on a very general approach to global optimization problems known as simulated annealing. In this case, one treats the error function as an energy function, and uses either molecular dynamics or other methods to sample conformations with a Boltzmann distribution at a given absolute temperature. By slowly lowering the temperature, the distribution gradually narrows into a single energy minimum, and as in crystallization and similar physical processes this minimum will often be a global minimum. Because of the numerous error function calculations required, many of the above-mentioned methods of accelerating these calculations are also used in simulated annealing.

3.3.1 Dynamical Simulated Annealing

One way to generate conformations with a Boltzmann distribution is via molecular dynamics. This is a general method for simulating the evolution of molecular systems under the influence of a classical Hamiltonian $\mathcal{H}$, by iteratively solving Newton's equations of motion:

$$m_i \frac{\mathrm{d}^2 \boldsymbol{p}_i}{\mathrm{d}t^2} = -\nabla\mathcal{H} \tag{4}$$

This may be done by using either the 'leap-frog' algorithm

$$v_i[(2k+1)\Delta t/2] = v_i[(2k-1)\Delta t/2] - \Delta t \frac{\nabla\mathcal{H}}{m_i} \tag{5a}$$

$$\boldsymbol{p}_i[(k+1)\Delta t] = \boldsymbol{p}_i(k\Delta t) + \Delta t\, v_i[(2k+1)\Delta t/2] \tag{5b}$$

or the Verlet algorithm

$$\boldsymbol{p}_i[(k+1)\Delta t] = 2\boldsymbol{p}_i(k\Delta t) + \boldsymbol{p}_i[(k-1)\Delta t] - (\Delta t)^2 \frac{\nabla\mathcal{H}}{m_i} \tag{6}$$

In the first applications of this method to NMR structure determination problems,[11,12] the error due to the NMR restraints was added to an empirical energy function, and the combined function treated as the Hamiltonian of the system. This had several disadvantages. First, the strong forces between bonded and overlapping atoms necessitated the use of a small time step, which in turn meant that a large number of function and gradient evaluations were needed to reach equilibrium at any given temperature. Second, the function and gradient evaluations themselves required a relatively large quantity of computer time, because the forces involved in

empirical energy functions are relatively long range. Third, careful weighting of the NMR restraints was necessary in order to keep them from 'drowning out' the energy, or vice versa.

Despite these problems, by changing the weights of the short- and long-range restraints versus the energy as the annealing proceeded in a fashion similar to that used in the variable target function algorithm, impressive results were attained, including the folding of small proteins starting from a completely random array of atoms.[13] Subsequently, it was found that the efficiency and reliability of the calculations could be further improved by dropping the energy entirely, and treating a simple error function as the Hamiltonian.[14,15] In fact, in most cases the energy has little effect on the spread of the resulting conformational ensembles as measured by the average RMSD,[16] although it does tend to sharpen the distribution of the torsion angles noticeably. As a rule, however, this can be achieved more efficiently by energy minimization once the overall structure has been determined.[17]

Although in actual attempts to simulate the physical evolution of chemical systems it is essential to keep the time step small enough to accurately conserve the energy of the system, when molecular dynamics is used as a heuristic for simulated annealing we have found it advantageous to use the largest possible time step consistent with numerical stability.[4] A further improvement in efficiency can be attained by using the same mass for all the atoms, since numerical stability prevents the time step from being made much longer than the inverse rate of the fastest bond vibration. The temperature of the system can be controlled by rescaling the velocities, or by simulating a temperature bath via a temperature dependent viscosity term. Annealing has also been achieved by slowly making all the force constants larger, until the system becomes essentially rigid at a fixed temperature. While molecular dynamics can be performed using the torsion angles as the variables, such simulations are relatively uncommon and have only recently been applied to NMR structure determination problems. Further information on dynamical simulated annealing, and its applications to both NMR and crystallographic structure determination, may be found in recent reviews.[18]

3.3.2 Other Stochastic Optimization Methods

The classical method of generating atomic configurations with a Boltzmann distribution, known as the *Monte Carlo method*,[19] dates back to the earliest days of scientific computing. This method does not use gradient information, and is applicable to either Cartesian coordinates, torsion angles, or even to discrete (combinatorial) optimization problems.[20] While several applications of Monte Carlo based simulated annealing to energy minimization have been reported, only one application to NMR structure determination has been published to date.[21] The reason is that the usual implementations appear to be substantially less efficient than the dynamical simulated annealing method described above. The efficiency and reliability of the Monte Carlo method, however, hinges critically on the rate at which the temperature is lowered and the way in which the positions of the atoms are perturbed in each iteration. Recently, a variety of sophisticated methods have been developed for energy minimization purposes, which generate larger changes with a better chance of being accepted.[22–24] It therefore seems likely that a Monte Carlo procedure could be devised that performs reasonably efficiently with distance geometry problems.

Another class of stochastic minimization methods that appear suitable for distance geometry problems are known as *genetic algorithms*. Unlike the methods described above, which are based on a physical analogy, genetic algorithms are based on an analogy with the optimization of the 'fitness' of populations by natural selection. These methods have actually been available for some years,[25] but have only recently begun to attract widespread interest.[26] Once again, the basic procedure is simple, but the efficiency and reliability depend critically on how the basic steps are implemented. Using torsion angles as the variables, these procedures have recently been successfully applied to energy minimization problems,[27] as well as at least one distance geometry problem involving NMR data.[28] Genetic algorithms have the attractive feature of intrinsically computing ensembles of conformations, and hence, if reasonably good ways of implementing the basic steps can be found, they may prove to be an improvement over other torsion angle based algorithms.

3.4 The EMBED Algorithm and its Variations

The EMBED algorithm is a method of randomly generating the Cartesian coordinates of structures that roughly fit the distance constraints, and hence are good starting points for minimization by any method that is applicable to Cartesian coordinates. It was actually developed[3,29] prior to the development of two-dimensional NMR, as part of a larger effort to demonstrate the applicability of distance geometry to a wide variety of experimental and theoretical information.[30] Shortly thereafter, it was employed to determine the conformation of fragments of micelle-bound glucagon from NMR data,[31] and then to determine the first protein solution structure ever solved by NMR.[17] It has since been used in the determination of more protein, DNA, and other biomolecular structures than the space available here permits us to present.

Structure calculations with the EMBED algorithm consist of three basic steps:

1. Using bound smoothing algorithms to estimate the best possible limits on the distances from the sparse and imprecise set of distance bounds given as input.
2. Guessing a random set of distances from within the limits, and computing Cartesian coordinates such that the distances calculated from these coordinates are a best fit to this guess.
3. Optimizing these coordinates by minimization of an error function so that both the distance and chirality constraints are satisfied.

By repeating steps (2) and (3) with different random number seeds in step (2), one obtains the desired conformational ensemble. Although all three steps have traditionally been considered to be part of the EMBED algorithm, steps (1) and (3) are of independent interest (as described above). For this reason we prefer to restrict our usage of the term to step (2). Since any method for minimizing error functions with respect to Cartesian coordinates can be used in step (3), the EMBED algorithm should be understood as being complementary to these methods, rather than a substitute for them. Indeed, the combination of the EMBED algorithm with simulated annealing is presently one of the most efficient and reliable methods available for NMR structure determination.[4,32]

3.4.1 Random Distance Matrices by Metrization

Early implementations of the EMBED algorithm generated their random distance matrices by choosing the trial distances $[\tilde{d}_{ij}]$ independently of one another with a uniform distribution from within their limits. It was subsequently found that, when the density of distance constraints was quite low, the coordinates obtained in this way were uniformly expanded compared with those obtained by other methods. This undesirable tendency is eliminated by *metrization*, an extension of triangle inequality bound smoothing that enables one to choose random distance matrices which obey the triangle inequality from within the triangle inequality limits.[33,34] In principle, by making the trial distances more realistic, this should also improve the quality of the embedded coordinates.

Metrization itself is based on a characterization of the triangle inequality limits which shows that if any distance is set to any value between its triangle inequality limits, values exist for the remaining distances so that all the distances satisfy both the triangle inequality and the limits. Thus by alternately setting one distance to some random value between its limits, then setting the corresponding lower and upper bounds to that distance and updating the limits by this change, one will eventually obtain a complete distance matrix satisfying both the triangle inequality and the limits. Provided that one uses a data structure known as a 'shortest-paths tree' to store the limits involving one atom, these updates can be accomplished in time proportional to the number of atoms, so that the overall time required is proportional to its cube.

Because triangle bound smoothing is more effective at lowering upper bounds than it is at raising lower bounds, it is necessary to randomize the order in which the atoms are considered for each metrization, in order to avoid having some parts of the structure come out systematically more compact than others. In applications to distance constraints derived from NMR data, it is also desirable to control the distribution with which the distances are selected so as to obtain average values that asymptotically tend towards some fixed fraction of the upper limits, since this ensures a correlation between the distances and the upper limits similar to that observed in practice (see Figure 2).

3.4.2 Embedding Distance Matrices

The trial distances chosen randomly from within the distance limits in the previous step are essentially always inconsistent, and hence cannot be realized by any possible conformation of the molecule. Nevertheless, if we can find coordinates that are a 'best fit' to these distances, then since the distances satisfy the constraints, the coordinates ought to at least come close. It turns out that a certain type of best fit can be rapidly calculated by eigenvalue methods.

To see how this works, suppose we are given a matrix of squared distances among a set of $N + 1$ points $\boldsymbol{p}_0, \ldots \boldsymbol{p}_N$, in three-dimensional space:

$$\mathbf{D} = [d_{ij}^2] = [\|\boldsymbol{p}_i - \boldsymbol{p}_j\|^2] \tag{7}$$

The symmetric, $N \times N$ matrix of dot products of the vectors from the zeroth point to all the rest is usually called the *metric* or *Gram matrix* $\mathbf{G}$, and can be calculated directly from $\mathbf{D}$ via the well-known law of cosines:

$$\mathbf{G} = [(\boldsymbol{p}_i - \boldsymbol{p}_0) \cdot (\boldsymbol{p}_j - \boldsymbol{p}_0)] = \tfrac{1}{2}[d_{0i}^2 + d_{0j}^2 - d_{ij}^2] \tag{8}$$

Let $\mathbf{G} = \mathbf{U}\boldsymbol{\Lambda}\,\mathbf{U}^{\mathrm{T}}$ denote the eigenvalue decomposition of $\mathbf{G}$, where $\mathbf{U}$ is the orthogonal matrix whose columns are the eigenvectors of $\mathbf{G}$ and $\boldsymbol{\Lambda} = \mathbf{diag}(\lambda_1, \ldots, \lambda_N)$ is a diagonal matrix containing its real eigenvalues sorted by decreasing value. Since $\mathbf{G} = \mathbf{P}^{\mathrm{T}}\mathbf{P}$, where $\mathbf{P} = [\boldsymbol{p}_1 - \boldsymbol{p}_0, \ldots, \boldsymbol{p}_N - \boldsymbol{p}_0]$ is a $3 \times N$ matrix, the matrix $\mathbf{G}$ is positive semidefinite of rank at most 3, so that $\lambda_1 \geq \lambda_2 \geq \lambda_3 \geq 0$ and $\lambda_4, \ldots, \lambda_N = 0$. Thus if we define the 3×3 diagonal matrix $\boldsymbol{\Lambda}_3^{1/2} = \mathbf{diag}(\lambda_1^{1/2}, \lambda_2^{1/2}, \lambda_3^{1/2})$ together with the $3 \times N$ matrix:

$$\mathbf{Q} = [\boldsymbol{q}_1, \ldots, \boldsymbol{q}_N] = \boldsymbol{\Lambda}_3^{1/2}[\boldsymbol{u}_1, \boldsymbol{u}_2, \boldsymbol{u}_3]^{\mathrm{T}} = \boldsymbol{\Lambda}_3^{1/2}\mathbf{U}_3^{\mathrm{T}} \tag{9}$$

it follows that the points $\boldsymbol{q}_0 = 0$ and $\boldsymbol{q}_1, \ldots, \boldsymbol{q}_N$ have the same Gram matrix as $\boldsymbol{p}_0, \ldots, \boldsymbol{p}_N$:

$$\begin{aligned}\mathbf{G} &= (\mathbf{U}_3\boldsymbol{\Lambda}_3^{1/2})(\boldsymbol{\Lambda}_3^{1/2}\mathbf{U}_3^{\mathrm{T}}) = \mathbf{Q}^{\mathrm{T}}\mathbf{Q} = [\boldsymbol{q}_i \cdot \boldsymbol{q}_j] \\ &= [(\boldsymbol{q}_i - \boldsymbol{q}_0) \cdot (\boldsymbol{q}_j - \boldsymbol{q}_0)]\end{aligned} \tag{10}$$

They also have the same distance matrix, since $\|\boldsymbol{p}_i - \boldsymbol{p}_0\|^2 = g_{ii} = \|\boldsymbol{q}_i - \boldsymbol{q}_0\|^2$ for $i = 1, \ldots, N$, while for all $0 \neq i \neq j \neq 0$, we have:

$$\begin{aligned}&\|\boldsymbol{p}_i - \boldsymbol{p}_j\|^2 \\ &\quad = \|\boldsymbol{p}_i - \boldsymbol{p}_0\|^2 + \|\boldsymbol{p}_j - \boldsymbol{p}_0\|^2 - 2[(\boldsymbol{p}_i - \boldsymbol{p}_0) \cdot (\boldsymbol{p}_j - \boldsymbol{p}_0)] \\ &\quad = \|\boldsymbol{q}_i\|^2 + \|\boldsymbol{q}_j\|^2 - 2(\boldsymbol{q}_i \cdot \boldsymbol{q}_j) = \|\boldsymbol{q}_i - \boldsymbol{q}_j\|^2\end{aligned} \tag{11}$$

Therefore, the new points are the same as the old up to translation and/or rotation, so that $\boldsymbol{q}_0, \ldots, \boldsymbol{q}_N$ can be regarded as $\boldsymbol{p}_0, \ldots, \boldsymbol{p}_N$ in a new coordinate system. Moreover, it follows from the orthogonality of the eigenvectors that these new coordinates are principal axes coordinates.

Although principal axes coordinates can be found more efficiently by diagonalizing the inertial tensor, the above method is applicable even if we do not have any coordinates for the points, but only the distances among them. The problem is that if the distances are inconsistent, the approximate Gram matrix $\tilde{\mathbf{G}}$ computed from the squared trial distances $\tilde{\mathbf{D}} = [\tilde{d}_{ij}^2]$ according to equation (8) will not be positive semidefinite of rank 3, and hence cannot be represented as a matrix of dot products among three-dimensional vectors. It can be shown, however, that if one sets all but the three largest eigenvalues to zero, then the matrix $\mathbf{G}$ obtained via equation (10) will be an optimum least-squares fit to $\tilde{\mathbf{G}}$ over all positive semidefinite rank 3 matrices.[1] It follows that the squared distances calculated from the coordinates

$$\|\boldsymbol{q}_i - \boldsymbol{q}_j\|^2 = g_{ii} + g_{jj} - 2g_{ij} \approx \tilde{g}_{ii} + \tilde{g}_{jj} - 2\tilde{g}_{ij} = \tilde{d}_{ij}^2 \tag{12}$$

will likewise be similar to the squared trial distances $\tilde{\mathbf{D}}$.

Note that the diagonal elements of the approximate Gram matrix $\tilde{g}_{ii} = \tilde{d}_{0i}^2$, which are just the squared trial distances involving the zeroth point, affect the fit to all the other

distances. This disproportionate influence can be eliminated by creating an additional point located at the centroid of the remaining N points, and treating it as the zeroth point. This is possible because the distances from the centroid to the remaining points can be calculated directly from the distances among them via the equation[29]

$$\tilde{d}_{0i}^2 = \frac{1}{N}\sum_{j=1}^{N}\tilde{d}_{ij}^2 - \frac{1}{N^2}\sum_{j<k}^{N}\tilde{d}_{jk}^2 \qquad (13)$$

Even so, the EMBED algorithm does not produce exactly a least-squares fit between the trial distances and those calculated from the coordinates. The coordinates obtained by embedding, however, can easily be improved by minimization of an appropriately weighted least-squares residual, using a method known as *majorization*.[4]

Because a variety of extremely efficient methods exist to locate the largest few eigenvalues and eigenvectors of a symmetric matrix without completely diagnonalizing it, the EMBED algorithm is by far the fastest known way of finding reasonably good approximate coordinates to serve as starting points for further optimization.

3.4.3 Variations on Embedding

In the years since it was developed, the EMBED algorithm has been improved and extended in many ways, some of which have been touched on above. In this section several recent developments which promise to be useful in NMR structure determination are described.

The first of these methods is derived from early work by Crippen, who applied ideas from the EMBED algorithm to energy minimization.[1,35] Since the EMBED algorithm can be viewed geometrically as projecting a higher dimensional structure onto a three-dimensional subspace, Crippen proposed minimizing the energy of the structures in spaces of successively lower dimension, eventually reaching a very low energy minimum constrained to three dimensions. He calls this approach *energy embedding*. Because even the simple conjugate gradients minimization of error functions converges quite reliably in four dimensions, it appears that only four dimensions are needed in applications of this approach to distance geometry. Unfortunately, it also turns out that the reduction of a four-dimensional structure to three dimensions is the most difficult step of the procedure, probably because it is in this step that the chirality and diastereomeric configuration of the molecule is determined.

Several investigators have found that by applying dynamical simulated annealing to four-dimensional error functions in which the sum of the squares of the fourth coordinates is added to the error as an additional restraint, the local minima encountered in reducing the structure to a three-dimensional one which satisfies the distance and chirality constraints can be overcome.[4,14] At the same time, since atoms in the structure can pass through one another without the four-dimensional distance between them falling below the sum of their hard-sphere radii, the method appears to alleviate the local minimum problem encountered in three-dimensions significantly. Problems with local minima still occur, however, which can only be avoided by careful annealing.

Other, somewhat more analytic, approaches to reducing the dimension without violating the distance constraints are currently being explored. For example, in the *WARP procedure* recently developed by the author, this is done by using the elements of a 3×4 matrix $\mathbf{C}$ as the variables while holding the $4 \times N$ matrix of coordinates $\mathbf{P}$ fixed, thus seeking the minimum of the error function E over all projections and affine transformations:

$$\text{minimize } E(\mathbf{CP}) \quad \text{with respect to } \mathbf{C} \qquad (14)$$

This minimization involves only 12 variables, and converges very rapidly. Although the error is only reduced by about a factor of 2 on average, the change in the coordinates can be very large. Thus, this method appears to provide an inexpensive means of improving the coordinates obtained by embedding.

Another extension of the ideas behind the EMBED algorithm is found in the work of Glunt, Hayden and co-workers. These investigators have developed a method, called *modified alternating projections* (*MAP*), which reliably locates an $(N-1)$-dimensional structure that satisfies arbitrary self-consistent distance bounds.[36] This procedure involves repeated diagonalization of an $(N+1) \times (N+1)$ matrix, and hence is much more time consuming than EMBED. The MAP procedure, however, constitutes the most powerful general method yet developed for testing distance bounds for consistency, since if the bounds cannot be satisfied by an $(N-1)$-dimensional structure, they certainly cannot be satisfied by any three-dimensional structure. If it should prove possible to not only detect, but also isolate, inconsistencies by this method, it may be well worth the computer time required.

In addition, Glunt, Hayden and co-workers have developed an analogous procedure, called the *data box algorithm*, for refining three-dimensional structures versus both distance and chirality constraints.[37] This procedure may be summarized as follows:

1. Let $\tilde{\mathbf{D}}_0$ be a matrix of squared trial distances which satisfy the distance limits l_{ij}, u_{ij} (obtained from, for example, triangle bound smoothing), and use one iteration of MAP to find an $(N-1)$-dimensional structure $\mathbf{P}_0$ whose distances are a least-squares fit to $\tilde{\mathbf{D}}_0$.
2. Let $\mathbf{P}_1$ be a three-dimensional projection of $\mathbf{P}_0$, set $\tilde{\mathbf{D}}_1 = \tilde{\mathbf{D}}_0$ and $k = 1$.
3. Use a more efficient version of the majorization algorithm, called the *spectral gradient algorithm*, to obtain coordinates $\mathbf{P}_{k+1}$ whose distances $[d_{ij}] = [\|\boldsymbol{p}_i - \boldsymbol{p}_j\|]$ are a weighted least-squares fit to those in $\tilde{\mathbf{D}}_k$, and which minimize suitable chirality restraints.
4. Define $\tilde{\mathbf{D}}_{k+1} = [\tilde{d}_{ij}^2]$ according to

$$\tilde{d}_{ij} = \begin{cases} l_{ij} & \text{if } d_{ij} < l_{ij} \\ u_{ij} & \text{if } d_{ij} \rangle u_{ij} \\ d_{ij} & \text{otherwise} \end{cases} \qquad (15)$$

5. If the constraints are satisfied, stop; else set $k = k + 1$ and go to step (3).

With the most recent improvements in the spectral gradient algorithm, the efficiency and reliability of this procedure appears to be roughly comparable to the other methods discussed above.

4 THE CONTRIBUTIONS OF DISTANCE GEOMETRY TO NMR

Distance geometry has not only played an important role in NMR structure determinations, but has also been used to evaluate the efficacy of the geometric information available from NMR. This is done by simulating the constraints that could be obtained from NMR experiments of varying quality and completeness, computing a conformational ensemble for each such set of simulated constraints, and quantifying the precision of these ensembles by, for example, the RMSD (see Section 2.4). In this way, distance geometry has been able to assist NMR spectroscopists in deciding what kinds of experiment are most useful in determining structure, and thereby has played a role in the development of the experimental methodology. In this final section, we highlight some of the contributions of this approach to present-day methods for determining protein structure from NMR.

The original motivation for distance geometry was to develop a formalism for representing the structural information available from a wide variety of experimental and theoretical methods, together with computational methods for determining biomolecular conformation from this information.[30] As part of this larger effort, the simulation method described above was used to evaluate the distance constraints available from a number of possible experiments on protein structure, using a simple 'one point per residue' model (which was about all the computers available at that time could handle).[38] The most interesting result of this study was that it is better to know many distances imprecisely than it is to know a few distances precisely. In particular, a complete list of all contacts (<1 nm) and noncontacts (>1 nm) present in a globular α-carbon chain was found to be sufficient to determine all its distances to within only 0.1 nm on average. An important implication of these results, which had a substantial influence on subsequent events, is that the information available from the NOESY experiment should be a powerful constraint on the tertiary structure of proteins.

Because the density of constraints available from NOESY at that time was significantly lower than that used in these simulations, and because it was not immediately certain how well the results would extend to more detailed atomic models of proteins, a similar study was later performed using both a more detailed atomic model as well as constraint sets which mimicked those available from a wide variety of solution NMR experiments.[39] The conclusions of this latter study not only supported the earlier results, but were actually a good deal better than expected. The reason for this, as is now known, is that a more detailed atomic model enables one to represent the intrinsic rigidity of the polypeptide chain and the steric restrictions on how the interior side chains can be packed together much more accurately than a one-point-per-residue model. The results of this study also enabled us to formulate some general guidelines concerning the optimum strategy for determining a protein structure from NMR data, which may be summarized as follows:

1. In determining the large-scale tertiary structure of a protein's polypeptide backbone, it is much more important to maximize the quantity of interresidue distance constraints than it is to maximize the quality (i.e. precision) of those constraints; sequential, intraresidue and torsion angle constraints play only a secondary role in this regard.
2. In order to determine the 'local' conformation of short segments of the polypeptide chain and their side chains with adequate precision, relatively precise sequential and intraresidue distance constraints are needed; torsion angle constraints derived from coupling constants are also, of course, very useful.

Since stereospecific assignments were not usually available at the time these studies were performed, their effect was not evaluated at that time. Once they became widely available, however, further studies were performed which showed they made a surprisingly strong contribution to the precision, particularly of the local conformation.[4,8] In part this is due to the elimination of 'pseudoatoms' and the consequent corrections to the distance constraints, but a more significant contribution seems to be due to the directionality information that these assignments provide.

Even though sophisticated refinement methods involving 'back-calculation' of the NOESY cross-peak intensities are coming into use which promise further to enhance the precision of NMR structure determinations,[40] distance geometry may be expected to continue to play an important role in the overall structure determination process. In the first place, it is a suitable formalism in which to eliminate errors from the data, determine its intrinsic structural implications, and to establish the basic features of the conformation. In the second, since these more complex refinements are ill-conditioned and extremely prone to becoming trapped by local minima, the excellent starting conformations that distance geometry yields are essential if they are to succeed. Finally, whereas these refinements all assume that the solution 'structure' can be adequately summarized by a single conformation, in reality the solution structure is an ensemble of rapidly exchanging conformations. The conformational ensembles that distance geometry yields are therefore a potentially more accurate representation of the solution structure, and in time methods may be developed which enable us to generate or refine these ensembles so as to make them representative of the actual solution ensemble.[41]

Several more detailed reviews covering the applications of distance geometry to structure determination by NMR are available.[42–46]

5 RELATED ARTICLES

Biological Macromolecules: Structure Determination in Solution; Biological Macromolecules; NOESY; Nuclear Overhauser Effect; Protein Structures: Relaxation Matrix Refinement; Structures of Larger Proteins, Protein-Ligand, and Protein-DNA Complexes by Multi-Dimensional Heteronuclear NMR.

6 REFERENCES

1. G. M. Crippen and T. F. Havel, *Distance Geometry and Molecular Conformation*, Research Studies Press, Taunton, 1988.
2. C. M. Oshiro, J. Thomason, and I. D. Kuntz, *Biopolymers*, 1991, **31**, 1049.
3. T. F. Havel, I. D. Kuntz, and G. M. Crippen, *Bull. Math. Biol.*, 1983, **45**, 665.

4. T. F. Havel, *Prog. Biophys. Mol. Biol.*, 1991, **56**, 43.
5. W. Braun and N. Gō, *J. Mol. Biol.*, 1985, **186**, 611.
6. W. Braun, *Q. Rev. Biophys.*, 1987, **19**, 115.
7. P. Güntert, W. Braun, and K. Wüthrich, *J. Mol. Biol.*, 1991, **217**, 517.
8. P. Güntert, W. Braun, M. Billeter, and K. Wüthrich, *J. Am. Chem. Soc.*, 1989, **111**, 3997.
9. P. Güntert and K. Wüthrich, *J. Biomol. NMR*, 1991, **1**, 447.
10. P. Koehl, J.-F. Lefèvre, and O. Jardetzky, *J. Mol. Biol.*, 1992, **223**, 299.
11. R. Kaptein, E. R. P. Zuiderweg, R. M. Scheek, R. Boelens, and W. F. van Gunsteren, *J. Mol. Biol.*, 1985, **182**, 179.
12. G. M. Clore, A. M. Gronenborn, A. T. Brünger, and M. Karplus, *J. Mol. Biol.*, 1985, **186**, 435.
13. M. Nilges, G. M. Clore, and A. M. Gronenborn, *FEBS Lett.*, 1988, **239**, 129.
14. W. Nerdal, D. R. Hare, and B. R. Reid, *J. Mol. Biol.*, 1988, **201**, 717.
15. R. Kaptein, R. Boelens, R. M. Scheek, and W. F. van Gunsteren, *Biochemistry*, 1988, **27**, 5389.
16. A. M. Gronenborn and G. M. Clore, *Biochemistry*, 1989, **28**, 5978.
17. M. P. Williamson, T. F. Havel, and K. Wüthrich, *J. Mol. Biol.*, 1985, **182**, 295.
18. A. T. Brünger and M. Karplus, *Acc. Chem. Res.*, 1991, **24**, 54; A. T. Brünger and M. Nilges, *Q. Rev. Biophnys.*, 1993, **26**, 49.
19. M. H. Kalos and P. A. Whitlock, *Monte Carlo Methods*, Wiley, New York, 1986.
20. S. Kirkpatrick, C. D. Gelatt, Jr, and M. P. Vecchi, *Science*, 1983, **220**, 671.
21. D. Bassolino, F. Hirata, D. B. Kitchen, D. Kominos, A. Pardi, and R. M. Levy, *Int. J. Supercomput. Appl.*, 1988, **2**, 41.
22. D. Bouzida, S. Kumar, and R. H. Swendsen, *Phys. Rev. A*, 1992, **45**, 8894.
23. Z. Li and H. A. Scheraga, *Proc. Natl. Acad. Sci. USA*, 1987, **84**, 6611.
24. B. von Freyberg and W. Braun, *J. Comput. Chem.*, 1991, **12**, 1065.
25. J. H. Holland, *Adaptation in Natural and Artificial Systems*, University of Michigan Press, Ann Arbor, MI, 1975.
26. S. Forrest, *Science*, 1993, **261**, 872.
27. R. Unger and J. Moult, *J. Mol. Biol.*, 1993, **231**, 75.
28. M. J. J. Blommers, C. B. Lucasius, G. Kateman, and R. Kaptein, *Biopolymers*, 1992, **32**, 45.
29. G. M. Crippen and T. F. Havel, *Acta Crystallogr., Sect. A*, 1978, **34**, 282.
30. I. D. Kuntz, G. M. Crippen, and P. A. Kollman, *Biopolymers*, 1979, **18**, 939.
31. W. Braun, C. Boesch, L. R. Brown, N. Gō, and K. Wüthrich, *J. Mol. Biol.*, 1983, **169**, 921.
32. M. Nilges, G. M. Clore, and A. M. Gronenborn, *FEBS Lett.*, 1988, **229**, 317.
33. T. F. Havel and K. Wüthrich, *Bull. Math. Biol.*, 1984, **46**, 673.
34. T. F. Havel, *Biopolymers*, 1990, **29**, 1565.
35. G. M. Crippen, *J. Comput. Chem.*, 1984, **5**, 548.
36. W. Glunt, T. L. Hayden, and W.-M. Liu, *Bull. Math. Biol.*, 1991, **53**, 769.
37. W. Glunt, T. L. Hayden, and M. Raydan, *J. Comput. Chem.*, 1993, **14**, 114.
38. T. F. Havel, G. M. Crippen, and I. D. Kuntz, *Biopolymers*, 1979, **18**, 73.
39. T. F. Havel and K. Wüthrich, *J. Mol. Biol.*, 1985, **182**, 281.
40. P. Yip and D. A. Case, *J. Magn. Reson.*, 1989, **83**, 643.
41. J.-X. Yang and T. F. Havel, *J. Biomol. NMR*, 1993, **3**, 355.
42. K. Wüthrich, *Methods Enzymol.*, 1989, **177**, 125.
43. I. D. Kuntz, J. F. Thomason, and C. M. Oshiro, *Methods Enzymol.*, 1989, **177**, 159.
44. R. M. Scheek, W. F. van Gunsteren, and R. Kaptein, *Methods Enzymol.*, 1989, **177**, 204.
45. G. P. Gippert, P. F. Yip, P. E. Wright, and D. A. Case, *Biochem. Pharmacol.*, 1990, **40**, 15.
46. G. Wagner, S. G. Hyberts, and T. F. Havel, *Ann. Rev. Biophys. Biomol. Struct.*, 1992, **21**, 167.

Biographical Sketch

Timothy Franklin Havel. *b* 1953. B.S., Reed College, 1975; Ph.D. University of California at Berkeley, 1982. Introduced to distance geometry by G. M. Crippen and I. D. Kuntz, and to NMR by K. Wüthrich. Assistant Member, Research Institute of Scripps Clinic, San Diego, CA, 1985–88; Associate research scientist, University of Michigan, Ann Arbor, MI, 1988–90; Lecturer, Harvard Medical School, Boston, MA, 1990–present. Approx. 40 publications; with Professor Crippen the book 'Distance Geometry and Molecular Conformation', Research Studies Press, Taunton, 1988. Research interests include the theory of molecular conformation, and methods for determining conformation from NMR spectroscopy.

Magic Angle Spinning Carbon-13 Lineshapes: Effect of Nitrogen-14

Charles A. McDowell

University of British Columbia, Vancouver, Canada

1	Introduction	1
2	Magic Angle Spinning	1
3	Effects of an Axially Symmetric Electric Field Gradient	2
4	^{14}N Effects of an Asymmetric Electric Field Gradient	3
5	Influence of J Coupling	6
6	Other Spin-$\frac{1}{2}$ Nuclei Bonded to ^{14}N: ^{1}H CRAMPS	6
7	Related Articles	8
8	References	8

1 INTRODUCTION

The introduction of the Hartmann–Hahn[1] technique of cross polarization into solid state nuclear magnetic resonance spectroscopy, particularly when combined with multiple pulse methods[2] to remove homo- and heteronuclear, dipolar broadening, was a significant addition to the methods available for the study of solid compounds by NMR. When cross polarization and proton decoupling were incorporated into the magic angle spinning technique,[3] there was produced a significant enlargement of the repertoire of sensitive NMR spectrometric procedures available for obtaining high-resolution spectra of solid state compounds and materials.[4] This important new spectroscopic method became known as cross polarization magic angle spinning (CP MAS) NMR. When the ^{13}C spectra of compounds containing nitrogen were studied by CP MAS some lines appeared as broadened asymmetric doublets. It was soon realized that this characteristic lineshape resulted from the ^{14}N nuclear quadrupole moment interfering with the ability of the magic angle spinning to average out the ^{13}C–^{14}N dipolar interactions. This interpretation was based on earlier observations of the ^{13}C lineshapes of carbon nuclei bonded to nitrogen in the NMR of single crystals. We shall now briefly describe the main features of such high-resolution NMR spectra of single crystals to provide a suitable background for understanding the theoretical interpretation of the asymmetrical ^{13}C–^{14}N lineshapes in CP MAS spectra.

1.1 Single Crystal NMR Spectra

Within a short time after their introduction, the new NMR spectroscopic techniques were applied to obtain ^{13}C chemical shielding data on a wide range of organic compounds. It was soon found in compounds containing a nitrogen nucleus adjacent to the carbon nucleus being studied that splittings from ^{13}C–^{14}N dipolar couplings were observed. Griffin et al.[5] found that the NMR spectrum of a single crystal of glycine at a certain orientation with respect to the magnetic field exhibited three lines from the methylene carbons split by adjacent ^{14}N nuclei. In measurements of the ^{13}C chemical shielding tensor in the metal complex $K_2Pt(CN)_4Br_{0.3}\cdot 3H_2O$, Stoll et al.[6] observed large effects clearly shown to be caused by ^{14}N quadrupolar interactions. In that compound, the electric quadrupolar interactions are of comparable size to the ^{13}C–^{14}N dipolar interaction; consequently, mixing with the pure Zeeman eigenfunctions occurs. These required eigenfunctions were obtained by the application of first-order perturbation theory and subsequent diagonalization of the combined Zeeman-quadrupole Hamiltonian. Stoll et al. assumed an axially symmetric electric field gradient tensor with its symmetry axis along the C–N bond. Good quantitative agreement was found between the theoretical and experimental spectral lineshapes for all the angular variations studied.

Because amino acids are of great biological importance, the observations of ^{13}C–^{14}N dipolar–quadrupolar interactions clearly meant that single crystal NMR spectra of amino acids would soon be investigated. Thus simultaneously there were reported such detailed studies of alanine[7] and glycine.[8] Though these two detailed single crystal studies cover similar ground, we shall give details about the more complete studies of alanine and use some of the theoretical ideas later in our discussion of the effects of ^{14}N quadrupolar interactions causing asymmetry in certain magic angle spectral lineshapes of compounds with C–N bonds.

The proton-enhanced proton-decoupled ^{13}C NMR spectra of a single crystal of L-alanine were studied by Naito et al.[7] The C-α line showed a triplet pattern arising from dipolar coupling with the ^{14}N ($S = 1$) nuclei (Figure 1). These splittings were asymmetric, especially in the a-axis orientation. The dipolar interactions in the presence of the ^{14}N quadrupolar interaction were calculated by applying ideas first employed by VanderHart et al.[9] to provide a theoretical analysis of the static proton resonance spectra of polycrystalline $HMn(CO)_5$ and $HCo(CO)_4$. The appropriate Hamiltonian for the case where the quadrupole asymmetry parameter η is zero is written in the following form for later convenience:

$$\mathcal{H} = -\gamma_N \hbar B_0 S_z + \frac{\chi h}{4S(2S-1)}[3S_z^2\cos^2\theta + 3S_x^2\sin^2\theta + 3(S_zS_x + S_xS_z)\sin\theta\cos\theta - S^2] \quad (1)$$

where the quadrupolar coupling constant is $\chi = e^2qQ/h$ This Hamiltonian was used to determine the required eigenfunctions of the ^{14}N nucleus, and these in turn employed to calculate the eigenfunctions of the ^{13}C–^{14}N dipolar interaction as a function of θ, the angle between the direction of the external magnetic field and the symmetry axis of the electric field gradient tensor, i.e., the C_θ–N bond direction. It was thus possible to calculate the three ^{13}C resonances predicted (and observed experimentally for the C-α nucleus) which correspond to the nitrogen Zeeman states $|+1\rangle$, $|0\rangle$, and $|-1\rangle$, respectively. When the sign of the quadrupole coupling constant was assumed to be positive, good agreement was found between the calculated and experimental data for all the angles studied. The experimental results thus give the sign of the quadrupole coupling constant.

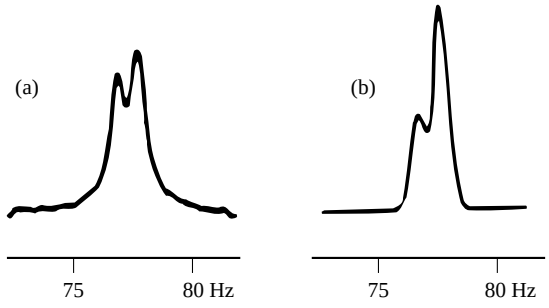

Figure 1 Lineshape of the C-α nucleus in the ^{13}C CP MAS spectrum of polycrystalline L-alanine taken at a field of 4.6 T. (a) Experimental spectrum; (b) computer-simulated spectrum assuming an axially symmetric quadrupolar parameter. (Reproduced by permission of the American Institute of Physics from Naito et al.[14])

2 MAGIC ANGLE SPINNING

As is well known, MAS tends to average out anisotropic interactions to their corresponding isotropic values when they are very weak as compared with their Zeeman interactions. Theoretical consideration of the effect of the ^{14}N quadrupolar interaction on the ^{13}C MAS spectra based on the above ideas, show that for ^{13}C nuclei bonded to ^{14}N an asymmetric doublet pattern is expected. Lippmaa et al.[10] reported that a high-resolution rotational-synchronized proton-enhanced magic angle spinning ^{13}C NMR spectrum of the polycrystalline solid of the one-dimensional compound tetrathiofulvalene–tetracyanoquinodimethane (TTF–TCQN) exhibited a three-line spectrum, one line of which consisted of an asymmetric doublet which they attributed to the C–N group. The splitting was found to be field-dependent and identified as arising from dipole–dipole interaction with the ^{14}N nuclei having a quadrupole interaction of comparable magnitude to their Zeeman interaction. This was the first observation of an asymmetric lineshape in a ^{13}C magic angle spinning NMR spectrum of a compound containing a ^{13}C–^{14}N bond.

3 EFFECTS OF AN AXIALLY SYMMETRIC ELECTRIC FIELD GRADIENT

The influence of spinning on the solid state NMR spectrum of a molecular system consisting of spin pairs in which one of the two spins has a quadrupole moment was first treated theoretically by Kundla and Alla.[11] The quadrupolar interaction fixes the spin moment at a definite orientation in the principal axis system (PAS) of the molecule. Rotation of the sample causes a rotational synchronized movement of the spin moment which does not permit the complete averaging of the dipole–dipole interaction between the spin-$\frac{1}{2}$ nucleus I and the quadrupole nucleus $S = 1$. The degree of the averaging depends on the ratio of the quadrupolar and Zeeman energies of the S nucleus.

The Hamiltonian may be written as

$$\mathcal{H} = \mathcal{H}_{\mathrm{Z}}^{I} + \mathcal{H}^{S} + \mathcal{H}_{\mathrm{D}}^{IS} \tag{2}$$

Here $\hat{\mathcal{H}}_{\mathrm{Z}}^{I}$ is the Zeeman term of the I nucleus, $\mathcal{H}^{S}$ is the quadrupolar Hamiltonian, and $\mathcal{H}_{\mathrm{D}}^{IS}$ the dipolar interaction Hamiltonian between the I and S spins. It is assumed that $\mathcal{H}_{\mathrm{D}}^{IS}$ is small so that first-order perturbation theory may be applied to calculate the resonance frequencies of the I-spin spectral lines. Because of the rotation of the sample at frequency ω_{r}, the eigenfunctions and eigenvalues of the unperturbed system become time-dependent. These were calculated for the case where the quadrupole coupling is symmetric. The energy levels were expressed in terms of parameters such as $k = \omega_{\mathrm{Q}}/\omega_{\mathrm{Z}}^{S}$; θ, the angle between the rotation axis and the magnetic field; the Euler angles α, β, and γ of the sample-fixed coordinate system, in which the α axis coincided with the rotational axis; and the PAS. When $\theta = 0$, the eigenvalue equations became the same as those giving the dependences of the spectral lines on the orientation of the nonrotating single crystal as described by Stoll et al.[6] To obtain the lineshapes and resonances of the polycrystalline sample at high spinning speeds, the average positions, $\overline{\Delta_n^{\mathrm{D}}}$, were obtained by averaging over all orientations represented by the angle β. Numerical calculations for the magic angle case showed that the line splittings and total widths depend strongly on the relative strengths of the Zeeman and quadrupolar interactions. Moreover, it was shown that in a strong magnetic field, the I-spin spectrum is an asymmetric doublet, one of the lines being the sum of two components, the full width of the single line being twice as large as that of the composite line. The splitting increased with increasing k leading to a regular triplet. The isotropic spin–spin interaction between the I and S nuclei was predicted to shift the I-spin spectral lines, the effect decreasing with increasing values of k.

Apparently unaware of the above work of the Estonian scientists, several groups reported CP MAS spectra of polycrystalline organic compounds containing C–N bonds such as amino acids, peptides, and proteins in which significant differences were observed between the solid state spectra and those in solution.[12,13] Most of the resonances from carbons bonded to nitrogens were split into broadened doublets, and some of the resonances from more distant carbons were also affected.

A classical and much studied example is the CP MAS spectrum of polycrystalline alanine.[14] The observed splittings of the asymmetric doublet of the C-α resonance was 45 Hz with a 200 MHz magnet and $\sim$ 100 Hz when measured at 90 MHz. The spectra can be fully interpreted and quantitatively explained by the following theoretical treatment.[14] First, the ^{14}N quadrupolar interaction is of comparable magnitude to the Zeeman interaction, so the ^{14}N spin eigenfunctions must be determined by diagonalizing the nitrogen Zeeman quadrupole Hamiltonian, and those eigenfunctions used in the calculation of the ^{13}C–^{14}N dipolar interactions. At the outset it should be understood that in this problem it is important to be mindful of the timescale of the magic angle spinning. In the experiments described by Naito et al.[14] the spinning frequency was 4.5 kHz, which is small compared with the ^{14}N quadrupolar interaction in L-alanine for which $\chi = 1.205$ MHz; the adiabatic approximation can therefore be employed to determine the nitrogen spin functions at time t from the following equation

$$\mathcal{H}_{\mathrm{ZQ}}\psi_{\mathrm{N}}(t) = E(t)\psi_{\mathrm{N}}(t) \tag{3}$$

Here, $\mathcal{H}_{\mathrm{ZQ}}(t)$ is the Zeeman quadrupole Hamiltonian of the nitrogen nuclei at time t. For the amino nitrogen in amino

acids and the cyano nitrogen in nitriles, one may assume with a high degree of accuracy that the electric field gradient tensor is axially symmetric, i.e., $\eta = 0$. Thus for the MAS spectrum of L-alanine we can write the Zeeman quadrupole Hamiltonian as

$$\mathcal{H}_{ZQ}(t) = -\gamma_N \hbar S_z B_0 + \frac{\chi h}{4S(2S-1)}[3S_z^2 \cos^2\theta(t) + 3S_x^2 \sin^2\theta(t) + 3(S_z S_x + S_x S_z)\sin\theta(t) \times \cos\theta(t) - S^2] \quad (4)$$

Here, $\theta(t)$ is the periodic value of the angle between the field direction $\boldsymbol{B}_0$ and the internuclear vector $\boldsymbol{r}_{CN}$. Under MAS, when a rigid array of nuclei is rotated with an angular velocity ω_r about an axis inclined at an angle β to the direction of the external magnetic field $\boldsymbol{B}_0$, and at an angle β' to $\boldsymbol{r}_{CN}$, we may write that $\theta(t)$ can vary as follows:

$$\cos\theta(t) = \cos\beta\cos\beta' + \sin\beta\sin\beta'\cos(\omega t + \psi) \quad (5)$$

where ψ is the azimuthal angle of $\boldsymbol{r}_{CN}$ at time $t = 0$.

In this case the $^{13}C-^{14}N$ dipolar interaction is very small compared with the Zeeman interaction, so first-order perturbation theory can be used to calculate the $^{13}C-^{14}N$ dipolar interaction at time t. The dipolar splitting of the ^{13}C resonance resulting from that calculation using the Hamiltonian $\mathcal{H}_{ZQ}$ represented by equation (3) yields

$$\Delta E_i(t) = -\gamma_C \gamma_N \hbar^2 / r_{CN}^3 \{[a_i(t)^2 - c_i(t)^3 2][1 - 3\cos^2\theta(t)] - (9/2)^{1/2}[a_i(t) + c_i(t)]b_i(t)\sin 2\theta(t)\} \quad (6)$$

Here, $a_i(t)$, $b_i(t)$, and $c_i(t)$ (i = 1, 2, and 3) are the coefficients at time t of the Zeeman quantized spin functions of the nitrogen nuclei, namely, $|1\rangle$, $|0\rangle$, and $|-1\rangle$, respectively. In L-alanine the $^{13}C-^{14}N$ dipolar interaction, 0.6636 kHz, is small compared with the spinning frequency 4.5 kHz, so in such cases the $\Delta E_i(t)$ have to be averaged from $t = 0$ to $t = \infty$ to obtain the $^{13}C-^{14}N$ dipolar energy of the spinning sample. The values of $\Delta E_i(t)$ were calculated for each 5° of $\omega t + \psi$ in the range 0° to 360° with constant β', and these values were then averaged to yield $\overline{\Delta E_{i\beta'}(t)}$. The theoretical lineshapes for polycrystalline samples rotating at the magic angle $\beta = 54.7°$ are obtained by calculating the numerical values of $\overline{\Delta E_{i\beta'}(t)}$ when β' is varied in steps of 2° in the interval 0° to 90°, each $\overline{\Delta E_{i\beta'}(t)}$ being weighted by its probability $\sin\beta'$. Finally, convoluting the theoretical lineshapes with a Gaussian function gave the actual lineshape. The linewidth of the Gaussian function is an adjustable parameter which takes into account any instrumental line broadening, such as effects arising from improper decoupling setting, any slight misalignment of the magic angle, and any magnetic field inhomogeneities, etc.

As shown in Figure 1, the calculated and experimental spectra agreed well. Clearly the calculated lineshape is an asymmetric doublet with a splitting of 48 Hz for a ^{13}C resonance frequency of 50.3 MHz and 108 Hz for a resonance frequency of 22.6 MHz, both values in good agreement with experimental observations.[12,14] This field-dependence of the asymmetric doublet splitting arises because a weak field causes a relative increase in the contributions from the off-diagonal elements of the matrix representation of the Hamiltonian $\hat{\mathcal{H}}_{ZQ}(t)$. Noteworthy also was the finding that when the sign of the term χh in the lineshape calculation was chosen as negative, the shape was reversed, i.e., the intensity of the high-frequency (low-field) peak was now stronger than the other one. This observation thus presents a means of determining the sign of the quadrupole coupling constant of ^{14}N bonded to ^{13}C by lineshape analysis of the CP MAS ^{13}C NMR spectra.

When the spectrum of cyanoacetamide was studied the same theoretical treatment was applicable because here also the $^{13}C-^{14}N$ dipolar interaction, 1.46 kHz, was smaller than the rotor spinning frequency. The lineshape exhibited a reversal of the intensities of the doublet components. When the value of χh was taken to be negative, the simulated lineshape was in good agreement with that observed experimentally. The splitting of the asymmetric doublet for the nitrile was 338 Hz in the simulated spectrum, in good agreement with the experimentally measured splittings of 305 Hz to 356 Hz for different cyano compounds.

The above theoretical treatment and the simulated MAS lineshapes were based on the important assumption that the rotor spinning speed was very small in comparison with the size of the quadrupole interaction of the ^{14}N nucleus in the molecule. It was, however, shown that if the spinning speeds were as large as the ^{14}N quadrupolar interaction (i.e., in the MHz range), which seems highly unlikely, the lineshape predicted is quite different from those obtained at low spinning frequencies. For the extremely high spinning frequency case, a truncated Zeeman quadrupole Hamiltonian $\overline{\mathcal{H}_{ZQ}(t)}$ (the time-dependent part is truncated) can be used for the MAS lineshape calculation. Using the same parameters as employed in the simulation of the spectra of nitrile compounds with a value of χ = 3.87 MHz and 24 Hz for the halfwidth of the Gaussian broadening function, it was found that the predicted splitting is less than one-third of the slow-spinning case, giving a broad powder pattern as the expected lineshape.

Contemporaneously with the above work, Zumbulyadis et al.[15] presented an extensive analysis of the influence of quadrupole nuclei on the magic angle spinning spectra of spin-$\frac{1}{2}$ nuclei. Here also, as above, the treatment was restricted to the case with an axially symmetric quadrupolar tensor. The formal theory described was similar to that described above; it also made use of the adiabatic approximation, in which a time-dependent wavefunction is approximated by an eigenfunction of the instantaneous Hamiltonian multiplied by a time-dependent phase factor. Theoretical powder patterns were calculated for a range of values of parameters typical of ^{13}C coupled to ^{14}N, the results being given as a function of ratio of the spin-1 Zeeman frequency Z to the quadrupole coupling constant χ. Each spectrum consisted of double-peaked bands with an intensity ratio of 1:2; the ratio of the S-spin Zeeman to the quadrupolar interaction (Z/χ) determined the widths of the bands and the splittings between them. This was also implicit in the theories of Naito et al.[14,16] as was the finding that both the widths and splittings of the bands decrease at higher magnetic fields where the quadrupolar interaction induces less mixing of the S-spin Zeeman eigenstates. It was also shown that the appearance of the bands depended critically on the mutual orientations of the unique principal axes of the dipolar and quadrupolar interaction tensors, the doublet splitting going through a minimum when the two principal axes were oriented at the magic angle *with respect to each other*.

4 ^{14}N EFFECTS OF AN ASYMMETRIC ELECTRIC FIELD GRADIENT

Though the above theoretical treatments[14,15] were successful in providing an interpretation of the CP MAS ^{13}C spectra of a number of nitrogen-containing compounds and, in particular, explaining the asymmetric lineshapes associated with C–N bonds, the restriction to cases with symmetric ^{14}N quadrupolar tensors was limiting. When the quadrupole coupling parameter $\eta \neq 0$, the C–N bond direction may not be parallel to the principal axis of the quadrupolar tensor. In this situation the off-diagonal elements in the matrix representation of the Hamiltonian $\mathcal{H}_{ZQ}$ will contain η, and hence a large value of the quadrupolar asymmetry parameter will be quite effective in determining the resulting MAS lineshape.

To extend the theory to include the ^{13}C CP MAS spectra of important organic molecules such as nitroanilines, and biomolecules like imidazoles, polypeptides, and proteins in which the influence of asymmetry of the ^{14}N quadrupole coupling tensor may play an important role in determining the lineshapes of the spectra, it was necessary to extend the theoretical formulation though the basic ideas were still sufficient to permit the required extension to encompass a wider range of molecular environments.[16]

The adiabatic approximation represented by equation (2) is still used but the Zeeman quadrupole Hamiltonian for ^{14}N must be modified to reflect the asymmetry of η, the nitrogen asymmetry parameter. The Hamiltonian is now written as

$$\mathcal{H}_{ZQ}(t) = -\gamma_N \hbar B_0 S_{z'} + \frac{eQq_{zz}}{4S(2S-1)} \times\{(3S_z^2(t) - S^2) + \eta[S_x^2(t) - S_y^2(t)]\} \qquad (7)$$

where $\eta = (q_{xx} - q_{yy})/q_{zz}$; eq_{ii} are the principal values of the electric field gradient tensor at the ^{14}N nucleus in the compound. They obey the convention that $|q_{zz}| \geq |q_{yy}| \geq |q_{xx}|$. The quantity e^2Qq_{ii} ($i = x, y, z$) is one of the principal values of the quadrupole coupling tensor and e^2Qq_{zz} is the quadrupole coupling constant. In this case there are two different coordinate systems to be considered. The Zeeman coordinate system is specified by (x', y', z'), and the principal axis system coordinates of the ^{14}N electric field gradient tensor of the compound by (x, y, z). The Euler angles of the spinner rotation axes (x^R, y^R, z^R) are written as β', θ, and ψ. The magic angle spinning axis, z^R, is inclined at an angle β' with the z axis, and at the magic angle β to the static magnetic field (Z'). The angle ψ is time-dependent and given by $\psi = \omega_r t + \psi_0$, where ψ_0 is the initial angle when $t = 0$ and ω_r is the angular velocity of spinning. Transformations of the coordinate systems (see Figure 2) give the ^{14}N Zeeman quadrupole Hamiltonian in the Zeeman coordinate system, and the resulting eigenstates are used to calculate the ^{13}C–^{14}N dipolar energy. Since, in general, the internuclear vector $\boldsymbol{r}_{CN}$ is not collinear with the z axis of the electric field gradient tensor, its direction is defined by the polar angles (θ, ψ) in the principal axis system of the electric field gradient tensor. First order perturbation theory can again be used to calculate the ^{13}C–^{14}N dipolar energy of the ^{13}C resonance of a certain

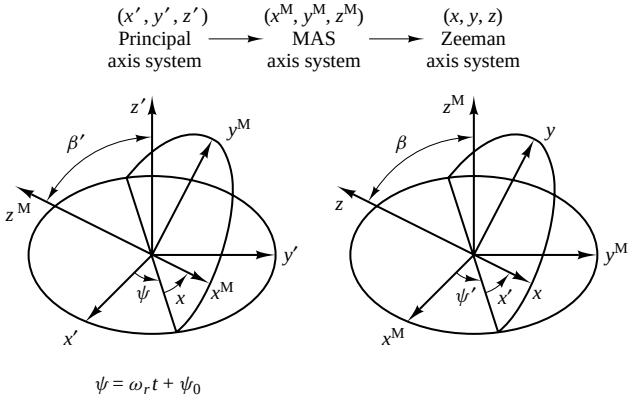

Figure 2 Diagrammatic representation of the coordinate transformations required to calculate the ^{13}C lineshapes when the quadrupolar parameter η is asymmetric. They can be summarized as follows:

x, y, z	x^R, y^R, z^R	x', y', z'
Principal $\xrightarrow{(\beta',\phi,\psi)}$	Rotating $\xrightarrow{(\beta,0,0)}$	Zeeman
axis system	axis system	axis system

molecular orientation at time t and is given by

$$\Delta E_{i\beta'\Phi}(t) = \langle\beta\psi_N(t)|\mathcal{H}_D(t)|\beta\psi_N(t)\rangle - \langle\alpha\psi_N(t)|\mathcal{H}_D(t)|\alpha\psi_N(t)\rangle \qquad (8)$$

Here, $|\alpha\rangle$ and $|\beta\rangle$ are the ^{13}C Zeeman spin functions. As before, the ^{13}C–^{14}N dipolar interaction is smaller than the spinning frequency, so $\Delta E_{i\beta'\Phi}(t)$ must be averaged over one rotor cycle, i.e., from $t = 0$ to $t = \infty$, to give the ^{13}C–^{14}N dipolar energy in the spinning sample, namely

$$\overline{\Delta E_{i\beta'\Phi}(t)} = (1/2\pi)\int_0^{2\pi} \Delta E_{i\beta'\Phi}(\psi)\,d\psi \qquad (9)$$

The values of $\overline{\Delta E_{i\beta'\Phi}(t)}$ were calculated numerically for small increments of the appropriate angles and the resulting values averaged. The resulting theoretical averaged line positions for the spinning sample were weighted by their probability, sin β', and then convoluted with a suitable lineshape function to yield the actual lineshape.

One of the first compounds chosen to test the above theory for calculating the MAS lineshapes of molecules containing ^{14}N nuclei with nonasymmetric quadrupolar tensors, i.e., with $\eta \neq 0$, was polycrystalline 2,6-dimethyl-3-nitroaniline. This molecule has two different types of ^{14}N nuclei. The ^{13}C MAS NMR spectrum showed that the resonances for both the nitro and amino carbon nuclei exhibited asymmetric doublet patterns (Figure 3). The high-frequency line in the nitro doublet was more intense than the other component, whereas the reverse was the case for the amino peak. Clearly the differences in the lineshapes arose from the different signs, orientations, and magnitudes of the respective electric field gradient tensors for the two ^{14}N nuclei. Calculations of the theoretical lineshapes by the method outlined above using the appropriate molecular parameters and a reasonable assignment for the orientation of the ^{14}N electric field gradient tensor based on that of *p*-nitrotoluene yielded lineshapes similar to those observed

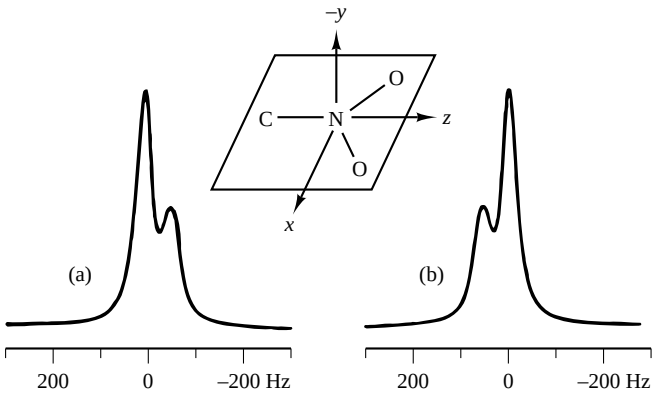

Figure 3 Lineshape of the resonance of the carbon nucleus adjacent to the NO_2 group in the ^{13}C CP MAS spectrum of 2,6-dimethyl-3-nitroaniline. Computer-simulated spectrum calculated with a quadrupolar asymmetry parameter $\eta = 0.408$ and (a) the ^{14}N quadrupolar coupling constant $e^2Qq_{zz}/h = -1.340$ MHz; (b) the quadrupolar coupling assumed to be positive. (Reproduced by permission of Academic Press from Naito et al.[16])

experimentally. With the value of χ being 1.340 MHz and η = 0.408 for ^{14}N of the $-NO_2$ group, good agreement was found with the experimental lineshape only when the sign of the quadrupole coupling constant was taken as negative. The simulation of the lineshape of the amino peak required more insight. Values for χ, η, and $\gamma_C\gamma_N\hbar/(2\pi r_{CN}^3)$, based on literature information, were chosen to be 3.977 MHz, 0.263, and 0.8466 kHz, respectively. In the case where the z axis of the quadrupole coupling constant was chosen to lie normal to the plane of the NH_2 group and the y axis assumed to be tilted 40° from the C–N bond direction, with the sign of the quadrupole coupling constant negative the resulting simulated lineshape was in excellent agreement with that observed experimentally. Also, the calculated value for the doublet splitting was 110 Hz, in good agreement with the observed value of 102 Hz.

It proved more difficult to provide an unambiguous interpretation of the lineshapes of the ^{13}C CP MAS NMR spectrum of polycrystalline glycylglycine and glycyl-L-alanine. Here again the orientation of the principal axes of the ^{14}N quadrupole coupling tensor was unknown. Proceeding as before, the calculated lineshapes for the case where the z axis was assumed to lie along the direction of the N–H bond led to a narrow singlet pattern not in agreement with the experimental spectrum. When the z axis was chosen to be normal to the C–N–C plane and the y axis along the N–H bond, the simulated lineshapes again did not agree with the observed lineshape. Several possible orientations of the axes were tried, but only when the z axis of the quadrupole tensor of the amino nitrogen was assumed to lie along the C–N bond direction and the sign of the quadrupole coupling constant taken as positive, together with acceptable values of the other constants, was a satisfactory lineshape simulation obtained. Moreover, the calculated doublet splitting for the C-α carbon in glycylglycine was 49 Hz, which was in good agreement with the experimental value of 41 Hz.

Given the satisfactory simulations of the observed lineshapes from the theory for amino acids and polypeptides, attention was then turned to a more sophisticated molecule of biological interest, namely, trimethylimidazole. This molecule has two different types of nitrogen nuclei. The quadrupole coupling constants and asymmetry constants of the two nitrogen nuclei are for N-1, χ = 1.424 MHz and η = 0.980, and for N-2 χ = 3.267 MHz and η = 0.129. The large difference in the two quadrupolar tensors for the two nitrogen nuclei is obviously mainly the cause of the notable difference between the lineshapes observed for the C-4 and C-5 carbon atoms in the CP MAS spectrum of ^{13}C in this compound. Nevertheless, it was only possibly to simulate the experimental lineshapes successfully after a judicious choice of the orientations with respect to the molecular axes of the respective quadrupolar tensor axes.

Furthermore, this work clearly showed that in nitrogen-containing organic compounds, if the correct quadrupole coupling tensor and the relative orientations of the principal axes with respect to the molecular axes are known for a particular nitrogen nucleus, it is possible to calculate the theoretical lineshape for the carbon nucleus bonded to the nitrogen. That the sign of the quadrupole coupling constant for the nitro and amino nitrogen atom in organic compounds differed was new. Since each group containing a nitrogen atom has a characteristic quadrupole coupling tensor, it follows that the ^{13}C resonances in the CP MAS NMR spectra of the carbon atoms in such groups, e.g., $-NO_2, -NH_2, \equiv N, -NH_3^+$, and −CN, all exhibit characteristic lineshapes. This information is obviously of considerable practical importance for the assignment of the solid state ^{13}C CP NMR spectra of organic compounds, particularly those of biological importance and heterocyclic compounds, pharmaceuticals, dyestuffs, etc.

Another approach to calculating the lineshapes of the ^{13}C MAS spectra of nitrogen-containing organic compounds was put forward by Hexem et al.[17] This was based on writing the Hamiltonian of the spin system in terms of irreducible spherical tensor operators, namely

$$\mathcal{H} = \sum_{\lambda} \sum_{l} \sum_{m=-l}^{l} (-1)^m R_{l-m}^{\lambda} T_{lm}^{\lambda} \qquad (10)$$

In this equation, λ represents the type of interaction, including the Zeeman interactions for the carbon, Z_C, and nitrogen spins, Z_N; the quadrupole interaction of the nitrogen spin, Q; D, the $^{13}C-^{14}N$ dipolar interaction; and CS, the chemical shielding of the carbon spins. The quantity J, the indirect spin–spin interaction, is ignored because it was assumed to be negligible. The rotational properties of the irreducible spherical tensors were used to obtain the Hamiltonian in a more convenient form. The time-dependence of the resulting Hamiltonian was removed by applying average Hamiltonian theory. The part of the average Hamiltonian representing the dominant interactions of the carbon atoms and which commutes with the appropriate Zeeman Hamiltonian can be written as

$$\mathcal{H}^C(\phi) = C^Z \rho_{00}^Z T_{00}^Z + C^{CS} \rho_{00}^{CS} T_{00}^{CS} + \sum_{m=-2}^{2} C^D (-1)^m R_2^D - (\phi) T^D 3_{2m} \qquad (11)$$

where $C^Z = \gamma_C\hbar$, $C^{CS} = \gamma_C$, $\rho_{00}^{CS} = \sigma_{iso}$, $T_{00}^Z = B_{00}I_z$, $C^D = -2\gamma_C\gamma_N\hbar^2$, and σ_{iso} is the isotropic chemical shift. Making use of Wigner rotation matrices, one set of Euler angles transforms the principal axis system of the dipolar interaction

to the principal axis system of the electric field tensor, while the angles (0, θ_M, ψ) transforms further the spatial components to the axis system of the spinning rotor. In this last transformation, θ_M is the magic angle (54.7°) and ψ is the azimuthal angle of rotation about the rotor axis.

The shifts in the energy levels of ^{13}C were calculated using zero-order average Hamiltonian theory, which is equivalent to first-order perturbation theory, this procedure being possible because the small size of the dipolar coupling means that it can be treated as a perturbation. Because of the relative orders of magnitude of the ^{14}N quadrupole coupling constant and the lower achievable spinning rates, one cannot use zero-order average Hamiltonian theory to average $\hat{\mathcal{H}}^D_{CN}$, the heteronuclear Hamiltonian over one rotational period. The ^{14}N matrix was diagonalized and the induced carbon shifts calculated. The carbon shifts were calculated for a sufficient number of points as described in the earlier theoretical treatments. These dipolar shifts were averaged over one rotation period $\overline{\omega_n^C}$ by numerical integration over the azimuthal angle of rotation, ϕ. This is equivalent to assuming the adiabatic approximation for calculating the change of the nitrogen states over the rotational period described in detail earlier by Naito et al.[14,16] and by Zumbulyadis et al.[15]

As a preliminary test of theory, and to compare the results from diagonalizing the nitrogen Hamiltonian matrix with those obtained by using first-order perturbation theory to obtain the coefficients in the eigenfunction $\Phi_n^N(\phi)$ representing a linear combination of the Zeeman spin states, Hexem et al.[17] calculated the expected powder ^{13}C spectrum for a C–N bond. Typical values of the parameters were used and the quadrupole coupling tensor was assumed to be axially symmetric with η = 0. When these theoretical predictions for the lineshapes were compared with the experimental observations for polycrystalline alanine, it was clear that the spectra lacked the resolution to show the fine structure predicted by the powder pattern. The calculated spectrum obtained using a value of 0.26 for the quadrupole asymmetry parameter, η, and taking its sign as positive was in good agreement with the experimental spectrum, in general accord with the findings of Naito et al.[16]

Explaining the ^{13}C lineshape of the α-carbon in *N*-acetylvaline was more challenging. In this case η = 0.31 and in the case of the polypeptide bond study of Naito et al.[16] it was necessary to consider carefully the relative orientations of the principal axes of the electric field gradient tensor with respect to the molecular axes. Consideration of several orientations soon yielded a set of parameters which produced good agreement between the computer simulated lineshape and that observed experimentally.

The extensive studies of Hexem et al.[17] and Naito et al.[16] showed clearly that comparing the experimental and computer-calculated spectra provides a ready method for obtaining information concerning the relative orientations of the dipolar and electric field gradient tensors from the manifestations of the influences of those parameters on the ^{13}C NMR lineshapes. Moreover, such studies also enable the sign of the asymmetry parameter of the ^{14}N nucleus bonded to the carbon to be established. Also, as is clearly apparent from the theoretical treatments outlined earlier in this article, the extent of the splitting between the doublet peaks characteristic of the ^{13}C resonance of a C–N bond depends on the magnitude and the asymmetry parameter of the ^{14}N quadrupole tensor, the internuclear distance, the strength of the applied magnetic field, and the orientation of the internuclear vector $\boldsymbol{r}_{CN}$ in the principal axis system of the electric field gradient tensor.[18]

Kundla and Alla[11] had earlier shown that the line splittings and total widths depended on the relative strengths of the Zeeman and quadrupolar interactions. The magnitude of the splitting is directly dependent on the dipolar interaction and the asymmetry parameter, which is different for differing values of the Euler angles defining its spatial orientation, with the Zeeman frequency of the ^{14}N nucleus being Z_N, the dipolar coupling $D = \gamma_C\gamma_N\hbar/4\pi^2 r_{CN}^3$, and the polar and azimuthal angles as β^D and α^D, the doublet splitting S is given by:

$$S = \tfrac{9}{20}(D\chi/Z_N)(3\cos^2\beta^D - 1 + \eta\sin^2\beta^D\cos 2\alpha^D) \quad (12)$$

which is in terms of all the geometric ($\boldsymbol{r}$, α^D, β^D) and energy variables (χ, Z_N, η) up to first order in (χ/Z_N). As a test of equation (13) the values of the splitting S predicted by that equation were plotted against the experimentally observed splittings for more than 20 compounds containing different types of C–N bonds.[19] An excellent linear relationship was found which may, at first sight, seem surprising because of the wide range of different molecular species involved.

5 INFLUENCE OF *J* COUPLING

In the Hamiltonians used in all the theoretical treatments described, the term $\mathcal{H}_J$ representing the indirect J coupling was ignored. This was because the value of J_{iso} was expected to be so small that it would have little, or no effect, on the CP MAS lineshapes of ^{13}C–^{14}N-containing compounds. The excellent agreements found between the experimental and theoretical lineshapes shows that this was usually an easily justifiable assumption. The inclusion of J coupling leads to the introduction of the term:[20]

$$[-(\Delta J/3)(3\cos^2\beta^J - 1 + \eta\sin^2\beta^J\cos 2\alpha^J)] \quad (13)$$

where β^J and α^J give the orientation of the unique z axis of the $\boldsymbol{J}$ tensor in the PAS of the quadrupole tensor. To illustrate the effect of the J coupling, Figure 4 shows how the normal two-peak powder spectrum becomes a three-peak spectrum for the case of ^{14}N. The theoretical spectra were calculated from the computer program of Naito et al.,[14,16] modified to include the term $\mathcal{H}_J$ in the Hamiltonian. The introduction of the indirect spin–spin coupling results in a splitting of the $m_{^{14}N} = -1$ and +1 levels, while the $m_{^{14}N} = 0$ peak is unaffected. In the calculations, the ^{14}N electric field gradient tensor was assumed to be axially symmetric with the largest principal component parallel to the ^{13}C–^{14}N dipolar vector. A similar procedure was employed by Eichele and Wasylishen,[21] though they used a different computer program based on the perturbation method to interpret and simulate the spectrum demonstrating the first observation of the indirect spin–spin coupling $^1J(^{14}N,^{13}C)$ effect which they discovered in the ^{13}C CP MAS NMR spectrum of [(*n*-$C_3H_7)_4N$][$Cd(SCN)_3$]. Because of the excellent agreement found between the simulated and the experimental spectra they estimated the value of $^1J(^{14}N,^{13}C)$ = 11 ± 3 Hz.

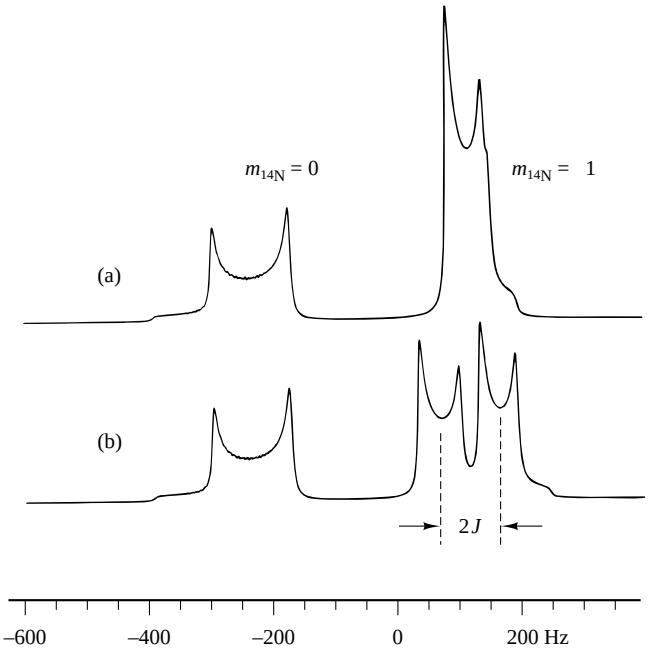

Figure 4 Diagrammatic representation of the effect of including the term $\mathcal{H}_J$ in the Hamiltonian before calculating the lineshape

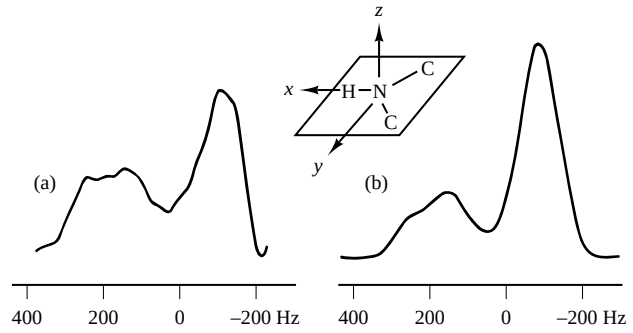

Figure 5 Lineshape of the CP MAS spectrum of a proton bonded to the peptide nitrogen nucleus in *N*-acetylglycine. (a) Experimental spectrum obtained by using CRAMPS with the MREV-8 pulse sequence. (b) Computer-simulated spectrum obtained using a quadrupolar asymmetry parameter $\eta = 0.32$ and $e^2Qq_{zz}/h = -3.21$ MHz. (Reproduced by permission of the American Chemical Society from Naito et al.[23])

6 OTHER SPIN-$\frac{1}{2}$ NUCLEI BONDED TO ^{14}N: ^{1}H CRAMPS

Protons are ubiquitous in nature and bond to many different types of nuclei. Of these the bonding to ^{14}N is important because N–H bonds are fundamental in the molecular composition of amino acids, polypeptides, and proteins. Unfortunately, the ^{1}H CP MAS spectra of such compounds were generally found to be lacking in structure because of the dipolar broadening caused by homonuclear interactions and magnetic shielding anisotropies. The introduction of the technique of combining sample rotation and multiple pulse NMR spectroscopy, the so-called CRAMPS procedure pioneered by Gerstein et al.,[22] was a major innovative addition to the CP MAS methodology which considerably enlarged its range of applications, making it possible to obtain high-resolution proton spectra of hydrogen-containing solids many of which are of great industrial importance. When applied to solid amino acids the CRAMPS technique yielded proton CP MAS spectra in which there were identified[23] asymmetric peaks clearly arising from the ^{1}H–^{14}N dipolar interaction and the ^{14}N quadrupole interaction not being averaged out, as earlier described for the analogous ^{13}C–^{14}N case. The resolution of the characteristic asymmetric lineshapes varied with the type of multiple pulse sequence used. This was presumably because a faster spinning frequency was required to reduce the N–H dipolar interactions. In all cases, characteristic asymmetric doublets were observed for the ^{1}H–^{14}N bonds, with the exception of the N-2 and N-3 nuclei in the imidazole ring of L-histidine hydrochloride monohydrate. Those two bonds exhibited broad asymmetric peaks, possibly being the result of strong hydrogen bonding.

The asymmetric peaks in the CRAMPS MAS spectra of amino acids were simulated by Naito et al.[23] using the computer programs based on the theoretical treatments described earlier.[14,16] In addition, it was necessary to multiply the quadrupole and Zeeman terms in the Hamiltonian by the scaling factors $S_m S_r$. The term S_m is the scaling factor for the multiple pulse scheme used, and $S_r = \frac{1}{2}(3\cos^2\theta - 1)$ is the scaling factor caused by a group rotation where θ is the angle between the rotation axis and the N–H direction. The lineshapes were simulated successfully. That of the peptide proton was well simulated (see Figure 5) using the ^{14}N coupling constant of -3.2 MHz and $\eta = 0.31$, the parameters having been determined in a single crystal ^{14}N NMR study on *N*-acetylvaline though the sign of the quadrupole coupling constant had been established previously from a comparison of the experimental and computer-simulated peptide carbon nuclei.[16] In addition, it was necessary to interchange the assigned axes of the electric field gradient tensor so that the *x* axis was parallel to the N–H bond direction. The spectral peaks for the proton bonded to the imidazole nitrogen N nuclei were simulated using the ^{14}N coupling constants earlier determined from ^{14}N NMR single crystal studies. The simulated spectra showed that broad lines were to be expected and that a clear asymmetric doublet was not to be anticipated in this case. It was also to be expected that the proton bonded to the N-2 nucleus should have a broader lineshape than that for the N-3 nucleus. These predicted lineshapes were in good agreement with those observed experimentally.

The interesting ^{14}N-containing spin-pairs ^{14}N≡^{15}N^{+}–and ^{15}N≡^{14}N^{+}–yield unusual lineshapes.[24] It should also be mentioned that the ^{13}C MAS lineshapes of the parent compounds 5-methyl-2-[α-^{15}N]diazobenzenesulfonic acid and its isotopomer with [β-^{15}N] exhibit characteristic novel lineshapes. It was, however, possible to obtain approximate lineshape simulations for the ^{13}C–^{14}N residual dipolar couplings even though the resulting ragged appearances of the simulations were clearly caused by the use of insufficient increments of the orientations of the angles β^Q and γ^Q in the calculations. Convolution of the two simulated spectra yielded a lineshape which was a good reproduction of the spectrum resulting from convoluting the observed ^{13}C MAS spectra of the two isotopomers. An apparent triplet lineshape was observed for the carbon nucleus bonded to the α- and β-^{14}N nuclei of the diazo group, which arises from two different residual ^{13}C–^{14}N dipolar couplings acting on the same carbon nucleus. It proved possible to simulate that feature.

Mention should be made of related studies of the lineshapes found for off-magic angle, or variable-angle, ^{13}C NMR spectra of compounds which exhibit $^{13}C-^{14}N$ dipolar–quadrupolar interaction effects.[25] Though to some extent peripheral to the main thrust of this article, the phenomena described in those studies are of considerable interest.

7 RELATED ARTICLES

Average Hamiltonian Theory; CRAMPS; Cross Polarization in Solids; Magic Angle Spinning; Quadrupolar Interactions; Quadrupolar Nuclei in Solids; Rotating Solids.

8 REFERENCES

1. S. R. Hartmann and E. L. Hahn, *Phys. Rev.*, 1962, **128**, 2042.
2. A. Pines, M. G. Gibby, and J. S. Waugh, *J. Chem. Phys.*, 1973, **59**, 569.
3. E. R. Andrew, A. Bradbury, and R. G. Eades, *Nature*, **182**, 1639; I. J. Lowe, *Phys. Rev. Lett.*, 1959, **2**, 285.
4. J. Schaefer, E. O. Stejskal, and R. Buchdahl, *Macromolecules*, 1975, **8**, 291.
5. R. G. Griffin, A. Pines, and J. S. Waugh, *J. Chem. Phys.*, 1975, **63**, 3676.
6. M. E. Stoll, R. W. Vaughan, R. B. Saillant, and T. Cole, *J. Chem. Phys.*, 1974, **61**, 2896.
7. A. Naito, S. Ganapathy, K. Akasaka, and C. A. McDowell, *J. Chem. Phys.*, 1981, **74**, 3190.
8. R. A. Haberkorn, R. E. Stark, H. van Willigen, and R. G. Griffin, *J. Am. Chem. Soc.*, 1981, **103**, 2534.
9. D. L. VanderHart, H. S. Gutowsky, and T. C. Farrar, *J. Am. Chem. Soc.*, 1967, **89**, 5056.
10. E. Lippmaa, M. Alla, H. Raude, R. Teeäär, I. Heinmaa, and E. Kundla, *Proc. 20th Congr. AMPERE, Tallin*, eds. E. Kundle, E. Lipmaa, and T. Saluvere, Springer-Verlag, Berlin, 1987, p. 87.
11. E. Kundla and M. Alla, *Proc. 20th Congr. AMPERE, Tallin*, eds. E. Kundle, E. Lipmaa, and T. Saluvere, Springer-Verlag, Berlin, 1987, p. 92.
12. C. J. Groombridge, R. K. Harris, K. J. Packer, B. J. Say, and S. F. Tanner, *J. Chem. Soc., Chem. Commun.*, 1980, 174.
13. M. H. Frey and S. J. Opella, *J. Chem. Soc., Chem. Commun.*, 1980, 474.
14. A. Naito, S. Ganapathy, and C. A. McDowell, *J. Chem. Phys.*, 1981, **74**, 5393.
15. N. Zumbulyadis, P. M. Hendricks, and R. L. Young, *J. Chem. Phys.*, 1981, **75**, 1603.
16. A. Naito, S. Ganapathy, and C. A. McDowell, *J. Magn. Reson.*, 1982, **48**, 367.
17. J. G. Hexem, M. H. Frey, and S. J. Opella, *J. Chem. Phys.*, 1982, **77**, 3847.
18. Z. Gan and D. M. Grant, *J. Magn. Reson.*, 1990, **90**, 522.
19. A. C. Olivieri, L. Frydman, and L. E. Diaz, *J. Magn. Reson.*, 1987, **75**, 50.
20. A. C. Olivieri, *J. Magn. Reson.*, 1988, **81**, 201.
21. K. Eichele and R. E. Wasylishen, *Solid State NMR*, 1992, **1**, 159.
22. B. C. Gerstein, R. G. Pembleton, R. C. Wilson, and L. M. Ryan, *J. Chem. Phys.*, 1977, **66**, 361.
23. A. Naito, A. Root, and C. A. McDowell, *J. Phys. Chem.*, 1991, **95**, 3578.
24. R. K. Harris, P. Jonsen, and K. J. Packer, *Magn. Reson. Chem.*, 1985, **23**, 565.
25. N. K. Sethi, D. W. Alderman, and D. M. Grant, *Mol. Phys.*, 1990, **71**, 217.

Biographical Sketch

Charles A. McDowell. *b* 1918. B.Sc., 1941, M.Sc., 1942, D.Sc., 1955, Queen's University of Belfast, UK; D.Sc., 1984, honoris causa, University of British Columbia, Canada. National service, UK, 1941–45; lecturer, University of Liverpool, UK, 1945–55; Professor and Head, Department of Chemistry, University of Liverpool, 1955–81; University Professor, 1981–84. Currently University Professor Emeritus, Department of Chemistry, University of British Columbia, Canada. Approx. 360 publications. Current research specialties; mainly in solid state NMR.

Magic Angle Spinning: Effects of Quadrupolar Nuclei on Spin-1/2 Spectra

Robin K. Harris
University of Durham, UK

1	Introduction	1
2	Theoretical Background	1
3	Consequences of Perturbation Theory	2
4	Results and Discussion	3
5	Departure from Perturbation Theory	4
6	Quadrupolar Coupling Dominant	5
7	Related Articles	6
8	References	6

1 INTRODUCTION

As explained in detail in ***Magic Angle Spinning Carbon-13 Lineshapes: Effect of Nitrogen-14***, magic angle spinning does not always eliminate from spin-$\frac{1}{2}$ spectra the influence of dipolar coupling to quadrupolar nuclei. In particular, when quadrupolar energies are not negligible compared with Zeeman energies, spin-$\frac{1}{2}$ spectra may show splittings and/or lineshapes which arise from residual dipolar coupling to quadrupolar nuclei. This phenomenon was first discovered and thoroughly investigated for the (^{13}C, ^{14}N) nuclear pair, but it soon became apparent that the effect was more widespread, indeed ubiquitous. The present article will discuss a wide range of examples and will place particular emphasis on the perturbation approach, which is adequate to explain many cases. The discussion will be limited to the centers of gravity of what are, strictly speaking, powder bandshapes. The reader is referred to ***Magic Angle Spinning Carbon-13 Lineshapes: Effect of Nitrogen-14*** for details of more exact theory, for questions of powder bandshapes, and for all examples involving ^{14}N. The whole subject has received attention in a review article[1] which summarizes the theoretical approaches and also lists cases for many different nuclear spin pairs.

2 THEORETICAL BACKGROUND

Consider a pair of nuclei I and S, where the former has the spin quantum number $\frac{1}{2}$ and the latter is quadrupolar. For simplicity in this discussion, it will be assumed that the electric field gradient at S is axially symmetric, but the reader must be careful not to infer that the results below apply to the general case of $\mu \neq 0$. The phenomenon mentioned above can be traced to the influence of terms in the quadrupolar Hamiltonian involving nuclear spin operators other than $\hat{S}_z$. When Zeeman terms dominate, the energy levels of quadrupolar nuclei are properly characterised by the spin component quantum number m_S, associated with $\hat{S}_z$. Since the relevant Hamiltonian terms have angular dependences $\frac{1}{2}(3\cos^2\theta_Q - 1)$, where θ_Q is the angle between the major principal axis of the quadrupolar tensor and the applied magnetic field ($\boldsymbol{B}_0$), their effects are averaged to zero by magic angle spinning at a fast enough rate. Moreover, in such circumstances, the only terms in the dipolar Hamiltonian connecting the quadrupolar nucleus with the spin-$\frac{1}{2}$ nucleus which are secular involve similar angular dependence $\frac{1}{2}(3\cos^2\theta_D - 1)$ where θ_D is the angle between $\boldsymbol{B}_0$ and the internuclear distance between the spin $\frac{1}{2}$ and the quadrupolar nuclei. Thus, magic angle spinning at a sufficiently high rate is enough to eliminate these dipolar interactions. Therefore, resonance frequencies in spin-$\frac{1}{2}$ MAS spectra are unaffected by dipolar interactions to quadrupolar nuclei in such circumstances. Similar considerations apply to anisotropy and asymmetry in the indirect ('scalar') coupling between a spin-$\frac{1}{2}$ nucleus and a quadrupolar nucleus: MAS suffices to remove the influence of such coupling components on the frequencies in the spin-$\frac{1}{2}$ spectrum, though the isotropic part of the coupling is retained.

However, when quadrupolar and Zeeman terms in the Hamiltonian become comparable, the situation is drastically changed. The detailed theoretical treatment using the full Hamiltonian is discussed in ***Magic Angle Spinning Carbon-13 Lineshapes: Effect of Nitrogen-14***. Here, the perturbation treatment, which is frequently applicable, will be presented. The use of perturbation theory was pioneered by Olivieri and co-workers[2] for the (^{13}C, ^{14}N) case (though it was implicit in earlier treatments), and rapidly extended[3] to situations involving higher-spin quadrupolar nuclei.

The spin-$\frac{3}{2}$ case is chosen here for illustration purposes. Consider the so-called 'alphabet expansion' of the dipolar and axially-symmetric quadrupolar interactions (Table 1). In the high-field approximation the Zeeman levels may be designated as $|m_S\rangle$, where $m_S = \frac{3}{2}, \frac{1}{2}, -\frac{1}{2}$ or $-\frac{3}{2}$. Under the influence of terms C, D, E, and F of the 'quadrupolar alphabet', these wavefunctions are mixed to become

$$|(-\tfrac{3}{2})'\rangle = \quad |-\tfrac{3}{2}\rangle + a_1^*|-\tfrac{1}{2}\rangle - a_2^*|\tfrac{1}{2}\rangle \tag{1a}$$

$$|(-\tfrac{1}{2})'\rangle = -a_1|-\tfrac{3}{2}\rangle + \quad |-\tfrac{1}{2}\rangle + a_3^*|\tfrac{1}{2}\rangle - a_2^*|\tfrac{3}{2}\rangle \tag{1b}$$

$$|(\tfrac{1}{2})'\rangle \quad = \quad a_2|-\tfrac{3}{2}\rangle - a_3|-\tfrac{1}{2}\rangle + \quad |\tfrac{1}{2}\rangle - a_1^*|\tfrac{3}{2}\rangle \tag{1c}$$

$$|(\tfrac{3}{2})'\rangle \quad = \quad +a_2|-\tfrac{1}{2}\rangle + a_1|\tfrac{1}{2}\rangle + \quad |\tfrac{3}{2}\rangle \tag{1d}$$

where, in the perturbation approach, $a_1 = \langle\frac{1}{2}|\hat{\mathcal{H}}_Q|\frac{3}{2}\rangle/\gamma_s\hbar B_0$, $a_2 = \langle-\frac{1}{2}|\hat{\mathcal{H}}_Q|-\frac{3}{2}\rangle/2\gamma_s\hbar B_0$ and $a_3 = \langle-\frac{1}{2}|\hat{\mathcal{H}}_Q|\frac{1}{2}\rangle/\gamma_s\hbar B_0$, etc.

The alphabet terms C and D are relevant for a_1 and a_3 whereas terms E and F are effective for a_2. However, it can be shown that $a_3 = 0$ and that a_2 cannot affect the I spectrum. Now, because of the mixed nature of the Zeeman levels, terms C and D of the (I, S) 'dipolar alphabet' become secular, the additional energy contributions being

$$\langle(-\tfrac{3}{2})'m_I|\hat{\mathcal{H}}_D|(-\tfrac{3}{2})'m_I\rangle = \langle(\tfrac{3}{2})'m_I|\hat{\mathcal{H}}_D|(\tfrac{3}{2})'m_I\rangle \propto -a_1 D m_I \tag{2a}$$

$$\langle(-\tfrac{1}{2})'m_I|\hat{\mathcal{H}}_D|(-\tfrac{1}{2})'m_I\rangle = \langle(\tfrac{1}{2})'m_I|\hat{\mathcal{H}}_D|(\tfrac{1}{2})'m_I\rangle \propto +a_1 D m_I \tag{2b}$$

Table 1 The NMR Internal Hamiltonian: The Alphabet Expansion

Term	Geometric factor[c]	Spin factors[a] Dipolar	Quadrupolar[b]	Connectivity
A	$1 - 3\cos^2\theta$	$I_z S_z$	$(I_z)^2$	Secular
B	$-\frac{1}{4}(1 - 3\cos^2\theta)$	$I_+S_- + I_-S_+$	$I_+I_- + I_-I_+$	Flip-flop[a]
C	$-\frac{1}{2}\sin\theta\cos\theta\exp(-i\phi)$	$I_zS_+ + I_+S_z$	$I_zI_+ + I_+I_z$	Single quantum
D	$-\frac{1}{2}\sin\theta\cos\theta\exp(i\phi)$	$I_zS_- + I_-S_z$	$I_zI_- + I_-I_z$	Single quantum
E	$-\frac{1}{4}\sin^2\theta\exp(-2i\phi)$	I_+S_+	$(I_+)^2$	Double quantum
F	$-\frac{1}{4}\sin^2\theta\exp(2i\phi)$	I_-S_-	$(I_-)^2$	Double quantum

[a] Secular for the quadrupolar and homonuclear dipolar interactions, but nonsecular for heteronuclear dipolar interactions.
[b] For the axially symmetric case ($\eta = 0$).
[c] There are also constant numerical factors (hD for the dipolar case and $h\chi/2S(2S-1)$ for the quadrupolar case).

where D is the dipolar coupling constant, $\gamma_I\gamma_S(\mu_0/4\pi)(\hbar/2\pi){r_{IS}}^{-3}$ (to be distinguished from the alphabet term D!). Therefore the energy levels are modified as shown in Figure 1, and the outer lines of the I multiplet will be shifted in one direction, while the inner lines will shift to the same extent but in the opposite direction. Of course the terms in the Hamiltonian also involve geometric factors which depend on the Euler angles connecting the dipolar and quadrupolar tensors with the magnetic field $\boldsymbol{B}_0$. Since these are *not* of the form $(3\cos^2\theta - 1)$, they are not eliminated by MAS although they are reduced. Thus each of the multiplet components in the I spectrum will be powder patterns under MAS. However, the structure of these powder patterns is not usually observed, and consequently the useful information normally comes from consideration of the centers of gravity of the bands. Of course the indirect coupling tensor $\boldsymbol{J}$ has some common features with $\boldsymbol{D}$, and therefore it will in principle also need to be considered.

Full evaluation for the general case results[1] in the following perturbation expression for the shift induced in the center of gravity of the spin-$\frac{1}{2}$ transition frequency associated with quadrupolar basis state m_S

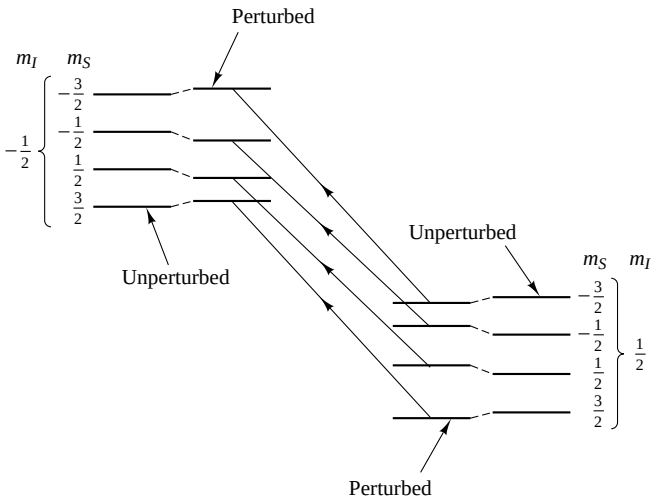

Figure 1 Energy-level diagram for an IS nuclear spin pair with $I = \frac{1}{2}$, $S = \frac{3}{2}$ to show the perturbations induced by quadrupolar and dipolar interactions. The extent of the perturbations is greatly exaggerated. It is assumed that γ_I, γ_S, and J_{iso} are all positive

$$ {}^2\Delta\nu(m_S) = \frac{3\chi}{20\nu_S}\left[\frac{S(S+1) - 3m_S^2}{S(2S-1)}\right] \times \left[Df(\alpha^D, \beta^D, \eta) - \frac{\Delta J}{3} f(\alpha^J, \beta^J, \eta)\right] \quad (3) $$

where $f(\alpha, \beta, \eta) = 3\cos^2\beta - 1 + \eta\sin^2\beta\cos 2\alpha$, α and β are the relevant Euler angles (see Harris and Olivieri[1]), η is the asymmetry in the electric field gradient, χ is the quadrupole coupling constant, ν_S is the Larmor frequency of the quadrupolar nucleus and ΔJ is the anisotropy in $\boldsymbol{J}$. The above equation assumes that $\boldsymbol{J}$ is an axially symmetric tensor. Simplifications result if there are further assumptions. In particular, if $\boldsymbol{J}$ and $\boldsymbol{D}$ are co-axial, and if η is ignored, the complete equation for the spin-$\frac{1}{2}$ transition frequency is

$$ \nu(m_S) = \nu_I - m_S J_{\text{iso}} + \frac{3D'\chi}{20\nu_S}\left[\frac{S(S+1) - 3m_S^2}{S(2S-1)}\right] \quad (4) $$

where ν_I is the Larmor frequency of the spin-$\frac{1}{2}$ nucleus, J_{iso} is the isotropic part of $\boldsymbol{J}$, and D' is an effective dipolar coupling constant, incorporating the anisotropy in J

$$ D' = D - \frac{\Delta J}{3} \quad (5) $$

The second-order shift itself, $\nu(m_S) - \nu_I + m_S J_{\text{iso}}$, depends only on the square of m_S, and for $m_S = \pm S$ it is independent of S. It is therefore convenient to normalize effects to the shift of the 'outermost' lines, defined as

$$ \Delta = -\frac{3}{10}\frac{\chi D'}{\nu_S} \quad (6) $$

This enables the second-order shifts of all lines to be written as

$$ {}^2\Delta\nu(m_S) = -\left[\frac{S(S+1) - 3m_S^2}{S(2S-1)}\right]\Delta \quad (7) $$

Table 2 lists the shifts of all lines, for various half-integral values of S, in terms of Δ.

Table 2 Second-Order Shifts in the Spectra of Spin-$\frac{1}{2}$ Nuclei Arising from Coupling to a Half-Integral Quadrupolar Nucleus S[a]

	m_S				
S	$\pm\frac{1}{2}$	$\pm\frac{3}{2}$	$\pm\frac{5}{2}$	$\pm\frac{7}{2}$	$\pm\frac{9}{2}$
$\frac{3}{2}$	-1	1			
$\frac{5}{2}$	$-\frac{4}{5}$	$-\frac{1}{5}$	1		
$\frac{7}{2}$	$-\frac{5}{7}$	$-\frac{3}{7}$	$\frac{1}{7}$	1	
$\frac{9}{2}$	$-\frac{2}{3}$	$-\frac{1}{2}$	$-\frac{1}{6}$	$\frac{1}{3}$	1

[a]Note: The values are normalized to the shift of the outermost lines as expressed in equation (6).

3 CONSEQUENCES OF PERTURBATION THEORY

A number of significant features can be understood from equations (3)–(7).

1. While perturbation theory holds, second-order shifts are inversely proportional to $\boldsymbol{B}_0$, so that no new information is obtained by using several spectrometers. However, such experiments can be used to check that the origin of splittings in the spectra does indeed involve second-order effects, since the behavior with $\boldsymbol{B}_0$ differs from that of splittings caused by either J_{iso} or differences in chemical shifts.
2. Since second-order shifts depend on m_S^2, their values occur in pairs, with the outermost multiplet lines moving most. Figure 2 illustrates the situation as a function of $\chi D/\nu_S$ when $\Delta J = 0$.
3. The average second-order shift is zero, so the isotropic chemical shift is simply obtained by averaging the frequencies of all the lines.
4. The isotropic coupling constant, $|J_{\text{iso}}|$, is also readily obtained as the average spacing between lines, though care must be taken if there is any crossover of frequencies. The value of $|J_{\text{iso}}|$ is also available from the central spacing $|\nu(m_S = \frac{1}{2}) - \nu(m_S = -\frac{1}{2})|$.
5. Since the innermost lines shift in the opposite direction to the effect on the outermost lines, there is a 'bunching' of lines at one end of the spectrum. The extent of coalescence is more apparent for lower values of S for a given $\chi D/\nu_S$. The sense depends on the sign of Δ, and in favorable cases it gives important information on relative signs.
6. In particular, if $\boldsymbol{J}$ and $\boldsymbol{D}$ are co-axial the following general rule results: 'bunching' occurs to low frequency (i.e. Δ is positive) if *either* χ is negative (with D and D' of the same sign) *or* χ is positive (with D and D' of opposite signs). An analogous statement can be made if Δ is negative. This rule takes into account the effects of signs of magnetogyric ratios. Thus, if the magnitude and sign of χ is known, together with r_{IS}, and if η is ignored, then ΔJ can be derived unambiguously. However, if only r_{IS} and $|\chi|$ are available, two possible values of ΔJ can be calculated but they cannot be distinguished.
7. When perturbation theory holds, neither the magnitude nor the sign of J_{iso} influences Δ.
8. If the value of $|J_{\text{iso}}|$ is negligible compared to linewidths, then there will be $S + \frac{1}{2}$ lines. The relative frequencies at which 'bunching' takes place will give the sign of χ. The magnitude of Δ will enable r_{IS} to be determined if $|\chi|$ is known, and vice versa. However, $S = \frac{3}{2}$ is a special case, since a 1:1 doublet will be seen [Figure 3(a)], of spacing $\frac{3}{10}(\chi D/\nu_S)(3\cos^2\beta^D - 1 + \eta\sin^2\beta^D\cos 2\alpha^D)$ in the general case, and information on the sign of χ is lost.
9. Since the denominator in equation (7) reflects the fact that the validity of the perturbation approach depends on $\chi/2S(2S-1)\nu_S$, higher spins are more accurately treated than lower spins for equivalent values of χ.

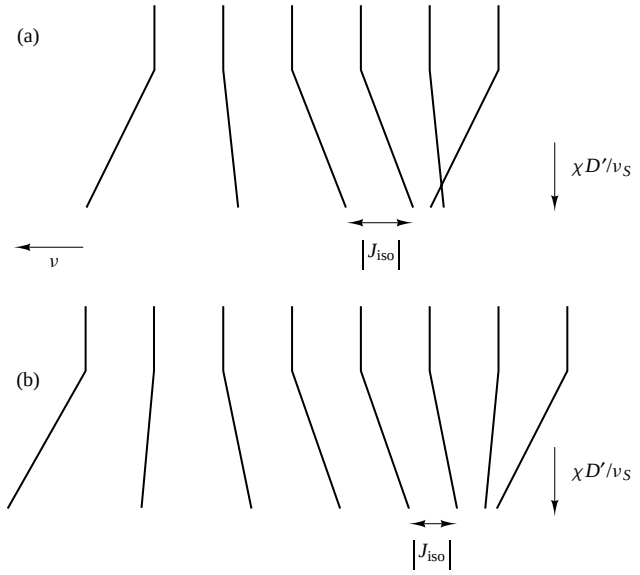

Figure 2 Second-order shifts in spin-$\frac{1}{2}$ MAS spectra arising from coupling to a quadrupolar nucleus S, as a function of the parameter $\chi D'/\nu_S$ under a perturbation approach according to equation (7): (a) $S = \frac{5}{2}$; (b) $S = \frac{7}{2}$. A positive value of Δ is assumed

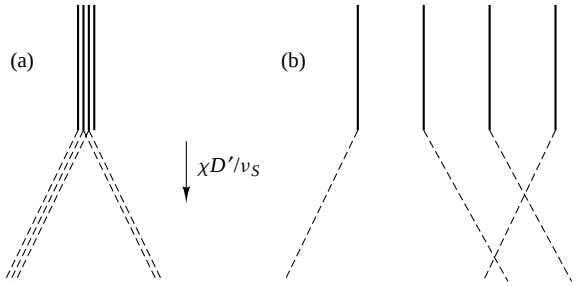

Figure 3 Second-order shifts in spin-$\frac{1}{2}$ MAS spectra arising from coupling to a quadrupolar nucleus $S = \frac{3}{2}$ as a function of the parameter $\chi D'/\nu_S$ under a perturbation approach according to equation (7): (a) $J_{\text{iso}} = 0$; (b) $-J_{\text{iso}}- > 0$. A positive value of Δ is assumed

4 RESULTS AND DISCUSSION

Many examples are now known where perturbation theory is reasonably applicable. In particular, the (^{119}Sn, $^{35/37}$Cl) situation is appropriate[3,4] since in such cases $|\chi|$ is generally modest (~35 MHz). Thus even for a 4.7 T spectrometer, the perturbation parameter $\chi/2S(2S-1)\nu_S$ is only in the region of 0.30. The splitting arising from $|J_{\text{iso}}|$ cannot be ignored. However, since chlorine is monovalent, coaxiality of $\boldsymbol{J}$ and $\boldsymbol{D}$ is a reasonable approximation for directly-bonded Sn–Cl groups except when chlorine is in a bridging situation. In fact,

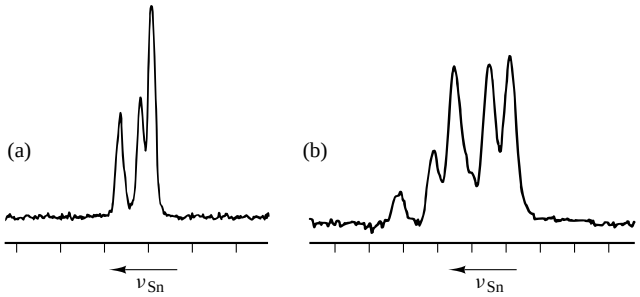

Figure 4 Tin-119 CP MAS NMR spectra at 74.63 MHz for (a) $(PhCH_2)_3SnCl$ and (b) Et_2SnCl_2, showing the second-order effects of coupling to the chlorine nuclei.[4] The markers are at 1 kHz and 0.5 kHz intervals for (a) and (b), respectively

a typical spectral pattern is a 1:1:2 triplet with relative spacings 2:1 [Figure 4(a)], which is strictly the case only when $|J_{iso}| = 2\Delta$. Values of $|J(\text{Sn,Cl})|$ have therefore been derived, as have approximate data for ΔJ. When more than one chlorine is coupled to the same Sn, simple convolution suffices to predict the spectral appearance. If the chlorines are equivalent, then $|J_{iso}| = 2\Delta$ leads to a 1:2:4:1:4:4 multiplet (with the first spacing twice the others), such as has been observed [Figure 4(b)] for Et_2SnCl_2.[4]

Cases involving ^{31}P coupled to metal nuclei are also common, and have been shown[5,6] to occur for a range of S-spin metals, e.g. $^{63/65}$Cu ($S = \frac{3}{2}$), ^{55}Mn ($S = \frac{5}{2}$), ^{59}Co ($S = \frac{7}{2}$), and ^{93}Nb ($S = \frac{9}{2}$). Figure 5 shows an example where the second-order effects are relatively small. In a number of such cases perturbation theory is not appropriate, and in others questions of nonaxiality reduce the usefulness of the observed second-order effects. However, the case of $Mn_2(CO)_9PPh_3$ proved[6] to be appropriate, since the molecular symmetry has axiality and spinning sideband analysis indicates that this is retained in the solid state. Such an analysis also gives a value for $|D'|$, so that $|\chi|$ can be derived (42 MHz). The value of $\chi/2S(2S-1)\nu_S$ for a spectrometer operating at 7.1 T is thus 0.028, which confirms that perturbation theory is applicable. Several (^{31}P, $^{63/65}$Cu) examples have been analyzed[7] using perturbation theory to yield data for $\Delta J \sim 0.6$ kHz.

Numerous other examples of residual dipolar coupling have been reported, some of which come into the category of a perturbation treatment. In particular, examples of (^{13}C, ^{2}H) have been given.[1,8,9] Although ^{2}H has a low value of χ, the residual effects of dipolar coupling are appreciable because r_{CH} is small and hence D is relatively large. With rigid molecules,[1,8] there is a nice contrast to the (^{13}C, ^{14}N) case since, although 2:1 doublets are observed in both instances, the origins differ. For the (^{13}C, ^{14}N) pair J_{iso} can usually be ignored, so there is overlap for the lines connected to states $|+1\rangle$ and $|-1\rangle$ for ^{14}N, whereas for (^{13}C, ^{2}H), the overlap is of transitions involving $|0\rangle$ and $|-1\rangle$ for ^{2}H. The latter situation arises coincidentally because $|J_{iso}(^{13}\text{C}, ^{2}\text{H})|$ is approximately equal to $\frac{9}{10}D\chi/\nu_S$. The spectra have a different appearance[9] for inclusion compounds of urea and thiourea with deuterated guest molecules, such as straight-chain alkanes and corresponding carboxylic acids. The guest molecules are relatively mobile, so that values of $\chi(^{2}\text{H})$ are substantially reduced (to ca. 50–70 kHz for CD_2 groups) by averaging. Second-order effects on the ^{13}C spectra are therefore relatively modest, simply resulting in a small asymmetry in the splittings

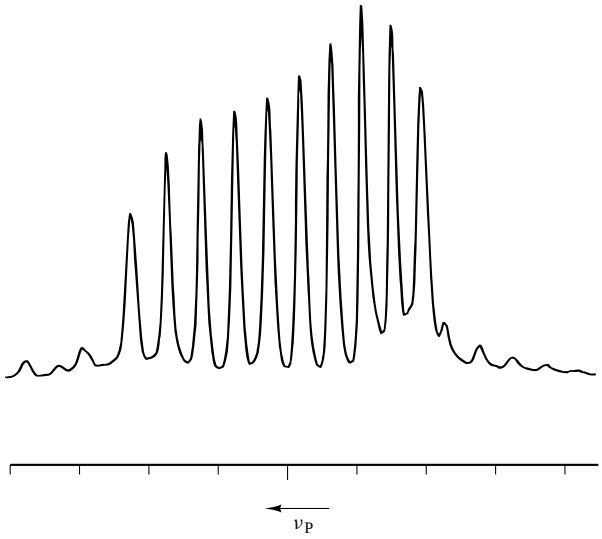

Figure 5 Phosphorus-31 CP MAS NMR spectra at 81.0 MHz for $(C_5H_5)(Me_3P)Cl_2Nb{=}N(o\text{-}tBuC_6H_4)$, showing the second-order effects of coupling to the niobium nucleus: the multiplet spacing decreases slightly from high to low frequency. The lines outside the main decet are spinning sidebands. The markers are at 1 kHz intervals

of the 1:2:3:2:1 quintet patterns. The spectra can be used to determine, at least qualitatively, the relative values of χ at different positions in a chain, which in turn depend on variations in local molecular mobility.

Of course, the appearance of splittings arising from either dipolar coupling, whether residual or full, or indirect coupling is contingent upon the lifetimes of the quadrupolar spin states being long compared with the frequency separations in the spin-$\frac{1}{2}$ spectra. If spin–lattice relaxation times of the quadrupolar nuclei become sufficiently short, the result is 'self-decoupling' (such as is frequently observed in solution state situations). In such cases a single line will be seen in the spin-$\frac{1}{2}$ spectrum. This is the situation[10] for the ^{31}P spectrum of PCl_5 where sharp singlets are observed for the PCl_4^+ and PCl_6^- ions at room temperature but multiplets at low temperature. Of course, molecular motion (e.g. rotation of ions, as for PCl_5) may affect residual dipolar splittings both directly (by averaging $\boldsymbol{D}$) and indirectly (by relaxing the S nucleus). 'Self-decoupling' can in principle also occur because of chemical exchange involving I–S bond breaking.

5 DEPARTURE FROM PERTURBATION THEORY

The first clear case of effects of dipolar coupling residual which did not involve the (^{13}C, ^{14}N) nuclear pair concerned the (^{31}P, ^{63}Cu) nuclei in bis(triphenylphosphine)copper(I) and related complexes, presented by Menger and Veeman.[5] These authors published detailed theory, but the situation was beyond the validity of perturbation theory. Many examples involving the (^{31}P, ^{63}Cu) pair have since come to light, though some are susceptible to the perturbation approach.

The (^{13}C, $^{35/37}$Cl) case is interesting.[11,12] Although there are simplifying features, since chlorine is univalent (and hence coaxiality of $\boldsymbol{J}$ and $\boldsymbol{D}$ can be assumed) and J(C, Cl) is negligibly small, the value of $|\chi|$ is sufficiently large (ca.

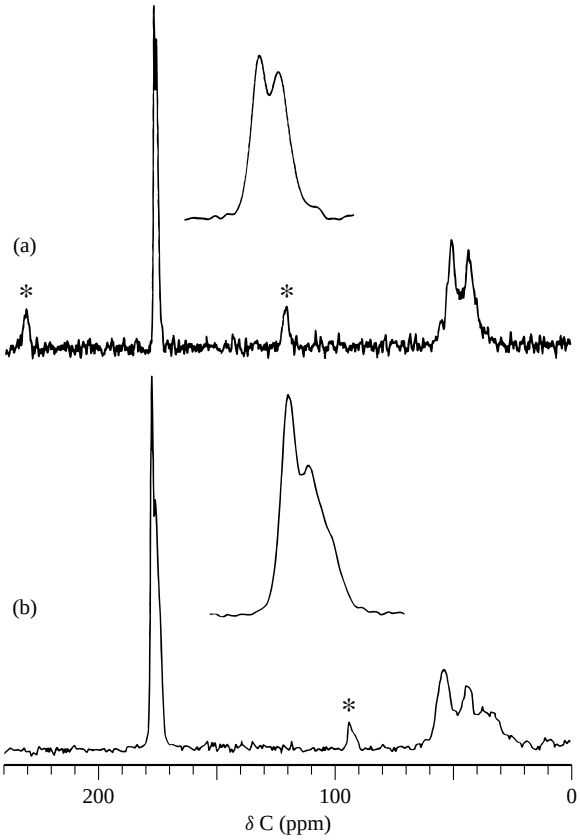

Figure 6 Carbon-13 CP MAS NMR spectra of sodium monochloroacetate: (a) 75.4 MHz; (b) 50.3 MHz, showing the second-order effects of coupling to chlorine.[12] The insets show expansions of the carboxyl region. The asterisks denote spinning sidebands

−70 MHz) that departures from perturbation theory can be observed. At modest magnetic fields (7.1 T and above), the 1:1 doublet predicted by perturbation theory is indeed observed [Figure 6(a)], but the splitting is smaller than predicted and is not inversely proportional to $\boldsymbol{B}_0$. However, it has been shown[13] by simulation using exact theory that for the case $S = \frac{3}{2}$ the doublet splitting, s, can be adequately represented in the range $0.8 < R = |\chi/\nu_S| < 3.0$ by the cubic polynomial

$$s = D(0.581R + 0.033R^2 - 0.021R^3) \tag{8}$$

A cubic equation for s has also been derived for the $S = \frac{3}{2}$ case in which J_{iso} cannot be ignored.

For the (^{13}C, $^{35/37}$Cl) case, even equation (8) is inadequate at 4.7 T, since a broad 2:1:1 triplet is both predicted and observed[11,12] [Figure 6(b)]. Figure 7 shows the theoretical line positions (centers of gravity) as a function of R for the case $I = \frac{1}{2}$, $S = \frac{3}{2}$ for positive χ and in the absence of $\boldsymbol{J}$. At high values of R, four lines are expected, and this links up with the expectation from inverse perturbation theory discussed below.

Molecular-level motion has a drastic effect on the ^{13}C spectra of sodium chloroacetates.[12] For the monochloro compound a clear doublet is seen for both the CH_2Cl and carbonyl carbons at 7.1 T and above, with the expected 2:1:1 triplet at 4.7 T. However sodium trichloroacetate shows a sharp line for each carbon at 7.1 T, not only at room temperature but also down to 163 K. The reason for this behavior undoubtedly lies in the facile internal rotation of the $C-CCl_3$ group.

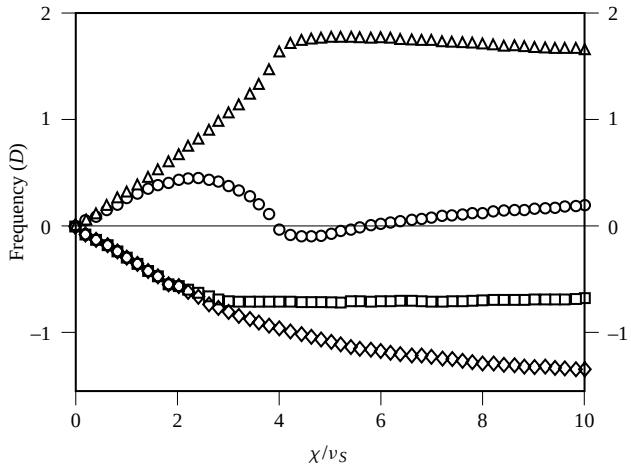

Figure 7 Line positions (centers of gravity, units of D) for a spin-1/2 nucleus coupled to a spin-3/2 nucleus as a function of $R = \chi/\nu_S$ as obtained[13] by the full theory for positive χ and assuming $J_{\text{iso}} = \Delta J = \eta = \beta^D = 0$

When J_{iso} needs to be taken into consideration and perturbation theory is inadequate, it has been shown[13] that the sign of J_{iso} can be obtained from the spectrum (if the sign of χ is known). Thence $J(^{63}\text{Cu}, ^{31}\text{P})$ has been found[13] to be negative.

6 QUADRUPOLAR COUPLING DOMINANT

Olivieri has considered[14,15] the case where the quadrupole coupling constant is very large. The dipolar and indirect couplings will still transfer the quadrupole information to the spin-$\frac{1}{2}$ nucleus under MAS conditions, giving rise to splittings in the spectra. For the case where $\boldsymbol{J}$ is axially symmetric and the three tensors $\boldsymbol{D}$, $\boldsymbol{q}$, and $\boldsymbol{J}$ are all co-axial, Olivieri showed[14] that a quartet results when $S = \frac{3}{2}$. Each component is a powder pattern, with the centers of gravity forming two doublets with splittings, independent of the applied magnetic field, given by

$$s(\pm\tfrac{1}{2}) = |1.709J_{\text{iso}} + D'| \tag{9a}$$

$$s(\pm\tfrac{3}{2}) = \tfrac{3}{2}|2D' - J_{\text{iso}}| \tag{9b}$$

When the Zeeman S term begins to be significant with respect to the quadrupolar interaction, an inverse perturbation approach ('inverse' when compared to the considerations of Section [2] above) may be used.[14] In this case equations (9a) and (9b) need to be modified, and the four centers of gravity are

$$\langle \Delta\nu(\pm\tfrac{1}{2})\rangle = \mp(0.8546J_{\text{iso}} + 0.5D') - 2(J_{\text{iso}} + D')\frac{\nu_S}{\chi} \tag{10a}$$

$$\langle \Delta\nu(\pm\tfrac{3}{2})\rangle = \pm\tfrac{3}{4}(2D' - J_{\text{iso}}) + 2(J_{\text{iso}} + D')\frac{\nu_S}{\chi} \tag{10b}$$

The spectrum is no longer symmetric, and the sense of the asymmetry depends on the relative signs of $J_{\text{iso}} + D'$, ν_S, and χ. Olivieri has also extended calculations[15] of this type to

situations where $\boldsymbol{q}$ is not axially symmetric and for arbitrary relative orientations of $\boldsymbol{q}$ and $\boldsymbol{D}$.

Frequently, large χ implies the likelihood of rapid spin–lattice relaxation and therefore self-decoupling of S from the spin-$\frac{1}{2}$ nucleus in question. However, (^{13}C, $^{79/81}$Br) systems have been shown[16] to approach the inverse perturbation case, and an example of a (^{31}P, ^{201}Hg) spin pair (with $D \ll J_{\mathrm{iso}}$ in magnitude) even nearer the low-field limit has been reported.[15,17]

7 RELATED ARTICLES

Magic Angle Spinning Carbon-13 Lineshapes: Effect of Nitrogen-14; Quadrupolar Interactions; Quadrupolar Nuclei in Solids.

8 REFERENCES

1. R. K. Harris and A. C. Olivieri, *Prog. NMR Spectrosc.*, 1992, **24**, 435.
2. A. C. Olivieri, L. Frydman, and L. E. Diaz, *J. Magn. Reson.*, 1987, **75**, 50; A. C. Olivieri, *J. Magn. Reson.*, 1989, **81**, 201.
3. R. K. Harris, *J. Magn. Reson.*, 1988, **78**, 389; D. C. Apperley, H. Bai, and R. K. Harris, *Mol. Phys.*, 1989, **68**, 1277.
4. R. K. Harris, A. Sebald, D. Furlani, and G. Tagliavini, *Organometallics* 1988, **7**, 388.
5. E. M. Menger and W. S. Veeman, *J. Magn. Reson.*, 1982, **46**, 257.
6. R. Gobetto, R. K. Harris, and D. C. Apperley, *J. Magn. Reson.*, 1992, **96**, 119.
7. A. C. Olivieri, *J. Am. Chem. Soc.*, 1992, **114**, 5758.
8. P. Jonsen, S. F. Tanner, and A. H. Haines, *Chem. Phys. Lett.*, 1989, **164**, 325; S. D. Swanson, S. Ganapathy, and R. G. Bryant, *J. Magn. Reson.*, 1987, **73**, 239.
9. A. E. Aliev, K. D. M. Harris, D. C. Apperley, R. K. Harris, and M. M. Sünnetçioglu, *J., Chem. Soc., Faraday Trans. 1*, 1993, **89**, 3791.
10. R. K. Harris and A. Root, *Mol. Phys.*, 1989, **66**, 993.
11. R. M. Cravero, M. González-Sierra, C. Fernández, and A. C. Olivieri, *J. Chem. Soc., Chem. Commun.*, 1993, 1253; R. K. Harris, M. M. Sünnetçioglu, K. S. Cameron, and F. G. Riddell, *Magn. Reson. Chem.*, 1993, **31**, 963.
12. S. H. Alarcón, A. C. Olivieri, S. A. Carss, and R. K. Harris, *J. Magn. Reson.*, 1995, in press..
13. S. H. Alarcón, A. C. Olivieri, and R. K. Harris, *Solid State NMR*, 1993, **2**, 325.
14. A. C. Olivieri, *J. Magn. Reson. Ser. A*, 1993, **101**, 313.
15. A. C. Olivieri, *Solid State NMR*, 1992, **1**, 345.
16. S. H. Alarcón, A. C. Olivieri, S. A. Carss, and R. K. Harris, *Magn. Reson. Chem.*, 1995, **33**, 603.
17. L.-J. Baker, G. A. Bowmaker, P. C. Healy, B. W. Skelton, and A. H. White, *J. Chem. Soc., Dalton Trans.*, 1992, 989.

Acknowledgments

The author is grateful to Professor A. C. Olivieri for fruitful collaborative research on the topic in question, and for valuable comments on the text of this article.

Biographical Sketch

Robin K. Harris. *b* 1936. B.A. (Nat.Sci.), Ph.D., (supervisor Norman Sheppard), Sc.D., University of Cambridge, UK. Postdoctoral work at Mellon Institute, Pittsburgh, PA (with Aksel Bothner-By). Successively lecturer, senior lecturer, and professor, University of East Anglia, UK. Currently Professor of Chemistry, University of Durham, UK. Secretary-General of ISMAR, 1986–92. Approx. 350 publications. Current research specialty: solid state NMR and its applications in materials chemistry.

Magnetic Field Induced Alignment of Molecules

Aksel A. Bothner-By

Carnegie Mellon University, Pittsburgh, PA, USA

1	Introduction	1
2	Energetics of a Rigid Molecule in Isotropic Solution in a Magnetic Field	1
3	Effects of Alignment on High-Resolution NMR Spectra	2
4	Applications	4
5	Related Articles	6
6	References	6

1 INTRODUCTION

If a sample of liquid benzene is exposed to the Earth's magnetic field passing through it along a north–south direction, there will be a slight tendency for the molecules to turn their faces east–west (or up–down) and away from north–south. The original meaning of 'orient' was to face the east, so one might describe the benzene as slightly oriented, or aligned. The normal thermal motions of the molecules largely overcome this tendency, and one can calculate that at any instant the excess of east–west facing molecules over north–south facing molecules is approximately 1 in 10^{15}. In the study of NMR, this tendency to align in the magnetic induction $\boldsymbol{B}_0$ has been ignored until recently, since the effects on the NMR spectra have been too small to observe. However, the degree of alignment increases as the square of $\boldsymbol{B}_0$, and in today's spectrometers with $\boldsymbol{B}_0$ values of 10^5 or more times the Earth's field, the alignment is sufficient that perturbations of the NMR spectrum are often readily observed. This article gives an outline of the origin of the alignment, the nature of the changes produced in the spectrum, and some applications of these to the structure determination of molecules in solution, to molecular angular correlation, to ions, and to paramagnetic species.

2 ENERGETICS OF A RIGID MOLECULE IN ISOTROPIC SOLUTION IN A MAGNETIC FIELD

All objects, molecules, men, or galaxies, possess the property called magnetic susceptibility,[1] usually denoted by χ. When the object is placed in a magnetic field $\boldsymbol{H}_0$, a magnetic dipole $\boldsymbol{m}$ is induced in it, according to the equation

$$\boldsymbol{m} = \chi \boldsymbol{H}_0 \tag{1}$$

For diamagnetic molecules or ions, χ is negative and small, for paramagnetic species, it is usually positive and larger.

The act of putting a molecule in the magnetic field results in a change in energy of the system:

$$\Delta E = -\chi \boldsymbol{H}_0 \cdot \boldsymbol{B}_0/2 \tag{2}$$

$\boldsymbol{B}_0$ is related to $\boldsymbol{H}_0$ by the fundamental relationship

$$\boldsymbol{B}_0 = \mu \boldsymbol{H}_0 \tag{3}$$

where μ is the permeability. In all cases discussed here, μ differs insignificantly from μ_0, the permeability of free space, so that one can rewrite equation (3) as

$$\Delta E = -\chi B_0^2/2\mu_0 \tag{4}$$

In the SI system, standardized in this Encyclopedia, the units of ΔE are joules, those of χ are m^3 per molecule, those of $\boldsymbol{B}_0$ are tesla, and those of μ_0 are $4\pi \times 10^{-7}$ tesla^2 m^3 joule^{-1}. Much of the experimental work performed on magnetic alignment has been reported using cgs units, in which $\mu_0 = 1$ and χ is in cm^3 per molecule. These literature values of χ can be converted into the SI system by multiplying by $4\pi \times 10^{-6}$. A few papers give χ in units of joule tesla^{-2}, collapsing μ_0 into χ.

For molecules which are not of tetrahedral or higher symmetry, χ is expected to be anisotropic, that is to differ when measured parallel to the x, y, and z axes of a molecule-fixed coordinate frame.[2] χ is then represented as a second-rank tensor, which, if the correct axes are chosen, will be diagonal:

$$\boldsymbol{\chi} = \begin{bmatrix} \chi_{xx} & 0 & 0 \\ 0 & \chi_{yy} & 0 \\ 0 & 0 & \chi_{zz} \end{bmatrix} \tag{5}$$

Equation (4) must then be written in tensor notation:

$$\Delta E = -\boldsymbol{B}_0 \cdot \boldsymbol{\chi} \cdot \boldsymbol{B}_0/2\mu_0 \tag{6}$$

In the absence of a magnetic induction, the molecules in solution undergo a random tumbling motion as a result of collisions with solvent molecules. However, in the presence of $\boldsymbol{B}_0$ there will be a torque tending to turn the molecule into its minimum energy position. Taking benzene as an example, we note that the susceptibility is most negative when measured along the six-fold axis, so the energy is highest when the six-fold axis is parallel to $\boldsymbol{B}_0$, and the alignment of benzene molecules with their planes parallel to $\boldsymbol{B}_0$ is preferred.

The degree of alignment of a particular axis i relative to $\boldsymbol{B}_0$ in the molecule is specified by the parameter S_{iB}, defined by[3]

$$S_{iB} = \langle \tfrac{3}{2} \cos^2 \theta_{iB} - \tfrac{1}{2} \rangle \tag{7}$$

where θ_{iB} is the angle between the axis i and $\boldsymbol{B}_0$, and the angle brackets indicate the expectation value of the enclosed expression. If $S_{iB} = 1$, the axis i is perfectly aligned parallel to $\boldsymbol{B}_0$, while if $S_{iB} = -\frac{1}{2}$ the axis i is always perpendicular to $\boldsymbol{B}_0$. $S_{iB} = 0$ implies completely random tumbling. S_{iB} may be evaluated assuming a Boltzmann distribution in the energies.[4] Then

$$S_{iB} = \frac{\int_0^{2\pi} \int_0^{\pi} \left(\frac{3}{2} \cos^2 \theta_{iB} - \frac{1}{2}\right) \mathrm{e}^{-\Delta E/kT} \sin \theta_{iB} \, \mathrm{d}\theta_{iB} \, \mathrm{d}\phi}{\int_0^{2\pi} \int_0^{\pi} \mathrm{e}^{-\Delta E/kT} \sin \theta_{iB} \, \mathrm{d}\theta_{iB} \, \mathrm{d}\phi} \tag{8}$$

Since ΔE is very small, the exponential can be approximated by $1 - \Delta E/kT$, and explicit integration of equation (8) gives

$$S_{iB} = \Delta\chi_{ii} B_0^2/15kT\mu_0 \tag{9}$$

with $\Delta\chi_{ii}$ equal to $\chi_{ii} - (\chi_{jj} + \chi_{kk})/2$. It is obvious that $S_{xB} + S_{yB} + S_{zB} = 0$. The degree of alignment increases as the square of the magnetic induction and is inversely proportional to the temperature. Taking benzene as an example, with a value of $\Delta\chi_{zz}$ of $-1.27 \times 10^{-33}\,\mathrm{m}^3$, and assuming B_0 = 14.1 T (600 MHz magnet), S_{zB} at 300 K is calculated to be -3.2×10^{-6}.

3 EFFECTS OF ALIGNMENT ON HIGH-RESOLUTION NMR SPECTRA

Two types of nuclear interaction have been observed to give rise to new or additional splittings in high-resolution spectra of samples in which the molecules are partially aligned by the magnetic induction: magnetic dipole interaction,[5] and electric quadrupole interaction.[6] Completely random tumbling averages these interactions to zero, so no splitting is observed. The rapidly fluctuating torques resulting from these interactions are evidenced, however, by the relaxation. However, if the tumbling is nonrandom, such that a small alignment occurs, these interactions are not completely averaged to zero, and effects on line positions and splittings are observed.

3.1 Magnetic Dipolar Interaction

An (oversimplified) model may be used. Two magnetic nuclei A and B are attached to the framework of a molecule, which is undergoing rapid tumbling. The magnetic moment of nucleus A is taken as parallel to the magnetic induction. The component of the magnetic field parallel to $\boldsymbol{B}_0$ generated by nucleus A at nucleus B is then given by[1]

$$H_\mathrm{B} = m_\mathrm{A}(3\cos^2\theta_{nB} - 1)/r_\mathrm{AB}^3 \tag{10}$$

where θ_{nB} is the angle between the internuclear axis and $\boldsymbol{B}_0$. If all orientations of the internuclear axis are equiprobable, equation (10) integrates to give $\langle H_\mathrm{B}\rangle = 0$. On the other hand, if the internuclear axis has a degree of alignment S_{nB}, then

$$\langle H_\mathrm{B}\rangle = 2m_\mathrm{A}S_{nB}/r_\mathrm{AB}^3 \tag{11}$$

This field would add to $\boldsymbol{H}_0$ causing a shift in the frequency of the NMR signal from nucleus B. If the moment of A were antiparallel to $\boldsymbol{B}_0$, the opposite shift would be observed. Thus a doublet would be produced. In the quantum mechanical formulation, the strength of the interaction is represented by D_AB, which is given by

$$D_\mathrm{AB} = -\gamma_\mathrm{A}\gamma_\mathrm{B}hS_{nB}/2\pi^2 r_\mathrm{AB}^3 \tag{12}$$

The observable splittings are directly related to D_AB. It is now necessary only to relate S_{nB} to χ:[4]

$$S_{nB} = \frac{2}{3}\sum_{i=x,y,z}\Delta\chi_{ii}(\tfrac{3}{2}\cos^2\theta_{in} - \tfrac{1}{2})B_0^2/15kT\mu_0 \tag{13}$$

where θ_{in} is the angle between the ith axis of the susceptibility tensor and the internuclear axis. Combining equations (12) and (13), and noting that the spectrometer frequency ν_A is equal to $\gamma_\mathrm{A}B_0/2\pi$, the practical formula is obtained:

$$D_\mathrm{AB} = -5.10 \times 10^{15}\nu_\mathrm{A}\nu_\mathrm{B} \times \sum_{i=x,y,z}\chi_{ii}(\tfrac{3}{2}\cos^2\theta_{in} - \tfrac{1}{2})/T a_\mathrm{AB}^3 \tag{14}$$

where a_AB is the internuclear distance (in nanometers).

The effect of D_AB on the spectrum has been thoroughly explored in studies of molecules partially aligned by solution in liquid crystal solvents.[7] For two spins with identical Larmor frequencies, the spectrum is a doublet with splitting $3D_\mathrm{AB}/2$. An example of such a splitting is shown in Figure 1. The signal arises from two methylene protons attached to a porphyrin ring in the zinc vinylphylloerythrin–pyridine complex (**1**), with the internuclear axis parallel to the four-fold symmetry axis of the ring. The observed doublet splitting of 1.98 Hz observed at 600 MHz, implies D_HH = 1.32 Hz. Taking a as 0.178 nm, T as 296 K, θ_{zn} = 0, and $\chi_{xx} = \chi_{yy}$, gives $\Delta\chi_{zz} = -11.9 \times 10^{-33}\,\mathrm{m}^3$. The $\Delta\chi_{zz}$ of the complex is the sum of $\Delta\chi_{zz}$ for the porphyrin ($-12.5 \times 10^{-33}\,\mathrm{m}^3$) and $-(\frac{1}{2})\Delta\chi_{zz}$ for the pyridine ligand ($-1.19 \times 10^{-33}\,\mathrm{m}^3$), in agreement with values obtained by other methods.[8]

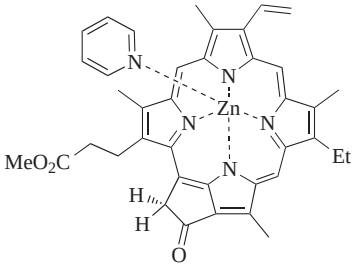

(1)

If the Larmor frequencies of the two nuclei differ by much more than D_AB and J_AB, the observed doublet spacing is simply $J_\mathrm{AB} + D_\mathrm{AB}$. The addition is algebraic,[7] so if the sign and magnitude of J_AB are known from other studies, the sign and magnitude of D_AB can be determined. As an example of this, a second porphyrin containing a similarly situated methylene group was studied in methyl pyropheophorbide A (**2**). The pyrrole ring adjacent to the methylene was reduced, rendering the methylene protons inequivalent. They now gave rise to AX type doublets, with a splitting $J_\mathrm{HH} + D_\mathrm{HH}$ of 20.17 Hz at 5.87 T, 19.95 Hz at 7.05 T, 19.51 Hz at 11.75 T, and 19.25 Hz at 14.09 T. The plot of these splittings versus B_0^2 is a straight line with intercept $J_\mathrm{HH} = -20.25$ Hz, and D_HH = +1.00 Hz at 14.09 T. Application of equation (14) yields $\Delta\chi = -10.1 \times 10^{-33}\,\mathrm{m}^3$. The reduction of the pyrrole ring has partially interrupted the circuit of π electrons responsible for the ring current and for the large anisotropic susceptibility of porphyrins.

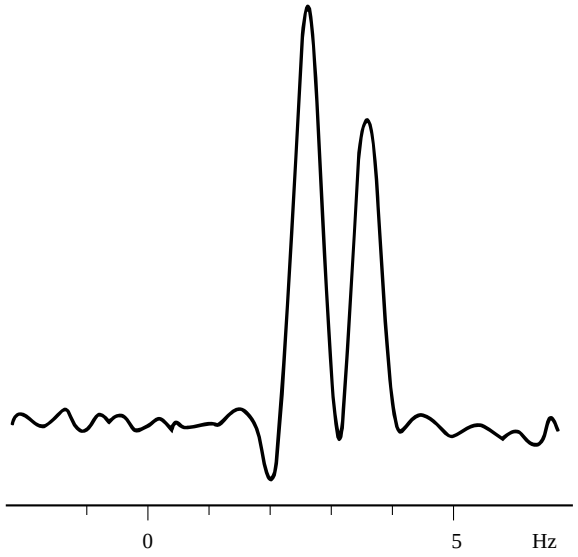

Figure 1 The doublet arising from the direct magnetic dipole interaction in zinc vinylphylloerythrin–pyridine complex

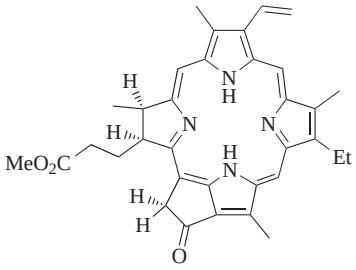

(2)

Finally, if the Larmor frequency difference between A and B and $J_{AB} \pm D_{AB}$ is of comparable magnitude, second-order effects are expected. The exact calculation of J_{AB} and D_{AB} from such spectra has been worked out in detail, in connection with the spectroscopy of solutes in liquid crystal solvents.[7] It has been shown[9] that the observation of the second order effects in suitable cases provides a sensitive method for detecting and measuring very small values of D_{AB}.

3.2 Electric Quadrupole Interaction

For most quadrupolar nuclei, the relaxation induced by the interaction of the nuclear quadrupole moment with the electric field gradient at the nucleus broadens the signals sufficiently to obscure the effects produced by molecular alignment. However, the quadrupole coupling constant for deuterium in a large variety of molecules is small, lying in the range 100–300 kHz, and the broadening is small enough that splittings arising from the quadrupole interaction can be seen in the ^{2}H NMR spectrum.

For a single deuterium atom, if molecular tumbling is not random, the signal consists of a doublet: the transitions correspond to the changes $m(-1 \rightarrow 0)$ and $m(0 \rightarrow 1)$. The frequency separation of the doublet $\Delta\nu_Q$ is given by

$$\Delta\nu_Q = 3eQ\langle V_{\boldsymbol{B}_0}\rangle/2h \qquad (15)$$

where eQ is the nuclear electric quadrupole moment, and $\langle V_{\boldsymbol{B}_0}\rangle$ is the expectation value of the electric field gradient along the direction of $\boldsymbol{B}_0$. It is convenient to establish a second molecule-fixed coordinate frame, x', y', z', in which the electric field gradient tensor is diagonal, and to define $\nu_{x'}$, $\nu_{y'}$, and $\nu_{z'}$ as the quadrupole splittings which would be observed if the molecule were fixed with the x', y', and z' axes parallel to $\boldsymbol{B}_0$, respectively. Then,[7]

$$\Delta\nu_Q = \frac{2}{3}\sum_{i=x',y',z'} \nu_i \sum_{j=x,y,z} \cos^2\theta_{ij}\, S_{jj} \qquad (16)$$

The electric field gradient tensor is traceless, implying $\nu_{x'} + \nu_{y'} + \nu_{z'} = 0$. Quadrupole coupling constants for carbon-bound deuterium have been measured by NMR relaxation methods, Zeeman microwave spectroscopy, NMR studies of deuterated molecules in liquid crystal solvents, and nuclear quadrupole resonance spectroscopy of solids.[10] The maximum splittings, $\nu_{z'}$ range from 225 to 300 kHz, with ^{2}H in similar chemical environments clustered together: ^{2}H attached to a benzene ring has $\nu_{z'}$ equal to 275 ± 5 kHz. Returning once again to benzene as an example, with $\nu_{z'} = 279$ kHz, $\nu_{x'} \approx \nu_{y'} = -139.5$ kHz, $\Delta\chi = -1.27 \times 10^{-33}\,\mathrm{m}^3$, $B_0 = 14.09$ T, $T = 300$ K, and $\theta_{zz'} = 90^\circ$, ν_Q is calculated using equation (16) to be 0.45 Hz. Figure 2 shows a ^{2}H NMR spectrum of monodeuterobenzene; the spectrum is resolution enhanced, with proton decoupling. The observed splitting (0.46 Hz) agrees well with the expected value.

Second-order effects are observed in the spectra when chemical shifts are zero or of comparable magnitude to J_{AB} and ν_{QA} or ν_{QB}. This complication prevents the direct observation of ν_Q in hexadeuterobenzene, which gives rise to a spectrum with numerous overlapping transitions.[11]

3.3 Anisotropic Chemical Shift

If the sample molecules possess anisotropic magnetic susceptibilities and also contain nuclei with anisotropic

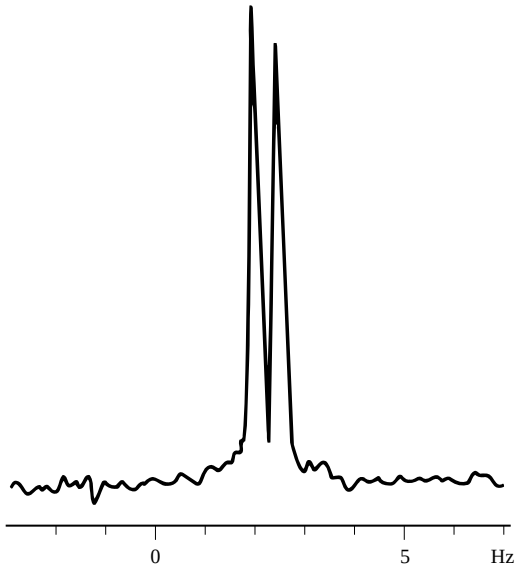

Figure 2 Deuteron quadrupole splitting of the deuteron signal from benzene-d_1, with proton decoupling

chemical shieldings, it is expected that the shift will not be linearly related to $\boldsymbol{B}_0$. The reason for this is clear: if the molecule is tumbling randomly, the average chemical shift $(\sigma_{xx} + \sigma_{yy} + \sigma_{zz})B_0/3$ will be observed; if the molecules are partly aligned, with alignment parameters S_{xB}, S_{yB}, and S_{zB}, the observed shift will be

$$2 \sum_{i=x,\,y,\,z} S_{iB}\sigma_{ii} B_0/3$$

Despite concerted effort, no such nonlinear shifts have been demonstrated to date. The difficulty is that the expected effects are very small, and easily masked by shifts arising from extraneous factors such as temperature.

4 APPLICATIONS

From the above, it can be seen that the dipolar splitting observed between two nuclei in a molecule in a high $\boldsymbol{B}_0$ relates the length and direction of the internuclear vector to $\boldsymbol{\chi}$. Similarly, the observed quadrupole splitting relates the electric field gradient tensor $\boldsymbol{V}$ and $\boldsymbol{\chi}$. If $\boldsymbol{\chi}$ is known, or can be estimated accurately, then information is obtained on the internuclear vector or on $\boldsymbol{V}$, i.e. structural information. On the other hand, if the structure is known (the length and direction of the internuclear vector relative to the principal axes, or direction and the strength of the electric field gradient), $\boldsymbol{\chi}$ may be determined. For organically bound ^{2}H, the largest component of $\boldsymbol{V}$ (V_{zz}) is directed along the C–^{2}H (or N–^{2}H, O–^{2}H, etc.) bond, and the asymmetry, $V_{xx} - V_{yy}$ is negligible. Even for ^{2}H attached to trigonal carbon, the asymmetry is normally less than 5% of V_{zz}.

4.1 $\boldsymbol{\chi}$, Systematics and Determination

In addition to the high-field NMR method, there are several methods for determining $\boldsymbol{\chi}$. In the crystal flip angle method,[2] a single crystal of the sample is suspended by a quartz fiber in a transverse magnetic induction and the torque required to cause the crystal to turn from its lowest energy state through its highest energy state is measured. In the Cotton–Mouton method,[12] the partial alignment of molecules in the liquid or gaseous state by $\boldsymbol{B}_0$ is measured by observing the optical birefringence. In the Zeeman microwave method,[13] the Zeeman effect on rotational spectra is observed. Extensive measurements have been made using all these methods, often on the same molecule; the results are generally in good agreement.[14] For example, for benzene, single crystal measurements yielded a value for $\Delta\chi$ of $-1.24 \times 10^{-33}\,\mathrm{m}^3$, three independent measurements by the Cotton–Mouton method gave -1.31, -1.32, and $-1.33 \times 10^{-33}\,\mathrm{m}^3$, and measurements by high-field NMR gave $-1.27 \times 10^{-33}\,\mathrm{m}^3$. With no electric dipole moment, benzene could not be studied directly by rotational spectroscopy.

All these measurements have demonstrated that Pascal's additivity scheme[15] for the isotropic diamagnetic susceptibility can be extended to $\boldsymbol{\chi}$, the molecular susceptibility tensor, i.e. that $\boldsymbol{\chi}$ can be expressed as the sum of bond susceptibility tensors $\boldsymbol{\chi}_\mathrm{b}$, or of atom susceptibilty tensors $\boldsymbol{\chi}_\mathrm{a}$, with the addition of $\boldsymbol{\chi}_\mathrm{e}$ (a susceptibility tensor ascribable to the delocalized circulation of electrons).[13] There is a considerable amount of literature covering $\boldsymbol{\chi}_\mathrm{e}$ in aromatic and antiaromatic compounds; an alternative name for this delocalized circulation is 'ring current'. In early studies the existence of the ring current and its magnitude were inferred from measurements of 'exaltation',[15] the amount by which χ exceeds $\Sigma\chi_\mathrm{b}$ or $\Sigma\chi_\mathrm{a}$. The circulation is in the plane of the aromatic or antiaromatic systems, so $\boldsymbol{\chi}_\mathrm{e}$ has zero elements for χ_{xx} and χ_{yy}; χ_{zz} is negative if the molecule is aromatic, and positive if it is antiaromatic.[16]

Acyclic compounds do not exhibit exaltations, and fit the additive scheme well, although multiple heavy atom substitution on carbon causes deviations. Single and triple bond susceptibility tensors are axial, that is $\chi_{xx} = \chi_{yy}$. If only single and triple bonds are present, S_{nB} for any axis can be determined using

$$S_{NB} = \sum_{\text{bonds}} (\tfrac{3}{2}\cos^2\theta_{nB} - \tfrac{1}{2})\Delta\chi_\mathrm{b} B_0^2/15kT\mu_0 \qquad (17)$$

Double bond susceptibility tensors have three different components, so the full version of equation (9) is required. Cyclic compounds, even saturated small ring compounds, such as cyclopropane, cyclobutane, and cyclopentane, show significant contributions from $\boldsymbol{\chi}_\mathrm{e}$. The exact nature of the delocalization is uncertain, but three- and five-membered rings have negative $\boldsymbol{\chi}_\mathrm{e}$, while four-membered rings have positive $\boldsymbol{\chi}_\mathrm{e}$.

The susceptibility tensor for most rigid molecules is a hard property, i.e. it is not affected appreciably by the environment. $\boldsymbol{\chi}$ is the same, within experimental error, whether measured in the gas, liquid, or solid phase. If the molecular electronic or geometrical structure is actually changed by the environment, $\boldsymbol{\chi}$ will change. For example, different solvents which produce a different weighting of the polar and nonpolar resonance forms in *N*-methyl-2-pyridone cause different quadrupole splittings to be observed for the deuterated compound.

Extensive analyses of bond susceptibility additivity schemes have been presented in articles by Flygare[13] and Haberditzl.[17]

4.2 Determination of Structure: Rigid Molecules

As an example of structural elucidation, we consider the study of the dihydrogen complex of the bridged bis(ruthenium porphyrin) · H_2 complex (**3**).[18] The structure of the $B(RuP)_2$ framework is well established. The structural question to be answered is: What is the arrangement of the H_2? How far apart are the hydrogen atoms, and what angle does the H–H axis make with the molecular *z* axis (Ru–Ru axis)?

The susceptibility tensor for the complex can be estimated within a few per cent by adding the known tensors for the two porphyrins, the phenylimidazolyl groups, and the biphenylene bridging group, using the summation

$$\Delta\chi_{zz} = \sum_{\text{groups}} (\tfrac{3}{2}\cos^2\theta_{zz} - \tfrac{1}{2})\Delta\chi_\mathrm{g} \qquad (18)$$

with $\theta_{zz'}$ being the angle between the molecular *z* axis and the normals to the ring planes of the individual groups. The anisotropy of the C–C bonds joining the biphenylene and porphyrin groups and of H_2 are less than $0.1 \times 10^{-33}\,\mathrm{m}^3$ and do not contribute significantly to the sum, which gives

$\Delta\chi_{zz} = -24.0 \times 10^{-33}\,\mathrm{m}^3$. Measurements of the H–H magnetic dipolar splitting were made at 620 MHz (14.56 T). S_{zB} is calculated to be -6.61×10^{-5} at this $\boldsymbol{B}_0$.

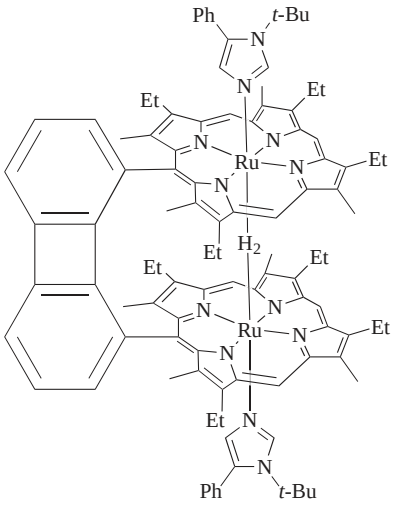

(3)

The H_2 signal at 620 MHz is a doublet with a splitting of $\pm 7.37 \pm 0.05$ Hz. D_{HH} is thus $\pm 4.91 \pm 0.03$ Hz. Using equation (14), one finds:

$$\langle \tfrac{3}{2}\cos^2\theta_{zn} - \tfrac{1}{2}\rangle / r_{HH}^3 = \pm 0.309 \times 10^{24} \tag{19}$$

The sign of D_{HH} was not known, but was determined by observing the field dependence of the splitting $J_{HD} + D_{HD}$ for the complex with HD. The sign of J_{HD} is known to be positive, so the decreasing magnitude of the splitting with increasing $\boldsymbol{B}_0$ means that D_{HD} and thus D_{HH} are negative. The internuclear distance was deduced by relaxation time measurements to be 0.121 ± 0.009 nm. This yields $\langle (3/2)\cos^2\theta_{zn} - (1/2)\rangle = -0.54 \pm 0.05$. Since $\langle (3/2)\cos^2\theta_{zn} - (1/2)\rangle$ cannot be more negative than $-\frac{1}{2}$, it appears that θ_{zn} must be very close to 90°; the H–H axis is perpendicular to the molecular z axis.

4.3 Study of Molecules with Internal Motion

As an example, a study of styrene and 1- and 2-vinylnaphthalene is outlined.[19] The motion of interest is the rotation of the vinyl group about the single bond joining it to the aromatic ring. The parameter measurable by high field studies is the expectation value, $\langle \sin^2\alpha\rangle$, where α is the dihedral angle between the planes of the vinyl group and the ring. In the study, the quadrupole splittings of the deuteron signals were measured for styrene with deuterium substituted in all positions of the vinyl and phenyl groups.

Addition of the known group susceptibility tensors for vinyl and phenyl groups suggests that the principal axis z of styrene is very nearly perpendicular to the phenyl ring, regardless of α, and that $\chi_{xx} \approx \chi_{yy}$. The equality of the observed splittings for the *ortho*, *meta*, and *para* deuterons in the phenyl group is consistent with this, and their magnitude at 14.57 T indicates a value of $\Delta\chi_{zz} = -1.45 \times 10^{-33}\,\mathrm{m}^3$. The determination of $\langle \sin^2\alpha\rangle$ is then an exercise in solid trigonometry: one has to calculate $\langle \cos^2\theta_{zz'}\rangle$ relating the molecular z axis to the z' axis of the electric field gradient tensor (the C–D bond axis) for the α and *trans*-β deuterons in the vinyl group. These are related by

$$\langle \cos^2\theta_{zz'}\rangle = \langle \sin^2\alpha\rangle \langle \sin^2\beta\rangle \tag{20}$$

where β is the angle between the C–D bond and the C–C bond joining the vinyl and phenyl groups. For the deuteron in the *cis*-β position, $\beta \approx 0°$, the C–D axis is parallel to that of the *para*-deuteron, regardless of internal rotation of the vinyl group. The ratio of the splittings is thus a measure of the ratio of the quadrupole couplings for the phenyl–D and vinyl–D nuclei (185 and 181 kHz, respectively), which is in agreement with previous measurements. For the α and *trans*-β deuterons, β is taken as 71°. From the observed splittings, it is then found that $\langle \sin^2\alpha\rangle$ is 0.081 and $\sin^{-1}\langle \sin^2\alpha\rangle^{1/2}$ is 16.5°. If the splitting were negative rather than positive, one would obtain $\langle \sin^2\alpha\rangle = 0.666$ and $\sin^{-1}\langle \sin^2\alpha\rangle^{\frac{1}{2}} = 55°$, but this can be eliminated, because the value of $\Delta\chi_{zz}$ obtained would be $-1.31 \times 10^{-33}\,\mathrm{m}^3$, which is a much smaller value than that indicated by the phenyl–D splittings. Similar measurements on 2-vinylnaphthalene indicated $\langle \sin^2\alpha\rangle$ gave values the same as those for styrene, within experimental error, while for 1-vinylnaphthalene, $\sin^{-1}\langle \sin^2\alpha\rangle^{-1/2} \approx 40°$, suggesting steric interference between the vinyl group and the *peri*-hydrogen atom in the planar arrangement.

4.4 Angular Correlation in the Liquid State

Even in the absence of a magnetic flux, a molecule (A) which is not isotropic interacts with neighboring anisotropic molecules (B) in such a way that they do not tumble randomly, but adopt preferred orientations with respect to A. A strong limiting case of this is association; if molecule A binds to molecule B, for example with a hydrogen bond or by ionic attraction, then A and B do not move independently, but tumble together synchronously. More subtle interactions can also induce molecular correlation: the electric polarizability, electric dipole moment, quadrupole moment, or higher moments, may interact with any of these of the B molecules; the shapes of molecules A and B may be conducive to better packing in particular mutual orientations. Molecule A may influence several molecules of molecule B, and vice versa. Finally, A and B may be different species (solute and solvent), or the same (neat liquids). Angular correlations may also be characterized by ordering parameters $S_{ij'} = \langle (3/2)\cos^2\theta_{ij'} - (1/2)\rangle$, where $\theta_{ij'}$ is the angle between the ith axis of A and the jth axis of B. If molecules A and B are identical, one may define Kirkwood's[20] parameter $g_{ii'}$ as

$$g_{ii'} = 1 + \sum_n S_{ii'} \tag{21}$$

The summation is taken over all neighboring B molecules, and the unity term represents the angular correlation of A with itself. For example, if $g_{zz'}$ were found to be 2.00 for neat benzene, a conceivable (though incorrect) explanation would be that neat benzene consists entirely of face-to-face dimers, with parallel z axes. For neat samples,

$$S_{iB}^{A} = g_{ii'}\Delta\chi_{ii}B_0^2/15kT\mu_0 \tag{22}$$

while for solute A in solvent B

$$S_{iB}^{A} = \left(\Delta\chi_{ii}^{A} + \frac{2}{3} \sum_{n} \sum_{j'=x',y',z'} (S_{ij'} \Delta\chi_{jj'}) \right) B_0^2 / 15kT\mu_0 \quad (23)$$

In order to measure the degree of molecular alignment caused by the induction, free of solvent angular correlation effects, it is customary to employ dilute solutions in solvents which are themselves exactly or nearly magnetically isotropic. Ideal solvents would include CCl_4, $SiMe_4$, CMe_4, and SF_6. Good, though not perfect, solvents include water, liquid ammonia, diethyl ether, and cyclohexane. The angular correlation in a number of neat liquids has been studied by comparing the alignments observed in dilute solution in isotropic solvents, and in the neat liquid. The value of $g_{zz'}$ found for benzene was 0.86, which implies a negative value for $S_{zz'}$. The rings of neighboring benzene molecules tend to form angles greater than 54.7°, rather than stack, pancake fashion.[10]

4.5 Paramagnetic and/or Charged Species

Paramagnetic or charged species are partially aligned in a magnetic field in the same way as neutral diamagnetic molecules. Since paramagnetic susceptibilities are usually much larger than diamagnetic susceptibilities, it is not surprising that the anisotropies of the paramagnetic susceptibilities are also much larger, and the degree of alignment correspondingly greater. Thus the first observation[5] of a dipolar splitting in isotropic solution was made on the paramagnetic cobalt complex bis[*p*-tolyl-tris(pyrazolyl)borato]cobalt(II) (**4**). Lanthanide shift reagents exert their effects by virtue of their large anisotropic susceptibilities; consequently, molecules complexed with shift reagents exhibit large dipolar and quadrupolar splittings of the type described here, even at moderate field strengths. A very interesting study of the susceptibility tensor for a ferric porphyrin has been reported.[21]

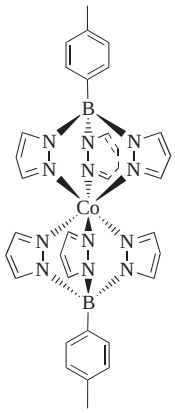

(4)

Studies of organic cations and anions have also been made.[22] Ion pairing probably occurs in the cases studied, although the counterions are expected to be nearly isotropic and thus correlation effects would be negligible. Of course the electronic structure of the organic ion itself may be strongly affected by the counterion. Values of χ_e have been deduced and related to the electronic structure of the ions.

5 RELATED ARTICLES

Anisotropy of Shielding and Coupling in Liquid Crystalline Solutions; Chemical Shift Tensors; Dipolar and Indirect Coupling Tensors in Solids; Liquid Crystalline Samples: Spectral Analysis; Quadrupolar Transition Metal and Lanthanide Nuclei.

6 REFERENCES

1. J. A. Stratton, *Electromagnetic Theory*, McGraw-Hill, New York, 1941, p. 10
2. C. V. Raman and K. S. Krishnan, *Proc. R. Soc. (London), Ser. A*, 1927, **A113**, 511.
3. A. Saupe and G. Englert, *Phys. Rev. Lett.*, 1963, **11**, 462.
4. P. C. M. Van Zijl, B. H. Ruessink, J. Bulthuis, and C. MacLean, *Acc. Chem. Res.*, 1984, **17**, 172.
5. A. A. Bothner-By, P. J. Domaille, and C. Gayathri, *J. Am. Chem. Soc.*, 1981, **103**, 5602.
6. J. A. B. Lohman and C. MacLean, *Chem. Phys.*, 1978, **35**, 269.
7. J. W. Emsley and J. C. Lindon, *NMR Spectroscopy in Liquid Crystal Solvents*, Pergamon, Oxford, 1975.
8. R. Havemann, W. Haberditzl, and P. Grzegorzewski, *Z. Phys. Chem.*, 1961, **217**, 91.
9. F. A. L. Anet, *J. Am. Chem. Soc.*, 1986, **108**, 1354.
10. A. Loewenstein, *Advances in Nuclear Quadrupole Resonance*, ed. J. A. S. Smith, Wiley, New York, 1983, Vol. 5, p. 53.
11. P. C. M. Van Zijl, C. MacLean, C. Gayathri, and A. A. Bothner-By, *J. Magn. Reson.*, 1984, **56**, 456.
12. H. Geschke, S. Pferrer, H. Haeussler, and W. Huettner, *Ber. Bunsenges. Phys. Chem.*, 1982, **86**, 790.
13. W. H. Flygare, *Chem. Rev.*, 1974, **74**, 653.
14. *Landolt-Börnstein, NSII*, eds. K.-H. Hellwege and O. Madelung, Springer-Verlag, Berlin, Vol. 16, p. 403.
15. P. Pascal, *Chemie General*, Masson, Paris, 1949.
16. H. J. Dauben, Jr., J. D. Wilson, and J. L. Laity, *Non-Benzenoid Aromatics*, ed. L. Snyder, Academic, New York, 1969, p. 167.
17. W. Haberditzl, *Angew. Chem., Int. Ed. Engl.*, 1966, 288.
18. J. P. Collman, P. S. Wagenknecht, A. A. Bothner-By, J. E. Hutchinson, N. S. Lewis, M. A. Lopez, R. Guilard, M. Lher, and P. K. Mishra, *J. Am. Chem. Soc.*, 1992, **114**, 5654.
19. K. Facchine, S. W. Staley, P. C. M. Van Zijl, P. K. Mishra, and A. A. Bothner-By, *J. Am. Chem. Soc.*, 1988, **110**, 4900.
20. J. G. Kirkwood, *J. Chem. Phys.*, 1939, **7**, 911.
21. S. H. Strauss, K. M. Long, M. Magerstaedt, and O. A. Gansow, *Inorg. Chem.*, 1987, **26**, 1185.
22. E. W. Bastiaan, P. C. M. Van Zijl, C. MacLean, and A. A. Bothner-By, *Annu. Rep. NMR Spectrosc.*, 1987, **19**, 35.

Biographical Sketch

Aksel A. Bothner-By. *b*. 1921. B.Chem., 1943, Ph.D., 1949 (with R. B. Woodward, Harvard), Brookhaven Natl. Lab. 1949–52. E.T.H. Zürich, 1952–53. Harvard, 1953–58. Mellon Institute, then Carnegie Mellon U. 1958–92. Began study of NMR in 1954. ~ 150 publications. Research specialties: molecular geometry by high-resolution NMR; Overhauser effects, longitudinal and transverse; molecular orientation by high magnetic field.

Multiple Quantum Coherence in Spin-1/2 Dipolar Coupled Solids

Bernard C. Gerstein

Ames Laboratory of US DOE & Iowa State University, Ames, IA, USA

1	Introduction	1
2	Single Quantum Coherence	2
3	Coherent Averaging	3
4	Development of Multiple Quantum Coherence: Use of a Double Quantum Propagator	4
5	Detection of Multiple Quantum Coherence	6
6	A Single Quantum Propagator	9
7	Related Articles	11
8	References	11

1 INTRODUCTION

Think for a moment about the area of the North American continent known as the 'Great Plains'. In the twenty thousand years before the coming of the Europeans to this area, the thirty millions of original peoples were able to see herds of antelope, and of native bison, so multitudinous that it took hours for a running herd to pass. There grew the native prairie grasses that sustained them, such as the Big Bluestem, Little Bluestem, and Indian Coneflower used by the indigenous peoples for medicinal purposes, and only recently found to be of medicinal use to the descendants of the descendants of the first Europeans. One of the stunning sights that these newcomers recorded in their arrival to the center of this 'New World' was the effect of the wind on the seas of prairie grasses, since replaced by corn and soybeans, which moved like 'waves of the sea'—seemingly endlessly abundant then, but since almost become extinct. Where had lived the peoples whose names themselves had the music of the prairies associated with them—the 'Illinois', 'Sioux', 'Ojibway', 'Menominee', 'Pawnee', 'Mesquakie' ... —were Katherine Lee Bates's (author of the song 'America the Beautiful') 'amber waves of grain', each stem coherently moving in concert with millions of others to produce the effect of being on an immense ocean, through which sailed the 'prairie schooner covered wagons' of those seeking more living room.

Now consider that sight, so vast and continuous that it drove some of the early invaders to madness with time. Here were countless billions of single, almost identical stems, enough to be called by Gibbs an 'ensemble' of those elegantly beautiful flora. The effect of waves of an ocean was produced by these two-meter high plants waving in phase with each other under the excitation of a wind, with wavelength long compared with the separation between the individual stems, and powerful enough to cause millions of them to move in concert so they appear to be a single body. In this example, we are given some hint of what the word 'coherence' can mean: the movement, in phase, in both time and space, of an ensemble of identical systems, such that vast portions of them can be detected being in a state which describes a macroscopic entity.

In magnetic resonance, we produce a coherence in phase among individual spins in an ensemble by excitation with a radiofrequency having a wavelength enormous compared with the separation between individual nuclear spins. We generally detect such coherence of an ensemble of spins waving in the static field of our magnet via the voltage induced by a sufficiently large number in an inductor such that a signal is detectable above the Johnson noise (but see ***Optically Enhanced Magnetic Resonance***). Since the inductor is a dipole producer, and a dipole detector, i.e., a detector of coherence associated with transitions between states differing in spin quantum number by a single quantum, we can only directly detect *single* quantum coherence ($\Delta k = 1$) of such an ensemble.

In the present discussion, we want to elucidate the meaning of multiple quantum coherence in the special case of dipolar coupled spin-$\frac{1}{2}$ systems, and to illustrate how the experiment is accomplished to produce and detect such a phenomenon. To do so, it is necessary to first amplify the meaning of 'coherence'. Then we shall proceed to discuss the production of multiple quantum coherence, and finally the means used for detection. To begin, we use the familiar example of the ideas behind the development and detection of single quantum coherence in spin-$\frac{1}{2}$ systems. Then the concepts used to produce *multiple* quantum coherence ($\Delta k \geq 2$) in ensembles of dipolar coupled spin-$\frac{1}{2}$ systems are developed. Thought experiments are used to illustrate conversion of populations ($\Delta k = 0$) into multiple quantum coherence with the use of coherent averaging to produce a multiple quantum propagator (quite a lovely introduction to the subject of propagators in quantum mechanics is given by Mattuck[1]). Propagators that develop multiple quantum coherence in steps of single and double quanta are discussed and illustrated. Experimental details concerning the manipulations necessary to perform the experiments are given. Experimental results using a single quantum propagator are shown for adamantane, and for a liquid crystal containing isolated clusters of 21 protons. The aim of this work is to present, in an easily understandable manner, and perhaps with a fresh perspective, the ideas behind the creation and detection of multiple quantum coherence in ensembles of homonuclear dipolar coupled spin-$\frac{1}{2}$ systems. To this end, both theoretical ideas and experimental details will be presented so that readers will have the background to perform such experiments on their own instruments, given the appropriate phase shifting capabilities.

Before beginning to discuss the specifics of coherence, and its production and detection, we note that spin counting by multiple quantum coherence is one of a variety of possible two-dimensional NMR experiments[2–4] that first began to appear in the mid 1970s and have since been extensively reviewed.[5–9] In the specific case of using multiple quantum coherence (MQC) to enumerate numbers of strongly coupled spins in ensembles of coupled clusters of protons in solids,[10,11] the initial work developed multiple quantum coherence in steps of two quanta, such that values of MQC, k, of 0, 2, 4, 6, ... , or (depending on the state of the system prepared before the use of multiple pulse techniques to produce MQC) 1, 3, 5, ... , might be detected. Later work (see below) resulted in the use of pulse sequences that developed MQC in steps of one quantum, such that values of $k = 0, 1, 2, \ldots$ could be detected.

In liquids, the coupling mechanism used to produce multiple quantum coherence is the two-body scalar or J coupling. The secular portion of the spin space part of this interaction is $\hat{I}_z\hat{S}_z$ for the heteronuclear case. In solids, the case to be discussed here, the interaction is the two-body homonuclear dipolar coupling between spin-$\frac{1}{2}$ systems, e.g., among protons in a solid. The secular portion of the 'spin space' part of this interaction is $\hat{\boldsymbol{I}}_1\cdot\hat{\boldsymbol{I}}_2 - 3\hat{I}_{z1}\hat{I}_{z2}$. The pulse sequences used to develop MQC in the latter case will therefore differ from those used for the former, in the same sense that the dipolar echo sequence (τ, $90_x{}^\circ$, τ, $90_y{}^\circ$, τ) (see ***CRAMPS***) differs from the spin echo sequence (τ, $180_x{}^\circ$, τ) (see ***Echoes in Solids***). However, the extension of the present description to heteronuclear dipolar coupling and to scalar coupling should be obvious, with the techniques used to generate and detect MQC being more easily achieved than in the present case.

2 SINGLE QUANTUM COHERENCE

We first ask: 'What do we observe in an NMR experiment?' The answer is always a transverse component of spin angular momentum. With phase detection along y in the rotating frame, what is observed is

$$\text{FID} \sim \langle \hat{I}_y(t)\rangle = \text{Tr}\{\hat{\rho}(t)\hat{I}_y\} \tag{1}$$

From this formalism, it is immediately obvious that we are invoking the use of the quantum statistical method, in that the density operator $\hat{\rho}$ must be used to describe the phenomena discussed here.[12] Statistical thermodynamics enters when we consider that the ensemble in question is prepared in some equilibrium state before observation, i.e., we expose an ensemble of nuclear spins I in a field until equilibrium is achieved under the Zeeman interaction $\hat{\mathcal{H}}$, and

$$\hat{\rho}(0) \equiv \hat{\rho}^{\text{equilibrium}} = \frac{1}{Z}\exp\left(-\frac{\hat{\mathcal{H}}}{k_\text{B}T}\right) \sim \sum_k \hat{I}_{zk}$$
$$k = 1, 2, \ldots \tag{2}$$

is the operator form of $\hat{\rho}$. Z is the ensemble partition function and k_B Boltzmann's constant.

The FID, whose time dependence is given by $\hat{\rho}(t)$, and whose phase is specified in this case by the operator $\hat{I}_y$, is driven by the presence of time-independent Hamiltonians $\hat{\mathcal{H}}$ as follows:

$$\hat{\rho}(t) = \exp(-\text{i}\hat{\mathcal{H}}t)\,\hat{\rho}(0)\exp(\text{i}\hat{\mathcal{H}}t) \tag{3}$$

The spectrum is obtained by Fourier transformation of the FID. We remind ourselves of the quantum mechanics involved in this statement with a short review.

We consider an ensemble of weakly interacting identical systems, each described by a set of single particle stationary states $|m_a\rangle$, which are eigenstates of the z component of nuclear spin angular momentum such that $\hat{I}_z|m_a\rangle = a|m_a\rangle$. These identical systems for purposes of the present discussion might be 'isolated' nuclear spins (e.g., ^{13}C nuclei at a natural abundance of 1.1% decoupled from other nuclei via strong rf decoupling), or isolated pairs of nuclear spins (e.g., pairs of protons in partially hydrated calcium sulfate, $CaSO_4{\cdot}xH_2O$, with $x < 2$), or many (of order 10^{23}) protons in strongly dipolar coupled solids. If a system consists of more than a single spin-$\frac{1}{2}$ nucleus then the stationary states describing the system can be arranged into linear combinations of products of single particle states, which we denote by $|M_a\rangle$, which are eigenfunctions of the square of the total spin angular momentum operator, $\hat{I}^2$, and of the z component of the angular momentum, $\hat{I}_z$.

Two of these many body states, $|M_a\rangle$, $|M_b\rangle$, differ by $k = a - b$ in the z component of the angular momentum. Further, the state of each system can in general be a time-dependent superposition of these stationary states:

$$|\Psi(t)\rangle = \sum_j c_j(t)|M_j\rangle \tag{4}$$

where the phase factor of the jth stationary state, $\text{e}^{\text{i}\phi_j}$ has been implicitly included in the time-dependent amplitude $c_j(t)$.

For example, in ensembles that consist of coupled pairs of spin-$\frac{1}{2}$ nuclei, each with stationary states α and β, where the coupling interaction is small compared with the Zeeman interaction, the normalized stationary states of the coupled systems, which can be arranged to be eigenfunctions of the square of the total spin operator, $\hat{I}^2$, and of the z component of spin, $\hat{I}_z$, are $|\alpha(1)\rangle|\alpha(2)\rangle$, $\sqrt{\frac{1}{2}}[|\alpha(1)\rangle|\beta(2)\rangle \pm |\beta(1)\rangle|\alpha(2)\rangle]$ and $|\beta(1)\rangle|\beta(2)\rangle$, which are the four two-particle functions describing the triplet and singlet spin states. Two coupled spins can have maximum total spin quantum number $I = 1$, and z component $-I < \langle\hat{I}_z\rangle < I$ in steps of unity. Three coupled spins can have maximum total spin quantum number $I = \frac{3}{2}$, etc.

We remember that the statistical probability of finding any system in stationary state $|M_s\rangle$ is

$$P_s = \overline{c_s^*(t)c_s(t)} = \overline{c_s(t)c_s^*(t)} \tag{5}$$

where the overbars mean an ensemble average. The operator $\hat{\rho}$ is defined by the ensemble average of the product $\hat{\rho} = |\psi\rangle\langle\psi|$ such that the i,jth matrix element is

$$\rho_{kj} = \overline{\langle k|\Psi\rangle\langle\Psi|\ j\rangle} = \overline{c_k c_j^*} \tag{6}$$

A nonvanishing value of ρ_{ss} therefore represents a population of the state $|M_s\rangle$. An observable signal in NMR means a nonvanishing value of $\rho_{s,s+1}$. This means that in the ensemble of systems being observed, there is a *phase coherence* associated with system states $|M_s\rangle$ and $|M_{s+1}\rangle$. We designate this a single quantum coherence. This is to say that we observe a decaying oscillation resulting from an ensemble in which the time-dependent state responsible for the behavior of each system is a superposition of two states differing from each other by a single quantum, *and having the same phase*. What does this mean? With the basis set for a spin-$\frac{1}{2}$ system being $|\alpha\rangle$ and $|\beta\rangle$, and for the kth basis state $|k\rangle$, the amplitude factor being $C_k = |C_k|\text{e}^{\text{i}\phi_k}$, an individual spin-$\frac{1}{2}$ system will have single particle wavefunction $|\psi\rangle = |C_\alpha|\text{e}^{\text{i}\gamma}|\alpha\rangle + |C_\beta|\text{e}^{\text{i}\phi}|\beta\rangle$. Here γ and ϕ are the phases of the single particle basis set functions, and the C_k will in general be time-dependent. A

very special kth single particle wavefunction in which the phase δ_k on the two basis functions is the same,

$$|\psi_k\rangle = e^{i\delta_k}\sqrt{\tfrac{1}{2}}(|\alpha_k\rangle + i|\beta_k\rangle) \tag{7}$$

is a *phase coherent superposition* of the two states that differ by $k = 1$ in the z component of the angular momentum. This system can be prepared by starting at time equal to zero with a single particle wavefunction $e^{i\delta_k}|\alpha\rangle$, and turning on an rf pulse, *operating on a timescale short compared with any dephasing tendency of the ensemble*, which rotates the z magnetization associated with the state $|\alpha\rangle$ by 90°, and converts it into the transverse magnetization described by the above superposition. *For this special combination*, $\langle\psi_k|\hat{I}_{yk}|\psi_k\rangle = \frac{1}{2}$. In an ensemble of spin-$\frac{1}{2}$ noninteracting systems represented by such a phase coherent superposition, $|\psi_{tot}\rangle = \Pi_k|\psi_k\rangle$, and for such an ensemble we find the ensemble average to be

$$\begin{aligned}\langle\hat{I}_y\rangle &= \langle\psi|\hat{I}_y|\psi\rangle \\ &= \frac{1}{N}\prod_k e^{-i\delta_k}\sqrt{\tfrac{1}{2}}(\langle\alpha_k| - i\langle\beta_k|)\Big(\sum_{k'}\hat{I}_{yk'}\Big)e^{i\delta_k} \\ &\quad\times\sqrt{\tfrac{1}{2}}(|\alpha_k\rangle + i|\beta_k\rangle) \\ &= \tfrac{1}{2}\end{aligned} \tag{8}$$

because the phase factors cancel! Another way of saying this is that

$$\rho_{\alpha\beta} = \frac{1}{N}\sum_k |C_{\alpha k}|e^{i\gamma_k}|C_{\beta k}|e^{i\phi_k} \equiv \overline{C_\alpha C_\beta} \neq 0 \tag{9}$$

Note that, in general, if γ and ϕ are not zero then the above sum is a superposition of sines and cosines that will average to zero—the random phase case.

The creation of multiple quantum coherence is equivalent to causing ρ to evolve in such a manner that $\rho_{rs} \neq 0$, and in the following discussion, we shall see how this inequality is achieved.

3 COHERENT AVERAGING

We next remind ourselves of the results of coherent averaging theory as applied to the spin portion of internal Hamiltonians.[13] We first note that a nuclear spin Hamiltonian may, in general, be expressed as the product of a constant characteristic of the interaction in question, and of 'spin space' operators. For example, for the heteronuclear dipolar interaction between spins $\hat{\boldsymbol{I}}$ and $\hat{\boldsymbol{S}}$, the constant is $\gamma_I\gamma_S/r_{IS}^3$, the 'real space' portion is $1 - 3\cos^2\theta$, and the 'spin space' portion is $\hat{I}_z\hat{S}_z$. It is assumed that the real space portions of the internal Hamiltonians are constant in the experiments under consideration, i.e., there is no molecular motion or experimenter-supplied sample spinning.

When we manipulate $\hat{\mathcal{H}}_{int}$ by rf pulse sequences that are cyclic [the ensemble is returned to its initial state after a cycle of rf pulses, meaning that the propagator $\hat{U}_{rf}(t_c,0)$ associated with the pulse train from time zero to time t_c is unity at cycle times t_c (and integer multiples of these times)] and periodic, the leading term in the result, observed at cycle times nt_c is

$$\hat{\rho}(nt_c) = \exp(-i\tilde{\hat{\mathcal{H}}}^{(0)}nt_c)\hat{\rho}(0)\exp(i\tilde{\hat{\mathcal{H}}}^{(0)}nt_c) \tag{10}$$

where $\tilde{\hat{\mathcal{H}}}^{(0)}$ is the time average of a static internal Hamiltonian made time-dependent by the rf pulses:

$$\tilde{\hat{\mathcal{H}}}^{(0)}_{int} = \frac{1}{t_c}\int_0^{t_c} dt\,\hat{\tilde{\mathcal{H}}}_{int}(t) \tag{11}$$

$\hat{\tilde{\mathcal{H}}}_{int}(t)$ is the instantaneous value of the internal Hamiltonian as determined by the rf pulses:

$$\hat{\tilde{\mathcal{H}}}_{int}(t) = \hat{U}^{\dagger}_{rf}(t,0)\hat{\mathcal{H}}_{int}\hat{U}_{rf}(t,0) \tag{12}$$

$\hat{U}_{rf}(t,0)$ is the propagation operator due to the rf pulses from time zero to time t. For n time intervals δ_1, followed by δ_2, followed by $\ldots$, δ_n, $\hat{U}_{rf}$ may be expressed as the product

$$\hat{U}_{rf}(t,0) = \hat{U}_{rf}(\delta_n)\cdots\hat{U}_{rf}(\delta_1) \tag{13}$$

whereby

$$\hat{U}^{-1}_{rf}(t,0) = \hat{U}^{-1}_{rf}(\delta_1)\cdots\hat{U}^{-1}_{rf}(\delta_n) \tag{14}$$

Equation (12) can always be expressed as a product of rotations in spin space acting on components of angular momentum operators. For example, if the rf pulse sequence $(\tau, 180_{y^\circ}, \tau)$ with perfect delta function rf pulses produces $\hat{U}_{rf}$, then at times $0 \le t \le \tau$, when the rf Hamiltonian is zero, $U_{rf}(t,0)$ takes the form $e^0 = 1$, and in this time interval, $\hat{\tilde{I}}_z = e^0\hat{I}_z e^0 = 1\cdot\hat{I}_z\cdot 1$, which we may formally identify as a rotation $\hat{R}$ of unity, performed on $\hat{I}_z$, symbolized by $\hat{R}\hat{I}_z = 1\cdot\hat{I}_z$. At time $t = \tau$, the rf Hamiltonian corresponds to an infinitely sharp 180° rotation about the y axis. $\hat{U}_{rf}(t = \tau) = \exp(i\pi\hat{I}_y)$, and the physical result is a 180_{y° rotation $\hat{R}_{180y}$. For $\tau < t < 2\tau$, the rf again is zero, and $\hat{U}_{rf}$ is unity. Under this sequence, therefore, with the spin portion of $\hat{\mathcal{H}}_{int}$ being proportional to $\hat{I}_z$, keeping in mind the time ordering dictated by equations (12) and (14), we find

$$0 \le t < \tau: \quad \hat{\tilde{I}}_z = 1\cdot\hat{I}_z = \hat{I}_z \tag{15a}$$

$$t = \tau: \quad \hat{\tilde{I}}_z = 1\cdot\hat{R}_{180y}\hat{I}_z = -\hat{I}_z \tag{15b}$$

$$\tau < t \le 2\tau: \quad \hat{\tilde{I}}_z = 1\cdot\hat{R}_{180y}\cdot 1\cdot\hat{I}_z = -\hat{I}_z \tag{15c}$$

The familiar result is that at cycle times $2n\tau$, under the spin echo sequence $(\tau, 180^\circ, \tau)^n$, chemical shifts and field inhomogeneities, with spin operators $\hat{I}_{zk}$, vanish (but other interactions, such as homonuclear dipolar coupling, do not). This is to say that at cycle times $2n\tau$, with the internal Hamiltonian being proportional to $\hat{I}_z$, that $\tilde{\hat{\mathcal{H}}}^{(0)}_{int}$ is zero, i.e.,

$$\begin{aligned}\tilde{\hat{\mathcal{H}}}^{(0)}_{cs} &\sim \int_0^{2n\tau} dt\,\hat{U}^{-1}_{rf}(t)\hat{\tilde{\mathcal{H}}}_{cs}\hat{U}_{rf}(t) \\ &= \omega_{cs}[\hat{I}_z\tau + (-\hat{I}_z)\tau] = 0\end{aligned} \tag{16}$$

where ω_{cs} is a product of a constant and the real space portion of the chemical shift Hamiltonian.

Another, perhaps less familiar, result is that under homonuclear dipolar decoupling sequences [τ, $90_{x}{}^{\circ}$, τ, $90_{y}{}^{\circ}$, τ], homonuclear dipolar terms vanish, but chemical shifts are scaled. Consider the dipolar echo sequence [τ, $90_{x}{}^{\circ}$, τ, $90_{y}{}^{\circ}$, 2τ, $90_{y}{}^{\circ}$, τ, $90_{x}{}^{\circ}$, τ]. Using equations (12)–(14), we find for ideal delta function rf pulses, the following values of $\hat{\tilde{I}}_z(t)$:

$$0 \le t < \tau: \quad \hat{\tilde{I}}_z = 1 \cdot \hat{I}_z = \hat{I}_z \tag{17a}$$

$$t = \tau: \quad \hat{\tilde{I}}_z \to 1 \cdot \hat{R}_{90x}\hat{I}_z = -\hat{I}_y \tag{17b}$$

$$\tau < t < 2\tau: \quad \hat{\tilde{I}}_z = 1 \cdot \hat{R}_{90x} \cdot 1\hat{I}_z = -\hat{I}_y \tag{17c}$$

$$t = 2\tau: \quad \hat{\tilde{I}}_z \to 1 \cdot \hat{R}_{90x} \cdot 1 \cdot \hat{R}_{90y}\hat{I}_z = -\hat{I}_x \tag{17d}$$

etc., from which we may immediately infer that, the scalar product $\hat{\boldsymbol{I}}_1 \cdot \hat{\boldsymbol{I}}_2$ being invariant to rotation, the time dependence of the operator $\hat{\tilde{\mathcal{H}}}_{zz} = (\hat{\boldsymbol{I}}_1 \cdot \hat{\boldsymbol{I}}_2 - 3\hat{I}_{z1} < \hat{I}_{z2})$ is as follows:

$$0 \le t < \tau: \quad \hat{\tilde{\mathcal{H}}}_{zz} = \hat{\mathcal{H}}_{tt} \tag{17e}$$

$$t = \tau: \quad \hat{I}_{z1}\hat{I}_{z2} \to \hat{I}_{y1}\hat{I}_{y2}, \quad \text{so} \quad \hat{\tilde{\mathcal{H}}}_{zz} \to \hat{\mathcal{H}}_{yy} \tag{17f}$$

etc. Then the two-body average homonuclear dipolar Hamiltonian is

$$\begin{aligned}\hat{\tilde{\mathcal{H}}}_{\mathrm{DII}}^{(0)} = \frac{\omega_{\mathrm{D}}}{6\tau}[&\tau(\hat{\boldsymbol{I}}_1 \cdot \hat{\boldsymbol{I}}_2 - 3\hat{I}_{z1}\hat{I}_{z2}) + \tau(\hat{\boldsymbol{I}}_1 \cdot \hat{\boldsymbol{I}}_2 - 3\hat{I}_{y1}\hat{I}_{y2}) \\ &+2\tau(\hat{\boldsymbol{I}}_1 \cdot \hat{\boldsymbol{I}}_2 - 3\hat{I}_{x1}\hat{I}_{x2}) + \tau(\hat{\boldsymbol{I}}_1 \cdot \hat{\boldsymbol{I}}_2 - 3\hat{I}_{y1}\hat{I}_{y2}) \\ &+\tau(\boldsymbol{I}_1 \cdot \boldsymbol{I}_2 - 3I_{z1}I_{z2})] \\ \equiv \tfrac{1}{3}\omega_{\mathrm{D}}&(\hat{\mathcal{H}}_{zz} + \hat{\mathcal{H}}_{yy} + \hat{\mathcal{H}}_{xx}) = 0\end{aligned} \tag{18}$$

where ω_{D} is a product of a constant and the real space portion of the space–spin product dipolar Hamiltonian.

An important result just seen is that the sum

$$(\hat{\mathcal{H}}_{xx} + \hat{\mathcal{H}}_{yy} + \hat{\mathcal{H}}_{zz})\tau = \sum_k \hat{\mathcal{H}}_{kk} = 0 \tag{19}$$

for two spins $\boldsymbol{I}_1$ and $\boldsymbol{I}_2$. *In both of the above cases*, the average Hamiltonian for a specific interaction is made to vanish, leaving remaining interactions to be observed. *However*, it is possible to manipulate certain internal interactions such that the average Hamiltonian is not zero, but something else that we want.

4 DEVELOPMENT OF MULTIPLE QUANTUM COHERENCE: USE OF A DOUBLE QUANTUM PROPAGATOR

What do we want as an average Hamiltonian in order to develop multiple quantum coherence? The answer is an average Hamiltonian that allows the density operator at zero time $\hat{\rho}(0)$ to evolve in such a manner that $\hat{\rho}_{1,1\pm k} \neq 0$, where k is the order of the multiple quantum coherence.

The process, then, is to manipulate some internal Hamiltonian with cyclic, periodic rf pulses such that at cycle times nt_{c}, we have an average Hamiltonian that allows a zero-time equilibrium density operator,

$$\hat{\rho}(0) \equiv \hat{\rho}_{\mathrm{eq}} \sim \sum_i \hat{I}_{zi}, \quad i = 1, 2, \ldots \tag{20}$$

containing only diagonal terms representing populations in the Zeeman basis set, to develop MQC, i.e., to develop in such a manner that $\hat{\rho}_{i,i\pm k} \neq 0$, for $1 \le k < \infty$. Since we can only detect single quantum coherence (SQC) with NMR, we note in advance that once produced, the MQC must be reduced to SQC *in a manner* that *reflects the* MQC *therein contained* in order to be detected.

Examples of terms in the density operator that exhibit SQC might be single spin terms $\hat{I}_i^+$ and $\hat{I}_i^-$, or two-spin products of the form $\hat{I}_1^+\hat{I}_{z2}$. Double quantum coherence is represented by two-spin product terms in the density operator such as $\sum_{ij}(\hat{I}_i^+\hat{I}_j^+ + \hat{I}_i^-\hat{I}_j^-)$. Triple quantum coherence would be represented by three-spin products such as $\hat{I}_j^+\hat{I}_k^+\hat{I}_m^+$.

We can understand how this process works by example. An ensemble of spin-$\frac{1}{2}$ systems (e.g., protons in solid adamantane) is allowed to come to equilibrium in a static field for a time that is long compared with T_1. Then

$$\hat{\rho}(0) \sim \sum_i \hat{I}_{zi} \tag{21}$$

The sum is over all spins in the sample. Under the influence of an average Hamiltonian, produced by coherent averaging in spin space, as discussed for the cases of the spin echo and the dipolar echo, this ensemble is allowed to evolve over time. The formal time evolution formula may be expressed in terms of the product

$$f(\hat{A}, \hat{B}) = \mathrm{e}^{\hat{A}}\hat{B}\,\mathrm{e}^{-\hat{A}} \tag{22}$$

where $\hat{A}$ and $\hat{B}$ are operators.

It may be shown (equation (4.19) in Gerstein and Dybowski[13]) that an equivalent form of this product is

$$\begin{aligned}\mathrm{e}^{\hat{A}} - \hat{B}\,\mathrm{e}^{-\hat{A}} = \hat{B} + [\hat{A}, \hat{B}] + [\hat{A}, [\hat{A}, \hat{B}]]/2! \\ +[\hat{A}, [\hat{A}, [\hat{A}, \hat{B}]]]/3! + \ldots\end{aligned} \tag{23}$$

i.e.,

$$\hat{\rho}(nt_{\mathrm{c}}) \sim \exp(-\mathrm{i}\hat{\tilde{\mathcal{H}}}nt_{\mathrm{c}}) \sum_i \hat{I}_{zi} \exp(\mathrm{i}\hat{\tilde{\mathcal{H}}}nt_{\mathrm{c}}) \tag{24}$$

and

$$\begin{aligned}\rho(nt_{\mathrm{c}}) = \sum_i \hat{I}_{zi} + \left[-\mathrm{i}nt_{\mathrm{c}}\hat{\tilde{\mathcal{H}}}, \sum_i \hat{I}_{zi} \right] \\ +\left[-\mathrm{i}nt_{\mathrm{c}}\hat{\tilde{\mathcal{H}}}, \left[-\mathrm{i}nt_{\mathrm{c}}\hat{\tilde{\mathcal{H}}}, \sum_i \hat{I}_{zi} \right] \right] \Big/ 2! + \cdots\end{aligned} \tag{25}$$

The leading term $\sum_i \hat{I}_{zi}$ represents populations. The following terms must then be arranged so as to evolve single and higher quantum coherences.

In order to understand how to choose an average Hamiltonian that will produce multiple quantum coherence in the time-developed density operator $\hat{\rho}(t)$ as given by equation (25), it is necessary to look at the commutation rules for angular momentum operators. We know that

$$[\hat{I}_{k1}, \hat{I}_{k2}] = [\hat{I}_{k1}, \hat{I}_{k1}] = 0, \quad k = x, y, z \tag{26a}$$

$$[\hat{I}_z, \hat{I}^{\pm}] = \pm\hat{I}^{\pm} \tag{26b}$$

$$[\hat{I}^{\pm}, \hat{I}^{+}] = \pm 2\hat{I}_z \tag{26c}$$

$$[\hat{I}^{\pm}, \hat{I}^{\pm}] = 0 \tag{26d}$$

Given the form of $\hat{\rho}_{\mathrm{eq}} \equiv \hat{\rho}(0) \sim \sum_i \hat{I}_{zi}$, equations (24) and (26a)–(26d) immediately tell us that we want $\tilde{\hat{\mathcal{H}}}$ to contain terms such as $\hat{I}_i^+$. Since we are using the internal homonuclear dipolar coupling Hamiltonian $\hat{\mathcal{H}}_{zz}$ as that which is to be manipulated in order to develop the multiple quantum coherence according to equation (27), we realize that we shall always be dealing with products between spins 1 and 2 containing terms such as $\hat{I}_{m1}\hat{I}_{m2}$, with $m = x, y, z$.

To begin to think about how rotations in spin space affect the two-body homonuclear dipolar Hamiltonian $\hat{\mathcal{H}}_{zz}$, it is useful to remember[13] that the effect of a rotation of the mth component of angular momentum, $\hat{I}_m$ by the operation

$$\begin{aligned}\hat{R}_j(\theta)\hat{I}_m &= \exp(\mathrm{i}\theta\hat{I}_j)\hat{I}_m \exp(-\mathrm{i}\theta\hat{I}_j) \\ &= \hat{I}_m \cos(\theta\epsilon_{jmp}) - \hat{I}_p \sin(\theta\epsilon_{jmp})\end{aligned} \tag{27}$$

where ϵ_{jmp} is zero if any two of j, m, and p are the same, unity if j, m, and p represent some cyclic order of x, y, and z, and -1 if the order is anticyclic. Then a result found after some algebra is that a rotation of the two-body Hamiltonian for spins 1 and 2, $\hat{\mathcal{H}}_{zz}$, by ξ about the y axis, followed by a rotation by ϕ about the z axis, yields

$$\begin{aligned}\hat{R}_z(\phi)\hat{R}_y(\xi)\hat{\mathcal{H}}_{zz} = {} & \tfrac{1}{2}\omega_{\mathrm{D}}(3\cos^2\xi - 1)\hat{\mathcal{H}}_{zz} \\ & -\tfrac{3}{2}\omega_{\mathrm{D}}(\hat{I}_{z1}\hat{I}_2^+ + \hat{I}_1^+\hat{I}_{z2})\mathrm{e}^{-\mathrm{i}\phi}\sin\xi\cos\xi \\ & +\tfrac{3}{2}\omega_{\mathrm{D}}(\hat{I}_1^+\hat{I}_2^+\mathrm{e}^{2\mathrm{i}\phi} + \hat{I}_1^-\hat{I}_2^-\mathrm{e}^{-2\mathrm{i}\phi}) \\ & \times \sin^2\xi\end{aligned} \tag{28}$$

The interesting result shown by equation (28) is that a general rotation of $\hat{\mathcal{H}}_{zz}$ in spin space yields a propagator (the exponential of the rotated Hamiltonian) containing populations ($\hat{\mathcal{H}}_{zz}$), single quantum terms ($\hat{I}_1^{\pm}\hat{I}_{z2}$) and double quantum terms ($\hat{I}_1^{\pm}\hat{I}_2^{\pm}$). As a special case of this result, we illustrate the formation of a two-quantum propagator under a particularly simple periodic and cyclic sequence.[11] This is the sequence (τ, 90°_x 4τ, $90^\circ_{\bar{x}}$, τ), which we shall denote by x, $\bar{x}$. We assume ideal delta function pulses. Under this sequence, the operator $\tilde{\hat{I}}_z(t)$ is as follows:

$$0 \le t < \tau: \quad \tilde{\hat{I}}_z = 1 \cdot \hat{I}_z = \hat{I}_z \tag{29a}$$

$$t = \tau: \quad \tilde{\hat{I}}_z = \hat{R}_{90x}\hat{I}_z = -\hat{I}_y \tag{29b}$$

$$\tau < t < 5\tau: \quad \tilde{\hat{I}}_z = -\hat{I}_y \tag{29c}$$

$$t = 5\tau: \quad \tilde{\hat{I}}_z = \hat{R}_{90x} \cdot 1 \cdot \hat{R}_{90x}\hat{I}_z = \hat{I}_z \tag{29d}$$

$$5\tau < t \le 6\tau: \quad \tilde{\hat{I}}_z = \hat{I}_z \tag{29e}$$

Then, for example, in the time interval $0 \le t < \tau$, $\tilde{\hat{\mathcal{H}}}_{zz} = \hat{\mathcal{H}}_{zz}$ [see equation (12)]. From an observation of the values of $\tilde{\hat{I}}_z(t)$, and the recognition that $\hat{\mathcal{H}}_{kk}$ contains the product $\tilde{\hat{I}}_k\tilde{\hat{I}}_k$ with $k = x, y, z$, it is possible to infer the values of $\tilde{\hat{\mathcal{H}}}_{zz}(t)$, immediately, and thus to calculate the average Hamiltonian corresponding to $\hat{\mathcal{H}}_{zz}$ to zeroth order:

$$\tilde{\hat{\mathcal{H}}}zz^{(0)} = \frac{1}{6\tau}\int_0^{6\tau} \mathrm{d}t\, \tilde{\hat{\mathcal{H}}}_{zz} = \tfrac{1}{3}(\hat{\mathcal{H}}_{zz} + 2\hat{\mathcal{H}}_{yy}) \tag{30}$$

With the identity $\sum_k \hat{\mathcal{H}}_{kk} = 0$, we find that, under the above sequence,

$$\tilde{\hat{\mathcal{H}}}_{zz}^{(0)} \simeq (\hat{\mathcal{H}}_{xx}\hat{\mathcal{H}}_{yy} + 2\hat{\mathcal{H}}_{yy}) = \hat{\mathcal{H}}_{yy} - \hat{\mathcal{H}}_{xx} \tag{31}$$

The reader will want to verify that under the sequence y, $\bar{y} \equiv (\tau, 90^\circ_y, 4\tau, 90^\circ_{\bar{y}}, \tau)$ the average homonuclear dipolar Hamiltonian is the negative of that found in equation (31), i.e. is proportional to $\hat{\mathcal{H}}_{xx} - \hat{\mathcal{H}}_{yy}$. Thus this sequence can be used to produce an average Hamiltonian that will act to reverse, in time, the effect of the average of the average Hamiltonian $\hat{\mathcal{H}}_{yy} - \hat{\mathcal{H}}_{xx}$ that was used to produce the MQC. As will be seen, this reconversion is performed in such a manner that the information content associated with the MQC is not lost. The means of doing so (see below) is to phase-shift the two quantum excitation sequence x, $\bar{x}$ with respect to the two quantum reconversion sequence y, $\bar{y}$ in steps of $2\pi/k_{\max}$, where $k_{\max}$ is the highest order of MQC to be observed.

With $\hat{I}^{\pm} = \hat{I}_x \pm \mathrm{i}\hat{I}_y$, we find that the average two-body homonuclear dipolar Hamiltonian under the two quantum excitation sequence x, $\bar{x}$ is proportional to

$$\hat{I}_1^+\hat{I}_2^+ + \hat{I}_1^-\hat{I}_2^- \tag{32}$$

for the pair of spins $\boldsymbol{I}_1$ and $\boldsymbol{I}_2$.

Now consider how this sequence can be used to develop multiple quantum coherence for an ensemble of *pairs* of dipolar coupled spins $\boldsymbol{I}_1$ and $\boldsymbol{I}_2$. We might anticipate in advance that for this simple case, using a two quantum propagator, all that will be seen are populations, and two quantum coherence. Under this sequence, repeated for n cycle times, $\tau_{\mathrm{c}} = 6\tau$, the time dependence of the density matrix becomes

$$\hat{\rho}(nt_{\mathrm{c}}) = \hat{U}_{2\mathrm{Q}}\hat{\rho}(0)\hat{U}_{2\mathrm{Q}}^{-1} \tag{33}$$

where $\hat{U}_{2\mathrm{Q}}$ is, to zeroth order,

$$\hat{U}_{2\mathrm{Q}} = \exp[-\tfrac{1}{2}\mathrm{i}nt_{\mathrm{c}}\omega_{\mathrm{D}}(\hat{I}_1^+\hat{I}_2^+ + \hat{I}_1^-\hat{I}_2^-)] \tag{34}$$

Then, with $\theta = \frac{1}{2}nt_{\mathrm{c}}\omega_{\mathrm{D}}$, equations (24) and (25) yield

$$\begin{aligned}\hat{\rho}(nt_{\mathrm{c}}) &\simeq \hat{I}_{z1} + \hat{I}_{z2} + \mathrm{i}\theta[\hat{I}_1^+\hat{I}_2^+ + \hat{I}_1^-\hat{I}_2^-, \hat{I}_{z1} + \hat{I}_{z2}] \\ &\quad + (i\theta)^2[\hat{I}_1^+\hat{I}_2^+ + \hat{I}_1^-\hat{I}_2^-, [\hat{I}_1^+\hat{I}_2^+ + \hat{I}_1^-\hat{I}_2^-, \hat{I}_{z1} + \hat{I}_{z2}]]/2! + \ldots \\ &= \hat{I}_{z1} + \hat{I}_{z2} - 2\mathrm{i}\theta(\hat{I}_1^+\hat{I}_2^+ + \hat{I}_1^-\hat{I}_2^-)\end{aligned} \tag{35}$$

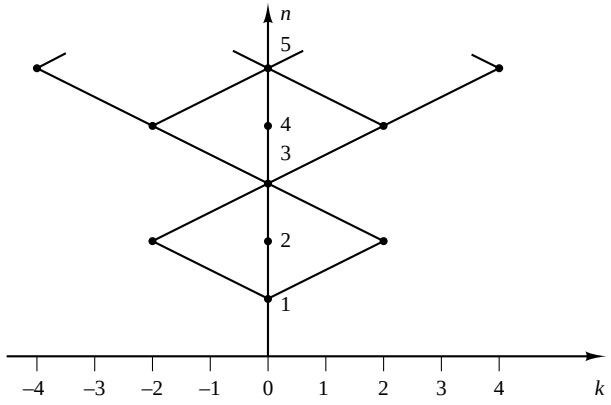

Figure 1 Selection rule for an n-spin operator after excitation with a double quantum propagator. The allowed values are $k = \pm 2, \pm 6, \ldots$, for n even, and $k = 0, \pm 4, \pm 8, \ldots$, for n odd

Only the first two terms in the series represented by equations (24) and (25) are nonzero. The remaining terms vanish. Only populations and double quantum coherence remains. At values of θ near zero, i.e., at times nt_c that are small compared with the inverse of the dipolar linewidth ω_D^{-1}, there exist only populations. As nt_c becomes of the order of the dipolar linewidth, two quantum coherence makes its appearance. No more than two quantum coherence is ever seen, regardless of how long the system is allowed to evolve, as one would physically expect from an ensemble consisting of coupled pairs of spins $\frac{1}{2}$. The reader will want to verify that for this representation of $\hat{\rho}(nt_c)$ only the terms ρ_{11}, ρ_{22}, ρ_{33}, ρ_{13}, and ρ_{31} are nonzero within the triplet basis set $|I, I_z\rangle$:

$$|m\rangle = |3\rangle = |1, 1\rangle = |\alpha\alpha\rangle \tag{36a}$$

$$|m-1\rangle = |2\rangle = |1, 0\rangle = \sqrt{\tfrac{1}{2}}|\alpha\beta + \beta\alpha\rangle \tag{36b}$$

$$|m-2\rangle = |1\rangle = |1, -1\rangle = |\beta\beta\rangle \tag{36c}$$

by performing the calculations $\langle m|\hat{\rho}(nt_c)|m-k\rangle$.

The results just calculated for an ensemble of dipolar coupled spin-$\frac{1}{2}$ pairs indicate that, under the propagator $\hat{U}_{2Q}$ developed by the sequence $(\tau, 90^\circ_x, 4\tau, 90^\circ_{\bar{x}}, \tau)$, the selection rules are such that populations and double quantum coherence is observed for an ensemble of pairs of dipolar coupled spins $\frac{1}{2}$. More generally, these selection rules for ensembles of n coupled spins may be exhibited by the diagram shown in Figure 1. This diagram states that, under this sequence, double quantum coherence will be exhibited by ensembles of 2, 4, 6, ... coupled spins, four quantum coherence will be exhibited by ensembles of 5, 7, 9, ... coupled spins, etc.

5 DETECTION OF MULTIPLE QUANTUM COHERENCE

We must now consider more closely what was meant by the past statement that the MQC, once produced, must be transferred to SQC in a manner that reflects the MQC previously produced. As a thought experiment to begin the process, recall the inversion–recovery experiment for measuring T_1. In this case, the system is prepared in a state of nonequilibrium populations by an inverting 180° pulse. After a time τ, during which the system is allowed to evolve under 'T_1 processes', these populations are converted into SQC using a 90° pulse. The initial intensity of the decay after the 'readout' 90° pulse is used, as a function of τ, to calculate T_1. A similar reasoning applies to detecting MQC. The MQC is developed as a function of multiples of the production sequence cycle time t_c. This development is only observable if it is converted into SQC. During the development, therefore, the MQC is manipulated in such a manner that, when converted back into SQC, the information content of the MQC is contained in the initial intensity of the SQC which is detected.

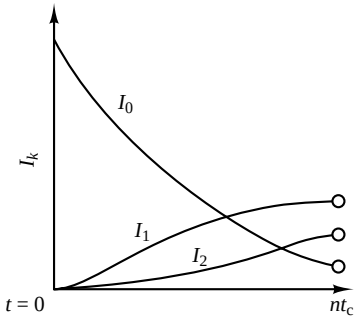

Figure 2 Time evolution of the order of n quantum coherence using a single quantum propagator. The intensity of (I_0) decreases as spin pairs begin to couple to develop the higher order of MQC and build up their intensity (I_1 and I_2)

To form a picture of how this works, it is useful to think about how the different orders of n quantum coherence evolve with time. As indicated in the example in equation (35), the higher orders of MQC develop as $\theta \approx nt_c\omega_{Dij}$ increases for the i,jth pair of spins. Therefore, it seems reasonable that the evolution of, e.g., populations, SQC, and two-quantum coherence (DQC) might look as shown in Figure 2. I_0 represents populations, I_1 the intensity of single quantum coherence, I_2 the intensity of DQC, etc. Initially, one starts with populations. As spin pairs begin to couple to form higher orders of n quantum coherence, there is a net loss in populations, and a build up [in the particular example for which the calculation using equation (35) was made], first of DQC, the second term in the expansion of the evolution of $\hat{\rho}$, and then of higher orders of MQC as time increases. In the example shown in Figure 2, we assume that we are allowed to build MQC in steps of single quanta, and we shall later provide a single quantum propagator $\hat{U}_{1Q}$ that allows this development to be performed.

Given the development of MQC shown in Figure 2, caused by the single quantum propagator U_{1Q}, it is simple to conceive how one reverses the process to convert back to an observable SQC. One simply causes the system to evolve under the propagator $\hat{U}_{1Q}^{-1}$. Since $\hat{U}_{1Q}$ will be of the form $\exp(-i\tilde{\hat{\mathcal{H}}}nt_c)$, with $\tilde{\hat{\mathcal{H}}}$ being an average Hamiltonian created by manipulating the homonuclear dipolar interaction, time reversal is achieved by manipulating the homonuclear dipolar Hamiltonian such that from time nt_c to $2nt_c$ the average Hamiltonian is $-\tilde{\hat{\mathcal{H}}}$. In the case of the two quantum propagator, we have seen that the sequence $(\frac{1}{4}\tau, 90^\circ_x, \tau, 90^\circ_{\bar{x}}, \frac{1}{4}\tau)$ produces the average Hamiltonian proportional to $\hat{\mathcal{H}}_{yy} - \hat{\mathcal{H}}_{xx}$. We have pointed out that the sequence $(\frac{1}{4}\tau, 90^\circ_y, \tau, 90^\circ_{\bar{y}}, \frac{1}{4}\tau)$ results in

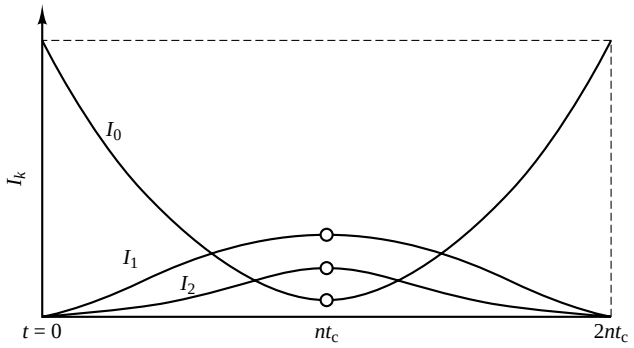

Figure 3 The MQC for higher orders are first created over a time period nt_c, and then collected this MQC back into ZQC at the time $2nt_c$ by using the negative of the average Hamiltonian. Aside from relaxation, the preparation ($0 \leq t < nt_c$) and mixing period ($nt_c \leq t < 2nt_c$) exactly mirror each other. This diagram illustrates the statement of the cyclic properties of $\hat{U}_{rf}$. At the end of $2nt_c$, I_0 ($t = 0$) = $I_0(t = 2nt_c)$

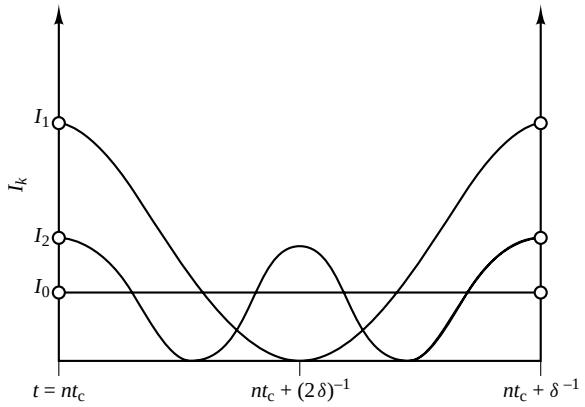

Figure 4 The behavior of ZQC, SQC, and DQC with a frequency offset δ (in Hz), after the preparation period nt_c. The n quantum coherence has the property of the cosine function, $I_n \propto \cos(n\delta/\text{Hz})$. See equation (42)

the average homonuclear dipolar Hamiltonian $\hat{\mathcal{H}}_{xx} - \hat{\mathcal{H}}_{yy} \equiv -(\hat{\mathcal{H}}_{yy} - \hat{\mathcal{H}}_{xx})$. Thus, the application of the sequence

$$(\tfrac{1}{4}\tau, 90^\circ_x, \tau, 90^\circ_x, \tfrac{1}{4}\tau)n, (\tfrac{1}{4}\tau, 90^\circ_y, \tau, 90^\circ_y, \tfrac{1}{4}\tau)n$$

would first create the MQC over a time of n cycle times t_c, and then, by time reversal accomplished by using the negative of the average Hamiltonian during the preparation period, 'collect' this MQC back into zero quantum coherence (ZQC) at time $2nt_c$. The process might be visualized as indicated in Figure 3.

At this point, however, there is no information content in the ZQC shown in Figure 3 at time $2nt_c$ that would be indicative of the MQC created during the times nt_c.

Therefore, as a second thought experiment, dictated by the knowledge that different orders of MQC (see below) oscillate at multiples of the SQC under a frequency offset, let us assume that after the production period nt_c, a frequency offset δ (in Hz) is imposed upon the experiment. Then the behavior of ZQC, SQC, and DQC might appear as indicated in Figure 4. The ZQC does not oscillate under an offset. The SQC will oscillate with period δ^{-1}. The DQC will oscillate with period $(2\delta)^{-1}$, etc.

Now suppose that the evolution time for MQC under the offset δ were set to be $(2\delta)^{-1}$. Then at that time I_1 would be zero, I_0 would retain its value at time $t = nt_c$, and I_2 would have oscillated to its value at time $(2\delta)^{-1}$, the period of its oscillation. Therefore, if the reconversion from nonvanishing off-diagonal elements of the density operator back to populations represented by diagonal elements were initiated at time $nt_c + (2\delta)^{-1}$, in the absence of an offset, the value of I_0 at time $2nt_c + (2\delta)^{-1}$ would contain *no contribution* from the SQC. The SQC monitored as the value of the initial intensity of the FID after a 90° pulse at time $nt_c + (2\delta)^{-1}$ would therefore be lower than that in the absence of an offset. One way of visualizing this result is shown in Figure 5, where different symbols are used to trace the imagined evolution of MQC back into populations after time $nt_c + (2\delta)^{-1}$. The symbol I_n, $n \geq 1$, means the n quantum coherence. The symbol I_n^0 means the contribution of the n quantum coherence developed at time $nt_c + (2\delta)^{-1}$ back into populations. The net

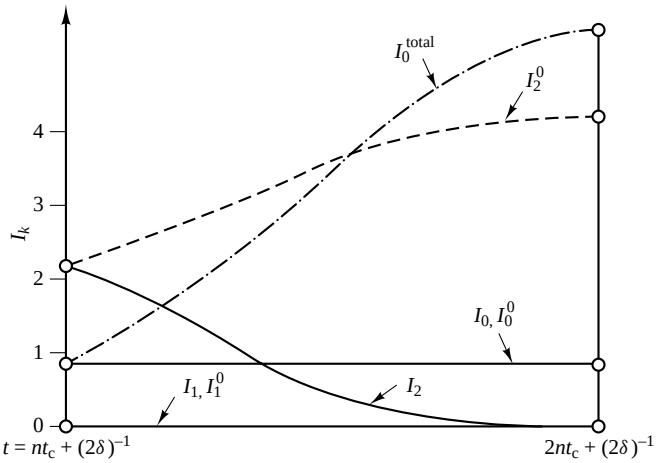

Figure 5 The behavior of the MQC at the evolution time $(2\delta)^{-1}$. $I0/k$ is the development of ZQC with k quantum coherence as its parent

magnetization associated with population differences, observed as the initial intensity of the FID after a 'readout' pulse converting population differences into SQC, is labeled I_0^{tot}. Clearly, I_0^{tot} will oscillate with time under a frequency offset during the evolution period, and this oscillation provides the means of detecting MQC therein contained, as indicated more analytically below.

The scheme of production and reconversion of MQC corresponding to the time development shown in Figure 3, i.e., in the absence of an offset, meaning in the absence of an evolution period, is indicated in Figure 6; a single quantum propagator acts on the ensemble of coupled spins from time zero to time nt_c, and the inverse of that propagator acts for an equal period of time afterwards. The ZQC at time $2nt_c$ is converted into observable SQC by a 90° 'readout' pulse, and is represented by the initial value of the FID. In the absence of irreversibility, the initial amplitude of the FID detected at time $2nt_c$ will be the same as that detected at time zero after a 'readout' 90° pulse. The equality of these two amplitudes, incidentally, is one means of detecting one's ability to perform time reversal effectively, which is a measure of the perfection of the pulse sequences used.

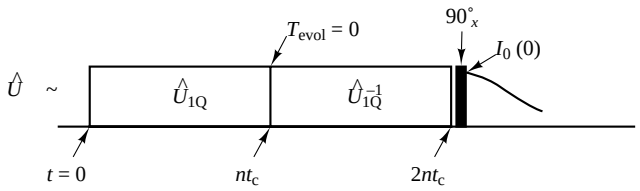

Figure 6 The scheme of a two-dimensional NMR pulse sequence, composed of preparation, evolution, mixing and detection periods, is adapted to develop multiple quantum coherence. The evolution period is set at zero

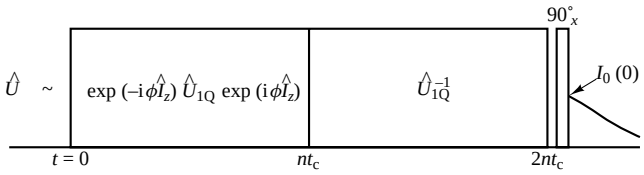

Figure 7 The arrangement of pulse sequence and the way of phase shifting during the multiple quantum experiment. The phases only of the pulses in the preparation period are shifted at the same time with the aid of a digital phase shifter, while the phases of the pulses in the mixing period remain unchanged

The imposition of a frequency offset δ during the evolution period, to detect MQC at the end of the mixing period, is not without its problems. One problem is that there is irreversible time evolution of the ensemble during the evolution period due to T_2 processes. A means of avoiding this problem is to realize that imposition of a phase shift[14] ϕ *during the preparation period* $0 \leq t < nt_c$ is formally equivalent to imposition to a frequency offset, and causes the same oscillations of the various orders of MQC as would be observed under a frequency offset. The effect of a phase increment during the preparation period on the detected signal intensity at the end of the mixing period is now considered. In the absence of an evolution period, the initial intensity of the FID detected at the end of the mixing period $t = 2nt_c$ is

$$\langle \hat{I}_z(t = 2nt_c)\rangle = \mathrm{Tr}\{\hat{\rho}(t = 2nt_c)\hat{I}_z\} \tag{37}$$

But

$$\hat{\rho}(2nt_c) = \hat{U}_{1Q}^{-1}\hat{U}_{1Q}\hat{I}_z\hat{U}_{1Q}^{-1}\hat{U}_{1Q} = \langle \hat{I}_z(t = 0)\rangle \tag{38}$$

in the absence of irreversibility due to imperfections, and interactions other than homonuclear dipolar coupling. Looking more carefully at the combination of equations (37) and (38), and leaving the subscript off the propagators $\hat{U}$ for simplicity, we find that

$$\begin{aligned}
\langle \hat{I}_z(t = 2nt_c)\rangle &= \mathrm{Tr}\{\hat{U}^{-1}\hat{U}\hat{I}_z\hat{U}^{-1}\hat{U}\hat{I}_z\} \\
&= \mathrm{Tr}\{\hat{U}\hat{I}_z\hat{U}^{-1}\hat{U}\hat{I}_z\hat{U}^{-1}\} \\
&= \sum_r \langle r|\hat{U}\hat{I}_z\hat{U}^{-1}\hat{U}\hat{I}_z\hat{U}^{-1}|r\rangle \\
&= \sum_{r,s} \langle r|\hat{U}\hat{I}_z\hat{U}^{-1}|s\rangle\langle s|\hat{U}\hat{I}_z\hat{U}^{-1}|r\rangle \\
&= \sum_{r,s} |\langle r|\hat{U}\hat{I}_z\hat{U}^{-1}|s\rangle|^2
\end{aligned} \tag{39}$$

Equation (39) has an interesting interpretation. The quantity $\hat{U}(nt_c,0)\hat{I}_z\hat{U}^{-1}(nt_c,0)$ measures how much multiple quantum coherence has been developed under the propagator $\hat{U}$. The quantity $\langle r|\hat{U}\hat{I}_z\hat{U}^{-1}|s\rangle$ measures the k quantum coherence, where $k = r - s$, as described earlier, and as will be again illustrated shortly. The term $|\langle r|\hat{U}\hat{I}_z\hat{U}^{-1}|s\rangle|^2$ is the intensity of the k quantum coherence. Thus the quantity detected as the SQC by a proper 'readout' pulse at time $t = 2nt_c$ is the result of producing multiple quantum coherence under a propagator $\hat{U}$ acting for a time $t = nt_c$, and converting this coherence back into populations via the inverse propagator $\hat{U}^{-1}$ during an equal time nt_c.

Now we need to ask: 'What is the effect of a phase change ϕ imposed on all of the pulses during the preparation period, but not on the pulses during the mixing period, at the total evolution time $t = 2nt_c$?' In this experiment, the 'evolution period' identified as the time between the preparation and mixing periods, is zero. A phase change ϕ is effected by physically rotating all excitation pulses during the preparation period by ϕ. This means that a 180°_x pulse, for example, becomes $180^\circ_{x+\phi}$, and a $180^\circ_{\bar{x}}$ pulse becomes $180^\circ_{\bar{x}+\phi}$, etc. The operator form of $\hat{U}$ rotated by ϕ is just $\hat{U}_\phi = \exp(-i\phi)\hat{I}_z\hat{U}\exp(i\phi\hat{I}_z)$. The experimental arrangement is indicated in Figure 7.

The expectation value of $\hat{I}_z$ detected at times $t = 2nt_c$ will be dependent upon ϕ, as follows:

$$\begin{aligned}
\langle \hat{I}_z(\phi, 2nt_c)\rangle &= \mathrm{Tr}\{\hat{U}(2nt_c, 0)\hat{\rho}(0)\hat{U}^{-1}(2nt_c, 0)\hat{I}_z\} \\
&= \mathrm{Tr}\{\hat{U}_{\phi=0}^{-1}(2nt_c, nt_c)\hat{U}_\phi(nt_c, 0)\hat{I}_z\hat{U}_\phi^{-1}(nt_c, 0) \\
&\quad \times \hat{U}_{\phi=0}(2nt_c, nt_c)\hat{I}_z\} \\
&\equiv \mathrm{Tr}\{\hat{U}_0^{-1}\hat{U}_\phi\hat{I}_z\hat{U}_\phi^{-1}\hat{U}_0\hat{I}_z\} \\
&= \sum_{r,s} \langle r|\exp(-i\phi\hat{I}_z)\hat{U}\exp(i\phi\hat{I}_z)\hat{I}_z \\
&\quad \times \exp(-i\phi\hat{I}_z)U^{-1}\exp(i\phi\hat{I}_z)|s\rangle\langle s|\hat{U}\hat{I}_z\hat{U}^{-1}|r\rangle \\
&= \sum_{k=r-s} \mathrm{e}^{-ik\phi}|\langle r|\hat{U}\hat{I}_z\hat{U}^{-1}|s\rangle|^2
\end{aligned} \tag{40}$$

We have noted that the quantity $\hat{U}\hat{I}_z\hat{U}^{-1}$ represents the time development of $\hat{I}_z$ under the propagator $\hat{U}$, in this case a propagator developing MQC. Nonzero values of $\langle r|\hat{U}\hat{I}_z\hat{U}^{-1}|s\rangle$ indicate nonzero values of $r - s = k$ quantum coherence $|\langle r|\hat{U}\hat{I}_z\hat{U}^{-1}|s\rangle|^2$ is the intensity of the k quantum coherence.

The result,

$$\langle \hat{I}_z(\phi, 2nt_c)\rangle = \sum_{k=-\infty}^{\infty} \mathrm{e}^{-ik\phi}|\langle r|U I_z U^{-1}|s\rangle|^2 \tag{41}$$

may be compared with the value of the free precession decay of a system containing an ensemble of spins oscillating with intensities A_n at frequencies ω_n with some phase ϕ_n with respect to the phase of detection, chosen to be y for the present example:

$$G(t) = \langle \hat{I}_y(t)\rangle = \sum_n A_n \cos(\omega_n t + \phi_n) \tag{42}$$

The FT to the frequency domain reveals the frequency content of $G(t)$ which, with appropriate phase correction, becomes the frequency spectrum $G(\omega) = F^{-}G(t)$. By direct analogy, the result (equation (41)) is the superposition in the phase domain $G(\phi)$ of oscillations with intensities $A_k = \langle r|\hat{U}\hat{I}_z\hat{U}^{-1}|s\rangle|^2$, and oscillations in the ϕ domain specified by k:

$$G(\phi) = \sum_k A_k \cos(k\phi + \delta_k) \tag{43}$$

The ϕ dependence is experimentally mapped by incrementing the phase of all pulses during the preparation period by $\Delta\phi$, in a series of m experiments at fixed preparation and mixing periods nt_c, and observing the initial value of the FID following a 90° sampling pulse immediately after $t = 2nt_c$. In practice the signal-to-noise ratio is increased if the entire on-resonant decay is integrated from a period after the receiver has recovered from the overload of the 90° pulse until no further signal is present. For strongly dipolar coupled systems with a properly operating solid state spectrometer operating at, say, 220 MHz for protons, this means a dead time of about 3 μs, and an integration period of less than 1 μs.

The k dependence of $G(\phi)$ is determined from the ϕ FT. Though it is not obvious from the above discussion, $G(\phi)$ is symmetric in k, so only the cosine transform is needed:

$$G(k) = \frac{1}{\sqrt{2\pi}} \int_0^\infty \mathrm{d}\phi\, G(\phi) \cos k\phi \tag{44}$$

Therefore, both positive and negative coherences are detected simultaneously. One need use $k_{\max}$ phase shifts $\delta\phi_i$,

$$0 \leq \delta\phi_i \leq \pi \tag{45}$$

in steps $\Delta\phi = \pi/k_{\max}$ to obtain all of the information necessary for the production of a multiple quantum spectrum $G(k)$ versus k, via Fourier transformation of the oscillatory signal $G(\phi)$ collected from the initial values of the FIDs after the multiple quantum production and collection sequences (i.e., after the preparation and mixing periods). This is to say that to see a multiple quantum spectrum $G(k)$ versus k, with k extending to $k_{\max}$, one carries out $n = k_{\max} + 1$ experiments with phase shifts $\Delta\phi_1 = 0$, $\Delta\phi_2 = \pi/k_{\max}$, $\Delta\phi_3 = 2\pi/k_{\max}$, ... ,$\Delta\phi_n = \pi$. In the absence of irreversibility, the value of $G(\phi)$ versus ϕ is symmetric about $\phi = \pi$. Therefore the values of $G(\phi)$ in the range $\pi < \phi \leq 2\pi$ are obtained from the data in the range $0 \leq \phi \leq \pi$; i.e. $G(2\pi) = G(0)$, $G(2\pi - \pi/k_{\max}) = G(\pi/k_{\max})$, etc. A suitably large number (e.g., 100) of periods of $G(\phi)$ versus ϕ are then stored as an array that can be apodized by the function $e^{-a\phi}$ and Fourier transformed on ϕ to produce the multiple quantum spectrum $G(k)$ versus k. This spectrum will show peaks differing by units of 2 quanta each if a two quantum propagator is used, or in steps of one quantum each if a single quantum (see below) is used.

The selection rules for exciting single quantum coherence are shown in Figure 8. With the system prepared only as polarization ($\boldsymbol{I}_z \neq 0$), two coupled spins ($n = 2$) will contribute single quantum coherence and zero quantum coherence, three coupled spins will contribute zero and double quantum coherence, etc.

An example of experimental data obtained for $G(\phi)$, with $0 \leq \phi \leq 2\pi$, using a single quantum propagator on adamantane,

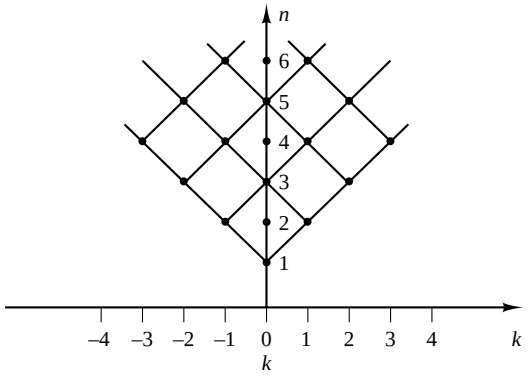

Figure 8 Selection rules for the single quantum propagator used in this work

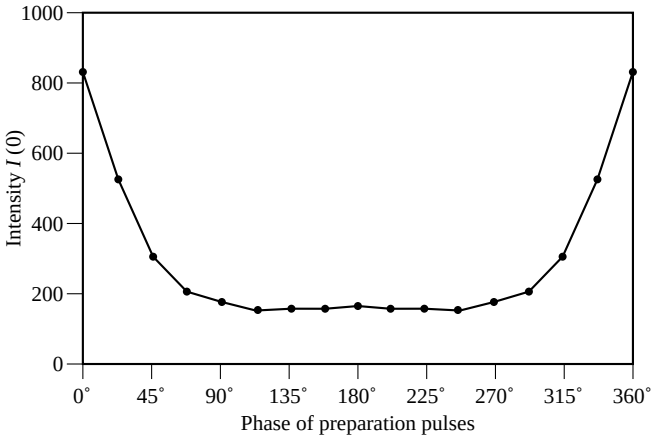

Figure 9 The intensity changes with the phase increment ($\Delta\phi = 22.5°$) of the preparation pulses, plotted in the phase domain (adamantane). The FID of each phase is transformed to frequency domain, and each point on the plot is obtained by integrating the whole spectrum area, normally from −50 kHz to 50 kHz

with phase increments chosen so as to see $k_{\max} = 8$ and with 312 μs of excitation time, is shown in Figure 9. These points repeated 128 times to fit to 2K size, and tapered by an appropriate apodization function, are shown in Figure 10. The baseline decay represents populations, so it may be subtracted from the oscillations shown in Figure 10 using a baseline adjustment technique before performing the transform on ϕ to yield the multiple quantum spectrum shown in Figure 11. Note that the zero quantum peak is not present in this spectrum.

We now discuss the development of multiple quantum coherence using a single quantum propagator.

6 A SINGLE QUANTUM PROPAGATOR

The development of MQC under pulse sequences resulting in a single quantum propagator for dipolar coupled spin-$\frac{1}{2}$ systems was first reported and discussed by Suter et al.[15] in 1987. The sequence that we have used to produce the data shown in Figures 9–11 was developed by M. Goldman,[16] and is essentially identical to that published in 1988 by the Pines group.[17]

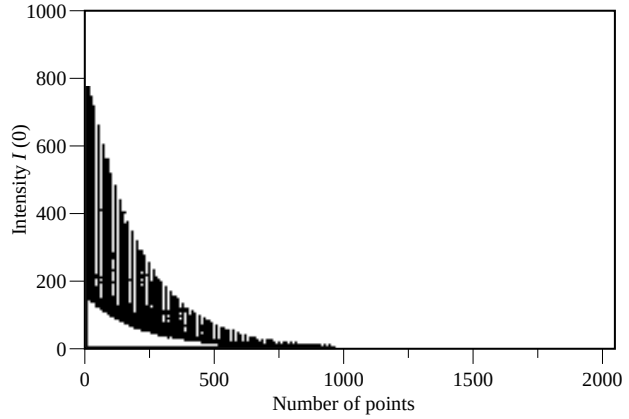

Figure 10 An extension of data point and tapering are performed to generate a data set in the phase domain. Figure 9 was repeated until the number of data points was 2K, and then tapered by using an appropriate apodization function

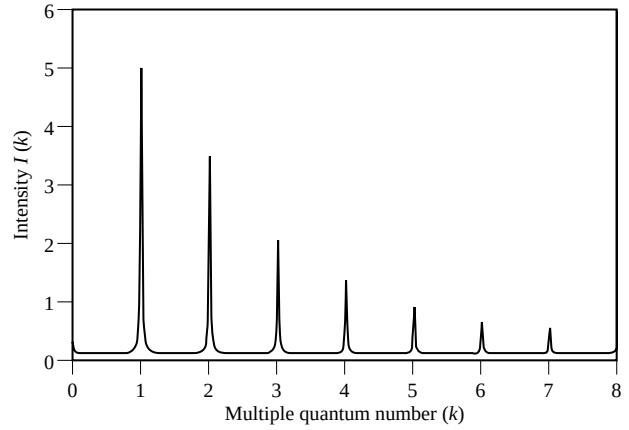

Figure 11 The Fourier transformed spectrum, from phase domain to multiple quantum number domain. The intensity distribution over the multiple quantum number $k = 8$ can be seen. The preparation time was 260 μs. The highest number of quanta $k_{\max}$ is not seen, due to the increment of the phase used

This sequence is shown in Figure 12. Important to understanding how this sequence works is an understanding of the development of internal Hamiltonians during finite pulses, an example of which is in Chapter 5, Section V of Pines[8] for the case of the 'flip-flop' phase tuning sequence (τ, 90°_x, τ, $90^\circ_{\bar{x}}$, τ). Applied to the sequence of Figure 12, the calculation proceeds as follows: consider the time interval $0 \le t < \frac{1}{4}\tau$. Immediately after a perfect delta function rotation by 45°_x at $t = 0$, $\hat{\tilde{\mathcal{H}}}_{zz}$ will be

$$\hat{R}_x(45^\circ)\hat{\mathcal{H}}_{zz} = \tfrac{1}{2}(\hat{\mathcal{H}}_{zz} + \hat{\mathcal{H}}_{yy}) - \tfrac{3}{2}(\hat{I}_{z1}\hat{I}_{y2} + \hat{I}_{y1}\hat{I}_{z2}) \quad (46)$$

The contribution to $\hat{\tilde{\mathcal{H}}}^{(0)}_{zz}$ for this period will then be

$$\frac{1}{t_c}\int_0^{\tau/4} \hat{\tilde{\mathcal{H}}}_{zz}\,\mathrm{d}t = \frac{1}{t_c}\frac{\tau}{8}[\hat{\mathcal{H}}_{zz} + \hat{\mathcal{H}}_{yy} - 3(\hat{I}_{z1}\hat{I}_{y2} + \hat{I}_{y1}\hat{I}_{z2})] \quad (47)$$

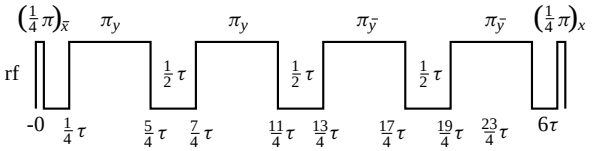

Figure 12 Pulse sequence for the single quantum propagator developed by Goldman,[16] and used in this work

During the period $\frac{1}{4}\tau \le t < \frac{5}{4}\tau$,

$$\begin{aligned}\hat{\tilde{\mathcal{H}}}_{zz}(t) &= \hat{R}_{45x}\hat{R}_{\xi y}\hat{\mathcal{H}}_{zz} \\ &= \hat{R}_{45x}\{\hat{\boldsymbol{I}}_1\cdot\hat{\boldsymbol{I}}_2 - 3[\hat{I}_{z1}\hat{I}_{z2}\cos^2\xi + \hat{I}_{x1}\hat{I}_{x2}\sin^2\xi \\ &\quad +(\hat{I}_{z1}\hat{I}_{x2} + \hat{I}_{x1}\hat{I}_{z2})\sin\xi\cos\xi]\} \\ &= \hat{\boldsymbol{I}}_1\cdot\hat{\boldsymbol{I}}_2 - \tfrac{3}{2}\{(\hat{z}_1\hat{z}_2 + \hat{y}_1\hat{y}_2 + \hat{z}_1\hat{y}_2 + \hat{y}_1\hat{z}_2)\cos^2\xi \\ &\quad +2\hat{x}_1\hat{x}_2\sin^2\xi \\ &\quad +\sqrt{2}[(\hat{z}_1 + \hat{y}_1)\hat{x}_2 + \hat{x}_1(\hat{z}_2 + \hat{y}_2)]\sin\xi\cos\xi\} \quad (48)\end{aligned}$$

where $\hat{z}_1\hat{z}_2$ is now used to designate $\hat{I}_{z1}\hat{I}_{z2}$, etc., to ease the notation.

During the period $\frac{1}{4}\tau < t < \frac{5}{4}\tau$, the flip angle ξ varies from zero to 180°. In the interval $\frac{1}{4}\tau < t \le \frac{5}{4}\tau$, the contribution of $\hat{\tilde{\mathcal{H}}}_{zz}$ to $\hat{\mathcal{H}}^{(0)}_{zz}$ can be calculated by assuming the flip angle ξ to be linear in t, so $\xi = \pi(t - \frac{1}{4}\tau)/\tau$, and $\mathrm{d}t = \tau\,\mathrm{d}\xi/\pi$. Then, in the period $\frac{1}{4}\tau \le t < \frac{5}{4}\tau$, or $0 \le \xi < \pi$, the contribution to $\hat{\mathcal{H}}^{(0)}_{zz}$ is

$$\begin{aligned}\hat{\tilde{\mathcal{H}}}_{zz(0)} &= \frac{1}{t_c}\int \hat{\tilde{\mathcal{H}}}_{zz}(t)\,\mathrm{d}t \\ &= \frac{1}{t_c}\left\{\tau\hat{\boldsymbol{I}}_1\cdot\hat{\boldsymbol{I}}_2 - 3[(\hat{z}_1\hat{z}_2 + \hat{y}_1\hat{y}_2 + \hat{z}_1\hat{y}_2 + \hat{y}_1\hat{z}_2)]\right. \\ &\quad \times\frac{\tau}{2\pi}\int_0^\pi \cos^2\xi\,\mathrm{d}\xi + \hat{x}_1\hat{x}_2\frac{\tau}{\pi}\int_0^\pi \sin^2\xi\,\mathrm{d}\xi \\ &\quad \left.+[(\hat{z}_1 + \hat{y}_1)\hat{x}_2 + \hat{x}_1(\hat{z}_2 + \hat{y}_2)]\frac{\tau}{\pi\sqrt{2}}\int_0^\pi \sin\xi\cos\xi\,\mathrm{d}\xi\right\} \\ &= \frac{\tau}{2t_c}[\tfrac{1}{2}(\hat{\mathcal{H}}_{zz} + \hat{\mathcal{H}}_{yy}) + \hat{\mathcal{H}}_{xx} - \tfrac{3}{2}(\hat{z}_1\hat{y}_2 + \hat{y}_1\hat{z}_2)] \quad (49)\end{aligned}$$

In the period immediately following $t = \frac{5}{4}\tau$, and before any other pulses are applied,

$$\hat{\tilde{\mathcal{H}}}_{zz} = \tfrac{1}{2}[\hat{\mathcal{H}}_{zz} + \hat{\mathcal{H}}_{yy} - 3(\hat{y}_1\hat{z}_2 + \hat{z}_1\hat{y}_2)] \quad (50)$$

Proceeding in this manner, it may be verified that the sequence shown in Figure 12, with cycle time $t_c = 6\tau$, yields the following values for the average Hamiltonian associated with the homonuclear dipolar coupling Hamiltonian $\hat{\mathcal{H}}_{zz}$ and the chemical shift $\hat{\mathcal{H}}_{cs} = \sum_{zz}\hat{I}_z$:

$$\begin{aligned}\hat{\tilde{\mathcal{H}}}_{zz} &= -(\hat{I}_{z1}\hat{I}_{y2} + \hat{I}_{y1}\hat{I}_{z2}) \\ &= -(\hat{I}_{z1}\hat{I}_2^+ - \hat{I}_{z1}\hat{I}_2 + \hat{I}_1^+\hat{I}_{z2} - \hat{I}_1^-\hat{I}_{z2})/2\mathrm{i} \quad (51)\end{aligned}$$

a pure single quantum operator, and $\hat{\tilde{\mathcal{H}}}_{cs}(0) = 0$.

7 RELATED ARTICLES

Average Hamiltonian Theory; CRAMPS; Double Quantum Coherence; Echoes in Solids; Optically Enhanced Magnetic Resonance.

8 REFERENCES

1. R. D. Mattuck, *A Guide to Feynman Diagrams in the Many Body Problem*, 2nd edn., McGraw-Hill, New York, 1976 (reprinted by Dover, New York, 1992).
2. H. Tanaka, T. Terao, and T. Hashi, *J. Phys. Soc. Jpn.*, 1975, **39**, 378.
3. H. Tanaka and T. Hashi, *J. Phys. Soc. Jpn.*, 1974, **39**, 1139.
4. W. P. Aue, E. Bertholdi, and R. R. Ernst, *J. Chem. Phys.*, 1976, **64**, 2229.
5. G. Bodenhausen, in *Progress in Nuclear Magnetic Resonance Spectroscopy*, eds. J. W. Emsley, J. Feeney, and L. H. Sutcliffe, Pergamon Press, Oxford, 1983, Vol. 14, p. 137.
6. D. Weitekamp, in *Advances in Magnetic Resonance*, ed. J. S. Waugh, Academic Press, New York, 1983, Vol. 11, p. 111.
7. M. Munowitz and A. Pines, in *Advances in Chemical Physics*, ed. I. Prigogine, Wiley, New York, 1987, Vol. 66, p. 1.
8. A. Pines, in *Proceedings of the 100th Fermi School on Physics, Varenna, 1986*, ed. B. Maraviglia, North-Holland, Amsterdam, 1988.
9. G. Drobny, *Annu. Rev. Phys. Chem.*, 1985, **262**, 451.
10. Y. S. Yen and A. Pines, *J. Chem. Phys.*, 1983, **78**, 3579.
11. J. Baum, M. Munowitz, A. N. Garroway, and A. Pines, *J. Chem. Phys.*, 1983, **83**, 2015.
12. M. Goldman *Quantum Description of High Resolution NMR in Liquids*, Oxford University Press, Oxford, 1988, Section 2.5.
13. B. C. Gerstein and C. R. Dybowski, *Transient Techniques in NMR of Solids: an Introduction to the Theory and Practice*, Academic Press, San Diego, 1985, Chapters 4 and 5.
14. S. Emid, *Physica B*, 1985, **128**, 79.
15. D. Suter, S. B. Liu, J. Baum, and A. Pines, *Chem. Phys.*, 1987, **114**, 103.
16. M. Goldman, personal discussions during the RMN Summer School organized by J. Virlet, 1987, Les Houches, France.
17. D. N. Shykind, J. Baum, S.-B. Liu, and A. Pines, *J. Magn. Reson*, 1988, **76**, 149.

Biographical Sketch

Bernard C. Gerstein. *b* 1932. B.S., 1953, Purdue, USA; Ph.D., 1960, Iowa State. Introduced to NMR by R. W. Vaughan. Faculty in Chemistry, Iowa State University, 1962–present. Approx. 150 publications. Research interests include the theory and practice of learning, and applications of solid state NMR to problems in the physics and chemistry of materials, fossil fuels, and heterogeneous catalysis.

Multiple Quantum Coherences in Extended Dipolar Coupled Spin Networks

Serge Lacelle
Université de Sherbrooke, Quebec, Canada

1	Background and Phenomenology	1
2	Ensemble Considerations	2
3	Quantum Mechanics of an N-Spin Subsystem	3
4	Quantum Statistical Mechanics of an Ensemble of N-Spin Subsystems	4
5	Development of Multiple Spin/Multiple Quantum Coherences in Dipolar Coupled Solids	5
6	Statistical Properties of Distributions of Dipolar Coupling Constants and Their Products in Large Spin Networks	7
7	Dynamical Scale Invariance in the Growth of Multiple Spin Correlations in Dipolar Coupled Solids	8
8	Related Articles	9
9	References	10

1 BACKGROUND AND PHENOMENOLOGY

In condensed matter, dipolar interactions among nuclear magnetic moments and their manipulation in multiple quantum (MQ) NMR experiments induce multiple spin correlations. The temporal and spatial development of these collective modes yield information about the structure and the dynamics of spin networks.[1–3] In this article, we examine the fundamental aspects of the growth of multiple spin/multiple quantum coherences in extended dipolar coupled spin networks driven by rf magnetic fields.

In MQ NMR, investigations of strongly dipolar coupled spin systems, such as rigid solids, the simplest relevant Hamiltonian needed to describe and understand experimental observations in a laboratory reference frame is given by

$$\hat{\mathcal{H}}(t) = \hat{\mathcal{H}}_{\mathrm{Z}} + \hat{\mathcal{H}}_{\mathrm{d}} + \hat{\mathcal{H}}_{\mathrm{rf}}(t) \tag{1}$$

The contributions to $\hat{\mathcal{H}}(t)$ in equation (1) include the interactions of the nuclear magnetic moments with a strong static magnetic field ($\hat{\mathcal{H}}_{\mathrm{Z}}$), with other nuclear magnetic moments through dipolar interactions ($\hat{\mathcal{H}}_{\mathrm{d}}$), and with time-dependent rf magnetic fields ($\hat{\mathcal{H}}_{\mathrm{rf}}$). Furthermore, $[\hat{\mathcal{H}}_{\mathrm{Z}}, \hat{\mathcal{H}}_{\mathrm{d}}] = 0$, and $[\hat{\mathcal{H}}_{\mathrm{Z}} + \hat{\mathcal{H}}_{\mathrm{d}}, \hat{\mathcal{H}}_{\mathrm{rf}}] \neq 0$.

In order to simplify the description and make connection with experiments, the Hamiltonian of equation (1) is transformed to a frame rotating about the z axis of the laboratory frame at the nuclear spin precession frequency. In this new reference frame, $\hat{\mathcal{H}}_{\mathrm{Z}}$ disappears. A further transformation to another noninertial frame, the rf toggling frame which 'follows' the directions of the rf fields during a pulse sequence, produces an effective Hamiltonian $\hat{\mathcal{H}}_{\mathrm{de}}(t)$. In this newest frame, $\hat{\mathcal{H}}_{\mathrm{de}}(t)$ results from the modulation of $\hat{\mathcal{H}}_{\mathrm{d}}$ by the time-dependent rf fields. The time average of $\hat{\mathcal{H}}_{\mathrm{de}}(t)$ over the period of a cycle of a multiple pulse excitation sequence yields, under appropriate conditions, a time-independent average Hamiltonian $\tilde{\hat{\mathcal{H}}}_{\mathrm{d}}$:

$$\tilde{\hat{\mathcal{H}}}_{\mathrm{d}} = \sum_{j>k} D_{jk}\, f(\hat{\boldsymbol{I}}_j, \hat{\boldsymbol{I}}_k) \tag{2}$$

where D_{jk} is a dipolar coupling constant between spins j and k

$$D_{jk} = \frac{\gamma^2\hbar^2(3\cos^2\theta_{jk} - 1)}{2r_{jk}^3} \tag{3}$$

and $f(\hat{\boldsymbol{I}}_j,\hat{\boldsymbol{I}}_k)$ is a function of bilinear operators involving the components of the spin angular momentum operators $\hat{\boldsymbol{I}}$, of spins j and k.

Formally, the geometrical interpretations of these transformations correspond to unitary transformations on the state of the spin system (i.e. the density operator) and its dynamical variables (i.e. the spin angular momentum and Hamiltonian operators). The resulting interaction pictures associate different parts of the time dependence of the physical system [i.e. the spins in the sample evolving under the Hamiltonian in equation (1)] to the state of the system and to the dynamical variables. This procedure is generic to all NMR experiments involving the manipulation of spin Hamiltonians. By a judicious choice of a reference frame, different portions of the Hamiltonian can be selected to appear to dominate the spin dynamics; hence, the possibility to discriminate among the various contributions in a spin Hamiltonian. Such an approach underlies the success of NMR spectroscopy. It is noteworthy that these transformations, from one frame to another, inertial or noninertial, do not necessarily preserve the invariance and conservation principles of physics. For example, spin energies measured in the laboratory frame are different from those measured in the rotating frame, while the spin quantum numbers, $I = \frac{1}{2}$ for protons, remain identical. However, observations restricted within a reference frame will be consistent with known laws of physics.

In pulsed NMR experiments, the evolution of the spin system is detected in the rotating frame. The time development of the spin system under $\tilde{\hat{\mathcal{H}}}_{\mathrm{d}}$ in the toggling frame is monitored directly, in multiple pulse line-narrowing sequences such as MREV-8, or indirectly, in MQ NMR, by stroboscopic observations when both the rotating and the toggling frames coincide.

A variety of rf multiple pulse sequences have been tailored to produce different average dipolar Hamiltonians $\tilde{\hat{\mathcal{H}}}_{\mathrm{d}}$. In MQ NMR experiments,[1–3] $[\hat{\mathcal{H}}_{\mathrm{Z}}, \tilde{\hat{\mathcal{H}}}_{\mathrm{d}}] \neq 0$. The spin portions [see equation (2)] $f(\hat{\boldsymbol{I}}_j,\hat{\boldsymbol{I}}_k)$ of these nonsecular average dipolar Hamiltonians include, among the bilinear spin operators, terms like $\hat{I}_{jz}\hat{I}_{k\pm}$, and $\hat{I}_{j\pm}\hat{I}_{k\pm}$, where $\hat{I}_+$ and $\hat{I}_-$ correspond to the raising and lowering (or ladder) spin angular momentum operators, respectively. These operators in $\tilde{\hat{\mathcal{H}}}_{\mathrm{d}}$ are responsible for the radiative coupling of Zeeman nuclear spin states with differing magnetic quantum numbers M_z by ±1 and ±2.

Evolution under $\bar{\mathcal{H}}_d$ for extended periods of time leads to nonstationary states with possibly larger differences in ΔM_z, as discussed in the next section. MQ NMR pulse excitation sequences for solids are specifically designed and optimized to generate multiple spin/multiple quantum coherences among the spins in a macroscopic sample.

The selection rules for the observation of transverse magnetization, or single spin/single quantum coherences, correspond to transitions with $\Delta M_z = \pm 1$. Thus, the creation and evolution of coherent superpositions of quantum states with $\Delta M_z \neq 1$ cannot be detected directly. Indirect piecewise mappings of multiple spin/multiple quantum coherences are accomplished through two-dimensional NMR methods as a function of the excitation and/or evolution times.[1–3] MQ NMR spectra obtained in this fashion reveal the presence of multiple spin/multiple quantum coherences with $\Delta M_z = n$, where n is the order of the coherences, in the sample during the excitation/evolution period (see Figure 1).

Figure 1 shows schematic MQ NMR spectra, obtained with time-resolved two-dimensional experiments, as a function of the excitation time. For a fixed excitation period, the spectral intensities decrease with increasing orders. With increasing excitation times, a redistribution of spectral intensities is observed to proceed or to 'flow' towards higher order coherences.

Understanding the behavior of the MQ NMR spectral intensity profiles of solids, as a function of order and excitation time, still poses an interesting challenge to NMR spectroscopists. Specifically, one would like to learn how the multiple spin dynamics depend on the lattice parameters and the space-filling properties of spin networks. Examples of the latter include spatial extent, morphologies, and effective dimensionalities of domain structures on mesoscopic length scales, i.e. in the range 1 nm to 1 μm, in condensed matter systems. More generally, the recognition of emergent properties, generic or universal behavior, amidst the complexities of this many-body problem with multiple scales, would deepen our understanding of the fundamental aspects of MQ NMR. These issues are addressed in the following sections, from the perspective of statistical mechanics.

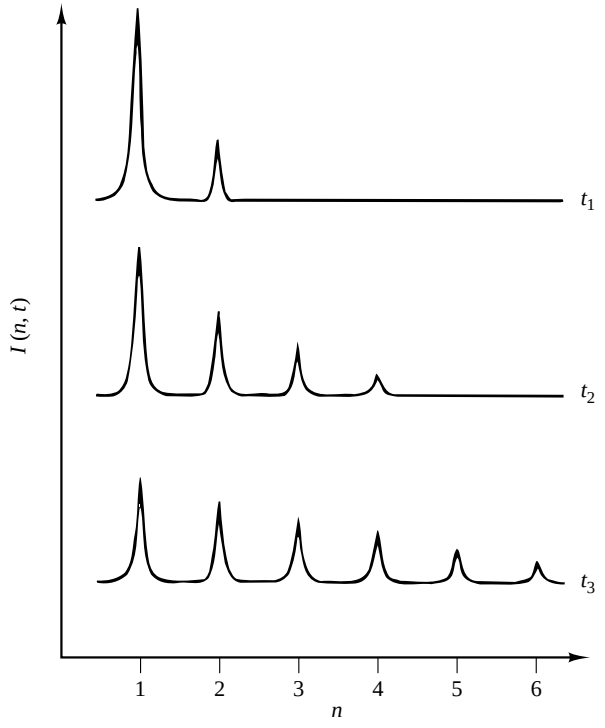

Figure 1 Typical MQ NMR spectra of a rigid solid: spectral intensities $I(n,t)$ as a function of order n and excitation time t, with $t_1 < t_2 < t_3$

2 ENSEMBLE CONSIDERATIONS

From a macroscopic point of view, in a MQ NMR experiment energy is pumped through rf magnetic fields produced by electronic devices into a solid sample residing in a strong static magnetic field. From a microscopic point of view, this injection of energy proceeds from individual nuclear magnetic moments, embedded in the lattice, to induce multiple spin correlations. Both the microscopic and macroscopic descriptions of the rf irradiation processes involve nonequilibrium driven systems: the macroscopic solid and the microscopic magnetic moments. As these experiments are performed in laboratories on a macroscopic scale, but interpreted microscopically, it is imperative to understand clearly how the macroscopic observables emerge from the numerous microscopic degrees of freedom.

A rigid solid is an aggregate of a large number of spatially fixed atoms. Various solids exist due to the nature of their constituents, which include atoms, ions, or molecules. In MQ NMR of rigid solids, ions and molecules lose their distinct identities on account of the through-space dipolar interactions among all magnetic moments. Hence, the spin network, consisting of the nuclear magnetic moments and their dipolar coupling constants, remains the only relevant and essential substratum onto which the microscopic degrees of freedom, the multiple spin coherences, evolve in MQ NMR experiments.

Solid samples used in MQ NMR investigations typically contain on the order of 10^{20} or more spins. The multiple spin correlations induced in spin networks by present-day MQ NMR methodologies involve coherences with up to possibly 10^2 spins. Consequently, the size difference between the sample and the multiple spin coherences suggests that the macroscopic observables, or responses, in MQ NMR experiments, arise from the random superposition of numerous multiple spin coherences. In other words, the sample could be viewed as an ensemble of loosely coupled subsystems.

Such a description of a macroscopic sample is certainly valid in liquid state NMR experiments, where under normal conditions, molecules behave as essentially independent subsystems. This outlook can also be extended to correlated molecular systems, as observed in critical fluctuations close to critical points.[4] For example, close to a consolute temperature, the intermolecular interactions among molecules in a critical binary fluid contrive and lead to composition fluctuations over length and timescales that can be quite large compared with those associated with the molecules, but still much smaller than those of the macroscopic sample. However, care must be exercised with such an analogy, since in critical phenomena systems are at equilibrium, while MQ NMR has to do with nonequilibrium driven systems. Possibly a more appropriate comparison for MQ NMR would be with the growth kinetics and processes of domain structures observed during phase

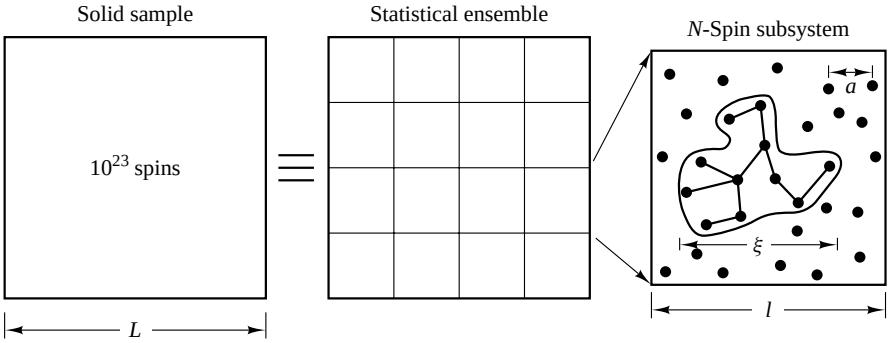

Figure 2 A macroscopic sample viewed as an ensemble of loosely coupled N-spin subsystems. Relevant length scales include: the lattice spacing a, the correlation length of a multiple spin coherence ξ, the extent of a subsystem l, and the sample size L, which satisfy $a < \xi < l \ll L$. Spins are denoted by •. An 11-spin coherence is also shown, with the lines representing the dipolar coupling constants appearing in the product, which multiplies the corresponding product operator term of the density operator

separation of binary fluids.[5] In this case, a similarity to critical phenomena exists; however, a richer behavior arises due to the nonequilibrium conditions and nonlinearity. In any event, the point at issue, that a macroscopic sample can be viewed, under certain conditions, as an ensemble of loosely coupled subsystems, where a subsystem can be one or several molecules, or even part of a spin network in a solid, would appear physically plausible.

Figure 2 shows a representation of a macroscopic sample as a statistical ensemble of N-spin subsystems. The number of spins N per subsystem is much smaller, by many orders of magnitude, than the total number of spins in the sample. The relevant length scales in this ensemble include the sample size L, the spatial extent of a subsystem l, the correlation length of the multiple spin coherences ξ, and the underlying lattice spacing a. This hierarchy of length scales satisfy the inequalities, $a < \xi < l \ll L$. Interaction energies between subsystems are assumed to be weak in comparison with interaction energies within the subsystems. This amounts to a neglect of surface effects for the MQ dynamics. Such approximation becomes more accurate in the limit when $\xi \ll l$. These effects are nevertheless necessary to achieve equilibrium or uniform spin temperature in the ensemble. The presence of the long-range dipolar interactions among the magnetic moments would appear to preclude or even invalidate this perspective of the sample as representing an ensemble of loosely coupled subsystems. However, as will be seen in Section 5, in time-resolved MQ NMR experiments, multiple spin coherences are 'weighted' by products of dipolar coupling constants. As it turns out, in spin networks, the distributions of dipolar coupling constants and their products are extremely wide. Since, at early excitation times, the MQ spin dynamics are dominated by the largest coupling constants and their products, the ensemble picture remains a good approximation for most experimental conditions. This approximation breaks down for mean field interpretations, e.g. MQ NMR experiments having infinite excitation periods.

Measurements performed over a short period of time on a macroscopic sample, made up of an ensemble of subsystems, correspond to averaging over the ensemble.[7] When a physical property of a macroscopic system is equal to this property averaged over the subsystems, spatial ergodicity exists. In statistical mechanics, the Gibbs canonical ensemble is composed of identical systems from the macroscopic point of view, i.e. they all have the same number of particles N, volume V, and temperature T. However, most systems are in different microscopic states. In the ensemble construction for a nonequilibrium driven macroscopic system, as described above, none of the subsystems need to be strictly identical. Instead, one assumes that statistical homogeneity is valid for the subsystems. On a subsystem scale, the statistical properties are stationary in space, i.e. a subsystem is statistically translationally invariant in space. Another feature of time-resolved MQ NMR measurements on such an ensemble, is the fact that, as the multiple spin coherences grow, so does their correlation length ξ. As the inequality $\xi < l$ must be satisfied for a consistent interpretation of the ensemble, this implies that the number of subsystems actually decreases as a function of time. This should be of no significant consequence, as long as $l \ll L$. Under present MQ NMR experimental conditions, these conditions are always satisfied, and the ensembles will consist of huge numbers of subsystems. Such ensembles yield asymptotic statistical states in experimental investigations.

Thus, a time-resolved MQ NMR measurement on a macroscopic solid is assumed to be equivalent to many independent measurements on the subsystems. Since the decomposition of the macroscopic sample into subsystems is not unique, the averaging process over the ensemble implied in a measurement is really a summation over the subsystems. As the spin dynamics are being probed on the scale of a subsystem, the response of the collective ensemble is taken to reflect the behavior of a typical subsystem. Underlying the spin dynamics are dipolar coupling constants and their products. Due to subtleties related to wide distributions and to averaging over products, the role of the couplings is more intricate than appears in the present discussion. For example, the distinction between average and typical behavior is very important in the MQ NMR of large spin networks.[6] We shall return to these issues in Section 6.

3 QUANTUM MECHANICS OF AN N-SPIN SUBSYSTEM

The focus on the spin dynamics within a subsystem and the subsequent averaging over a large collection of subsystems, yields a more tractable avenue to the understanding of

MQ NMR of solids, rather than treating a single spin system consisting of 10^{20} or more spins. Nevertheless, on the timescale of MQ NMR experiments, the spin dynamics within a subsystem still retain some of complexities of the many-body problem.

In a subsystem consisting of N spins I, there are $(2I + 1)^N$ stationary states of $\hat{\mathcal{H}}_Z$. For $I = \frac{1}{2}$, these 2^N energy levels can be classified according to the magnetic quantum numbers M_z given by

$$M_z = \sum_i^N m_{iz} \tag{4}$$

where m_{iz} is the eigenvalue ($m_z = \pm\frac{1}{2}$) of the ith spin. These Zeeman states, in the magnetic field $\boldsymbol{B}_0$, have corresponding energies

$$E_z = -\gamma\hbar B_0 M_z \tag{5}$$

and degeneracies

$$\Omega = \frac{N!}{(\frac{1}{2}N + M_z)!(\frac{1}{2}N - M_z)!} \tag{6}$$

The Zeeman manifolds are further broadened by homonuclear dipolar perturbations $\hat{\mathcal{H}}_d$. The resulting energy level diagram can be characterized, in principle, by the combined eigenvalues and eigenfunctions of $\hat{\mathcal{H}}_Z$ and $\hat{\mathcal{H}}_d$. However, due to the presence of bilinear spin operators in $\hat{\mathcal{H}}_d$, the combined eigenfunctions are constructed from direct products of $\hat{\mathcal{H}}_Z$ eigenfunctions. As a consequence, the m_{iz} eigenvalues are not good quantum numbers. In addition, the presence of large N rapidly makes this approach analytically intractable.

Therefore, as a first approximation, only the energy level diagram due to $\hat{\mathcal{H}}_Z$ is considered. This is justifiable, since the Zeeman splittings are usually of the order of tens to hundreds of megahertz as compared with tens of kilohertz for dipolar splittings. Radiative coupling of pairs of Zeeman levels leads to

$$\binom{2^N}{2} = 2^N(2^N - 1)/2 \tag{7}$$

possible transitions. The distinction between $+n$ and $-n$ coherences results in $2^N(2^N - 1)$ transitions. These transitions, or coherences, are classified according to their orders n. The number of coherences of order $n \neq 0$, Z_n, where $|n| \leq N$, is obtained from the constrained sum over the products of degeneracies of coupled Zeeman manifolds,

$$Z_n = \sum_{M_i - M_j = n} \binom{N}{\frac{1}{2}N + M_i}\binom{N}{\frac{1}{2}N + M_j} = \binom{2N}{N - n} \tag{8}$$

The number of coherences within a Zeeman manifold or with $n = 0$, Z_0, is given by

$$Z_0 \sum_{M_i = N/2+1}^{-N/2+1} \binom{N}{\frac{1}{2}N + M_i}\left[\binom{N}{\frac{1}{2}N + M_i} - 1\right] = \binom{2N}{N} - 2^N \tag{9}$$

Radiative coupling within a subsystem of N dipolar coupled spins $\frac{1}{2}$ can be rationalized, to a very good degree of approximation, on the basis of the possible $2^N(2^N - 1)$ transitions which connect the 2^N energy levels. The information content needed to describe this physical situation involves $2^N(2^N - 1)$ coherences and 2^N populations, or a total of 4^N parameters.

The 2^N eigenfunctions of $\hat{\mathcal{H}}_Z$, $|r\rangle$, for an N-spin-$\frac{1}{2}$ subsystem, constitute a complete basis set to characterize any spectroscopic experiments involving coherences and populations. As a consequence, any state $|\psi\rangle$ of a subsystem, can be expanded with the complete Zeeman basis set,

$$|\psi\rangle = \sum_{r=1}^{2^N} |r\rangle\langle r|\psi\rangle = \sum_{r=1}^{2^N} c_r|r\rangle \tag{10}$$

$$\langle r|\psi\rangle = c_r \tag{11}$$

Similarly, the observables or expectation values corresponding to any dynamical variables, such as the magnetization M_x, detected in a spectroscopic measurement on a subsystem, can be represented in this basis set with the corresponding operator $\hat{M}_x$ as,

$$\begin{aligned}\langle\psi|\hat{M}_x|\psi\rangle &= \sum_{r,s}\langle\psi|s\rangle\langle s|\hat{M}_x|r\rangle\langle r|\psi\rangle \\ &= \sum_{r,s} c_s^* c_r \langle s|\hat{M}_x|r\rangle\end{aligned} \tag{12}$$

where $c_r = \langle r|\psi\rangle$. The matrix elements $\langle s|\hat{M}_x|r\rangle$ are numbers related to the values of the dynamical variable M_x. The matrix elements, $c^*_s c_r$, are numbers describing the state $|\psi\rangle$ of the subsystem; there are 4^N such matrix elements. As a consequence, this matrix is isomorphic to, or has the same information content as, the description in terms of coherences and populations.[8,9] The diagonal elements are proportional to the probabilities of occupation of the energy levels, and consequently to the populations. The off-diagonal elements correspond to correlations between the values of the coefficients c_r. For time-dependent problems, as in spectroscopic measurements, these off-diagonal elements are related to coherent superpositions of the stationary states, i.e. coherences or transitions, present in a spin subsystem.

Different states $|\psi\rangle$ yield different values for the same observable, as can be seen from equation (12). The products, $c^*_s c_r$, vary according to the states $|\psi\rangle$, while the matrix elements $\langle s|\hat{M}_x|r\rangle$ remain invariant. It proves convenient to describe the state of the subsystem, with a projection operator for a single state, $\hat{P}_\psi = |\psi\rangle\langle\psi|$, in the Zeeman basis set:

$$\langle r|\hat{P}_\psi|s\rangle = c_s^* c_r \tag{13}$$

With this projection operator, the expectation value of $\hat{M}_x$ in a subsystem becomes [see equation (12)]:

$$\begin{aligned}\langle\hat{M}_x\rangle = \langle\psi|\hat{M}_x|\psi\rangle &= \sum_{r,s}\langle r|\hat{P}_\psi|s\rangle\langle s|\hat{M}_x|r\rangle \\ &= \mathrm{Tr}\{\hat{P}_\psi\hat{M}_x\}\end{aligned} \tag{14}$$

4 QUANTUM STATISTICAL MECHANICS OF AN ENSEMBLE OF N-SPIN SUBSYSTEMS

A measurement of M_x over an ensemble of subsystems is equivalent to averaging over $\langle \hat{M}_x \rangle$ in equation (14). As the state $|\psi\rangle$ or $c^*_s c_r$ of each subsystem will generally be different, while the dynamical variable will be identical, the averaging gives

$$\overline{\langle \hat{M}_x \rangle} = \sum_{r,s} \overline{\langle r|\hat{P}_\psi|s\rangle} \langle s|\hat{M}_x|r\rangle = \mathrm{Tr}\{\hat{\rho}\hat{M}_x\} \tag{15}$$

with $\hat{\rho}$, the density matrix of the ensemble,[8,9] defined as

$$\langle r|\hat{\rho}|s\rangle = \sum_\psi p_\psi \langle r|\hat{P}_\psi|s\rangle = \overline{\langle r|\hat{P}_\psi|s\rangle} = \overline{c^*_s c_r} \tag{16}$$

where p_ψ is the statistical weight of $|\psi\rangle$ in the ensemble.

For NMR experiments, the density matrix is represented by a density operator, corresponding to the Boltzmann weight of the canonical ensemble with the appropriate Hamiltonian operator defined with respect to some convenient reference frame,

$$\hat{\rho} = Q^{-1} \mathrm{e}^{-\hat{\mathcal{H}}/kT} \tag{17}$$

where Q is the ensemble partition function,

$$Q = \sum_{r=1}^{2^N} \langle r|\mathrm{e}^{-\hat{\mathcal{H}}/kT}|r\rangle \tag{18}$$

The description of any spectroscopic experiment will involve the time dependence, due to evolution under some Hamiltonian $\hat{\mathcal{H}}$ of $\hat{\rho}$ to characterize the ensemble, or $\hat{P}$ to represent a subsystem. In the Schrödinger picture, the time dependence is assigned to the state of the system, specifically, to the coefficients $c_r(t)$ of equation (11).[8,9] In MQ NMR experiments of solids, the relevant Hamiltonian corresponds to the time average of $\hat{\mathcal{H}}_\mathrm{d}$ in the rf toggling frame, $\tilde{\hat{\mathcal{H}}}_\mathrm{d}$ [see equation (2)], over a cycle of the rf excitation sequence. The equation of motion for $\hat{P}$ is obtained by inserting $|\psi\rangle$ into the time-dependent Schrödinger equation to yield[8,9]

$$\frac{\mathrm{d}\hat{P}}{\mathrm{d}t} = \frac{\mathrm{i}}{\hbar}[\hat{P}, \tilde{\hat{\mathcal{H}}}_\mathrm{d}] \tag{19}$$

The averaging of equation (19) over the ensemble of subsystems with identical $\tilde{\hat{\mathcal{H}}}_\mathrm{d}$ gives the equation of motion for $\hat{\rho}$:

$$\frac{\mathrm{d}\hat{\rho}}{\mathrm{d}t} = \frac{\mathrm{i}}{\hbar}[\hat{\rho}, \tilde{\hat{\mathcal{H}}}_\mathrm{d}] \tag{20}$$

Equation (20) is also known as the Liouville–von Neumann equation.

For a time independent average Hamiltonian, a formal solution to equation (20) is

$$\hat{\rho}(t) = \hat{U}\hat{\rho}(0)\hat{U}^{-1} \tag{21}$$

where the propagator $\hat{U}$ is defined as

$$\hat{U} = \exp\left(-\frac{\mathrm{i}}{\hbar}\tilde{\hat{\mathcal{H}}}_\mathrm{d} t\right) \tag{22}$$

The interpretation of equation (21) is of importance for understanding the development of multiple spin coherences in time resolved MQ NMR experiments. Insight in this many-body problem, as discussed in the next section, can be gained through a Taylor expansion of $\hat{\rho}(t)$ about $t = 0$:

$$\hat{\rho}(t) = \hat{\rho}(0) + \sum_{n=1}^{\infty} \frac{t^n}{n!} \frac{\mathrm{d}^n}{\mathrm{d}t^n} \hat{\rho}(t)|_{t=0} \tag{23}$$

From equations (21) and (22), one finds the derivatives of $\hat{\rho}(t)$, of which only the first two are given here:

$$\frac{\mathrm{d}\hat{\rho}(t)}{\mathrm{d}t} = \frac{\mathrm{i}}{\hbar}[\hat{\rho}(0), \tilde{\hat{\mathcal{H}}}_\mathrm{d}] \tag{24}$$

$$\frac{\mathrm{d}^2\hat{\rho}(t)}{\mathrm{d}t^2} = -\frac{1}{\hbar}[[\hat{\rho}(0), \tilde{\hat{\mathcal{H}}}_\mathrm{d}], \tilde{\hat{\mathcal{H}}}_\mathrm{d}] \tag{25}$$

Finally, by substituting equations (24) and (25) and all the other derivatives into equation (23), one obtains:

$$\hat{\rho}(t) = \hat{\rho}(0) + \frac{\mathrm{i}t}{\hbar}[\hat{\rho}(0), \tilde{\hat{\mathcal{H}}}_\mathrm{d}] - \frac{t^2}{2\hbar^2}[[\hat{\rho}(0), \tilde{\hat{\mathcal{H}}}_\mathrm{d}], \tilde{\hat{\mathcal{H}}}_\mathrm{d}] + \cdots \tag{26}$$

5 DEVELOPMENT OF MULTIPLE SPIN/MULTIPLE QUANTUM COHERENCES IN DIPOLAR COUPLED SOLIDS

The power series in time for $\hat{\rho}(t)$ in equation (26) describes the evolution of the spin dynamics in MQ NMR experiments. With the initial conditions corresponding to the spin system at equilibrium in a strong Zeeman field at a high temperature, equation (17) implies

$$\hat{\rho}(0) \propto \hat{I}_z = \sum_i \hat{I}_{zi} \tag{27}$$

As pointed out in Section 3, since $|\hat{\mathcal{H}}_\mathrm{Z}| \gg |\hat{\mathcal{H}}_\mathrm{d}|$, it is appropriate to neglect the contributions of $\hat{\mathcal{H}}_\mathrm{d}$ in the initial conditions. However, in the toggling reference frame, $\tilde{\hat{\mathcal{H}}}_\mathrm{d}$ is crucial for determining the evolution of the spin dynamics. By inserting $\hat{\rho}(0)$ and the nonsecular average Hamiltonian $\mathcal{H}_\mathrm{d}$ suitable for a particular MQ NMR experiment into equation (26), it is possible to examine the qualitative features of the growth of multiple spin/multiple quantum coherences in a solid.

With $\rho(0)$ corresponding to single-spin interactions and $\tilde{\hat{\mathcal{H}}}_\mathrm{d}$ to two-spin interactions, the ascending terms in the expansion of $\hat{\rho}(t)$ describe the sequential growth of multiple spin coherences due to the evolution under $\tilde{\hat{\mathcal{H}}}_\mathrm{d}$. In the first-order terms t^1, the commutators produces two-spin correlations of the form $\hat{I}_{i\alpha}\hat{I}_{j\beta}$, where the components α and β of the spin angular momentum operators are determined by the actual

details of $\hat{\mathcal{H}}_d$. The nested commutators in the second-order terms t^2 yield three-spin operators, $\hat{I}_{i\alpha}\hat{I}_{j\beta}\hat{I}_{k\gamma}$. The hierarchy of nested commutators from the higher order terms t^n generate $(n-1)$-spin operators. By introducing ladder (raising and lowering) operators in these product operators, the order n of the corresponding MQCs becomes explicit; the sum of raising operators minus the sum of the lowering operators in a product operator gives the order of the coherence. Thus, to observe an n quantum coherence it is necessary to have, at the minimum, a contribution of order t^{n+1}, implying the presence of an n-spin/n quantum operator in the expansion of $\hat{\rho}(t)$. Higher order terms can also produce n quantum coherences. The distinction between these different n quantum coherences comes from the number of spins participating in the correlations. Since multiple spin coherences contribute to equation (26) through the product of dipolar coupling constants (as discussed below and in Section 6), the lattice parameters r_{ij} and θ_{ij} will ultimately control and distinguish between the various n quantum coherences.

The interplay between the development of multiple spin coherences and the order of the resulting multiple quantum coherences depends on selection rules associated with the nature of $\hat{\mathcal{H}}_d$ and equation (26). With respect to the time development of the number of spins in multiple spin coherences, the bilinear spin operators of $\hat{\mathcal{H}}_d$ and the algebra of the nested commutators in equation (26) imply a cascade process in the growth of correlations. An n-spin coherence can only grow by sequentially incorporating one single spin at a time, one after another. The time development of multiple quantum coherences is constrained to pathways, in a K-spin/n quantum space, which depend uniquely on the nature of $\hat{\mathcal{H}}_d$.[2,10] The pulse excitation sequences for MQ NMR of solids produce generic classes of $\hat{\mathcal{H}}_d$ terms: 2-spin/0,2 quantum operators, 2-spin/1-quantum operators, and 2-spin/2 quantum operators. These excitation sequences achieve a redistribution of MQ NMR spectral intensities according to selections rules on ΔK and Δn. For example, with 2-spin/2 quantum operators in $\hat{\mathcal{H}}_d$, and an $\hat{I}_z$ initial condition, equation (26) and the selection rules $\Delta K = \pm 1$ and $\Delta n = \pm 2$, demonstrate that only even coherences develop; in addition, the evolution cannot generate 4-spin/4 quantum coherences. The redistribution of spectral intensities produced by the different $\hat{\mathcal{H}}_d$ terms is optimized according to the size or spatial distribution of the spins within a subsystem, e.g. for the detection of spin clusters, or extended spin networks.

One of the simplest models, the so-called statistical or Gaussian model,[1] used to interpret MQ NMR spectra of solids, consists of assuming that all the individual coherences possible in an N-spin subsystem have the same magnitudes with random phases, and that all have been excited at long excitation times in the sample or ensemble of subsystems. Time-reversal excitation produces transitions with identical phases within an order.[11] Hence, the assumption of a priori equal weight of the different coherences implies that the MQ NMR spectral intensities $I(n,t)$ are proportional to Z_n, [see equation (8)]. Stated differently, the distribution of coherences in the ensemble of subsystems is proportional to Z_n. For large N and small n, it is possible to transform Z_n in equation (8) with Stirling's approximation $y! \approx (2\pi y)^{\frac{1}{2}}\, y^y\, e^{-y}$ to give

$$Z_n \approx 4^N (\pi N)^{-\frac{1}{2}} e^{-n^2/N} \tag{28}$$

As a consequence, according to the statistical model, a MQ NMR spectral intensity profile as a function of order $I(n,t)$ should be Gaussian, as suggested by equation (28).

The time dependence of these profiles arises from the growth of the subsystem size $N(t)$. The variance $N(t)$ obtained from fitting $I(n,t)$ to a Gaussian function of n represents the effective number of dynamically coupled spins, in a typical subsystem, following an excitation period of duration t under $\hat{\mathcal{H}}_d$. In addition to spin counting with this variance, it has been suggested that the rate of change in $N(t)$ with time reflects on some of the space-filling properties, such as dimensionality effects, of spin networks.[1,1,12–14] Qualitatively, three generic classes of behavior have been observed for $N(t)$. Saturation in $N(t)$ implies the presence of isolated clusters of spins. Unbounded growth curves are observed in extended spin networks. Saturation behavior seen at early excitation times, followed by unbounded growth, indicates the occurrence of coupled clusters of spins.

The simplicity of the statistical model accounts for its widespread use in the MQ NMR literature of solids.[2,3] However, some questions have been raised concerning the validity of the assumption of the a priori equal weight of all coherences.[2,6] In addition, the convenience of the Gaussian model with the use of simple fitting procedures to analyze MQ NMR spectral intensity profiles is not successful with extended spin networks.[15] To appreciate the nature of these problems, and to understand the development of multiple spin/multiple quantum coherences in solids beyond the level of the statistical model, it is necessary to consider further fundamental aspects of the spin dynamics in MQ NMR.

As discussed in previous sections, the interpretation of MQ NMR experiments of solids relies on the spin dynamics within a subsystem, followed by averaging over an ensemble of subsystems. The density operator $\hat{\rho}$ in equation (17) and its equation of motion [equation (26)] reflect this two-fold averaging: a quantum mechanical averaging or the determination of expectation values in a subsystem [equation (14)], and a statistical averaging over the expectation values due to the distribution of subsystem states in the ensemble [equations (15) and (16)].

It is possible to construct a statistical ensemble of diagrams or graphs, including evolution, which is completely isomorphic with the density operator formalism used to describe MQ NMR.[2] This approach provides complementary physical insights into MQ NMR spin dynamics, averaging, and measurements. The diagrams include vertices corresponding to spins, and edges or links to delineate dipolar coupling constants between spins. The weight of an edge is proportional to the absolute value of the dipolar coupling constant. The state of a spin is represented by a color. For a spin $\frac{1}{2}$ there are three colors, $\hat{I}_x$, $\hat{I}_y$, and $\hat{I}_z$; generalization to higher spins is possible.

The decomposition of the density operator proceeds by examining an N-spin subsystem, under rigid lattice conditions and without any symmetry elements. In such an N-spin subsystem, the number of distinct subsets n_i each containing i spins is given by the binomial coefficient:

$$n_i = \binom{N}{i} \tag{29}$$

For example, the number of pairs of spins or dipolar coupling constants in a single subsystem is n_2. The subsets can range in size from $i = 1$ to N. The sum over all possible subsets is:

$$n_{\mathrm{T}} = \sum_{i=1}^{N} n_i = \sum_{i=1}^{N} \binom{N}{i} = 2^N - 1 \tag{30}$$

In equation (30), n_{T} is the sum of all possible spin correlations in the spin subsystem. By including the states of the spins or colors within the spin correlations, one obtains

$$n_{\mathrm{T}}^{\mathrm{c}} = \sum_{i=1}^{N} n_i 3^i = \sum_{i=1}^{N} \binom{N}{i} 3^i = 4^N - 1 \tag{31}$$

where $n_{\mathrm{T}}^{\mathrm{c}}$ is the total number of distinct colored subsets, and is equal to the number of elements (coherences and populations) of the normalized density operator in an N-spin-$\frac{1}{2}$ subsystem.

The growth of multiple spin/multiple quantum coherences is described by equation (26). From the interpretation of this equation, the coherences were seen to grow sequentially by adding one spin after another with increasing time. It is clear that this description is valid for the density operator, either in the product operator formalism or in the ensemble of colored spin correlations described above.

However, there is an essential feature related to the growth processes and the averaging over the subsystems, which becomes more obvious with the diagrams. Consider a generic term of $(n + 1)$th order in the Taylor expansion of equation (19) for the time dependence of the projection operator $\hat{P}_\psi$. The resulting equation is analogous to equation (26) with $\hat{P}_\psi$ replacing $\hat{\rho}$. The product of spin operators will include n-spin operators corresponding to different spins in the subsystem. As $\hat{\mathcal{H}}_{\mathrm{d}}$ is present in the nested commutators, there will also be products of $(n - 1)$ dipolar coupling constants which multiply the n-spin product operators. For example, a 3-spin coherence involving spins i, j, and k, will have a corresponding product operator of the form $\hat{I}_{i\alpha}\hat{I}_{j\beta}\hat{I}_{k\gamma}$, multiplied by a product of dipolar coupling constants $D_{ij}D_{jk}$. Hence, in general, the contributions or weights of n-spin coherences in the equation of motion are determined by products of $(n - 1)$ dipolar coupling constants. A diagram, consisting of n vertices connected with $(n - 1)$ edges is called a tree; no loops are permitted in such a graph. The number of ways to connect n vertices, with $(n - 1)$ edges chosen among $\binom{n}{2}$ distinct edges, corresponds to the number of distinct trees given by

$$n^{n-2} \tag{32}$$

Equation (32) also gives the number of products of n dipolar coupling constants for a particular n-spin coherence. In an N-spin subsystem, the total number of products of n dipolar coupling constants for n-spin coherences is

$$\binom{N}{n} n^{n-2} \tag{33}$$

The averaging over an ensemble of subsystems, in order to obtain $\hat{\rho}$, as discussed in Section 4 and in NMR texts,[8,9] proceeds by assuming that the Hamiltonians are identical for all subsystems [see equations (19) and (20)]. This is certainly true for a hypothetical representative ensemble, or approximately true for a sample viewed as an ensemble of loosely coupled subsystems, as presented in Section 2. However, when the averaging is done over a nonequilibrium ensemble for a finite sample, care must be taken to distinguish between the sum in the Hamiltonian [see equations (2), (19) and (20)] and the realizations of multiple spin correlations (with corresponding product operators) present in the ensemble. As an example, consider a 25-spin subsystem. In this subsystem, there is only a single MQ coherence of order 25 represented by a product operator consisting of 25 raising operators. According to equation (26), the 25-spin/25 quantum coherence is weighted by a product of 24 dipolar coupling constants. Among these spins, there are $\binom{25}{2} = 300$ distinct dipolar coupling constants. The number of distinct products of 24 dipolar coupling constants corresponds to the number of trees, in this case $25^{23} \approx 10^{32}$ realizations. It should be clear that a macroscopic sample consisting of 10^{20} spins will not have enough 25-spin subsystems to represent all trees or possible realizations of the 25-MQ coherence. An MQ NMR measurement on a macroscopic sample, consisting of an ensemble of subsystems, is really an average over the subsystems [see equation (16)]. The average over multiple spin coherences is really performed over the distribution of corresponding trees present in the ensemble, i.e. over products of dipolar coupling constants. To appreciate the intricacies of such a measurement or averaging procedure, we now examine the distributions of dipolar coupling constants and their products in spin networks.

6 STATISTICAL PROPERTIES OF DISTRIBUTIONS OF DIPOLAR COUPLING CONSTANTS AND THEIR PRODUCTS IN LARGE SPIN NETWORKS

Consideration of equation (26) demonstrated that different multiple spin coherences contribute to the evolution of ρ according to the values of the products of dipolar coupling constants. Thus, for a finite excitation time, coherences cannot be treated equally, as is assumed in the Gaussian statistical model.[1] Only in the limit of an infinite excitation time will all the coherences contribute equally to the spin dynamics.[6] The recognition that in spin networks the distributions of dipolar coupling constants and their products are characterized by asymmetry associated with extreme widths is important for understanding MQ NMR spin dynamics.[6] Difficulties encountered with the interpretation of equation (26), due to the presence of multiple length- and timescales, actually arise from these broad and peculiar distributions.

In three-dimensional solids, lattice sums of dipolar coupling constants can be replaced by a continuum approximation involving integrals such as

$$\sum_{i\rangle j}^{N} D_{ij} \propto \int_r (1/r^3) r^2 \, \mathrm{d}r \propto \ln r \tag{34}$$

For an infinite sample, the lattice sum diverges, while for finite spin networks the sum is conditionally convergent, i.e. it depends on the sample shape. Some approaches, such as the Ewald summation and the Lorentz cavity method, have

been devised to study these distributions in samples of general shapes.

In one-dimensional solids, the lattice sums can be performed analytically. Consider an infinite crystalline one-dimensional chain of spins with lattice parameter r oriented perpendicular to the Zeeman field. The average dipolar coupling constant per spin $\langle D \rangle_s$ is

$$\langle D \rangle_s = 2 \sum_{k=1}^{\infty} \tfrac{1}{2} \gamma^2 \hbar^2 (kr)^{-3} \approx 1.20 \gamma^2 \hbar^2 / r^3 \qquad (35)$$

In this case, 83% of the average is determined by the value of two nearest neighbor couplings out of an infinity of couplings!

Figure 3 shows a schematic distribution of the absolute values of dipolar coupling constants and their logarithms for a large spin subsystem. One should note that the distribution in Figure 3(a) is really a caricature, since in large networks the width essentially cannot be observed on linear scales.[6] Several statistical features are illustrated by Figure 3. The average $\langle |D| \rangle$ is determined by the coupling constants in the tail of the distribution, while the most probable value $|D|_{\mathrm{MPV}}$ is sensitive to the small and numerous long-range couplings. The transformation of the distribution on a logarithmic scale demonstrates the huge dynamic range of the distribution. For example in a two-dimensional square lattice of $10^2 \times 10^2$ spins, the distribution of coupling constants covers over 10 orders of magnitude. Differences between $\langle \ln |D| \rangle$ and $\ln \langle |D| \rangle$ are important to reconcile with measurements on an ensemble. The value of $\langle |D| \rangle$ is sensitive to the largest coupling constants, while $\langle \ln |D| \rangle$ is more sensitive to the details of the overall distribution. Such distinctions are significant in the physics of

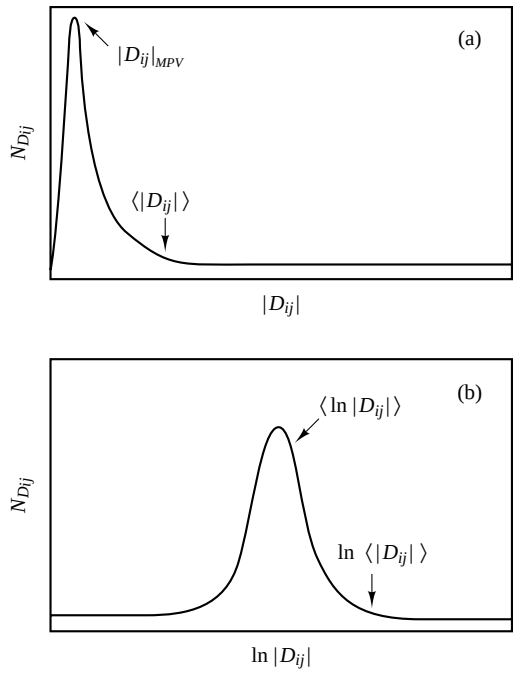

Figure 3 (a) Schematic distribution of the absolute values of dipolar coupling constants in an N-spin subsystem. (b) Schematic distribution of the logarithm of the absolute values of dipolar coupling constants in the same subsystem. Note the difference between $\langle \ln |D_{ij}| \rangle$ and $\ln \langle |D_{ij}| \rangle$. The analogous distributions, involving products of dipolar coupling constants, show similar behavior, but with wider distributions

disordered systems.[16,17] Products of dipolar coupling constants show similar features; however, the distributions are even wider.[6]

Probably the most interesting feature of these distributions arises from the scaling behavior of the statistical properties as a function of N, the number of spins. The relative fluctuations RF,

$$\mathrm{RF} = \frac{(\langle |D|^2 \rangle - \langle |D| \rangle^2)^{\frac{1}{2}}}{\langle |D| \rangle} \qquad (36)$$

measure the relative spread about the mean. In the limit of large spin networks,

$$\mathrm{RF} \propto N^{+\frac{1}{2}} \qquad (37)$$

This result implies that the distributions become wider as N increases, i.e. there is no self-averaging. The ratio of the most probable value to the first moment can be shown to scale as $N^{+\frac{3}{2}}$. The product of dipolar coupling constants shows a similar behavior with the same scaling exponents.[6] Such behavior is highly counterintuitive, since in random additive processes, within the central limit theorem, the relative fluctuations scale as $N^{-\frac{1}{2}}$, and the most probable value coincides with the first moment in the thermodynamic limit.

Some implications of these results for the growth of multiple spin coherences/multiple quantum coherences are beginning to emerge.[2,18] For example, anisotropy effects in the growth process should be determined by the products of the angular contributions of dipolar coupling constants. In a measurement on an ensemble of subsystems, the realizations of multiple spin coherences which are detected should be those with the largest products of dipolar coupling constants. However, these products are the least numerous but still dominate the dynamics due to their large weights. This last result would suggest that a single subsystem, where a multiple spin coherence with the largest possible product has been excited, could eventually dominate a macroscopic measurement. The statistical properties of the distributions of dipolar coupling constants and their products should also be relevant for other aspects of strongly dipolar coupled spin systems; examples include problems associated with FIDs[19] and the lineshapes,[20] spin diffusion,[21] and spin temperature.[22]

7 DYNAMICAL SCALE INVARIANCE IN THE GROWTH OF MULTIPLE SPIN CORRELATIONS IN DIPOLAR COUPLED SOLIDS

Dilation or scaling symmetry, observed under certain conditions in some physical systems, is a generalization of the concept of similarity among geometrical objects. In geometry, the properties of two circles with different radii are similar to one another by simple transformations of scales. In physical sciences, the practical aspects of scaling involve the determination of the relevant scaled variables to describe a phenomenon, such that all data acquired under a range of conditions collapse onto some single universal plot. Thus, scaling reveals an invariance or a kind of unification among the relevant scaled variables, which was not obvious

in the original unscaled variables. Understanding the physical reasons underlying scaling symmetry usually leads to deeper insights into the phenomenon.

Some scaling arguments have been applied to various aspects of the growth of multiple spin/multiple quantum coherences in solids.[1,2,15,23] In the context of the Gaussian statistical model, studies have focused on the behavior of the variance $N(t)$ in dilution effects[1] and power law growth[2] in spin networks, and dimensional analysis of growth curves.[23] A more elaborate scaling analysis of MQ NMR spectral intensity profiles, as a function of order and excitation time, demonstrated non-Gaussian behavior in extended spin networks.[15] These studies also provided additional support for the case of exponentially decaying intensity profiles. Behind these approaches lies the belief that the physics of the growth processes should be invariant or scale free, for some range of length- and timescales.

Baum et al.[1] have studied the effects of dilution of spin networks with MQ NMR. With increasing dilution, the growth curves $N(t)$ were shifted to longer excitation times. When the excitation time was multiplied by a scaling factor, all growth curves for the diluted systems could be collapsed onto the data of the undiluted or 'pure' spin network. In this case, the scaling symmetry demonstrates the invariance of the physics of the growth processes in the pure and diluted spin networks. A simple dilution in time relates these different systems. The scaling factor was observed to be a function of dilution; no serious attempts were made to understand this phenomenology.

Lacelle[2] has studied the growth curves $N(t)$ of a large variety of solid samples. All the data were seen to follow power law behavior,

$$N(t) \propto t^{\alpha} \tag{38}$$

where α is a growth exponent characteristic of the samples and the growth mechanism. The presence of power law growth indicates a scale invariant process, such that the functional

$$N(\lambda t) = \lambda^{\alpha} N(t) \tag{39}$$

exists for any values of the scaling factor λ. The solution of equation (39), i.e. equation (38), is obtained by setting $\lambda = 1/t$ in equation (39). In order to determine the physics behind the growth exponents, several models were considered. For example, in diffusive growth, the length scale ξ of the multiple spin correlations should follow

$$\xi \propto t^{\frac{1}{2}} \tag{40}$$

The space-filling properties of a homogeneously embedded solid in D dimensions imply that

$$N \propto \xi^{D} \tag{41}$$

Equations (40) and (41) yield

$$N \propto t^{D/2} \tag{42}$$

from which the growth exponent $\alpha = D/2$ is deduced for a diffusive growth mechanism. None of the models developed could account successfully for all the observed growth exponents. However, a classification of the spin networks could be achieved with the long time behavior of the growth rates

$$\frac{\mathrm{d}N}{\mathrm{d}t} \propto t^{\alpha-1} \tag{43}$$

When $\alpha < 1$, the growth rates converge to zero at long excitation times, implying the presence of clusters of spins. When $\alpha > 1$, a divergence in the growth rates should occur, which indicates the presence of an extended network. The case of $\alpha = 1$ corresponds to the threshold between these regimes. In a sense, α serves as a localization/delocalization criterion for multiple spin coherences.

Scruggs and Gleason[23] have examined the growth curves of different simple crystalline materials. By assuming that the growth processes were only determined by a relevant time-independent scale, the inverse of the square root of the second moment of the dipolar linewidths, the different growth curves collapsed onto a single universal curve for early excitation times. Their assumption for this empirical scaling is implicitly equivalent to assuming that the growth processes are dominated by nearest neighbor couplings, since Van Vleck's second moment is also dominated by such couplings.

One could argue about the quality and the quantitative aspects of the fitting procedures with the Gaussian approximation in these studies.[1,2,23] However, the value of such studies really lies in the efforts made to explore the possible facets of scaling in the growth processes of multiple spin/multiple quantum coherences. To ascertain any quantitative aspects of scaling, for example, growth exponents, under these circumstances it is clear that many more experiments involving high quality data will be required.

Lacelle et al.[15] have developed some scaling arguments in order to test the validity of the Gaussian statistical model. In particular, they strived to observe the scaling of MQ NMR spectra, as a function of order and excitation times, in extended spin networks. The Gaussian dependence suggested for the spectral intensity profiles $I(n,t)$ in equation (28) is actually a generalized homogeneous equation. With the time dependence of the variance $N(t)$ corresponding to a random walk model in product operator space,[1,10] the expected scaling, $I(n,t)/t^{-\frac{1}{2}}$ versus $n/t^{\frac{1}{2}}$, should have collapsed all MQ NMR spectra for a sample onto a single universal spectrum. The lack of scaling clearly demonstrated non-Gaussian behavior. Instead, consideration of the multiplicative nature of the coupling constants associated with product operators in equation (26) led to a heuristic argument predicting exponential decaying intensity profiles. The ensuing scaling analysis collapsed MQ NMR spectra, obtained at different excitation times, onto a single universal spectrum, thereby demonstrating dynamical scale invariance in the growth process of multiple spin/multiple quantum coherences. Such an approach reveals some aspects of the complexities, richness, and subtleness of multiple spin dynamics in MQ NMR of solids.

8 RELATED ARTICLES

Average Hamiltonian Theory; Double Quantum Coherence; Multiple Quantum Coherence in Spin-1/2 Dipolar Coupled Solids; Multiple Quantum NMR in Solids; Spin Diffusion in Solids.

9 REFERENCES

1. J. Baum, M. Munowitz, A. N. Garroway, and A. Pines, *J. Chem. Phys.*, 1985, **83**, 2015.
2. S. Lacelle, *Adv. Magn. Opt. Reson.*, 1991, **16**, 173.
3. K. K. Gleason, *Concepts Magn. Reson.*, 1993, **5**, 199.
4. H. E. Stanley, *Introduction to Phase Transitions and Critical Phenomena*, Oxford University Press, New York, 1971, Chap. 9
5. J. D. Gunton, M. San Miguel, and P. S. Sahni, in *Phase Transitions and Critical Phenomena*, ed. C. Domb and J. L. Lebowitz, Academic, London, 1983, Vol. 8, Chap. 3
6. S. Lacelle and L. Tremblay, *J. Chem. Phys.*, 1993, **98**, 3642.
7. D. Chandler, *Introduction to Modern Statistical Mechanics*, Oxford University Press, New York, 1987, Section 3.1.
8. C. P. Slichter, *Principles of Magnetic Resonance*, 3rd edn., Springer, Berlin, 1990, Section 5.4.
9. M. Goldman, *Quantum Description of High-Resolution NMR in Liquids*, Oxford University Press, New York, 1988, Section 4.1.
10. M. Munowitz, A. Pines, and M. Mehring, *J. Chem. Phys.*, 1987, **86**, 3172.
11. Y. S. Yen and A. Pines, *J. Chem. Phys.*, 1982, **78**, 3579.
12. D. H. Levy and K. K. Gleason, *J. Phys. Chem.*, 1992, **96**, 8125.
13. B. E. Scruggs and K. K. Gleason, *Chem. Phys.*, 1992, **166**, 367.
14. G. Cho and J. P. Yesinowski, *Chem. Phys. Lett.*, 1993, **205**, 1.
15. S. Lacelle, S. J. Hwang, and B. C. Gerstein, *J. Chem. Phys.*, 1993, **99**, 8407.
16. B. Derrida, *Phys. Rep.*, 1984, **103**, 29.
17. S. Redner, *Am. J. Phys.*, 1990, **58**, 267.
18. S. Lacelle and L. Tremblay, *Bull. Magn. Reson.*, 1994, in press.
19. I. J. Lowe and R. E. Norberg, *Phys. Rev.*, 1957, **107**, 46.
20. J. H. Van Vleck, *Phys. Rev.*, 1948, **74**, 1168.
21. N. Bloembergen, *Physica*, 1949, **15**, 386.
22. M. Goldman, *Spin Temperature and Nuclear Magnetic Resonance in Solids*, Clarendon, Oxford, 1970.
23. B. E. Scruggs and K. K. Gleason, *J. Magn. Reson.*, 1992, **99**, 149.

Biographical Sketch

Serge Lacelle. *b* 1955. B.Sc., Ottawa, 1978; Ph.D., Iowa State, 1984. Introduced to NMR by B. C. Gerstein. Faculty, Chimie Université de Sherbrooke, 1985–present. Research interests: the development and understanding of NMR methods to probe mesoscopic length scales (1 nm to 1 μm) in condensed matter; statistical mechanics of spin networks; multiple quantum NMR of solids; phase separation and critical phenomena; fluid mechanics; and pattern formation.

Multiple Quantum NMR in Solids

Karen K. Gleason

Massachusetts Institute of Technology, Cambridge, MA, USA

1	Introduction	1
2	MQ Coherence Intensities	1
3	MQ Excitation by $\hat{\mathcal{H}}_{yx}$	2
4	Measuring MQ Intensities	3
5	Small Dipole Coupled Networks	4
6	Large Dipole Coupled Networks	5
7	Dimensionality of a Nuclear Spin Distribution	6
8	Relaxation and Effect of Molecular Motion	8
9	Related Articles	9
10	References	9

1 INTRODUCTION

Multiple quantum (MQ) NMR can provide unique insight into the distribution and motion of nuclei in solids. In this article, we consider multiple quantum coherences associated with homonuclear dipolar coupling among spin-$\frac{1}{2}$ nuclei in solids. Therefore, we consider nuclei with high natural isotopic abundance and a high gyromagnetic ratio. ^{1}H MQ NMR has been applied to study organic solids,[1–3] amorphous semiconductors,[4–7] and adsorbates on catalysts[8–14] and chromatography columns.[15] In addition, ^{19}F MQ NMR has been used to study bulk salts,[16] photosensitive salt/polymer mixtures,[17–19] and bulk polymers.[20] MQ NMR of ^{31}P in solids has also been demonstrated.[21] Several review articles and textbook chapters on MQ NMR experiments and their applications are available.[21–29]

The rate of MQ coherence development depends on the strength and time dependence of each pairwise homonuclear dipolar coupling as well as the number of such pairs. For a network of N equivalent nuclei, the second moment M_2 of the distribution of all the pairwise homonuclear dipole couplings can be related to the geometry of the spin distribution through the van Vleck equation:[30]

$$M_2 = \tfrac{3}{4}\gamma^4\hbar^2 \frac{I(I+1)}{2} \sum_{i<j}^{N-1} \frac{(1-3\cos^2\theta_{ij})^2}{r_{ij}^6} \qquad (1)$$

Thus, many combinations of internuclear distances r_{ij} and the total number of pairs in the summation $N-1$ can give rise to identical M_2. Using MQ NMR, the number and distribution of dipolar couplings can be investigated independently, thus allowing the distribution of nuclei in a solid to be explored.

Observation of MQ coherence development in solids is accomplished interferometrically via a two-dimensional NMR technique.[1,29] By incrementing the MQ preparation time τ, the presence of finite clusters of nuclei can be distinguished from nuclear distributions which are homogeneous on the 1–2 nm length scale of this experiment.[2,3] Coherences arising from a cluster of nuclei will saturate with increasing MQ excitation time, because no additional nuclei are available for correlation in the surrounding region. In contrast, the number of nuclei coupled together in a large homogeneous dipole network will increase monotonically with time until relaxation occurs.

Furthermore, a simple scaling exists for the growth of MQ coherences among many bulk materials.[16,31] This behavior allows homogeneous three-dimensional distributions of nuclei to be differentiated from one- and two-dimensional distributions.[31–33] Identification of two-dimensional distributions is particularly valuable for determining whether a given nuclear species, such as ^{1}H, ^{19}F, or ^{31}P, is segregated at a surface,[31,34] such as a grain boundary in a polycrystalline material. A model which expands the density matrices in terms of average product operators allows these differences to be evaluated numerically.[31]

More complex distributions of nuclei can also be analyzed using MQ NMR. For example, both isolated salt molecules and large aggregates of salt have been observed simultaneously within polymeric matrices.[17–19] Finally, MQ NMR and its relaxation may serve as a valuable probe of molecular reorientation in solids which modulate the dipolar coupling network at frequencies in the kilohertz range.[20,35,36]

2 MQ COHERENCE INTENSITIES

Analysis of MQ intensities is the underlying principle for using MQ NMR as a 'spin-counting' technique, allowing the number of dipole coupled nuclei in a isolated cluster to be determined.[3] Although only two possible states, α and β, exist for an individual spin-$\frac{1}{2}$ nucleus, when N of these nuclei are dipole coupled there are 2^N possible product states. Thus, a $2^N \times 2^N$ density matrix is required to represent fully the time development of MQ coherence intensity among N dipolar coupled spin-$\frac{1}{2}$ nuclei. A schematic representation of ρ for $N = 3$ is shown in Figure 1, where the indices of the matrix are the eight possible product states. Diagonal elements can be used to calculate the populations of the product states, while the off-diagonal elements indicate the MQ coherences between two different states.

The MQ coherence order, n, is equal to the difference in m_z between the two states. Since the z component of angular momentum m_z of an individual spin state is $\pm\frac{1}{2}$, m_z for the product states ranges from $-N/2$ to $+N/2$. Thus, MQ orders can be positive, negative, or zero, provided that $|n| \leq N$. This limitation provides a very elegant way of determining the number of dipole coupled spins in a spatially isolated cluster. However, there is only one way to achieve such an $n = N$ coherence, making it statistically difficult to observe intensity in highest MQ order for large N. Fortunately, the number of density matrix elements Z_n for lower order coherences ($|n| < N$) also depends on the number of coupled nuclei:

$$Z_n = \sum_{i<j} \delta_{[(m_{zi}-m_{zj}),n]} = \binom{2N}{N-|n|} \qquad (2)$$

In this equation, Z_0 includes both off-diagonal elements with $n = 0$, representing true zero quantum coherence (0Q), and diagonal elements representing self-correlation among the

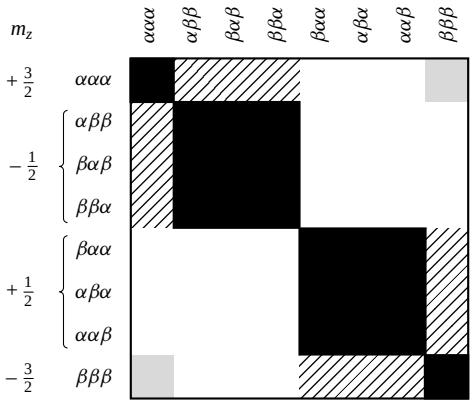

Figure 1 Schematic representation of ρ for $N = 3$. The 2^3 product states are sorted by m_z so that elements corresponding to even MQ coherences ($n = 0$, black; $|n| = 2$, striped) appear in the upper left and lower right quadrants. The remaining elements correspond to odd MQ orders ($|n| = 1$, white; $|n| = 3$, grey)

states, as no difference is resolved between these two types of element by most MQ experiments.

Each element in Figure 1 is shaded according to the absolute value of its corresponding MQ order. Note that the first $4^N/2$ indices in Figure 1 represent the states with $m_z = (N - k)$, where k is an integer. Thus, elements corresponding to even order MQ coherences will appear only in the upper left and lower right quadrants of the density matrix. The remainder of the elements in the upper right and lower left quadrants correspond to odd order MQ coherences. If only even order MQ coherences are excited, this density matrix will be block diagonal with only $4^N/2 = 32$ possible nonzero elements. For $N = 3$, the number of elements contributing to the even orders will be $Z_0 = 20$ and $(Z_2 + Z_{-2}) = 12$.

At equilibrium, the density matrix is proportional to I_z. Thus, only the diagonal elements are nonzero. As MQ excitation begins, intensity develops in density matrix elements of low MQ order. Longer excitation times are required for growth of high-order MQ coherences. The n quantum intensity at any time τ after MQ excitation is begun $I_n(\tau)$, contains contributions from all Z_n density matrix elements comprising that order:[37]

$$I_n(\tau) = \sum_{i<j} \delta_{[(m_{zi}-m_{zj}),n]} |\rho_{ij}(\tau)|^2 \tag{3}$$

Thus, calculation of MQ dynamics requires following the time evolution of the density matrix under the influence of the Hamiltonian corresponding to the MQ excitation sequence during the experiment.

The Liouville von Neumann equation of motion can be used to calculate $\hat{\rho}(\tau)$ explicitly:

$$\frac{\mathrm{d}\hat{\rho}(\tau)}{\mathrm{d}\tau} = \mathrm{i}[\hat{\rho}(\tau), \tilde{\hat{\mathcal{H}}}] \tag{4}$$

where $\hat{\mathcal{H}}$ is the Hamiltonian applied to the system for a duration τ in order to develop MQ coherences. If average Hamiltonian theory can be applied, the solution of equation (4) is

$$\hat{\rho}(\tau) = \exp(-\mathrm{i}\tilde{\hat{\mathcal{H}}}\tau)\rho(0)\exp(\mathrm{i}\tilde{\hat{\mathcal{H}}}\tau) \tag{5}$$

For small numbers of spins ($N \leq 9$), the development of $I_n(\tau)$ has been calculated explicitly using equations (3) and (5).[32,37,38]

However, tracking the time development of the 4^N density matrix elements is a large task for any significant number of coupled spins. For $N = 95$, the number of density matrix elements exceeds the number of hydrogen atoms in the Earth's sun! Thus for a large N, statistical limit behavior is often assumed, in which all MQ coherences have equal probability, allowing the magnitude of all density matrix elements to become equal at long excitation times.

The assumption of a statistical limit[37] greatly simplifies the analysis of MQ coherence intensities since the intensity of an n quantum coherence depends only on the number of elements of that order Z_n:

$$I_n = \frac{C Z_n}{4^N} \tag{6a}$$

The inverse of the constant C represents the fraction of density matrix elements where nonzero intensity could be excited. This fraction depends upon the selectivity of the Hamiltonian applied to the system. When nonselective excitation is used, all MQ orders are excited and $C = 1$. However, selective MQ excitation is often used. For instance, if only even MQ orders are excited, $C = 2$. Since equation (2) shows that Z_n is a function of n and N only, the distribution of $I_n(\tau)$ allows N to be determined. When $N \geq 6$, the right-hand side of equation (6a) can be approximated by a Gaussian distribution:

$$I_n \simeq \frac{C}{\sqrt{N\pi}} \exp(-n^2/N) \tag{6b}$$

Equations (6a) and (6b) are valid for all positive, negative and zero integer values of n, and are normalized such that

$$\sum_{n=-\infty}^{\infty} I_n = 1 \tag{7}$$

In addition, note that the MQ intensity distribution is symmetric, $I_n = I_{-n}$, and that I_0 contains both populations and true 0Q coherences. Furthermore, higher order coherences are statistically more difficult to achieve than lower order coherences. As will be shown below, I_0 tends to deviate more from the predicted values than the positive orders; only the latter are generally utilized to determine N. Statistical limit behavior is often a poor assumption for very small groups of spins, due to presence of symmetry forbidden transitions.

3 MQ EXCITATION BY $\hat{\mathcal{H}}_{yx}$

One of the most desirable Hamiltonians for exciting MQ coherences in solids is $\hat{\mathcal{H}}_{yx}$:

$$\tilde{\hat{\mathcal{H}}}_{yx} = -\frac{1}{2}\sum_{i<j} R_{ij}(\hat{I}_{i+}\hat{I}_{j+} + \hat{I}_{i-}\hat{I}_{j-}) \tag{8}$$

Other Hamiltonians such as $\hat{\mathcal{H}}_{zx}$ have been used for exciting MQ coherences. However, higher orders develop more quickly under $\hat{\mathcal{H}}_{yx}$,[38] maximizing the number of spins that can be correlated before relaxation effects become significant.

The bilinear raising and lowering operators $\hat{I}_{+i}\hat{I}_{+j}$, and $\hat{I}_{-i}\hat{I}_{-j}$ allow only even-order MQ coherence intensity to evolve when $\hat{\mathcal{H}}_{yx}$ is utilized in conjunction with an equilibrium initial density matrix $\rho(0)$ that is proportional to $\hat{I}_z$. When only half of all possible orders are excited, the intensity of each is twice that of a nonselective experiment [equation (6)]. The increased intensity is particularly important for detecting high-order coherences, which are statistically less likely than lower order coherences. Odd order and nonselective excitation using $\hat{\mathcal{H}}_{yx}$ results when prepulses create an initial density matrix proportional to the single quantum operator $\hat{I}_x$ or it can be made nonselective if $\rho(0)$ is a mixture of $\hat{I}_z$ and $\hat{I}_x$, respectively.[40]

For spin counting applications it is important to note that the selection rules for $\hat{\mathcal{H}}_{yx}$ from an initial density matrix proportional to $\hat{I}_z$ result in the inability to create $n = N$ quantum coherence. Obviously, N quantum coherence cannot be developed when N is odd. More surprisingly, N quantum coherence cannot be achieved among $N = 4k$ dipole coupled spins, where k is a positive integer.[40] Thus, four quantum coherence cannot develop among an isolated cluster of four coupled nuclei. While these limitations appear problematic, the ability to achieve N quantum coherence via other MQ propagators can be even more restrictive. For instance, under $\hat{\mathcal{H}}_{zx}$ the N quantum order can never be achieved when starting from the equilibrium density matrix. The restrictions on creating N quantum coherence are only significant for size determination among very small clusters of nuclei. In larger dipole coupled networks, the signal-to-noise ratio of the highest order MQ coherence is generally below the detection limit, rendering the ability to achieve this coherence insignificant.

To carry out the MQ experiment in the laboratory, the phase ϕ of $\hat{\mathcal{H}}_{yx}$ is generally varied.[1,2] One or more repetitions of the eight-pulse cycle shown below have been used to create $\hat{\mathcal{H}}_{yx}(\phi)$:

$$(\Delta/2) - 90^\circ_\phi - (\Delta') - 90^\circ_\phi - (\Delta) - 90^\circ_\phi - (\Delta') - 90^\circ_\phi - (\Delta) - 90^\circ_{\phi+180^\circ} - (\Delta') - 90^\circ_{\phi+180^\circ} - (\Delta) - 90^\circ_{\phi+180^\circ} - (\Delta') - 90^\circ_{\phi+180^\circ} - (\Delta/2)$$

where $\phi = 0^\circ$ corresponds to an x pulse. The relationships between the delays is $\Delta' = 2\Delta + t_p$, where t_p is the pulse length. The average Hamiltonian, $\tilde{\hat{\mathcal{H}}}_{yx}(\phi)$ is then

$$\tilde{\hat{\mathcal{H}}}_{yx}(\phi) = -\frac{1}{2}\sum_{i<j} R_{ij}[\hat{I}_{i+}\hat{I}_{j+}\exp(2i\phi) + \hat{I}_{i-}\hat{I}_{j-}\exp(-2i\phi)] \quad (9)$$

Considering $0^\circ \le \phi < 360^\circ$, $\tilde{\hat{\mathcal{H}}}_{yx}(\phi) = \hat{\mathcal{H}}_{yx}$ at $\phi = 0^\circ$ or 180° and $\tilde{\hat{\mathcal{H}}}_{yx}(\phi) = -\hat{\mathcal{H}}_{yx}$ at $\phi = 90^\circ$ or 180°. During the mixing period, the value of ϕ is fixed at 90°, corresponding to $-\hat{\mathcal{H}}_{yx}$.

In the presence of heteronuclear couplings, the $\hat{\mathcal{H}}_{yx}$ sequence can be used to examine the distribution of I spins without irradiation of the S spin frequency or reduction of the $I-S$ couplings by isotopic exchange.[16] This is particularly important when both ^{19}F and ^{1}H are present in the sample of interest.

As in any multiple pulse NMR experiment, deviations from perfect delta pulses, finite pulse cycle times with respect to the inverse frequences of the interactions in the sample, and off-resonance effects can lead to undesirable effects.[42] The sensitivity to chemical shift offset has recently been exploited to measure the correlation length of the chemical shift shielding tensor in polycrystalline solids.[43] This increased sensitivity of higher order coherences to magnetic field gradients has also been exploited to enhance the spatial resolution of NMR imaging of solids.[44] In the future, excitation using shaped rf pulses has the potential for improving experimental implementation of the MQ experiment.[45] In practice, rectangular pulses with $t_p \le 3\,\mu$s and eight-pulse cycle times t_c, of $30-72\,\mu$s are generally employed, and the experiment is carried out on resonance.

4 MEASURING MQ INTENSITIES

Although MQ coherences have sometimes been detected directly by CW NMR,[22] MQ coherences cannot be detected directly by FT NMR. Since MQ intensities are nonlinear under CW experiments, two-dimensional NMR experiments are currently employed for this purpose. Only an overview of the required experimental procedure is provided below. Additional descriptions can be found in Yen and Pines,[1] Baum et al.,[2] Baum and Pines,[3] and Gleason.[21]

As in most two-dimensional NMR experiments, there are four distinct periods: preparation, evolution, mixing, and detection. During the preparation period, of length τ and phase ϕ, MQ coherences are excited as a result of homonuclear dipole couplings, and nonzero intensity is developed in the off-diagonal elements of the density matrix [equation (9)]. However, no observable magnetization from these elements can be detected experimentally. These coherences evolve during t_1, the evolution period time. The mixing period of length τ (identical to the preparation period length) and phase $\phi = 90^\circ$, converts MQ coherences in the off-diagonal elements back into diagonal elements, corresponding to z magnetization. Finally, the detection period is used to create observable signal $S(\phi, \tau)$.

In order to resolve the various n quantum coherences, the phase of the preparation period ϕ is changed from 0 to 360° in increments of $\Delta\phi$, while the preparation period length, the mixing period length, and the phase of mixing period are held fixed. Fourier transformation of this series of $S(\phi,\tau)$ at constant τ with respect to ϕ yields the intensities of the n quantum orders $I_n(\tau)$. At least $2n$ phase shifts must be performed when detectable n quantum intensity is present. Fewer phase shifts will alias high-order coherence intensity to lower values of n. Most commonly, $\Delta\phi$ is set at 5.6° or 2.8°, allowing detection of $|n| \le 16$ and 32, respectively.

In order to determine the local distribution of nuclei within a sample, $I_n(\tau)$ is measured for a series of τ. Generally,

$\tau = n_c t_c$ which corresponds to changing the integer number of repetitions n_c, of the basis eight-pulse MQ subcycle for $\hat{\mathcal{H}}_{yx}$. In a given sample, longer τ values correspond to probing the dipolar network over increasing distances.

The length of the evolution period t_1 can also be incremented, allowing MQ coherences to evolve under the internal Hamiltonian of the spin system, yielding the n quantum coherence lineshapes.[1] However, for many applications, only the integrated intensity of the coherence is required. Thus, the evolution period time t_1 is often set to zero,[5,46] maximizing the final signal intensity and significantly decreasing acquisition time. This also eliminates the effects of couplings linear in $\hat{I}_z$ such as chemical shift and heteronuclear dipole coupling during the evolution period.

When $t_1 = 0$ and relaxation effects are neglected, the density matrices at times 0 and 2τ are identical when $\phi = 0^\circ$ or 180°, so called 'time reversal'. At other ϕ some transverse magnetization will also be present at the end of the mixing period and the magnitude of z magnetization will be reduced. Thus, prior to the detection period, a delay which is long compared to T_2 but short compared to T_1 allows for decay of any transverse magnetization transients. Then, a $\pi/2$ pulse can be applied to detect $S(\phi,\tau)$. Spin locking with periodic sampling can be employed during the detection period to enhance the signal-to-noise ratio of $S(\phi,\tau)$.

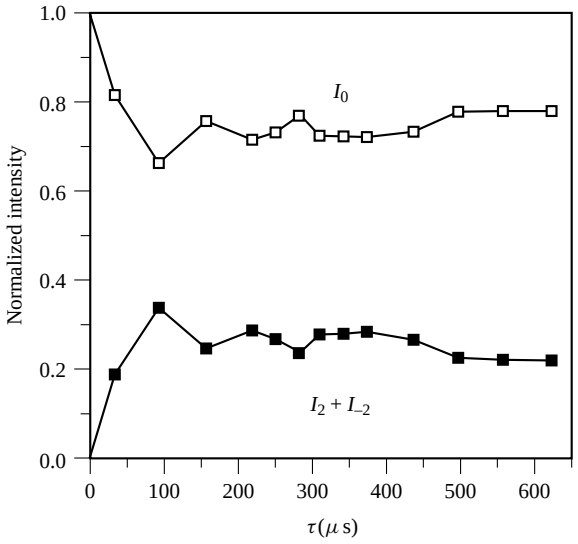

Figure 2 The ^{19}F zero quantum and +2 and −2 quantum intensities from an even-selective experiment on 2 wt.% NH_4+$CF_3SO_3^-$ in poly(*p*-hydroxystyrene). The salt is well dispersed in the polymer, and thus its CF_3 group behaves as expected for $N = 3$. Oscillations are distinct at early τ and destructive interference leads to steady-state values at long τ. (Reproduced by permission of the American Chemical Society from Limb et al.[19]

5 SMALL DIPOLE COUPLED NETWORKS

Even when the number of dipole coupled spins is small, the dynamics of MQ coherence growth can become quite complicated. The simplest possible system to consider is isolated pairs ($N = 2$) of spin-$\frac{1}{2}$ nuclei with identical internuclear separations and orientations with respect to the external magnetic field. Thus, all intrapair dipole coupling constants R are identical and much stronger than any interpair coupling. Then, even order selective excitation by $\hat{\mathcal{H}}_{yx}$ allows only the zero quantum and ± 2 quantum intensity to develop as given by the analytical solution to equation (5):

$$I_2(\tau) = I_{-2}(\tau) = \tfrac{1}{2}[1 - I_0(\tau)] = \tfrac{1}{2}[1 - \cos(R\tau)] \quad (10)$$

In the absence of relaxation, the oscillatory exchange of MQ coherence intensity between the orders will continue indefinitely.[38]

In a macroscopic NMR sample, such as a single crystal or a liquid crystal, identical orientations of internuclear vectors with respect to the external magnetic field can occur. By contrast, polycrystalline powders are the most commonly used samples for MQ NMR. Even for isolated pairs with identical internuclear spacings, the angular dependence of the dipolar coupling interaction leads to destructive interference among the characteristic frequencies which contribute to the MQ intensity development, leading to steady state values of I_n at long τ.

The appearance of oscillations which are damped at long times is characteristic of the powder average of a small number of coupled spins.[41] Figure 2 shows the ^{19}F MQ coherence development for sodium triflate salt ($NH_4^+CF_3SO_3$) well dispersed in polyhydroxystyrene.[19] Only the $n = 0$, 2, and −2 quantum orders have nonzero intensity under the even-selective MQ excitation employed. This is the same behavior expected for an isolated network of three dipole coupled ^{19}F nuclei, where only even MQ orders with $|n| \leq 3$ develop. This result indicates that the average spacing between the salt anions is large, allowing its CF_3 group to act as an isolated $N = 3$ cluster. Note that this configuration can be represented by the density matrix shown in Figure 1. Furthermore, the development of ± 2 quantum coherence intensity indicates that the time average of the intraion dipole couplings is nonzero. Thus, the triflate anion is not reorienting rapidly and isotropically within the polymeric matrix.

Clear oscillations in the MQ intensities are initially observed in Figure 2, while steady state is approached at $\tau >$ 500 ms. The observed long time values are 0.78 for the zero quantum coherence and 0.22 for the sum of the +2 and −2 quantum coherences. These values differ significantly from the predictions of equation (6a), utilizing $N = 3$ and $C = 2$, of 0.625 and 0.375, respectively. This difference shows that the statistical limit has not been achieved, a problem that was anticipated for very small numbers of coupled spins due the presence of symmetry disallowed MQ transitions. Thus, it is desirable to determine N for very small networks by detecting the highest order coherence present, rather than by assuming that the statistical limit holds.

For larger groups of spins, good agreement with the statistical limit behavior has been found. The liquid crystal, *p*-hexyl-*p*′-cyanobiphenyl ($C_{19}H_{21}N$) is a finite cluster of dipole coupled spins, since translation and anisotropic rotation serve to destroy intermolecular dipole couplings, while intramolecular dipole couplings maintain nonzero values. As expected, the positive order MQ coherences grow with τ until all the protons on the liquid crystal molecule are coupled on the experimental timescale. No further increase occurs as the preparation time increases further. The distribution of the steady state MQ intensities is well described by equation (6b)

with $N = 20 \pm 1$. This result is in excellent agreement with the known structural formula.[3]

Thus, MQ NMR gives quantitative information on the number of nuclei in a limited network of dipole, when the structure is unknown. For instance, the size of small hydrogenated defects in amorphous semiconductors has been determined.[4–7] The clustering of molecules inside zeolites[9,11–14] and the distribution of molecules on catalysts[8,10,29] and on chromatographic supports[15] have also been investigated using the MQ spin counting technique.

6 LARGE DIPOLE COUPLED NETWORKS

Although the MQ dynamics of spin systems for which the dipole coupling network extends beyond the typical 1–2 nm length scale of a MQ NMR experiment are nearly impossible to calculate exactly, similar development of $I_n(\tau)$ is observed in many samples. Figure 3 shows the development of positive even-order MQ coherence intensity for CaF_2 powder for increasing τ created from integral multiple repeats of t_c between 30 and 60 μs. The smooth MQ development in Figure 3 is a result of the distribution of dipole coupling present in this polycrystalline sample. Significant oscillations in $I_n(\tau)$ can be seen in a single crystal CaF_2 with its (111) direction oriented perpendicular to the applied magnetic field (Figure 4). For this configuration, all internuclear vectors to the nearest ^{19}F neighbors are at either 54.7°, the magic angle, or (54.7 + 180)°. Thus, all four dipole couplings between nearest neighbors are zero for this configuration. The strongest couplings in this system are actually between next nearest neighbors. The lack of angular dispersion and relative weak dipole couplings lead to only slow damping of the oscillation of the MQ coherences which arises from the even weaker dipolar coupling to neighbors in other shells. The small dipolar couplings in the (111) oriented crystal also lead to slower growth of positive MQ intensities than is observed for the powdered CaF_2 sample.

The observed distributions of $I_n(\tau)$ for polycrystalline powders are often described empirically as a Gaussian distribution, as can be seen in Figure 5 for powdered CaF_2 and GaP, where the solid lines are given by equation (7). The slow development of MQ coherence intensity in GaP allows the comparison to be made for low $N(\tau)$ while CaF_2 provides information at higher $N(\tau)$ values. This description is convenient, as the single parameter $N(\tau)$ can be used to describe an entire MQ spectrum.[2] However, the interpretation of $N(\tau)$ via equation [6,7]6 is not straightforward, since the number of coupled spins is ill defined in this situation. Materials with the highest dipolar couplings also display the fastest growth of $N(\tau)$. Thus $N(\tau)$ has been considered as a parameter that is dependent on the size, structure, and motion of the dipolar coupling network.

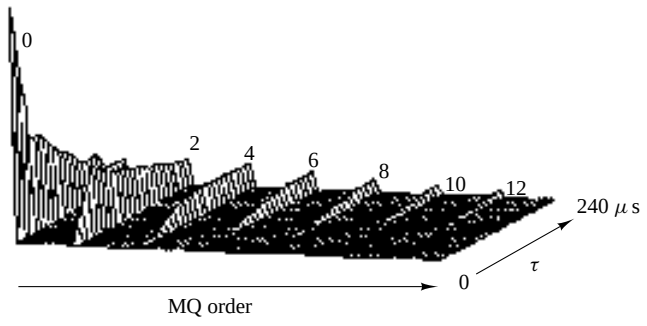

Figure 3 Even-order selective ^{19}F MQ spectra of a polycrystalline powder of CaF_2. As τ increases, high-order coherence intensities grow monotonically

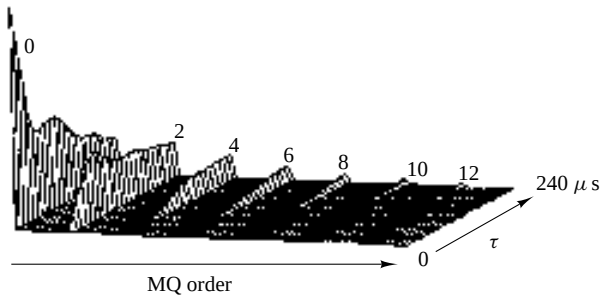

Figure 4 Even-order selective ^{19}F MQ spectra of a single crystal of CaF_2 oriented with its (111) direction along the external magnetic field. The lack of angular orientation distribution, as compared to the powder (Figure 3), leads to oscillatory growth of the zero and two quantum coherences, while the smaller magnitude of the dipole couplings in this sample leads to slower higher order coherence growth

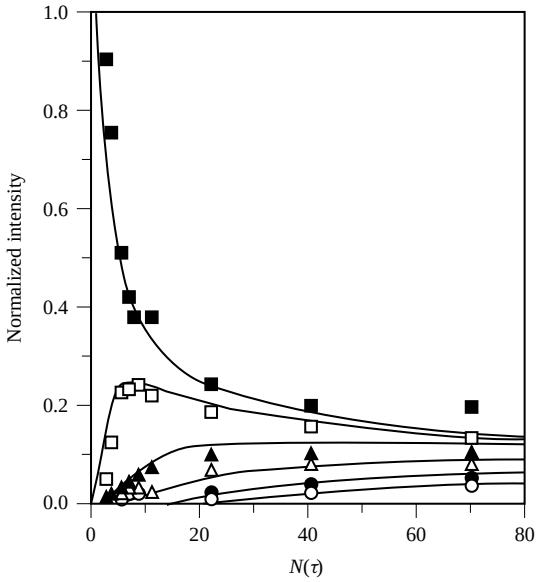

Figure 5 Gaussian distribution (——) and experimentally measured intensities versus $N(\tau)$ for two large dipole coupled networks, $Ca^{19}F_2$ (squares) and $Ga^{31}P$ (other symbols), showing reasonable agreement for $N(\tau) < 70$: (■) I_0, (□) I_2, (▲) I_4, (△) I_6, (●) I_8, (○) I_{10}

Non-Gaussian behavior of the distribution of positive MQ orders for infinite spin systems at long τ has been noted, usually becoming significant when $N(\tau)$ is greater than about 70. In addition, a least-squares fit to equation (6) underpredicts the intensity of the nonzero orders while overpredicting the zero quantum intensity. This may indicate relaxation of intensity in the off-diagonal density matrix elements back to diagonal elements. These effects are not seen in the 21-spin system, liquid crystal *p*-hexyl-*p*′-cyanobiphenyl ($C_{19}H_{21}N$), experiments at similar τ, and thus cumulative pulse errors cannot be the sole cause of the deviation. Experimentally,

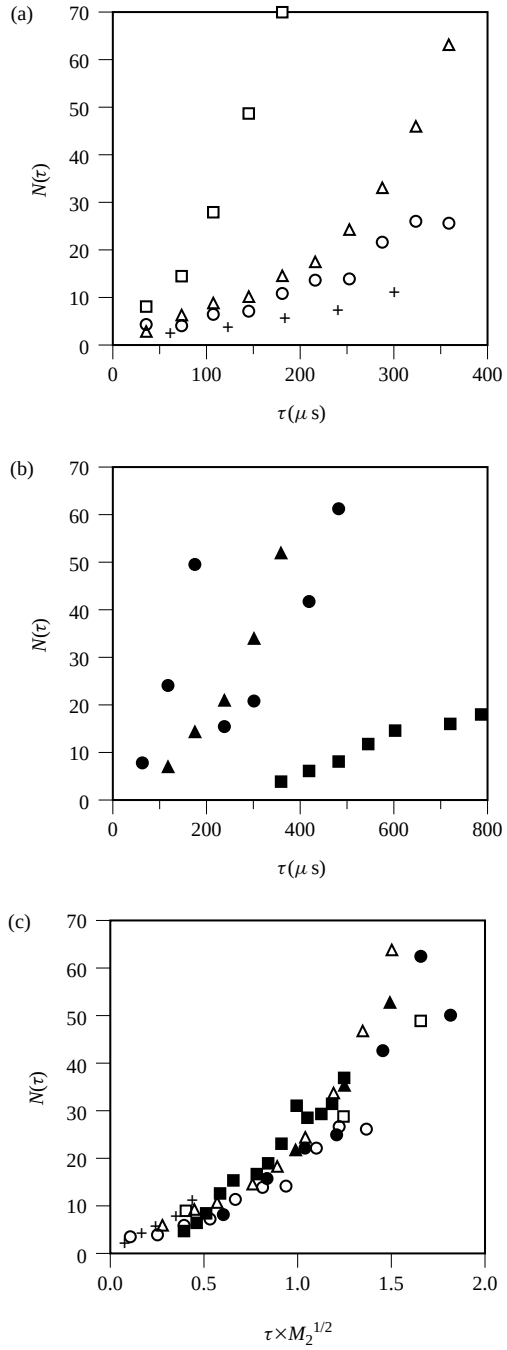

Figure 6 Effective number of correlated nuclei, $N(\tau)$ as function of τ for three-dimensional distributions (a): (□) CaH_2 (^{1}H),[31] (△) adamantane (^{1}H),[31] (○) sodium bicarbonate (^{1}H),[31] (+) Ga P (^{31}P).[21] (b) All ^{19}F:[16] (+) CaF_2, (▲) $NaAsF_6$, (●) CsF, (■) $(C_6F_5)_3SAsF_6$. (c) A universal MQ growth curve is seen for all the samples in (a) and (b), when a nondimensional time axis is created by multiplying τ by $M_2^{1/2}$ (equation (1))

the zero quantum intensity deviates from Gaussian behavior at the smallest number of correlated spins, making it a strong indicator of the onset of relaxation effects.

However, as shown in Figure 6(a) and 6(b) for $N(\tau) < 70$, $N(\tau)$ does grow as the MQ excitation time τ increases. This development of $N(\tau)$ can be described by a universal growth curve when a dimensionless MQ excitation time is created by multiplying τ by $M_2^{\frac{1}{2}}$.[18,21,31] The result of this scaling is shown in Figure 6(c), where $M_2^{\frac{1}{2}}$ has been calculated from equation (1) using the known crystal structures of the materials. The solids represented in Figure 6 fall into one of two catagories. In both categories the dipolar field at each nucleus in a three-dimensional crystal lattice is equivalent and time independent on the MQ timescale. For the first class of materials, no translation or rotation occurs on the NMR timescale. Examples of this category include Ca^1H_2, $Ca^{19}F_2$, and $Ga^{31}P$. In the second class, rapid isotropic rotation exists in the absence of translation, allowing only intermolecular dipole couplings to survive. Examples of such behavior are ^{1}H in adamantane or ^{19}F in salts containing hexafluoroarsenate anions (AsF_6^-). For this second category, the high concentration of NMR active nuclei with relatively low dipole couplings allows larger numbers of spins to be correlated before relaxation effects become significant.

The MQ dynamics of many molecular solids do not follow the universal growth curve, since these solids possess a variety of short internuclear spacings and motion which is neither fast nor isotropic. Sometimes, lowering the sample temperature can eliminate such undesirable motion. In addition, some nuclear distributions are inherently nonuniform, and non-Gaussian intensity distributions are observed even at short τ. For example, both isolated salt molecules and salt aggregates can exist within the same salt/polymer mixture.[17,19] The fraction of each environment can be quantitated by treating the observed MQ spectra as a linear combination of the two MQ intensity distributions. Treatment of MQ coherence growth from nuclei within tightly coupled clusters in addition to slower intercluster growth has also been used to analyze proton distributions in amorphous hydrogenated semiconductors[4–7] and to characterize the distribution of molecules absorbed in zeolites.[11,12]

7 DIMENSIONALITY OF A NUCLEAR SPIN DISTRIBUTION

Certain deviations from the MQ universal behavior [Figure 6(c)] for large dipole coupled networks cannot be accounted for by the presence of molecular motion. Such deviations may indicate that the nuclear distribution is not three dimensional. Hydrogen existing on the surface of a treated natural diamond powder is an example of a two-dimensional distribution.[31] For the diamond powder, the $N(\tau)$ versus τ curve exhibits a concave upward shape, unlike $N(\tau)$ for the 21-spin liquid crystal, which saturates at large preparation times. Thus, the diamond powder represents a large dipole coupled network. However, its MQ growth does not follow the universal scaling behavior of the three-dimensional model compounds. Even greater deviation from the universal curve was found for the initial MQ growth among protons in hydroxyapatite which provides a pseudo-one-dimensional distribution of spin-$\frac{1}{2}$ nuclei.[33]

To predict the influence of dimensionality on the rate of MQ coherence in large dipolar networks, a solution to equation (4) is required. For this purpose $\hat{\rho}(\tau)$ is expanded in terms of product operators, as an alternative to tracking the time development of each of the 4^N individual elements.[41] These product operators are formed from the multiplication

of individual spin operators ($\hat{I}_{iz}$, $\hat{I}_{i+}$ or $\hat{I}_{i-}$) from M of the N nuclei in the dipole network. For example, $\hat{I}_{5z}\hat{I}_{6-}\hat{I}_{7+}\hat{I}_{8z}$, represents $M = 4$ possible product operators when $N \geq 8$.

Two simplifications[31] allow $\hat{\rho}(\tau)$ to be approximated by an expansion requiring only N coefficients:

$$\hat{\rho}(\tau) \approx \sum_{M=1}^{N} C_M(\tau)\hat{P}_M \tag{11}$$

Here, $\hat{P}_M$ is a time independent average product operator, representing all the possible product operators containing M spins. Thus, the time evolution of the MQ coherence and multiplicity of all possible product operators with respect to M is contained in the coefficients $C_M(\tau)$.

When $\hat{\rho}(0) = \hat{I}_z$, only $C_1(0)$ has nonzero intensity. Intensity develops in C_M for $M > 1$ with increasing τ through the commutator obtained when equation (11) is substituted into equation (4) under excitation by $\hat{\mathcal{H}}_{yx}$:

$$\sum_M \left(\frac{\mathrm{d}C_M}{\mathrm{d}\tau}\hat{P}_M\right) = \frac{-\mathrm{i}}{4}\sum_M C_M\left\{\sum_i^N\sum_{i\neq j}^N R_{ij}[\hat{P}_M, (\hat{I}_{i+}\hat{I}_{j+}\hat{I}_{i-}\hat{I}_{j-})]\right\} \tag{12}$$

This summation represents only N coupled differential equations, thus significantly reducing the volume of calculation required compared to the exact solution. Information on the order of the MQ coherences has been averaged away. However, approximating the effective spin correlation size $N(\tau)$ as the center of mass of the distribution of C_M over M allows the results of the average product operator model to be compared directly with experimental measurements of $N(\tau)$.[31]

To emphasize that the rate of MQ coherence development through equation (12) is strongly dependent on the geometry of the dipole coupled network, only two values of R_{ij} will be considered. All nearest neighbor dipole couplings are taken to be equal to the root-mean-square value over the powder average for the nearest neighbor separation, and all R_{ij} for all non-neighboring nuclei are set equal to zero. This is a stepwise approximation to the true decay in the magnitude of dipole coupling constants with internuclear distance cubed.

Because R_{ij} is nonzero only for nearest neighbors, only product operators representing M spins occupying a contiguous region of space will contribute to the average product operator $\hat{P}_M$. For simplicity, lines, squares, and cubes are the shapes assumed to be associated with $\hat{P}_M$ for nuclei distributed uniformly over one-, two-, and three-dimensional lattices, respectively. A schematic drawing of P_9 for a two-dimensional (surface) distribution of nuclei is shown in Figure 7. In order to compute MQ dynamics, the commutator in equation (11) must be evaluated. Only adjacent i,j spin pairs need to be considered because only these have nonzero values of R_{ij}. Thus, the larger the number of nearest neighbors, the greater the possibilities for high-order MQ development. As shown in Figure 7, the spin pair i,j and the M spins comprising $\hat{P}_M$ will have zero, one, or two of their spins in common; these cases correspond to pairs external to, at the surface of, or internal to $\hat{P}_M$, respectively. The commutator for external pairs is identically zero, resulting in no change in the size of the MQ coherence. Products of $M + 1$ and $M - 1$ spin operators result from commutators involving surface and internal pairs, respectively.

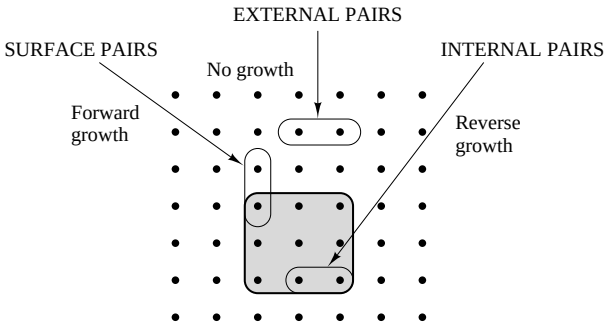

Figure 7 Schematic drawing of $\hat{P}_M$, the average product operator for nine spins on a two-dimensional square lattice. Surface pairs lead to forward MQ growth, while internal pairs reduce the coherence size. Faster MQ coherence growth rates are anticipated as the dimensionality of the lattice increases, since the ratio of surface pairs to internal pairs increases

The $\hat{P}_{M+1}$ operators represent forward growth of the MQ coherence size, while the $\hat{P}_{M-1}$ operators correspond to reverse growth, allowing equation (12) to be simplified to

$$\sum_M (\mathrm{d}C_M/\mathrm{d}\tau)\hat{P}_M = \frac{-\mathrm{i}}{4}\sum_M C_M \times (W^{\mathrm{f}}_{M+1}\hat{P}_{M+1} + W^{\mathrm{r}}_{M-1}\hat{P}_{M-1}) \tag{13}$$

Note that the $\Delta M = \pm 1$ selection rule for product operator evolution under $\hat{\mathcal{H}}_{yx}$ is evident from this equation. The forward and reverse growth rate coefficients W^{f}_M and W^{r}_M depend on the number of pairs at the surface of and internal to $\hat{P}_M$. Since the surface-to-volume ratio for $\hat{P}_M$ depends on its dimensionality, higher MQ growth rates are anticipated for homogeneous distributions of nuclei of increasing dimensionality.

Thus, using average product operators, an N-spin system can be represented by a set of N simultaneous differential equations, allowing the MQ dynamics of large numbers of spins, arranged in varying morphologies, to be easily simulated. Figure 8 shows the growth of $N(\tau)$ predicted by the average product operator model using only nearest neighbor couplings of 1.0 kHz. The analytical formulae used to calculate W^{f}_M and W^{r}_M in equation (13) are given in Levy and Gleason.[31] The three curves were obtained by considering 2500 nuclei arranged uniformly on linear, square, or cubic lattices. As expected, the three-dimensional configuration of nuclei yields the fastest MQ growth. The linear geometry yields slow linear growth of $N(\tau)$. The model can be used to simulate the MQ dynamics of various types of spin distribution and has been extended to nuclear distributions having more than one characteristic nearest neighbor dipole coupling.[31]

The model and experimental data can be compared by scaling the time axis in Figure 7. The experimental data for CaH_2 and for hydrogenated diamond powder given in Figure 9 are in good agreement with the computer simulations of MQ coherence growth for two- and three-dimensional nuclear distributions based on the average product operator

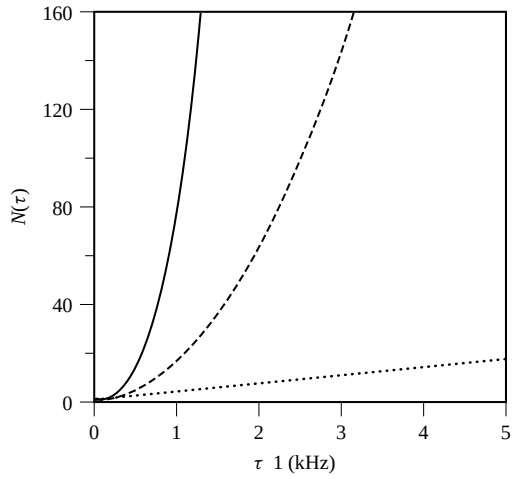

Figure 8 Values of $N(\tau)$ predicted by the average product operator model for spin-$\frac{1}{2}$ nuclei evenly spaced on a line, square lattice, or cubic lattice. In each case, the nearest neighbor dipole coupling was fixed at 1 kHz. The most rapid growth of $N(\tau)$ results for the cubic lattice which has the largest number of nearest neighbors, while the linear arrangement, with the lowest number of nearest neighbors, yields the slowest development of $N(\tau)$. (Reproduced by permission of NMR Concepts from Gleason[21]

model with only one adjustable parameter. In addition, the initial MQ growth of the pseudo-one-dimensional distribution of protons in hydroxyapatite has been found to agree with the slow, nearly linear growth predicted by the results of the product operator calculation for the one-dimensional distribution of nuclei.[33]

8 RELAXATION AND EFFECT OF MOLECULAR MOTION

MQ relaxation rates have been considered in detail by Ernst in terms of the Redfield formalism.[35] The zero quantum and

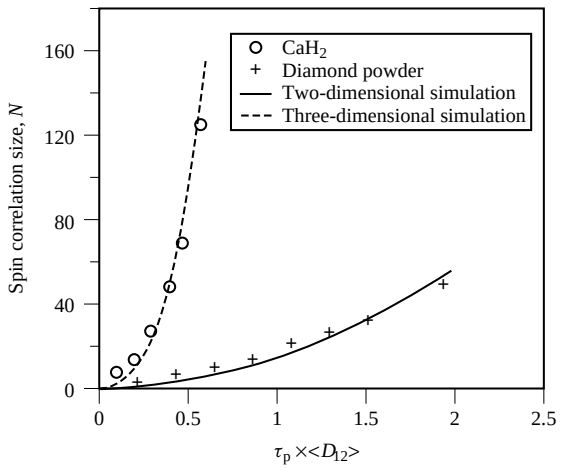

Figure 9 Comparison of MQ dynamics predicted by average operator theory and experimental data for infinite two- and three-dimensional systems. (Reproduced by permission of the American Chemical Society from Levy and Gleason[30]

$n \geq 2$ MQ relaxation rates provide information on the spectral densities of autocorrelation and cross-correlation functions which is not obtainable from the more traditionally measured single quantum relaxation rates. Since the sensitivity to static magnetic field inhomogeneity is proportional to the MQ order, this effect can be problematic when measuring higher order MQ relaxation rates. However, zero quantum relaxation rates have the desirable property of not being influenced by such gradients. This exact theoretical treatment of MQ relaxation has been applied to the external paramagnetic relaxation of two spin-$\frac{1}{2}$ nuclei in a liquid[35] and of an oriented CH_3 group in a liquid crystal.[36] However, application of this exact theory becomes increasingly difficult as the size of the coupled spin-$\frac{1}{2}$ network increases and when the results must be averaged over many possible orientations. Thus, although general considerations have been addressed,[23,28] the measurement and quantitive analysis of MQ relaxation in polycrystalline solids have been limited to date.

Empirically it has been observed that the total signal present in the detection period after MQ excitation of a rigid solid decreases with τ, often becoming negligible for $\tau > 1$ ms. The largest number of spins correlated is thus generally limited to between 100 and 1000, corresponding to a 1–2 nm length scale in a bulk three-dimensional solid. In addition, models for the growth of MQ coherence are difficult to validate because spin correlation data are generally only available for relatively very short τ.

Additional effects are observed when molecular motion modulates the dipolar couplings in solids through variations in internuclear distances and/or the orientation of the internuclear vectors with respect to the applied magnetic field.[20] When the timescale for motion is comparable to τ, complete time reversal of the preparation period is not achievable during the mixing period. Thus, the fraction of magnetization which is actually refocused by the MQ experiment f_{MQ} will generally be < 1. However, efficient refocusing can occur if the frequency of the molecular motion and the MQ experiment are matched correctly. Since τ is generally between 30 μs and 1 ms, motions with frequencies between 1 and 33 kHz can be probed. Since MQ coherences can involve anywhere from 2 to >100 nuclei, the correlated motion for atomic groups of various sizes can be probed, rather than tracking the motion of a single site.

As temperature is monotonically increased and the MQ preparation time is fixed, the frequency of motion can take on several of these special refocusing frequencies, interspersed by defocusing frequencies. Thus, a series of oscillations in f_{MQ} with temperature is expected. In addition to identifying the frequency of motion, the shapes of these oscillations are signatures of the underlying mechanism of molecular motion, e.g. multisite hops versus continuous rotations. Only motions which restore the relative positions of the nuclei after the MQ experiment will cause refocusing. Motions, such as translational diffusion, which do not restore the initial configuration of the nuclei will not produce refocusing under any condition.

Figure 10 shows the temperature dependent ^{19}F f_{MQ} for two polytetrafluoroethylene samples of different crystallinity.[19] Each line indicates a fixed value of the MQ preparation period τ. The overall decrease in f_{MQ} with increasing τ indicates that relaxation is not associated with molecular motion. However, at each fixed τ, oscillations in f_{MQ} can be seen. Oscillations in

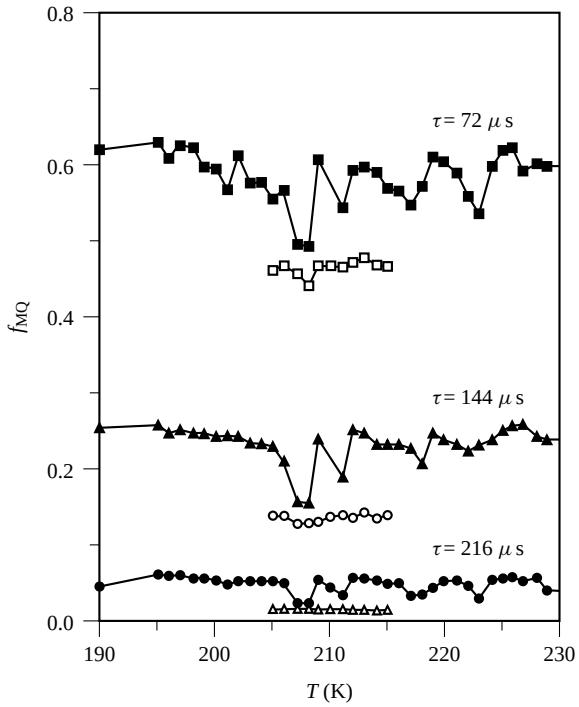

Figure 10 The fraction of refocused magnetization, f_{MQ} at three different values of τ as a function of temperature for *as*-polymerized (■, ▲, ●, ——) and melt-crystallized (□, ○, △, ------) polytetrafluoroethylene. Oscillations are seen only in the *as*-polymerized polymer, corresponding to the motion of a point defect

f_{MQ} are observed from 208 to 230 K for the 98% crystalline sample, while this ratio is constant over the same temperature range for the 64% crystalline sample. These oscillations may be associated with paracrystalline defects found only in the first sample. Thus, the MQ refocusing experiment is able to differentiate clearly between polymer samples which have different thermal histories. The sharpness of the MQ refocusing features and their variations in magnitude, shape, and sign with temperature are signatures of the molecular level details of the underlying dynamics which produce them.

9 RELATED ARTICLES

Amorphous Silicon Alloys; Average Hamiltonian Theory; Diamond Thin Films; Double Quantum Coherence; Liquid Crystals: General Considerations; Molecular Sieves: Crystalline Systems; Multiple Quantum Coherence in Spin-1/2 Dipolar Coupled Solids; Multiple Quantum Coherences in Extended Dipolar Coupled Spin Networks; Multiple Quantum Spectroscopy in Liquid Crystalline Solvents; Multiple Quantum Spectroscopy of Liquid Samples; Polymer Dynamics and Order from Multidimensional Solid State NMR.

10 REFERENCES

1. Y.-S. Yen and A. Pines, *J. Chem. Phys.*, 1983, **78**, 3579.
2. J. Baum, M. Munowitz, A. N. Garroway, and A. Pines, *J. Chem. Phys.*, 1985, **83**, 2015.
3. J. Baum and A. Pines, *J. Am. Chem. Soc.*, 1986, **108**, 7447.
4. J. Baum, K. K. Gleason, A. Pines, A. N. Garroway, and J. A. Reimer, *Phys. Rev. Lett.*, 1986, **56**, 1377.
5. K. K. Gleason, M. A. Petrich, and J. A. Reimer, *Phys. Rev. B*, 1987, **36**, 3259.
6. M. A. Petrich, K. K. Gleason, and J. A. Reimer, *Phys. Rev. B*, 1987, **36**, 9722.
7. S. Mitra, K. K. Gleason, H. Jia, and J. S. Shinar, *Phys. Rev. B*, 1993, **48**, 2175.
8. P.-K. Wang, C. P. Slichter, and J. H. Sinfelt, *Phys. Rev. Lett.*, 1984, **53**, 82.
9. R. Ryoo, S. B. Liu, L. C. de Menoval, K. Takegushi, B. Chmelka, M. Tresoshe, and A. Pines, *J. Phys. Chem.*, 1987, **91**, 6575.
10. S. J. Hwang, T. S. King, and B. C. Gerstein, *Catal. Lett.*, 1991, **8**, 367.
11. B. F. Chmelka, J. G. Pearson, S. B. Liu, R. Ryoo, L. C. de Menorval, and A. Pines, *J. Phys. Chem.*, 1991, **95**, 303.
12. J. G. Pearson, B. F. Chmelka, D. N. Shykind, and A. Pines, *J. Phys. Chem.*, 1992, **96**, 8517.
13. S. B. Hong, H. M. Cho, and M. E. Davis, *J. Phys. Chem.*, 1993, **97**, 1622.
14. S. B. Hong, H. M. Cho, and M. E. Davis, *J. Phys. Chem.*, 1993, **97**, 1629.
15. W. V. Gerasimowicz, A. N. Garroway, J. B. Miller, and L. C. Sander, *J. Phys. Chem.*, 1992, **96**, 3658.
16. B. E. Scruggs and K. K. Gleason, *J. Magn. Reson.*, 1992, **99**, 149.
17. B. E. Scruggs and K. K. Gleason, *Macromolecules*, 1992, **25**, 1864.
18. B. E. Scruggs and K. K. Gleason, *J. Magn. Reson.*, 1992, **99**, 149.
19. S. J. Limb, B. E. Scruggs, and K. K. Gleason, *Macromolecules*, 1993, **26**, 3750.
20. D. A. Lathrop and K. K. Gleason, *Macromolecules*, 1993, **26**, 4652.
21. K. K. Gleason, *Concepts Magn. Reson.*, 1993, **5**, 199.
22. G. Bodenhausen, *Prog. NMR Spectrosc.*, 1981, **14**, 137.
23. D. P. Weitekamp, *Adv. Magn. Reson.*, 1983, **11**, 111.
24. M. Munowitz and A. Pines, *Science*, 1986, **233**, 525.
25. S. Lacelle, *Adv. Magn. Opt. Reson.*, 1991, **16**, 173.
26. M. Mehring, *Principles of High Resolution NMR in Solids*, Springer, Berlin, 1983, pp. 233–259.
27. M. Munowitz, *Coherence and NMR*, Wiley, New York, 1988, pp. 123–124, 200–218.
28. T. J. Norwood, *Prog. Nucl. Magn. Reson. Spectrosc.*, 1992, **24**, 295.
29. B. C. Gerstein, M. Pruski, and S. J. Hwang, *Bull. Magn. Reson.*, 1993, **15**, 211.
30. A. Abragam, *The Principles of Nuclear Magnetism* Clarendon, Oxford, 1961.
31. D. H. Levy and K. K. Gleason, *J. Phys. Chem.*, 1992, **96**, 8125.
32. B. E. Scruggs and K. K. Gleason, *Chem. Phys.*, 1992, **166**, 367.
33. G. Cho and J. P. Yesinowski, *Chem. Phys. Lett.*, 1993, **205**, 1.
34. B. E. Scruggs and K. K. Gleason, *J. Phys. Chem.*, 1993, **97**, 9187.
35. A. Wokaun and R. R. Ernst, *Mol. Phys.*, 1978, **36**, 317.
36. J. Tang and A. Pines, *J. Chem. Phys.*, 1980, **72**, 3290.
37. J. B. Murdock, W. S. Warren, D. P. Weitekamp, and A. Pines, *J. Magn. Reson.*, 1984, **60**, 205.
38. M. Munowitz, *Mol. Phys.*, 1990, **71**, 959.
39. D. Suter, S. B. Liu, J. Baum, and A. Pines, *Chem. Phys.*, 1987, **114**, 103.

40. Y. Ba and W. S. Veeman, *Isr. J. Chem.*, 1992, **32**, 173.
41. M. Munowitz, A. Pines, and M. Mehring, *J. Chem. Phys.*, 1987, **86**, 3172.
42. B. C. Gerstein and C. R. Dybowski, *Transient Techniques in NMR of Solids*, Academic, Orlando, 1985, Chap. 5
43. L. M. Moran and J. P. Yesinowski, *Chem. Phys. Lett.*, 1994, **222**, 363.
44. A. N. Garroway, J. Baum, M. G. Munowitz, and A. Pines, *J. Magn. Reson.*, 1984, **60**, 337.
45. C. J. Lee, N. Murali, and N. S. Warren, *Adv. Magn. Reson.*, 1990, **14**, 241.
46. S. Emid, *Physica B*, 1985, **128**, 79.

Biographical Sketch

Karen K. Gleason. *b* 1960. B.S., 1982, M.S., 1982, MIT; Ph.D., University of California, Berkeley, 1987. Introduced to NMR by J.A. Reimer. Faculty, Chemical Engineering, MIT, 1987–present. Approx. 50 publications. Research interests: application of NMR to thin films and interfaces, particularly for detecting low concentrations of hydrogen, and development of multiple quantum NMR spectroscopy.

Multiple-quantum Magic-angle Spinning Experiments on Half-integer Nuclei: Fundamentals

Lucio Frydman

Department of Chemical Physics, Weizmann Institute of Sciences, Rehovot, Israel

1	Introduction	1
2	Second Order Quadrupole Effects: Origins and Averaging Approaches	2
3	MQMAS NMR Pulse Sequences	5
4	Fine Structure of the MQMAS NMR Line Shapes	10
5	Outlook	11
6	Related Articles in this Volume	12
7	Related Articles in Volumes 1–8	12
8	References	12

1 INTRODUCTION

A majority of magnetically active nuclides in the Periodic Table possesses half-integer spin numbers: $S = 3/2$, 5/2, 7/2 and 9/2 (Figure 1).[1] Unlike their more common spin-1/2 counterparts, these nuclei possess quadrupole moments and thus interact not only with external or internal magnetic fields, but also with the electric field gradients (EFG) originating from asymmetries in the distribution of charges that surrounds them.[2,3] Depending on the degree of distortion in this local charge distribution, the resulting quadrupole couplings can be small or large when compared to the Zeeman coupling ν_O between the nuclear magnetic moment and the external magnetic field B_o. If sufficiently small, quadrupole effects can often be neglected and the NMR of the spins treated as their $S = 1/2$ counterparts;[4] if comparatively large NMR observations are seldom successful and zero-field nuclear quadrupole resonance (NQR) analyses become the alternative of choice.[3] By contrast to these cases, the majority of scenarios, including those to be considered here, are those where quadrupolar couplings are sizable yet still enable the acquisition of solid state NMR spectra. The resulting quadrupole couplings can then be treated as minor perturbations to a main Zeeman interaction; this leads to broadenings that to first order are orientation-dependent and proportional to the square of the z component of the angular momentum S.[2] For moderately strong quadrupole couplings this implies that when analyzing powdered or disordered samples, all the allowed $\Delta S_z = \pm 1$ transitions will be broadened beyond the NMR detection limit except for the central $-1/2 \leftrightarrow 1/2$ one. It is consequently on these central transitions, which end up being much sharper than the remaining single-quantum signals in the spin manifold, that most solid state NMR studies of half-integer quadrupolar nuclei are generally focused.

In spite of this consideration, central transition quadrupolar NMR spectra do not generally render sharp resonances from powdered samples. This is due to the presence of residual second order quadrupolar broadenings.[2–6] Such higher order effects are proportional to the square of the internal perturbation divided by the main Zeeman interaction, and therefore usually negligible in $S = 1/2$ cases involving shielding or dipolar couplings. They will, however, affect half-integer quadrupoles to an extent proportional to the (quadrupole coupling)$^2/\nu_O$, broadening their central transitions resonances by tens or hundreds of kilohertz whenever EFGs are significant. Analyzing the resulting second order quadrupolar line shapes is not inherently difficult when dealing with individual chemical sites,[4] yet overlap among inequivalent powder patterns precludes these analyses if several inequivalent sites are present. An improvement in the resolution of these solid state line shapes can be achieved by variable-angle sample spinning.[7–9] Yet by contrast to the spin-1/2 case, where first order anisotropies such as the chemical shielding or dipole–dipole interaction can be successfully removed via fast magic angle spinning (MAS), no single 'magic' spinning angle exists capable of removing all the second order effects originated by quadrupolar couplings. This complication stood out as one of the main limitations in the application of solid state quadrupolar NMR, particularly when it came to characterizations of complex materials such as minerals, catalysts, ceramics and glasses.[10]

A better understanding of the nature of second order quadrupole effects has changed this state of affairs. During recent years, a number of different averaging procedures have been proposed, capable of achieving the long-sought goal of bringing high resolution NMR to quadrupolar nuclei.[11–14] All these techniques have in common the introduction of an additional degree of freedom in the manipulation of the spins' evolution; manipulating this extra variable then enables the refocusing of residual second order anisotropies, usually in a two-dimensional (2D) NMR fashion. One approach for implementing such high resolution acquisitions is based on the use of multiple quantum (MQ) spectroscopy in combination with conventional MAS. The resulting technique became known as multiple quantum magic angle spinning (MQMAS),[14,15]

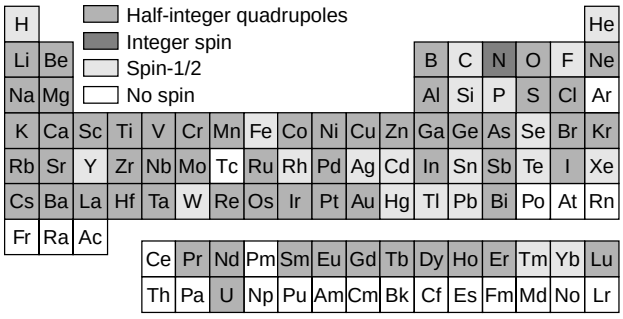

Figure 1 Periodic Table of the Elements indicating the nature of the most abundant NMR-active isotopes. Notice the predominance of half-integer quadrupolar species

and thanks to its ease of implementation it quickly became a method of choice for studies of quadrupolar nuclei in powdered samples. The present article summarizes basic theoretical and practical aspects of MQMAS, as well as limitations to its resolution performance. In its conclusions it also reflects on some of the challenges opened up by the development of this technique.

2 SECOND ORDER QUADRUPOLE EFFECTS: ORIGINS AND AVERAGING APPROACHES

2.1 Second Order Quadrupole Effects

Just as their spin-1/2 counterparts, quadrupolar nuclei possess magnetic moments through which they can interact with magnetic fields. These include the external field B_O, pulsed radiofrequency (rf) fields B_1, local fields generated by the chemical shielding as well as by the dipolar moments of other nuclei. Such magnetic couplings are usually represented by quantum mechanical Hamiltonians: H_Z, H_{RF}, H_{CS}, H_D. In addition, nuclei with $S > 1/2$ are distinguished by a nonspherical shape (Figure 2), associated with a nuclear quadrupole moment capable of coupling with the surrounding electric field gradients. The result is a quantum-mechanical Hamiltonian H_Q that may also end up affecting the NMR transitions. All these local Hamiltonians can be represented by scalar products of spatial and spin tensors of rank $k \leq 2$:[16,17]

$$H_\lambda = C_\lambda \overline{\overline{R}} \cdot \overline{\overline{T}} = C_\lambda \sum_{k=0}^{2} \sum_{m=-k}^{k} (-1)^m R_{k-m}^{(\lambda)} T_{km}^{(\lambda)} e^{-im\omega_0 t} \qquad (1)$$

where $R_{k-m}^{(\lambda)}$, $T_{km}^{(\lambda)}$ define the spatial and spin components of the Hamiltonian, and C_λ is the corresponding coupling constant. Except for $m = 0$ the matrix representation of the T_{km} spin operators is off-diagonal in the usual basis set of Zeeman eigenstates $\{|S_z\rangle\}_{-S \leq S_z \leq S}$. Consequently, analyzing the effects of arbitrary internal Hamiltonians in the presence of the Zeeman coupling is a complex task not always susceptible to analytical treatment. This problem can be simplified when it is possible to assume that all internal interactions H_λ act only as minor perturbations to the main Zeeman coupling. To first order this approximation allows one to consider only those terms that commute with H_Z, which in turn is proportional to T_{10}. Since all internal anisotropies possess rank $k = 2$ this implies that only T_{20} contributions remain. For the quadrupolar Hamiltonian, the resulting first order coupling can be written as

$$H_Q^{(1)} = C_Q R_{20}^{(Q)} T_{20}^{(Q)} = C_Q \sqrt{\frac{1}{6}} R_{20}^{(Q)} [3S_z^2 - S(S+1)] \qquad (2)$$

where $C_Q = \frac{e^2 q Q}{4S(2S-1)h}$ defines the strength of the nuclear quadrupole coupling to the surrounding EFG, and $R_{20}^{(Q)}$ is an irreducible second-rank spherical tensor element depending on the relative orientation between the quadrupole tensor of a given site in a particular crystallite and the Zeeman field. A similar orientation dependence characterizes other first order effects like the dipolar or the chemical shift anisotropies. In principle, all of these anisotropies are susceptible to averaging when executing fast MAS at rates $\nu_r \gg C_\lambda$. Indeed upon mechanical spinning the sample all R_{20}^{λ} will acquire a time dependence whose average is[3,7,18]

$$\langle R_{20}^{\lambda}(t) \rangle = R_{20}^{\lambda} \cdot P_2(\cos\chi) \qquad (3a)$$

where

$$P_2(\cos\chi) = \frac{3\cos^2\chi - 1}{2} \qquad (3b)$$

is the second order Legèndre polynomial possessing a root at $\cos\chi = 1/\sqrt{3}$. Setting the spinning axis at the magic angle $\chi = 54.7°$ with respect to B_O effectively nulls this geometric scaling factor, thereby removing all anisotropic contributions to the solid NMR Hamiltonian.

Achieving such a fast spinning regime in quadrupolar cases is actually difficult in a majority of nuclei by virtue of the large size of their quadrupole moments. Even so, it is possible to avoid the effects of first order quadrupolar anisotropies thanks to the T_{20}-type dependence that characterizes these effects [equation (2)]. The S_z^2 factor in T_{20} then frees the $-1/2 \leftrightarrow +1/2$ transition of first order quadrupolar influences, and is in turn the reason why half-integer quadrupolar studies have generally focused on this central transition.

In spite of this consideration, central transition experiments do not generally afford well resolved resonances. This is due to the large magnitudes of the quadrupolar couplings usually involved, which do not justify the neglect of higher order effects. Particularly important to consider are the second order corrections that the full quadrupolar Hamiltonian will impart onto the spin energy eigenvalues. Standard perturbation theory enables one to represent these effects by[5]

$$H_Q^{(2)} = \frac{C_Q^2}{\nu_O} \sum_{m \neq 0} \frac{R_{2m}^{(Q)} R_{2-m}^{(Q)} [T_{2m}, T_{2-m}]}{2m} \qquad (4a)$$

$$H_Q^{(2)} = -\frac{C_Q^2}{2\nu_O} \left\{ \begin{array}{l} R_{2-1}^{(Q)} R_{21}^{(Q)} S_z [4S(S+1) - 8S_z^2 - 1] \\ + R_{2-2}^{(Q)} R_{22}^{(Q)} S_z [2S(S+1) - 2S_z^2 - 1] \end{array} \right\} \qquad (4b)$$

These correction terms are proportional to the square of the quadrupolar couplings scaled by Zeeman interaction, hence leading to the C_Q^2/ν_O dependence characteristic of second order effects. The multiplication of quadrupolar terms in equation (4) also leads to spatial components that transform as *products* of second-rank spherical tensor elements, as opposed to the simpler R_{20} dependence that characterized all first order

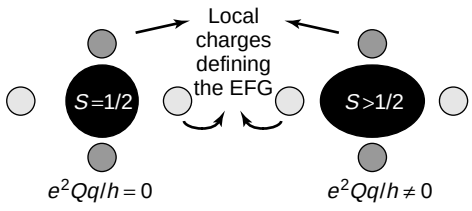

Figure 2 Origin of the electrostatic quadrupole interaction in spins $S \geq 1$, arising from placing the ellipsoidal nuclear positive charge into local electrostatic field gradients. The ensuing coupling ends up depending on the moments of the nucleus, which according to the Wigner–Eckart theorem are in turn proportional to the quantum operators $\{S_\alpha\}_{\alpha=x,y,z}$

effects. Such products result from taking cross correlations of the quadrupolar interaction with itself, and imply that line shapes derived from $H_Q^{(2)}$ will be affected by a net isotropic quadrupolar shift ν_O^Q even though H_Q's original center of mass was zero for all transitions. Also worth mentioning are the products involved in the T_{2m} commutators; these endow $H_Q^{(2)}$ with a spin-space dependence that is different from either T_{10} (linear in S_z) or T_{20} (quadratic in S_z), a feature that will eventually enable MQMAS to refocus second order effects via spin-space manipulations which do not simultaneously remove all chemical shift information.

The presence of isotropic quadrupolar shifts provides a mechanism for distinguishing among chemically inequivalent sites acting in addition to the usual isotropic chemical shift. The anisotropic character of $H_Q^{(2)}$, however, implies that sites in a powder will now also show broad line shapes even when focusing on the central transitions. Furthermore, by contrast to what happened with first order effects, fast MAS of the sample will then be of limited use for assisting in the narrowing of these powder patterns. This is a consequence of the higher complexity associated with the spatial terms of $H_Q^{(2)}$, involving products of second-rank tensors and thus giving origin to both second-(R_{20}) and fourth-rank (R_{40}) anisotropies. The former transform in the usual $P_2(\cos\chi)$ fashion and can thus be removed by MAS; the latter by contrast scale upon sample spinning as the fourth-rank Legèndre polynomial $P_4(\cos\chi) = (35\cos^4\chi - 30\cos^2\chi + 3)/8$, which can be set to zero at some spinning angles but not when $\chi = 54.7°$ (Figure 3). The noncoincident roots of these two polynomials implies that no single choice of spinning axis will simultaneously remove all second order quadrupolar broadenings from a central transition spectrum.[5,11,19]

2.2 Alternatives to Refocus the Anisotropies

One way of remedying this single-axis spinning deficiency is by introducing more complex forms of mechanical reorientation; for instance, by consecutively spinning the sample about two different spinning axes. The two sample spinning angles (χ_1, χ_2) will then be associated with corresponding evolution times (t_1, t_2), bringing in turn the idea and the possibility of refocusing anisotropies via a bidimensional (2D) NMR approach. The choice of spinning angles in these dynamic angle spinning (DAS) experiments demands the simultaneous cancellation, at a given time and for all crystallites in the powder, of both the second- and fourth-rank anisotropies arising from the second order effects. It follows from the considerations above that this can be achieved when setting[11,13]

$$P_2(\cos\chi_1)t_1 = -P_2(\cos\chi_2)t_2$$
$$P_4(\cos\chi_1)t_1 = -P_4(\cos\chi_2)t_2 \qquad (5)$$

conditions which do not affect the normal course of the isotropic evolution. At the conclusion of the total $t_1 + t_2$ evolution time, this choice of spinning angles will lead to the formation of an echo signal encoding a purely isotropic evolution, and by synchronous increases in the duration of (t_1, t_2), this procedure can end up affording a high resolution time-domain signal. This stepwise t_1, t_2 refocusing is different from that occurring in MAS, where anisotropies are being continuously removed. Indeed, in DAS, anisotropies are not removed but show up, after Fourier transformation of the 2D time domain signal, correlated along a sharp ridge for each site in the sample. Therefore unlike MAS, DAS does not bring with its higher resolution an effective increase in signal-to-noise; in fact, signal will be lost by virtue of the need for storing the evolving coherences along B_O while the spinning axis is mechanically reoriented from χ_1 to χ_2.

A refocusing similar to that carried out by DAS but involving a single axis of sample rotation is feasible if the restriction to central transition observations is lifted. Indeed it follows from the arguments given earlier that for any half-integer quadrupole nucleus not only the central but in fact any $S_z = -m \leftrightarrow S_z = +m$ MQ transition will be free from the dominant first order quadrupole broadenings (Figure 4). Yet these transistions will still be affected by second order quadrupole effects, opening up the possibility of compensating the residual broadenings affecting their line shapes with those arising in the central $-1/2 \leftrightarrow +1/2$ transition. To explore such a possibility it is necessary to incorporate the transition order m into the explicit description of the second order NMR frequencies. Under rapid sample spinning conditions this calculation leads to the angle- and order-dependent evolution frequency

$$\nu_Q^{(2)}(m,\chi) = A_0^Q C_0^S(m) + A_2^Q(\varphi,\theta)C_2^S(m)P_2(\cos\chi) + A_4^Q(\varphi,\theta)C_4^S(m)P_4(\cos\chi) \qquad (6)$$

where the $\{A_l^Q\}_{l=0,2,4}$ denote the isotropic, second- and fourth-rank quadrupolar contributions, and the $\{C_l^S(m)\}_{l=2,4}$ are polynomials which depend on the spin S and transition order m involved:

$$C_0^S(m) = 2m[S(S+1) - 3m^2] \qquad (7a)$$
$$C_2^S(m) = 2m[8S(S+1) - 12m^2 - 3] \qquad (7b)$$
$$C_4^S(m) = 2m[18S(S+1) - 34m^2 - 5] \qquad (7c)$$

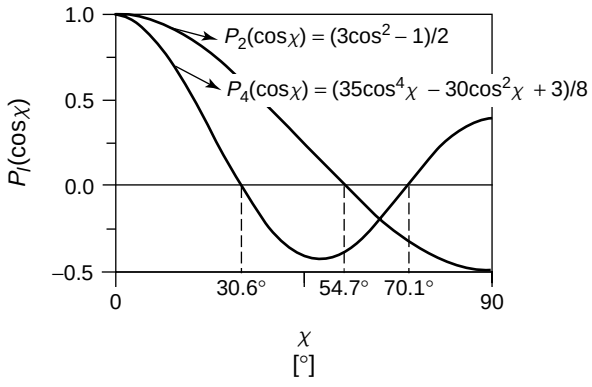

Figure 3 Orientation dependence of the two Legèndre polynomials $\{P_l(\cos\chi)\}_{l=2,4}$ that define the line broadening of central transition quadrupolar patterns. Also shown are the positions of the polynomials' roots: $\chi_m = 54.7°$, the usual magic angle for averaging second-rank anisotropies, and $\chi = 30.6°$, 70.1° for the fourth-rank anisotropies that show up on considering second order effects. The presence of two anisotropic contributions whose zeroes do not coincide deprives sample spinning from the possibility of averaging away central transition broadenings

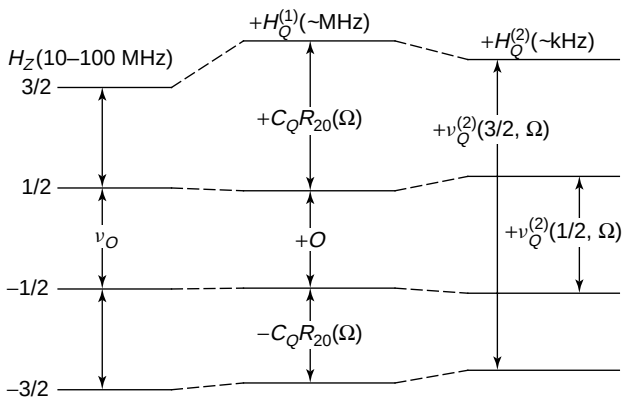

Figure 4 Hierarchical energy level diagram for an $S = 3/2$ nucleus interacting with a dominating external magnetic field coupling and an electric field gradient perturbation

Equation (6) shows the analogous roles that spinning angles and quantum numbers play in defining the second order evolution frequency: the former will scale anisotropies according to the $\{P_l(\cos\chi)\}_{l=2,4}$ polynomials, the latter according to the $\{C_l^S(m)\}_{l=2,4}$ coefficients. Thus instead of fixing m at 1/2 and using χ as a degree of freedom as is done in DAS, it is possible to propose a 2D refocusing experiment whereby for a fixed spinning angle χ spins evolve during initial and final times t_1, t_2 under the effects of two different transition orders m_1 and m_2 (Figure 5). $H_Q^{(2)}$-driven anisotropies will then dephase both of these coherence orders along their respective evolution times, but since these anisotropies can be made proportional to one another for every crystallite the result of such 2D correlation will be powder line shapes that show up as sharp parallel ridges for different sites in the sample.

In analogy to equation (5), the spectral correlation of anisotropic broadenings that is introduced by this MQ strategy can be associated with the time-domain refocusing conditions

$$C_2^S(m_1)t_1 = C_2^S(m_2)t_2 \tag{8a}$$

$$C_4^S(m_1)t_1 = C_4^S(m_2)t_2 \tag{8b}$$

At this (t_1, t_2) point in the MQ correlation, a purely isotropic signal can be detected, which if Fourier transformed would lead to a 1D high resolution NMR spectrum. Although a range of spinning angles χ are compatible with equations (8a,b), the most convenient choice is naturally $\chi_{MAS} = 54.7°$, since under these conditions the hitherto neglected chemical shift and dipolar anisotropies will also be effectively averaged away by the spinning. Simultaneously, MAS makes the second-rank refocusing condition (equation (8a)) immaterial. The selection rules for NMR also need to be considered at this point; these state that in the directly detected domain only single quantum coherences can yield measurable signals, restricting the coherence order to be employed during t_2 to $m_2 = 1/2$; the central single quantum transition. As for the choice of m_1 this may in principle be dictated by the spin number (for $S = 3/2$ only $m_1 = 3/2$ is available; for $S = 5/2 m_1 \leq 5/2$, etc.); yet in all cases at least one such MQ transition is available, and it is the indirect domain that will encode its evolution. Standard phase cycling procedures

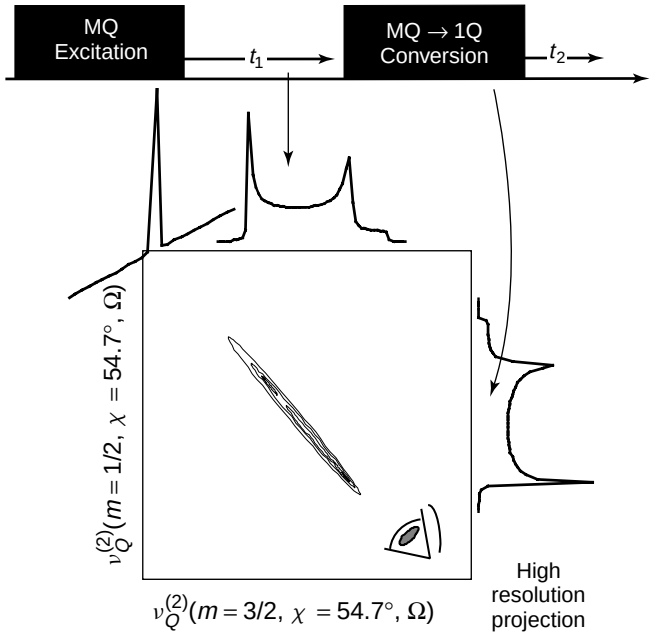

Figure 5 (Top) Schematic diagram of the MQMAS pulse sequence. (Bottom) 2D diagram illustrating how the proportionality among second order MAS broadenings in both the central and MQ transitions, enables high resolution acquisitions when data are considered at appropriate angles in the $MQ \rightarrow 1Q$ 2D correlation spectrum

also put under the experimentalist's control the apparent sense of evolution of the spins during t_1;[20] enabling the stepwise refocusing of all fourth-rank anisotropies regardless of the relative sign of the $C_4^S(m_1)$, $C_4^S(1/2)$ coefficients. As a result of all these considerations, it follows that in MQMAS, second order anisotropies will refocus for all crystallites in the sample simultaneously, at times fulfilling the condition

$$t_2 = \left\{ \frac{|C_4^S(m_1)|}{C_4^S(1/2)} \right\} t_1 \tag{9}$$

The appearance of such long-lived echoes at these particular (t_1, t_2) combinations is one of the most basic features displayed by MQMAS experiments. Their formation is illustrated in Figure 6 for a variety of S and m_1 cases, using ^{23}Na (spin-3/2) and ^{55}Mn (spin-5/2) MQMAS NMR as examples. Rapidly decaying anisotropic evolutions are evident here along both the MQ and 1Q (t_1 and t_2) domains, yet as predicted by equation (9), a much slower decay is noticed along the ideal $|C_4^S(m_1)|/C_4^S(1/2)$ slope.

The capacity of MQMAS NMR to resolve chemically inequivalent sites is further illustrated in Figure 7(a), which shows how this experiment can distinguish four inequivalent ^{23}Na sites that overlap in the conventional MAS spectrum of the Na_2ATP complex. As in the DAS case, it may be convenient to transform the tilted powder patterns that result from these MQMAS experiments into a format that can yield a 1D high resolution trace by conventional projection. This can be done by a shearing transformation defined by the $|C_4^S(m_1)|/C_4^S(1/2)$ ratio; which is in essence a rotation of the line shapes, and can be carried out in such a way as to leave a conventional MAS pattern along one of the

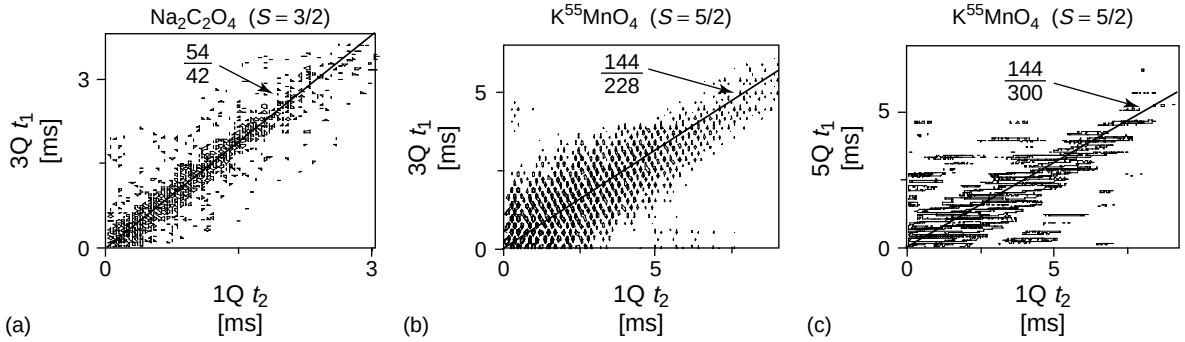

Figure 6 ^{23}Na ($S = 3/2$) and ^{55}Mn ($S = 5/2$) MQMAS NMR time-domain data illustrating the formation of long-lived isotropic echoes at the theoretically expected slopes. (a, b) Triple- to single-quantum correlation experiments; (c) five- to single-quantum correlation experiment

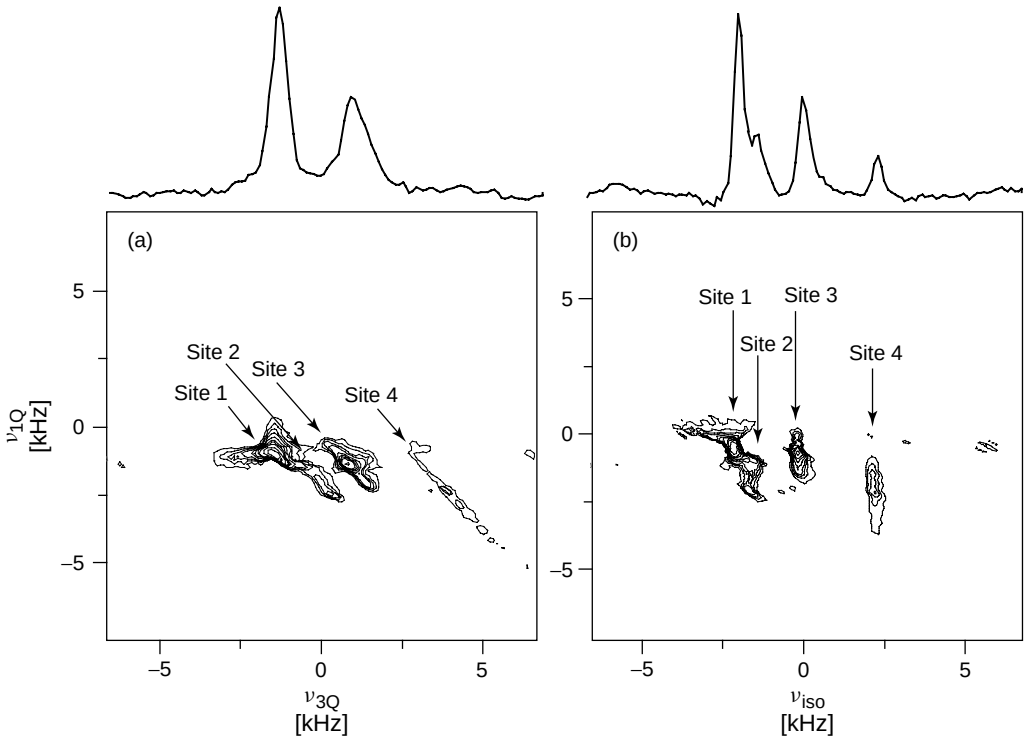

Figure 7 2D 7.1 T ^{23}Na NMR spectrum arising from the $Na_2ATP{\cdot}10H_2O$ complex crystallized from water/dioxane after (a) standard FFT of the 3QMAS time-domain data; (b) subjecting the 2D MQMAS data to a shearing transformation. In both cases the 1Q domain contains the conventional MAS line shapes, distorted by the relative powder efficiencies of the MQ excitation and conversion processes. Sites in (a) appear resolved when regarded at a slope depending on the $|C_4(3/2)/C_4(1/2)|$ ratio; in (b) by contrast, a projection along the indirect domain leads to a purely isotropic high resolution 1D dimension showing four partially resolved resonances (adapted from Ref.[74])

spectral axes and only isotropic components along the other (Figure 7b). An alternative procedure involves redefining the first evolution period so as to contain all the MQ evolution plus the fraction of 1Q evolution needed for a complete refocusing of anisotropies; such a redefined t_1 time will thus encode a purely isotropic evolution.[21] Pros and cons involved in these and other MQMAS procedures are described in greater detail in the article by Pruski and Amoureux (see **MQMAS Advances**). Also worth noting is a recently proposed alternative whereby second order effects of the central 1Q transition are refocused not by symmetric MQ transitions, but by their single-quantum counterparts in the satellite transitions[22] (see **Satellite Transition NMR Spectroscopy of Half-Integer Quadrupolar Nuclei under Magic-Angle Spinning**).

3 MQMAS NMR PULSE SEQUENCES

3.1 General Considerations

The previous section introduced some of the problems associated with the acquisition of high resolution NMR spectra in the presence of second order effects, and the manner by which MQMAS enables the removal of the anisotropies via the

stepwise refocusing of MQ dephasings by 1Q spin evolutions. Two active steps are required for the generation of the ensuing MQMAS echoes: a first one involving the excitation of the MQ coherence starting from an equilibrium state, $S_z \rightarrow S_{x,y}^{MQ}$, and a second one involving the conversion of MQ coherences that evolved during t_1 into 1Q coherences whose signals can be detected: $S_{x,y}^{MQ} \rightarrow S_{x,y}^{1Q}$. Several pulse sequences have already been proposed to implement these two steps while undergoing MAS,[14,15,21,23–48] and it is likely that new and better protocols to achieve these goals will continue to arise in the near future. Therefore in an effort to avoid premature obsolescence, this section focuses on general considerations of what such pulse sequences incorporate rather than on their comprehensive individual descriptions.

Before going into specifics, it is worth dwelling on generalities about what a good MQMAS pulse sequence should achieve. As manipulations of MQ coherences by means of rf fields are to first order forbidden by the conventional NMR transition rules, the excitation of MQ coherences and their subsequent transformation into 1Q observables is rarely a very efficient process. Hence if summarizing the initial excitation of MQ coherences according to

$$S_z \xrightarrow[\text{excitation}]{} e_x S_x^{MQ} + e_y S_y^{MQ} \tag{10a}$$

and the subsequent conversion process by

$$\begin{aligned} S_x^{MQ} &\xrightarrow[\text{conversion}]{} c_{xx} S_x^{1Q} + c_{xy} S_y^{1Q} \\ S_y^{MQ} &\xrightarrow[\text{conversion}]{} c_{yx} S_x^{1Q} + c_{yy} S_y^{1Q} \end{aligned} \tag{10b}$$

one of the main goals usually being sought in MQMAS is simply the maximization of the excitation $\{e_i\}_{i=x,y}$ and the conversion $\{c_{ij}\}_{i,j=x,y}$ coefficients. Furthermore the free spin evolutions occurring during t_1 and t_2 are unitary processes involving relatively long spin–spin relaxation decays which preserve the norm of the spin coherences; it is then convenient to introduce a description of the MQMAS signal intensity in terms of a single complex number $\varepsilon = (\varepsilon_x, \varepsilon_y)$ given by[42]

$$\begin{aligned} \varepsilon_x &= [e_x(c_{xx} + c_{yy}) + e_y(c_{yx} - c_{xy})]; \\ \varepsilon_y &= [e_x(c_{xy} + c_{yx}) + e_y(c_{xx} - c_{yy})] \end{aligned} \tag{11}$$

The MQ processes in equations (10a,b) are usually mediated by the simultaneous action of the rf plus the orientation dependent first order quadrupole interaction, and therefore all coefficients in equation (11) will vary from crystallite to crystallite. In view of this, it becomes meaningful to associate an efficient MQMAS sequence with the largest powder averaged value of $|\varepsilon|^2$

$$|\varepsilon|^2 \approx \left\{ \left[\int_{\text{powder}} d\Omega \varepsilon_x(\Omega) \right]^2 + \left[\int_{\text{powder}} d\Omega \varepsilon_y(\Omega) \right]^2 \right\} \tag{12}$$

Yet it also follows from this analysis that there is more to an optimum pulse sequence than achieving the largest possible $|\varepsilon|^2$ value. This stems from the echo character of the MQMAS experiment, which requires all spins to evolve solely from the second order effects active during t_1 and t_2. Conspiring against this requirement is the fact that both the rf-driven excitation and conversion of MQ coherences are orientation dependent processes, a feature which opens up the possibility of imparting extra evolution phases to the spin coherences that do not relate to the second order effects, and hence may fail to refocus during the course of the experiment (Figure 8). For instance a sequence which efficiently transforms S_x^{MQ} into S_x^{1Q} but which at the same time generates an appreciable S_y^{1Q} component may be associated with a large $|\varepsilon|^2$ value, but will at the same time induce a net rotation in the $\{S_x^{1Q}, S_y^{1Q}\}$ space that prevents the full refocusing of anisotropies via the $MQ \rightarrow 1Q$ correlation. It is possible to associate the overall anisotropy of the excitation and conversion processes with the powder distribution of the ε phase factor: $\phi(\Omega) = arctan[\varepsilon_y(\Omega)/\varepsilon_x(\Omega)]$. This parameter describes the relative phase with which the rf pulse sequence itself (as opposed to the actual internal spin interactions) transforms the equilibrium magnetization into observable x and y components via an intermediate MQ step. A narrow distribution of the $\phi(\Omega)$ values over the powdered sample is therefore another important goal to achieve for maximizing the sensitivity. It is also possible to decompose the various x and y pulse sequence coefficients into spherical coordinates and re-express this whole treatment in terms of $\{S_\alpha^{1Q}, S_\alpha^{MQ}\}_{\alpha=\pm}$ spin coherences. One would then state that an important characteristic of any given pulse sequence is not only the absolute efficiencies of its various processes, but also the relative efficiency with which it transforms the $S_z = 0$ magnetization first into separate $+m$ and $-m$ coherences, and subsequently each of these into observable magnetization of coherence order -1. Considerations on the line shape distortions that may then arise in connection with the different efficiencies of the $0 \rightarrow \pm m \rightarrow -1$ coherence transfer pathways are further discussed below, as well as elsewhere (see **MQMAS Advances**).

3.2 Overview of MQMAS Pulse Sequences

As mentioned, the main actors in the MQMAS pulse sequence excitation and conversion processes are the rf and the first order quadrupole interactions. The former creates the various nonequilibrium states while the latter, even though absent during the evolution and acquisition periods, is in fact the coupling that enables the generation of MQ states. There are also other factors affecting the various stages of the pulse sequence including the spinning speed, which controls the temporal oscillations of the quadrupole coupling during the course of the rf pulses, as well as the shifts arising from the chemical shielding and second order quadrupolar interactions. Additional variables available in the design of the pulse sequences include the amplitudes, phases and frequencies of the various rf pulses involved in the MQ excitation and conversion, as well as the number of pulses involved in each stage. Figure 9 presents a number of strategies that have hitherto been proposed for the implementation the excitation and conversion steps of MQMAS acquisitions on spin-3/2.

Although simple, a sequence composed by two short pulses (Figure 9a) is capable of affording MQMAS spectra and provides insight into the general spin physics of more complex procedures. This experiment involves a short initial pulse which transforms the initial equilibrium polarization into high order MQ coherences, a free evolution period t_1, and a second short pulse that converts the evolving MQ coherences into observable 1Q magnetization. Such pulse sequence was

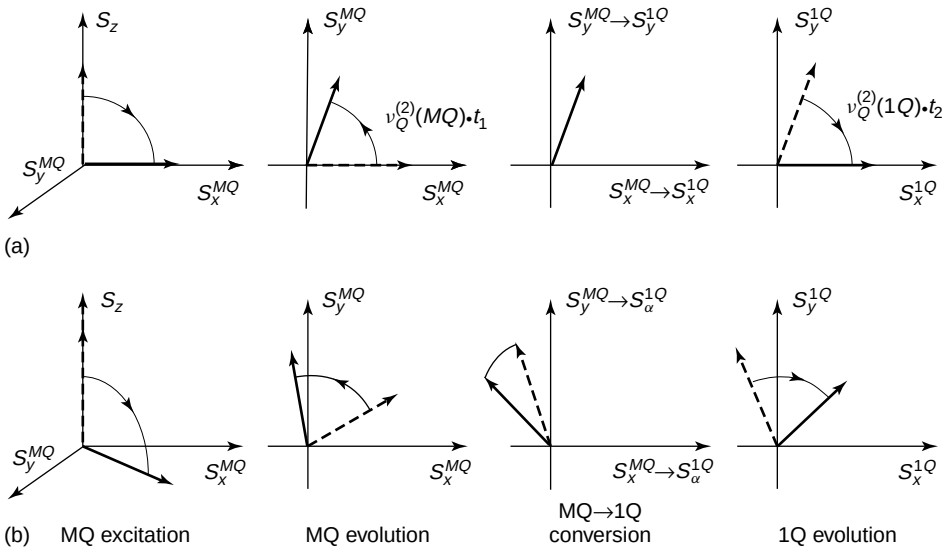

Figure 8 Potential echo spoiling effects of pulses throughout an MQMAS sequence. Dashed lines correspond to the starting spin states, full lines illustrate the finishing states. In an ideal pulse sequence (a) the spin packets of different crystallites evolve under the effects of internal anisotropies and pulses are only responsible for the direct excitation and transfer of coherences among the subspaces. A complete reversal of the anisotropic evolution occurs, and hence magnetizations of all crystallites refocus along a common axis (assumed here to be the x-axis). In actual experiments (b) the orientation dependence of the excitation and conversion processes may induce net evolution phases which prevent a full reversal of anisotropies

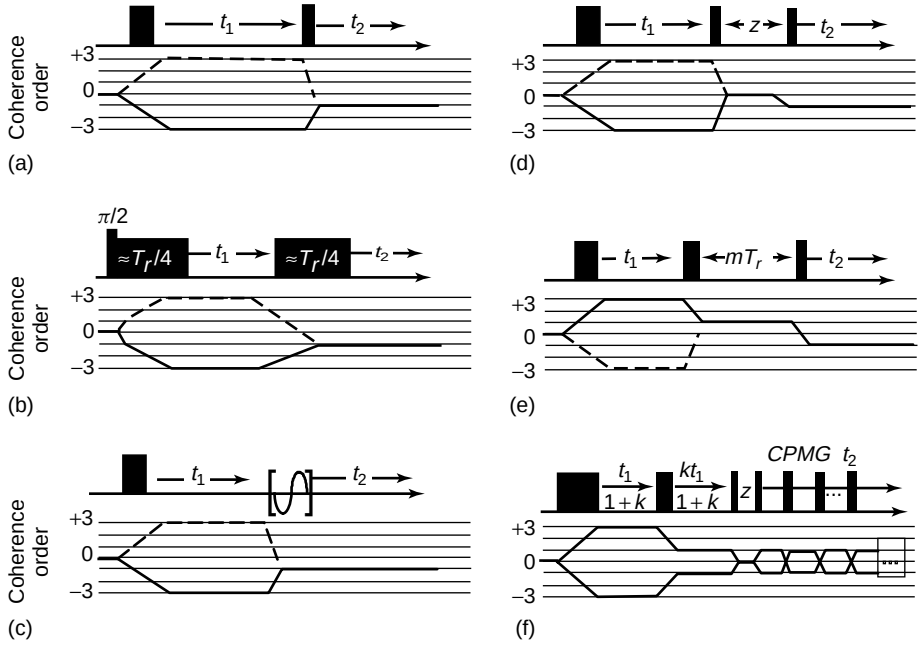

Figure 9 Some of the pulse sequences proposed for the acquisition of 2D MQMAS spectra. (a) Basic two-pulse sequence implementing the excitation and conversion of the multiple-quantum coherences with short CW pulses. (b) Variant based on MQ coherence manipulations driven by adiabatic passages between $MQ \leftrightarrow 1Q$ states, with the initial MQ excitation being aided by a central transition 90 °excitation pulse. (c) Sequence incorporating a fast-amplitude modulation (FAM) of the MQ conversion pulse. In general short CW, RIACT and FAM pulses (as well as other rf pulse modules, such as composite pulses or double-frequency-sweep pulses) can be combined in various forms to achieve a maximization of the MQMAS signal and optimization of the line shapes. Alternatives to the simple MQ(t_1)−1Q(t_2) scheme are shown on the right-hand column and include the introduction of a z-filter (d), whole echo detection during t_2 (e), and a split-t_1 scheme followed by a z-filter and Carr−Purcell−Meiboom−Gill acquisition. Staffs underneath each pulse sequence describe the corresponding coherence transfer pathways required for detecting the MQMAS echo and anti-echo signals (full and dashed lines, respectively). The actual coherence transfer pathway executed during the pulse sequence can be selected either by phase cycling[20,75] or via the application of pulsed field gradients[76]

initially proposed for performing double- and triple-quantum NMR spectroscopy on static powders and single crystals,[49–51] and currently finds widest application in MQMAS experiments on half-integer quadrupolar nuclei. An exact analysis on the nature of this sequence requires propagating the evolution of the spins as a function of all the coupling parameters mentioned earlier (spin number S, transition order m, quadrupole coupling parameters C_Q, η_Q, shielding parameters $\nu_{\rm iso}^{\rm CS}$, $\nu_{\rm aniso}^{\rm CS}$, Larmor frequency ν_O, spinning rate ν_r, transverse rf nutation field ν_1). Such calculations have been carried out for a range of conditions;[23,28,34,40] they are useful and eventually even necessary, yet sometimes some basic features of the experiment can also be gathered from simpler analytical treatments. One such analysis assumes only static first order quadrupolar and rf Hamiltonians:[15]

$$H_{\rm irr} = C_Q\sqrt{\frac{1}{6}}R_{20}(\theta,\varphi)[3S_z^2 - S(S+1)] + \nu_1 S_x \qquad (13)$$

Nuclear spins initially in a thermodynamic equilibrium state parallel to the z-axis will be excited by this irradiation to yield, among other states, the desired 3Q coherences. The origins of this MQ excitation process can be appreciated by diagonalizing $H_{\rm irr}$, and describing the resulting Hamiltonian in terms of fictitious spin-1/2 operators.[51,52] It can then be shown that for a spin $S = 3/2$ the result contains, among other components, a triple-quantum transverse excitation term proportional to S_x^{1-4}. This MQ excitation operator comes as a higher order rf effect mediated by the quadrupolar term, which excites the initial population into S_y^{1-4} coherences according to

$$S_z \xrightarrow{H_{\rm irr}\tau_{\rm exc}} 3\sin\left(\frac{3}{8}\frac{\nu_1^3}{\nu_Q^2(\theta,\varphi)}\tau_{\rm exc}\right)S_y^{1-4} \qquad (14)$$

Note the unusual dependence of the nutation rate, as well as a factor of three magnifying the MQ coherence. The former derives from the higher order nature of this excitation, which scales the effective rf by a factor $(\nu_1/\nu_Q)^2$. The latter derives from the direct $S_z^{1-4} \rightarrow S_y^{1-4}$ process promoted by the S_x^{1-4} excitation term in $H_{\rm irr}$. Although this prediction of a single nutation frequency for the buildup of single-crystallite triple-quantum coherences is just an approximation, it is quite a good one, mainly if the rf pulse is short enough to neglect other factors such as sample rotation, second order effects, and isotropic/anisotropic offsets. The nutation curves for a powdered sample can then be computed as a weighted superposition of single crystal nutation patterns for all possible (φ, θ); angles (Figure 10a). These theoretical predictions match well with MQMAS NMR experiments and predict that over a range of ν_1/ν_Q ratios, a growth in the MQ excitation occurs for increasing rf fields. This feature has led to the development of customized MQMAS probes capable of delivering intense pulses for short periods of time, reaching in favorable cases nutation rates in excess of 200 kHz. As for more conventional rf settings, one of the main reasons precluding the efficient excitation of MQ coherences with low nutation fields is the relatively long periods required for achieving the desired buildup. These then become comparable to the duration of the rotor period, and the MAS-driven averaging of $H_Q^{(1)}$ deprives the process from much of its effectiveness. Even under such conditions it has been observed

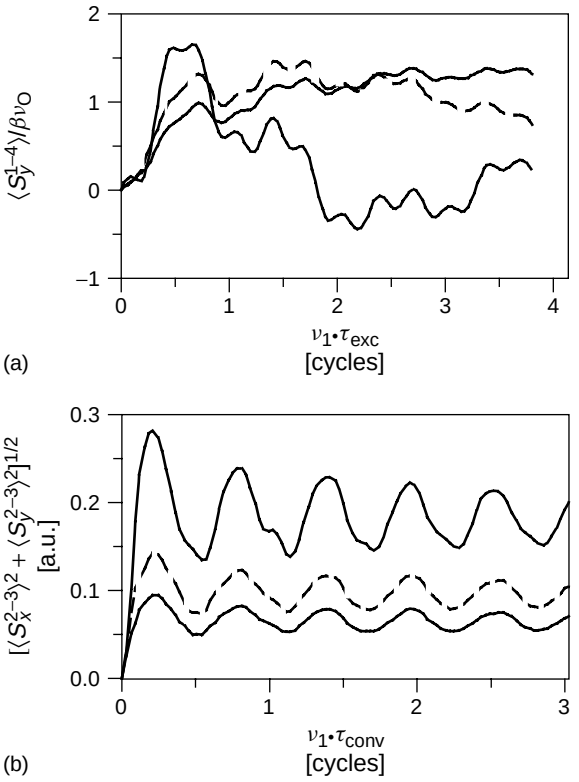

Figure 10 Triple-quantum excitation (a) and conversion (b) nutation behavior expected for a $S = 3/2$ nucleus subject to short CW pulses (sequence in Figure 9a), calculated for a static powdered sample as a function of different C_Q/ν_1 ratios: $C_Q/\nu_1 = 2$ (dotted lines), $C_Q/\nu_1 = 4$ (dashed lines), $C_Q/\nu_1 = 6$ (continuous lines). In all cases an axially symmetric quadrupole tensor with $C_Q = 400$ kHz was assumed; spins were assumed at thermal equilibrium for the excitation calculations, and at $S_x^{1-4} = S_y^{1-4} = 1$ for the $3Q \leftrightarrow 1Q$ conversion ones (adapted from Ref.[15])

that the excitation of MQ coherences can still be carried out continuously through the course of several rotor periods, provided that the amplitudes of the rf nutation fields are set between multiples of the sample spinning speed.[47]

A MQ excitation mechanism approach different from the one just discussed is the rotationally induced adiabatic coherence transfer (RIACT).[26] This effect exploits the fact that MAS will effectively null the quadrupolar frequency of a crystallite a number of times during the course of a rotor period, and that at these zero crossings a transverse rf field may redistribute the spin coherences among all eigenstates within the spin manifold.[53] Coherences that had been initially excited into transverse $\{S_i^{2-3}\}_{i=x,y}$ magnetizations of the central transition may end up during these zero crossings redistributed into higher $\{S_i^{1-4}\}_{i=x,y}$, giving rise to the desired MQ excitation. These experiments will therefore involve an initial central transition pulse, which can usually be made highly efficient for all crystallites in the sample, followed by a spin locking period during which the $1Q \rightarrow MQ$ transfer occurs (Figure 9b). In order to ensure that most crystallites in the sample undergo at least one zero crossing but avoid the occurrence of multiple crossings (which would transfer coherence back from $MQ \rightarrow 1Q$), the RIACT spin-lock excitation is usually kept within 1/4–1/3 of a rotor period.

Under optimal conditions of adiabatic passage, the transfer will be complete for all crystallites regardless of their individual quadrupolar frequencies and thus exhibit an improvement over the short-pulse approach in Figure 9(a).

Both short continuous wave (CW) as well as spin-locking pulses can be used as starting points for implementing the $MQ \rightarrow 1Q$ conversion process. Indeed it can be shown that such conversions involve simultaneous manipulations of the satellite $\pm 1/2 \leftrightarrow \pm 3/2$, amenable to both kinds of pulse sequences. Furthermore, similar theoretical approaches to those used in the excitation can be employed to design sequences that optimize the MQ to single-quantum conversion processes. These show that in the presence of large first and second order quadrupolar effects both strategies are actually challenged; the short CW one by the high rf fields that it requires for meaningful excitations of the satellite transitions, and RIACT by its marked orientation and offset dependencies. For instance, in the short pulse case it can be shown that in contrast to the MQ excitation case [equation (14)], the conversion process possesses no well-defined nutation frequency for the various crystallites. This in turn leads to a relatively poor conversion efficiency even for a single crystal orientation, as well as to one which rapidly decreases with increasing C_Q/ν_1 ratios. Still, even for powder samples, a maximum at $\nu_1/\tau_{\text{conv}} \approx 0.2$ cycles can be localized corresponding to a transient coherent superposition of the individual single crystal signals (Figure 10b).[15,23] Furthermore, rotational resonance excitation conditions for rf nutation rates $\nu_1 \approx \nu_r$, $2\nu_r$ have again been observed for these process.[47] In many instances the RIACT approach performs a better conversion than its CW counterpart, opening the possibility of using mixed short-pulse/RIACT sequences that become less sensitive to the strength of quadrupolar couplings and therefore more quantitative than either option in Figure 9(a,b). Yet the actual fate of the spin-locked states will also depend on a competition between the strengths of the first order quadrupole coupling separating central from satellite transitions, the rf field recoupling these transitions, the spinning rate controlling the time that central and satellite transitions will stay in contact during the zero-crossings, and the various offsets involved. It is in fact illustrative to compare the predictions that the echo efficiency parameter ε introduced earlier yields for the two kinds of pulse sequences. For a typical case $S = 3/2$, the overall magnitudes of these coefficients are indeed larger for an optimized RIACT than for the short CW pulse sequence (Figure 11), yet the fact that they are also further spread out in their ϕ powder values is indicative of larger line shape distortions[54] and may prevent RIACT from achieving a more effective refocusing performance.

In addition to these sequences based on the implementation of $MQ \rightarrow 1Q$ conversions via the use of square CW rf pulses, a series of recent papers has focused on the application of shaped and variable-frequency pulses to MQMAS. A promising shaped-pulse proposition involves replacing the square conversion pulses by amplitude modulated ones.[38,39,42,45] This can be achieved via an actual modulation of the pulses' envelop, or by applying fast 180° phase shifts to the rf that will effectively split the on-resonance pulse into symmetric off-resonance components. Either approach can be used to efficiently excite the outlying satellite transitions involved in the 3Q → 1Q conversion step (Figure 9c). In spin-3/2 MQMAS experiments of simple model compounds, enhancement of over

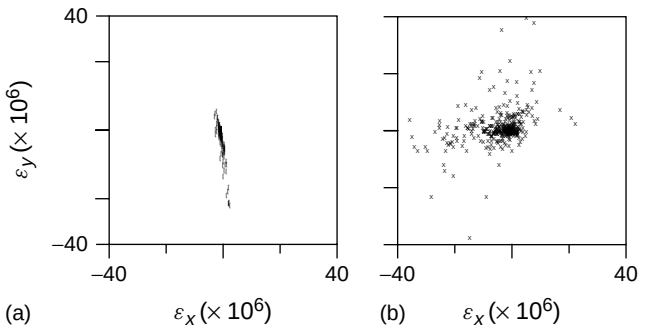

Figure 11 Comparison between the powder values taken by the $\{\varepsilon_\alpha\}_{\alpha=x,y}$ values in short-pulse (a) and RIACT MQMAS pulse sequences (b). Each point represents a different crystallite in the sample distributed over a solid sphere; both plots were calculated for identical MAS conditions: $S = 3/2$, $\nu_r = 10$ kHz, $C_Q =$ kHz, $\nu_1 = 100$ kHz. Notice the overall larger magnitudes but also the spread of coefficients in the RIACT case (courtesy of A. Goldbourt and S. Vega, Weizmann Institute)

300% have recently been reported with this simple procedure. A closely related approach involves using double-frequency-swept chirp pulses, capable of enhancing the MQ conversion steps by sweeping through the off-resonance satellite transitions.[36,43] Theory predicts that either of these approaches may not perform as well for $S \geq 5/2$ spin systems as for their $S = 3/2$ counterparts. Still it has been shown that improvements can be achieved in some of these cases using pulses possessing a different amplitude modulation;[41,46] these approaches also appear promising for manipulating higher orders of MQ coherences.

Additional ways to improve the line shape and signal-to-noise in half-integer quadrupolar NMR in general have also been proposed; these are worth considering when implementing a low sensitivity experiment such as MQMAS. One of them takes advantage of the inhomogeneous nature of the anisotropies in MQMAS' direct dimension, to generate multiple 1Q signals from a single scan using a Carr–Purcell–Meiboom–Gill echo train during the acquisition period (Figure 9f).[44] Another involves transferring spin order from the satellite to the central spin transitions of a $S = 3/2$ prior to the beginning of the experiment, an approach that proves helpful when starting the spin excitation directly from central S_z^{2-3} magnetization as in the RIACT case.[48,55]

Most of these developments in pulse sequence focused on optimizing the MQMAS signal intensities in the presence of small off-resonance irradiation offsets. This is usually a very good approximation if alkali metals or light main group elements, possessing relatively small shielding contributions ($\leq 0.1\nu_1$). But for the case of heavier elements possessing much large magnitudes in their chemical shift scales, these offsets may severely interfere with the excitation of the MQ coherences. In some situations extreme shielding effects may prevent the acquisition of MQMAS signals altogether, even when dealing with sites possessing small quadrupole couplings. The effects of chemical shielding offsets can be compensated in part by manipulating the MQ coherences via the use of amplitude-modulated or composite pulses.[33] Still, even under these optimal conditions the overall MQMAS signal is usually poorer than that observed in the absence of large chemical or second order quadrupolar shifts.

Although more complete discussions on the optimization of these various MQMAS sequences can be found in the cited literature, it should be remembered that usually 'optimal' pulse values are just good initial starting points, susceptible to considerable improvement by even small variations in their timings. Before setting up a complete 2D MQMAS NMR acquisition it is therefore convenient to monitor the t_2 echo formation for a particular t_1 value, usually fixed at a small integer multiple of rotor periods in order to avoid the intense rotor-modulation imposed by spinning on MQMAS signals, and then vary the individual pulse width parameters around the suggested values until the strongest MQ signal has been detected. Only with these optimized values is it worth devoting the amount of spectrometer time that is required for the acquisition of a complete 2D MQMAS NMR spectrum.

4 FINE STRUCTURE OF THE MQMAS NMR LINE SHAPES

In addition to a successful refocusing of the interactions, retrieving quality half-integer quadrupolar line shapes by MQMAS demands dealing with a number of peculiarities related to the nature of this experiment. Most important among these is the presence of mixed-phase peak distortions. Mixed phase line shapes comprise one of the well-known limitations of 2D Fourier transform NMR, stemming from the indirect detection of one (or more) of the evolving frequencies.[20] Avoiding the dispersive artifacts that arise in these peaks requires some form of time-reversal involving either the formation of a spin-echo, the acquisition of separate echo/anti-echo or cosine/sine MQ-modulated signals (corresponding to different combinations of $+t_1$ and $-t_1$ evolutions), or the simultaneous acquisition of echo + anti-echo amplitude-modulated signals followed by their disentanglement via techniques such as time-proportional phase incrementation (TPPI) or off-resonance irradiation (discouraged for this experiment due to the reasons mentioned in the previous paragraph). Since MQMAS is actually an echo experiment, these mixed phase artifacts are not usually too severe. But when requiring highly-resolved or purely absorptive line shapes, the acquisition of echo and anti-echo signals with identical intensities for all crystallites is required. As mentioned earlier such acquisitions are in many instances hard or impossible to implement due to the different phase factors adopted by the ε parameter of the crystallites as a function of their orientation. Similar problems have been encountered in solution phase NMR, where it was shown they can be alleviated by introducing an intermediate step where coherences are momentarily stored along the z-axis and only then made into observable 1Q magnetizations. The resulting so-called z-filter approach (Figure 9d) ends up using a $0 \rightarrow \pm MQ(t_1) \rightarrow 0 \rightarrow -1(t_2)$ coherence transfer scheme, thereby requiring the addition of an extra pulse into the MQMAS sequence and sacrificing part of the signal.[24] On the other hand, the advantage of this z-filter lies in the fact that since efficiencies for $+MQ(t_1) \rightarrow 0 \rightarrow -1(t_2)$ and $-MQ(t_1) \rightarrow 0 \rightarrow -1(t_2)$ can now be made equal, purely absorptive 2D peaks result. Alternatively, mixed t_1 periods including both MQ and 1Q evolutions followed by acquisition of whole echoes over t_2 (Figure 9e,f) can be used to retrieve purely absorptive line shapes.[29,56] Further details on the nature of these distortions and on strategies for avoiding them are given in detail in (see **MQMAS Advances**).

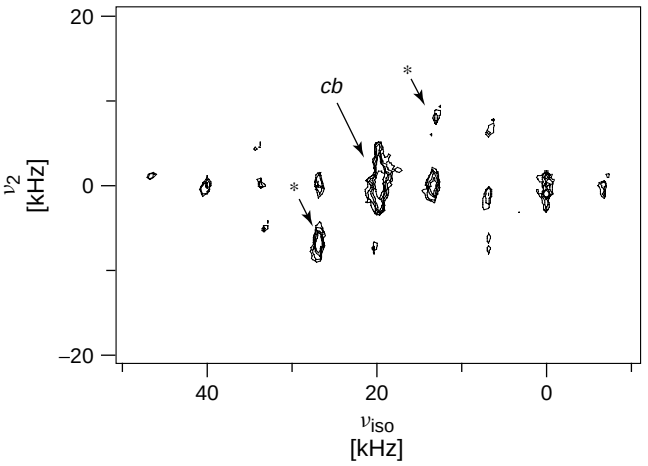

Figure 12 Spinning sideband structure displayed by the ^{23}Na MQMAS NMR spectrum of Na_2SO_4 recorded at 4.7 T with sample spinning at $\nu_r = 6$ kHz. Data were acquired using a two-pulse sequence (Figure 9a) and subject to a shearing to yield a high resolution dimension; they should lead to a single centerband (cb) peak. Asterisks indicate spinning sidebands originating from modulations of the central transition anisotropies, shifted along ν_1 as a result of a shearing of the data. All remaining spinning sidebands, appearing mainly along the indirectly detected ν_1 axis, are artifacts peculiar to the excitation and conversion orientation dependencies of the MQMAS pulse sequence (adapted from Ref.[57])

Another line shape feature characterizing MQMAS NMR spectra is the occurrence of extensive spinning sidebands in the indirectly detected MQ frequency domain (Figure 12). These sidebands behave like their conventional spin-1/2 counterparts in that they are absorptive and appear at multiples of the rotor frequency with decreasing intensities as the spinning speed is increased; their origin, however, does not necessarily relate to the usual spinning-induced time modulation of chemical shift, dipolar or second order quadrupolar interactions. Indeed MQMAS spinning sidebands can span a significantly larger frequency range than those corresponding to the static magnitudes of these nuclear interactions, and are often a consequence of the orientation dependencies associated with the nutation pulses used for MQ excitation and MQ detection.[57,58] A rigorous analysis of such problems requires introducing into the effects of the rf pulse involved in the MQMAS sequence, the explicit time-dependent oscillations of the first order quadrupolar frequencies during t_1. Such an approach reveals that the rotational sideband intensities are mainly a function of e^2qQ/h and η_Q; since analyses of the MQMAS frequency line shape can yield these internal coupling parameters, simulating these indirect-domain spinning sideband patterns often yields only redundant information. From this theoretical analysis it also follows that either orientation-independent excitation or conversion processes will be needed to remove the appearance of these artifacts; these goals have hitherto proved elusive to achieve.

Another source of MQMAS line shape distortions worth discussing are the nonsecular dipolar couplings that arise from other proximate quadrupole nuclei I. Such couplings have been extensively documented in ^{13}C MAS NMR, and are known to arise due to the quadrupole-induced tilting of I's

nuclear spin quantization axes.[59] These effects also show up in MQMAS NMR,[60–63] as neither the spin nor the spatial manipulations involved in this experiment can take care of their averaging. Such residual couplings can be of either homo- or heteronuclear nature, and their effects are usually smaller as magnetic fields increase. Of the various coupling scenarios, the simplest to describe is the high field heteronuclear one;[62] MQMAS line shapes here are made up of $2I + 1$ components whose centers of mass are placed at offsets

$$\nu_{\rm iso}(m_I) = \frac{[|C_S^4(m)| + 2mC_S^4\left(\frac{1}{2}\right)]}{C_S^4\left(\frac{1}{2}\right) + |C_S^4(m)|} \times \{[3m_I^2 - I(I+1)]\Delta + m_I J\} \qquad (15a)$$

where

$$\Delta = \frac{3}{20}\frac{D_{zz}^{\rm eff} C_Q^I}{\nu_O^I}(3\cos^2 b - 1 + \eta_Q^I \sin^2 b \cos 2a) \qquad (15b)$$

is a parameter depending on I's quadrupolar and Larmor as well as on $I-S$'s dipolar coupling. As can be gathered from these expressions, such couplings are usually magnified by the MQMAS experiments, leading to complex multiplets that may impair the method's resolution (Figure 13) but which can also convey valuable coupling information.

Before concluding, it is worth dwelling on other issues affecting line shape resolution. When dealing with heteronuclear couplings to abundant spin-1/2 nuclei, such as in organic systems, the highest resolution proves hard to achieve by simple MAS averaging. This can be aided via heteronuclear decoupling, yet the magnification brought about by dealing with MQ evolutions may demand in these cases the use of efficient decoupling schemes for maximizing resolution.[64,65] Considerable resolution limitations can also arise in homonuclear systems from a different source: the flip-flop terms present in such dipole–dipole couplings, which do not commute with the longitudinal terms in the quadrupolar Hamiltonians.[74,78] If such homonuclear effects are present and strong, a fast-decaying MQMAS echo showing little resolution enhancement when compared to conventional MAS line shapes may result. Furthermore these effects may result in broadenings which decay only slowly or sometimes even increase with spinning speeds, at least within the range of normally used ν_r values.[66] Finally, it is also worth noting that a dependence of the spectral resolution has also been noted on the order m used in MQMAS experiments:[30,67,68] for $S \geq 5/2$ nuclei, a higher resolution tends to be achieved for the maximum MQ order available in the manifold. This can be rationalized by the different m-dependencies exhibited by the isotropic chemical and quadrupolar shifts, transforming as $2m$ and $C_O^S(m)$, respectively. The largest values of these weighting coefficients are usually found for the $m_1 = S$ condition; a $-S \rightarrow -1$ coherence transfer pathway is then required for achieving a refocusing of anisotropies and this choice further reinforces the resolving power of the various isotropic contributions along the high resolution domain. Even further refinements on this approach can be proposed if one allows the pulse sequence to subsequently encode several MQ orders throughout the course of the indirect t_1 evolution;[69] it then becomes feasible to devise acquisition schemes that maximize resolution for almost arbitrary shift values, even if at the expense of substantial sacrifices in signal-to-noise.

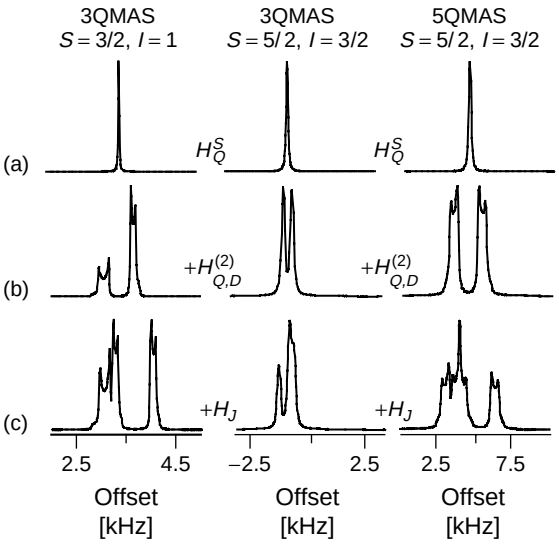

Figure 13 Progressive broadening introduced into the isotropic dimension of MQMAS line shapes (a) by the residual dipolar (b) and J (c) couplings between a spin S and a quadrupolar heteronucleus. Tensors were in all cases assumed axially symmetric and coincident, and the frequency scales refer to an isotropic shift $\delta_S = 0$ kHz. Spectra on the left assumed 3QMAS NMR on an $S = 3/2$ ($e^2qQ/h = 2$ MHz, $\nu_O = 64.4$ MHz) coupled to an $I = 1$ ($e^2qQ/h = 3$ MHz, $\nu_O = 14.5$ MHz) with a $D_{zz}^{\rm eff} = 1.7$ kHz; the center and right columns describe the 3QMAS and 5QMAS spectra of an $S = 5/2$ ($e^2qQ/h = 3$ MHz, $\nu_O = 52$ MHz) coupled to an $I = 3/2$($e^2qQ/h = 12$ MHz, $\nu_O = 20$ MHz). J couplings throughout row (c) were set at 100 Hz (adapted from Ref.[62])

5 OUTLOOK

This review discussed some of the basic features of 2D MQMAS NMR as they apply to the acquisition of high resolution spectra from half-integer quadrupolar nuclei. As an analytical tool for resolving inequivalent chemical sites, the technique appears to be experimentally simple and applicable to a large number of elements. It can be used to distinguish isotropic chemical from isotropic quadrupolar shifts, as well as to pinpoint the quadrupolar coupling parameters e^2Qq/h and η_Q of individual chemical sites. Remarkable also is the extensive spin-physics that have been triggered by this experiment, reawakening a mostly dormant interest in the field of MQ quadrupolar NMR in solids. Due to space constraints many of the underlying principles developed in connection with the manipulation of MQ coherences throughout this experiment have only been briefly discussed. As mentioned, this material is covered in further detail in the original literature, in a number of recent reviews[70–73] as well as in accompanying articles in this Encyclopedia.

As the number of MQMAS applications continues to grow, a number of challenges to be resolved are also becoming increasingly clear. Some of these are of a technical nature, and involve issues such as employing MQMAS data for quantifying the abundance of chemical sites and/or for improving the signal-to-noise ratio of the experiment. Indeed, although significant advances have been made in these areas important

obstacles to overcome still remain, for instance when it comes to observing low-γ nuclei, to characterizing systems affected by substantial chemical shieldings, or to unlocking the potential of 5Q and 7Q MAS spectroscopies towards improving the spectral resolution. Yet it is also clear that even in its present form MQMAS can be a significant aid in enhancing the NMR information afforded by a variety of chemical systems.

A second and perhaps longer-range type of problem triggered by MQMAS, stems from the nature of the method as a mean rather than as an end. Indeed, once inequivalent resonances appear resolved by MQMAS, the real problem of analyzing the meaning of these NMR data begins. For many of the spin isotopes being analyzed by MQMAS this challenge is currently hard to overcome, as the assignment of quadrupolar and shielding parameters to individual chemical sites remains for the most part uncharted. Quantum chemical calculations of NMR coupling parameters are a potentially good starting point for establishing such correlations, yet in many instances their usefulness is compromised by the heavy-element and multi-electronic nature of the isotopes being analyzed. An alternative to this assignment approach relies on employing the X-ray structures available for model systems, in combination with spectral editing techniques based on the dipolar dephasing imposed by nearby nuclei, in order to empirically correlate MQMAS-resolved coupling parameters with specific coordination and bonding motifs. This in turn highlights the need to further develop homo- and heteronuclear recoupling techniques on quadrupole nuclei, and for making these recoupling protocols integral parts of the MQMAS methodology. Driven by this need, it is reasonable to expect this research area to become within the near future as active a topic of investigation as it has become for its spin-1/2 counterparts.

6 RELATED ARTICLES IN THIS VOLUME

MQMAS Advances; Satellite Transition NMR Spectroscopy of Half-Integer Quadrupolar Nuclei under Magic-Angle Spinning.

7 RELATED ARTICLES IN VOLUMES 1–8

Dynamic Angle Spinning, Volume 3; Magic Angle Spinning, Volume 5; Multidimensional Spectroscopy: Concepts, Volume 5; Multiple Quantum Spectroscopy of Liquid Samples, Volume 5; Quadrupolar Interactions, Volume 6; Quadrupolar Nuclei in Solids, Volume 6.

8 REFERENCES

1. R. K. Harris and B. E. Mann, 'NMR and the Periodic Table', Academic Press: New York, 1970.
2. M. H. Cohen and F. Reif, *Solid State Phys.*, 1957, **5**, 321–438.
3. C. P. Slichter, 'Principles of Nuclear Magnetic Resonance', 3rd edn., Springer-Verlag: New York, 1990.
4. D. Freude and J. Haase, *NMR Basic Principles Prog.*, 1993, **29**, 1–90.
5. B. F. Chmelka and J. W. Zwanziger, *NMR Basic Principles Prog.*, 1994, **33**, 79–123.
6. A. J. Vega, in 'Encyclopedia of NMR', eds D. M. Grant and R. K. Harris, Wiley: New York, 1996, pp 3869–3888.
7. M. M. Maricq and J. S. Waugh, *J. Chem. Phys.*, 1979, **70**, 3300–3316.
8. G. E. Maciel, *Science*, 1984, **226**, 282–288.
9. E. Oldfield and R. J. Kirkpatrick, *Science*, 1985, **227**, 1537–1544.
10. J. Fitzgerald, 'Solid State NMR of Inorganic Materials', ACS Symposium Series No. 717, ACS: Washington, DC, 1999.
11. A. Llor and J. Virlet, *Chem. Phys. Lett.*, 1988, **152**, 248–253.
12. A. Samoson, A. Lippmaa, and A. Pines, *Mol. Phys.*, 1988, **65**, 1013–1016.
13. K. T. Mueller, B. Q. Sun, G. C. Chingas, J. W. Zwanziger, T. Terao, and A. Pines, *J. Magn. Reson.*, 1990, **86**, 470–487.
14. L. Frydman and J. S. Harwood, *J. Am. Chem. Soc.*, 1995, **117**, 5367–5368.
15. A. Medek, J. S. Harwood, and L. Frydman, *J. Am. Chem. Soc.*, 1995, **117**, 12 779–12 787.
16. U. Haeberlen, in 'Advances in Magnetic Resonance', ed J. S. Waugh, Academic Press: New York, 1976.
17. L. Frydman, *Ann. Rev. Phys. Chem.*, 2001, **52**, 463–498.
18. E. R. Andrew, A. Bradbury, and R. G. Eades, *Nature*, 1958, **182**, 1659–1659.
19. E. W. Wooten, K. T. Muller, and A. Pines, *Acc. Chem. Res.*, 1992, **25**, 209–215.
20. R. R. Ernst, G. Bodenhausen, and A. Wokaun, 'Principles of Nuclear Magnetic Resonance in One and Two Dimensions', Clarendon: Oxford, 1987.
21. S. P. Brown, S. J. Heyes, and S. Wimperis, *J. Magn. Reson.*, 1996, **A119**, 280.
22. Z. H. Gan, *J. Am. Chem. Soc.*, 2000, **122**, 3242–3243.
23. J. P. Amoureux, C. Fernandez, and L. Frydman, *Chem. Phys. Lett.*, 1996, **259**, 347–355.
24. J. P. Amoureux, C. Fernandez, and S. Steuernagel, *J. Magn. Reson.*, 1996, **A123**, 116–118.
25. D. Massiot, *J. Magn. Reson.*, 1996, **A122**, 240–244.
26. G. Wu, D. Rovnyak, and R. G. Griffin, *J. Am. Chem. Soc.*, 1996, **118**, 9326–9332.
27. G. Wu, D. Rovnyak, B. Sun, and R. G. Griffin, *Chem. Phys. Lett.*, 1996, **249**, 210–217.
28. J. P. Amoureux and C. Fernandez, *Solid State NMR*, 1996, **5**, 315–321.
29. S. P. Brown and S. Wimperis, *J. Magn. Reson.*, 1997, **128**, 42–61.
30. M. J. Duer and C. Stourton, *J. Magn. Reson.*, 1997, **124**, 189–199.
31. M. Hanaya and R. K. Harris, *J. Phys. Chem.*, 1997, **A101**, 6903–6910.
32. F. H. Larsen, H. J. Jakobsen, P. D. Ellis, and N. C. Nielsen, *J. Phys. Chem. A*, 1997, **101**, 8597–8606.
33. L. Marinelli, A. Medek, and L. Frydman, *J. Magn. Reson.*, 1998, **132**, 88–95.
34. J. P. Amoureux, M. Pruski, D. P. Lang, and C. Fernandez, *J. Magn. Reson.*, 1998, **131**, 170–175.
35. S. Ding and C. A. McDowell, *J. Magn. Reson.*, 1998, **135**, 61.
36. A. P. M. Kentgens and R. Verhagen, *Chem. Phys. Lett.*, 1999, **300**, 435–443.
37. F. H. Larsen and N. Nielsen, *J. Phys. Chem. A*, 1999, **103**, 10 825–10 832.
38. P. K. Madhu, A. Goldbourt, L. Frydman, and S. Vega, *Chem. Phys. Lett.*, 1999, **307**, 41–47.
39. P. K. Madhu, A. Goldbourt, L. Frydman, and S. Vega, *J. Chem. Phys.*, 2000, **112**, 2377.
40. J. P. Amoureux, J. W. Wiench, and M. Pruski, *J. Magn. Reson.*, 2000, **147**, 286–295.
41. A. Goldbourt, P. K. Madhu, and S. Vega, *Chem. Phys. Lett.*, 2000, **320**, 448–456.
42. A. Goldbourt, P. K. Madhu, S. Kababya, and S. Vega, *Solid State NMR*, 2000, **18**, 1–16.
43. D. Iuga, H. Schafer, R. Verhagen, and A. P. M. Kentgens, *J. Magn. Reson.*, 2000, **147**, 192–209.

44. T. Vosegaard, F. H. Larsen, H. J. Jakobsen, P. D. Ellis, and N. C. Nielsen, *J. Am. Chem. Soc.*, 1997, **11**, 9055.
45. T. Vosegaard, P. Florian, P. J. Grandinetti, and D. Massiot, *J. Magn. Reson.*, 2000, **143**, 217–222.
46. T. Vosegaard, D. Massiot, and P. J. Grandinetti, *Chem. Phys. Lett.*, 2000, **326**, 454–460.
47. T. Vosegaard, P. Florian, D. Massiot, and P. J. Grandinetti, *J. Chem. Phys.*, 2001, **114**, 4618.
48. H.-T. Kwak, S. Prassad, Z. Yao, L. Emsley, J. Sachleben, and P. J. Grandinetti, *J. Magn. Reson.*, 2001, **150**, 71–80.
49. A. Wokaun and R. R. Ernst, *J. Chem. Phys.*, 1977, **67**, 1752–1758.
50. S. Vega, *J. Chem. Phys.*, 1978, **68**, 5518.
51. S. Vega and Y. J. Naor, *J. Chem. Phys.*, 1981, **75**, 75–86.
52. R. Jannsen and W. S. Veeman, *J. Chem. Soc., Faraday Trans.*, 1988, **84**, 3747.
53. A. J. Vega, *J. Magn. Reson.*, 1992, **96**, 50–68.
54. K. H. Lim and C. P. Grey, *Solid State NMR*, 1998, **13**, 101.
55. Z. Yao, H.-T. Kwak, D. Sakellariou, L. Emsley, and P. J. Grandinetti, *Chem. Phys. Lett.*, 2000, **327**, 85–90.
56. D. Massiot, B. Tonzo, D. Trumeau, J. P. Coutures, J. Virlet, P. Florian, and P. J. Grandinetti, *Solid State NMR*, 1996, **6**, 73–83.
57. L. Marinelli and L. Frydman, *Chem. Phys. Lett.*, 1997, **275**, 188–198.
58. U. Friedrich, I. Schnell, S. P. Brown, A. Lupescu, D. E. Demco, and H. W. Spiess, *Mol. Phys.*, 1998, **95**, 1209–1227.
59. R. K. Harris and A. C. Olivieri, *Prog. NMR Spetrosc.*, 1992, **24**, 435–456.
60. J. McManus, R. Kemp-Harper, and S. Wimperis, *Chem. Phys. Lett.*, 1999, **311**, 292–298.
61. G. Wu and K. Yamada, *Chem. Phys. Lett.*, 1999, **313**, 519–524.
62. S. Wi and L. Frydman, *J. Chem. Phys.*, 2000, **112**, 3248–3261.
63. S. Wi, V. Frydman, and L. Frydman, *J. Chem. Phys.*, 2001, **114**, 8511–8519.
64. V. Lacassagne, P. Florian, V. C. Montouillout, F. B. Gervais, and D. Massiot, *Magn. Reson. Chem.*, 1998, **36**, 956.
65. A. E. Bennett, C. M. Rienstra, M. Auger, K. V. Lakshmi, and R. G. Griffin, *J. Chem. Phys.*, 1995, **103**, 6951–6958.
66. M. Eden and L. Frydman, *J. Chem. Phys.*, 2001, **114**, 4116–4123.
67. S. H. Wang, Z. Xu, J. H. Baltisberger, L. M. Bull, J. F. Stebbins, and A. Pines, *Solid State NMR*, 1997, **8**, 1–16.
68. K. J. Pike, R. P. Malde, S. E. Ashbrook, J. McManus, and S. Wimperis, *Solid State NMR*, 2000, **16**, 203.
69. A. Jerschow, J. W. Logan, and A. Pines, *J. Magn. Reson.*, 2001, **149**, 268–270.
70. A. Medek and L. Frydman, *J. Braz. Chem. Soc.*, 1999, **10**, 263–277.
71. D. Freude, in 'Encyclopedia of Analytical Chemistry', ed R. A. Meyers, Wiley: Chichester, 2000, pp 12 188–12 224.
72. M. E. Smith and E. R. H. vanEck, *Prog. NMR Spectrosc.*, 1999, **34**, 159–201.
73. M. W. Anderson and M. J. Duer eds, New NMR Techniques for Quadrupolar Nuclei, in *Solid State NMR*, 1999, **15**.
74. C. V. Grant, D. McElheny, V. Frydman, and L. Frydman, manuscript in preparation.
75. H. Kessler, M. Gehrke, and C. Griesinger, *Angew. Chem. Int. Ed. Engl.*, 1988, **27**, 490–536.
76. C. A. Fyfe, J. Skibsted, H. Grodney, and H. M. Altenschildesche, *Chem. Phys. Lett.*, 1997, **281**, 44–48.
77. M. J. Duer, *Chem. Phys. Lett.*, 1997, **277**, 167–174.
78. M. J. Duer and A. J. Painter, *Chem. Phys. Lett.*, 1999, **313**, 763–770.

Acknowledgements

The development of the material described in this paper was enriched by valuable discussions with Dr Ales Medek, Ms Laura Marinelli, Dr John S. Harwood, Dr Chris Grant, Dr P. K. Madhu and Professor S. Vega.

Biographical Sketch

Lucio Frydman, *b* 1965, Buenos Aires, Argentina. B.Sc. 1986 Chemistry, Ph.D. 1990 Physical Chemistry, University of Buenos Aires. Research Associate, Lawrence Berkeley Laboratory, 1990–1992 with A. Pines. Assistant-Associate-Full Professor, University of Illinois at Chicago, 1992–2001. Adjunct Professor, University of Illinois at Chicago, since 2001. Professor, Weizmann Institute of Sciences, since 2001. Approximately 70 publications. Current research interests: development and application of new methods in solution solid state and liquid crystalline NMR.

REDOR and TEDOR

Jacob Schaefer

Department of Chemistry, Washington University, St. Louis, MO, USA

1	Refocusing and Dephasing	1
2	REDOR Dephasing for Recrystallized Labeled Alanines	1
3	Long-Range Couplings and the Natural-Abundance Background	3
4	Coherence Transfer and Selectivity	5
5	Combination Experiments and Synchronous Detection	6
6	Related Articles	7
7	References	7

1 REFOCUSING AND DEPHASING

Rotational echo double resonance (REDOR) NMR is a new analytical spectroscopic technique for solids spinning at the magic angle which has been developed during the last 6 years.[1] REDOR provides a direct measure of heteronuclear dipolar coupling between isolated pairs of labeled nuclei. In a solid with a $^{13}C-^{15}N$ labeled pair, for example, the ^{13}C rotational echoes that form each rotor period following a $^{1}H-^{13}C$ cross polarization transfer can be prevented from reaching full intensity by insertion of a ^{15}N π pulse each half rotor period (Figure 1). The ^{15}N pulse in the middle of the evolution period is replaced by a ^{13}C pulse so that isotropic carbon chemical shifts are in phase at the beginning of data acquisition. The REDOR difference (the difference between a ^{13}C NMR spectrum obtained under these conditions and one obtained with no ^{15}N π pulses) has a strong dependence on the $^{13}C-^{15}N$ dipolar coupling and hence the $^{13}C-^{15}N$ internuclear distance.[2] REDOR is described as double resonance even though three radiofrequencies (typically ^{1}H, ^{13}C, and ^{15}N) are used because the protons are removed from the important evolution part of the experiment by resonant decoupling. The dephasing of magnetization in REDOR arises from a local dipolar $^{13}C-^{15}N$ field gradient and involves no polarization transfer. REDOR has no dependence on ^{13}C or ^{15}N chemical shift tensors and does not require resolution of a $^{13}C-^{15}N$ coupling in the chemical shift dimension.[2]

The evolution of observable S-spin magnetization for a single crystallite on resonance under magic angle spinning and an $I-S$ dipolar coupling is shown in Figure 2 (left). Each dot represents the result of evolution for an equal fraction of a rotor period, with a minor homogeneous decay superimposed for display purposes. At the beginning of the rotor cycle, the magnetization is the observable, $\langle\hat{S}_x\rangle$. Under sample rotation and $I-S$ dipolar coupling, the observable magnetization is transformed into nonobservable bilinear coherence, $\langle\hat{I}_z\hat{S}_y\rangle$, and then back into $\langle\hat{S}_x\rangle$. By the end of the rotor cycle the full observable magnetization has been recovered. For a collection of crystallites in a powder, individual phase accumulations (the product of resonance frequency and time) vary in size and sign depending on crystallite orientation in the magnetic field. This causes phase interference during the rotor cycle and an apparent decay of the observable signal for the powder. Nevertheless, because the magnetization from each crystallite refocuses completely, the dephasing for the powder is also refocused into a full rotational echo at the end of the rotor cycle.

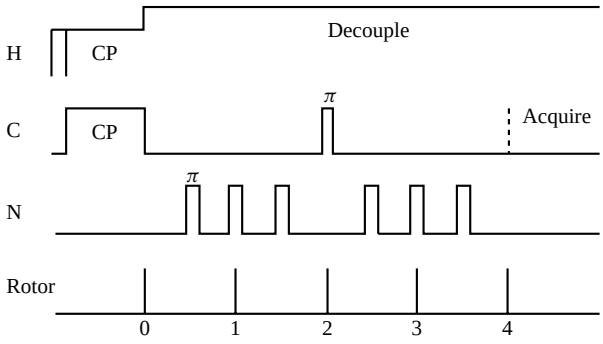

Figure 1 Pulse sequence for a version of REDOR ^{13}C NMR. Two equally spaced, ^{15}N 180° pulses per rotor period result in the dephasing of transverse carbon magnetization produced by a cross-polarization (CP) transfer from dipolar-coupled protons. Carbon–nitrogen dipolar coupling determines the extent of dephasing. A ^{13}C 180° pulse replaces the ^{15}N pulse in the middle of the dephasing period and refocuses isotropic ^{13}C chemical shift differences at the beginning of data acquisition. After the CP transfer, resonant decoupling removes the protons from the experiment. The illustration is for four rotor cycles

However, even for a single crystallite, the refocusing is incomplete in the presence of dephasing I-spin π pulses (Figure 2, right). Evolution for the crystallite is identical to that shown at the left of the figure between times '1' and '2'. The I-spin inverting π pulse, which ends at time '3', changes the sign of $\langle\hat{I}_z\hat{S}_y\rangle$. This process is repeated under the second I-spin π pulse which ends at time '5'. At the end of the rotor cycle (time '6'), the transformation of bilinear coherence created during the rotor cycle into observable magnetization is incomplete. For a powder, a rotational echo of diminished intensity is observed. The extent of the diminution depends on the $I-S$ coupling. The diminution is maximum for two dephasing pulses and is independent of their exact placement so long as the pulse spacing is one-half of the rotor period.[2]

2 REDOR DEPHASING FOR RECRYSTALLIZED LABELED ALANINES

The results of a REDOR experiment performed using the pulse sequence of Figure 1 on an equimolar, recrystallized mixture of L-[2-^{13}C,^{15}N]alanine and L-[1-^{13}C]alanine are shown in Figure 3.[3] The full echo ^{13}C NMR spectrum (S_0) after two rotor cycles with no dephasing is at the bottom of the Figure, and the REDOR difference ($\Delta S = S_0 - S$, where S is the spectrum with dephasing) as a function of the number of rotor cycles, is shown at the top of the Figure. The 900 Hz intramolecular $^{13}C-^{15}N$ coupling results in a sizeable ΔS for the methine carbon atom after only two rotor cycles; this ΔS reaches a maximum after four rotor cycles, and then oscillates in amplitude. The average 100 Hz intermolecular coupling produces a small carboxyl carbon atom ΔS after two rotor cycles, which increases monotonically with dephasing time.

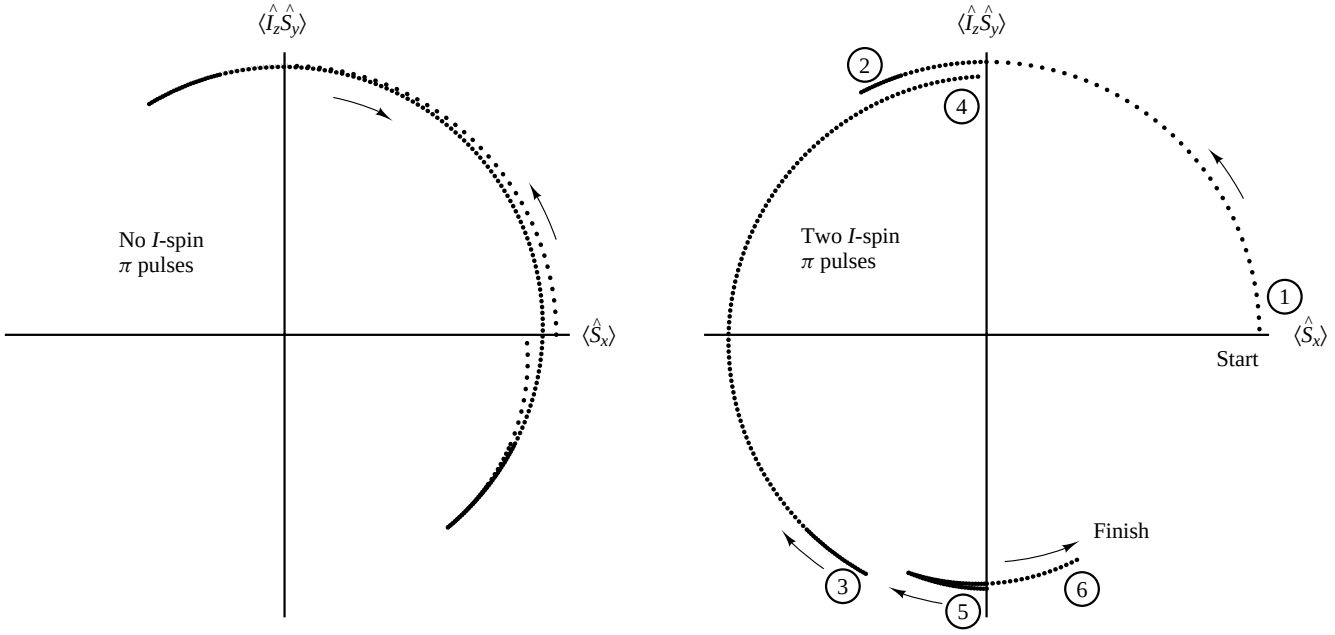

Figure 2 Schematic diagram of the evolution of the IS density matrix for a single crystal under magic angle spinning and $I-S$ dipolar coupling during a REDOR pulse sequence with no dephasing pulses (left) and with dephasing pulses (right)

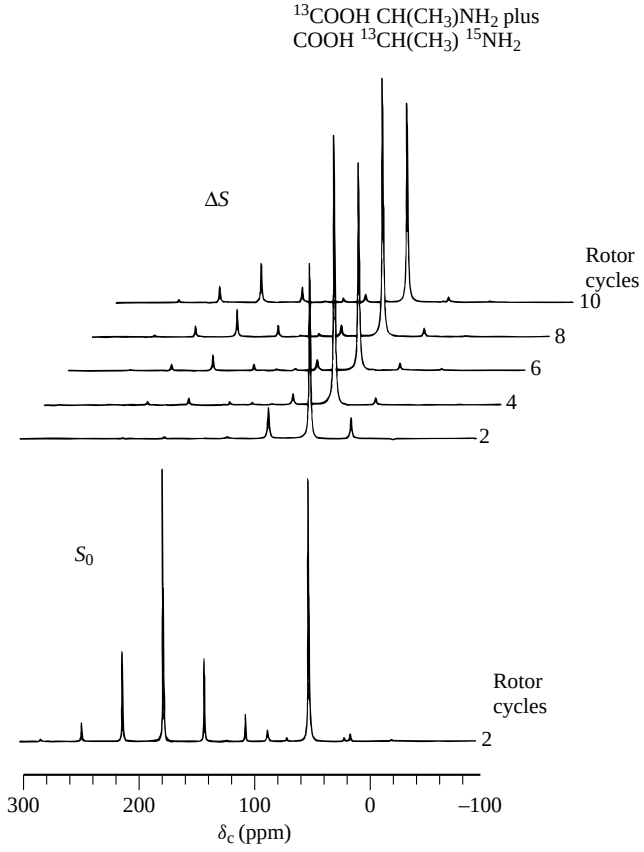

Figure 3 The 50.3-MHz REDOR ^{13}C NMR spectra of an equimolar, recrystallized mixture of L-[2-^{13}C,^{15}N]alanine and L-[1-^{13}C]alanine, as a function of the number of rotor cycles. A full echo spectrum (S_0) after two rotor cycles is shown at the bottom of the Figure and REDOR difference spectra (ΔS) at the top. Magic angle spinning was at 2702 Hz

The $\Delta S/S_0$ ratios for both carbon atoms have the same dependence on the dimensionless parameter, λ_D (Figure 4, solid circles and squares). The theoretical dependence (Figure 4, solid line) was calculated by performing an isotropic powder average over the dephasing for individual crystallites (Figure 2, right). Thus, the angular dependence of the dipolar interaction is suppressed. The resulting universal dephasing behavior needs to be calculated only once for all heteronuclear spin-1/2 pairs. (REDOR applications also include quadrupolar nuclei like ^{2}H, with either direct observation of deuterium or indirect observation through REDOR dephasing. Calculation of the theoretical $\Delta S/S_0$ behavior is slightly more complicated.)[4]

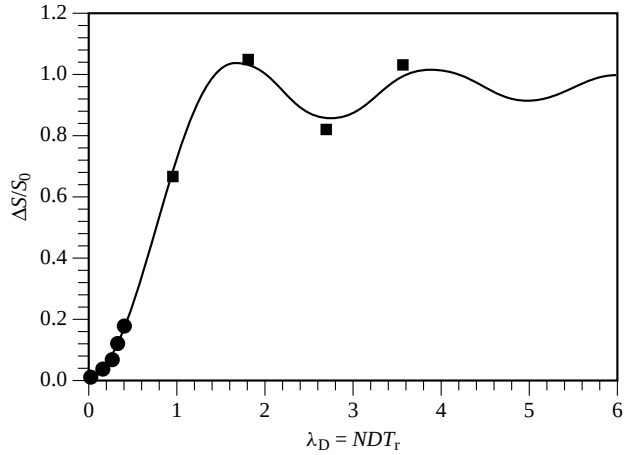

Figure 4 Observed dependence of $\Delta S/S_0$ on the universal parameter, λ_D, for the ^{13}C–^{15}N double-labeled alanine mixture of Figure 3. (N is the number of rotor cycles with dephasing, D is the dipolar coupling constant, and T_r is the rotor period)

A few experimental values of $\Delta S/S_0$ determine λ_D, which then establishes D since the total dephasing time (the product of the number of rotor cycles of dephasing and the rotor period) is known. Because $D = \gamma_I\gamma_S h/2\pi r^3_{IS}$, the observed dephasing can be translated into an internuclear distance directly. If $\Delta S/S_0$ and hence D are known experimentally to 10%, the distance is known with 2% accuracy. Weak dipolar couplings associated with large internuclear distances can be effectively amplified in REDOR by simply allowing the rotor to go around. The only practical problem is holding the echo train together. This depends on the technical difficulty of completely decoupling the protons, which may require low temperatures to suppress kHz regime molecular motions.[5] Translating dipolar couplings into distances in the presence of large-amplitude motions involves specifying a model for the motion.[6]

3 LONG-RANGE COUPLINGS AND THE NATURAL-ABUNDANCE BACKGROUND

In the early applications of REDOR to C–N distance determinations in peptides, relatively few dephasing pulses were used so that sometimes large natural-abundance corrections were necessary.[7] More recently, increased dephasing has been possible as a result of the development of phase routing schemes[8] (Figure 5) that eliminate the dependence of REDOR determinations on frequency offsets and pulse imperfections.[9]

For example, the ^{13}C signal for the label in the nine-residue emerimicin fragment, Ac-Phe-[1-^{13}C]MeA$_2$-MeA-MeA-Val-[^{15}N]Gly$_6$-Leu-MeA-MeA-*O*-Bzl, where Ac = acetyl, Phe = phenylalanine, MeA = methylalanine, Val = valine, Gly = glycine, Leu = leucine, Bzl = benzyl is not resolved from that of natural-abundance peptide carbonyl carbon atoms, which make a constant 7.7% contribution to the full echo signal, S_0. This correction can either be measured in a separate experiment on a natural-abundance sample, or calculated from the known structure.[10] In addition, the natural-abundance ^{13}C carbonyls of Val$_5$ and Gly$_6$ are, respectively, one and two bonds away from the ^{15}N label and so will make a contribution to ΔS that reaches a maximum value of 2% by about N_c = 16. The other natural-abundance carbonyl ^{13}C atoms are all farther away from the ^{15}N label than is the carbonyl label at MeA$_2$. Thus, for $N_c > 32$, the observed ΔS is dominated by the coupling of the ^{15}N–^{13}C labels and additional natural-abundance corrections are unimportant. By N_c = 96, $\Delta S/S_0$ is greater than 0.7 (Figure 6), consistent with a D value of 40 Hz, corresponding to a C–N distance of 4.2 ± 0.1 Å. The distance by X-ray analysis[11] is 4.16 Å. The natural-abundance correction to D is less than 2 Hz when N_c = 96, which means that less than a 0.05-Å correction for the C–N distance is required. The agreement between X-ray and REDOR determinations of the [1-^{13}C]MeA$_2$–[^{15}N]Gly$_6$ distance for this calibration sample for N_c = 8 to N_c = 112

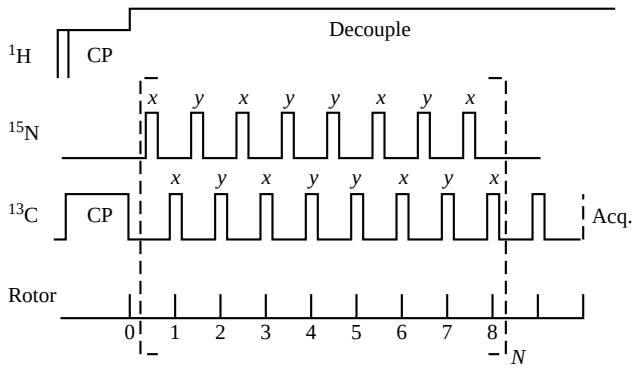

Figure 5 REDOR pulse sequence with dephasing π pulses on both the nitrogen and carbon channels. The pulses are applied using an *xy*-8 phase cycling scheme to eliminate offset effects and pulse imperfections. Signal acquisition begins two rotor cycles after the completion of a full 8*N* rotor cycles of dephasing. CP = cross polarization. Acq = acquisition

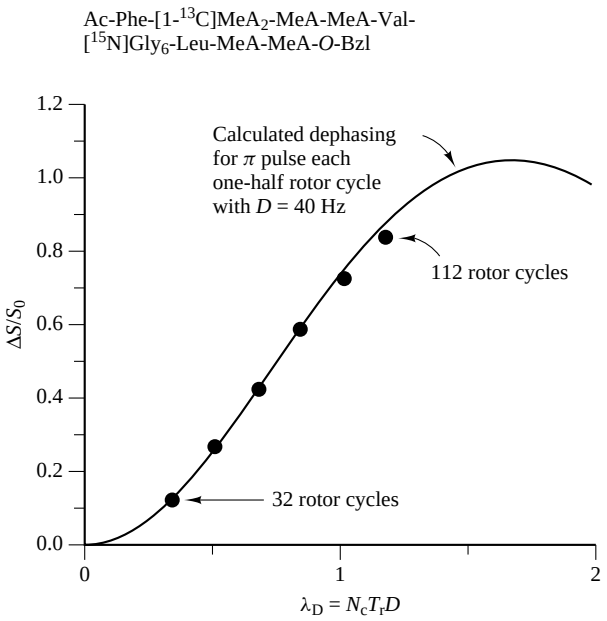

Figure 6 Observed dependence of $\Delta S/S_0$ on the universal parameter, λ_D, for a ^{13}C–^{15}N double-labeled fragment of emerimicin. The pulse sequence of Figure 5 was used. The experimental results (solid circles) are in agreement with calculation (solid line) assuming a ^{13}C–^{15}N dipolar coupling of 40 Hz corresponding to a C–N distance of 4.1 ± 0.1 Å. The natural-abundance correction to $\Delta S/S_0$ at N_c = 8 is 50% and at N_c = 100 is 4%

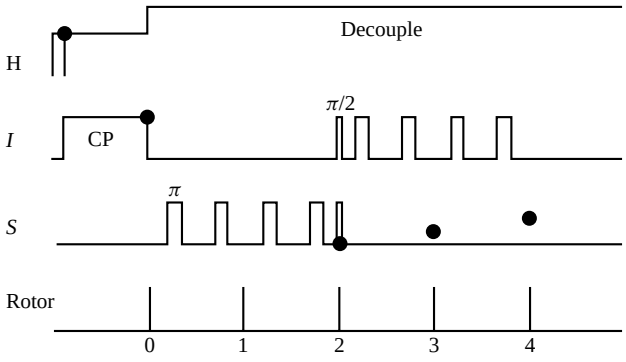

Figure 7 Pulse sequence for TEDOR *I*–*S* NMR. Following a cross-polarization (CP) transfer from abundant protons to generate initial *I*-spin magnetization, the effect of the protons is removed by resonant decoupling. The π pulses are shown separated by one-half rotor periods. The coherence transfer is achieved by simultaneous $\pi/2$ pulses in the middle of the evolution period. The solid circles represent observable magnetization

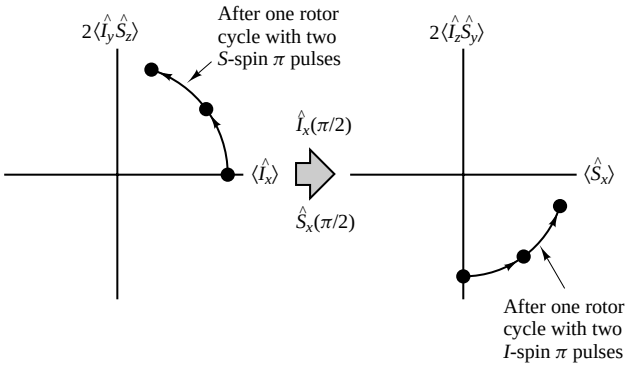

Figure 8 Schematic diagram of the evolution of the density matrix for a powder during the TEDOR pulse sequence of Figure 7 before the coherence transfer pulses (left) and after the application of the transfer pulses (right). The phase angle between $\langle\hat{I}_x\rangle$ and $\langle\hat{I}_y\hat{S}_z\rangle$ for each rotor cycle is indicated by the solid circles and is calculated using the technique illustrated in Figure 2 (right) together with a powder average. The effect of the 90° pulses is to permute I and S subscript indices

confirms that with the compensation of the *xy*-8 phase cycling scheme, hundreds of dephasing pulses can be used with no significant accumulation of error for a REDOR difference.[10] A few, accurate long range distance determinations are often sufficient to establish unambiguously the local conformation of a peptide or protein.[12]

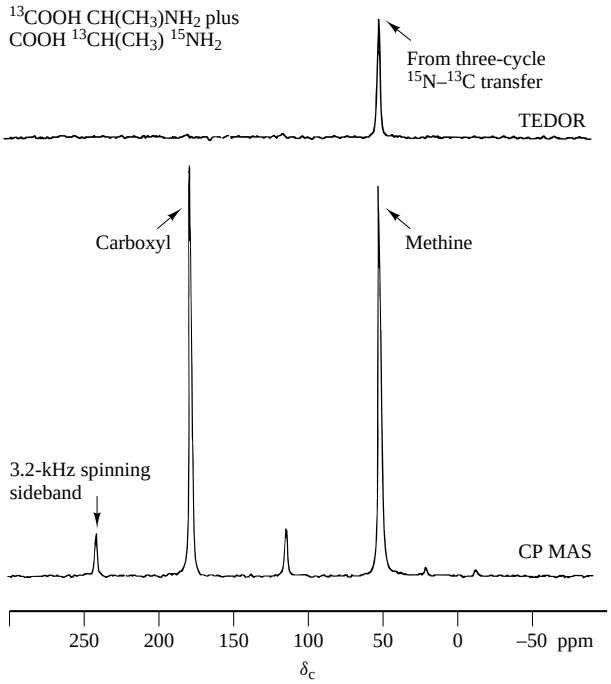

Figure 9 Transferred-echo double-resonance (top) and cross-polarization, magic angle spinning (CP MAS, bottom) ^{13}C NMR spectra of a recrystallized equimolar mixture of L-[2-^{13}C,^{15}N]alanine and L-[1-^{13}C]alanine. The TEDOR spectrum was obtained using three rotor cycles each of dephasing and refocusing. This is insufficient to generate significant carboxyl-carbon magnetization because the average intermolecular C–N dipolar coupling is weak

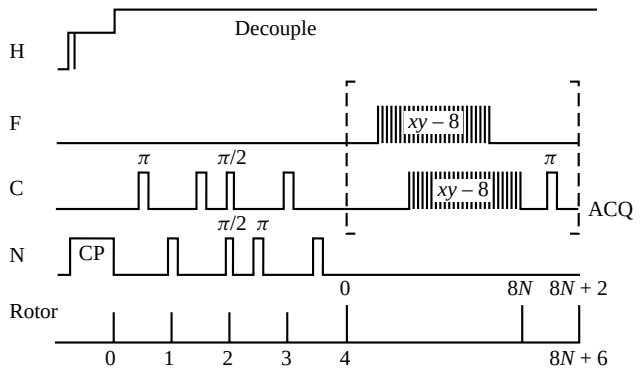

Figure 10 Pulse sequence for TEDOR combined with REDOR. The TEDOR part of the experiment (which for this illustration extends over the first four rotor cycles following the H–N cross polarization transfer) selects ^{13}C magnetization by a coherence transfer from ^{15}N. The REDOR part of the experiment (broken brackets) immediately follows the TEDOR preparation and measures dipolar coupling of the selected ^{13}C to ^{19}F. REDOR dephasing is performed using the phase-routing scheme illustrated in Figure 5. Two rotor cycles are added to the sequence so that the start of data acquisition is not coincident with a pulse

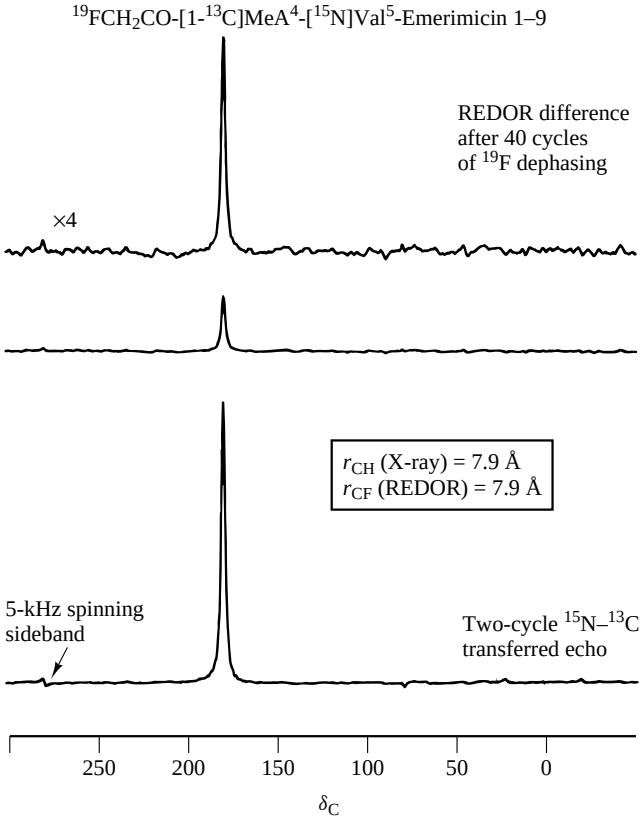

Figure 11 TEDOR–REDOR ^{13}C NMR spectra of a ^{19}F, ^{13}C, ^{15}N-labeled emerimicin (see Figure 6). The TEDOR spectrum (bottom) was obtained using an N–C coherence transfer as illustrated in Figure 7. The TEDOR–REDOR difference spectrum (the difference between TEDOR spectra with and without dephasing REDOR pulses) is shown at the top of the Figure. This spectrum was obtained by ^{19}F dephasing of the ^{15}N-TEDOR-selected ^{13}C magnetization over 40 rotor cycles

Background corrections for ^{13}C-observe ^{15}N-dephase REDOR are relatively simple to calculate because the ^{15}N natural abundance is low and γ_N is small. A measured value involves a separate sample with no ^{15}N label. The minor, observed $\Delta S/S_0$ for the single-labeled sample is then usually just subtracted from that for the double-labeled sample.[3] The correction is more involved for ^{13}C–^{31}P and ^{13}C–^{19}F pairs. For example, a ^{19}F-observe ^{13}C-dephase REDOR experiment designed to measure the dipolar coupling for a labeled ^{19}F–^{13}C pair separated by 10 Å must take into account the sizeable number of natural-abundance ^{13}C atoms within dephasing range of the ^{19}F. One way[13] to interpret the observed $\Delta S/S_0$ is to generate a model lattice with 1% randomly distributed ^{13}C. If all ^{13}C–^{13}C coupling is ignored, the ^{19}F-observed, ^{13}C-dephase REDOR ΔS can be interpreted in terms of a collection of independent, ^{19}F(label)-^{13}C(label)-^{13}C(natural abundance), three-spin clusters, whose dipolar-tensor orientations are known from the lattice parameters.

4 COHERENCE TRANSFER AND SELECTIVITY

Sometimes a natural-abundance background cannot be measured or calculated easily. In this situation, the dipolar-coupled spins can be selected from among the background of uncoupled spins by a coherence transfer from one spin of the heteronuclear pair to the other. The pulse sequence for this selection is shown in Figure 7. Transverse magnetization is first established in the I-spin system by a cross-polarization transfer from abundant protons. The dephasing of I-spin magnetization by dipolar-coupled S spins through rotor-synchronized S-spin π pulses leads to a bilinear coherence (Figure 8, left) that is transferred by an I,S pair of $\pi/2$ pulses (Figure 8, shaded arrow). These pulses occur together at the completion of a rotor cycle (Figure 7) and interchange the indices of the bilinear coherence. Finally, the transferred bilinear coherence is transformed into observable S-spin transverse magnetization by rotor-synchronized I-spin π pulses (Figure 8, right). The entire procedure is called transferred echo double resonance (TEDOR).[14] TEDOR is a rotor-synchronized solid state experiment which is based on some of the same coherence transfer principles as the INEPT solution state experiment.

The results of a TEDOR experiment using the pulse sequence of Figure 7 performed on the mixed double-labeled alanine sample discussed above are shown in Figure 9. Proton polarization is first transferred to nitrogen atoms. Then three rotor cycles are used to create bilinear ^{15}N–^{13}C coherence, and three more rotor cycles to produce observable methine carbon atom magnetization following the coherence transfer. The TEDOR theoretical transfer efficiency[14] is 50% compared with the observed 35% (Figure 9). Because TEDOR is not a difference experiment, TEDOR has the same theoretical sensitivity as REDOR. No sizeable carboxyl

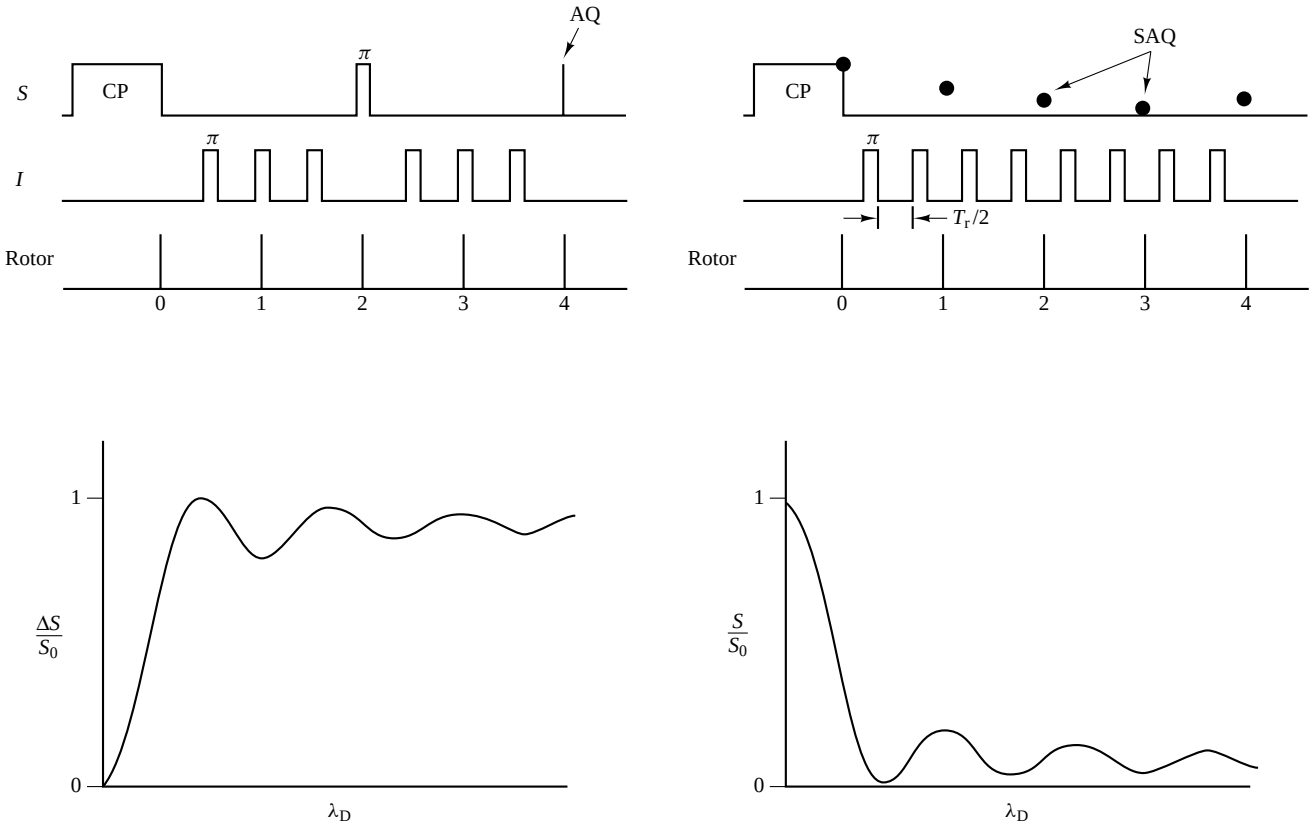

Figure 12 Two schemes for REDOR. (Left) Acquisition of a time domain signal follows evolution during which dephasing pulses diminish observable magnetization and create nonobservable $I-S$ bilinear coherence. This scheme is suitable for multiline spectra and a separate $\Delta S/S_0$ is measured for each line in the spectrum. The dependence on λ_D is determined by varying the number of rotor cycles. (Right) Synchronous detection of a time domain signal during evolution is suitable for a single-line spectrum. The observed S/S_0 is $1 - (\Delta S/S_0)$. AQ = acquisition; SAQ = synchronous acquisition

carbon magnetization is observed in Figure 9 because the short evolution time was insufficient for the weak intermolecular $^{15}N-^{13}C$ coupling to create significant bilinear coherence. If there had been a collection of nitrogen atoms all with comparable strong, couplings to carbon atoms, the TEDOR coherence transfer could still have been made selective by alternating the sign of the starting nitrogen magnetization for just one type of ^{15}N by DANTE inversion of the selected nitrogen atom signal every other scan.[15] The sign of the transferred bilinear coherence would then alternate, as would that of the observed carbon atom magnetization corresponding to the selected $^{15}N-^{13}C$ coupling. Data routing could then discriminate between carbon signals.

5 COMBINATION EXPERIMENTS AND SYNCHRONOUS DETECTION

TEDOR can be used alone or in combination to make highly selective TEDOR–TEDOR and TEDOR–REDOR experiments.[16] The pulse sequence for the latter is illustrated in Figure 10. A TEDOR sequence is tailored to select the carbonyl carbon atom signal of residue 4 of a ^{19}F, ^{13}C, ^{15}N triple-labeled emerimicin fragment (Figure 11). The $^{15}N-^{13}C$ selected magnetization is then dephased by REDOR ^{19}F π pulses resulting in the determination of a selected 8-Å C–F distance. This combination experiment involves four radiofrequencies in the same sequence which is possible using transmission-line probe technology.[17] The tuning elements in these probes are outside the magnet in a large, shielded box with isolation of all radiofrequencies, making high power on four channels practical.[18]

The observed signal in the TEDOR–REDOR experiment can be detected either as part of a two-dimensional experiment in which full S and S_0 spectra are obtained by normal acquisition starting with a rotor cycle (Figure 12, left), or synchronously with one sampling per rotor cycle (Figure 12, right). The former is used for complicated spectra with more than one resonance even after selection by TEDOR. The latter is used for the simple, one-line spectra that usually result from a TEDOR preparation. Synchronous detection[2] has the sensitivity advantage of generating the entire REDOR dephasing pattern in real time. The dipolar evolution dimension can be mapped by variation of the number of rotor cycles,[1] or variation of the position of the dephasing pulse within the rotor period.[2] The latter has a constant total dipolar evolution time which eliminates the echo-train lifetime from the analysis. In both of these two-dimensional methods, spins which contribute to the S-spin signal but have no $I-S$ coupling (a common situation for a natural-abundance background) do not interfere with the determination of the $I-S$ interaction.[16] Such spins produce a constant offset in the dipolar time domain and so a zero-frequency spike in the dipolar frequency domain. The $I-S$ coupling is determined by the width of the dipolar spectrum.[2]

Even an efficient TEDOR transfer does not result in observable magnetization associated with an isotropic powder. Thus, some crystallite orientations are discriminated against depending on the orientation of the *IS* and *SX* dipolar tensors in an $I-S-X$ three-spin TEDOR–REDOR experiment. Nevertheless, following an efficient $I-S$ TEDOR transfer, the *initial* S-observe, X-dephase REDOR behavior depends only on the size of the dipolar tensors and not on their orientation (Figure 13). Thus, interpretation of the 20% dephasing (Figure 14) in a TEDOR–REDOR experiment on the triple-labeled peptide of Figure 11 does not require knowledge of $^{15}N-^{13}C-^{19}F$ geometry in order to extract a C–F distance.[16] This will be the situation for most long-range distance determinations in general, simply because little dephasing is observed and determination of the dipolar coupling is based on the initial S/S_0 behavior. However, for systems with stronger couplings, Fourier transforms of the TEDOR–REDOR dipolar evolution offer the opportunity to establish geometry by comparisons with theoretical dipolar lineshapes (Figure 15).

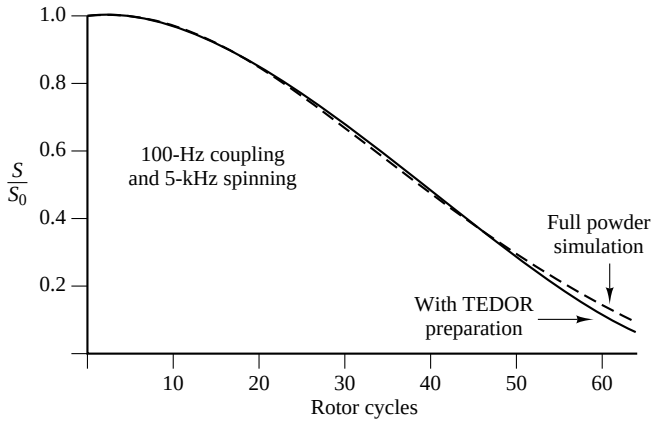

Figure 13 Simulation of X-spin REDOR dephasing of $I-S$ TEDOR-selected S-spin magnetization (solid line). The simulation assumed an $I-S$ coherence transfer after two rotor cycles of dephasing, followed by two rotor cycles of transformation of coherence into observable S-spin magnetization (see Figure 7). For $S/S_0 > 0.5$, the simulation is almost independent of orientation of $I-S$ and $S-X$ dipolar tensors (results not shown) and closely matches that for a full isotropic powder (dotted line). All simulations were performed assuming that the $I-S$ coupling was 1.2 kHz, the $S-X$ coupling was 100 Hz, and the magic angle spinning was 5 kHz

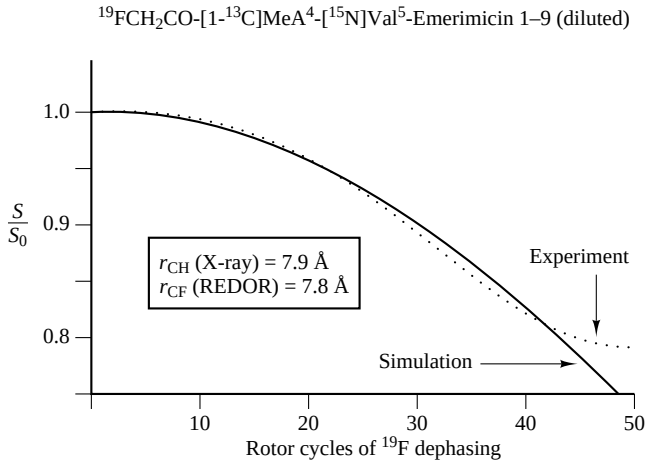

Figure 14 Synchronously sampled time domain ^{13}C signal of a ^{19}F, ^{15}N, ^{13}C-triple-labeled emerimicin diluted by natural-abundance peptide. The ^{15}N TEDOR-selected ^{13}C signal is sampled once each rotor period either with (S) or without (S_0) ^{19}F dephasing pulses. Magic angle spinning was at 5 kHz

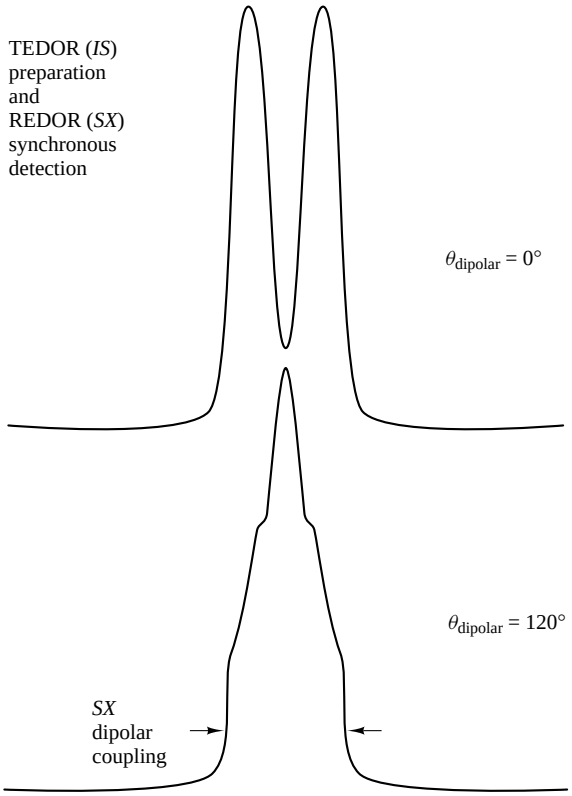

Figure 15 Dipolar spectra obtained by Fourier transforms of time domain simulations performed as described in the caption to Figure 13. The widths of both dipolar spectra are determined by the 100-Hz $S-X$ coupling. Details of the lineshape are determined by orientation of $I-S$ and $S-X$ dipolar tensors

6 RELATED ARTICLES

Cross Polarization in Solids; Electron– Nuclear Multiple Resonance Spectroscopy; INEPT; Magic Angle Spinning; Rotating Solids; Selective Excitation in MRI and MR Spectroscopy.

7 REFERENCES

1. T. Gullion and J. Schaefer, *J. Magn. Reson.*, 1989, **81**, 196.
2. T. Gullion and J. Schaefer, *Adv. Magn. Reson.*, 1989, **13**, 55.
3. Y. Pan, T. Gullion, and J. Schaefer, *J. Magn. Reson.*, 1990, **90**, 330.
4. A. Schmidt, R. A. McKay, and J. Schaefer, *J. Magn. Reson.*, 1992, **96**, 644.
5. B. A. Lewis, G. S. Harbison, J. Herzfeld, and R. G. Griffin, *Biochemistry*, 1985, **24**, 4671.
6. J. Schaefer, E. O. Stejskal, R. A. McKay, and W. T. Dixon, *Macromolecules*, 1984, **17**, 1479.
7. G. R. Marshall, D. D. Beusen, K. Kociolek, A. S. Redlinski, M. T. Leplawy, Y. Pan, and J. Schaefer, *J. Am. Chem. Soc.*, 1990, **112**, 963.
8. T. Gullion, D. B. Baker, and M. S. Conradi, *J. Magn. Reson.*, 1990, **89**, 479.
9. T. Gullion and J. Schaefer, *J. Magn. Reson.*, 1991, **92**, 439.
10. A. W. Hing, N. Tjandra, P. F. Cottam, J. Schaefer, and C. Ho, *Biochemistry*, 1994, **33**, 8651.
11. G. R. Marshall, E. E. Hodgkin, D. A. Langs, G. D. Smith, J. Zabrocki, and M. T. Leplawy, *Proc. Natl. Acad. Sci. U.S.A.*, 1990, **87**, 487.
12. A. M. Christensen and J. Schaefer, *Biochemistry*, 1993, **32**, 2868.
13. L. M. McDowell, C. A. Klug, D. D. Beusen, and J. Schaefer, *Biochemistry*, submitted.
14. A. W. Hing, S. Vega, and J. Schaefer, *J. Magn. Reson.*, 1992, **96**, 205.
15. D. D. Mueller, A. Schmidt, K. L. Papan, R. A. McKay, and J. Schaefer, 1995, **34**, 5597.
16. S. M. Holl, G. R. Marshall, D. D. Beusen, K. Kociolek, A. S. Redlinski, M. T. Leplawy, R. A. McKay, S. Vega, and J. Schaefer, *J. Am. Chem. Soc.*, 1992, **114**, 4830.
17. S. M. Holl, R. A. McKay, T. Gullion, and J. Schaefer, *J. Magn. Reson.*, 1990, **89**, 620.
18. R. A. McKay, US Patent 4446431, 1994.

Acknowledgments

This work was supported by NIH grant GM-40634.

Biographical Sketch

Jacob Schaefer, *b* 1938. B.S., 1960, Ph.D., 1964, physical chemistry, University of Minnesota, USA. Research scientist at Monsanto Company, St. Louis, 1964–1986; collaborated with E. O. Stejskal in 1976 to combine cross polarization with magic angle spinning. Faculty in Chemistry, Washington University in St. Louis, 1986–present. Approx. 200 publications. Research specialty: development of techniques for the NMR of polymeric and biological solids.

Spin Diffusion in Solids

T. T. Peter Cheung

Phillips Petroleum Company, Bartlesville, OK, USA

1	Introduction	1
2	Effects of Spin Diffusion on Nuclear Spin Relaxation	2
3	Studies of Polymer Morphology by Proton Spin Diffusion	4
4	Related Articles	6
5	References	6

1 INTRODUCTION

Spin diffusion is a phenomenon in which spin information, or more specifically the spin magnetization, at one location of a substance is transported to other locations. In solids, where the translations of the spin-bearing atoms are highly restricted, the transport of spin information is mediated by spin–spin interactions. In the following, this transport phenomenon and its effects on NMR will be described. Historically, spin diffusion was considered a nuisance, because it tends to average out useful spin information that reflects the spatial heterogeneity of a solid. As will be described below, with an understanding of spin diffusion and appropriate NMR pulse sequences, one can actually extract spatial information about disordered solids such as polymers by following how the local magnetization is transported by spin diffusion.

Consider an isolated pair of identical spins $\frac{1}{2}$, $\boldsymbol{I}_1$ and $\boldsymbol{I}_2$, in a strong external magnetic field. They are coupled to each other by an exchange interaction $\lambda\hat{\boldsymbol{I}}_1 \cdot \hat{\boldsymbol{I}}_2$. If the system is initially in the spin state $|\uparrow\ \downarrow\rangle$, the spins will evolve under the influence of the exchange interaction to the $|\downarrow\ \uparrow\rangle$ state in which there are opposite flips in the 'directions' of the two spins. The total wavefunction of the system can be expressed as

$$\varphi(t) = c_1(t)|\uparrow\downarrow\rangle + c_2(t)|\downarrow\uparrow\rangle \tag{1}$$

By solving the time-dependent Schrödinger equation, the probability that the system remains in $|\uparrow\ \downarrow\rangle$ is

$$|c_1(t)|^2 = \cos^2[(\lambda/\hbar)t] \tag{2}$$

and the probability that it evolves to $|\downarrow\ \uparrow\rangle$ is

$$|c_2(t)|^2 = 1 - \cos^2[(\lambda/\hbar)t] \tag{3}$$

Therefore, the exchange interaction leads to a cyclic transfer of spin information, which, in this case, is the magnetization of spin $\boldsymbol{I}_1$, represented by $|c_1(t)|^2 - |c_2(t)|^2$, from spin $\boldsymbol{I}_1$ to spin $\boldsymbol{I}_2$, and then back to spin $\boldsymbol{I}_1$ again, with a frequency of $\lambda/\hbar$.

In solids, nuclear spins like ^{1}H are strongly coupled by dipole–dipole interactions, the secular part of which has the form

$$\hat{\mathcal{H}}_{\mathrm{d}}^0 = \frac{1}{4}\sum_i \sum_j \frac{(3\cos^2\theta_{ij} - 1)\hbar^2\gamma^2}{r_{ij}^3}(\hat{\boldsymbol{I}}_i \cdot \hat{\boldsymbol{I}}_j - 3\hat{I}_{iz}\hat{I}_{jz}) \tag{4}$$

where θ_{ij} is the angle between the direction of the external magnetic field and the vector joining the spin $\boldsymbol{I}_i$ at location $\boldsymbol{r}_i$ and the spin $\boldsymbol{I}_j$ at $\boldsymbol{r}_j$, and $\boldsymbol{r}_{ij} = |\boldsymbol{r}_i - \boldsymbol{r}_j|$. The exchange term $\hat{\boldsymbol{I}}_i \cdot \hat{\boldsymbol{I}}_j$ in equation (4) allows the exchange of magnetization between two coupled spins $\boldsymbol{I}_i$ and $\boldsymbol{I}_j$. Because of the r_{ij}^{-3} dependence, the interaction can be restricted to nearest-neighbor spins. If the spins $\boldsymbol{I}_1$ and $\boldsymbol{I}_2$ mentioned earlier are a part of the solid and interact with many other spins $\boldsymbol{I}_i$ of the same kind, it becomes very likely that before the magnetization from spin $\boldsymbol{I}_2$ returns to the spin $\boldsymbol{I}_1$, it will spread to other spins coupled to spin $\boldsymbol{I}_2$. This transfer of magnetization will continue to spins at farther distances from spin $\boldsymbol{I}_1$ in a manner very similar to that of the random walk. Hence the term 'spin diffusion' was coined.[1,2]

The spin diffusion equation can be formally derived from the dipole–dipole Hamiltonian in equation (4) using linearized projection operator techniques.[3] However, it is much easier to understand in terms of the rate equation for the *local* magnetization $m(\boldsymbol{r}_i,t)$, which is defined as the thermal average of $\hat{I}_{iz}$ at time t:

$$\frac{\partial m(\boldsymbol{r}_i, t)}{\partial t} = \sum_j{}' W(\boldsymbol{r}_i, \boldsymbol{r}_j)[m(\boldsymbol{r}_j, t) - m(\boldsymbol{r}_i, t)] \tag{5}$$

This equation is an expression of linear response theory stating that the rate of change of the local magnetization at site $\boldsymbol{r}_i$ has a linear (i.e., first-order) dependence on the differences in the local magnetization between site $\boldsymbol{r}_i$ and its nearest-neighbor sites $\boldsymbol{r}_j$. $W(\boldsymbol{r}_i,\boldsymbol{r}_j)$ is the rate of the spin flip–flop induced by the dipole–dipole interaction between spins $\boldsymbol{I}_i$ and $\boldsymbol{I}_j$, and is of the order of the spin–spin relaxation rate $(T_2)^{-1}$. The prime on the summation above indicates that the summation over j is restricted to nearest neighbors of the spin $\boldsymbol{I}_i$. In the simple case where the nuclear spins are arranged in a cubic array, the summation along the x axis can be expressed as

$$a^2 W(\boldsymbol{r}_i, \boldsymbol{r}_i + a\boldsymbol{i}) \frac{\left(\frac{m(\boldsymbol{r}_i + a\boldsymbol{i}, t) - m(\boldsymbol{r}_i, t)}{a}\right) - \left(\frac{m(\boldsymbol{r}_i, t) - m(\boldsymbol{r}_i - a\boldsymbol{i}, t)}{a}\right)}{a} \tag{6}$$

where $\boldsymbol{i}$ is the unit vector along the x axis and a is the lattice constant. In the continuum limit, this reduces to

$$a^2 W(\boldsymbol{r}, \boldsymbol{r} + a\boldsymbol{i}) \frac{\partial^2 m(\boldsymbol{r}, t)}{\partial x^2} \tag{7}$$

Similar expressions can be obtained for the sums along the y and z directions. Neglecting the anisotropy of $W(\boldsymbol{r},\boldsymbol{r} + a\boldsymbol{i})$ or replacing it with W, the average over the three directions, the rate equation becomes the diffusion equation

$$\frac{\partial m(\boldsymbol{r}, t)}{\partial t} = D\nabla^2 m(\boldsymbol{r}, t), \quad \text{with} \quad D = a^2 W \tag{8}$$

Because the nonsecular part of the dipole–dipole interaction as well as other magnetic interactions that we have not considered can lead to spin–lattice relaxation of the nuclear magnetization, one should also include a relaxation term $-m(\boldsymbol{r},t)/T_1(\boldsymbol{r})$ on the right-hand side of the spin diffusion equation when the spin relaxation rate is comparable to the diffusion rate.

Using the Fermi golden rule, the spin flip rate W can be expressed as

$$W \approx |\hat{H}_{\mathrm{d}}^0|^2 f(\omega_i - \omega_j) \tag{9}$$

where ω_i and ω_j are the Larmor frequencies of the spins $\boldsymbol{I}_i$ and $\boldsymbol{I}_j$, and $f(\omega)$ is the lineshape function of the spin pair due to

the action of all the other spins. It has a width of order T_2^{-1} and decays rapidly to zero with increasing ω. The difference in the Larmor frequencies $(\omega_i - \omega_j)$ represents the amount of energy required to flip the two spins in opposite directions. The implication of equation (9) is that the rate of the spin flip is fastest; thus, the spin diffusion is most efficient when the spins have the same Larmor frequency, i.e., when the process is energy-conserving. If the difference in the Larmor frequencies is much larger than T_2^{-1} then the spin flip stops and the spin diffusion is quenched.

Equation (8) holds not only in the laboratory frame but also in the rotating frame, provided that the spin locking field is much larger than the dipolar interactions. For simplicity, we shall not distinguish between spin diffusion in these two frames unless the circumstance requires it and we shall adopt the notation T_{L} for the spin–lattice relaxation time in either frame.

Spin diffusion plays an important role in the understanding of spin–lattice relaxation phenomena in solids when spin relaxation can occur mainly at few isolated locations. For instance, at very low temperatures, spin relaxation in polymers with long molecular chains takes place mainly at the end groups, where motions are still possible. Paramagnetic impurities in crystalline materials also act as relaxation centers for the nuclear spins because of the rapid fluctuations of the electronic spin moments. The relaxation of the total magnetization

$$M(t) = \int_V m(\boldsymbol{r}, t)\, \mathrm{d}^3 r \tag{10}$$

where V is the sample volume, depends on both the relaxation rate at these centers and the rate at which the local magnetization is transported to these centers by spin diffusion.

The question of how well spin diffusion can be utilized to extract information about a system depends largely on one's ability to solve the diffusion equation according to appropriate sets of initial and boundary conditions. The methods of solving the spin diffusion equation are very similar to those used in heat conduction, and there are a number of excellent texts[4,5] treating the latter in great detail. There is one fundamental fact about the diffusion process that should be borne in mind, namely, spin information will travel a distance l in a time $t \approx l^2/D$. In other words, a spin will know what happens to another spin a distance l away in a time t. The consequence is that a spatial inhomogeneity in the local magnetization with a characteristic length l will disappear in a time $t \approx l^2/D$. Let us put this another way: the inhomogeneity will not occur if it requires a time much longer than l^2/D to develop. A good example is the spin–lattice relaxation of protons in solid polymers at ambient temperature. In semicrystalline polymers[6] there are at least two different intrinsic T_1s associated with the crystalline and amorphous phases because of the difference in segmental motions of the polymer chains. However, typically, one observes only a single decay in the total magnetization $M(t)$, with a ${T_1}^{-1}$ being the weighed average of the intrinsic ${T_1}^{-1}$ of each phase. The reason is that the intrinsic T_1s are much longer than the time it takes spin diffusion to occur across the domains of each phase; any inhomogeneity that would have been developed in the magnetization due to the different intrinsic T_1s is averaged out by the spin diffusion.

On the other hand, by using appropriate NMR pulse sequences, one can create a nonuniform magnetization in a solid with a characteristic length l on a timescale much shorter than l^2/D. Then the transfer of the magnetization by spin diffusion can be observed by NMR. Very often, the nonuniform magnetization that can be created reflects the spatial heterogeneity of the solid itself. Therefore, spin diffusion provides an useful means to study the spatial properties of disordered materials. We shall discuss more of this later.

2 EFFECTS OF SPIN DIFFUSION ON NUCLEAR SPIN RELAXATION

2.1 Spin–Lattice Relaxation by Paramagnetic Impurities

Spin diffusion in solids was first discovered[1] in spin–lattice relaxation experiments with crystalline substances, like CaF_2, doped with paramagnetic impurities. The dipolar coupling between the electronic spin of the paramagnetic center and the nuclear spin leads to spin–lattice relaxation at the nuclear site with a rate[2]

$$\frac{1}{T_1(r)} = \frac{C}{r^6} \tag{11}$$

where r is the distance between the nuclear and electronic spins. It turned out that the experimental relaxation time was several orders of magnitude shorter[1,2] than that calculated from equation (11). It was realized that, while the nuclear spins in the vicinity of the paramagnetic site relaxed very rapidly, those at a distance did not because of the r^{-6} dependence in the relaxation rate. In order for the whole spin system to relax, spin diffusion must have transported the magnetization to the vicinity of the paramagnetic sites. The time evolution of the local magnetization due to a single impurity is given by

$$\frac{\partial m(\boldsymbol{r}, t)}{\partial t} = D\nabla^2 m(\boldsymbol{r}, t) - \frac{C}{r^6}[m(\boldsymbol{r}, t) - m_0] \tag{12}$$

where m_0 is the thermal equilibrium value of $m(\boldsymbol{r},t)$. There is a critical radius b_0 around the impurity, inside which the local magnetic field due to the electronic spin is so large that the Larmor frequencies of the nuclei there will be very different from those in the bulk of the solid, and they will escape detection. Furthermore, the large gradient in the Larmor frequency essentially quenches the spin diffusion within the critical radius b_0, because the spin flips in the diffusion process are no longer energy-conserving.

Equation (12) can be solved either by numerical methods[7] or by using the steady state approximation $\partial m(\boldsymbol{r},t)/\partial t = 0$. To solve the steady-state equation,[8–10] the following assumptions are usually made:

1. there is a 'pseudopotential' radius

$$b = 0.7(C/D)^{1/4} \tag{13}$$

   around an impurity, inside which the nuclear spins relax so rapidly that the local magnetization is always at the equilibrium value;
2. the concentration ρ of the impurities is sufficiently low that the average distance $2R$ between them is much larger than b;
3. the pseudopotential radius b is larger than the critical radius b_0.

These assumptions can be summarized as

$$R \gg b \rangle b_0, \quad \text{with} \quad \rho^{-1} = \tfrac{4}{3}\pi R^3 \tag{14}$$

By matching the boundary condition at b, the steady-state solution yields

$$1/T_1 = 4\pi\rho b D \tag{15a}$$

for $M(t)$. Equation (15a) agrees qualitatively with experimental data.[2] The fact that the spin–lattice relaxation depends on C as well as the diffusion coefficient D indicates that spin diffusion plays an important role in the process, but it is not the rate-determining step.

A $1/T_1$ similar to that in equation (15a) can also be obtained by an order-of-magnitude argument. It may serve to illustrate the role of spin diffusion without using complicated mathematics. As indicated in equation (11), the spin–lattice relaxation of a nuclear spin due to a paramagnetic impurity decreases very rapidly with increasing distance between them. Therefore, when the concentration of impurities is low, the spin relaxation times of the majority of the nuclear spins are much longer than the diffusion time between them, except for those within a radius b_d from the impurity. This radius b_d is determined by the condition that the spin diffusion time for the distance from the impurity to the radius b_d be of the order of $(C/b_\mathrm{d}^6)^{-1}$. That is, $b_\mathrm{d}^2/D \approx b_\mathrm{d}^6/C$. This yields $b_\mathrm{d} \approx (C/D)^{\frac{1}{4}} \approx b$. Because of the condition in equation (14), the number of nuclei inside the radius b_d is much smaller than that in the bulk, and can be neglected. In the limit of rapid diffusion, the spin–lattice relaxation rate of $M(t)$ is given by the weighed average of $1/T_1(r)$ in equation (11) for the nuclei outside radius b_d:

$$\begin{aligned}\frac{1}{T_1} &\approx \frac{\int_{b_\mathrm{d}}^{R} Cr^{-6} 4\pi r^2 \,\mathrm{d}r}{\int_{b_\mathrm{d}}^{R} 4\pi r^2 \,\mathrm{d}r} \\ &\approx \rho \tfrac{4}{3}\pi (C/b_\mathrm{d}^3) \\ &\approx \rho b D\end{aligned} \tag{15b}$$

where b_d has been replaced by b and a numerical factor of the order of unity has been neglected. Since $T_1 \approx (R^2/D)R/b$ in equation (15b), it is much longer than R^2/D, the time it takes spin diffusion to transverse a distance R. Therefore, the rapid diffusion approximation is indeed valid.

2.2 Proton Spin Relaxation via End Groups in Polymers

At low temperatures, spin–lattice relaxation of polymers occurs mainly at the end groups of the polymer chains, since the motions of the backbones of the polymers are 'frozen' out. End groups like methyl groups retain considerable motions even at very low temperatures, and act as sinks that relax the whole spin system by means of spin diffusion. Spin–lattice relaxation in solid n-alkanes[11] is a classic example of how spin relaxation is affected by the spin diffusion process. Here the role of spin diffusion can be followed mathematically, because the diffusion is essentially one-dimensional along the chain axis. Taking the center of the chain as the origin of the x axis and using the symmetry requirement $\partial m(x,t)/\partial x|_0 = 0$, the solution for $m(x,t)$ is

$$m(x,t) = \sum_{n=0}^{\infty} A_n \cos p_n x \exp(-D p_n^2 t) \tag{16}$$

For an alkane molecule of length L with N carbon atoms, the lattice constant a is roughly L/N. The boundary condition is

$$D\frac{\partial m(x,t)}{\partial x}\bigg|_{x=L/2} = -\frac{am(x,t)}{T_\mathrm{e}}\bigg|_{x=L/2} \tag{17}$$

which equates the flux of the magnetization to the methyl group to the rate $1/T_\mathrm{e}$ by which the magnetization is relaxed by the rotation of the methyl group. This leads to the equation

$$\tfrac{1}{2}Lp_n \tan \tfrac{1}{2}Lp_n = \frac{La}{2DT_\mathrm{e}} \tag{18}$$

which relates p_n to the length of the chain, the diffusion coefficient, and the relaxation rate at the end group.

In the limit of rapid spin diffusion, i.e., $DT_\mathrm{e} \gg L^2$, we have

$$p_n^2 = \frac{2}{NDT_\mathrm{e}} \tag{19}$$

Since all the terms in the sum in equation (16) have the same time constant, the spin–lattice relaxation rate of $M(t)$ is

$$\begin{aligned}T_\mathrm{L}^{-1} &= Dp_n^2 \\ &= (2/N)(T_\mathrm{e})^{-1}\end{aligned} \tag{20}$$

which is the weighed average of the relaxation rate at the end groups. The factor of 2 is due to the fact that there are two methyl groups in each alkane molecule.

On the other hand, in the opposite limit of $DT_\mathrm{e} \ll L^2$, where now the spin diffusion is the rate limiting step, one has instead

$$p_n \approx (2n+1)\pi/L \tag{21}$$

Because of the n dependence of p_n, only the first term in the sum in equation (16) is important, and the spin–lattice relaxation rate becomes

$$T_\mathrm{L}^{-1} = D(\pi/aN)^2 \tag{22}$$

It is independent of T_e! One important difference between the spin–lattice relaxation rates in the fast and slow diffusion limits is their dependence on the size of the molecules. The former is proportional to N^{-1}, while the latter has a N^{-2} dependence. Experimentally, the spin–lattice relaxation rate in the rotating frame $T_{1\rho}^{-1}$ of n-alkanes[11] at $-190\,^\circ$C was found to have an $N^{-1.7}$ dependence. This indicates that the spin–lattice relaxation in the rotating frame is governed, to a large extent, by how fast the local magnetization is transported by spin diffusion to the end groups.

2.3 Proton Spin Relaxation in Semicrystalline Polymers in the Rotating Frame

The above discussion can be extended to ^{1}H spin relaxation in semicrystalline polymers at ambient temperature. The polymers consist of domains of crystalline and amorphous phases. Owing to different backbone motions available at ambient temperature, each phase has a different intrinsic T_1 and $T_{1\rho}$. Since the proton spin–spin interactions may be different, different spin diffusion coefficients can also be assigned to the two phases. Because the T_1s are typically

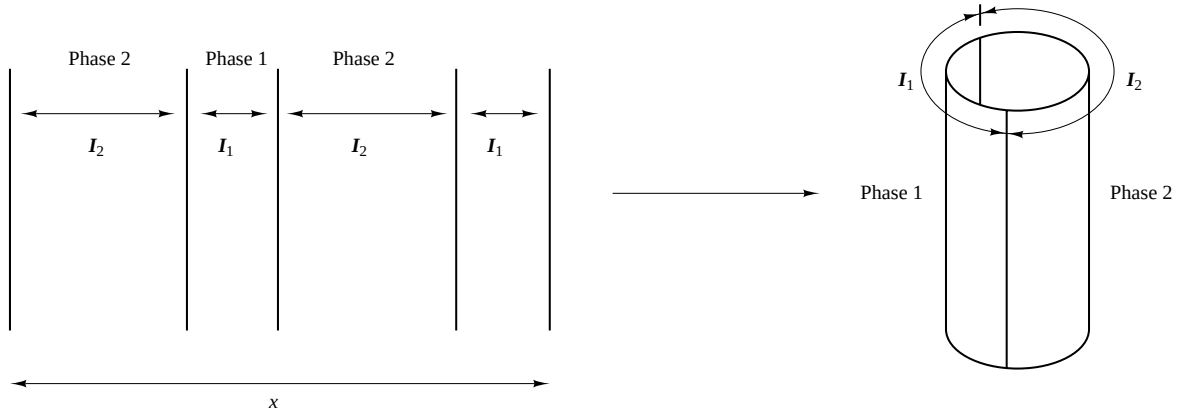

Figure 1 A two-phase, one-dimensional model of spin diffusion in a polymer. The multiple domain arrangement on the left is reduced to a two-domain system with a cyclic boundary condition

much longer than the spin diffusion time across a domain, only a simple exponential decay is observed in the total magnetization, with T_1^{-1} being the weighed average of the intrinsic T_1^{-1}s. However, the $T_{1\rho}$s are found to be sufficiently short that the spatial averaging by spin diffusion is not complete, and multiple component decay can be observed.[6,12,13] To treat the effects of spin diffusion on $T_{1\rho}$ in the general case would require solving the diffusion equation numerically. To simplify the matter, the following approximations are often made.

1. The domains have the form of parallel layers. The spin diffusion is one-dimensional perpendicular to the layers.
2. Only one domain of each of the crystalline and amorphous phases is considered. They are arranged in such a way that they are joined to each other at both ends.

This arrangement is depicted in Figure 1. Pairs of diffusion coefficients D_1 and D_2, intrinsic relaxation times $T_{1\rho}(1)$ and $T_{1\rho}(2)$, and thicknesses l_1 and l_2 are assigned to the amorphous and crystalline layers, respectively.

To see how the spin diffusion affects the spin relaxation times, let us consider the case in which the spin relaxation time $T_{1\rho}(1)$ of the amorphous phase is short and satisfies the condition $T_{1\rho}(1) \ll T_{1\rho}(2)$, l_1^2/D_1 and l_2^2/D_2. This amounts to treating the amorphous phase as a sink that relaxes the magnetization of the crystalline phase via spin diffusion. At the same time, the magnetization in the crystalline phase is also relaxed by the direct coupling to the lattice, with a rate $1/T_{1\rho}(2)$. Define the center of the crystalline layer as the origin of the x axis. The spin diffusion equation in the crystalline region is

$$\frac{\partial m(x,t)}{\partial t} = D_2 \frac{\partial^2}{\partial x^2} m(x,t) - \frac{m(x,t)}{T_{1\rho}(2)} \quad \text{for} \quad -\tfrac{1}{2}l_2 < x < \tfrac{1}{2}l_2 \qquad (23)$$

The substitution

$$m(x,t) \equiv \exp[-t/T_{1\rho}(2)]\, m^*(x,t) \qquad (24)$$

reduces equation (23) to the one-dimensional diffusion equation for $m^*(x,t)$, but now without the decay term. The solution of $m^*(x,t)$ has the same form as that on the right-hand side of equation (16). The condition $T_{1\rho}(1) \ll T_{1\rho}(2)$ and l_1^2/D_1 indicates that the magnetization relaxes uniformly across the amorphous domain, which leads to the same boundary condition for $m^*(x,t)$ as that in equation (17) except that T_e is replaced by $T_{1\rho}(1)$ and L by l_2. The diffusion problem is therefore reduced to that of the spin relaxation via the end groups described earlier. Furthermore, because $T_{1\rho}(1)$ is much shorter than l_2^2/D_2, the coefficient p_n is given by the diffusion limiting solution in equation (21). With equation (24), one finds that the relaxation time constants of the multiple component decay of the total magnetization are $T_{1\rho}(1)$ and the $T_{1\rho}(2,n)$s, where

$$\frac{1}{T_{1\rho}(2,n)} = \frac{1}{T_{1\rho}(2)} + \frac{D_2(2n+1)^2\pi^2}{l_2^2} \qquad (25)$$

with $n = 0, \ldots, \infty$. The relative intensities of the decay components associated with each $T_{1\rho}(2,n)$ are directly proportional to $(2n+1)^{-2}$. If $T_{1\rho}(2)$ is much longer than l_2^2/D_2 then only the $T_{1\rho}(2,n=0)$ term is important, and the number of components in the decay is reduced to two: one with a time constant $[1/T_{1\rho}(2) + D_2\pi^2/l_2^2]^{-1}$ and the other with $T_{1\rho}(1)$. It is important to realize that when more than one $T_{1\rho}(2,n)$ contribute to the decay of $M(t)$, the intensities of these components in the decay have no direct relationship to the number of nuclei contributing to them.

The dependence of $T_{1\rho}(2,n)$ on l_2 suggests that the domain size in polymers may be extracted indirectly from the proton spin relaxation measurements. In the general case, one may solve the diffusion equation numerically and fit the results to the experimental data.[12,13] In the special case where $T_{1\rho}(1) \ll T_{1\rho}(2)$, l_1^2/D_1 and l_2^2/D_2, the data are simply fitted with a multiple component decay with the time constants given by equation (25). $T_{1\rho}(1)$, $T_{1\rho}(2)$, and l_2 are usually treated as the adjustable parameters.[14]

3 STUDIES OF POLYMER MORPHOLOGY BY PROTON SPIN DIFFUSION

Information about domain size can be obtained directly using the Goldman–Shen method.[15] This is based on the idea that with appropriate NMR pulse sequences, nonuniform magnetization associated with the spatial inhomogeneity of a solid can be created on a timescale much shorter than that of the spin diffusion. By monitoring the return of the magnetization to the uniform state by spin diffusion, the sizes of the spatial inhomogeneities can be deduced. As the most

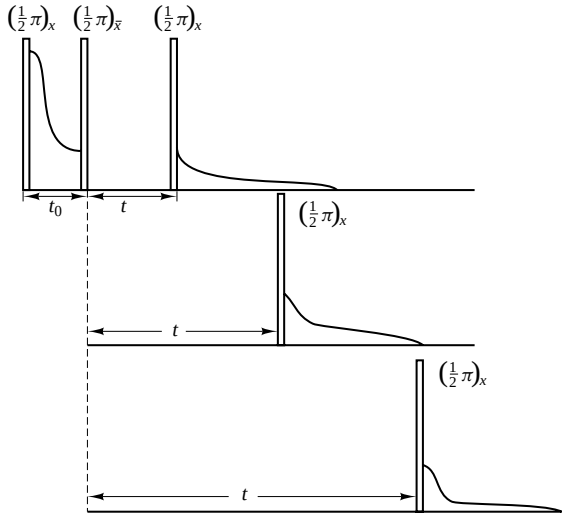

Figure 2 The Goldman–Shen NMR pulse sequence. The magnetization in the crystalline phase is randomized in a time t_0. The transfer of magnetization by spin diffusion from the amorphous domain to the crystalline one occurs during the time t

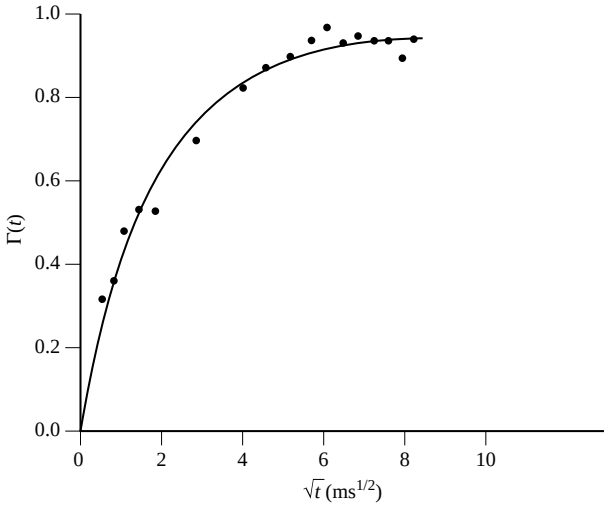

Figure 3 The recovery of the magnetization $\Gamma(t)$ in the crystalline phase of a polypropylene film as a function of the diffusion time t. The experimental data are represented by the solid circles. The theoretical fit according to equations (30) and (31) is given by the solid line

abundant and strongly coupled spin in polymers, ^{1}H is usually the nucleus of choice for such studies.

The original Goldman–Shen pulse sequence $[(\frac{1}{2}\pi)_x - t_0 - (\frac{1}{2}\pi)_x - t - (\frac{1}{2}\pi)_x]$ was first applied to homopolymers with rigid and mobile phases.[16–18] We shall use semicrystalline polymers as an example for our discussion. To a large extent, the free induction decay (FID) of semicrystalline polymers consists of two components associated with the crystalline (rigid) and amorphous (mobile) phases. The spin–spin relaxation time T_2 of the crystalline domain is usually shorter than that of the amorphous domain. By decomposing the FID with curve fitting techniques, one determines the fraction of the total proton magnetization in each phase. The Goldman–Shen pulse sequence shown in Figure 2 exploits this difference. After the initial $(\frac{1}{2}\pi)_x$ pulse, one waits for a fixed time t_0 during which the total magnetization of the crystalline phase M_2 is allowed to decay to zero while there is still sufficient magnetization left in the amorphous phase. The second pulse returns the remaining magnetization M_1 in the amorphous phase to the direction of the external magnetic field. The magnetization in the amorphous phase is allowed to diffuse back to the crystalline phase for a variable time t. By decomposing the FID observed after the third pulse, one determines the amount of magnetization that has been transferred back to the crystalline phase. The spin diffusion period t should be shorter than the T_1 of the system, so that the return of the magnetization to the crystalline phase is due to spin diffusion and not because of spin–lattice relaxation. The sizes of domain structures suitable for spin diffusion studies are those which the spin diffusion can transverse in a time of the order of T_1. For a typical T_1 of the order of 0.1 s and ^{1}H spin diffusion coefficient of $6 \times 10^{-12}\,\mathrm{cm^2\ s^{-1}}$, they are about 8 nm.

The recovery of the magnetization in the crystalline phase is defined as

$$\Gamma(t) = \frac{M_2(t)}{M_2(t \to \infty)} = 1 - \frac{M_1(t) - M_1(t \to \infty)}{M_1(t=0) - M_1(t \to \infty)} \tag{26}$$

An example of $\Gamma(t)$ for polypropylene film is shown in Figure 3. To extract spatial information from $\Gamma(t)$, one needs to solve the diffusion equation according to the initial and boundary conditions appropriate to the problem. In general, solutions can be obtained only by numerical methods,[19] even for the simplest polymer models. Fortunately, analytical solutions are available if one assumes either (i) that the diffusion coefficient is the same for both the amorphous and crystalline phases or (ii) that the diffusion coefficient of the crystalline phase is much shorter than that of the amorphous phase.

The solution to the first case is described in detail by Cheury and Gerstein.[18] We shall present a simplified account here. Again, we consider the model given in Figure 1. Let the center of the amorphous domain be the origin of the x axis. The amorphous domain occupies the region $-\frac{1}{2}l_1 < x < \frac{1}{2}l_1$, while the crystalline domain extends from $-\frac{1}{2}l_1$ to $-\frac{1}{2}(l_1 + l_2)$ and from $\frac{1}{2}l_1$ to $\frac{1}{2}(l_1 + l_2)$. For simplicity, we shall assume that l_2 is much larger than l_1, which is appropriate when the polymer has a high degree of crystallinity. With the initial conditions

$$m(x, t=0) = \begin{cases} 1 & \text{for } x \in \text{amorphous phase} \\ 0 & \text{for } x \in \text{crystalline phase} \end{cases} \tag{27}$$

and the boundary condition

$$\left.\frac{\partial m(x,t)}{\partial x}\right|_{x=\pm(l_1+l_2)/2} = 0 \tag{28}$$

one obtains

$$\begin{aligned} \psi(t) &\equiv \int_{-l_1/2}^{l_1/2} [m(x,t) - m(x, t \to \infty)]\,\mathrm{d}x \\ &= \frac{8}{l_1 + l_2} \sum_{n=1}^{\infty} \frac{\sin^2(\frac{1}{2}p_n l_1)}{p_n^2} \exp(-D p_n^2 t), \quad \text{with} \quad p_n = \frac{2\pi n}{l_1 + l_2} \\ &\approx l_1 \left\{ 1 - \int_0^t \mathrm{d}\tau \left(\frac{D}{\pi l_1^2 \tau}\right)^{1/2} \left[1 - \exp\left(-\frac{l_1^2}{4D\tau}\right)\right]\right\} \\ &\qquad \text{for} \quad l_1 \ll l_2 \end{aligned} \tag{29}$$

For a single layer of the amorphous and crystalline phase, $\Gamma(t) = 1 - \psi(t)/\psi(0)$. This expression for $\Gamma(t)$ is applicable to oriented polymers with lamellar domains. However, if the distribution of the domains is isotropic, spin diffusion in each of the directions (whether along the x, y, or z axis) is equivalent. The general form of $\Gamma(t)$, taking this into account, is

$$\Gamma(t) = 1 - [\psi(t)/\psi(0)]^3 \tag{30}$$

In semicrystalline polymers, there is always a distribution of the width of the domains. The result in equation (29) amounts to assuming a delta function for the distribution of l_1. On the other hand, averaging equation (29) over a Poisson distribution $(1/\langle l_1\rangle)\exp(-l_1/\langle l_1\rangle)$ for l_1, where $\langle l_1\rangle$ is the average l_1, $\psi(t)/\psi(0)$ becomes

$$\frac{\psi(t)}{\psi(0)} = \exp\left(\frac{Dt}{\langle l_1\rangle^2}\right)\operatorname{erfc}\left(\sqrt{\frac{Dt}{\langle l_1\rangle^2}}\right) \tag{31}$$

where erfc is the complementary error function. Regardless of the form of the distribution of l_1, the short-time behavior of $\Gamma(t)$ depends only on $\langle l_1\rangle$, the average value of l_1. This can be seen by expanding equation (29) in the limit of small t and substituting the result into equation (30):

$$\Gamma(t) = \frac{6}{\sqrt{\pi}}\left(\frac{Dt}{\langle l_1\rangle^2}\right)^{1/2} \quad \text{for} \quad t \ll \frac{\langle l_1\rangle^2}{D} \tag{32}$$

In Figure 3, equation (30) with $\psi(t)/\psi(0)$ given by equation (31) is fitted to the data for the polypropylene film. For $D = 6.75 \times 10^{-12}\,\mathrm{cm^2\ s^{-1}}$, a value of $\langle l_1\rangle = 4.9\,\mathrm{nm}$ is obtained from the fit.

In block copolymers[13] and polymer blends,[6] one sometimes encounters two polymers with very different T_2s. The approximation of a single spin diffusion coefficient is clearly invalid. In this case, one may consider the two-domain model in Figure 1 in the limits

$$D_1 \ll D_2, \quad l_1 \ll l_2 \tag{33}$$

where subscripts 1 and 2 represent the phases with long and short T_2, respectively. We shall refer to these as the slow and fast diffusion domains. With the conditions in equation (33), the spin diffusion in the slow domain is again reduced to the diffusion limiting case of what we have discussed for spin relaxation via end groups. With the initial condition that there is only magnetization in the slow diffusion region, one obtains

$$\begin{aligned}\frac{\psi(t)}{\psi(0)} &= \sum_{n=0}\frac{8}{(2n+1)^2\pi^2}\exp\left[-D_1\left(\frac{2n+1}{l_1}\right)^2\pi^2 t\right] \\ &\approx 1 - \frac{4}{\sqrt{\pi}}\left(\frac{D_1 t}{l_1^2}\right)^{1/2} \quad \text{for} \quad t \ll l_1^2/D_1\end{aligned} \tag{34}$$

The recovery of the magnetization in the fast diffusion domain (assuming isotropic distribution of the domains and spin diffusion in three directions) becomes

$$\Gamma(t) = \frac{12}{\sqrt{\pi}}\left(\frac{D_1 t}{l_1^2}\right)^{1/2} \quad \text{for} \quad t \ll l_1^2/D_1 \tag{35}$$

which should be compared with equation (32). As a function of $\sqrt{t}$, the slope of $\Gamma(t)$ in equation (35) is twice as large as that in equation (32). [The short-time ($t \ll {l_1}^2/D_1$) result in equation (34) is slightly different from that in equation (17) of Cheung and Gerstein.[18] The latter is based on the transfer of magnetization from the slow diffusion domain to the fast diffusion one at only one interface between the domains. However, the transfer in the two-domain model in Figure 1 occurs at two interfaces. The result is that the slope of $\Gamma(t)$ as a function of $\sqrt{t}$ in equation (35) is twice as large as that obtained from equation (17) of Cheung and Gerstein.[18]] We can summarize the results in both equations (32) and (35) by the following statement. In the Goldman–Shen experiment, the *initial* return of the magnetization to the domain, which has been depleted of magnetization, increases linearly with $\sqrt{t}$, and the slope is proportional to $(D/l^2)^{\frac{1}{2}}$, with D and l being the spin diffusion coefficient and the size of the domain from which the magnetization emanates.

Several modifications of the Goldman–Shen pulse sequence have been proposed. Two of the significant ones are

1. the use of multiple pulse techniques[19,20] to suppress spin diffusion during the creation of the nonuniform magnetization (i.e., in the time window t_0) and to enhance the ^{1}H spectral resolution at the detection period;[21]
2. identification of domains with ^{13}C NMR after ^{1}H–^{13}C cross polarization.[22–24]

The latter is used in the detection period, and is particularly suitable for polymer blends[25] consisting of two polymers with very different structures.

4 RELATED ARTICLES

Dynamic NMR in Liquid Crystalline Solvents; Electron–Nuclear Multiple Resonance Spectroscopy; Rotating Frame Spin–Lattice Relaxation Off-Resonance.

5 REFERENCES

1. N. Bloembergen, *Physica*, 1949, **15**, 386.
2. A. A. Abragam, *The Principles of Nuclear Magnetism*, Clarendon Press, Oxford, 1961.
3. T. T. P. Cheung, *Phys. Rev. B*, 1981, **23**, 1404.
4. J. Crank, *The Mathematics of Diffusion*, Clarendon Press, Oxford, 1975.
5. H. S. Carslaw and J. C. Jaeger, *Conduction of Heat in Solids*, Clarendon Press, Oxford, 1959.
6. V. J. McBrierty and D. C. Douglass, *J. Polym. Sci., Macromol. Rev.*, 1981, **16**, 295; *Phys. Rep.*, 1980, **63**, 63, and references therein.
7. J. I. Kaplan, *Phys. Rev. B*, 1971, **3**, 604.
8. G. R. Khutsishvili, *Proc. Inst. Phys. Acad. Sci. Georgia (USSR)*, 1956, **4**, 3.
9. P. G. de Gennes, *J. Phys. Chem. Solids*, 1958, **7**, 345.
10. H. E. Rorschach Jr., *Physica*, 1964, **30**, 38.
11. D. C. Douglass and G. P. Jones, *Phys. Rev.*, 1966, **45**, 956.
12. K. J. Packer, J. M. Pope, R. R. Young, and M. E. A. Cudby, *J. Polym. Sci., Polym. Phys. Ed.*, 1984, **22**, 589.
13. H. Tanaka and T. Nishi, *Phys. Rev. B*, 1986, **33**, 32.
14. K. J. Packer, I. J. F. Poplett, M. J. Taylor, M. E. Vickers, A. K. Whittaker, and K. P. J. Williams, *Makromol. Chem. Macromol. Symp.*, 1990, **34**, 161.
15. M. Goldman and L. Shen, *Phys. Rev.*, 1966, **144**, 321.
16. R. A. Assink, *Macromolecules*, 1978, **11**, 1233.

17. K-L. Li, A. A. Jones, P. T. Inglefield, and A. D. English, *Macromolecules*, 1989, **22**, 4198.
18. T. T. P. Cheung and B. C. Gerstein, *J. Appl. Phys.* 1981, **52**, 5517.
19. J. R. Havens and D. L. VanderHart, *Macromolecules*, 1985, **18**, 1663.
20. K. Schmidt-Rohr, J. Clauss, B. Blumich, and H. W. Spiess, *Magn. Reson. Chem.*, 1990, **28**, S3.
21. T. T. P. Cheung, B. C. Gerstein, L. M. Ryan, R. E. Taylor, and C. Dybowski, *J. Chem. Phys.*, 1980, **73**, 6059.
22. N. Zumbulyadis, *J. Magn. Reson.*, 1983, **53**, 486.
23. R. H. Newman, *Chem. Phys. Lett.*, 1991, **180**, 301.
24. S. Zhang, B. H. Meier, and R. R. Ernst, *Solid State Nucl. Magn. Reson.*, 1992, **1**, 313.
25. D. L. VanderHart, *Makromol. Chem., Macromol. Symp.*, 1990, **34**, 125.

Biographical Sketch

T. T. Peter Cheung. *b* 1952. B.S., 1974, Rockhurst College; Ph.D., 1978, Princeton University. Postdoctoral Fellow, Washington University, 1979; Postdoctoral Fellow, Iowa State University, 1980. Senior research chemist, Phillips Petroleum Company, 1981–present. Approx. 40 publications. Research interests include stochastic processes in disordered solids, statistical theory of condensation, ^{129}Xe NMR, X-ray photoelectron spectroscopy of alloys, and applied catalysis.

Three-dimensional Molecular Structures in Uniformly Labelled Solids Determined Using Rotational Resonance in the Tilted Rotating Frame

K. Takegoshi and Takehiko Terao

Department of Chemistry, Graduate School of Science, Kyoto University, Kyoto, Japan

1 Introduction 1
2 Theory 1
3 Method 2
4 Application to Glycylisoleucine 4
5 Concluding Remarks 10
6 References 10

1 INTRODUCTION

While solution NMR methods have been successfully applied for elucidating three dimensional (3D) structures of molecules including proteins (see **Biological Macromolecules: Structure Determination in Solution,** Volume 2), solid-state NMR has not attained such a stage. This review demonstrates the state of the art of structural determination of a whole molecule by solid state NMR, which should be complementary to solution NMR and irreplaceable for insoluble systems. In NMR of solids, measurements of dipolar interactions provide direct information on geometrical structures; they are most conveniently made under magic angle spinning (MAS) (see **Magic Angle Spinning,** Volume 5) with hidden potential of determining more than one distance using a single sample. However, most of the methods developed so far are of non-selective measurements of dipolar couplings, by which it is difficult to deduce quantitative structural information when more than two spins are involved. Hence, only one specific internuclear distance or dihedral angle is commonly determined by selectively isotope-labeling a particular pair of atoms. Then, many doubly-labeled samples must be prepared, if one tries to determine the 3D structure composed of sizable atoms by such non-selective approaches. On the other hand, if a specific dipolar interaction in a multiply or uniformly labeled system can selectively be recoupled, all the structural parameters necessary to determine the 3D structure can be obtained one by one using a single sample, significantly saving labor for sample preparation.

To achieve frequency-selective recoupling, it is required to remove all dipolar couplings at once, and recouple a specific pair. Using MAS, one can remove all the dipolar couplings together with chemical shift anisotropies under proton decoupling, and therefore the remaining problem is to achieve selective recoupling under MAS fast enough to remove all the other dipolar interactions simultaneously. For homonuclear dipolar interactions, rotational resonance (R^2)[1–8] has been developed as a simple selective recoupling method, and in fact, has been applied to biologically interesting molecules.[9] In the R^2 method, selection of a pair of spins is made by adjusting an integral multiple of the MAS frequency ν_R to the difference of the chemical shifts of the two spins. Therefore, R^2 is frequency-difference selective, and if more than one spin pair with the same separation exists, they are simultaneously recoupled. Further, when the chemical shift difference for the two spins is relatively small, the MAS frequency must be lowered, leading to imperfect decoupling of the other dipolar interactions.

Selective recoupling among homonuclear spins can also be achieved in a tilted rotating frame.[10] Under rf irradiation, the Zeeman interaction for a spin system can be written in a tilted rotating frame (X, Y, Z) as

$$\frac{\mathcal{H}}{\text{Hz}} = \sum_i \nu_{ei} \hat{I}_{Zi} \tag{1}$$

while the conventional Zeeman interaction in the rotating frame (x, y, z) is written as

$$\mathcal{H} = \sum_i \Delta\nu_i \hat{I}_{zi} \tag{2}$$

where ν_e denotes the effective field and $\Delta\nu$ is the resonance offset. By comparing these two equations, it may be expected that the R^2 condition in the rotating frame:

$$|\Delta\nu_1 - \Delta\nu_2| = n\nu_R \tag{3}$$

would be modified in the tilted rotating frame as

$$|\nu_{e1} - \nu_{e2}| = n\nu_R \tag{4}$$

In fact, this is one of the recoupling conditions in the tilted rotating frame. There are additional recoupling conditions, namely, $\nu_{e1} + \nu_{e2} = n\nu_R$ and $\nu_{eX} = n\nu_R$ ($X = I$ or S), as derived in the following section. These conditions are referred to as the R2TR (rotational resonance in the tilted rotating frame) conditions. There are three adjustable parameters to achieve one of the R2TR conditions, namely, the intensity ν_1 and the frequency ν of the rf irradiation and the MAS frequency ν_R. This diversity makes it possible to find an R2TR condition even for a pair of spins with a small chemical shift difference without relaxing the fast MAS condition necessary for decoupling all other dipolar couplings. Further, it should be pointed out here that, while R^2 is frequency-difference selective, R2TR is frequency selective. Hence, a particular dipolar coupling can be recoupled by properly choosing the experimental parameters even when more than two lines have equal chemical-shift differences.

2 THEORY

First, we briefly touch upon rotational resonance recoupling. A dipolar-coupled homonuclear two-spin $I - S$ system in a

rotating powdered sample is considered. For simplicity, the chemical shift anisotropies (CSAs) are neglected. The total spin Hamiltonian can be written as

$$\mathcal{H} = \Delta\nu_I \hat{I}_z + \Delta\nu_S \hat{S}_z + \mathcal{H}_D(t) \tag{5}$$

where $\mathcal{H}_D(t)$ is the homonuclear dipolar interaction

$$\mathcal{H}_D(t) = D(t)\left\{\hat{I}_z\hat{S}_z - \frac{1}{4}(\hat{I}_+\hat{S}_- + \hat{I}_-\hat{S}_+)\right\} \tag{6}$$

with the spatial part modulated by MAS

$$D(t) = \sum_{n=\pm1,\pm2} \nu_{Dn} \exp(in\nu_R t) \tag{7}$$

Here, ν_{Dn} is a function of the internuclear distance and the polar angles defining the direction of the $I-S$ vector in a rotor-fixed frame. $\mathcal{H}_D(t)$ is transferred into the frame of the Zeeman interaction by using the unitary operator

$$U(t) = \exp(i\Delta\nu_I \hat{I}_z t)\exp(i\Delta\nu_S \hat{S}_z t) \tag{8}$$

as

$$\begin{aligned}\widetilde{\mathcal{H}_D}(t) &= U(t)\mathcal{H}_D(t)U^{-1}(t)\\ &= \sum_{n=\pm1,\pm2} \nu_{Dn}\Big[\hat{I}_z\hat{S}_z\exp(in\nu_R t)\\ &\quad -\frac{1}{4}(\hat{I}_+\hat{S}_- + \hat{I}_-\hat{S}_+)\exp\{i(n\nu_R - \Delta)\}\Big]\end{aligned} \tag{9}$$

where Δ is the difference of the isotropic chemical shift: $\Delta = \nu_I - \nu_S$. This equation shows that the rotational resonance recoupling occurs at $\Delta = n\nu_R$ with $n = \pm1, \pm2$. If one takes account of the chemical shift anisotropies, one can prove that recoupling occurs even under higher-order ($|n| > 2$) conditions.[4]

Second, we examine the effect of continuous wave rf irradiation along the x-axis of the rotating frame for the two-spin system. The total Hamiltonian

$$\mathcal{H} = \Delta\nu_I \hat{I}_z + \Delta\nu_S \hat{S}_z + \nu_1(\hat{I}_x + \hat{S}_x) + \mathcal{H}_D(t) \tag{10}$$

is transformed into the tilted rotating frame (X, Y, Z) by the unitary transformation of

$$U_{TR} = \exp(i\beta_I \hat{I}_y)\exp(i\beta_S \hat{S}_y) \tag{11}$$

where β_X denotes the angle between the z-axis of the rotating frame (i.e., the direction of the static field) and the Z-axis of the tilted rotating frame (i.e., the direction of the effective field) for the X spin. The total spin Hamiltonian in the tilted rotating frame can be given by

$$\begin{aligned}\mathcal{H}^{TR} &= U_{TR}\mathcal{H}U_{TR}^{-1}\\ &= \nu_{eI}\hat{I}_Z + \nu_{eS}\hat{S}_Z + U_{TR}\mathcal{H}_D(t)U_{TR}^{-1}\end{aligned} \tag{12}$$

where ν_{eX} denotes the strength of the effective field for the X spin. This is further transferred into the interaction frame using the following unitary operator

$$U_{\text{eff}}(t) = \exp(i\nu_{eI}\hat{I}_Z t)\exp(i\nu_{eS}\hat{S}_Z t) \tag{13}$$

and the result is

$$\begin{aligned}\mathcal{H}_D^*(t) &= U_{\text{eff}}(t)U_{TR}\mathcal{H}_D(t)U_{TR}^{-1}U_{\text{eff}}^{-1}(t)\\ &= \sum_{n=\pm1,\pm2}\nu_{Dn}[A\hat{I}_Z\hat{S}_Z\exp(-in\nu_R t)\\ &\quad + B[\hat{I}_+\hat{S}_-\exp\{i(n\nu_R + \Delta_{\text{eff}})t\}\\ &\quad + \hat{I}_-\hat{S}_+\exp\{i(n\nu_R - \Delta_{\text{eff}})t\}]\\ &\quad + R[\hat{I}_Z\hat{S}_+\exp\{i(n\nu_R + \nu_{eS})t\}\\ &\quad + \hat{I}_Z\hat{S}_-\exp\{i(n\nu_R - \nu_{eS})t\}]\\ &\quad + S[\hat{I}_+\hat{S}_Z\exp\{i(n\nu_R + \nu_{eI})t\}\\ &\quad + \hat{I}_-\hat{S}_Z\exp\{i(n\nu_R - \nu_{eI})t\}]\\ &\quad + Q[\hat{I}_+\hat{S}_+\exp\{i(n\nu_R + \Sigma_{\text{eff}})t\}\\ &\quad + \hat{I}_-\hat{S}_-\exp\{i(n\nu_R - \Sigma_{\text{eff}})t\}]]\end{aligned} \tag{14}$$

where the coefficients A, B, R, S, and Q are functions of the angle β_X, whose explicit forms are found in Ref.[11]. It can be shown that the spatial part of $\mathcal{H}_D^*(t)$ is modulated by MAS with the spinning frequency ν_R and $2\nu_R$, while the spin part is modulated by the effective field with the frequencies of $\Sigma_{\text{eff}} = \nu_{eI} + \nu_{eS}$, $\Delta_{\text{eff}} = \nu_{eI} - \nu_{eS}$, ν_{eI}, and ν_{eS}. When any of the conditions Σ_{eff}, Δ_{eff}, ν_{eI}, or $\nu_{eS} = m\nu_R$ ($m = \pm1$ or ±2) is met, the time dependence of the spatial part and the spin part in $\mathcal{H}_D^*(t)$ is partially canceled with each other to give a static dipolar interaction $\overline{\mathcal{H}_D}^*$.

3 METHOD

Determination of the 3D structure of a multiply labeled molecule can be accomplished by obtaining all bond lengths, bond angles, and dihedral angles. For a peptide, however, one may use typical bond lengths and angles because they differ only slightly among peptides, and the peptide 3D structure can be constructed by determining dihedral angles.

Figure 1 illustrates the strategy. For a multiply $^{13}C/^{15}N$ labeled peptide, all dipolar interactions are removed uniformly by fast MAS and proton decoupling. Then, a specific three-bonds distant pair of spins is selectively recoupled by applying an rf field satisfying a proper R2TR condition. The time development of the magnetization of either of the paired spins is measured, from which the corresponding dihedral angle is deduced. This procedure is repeated for other spin pairs, until all the dihedral angles are determined.

The pulse sequence for the selective recoupling experiments is shown in Figure 2(a). During the recoupling period (t_m), the rf field satisfying a R2TR condition $\nu_{eI} + \nu_{eS} = \nu_R$ is applied to one of the paired spins concerned. This rf field also functions for spin-locking the magnetization. Then, the t_m dependence of the spin-locked magnetization is monitored after removing the possible small y component of the magnetization by applying a 90°_X pulse. The t_m dependence of the magnetization is also affected by $T_{1\rho}$ relaxation. Measuring $T_{1\rho}$ under the same irradiation condition but with a slightly ($\sim$500 Hz) different spinning frequency so as not to satisfy the DQ R2TR condition, we can remove the relaxation effect from the t_m dependence by multiplying it by $\exp(t_m/T_{1\rho})$.

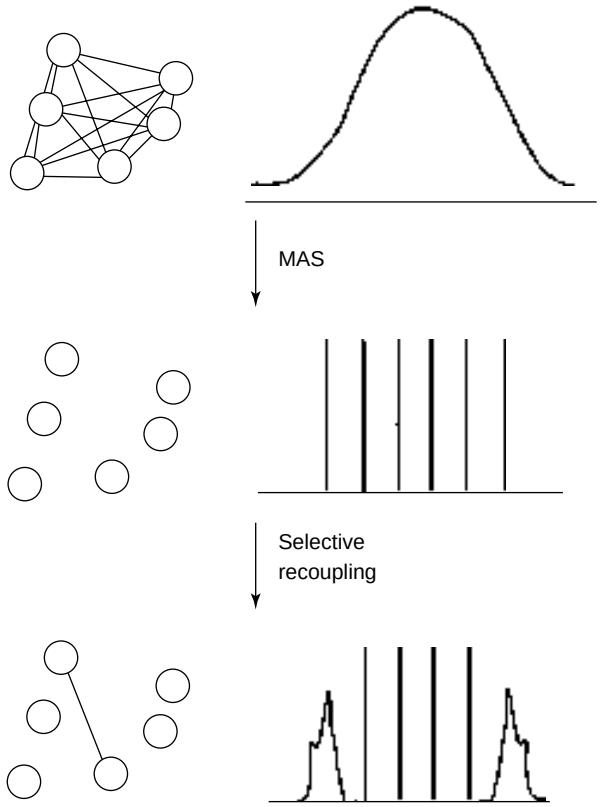

Figure 1 Schematic illustration of uniform decoupling by MAS and selective recoupling

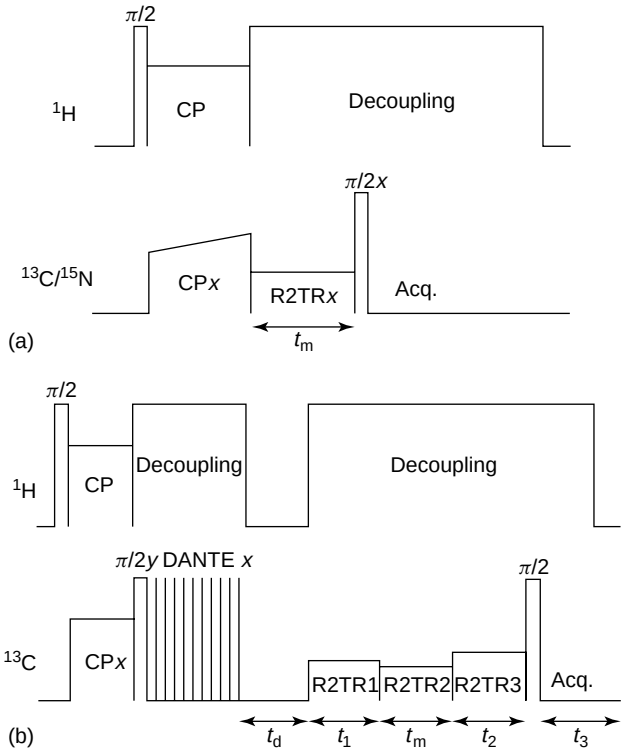

Figure 2 Pulse sequences to determine dihedral angles. (a) Dipolar recoupling experiment. After CP, a rf field satisfying a DQ condition for a particular pair of ^{13}C spins is applied on resonance to one of the spins for a recoupling time t_m. Then, the transverse magnetization of the spin is observed as a function of t_m. (b) 2D dipolar correlation experiment. After CP, the C magnetization in a four ^{13}C spin (A–B–C–D) system is suppressed by a DANTE pulse train. The A–B and the C–D dipolar interactions are selectively recovered in the t_1 and t_2 periods, respectively. These dipolar powder patterns are correlated by transferring magnetization from A or B to C or D in the mixing period. The AB/CD dipolar correlation spectrum is obtained by observing the C magnetization in the detection period t_3. (Reproduced from Nomura et al.[13] with kind permission from Kluwer Academic Publishers)

The other conditions of ZQ, SQ, and DQ ($n > 1$) are not suitable for the present experiments for the following reasons. First, to satisfy a ZQ condition, the chemical shift difference between a specific pair of spins must be larger than ν_R. However, chemical shift differences of ^{13}C or ^{15}N spin pairs at a common magnetic-field intensity are not so large as to satisfy a ZQ condition for ν_R fast enough to completely decouple the other dipolar couplings. Second, under a SQ condition, both chemical shift anisotropies (CSAs) of the relevant carbons are dominantly recovered, obscuring the effect of dipolar recoupling. Last, a DQ condition with $n > 1$, which requires a large rf-field intensity for ν_R fast enough to decouple the other dipolar couplings, lowers the selectivity of recoupling.

The influence of intermolecular dipolar couplings on the dipolar recoupling experiments was reduced by diluting a uniformly labeled sample (10%) with natural abundance material (90%). In the recoupling-time dependence experiments for the 10% uniformly labeled sample, 10% of the signal intensity at $t_m = 0$ was subtracted from the intensity observed at each recoupling time t_m, because it was found that the magnetization of the natural abundance material is kept almost constant during t_m.

An alternative approach to determine a dihedral angle is to measure mutual orientations of two or more anisotropic spin interactions. In the R2TR method, one can easily and quickly switch the dipolar interaction to be recoupled from one to another by changing ν and ν_1 under a constant spinning speed contrary to the normal R^2 method. This makes it possible to realize a 2D experiment which correlates the AB and CD dipolar powder patterns in an A–B–C–D ^{13}C spin system. Figure 2(b) shows the pulse sequence for the 2D dipolar correlation experiment. After cross polarization (CP), the C magnetization is suppressed by a selective 90° (DANTE) pulse followed by a dephasing period (t_d). In the first evolution period (t_1) the AB dipolar interaction is selectively recoupled, in the mixing period the A or B magnetization is selectively transferred to the C or D spin, and in the second evolution period (t_2) the C magnetization evolves under the selectively recoupled CD dipolar interaction. The AB/CD dipolar correlated 2D powder pattern is selectively obtained by observing the C spin in the detection period (t_3).

Recoupling may take place even in off-R2TR conditions to some extent, making the selectivity incomplete. The incompleteness of selectivity can be taken into account by including several spins into simulations in addition to the relevant two spins. To examine selectivity, we studied magnetization transfer in uniformly ^{13}C labeled L-alanine.[11] Figure 3(a) shows the ^{13}C 2D exchange NMR spectrum observed without applying any ^{13}C rf field during a mixing time of 4 ms under a MAS frequency of 5718 Hz. No conventional R^2 effects were observed at this spinning speed. The spectrum in Figure 3(b)

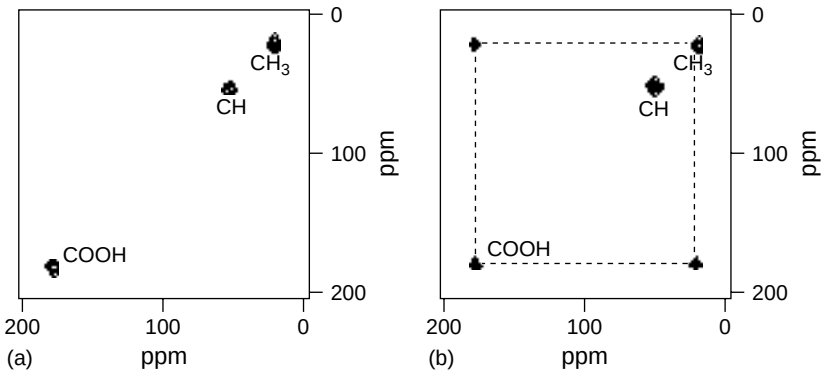

Figure 3 ^{13}C 2D exchange NMR spectra of uniformly ^{13}C labeled L-alanine. It was observed (a) without and (b) with applying a ^{13}C rf field during a mixing time of 4 ms under the MAS frequency of 5718 Hz. The rf field with the intensity of 4 kHz was applied at 296.7 ppm for the spectrum (b) to satisfy a R2TR condition $\Delta_{\text{eff}} = 2\nu_{\text{R}}$ for the carboxyl and the methyl carbons

was obtained at the same spinning speed while applying an rf field with the intensity of 4 kHz during the same mixing time to satisfy the ZQ R2TR condition $\Delta_{\text{eff}} = 2\nu_{\text{R}}$ for the carboxyl and methyl ^{13}C spins. Cross peaks appear between the carboxyl and methyl carbons, but no cross peaks can be seen between the carboxyl and methine carbons or between the methine and methyl carbons. This result confirms that the dipolar interaction between the carboxyl and the methyl carbons can be selectively recovered by the R2TR experiment, in spite of the fact that the recoupled dipolar coupling is below one fourth the other couplings. The stronger couplings remain completely decoupled by MAS.

Figure 4 shows the observed and the calculated mixing-time dependence of the individual ^{13}C magnetizations after saturation of the methyl carbon signal. The initial rapid oscillation of the carboxyl ^{13}C magnetization can be ascribed to the spinning sidebands in the tilted rotating frame,[11] which is damped quickly within a few milliseconds due to rf-field inhomogeneity. Hence, in the following, this oscillation in the simulation was damped to the same extent as the experimental data. Except for this initial oscillation and slight decay due to relaxation, the sum of the ^{13}C magnetizations of the carboxyl and the methyl carbons, $M_{0I} + M_{0S}$, is shown to be conserved. Further, the observed and the calculated curves for the methine carbon in Figure 4(b) again shows that the polarization transfer occurs selectively between the carboxyl and the methyl carbons, and further that a mixing time of 5 ms is enough for the polarization transfer between two carbons separated by 0.25 nm.

Further, to examine how large the chemical shift difference between non-relevant spins should be to achieve high selectivity, several isotropic chemical-shift values were assumed for the methine carbon, keeping its chemical shift anisotropy constant. Figure 5 shows the calculated mixing-time dependence of the methine ^{13}C magnetization for four chemical shift differences between the methyl and the methine carbons: 0, 500, 1000, and 2340 Hz. From Figure 5, it can be concluded that the chemical shift difference should be larger than 1000 Hz for selective transfer, leading to the following practical criteria of spins being added in simulations: For the selective recoupling experiment of A and D in a A–B–C–D ^{13}C system with observing the D magnetization, not only all the four spins, but also the following ^{13}C spin(s), if any: ^{13}C directly bonded to D (A), and ^{13}C within about 0.25 nm from D (A) with the ν_{e} difference between the ^{13}C and A (D) less than 1000 Hz.

4 APPLICATION TO GLYCYLISOLEUCINE

In the following, the complete 3D structure of a glycylisoleucine (Gly-Ile) molecule by R2TR is determined using a powder sample of uniformly ^{13}C,^{15}N-labeled Gly-Ile molecules, including all the positions of carbons, nitrogens, and oxygens in both main and side chains.[12,13] The 3D structure of a Gly-Ile molecule is obtained by measuring the six dihedral angles shown in Figure 6. In this study, ψ_{G}, ω_{G}, ϕ_{I}, χ_{I1}, and χ_{I2} are defined as dihedral angles N_{G}–$\text{C}^{\alpha}_{\text{G}}$–$\text{C}'_{\text{G}}$–$\text{N}_{\text{I}}$, $\text{C}^{\alpha}_{\text{G}}$–$\text{C}'_{\text{G}}$–$\text{N}_{\text{I}}$–$\text{C}^{\alpha}_{\text{I}}$, C'_{G}–N_{I}–$\text{C}^{\alpha}_{\text{I}}$–$\text{C}'_{\text{I}}$, C'_{I}–$\text{C}^{\alpha}_{\text{I}}$–$\text{C}^{\beta}_{\text{I}}$–$\text{C}^{\gamma 1}_{\text{I}}$, and $\text{C}^{\alpha}_{\text{I}}$–$\text{C}^{\beta}_{\text{I}}$–$\text{C}^{\gamma 1}_{\text{I}}$–$\text{C}^{\delta}_{\text{I}}$, respectively, by taking zero degrees for the *cis* conformation. ψ_{I} is defined as the angle between the N_{I}–$\text{C}^{\alpha}_{\text{I}}$ bond and the O^{1}_{I}–C'_{I}–O^{2}_{I} plane, being between 0 and 180°. ψ_{G}, ω_{G}, ϕ_{I}, and χ_{I1} were determined by performing the R2TR dipolar recouping experiment for a proper three or four-bonds distant spin pair, and χ_{I2} by a 2D dipolar correlation experiment because of the reason mentioned later, assuming the typical bond lengths and angles shown in Figure 6. The planar configuration of the peptide plane was also assumed.

Although the CSA interaction was neglected in Theory for simplicity, it does contribute to the results, and should thus be included into numerical calculations. Especially, the contribution of the CSA tensors for carbonyl carbons and amide nitrogens in the main chain are important owing to their large anisotropies (see **Chemical Shift Tensors,** Volume 2). However, the CSA tensors for carbonyl carbons are not very different from peptide to peptide. Hence, the mean values of δ and η for the carbonyl carbon tensors reported for some peptides are adopted (Table 1). For the directions of the principal axes, it is generally observed that the σ_{33} axis is perpendicular to the sp^2 plane.[14] On the other hand, the σ_{22} axis may make a small angle with the C=O bond direction. For C'_{G}, the σ_{33} axis is assumed to be perpendicular to the sp^2 plane and the σ_{22} axis makes the angle of 4.5° with the C'_{G}–O_{G} bond toward the C'_{G}–$\text{C}^{\alpha}_{\text{G}}$ bond.[15] For C'_{I}, the σ_{33} axis is perpendicular to the sp^2 plane and the σ_{11} axis is along the $\text{C}^{\alpha}_{\text{I}}$–$\text{C}'_{\text{I}}$ bond. The δ and η values for N_{I} and N_{G} were

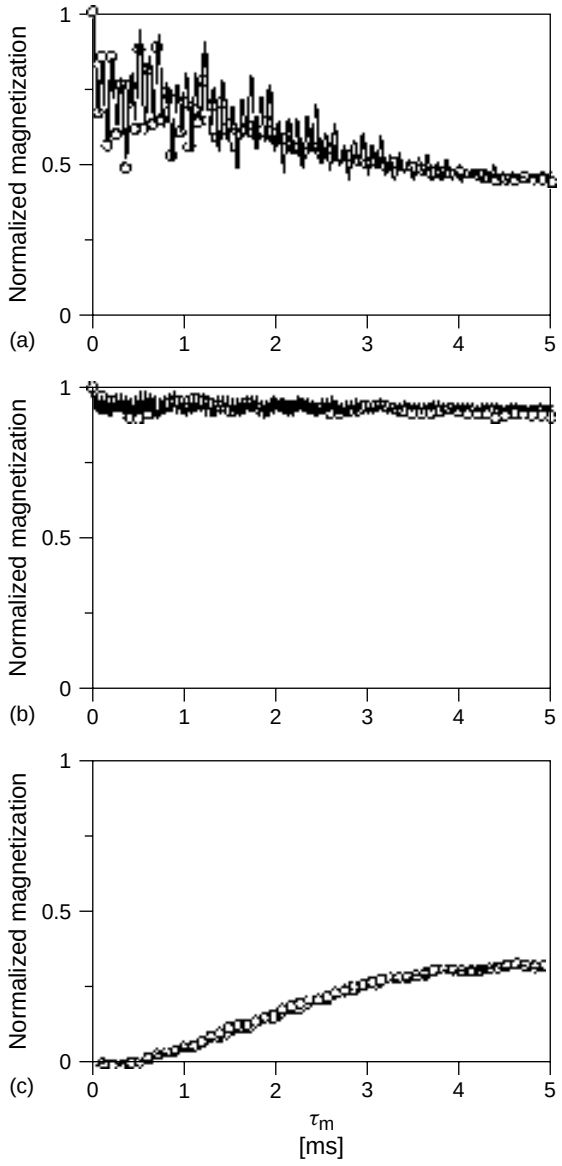

Figure 4 Experimental (○) and simulated (−) mixing-time dependence of the normalized magnetizations of (a) the carboxyl, (b) the methine, and (c) the methyl carbons under the condition $\Delta_{eff} = 2\nu_R$ satisfied between the carboxyl and the methyl carbons after saturation of the methyl carbon signal. The experiments were performed with the same parameters as described in the caption of Figure 3, excluding the initial magnetization for the methyl carbon. (Reproduced from Takegoshi et al.[11] with kind permission from Academic Press)

determined from spinning side bands observed at a low speed. The σ_{22} axis for N_I is assumed to be perpendicular to the peptide plane and the σ_{11} axis is along the N–C=O bond.[16] For N_G, the σ_{33} direction is along the N_G–C_G^α bond direction and the σ_{11} axis is perpendicular to the N_G–C_G^α–C'_G plane.[16] For the aliphatic carbons, it will be shown that the CSA interactions do not significantly affect simulated results. The ^{13}C and ^{15}N chemical shift parameters used for numerical simulations are collected in Table 1.

Figure 7 shows a ^{13}C COSY spectrum observed at $\nu_R = 17.5$ kHz under TPPM decoupling, presenting the connectivity between the observed eight signals (C_1–C_8) splitted by the

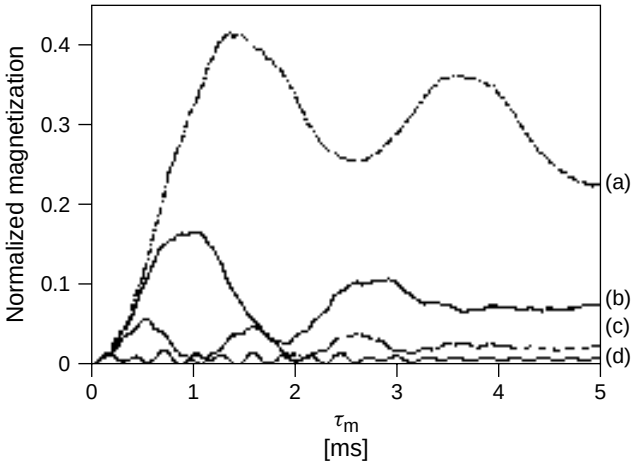

Figure 5 Simulated mixing-time dependence of the methine carbon magnetization under the same conditions as described in the caption of Figure 4, excluding the isotropic chemical shift of the methine carbon. The assumed chemical shift relative to the methyl carbon is: (a) 0 Hz, (b) 500 Hz, (c) 1000 Hz, and (d) 2340 Hz

^{13}C–^{13}C spin−spin couplings. From the connectivity and common knowledge of ^{13}C chemical shifts, all the signals can straightforwardly be assigned as $C_2 = C'_G$, $C_4 = C_G^\alpha$, $C_1 = C'_I$, $C_3 = C_I^\alpha$, $C_5 = C_I^\beta$, $C_6 = C_I^{\gamma 1}$, $C_7 = C_I^{\gamma 2}$, and $C_8 = C_I^\delta$. The observed isotropic chemical shifts are collected in Table 1.

Firstly, determination of the main-chain structure, which is described by dihedral angles conventionally named as ψ, ω, and ϕ (Figure 6), is discussed. ψ_G was determined by the selective-recoupling experiment of N_G and N_I. For the selective recoupling, an rf field with the intensity of 8300 Hz was applied on resonance to N_G, which satisfies a DQ condition under $\nu_R = 17.5$ kHz, and the recoupling-time dependence of the spin-locked magnetization of N_G was observed (Figure 8a). ψ_G was determined to be 180° from the root-mean-square deviation (RMSD) between the experimental data and the curves calculated for various ψ_G (Figure 8b). Let us examine to what extent the assumptions for the chemical shift tensors lead to error for determination of ψ_G. It was found that a deviation of 10° in the σ_{11} direction for N_I from the peptide bond direction to the N–C_α direction hardly changes the simulation curve. The deviation of 10° in the σ_{33} axis for N_G from the C_G^α–N_G bond direction does not change it either. The averages of the CSA parameters of the amide nitrogens[16] in $AcGlyGlyNH_2$, $AcGlyAlaNH_2$, $AcGlyTyrNH_2$, and GlyGly·HCl gives $(\delta, \eta) = (103.2\,\text{ppm}, 0.22)$, which are similar to the observed ones, leads to the same ψ_G value of 180° as above. It should be pointed out, however, that changing the observed CSA parameters of N_I to those for the amide nitrogen in $AcGlyTyrNH_2$ ($(\delta, \eta) = (96.4\,\text{ppm}, 0.26)$) or GlyGly·HCl ($(\delta, \eta) = (101.0\,\text{ppm}, 0.02)$)[16] results in the best-fit values of $\psi_G = \pm 154$ or $\pm 159°$, respectively. Such sensitivity of the recoupling-time dependence to the CSA parameters δ and η would be found particularly around $\psi = 180°$ at which the ^{15}N–^{15}N dipolar interaction becomes the weakest and thus insensitive to the dihedral angle. Nevertheless, the plot of $\Delta\chi^2$ shown in Figure 8(b) indicates that the 68% confidence interval ($\Delta\chi^2 < 1$) is still ±10°. For a better precision, it is desirable to measure the CSA parameters of amide nitrogens and use them in the simulations for determining ψ.

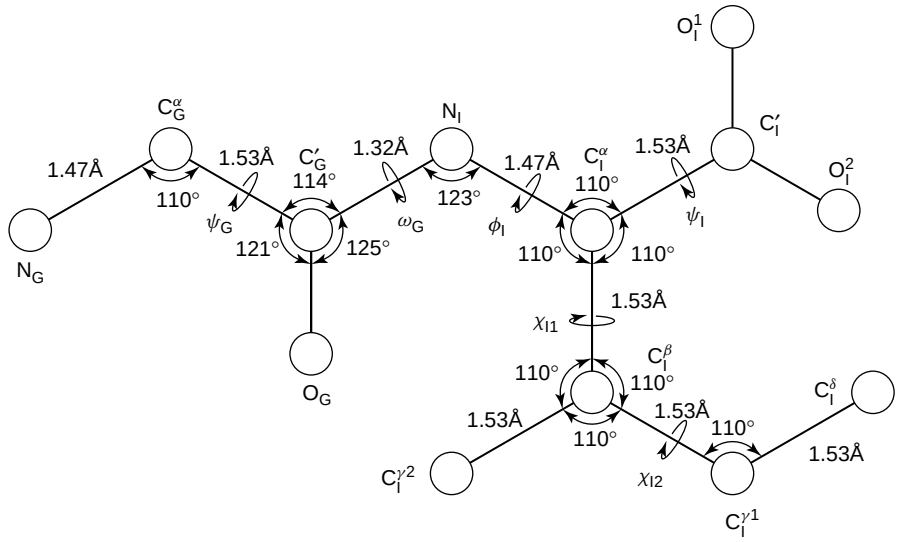

Figure 6 Schematic representation of a glycylisoleucine molecule. Typical values of the bond distances in Å and the bond angles in degrees are shown, which were used to simulate experimental results and construct the three dimensional structure of glycylisoleucine. The glycine carbonyl and C_α carbons are labeled as C'_G and C^α_G, and the isoleucine carboxyl, C_α, C_β, $C_{\gamma 1}$, $C_{\gamma 2}$, C_δ carbons are as C'_I, C^α_I, C^β_I, $C^{\gamma 1}_I$, $C^{\gamma 2}_I$, and C^δ_I, respectively. The glycine amine and the isoleucine amide nitrogens are labeled as N_G and N_I, respectively, and the glycine carbonyl oxygen as O_G, and the two isoleucine carboxyl oxygens as O^1_I and O^2_I. The dihedral angles ϕ_I, ω_G, ψ_G, ψ_I, χ_{I1}, and χ_{I2} are also shown. (Reproduced from Nomura et al.[13] with kind permission from Kluwer Academic Publishers)

Table 1 Chemical shift parameters used for the numerical simulations of the R2TR dipolar recoupling experiments in glycylisoleucine. (Reproduced by permission of Kluwer Academic Publishers from Nomura et al.[13])

	C'_I	C'_G	C^α_I	C^α_G	C^β_I	$C^{\gamma 1}_I$	$C^{\gamma 2}_I$	C^δ_I	N_I	N_G
δ_{iso}[a], ppm	178.9	169.3	64.0	40.3	36.3	26.7	17.0	12.4	120.9	23.1
δ[b], ppm	−71.0[c]	−79.3[d]	−19.7[e]	20.0[f]	6.67[g]	−12.3[h]	–	−13.9[i]	103.0[j]	19.5[j]
η[b]	0.84[c]	0.82[d]	0.44[e]	0.94[f]	0.60[g]	0.58[h]	–	0.32[i]	0.31[j]	0.68[j]

[a] ^{13}C and ^{15}N isotropic chemical shifts were obtained with respect to Me_4Si and liquid NH_3, respectively.
[b] The anisotropy δ and the asymmetry parameter η are defined as $\delta = \delta_{zz} - \delta_{iso}$ and $\eta = (\delta_{yy} - \delta_{xx})/\delta$, where δ_{iso} is the isotropic shift and $|\delta_{yy} - \delta_{iso}| \leq |\delta_{xx} - \delta_{iso}| \leq |\delta_{zz} - \delta_{iso}|$.
[c] Average of the values for the carboxyl carbons in glycine,[17] L-alanine,[18] L-serine,[19] L-threonine,[20] L-asparagine.[20]
[d] Average of the values for the carbonyl carbons in some peptides.[15]
[e] Values for the α carbon in L-alanine.[18]
[f] Values for the α carbon in glycine.[17]
[g] Values for the β carbon in isobutane.[22]
[h] Values for the α-methylene carbon in n-eicosane.[23]
[i] Values for the methyl carbon in n-eicosane.[23]
[j] Determined by the sideband analysis of a low-speed MAS spectrum.

To determine ϕ_I, the selective recoupling experiment was done for C'_G and C'_I, where an rf field with an intensity of 8500 Hz was applied on resonance to the C'_I carbon while spinning with $\nu_R = 17.054$ kHz. Figure 9(a) shows the observed recoupling-time dependence of the magnetization of C'_I. If only the dipolar interaction between C'_G and C'_I contributes to the result, only the absolute value of the dihedral angle ϕ_I can be determined from this experiment. In the present case, however, the large CSAs of both carbons and the relative orientations between the CSA tensors, and some dipolar tensors significantly affect the experimental result. Hence, there may be a good chance of determining not only ϕ_I but also ψ_I with the signs. Since peptide planes take the *trans* configuration except for cyclic peptides or peptides with proline, ω_G was assumed to be 180°. Therefore, the experimental curve was simulated, taking ϕ_I and ψ_I as adjustable parameters.

Figure 9(b) and (c) show the contour plots of RMSD between the experimental data and the curves calculated for various values of (ϕ_I, ψ_I) and $\Delta\chi^2$ around the global minimum of RMSD, respectively. These results provide the best-fit values of $(\phi_I, \psi_I) = (-76°, 147°)$ and the 68% confidence regions ($\Delta\chi^2 \sim 1$) of $(-1° \sim 1°)$ for ϕ_I and $(-9° \sim 6°)$ for ψ_I. Due to the imperfect selectivity of R2TR, C^α_G, C^α_I, and C^β_I in addition to C'_G and C'_I had to be included to best simulate the recoupling curve. This resolves the degeneracy for (ϕ_I, ψ_I) and $(-\phi_I, -\psi_I$ or $180 - \psi_I)$, which occurs if only C'_G and C'_I contribute to the recoupling curve. In fact, the $\Delta\chi^2$ value around $(\phi_I, \psi_I) = (76°, 33°)$ is relatively large (ca. 34). Hence, both ϕ_I and ψ_I could be uniquely determined. It should,

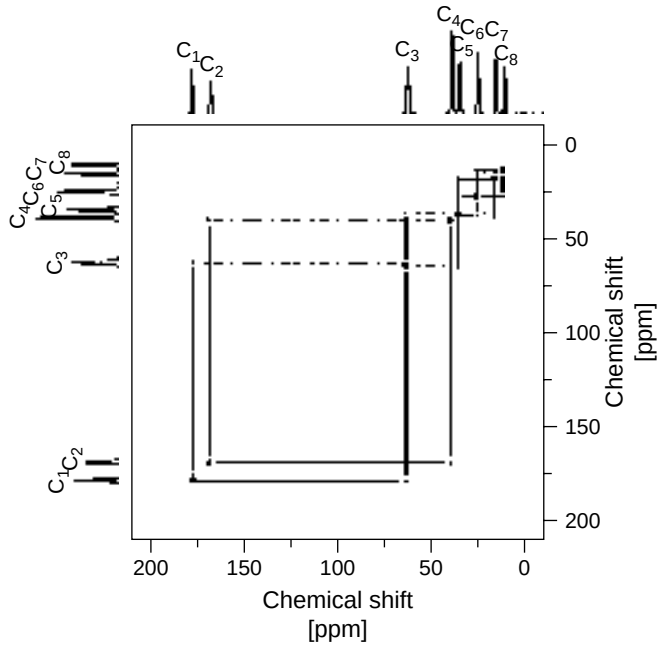

Figure 7 ^{13}C COSY spectrum of uniformly ^{13}C,^{15}N-labeled glycylisoleucine. It was obtained under the spinning speed of 17.5 kHz and TPPM decoupling. (Reproduced from Nomura et al.[13] with kind permission from Kluwer Academic Publishers)

however, be pointed out that ϕ_I is precisely determined but ψ_I is not. This is because the dipolar coupling directly contributes to the determination of ϕ_I, but ψ_I is obtained only through the relative orientation of the C'_I CSA tensor to the other tensors. Therefore, the validity of the use of the CSA tensors assumed for C'_G and C'_I in the above simulations should be examined.

First, as for C'_G, the experimental result was simulated using the CSA parameters and orientations determined for $AcGlyGlyNH_2$, $AcGlyAlaNH_2$, $AcGlyTyrNH_2$, and GlyGly·HCl.[15] The best-fit values of (ϕ_I, ψ_I) do not deviate significantly for the four sets of parameters ($-71° \sim -78°$, $139° \sim 148°$). As for the tensor orientation of C'_I, it was assumed that σ_{11} is parallel to the C^α_I–C'_I bond, while it may deviate from the bond direction by about 10°.[14] It was found that the 10° deviation leads to (ϕ_I, ψ_I) = ($-76°$, 138°). For the CSA parameters (δ, η), the values for glycine,[17] L-alanine,[18] L-serine,[19] L-threonine,[20] and L-asparagine[21] were used to find (ϕ_I, ψ_I) to be ($-75° \sim -76°$, $137° \sim 150°$).

These results show that the use of likely CSA tensors for C'_G and C'_I in the simulations causes only a small error in the determination of ϕ_I, but leads to a considerable error in ψ_I. This is also because the ϕ_I value is directly related to the distance, while the ψ_I value is related mainly to the relative orientations of the CSA tensors, being more sensitive to them. To obtain a more precise value for ψ_I, (δ, η) for C'_I should be measured by some method.

The present result of the recoupling experiment for C'_G and C'_I indicates that one dipolar recoupling experiment per amino acid residue is enough to determine dihedral angles (ψ, ω, ϕ) which provide the 3D backbone structure of a peptide. In the above, however, $\omega_G = 180°$ was assumed, while in cyclic peptides or peptides with proline, ω_G may be 0°. Hence, the possibility of determining whether $\omega_G = 0°$ or 180° was examined. The dotted line in Figure 9(a) shows

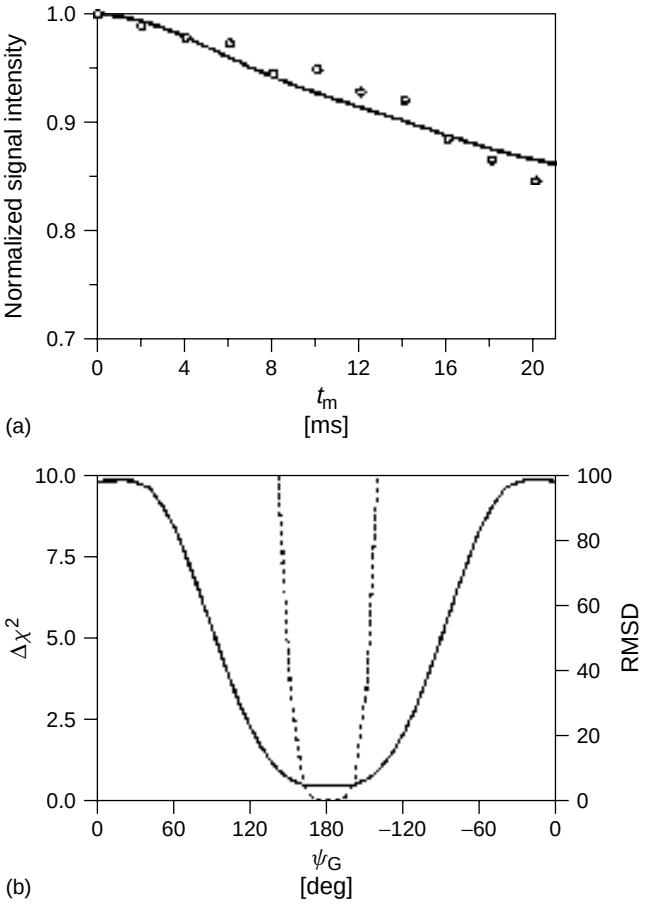

Figure 8 (a) Recoupling-time dependence of the normalized magnetization of N_G in 10% uniformly ^{13}C,^{15}N-labeled glycylisoleucine. The dipolar recoupling experiment was carried out using the pulse sequence in Figure 2(a) under a R2TR condition ($\nu_{eI} + \nu_{eS} = \nu_R$) satisfied for N_G and N_I by applying a rf field with the intensity of 8300 Hz on resonance to N_G under MAS with $\nu_R = 17.5$ kHz. Experimental points are shown by circles. The standard deviation for each point is ca. ±0.05. The curves are calculated for the dihedral angle ψ_G of 180°. $T_{1\rho}$ was determined to be 70 ms by an off-R2TR experiment, and used to remove the relaxation effect from the dipolar recoupling data. (b) Dihedral angle (ψ_G) dependence of RMSD (- - - - -) between the experimental (Figure 8a) and simulated data and of $\Delta\chi^2$ (———). (Reproduced from Nomura et al.[13] with kind permission from Kluwer Academic Publishers)

the curve simulated with $\omega_G = 0°$ and the best-fit values of (ϕ_I, ψ_I) = ($-86°$, 167°), showing that it is difficult to determine the difference between the two possibilities $\omega_G = 0°$ and $\omega_G = 180°$ by this experiment. Therefore, another recoupling experiment was made for C^α_G and C'_I, by applying an rf field with an intensity of 2800 Hz on resonance to the C'_I carbon which satisfies a DQ condition under spinning with $\nu_R = 17.03$ kHz. Figure 10 shows the recoupling-time dependence of the magnetization of C'_I together with the simulated curves obtained for the two sets of (ω_G, ϕ_I, ψ_I), namely, (180°, $-76°$, 147°) and (0°, $-86°$, 167°). Clearly, the former set reproduces the observation as expected. It indicates that even when one does not know whether $\omega = 0°$ or 180°, one can determine the three dihedral angles (ψ, ω, ϕ) by two dipolar recoupling experiments per amino acid residue.

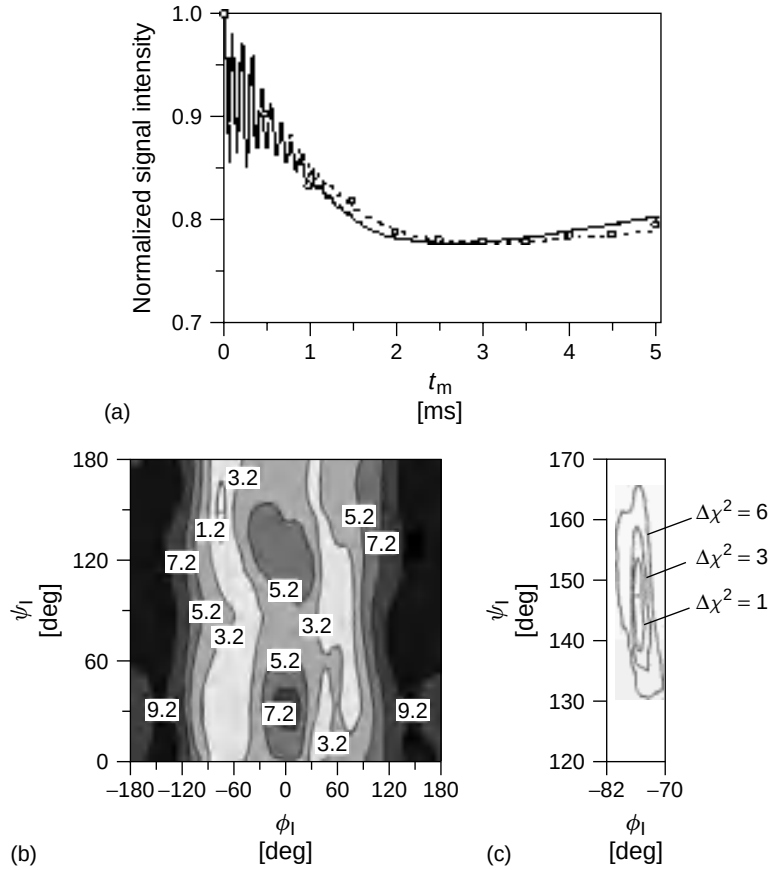

Figure 9 (a) Recoupling-time dependence of the normalized magnetization of C'_I in 10% uniformly ^{13}C,^{15}N-labeled glycylisoleucine. The dipolar recoupling experiment was carried out using the pulse sequence in Figure 2(a) under a R2TR condition ($\nu_{eI} + \nu_{eS} = \nu_R$) satisfied for C'_I and C'_G by applying a rf field with the intensity of 8500 Hz on resonance to the C'_I carbon under MAS with $\nu_R = 17.054$ kHz. Experimental points are shown by circles. The standard deviation for each point is ca. ± 0.03. The solid line is the curve calculated for the dihedral angles (ω_G, ϕ_I, ψ_I) = (180°, −76°, 147°), whereas the dotted line for (ω_G, ϕ_I, ψ_I) = (0°, −86°, 167°). $T_{1\rho}$ was determined to be 500 ms for C'_I in 10% uniformly ^{13}C,^{15}N-labeled glycylisoleucine, and used to correct the experimental data. (b) The contour plot of RMSD between the experimental spectrum (Figure 5a) and the simulations for various sets of (ϕ_I, ψ_I) and $\omega_G = 180°$. The global minimum is indicated by a dot. (c) Dihedral angles (ϕ_I and ψ_I) dependence of $\Delta\chi^2$ for $\omega_G = 180°$. (Reproduced from Nomura et al.[13] with kind permission from Kluwer Academic Publishers)

As exemplified here, the recoupling-time behavior in a general sp^2–sp^2 ^{13}C spin pair depends not only on the internuclear distance, but also on the relative orientations between the CSA tensors and the dipolar vector as well as the CSA parameters. Owing to the dependence caused by CSA, the magnitudes of not only ϕ but also ψ can be determined. Moreover, a few more carbons also contribute to the experimental result due to the incomplete selectivity; however, it provides the benefit of being able to determine the signs of ϕ and ψ. While the contribution of CSA tensors and other spins makes the simulation troublesome and somewhat reduces the accuracy in determination of dihedral angles, it provides information which cannot easily be obtained by other means.

As described above, the dihedral angles for the main chain were determined. The dihedral angles for the side chain in the isoleucine residue can also be determined in a similar manner. However, since their chemical-shift values are very similar to each other and moreover the atomic positions are close to each other, selective recoupling of one of these pairs is indeed difficult. In this sense, the isoleucine residue is one of the most demanding ones for the present approach.

The χ_{I1} angle was obtained by selective dipolar recoupling between C'_I and $C_I^{\gamma 1}$, which was attained by applying a rf field with the intensity of 2000 Hz on resonance to the C'_I carbon under MAS with $\nu_R = 17.46$ kHz. In the simulation, C_I^{α}, C_I^{β}, and C_I^{δ} besides C'_I and $C_I^{\gamma 1}$ were included, and χ_{I1} was determined to be 178°. The effect of the chemical shift tensors of C'_I on the χ_{I1} value were examined using the literature (δ, η) values of C′ in L-alanine, L-serine, L-threonine, and L-asparagine, and it was found that the best-fit values of χ_{I1} are virtually unaffected (175° ∼ 178°). Also, changing the CSA parameters for $C_I^{\gamma 1}$ to those determined for the α-methylene carbon of *n*-eicosane[23] provides essentially the same value of $\chi_{I1} = -176°$.

As exemplified by the present case, in a general sp^3–sp^2 ^{13}C spin pair, possible variations of the parameters and orientations of their CSA tensors barely affects the recoupling-time dependence. Thus, likely CSA parameters (δ, η) and tensor orientations for both carbons may be used safely.

To determine the χ_{I2} angle in the same way as above, it is necessary to selectively recouple C_I^{α} and C_I^{δ}, or $C_I^{\gamma 2}$ and C_I^{δ}. Due to the spectral congestion, it is difficult to find a R2TR

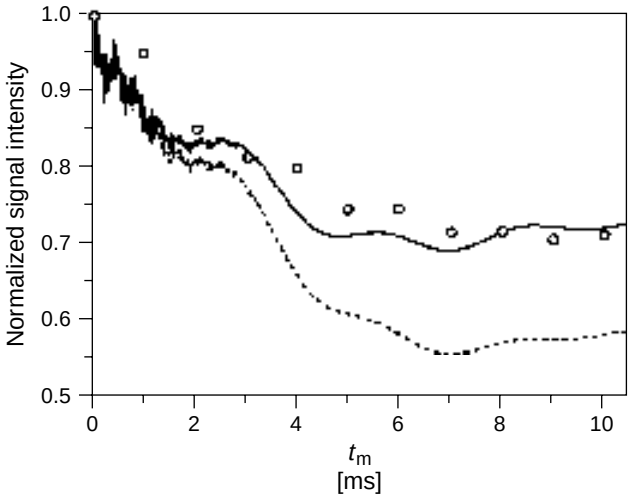

Figure 10 Recoupling-time dependence of the normalized magnetization of C'_I in 10% uniformly ^{13}C,^{15}N-labeled glycylisoleucine. The dipolar recoupling experiment was carried out using the pulse sequence in Figure 2(a) under a R2TR condition ($\nu_{eI} + \nu_{eS} = \nu_R$) satisfied for C'_I and C^{α}_G by applying a rf field with the intensity of 2800 Hz on resonance to the C'_I carbon under MAS with $\nu_R = 17.03$ kHz. Experimental points are shown by circles. The standard deviation for each point is ca. ± 0.04. The solid line is the curve calculated for the dihedral angles (ω_G, ϕ_I, ψ_I) = (180°, −76°, 147°), whereas the dotted line for (ω_G, ϕ_I, ψ_I) = (0°, −86°, 167°). $T_{1\rho}$ was determined to be 500 ms for C'_I in 10% ^{13}C,^{15}N-labeled glycylisoleucine, and used to correct the experimental data. (Reproduced from Nomura et al.[13] with kind permission from Kluwer Academic Publishers)

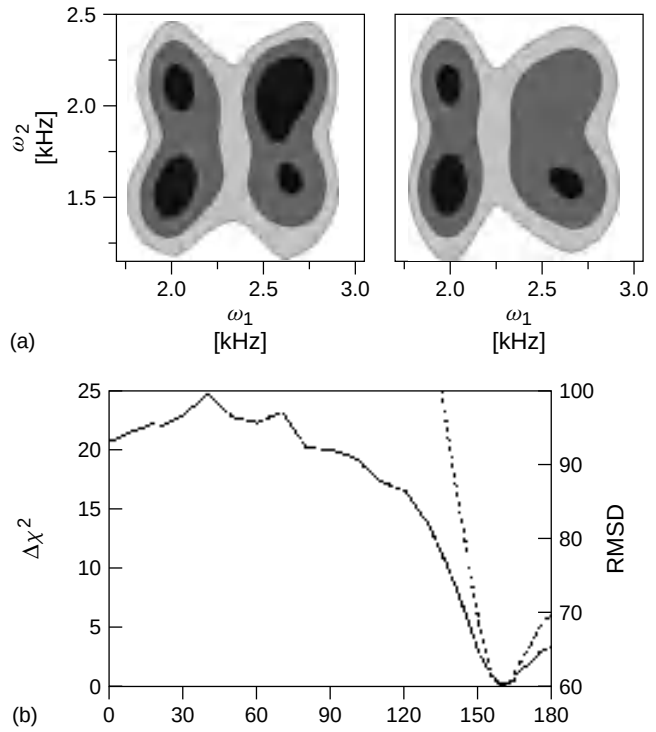

Figure 11 (a) The 2D C^{α}_I–C^{δ}_I/$C^{\gamma 2}_I$–C^{δ}_I dipolar correlation spectrum for uniformly ^{13}C,^{15}N-labeled glycylisoleucine. The experiment was performed using the pulse sequence in Figure 2(b). The spinning frequency ν_R is 5110 Hz. The ^{13}C rf-field intensities during the t_1 period, the mixing time, and the t_2 period are $\nu_1 = 2540$ (on resonance to the C^{δ}_I carbon), 0, and 1825 Hz (on resonance to the C^{α}_I carbon), respectively. (left) Experimental 2D spectrum. (right) Simulated 2D spectrum calculated for the $C^{\gamma 1}_I$–C^{δ}_I distance of 1.62 Å and the dihedral angle χ_{I2} of 160°. The contour lines are plotted at 65, 77, and 88% of the maximum intensity. (b) Dihedral angle (χ_{I2}) dependence of RMSD (- - - - -) between the experimental (Figure 11a) and simulated 2D dipolar correlation spectra and of $\Delta\chi^2$ (———). (Reproduced from Nomura et al.[13] with kind permission from Kluwer Academic Publishers)

condition suitable for these pairs. Therefore, a C^{α}_I–C^{β}_I/$C^{\gamma 1}_I$–C^{δ}_I dipolar correlation 2D powder pattern was observed using the sequence shown in Figure 2(b). In this experiment, a 100% uniformly labeled sample was used for obtaining a high signal-to-noise ratio. The use of the undiluted sample is justified, because the dipolar interactions recoupled in the t_1 and t_2 periods are of directly bonded ones, and thus much stronger than the intermolecular dipolar interactions.

The spinning speed ν_R was set to 5110 Hz, satisfying the R^2 condition for C^{δ}_I and C^{α}_I. In the t_1 period, a DQ condition is matched for $C^{\gamma 1}_I$ and C^{δ}_I by applying an rf field with an intensity of 2540 Hz on resonance to C^{δ}_I. During the mixing time t_m, the magnetization of C^{δ}_I is selectively transferred to C^{α}_I by R^2. In the t_2 period, a DQ condition is fulfilled for C^{α}_I and C^{β}_I by applying an rf field with an intensity of 1825 Hz on resonance to C^{α}_I. Figure 11(a) compares the experimental and the simulated 2D spectra, while Figure 11(b) shows the χ_{I2} dependence of RMSD between the experimental and calculated 2D spectra. Even though the agreement is not excellent, the $\Delta\chi^2$ plot in Figure 11(b) shows that the 68% confidence interval is ±5°, and χ_{I2} was determined to be 160°. The sign of χ_{I2} cannot be determined from this experiment. The dihedral angle ($C^{\gamma 2}_I$–C^{β}_I–$C^{\gamma 1}_I$–C^{δ}_I) was calculated to be 39° from $\chi_{I2} = -160°$, and to be 79° from $\chi_{I2} = 160°$; it suggests that the steric hindrance between the two methyl groups is smaller for the latter case. Therefore, the positive sign was preferred.

In the simulation, $C^{\gamma 2}_I$ in addition to C^{α}_I, C^{β}_I, $C^{\gamma 1}_I$, and C^{δ}_I were included, and a somewhat long $C^{\gamma 1}_I$–C^{δ}_I bond length of 1.62 Å had to be assumed for the best fitting. This unusual bond length was attributed to a thermal vibration of C^{δ}_I. It is worthy to be noted that with the existence of molecular motion, dihedral angles cannot be correctly determined from distance measurements. However, in a theoretical study of vibrational effects,[24] it has been proved that the dipolar 2D powder patterns provide correct dihedral angles even under the presence of molecular vibrations as long as the asymmetry of the vibration is negligible. It is a common problem for various methods of structure determination that we must pay attention to the presence of local motion.

In these simulations, chemical shift anisotropies are not included, but it was found that even if likely chemical shift tensors are included, the spectrum does not appreciably change, under the MAS frequency of ∼5 kHz. This is fortunate, because the CSA tensors of sp^3 carbons depend heavily on circumstances, so that it is very difficult to assume them appropriately for simulations. For a directly bonded sp^3–sp^3 ^{13}C spin pair, the effect of CSAs can indeed be neglected in comparison with the contribution of the dipolar coupling under MAS with a spinning speed a few times faster than $|\delta|$, according to

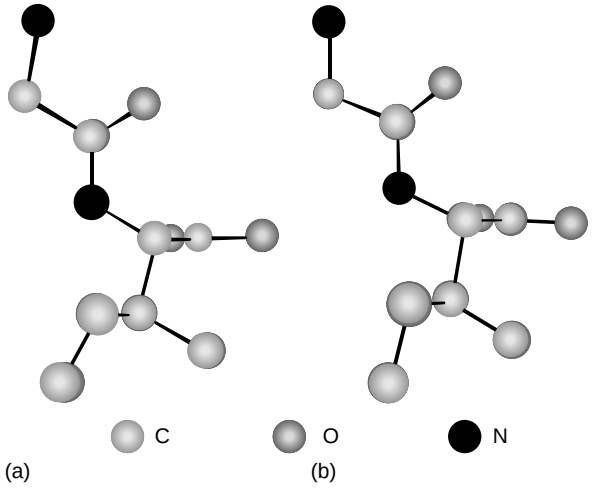

Figure 12 Three dimensional structure of glycylisoleucine. (a) NMR study; (b) X-ray crystallography. (Reproduced from Nomura et al.[13] with kind permission from Kluwer Academic Publishers)

our simulations. On the other hand, for a nonbonded, namely weakly dipolar coupled sp^3-sp^3 ^{13}C spin pair, the effect of the CSAs becomes more important than for a directly bonded pair. Therefore, the CSA effect must be reduced for accurate determination of dihedral angles by using a sufficiently fast spinning speed. Then large ν_1 is needed for satisfying a DQ recoupling condition, so that selectivity is declined. Therefore, when some other sp^3 carbons exist close to the relevant carbons, the dipolar recoupling experiment (Figure 2a) does not work well, and the 2D dipolar correlation experiment (Figure 2b) is recommended.

Figure 12 shows the 3D structure constructed from the dihedral angles determined by the R2TR experiments, and that determined by X-ray crystallography. The dihedral angles determined by NMR and X-ray are (ψ_G, ω_G, ϕ_I, ψ_I, χ_{I1}, χ_{I2}) = (180°, 180°, −76°, 147°, 178°, 160°) and (165°, 170°, −70°, 156°, 178°, 170°), respectively. Although of course the result by NMR includes errors, we note that the structure determined by X-ray diffraction is not very accurate either. Nevertheless, both structures are in good agreement, indicating that the present approach is useful for structure determination. Further, the X-ray diffraction showed that the thermal vibration parameters of C_I^{δ} are very large, agreeing with our observation by NMR.

5 CONCLUDING REMARKS

The complete 3D structure of a uniformly ^{13}C,^{15}N-labeled Gly-Ile molecule were determined using the R2TR method. All the dihedral angles were individually determined by selectively recoupling some dipolar interactions between three or four-bonds distant spins or observing a dipolar correlation 2D powder pattern. Choosing three adjustable parameters ν_1, ν_0, and ν_R properly, it was possible to find a R2TR condition suitable for selective recoupling of the pair of spins concerned. Furthermore, it is not always necessary that all resonances are resolved; it is possible to monitor the recoupling-time dependence if only one of the pair of the spins concerned is resolved well from the others.

The present approach can be applied to determine the 3D structure of a small molecule and also the structure of a restricted region important to the biological function of a large system using a sample in which the region is uniformly or multiply labeled. So far quantitative structural information obtained by solid state NMR has been almost limited to a single internuclear distance or dihedral angle. The present approach increases the obtainable quantity of structural information in a single powder sample.

6 REFERENCES

1. E. R. Andrew, S. Clough, L. F. Farnell, T. D. Gledhill, and I. Roberts, *Phys. Lett.*, 1966, **21**, 505.
2. D. P. Raleigh, G. S. Harbison, T. G. Neiss, J. E. Roberts, and R. G. Griffin, *Chem. Phys. Lett.*, 1987, **138**, 285.
3. B. H. Meier and W. L. Earl, *J. Am. Chem. Soc.*, 1987, **109**, 7937.
4. M. G. Colombo, B. H. Meier, and R. R. Ernst, *Chem. Phys. Lett.*, 1988, **146**, 189.
5. A. Kubo and C. A. McDowell, *J. Chem. Soc. Faraday Trans.*, 1988, **84**, 3713.
6. W. E. J. R. Maas and W. S. Veeman, *Chem. Phys. Lett.*, 1988, **149**, 170.
7. T. Nakai and C. A. McDowell, *J. Chem. Phys.*, 1992, **96**, 3452.
8. T. Nakai and C. A. McDowell, *Mol. Phys.*, 1996, **88**, 1263.
9. S. O. Smith, in 'Encyclopedia of NMR', eds D. M. Grant and R. K. Harris, Wiley: Chichester, 1996, Vol. 7, p. 4185.
10. K. Takegoshi, K. Nomura, and T. Terao, *Chem. Phys. Lett.*, 1995, **232**, 424.
11. K. Takegoshi, K. Nomura, and T. Terao, *J. Magn. Reson.*, 1997, **127**, 206.
12. K. Nomura, K. Takegoshi, T. Terao, K. Uchida, and M. Kaisnosho, *J. Am. Chem. Soc.*, 1999, **121**, 4064.
13. K. Nomura, K. Takegoshi, T. Terao, K. Uchida, and M. Kaisnosho, *J. Biol. NMR*, 2000, **17**, 111.
14. W. S. Veeman, *Prog. Nucl. Magn. Reson. Spectrosc.*, 1984, **16**, 193.
15. T. G. Oas, C. J. Hartzell, T. J. McMahon, G. P. Drobny, and F. W. Dahlquist, *J. Am. Chem. Soc.*, 1987, **109**, 5956.
16. T. G. Oas, C. J. Hartzell, F. W. Dahlquist, and G. P. Drobny, *J. Am. Chem. Soc.*, 1987, **109**, 5962.
17. R. A. Haberkorn, R. E. Stark, H. van Willigen, and R. G. Griffin, *J. Am. Chem. Soc.*, 1981, **103**, 2534.
18. A. Naito, S. Ganapathy, K. Akasaka, and C. A. McDowell, *J. Chem. Phys.*, 1981, **74**, 3190.
19. A. Naito, S. Ganapathy, P. Raghunathan, and C. A. McDowell, *J. Chem. Phys.*, 1983, **79**, 4173.
20. N. Janes, S. Ganapathy, and E. Oldfield, *J. Magn. Reson.*, 1983, **54**, 111.
21. A. Naito and C. A. McDowell, *J. Chem. Phys.*, 1984, **81**, 4795.
22. J. C. Facelli, A. M. Orendt, M. S. Solum, G. Depke, D. M. Grant, and J. Michl, *J. Am. Chem. Soc.*, 1986, **108**, 4268.
23. D. L. VanderHart, *J. Chem. Phys.*, 1976, **64**, 830.
24. Y. Ishii, T. Terao, and S. Hayashi, *J. Chem. Phys.*, 1997, **107**, 2760.

Biographical Sketches

K. Takegoshi, *b* 1956. B.Sc., 1979, Ph.D., 1984, Chemistry, Kyoto University, Japan. Postdoctoral Fellow at University of British Columbia (Canada) 1984–1986 and at University of California (Berkeley, USA) 1986–1987. Staff scientist at Foundation of Material Science and Technology of Japan 1987–1988. Assistant Professor at Hokkaido University 1988–1993. Associate Professor at Kyoto University 1993-present.

Takehiko Terao, *b* 1941. B.Sc., 1966, Ph.D., 1973, Physics, Kyoto University, Japan, where he was introduced to NMR by Tsuneo Hashi. Faculty of Science, Kyoto Sangyou University, 1971–75. Department of Chemistry, Graduate School of Science, Kyoto University, 1975-present. Research speciality: solid state NMR and its applications to chemistry and biology.

Anisotropy of Shielding and Coupling in Liquid Crystalline Solutions

Jukka Jokisaari

Department of Physics, University of Oulu, FIN-90570 Oulu, Finland

1	Introduction	1
2	Liquid Crystals	1
3	The Hamiltonian Operator and Observables	2
4	Shielding Anisotropy	2
5	Spin–Spin Coupling Anisotropy	7
6	Related Articles	9

1 INTRODUCTION

In the beginning of the 1960s, NMR spectroscopists started to look for means to orient molecules with a particular goal in mind, i.e. to find a situation where the intermolecular direct dipolar couplings would average out whereas the corresponding intramolecular couplings would average to a nonzero value. Various methods were tried until, in 1963, Saupe and Englert[1] proposed that the sought-after properties can be reached by using liquid crystals as solvents.

The anisotropic orientational distribution of solute molecules in liquid crystals makes it possible to use the NMR observables (anisotropic couplings including both the direct dipole–dipole couplings and a contribution from the anisotropy of the indirect spin–spin coupling tensor, chemical shifts, and nuclear quadrupole splittings) for the determination of molecular structures, the anisotropies of nuclear shielding and spin–spin couplings, and quadrupole couplings for nuclei with spin ≥ 1. In principle, the method is quite straightforward but in practice some complications may appear. In particular, the determination of molecular structures necessitates the introduction of the vibrational[2] and deformational[3–5] corrections (see ***Structure of Rigid Molecules Dissolved in Liquid Crystalline Solvents***). Since the anisotropic contribution of the spin–spin coupling tensor can only be separated from the experimental coupling when the direct dipole–dipole coupling is known, the corresponding effects have also to be considered here. To obtain reliable shielding anisotropies for protons and for nuclei with small anisotropy in general, various disturbing effects on the experimentally determined chemical shifts, such as local anisotropy due to solvent molecules, have to be taken into account.

A comprehensive review on the anisotropies of shielding and spin–spin coupling tensors determined using liquid crystalline solvents appeared in 1982.[6] Since then, however, remarkable progress has taken place. This concerns spin–spin coupling anisotropy, in particular, where the inclusion of the deformational corrections leads to unambiguous, solvent independent results.

The NMR spectra observable from the spin-$\frac{1}{2}$ nuclei in molecules dissolved in liquid crystals resemble those in isotropic liquids; relatively sharp, well resolved lines can be detected. Hence, analyses of spectra taken in the two phases are, in principle, similar (see ***Liquid Crystalline Samples: Spectral Analysis***, and ***Analysis of High-Resolution Solution State Spectra***). There are, however, also a few basic differences. Firstly, the anisotropic couplings between magnetically and chemically equivalent nuclei affect the structure of the spectrum. Thus, for example, the ^{1}H NMR spectrum of three methyl protons is a triplet and the six benzene protons give a spectrum very rich in resonance lines. Secondly, the dipole–dipole coupling constants are often large, of the order of kHz, and consequently the first-order approximation can usually be carried out only when the coupled nuclei are of different species.

2 LIQUID CRYSTALS

The liquid crystals most applicable in NMR spectroscopy are the thermotropic ones which have mesophases within certain temperature ranges.[7] In a few cases, lyotropic liquid crystals have also been used. They are formed by mixing, for example, alkyl sulfates and the corresponding alcohols, sodium sulfate, and water.[8]

Thermotropic liquid crystals which are mainly used as solvents in NMR spectroscopy, can be classified into two main categories; nematic (N) and smectic (S). In the nematic phases, the molecules have only a short range positional order. However, if the liquid crystals consist of elongated molecules, as those used in the applications described in this context usually do, they tend to align with their long axes parallel to a common axis which defines the director (often called also the optic axis), $\boldsymbol{n}$, of the liquid crystal. The nematic phases are almost in all known cases uniaxial (rotational symmetry exists around the director) and apolar (the directions $\boldsymbol{n}$ and $-\boldsymbol{n}$ are equivalent). In the smectic phases the liquid crystal molecules possess long range order. A specific feature of smectic phases is the appearance of one-dimensional density waves or, as often called, layered structures. Smectic phases are divided into subgroups of which the smectic A phase (S_A) is the one used in the present applications. In this phase, the director coincides with the normal of the layer, and $\boldsymbol{n}$ and $-\boldsymbol{n}$ are equivalent. The structures of the nematic and smectic A phases are shown in Figure 1.

When a liquid crystalline sample is placed in an external magnetic field $\boldsymbol{B}$, the sample is magnetized so that the magnetization $\boldsymbol{M}$ is given by

$$M_\alpha = \mu_0^{-1} \chi_{\alpha\beta} B_\beta \tag{1}$$

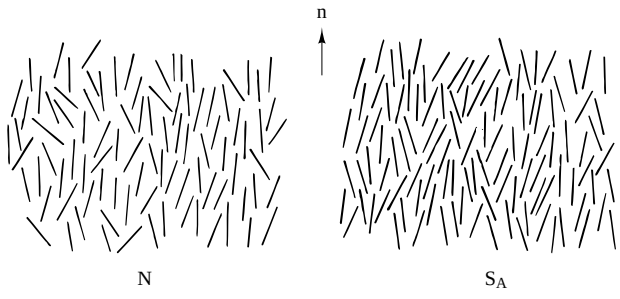

Figure 1 Structures of thermotropic nematic (N) and smectic A (S_A) liquid crystalline phases. The direction of the director is shown by **n**

where μ_0 is the permeability in vacuo and the $\chi_{\alpha\beta'}$s are elements of the diamagnetic (volume) susceptibility tensor, χ_{m}, which is diagonal in uniaxial phases.

The energy density, ρ_{B}, due to the magnetization $\boldsymbol{M}$ is:

$$\rho_B = -\int_0^B M \cdot \mathrm{d}B = -\frac{B^2}{2\mu_0}\left[\chi_{\mathrm{m}} + \frac{2}{3}\Delta\chi_{\mathrm{m}} P_2(\cos\theta)\right] \tag{2}$$

where $\chi_{\mathrm{m}} = \frac{1}{3}\,\mathrm{Tr}\chi_{\mathrm{m}}$ is the isotropic susceptibility, $\Delta\chi_{\mathrm{m}}$ is the anisotropy of the susceptibility tensor, and $P_2(\cos\theta) = \frac{1}{2}(3\cos^2\theta - 1)$ is the second Legendre polynomial (θ being the angle between $\boldsymbol{B}$ and $\boldsymbol{n}$). Considering the condition of minimum energy density, one can conclude the following:

1. When $\Delta\chi_{\mathrm{m}}$ is positive, ρ_{B} reaches a minimum with $P_2(\cos\theta) = 1$, i.e. the director is oriented parallel with the external magnetic field.
2. When $\Delta\chi_{\mathrm{m}}$ is negative, ρ_{B} reaches a minimum with $P_2(\cos\theta) = -\frac{1}{2}$, i.e. when the director is oriented perpendicular to the external field.

Both types of thermotropic liquid crystals exist and have been used in studies of the properties of solute molecules. Furthermore, proper mixtures of liquid crystals with opposite signs of diamagnetic anisotropies have been utilized. (See ***Liquid Crystals: Mixed Magnetic Susceptibility Solvents***.)

3 THE HAMILTONIAN OPERATOR AND OBSERVABLES

When considering the NMR spectra of spin-$\frac{1}{2}$ nuclei in molecules partially oriented in liquid crystals, the transition frequencies are dependent upon the nuclear shielding tensor, σ_i, the indirect spin–spin coupling tensor, $\boldsymbol{J}_{ij}$, and the direct dipole–dipole coupling tensor, $\boldsymbol{D}_{ij}$ (see ***Liquid Crystals: General Considerations***). Then the total Hamiltonian operator is (in energy units):

$$\hat{\mathcal{H}} = -\hbar\sum_i \gamma_i \hat{\boldsymbol{I}}_i \cdot (\boldsymbol{1} - \boldsymbol{\sigma}_i)\cdot B + h\sum_{i<j} \hat{\boldsymbol{I}}_i \cdot (\boldsymbol{J}_{ij} + \boldsymbol{D}_{ij})\cdot \hat{\boldsymbol{I}}_j \tag{3}$$

where $\hbar$ is Planck's constant divided by 2π, γ_{i} is the magnetogyric ratio of nucleus i, and $\boldsymbol{1}$ is the unit tensor. On the basis of perturbation theory one can conclude that the terms of the Hamiltonian operator which do not commute with the total spin component, $\hat{I}_z$,in the direction of $\boldsymbol{B}$ (defined as the z direction of the laboratory frame) can be safely neglected. Furthermore, taking the time average of the observables over the anisotropic molecular tumbling, the operator shown in equation (3) can be approximated by:

$$\begin{aligned}\hat{\mathcal{H}} = &-\hbar\sum_i \gamma_i(1-\sigma_i)B\hat{I}_{iz} \\ &+ h\sum_{i<j} J_{ij}\left[\hat{I}_{iz}\hat{I}_{jz} + \frac{1}{2}(\hat{I}_{i+}\hat{I}_{j-} + \hat{I}_{i-}\hat{I}_{j+})\right] \\ &+ h\sum_{i<j}(2D_{ij} + J_{ij}^{\mathrm{aniso}})\left[\hat{I}_{iz}\hat{I}_{jz} - \frac{1}{4}(\hat{I}_{i+}\hat{I}_{j-} + \hat{I}_{i-}\hat{I}_{j+})\right]\end{aligned} \tag{4}$$

In the operator shown in equation (4), the shielding is represented as

$$\begin{aligned}\sigma_i = \langle\sigma_{izz}\rangle &= \frac{1}{3}\sum_\alpha \sigma_{i\alpha\alpha} + \frac{2}{3}\left(\sum_{\alpha,\beta} S_{\alpha\beta}\sigma_{i\alpha\beta}\right)P_2(\cos\theta) \\ &= \sigma_i^{\mathrm{iso}} + \sigma_i^{\mathrm{aniso}}\end{aligned} \tag{5}$$

The isotropic spin–spin coupling constant, J_{ij}, and the anisotropic contribution, $J_{\mathrm{ij}}^{\mathrm{aniso}}$, are

$$J_{ij} = \frac{1}{3}\sum_\alpha J_{ij\alpha\alpha} \tag{6}$$

and

$$J_{ij}^{\mathrm{aniso}} = \left(\frac{2}{3}\sum_{\alpha,\beta} S_{\alpha\beta}J_{ij\alpha\beta}\right)P_2(\cos\theta) \tag{7}$$

In equations (5)–(7), $\sigma_{\mathrm{i}\alpha\beta}$ and $J_{\mathrm{ij}\alpha\beta}$ are the elements of the shielding and spin–spin coupling tensor, respectively, in the molecule fixed coordinate system while the $S_{\alpha\beta}$ terms in turn, are the elements of the Saupe ordering tensor[9] which are defined as

$$S_{\alpha\beta} = \frac{1}{2}\langle 3\cos\theta_{\alpha n}\cos\theta_{\beta n} - \delta_{\alpha\beta}\rangle \tag{8}$$

where $\theta_{\alpha n}$ is the angle between the director $\boldsymbol{n}$ and the α axis of the coordinate system, the $\langle\ \rangle$ brackets indicate a time average, and $\delta_{\alpha\beta}$ is the Kronecker delta. The dipole–dipole coupling constant, D_{ij}, appearing in the operator shown in equation (4) is defined (when the correlation of the molecular reorientational and vibrational motions is neglected) as

$$D_{ij} = -\frac{\mu_0\hbar\gamma_i\gamma_j}{8\pi^2 r_{ij}^3}S_{ij} \tag{9}$$

where r_{ij} is the internuclear distance, and

$$S_{ij} = \frac{1}{2}\langle 3\cos^2\theta_{ijB} - 1\rangle \tag{10}$$

is called the order parameter (with respect to the external magnetic field) of the axis passing through i and j, and θ_{ijB} is the angle between the ij direction and the magnetic field. Since the order tensor is traceless and symmetric, it consists of five independent elements which are usually chosen as S_{cc}, $(S_{\mathrm{aa}} - S_{\mathrm{bb}})$, S_{ab}, S_{ac}, and S_{bc} (a, b and c are the axes of the molecule fixed coordinate system). Utilizing the coordinate transformation equation

$$S_{ij} = \sum_{\alpha,\beta}\cos\theta_{ij\alpha}\cos\theta_{ij\beta}\ S_{\alpha\beta} \tag{11}$$

S_{ij} can be written as:

$$\begin{aligned}S_{ij} = \Big[&\frac{1}{2}S_{cc}(3\cos^2\theta_{ijc} - 1) + \frac{1}{2}(S_{aa} - S_{bb})(\cos^2\theta_{ija} - \cos^2\theta_{ijb}) \\ &+ 2S_{ab}\cos^2\theta_{ija}\cos^2\theta_{ijb} + 2S_{ac}\cos^2\theta_{ija}\cos^2\theta_{ijc} \\ &+ 2S_{bc}\cos^2\theta_{ijb}\cos^2\theta_{ijc}\Big]P_2(\cos\theta)\end{aligned} \tag{12}$$

The number of the independent elements of the order tensor can be reduced by taking into account molecular symmetry. The values of the order tensor elements are obtained from the dipole–dipole coupling constants provided that at least one internuclear distance is known.

4 SHIELDING ANISOTROPY

For a moment let us forget the complications that may occur particularly when determining small anisotropies of nuclear shieldings, and concentrate on the principles of how the shielding anisotropy is obtained from an NMR spectrum of a molecule partially oriented in a liquid crystal. Let us choose as an example a molecule possessing at least a

threefold symmetry axis, e.g. acetonitrile (CH_3CN). In such a case, the molecular orientation is completely determined by one order tensor element. Thus the experimental chemical shift, δ^{exp}, can be expressed in the form (note that δ increases to high frequency whereas σ increases to low frequency; for simplifying notations the subscript i will be omitted):

$$\begin{aligned}\delta^{exp} &= \delta^{iso} - \frac{2}{3}\left[\sigma_{zz} - \frac{1}{2}(\sigma_{xx} + \sigma_{yy})\right] SP_2(\cos\theta) \\ &\equiv \delta^{iso} - \frac{2}{3}\Delta\sigma SP_2(\cos\theta)\end{aligned} \tag{13}$$

where $\sigma_{zz} - \frac{1}{2}(\sigma_{xx} + \sigma_{yy}) \equiv \Delta\sigma$ is the anisotropy of the shielding tensor [(x, y, z) is a molecule fixed coordinate system] and S is the order parameter of the molecular symmetry axis (which in the case of acetonitrile lies along the $-C-C\equiv N$ direction). Equation (13) contains two unknown parameters δ^{iso} and $\Delta\sigma$; the order parameter S is obtained from the experimental dipole–dipole couplings [defined in equation (9)] which do not contain an anisotropic contribution, J_{ij}^{aniso}, and are corrected for harmonic vibrations and preferably also for deformational contributions. Usually couplings of the type D_{HX} with ^1H as a coupling partner (D_{HH} in CH_3CN) are a safe choice.

The shielding anisotropy can be determined by changing either S or $P_2(\cos\theta)$. There exist several possibilities for both. They are described below.

4.1 Use of Isotropic–Nematic Phase Transitions

In this method, $\delta^{iso} = \delta^{exp}$(isotropic) is determined in the liquid crystal heated to the isotropic state (when $S \equiv 0$) and assumed not to be affected by the change of phase. Then the sample is cooled to the nematic state and δ^{exp}(nem.) is measured. Consequently,

$$\Delta\sigma = -\frac{3}{2}\left[\frac{\delta^{exp}(\text{nem.}) - \delta^{exp}(\text{isotropic})}{SP_2(\cos\theta)}\right] \tag{14}$$

4.2 Gradient Method

One disadvantage of the previous method is that the experiments have to be carried out at two different phases, isotropic and nematic. This can be avoided by working exclusively in a nematic or smectic phase and changing the molecular degree of order, i.e. the order parameter S. This is achieved by changing the temperature or concentration of the sample. When δ^{exp} is expressed graphically as a function of $SP_2(\cos\theta)$, the slope of the resulting straight line gives $\Delta\sigma$ and the intercept δ^{iso}.

4.3 Use of Smectic Phases

The smectic A phases of thermotropic liquid crystals often possess the property that once oriented in a magnetic field they keep the orientation for a long time. This makes it possible to change in a very straightforward way the angle between the director $\boldsymbol{n}$ and the magnetic field $\boldsymbol{B}$, i.e. the factor $P_2(\cos\theta)$ in equation (13), while S remains unchanged.[10] The shielding anisotropy is then obtained without changing solvent properties.

When the liquid crystal is heated to the isotropic state and then cooled in the magnetic field to the smectic state, the director orients (when $\Delta\chi_m > 0$) along the magnetic field and $\theta = 0$. Thus

$$\delta^{exp}(0) = \delta^{iso} - \frac{2}{3}\Delta\sigma S \tag{15}$$

The rotation of the sample (in a conventional electromagnet) around the tube axis by 90° [generally, the rotation angle is obtained from the ratio of the dipolar couplings: $D_{ij}(\theta)/D_{ij}(0) = P_2(\cos\theta)$] gives:

$$\delta^{exp}(90) = \delta^{iso} + \frac{1}{3}\Delta\sigma\ S \tag{16}$$

and consequently,

$$\Delta\sigma = \frac{\delta^{exp}(90) - \delta^{exp}(0)}{S} \tag{17}$$

In the smectic phases the degree of solute molecular orientation is usually high, when both S and the chemical shift difference [nominator in equation (17)] are large, leading to a good relative precision in $\Delta\sigma$. Figure 2, which shows the ^{199}Hg NMR spectrum of dimethylmercury $(CH_3)_2Hg$ at the orientation described above, illustrates the method.

4.4 Use of Mixtures of Thermotropic Nematic Liquid Crystals

4.4.1 Liquid Crystals with Opposite Diamagnetic Anisotropy

This method, called NEMIX, is comparable with the one described in Section 4.3. When two thermotropic nematic liquid crystals possessing opposite anisotropies of diamagnetic susceptibility, $\Delta\chi_m$, are mixed at a certain critical concentration ratio ($\Delta\chi_m$ of the critical mixture is equal to 0), the 90°

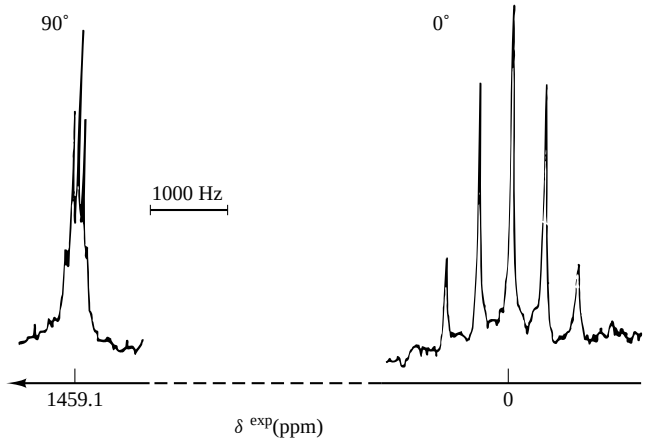

Figure 2 ^{199}Hg NMR spectrum of dimethylmercury [$(CH_3)_2Hg$] in the smectic A phase of HAB: 0°, director parallel with the external magnetic field, 90°, director perpendicular to the external magnetic field. (Reproduced with permission of Heyden & Sons from J. Jokisaari and P. Diehl[26])

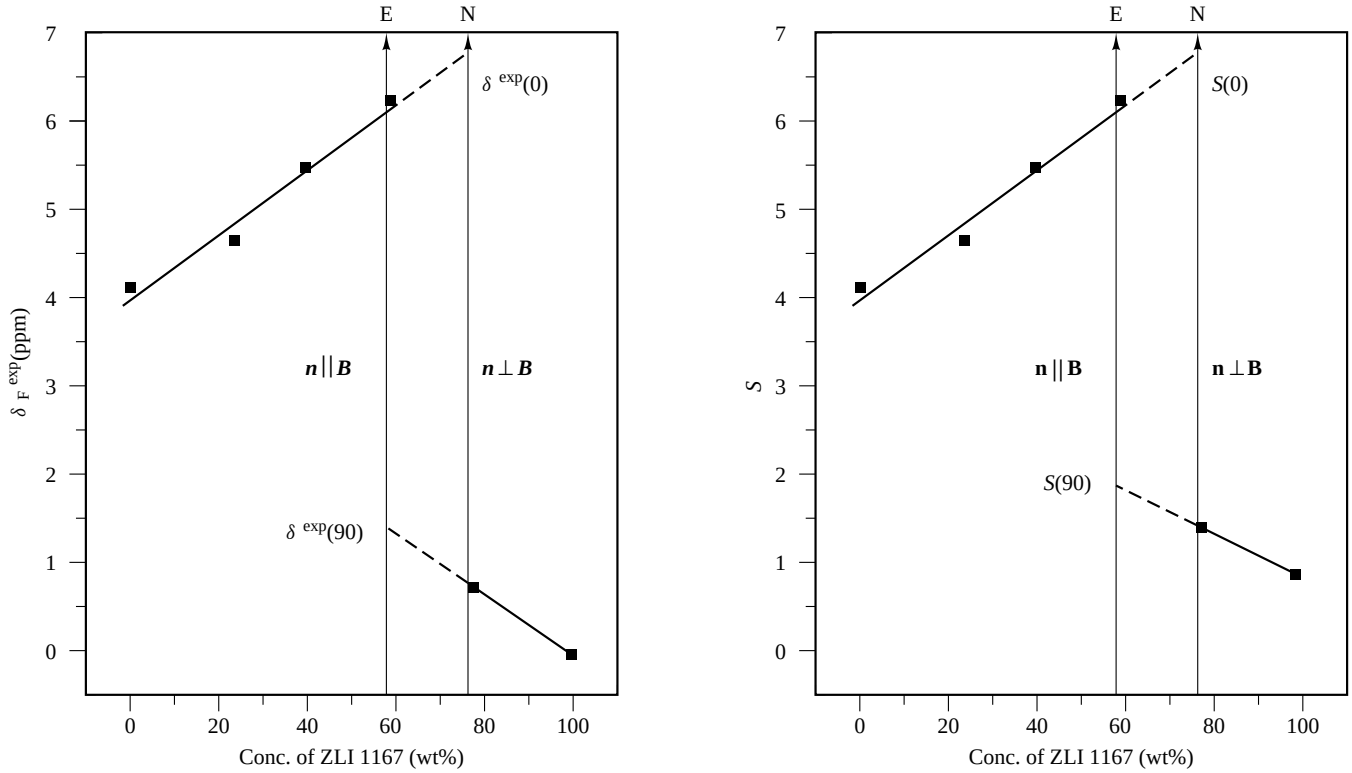

Figure 3 The experimental chemical shift, $\delta_F{}^{exp}$, of the ^{19}F nucleus and the order parameter of the C_3 symmetry axis, S, for methyl fluoride (CH_3F) as a function of the liquid crystal composition in mixtures of ZLI 1167 and EBBA. The mixtures used in the NEMIX and ENEMIX methods are indicated by N and E, respectively

rotation of the liquid crystal director is achieved by changing the sign of $\Delta\chi_m$ with the aid of a slight temperature change or a small temperature gradient over the sample volume (see ***Liquid Crystals: Mixed Magnetic Susceptibility Solvents***). In the latter case, the NMR spectra corresponding to the two director orientations can be detected simultaneously.[11,12] The shielding anisotropy can be calculated from equation (17). Figure 3 shows how the method works.

4.4.2 Liquid Crystals with Opposite Deformational Effects on Molecular Structure

The anisotropic forces that cause the orientation of solute molecules at the same time deform their structure leading to the solvent dependence of structure. It has appeared that ^{13}C-enriched methane ($^{13}CH_4$) is a convenient and practical reference, not only for chemical shifts but also for structural deformations. It has been found that in certain mixtures of thermotropic liquid crystals the methane molecule is not deformed.[13] The components of the mixture may be selected so that they possess opposite diamagnetic anisotropies and, consequently, parallel and perpendicular orientations of the director with respect to the external magnetic field can be produced in a similar way to that discussed above. Figure 3 also demonstrates this method, which is called ENEMIX. In contrast to the NEMIX method and the method based on the utilization of smectic liquid crystals, the ratio of the S parameters corresponding to the two director orientations may not exactly equal -2, whence

$$\Delta\sigma = -\frac{3}{2}\left[\frac{\delta^{exp}(0) - \delta^{exp}(90)}{S(0) - S(90)}\right] \tag{18}$$

4.5 Use of Sample Spinning

4.5.1 Sample Tube Axis Perpendicular to the Magnetic Field

As discussed above, the liquid crystals director orients either along the external magnetic field or perpendicular to it depending upon the sign of the diamagnetic anisotropy. In a conventional electromagnet, the director orients perpendicular to the tube axis (when $\Delta\chi_m > 0$; if $\Delta\chi_m < 0$ the director orients along the tube axis and no change in the orientation can be achieved by spinning the sample tube). When the sample is spinning around the tube axis the liquid crystal experiences a viscous torque

$$N_v = \lambda_1\Omega \tag{19}$$

where Ω is the angular speed and λ_1 a coefficient proportional to the viscosity of the solution. The magnetic torque opposes the viscous torque, and in equilibrium $N_B = N_v$. Thus the angle θ_0 between the magnetic field and the director is determined by

$$\sin 2\theta_0 = -\frac{2\mu_0\lambda_1}{B^2\Delta\chi_m}\Omega \tag{20}$$

The value of $SP_2(\cos\theta_0)$ can be determined from the dipolar coupling constants and the shielding anisotropy calculated as in the previous method. On the other hand, θ_0 can be varied by varying the angular speed Ω. There is, however, an upper limit for Ω, the so-called critical speed, $\Omega_c = -B_2\Delta\chi_m/2\,\mu_0\lambda_1$, above which no equilibrium state can be reached but the director rotates with the tube. When the experimental chemical shift is plotted as a function of $SP_2(\cos\theta_0)$, the shielding

anisotropy is obtained from the slope of the resulting straight line.

4.5.2 *Variable Angle Spinning*

Let us consider a general case where the spinning axis of a sample tube forms an angle β with the magnetic field. Transforming the susceptibility tensor into the principal axis system rotating around the magnetic field direction and taking a time average,[14] the magnetic energy density can be represented in the form

$$\langle \rho_B \rangle = -\frac{B^2}{2\mu_0}\left[\chi_m + \frac{2}{3}\Delta\chi_m P_2(\cos\beta)P_2(\cos\delta)\right] \quad (21)$$

where δ is the angle between the spinning axis and the liquid crystal director. From the condition of minimum energy density, one can conclude the following: (a) when $\Delta\chi_m > 0$ and $0 \leq \beta < \beta_m$ (β_m is the magic angle, 54.7°), the liquid crystal director orients parallel with the spinning axis, i.e. the angle between the director and the magnetic field equals β; (b) when $\Delta\chi_m > 0$ and $\beta_m < \beta \leq \pi/2$, the directors are equally distributed in the plane perpendicular to the spinning axis; (c) when $\Delta\chi_m < 0$ and $0 \leq \beta < \beta_m$, the situation is similar to (b); and (d) when $\Delta\chi_m < 0$ and $\beta_m < \beta \leq \pi/2$, the situation is similar to (a).

The slope of the resulting straight line obtained by plotting the experimental chemical shift as a function of $SP_2(\cos\beta)$, or as a function of a dipolar coupling constant as shown in Figure 4, gives the shielding anisotropy.

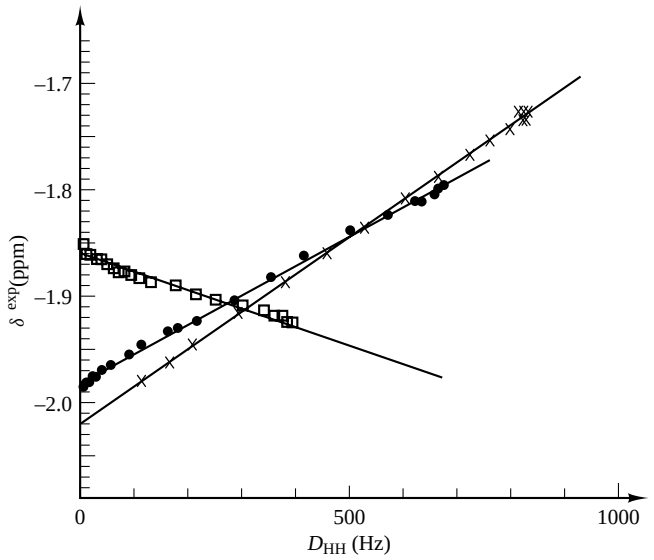

Figure 4 Plot of δ^{exp} for the ^{1}H nucleus (referenced to internal TMS) as a function of D_{HH} for methyl iodide (CH_3I) in three liquid crystals: phase 4 (□); ZLI 1167 (39.1%)/phase 4 (60.9%) (•); and ZLI 1167 (57.6%)/phase 4 (42.4%) (x). The data were produced on a VAS system by varying the angle between the spinning axis and the external magnetic field. The slope, κ, of the straight line yields the proton shielding anisotropy $\delta\sigma_H = (3/4)\,(K_{HH}/r^3_{HH})\kappa$, where $K_{HH} = \mu_0\hbar{\gamma_H}^2/8\pi^2$. (Reproduced with permission of Academic Press from T. Väänänen, J. Jokisaari, and M. Seläntaus[33]). Note: the δ scale is opposite to the one used in the present text

4.6 Examples and Reliability of Results

4.6.1 *Molecules Whose Orientation Can Be Described by One Order Parameter*

Tables (1)-(3) show $\Delta\sigma$ values determined by applying various liquid crystals and methods described above. The examples are chosen so that they cover a wide range of values, and consequently yield the weaknesses on the one hand and the reliability on the other hand of liquid crystal NMR spectroscopy as applied to the determination of shielding anisotropies. Table 1 lists the proton shielding anisotropy values measured for acetonitrile (CH_3CN). As can be seen, they vary over a relatively wide range, and both positive and negative values have been reported. The $\Delta\sigma_H$ value seems to depend upon the method used, liquid crystal solvent, and reference method and substance. This is due to the fact that the measured shielding is affected by three different anisotropic contributions:

$$\sigma^{exp} = \sigma^{mol} + \sigma^{local} + \sigma^{bulk} \quad (22)$$

where σ^{mol} (the quantity of interest) arises from the electron distribution in the molecule, σ^{local} (the local effect) from the nearest neighbor molecules, and σ^{bulk} (the bulk effect) from the other parts of the sample. The greatest problem is caused by the local effects; obviously the solute and reference molecules do not probe exactly the same local fields, leading to an erroneous $\Delta\sigma$. Local effects in a smectic liquid crystal, and in mixtures of thermotropic nematic liquid crystals with opposite diamagnetic anisotropies, have been studied by using globular solutes (which do not orient in liquid crystals, i.e. $S - 0$) and found to be from -0.2 to -0.5 ppm for protons.[15–17] These experiments and the earlier ones[18,19] mean that the anisotropic contribution of the local effects may be of the same magnitude as σ^{aniso} for protons, but also for other nuclei if their shielding anisotropy is not very large.

The first column of Table 2 shows that the shielding anisotropy of the methyl carbon, $\Delta\sigma CH_3$ in acetonitrile, being of the order of 20 ppm, also depends markedly on the applied experimental method and liquid crystal solvent. On the contrary, the shielding anisotropies measured for the $-C{\equiv}N$ carbon, $\Delta\sigma_{CN}$, in acetonitrile as well as those for the ^{199}Hg nucleus in dimethylmercury [$(CH_3)Hg$] (see Table 3) are virtually insensitive to all these factors. The small scatter arises from the internuclear distance chosen as a basis in calculating the order parameter S and from whether vibrational corrections are taken into account or not.

The experiments carried out until now and comparisons made with the values produced by other techniques or theoretical calculations provide strong support for the modified ENEMIX method giving the most reliable estimates for small $\Delta\sigma$s.[21]

4.6.2 *Molecules Whose Orientation Can Be Described by Two Order Parameters*

In cases where molecules possess two perpendicular planes of symmetry as, for example, monosubstituted benzenes and heteroatomic five-membered rings, the experimental chemical shift can be represented in the form:

$$\delta^{exp} = \delta^{iso} - \frac{2}{3}\left\{S_{zz}\left[\sigma_{zz} - \frac{1}{2}(\sigma_{xx} + \sigma_{yy})\right] + \frac{1}{2}(S_{xx} - S_{yy})(\sigma_{xx} - \sigma_{yy})\right\} P_2(\cos\theta) \quad (23)$$

Table 1 Proton Shielding Anisotropy of Acetonitrile Determined by Various Methods in Different Liquid Crystals

$\Delta\sigma_H$ (ppm)	Method	Liquid crystal	Chemical shift reference[a]
+3.9 ± 0.2	Gradient method[20]	ZLI 1167	$^{13}CH_4$
+2.3 ± 0.1	Gradient method[20]	ZLI 1167	TMS
+2.1	Modified ENEMIX[21]	ZLI 1167/Phase 4	$^{13}CH_4$
+0.30 ± 0.08 to +1.06 ± 0.8	NEMIX[20]	Various LCs mixed with ZLI 1167	TMS
−2.7 ± 0.1	Smectic phase[20]	HAB	$^{13}CH_4$
−4.5 ± 0.8	Gradient method[20]	EBBA	$^{13}CH_4$
−4.7 ± 0.1	Smectic phase[20]	HAB	TMS

[a]Internal reference.

Table 2 ^{13}C Shielding Anisotropies in Acetonitrile Determined by Various Methods in Different Liquid Crystals. For Comparison, Theoretical Values are Also Included

$\Delta\sigma CH_3$ (ppm)	$\Delta\sigma_{CN}$ (ppm)	Method	Liquid crystal	Chemical shift reference[a]
22.9	324.6	Modified ENEMIX[21]	ZLI 1167/phase 4	$^{13}CH_4$
20.5 ± 0.7	328 ± 8	Gradient[20]	ZLI 1167	$^{13}CH_4$
15.7 ± 1.5		Smectic phase[20]	HAB	$^{13}CH_4$
13.6 ± 0.6	311 ± 6	Gradient[20]	EBBA	$^{13}CH_4$
	304 ± 5	Gradient[22]	MIX	ext. $^{13}CS_2$
	307 ± 4	I–N phase transition[23]	EBBA	^{1}H reson. of CH_3CN
	299 ± 5	I–N phase transition[22]	MIX	ext. $^{13}CS_2$
21, 15	340, 348	Theory[24b]		

[a]Internal reference if not otherwise indicated.
[b]IGLO method with two different basis sets. Large basis set results on the right.

The shielding anisotropy, $\Delta\sigma = \sigma_{zz} - \frac{1}{2}(\sigma_{xx} + \sigma_{yy})$, and the difference $(\sigma_{xx} - \sigma_{yy})$ are obtained separately only if the ratio $(S_{xx} - S_{yy})/S_{zz}$ can be varied. Consequently, none of the methods described above which are based on the change of direction of the liquid crystal director with respect to the external magnetic field, i.e. the variation of the $P_2(\cos\theta)$ factor, is applicable here. The variation of the ratio $(S_{xx} - S_{yy})/S_{zz}$ may be produced by changing the sample temperature or by using different liquid crystal solvents. Then one has to assume that the shielding tensor elements are not affected by the experimental conditions.

The determination of the ^{13}C shielding anisotropies in molecules which are large in the liquid crystal NMR scale (when the number of magnetic nuclei increases, the NMR spectrum of an oriented molecule becomes very complex; in practice the upper limit for the number of active, interacting nuclei is 10–12), and contain several carbon atoms and ^{13}C in natural abundance, is usually at least very cumbersome if not impossible from the proton coupled spectra. Therefore, a method has been proposed which uses a spin echo sequence $[90^\circ - \tau - 180^\circ - 2\tau - 180^\circ - \tau - \text{acquisition}]$ and phase-alternated broadband decoupling.[30] The echo sequence cancels the possible overlap of the solute signals by the solvent signals.

Table 3 ^{199}Hg Shielding Anisotropy in Dimethylmercury Determined by Various Methods in Different Liquid Crystals. For Comparison, Results obtained from Spin–Lattice Relaxation Time Measurements are also Included

$\Delta\sigma^{199}Hg$ (ppm)	Method	Liquid crystal	Comments
7475 ± 80	Gradient[25]	EBBA	No vibr. corr.
7799 ± 55	Smectic phase[26]	HAB	No vibr. corr.
7325 ± 55	Smectic phase[26]	HAB	D_{ij}s corrected for harm. vibr.
7260 ± 90	ENEMIX[27]	ZLI 1167	D_{ij}s corrected for harm. vibr.
4600 ± 1000	T_1[28]		Saturation-recovery method
5820 ± 10%	T_1[28]		Inversion–recovery method

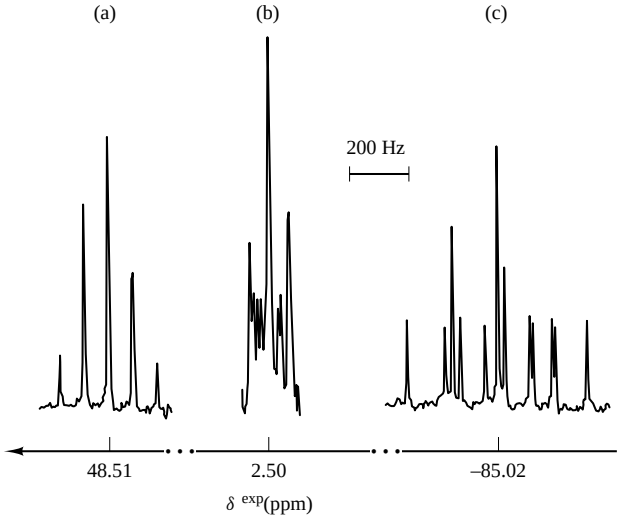

Figure 5 The ^{125}Te NMR spectrum of tellurophene (C_4H_4Te) in (a) ZLI 1167 (58%)/phase 4(42%), (b) EBBA and (c) ZLI 1167. (Reproduced with permission of Taylor & Francis from J. Jokisaari and T. Väänänen[31])

The ^{13}C NMR spectrum yields the chemical shifts whereas the order parameters appearing in equation (23) are obtained from the ^{1}H spectrum.

The NMR spectroscopy of solute molecules in liquid crystals has not been applied very much to the investigations of shielding anisotropies of the so-called heavy nuclei. Most of the studies deal with the ^{1}H, ^{13}C, ^{19}F, and ^{31}P nuclei, and highly symmetrical molecules.[6] This is somewhat surprising because the method is best when the shielding anisotropy is fairly large. There has been, however, some work carried out for ^{111}Cd, ^{113}Cd, and ^{199}Hg in molecules with C_3 symmetry, and one work for the ^{125}Te nucleus in a C_{2v} symmetric molecule, tellurophene (C_4H_4Te).[31] The ^{125}Te NMR spectra of tellurophene in three liquid crystals are shown in Figure 5.

Equation (23) can be rewritten in the form

$$-\frac{3}{2}\left[\frac{\delta^{\text{exp}}-\delta^{\text{iso}}}{S_{zz}}\right]=\left[\sigma_{zz}-\frac{1}{2}(\sigma_{xx}+\sigma_{yy})\right]+\frac{\sigma_{xx}-\sigma_{yy}}{2}\,\frac{S_{xx}-S_{yy}}{S_{zz}} \quad (24)$$

The intercept of the straight line obtained by plotting the left hand side of equation (24) as a function of $(S_{xx} - S_{yy})/S_{zz}$ yields $[\sigma_{zz} - \frac{1}{2}(\sigma_{xx} + \sigma_{yy})]$ whereas the slope gives $(\sigma_{xx} - \sigma_{yy})$. The results derived for ^{125}Te in tellurophene are collected in Table 4.

5 SPIN–SPIN COUPLING ANISOTROPY

The determination of reliable anisotropies, ΔJ_{ij}, of the spin–spin coupling tensors using NMR spectroscopy of molecules dissolved in liquid crystals may be a fairly difficult task. This is due to the fact that the experimental couplings, D_{ij}^{exp}, are dominated by the direct dipole–dipole coupling tensor elements, and moreover, in real molecules the dipole–dipole as well as spin–spin coupling tensors are averages over intramolecular motions. However, when performing proper analyses of data (sets of D_{ij}^{exp} values) preferably (often necessarily) produced in many liquid crystal solvents, most reliable and accurate ΔJ_{ij} values can be determined.

5.1 Quantitative Determination of *J* Anisotropy

The experimentally available couplings D_{ij}^{exp} can be expressed as a sum of several contributions (***Structure of Rigid Molecules Dissolved in Liquid Crystalline Solvents***):

$$D_{ij}^{\text{exp}}=D_{ij}^{\text{e}}+D_{ij}^{\text{ah}}+D_{ij}^{\text{h}}+D_{ij}^{\text{d}}+\frac{1}{2}J_{ij}^{\text{aniso}} \quad (25)$$

In equation (25), the first four terms on the right-hand side constitute the direct dipolar part of the coupling: D_{ij}^{c} is the dipole–dipole coupling corresponding to the equilibrium structure of the molecule; D_{ij}^{aff} is the contribution from the anharmonicity of the vibrational potential (the sum of these terms $D_{ij}^{\text{e}} + D_{ij}^{\text{ah}} = D_{ij}^{\alpha}$ is the dipole–dipole coupling corresponding to the so-called r_α structure of the molecule; the anharmonic force constants are often not available and thus only the r_α structure can be determined); D_{ij}^{h} is the contribution from the harmonic vibrations; and D_{ij}^{d} (the so-called deformational contribution which is responsible for the solvent dependence of structure) from the correlation between

Table 4 The Results of the ^{125}Te NMR Study of Tellurophene Dissolved in three Liquid Crystals.[31] The Signs of δ^{exp} and δ^{iso} are Opposite to those in the Original Paper due to the Different Definition of the δ scale

Liquid crystal	δ^{exp} (ppm)	δ^{iso} (ppm)[a]	$S_{xx} - S_{yy}/S_{zz}$	S_{zz}[b]
EBBA	2.41	1.55	0.5033	0.1563
ZLI 1167/phase 4	48.51	−2.18	1.7478	0.1954
ZLI 1167	−85.02	15.65	1.9992	−0.0592

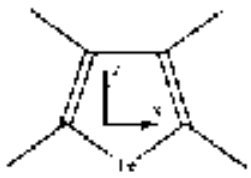

$\Delta\sigma = \sigma_{zz} - \frac{1}{2}(\sigma_{xx} + \sigma_{yy}) = 1560 \pm 21$ ppm

$\sigma_{xx} - \sigma_{yy} = 307 \pm 36$ ppm

[a] Assumed to be a simple hexagonal benzenic state.
[b] Determined from the ^{13}C–^{125}Te dipolar coupling constants assuming the corresponding J^{aniso} to be negligible.
[c] With respect to the external magnetic field.

vibrational and reorientational motions (time averages of S_{ij} and r_{ij}^{-3} appearing in the definition of the dipole–dipole coupling, equation (9), cannot be taken independently).

In order to get a reliable value for J_{ij}^{aniso} (which is normally small and in many cases comparable in magnitude with the vibrational and deformational correction terms), the molecular structure should be determined as completely as possible with the aid of the D_{ij}^{exp} values. This necessarily means a full analysis of data taking into account the interactions (the anisotropic forces that tend to orient molecules) between the solute and solvent molecules. In such an analysis the number of unknown parameters often exceeds the number of D_{ij}^{exp} values obtainable from one experiment, i.e. the problem becomes underdetermined. This increasing number of parameters is a consequence of the deformational effects. For example, in order to be able to calculate deformational corrections to J^{aniso}, one should know the derivatives of the spin–spin coupling tensor with respect to the vibrational normal coordinates. These are not available, and consequently must be used as adjustable parameters.[32] The problem of underdetermination can, however, be overcome by carrying out experiments in several liquid crystalline solvents.

Another uncertainty in the determination of J_{ij}^{aniso} may appear in cases of spin systems consisting of different nuclear species, for instance I and S spins. Thus, the NMR spectrum yields only the sum $|2D_{is}^{exp} + J_{is}|$. If the spin–spin coupling constant, J_{IS}, cannot be determined under the same experimental conditions (the same solvent, temperature, concentration, etc.) as the sum, an additional uncertainty is introduced into D_{IS}^{exp}, and consequently, also into J_{IS}^{aniso}. In principle, J_{IS} can be determined in liquid crystalline phases by performing, for instance, VAS (Variable Angle Spinning) experiments.[33]

Let us consider the determination of the anisotropy of the $^{13}C-^{19}F$ spin–spin coupling in the methyl fluoride (CH_3F) molecule. Due to the C_3 symmetry of the molecule, its orientation can be described by one order parameter, S, of the symmetry axis. Then the anisotropic contribution to the experimental coupling $D_{CF}{}^{exp}$ can be expressed in the form:

$$J_{CF}^{aniso} = \frac{2}{3}\Delta J_{CF} S P_2(\cos\theta) \tag{26}$$

where $\Delta J_{CF} = J_{CFzz} - \frac{1}{2}(J_{CFxx} + J_{CFyy})$ is the anisotropy of the coupling tensor $\boldsymbol{J}_{CF}$. When the experimental dipolar couplings are corrected for harmonic vibrations but the deformational corrections are neglected, ΔJ_{CF} appears to be solvent dependent to a very great extent, as shown in Table 5. This large scatter of results is removed when all the dipolar couplings and J_{CF}^{aniso} are corrected for deformational effects and a joint analysis of nine experiments (44 couplings, D_{CF}^{exp} in one liquid crystal could not be obtained, and 23 parameters) is carried out. This analysis results in $\Delta J_{CF} = 404 \pm 31$ Hz. The relative anisotropy, $\Delta J_{CF}/J_{CF}$, is -2.50 ± 0.20 (J_{CF} appears to be slightly dependent upon the liquid crystal solvent, its average value is -161.43 Hz) and should be compared with -2.70 obtained by Hartree–Fock theory (ab initio) and by a semiempirical finite perturbation method at the INDO MO level of approximation.[34] The first-order polarization propagator approach has led to the ΔJ_{CF} value of 296.41 Hz.[35] Consequently, the experimental results of a joint analysis and the theoretical results are in fair agreement.

Reinforcement for the workability of the method is provided by the studies on acetonitrile (CH_3CN) and methyl isocyanide (CH_3NC). Table 6 clearly shows that when the harmonic vibrational and deformational effects are taken into account in the experimental dipolar couplings, the ΔJ values are in nice accord with the theoretical ones.

Table 5 The Anisotropy ΔJ_{CF} of the $^{13}C-^{19}F$ Spin–Spin Coupling Tensor for Methyl Fluoride ($^{13}CH_3F$) in Various Liquid Crystals. The Dipolar Couplings are Corrected for Harmonic Vibrations but not for Deformational Effects. The Result of the Joint Analysis (which takes into account also the Deformational Effects) of Nine Sets of D_{ij}^{exp} Values (44 Couplings and 23 Parameters) is also given for Comparison[32]

ΔJ_{CF} (Hz)	Liquid crystal solvent[a]
690 ± 60	ZLI 1167
646 ± 46	ZLI 1167 (78.4)/EBBA (21.6)
390 ± 82	ZLI 1167 (58.7)/EBBA (41.3)
49 ± 49	ZLI 1167 (40.1)/EBBA (59.9)
-653 ± 103	ZLI 1167 (23.6)/EBBA (76.4)
-4955 ± 260	EBBA
-1365 ± 72	Phase 4
546 ± 14	Phase 1221
404 ± 31[b]	
296[c]	

[a]The figures in parentheses show the concentration (in wt.%) of the component in the mixture.
[b]Results of the joint analysis. For details, see text.
[c]Theoretical value obtained by first-order polarization propagator approach.[35]

5.2 Qualitative Revelation of J Anisotropy

Molecular symmetry can place very restrictive conditions for the ratios of dipolar coupling constants. Consequently, this can be used to reveal whether D^{exp} includes a contribution from J^{aniso} or not. If the examination of the ratios $D_{ij}{}^{exp}/D_{kl}{}^{exp}$ shows that they differ from the corresponding ratios of direct dipolar couplings ($D^{dir} = D^{exp} - \frac{1}{2}J^{aniso} = D^{e} + D^{ah} + D^{h} + D^{d}$, see equation (26)), they (or at least some of them) may be affected by J^{aniso}.

Benzene is a good example of a molecule in which symmetry completely fixes the ratios of the dipolar couplings. The order parameter of each ij direction equals $-\frac{1}{2}S$ (S is the order parameter of the sixfold symmetry axis) and consequently the following equation is valid:

$$\frac{D_{ij}^{dir}}{D_{kl}^{dir}} = \frac{\gamma_i\gamma_j}{\gamma_k\gamma_l}\left(\frac{r_{kl}}{r_{ij}}\right)^3 \tag{27}$$

It follows from the hexagonal symmetry of benzene that $r_m = \sqrt{3}r_o$ and $r_p = 2r_o$ (o = *ortho*, m = *meta*, p = *para*). Thus for the nuclei of same isotopic species, $D_o/D_m/D_p = 1 : \sqrt{3}/9 : 1/8 \sim 1 : 0.1925 : 0.1250$. It has been found that the $^1H-^1H$ couplings in benzene indeed fulfil these ratios (in particular, when the experimental couplings are corrected for harmonic vibrational and deformational effects) and thus the $J_{HH}{}^{aniso}$ values are obviously negligible.[4] In contrast, remarkable deviations have been detected for the $^{13}C-^{13}C$ couplings (corrected for harmonic vibrations).[39]

Equation (27) is not only valid for benzene but more generally. Thus, if S_{ij} for the nuclei i and j is the same as S_{kl} for the nuclei k and l, in other words the axes passing through

Table 6 Anisotropies of the $^{13}C-^{13}C$ and $^{13}C-^{15}N$ Spin–Spin Coupling Tensors in Acetonitrile (CH_3CN) and Methyl Isocyanide (CH_3NC)

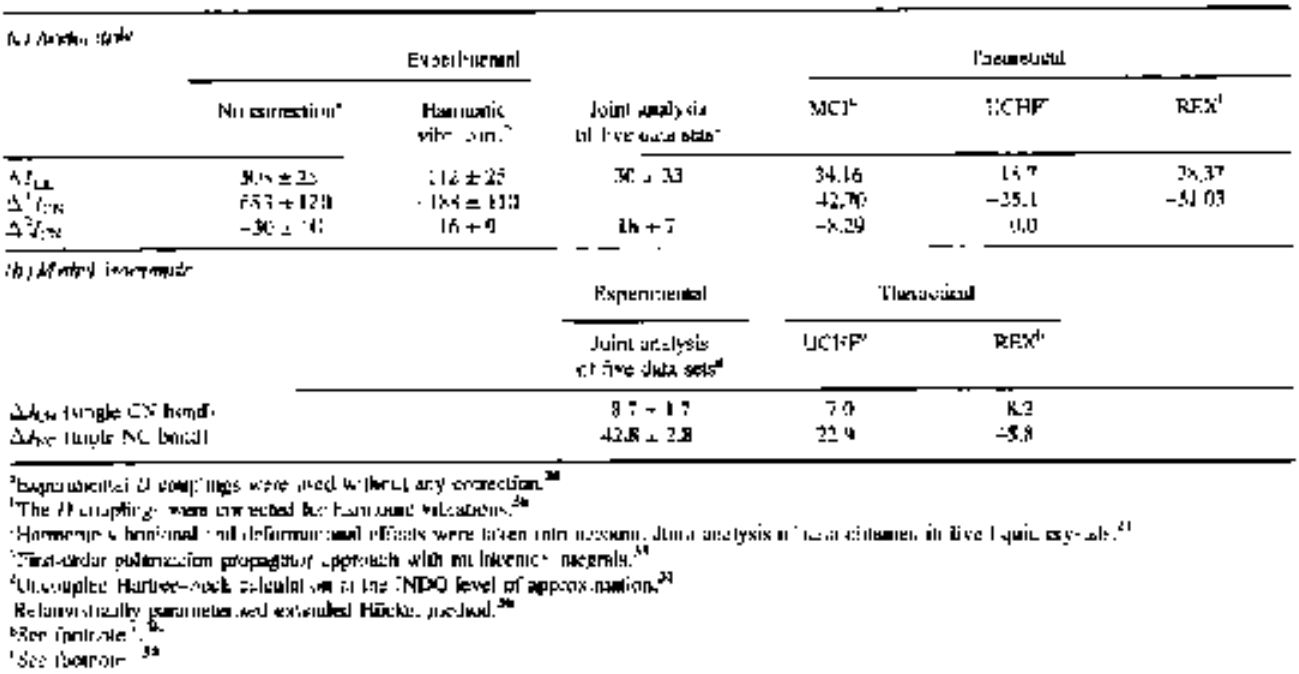

Table 7 Code Names and Compositions of the Liquid Crystals Mentioned in the Text

Code name[a]	Composition
ZLI 1167 ($\Delta\chi_m < 0$)	Mixture of 4-propyl-*trans*,*trans*-bicyclohexyl-4′-carbonitrile (36%), 4-pentyl-*trans*,*trans*-bicyclohexyl-4′-carbonitrile (34%), and 4-heptyl-*trans*,*trans*-bicyclohexyl-4′-carbonitrile (30%)
Phase 4 ($\Delta\chi_m > 0$)	Eutectic mixture of *p*-methoxy-*p*′-butylazoxybenzenes
HAB ($\Delta\chi_m > 0$)	*p*,*p*′-diheptylazoxybenzene
EBBA ($\Delta\chi_m > 0$)	(*p*-Ethoxybenzylidene)-*p*-butylaniline
ZLI 1132 ($\Delta\chi_m > 0$)	Mixture of *trans*-4-propyl-(4-cyanophenyl)cyclohexane (24%), *trans*-4-pentyl-(4-cyanophenyl)cyclohexane (36%), *trans*-4-heptyl-(4-cyanophenyl)cyclohexane (25%), and *trans*-4-pentyl-(4′-cyanobiphenyl-4)cyclohexane (15%)
Phase 1221 ($\Delta\chi_m > 0$)	Mixture of phenylcyclohexanes, biphenylcyclohexane, and phenylcyclohexane esters
MIX ($\Delta\chi_m > 0$)	Mixture of butyl-*p*-(*p*-ethoxyphenoxycarbonyl)phenyl carbonate (75%) and *p*-capronyloxy-*p*′-ethoxyazoxybenzene (25%)

[a]The sign of the anisotropy of diamagnetic susceptibility is shown below; when $\Delta\chi_m > 0$ the liquid crystal director orients along, and when $\Delta\chi_m < 0$ the director orients perpendicular to the external magnetic field.

the nuclear pairs *ij* and *kl* are parallel, the ratio $D_{ij}^{dir} : D_{kl}^{dir}$ is independent of the orientation. If the corresponding ratio of the experimental couplings is found to vary, it suggests anisotropic contribution at least in one of the couplings.[40,41] The code names and compositions of the liquid crystals mentioned above are defined in Table 7.

6 RELATED ARTICLES

Average Hamiltonian Theory; Chemical Shift Tensor Measurement in Solids; Chemical Shift Tensors; Dipolar and Indirect Coupling Tensors in Solids; Indirect Coupling: Semiempirical Calculations; Liquid Crystalline Samples: Spectral Analysis; Liquid Crystals: General Considerations; Liquid Crystals: Mixed Magnetic Susceptibility Solvents; Shielding Calculations: IGLO Method; Shielding Calculations: Perturbation Methods; Spinning Liquid Crystalline Samples; Structure of Rigid Molecules Dissolved in Liquid Crystalline Solvents.

7 REFERENCES

1. A. Saupe and G. Englert, *Phys. Rev. Lett.*, 1963, **11**, 462.
2. S. Sýkora, J. Vogt, H. Bösiger, and P. Diehl, *J. Magn. Reson.*, 1979, **36**, 53.
3. J. Lounila and P. Diehl, *J. Magn. Reson.*, 1984, **56**, 254.

4. J. Lounila and P. Diehl, *Mol. Phys.*, 1984, **52**, 827.
5. J. Lounila, *Mol. Phys.*, 1986, **58**, 897.
6. J. Lounila and J. Jokisaari, *Prog. NMR Spectrosc.*, 1982, **15**, 249.
7. A. J. Leadbetter, in *Thermotropic Liquid Crystals*, ed. G. W. Gray, John Wiley & Sons, Guildford, 1987, Chap. 1
8. C. L. Khetrapal, A. C. Kunwar, A. S. Tracey, and P. Diehl, in *NMR Basic Principles and Progress*, eds. P. Diehl, E. Fluck, and R. Kosfeld, Springer-Verlag, Heidelberg, 1975, Vol. 9.
9. A. Saupe, *Z. Naturforsch.*, 1964, **19a**, 161.
10. A. J. Montana and B. P. Dailey, *Mol. Phys.*, 1975, **30**, 1521.
11. C. L. Khetrapal and A. C. Kunwar, *Mol. Cryst. Liq. Cryst.*, 1981, **72**, 13.
12. C. L. Khetrapal and A. C. Kunwar, *Chem. Phys. Lett.*, 1981, **82**, 170.
13. J. Jokisaari and Y. Hiltunen, *Mol. Phys.*, 1983, **50**, 1013.
14. R. Teeäär, M. Alla, and E. Lippmaa, *Org. Magn. Reson.*, 1982, **19**, 134.
15. P. Diehl, J. Jokisaari, F. Moia, and J. Lounila, *Mol. Cryst. Liq. Cryst.*, 1982, **87**, 319.
16. Y. Hiltunen and J. Jokisaari, *J. Magn. Reson.*, 1987, **75**, 213.
17. E. E. Burnell and C. A. de Lange, *Chem. Phys. Lett.*, 1987, **136**, 87.
18. R. A. Bernheim and T. R. Krugh, *J. Am. Chem. Soc.*, 1967, **89**, 6784.
19. A. D. Buckingham, E. E. Burnell, and C. A. de Lange, *J. Am. Chem. Soc.*, 1968, **90**, 2972.
20. P. Diehl, J. Jokisaari, and F. Moia, *J. Magn. Reson.*, 1982, **49**, 498.
21. J. Lounila, M. Ala-Korpela, and J. Jokisaari, *J. Chem. Phys.*, 1990, **93**, 8514.
22. P. K. Bhattacharyya and B. P. Dailey, *Chem. Phys. Lett.*, 1975, **32**, 305.
23. J. D. Kennedy and W. McFarlane, *Mol. Phys.*, 1975, **29**, 593.
24. M. Schindler, *J. Am. Chem. Soc.*, 1987, **109**, 5950.
25. J. D. Kennedy and W. McFarlane, *J. Chem. Soc., Faraday Trans. 2*, 1976, **72**, 1653.
26. J. Jokisaari and P. Diehl, *Org. Magn. Reson.*, 1980, **13**, 359.
27. A. Pulkkinen, Y. Hiltunen, and J. Jokisaari, *Liq. Cryst.*, 1988, **3**, 737.
28. C. R. Lassigne and E. J. Wells, *Can. J. Chem.*, 1977, **55**, 1303.
29. R. E. Wasylishen, R. E. Lenkinski, and C. Rodger, *Can. J. Chem.*, 1982, **60**, 2113.
30. B. M. Fung, *J. Am. Chem. Soc.*, 1983, **105**, 5713.
31. J. Jokisaari and T. Väänänen, *Mol. Phys.*, 1986, **58**, 959.
32. J. Jokisaari, Y. Hiltunen, and J. Lounila, *J. Chem. Phys.*, 1986, **85**, 3198.
33. T. Väänänen, J. Jokisaari, and M. Seläntaus, *J. Magn. Reson.*, 1987, **72**, 414.
34. H. Nakatsuji, K. Hirao, H. Kato, and T. Yonezawa, *Chem. Phys. Lett.*, 1970, **6**, 541.
35. J. C. Facelli and M. Barfield, *J. Magn. Reson.*, 1984, **59**, 452.
36. P. Diehl, J. Jokisaari, J. Amrein, T. Väänänen, and P. Pyykkö, *J. Magn. Reson.*, 1982, **48**, 495.
37. H. Nakatsuji, I. Morishima, H. Kato, and T. Yonezawa, *Bull. Chem. Soc. Jpn.*, 1971, **44**, 2010.
38. Y. Hiltunen, J. Jokisaari, J. Lounila, and A. Pulkkinen, *J. Am. Chem. Soc.*, 1989, **111**, 3217.
39. P. Diehl, H. Bösiger, and J. Jokisaari, *Org. Magn. Reson.*, 1979, **12**, 282.
40. J. Gerritsen and C. MacLean, *J. Magn. Reson.*, 1971, **5**, 44.
41. J. Gerritsen and C. MacLean, *Mol. Cryst. Liq. Cryst.*, 1971, **12**, 97.

Biographical Sketches

Jukka P. Jokisaari. *b* 1944. M.S., 1968, Ph.D., 1974, University of Oulu, Finland; Postdoctoral work at University of Basel, Switzerland (with Peter Diehl). Professor of Physics (Atomic and Molecular Spectroscopy), University of Oulu, Finland. Approx. 100 publications. Current research specialty: NMR of small molecules and noble gases in liquid crystals.

Coupling Through Space in Organic Chemistry

Frank B. Mallory
Bryn Mawr College, PA, USA
&
Clelia W. Mallory
University of Pennsylvania, Philadelphia, PA, USA

1	Introduction	1
2	FF Systems	2
3	NF and PF Systems	6
4	HF, CF, and CP Systems	7
5	HH Systems	8
6	F–F Coupling Through Nonbonded Interactions with an Intervening Orbital	9
7	Related Articles	9
8	References	9

1 INTRODUCTION

The concept that nuclear spin–spin coupling might occur by through-space as well as through-bond interactions was introduced many years ago to account for the observations that certain atoms which are crowded against one another intramolecularly exhibit unusually large coupling constants as measured by NMR spectroscopy.[1,2] The early work on through-space coupling was reviewed in 1975,[3] and a review of various theoretical treatments of the phenomenon appeared in 1985.[4]

This article is concerned only with spin–spin coupling between pairs of magnetic nuclei in molecules that are freely tumbling in fluid solution such that direct 'through-space' dipole–dipole interactions between the two nuclei are averaged to zero. The observed coupling arises instead from intramolecular Fermi contact and Hund interactions involving the nuclear spins and the spins of electrons in the molecule. Fermi contact interaction between a magnetic nucleus and an electron requires these two particles to be essentially coincident in space, which is possible only if the electron is in an orbital with s character at that nucleus. The system is lower in energy if the electron and the nucleus with which it is in intimate contact have antiparallel spins. Hund interactions are operative between two electrons that are contained in two different orbitals that have some spatial overlap of their electron densities. When an electron from one of the orbitals inhabits the same region of space as an electron from the other orbital the system has a lower energy if the two electrons have parallel spins.

The phenomenon of through-space coupling has been reported for spatially proximate pairs of nuclei of various types, including $^{19}F-^{19}F$, $^{1}H-^{19}F$, $^{13}C-^{19}F$, $^{1}H-^{1}H$, $^{15}N-^{19}F$, $^{31}P-^{19}F$, and $^{13}C-^{31}P$ systems. Some examples are shown in Figure 1.

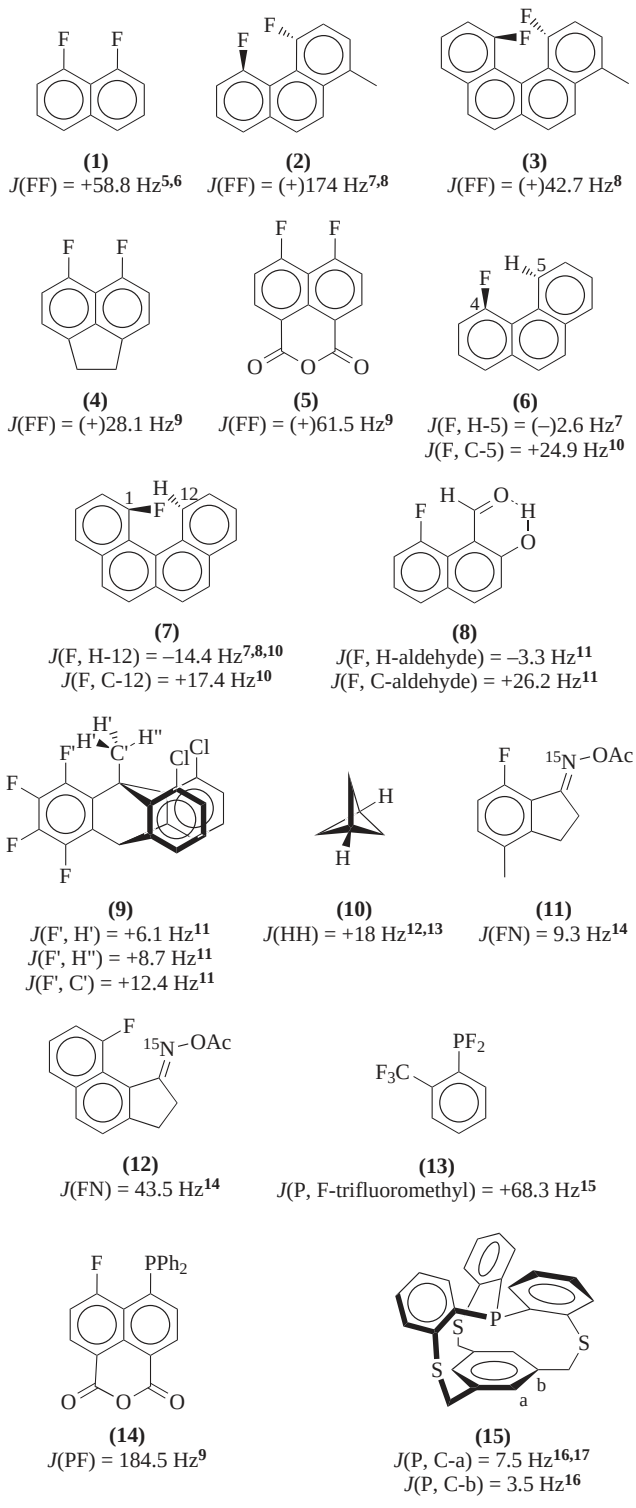

Figure 1 Examples of through-space coupling

Initially the proposals for the existence of a special through-space mode of coupling were greeted with some skepticism. For example, there seemed no convincing way to rule out the alternative possibility that the large coupling

constants observed for various molecules related to 1,8-difluoronaphthalene (**1**) result instead from peculiarly effective through-bond interactions in the U-shaped array of the four relevant bonds in the FCCCF fragment. The early history of the study of the through-space coupling phenomenon was marked by attempts to dispel this skepticism. One compeling piece of evidence in this context was the report that several disubstituted 4,5-difluorophenanthrenes, in which the shortest through-bond pathway is one bond longer than that in the 1,8-difluoronaphthalene system but the intramolecular crowding between the two fluorine atoms is greater, exhibited astonishingly large coupling constants in the range 167–170 Hz;[18] a value of 174 Hz was reported subsequently for the monosubstituted derivative (**2**).[7,8] Another convincing piece of evidence was provided by a study of the analog of the enzyme dihydrofolate reductase in which the four tryptophan residues in the native enzyme had been replaced biosynthetically by 6-fluorotryptophan residues.[19] It happens that the tertiary structure of this enzyme places two of these four tryptophan (or fluorotryptophan) residues, namely residues 133 and 158, in van der Waals contact with one another. The ^{19}F NMR spectrum of a fluorine-substituted enzyme shows four fluorine signals, two singlets and two doublets with a coupling constant of 17 Hz.[19] There is no reasonable way to attribute this F–F coupling to through-bond interactions, because the shortest through-bond pathway connecting the two spatially proximate fluorines is 89 bonds long!

Both through-space and through-bond interactions contribute to the observed coupling in molecules such as those shown in Figure 1. That is, the experimentally measured coupling constant J can be expressed as a sum of through-space and through-bond components, J^{TS} and J^{TB}, respectively:

$$J = J^{TS} + J^{TB} \quad (1)$$

Perhaps the central unsolved problem in the quest for a precise understanding of the dependence of through-space coupling on molecular structure is the lack of a reliable means of dissecting the observed coupling into its through-space and through-bond components. In a few atypical cases, such as the F–F coupling in the enzyme system discussed above, this dissection is easily made because it is clear that the through-bond component is zero. Although the experimentally determined values of J(FF) for molecules such as **(1)–(3)** are sufficiently large that it seems safe to conclude qualitatively that the through-space mode of coupling plays a dominant role, the actual magnitudes of the through-space components cannot be assessed quantitatively in any of these systems because there is no reliable way to determine experimentally the magnitudes of the accompanying through-bond contributions. At this time it appears that theoretical calculations offer the best, or perhaps the only, hope for evaluating the relative importance of the through-space and through-bond modes of coupling in particular molecules. Some computational methods currently under development appear promising in this context.[4,20,21]

In the early days of the study of through-space F–F coupling a conceptual view of the mechanism of this type of coupling was put forward by one of us based on the mixing of lone-pair orbitals through overlap interactions.[22] In the next section we present a modified version of this conceptual approach for various F–F systems, and then in subsequent sections we describe how this approach can be extended to account for through-space coupling between other kinds of magnetic nuclei, as exemplified in Figure 1. It should be acknowledged at the outset that various mathematically sophisticated and computationally oriented quantum mechanical theories of through-space F–F coupling have been presented in the past by other workers.[4] However, although quantum mechanical approaches are intrinsically superior to our conceptual approach, they have not yet proved wholly successful in giving theoretical values of F–F coupling constants that are in consistently good agreement with the experimentally observed values. Therefore we continue to think it useful to offer our orbital overlap description as a basis on which to consider the phenomenon of through-space coupling.

2 FF SYSTEMS

Through-space F–F coupling can be attributed to the overlap of a pair of nominally lone-pair orbitals, one from each of the two coupled fluorine atoms.[22] The situation for the particular intramolecular orientation found in the 1,8-difluoronaphthalene system (**1**), in which the C–F bonds are coplanar and approximately parallel to one another, is illustrated by the rough diagrams given in Figure 2. The relevant basis orbitals are the two in-plane one-center atomic lone-pair orbitals $p_{F\sigma}$ and $p'_{F\sigma}$ that would be characteristic of the fluorines if they were too far apart for these two orbitals to experience overlap interactions with each other. (For simplicity we neglect here the strong mixing of these $p_{F\sigma}$ and $p'_{F\sigma}$ orbitals with σ orbitals that are part of the carbon framework of the naphthalene system.) The F–F distance in (**1**), as measured by X-ray crystallography, is 0.2584 nm.[23] This is less than twice the 0.14 nm van der Waals radius of fluorine, so in fact the $p_{F\sigma}$ and $p'_{F\sigma}$ orbitals do overlap to a small extent. As shown schematically in Figure 2, this small F–F overlap transforms the pair of one-center atomic $p_{F\sigma}$ and $p'_{F\sigma}$ orbitals into a pair of two-center molecular orbitals, a weakly bonding orbital σ_{FF} and a weakly antibonding orbital σ^*_{FF}. Although

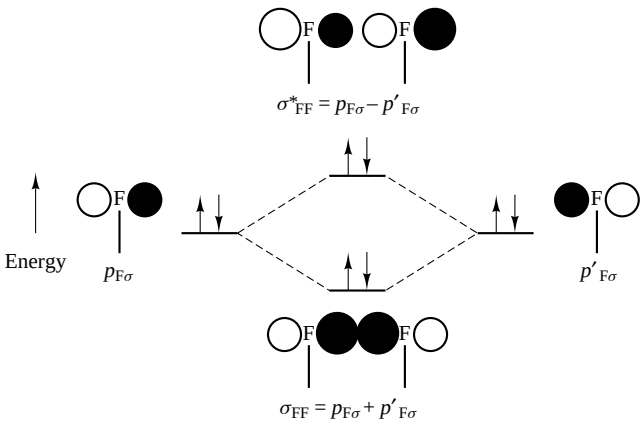

Figure 2 Schematic representations of the approximate shapes and relative energies of the bonding and antibonding molecular orbitals, σ_{FF} and σ^*_{FF}, that result from the overlap of the in-plane lone-pair orbitals, $p_{F\sigma}$ and $p'_{F\sigma}$, on two spatially proximate fluorine atoms oriented with their C–F bonds coplanar and essentially parallel, as in 1,8-difluoronaphthalene (**1**)

this combination of one filled bonding orbital and one filled antibonding orbital leads to no net chemical bonding between the two fluorine atoms, we believe it does provide a direct four-electron linkage that allows the transmittal of nuclear spin information between the two fluorine nuclei, and thereby gives rise to through-space F–F coupling.

In this lone-pair overlap theory through-space coupling is attributed to exactly the same kinds of interactions that are involved in through-bond coupling, namely Fermi contact interactions of the spins of the two magnetic nuclei with the spins of the surrounding electrons, electron correlation in accord with the Pauli principle for the two electrons within any given orbital, and Hund interactions between the spins of electrons in different orbitals. From this perspective the only distinction between through-space and through-bond coupling is a trivial one: through-space F–F coupling is transmitted by electrons that occupy weakly bonding and weakly antibonding orbitals, whereas through-bond coupling is transmitted by electrons that occupy strongly bonding orbitals. Given this picture, the term 'through-space coupling' can be seen as a misnomer. Perhaps this type of coupling would be more appropriately designated 'proximate coupling', 'direct coupling', or 'nonbonded coupling' but it seems unlikely that chemists will readily abandon the long-used term 'through-space coupling' and its juxtaposition with the term 'through-bond coupling'.

In principle, there are five different valence-level fluorine basis orbitals whose overlap interactions should be considered with regard to through-space F–F coupling: the 2*s* lone-pair orbital s_F; the in-plane 2*p* lone-pair orbital $p_{F\sigma}$; the out-of-plane 2*p* lone-pair orbital $p_{F\pi}$; the two-center bonding orbital σ_{CF}; and the empty two-center antibonding orbital σ^*_{CF}. The $p_{F\sigma}-p'_{F\sigma}$ interaction illustrated in Figure 2 is only one of 14 different pairwise overlap interactions whose potential role in through-space F–F coupling should be taken into account. We have chosen to begin our presentation with the 1,8-difluoronaphthalene system because of its relative simplicity; each of the other 13 overlap interactions in this system can be considered to be either nonexistent or negligibly small in magnitude for various reasons. For example, the $s_F-p'_{F\pi}$, $p_{F\sigma}-p'_{F\pi}$, $p_{F\pi}-\sigma'_{CF}$, and $p_{F\pi}-\sigma^*{}'_{CF}$ interactions are all zero by symmetry, as illustrated by the diagrams in Figure 3, and four other overlap interactions, $s_F-\sigma'_{CF}$, $s_F-\sigma^*{}'_{CF}$, $p_{F\sigma}-\sigma'_{CF}$, and $p_{F\sigma}-\sigma^*{}'_{CF}$, are nearly zero in magnitude because of local symmetry considerations as illustrated in Figure 4.

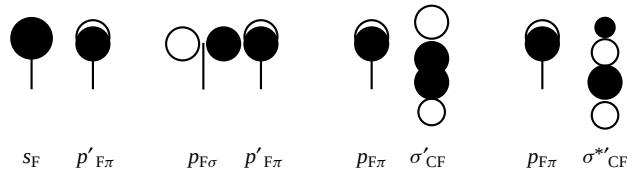

Figure 3 Schematic representations of F–F overlap interactions in the 1,8-difluoronaphthalene system (**1**) that are forbidden by symmetry

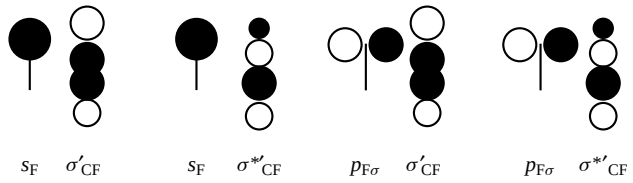

Figure 4 Schematic representation of overlap interactions in the 1,8-difluoronaphthalene system (**1**) that are nearly forbidden by symmetry

Furthermore, all of the pairwise orbital interactions other than $p_{F\sigma}-p'_{F\sigma}$ suffer from the fact that their spatial overlaps at the F–F distance of about 0.258 nm are small relative to the spatial overlap involved in the dominant $p_{F\sigma}-p'_{F\sigma}$ interaction. Finally, many of the orbital interactions are unfavorable because of a large mismatch in the energies of the interacting pairs of basis orbitals. This information is summarized in Table 1.

The σ_{FF} and σ^*_{FF} molecular orbitals shown in Figure 2 both have nodes at or very near each fluorine nucleus, so the four electrons in these two orbitals do not have significant Fermi contact with the fluorine nuclei. Instead, the Fermi contact that is relevant for the observed F–F coupling involves the electrons in the 2*s* lone-pair orbitals, s_F and s'_F. (For simplicity, the Fermi contact interactions involving the electrons in the 1*s* orbital at each fluorine nucleus are ignored here.) For a fluorine atom whose nucleus has a spin-up alignment, for example, Fermi contact interactions give rise to an enhanced probability of finding the spin-down s_F electron in the region of the s_F orbital closer to the fluorine nucleus and a correspondingly enhanced probability of finding the spin-up

Table 1 Evaluation of the Relative Magnitudes of 14 Different Types of Pairwise Orbital Overlap Interactions between the Two Fluorine Atoms in 1,8-Difluoronaphthalene (**1**)

Orbital	Orbital′	Interaction Magnitude	Explanation Regarding Magnitude (see text)
s_F	s'_F	Negligible	Long distance
	$p'_{F\sigma}$	Negligible	Long distance, energy mismatch
	$p'_{F\pi}$	Zero	Symmetry, long distance, energy mismatch
	σ'_{CF}	Negligible	Local symmetry, long distance, energy mismatch
	$\sigma^*{}'_{CF}$	Negligible	Local symmetry, long distance, energy mismatch
$p_{F\sigma}$	$p'_{F\sigma}$	Large	Good spatial overlap, perfect energy match
	$p'_{F\pi}$	Zero	Symmetry, long distance
	σ'_{CF}	Negligible	Local symmetry, long distance
	$\sigma^*{}'_{CF}$	Negligible	Local symmetry, long distance, energy mismatch
$p_{F\pi}$	$p'_{F\pi}$	Negligible	Long distance
	σ'_{CF}	Zero	Symmetry, long distance
	$\sigma^*{}'_{CF}$	Zero	Symmetry, long distance, energy mismatch
σ_{CF}	σ'_{CF}	Negligible	Long distance
	$\sigma^*{}'_{CF}$	Negligible	Long distance, energy mismatch

s_F electron in the region of the s_F orbital more remote from the fluorine nucleus. This phenomenon, in which the spin-up and spin-down electrons in a given orbital have different spatial distributions of their electron densities, is known as spin polarization. The transmission pathway for the communication of nuclear spin information between the two fluorine nuclei is completed by way of Hund interactions between the electrons in the spin-polarized s_F and s'_F orbitals and the electrons in the σ_{FF} and σ^*_{FF} orbitals. As background for our explanation about how these particular Hund interactions control through-space F–F coupling we first consider three simpler systems: an isolated fluorine atom, the hydrogen fluoride molecule, and a C–F bond.

Theoretical calculations for an isolated fluorine atom have shown that Hund interactions between the electron in the half-occupied 2*p* orbital and the electrons in the spin-polarized 2*s* orbital lead to a preference for this 2*p* electron to have its spin aligned parallel to the net electron spin density in the inner region of the 2*s* orbital (and therefore antiparallel to the spin of the nucleus) as shown in Figure 5(a).[24]

In the hydrogen fluoride molecule electron correlation effects cause one of the two electrons in the σ_{HF} bonding orbital to be closer to the fluorine nucleus and the other σ_{HF} electron to be closer to the hydrogen nucleus at a typical instant of time. This σ_{HF} orbital closely resembles a simple $2p_F$ orbital in the spatial distribution of its electron density, and as a consequence these two orbitals have analogous Hund interactions with their spin-polarized $2s_F$ orbitals. That is, the σ_{HF} electron that is closer to the fluorine nucleus prefers to have its spin aligned parallel to the electron spin density in the inner region of the spin-polarized fluorine 2*s* orbital. The net result is that a spin-up fluorine nucleus will cause the spin-down σ_{HF} electron to be located preferentially near the fluorine end of the hydrogen fluoride molecule as illustrated in Figure 5(b). As a consequence, the spin-up σ_{HF} electron will be located preferentially near the hydrogen end of the molecule. This spin-up σ_{HF} electron can experience direct Fermi contact interactions with the hydrogen nucleus, which means that there will be an energetic advantage if the hydrogen nucleus has a spin-down alignment as shown in Figure 5(b). This simple picture predicts that the fluorine and hydrogen nuclei will prefer to have antiparallel nuclear spins, which accounts for the fact that the one-bond J(FH) coupling constant for hydrogen fluoride molecule has been found to be positive in sign by both experimental and theoretical methods.[25]

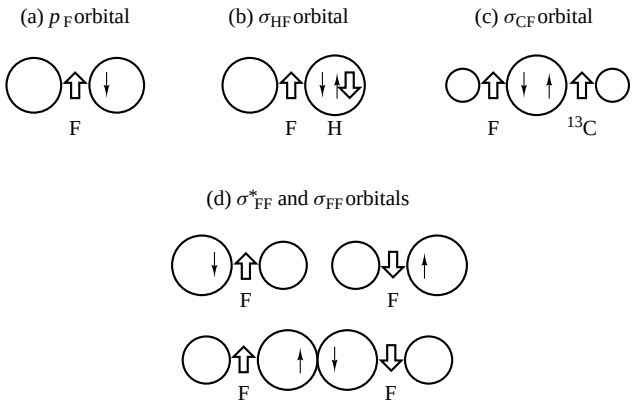

Figure 5 Schematic representations of the preferred electron and nuclear spin alignments for various systems: (a) the half-occupied 2*p* orbital of an isolated fluorine atom; (b) the σ_{HF} bonding orbital of the hydrogen fluoride molecule; (c) the σ_{CF} bonding orbital of a carbon–fluorine fragment; (d) the σ^*_{FF} antibonding and σ_{FF} bonding orbitals thought to be involved in through-space F–F coupling in a molecule such as (**1**)

In contrast, the one-bond J(FC) coupling constant for directly bonded carbon-13 and fluorine nuclei has been found to be negative in all known cases. Because of the usual electron correlation behavior the typical instantaneous configuration within the σ_{CF} orbital will have the two electrons located near opposite ends of the C–F bond. It has been argued earlier that the σ_{CF} electron that is located closer to the fluorine end of the bond experiences greater Hund interactions with the electron spin density in the outer region of the spin-polarized fluorine 2*s* orbital.[26] This reversal in the Hund behavior for the electrons in the C–F bond as compared with the H–F bond was attributed to the fact that the C–F bond is longer than the H–F bond.[26] The net result is a preference for the spin alignments shown in Figure 5(c), with the spin-up σ_{CF} electron located near the spin-up flourine nucleus and therefore with the spin-down σ_{CF} electron located near the carbon nucleus. This spin-down σ_{CF} electron can experience direct Fermi contact interaction with the carbon-13 nucleus, which means that there will be an energy advantage if the carbon-13 nucleus has a spin-up alignment as shown in Figure 5(c). This simple picture predicts that the carbon-13 and fluorine nuclei will prefer to have parallel nuclear spins, consistent with the experimentally observed negative signs for carbon-fluorine one-bond coupling constants.

We turn now to the σ_{FF} and σ^*_{FF} orbitals (Figure 2) that are of interest for through-space F–F coupling. As illustrated in Figure 5(d) the orbital amplitudes are such that the two electrons in the bonding σ_{FF} orbital will be located preferentially in the region between the two nuclei, whereas the two electrons in the antibonding σ_{FF}* orbital will be located preferentially in the two outer lobes of that orbital. As a consequence of electron correlation effects, one of the electrons in each orbital will be located preferentially near one of the fluorine nuclei while the other electron in each orbital will be located preferentially near the other fluorine nucleus. We hypothesize that because of the pronounced elongation of the bonding σ_{FF} orbital [the F–F distance of about 0.258 nm in a system such as (**1**) is considerably longer than the typical C–F bond distance of about 0.135 nm] the two σ_{FF} electrons experience Hund interactions preferentially with the outer regions of the spin-polarized s_F and s'_F orbitals, respectively, giving rise to a preference for the electron and nuclear spin alignments shown in Figure 5(d). This spin-polarization behavior is analogous to that noted for the C–F bond in Figure 5(c). We hypothesize further that the antibonding σ^*_{FF} orbital, which lacks the elongation of the σ_{FF} orbital because of the nodal plane at the midpoint of the line joining the two fluorine nuclei, shows spin-polarization behavior analogous to that of an isolated fluorine 2*p* orbital such that the two σ^*_{FF} electrons experience Hund interactions preferentially with the inner regions of the spin-polarized s_F and s'_F orbitals, respectively. This gives rise to a preference for the electron and nuclear spin alignments shown in Figure 5(d), which is analogous to the spin-polarization behavior noted for the F and HF systems in Figure 5(a) and (b). As a consequence of the cooperative effect

of all four electrons in the σ_{FF} and σ^*_{FF} orbitals there is an energetic advantage if the two fluorine nuclei have antiparallel spins rather than parallel spins. In this way we can account for the fact that in all of the cases in which the signs of the F–F coupling constants have been determined experimentally for molecules in which the through-space mode of F–F coupling is thought to predominate, these signs have been found to be positive.[6] Furthermore, the theory presented here leads to the conclusion that the magnitude of the through-space component of F–F coupling should depend on the extent to which the σ_{FF} and σ^*_{FF} orbitals are differentiated from one another in their electron densities in the region near the midpoint of the line connecting the two fluorine nuclei. This differentiation should depend in turn on the extent of overlap of the $p_{F\sigma}$ and $p'_{F\sigma}$ basis orbitals (see Figure 2), and this expectation leads to three experimentally testable predictions about the magnitude of $J(FF)^{TS}$: it should fall off exponentially with the distance between the two fluorine atoms, it should depend on orientation effects as well as distance effects, and it should not depend heavily on the π-electron withdrawing or π-electron supplying effects of any substituents that are located on the carbon framework that bears the two fluorine atoms. These implications are elaborated in the following paragraphs.

Many experimental studies have indicated that through-space F–F coupling has a very steep dependence on the distance between the coupled fluorine nuclei. One such study involves 15 compounds of types (**16**) and (**17**) (Figure 6) in which various peri substituents X and Y serve to perturb the F–F distance in predictable ways.[9,27] Systems (**16**) and (**17**) have the disadvantage that the through-bond components of the experimentally measured total F–F coupling may be large enough to muddle the interpretation of the results. But these systems have two advantages: there is no complication from out-of-plane distortions of the fluorines of the kind found, for example, in systems related to (**2**) and (**3**); and the molecules are relatively straightforward to synthesize. The experimental results for (**16**) and (**17**) are given in Table 2.

The total coupling constants $J(FF)$ were measured by ^{19}F NMR spectroscopy and the distances between the two fluorine nuclei d_{FF} were determined by averaging the results obtained by MM2 and AM1 computations. The values of $J(FF)$ cover a wide range: from 28.1 Hz for 5,6-difluoroacenaphthene,

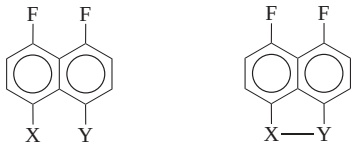

(16) **(17)**

Figure 6 The types of 1,8-difluoronaphthalene (**16**) and 5,6-difluoroacenaphthene (**17**) derivatives for which $J(FF)$ values are listed in Table 2 and plotted in Figure 7

in which the two fluorine atoms are splayed apart as a consequence of the distortions in the peri-angles caused by the strained five-membered ring, to 82.3 Hz for 4,5-dicyano-1,8-difluoronaphthalene, in which the two fluorine atoms are pushed together as a consequence of the distortions of the peri-angles in the opposite sense caused by van der Waals repulsion between the two cyano groups. A semilogarithmic plot of $J(FF)$ against d_{FF} is shown in Figure 7. The data appear to be well correlated by the straight line shown in Figure 7, which leads to the relationship:

$$J(FF) = (9.64 \times 10^5)e^{-3.78d_{FF}} \quad (2)$$

The average vertical deviation of points from the line in Figure 7 is ±2.6 Hz and the correlation coefficient is 0.99. [We did not include in Figure 7 the data of 5,6-difluoroacenaphthylene, which would have given a point about 9.6 Hz above the correlation line. The reason for this large discrepancy remains obscure, although we suspect that the –CH=CH– bridge might give rise to an enhanced through-bond component $J(FF)^{TB}$.]

Of course in order to use these data to provide a rigorous test of the validity of the lone-pair overlap theory one would need to plot not the total coupling constant $J(FF)$, but rather the through-space component $J(FF)^{TS}$, which is given by $J(FF) - J(FF)^{TB}$ where $J(FF)^{TB}$ is the through-bond component. Unfortunately, neither the magnitude nor the sign of $J(FF)^{TB}$ is known for any of the compounds in the series, although it seems likely from the large magnitudes of the observed coupling constants that the magnitude of $J(FF)^{TyB}$ is small relative to $J(FF)$. Granted that the interpretation of

Table 2 Values of the Measured F–F Coupling Constants $J(FF)$ and the Calculated F–F Distances d_{FF} for Various Molecules of Types (**16**) and (**17**), and the Amounts by which these Experimental Coupling Constants Deviate from the Linear Correlation Plotted in Figure 7 and Expressed by Equation (2)

System	Perisubstituents X and Y	d_{FF} (nm)	$J(FF)$ (Hz)	Deviation from plot (Hz)
17	$-CH_2-CH_2-$	0.2740	28.1	−2.2
17	–C(=NOH)–C(=NOH)–	0.2735	31.0	+0.1
17	–C(=O)–C(=O)–	0.2745	31.5	+1.8
17	Quinoxaline deriv. of diketone	0.2720	33.0	+0.3
16	–CH=CH–	0.2775	36.1	+9.6
16	H, H	0.2560	58.8	−1.0
16	–C(=O)–O–C(=O)–	0.2570	61.5	+3.9
16	H, NH_2	0.2520	61.8	−7.8
16	H, CH_3	0.2540	64.4	−0.1
16	H, $NHCOCH_3$	0.2525	64.6	−3.7
16	H, Cl	0.2530	65.7	−1.3
16	H, CN	0.2540	65.9	+1.4
16	H, Br	0.2525	67.4	−0.9
16	H, NO_2	0.2520	75.2	+5.6
16	CN, CN	0.2495	82.3	+5.8

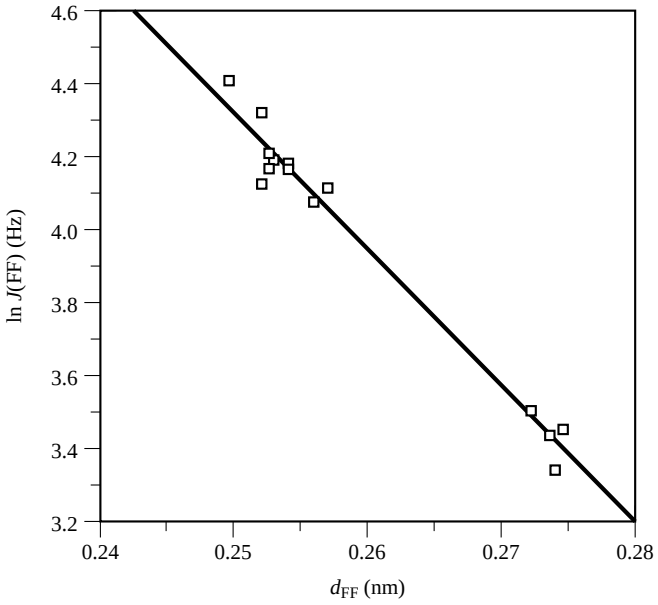

Figure 7 Semilogarithmic plot of J(FF) vs. d_{FF} for the derivatives of 1,8-difluoronaphthalene and 5,6-difluoroacenaphthene listed in Table 2 and pictured in Figure 6

the plot in Figure 7 is flawed by this uncertainty about the magnitude of the through-bond contribution to the observed J(FF) values, it nonetheless can be argued that the linear trend in this semilogarithmic plot provides at least qualitative support for the idea that through-space F–F coupling falls off exponentially with distance.

As an aside, an indication that there is a small through-bond component in the observed coupling constants in this series can be seen from the pattern exhibited by the small deviations of the experimental J(FF) values from the line plotted in Figure 7. The points for all seven of the compounds with π-acceptor substituents lie above the line: dicyano, +5.8; nitro, +5.6; anhydride, +3.9; diketone, +1.8; cyano, +1.4; quinoxaline, +0.3; and dioxime, +0.1 Hz. In contrast, the points for all six of the compounds with π-donor substituents lie below the line: methyl, −0.1; bromo, −0.9; chloro, −1.3; $-CH_2CH_2-$, −2.2; acetamido, −3.7; and amino, −7.8 Hz. The trend in these substituent effects is similar to the trend reported for the through-bond F–F coupling that takes place through the π-electron system in the 4-substituted-1,3-difluorobenzenes.[28] Relative to the F–F coupling constant of +6.6 Hz for 1,3-difluorobenzene itself, π-acceptor substituents at C-4 make J(FF) more positive and π-donor substituents at C-4 make J(FF) less positive by the following increments: nitro, +5.6; cyano, +4.3; chloro, −0.4; bromo, −0.5; methyl, −2.0; and amino, −8.7 Hz. It is perhaps not unreasonable to suspect that the 4-substituted-1,3-difluorobenzenes and the 4-substituted-1,8-difluoronaphthalenes may be analogous with respect to through-bond coupling through the π system because these two families of molecules share some common structural features; in each family the two fluorines are unconjugated with each other and separated by four bonds, and the substituent is *para* with respect to one of the fluorine atoms and also conjugated with the other fluorine atom.

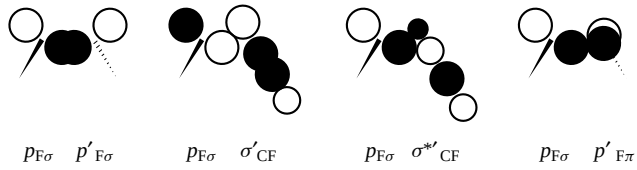

Figure 8 Schematic representations of several types of orbital overlap that may play a role in through-space F–F coupling in 4,5-difluorophenanthrene systems such as (**2**)

For 4,5-difluorophenanthrenes such as (**2**), the C–F bonds are neither parallel nor coplanar, which makes the orbital overlap picture of through-space F–F coupling more complicated than that described above for the 1,8-difluoronaphthalenes such as (**1**). As illustrated in Figure 8, the orientation of the two fluorine atoms in the 4,5-difluorophenanthrene system may allow contributions to through-space F–F coupling from overlap interactions of the $p_{F\sigma}-\sigma'_{CF}$, $p_{F\sigma}-\sigma^{*\prime}_{CF}$, and $p_{F\sigma}-p'_{F\pi}$ types in addition to the major contribution arising from overlap interaction of the $p_{F\sigma}-p'_{F\sigma}$ type. These additional modes of overlap may be responsible for the fact that the measured value of 174 Hz for the F–F coupling constant for 4,5-difluoro-1-methylphenanthrene (**2**) is so much larger than the value of 97 Hz that would have been predicted from the correlation line in Figure 7 for the F–F distance of 0.2434 nm found experimentally for (**2**).[29] One should be cautious, however, about attempting quantitative comparisons involving J(FF) values in different systems such as 1,8-difluoronaphthalenes and 4,5-difluorophenanthrenes because of the uncertainties about the magnitudes and the signs of the through-bond components.

Yet another spatial array that leads to through-space F–F coupling is found in 1,12-difluorobenzo[*c*]phenanthrenes such as (**3**). For steric reasons this ring system adopts a helical structure such that the dominant orbital overlap interaction leading to through-space coupling between the two fluorine atoms involves the 'out-of-plane' $p_{F\pi}$ and $p'_{F\pi}$ lone-pair orbitals as illustrated in Figure 9. (For simplicity in this conceptual presentation we have neglected the strong mixing of these $p_{F\pi}$ and $p'_{F\pi}$ orbitals with various π orbitals that are characteristic of the benzo[*c*]phenanthrene ring system.) For the particular example of 4-bromo-1,12-difluorobenzo[*c*]phenanthrene the F–F distance is 0.2535 nm and the value of J(FF) is 45 Hz.[8,29] At this F–F distance the correlation line for the 1,8-difluoronaphthalene system in Figure 7 would predict a significantly larger value of 66 Hz for J(FF). This discrepancy may reflect an orientation effect: the $p_{F\sigma}-p'_{F\sigma}$ overlap in the 1,8-difluoronaphthalene system is nearly optimum because the orbital axes are almost colinear, whereas the $p_{F\pi}-p'_{F\pi}$ overlap in the 1,12-difluorobenzo[*c*]phenanthrene system is less than optimum because of the significant departure of the orbital axes from colinearity, as shown in Figure 9. Once again, however, such comparisons between two different systems are risky because of our lack of knowledge of the through-bond contributions to the observed values of J(FF).

3 NF AND PF SYSTEMS

The lone-pair overlap theory presented here can be extended in a simple way to account for two other types of through-space coupling between spatially proximate atoms bearing lone

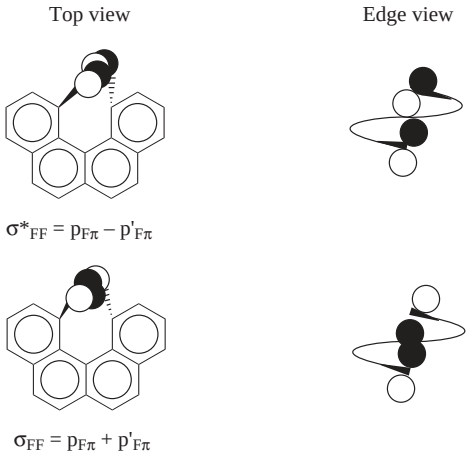

Figure 9 Schematic representations from two vantage points of the bonding and antibonding orbitals, σ_{FF} and σ^*_{FF}, resulting from the mutual overlap of the two 'out-of-plane' lone-pair orbitals, $p_{F\pi}$ and $p'_{F\pi}$, in 1,12-difluorobenzo[*c*]phenanthrene systems such as (**3**)

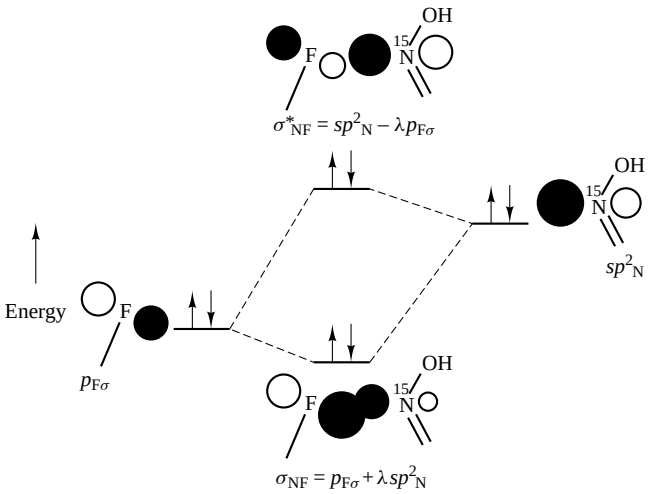

Figure 10 Schematic representations of the approximate shapes and relative energies of the bonding and antibonding molecular orbitals, σ_{NF} and σ^*_{NF}, that result from the overlap of an in-plane p_F lone-pair orbital and an $sp^2{}_N$ lone-pair orbital on spatially proximate fluorine and nitrogen atoms oriented as in oxime acetate (**12**)

pairs, namely N–F and P–F coupling. The lone-pair orbital overlap interactions thought to be important for through-space N–F coupling are illustrated in Figure 10 for a structural array similar to that in oxime acetate (**12**). Through-space P–F coupling in molecules such as (**14**) can be accounted for in an analogous fashion. The dependence of N–F and P–F through-space coupling on distance and orientation effects appears to be similar to the dependence on these two factors found for the much more thoroughly studied through-space coupling in F–F systems.[9,14,30]

4 HF, CF, AND CP SYSTEMS

The lone-pair overlap theory can be extended yet further by hypothesizing that through-space coupling can result from lone-pair–bond-pair overlap as well as from lone-pair–lone-pair overlap as considered above. Through-space H–F and C–F coupling has been extensively documented in a variety of molecules in which either the hydrogen end or the carbon-13 end of a C–H bond is in close spatial contact with a fluorine 2*p* lone pair. As illustrated in Figure 11 and Figure 12, respectively, this coupling can be attributed to the overlap of the fluorine lone-pair orbital with the CH bonding orbital, augmented by some overlap of the fluorine lone pair with the corresponding CH antibonding orbital. The orbital mixing that arises from this overlap of these three basis orbitals creates three three-center molecular orbitals in each case, a pair of filled bonding and antibonding orbitals that are involved in the through-space coupling, and also one high-energy antibonding orbital that is empty and therefore plays no role in coupling.

In the F ··· HC orientation, for which the two filled three-center orbitals σ_{FHC} and σ^*_{FHC} are depicted in Figure 11, the amplitudes of the wave functions are such that the electron density in the bonding σ_{FHC} orbital is concentrated mostly in the middle region of the three-atom array, whereas the electron density in the antibonding σ^*_{FHC} orbital is concentrated mostly at the ends of the three-atom array. The spin-polarization pattern of these two pairs of electrons that appears to lead overall to the most favorable combination of Hund and Fermi interactions in the F ··· HC system is shown in Figure 13(a). By analogy with the F–F system discussed in the preceding section, we believe that the σ_{FHC} electron will experience Hund interactions at the fluorine atom primarily with the outer region of the spin-polarized s_F orbital, and therefore will prefer to have its spin aligned parallel to the spin of the fluorine nucleus. Also by analogy with the F–F system discussed above, we believe that the σ^*_{FHC} electron will experience Hund interactions at the fluorine atom primarily with the inner region of the spin-polarized s_F orbital, and therefore will prefer to have its spin aligned antiparallel to

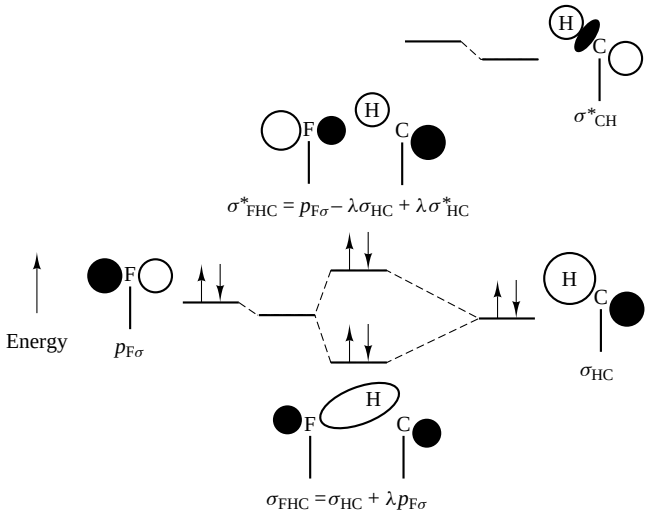

Figure 11 Schematic representations of the approximate shapes and relative energies of the three-center bonding and antibonding molecular orbitals, σ_{FHC} and σ^*_{FHC}, that result from the overlap of a $p_{F\sigma}$ lone-pair orbital with a σ_{HC} orbital and a σ^*_{HC} orbital in a system such as (**6**) or (**8**) in which the fluorine atom is crowded against the hydrogen end of the CH fragment

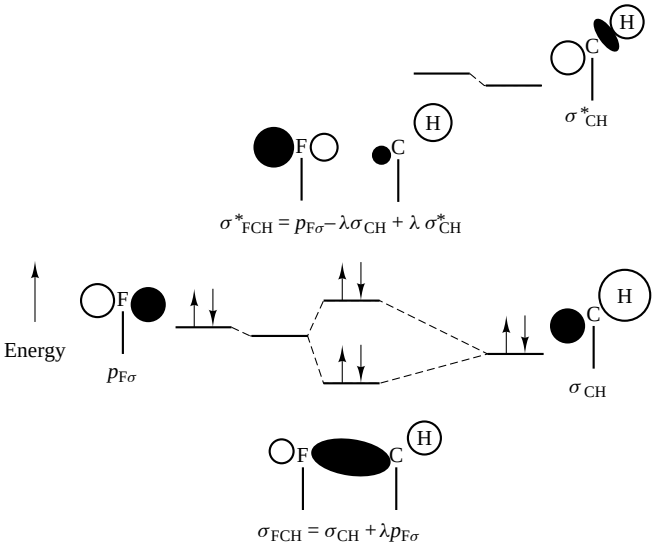

Figure 12 Schematic representations of the shapes and relative energies of the three-center bonding and antibonding molecular orbitals, σ_{FCH} and σ^*_{FCH}, that result from the overlap of a $p_{F\sigma}$ lone-pair orbital with a σ_{CH} orbital and a σ^*_{CH} orbital in a system such as (**9**) in which the fluorine atom is spatially proximate to the carbon end of the CH fragment

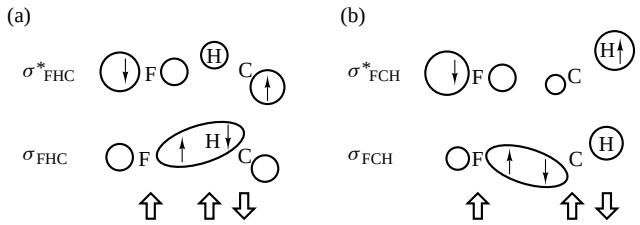

Figure 13 Schematic representations of the preferred relative alignments of electron spins and nuclear spins in two systems: (a) the F ··· HC system depicted in Figure 11, and (b) the F ··· CH system depicted in Figure 12

the spin of the fluorine nucleus. The hydrogen and carbon-13 nuclei in this system interact with the σ_{FHC} and σ^*_{FHC} electrons by direct Fermi contact, which results in a preference for an antiparallel alignment of nuclear and electron spins in the regions around each of these nuclei. This analysis leads to the overall prediction that with respect to the through-space components of the H–F and C–F coupling in this system the hydrogen and fluorine nuclei in the F ··· HC system will prefer to have parallel nuclear spins, while the carbon and fluorine nuclei and also the carbon and hydrogen nuclei will prefer to have antiparallel nuclear spins, as shown in Figure 13(a). This prediction is in accord with the experimental demonstrations in these F ··· HC systems that the H–F coupling constants are negative and the C–F and C–H coupling constants are positive.[10,11,31]

In the F ··· CH orientation, for which the two filled three-center orbitals σ_{FCH} and σ^*_{FCH} are depicted in Figure 12, the electron density in the bonding σ_{FCH} orbital is once again concentrated mostly in the middle region of the three-atom array while the electron density in the antibonding σ^*_{FCH} orbital is concentrated mostly at the ends of the three-atom array. The spin-polarization pattern of these two pairs of

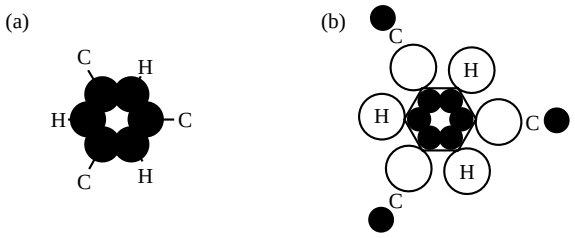

Figure 14 Top views of (a) the lowest-energy π orbital and (b) one of the σ orbitals of the basal trisubstituted benzene ring in phosphorus compound (**15**)

electrons that appears to lead overall to the most favorable combination of Hund and Fermi interactions in the F ··· CH system is shown in Figure 13(b). This analysis leads to the overall prediction that with respect to the through-space components of H–F and C–F coupling in this system the hydrogen and fluorine nuclei and also the carbon and hydrogen nuclei will prefer to have antiparallel nuclear spins, consistent with the experimental observations that the H–F and C–H coupling constants in these F ··· CH systems are each positive in sign. The pattern in Figure 13(b) also predicts that $J(FC)^{TS}$ in this system should be negative. In fact, the total coupling constant $J(FC)$ is found to be small and negative in a particular F ··· CH system similar to (**9**),[11] but in contrast $J(FC)$ is found to be positive in system (**9**) itself and other F ··· CH systems.[31] Perhaps this discrepancy arises because the through-bond component of the C–F coupling in molecules such as (**9**) is positive in sign and sufficiently large in magnitude to override the small negative through-space component of the C–F coupling that is predicted by the analysis shown in Figure 13(b). Alternatively, perhaps that analysis is simply not a reliable basis on which to predict the sign of $J(FC)$ in such systems.

The recently reported novel through-space coupling between phosphorus and carbon-13 nuclei in molecules such as (**15**) has been attributed to overlap interactions involving the lowest-energy π orbital of the basal trisubstituted benzene ring shown in Figure 14(a).[16,17] This π orbital has the proper symmetry to mix with the lone-pair orbital on the phosphorus atom to generate two new filled seven-center molecular orbitals, one bonding and the other antibonding in the region between the phosphorus atom and the benzene ring. As an alternative possibility for consideration we suggest that the observed P–C coupling in (**15**) might involve mixing of the phosphorus lone-pair orbital with the σ orbital of the basal benzene ring shown in Figure 14(b). This mixing would generate a bonding and antibonding pair of filled 13-center molecular orbitals.

5 HH SYSTEMS

Having considered above how through-space coupling can be viewed as arising mainly from overlap interactions between two lone pairs or between one lone pair and one bond pair, it remains to consider the through-space coupling that arises from overlap interactions between two bond pairs. The large 18 Hz coupling between the two bridgehead hydrogen atoms in bicyclo[1.1.1]pentane (**10**) can be attributed to such interactions.[12,13] As shown in Figure 15, the mutual overlap of the rear lobes of the two filled C–H bond orbitals σ_{CH} and

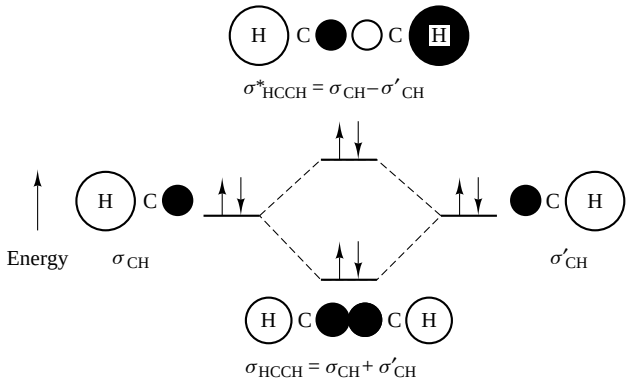

Figure 15 Schematic representations of the approximate shapes and relative energies of the four-center bonding and antibonding molecular orbitals, σ_{HCCH} and σ^*_{HCCH}, that result from the overlap of two filled CH bond-pair orbitals (with slight admixture of the corresponding two empty CH antibonding orbitals that are not shown explicitly here) oriented with their carbon ends spatially proximate as for the bridgehead C–H bonds in bicyclo[1.1.1]pentane (**10**)

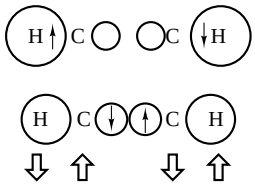

Figure 16 Schematic representations of the preferred relative alignments of electron spins and nuclear spins in the HC ··· CH system depicted in Figure 15

σ'_{CH}, modified slightly by overlap interactions of these filled orbitals with the empty antibonding orbitals σ^*_{CH} and $\sigma^{*\prime}_{CH}$, would give rise to two new four-center molecular orbitals, one bonding and the other antibonding. This orbital mixing creates a four-center four-electron HCCH linkage for the transmittal of nuclear spin information among the four nuclei. As illustrated in Figure 16, this analysis correctly predicts a positive sign for J(HH) in bicyclo[1.1.1]pentane (**10**).

One could imagine that through-space H–H coupling also might result when the hydrogen ends of two C–H bonds are brought into close proximity with one another. Many examples of through-space H–H couplings in this latter type of orientation have been reported, but they are very small in magnitude.

6 F–F COUPLING THROUGH NONBONDED INTERACTIONS WITH AN INTERVENING ORBITAL

Finally, the lone-pair overlap theory has proved itself to be useful by predicting the existence of a new type of through-space F–F coupling in which the two coupled fluorines are not crowded directly against one another but rather are each crowded in a nonbonding way against an intervening group X in molecules such as 1,8-difluoro-9-X-anthracenes.[32] For example, various 1,8-difluoro-9-phenylanthracenes show values of J(FF) in the range of 5–6 Hz as compared with

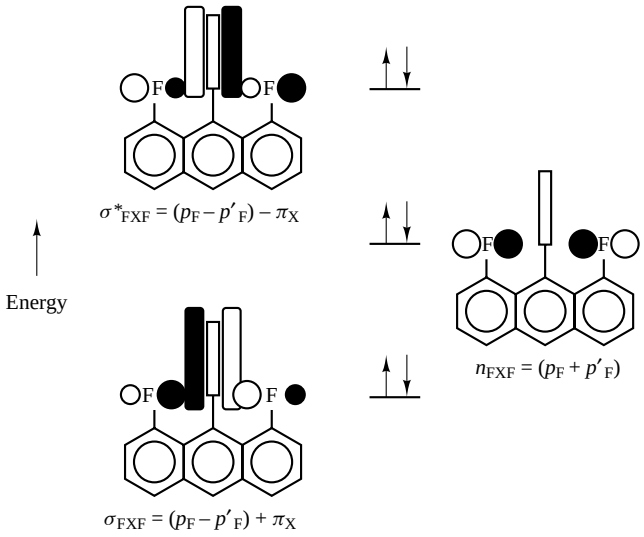

Figure 17 Schematic representations of the three mixed orbitals thought to be involved in through-space F–F coupling in the 1,8-difluoro-9-phenylanthracene system

J(FF) values of less than 1 Hz for the corresponding 1,8-difluoroanthracenes.[9,32] As a result of the steric demands in this system the phenyl group is oriented with its plane perpendicular to the plane of the anthracene ring. The pathway for the transmission of nuclear spin information in this system is believed to result from the overlap interactions of three basis orbitals, including two fluorine lone-pair orbitals and the lowest-energy filled π orbital on the intervening phenyl group. These interactions generate a set of three mixed orbitals, including one three-center bonding orbital σ_{FXF}, one three-center nonbonding orbital n_{FXF}, and one three-center antibonding orbital σ^*_{FXF} as in Figure 17. The lowest-energy π orbital is expected to have the most effective interactions here because ab initio molecular orbital calculations indicate that its energy is very close to that of the fluorine lone-pair orbitals.[9] In addition, however, other π and π^* orbitals on the phenyl that possess the correct symmetry for overlap with the fluorine orbitals also may play a role in the F–X–F coupling.

7 RELATED ARTICLES

NF153-Fluorine-19 NMR; NN303-Nuclear Spin Properties and Notation; NS465-Stereochemistry and Long Range Coupling Constants

8 REFERENCES

1. J. D. Roberts, D. R. Davies, and R. P. Lutz, *J. Am. Chem. Soc.*, 1961, **83**, 246.
2. L. Petrakis and C. H. Sederholm, *J. Chem. Phys.*, 1961, **35**, 1243.
3. J. Hilton and L. H. Sutcliffe, *Prog. NMR Spectrosc.*, 1975, **10**, 27.
4. R. H. Contreras, M. A. Natiello, and G. E. Scuseria, *Magn. Reson. Rev.*, 1985, **9**, 239.

5. S. L. Manatt, M. A. Cooper, C. W. Mallory, and F. B. Mallory, *J. Am. Chem. Soc.*, 1973, **95**, 975.
6. S. L. Manatt and M. A. Cooper, *J. Am. Chem. Soc.*, 1977, **99**, 4651.
7. F. B. Mallory, C. W. Mallory, and W. M. Ricker, *J. Am. Chem. Soc.*, 1975, **97**, 4770.
8. F. B. Mallory, C. W. Mallory, and W. M. Ricker, *J. Org. Chem.*, 1985, **50**, 457.
9. Some of the information in this article derives from unpublished experiments and calculations carried out at Bryn Mawr College in collaboration with: Eddie Luzik and Mercy Ramanjulu (graduate students); Laura Fredenburgh, Kelly Butler, Que Van, Mary Beth Lewis, Chandra Wray, Maia Whang, and Christine Hann (undergraduate students); and Michelle Francl, Maryellen Nerz-Stormes, and Lisa Chirlian (faculty colleagues).
10. L. C. Hsee and D. J. Sardella, *Magn. Reson. Chem.*, 1990, **28**, 688.
11. I. D. Rae, J. A. Weigold, R. H. Contreras, and G. Yamamoto, *Magn. Reson. Chem.*, 1992, **30**, 1047.
12. K. B. Wiberg, G. M. Lampman, R. P. Ciula, D. S. Connor, P. Schertler, and J. Lavanish, *Tetrahedron*, 1965, **21**, 2749.
13. M. Barfield, E. W. Della, P. E. Pigou, and S. R. Walter, *J. Am. Chem. Soc.*, 1982, **104**, 3549.
14. F. B. Mallory, E. D. Luzik, Jr, C. W. Mallory, and P. J. Carroll, *J. Org. Chem.*, 1992, **57**, 366.
15. T. Schaefer, K. Marat, A. Lemire, and A. F. Janzen, *Org. Magn. Reson.*, 1982, **18**, 90.
16. R. P. L'Esperance, A. P. West, Jr., D. Van Engen, and R. A. Pascal, Jr, *J. Am. Chem. Soc.*, 1991, **113**, 2672.
17. A. P. West, Jr, N. Smyth, C. M. Kraml, D. M. Ho, and R. A. Pascal, Jr, *J. Org. Chem.*, 1993, **58**, 3502.
18. K. L. Servis and K. Fang, *J. Am. Chem. Soc.*, 1968, **90**, 6712.
19. B. J. Kimber, J. Feeney, G. C. K. Roberts, B. Birdsall, D. V. Griffiths, A. S. V. Burgen, and B. D. Sykes, *Nature*, 1978, **271**, 184.
20. A. C. Diz, C. G. Giribet, M. C. Ruiz de Azua, and R. H. Contreras, *Int. J. Quantum Chem.*, 1990, **37**, 663.
21. M. C. Ruiz de Azua, A. C. Diz, C. G. Giribet, and R. H. Contreras, *Int. J. Quantum Chem.*, 1986, **S20**, 585.
22. F. B. Mallory, *J. Am. Chem. Soc.*, 1973, **95**, 7747.
23. A. Meresse, C. Courseille, F. Leroy, and N. B. Chanh, *Acta Crystallogr., Sect. B*, 1975, **31**, 1236.
24. D. A. Goodings, *Phys. Rev.*, 1961, **123**, 1706.
25. J. Kowalewski, *Prog. NMR Spectrosc.*, 1978, **11**, 1.
26. C. J. Jameson and H. S. Gutowsky, *J. Chem. Phys.*, 1969, **51**, 2790.
27. F. B. Mallory, C. W. Mallory, and M.-C. Fedarko, *J. Am. Chem. Soc.*, 1974, **96**, 3536.
28. R. J. Abraham, D. B. Macdonald, and E. S. Pepper, *J. Am. Chem. Soc.*, 1968, **90**, 147.
29. These F–F distances were determined through single-crystal X-ray diffraction studies carried out by P. J. Carroll at the University of Pennsylvania, PA, USA.
30. F. B. Mallory and C. W. Mallory, *J. Am. Chem. Soc.*, 1985, **107**, 4816.
31. M. Barfield, S. R. Walter, K. A. Clark, G. W. Gribble, K. W. Haden, W. J. Kelly, and C. S. Le Houllier, *Org. Magn. Reson.*, 1982, **20**, 92.
32. F. B. Mallory, C. W. Mallory, and M. B. Baker, *J. Am. Chem. Soc.*, 1990, **112**, 2577.

Biographical Sketches

Frank B. Mallory. *b* 1933. B.S., 1954, Chemistry, Yale University, USA, Ph.D., 1958, Chemistry, California Institute of Technology, USA. Faculty, Bryn Mawr College, USA, 1957–present. Currently W. Alton Jones Professor of Chemistry. Approx. 70 publications. Research specialties: ^{19}F NMR studies, photocyclizations of stilbenes, nuclear spin relaxation measurements of methyl rotation barriers in crystalline solids.

Clelia W. Mallory. *b* 1938. A.B., 1959, M.A., 1960, Ph.D., 1963, Chemistry, Bryn Mawr College, USA. Postdoctoral work at Bryn Mawr College, 1963–present. Faculty, Yale University, USA, 1977–80. Faculty, University of Pennsylvania, USA, 1980–present. Currently senior lecturer in Chemistry. Approx. 30 publications. Research specialties: ^{19}F NMR studies, photocyclizations of stilbenes.

Dipolar and Indirect Coupling Tensors in Solids

Roderick E. Wasylishen

Dalhousie University, Halifax, Nova Scotia, Canada

1	Introduction	1
2	Direct Dipolar Coupling	2
3	Indirect Spin–Spin Coupling	4
4	Summary	10
5	Related Articles	10
6	References	10

1 INTRODUCTION

Nuclei which possess the property of spin also have an associated nuclear magnetic moment. It is the interaction between these nuclear magnetic moments and a strong applied magnetic field $\boldsymbol{B}_0$ which forms the basis of the NMR experiment. This interaction, known as the Zeeman interaction, is always the most important spin interaction for spin-$\frac{1}{2}$ nuclei. In addition to the externally applied magnetic field, nuclei may also experience much smaller internal magnetic fields. For example, the field-induced motion of electrons generates small magnetic fields which modify the applied magnetic field and result in the phenomenon known as nuclear magnetic shielding or chemical shielding. In addition, neighboring nuclear spins may also create small magnetic fields which modify the applied magnetic field. There are two fundamental mechanisms by which one nuclear magnetic moment may interact with another: the *direct* magnetic dipole–dipole interaction and the *indirect* spin–spin interaction. The magnitude of the direct dipolar interaction is directly proportional to the inverse cube of the separation between two spins, while the indirect interaction does not depend on distance in any simple way since it is a two-stage process mediated by the intervening electrons. Because the mechanism of indirect spin–spin coupling involves electrons, this parameter depends on the detailed electronic structure of a molecule. Both the direct and indirect coupling interactions are bilinear in the nuclear spin operators (see below). In principle, the direct dipolar and indirect spin–spin interactions couple every spin of the sample with all others.

Most early NMR investigations were ^{1}H NMR studies, because of the relatively large magnetic moment of ^{1}H (hence its high inherent sensitivity to NMR detection), its large natural abundance (99.985%), and its ubiquitous presence in chemical compounds. The direct dipolar interaction has special significance in these studies since proton–proton direct dipolar interactions are largely responsible for the general appearance of ^{1}H NMR spectra of solid materials. Furthermore, the ^{1}H–^{1}H dipolar interaction provided the first important application of NMR in chemistry. Specifically, Pake[1] used the ^{1}H–^{1}H direct dipolar interaction to determine the H–H separation of water molecules in gypsum ($CaSO_4.2H_2O$): $r_{H-H} = 0.158$ nm.

The indirect spin–spin coupling interaction was first observed as magnetic field-independent splittings in the NMR spectra of solution samples.[2–4] In solution, the direct dipolar interaction averages to zero because of the rapid random tumbling motion of molecules. The first indirect spin–spin coupling constant J was reported by Proctor and Yu in 1951.[2] It involved the indirect spin–spin coupling between the antimony and fluorine nuclei of the SbF_6 anion in an aqueous solution of $NaSbF_6$; $J(^{121}Sb, ^{19}F)$ = 1.9 kHz. Shortly after this report, Gutowsky and co-workers reported the observation of $J(^{31}P, ^{19}F)$ in $P(O)Cl_2F$ (1.2 kHz), $P(O)ClF_2$ (1.1 kHz), and $CH_3(O)PF_2$ (1.3 kHz).[3] The first ^{1}H–^{1}H electron-mediated spin–spin couplings were reported in the same year by Hahn and Maxwell.[4] They studied the frequency modulation of ^{1}H NMR spin echoes arising from molecules with chemically nonequivalent hydrogen nuclei. For dichloroacetaldehyde ($CHCl_2CHO$), two distinct modulation frequencies were observed on the ^{1}H spin echo envelope: one corresponding to the difference in ^{1}H chemical shifts, and a second, much smaller frequency J which was independent of the applied magnetic field [$^3J(^1H, ^1H) = 0.7$ Hz]. On the basis of their measurements, Hahn and Maxwell proposed that the Hamiltonian describing electron coupled spin interactions in isotropic fluids should be of the form $J_{N,N'}\boldsymbol{I}_N \cdot \boldsymbol{I}_{N'}$. However, for a pair of coupled spins residing in a molecule which is not rapidly tumbling in an isotropic fluid, Ramsey[5] later pointed out that the energy of interaction $E_{N,N'}$ depends on the orientation of the spin pair in the applied magnetic field. In general, the energy of interaction is given by

$$E_{N,N'} = h\boldsymbol{I}_N \cdot \boldsymbol{J}_{N,N'} \cdot \boldsymbol{I}_{N'} + hJ_{N,N'}\boldsymbol{I}_N \cdot \boldsymbol{I}_{N'} \qquad (1)$$

where $\boldsymbol{J}_{N,N'}$ is a second rank tensor whose trace is zero and $J_{N,N'}$ is the isotropic indirect spin–spin coupling constant.

In solid samples, splittings arising from indirect spin–spin coupling were not observed until 1967.[6] In the solid state, the magnitude of direct dipolar interactions among magnetically abundant spins, such as ^{1}H or ^{19}F, precluded the measurement of much smaller indirect spin–spin interactions. However, by spinning samples rapidly about an axis inclined at 54° 44′ with respect to the applied magnetic field, broadening due to anisotropic chemical shielding and direct dipolar interactions can be largely removed. Using this technique, known as magic angle spinning (MAS), Andrew et al.[6] observed splittings due to $J(^{75}As, ^{19}F)$ of 905 Hz, and $J(^{121}Sb, ^{19}F)$ of 1820 Hz in the ^{19}F NMR spectra of solid $KAsF_6$ and $KSbF_6$, respectively. From the ^{19}F NMR linewidths observed in nonspinning samples of these salts, the authors were able to conclude that the hexafluoroarsenate and hexafluoroantimonate anions are dynamically disordered. Rapid jumps of the MF_6 octahedra about their symmetry axes average *intra*molecular dipolar interactions to zero. Subsequently, VanderHart et al.[7] studied the ^{19}F and ^{31}P NMR lineshapes of static samples of polycrystalline $BaFPO_3$ where the directly bonded ^{19}F and ^{31}P nuclei are coupled by both the direct dipolar and the indirect spin–spin coupling interactions. The authors indicated that with an accurate value of the ^{19}F–^{31}P separation r_{FP}, one could calculate the contribution that the direct dipolar interaction makes to the overall ^{19}F or ^{31}P NMR lineshape and, in principle, determine the anisotropy in the indirect spin–spin coupling, a parameter which is usually inaccessible.

The objective of this article is to present an introductory discussion of how spin–spin coupling interactions are described

and how they manifest themselves in the NMR spectra of diamagnetic systems, particularly in NMR studies of solids. The discussion will focus on the indirect spin–spin coupling tensor $\boldsymbol{J}$, since detailed discussions of the direct dipolar interaction can be found in several textbooks on NMR.[8–11] For pedagogical reasons, it is most convenient to focus the discussion on simple two-spin systems.

2 DIRECT DIPOLAR COUPLING

A nucleus with nonzero total spin angular momentum $\hbar\boldsymbol{I}$ also possesses a magnetic moment $\boldsymbol{\mu}$. The magnetic moment and angular momentum vectors are related by the magnetogyric ratio γ, a unique constant for any given isotope:

$$\boldsymbol{\mu} = \gamma\hbar\boldsymbol{I} \tag{2}$$

It is useful to consider the total static magnetic field emanating from a magnetic dipole. At a point P, the static field depends on the distance r and the angle θ between the magnetic dipole and P; the z component of the local field is $\gamma r^{-3}\hbar\,(3\cos^2\theta - 1)\,(\mu_0/4\pi)$. With $\theta = 0^\circ$, the local field 0.1 nm from a proton is 5.64 mT, several orders of magnitude less than the magnitude of typical external fields employed in NMR experiments.

From classical electrodynamics, the energy of interaction E between two magnetic dipoles, $\boldsymbol{\mu}_1$ and $\boldsymbol{\mu}_2$, separated by a distance r may be written as

$$E = [(\boldsymbol{\mu}_1 \cdot \boldsymbol{\mu}_2)r^{-3} - 3(\boldsymbol{\mu}_1 \cdot \boldsymbol{r})(\boldsymbol{\mu}_2 \cdot \boldsymbol{r})r^{-5}](\mu_0/4\pi) \tag{3}$$

where μ_0 is the permeability constant, $\mu_0 = 4\pi \times 10^{-7}$ kg m s^{-2} A^{-2}. If the two dipoles $\boldsymbol{\mu}_1$ and $\boldsymbol{\mu}_2$ have the same orientation with respect to $\boldsymbol{r}$ then equation (3)becomes:

$$E = (\boldsymbol{\mu}_1 \cdot \boldsymbol{\mu}_2)r^{-3}(1 - 3\cos^2\theta)(\mu_0/4\pi) \tag{4}$$

where θ is the angle between the direction of the two magnetic dipoles and the vector $\boldsymbol{r}$ which separates them.

In NMR studies, one is generally concerned with nuclear magnetic moments. Consider two nuclei (1 and 2) separated by a distance r in a magnetic field (Figure 1). The quantum mechanical Hamiltonian describing the direct dipolar interaction, $\hat{\mathcal{H}}_{\mathrm{DD}}$, is constructed by replacing the vectors $\boldsymbol{\mu}_1$ and $\boldsymbol{\mu}_2$ in equation (3) by their corresponding operators, $\gamma_1\hbar\hat{\boldsymbol{I}}_1$ and $\gamma_2\hbar\hat{\boldsymbol{I}}_2$:

$$\hat{\mathcal{H}}_{\mathrm{DD}} = \gamma_1\gamma_2\hbar^2[(\hat{\boldsymbol{I}}_1 \cdot \hat{\boldsymbol{I}}_2)r^{-3} - 3(\hat{\boldsymbol{I}}_1 \cdot \boldsymbol{r})(\hat{\boldsymbol{I}}_2 \cdot \boldsymbol{r})r^{-5}](\mu_0/4\pi) \tag{5}$$

where γ_i is the magnetogyric ratio of nucleus i (in rad s^{-1} T^{-1}), $\hat{\boldsymbol{I}}_i$ is the nuclear spin angular momentum operator, and $\boldsymbol{r}$ is the internuclear vector. In an NMR experiment, the direction of the magnetic moments is defined by the direction of the applied magnetic field $\boldsymbol{B}_0$.

If one expands the scalar products in equation (5),

$$\hat{\boldsymbol{I}}_1 \cdot \hat{\boldsymbol{I}}_2 = \hat{I}_{1x}\hat{I}_{2x} + \hat{I}_{1y}\hat{I}_{2y} + \hat{I}_{1z}\hat{I}_{2z} \tag{6}$$

$$\hat{\boldsymbol{I}}_1 \cdot \boldsymbol{r} = \hat{I}_{1x}x + \hat{I}_{1y}y + \hat{I}_{1z}z \tag{7}$$

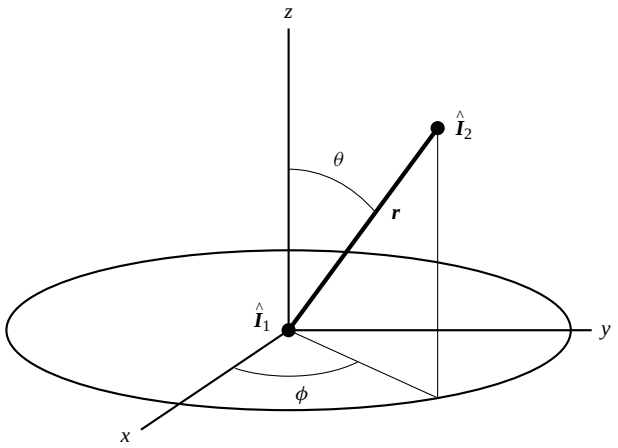

Figure 1 Coordinate system used to describe the coupling of two spins $\hat{\boldsymbol{I}}_1$ and $\hat{\boldsymbol{I}}_2$ separated by a distance r. A strong applied magnetic field lies along the z axis

$$\hat{\boldsymbol{I}}_2 \cdot \boldsymbol{r} = \hat{I}_{2x}x + \hat{I}_{2y}y + \hat{I}_{2z}z \tag{8}$$

the direct dipolar Hamiltonian may be expanded and rewritten as

$$\begin{aligned}\hat{\mathcal{H}}_{\mathrm{DD}} = \gamma_1\gamma_2\hbar^2 r^{-5}[&\hat{I}_{1x}\hat{I}_{2x}(r^2 - 3x^2) + \hat{I}_{1y}\hat{I}_{2y}(r^2 - 3y^2)\\ &+\hat{I}_{1z}\hat{I}_{2z}(r^2 - 3z^2) - (\hat{I}_{1x}\hat{I}_{2y} + \hat{I}_{1y}\hat{I}_{2x})3xy\\ &-(\hat{I}_{1y}\hat{I}_{2z} + \hat{I}_{1z}\hat{I}_{2y})3yz - (\hat{I}_{1z}\hat{I}_{2x} + \hat{I}_{1x}\hat{I}_{2z})3zx]\\ &\times(\mu_0/4\pi)\end{aligned} \tag{9}$$

This equation can be expressed in matrix form:

$$\hat{\mathcal{H}}_{\mathrm{DD}} = hR\left\{[\hat{I}_{1x} \quad \hat{I}_{1y} \quad \hat{I}_{1z}]\right.$$
$$\left.\begin{bmatrix} (r^2 - 3x^2)/r^2 & -3xy/r^2 & -3xz/r^2 \\ -3xy/r^2 & (r^2 - 3y^2)/r^2 & -3yz/r^2 \\ -3xz/r^2 & -3yz/r^2 & (r^2 - 3z^2)/r^2 \end{bmatrix} \begin{bmatrix} \hat{I}_{2x} \\ \hat{I}_{2y} \\ \hat{I}_{2z} \end{bmatrix}\right\} \tag{10}$$

where R is defined as the direct dipolar coupling constant,

$$R = \gamma_1\gamma_2 r^{-3}(\hbar/2\pi)(\mu_0/4\pi) \tag{11}$$

Equation (10) can be abbreviated as

$$\hat{\mathcal{H}}_{\mathrm{DD}} = hR(\hat{\boldsymbol{I}}_1 \cdot \boldsymbol{D} \cdot \hat{\boldsymbol{I}}_2) \tag{12}$$

where $\boldsymbol{D}$; is the direct dipolar tensor.

It is easy to see that if the internuclear vector $\boldsymbol{r}$, lies along the z axis, then the dipolar tensor becomes diagonal:

$$\boldsymbol{D} = \begin{bmatrix} 1 & 0 & 0 \\ 0 & 1 & 0 \\ 0 & 0 & -2 \end{bmatrix} \tag{13}$$

This is the so-called principal axis system (PAS) of the dipolar tensor. Note that the principal components of the dipolar tensor

are axially symmetric, i.e. $D_{11} = D_{22}$. From equation (10) it is also obvious that the dipolar tensor is symmetric (i.e. $D_{\alpha\beta} = D_{\beta\alpha}$). Finally, it is also clear that the trace of the dipolar tensor is zero. This result indicates that the direct dipolar interaction does not influence the positions of peaks in liquid phase NMR spectra. It can also be shown that for isolated spin pairs in solid samples the time averaged expectation value of $\hat{\mathcal{H}}_{\mathrm{DD}}$ is zero under conditions of MAS.[12] The sample must be spun rapidly with respect to the direct dipolar coupling constant R.

In order to discuss the NMR spectrum of two dipolar coupled spins in the solid state, it is convenient to transform equation (5) from Cartesian coordinates to spherical polar coordinates. This is readily accomplished by setting: $x = r \sin\theta \cos\phi$, $y = r \sin\theta \sin\phi$, $z = r \cos\theta$ and expressing $\hat{I}_x$ and $\hat{I}_y$ in terms of the raising and lowering operators $\hat{I}^+$ and $\hat{I}^-$, respectively:

$$\hat{\boldsymbol{I}}^+ = \hat{I}_x + \mathrm{i}\hat{I}_y, \quad \hat{\boldsymbol{I}}^- = \hat{I}_x - i, \hat{I}_y \tag{14}$$

Spin functions used to describe a nuclear spin state are eigenfunctions of the Zeeman Hamiltonian; they are often denoted by $|\, I,\, m\rangle$, where I is the nuclear spin quantum number and m is the z component of the spin angular momentum in units of $\hbar$ (i.e. $\hat{I}_z \mid I,\, m\rangle = m|I,\, m\rangle$). The spin quantum number m may take on values of $-I, -I+1, \ldots, +I$. Thus, for spin-$\frac{1}{2}$ nuclei there are only two states $|\, \frac{1}{2}, \frac{1}{2}\rangle$ and $|\, \frac{1}{2}, -\frac{1}{2}\rangle$, which are generally denoted by $|\, \alpha\rangle$ and $|\, \beta\rangle$, respectively: $\hat{I}_z \mid \alpha\rangle = \frac{1}{2}|\alpha\rangle$ and $\hat{I}_z|\beta\rangle = -\frac{1}{2}|\beta\rangle$, while $\hat{I}^+|\alpha\rangle = 0$, $\hat{I}^+|\beta\rangle = |\alpha\rangle$, $\hat{I}^-|\alpha\rangle = |\beta\rangle$ and $\hat{I}^-|\beta\rangle = 0$. Further details concerning the quantum mechanics of angular momentum can be found elsewhere.[8–11,13,14]

In spherical polar coordinates, the dipolar Hamiltonian can be expressed in terms of the so-called dipolar alphabet:

$$\hat{\mathcal{H}}_{\mathrm{DD}} = hR(\hat{A} + \hat{B} + \hat{C} + \hat{D} + \hat{E} + \hat{F}) \tag{15}$$

Each of the terms $\hat{A}$ to $\hat{F}$ contains spin operators and a spatial term generally involving both θ and ϕ. Each term alters the spin functions used to describe a spin pair in a characteristic way. Explicit expressions for the terms $\hat{A}$ to $\hat{F}$ are given in several NMR textbooks.[8–11]

To describe the NMR spectrum of a pair of equivalent homonuclear spins in a strong magnetic field, it is only necessary to consider the terms $\hat{A}$ and $\hat{F}$:

$$\hat{A} = -\hat{I}_{1z}\hat{I}_{2z}(3\cos^2\theta - 1) \tag{16}$$

$$\hat{B} = \tfrac{1}{4}[\hat{\boldsymbol{I}}_1^+ \cdot \hat{\boldsymbol{I}}_2^- + \hat{\boldsymbol{I}}_1^- \cdot \hat{\boldsymbol{I}}_2^+](3\cos^2\theta - 1) \tag{17}$$

Clearly, the $\hat{A}$ term does not alter the simple product spin functions $|\, \alpha\alpha\rangle$, $|\, \alpha\beta\rangle$, $|\, \beta\alpha\rangle$, and $|\, \beta\beta\rangle$ (e.g. $\hat{I}_{1z}\hat{I}_{2z}|\alpha\beta\rangle = (\frac{1}{2})(-\frac{1}{2})|\alpha\beta\rangle$). On the other hand, the $\hat{B}$ term contains the 'flip-flop' operator $\hat{I}_1^+\hat{I}_2^- + \hat{I}_1^-\hat{I}_2^+$, which alters the spin functions $|\, \alpha\beta\rangle$ to $|\, \beta\alpha\rangle$, and vice versa. For a pair of magnetically equivalent spins which are dipolar coupled in a strong applied magnetic field $\boldsymbol{B}_0$, the appropriate Hamiltonian operator is

$$\hat{\mathcal{H}} = \hat{\mathcal{H}}_{\mathrm{Z}} + \hat{\mathcal{H}}_{\mathrm{DD}} \tag{18}$$

where $\hat{\mathcal{H}}_{\mathrm{Z}} = -\nu_0 h(\hat{I}_{1z} + \hat{I}_{2z}$, and $\nu_0 = \gamma B_0/2\pi$. To describe such a spin system, it is convenient to use the following basis functions:

$$|t_1\rangle = |\alpha\alpha\rangle \tag{19a}$$

$$|t_0\rangle = 2^{-1/2}(|\alpha\beta\rangle + |\beta\alpha\rangle)$$

$$|s\rangle = 2^{-1/2}(|\alpha\beta\rangle - |\beta\alpha\rangle) \tag{19b}$$

$$|t_{-1}\rangle = |\beta\beta\rangle \tag{19c}$$

Using these basis functions, the total matrix of the truncated dipolar Hamiltonian operator is diagonal. The resulting eigenvalues of $\hat{\mathcal{H}}$ (in frequency units) are:

$$|t_1\rangle: \quad -\nu_0 - \tfrac{1}{4}R(3\cos^2\theta - 1) \tag{20a}$$

$$|t_0\rangle: \quad \tfrac{1}{2}R(3\cos^2\theta - 1) \tag{20b}$$

$$|t_{-1}\rangle: \quad \nu_0 - \tfrac{1}{4}R(3\cos^2\theta - 1) \tag{20c}$$

$$|s\rangle: \quad 0 \tag{20d}$$

where θ is the angle between the dipolar vector and the applied magnetic field $\boldsymbol{B}_0$. Transitions involving the antisymmetric $|\, s\rangle$ level are symmetry-forbidden; therefore only two transitions, $\nu_0 \pm \frac{3}{4}R(3\cos^2\theta - 1)$, are allowed.

For any general orientation of a spin pair in an applied magnetic field, the two peaks are separated by $(\frac{3}{2})R(3\cos^2\theta - 1)$. Spectra from an isolated homonuclear spin pair in a hypothetical single crystal and powder sample are shown in Figure 2. The powder spectrum, known as a Pake powder pattern, is obtained by considering all orientations of the dipolar vector in $\boldsymbol{B}_0$ ($0^\circ \le \theta \le 180^\circ$; $0^\circ \le \phi \le 360^\circ$). The separation between the discontinuities, $(\frac{3}{2})R$, corresponds to $\theta = 90^\circ$ while the shoulders are separated by $3R$, which corresponds to the $\theta = 0^\circ$ orientation.

For a pair of unlike spins A and X, where the two spins have different magnetogyric ratios but both are spin $\frac{1}{2}$, it is only necessary to consider the A term of $\hat{\mathcal{H}}_{\mathrm{DD}}$ since this is the only term in the dipolar alphabet which commutes with $\hat{\mathcal{H}}_{\mathrm{Z}}$. The A-spin NMR spectrum consists of two peaks at $\nu_{\mathrm{A}} \pm (\frac{1}{2})R(3\cos^2\theta - 1)$, where $\nu_{\mathrm{A}} = \gamma_{\mathrm{A}}B_0/2\pi$; the X-spin spectrum will be identical, except for the fact that it is centered about ν_{X} instead of ν_{A}. For unlike spins, the separation between the discontinuities in the A-spin or X-spin Pake powder pattern is R. If the X spin is a quadrupolar nucleus, calculation of the A-spin NMR spectrum may be more difficult, particularly if the high-field approximation is not applicable [i.e. $\hat{\mathcal{H}}_{\mathrm{Z}}(X) \approx \hat{\mathcal{H}}_{\mathrm{Q}}(X)$]. An instructive example of this problem was provided by Stoll et al.[15] who discussed the ^{13}C NMR spectra of the $^{13}\mathrm{C} - {}^{14}\mathrm{N}$ spin pair in a single crystal of $K_2Pt(CN)_4Br_{0.3}{\cdot}3H_2O$.

In practice, the chemical shielding interaction is orientation dependent, and thus it will also influence the detailed NMR lineshape. For protons, anisotropic chemical shielding generally causes a minor perturbation on the Pake doublet powder pattern, since it will be several orders of magnitude smaller than the direct dipolar interaction. However, for most other nuclei, the anisotropic chemical shielding (in frequency units) may be comparable to or greater than the dipolar interactions with adjacent nuclei. Under such conditions the

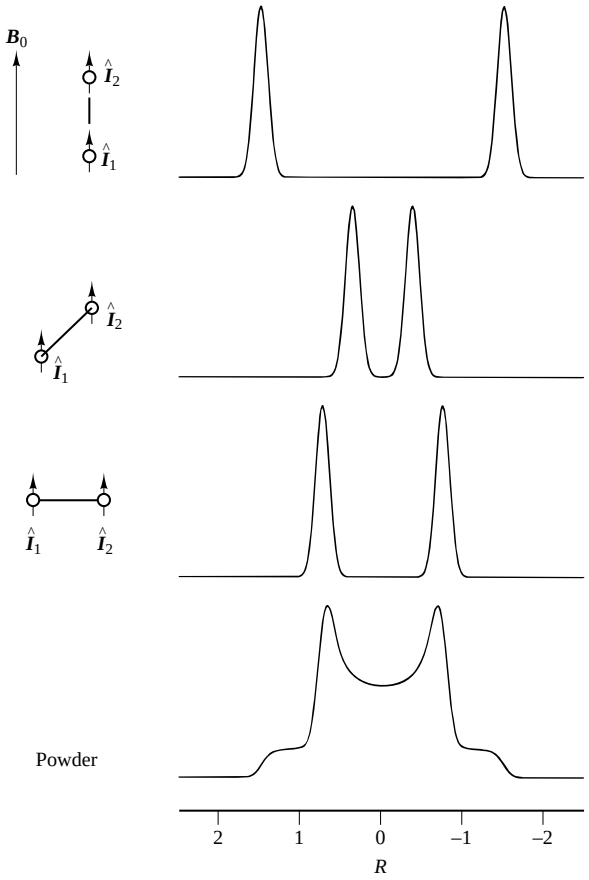

Figure 2 Calculated NMR spectra for two equivalent spins $\hat{\boldsymbol{I}}_1$ and $\hat{\boldsymbol{I}}_2$ which interact with one another by the direct dipolar interaction. From top to bottom: calculated spectra for three orientations of the internuclear vector in the applied magnetic field $\boldsymbol{B}_0$, θ = 0°, 45°, 90°, respectively. The bottom spectrum is the Pake powder pattern which results from a sum of spectra of individual crystallites which are randomly distributed in the sample. The calculated spectra have been convoluted with a Gaussian function to simulate weak dipolar interactions with more remote nuclei

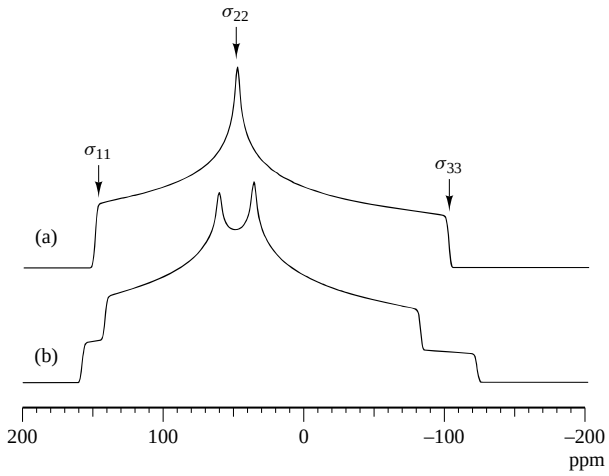

Figure 3 (a) A typical spin-$\frac{1}{2}$ NMR powder pattern of an isolated spin with anisotropic chemical shielding. The principal components of the chemical shielding tensor are easily identified from the powder pattern by the shoulders at σ_{11} and at σ_{33} and the discontinuity at σ_{22}. (b) Same as (a), but the influence of direct dipolar coupling with an adjacent spin-$\frac{1}{2}$ nucleus is illustrated. The direct dipolar interaction causes an apparent splitting of the chemical shielding powder pattern

Table 1 Typical Direct and Indirect Spin–Spin Coupling Constants Involving Carbon

X	Compound	R [a](Hz)	$J(\mathrm{M},^{13}\mathrm{C})_{\mathrm{iso}}$ (Hz)	$K(\mathrm{M,C})_{\mathrm{iso}}$ [b]
^{13}C	$C(CH_3)_4$ [c]	2080	37	4.9
^{29}Si	$Si(CH_3)_4$ [c]	−920	−50	8.4
^{73}Ge	$Ge(CH_3)_4$ [c]	−140	−19	17.7
^{119}Sn	$Sn(CH_3)_4$ [c]	−1090	−340	30.1
^{207}Pb	$Pb(CH_3)_4$ [c]	590	250	39.9
^{113}Cd	$Cd(CH_3)_2$ [d]	−740	−513	76.3
^{199}Hg	$Hg(CH_3)_2$ [e]	660	690	127
^{199}Hg	$Hg(CH_3)(NO_3)$ [e]	660	1800	331

[a]Approximate values. [b]$K_{\mathrm{N,N'}} = 4\pi^2 J_{\mathrm{N,N'}}/h\gamma_{\mathrm{N}}\gamma_{\mathrm{N'}}$ (units 10^{20} N A^{-2} m^{-3}). [c]Dalling and Gutowsky.[57] [d]Dreeskamp and Hildenbrand.[58] [e]Jokisaari et al.[59]

'A'-spin NMR spectrum of an AX-spin system in a static powder sample will consist of $2I$ + 1 overlapping powder patterns, where I is the spin quantum number of X (Figure 3). One can often obtain valuable information concerning the orientation of chemical shielding tensors by analyzing dipolar chemical shift NMR spectra.[14,16–18]

Typical values of the direct dipolar coupling constant involving directly bonded spin pairs range from a few hundred hertz to several kilohertz. For example, for the directly bonded ^{13}C–^{15}N spin pair in the amide fragment of a peptide, $R \approx 1.3$ kHz; for the directly bonded ^{13}C–^{1}H spin pair in a typical organic compound, $R \approx 23$ kHz. Further examples of direct dipolar coupling constants involving carbon are given in Table 1.

Much recent research is being focused on recoupling of dipolar interactions in high-resolution MAS experiments, e.g. the rotational resonance and rotational echo double resonance (REDOR) techniques.[19–21] The objective of these experiments is to determine internuclear separations from small dipolar coupling constants. In fact, as will be outlined in Section 3.2, these experiments yield only an effective dipolar coupling constant which is dependent on the anisotropy in the indirect coupling as well as the direct dipolar coupling constant R.

As an aside, it is important to indicate that anisotropic molecular vibrations can result in a subtle vibrationally induced asymmetry of the dipolar coupling tensor; this will be most important when the direct dipolar coupling involves a hydrogen nucleus.[22,23]

The discussion presented here can be extended to more complex spin systems. For example, Van Hecke et al.[24] studied the ^{1}H and ^{19}F NMR spectra of the bifluoride ion in a single crystal of KHF_2. In addition, systems containing the $^{13}CH_2$ fragment have attracted considerable attention.[25–27]

3 INDIRECT SPIN–SPIN COUPLING

As mentioned in Section 1, indirect spin–spin coupling is a two-stage process. One can imagine the spin at one nucleus perturbing the electrons in its vicinity. The resulting

perturbation is transferred via the electronic framework of the molecule to electrons in the vicinity of the second nucleus. The distinctive ways in which a nuclear moment perturbs the surrounding electrons is known as a mechanism for indirect spin–spin coupling (see below). The total indirect spin–spin coupling constant J is a sum of the contributions arising from each mechanism. Clearly, the contribution that each coupling mechanism makes to J is directly proportional to the product of the nuclear magnetic moments of the two coupled nuclei. The sign of indirect spin–spin coupling constants can be either positive or negative. If the indirect spin–spin coupling interaction stabilizes the antiparallel arrangement of the nuclear spins, then the indirect spin–spin coupling is positive. The magnitudes of isotropic indirect spin–spin coupling constants are readily measured in solution NMR studies. Values as small as 0.10 Hz are routinely measured. Isotropic values rarely exceed 30 kHz; however, a ^{199}Hg,^{199}Hg indirect spin–spin coupling constant of 139.6 kHz has been reported for the Hg_3^{2+} ion.[28] Typical values of one-bond indirect spin–spin coupling constants involving carbon, $^1J(\mathrm{M},^{13}\mathrm{C})_{\mathrm{iso}}$, are given in Table 1. The literature on isotropic indirect spin–spin coupling constants is extensive.[29] Over the past 45 years many important relationships between spin–spin coupling constants J_{iso} and molecular structure have been established. On the other hand $\boldsymbol{J}$ tensors are difficult to characterize experimentally. Furthermore, reliable quantum mechanical calculations of $\boldsymbol{J}$ tensors or their corresponding isotropic values are a challenge.[30] Here, the properties of the $\boldsymbol{J}$ tensor are outlined. This is followed by a discussion of how the $\boldsymbol{J}$ tensor can be experimentally characterized from solid state NMR measurements.

3.1 Nature of $\boldsymbol{J}$ Coupling Tensors

The Hamiltonian describing the indirect spin–spin coupling of two spins, $\boldsymbol{I}_1$ and $\boldsymbol{I}_2$, may be expressed as

$$\hat{\mathcal{H}}_J = h\hat{\boldsymbol{I}}_1 \cdot \boldsymbol{J} \cdot \hat{\boldsymbol{I}}_2 \tag{21}$$

where $\boldsymbol{J}$ is the indirect spin–spin coupling tensor. The $\boldsymbol{J}$ tensor is a second rank tensor which is described by nine matrix elements in a Cartesian coordinate system. For example, in a particular molecular fixed axis system, the $\boldsymbol{J}$ tensor might be represented by the matrix:

$$\boldsymbol{J} = \begin{bmatrix} J_{aa} & J_{ab} & J_{ac} \\ J_{ba} & J_{bb} & J_{bc} \\ J_{ca} & J_{cb} & J_{cc} \end{bmatrix} \tag{22}$$

In contrast to the direct dipolar tensor, the $\boldsymbol{J}$ tensor has a nonvanishing trace.

A general second-rank tensor can be decomposed into a sum of irreducible tensors of rank l = 0, 1, 2.[31,32] Thus the indirect spin–spin coupling tensor can be written as

$$\boldsymbol{J} = \boldsymbol{J}^{(0)} + \boldsymbol{J}^{(1)} + \boldsymbol{J}^{(2)} \tag{23}$$

In equation (23) the l = 0 tensor is the isotropic part of the tensor,

$$\boldsymbol{J}^{(0)} = (\tfrac{1}{3}\ \mathrm{Tr}\ \boldsymbol{J})\boldsymbol{1} = J_{\mathrm{iso}}\boldsymbol{1} \tag{24}$$

where $\mathrm{Tr}\ \boldsymbol{J} = (J_{aa} + J_{bb} + J_{cc})$ and $\boldsymbol{1}$ is the unit tensor with diagonal components equal to 1 and all off-diagonal elements zero. The second term in equation (23), l = 1, is the antisymmetric part of the tensor,

$$\boldsymbol{J}^{(1)} = \tfrac{1}{2}(\boldsymbol{J} - \boldsymbol{J}^{\mathrm{t}}) \tag{25}$$

where $\boldsymbol{J}^{\mathrm{t}}$ is the transpose of $\boldsymbol{J}$. The transpose of a 3 × 3 matrix is obtained by replacing the first column by the first row, the second column by the second row, and the third column by the third row. Since the diagonal elements of $\boldsymbol{J}$ and $\boldsymbol{J}^{\mathrm{t}}$ are identical, the diagonal elements of the antisymmetric tensor are zero. The third term in equation (23), l = 2, is the symmetric part of the tensor, defined as

$$\boldsymbol{J}^{(2)} = \tfrac{1}{2}(\boldsymbol{J} + \boldsymbol{J}^{\mathrm{t}}) - J_{\mathrm{iso}}\boldsymbol{1} \tag{26}$$

Although the trace of the symmetric part is zero, the diagonal elements are, in general, not zero.

To a very good approximation, only tensors with l = 0 and l = 2 affect the general appearance of an NMR spectrum.[32] That is, even though the antisymmetric components of a particular $\boldsymbol{J}$ tensor may be non zero, these components do not perturb the observed spectrum in first order. In fact, the existence of antisymmetric components in any indirect spin–spin coupling tensor has never been demonstrated experimentally.[33]

For each symmetric $\boldsymbol{J}$ tensor ($\boldsymbol{J}^{(0)} + \boldsymbol{J}^{(2)}$), there exists a principal axis system for which the matrix $\boldsymbol{J}^{(2)}$ is diagonal. The diagonal elements, denoted by J_{xx}, J_{yy}, and J_{zz}, are called the principal elements, with the convention:

$$|J_{zz}| \geq |J_{xx}| \geq |J_{yy}| \tag{27}$$

The principal axis system of the $\boldsymbol{J}$ tensor is often fixed by the molecular symmetry. For a linear molecule there are only two components, $J_{\parallel}$ and $J_{\perp}$, describing the coupling of the nuclear spin components parallel and perpendicular to the internuclear axis, respectively. Similarly, there are only two non-zero components of the symmetric $\boldsymbol{J}$ tensor for a pair of nuclei sitting on the highest order symmetry axis of molecules in the point groups D_{nd}, D_{nh}, C_{nh}, C_{nv}, and S_n, with $n \geq 3$. The number of independent components in the $\boldsymbol{J}$ tensor for other group symmetries has been tabulated by Buckingham et al.[33] and by Robert and Wiesenfeld.[34]

In describing the orientation dependence of NMR parameters, it is often useful to define the anisotropy of the parameter. This provides a measure of the maximum orientation dependence of that particular parameter. The anisotropy of the indirect spin–spin coupling tensor is usually defined as

$$\Delta J = J_{zz} - \tfrac{1}{2}(J_{xx} + J_{yy}) \equiv \tfrac{3}{2}(J_{zz} - J_{\mathrm{iso}}) \tag{28}$$

In the case of axial symmetry, equation (28) simplifies to

$$\Delta J = J_{\parallel} - J_{\perp} \tag{29}$$

In such cases it is straightforward to show that

$$\boldsymbol{J} = \begin{bmatrix} J_{\perp} & 0 & 0 \\ 0 & J_{\perp} & 0 \\ 0 & 0 & J_{\parallel} \end{bmatrix} = J_{\mathrm{iso}}\boldsymbol{1} + \begin{bmatrix} -\Delta J/3 & 0 & 0 \\ 0 & -\Delta J/3 & 0 \\ 0 & 0 & 2\Delta J/3 \end{bmatrix} \tag{30}$$

Under these conditions the Hamiltonian equation (21), becomes

$$\hat{\mathcal{H}}_{\boldsymbol{J}} = hJ_{\rm iso}\hat{\boldsymbol{I}}_1 \cdot \hat{\boldsymbol{I}}_2 + h\hat{\boldsymbol{I}}_1 \cdot \boldsymbol{J}' \cdot \hat{\boldsymbol{I}}_2 \tag{31}$$

where $\boldsymbol{J}'$ is the traceless '$\Delta\boldsymbol{J}$' tensor which is of the same form as the dipolar tensor [equation (13)]. Since the trace of $\boldsymbol{J}'$ is zero, it is clear that the anisotropy in the principal components of $\boldsymbol{J}$ has no influence on the NMR spectra of isotropic fluids. In principle, ΔJ could provide a mechanism for spin–lattice relaxation, but this mechanism has never been identified as being important.[35]

Ramsey's theory[5] serves as the basis for most theoretical discussions of indirect spin–spin coupling tensors. Following Ramsey, the nonrelativistic Hamiltonian describing nuclear spin, electron spin interactions can be represented by

$$\hat{\mathcal{H}} = \hat{\mathcal{H}}^{(1a)} + \hat{\mathcal{H}}^{(1b)} + \hat{\mathcal{H}}^{(2)} + \hat{\mathcal{H}}^{(3)} \tag{32}$$

The first two terms are the so-called orbital diamagnetic (OD) and orbital paramagnetic (OP) terms which account for the interaction between the nuclear magnetic moments and the orbital motion of the electrons. The third term, $\hat{\mathcal{H}}^{(2)}$, accounts for the spin-dipolar (SD) interactions between the nuclear and electronic magnetic moments. The last term, $\hat{\mathcal{H}}^{(3)}$, accounts for the interaction of the nucleus and the electron spin at the nucleus; this interaction is known as the Fermi contact (FC) interaction. Using these interactions, various approaches, generally based on second-order perturbation theory, are used to calculate indirect nuclear spin–spin coupling tensors. Five separate terms contribute to the overall $\boldsymbol{J}$ tensor:

$$\boldsymbol{J} = \boldsymbol{J}^{(1a)} + \boldsymbol{J}^{(1b)} + \boldsymbol{J}^{(2)} + \boldsymbol{J}^{(3)} + \boldsymbol{J}^{(4)} \tag{33}$$

The orbital diamagnetic contribution $\boldsymbol{J}^{(1a)}$ involves only the ground electronic state of the system. The other four terms involve the following combination of interactions: OP–OP, SD–SD, FC–FC, and FC–SD. The OP term has matrix elements between the ground state and excited singlet states while the SD and FC interactions have matrix elements between the ground state and excited triplet states. The FC–FC contribution to the $\boldsymbol{J}$ tensor is completely isotropic. In contrast, the FC–SD cross term does not contribute to the isotropic value of the spin–spin coupling tensor, but only to its anisotropy, thus the trace of the tensor arising from this term is zero. The other two terms contribute to both the isotropic and anisotropic portion of the total $\boldsymbol{J}$ tensor.

Explicit expressions for each of the five terms in equation (33) are given in several standard NMR texts and review articles.[29,36] It should be mentioned that the theory of Ramsey is a nonrelativistic theory which assumes that orbital and spin angular momenta are L–S coupled. Pyykkö[37] has developed a relativistic analogue of Ramsey's theory based on j–j coupling. Undoubtedly, relativistic effects will be important for indirect spin–spin coupling constants involving nuclei beyond the second row. Furthermore, it has been found that consideration of relativistic effects in extended Hückel calculations tends to increase the calculated anisotropy of spin–spin coupling tensors.[38]

In equation (33), each term is of the form $\gamma_N\gamma_{N'}h\boldsymbol{K}_{N,N'}/4\pi^2$, where $\boldsymbol{K}_{N,N'}$ is called the reduced indirect spin–spin coupling tensor involving nuclei N and N'. The reduced coupling tensor is independent of the magnitude of the nuclear magnetic moments and, therefore, it is useful in comparing indirect spin–spin coupling tensors involving different spin pairs. Note that $\boldsymbol{J}_{N,N'}$ has units of Hz (s^{-1}) and $\boldsymbol{K}_{N,N'}$ has units of N A^{-2} m^{-3} (or, equivalently, T^2 J^{-1}).[39] The isotropic indirect spin–spin coupling constants involving carbon in Table 1 have also been expressed as reduced coupling constants. As one descends the group 14 elements, M, of the Periodic Table in the series $M(CH_3)_4$, $\boldsymbol{K}$(M,C) increases with atomic number Z_M. Similarly, in the series X_3MPR_3, where M is a group 13 element, $\boldsymbol{K}$(M,P) increases as follows: $\approx 10 \times 10^{20}$ N A^{-2} m^{-3} (M = B), $\approx 20 \times 10^{20}$ (Al), $\approx 65 \times 10^{20}$ (M = Ga), and $\approx 100 \times 10^{20}$ (M = In).[40] Qualitatively, these trends can be rationalized by considering only the Fermi contact mechanism; however, there is evidence that the tensor, $\boldsymbol{K}$(In,P), in $Br_3InP[4\text{-}(CH_3O)\text{-}C_6H_4]_3$ is anisotropic, implying that mechanisms other than the Fermi contact contribute to this particular $\boldsymbol{J}$ tensor.[40]

3.2 Measurement of $\boldsymbol{J}$ Coupling Tensors

Using NMR spectroscopy, $\boldsymbol{J}$ tensors can be characterized by studying the spectra of single crystals,[41–43] solid powder samples,[44–47] or samples oriented in liquid crystalline solvents.[48,49] In isotropic fluids, only the isotropic indirect spin–spin coupling constant (a scalar) is measured. For simple molecules in the gas phase ΔJ can, in principle, be measured using molecular beam magnetic resonance techniques.[50] So far, the latter technique has only been successfully applied to thallium fluoride.[51] In this case, $J(^{205}\text{Tl}, {}^{19}\text{F})_{\rm iso} = -13.3 \pm 0.7$ kHz and $\Delta J(^{205}\text{Tl}, {}^{19}\text{F}) = 11.1 \pm 0.7$ kHz. Below, the NMR spectra of a simple heteronuclear two-spin system residing in a rigid solid will be discussed. Particular emphasis is placed on describing how the NMR spectra depend on ΔJ.

Consider a pair of heteronuclear spins A and X, also denoted by '1' and '2', respectively, which are coupled to one another via direct and indirect spin–spin interactions in a strong applied magnetic field. Furthermore, if the $\boldsymbol{J}$ tensor is axially symmetric and coincident with the direct dipolar tensor, $J_\parallel$ and $J_\perp$ correspond to orientations where the internuclear vector is parallel and perpendicular, respectively, to the applied magnetic field. Under these conditions the appropriate nuclear spin Hamiltonian for the A spin is:

$$\hat{\mathcal{H}} = \hat{\mathcal{H}}_{\rm Z} + \hat{\mathcal{H}}_{\rm CS} + \hat{\mathcal{H}}_{\rm DD} + \hat{\mathcal{H}}_J \tag{34}$$

where $\hat{\mathcal{H}}_{\rm CS}$ accounts for the anisotropic chemical shielding. For now it is assumed that the chemical shielding is independent of the orientation of the molecule in the applied magnetic field. Both $\hat{\mathcal{H}}_{\rm DD}$ and $\hat{\mathcal{H}}_J$ are of the same form. As already indicated

$$\hat{\mathcal{H}}_{\rm DD} = hR\hat{\boldsymbol{I}}_1 \cdot \boldsymbol{D} \cdot \hat{\boldsymbol{I}}_2 = -hR\hat{I}_{1z}\hat{I}_{2z}(3\cos^2\theta - 1) \tag{35}$$

Similarly, equation (31) becomes

$$\hat{\mathcal{H}}_J = h\hat{\boldsymbol{I}}_1 \cdot \boldsymbol{J} \cdot \hat{\boldsymbol{I}}_2 = hJ_{\rm iso}\hat{I}_{1z}\hat{I}_{2z} + h(\Delta J/3)\hat{I}_{1z}\hat{I}_{2z} \times (3\cos^2\theta - 1) \tag{36}$$

Using the basic product functions for an AX spin system consisting of two spin-$\frac{1}{2}$ nuclei, it is straightforward to calculate the four energy levels. The A spectrum results from two allowed transitions at:

$$\nu = \nu_A - m_X J_{iso} + m_X[R - (\Delta J/3)](3\cos^2\theta - 1) \quad (37)$$

where $m_X = +\frac{1}{2}$ or $-\frac{1}{2}$. The two A peaks are separated by

$$\Delta\nu = J_{iso} - [R - (\Delta J/3)](3\cos^2\theta - 1) \quad (38)$$

Often, the term $R - (\Delta J/3)$ in equations (37) and (38) is called the effective dipolar coupling constant R_{eff}; thus,

$$\Delta\nu = J_{iso} - R_{eff}(3\cos^2\theta - 1) \quad (39)$$

The splittings, $\Delta\nu$, that would be observed as the A–X bond axis, $\boldsymbol{r}_{AX}$, in a single crystal is rotated about an axis perpendicular to $\boldsymbol{B}_0$ are shown in Figure 4. Several important points emerge from equations (37)–(39) and Figure 4:

1. For a single crystal sample, equation (39) also applies if the chemical shielding is anisotropic.
2. From Figure 4 it is apparent that the maximum *variation* in the splitting of the A peaks is $3R_{eff}$. Experimentally, one cannot separately determine R and ΔJ; only R_{eff} can be measured. If a value for the internuclear separation r_{AX} can be determined independently by diffraction techniques, R can be calculated from equation (11), and ΔJ can be obtained from the experimental value of R_{eff}.
3. The relative sign of J_{iso} and R_{eff} can be deduced from single crystal measurements. If J_{iso} and R_{eff} have the same sign, the maximum splitting will be $|J_{iso}| + |R_{eff}|$, while the minimum splitting will be $|J_{iso}| - 2|R_{eff}|$. On the other hand, if J_{iso} and R_{eff} have opposite signs, the maximum splitting will be $|J_{iso}| + 2|R_{eff}|$ and the minimum splitting will be $|J_{iso}| - |R_{eff}|$.

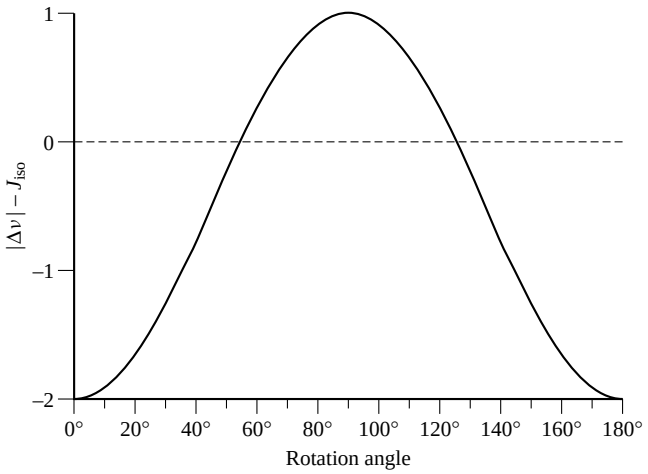

Figure 4 Separation between the two allowed A spin transitions for an AX spin system in a single crystal as a function of the orientation in the applied magnetic field $\boldsymbol{B}_0$. Splittings are given in units of R_{eff}. The rotation axis is perpendicular to $\boldsymbol{B}_0$ and the rotation angle θ is defined as the angle between $\boldsymbol{r}_{AX}$ and $\boldsymbol{B}_0$

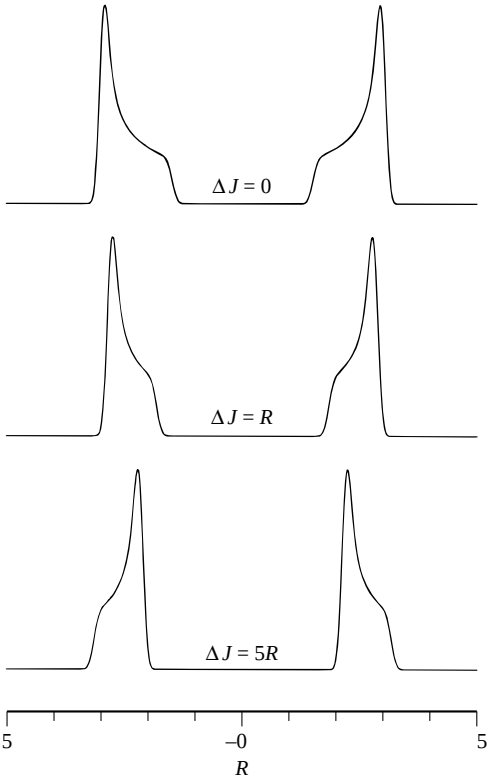

Figure 5 The effect of ΔJ on the A-spin NMR spectrum of a powder sample containing a heteronuclear AX spin pair. In each case $J_{iso} = 5R$. With $\Delta J = 3R$, each subspectrum collapses into an isotropic peak

In the case of a powder sample, the A spectrum consists of two subspectra corresponding to $m_X = +\frac{1}{2}$ and $m_X = -\frac{1}{2}$. Each subspectrum is one-half of a conventional Pake powder pattern (Figure 5). The isotropic frequencies of the two subspectra are separated by J_{iso}. (Note that if $J_{iso} = 0$, conventional Pake powder patterns would be observed except for the case where $\Delta J = 3R$.)

In calculating the spectra shown in Figure 5, the chemical shielding is assumed to be isotropic (i.e. independent of orientation). In order to calculate the A-spin NMR powder lineshape, allowing for the possibility of anisotropic chemical shielding, it is convenient to define the orientation of the internuclear vector in the PAS of the chemical shielding tensor (Figure 6). In this case one can show that the frequency of the A-spin transitions are given by:

$$\nu_m(\theta,\phi) = \nu_L - \nu_{CS} - m_X\nu_D - m_X J_{iso} \quad (40)$$

$$\nu_L = \gamma_A B_0/2\pi \quad (41)$$

$$\nu_{CS} = \left(\frac{\gamma_A B_0}{2\pi}\right)(\sigma_{11}\sin^2\theta\cos^2\phi + \sigma_{22}\sin^2\theta\sin^2\phi + \sigma_{33}\cos^2\theta) \quad (42)$$

$$\nu_D = R_{eff}\{1 - 3[\sin\beta\sin\theta\cos(\phi - \alpha) + \cos\beta\cos\theta]^2\} \quad (43)$$

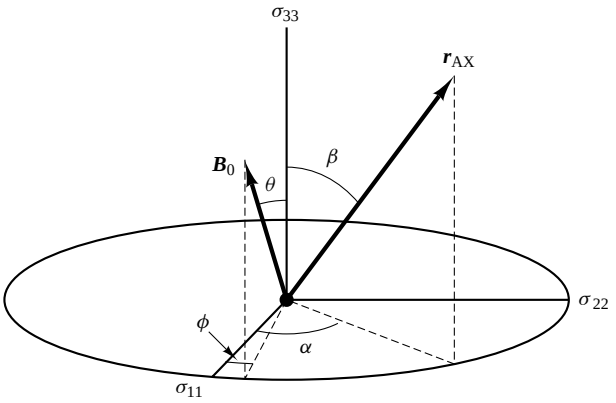

Figure 6 The orientation of an internuclear vector $\boldsymbol{r}_{AX}$ in the principal axis system (PAS) of the A-spin shielding tensor. The angles θ and ϕ define the orientation of $\boldsymbol{B}_0$ in the PAS of the shielding tensor

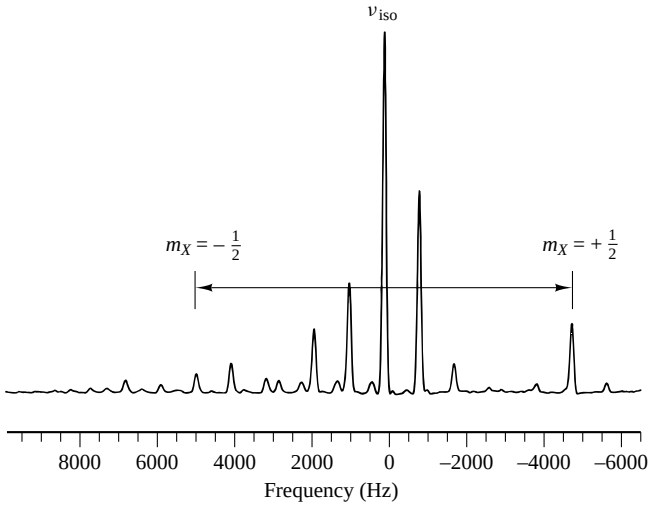

Figure 7 The ^{31}P NMR spectrum of a powder sample of [HgP(*o*-tolyl)$_3$(NO$_3$)$_2$]$_2$ obtained with relatively slow magic angle sample spinning (ν_r = 892 Hz). The spectrum was obtained with high-power ^{1}H decoupling and cross polarization in an applied magnetic field of 4.7 T, corresponding to a ^{31}P NMR Larmor frequency of 81.0 MHz. Frequencies are given with respect to the isotropic ^{31}P NMR peak of solid $NH_4H_2PO_4$. The horizontal arrow indicates the separation between the isotropic peak positions of the ^{199}Hg satellite peaks (J_{iso} = 9660 Hz). Note that the spinning sidebands of the high-frequency satellite peak, $m_{Hg-199} = -\frac{1}{2}$, extend over a much larger range than do those of the low-frequency satellite corresponding to $m_{Hg-199} = \frac{1}{2}$

where the principal components of the chemical shielding tensor σ_{11}, σ_{22}, and σ_{33} are defined such that $\sigma_{11} \leq \sigma_{22} \leq \sigma_{33}$. All angles are defined in Figure 6. In deriving equations (40)–(43), it is assumed that the $\boldsymbol{J}$ tensor is axially symmetric and that the $\boldsymbol{J}$ and $\boldsymbol{D}$ tensors are coincident. Even with these assumptions, the A-spin NMR powder spectrum may prove difficult to analyze.[18]

From the above discussion, it should be clear that if one is interested in characterizing a particular $\boldsymbol{J}$ tensor using solid state NMR techniques, single crystal NMR studies are desirable. Unfortunately, few studies have been reported to date.[41–43] Such studies are generally tedious, require relatively large single crystals (e.g. sides of 1 mm or greater), and the results of an X-ray or neutron diffraction investigation. In some cases, values of ΔJ can be obtained from the analysis of NMR powder spectra which arise from isolated spin pairs.[44–47] For example, for a series of mercury phosphine complexes values of $\Delta J(^{199}\text{Hg}, ^{31}\text{P})$ of the order of 5 kHz have been estimated from the analysis of static ^{31}P NMR spectra.[46,47] Below, the general procedure used to analyze such spectra is outlined.

The ^{31}P CP MAS spectrum of one of these complexes, [HgP(*o*-tolyl)$_3$(NO$_3$)$_2$]$_2$, is shown in Figure 7. The natural abundance of ^{199}Hg is 16.84% ($I = \frac{1}{2}$), therefore the ^{31}P NMR spectrum of the molecules containing the ^{199}Hg–^{31}P spin pair is a doublet with separation $J(^{199}\text{Hg},^{31}\text{P})_{iso}$ = 9660 Hz. The sign of this indirect spin–spin coupling constant is assumed to be positive on the basis of double resonance NMR experiments carried out on related molecules in solution. The only other naturally occurring isotope of mercury with nonzero spin is ^{201}Hg ($I = \frac{3}{2}$; natural abundance 13.22%), but the ^{31}P NMR spectrum of the ^{201}Hg–^{31}P spin pair is very broad and difficult to observe at room temperature. Molecules containing other naturally occurring isotopes of mercury give rise to a single isotropic peak, since the mercury nuclei of these isotopes have $I = 0$. In order to obtain R_{eff}, it is most advantageous to obtain a ^{31}P NMR spectrum of a static powder sample (Figure 8). Again, the intense central feature in the ^{31}P NMR spectrum corresponds to molecules where mercury nuclei have a spin $I = 0$.

Analysis of this central lineshape provides the principal components of the phosphorus shielding tensor, information required to analyze the subspectra arising from the ^{199}Hg–^{31}P spin pairs. In this case, the phosphorus shielding tensor is

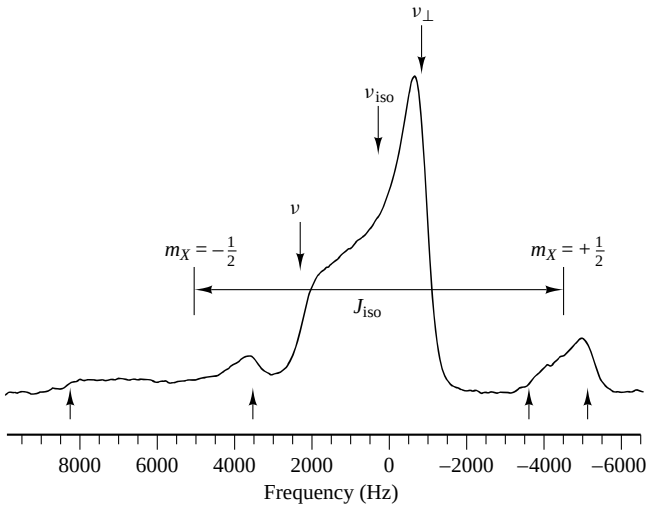

Figure 8 The ^{31}P NMR spectrum of a static powder sample of [HgP(*o*-tolyl)$_3$(NO$_3$)$_2$]$_2$ obtained at 81.0 MHz

approximately axially symmetric with the unique component along the Hg–P bond axis. Inspection of the spectrum shown in Figure 8 indicates that the high-frequency subspectrum corresponding to $m_{Hg-199} = -\frac{1}{2}$ is stretched (breadth ≈4.75 kHz), while the low-frequency subspectrum corresponding to $m_{Hg-199} = \frac{1}{2}$ is squeezed (breadth ≈1.45 kHz) relative to the intense central powder pattern [$(\nu_\parallel - \nu_\perp) \approx 3.10$ kHz]. In this particular case it is straightforward to show that the

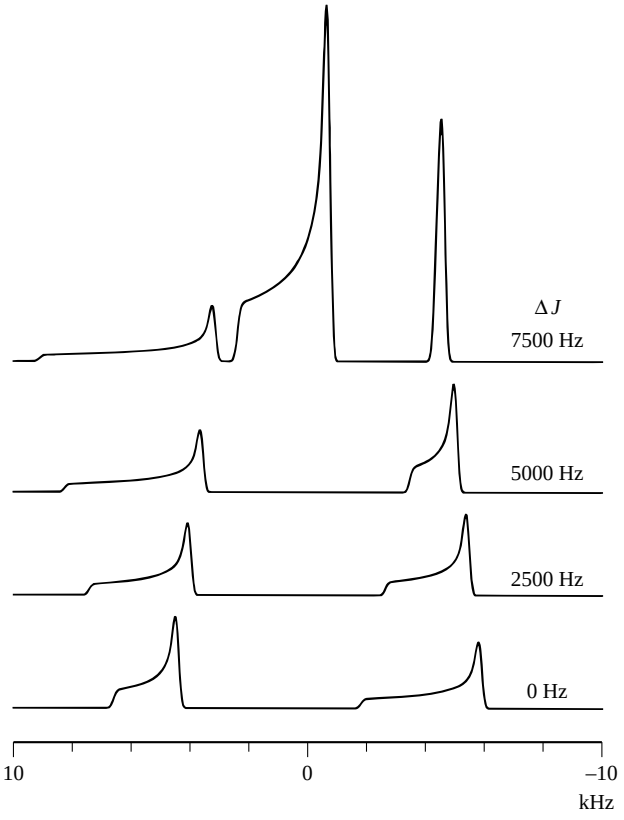

Figure 9 Calculated ^{31}P NMR powder spectra of [HgP(*o*-tolyl)$_3$(NO$_3$)$_2$]$_2$ as a function of ΔJ. The direct dipolar coupling constant, R = 0.64 kHz, and ($\nu_{\parallel} - \nu_{\perp}$) $\approx$ 3.10 kHz were held constant in each calculation. The central uncoupled ^{31}P NMR spectrum is only shown in the top spectrum; its intensity has been suppressed to emphasize the variations in the satellite subspectra as a function of ΔJ

breadth of each subspectrum is given by

$$\Delta\nu_{\pm m(Hg-199)} = (\nu_{\parallel} - \nu_{\perp}) \pm 3m_{Hg-199}R_{eff} \qquad (44)$$

Solving equation (44), one obtains R_{eff} = −1.10 kHz. From the known values of r_{Hg-P} in closely related compounds, R = 0.64 kHz; thus (ΔJ/3) = 1.74 kHz and ΔJ = 5.2 kHz. Note that if the relative signs of R_{eff} and J_{iso} were not known, another acceptable solution would be R_{eff} = + 1.10 kHz, hence ΔJ = −1.38 kHz. The sensitivity of the ^{31}P NMR spectrum of [HgP(*o*-tolyl)$_3$(NO$_3$)$_2$]$_2$ to ΔJ is illustrated in Figure 9. A complete single crystal ^{31}P NMR study of a closely related compound, HgP(cyclohexyl)$_3$(NO$_3$)$_2$, has recently been completed.[52] A typical rotation pattern is shown in Figure 10. Analysis indicates that R_{eff} = −1.07 kHz, leading to comparable values of ΔJ(^{199}Hg,^{31}P).[52] The results of these studies are significant in that they indicate that mechanisms other than the Fermi contact contribute to the $\boldsymbol{J}$(^{199}Hg, ^{31}P) tensor.

For AX spin systems in powder samples, one can also obtain R_{eff} from slow spinning MAS or variable angle spinning NMR studies; however, the errors tend to be large. Therefore, unless R_{eff} is significantly different than R, any estimate of ΔJ may be meaningless.

If a spin-$\frac{1}{2}$ nucleus is coupled to a neighboring quadrupolar nucleus, the spin-$\frac{1}{2}$ MAS NMR lineshape will often exhibit

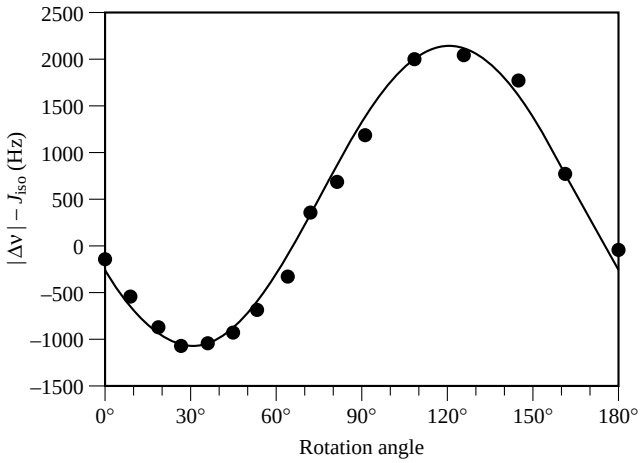

Figure 10 Plot of $\Delta\nu - J$(^{199}Hg,^{31}P)$_{iso}$ versus the rotation angle for a single crystal of HgP(cyclohexyl)$_3$(NO$_3$)$_2$. In this case the rotation axis is approximately perpendicular to the vector $\boldsymbol{r}_{Hg-P}$ so that the maximum observed variation in frequency (3.21 kHz) is approximately $3R_{eff}$

residual 'dipolar splittings' due to coupling with the quadrupolar nucleus.[53] In such cases the magic angle is no longer 'magic' because of the breakdown of the high-field approximation. Qualitatively, the Zeeman states of the quadrupolar nuclei are perturbed by the quadrupolar interaction. Thus, the detailed spin-$\frac{1}{2}$ MAS NMR lineshape depends on R_{eff}, $\boldsymbol{B}_0$, the nuclear quadrupolar coupling constant, and the orientation of the EFG tensor at the quadrupolar nucleus with respect to R_{AX}. Unless information concerning the EFG tensor at the quadrupolar nucleus is available from independent NMR or NQR studies, analysis of the spin-$\frac{1}{2}$ MAS NMR spectrum will be problematic.

Information concerning ΔJ is also available from NMR studies of solute molecules partially ordered in liquid crystalline solvents; however, again one can only determine $\boldsymbol{R}_{AX}$. In fact, from such experiments one measures a parameter which is related to $-S_{zz}[R - (\Delta J/3)]$, where S_{zz} is an order parameter, typically of the order of 0.1. In addition, it is necessary to make vibrational corrections and consider solute–liquid crystal solvent interactions. In spite of these problems, reliable values of ΔJ appear to be available for several compounds. For example, for methyl fluoride, ΔJ(^{19}F,^{13}C) = 404 ± 31 Hz, and thus ΔJ(^{19}F,^{13}C)/J(^{19}F,^{13}C)$_{iso}$ = −2.5 ± 0.2;[54] for dimethylmercury, ΔJ(^{199}Hg,^{13}C) = 855 ± 14 Hz, and thus ΔJ(^{199}Hg,^{13}C)/ J(^{199}Hg,^{13}C)$_{iso}$ = 1.25 ± 0.02.[55]

As mentioned in Section 2, several NMR experiments have been developed to recouple the direct dipolar interaction under conditions of MAS. Although such experiments actually measure R_{eff}, and not R, it is probably reasonable to assume that (ΔJ/3) $\ll R$, if the coupled nuclei are both first row elements (e.g. ^{13}C and ^{15}N), where J_{iso} is probably at least an order of magnitude less than R. Clearly, reliable theoretical calculations could be of value in assessing the validity of this assumption for any given spin pair.

Finally, it is of interest to mention that, several years ago, Andrew and Farnell[56] investigated the effect of magic angle sample spinning on each of the irreducible tensors which describe the indirect spin–spin coupling tensor [equation (23)]. Of course, MAS does not influence the term $J\mathbf{1}$; also, the traceless symmetric components do not influence

the MAS spectrum. However, for a homonuclear spin pair, they found that MAS will not necessarily result in a complete averaging of the antisymmetric components of the **J** tensor [i.e. components of $\boldsymbol{J}^{(1)}$ in equation (23)]. The contribution of the antisymmetric components was predicted to be most important when the chemical shift difference between the two coupled spins was very small. Further discussions of the possibility of measuring antisymmetric components of the **J** tensor are given in the excellent review by Robert and Wiesenfeld.[34] As already mentioned, the antisymmetric components of any indirect spin–spin coupling tensor have not been experimentally characterized.

4 SUMMARY

From the experimental point of view, it is clear that the mathematical properties of the anisotropic indirect **J** tensor are analogous to those of the direct dipolar tensor. As a result, it is impossible to measure separately the anisotropic **J** tensor and the direct dipolar tensor. Fortunately, for isolated spin pairs in rigid solid samples, the direct dipolar tensor can always be calculated if structural data are available. The most reliable procedure for characterizing **J** tensors in the solid state involves single crystal NMR experiments. For solid powder samples the determination of ΔJ is often problematic. The reliability of a powder analysis will always be greatest when: (i) the spin pair of interest lies along a symmetry axis, (ii) J_{iso} is large enough so that the individual subspectra are well resolved, and (iii) R is small or at least comparable to $\Delta J/3$. With the availability of higher sensitivity NMR hardware and advanced single crystal NMR experiments one can hope that more reliable experimental data will become available. In the future, one can also anticipate significant advances in computational techniques, particularly for relatively small molecules involving atoms of the first two rows of the Periodic Table. Unfortunately, these are the systems where it is most difficult to obtain reliable experimental data concerning the anisotropy in the **J** tensor. In any case, it is clear that in order to formulate meaningful models relating J couplings to molecular structure, a better understanding of the **J** tensor is essential. Obviously, any information that indicates which mechanisms are or are not operative is critically important in leading to a better understanding of J coupling phenomena.

5 RELATED ARTICLES

Anisotropy of Shielding and Coupling in Liquid Crystalline Solutions; CRAMPS; Electron–Nuclear Multiple Resonance Spectroscopy; Indirect Coupling: Semiempirical Calculations; Indirect Coupling: Theory and Applications in Organic Chemistry; Internal Spin Interactions and Rotations in Solids; Magic Angle Spinning; REDOR and TEDOR; Rotating Solids.

6 REFERENCES

1. G. E. Pake, *J. Chem. Phys.*, 1948, **16**, 327.
2. W. G. Proctor and F. C. Yu, *Phys. Rev.*, 1951, **81**, 20.
3. H. S. Gutowsky and D. W. McCall, *Phys. Rev.*, 1951, **82**, 748.
4. E. L. Hahn and D. E. Maxwell, *Phys. Rev.*, 1951, **84**, 1246.
5. N. F. Ramsey, *Phys. Rev.*, 1953, **91**, 303.
6. E. R. Andrew, L. F. Farnell, and T. D. Gledhill, *Phys. Rev. Lett.*, 1967, **19**, 6.
7. D. L. VanderHart, H. S. Gutowsky, and T. C. Farrar, *J. Chem. Phys.*, 1969, **50**, 1058.
8. M. Mehring, *High Resolution NMR in Solids*, 2nd edn, Springer, Berlin, 1983.
9. B. C. Gerstein and C. R. Dybowski, *Transient Techniques in NMR of Solids*, Academic, Orlando, Fl., 1985.
10. R. K. Harris, *Nuclear Magnetic Resonance Spectroscopy*, Longman, Burnt Mill, 1986.
11. C. P. Slichter, *Principles of Magnetic Resonance*, 3rd edn, Springer, Berlin, 1989.
12. E. R. Andrew, *Progr. NMR Spectrosc.*, 1971, **8**, 1.
13. P. L. Corio, *Structure of High-Resolution NMR Spectra*, Academic, New York, 1966.
14. M. Munowitz, *Coherence and NMR*, Wiley, New York, 1988.
15. M. E. Stoll, R. W. Vaughan, R. B. Saillant, and T. Cole, *J. Chem. Phys.*, 1974, **61**, 2896.
16. K. W. Zilm and D. M. Grant, *J. Am. Chem. Soc.*, 1981, **103**, 2913.
17. R. K. Harris, K. J. Packer, and A. M. Thayer, *J. Magn. Reson.*, 1985, **62**, 284.
18. K. Eichele and R. E. Wasylishen, *J. Magn. Reson., Ser A*, 1994, **106**, 46, and references therein.
19. M. H. Levitt, D. P. Raleigh, F. Creuzet, and R. G. Griffin, *J. Chem. Phys.*, 1990, **92**, 6347.
20. T. Gullion and J. Schaefer, *Adv. Magn. Reson.*, 1989, **13**, 57.
21. J. M. Griffiths and R. G. Griffin, *Anal. Chim. Acta*, 1993, **283**, 1081.
22. T. Nakai, J. Ashida, and T. Terao, *Mol. Phys.*, 1989, **67**, 839.
23. J. M. Millar, A. M. Thayer, D. B. Zax, and A. Pines, *J. Am. Chem. Soc.*, 1986, **108**, 5113.
24. P. Van Hecke, H. W. Spiess, U. Haeberlen, and S. Haussühl, *J. Magn. Reson.*, 1976, **22**, 93 (see also p. 103).
25. T. Terao, H. Miura, and A. Saika, *J. Chem. Phys.*, 1986, **85**, 3816.
26. A. J. Kim, M. I. Altbach, and L. G. Butler, *J. Am. Chem. Soc.*, 1991, **113**, 4831.
27. K. Schmidt-Rohr, M. Wihelm, A. Johansson, and H. W. Spiess, *Magn. Reson. Chem.*, 1993, **31**, 352.
28. R. J. Gillespie, P. Granger, K. R. Morgan, and G. J. Schrobilgen, *Inorg. Chem.*, 1984, **23**, 887.
29. C. J. Jameson, in *Multinuclear NMR*, ed. J. Mason, Plenum, New York, 1987, Chap. 4, pp. 89–131.
30. R. H. Contreras and J. C. Facelli, *Ann. Rep. NMR Spectrosc.*, 1993, **27**, 255.
31. R. F. Schneider, *J. Chem. Phys.*, 1968, **48**, 4905.
32. H. W. Spiess, *NMR, Basic Principles Prog.*, 1978, **15**, 55.
33. A. D. Buckingham, P. Pyykkö, J. B. Robert, and L. Wiesenfeld, *Mol. Phys.*, 1982, **46**, 177.
34. J. B. Robert and L. Wiesenfeld, *Phys. Rep.*, 1982, **86**, 363.
35. J. S. Blicharski, *Z. Naturforsch., Teil a*, 1972, **27**, 1355.
36. J. Kowalewski and A. Laaksonen, in *Theoretical Models in Chemical Bonding*, Part 3, ed. Z. B. Maksić, Springer, Berlin, 1991, p. 387.
37. P. Pyykkö, *Chem. Phys.*, 1977, **22**, 289.
38. A. Viste, M. Hotokka, L. Laaksonen, and P. Pyykkö, *Chem. Phys.*, 1982, **72**, 225.

39. W. T. Raynes, *Magn. Reson. Chem.*, 1992, **30**, 686.
40. R. E. Wasylishen, K. C. Wright, K. Eichele, and T. S. Cameron, *Inorg. Chem.*, 1994, **33**, 407.
41. A. Nolle, *Z. Phys. B*, 1979, **34**, 175.
42. P. N. Tutunjian and J. S. Waugh, *J. Chem. Phys.*, 1982, **76**, 1223; *J. Magn. Reson.*, 1982, **49**, 155.
43. K. Eichele, G. Wu, R. E. Wasylishen, and J. F. Britten, *J. Phys. Chem.*, 1995, **99**, 1030.
44. D. L. VanderHart and H. S. Gutowsky, *J. Chem. Phys.*, 1968, **49**, 261.
45. U. Haubenreisser, U. Sternberg, and A.-R. Grimmer, *Mol. Phys.*, 1987, **60**, 151.
46. G. H. Penner, W. P. Power, and R. E. Wasylishen, *Can. J. Chem.*, 1988, **66**, 1821.
47. W. P. Power, M. D. Lumsden, and R. E. Wasylishen, *J. Am. Chem. Soc.* 1991, **113**, 8257.
48. J. W. Emsley and J. C. Lindon, *NMR Spectroscopy Using Liquid Crystal Solvents*, Pergamon, Oxford, 1975.
49. J. Lounila and J. Jokisaari, *Prog. NMR Spectrosc.*, 1982, **15**, 249.
50. N. F. Ramsey, *Molecular Beams*, Oxford University Press, Oxford, 1956.
51. R. von Boeckh, G. Gräff, and R. Ley, *Z. Phys.*, 1964, **179**, 285.
52. M. D. Lumsden, K. Eichele, R. E. Wasylishen, T. S. Cameron, and J. F. Britten, *J. Am. Chem. Soc.*, 1994, **116**; 11129.
53. R. K. Harris and A. C. Olivieri, *Prog. NMR Spectrosc.*, 1992, **24**, 435.
54. J. Jokisaari, Y. Hiltunen, and J. Lounila, *J. Chem. Phys.*, 1986, **85**, 3198.
55. A. Pulkkinen, Y. Hiltunen, and J. Jokisaari, *Liq. Cryst.*, 1988, **3**, 737.
56. E. R. Andrew and L. F. Farnell, *Mol. Phys.*, 1968, **15**, 157.
57. D. K. Dalling and H. S. Gutowsky, *J. Chem. Phys.*, 1971, **55**, 4959.
58. H. Dreeskamp and K. Hildenbrand, *Z. Naturforsch., Teil a*, 1968, **23**, 940.
59. J. Jokisaari, K. Räisänen, J. Kuonanoja, P. Pyykkö, and L. Lajunen, *Mol. Phys.*, 1980, **39**, 715.

Acknowledgments

I wish to thank Dr. Klaus Eichele and Michael D. Lumsden for their assistance in preparing the figures for this contribution. Also, I wish to thank Klaus, Mike, Gang Wu, and Professor Aatto Laaksonen for many helpful comments. Our research has been generously supported by NSERC of Canada.

Biographical Sketch

Roderick Wasylishen. *b* 1944. B.Sc., 1968, Waterloo, Ph.D., 1972, Manitoba. Introduced to NMR by Terry Gough at the University of Waterloo and Ted Schaefer at the University of Manitoba. NRC of Canada PDF at the National Institutes of Health, Bethesda, Maryland with Ted Becker. 1972–74. Department of Chemistry, University of Winnipeg, 1974–82; Dalhousie University, 1982–present. Approx. 180 publications. Current research specialty: NMR studies of solids, chemical shielding, spin–spin coupling, EFG tensors, NMR lineshapes, NMR relaxation.

Indirect Coupling: Theory and Applications in Organic Chemistry

Michael Barfield

Department of Chemistry, University of Arizona, Tucson, AZ, USA

1	Introduction	1
2	Observations and Early Interpretations	1
3	Theoretical Formulations for Nuclear Spin–Spin Coupling	2
4	Applications to Specific Coupling Situations	9
5	References	11

1 INTRODUCTION

Nuclear spin−spin coupling theory has been the subject of several reviews[1−4] and it has been an annual topic in the Royal Society of Chemistry Reports since 1972.[5,6] In recent years there has been a renewed interest in the factors controlling heteronuclear spin−spin coupling constants. This is partially attributable to the emergence of multiple pulse techniques for spectral editing as these have produced a wealth of new data.

Like many other topics in NMR an exhaustive review of indirect nuclear spin−spin coupling theory would not be possible within the limitations of this review. Moreover, various aspects of J coupling will appear in other chapters of this monograph. Thus, the scope of this chapter is narrowed to reflect the author's interests in this topic for the past 30 years and to bring some coherence to this material. The coverage of the literature is fairly complete up until the early 1970s. It was at about this time that the FPT-INDO method [finite perturbation theory in the intermediate neglect of differential overlap approximation of self-consistent field molecular orbital (SCF-MO) theory] became generally available and was applied to an enormous number of problems.[7] In recent years high quality ab initio computations have appeared. These use large basis sets and include extensive correlation corrections applied to both Fermi contact and noncontact mechanisms.[8−15]

The spin−spin coupling phenomenon quickly emerged as a powerful tool for structural and conformational studies, in part, because of the general applicability of semiempirical methods in reproducing conformational and substituent trends. This is in marked contrast with chemical shielding where the data are even more abundant but semiempirical methods have not been as useful. The first part of this chapter will describe the observation and early interpretation of the spin−spin coupling phenomenon. The second part will present an overview of theoretical descriptions as expressed in density matrix notation and exemplified by semiempirical methods. The final section applies the theory to some organic structural aspects of J coupling, again emphasizing topics of interest to the author.

2 OBSERVATIONS AND EARLY INTERPRETATIONS

The early work in the observation of spin−spin coupling will be described elsewhere in this article and will only be described briefly here. In 1950 the application of spin echo methods to ethanol by Hahn[16] showed 'slow beats' in the echo. These were later shown to arise from nuclear spin−spin coupling. Using slow passage conditions, the fine structure in the ^{121}Sb resonance of a solution of $NaSbF_6$, which was observed by Proctor and Yu,[17] was thought to arise from the magnetic dipole interaction of the Sb nucleus with the surrounding F nuclei. Gutowsky and McCall[18] also observed fine structure in ^{31}P and ^{19}F spectra. In 1951 there were several other papers on this topic[19,20] and it was soon concluded that the interaction is independent of the external field but that it does depend on the product of the nuclear spin vectors,[21−23]

$$\Delta E_{\mathrm{NN}'} = h J_{\mathrm{NN}'} \boldsymbol{I}_{\mathrm{N}} \cdot \boldsymbol{I}_{\mathrm{N}'} \tag{1}$$

where $J_{\mathrm{NN}'}$ is the nuclear spin−spin coupling constant in hertz. The physical basis for these splittings was disputed until the appearance of papers by Ramsey and Purcell[24] and Ramsey.[25] They concluded that the interaction arises from 'the magnetic interaction between each nucleus and the electron spin of its own atom together with the exchange coupling of the electron spin with each other'. In the absence of a magnetic field the spin−spin coupling constant for H_2 is simply the energy difference in hertz between *ortho*- and *para*-hydrogen, e.g. in the absence of a magnetic field it is the difference between the triplet and singlet nuclear spin levels. This is depicted in Figure 1 for a pair of equivalent spin-$\frac{1}{2}$ nuclei. The nuclear Zeeman levels are plotted as a function of the magnetic induction B_0. The J coupling is taken to be of positive sign if the nuclear spin singlet energy is lower than the triplet energy. This is the case for H_2 because the Fermi contact mechanism (which is dominant) favors the antiparallel arrangement of electron and nuclear spins.

In his 1953 paper Ramsey developed a general formulation for nuclear spin−spin coupling. Equation (1) implies that coupling constant terms will occur in first order perturbation theory if the operators contain the product $\boldsymbol{I}_{\mathrm{N}} \cdot \boldsymbol{I}_{\mathrm{N}'}$, e.g. the one-electron or orbital diamagnetic term. Contributions will also arise in second order perturbation theory as products of operators ($\boldsymbol{A}_{\mathrm{N}} \cdot \boldsymbol{I}_{\mathrm{N}}$ and $\boldsymbol{A}_{\mathrm{N}'} \cdot \boldsymbol{I}_{\mathrm{N}'}$) containing the two nuclear spins. Ramsey identified three interaction terms of this form, those involving the electron orbital motion with the nuclear spin, the dipolar term involving the electronic spins and the nuclear spins, and the Fermi contact interaction associated with the electronic and the nuclear spins. Ramsey's expression for the (isotropic) Fermi contact term, which is of primary interest here, in Gaussian units is

$$J_{\mathrm{NN}'} = -(2/3h)\left(16\pi\beta\frac{\hbar}{3}\right)^2 \gamma_{\mathrm{N}}\gamma_{\mathrm{N}'} \sum_{\kappa} ({}^3E_\kappa - {}^1E_0)^{-1} \times \left\langle 0 \left| \sum_j \delta(r_{j\mathrm{N}}) S_j \right| \kappa \right\rangle \left\langle \kappa \left| \sum_k \delta(r_{k\mathrm{N}'}) S_k \right| 0 \right\rangle \tag{2}$$

where $J_{\mathrm{NN}'}$ denotes the isotropic coupling between nuclei N and N′ having magnetogyric ratios γ_{N} and $\gamma_{\mathrm{N}'}$, respectively. The first summation is over all triplets κ. In the Fermi contact

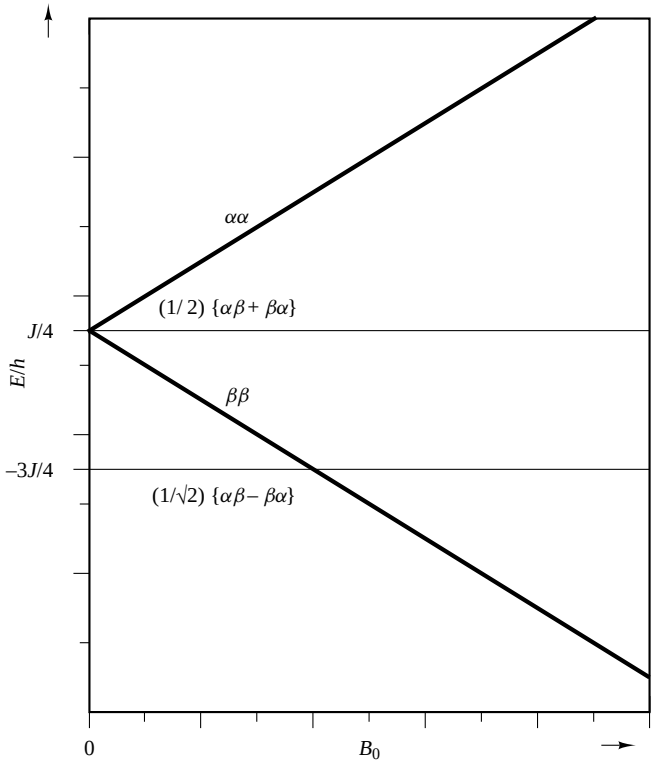

Figure 1 Energy level diagram for two equivalent spin-$\frac{1}{2}$ nuclei plotted as a function of the magnetic induction B_0. The coupling constant J is the separation between the nuclear spin singlet and the nuclear spin triplet

operators $\delta(r_{j\mathrm{N}})$, for example, denotes the Dirac delta function for electron j at nucleus N, S_j is the electron spin operator for the jth electron, and the summation is taken over all electrons j. Matrix elements connect the singlet states $\langle 0|$ having energy ${}^1E_0$ and triplet states $|\kappa\rangle$ having energies ${}^3E_\kappa$. Equation (2) is the starting point for most discussions of Fermi contact coupling. Ramsey also recognized the tensor nature of the J coupling but for the HD molecule only reported numerical estimates of the *isotropic* terms. Based on the James and Coolidge wavefunction, a value of 40 Hz for the Fermi contact term is in reasonable accord with the experimental value of 42.7 ± 0.7 Hz.[26] This also supported arguments for small contributions from noncontact mechanisms. Following speculation that the H–D spin–spin coupling constant had a negative sign,[27] Code and Ramsey used molecular beam methods to demonstrate[28] that the sign was indeed positive.

Ramsey also made the interesting observation that as the atoms of HD are pulled apart, the denominator in equation (2) approaches zero, a situation in which perturbation theory would not be applicable. Because of a possible relationship to long-range coupling, the dependence of the H–H nuclear spin–spin coupling on $r_{\mathrm{HH}'}$ was examined[29] using a variational method with Heitler–London wavefunctions including both the electron and nuclear spins. In the dissociation limit the splitting is the electron–nuclear hyperfine coupling. The total electronic spin S cannot be a good quantum number as the molecule dissociates as this would have the contradiction of nuclear spin–spin coupling being nonzero at infinite separation. In the simple Heitler–London picture for which the singlet and triplet energies are asymptotic as $R \rightarrow \infty$, the four basic product electron spin functions necessarily assume equal weights corresponding to two uncorrelated spins. Had effects as small as the indirect nuclear spin–spin coupling been of interest, these would have been implicit in the detailed work of the Wisconsin group on the H_2 hyperfine splitting.[30] The previous reviews[1–6] should be consulted for references to the many papers concerned with calculation of the HD coupling constant.

Before looking at specific molecular formulations, it will be convenient in the next section to transcribe the various expressions for (Fermi contact) nuclear spin–spin coupling constants into density matrix notation. These techniques will then be used in Sections 3.2–3.4 to discuss the specific quantum mechanical formulations.

3 THEORETICAL FORMULATIONS FOR NUCLEAR SPIN–SPIN COUPLING

3.1 Density Matrix Notation

The density matrix notation adopted here follows that introduced by McWeeny and co-workers.[31,32] This formalism was used extensively in these laboratories to investigate nuclear spin–spin coupling and a number of other types of NMR parameters. The one-electron *transition density matrix* associated with states Ψ_κ and Ψ_λ is given by

$$\rho_1(\kappa\lambda \mid 1; 1') = N \int \Psi_\kappa(1, 2, 3, \ldots, N)\Psi^*_\lambda \times \Psi_\lambda(1', 2, 3, \ldots, N)\ \mathrm{d}r_2\ \mathrm{d}r_3 \ldots\ \mathrm{d}r_N \quad (3)$$

where N is the number of electrons and the integrations are to be taken over the space and spin coordinates r_i of all but one electron. It is sometimes convenient to write the one-electron density matrix in terms of spinless components,

$$\rho_1(\kappa\lambda \mid 1; 1') = P_1(\kappa\lambda \mid \overset{\alpha}{1}; \overset{\alpha}{1'})\alpha(1)\alpha^*(1') + P_1\kappa\lambda \mid \overset{\beta}{1}; \overset{\beta}{1'})\beta(1)\beta^*(1') \quad (4)$$

from which it follows that for a given state ($\kappa = \lambda$) the diagonal element denotes the probability of finding an electron in volume element at point 1. *Transition spin densities* occur when spin operators are involved and these can be written in terms of the spinless components,

$$Q_1(\kappa\lambda \mid 1; 1') = P_1(\kappa\lambda \mid \overset{\alpha}{1}; \overset{\alpha}{1'}) - P_1(\kappa\lambda \mid \overset{\beta}{1}; \overset{\beta}{1'}) \quad (5)$$

For a given state ($\kappa = \lambda$) $Q_1(\kappa\kappa|1;1)$ is just a *spin density* for which integration over all space gives the number of unpaired spins.

From equations (2)–(5) the expression for the Fermi contact (FC) contribution to the isotropic spin–spin coupling is

$$J_{\mathrm{NN}'} = -(2h)^{-1}(16\pi\beta\hbar/3)^2\gamma_{\mathrm{N}}\gamma_{\mathrm{N}'}\sum_\kappa({}^3E_\kappa - {}^1E_0)^{-1} \times Q_1(0\kappa_0 \mid 1_{\mathrm{N}}; 1_{\mathrm{N}})Q_1(0\kappa_0 \mid 1_{\mathrm{N}'}; 1_{\mathrm{N}'}) \quad (6)$$

where $Q_1(0\kappa_0|1_N;1_N)$, for example, denotes the transition spin density evaluated at the position of nucleus N. The advantages of using density matrix notation rather than the integrals in equation (2) are the removal of the spin operators and the ease of writing general density matrix expressions. General density matrix expressions analogous to equation (6) can also easily be written for coupling constant contributions associated with the spin dipolar (SD), and orbital paramagnetic (OP) contributions, as well as the various cross terms.[33,34]

The initial theoretical work on J coupling invoked the so called 'average energy approximation' to simplify the second order expressions. This procedure invokes closure in the second order sum and replaces the excitation energies by an average value ΔE. Although it has long been clear that this procedure is not an approximation in the usual sense of the word,[35,36] it has led to some very important relationships between J couplings and molecular structures as well as some useful qualitative insights that have permitted correlations of many structural features. The 'average energy approximation' was particularly appealing in its very simple relationship to the electron correlation features in n-particle systems.[32,37,38] In density matrix notation the FC contribution to the spin–spin coupling between nuclei N and N′ at this level of theory is given by[32]

$$J_{NN'} = -(3h\Delta E)^{-1}(16\pi\beta\hbar/3)^2\gamma_N\gamma_{N'}Q_c(1_N, 2_{N'}; 1_N, 2_{N'}) \tag{7}$$

where $Q_c(1_N, 2_{N'}; 1_N, 2_{N'})$ denotes a two-electron spin density (or spin coupling matrix) evaluated at the positions of the coupled nuclei, and ΔE is an 'average excitation energy'. The usual state labels of density matrix notation are not used here because only the ground state wavefunction is involved. The two-electron spin density matrix is related to the two-electron spinless components of the density matrix,

$$Q_c(1, 2; 1', 2') = 3[P_2(\overset{\alpha}{1}, \overset{\alpha}{2}; \overset{\alpha}{1'}, \overset{\alpha}{2'}) - P_2(\overset{\alpha}{1}, \overset{\beta}{2}; \overset{\alpha}{1'}, \overset{\beta}{2'})] \tag{8}$$

where the first term on the right denotes the simultaneous probability of finding the two electrons with α spin in differential volume elements at points 1 and 2, and the second term denotes the corresponding probability for electrons of opposite spin. We now look at some important implications of these relationships. The spinless components in equation (8) are related to the one-particle spinless density matrix components in equation (4) and correlation functions for electrons of the same and opposite spins,

$$P_2(\overset{\alpha}{1}, \overset{\alpha}{2}; \overset{\alpha}{1}, \overset{\alpha}{2}) = P_1(\overset{\alpha}{1}; \overset{\alpha}{1})P_1(\overset{\alpha}{2}; \overset{\alpha}{2})[1 + f(\overset{\alpha}{1}, \overset{\alpha}{2})] \tag{9}$$

$$P_2[(\overset{\alpha}{1}, \overset{\beta}{2}; \overset{\alpha}{1}, \overset{\beta}{2})] = P_1(\overset{\alpha}{1}; \overset{\alpha}{1})P_1(\overset{\beta}{2}; \overset{\beta}{2})[1 + f(\overset{\alpha}{1}, \overset{\beta}{2})] \tag{10}$$

where $f(\overset{\alpha}{1}, \overset{\alpha}{2})$ and $f(\overset{\alpha}{1}, \overset{\beta}{2})$ denote correlation functions for electrons of the same and of opposite spins, respectively. The Pauli Exclusion Principle requires that as the coordinates of particle 2 approach those of particle 1,

$$f(\overset{\alpha}{1}, \overset{\alpha}{2}) \to -1 \quad \text{and} \quad f(\overset{\alpha}{1}, \overset{\beta}{2}) \to -1 \tag{10a}$$

corresponding to 100% negative correlation which prevents particles of like spin being found at the same point in space.[31]

Since essentially all of the molecules of interest are in singlet ground states

$$P_1(\overset{\alpha}{1}; \overset{\alpha}{1}) = P_1(\overset{\beta}{2}; \overset{\beta}{2}) = (\tfrac{1}{2})P_1(1; 1) \tag{11}$$

so that both the two-electron spin density matrix and the *nuclear spin–spin coupling are proportional to the differences in the correlation functions for electrons of the same and opposite spins*,

$$Q_c(1, 2; 1, 2) = (\tfrac{3}{4})P_1(1; 1)P_1(2; 2)[\, f(\overset{\alpha}{1}, \overset{\alpha}{2}) - f(\overset{\alpha}{1}, \overset{\beta}{2})] \tag{12}$$

At this level of theory the various bond orders provide estimates for the differences in the correlation functions in equation (12).

3.2 Early Theory

The recognition of the spin coupling phenomenon quickly led to theoretical discussion using the Heitler–London formulation.[39] It also provided an explanation for linewidths in solids which were larger than could be accounted for on the basis of the direct dipole–dipole interactions.[40,41]

3.2.1 Molecular Orbital Methods

In the period 1955–1957 McConnell considered the J coupling problem from several points of view including a molecular orbital description,[42] a Dirac vector model,[43] and a spin-exchange model.[44,45] The MO model was used by Saika[46] to investigate the J coupling in ammonia. On the basis of MO results in which interproton spin–spin coupling constants were proportional to the square of the MO bond order, McConnell speculated that interproton coupling constants were probably all positive in sign.[47] In the light of subsequent sign measurements, a formulation was used to rationalize the negative $J(H, H')$ in aromatic systems.[48] During this period Pople related the orbital contributions to nuclear spin–spin coupling to the anisotropy of the magnetic screening.[49]

In single determinant Hartree–Fock theory the correlation function for electrons of opposite spins in equation (12) vanishes identically, and assuming that the molecule has a singlet ground state,

$$Q_c(1, 2; 1, 2) = (\tfrac{3}{4})P_1(1; 1)P_1(2; 2)\, f(\overset{\alpha}{1}, \overset{\alpha}{2}) \tag{13}$$

which is negative because the correlation function $f(\overset{\alpha}{1}, \overset{\alpha}{2})$ is inherently negative (it is zero if the electrons are uncorrelated).

Expanding a Slater determinant via Laplace's development leads to an expression for the two-particle density matrix in terms of the Fock–Dirac density matrix $\rho_1(1;1')$,[32]

$$\rho_2(1, 2; 1', 2') = \rho_1(1; 1')\rho_1(2, 2') - \rho_1(1; 2')\rho_1(2; 1') \tag{14}$$

Rewriting the one-particle density matrices in terms of the spinless components provides an expression for the two-electron spinless components,

$$P_2(\overset{\alpha}{1},\overset{\alpha}{2};\overset{\alpha}{1'},\overset{\alpha}{2'}) = P_1(\overset{\alpha}{1};\overset{\alpha}{1'})P_1(\overset{\alpha}{2},\overset{\alpha}{2'}) - P_1(\overset{\alpha}{1};\overset{\alpha}{2'})P_1(\overset{\alpha}{2};\overset{\alpha}{1'}) \tag{15}$$

$$P_2(\overset{\alpha}{1},\overset{\beta}{2};\overset{\alpha}{1'},\overset{\beta}{2'}) = P_1(\overset{\alpha}{1};\overset{\alpha}{1'})P_1(\overset{\beta}{2};\overset{\beta}{2'}) \tag{16}$$

From equation (8) the spin coupling function can, therefore, be written in terms of the off-diagonal elements of the one-particle density matrix

$$Q_c(1,2;1,2) = -(\tfrac{3}{4})P_1(1;2)P_1(2;1) \tag{17}$$

where the off-diagonal elements of the one-particle density matrix can be written in terms of the molecular orbitals

$$P_1(1;2) = \sum_i n_i \chi_i(1)\chi_i^*(2) = \sum_{\mu\nu}\sum_i n_i c_{i\mu}c_{i\nu}^*\phi_\mu(1)\phi_\nu^*(2)$$
$$= \sum_{\mu\nu}\eta_{\mu\nu}\phi_\mu(1)\phi_\nu^*(2) \tag{18}$$

In the ith molecular orbital $c_{i\mu}$ and $c_{i\nu}$ are the coefficients of orbitals μ and ν, respectively, n_i is the occupation number, and $\eta_{\mu\nu}$ is the bond order between orbitals μ and ν as defined by Coulson and Longuet-Higgins,[50]

$$\eta_{\mu\nu} = \sum_i n_i c_{i\mu}c_{i\nu}^* \tag{19}$$

Substituting equation (18) into equation (17), one sees that at this level of MO theory the coupling constant is proportional to the square of the bond order. This is awkward, not only because of the single sign problem noted above, but also because this type of bond order vanishes for even alternant systems if orbitals μ and ν are in the same subset.[50] Of course, this result is not consistent with a large number of examples of sizable spin–spin coupling constants of either sign for atoms separated by an even number of bonds. These problems can be circumvented in alternant MO methods[38] in which both types of correlation are included in an easily visualized way. For the specific case of a molecule with two electrons, e.g. H_2 $P_2(\overset{\alpha}{1},\overset{\alpha}{2};\overset{\alpha}{1},\overset{\alpha}{2}) = 0$, so the coupling constant is proportional to

$$Q_c(\overset{\alpha}{1},\overset{\beta}{2};\overset{\alpha}{1},\overset{\beta}{2}) = -3P_2(\overset{\alpha}{1},\overset{\alpha}{2};\overset{\beta}{1},\overset{\beta}{2})$$
$$= -3P_1(1;1)P_1(2,2)[1 + f(\overset{\alpha}{1},\overset{\beta}{2})] \tag{20}$$

Since $f(\overset{\alpha}{1},\overset{\beta}{2}) = 0$ at the Hartree–Fock level, equation (13) becomes simply

$$Q_c(1,2;1,2) = -(\tfrac{3}{4})P_1(1;1)P_1(2,2) \tag{21}$$

For a two-electron system in terms of the occupied MO χ the diagonal element is simply

$$P_1(1;1) = 2\chi(1)\chi^*(1') \tag{22}$$

Taking χ to be a linear combination of atomic orbitals ϕ_μ and ϕ_ν, associated with nuclei N and N′, then

$$P_1(1;1') = \phi_\mu(1)\phi_\mu^*(1') + \phi_\nu(1)\phi_\nu^*(1')$$
$$+\phi_\mu(1)\phi_\nu^*(1') + \phi_\nu(1)\phi_\mu^*(1') \tag{23}$$

Neglecting terms like $\phi_\mu(1_N)\phi_\nu{}^*(1_N)$ in comparison with terms like $\phi_\mu{}^2(1_N)$, it then follows from equations (7) and (22) that the directly bonded coupling constant expression is

$$J_{NN'} = (h\Delta E)^{-1}(16\pi\beta\hbar/3)^2\gamma_N\gamma_{N'}\phi_\mu^2(1_N)\phi_\nu^2(1_{N'}) \tag{24}$$

Substitution of the form for a hybrid orbital for one or both of ϕ_μ and ϕ_ν where ϕ_μ is of the form

$$\phi_\mu = as_\mu + (1-a^2)^{1/2}p_{\sigma\mu} \tag{25}$$

where s_μ and $p_{\sigma\mu}$ denote 2s and 2p atomic orbitals on atom μ and a^2 is the s character. The resulting equation relates directly bonded, e.g. $^{13}C–H$ and $^{13}C–^{13}C$ coupling constants to the s characters at the carbon atoms.[51–53] Equation (25) neglects a factor of $(1 + S)^{-2}$, where S is the overlap integral between bonded orbitals ϕ_μ and ϕ_ν. By means of an alternant molecular orbital method it was noted[38] that *the neglect of overlap compensates to some extent for the neglect of electron correlation*!

3.2.2 Valence Bond (VB) Methods

These methods were used extensively in the early work in nuclear spin–spin coupling.[54–71] Certainly, the most widely known application is that for the angular dependence of the vicinal H–H coupling constants in ethane.[58] Since the VB method had an important impact on the development of spin–spin coupling theory, its application in conformational analyses, and some intuition regarding the electronic factors leading to the phenomenon, a brief review seems appropriate here. Even though VB concepts are closely tied to chemists' ideas of formulas, resonance, etc., the quantum mechanical methods are unfamiliar to many chemists. The derivation of VB coupling constant expressions demonstrates the simplicity provided by the density matrix formalism. In the simple VB method the singlet ground state wavefunction $^1\Psi_0$ is written as a linear combination of independent, nonpolar VB structures $^1\Phi_j$,[72]

$$^1\Psi_0 = \sum_j c_j\,{}^1\Phi_j \tag{26}$$

The $^1\Phi_j$ can be constructed formally by placing $2n$ points on the circumference of a circle and then drawing all possible structures which have all of the points connected, but in which no two lines cross. For example, depicted in Figure 2(a) are the two independent, singlet VB structures $^1\Phi_1$ and $^1\Phi_2$. These are useful for investigating geminal, vicinal, and long range H–H coupling as described simply by two C–H bonds as depicted in Figure 2(b). The perfect pairing structure is that in which there are covalent bonds between the carbon hybrid orbitals and the hydrogenic 1s atomic orbitals $c–h$ and $c'–h'$. The nonperfect pairing structure is of

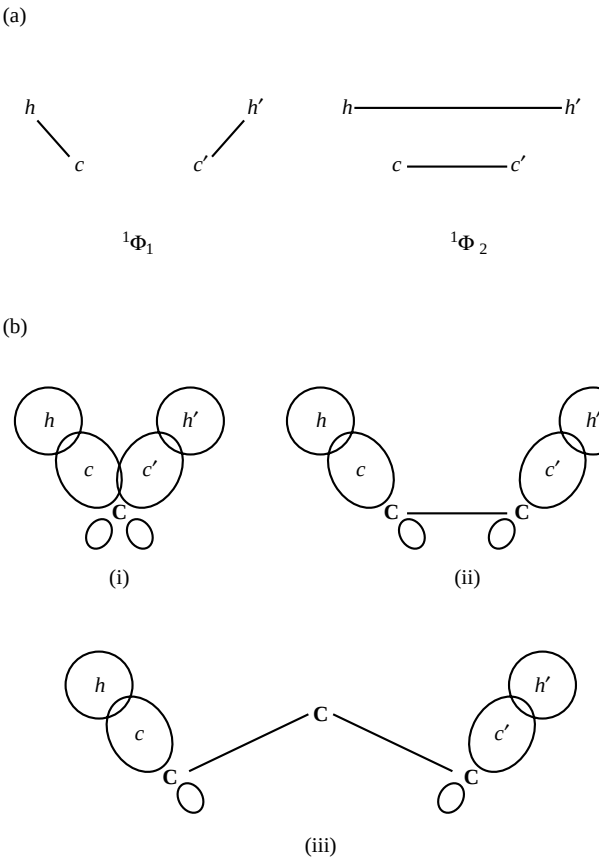

Figure 2 (a) Valence bond singlet structures for a system of four electrons associated with two C–H bonds. Structure $^1\Phi_1$ is the perfect pairing structure and $^1\Phi_2$ is the non-perfect pairing structure. (b) Schematic representations of four electron fragments for (i) geminal coupling in a CH_2 moiety, (ii) vicinal coupling in an ethanic moiety, and (iii) long-range coupling in a propanic moiety

higher energy since it involves breaking the two C–H bonds and forming bonds between h and h' and c and c'. In the VB formulation nonvanishing H–H coupling arises from the contributions of $^1\Phi_2$ to the ground state wavefunction. Matrix elements entering the secular determinant associated with equation (26) are constructed by superimposing the various structures.[73] The matrix elements are written as a sum of terms involving Coulomb and exchange integrals multiplied by a function which is determined by superimposing the VB structures. For a $2n$ electron system the coefficients of the Coulomb integrals are $(\frac{1}{2})^{n-i_{jl}}$ where i_{jl} is the number of islands (closed polygons) which occur in the superposition diagram of structures j and l. The coefficients of the exchange integrals are $(\frac{1}{2})^{n-i_{jl}} f_{jl}^{\mu\nu}$ where $f_{jl}{}^{\mu\nu}$ assumes the values 1, -2, and $-\frac{1}{2}$ depending on whether orbital μ and ν are in the same island separated by an odd number of bonds, or an even number of bonds, or are in different islands, respectively. The two-electron density matrix follows directly from the expression for the ground state energy,

$$P_2(1,2;1',2') = \sum_{j,l} c_j c_l (\tfrac{1}{2})^{n-i_{jl}} \sum_{\mu,\nu} [\phi_\mu(1)\phi_\nu(2)\phi_\mu(1')\phi_\nu(2') + f_{jl}^{\mu\nu}\phi_\mu(1)\phi_\nu(2)\phi_\nu(1')\phi_\mu(2')] \quad (27)$$

where c_j is the coefficient of the jth VB structure, and ϕ_μ and ϕ_ν are atomic orbitals. The spin–spin coupling function is obtained from equations (7) and (8) and the spinless components of $P_2(1, 2; 1', 2')$,[32,74]

$$Q_c(1,2;1',2') = -(\tfrac{1}{2}) \sum_{j,l} c_j c_l (\tfrac{1}{2})^{n-i_{jl}} \times \sum_{\mu,\nu} [(1 + 2f_{jl}^{\mu\nu})\phi_\mu(1)\phi_\nu(2)\phi_\mu(1')\phi_\nu(2') + (2 + f_{jl}^{\mu\nu})\phi_\mu(1)\phi_\nu(2)\phi_\nu(1')\phi_\mu(2')] \quad (28)$$

Equation (28) can immediately be rewritten in terms of the Penney–Dirac bond orders $p_{PD}(\mu, \nu)$,

$$Q_c(1,2;1',2') = -(\tfrac{3}{2}) \sum_{\mu\nu} \{p_{PD}(\mu,\nu)\phi_\mu(1)\phi_\nu(2)\phi_\mu \times(1')\phi_\nu(2') + (\tfrac{1}{2})[1 + p_{PD}(\mu,\nu)]\phi_\mu(1) \times\phi_\nu(2)\phi_\nu(1')\phi_\mu(2')\} \quad (29)$$

where[75]

$$p_{PD}(\mu,\nu) = (\tfrac{1}{3}) \sum_{j,l} c_j c_l (\tfrac{1}{2})^{n-i_{jl}} (1 + 2f_{jl}^{\mu\nu}) \quad (30)$$

Neglecting two-center overlap terms of the type $\phi_\mu(1_N)\phi_\nu(1_N)$ in equation (27) shows that the nuclear spin–spin (FC contribution) coupling is linearly related to the Penney–Dirac bond order $p_{PD}(\mu, \nu)$.[66] Consider several situations for H–H coupling represented by the two C–H bonds in Figure 2(b). Depending on whether the hybrid orbitals c and c' constitute (i) a geminal pair, (ii) a vicinal pair, or (iii) are hybrid carbon orbitals separated by two or more bonds, these structures provide a useful, but simplistic, representation of the corresponding coupling situations. Note that the PD bond order $p_{PD}(h, h')$ has no contribution from the perfect pairing structure [see Figure 2(a)] because $f_{11}{}^{hh'} = -\frac{1}{2}$ in equation (30). However, in the superposition diagram for $^1\Phi_1$ and $^1\Phi_2$, $f_{12}{}^{hh'} = 1$ leading to a nonvanishing contribution to $p_{PD}(h, h')$. Using perturbation theory $c_1 \approx 1$,[54,74] hence

$$c_2 \approx (\tfrac{1}{2}) \left[\frac{K(h,h') + K(c,c') - K(c,h') - K(c',h)}{K(c,h) + K(c',h') - K(c,c') - K(h,h')} \right] \quad (31)$$

where $K(\mu, \nu)$ is a two-center exchange integral associated with orbitals ϕ_μ and ϕ_ν,

$$K(\mu,\nu) = \int\int \phi_\mu(1)\phi_\nu(2)[(R_{ab})^{-1} + (r_{12})^{-1} - (r_{1b})^{-1} - (r_{2a})^{-1}]\phi_\nu(1)\phi_\mu(2)\ d\tau_1\ d\tau_2 \quad (32)$$

From equation (30) the PD bond order associated with the hydrogens is simply,

$$p_{PD}(h,h') = c_1c_2 + c_2^2 \approx c_1c_2 \approx c_2 \quad (33)$$

Since $c_2 \ll c_1 \approx 1$ for saturated systems, in this simple model the coupling constant is proportional to the contribution of the nonperfect pairing structure to the ground state wavefunctions,

and it related to the exchange integrals in equation (31). As the numerator and any one of the exchange integrals can be of either sign, the Penney–Dirac bond orders and coupling constants can be either positive or negative. This is a more plausible result than the quadratic dependence on the MO bond order, which occurs because of the very different ways in which electron correlation appears in these two methods! Because of the extreme importance of electron correlation effects for nuclear spin–spin coupling, the early successes of valence bond methods compared with simple MO methods should come as no surprise.

At an early stage in the development of NMR this simple VB theory qualitatively explained a number of aspects of interproton coupling: geminal H–H coupling is quite sensitive to exchange integral cancelation in the numerator of equation (31). In comparison with vicinal H–H coupling constants, geminal H–H coupling constants are very sensitive to H–C–H angles, substituent and solvent effects. The original VB calculations for vicinal H–H coupling constants in an ethanic fragment were based on a six-electron fragment for the ethane molecule. However, all of the important aspects are implicit in the four-electron model described herein. In the original paper[58] describing the dihedral angle dependence of vicinal H–H coupling constants, the only necessary nonbonded exchange integral was $K(c, c')$ occurring in the numerator of equation (29). The hybrid orbitals c and c' are depicted in Figure 2(b). The most general form of a, e.g., carbon hybrid orbital ϕ_μ can be written in terms of atomic s- and p-type atomic orbitals, the angle θ_μ that the hybrid orbital makes with the z axis, and the dihedral angle φ about the z axis,

$$\phi_\mu = a_\mu s_\mu + (1 - a_\mu^2)^{1/2}(\cos\varphi \sin\theta_\mu p_{x\mu} + \sin\varphi \sin\theta_\mu p_{y\mu} + \cos\theta_\mu p_{\sigma\mu}) \quad (34)$$

where s_μ, $p_{x\mu}$, $p_{y\mu}$, and $p_{\sigma\mu}$ denote the 2s and 2p atomic orbitals associated with the μth hybrid orbital, and a_μ is defined such that ${a_\mu}^2$ is the s character of the hybrid orbital. If equation (4) is specialized, for example, to tetrahedral hybrids with appropriate bond angles and a single dihedral angle φ, substitution of equation (34) into equation (32) gives the mathematical form for the vicinal exchange integral

$$K(c, c') = A\cos^2\varphi + B\cos\varphi + C \quad (35)$$

From equations (28)–(31), (33) and (7) this will also be the approximate form for dependence of vicinal coupling constants on dihedral angles.

This simple, qualitative VB model can be extended to systems which have more than four electrons by means of 'fragment' bond orders of the type given in equations (31) and (33). The fragment bond order $p^0(r, s)$ associated with bonds $r–r'$ and $s–s'$ is

$$p^0(r, s) = (\tfrac{1}{2})\left[\frac{K(r, s) + K(r', s') - K(r, s') - K(r', s)}{K(r, r') + K(s, s') - K(r, s) - K(r', s')}\right] \quad (36)$$

Consider the calculation of the PD bond order $p_{\mathrm{PD}}(h, h')$ for the molecular system depicted in Figure 3. In addition to the two C–H bonds there are N bond pairs $(t–t')_j$. The Penney–Dirac bond orders can be determined from the coefficients obtained by perturbation theory. Up to second order the bond order associated with the two hydrogens is written in terms of the fragment bond orders. An approximate expression is[74]

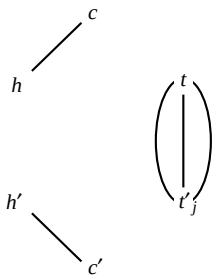

Figure 3 Schematic representations of a four-electron fragment plus n-bonds $(t–t')_j$

$$p_{\mathrm{PD}}(h, h') = p^0(h, h') + (\tfrac{3}{2})\sum_j p^0(h, t_j)p^0(t'_j, h') \quad (37)$$

where each of the fragment bond orders is of form of equation (36). The first term on the right hand side of equation (37) has been associated with a *direct* coupling mechanism and the second with the many possible *indirect* coupling mechanisms.[74] It seems likely that the widely but undefined terms 'through space' and 'through bond' have led to substantial confusion regarding the factors responsible for spin–spin coupling. Additional relationships among the bond order expressions are as follows:

$$p^0(h, h') = p^0(c, c') = -p^0(c, h') = -p^0(h, c') \quad (38)$$

These equations provide a basis for interrelating the various coupling constants and the simple VB bond order model provides a qualitative basis for interpreting a wide variety of substituent and conformational effects.[74,76–80]

3.3 Sum-Over-States Methods

3.3.1 Molecular Orbital Descriptions

Where the ground state wavefunction is given as an antisymmetrized product of molecular orbitals,

$${}^1\Psi_0 = \mathcal{A}[\chi_1(1)\overline{\chi_1(2)}\chi_2(3)\ldots\chi_i(k)\overline{\chi_i(k+1)}\ldots] \quad (39)$$

and triplet state wavefunctions are produced by exciting an electron from the ith occupied MO to the jth unoccupied MO,

$${}^3\Psi_{km} = \mathcal{A}[\chi_1(1)\overline{\chi_1(2)}\chi_2(3)\ldots\chi_i(k)\ldots\chi_j(k+1)\ldots] \quad (40)$$

In equation (40) electrons k and $k + 1$ have parallel spins and $m = +1$, 0, and -1. The transition density matrix associated with the ground state and $m = 0$ components of the triplet levels is given from equations (3), (32) and (33),

$$\rho_1(0\kappa_0 \mid 1; 1') = 2\int \chi_i(1)\chi_i(2)(1/\sqrt{2})[\alpha(1)\beta(2) - \beta(1)\alpha(2)] \times (1/\sqrt{2})[\chi_i^*(1')\chi_j^*(2) + \chi_j^*(1')\chi_i^*(2)] \times (1/\sqrt{2})[\alpha^*(1')\beta^*(2) + \beta^*(1')\alpha^*(2)]\ \mathrm{d}r_2 \quad (41)$$

Integration over the space and spin coordinates of electron 2 yields the transition density matrix

$$\rho_1(0\kappa_0 \mid 1; 1') = -(1/\sqrt{2})\chi_i(1)\chi_j^*(1')[\alpha(1)\alpha^*(1') - \beta(1)\beta^*(1')] \quad (42)$$

which defines the spinless components. These provide an expression for the transition spin density matrix

$$Q_1(0\kappa_0 \mid 1; 1') = -\sqrt{2}\chi_i(1)\chi_j^*(1') \quad (43)$$

Substituting equation (43) into equation (6) leads to an expression for the FC contribution

$$J_{\mathrm{NN}'} = -h^{-1}(16\pi\beta\hbar/3)^2\gamma_{\mathrm{N}}\gamma_{\mathrm{N}'}\sum_{i,j}(\epsilon_j - \epsilon_i)^{-1} \times \chi_i(1_{\mathrm{N}})\chi_j^*(1_{\mathrm{N}})\chi_i(1_{\mathrm{N}'})\chi_j^*(1_{\mathrm{N}'}) \quad (44)$$

where the sum is over the occupied and unoccupied MOs i and j, respectively. Expanding the MOs as a linear combination of atomic orbitals and neglecting contributions other than the s-type orbitals centered on atoms N and N′, this becomes

$$J_{\mathrm{NN}'} = -h^{-1}(16\pi\beta\hbar/3)^2\gamma_{\mathrm{N}}\gamma_{\mathrm{N}'}\sum_{i,j}(\epsilon_j - \epsilon_i)^{-1}c_{i\mu}c_{j\nu}c_{i\nu}c_{j\mu} \times \phi_\mu^2(1_{\mathrm{N}})\phi_\nu^2(1_{\mathrm{N}'}) \quad (45)$$

where orbitals ϕ_μ and ϕ_ν are associated with nucleus N and N′, respectively. Equation (44) is more conveniently written in the form

$$J_{\mathrm{NN}'} = -(4h)^{-1}(16\pi\beta\hbar/3)^2\gamma_{\mathrm{N}}\gamma_{\mathrm{N}'}\phi_\mu^2(1_{\mathrm{N}})\phi_\nu^2(1_{\mathrm{N}'})\pi_{\mu\nu} \quad (46)$$

where the mutual atom–atom polarizability $\pi_{\mu\nu}$ is given by[50]

$$\pi_{\mu\nu} = -4\sum_{i,j}(\epsilon_j - \epsilon_i)^{-1}c_{i\mu}c_{i\nu}c_{j\mu}c_{j\nu} \quad (47)$$

This equation has been used extensively to calculate contact contributions to spin–spin coupling constants and to rationalize substituent trends. Pople and Santry used this formulation and an independent electron MO model[81] to investigate spin–spin coupling constants in hydrocarbons. Perturbation theory was used to relate the mutual atom–atom polarizabilities in equation (47) to the off-diagonal elements of the Hamiltonian.[81] These techniques were extended by several groups to investigate J couplings in a variety of situations.[82–86] Murrell and Gil also used a perturbation approach but for hydrocarbons included the additional integrals which involve the hydrogens.[82] This formulation was also used with a variety of different types of approximate methods, including extended Hückel,[87–91] complete neglect of differential overlap (CNDO),[92] INDO,[93] and wavefunctions[94] based on a modified Mulliken approximation.[95]

The Pople–Santry sum-over-states formulation (usually with a modified denominator to account for triplet energies) or the finite perturbation theory (FPT) method described in the next section was used for ab initio calculations.[33,96–102] The results were unsatisfactory. For example, nonempirical results with SCF wavefunctions (with the exception of values for HFC=O) led to coupling constants which were 2–4 times too large in magnitude.[102]

In a number of cases molecular symmetry has been exploited in the sum-over-states formulation to provide elegant descriptions of substituent effects. These include geminal H–H,[103,104] long range H–H,[105,106] and coupling in ethylenic and aromatic systems.[107] The Pople–Santry method[81] was also used to investigate the importance of noncontact mechanisms, e.g. F–F coupling constants,[108,109] and ^{13}C–^{13}C coupling constants.[110]

Hiroike[111] noted that the simple VB and MO methods based on equation (46) without configuration interaction (CI) represent different contributions to the spin–spin coupling constant. In fact, for the case of long range H–H coupling over four bonds it was found that the sum of the two results gives a much better representation than either of the MO or VB results.[112]

3.3.2 *Valence Bond Sum-Over-Triplet Description*

In the VB sum-over-triplet level scheme from these laboratories,[113,114] the ground state wavefunction is written as before, and the wavefunctions for the manifold of triplets are written,

$$^3\Psi_\kappa = \sum_l c_{\kappa l}\,^3\Phi_l \quad (48)$$

where for a system of $2n$ electrons $^3\Phi_l$ denotes a set of $3[(2n)!/(n+2)!(n-1)!]$ linearly independent, nonpolar triplet canonical structures. These structures can most easily be obtained from the usual Rumer structures according to a scheme devised by McLachlan.[115] For the system of two c–h bonds these structures are depicted in Figure 4. The transition spin densities follow from equations (3)–(5), (26) and (48)

$$Q_1(0\kappa_0 \mid 1; 1') = \sum_{j,l} c_j c_{\kappa l}(\tfrac{1}{2})^{n-i_{jl}}\sum_\mu \phi_\mu(1)\phi_\mu^*(1')f_{jl}^\mu \quad (49)$$

where in the superposition diagrams of the singlet and triplet canonical structures, i_{jl} is the number of islands and $f_{jl}{}^\mu$ = +1 or −1 if orbital ϕ_μ is part of an island which contains a broken bond and is in the even or odd subset respectively.

The VB method with a sum-over-triplets has not been extensively applied. Even in its semiempirical form, a

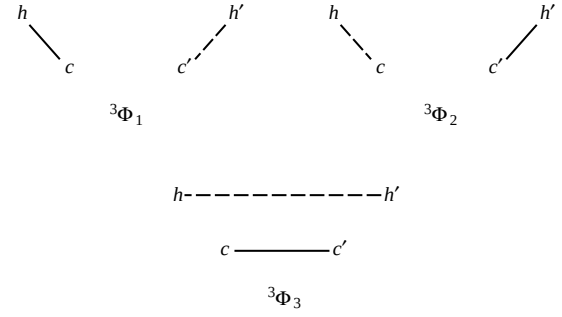

Figure 4 Valence bond triplet structures for a system of four electrons associated with two C–H bonds

molecule with $2n$ electrons requires the calculation of a ground state wavefunction having $[(2n!/n!(n+1)!]$ nonpolar singlet structures and $3[(2n)!/(n+2)!(n-1)!]$ nonpolar triplets. A general scheme for calculating coupling constants, which was developed within the framework of the generalized product approximation, permitted calculations of a large number of coupling constants via VB and other methods.[116–118] Since correlation effects are implicit in the ground state and triplet state VB functions, it is not surprising that it provides an excellent semiempirical description of nuclear spin–spin coupling.

3.3.3 *The Generalized Product Approximation with Intergroup Configuration Interaction*

This method provides a generalization of existing methods for FC spin–spin coupling in terms of the second order perturbation approaches of equations (2) and (6). The recognition of distinct groups in the molecule such as bonds and π-electron systems, permits a simplification of the discussion of many-electron systems.[32] However, for cases of more than one group, an adequate description of spin coupling requires intergroup CI. Group function methods have proved to be a convenient framework for investigating, e.g. long range coupling transmitted via the π-electron systems.[119–126] Although not originally cast in terms of density matrix notation, the various formulations for π-electron contributions to spin–spin coupling can conveniently be described by the generalized product approximation with intergroup CI.[127] For a molecular system in which distinct groups A, B, C, etc. are recognized, a single configuration wavefunction is of the form

$$^1\Phi_0 = \mathcal{A}[^1\phi_{A0}(1, 2, \ldots, N_A)\,{}^1\phi_{B0}(N_A+1, N_A+2, \ldots, N_A+N_B)\ldots] \quad (50)$$

where $\mathcal{A}$ is an operator which gives a normalized, antisymmetric wavefunction, and $^1\phi_{R_0}$ is the lowest energy singlet state wavefunction for the N_R electron group R. Triplet wavefunctions $^3\phi_{R_m}$ ($m = +1, 0, -1$) are obtained by exciting group R to the r_mth triplet state,

$$^3\Phi_{Rrm} = \mathcal{A}[^1\phi_{A0}\,{}^1\phi_{B0}\ldots{}^3\phi_{Rrm}\ldots] \quad (51)$$

In the single configuration approximation, transition spin densities between $^1\phi_0$ and $^3\phi_{R_m}$ only arise for group R,

$$Q_1(0\kappa_0 \mid 1; 1') = Q_1(0r_m \mid 1; 1') \quad (52)$$

Therefore, the only nonzero contributions to the nuclear spin coupling constant from equation (6) would be those for which electrons in group R have nonvanishing densities at nuclei N and N′. Presumably, this would only be the trivial situation in which there was only one group describable by the previous formulations. As a more interesting alternative, consider configurational mixing between the ground state and those singlets $^1\phi_{RS}$ produced by exciting two groups R and S to triplets and spin coupling to a singlet,

$$^1\Psi_0 = c_0\,{}^1\Phi_0 + \sum_{RS} c_{rs}\,{}^1\Phi_{RS} \quad (53)$$

where

$$^1\Phi_{RS} = 3^{-1/2}(\Phi_{Rr_{+1}\,Ss_{-1}} - \Phi_{Rr_0s_0} + \Phi_{Rr_{-1}r_{+1}}) \quad (54)$$

in which

$$\Phi_{Rr_{+1}Ss_{-1}} = \mathcal{A}(^3\phi_{Rr_{+1}}\,{}^3\phi_{Ss_{-1}}) \quad (55)$$

The summation in equation (53) is over all of the triplets. If one considers all possible coupling schemes, this would eventually produce all of the singlet, nonpolar VB structures. Furthermore, in the triplet manifold configurational mixing occurs, for example, between a given triplet and those obtained by exciting all the other groups to triplets,

$$^3\Psi_{\rho_0} = \sum_{r_0} c_{\rho_0 r_0}\,{}^3\Phi_{Rr_0} + \sum_{\rho_0 s_0} c_{\rho_0 s_0}\,{}^3\Phi_{Ss_0} \quad (56)$$

The transition spin densities which enter the FC coupling expression in equation (6) follow from equation (3), equations (53) and (56). The coefficients entering equations (53) and (56) and the energies appropriate to equation (6) can easily be obtained directly by solving the secular determinants[116–118] or by means of perturbation theory.[127,128]

3.4 Coupled Hartree–Fock/Finite Perturbation Descriptions

One of the most widely used methods for J coupling makes use of coupled Hartree–Fock theory. In coupled Hartree–Fock theory the nuclear perturbation of the electronic system is included in the Hamiltonian,

$$\mathcal{H} = \mathcal{H}_0 + \boldsymbol{A}_N \cdot \boldsymbol{\mu}_N + \boldsymbol{A}_{N'} \cdot \boldsymbol{\mu}_{N'} \quad (57)$$

and the Hartree–Fock equations are solved in the usual Roothaan type of formulation. Some of the previous equations, e.g. equation (44) conform to one type of uncoupling scheme for the Hartree–Fock equations.[129] There are several ways to perform calculations of J couplings that are equivalent to the coupled Hartree–Fock method. The most widely used is the FPT of Pople and co-workers.[7,130]

Expanding the energy in a Taylor's series over the magnetic moments, then the coupling constant is proportional to the second derivative of the energy,

$$J_{NN'} \propto \left[\frac{\partial^2 E(\mu_N, \mu_{N'})}{\partial\mu_N \partial\mu_{N'}}\right]_{\mu_N=\mu_{N'}=0} \quad (58)$$

From the Hellman–Feynman theorem the authors[7] further showed that

$$J_{NN'} \propto \left[\frac{\partial}{\partial\mu_{N'}}\langle\Psi(\mu_{N'})|A_N|\Psi(\mu_{N'})\rangle\right]_{\mu_{N'}=0} \quad (59)$$

where the matrix elements can be written in terms of the spin density matrix,

$$\rho = P_1(\overset{\alpha}{1}, \overset{\alpha}{1}) - P_1(\overset{\beta}{1}, \overset{\beta}{1}) \quad (60)$$

For FC coupling it follows from equation (59) that

$$\langle \Psi(\mu_{N'})|A_N|\Psi(\mu_{N'})\rangle = (8\pi\beta/3)\sum_{\mu\nu}\rho_{\mu\nu}(\mu_N)\langle\phi_\mu|\delta(r_N)|\phi_\nu\rangle \quad (61)$$

where μ and ν denote atomic orbitals and it is assumed as usual that matrix elements of $\delta(r_N)$ in equation (61) vanish except for s-type orbitals on N.

The self-consistent perturbation theory (SCPT) method was introduced by Blizzard and Santry[131] as a less computationally demanding alternative to the FPT approach. An alternative method makes use of the first-order polarization propagator (FOPPA).[132] This has been used extensively by Engelmann and Contreras[133] and co-workers. Applications of coupled Hartree–Fock methods including FPT, SCPT, and FOPPA formulations are far too numerous to be included here. Since noncontact mechanisms have not otherwise been emphasized here, mention should be made of the studies of ^1J(C,C)[134,135] coupling, those involving second row atoms,[135,136] and nonempirical calculations.[137–140] Within the semiempirical INDO framework, the FOPPA method (with respect to the inclusion of multicenter integrals)[141] leads to values of FC, OP, and SD contributions which are generally in accord with the nonempirical results.

A comparison of coupled Hartree–Fock methods with sum-over-states approaches indicated that the FPT method also introduces doubly excited states in a restricted way and should give quite different results when correlation is important for the unperturbed wavefunction.[142,143]

4 APPLICATIONS TO SPECIFIC COUPLING SITUATIONS

To examine the topic of scalar coupling from a qualitative point of view, it is often convenient to work with a simple VB bond order picture.[74] An alternative model, which leads to similar conclusions makes use of a MO model in which the MOs χ_i are written as a linear combination of hybrid type orbitals ϕ_μ (HTOs),

$$\chi_i = \sum_\mu c_{i\mu}\phi_\mu \quad (62)$$

where the ϕ_μ can be written in terms of atomic s- and p-type atomic orbitals as in equations (25) or (34). In the basis set of HTOs the expression for the FC contribution to $J_{NN'}$ is identical to the one obtained by Pople and Santry.[81] The nuclear spin–spin coupling constant is proportional to the mutual atom–atom polarizability in equations (46) and (47). For geminal, vicinal coupling, or long-range H–H coupling perturbation theory can be used to relate $\pi_{hh'}$ to the off-diagonal elements of the Hamiltonian,[81–86]

$$\pi_{hh'} = (-5\beta_{cc'}^2 - 2\beta_{hh'}^2 + 4\beta_{hc'}^2 + 2\beta_{cc'}\beta_{hh'})/(16\beta^3) \quad (63)$$

where $\beta_{cc'}$, for example, is the matrix element of the Hamiltonian operator between HTOs c and c', which are directed toward hydrogenic orbitals h and h' as in Figure 2(b).

$$\beta_{cc'} = \langle\phi_c|\mathcal{H}|\phi_{c'}\rangle \quad (64)$$

The off-diagonal element beta; in the denominator of equation (63) corresponds to an average of those between orbitals which are bonded in the primary valence structure. As a consequence of the assumptions which are implicit in the expressions for $\pi_{hh'}$, and others associated with the relation to the spin–spin coupling, this formulation is appropriate for *qualitative interpretations*. These methods will be used here to examine briefly some of the structural factors associated with geminal and vicinal H–H coupling constants.

4.1 Geminal Coupling Constants

Many features of geminal coupling can be rationalized by means of equations (46) and (63). Various terms in the numerator have opposite signs. Depending on the magnitudes of the various matrix elements, geminal H–H coupling constants could represent a delicate balance between terms of comparable magnitude but of opposite sign. The difficulty with early calculations of geminal coupling constants and the unusual sensitivity of geminal coupling constants to substituents and solvents would tend to support this view. Because of the renewed interest in the H–C–H angle dependence of ^2J(H,H′),[144,145] it may be useful to reexamine the proposed dependence of ^2J on the carbon hybridization. In equation (63) the most important term appears to be the geminal interaction integral $\beta_{cc'}$ since it is multiplied by 5. When expressed in terms of the diagonal matrix elements α_s and α_p in the s,p basis set, this term is proportional to the carbon s character a^2,

$$\beta_{cc'} = a^2(\alpha_s - \alpha_p) \quad (65)$$

If all of the integrals except this one could be neglected in the numerator of equation (63), the geminal coupling constants would be proportional to the products of the s character a^4 at the carbon atom. Therefore, the dependence of the coupling constants on the valence angle θ follows from the proportionality to a^4 and the relationship of a^2 to θ,

$$a^2 = -\cos\theta/(1-\cos\theta) \quad (66)$$

The slope of this function is 0.25 + 0.02 between θ = 102 and 129°.[144] Small variations of $\Delta\theta$ around both the tetrahedral and the trigonal interorbital angles should lead to approximately linear dependences of the geminal coupling constants on $\Delta\theta$. The recent ab initio MO data for ^2J(H,H′) of Geertsen et al.[145] indicate that this is the case. Their nonempirical results can also be fit to the expression

$$^2J(\mathrm{H,H'}) = 160.6a_C^4 - 24.6 \ \mathrm{Hz} \quad (67)$$

which has a standard deviation of only 0.2 Hz.

4.2 Vicinal Coupling Constants

Because of their sensitivity to variations of dihedral angles, vicinal H–H nuclear spin–spin coupling constants $^3J(H,H')$ have been used extensively for conformational studies. Much effort has been expended in specifying parameters for the torsion angle dependence for this type of coupling. Factors such as H–C–C internal angle dependence, C–C bond length dependence, and substituent electronegativity are also involved. Subsequent efforts have identified other factors, including substituent orientation and electronic contributions to $^3J(H,H')$ from other groups in the molecule. Based on either the VB bond order formulation, MO sum-over-states perturbation, or group function formulations, there can be important contributions to the nuclear spin–spin coupling constants arising from groups that are outside the coupling path. An interesting example of this is the nonequivalence of the *exo–exo* and *endo–endo* vicinal coupling constants in bicyclo[2.2.1]heptanes.[146]

4.2.1 Contributions from Remote Groups, e.g. Reasons for the Nonequivalence of Exo–Exo and Endo–Endo Coupling Constants

Attempts to refine the dihedral angle dependences of vicinal H–H coupling constants have demonstrated the importance of electronic factors outside the coupling path. An example of such an effect was the reason for the nonequivalence of the *exo–exo* and *endo–endo* coupling constants in the norbornane series.[146] In norbornanes it was observed that *exo–exo* coupling constants are several hertz larger than the *endo–endo* values even though both correspond to situations in which the dihedral angles are near 0°. These experimental trends were satisfactorily reproduced at the semiempirical (INDO-FPT) level. To investigate this nonequivalence a procedure was used in which certain nonbonded interactions between the ethanic bridge and other parts of the molecule were eliminated from the SCF procedure. Our first guess, that the most important interactions were between the two ethanic bridges of norbornane, turned out to be incorrect. Only on elimination of the interactions between the ethanic bridge and the methylene bridge did the two types of coupling become equivalent. These ideas have been incorporated into procedures for conformational analyses of 5-membered rings.[147,148] It is not our intent to minimize the practical applicability of the many empirical equations, but this provides one example of the reason that there can be no universal equations to describe the conformation dependences of nuclear spin–spin coupling constants.

4.2.2 Dependence on H–C–C Internal Angles as well as Dihedral Angles

Substantial deviations of internal H–C–C angles from the tetrahedral values are common in strained, multicyclic compounds. Because of their relative rigidity, such compounds are most appropriate for unambiguously relating spin–spin coupling constants to molecular structures. There are some interesting examples which clearly show the importance of internal angle change, e.g. the monotonic decrease of H–C=C–H coupling with decreasing ring size in cycloalkenes. The 5.3 Hz $^3J(H,H')$ in cubanes, which have C–C–H angles near 125°, is just about one-half of the value expected in molecules with tetrahedral angles.

An explicit expression was derived[149] for vicinal H–H coupling constants $^3J_{(H,H')}(\theta_1, \theta_2, \varphi)$ in terms of the two internal H–C–C angles θ_1 and θ_2 and the torsion angle φ. The resulting expression provides excellent correlations of most features of vicinal H–H coupling in ethanic (–CH–CH–), ethylenic (–CH=CH–), allylic (C=CH–CH–), and diene (C=CH–CH=C) moieties, and provide criteria for assessing the importance of internal angle changes. Because of the obvious extension of these equations to other spin–spin coupling situations, it is of interest to include a brief description of the results.

From equations (34) and (63) (and the proportionality of the matrix elements to overlap integrals in equation (64)) the vicinal coupling constants can be written in the form

$$^3J_{(H,H')}(\theta_1, \theta_2, \varphi) = c_a a(\theta_1, \theta_2)\cos^2\varphi + \sum_i c_{bi} b_i(\theta_1, \theta_2)\cos\varphi + C \quad (68a)$$

where

$$a(\theta_1, \theta_2) = (1 + \cos\theta_1)(1 + \cos\theta_2) \quad (68b)$$

$$b_1(\theta_1, \theta_2) = \cot(\theta_1/2)\ \cot(\theta_2/2)\cos\theta_1\cos\theta_2 \quad (68c)$$

$$b_2(\theta_1, \theta_2) = \cot(\theta_1/2)\ \cot(\theta_2/2)(\cos\theta_1\cos\theta_2)^{1/2} \quad (68d)$$

$$b_3(\theta_1, \theta_2) = \cot(\theta_1/2)\ \cot(\theta_2/2)[\cos\theta_2(-\cos\theta_1)^{1/2} + \cos\theta_1(-\cos\theta_2)^{1/2}] \quad (68e)$$

The C term is usually small in magnitude when $^3J(H,H')$ is written in the form of equation (35).[149] Equation (68) is an analytic expression but is subject to the many approximations that are implicit in the derivation.

In equations (68a)–(68e) the dependence of $^3J_{(H,H')}$ on C–C internuclear separations occurs in the overlap integrals, which are implicit in the coefficients c_a, c_{bi} and C. Therefore, there will be a set of coefficients for each value of r(C–C). In the spirit of semiempirical MO methods, where the β integrals are determined empirically, these coefficients were based on a least squares analysis of the available experimental data. In deriving this equation from equation (64) it was assumed that the $\beta_{cc'}$ term is dominant and that other integrals will have the effect of slightly modifying the empirically determined coefficients.

The term containing $\cos^2\varphi$ (the A term) in equation (68a) is the most important term controlling the vicinal coupling constants. The θ-dependence of the coefficient of this term [equation (68b)] is relatively simple when compared with the coefficients [equations (68c)–(68e)] of the cos φ term. Depicted in Figure 5 for ethanic coupling is a surface and contour plot of $^3J_{(H,H')}(\theta_1, \theta_2, \varphi)$ on the internal angles $\theta_1 = \theta_2$ and the dihedral angle φ. The decrease in the magnitude of the vicinal coupling constants with increasing H–C–C angle is substantial, especially for the *trans* coupling. Clearly, the usual tendency to neglect the effects of internal angle changes

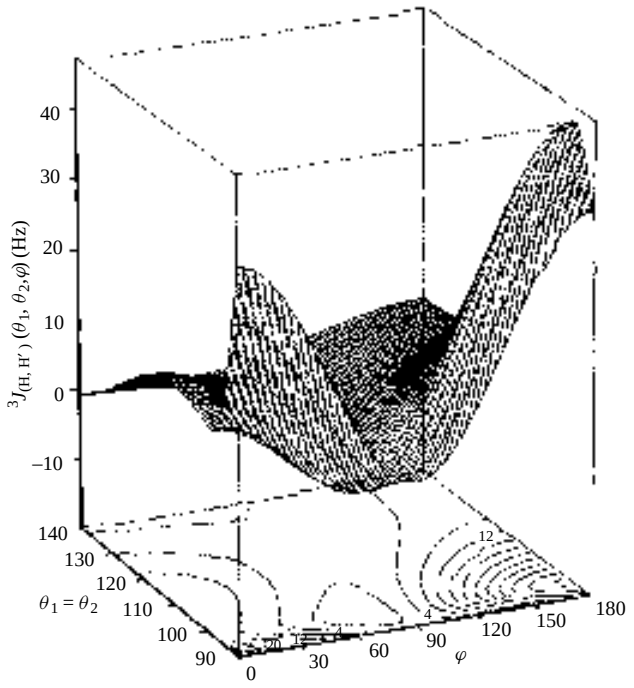

Figure 5 Surface and contour plots depicting the dependence of vicinal H–H coupling constants in an ethanic system as a function of the dihedral angle ϕ and the internal H–C–C angles θ_1=θ_2

cannot be justified in strained molecules or those with unusual bonding patterns.

5 REFERENCES

1. M. Barfield and D. M. Grant, *Adv. Magn. Reson.*, 1965, **1**, 149.
2. J. N. Murrell, *Prog. NMR Spectrosc.*, 1971, **6**, 1.
3. P. D. Ellis and R. Ditchfield, in *Topics in Carbon-13 NMR Spectroscopy*, ed. G. Levy, Wiley, New York, 1976, Vol. 2, p. 434.
4. J. Kowalewski, *Annu. Rep. NMR Spectrosc.*, 1982, **12**, 81.
5. H. Fukui, in *Nuclear Magnetic Resonance*, Specialist Periodical Reports, The Chemical Society, London, No. 22, 1993 and previous chapters in this series.
6. K. Kamienska-Trela, in *Nuclear Magnetic Resonance*, Specialist Periodical Reports, The Chemical Society, London, No. 22, 1993 and previous chapters in this series.
7. J. A. Pople, J. W. McIver, Jr., and N. S. Ostlund, *J. Chem. Phys.*, 1968, **49**, 2960, 2965.
8. J. Geertsen, J. Oddershede, W. T. Raynes, and G. E. Scuseria, *J. Magn. Reson.*, 1991, **93**, 458; W. T. Raynes, J. Geertsen, and J. Oddershede, *Chem. Phys. Lett.*, 1992, **197**, 516.
9. O. Vahtras, H. Ågren, P. Jorgensen, H. J. Aa. Jensen, S. B. Padkjaer, and T. Helgaker, *J. Chem. Phys.*, 1992, **96**, 6120; O. Vahtras, H. Ågren, P. Jorgensen, T. Helgaker, and H. J. Aa. Jensen, *Chem. Phys. Lett.*, 1993, **209**, 201.
10. H. Fukui, K. Miura, H. Matsuda, and T. Baba, *J. Chem. Phys.*, 1992, **97**, 2299; H. Fukui, K. Miura, and H. Matsuda, *J. Chem. Phys.*, 1991, **94**, 533.
11. I. Carmichael, *J. Phys. Chem.*, 1993, **97**, 1789.
12. I. Carmichael, D. M. Chipman, C. A. Podlasek, and A. S. Serianni, *J. Am. Chem. Soc.*, 1993, **115**, 10 863.
13. J. San-Fabián, J. Guilleme, E. Díez, P. Lazzeretti, M. Malagoli, and R. Zanasi, *Chem. Phys. Lett.*, 1993, **206**, 253.
14. A. S. Edison, J. L. Markley, and F. Weinhold, *J. Phys. Chem.*, 1993, **97**, 11 657.
15. G. A. Aucar and J. Oddershede, *Int. J. Quantum Chem.*, 1993, **47**, 425.
16. E. L. Hahn, *Phys. Rev.*, 1950, **80**, 580.
17. W. G. Proctor and F. C. Yu, *Phys. Rev.*, 1951, **81**, 20.
18. H. S. Gutowsky and D. W. McCall, *Phys. Rev.*, 1951, **82**, 748.
19. E. R. Andrew, *Phys. Rev.*, 1951, **82**, 443.
20. M. E. Packard and J. T. Arnold, *Phys. Rev.*, 1951, **83**, 210A.
21. H. S. Gutowsky, D. W. McCall, and C. P. Slichter, *Phys. Rev.*, 1951, **84**, 589.
22. E. B. McNeil, C. P. Slichter, and H. S. Gutowsky, *Phys. Rev.*, 1951, **84**, 1245.
23. E. L. Hahn and D. E. Maxwell, *Phys. Rev.*, 1951, **84**, 1246.
24. N. F. Ramsey and E. M. Purcell, *Phys. Rev.*, 1952, **85**, 143.
25. N. F. Ramsey, *Phys. Rev.*, 1953, **91**, 303.
26. T. F. Wimett, *Phys. Rev.*, 1953, **91**, 476A.
27. J. Musher, *Phys. Rev. Lett.*, 1965, **15**, 1015; 1966, **16**, 675E.
28. R. F. Code and N. F. Ramsey, *Phys. Rev. A*, 1971, **4**, 1945.
29. M. Barfield, unpublished results, 1967.
30. J. E. Harriman, M. Twerdochlib, M. B. Milleur, and J. O. Hirschfelder, *Proc. Natl. Acad. Sci. U.S.A.*, 1967, **57**, 1558; M. B. Milleur, L. A. Curtiss, M. Twerdochlib, and J. O. Hirschfelder, *J. Chem. Phys.*, 1968, **48**, 4261.
31. R. McWeeny, *Proc. R. Soc. London, Ser. A*, 1959, **253**, 242; R. McWeeny and Y. Mizuno, *Proc. R. Soc. London, Ser. A*, 1961, **259**, 554; R. McWeeny, *Rev. Mod. Phys.*, 1960, **32**, 335.
32. R. McWeeny and B. T. Sutcliffe, *Methods of Molecular Quantum Mechanics*, Academic Press, New York, 1969.
33. J. J. Reed, *Theoretical Studies of Nuclear Spin-Spin Coupling*, Ph.D. Thesis, University of Arizona, 1971.
34. M. Barfield, *Chem. Phys. Lett.*, 1970, **4**, 518.
35. A. D. McLachlan, *J. Chem. Phys.*, 1960, **32**, 1263.
36. M. Karplus, *J. Chem. Phys.*, 1960, **33**, 941.
37. J. A. Pople, W. G. Schneider, and H. J. Bernstein, *High Resolution Nuclear Magnetic Resonance*, McGraw-Hill, New York, 1959, p. 190.
38. M. Barfield, *J. Chem. Phys.*, 1966, **44**, 1836.
39. H. S. Gutowsky, D. W. McCall, and C. P. Slichter, *J. Chem. Phys.*, 1953, **21**, 279.
40. M. A. Ruderman and C. Kittel, *Phys. Rev.*, 1954, **96**, 99.
41. N. Bloembergen and J. T. Rowland, *Phys. Rev.*, 1955, **97**, 1679.
42. H. M. McConnell, *J. Chem. Phys.*, 1955, **23**, 760; 1956, **24**, 460.
43. H. M. McConnell, *J. Chem. Phys.*, 1955, **23**, 2454.
44. H. M. McConnell, *J. Mol. Spectrosc.*, 1957, **1**, 11.
45. A. D. McLachlan, *Mol. Phys.*, 1958, **1**, 233.
46. A. Saika, *Physica*, 1959, **25**, 51.
47. H. M. McConnell, *Annu. Rev. Phys. Chem.*, 1957, **8**, 105.
48. H. M. McConnell, *J. Chem. Phys.*, 1959, **30**, 126.
49. J. A. Pople, *Mol. Phys.*, 1958, **1**, 216.
50. C. A. Coulson and H. C. Longuet-Higgins, *Proc. R. Soc. London, Ser. A*, 1947, **191**, 39; 1947, **192**, 16; 1948, **193**, 447.
51. N. Muller and D. E. Pritchard, *J. Chem. Phys.*, 1959, **31**, 768.
52. J. N. Shoolery, *J. Chem. Phys.*, 1959, **31**, 1427.
53. H. S. Gutowsky and C. S. Juan, *J. Am. Chem. Soc.*, 1962, **84**, 307.
54. E. Aihara, *J. Chem. Phys.*, 1957, **26**, 1347.

55. M. Karplus, D. H. Anderson, T. C. Farrar, and H. S. Gutowsky, *J. Chem. Phys.*, 1957, **27**, 597.
56. M. J. Stephen, *Proc. R. Soc. London, Ser. A*, 1957, **243**, 274.
57. M. Karplus and D. H. Anderson, *J. Chem. Phys.*, 1959, **30**, 6.
58. M. Karplus, *J. Chem. Phys.*, 1959, **30**, 11; *J. Am. Chem. Soc.*, 1963, **85**, 2870.
59. H. S. Gutowsky, M. Karplus, and D. M. Grant, *J. Chem. Phys.*, 1959, **31**, 1278.
60. M. Karplus and D. M. Grant, *Proc. Natl. Acad. Sci. U.S.A.*, 1959, **45**, 1269.
61. E. Hiroike, *J. Phys. Soc. Jpn.*, 1960, **15**, 270; *Prog. Theor. Phys.*, 1961, **26**, 283.
62. S. Alexander, *J. Chem. Phys.*, 1961, **34**, 106.
63. J. Ranft, *Ann. Phys.*, 1961, **8**, 322; 1962, **9**, 124.
64. C. Juan and H. S. Gutowsky, *J. Chem. Phys.*, 1962, **37**, 2198; H. S. Gutowsky and C. Juan, *Discuss. Faraday Soc.*, 1962, **34**, 1.
65. M. Barfield and D. M. Grant, *J. Chem. Phys.*, 1962, **36**, 2054; *J. Am. Chem. Soc.*, 1963, **85**, 1899.
66. H. G. Hecht, *Theor. Chim. Acta*, 1963, **1**, 222.
67. S. Koide and E. Duval, *J. Chem. Phys.*, 1964, **41**, 315.
68. M. Barfield, *J. Chem. Phys.*, 1964, **41**, 3825.
69. P. Chandra and P. T. Narasimhan. *Mol. Phys.*, 1966, **11**, 189; 1967, **12**, 523.
70. E. Sackmann and H. Dreeskamp, *Spectrochim. Acta*, 1965, **21**, 2005.
71. R. A. Bernheim and T. P. Das, *J. Chem. Phys.*, 1960, **33**, 1813; T. P. Das and R. Bersohn, *Phys. Rev.*, 1959, **115**, 897.
72. G. Rumer, *Nachr. Ges. Wiss. Goettingen, Math. Phys. Kl, Fachgruppe 1*, 1932, 337.
73. L. Pauling and E. B. Wilson, Jr., *Introduction to Quantum Mechanics*, McGraw-Hill, New York, 1935, pp. 374–380.
74. M. Barfield and M. Karplus, *J. Am. Chem. Soc.*, 1969, **91**, 1.
75. W. G. Penney, *Proc. R. Soc. London, Ser. A*, 1937, **158**, 306.
76. S. Karplus and M. Karplus, *Proc. Natl. Acad. Sci. U.S.A.*, 1972, **69**, 3204.
77. D. Doddrell, M. Barfield, W. Adcock, M. Aurangzeb, and D. Jordan, *J. Chem. Soc., Perkin Trans. 2*, 1976, 402.
78. M. Barfield, S. A. Conn, J. L. Marshall, and D. E. Miiller, *J. Am. Chem. Soc.*, 1976, **98**, 6253.
79. M. Barfield, R. J. Spear, and S. Sternhell, *Chem. Rev.*, 1976, **76**, 593.
80. M. Barfield and S. R. Walter, *J. Am. Chem. Soc.*, 1983, **105**, 4191.
81. J. A. Pople and D. P. Santry, *Mol. Phys.*, 1964, **7**, 269; 1964, **8**, 1; 1965, **9**, 301, 311.
82. J. N. Murrell and V. M. S. Gil, *Theor. Chim. Acta*, 1966, **4**, 114.
83. F. B. van Duijneveldt, V. M. S. Gil, and J. N. Murrell, *Theor. Chim. Acta*, 1966, **4**, 85.
84. R. Ditchfield, G. T. Jones, and J. N. Murrell, *Theor. Chim. Acta*, 1968, **9**, 253.
85. V. M. S. Gil and J. J. C. Teixeira-Dias, *Mol. Phys.*, 1968, **15**, 47.
86. C. J. Jameson and H. S. Gutowsky, *J. Chem. Phys.*, 1969, **51**, 2790; C. J. Jameson and M. C. Damasco, *Mol. Phys.*, 1970, **18**, 491.
87. R. C. Fahey, G. C. Graham, and R. L. Piccioni, *J. Am. Chem. Soc.*, 1966, **88**, 193.
88. S. Polezzo, P. Cremaschi, and M. Simonetta, *Chem. Phys. Lett.*, 1967, **1**, 357.
89. W. H. de Jeu and G. P. Beneder, *Theor. Chim. Acta*, 1969, **13**, 349.
90. T. Yonezawa, I. Morishima, M. Fujii, and H. Kato, *Bull. Chem. Soc. Jpn.*, 1967, **40**, 487.
91. K. G. R. Pachler, *Tetrahedron Lett.*, **1970**, 1955.
92. R. Ditchfield and J. N. Murrell, *Mol. Phys.*, 1968, **14**, 481.
93. R. Ditchfield, *Mol. Phys.*, 1969, **17**, 33.
94. H. Frischleder and D. Klöpper, *Mol. Phys.*, 1970, **18**, 113.
95. M. D. Newton, F. P. Boer, and W. N. Lipscomb, *J. Am. Chem. Soc.*, 1966, **88**, 2353.
96. D. S. Bartow and J. W. Richardson, *J. Chem. Phys.*, 1965, **42**, 4018.
97. P. Loève and L. Salem, *J. Chem. Phys.*, 1965, **43**, 3402.
98. Y. Kato and A. Saika, *J. Chem. Phys.*, 1967, **46**, 1975.
99. E. A. G. Armour and A. J. Stone, *Proc. R. Soc. London, Ser. A*, 1967, **302**, 25.
100. E. A. G. Armour, *J. Chem. Phys.*, 1968, **49**, 5445.
101. N. S. Ostlund, M. D. Newton, J. W. McIver, Jr., and J. A. Pople, *J. Magn. Reson.*, 1969, **1**, 298.
102. Alan W. Douglas, *A Priori Calculations of Nuclear Spin Coupling Constants*, Ph.D. Thesis, State University of New York at Stony Brook, 1969.
103. J. A. Pople and A. A. Bothner-By, *J. Chem. Phys.*, 1965, **42**, 1339.
104. V. M. S. Gil and S. J. S. Formosinho-Simoes, *Mol. Phys.*, 1968, **15**, 639; V. M. S. Gil and C. F. G. C. Geraldes, *Rev. Port. Quim.*, 1970, **12**, 32.
105. M. Barfield and B. Chakrabarti, *Chem. Rev.*, 1969, **69**, 757.
106. M. Barfield, R. J. Spear, and S. Sternhell, *J. Am. Chem. Soc.*, 1971, **93**, 5322.
107. V. M. S. Gil, *Mol. Phys.*, 1968, **15**, 645.
108. H. Nakatsuji, I. Morishima, H. Kato, and T. Yonezawa, *Bull. Chem. Soc. Jpn.*, 1971, **44**, 2010; K. Hirao, H. Nakatsuji, H. Kato, and T. Yonezawa, *J. Am. Chem. Soc.*, 1972, **94**, 4078; K. Hirao, H. Nakatsuji, and H. Kato, *J. Am. Chem. Soc.*, 1973, **95**, 31.
109. A. D. C. Towl and K. Schaumburg, *Mol. Phys.*, 1971, **22**, 49; H. Jensen and K. Schaumburg, *Mol. Phys.*, 1971, **22**, 1041.
110. C. Barbier, H. Foucher, and G. Berthier, *Theor. Chim. Acta*, 1971, **21**, 105.
111. E. Hiroike, *J. Phys. Soc. Jpn.*, 1967, **22**, 379.
112. M. Barfield, A. M. Dean, C. J. Fallick, R. J. Spear, S. Sternhell, and P. W. Westerman, *J. Am. Chem. Soc.*, 1975, **97**, 1482.
113. M. Barfield, *J. Chem. Phys.*, 1967, **46**, 811; 1968, **49**, 4458.
114. M. Barfield, *J. Chem. Phys.*, 1968, **49**, 4463.
115. A. D. McLachlan, *J. Chem. Phys.*, 1960, **33**, 663.
116. M. Barfield, *J. Chem. Phys.*, 1968, **49**, 2145.
117. M. Barfield and J. J. Reed, *J. Chem. Phys.*, 1969, **51**, 3039.
118. M. Barfield and B. Chakrabarti, *J. Am. Chem. Soc.*, 1969, **91**, 4346.
119. M. Karplus, *J. Chem. Phys.*, 1960, **33**, 1842; *J. Am. Chem. Soc.*, 1960, **82**, 4431.
120. J. V. Acrivos, *Mol. Phys.*, 1962, **5**, 1.
121. A. V. Cunliffe and R. K. Harrris, *Mol. Phys.*, 1967, **13**, 269.
122. R. Ditchfield and J. N. Murrell, *Mol. Phys.*, 1968, **15**, 533.
123. A. V. Cunliffe, R. Grinter, and R. K. Harrris, *J. Magn. Reson.*, 1970, **3**, 299.
124. D. E. O'Reilly, *J. Chem. Phys.*, 1962, **36**, 274.
125. H. Frischleder and G. Bär, *Mol. Phys.*, 1966, **11**, 359.
126. T. Vladimiroff and E. R. Malinowski, *J. Chem. Phys.*, 1967, **46**, 1830.

127. W. J. van der Hart, *Mol. Phys.*, 1971, **20**, 385, 399, 407.
128. N. D. Chuvylkin, G. M. Zhidomirov, and R. B. Schastnev, *Mol. Phys.*, 1972, **23**, 639.
129. P. W. Langhoff, M. Karplus, and R. P. Hurst, *J. Chem. Phys.*, 1966, **44**, 505.
130. G. E. Maciel, J. W. McIver, Jr., N. S. Ostlund, and J. A. Pople, *J. Am. Chem. Soc.*, 1970, **92**, 1, 11, 4151, 4497, 4506.
131. A. C. Blizzard and D. P. Santry, *J. Chem. Phys.*, 1971, **55**, 950; 1973, **58**, 4714.
132. J. Linderberg and Y. Öhrn, *Propagators in Quantum Chemistry*, Academic Press, New York, 1973.
133. A. R. Engelmann and R. H. Contreras, *Int. J. Quantum Chem.*, 1983, **23**, 1033.
134. M. D. Newton and J. M. Schulman, *J. Am. Chem. Soc.*, 1972, **94**, 767, 773; M. D. Newton, J. M. Schulman, and M. M. Manus, *J. Am. Chem. Soc.*, 1974, **96**, 17; J. M. Schulman and M. D. Newton, *J. Am. Chem. Soc.*, 1974, **96**, 6295.
135. P. Lazzereti, F. Taddei, and R. Zanasi, *J. Am. Chem. Soc.*, 1976, **98**, 7989.
136. T. A. Albright, *Org. Magn. Reson.*, 1976, **8**, 489.
137. M. D. Beer and R. Grinter, *J. Magn. Reson.*, 1978, **31**, 187.
138. R. Ditchfield and L. C. Snyder, *J. Chem. Phys.*, 1972, **56**, 5823.
139. J. Oddershede, P. Jorgensen, and N. H. F. Beebe, *J. Chem. Phys.*, 1975, **63**, 2996.
140. M. F. Guest, V. R. Saunders, and R. E. Overill, *Mol. Phys.*, 1978, **35**, 427.
141. J. C. Facelli and M. Barfield, *J. Am. Chem. Soc.*, 1984, **106**, 3407; *J. Magn. Reson.*, 1984, **59**, 452.
142. R. Ditchfield, N. S. Ostlund, J. N. Murrell, and M. A. Turpin, *Mol. Phys.*, 1970, **18**, 433.
143. M. D. Johnston, Jr.and M. Barfield, *J. Chem. Phys.*, 1971, **54**, 3083.
144. M. Klessinger and M. Barfield, in *Modelling of Structure and Properties of Molecules*, ed. Z. B. Maksic, Ellis Horwood, Chichester, 1987, pp. 269–284.
145. J. Geertsen, J. Oddershede, and W. T. Raynes, *Magn. Reson. Chem.*, 1993, **31**, 722.
146. J. L. Marshall, S. R. Walter, M. Barfield, A. P. Marchand, N. W. Marchand, and A. L. Segre, *Tetrahedron*, 1976, **32**, 537.
147. A. Jaworski, I. Ekiel, and D. Shugar, *J. Am. Chem. Soc.*, 1978, **100**, 4357; A. Jaworski and I. Ekiel, *Int. J. Quantum Chem.*, 1979, **16**, 615.
148. C. A. G. Haasnoot, F. A. A. M. de Leeuw, and C. Altona, *Tetrahedron*, 1980, **36**, 2783; F. A. A. M. de Leeuw, C. Altona, H. Kessler, W. Bermel, A. Friedrich, G. Krack, and W. E. Hull, *J. Am. Chem. Soc.*, 1983, **105**, 2237; F. A. A. M. de Leeuw, A. A. van Beuzekom, and C. Altona, *J. Comput. Chem.*, 1983, **4**, 438.
149. M. Barfield and W. B. Smith, *J. Am. Chem. Soc.*, 1992, **114**, 1574; W. B. Smith and M. Barfield, *Magn. Reson. Chem.*, 1993, **31**, 696.

Biographical Sketch

Michael Barfield. *b* 1934. B.A., 1957, Ph.D., Chemistry, University of Utah, USA, 1962 (advisor David M. Grant). Postdoctoral Fellow, Harvard University, 1962–63 (with John D. Baldeschwieler). Assistant Professor, University of South Florida, 1963–65. Assistant Professor, Associate Professor, Professor, University of Arizona, 1965–present. Approx. 100 publications. Research specialties: studies of NMR parameters, especially nuclear spin–spin coupling and chemical shielding.

Indirect Coupling: Intermolecular and Solvent Effects

Isao Ando

Tokyo Institute of Technology, Tokyo, Japan

1	Introduction	1
2	The Effect of Nonbonded Interactions on J Couplings	1
3	Effect of Pressure on J Couplings	4
4	Related Articles	4
5	References	4

1 INTRODUCTION

In general, J couplings (spin–spin couplings) are solvent dependent. This arises from subtle electronic changes which occur in the solute molecule as a result of intermolecular solute–solvent interactions. Therefore, a study of medium effects on J couplings is potentially able to provide intimate information on solute–solvent interactions.

Generally, there are a number of nonbonded and bonded solute–solvent interactions that may influence NMR parameters.[1] Clearly, the relative importance of these various interactions needs to be elucidated prior to any detailed investigation. The nonbonded interactions arise from electric field influences. These appear to operate by means of some type of electrostatic interaction between the solute and solvent molecules. Consequently, a model containing an account of the charge distribution in the interacting molecules would appear to be reasonable for the nonbonded interactions. A number of specific solute–solvent bonded interactions may also occur. Examples of these are weak molecular association, hydrogen bonding, ionic interactions and intramolecular change. From a knowledge of the chemistry of the solute and solvent concerned it is often possible to estimate the extent of any bonded interactions present. Such influences should be removed from consideration before turning to the effects of the nonbonded interactions.

A satisfactory model for quantitatively understanding solvent effects will inevitably include a realistic description of the charge distribution of the solute molecule. However, the solvent molecules need not be treated so specifically. The simplest approach is to consider the solvent as a continuum surrounding the solute molecule. Several different models of this type have been proposed to understand nonbonded solute–solvent effects on J coupling. Inevitably, the polarity of the solvent medium enters into their formulation. The main purpose of this section is to provide a substantial elucidation of the nature of solute–solvent interactions in J coupling through theoretical and experimental estimates of J coupling.

2 THE EFFECT OF NONBONDED INTERACTIONS ON J COUPLINGS

The three major contributions to J coupling arise from the contact, orbital, and dipolar interactions.[2] The J coupling involving hydrogen nuclei is predominantly governed by only the contact interaction. However, the J coupling between non-hydrogen nuclei is governed by all three interactions. Within the self-consistent perturbation framework these contributions to J(A,B), the spin–spin coupling interaction between nuclei A and B, are given by equations (1)–(3).

The contact contribution, J_c, can be defined as

$$J_c(\mathrm{A,B}) = (32/9)h\pi\mu_0\mu_B^2\gamma_A\gamma_B S_A^2(0)S_B^2(0)P^{\alpha}_{S_B S_B} \quad (1)$$

where μ_0 is the permeability of a vacuum, μ_B is the Bohr magneton, $[\gamma]$ is the nuclear magnetogyric ratio divided by 2π, $S^2(0)$ is the s electron density at the nucleus concerned and $P^{\alpha}_{S_B S_B}$ refers to a diagonal element of the charge density, bond order matrix for s electron spin orbitals on nucleus B with α spin.

The orbital term, J_O, is given by

$$J_O(\mathrm{A,B}) = (2\mu_0\mu_B^2 h\gamma_A\gamma_B/3\pi)\langle r_A^{-3}\rangle_p\langle r_B^{-3}\rangle_p \times(P_{x_B y_B} + P_{z_B y_B} + P_{x_B z_B}) \quad (2)$$

where $\langle r^{-3}\rangle_p$ refers to the expectation value of the inverse cube of the separation between the nucleus concerned and its p electrons and $P_{x_B y_B}$ is the charge density, bond order matrix element for the p_x and p_y orbitals on atom B.

Finally, the dipolar expression, J_D, is

$$J_D(\mathrm{A,B}) = (\mu_0\mu_B^2 h^3\gamma_A\gamma_B/20\pi^3)\langle r_A^{-3}\rangle_p\langle r_B^{-3}\rangle_p \times(2P^{\alpha\alpha}_{z_B z_B} - P^{\alpha\alpha}_{x_B x_B} - P^{\alpha\alpha}_{y_B y_B} + 3P^{\alpha\beta}_{x_B z_B} - 3Q^{\alpha\beta}_{y_B y_B}) \quad (3)$$

where Q refers to the imaginary part of the charge density, bond order matrix.

As shown by equations (2) and (3), the orbital and dipolar contributions arise for nuclei with p valence electrons whereas equation (1) reveals that the presence of s electrons is necessary for the contact interaction.

In the absence of specific association effects the solvent dependence of coupling interactions is related to the polarity of the medium. This dependence has been studied theoretically by means of the reaction field model, a cubic closest packed cluster model and solvation model (see Section 2.2 below).

2.1 Reaction-Field Type Solvent Effect

This provides the simplest theoretical description of the interactions occurring between polar solute and polar solvent molecules.[3–5] The model treats the solute as a polarizable point dipole centered in a spherical cavity within the dielectric continuum formed by the solvent molecules. It is assumed that the solute point dipole polarizes the surrounding medium, thus creating a reaction field which is parallel to its dipole moment. By taking the direction of the dipole moment vector,

μ, to be from the positive to negative charge on the solute, the reaction field, R, lies in the same direction as μ. The relationship between R and μ is given by equation (4).

$$R = 2\mu(\epsilon - 1)(n^2 - 1)/3\alpha(2\epsilon + n^2) \tag{4}$$

where n is the refractive index of the solute, α is its polarizability, μ refers to the solute point dipole and ϵ is the dielectric constant of the solvent. Linear relationships have been reported between J coupling interactions and the reaction field parameter.

Since ^{1}H and ^{19}F nuclei are often on the surface of the solute molecule they are more directly exposed to solvent molecules than are skeletal nuclei such as ^{13}C, ^{15}N or ^{31}P. Consequently, equation (4) may need to be modified to include local effects due to polar groupings on neighboring solvent molecules when considering J couplings between peripheral nuclei.

In calculations of the effects of the reaction field on J couplings both magnetic and electric reaction fields have been considered. The inclusion of reasonable numbers in the expression obtained in the magnetic field case results in solvent effects of about 1 Hz, which is much smaller than those observed for a number of J couplings. Thus, only electrostatic interactions between the solute and solvent molecules have been extensively considered in the reaction field. A simplified sum-over-states perturbation theory was applied to the study of the electrostatic interaction. In this approach the contact contribution to the J coupling is given by[6]

$$J_c(\mathrm{A,B}) = \pi h \mu_0 \mu_B^2 \gamma_A \gamma_B S_A^2(0) S_B^2(0) \pi_{AB} \tag{5}$$

where the mutual atom–atom polarizability, π_{AB}, is expressed as

$$\pi_{AB} = 4 \sum_{j}^{\mathrm{occ}} \sum_{k}^{\mathrm{unocc}} (\epsilon_j - \epsilon_k)^{-1} C_{j,S_A} C_{k,S_A} C_{j,S_B} C_{k,S_B} \tag{6}$$

where ϵ_j and ϵ_k refer to the energies of the j occupied and k unoccupied molecular orbitals, respectively, and the C terms are the coefficients for the s orbitals on atoms A and B in these molecular orbitals. The value of π_{AB} is related to the empirical resonance and Coulomb integrals. The electric field dependence of π_{AB} is introduced by means of these empirical parameters to obtain an estimate of the solvent dependence of J_c(A,B). However, the formulation employed for the electric field effects on these parameters has been criticized. Additionally, it is claimed that the reported results are fortuitous since the transfer of electron density out of the C–H bonding region is not considered. The inclusion of this electron transfer produces satisfactory agreement between the calculated and observed solvent effects on ^2J(H,H) when Intermediate Neglect of Differential Overlap (INDO) parameters are employed.

More comprehensive calculations of J couplings, within the reaction field framework, have included a term describing the interaction between the solute molecule and neighboring electrostatic fields in the Hamiltonian governing the J coupling interaction. The solvent effects on the J couplings, ΔJ(A,B), are calculated from[7]

$$\Delta J(\mathrm{A,B}) = 10^{-5}(|R| - |R_0|)[\Delta J(\mathrm{A,B})_E] \tag{7}$$

where $|R|$ and $|R_0|$ are the magnitudes of the reaction field, given by equation (4), in the solvent of interest and in cyclohexane, respectively. ΔJ(A,B) is the difference in the J coupling constant calculated for the isolated molecule, ϵ = 1, and that due to the addition of an electric field of 10^5 esu cm^{-2}. The use of equation (8) is apparently justified by the linearity of changes in the calculated J coupling constants as a function of the reaction field for values of the latter as large as 3×10^5 esu cm^{-2}. The calculation explains well the experimental data.

2.2 Solvation Type Solvent Effect

Some attempts to perform direct quantum chemical calculations on a solvated molecule have been reported.[8] Treatments of solvent effects on nuclear shielding[9,10] and the J coupling constant[11–14] by means of the solvaton theory in conjunction with MO methods have been published. This procedure has been used to compute the wavefunctions of molecules under the influence of the solvent considered as a perturbation.

According to the solvaton model, it is assumed that the solvent molecule induces a number of charges, the solvatons, in a solvent of dielectric constant ϵ: one solvaton is associated with each atom of the solute, and its charge is equal in magnitude but opposite in sign to the net charge of the atom to which it is attached. There are no interactions between the solvatons. On the basis of this model, the Hamiltonian, $\hat{\mathcal{H}}$, of a particular molecule with M electrons and N nuclei consists of the inherent term, $\hat{\mathcal{H}}_{\mathrm{inh}}$, and the solute–solvent interaction term, $\hat{\mathcal{H}}_{\mathrm{solv}}$, and is given, in atomic units, by equations (8)–(10).[9]

$$\hat{\mathcal{H}} = \hat{\mathcal{H}}_{\mathrm{inh}} + \hat{\mathcal{H}}_{\mathrm{solv}} \tag{8}$$

$$\hat{\mathcal{H}}_{\mathrm{inh}} = \sum_{i=1}^{M} \left(-\nabla_i^2 - \sum_{n=1}^{N} \frac{Z_n}{r_{ni}} \right) + \frac{1}{2} \sum_{i}^{M} \sum_{j}^{M} \frac{1}{r_{ij}} + \frac{1}{2} \sum_{k}^{N} \sum_{l}^{N} \frac{Z_k Z_l}{r_{kl}} \tag{9}$$

$$\hat{\mathcal{H}}_{\mathrm{solv}} = \frac{\epsilon - 1}{2\epsilon} \left(\sum_{i}^{M} \sum_{s}^{N} \frac{Q_s}{r_{si}} - \sum_{r}^{M} \sum_{k}^{N} \frac{Q_s Z_k}{r_{sk}} \right) \tag{10}$$

where Q_s is the induced solvaton charge, r_{si} and r_{sk} are the solvaton–electron and solvaton–nucleus separations, respectively, and Z is the nuclear charge. The Born equation is used to approximate the solvent–solute interactions. If the atomic orbitals (AOs) and solvaton are associated with the same center, the solvaton–electron distance, r_{si}, is approximated by the van der Waals radius of the particular type of atom. If the AOs and solvaton are associated with different atomic centers, the solvaton is assumed to be centered on the atom associated with it and then r_{si} is evaluated accordingly.

This model has been employed within the Finite Perturbation Theory (FPT) formalism, in an attempt to understand the effects of solvents on ^1J(C,H), ^3J(H,H) and ^3J(C,H) couplings. The approach adopted considered only the contact interaction and the spin-unrestricted self-consistent field

equations of the Fock matrices, $F_{\mu\nu}{}^{\alpha}$ and $F_{\mu\nu}{}^{\beta}$, for α and β electron spins become[10]

$$F^{\alpha}_{\mu\nu} = H^{\text{core}}_{\mu\nu} + \sum_{\lambda\sigma}[P_{\lambda\sigma}(\mu\nu \mid \lambda\sigma) - P^{\alpha}_{\lambda\sigma}(\mu\sigma \mid \lambda\sigma)] + \frac{\epsilon - 1}{\epsilon} \times \int \phi_{\mu}\left(\sum_{s}^{N} \frac{Q^{\alpha}_{s}}{r_{sl}}\right)\phi_{\nu}\,\mathrm{d}\tau + \tfrac{8}{3}\pi\beta_{\mu}\int \phi_{\mu}\delta(r_{\mathrm{B}})\phi_{\nu}\,\mathrm{d}r \quad (11)$$

$$F^{\beta}_{\mu\nu} = H^{\text{core}}_{\mu\nu} + \sum_{\lambda\sigma}[P_{\lambda\sigma}(\mu\nu \mid \lambda\sigma) - P^{\beta}_{\lambda\sigma}(\mu\sigma \mid \lambda\nu)] - \frac{\epsilon - 1}{\epsilon} \times \int \phi_{\mu}\left(\sum_{s}^{N} \frac{Q^{\beta}_{s}}{r_{sl}}\right)\phi_{\nu}\,\mathrm{d}\tau - \tfrac{8}{3}\pi\beta_{\mu}\int \phi_{\mu}\delta(r_{\mathrm{B}})\phi_{\nu}\,\mathrm{d}r \quad (12)$$

where the fourth terms in equations (11) and (12) represent the contact interaction and $\delta(r_{\mathrm{B}})$ is the Dirac delta function which describes the contact between electrons and nucleus B; the other symbols have their usual meaning. The charges $Q_s{}^{\alpha}$ and $Q_s{}^{\beta}$ for the α and β spins, respectively, on the solvaton are assumed to be equal in magnitude but opposite in sign to those on the atom to which it is attached. The J coupling is calculated by means of the FPT method incorporating the Fock matrices given by equations (11) and (12).

The effects of solvents on the directly bonded ^{13}C–H couplings of acrylonitrile, dichloromethane, chloroform, difluoromethane and trifluoromethane have been estimated by this procedure. The tendency for the calculated values to increase with increasing ϵ agrees qualitatively with the observed tendency, except in the case of ^{1}J(C-1,H–B) + ^{1}J(C-1,H–C) for acrylonitrile.[11,12]

The values of ^{1}J(C,H) produced by the solvaton model can be fit approximately by equation (13).

$$^{1}J(\mathrm{C,H}) = a(\epsilon - 1)/\epsilon + b((\epsilon - 1)/\epsilon)^2 + c \quad (13)$$

The observed values of ^{1}J(C,H) fall approximately on a straight line when plotted against $(\epsilon - 1)/\epsilon$. Consequently the second term in equation (13) can be neglected. By plotting ^{1}J(C,H) against $(\epsilon - 1)/\epsilon$, the values of a and c are obtained: in acetonitrile the ^{1}J(C-2,H–A) data give a = 3.9 Hz and c = 176.1 Hz; in dichloromethane a = 28.0 Hz and C = 153.0 Hz; in chloroform a = 36.0 Hz and c = 182.0 Hz; in difluoromethane a = 7.7 Hz and c = 178.0 Hz; in trifluoromethane a = 22.5 Hz and c = 225.0 Hz.[11,12] By comparing various substituted methanes the values of a are found to be larger for chlorine-substituted than fluorine-substituted molecules, and those for trisubstituted methanes are larger than for disubstituted methanes. The magnitude of a provides a measure of the solvent effect on ^{1}J(C,H); thus an increase in the number of halogen-substituted atoms in methane leads to an increase in the solvent effect. In general, it seems that the solvaton model is able to reproduce the gross experimental trends of the effects of solvation on the J couplings considered.

2.3 Solvent Effects on the J Couplings of Flexible Molecules

The molecules mentioned above are considered to be rigid. However, there is another category of solvent effects of J couplings, namely, those on the coupling constants of molecules that can adopt two or more conformations. For these molecules, the observed J coupling $\langle J\rangle_{\mathrm{obs}}$ is given by

$$\langle J\rangle_{\mathrm{obs}} = \sum_{i} X_i J_i \quad (14)$$

where X_i and J_i are the molar fraction and J coupling, respectively, of conformer i. It is shown that the solvent-induced changes of ^{1}J(C,H) are very large when compared with temperature-induced changes and the greater change is proof of the larger contribution of the solvent-induced electronic changes in the solute molecules to the solvent effects of ^{1}J(C,H) than of the contribution arising from changes in the relative populations of the conformers.

Since Karplus's prediction of a strong conformational dependence of vicinal proton–proton J couplings of ethane derivatives, peptide systems and various other molecules have received the attention of many investigators. They have considered the dihedral angle, ϕ, dependence of vicinal J couplings in an isolated molecule in a similar manner to that given by the Karplus relationship.[15]

$$^{3}J(\mathrm{H,H}) = A + B\cos\phi + C\cos 2\phi \quad (15)$$

where A, B and C are coefficients to be determined for the system under consideration. In order to provide a more exact insight into the relationship between the magnitude of the vicinal coupling and the conformation, solvent effects must be taken into account. Ando and co-workers have provided a theoretical prediction of solvent effects on vicinal proton–proton and proton–carbon J couplings.[12,16–18]

The values of the coefficients A, B and C for ethane, $CHCl_2CHCl_2$ and *trans*-*N*-methylformamide, have been calculated as a function of ϵ by means of the FPT-INDO and FPT-Complete Neglect of Differential Overlap/2 approximations within the solvaton model.[12] For the H–C–N–H J couplings the values of the coefficients are smaller than those appropriate to the H–C–C–H and H–C–N–H couplings. The value of B in the former is somewhat larger than in the latter case. The calculated absolute values of the coefficients A, B and C show an increase with increasing ϵ except for the case of the coefficient C for ^{3}J(C,H) in *trans*-*N*-methylformamide obtained from INDO calculations. The values of A, B and C show the following dependence on ϵ:

$$A, B \text{ or } C = a'(\epsilon - 1)/\epsilon + b' \quad (16)$$

where a' is a measure of the strength of the dielectric solvent effect on the A, B and C coefficients and b' is the value of A, B or C at ϵ = 1. From these results, the calculated solvent dependence may be represented by

$$J = b(\epsilon - 1)/\epsilon + c \quad (17)$$

where b is a measure of the strength of the dielectric solvent effect on the vicinal J coupling constants, and c represents the

J coupling values of the *trans* and *gauche* conformers for an isolated molecule (at $\epsilon = 1$).

An oriented clustering of the polar solvent molecules around the polar solute molecule is assumed for solvent effects of J couplings.[19] The solute molecule has its dipole moment parallel to the z axis and the directions of the solvent dipoles are as indicated. Such a model may be reasonably expected to be more satisfactory than the simple reaction field model for peripheral solute nuclei which are more exposed to the influences of individual solvent molecules. In this approach the solvent and solute molecules are recognized as belonging to distinct groups with the assumption of strong orthogonality between them. The interactions between these groups are described by including attraction terms between the electrons of the solute and the nuclei of the solvents as well as intermolecular Coulomb repulsion integrals in the Hamiltonian accounting for the spin−spin interaction. In comparison with the reaction field results, it is noteworthy that those presented for formaldehyde show the correct sign and magnitude for the solvent effect on ^2J(H,H) in acetonitrile as solvent.

3 EFFECT OF PRESSURE ON J COUPLINGS

The application of pressure to pure liquids and solutions leads to a decrease of intermolecular distance.[20] Such an intermolecular change is reflected in a variation of the electronic distribution within a given molecule. This will, inevitably, be revealed by changes in the J coupling.

The pressure dependence of the directly bonded ^{13}C−H couplings for the methyl groups of ^{13}C-enriched acetaldehyde and methanol have been reported.[21,22] The value of ^1J(C,H) is found to increase linearly with increasing pressure. The experimental data have been clarified by the solvaton theory. As mentioned above, an increase in pressure usually results in a decrease in intermolecular distance and in an increase in the value of the dielectric constant for acetaldehyde and methanol. Thus, the pressure dependence of ^1J(C,H) contains the pressure effect on the intermolecular distance and on the dielectric constant. The solvaton−nucleus distance r_{sk} in equation (10) corresponds to the intermolecular distance. In the calculation, it is assumed that a variation in r_{sk} mimics the effect of changing the external pressure of the experimental system. Calculations containing such an interaction show that the pressure dependence of the J coupling arises predominantly from a change in the intermolecular distances, and is not due to the simultaneous change in the dielectric constant.

4 RELATED ARTICLES

Coupling Through Space in Organic Chemistry; Dipolar and Indirect Coupling Tensors in Solids; Indirect Coupling: Semiempirical Calculations; Indirect Coupling: Theory and Applications in Organic Chemistry.

5 REFERENCES

1. I. Ando and G. A. Webb, *Org. Magn. Reson.*, 1981, **15**, 111.
2. I. Ando and G. A. Webb, *Theory of NMR Parameters*, Academic Press, New York, 1983.
3. L. Onsager, *J. Am. Chem. Soc.*, 1936, **58**, 1486.
4. A. D. Buckingham, *Can. J. Chem.*, 1960, **38**, 300.
5. W. T. Raynes, *Mol. Phys.*, 1968, **15**, 435.
6. J. A. Pople and D. P. Santry, *Mol. Phys.*, 1964, **8**, 1.
7. M. D. Johnston and M. Barfield, *J. Chem. Phys.*, 1971, **54**, 3083.
8. G. Klopman, *Chem. Phys. Lett.*, 1967, **1**, 200.
9. I. Ando, A. Nishioka, and M. Kondo, *J. Magn. Reson.*, 1976, **21**, 429.
10. I. Ando, Y. Kato, M. Kondo, and A. Nishioka, *Makromol. Chem.*, 1977, **178**, 803.
11. M. Kondo, S. Watanabe, and I. Ando, *Mol. Phys.* 1979, **37**, 1521.
12. S. Watanabe and I. Ando, *Bull. Chem. Soc. Jpn.*, 1980, **53**, 1257.
13. K. A. K. Eraheem, S. N. Shargi, and S. A. Kadnm, *Monatsh. Chem.*, 1989, **120**, 923.
14. H. Fukui (G. A. Webb (ed.)), *Nucl. Magn. Reson.*, 1992, **21**, 106.
15. M. Karplus, *J. Chem. Phys.*, 1959, **30**, 11.
16. I. Ando, T. Asakura, and S. Watanabe, *J. Mol. Struct. (Theochem)*, 1981, **76**, 93.
17. S. Watanabe and I. Ando, *J. Mol. Struct.*, 1982, **84**, 77.
18. S. Watanabe and I. Ando, *J. Mol. Struct.*, 1983, **104**, 155.
19. M. D. Johnston and M. Barfield, *J. Chem. Phys.*, 1971, **55**, 3483.
20. I. Ando and G. A. Webb, *Magn. Reson. Chem.*, 1986, **24**, 557.
21. I. Ando, Y. Inoue, S. Watanabe, Y. Sakamoto, and G. A. Webb, *J. Mol. Liq.*, 1984, **27**, 179.
22. I. Ando, T. Sanefuji, T. Yamanobe, S. Watanabe, and G. A. Webb, *J. Mol. Liq.*, 1985, **31**, 31.

Biographical Sketch

Isao Ando. *b* 1941. Ph.D., 1972, (supervisor Atsuo Nishioka), Polymer Chemistry, Tokyo Institute of Technology. Postdoctoral work at University of Illinois, Urbana (with Herb Gutowsky). Successively research associate, Associate Professor and Professor, Tokyo Institute of Technology. Approx. 250 publications. Research specialties: structures and electronic states of solid polymers and biopolymers, solid state NMR and nuclear shielding.

Indirect Coupling: Semiempirical Calculations

Julio C. Facelli
The University of Utah, Salt Lake City, UT, USA

1	Introduction	1
2	Early Semiempirical Methods	1
3	Finite Perturbation Theory	1
4	Transmission Mechanisms of the Coupling Constants	3
5	Conclusions	4
6	Related Articles	4
7	References	4

1 INTRODUCTION

In many fields, semiempirical calculations have been replaced by more reliable ab initio calculations, but this is not the case for the calculations of J coupling constants in organic molecules of chemical interest. The presence of triplet instabilities, a common feature for ab initio wavefunctions, requires higher levels of perturbation theory to obtain even approximate results when using ab initio methods to calculate J couplings, making ab initio methods almost inapplicable to calculating J couplings in large molecules. Therefore, the discussion of the semiempirical methods commonly used to calculate J couplings has not only an historical value but also provides important practical information on how to calculate and to analyze J couplings.

The calculation of spin–spin J couplings has been discussed in four comprehensive reviews on the subject during the last 20 years[1–4] where the interested reader can find in great detail the advances achieved in this field. The theoretical formulation of the coupling constants is also discussed in Barfield's article in this Encyclopedia (see ***Indirect Coupling: Theory and Applications in Organic Chemistry***).

2 EARLY SEMIEMPIRICAL METHODS

Early attempts to calculate J couplings using molecular quantum mechanical methods were characterized by the use of the so called ΔE approximation. This approximation involves the use of ad hoc empirical or semiempirical parameters instead of the direct evaluation of the Ramsey formulae[5] using perturbation theory. The limited space of this article precludes a detailed derivation of the relevant expressions for the coupling constants under these approximations, but it is sufficient to say that using the ΔE and the LCAO (Linear Combination of Atomic Orbitals) approximations for the molecular wavefunction we can write the contributions to the J couplings from the different interaction mechanisms as:

Fermi Contact (FC) term

$$K^{(3)}_{\mathrm{NN'}} = \frac{64\pi^2\beta^2}{9}({}^3\Delta E)^{-1} P^2_{\mathrm{NN'}}\phi^2_{\mathrm{N}}(0)\phi^2_{\mathrm{N'}}(0) \qquad (1)$$

Paramagnetic Spin Orbital (PSO) term

$$K^{(1)}_{\mathrm{NN'}} = \frac{8\beta^2}{3}({}^1\Delta E)^{-1}\langle r^{-3}_{\mathrm{N}}\rangle\langle r^{-3}_{\mathrm{N'}}\rangle(P_{x_{\mathrm{N}}x_{\mathrm{N'}}}P_{y_{\mathrm{N}}y_{\mathrm{N'}}} + P_{y_{\mathrm{N}}y_{\mathrm{N'}}}P_{z_{\mathrm{N}}z_{\mathrm{N'}}} + P_{z_{\mathrm{N}}z_{\mathrm{N'}}}P_{x_{\mathrm{N}}x_{\mathrm{N'}}} - P_{x_{\mathrm{N}}y_{\mathrm{N'}}}P_{y_{\mathrm{N}}x_{\mathrm{N'}}} - P_{y_{\mathrm{N}}z_{\mathrm{N'}}}P_{z_{\mathrm{N}}y_{\mathrm{N'}}} - P_{z_{\mathrm{N}}x_{\mathrm{N'}}}P_{x_{\mathrm{N}}z_{\mathrm{N'}}}) \qquad (2)$$

Spin Dipolar (SD) term

$$K^{(1)}_{\mathrm{NN'}} = \frac{4\beta^2}{25}({}^3\Delta E)^{-1}\langle r^{-3}_{\mathrm{N}}\rangle\langle r^{-3}_{\mathrm{N'}}\rangle \times [2(P^2_{x_{\mathrm{N}}x_{\mathrm{N'}}} + P^2_{y_{\mathrm{N}}y_{\mathrm{N'}}} + P^2_{z_{\mathrm{N}}z_{\mathrm{N'}}}) + 3(P_{x_{\mathrm{N}}x_{\mathrm{N'}}}P_{y_{\mathrm{N}}y_{\mathrm{N'}}} + P_{y_{\mathrm{N}}y_{\mathrm{N'}}}P_{z_{\mathrm{N}}z_{\mathrm{N'}}} + P_{z_{\mathrm{N}}z_{\mathrm{N'}}}P_{x_{\mathrm{N}}x_{\mathrm{N'}}}) - (P^2_{x_{\mathrm{N}}y_{\mathrm{N'}}} + P^2_{y_{\mathrm{N}}x_{\mathrm{N'}}} + P^2_{y_{\mathrm{N}}z_{\mathrm{N'}}} + P^2_{z_{\mathrm{N}}y_{\mathrm{N'}}} + P^2_{z_{\mathrm{N}}x_{\mathrm{N'}}} + P^2_{x_{\mathrm{N}}z_{\mathrm{N'}}}) + 3(P_{x_{\mathrm{N}}y_{\mathrm{N'}}}P_{y_{\mathrm{N}}x_{\mathrm{N'}}} + P_{y_{\mathrm{N}}z_{\mathrm{N'}}}P_{z_{\mathrm{N}}y_{\mathrm{N'}}} + P_{z_{\mathrm{N}}x_{\mathrm{N'}}}P_{x_{\mathrm{N}}z_{\mathrm{N'}}})] \qquad (3)$$

where we have used standard quantum chemical notation for the quantities describing the wavefunction and assumed that the LCAO expansion contains only 1s, 2s and 2p orbitals. ΔE is an empirical parameter which represents the average excitation energy between the ground state and the excited electronic states (triplets for the FC and SD terms and singlets for the PSO term). In many cases this parameter has been correlated with the UV spectrum of the molecules under consideration. $\langle r^{-3}\rangle$ is an empirical parameter which represents the average of the cube of the distance between the electrons and the nucleus; this parameter takes into consideration the contraction and expansion of the atomic orbitals due to different bonding strengths. Finally, $\phi^2_{\mathrm{N}}(0)$ is the electron density at the position of the nucleus and $\mathbf{P}$ is the electronic density matrix.

Equations (1)–(3) provide a very simple way to calculate and to analyze some of the most relevant features of the coupling constants, but also predict some disturbing properties. Perhaps the most serious drawback of equations (1)–(3) is that they predict zero paramagnetic spin orbital and dipolar contributions for any coupling constant involving protons. Note that because protons do not have p orbitals, equations (2) and (3) are exactly zero when one of the nuclei is a proton. This has been a common assumption in many semiempirical calculations of coupling constants that is not supported either by more elaborate semiempirical calculations or by ab initio results. Nevertheless, equations (1)–(3) are usually successful in predicting qualitative trends in molecules belonging to the same family. In many cases the deficiencies and/or systematic errors of the calculations can be taken into account by adjusting the empirical parameters, ΔE, $\phi^2_{\mathrm{N}}(0)$ and $\langle r^{-3}\rangle$ to reproduce the experimental values of the coupling constants in a selected set of coupling constants.

The early semiempirical formulations totally ignored the diamagnetic spin orbital (DSO) term, which until recent years was considered negligible.[6] Recent calculations using ab initio as well as semiempirical methods have shown that this assumption is incorrect for many kinds of coupling constants.[4]

3 FINITE PERTURBATION THEORY

The most significant advance in the semiempirical calculation of J coupling constants has been the introduction of the INDO-FPT (Intermediate Neglect of Differential Overlap-Finite Perturbation Theory) method by Pople and co-workers in 1968.[7] The success of this method has been extensively documented and it is still today the most popular method for semiempirical calculations of coupling constants. The original formulation of the method calculated only the FC interaction but later, using the equivalent CHF (Coupled Hartree–Fock) perturbation scheme, was extended by Blizzard and Santry to include all the second order noncontact interactions.[8]

The original idea behind Pople's work was to realize that the coupling constants or their reduced couplings can be expressed as the second derivative of the total energy of the molecule with respect to the magnetic moments, μ_N and μ_N, of the coupled nuclei:

$$K_{NN'} = \left[\frac{\partial^2 E(\mu_N, \mu_{N'})}{\partial \mu_N \partial \mu_{N'}}\right]_{\mu_N=\mu_{N'}=0} \tag{4}$$

For the FC term this derivative can be transformed using the Hellmann–Feynman theorem and the INDO approximation into a compact expression in terms of the derivative of the spin density at the position of the nucleus N with respect to the magnetic moment of the nucleus N′. The final expression for the FPT-INDO calculations of the FC term is:

$$K^{(3)}_{NN'} = \left(\frac{8\pi\beta}{3}\right)^2 s^2_N(0) s^2_{N'}(0) \frac{\rho_{s_N s_N}(h_{N'})}{h_{N'}} \tag{5}$$

where $s_N(0)$ is the electronic density at the position of the nucleus N and the derivative of the spin density has been calculated by its finite difference quotient. $\rho_{s_N s_N}(h'_N)$ is the spin density at the nucleus N when a magnetic moment of intensity $h_{N'}$ is placed at the position of the nucleus N′. The spin density can be estimated, in an open shell calculation, as the difference between the electronic density of the electrons with α and β spins. This formulation of the FPT-INDO theory is straightforward to implement, requiring only minor modifications of any standard program for molecular orbital (MO) calculations. Unfortunately the FPT method is computationally very inefficient, requiring a large number of self-consistent field calculations when all of the noncontact interactions are considered. In recent years the FPT-INDO and the CHF-INDO methods of calculating coupling constants have been reformulated in terms of the computationally more efficient Polarization Propagator Approach. A comprehensive program to perform semiempirical calculations of coupling constants including all the interactions as well as certain capabilities to analyze their transmission mechanisms is available from the Daresbury Library of computer programs.[9]

In Figure 1 we present the correlation between calculated and experimental J couplings for selected J(C,H), J(C,C) and J(H,H) in a variety of compounds. Results for J values involving other nuclei are in general satisfactory, but serious difficulties have been found for couplings involving fluorine and other electronegative atoms. Unfortunately, there is no systematic way to improve the quality of the semiempirical methods and therefore it is necessary to test the validity of the method for each type of coupling constant.

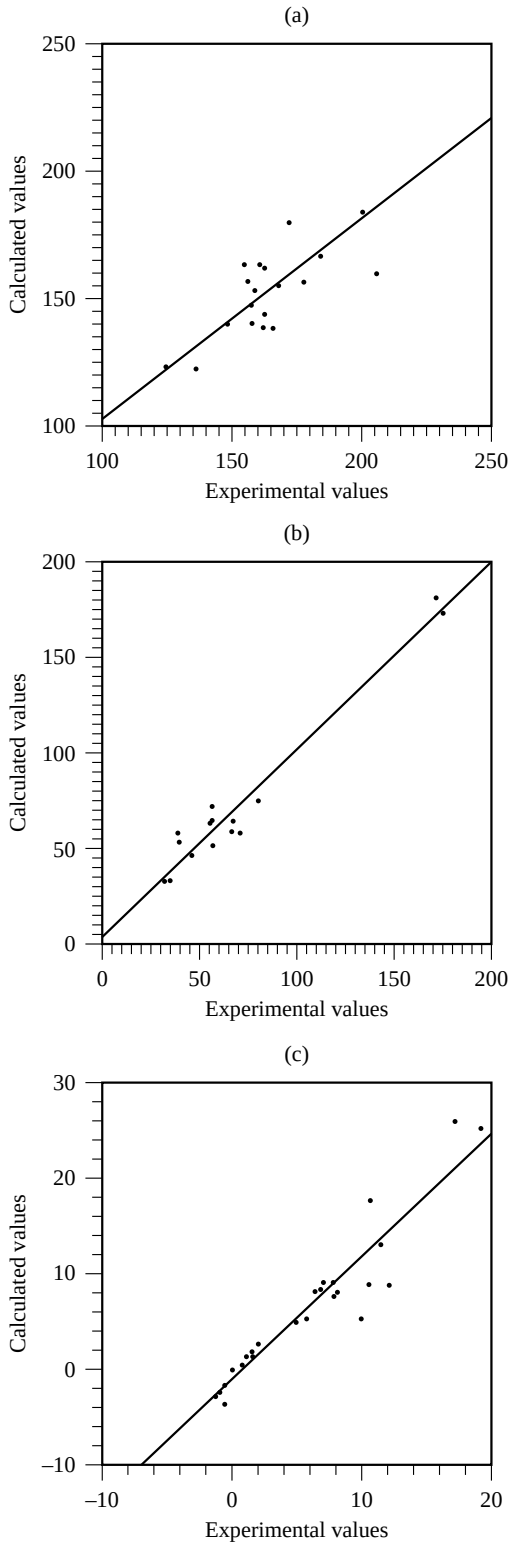

Figure 1 Comparison of the experimental and calculated values of selected J coupling constants. The calculations were done using the CHF (Coupled Hartree–Fock) method with the INDO parameterization. (a) J(C,H), R^2 = 0.8099; (b) J(C,C), R^2 = 0.9576; (c) J(H,H), R^2 = 0.9248. All the values are in Hz; the calculations of the J(C,H) and J(H,H) include only the Fermi contact term while the calculations for J(C,C) include all the second order terms

Over the years many attempts have been made to improve the results obtained using the original INDO parameterization, but most of them have been either unsuccessful or produced marginally better results. The Modified Neglect of Differential Overlap (MNDO) method of Dewar and Thiel,[10] which has become the most common method for the semiempirical calculation of molecular properties, has not been successful in the calculations of J couplings because the MNDO wavefunctions in unsaturated compounds exhibit triplet instabilities which preclude CHF calculations of J couplings. The origin of the triplet instabilities has been traced to the large difference between the β^0 parameters used in the MNDO method for the s and p orbitals.[11]

The INDO based semiempirical methods were originally formulated to calculate coupling constants involving first row atoms (H–F), but a number of extensions have been reported and now this method is commonly used for calculations of couplings between nuclei in the first two rows of the Periodic Table. Calculations including heavier atoms can also be found in the literature but they are less common and their results are less reliable.

Extensive calculations of coupling constants involving heavy atoms have been performed using the REX (Relativistic Extended Hückel Theory) and the ITREX (Iterative Relativistic Hückel Theory) methods.[12] A computer program, REXNMR,[13] is available from the Quantum Chemistry Program Exchange to perform this kind of calculation in molecules including any element of the Periodic Table. The results achievable with these methods are dependent on the type of coupling constant considered, but in general the comparison of the results obtained with the EHT (Extended Hückel Theory) without relativistic corrections and those with the corrections shows that the relativistic corrections are quite important when one of the coupled nuclei belongs to the third row or higher. Some examples of this behavior are depicted in Figure 2.

C 23.3 41.3	N 32. 50.	O 36.6 48.	F 33. 46.9
Si 53.1 84.9	P 30. 37.8	S 28.5	Cl 8. 32.
Ge 142.4 232.	As 36. (41) 45.	Se 2.6 (14.1) 28.4	Br –69. (–47) 19
Sn 289. (219) 430.	Sb 5. (40)	Te –98. (–16) ±15.5	I –223. (–128)
Pb 844. (373) 938.	Bi –572. (19)		

Figure 2 Reduced coupling constants between directly bonded atoms, ^1K(H,X), in simple hydrides. The uppermost value is the calculated REX value, the number in parentheses is the nonrelativistic EHT value (when different from the relativistic one). The lowest value is the experimental coupling. The calculated results are from Pyykkö and Wiesenfeld.[13] All the values are in $10^{19}\,m^{-2}\,kg\,s^{-2}\,Å^{-2}$. (Reproduced by permission of Academic Press from J. Kowalewski.[3])

4 TRANSMISSION MECHANISMS OF THE COUPLING CONSTANTS

The understanding of the transmission mechanisms of the coupling constants is important in gaining information on the intimate relationship between the electronic structure of molecules and the coupling constants. The semiempirical MO formulations, like the FPT-INDO method discussed above, cannot provide a direct interpretation of the origin of the couplings as in equations (1)–(3), but in recent years a great deal of effort has been dedicated to the development of methods to provide a better understanding of the transmission mechanisms of the coupling constants.

While the methods of studying transmission mechanisms are independent of the kind of wavefunction used in the calculation of the coupling constants, most of the applications of these methods have used semiempirical approximations of the wavefunctions.[14] The early work in this field was based on the PRMO (Partially Restricted Molecular Orbitals)[15] and the NNBI (Neglect of Non Bonded Interactions)[16] methods, which use the FPT-INDO formulation to calculate coupling constants. Both methods are based on the selective exclusion from the calculations of certain transmission paths by either the equalization of the spin populations along the paths (PRMO) or neglecting electronic interactions between the electrons localized along the paths and the rest of the molecule (NNBI). The first applications of these methods were concentrated on the study of the separation of the electronic $\sigma-\pi$ components[15] and the through-space or nonbonded contributions[16] to the coupling constants. These approaches to analyzing the transmission mechanisms were very successful in reproducing well established empirical rules like the methyl replacement rule, the sign alternation of the π electron transmitted contributions, the dominance of π electron transmitted contributions in long-range couplings, the W rule for the σ transmitted contributions, etc. As an example, in Table 1 we present PRMO results that show how the methyl substituent rule is verified in toluene.

The success of these methods prompted the extension of the PRMO ideas to the more general formulation of the CLOPPA (Contributions from Localized Orbitals within the Polarization Propagator Approach) method.[17] This approach allows the expression of any coupling constant as a sum-over-contributions arising from arbitrarily defined molecular fragments. The CLOPPA method has been formulated for all of the interaction mechanisms. It is self evident that the first order DSO contribution can be written as a sum-over-molecular fragments. This is done by summing the average value of the interaction Hamiltonian over the projection of the wavefunction onto the localized orbitals representing the different fragments:

$$J_{NN'}^{DSO} = \sum_{i=occ} \langle i|\hat{\mathcal{H}}(1,1)|i\rangle \qquad (6)$$

where $|i\rangle$ is an occupied localized MO and $\hat{\mathcal{H}}(1,1)$ is the Hamiltonian for the DSO contribution. The decomposition of the second-order contributions presents more complicated

Table 1 Comparison of the Experimental Benzylic Couplings in Toluene with their PRMO Calculated π-Transmitted Components and the π-Transmitted Components of the Respective ^{n-1}J(H,H) Couplings in Benzene. All Values in Hz. (Values from A. R. Engelmann et al.[15])

Coupling	Experimental	Full INDO	π-transmitted components	
			^{n}J(H,H) in toluene	^{n-1}J(H,H) in benzene
^{4}J(H, CH_3)	−0.75	−0.92	−0.67	0.60
^{5}J(H, CH_3)	0.36	0.69	0.41	−0.43
^{6}J(H, CH_3)	−0.62	−0.64	−0.57	0.51

expressions which involve the use of the polarization propagator inner projected onto the localized orbitals defining the molecular fragments. This is:

$$J^2_{\mathrm{NN}'} = \sum_{ia,jb} U_{ia,\mathrm{N}} W_{ia,jb} U_{jb,\mathrm{N}'} \tag{7}$$

where the sum runs over all possible transitions between localized occupied (i,j) and unoccupied (a,b) molecular orbitals. W is the inner projector of the singlet (PSO term) or triplet (FC and SD terms) polarization propagator. The U operators are the perturbators given by:

$$U^{\mathrm{FC}}_{ia,\mathrm{N}} = \langle i|\delta(\boldsymbol{r}_{\mathrm{N}})|a\rangle \tag{8}$$

$$U^{\mathrm{PSO}}_{ia,\mathrm{N}} = -\mathrm{i}\left\langle i \left| \frac{\hat{\boldsymbol{L}}_{\mathrm{N}}}{r^3_{\mathrm{N}}} \right| a \right\rangle \tag{9}$$

$$U^{\mathrm{SD},\alpha\beta}_{ia,\mathrm{N}} = \left\langle i \left| \frac{3r_{\mathrm{N}\alpha}r_{\mathrm{N}\beta} - r^2_{\mathrm{N}}\delta_{\alpha\beta}}{r^5_{\mathrm{N}}} \right| a \right\rangle \tag{10}$$

for the FC, PSO and SD terms, respectively. If all the MOs are included in equations (6) and (7) then the equations give expressions for the total couplings; a partial sum over the localized MOs belonging to a particular molecular fragment provides an estimate of the contribution to the coupling constant from that particular fragment. The CLOPPA analysis is a powerful tool for understanding the mechanisms of transmission of the coupling constants and in principle can be implemented for any approximation of the molecular wavefunction. In analyzing the results of this method it is always important to remember that the partition of the molecule into fragments is arbitrary and that the projections of wavefunctions onto the different molecular fragments do not always form an orthogonal set. Therefore the additivity of the contributions from different molecular fragments does not hold exactly.

The CLOPPA partition of the spin coupling constants has been used mostly with the INDO approximation of the molecular wavefunction because of the great success of the INDO parameterization in calculating the spin−spin coupling constants. Note that when using the first order approximation for the propagator and the INDO parameterization for the Hamiltonian, equations (6) and (7) are exactly equivalent to the FPT or CHF methods discussed above if all the occupied and vacant orbitals are included in the calculation.

5 CONCLUSIONS

Semiempirical calculations using the INDO parameterization are still the state of the art for calculating coupling constants in organic molecules with more than a handful of atoms. The lack of systematic ways of improving semiempirical calculations has been a significant hurdle in this field and we do not expect that it will be overcome soon. Progress in ab initio methods has been slow and its applicability to medium and large organic molecules has to wait for the development of efficient computer programs to calculate J couplings including correlation effects. In the meantime judicious semiempirical calculations and analysis of the transmission mechanisms of the J coupling constants can be used as tools for electronic structure determination.

6 RELATED ARTICLES

Anisotropy of Shielding and Coupling in Liquid Crystalline Solutions; Coupling Through Space in Organic Chemistry; Indirect Coupling: Intermolecular and Solvent Effects; Indirect Coupling: Theory and Applications in Organic Chemistry; Isotope Effects on Chemical Shifts and Coupling Constants; Vicinal Coupling Constants and Conformation of Biomolecules; Vicinal ^{1}H, ^{1}H Coupling Constants in Cyclic π-Systems.

7 REFERENCES

1. J. N. Murrell, *Prog. Nucl. Magn. Reson.*, 1971, **6**, 1.
2. J. Kowalewski, *Prog. Nucl. Magn. Reson.*, 1978, **11**, 1.
3. J. Kowalewski, *Annu. Rep. NMR Spectrosc.*, 1982, **12**, 81.
4. R. H. Contreras and J. C. Facelli, in *Annu. Rep. NMR Spectrosc.*, 1993, **27**, 255.
5. N. F. Ramsey, *Phys. Rev.*, 1953, **91**, 323.
6. W. S. Lee and J. M. Schulman, *J. Chem. Phys.*, 1979, **70**, 1530.
7. J. A. Pople, J. W. McIver, and N. S. Ostlund, *J. Chem. Phys.*, 1968, **49**, 2960, 2965.
8. A. C. Blizzard and D. P. Santry, *J. Chem. Phys.*, 1971, **55**, 950; 1973, **58**, 4714.
9. A. R. Engelmann, M. A. Natiello, G. E. Scuseria, and R. H. Contreras, *Comput. Phys. Commun.*, 1986, **39**, 409.
10. M. J. S. Dewar and W. Thiel, *J. Am. Chem. Soc.*, 1977, **99**, 4899, 4907.
11. G. E. Scuseria, A. R. Engelmann, and R. H. Contreras, *Theor. Chim. Acta*, 1982, **61**, 49.
12. P. Pyykkö, *Chem. Rev.*, 1988, **88**, 563.
13. P. Pyykkö and L. Wiesenfeld, *Mol. Phys.*, 1981, **43**, 557.
14. R. H. Contreras, M. A. Natiello, and G. E. Scuseria, *Magn. Reson. Rev.*, 1985, **9**, 239.

15. A. R. Engelmann, R. H. Contreras, and J. C. Facelli, *Theor. Chim. Acta*, 1981, **59**, 17.
16. M. Barfield, *J. Am. Chem. Soc.*, 1980, **102**, 1.
17. R. H. Contreras, C. G. Giribet, M. C. Ruiz de Azúa, and M. B. Ferraro, in *Computational Chemistry: Structure, Interactions and Reactivity*, ed. S. Fraga, Elsevier, Amsterdam, 1992, Vol. 2, p. 212.

Biographical Sketch

Julio C. Facelli. *b* 1953. Licenciado in Physics, 1977 and Doctor in Physics, 1981, University of Buenos Aires, Argentina. Postdoctoral work at the University of Arizona 1983–84. University of Utah 1984–present. Approx. 80 publications. Current research interests: quantum chemical calculations of NMR parameters, relationships between NMR parameters and molecular structure and large scale scientific computing.

Indirect Nuclear Spin–Spin Coupling Tensors

Roderick E. Wasylishen

University of Alberta, Edmonton, Canada

1 Introduction 1
2 Theoretical Background 2
3 Symmetry Properties 2
4 Characterization of **J**-Tensors by Experiment 3
5 Conclusions 7
6 Related Articles in this Volume 7
7 Related Articles in Volumes 1–8 7
8 References 8

1 INTRODUCTION

Nuclear spins can interact with one another by two fundamentally different mechanisms: (1) a direct-dipolar interaction and (2) an indirect nuclear spin-nuclear spin coupling involving the intervening electrons in a molecule (see **Dipolar & Indirect Coupling Tensors in Solids,** Volume 3). The latter interaction may be thought of as a two-stage process whereby the spin of one nucleus, N, polarizes a nearby electron spin and the resulting infinitesimally small spin polarization is transferred to other electrons which in turn transfer their polarization to a second nucleus, N′. On the other hand, the direct dipolar interaction between two nuclei does not involve the electronic framework of the molecule. The classical analogue is the direct through-space interaction between two magnetic point dipoles, μ_N and $\mu_{N'}$, which is known to depend on the value of $\langle r_{N,N'}^{-3} \rangle$ where r is the internuclear separation. The interaction energy of a pair of isolated nuclear spins N and N′ may be represented by

$$E_{NN'} = h\mathbf{I}_N \cdot (\mathbf{D} + \mathbf{J}) \cdot \mathbf{I}_{N'} \quad (1)$$

where h is Planck's constant, $\mathbf{I}_N$ and $\mathbf{I}_{N'}$ represent the nuclear spin angular momentum vectors associated with nuclei N and N′, respectively, **D** is the direct dipolar spin–spin coupling tensor and **J** is the indirect spin–spin coupling tensor. Both **D** and **J** are general second-rank tensors. While **D** is traceless, **J** in general has a non-zero trace. Thus, in isotropic fluids where molecules tumble rapidly, the direct-dipolar coupling interaction generally does not influence the nuclear magnetic resonance (NMR) line shape of spins N or N′; however, as will be described below, the indirect interaction generally results in splitting(s), J_{iso}, in the NMR spectrum of both the spins N and N′.

It is often convenient to simplify equation (1) by separating the isotropic portion, J_{iso}, of the indirect spin–spin coupling from the traceless anisotropic portion, $\mathbf{J}_T$,

$$E_{N,N'} = hJ_{iso}\mathbf{I}_N \cdot \mathbf{I}_{N'} + h\mathbf{I}_N \cdot (\mathbf{D} + \mathbf{J}_T) \cdot \mathbf{I}_{N'} \quad (2)$$

where J_{iso} is 1/3 the trace of **J** (simply the average value of the three diagonal elements of the **J**-tensor), often called the scalar coupling. The sign of J_{iso} may be positive or negative depending on the detailed electronic and molecular structure of the fragment under consideration and the signs of the magnetogyric ratios γ_N and $\gamma_{N'}$. If the sign of J_{iso} is positive, the lowest energy configuration of the two coupled nuclear magnetic moments is antiparallel provided that γ_N and $\gamma_{N'}$ have the same sign. In general, solution NMR spectra are insensitive to the absolute sign of J_{iso}.

It is instructive to consider the case of a heteronuclear diatomic molecule, for example, $^{35}Cl–^{19}F$, where the principal axis system (PAS) is defined by the C_∞ symmetry axis of the molecule. In this case, both the anisotropic **D** and $\mathbf{J}_T$-tensors take a very simple form,

$$\mathbf{D} = R_{DD}\begin{bmatrix} 1 & 0 & 0 \\ 0 & 1 & 0 \\ 0 & 0 & -2 \end{bmatrix} \text{ and } \mathbf{J}_T = -\frac{\Delta J}{3}\begin{bmatrix} 1 & 0 & 0 \\ 0 & 1 & 0 \\ 0 & 0 & -2 \end{bmatrix} \quad (3)$$

where the direct dipolar coupling constant, R_{DD}, is defined by equation (4):

$$R_{DD} = \frac{\mu_0}{4\pi}\frac{\hbar}{2\pi}\gamma_N\gamma_{N'}\langle r_{NN'}^{-3} \rangle \quad (4)$$

and ΔJ is the anisotropy of the indirect spin–spin coupling tensor:

$$\Delta J = J_\parallel - J_\perp \quad (5)$$

Both R_{DD} and ΔJ are in frequency units, Hz; μ_0 is the permeability constant, $4\pi \times 10^{-7}\,\mathrm{kg\,m\,s^{-2}\,A^{-2}}$, $\hbar$ is Planck's constant divided by 2π, and γ_N and $\gamma_{N'}$ are the magnetogyric ratios of nuclei N and N′, respectively. Equation (2) can be expressed as follows:

$$E_{NN'} = hJ_{iso}\mathbf{I}_N \cdot \mathbf{I}_{N'} + hR_{eff}\mathbf{I}_N \cdot \begin{bmatrix} 1 & 0 & 0 \\ 0 & 1 & 0 \\ 0 & 0 & -2 \end{bmatrix} \cdot \mathbf{I}_{N'} \quad (6)$$

where the effective dipolar coupling constant, R_{eff}, is $R_{DD} - \Delta J/3$. Equation (6) is general in that it demonstrates that one cannot separately measure R_{DD} and ΔJ. However, if one knows $r_{NN'}$ and can measure R_{eff}, then values of ΔJ can be obtained. Isotropic spin–spin coupling constants as small as 0.1 Hz are readily measured for small molecules in isotropic fluids. The largest known value of an isotropic indirect spin–spin coupling constant is $^1J(^{199}Hg,^{199}Hg)_{iso} = 284\,100 \pm 860$ Hz for [Hg_2(18-crown-6)(15-crown-5)(MeOH)](O_3SCF_3)$_2$.[1]

The purpose of this contribution is to focus on a discussion of the indirect spin–spin coupling. After a brief historic summary of the background theory, the symmetry properties of the **J**-tensor will be reviewed. Methods of characterizing **J**-tensors will be discussed and illustrated by several examples. Finally, some experimental and theoretical developments will be summarized.

2 THEORETICAL BACKGROUND

Experimental evidence of splittings due to indirect spin–spin coupling was first recognized in the NMR spectra of molecules in isotropic fluids. Several groups reported such splittings in the Physical Review in 1951.[2–4]

Initial observations indicated that splittings in frequency units (Hz = cycles per second, cps, in the original NMR literature) due to spin–spin coupling were independent of the applied magnetic field. As well, splittings were found to be the same regardless of which nucleus was probed, N, or N′. For example, in the case of hydrogen deuteride, Carr and Purcell[5] observed a doublet splitting of 43.5 ± 1 Hz in the ^{2}H NMR spectrum arising from deuterium transitions taking place with the ^{1}H (spin 1/2) either being $m_I = +1/2$ or $m_I = -1/2$. Similarly, the ^{1}H NMR spectrum appeared as three equally spaced peaks of equal intensity, each separated by 43.5 ± 1 Hz, corresponding to the deuterium nucleus (spin 1) being in any one of its three allowed spin states, $m_I = +1, 0, -1$.

Ramsey presented a comprehensive theory of indirect spin–spin coupling in 1953.[6] Three interactions between nuclear spins and electron spins were identified as mechanisms for indirect nuclear spin–spin coupling,

$$\widehat{\mathcal{H}}' = \widehat{\mathcal{H}}_{1a} + \widehat{\mathcal{H}}_{1b} + \widehat{\mathcal{H}}_2 + \widehat{\mathcal{H}}_3 \tag{7}$$

Here, $\widehat{\mathcal{H}}_{1a}$ and $\widehat{\mathcal{H}}_{1b}$ result from the interaction of the nuclear magnetic moment with the orbital magnetic moment of the electrons; $\widehat{\mathcal{H}}_{1a}$ and $\widehat{\mathcal{H}}_{1b}$ are known as the orbital 'diamagnetic' and 'paramagnetic' terms, respectively. $\widehat{\mathcal{H}}_2$ represents the dipole–dipole interaction between the nuclear magnetic moment and the electron magnetic moment provided the electron does not reside at the nucleus (the "spin-dipolar" interaction), and $\widehat{\mathcal{H}}_3$ is the Fermi-contact Hamiltonian which is non-zero when electrons have a finite probability of being at the nucleus. Ramsey's second-order perturbation treatment lead to contributions of the form,

$$E_{NN'}\ (\text{indirect}) = \sum_n \frac{\langle\psi_0|\widehat{\mathcal{H}}'|\psi_n\rangle\langle\psi_n|\widehat{\mathcal{H}}'|\psi_0\rangle}{E_0 - E_n} \tag{8}$$

where the sum is over all excited states of the unperturbed system. Although the energy expression, in principle, contains cross terms, Ramsey showed that in the non-relativistic limit only cross terms between $\widehat{\mathcal{H}}_2$ and $\widehat{\mathcal{H}}_3$ are non-zero. Thus, the indirect spin–spin coupling tensor may be written as

$$\mathbf{J} = \mathbf{J}_{1a} + \mathbf{J}_{1b} + \mathbf{J}_2 + \mathbf{J}_3 + \mathbf{J}_4 \tag{9}$$

where $\mathbf{J}_4$ is the contribution due to the so-called spin-dipolar Fermi-contact cross term. The latter tensor has a zero trace but contributes to the anisotropy of the coupling tensor. In contrast, the Fermi-contact contribution, $\mathbf{J}_3$, is isotropic. The other terms make isotropic and anisotropic contributions to the total coupling tensor. Each of the contributions to $\mathbf{J}(N,N')$ are proportional to the product of the magnetogyric ratios, $\gamma_N\gamma_{N'}$, thus it is convenient to define a reduced indirect spin–spin coupling tensor which is independent of the nuclear magnetic moments:

$$\mathbf{K}(NN') = \frac{4\pi^2\mathbf{J}(NN')}{h\gamma_N\gamma_{N'}} \tag{10}$$

where $\mathbf{K}$ has units of $N\,A^{-2}\,m^{-3}$ or equivalently $T^2\,J^{-1}$ (SI units) or cm^{-3} (in cgs units). In the case of hydrogen deuteride, $^1J(^2H,^1H)_{iso} = 42.94 \pm 0.04$ Hz at 300 K[7] which corresponds to $^1K(H,H)_{iso} = 2.329 \times 10^{20}\,T^2\,J^{-1}$ or $23.29 \times 10^{20}\,cm^{-3}$.

Early theoretical calculations indicated that the Fermi-contact mechanism was largely responsible for indirect spin–spin coupling constants involving hydrogen nuclei. However, for molecules such as ClF, it is now known that both the paramagnetic orbital and spin-dipolar contributions to $^1\mathbf{K}$(Cl,F) are much greater than the Fermi-contact contributions.[8] The expressions derived by Ramsey remain exact at the non-relativistic limit.[9]

A relativistic analogue of Ramsey's theory of nuclear spin–spin coupling in molecules was presented by Pyykkö in 1977.[10] A survey of the results using this theory and relativistically-parameterized extended Hückel calculations were presented by Pyykkö and Wiesenfeld in 1981.[11]

More recently, Autschbach and Ziegler have presented a relativistic formulation of spin–spin coupling based on the two-component zeroth-order regular approximate (ZORA) Hamiltonian.[12] This formalism has been implemented into a density functional program which permits calculations on molecules containing heavy nuclei. Qualitatively, relativistic effects can be very important, even dominant, particularly if heavy nuclei are involved. Although electron orbital and spin moments are independent of each other in the non-relativistic limit, this is not the case when spin-orbit coupling (i.e., PSO) is significant. In such cases, the $\widehat{\mathcal{H}}_{1b}$, $\widehat{\mathcal{H}}_2$ cross term is non-zero and may be important.

Progress in the computation of indirect spin–spin coupling tensors is reviewed annually.[13] For recent 'state-of-the-art' calculations of **J**-tensors for the hydrogen halides, see Visscher et al. and Vaara et al.[14] Several recent reviews are highly recommended.[15–18]

3 SYMMETRY PROPERTIES

As already mentioned, the indirect nuclear spin–spin coupling tensor is a general second-rank tensor, with up to nine independent components. The tensor may be decomposed into three parts: isotropic, J_{iso}, symmetric (J^{sym}), and antisymmetric ($J^{antisym}$).[19]

The isotropic component, a scalar, is one third the trace of **J**. The symmetric part of the tensor is constructed from **J** and its transpose, $\mathbf{J}^t$,[20]

$$\mathbf{J}^{sym} = \frac{(\mathbf{J} + \mathbf{J}^t)}{2} - J_{iso}\mathbf{1} \tag{11}$$

and may possess up to five independent components. In its principal axis system, $\mathbf{J}^{sym} + J_{iso}\mathbf{1}$ is diagonal and has up to three independent elements: J_{11}, J_{22}, and J_{33}, ordered according to the convention $|J_{33} - J_{iso}| \geq |J_{11} - J_{iso}| \geq |J_{22} - J_{iso}|$.[21]

The diagonalization of $\mathbf{J}^{sym} + J_{iso}\mathbf{1}$ yields its orientation in the molecular framework which may be defined by three Euler angles. The anisotropy of the indirect spin–spin coupling tensor, ΔJ, may be defined as,

$$\Delta J = J_{33} - \frac{J_{11} + J_{22}}{2} \tag{12}$$

For a tensor with only two unique principal components this reduces to equation (5). The asymmetry of the indirect spin–spin coupling tensor may be defined as

$$\eta = \frac{J_{22} - J_{11}}{J_{33} - J_{\text{iso}}} \tag{13}$$

where $0 \leq \eta \leq 1$. The antisymmetric portion of **J** is defined as,

$$\mathbf{J}^{\text{antisym}} = \frac{(\mathbf{J} - \mathbf{J}^{\text{t}})}{2} \tag{14}$$

and may have up to three independent components.

The number of independent components of the **J**-tensor will depend on the symmetry properties of the molecule, and more specifically the local symmetry that is appropriate for the two coupled nuclei.[22]

For CH_3F, the molecule belongs to the point group C_{3v} and the C–F bond lies along the principal axis; thus, there are only two unique components in the symmetric **J**(^{19}F,^{13}C)-tensor. On the other hand, for the **J**(^{19}F,^{1}H)-tensor, the relevant symmetry is C_s and it can be shown that the **J**-tensor has four symmetric components and one antisymmetric component. The number of non-vanishing symmetric and antisymmetric components of the indirect spin–spin coupling tensor when N and N′ cannot be exchanged by symmetry (e.g., any heteronuclear spin-pair) is given in Table 1. More extensive discussions of symmetry rules for the indirect spin–spin coupling tensor have been given in the literature and are highly recommended.[19,22,23] While experiments to characterize the antisymmetric component(s) have been proposed,[19,20,24] successful measurements have not been reported. High-level first-principles calculations might be useful in suggesting appropriate molecules to investigate.[25] In the discussion that follows we will not consider the antisymmetric portion of the **J**-tensor further as it does not influence NMR spectra to first order.

4 CHARACTERIZATION OF J-TENSORS BY EXPERIMENT

Evidence for indirect spin–spin coupling and anisotropy in the **J**-tensor in a non-conducting solid was first inferred from ^{203}Tl and ^{205}Tl NMR measurements on powder samples of Tl_2O_3.[26] The contribution of the ^{203}Tl–^{205}Tl indirect spin–spin coupling anisotropy to the observed effective direct dipolar coupling was referred to as the 'pseudo-dipolar' character of the spin–spin coupling. In fact, any procedure for characterizing **J**-tensors involves experimentally measuring the effective dipolar tensor, $\mathbf{D} + \mathbf{J}_{\text{T}}$, and subtracting from it the direct dipolar tensor, **D**. Clearly, knowledge of the direct dipolar tensor is required for any experimental characterization of the **J**-tensor. For isolated spin-pairs, the direct dipolar coupling tensor is readily calculated if the molecular structure is known (i.e., $\langle r^{-3} \rangle$). Accurate calculation of the dipolar tensor requires taking into account motional averaging (e.g., rovibrational averaging of R_{DD}).[8,27]

Table 1 Number of Independent Components of the **J**-tensor for Some Important Group Symmetries (adapted from Ref.[22])[a]

Point Group	Number of Unique Symmetric Components	Number of Unique Antisymmetric Components
C_1	6	3
C_s	4	1
C_2	4	1
C_{2v}	3	0
C_n (n > 2)	2	1
C_{nv} (n > 2)	2	0

[a] Assuming the two nuclei are not exchanged by a symmetry operation.

In the solid-state physics literature (e.g., see Ref.[28]), isotropic spin–spin coupling via conduction electrons is generally referred to as Ruderman–Kittel (RK) coupling.[29]

Most experimental efforts to characterize the symmetric components of **J**-tensors have been confined to directly bonded spin-pairs that lie along a C_n-axis (n > 2) of symmetry. This ensures that the **J**-tensor is axially symmetric.

There are essentially three experimental techniques that may be used to characterize **J**-tensors: 1) high-resolution rotational spectroscopy including molecular beam magnetic resonance (MBMR) and molecular beam electric resonance (MBER),[30,31] 2) nuclear magnetic resonance (NMR) studies of powder or single-crystal samples[19] and 3) NMR studies of solutes in partially oriented fluids (i.e., liquid-crystalline solvents).[32] An example illustrating an application of each of these techniques for deriving information on **J**-tensors will be described in the following section. In addition, strong electric fields can be used to partially align molecules in liquids with electric dipole moments.[33] This technique can also in principle be used to characterize **J**-tensors.[34] Buckingham and McLauchlan[35] demonstrated that partial alignment using electric fields can be used to determine the absolute sign of $^{3}J(^{1}\text{H},^{1}\text{H})_{\text{iso}}$ for *p*-nitrotoluene. Finally, anisotropy of the indirect spin–spin coupling could in principle provide a mechanism for nuclear spin relaxation in isotropic fluids[21] but so far no experimental evidence for this mechanism exists.

4.1 Hyperfine Structure in High-Resolution Rotational Spectroscopy

The importance of molecular beam techniques to characterize **J**-tensors has not been well appreciated. Accurate experimental data are now available for more than 15 diatomic molecules[8] (see Table 2 for a partial list). Since the measurements are performed on gaseous samples at very low pressures, the results from these experiments are important because they provide 'benchmark' data for isolated molecules that can be used to establish the reliability of first-principles calculations. For example, in the case of hydrogen fluoride, $^{1}J(^{19}\text{F},^{1}\text{H})_{\text{iso}} = +529 \pm 23$ Hz from gas phase measurements[36] while in acetonitrile solution, $^{1}J(^{19}\text{F},^{1}\text{H})_{\text{iso}} = +479 \pm 4$ Hz.[37] Clearly solvent effects on indirect spin–spin coupling constants can be significant, particularly in cases where intermolecular interactions are important.

To outline the molecular beam procedure for the characterization of indirect spin–spin coupling tensors, we will consider the diatomic molecule, ^{35}Cl–^{19}F where the ^{35}Cl and ^{19}F nuclei are spin 3/2 and 1/2, respectively.[38,39] In the absence of any external fields, the effective hyperfine Hamiltonian for this

Table 2 Reduced Spin–Spin Coupling Tensors and Relative Anisotropy Ratios Derived From Available Experimental Hyperfine Data[a,b]

	$K_{iso}/10^{20}$ N A^{-2} m^{-3}	$\Delta K/10^{20}$ N A^{-2} m^{-3}	$\Delta J/J_{iso}$ (%)	$\Delta J/R_{DD}$ (%)
^{7}LiH	2.89	−1.22	−8.4	−0.12
^{7}LiF	3.92	3.94	91.9	1.55
^{7}Li^{79}Br	5.15	18.1	351	19
^{7}Li^{127}I	6.65	18.4	277	25
^{35}ClF	75.7	−81.8	−108	−35
^{79}BrF	171	−206	−120	−113
^{127}IF	252	−257	−102	−179
^{205}TlF	−202	173	−85.6	156
^{205}Tl^{35}Cl	−224	262	−117	400
^{205}Tl^{81}Br	−361	448	−124	800
^{205}Tl^{127}I	−474	664	−140	1470

[a]Rovibrational states: $v = 0$, $J = 0$ (LiF, LiI, BrF, IF); $v = 0$, $J = 1$ (LiH, LiBr, TlF, TlCl, ClF); $v = 0$, $J = 2$ (TlBr); $v = 0$, $J = 3$ (TlI). [b]see reference 8 for references to the original literature.

molecule is generally expressed in the molecular beam literature as:[30,31]

$$h^{-1}\widehat{\mathcal{H}}_{hf} = \mathbf{V}_{Cl} \cdot \mathbf{Q}_{Cl} + c_{Cl}\mathbf{I}_{Cl} \cdot \mathbf{J} + c_F\mathbf{I}_F \cdot \mathbf{J} + c_3\mathbf{I}_{Cl} \cdot \mathbf{d}_T \cdot \mathbf{I}_F + c_4\mathbf{I}_{Cl} \cdot \mathbf{I}_F \quad (15)$$

The first term accounts for the ^{35}Cl nuclear quadrupolar interaction, c_{Cl} and c_F are the nuclear spin-rotation constants for ^{35}Cl and ^{19}F respectively, c_3 is the effective ^{35}Cl–^{19}F dipolar coupling constant, and c_4 is $J(^{35}\text{Cl},^{19}\text{F})_{iso}$. The spin-rotation constants are related to the paramagnetic nuclear magnetic shielding and are important to those interested in absolute shielding tensors (see also **Chemical Shift Scales on an Absolute Basis,** Volume 2).[40,41] For the $v = 0$, $J = 1$ state of ^{35}Cl–^{19}F, Fabricant and Muenter[38] have reported $c_3 = 2859 \pm 9$ Hz and $c_4 = 840 \pm 6$ Hz. Although the equilibrium bond length of the Cl–F molecule is known to more than five significant figures, one must make a rovibrational correction so that $\langle r^{-3} \rangle$ can be evaluated for the $v = 0$, $J = 1$ state. Procedures for carrying out rovibrational averaging in diatomics have been discussed by Bryce and Wasylishen[8] and references therein. Using accepted values of the fundamental constants,[42] $r = 1.628\,3323$ Å, $R_{DD} = 2557$ Hz, thus $\Delta J/3 = -302 \pm 9$ Hz and $\Delta J = -906 \pm 27$ Hz. Results for several other diatomics are presented in Table 2 and Ref.[8] Consider the experimental results for the interhalogen fluorides: ^{35}ClF, ^{79}BrF, and ^{127}IF. As one descends the group 17 interhalogen fluorides, the magnitudes of K_{iso} and ΔK increase. Similarly for the thallium halides, the magnitudes of these parameters also increase as one descends group 17 (Table 2). This appears to be a general periodic trend.

4.2 Solid-state NMR Experiments

NMR investigations of **J**-tensors have been performed on both powder and single-crystal samples.[19,43] Magic angle spinning (MAS) experiments[20] performed on samples containing spin–spin coupled spin-pairs readily provide J_{iso}; however, analysis of the non-spinning samples is more difficult. For example, the ^{31}P NMR spectrum of $[Ph_3P\text{-}PPh_2][GaCl_4]$ acquired with MAS (Figure 1b) clearly demonstrates that

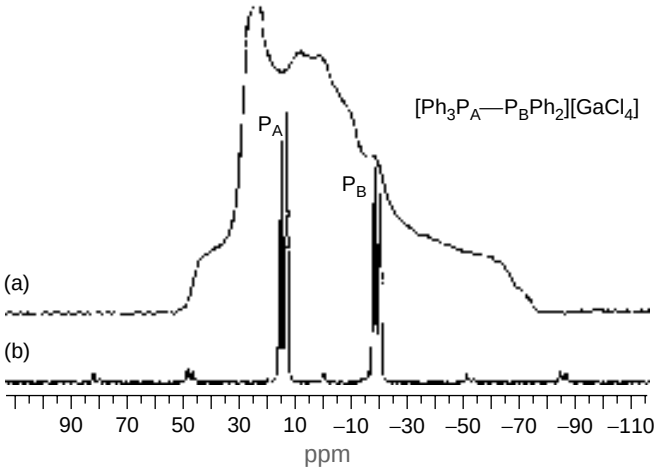

Figure 1 Phosphorus-31 NMR spectra of $[Ph_3P\text{–}PPh_2][GaCl_4]$ obtained at a spectrometer frequency of 161.98 MHz for (a) a stationary powder sample and (b) with magic angle spinning at 10.8 kHz

$|^1J(^{31}\text{P}_A, ^{31}\text{P}_B)_{iso}| = 323 \pm 2$ Hz. The corresponding spectrum acquired on a powder sample without MAS (Figure 1a) also consists of four transitions but is complicated by the orientation dependence of the phosphorus magnetic shielding of both nuclei as well as the direct-dipolar and anisotropic indirect ^{31}P, ^{31}P coupling interactions (vide infra). In the case of powder samples, it is difficult and often impossible to obtain reliable information about **J**-tensors unless the spin-pair of interest lies along a C_3 principal axis of a molecule which has C_{3v} or higher symmetry.

Here we discuss the powder NMR spectra of an isolated spin-pair where the two nuclei, A and X, are spin 1/2 nuclei and lie on the axis of symmetry such that both the nuclear magnetic shielding and the indirect spin–spin coupling tensors are axially symmetric and co-linear with the dipolar tensor. To predict the NMR spectra of such a spin system, we need to consider the following NMR Hamiltonian,

$$\widehat{\mathcal{H}} = \widehat{\mathcal{H}}_Z + \widehat{\mathcal{H}}_{CS} + \widehat{\mathcal{H}}_D + \widehat{\mathcal{H}}_J \quad (16)$$

where $\widehat{\mathcal{H}}_Z$ describes the interaction of the spins A and X with $\mathbf{B}_0$ and H_{CS} describes the nuclear magnetic shielding interaction. Here we will focus on the NMR spectrum of the A spins. Together H_Z and H_{CS} may be written as:

$$\widehat{\mathcal{H}}_Z + \widehat{\mathcal{H}}_{CS} = \frac{h}{2\pi}\gamma_A\mathbf{I}_A \cdot (\mathbf{1} - \boldsymbol{\sigma}_A) \cdot \mathbf{B}_0 \quad (17)$$

where $\boldsymbol{\sigma}_A$ is the nuclear magnetic shielding tensor. The direct and indirect spin–spin coupling Hamiltonians may be written:

$$\widehat{\mathcal{H}}_D = \gamma_A\gamma_X\frac{\hbar}{2\pi}\mathbf{I}_A \cdot \mathbf{D} \cdot \mathbf{I}_X \quad (18)$$

and

$$\widehat{\mathcal{H}}_J = \gamma_A\gamma_X\frac{\hbar}{2\pi}\mathbf{I}_A \cdot \mathbf{J} \cdot \mathbf{I}_X \quad (19)$$

As already mentioned, the magnetic shielding tensor for the systems considered must be axially symmetric with the $\sigma_\parallel$ and

$\sigma_\perp$ components corresponding to the shielding with $\mathbf{B}_0$ parallel and perpendicular to the A-X axis, respectively. The anisotropy or span of the magnetic shielding tensor may be defined as:

$$\Delta\sigma = \sigma_\parallel - \sigma_\perp \tag{20}$$

and the isotropic shielding, σ_{iso}, is $(2\sigma_\perp + \sigma_\parallel)/3$. It is straightforward to show that the spectrum of the A spins is given by:

$$\nu_A = \nu_{iso} - \nu_{iso}\frac{\Delta\sigma}{3}(3\cos^2\theta - 1) + m_X R_{eff}(3\cos^2\theta - 1) - m_X J_{iso} \tag{21}$$

where ν_{iso} is $\gamma_A B_0(1 - \sigma_{iso})/2\pi$, θ is the angle between $\mathbf{B}_0$ and the AX axis and $m_X = 1/2$ or $-1/2$[43,44] (see also **Dipolar & Indirect Coupling Tensors in Solids,** Volume 3). In Figure 2, we consider three cases: a) all spin–spin coupling interactions are zero, b) $R_{eff} = 0$ with $J_{iso} = 4\nu_{iso}\Delta\sigma$, and c) as above, except $R_{eff} = (\nu_{iso}\Delta\sigma)/3$. Spectrum 2a corresponds to the spectrum one would observe if the X-spins were decoupled. The discontinuity on the left corresponds to $\sigma_\perp$ while the shoulder on the right corresponds to $\sigma_\parallel$. In the hypothetical case where $R_{eff} = 0$ (Figure 2b), it is clear that the effect of J_{iso} is to produce two identical sub-spectra, one corresponding to $m_X = -1/2$ (on the left) and the other corresponding to $m_X = +1/2$ (on the right). Here we have assumed J_{iso} is positive. With $R_{eff} \neq 0$ (Figure 2c), the two sub-spectra now become different, one powder-pattern is stretched while the other is squeezed. Using equation (21) it is easy to demonstrate that the sub-spectrum corresponding to $m_X = +1/2$ becomes isotropic when $R_{eff} = \nu_{iso}\Delta\sigma/3$. If $R_{eff} > \nu_{iso}\Delta\sigma/3$, then the sense of the low-frequency sub-spectrum is opposite that of the high-frequency sub-spectrum. Note that in order to calculate the powder patterns one must average over all orientations of the A-X axis with respect to $\mathbf{B}_0$.[21,45]

To illustrate an example where equation (21) may be used to extract ΔJ, consider the ^{31}P NMR spectra of the

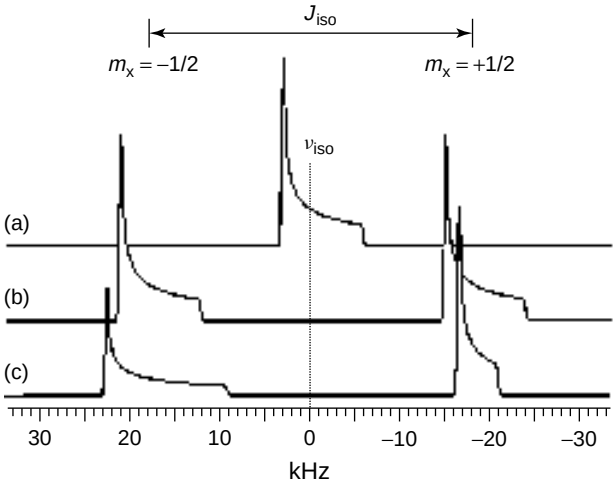

Figure 2 Line shape for the A spin NMR spectrum of an AX spin-pair in a stationary powder sample, (a) where the X spins are decoupled, hence only the magnetic shielding interaction is present. If $R_{eff} = 0$ Hz and $J_{iso} = 4\nu_{iso}\Delta\sigma$ spectrum (b) is obtained. If $R_{eff} = (\nu_{iso}\Delta\sigma)/3$ and $J_{iso} = 4\nu_{iso}\Delta\sigma$, spectrum (c) is predicted. The spectra were calculated using $J_{iso} = 36$ kHz, $R_{eff} = 3$ kHz, and an axially symmetric nuclear magnetic shielding tensor with $\nu_{iso}\Delta\sigma = 9$ kHz

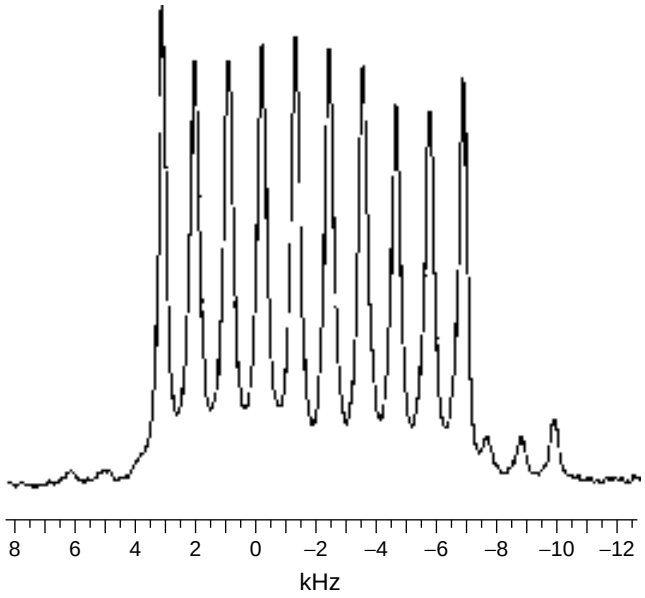

Figure 3 Phosphorus-31 NMR spectrum of solid tribromo(tris(4-methoxyphenyl)phosphine)indium(III), $Br_3In{\cdot}P[4\text{-}(CH_3O)C_6H_4]_3$ obtained at a spectrometer frequency of 81.033 MHz. The spectrum was acquired with CP and magic angle spinning at 3.0 kHz

^{115}In–^{31}P spin-pair in a powder sample of tribromo(tris(4-methoxyphenyl)phosphine)indium(III), $Br_3In{\cdot}P(4\text{-}(CH_3O)C_6H_4)_3$[43] shown in Figures 3 and 4. Indium-115 has a natural abundance of 95.72% and a spin of 9/2. X-ray diffraction measurements indicate that the In-P bond lies along a C_3 axis and the In-P bond length is 2.583 Å, thus $R_{DD} = +623$ Hz.[46] The ^{31}P NMR spectrum obtained with rapid spinning about the magic angle is shown in Figure 3. Magic-angle spinning averages the phosphorus shielding and the effective ^{115}In,^{31}P dipolar coupling tensor leaving only splittings due to J_{iso}. The equal spacing of all pairs of adjacent peaks indicates that the high-field approximation is reasonable here (i.e., the ^{115}In nuclei are quantized along $\mathbf{B}_0$).[47,48] This spacing, 1109 ± 9 Hz, corresponds to $^1J(^{115}\text{In},^{31}\text{P})_{iso}$, and there are ten peaks in the spectrum because there are $2I_X + 1$ allowed values of m_X. The ^{31}P NMR spectrum of a stationary sample is shown in Figure 4. Noting the frequencies of the peak maxima in Figure 4(a) and comparing these frequencies with those in Figure 3, consideration of equation (21) indicated that $-9/2R_{eff} \simeq \nu_{iso}\Delta\sigma/3$. Spectral simulation shows that $R_{eff} = \pm 230 \pm 50$ Hz, thus $\Delta J = +1179 \pm 150$ Hz or -2559 ± 150 Hz corresponding to R_{eff} being positive or negative, respectively. Since analysis of the spectrum of the stationary sample indicated that $^1J(^{115}\text{In},^{31}\text{P})_{iso}$ and R_{eff} have the same signs and given that $^1K(\text{P,B})_{iso}$ is positive in analogous compounds, it is reasonable to assume that ΔJ is positive and therefore the value of $+1179 \pm 150$ Hz is preferred. The squeezing and stretching of each of the isotropic transitions in the calculated spectrum are illustrated for the ten transitions in Figure 4(c) and for just the $m_X = -9/2$ (to high frequency) and the $m_X = +9/2$ (to low frequency) sub-spectra in Figure 4(d).

The indirect spin–spin coupling tensor involving ^{115}In and ^{31}P has also been measured in the semiconductor material,

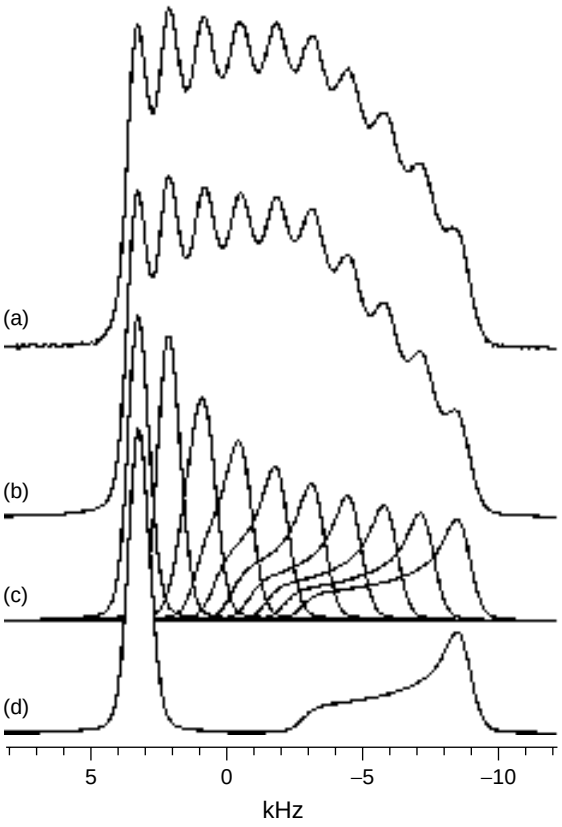

Figure 4 Phosphorus-31 NMR spectra of solid tribromo(tris-(4-methoxyphenyl)phosphine)indium(III), $Br_3In{\cdot}P(4\text{-}(CH_3O)C_6H_4)_3$ obtained at a spectrometer frequency of 81.033 MHz. The experimental spectrum (a) was acquired with CP using a stationary powder sample. The calculated powder line shape is shown in (b) with the sub-spectra shown in (c). For clarity, the sub-spectra corresponding to just the $m_X = -9/2$ (to high frequency) and $m_X = +9/2$ (to low frequency) indium-115 spin states are shown in (d)

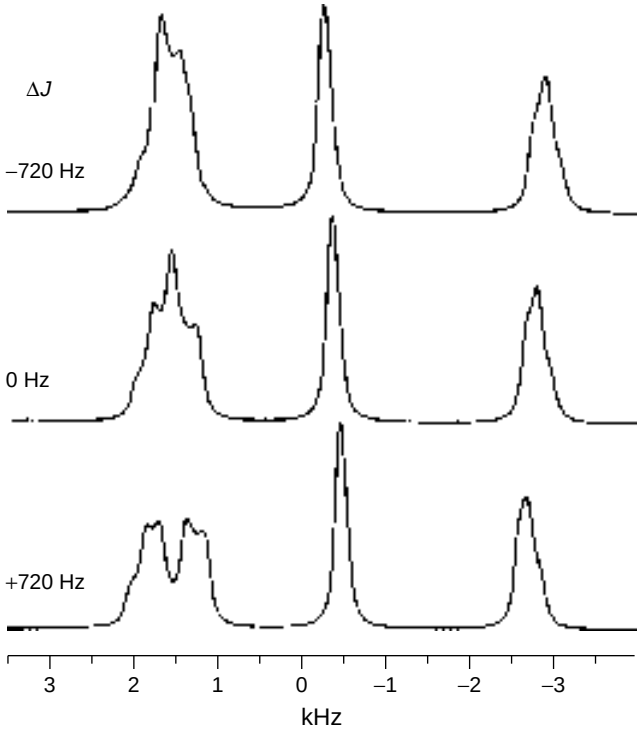

Figure 5 Phosphorus-31 NMR spectra calculated at 4.7 T for $[P(Bz)_3]_2Cu[PF_6]$ spinning at the magic angle, showing the sensitivity of the line shape to the sign and magnitude of $\Delta^1J(^{63/65}Cu,^{31}P)$. The experimental spectrum corresponds to that calculated with $\Delta^1J(^{63}Cu,^{31}P) = +720$ Hz[50]

InP, by Pines et al.[49] The magnitude of $^1J(^{115}In,^{31}P)_{iso}$ for undoped InP is 225 ± 10 Hz while $\Delta J = 1220 \pm 75$ Hz or 2600 ± 75 Hz, the two possible values arising because the absolute sign of R_{eff} could not be determined.

For a spin-pair of a quadrupolar nucleus coupled to a spin-1/2 nucleus, R_{eff} can often be derived from the spin-1/2 NMR spectra obtained with MAS. For example, consider the $^{63}Cu-^{31}P$ and $^{65}Cu-^{31}P$ spin-pairs of a bisphosphine of Cu(I) where the phosphine ligands are related by a center of inversion.[50] Both naturally occurring isotopes of copper, ^{63}Cu and ^{65}Cu, are spin 3/2 with natural abundances of 69.09 and 30.91%, respectively. In this case, the high-field approximation does not hold and the heteronuclear dipolar interaction is not completely averaged by MAS.[47] For example at 4.7 T, the Larmor frequency for ^{63}Cu is approximately 53.1 MHz and the nuclear quadrupolar coupling constant, $C_Q(^{63}Cu)$, for $[P(Bz)_3]_2Cu[PF_6]$ is 82.96 MHz. In this case, the calculated ^{31}P NMR spectra are sensitive to R_{eff} and hence to ΔJ (see Figure 5). Simulations of experimental ^{31}P NMR spectra acquired under MAS conditions at three different applied magnetic fields demonstrated that $^1J(^{63}Cu,^{31}P)_{iso} = +1550 \pm 10$ Hz and $\Delta J(^{63}Cu,^{31}P) = +720 \pm 50$ Hz. A related ^{199}Hg NMR study of $K_2Hg(CN)_4$ provided information about the **J**-tensor over two bonds; $|^2J(^{199}Hg,^{14}N)_{iso}| = 20.6$ Hz and $\Delta^2J(^{199}Hg,^{14}N) = 69 \pm 15$ Hz.[51] Again, this measurement of ΔJ is possible because the high-field approximation breaks down for ^{14}N ($I = 1$).

In cases where both A and X are spin-1/2 nuclei, R_{eff} can also readily be obtained from slow-spinning MAS experiments provided that $J(A,X)_{iso}$ is well-resolved and the intensities of several sidebands in each sub-spectrum of either the A- or the X-spin NMR spectrum can be measured. Consider Figure 2(c) where the span or breadth of each 'A' sub-spectrum is very different. Clearly, under conditions of MAS, the spinning sideband pattern of each sub-spectrum could be analyzed to obtain the principal components of each sub-spectrum using the Herzfeld–Berger method.[52] Harris, Packer, and Thayer[53] have provided a detailed account of the background theory necessary to analyze such a spin system. Grossmann et al.[54] have recently applied this technique to measure $\Delta^1J(^{77}Se,^{31}P)$ in trimethyl and triphenyl phosphine selenide. Earlier, Penner, Power, and Wasylishen[55] applied this technique to measure $\Delta^1J(^{199}Hg,^{31}P)$ in a 1 : 1 mercury phosphine complex. Initial results obtained for powder samples were later verified by single-crystal ^{31}P NMR experiments involving a related compound.[56]

A discussion of the single-crystal NMR experiments as applied to AX spin systems and mercury phosphine complexes was presented in the Encyclopedia of NMR (see **Dipolar & Indirect Coupling Tensors in Solids,** Volume 3).

For homonuclear spin-pairs, **J**-tensors have been characterized using single-crystal NMR.[57,58] For powder samples, a 2D spin-echo experiment provides valuable information about R_{eff}.[57,59] As well, slow spinning at the magic angle[60] (see

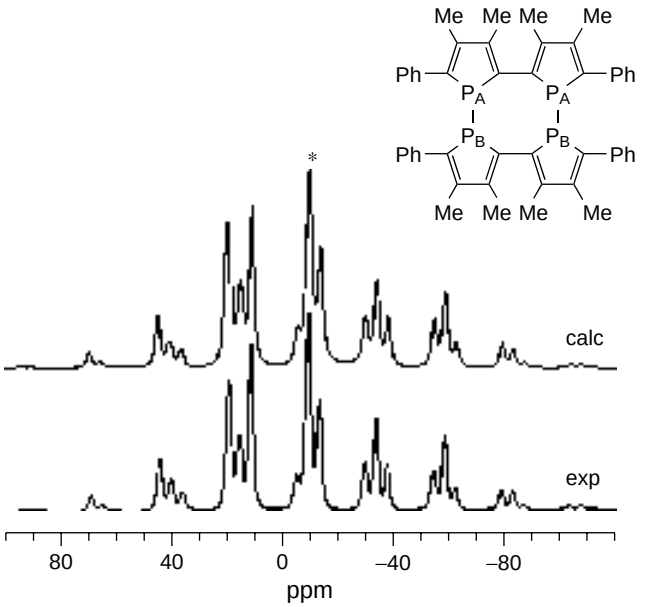

Figure 6 Phosphorus-31 NMR spectrum of a phosphole tetramer at 4.7 T. The sample spinning frequency was 1.5 kHz and the isotropic chemical shifts of P_A and P_B differ by 1.7 ppm. The asterisk indicates the average position of δ_{iso}. $^1J(^{31}P,^{31}P)_{iso} = -362$ Hz and $R_{eff} = 1.80 \pm 0.05$ kHz. The exact line shape and intensities of the numerous spinning sidebands shown here are very sensitive to the magnitudes and relative orientations of the shielding and dipolar tensors. See Ref.[60] for details

Figure 6) or fast spinning off the magic angle[61] can also provide information about R_{eff}.

Finally, numerous dipolar recoupling experiments[62] have been devised to 'determine' $r_{NN'}$; however, it is important to note that these experiments measure R_{eff} and not R_{DD}. Furthermore, the principal axis system of the direct dipolar tensor may not be coincident with the indirect spin–spin coupling tensor unless dictated by molecular symmetry.

4.3 Partially Oriented Fluids

In an applied magnetic field, the molecules of liquid crystalline solvents become partially aligned. As a result, the motion of solute molecules in such a medium becomes anisotropic and their resulting NMR spectra become dependent on both the anisotropic magnetic shielding and the intramolecular spin–spin coupling tensors ($\mathbf{D} + \mathbf{J}$); intermolecular dipole–dipole interactions are nearly averaged to zero. In liquid crystal NMR experiments, one must determine the degree of orientation of the solute molecules with respect to the magnetic field, which is described by one or more order parameters.[32,63] Similar to solid-state NMR investigations of powder samples, reliable measurements of $\Delta\boldsymbol{J}$ are generally impossible without high symmetry. As an example of a 'state-of-the-art' investigation of a **J**-tensor using liquid-crystal NMR, we refer the reader to recent papers involving methylfluoride, CH_3F.[64,65] To obtain $\Delta^1J(^{19}F,^{13}C)$, one requires the motionally averaged direct dipolar coupling constant corrected for harmonic and anharmonic vibrations. Also, a correction due to solvent deformations must be made in order to obtain reliable values of ΔJ.[66] For CH_3F, $^1J(^{19}F,^{13}C)_{iso} = -163$ Hz and $\Delta^1J(^{19}F,^{13}C) = 350$ Hz; high-level ab initio calculations yield -156.6 Hz and 207.8 Hz, respectively, for these parameters.

The liquid crystal technique used for characterizing **J**-tensors was reviewed in 1982[32] and in the Encyclopedia of NMR (see **Anisotropy of Shielding & Coupling in Liquid Crystalline Solutions,** Volume 2). A comprehensive review on **J**-tensors is currently being prepared.[17]

5 CONCLUSIONS

From the brief overview presented here it should be clear that it is possible to experimentally characterize the symmetric portion of indirect spin–spin coupling tensors. The accuracy of any experimental determination of a **J**-tensor is dependent on the experimentalist's ability to characterize the accompanying direct-dipolar tensor. As indicated in sections 3 and 4 the reliability of **J**-tensor data will improve if the spin-pairs of interest lie on a principal axis of symmetry. In systems where symmetry does not require the dipolar and **J**-tensors to be coincident, most experimental techniques yield **J**-tensor data that are ambiguous at best, the exception being single-crystal NMR experiments.

Over the past few years there have been significant advances in the computation of **J**-tensors using both ab initio and density functional methods.[13,17] Observation of J-coupling across hydrogen bonds[67] in nucleic acid base pairs has led to a renewed interest in 'through-space' indirect spin–spin coupling.[68]

Many NMR experiments have been developed to measure dipolar coupling constants in solids under conditions of magic angle spinning. In these so-called "dipolar-recoupling" experiments it is important to recognize that one obtains R_{eff}. While the assumption that $R_{DD} = R_{eff}$ may be valid for many systems, there is growing evidence that $\Delta J/3$ can be significant particularly if heavy nuclei are involved in the spin–spin coupling. Finally, it is intriguing that magnetic field oriented media and residual dipolar couplings are being used to determine the structure of biomolecules.[69] Thus there is an apparent merging of traditional high-resolution solution-state NMR and solid-state NMR. Clearly some appreciation or knowledge of **J**-tensors is beneficial to a wide audience of NMR spectroscopists.

6 RELATED ARTICLES IN THIS VOLUME

Three-dimensional Molecular Structures in Uniformly Labelled Solids Determined Using Rotational Resonance in the Tilted Rotating Frame; Accuracy Limitations on Internuclear Distances Measured by REDOR; Liquid Crystalline Samples: Application to Macromolecular Structure Determination.

7 RELATED ARTICLES IN VOLUMES 1–8

Anisotropy of Shielding & Coupling in Liquid Crystalline Solutions, Volume 2; Chemical Shift Scales on an Absolute Basis, Volume 2; Dipolar & Indirect Coupling Tensors in Solids, Volume 3.

8 REFERENCES

1. R. Malleier, H. Kopacka, W. Schuh, K. Wurst, and P. Peringer, *Chem. Commun.*, 2001, 51.
2. W. G. Proctor and F. C. Yu, *Phys. Rev.*, 1951, **81**, 20.
3. H. S. Gutowsky and D. W. McCall, *Phys. Rev.*, 1951, **82**, 748.
4. E. L. Hahn and D. E. Maxwell, *Phys. Rev.*, 1951, **84**, 1246.
5. H. Y. Carr and E. M. Purcell, *Phys. Rev.*, 1952, **88**, 415.
6. N. F. Ramsey, *Phys. Rev.*, 1953, **91**, 303.
7. W. T. Raynes and N. Panteli, *Chem. Phys. Lett.*, 1983, **94**, 558.
8. D. L. Bryce and R. E. Wasylishen, *J. Am. Chem. Soc.*, 2000, **122**, 3197.
9. P. Pyykkö, *Theor. Chem. Acc.*, 2000, **103**, 214.
10. P. Pyykkö, *Chem. Phys.*, 1977, **22**, 289.
11. P. Pyykkö and L. Wiesenfeld, *Mol. Phys.*, 1981, **43**, 557.
12. J. Autschbach and T. Ziegler, *J. Chem. Phys.*, 2000, **113**, 936.
13. H. Fukui, in 'A Specialist Periodic Report: Nuclear Magnetic Resonance', ed G. A. Webb, The Royal Society of Chemistry: Cambridge, 2000, Vol. 29, Chap. 4.
14. (a) L. Visscher, T. Enevoldsen, T. Saue, H. J. Aa. Jensen, and J. Oddershede, *J. Comput. Chem.*, 1999, **20**, 1262; (b) J. Vaara, K. Ruud, and O. Vahtras, *J. Comput. Chem.*, 1999, **20**, 1314.
15. H. Fukui, *Prog. NMR Spectrosc.*, 1997, **31**, 317.
16. T. Helgaker, M. Jaszuński, K. Ruud, *Chem. Rev.*, 1999, **99**, 293.
17. J. Vaara, J. Jokisaari, R. E. Wasylishen, and D. L. Bryce, *Prog. NMR Spectrosc.*, submitted.
18. R. H. Contreras, J. E. Peralta, C. G. Giribet, M. C. De Azua, and J. C. Facelli, *Annu. Rep. NMR Spectrosc.*, 2000, **41**, 55.
19. J. B. Robert and L. Wiesenfeld, *Phys. Rep.*, 1982, **86**, 363.
20. E. R. Andrew, in 'Progress in Nuclear Magnetic Resonance Spectroscopy', eds J. W. Emsley, J. Feeney, and L. H. Sutcliffe, Pergamon Press: Oxford, 1972, Vol. 8, p. 1.
21. H. W. Spiess, in 'NMR Basic Principles and Progress', eds P. Diehl, E. Fluck, and R. Kosfeld, Springer-Verlag: Berlin, 1978, Vol. 15, p. 55.
22. A. D. Buckingham, P. Pyykkö, J. B. Robert, and L. Wiesenfeld, *Mol. Phys.*, 1982, **46**, 177.
23. A. L. Barra and J. B. Robert, *Mol. Phys.*, 1996, **88**, 875.
24. E. R. Andrew and L. F. Farnell, *Mol. Phys.*, 1968, **15**, 157.
25. D. L. Bryce and R. E. Wasylishen, *J. Am. Chem. Soc.*, 2000, **122**, 11 236.
26. N. Bloembergen and T. J. Rowland, *Phys. Rev.*, 1955, **97**, 1679.
27. K. Ruud, P.-O. Åstrand, and P. R. Taylor, *J. Chem. Phys.*, 2000, **112**, 2668.
28. (a) A. S. Oja and O. V. Lounasmaa, *Rev. Mod. Phys.*, 1997, **69**, 1; (b) R. C. Patnaik, R. L. Hota, and G. S. Tripathi, *Phys. Rev. B*, 1998, **58**, 3924.
29. M. A. Ruderman and C. Kittel, *Phys. Rev.*, 1954, **96**, 99.
30. (a) J. C. Zorn and T. C. English, in 'Advances in Atomic and Molecular Physics', eds D. R. Bates and I. Estermann, Academic Press: New York, 1973, Vol. 9, p. 243; (b) T. C. English and J. C. Zorn, in 'Methods of Experimental Physics', ed D. Williams, Academic Press: New York, 1973, Vol. 3.
31. T. R. Dyke and J. S. Muenter, in 'Molecular Structure and Properties', ed A. D. Buckingham, Butterworth: London, 1975, p. 27.
32. J. Lounila and J. Jokisaari, *Prog. NMR Spectrosc.*, 1982, **15**, 249.
33. A. D. Buckingham and J. A. Pople, *Trans. Faraday Soc.*, 1963, **59**, 2421.
34. S. A. Riley and M. P. Augustine, *J. Phys. Chem. A*, 2000, **104**, 3326.
35. A. D. Buckingham and K. A. McLauchlan, *Proc. Chem. Soc., London*, 1963, 144.
36. J. S. Muenter and W. Klemperer, *J. Chem. Phys.*, 1970, **52**, 6033.
37. J. S. Martin and F. Y. Fujiwara, *J. Am. Chem. Soc.*, 1974, **96**, 7632.
38. B. Fabricant and J. S. Muenter, *J. Chem. Phys.*, 1977, **66**, 5274.
39. R. E. Davis and J. S. Muenter, *J. Chem. Phys.*, 1972, **57**, 2836.
40. D. L. Bryce and R. E. Wasylishen, *J. Chem. Educ.*, 2001, **78**, 124.
41. C. J. Jameson, in 'Multinuclear NMR', ed J. Mason, Plenum Press: New York, 1987, Chap. 4.
42. I. Mills, T. Cvitaš, K. Homann, N. Kallay, and K. Kuchitsu, 'Quantities, Units and Symbols in Physical Chemistry', 2nd edn., Blackwell Science: Cambridge, 1993.
43. D. L. VanderHart and H. S. Gutowsky, *J. Chem. Phys.*, 1968, **49**, 261.
44. K. W. Zilm and D. M. Grant, *J. Am. Chem. Soc.*, 1981, **103**, 2913.
45. U. Haeberlen, in 'Advances in Magnetic Resonance', ed J. S. Waugh, Academic Press: New York, 1976, Supplement 1.
46. R. E. Wasylishen, K. C. Wright, K. Eichele, and T. S. Cameron, *Inorg. Chem.*, 1994, **33**, 407.
47. R. K. Harris and A. C. Olivieri, *Prog. NMR Spectrosc.*, 1992, **24**, 435.
48. P. Grondona and A. C. Olivieri, *Concepts Magn. Reson.*, 1993, **5**, 319.
49. M. Tomaselli, D. deGraw, J. L. Yarger, M. P. Augustine, and A. Pines, *Phys. Rev. B*, 1998, **58**, 8627.
50. S. Kroeker, J. V. Hanna, R. E. Wasylishen, E. W. Ainscough, and A. M. Brodie, *J. Magn. Reson.*, 1998, **135**, 208.
51. G. Wu and R. E. Wasylishen, *J. Phys. Chem.*, 1993, **97**, 7863.
52. J. Herzfeld and A. E. Berger, *J. Chem. Phys.*, 1980, **73**, 6021.
53. R. K. Harris, K. J. Packer, and A. M. Thayer, *J. Magn. Reson.*, 1985, **62**, 284.
54. G. Grossmann, M. J. Potrzebowski, U. Fleischer, K. Krüger, O. L. Malkina, and W. Ciesielski, *Solid State NMR*, 1998, **13**, 71.
55. G. H. Penner, W. P. Power, and R. E. Wasylishen, *Can. J. Chem.*, 1988, **66**, 1821.
56. M. D. Lumsden, K. Eichele, R. E. Wasylishen, T. S. Cameron, and J. F. Britten, *J. Am. Chem. Soc.*, 1994, **116**, 11 129.
57. K. Eichele, G. Wu, R. E. Wasylishen, and J. F. Britten, *J. Phys. Chem.*, 1995, **99**, 1030.
58. M. Gee, R. E. Wasylishen, K. Eichele, and J. F. Britten, *J. Phys. Chem. A*, 2000, **104**, 4598.
59. T. Nakai and C. A. McDowell, *J. Am. Chem. Soc.*, 1994, **116**, 6373.
60. M. Gee, R. E. Wasylishen, K. Eichele, G. Wu, T. S. Cameron, F. Mathey, and F. Laporte, *Can. J. Chem.*, 2000, **78**, 118.
61. C. Marichal and A. Sebald, *Chem. Phys. Lett.*, 1998, **286**, 298.
62. S. Dusold and A. Sebald, *Annu. Rep. NMR Spectrosc.*, 2000, **41**, 185.
63. J. W. Emsley and J. C. Lindon, 'NMR Spectroscopy Using Liquid Crystal Solvents', Pergamon Press: Oxford, 1975.
64. P. Lantto, J. Kaski, J. Vaara, and J. Jokisaari, *Chem. Eur. J.*, 2000, **6**, 1395.
65. J. B. S. Barnhoorn and C. A. De Lange, *Mol. Phys.*, 1996, **88**, 1.
66. J. Jokisaari, Y. Hiltunen, and J. Lounila, *J. Chem. Phys.*, 1986, **85**, 3198.
67. (a) A. J. Dingley and S. Grzesiek, *J. Am. Chem. Soc.*, 1998, **120**, 8293; (b) D. L. Bryce and R. E. Wasylishen, *J. Biomol. NMR*, 2001, **19**, 371 (and references therein).
68. D. L. Bryce and R. E. Wasylishen, *J. Mol. Struct.*, 2002, **602–603**, 463.
69. J. H. Prestegard, H. M. Al-Hashimi, and J. R. Tolman, *Q. Rev. Biophys.*, 2000, **33**, 371.

Acknowledgements

I wish to thank Dr. Myrlene Gee, David Bryce, Kirk Feindel, and Dr. Klaus Eichele for technical assistance preparing this manuscript. Also, I wish to thank Myrlene, David and Klaus for several helpful comments, and past and present members of my research group who have contributed to our work involving **J**-tensors. Finally, I wish to acknowledge the University of Alberta, the Natural Sciences and Engineering Research Council (NSERC) of Canada and the Canada Research Chairs Program for supporting our research program.

Biographical Sketch

Roderick E. Wasylishen, *b* 1944. B.Sc., 1968, Waterloo, Ph.D., 1972, Manitoba. Introduced to NMR by Terry Gough at the University of Waterloo and Ted Schaefer at the University of Manitoba. National Research Council of Canada PDF at the National Institutes of Health, Bethesda, Maryland with Ted Becker, 1972–1974. Department of Chemistry, University of Winnipeg, 1974–82, Dalhousie University, 1982–2000, University of Alberta, 2000–present. Canada Research Chair in Physical Chemistry at the University of Alberta, 2001–present. Approx. 230 publications. Current research specialties: NMR studies of solids, nuclear magnetic shielding, spin–spin coupling, EFG tensors, NMR line shapes, NMR relaxation, materials characterization, and computational chemistry.

Isotope Effects on Chemical Shifts and Coupling Constants

Cynthia J. Jameson

University of Illinois, Chicago, IL, USA

1	Introduction	1
2	Isotope Shifts: Observations	1
3	Rovibrational Theory of Isotope Shifts	2
4	General Trends in the Electronic Factors	11
5	Isotope Shifts Over Two or More Bonds	11
6	Isotope Effects on Spin–Spin Coupling	13
7	Related Articles	16
8	References	16

1 INTRODUCTION

Where an isotopic label is introduced into a molecule, every neighboring resonant nucleus experiences a slight chemical shift. If the labeling is less than 100%, the resonant nuclei in both the labeled and the unlabeled molecules are observed, with intensities according to statistical distribution. The magnitude of the shift depends on the fractional mass change at the isotope substitution site, on the remoteness of the resonant nucleus from the substitution site, and on the sensitivity of the shielding of the resonant nucleus. Every resonant nucleus in the isotopically labeled molecule experiences this chemical shift due to isotopic substitution, but the shift is only observable under favorable conditions, such as when the shift is larger than the halfwidth of the peaks. Isotope shifts as small as a few ppb have been observed, from zero bonds (the isotopic label itself is the resonant nucleus) to 12 bonds away from the substitution site.[1–3] When the isotopic label itself is the resonant nucleus, the isotope shift is called a primary isotope shift. Such primary isotope shifts can only be observed indirectly, when two in different molecules are compared. There are also attendant effects on the spin–spin coupling constants in the molecule.[4] Here, the primary and secondary effects have to be deduced from the proper combination of observed couplings, and it is more appropriate to do this in the reduced coupling constant from which the gyromagnetic ratios have been removed altogether.

Isotope effects on chemical shifts and coupling constants are very important in two distinct ways. First, they have a multitude of practical applications, such as in the determination of molecular structure and the verification of mechanisms of reactions. This is just one more powerful tool in which a very selective tag carries with it the same wealth of information as the chemical shift itself. Second, isotope shifts provide a more stringent test of ab initio calculations of chemical shifts in specific molecules, being directly related to the slopes on the shielding surface (a mathematical surface), and, in a more general sense, the trends in the thousands of isotope shifts that have been accumulated[1–3] provide insight into the general nature of these shielding surfaces, in terms of the dependence of the details of the surface on the nature of the chemical bond, the net charge of the molecule, bond orders, presence of lone pairs, etc.[5,6] Isotope effects on coupling constants lack practical applications, but are invaluable from the second point of view. For the most part, coupling constants are obtained in rapidly tumbling systems, and only the isotropic average of the tensor is obtained. The full tensor is very difficult to extract from experiments in oriented molecules, since it is always observed as a sum with the larger dipolar tensor. Since coupling mechanisms other than the Fermi contact mechanism are the ones that give rise to the anisotropy of the tensor, the lack of tensor information leaves us with a severe dearth of critical tests of the ab initio calculations. Isotope effects on coupling constants provide additional critical tests, since they depend on the spin–spin coupling surface, not just a single calculated value. The earliest questions asked of theoretical calculations of chemical shifts demanded only that the relative order of chemical shifts be reproduced and that the relative magnitudes agree with experiment. More recently, we have asked how well the calculations reproduce the absolute shielding in specific molecules, not just their relative shifts, and also how well they reproduce the shielding tensor components. These are more stringent tests of theory. In the isotope shift experiments, we ask for even more detailed agreement: how well do the calculations reproduce the shapes of the shielding surfaces as the nuclear coordinates are displaced away from the immediate vicinity of the equilibrium geometry of the molecule? A similar question is posed for the spin–spin coupling surface by the primary and secondary isotope effects on J.

2 ISOTOPE SHIFTS: OBSERVATIONS

We follow the notation introduced by Gombler[7] for the isotope shift observed for nucleus A upon substitution of the neighboring $^{m'}$X isotope:

$$ {}^{n}\Delta\mathrm{A}(^{m'/m}\,\mathrm{X}) = \frac{\nu_{\mathrm{A}}(\mathrm{A}^{\,m'}\mathrm{X}\ldots) - \nu_{\mathrm{A}}(\,\mathrm{A}^{\,m}\mathrm{X}\ldots)}{\nu_{\mathrm{A}}(\mathrm{A}^{\,m}\mathrm{X}\ldots)} \quad (m'\rangle m) \tag{1} $$

where $\nu_{\mathrm{A}}(\mathrm{A}^{\,m'}\mathrm{X}\ \ldots\ )$ is the resonance frequency of the A nucleus in the molecule having the heavier $^{m'}$X isotope, which is n bonds away from the observed nucleus. The molecules (A $^{m'}$X …) and (A ^{m}X …) are isotopomers. The isotope shift can also be written in terms of the nuclear shielding difference:

$$ \begin{aligned} {}^{n}\Delta\ \mathrm{A}(^{m'/m}\,\mathrm{X}) &= \sigma^{\mathrm{A}}(\,\mathrm{A}^{\,m}\,\mathrm{X}\ldots) - \sigma^{\mathrm{A}}(\,\mathrm{A}^{\,m'}\,\mathrm{X}\ldots) \\ &= \sigma - \sigma^{*} \end{aligned} \tag{2} $$

where the asterisk applies to the heavy isotopomer. Just as for spin–spin couplings, this notation becomes ambiguous when A and X are atoms in cyclic compounds in which there are at least two paths connecting the observed nucleus and substituted atom, in which case the observed quantity is an isotope shift corresponding to two or more bond paths.

There are several general observations that have been made about magnitudes and signs of isotope shifts:[1,8]

1. Upon substitution with a heavier isotope, the NMR signal of the nearby nucleus usually shifts towards lower frequencies (higher shielding). Thus, as defined in equations (1) and (2), isotope shifts are generally negative in sign.
2. The magnitude of the isotope shift depends on how remote the isotopic substitution is from the observed nucleus. Although there are exceptions, one-bond isotope shifts are larger than two-bond or three-bond shifts. In the examples shown in Table 1, there is a clear attenuation of the isotope shift with the number of bonds separating the NMR nucleus and the substitution site.[9,10]
3. The magnitude of the isotope shift is a function of the observed nucleus, and reflects its chemical shift range. Comparisons can be made in analogous compounds, as in Table 2.
4. The magnitude of the shift is related to the fractional change in mass upon isotopic substitution. The larger the fractional change in mass, $(m' - m)/m'$, the larger the isotope shift, as is obvious in the examples in Table 3. (The signals can be easily assigned according to the abundance of the masses m' and m.) When two different atoms can be substituted in the molecule, the isotopic shifts are commensurate with the fractional change in masses, as in the example in Table 4.
5. The magnitude of the shift is approximately proportional to the number of equivalent atoms that have been substituted by isotopes. In other words, isotope shifts exhibit additivity. When there are multiple equivalent sites and the labeling is less than 100%, the resonant nuclei in the variously labeled and the unlabeled molecules are observed. For example, for a deuterium fraction d (based on the solvent isotopic composition for the exchange), for N equivalent replaceable hydrogens, the statistical limit for the relative intensity of the $XH_{N-n}D_n$ isotopomer will be

$$I_n = \frac{N!}{n!(N-n)!}(1-d)^{(N-n)}d^n \tag{3}$$

This strictly statistical formula neglects any isotope effects on the equilibrium constant for the exchange. By doing more than one labeling experiment (using different heavy atom fractions), the identification of the signals with the isotopomers can be unequivocal. Fortunately, in many cases, there is also spin–spin coupling information in the NMR spectrum, so that only one labeling experiment is necessary. When there are several equivalent substitution sites, the additivity of the isotope shifts is obvious, as in the examples in Table 5.[15–18] Deviations from strict additivity are small, and their 0:3:4:3:0 ratio in CH_4-like systems has been explained.[19] Additivity is observed in long-range isotope shifts as well. For example, the two-bond deuterium-induced isotope shifts of ^{59}Co in hexaamminecobalt(III) chloride are all −5.2 ppm per D in each of the 18 different isotopomers of $[Co(NH_3)_6]^{3+}$. Less obvious, but also observed, is the additivity of isotope shifts due to substitution at nonequivalent sites.

Table 1

n	$^n\Delta^{31}$P($^{13/12}$C) in Ph_3P (ppm)	$^n\Delta^{13}$C($^{2/1}$H) in butane-1-d_1 (ppm)
1	−0.0227	−0.298
2	−0.0039	−0.088
3	−0.0018	−0.0291
4	—	+0.0051

Table 2

X	$^1\Delta$X($^{13/12}$C) (ppm)	Chemical shift range (ppm)
^{77}Se in Me_2Se	−0.228	2200
^{125}Te in Me_2Te	−0.341	3160
^{29}Si	−0.006	600
^{119}Sn	−0.018	3000
^{207}Pb	−1.089	9000
X	$^1\Delta$X($^{18/16}$O) (ppm)	Chemical shift range (ppm)
^{29}Si	−0.0218	600
^{13}C	−0.019	680
^{31}P	−0.018 to −0.036	950
^{15}N	−0.056, −0.138	1200
^{55}Mn	−0.599	3440
^{99}Tc	−0.22	4500
^{95}Mo	−0.25	7000
^{129}Xe	−0.58	7850
X	$^1\Delta$X($^{2/1}$H) (ppm)	Chemical shift range (ppm)
^{51}V in $[CpVH(CO)_3]^-$	−4.7	6000
^{93}Nb in $[CpNbH(CO)_3]^-$	−6.0	5000
^{183}W in $CpWH(CO)_3$	−10.0	11500

These are the general trends found for all isotope shifts. These general experimental trends provide the testing grounds for the theory of isotope shifts. There are also some tendencies that are less global in nature but that are perceived as correlations in observations of related classes of compounds; for example, one-bond isotope shifts tend to be larger when the bond order between the observed nucleus and the substituted nucleus is higher. These correlations have to be considered separately, since they involve comparisons between different molecules that have many differences other than in the parameters that are being correlated with the isotope shifts.

3 ROVIBRATIONAL THEORY OF ISOTOPE SHIFTS

The effects of intramolecular dynamics (vibration and rotation) on nuclear shielding were theoretically predicted by Ramsey,[20] and have been observed in two ways. First, there is an observable temperature dependence of the resonance frequency, even for the 'isolated' molecule (apart from the temperature dependence due to intermolecular interactions). Second, there is an observable shift upon isotopic substitution of neighboring nuclei. Both are effects of differences in averaging over nuclear configuration as the molecule undergoes vibration and rotation.[21] The temperature dependence of nuclear shielding is observed in the dilute gas phase.[22–25] The nuclear shielding in an 'isolated' molecule, $\sigma_0(T)$, is an average of the nuclear magnetic shielding tensor over all possible orientations of the molecule in the magnetic field, and is actually observed as the nuclear shielding in the limit as the pressure approaches zero. One does not extrapolate the results to a true zero pressure, but to a pressure so low that collisional deformation of the molecule no longer contributes to σ, while there are still enough collisions to provide the required rate of transition between vibrational and rotational states. Thus, $\sigma_0(T)$ is an average over all possible rovibrational states of

Table 3

Molecule	m'	m	Isotope shifts (ppm)	Reference
$(CH_3)_2CO$	3	1	$^2\Delta\ ^{13}C(^{3/1}H) = +0.076$	Arrowsmith et al.[11]
	2	1	$^2\Delta\ ^{13}C(^{2/1}H) = +0.054$	
$(CH_3)_2CO$	3	1	$^1\Delta\ ^{13}C(^{3/1}H) = -0.356$	Arrowsmith et al.[11]
	2	1	$^1\Delta\ ^{13}C(^{2/1}H) = -0.250$	
CO	17	16	$^1\Delta\ ^{13}C(^{17/16}O) = -0.0247$	Wasylishen et al.[12]
	18	16	$^1\Delta\ ^{13}C(^{18/16}O) = -0.0476$	
SeF_6	76	74	$^1\Delta\ ^{19}F(^{76/74}Se) = -0.0154$	Jameson et al.[13]
	77	74	$^1\Delta\ ^{19}F(^{77/74}Se) = -0.021$	
	78	74	$^1\Delta\ ^{19}F(^{78/74}Se) = -0.0301$	
	80	74	$^1\Delta\ ^{19}F(^{80/74}Se) = -0.0442$	
	82	74	$^1\Delta\ ^{19}F(^{82/74}Se) = -0.0576$	

Table 4

Molecule	m'	m	Isotope shift[14] (ppm)
$[CpVH(CO)_3]^-$	2	1	$^1\Delta\ ^{51}V(^{2/1}H) = -4.7$
	13	12	$^1\Delta\ ^{51}V(^{13/12}C) = -0.51$

the molecule, weighted according to the fraction of molecules occupying that state at that temperature.

The average shielding for a given rovibrational state is different for each of several isotopically related species, because the masses enter into the solution of the vibrational–rotational Hamiltonian.[26] Thus, the thermal average shielding $\sigma_0(T)$ is different for the isotopomers. These differences are measured as isotope shifts. It is important to know which aspects of isotope shifts are due to dynamical factors (rovibrational averaging of internuclear separations) and which can be attributed to electronic factors (changes in nuclear shielding with bond extension or bond angle deformation). If the theory can sort out the former, isotope shifts can be used to extract the latter, thus providing chemically interesting information that would establish the isotope shift as an easily measurable index of the chemical bond.

3.1 Vibrational Averaging in Diatomic Molecules

The potential energy surface (PES) of a diatomic molecule can be written in terms of a Dunham potential, or more approximately in terms of a Morse potential. The Dunham potential function expresses the potential energy in terms of a Taylor series expansion in $x = (r - r_e)/r_e$:

$$V = a_0x^2(1 + a_1x + a_2x^2 + a_3x^3 + \dots) \tag{4}$$

The potential parameters a_0, a_1, ... can be obtained from the spectroscopic constants of the molecule. The vibrational levels and functions shown in Figure 1 for the H_2^+ molecule are typical. The first thing to note is that the anharmonic nature of the potential function leads to an unsymmetrical probability distribution function: there is a higher probability of finding the diatomic molecule extended than compressed. Second, this asymmetry becomes more pronounced as we move up in the potential well. Third, the vibrational levels for D_2^+ (shown also as dashed lines) lie lower in the potential well than those for H_2^+, corresponding to its lower vibrational frequency, $\omega_e = 1643.0\,cm^{-1}$ for D_2^+ compared with $2323.5\,cm^{-1}$ for H_2^+. Since we are interested in vibrational averaging and the mass dependence of shielding, we show in Figure 2 the vibrational functions of D_2^+ and H_2^+. It is obvious that the anharmonic potential will give rise to different vibrational averages for the isotopomers, since the more sharply peaked and compact probability density of D_2^+ should lead to a different average than that for H_2^+, in which the probability density is more spread out at the larger separations. This is true for the vibrational ground state, and the differences become even more pronounced at higher vibrational levels. The average values $\langle x^n \rangle$ can be obtained. Complete calculations for some isotopomers of H_2^+ lead to the results for the ground vibrational state shown in Table 6, which also shows the results for the case where the vibration is truly that of a harmonic oscillator (HO).

In order to observe more easily the largest terms that contribute to the above equations and explicitly express their mass dependence, we write only the leading terms, expressed in the measured spectroscopic constants of the molecule.[8]

$$\langle x \rangle_{vJ} = -3(v + \tfrac{1}{2})a_1\frac{B_e}{\omega_e} + 4J(J+1)\frac{B_e}{\omega_e^2} \tag{5}$$

$$\langle x^2 \rangle_{vJ} = 2(v + \tfrac{1}{2})\frac{B_e}{\omega_e} \tag{6}$$

Of these quantities, a_1 is mass-independent, and the others depend on the reduced mass of the diatomic molecule as follows:

$$\omega_e^* = \left(\frac{\mu}{\mu^*}\right)^{1/2}\omega_e, \quad B_e^* = \frac{\mu}{\mu^*}B_e \tag{7}$$

Furthermore, the thermal average $\langle v + \frac{1}{2} \rangle^T$ is also mass-dependent, since the populations of the vibrational energy levels over which this average is taken depend on the vibrational frequency ω_e. Note that $B_e/{\omega_e}^2$ is mass-independent, so the rotational contribution to the thermal average shielding in the diatomic molecule is independent of mass.

Note also that if we include only the leading terms then

$$\langle x \rangle_v = -\tfrac{3}{2}a_1\langle x^2 \rangle_v \tag{8}$$

The difference between two isotopomers is

$$\langle x^2 \rangle_{vJ} - \langle x^2 \rangle_{vJ}^* = 2\frac{B_e}{\omega_e}\left[1 - \left(\frac{\mu}{\mu^*}\right)^{1/2}\right](v + \tfrac{1}{2}) + \dots \tag{9}$$

Table 5

	Isotopomer	δ, observed (ppm)	δ, if exactly additive (ppm)	Deviation (ppm)
^{119}Sn	SnH_3^-	0.0	0.0	0
	SnH_2D^-	−3.093	−3.108	−0.015
	$SnHD_2^-$	−6.202	−6.217	−0.015
	SnD_3^-	−9.325	−9.325	0
^{119}Sn	SnH_4	0.0	0.0	0
	SnH_3D	−0.4266	−0.4026	+0.024
	SnH_2D_2	−0.8369	−0.8052	+0.032
	$SnHD_3$	−1.2306	−1.2077	+0.023
	SnD_4	−1.6103	−1.6103	0
^{31}P	PH_3	0.0	0.0	0
	PH_2D	−0.8045	−0.8458	−0.041
	PHD_2	−1.6491	−1.6916	−0.042
	PD_3	−2.5373	−2.5373	0
^{15}N	NH_3	0.0	0.0	0
	NH_2D	−0.6264	−0.6229	0.0035
	NHD_2	−1.2491	−1.2458	0.0033
	ND_3	−1.8687	−1.8687	0
^{15}N	NH_4^+	0.0	0.0	0
	NH_3D^+	−0.3077	−0.2933	+0.0144
	$NH_2D_2^+$	−0.6048	−0.5865	+0.0183
	NHD_3^+	−0.8937	−0.8798	+0.0139
	ND_4^+	−1.1730	−1.1730	0
^{13}C	CH_4	0.0	0.0	0
	CH_3D	−0.2016	−0.19865	+0.003
	CH_2D_2		−0.3973	
	CHD_3	−0.6006	−0.5960	+0.004
	CD_4	−0.7946	−0.7946	0

$$\langle x\rangle_{vJ} - \langle x\rangle^*_{vJ} = -3a_1\frac{B_e}{\omega_e}\left[1-\left(\frac{\mu}{\mu^*}\right)^{1/2}\right](\,v+\tfrac{1}{2}) + \ldots \qquad (10)$$

The leading term in $\langle x^3\rangle_{vJ}$ has the same mass dependence as the next higher order term in $\langle x\rangle$ and $\langle x^2\rangle$; thus, it is consistent to include only the above two terms. We find the ratios from the full calculations:

$$\frac{\langle x\rangle_{H_2^+} - \langle x\rangle_{HT^+}}{\langle x\rangle_{H_2^+} - \langle x\rangle_{HD^+}} = 1.370 \qquad (11)$$

$$\frac{\langle x^2\rangle_{H_2^+} - \langle x^2\rangle_{HT^+}}{\langle x^2\rangle_{H_2^+} - \langle x^2\rangle_{HD^+}} = 1.369 \qquad (12)$$

whereas using *only* the leading terms leads in both cases to the ratio

$$\frac{1-(\mu_{H_2^+}/\mu_{HT})^{1/2}}{1-(\mu_{H_2^+}/\mu_{HD^+})^{1/2}} = 1.370 \qquad (13)$$

Qualitatively, the mass change accompanying the replacement of ^{m}X by its heavier isotope $^{m'}$X leads to a shorter average bond length. In Figure 2, we show for the lowest vibrational levels the probabilities of finding the diatomic molecule at the various internuclear separations. For the same anharmonic potential, the lighter isotopomer H_2^+ clearly shows greater probabilities of being found in a more extended configuration compared with D_2^+ at each vibrational state. Since the vibrational frequencies are lower for the heavier isotopomer, the populations of its higher vibrational states are somewhat greater. Both effects constitute the mass dependence of the thermal average $\langle x\rangle^T$, with the latter being less important than the former:

$$\{\langle x\rangle^T - \langle x\rangle^{*T}\} \approx -3a_1\frac{B_e}{\omega_e}\left[1-\left(\frac{\mu}{\mu^*}\right)^{1/2}\right]\langle\, v+\tfrac{1}{2}\rangle^T \qquad (14)$$

If we use a harmonic oscillator density of vibrational states, we get a simple form

$$\langle\, v+\tfrac{1}{2}\rangle^T_{HO} = \tfrac{1}{2}\coth(hc\omega_e/2k_BT) \qquad (15)$$

which itself has a mild mass dependence, which is not too important when ω_e is large, in which case coth $(hc\omega_e/2k_\beta T)$

Table 6

$x = (r - r_e)/r_e$	H_2^+	HD^+	HT^+	D_2^+
$\langle x\rangle_{v=0}$	0.033 12	0.028 63	0.026 97	0.023 32
$\langle x^2\rangle_{v=0}$	0.014 47	0.012 35	0.011 58	0.009 90
$\langle x^3\rangle_{v=0}$	0.001 66	0.001 24	0.001 09	0.000 81
HO $\langle x\rangle_v$, $\langle x^3\rangle_v$	0	0	0	0
HO $\langle x^2\rangle_{v=0}$	0.012 98	0.011 24	0.010 598	0.009 178
ω_e (cm^{-1})	2323.5	2012.2	1897.2	1643.0

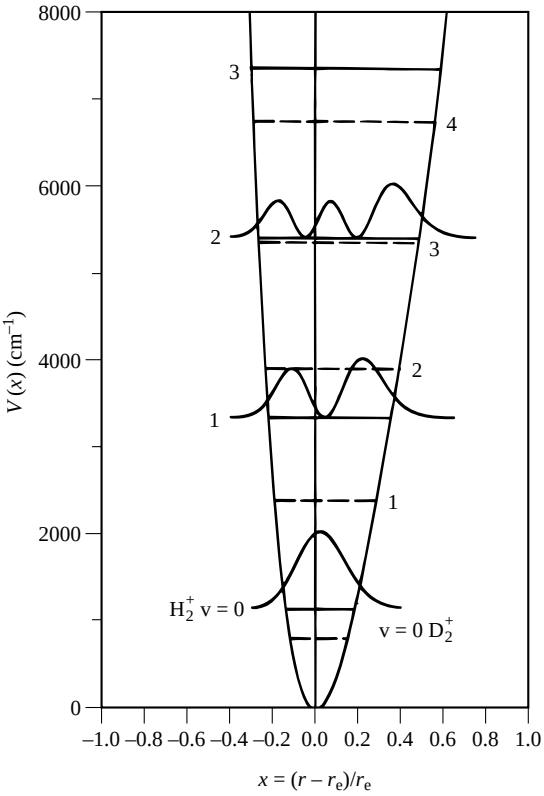

Figure 1 Vibrational levels and wavefunctions (squared) for the $H_2{}^+$ molecule. Also shown, by dashed lines, are the vibrational levels of the $D_2{}^+$ molecule

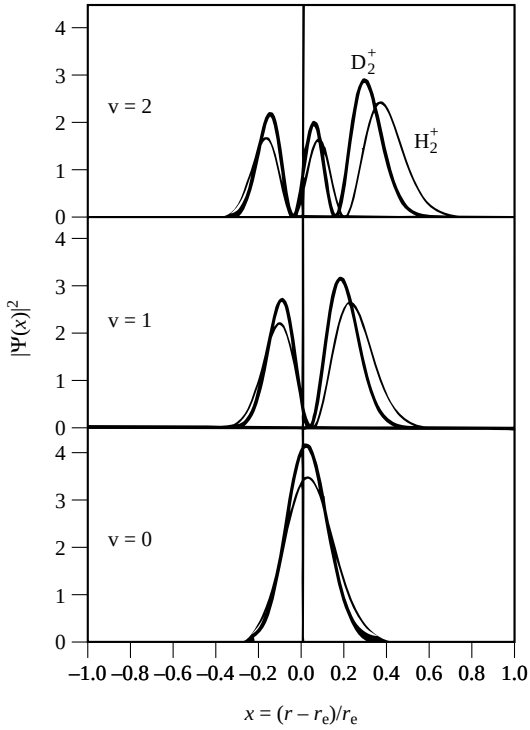

Figure 2 Vibrational wavefunctions (squared) for the $D_2{}^+$ molecule (heavy lines) and the $H_2{}^+$ molecule (light lines)

is very close to 1. A useful form of an approximate potential for the diatomic molecule is the Morse function

$$V = D_e\{1 - \exp[-a(r - r_e)]\}^2 \tag{16}$$

where D_e is the dissociation energy and a is called the Morse parameter, ar_e being a dimensionless quantity related to the ratio

$$\frac{1}{3!}\left(\frac{d^3V}{dx^3}\right)_e \Big/ \frac{1}{2!}\left(\frac{d^2V}{dx^2}\right)_e = -ar_e = a_1 \tag{17}$$

and

$$\langle x\rangle = \tfrac{3}{2}ar_e\langle x^2\rangle \tag{18}$$

At this level of theory, the mass dependence of $\langle x^2\rangle$ is the same as that of $\langle x\rangle$. Thus, we find that for diatomic molecules, neglecting the mass dependence in the coth function,

$$\langle x\rangle^T - \langle x\rangle^{*T} \approx \frac{3ar_e}{2}\frac{B_e}{\omega_e}\left[1 - \left(\frac{\mu}{\mu^*}\right)^{1/2}\right]\coth\left(\frac{hc\omega_e}{2k_BT}\right)$$
$$\approx \langle x\rangle^T\left[1 - \left(\frac{\mu}{\mu^*}\right)^{1/2}\right] \tag{19}$$

or

$$\langle \Delta r\rangle^T - \langle \Delta r\rangle^{*T} \approx \langle \Delta r\rangle^T_{vib}\left[1 - \left(\frac{\mu}{\mu^*}\right)^{1/2}\right] \tag{20}$$

$$\langle \Delta r\rangle^T_{vib} \approx \frac{3ar_e^2}{2}\frac{B_e}{\omega_e}\coth\left(\frac{hc\omega_e}{2k_BT}\right) \tag{21}$$

When μ/μ^* is very close to 1 (which is true for most situations not involving hydrogen), $1 - (\mu/\mu^*)^{1/2}$ can be further approximated by $(\mu^* - \mu)/2\mu^*$ or, in the comparison of the isotopomers A ^{m}X and A $^{m'}$X, by[27]

$$1 - \left(\frac{\mu}{\mu^*}\right)^{1/2} \approx \frac{1}{2}\frac{(m' - m)}{m'}\frac{m_A}{(m_A + m)} \tag{22}$$

$$\langle \Delta r\rangle^T - \langle \Delta r\rangle^{*T} \approx \langle \Delta r\rangle^T_{vib}\frac{1}{2}\frac{(m' - m)}{m'}\frac{m_A}{(m_A + m)} \tag{23}$$

with an analogous expression for $\langle(\Delta r)^2\rangle$. Here we find already the origin of general trend 4 in Section 2. The dynamic factors contain the mass dependence, and in diatomic molecules this mass dependence takes a simple form. It is interesting to point out here that, even for polyatomic molecules, this mass dependence has been found to hold: for $^{m'/m}SeF_6$, a plot of $\langle \Delta r_{SeF}\rangle^T$ and $\langle(\Delta r_{SeF})^2\rangle^T$ versus $(m' - m)/m'$ for m = 74 and m' = 76, 77, 78, 80, 82 leads to straight lines passing through the origin.[28]

A very interesting global description of potential functions for diatomic molecules was given by Herschbach and Laurie.[29] They found that the second and third derivatives of the potential could be described by exponential functions of the equilibrium internuclear distance, each described by a family of curves which are determined by the locations of the bonded atoms in rows of the Periodic Table:

$$(-1)^n F_n = 10^{-(r_e - p_n)/q_n} \tag{24}$$

where

$$F_3 \equiv \frac{1}{3}\left(\frac{\mathrm{d}^3V}{\mathrm{d}r^3}\right)_\mathrm{e}, \quad F_2 \equiv \left(\frac{\mathrm{d}^2V}{\mathrm{d}r^2}\right)_\mathrm{e} \tag{25}$$

and p_n and q_n are parameters that characterize any two rows of the Periodic Table. It was proposed by Jameson and Osten[27] that the averages $\langle x\rangle_\mathrm{v}$ and $\langle x^2\rangle_\mathrm{v}$ can be determined entirely from a knowledge of the r_e and the rows of the Periodic Table to which the atoms belong, using the following relations:

$$\langle \Delta r\rangle_\mathrm{v} = r_\mathrm{e}\langle x\rangle_\mathrm{v} \approx \frac{3h}{8\pi}\mu^{-1/2}10^{-D}(2\ \mathrm{v}+1) \tag{26}$$

$$\langle(\Delta r)^2\rangle_\mathrm{v} = r_\mathrm{e}^2\langle x^2\rangle_\mathrm{v} \approx \frac{h}{4\pi}\mu^{-1/2}10^{-d}(2\ \mathrm{v}+1) \tag{27}$$

where

$$D \equiv \frac{r_\mathrm{e}-p_3}{q_3} - \frac{3(r_\mathrm{e}-p_2)}{2q_2} \tag{28}$$

$$d \equiv \frac{r_\mathrm{e}-p_2}{2q_2} \tag{29}$$

Figure 3 shows a plot of $\langle\Delta r\rangle_\mathrm{vib}$ calculated at 300 K for a large set of diatomic molecules using their individual spectroscopic constants. It appears that the global relation given in equation (26) provides a reasonably good description of the vibrationally averaged bond displacement for diatomic molecules. It has been shown that these equations can be used as well to estimate the dynamic parts for polyatomic molecules, except that the constant factor is closer to $\frac{3}{7}$ than $\frac{3}{8}$.

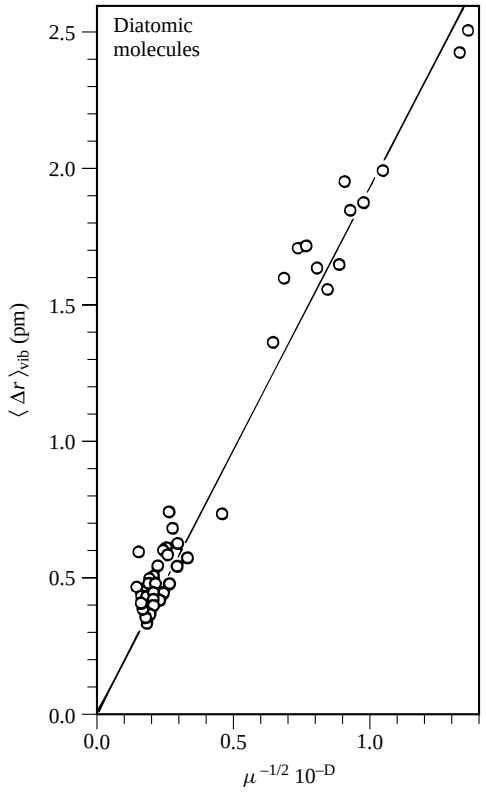

Figure 3 Mean bond displacement in diatomic molecules calculated by vibrational averaging over their individual potential surfaces compared with the global form $\langle\Delta r\rangle_\mathrm{vib} \approx (3\mathrm{h}/8\pi)\mu^{-1/2}10^{-D}$ (the straight line), where D is defined in equation (28). (Reproduced by permission of the American Insitute of Physics from Jameson and Osten[27])

3.2 The Shapes of Shielding Surfaces

In the context of the Born–Oppenheimer approximation, analogous to the potential energy surface, which is a mass-independent electronic property of a molecule in a given electronic state, there is likewise a mass-independent nuclear shielding surface that describes the variation of the shielding as a function of nuclear configuration. For a diatomic molecule, this surface can be described entirely in terms of the internuclear separation. Two examples are shown in Figures 4 and 5. At the united atom limit (r = 0), the diamagnetic shielding of the He^+ ion is (not shown) 35.5009 ppm. At the equilibrium geometry of $H_2{}^+$, the proton shielding is 11.4296 ppm, and at the separated atom limit, the diamagnetic shielding corresponds to half that of the free hydrogen atom ($\frac{1}{2}$)17.75 ppm.[30] The other example is ^{23}Na shielding in NaH, in which the shielding at the equilibrium geometry is lower than for the separated system (either Na^+ or Na atom).[31] Figure 4 is a typical shielding surface for diatomic molecules in that the shielding surface has negative first and second derivatives.[32,33] For example, ^{19}F in the HF molecule and in the F_2 molecule, and ^{35}Cl in the HCl molecule and in the ClF molecule, all have negative first and second derivatives; that is, deshielding accompanies bond extension. It is also typical for the proton shielding in the molecule at its equilibrium geometry to be greater than that for the free H atom in the separated systems. On the other hand, the heavy nuclei are generally deshielded in the molecule at its equilibrium geometry compared with the diamagnetic shielding of the free atom. For example, nearly all ^{19}F nuclei have shielding less than 470.71 ppm. (^{19}F in ClF is a notable exception, and ^{19}F in CH_3F has an isotropic shielding nearly the same as that of the free F atom.) Every ^{19}F shielding first derivative at the equilibrium geometry, including ^{19}F in the ClF molecule, has been found to be negative, and the second derivative is negative as well.[34] On the other hand, the shielding surfaces for ^{23}Na in NaH and ^{7}Li in LiH have positive first derivatives at the equilibrium geometry.[31] The shapes of the shielding surfaces in Figures 4 and 5 are fairly similar; the major difference is which point on the shielding surface corresponds to the pocket in the PES and to which side of the shielding minimum this point corresponds. We have seen that the general behavior in vibrational averaging in the anharmonic PES is that the probabilities are greater on the $r > r_\mathrm{e}$ side. Thus, dynamic averaging always leads to deshielding when the pocket in the PES is to the short-r side of the shielding minimum, whereas dynamic averaging leads to increased shielding relative to the shielding at the equilibrium geometry when the pocket in the PES is to the longer-r side of the shielding minimum. Most nuclei that are observed in NMR are found on the right-hand side of the Periodic Table, where the shielding surface and the PES are related as in Figure 4; there are fewer observations of the alkali and alkaline earth nuclei, whose shielding surfaces and PES are related as in Figure 5. Therefore, the usual case

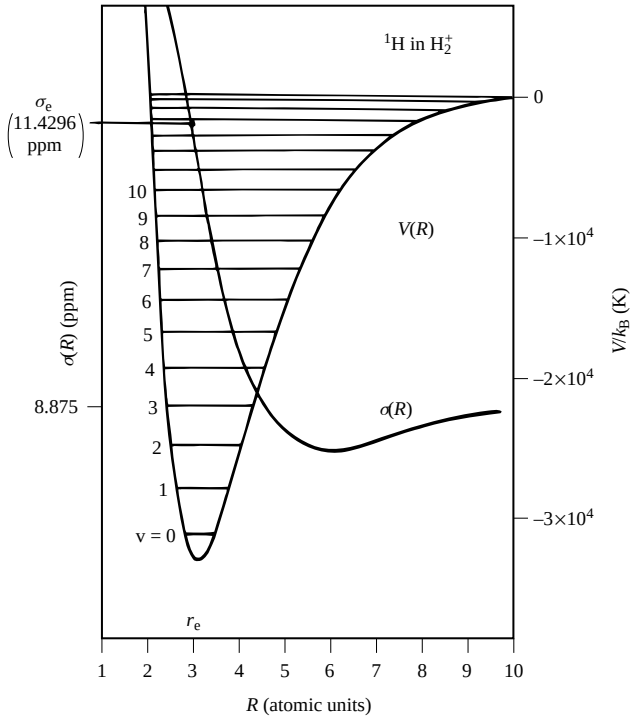

Figure 4 The ^{1}H shielding surface for the H_2^+ molecule is shown with the potential energy surface. The shielding surface is from ab initio calculations by Hegstrom.[30] (Reproduced by permission of the American Institute of Physics from Jameson and de Dios[31])

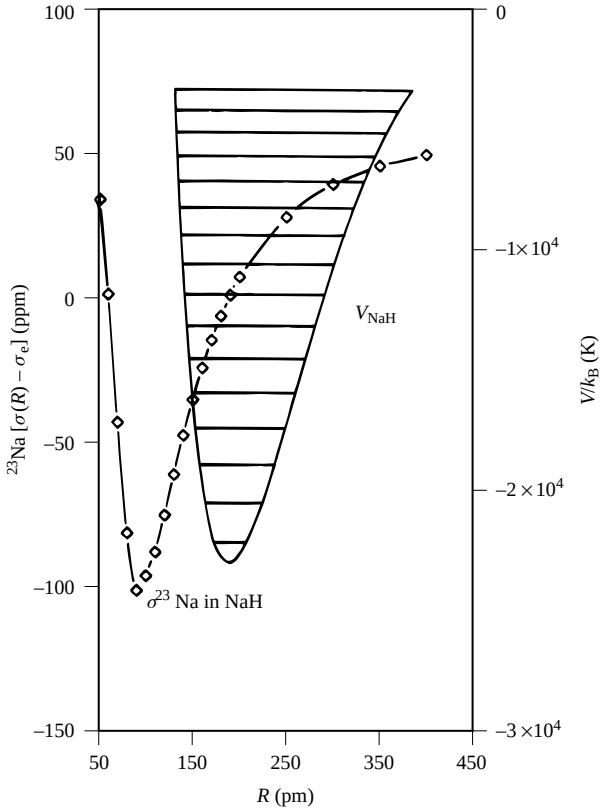

Figure 5 The ^{23}Na shielding surface for the NaH molecule is shown with the potential energy surface. The shielding surface is from ab initio calculations by Jameson and de Dios. (Reproduced by permission of the American Institute of Physics from Jameson and de Dios[31])

is more like Figure 4. Here then is the explanation for general trend 1 in Section 2: superposition of Figure 2 on Figure 4 would lead to a nucleus in the lighter isotopomer being less shielded than the same nucleus in the heavy isotopomer. Preponderance of this situation would lead to a nearly universal sign of one-bond isotope shifts. The exceptions will be Li and Na in the hydrides, for example.

The magnitudes of the isotope shifts would correspond to the ranges of chemical shifts of the observed nucleus if the shielding surfaces themselves scale to these. Let us see. We present the shielding surfaces in the vicinity of the equilibrium geometry in analogous compounds in Figure 6, where ^{19}F in F_2 is compared with ^{35}Cl in ClF (both are bonded to fluorine). ^{19}F in HF is compared with ^{35}Cl in HCl (both are bonded to an H atom). Finally, ^{23}Na in NaH is compared with ^{7}Li in LiH. It is found that if the change in shielding, $\sigma(r) - \sigma(r_e)$, is scaled by the factor $r_e\langle a_0^3/r^3\rangle$, the equilibrium bond distance in the molecule and the purely electronic quantity $\langle a_0^3/r^3\rangle$ characteristic of the atom, for the observed nucleus, the surfaces that describe the change in the shielding of different nuclei in analogous bonding situations superimpose.[31] This then is an explanation for general trend 3 in Section 2: the magnitude of the isotope shift is a function of the observed nucleus and reflects its chemical shift range. A general discussion of shielding surfaces is given by de Dios and Jameson.[35]

3.3 Averaging Over Shielding Surfaces

It is sometimes actually necessary to evaluate the average over a large part of the shielding surface.[36] For example, the PES of the NH_3 molecule has a rather broad double minimum in the inversion coordinate. The trace on the ^{15}N shielding surface along this inversion coordinate is shown in Figure 7. To obtain the contribution to the average ^{15}N shielding from this degree of freedom, it was necessary to find the numerical PES (which are highly anharmonic) and solve for the vibrational wavefunctions. These are shown in Figure 7. The average for each state 0^s, 0^a, 1^s, 1^a, 2^s, 2^a was numerically calculated with these functions, $\langle\Psi_v|\hat{\sigma}|\Psi_v\rangle$, and the thermal average is obtained as

$$\langle\sigma\rangle^T = \frac{\sum_v e^{-E_v/k_BT}\langle\sigma\rangle_v}{\sum_v e^{-E_v/k_BT}} \tag{30}$$

For semirigid molecules that we often observe in NMR (excluding molecules that are fluxional or that undergo low-frequency torsion), the motions involved in the averaging take place in a small pocket of the potential energy surface close to the equilibrium configuration. It is therefore not necessary to calculate the entire shielding surface, as we have shown in Figures 4, 5, and 7. In the same way that averages such as $\langle x\rangle$, $\langle x^2\rangle$, $\langle x^3\rangle$, etc. could be evaluated in terms of the derivatives of the PES such as represented by the quantities a_0, a_1, a_2, a_3, etc. in the Dunham potential function, it is possible to calculate the average shielding from derivatives of the shielding surface at the equilibrium geometry, since we only need to average over very small displacements away from the minimum in the PES.

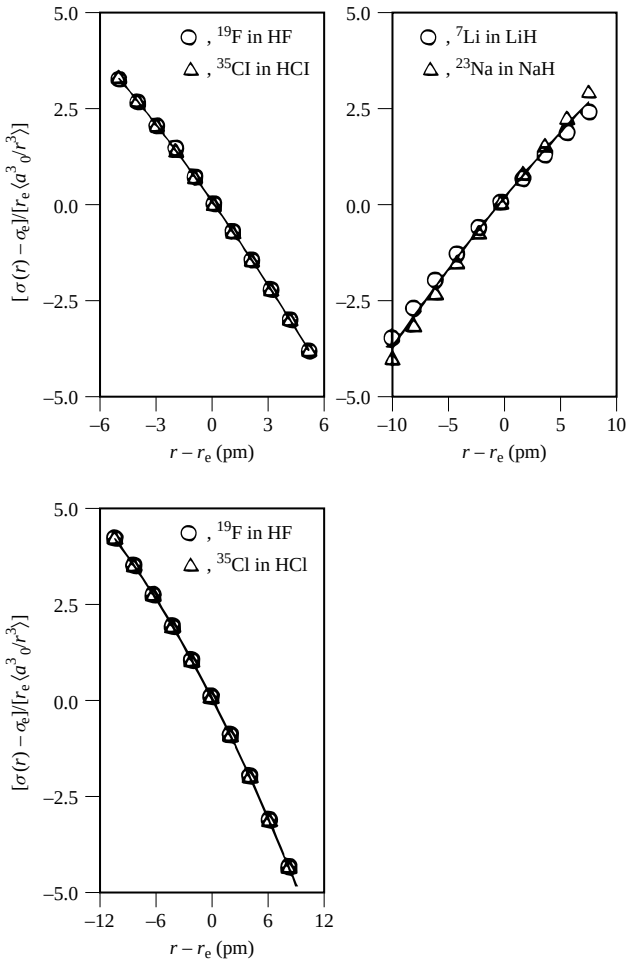

Figure 6 The shielding surfaces of analogous diatomic molecules in the vicinity of the equilibrium geometry, in the range of nuclear displacements spanning the classical turning points of the ground vibrational state. (Reproduced by permission of the American Institute of Physics from Jameson and de Dios[31])

For a diatomic molecule, it is convenient to expand the shielding surface as a power series in $x = (r - r_e)/r_e$. For a particular molecular state characterized by vibrational and rotational quantum numbers v and J,

$$\langle\sigma\rangle_{vJ} = \sigma_e + \left(\frac{d\sigma}{dx}\right)_e \langle x\rangle_{vJ} + \frac{1}{2}\left(\frac{d^2\sigma}{dx^2}\right)_e \langle x^2\rangle_{vJ} + \cdots \qquad (31)$$

Here $\langle x\rangle_{vJ}$, $\langle x^2\rangle_{vJ}$, ... are the averages over the vibrational–rotational wavefunctions corresponding to the (v, J) level, which we have already described in Section 3.1. The isotope shift is therefore given by

$$\langle\sigma\rangle^T - \langle\sigma\rangle^{*T} = \left(\frac{d\sigma}{dx}\right)_e (\langle x\rangle^T - \langle x\rangle^{*T}) + \frac{1}{2}\left(\frac{d^2\sigma}{dx^2}\right)_e (\langle x^2\rangle^T - \langle x^2\rangle^{*T}) + \cdots \qquad (32)$$

With the approximations described in Section 3.1, using the Morse parameter,

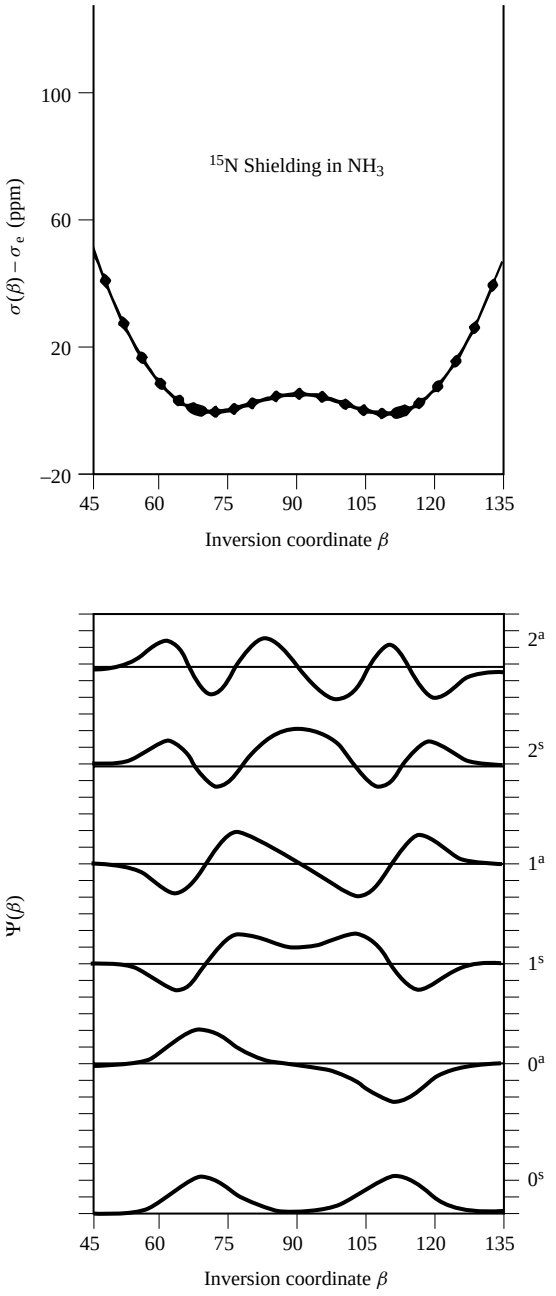

Figure 7 The ^{15}N shielding surface of NH_3 along the inversion coordinate β (the angle between the symmetry axis and a N–H bond) is shown with the vibrational wavefunctions for the lowest inversion levels. The shielding average can be obtained by numerical integration as $\langle\sigma\rangle_v = \int \Psi_v^*(\beta)\sigma(\beta)\Psi_v(\beta)\, d\beta$. (Reproduced by permission of the American Institute of Physics from Jameson et al.[36])

$$\langle x\rangle^T \approx \tfrac{3}{2} a r_e \langle x^2\rangle^T \qquad (33)$$

the isotope shift in diatomic molecules is given by

$$\langle\sigma\rangle^T - \langle\sigma\rangle^{*T} \approx \left[\left(\frac{d\sigma}{dx}\right)_e + \frac{1}{3ar_e}\left(\frac{d^2\sigma}{dx^2}\right)_e\right](\langle x\rangle^T - \langle x\rangle^{*T}) + \cdots \approx \left[\left(\frac{d\sigma}{dr}\right)_e + \frac{1}{3a}\left(\frac{d^2\sigma}{dr^2}\right)_e\right](\langle\Delta r\rangle^T - \langle\Delta r\rangle^{*T}) \qquad (34)$$

and, when coth ($hc\omega_e/2k_BT$) is close to 1,

$$\langle\sigma\rangle^T - \langle\sigma\rangle^{*T} \approx \left[\left(\frac{d\sigma}{dr}\right)_e + \frac{1}{3a}\left(\frac{d^2\sigma}{dr^2}\right)_e\right] \times \langle\Delta r\rangle^T_{vib}\left[1 - \left(\frac{\mu}{\mu^*}\right)^{1/2}\right] \quad (35)$$

In equations (34) and (35), the first quantity (in square brackets) is a mass-independent purely electronic quantity; the second quantity is a mass-dependent dynamic factor. As we have seen, both the first and second derivatives of the shielding surface are most often negative. Right here, we see that the sign of the isotope shift is negative owing to $(d\sigma/dr)_e$ being negative, since the shift is defined such that the dynamic factor is positive; that is, the nucleus in the light isotopomer is less shielded (appears at higher frequency) than the nucleus in the heavy isotopomer. The unusual (positive) sign of the isotope shift will be observed when the shielding derivative is positive, such as for ^{23}Na in NaH or ^{7}Li in LiH. For polyatomic molecules, it makes physical sense to expand the nuclear shielding in terms of the normal coordinates Q_s (a concept of significance only for small displacements):[21,37]

$$\sigma = \sigma_e + \sum_s \left(\frac{\partial\sigma}{\partial Q_s}\right)_e Q_s + \frac{1}{2}\sum_{s,r}\left(\frac{\partial^2\sigma}{\partial Q_r\,\partial Q_s}\right)_e Q_r Q_s + \cdots \quad (36)$$

where the shielding derivatives are taken at the equilibrium configuration. Normal coordinates are a logical choice for this expansion, since methods of evaluating the average values $\langle Q_s\rangle$ and $\langle Q_r Q_s\rangle$ are well known in vibrational spectroscopy. However, the derivatives of the nuclear shielding with respect to the mass-dependent normal coordinates are not invariant under isotopic substitution. For the purpose of discussing the isotope shift, it is more convenient to expand the shielding in terms of mass-independent internal displacement coordinates:[5,21]

$$\sigma = \sigma_e + \sum_i \left(\frac{\partial\sigma}{\partial\mathcal{R}_i}\right)_e \mathcal{R}_i + \frac{1}{2}\sum_{i,j}\left(\frac{\partial^2\sigma}{\partial\mathcal{R}_i\,\partial\mathcal{R}_j}\right)_e \mathcal{R}_i\mathcal{R}_j + \cdots \quad (37)$$

where $\mathcal{R}$ stands for the bond displacements (Δr_i) and the bond angle deformations ($\Delta\alpha_{ij}$).

The theoretical interpretation of isotope shifts in polyatomics therefore involves the mass-independent electronic quantities such as

$$\left(\frac{\partial\sigma}{\partial\mathcal{R}_i}\right)_e = \left(\frac{\partial\sigma}{\partial r_i}\right)_e \quad \left(\frac{\partial\sigma}{\partial\alpha_{ij}}\right)_e \quad (38)$$

which describe the change in nuclear shielding with bond extension or angle deformation, and the mass-dependent thermal averages $\langle\mathcal{R}_i\rangle^T$, which are $\langle\Delta r\rangle^T$, $\langle\Delta\alpha\rangle^T$, ... and $\langle\mathcal{R}_i\mathcal{R}_j\rangle^T$, which are $\langle(\Delta r)^2\rangle^T$, $\langle(\Delta\alpha)^2\rangle^T$, $\langle\Delta r\ \Delta\alpha\rangle^T$, ... The isotope shift is given by

$$\sigma - \sigma = \sum_i \left(\frac{\partial\sigma}{\partial\mathcal{R}_i}\right)_e \langle\mathcal{R}_i\rangle^T + \frac{1}{2}\sum_{i,j}\left(\frac{\partial^2\sigma}{\partial\mathcal{R}_i\,\partial\mathcal{R}_j}\right)_e \langle\mathcal{R}_i\mathcal{R}_j\rangle^T + \cdots \quad (39)$$

In order to be able to evaluate $\langle\mathcal{R}_i\rangle^T$, $\langle\mathcal{R}_i\mathcal{R}_j\rangle^T$ etc., we need a potential surface in which the vibrational motion of the molecule takes place. The known derivatives of this surface are the quadratic, cubic, etc. force constants. Normal coordinate analysis with the quadratic force constants gives the solutions to the harmonic problem, which are the harmonic frequencies ω_s, the normal coordinates Q_s, and the **L** matrix. The internal displacement coordinates $\mathcal{R} = \Delta r_i, \Delta\alpha_{ij}$, etc. can be expressed in terms of these normal coordinates in the general relation[38]

$$\mathcal{R} = \mathbf{L}Q \quad (40)$$

where is a tensor containing the transformation coefficients between the curvilinear internal coordinates and various powers of Q_s. The vibrational part of Δr_i is then

$$\Delta r_i = \sum_i L_i^r Q_r + \frac{1}{2}\sum_{r,s} L_i^{rs} Q_r Q_s + \frac{1}{6}\sum_{r,s,t} L_i^{rst} Q_r Q_s Q_t + \cdots \quad (41)$$

Thus, the vibrational average $(\Delta r)_{vib}$ can be expressed in terms of $\langle Q_r\rangle$, $\langle Q_r Q_s\rangle$, etc. The analytical expressions for elements of the **L** tensor are given by Hoy et al.,[38] in which the linear terms L_i^r are identical to the elements L_{ir} of the **L** matrix. The above equation is exact, but in practice, of course, the series must be truncated; in general, it converges well, each term being smaller than the preceding by a factor of about 10 for typical vibrational amplitudes. The expectation values of only totally symmetric coordinates Q_s are required:[39]

$$\langle Q_s\rangle = \left(\frac{h}{4\pi^2 c}\right)^{1/2}\omega_s^{-3/2}\left[3k_{sss}(\mathrm{v}_s + \tfrac{1}{2}) + \sum_r{}' k_{srr}(\mathrm{v}_r + \tfrac{1}{2}g_r)\right] \quad (42)$$

where ω_s are the normal frequencies and k_{srr} are the cubic force constants, both in wavenumbers. g_r denotes the degeneracy of the rth vibration. $\langle Q_r Q_s\rangle = 0$ if $\omega_r \neq \omega_s$, and

$$\langle Q_s^2\rangle = \frac{h}{4\pi^2 c\omega_s}(\mathrm{v}_s + \tfrac{1}{2}) \quad (43)$$

To obtain the thermal average shielding, we again need $\langle \mathrm{v}_s + \frac{1}{2}\rangle^T$. For larger molecules, it becomes impossible to calculate a sufficient number of rovibrational states in order to use the exact method for the thermal averaging, so the only practical way of calculating expectation values of molecular properties over different rotational and vibrational states for a given temperature is by using the harmonic approximation for the vibrational partition function, that is,

$$\langle \mathrm{v}_s + \tfrac{1}{2}\rangle^T = \tfrac{1}{2}\coth(hc\omega_s/2k_BT) \quad (44)$$

3.4 Relative Magnitudes of Terms That Contribute to the Isotope Shift

Mass substitution at one site in the molecule affects dynamic averages of all electronic properties. If, in particular, we have nuclear spins at various sites, all of these will have different average shifts; some will experience larger changes than others. In general, the entire molecule participates in the dynamic averaging. Depending on the nature of each nuclear shielding surface, the change in chemical shift may be of either sign. Each molecule offers a unique situation, and, especially for the long-range isotope effects, vibrations involving many atoms may play a part. To illustrate the types of terms that contribute to a one-bond isotope shift, we use the

$^1\Delta\ ^{13}C\ (^{2/1}H)$ in CH_4 as an example. During vibration, the displacements away from the equilibrium nuclear configuration can be small enough that a Taylor series expansion can be used:[40]

$$\begin{aligned}\langle\sigma^C\rangle = \sigma_e &+ P_r(\langle\Delta r_1\rangle + \langle\Delta r_2\rangle + \langle\Delta r_3\rangle + \langle\Delta r_4\rangle)\\ &+\tfrac{1}{2}P_{rr}[\langle(\Delta r_1)^2\rangle + \langle(\Delta r_2)^2\rangle + \langle(\Delta r_3)^2\rangle + \langle(\Delta r_4)^2\rangle]\\ &+P_{rs}(\langle\Delta r_1\Delta r_2\rangle + \langle\Delta r_1\Delta r_3\rangle + \langle\Delta r_1\Delta r_4\rangle\\ &+\langle\Delta r_2\Delta r_3\rangle + \langle\Delta r_2\Delta r_4\rangle + \langle\Delta r_3\Delta r_4\rangle)\\ &+\tfrac{1}{2}P_{\alpha\alpha}[\langle(\Delta\alpha_{12})^2\rangle + \cdots] + P_{\alpha\beta}(\langle\Delta\alpha_{12}\Delta\alpha_{13}\rangle + \cdots)\\ &+P_{r\alpha}(\langle r_1\Delta\alpha_{12}\rangle + \cdots) + P_{\alpha\omega}(\langle\Delta\alpha_{12}\Delta\alpha_{34}\rangle + \cdots)\\ &+ \text{higher-order terms}\end{aligned} \tag{45}$$

where $P_r \equiv (\partial\sigma^C/\partial r_1)_e$, while P_{rr} and P_{rs} are the second derivatives of the ^{13}C shielding with respect to the C–H bond distances; $P_{\alpha\alpha}$, $P_{\alpha\beta}$, and $P_{\alpha\omega}$ are the second derivatives of the ^{13}C shielding with respect to the HCH bond angles, and $P_{r\alpha}$ is the mixed second derivative $(\partial^2\sigma^C/\partial r_1\ \partial\alpha_{12})_e$. In some molecules, there are first derivatives with respect to the angle as well, for example, for ^{17}O in H_2O and ^{31}P in PH_3.[41,42] In yet others, the averaging cannot be carried out by considering small displacements, as in the inversion motion of the NH_3 molecule. The complexity of the equation increases with increasing number of atoms. Nevertheless, many general trends may be observed in the huge body of information represented in tables of thousands of isotope shifts.[1–3] These trends have become apparent, despite the uniqueness of the dynamic averaging of each molecule, because some terms in the full theory are more dominant than others. It is the persistence of the dominant contributions in most molecules that allows us to consider isotope shifts in much simpler terms, short of full averaging of full shielding surfaces in every case. In Table 7, we examine the relative magnitudes of terms that contribute to the isotope shift in selected molecules, where the calculations of the many terms (as shown above for CH_4) have been carried out to gain some insight into what might be expected in other molecules.[36,42–46] Clearly, the mixed terms and higher-order terms (listed in Table 7 as 'Other') are negligible compared with the total isotope shift. The P_r term, which is due entirely to the anharmonicity of the vibration, provides the largest contribution, but P_{rr} terms are not negligible. The stretch (P_r and P_{rr} terms together) dominate, even in the case of NH_3, where the inversion mode gives significant angle deformation contributions. If we can extrapolate these results to larger molecules, we can say that the bond stretching contributions dominate one-bond isotope shifts, and the anharmonic part of this, which goes with the first shielding derivative $(\partial\sigma/\partial r)_e$, gives the largest contribution. However, the terms involving the second derivative $(\partial^2\sigma/\partial r^2)_e$ are also important. Bond angle contributions are uniformly less important than the bond stretching contributions to the isotope shift.

Table 8 Comparison of Shielding Derivatives Estimated from Isotope Shifts with Those Obtained from Ab Initio Quantum Mechanical Calculations

	$(\partial\sigma/\partial r)_e$ (ppm Å^{-1})	
	Estimated from isotope shifts	Ab initio theoretical
^{15}N in CN^-	−872[47]	−809.8[34]
^{13}C in CN^-	−473[47]	−494.4[34]
^{15}N in NH_3	−124[17]	−123.2[36]
^{15}N in NH_4^+	−65[27]	−67.9[52]
^{31}P in PH_3	−180[15]	−148.83[42]
^{13}C in CH_4	−38[48]	−52.62[53]
^{17}O in H_2O	−294[17]	−270.9[41]
^{77}Se in H_2Se	−1250[49]	−1056.5[46]
^{13}C in CO	−456[12]	−538.1[34]
^{17}O in CO	−1150[12]	−1061.1[34]
^{15}N in N_2	−912[50]	−1011.4[34]
^{11}B in BH_4^-	−26.7[27]	−27.0[52]
^{13}C in CO_2	−214[51]	−156.4[34]
^{15}N in NO_2^-	−990[51]	−1438.1[34]
^{15}N in NO_3^-	−410[51]	−498.0[34]

If we take the experimental isotope shift and use an estimate for the dynamic factor $\langle\Delta r_{XH}\rangle - \langle\Delta r_{XD}\rangle$, we arrive at a reasonable estimate of the shielding derivative $(\partial\sigma/\partial r)_e$ in the molecule. Indeed, Table 8 shows that the estimated shielding derivatives compare reasonably well with the derivatives obtained from the ab initio shielding surfaces.

3.5 Additivity of Isotope Shifts

We can use the isotopomers of the CH_4 molecule to illustrate the additivity of NMR isotope shifts. The mean bond displacements in the methane family $CX_{4-n}Y_n$ (where X,Y = H,D,T) have been calculated using the anharmonic force field of methane.[19] It has been found that the substitution effects on the vibrational contribution to mean bond displacements are strictly additive. Each substitution of a hydrogen by a deuterium shortens the appropriate bond by nearly the same amount Δ. The mean bond displacements in $^{12}CH_{4-n}T_n$ and $^{12}CD_{4-n}T_n$ exhibit the same strictly linear dependence on n. We can express $\langle\Delta r_{CH}\rangle$ and $\langle\Delta r_{CD}\rangle$ in $^{12}CH_{4-n}D_n$ as follows. If we let

$$d = \langle\Delta r_{CH}\rangle \quad \text{in } CH_4 \text{ at } 300\,K \tag{46}$$

Table 7 Isotope Shifts $\sigma^X(XH_n) - \sigma^X(XD_n)$ (in ppm) Calculated for ^{13}C, ^{15}N, ^{31}P, ^{17}O, and ^{77}Se Nuclei

Term	CH_4[43]	NH_3[36]	PH_3[42]	H_2O[44]	H_2Se[a]
P_r	−1.169	−2.05	−2.44	−2.847	−11.66
P_{rr}	0.453	−0.97	−1.68	−1.316	−5.59
$P_\alpha + P_{\alpha\alpha}$	+0.686	+0.66	+0.67	+0.404	+1.25
Other	−0.042	−0.004	0.002	+0.08	neglect
Total	−0.978	−2.36	−3.45	−3.68	−16.0
Experimental	−0.774	−1.87	−2.53	−3.09	−14.04

[a]Calculated by Jameson,[45] based on the points on the ab initio shielding surface of Tossell and Lazzeretti.[46]

$$d - \Delta = \langle \Delta r_{CD} \rangle \quad \text{in } CD_4 \text{ at } 300\,K \tag{47}$$

where d = 2.0881 pm and Δ = 0.553 45 pm, we find for $CH_{4-n}D_n$ that

$$\langle \Delta r_{CD} \rangle = d - \Delta + (4-n)\delta_D \tag{48}$$

$$\langle \Delta r_{CH} \rangle = d + n\delta_H \tag{49}$$

Similar relations can be found for the other series of isotopomers. That is, for a given bond, substitution of an isotope involved in this bond had an effect Δ on its own mean bond length (a primary effect on the mean bond displacement); each substitution of an isotope at some other bond has a much smaller effect δ (a secondary effect). The $^{2/1}$H-induced ^{13}C NMR isotope shift between any two isotopomers of $CH_{4-n}D_n$ can then be expressed as

$$\begin{aligned} \sigma^C(\,CH_{4-n}\,D_n) - \sigma^C(\,CH_{4-n'}\,D_{n'}) &= \left(\frac{\partial\sigma^C}{\partial r}\right)_e \\ &\quad \times[(n'-n)\Delta + \text{ terms in } \delta] \\ &\approx \left(\frac{\partial\sigma^C}{\partial r}\right)_e (n'-n)\Delta \end{aligned} \tag{50}$$

This is the basis for the near-additivity of isotope shifts due to substitution at equivalent sites. If we leave out the terms in δ (which are about two orders of magnitude smaller than Δ), we have strict additivity: the magnitude of the shift is proportional to the number $n' - n$ of atoms that have been substituted by isotopes. Even when all the terms in P_{rr}, P_{rs}, $P_{r\alpha}$, etc. are included and calculated properly, the nearly strict additivity of isotope shifts is preserved. Although there are many smaller changes that are not quite the same as each ^{m}X is replaced by $^{m'}$X, it has been shown that these smaller changes lead to only slight deviations from additivity, which deviations incidentally have been observed[15–18] just as predicted.[19]

4 GENERAL TRENDS IN THE ELECTRONIC FACTORS

We have already seen that the dynamical factors in one-bond isotope shifts are fairly predictable, and can even be estimated without a good force field because the mass-independent part of the dynamic factor is largely determined by the bond length and the rows of the Periodic Table of the pair of bonded atoms. We have also seen that the mass dependence of the isotope shift and its additivity can be explained entirely by the dynamic factors for one-bond isotope shifts. All other trends must therefore be attributable to trends in the electronic factor and the first and second derivatives of the nuclear shielding. If we estimate the dynamic factors $\langle \Delta r \rangle - \langle \Delta r \rangle^*$ as described in Section 3.1, it is possible to obtain the magnitudes and signs of the electronic factor $[(\partial\sigma/\partial r)_e + (1/3a)(\partial^2\sigma/\partial r^2)_e]$, which we shall denote simply by $(\partial\sigma/\partial r)_e$, with the understanding that the first-derivative terms nearly always dominate, although the ratio of the above two terms may range from 10:1 to 3:1.

Some trends in $(\partial\sigma/\partial r)_e$ have been predicted from the observed trends in isotope shifts.[5,6] Recent ab initio calculations have explored the generality of these trends and the limits and conditions of their applicability.[34]

1. $(\partial\sigma/\partial r)_e$ is usually negative. The general shape of the shielding surface shown in Figure 4 seems to be typical for a diatomic molecule, and, for most nuclei, the minimum in the shielding surface occurs at separations larger than the equilibrium internuclear separation, leading to a negative $(\partial\sigma/\partial r)_e$. The exceptional sign of $(\partial\sigma/\partial r)_e$ arises when the minimum in the shielding surface lies inside the equilibrium internuclear separation, as in Figure 5. In polyatomic molecules, negative $(\partial\sigma/\partial r)_e$ are also much more commonly found than positive ones, leading to the usual (negative) sign of the isotope shift.
2. $(\partial\sigma/\partial r)_e$ generally increases with the chemical shift range of the nucleus. We have seen in Figure 6 that changes in the shielding upon displacement away from the equilibrium geometry do scale in analogous compounds according to $\langle a_0^3/r^3 \rangle$ for the free atom, which is the same factor that varies periodically across the Periodic Table in the same way as the ranges of chemical shifts.[54,55] Because of this correlation, an easy way to obtain an estimate of an isotope shift is to use the scaling factor of $\langle a_0^3/r^3 \rangle$ values to provide a Periodic-Table-wide set of 'reduced isotope shifts', which need only be multiplied by the mass factors $[(m' - m)/m']$ $\times (m_A + m)/2m_A$ to get an estimate of the one-bond isotope shift induced by any isotopic substitution for any nucleus in any molecule.[56]
3. $(\partial\sigma/\partial r)_e$ has been found to correlate with the absolute shielding σ_0 in related molecules: at the equilibrium geometry, the most deshielded environments have more steeply changing shielding surfaces. When the dynamic terms are very similar, this forms the basis for the correlations of $^1\Delta$ with chemical shifts, which have been observed in some cases. Such correlations of isotope shifts are more likely to be noticed in diatomic-like situations such as $^{13/12}$C-induced ^{19}F isotope shifts or $^{18/16}$O-induced ^{13}C isotope shifts in O=C situations.[57] Chesnut and Wright have found that calculated shielding derivatives do roughly correlate with shielding itself for ^{19}F and for ^{13}C, ^{15}N, and ^{17}O involved in multiple bonds.
4. The magnitudes of the derivatives of shielding with respect to extension of a bond increase with increasing bond order. Since bond lengths tend to anticorrelate with bond order (higher bond order, shorter bond length), this trend in the shielding derivative is also the basis for the observed increasing magnitudes of one-bond isotope shifts for shorter bond lengths between the NMR nucleus and the substitution site.
5. The shielding derivative tends to be more negative with increasing negative net charge and with the presence of lone pairs on the observed nucleus. This has been found in the comparisons of ^{15}N in NO_2^- and NO_3^-, ^{15}N in NH_3 and NH_4^+, ^{31}P in PH_4^+, PH_3 and PH_2^-, ^{119}Sn in SnH_3^+, SnH_4 and SnH_3^-, and ^{13}C and also ^{15}N in HCN and CN^-.
6. Since the one-bond coupling constant is a purely electronic quantity, it must be the electronic factors in the one-bond isotope shifts that allow the observation of linear correlations with the one-bond coupling constant, and likewise the incremental effects of substitution of H by Ph or H by CH_3 in the examples in Table 9.[10–61] These above data translate to increasingly negative $(\partial\sigma^X/\partial r_{XH})_e$ upon successive Ph substitution at X.

Table 9

	$^1\Delta$ (ppm per D)		$^1\Delta^{13}C(^{2/1}H)$ (ppm per D)
^{15}N in NH_3	−0.623	^{13}C in CH_3D	−0.187
in $PhNH_2$	−0.715	in $PhCH_2D$	−0.2755
^{31}P in PH_3	−0.846	in $(Ph)_2CHD$	−0.342
in $PhPH_2$	−1.21	in $(Ph)_3CD$	−0.4377
^{13}C in CH_4	−0.192	^{13}C in CH_3D	−0.187
in $PhCH_3$	−0.28	in H_3CCH_2D	−0.284
^{77}Se in SeH_2	−7.02	in $(H_3C)_2CHD$	−0.3759
in PhSeH	−7.96	in $(H_3C)_3CD$	−0.4722

5 ISOTOPE SHIFTS OVER TWO OR MORE BONDS

Isotope shifts due to substitution with a heavier atom at a site remote from the observed nucleus show the same general trends as one-bond isotope shifts.

1. The sign is still generally negative, although some are positive, with some alternation of signs being observed in the same molecule.
2. The magnitude reflects the chemical shift range of the observed nucleus.
3. The magnitude is related to the fractional mass change.
4. The effect is additive.

These are generally smaller than one-bond shifts; nevertheless, a large number of them have been observed, some over a distance of seven or more bonds. The question is, what information is contained in these long-range shifts? What we propose to show here is that these long-range shifts are a property of the electronic transmission path from the site of substitution up to the resonant nucleus.

To illustrate the types of terms that contribute to a long-range isotope shift, let us consider a two-bond isotope shift such as $^2\Delta\ ^1H(^{2/1}H)$ in CH_4.[19] The average proton shielding for proton H_1 can be written as

$$\begin{aligned}\langle\sigma^{H_1}\rangle = {} & \sigma_e + P_r\langle\Delta r_1\rangle + P_s(\langle\Delta r_2\rangle + \langle\Delta r_3\rangle + \langle\Delta r_4\rangle) \\ & + \tfrac{1}{2}P_{rr}\langle(\Delta r_1)^2\rangle + \tfrac{1}{2}P_{ss}[\langle(\Delta r_2)^2\rangle + \langle(\Delta r_3)^2\rangle + \langle(\Delta r_4)^2\rangle] \\ & + P_{rs}(\langle\Delta r_1\Delta r_2\rangle + \langle\Delta r_1\Delta r_3\rangle + \langle\Delta r_1\Delta r_4\rangle) \\ & + P_{st}(\langle\Delta r_2\Delta r_3\rangle + \langle\Delta r_2\Delta r_4\rangle + \langle\Delta r_3\Delta r_4\rangle) + \cdots \end{aligned} \tag{51}$$

where

$$P_r \equiv \left(\frac{\partial\sigma^{H_1}}{\partial r_1}\right)_e, \quad P_s \equiv \left(\frac{\partial\sigma^{H_1}}{\partial r_2}\right)_e \tag{52}$$

and P_{rr}, P_{ss}, P_{rs}, and P_{st} are the appropriate second derivatives of the shielding with respect to the various C–H distances. Therefore, the two-bond deuterium-induced proton isotope shifts between CH_3D and CH_4 is (with D replacing proton number 2)

$$\begin{aligned}{}^2\Delta^1\,H(^{2/1}\,H) = {} & \langle\sigma^{H_1}\rangle_{CH_4} - \langle\sigma^{H_1}\rangle_{CH_3D} \\ = {} & (P_r + 2P_s)(\langle\Delta r_1\rangle_{CH_4} - \langle\Delta r_1\rangle_{CH_3D}) \\ & + P_s(\langle\Delta r_2\rangle_{CH_4} - \langle\Delta r_2\rangle_{CH_3D}) \\ & + (\tfrac{1}{2}P_{rr} + P_{ss})[\langle(\Delta r_1)^2\rangle_{CH_4} - \langle(\Delta r_1)^2\rangle_{CH_3D}] \\ & + \tfrac{1}{2}P_{ss}[\langle(\Delta r_2)^2\rangle_{CH_4} - \langle(\Delta r_2)^2\rangle_{CH_3D}] \\ & + (P_{rs} + 2P_{st})(\langle\Delta r_1\Delta r_2\rangle_{CH_4} - \langle\Delta r_1\Delta r_2\rangle_{CH_3D}) \\ & + (2P_{rs} + P_{st})(\langle\Delta r_1\Delta r_3\rangle_{CH_4} - \langle\Delta r_1\Delta r_3\rangle_{CH_3D}) \\ & + \cdots \end{aligned} \tag{53}$$

With D replacing proton number 2, $\delta = \langle\Delta r_i\rangle_{CH_4} - \langle\Delta r_i\rangle_{CH_3D}$ is (the same for i = 1,3,4) a slight change of about 10^{-3} pm in the other C–H average bond lengths due to deuteration, and $\langle\Delta r_2\rangle_{CH_4} - \langle\Delta r_2\rangle_{CH_3D}$ is the typical $\Delta = \langle r_{CH}\rangle - \langle\Delta r_{CD}\rangle$, which is of order about 0.5 pm:

$$\begin{aligned}{}^2\Delta^1\,H(^{2/1}\,H) \approx {} & (P_r + 2P_s)\delta + P_s\Delta + \left(\tfrac{1}{2}P_{rr} + P_{ss}\right)\delta_{rr} + \tfrac{1}{2}P_{ss}\Delta_{rr} \\ & + (P_{rs} + 2P_{st})\Delta_{rs} + (2P_{rs} + P_{st})\delta_{rs} \end{aligned} \tag{54}$$

If we invoke the relationship $\langle\Delta r\rangle \approx \frac{3}{2}ar_e\ \langle(\Delta r)^2\rangle$ used earlier, we find

$$\begin{aligned}{}^2\Delta^1\,H(^{2/1}\,H) \approx {} & \left(P_s + \frac{1}{3a}P_{ss}\right)\Delta + \left(P_r + \frac{1}{3a}P_{rr} + 2P_s + \frac{2}{3a}P_{ss}\right)\delta \\ & + \text{mixed terms} + \text{higher-order terms} \end{aligned} \tag{55}$$

or, more succinctly,

$$\begin{aligned}2\Delta^1\,H(^{2/1}\,H) \approx {} & \mathcal{S}\Delta + (\mathcal{P} + 2\mathcal{S})\delta \\ & + \text{mixed terms} + \text{higher-order terms} \end{aligned} \tag{56}$$

Here $\mathcal{P}$ stands for the following combination of primary first and second derivatives:

$$\mathcal{P} \equiv \left(\frac{\partial\sigma^{H_1}}{\partial r_1}\right)_e + \frac{1}{3a}\left(\frac{\partial^2\sigma^{H_1}}{\partial r_1^2}\right)_e \tag{57}$$

and is a measure of the sensitivity of the shielding of a nucleus to stretching of a bond to it. $\mathcal{S}$ stands for the following combination of secondary first and second derivatives:

$$\mathcal{S} \equiv \left(\frac{\partial\sigma^{H_1}}{\partial r_2}\right)_e + \frac{1}{3a}\left(\frac{\partial^2\sigma^{H_1}}{\partial r_2^2}\right)_e \tag{58}$$

and is a measure of the sensitivity of the shielding of a nucleus to stretching of a remote bond.[19] When we recall that $\Delta \approx 0.5$ pm whereas $\delta \approx 10^{-3}$ pm, we see that the term $\mathcal{S}\Delta$ would dominate the isotope shift unless $\mathcal{P}$ is two orders of magnitude larger than $\mathcal{S}$. It is therefore valid to consider a long-range isotope shift as largely described by a product of a primary change in the average bond length at the heavy atom substitution site (the dynamic factor) and a secondary shielding derivative(s) that measures the change in shielding upon a change with bond length at the remote site. This is very encouraging, because the secondary dynamic factor δ is so dependent on the entire molecular framework and potential energy surface in which vibrations take place that it is difficult to estimate. On the other hand, we have seen that Δ has a very straightforward dependence on r_e and the masses in the local fragment, and can be easily estimated. This means that if the δ terms are unimportant, the sign and magnitude of the long-range isotope shifts are a direct measure of the sign and

magnitude of $(\partial\sigma/\partial r_{\text{remote}})_e$. This derivative is stereospecific, dependent on electron-withdrawing/donating abilities of substituents, and has the usual electronic-transmission-path dependence of various observables such as long-range spin–spin coupling and substituent effects on chemical shifts. Thus, in $^{13}CH_3(CH_2)_{n-2}NHD$, for example,

$$ {}^{n}\Delta\,{}^{13}\mathrm{C}(^{2/1}\mathrm{H}) \approx \left[\left(\frac{\partial\sigma^{\mathrm{C}}}{\partial r_{\mathrm{NH}}}\right)_e + \frac{1}{3a}\left(\frac{\partial^2\sigma^{\mathrm{C}}}{\partial r_{\mathrm{NH}}^2}\right)_e\right] \times(\langle\Delta r_{\mathrm{NH}}\rangle - \langle\Delta r_{\mathrm{ND}}\rangle) \tag{59} $$

it is easy to see why *n*-bond isotope shifts are in general smaller than one-bond isotope shifts. The farther away the substitution site is from the observed nucleus, the smaller the secondary derivative is expected to be. For example, in the H_2O molecule,[41]

$$ \left(\frac{\partial\sigma^{\mathrm{H}_1}}{\partial r_{\mathrm{OH}_1}}\right)_e = -0.353 \text{ ppm pm}^{-1} $$
$$ \left(\frac{\partial\sigma^{\mathrm{H}_1}}{\partial r_{\mathrm{OH}_2}}\right)_e = -0.046 \text{ ppm pm}^{-1} \tag{60} $$

that is, a trace along the increasing coordinate r_{OH_1} gives a sharply decreasing H_1 shielding surface near the equilibrium geometry, but a trace along the coordinate r_{OH_2} on the same shielding surface is rather flat. Also, the nearly flat portion of the shielding surface could be sloping slightly in either direction; thus, either sign is possible for long-range isotope shifts. The secondary derivatives should still reflect the shielding sensitivity of various nuclei as manifested in the ranges of their chemical shifts.

The experimental evidence for the dominance of the term $\mathcal{S}\Delta$ is convincing.

1. The observed additivity of long-range isotope shifts is completely consistent with this. Isotope shifts from equivalent substitution sites such as a remote CH_3 group involve the secondary derivative multiplied by one Δ term for each C–D replacing a C–H.
2. The mass dependence of the two-bond isotope shift is the same as that of the one-bond shift, that is, $1\text{-}(\mu/\mu^*)^{1/2}$, where μ and μ^* are the local reduced masses *at the substitution site*. Furthermore, the ratio of the effects of substitution of H by T to that of H by D is the same as would be expected if the Δ term dominated the isotope shift. Vibrational calculations show that[48]

$$ \frac{\langle\Delta r_{\mathrm{CH}}\rangle_{\mathrm{CH_4}} - \langle\Delta r_{\mathrm{CT}}\rangle_{\mathrm{CT_4}}}{\langle\Delta r_{\mathrm{CH}}\rangle_{\mathrm{CH_4}} - \langle\Delta r_{\mathrm{CD}}\rangle_{\mathrm{CD_4}}} = 1.426 \tag{61} $$

   In $(CH_3)_2C{=}O$, the observed ratio of isotope shifts for tritium and deuterium substitution is[11]

$$ \frac{{}^{1}\Delta\,{}^{13}\mathrm{C}(^{3/1}\mathrm{H})}{{}^{1}\Delta\,{}^{13}\mathrm{C}(^{2/1}\mathrm{H})} = 1.424 \pm 0.025 \tag{62} $$

   That this ratio is indistinguishable from 1.426 serves to reassure us that the leading term is dominant in one-bond shifts, with $(\partial\sigma/\partial r)_e$ $(\langle\Delta r_{\mathrm{CH}}\rangle - \langle\Delta r_{\mathrm{CD}}\rangle)$ for deuterium substitution and $(\partial\sigma/\partial r)_e$ $(\langle\Delta r_{\mathrm{CH}}\rangle - \langle\Delta r_{\mathrm{CT}}\rangle)$ for tritium substitution. The two-bond isotope shifts have also been observed in $CH_3{}^{13}C(O)CH_3$, and these have the ratio[11]

$$ \frac{{}^{2}\Delta\,{}^{13}\mathrm{C}(^{3/1}\mathrm{H})}{{}^{2}\Delta\,{}^{13}\mathrm{C}(^{2/1}\mathrm{H})} = 1.41 \pm 0.12 \tag{63} $$

   This ratio is also indistinguishable from 1.426, which indicates that the dominant contribution is $(\partial\sigma^{\mathrm{C(O)}}/\partial r_{\mathrm{CH}})_e \times (\langle\Delta r_{\mathrm{CH}}\rangle - \langle\Delta r_{\mathrm{CT}}\rangle)$ for tritium substitution and $(\partial\sigma^{\mathrm{C(O)}}/\partial r_{\mathrm{CH}})_e(\langle\Delta r_{\mathrm{CH}}\rangle - \langle\Delta r_{\mathrm{CD}}\rangle)$ for deuterium substitution.
3. The relative signs of one-bond and *n*-bond isotope shifts for the same nucleus in the same molecule are not always the same. Consider, for example, the carbonyl carbon isotope shifts in $(CH_3)_2$ $^{13}C{=}O$. The $^{1}\Delta$ $^{13}C(^{18/16}O)$ and $^{2}\Delta$ $^{13}C(^{2/1}H)$ are opposite signs. Thus, the important term in $^{2}\Delta$ $^{13}C(^{2/1}H)$ must not involve $(\partial\sigma^{\mathrm{C(O)}}/\partial r_{\mathrm{CO}})_e$ δ.
4. The long-range isotope shifts correlate with indicators of electronic transmission paths such as dihedral angle dependence of three-bond isotope shifts (similar to the Karplus relation for three-bond coupling constants, although not with one set of coefficients), stereospecificity (*cis* versus *trans* versus *gauche*, and *syn* versus *anti*) of isotope shifts parallels that of spin–spin coupling, and the correlation of long-range isotope shifts with electron-withdrawing/donating ability of substituents, even across a path traversing seven bonds. These correlations of long-range isotope shifts with purely electronic quantities can only be observed if the isotope shift is itself dominated by an electronic factor that depends on the transmission of electronic information between the observed nucleus and the mass-modified site: a fortunate occurrence, since the long-range electronic factor is far more interesting and useful than the long-range dynamic factor. Since the primary dynamic factor Δ is easily estimated, long-range isotope shifts can provide direct invaluable information about the changes in shielding of a nucleus upon a minor perturbation at a distant site.

In summary, the electronic factor $(\partial\sigma^{\mathrm{A}}/\partial r_{\mathrm{XY}})_e$ in the long-range isotope shifts is found to have the following attributes.

1. The magnitude decreases (usually) as the Y–X bond becomes more remote from nucleus A. Ab initio calculations have shown that for the first- and second-row hydrides XH_n, the ratio $(\partial\sigma^{\mathrm{H}_1}/\partial r_2)_e/(\partial\sigma^{\mathrm{H}_1}/\partial r_1)_e = 0.06\text{–}0.14$. However, the two-bond secondary derivative is not necessarily much smaller than primary derivatives, especially when multiple bonds are involved.[34]
2. It is stereospecific. For three-bond isotope shifts, it is found that *cis*, *trans* > *gauche*, and in some cases the dihedral angle dependence has been clearly observed and it is not unlike the Karplus relation of three-bond spin–spin coupling with angle ϕ. This stereospecificity is purely electronic in nature.
3. It correlates with other purely electronic quantities that are dependent on the same electronic transmission path, such as substituent effects on chemical shifts by electron-withdrawing or -donating groups. The electronic transmission path is most easily explored by the isotope shift, because substitution of an atom by a heavier one leads to the fewest complications compared with other methods of investigation such as replacement by atoms or groups of different electronegativity or size.

6 ISOTOPE EFFECTS ON SPIN–SPIN COUPLING

The indirect spin–spin coupling constant J is a useful index of the chemical bond, and isotope effects on it provide

information about the sensitivity of J to bond extension. Since the isotope effects on the isotropic average J can be determined more precisely than the individual J tensor components or the anisotropy, the isotope effects can be considered as *the* major source of experimental information for assessing the quality of ab initio theoretical calculations of indirect spin–spin coupling.

The working definitions of the isotope effects on J are as follows.[4] $\Delta_s\, {}^nJ(\mathrm{AB})[{}^{m'/m}\mathrm{X}]$ is the *secondary* isotope effect on the n-bond coupling constant between nuclei A and B due to the substitution of ${}^m\mathrm{X}$ by the heavier isotope ${}^{m'}\mathrm{X}$ somewhere in the molecule:

$$\Delta_s\, {}^nJ(\mathrm{AB})[{}^{m'/m}\mathrm{X}] = |{}^nJ(\mathrm{AB})|^* - |{}^nJ(\mathrm{AB})| \tag{64}$$

$\Delta_p\, {}^nJ(\mathrm{A}^{2/1}\mathrm{H})$ is the *primary* isotope effect on the coupling constant between nuclei A and H due to the substitution of H by D, the coupled nuclei being separated by n bonds:

$$\Delta_p\, {}^nJ(\mathrm{A}^{2/1}\mathrm{H}) = |{}^nJ(\mathrm{AD})|^* \frac{\gamma_\mathrm{H}}{\gamma_\mathrm{D}} - |{}^nJ(\mathrm{AH})| \tag{65}$$

where $\gamma_\mathrm{H}/\gamma_\mathrm{D} = 6.514\,398\,04(120)$. Of course, if we instead use the purely electronic quantities, namely, the reduced coupling constants

$${}^nK(\mathrm{AH}) \equiv 4\pi^2 \frac{{}^nJ(\mathrm{AH})}{h\gamma_\mathrm{A}\gamma_\mathrm{H}} \tag{66}$$

usually expressed in reduced units of $10^{19}\,\mathrm{J^{-1}\,T^2}$, then the primary isotope effect is simply a difference:

$$\Delta_p\, {}^nK(\,{}^{2/1}\mathrm{H}) = |{}^nK(\mathrm{AD})|^* - |{}^nK(\mathrm{AH})| \tag{67}$$

Only the absolute values are compared, for practical reasons, since the absolute signs of spin–spin coupling constants are not always known. As in isotope shifts, the asterisk * denotes the heavier isotopomer. Where both secondary and primary isotope effects are observed, the primary isotope effect should be obtained from, for example, $J(\mathrm{SnD})$ in SnH_2D^- and $J(\mathrm{SnH})$ in SnH_3^-, rather than $J(\mathrm{SnD})$ and $J(\mathrm{SnH})$ in the same isotopomer SnH_2D^-. The latter difference includes both primary and secondary isotope effects.

Isotope effects on nuclear shielding are usually visually obvious in a high-resolution NMR spectrum, since the peaks of the isotopomer are shifted from the parent species. On the other hand, isotope effects on coupling constants are only observed as very slightly different multiplet splittings for each isotopomer (secondary isotope effects) or as a slightly smaller (usually) or larger $J(\mathrm{AD})$ than that expected from $J(\mathrm{AH})/6.514\,398\,04$ (primary isotope effects). Because of this factor of $6.514\ldots$, the isotope effects on J are less precisely determined than the isotope effects on shielding. According to these working definitions, a positive isotope effect on J means that the reduced coupling is larger in the deuterated species.

6.1 Observed General Trends in Isotope Effects on J

The general trends and their theoretical explanation have been presented by Jameson and Osten.[4]

1. The sign of the primary or secondary isotope effect on the coupling constant is not directly related to the absolute sign of the coupling constant. Whether it is related to the absolute sign of the reduced coupling constant is not yet established, since one-bond coupling isotope effects are presently available for positive reduced coupling constants only.
2. Primary isotope effects are negative or positive, the positive signs being found only in molecules involving one or more lone pairs of the coupled nuclei. For example, primary isotope effects are positive in H_2Se, in PH_3, and in other 3-coordinate phosphorus, but negative in PH_4^+ and in 4- and 5-coordinate phosphorus. It is positive in SnH_3^- (one lone pair) and negative in SnH_4 and SnH_3^+ (no lone pairs).
3. Secondary isotope effects can have either sign, but are often negative. Positive signs have been observed where triple bonds are involved (as in HC≡CH and HC≡N), but also in some of the same systems with positive primary isotope effects.
4. Secondary isotope effects are roughly additive upon substitution of several equivalent sites neighboring the coupled nuclei. For example, in the NH_4^+ ion, each D substitution decreases ${}^1J({}^{14}\mathrm{NH})$ by $0.05 \pm 0.02\,\mathrm{Hz}$, and in PH_3, each D substitution decreases ${}^1J(\mathrm{PH})$ by $2.5\,\mathrm{Hz}$. Small deviations from additivity have been observed.
5. The magnitudes of isotope effects are small, the largest primary effect being about 10% of the coupling constant in SnH_3^-, so that only the effects of deuterium (and tritium) substitution, where the largest fractional changes in mass are involved, have been observed. Some of the larger primary isotope effects are $+11.5\,\mathrm{Hz}$ for $\Delta_p\, {}^1J(\mathrm{PH})$ in PH_3 and $+10.5\,\mathrm{Hz}$ in SnH_3^-. Secondary isotope effects as large as $-2.0\,\mathrm{Hz}$ per D [for ${}^1J(\mathrm{SiF})$] and $+3.0\,\mathrm{Hz}$ per D [for ${}^1J(\mathrm{SnH})$] have been observed.
6. The magnitudes of the isotope effects are roughly proportional to the fractional change in mass, in the very few instances where effects of isotopic substitution of ${}^1\mathrm{H}$ by ${}^2\mathrm{H}$ and ${}^3\mathrm{H}$ have been reported.

6.2 Rovibrational Averaging of J, the Leading Terms

Just as in isotope shifts, the isotope effect on J can be written in terms of products of electronic and dynamic factors as follows.[6] For a diatomic molecule,

$$\langle J\rangle^* - \langle J\rangle = \left(\frac{\partial J}{\partial r}\right)_\mathrm{e} (\langle \Delta r\rangle^* - \langle \Delta r\rangle) + \frac{1}{2}\left(\frac{\partial^2 J}{\partial r^2}\right)_\mathrm{e} [\langle (\Delta r)^2\rangle^* - \langle (\Delta r)^2\rangle] + \ldots \tag{68}$$

The dynamic factors are the same as we have already discussed (and, indeed, the same for all rovibrational averaging of any molecular electronic properties). Only the electronic factors need be discussed here. Of course, γ of some nuclei are negative, so we really should compare derivatives of the reduced coupling such as $(\partial K/\partial r)_\mathrm{e}$, etc., where

$$\left(\frac{\partial J}{\partial r}\right)_\mathrm{e} = \frac{h\gamma_\mathrm{N}\gamma_{\mathrm{N}'}}{4\pi^2}\left(\frac{\partial K}{\partial r}\right)_\mathrm{e} \tag{69}$$

One important difference between J and σ is that the latter is a one-center property whereas the former is a two-center

Table 10

	Experimental[15]		Calculated	
	K(SnH) (reduced units)	K(SnD) (reduced units)	K(SnH) (reduced units)	K(SnD) (reduced units)
SnH_3^-	24.09 ± 0.01		24.09	
SnH_2D^-	24.76 ± 0.02	27.09 ± 0.14	24.76	27.08
$SnHD_2^-$	25.40 ± 0.03	27.72 ± 0.22	25.43	27.75
SnD_3^-		28.53 ± 0.43		28.42

property. In polyatomic molecules, there are usually several electronic factors of comparable size that contribute to the isotope effects on J. For polyatomic molecules, if ^1J is most sensitive to the bond length, the one-bond shifts can also be written in the same way as for diatomic molecules, with the terms such as $(\partial J/\partial\alpha)_e(\langle\Delta\alpha\rangle^* - \langle\Delta\alpha\rangle) + \ldots$ being less important. ^2J and ^3J, on the other hand, are very sensitive to bond and torsion angles.[62]

Let us consider SnH_4 as an example rather than CH_4, since fairly large isotope effects on SnH coupling have been observed. The types of terms that contribute to the vibrationally averaged spin–spin coupling are the same as those that contribute to the proton shielding in CH_4 as given in equation (51):

$$\langle K(\mathrm{SnH_1})\rangle = K_e + P_r\langle\Delta r_1\rangle + P_s(\langle\Delta r_2\rangle + \langle\Delta r_3\rangle + \langle\Delta r_4\rangle) + \text{terms in } P_{rr}, P_{ss}, P_{rs}, P_{st}, P_\alpha, \text{ etc.} \quad \ldots \tag{70}$$

where the primary derivative is $P_r \equiv (\partial K(\mathrm{SnH_1})/\partial r_{\mathrm{SnH_1}})_e$ and the secondary derivative is $P_s \equiv (\partial K(\mathrm{SnH_1})/\partial r_{\mathrm{SnH_2}})_e$. If we let $d \equiv \langle\Delta r_{\mathrm{SnH}}\rangle$ in SnH_4 and $d - \Delta \equiv \langle\Delta r_{\mathrm{SnD}}\rangle$ in SnD_4 then $d \approx 1.780$ pm and $\Delta \approx 0.5161$ pm can be obtained for $r_e = 170$ pm using the method described in Section 3.1. K_e is the reduced coupling constant at the equilibrium molecular geometry. The leading terms are[6]

$$\mathrm{SnH_4}: \quad \langle K(\mathrm{SnH})\rangle = K_e + (P_r + 3P_s)d + \ldots \tag{71}$$

$$\mathrm{SnH_3D}: \quad \langle K(\mathrm{SnH})\rangle = K_e + (P_r + 2P_s)d + P_s(d - \Delta) + \ldots \tag{72}$$

$$\langle K(\mathrm{SnD})\rangle = K_e + P_r(d - \Delta) + 3P_s d + \ldots \tag{73}$$

$$\mathrm{SnH_2D_2}: \quad \langle K(\mathrm{SnH})\rangle = K_e + (P_r + P_s)d + 2P_s(d - \Delta) + \ldots \tag{74}$$

$$\langle K(\mathrm{SnD})\rangle = K_e + (P_r + P_s)(d - \Delta) + 2P_s d + \ldots \tag{75}$$

$$\mathrm{SnHD_3}: \quad \langle K(\mathrm{SnH})\rangle = K_e + P_r d + 3P_s(d - \Delta) + \ldots \tag{76}$$

$$\langle K(\mathrm{SnD})\rangle = K_e + (P_r + 2P_s)(d - \Delta) + P_s d + \ldots \tag{77}$$

$$\mathrm{SnD_4}: \quad \langle K(\mathrm{SnH})\rangle = K_e + (P_r + 3P_s)(d - \Delta) + \ldots \tag{78}$$

From the above, we see that the primary isotope effect, the difference[63]

$$\Delta_p{}^1K(\mathrm{Sn}^{2/1}\mathrm{H}) = |^1K(\mathrm{SnD})|^*_{\mathrm{SnH_3D}} - |^1K(\mathrm{SnH})|_{\mathrm{SnH_4}} = (428.21 \pm 0.14) - (429.19 \pm 0.02) \approx -P_r\Delta \tag{79}$$

leads to $P_r \approx 1.90$ reduced units pm^{-1}. The primary isotope effect may also be taken from any of the differences $|^1K(\mathrm{SnD})|_{\mathrm{SnH_2}D_2} - |^1K(\mathrm{SnH})|_{\mathrm{SnH_3D}}$ or $|^1K(\mathrm{SnD})|_{\mathrm{SnHD_3}} - |^1K(\mathrm{SnH})|_{\mathrm{SnH_2D_2}}$ or $|^1K(\mathrm{SnD})|_{\mathrm{SnD_4}} - |^1K(\mathrm{SnH})|_{\mathrm{SnHD_3}}$, leading to an average value $P_r = (\partial K(\mathrm{SnH_1})/\partial r_{\mathrm{SnH_1}})_e \approx 2.00$ reduced units pm^{-1}. Note that at this level of approximation, only the primary derivative P_r is involved in the primary isotope effect.

At the same time, the difference

$$\Delta_s{}^1K(\mathrm{SnH})[^{1/2}\mathrm{H}] = |K(\mathrm{SnH})|^*_{\mathrm{SnH_3D}} - |K(\mathrm{SnH})|_{\mathrm{SnH_4}} = (428.81 \pm 0.02) - (429.19 \pm 0.02) \approx -P_s\Delta \tag{80}$$

leads to $P_s \approx 0.74$ reduced units pm^{-1}. Since this secondary isotope effect may be taken from three other differences such as $|^1K(\mathrm{SnH})|_{\mathrm{SnH_2D_2}} - |^1K(\mathrm{SnH})|_{\mathrm{SnH_3D}}$, etc., we get an average value $P_s = (\partial K(\mathrm{SnH_1})/\partial r_{\mathrm{SnH_2}})_e \approx 0.75$ reduced units pm^{-1} and $K_e = 421.63$ reduced units. The primary isotope effect involves largely the primary derivative of the coupling constant, and the secondary isotope effect on the coupling involves largely the (secondary) derivative of the coupling constant with respect to stretching a remote bond.

We can do the same analysis for the isotopomers of SnH_3^-, and we find that the values $P_r = -5.80$ reduced units pm^{-1}, $P_s = -1.30$ reduced units pm^{-1}, and $K_e = 39.04$ reduced units reproduce the experimental values reasonably well, as seen in Table 10.

The agreement with the six experimental numbers is very good. These quantities can be translated back to Hz pm^{-1} as in Table 11.

It is interesting that, although the magnitude of the SnH coupling constant is about one order of magnitude smaller in SnH_3^- than in SnH_4, the sensitivity of the spin–spin coupling to bond extension is almost three times as great. The lone pair is generally known to be responsible for negative contributions to the reduced coupling, leading to a much smaller magnitude of the spin–spin coupling. Apparently, it is also the lone pair (on Sn in SnH_3^-) that is responsible for the greater sensitivity to bond extension. By similar procedures, the changes in the reduced coupling constant with extension of the bond, $(\partial K/\partial r)_e$, or of an adjacent bond, $(\partial K/\partial r')_e$, can be estimated in other systems such as SnH_3^+, PH_4^+, PH_3, PH_2^-, and SeH_2 from experimental values of J(AH) and

Table 11

	SnH_4	SnH_3^-
$(\partial J(\mathrm{SnH})/\partial r)_e$ (Hz pm^{-1})	−9.00	+26.00
$(\partial J(\mathrm{SnH})/\partial r')_e$ (Hz pm^{-1})	−3.40	+5.80
$\langle J(\mathrm{SnH})\rangle - J_e$ (Hz)	−34.1	+67.3
J_e (Hz)	−1899.3	−175.8

Table 12 Derivatives of the Reduced Spin–Spin Coupling Constant with Respect to Extension of the Bond Between the Coupled Nuclei (r) and With Respect to Extension of the Other Bond (r')[6]

	Empirical		Theoretical	
Molecule	$(\partial K/\partial r)_e$ (reduced units pm^{-1})	$(\partial K/\partial r')_e$ (reduced units pm^{-1})	$(\partial K/\partial r)_e$ (reduced units pm^{-1})	$(\partial K/\partial r')_e$ (reduced units pm^{-1})
Without lone pairs:				
HD			+1.4979	
CH_4			+0.973 24	+0.5884
PH_4^+	+1.04 ± 0.20	+0.075 ± 0.02		
SnH_4	+2.00 ± 0.30	+0.75 ± 0.07		
SnH_3^+	+6.00 ± 4.00	≈0		
With lone pairs:				
$^{13}C^{17}O$			negative	
$^{14}N^{15}N$			negative	
HF			−0.5156	
PH_3	−4.22	+0.465		
PH_2^-	−1.25	−0.26		
SeH_2	−1.90 ± 0.60	−0.71 ± 0.09		
SnH_3^-	−5.80 ± 0.40	−1.30 ± 0.10		

J(AD) combined with values of the dynamic factor calculated by the methods described in Section 3.1. These values are compared with some published theoretical values in Table 12. Since all are expressed as γ-free reduced coupling constants, these are purely electronic quantities, which can be directly compared with each other in sign and magnitude. Theory has shown that the Fermi contact term is most sensitive to bond stretch.[64,65] Thus, it is not surprising that the magnitudes of the empirical derivatives in Table 12 increase with increasing spin density at the nucleus, just as the reduced coupling constants are known to do. The secondary derivative is generally smaller than the primary derivative, and both usually have the same sign. The earlier prediction by Jameson and Osten[4] that $(\partial K(\mathrm{AH})/\partial r)_e$ will generally be negative when A has lone pairs but will be positive otherwise appears to be correct.

In summary, the electronic factor in the one-bond coupling constant $(\partial K(\mathrm{AH})/\partial r_{\mathrm{AH}})_e$ has been found to have the following attributes that explain the observed trends.

1. For A without lone pairs, it is positive; that is, the magnitude of the coupling increases as the bond becomes stretched.
2. It is largely dominated by the Fermi contact term, which is very sensitive to the distance between the two nuclei, much more so than the spin–dipolar and orbital contributions to coupling.
3. Probably because of the dominance of the Fermi contact term, it is larger for nucleus A having larger atomic number.
4. For A with lone pairs, this electronic factor is negative. It is known that lone pairs make negative contributions to the spin–spin coupling. The sign of this electronic factor confirms that the lone pair contributions are very sensitive to bond extension.
5. The secondary electronic factor $(\partial K(\mathrm{AH})/\partial r_{\mathrm{AX}})_e$ is generally 2–5 times smaller than the primary electronic factor, and is a measure of the sensitivity of the coupling across one bond to the lengthening of another bond involving one of the coupled atoms.

In summary, the dynamic factors and electronic factors in isotope effects on NMR parameters have been characterized. The theoretical model is general for any molecular electronic property.[26] The effects can be completely understood within the context of the Born–Oppenheimer approximation. Complete calculations can be carried out for individual molecules within this theoretical framework. Where such calculations have been carried out, the agreement with experiment is good. Under conditions where the leading terms are dominant, the molecule-specific higher order terms can be neglected so as to find explanations for and make predictions of the sweeping generalities that have surfaced empirically in isotope effects on NMR parameters. The dynamic factor that has been derived by assuming dominance of the bond stretching successfully predicted the mass dependence of the isotope effects observed later. The empirical electronic factors deduced from this model are found to be consistent (in sign, in magnitude, and in correlations with various quantities such as net charge, presence or absence of lone pairs, bond order, etc.) with the theoretical electronic factors obtained by ab initio calculations.

7 RELATED ARTICLES

Chemical Shift Scales on an Absolute Basis; Gas Phase Studies of Intermolecular Interactions and Relaxation.

8 REFERENCES

1. H. Batiz-Hernandez and R. A. Bernheim, in *Progress in Nuclear Magnetic Resonance Spectroscopy*, eds. J. W. Emsley, J. Feeney, and L. H. Sutcliffe, Pergamon Press, Oxford, 1967, Vol. 3, p. 63
2. P. E. Hansen, in *Annual Reports on NMR Spectroscopy*, ed. G. A. Webb, Academic Press, London, 1983, Vol. 15, p. 105.
3. P. E. Hansen, in *Progress in Nuclear Magnetic Resonance Spectroscopy*, eds. J. W. Emsley, J. Feeney, and L. H. Sutcliffe, Pergamon Press, Oxford, 1988, Vol. 20, p. 207.
4. C. J. Jameson and H. J. Osten, *J. Am. Chem. Soc.*, 1986, **108**, 2497.
5. C. J. Jameson and H. J. Osten, in *Annual Reports on NMR Spectroscopy*, ed. G. A. Webb, Academic Press, London, 1986, Vol. 17, p. 1.

6. C. J. Jameson, in *Isotopes in the Physical and Biomedical Sciences*, eds. E. Buncel and J. R. Jones, Elsevier, Amsterdam, 1991, Vol. 2, p. 1.
7. W. Gombler, *J. Am. Chem. Soc.*, 1982, **104**, 6616.
8. C. J. Jameson, *J. Chem. Phys.*, 1977, **66**, 4983.
9. R. Maple, J. E. Carson, and A. Allerhand, *J. Am. Chem. Soc.*, 1989, **111**, 7293.
10. J. R. Wesener, D. Moskau, and H. Gunther, *J. Am. Chem. Soc.*, 1985, **107**, 7307.
11. C. H. Arrowsmith, L. Baltzer, A. J. Kresge, M. F. Powell, and Y. S. Tang, *J. Am. Chem. Soc.*, 1986, **108**, 1356.
12. R. E. Wasylishen, J. O. Friedrich, S. Mooibroek, and J. B. Macdonald, *J. Chem. Phys.*, 1985, **83**, 548.
13. C. J. Jameson, A. K. Jameson, and D. Oppusunggu, *J. Chem. Phys.*, 1986, **85**, 5480.
14. M. Hoch and D. Rehder, *Inorg. Chim. Acta*, 1986, **111**, L13.
15. R. E. Wasylishen and N. Burford, *Can. J. Chem.*, 1987, **65**, 2707.
16. A. K. Jameson and C. J. Jameson, *J. Magn. Reson.*, 1978, **32**, 455.
17. R. E. Wasylishen and J. O. Friedrich, *Can. J. Chem.*, 1987, **65**, 2238.
18. B. Bennett and W. T. Raynes, *Spectrochim. Acta A*, 1989, **45**, 1267.
19. C. J. Jameson and H. J. Osten, *J. Chem. Phys.*, 1984, **81**, 4293.
20. N. F. Ramsey, *Phys. Rev.*, 1952, **87**, 1075.
21. C. J. Jameson, *J. Chem. Phys.*, 1977, **66**, 4977.
22. C. J. Jameson, A. K. Jameson, and S. M. Cohen, *J. Chem. Phys.*, 1977, **67**, 2771.
23. A. K. Jameson, K. Schuett, C. J. Jameson, S. M. Cohen, and H. Parker, *J. Chem. Phys.*, 1977, **67**, 2821.
24. C. J. Jameson, *Bull. Magn. Reson.*, 1980, **3**, 3.
25. C. J. Jameson, *Chem. Rev.*, 1991, **91**, 1375.
26. C. J. Jameson, in *Theoretical Models of Chemical Bonding*, ed. Z. B. Maksic, Springer-Verlag, Berlin, 1991, Part 3, p. 457.
27. C. J. Jameson and H. J. Osten, *J. Chem. Phys.*, 1984, **81**, 4300.
28. C. J. Jameson and A. K. Jameson, *J. Chem. Phys.*, 1986, **85**, 5484.
29. D. R. Herschbach and V. W. Laurie, *J. Chem. Phys.*, 1961, **35**, 458.
30. R. A. Hegstrom, *Phys. Rev. A*, 1979, **19**, 17.
31. C. J. Jameson and A. C. de Dios, *J. Chem. Phys.*, 1993, **98**, 2208.
32. R. Ditchfield, *Chem. Phys.*, 1981, **63**, 185.
33. D. B. Chesnut and C. K. Foley, *J. Chem. Phys.*, 1986, **84**, 852.
34. D. B. Chesnut and D. W. Wright, *J. Comput. Chem.*, 1991, **12**, 546.
35. A. C. de Dios and C. J. Jameson, in *Annual Reports on NMR Spectroscopy*, ed. G. A. Webb, Academic Press, London, 1994, vol. 29, p. 1.
36. C. J. Jameson, A. C. de Dios, and A. K. Jameson, *J. Chem. Phys.*, 1991, **95**, 1069.
37. G. Riley, W. T. Raynes, and P. W. Fowler, *Mol. Phys.*, 1979, **38**, 877.
38. A. R. Hoy, I. M. Mills, and G. Strey, *Mol. Phys.*, 1972, **24**, 1265.
39. M. Toyama, T. Oka, and Y. Morino, *J. Mol. Spectrosc.*, 1964, **13**, 193.
40. W. T. Raynes, P. W. Fowler, P. Lazzeretti, R. Zanasi, and M. Grayson, *Mol. Phys.*, 1988, **64**, 143.
41. P. W. Fowler, G. Riley, and W. T. Raynes, *Mol. Phys.*, 1981, **42**, 1463.
42. C. J. Jameson, A. C. de Dios, and A. K. Jameson, *J. Chem. Phys.*, 1991, **95**, 9042.
43. W. T. Raynes, *Mol. Phys.*, 1988, **63**, 719.
44. P. W. Fowler and W. T. Raynes, *Mol. Phys.*, 1981, **43**, 65.
45. C. J. Jameson, in *Specialist Periodical Reports on NMR*, ed. G. A. Webb, Royal Society of Chemistry, London, 1989, Vol. 19, p. 1.
46. J. A. Tossell and P. Lazzeretti, *J. Magn. Reson.*, 1988, **80**, 39.
47. R. E. Wasylishen, *Can. J. Chem.*, 1982, **60**, 2194.
48. H. J. Osten and C. J. Jameson, *J. Chem. Phys.*, 1985, **81**, 4288.
49. H. J. Osten and C. J. Jameson, *J. Chem. Phys.*, 1985, **82**, 4595.
50. J. O. Friedrich and R. E. Wasylishen, *J. Chem. Phys.*, 1985, **83**, 3707.
51. C. J. Jameson and H. J. Osten, *J. Chem. Phys.*, 1984, **81**, 2556.
52. D. B. Chesnut, *Chem. Phys.*, 1986, **110**, 415.
53. P. Lazzeretti, R. Zanasi, A. J. Sadlej, and W. T. Raynes, *Mol. Phys.*, 1987, **62**, 605.
54. C. J. Jameson and H. S. Gutowsky, *J. Chem. Phys.*, 1964, **40**, 1714.
55. C. J. Jameson and J. Mason, in *Multinuclear Nuclear Magnetic Resonance*, ed. J. Mason, Plenum Press, London, 1987, p. 51.
56. C. J. Jameson and H. J. Osten, *J. Am. Chem. Soc.*, 1985, **107**, 4158.
57. C. J. Jameson, *Mol. Phys.*, 1985, **54**, 73.
58. A. A. Borisenko, N. M. Sergeyev, and Y. A. Ustynyuk, *Mol. Phys.*, 1971, **22**, 715.
59. M. Alei and W. E. Wageman, *J. Chem. Phys.*, 1978, **68**, 783.
60. T. Schaefer, J. Peeling, and R. Sebastian, *Can. J. Phys.*, 1987, **65**, 534.
61. H. J. Jakobsen, A. J. Zozulin, P. D. Ellis, and J. D. Odom, *J. Magn. Reson.*, 1980, **38**, 219.
62. W. T. Raynes, J. Geertsen, and J. Oddershede, *Chem. Phys. Lett.*, 1992, **197**, 516.
63. K. L. Leighton and R. E. Wasylishen, *Can. J. Chem.*, 1987, **65**, 1469.
64. J. Oddershede, J. Geertsen, and G. Scuseria, *J. Phys. Chem.*, 1988, **92**, 3056.
65. J. Geertsen, J. Oddershede, and G. E. Scuseria, *J. Chem. Phys.*, 1987, **87**, 2138.

Biographical Sketch

Cynthia J. Jameson. *b* 1937. B.S., University of the Philipines; Ph.D., 1963, University of Illinois at Urbana-Champaign. Introduced to NMR by Herb Gutowsky. Faculty in Chemistry, University of Illinois at Chicago, 1968–present. Approx. 130 publications. Research interests include theoretical and experimental studies of the chemical shift in simple systems in the gas phase and in molecules absorbed in microporous solids, with particular emphasis on intramolecular and intermolecular shielding surfaces and averages therein; also, spin relaxation in gases and their connection with the anisotropy of intermolecular potentials and molecular dynamics.

Quantum Exchange

Kurt W. Zilm
Yale University, New Haven, CT, USA

1	Introduction	1
2	Experimental Observations	1
3	Theory	1
4	Examples	7
5	Summary	8
6	References	9

1 INTRODUCTION

By the late 1950s, all of the physics important to high-resolution solution NMR seemed to have been identified. The basic interactions of chemical shift and scalar or J couplings, as well as the dynamics leading to spin relaxation and chemical exchange, were understood—at least in principle. It seemed that all of the relevant terms in the Hamiltonian that applied to NMR in isotropic solutions were known. Advances in NMR theory focused on the details of dealing with complex spin systems and their manipulation by pulse trains, or how the spins reflected molecular dynamics, as exemplified in this Encyclopedia. This article deals with the recent recognition of an additional term in the solution NMR Hamiltonian, namely, that for nuclear–nuclear exchange coupling, and the dramatic effects it can have on solution NMR spectra. The purpose is to provide the reader with as intuitive and physical a picture of this purely quantum mechanical effect as possible. More rigorous treatments of the details of the underlying physics may be found in the references.

2 EXPERIMENTAL OBSERVATIONS

The discovery of nuclear–nuclear exchange couplings or quantum exchange couplings in solution NMR spectroscopy[1–3] grew out of NMR studies of transition metal polyhydrides in the 1980s. Kubas at Los Alamos National Laboratory had discovered a class of transition metal complexes that bind H_2 as an intact ligand, rather than oxidatively adding the H_2 to the metal center.[4] This prompted a great deal of activity among inorganic chemists in the synthesis of new hydride and dihydrogen complexes, as well as the reinvestigation of many previously known systems. At the time, the synthetic chemists also postulated that species such as H_3^+ might also be stabilized as ligands in transition metal complexes. Solution NMR spectroscopy of ^{1}H was usually the structural method of choice in these investigations, and the classic signature of an H_2 complex became a measurable value for $^1J(^1\mathrm{H}, ^2\mathrm{D})$ in the HD isotopomer, usually of the order of 20–35 Hz. It was widely assumed that a large value of $^1J(^1\mathrm{H}, ^1\mathrm{H})$ would be found in any H_3 complex.

In the late 1980s, Heinekey at Yale and Chaudret at Toulouse independently[5,6] made some somewhat startling observations in the ^{1}H NMR of several transition metal trihydrides. In these systems, the spectra indicated that $^1J(^1\mathrm{H}, ^1\mathrm{H})$ could be over 200 Hz. Since the coupling in molecular H_2 itself is only 280 Hz as inferred from the NMR of HD, these large values for ^1J were at first glance evidence for the putative H_3^+ complexes. However, it soon became clear that these systems were not to be explained so simply. During the next few years, Heinekey carried out a set of classic experiments that formed the basis on which it is now accepted that these splittings are exchange couplings.

One of the first indications that the observed splittings were not due to the usual Fermi-contact mediated scalar coupling mechanism was their extreme sensitivity to temperature. Early on, the apparent J couplings seemed to be field-dependent. However, careful experiments by Heinekey showed that this apparent B_0 dependence arose from slight variations in the probe temperature on different instruments. The splittings in fact did not depend upon field, but instead were hypersensitive to temperature. Many alternate models were considered for explaining these observations at the time. Some invoked chemical equilibria involving an unusual thermally accessible state that would have unprecedently large J couplings. Several tunneling-type mechanisms were also considered, but these seemed difficult to resolve with the observation of these splittings in fluid media at close to ambient temperatures. (For a review of previous experimental observations, other models eliminated, and pertinent references, see Zilm and Miller.[7]) Heinekey then carried out some very important experiments employing ^{2}D substitution. The resulting pattern of isotope shifts and the isotopic variations on the apparent values of $^1J(^1\mathrm{H}, ^1\mathrm{H})$ in the remaining protons ruled out any sensible model involving chemical equilibrium.[2] Unfortunately, the spectra of the partially deuterated isotopomers themselves did not provide convincing evidence for the involvement of tunneling. While no $^1J(^1\mathrm{H}, ^2\mathrm{D})$ couplings were observed, this observation could be explained just as convincingly by self-decoupling due to the rapid ^{2}D relaxation in concert with chemical exchange as by a tunneling mechanism. The key experiment to perform became clear. The NMR of a partially tritiated isotopomer would have none of the complications encountered with deuterium. Given the difficulties in handling radioactive samples, this experiment was more than difficult to perform. The results were well worth Heinekey's efforts: a coupling that started as over 500 Hz in a perprotio molecule was reduced to a $^1J(^1\mathrm{H}, ^3\mathrm{T})$ of less than 30 Hz at the same temperature.[1] This was the first conclusive evidence obtained in favor of the exchange coupling mechanism for these large temperature dependent couplings. The initial report[1] of this result and a theoretical framework for quantitatively accounting for these couplings and their temperature dependence was soon published. Simultaneously with this report, Jones and Weitekamp[8] also proposed an exchange coupling mechanism in these systems, which utilized symmetry arguments, but with no additional experimental data.

3 THEORY

Exchange interactions among electrons are familiar to any student of solid state physics or quantum chemistry. They are central to the quantum mechanical description of bonding in

molecules and the mechanism of phenomena such as high-temperature superconductivity. The appearance of $J\boldsymbol{I}_1\cdot\boldsymbol{I}_2$ type couplings in ESR spectra of triplet biradicals is a well-known spectroscopic manifestation of the electron–electron exchange interaction. For nuclei, quantum mechanical exchange interactions are less familiar, and until recently they were not known to affect high-resolution magnetic resonance spectra in any manner. (For references on quantum exchange in solid ^{3}He and in related electronic structure problems, see Zilm and Miller.[7]) The best-known example of heavy particle quantum exchange is in solid ^{3}He. In this system, diffusion rates and other properties are known in large part to be determined by ^{3}He–^{3}He exchange interactions. NMR spectra of tunneling methyl groups at low temperature also display features related to rotational tunnel splittings, but these have not usually been considered as manifestations of an exchange interaction per se. Given that quantum effects such as these have typically been considered as purely low-temperature phenomena, it is not surprising that quantum exchange involving nuclei has not until recently been recognized as having any role in solution NMR spectroscopy.

Any theory accounting for quantum exchange must consider the total wavefunctions for the nuclei being observed, spanning both spin and spatial coordinates. In this respect, quantum exchange is quite distinct from the other terms in the NMR Hamiltonian. A typical NMR interaction can usually be written as a product of a spin operator and an interaction constant or tensor, which is an expectation value of the rest of the system Hamiltonian over all coordinates except spin. In quantum exchange, however, the spin coordinate and the spatial coordinate are correlated, and such a separation is not possible. To illustrate this, we shall consider a simple two-spin system where the spins occupy chemically inequivalent sites.

3.1 Molecular Dynamics

To understand quantum exchange in the context of NMR spectroscopy, we must first consider the quantum mechanics governing the Cartesian displacements of the NMR active nuclei, i.e., their orbital wavefunctions, and then see how this is coupled to their spin coordinates, i.e., the spin functions. For a start, we shall consider a simple two-particle quantum mechanics problem that is often somewhat misunderstood. Although our treatment will be quite similar to a number of familiar problems in tunneling (see, e.g., Atkins[9]), we should like to emphasize now that quantum exchange does not in fact imply that tunneling motions occur. This point will be clarified in the following discussion.

The molecular systems in which quantum exchange has been observed by NMR all are of the form (**1**)

(1)

where the other ligands collectively denoted by L_3 are typically another hydride, a cyclopentadienyl, and a phosphine. Single crystal neutron diffraction studies[3] indicate that the hydrides are typical terminal hydrides having a single bond to the central transition metal atom M. Although the M–H linkages are significantly more 'floppy' than C–H bonds, these hydrides are basically localized at their binding sites. To a very good approximation, the potential well that each of these hydrides experiences can be approximated by the harmonic oscillator potential as depicted in Figure 1(a).

A complete quantum mechanical treatment of the pair of hydrides under consideration would involve a six-dimensional potential energy surface describing the energy of all configurations of the two hydrides as they are moved relative to each other and to the metal center. As long as the hydrides remain outside each other's van der Waals radii, the potential experienced by either is still roughly harmonic. If the hydrides do not have any appreciable interaction with one another, the problem reduces to that of two uncoupled harmonic oscillators.[7]

As a simple model for this system, consider two hydrides bound to a surface, each in locally harmonic single particle potentials, (**2**) and (**3**).

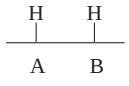

(2)

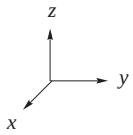

(3)

If the interaction between the two protons is sufficiently weak, their displacements are approximately harmonic except for the symmetric displacement towards one another. In this instance, each hydride feels a repulsive force, which rises rapidly as they near one another. The hydrides are also attracted to the potential minimum at the other binding site. It is the displacement of the hydrides along this type of coordinate that we shall focus upon.

A good model potential for displacements along this exchange coordinate is a double well potential such as that in Figure 1(b). Movement along this coordinate exchanges the two hydrides between the two wells. The reaction coordinate is a two-particle potential, and is necessarily somewhat complicated. If the hydrides simply each moved along the y axis towards one another, there would be an essentially infinite barrier separating the two configurations. The model we want to consider instead takes the coordinate to be a minimum energy type of path along which exchange is possible. At the barrier the two particles must move out of each other's way along a path that takes them out of the (y, z) plane.

It worthwhile to note what is, and what is not, important in the choice of this potential energy curve. The double well model is only one approach to connecting the two different possible ground state configurations of the hydrides. Displacement on a periodic rotational coordinate would also produce the type of effects to be discussed.[10] The required features are only that the potential has two wells representing two distinct configurations and that there be a finite barrier separating them.

Having reduced the two-particle problem to a single internal reaction coordinate in a double well makes the problem fairly simple. We shall only consider the vibrational ground state in this potential, since we know that the hydrides are basically bound fairly tightly to their binding sites. This places them in one of the two configurations representing the double well minima. Near the bottom of either well, the potential is close to harmonic, and a good approximate two-particle ground state

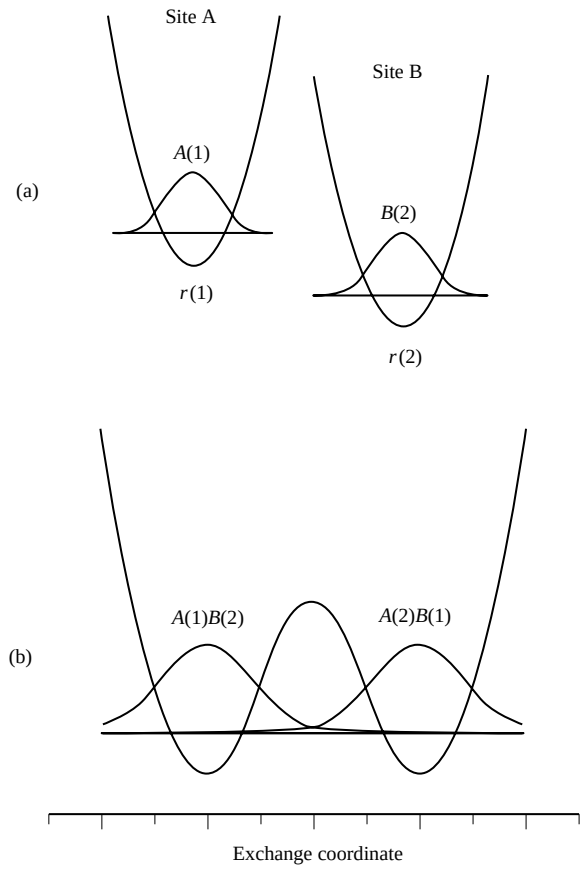

Figure 1 (a) Depiction of two harmonic potentials at two different sites, with vibrational ground state wavefunctions. This is a reasonable description of two largely uncoupled M–H vibrators in a transition metal hydride. The coordinates are the displacements of the individual hydrides. (b) A model two-particle potential describing the change in potential energy as the two hydrides in the two sites shown in (a) are exchanged between the two sites. The coordinate is the reaction coordinate along which the exchange takes place. The wavefunctions shown are two-particle wavefunctions for the two degenerate configurations

wavefunction would be a Gaussian centered in either of the two wells. We define $\psi(\mathrm{L})$ as the configuration where the protons 1 and 2 were at sites A and B, respectively. This configuration can be written as a product of one-particle wavefunctions, i.e., $A(1)B(2)$, where $A(1)$ and $B(2)$ are the Gaussians representing the one-particle ground state vibrational wavefunctions in the single particle potentials representing the two binding sites. The other side of the double well would then be represented by the two-particle wavefunction $\psi(\mathrm{R})$=$A(2)B(1)$ [see Figure 1(b)].

It is tempting to apply what we know about the quantum mechanics of a single particle in a double well directly to this two-particle problem, since the mathematical formulation is now the same at this point (see, e.g., Atkins[9]). Because the wells are a finite distance apart, the wavefunctions for the two ground state basis configurations we have chosen overlap each well. This produces an off-diagonal element in the matrix for the system Hamiltonian $\hat{\mathcal{H}}_{\mathrm{L}}$ that includes the interaction of the particles with both wells and each other. To get the best possible description of the ground state within this restricted basis set, we must diagonalize this matrix. If

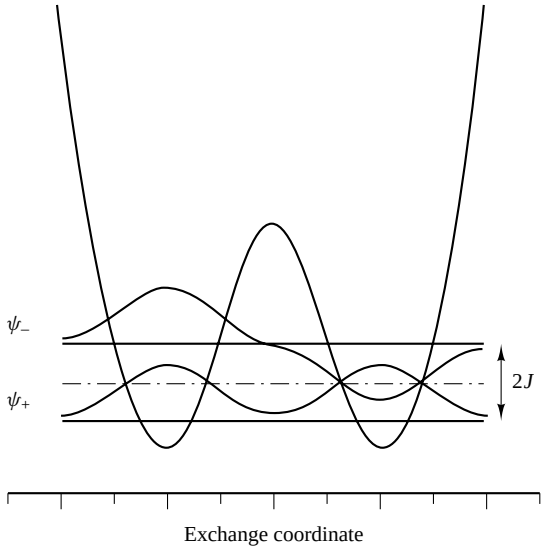

Figure 2 Model double well exchange potential showing the two lowest energy eigenfunctions ψ_+ and ψ_-. The energies of these two states are split by $2J$ symmetrically about the energy of the two degenerate localized basis states

the two sides of the double well have the same depth, the basis states are degenerate. No matter how small the off-diagonal term, the two basis set wavefunctions will be mixed. As every student of quantum mechanics knows, in the single particle case the symmetric and antisymmetric combinations of the two Gaussians are then good approximations to the proper wavefunctions. The eigenenergies of the two eigenstates $\psi_\pm = \frac{1}{2}[\psi(\mathrm{L}) \pm \psi(\mathrm{R})]$ for the symmetrical potential are $E_\pm = E \pm J$ (see Figure 2). E is the unperturbed energy of either of the degenerate configurations given by

$$\int\int [A(1)B(2)]^* \hat{\mathcal{H}}_{\mathrm{L}} A(1)B(2)\,\mathrm{d}\tau_1\,\mathrm{d}\tau_2 \qquad (1)$$

and J is the value of the off-diagonal matrix element

$$\int\int [A(1)B(2)]^* \hat{\mathcal{H}}_{\mathrm{L}} A(2)B(1)\,\mathrm{d}\tau_1\,\mathrm{d}\tau_2 \qquad (2)$$

In the case of a single particle in the double well, the energy difference $2J$ is a tunnel splitting. The wavefunctions indicate that the particle is equally likely to be in either well. This is interpreted to mean that the particle is 'delocalized' over both sides of the potential. If a localized state is prepared by a superposition of ψ_+ and ψ_-, it will evolve in time according to the usual rules of time-dependent quantum mechanics. The picture that emerges is one of the maximum in the probability density oscillating between the two wells at a frequency $2J/h$. One usually describes the particle as coherently tunneling from one well to the other at this rate. On the other hand, when the two wells are of differing depths, the particle quickly becomes localized. As long as the difference in the energies of the two states $\psi(\mathrm{L})$ and $\psi(\mathrm{R})$ is larger than the off-diagonal term J, these remain good states to first order in the perturbation treatment.

The mapping of the two-particle case onto this reduced one-particle description contains some subtleties. If the two

sites are energetically the same, i.e. the one-particle potentials at the two binding sites are identical, the configurations $A(1)B(2)$ and $A(2)B(1)$ will clearly have the same energies. The degeneracy will again be lifted by any finite matrix element connecting the functions $A(1)B(2)$ and $A(2)B(1)$, and there will be two states separated by a tunnel splitting. In the molecules we are considering, however, the hydrides are chemically inequivalent. This means that the local one-particle potentials are different, if only slightly so on a cm^{-1} scale. However, this does necessarily break the symmetry of the two-particle potential along the exchange coordinate. If the two particles are identical, the basis configurations $A(1)B(2)$ and $A(2)B(1)$ representing $\psi(\mathrm{L})$ and $\psi(\mathrm{R})$ will still have the same energies. Exchange of identical particles can then be described by a mirror-symmetric two-particle potential in the exchange coordinate. If the hydrides are not identical (e.g., a proton and a triton), this symmetry will be broken, since the two basis configurations will have different energies. The eigenstates will then be localized, and no tunneling will occur. In this case of two distinguishable particles, the two sites would have to be identical for the exchange potential to remain symmetric.

The appearance of a potential for particle exchange with mirror symmetry is then a prerequisite for exchange splittings to appear in the energy level diagram for this two-particle system. Many familiar systems have this type of symmetry, but not all can display quantum exchange. For example, consider the umbrella mode of ammonia, or the chair-to-chair inversion of cyclohexane. In the gas phase, both displacements can be described by mirror-symmetric double wells. Placing these molecules into a condensed phase, however, breaks this symmetry. When either molecule inverts, it moves from one region of space to another. The presence of an anisotropic solvent shell around each site gives the configurations distinct energies. This is not the case for the transition metal polyhydrides we are considering, or other systems such as rotating methyl groups. In the transition metal hydrides, the configuration before and after the exchange of two hydrides occupies the same region of space. Rotation of a methyl group by 120° likewise results in a new configuration that occupies the same space as before the rotation. These displacements are then always instantaneously described by mirror-symmetric potentials, and thus will have exchange-type splittings appearing in their energy level structure. It should be emphasized that whether particles are identical or not depends only on the nature of the particles and not on their location in the molecule or lattice. However, whether a molecular rearrangement that exchanges identical particles is a truly degenerate rearrangement energetically depends on the relation of the molecule to the lattice at the beginning and the end of the rearrangement.

The above treatment of the two-particle exchange problem as a single pseudoparticle in a double well is only partially correct. This is because the two-particle wavefunctions have additional constraints. One must remember that the spatial portion of a wavefunction describes the probability of a particle's location. When several particles are described by a single wavefunction, the probabilities can only be ascribed individually to particles that are distinguishable. For indistinguishable particles, the identity (e.g., particle number) is irrelevant.[11] The wavefunction for a pair of identical particles can then only give the probability of finding a particle of that type at any position. It cannot tell us the probability for finding a particular particle there.

Our interpretation of $\psi_\pm$ in the one- and two-particle cases, then, is somewhat different. For the single particle in the double well, the equal probability amplitudes on the left and right sides is taken as an indication that the particle is 'delocalized' over both sides. This notion is reinforced by the time-dependent behavior of a single particle in this potential if the initial state is localized as just discussed. On the other hand, the two-particle wavefunctions $\psi_\pm$ do not imply delocalization of the two particles, or of the configuration. These functions now simply state that the system is most likely in a configuration with one particle on the left and one on the right, but the identity of the configuration is indeterminate. We may not ask about the location of individual particles, since they are identical, and as such their labels are simply irrelevant. Thus, we see in the two-particle case that the indeterminacy as to which particle is on the left or on the right has replaced the delocalization that arises in the one-particle problem.

This statistical interpretation of the two-particle wavefunctions requires that any relabeling of the particle identities must leave the probability densities unchanged. Thus, the wavefunction must be the same, or at most change sign, when the particle labels are permuted. In accord with the well-known symmetrization postulate, wavefunctions for identical bosons are symmetric or remain the same, while those for identical fermions are antisymmetric or change sign, under particle label exchange. With this in mind, we return to the problem of two particles in the double well. Consider the case where the particles are of zero spin and are therefore bosons. The function ψ_+ has the proper symmetry, while ψ_- does not. The ground state can then only exist as ψ_+, since ψ_- is an unacceptable wavefunction. The consequence of this is that a 'localized' state cannot be constructed by combining ψ_+ and ψ_-. The picture we arrived at in the one-particle state of an initially localized state periodically moving between the two wells is then inappropriate. The system can only remain in the ground state ψ_+. This is most easily interpreted as the system being localized in one of the two possible indistinguishable configurations.

3.2 Including the Spin Coordinate

When the spin functions are included in the two-particle problem, the symmetry of the total wavefunction including spin must be considered. One place to start is to write the individual spatial and spin functions as separate symmetrized sets. For a pair of spin-$\frac{1}{2}$ nuclei the symmetrized functions are the symmetric triplet functions T_0, T_{-1}, T_{+1}, and the antisymmetric singlet spin function S_0. The total wavefunction for identical fermions must be antisymmetric with respect to exchange, and therefore ψ_+S_0, ψ_-T_0, ψ_-T_{-1}, and ψ_-T_{+1} are the only acceptable combinations. Now that spin has been introduced, the system can have an energy of either $E + J$ or $E - J$, depending upon the spin state of the nuclei. Any additional small interaction of the magnetic field would not be expected to change the situation with respect to the energy associated with the orbital or lattice terms of the Hamiltonian. On the other hand, magnetic interactions will mix the singlet and triplet spin manifolds. Any spin flip that occurs must also make up any difference in lattice energy accompanying the transition. The appearance of the exchange energy in an

NMR transition is then a consequence of the correlation of the spin states with the orbital energies associated with the displacements of the NMR active nuclei.

In general, the above type of prescription for determining properly symmetrized total spin + spatial wavefunctions is cumbersome. The resulting functions can be recast in a more physical and convenient basis, which we call the site spin basis.[11] Rather than deriving the site spin basis, we shall develop it directly from some basic symmetry considerations. Let us start by considering a pair of protons in chemically equivalent sites that comprise an AX spin system. Normally we ignore the complications brought on by the coordinate or orbital part of the wavefunction, and simply write the spin eigenfunctions as $|+\ +\rangle$, $|+\ -\rangle$, $|-\ +\rangle$, and $|-\ -\rangle$, where the labels refer to m_S for particles 1 and 2 in that order. These two-particle product basis spin functions themselves, however, do not have the proper symmetry with respect to particle exchange, i.e., $|+\ -\rangle \neq \pm|-\ +\rangle$. This at first sight seems perplexing, since every NMR spectroscopist knows that these wavefunctions are what are always used for an AX spin system. The answer is that in actuality the spin labels do not refer to the particle identities. Instead, the functions are of the form $|m_S(\mathrm{A}), m_S(\mathrm{B})\rangle$, i.e., the labels are according to the site identity, not the particle numbers. The function $|+\ -\rangle$ says the particle in site A is in the + state, and the particle in site B is in the − state. What the function does not tell us is which particle is in which site. Therefore, the spin functions labeled according to the m_S in each site are automatically symmetric with respect to particle exchange. To differentiate the product basis labeled according to sites, we shall write these kets as $[+\ -\rangle'$.

In using this site labeling convention, we must also relabel our spin Hamiltonian.[11] For instance, the Zeeman plus chemical shift term in frequency units for two spins would be written as

$$\hat{\mathcal{H}}_{\mathrm{cs}} = -\nu_{\mathrm{A}}\hat{I}_{z\mathrm{A}} - \nu_{\mathrm{B}}\hat{I}_{z\mathrm{B}} \tag{3}$$

The resonance frequencies and spin operators are thus identified with the molecular site instead of a particle number. In most instances, this is in fact how NMR problems are typically handled, even though one may have the impression that one is using particle labels instead of site labels.

The overall symmetry of the total site spin basis function $\psi_{\mathrm{site}} = \psi_{\mathrm{orbital}}\psi_{\mathrm{spin}}$ is then determined solely by the symmetry of the orbital wavefunction. For this pair of spin-$\frac{1}{2}$ nuclei, ψ_{orbital} must always be the antisymmetric function ψ_-, since ψ_{spin} is always symmetric with this site labeling convention. The total wavefunction for the $[+\ -\rangle'$ spin state is then $\sqrt{\frac{1}{2}}[A(1)B(2) - A(2)B(1)][+\ -\rangle'$ (the normalization is only approximate, since we have ignored the small overlap term). As a shorthand, these site spin basis functions will be written as $[m_S(\mathrm{A}), m_S(\mathrm{B})\rangle$, dropping the prime notation to imply the inclusion of the orbital portion. Remember that the labeling of the spin portion is according to site A and B, not particle 1 and 2, in these functions with the '[' notation. In order to calculate a spectrum, it is instructive first to explicitly calculate a few matrix elements. We shall use the sum of the coordinate Hamiltonian for the particles, $\hat{\mathcal{H}}_{\mathrm{L}}$, and $\hat{\mathcal{H}}_{\mathrm{cs}}$ as an example.

First consider $\langle+-]\hat{\mathcal{H}}_{\mathrm{cs}}[+-\rangle$. Using the site labeling convention, this is evaluated as $\frac{1}{2}(\nu_{\mathrm{B}} - \nu_{\mathrm{A}})$ in the usual fashion. The integral over the particle coordinates is unity, since the orbital function is normalized. To calculate $\langle-]\hat{\mathcal{H}}_{\mathrm{L}}[+-\rangle$, we must expand $[+\ -\rangle$ in terms of functions with particle labels:

$$[+-\rangle = \tfrac{1}{2}[A(1)B(2)|+-\rangle - A(2)B(1)|-+\rangle] \tag{4}$$

Since the spins have particle number designations on the right-hand side, the + and − labels have been arranged to keep the + spin in the A site and the − spin in the B site. The quantity $\langle+-]\hat{\mathcal{H}}_{\mathrm{L}}[+-\rangle$ can be written as a sum of products of integrals over spin and space separately:

$$\begin{aligned}
&\langle+-]\hat{\mathcal{H}}_{\mathrm{L}}[+-\rangle \\
&= \tfrac{1}{2}\langle+-\,|\,+-\rangle \int\int [A(1)B(2)]^*\hat{\mathcal{H}}_{\mathrm{L}}A(1)B(2)\,\mathrm{d}\tau_1\,\mathrm{d}\tau_2 \\
&\quad +\tfrac{1}{2}\langle-+\,|\,-+\rangle \int\int [A(2)B(1)]^*\hat{\mathcal{H}}_{\mathrm{L}}A(2)B(1)\,\mathrm{d}\tau_1\,\mathrm{d}\tau_2 \\
&\quad -\tfrac{1}{2}\langle-+\,|\,+-\rangle \int\int [A(2)B(1)]^*\hat{\mathcal{H}}_{\mathrm{L}}A(1)B(2)\,\mathrm{d}\tau_1\,\mathrm{d}\tau_2 \\
&\quad -\tfrac{1}{2}\langle+-\,|\,-+\rangle \int\int [A(1)B(2)]^*\hat{\mathcal{H}}_{\mathrm{L}}A(2)B(1)\,\mathrm{d}\tau_1\,\mathrm{d}\tau_2
\end{aligned} \tag{5}$$

Note again that the spin labels on the left refer to sites A and B, while those on the right refer to particle numbers 1 and 2. The first two integrals each give $\frac{1}{2}E$, and the last two are zero because of the vanishing integral over the spin coordinate. The net value of the element $\langle+-]\hat{\mathcal{H}}_{\mathrm{L}}[+-\rangle$ is then the lattice energy E. Now consider the element $\langle-+]\hat{\mathcal{H}}_{\mathrm{L}}[+-\rangle$. In a similar fashion, the integral can be expanded as

$$\begin{aligned}
&\langle-+]\hat{\mathcal{H}}_{\mathrm{L}}[+-\rangle \\
&= \tfrac{1}{2}\langle-+\,|\,+-\rangle \int\int [A(1)B(2)]^*\hat{\mathcal{H}}_{\mathrm{L}}A(1)B(2)\,\mathrm{d}\tau_1\,\mathrm{d}\tau_2 \\
&\quad +\tfrac{1}{2}\langle+-\,|\,-+\rangle \int\int [A(2)B(1)]^*\hat{\mathcal{H}}_{\mathrm{L}}A(2)B(1)\,\mathrm{d}\tau_1\,\mathrm{d}\tau_2 \\
&\quad -\tfrac{1}{2}\langle+-\,|\,+-\rangle \int\int [A(2)B(1)]^*\hat{\mathcal{H}}_{\mathrm{L}}A(1)B(2)\,\mathrm{d}\tau_1\,\mathrm{d}\tau_2 \\
&\quad -\tfrac{1}{2}\langle-+\,|\,-+\rangle \int\int [A(1)B(2)]^*\hat{\mathcal{H}}_{\mathrm{L}}A(2)B(1)\,\mathrm{d}\tau_1\,\mathrm{d}\tau_2
\end{aligned} \tag{6}$$

In this case, the first two integrals are zero, and the second pair give contributions of $-\frac{1}{2}J$ for a total value of $-J$.

The reader may already see that these matrix elements can be evaluated on inspection following a few simple rules. When dealing with the NMR or spin Hamiltonian, we proceed as normally, using spin operators, interaction coefficients, and spin functions labeled according to site. The coordinate part seems trickier, but can be simply treated as a permutation operator over the spin. For a term $\langle ij]\hat{\mathcal{H}}_{\mathrm{L}}[kl\rangle$, a value of E is returned if $i = k$ and $j = l$. If $i = l$ and $j = k$, a contribution of $-J$ is obtained. The additional terms that the exchange interaction brings to the NMR Hamiltonian can then be recognized as having the same form as the classical exchange matrix familiar to students of dynamic NMR lineshape analysis.

Table 1 Hamiltonian Matrix in the Site Spin Basis for a Simple AX Spin System

	$\|+\,+\rangle$	$\|+\,-\rangle$	$\|-\,+\rangle$	$\|-\,-\rangle$
$\langle++\|$	$-\frac{1}{2}\nu_A - \frac{1}{2}\nu_B + E - J$	0	0	0
$\langle+-\|$	0	$-\frac{1}{2}\nu_A + \frac{1}{2}\nu_B + E$	$-J$	0
$\langle-+\|$	0	$-J$	$+\frac{1}{2}\nu_A - \frac{1}{2}\nu_B + E$	0
$\langle--\|$	0	0	0	$+\frac{1}{2}\nu_A + \frac{1}{2}\nu_B + E - J$

For our simple AX spin system, the full Hamiltonian matrix in the site spin basis can then be written on inspection as in Table 1. Since the orbital energy E only adds to the diagonal, it just represents a shift of the energy scale and can arbitrarily be set to zero. If the chemical shift difference $|\nu_A - \nu_B| \gg |J|$ then the off-diagonal terms will be truncated, and the NMR transitions will give two doublets centered at ν_A and ν_B with splittings of $-2J$. This Hamiltonian then gives the same spectrum as that for an AX spin system with an effective J coupling of $-2J$. Since the matrix element that J represents is inherently negative, the apparent coupling in the spectrum is positive. For spin-$\frac{1}{2}$ nuclei, it can be shown that any pairwise exchange interaction gives rise to a term that behaves just as if there were a scalar coupling $-2J$ between those two sites. Higher-spin systems, however, cannot be described by such a simple effective spin Hamiltonian.[11]

One could incorrectly infer from the energy level structure of this simple example that the identity of the particles can somehow be made known by the fact that they experience different chemical shifts at the two different sites. A question that might be asked is how often the spins can change places by tunneling. The answer turns out to be that one cannot tell. The probability that a spin in site A has exchanged with a spin in site B becomes a maximum when their spin quantum numbers are identical. In other words, the spins can tunnel when one cannot tell them apart, even by their spin. Therefore, the most straightforward interpretation is that the spins remain localized, but which spin is localized where is something that cannot be known, since the particles are indistinguishable.

The advantage of the site spin basis approach to treating exchange coupling in NMR spectroscopy is that it is very easily extended to more complicated permutations or exchanges of spins, and is easily applied to problems involving nuclei of arbitrarily large I. The general form of the exchange Hamiltonian in the site spin basis can be shown[11] to be

$$\hat{\mathcal{H}}_{ex} = \sum_i \xi^{p(i)} J_i \hat{\mathcal{P}}_i(k, l, m, \ldots) \tag{7}$$

where $\xi = e^{2\pi i I}$ and I is the spin quantum number of the nucleus in question. The permutation of the spins among the sites k, l, m, ... is represented by the operator $\hat{\mathcal{P}}_i(k, l, m, \ldots)$, which acts on the spin labels within the site spin basis functions. Each site spin basis function has the same orbital function implied. For fermions, this is formed using a Slater determinant for the orbital states for each site. If the nuclei are bosons, an antideterminant is used instead. The exchange matrix element is given by J_i. It is calculated by taking the matrix element of $\hat{\mathcal{H}}_L$ between an orbital state for one configuration and that of the configuration resulting from the permutation. For example, consider a three-site problem (e.g., a methyl group). A starting configuration would be $A(1)B(2)C(3)$. If the three particles are subjected to a cyclic permutation, this state would become $A(3)B(1)C(2)$. The value of J_c would be

$$J_c = \int\int\int [A(1)B(2)C(3)]^* \hat{\mathcal{H}}_L A(3)B(1)C(2)\, d\tau_1\, d\tau_2\, d\tau_3 \tag{8}$$

Different permutations have different parities. For bosons, this is irrelevant. However, for fermions, permutations of even parity produce negative elements, and those of odd parity give positive exchange integrals. This is handled by the $\xi^{p(i)}$ term. If the nuclei are fermions with spin $I = n + \frac{1}{2}$ then $\xi = -1$. If they are bosons then $\xi = +1$. For fermions, a single pairwise permutation has odd parity, and $p(i) = 1$, which produces a negative sign for the exchange matrix element. On the other hand, a permutation that can be written as the product of two pairwise permutations has even parity, and $p(i) = 2$. These permutations give positive exchange coupling elements in the Hamiltonian matrix. One can show by straightforward but tedious calculations that the results of this prescription are to reproduce the matrix elements that would be obtained by expanding the site spin basis functions as products of properly symmetrized orbital functions and spin functions with particle labels, and performing the integration explicitly.

In practice, one simply associates a different J value with each particular topological rearrangement or permutation of the nuclei between the different locations in a molecule. High barrier permutations give low J values, and facile permutations give larger ones. The states that are connected are those where the permutation operation shuffles the spin labels so that they match those of the state to which it is coupled. The procedure is exactly the same as filling an exchange matrix for a classical chemical exchange lineshape problem. The signs of the elements are determined by whether the spins are fermions or bosons, and whether the permutation has even or odd parity. These elements are added to the rest of the standard NMR Hamiltonian, and the spectrum is determined by finding the eigenstates and determining the transition moments in the usual fashion.

A convenient starting point for computer simulation of exchange-coupled spectra in the presence of chemical exchange is to start with any of the many programs for dynamic NMR lineshape simulation. One simply duplicates the code for calculating the elements of the classical exchange matrix, and uses it to add exchange coupling elements to the Hamiltonian matrix. In this manner, we have been able to computer-simulate exchange-coupled NMR spectra for systems of up to four chemically exchanging protons or deuterons.

3.3 Temperature Dependence

Our main purpose so far has been to provide a physical picture of how exchange interactions produce splittings in

NMR spectra. The theory accounts for the disappearance of exchange couplings between different isotopes of the same element, for the persistence at ambient temperatures of an effect that is similar to tunneling, and for the different spectral patterns that are observed for spin-$\frac{1}{2}$ and spin-1 systems (see below). Accounting for the size of these splittings and their temperature dependence is another matter. Several models have been proposed, and probably all are correct to some extent. A definitive calculation of the exchange coupling would require an accurate $3N$-dimensional potential energy surface for N identical nuclei. This is at present out of reach, so the models are either approximate analytical or computational attempts to focus on key features of the exchange process.

The model we have favored most is based on a treatment of exchange in solid ^{3}He by Landesmann.[2,7] Landesmann has analytically calculated the ground state exchange splitting for two atoms in harmonic wells and repelled by a hard sphere potential. To account for the temperature dependence, thermal excitations that place the molecules in higher vibrational states are involved. Since these vibrationally excited states are more delocalized, there is more overlap of the individual particles with the neighboring sites, and the size of J goes up with vibrational quantum number. In the double well description, the splittings of the higher states increase exponentially as one moves beyond the ground state. In solution, the vibrational states are short-lived, and the NMR experiment measures a Boltzmann population weighted average of the splittings over the vibrational ladder. The spin state is conserved in these transitions, and the sign of J remains the same; therefore, the weighted average of J increases with temperature. We have shown that the sum over vibrational states can be effectively accomplished by first calculating a Boltzmann population weighted overlap function.[7] This can be shown to be approximated by a Gaussian of increasing width with increasing temperature. As Landesmann's ground state calculation used a Gaussian basis set, this result can then be applied to the averaged splitting as a function of temperature also. The final expression obtained is

$$J(T) = \frac{-3\hbar a}{8\pi m\delta(T)^3}\sqrt{\frac{3}{\pi}}\exp\left[-\frac{3}{4}\frac{a^2+\lambda^2}{\delta(T)^2}\right] \qquad (9a)$$

where

$$\delta(T)^2 = \frac{3h}{4\pi m\nu}\coth\left(\frac{h\nu}{2kT}\right) \qquad (9b)$$

Here a is the inter-hydride equilibrium distance, λ is a hard sphere radius (usually taken as 10 nm), ν is the bending frequency of the M–H bonds, and m is the proton mass. When deuterium or tritium is involved, the mass and bending frequency are adjusted accordingly.

Equation (9a) can be used to fit J versus T data, and both a and ν determined. The values found in a large number of fits are quite close to the distances a found by single crystal neutron diffraction and the few ν bending frequencies that have been measured.[2] For systems with very large ^{1}H–^{1}H exchange interactions, this equation has correctly predicted the size of the ^{2}D–^{2}D exchange couplings when they can be measured. This equation also explains why exchange couplings are not observed in organic molecules. The exchange coupling decreases about two orders of magnitude for every 100 cm^{-1} increase in ν. Since C–H bends are of the order of 600 cm^{-1} higher than M–H bends, the exchange couplings in organic systems are about 10^{12} smaller and thus unobservable.

Jones and Weitekamp have developed a similar model using numerical diagonalization of model double well potentials.[12] The behavior of J versus T is calculated by a sum over the thermally populated states. One difficulty with this approach is making a connection between the model reaction coordinate and the molecular structure. Harris and co-workers[13] have studied exchange using muffin-tin-type potentials. They are also able to account for the observed data, and have offered some insight into the types of reaction coordinates that may play an important role.

Limbach[10] has proposed an alternative model to these that is most different in the assumed exchange coordinate. This is a rotational model that produces an exchange splitting from a periodic exchange potential. In the rotational tunneling problem, the tunnel splittings alternate in sign with increasing rotational quantum number. One might then expect that the exchange coupling would have to decrease with temperature in this model instead of increasing as is observed. To circumvent this problem, Limbach proposes that in the ground state the hydrides have no appreciable rotational tunnel splitting. Thermal excitations then allow the system to access a state that is a nascent H_2 complex. The H_2 ligand in this state has a substantial tunnel splitting, which produces the appearance of the exchange coupling. The temperature dependence arises from the thermal population of essentially just the lowest rotational state of the H_2 complex. Such a model can also be used to fit all of the experimental data collected on perprotio systems to date. The main difficulty with this model is rationalizing the existence of an H_2 complex that must lie only 4–8 kJ mol^{-1} above the ground state trihydride structure. In addition, the barrier to rotation of the H_2 ligand in the thermally excited state must be well over 40 kJ mol^{-1} to properly account for the apparent tunnel splitting in the lowest rotational state of this nascent H_2 complex.

Differentiation of how well these and other models describe these systems is being tested by several computational groups at present.[14,15] Potential energy surfaces are calculated for a model system, and the Hamiltonian is then numerically diagonalized. A Boltzmann population-weighted average over the calculated exchange splittings is computed for comparison to the experimentally observed variation of J with temperature. Such calculations can be made to reproduce the trends observed experimentally. However, it remains to be seen how high a level of calculation will be needed to do a better job than the approximate analytical theories.

4 EXAMPLES

A large number of transition metal hydride systems that display exchange couplings have been discovered or rediscovered. One of the most striking is the $Cp^*(CO)IrH_3^+$ cation. At 500 MHz, spectra similar to the simulations shown in Figure 3 are observed.[16] This is a deceptively simple AB_2 spectrum, which at first glance is a single line. On closer inspection, one sees that the central line is flanked by two broader lines with integrated intensities of approx. one-tenth of the central peak. This is an example of a dynamically broadened spectrum with a very large $J(^1H,^1H)$. The apparent

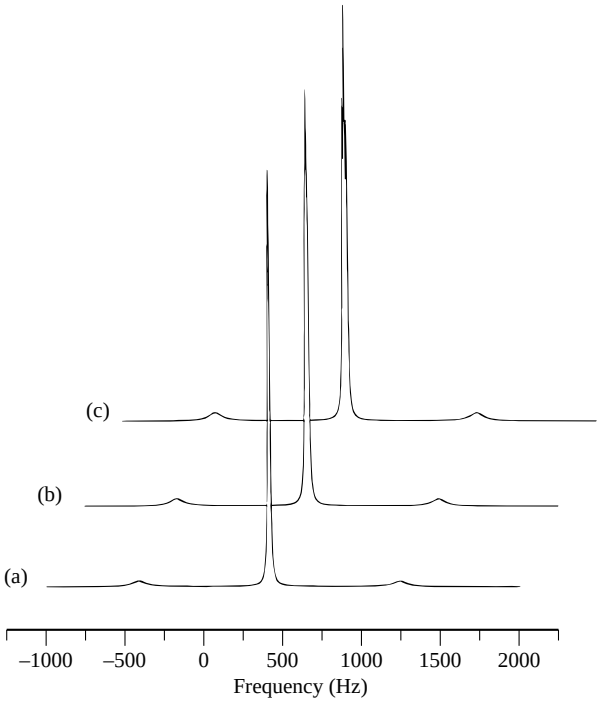

Figure 3 Simulated AB_2 dynamic ^1H NMR spectra similar to what are observed at 500 MHz and about 140 K for the $Cp^*(CO)IrH_3^+$ cation.[16] $J = -2J$ in these simulations is (a) 50 kHz, (b) 25 kHz, and (c) 18 kHz. The central line appears at the weighted average of the A and B chemical shifts. One of the dynamically broadened wings appears at the A-site chemical shift. In comparison with the experimental spectra, only simulations with $J = -2J > 50$ kHz produce a narrow enough central peak. In such cases where $|\nu_A - \nu_B| \ll J$, the central line does not broaden as the decoalescence temperature is reached—rather, only the outer wings narrow. This can lead to the impression that such a molecule is fluxional when in fact it is not

$J = -2J$ must be over 50 kHz as judged from comparison of these simulations with the experimental spectra. This large J lead us to predict that the exchange interaction in the perdeutero system would be of the order of 30–60 Hz and thus observable. Figure 4 shows an example of ^2D–^2D exchange coupling observed in this molecule. Simulation of this spectrum requires an exchange coupling. This is because, for spin $I = 1$, the Hamiltonian no longer has the same symmetry as a scalar coupling; therefore, these data cannot be simulated using a scalar coupling network. From the dependence of J on T, one can extract the parameters a and ν, which predict that $J(^1H,^1H)$ should be approx. 75 kHz, in accordance with the observed ^1H spectra. In future, it will be important to find systems in which both the ^1H and ^2D exchange interactions can be accurately measured as a test of exchange coupling theories.

As a final example, Figure 5 displays some calculated ^2D exchange-coupled spectra for AB_2 spin systems with various ratios of exchange coupling to the chemical shift difference. A D_B–D_B scalar coupling has also been included. Note that the scalar coupling between two magnetically equivalent nuclei is now seen to have an effect upon the spectrum! This result is expected, since the D_A–D_B exchange interactions do not commute with the D_B–D_B scalar coupling Hamiltonian, making it possible now to observe it in the spectra.

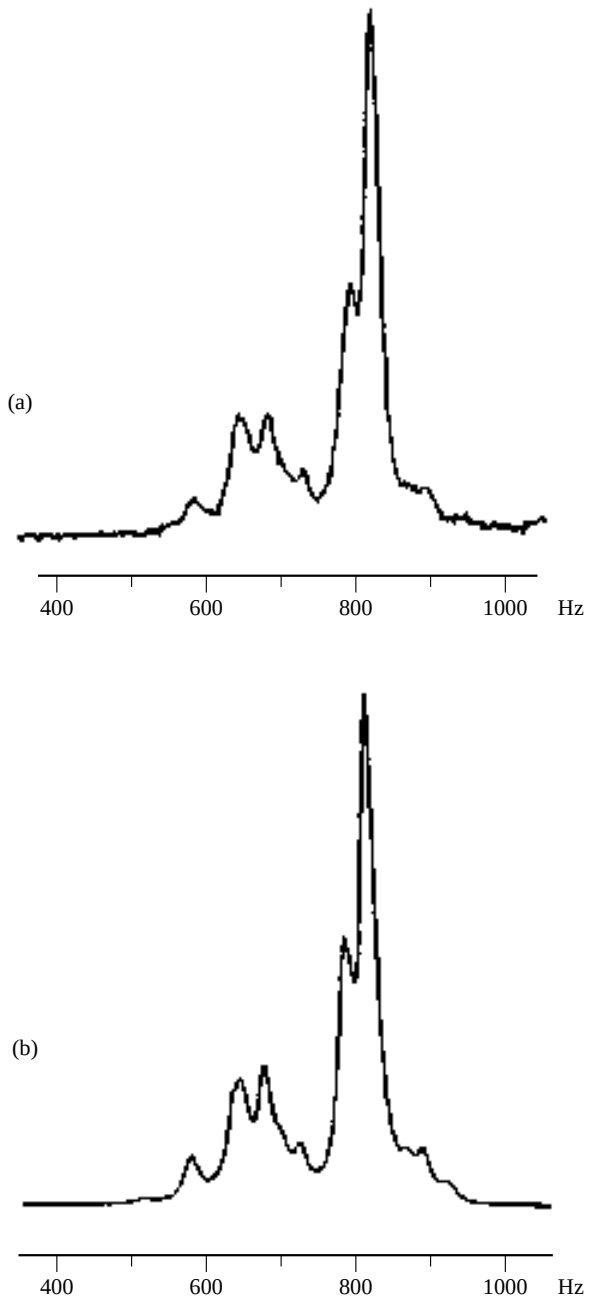

Figure 4 (a)Experimental ^2D NMR spectrum of a mixture of deuterated isotopomers of the $Cp^*(CO)IrH_3^+$ cation (approx. 60% D) at about 145 K. (b) Simulated spectrum giving a D–D exchange coupling between the A and B sites of approx. 40 Hz. Such spectra cannot be fitted using a scalar coupling network

5 SUMMARY

Exchange couplings in solution NMR spectra are manifestations of a purely quantum mechanical effect on the energy levels of sets of identical nuclei in molecules. These effects are related to rotational tunnel splittings in systems such as H_2 or methyl groups, and have the same origins as quantum exchange in solid ^3He. The unique feature of exchange coupling in transition metal polyhydride systems is that it persists to relatively high temperatures in the solution phase, making it possible to observe very small exchange splittings by

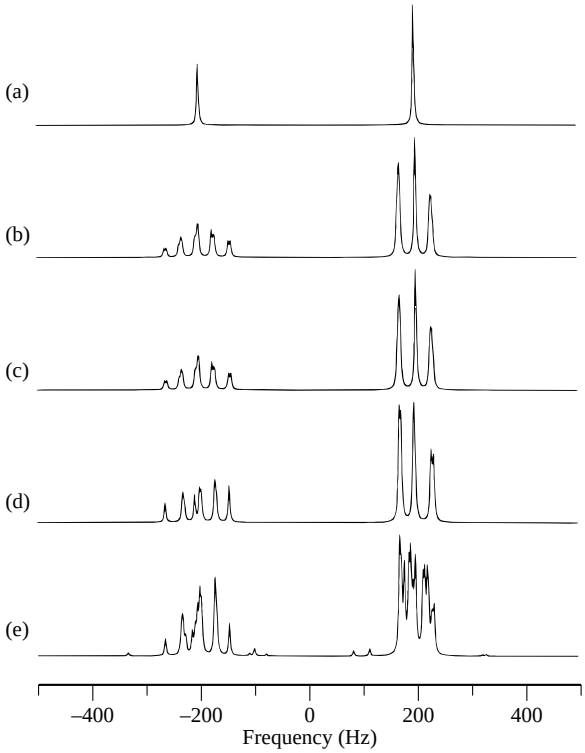

Figure 5 Calculated ^{2}D NMR spectra for an AB_2 spin system with scalar and exchange couplings (the chemical shift difference has been set at 400 Hz): (a) no couplings; (b) scalar couplings J(A, B) = 30 Hz, J(B, B) = 0; (c) scalar couplings J(A, B) = 30 Hz, J(B, B) = 100 Hz; (d) AB exchange coupling $|-2J|$ = 30 Hz, scalar J(B, B) = 0; (e) AB exchange coupling $|-2J|$ = 30 Hz, scalar J(B, B) = 100 Hz. Note that in (c) the inclusion of J(B, B) = 100 Hz has no visible effect, while the spectrum in (e) is dramatically different from that in (d) when J(B, B) is introduced

high-resolution NMR. While these splittings are related to tunnel splittings, they do not imply that coherent tunneling motions occur. Rather, they are a consequence of shifts in the orbital energies of the nuclei that are correlated with their spin states. This correlation of spatial and spin variables results in the exchange energy appearing in the transition frequencies observed in NMR spectra.

6 REFERENCES

1. K. W. Zilm, D. M. Heinekey, J. M. Millar, N. G. Payne, and P. G. Demou, *J. Am. Chem. Soc.*, 1989, **111**, 3088.
2. K. W. Zilm, D. M. Heinekey, J. M. Millar, N. G. Payne, S. P. Neshyba, J. C. Duchamp, and J. Szczyrba, *J. Am. Chem. Soc.*, 1990, **112**, 920.
3. D. M. Heinekey, J. M. Millar, T. F. Koetzle, N. G. Payne, and K. W. Zilm, *J. Am. Chem. Soc.*, 1990, **112**, 909.
4. G. J. Kubas, *Acc. Chem. Res.*, 1988, **21**, 120.
5. D. M. Heinekey, N. G. Payne, and G. K. Schulte, *J. Am. Chem. Soc.*, 1988, **110**, 2302.
6. T. Arliguie, B. Chaudret, J. Devillers, and R. Poilblanc, *C. R. Hebd. Seances Acad. Sci., Ser. 2*, 1987, **305**, 1523.
7. K. W. Zilm and J. M. Millar, *Adv. Magn. Opt. Reson.*, 1990, **15**, 163.
8. D. H. Jones, J. A. Labinger, and D. P. Weitekamp, *J. Am. Chem. Soc.*, 1989, **111**, 3087.
9. P. W. Atkins, *Molecular Quantum Mechanics*, 2nd edn., Oxford University Press, Oxford, 1983, pp. 314–316.
10. H. Limbach and B. Chaudret, *Angew. Chem., Int. Ed. Engl.*, 1992, **31**, 1369.
11. S. J. Inati and K. W. Zilm, *Phys. Rev. Lett.*, 1992, **68**, 3273.
12. C. R. Bowers, D. H. Jones, N. D. Kurur, J. A. Labinger, M. G. Pravica, and D. P. Weitekamp, *Adv. Magn. Opt. Reson.*, 1990, **14**, 269.
13. E. M. Hiller and R. A. Harris, *J. Chem. Phys.*, 1993, **98**, 2077.
14. A. Jarid, M. Moreno, A. Lledos, J. M. Lluch, and J. Bertran, *J. Am. Chem. Soc.*, 1993, **115**, 5861.
15. O. Eisenstein and P. Daudey, to appear.
16. D. M. Heinekey, personal communication.

Acknowledgments

My work in this area has benefited from many interactions with NMR spectroscopists, inorganic chemists, and theoreticians interested in transition metal hydride chemistry. Especially important to me has been my close and very enjoyable collaboration with Professor D. Michael Heinekey and his group. Without his careful attention to experimental detail, the phenomenon of exchange coupling in solution NMR spectra would probably still remain undiscovered.

Biographical Sketch

Kurt Z. Zilm. *b* 1955. B.S., 1976, Ph.D., 1981, University of Utah, USA. Introduced to NMR by D. M. Grant. Faculty in Chemistry Yale University, 1983–present. Approx. 80 publications. Research interests: theory and development of NMR techniques for solving problems of chemical interest, studies of transition metal polyhydrides, supported metal catalysts, matrix-isolated organic intermediates and metal clusters, applications of optical pumping in gas phase NMR, tunneling in NMR, dipolar demagnetizing field effects in NMR and development of new solids NMR techniques for structural studies in polymers and organic geochemistry.

Relativistic Computation of NMR Shieldings and Spin–Spin Coupling Constants

Jochen Autschbach and Tom Ziegler

University of Calgary, Calgary, Canada

1 Introduction 1
2 Relativistic Theory of NMR Shieldings and Spin–Spin Coupling Constants 1
3 Heavy Atom Nuclear Shieldings 8
4 Heavy Atom Spin–Spin Couplings 13
5 Summary 16
6 Related Articles in this Volume 16
7 Related Articles in Volumes 1–8 16
8 References 16

1 INTRODUCTION

A long time has passed since the formulation of relativistic quantum mechanics. Meanwhile, it has become chemistry textbook knowledge that atoms and molecules containing heavy nuclei exhibit so-called relativistic effects which, e.g., cause mercury to be liquid and are responsible for the color and the chemical inertness of gold. A qualitative explanation based on the Bohr model for one-electron atoms is straightforward. Special relativity has to be considered when velocities are no longer small compared to the speed of light. The Bohr formulae can be interpreted such that, in atomic units (see below), the electron in the ground state has a velocity of Z, with Z being the nuclear charge. The speed of light, c, has a value of approximately 137 in the same units. This illustrates that electrons in heavy atoms can reach a substantial fraction of the speed of light, and it is therefore clear that core orbitals in heavy atoms show sizable relativistic effects. It has been somewhat surprising, however, that valence orbitals exhibit relativistic effects of the same order in c^{-2} as core orbitals, which cause significant changes in the chemical properties of heavy element compounds. Relativistic effects for valence orbitals are nowadays well investigated and understood. For elements of the 6th row of the periodic table (Cs–Rn), the correction terms are so large that nonrelativistic quantum chemical computations often do not yield even a qualitatively correct answer. It is generally accepted that relativistic computations have to be carried out for such atoms and their compounds. c^{-2} appears in the relativistic theory – due to its smallness – as an expansion parameter, by which perturbational orders of relativistic corrections are characterized. The nonrelativistic limit is approached for $c \to \infty$.

Nuclear shieldings and spin–spin couplings are very sensitive experimental probes for the electronic and geometrical structure of a compound. For the same reason, however, they are difficult to compute accurately. In the presence of heavy nuclei, any attempt to achieve a reasonable agreement between theory and experiment has to consider relativistic effects in the computations. Both the current state of relativistic quantum chemical methods and the art of computing NMR parameters have advanced far enough that a large body of computational results for heavy element systems obtained with a variety of methods is available. Remarkable results have been achieved, e.g., the explanation of certain experimental trends such as the 'halogen dependence', or the ability to compute NMR parameters with the heavy nuclei as the probe. Therefore it is appropriate to give a short overview here of the methodologies being used so far as well as results that have been obtained for a number of heavy atom systems.

Concerning the methodology, we focus on methods that are capable of treating both light and heavy nuclei with respect to NMR shieldings and spin–spin couplings on a first-principles basis (meaning ab initio methods and approximate Kohn–Sham density functional theory (DFT)). Variational methods are emphasized, but the possibility of treating relativity as a perturbation is frequently mentioned. In particular for nuclear shieldings, certain chemical trends have successfully been explained upon inclusion of spin-orbit coupling to first order alone, and a number of such results are quoted in Section 3. Concerning the spin–spin couplings, we focus on couplings involving a heavy nucleus. Dimensionless atomic units (unit of charge $e = 1$, electron mass $m = 1$, $4\pi\varepsilon_0 = 1$, $h = 2\pi$, $c \approx 137.036$) are used in the theoretical section. The electronic g-factor is assumed to be exactly 2, as predicted by the Dirac equation, and not written explicitly.

Computed or experimental nuclear shieldings and chemical shifts are quoted in ppm (10^{-6}), spin–spin couplings either as reduced couplings K in SI units of $\mathrm{kg\,m^{-2}\,s^{-2}\,A^{-2}}$, or as coupling constants J in Hertz ($\mathrm{s^{-1}}$). The discussion of theoretical results and interpretations refer to a time-independent treatment of closed-shell molecules with fixed nuclei.

In Section 2, we outline the theoretical approach to heavy atom NMR. Illustrative results and interpretations for chemical shifts and spin–spin couplings presented in Sections 3 and 4, respectively, are chosen in order to cover a range of chemical applications and trends and a number of different methodologies.

2 RELATIVISTIC THEORY OF NMR SHIELDINGS AND SPIN–SPIN COUPLING CONSTANTS

In this section the theoretical methodology that allows for the relativistic computation of NMR parameters of molecules is outlined. Due to the vast amount of literature and the many different techniques in the field of relativistic quantum chemistry, no attempt has been made to give a complete overview. Instead, a hierarchy of currently common approximations from which magnetic properties can be extracted is sketched in a pragmatic way. For details we refer to some of the books and review articles on relativistic quantum chemistry.[1–4]

2.1 Relativity in Quantum Chemistry

'Ordinary' nonrelativistic quantum chemistry deals with the solution of the time-independent many-electron Schrödinger equation

$$\hat{\mathcal{H}}^{\mathrm{nrel}}\Psi = \Psi E \tag{1}$$

where Ψ is the many-electron wavefunction of an atom or molecule with fixed nuclei, and E is the total energy.

$$\hat{\mathcal{H}}^{\mathrm{nrel}} = \sum_{i=1} \frac{\hat{\boldsymbol{p}}_i^2}{2} + \sum_{i=1} V_{Ni} + V_{ee} + V_{\mathrm{nuc}} \tag{2}$$

is the nonrelativistic Hamiltonian consisting of the nonrelativistic kinetic energy operator $\hat{\boldsymbol{p}}_i^2/2$ for each electron i, the electron-nucleus attraction potential V_{Ni} for each electron, the nonrelativistic electron−electron Coulomb repulsion $V_{ee} = \sum_{j>i} 1/r_{ij}$, and the internuclear repulsion potential V_{nuc}. $\hat{\boldsymbol{p}} = -i\boldsymbol{\nabla}$ is the momentum operator in space representation. Since analytic solutions of equation (1) for many electron systems are not known, approximations have to be made. As a starting point, the N-electron equation is usually separated into N effective one-electron equations for one-particle wavefunctions ψ (so called atomic or molecular orbitals) which depend on an effective potential V. For simplicity, we implicitly refer to such effective one-electron equations (or true one-electron systems) in the following, by using the symbol ψ for the one-electron wavefunction or orbital. Particular details of common approximations are not discussed in this section.

In relativistic quantum chemistry, $\hat{\mathcal{H}}^{\mathrm{nrel}}$ in equation (1) is replaced by its relativistic counterpart. All of the problems of the nonrelativistic many-electron theory are present in the relativistic formulation as well. Hence, similar techniques are common in order to find approximate solutions; in particular, use of orbitals is made. However, relativistic quantum chemistry has its own specific problems associated with it, one of them being the lack of a consistent relativistic many-particle Hamiltonian being derived from quantum electrodynamics. Therefore, relativistic many-electron atomic and molecular computations rely on the use of the four-component 'no-pair' Dirac−Coulomb−Breit Hamiltonian or some approximation obtained from it:

$$\hat{\mathcal{H}}^{\mathrm{DCB}} = \hat{P}^+ \left[\sum_{i=1}^{N} (c\boldsymbol{\alpha}_i\hat{\boldsymbol{p}}_i + \beta_i c^2) + V_{Ni} + V_{ee} + \sum_{j>i=1}^{N} \hat{\mathcal{H}}_{ij}^{\mathrm{B}} + V_{\mathrm{nuc}} \right] \hat{P}^+ \tag{3}$$

Here, $\boldsymbol{\alpha}$ and β are 4×4 matrices introduced by Dirac in order to obtain a relativistic wave equation for spin-1/2 particles from the 'classical' relativistic Hamilton function. In its standard representation, $\boldsymbol{\alpha}$ is written in terms of the well-known Pauli spin-matrices $\boldsymbol{\sigma}_s$ (not to be confused with the symbol for the nuclear shielding tensor). The $\hat{\mathcal{H}}_{ij}^{\mathrm{B}}$ (Breit interaction, see, e.g., Ref.[4]) are relativistic corrections to V_{ee} that contain the so-called magnetic interaction and further account for the fact that the electron−electron interaction is not instantaneous but is transmitted with a finite speed. Use of the projection operators $\hat{P}^+$ cures some of the problematic features of the Dirac−Coulomb(−Breit) operator by restricting its solutions to the positive energy spectrum, the eigenfunctions of which are identified with the desired electronic states (no-pair approximation[2,5]). We have to stress here that though $\hat{\mathcal{H}}^{\mathrm{DCB}}$ is in general not truly Lorentz invariant, it "provides an excellent approximation to the full theory".[3]

The main difference between the four-component relativistic and the nonrelativistic Hamiltonian is seen to be in the kinetic energy operator for an electron, which is $c\boldsymbol{\alpha}\hat{\boldsymbol{p}} + \beta c^2$ in equation (3) instead of $\hat{\boldsymbol{p}}^2/2$ in $\hat{\mathcal{H}}^{\mathrm{nrel}}$. It takes into account the relativistic increase of electron mass due to high velocities, it includes the electron's rest mass energy, it incorporates the electron spin, and also causes the spin-orbit coupling. Although electron spin needs to be considered in the nonrelativistic theory in an ad hoc manner in order to account for experimental facts, a coupling between spin and spatial degrees of freedom occurs only in the relativistic theory. For simplicity of notation, we omit the $\hat{P}^+$ in the following, and we do not explicitly consider the Breit interaction since it is actually being neglected in many computations. Its relative importance to, e.g., total atomic energies was found to decrease with increasing nuclear charge from ∼50% in He to ∼2% in Hg relative to the one-electron relativistic corrections.[6]

A conceptually straightforward way of performing a relativistic molecular computation in order to obtain a starting point for a calculation of NMR properties is to use directly the time-independent Dirac equation

$$\hat{\mathcal{H}}^{\mathrm{D}}\psi^{\mathrm{D}} = \psi^{\mathrm{D}}E \tag{4}$$

with

$$\hat{\mathcal{H}}^{\mathrm{D}} = c\boldsymbol{\alpha}\hat{\boldsymbol{p}} + \beta c^2 + V \tag{5}$$

Note that we used here the aforementioned simple notation for (effective) one-electron equations. ψ^{D} is a four-component relativistic orbital. Because $\boldsymbol{\alpha}$ and β are 4×4 matrices, the wavefunction has to be a four-component vector for which each component is a complex function of space. Due to the four components, such molecular computations are unfortunately quite expensive as compared to nonrelativistic ones, and the explicit inclusion of electron correlation is a formidable task.

Many attempts have been made to transform the four-component equation (4) into two-component form, in order to keep interpretations simpler and to reduce the computational effort. However, so-called picture change effects occur, a discussion of which is beyond the scope of this overview (see, e.g., Ref.[7] and references cited therein.) Here we give an account of some of these methods. Writing $\boldsymbol{\alpha}$ explicitly in terms of the 2×2 Pauli spin-matrices $\boldsymbol{\sigma}_s$, the Dirac equation (4) reads

$$(\hat{\mathcal{H}}^{\mathrm{D}} - E)\psi^{\mathrm{D}} = \begin{pmatrix} V - E & c\boldsymbol{\sigma}_s\hat{\boldsymbol{p}} \\ c\boldsymbol{\sigma}_s\hat{\boldsymbol{p}} & V - E - 2c^2 \end{pmatrix} \begin{pmatrix} \varphi \\ \chi \end{pmatrix} = 0 \tag{6}$$

The zero of the energy scale has been shifted in equation (6) to $+mc^2$, $m = 1$, the rest mass energy of the electron, so that bound states have negative energy as usual in nonrelativistic quantum chemistry. Here, φ and χ are the so-called 'upper' and 'lower' components of the four-component orbital ψ^{D}, each of them made up of two components. The functions φ

and χ are also frequently referred to as the 'large' and 'small' components because of the $1/2c$ prefactor in equation (7) below. (Note, however that, depending on the potential and the location, the 'small component' can be much larger than the 'large' one, e.g., for $p_{1/2}$ orbitals close to the nucleus.) From the second row of the matrix one obtains explicitly

$$\chi = X\varphi = \frac{1}{2c} k \boldsymbol{\sigma}_s \hat{\boldsymbol{p}} \varphi \tag{7}$$

with $k = (1 - [(V - E)/2c^2])^{-1}$, which yields the relation between the upper and the lower component. Because φ and χ are not independent of each other, it should be possible to obtain a relativistic two-component equation for φ or χ alone, the solutions of which contain the same information as ψ^{D}. In the elimination of the small component (ESC) scheme, equation (7) is directly substituted in the equation obtained from the first row of the matrix in (6) and yields the two-component Hamiltonian:

$$\hat{\mathcal{H}}^{\mathrm{ESC}} = V + \frac{1}{2}(\boldsymbol{\sigma}_s \hat{\boldsymbol{p}}) k (\boldsymbol{\sigma}_s \hat{\boldsymbol{p}}) \tag{8}$$

In the nonrelativistic limit, $c \to \infty$, $k \to 1$, and then, with $(\boldsymbol{\sigma}_s \hat{\boldsymbol{p}})^2 = \hat{\boldsymbol{p}}^2$, the nonrelativistic Schrödinger Hamiltonian is recovered from the ESC operator (8):

$$\hat{\mathcal{H}}^{\mathrm{nrel}} = V + \frac{1}{2}(\boldsymbol{\sigma}_s \hat{\boldsymbol{p}})^2 \tag{9}$$

Another way in which to obtain the nonrelativistic limit is to multiply (4) with $\hat{\mathcal{H}}^{\mathrm{D}}$ before taking the limit $c \to \infty$. Although the ESC equation appears to be very illustrative, the Hamiltonian depends (through k) on the unknown energy and is not usable in actual linear variational calculations. In order to arrive at an energy-independent two-component equation, the Foldy–Wouthuysen (FW) transformation of $\hat{\mathcal{H}}^{\mathrm{D}}$ to block-diagonal form is achieved by

$$\hat{\mathcal{H}}^{\mathrm{FW}} = U \hat{\mathcal{H}}^{\mathrm{D}} U^{-1} \tag{10}$$

When $\hat{\mathcal{H}}^{\mathrm{FW}}$ is block diagonal, this completely uncouples the upper and lower component and yields the desired two-component equation and $\chi = X\varphi$, an energy-independent relation between upper and lower component [see equation (7)]. U can be written in terms of X, see, e.g., the literature cited in Ref.[7] For many-electron systems, the exact form of X and U and therefore the exact form of $\hat{\mathcal{H}}^{\mathrm{FW}}$ are not known. Different approximations for X yield different approximate two-component Hamiltonians in which the uncoupling of the two components is only achieved to a certain order in c^{-2}. These approximate two-component Hamiltonians are sometimes collectively denoted as 'quasi relativistic'.

A rather simple approach is to expand (7) to zeroth order in c^{-2}. This yields $X \approx c\boldsymbol{\sigma}_s \hat{\boldsymbol{p}}/2c^2$, which results in the famous Pauli Hamiltonian[8] after carrying out the transformation (10) with $U(X)$:

$$\hat{\mathcal{H}}^{\mathrm{Pauli}} = \hat{\mathcal{H}}^{\mathrm{nrel}} - \frac{\hat{\boldsymbol{p}}^4}{8c^2} - \frac{(\hat{\boldsymbol{p}}^2 V)}{8c^2} + \frac{i}{4c^2}\boldsymbol{\sigma}_s[(\hat{\boldsymbol{p}} V) \times \hat{\boldsymbol{p}}] \tag{11}$$

The second, third, and fourth term on the right-hand side of (11) are the mass–velocity (MV), Darwin (DAR), and spin-orbit (SO) terms, respectively, representing corrections of order c^{-2} to the nonrelativistic Hamiltonian. The Pauli operator has certain pathological features due to the fact that close to a nucleus where V is very large (it goes to $-\infty$ for point-like nuclei), $(V - E)/2c^2$ is not small and neglecting this term in equation (7) is not justified. As a result, the Pauli operator affords severe singularities. Moreover, it is not variationally stable and permits only a perturbational treatment to first order. Higher order contributions yield diverging terms. Variational computations based on the Pauli operator have been frequently carried out, by using frozen cores and minimal basis sets in the core regions for valence orbitals, under which circumstances the variational instability can be kept somewhat under control in many cases. We refer to such frozen core methods in Sections 3 and 4 when speaking about variational Pauli computations. A *scalar relativistic* approach is obtained by omitting the SO term. This yields a one-component formalism analogous to the nonrelativistic scheme with pure α- and β-spin orbitals, that contain the – in many cases dominant – scalar relativistic effects. It is also possible to separate off a spin-orbit part in the Dirac equation.

One of the possible alternatives for the Pauli Hamiltonian is offered by the so-called zeroth order regular approximation (ZORA) method.[9] Some authors refer to the ZORA Hamiltonian as the Chang–Pélissier–Durand (CPD) operator. It is obtained from the zeroth order of an expansion of k in powers of $E/(2c^2 - V)$ in equation (7). This expansion parameter remains rather small in particular where the potential V goes to $-\infty$. The two-component ZORA Hamiltonian resulting from the transformation (10) reads

$$\hat{\mathcal{H}}^{\mathrm{ZORA}} = V + \frac{1}{2}(\boldsymbol{\sigma}_s \hat{\boldsymbol{p}}) \mathcal{K} (\boldsymbol{\sigma}_s \hat{\boldsymbol{p}}) \tag{12a}$$

$$= V + \frac{1}{2}\hat{\boldsymbol{p}} \mathcal{K} \hat{\boldsymbol{p}} + \frac{i}{2}\boldsymbol{\sigma}_s[(\hat{\boldsymbol{p}}\mathcal{K}) \times \hat{\boldsymbol{p}}] \tag{12b}$$

with $\mathcal{K} = 2c^2/(2c^2 - V)$. Note the formal similarity to the ESC Hamiltonian in (8), with k replaced by $\mathcal{K}$. The nonrelativistic limit corresponds to $\mathcal{K} \to 1$, $(\hat{\boldsymbol{p}}\mathcal{K}) = 0$. The first and the second term in (12b) yield $\hat{\mathcal{H}}^{\mathrm{nrel}}$ plus scalar relativistic corrections, while the third term is the ZORA SO operator. For small V, $(\hat{\boldsymbol{p}}\mathcal{K}) \approx (\hat{\boldsymbol{p}} V)/2c^2$, and the ZORA SO term is similar to the Pauli SO term. Close to a nucleus, both operators differ substantially. The use of the ZORA method in heavy element computations is becoming increasingly popular, and the results are in most cases superior to those obtained with the Pauli operator. Conceptually, the ZORA operator has the disadvantage of not being invariant with respect to a change of the origin of the energy scale (gauge invariance), as can be seen from the fact that only V but not $(V - E)$ occurs in the operator. The standard choice for the potential is $V(\boldsymbol{r}) \to 0$ for $\boldsymbol{r} \to \infty$. Most of the resulting problems can be circumvented by a "scaling" procedure or by the use of frozen core potentials or model potentials for the construction of $\mathcal{K}$.

A different way of transforming the Dirac Hamiltonian to two-component form is used in the Douglas–Kroll (DK) method. Here, U in equation (10) is obtained via subsequent transformations that uncouple the upper and lower components to some order n in c^{-2} written as

$$U_n = \sqrt{1 + W_n^2} + W_n \tag{13}$$

where W_n is anti-hermitian. For U_0, the FW transformation for the free electron is used. To higher orders, equations for W_n have to be solved in order to achieve further uncoupling. Already with U_1, most of the relativistic effects are recovered. We refer the reader to, e.g., Ref.[3] for details and original references. In particular due to the work of Hess and coworkers, the DK method has been established as a reliable tool in quantum chemistry for the computation of heavy element compounds. To some extent, the ZORA and the DK method to lowest order yield quite comparable results for many molecular properties. As an advantage, the DK method does not suffer from a gauge invariance problem, at the disadvantage of a somewhat more complicated formalism, if spin-orbit coupling and magnetic fields are included.

In order to arrive at a relativistic perturbation theory that avoids the infinities of the Pauli Hamiltonian to higher orders, so-called 'direct' or 'Dirac' four-component perturbation theory (DPT) can be employed. By a simple change of metric between upper and lower components in the Dirac equation (6), an expansion of the resulting four-component equation in powers of c^{-2} is straightforward and leads to nonsingular first and higher order expressions for E and ψ. A treatment of magnetic properties has been described in detail in the literature.[10] However, higher order expressions become computationally rather expensive, while at the same time it is well known that first-order relativistic perturbation theory is not sufficient for such 'relativistic' elements as, e.g., Au, Hg or Pb for the determination of bond energies or molecular geometries. It can be assumed that relativistic corrections up to order c^{-4} at least are also necessary for NMR parameters for such nuclei, in which case a variational procedure (Dirac, ZORA, DK) might be easier to implement and computationally not much more or even less expensive.

As an alternative to the aforementioned methods which incorporate relativity directly into the calculations, the use of relativistic effective core potentials (ECPs) allows for consideration of relativistic effects in molecular computations. Inclusion of spin-orbit coupling is also possible in these methods. Recent benchmark calculations[11] have shown that ECPs can yield very reliable properties of heavy element compounds.

As already mentioned, the potential V in the equations in this section might not simply refer to the external potential (e.g., V_{Ni}) for one-electron systems but to an effective many-electron potential. In this case, V implicitly contains effects that are due to the electron–electron Coulomb repulsion $1/r_{ij}$. The explicit transformation of $1/r_{ij}$ to two-component form yields new relativistic operators of order c^{-2} instead, for example the two-electron spin-orbit operator. Use of the effective electronic potential in V in the one-electron SO operator accounts, to some extent, for these two-electron terms in a mean-field sense. Transformation of the Breit interaction to two-component form yields further two-electron terms, such as the spin-other-orbit operator.

2.2 Nuclear Shieldings and Spin–Spin Couplings

A basic quantity that formally allows access to many properties of atoms and molecules is the total (electronic + nuclear repulsion) energy E of the system. It is readily available, to some degree of accuracy depending on the approximations that have been made, from quantum chemical computations, either from a relativistic or nonrelativistic formalism, based on variational or perturbational approaches. We refer to the wavefunction or the set of orbitals that produced this energy as the 'zeroth order solution'. In practice, it does not initially contain the effects from external magnetic fields or nuclear spins, but it might incorporate relativistic effects. Many observables, among them NMR shielding and spin–spin coupling tensors, can be defined as derivatives of the total energy of the system under investigation. The shielding tensor $\boldsymbol{\sigma}$ for a nucleus A is given by

$$\boldsymbol{\sigma}(A) = \left.\frac{\partial^2 E}{\partial \boldsymbol{B}^{\mathrm{ext}} \partial \boldsymbol{\mu}_A}\right|_{\boldsymbol{B}^{\mathrm{ext}}=0, \boldsymbol{\mu}_A=0} \tag{14a}$$

while the reduced nuclear spin–spin coupling tensor $\mathbf{K}$ involving two nuclei A and B is obtained from

$$\mathbf{K}(A, B) = \left.\frac{\partial^2 E}{\partial \boldsymbol{\mu}_A \partial \boldsymbol{\mu}_B}\right|_{\boldsymbol{\mu}_A=0, \boldsymbol{\mu}_B=0} \tag{14b}$$

Here, $\boldsymbol{B}^{\mathrm{ext}}$ is the applied external magnetic field, and $\boldsymbol{\mu}_A$ is the magnetic moment of nucleus A, related to its intrinsic angular momentum $\boldsymbol{I}_A$ by $\boldsymbol{\mu}_A = \gamma_A \hbar \boldsymbol{I}_A$ with γ_A being the magnetogyric ratio of the nucleus. We refer to some of the many excellent review articles focusing on the nonrelativistic computation of NMR parameters for details.[12–15] Equations (14a,b) conceptually serve as the starting point for a perturbational approach by which the energy derivatives can be evaluated once the zeroth order solution has been obtained. For the spin–spin coupling, the direct (through space) coupling between two nuclei does not yield a contribution to the coupling constants for rapidly rotating molecules (i.e., for measurements in gas phase or in solution) and is not discussed further. We implicitly refer to indirect spin–spin couplings throughout the rest of this article.

For the general case of two perturbations, described by the perturbation parameters $\boldsymbol{\kappa}$ and $\boldsymbol{\lambda}$ with Cartesian components κ_x, κ_y, κ_z etc., the mixed second derivative of the total energy

$$E = \langle \Psi | \hat{\mathcal{H}} | \Psi \rangle \tag{15}$$

with respect to the perturbation parameters is given from standard double perturbation theory by equation (16). There it is assumed that the Hellmann–Feynman theorem holds with respect to the first perturbation $\boldsymbol{\lambda}$ for approximate zeroth-order solutions. In the NMR case, the nuclear magnetic moments or the external magnetic field are directly interpreted as the perturbation parameters due to their relative 'smallness'.

$$\begin{aligned} E^{(1,1)} :&= \left.\frac{\partial^2 E}{\partial \boldsymbol{\kappa} \partial \boldsymbol{\lambda}}\right|_{\boldsymbol{\kappa}=0, \boldsymbol{\lambda}=0} \\ &= \langle \Psi^{(0,0)} | \hat{\mathcal{H}}^{(1,1)} | \Psi^{(0,0)} \rangle + 2\mathrm{Re} \langle \Psi^{(0,1)} | \hat{\mathcal{H}}^{(1,0)} | \Psi^{(0,0)} \rangle \end{aligned} \tag{16}$$

The superscripts denote the order of perturbation with respect to $\boldsymbol{\lambda}$ and $\boldsymbol{\kappa}$, respectively. Because $\boldsymbol{\lambda}$ and $\boldsymbol{\kappa}$ are vectors, $E^{(1,1)}$ is a 2nd rank tensor. $\hat{\mathcal{H}}^{(1,0)} = \partial \hat{\mathcal{H}} / \partial \boldsymbol{\lambda}|_{\boldsymbol{\lambda}=0}$, $\Psi^{(0,1)} = \partial \Psi / \partial \boldsymbol{\kappa}|_{\boldsymbol{\kappa}=0}$, etc. $\Psi^{(0,1)}$ represents the change of the wavefunction due to the presence of the perturbation denoted by $\boldsymbol{\kappa}$, i.e., either the external magnetic field, or the magnetic field arising from one

of the nuclear spins. $\Psi^{(0,1)}$ can be formally obtained from solving the first-order perturbed wave equation

$$(\hat{\mathcal{H}}^{(0,0)} - E^{(0,0)})\Psi^{(0,1)} + (\hat{\mathcal{H}}^{(0,1)} - E^{(0,1)})\Psi^{(0,0)} = 0 \qquad (17)$$

showing that $\hat{\mathcal{H}}^{(0,1)}$ has to be known in order to compute $\Psi^{(0,1)}$. In DFT, formally similar expressions involving a sum over the Kohn–Sham orbitals instead of the many-electron wavefunction Ψ are used to compute $\boldsymbol{\sigma}$ and $\mathbf{K}$.

In the sum-over-states formulation it is assumed that the unperturbed ground state $\Psi_0 = \Psi^{(0,0)}$ with $E_0 = E^{(0,0)}$ and *all* the excited states (energies E_i and wavefunctions Ψ_i) corresponding to the field-free Hamiltonian $\hat{\mathcal{H}}^{(0,0)}$ are known. The Ψ_i form a complete basis set in which $\Psi^{(0,1)}$ can be expressed as

$$\Psi^{(0,1)} = \sum_{a\neq 0} \Psi_a C_a \qquad (18)$$

with yet unknown coefficients C_a. With the first-order equation (17), one obtains for the C_a after some manipulation

$$C_a = \sum_{a\neq 0} \frac{\langle\Psi_a|\hat{\mathcal{H}}^{(0,1)}|\Psi_0\rangle}{E_0 - E_a} \qquad (19)$$

and therefore for the nuclear shielding or spin–spin coupling

$$E^{(1,1)} = \langle\Psi_0|\hat{\mathcal{H}}^{(1,1)}|\Psi_0\rangle + 2\mathrm{Re}\sum_{a\neq 0} \frac{\langle\Psi_0|\hat{\mathcal{H}}^{(0,1)}|\Psi_a\rangle\langle\Psi_a|\hat{\mathcal{H}}^{(1,0)}|\Psi_0\rangle}{E_0 - E_a} \qquad (20)$$

We have to stress here that although equation (20) is *formally* correct, in practice not all (or any) of the excited states of $\hat{\mathcal{H}}^{(0,0)}$ are (or can be) known. However, equation (20) serves as a convenient basis for an interpretation of the final results and approximations to it can be easily identified within orbital models. Employing variational perturbation theory, $E^{(1,1)}$ is in practice usually directly computed from the zeroth order solution based upon the set of occupied and unoccupied (virtual) orbitals that serve as a one-particle basis in most theoretical methods.[16] In simple cases, for each occupied orbital a sum over virtual orbitals similar to (20) can be derived as the contributions to $E^{(1,1)}$, in which $E_0 - E_a$ is replaced by differences between occupied and virtual orbital energies, $\epsilon_i - \epsilon_a$. However, these orbital contributions also take into account possible first-order change in the potential caused by the perturbation, and a possible dependence of the basis set on the perturbation. Neglecting any change in the potential V leads to so-called uncoupled equations that are much easier and computationally cheaper to solve. (In DFT, neglecting the current-density dependence of the density functional leads to the mentioned uncoupled approach when the first-order perturbations of the orbitals due to the external magnetic field are evaluated.) For interpretation purposes, the potential change is often negligible, in which case the orbital contributions can have exactly the form (20), but with Ψ_0 replaced by an occupied orbital ψ_i (with energy ϵ_i) and Ψ_a and E_a replaced by virtual orbitals ψ_a and their energies ϵ_a. In particular the HOMO-LUMO gap plays an important role here, since it leads to the largest individual $1/(\epsilon_i - \epsilon_a)$. Another factor is, of course, the magnitude of the $\langle\psi_i|\hat{\mathcal{H}}^{(0,1)}|\psi_a\rangle$ and $\langle\psi_a|\hat{\mathcal{H}}^{(1,0)}|\psi_i\rangle$ matrix elements. For chemical shifts (not shieldings) and spin–spin couplings, it turns out that $\langle\Psi_0|\hat{\mathcal{H}}^{(1,1)}|\Psi_0\rangle$, the diamagnetic term (see below), is often of only minor importance. It is also possible to write the diamagnetic term in a sum-over-states form.[17] *For simplicity of notation, we refer to equation (20) as the working equation for evaluating* $\boldsymbol{\sigma}$ *and* $\mathbf{K}$ *regardless of the actual method being used.*

Once the zeroth order solution is known, and the perturbation operators with respect to $\boldsymbol{\mu}_A$ and $\boldsymbol{B}^{\mathrm{ext}}$ have been formulated, $\boldsymbol{\sigma}$ and $\mathbf{K}$ can be computed based on equation (20) in some chosen computational approximation. For the relativistic case of heavy element systems, E, Ψ and the perturbation operators refer to a relativistic zeroth-order treatment. In case relativity is treated as a perturbation itself, this leads to at least second- and third-order perturbation expressions for $\boldsymbol{\sigma}$ and $\mathbf{K}$ in which the order of derivatives is arbitrary. In this case, relativity can be conceptually regarded as a perturbation of an initially nonrelativistic expression for (14a,b).

In order to apply equation (20) for the computation of NMR shieldings or spin–spin couplings, the presence of the external magnetic field $\boldsymbol{B}^{\mathrm{ext}}$ and the magnetic field due to the nuclear spins has thus to be considered in the theory. More specifically, within a chosen theoretical level (nonrelativistic, four-component, a variational two-component scheme, relativistic perturbation theory, ...) the Hamiltonian $\hat{\mathcal{H}}(\boldsymbol{B}^{\mathrm{ext}}, \boldsymbol{\mu})$ is to be formulated in order to determine $\hat{\mathcal{H}}^{(1,1)}$, $\hat{\mathcal{H}}^{(1,0)}$ and $\hat{\mathcal{H}}^{(0,1)}$. Magnetic fields $\boldsymbol{B}$ are usually incorporated into quantum chemistry by finding the corresponding magnetic vector potential $\boldsymbol{A}$ which is related to the magnetic field $\boldsymbol{B}$ by $\boldsymbol{B} = \nabla \times \boldsymbol{A}$, and making the so-called minimal substitution for the momentum operator in the field-free Hamiltonian,

$$\hat{\boldsymbol{p}} \longrightarrow \hat{\boldsymbol{\pi}} = \hat{\boldsymbol{p}} - q\boldsymbol{A} \qquad (21)$$

with respect to a particle of charge q. We use $q = -e = -1$ for an electron in the following.

The well-known gauge-invariance problem arises here, viz. a given magnetic field does not uniquely define the vector potential, since adding the gradient $\nabla f(\boldsymbol{r})$ of any scalar function to $\boldsymbol{A}$ does not change $\boldsymbol{B}$, because $\nabla \times \nabla f(\boldsymbol{r}) = 0$. Often, f is chosen such that $\nabla\boldsymbol{A} = 0$ (Coulomb gauge). We use this gauge in the following. A different gauge of $\boldsymbol{A}$ can, e.g., be represented by choosing a different origin for the coordinate representation of $\boldsymbol{A}$. Although for a large class of variationally determined *exact* wavefunctions, expectation values do not depend on the chosen gauge, this is not generally true for approximate wavefunctions in a finite basis.[16]

For a point-like nuclear magnetic dipole, the vector potential is

$$\boldsymbol{A}^{\mu}_A = \frac{1}{c^2}\frac{\boldsymbol{\mu}_A \times \boldsymbol{r}_A}{r_A^3} \qquad (22)$$

$\boldsymbol{r}_A$ being the distance vector with respect to nucleus A, and r_A its length. Due to the strong inhomogeneity of $\boldsymbol{A}^{\mu}_A$, the position of the nucleus A is generally used as the origin for $\boldsymbol{A}^{\mu}_A$. The vector potential of an external, homogeneous magnetic field reads

$$\boldsymbol{A}^{\mathrm{ext}} = \frac{1}{2}\boldsymbol{B}^{\mathrm{ext}} \times \boldsymbol{r} \qquad (23)$$

For a molecule with many atoms there exists no obvious gauge origin since $\boldsymbol{r}$ refers to an arbitrarily chosen coordinate system. Nuclear shieldings obtained with wavefunctions approximated in a finite basis depend more or less strongly on the chosen origin. The $\boldsymbol{A}^{\text{ext}}$ gauge problem is circumvented in, e.g., the gauge-independent or gauge-including atomic orbitals (GIAO) or the individual gauge for localized orbitals (IGLO) methods. In these methods, field dependent basis functions or molecular orbitals are employed to ensure gauge invariance of expectation values. Such distributed gauge origin methods are commonly used in computations of nuclear shieldings. Another, less effective procedure is to supplement the basis sets by functions that are chosen such as to remove the gauge dependence to some extent without being of critical importance for the determination of the energy or the molecular structure. The gauge origin problem has been extensively discussed in the literature (see, e.g., Refs.[12,13,18] and literature cited therein for details).

Equation (22) is the most frequently used expression for the nuclear magnetic vector potential. It is known that for very accurate relativistic results, a finite nucleus model should be adopted both to obtain the zeroth-order solution as well as in the NMR perturbation calculation. However, almost all of the results quoted later in this work have been obtained with the point-nucleus approximation, and the influence of finite-nucleus corrections on the final results does not seem to be of critical importance.

Substituting (21) into the nonrelativistic one-electron Schrödinger Hamiltonian, equation (9), yields the additional 'magnetic' terms

$$\hat{\mathcal{H}}^{\text{mag}}_{\text{nrel}} = \frac{1}{2}(\boldsymbol{A}\hat{\boldsymbol{p}} + \hat{\boldsymbol{p}}\boldsymbol{A} + i\boldsymbol{\sigma}_s[\hat{\boldsymbol{p}} \times \boldsymbol{A} + \boldsymbol{A} \times \hat{\boldsymbol{p}}] + \boldsymbol{A}^2) \tag{24}$$

The operators linear in $\boldsymbol{A}$ are called the paramagnetic terms, while those proportional to $\boldsymbol{A}^2$ are called the diamagnetic terms. The second term on the right-hand side of equation (24) describes the interaction of the electronic spin with a magnetic field and is not present if one starts with the one-component Schrödinger equation where $(\boldsymbol{\sigma}_s\hat{\boldsymbol{p}})^2$ of equation (9) is replaced by $\hat{\boldsymbol{p}}^2$ before the minimal substitution is made (this implies that the substitution $\hat{\boldsymbol{p}} \rightarrow \hat{\boldsymbol{\pi}}$ has to be made before transformation to two-component form and then the limit $c \rightarrow \infty$ is taken). In the ZORA or ESC case, formally very similar magnetic operators are obtained that contain relativistic corrections due to the presence of $\mathcal{K}$ or k. For the ZORA case, see Refs.[19,20] For a derivation of the magnetic terms arising from the second-order DK transformation and from the Pauli Hamiltonian, see Refs.[21,22] The ESC case is illustrated elsewhere.[23]

Substituting $\hat{\boldsymbol{p}}$ with $\hat{\boldsymbol{\pi}}$ in the one-electron Dirac operator (5) yields a single paramagnetic term

$$\hat{\mathcal{H}}^{\text{mag}}_{\text{D}} = c\boldsymbol{\alpha}\boldsymbol{A} \tag{25}$$

Since the nonrelativistic limit (24) as well as relativistic two-component Hamiltonians afford a diamagnetic term, this should be contained in a result for $E^{(1,1)}$ obtained from (25). It has been shown that a diamagnetic contribution to $E^{(1,1)}$ in equation (16) indeed arises in the four-component scheme due to the contributions from negative energy eigenfunctions of $\hat{\mathcal{H}}^{\text{D}}$, that are used as a basis set in a sum-over-states expression for $\Psi^{(0,1)}$ in equation (16),[24] even though there is only a paramagnetic perturbation operator (25).

Upon explicit substitution of $\boldsymbol{A} = \boldsymbol{A}^{\text{ext}} + \sum_A \boldsymbol{A}^{\mu}_A$ from equation (23), and equation (22) or a finite-size magnetic dipole version of it, $\hat{\mathcal{H}}^{\text{mag}}(\boldsymbol{B}^{\text{ext}}, \boldsymbol{\mu})$ is finally obtained. Taking the derivatives with respect to $\boldsymbol{B}^{\text{ext}}$ and $\boldsymbol{\mu}_A$, $\boldsymbol{\mu}_B$ then yields $\hat{\mathcal{H}}^{(1,1)}$, $\hat{\mathcal{H}}^{(0,1)}$ and $\hat{\mathcal{H}}^{(1,0)}$ for a specific nonrelativistic or relativistic theoretical scheme. In the case of nuclear shieldings, it is most economic to take $\hat{\mathcal{H}}^{(1,0)} = \partial\hat{\mathcal{H}}/\partial\boldsymbol{\mu}_A|_{\boldsymbol{\mu}_A=0}$, while $\Psi^{(0,1)} = \partial\Psi/\partial\boldsymbol{B}^{\text{ext}}|_{\boldsymbol{B}^{\text{ext}}=0}$. In the nonrelativistic case, one obtains the one-electron operators

$$\begin{aligned}\hat{\mathcal{H}}^{\text{mag}}_{\text{nrel}}(\boldsymbol{B}^{\text{ext}}, \boldsymbol{\mu}) = \boldsymbol{A}^{\text{ext}^2} + \hat{\mathcal{H}}^{\text{OZ}} + \hat{\mathcal{H}}^{\text{SZ}} + \hat{\mathcal{H}}^{\text{OP}} \\ + \hat{\mathcal{H}}^{\text{DS}} + \hat{\mathcal{H}}^{\text{FC}} + \hat{\mathcal{H}}^{\text{SD}} + \hat{\mathcal{H}}^{\text{OD}}\end{aligned} \tag{26}$$

Here,

$$\hat{\mathcal{H}}^{\text{OZ}} = \frac{1}{2}\boldsymbol{B}^{\text{ext}} \cdot (\boldsymbol{r} \times \hat{\boldsymbol{p}}) = \frac{1}{2}\boldsymbol{B}^{\text{ext}} \cdot \hat{\boldsymbol{L}} \tag{27a}$$

$$\hat{\mathcal{H}}^{\text{SZ}} = \frac{1}{2}\boldsymbol{B}^{\text{ext}} \cdot \boldsymbol{\sigma}_s \tag{27b}$$

$$\hat{\mathcal{H}}^{\text{OP}} = \frac{1}{c^2}\sum_A \boldsymbol{\mu}_A \left(\frac{\boldsymbol{r}_A}{r_A^3} \times \hat{\boldsymbol{p}}\right) \tag{27c}$$

$$\begin{aligned}\hat{\mathcal{H}}^{\text{DS}} = \frac{1}{2c^2}\sum_A \Bigg[(\boldsymbol{\mu}_A \cdot \boldsymbol{B}^{\text{ext}})\left(\frac{\boldsymbol{r}_A}{r_A^3} \cdot \boldsymbol{r}\right) \\ -(\boldsymbol{\mu}_A \cdot \boldsymbol{r})\left(\boldsymbol{B}^{\text{ext}} \cdot \frac{\boldsymbol{r}_A}{r_A^3}\right)\Bigg]\end{aligned} \tag{27d}$$

$$\begin{aligned}\hat{\mathcal{H}}^{\text{FC}} + \hat{\mathcal{H}}^{\text{SD}} = \frac{1}{2c^2}\sum_A \boldsymbol{\sigma}_s \Bigg[\boldsymbol{\mu}_A \left(\nabla \cdot \frac{\boldsymbol{r}_A}{r_A^3}\right) \\ -(\boldsymbol{\mu}_A \cdot \nabla)\frac{\boldsymbol{r}_A}{r_A^3}\Bigg]\end{aligned} \tag{27e}$$

$$\hat{\mathcal{H}}^{\text{OD}} = \frac{1}{2c^4}\sum_{B\neq A} \frac{(\boldsymbol{\mu}_A \cdot \boldsymbol{\mu}_B)(\boldsymbol{r}_A \cdot \boldsymbol{r}_B) - (\boldsymbol{\mu}_A \cdot \boldsymbol{r}_B)(\boldsymbol{\mu}_B \cdot \boldsymbol{r}_A)}{r_A^3 r_B^3} \tag{27f}$$

(27a) is the orbital Zeeman term, (27b) spin Zeeman, (27c) paramagnetic orbital, (27d) diamagnetic shielding, (27e) Fermi-contact + spin-dipole, (27f) diamagnetic orbital term, respectively. The individual FC and SD operators, in particular the well-known δ function for the FC term, are obtained by explicitly carrying out the differentiation of $\boldsymbol{r}_A/r_A^3$ in (27e). Note that the presence of c in the nonrelativistic magnetic operators does *not* denote any relativistic terms, but c emerges from the magnetic units in equation (22) and the fact that the fine structure constant equals $1/c$ in the chosen atomic units. As already mentioned, the operators in the ZORA or ESC case are formally quite similar to the nonrelativistic ones, but include $\mathcal{K}$ or k and their derivatives, yielding different spatial contributions in particular for the FC term, but similar physical interpretations. We therefore use the same names for the operators when referring to these two-component relativistic schemes.

As compared to the nonrelativistic or two-component ones, the Dirac form of the one-electron magnetic operators look rather simple:

$$\hat{\mathcal{H}}^{\text{mag}}_{D}(\boldsymbol{B}^{\text{ext}}, \boldsymbol{\mu}) = -\frac{c}{2}\boldsymbol{B}^{\text{ext}} \cdot (\boldsymbol{\alpha} \times \boldsymbol{r}) - \frac{1}{c}\sum_A \boldsymbol{\mu}_A \cdot \left(\boldsymbol{\alpha} \times \frac{\boldsymbol{r}_A}{r_A^3}\right) \tag{28}$$

Taking the derivatives with respect to $\boldsymbol{B}^{\mathrm{ext}}$ and $\boldsymbol{\mu}_A$ in order to apply equation (20) is conceptually straightforward. Since (26) is connected to (28) as its nonrelativistic limit, the apparent simplicity of the four-component operators results in the many two-component terms through the coupling of the upper and lower components of the wavefunction by the Dirac operators. The 'Gordon-decomposition' of the Dirac shielding tensor provides a route to interpret the four-component results in the more common way of paramagnetic and diamagnetic contributions.[25] See, e.g., Ref.[26] for numerical examples.

Referring to the two-component scheme, equations (27a–f), it can be seen that the OZ, OP and DS operators contribute to the nuclear shielding. Explicitly,

$$\hat{\mathcal{H}}^{(1,1)} = \left.\frac{\partial^2 \hat{\mathcal{H}}^{\mathrm{DS}}}{\partial \boldsymbol{B}^{\mathrm{ext}} \partial \boldsymbol{\mu}_A}\right|_{\boldsymbol{B}^{\mathrm{ext}}=0,\,\boldsymbol{\mu}_A=0}$$

$$\hat{\mathcal{H}}^{(1,0)} = \left.\frac{\partial (\hat{\mathcal{H}}^{\mathrm{OP}} + \hat{\mathcal{H}}^{\mathrm{FC}} + \hat{\mathcal{H}}^{\mathrm{SD}})}{\partial \boldsymbol{\mu}_A}\right|_{\boldsymbol{\mu}_A=0}$$

$$\hat{\mathcal{H}}^{(0,1)} = \left.\frac{\partial \hat{\mathcal{H}}^{\mathrm{OZ}}}{\partial \boldsymbol{B}^{\mathrm{ext}}}\right|_{\boldsymbol{B}^{\mathrm{ext}}=0} \tag{29}$$

are used in equation (20). Here, the external field and the nuclear spin induce electronic paramagnetic orbital currents through $\hat{\mathcal{H}}^{\mathrm{OZ}}$ and $\hat{\mathcal{H}}^{\mathrm{OP}}$, respectively, the magnetic fields of which cause the paramagnetic nuclear shielding. The diamagnetic shielding contribution from $\hat{\mathcal{H}}^{\mathrm{DS}}$ is due to the diamagnetic electronic currents induced in the electronic system. As already mentioned, we restrict the discussion here to the spin-compensated case (closed-shell molecules). Without spin-orbit coupling, the FC and SD terms do not contribute to the nuclear shielding in closed shell systems, i.e., with pure spin-orbitals the contributions from spin-up and spin-down orbitals due to $\hat{\mathcal{H}}^{\mathrm{FC}}$, $\hat{\mathcal{H}}^{\mathrm{SD}}$ exactly cancel because the external magnetic field does not induce spin density.

For nonrelativistic spin–spin couplings, one uses

$$\hat{\mathcal{H}}^{(1,1)} = \left.\frac{\partial^2 \hat{\mathcal{H}}^{\mathrm{OD}}}{\partial \boldsymbol{B}^{\mathrm{ext}} \partial \boldsymbol{\mu}_A}\right|_{\boldsymbol{\mu}_A=0,\,\boldsymbol{\mu}_B=0}$$

$$\hat{\mathcal{H}}^{(1,0)} = \left.\frac{\partial (\hat{\mathcal{H}}^{\mathrm{OP}} + \hat{\mathcal{H}}^{\mathrm{FC}} + \hat{\mathcal{H}}^{\mathrm{SD}})}{\partial \boldsymbol{\mu}_A}\right|_{\boldsymbol{\mu}_A=0}$$

$$\hat{\mathcal{H}}^{(0,1)} = \left.\frac{\partial (\hat{\mathcal{H}}^{\mathrm{OP}} + \hat{\mathcal{H}}^{\mathrm{FC}} + \hat{\mathcal{H}}^{\mathrm{SD}})}{\partial \boldsymbol{\mu}_B}\right|_{\boldsymbol{\mu}_B=0} \tag{30}$$

Similar to NMR shieldings, the OP and OD terms introduce paramagnetic and diamagnetic electronic currents due to a nuclear magnetic moment that can further interact with the perturbations from another nucleus. The SD and in particular the FC term both yield nonzero contributions and cause a different coupling mechanism. These operators introduce a net electronic spin density at or around, say, nucleus A, which is transferred through the electronic system (chemical bonds) to nucleus B and interacts with its spin magnetic moment there. There is also a mixed term between the FC and the SD contribution, that contributes to the anisotropy of the $\mathbf{K}$ tensor. Again, in the nonrelativistic case, where spin and spatial degrees of freedom are completely independent from each other, all 'mixed' contributions to $\mathbf{K}$ between orbital- and spin-dependent operators yield zero (e.g., the contribution due to $\hat{\mathcal{H}}^{\mathrm{FC}}$ in $\hat{\mathcal{H}}^{(1,0)}$ with the one due to $\hat{\mathcal{H}}^{\mathrm{OP}}$ in $\hat{\mathcal{H}}^{(0,1)}$ and vice versa in equation (20)). The same arguments concerning vanishing terms involving both spin- and orbital-dependent operators apply in the scalar relativistic case.

The situation is much different at the presence of SO coupling. Spatial and spin degrees of freedom are then coupled and not longer independent from each other. Not unexpectedly therefore, in, e.g., the Pauli, ESC, DK, or ZORA case including the one-electron spin-orbit (1e-SO) operator, mixed contributions involving both spin- and orbital-dependent operators occur for $\boldsymbol{\sigma}$ and $\mathbf{K}$ in this case. In particular, the spin-dependent FC and SD terms contribute to the chemical shielding because, through SO coupling, an external magnetic field induces net spin-density even in a closed-shell system. Likewise, for spin–spin couplings, mixed terms between spin- and orbital-dependent operators in $\hat{\mathcal{H}}^{(1,0)}$ and $\hat{\mathcal{H}}^{(0,1)}$ are no longer zero. In variational two-component procedures in which the zeroth-order computation and the magnetic operators are based on the same formalism and no terms have been omitted initially, no new operators or new terms in the expressions for $\boldsymbol{\sigma}$ or $\mathbf{K}$ arise due to SO coupling. In case that the (usually Pauli) 1e-SO operator is introduced as a first-order perturbation, the additional terms are formulated and calculated explicitly, which is convenient for interpretations. The same holds for additional scalar relativistic corrections. The operators arising from the minimal substitution $\hat{\boldsymbol{p}} \rightarrow \hat{\boldsymbol{\pi}}$ in the spin-orbit operator itself have thereby been overlooked for a long time.[22] For nuclear shielding, the most important contribution due to spin-orbit coupling has been shown to arise from the FC term in the external magnetic field, while for spin–spin couplings, the FC-OP cross term appears to be dominant in the cases being investigated so far. See Sections 3.1 and 4.2 for further comments and explanations. All the 1e-SO contributions are, of course, contained in the four-component treatment based on equation (28).

As already mentioned, transformation of the electron–electron interaction to two-component form yields various new terms, among them the two-component two-electron spin-orbit and spin-other-orbit operators (collectively being denoted here by '2e-SO'), which give rise to various additional magnetic contributions in the presence of magnetic fields. See, e.g., Refs.[4,16,27] for theoretical details. Unless explicitly mentioned, we refer to the 1e-SO effects in the following. Actual program implementations may make use of an effective potential in the 1e-SO operator and the results may therefore contain two-electron SO effects to some extent.

2.3 Computational Methods

While the importance of Hartree–Fock computations in quantum chemistry is generally decreasing in favor of either correlated ab initio methods or DFT, it is still one of the common methods in the field of computation of heavy atom NMR parameters. A four-component implementation of Hartree–Fock shielding tensors and spin–spin couplings has been reported by Visscher and co-workers[28,29] and an implementation for nuclear shieldings by Nakatsuji and co-workers.[26,30,31] Both implementations use a common gauge origin for the external magnetic field. Pioneering NMR Hartree–Fock calculations including scalar relativistic effects based on the Pauli operator or the DK transformation, and

spin-orbit effects based either upon explicit consideration of the Pauli SO operator or the use of spin-orbit ECPs, have been reported by Nakatsuji et al.[32,33] and by Fukui et al.[21,22,34] Theoretically somewhat less justified 'mixed' methods such as using the scalar part of the DK operator together with Pauli SO for the zeroth-order solution and nonrelativistic + Pauli SO operators for NMR shieldings have also been used with reasonable success.[35] The main disadvantage of the Hartree–Fock based methods is, of course, the neglect of electron correlation, that has been demonstrated to be of high importance for the determination of NMR parameters in general and of heavy atom spin–spin couplings in particular.

To the best of our knowledge, four-component post Hartree–Fock or DFT implementations of NMR parameters have not yet been carried out, but can be expected in the near future at least for the DFT case. Post Hartree–Fock MCSCF computations of heavy atom nuclear shieldings (employing GIAO) and spin–spin couplings have so far considered spin-orbit effects only, based on a perturbational first-order treatment of the Pauli SO operator.[36–40] Scalar relativistic effects from the heavy atom were neglected in this case. This method is often suitable for NMR of light nuclei close to a heavy atom and has been successfully applied to small molecules. Likewise, SO ECPs are able to recover the important spin-orbit effects on neighbor atom shieldings that are being neglected by scalar relativistic ECPs.

The first-order SO approach has already been utilized in the pioneering approaches for the computation of nuclear shieldings in heavy atom compounds, involving simple semiempirical wavefunctions.[41–44] For spin–spin couplings, relativistic effects have been first considered in the form of correction factors applied on top of nonrelativistic Hartree–Fock or semiempirical wavefunctions.[45,46] Four-component extended Hückel theory (REX) has been developed and extensively applied to both heavy atom shieldings and spin–spin couplings by Pyykkö and co-workers.[47]

The restriction of excluding the heavy nuclei in the NMR computations applies technically to a common use of ECPs in heavy element computations. Existing methodology for NMR parameters that has been derived for all-electron calculations cannot be used without modification for NMR parameters of those atoms for which an ECP is used. In this case, either a NMR methodology directly derived from the pseudopotential formalism would have to be used, or at least the pseudo-orbitals need to be orthogonalized on the relativistic heavy atom cores before applying a standard all-electron code.

Density functional theory (DFT)[48] has been very successful in the field of heavy atom NMR computations. Methodological development for relativistic NMR computations has been performed in particular by Kaupp, Malkin, Malkina and co-workers[49–51] (using the IGLO method for shieldings), and by Ziegler and co-workers (GIAO for shieldings).[19,20,52–54] Taking into account that the electron density, the spin density and the current density define the one-electron magnetic contributions to $\boldsymbol{\sigma}$ and $\mathbf{K}$, and that these densities are (of course only in principle) obtained exactly from Kohn–Sham DFT,[55] its application to NMR parameters has a theoretically well founded base. From the experience gained so far it seems that the current-density dependence and also relativistic corrections of the exchange-correlation functional are not very large, and quite reasonable results can be obtained with standard nonrelativistic local-density (LDA) or generalized gradient (GGA) approximations (in which, however, the density can be a relativistic one). The fact that electron correlation is to some extent accounted for in contemporary Kohn–Sham DFT, and due to its computational effectiveness with regard to the number of atoms that can be treated simultaneously, most of the relativistic NMR computations on larger systems such as transition metal complexes are currently based on DFT. For the heavy atom DFT NMR computations carried out so far, various relativistic methods have been utilized, among them perturbational use of the Pauli SO operator, variational computations with the Pauli operator and frozen cores excluding or including SO coupling, the use of the ZORA Hamiltonian, and use of scalar relativistic and spin-orbit ECPs.

We further note that some authors subdivide the relativistic effects of NMR parameters into 'direct' and 'indirect' effects, the latter being related to the change of the NMR parameters with respect to a change of the computed molecular structure due to relativity. It is known that small geometrical changes can result in sizeable changes of shieldings and couplings. The choice of experimentally determined structures, if available, for the computations is unambiguous and leaves only the 'direct' effects to be discussed.

Apart from acronyms already specified in the previous sections, we make use of the following abbreviations from now on: vPSO, vPSC, vPauli for variational Pauli SO only, scalar only, and scalar + SO, respectively; similarly, pPSO, pPSC, pPauli denote first-order perturbational relativistic calculations; HF for Hartree–Fock; DKSC, DK for Douglas–Kroll, first order without and with SO corrections, respectively, and MCSCF for multiconfigurational Hartree–Fock (ab initio).

3 HEAVY ATOM NUCLEAR SHIELDINGS

Suggestions on the importance of relativistic corrections to nuclear shieldings and first numerical estimates for atoms date back to the 1960s. In 1969, Nakagawa argued that spin-orbit coupling would be an important factor for nuclear shieldings of light nuclei in the neighborhood of heavy halides.[56] Subsequently, semiempirical calculations of the respective SO effect in hydrogen and methyl halides were carried out by Morishima et al.,[41] Volodicheva and Rebane[42] and Cheremisin and Schastnev.[43] In the early 1980s, several authors published the formalism of nuclear shieldings within the four-component (Dirac) scheme.[25,57,58] This work and its future importance was subsequently reviewed by Jameson.[59] We also refer the reader to subsequent articles by Jameson and Jameson et al. who review the literature in the computational NMR field on a yearly basis. In particular the more recent articles show a large increase of publications based on relativistic methods. See, e.g., Ref.[60] for a relativistic NMR application in solid-state physics. Already anticipated by Pyykkö[57] in his remark "A rigorous implementation of the present theory will [...] probably take some time", four-component ab initio (Hartree–Fock) calculations of NMR shieldings in molecules have been reported only rather recently.[26,28,31]

Following the historical computational development we discuss SO effects on NMR shieldings prior to scalar relativistic effects.

3.1 Spin-orbit Coupling Effects

The proton chemical shift in the series of hydrogen halides HX (X = F, Cl, Br, I) and the ^{13}C shifts in CH_3X are probably the most thoroughly studied parameters in heavy atom NMR computations. The reason is that these molecules are among the smallest samples in which the strong SO dependence of NMR chemical shifts can be computed and compared to experiment. The HX and CH_3X series therefore serve as benchmarks for heavy atom NMR computations where, due to the smallness of the systems, high quality basis sets can be employed nowadays. The trend being obtained from the computations is always similar, regardless of which method has been used: excluding SO coupling does not recover the experimentally observed trend, but with inclusion of SO effects the calculated values follow the experimental trend. The numerical quality of the results is, of course, much dependent on the chosen method, and also somewhat on whether scalar relativistic effects have been additionally considered or not. Table 1 displays some of the results for the HX series that have been obtained during the last three decades. The data establish that the experimental trend can indeed be explained on the basis of SO effects only, while exclusion of SO effects does not reproduce the right trend even if scalar relativistic effects are considered.

Explanations of the SO contribution to nuclear shielding have been given in almost all of the articles quoted in Table 1 and many other papers. Qualitatively, let us consider the singlet (closed shell) ground state wavefunction without SO coupling first. As in equation (18), we assume that Ψ_0 and all the excited states of the Hamiltonian (without SO coupling) are available as a complete basis set. Expanding the spin-orbit coupled wavefunction on this basis means that, due to the nature of the SO operator, contributions also from excited triplet states will enter the SO wavefunction. Now the perturbed SO wavefunction in an external magnetic field, represented in the same basis, will have different coefficients for the singlet and triplet states and thereby the magnetic field can effectively induce a net spin density in the electronic system. The FC and SD operators also induce spin density and therefore the contribution from these operators to the NMR shielding are no longer zero.

In the case of the shielding of a light nucleus L in the neighborhood of a heavy atom Y, the spin density is induced by the external field around Y, transferred through the chemical bond(s) to the light nucleus L, and is there 'detected' by the FC and SD perturbations (heavy-atom effect on the light-atom shielding (HALA) in contrast to the heavy atom effect on the heavy nucleus shielding itself, HAHA[61]). This suggests a qualitative similarity to the nonrelativistic FC/SD mechanism of nuclear spin–spin coupling, where the spin density is not induced by the external field but by the FC and SD perturbation from another nucleus. This similarity has already been proposed in 1969 by Nakagawa et al.,[56] but no unambiguous numerical evidence could be provided. Recent DFT computations[62] on a number of systems convincingly demonstrate the correlation between K(L,Y) and the spin-orbit contribution to σ(L) induced by Y. In particular, a familiar Karplus-type dihedral angle relation known for three-bond spin–spin couplings has been obtained for the SO contribution to proton shielding in iodoethane that closely follows the behavior of ^3K(H,I). Many numerical results obtained by different authors show that the SD contribution to spin-orbit induced shielding can often be neglected, and the FC part is usually dominant. The same holds for nuclear spin–spin couplings (Section 4). Similar to spin–spin couplings, too, is that the magnitude of the FC contribution to nuclear shielding depends on the σ-character of the L–Y bond(s). This allows for similar chemical interpretations.[51,62]

The case of $\delta(^{13}C)$ in methyl halides is not as spectacular as the hydrogen halides. Still, qualitative agreement with experimental data can only be achieved upon inclusion of SO coupling in the shieldings calculation, while scalar relativistic corrections are of minor importance. Benchmark data for

Table 1 Proton Chemical Shifts in Hydrogen Halidex HX

$-\delta(^1H)$[a] method/year	X = Cl		X = Br		X = I	
	nrel[d]	rel	nrel	rel	nrel	rel
Semiemp. pPSO/1973[41]	8.02	8.24	11.24	13.85	13.08	20.92
Semiemp. pPSO/1978[42]	2.1	2.7	5.75	10.0	3.22	16.8
REX/1987[47]		0.45		3.35		11.01
HF pPSO/1995[32]	2.43	3.17	2.57	7.72	3.07	18.93
HF DK + vPSO/1996[35]	1.92	2.69	2.36	7.87	0.04	19.93
DFT pPSO/1996[49]	1.68	2.31	1.23	5.34	1.61	13.24
DFT vPSC/1997[52]	1.4	1.5	1.7	1.8	2.1	2.3
MCSCF pPSO/1998[36]	1.98	2.57	2.19	6.04	2.74	14.68
DFT vPauli/1998[53]		1.43		5.34		11.79
HF SCDK/1999[34]	2.08	2.17	2.39	3.06	2.62	4.95
HF Dirac/1999[28]	2.39	3.13	2.82	8.21	3.32	20.11
HF Dirac/1999[26]		2.68		4.91		10.71
DFT ZORA/2001[b]	1.57	2.45	1.84	5.31	2.19	13.6
DFT SO-ECP/2001[63]	1.68	2.39	1.21	6.42	1.61	14.87
exp ($\pm$0.02)[c]		2.58		6.43		15.34

[a]In ppm, with respect to HF, all values $\times$ (−1).
[b]This work, DFT ZORA, (BP86 functional).
[c]Experimental values as quoted in Ref.[53] Uncertainty due to the experimental value for HF (measured with respect to CH_4).
[d]Nonrelativistic values listed if reported in reference.

these and other small molecules have been published, e.g., in Refs.[32,36,43,47,49,53,63]

The importance of the influence of two-electron (2e−) SO operators or the Breit correction in the Dirac scheme has been investigated by some authors.[30,36,50] For $\sigma(^1H)$ in HX and $\sigma(^{13}C)$ in MeX, the 2e-SO contributions were found to be small and of opposite sign to the 1e-SO shielding terms. The relative importance of the two-electron terms appears to be generally decreasing for these cases as the heavy atom becomes heavier, contributing about 30% to the (small) SO shift caused by F substituents and about 7% to the (large) SO shift caused by iodine substituents. Similar conclusions for the relative importance of the 2e-SO terms were obtained for the shielding of the heavy atom,[36] for which (see next section) the scalar relativistic effects should not be neglected. For increasingly heavy X, the scalar relativistic corrections may be of higher importance than the two-electron SO terms. See, e.g., the DK results in Table 1. On the other hand, the vPSC DFT values of Ref.[52] do not indicate such large scalar relativistic corrections. At the present level of accuracy that can currently be achieved by either nonrelativistic + pPSO or four component ab initio methods, or relativistic DFT, the two-electron SO contributions appear to be rather negligible for heavy element molecules.

One of the major successes of relativistic NMR shieldings computations has been the explanation of the origin of the 'normal' and 'inverse' halogen dependence (NHD and IHD) in many compounds. Well known to experimentalists and theoreticians, shieldings of light atoms L bound to a halogen X quite often strongly increase as X becomes heavier (NHD) and its electronegativity decreases. Examples are HX, shown above, CH_3X, CH_2X_2, etc., and many other main group compounds in particular in high oxidation states. However, counter examples are known, where the L nucleus becomes less shielded for decreasing electronegativity (and increasing nuclear charge) of X, at least for Cl (sometimes Br) compared to F. Sometimes, in those compounds the NHD is observed again for X = I (and sometimes Br). Examples are SiX_4, AlX_4^-, and many transition metal compounds. As in HX (Table 1), in the investigated cases the NHD is caused by the SO contribution to nuclear shielding, while the nonrelativistic computations predict an IHD behavior. Figure 1 displays the Hartree–Fock data obtained for some silicon halides in 1995. Very similar results for these and other compounds were obtained in the same year by a semiempirical approach.[44]

Extremely large SO corrections to the phosphorus chemical shift in PX_4^+ have been reported in Ref.[64] and were attributed to the pronounced s-character of the L–X bonds due to the high oxidation state of phosphorus. Similar NHD results can be found in many theoretical studies of the SO shielding contribution. The authors of Ref.[65] investigated a number of Ti tetrahalides and Nb hexahalides. Rather typical for early transition metal halides, almost vanishing net SO effects on the metal shielding were observed even for the tetra- and hexa-iodides, caused by a cancellation of positive SO contributions from the FC term and negative changes of the paramagnetic shielding at the presence of SO coupling. In this case, IHD for the series F → I is observed for the chemical shifts in agreement with experiment. This has been interpreted in terms of the different nature of the metal d-orbitals binding to the ligands as compared to (s- and) p-orbitals in the case of main group elements exhibiting NHD.

If one bases the interpretation for the IHD on equation (20), the decreasing HOMO-LUMO gap due to decreasing electronegativity of the halogen in the series X = F → I results in a larger magnitude of the paramagnetic shielding, if the matrix elements in the sum over excited states are assumed to be approximately constant. (In Ref.[66], excellent linear correlation of ^{95}Mo chemical shifts with the lowest magnetically allowed d-d* excitation energy has been observed for a number of Mo complexes.) Since the nonrelativistic paramagnetic shielding contribution is typically negative, this results in increasingly positive chemical shifts (IHD). From the investigations quoted above it becomes clear that the NHD, on the other hand, is due to the more pronounced influence of spin-orbit coupling, which often increases the shielding and therefore causes increasingly negative chemical shifts. The diamagnetic shielding, as a core property, is usually found to be of small influence concerning the chemical shifts. From the relativistic nature of the NHD it becomes clear why previous

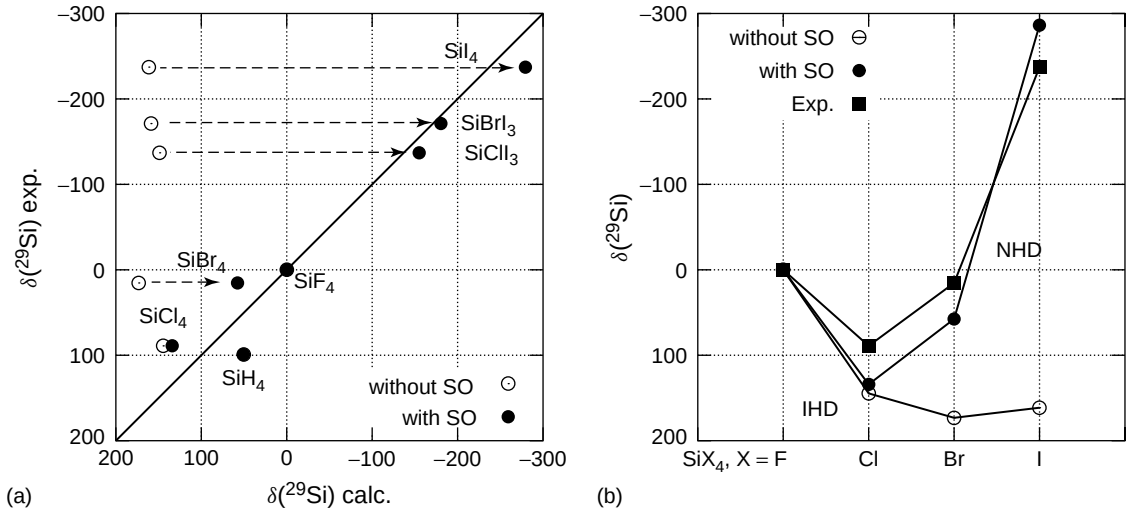

Figure 1 ^{19}Si chemical shifts with respect to SiF_4 in silane and some silicon halides, from Hartree–Fock data.[33] Scalar rel. and SO effects considered here via ECPs on the halide ligands. (a) experimental vs. computed Si shifts. (b) NHD and IHD along the SiX_4 series. See Section 3.1

explanations of the NHD that only take the (nonrelativistic) paramagnetic shielding into account have not generally been convincing.

Density functional theory (DFT) has been particularly successful in the case of transition metal compounds, and generally in cases for which electron correlation has a strong influence on the NMR shielding, and where a correlated ab initio method including relativistic effects has not been available or has not been applicable due to the size of the system (see also the section on spin–spin couplings). An example where electron correlation is believed to be very important is the ^{13}C shift in the series of CX_3^+. Nonrelativistic DFT and MP2 calculations show very similar results exhibiting IHD. This trend is also observed, but strongly overestimated, by nonrelativistic Hartree–Fock calculations, indicating the importance of electron correlation. Further inclusion of SO coupling in the DFT calculations recovers the experimentally observed NHD for $X = Cl \rightarrow Br \rightarrow I$ with good accuracy.[67]

Most of the relativistic DFT studies of transition metal compounds include scalar relativistic effects and are discussed in the next section.

3.2 Including Scalar Relativistic Effects

From a computational point of view, the most simple way of including scalar relativistic effects in a NMR shieldings calculation is to use an available scalar relativistic ECP on the heavy atom. When HALA effects are studied, existing nonrelativistic NMR code can be (and is) used without modifications. Many studies have been carried out using this approach, see, e.g., Refs.[51,68] for overviews of density functional applications in particular to transition metal complexes. In view of the importance of SO corrections to $\boldsymbol{\sigma}$ as seen in the previous section, however, the range of applications of this method seems to be limited. Spin-orbit ECPs have been applied to a number of NMR ligand shieldings including heavy main group and transition metal compounds.[33,63] Restrictions with respect to HALA effects also apply to the purely scalar relativistic approach of Ref.[52], in which HX and a number of transition metal complexes are studied. However, the method is capable of treating the heavy metal shift (and HAHA effects) itself, with reasonable accuracy as shown for the W shifts in Table 2. In Ref.[69], an overview of this variational scalar Pauli method is given. Among other data, a large number of ^{125}Te shifts are presented. In comparison with experiment, the relativistic computations achieved good accuracy, therefore SO effects can be regarded as mostly unimportant for Te chemical shifts. An increase of the scalar relativistic effects of the shielding of the heavy nucleus X with $\sim Z^{3.5}$ has been found from SCDK calculations for the HX series.[21] This underlines the importance of scalar relativistic corrections for heavy nucleus shieldings. Computational methods that include both scalar relativistic and SO effects and have been applied to both light and heavy nucleus shieldings are, of course, the four-component methods,[26,28,30] and, e.g., Douglas–Kroll including SO effects,[70–72] Pauli including SO,[22,53] or the ZORA approach.[19,73] A collection of transition metal tetroxo- and hexacarbonyl complexes appears to represent a benchmark test set for DFT NMR implementations. Oxygen shifts of group 6–8 transition metal tetroxo-complexes were studied, e.g., in Refs.[52,74] with a scalar relativistic approach. The rather good agreement with experimental shifts suggests that SO coupling does not play an important role in this case. Scalar relativistic effects on the ligand shifts appeared to be of high importance only for the 5d metals and are almost negligible for the 3d metals. The metal shifts in the same set of complexes were studied by variational scalar + SO Pauli and ZORA SO DFT.[75] Unfortunately, no oxygen shifts were reported there for comparison. The results for the metal shifts have been satisfactory, with ZORA emerging as the superior method in this case. Table 2 displays some ^{183}W shifts that were obtained by DFT methods and by a Hartree–Fock approach[70] including scalar + SO effects. The results indicate that scalar and SO effects are probably of equal importance for the W shifts. In Ref.[76], a larger number of W shifts than quoted in Table 2 have been computed by both vPauli and by ZORA DFT. ZORA resulted in a mean error of approximately 3% of the total shift range of 7000 ppm for the investigated samples when compared to experiment. The Pauli approach performed worse in this case, with an error of about 6%. ZORA produced a similar accuracy for a number of ^{207}Pb chemical shifts reported in the same study (4% error compared to the covered shift range), whereas the mean error from the Pauli approach was found to be four times larger in this case. The ZORA computations predicted an enormous SO shift of the Pb shielding of PbI_4 of more than −8000 ppm, a number yet to be supported by experimental results.

Carbon chemical shifts for 5d transition metal carbonyl complexes studied with DFT are displayed in Table 3. SO effects play a less significant role for the ^{13}C chemical shift in these complexes as compared to HX, but systematically improve the computed results. The SO shifts do not easily follow intuitive arguments based on the size of the HOMO-LUMO gap (HLG).[53] From equation (20) the individual contributions to the shielding can be expected to decrease with increasing HLG along a row of the periodic table. Despite the fact that the HLG increases from approximately 2 to 6 eV from $[Hf(CO)_6]^{2-}$ to $[Ir(CO)_6]^{3+}$, the spin-orbit contribution to the nuclear shielding and to the chemical shift is nevertheless seen to be increasing from Hf to Ir. As illustrated in Ref.[53], the trend can be rationalized on the basis that, due to the relative energies of the metal d_σ, d_π and the CO σ and π^*

Table 2 Some ^{183}W Chemical Shifts

Compound	δ exp.[a]	DFT vPSC[52]		DFT vPauli[76]	DFT ZORA[76]	HF SCDK + vPSO[70b]	
		nrel	rel	rel	rel	nrel	rel
$W(CO)_6$	−3446	−4075	−3703	−3306	−3876		
WF_6	−1121			−107	−630	−1795	−1135
WCl_6	2181			1773	1932	2266	2686

[a]With respect to WO_4^{2-}, as compiled in Ref.[76]
[b]Reported in [70] with respect to WF_6.

orbitals, the bonding in Hf carbonyl is dominated by $d_\pi - \pi^*_{CO}$ interaction, whereas the bonding in Ir carbonyl is dominated by $d_\sigma - \sigma_{CO}$ interaction. CO is more likely to σ-donate charge to the highly positively charged Ir, whereas metal-ligand π-back-donation dominates in the Hf complex. Only in the former case, however, can spin density be effectively transferred to the carbon nucleus, therefore the magnitude of the SO induced carbon shift is increasing along the 5d transition metal carbonyl series despite the increasing HLG. It has been shown previously that the decreasing $\delta(^{13}C)$ along the series at the scalar relativistic level is due to a complex interplay of different factors in which the amount of π-back-donation is predominant.[77,78]

In a ZORA DFT study of ^{195}Pt chemical shifts,[79] the authors also found that simple arguments based on the magnitude of $1/(\epsilon_i - \epsilon_a)$ are not always able to provide an explanation of the observed trends. The magnitude of the matrix elements in the numerator of the sum in equation (20) has to be considered as well and needs to be explained by intuitive chemical arguments. In the case of Pt shifts, NHD is observed in many cases. An analysis of the computational data shows that both the SO contributions and the paramagnetic shielding approximately equally contribute to the NHD. For the paramagnetic Pt shielding, this was attributed to a preference of the soft acid Pt(II) to bind to the soft base I instead of Cl. The authors in Ref.[79] could numerically and graphically illustrate that this results in a smaller magnitude of the (negative) paramagnetic shielding for iodine ligands due to smaller paramagnetic matrix elements in equation (20) that overcompensate the opposite HLG influence. The overall accuracy of the ZORA DFT method for Pt shieldings resulted in a mean error of approximately 10% of the investigated chemical shift range for 23 samples.[79]

Mercury shieldings have been computed by DFT and Hartree–Fock methods.[19,71,72] Table 4 lists some results that have been obtained. As can be seen from the data for HgMeX and HgX_2, the mercury halide compounds exhibit NHD, largely caused by the SO effects on the nuclear shieldings.[19,71] Large 'coupling' between scalar and SO corrections to mercury shifts were noted in Ref.[71] This means that the inclusion of both relativistic mechanisms is important in order to achieve reasonable results, because the SO correction based on a nonrelativistic zeroth order solution is much different from the one obtained from a scalar relativistic one. It is well known that scalar relativistic effects substantially stabilize and contract the 6s orbital in Hg, while the Hg 5d shell is destabilized and spatially expanded as compared to nonrelativistic computations.

Table 3 ^{13}C Chemical Shifts in 5d Transition Metal Carbonyls, from DFT Calculations

Compound	δ exp.[a]	vPSC [78]	vPauli [53]	SO ECP [63]
$[Hf(CO)_6]^{2-}$	244	228.3	234.5	228.2
$[Ta(CO)_6]^{-}$	211	211.8	214.8	206.0
$W(CO)_6$	192	197.7	196.7	188.6
$[Re(CO)_6]^{+}$	171	183.9	176.2	173.7
$[Os(CO)_6]^{2+}$	147	172.4	149.5	153.9
$[Ir(CO)_6]^{3+}$	121	153.6	125.8	130.9
$[Au(CO)_2]^{+}$	174		165.3	164.0
$[Hg(CO)_2]^{2+}$	169		158.2	154.0

[a]As compiled in Refs.[53,63], with respect to TMS.

Table 4 ^{199}Hg Chemical Shifts

Compound[a]	δ exp.[b]	DFT ZORA[19]	HF DK
$Hg(SiH_3)_2$	+196		+232[72]
$Hg(GeH_3)_2$	−147		−289[72]
HgMe(CN)	−766	−861	
$Hg(CN)_2$	−1386	−1724	
HgMeCl	−861	−943	
HgMeBr	−915	−1068	
HgMeI	−1097	−1025	
$HgCl_2$	−1519	−1556	(−1519)[c]
$HgBr_2$	−2213	−2684	−2134/−3191[c]
HgI_2	−3447	−3506	−2371/−4130[c]
$HgCl_2\ (NH_3)_2$[d]	−1280[e]	−1086	
$HgBr_2\ (NH_3)_2$[d]	−1622[e]	−1858	
$HgI_2\ (NH_3)_2$[d]	−2355[e]	−2836	

[a](Me = CH_3).
[b]With respect to $HgMe_2$, as compiled in Refs.[19,72]. Solvent for HgX_2 has been THF.
[c]SCDK + vPSO, Ref.[71] Data reported with respect to $HgCl_2$, therefore the value for $HgCl_2$ has been set equal to the experimental shift here. Results were obtained with two different basis sets. The shifts obtained with the external field projectors are displayed.
[d]NH_3 to simulate the solvent pyridine in the computations.
[e]Experimental values for HgX_2 in pyridine.

In effect, the scalar relativistic Hg–ligand bonds are much different from the nonrelativistic ones, meaning that the s and d contributions in the occupied and virtual metal-ligand orbitals, that determine to some extent the magnitude of the SO corrections to the chemical shifts, will be very different as well. In Ref.[71], the rather unsatisfactory performance of the computations, in particular the strong overestimation of the SO shift corrections for the HgX_2 series (Table 4, large basis set) was attributed to the missing treatment of 2e-SO terms. The authors proposed that 20–40% of the 1e-SO contribution to the chemical shift may be canceled by the two-electron contributions, which seems to be excessive taking the previously quoted findings about the relative importance of the two-electron SO terms for heavy atom compounds into account. Considering the reasonable overall performance of the DFT calculations for Hg shifts (they do not include 2e-SO operators explicitly), the inaccuracies of the Hartree–Fock results for HgX_2 could also be attributed to the missing treatment of electron correlation. Another problem might be the inconsistent treatment of relativity, viz. the use of the problematic Pauli SO operator in conjunction with the scalar relativistic DK Hamiltonian. This has been criticized by Fukui.[21]

For the series $Hg(LCH_3)_2$, L = C, Si, Ge, which has been computed with a DK transformed Hamiltonian including SO coupling, it was found that the rather small magnitudes of Hg chemical shifts are caused by cancellation of large relativistic and nonrelativistic contributions.[72] Even the usually negligible SD contribution to the chemical shift is here comparable in magnitude to the shift itself. In that respect, the achieved results must be regarded as quite accurate and testify to the accuracy of the relativistic treatment with the DK Hamiltonian. The authors also consider missing solvent effects as a possible source of error, an issue that has already been addressed regarding mercury chemical shifts.[19] Experimentally confirmed, the solvent dependence of, e.g., the Hg shift in HgI_2 can amount to more than 1000 ppm (pyridine vs.

THF). It has been computationally demonstrated in Ref.[19], that direct coordination of the metal by a nucleophilic solvent (pyridine, simulated by NH_3 in the ZORA computations) is largely responsible for the large experimental solvent effects on chemical shifts. The computations were able to qualitatively simulate a strong positive contribution to $\delta(^{199}\mathrm{Hg})$ due to the coordination of the solvent to Hg. The resulting geometry change (bending of X–Hg–X by approximately 30°) upon complexation was found to increase the magnitude of the (negative) chemical shift by ∼600 ppm for $HgCl_2$, while the direct interaction of the solvent with the heavy atom caused a large shift of δ by ∼+1100 ppm. THF was supposed to coordinate much less strongly to Hg and not to cause a significant change of the linear structure of HgX_2. A possible influence on the chemical shift due to THF that might account for the differences between theory and experiment in Table 4 has therefore not been investigated.

It should be noted here that absolute shielding values of, e.g., 8020 ppm from ZORA DFT,[19] and of 15 128 ppm from spin-orbit DK Hartree–Fock[72] for ^{199}Hg in $Hg(CH_3)_2$ have been reported. While the paramagnetic and diamagnetic shieldings are approximately equal in both methods, the reported spin-orbit corrections differ by ∼7000 ppm. The differences obviously largely cancel regarding the chemical shift and demonstrate that due to cancellation of systematic errors, chemical shifts are much easier to compute accurately than absolute shieldings in particular for such heavy nuclei. We therefore do not list reported absolute shielding values in the tables.

Chemical shifts in compounds containing elements as heavy as uranium have been investigated[73,80] with DFT. In Ref.[80], variational Pauli and ZORA calculations have been employed together with standard GGA functionals, as well as a scalar relativistic ECP in conjunction with the B3LYP hybrid functional. ^{19}F chemical shifts in a number of U-halide complexes were obtained with moderate absolute accuracy with both the ZORA and the Pauli approaches, while certain trends between different compounds could not be reproduced by the GGA functionals. SO effects for the F shifts were found to be of low importance (typically ∼30 ppm for Pauli and somewhat less for ZORA, as compared to experimental shifts between 750 and 790 ppm). The scalar relativistic ECP/B3LYP did yield systematically between 80 and 270 ppm too large chemical shifts, but certain trends were better reproduced. From this, the authors concluded that the ECP approach is beyond its limit for actinide NMR and that improved XC functionals are needed for the nonhybrid DFT methods in order to reproduce some trends among a series of compounds more accurately. A clearly better performance of ZORA vs. Pauli could not be observed in this study.

Many of the studies cited so far also provide relativistic effects on the shielding tensor anisotropy, $\Delta\sigma$. See Refs.[28,36,37] for examples. The practical application of these quantities for heavy atom systems is, however, rather limited so far. We therefore refer to the literature for detailed discussions of relativistic effects on $\Delta\sigma$, and only mention here that huge effects have been reported so far.

4 HEAVY ATOM SPIN–SPIN COUPLINGS

Nuclear spin–spin couplings are not very easy to compute accurately, in particular for heavy elements, but can often be measured with high precision. Unlike the case of chemical shifts, where systematic errors in the computation may cancel when the shifts are obtained from the difference of the two computed shielding values of the probe and the reference compounds, there is no such cancellation of errors for spin–spin couplings. Another problem is that the interest is often in couplings involving a heavy nucleus itself, and scalar relativistic effects can be enormously large. Therefore, attempts to calculate spin–spin couplings similarly to the NMR shieldings case just by considering the Pauli SO operator to first order did not yield very satisfactory results for couplings involving a heavy nucleus.[38–40] However, this method seems to be applicable for the study of HALA effects in some cases.[38] Likewise, ECPs can be employed for this type of application (e.g., in Ref.[81]). However, in the following we focus on couplings to a heavy nucleus itself. As compared to chemical shieldings, much less computational data are yet available.

4.1 (Mostly) Scalar Relativistic Effects

Scalar relativistic effects are usually believed to yield the major influence on heavy nuclear spin–spin couplings. The reason for this is related to the fact that the FC term (27e) was found to represent the dominant contribution for an overwhelming number of couplings that have been investigated (of course, counter examples are known). In its usual nonrelativistic form for point-like nuclei, the FC term originates from the value of the induced spin-density *directly at* the nuclei, while its relativistic generalizations probe the space very close to the nuclei.[20,29] There, in particular, the electron density is substantially modified due to the scalar relativistic operators (MV + DAR in the Pauli formalism, equation (11)), and a huge influence on the FC perturbations can be expected. This was noted in 1968[82] regarding the contact term in NMR spin–spin coupling and has been known since 1930[83] from the theory of atomic hyperfine splittings.

The authors of Refs.[45,46] introduced relativistic correction factors (RCFs) for hyperfine integrals of atomic orbitals (AOs), which account for the relativistic increase of the electron density at the respective nucleus. The RCFs can then be used in nonrelativistic molecular computations to scale the AO integrals entering the FC expression for the coupling tensor in equation (20). The authors of Ref.[84] reported a somewhat related procedure that is applicable to couplings involving a heavy nucleus, based on the variational scalar Pauli treatment. The semiempirical approaches described in, e.g., Refs.[85–88] also make use of integrals based on four-component atomic computations in an otherwise nonrelativistic formalism.

To give the reader an idea of the magnitude of the RCFs, we note that, e.g., a value of 2.4386 has been reported[45] for the Hg 6s orbital. This means that, if the coupling Hg–L (L = light nucleus) is dominated, as it is often the case, by the FC contribution and by the 6s orbital on the Hg side, the coupling relativistically increases by almost a factor of 3. Likewise, Hg–Hg and other couplings between 6th row elements can be expected to relativistically increase by almost an order of magnitude. Even for rather light fourth row nuclei, nonnegligible relativistic effects on coupling constants of ∼10% can be expected. This should be compared to the celebrated huge relativistic bond contraction of many Au(I) compounds, which is of the order of 10%.

A problem connected with the RCFs is that they do not account for relativistic changes of the molecular orbitals that determine the spin–spin coupling. Such changes would be obtained from a variational or higher than first-order perturbational relativistic molecular computation. The RCFs are also not able to describe relativistic effects of L–L′ couplings in the neighborhood of a heavy nucleus for the same reason. In many cases, relativistic changes of the zeroth-order solution may either enhance or quench the strong relativistic effects of the AO integrals and lead to much different answers than obtained from the RCFs. In these, and other cases for which the coupling is not dominated by the FC term, a consistent first-principles variational or perturbational scheme for molecules is desirable.

The four-component formalism of nuclear spin–spin couplings has been subsequently published by Pyykkö, who provided a simple LCAO example for K(Hg–C) in dimethylmercury.[89] The results are very typical for heavy-atom spin–spin couplings. They exhibit a huge relativistic increase of K(Hg–C) by a factor of 2.7, with the new mixed contributions due to spin-orbit coupling being almost negligible for the isotropic coupling and yielding a somewhat larger contribution to the anisotropy ΔK of the coupling tensor. ΔK thereby increased even stronger by a factor of 3.3 due to relativity. A formulation for spin–spin couplings within the four-component scheme based on the polarization propagator method has been published by Aucar and Oddershede.[90] An implementation for spin–spin couplings within the relativistic extended Hückel theory (REX) was applied to many systems and often recovered the experimentally observed trends and provided explanations.[91] Recently, an ab initio Hartree–Fock four-component implementation and benchmark results for HX, H_2Y, (Y = O, S, Se, Te), and some plumbanes have been reported.[24,28,29] Also rather recently, the two-component ZORA DFT approach for spin–spin couplings has been formulated and implemented by the present authors.[20,54] Earlier semiempirical approaches based on the MNDO, AM1 and PM3 Hamiltonians, and ab initio methods including the Pauli SO operator, have already been mentioned. See Ref.[23] for a review on hyperfine interaction in metals from the solid-state physics point of view.

The series YH_4, Y = C, Si, Ge, Sn, Pb, has been studied as benchmark systems in many of the references cited so far. The results show a strong scalar relativistic increase in the FC contribution to the Y–H coupling, that amounts to roughly a factor of two in the case of Y = Pb. Table 5 displays spin–spin couplings in plumbanes obtained from different theoretical methods. Nonrelativistically, the FC term to the couplings is dominant and all other contributions are almost negligible. In the relativistic case, the situation is not much different. The new mixed contributions due to SO coupling are not negligible, but rather small.[40,54,91] The scalar relativistic corrections to FC terms of the Pb–L couplings clearly dominate and it can be seen from Table 5 that the total relativistic corrections to the Pb–L couplings are very substantial. The correlated ab initio study of Kirpekar et al.,[40] only including SO effects, was not able to achieve qualitative agreement with experiment, but could provide evidence that SO effects on K(Pb–H) in PbH_4 are indeed not very large (and negative in this case). The largest SO contribution is due here to the OP-FC cross term (which is zero in the nonrelativistic limit).[40,54] Therefore, large SO effects on the coupling constants can be expected only for those systems where SO coupling is of high importance (typically heavy p-block elements such as Tl, Bi, Pb), and both the FC and the paramagnetic coupling contribution are not very small already at the non- or scalar-relativistic limit. This is not the case for the plumbanes, and therefore the scalar relativistic effects on the FC term dominate the picture. This also rationalizes the quite accurate results for PbH_4 and $PbMe_4$ in Refs.[84,86]. Compared to other studies of sixth row element one-bond couplings, the data in Table 5 appear to be rather typical and qualitatively similar results have been, e.g., obtained for couplings involving W, Pt and Hg in a number of heavy metal complexes.[20,84] As for the plumbanes in Table 5, chemical trends for very similar compounds are often already reproduced at the nonrelativistic level while magnitudes of coupling constants typically increase by a factor of two due to scalar relativistic corrections. Already at the scalar relativistic level, good agreement with experiment has been achieved for most of the systems in Refs.[20,84].

From the data in Table 5, the importance of electron correlation for obtaining reasonable estimates of spin–spin coupling constants becomes obvious. The effect of correlation

Table 5 Reduced Pb–L Spin–Spin Coupling Constants in Plumbanes, in $10^{20}\,kg\,m^{-2}\,s^{-2}\,A^{-2}$

Compound coupling[a]	PbH_4 Pb–H	$PbMe_2H_2$ Pb–H	$PbMe_3H$ Pb–H	$PbMe_4$ Pb–C	$PbCl_4$ Pb–Cl
REX[91]	84.4			46.5	
	(37.3)			(16.4)	
AM1[86]	97.2			33.5	−32.0
DFT vPSC[84]	85.1			20.7	
DFT ZORA[20,54]	122.8	98.3	89.1	−26.8[b]	−321.5[b]
	(59.9)	(57.8)	(56.6)	(10.4)	(−211.6)
HF Dirac[29]	181.9		166.8		
	(71.1)				
MCSCF pPSO[40]	48.3				
	(56.2)				
Experiment[95]	112[c]	98.7	92.3	39.6	288.9[d]

[a]Nonrelativistic values in parentheses, Me = CH_3.
[b]$PbMe_4$, this work BP86 functional; $PbCl_4$, scalar ZORA.
[c]Extrapolated from $PbMe_2H_2$ and $PbMe_3H$.
[d]Not directly measured, sign not determined.

at the nonrelativistic ab initio level is seen from a comparison of the nrel. number in parentheses listed for the Dirac approach with the one from the MCSCF computation. Based on a respective nonrelativistic ratio for SiH_4, Enevoldsen et al.[29] estimated a Pb–H coupling constant in PbH_4 of $\sim 138 \times 10^{20}\,\mathrm{kg\,m^{-2}\,s^{-2}\,A^{-2}}$ for a correlated approach. This is very close to the ZORA DFT result and underlines on the one hand the sensitivity of spin–spin coupling constants with respect to the quality of the zeroth-order solution and on the other hand the fact that standard DFT functionals partially account for the influence of correlation. The semiempirical methods try to incorporate these effects via their parametrization. As seen from Table 5, the results for PbH_4 and $PbMe_4$ are in rather good agreement with experiment. However, the Pb–Cl coupling in $PbCl_4$ appears to be strongly underestimated by the AM1 method. The authors list a better coupling constant of $-80.6 \times 10^{20}\,\mathrm{kg\,m^{-2}\,s^{-2}\,A^{-2}}$ obtained with the PM3 semiempirical Hamiltonian in Ref.[86], but on the other hand K(Pb–H) in PbH_4 is overestimated by more that a factor of five with PM3. In a comparison of theory and experiment for the YCl_4 series, Y = C, Si, Sn, Pb, the semiempirical methods systematically underestimate the magnitude of the Y–Cl coupling constant, with the PM3 results being substantially larger than the AM1 (and MNDO) results. REX performs rather well in comparison.[91] The strong overestimation of some coupling constants in the semiempirical methods has been attributed to the 'triplet instability' problem that also plagues the Hartree–Fock approaches.[12] The DFT methods seem to be much more robust in this case. Both scalar and SO ZORA DFT have predicted a negative Pb–C coupling constant for $PbMe_4$ despite the fact that the nonrelativistic limit, other computations, and the quoted experimental coupling (from 1978) agree on a positive value. In all other cases we have investigated so far, ZORA did yield the experimentally predicted sign of K and in most cases the magnitudes were reproduced with good accuracy.

As already mentioned in Section 3, solvent effects can substantially influence NMR parameters for heavy atom compounds. In particular, it was found that complexation of the heavy atom by solvent molecules, if possible, yields huge effects on shieldings of the heavy nucleus. It is therefore not very surprising that this is the case for NMR spin–spin couplings as well. More surprising, however, is the magnitude of the effects even for rather weakly coordinating solvents that do not cause a significant change in the geometry of the compound under investigation. In Ref.[92], a number of linear mercury and square-planar platinum complexes have been investigated. Even for such weakly coordinating solvents such as $CHCl_3$ or CH_2Cl_2, a significant shift of the FC contribution to the spin–spin coupling has been observed. Experimental trends for different solvents ($CHCl_3$ vs. DMSO) have been quantitatively reproduced. The solvent coordination effect has been analyzed in detail for $Hg(CN)_2$. K(Hg–C) increases from 237.9 to 443.4 to $576.2 \times 10^{20}\,\mathrm{kg\,m^{-2}\,s^{-2}\,A^{-2}}$ at the nonrelativistic, scalar ZORA relativistic, scalar rel. + $4CH_3OH$ solvent molecules level, respectively (DFT, VWN functional). SO corrections were small in the samples studied in Ref.[92] It was found that charge donation from the solvent into the metal-ligand σ bonds is responsible for the large positive shift of K(Hg–C). It does not seem very likely that unspecific solvent effects for coordinatively saturated complexes are of such high importance, but they will be not negligible for high-accuracy computations. In Ref.[93], complexation of the complex $[(NC)_5Pt–Tl(CN)]^-$ by water was found to explain a rather unintuitive experimental result for the Tl–C couplings. In aqueous solution, $^2K(\mathrm{Tl–C}) \gg {}^1K(\mathrm{Tl–C})$ has been observed experimentally. In the same complex, the huge Pt–Tl coupling (expt. $\sim$57 kHz in water) has been shown to increase by more than 20 kHz upon coordination by solvent molecules in the ZORA DFT computations.

4.2 Spin-orbit Effects

Not many cases have been investigated so far, where SO coupling is of essential importance for heavy nucleus spin–spin coupling constants. Very often it is possible to achieve a good comparison between theory and experiment at the computationally much cheaper and easier to interpret scalar relativistic level. As a counter example, we would like to emphasize the case of Tl halides, TlX.

Figure 2 shows the coupling constants that have been obtained with the ZORA DFT approach[54] on different levels of approximation. Clearly, SO effects yield the dominant contribution to the coupling constants for TlI and a completely wrong trend for the series is obtained at the scalar relativistic level. The explanation for the SO effects follows that for the chemical shieldings. Mixed terms between the spin-dependent FC and SD operators and the orbital dependent OP operator are no longer zero in the presence of SO coupling. Through SO coupling, the spin-density that is induced by the FC perturbation at a nucleus 'leaks' through into the orbital shapes and causes orbital current densities that yield nonzero coupling contributions with the orbital currents induced by the OP term at the other nucleus. Likewise, the OP operator induces spin-density in the SO coupled system. As for nuclear shieldings, the FC-OP cross term was found to be dominant and the SD-OP term small.[39,40,54] For TlX, the paramagnetic contribution is dominant at the nonrelativistic level and the FC term represents

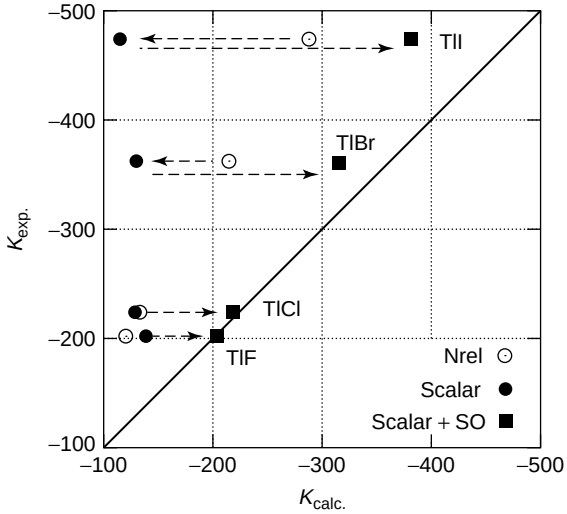

Figure 2 Reduced spin–spin coupling constants in thallium halides TlX from ZORA DFT computations (Ref.[54], BP86 functional), in $10^{20}\,\mathrm{kg\,m^{-2}\,s^{-2}\,A^{-2}}$. Calculated vs. experimental values. Experimental data compiled in Ref.[94]

the second largest contribution. This leads to the large FC-OP cross terms at the SO coupled level. In the case of TlI, this cross term represents the largest individual relativistic correction to the coupling constant and is essential in order to obtain the correct trend for the TlX series.[54] The DFT approach appears to be of somewhat reduced accuracy for the case of TlBr and TlI which has been largely attributed to deficiencies in the GGA functional.[54]

The authors of Ref.[38] concluded from a study of K(H−H) in H_2Y (Y = O, S, Se, Te) that the SO effects may generally yield the dominant contribution for HALA effects as is the case for many nuclear shieldings. A large relativistic change of K(H−H) in PbH_4 has been observed from four-component Hartree−Fock computations[29] where SO effects are naturally present. On the other hand, Ref.[40] reports rather small SO corrections to K(H−H) in PbH_4, based on a nonrelativistic Hartree−Fock wavefunction. Furthermore, huge changes of the FC term due to electron correlation were found. Clearly, more relativistic studies including both scalar and SO effects are needed in this case in order to draw a definite conclusion.

Available studies have shown that even in those cases where the SO effect on the coupling constant is rather small, the anisotropy ΔK can be quite strongly influenced by SO coupling. Relativistic changes of ΔK have been reported in several of the papers cited so far, e.g., in Refs.[24,28,38,54,87,91] However, the applications of ΔK for the heavy atom case are, as in the $\Delta\sigma$ case, very limited so far. It is already established that future investigations of ΔK and interpretations of respective experimental findings will need to include relativistic effects if heavy atom systems are studied, and both scalar and SO effects will be of importance in this case. Experimental data for the TlX series have, along with a number of other light and heavy diatomic systems, been investigated in Ref.[94] and periodic trends of K and ΔK have been analyzed. ΔK can generally be expected to increase with increasing charge of the heavy nuclei involved, with very large anisotropies for couplings with sixth row atoms in particular at the right end of the periodic table.

5 SUMMARY

It is nowadays possible to compute relativistic heavy nucleus NMR parameters by a variety of different approaches at different levels of accuracy and computational expense. A number of available quantum chemical program systems are capable of such computations. From the numerical evidence provided so far by many computational studies of NMR parameters in heavy atom systems, it becomes obvious that relativistic effects can be responsible for the main chemical trends that have been observed experimentally. In particular, spin-orbit coupling must be considered for shieldings of light nuclei in the neighborhood of heavy p-block elements. Both scalar and spin-orbit relativistic corrections are important for shielding tensors of heavy nuclei and ligand shieldings in heavy transition metal complexes. It is imperative to use scalar relativistic corrections in order to compute reliable magnitudes for spin−spin couplings involving heavy nuclei. Spin-orbit corrections to spin−spin couplings can be very substantial if both the paramagnetic and the Fermi-contact contributions to the coupling are large and a heavy p-block element is involved.

6 RELATED ARTICLES IN THIS VOLUME

Shielding Calculations; Indirect Nuclear Spin−Spin Coupling Tensors.

7 RELATED ARTICLES IN VOLUMES 1–8

Chemical Shift Tensors, Volume 2; Dipolar & Indirect Coupling Tensors in Solids, Volume 3; Indirect Coupling: Semiempirical Calculations, Volume 4; Indirect Coupling: Theory & Applications in Organic Chemistry, Volume 4; Shielding Calculations: IGLO Method, Volume 7; Shielding Calculations: LORG & SOLO Approaches, Volume 7; Shielding Calculations: Perturbation Methods, Volume 7; Shielding in Small Molecules, Volume 7; Shielding: Overview of Theoretical Methods, Volume 7; Shielding Tensor Calculations, Volume 7.

8 REFERENCES

1. P. Pyykkö, *Chem. Rev.*, 1988, **88**, 563.
2. J. Almlöf and O. Gropen, in 'Reviews in Computational Chemistry', eds K. B. Lipkowitz and D. B Boyd, VCH Publishers: New York, Vol. 8, pp. 203−244.
3. B. A. Hess, in 'Encyclopedia of Computational Chemistry', ed P. v. R. Schleyer, John Wiley & Sons: Chichester, 1998, pp. 2499−2508.
4. R. E. Moss, 'Advanced Molecular Quantum Mechanics', Chapman and Hall: London, 1973.
5. A. J. Sadlej, in 'Lecture Notes in Chemistry II', ed B. O. Roos, Springer: Berlin, 1994, Vol. 64, pp. 203−230.
6. S. Okada, M. Shinada, and O. Matsuoka, *J. Chem. Phys.*, 1990, **93**, 5013.
7. J. Autschbach and W. H. E. Schwarz, *Theor. Chem. Acc.*, 2000, **104**, 82.
8. W. Pauli, in 'Handbuch der Physik', Springer: Berlin, 1958, Vol. 5.
9. E. van Lenthe, E. J. Baerends, and J. G. Snijders, *J. Chem. Phys.*, 1993, **99**, 4597.
10. W. Kutzelnigg, *J. Comput. Chem.*, 1999, **20**, 1199.
11. P. Schwerdtfeger, J. R. Brown, J. K. Laerdahl, and H. Stoll, *J. Chem. Phys.*, 2000, **113**, 7110.
12. T. Helgaker, M. Jaszuński, and K. Ruud, *Chem. Rev.*, 1999, **99**, 293.
13. U. Fleischer, C. van Wüllen, and W. Kutzelnigg, in 'Encyclopedia of Computational Chemistry', ed P. v. R. Schleyer, John Wiley & Sons: Chichester, 1998, pp. 1827−1835.
14. D. B. Chesnut, in 'Reviews in Computational Chemistry', eds K. B. Lipkowitz and D. B Boyd, VCH Publishers: New York, 1996, Vol. 8, pp. 245−297.
15. J. Kowalewski, *Annu. Rep. NMR Spectrosc.*, 1982, **12**, 81.
16. R. McWeeny, 'Methods of Molecular Quantum Mechanics', 2nd edn., Academic Press: London, 1992.
17. S. P. A. Sauer, *J. Chem. Phys.*, 1993, **98**, 9220.
18. H. Fukui, *Nucl. Magn. Reson.*, 1994, **23**, 124.
19. S. K. Wolff, T. Ziegler, E. van Lenthe, and E. J. Baerends, *J. Chem. Phys.*, 1999, **110**, 7689.
20. J. Autschbach and T. Ziegler, *J. Chem. Phys.*, 2000, **113**, 936.
21. H. Fukui and T. Baba *J. Chem. Phys.*, 1998, **108**, 3854.
22. H. Fukui, T. Baba, and H. Inomata, *J. Chem. Phys.*, 1996, **105**, 3175.

23. H. Akai, M. Akai, S. Blügel, B. Drittler, H. Ebert, K. Terakura, R. Zeller, and P. H. Dederichs, *Prog. Theor. Phys. Suppl.*, 1990, **101**, 11.
24. G. A. Aucar, T. Saue, L. Visscher, and H. J. A. Jensen, *J. Chem. Phys.*, 1999, **110**, 6208.
25. N. C. Pyper, *Chem. Phys. Lett.*, 1983, **96**, 204; **96**, 211.
26. M. Hada, Y. Ishikawa, J. Nakatani, and H. Nakatsuji, *Chem. Phys. Lett.*, 1999, **310**, 342.
27. J. E. Harriman, 'Theoretical Foundations of Electron Spin Resonance', Academic Press: New York, 1978.
28. L. Visscher, T. Enevoldsen, T. Saue, H. J. A. Jensen, and J. Oddershede, *J. Comput. Chem.*, 1999, **20**, 1262.
29. T. Enevoldsen, L. Visscher, T. Saue, H. J. A. Jensen, and J. Oddershede, *J. Chem. Phys.*, 2000, **112**, 3493.
30. Y. Ishikawa, T. Nakajima, M. Hada, and H. Nakatsuji *Chem. Phys. Lett.*, 1998, **283**, 119.
31. M. Hada, R. Fukuda, and H. Nakatsuji, *Chem. Phys. Lett.*, 2000, **321**, 452.
32. H. Nakatsuji, H. Takashima, and M. Hada, *Chem. Phys. Lett.*, 1995, **233**, 95.
33. H. Nakatsuji, T. Nakajima, M. Hada, H. Takashima, and S. Tanaka, *Chem. Phys. Lett.*, 1995, **247**, 418.
34. T. Baba and H. Fukui, *J. Chem. Phys.*, 1999, **110**, 131.
35. C. B. Ballard, M. Hada, H. Kaneko, and H. Nakatsuji, *Chem. Phys. Lett.*, 1996, **254**, 170.
36. J. Vaara, K. Ruud, O. Vahtras, H. Ågren, and J. Jokisaari, *J. Chem. Phys.*, 1998, **109**, 1212.
37. J. Vaara, K. Ruud, and O. Vahtras, *J. Chem. Phys.*, 1999, **111**, 2900.
38. J. Vaara, K. Ruud, and O. Vahtras, *J. Comput. Chem.*, 1999, **20**, 1314.
39. S. Kirpekar, H. J. A. Jensen, and J. Oddershede, *Theor. Chim. Acta.*, 1997, **95**, 35.
40. S. Kirpekar and S. P. A. Sauer, *Theor. Chem. Acc.*, 1999, **103**, 146.
41. I. Morishima, K. Endo, and T. Yonezawa, *J. Chem. Phys.*, 1973, **59**, 3356.
42. M. I. Volodicheva and T. K. Rebane, *Teoreticheskaya i Éksperimental'naya Khimiya (engl. ed Theor. and Exp. Chemistry)* 1978, **14**, 348.
43. A. A. Cheremisin and P. V. Schastnev, *J. Magn. Reson.*, 1980, **40**, 459.
44. K. Endo, K. Yamamoto, and H. Okada, *Bull. Chem. Soc. Jpn.*, 1995, **68**, 3341.
45. P. Pyykkö, E. Pajanne, and M. Inokuti, *Int. J. Quantum Chem.*, 1973, **7**, 785.
46. D. K. Dalling and H. S. Gutowsky, *J. Chem. Phys.*, 1971, **55**, 4959.
47. P. Pyykkö, A. Görling, and N. Rösch, *Mol. Phys.*, 1987, **61**, 195.
48. R. G. Parr and W. Yang, 'Density Functional Theory of Atoms and Molecules', Oxford University Press: New York, 1989.
49. V. G. Malkin, O. L. Malkina, and D. R. Salahub, *Chem. Phys. Lett.*, 1996, **261**, 335.
50. O. L. Malkina, B. Schimmelpfennig, M. Kaupp, B. A. Hess, P. Chandra, U. Wahlgren, and V. G. Malkin, *Chem. Phys. Lett.*, 1998, **296**, 93.
51. M. Kaupp, V. G. Malkin, and O. L. Malkina, in 'Encyclopedia of Computational Chemistry', ed P. v. R. Schleyer, John Wiley & Sons: Chichester, 1998, pp. 1857–1866.
52. G. Schreckenbach and T. Ziegler, *Int. J. Quantum Chem.*, 1997, **61**, 899.
53. S. K. Wolff and T. Ziegler, *J. Chem. Phys.*, 1998, **109**, 895.
54. J.Autschbach and T. Ziegler, *J. Chem. Phys.*, 2000, **113**, 9410.
55. E. K. U. Gross, J. F. Dobson, and M. Petersilka, *Top. Curr. Chem.*, 1996, **81**, 181.
56. Y. Nomura, Y. Takeuchi, and N. Nakagawa, *Tetrahedron Lett.*, 1969, **8**, 639.
57. P. Pyykkö, *Chem. Phys.*, 1983, **74**, 1.
58. Z. C. Zhang and G. A. Webb, *J. Mol. Struct.*, 1983, **104**, 439.
59. C. J. Jameson, *Nucl. Magn. Reson.*, 1984, **13**, 1.
60. R. L. Hota, R. C. Patnaik, G. S. Tripathi, and P. K. Misra, *Phys. Rev. B*, 1995, **51**, 7291.
61. U. Edlund, T. Lejon, P. Pyykkö, T. K. Venkatachalam, and E. Buncel, *J. Am. Chem. Soc.*, 1987, **109**, 5982.
62. M. Kaupp, O. L. Malkina, V. G. Malkin, and P. Pyykkö, *Chem. Eur. J.*, 1998, **4**, 118.
63. J. Vaara, O. L. Malkina, H. Stoll, V. G. Malkin, and M. Kaupp, *J. Chem. Phys.*, 2001, **114**, 61.
64. M. Kaupp, C. Aubauer, G. Engelhardt, T. M. Klapötke, and O. L. Malkina, *J. Chem. Phys.*, 1999, **110**, 3897.
65. H. Nakatsuji, Z.-M. Hu, and N. Nakajima, *Chem. Phys. Lett.*, 1997, **275**, 429.
66. H. Nakatsuji, M. Sugimoto, and S. Saito, *Inorg. Chem.*, 1990, **29**, 3095.
67. M. Kaupp, O. L. Malkina, and V. G. Malkin, *Chem. Phys. Lett.*, 1997, **265**, 55.
68. M. Bühl, M. Kaupp, O. L. Malkina, and V. G. Malkin, *J. Comput. Chem.*, 1998, **20**, 91.
69. G. Schreckenbach and T. Ziegler, *Theor. Chem. Acc.*, 1998, **99**, 71.
70. M. Hada, H. Kaneko, and H. Nakatsuji, *Chem. Phys. Lett.*, 1996, **261**, 7.
71. H. Nakatsuji, M. Hada, H. Kaneko, and C. C. Ballard, *Chem. Phys. Lett.*, 1996, **255**, 195.
72. J. Wan, R. Fukuda, M. Hada, and H. Nakatsuji, *J. Phys. Chem., A* 2001, **105**, 128.
73. G. Schreckenbach, S. K. Wolff, and T. Ziegler, in 'Modeling NMR Chemical Shifts', ACS Symposium Series no. 732, eds J. C. Facelli and A. C. de Dios, American Chemical Society: Boston, MA, 1999, pp. 101–114.
74. M. Kaupp, V. G. Malkin, O. L. Malkina, and D. R. Salahub, *J. Am. Chem. Soc.*, 1995, **117**, 1851; erratum 1995, **117**, 8492.
75. R. Bouten, E. J. Baerends, E. van Lenthe, L. Visscher, G. Schreckenbach, and T. Ziegler, *J. Chem. Phys.*, 2000, **104**, 5600.
76. A. Rodriguez-Fortea, P. Alemany, and T. Ziegler, *J. Phys. Chem. A*, 1999, **103**, 8288.
77. Y. Ruiz-Morales, G. Schreckenbach, and T. Ziegler, *J. Phys. Chem.*, 1996, **100**, 3359.
78. A. W. Ehlers, Y. Ruiz-Morales, E. J. Baerends, and T. Ziegler, *Inorg. Chem.*, 1997, **36**, 5031.
79. T. M. Gilbert and T. Ziegler, *J. Phys. Chem. A*, 1999, **103**, 7535.
80. G. Schreckenbach, S. K. Wolff, and T. Ziegler, *J. Phys. Chem. A*, 2000, **104**, 8244.
81. G. B. Bacskay, I. Bytheway, and N. S. Hush, *J. Am. Chem. Soc.*, 1996, **118**, 3753.
82. J. Feeney, R. Haque, L. W. Reeves, and C. P. Yue, *Can. J. Chem.*, 1968, **46**, 1389.
83. G. Breit, *Phys. Rev.* 1930, **35**, 1447.
84. J. Khandogin and T. Ziegler, *J. Phys. Chem. A*, 2000, **104**, 113.
85. G. A. Aucar and R. H. Contreras, *J. Magn. Reson.*, 1991, **93**, 413.
86. R. M. Lobayan and G. A. Aucar, *J. Mol. Struct.*, 1998, **452**, 1.
87. J. A. Gonzaléz, G. A. Aucar, M. C. Ruiz de Azúa, and R. H. Contreras, *Int. J. Quantum Chem.*, 1997, **61**, 823.
88. G. A. Aucar, E. Botek, S. Gómez, F. Sproviero, and R. H. Contreras, *J. Organomet. Chem.*, 1996, **524**, 1.
89. P. Pyykkö, *Chem. Phys.*, 1977, **22**, 289.
90. G. A. Aucar and J. Oddershede, *Int. J. Quantum Chem.*, 1993, **47**, 425.
91. P. Pyykkö and L. Wiesenfeld, *Mol. Phys.*, 1981, **43**, 557.
92. J. Autschbach and T. Ziegler, *J. Am. Chem. Soc.*, 2001, **123**, 3341.
93. J. Autschbach and T. Ziegler, *J. Am. Chem. Soc.*, 2001, **123**, 5320.
94. D. L. Bryce and R. E. Wasylishen, *J. Am. Chem. Soc.*, 2000, **122**, 3197.
95. B. Wrackmeyer and K. Horchler, *Annu. Rep. NMR Spectrosc.*, 1989, **22**, 249.

Acknowledgements

This work has received financial support from the National Science and Engineering Research Council of Canada (NSERC). J. A. thanks Dr. S. Patchkovskii for stimulating discussions.

Biographical Sketches

Jochen Autschbach, *b* 1968. M.Sc. (Chemistry), 1996, Ph.D., 1999, Siegen, Germany. Ph.D. thesis on relativistic effects in atoms and chemical bonds. Since 1999 member of Tom Ziegler's research group in Calgary, Canada. Current research interests: computation of heavy atom NMR spin–spin coupling constants and chemical shifts, solvent effects in spectroscopy, theory of optical activity, density functional response theory, relativistic quantum chemistry. J. A. has contributed, among other code, a program for the computation of heavy atom spin–spin couplings to the Amsterdam Density Functional program.

Tom Ziegler, *b* 1944. T. Z. was raised in Denmark and graduated from the University of Copenhagen in 1972 with a Cand. Scient. degree in theoretical chemistry. He obtained a Ph.D. from University of Calgary (1978) where he has been a full professor since 1991. He has in the last 25 years worked with the development of density functional theory as a practical tool in transition metal chemistry and homogeneous catalysis. This has led to computational methods of use in spectroscopy, thermochemistry, structure determination and molecular dynamics. He is a fellow of both the Royal Danish and Royal Canadian Societies.

Relaxation of Transverse Magnetization for Coupled Spins

Thomas C. Farrar and Thomas C. Stringfellow
University of Wisconsin, Madison, WI, USA

1	Introduction	1
2	Redfield Theory and Transverse Relaxation	1
3	Application to Molecular Structure and Dynamics in Na_2PHO_3	3
4	Discussion	5
5	Summary	5
6	Related Articles	6
7	References	6

1 INTRODUCTION

Several excellent articles on Redfield relaxation theory are presented elsewhere in this Encyclopedia (see, e.g., ***Relaxation Theory: Density Matrix Formulation***), and the applications given here are based on that work. The theory is not only simple and elegant, it is also a very powerful and useful tool for the experimental NMR spectroscopist. As shown below, NMR relaxation time measurements of coupled spin systems provide a wealth of information about molecular structure and molecular dynamics in solution that is available in no other way. Such studies are especially important, since a large fraction of chemistry takes place in solution or at interfaces where molecules are still mobile.

For an isolated spin system consisting of two spins of $\frac{1}{2}$ (e.g., C–H, P–H, C–F, P–F, etc.) at low magnetic fields (2.3 T or lower) where only dipolar relaxation is important, the NMR relaxation in a nonviscous fluid sample can be characterized by a single parameter, R_1, the spin–lattice relaxation rate, since in this case the longitudinal relaxation, R_1, and the transverse relaxation, R_2, are equal. That is, all four spectral lines (two for each nucleus) have the same relaxation rate. For magnetic fields of 4.7 T (200 MHz for protons) and higher, most nuclei other than hydrogen are relaxed by both the dipolar and by the chemical shift anisotropy (CSA) mechanisms. In this event, for a coupled system, the observed relaxation rate cannot be described as the sum of the relaxation rates of the contributing mechanisms, that is, $R_{\text{total}} \neq R_{\text{dipolar}} + R_{\text{CSA}}$. Furthermore, four parameters are required to describe the transverse relaxation (each of the four lines has a different R_2 value);[1–9] and for longitudinal relaxation, each line relaxes as a triple exponential.[6–12]

A clear understanding of such relaxation processes is essential, since it has recently been shown that in coherence transfer experiments on large molecules (with long correlation times), anomalous peaks may arise in 2D multiple quantum filtered correlation spectra owing to the presence of such multiple relaxation processes.[10] Differential relaxation can also affect two-dimensional correlation (COSY) experiments.[13,14] The experiments in an aqueous solution of Na_2PHO_3 discussed below provide insight into these differential longitudinal and transverse relaxation processes.

For the general case of two coupled spins of $\frac{1}{2}$, A and K, the parameters that affect the longitudinal and the transverse relaxation are the CSA values of spin A and spin K, the A–K bond distance, the molecular correlation time, and the random field terms. The simultaneous determination of all these parameters at a given temperature presents the opportunity to measure their temperature dependence, a situation that is not possible when relaxation is due to a single relaxation mechanism[15] or when one of the two spins is decoupled. In addition, in the coupled experiments described here, the temperature dependence of the random field terms provides information about the molecular motion of those solvent molecules that are in close proximity to the spin pair.

2 REDFIELD THEORY AND TRANSVERSE RELAXATION

The theory of spin–lattice relaxation in coupled spin systems has been treated thoroughly by a number of authors,[1–12] and is not repeated in detail here. For the most general case, the time evolution of the density matrix $\boldsymbol{\sigma}$ is given by

$$\frac{\mathrm{d}\boldsymbol{\sigma}}{\mathrm{d}t} = \mathbf{R}[\boldsymbol{\sigma} - \boldsymbol{\sigma}(\infty)] \tag{1}$$

This equation can in most cases be greatly simplified. If the basis functions for the density matrix are eigenstates of the Hamiltonian then the diagonal elements σ_{ii} of the density matrix represent the populations of the energy levels, and are related to the longitudinal ('T_1') relaxation. Furthermore, in this eigenbasis representation, if the eigenstates are not degenerate, the density matrix elements σ_{ij} are not connected via the relaxation superoperator to any other matrix elements, and the time evolution of these states is given by

$$\frac{\mathrm{d}\sigma_{ij}}{\mathrm{d}t} = -R_{ijij}[\sigma_{ij} - \sigma_{ij}(\infty)] \tag{2}$$

Given the boundary condition that the transverse magnetization at time $t = 0$ is $\sigma_{ij}(\max)$, the solution of the above differential equation is

$$\sigma_{ij}(t) = \sigma_{ij}(\max)\exp(-t/T_2) \tag{3}$$

Equation (3) tells us that the free induction decay (FID) signal for the coherence σ_{ij} will decay as a single exponential with a time constant T_2. The Fourier transform of this FID is consequently a Lorentzian line with a linewidth, $\pi\Delta\nu_{1/2}(i \rightarrow j) = R_{ijij}$ (see Figure 1). The matrix elements R_{ijij} are then related in a simple fashion to the linewidths of the six transverse coherences for the two-spin system. There are four single quantum coherences: R_{1212} and R_{3434}, the low- and high-frequency lines, respectively, in the carbon spectrum (for a carbon–hydrogen spin pair), and R_{1313} and R_{2424}, the low- and high-frequency lines, respectively, in the proton spectrum (a similar situation would hold, of course, for a proton–phosphorus spin pair or a fluorine–phosphorus spin

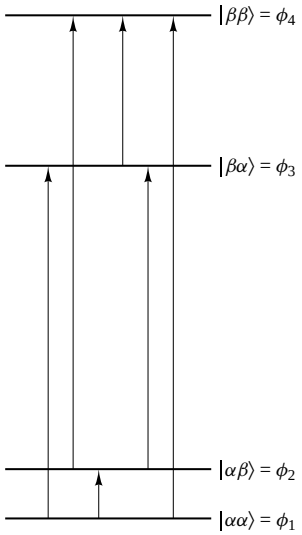

Figure 1 The energy level diagram for PHO_3^{2-}. The labeled wavefunctions correspond to the weak coupling limit. The transitions are as follows: $1 \rightarrow 3$ and $2 \rightarrow 4$ correspond to the low- and high-frequency proton peaks, $1 \rightarrow 2$ and $3 \rightarrow 4$ correspond to the low- and high-frequency phosphorus peaks, $2 \rightarrow 3$ corresponds to the zero quantum transition, and $1 \rightarrow 4$ corresponds to the double quantum transition

pair). We may indirectly measure the zero quantum coherence rate constant R_{2323} and the double quantum coherence rate constant R_{1414}. These relaxation matrix elements are related in a straightforward fashion to the dipolar parameter p, the two chemical shift anisotropies $\Delta\sigma_I = \delta_I$ and $\Delta\sigma_S = \delta_S$, the molecular correlation time, τ_c, and random field terms as indicated in Table 1.

This is, in principle, an attractive way to obtain a wealth of information about molecular structure and molecular dynamics, since it would appear that one need only measure six relaxation rates. As mentioned above, in a completely homogeneous magnetic field, the rate constant is related to the spectral linewidth:

$$R_{ijij} = (1/T_2)_{(i \rightarrow j)} = \pi \Delta\nu_{1/2}(i \rightarrow j) \tag{4}$$

where $\Delta\nu_{1/2}(i \rightarrow j)$ is the full width at halfheight of a peak with Lorentzian lineshape.

In practice, accurate values of the transverse relaxation time may be obtained using the experimental linewidth only when the relaxation time is short. In this event, the linewidth is usually very large compared with any magnetic field inhomogeneities. In principle, accurate values for the linewidth may be obtained by a spin echo experiment, which circumvents the errors arising from pulse imperfections and self-diffusion through an inhomogeneous field. One popular and often used version of the spin echo experiment is the one proposed by Meiboom and Gill.[16] This experiment uses the pulse sequence

$$90^\circ_x - (\tau - 180^\circ_y - \tau)_n \tag{5}$$

This is a variation of the Carr–Purcell pulse sequence.[17] This experiment is, in principle, quite straightforward. In practice, it is very difficult to obtain accurate, meaningful results in the laboratory. If done with great care, however, this experiment is capable of providing accurate results. Vold et al.[18] used numerical analysis of the Bloch equations to evaluate the effects of several experimental conditions. To obtain an accuracy of 1–2% in CPMG experiments, they suggested that the following conditions be satisfied.

Table 1 Relaxation Matrix Elements for a Weakly Coupled System of Two Spins of $\frac{1}{2}$ in the Population Basis; the Y_{ijij} and Z_{ijij} Random Field Terms Include the Longitudinal Random Field Terms A and B

Longitudinal

$R_{1111} = -3(p - \delta_I)^2 k_I - 3(p - \delta_S)^2 k_S - 12p^2 k_+ - \frac{1}{2}(A + B)$
$R_{1122} = 3(p - \delta_S)^2 k_S + \frac{1}{2}A$
$R_{1133} = 3(p - \delta_I)^2 k_I + \frac{1}{2}B$
$R_{1144} = 12p^2 k_+$
$R_{2222} = -3(p + \delta_I)^2 k_I - 3(p - \delta_S)^2 k_S - 2p^2 k_- - \frac{1}{2}(A + B)$
$R_{2233} = 2p^2 k_-$
$R_{2244} = 3(p + \delta_I)^2 k_I + \frac{1}{2}B$
$R_{3333} = -3(p - \delta_I)^2 k_I - 3(p + \delta_S)^2 k_S - 2p^2 k_- - \frac{1}{2}(A + B)$
$R_{3344} = 3(p + \delta_S)^2 k_S + \frac{1}{2}A$
$R_{4444} = -3(p + \delta_I)^2 k_I - 3(p + \delta_S)^2 k_S - 12p^2 k_+ - \frac{1}{2}(A + B)$

Transverse

$R_{1212} = -3(p^2 + \delta_I^2)k_I - 3(p - \delta_S)^2 k_S - 4(p - \delta_S)^2 k_0 - 6p^2 k_+ - p^2 k_- - Y_{1212}$
$R_{1313} = -3(p^2 + \delta_S^2)k_S - 3(p - \delta_I)^2 k_I - 4(p - \delta_I)^2 k_0 - 6p^2 k_+ - p^2 k_- - Z_{1313}$
$R_{2424} = -3(p^2 + \delta_S^2)k_S - 3(p + \delta_I)^2 k_I - 4(p + \delta_I)^2 k_0 - 6p^2 k_+ - p^2 k_- - Z_{2424}$
$R_{3434} = -3(p^2 + \delta_I^2)k_I - 3(p + \delta_S)^2 k_S - 4(p + \delta_S)^2 k_0 - 6p^2 k_+ - p^2 k_- - Y_{3434}$

Zero/multiple quantum

$R_{2323} = -3(p^2 + \delta_I^2)k_I - 3(p^2 + \delta_2^2)k_S - 4(\delta_I - \delta_S)^2 k_0 - 2p^2 k_- - X_{2323}$
$R_{1414} = -3(p^2 + \delta_I^2)k_I - 3(p^2 + \delta_S^2)k_S - 4(\delta_I + \delta_S)^2 k_0 - 12p^2 k_+ - X_{1414}$
$p = \gamma_I \gamma_S \mu\hbar/8\pi r_{IS}^3$
$\delta = \frac{1}{3}\gamma B_0[\sigma_{33} - \frac{1}{2}(\sigma_{11} + \sigma_{22})]$
$k_0 = \frac{1}{5}\tau_c$
$k_i = \tau_c/5(1 + \omega_i^2 \tau_c^2)$
$\omega_+ = \omega_I + \omega_S$
$\omega_- = \omega_I - \omega_S$

1. Pulse widths must be calibrated and accurate to within about 5% of ideal.
2. Data from the first part of the relaxation curve should not be used in the least-squares fit.
3. The transmitter should be as close to on resonance as possible to eliminate off-resonance effects.
4. Amplitudes of the spin echoes must be calculated relative to an experimentally determined steady-state value.
5. The sample should remain static so that the gradients in the magnetic field are not time-dependent.
6. Refocusing pulse spacings should be less than approximately 100 ms so that diffusion effects are eliminated.

Another method of measuring relaxation in the transverse plane is the spin locking experiment,[19,20] in which one employs a continuous $\boldsymbol{B}_1$ field in lieu of the sequence of 180° pulses used in spin echo experiments. This field locks the magnetization along the applied axis in the transverse plane. By varying the duration of the spin locking period, one may fit the peak intensity versus time to a decaying exponential and obtain the spin–lattice relaxation time in the rotating frame, $T_{1\rho}$. For most liquid samples, $T_{1\rho}$ is essentially equivalent to T_2.[19,21]

To obtain information about the relaxation rates for zero and multiple quantum coherences, a number of different pulse sequences have been proposed.[22] For heteronuclear spin systems, the following pulse sequence may be used to generate double quantum coherences:[23]

$$\left.\begin{array}{lllll} I: & 90^\circ_y - \frac{1}{2}\tau - & 180^\circ - \frac{1}{2}\tau - 90^\circ_x - t_1 - \text{acquire} \\ S: & & 180^\circ - \frac{1}{2}\tau - 90^\circ - t_1 \end{array}\right\} \quad (6)$$

where $\tau = \pi/2J$. The purpose of the 180° pulses is to refocus the dephasing of the magnetization due to magnetic field inhomogeneities and chemical shifts and suppress the dependence of the transmitter offset frequency. Yang et al.[24] proposed using a similar pulse sequence with explicit pulse phasings to separate the zero and double quantum coherences. This sequence is as follows:

$$\left.\begin{array}{llll} I: & 90^\circ_1 - \frac{1}{2}\tau - & 180^\circ_y - \frac{1}{2}\tau/2 & 180^\circ_x - \frac{1}{2}t_1 - 90^\circ_2 \\ S: & & 180^\circ_y - \frac{1}{2}\tau - 90^\circ_y - \frac{1}{2}t_1 - & 180^\circ_x - \frac{1}{2}t_1 - \text{acquire}_3 \end{array}\right\} \quad (7)$$

To obtain purely zero quantum coherence, the relative phasing of the pulses is

$$\left.\begin{array}{llll} (1) & x & x & -x & -x \\ (2) & x & y & x & y \\ (3) & x & y & -x & -y \end{array}\right\} \quad (8)$$

which is arranged to eliminate any magnetization from the S spin. The recovery curve may then be fit to the following equation to obtain the zero quantum relaxation time T_{ZQ}:

$$\begin{aligned} I(t_1) &= I(\infty) + B' \mathrm{e}^{-t_1/T_{\text{ZQ}}} \sin(\pi J \tau) \\ &= A + B \mathrm{e}^{-t_1/T_{\text{ZQ}}} \end{aligned} \quad (9)$$

To obtain purely double quantum coherence, the relative phasing of the pulses is

$$\left.\begin{array}{llll} (1) & x & x & -x & -x \\ (2) & x & -y & x & -y \\ (3) & x & y & -x & -y \end{array}\right\} \quad (10)$$

The recovery curve may then be fit to an equation similar to that for a zero quantum coherence to obtain the double quantum relaxation time T_{DQ}.

3 APPLICATION TO MOLECULAR STRUCTURE AND DYNAMICS IN NA_2PHO_3

It is important to test the development of a new theory by carrying out experiments on a sample for which one knows the experimental results. All of the pertinent NMR parameters for a sample of Na_2PHO_3 have been measured by a number of independent methods. We therefore decided to carry out a set of transverse relaxation experiments with a solution of sodium phosphite, Na_2PHO_3, dissolved in a 60%/40% mixture of ethylene glycol-d_6 and methanol-d_4. They were performed at −25.4°C, a temperature slightly higher than the temperature of the proton-decoupled T_1 minimum of the phosphorus nuclei at a field of 4.7 T. Figure 2 shows the ^{31}P NMR spectra of the sample in a field of 11.5 T. The upper trace was recorded at 300 K, the middle trace at 250 K, and the bottom trace at 225 K. At 225 K, the low-frequency line has become so broad that it has disappeared into the baseline noise.

Fitting the data to equation (1) produced the following best fit parameters: the P–H bond length r = 150.4 pm, the proton chemical shift anisotropy $\Delta\sigma_{\text{H}}$ = 5.3 ppm, the phosphorus chemical shift anisotropy $\Delta\sigma_{\text{P}}$ = −137.5 ppm, the rotational correlation time, assuming a Lorentzian spectral density function, τ_{c} = 818 ps, the phosphorus intermolecular term $A = 0.27\,\text{s}^{-1}$, and the proton intermolecular term $B = 0.22\,\text{s}^{-1}$. The theoretical transverse relaxation times may be calculated using these molecular parameters and the equations given in Table 1. Independent values for the P–H bond length were obtained from X-ray and neutron diffraction experiments.[25] Independent values for the phosphorus and proton chemical shift anisotropies were obtained from NMR

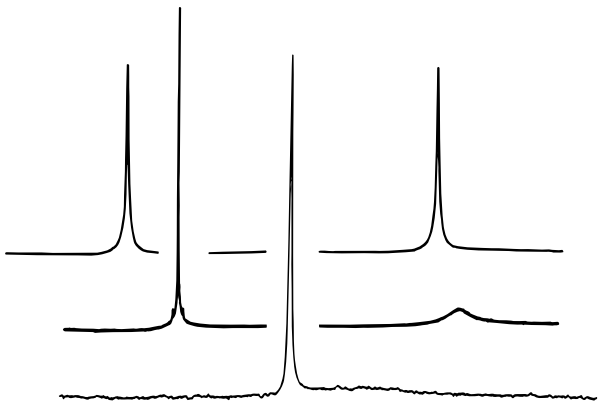

Figure 2 The ^{31}P NMR spectra of a sample of Na_2PHO_3 in a magnetic field of 11.5 T (202 MHz resonance frequency for phosphorus). The upper trace was recorded at 300 K, the middle trace at 250 K, and the bottom trace at 225 K. At 225 K, $\omega_0\tau_{\text{c}} \sim 1$, and the low-frequency line has become so broad that it has disappeared into the baseline noise

experiments on a solid sample of Na_2PHO_3 (T. C. Farrar, unpublished results).

These results show clearly that the two lines in the phosphorus spectrum will have different widths and the two lines in the proton spectrum will have different widths. The width of the $(1 \rightarrow 2)$ phosphorus line in PHO_3^{2-} must be broad, since the sign of the phosphorus CSA is negative and R_{1212} contains terms with the difference between δ_P and p. Similarly, the width of the $(3 \rightarrow 4)$ phosphorus line must be narrow, since R_{3434} contains terms with the sum of the CSA and dipolar terms. In the phosphorus spectra shown in Figure 2, the low-frequency line is broad; consequently, the sign of the phosphorus–proton coupling constant J(P,H) must be positive. The equations for R_{ijij} above also show that the greatest differential line broadening will occur at that field for which the CSA and the dipolar parameters are approximately equal, and under those sample conditions for which $\omega\tau_c \sim 1$. This is exactly what we have found experimentally.

The theory clearly tells us what to expect, but it is always a bit more satisfying if one can obtain a simple physical picture of what is happening. Consider, then, a single crystal of Na_2PHO_3 with the various orientations shown in Figure 3(a). The resonance frequency for the phosphorus nuclei that are bonded to protons will change as a function of Θ in the following manner:

$$f_\alpha = f_0 - \frac{\gamma_H \gamma_P \hbar}{r^3}(3\cos^2\Theta - 1) \tag{11}$$

$$f_\beta = f_0 + \frac{\gamma_H \gamma_P \hbar}{r^3}(3\cos^2\Theta - 1) \tag{12}$$

where f_α and f_β are the two frequencies in the phosphorus spectrum, Θ is the angle between the P–H internuclear vector and the magnetic field $\boldsymbol{B}_0$, and r is the P–H bond length. The other constants are defined in Table 1. Note that the f_α line arises from that half of the molecules in which the phosphorus is bonded to a proton nucleus in the α spin state (i.e., those proton nuclei that have their spins aligned parallel with the magnetic field $\boldsymbol{B}_0$), and the f_β line arises from that half of the molecules in which the phosphorus is bonded to a proton nucleus in the β spin state. If the chemical shift of the phosphorus is isotropic ($\delta_P = 0$), there will be a maximum splitting of $2p$ (about 15 kHz) for the two lines at a value of $\Theta = 0$. For $\Theta = 54.7^\circ$ (the 'magic angle'), the two lines will coalesce, and at $\Theta = 90^\circ$ the splitting is p (about 7.5 kHz, see the definition of p in Table 1). The spectra for these orientations are depicted in Figure 3(a). The hatched lines below the spectra show the total variation in the magnetic field at the phosphorus nuclei as Θ varies.

If the phosphorus and/or proton chemical shifts are anisotropic (which they are for PHO_3^{2-}) then the local field experienced by the phosphorus nuclei will be very different. Figure 3(b) shows the single crystal spectra for the phosphorus for the same orientations as in Figure 3(a). The frequencies of the two lines are now given by

$$f_\alpha = f_0 - \frac{\gamma_H \gamma_P \hbar}{r^3}(3\cos^2\Theta - 1) + \delta_P(3\cos^2\Theta - 1) \tag{13}$$

$$f_\beta = f_0 + \frac{\gamma_H \gamma_P \hbar}{r^3}(3\cos^2\Theta - 1) + \delta_P(3\cos^2\Theta - 1) \tag{14}$$

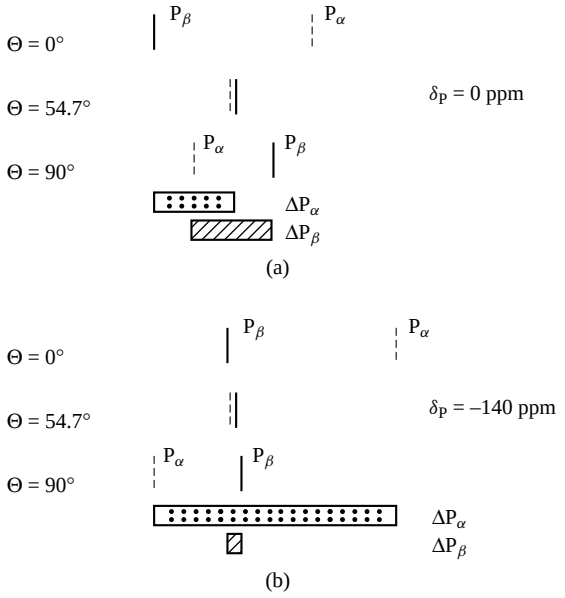

Figure 3 (a) ^{31}P NMR spectra for a single crystal of Na_2PHO_3 at three different orientations of Θ, the angle between the P–H internuclear vector and the magnetic field direction, assuming a phosphorus CSA of zero. (b) As (a), but with a phosphorus CSA value of -140 ppm

If the magnitudes of the phosphorus dipolar and CSA terms are about equal then one of the lines in the single crystal spectrum will experience almost no change in frequency as a function of Θ, since any change in the local field due to the dipolar term will be canceled by the CSA term. The other line will experience a change almost twice as great, since local fields generated by the dipolar and CSA terms add constructively. For PHO_3^{2-}, the phosphorus CSA, $\delta_P = (\sigma_\parallel - \sigma_\perp)_P = -125$ ppm.[6,7] In this case, the total range of magnetic fields experienced as a function of Θ is very small for the P_β nuclei, the phosphorus nuclei spin-coupled to proton nuclei in the β spin state. At a magnetic field of about 6.3 T, the local magnetic field for the P_β nuclei is almost independent of orientation. For the P_α nuclei, the local field changes over a range almost twice as great as that expected for the dipolar interaction. In other words, the dipolar field fluctuations at the P_β nuclei due to changes in orientation are largely canceled by field changes of the opposite sign due to the CSA. The hatched bars below the spectra in Figure 3(b) show schematically this very small range in the local field for the P_β nuclei and the twofold greater-than-normal dipolar range in the dipolar field for the P_α nuclei.

When the molecules begin to move, the magnetic fields at the P_α and P_β nuclei are modulated by the molecular motion. And it is the magnitude of this motion-induced magnetic field modulation [represented by the hatched bars in Figure 3(a) and (b)] that couples the precessional motion of the nuclear spins to the molecular motion and brings about relaxation of the nuclear spin system. When the CSA and dipolar interactions are comparable, as they are in the present case, relatively little magnetic field modulation occurs at the P_β nuclei. Consequently, they will have a very long relaxation time, even for slow molecular motions where $\omega_P\tau_c \sim 1$. The P_α nuclei, however, will experience much larger than normal magnetic field fluctuations, and as a result will have short relaxation times.

Normally, one cannot determine which of the lines in a high-resolution NMR spectrum are associated with the transitions between the various energy levels. For example, in a spectrum such as that in Figure 2, it is not usually possible to determine whether the high-frequency phosphorus line arises from the transition between energy levels 1 and 2 or between levels 3 and 4. However, when differential line broadening is present, one can easily determine which line is associated with the transitions between the energy levels. As pointed out above, since we know from solid state NMR experiments that the phosphorus CSA is negative and since we know from the spectrum that it is the low-frequency phosphorus line that is broad, by looking at the expression for R_{1212} above, we know that the broad line must be associated with the R_{1212} transition. Consequently, the absolute sign of the phosphorus–hydrogen spin coupling constant, J(P,H) must be positive; in this case, J(P,H) = +565 Hz. In a similar fashion, we have shown that the absolute sign of directly bonded carbon–hydrogen spin coupling is positive.[8]

The transverse relaxation times for all four lines were measured using the CPMG sequence [see equation (5)] and $T_{1\rho}$ experiments. The experiments were performed on resonance at the same temperature as the longitudinal relaxation experiments. The sample was static, and field/frequency locking was not used. A three-parameter fit to an equation similar to equation (9) gives the transverse relaxation time. For the $R_{1\rho}$ experiments, the spin locking fields γB_1 were 340 and 746 s^{-1}, respectively, for the proton and phosphorus nuclei. Table 2 shows a comparison of the results from these experiments.

4 DISCUSSION

Examining Table 2, one sees that the experimentally determined transverse relaxation times do not agree with the theoretical relaxation times calculated from the bond length, the two CSAs, and the correlation time obtained from the longitudinal relaxation studies. The calculated T_{ij} values are appreciably longer than the experimentally determined values. The differences are due to several factors. The largest source of the differences probably arises from the intermolecular, random field terms. These terms account for relaxation mechanisms of rank one, such as scalar relaxation, spin rotation, chemical exchange, and relaxation due to the presence of paramagnetic species. Since the experiments were done at low temperature, spin rotation can be ruled out. Very careful sample preparation allows one also to rule out paramagnetic impurities. Since the random field terms for the longitudinal relaxation also contribute to the transverse relaxation, and have been included in the Y_{ijij} and Z_{ijij} terms in the calculated values, the difference must arise from additional random field terms that are unique to the transverse relaxation. Such terms would include those due to chemical exchange and other relatively slow random dynamic processes. Neglect of these terms will result in calculated values for the transverse relaxation rates that are smaller (and calculated relaxation times that are longer) than the experimentally measured values.

If one assumes that the additional intermolecular contribution is the same for both single quantum coherences of a given nucleus, one may subtract the relaxation rates and get a relation independent of the intermolecular interactions:

$$\Delta_{\mathrm{P}} = R_{1212} - R_{3434} = 12p\delta_{\mathrm{P}}k_{\mathrm{P}} + 16p\delta_{\mathrm{P}}k_0 \qquad (15)$$

$$\Delta_{\mathrm{H}} = R_{1313} - R_{2424} = 12p\delta_{\mathrm{H}}k_{\mathrm{H}} + 16p\delta_{\mathrm{H}}k_0 \qquad (16)$$

where k_i and k_0 are defined in Table 1. Comparing the experimentally obtained values of these parameters with those calculated from T_1 data, the results still do not agree, implying either that these additional intermolecular terms are not the sole factor causing the difference or that there are still additional random field terms operating that do not equally affect the two different coherences for a given nucleus. This suggests, for example, that Y_{1212} and Y_{3434} (see Table 1) are not equal.

Another factor that may lead to the discrepancies seen between the theoretical relaxation rates and the experimentally determined rates is the form of the spectral density function. Longitudinal relaxation depends on rapidly fluctuating fields near the Larmor frequency γB_0. Transverse relaxation times depend on fluctuating fields near the Larmor frequency as well as slowly fluctuating fields described by k_0. The Lorentzian spectral density function may not be valid for this range of molecular motions. Finally, the experiments may not be measuring the true transverse or zero/multiple quantum relaxation rates.

5 SUMMARY

In principle, transverse relaxation studies, including zero and multiple quantum coherences, can provide structural and dynamic information. They complement longitudinal relaxation studies in that they provide information concerning low-frequency motions and cross-correlation functions. Preliminary work comparing longitudinal and transverse relaxation results obtained for PHO_3^{2-} in solution indicates that great caution

Table 2 Theoretical and Experimental Results of Transverse Relaxation Studies on PHO_3^{2-}

Source	T_{12} (ms)	T_{34} (ms)	T_{13} (ms)	T_{24} (ms)	T_{23} (ms)	T_{14} (ms)
Theory and T_1 study[a]	151	537	279	254	406	320
CPMG	121	386	185	165		
Zero quantum					319	
Double quantum						205
$T_{1\rho}$	125	369	215	181		

[a]The values for p, $\Delta\sigma_{\mathrm{P}}$, $\Delta\sigma_{\mathrm{H}}$, τ_{c}, and the random field terms A and B were taken from longitudinal NMR experiments, solid state NMR experiments, and neutron diffraction work, and were used in the equations for the R_{ijij} matrix elements given in Table 1.

should be used in using the transverse experiments to obtain structural and dynamic information. This is in part due to the difficulty in executing accurate, meaningful CPMG and $T_{1\rho}$ experiments. It may also be due to the fact that a single spectral density function is not a faithful representation of the molecular motions over the entire range of motion.

Given the six equations for the six different coherences and the up to 10 unknown parameters (δ_H, δ_P, p, and τ_c, and the six transverse random field terms; see Table 1), a measurement of the six coherences is not enough information to give one accurate, uniquely determined values for all of those parameters. In addition, as we have seen in the example presented above, there are experimental problems, since it is very difficult indeed to measure linewidths (coherences) accurately, especially for very narrow lines. In our experience, neither linewidth measurements nor Carr–Purcell–Meiboom–Gill spin echo experiments give highly reliable results, especially at the higher temperatures where some of the linewidths are relatively narrow. $T_{1\rho}$ experiments, if done carefully, give reasonably good results.

The most fundamental difficulty is that one has 6 equations and there are probably 10 unknown parameters. This would seem to indicate that experimental information about the transverse relaxation must be complemented by additional data from longitudinal relaxation experiments. In practice, a better way to obtain information about the molecular parameters is to carry out longitudinal relaxation time experiments. Although the data analysis is considerably more difficult, the experiments are easier to execute, and give more reliable and more reproducible results.[6–8]

6 RELATED ARTICLES

Relaxation of Coupled Spins from Rotational Diffusion; Relaxation Mechanisms: Magnetization Modes; Relaxation Processes in Coupled-Spin Systems; Relaxation Processes: Cross Correlation and Interference Terms; Relaxation Theory: Density Matrix Formulation.

7 REFERENCES

1. A. G. Redfield, in *Advances in Magnetic Resonance*, ed. J. S. Waugh, Academic Press, New York, Vol. 1, p. 1.
2. H. J. Shimizu, *J. Chem. Phys.*, 1964, **40**, 3357.
3. E. L. Mackor and C. MacLean, in *Progress in Nuclear Magnetic Resonance Spectroscopy*, eds. J. W. Emsley, J. Feeney, and L. H. Sutcliffe, Pergamon Press, Oxford, 1967, Vol. 3, p. 129.
4. L. G. Werbelow and D. M. Grant, in *Advances in Magnetic Resonance*, ed. J. S. Waugh, Academic Press, New York, 1977, Vol. 9, p. 189.
5. R. L. Vold and R. R. Vold, in *Progress in Nuclear Magnetic Resonance Spectroscopy*, eds. J. W. Emsley, J. Feeney, and L. H. Sutcliffe, Pergamon Press, Oxford, 1978, Vol. 12, p. 79.
6. T. C. Farrar and I. C. Locker, *J. Chem. Phys.*, 1987, **87**, 3281; see also *Z. Phys. Chem.*, 1987, **151**, 24.
7. T. C. Farrar and J. D. Decatur, *J. Phys. Chem.*, 1990, **94**, 7395.
8. T. C. Farrar, M. A. Jablonsky, and J. L. Schwartz, *J. Phys. Chem.*, 1994, **98**, 4780; see also T. C. Farrar, B. A. Adams, G. C. Grey, R. A. Quintero, and Q. Zuo, *J. Am. Chem. Soc.*, 1986, **108**, 8190.
9. T. C. Farrar and R. A. Quintero, *J. Phys. Chem.*, 1987, **91**, 3224.
10. N. Mueller, G. Bodenhausen, K. Wuethrich, and R. R. Ernst, *J. Magn. Reson.*, 1985, **65**, 531.
11. K. Elbayed and D. Canet, *Mol. Phys.*, 1989, **68**, 1033.
12. E. Koenigsberger and H. Sterk, *J. Chem. Phys.*, 1985, **83**, 2723.
13. S. Wimperis and G. Bodenhausen, *Chem. Phys. Lett.*, 1987, **140**, 41.
14. S. Wimperis and G. Bodenhausen, *Mol. Phys.*, 1989, **66**, 897.
15. H. G. Hertz, in *Progress in Nuclear Magnetic Resonance Spectroscopy*, eds. J. W. Emsley, J. Feeney, and L. H. Sutcliffe, Pergamon Press, Oxford, 1983, Vol. 16, p. 115; see also H. G. Hertz, ibid., 1967, Vol. **3**, p. 159.
16. S. Meiboom and D. Gill, *Rev. Sci. Instrum.*, 1958, **29**, 688.
17. H. Y. Carr and E. M. Purcell, *Phys. Rev.*, 1954, **94**, 630.
18. R. L. Vold, R. R. Vold, and H. E. Simon, *J. Magn. Reson.*, 1973, **11**, 283.
19. Farrar, T. C., *Introduction to Pulse NMR Spectroscopy*, The Farragut Press, Chicago, 1989.
20. T. K. Leipert, J. H. Noggle, W. J. Freeman, and D. L. Dalrymple, *J. Magn. Reson.*, 1975, **19**, 208.
21. J. S. Blicharski, *Z. Naturforsch. A*, 1972, **27**, 1355; *Acta Phys. Polon. A*, 1972, **41**, 223.
22. A. Wokaun and R. R. Ernst, *Mol. Phys.*, 1978, **36**, 317.
23. A. Minoretti, W. P. Aue, M. Reinhold, and R. R. Ernst, *J. Magn. Reson.*, 1980, **40**, 175.
24. J. Yang, W. Qin-yi and Y. Chao-hui, *Chin. J. Phys.*, 1987, **7**, 905.
25. T. C. Farrar, D. R. Powell, S. K. Smith, and F. K. Ross, *Acta Crystallogr., Sect. C*, 1994, **50**, 342.

Biographical Sketches

Thomas C. Farrar. *b* 1933. B.Sc. (mathematics and chemistry), 1954, Wichita State University, USA; Ph.D. (chemistry), 1959, University of Illinois, Urbana. National Science Foundation Postdoctoral fellow at Cambridge University, Department of Theoretical Chemistry, 1959–61. Introduced to NMR by H. S. Gutowsky and M. Karplus. Faculty in Chemistry, University of Oregon, 1961–63. National Bureau of Standards, Chief of Magnetism Section, 1963–71. Director of Research and Development, JEOL, 1971–75. Director of Chemical Instrumentation Program, National Science Foundation, 1975–79. Professor of Chemistry, University of Wisconsin–Madison, 1979–present. Approx. 100 publications. Current research interests: molecular structure and molecular dynamics, ab initio calculations of molecular structure and of NMR parameters, experimental and theoretical development of density matrix theory and its applications in spectroscopy, and NMR relaxation time studies of molecular structure and dynamics.

Thomas C. Stringfellow. *b* 1957. B.A. (chemistry), 1991, Indiana State University, where magnetic resonance studies were begun under the guidance of Professor Myong-Ku Ahn. Graduate student at the University of Wisconsin–Madison, in the laboratory of Professor Thomas C. Farrar, 1991–present. Current research interests include the use of NMR relaxation measurements, Raman light scattering, and ab initio calculations to obtain information about the dynamics, structure and interactions of molecules in solution.

Relaxation Processes in Coupled-Spin Systems

Charles L. Mayne and Scott A. Smith
University of Utah, Salt Lake City, UT, USA

1	Introduction	1
2	Time-Dependent Perturbation Theory	2
3	Relaxation Mechanisms and Cross Correlation	10
4	Some Examples	13
5	References	19

1 INTRODUCTION

Nuclear magnetic resonance is uniquely capable of revealing structure and dynamics on a molecular level. An understanding of nuclear spin relaxation is fundamental to an understanding of nuclear magnetic resonance in general. The theoretical framework needed to promote this understanding is conveniently constructed in terms of the time evolution of the density operator under the influence of some Hamiltonian as expressed by the Liouville–von Neumann equation. The basic theory needed for what follows may be found in ***Liouville Equation of Motion***. It will be presumed that the reader is familiar with the contents of this article.

The emphasis here will be on molecules in liquids, though many of the principles presented are applicable to solids and gases. The experimental observables of NMR are magnetizations induced in a sample as a consequence of subjecting it to various static and time-varying magnetic fields. The quantum mechanical operators corresponding to these observables act only on the nuclear spin degrees of freedom of the system. Furthermore, these operators are proportional to the spin angular momentum operators or products thereof and, hence, can be dealt with using finite basis sets of states or operators. Relaxation, however, is a consequence of interactions between the nuclear spins and the rest of the system, referred to as the 'lattice' or 'bath'. In most cases, the lattice cannot be treated exactly using quantum mechanics, because the density operator and the Hamiltonian cannot be defined in explicit mathematical detail. The strategy generally employed, then, is to treat the effects of the lattice classically as a random time-dependent modulation of the nuclear spin operators while retaining a quantum mechanical description of the nuclear spins themselves. All externally applied magnetic fields are likewise treated classically. Our goal is to derive equations that correctly describe the observed temporal behavior of the experimental observables. This is done by proposing a Hamiltonian for the system under study, solving the Liouville–von Neumann equation for the time evolution of the density operator, computing the expected time evolution of the experimental observables, and comparing the result with measured values of these observables. Secondly, one wants to extract from this temporal behavior of the observables information about the fundamental nature of the system under investigation. For example, bond angles and rates of molecular reorientation due to Brownian motion dramatically affect the results of an NMR experiment. How can this kind of information be extracted from the behavior of the magnetization in a sample as a function of time? This article will present the time-dependent perturbation theory methods commonly used in NMR to explain observed phenomena, discuss the various mechanisms that influence relaxation in liquids, and present some simulations exemplifying how nuclear spins behave as a consequence of these mechanisms.

This article presumes a basic knowledge of the nuclear magnetic resonance phenomenon, including nuclear spin polarization in an external static magnetic field and interaction of nuclear spins with applied radiofrequency fields. For those not acquainted with these concepts, several basic texts may be consulted.[1–3] The reader is assumed to have some grasp of basic quantum mechanics and angular momentum theory at the level generally taught in undergraduate physical chemistry courses. Some command of linear algebra and integral and differential calculus is also assumed. All abbreviations and symbols are either defined in the endpapers or are defined in context. Vectors will be distinguished by bold italic type, and the same symbol in normal weight type will denote the magnitude of a vector or, with appropriate subscripts, its components. Quantum mechanical operators will have a hat, for example $\hat{\mathcal{H}}$. Liouville space operators or superoperators will have a double hat, for example $\hat{\hat{\mathcal{L}}}$.

No experimental data will be presented in this article. The experimental literature on coupled relaxation has been recently reviewed.[4] Rather, many simulations using the GAMMA magnetic resonance simulation platform[5] will be used, so that particular aspects of the subject may be illustrated and contrasted without lengthy digressions into experimental detail. While some references to the original literature will be given, most references will be to texts where additional details of the concepts discussed can be found.

1.1 What Is Nuclear Spin Relaxation?

To begin, let us consider nuclear spin relaxation from a phenomenological viewpoint. When a sample containing nuclear spins (e.g., water, which contains ^{1}H nuclei) is placed in a strong, uniform, static magnetic field $\boldsymbol{B}_0$, the sample is observed to develop a macroscopic magnetization $\boldsymbol{M}_0$ parallel to $\boldsymbol{B}_0$. The direction of $\boldsymbol{B}_0$ is taken to be the z direction of a laboratory-fixed coordinate system. Certain nuclei, for example ^{15}N, develop magnetization antiparallel to $\boldsymbol{B}_0$. The magnetization of a sample placed suddenly in a strong field increases with time and asymptotically approaches a steady state value. The magnitude of the steady state magnetization is proportional to the number of magnetic nuclei in the sample and to the strength of $\boldsymbol{B}_0$ (it depends on temperature also, but constant temperature will be assumed for now). Each nucleus of an isotope having a nonzero nuclear spin contributes an amount of magnetization characteristic of that particular isotope. If one used deuterium oxide rather than normal water, for example, both the rate of approach to the steady state and the steady-state magnetization would be different. If the sample is left in the magnet for a long time so that it has closely approached the steady state, this condition is called *thermal equilibrium*. If the magnetization is perturbed from thermal equilibrium, by a pulse of radiofrequency

field at the appropriate frequency, it will return to thermal equilibrium—again asymptotically. This process that causes the magnetization to approach thermal equilibrium is called *nuclear spin relaxation*. The time needed for a sample to achieve thermal equilibrium is, of course, infinite, since the approach is asymptotic. However, the time needed to reasonably approximate thermal equilibrium is in the range of milliseconds to hundreds of seconds for liquids, depending on the nature of the sample and the nuclei involved.

The rest of this article will consist mainly of a detailed discussion of the behavior of the magnetization as a function of time and how measurement of this behavior can be used to determine the structural and dynamical features of the molecules bearing the magnetic nuclei.

1.2 Classical Treatment: Bloch's Equations

The first investigations of nuclear-spin relaxation were conducted soon after the discovery of NMR.[6–8] The main results of this work can be summarized by the following equations:

$$\left.\begin{aligned}\frac{dM_x}{dt} &= [M_y(\gamma B_0 - \omega) - M_z\gamma B_y] - \frac{M_x}{T_2}\\ \frac{dM_y}{dt} &= -[M_x(\gamma B_0 - \omega) - M_z\gamma B_x] - \frac{M_y}{T_2}\\ \frac{dM_z}{dt} &= [M_x\gamma B_y - M_y\gamma B_x] - \frac{M_z - M_0}{T_1}\end{aligned}\right\} \quad (1)$$

These phenomenological equations are generally referred to as the Bloch equations and are cast here in terms of a reference frame rotating at an angular frequency ω about the z axis with respect to a laboratory-fixed frame. A particularly lucid discussion of the Bloch equations may be found in the text by Slichter.[9] This system of coupled linear differential equations with constant coefficients has solutions wherein the magnetization precesses about the effective field in the rotating frame having components (B_x, B_y, $B_0 - \omega/\gamma$). In order for B_x and B_y to be stationary in the rotating frame, they must be oscillating in the laboratory frame so that their sum rotates at frequency ω. This will be discussed in mathematical detail in Section 2.7. For usual high-resolution experiments with liquids, ω will be of the order of tens or hundreds of megahertz, thus, radiofrequency technology is used to produce B_x and B_y in the laboratory frame.

However, the main interest here is in the terms involving T_1 and T_2. If $\omega = \gamma B_0$ and $B_x = B_y = 0$ then equation (1) uncouple and yield particularly simple solutions wherein M_x and M_y relax exponentially to zero governed by T_2 while M_z relaxes exponentially toward M_0 governed by T_1. Specifically, the solution of equation (1) is given by

$$\left.\begin{aligned}M_x(t) &= M_x(0)\exp(-t/T_2)\\ M_y(t) &= M_y(0)\exp(-t/T_2)\\ M_z(t) &= M_0 + [M_z(0) - M_0]\exp(-t/T_1)\end{aligned}\right\} \quad (2)$$

where $\boldsymbol{M}(0)$ is the magnetization at time zero. These equations accurately describe the evolution of the macroscopic magnetization whenever the system under study may be regarded as an ensemble of spins interacting only with the lattice and not with each other. The relaxation of a surprisingly large number of materials that have been studied is satisfactorily explained by equation (2).

The fact that the magnetization changes with time implies that the nuclei are undergoing transitions among the available quantum mechanical states. Just as the magnetization may be manipulated by inducing transitions with externally applied rf pulses, any natural phenomenon that produces a time-varying field at a nucleus can induce transitions. The effect of all of these natural phenomena is to drive the macroscopic magnetization toward the thermal equilibrium value. See Section 3 for a discussion of specific examples of natural phenomena that can be mechanisms of spin relaxation. The decay of M_x and M_y involves exchange of energy among the spins, whereas the evolution of M_z toward its steady state value involves transfer of energy between the spins and the lattice.

1.3 When There Are Two or More Coupled Spins

When two or more spins are coupled by some sort of interaction, equation (1) may not be sufficient to explain the observed evolution of the magnetization. Consider, for example, a ^{13}C–^{1}H moiety such as might be found in the formate ion.[10] In a conceptually simple experiment, the ^{1}H magnetization is inverted, and then the ^{1}H and ^{13}C magnetizations are followed as a function of time. Additional details of this experiment can be found in Section 4.1.1. If there were no interaction between ^{1}H and ^{13}C then each of the spins could be treated separately according to equation (1), and the resulting evolution would be as shown in Figure 1(a). The ^{1}H magnetization recovers to thermal equilibrium exponentially as expected, and the ^{13}C magnetization remains unperturbed; however, when one actually performs this experiment, the results are as shown in Figure 1(b). The ^{13}C magnetization grows beyond thermal equilibrium, and then decays back to thermal equilibrium. Apparently, magnetization is flowing from the ^{1}H to the ^{13}C nuclei; this behavior cannot be predicted by equation (1). The mechanism that has been introduced to produce this effect is dipole–dipole (DD) coupling between the two nuclei. This is an example of cross relaxation. The theory of which this is a simple example will be the subject of the rest of this article.

2 TIME-DEPENDENT PERTURBATION THEORY

The theoretical model generally adopted for high-resolution NMR of liquids is that of a molecule bearing the spin system of interest immersed in a solvent. The concentration of such molecules is sufficiently low that intermolecular interactions among the spins of interest need not be considered. Because of the short range and random nature of the interactions involved, this assumption is adequately met even at fairly high concentrations. The macroscopic sample may then be considered as an ensemble of isolated systems each consisting of a single spin system of interest immersed in a bath or lattice the exact state of which is of no interest. The terms 'bath' and 'lattice' will be used interchangeably to refer to all the degrees of freedom of one member of the ensemble not directly associated with the nuclear spins in which we

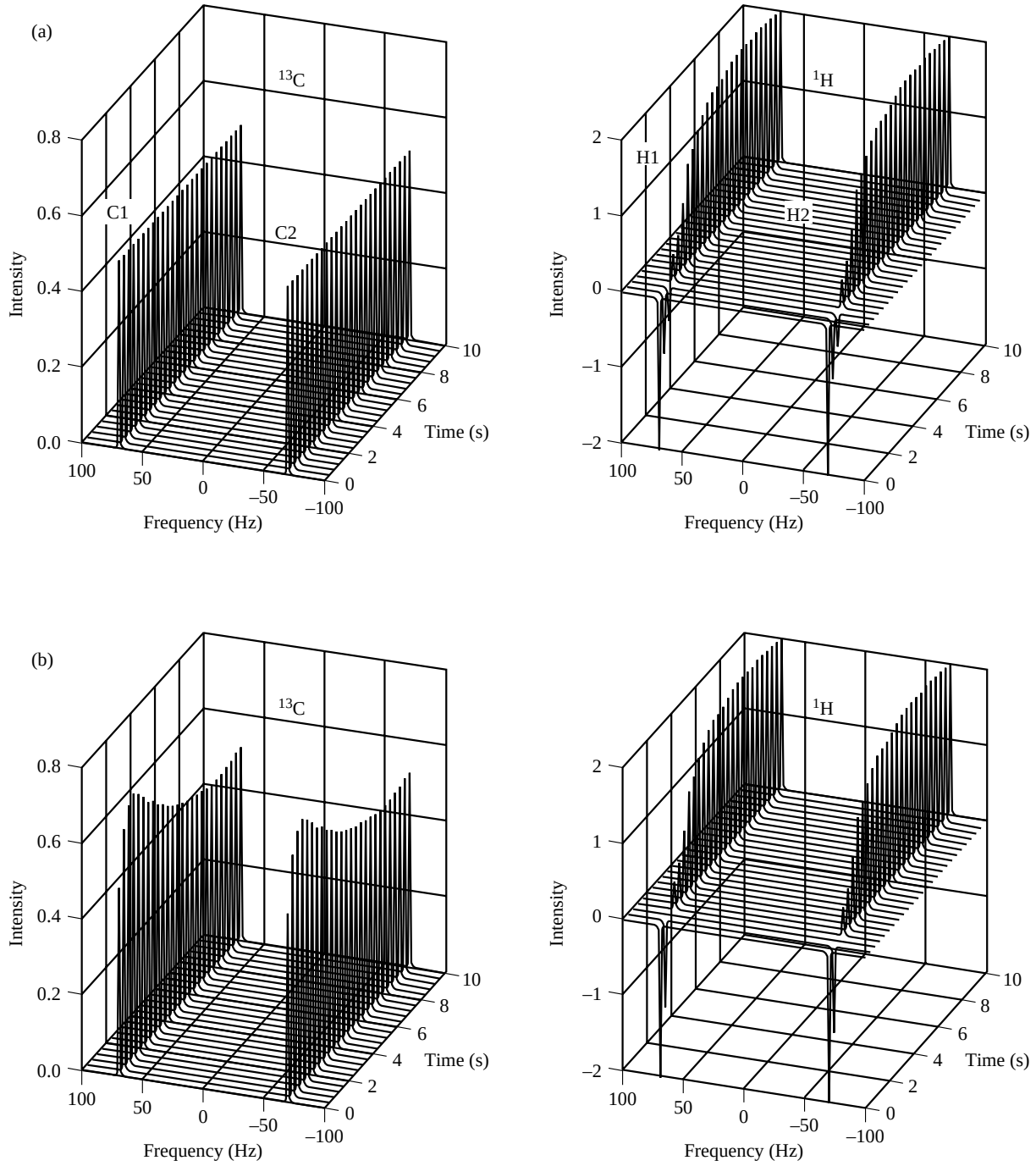

Figure 1 Simulation of relaxation of a two-spin (^{13}C–^{1}H) system after a proton π nonselective pulse: (a) relaxed only by external random fields (T_1 = 1.6 s, J = 140 Hz); (b) relaxed also by dipole–dipole coupling between the two spins (internuclear distance 0.109 nm, spherical top, correlation time 10 ps). The intensity is scaled so that the total ^{13}C magnetization at thermal equilibrium is unity, and that of ^{1}H is then greater by a factor γ_H/γ_C, or about four. See Section 4.1.1 for a more detailed discussion of the experiment

are interested. For example, the translational, rotational, and vibrational states of the molecule bearing the spin system of interest as well as the states of any nuclear or electron spins in solvent molecules would be in this category. The number of degrees of freedom of the lattice is so great as to be effectively infinite, with essentially a continuum of energy eigenstates. Using the terms somewhat loosely, the 'heat capacity' of the lattice is assumed to be so much greater than that of the nuclear spins that no interaction between the two can change the 'temperature' of the lattice. The nuclear spins also interact with externally applied magnetic fields, which are treated classically. In this discussion, the external magnetic field will be only the usual static field $\boldsymbol{B}_0$, the direction of which is taken to be the z axis of our laboratory coordinate system. Pulses will be treated as instantaneous rotations. A more general treatment of pulses and time-dependent external fields in general has been given by Smith et al.[11–13]

To begin our theoretical development, the Hamiltonian for one member of our ensemble can be expressed as a combination of terms acting on the spin system $\hat{\mathcal{H}}_s$, terms acting on the bath $\hat{\mathcal{H}}_b$, and terms for the interaction between the two $\hat{\mathcal{H}}_I$:

$$\hat{\mathcal{H}} = \hat{\mathcal{H}}_s + \hat{\mathcal{H}}_b + \hat{\mathcal{H}}_I \tag{3}$$

The density operator $\hat{\rho}(t)$ encompasses both spin system and bath. The Liouvillian $\hat{\hat{\mathcal{L}}}$ is a commutation or derivation superoperator relating to the Hamiltonian according to

$$\hat{\hat{\mathcal{L}}} = \hat{\mathcal{H}} \otimes \hat{E} - \hat{E} \otimes \hat{\mathcal{H}} \tag{4}$$

For a discussion of superoperators and their relationship to operators see Section 5 of ***Liouville Equation of Motion***. The Hamiltonian for a spin system $\hat{\mathcal{H}}_s$ interacting only with $\boldsymbol{B}_0$ contains terms from Zeeman interactions, chemical shieldings, scalar couplings, etc. A detailed discussion of high-resolution NMR Hamiltonians may be found in the first of the series of articles by Smith et al.[11] Some of these interactions involve terms that are dependent upon spin system orientation relative to $\boldsymbol{B}_0$, in which case interaction terms involving the rotational state of the molecule will be of interest. Such terms are of principal interest for spin relaxation studies in liquids, since molecules in liquids are rotating rapidly and changing rotational state frequently owing to collisions. Because of this, it is useful to express individual terms of the Hamiltonian in a general spherical tensor format. The Hamiltonian may be expressed as[11]

$$\hat{\mathcal{H}} = \sum_{\mu} \xi_{\mu} \sum_{m=-l}^{l} (-1)^m \hat{T}^{\mu}_{m} \hat{F}^{\mu}_{-m} \tag{5}$$

These tensors can be easily rotated from one coordinate system to another.[14] Here the $\hat{T}^{\mu}_{m}$ are spin operators acting on the system of interest, the $\hat{F}^{\mu}_{-m}$ are operators on the lattice states or functions relating to the externally applied magnetic fields, and ξ_{μ} are interaction constants, which will vary depending upon the nature of the interaction. The index μ is used to label a particular interaction, and each interaction has one or more associated values of the rank l. For each l, one must sum over the projection index m as shown. All of the terms in this sum can be assigned to one of the three Hamiltonians on the right-hand side of equation (3). Terms involving $l = 0$ and $m = 0$ for the spin operators are bath terms. Those involving $l = 0$ and $m = 0$ for the lattice operators as well as those depending only on the applied external field are spin terms. All others are interaction terms.

Both $\hat{T}^{\mu}_{m}$ and $\hat{F}^{\mu}_{-m}$ transform like spherical harmonics under rotations,[14] and are related to their adjoints as follows:

$$\left.\begin{aligned} (\hat{F}^{\mu}_{m})^{\dagger} &= (-1)^m \hat{F}^{\mu}_{-m} \\ (\hat{T}^{\mu}_{m})^{\dagger} &= (-1)^m \hat{T}^{\mu}_{-m} \end{aligned}\right\} \tag{6}$$

The superscript † indicates the adjoint or Hermitian conjugate of the operator. When the operator is represented in Liouville space using some operator basis, this means transpose the vector and take the complex conjugate of each element.

The Liouville equation in the Schrödinger representation is

$$\frac{\mathrm{d}|\hat{\rho}(t)\rangle}{\mathrm{d}t} = -\frac{\mathrm{i}}{\hbar}\hat{\hat{\mathcal{L}}}|\hat{\rho}(t)\rangle \tag{7}$$

(For a more detailed development of this type of equation, see Section 5 of ***Liouville Equation of Motion***). It defines the time evolution of the density operator for the entire system, spins and lattice, in terms of the Liouvillian of equation (4). In this representation, the density superket is time-dependent whereas the Liouvillian is not. This implies, as mentioned above, that no time-varying magnetic fields are applied. Unfortunately, equation (7) is completely intractable, because the lattice and interaction Hamiltonians $\hat{\mathcal{H}}_b$ and $\hat{\mathcal{H}}_I$ cannot be clearly defined and the dimension of the Liouville space of the lattice would be far too large for meaningful calculations to be performed. Hence, we are forced to seek an approximate method for solving the Liouville equation. Nuclear spins relax very slowly compared with most events on a molecular scale, so it is reasonable to suppose that the interaction $\hat{\mathcal{H}}_I$ is very weak. Further, collisions between the molecule of interest and solvent molecules should be treatable as a random process amenable to statistical methods. These two facts lead one to attempt a solution of equation (7) using perturbation theory and statistical mechanics.

2.1 The Interaction Representation

We begin the application of time-dependent perturbation theory by making use of the interaction picture of the problem to permit focusing on the small interaction terms. If we transform all the operators in the Liouville equation into an interaction representation based on the combined bath and spin system Hamiltonians, we can effectively 'remove' the pure bath and pure spin system contributions, a procedure that simplifies equation (7) and, it is to be hoped, facilitates its integration:

$$\frac{\mathrm{d}|\hat{\rho}'(t)\rangle}{\mathrm{d}t} = -\frac{\mathrm{i}}{\hbar}\hat{\hat{\mathcal{L}}}'_{\mathrm{I}}(t)|\hat{\rho}'(t)\rangle \tag{8}$$

(for a discussion of interaction representations and transformations, see Section 4.1 of ***Liouville Equation of Motion***). Operators (superkets) and superoperators in the interaction representation are indicated by a prime. These relate to the Schrödinger representation via

$$\left.\begin{aligned} \hat{\hat{\mathcal{L}}}_0 &= \hat{\hat{\mathcal{L}}}_s + \hat{\hat{\mathcal{L}}}_b \\ |\hat{\rho}'(t)\rangle &= \exp\left(\frac{\mathrm{i}}{\hbar}\hat{\hat{\mathcal{L}}}_0 t\right)|\hat{\rho}(t)\rangle \\ \hat{\hat{\mathcal{L}}}'_{\mathrm{I}}(t) &= \exp\left(\frac{\mathrm{i}}{\hbar}\hat{\hat{\mathcal{L}}}_0 t\right)\hat{\hat{\mathcal{L}}}_{\mathrm{I}}\exp\left(-\frac{\mathrm{i}}{\hbar}\hat{\hat{\mathcal{L}}}_0 t\right) \end{aligned}\right\} \tag{9}$$

2.2 Second-Order Perturbation Theory

Because of the inherently complex interaction between bath and spin system, as embodied in the superoperator $\hat{\hat{\mathcal{L}}}'_{\mathrm{I}}(t)$, the equation of motion must be solved using some sort of approximation technique. One approach is to use

a Dyson expansion of the integral. The initial steps are trivial—equation (8) is integrated formally from an arbitrary starting time t_0 to some later time t:

$$\left.\begin{aligned}\int_{t_0}^{t} \mathrm{d}|\hat{\rho}'(t_1)\rangle &= -\frac{\mathrm{i}}{\hbar}\int_{t_0}^{t} \mathrm{d}t_1\, \hat{\hat{\mathcal{L}}}'_{\mathrm{I}}(t_1)|\hat{\rho}'(t_1)\rangle \\ |\hat{\rho}'(t)\rangle &= |\hat{\rho}'(t_0)\rangle - \frac{\mathrm{i}}{\hbar}\int_{t_0}^{t} \mathrm{d}t_1\, \hat{\hat{\mathcal{L}}}'_{\mathrm{I}}(t_1)|\hat{\rho}'(t_1)\rangle\end{aligned}\right\} \tag{10}$$

We can now make a change of variable in equation (10),

$$|\hat{\rho}'(t_1)\rangle = |\hat{\rho}'(t_0)\rangle - \frac{\mathrm{i}}{\hbar}\int_{t_0}^{t_1} \mathrm{d}t_2\, \hat{\hat{\mathcal{L}}}'_{\mathrm{I}}(t_2)|\hat{\rho}'(t_2)\rangle \tag{11}$$

and substitute back into the integrand of equation (10) to produce

$$\begin{aligned}|\hat{\rho}'(t)\rangle &= |\hat{\rho}'(t_0)\rangle \\ &\quad -\frac{\mathrm{i}}{\hbar}\int_{t_0}^{t} \mathrm{d}t_1\, \hat{\hat{\mathcal{L}}}'_{\mathrm{I}}(t_1)\left[|\hat{\rho}'(t_0)\rangle - \frac{\mathrm{i}}{\hbar}\int_{t_0}^{t_1} \mathrm{d}t_2\, \hat{\hat{\mathcal{L}}}'_{\mathrm{I}}(t_2)|\hat{\rho}'(t_2)\rangle\right] \\ &= |\hat{\rho}'(t_0)\rangle - \frac{\mathrm{i}}{\hbar}\int_{t_0}^{t} \mathrm{d}t_1\, \hat{\hat{\mathcal{L}}}'_{\mathrm{I}}(t_1)|\hat{\rho}'(t_0)\rangle \\ &\quad -\frac{1}{\hbar^2}\int_{t_0}^{t} \mathrm{d}t_1 \int_{t_0}^{t_1} \mathrm{d}t_2\, \hat{\hat{\mathcal{L}}}'_{\mathrm{I}}(t_1)\, \hat{\hat{\mathcal{L}}}'_{\mathrm{I}}(t_2)|\hat{\rho}'(t_2)\rangle\end{aligned} \tag{12}$$

This process is iterated, substituting equation (11), with the appropriate change of variable for $|\hat{\rho}'(t_2)\rangle$, into equation (12). With each iteration, the lower order integrals involve only the initial density superket. Continuing the iterations and assuming that the series eventually converges so that the last term involving $|\hat{\rho}'(t_n)\rangle$ may be ignored produces the Dyson series

$$\begin{aligned}|\hat{\rho}'(t)\rangle = |\hat{\rho}'(t_0)\rangle + \sum_{n=1}^{\infty}\left(-\frac{\mathrm{i}}{\hbar}\right)^n \int_{t_0}^{t} \mathrm{d}t_1 \int_{t_0}^{t_1} \mathrm{d}t_2 \cdots \\ \times \int_{t_0}^{t_{n-1}} \mathrm{d}t_n\, \hat{\hat{\mathcal{L}}}'_{\mathrm{I}}(t_1)\, \hat{\hat{\mathcal{L}}}'_{\mathrm{I}}(t_2) \cdots \hat{\hat{\mathcal{L}}}'_{\mathrm{I}}(t_n)|\hat{\rho}'(t_0)\rangle\end{aligned} \tag{13}$$

If it could be shown that the interaction Liouvillians at different times commute then the time ordering would be inconsequential, and equation (12) would be equivalent to a Taylor series for an exponential:

$$|\hat{\rho}'(t)\rangle = \exp\left[-\frac{\mathrm{i}}{\hbar}\int_{t_0}^{t} \mathrm{d}t_1\, \hat{\hat{\mathcal{L}}}'_{\mathrm{I}}(t_1)\right]|\hat{\rho}'(t_0)\rangle \tag{14}$$

If the interaction Liouvillian (in the interaction representation) were time-independent then the integral would be trivial and the solution in the interaction representation would be

$$|\hat{\rho}'(t)\rangle = \exp\left[-\frac{\mathrm{i}}{\hbar}\,\hat{\hat{\mathcal{L}}}'_{\mathrm{I}}(t - t_0)\right]|\hat{\rho}'(t_0)\rangle \tag{15}$$

We shall assume that the Liouvillians at different times do not commute, but that terms higher than second order are negligible, i.e., that *second-order perturbation theory* is adequate to describe the system. The equation of motion is then approximated by

$$\begin{aligned}|\hat{\rho}'(t)\rangle = |\hat{\rho}'(t_0)\rangle - \frac{\mathrm{i}}{\hbar}\int_{t_0}^{t} \mathrm{d}t_1\, \hat{\hat{\mathcal{L}}}'_{\mathrm{I}}(t_1)|\hat{\rho}'(t_0)\rangle \\ -\frac{1}{\hbar^2}\int_{t_0}^{t} \mathrm{d}t_1 \int_{t_0}^{t_1} \mathrm{d}t_2\, \hat{\hat{\mathcal{L}}}'_{\mathrm{I}}(t_1)\, \hat{\hat{\mathcal{L}}}'_{\mathrm{I}}(t_2)|\hat{\rho}'(t_0)\rangle\end{aligned} \tag{16}$$

2.3 Application of the Wangsness–Bloch–Redfield Assumptions

Equation (16) is still not in a form that can be handled either analytically or numerically for useful systems. We therefore apply several additional approximations that will eventually lead to a manageable expression. Recognizing that the first integral term in equation (16) is nondissipative, it can at most add a constant term to the density matrix. Furthermore, we shall shortly deal with an ensemble of spin systems, and the average effect of the interaction Liouvillian at any point in time is zero for an isotropic liquid. This is true for a bath interacting in an essentially random fashion with the system of interest. Therefore the first integral term in equation (16) may be ignored, giving

$$|\hat{\rho}'(t)\rangle = |\hat{\rho}'(t_0)\rangle - \frac{1}{\hbar^2}\int_{t_0}^{t} \mathrm{d}t_1 \int_{t_0}^{t_1} \mathrm{d}t_2\, \hat{\hat{\mathcal{L}}}'_{\mathrm{I}}(t_1)\, \hat{\hat{\mathcal{L}}}'_{\mathrm{I}}(t_2)|\hat{\rho}'(t_0)\rangle \tag{17}$$

If the integrand is continuous over the integration range then we can differentiate equation (17) to obtain a differential equation again:

$$\frac{\mathrm{d}|\hat{\rho}'(t)\rangle}{\mathrm{d}t} = -\frac{1}{\hbar^2}\int_{t_0}^{t} \mathrm{d}t_1\, \hat{\hat{\mathcal{L}}}'_{\mathrm{I}}(t)\, \hat{\hat{\mathcal{L}}}'_{\mathrm{I}}(t_1)|\hat{\rho}'(t_0)\rangle \tag{18}$$

It is assumed that the integral really only depends upon the difference $\tau = t - t_1$, so that the variable of integration may be changed as follows:

$$\frac{\mathrm{d}|\hat{\rho}'(t)\rangle}{\mathrm{d}t} = -\frac{1}{\hbar^2}\int_{t_0}^{t} \mathrm{d}\tau\, \hat{\hat{\mathcal{L}}}'_{\mathrm{I}}(t)\, \hat{\hat{\mathcal{L}}}'_{\mathrm{I}}(t - \tau)|\hat{\rho}'(t_0)\rangle \tag{19}$$

It is further assumed that the density superket does not change rapidly over the range of the integral, so that replacing $|\hat{\rho}'(t_0)\rangle$ with $|\hat{\rho}'(t)\rangle$ does not introduce significant error. This yields

$$\frac{\mathrm{d}|\hat{\rho}'(t)\rangle}{\mathrm{d}t} = -\frac{1}{\hbar^2}\int_{0}^{t} \mathrm{d}\tau\, \hat{\hat{\mathcal{L}}}'_{\mathrm{I}}(t)\, \hat{\hat{\mathcal{L}}}'_{\mathrm{I}}(t - \tau)|\hat{\rho}'(t)\rangle \tag{20}$$

A final assumption is that t will be long enough that the integrand will have decayed to zero and no error will be introduced by extending the limit of integration to infinity. Then we have

$$\frac{\mathrm{d}|\hat{\rho}'(t)\rangle}{\mathrm{d}t} = -\frac{1}{\hbar^2}\int_{0}^{\infty} \mathrm{d}\tau\, \hat{\hat{\mathcal{L}}}'_{\mathrm{I}}(t)\, \hat{\hat{\mathcal{L}}}'_{\mathrm{I}}(t - \tau)|\hat{\rho}'(t)\rangle \tag{21}$$

2.4 The Semiclassical Liouville Equation

At this point, it is essential to depart from the treatment of the entire system of spins and bath and focus only on the smaller system of interest, namely, the spin system. The total system density operator can always be represented as a tensor product of two density operators, one spanning the spin system subspace and one spanning the lattice subspace:

$$|\hat{\rho}(t)\rangle = |\hat{\sigma}(t)\rangle|\hat{\rho}_{\mathrm{b}}(t)\rangle \tag{22}$$

Keep in mind that it is the smaller spin system represented by the reduced density operator $|\hat{\sigma}(t)\rangle$ that is of interest, not the entire system $|\hat{\rho}(t)\rangle$. The latter resides in a Liouville space of unmanageable dimensionality whereas the dimension of the former is normally small enough that its evolution in time can be mathematically detailed with some precision. One can define a superket $|\hat{\rho}_{\mathrm{s}}(t)\rangle$ that resides in the full Liouville space of the spin system and bath, and yet contains only the information regarding the spin system of interest:

$$\left.\begin{aligned} |\hat{\rho}_{\mathrm{s}}(t)\rangle &= \hat{\hat{P}}|\hat{\rho}(t)\rangle = \hat{\hat{E}}_{\mathrm{s}} \otimes (|\hat{\rho}_{\mathrm{b}}(t)\rangle \otimes \langle\hat{E}_{\mathrm{b}}|) \\ |\hat{\sigma}(t)\rangle &= (\hat{\hat{E}}_{\mathrm{s}} \otimes \langle\hat{E}_{\mathrm{b}}|)|\hat{\rho}_{\mathrm{s}}(t)\rangle = (\hat{\hat{E}}_{\mathrm{s}} \otimes \langle\hat{E}_{\mathrm{b}}|)\,\hat{\hat{P}}|\hat{\rho}(t)\rangle \\ &= (\hat{\hat{E}}_{\mathrm{s}} \otimes \langle\hat{E}_{\mathrm{b}}|)\,\hat{\hat{E}}_{\mathrm{s}} \otimes (|\hat{\rho}_{\mathrm{b}}(t)\rangle \otimes \langle\hat{E}_{\mathrm{b}}|) \end{aligned}\right\} \tag{23}$$

The equation of motion for $|\hat{\rho}_{\mathrm{s}}(t)\rangle$ is obtained by use of the projection superoperator $\hat{\hat{P}}$ in the approximate equation of motion:

$$\frac{\mathrm{d}|\hat{\rho}'_{\mathrm{s}}(t)\rangle}{\mathrm{d}t} = -\frac{1}{\hbar^2}\,\hat{\hat{P}}\int_0^\infty \mathrm{d}\tau\;\hat{\hat{\mathcal{L}}}'_1(t)\,\hat{\hat{\mathcal{L}}}'_1(t-\tau)\,\hat{\hat{P}}|\hat{\rho}'_{\mathrm{s}}(t)\rangle \tag{24}$$

Back-transformation into the Schrödinger representation produces

$$\begin{aligned} \frac{\mathrm{d}|\hat{\rho}'_{\mathrm{s}}(t)\rangle}{\mathrm{d}t} = &-\frac{\mathrm{i}}{\hbar}\,\hat{\hat{\mathcal{L}}}_{\mathrm{s}}|\hat{\rho}_{\mathrm{s}}(t)\rangle - \frac{1}{\hbar^2}\,\hat{\hat{P}}\int_0^\infty \mathrm{d}\tau\;\hat{\hat{\mathcal{L}}}'_1(t)\exp\left(-\frac{\mathrm{i}}{\hbar}\,\hat{\hat{\mathcal{L}}}_0\tau\right) \\ &\times\hat{\hat{\mathcal{L}}}'_1(t-\tau)\exp\left(\frac{\mathrm{i}}{\hbar}\,\hat{\hat{\mathcal{L}}}_0\tau\right)\hat{\hat{P}}|\hat{\rho}'_{\mathrm{s}}(t)\rangle \end{aligned} \tag{25}$$

This equation is general for any system interacting with a large bath, so long as the constraints outlined in Section 2.3 are fulfilled. The Liouvillians $\hat{\hat{\mathcal{L}}}_{\mathrm{s}}$ and $\hat{\hat{\mathcal{L}}}_{\mathrm{b}}$ commute, and $\hat{\hat{\mathcal{L}}}_{\mathrm{b}}$ cannot operate on $|\hat{\rho}_{\mathrm{s}}(t)\rangle$, so that $\exp(-\mathrm{i}\hbar^{-1}\hat{\hat{\mathcal{L}}}_0\tau)\,\hat{\hat{P}} = \exp(-\mathrm{i}\hbar^{-1}\hat{\hat{\mathcal{L}}}_{\mathrm{s}}\tau)\,\hat{\hat{P}}$. Then,

$$\begin{aligned} \frac{\mathrm{d}|\hat{\rho}_{\mathrm{s}}(t)\rangle}{\mathrm{d}t} = &-\frac{\mathrm{i}}{\hbar}\,\hat{\hat{\mathcal{L}}}_{\mathrm{s}}|\hat{\rho}_{\mathrm{s}}(t)\rangle - \frac{1}{\hbar^2}\,\hat{\hat{P}}\int_0^\infty \mathrm{d}\tau\;\hat{\hat{\mathcal{L}}}'_1(t)\exp\left(-\frac{\mathrm{i}}{\hbar}\,\hat{\hat{\mathcal{L}}}_0\tau\right) \\ &\times\hat{\hat{\mathcal{L}}}'_1(t-\tau)\exp\left(\frac{\mathrm{i}}{\hbar}\,\hat{\hat{\mathcal{L}}}_{\mathrm{s}}\tau\right)\hat{\hat{P}}|\hat{\rho}'_{\mathrm{s}}(t)\rangle \end{aligned} \tag{26}$$

It is beyond the scope of this article to show that the net result of continued manipulations produces

$$\begin{aligned} &\hat{\hat{P}}\int_0^\infty \mathrm{d}\tau\;\hat{\hat{\mathcal{L}}}'_1(t)\exp\left(-\frac{\mathrm{i}}{\hbar}\hat{\hat{\mathcal{L}}}_0\tau\right)\hat{\hat{\mathcal{L}}}'_1(t-\tau)\exp\left(\frac{\mathrm{i}}{\hbar}\hat{\hat{\mathcal{L}}}_{\mathrm{s}}\tau\right)\;\hat{\hat{P}}|\hat{\rho}'_{\mathrm{s}}(t)\rangle \\ &= \;\hat{\hat{P}}\int_0^\infty \mathrm{d}\tau\;\hat{\hat{\mathcal{L}}}'_1(t)\exp\left(-\frac{\mathrm{i}}{\hbar}\hat{\hat{\mathcal{L}}}_{\mathrm{s}}\tau\right)\hat{\hat{\mathcal{L}}}'_1(t-\tau)\exp\left(\frac{\mathrm{i}}{\hbar}\hat{\hat{\mathcal{L}}}_{\mathrm{s}}\tau\right) \\ &\quad\times\hat{\hat{P}}|\hat{\rho}'_{\mathrm{s}}(t)-\hat{\rho}'_{\mathrm{s}}(\infty)\rangle \end{aligned} \tag{27}$$

Further details of this step may be found in an article by Szymanski et al.[15] The projection operators allow us now to work exclusively with the reduced density operator and place all operators into the corresponding reduced space. Switching to the difference (reduced) density operator $\Delta\hat{\sigma}$, we now perform an ensemble average over all the spin systems in the sample to yield

$$\begin{aligned} \frac{\mathrm{d}|\hat{\sigma}(t)\rangle}{\mathrm{d}t} = &-\frac{\mathrm{i}}{\hbar}\,\overline{\hat{\hat{\mathcal{L}}}_{\mathrm{s}}}|\hat{\sigma}(t)\rangle - \frac{1}{\hbar^2}\int_0^\infty \mathrm{d}\tau\;\hat{\hat{\mathcal{L}}}'_1(t) \\ &\times\overline{\exp\left(-\frac{\mathrm{i}}{\hbar}\hat{\hat{\mathcal{L}}}_{\mathrm{s}}\tau\right)\hat{\hat{\mathcal{L}}}'_1(t-\tau)\exp\left(\frac{\mathrm{i}}{\hbar}\hat{\hat{\mathcal{L}}}_{\mathrm{s}}\tau\right)} \\ &\times|\hat{\sigma}(t)-\hat{\sigma}(\infty)\rangle \\ = &-\frac{\mathrm{i}}{\hbar}\,\overline{\hat{\hat{\mathcal{L}}}_{\mathrm{s}}}|\hat{\sigma}(t)\rangle - \frac{1}{\hbar^2}\int_0^\infty \mathrm{d}\tau\;\hat{\hat{\mathcal{L}}}'_1(t) \\ &\times\overline{\exp\left(-\frac{\mathrm{i}}{\hbar}\hat{\hat{\mathcal{L}}}_{\mathrm{s}}\tau\right)\hat{\hat{\mathcal{L}}}'_1(t-\tau)\exp\left(\frac{\mathrm{i}}{\hbar}\hat{\hat{\mathcal{L}}}_{\mathrm{s}}\tau\right)} \\ &\times|\Delta\hat{\sigma}(t)\rangle \end{aligned} \tag{28}$$

As in the Hilbert space formulation of Wangsness–Bloch–Redfield theory, it remains to isolate the time dependence in the integral function in order to formulate spectral densities.

2.5 The Spin and Interaction Hamiltonians

The lattice Hamiltonian $\hat{\mathcal{H}}_{\mathrm{b}}$ now influences the equation of motion only in that the system relaxes toward thermal equilibrium at the temperature of the bath $|\hat{\sigma}(\infty)\rangle$. We must now define in detail the form of the spin and interaction Hamiltonians. The principal influence of the lattice is to reorient the spin system. Equation (5) can then be interpreted as follows to account for both the spin system and its interaction with the lattice:

$$\hat{\mathcal{H}}_{\mathrm{s}} + \hat{\mathcal{H}}_1(t) = \sum_\mu \xi_\mu \sum_{m=-l}^{l} (-1)^m \hat{T}^\mu_m F^\mu_{-m}(t) \tag{29}$$

The lattice operators are now manifested as random functions of time that reorient the spin system. This is referred to as the *semiclassical model* for the Hamiltonian; the interaction terms of the Hamiltonian are time-dependent through the lattice functions $F^\mu_{-m}(t)$, but the operators that act on the spin system are independent of time. Invoking the ergodic hypothesis, the ensemble average can be replaced by a time average, and, if all orientations are equally probable (an isotropic liquid), many of the interactions average to zero in first order. The isotropic terms, $l = m = 0$, in equation (29) are independent of spin system orientation, and, hence, do not need to be time-averaged. These terms yield for a system of n spins the isotropic Hamiltonian commonly found in texts on high-resolution NMR:

$$\hat{\mathcal{H}}_{\mathrm{s}} = \hat{\mathcal{H}}_0 = -\sum_{i=1}^{n}\hbar\omega_i\hat{I}_{iz} + 2\pi\hbar\sum_{i=2}^{n}\sum_{j=1}^{i-1}J_{ij}\hat{\boldsymbol{I}}_i\cdot\hat{\boldsymbol{I}}_j \tag{30}$$

The symbol J is widely used in the literature for both scalar couplings and spectral densities, which will be introduced in equation (41). We prefer to retain this notation in both cases, trusting that the reader will be able to discern from the context which is meant in a given case. Other Hamiltonian components that are orientation-dependent and, therefore, time-dependent will be categorized in the interaction Hamiltonian term of equation (29):

$$\hat{\mathcal{H}}_{\mathrm{I}}(t) = \sum_{\mu} \xi_{\mu} \sum_{m=-l}^{l} (-1)^m \hat{T}^{\mu}_{m} F^{\mu}_{-m}(t) \tag{31}$$

Although it is not explicit, note that the sum over μ in equation (29) includes the rotationally invariant components, whereas the sum in equation (31) does not include them. Furthermore, since the lattice operators are now simply functions, the adjoint used in equation (6) is replaced by a complex conjugate, so that $[F^{\mu}_{m}(t)]* = (-1)^m F^{\mu}_{-m}(t)$. The equation of motion is then

$$\frac{\mathrm{d}|\hat{\sigma}(t)\rangle}{\mathrm{d}t} = -\frac{\mathrm{i}}{\hbar}\hat{\hat{\mathcal{L}}}_0|\hat{\sigma}\rangle - \frac{1}{\hbar^2}\int_0^{\infty} \mathrm{d}\tau\, \hat{\hat{\mathcal{L}}}_{\mathrm{I}} \times \overline{\exp\left(-\frac{\mathrm{i}}{\hbar}\hat{\hat{\mathcal{L}}}_0\tau\right)\hat{\hat{\mathcal{L}}}_{\mathrm{I}}\exp\left(\frac{\mathrm{i}}{\hbar}\hat{\hat{\mathcal{L}}}_0\tau\right)}|\Delta\hat{\sigma}\rangle \tag{32}$$

2.6 The Relaxation Superoperator

Making use of the semiclassical interaction model for $\hat{\mathcal{H}}_{\mathrm{I}}$ given in equation (29), the interaction Liouvillian can be constructed:

$$\begin{aligned}\hat{\hat{\mathcal{L}}}_{\mathrm{I}}(t) &= \sum_{\mu}\xi_{\mu}\sum_{m=-l}^{l}(-1)^m(\hat{T}^{\mu}_{m}\otimes\hat{E} - \hat{E}\otimes\hat{T}^{\mu}_{m})F^{\mu}_{-m}(t)\\ &= \sum_{\mu}\xi_{\mu}\sum_{m=-l}^{l}(-1)^m\hat{\hat{\Gamma}}^{\mu}_{m}F^{\mu}_{-m}(t)\end{aligned} \tag{33}$$

Substitution of this relationship into equation (32) produces

$$\begin{aligned}\frac{\mathrm{d}|\hat{\sigma}(t)\rangle}{\mathrm{d}t} = -\frac{\mathrm{i}}{\hbar}\hat{\hat{\mathcal{L}}}_0|\hat{\sigma}\rangle - \frac{1}{\hbar^2}\sum_{\mu}\sum_{\mu'}\xi_{\mu}\xi_{\mu'}\sum_{m=-l}^{l}\sum_{m'=-l'}^{l'}(-1)^{m+m'}\hat{\hat{\Gamma}}^{\mu}_{m}\\ \times\int_0^{\infty}\mathrm{d}\tau\,\overline{F^{\mu}_{-m}(t)F^{\mu'}_{-m'}(t-\tau)}\exp\left(-\frac{\mathrm{i}}{\hbar}\hat{\hat{\mathcal{L}}}_0\tau\right)\\ \times\hat{\hat{\Gamma}}^{\mu'}_{m'}\exp\left(\frac{\mathrm{i}}{\hbar}\hat{\hat{\mathcal{L}}}_0\tau\right)|\Delta\hat{\sigma}\rangle\end{aligned} \tag{34}$$

Our objective is to separate quantities that depend on the time variable τ from the spin operators, which do not. The spherical spin tensor operator components $\hat{T}^{\mu}_{m}$ generally will not commute with $\hat{\mathcal{H}}_0$ and, hence, will not commute with $\hat{\hat{\mathcal{L}}}_0$ either, so one cannot isolate the exponentials involving τ.

One can express the spherical tensor operators in a basis comprising the eigenoperators of the static Hamiltonian superoperator $\hat{\hat{\mathcal{L}}}_0$:

$$\left.\begin{aligned}|\hat{T}^{\mu}_{m}\rangle &= \sum_{p}|\hat{T}^{\mu}_{m,p}\rangle\\ |\hat{T}'^{\mu}_{m}(t)\rangle &= \exp\left(-\frac{\mathrm{i}}{\hbar}\hat{\hat{\mathcal{L}}}_0\tau\right)|\hat{T}^{\mu}_{m}\rangle\\ &= \sum_{p}\exp\left(-\frac{\mathrm{i}}{\hbar}\hat{\hat{\mathcal{L}}}_0\tau\right)|\hat{T}^{\mu}_{m,p}\rangle = \sum_{p}\mathrm{e}^{-\mathrm{i}\Omega_p\tau}|\hat{T}^{\mu}_{m,p}\rangle\end{aligned}\right\} \tag{35}$$

The Ω_p are the transition frequencies in the laboratory frame, eigenvalues of the Liouvillian $\hat{\hat{\mathcal{L}}}_0$. The range of p is from 1 to the dimension of the spin system Liouville space. For a system of n spin-$\frac{1}{2}$ nuclei, this would be 2^{2n}. Such a treatment is equivalent to expanding the spin operators in terms of a basis consisting of the eigenfunctions of the static Hamiltonian $\hat{\mathcal{H}}_0$, as is done in the usual Hilbert space development of the Redfield equation.[9,16] Using these relations, the equation of motion now becomes

$$\begin{aligned}\frac{\mathrm{d}|\hat{\sigma}(t)\rangle}{\mathrm{d}t} = -\frac{\mathrm{i}}{\hbar}\hat{\hat{\mathcal{L}}}_0|\hat{\sigma}(t)\rangle - \frac{1}{\hbar^2}\sum_{\mu}\sum_{\mu'}\xi_{\mu}\xi_{\mu'}\sum_{m=-l}^{l}\sum_{m'=-l'}^{l'}(-1)^{m+m'}\\ \times\int_0^{\infty}\mathrm{d}\tau\,\overline{F^{\mu}_{-m}(t)F^{\mu'}_{-m'}(t-\tau)}\\ \times\hat{\hat{\Gamma}}^{\mu}_{m}\sum_{p}\hat{\hat{\Gamma}}^{\mu'}_{m',p}\mathrm{e}^{-\mathrm{i}\Omega_p\tau}|\Delta\hat{\sigma}(t)\rangle\end{aligned} \tag{36}$$

This expansion uses the close relationship between a similarity transformation superoperator and the exponential of a commutation superoperator. The commutation superoperator of the isotropic spin system Hamiltonian is given by

$$\hat{\hat{\mathcal{L}}}_0 = \hat{\mathcal{H}}_0\otimes\hat{E} - \hat{E}\otimes\hat{\mathcal{H}}_0 \tag{37}$$

The similarity transformation superoperator will, in this instance, be given by

$$\begin{aligned}\hat{\hat{G}}|\hat{T}^{\mu}_{m}\rangle &= \exp\left(-\frac{\mathrm{i}}{\hbar}\hat{\mathcal{H}}_0 t\right)\otimes\exp\left(\frac{\mathrm{i}}{\hbar}\hat{\mathcal{H}}_0 t\right)|\hat{T}^{\mu}_{m}\rangle\\ &= \left|\exp\left(-\frac{\mathrm{i}}{\hbar}\hat{\mathcal{H}}_0 t\right)\hat{T}^{\mu}_{m}\exp\left(\frac{\mathrm{i}}{\hbar}\hat{\mathcal{H}}_0 t\right)\right\rangle = |\hat{T}'^{\mu}_{m}\rangle\end{aligned} \tag{38}$$

The two superoperators are related by

$$\hat{\hat{G}} = \exp\left(-\frac{\mathrm{i}}{\hbar}\hat{\hat{\mathcal{L}}}_0 t\right) \tag{39}$$

The exponential term in τ can now be grouped with the rest of the variables involving τ, and the desired separation of spin operators and τ-dependent lattice functions is thus achieved:

$$\begin{aligned}\frac{\mathrm{d}|\hat{\sigma}(t)\rangle}{\mathrm{d}t} = -\frac{\mathrm{i}}{\hbar}\hat{\hat{\mathcal{L}}}_0|\hat{\sigma}(t)\rangle - \frac{1}{\hbar^2}\sum_{\mu}\sum_{\mu'}\xi_{\mu}\xi_{\mu'}\sum_{m=-l}^{l}\sum_{m'=-l'}^{l'}(-1)^{m+m'}\\ \times\sum_{p}\hat{\hat{\Gamma}}^{\mu}_{m}\hat{\hat{\Gamma}}^{\mu'}_{m',p}\int_0^{\infty}\mathrm{d}\tau\,\overline{F^{\mu}_{-m}(t)F^{\mu'}_{-m'}(t-\tau)}\mathrm{e}^{-\mathrm{i}\Omega_p\tau}|\Delta\hat{\sigma}(t)\rangle\end{aligned} \tag{40}$$

The integral is defined as the spectral density function by

$$\mathcal{J}^{\mu\mu'}_{mm'}(\Omega) = \int_0^\infty \mathrm{d}\tau\ \overline{F^{\mu}_{-m}(t)F^{\mu'}_{-m'}(t-\tau)}\mathrm{e}^{-\mathrm{i}\Omega\tau} \qquad (41)$$

The spherical tensor properties of the $F^{\mu}_{-m}(t)$ guarantee that the integrand averaged over all orientations with equal probability will be nonzero only when $m' = -m$ and the result will be independent of m. Thus, one can write equation (41) in terms of a reduced spectral density $J^{\mu\mu'}$:

$$\mathcal{J}^{\mu\mu'}_{mm'}(\Omega) = (-1)^m \delta_{-mm'} J^{\mu\mu'}(\Omega) \qquad (42)$$

Furthermore, it is presumed that the lattice functions are stationary random variables, i.e., that the result of a time average does not depend on the time at which the averaging process is started, and we may set $t = 0$ in the integrand of equation (41). The reduced spectral density is then

$$J^{\mu\mu'}(\Omega) = \int_0^\infty \mathrm{d}\tau\ \overline{F^{\mu}_{-m}(0)F^{\mu'}_{m}(\tau)}\mathrm{e}^{-\mathrm{i}\Omega\tau} \qquad (43)$$

A detailed discussion of spectral densities and how they relate to the dynamical and geometrical parameters of the spin system is found in ***Relaxation of Coupled Spins from Rotational Diffusion***.

The relaxation superoperator is defined by

$$\hat{\hat{\Gamma}} = \sum_{\mu}\sum_{\mu'} \xi_\mu \xi_{\mu'} \sum_{m=-l}^{l} (-1)^m \sum_{p} \hat{\hat{\Gamma}}^{\mu}_{m} \hat{\hat{\Gamma}}^{\mu'}_{-m,p} J^{\mu\mu'}(\Omega_p) \qquad (44)$$

The equation of motion for the density superket may be written very compactly using these definitions:

$$\frac{\mathrm{d}|\hat{\sigma}(t)\rangle}{\mathrm{d}t} = -\frac{\mathrm{i}}{\hbar}\hat{\hat{\mathcal{L}}}_0|\hat{\sigma}(t)\rangle - \frac{1}{\hbar^2}\hat{\hat{\Gamma}}|\Delta\hat{\sigma}(t)\rangle \qquad (45)$$

The relaxation superoperator may be written as a sum of terms of the form

$$\hat{\hat{\Gamma}} = -\sum_{\mu}\sum_{\mu'} \hat{\hat{\Gamma}}^{\mu\mu'} \qquad (46)$$

with the individual terms defined by

$$\hat{\hat{\Gamma}}^{\mu\mu'} = \xi_\mu \xi_{\mu'} \sum_{m=-l}^{l} (-1)^m \sum_{p} \hat{\hat{\Gamma}}^{\mu}_{m} \hat{\hat{\Gamma}}^{\mu'}_{-m,p} J^{\mu\mu'}(\Omega_p) \qquad (47)$$

The $\hat{\hat{\Gamma}}^{\mu\mu'}$ terms express how the various interactions characterizing the spin system correlate with one another to produce relaxation. If $\mu = \mu'$, the relaxation is termed *autocorrelated*; otherwise, it is called *cross correlated*. This latter term must not be confused with *cross relaxation*, which is simply the flow of magnetization from one nucleus to another rather than from a nucleus to the lattice. Cross relaxation may involve either autocorrelated or cross-correlated relaxation mechanisms. This concept will be discussed further in Section 3.

2.7 The Rotating Frame

It is common practice in NMR to work in a rotating frame, or simultaneously in multiple rotating frames. One use of the rotating frame is to remove Zeeman contributions to the Hamiltonian by rotating about the field axis at or near the Larmor frequency of a spin. Although not of significance in rendering a formal solution to the Liouville equation in the case presented here, in numerical solutions of the equation of motion this avoids computational roundoff, which can occur in mixing frequencies on a megahertz scale (from the static magnetic field) with those on a hertz scale (from chemical shifts and scalar couplings).

Transformation into a rotating frame about the static magnetic field axis, the z axis, is accomplished using the rotation operator

$$\hat{R}_z(\theta) = \exp\left(-\frac{\mathrm{i}}{\hbar}\hat{F}_z\theta\right) \qquad (48)$$

In this case, the angle of rotation is written as $\theta = \Omega t$, where Ω is the angular frequency of the rotation. The form of the Liouville equation in the rotating frame is only a slight modification of that in the laboratory frame. In the frame rotating about the z axis at angular frequency Ω,

$$\frac{\mathrm{d}|\underline{\hat{\rho}}(t)\rangle}{\mathrm{d}t} = -\frac{\mathrm{i}}{\hbar}\left[\hat{\hat{\underline{\mathcal{L}}}}(t) + \hat{\hat{\Gamma}}_z(\Omega)\right]|\underline{\hat{\rho}}(t)\rangle \qquad (49)$$

The superoperator $\hat{\hat{\Gamma}}_z(\Omega)$ is formed as the commutator of $\Omega\hat{F}_z$. Superkets and superoperators in the rotating frame are indicated by an underscore and relate to the laboratory frame via the rotation superoperator

$$\hat{\hat{R}}_z(\Omega t) = \hat{R}_z(\Omega t) \otimes \hat{R}^*_z(\Omega t) \qquad (50)$$

The transformations have the form

$$\left.\begin{aligned} |\underline{\hat{O}}(t)\rangle &= \hat{\hat{R}}_z(\Omega t)|\hat{O}\rangle \\ \hat{\hat{\underline{\mathcal{L}}}}(t) &= \hat{\hat{R}}_z(\Omega t)\hat{\hat{\mathcal{L}}}\ \hat{\hat{R}}_z^{-1}(\Omega t) \end{aligned}\right\} \qquad (51)$$

That equations (49) and (7) are equivalent is shown by carrying out the differentiation as follows, making the indicated substitutions:

$$\begin{aligned} \frac{\mathrm{d}|\underline{\hat{\rho}}(t)\rangle}{\mathrm{d}t} &= \frac{\mathrm{d}}{\mathrm{d}t}\left[\ \hat{\hat{R}}_z(\Omega t)|\hat{\rho}(t)\rangle\right] \\ &= \frac{\mathrm{d}}{\mathrm{d}t}\left[\ \hat{\hat{R}}_z(\Omega t)\right]|\hat{\rho}(t)\rangle + \ \hat{\hat{R}}_z(\Omega t)\frac{\mathrm{d}|\hat{\rho}(t)\rangle}{\mathrm{d}t} \\ &= -\frac{\mathrm{i}}{\hbar}\hat{\hat{\Gamma}}_z(\Omega)\ \hat{\hat{R}}_z(\Omega t)|\hat{\rho}(t)\rangle + \ \hat{\hat{R}}_z(\Omega t)\frac{\mathrm{d}|\hat{\rho}(t)\rangle}{\mathrm{d}t} \\ &= -\frac{\mathrm{i}}{\hbar}\hat{\hat{\Gamma}}_z(\Omega)\ \hat{\hat{R}}_z(\Omega t)|\hat{\rho}(t)\rangle \\ &\quad -\frac{\mathrm{i}}{\hbar}\ \hat{\hat{R}}_z(\Omega t)\hat{\hat{\mathcal{L}}}\ \hat{\hat{R}}_z^{-1}(\Omega t)\ \hat{\hat{R}}_z(\Omega t)|\hat{\rho}(t)\rangle \\ &= -\frac{\mathrm{i}}{\hbar}\left[\ \hat{\hat{\underline{\mathcal{L}}}}(t) + \hat{\hat{\Gamma}}_z(\Omega)\right]|\underline{\hat{\rho}}(t)\rangle \end{aligned} \qquad (52)$$

From spherical tensor arguments, we know that the static Hamiltonian $\hat{\mathcal{H}}_0$ is isotropic and rotationally invariant. Thus, it is left unaffected by transformation into the rotating frame, as we might suspect since $[\hat{\mathcal{H}}_0, \hat{F}_z] = 0$, and from equation (30), we can write

$$\underline{\hat{\mathcal{H}}}_0 = \hat{\mathcal{H}}_0 = \sum_{i=1}^{n} \hbar\omega_i \hat{I}_{iz} + 2\pi\hbar \sum_{i=1}^{n} \sum_{j=1}^{i-1} J_{ij} \hat{\boldsymbol{I}}_i \cdot \hat{\boldsymbol{I}}_j \qquad (53)$$

The interaction Hamiltonian as given by equation (31) will become as follows in the rotating frame:

$$\hat{\mathcal{H}}_1(t) = \sum_{\mu} \xi_\mu \sum_{m=-l}^{l} (-1)^m \underline{\hat{T}}^{\mu}_{m} F^{\mu}_{-m}(t) \qquad (54)$$

The bath variables are functions of time in this semiclassical treatment, and are unaffected by the rotation operator, which acts only on spin operators.

The question now is how the solution of equation (49) differs from that already presented in the laboratory frame. The form of the rotating frame Liouville equation is very similar to that in the laboratory frame, and the approach to a solution is the same. We define an effective Hamiltonian according to

$$\hat{\mathcal{H}}_{\text{eff}} = \hat{\mathcal{H}}_0 + \Omega \hat{F}_z \qquad (55)$$

and transform into an interaction representation based on $\hat{\mathcal{H}}_{\text{eff}}$ rather than $\hat{\mathcal{H}}_0$ to remove the static components of the rotating frame Hamiltonian from our differential equation. It is of some interest to note that this particular $\hat{\mathcal{H}}_{\text{eff}}$ is time-independent both in the frame rotating about the z axis and in the laboratory frame. The new equation of motion has exactly the same form as equation (8), but all quantities have been transformed into the rotating frame:

$$\frac{\mathrm{d}|\underline{\hat{\rho}}'(t)\rangle}{\mathrm{d}t} = -\frac{\mathrm{i}}{\hbar}\, \underline{\hat{\mathcal{L}}}'_{\mathrm{I}}(t)|\underline{\hat{\rho}}'(t)\rangle \qquad (56)$$

We are still using a prime to signify the interaction representation. Equation (56) is the analog to equation (8), and a modified equation (9) is used to relate the interaction representation to the rotating frame:

$$|\underline{\hat{O}}'\rangle = \exp\left(\frac{\mathrm{i}}{\hbar}\hat{\hat{\mathcal{L}}}_{\text{eff}} t\right) \qquad (57)$$

The order in which one alters these reference frames can, in this instance, be switched, because $\hat{\mathcal{H}}_{\text{eff}}$ commutes with $\hat{R}_z$. That is to say, for the effective Hamiltonian of this treatment, the following relations hold:

$$\begin{aligned} |\underline{\hat{O}}'\rangle &= \exp\left(\frac{\mathrm{i}}{\hbar}\hat{\hat{\mathcal{L}}}_{\text{eff}} t\right)|\underline{\hat{O}}\rangle = \exp\left(\frac{\mathrm{i}}{\hbar}\hat{\hat{\mathcal{L}}}_{\text{eff}} t\right) \\ &\quad \times \exp\left(\frac{\mathrm{i}}{\hbar}\,\hat{\hat{F}}_z \Omega t\right)|\hat{O}\rangle \\ &= \exp\left(\frac{\mathrm{i}}{\hbar}\,\hat{\hat{F}}_z \Omega t\right)\exp\left(\frac{\mathrm{i}}{\hbar}\hat{\hat{\mathcal{L}}}_{\text{eff}} t\right)|\hat{O}\rangle \end{aligned} \qquad (58)$$

The steps taken towards the solution of equation (56) are virtually identical to the treatment performed in the laboratory frame, we simply write the analog to equation (34):

$$\begin{aligned} \frac{\mathrm{d}|\underline{\hat{\sigma}}\rangle}{\mathrm{d}t} &= -\frac{\mathrm{i}}{\hbar}\hat{\hat{\mathcal{L}}}_{\text{eff}}|\underline{\hat{\sigma}}\rangle - \frac{1}{\hbar^2}\sum_{\mu}\sum_{\mu'}\xi_\mu\xi_{\mu'}\sum_{m=-l}^{l}\sum_{m'=-l'}^{l'}(-1)^{m+m'}\hat{\underline{\Gamma}}^{\mu}_{m} \\ &\quad \times \int_0^\infty \mathrm{d}\tau\, \overline{F^{\mu}_{-m}(t)F^{\mu'}_{-m'}(t+\tau)} \\ &\quad \exp\left(-\frac{\mathrm{i}}{\hbar}\hat{\hat{\mathcal{L}}}_{\text{eff}}\tau\right)\hat{\underline{\Gamma}}^{\mu'}_{m'}\exp\left(\frac{\mathrm{i}}{\hbar}\hat{\hat{\mathcal{L}}}_{\text{eff}}\tau\right)|\Delta\hat{\sigma}\rangle \end{aligned} \qquad (59)$$

The difference is that now we perform the expansion in terms of eigenoperators of the effective Hamiltonian and note that these are still in the rotating frame. Analogs of equation (35) in this treatment are

$$\left.\begin{aligned} |\hat{\underline{T}}^{\mu}_{m}\rangle &= \sum_p |\hat{\underline{T}}^{\mu}_{m,p}\rangle \\ |\hat{\underline{T}}'^{\mu}_{m}(t)\rangle &= \exp\left(-\frac{\mathrm{i}}{\hbar}\hat{\hat{\mathcal{L}}}_{\text{eff}}\tau\right)|\hat{\underline{T}}^{\mu}_{m}\rangle \\ &= \sum_p \exp\left(-\frac{\mathrm{i}}{\hbar}\hat{\hat{\mathcal{L}}}_{\text{eff}}\tau\right)|\hat{\underline{T}}^{\mu}_{m,p}\rangle \\ &= \sum_p \mathrm{e}^{-\mathrm{i}\omega_p\tau}|\hat{\underline{T}}^{\mu}_{m,p}\rangle \end{aligned}\right\} \qquad (60)$$

This choice of representing the interaction Hamiltonian produces an important relationship between the spin operators and the commutator superoperator of $\hat{F}_z$:

$$\hat{\hat{F}}^{\mathrm{D}}_{z}|\hat{T}^{\mu}_{m}\rangle = m|\hat{T}^{\mu}_{m}\rangle \qquad (61)$$

Equation (59) then becomes

$$\begin{aligned} \frac{\mathrm{d}|\underline{\hat{\sigma}}(t)\rangle}{\mathrm{d}t} &= -\frac{\mathrm{i}}{\hbar}\hat{\hat{\mathcal{L}}}_{\text{eff}}|\underline{\hat{\sigma}}(t)\rangle - \frac{1}{\hbar^2}\sum_{\mu}\sum_{\mu'}\xi_\mu\xi_{\mu'}\sum_{m=-l}^{l}\sum_{m'=-l'}^{l'} \\ &\quad \times(-1)^{m+m'}\int_0^\infty \mathrm{d}\tau\, \overline{F^{\mu}_{-m}(t)F^{\mu'}_{-m'}(t+\tau)} \\ &\quad \times\hat{\underline{\Gamma}}^{\mu}_{m}\sum_p \mathrm{e}^{-\mathrm{i}m_p\omega_0\tau}\hat{\underline{\Gamma}}^{\mu'}_{m',p}\mathrm{e}^{\mathrm{i}\omega_p\tau}|\Delta\underline{\hat{\sigma}}(t)\rangle \end{aligned} \qquad (62)$$

In these equations, we are using ω_p for the transition frequencies associated with the effective Hamiltonian $\hat{\mathcal{H}}_{\text{eff}}$ in order to distinguish them from the transition frequencies Ω_p associated with the isotropic Hamiltonian $\hat{\mathcal{H}}_0$. Another, more common, viewpoint is that ω_p are the transition frequencies in the rotating frame whereas Ω_p are the transition frequencies in the laboratory frame.

When we transform the spin tensor superoperator components out of the rotating frame, the rotating frame frequencies disappear from the relaxation matrix in that the spectral densities are always evaluated at laboratory frame frequencies as

follows:

$$\frac{\mathrm{d}|\hat{\underline{\sigma}}(t)\rangle}{\mathrm{d}t} = -\frac{\mathrm{i}}{\hbar}\hat{\hat{\mathcal{L}}}_{\mathrm{eff}}|\hat{\underline{\sigma}}(t)\rangle - \frac{1}{\hbar^2}\sum_{\mu}\sum_{\mu'}\xi_\mu\xi_{\mu'}\sum_{m=-l}^{l}\sum_{m'=-l'}^{l'} \times(-1)^{m+m'}\int_0^\infty \mathrm{d}\tau\ \overline{F^{\mu}_{-m}(t)F^{\mu'}_{-m'}(t+\tau)} \times\hat{\hat{\Gamma}}^{\mu}_{m}\sum_{p}\mathrm{e}^{-\mathrm{i}m_p\Omega_0\tau}\hat{\hat{\Gamma}}^{\mu'}_{m',p}\mathrm{e}^{\mathrm{i}\omega_p\tau}|\Delta\hat{\underline{\sigma}}(t)\rangle \tag{63}$$

$$\frac{\mathrm{d}|\hat{\underline{\sigma}}(t)\rangle}{\mathrm{d}t} = -\frac{\mathrm{i}}{\hbar}\hat{\hat{\mathcal{L}}}_{\mathrm{eff}}|\hat{\underline{\sigma}}(t)\rangle - \frac{1}{\hbar^2}\sum_{\mu}\sum_{\mu'}\xi_\mu\xi_{\mu'}\sum_{m=-l}^{l}\sum_{m'=-l'}^{l'} \times(-1)^{m+m'}\int_0^\infty \mathrm{d}\tau\ \overline{F^{\mu}_{-m}(t)F^{\mu'}_{-m'}(t+\tau)} \times\hat{\hat{\Gamma}}^{\mu}_{m}\sum_{p}\hat{\hat{\Gamma}}^{\mu'}_{m',p}\mathrm{e}^{\mathrm{i}\Omega_p\tau}|\Delta\hat{\underline{\sigma}}(t)\rangle \tag{64}$$

The end result is that the relaxation matrix is unaffected by rotation about the z axis. The solution in the rotating frame—highly preferred over that in the laboratory frame in computation—is often used as is; i.e., no transformation is performed to place the density matrix back into the laboratory frame after the solution of $|\hat{\underline{\sigma}}(t)\rangle$ is obtained.

A word of caution is in order. Although the transformation into a single rotating frame about the static field axis does not affect the relaxation matrix, this is not true for a transformation into a multiple rotating frame. Multiple rotating frames are particularly useful in dealing with heteronuclear spin systems, but in such cases a secular approximation must be applied. Fortunately, the nonsecular terms will be oscillating at frequencies that are on the order of the difference between the isotope Larmor frequencies. For the vast majority of cases, these will be at least several megahertz at common field strengths. At low field strengths or in the event that two isotopes have very similar Larmor frequencies, only a single rotating frame can be used, but will typically suffice to place all transition frequencies on a reasonable scale for accurate computation.

3 RELAXATION MECHANISMS AND CROSS CORRELATION

We have shown that spin system relaxation is dictated by the superoperator $\hat{\hat{\Gamma}}$, and, according to equation (46), it is a sum over products of superoperators corresponding to the active interactions as indexed by symbols μ and μ'. Using this equation, we can proceed to formulate superoperators for individual relaxation mechanisms. To complete the formulation of $\hat{\hat{\Gamma}}$, it is only necessary to give explicit form to equation (31) for each of the relaxation mechanisms active in the spin system under study. In this section, such will be done for several of the mechanisms most frequently encountered in liquid samples.

3.1 Intramolecular Dipole–Dipole Coupling

Relaxation by dipolar interactions is the most commonly treated relaxation mechanism in NMR. As such, we shall begin our specific relaxation discussions with the dipolar interaction and the dipole–dipole relaxation mechanism. The dipolar Hamiltonian for a system of n spins is given by

$$\hat{\mathcal{H}}^{\mathrm{D}} = \sum_{i=2}^{n}\sum_{j=1}^{i-1}\xi^{\mathrm{D}}_{ij}\sum_{m=-2}^{2}(-1)^m F^{(2)}_{-m}(\mathrm{D},\theta_{ij},\phi_{ij})\hat{T}^{(2)}_{m} \times(\mathrm{D},i,j) \tag{65}$$

The index μ has been resolved into the label D and a sum over all pairs of spins in the system. The spherical polar coordinates (θ_{ij}, ϕ_{ij}) specify the orientation of the internuclear vector for each pair of spins relative to the laboratory fixed coordinate system, and are implicitly time-dependent through the rotational diffusion of the molecule. Only the $l = 2$ spherical tensor components contribute to this mechanism. The dipolar interaction is symmetric about the internuclear vector, so that only two orientational parameters are required. The two spins interact through space, so that it is immaterial whether they are proximate through chemical bonds or not. The dipolar interaction constant is given by

$$\xi^{\mathrm{D}}_{ij} = -2\sqrt{\frac{6\pi}{5}}\frac{\gamma_i\gamma_j}{r^3_{ij}} \tag{66}$$

The required rank-2 spatial functions are identical to the spherical harmonic functions as given by

$$\left.\begin{aligned} F^{(2)}_0(\mathrm{D},\theta_{ij},\phi_{ij}) &= Y^{(2)}_0(\theta_{ij},\phi_{ij}) \\ &= \sqrt{\frac{5}{16\pi}}(3\cos^2\theta_{ij}-1) \\ F^{(2)}_{\pm1}(\mathrm{D},\theta_{ij},\phi_{ij}) &= Y^{(2)}_{\pm1}(\theta_{ij},\phi_{ij}) \\ &= \mp\sqrt{\frac{15}{8\pi}}(\cos\theta_{ij}\sin\theta_{ij}\,\mathrm{e}^{\pm\mathrm{i}\phi_{ij}}) \\ F^{(2)}_{\pm2}(\mathrm{D},\theta_{ij},\phi_{ij}) &= Y^{(2)}_{\pm2}(\theta_{ij},\phi_{ij}) \\ &= \sqrt{\frac{15}{32\pi}}(\sin^2\theta_{ij}\,\mathrm{e}^{\pm2\mathrm{i}\phi_{ij}}) \end{aligned}\right\} \tag{67}$$

Since the molecule reorients in a liquid, these angles are time-dependent and contribute to the lattice spectral densities as described in Section 2.6.

The rank-2 spherical tensor operators are given by

$$\left.\begin{aligned} \hat{T}^{(2)}_0(\mathrm{D},i,j) &= \sqrt{\tfrac{1}{6}}(3\hat{I}_{iz}\hat{I}_{jz} - \hat{\boldsymbol{I}}_i\cdot\hat{\boldsymbol{I}}_j) \\ \hat{T}^{(2)}_{\pm1}(\mathrm{D},i,j) &= \mp\tfrac{1}{2}(\hat{I}_{i\pm}\hat{I}_{jz} + \hat{I}_{iz}\hat{I}_{j\pm}) \\ \hat{T}^{(2)}_{\pm2}(\mathrm{D},i,j) &= \tfrac{1}{2}\hat{I}_{i\pm}\hat{I}_{j\pm} \end{aligned}\right\} \tag{68}$$

For a system composed of two spins, both $I = \frac{1}{2}$, the spin operators take on the following matrix representations when

expressed in the product basis $\{|\alpha\alpha\rangle, |\alpha\beta\rangle, |\beta\alpha\rangle, |\beta\beta\rangle\}$:

$$\left.\begin{array}{c} \hat{T}_0^{(2)} \\ \frac{1}{2\sqrt{6}}\begin{bmatrix} 1 & 0 & 0 & 0 \\ 0 & -1 & -1 & 0 \\ 0 & -1 & -1 & 0 \\ 0 & 0 & 0 & 1 \end{bmatrix}, \end{array} \quad \begin{array}{c} \hat{T}_1^{(2)} = -(\hat{T}_{-1}^{(2)})^{\mathrm{T}} \\ \frac{1}{4}\begin{bmatrix} 0 & -1 & -1 & 0 \\ 0 & 0 & 0 & 1 \\ 0 & 0 & 0 & 1 \\ 0 & 0 & 0 & 0 \end{bmatrix} \end{array} \right\} \quad \begin{array}{c} \hat{T}_2^{(2)} = (\hat{T}_{-2}^{(2)})^{\mathrm{T}} \\ \frac{1}{2}\begin{bmatrix} 0 & 0 & 0 & 1 \\ 0 & 0 & 0 & 0 \\ 0 & 0 & 0 & 0 \\ 0 & 0 & 0 & 0 \end{bmatrix} \end{array} \right\} \tag{69}$$

The commutation superoperators required for equation (44) are formed from the spin tensor components as follows:

$$\hat{\hat{\Gamma}}_m^{\mathrm{D}ij} = \hat{T}_m^{(2)}(\mathrm{D}, i, j) \otimes \hat{E} - \hat{E} \otimes \hat{T}_m^{(2)}(\mathrm{D}, i, j) \tag{70}$$

The dipole–dipole contribution to relaxation is thus given by

$$\hat{\hat{\Gamma}}^{\mathrm{DD}} = \sum_{i=2}^{n}\sum_{j=1}^{i-1}\sum_{k=2}^{n}\sum_{l=1}^{k-1}\xi_{ij}^{\mathrm{D}}\xi_{kl}^{\mathrm{D}}\sum_{m=-2}^{2}(-1)^m \times \sum_{p}\hat{\hat{\Gamma}}_m^{\mathrm{D}ij}\hat{\hat{\Gamma}}_{-m,p}^{\mathrm{D}kl}J^{\mathrm{DD}ijkl}(\Omega_p) \tag{71}$$

3.2 Chemical Shielding Anisotropy

Another important interaction contributing to relaxation arises from the anisotropic part of the chemical shielding Hamiltonian (SA). Because the energies involved are dependent on the static magnetic field strength, this type of relaxation becomes more important as the spectrometer field strength increases. The Hamiltonian for shielding anisotropy is given by

$$\hat{\mathcal{H}}^{\mathrm{S}} = \sum_{i=1}^{n}\xi_i^{\mathrm{S}}\sum_{m=-2}^{2}(-1)^m F_{-m}^{(2)}(\mathrm{S}, \theta_i, \phi_i, \chi_i)\hat{T}_m^{(2)}(\mathrm{S}, i) \tag{72}$$

In this case, the index μ has been resolved into the label S and a sum over all the spins in the system. Only the $l = 2$ tensors are required. The set $\{\theta_i, \phi_i, \chi_i\}$ are the three Euler angles that orient the principal axes of a given shielding tensor into a common coordinate system according to

$$F_m^{(2)}(\mathrm{S}, \theta_i, \phi_i, \chi_i) = \sum_{m'=\pm 2}\mathcal{D}_{mm'}^{(2)}(\theta_i, \phi_i, \chi_i)F_{m'}^{(2)}(\mathrm{S}, \mathrm{PAS}_i) \tag{73}$$

If the shielding tensor is symmetric ($\eta = 0$) then the spherical harmonic is sufficient to describe the lattice fluctuations, and equation (73) reduces to

$$F_m^{(2)}(\mathrm{S}, \theta_i, \phi_i, \chi_i) = Y_m^{(2)}(\theta_i, \phi_i) \tag{74}$$

Here PAS is used to indicate the principal axis system in which the rank-2 irreducible tensor is diagonal, and $\mathcal{D}_{mm'}^{(2)}$ are the elements of the rank-2 Wigner rotation matrices. We have neglected the $l = 1$ component in equation (72) because it is very small in almost all cases. Although the isotropic component ($l = 0$) does not vanish for this interaction, as it does for the DD interaction in liquid systems, we have combined it with the Zeeman term in the Hamiltonian to produce the chemical shielding contribution to $\hat{\mathcal{H}}_0$, i.e., these contributions are absorbed into the ω_i of equation (30).

It is important to note that in the treatment of shielding anisotropy, the 'spin' tensors are actually 'spin–space' tensors in that they contain normalized components of the static magnetic field and are thus dependent upon its spatial orientation. Since this is stationary and oriented along the z axis in the laboratory frame, it is of no concern to the theory presented. However, using this type of formulation, one cannot rotate this tensor in spin space, as conceivably could be done for the dipolar Hamiltonian spin tensor. The shielding interaction constant, spatial functions, and 'spin–space' tensor components are given below, the latter having field components that stem from a normalized field vector $\boldsymbol{B}_{\mathrm{n}} = \boldsymbol{B}_0/|\boldsymbol{B}_0| = \boldsymbol{B}_0/B_0$. The interaction constants are given by

$$\xi_i^{\mathrm{S}} = \sqrt{\frac{6\pi}{5}}\nu_i B_0 \delta_{zz}(i) = \sqrt{\frac{6\pi}{5}}\frac{\gamma_i}{\gamma_{\mathrm{H}}}\Omega_{\mathrm{spec}}\delta_{zz}(i) \tag{75}$$

The SA tensor functions in the PAS are given by

$$\left.\begin{aligned} F_0^{(2)}(\mathrm{S}, \mathrm{PAS}) &= \sqrt{\frac{5}{4\pi}} \\ F_{\pm 1}^{(2)}(\mathrm{S}, \mathrm{PAS}) &= 0 \\ F_{\pm 2}^{(2)}(\mathrm{S}, \mathrm{PAS}) &= \sqrt{\frac{5}{24\pi}}\eta \end{aligned}\right\} \tag{76}$$

The spherical tensor operators are given by

$$\left.\begin{aligned} \hat{T}_0^{(2)}(\mathrm{S}, i) &= \sqrt{\tfrac{1}{6}}(3\hat{I}_{iz}B_z - \hat{\boldsymbol{I}}_i \cdot \boldsymbol{B}_n) \\ \hat{T}_{\pm 1}^{(2)}(\mathrm{S}, i) &= \mp\tfrac{1}{2}(\hat{I}_{i\pm}B_z + \hat{I}_{iz}B_{\pm}) \\ \hat{T}_{\pm 2}^{(2)}(\mathrm{S}, i) &= \tfrac{1}{2}\hat{I}_{i\pm}B_{\pm} \end{aligned}\right\} \tag{77}$$

For a treatment of a single spin-$\frac{1}{2}$ particle, the rank-2 shielding 'spin–space' tensor components take on the following matrix forms when expressed in the standard spin basis $\{|\alpha\rangle, |\beta\rangle\}$ in the laboratory frame, with the field axis along $+z$:

$$\begin{array}{ccccc} \hat{T}_0^{(2)} & & \hat{T}_1^{(2)} = [\hat{T}_{-1}^{(2)}]^{\mathrm{T}} & & \hat{T}_2^{(2)} = [\hat{T}_{-2}^{(2)}]^{\mathrm{T}} \\ \frac{1}{\sqrt{6}}\begin{bmatrix} 1 & 0 \\ 0 & -1 \end{bmatrix}, & & -\frac{1}{2}\begin{bmatrix} 0 & 1 \\ 0 & 0 \end{bmatrix}, & & \begin{bmatrix} 0 & 0 \\ 0 & 0 \end{bmatrix} \end{array} \tag{78}$$

Although the shielding Hamiltonian is of rank 2, the $m = 2$ component disappears, and the shift anisotropy–shift anisotropy contribution to relaxation is thus given by

$$\hat{\hat{\Gamma}}^{\mathrm{SS}} = \sum_{i=1}^{n}\sum_{j=1}^{n}\xi_i^{\mathrm{S}}\xi_j^{\mathrm{S}}\sum_{m=-1}^{1}(-1)^m\sum_{p}\hat{\hat{\Gamma}}_m^{\mathrm{S}i}\hat{\hat{\Gamma}}_{-m,p}^{\mathrm{S}j}J^{\mathrm{SS}ij}(\Omega_p) \tag{79}$$

The $\hat{\hat{\Gamma}}_m^{\mathrm{S}i}$ are commutation superoperators are formed from the spin tensor component for spin i according to

$$\hat{\hat{\Gamma}}_m^{\mathrm{S}i} = \hat{T}_m^{(2)}(\mathrm{S}, i) \otimes \hat{E} - \hat{E} \otimes \hat{T}_m^{(2)}(\mathrm{S}, i) \tag{80}$$

3.3 Quadrupolar Interactions

Spins having spin angular momentum quantum numbers larger than $\frac{1}{2}$, $I \geq 1$, may possess an appreciable electric quadrupole moment, which can provide important relaxation mechanisms. The Hamiltonian for quadrupolar interactions is given by

$$\hat{\mathcal{H}}^{\mathrm{Q}} = \sum_{i=1}^{n} \xi_i^{\mathrm{Q}} \sum_{m=-2}^{2} (-1)^m F_{-m}^{(2)}(\mathrm{Q}, \theta_i, \phi_i, \chi_i) \hat{T}_m^{(2)}(\mathrm{Q}, i) \quad (81)$$

As for the Q mechanism, the index μ has been resolved into the label Q and a sum over all the spins in the system. Only the $l = 2$ tensors are required. The set $\{\theta_i, \phi_i, \chi_i\}$ are the three Euler angles that orient the principal axes of the quadrupolar tensor into a common coordinate system according to

$$F_m^{(2)}(\mathrm{Q}, \theta_i, \phi_i, \chi_i) = \sum_{m=\pm 2} \mathcal{D}_{mm'}^{(2)}(\theta_i, \phi_i, \chi_i) F_{m'}^{(2)}(\mathrm{Q}, \mathrm{PAS}_i) \quad (82)$$

When the quadrupolar tensor is symmetric ($\eta = 0$), the spherical harmonic is sufficient to describe the lattice fluctuations and equation (82) reduces to

$$F_m^{(2)}(\mathrm{Q}, \theta_i, \phi_i, \chi_i) = Y_m^{(2)}(\theta_i, \phi_i) \quad (83)$$

As for the shielding Hamiltonian, three angles are necessary for specification of the spatial tensor orientation. For an axially symmetric quadrupolar tensor, $\eta = 0$, only two angles are necessary, and in that case the spatial functions are equivalent to the rank-2 spherical harmonics given for the dipolar interaction. The quadrupolar interaction constants are given by

$$\begin{aligned} \xi_i^{\mathrm{Q}} &= \hbar \sqrt{\frac{6\pi}{5}} \frac{\delta_{zz}(i)}{2I_i(2I_i - 1)} = \hbar \sqrt{\frac{6\pi}{5}} \frac{\mathrm{QCC}_i}{2I_i(2I_i - 1)} \\ &= \hbar \sqrt{\frac{6\pi}{5}} \frac{2\pi \nu_i^{\mathrm{Q}}}{2I_i(2I_i - 1)} \end{aligned} \quad (84)$$

where QCC is the quadrupolar coupling constant. The lattice interaction functions are given by

$$\left.\begin{aligned} F_0^{(2)}(\mathrm{PAS}) &= \sqrt{\frac{5}{4\pi}} \\ F_{\pm}^{(2)}(\mathrm{PAS}) &= 0 \\ F_{\pm 2}^{(2)}(\mathrm{PAS}) &= \sqrt{\frac{5}{24\pi}} \eta \end{aligned}\right\} \quad (85)$$

The spherical tensor operators are given by

$$\left.\begin{aligned} \hat{T}_0^{(2)}(\mathrm{Q}, i) &= \sqrt{\tfrac{1}{6}}(3\hat{I}_{iz}^2 - \hat{\boldsymbol{I}}_i^2) \\ \hat{T}_{\pm 1}^{(2)}(\mathrm{Q}, i) &= \mp \tfrac{1}{2}(\hat{I}_{i\pm}\hat{I}_{iz} + \hat{I}_{iz}\hat{I}_{i\pm}) \\ \hat{T}_{\pm 2}^{(2)}(\mathrm{Q}, i) &= \tfrac{1}{2}\hat{I}_{i\pm}^2 \end{aligned}\right\} \quad (86)$$

For treatment of a spin-1 particle, the rank-2 quadrupolar spin tensor components are expressed in their matrix form as

$$\begin{matrix} \hat{T}_0^{(2)} & \hat{T}_1^{(2)} = [\hat{T}_{-1}^{(2)}]^{\mathrm{T}} & \hat{T}_2^{(2)} = [\hat{T}_{-2}^{(2)}]^{\mathrm{T}} \end{matrix}$$

$$\frac{1}{\sqrt{6}} \begin{bmatrix} 1 & 0 & 0 \\ 0 & -2 & 0 \\ 0 & 0 & 1 \end{bmatrix}, \quad \frac{1}{\sqrt{2}} \begin{bmatrix} 0 & -1 & 0 \\ 0 & 0 & 1 \\ 0 & 0 & 0 \end{bmatrix}, \quad \begin{bmatrix} 0 & 0 & 1 \\ 0 & 0 & 0 \\ 0 & 0 & 0 \end{bmatrix} \quad (87)$$

The spin index is implicit and the matrices are in the standard single spin basis $\{|\alpha\rangle, |\beta\rangle, |\gamma\rangle\}$. The quadrupole–quadrupole contribution to relaxation is thus given by

$$\hat{\hat{\Gamma}}^{\mathrm{QQ}} = \sum_{i=1}^{n} \sum_{j=1}^{n} \xi_i^{\mathrm{Q}} \xi_j^{\mathrm{Q}} \sum_{m=-2}^{2} (-1)^m \sum_{p} \hat{\hat{\Gamma}}_m^{\mathrm{Q}i} \hat{\hat{\Gamma}}_{-m,p}^{\mathrm{Q}j} J^{\mathrm{QQ}ij}(\Omega_p) \quad (88)$$

The superoperator $\hat{\hat{\Gamma}}_m^{\mathrm{Q}i}$ is formed from the spin tensor operators as follows:

$$\hat{\hat{\Gamma}}_m^{\mathrm{Q}i} = \hat{T}_m^{(2)}(\mathrm{Q}, i) \otimes \hat{E} - \hat{E} \otimes \hat{T}_m^{(2)}(\mathrm{Q}, i) \quad (89)$$

3.4 External Random Fields

Relaxation by random fields is often used as a 'catch-all' in order to account for relaxation that cannot be attributed to other relaxation mechanisms. The origin of the random fields is not precisely specified. They could, for example, arise from DD interactions with paramagnetic species or nuclear spins of solvent molecules. Consider a random field at spin i given by $\boldsymbol{B}(\mathrm{R}, i, t)$. The time average of the field must be zero, since all constant terms have been absorbed into the static Hamiltonian. However, the time-averaged amplitude of the field irrespective of its direction is nonzero, and this quantity $\boldsymbol{B}(\mathrm{R}, i) = \overline{|\boldsymbol{B}(\mathrm{R}, i, t)|}$ will define the interaction strength according to

$$\xi_i^{\mathrm{R}} = \gamma_i B(\mathrm{R}, i) \quad (90)$$

A normalized random field with unit time-averaged amplitude can now be defined as follows:

$$\boldsymbol{b}(\mathrm{R}, i, t) = \frac{\boldsymbol{B}(\mathrm{R}, i, t)}{B(\mathrm{R}, i)} \quad (91)$$

The spherical components of this vector are

$$\left.\begin{aligned} b_0^{(1)}(\mathrm{R}, i, t) &= b_z(\mathrm{R}, i, t) \\ b_{\pm 1}^{(1)}(\mathrm{R}, i, t) &= \mp \sqrt{\tfrac{1}{2}} b_{\pm}(\mathrm{R}, i, t) \end{aligned}\right\} \quad (92)$$

These spherical components of the normalized random field may be identified with the lattice fluctuation functions as follows, and expressed in terms of the spherical harmonics and the time-dependent norm of the scaled random field:

$$F_m^{(1)}(\mathrm{R}, i, t) = b_m^{(1)}(\mathrm{R}, i, t) = |\boldsymbol{b}(\mathrm{R}, i, t)| Y_m^{(1)}(\theta_i, \phi_i) \quad (93)$$

In contrast to the other interactions we have discussed, all of which have constant amplitude but random orientation, the random field interaction must be assumed to vary randomly in both orientation and amplitude. All the time dependence of the lattice functions then cannot be vested in the spherical harmonics. The Hamiltonian for the random field interaction is

$$\hat{\mathcal{H}}^{\mathrm{R}} = \sum_{i=1}^{n} \xi_i^{\mathrm{R}} \sum_{m=-1}^{1} (-1)^m F_{-m}^{(1)}(\mathrm{R}, i, t) \hat{T}_m^{(1)}(\mathrm{R}, i) \quad (94)$$

The spherical tensor operators are given by

$$\left.\begin{aligned}\hat{T}_0^{(1)}(\mathrm{R},i) &= \hat{I}_{iz}\\ \hat{T}_{\pm1}^{(1)}(\mathrm{R},i) &= \mp\sqrt{\tfrac{1}{2}}\hat{I}_{i\pm}\end{aligned}\right\} \tag{95}$$

For a single spin-$\frac{1}{2}$ particle, the random field spin tensor components are

$$\begin{matrix}\hat{T}_0^{(1)} & \hat{T}_1^{(1)} = -[\hat{T}_{-1}^{(1)}]^{\mathrm{T}}\\ \frac{1}{2}\begin{bmatrix}1 & 0\\ 0 & -1\end{bmatrix}, & \frac{1}{\sqrt{2}}\begin{bmatrix}0 & 0\\ 1 & 0\end{bmatrix}\end{matrix} \tag{96}$$

The random field–random field contribution to relaxation is thus given by

$$\hat{\hat{\Gamma}}^{\mathrm{RR}} = \sum_{i=1}^{n}\sum_{j=1}^{n}\xi_i^{\mathrm{R}}\xi_j^{\mathrm{R}}\sum_{m=-1}^{1}(-1)^m\sum_{p}\hat{\hat{\Gamma}}_m^{\mathrm{R}i}\hat{\hat{\Gamma}}_{-m,p}^{\mathrm{R}j} J^{\mathrm{RR}ij}(\Omega_p) \tag{97}$$

3.5 Cross Correlation Effects

According to equation (47), the relaxation matrix is a sum of terms, each of which involves two interactions. The index μ implicitly contains a spin or spin pair index, the type of interaction, and the interaction rank. Since there is no restriction on the double sum, there are a great many terms involving different spins or spin pairs and different mechanisms. If the value of any of the indices associated with μ' is different from that associated with μ, the term is referred to as a cross-correlation term. Such terms can involve two different spins or spin pairs of the same mechanism, or two different mechanisms. Some of these terms are zero because the interactions involved are not correlated, so the time average over the product of lattice functions yields zero, but many of them are not negligible and contribute dramatically to relaxation, as will be demonstrated in Section 4. Consider the DD mechanism with three or more spins in the system of interest as shown in equation (71). If $i \neq k$ or $j \neq l$ (both of these inequalities can hold if there are four or more spins) then we have an example of cross correlation. Interactions of different ranks will never correlate, but dipolar and shielding anisotropy interactions are both of rank-2, and cross terms like the following will occur in addition to those enumerated previously:

$$\left.\begin{aligned}\hat{\hat{\Gamma}}^{\mathrm{DS}} &= \sum_{i=2}^{n}\sum_{j=1}^{i-1}\sum_{k=1}^{n}\xi_{ij}^{\mathrm{D}}\xi_k^{\mathrm{S}}\sum_{m=-2}^{2}(-1)^m \times\sum_{p}\hat{\hat{\Gamma}}_m^{\mathrm{D}ij}\hat{\hat{\Gamma}}_{-m,p}^{\mathrm{S}k}J^{\mathrm{DS}ijk}(\Omega_p)\\ \hat{\hat{\Gamma}}^{\mathrm{SD}} &= \sum_{i=1}^{n}\sum_{j=2}^{n}\sum_{k=1}^{j-1}\xi_i^{\mathrm{S}}\xi_{jk}^{\mathrm{D}}\sum_{m=-2}^{2}(-1)^m \times\sum_{p}\hat{\hat{\Gamma}}_m^{\mathrm{S}i}\hat{\hat{\Gamma}}_{-m,p}^{\mathrm{D}jk}J^{\mathrm{SD}ijk}(\Omega_p)\end{aligned}\right\} \tag{98}$$

Some simulations showing the effects of cross correlation may be found in Sections 4.2 and 4.4.

4 SOME EXAMPLES

Now that the mathematical tools needed are at our disposal and several relaxation mechanisms have been presented, we can explore their effects using some simple spin systems as examples. This will be done by means of simulations using the GAMMA magnetic resonance simulation platform[5] so that the various mechanisms can be turned on and off or adjusted at will to illustrate their effects. Most of our attention will be focused on longitudinal relaxation, though some transverse effects will be noted. In addition, the influence of molecular motion and geometry on the results of our 'experiments' will be examined. A growing body of experimental results[4] indicates that the theoretical framework developed above predicts the results of experiments very accurately. Thus, we can proceed with some confidence to predict the results of experiments, though they may not yet be in the literature. The complexity of the relationship between these geometrical and dynamical parameters is such that it is clearly impossible to explore every variable fully here, but selected examples will be used to exhibit the sensitivity of experimental results to various physical parameters.

4.1 Coupled Relaxation Experiments: The AX Spin System

In this section, several experiments will be described that are used for studying longitudinal relaxation in coupled spin systems. Examples of their application to a $^{13}\mathrm{C}-^{1}\mathrm{H}$ (AX) spin system will be given. Many of the basic principles of coupled relaxation can be illustrated using only this simple spin system. Some other pair of heteronuclei or a homonuclear spin system could be treated equally well.

The return to thermal equilibrium of magnetization that has been perturbed is governed by equation (45). Experiments to study spin relaxation normally consist of

1. preparing the spin system in a nonequilibrium state using rf pulses;
2. allowing the magnetization to relax for a period of time t_1;
3. projecting the magnetization of interest onto the observable single quantum coherences, again using rf pulses;
4. observing the resulting FID as a function of the time t_2;
5. Fourier transforming the FID to obtain a spectrum exhibiting the partially relaxed magnitudes of the various magnetizations.

This procedure is repeated for various values of t_1 and for various preparations of the nonequilibrium state until a sufficient body of data has been accumulated to elucidate all desired aspects of the relaxation of the system under study. Generally, one acquires enough data to overdetermine the relaxation, and then utilizes nonlinear least-squares fitting techniques to extract the values of the physical parameters of interest from the experimental data. Using the theory given above as implemented in the GAMMA platform, one can numerically simulate all of these steps. To exhibit all aspects of the relaxation behavior, it is generally necessary to perform several experiments, preparing the spin system in various ways. In each case, the relaxation during the evolution time t_1 is governed by equation (45), but the initial condition for the differential equation (i.e., the density operator at the start of the evolution period) is different in each case. Several

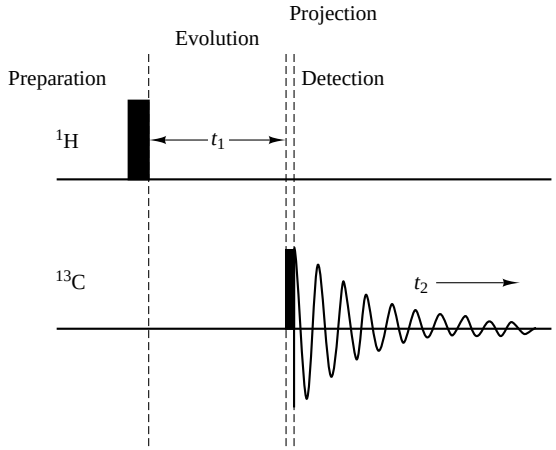

Figure 2 The proton hard pulse experiment used to create Figure 1. The wide pulse is a π pulse; the narrow one is a $\frac{1}{2}\pi$ pulse

such experiments are described below. More experimental details can be found in the review by Grant et al.[4] We shall confine ourselves to exploring the effects of several relaxation mechanisms on some simple spin systems to illustrate the kinds of physical parameters to which spin relaxation is sensitive. Using the $^{13}C-^{1}H$ (AX) spin system as a simple example, several typical experiments for studying coupled relaxation will be presented.

4.1.1 Nonselective Inversion: Hard Pulse

In the introduction (Section 1.3) the concept of cross relaxation due to dipolar coupling between the spins was introduced, and was illustrated in Figure 1. Figure 2 shows the proton hard pulse or nonselective inversion procedure used to create the simulations in Figure 1. This experiment illustrates many of the features of coupled relaxation and many of the effects of the various relaxation mechanisms. The protocol of the experiment is as follows:

1. Preparation: the system is started at thermal equilibrium, then a nonselective π pulse is applied at the proton resonance frequency. All the proton magnetization is now aligned along the negative z axis; the carbon magnetization remains at thermal equilibrium.
2. Evolution: the system is allowed to evolve for a time t_1. The proton magnetization returns toward thermal equilibrium, with cross relaxation to the carbon.
3. Projection: a $\frac{1}{2}\pi$ pulse is applied at the carbon resonance frequency to project the z components of the carbon magnetization onto the carbon single quantum coherences.
4. Detection: the carbon FID is digitized.
5. The FID is Fourier transformed.

A series of values of t_1 was chosen and the procedure repeated for each value. The resulting spectra are shown in Figure 1. The ^{1}H spectra shown there were obtained by shifting the projection and observation steps to the proton frequency. Note that the two lines in each doublet evolve identically; this leads naturally to the idea of magnetization modes. More on this subject can be found in ***Relaxation Mechanisms: Magnetization Modes***. It is generally more convenient and instructive to plot linear combinations of peak intensities corresponding to these magnetization modes. In Figure 1 note that the four lines have been designated as C1, C2, H1, and H2. The magnetization modes for this AX system are

$$\left.\begin{aligned} M_{\mathrm{C}} &= M_{\mathrm{C1}} + M_{\mathrm{C2}} \\ M_{\mathrm{H}} &= M_{\mathrm{H1}} + M_{\mathrm{H2}} \\ M_{\Delta} &= M_{\mathrm{C1}} - M_{\mathrm{C2}} = M_{\mathrm{H1}} - M_{\mathrm{H2}} \\ M_{\mathrm{T}} &= \text{sum over all state populations} \end{aligned}\right\} \tag{99}$$

The M_{T} mode is just the sum of the populations of all the states, which is assumed to be constant, since the number of spins in the sample is constant. This corresponds to using the irreducible spherical tensor operators for two nonidentical spins as basis operators. The procedure for generating these operators is discussed in detail by Wang and Grant.[17] Figure 3 shows the effect of several relaxation mechanisms on the spin system of Figure 1. The dotted line shows evolution under DD relaxation alone; random field effects have been turned off. The system relaxes much more slowly than shown in Figure 1. The addition of SA relaxation results in evolution as shown by the light line. To this point, M_{Δ} has not been perturbed at all. However, when cross correlation between DD and SA (see Section 3.5) is added, the evolution shown by the heavy lines results. Thus, only the DD–SA cross correlation relaxation couples M_{Δ} to the other modes. Figure 4 shows expanded views of the lines of the doublet at thermal equilibrium for these same cases. When DD–SA relaxation is considered, the two linewidths, i.e., the T_2 values of the lines, are no longer equal, and the doublet is not symmetric. In this case, lineheights may not be used to follow the evolution of the magnetization modes, but integrated intensities must be used. This has been done in Figure 3.

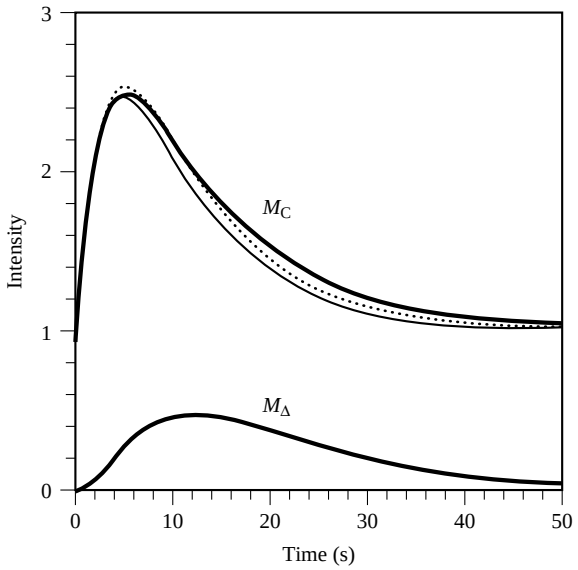

Figure 3 Magnetization mode evolution plots showing the effect on a $^{13}C-^{1}H$ spin system of DD relaxation (dotted line), the addition of SA on the ^{13}C of 100 ppm (light line), and finally with cross correlation between DD and SA (heavy lines). The spin system is as in Figure 1. The shielding tensor is axially symmetric, with the unique axis along the internuclear vector. A hard pulse perturbation as in Figure 2 is used. There is no random field relaxation. The M_{Δ} mode is shown only for the last case, since it is always zero in the first two cases

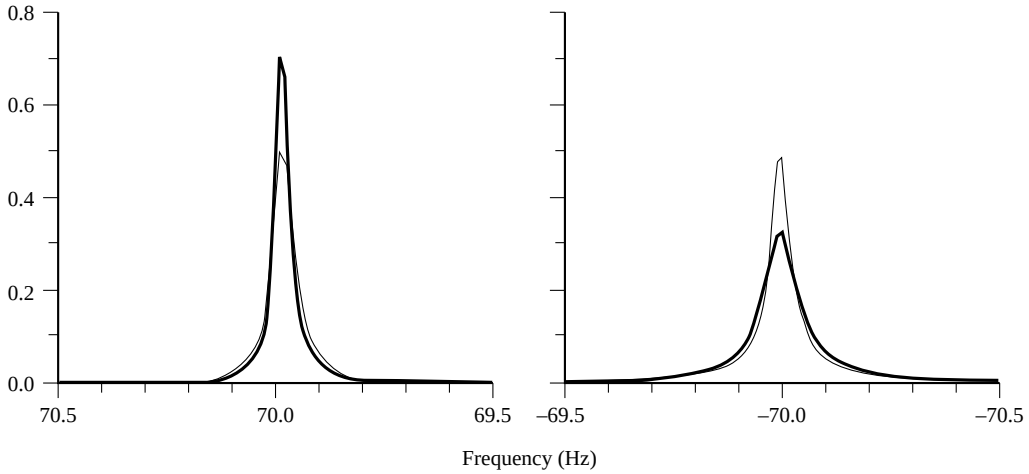

Figure 4 Expanded plots showing thermal equilibrium ^{13}C spectra from the data set of Figure 3. The light line shows only DD relaxation, while the heavy line includes DD–SA cross correlation. The doublet remains symmetric for DD relaxation, but addition of DD–SA cross correlation affects T_2 differentially for the two transitions, yielding an unsymmetrical doublet

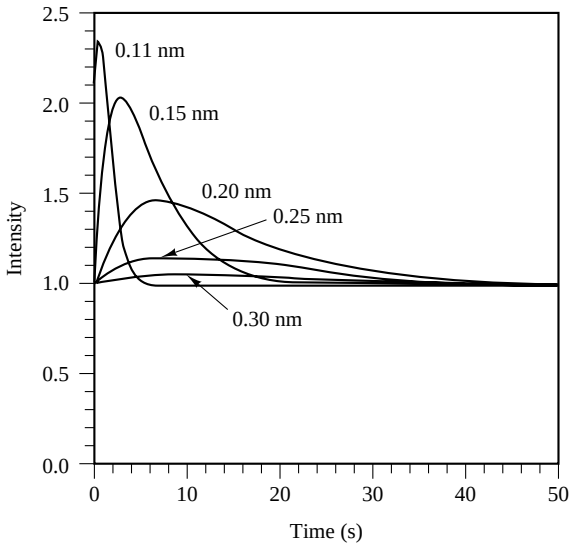

Figure 5 The effect of internuclear distance on DD cross relaxation from M_H to M_C. Random field relaxation of T_1 = 10 s is also present for both ^{13}C and ^{1}H. All other aspects of the experiment are the same as for Figure 1

In Figure 1, relaxation following a π ^{1}H pulse has already been illustrated for a nominal bond distance of 0.109 nm. The DD relaxation mechanism depends on the inverse sixth power of the internuclear separation. Suppose, now, that the proton is more remote. Figure 5 shows a plot of M_C as a function of the proton carbon distance from 0.11 to 0.30 nm. The random field mechanism has been set for a T_1 of 10 s. The internuclear distance has a dramatic effect on the cross relaxation, and one would expect to be able to measure distances quite accurately by studying cross relaxation. However, the rotational diffusion correlation time has a similar effect, as shown in Figure 6. It is only possible to determine the ratio of these two quantities. In a large molecule where a number of internuclear distances are sought, it is often possible to determine at least one internuclear distance a priori, for example, by assuming that one C–H bond has its usual value for similar hybridization of the carbon; then all other internuclear distances can be calculated. This calculation presumes that nuclei involved all reorient at the same rate, i.e., that the molecule is rigid. As the internuclear distance is increased, the DD mechanism weakens rapidly, but, even at 0.3 nm, the DD mechanism is still evident in that it produces cross relaxation. It is not the weakening of the DD mechanism that imposes this limit, but rather that it becomes weak compared to the combined effect of all other mechanisms.

So far, we have assumed that the molecule under study undergoes rotational diffusion as a spherical top, and the orientation of the internuclear vector with respect to some molecule-fixed coordinate system is irrelevant. If the molecule is diffusing as a symmetric top, this is no longer the case. Let the molecule-fixed coordinate system be that which diagonalizes the rotational diffusion tensor. Then Figure 7 shows the dependence of M_C on the angle θ between the

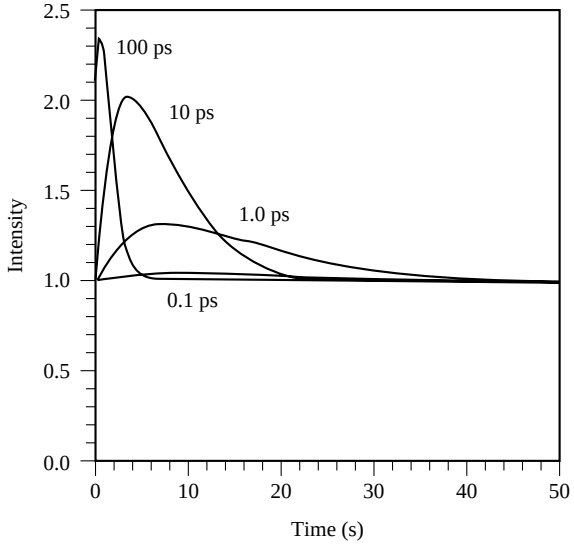

Figure 6 The effect of rotational correlation time on cross relaxation. A random field relaxation of T_1 = 10 s is present for both ^{13}C and ^{1}H. All other aspects of the experiment are the same as for Figure 5

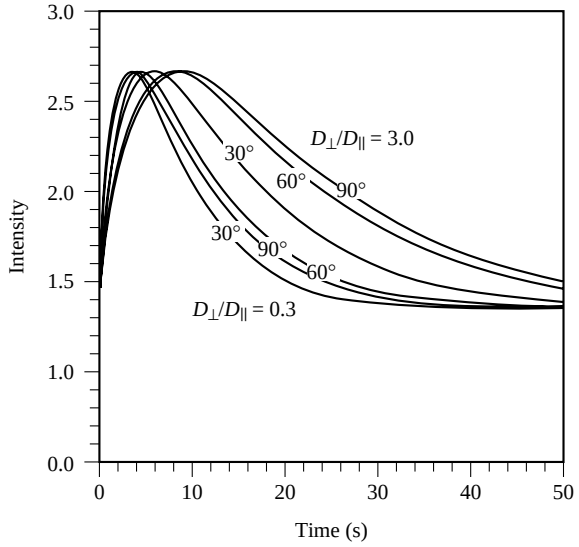

Figure 7 The effect of motional anisotropy on cross relaxation from M_H to M_C for various angles between the internuclear vector and the unique axis of the rotational diffusion tensor. Curves are given for an oblate and a prolate top as shown. All other aspects of the experiment are the same as for Figure 1

unique axis of the top and the internuclear vector for motional anisotropies $D_\perp/D_\parallel$ of 0.3 and 3.0. To effect DD relaxation, molecular motion must change the direction of the internuclear vector. Thus, if the C–H vector is oriented parallel to the direction of $D_\parallel$ then changing the value of $D_\parallel$ has no effect on the relaxation. In Figure 7, $D_\perp$ has been kept constant as in Figure 1, and $D_\parallel$ has been altered to produce the anisotropies.

4.1.2 Inversion–Recovery

Figure 8 illustrates the inversion–recovery experiment. This procedure is identical to that commonly used for measuring ^{13}C T_1 values under ^1H decoupling, but here no decoupling is applied. The protocol for the experiment is as follows:

1. Preparation: the system is started at thermal equilibrium; then a π pulse is applied at the carbon resonance frequency. All the carbon magnetization is now aligned along the negative z axis; the proton magnetization remains at thermal equilibrium.
2. Evolution: the system is allowed to evolve for a time t_1. The carbon magnetization returns to thermal equilibrium, with cross relaxation to the protons.
3. Projection: a $\frac{1}{2}\pi$ pulse is applied at the carbon resonance frequency to project the z components of the carbon magnetization onto the carbon single quantum coherences.
4. Detection: the carbon FID is digitized.
5. The FID is Fourier transformed.

Figure 9 shows the resulting simulated spectra for the AX spin system as in Figure 1. As before, the ^1H spectra shown in Figure 9 were obtained by shifting the projection and observation steps to the proton frequency. Note that magnetization flows from the ^{13}C to the ^1H in this case—the reverse of what was observed in Figure 1. For this simulation, only DD relaxation was used, to accentuate the effects of cross relaxation; thus, the relaxation times are substantially longer. Figure 10 shows a plot of M_C taken from the spectra of

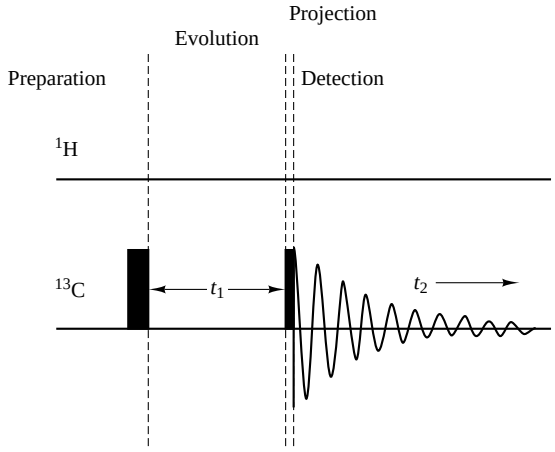

Figure 8 The inversion–recovery experiment. The wide pulse is a π pulse; the narrow one is a $\frac{1}{2}\pi$ pulse

Figure 9. The dotted line shows a single exponential with the T_1 adjusted to best fit the actual evolution. The nonexponential behavior indicates that the ^{13}C magnetization is perturbed by the presence of the ^1H, i.e., by cross relaxation to the protons. The departure is slight, and might be overlooked in a real experiment unless careful studies were done with high S/N data. Thus, the hard pulse experiment of the previous section is a much more sensitive measure of the effects of cross relaxation. Again, the M_Δ mode is unperturbed.

4.1.3 Selective Inversion: Polarization Transfer

There are several variations of the selective inversion or soft pulse experiment, depending on which of the spectral lines are to be inverted and the method to be used for inversion. A simple low-power 'soft' rectangular pulse or a shaped pulse can be used to invert a single line. One member of a doublet can be inverted by adjusting the pulse amplitude so that the on-resonance peak experiences a π nutation while the off-resonance one experiences an effective field producing a 2π precession and is thus unchanged. These methods have been used before the advent of modern spectrometers with sufficient phase agility to accomplish polarization transfer or INEPT-type procedures such as the one described in Figure 11. This latter procedure is now the preferable one in most cases. It proceeds as follows:

1. Preparation: the system is started at thermal equilibrium; then a proton $(\frac{1}{2}\pi)_x$ pulse is applied to orient the two members of the proton doublet along the y axis. Precession due to scalar coupling for a period of $\frac{1}{2}J$ produces antiphase proton magnetization along the x axis that is then rotated back onto the z axis with a $(\frac{1}{2}\pi)_y$ pulse. The simultaneous π pulses in the center of the preparation period cause the evolution due to chemical shift to refocus, but do not affect the evolution due to scalar coupling. The carbon thermal equilibrium magnetization is inverted by the π pulse, and to this is added the antiphase magnetization generated in the proton domain. This yields a $1.5 : -2.5$ doublet intensity ratio.
2. Evolution: the system is allowed to evolve for a time t_1. Both the carbon and proton magnetizations return toward thermal equilibrium.

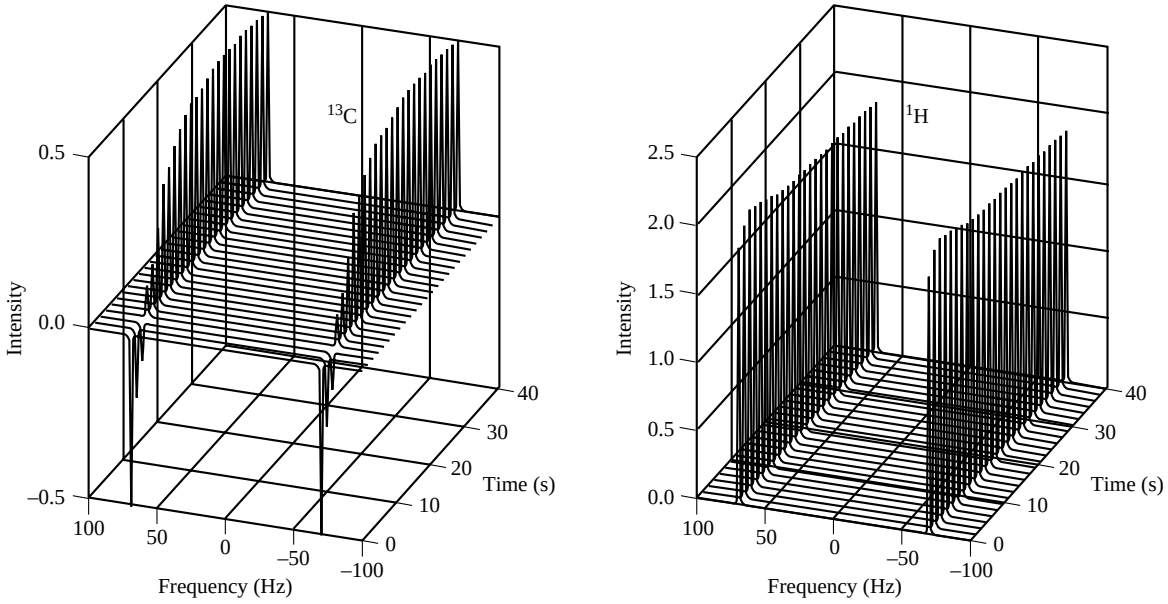

Figure 9 Simulated spectra resulting from the inversion–recovery experiment described in Figure 8. The spin system is the same as for Figure 1. Only DD relaxation is enabled

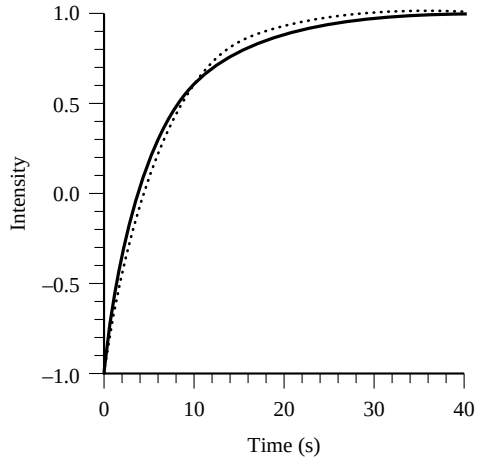

Figure 10 The M_C mode taken from the spectra of Figure 9 plotted versus time. The solid line is the actual evolution of the magnetization; the dotted line is the corresponding single exponential evolution

3. Projection: a $\frac{1}{2}\pi$ pulse is applied at the carbon or the proton resonance frequency to project the z components of the corresponding magnetization onto the single quantum coherences.
4. Detection: the carbon or proton FID is digitized.
5. The FID is Fourier transformed.

Figure 12 shows the spectra obtained by applying this sequence to the spin system of Figure 1. Note how proton magnetization is transferred to the ^{13}C in much the same way as happens in an INEPT experiment. In this case, the M_Δ mode is strongly perturbed, but, as shown in Figure 13, it is mono-exponential because this mode is not coupled to any other for an AX system with only DD relaxation. Even though the spectral lines evolve in a more complicated way and evolve differently for the ^{1}H than for the ^{13}C doublet, the difference of the two lines of the doublet M_Δ evolves identically and mono-exponentially, whether measured in the ^{1}H or the ^{13}C spectrum as stated in equation (99). This is a manifestation of the fact that the operator corresponding to M_Δ is identical whether it is measured in the proton spectrum or the carbon spectrum. These two differences of line intensities are just two different views of the same measurable, and this measurable is not coupled to any other mode.

4.2 Angles Between Internuclear Vectors: The AX_2 Spin System

In Section 4.1.3, we observed how cross correlation between DD and SA interactions can influence relaxation. The AX_2 spin system introduces the possibility to have cross correlation between two different DD interactions. There are

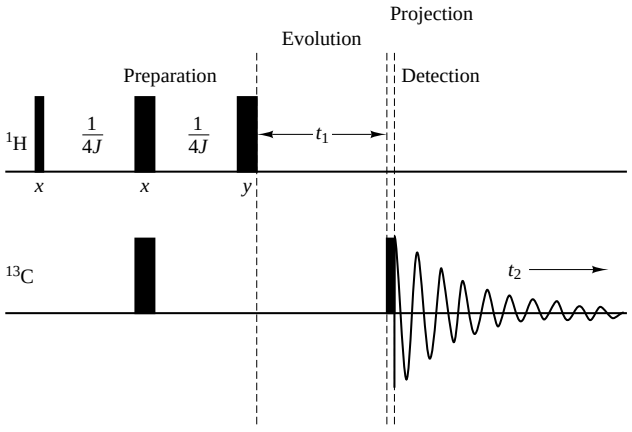

Figure 11 Selective inversion of a proton doublet using nonselective pulses. The wide pulses are π; the narrow ones are $\frac{1}{2}\pi$. The letters under the pulses indicate relative phases. If no phase is indicated, it is arbitrary

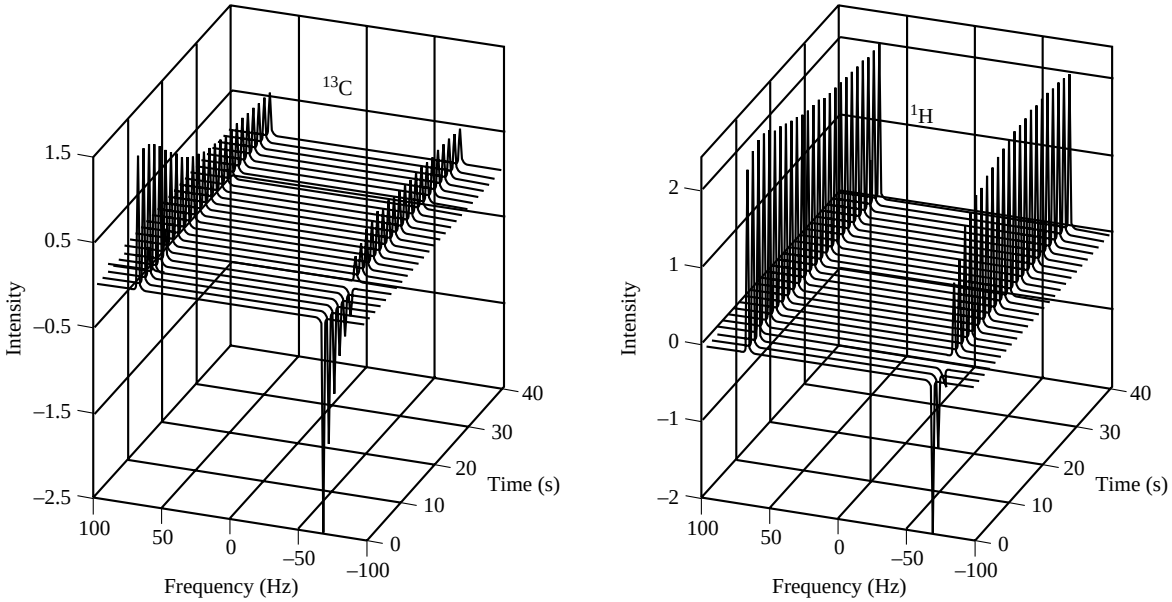

Figure 12 Spectra obtained by applying the selective inversion procedure of Figure 11 to the proton spin system described in Figure 1. Only the DD mechanism is enabled

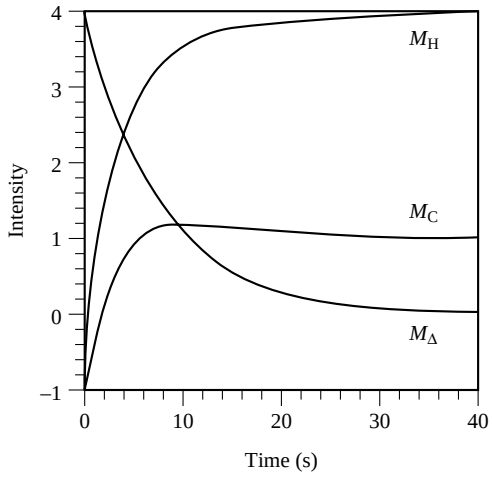

Figure 13 Magnetization modes taken from the spectra of Figure 12 plotted as a function of evolution time. Here the single exponential (dotted) line precisely superimposes on M_Δ and is not visible. Compare with Figure 10

three different spin pairs (AX, AX′, and XX′), each of which has a DD interaction, and there can be cross correlation among these various interactions (see Section 3.5). Because of the complexity of the way in which these cross correlations are folded into the elements of the relaxation superoperator, it is difficult to show how they influence relaxation in a clear way. However, the AX_2 spin system also introduces the angle between two internuclear vectors as a parameter of interest that is affected by this DD–DD cross-correlation. In Section 4.1.1, it was noted that for an AX spin system, the orientation of the internuclear vector with respect to some molecule-fixed frame is irrelevant for a spherical top. However, Figure 14 shows the influence of the angle between two internuclear vectors on the results of a proton hard pulse experiment. The magnetization modes of interest here are

$$\left.\begin{aligned} M_C &= M_{C1} + M_{C2} + M_{C3} \\ M_{+-+} &= M_{C1} - M_{C2} + M_{C3} \end{aligned}\right\} \tag{100}$$

The M_{+-+} mode was not present in the AX spin system, and is coupled to both the total proton and total carbon magnetizations. Both of these modes show dramatic sensitivity to the HCH angle for spherical top diffusion.

4.3 Rotational Anisotropy: The AX_3 Spin System

The prototypical AX_3 spin system is a ^{13}C methyl group. If a methyl is attached to a larger molecule, the free rotation

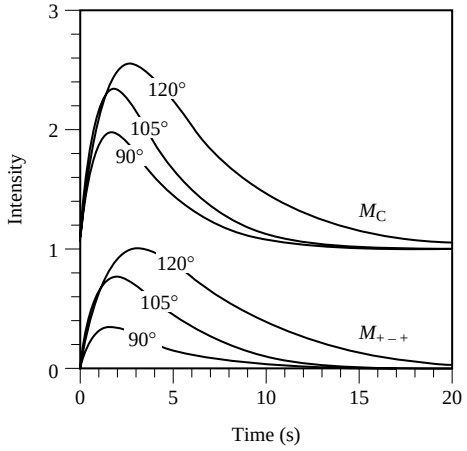

Figure 14 For a ^{1}H–^{13}C–^{1}H (AX_2) system, the effect of the HCH angle on the cross relaxation of the observable magnetization modes. Only the DD mechanism is enabled in the simulations. The perturbation is a proton hard pulse as in Figure 2. All other conditions are the same as for Figure 1

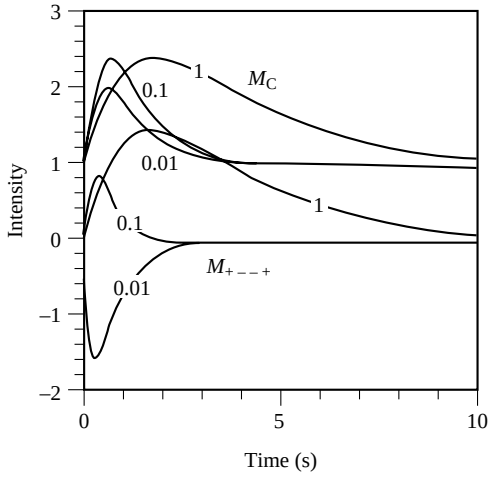

Figure 15 For a $^{13}C–^{1}H_3$ (AX_3) system, the effect of motional anisotropy (shown as $D_\perp/D_\parallel$ for the various curves) on the cross relaxation of the M_C and M_{+--+} magnetization modes. Only the DD mechanism is enabled in the simulations. The geometry is tetrahedral, with the threefold axis of the methyl collinear with $D_\parallel$. The perturbation is a proton hard pulse as in Figure 2. All other conditions are the same as for Figure 1

about the threefold axis of the methyl combined with the much slower overall tumbling of the molecule as a whole results in high motional anisotropy. This situation is a good case for exploring the effect of motional anisotropy on spin relaxation. The magnetization modes of interest in this case can be written as linear combinations of the four transitions of the carbon quartet:

$$\left.\begin{aligned} M_C &= M_{C1} + M_{C2} + M_{C3} + M_{C4} \\ M_{+--+} &= 3M_{C1} - M_{C2} - M_{C3} + 3M_{C4} \end{aligned}\right\} \quad (101)$$

Figure 15 shows these ^{13}C magnetization modes as they evolve in a proton hard pulse experiment. Beginning with a spherical top, cross relaxation is observed much as in previous cases; however, as the anisotropy of the reorientation increases, the M_{+--+} mode is very sensitive, even switching to a negative excursion rather than a positive one under highly unsymmetrical reorientation.

4.4 *o*-Dichlorobenzene

The simulation in Figure 16 uses experimental parameters as for the protons of *o*-dichlorobenzene (an AA′BB′ spin system.) The basic parameters for this simulation were taken from a paper by Stark et al.[18] The lower traces show spectra with full DD relaxation, including both autocorrelation and cross-correlation terms, whereas the upper traces have only autocorrelated DD terms. Under extreme narrowing (the two left traces), there is no apparent difference. When the correlation times are increased by a factor of 10, however, differences in maximum peak heights and linewidths are clearly visible. This simulation includes only dipolar relaxation terms, and uses a rigid asymmetric top as the motional model.

These few examples show the wealth of information available from coupled relaxation studies. Furthermore, many of the

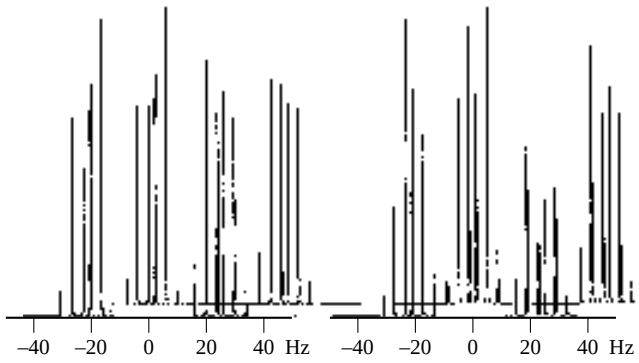

Figure 16 Simulated proton spectra at 220 MHz of *o*-dichlorobenzene with DD relaxation including both autocorrelated and cross-correlated relaxation terms (lower traces) and with only autocorrelated terms (upper traces). The motion was modeled as a rigid asymmetric top with correlation times of 3.4, 5.4, and 1.9 ps (left traces) and 34, 54, and 19 ps (right traces). Artificial line broadening of 0.05 Hz was used for the spectra on the left to suppress truncation artifacts

multidimensional experiments that have become commonplace tools for the chemist and biochemist involve placing coupled spin systems in nonequilibrium states. In many cases, the cross relaxation and cross-correlation effects illustrated here markedly influence the results of such experiments, and due consideration must be given when interpreting these experiments.

The GAMMA platform has been made available to the public by its authors. The source code of the GAMMA-based program that generated all the simulations herein, as well as online simulations of these effects, are available courtesy of the National High Magnetic Field Laboratory at **http://gamma1.magnet.fsu.edu/~gamma/**.

5 REFERENCES

1. T. C. Farrar and E. D. Becker, *Pulse and Fourier Transform NMR: Introduction to Theory and Methods*, Academic Press, New York, 1971.
2. H. Friebolin, *Basic One- and Two-Dimensional NMR Spectroscopy*, VCH, New York, 1991.
3. A. E. Derome, *Modern NMR Techniques for Chemistry Research*, Pergamon Press, Oxford, 1987.
4. D. M. Grant, C. L. Mayne, F. Liu, and T. Xiang, *Chem. Rev.*, 1991, **91**, 1591.
5. S. A. Smith, T. O. Levante, B. H. Meier, and R. R. Ernst, *J. Magn. Reson. Ser. A*, 1994, **106**, 75.
6. E. M. Purcell, H. C. Torrey, and R. V. Pound, *Phys. Rev.*, 1946, **69**, 37.
7. F. Bloch, W. W. Hansen, and M. Packard, *Phys. Rev.*, 1946, **70**, 474.
8. F. Bloch, *Phys. Rev.*, 1946, **70**, 460.
9. C. P. Slichter, *Principles of Magnetic Resonance*, 3rd edn., Springer-Verlag, Berlin, 1990.
10. C. L. Mayne, D. W. Alderman, and D. M. Grant, *J. Chem. Phys.*, 1975, **63**, 2514.
11. S. A. Smith, W. E. Palke, and J. T. Gerig, *Concepts Magn. Reson.*, 1992, **4**, 107.
12. S. A. Smith, W. E. Palke, and J. T. Gerig, *Concepts Magn. Reson.*, 1992, **4**, 181.

13. S. A. Smith, W. E. Palke, and J. T. Gerig, *Concepts Magn. Reson.*, 1993, **5**, 151.
14. R. N. Zare, *Angular Momentum*, Wiley, New York, 1988.
15. S. Szymanski, A. M. Gryff-Keller, and G. Binsch, *J. Magn. Reson.*, 1986, **68**, 399.
16. A. G. Redfield, in *Advances in Magnetic Resonance*, ed. J. S. Waugh, Academic Press, New York, 1965, Vol. 1, p. 1.
17. C. H. Wang and D. M. Grant, *J. Chem. Phys.*, 1976, **64**, 1522.
18. R. E. Stark, R. L. Vold, and R. R. Vold, *J. Magn. Reson.*, 1979, **33**, 421.

Biographical Sketch

Charles L. Mayne. *b* 1942. B.S., 1970, New Mexico State University, U.S.A.; Ph.D., 1976, University of Utah. Introduced to NMR by George A. Gray and subsequently tutored by David M. Grant. Manager of NMR Laboratories, University of Utah, Department of Chemistry, 1973–present; academic appointment as Adjunct Associate Professor of Chemistry, University of Utah. Approx. 40 publications in NMR. Research interests include nuclear-spin relaxation, NMR at high pressure, structure elucidation of natural products, various aspects of multidimensional NMR, and computerized analysis of NMR data.

Scott A. Smith. *b* 1955. B.S., 1980, San Diego State University, U.S.A.; Ph.D., 1989, University of California, Santa Barbara. Introduced to NMR by Dr Stephen B. W. Roeder. Currently working for Dr R. R. Ernst with Tilo Levante on the GAMMA project and its release to the public. 5 publications in computer simulation of NMR experiments. Research interests include nuclear-spin relaxation and computer simulation of magnetic resonance phenomena.

Stereochemistry and Long Range Coupling Constants

Ted Schaefer

University of Manitoba, Winnipeg, MB, Canada

1	Introduction	1
2	Stereochemistry	1
3	The Coupling Constant Between Nuclei	2
4	$^nJ(n \geq 4)$ in Saturated Molecules	4
5	$^nJ(n \geq 4)$ in Unsaturated Molecules	5
6	Aromatic Molecules	7
7	Proximate Long Range Coupling Constants	9
8	The Future of Long Range Coupling Constants	10
9	Related Articles	10
10	References	10

1 INTRODUCTION

Stereochemistry (from the Greek *stereos*, meaning 'solid'), the three-dimensional architecture of molecules at the atomic level, underlies our world of appearances, from the grit of grains of sand to the intricacies of an infant's hand. It is a tenet that the macroscopic properties of solids are a consequence of this architecture. It is also thought that the myriad of chemical transformations depends in a subtle way on stereochemistry; the living cell, a microscopic center for the chemical reactions essential to life, depends on stereochemistry for the 'recognition' of one molecule by another during the initiation of reactions which, in turn, produce molecules whose biological utility again has an exquisite dependence on their architecture. Such are the working hypotheses at the root of an enormous effort to establish the stereochemistry of animate and inanimate materials.

NMR is playing an important role in this quest—witness the ubiquity of NMR spectrometers in chemical laboratories. One stereosensitive property of a molecule is the scalar interaction between magnetic nuclei ^nJ, in which n represents the number of intervening chemical bonds; n can run from unity, in all molecules, to at least 14 in some molecules (see ***Indirect Coupling: Theory and Applications in Organic Chemistry***). For $n \geq 4$, ^nJ is often relatively small. As the resolution of NMR spectra improved, the presence of such long range coupling constants became clear and their relationship to stereochemistry became a subject of study. Among the earliest theoretical and experimental investigators of this topic were F. A. L. Anet, M. Barfield, A. A. Bothner-By, D. M. Grant, H. Günther, R. A. Hoffman, H. S. Gutowsky, G. J. Karabatsos, M. Karplus, J. Meinwald, and H. M. McConnell. Barfield has been particularly active over a long period in providing theoretical stimulation to experimentalists. A number of extensive reviews[1–8] of the theory of long range coupling constants and their stereochemical applications are recommended.

The aim of this article is to provide an overview of the utility of long range coupling constants in stereochemical analysis. A very brief discussion is given of stereochemical concepts, followed by a heuristic description of the origins of ^nJ, which is elaborated by specific examples drawn mainly from organic chemistry. This choice is dictated by the available space and is also colored by personal taste. Apologies are in order to those authors whose work may well have been cited. Only a few of the thousands of long range coupling constants can be included; even if only the more familiar NMR-active nuclei (^{1}H, ^{13}C, ^{19}F, and ^{31}P) were included for $4 \leq n \leq 12$, then the variety of chemical bonding patterns would require a substantial book for an adequate discussion.

2 STEREOCHEMISTRY

The electrons in a molecule move with speeds near a million meters per second and therefore traverse the space of a moderately sized molecule about a thousand million million times in one second. In so doing, the electrons tie the very small but relatively massive nuclei into a floppy, pulsating, rotating object, which is stable at ambient temperatures. At certain distances between the nuclei, the Coulombic forces of attraction between the nuclei and electrons outweigh those of repulsion between nuclei and between electrons. For nearest-neighbor nuclei these distances are called 'bond lengths'; intuition is correct in suggesting that the electrons tend to concentrate in the regions between neighboring nuclei. If two electrons undergo this concentration one has a single bond, if four, a double bond, and so forth.

The diversity of molecular size and shape is breathtaking. The diatomic oxygen molecule, so necessary to our very existence, contains two nuclei and sixteen electrons. A small diamond, also thought necessary by some, is a single molecule containing some 10^{22} nuclei and six times as many electrons. When diamond burns in oxygen, one obtains the linear, triatomic molecule, carbon dioxide, which is considered obnoxious, yet is essential for photosynthesis. One of the aims of modern experimental and theoretical chemistry is the elucidation of the detailed shapes of these various three-dimensional objects, i.e. their stereochemistry.

Consider a tetra-atomic molecule ABCD. In (**1**), the four different nuclei are connected in a unique way: A is attached to B by a single bond and not to C, and so forth. This connection scheme defines the *connectivity* or *constitution* of the molecule and represents the first step in the stereochemical description. The angles between the internuclear vectors, A–B and B–C, for example, are called 'bond angles'. An important angle θ, the torsion or dihedral angle between the two planes containing ABC and BCD, defines the *configuration* or the *conformation* of the molecule. If a very large energy input is needed to interconvert (**1**) and (**3**), i.e. if the thermal kinetic energy (motion of the molecules through space may lead to a collision in which one molecule receives energy from another) is small compared to the energy needed to twist (**1**) into (**3**), or vice versa, then one may speak of two configurations of the molecule, or of *configurational isomers*. If you have configuration (**1**) and, some time later, say days, (**1**) has not turned even partially into (**3**), even under heat, then you may speak of configuration. Often, such a situation requires a double bond between C and D, indicated by two strokes (double bond), and one refers to 'breaking the double bond' during configurational isomerization. If the energy needed

to interconvert (**1**) and (**3**) is not large compared to the thermal energies, then the sample of the substance ABCD may well contain appreciable amounts of (**1**) to (**3**). One has an equilibrium among conformational isomers or *conformers*. The relative amounts, or populations, of the conformers usually change as the temperature changes.

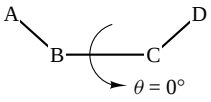

(**1**)

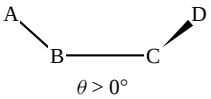

(**2**)

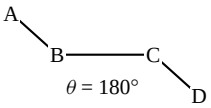

(**3**)

The two terms 'configuration' and 'conformation' relate to the human timescale. Near absolute zero in temperature, there would be little need for both terms; one would suffice in most instances. It all depends on the flexibility or floppiness of the molecule. A certain care is therefore needed in the description of the stereochemistry of a molecule. If the energy barrier to interconversion among (**1**) to (**3**) is small, then ABCD takes on all conformations, defined by θ, with similar probabilities. All angles from 0° to 180° are then significantly represented in the sample (ensemble). A molecule's reactivity, how it combines with other molecules to form one or more product molecules, and how rapidly it does so, can depend strongly on its conformation/configuration; this is one reason for the study of stereochemistry.

A complete stereochemical description requires precise values of bond lengths and bond and torsion angles, preferably with a potential function describing the energy of a molecule as a function of θ. Furthermore, because the molecule vibrates (pulsates), a knowledge of all the other vibrational motions, such as bond stretches and bond angle deformations, together with their frequencies and amplitudes, is desirable. Finally, a map of the electron density, at least up to distances of 10^{-9} m from the molecular periphery, is also needed.

Needless to say, a variety of experimental and theoretical techniques is necessary for these purposes. Most techniques utilize the fact that rotational, vibrational and electronic energies of molecules are quantized and directly related to the stereochemical properties. The energies, or at least their differences, can be ascertained by stimulating transitions between the various states of different energies with the photons available from electromagnetic radiation. Other methods scatter the photons from the molecule in the gas or solid and, from interference patterns formed by the scattered photons, deduce electron densities and, by inference, the sites of the nuclei.

NMR techniques, by way of contrast, use the magnetic properties of nuclei and their magnetic interactions with other nuclei and/or electrons to deduce molecular stereochemistry. The magnetic interactions between the nuclei and electrons in molecules are about a million times smaller than the electrostatic interactions which actually determine the stereochemistry. Therefore, at first sight it appears unreasonable to focus on the magnetic interactions as a source of stereochemical information. After all, the magnetic dipole moment of the nucleus is only weakly coupled to the very forces which mould the molecular shape. Paradoxically, it is this fact which allows NMR to be perhaps the single most general tool for stereochemical analysis. The magnetic field $\boldsymbol{B}_0$ of the NMR spectrometer penetrates the molecular space almost unaltered and orients the magnet moment of the nucleus into certain definite directions. Under certain conditions the magnetic interactions between the nuclei and between the nuclei and the electrons appear as perturbations of the interaction between $\boldsymbol{B}_0$ and the nuclei. As a consequence, the NMR spectrum, whose basic frequency represents the $\boldsymbol{B}_0$/nucleus energy, is somewhat shifted and split into a number of peaks or frequencies. These shifts and splittings, the latter being related to the J values, can be interpreted in terms of stereochemistry.

3 THE COUPLING CONSTANT BETWEEN NUCLEI

The scalar spin–spin interaction energy between two nuclei is represented by $hJ\hat{I}_i \cdot \hat{I}_j$, where $\hat{I}_i$ is the spin angular momentum vector operator of nucleus i. Because the magnetic moment μ is proportional to $\hat{I}$, J is also proportional to the product of the two nuclear moments (see ***Nuclear Spin Properties and Notation***). In this article, J is given in units of hertz. The dot, or scalar, product in the expression above applies to molecules in the isotropic liquid or gaseous states. It depends on the relative orientations of the two spins, not on their positions in space. Therefore J is unchanged by molecular reorientations, unlike the dipolar interactions which average to zero during such reorientations (see ***Dipolar and Indirect Coupling Tensors in Solids***). The directions of the nuclear spins are only very slightly coupled to the orientation of the molecule in space, but are coupled to $\boldsymbol{B}_0$. The scalar interaction modifies this latter coupling by definite amounts, proportional to J, and hence appears in the fine structure of the NMR spectrum. Figure 1 shows the ^{1}H NMR spectrum of the methyl protons of 1-phenylpropyne (**4**). In the absence of J only a single peak would occur; instead there exist many peaks arising from $^{6,7,8}J$, long range proton–proton coupling constants, over six, seven and eight formal bonds (n = 6, 7, 8). The long range coupling constants can be extracted by standard procedures (see ***Analysis of High-Resolution Solution State Spectra***).

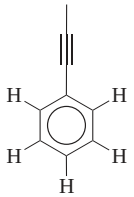

(**4**)

How does J come about? Consider a hydrogen atom. In addition to the electrostatic attraction between the electron and the proton, an energy of 13.6 eV, there exists a magnetic interaction of 6.0×10^{-6} eV (the hyperfine interaction, that is, very small), which aligns the spins of the proton and

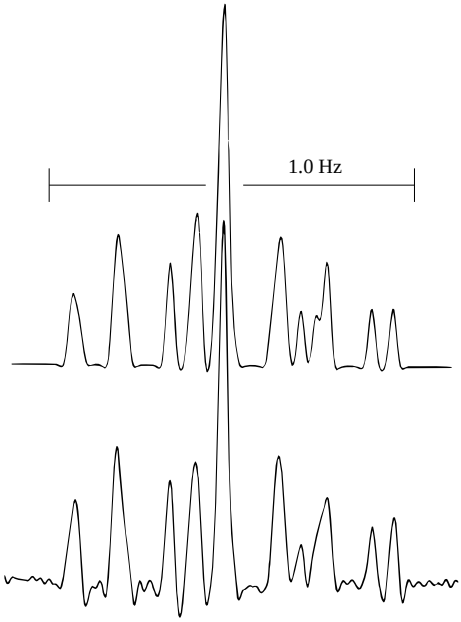

Figure 1 The ^{1}H NMR spectrum at 300 MHz of the methyl protons of 1-phenylpropyne ($C_6H_5C{\equiv}CCH_3$) as a dilute solution in acetone-d_6 at 300 K, has a linewidth at halfheight of somewhat less than 0.03 Hz. The upper, theoretical, spectrum comes from a precise spectral analysis and has the long range coupling constants ^6J(**H**,C**H**$_3$), ^7J(**H**,C**H**$_3$), and ^8J(**H**,C**H**$_3$) of −0.298(1), 0.145(1), and −0.254(1) Hz, respectively. (Reproduced with permission of The National Research Council of Canada from T. Schaefer, R. Sebastian, and R. W. Schurko, *Can. J. Chem.*, 1992, **70**, 2365)

electron in an antiparallel fashion, as in (**5**). Mutual flips of these alignments give rise to radiation at 1420 MHz which is detectable in radioastronomy, exemplifying the underlying unity of the natural sciences. The hyperfine interaction operates when the electron is very near the proton (the contact interaction).

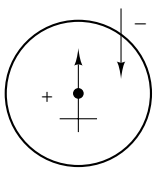

(**5**)

3.1 A Model of ^1J

Now consider the hydrogen molecule (**6**). Because the electrostatic energies ensure the antiparallel spin alignment of the two electrons (paired off, singlet state), a consequence of the quantum properties of small particles, the contact interaction favors the overall spin orientations shown in (**6**). The nuclear spin is said to 'spin polarize' the electrons in the sense that—although the net electron spin in the bond, 'down' minus 'up', is zero when averaged over the space of the bond—at the left of the bond in (**6**) there occurs more 'down' than 'up' spin, and vice versa on the right. The net result is that an antiparallel arrangement, defining a positive J, of the proton spins (crossed arrows) is favored by about 10^{-12} eV. This magnetic energy is tiny compared with the electrostatic energies yet, paradoxically, is easily measured by NMR. In the hydrogen molecule, J is 280 Hz or 1.1×10^{-3} kJ mol^{-1}, which is miniscule compared with the bond energy of 460 kJ mol^{-1}. It is clear that J, transmitted via the electrons, is proportional, at each end of the coupling path, to the size of the magnetic moment of the nucleus and, therefore, to the product of the two nuclear magnetic moments.

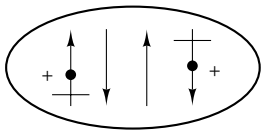

(**6**)

J is a second-order property of the molecule in the sense that it results from the product of two first-order interactions; here, two contact interactions. In another sense, because that contact interaction perturbs the ground state molecular wavefunction, the theoretical computation of J must take this perturbation into account; it does so by mixing electronically excited states into the ground state in a complicated fashion. Hence the quantitative computation of J from first principles is not easy (see ***Indirect Coupling: Theory and Applications in Organic Chemistry***). In the present article, qualitative models of ^nJ, $n \geq 4$, which nevertheless can be made semiquantitative, are used to illustrate its stereochemical applications. As will be seen, the torsional dependence of J can sometimes be ascertained by empirical methods which allow rather precise stereochemical conclusions.

3.2 Models of ^2J and ^3J

In (**7**), a pair of protons separated by two formal bonds, as in a CH_2 fragment of a molecule, is indicated to have a negative ^2J. The coupling mechanism favors a parallel orientation of the proton spin vectors. This is so because the two electrons, in different bonds but near carbon, have a lower electrostatic energy if their spins are parallel than if they are antiparallel. The lower energy, an illustration of Hund's rule, is probably a consequence of the fact that these two electrons move in such a way that they are attracted more strongly by the carbon nucleus when their spins are parallel—the spin serves as a sort of traffic policeman, one electron tending not to get between the other electron and the nucleus. The picture in (**7**) is called the 'Dirac vector model' of ^2J, predicting a negative value, for example, in methane, where ^2J is indeed −12.4 Hz. However, ^2J(H,H) is positive in some molecules. This failure of the model is shared by another kind of model, which is now illustrated for ^3J.

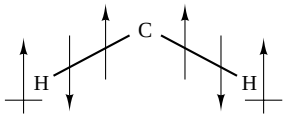

(**7**)

The HCCH or ethanic fragment in (**8**) is the prototype of an important class of vicinal or ^3J interactions (***Vicinal Coupling Constants and Conformation of Biomolecules***). The Dirac vector model correctly predicts a positive ^3J, but it cannot account for its dependence on the torsion angle θ in (**9**). In fact, it is a direct interaction (not a dipolar interaction, which is also sometimes called 'direct') between the electrons in the two C–H bonds which is important in correlating the electron, and hence the proton, spins. The direct interaction, proportional to valence bond exchange integrals, is minimal when the two C–H bonds lie in mutually perpendicular planes ($\theta = 90^\circ$). An acquaintance with trigonometry, together with the constraint that ^3J be positive, suggests that the θ dependence between 0° and 180° is mainly on $\cos^2\theta$, and perhaps slightly on $\cos\theta$. This is indeed true. The stereochemical significance is obvious. Note that the 'through bond' mechanism, as in (**8**), is relatively unimportant.

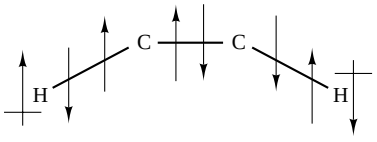

(**8**)

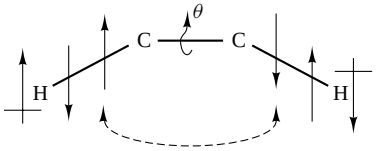

(**9**)

This manner of argument implies that geminal spin correlations, as in (**7**), could combine with vicinal spin correlations, as in (**9**), to yield long range coupling constants ^nJ ($n \geq 4$) in larger molecular fragments and is therefore related to their geometrically extended stereochemistry. This is also true. One drawback concerns the magnitude of long range coupling constants. Generally speaking, for saturated fragments (single bonds) the magnitude decreases as n increases, simply because ^nJ arises either from the product of small interactions of the kind shown in (**8**) and (**9**), or because the direct interaction between bonds decreases with their separation; the bond exchange integrals (interactions) giving rise to spin correlation between electrons in different bonds depend on interelectronic distances in these structures. In (**9**), ^3J is of the order of 10 Hz at $\theta = 0^\circ$ or 180°, whereas ^4J has a magnitude of about 1 Hz in the propanic fragment below. Note that at least some deviation from perfect pairing is necessary for a finite J. However, for unsaturated molecules, in which extensive electron delocalization occurs, ^nJ can be sizeable and does not necessarily drop off monotonically as n increases. As an extreme example,[10] ^{14}J(F,F) in (**10**) is 0.2 Hz in magnitude.

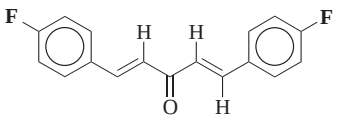

(**10**)

4 $^nJ(n \geq 4)$ IN SATURATED MOLECULES

In the propanic fragment (**11**) to (**14**), direct and indirect mechanisms can contribute to ^4J(H,H). The direct mechanisms are important[11] in conformations (**12**) and (**13**). In (**12**), the two C–H bonds are proximate in space and $1 \rightarrow 3$ interactions are important. Coupling constants arising in this way are often called 'through space', which is a misnomer because the molecule itself is largely empty space; perhaps, 'proximate' ^nJ would be a better name. In (**13**), an all-*trans* or zig-zag conformer, there is a direct interaction between the orbitals on the carbon atoms (rear lobes) to which the coupled protons are bonded, resulting in a relatively large positive ^4J(H,H). Indirect mechanisms are associated with $1 \rightarrow 2'' \rightarrow 3$ and $1 \rightarrow 2''' \rightarrow 3$, vicinal–vicinal, and with $1 \rightarrow 2 \rightarrow 3$ or $1 \rightarrow 2' \rightarrow 3$, geminal–vicinal, interactions in (**11**); the latter are difficult to evaluate. The indirect mechanisms can contribute to ^4J(H,H) with either sign, so that ^4J(H,H) can be positive or negative,[11] depending on the dihedral angles θ and $z\theta'$. In (**14**), the value of ^4J(H,CH_3) is large, corresponding to $\theta = 180^\circ$.

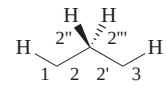

(**11**)

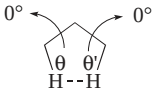

(**12**)

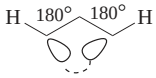

(**13**)

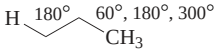

(**14**)

A recent analysis (Schaefer et al., 1993) of the ^{1}H NMR spectrum of 2-phenyl-1,3-dithiane, (**15**), illustrates the stereochemical dependence of ^4J(H,H). The approximate torsion (dihedral) angles are given in (**15**). Note the positive shift of ^4J(H,H) as HCSCH, containing the heteroatom, sulfur, replaces the propanic fragment. A heteroatom attached to the propanic fragment can also alter ^4J. Such substituent perturbations complicate stereochemical assignments and present challenges to the theorist [in fact, the positive shift noted for (**15**) can be reproduced with the INDO MO FPT formalism,[12] which takes a number of coupling mechanisms into account]. In principle, ^4J(H,H) is useful in the stereochemical analysis of other six-membered alicyclic rings which can occur in sugars and steroids, for example. Another example is provided[13] by the five-membered ring in the anhydronucleoside (**16**). The signs and magnitudes of ^4J(H,H) are related to torsion angles[14] in the furanose ring. Also, coupling constants over five bonds exist between H-1′ and the methylene protons in (**16**).

As the molecular mass increases, the ^{1}H NMR spectra become very complex and the peak widths also increase due to unresolved long range coupling constants and to shorter relaxation times. Nevertheless, the presence of ^4J(P,H), as in the nucleotide (**17**) and whose magnitude is determined[15] by the geometry of the P–O–C-5′–C-4′ fragment, allows[15] the assessment of ^3J(H-4′,H-5′) and ^3J(H-4′,H-5″) in a double-helical dodecanucleotide (a DNA fragment). The vicinal coupling constants help in fixing the torsion angle in the fragment O–C-5′–C-4′–C-3′.

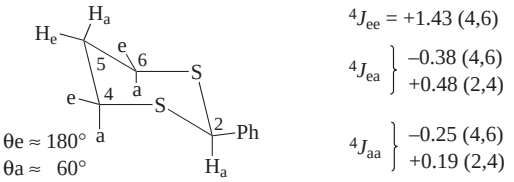

(15)

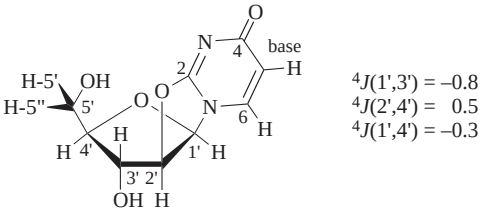

(16)

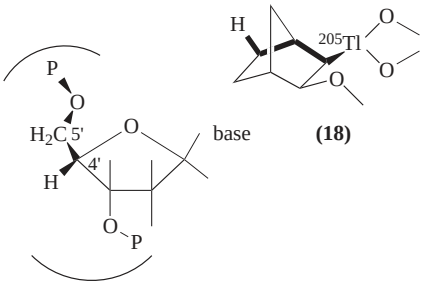

(17)

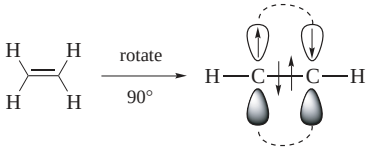

(19)

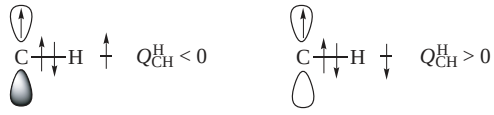

(20) **(21)**

In rigid bicyclic systems,[5] extended or multiple, all-*trans*, coupling pathways can exist, so that $^{4,5,6}J$(H,H) can be large [propanic (**11**), butanic, and pentanic paths]. Furthermore, C–H, F–H, P–H, F–F, Tl–H, and C–C long range couplings are known in such molecules; some of these are large for conformations analogous[16] to (**12**) (proximate couplings). Many are tens of hertz in magnitude, or even as large[17] as 820 Hz as in (**18**), a norbornane derivative; the electron density at the thallium nucleus is very large for this nucleus of atomic number 81.

5 $^nJ(n \geq 4)$ IN UNSATURATED MOLECULES

5.1 Alkenes and Acetylenes: σ, π Model

In unsaturated molecules such as alkenes and acetylenes the valence electrons are usually considered to be of two different types: σ and π electrons. Thus, in planar ethylene (**19**), the double bond between the carbon atoms is thought of as a single σ bond and a single π bond; the latter is formed from electrons in p orbitals on the carbon atoms and yields maximum electron density above and below the plane of the molecule (the six nuclei lie in a plane in the most stable state of the molecule). This σ, π model has been very successful in the description of long range coupling constants although, again, it is a topic of critical discussion.[18]

The σ, π model of ^nJ begins with the recognition that the contact contribution depends on the probability that the electrons, involved in the transmission of ^nJ, are found at the sites of the coupled nuclei; the protons in ethylene, for example. However, electrons in π orbitals have a zero probability of being found at the nuclear sites—p orbitals have nodes in the plane of the nuclei.

This conundrum is resolved by the invocation of a σ, π spin polarization mechanism, rather similar to that involving the σ electrons in (**7**). The single p or π electron in (**20**) and (**21**) spin polarizes the σ electrons in the C–H bond and leads to an 'up' or a 'down' arrangement of the proton spin (crossed arrow). By Hund's rule, (**20**) is energetically favored. This fact is represented by the σ, π hyperfine interaction parameter $Q^{\mathrm{H}}_{\mathrm{CH}} < 0$ (in the subscript the first symbol represents the atom carrying the unpaired spin, the two subscripts together indicate the bond being spin polarized, and the superscript designates the nucleus coupled to the unpaired electron). $Q^{\mathrm{H}}_{\mathrm{CH}}$ is negative by definition—the p electron and the proton spins are parallel. Consolidation of this fact with the bonding in ethene (**22**) where the π electrons are spin correlated (paired off), leads to a π electron spin coupling pathway as shown, in addition to that through the σ bond. It is then found that $^3J^{\pi} \propto Q^{\mathrm{H}}_{\mathrm{CH}} \times Q^{\mathrm{H}}_{\mathrm{CH}}$, yielding about +1.5 Hz, which adds to $^3J^{\sigma}$ which is an order of magnitude larger, to give $^3J^{\pi} + {}^3J^{\sigma}$.

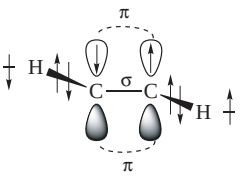

(22)

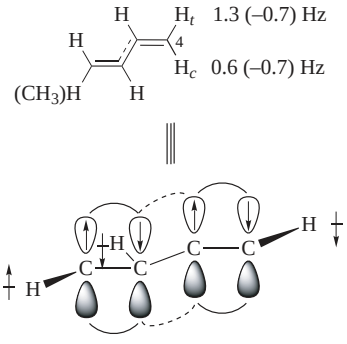

(23)

Now, consider butadiene (**23**). The bond between the middle carbon atoms is not a single bond but has considerable 'double-bond character'; it is said to have a mobile bond order between zero and one, a result of the relatively easy delocalization of π electrons (unlike σ electrons). The magnitude of $^5J^{\pi}$ depends on how strongly the p electrons at the central carbon atoms [dashed lines in (**23**)] are spin correlated. The

hyperfine interaction at each end of the coupling pathway provides the link between the σ and π electron systems. Note that $^5J^\pi > 0$, the proton spins in (**23**) being antiparallel, even though $Q^{\mathrm{H}}_{\mathrm{CH}} < 0$. The sign of J^π depends on the number of intervening bonds, being positive for n odd and negative for n even. Note also that this mechanism implies equal ^5J(H,H) values in (**23**), i.e. the values are independent of the configuration at C-4. The observation that ^5J_t is 1.3 Hz whereas ^5J_c is 0.6 Hz implies a contribution to ^5J_t from the σ electrons, $^5J^\sigma$. The coupling mechanisms discussed above for ^4J(H,H) allow for two vicinal–vicinal interactions involving the central C–C bond in each and thus are expected to contribute most efficiently for an all-*trans* arrangement of the intervening bonds [extend structure (**13**)].

An estimate of $^5J^\pi$ can be made using the 'methyl group replacement technique', the use of which involves the following argument. In (**24**), a proton in one C–H bond of a methyl group has a positive hyperfine interaction $Q^{\mathrm{H}}_{\mathrm{CCH}} \rangle 0$ with the electron in the p orbital on the neighboring carbon atom [a so-called β-interaction, contrasting with the α-interaction in (**20**)]. Furthermore, $Q^{\mathrm{H}}_{\mathrm{CCH}} \propto \sin^2\theta$ so that $Q^{\mathrm{H}}_{\mathrm{CCH}}$ is largest when the sigma C–H bond lies in the plane containing the p orbital (best overlap). For a rotating methyl group, with three C–H bonds, $\sin^2\theta$ has an average value of 0.5.

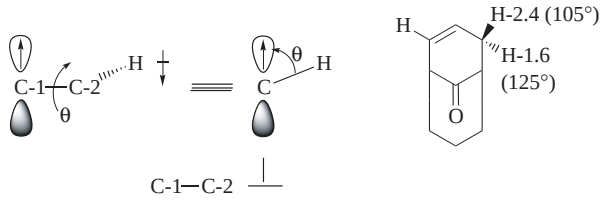

(24) **(26)**

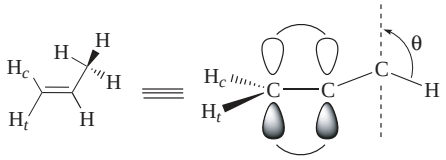

(25)

It then turns out that $Q^{\mathrm{H}}_{\mathrm{CCH}} \approx -Q^{\mathrm{H}}_{\mathrm{CH}}$, with the consequence that $^6J^\pi$(H,CH_3) $\approx -\ ^5J^\pi$(H,H). From the data on (**23**) it follows that $^5J^\pi \approx 0.7$ Hz and $^5J^\sigma \approx 0.6$ Hz. The model is not exact, of course, but has been used to estimate π electron contributions to ^nJ in a variety of molecules, including cumulenes ($CH_2{=}C_n{=}CH_2$) and acetylenes [HC–$(C{\equiv}C)_n$–CH]. In such molecules, the extended spin correlation of the π electrons is relatively high,[2] leading to significant ^nJ for n as large as 9. Note that, as the mobile bond order of the central C–C bond in (**23**) decreases (dashed lines), $^5J^\pi$ will also decrease in magnitude. In this sense $^nJ^\pi$ is a measure of π electron delocalization: the mobile bond order in ethene (**22**) is unity, is about 0.4 for the central C–C bond in (**23**), and is less than unity for the other two C–C bonds. The use of ^nJ(H, CH_3) in testing the extent of delocalization in various molecules is described in a later section of this article.

5.2 Allylic and Homoallylic Couplings: ^4J(H,H) and ^5J(H,H)

The $\sin^2\theta$ dependence of $Q^{\mathrm{H}}_{\mathrm{CCH}}$ has many stereochemical applications, only two examples of which can be given here. ^4J_c(H,CH_3) $\equiv\ ^4J_c$ and ^4J_t(H,CH_3) $\equiv\ ^4J_t$ in propene (**25**) are called 'allylic coupling constants' and have values of -1.7 and -1.3 Hz, respectively. If the σ component of ^4J were to vanish and the conformation of the methyl group was exactly the same as that in (**25**), but with rapid interconversion so that each C–H bond sampled each of the three values of θ (namely 0°, 120°, and 240°), then $\langle\sin^2\theta\rangle$, the average value of $\sin^2\theta$, would be 0.5. Actually, for free rotation of the methyl group, $\langle\sin^2\theta\rangle$ is also 0.5, a consequence of the three-fold symmetry of a methyl group (a CH_2X group has lower symmetry, with important consequences for the derivation of internal rotational potentials, as described below). It would follow that ^4J is a measure of the magnitude of $^3J^\pi$ in ethene ($Q^{\mathrm{H}}_{\mathrm{CH}} \approx -Q^{\mathrm{H}}_{\mathrm{CCH}}$).

However, because in (**25**) $^4J_c \neq\ ^4J_t$, the argument is only semiquantitative. The inequality may be attributable to the presence of $^4J^\sigma$. Thus, if the all-*trans* arrangement [see (**13**)] is most effective for $^4J^\sigma$, giving a positive contribution to ^4J_t, a rough assessment of $^3J^\pi$ in ethene would be +1.7 Hz. The true situation is more complex;[11] nevertheless, large negative ^4J values are expected and observed for $\theta \approx 90°$. An example in which $^4J \propto \sin^2\theta$ is (**26**), where the ratio of the two coupling constants is 1.5, as compared with a ratio of 1.4 for the corresponding values of $\sin^2\theta$. To within the combined errors of the J values and the two angles, the relationship is very likely satisfied.

Homoallylic coupling constants ^5J(H,H) arise from protons in C–H bonds flanking the double bond at both ends. Hence ^5J(H,H) $\propto Q^{\mathrm{H}}_{\mathrm{CCH}} Q^{\mathrm{H}}_{\mathrm{CCH}} \propto \sin^2\theta \sin^2\theta'$, where the two torsional angles θ and θ' are analogous to those in (**25**).

A somewhat subtle stereochemical problem involves the degree of nonplanarity of 1,4-dihydrobenzene (**27a**)–(**27c**). If the equivalent (isoenergetic), nonplanar conformers (**27a**) and (**27c**) are the most stable ones, they may interconvert via the planar conformer (**27b**). The molecule is then said to undergo 'conformational isomerization by inversion'. The potential energy function opposing inversion has two minima, as indicated; the speed of inversion depends on how the available thermal energy compares to the potential hindering the inversion. Alternatively, the most stable conformer may be (**27b**). Then the internal potential has a single minimum; nonplanar conformers occur with decreasing probabilities as the bending angle α deviates increasingly from 180°.

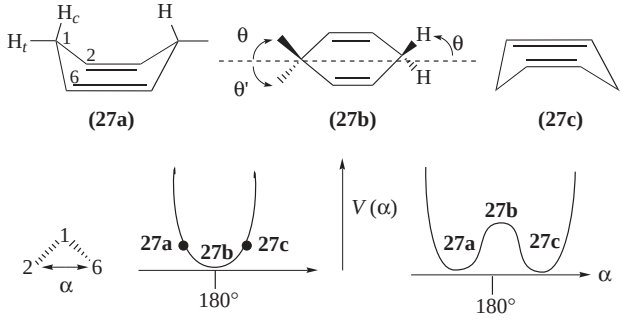

(27a) **(27b)** **(27c)**

In (**27b**), the angles θ and θ' are 60° for an idealized geometry, but are not equal in (**27a**). Hence ${}^5J_c = J_t$ in (**27b**), but ${}^5J_c \neq {}^5J_t$ in (**27a**). In solution ${}^5J_c = 1.2\ {}^5J_t$, from which it might be deduced[19] that α is about 172°. The derivation of α assumes two rigid forms (**27a**) and (**27c**), a so-called 'two-site analysis' in which the measured values of ${}^5J_c$ and ${}^5J_t$ are simple averages of their values in these conformers. However, another interpretation holds that torsion about the C–C bonds of a stable, planar (**27b**), producing nonplanar conformers, would also cause the inequality ${}^5J_c > {}^5J_t$, so that either potential curve could correspond to observation. In fact, today the available evidence from various sources is that (**27b**) is the stable form.

6 AROMATIC MOLECULES

6.1 Some Coupling Mechanisms

In benzene (**28**) the indicated ${}^{3,4,5}J$(H,H) are of obvious use in assigning substitution sites in derivatives of (**28**). ${}^4J$(H,H), corresponding to an all-*trans* arrangement, has only a small π component. The ${}^6J$(**H**,C**H**$_3$) value of −0.60 Hz in toluene (**29**) indicates that ${}^5J$(H,H) in (**28**) is mainly J^π, while the ${}^7J$(C**H**$_3$,C**H**$_3$) value of −0.60 Hz in (**30**) implies $Q^{\mathrm{H}}_{\mathrm{CH}} = -Q^{\mathrm{H}}_{\mathrm{CCH}}$ in these compounds. Furthermore,[20] in (**31**), which represents derivatives of anisole (X = O), thioanisole (X = S), and ethylbenzene (X = CH_2), it is true that ${}^5J$(C,C) = −1.50 ${}^6J$(C,H) + 0.02 and ${}^6J$(C,C) = −0.37 ${}^5J$(C,C) + 0.02. The signs and relative magnitudes of the corresponding hyperfine interaction parameters near C-4, as in (**32**), are then $Q^{\mathrm{H}}_{\mathrm{CH}} = -Q^{\mathrm{H}}_{\mathrm{CCH}}$, $Q^{\mathrm{C}}_{\mathrm{CH}} = -1.50\,Q^{\mathrm{H}}_{\mathrm{CH}}$, and $Q^{\mathrm{C}}_{\mathrm{CC}} = 0.56\,Q^{\mathrm{H}}_{\mathrm{CH}}$. Such relationships also hold for other nuclei in the side chain, such as ^{19}F, typified by (**33**), showing that the π-electron mechanism is dominant for the indicated ${}^{5,6,7}J$ couplings and that they depend on $\sin^2\theta$.

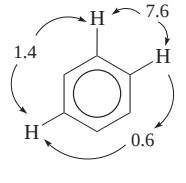

(28)

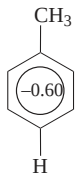

(29)

(30)

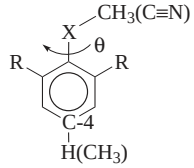

X = O, S, CH_2
R = H, F, Cl, Br

(31)

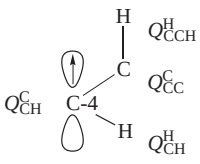

(32)

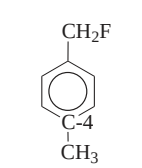

^7J(F, H) = 2.1$_5$
^6J(F, C) = 1.1$_5$
^5J(F, C) = 3.1$_5$

(33)

6.2 Internal Rotational Potentials from Long-Range Coupling Constants

When conformations are well defined, that is when the barrier to interconversion between conformers is large compared to the thermal energies (see Section 1), the angle dependence of a long-range coupling constant is a good indicator of conformation. An example from aromatic chemistry is a benzaldehyde derivative (**34**). ${}^5J$(**H**,C**H**O) is apparently a ${}^5J^\sigma$ and, as such, is large for the all-*trans* pathway. If the indicated J values are correct, then measurement of ^{5}J(**H**,C**H**O) yields the populations of (**34a**) and (**34b**) by simple proportion. This simple strategy works well because nonplanar conformers are negligible at ambient temperatures.

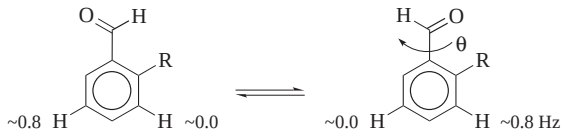

(34a) **(34b)**

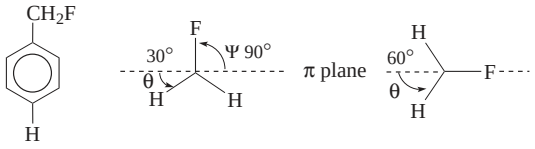

(35a) **(35b)** **(35c)**

Suppose, however, that the barrier to rotation about the ring–CHO bond were very small compared with thermal energies. In such circumstances the idea of one or a few conformations would lose utility because many angles θ would be of similar probability. In the limit of a zero barrier, an infinite number of conformations (all values of θ) would be present.

When the barrier to internal rotation about a bond is small, it is advantageous to discuss stereochemical problems in terms of the internal rotational potential $V(\theta)$, which gives the relative energy of the molecule at each value of θ. Can long range coupling constants be used to determine $V(\theta)$? In some instances, certainly. These statements are best illustrated with one of the many examples available.

Consider benzyl fluoride (**35**) and the potential hindering rotation about the exocyclic C–C bond. If (**35b**) and (**35c**) represent extrema in the potential, the barrier $V(\psi)$ [or $V(\theta)$] is said to be two-fold because it repeats itself twice between 0° and 360° [see (**36**)]. The barrier turns out to be solvent dependent,[21] which is an advantage in the following logic. One has ${}^6J$(F,H) = ${}^6J^{\mathrm{F}}_{90}\langle\sin^2\psi\rangle$ and ${}^6J$(H,H) = ${}^6J^{\mathrm{H}}_{90}\langle\sin^2\theta\rangle$; here ${}^6J_{90}$ is the value when C–F or C–H lies 90° out of the benzene ring plane, and the angle brackets indicate an average over the internal motion controlled by the potential. The roughly tetrahedral geometry at the carbon atom of the CH_2F group implies $\langle\sin^2\theta\rangle = 0.75 - 0.5\langle\sin^2\psi\rangle$. It follows that measurements of the two coupling constants in two different solvents yield both the ${}^6J_{90}$ values as well as $\langle\sin^2\psi\rangle$ and $\langle\sin^2\theta\rangle$ in each solvent. The latter can be calculated[22] by quantum mechanical or classical methods as a function of the internal potential, V_2. A comparison between the theoretical $\langle\sin^2\psi\rangle$, say, and its experimental values yields V_2 in the two solvents. Together with measurements of ${}^5J$(F,C), also a J^π, one finds that V_2 is 3.2 kJ mol^{-1} in very polar solvents and 0.7 kJ mol^{-1} in nonpolar solvents. Curve (a) in Figure 2 describes the potential form. Extrapolation to the vapor phase implies that the potential is now as in curve

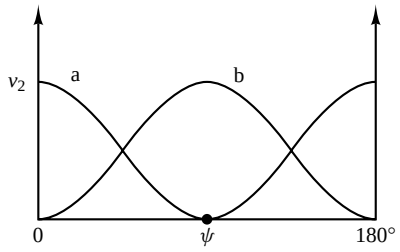

Figure 2 Twofold internal rotational potential, as applicable to (**35b**)

(b) in Figure 2, which is qualitatively confirmed by high-level molecular orbital computations on the free molecule. The change in phase of the potential is of interest in the theory of solutions. A phase change can also be induced by substituents on the ring. Each derivative will possess its own, distinctive, solvent dependent, internal rotational potential, the determinations of which present as yet unmet challenges for the various spectroscopic and theoretical methods (***Liquid Crystalline Samples: Structure of Nonrigid Molecules***).

6.3 Stereospecific Long Range Coupling Constants in Extended Aromatic Molecules

Examples of ^nJ with n as large as 11 are provided by ^nJ(F,F) and ^nJ(F,C) in (**36**) and (**37**). It is known that the torsion angle θ in (**37**) is effectively 90°, the two benzene planes being perpendicular, and that it is near 45° in (**36**). Note that $^{7,8}J$(F,C) and ^9J(F,F) vanish when $\theta \approx 90°$, indicating that π electron spin correlation has been broken across the central C-4–C-5 bond; there is no π electron conjugation or delocalization between the two aromatic moieties in (**37**). The finite values of these ^nJ can be related[23] to $\cos^2\theta$ in (**36**), as can ^{11}J(F,F) when the fluorine atoms in (**36**) are replaced[24] by CH_2F groups. Of course, ^{11}J(F,F) will, in addition, be proportional to $\sin^2\psi$, where ψ is the angle by which the C–F bond turns out of the benzene plane, as in (**35b**); thus $^{11}J(\text{F,F}) \propto \sin^2\psi\cos^2\theta$.

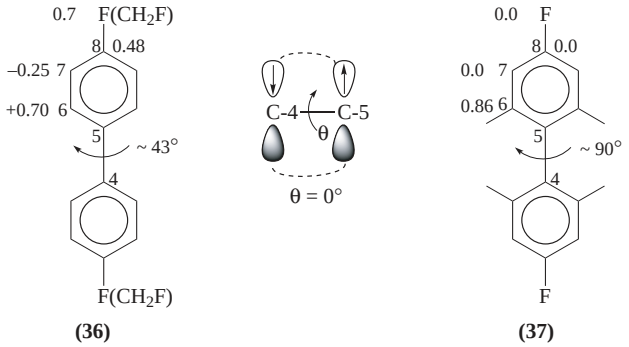

(36) **(37)**

A composite mechanism must also operate for ^6J(F,C) at site 6 in (**36**) and (**37**) because it is larger in (**37**). The C-5–C-6 bond undergoes a hyperfine interaction with the π electron at C-4, characterized by $Q^{\text{C}}_{\text{CCC}}$ and analogous to $Q^{\text{H}}_{\text{CCH}}$ in (**32**), which is maximal in (**37**) and hence varies as $\sin^2\theta$. The other part of the mechanism varies as $\cos^2\theta$, just as for $^{7,8}J$(F,C); hence $^6J(\text{F,C}) = A\sin^2\theta + B\cos^2\theta$. Such composite mechanisms also occur in other conjugated systems, an excellent example being styrene,[25] where an alkenic group is bonded to an aromatic system.

6.4 Electron Delocalization and Long Range Coupling Constants

Aromaticity is related to the delocalization of π electrons, leading to mobile bond orders. The structure and reactivity of a molecule are sensitive to the extent of delocalization. There are various definitions of mobile bond order, but all agree that the bond order is zero for a C–C bond, unity in ethene (**19**) or propene (**25**) and 2 for a triple bond, as in (**4**). Clearly, the allylic $^4J(\text{H,CH}_3)$ in (**25**) depends on the π electrons. If delocalization were to decrease the mobile bond order, then the magnitude of $^4J(\text{H,CH}_3)$ would also decrease. This idea has been exploited, particularly by Sternhell and co-workers,[26] to determine the mobile bond orders in aromatic systems; however, in this case ^4J is called a 'benzylic J'. In (**38**)–(**45**), the degree of delocalization is evident from the indicated ^4J. If -0.70 Hz in (**41**) is a measure of the delocalization of the π electrons in the prototypical aromatic molecule, benzene, then in (**42**), for example, some localization (double bond fixation) has been induced by the strong conjugation between the hydroxyl and nitro groups. In the cyclophane (**45**) the benzene moiety is strongly nonplanar, yet delocalization of the π electrons is still substantial.

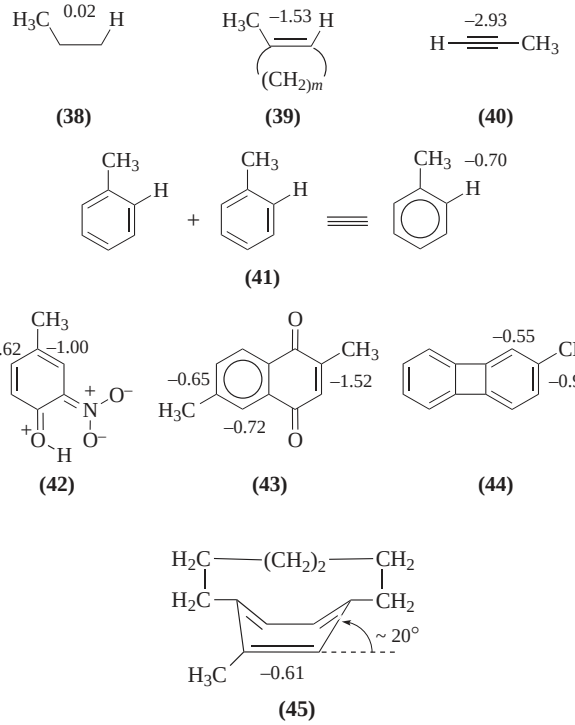

(38) **(39)** **(40)**

(41)

(42) **(43)** **(44)**

(45)

Of course, $^7J(\text{CH}_3,\text{CH}_3) \equiv {}^7J = 0.60$ Hz in 1,4-dimethylbenzene (**30**) is also a measure of delocalization of π electrons. The pyridine derivatives (**46**)–(**48**) are delocalized, whereas the benzoquinone (**49**) and the borazine (**50**) are not. Borazine itself is isoelectronic and isostructural with benzene and is sometimes considered as an inorganic analog of benzene.

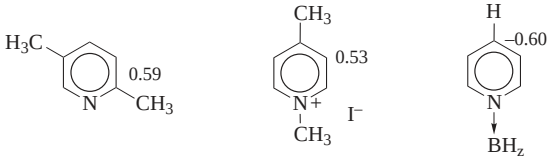

(46) **(47)** **(48)**

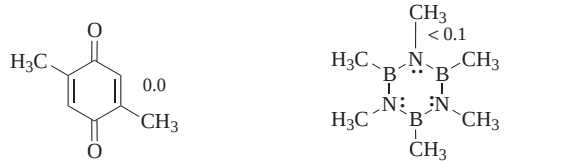

(49) **(50)**

6.5 ^4J(C,C) in Some Condensed Aromatics

^4J(C,C) in condensed aromatics such as (**51**)–(**54**) are thought[27] to be transmitted mainly via the π electrons, which are delocalized to a large extent. ^4J(C,C) was measured by enriching with ^{13}C at the position marked by an asterisk; the sign of ^4J(C,C) is known only in the case where it is given in the structures. The generalized mobile bond order between the coupled sites vanishes for these even alternant hydrocarbons,[28] which suggests very little spin correlation of the electrons at these sites. Furthermore, the atom–atom polarizabilities, which might in this connection be thought of as indicating how the π electron at the second site responds to a perturbation at the first site, are also very small for the indicated atoms. However, the atom–atom polarizability involving the penultimate site in the shortest coupling path, indicated by solid triangles in (**51**) and (**52**), is relatively large except for the ^4J of 0.3 Hz in (**53**) and that of 0.0 Hz in (**54**). This observation may represent an accidental coincidence; it has not been discussed in the scientific literature, but may be worth further study. It may be noted that $Q^{\mathrm{C}}_{\mathrm{C'C}}$ is sizeable and negative, and contributes to a negative ^4J(C,C) because it measures the hyperfine interaction of a π electron at the nearest carbon atom (solid spade) with the ^{13}C nucleus at the coupled site (solid circle). In this connection it would be useful to have many more ^nJ(C,C) values. There now exist methods[29] for finding ^nJ for unenriched molecules.

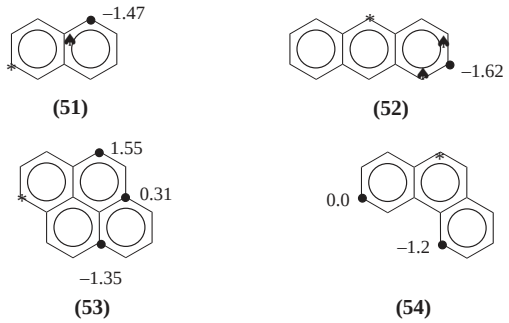

(51) **(52)** **(53)** **(54)**

6.6 A Unique Conformation Determined from ^nJ(H,H)

Were a chemist asked to predict the conformation of 2-hydroxythiophenol (**55**) in solution, he or she might well suggest an equilibrium among three planar structures, HS···OH, HS···HO, and SH···OH. This suggestion depends on the knowledge that conjugation of the lone pairs of electrons on oxygen or sulfur with the aromatic π electrons creates a mobile bond order, C···S and C···O (partial double bonds), leading to planar structures with concomitant barriers to rotation about the exocyclic bonds. A more sophisticated chemist might also suggest that the HS···HO structure would be most stable because the electrically polar $O^- - H^+$ bond would seek the lone pair on sulfur, forming an intramolecular hydrogen bond, thereby stabilizing this structure. Indeed, the vibrational spectrum of (**55**) in CCl_4 solution has been interpreted in terms of an equilibrium among three planar forms.

^5J(OH, SH), –0.14; ^5J(SH, H-3), 0.36;
^4J(OH, H-3), –0.11; ^5J(SH, H-5), 0.39

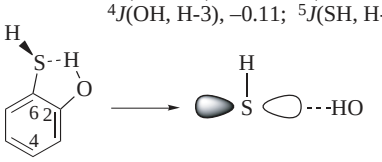

^6J(OH, H-5), 0.00; ^4J(SH, H-6), –1.07;
^5J(OH, H-4), 0.42; ^6J(SH, H-4), –0.96;
^5J(OH, H-6), 0.00

(55)

On analysis,[30] the ^{1}H NMR spectrum of such a solution yields nine ^nJ(H,H) ($4 \leq n \leq 6$) for protons in the side chains. These demonstrate unequivocally that the perpendicular conformation depicted in (**55**) is dominant. In view of the previous discussions, the large magnitudes of ^nJ(SH,H) and the stereospecific ^5J(OH,H-4) are consistent only with the indicated conformation, the one in which the S–H bond lies in a plane roughly perpendicular to that of the rest of the molecule. The polar O–H bond twists the 3p lone pair into the molecular plane, forming a hydrogen bond, and the S–H bond must therefore twist out of that plane. The formal ^5J(OH,SH) is an example of one kind of proximate J, in this case most probably being transmitted via the hydrogen bond.

7 PROXIMATE LONG RANGE COUPLING CONSTANTS

The stereochemistry of a molecule may be such that two of its fragments, while separated by many formal bonds, may still be proximate. Couplings between nuclei in the different fragments[6,31] are called 'proximate' (originally, 'through space'). An example is the ^5J(F,F) of 174 Hz in (**56**),[32] which is thought to be transmitted by the interaction of the lone pair electrons on the two fluorine atoms. The internuclear distance is well within the sum of the van der Waals radii of the atoms. Another example is (**57**) where the proximity mechanism is relayed via an H–F overlap to yield a ^4J(F,C) the magnitude of which decays exponentially with the H–F distance.[33] The scientific literature abounds with examples of proximate coupling constants between many different pairs of nuclei. Their stereochemical use is obvious. (See also ***Coupling Through Space in Organic Chemistry***)

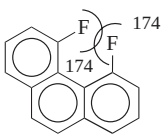

(56)

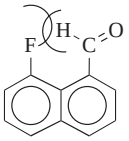

(57)

The most striking example[34] is a J of about 17 Hz between fluorine nuclei of 5-fluorotryptophan residues placed in the enzyme dihydrofolate reductase. The fluorine atoms are separated by dozens (n) of covalent bonds, yet must approach each other to within about 0.3 nm, a consequence of the folding pattern of the protein. The value of n may well be a record.

8 THE FUTURE OF LONG RANGE COUPLING CONSTANTS

One of the goals of mathematical chemistry is the computation of accurate stereochemical properties of molecules. Great progress has been made towards this goal, particularly for molecules for which the accurate measurement of small ^nJ values is feasible. As computers become faster, the general computation of ^nJ for reliable theoretical stereochemistries may also become a reliable procedure. Until then, measurements of ^nJ will likely retain their empirical utility. Furthermore, ^nJ values are normally measured in solution, in which perturbations by solvent molecules of conformational equilibria can be large; the ^nJ values may serve as checks of the theoretical descriptions or models of such perturbations.

9 RELATED ARTICLES

Analysis of High-Resolution Solution State Spectra; Analysis of Spectra: Automatic Methods; Coupling Through Space in Organic Chemistry; Double Resonance; Electron–Nuclear Hyperfine Interactions; Fluxional Motion; Hydrogen Bonding; Indirect Coupling: Intermolecular and Solvent Effects; Indirect Coupling: Theory and Applications in Organic Chemistry; Magnetic Equivalence; Organic Chemistry Applications; Quantitative Measurements; Recording One-Dimensional High Resolution Spectra; Vicinal ^{1}H, ^{1}H Coupling Constants in Cyclic π-Systems.

10 REFERENCES

1. L. M. Jackman and S. Sternhell, *Nuclear Magnetic Resonance Spectroscopy in Organic Chemistry*, 2nd edn, Pergamon, Oxford, 1969.
2. M. Barfield and B. Chakrabarti, *Chem. Rev.*, 1969, **69**, 757.
3. J. Kowalewski, *Prog. NMR Spectrosc.*, 1977, **11**, 1; *Ann. Rep. NMR Spectrosc.*, 1982, **12**, 81.
4. P. E. Hansen, *Prog. NMR Spectrosc.*, 1981, **14**, 175.
5. A. P. Marchand, *Stereochemical Applications of NMR Studies in Rigid Bicyclic Systems*, Verlag Chemie, Deerfield Beach, FL, 1982.
6. R. H. Contreras, M. A. Natiello, and G. E. Scuseria, *Magn. Reson. Rev.* 1985, **9**, 239.
7. L. B. Krivdin and E. W. Della, *Prog. NMR Spectrosc.*, 1991, **23**, 301.
8. R. H. Contreras, M. C. Ruiz de Azúa, C. G. Giribet, G. A. Aucar, and R. Lobayan de Bonczok, *J. Mol. Struct. (Theochem)*, 1993, **284**, 249.
9. M. Barfield and M. Karplus, *J. Am. Chem. Soc.*, 1969, **91**, 1.
10. P. J. Mitchell, L. Phillips, S. J. Roberts, and V. Wray, *Org. Magn. Reson.*, 1974, **6**, 127.
11. M. Barfield, A. M. Dean, C. J. Fallick, R. J. Spear, S. Sternhell, and P. W. Westerman, *J. Am. Chem. Soc.*, 1975, **97**, 1482.
12. J. A. Pople and D. L. Beveridge, *Approximate Molecular Orbital Theory*, McGraw-Hill, New York, 1970.
13. F. E. Hruska, J. G. Dalton, and M. Remin, *Can. J. Chem.*, 1979, **57**, 2191.
14. D. B. Davies, *Prog. NMR Spectrosc.*, 1978, **12**, 135.
15. R. H. Sarma, R. J. Mynott, D. J. Wood, and F. E. Hruska, *J. Am. Chem. Soc.*, 1973, **95**, 6457.
16. K. V. R. Chary, V. K. Rastogl, and G. Govil, *J. Magn. Reson., Ser. B*, 1993, **102**, 81.
17. F. A. L. Anet, *Tetrahedron Lett.*, **1964**, 3399.
18. P. A. Schultz and R. P. Messmer, *J. Am. Chem. Soc.*, 1993, **115**, 10 925; 10 938; 10 943.
19. E. W. Garbisch, Jr, and M. G. Griffith, *J. Am. Chem. Soc.*, 1968, **90**, 3590.
20. T. Schaefer and G. H. Penner, *Can. J. Chem.*, 1988, **66**, 1229.
21. T. Schaefer, C. Beaulieu, R. Sebastian, and G. H. Penner, *Can. J. Chem.*, 1990, **68**, 581.
22. W. J. E. Parr and T. Schaefer, *Acc. Chem. Res.*, 1980, **13**, 400.
23. T. Schaefer, J. Peeling, and G. H. Penner, *Can. J. Chem.*, 1986, **64**, 2162.
24. L. Ernst and S. Pulmann, *Org. Magn. Reson.*, 1981, **16**, 63.
25. M. Barfield, C. J. Macdonald, I. R. Peat, and W. F. Reynolds, *J. Am. Chem. Soc.*, 1971, **93**, 4195.
26. J. E. Gready, T. W. Hambley, K. Kakiuchi, K. Kobiro, S. Sternhell, C. W. Tansey, and Y. Tobe, *J. Am. Chem. Soc.*, 1990, **112**, 7537.
27. J. L. Marshall, *Carbon–Carbon and Carbon–Proton NMR Couplings: Applications to Organic Stereochemistry and Conformational Analysis*, Verlag Chemie, Deerfield Beach, FL, 1983.
28. C. A. Coulson and A. Streitwieser, Jr, *Dictionary of π Electron Calculations*, W. H. Freeman, San Francisco, 1965.
29. É. Kupče and R. Freeman, *J. Magn. Reson., Ser. A*, 1993, **104**, 234.
30. T. Schaefer, T. A. Wildman, and S. R. Salman, *J. Am. Chem. Soc.*, 1980, **102**, 107.
31. J. Hilton and L. H. Sutcliffe, *Prog. NMR Spectrosc.*, 1975, **10**, 27.
32. F. B. Mallory, E. D. Luzik, Jr, C. W. Mallory, and R. J. Carroll, *J. Org. Chem.*, 1992, **57**, 366.
33. I. D. Rae, A. Staffa, A. C. Diz, C. A. Giribet, M. C. Ruiz de Azúa, and R. H. Contreras, *Austr. J. Chem.*, 1987, **40**, 1923.
34. B. J. Kimber, J. Feeney, G. C. K. Roberts, B. Birdsall, D. V. Griffiths, A. S. V. Burgen, and B. D. Sykes, *Nature*, 1978, **271**, 184.

Biographical Sketch

Theodore P. Schaefer. *b* 1933. B.Sc., 1954, M.Sc., 1955, chemistry, University of Manitoba, Canada, D. Phil, 1958, University of Oxford, (supervisor, R. E. Richards). Faculty in Chemistry, University of Manitoba, 1958–present. Approx. 300 publications. Research interests: very high resolution NMR yielding precise long-range spin–spin coupling constants and their relationship to conformation and internal motions in highly flexible molecules.

Through-Bond Experiments in Solids

Dimitris Sakellariou and Lyndon Emsley

Laboratoire de Stéréochimie et des Interactions Moléculaires, Ecole Normale Supérieure de Lyon, Lyon, France

1 Introduction 1
2 Using Homonuclear *J* Couplings 1
3 Using Heteronuclear *J* Couplings 6
4 Related Articles in Volumes 1–8 15
5 References 15

1 INTRODUCTION

In modern solid-state NMR, resolution and sensitivity can be enhanced by means of cross polarization (CP) (see **Cross Polarization in Solids,** Volume 3, **Cross Polarization in Rotating Solids: Spin-1/2 Nuclei,** Volume 3), spin decoupling (see **Line Narrowing Methods in Solids,** Volume 4) and magic angle spinning (MAS) (see **Magic Angle Spinning,** Volume 5). Spectra of either crystalline or amorphous samples can be recorded. The assignment of these spectra is usually performed on the basis of chemical shift considerations in conjunction with multidimensional correlation experiments relying mostly on the use of dipolar couplings.

Due to their large size, dipolar couplings are the obvious interaction to use in solid-state NMR in order to perform coherence transfer and thus correlate nuclei. Thus, a large number of methods have been developed in order to reintroduce heteronuclear or homonuclear dipolar couplings under magic angle spinning (see **Homonuclear Recoupling Schemes in MAS NMR,** Volume 4). Since dipolar coupling is a through-space interaction, these methods yield information about short and long range distances. In liquids, analogous experiments using the nuclear Overhauser effect (NOE) (see **Nuclear Overhauser Effect,** Volume 5) are the basic components for molecular structure determination (see **Protein Structures: Relaxation Matrix Refinement,** Volume 6).

In this entry we present an overview of techniques analogous in many respects to some liquid-state NMR techniques (see **Polarization Transfer Experiments via Scalar Coupling in Liquids,** Volume 6), which make use of *scalar* couplings in solid-state NMR. Until the end of the 1990s, only highly mobile solids, such as plastic crystals, yielded spectra with enough resolution to observe directly scalar couplings.[1,2] In such compounds, the dipolar couplings are partially averaged, and the *J* couplings are naturally resolved; thus, liquid-like sequences perform reasonably well. On the other hand, in more ordinary organic compounds, where motion is reduced, the strong dipolar couplings (say 20 kHz) hide the much smaller *J* couplings (say 100 Hz).

As we show in the following, improvements in magic angle spinning and spin decoupling techniques[3–6] have led to reduced intrinsic linewidths, thereby making it possible to resolve homonuclear and heteronuclear scalar couplings. Under such conditions, techniques using scalar couplings have great potential for unambiguous spectral assignment, since the coherence transfer is performed by means of a through-bond interaction, and not through-space. Indeed, as in liquid-state NMR,[7] an ideal approach to structure determination exploits the complementarity of through-space and through-bond interactions by using through-bond techniques to establish an unambiguous assignment of the NMR spectra before using through-space interactions to determine three-dimensional structure (see **Biological Macromolecules: Structure Determination in Solution,** Volume 2) and dynamics (see Figure 1).

2 USING HOMONUCLEAR *J* COUPLINGS

For the moment $^{1}H–^{1}H$ *J* couplings (∼10 Hz) are too small compared to residual linewidths (at best ∼100 Hz) to be exploited to obtain correlations. However, homonuclear *J* couplings of nuclei such as ^{13}C, ^{31}P and ^{29}Si are large enough to be observed, and in this section we discuss experiments which make use of them.

2.1 ^{13}C Homonuclear Scalar Couplings

Because of the low (1.1%) natural abundance of ^{13}C, sensitivity is the primary problem when trying to observe carbon–carbon *J* couplings. There are some examples where experiments were successfully performed on natural abundance samples, but in general the techniques discussed below are aimed at (partially or fully) carbon-13 enriched samples. The size of the ^{1}J coupling constants between directly bonded nuclei, which depends on the hybridization of the carbon orbitals and on the nature of the substituents, is usually found

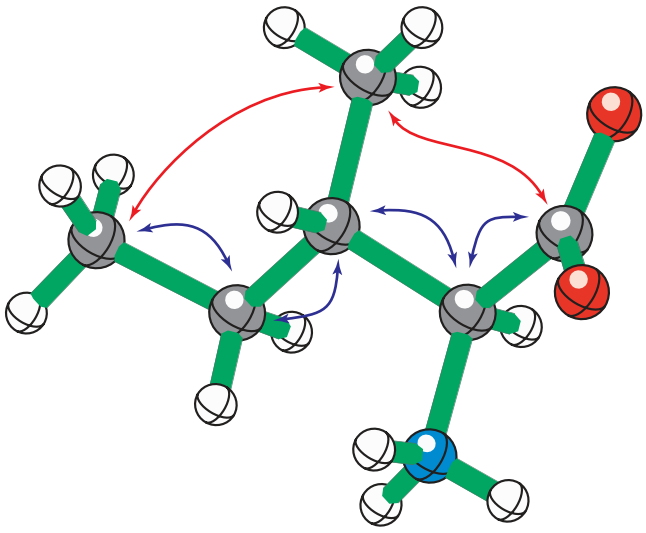

Figure 1 Through-bond correlations are necessary to assign the spectrum. Through-space correlations are used to establish the three-dimensional structure

between 35 and 75 Hz. ^2J and ^3J coupling constants are much smaller, typically between 0 and 5 Hz in liquids. The J coupling is thus usually approximately 40 times smaller than the dipolar coupling between two carbon nuclei (see **Dipolar & Indirect Coupling Tensors in Solids,** Volume 3).

2.1.1 *INADEQUATE*

The most straightforward approach to obtaining carbon–carbon through-bond connectivities is by using an INADEQUATE experiment adapted for solids. The liquid-state version of this experiment was first proposed by Bax, Freeman and co-workers[8,9] (see **INADEQUATE Experiment,** Volume 4). The INADEQUATE experiment selects only carbons that are directly bonded and filters any signals coming from isolated carbon nuclei (such as most of the natural abundance signal) The equivalent solid-state sequence is presented in Figure 2(a). Apart from the cross polarization period, and the fact that the sample is spinning at the magic angle, the experiment is completely analogous to its liquid-state cousin. After cross polarization from ^{1}H, the ^{13}C magnetization evolves during the delay 2τ under the homonuclear J coupling Hamiltonian

$$\mathcal{H} = \pi \sum_{i<j} J_{ij} 2I_{iz} I_{jz} \tag{1}$$

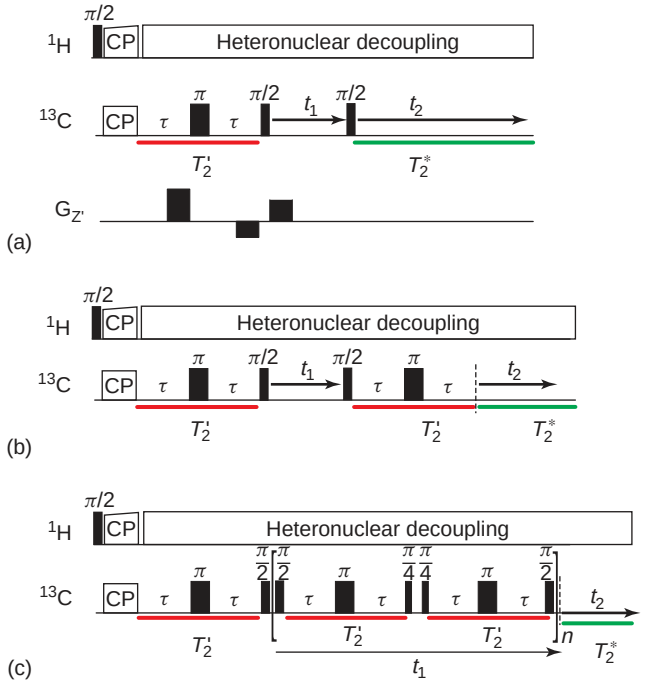

Figure 2 (a) The solid-state INADEQUATE pulse sequence. A 32 step phase cycle can be used, or alternatively the coherence transfer pathway can be selected using gradients. (b) Pulse sequence for solid-state refocused INADEQUATE. An extra Hahn echo period is added in order to refocus the signal after t_1. The τ delay should be synchronized to be an integral number of rotor periods. By T_2' and T_2^* we note the effective and the apparent damping time constants during the $\tau-\pi-\tau$ and the acquisition periods. (c) Pulse sequence for INADEQUATE-ce (see text for details)

Here we assumed that the chemical shift differences between the carbon nuclei are larger than the homonuclear J couplings, and thus only the truncated part of the Hamiltonian is effective. This is because the averaging of the chemical shift occurs over larger time scales than in the TOBSY scheme we analyze later.

The carbon–carbon homonuclear dipolar interactions, together with any anisotropies (chemical shift, or even J), are removed by fast MAS, and the isotropic chemical shift is refocused by the π pulse. The τ delay should be synchronized to be an integral number of rotor periods in order to average out completely the homonuclear carbon dipolar couplings. The heteronuclear dipolar and scalar interactions are averaged out by heteronuclear dipolar decoupling schemes, usually continuous wave (CW) decoupling, or the more efficient two-pulse phase modulation (TPPM) decoupling.[3] The solid-state INADEQUATE experiment is particularly simple to implement, and can be performed at high spinning frequencies.

The double quantum coherence created by the first carbon 90° pulse evolves during t_1, at a frequency which is the sum of the single-quantum frequencies of the two spins

$$\omega_{\mathrm{DQ}} = \omega_{\mathrm{SQ}}^A + \omega_{\mathrm{SQ}}^B \tag{2}$$

and is converted back into antiphase coherence by the last 90° pulse. This sequence leads to anti-phase lineshapes which were previously considered to be impractical in ordinary solids due to the residual linewidth. Nevertheless, such experiments were shown to be practical on plastic crystals[10,11] where the linewidth is only a few hertz, and, more recently, on *crystalline* organic compounds[12] where the linewidth in the one-dimensional carbon spectrum is comparable to the size of the scalar couplings.

The INADEQUATE experiment has been successfully applied to small molecules,[12] and an example of a two-dimensional spectrum is shown in Figure 3. Using fully labeled samples leads to a very good signal to noise ratio and, in this particular case, gradients were used to select the coherence transfer pathway in order to reduce the total experimental time (the spectrum was acquired with 10 mg of sample in 13 min). From the two-dimensional map, the atomic connectivity can be traced throughout the carbon skeleton in an unambiguous way. This experiment is sufficiently sensitive to obtain a spectrum of a powdered sample of *natural abundance* L-alanine with good signal to noise ratio over a weekend.[12]

Linewidths in *amorphous* solids can be much larger (hundreds of hertz) than those for the examples above and one might think that this would compromise the performance of the INADEQUATE experiment. However, the linewidth in solids arises from several different sources,[13] such as:

- the degree of crystallinity of the sample, which yields a more or less broad chemical shift distribution;
- the local magnetic field inhomogeneity (B_0 inhomogeneity, magnetic susceptibility effects . . .);
- dipolar couplings and higher order cross terms with chemical shift anisotropy (CSA) unaveraged by MAS;
- the incoherent effects of stochastically fluctuating local fields that yield T_2 relaxation.

These contributions can be divided into two categories depending on whether they are inhomogeneous or homogeneous.[14] Inhomogeneously broadened lineshapes, resulting from such

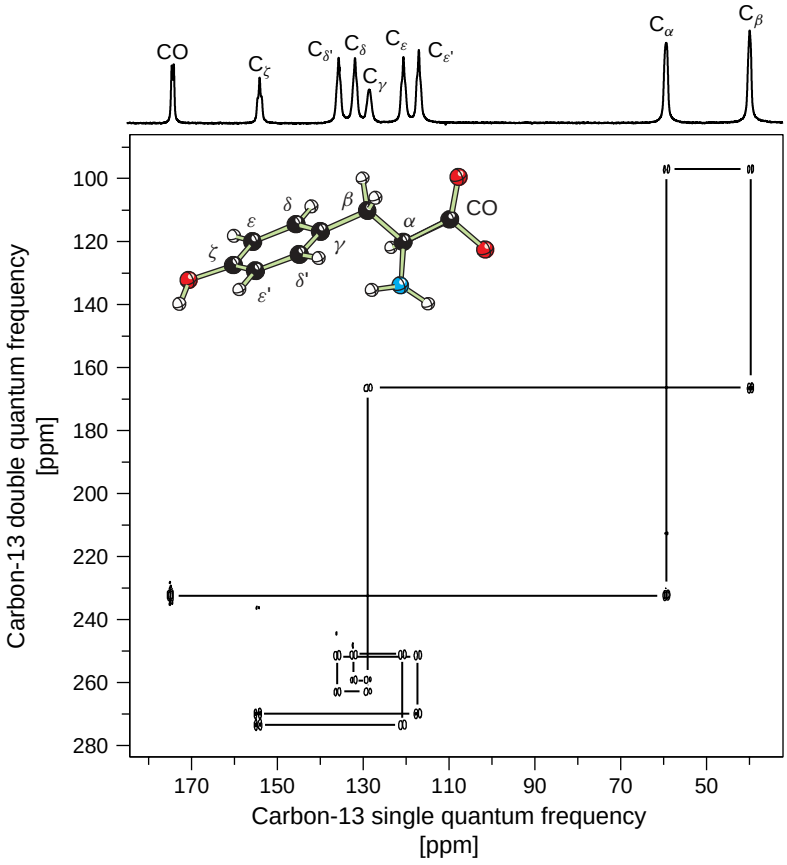

Figure 3 Two-dimensional INADEQUATE spectrum of a fully ^{13}C labeled sample of L-tyrosine hydrochloride. The one-dimensional carbon spectrum is also shown. The spinning frequency was 20 kHz and the decoupling radio-frequency field strength was 120 kHz. Starting from the carbonyl carbon, we can trace out the whole carbon skeleton of the molecule, yielding an unambiguous assignment of the carbon backbone of the molecule. This spectrum was obtained by Dr S. Steuernagel (Bruker Analytik Germany) and is reproduced from Ref.[50] with permission. A 10-mg sample was used and the coherence transfer pathway was selected using gradients (shown in Figure 2a) and led to an experimental time of 13 mins

mechanisms as chemical shift distributions or field inhomogeneity, consist of a continuum of independent lines that can be manipulated individually whereas homogeneously broadened lines due to multispin dipolar couplings or T_2 relaxation, react to pulses as an indivisible entity. The refocused INADEQUATE sequence in Figure 2(b) can be applied successfully to disordered samples since it leads to in-phase lineshapes due to the last $\tau - \pi - \tau$ refocusing period.[15] Assuming a short apparent relaxation time T_2^*, deduced from the linewidth, the efficiency of the refocused INADEQUATE experiment depends on the ratio T_2'/T_2^*, where T_2' is the transverse dephasing time measured in a spin echo experiment. We show where these respective damping constants are 'active' during the experiment in Figure 2. Another approach using composite refocusing (INADEQUATE-CR) was also introduced.[16] The magnetization in this experiment is channeled into one line of the J structure (α or β) and this leads to single absorptive peaks. The pulse sequence is shown in Figure 2(c). As in the refocused INADEQUATE experiment, in the case of broad peaks, the efficiency of INADEQUATE-CR depends on the ratio between the homogeneous and the inhomogeneous linewidth.

Figure 4 shows the refocused INADEQUATE spectrum of a sample of 10% randomly carbon-13 labeled purified cellulose recorded in a total experiment time of 16 h (250 mg of sample). As pointed out previously, in the two-dimensional map two directly bonded carbons share a common frequency in the double quantum dimension, and, provided that one carbon resonance can be identified a priori, assignment is quite straightforward. The cellulose spectrum contains resonances which have already been identified in previous studies, mainly by comparison with liquid spectra, and more recently by two-dimensional NMR.[17,18] The assignment shown in Figure 4 differs from the ones obtained using spin diffusion experiments, i.e., dipolar interactions, which underlines the fact that data from dipolar correlation techniques must be interpreted with caution as they may yield incorrect assignments.

2.1.2 TOBSY

The INADEQUATE experiment in solids can be considered to play the role of COSY in liquids, by establishing one-bond connectivities. In liquids, COSY is often complemented by TOCSY, which correlates all the spins in a coupled spin system with each other. Originally proposed in the liquid state by Braunschweiler and Ernst,[19] this experiment has been used extensively in liquids, together with COSY, INADEQUATE and NOESY, to provide assignment information for organic and biological molecules. Recently a solid-state version named TOBSY (for Total Through Bond Spectroscopy)

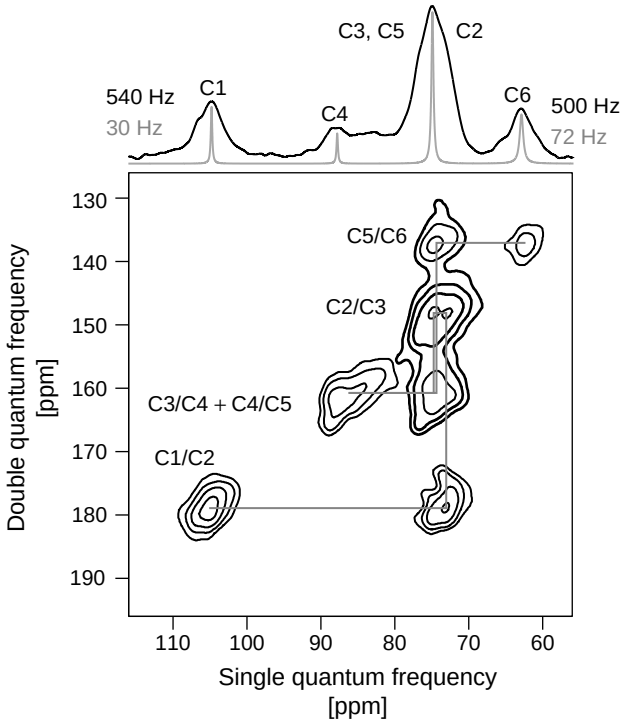

Figure 4 Two-dimensional refocused INADEQUATE spectrum of cellulose. The spectrum was obtained at 125 MHz on a Bruker DSX 500 spectrometer using a 7-mm double-tuned MAS probe. A total of 100 t_1 increments with 192 scans each were collected. The τ delay was set to 3 ms, and the contact time for cross polarization to 500 ms. The spinning speed was 6 kHz and the proton decoupling field strength was 100 kHz using continuous wave decoupling. The various connectivities between the directly bonded carbons are indicated by solid lines. The experimental one-dimensional spectrum is shown above the contour plot with a solid line. The homogeneous linewidth can be measured by a spin echo sequence, and from it we indicate the linewidths which are responsible for the damping during the two τ periods as a schematic spectrum as a thin line, for comparison, together with the measured linewidths. (Adapted from Lesage et al.[15] with permission, © 1999 American Chemical Society)

has been originally proposed by Baldus and Meier[20] and further improved.[21,22]

The correlation between nuclei is obtained by means of an isotropic Hamiltonian:

$$\mathcal{H} = 2\pi \sum_{i<j} J_{ij} \vec{I}_i \cdot \vec{I}_j \tag{3}$$

This Hamiltonian leads to a *net* polarization transfer as well as to antiphase signals[19] in the resulting two-dimensional spectra. The *net* polarization transfer $I_{1x} \rightarrow I_{2x}$ gives positive in-phase cross peaks while the anti-phase signals (originating from the transfer $I_{1x} \rightarrow I_{1y}I_{2z} - I_{1x}I_{2y}$) lead to dispersion signals in the detection period. These anti-phase components do not contribute to the signal at $t_2 = 0$, but evolve into observable coherences under the influence of the J interaction. In solids where the J interaction is not resolved, these anti-phase components are not observable, especially in the case of homogeneously broadened spectra. Under these conditions, the TOBSY experiment leads to pure absorption lineshapes in the two-dimensional spectrum.

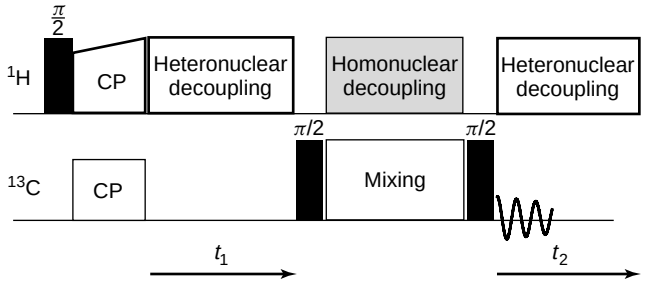

Figure 5 Two-dimensional TOBSY pulse scheme. During the t_1 evolution period, on-resonance high-power proton decoupling is used. The first 90° pulse on ^{13}C places magnetization along the z axis and then J-induced polarization transfer occurs during the mixing $\tau_{\text{mix}} = m\tau_{\text{MAS}}$ (where $m = 1, 2, 3, \ldots$) under simultaneous homonuclear proton decoupling. In the original TOBSY experiments[20] the mixing scheme $\text{R} = \overline{2}4\overline{2}3\overline{1}$, is applied such that $k = 4$ or $k = 8$ cycles cover one rotor period τ_{MAS}. For detection during t_2, high power on-resonance proton decoupling is applied. More recently the $\text{C}N_n^\nu$ schemes were proposed in order to perform the J-induced polarization transfer.[21,22] Usually cycles like WALTZ-4, POST-C7 and permuted WALTZ-4 can be used in order to improve the robustness of the pulse sequence with respect to rf field inhomogeneities. This pulse sequence can be easily adapted to cases where no proton nuclei are present (No proton channel in the above diagram)

To obtain an isotropic J mixing sequence (this means that the transfer does not depend on the initial condition of the magnetization), the Hamiltonian of equation (1) has to be crafted. The pulse sequence shown in Figure 5 achieves such an effective Hamiltonian. The philosophy of this pulse sequence is that MAS, together with rotor synchronized π pulses, can lead to a zeroth order average Hamiltonian that contains only the J couplings [see equation (3)]. The composite π pulses from the WALTZ decoupling scheme[23] have been used, and particular synchronization conditions have to be chosen in order to achieve pure J transfer.[20] The spin dynamics of rotor synchronized multiple pulse schemes is governed by the symmetry properties of the spin and space tensors of the interactions, and have been recently described at length using average Hamiltonian theory[24,25] (see **Symmetry-Based Pulse Sequences in Magic-Angle Spinning Solid-State NMR**). Introducing pulse sequences having the generic symmetry $\text{C}N_n^\nu$, where N cycles C_p with $p = 0, \ldots, N-1$, occupy n rotor periods, one can prove that appropriate choice of N, ν and n can be used to selectively average out given interactions. In fact the $\text{C}9_3^1$ symmetric class provides the basis for pure J magnetization transfer.[21] Studies using such symmetric pulse schemes have led to improved magnetization transfer efficiencies, and have allowed these experiments to perform well under faster MAS frequencies.[22] Heteronuclear dipolar decoupling of the protons is obtained using homonuclear proton decoupling in combination with MAS. We explain in detail how this works in the next section.

Experimental results using TOBSY are shown in Figure 6 for a powder sample of fully (^{13}C, ^{15}N)-labeled arginine. All one bond correlations are represented through cross peaks using a short mixing time, whereas long range connectivity coming from long-range and indirect couplings can be observed using a much longer mixing time.[20] The TOBSY spectrum of U–^{13}C, ^{15}N bacteriochlorophyll a is presented in Figure 7 as another example of the applicability of the

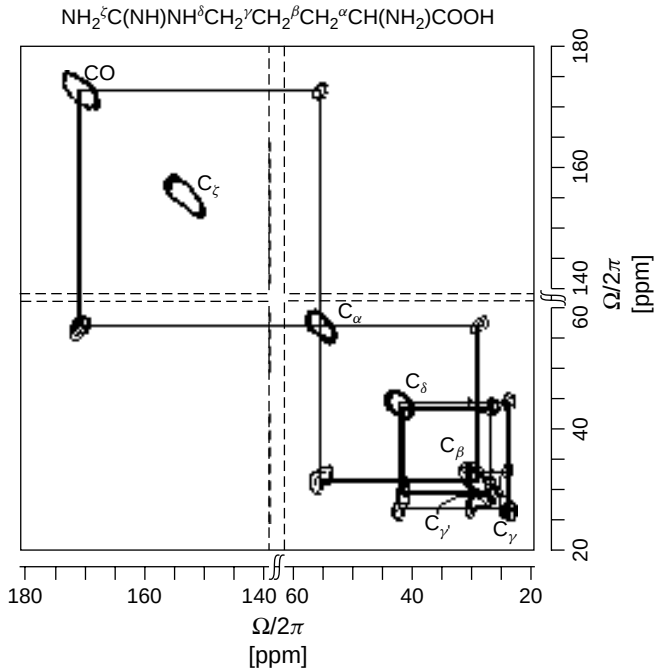

Figure 6 TOBSY initial-rate spectrum from a fully ^{13}C, ^{15}N-labeled arginine powder sample after a mixing time of 3 ms. Only the aromatic and aliphatic regions of the total two-dimensional spectrum are shown. All one-bond correlations are represented through cross-peaks. The spinning frequency was set to 8.5 kHz, and four R cycles per MAS period were used. A total of 256 t_1 experiments averaging eight transients in the t_2 was performed. Contour levels between 5 and 15 of the maximum signal intensity are shown. (Reproduced from Baldus and Meier,[20] © 1996, with permission from Academic Press)

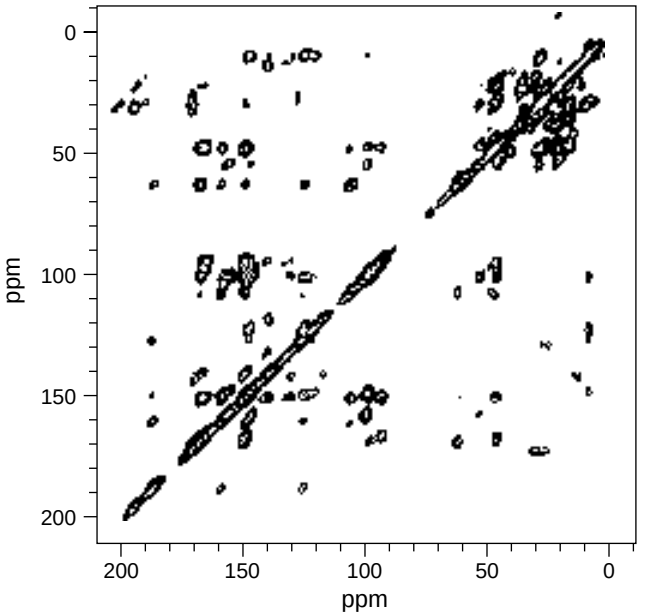

Figure 7 Part of a scalar correlation spectrum of U–^{13}C,^{15}N bacteriochlorophyll *a* recorded using POST-C9 as the isotropic mixing sequence at a MAS rate of 13 kHz, a mixing time of 9 ms, an rf amplitude for proton decoupling of 140 kHz, carbon rf amplitude of 78 kHz during POST-C9 and 113 kHz for the $\pi/2$ pulse, spectral width 30 kHz in each dimension, acquisition time 34 ms, 165 t_1 increments. Eight contour levels between 1% and 20% of the maximum positive spectra intensity are plotted. (Reproduced from Heindrichs et al.,[21] © 2001, with permission from Elsevier Science)

improved TOBSY sequences. Once again atomic connectivities along the carbon skeleton can be unambiguously determined.

2.2 Homonuclear Correlations for Other Nuclei

Up to now we have shown how homonuclear scalar couplings can be used for spectral assignment. Here we present an example in which *J* couplings can be used to probe geometric properties. In liquids, the well-known Karplus rule for the ^3J proton couplings is a useful tool for the determination of dihedral angles[7] (see **Vicinal Coupling Constants & Conformation of Biomolecules,** Volume 8). However, such couplings are not currently observable in solids. Homonuclear ^{31}P couplings have been used in order to determine bond angles in solid inorganic compounds.[26] The angle between two ^{31}P CSA tensors can be determined if polarization can be transferred between the two spins involved. By exploiting prior knowledge about the orientation of the CSA tensors relative to the molecular frame, bond angles can then be evaluated.

In many spin systems, such as SiP_2O_7, the evaluation of the experimental sideband patterns using dipolar techniques becomes difficult because cross-peaks between all resonances appear and greatly reduce the individual cross-peak intensities. The partial overlap of cross-peaks makes a quantitative analysis of the cross-peak intensity even more difficult. Therefore, the scalar *J* couplings are used as the polarization transfer mechanism, and only two ^{31}P spins within the P–O–P unit exchange polarization through the $^2J_{P-P}$ scalar coupling. Thus, the relative orientation of each unit can be measured selectively.

In Figure 8(a) the two-dimensional scalar correlation spectrum of a powder sample of the cubic phase of SiP_2O_7 is shown together with its one-dimensional spectrum. Only the centerband and the first sideband regions are shown. The intensity of the cross-peaks between different sidebands of chemically inequivalent spins contains information about the P–O–P angles, which can be obtained by numerical fitting. The results of such a fitting procedure are shown in Figure 8(b) and show that three pairs of P–O–P groups are bent, while one is linear.[26] These NMR data suggest that the "linear" pyrophosphate groups in SiP_2O_7 are in fact linear on the NMR time scale ($\sim$100 μs). A static disorder of 'normal' bent units, postulated previously, is clearly excluded.[26]

Other more exotic nuclei have also been investigated. One of the first examples of the application of INADEQUATE in the solid state was performed on the Sn nuclei.[11] ^{29}Si, whose natural abundance is 4.7%, has also been used to obtain scalar correlations. The ^1J couplings are of the order of 50 Hz and the ^2J couplings vary from 1 to 15 Hz. INADEQUATE helped find the correct structure of silanes in liquids. The technique was applied in the solid state by Benn et al.[27] to study very highly crystalline zeolites, where the linewidths are of the order of 1–20 Hz under proton decoupling. COSY-type experiments using J_{Si-Si} couplings have also been reported on glasses[28,29] (see **Silicon-29 NMR of Solid Silicates,** Volume 7).

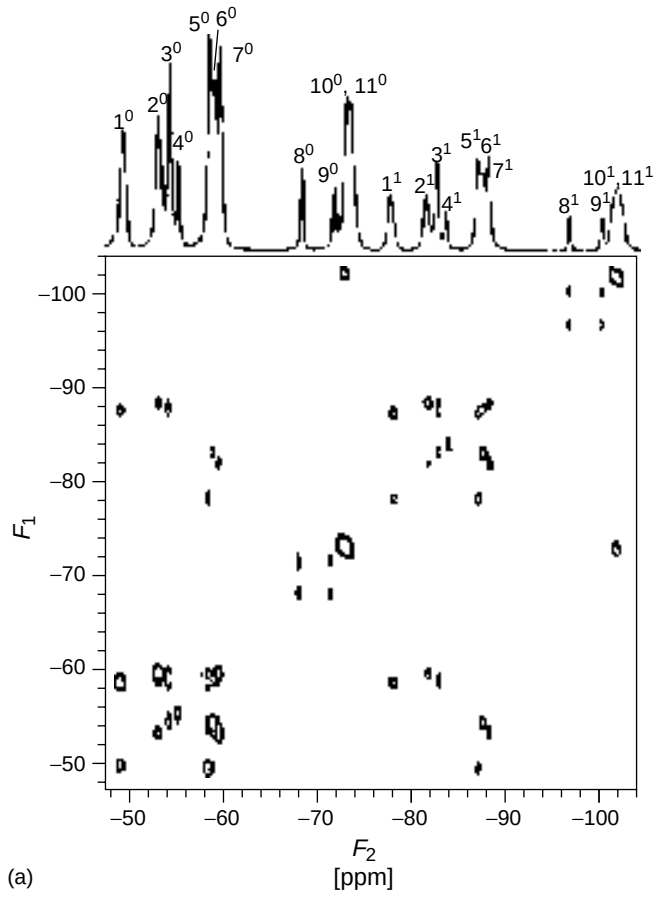

Figure 8 (a) Rotor-synchronized two-dimensional ^{31}P TOBSY spectrum of the cubic phase of SiP_2O_7 recorded with a MAS frequency of 4.63 kHz at a static field of 9.4 T. Only the region showing the centerband and the +1 sideband is reproduced. The pulse sequence from Figure 5 was used. The mixing time period was set to 21 ms at a rf field strength of 111 kHz. The ^{31}P chemical shift scale is referenced externally to phosphoric acid. (b) Normalized root-mean-square deviation between the experimental cross-peak intensities (taken into account were cross-peaks of order $n - m = 0, \pm 1, \pm 2$) as a function of the angle β for four sets of P–O–P units in SiP_2O_7. (Reproduced from Iulliucci and Meier[26] with permission, © 1998 American Chemical Society)

3 USING HETERONUCLEAR *J* COUPLINGS

The key step in characterizing and assigning *natural abundance* organic solids is through *heteronuclear* proton–carbon correlations. Until recently heteronuclear correlations in solids were obtained exclusively by dipolar correlations.[30–35] In the following, we review how heteronuclear coherence transfer can be obtained using scalar couplings leading to new sequences for spectral editing and heteronuclear *J* correlation.

3.1 How to Observe Heteronuclear Scalar Couplings: Homonuclear Proton Decoupling

The total Hamiltonian $\mathcal{H}$, under MAS and RF irradiation, is time dependent and can be written:

$$\mathcal{H}(t) = \mathcal{H}_I(t) + \mathcal{H}_S(t) + \mathcal{H}_{II}(t) + \mathcal{H}_{SS}(t) + \mathcal{H}_{IS}(t) + \mathcal{H}_{\mathrm{RF}}(t) \quad (4)$$

where $\mathcal{H}_X(t)$ accounts for the time dependent CSA interactions for the spin species X, $\mathcal{H}_{XY}$ for the dipolar and scalar coupling interactions between the spin species X and Y, and $\mathcal{H}_{\mathrm{RF}}(t)$ for the time dependent radio frequency fields that can be applied. In the following, we consider ordinary natural abundance organic solids (I refers to the ^{1}H nuclei and S refers to a rare nucleus such as ^{13}C or ^{15}N). Thus, it is reasonable to neglect the homonuclear Hamiltonian between rare spins $\mathcal{H}_{SS}(t)$.

To use the scalar couplings, one must first remove the dominant dipolar interactions (see **Average Hamiltonian Theory,** Volume 2, **Line Narrowing Methods in Solids,** Volume 4). Under homonuclear proton–proton decoupling (and assuming a fast radio-frequency averaging compared with the MAS time scale), the proton–proton dipolar interaction is, at least to first order, averaged to zero. The efficiency of the proton–proton decoupling depends on the decoupling sequence and many experimental parameters. Additionally, the proton chemical shift *and* the heteronuclear coupling interactions (dipolar and scalar) are scaled down by a scaling factor λ. In the absence of homonuclear interactions, the Hamiltonian becomes *inhomogeneous*[14,36,37] allowing for the averaging to zero, to first order, of the heteronuclear dipolar interactions and the CSA under MAS. The homonuclear scalar coupling terms between I spins, which are relatively small, are neglected. This leads to a considerable simplification of the effective Hamiltonian under homonuclear decoupling and MAS conditions. This effective Hamiltonian in the doubly rotating frame, can be written

$$\mathcal{H}_{\mathrm{eff}} = \lambda \sum_n \delta_n^I I_{nz} + \sum_m \delta_m^S S_{nz} + \lambda\pi \sum_{n,m} J_{nm}^{IS} 2 I_{nz} S_{mz} \quad (5)$$

and is very similar to the 'liquid state' NMR Hamiltonian that contains only the isotropic interactions.

In Figure 9(a) we show the carbon-13 spectrum of a powder sample of L-alanine recorded under proton-homonuclear decoupling and MAS. Figure 9(b) shows the methyl resonance of a powder sample of [2-^{13}C]sodium acetate recorded under the same conditions. Figure 9(c) shows the nitrogen-15 spectrum of a powder sample of glycine recorded under the same conditions. The frequency switched Lee–Goldburg (FSLG)[4,38] decoupling scheme was used with a rf decoupling amplitude of 100 kHz, and the MAS spinning frequency was set to 12 kHz. Splittings are observable in these spectra corresponding to

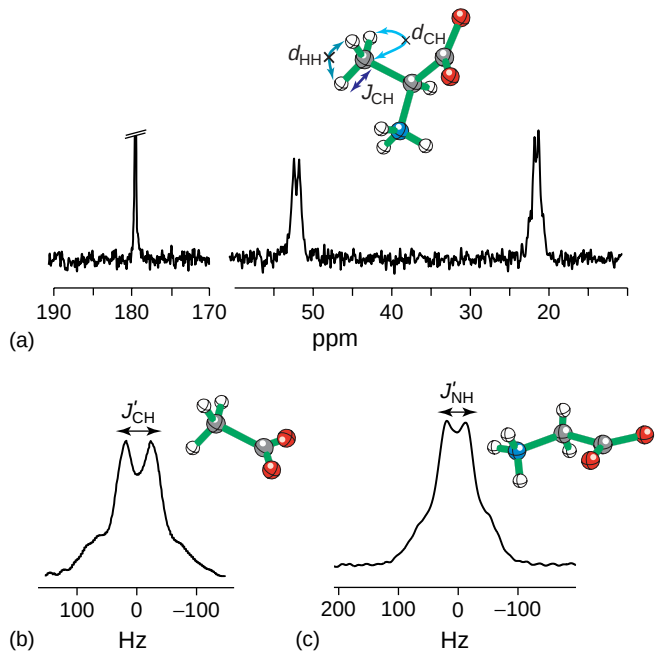

Figure 9 Carbon-13 (a,b) and nitrogen-15 (c) NMR spectra of powdered organic compounds under MAS and homonuclear proton dipolar decoupling. The homonuclear dipolar couplings are averaged by the rf sequence and the heteronuclear dipolar couplings by MAS, leaving only the heteronuclear scalar couplings. (a) In the carbon spectrum of L-alanine we can distinguish the doublet of the α carbon and the quartet of the methyl carbon. (b) Carbon spectrum of a sample of sodium acetate enriched at the methyl position. Only the methyl resonance is shown. A quartet is expected for the CH_3 group, which appears as a doublet in the spectrum because of the poor resolution of the outer transitions. (c) The same 'doublet' appears in the nitrogen-15 spectrum of glycine and hides the fine structure of the 1 : 3 : 3 : 1 quartet. Note that the heteronuclear proton–nitrogen couplings are smaller than the proton–carbon couplings. In all spectra the scalar couplings are scaled by the scaling factor of the decoupling sequence. In these experiments the FSLG decoupling sequence was used but other decoupling sequences can be used as well

the multiplet fine structure due to the heteronuclear J couplings. The α-carbon in L-alanine gives a doublet, while the methyl carbon in alanine and in sodium acetate gives a 'quartet', which is poorly resolved and appears in the spectrum as a doublet. Even though the proton–nitrogen J interactions are smaller (∼90 Hz) than the proton–carbon couplings (∼130 Hz), they can also be resolved, as we can see from the "quartet" present in the spectrum of glycine. It corresponds to the 1 : 3 : 3 : 1 fine structure of the NH_3^+ group.

3.2 Spectral Editing

One-dimensional spectral editing techniques such as INEPT, DEPT and APT, are very popular in the liquid state since they provide a quick and easy way of assigning carbon-13 resonances in many organic compounds (see **INEPT,** Volume 4, **Polarization Transfer Experiments via Scalar Coupling in Liquids,** Volume 6). They also constitute a first step towards the use of J couplings to perform heteronuclear correlation spectroscopy (see also **Heteronuclear Assignment Techniques,** Volume 4, **Spectral Editing Techniques: Hydrocarbon Solids,** Volume 7).

3.2.1 *Solid-State APT*

The attached proton test (APT) sequence is one of the simplest liquid-state spectral editing techniques,[39–41] and it has been modified and used for the solid state by Lesage et al.[42] The pulse sequence for the experiments is shown in Figure 10(a). Cross polarization is used to enhance the carbon polarization and homonuclear dipolar decoupling is introduced during the evolution periods to remove proton–proton dipolar couplings. As described above, under these conditions the inhomogeneous interactions, i.e., the chemical shift anisotropy and the heteronuclear dipolar couplings, are averaged out by rapid magic angle spinning, leaving only the isotropic chemical shift and the scalar J couplings. The π pulses applied simultaneously to proton and carbon in the center of the 2τ period, have the net effect of refocusing the carbon chemical shift evolution, while maintaining the evolution under the scaled scalar λJ_{IS} coupling. Thus, after cross polarization, carbon coherences evolve only under the effect of a scaled heteronuclear scalar coupling. The scaling factor λ varies according to the dipolar decoupling sequence that is used; for the FSLG sequence[4] the theoretical scaling factor is $1/\sqrt{3}$.

If the dynamics can be described by the simple Hamiltonian of equation (5), the theoretical evolution of carbon signals can easily be calculated using product operator algebra[43] since all terms in the Hamiltonian commute with each other. This formalism proves to be very useful since all of the following sequences can be calculated, to first order at least, as if they were liquid-state sequences. In the case of the APT sequence, since the carbon and the proton chemical shift evolution is refocused, the effective Hamiltonian during the 2τ period is

$$\mathcal{H}_{\text{eff}}^{\text{APT}} = \lambda\pi \sum_{n,m} J_{nm}^{IS} 2I_{nz}S_{mz} \tag{6}$$

and the observable signal intensity is

$$I_{I_nS}^{\text{APT}}(2\tau) = \cos^n(2\pi J'\tau)\exp\left(\frac{-2\tau}{T_2'^{I_nS}}\right) I_{I_nS}^0 \tag{7}$$

where I^0 is the signal intensity after cross polarization and T_2' is the transverse relaxation (dephasing) time during the period 2τ (equal to $1/\pi\Delta$). For each CH_n group ($n = 0$, 1, 2, 3), the intensities are shown in Figure 11(a) as functions of the delay τ. The calculations are shown for two different values of the linewidth Δ (1 Hz and 130 Hz, respectively, for the left and right panel) and J coupling (and 50 Hz and 70 Hz, respectively), corresponding to the 'ideal liquid state' case, and to the equivalent solid-state case. Note that the linewidth Δ indicated in the figures is the full linewidth at half-height of the signals evolving during 2τ (i.e., the linewidth for a single component of the fine structure of the multiplet), and is different from the overall linewidth of the signals observed during acquisition. The calculations were done in the ideal case where all protonated carbon groups have the same heteronuclear scalar couplings; 130 Hz is a typical value for a one-bond J_{CH} coupling for an aliphatic carbon, and the value of 70 Hz corresponds approximately to a scaling factor $\lambda = 1/\sqrt{3}$, due to the homonuclear proton decoupling. A τ value of $1/(2J)$ will produce a spectrum in which the C and CH_2 carbon peaks will be positive in sign, while the CH and CH_3 peaks will be inverted. Note that the sign of the

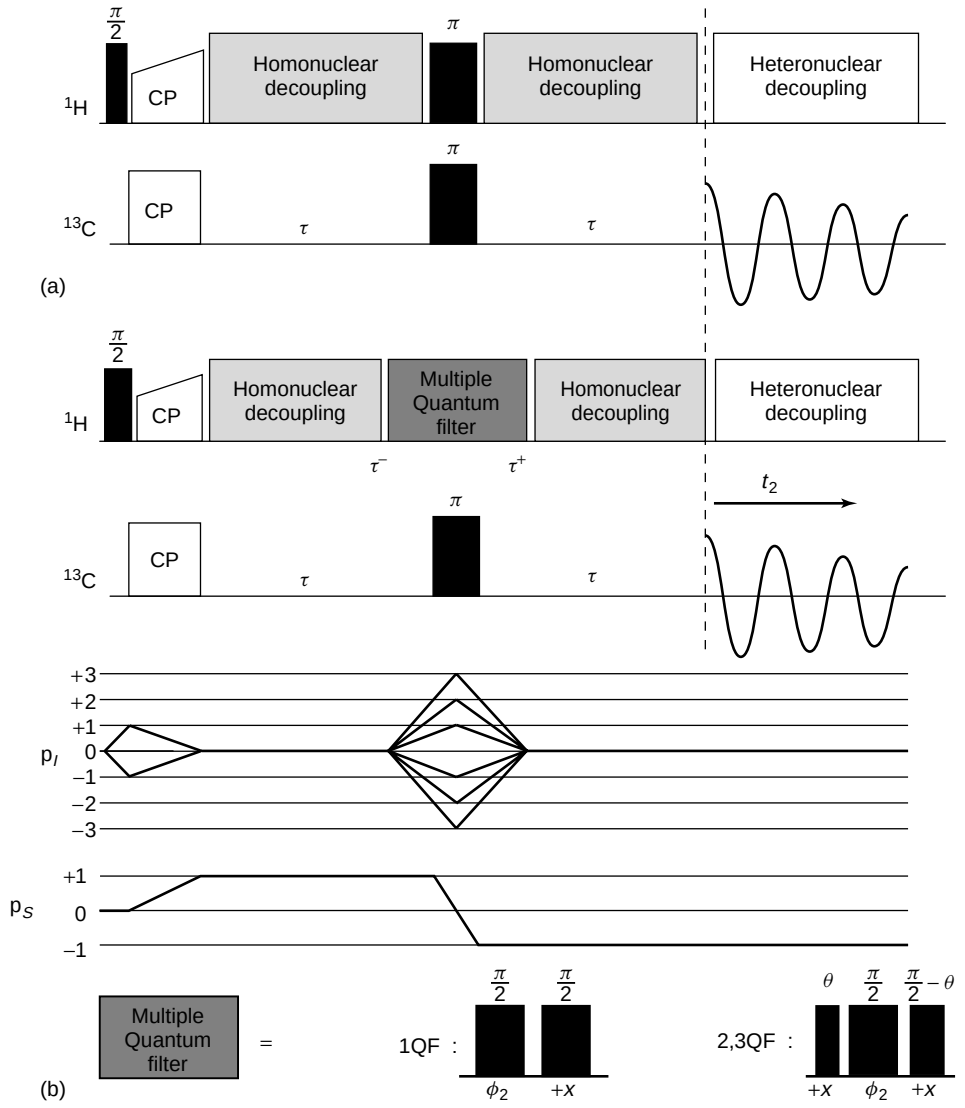

Figure 10 (a) The pulse sequence suitable for the solid-state APT and the corresponding coherence transfer pathway. (b) Pulse sequence and coherence transfer pathways for the J-MQ-Filter experiment. In the experiments presented in Figure 12 we used the FSLG sequence as the homonuclear proton decoupling scheme, thus θ is 54.7° pulse. Other homonuclear decoupling sequences can also be used instead of FSLG, by appropriately fixing θ. The MQ-Filter block is given at the bottom of the figure. (Detailed information about the implementation of these sequences is given in Refs.[42,44])

peaks is independent of the linewidth. Variations in linewidths will simply lead to a modulation of the amplitude of the signals but will not prevent discrimination between positive (CH_2) and negative (CH) signals. Note especially that, in cases where some groups are more flexible than others, partial averaging of the dipolar couplings through molecular motion will simply increase the signal amplitude (by decreasing the linewidth). Figure 11(b) shows a typical experimental example of this technique applied to L-histidine monohydrochloride monohydrate.

3.2.2 MAS-J-MQF

The APT sequence essentially serves as a parity test rather than removing resonances according to their multiplicity. An alternative sequence using the same principles but including a multiple-quantum filter block has been demonstrated to be capable of removing resonances from the spectrum according to their multiplicity.[44] The sequence is shown in Figure 10(b). Note that this experiment is applicable even when a carbon chemical shift distribution leads to inhomogeneous line broadening, since the π pulse on the carbon channel refocuses this effect. Thus, this technique (and the others considered in this section) should be applicable even in amorphous solids. Figure 12 shows an example of this approach applied to a protected tripeptide sample.

3.3 Two-dimensional Techniques

Multidimensional heteronuclear correlation spectroscopy is the cornerstone for assignment and structure determination in the liquid-state.[7] In analogy to liquid-state experiments (see **Two-Dimensional Carbon-Heteroelement Correlation,** Volume 8), the solid-state MAS-J-HMQC[45] and MAS-J-HSQC[46] sequences use heteronuclear multiple-quantum and heteronuclear single-quantum coherences, respectively, to

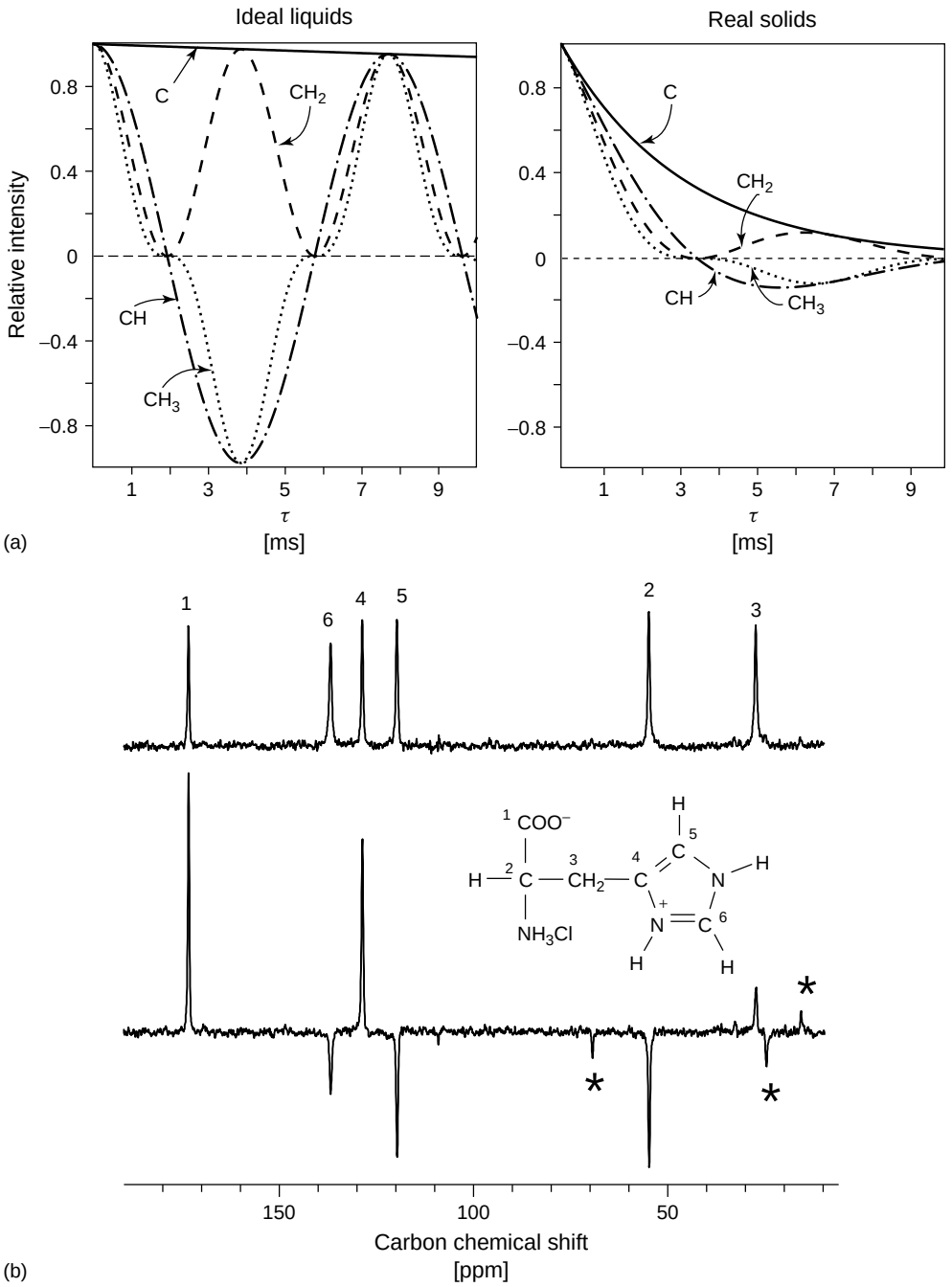

Figure 11 (a) Functional dependence of the observable signal as a function of the τ delay in the ATP sequence for the case of an ideal liquid and the solid-state. See text for details. A τ value of $1/(2J_{CH})$ will produce a spectrum in which the C and CH_2 carbon resonances will be positive in sign, while the CH and CH_3 resonances will be inverted. (b) One-dimensional CP/MAS spectrum (upper spectrum) and solid-state APT spectrum (lower spectrum) of L-histidine monohydrochloride monohydrate. A contact time of 1 ms was used and the spectra were recorded with 200 scans and 2048 scans, respectively. τ was set to 4 ms for the editing experiment. The spinning sidebands are marked with asterisks. (Reproduced from Lesage et al.[42] with permission, © 1998 American Chemical Society)

provide chemical-shift correlations between pairs of directly bonded nuclei in powder samples. Long range heteronuclear J couplings can also be used to probe multiple bond correlations, leading to the MAS-J-HMBC experiment.[47]

3.3.3 MAS-J-HMQC

This two-dimensional experiment is based on the polarization transfer techniques using scalar interactions that have been described in the spectral editing paragraph. The only difference is that a t_1 evolution time is included during which the multiple spin multiple quantum coherences evolve under the isotropic chemical shifts of the proton nuclei. The sequence is shown in Figure 13(a) and leads to two-dimensional spectra containing correlations between rare nuclei (carbons, nitrogens) along ω_2, and protons along ω_1 of the kind shown in Figure 14. The time τ is responsible for the polarization transfer, and it has been shown that for short τ evolutions only correlations from

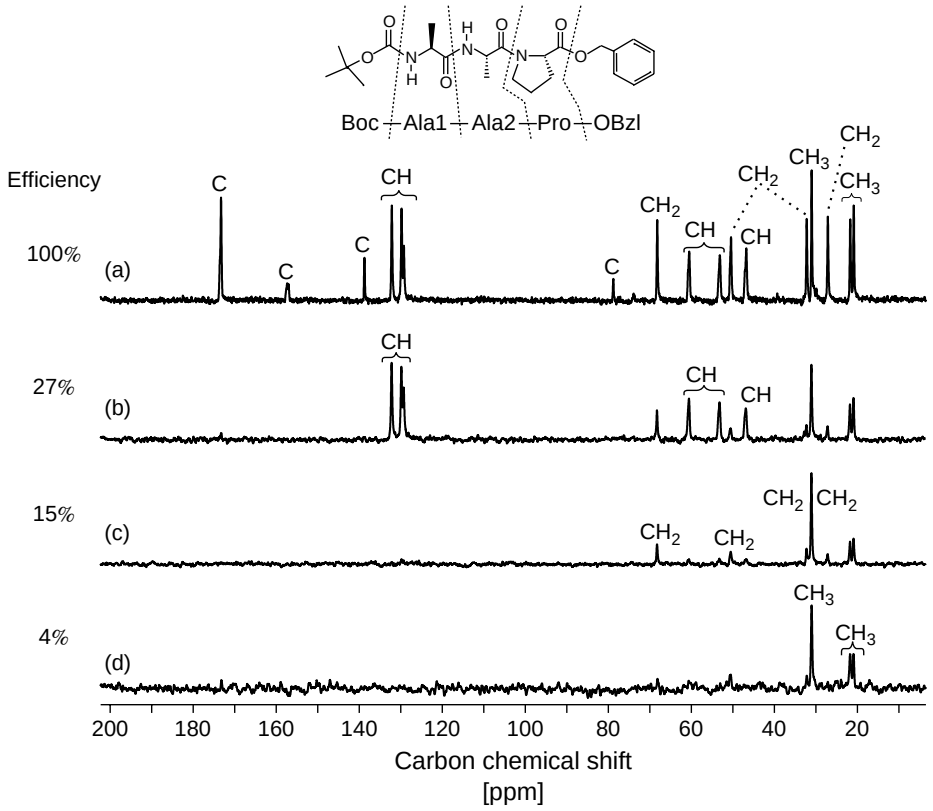

Figure 12 J-MQ-Filtered solid-state NMR spectra of the tripeptide Boc-Ala-Ala-Pro-O-Bzl. (a) Standard CP/MAS spectrum of 20 mg of a powder sample of the tripeptide. The spinning frequency was set to 12.5 kHz and a 1-ms cross polarization contact time was used. TPPM heteronuclear decoupling ($\omega_1/2\pi = 100$ kHz) was applied during acquisition; 64 scans were recorded. (b) 1Q-Filtered spectrum. As predicted, signals from the CH, CH_2 and CH_3 groups are present; 128 scans were recorded. (c) 2Q-Filtered spectrum. Only signals from the CH_2 and CH_3 groups are present; 2560 scans were recorded. (d) 3Q-Filtered spectrum. Only signals from the CH_3 groups are present; 4800 scans were recorded. The evolution time τ was set to 3.2 ms (synchronized with the MAS) for (b) and (c) and to 7.0 ms for (d) in order to enhance 3Q coherence creation. Spectra (c) and (d) were acquired within 2 and 4 h, respectively. The signal to noise ratio relative to the CP/MAS experiment, corrected for the number of scans, is given next to the spectrum for each experiment. (Reproduced by permission from Sakellariou et al.,[44] © 2001, with permission from Academic Press)

directly bonded nuclei are obtained. For longer τ periods, long range correlations are observed, and, in the case of camphor, fit well when ^2J and ^3J are included in spin Hamiltonian. Such correlations are thus exploited to explore long range connectivities like the HMBC experiment in liquids.[47] In what follows, we concentrate on the possibility of obtaining the full assignment of medium-size organic molecules using these correlation techniques.

3.3.4 Complete Assignment Using Multiple-Bond Correlations

For an approach to the complete assignment of the ^{13}C spectrum, we start with the one-bond (^1H, ^{13}C) correlations. This approach has yielded the complete assignment of the protected tripeptide shown in Figure 15, and here we demonstrate the assignment protocol only for one of the residues.

As mentioned above, for short values of the evolution period τ (typically 2 ms), the carbon–proton magnetization transfer is highly selective, i.e., it leads to only one-bond chemical shift correlations. Figure 15(a) shows the one-bond MAS-J-HMQC spectrum of the tripeptide Boc-Ala-Ala-Pro-O-Bzl (the three amino acids are referred to in the text as A1, A2 and P). Some resonance lines of the ^{13}C spectrum can be identified from this two-dimensional correlation map alone. We can readily identify the three carbon resonances at low field as well as the one around 77.3 ppm as quaternary carbons since they are not correlated with any proton in the ω_1 dimension. From carbon chemical shift considerations, the carbon resonance at 77.3 ppm can be assigned to the quaternary carbon of the ter-butyl group, and that at 137.3 ppm to the quaternary carbon of the benzyl group; the remaining two quaternary resonances must therefore correspond to the three amino acid carbonyl groups (171.9 ppm) and to the carbonyl carbon of the Boc group (155.7 ppm). The carbon peaks between 127 and 131 ppm yield correlations with protons at about 7 ppm, and are therefore likely to correspond to the protonated carbons of the benzyl group. From carbon peak intensity, the high-field resonance must correspond to the para carbon. A specific assignment of the two other aromatic resonances is not possible. In the high-field part of the spectrum, the three carbon resonances at 19.4, 20.3 and 29.6 ppm can be assigned to the three methyl groups since they correlate with protons around 1.5 ppm. Tentatively, from carbon chemical shifts and peak intensity, we assume that the peak at 29.6 ppm corresponds to the ter-butyl methyl groups,

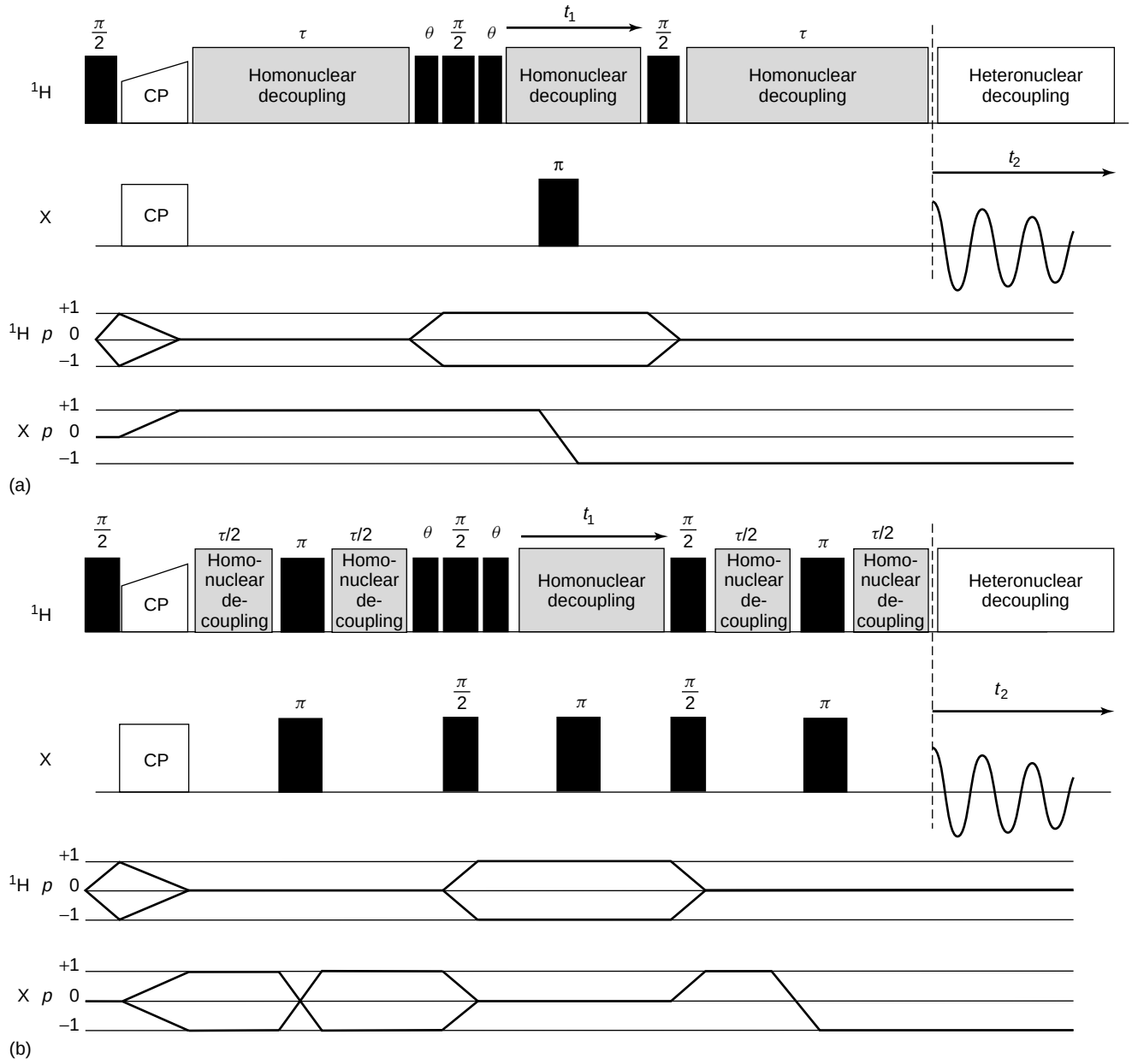

Figure 13 (a) Pulse sequence for the MAS-J-HMQC experiment. θ is a prepulse whose flip angle depends on the homonuclear decoupling scheme (for FSLG $\theta = \theta_m$, i.e., the magic angle). After cross polarization from ^{1}H (I spins), the magnetization of the rare S spins evolves during the delay τ only under an isotropic scaled heteronuclear J coupling Hamiltonian. For a pair of covalently bonded ^{1}H-S spins, the carbon magnetization evolves from in-phase (S_x) into antiphase ($2I_zS_y$) coherence with respect to the attached proton. A 90° pulse applied on protons transforms the antiphase carbon coherence into a multiple-quantum heteronuclear coherence which evolves during t_1 only under the effect of the proton chemical shift. At the end of the t_1 evolution period, the MQ coherence is converted back into an antiphase carbon coherence by the second 90° proton pulse. During the second τ period this coherence evolves to become an in-phase observable carbon coherence. (b) Pulse sequence for the MAS-J-HSQC experiment. During the t_1 evolution period only single quantum proton coherence evolves under the isotropic proton chemical shift

and the other two, to the Cβ of alanine residues. At this stage, however, it is not possible to determine to which alanine residue (A1 or A2) each methyl carbon resonance belongs. Of the remaining peaks, the two carbons at 25.7 and 30.8 ppm, which correlate with protons at around 2.5 ppm, are likely to correspond to the proline γ and β carbons, respectively. The remaining five peaks between 40 and 70 ppm therefore correspond to the proline α and δ carbons, to the two alanine α carbons, and to the O–CH_2 group.

Thus, multiple-bond proton–carbon correlations are required to lift this ambiguity. Geminal ^{13}C–^{1}H couplings ($^2J_{CH}$) and vicinal ^{13}C–^{1}H couplings ($^3J_{CH}$) are also active during the evolution periods, and thus contribute to the creation of heteronuclear multiple-quantum coherences. If the evolution periods τ are long enough, in theory of the order of $1/(2\,{}^nJ_{CH})$, multiple-bond couplings may yield significant correlations. Note that, in this case, the MAS-J-HMQC experiment should rather be compared to the liquid-state

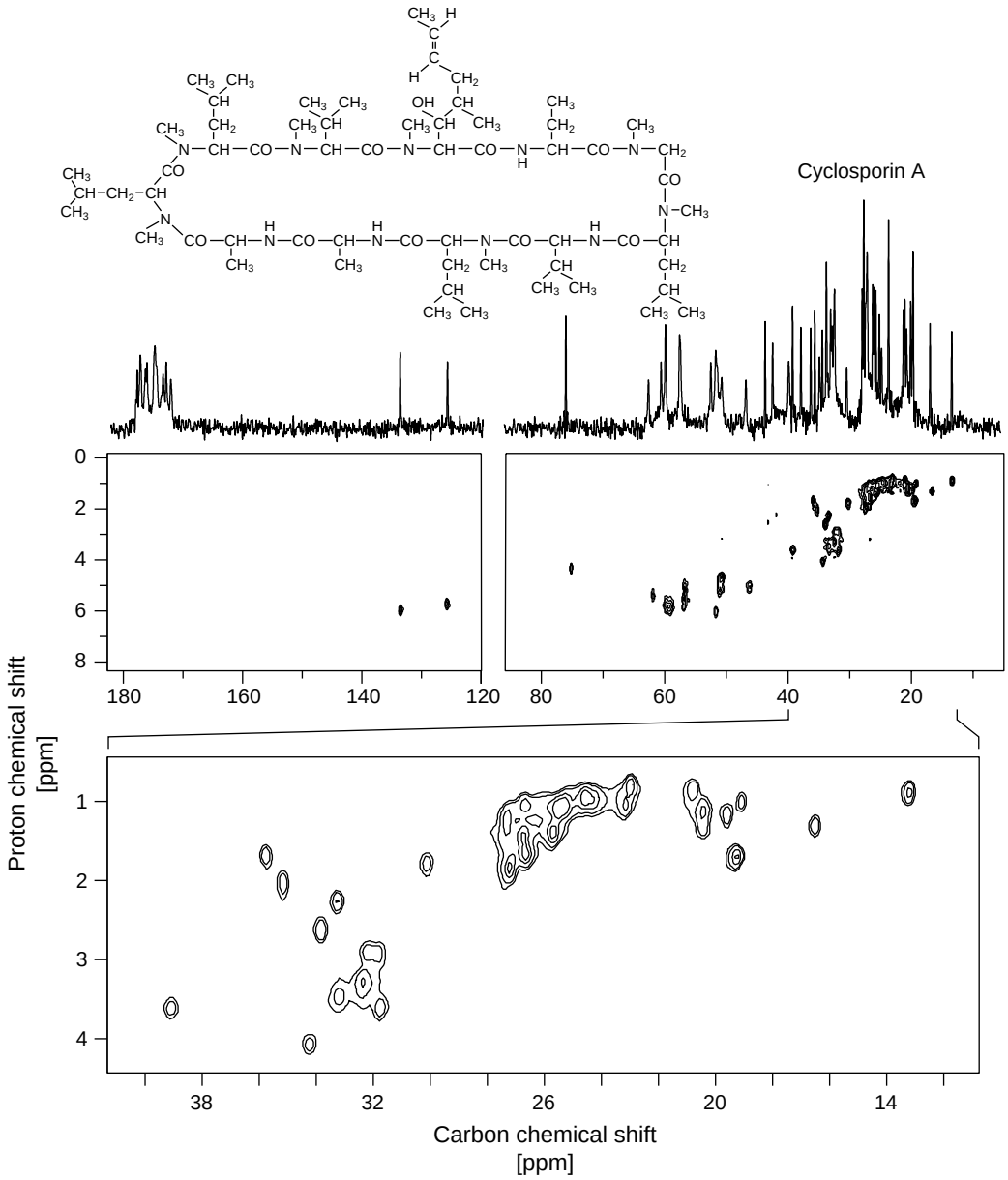

Figure 14 MAS-*J*-HMQC spectrum of Cyclosporin A. This spectrum was obtained at 500 MHz and shows one-bond carbon–proton correlations for the undecapeptide

heteronuclear multiple-bond correlation (HMBC) experiment. In organic compounds in the liquid-state, values between −10 and +66 Hz are usually found for $^{2}J_{CH}$ couplings, whereas the $^{3}J_{CH}$ couplings have values between 0 and 16 Hz.[48] In amino acids, the (CO–Hα) coupling constants range from −4 to −7 Hz while (CO–Hβ) coupling constants range from 2 to 6 Hz.

The apparent carbon linewidths under FSLG decoupling are obviously much larger than these multiple-bond scalar interactions. However, the dephasing time constant which is effective for the creation of the heteronuclear MQ coherences (τ periods) is related to the refocused linewidth (or the homogeneous linewidth), for which all the inhomogeneous broadening is removed by the carbon π pulse. It was recently shown that, under CW decoupling, the carbon line broadening for crystalline organic compounds is mainly inhomogeneous, and refocused linewidths as small as a few hertz on model organic samples have been measured.[15] Under homonuclear proton decoupling, the homogeneous linewidth increases for protonated carbons. However, it remains about the same for nonprotonated carbons, i.e., of the order of a few hertz, thus rendering the observation of multiple-bond correlations feasible for these nuclei. Figure 15(b) shows the MAS-*J*-HMQC spectrum of the tripeptide recorded with an evolution period τ equal to 16 ms. Besides the one-bond connectivity (except for those corresponding to CH_2 groups, all of them are present), many additional through-bond 'long-range' correlation peaks are observed. As expected, all the nonprotonated carbons (four resonance lines in the carbon spectrum) yield multiple-bond connectivity. For example, the carbonyl carbon of the Boc group at 155.7 ppm is expected to correlate with the amide proton of the N-terminal alanine residue (A1), and also with

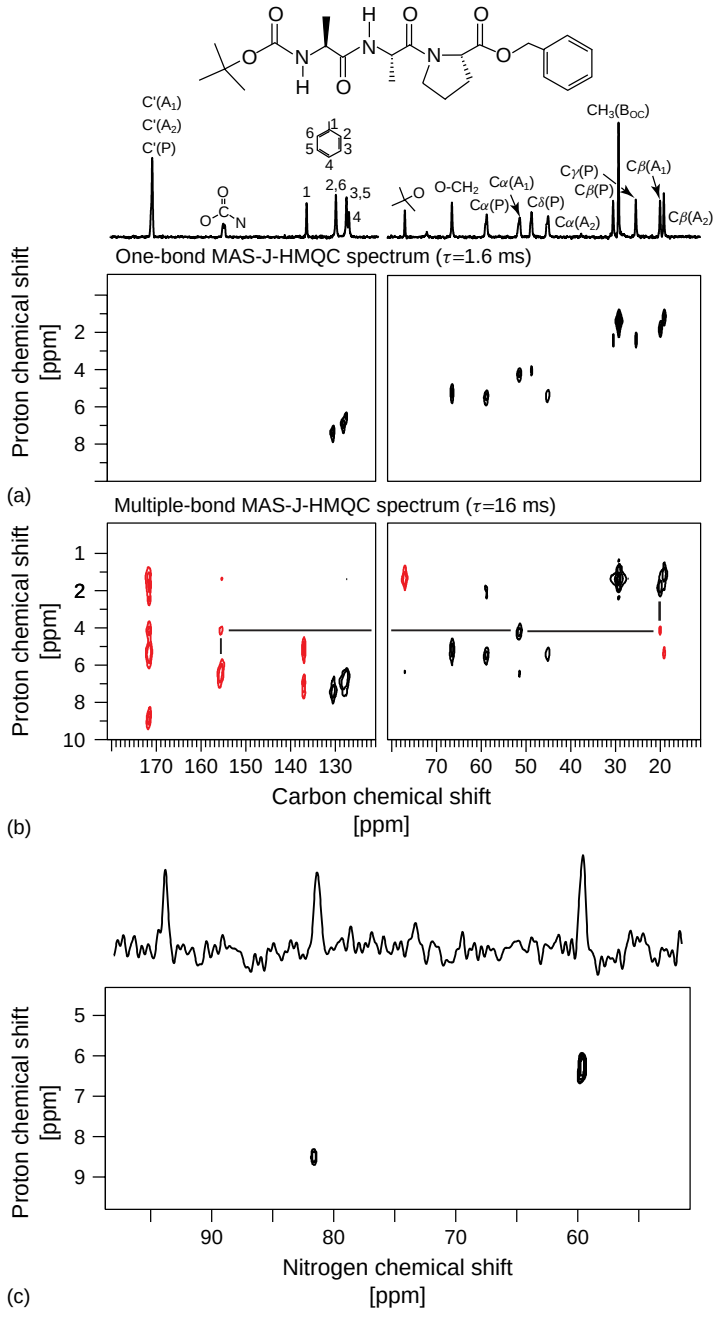

Figure 15 Carbon–proton two-dimensional MAS-*J*-HMQC spectra of the natural abundance tripeptide Boc-Ala-Ala-Pro-O-Bzl recorded with an evolution period (τ value) of (a) 1.6 ms, and (b) 16 ms. The one-dimensional CP/MAS ^{13}C spectrum is shown above the two-dimensional spectrum. The proton linewidths depend on the efficiency of the homonuclear decoupling scheme. Under our experimental conditions, we measured proton linewidths of about 200 Hz, 250 Hz and 400 Hz for the CH_3, CH and CH_2 groups, respectively. However, for CH_2 groups, the proton resonance may correspond to two magnetically nonequivalent protons. Note that, despite the long evolution periods (16 ms) which are required for the excitation of the long-range MQ coherences, the multiple-bond experiment remains quite sensitive since, as pointed out in the text, the effective time constants which characterize the decay of carbon magnetization during the τ delays, are 'refocused' time constants and thus, are longer than the apparent relaxation times. (c) ^{15}N-^{1}H two-dimensional MAS-*J*-HMQC spectra of the tripeptide. The spinning frequency was 12.5 kHz and τ was 4.32 ms. A total of 110 t_1 increments with 256 scans each were acquired. The other experimental conditions are the same as in (a) and (b). The one-dimensional CP/MAS ^{15}N spectrum is shown above the two-dimensional spectrum; 4 mm MAS probe ~20 mg, $\omega_{1H} = 100$ kHz. (Reproduced from Lesage et al.[47] with permission, © 2000 American Chemical Society)

the α proton of the same residue. Indeed, two cross-peaks, one very intense at 6.5 ppm and the other weaker at 4.25 ppm, are observed in the ω_1 dimension. From the proton chemical shifts, they must correspond respectively to the HN and Hα protons of A1. In the one-bond (^{1}H, ^{13}C) MAS-*J*-HMQC spectrum, the carbon resonance at 51.7 ppm is also correlated to the Hα(A1) proton, and can therefore be assigned to the Cα(A1). In addition to the quaternary carbons, the Cβ carbons of the alanine residues (methyl groups) yield weak multiple-bond correlations with the neighboring α protons. As the Hα(A1) proton

could be previously assigned at 4.25 ppm from its correlation with the carbonyl carbon of the Boc group (at 155.7 ppm), the assignment of the methyl carbons is now straightforward: the carbon resonance at 20.3 ppm corresponds to the Cβ(A1) and, by deduction, the resonance at 19.4 ppm to the Cβ(A2). By continuing in this way, all the proton, carbon and nitrogen resonances in the spectrum can be assigned (the nitrogen-15 assignment being obtained simply from the natural abundance proton–nitrogen HMQC experiment shown in Figure 15(c)).

MAS-*J*-HMQC experiments constitute a powerful tool for the characterization of the NMR spectra of solid-state natural abundance organic molecules. Despite the small size of multiple-bond scalar couplings, it has been shown experimentally[47] that it is possible to observe long-range connectivities that can be assigned to through-bond correlations, which is an important step towards complete assignment of ^{13}C CP/MAS spectra.

Note that it would be difficult to reliably identify multiple-through-bond correlations using dipolar based techniques, since, at long contact times, dipolar methods usually lead to a wide range of through-space interactions, often including inter-molecular contacts. In fact, long range dipolar and scalar experiments are complementary techniques, and differences in the correlation patterns could be very informative to identify, for example, effects such as hydrogen bonding in solids.

3.3.5 *MAS-J-HSQC*

The spin dynamics in the MAS-*J*-HMQC experiment can be very easily modified to have only a single quantum proton coherence evolution during the t_1, leading to the MAS-*J*-HSQC experiment. At first sight there should not be a significant difference between the two experiments. In fact, for natural abundance compounds, the MAS-*J*-HMQC and the MAS-*J*-HSQC experiments give about the same proton resolution in the indirect dimension, although the HSQC version is more prone to artifacts such as quadrature images or axial peaks, since there are more pulses in the sequence. On the other hand, for ^{13}C enriched materials, substantially narrower proton linewidths are obtained with the MAS-*J*-HSQC experiment, since homonuclear carbon–carbon couplings have no influence on the evolution of the single quantum proton coherence. The pulse sequence of the MAS-*J*-HSQC experiment is shown in Figure 13(b). The comparison between the two approaches is discussed in detail in Ref.[46]

3.3.6 *J-WISE*

The experiments discussed above are aimed at assigning complex spectra. However, controlled coherence transfer through scalar couplings can also be put to use in structural studies by comparing the results of polarization transfer using dipolar and scalar couplings. A striking example has recently been demonstrated for wideline proton (WISE) spectra in polymer systems to study hydration effects (see **Polymer Dynamics & Order from Multidimensional Solid State NMR,** Volume 6). Figure 16 shows a comparison between an 'ordinary' dipolar WISE spectrum,[49] recorded for a sample of partially rehydrated onion cell-wall material with a similar wideline spectrum where the proton–carbon correlation is obtained using a derivative of the MAS-*J*-HSQC experiment without applying decoupling during t_1 (dubbed *J*-WISE). Interestingly, all of the proton signals in the cell-wall material dipolar WISE spectra contain a broad signal split into spinning sidebands superimposed on a narrow component occurring at the centerband. By performing a *J*-WISE experiment, it was shown that the narrow line arises from water molecules close

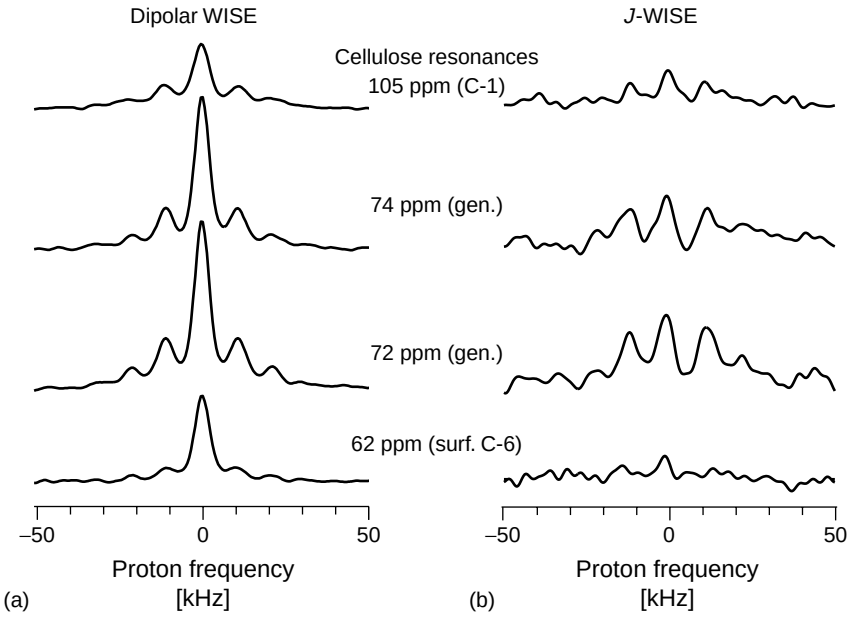

Figure 16 Comparative study of onion cell-wall material using the standard WISE and *J*-WISE experiments. Proton signals arising from immobile regions of the molecule give the broad signal split into sidebands onto which is clearly superimposed a narrow center component in the dipolar spectra (a). In the *J*-WISE spectra (b) this narrow component is absent, indicating that it belongs to 'bound water'. (Courtesy of Dr S. Hediger)

to the polysaccharides ('bound water'), since the narrow component disappears from the spectrum, indicating that there is no covalent connection between these protons and the carbon atoms of the polysaccharides. This is a particularly elegant demonstration of the complementarity between through-space and through-bond correlation techniques with which we conclude this entry.

4 RELATED ARTICLES IN VOLUMES 1–8

CRAMPS, Volume 3, Cross Polarization in Rotating Solids: Spin-1/2 Nuclei, Volume 3, Cross Polarization in Solids, Volume 3, Heteronuclear Assignment Techniques, Volume 4, Magic Angle Spinning, Volume 5, Rotating Solids, Volume 7, Spectral Editing Techniques: Hydrocarbon Solids, Volume 7.

5 REFERENCES

1. T. Terao, H. Miura, and A. Saika, *J. Chem. Phys.*, 1981, **75**, 1573.
2. K. W. Zilm and D. M. Grant, *J. Magn. Reson.*, 1982, **48**, 524.
3. A. E. Bennett, C. M. Rienstra, M. Auger, K. V. Lakshmi, and R. G. Griffin, *J. Chem. Phys.*, 1995, **103**, 6951.
4. A. Bielecki, A. C. Kolbert, and M. H. Levitt, *Chem. Phys. Lett.*, 1989, **155**, 341.
5. E. Vinogradov, P. K. Madhu, and S. Vega, *Chem. Phys. Lett.*, 1999, **314**, 443.
6. D. Sakellariou, A. Lesage, P. Hodgkinson, and L. Emsley, *Chem. Phys. Lett.*, 2000, **319**, 253.
7. K. Wüthrich, 'NMR of Proteins and Nucleic Acids', Wiley-Interscience: New York, 1986.
8. A. Bax, R. Freeman, and S. P. Kempsell, *J. Am. Chem. Soc.*, 1980, **102**, 4849.
9. A. Bax, R. Freeman, and T. A. Frenkiel, *J. Am. Chem. Soc.*, 1981, **103**, 2102.
10. T. A. Early, B. K. John, and L. F. Johnson, *J. Magn. Reson.*, 1987, **79**, 134.
11. I. D. Gay, C. H. Jones, and R. D. Sharma, *J. Magn. Reson.*, 1991, **91**, 186.
12. A. Lesage, C. Auger, S. Caldarelli, and L. Emsley, *J. Am. Chem. Soc.*, 1997, **119**, 7867.
13. D. L. VanderHart, W. L. Earl, and A. N. Garroway, *J. Magn. Reson.*, 1981, **44**, 361.
14. M. M. Maricq and J. S. Waugh, *J. Chem. Phys.*, 1979, **70**, 3300.
15. A. Lesage, M. Bardet, and L. Emsley, *J. Am. Chem. Soc.*, 1999, **121**, 10 987.
16. R. Verel, J. D. van Beek, and B. H. Meier, *J. Magn. Reson.*, 1999, **140**, 300.
17. M. Bardet, D. Gagnaire, R. Nardin, D. Robert, and M. Vincendon, *Holzforschung*, 1986, **40**, 17.
18. M. Bardet, L. Emsley, and M. Vincendon, *Solid State NMR*, 1997, **8**, 25.
19. L. Braunschweiler and R. R. Ernst, *J. Magn. Reson.*, 1983, **53**, 521.
20. M. Baldus and B. H. Meier, *J. Magn. Reson. A*, 1996, **121**, 65.
21. A. S. D. Heindrichs, H. Geen, C. Giordani, and J. J. Titman, *Chem. Phys. Lett.*, 2001, **335**, 89.
22. E. H. Hardy, R. Verel, and B. H. Meier, *J. Magn. Reson.*, 2001, **148**, 459.
23. A. J. Shaka, J. Keeler, T. Frenkiel, and R. Freeman, *J. Magn. Reson.*, 1983, **52**, 335.
24. M. Edén and M. H. Levitt, *J. Chem. Phys.*, 1999, **111**, 1511.
25. M. Carravetta, M. Edén, X. Zhao, A. Brinkmann, and M. H. Levitt, *Chem. Phys. Lett.*, 2000, **321**, 205.
26. R. J. Iuliucci and B. H. Meier, *J. Am. Chem. Soc.*, 1998, **120**, 9059.
27. R. Benn, H. Grondey, C. Brevard, and A. Pagelot, *J. Chem. Soc., Chem. Commun.*, 1988, **2**, 102.
28. C. A. Fyfe, H. Gies, and Y. Feng, *J. Chem. Soc., Chem. Commun.*, 1989, **17**, 1240.
29. C. T. G. Knight, R. J. Kirkpatrick, and E. Oldfield, *J. Noncryst. Solids*, 1990, **116**, 140.
30. P. Caravatti, G. Bodenhausen, and R. R. Ernst, *Chem. Phys. Lett.*, 1982, **89**, 363.
31. P. Caravatti, L. Braunschweiler, and R. R. Ernst, *Chem. Phys. Lett.*, 1983, **100**, 305.
32. J. E. Roberts, S. Vega, and R. G. Griffin, *J. Am. Chem. Soc.*, 1984, **106**, 2506.
33. C. H. Wu, A. Ramamoorthy, and S. J. Opella, *J. Magn. Reson. A*, 1994, **109**, 270.
34. Z. Gu, C. F. Ridenour, C. E. Bronnimann, T. Iwashita, and A. McDermott, *J. Am. Chem. Soc.*, 1996, **118**, 822.
35. B. J. Van Rossum, H. Forster, and H. J. M. De Groot, *J. Magn. Reson.*, 1997, **124**, 516.
36. R. K. Hester, J. L. Ackerman, B. L. Neff, and J. S. Waugh, *Phys. Rev. Lett.*, 1976, **36**, 1081.
37. T. Terao and S. Matshui, *Phys. Rev. B*, 1980, **21**, 3781.
38. A. Bielecki, A. C. Kolbert, H. J. M. De Groot, R. G. Griffin, and M. H. Levitt, *Adv. Magn. Reson.*, 1990, **14**, 111.
39. C. LeCocq and J.-Y. Lallemand, *J. Chem. Soc., Chem. Commun.*, 1981, **119**, 150.
40. F.-K. Pei and R. Freeman, *J. Magn. Reson.*, 1982, **48**, 318.
41. H. J. Jakobsen, O. W. Sørensen, W. S. Brey, and P. Kanya, *J. Magn. Reson.*, 1982, **48**, 328.
42. A. Lesage, S. Steuernagel, and L. Emsley, *J. Am. Chem. Soc.*, 1998, **120**, 7095.
43. O. W. Sørensen, G. W. Eich, M. H. Levitt, G. Bodenhausen, and R. R. Ernst, *Prog. NMR Spectrosc.*, 1983, **16**, 163.
44. D. Sakellariou, A. Lesage, and L. Emsley, *J. Magn. Reson.*, 2001, **151**, 40.
45. A. Lesage, D. Sakellariou, S. Steuernagel, and L. Emsley, *J. Am. Chem. Soc.*, 1998, **120**, 13 194.
46. A. Lesage and L. Emsley, *J. Magn. Reson.*, 2001, **148**, 449.
47. A. Lesage, P. Charmont, S. Steuernagel, and L. Emsley, *J. Am. Chem. Soc.*, 2000, **122**, 9739.
48. H. O. Kalinowski, S. Berger, and S. Braun, 'Carbon-13 NMR Spectroscopy', John Wiley & Sons: Chichester, 1988.
49. K. Schmidt-Rohr, J. Clauss, and H. W. Spiess, *Macromolecules*, 1992, **25**, 3273.
50. C. Auger, 'Une nouvelle technique de correlation deuterium-carbone pour l'attribution et la mesure des couplages quadrupolaires dans les materiaux orientes', Ph.D. thesis, ENS Lyon, 1998.

Acknowledgements

We would particularly like to acknowledge the invaluable contribution of Anne Lesage to the work we review here, we simply regret that she was not available to write this entry with us. We would like to dedicate this article to Alix. We would also like to thank Sabine Hediger, Paul Hodgkinson, Stefano Caldarelli, Celine Auger, Patrick Charmont, Stefan Steuernagel and all the other members of our group who have contributed to this work. We thank Jamie Walls, Malgorzata Marjanska and Steven P. Brown for helpful discussions and criticisms on this manuscript.

Biographical Sketches

Dimitris Sakellariou, *b* 1974. B.Sc. École Normale Supérieure de Lyon, 1996, Ph.D., École Normale Supérieure de Lyon, France, 2000 under the direction of Lyndon Emsley, Fellow of the Lawrence Berkeley National Laboratory, UC Berkeley, currently working with Alex Pines. Current research interests focus on NMR.

Lyndon Emsley, *b* 1964. B.Sc. Imperial College, London, 1986, Ph.D., Université de Lausanne, Switzerland, 1991 under the direction of Geoffrey Bodenhausen. Fellow of the Miller Institute for Basic Research in Science, UC Berkeley, 1991–1993 (collaboration with Alex Pines). Foreign member of the Institut Universitaire de France, 1994. Professor of Chemistry, École Normale Supérieure de Lyon 1995–present. Current research interests focus on fundamental aspects of NMR, with an emphasis on the solid state.

Vicinal ^{1}H,^{1}H Coupling Constants in Cyclic π-Systems

Harald Günther

University of Siegen, Germany

1	Discussion	1
2	Related Articles	2
3	References	3

1 DISCUSSION

According to the Karplus theory of vicinal ^{1}H,^{1}H coupling constants, i.e. $^3J(^1\mathrm{H},^1\mathrm{H})$, such parameters depend on the structural features of the corresponding HC–CH fragment (dihedral angle Φ, bond length R_{cc}, and HCC valence angles) as well as on the electronic effects of substituents.[1,2] These results form the basis for numerous applications of ^{1}H NMR spectroscopy in organic, bio-organic, and organometallic chemistry.

While the dihedral angle dependence of $^3J(^1\mathrm{H},^1\mathrm{H})$—the well-known *Karplus curve*—is one of the major tools in conformational analysis,[3] structural research in the field of cyclic π-systems profits from the R_{cc} and valence angle dependence which dominates $^3J(^1\mathrm{H},^1\mathrm{H})$ values in planar unsaturated hydrocarbons, where $\Phi = 0^\circ$ for a *cis*-HC$_\mu$⋯C$_\nu$H arrangement and where substitutents are absent. This aspect was first highlighted as a linear dependence between $^3J(^1\mathrm{H},^1\mathrm{H})_{cis}$ and the Hückel (HMO) π-bond order, $P_{\mu\nu}$, of the C$_\mu$⋯C$_\nu$ bond was found for benzenoid aromatics[4] and later extended to olefinic systems.[5,6] At the same time, related correlations between $^3J(^1\mathrm{H},^1\mathrm{H})$ and the CC bond length $R_{\mu\nu}$ were established for aromatics[7] and polyenes.[8] An early application of $^3J(^1\mathrm{H},^1\mathrm{H})$ data for the analysis of the bonding situation in a cyclic π system was the detection of partial π-bond fixation in biphenylene (**1**),[9] which in terms of resonance theory demonstrated the preference for Kekulé structures with exocyclic double bonds at the central four-membered ring. Later, the olefinic nature of tropone (**2**) was established from its $^3J(^1\mathrm{H},^1\mathrm{H})$ values,[10] partial bond fixation in heterocyclic compounds was detected,[11,12] and the characteristic $^3J(^1\mathrm{H},^1\mathrm{H})$ data measured for cyclic dienes and trienes were recognized as important tools for the structural analysis of cyclic diene–triene isomers like norcaradienes and cycloheptatrienes.[13]

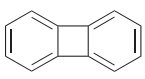

(1)

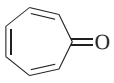

(2)

A detailed investigation of the $^3J(^1\mathrm{H},^1\mathrm{H})_{cis}/R_{\mu\nu}$ and $P_{\mu\nu}$ relations in unsaturated six-membered rings of various benzenoid aromatics and other hydrocarbons,[14,15] where the magnitude of these constants ranges between 5 and 9 Hz (and—as for other $^3J(^1\mathrm{H},^1\mathrm{H})$ values—a positive sign is found[16]), finally led to equations (1) and (2) which can be used to derive bond length and π-bond order information from experimental $^3J(^1\mathrm{H},^1\mathrm{H})_{cis}$ data:

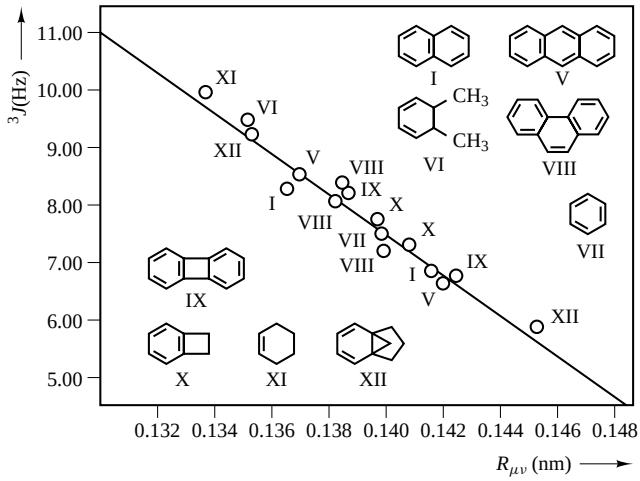

Figure 1 Dependence of $^3J(^1\mathrm{H},^1\mathrm{H})_{cis}$ on the CC bond length in the HC⋯CH fragment of six-membered rings [equation (1)]. (Reproduced with permission from H. Günther, 'NMR Spectroscopy', 2nd edn., Wiley, Chichester, 1995)

$$^3J(^1\mathrm{H},^1\mathrm{H})_{cis} = -351.0R_{\mu\nu}(\mathrm{nm}) + 56.65 \quad (1)$$

$$^3J(^1\mathrm{H},^1\mathrm{H})_{cis} = 12.47P_{\mu\nu}(\mathrm{HMO}) - 0.71 \quad (2)$$

The sensitivity of $^3J(^1\mathrm{H},^1\mathrm{H})_{cis}$ for bond length changes is high (Figure 1) and provides a valuable probe for the bonding situation in various cyclic π systems and annulenes. Steric compression and strain effects may cause deviations from equation (1) if changes of the HCC valence angles are induced.[17,18] This becomes apparent if one compares the data for 1,4-di-*t*-butylnaphthalene[18] with those of naphthalene[15] or data for *o*-di-*t*-butylbenzene[19] and the highly strained benzocyclopropene[17] with those of the unstrained 9,10-dihydroanthracene[17] (Figure 2).

Strain and steric compression are frequently encountered in fused ring systems where these factors cause a decrease in $^3J(1,2)$ and an increase in $^3J(2,3)$ if a small ring ($n < 6$) is fused to a large ring (**3**). The reverse trend—an increase of $^3J(1,2)$ and a decrease of $^3J(2,3)$—is found if a larger ring is fused to a smaller one (**4**).[20]

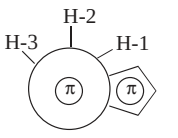

(3)

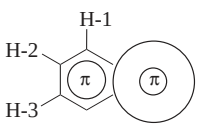

(4)

More drastic changes of the HCC valence angles are induced in π systems of different ring size and modified correlations have been derived for these cases:

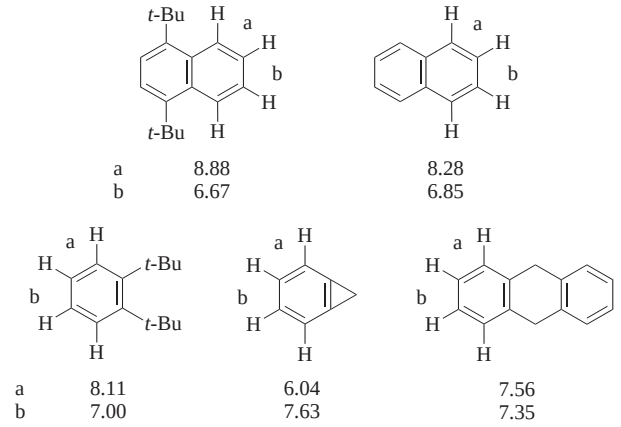

Figure 2 The effect of steric compression and strain on $^3J(^1H,^1H)_{cis}$ values (in Hz) of various HC⎓CH fragments (a, b)

Table 1 The Ring Size Dependence of $^3J(^1H,^1H)_{cis}$ Values

Cycloalkene ring size	^3J(Hz)
3[28]	1.3
4[29]	2.85
5[27]	5.57
6[27]	10.11
7[27]	11.02
8[27]	10.41

Five -membered rings:[5,21]

$$^3J(^1H,^1H)_{cis} = -322.6R_{\mu\nu}(\text{nm}) + 48.45 \quad (3)$$

$$^3J(^1H,^1H)_{cis} = 7.12P_{\mu\nu}(\text{HMO}) - 1.18 \quad (4)$$

Seven-membered rings:[20,22]

$$^3J(^1H,^1H)_{cis} = -367.4R_{\mu\nu}(\text{nm}) + 60.68 \quad (5)$$

$$^3J(^1H,^1H)_{cis} = 21.91P_{\mu\nu}(\text{HMO}) - 3.85 \quad (6)$$

The ring size dependence of the HCC valence angles is a consequence of the changes in internal CCC valence angles for the respective perimeters and a linear correlation of ∢CCC with $^3J(^1H,^1H)_{cis}$ is thus not unexpected. Using five-, six-, seven-, and eight-membered ring systems, an increment of 0.29 Hz per degree was found after correcting for different π-bond orders.[23] Similar relations were established for the long-range ^{1}H,^{1}H couplings ^4J and ^5J.[23] For isolated double bonds, the effect of HCC valence angle changes is most clearly seen by the ring size dependence of $^3J(^1H,^1H)_{cis}$ in cycloalkenes,[24–27] as shown in Table 1.

A systematic study of $^3J(^1H,^1H)_{cis}$ for benzo-annelated annulenes[30] has shown that in addition to steric effects the electronic nature of the annulenes, i.e. the number of π electrons and the degree of delocalization, influences the $^3J(^1H,^1H)_{cis}$ data in the annelated benzene ring in a characteristic way. Thus, the π-electron structure of annulenes can be monitored by the $^3J(^1H,^1H)_{cis}$ data for the benzene ring in the corresponding benzoannulene. The π-bond orders P_{12} and P_{23} are determined from the measured coupling constants according to equation (7), which is based on PPP–SCF π-electron calculations,[31,32]

$$P_{\mu\nu}(\text{SCF}) = 0.104^3J(^1H,^1H)_{cis} - 0.120 \quad (7)$$

a Q value being defined as $Q = P_{12}/P_{23}$. The magnitude of Q is related to the bonding situation in the annulene: $Q < 1.00$ for antiaromatic ($4n$) π systems, $Q > 1.10$ for aromatic ($4n + 2$) π systems, and $1.00 < Q > 1.10$ for olefinic systems. Typical examples are found with the benztropylium ion (**5**)[23] and benzocycloheptatriene-id (**6**)[33] or the two dehydroannulenes (**7**) and (**8**).[34]

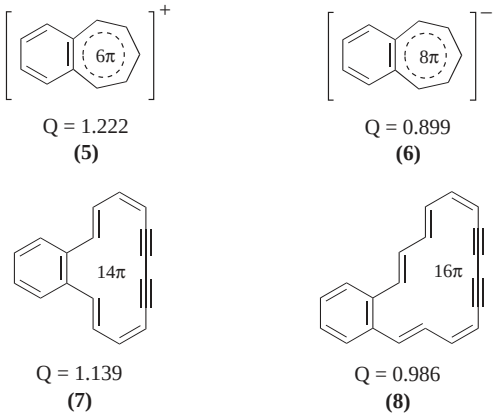

Substituent effects have mostly been studied with substituted benzenes, where a careful determination of the $^3J(^1H,^1H)$ values[35] has established the effect of electronegativity: ^3J(a,b) increases in the (X)C–CH_a–CH_b–CH_c–fragment if X is more electronegative than hydrogen, while a small decrease is found for the coupling ^3J(b,c).

;Vicinal ^{1}H,^{1}H coupling via a *trans*-HC–CH fragment, $^3J(^1H,^1H)_{trans}$, is found only in larger annulene rings which tolerate *trans* double bonds. As a consequence of the different dihedral angle $\Phi = 180°$, such couplings are larger than the *cis* values, as the data reported for [18]annulene [$^3J(^1H,^1H)_{cis}$ = 8.0 and $^3J(^1H,^1H)_{trans}$ = 15.5 Hz][36] demonstrate. Other values have been collected in the literature,[34,37] but a detailed analysis of these data was not attempted. For bridged annulenes, various steric requirements imposed on the perimeter geometry by the bridging group usually lead to a loss of coplanarity of all HC–CH fragments and the magnitude of the vicinal ^{1}H,^{1}H coupling constants is subject to additional factors such as varying dihedral angles.[38–40] Early theoretical calculations for $^3J(^1H,^1H)_{cis}$ have been reviewed.[41]

In conclusion, vicinal ^{1}H,^{1}H coupling constants provide the basis for detailed insights into the electronic structure of annulenes and other cyclic π systems and complement the information obtained from shielding properties such as, for example, ring current effects.

2 RELATED ARTICLES

Heterocycles; Indirect Coupling: Theory and Applications in Organic Chemistry.

3 REFERENCES

1. M. Karplus, *J. Chem. Phys.*, 1959, **30**, 11.
2. M. Karplus, *J. Am. Chem. Soc.*, 1963, **85**, 2870.
3. H. Booth, *Prog. Nucl. Magn. Reson. Spectrosc.*, 1969, **5**, 149; C. Altona, J. H. Ippel, A. J. A. W. Hoekzema, C. Erkelenz, M. Groesbeek, and L. A. Donders, *Magn. Reson. Chem.*, 1989, **27**, 564.
4. N. Jonathan, S. Gordon, and B. P. Dailey, *J. Chem. Phys.*, 1962, **36**, 2443.
5. W. B. Smith, W. H. Watson, and S. Chiranjeevi, *J. Am. Chem. Soc.*, 1967, **89**, 1438.
6. H. Günther, *Tetrahedron Lett.*, 1967, 2967.
7. D. R. Eaton, A. D. Josey, W. D. Phillips, and R. E. Benson, *J. Chem. Phys.*, 1963, **39**, 3513.
8. G. Scheibe, W. Seiffert, G. Hohlneicher, C. Jutz, and H. J. Springer, *Tetrahedron Lett.*, 1966, 5053.
9. A. R. Katritzky and R. E. Reavill, *Recl. Trav. Chim. Pays-Bas*, 1964, **83**, 1230.
10. D. J. Bertelli, T. G. Andrews, Jr., and P. O. Crews, *J. Am. Chem. Soc.*, 1969, **91**, 5286.
11. N. M. D. Brown and P. Bladon, *Spectrochim. Acta*, 1968, **24A**, 1869.
12. A. J. Boulton, P. J. Halls, and A. R. Katritzky, *Org. Magn. Reson.*, 1969, **1**, 311.
13. H. Günther and H. H. Hinrichs, *Tetrahedron Lett.*, 1966, 787.
14. M. A. Cooper and S. L. Manatt, *J. Am. Chem. Soc.*, 1969, **91**, 6325.
15. J. B. Pawliczek and H. Günther, *Tetrahedron*, 1970, **26**, 1755.
16. P. C. Lauterbur and R. J. Kurland, *J. Am. Chem. Soc.*, 1962, **84**, 3405.
17. M. A. Cooper and S. L. Manatt, *J. Am. Chem. Soc.*, 1970, **92**, 1605.
18. M. A. Cooper and S. L. Manatt, *J. Am. Chem. Soc.*, 1970, **92**, 4646.
19. S. Castellano and R. Kostelnik, *Tetrahedron Lett.*, 1967, 5211.
20. H. Günther, H. Schmickler, M.-E. Günther, and D. Cremer, *Org. Magn. Reson.*, 1977, **9**, 420.
21. H. L. Ammon and G. L. Wheeler, *J. Am. Chem. Soc.*, 1975, **97**, 2326.
22. S. Braun and J. Kinkeldei, *Tetrahedron*, 1977, **33**, 3127.
23. H. Günther, A. Shyoukh, D. Cremer, and K.-H. Frisch, *Liebigs Ann. Chem.*, 1978, 150.
24. O. L. Chapman, *J. Am. Chem. Soc.*, 1963, **85**, 2014.
25. G. V. Smith and H. Kriloff, *J. Am. Chem. Soc.*, 1963, **85**, 2016.
26. P. Laszlo and P. v. R. Schleyer, *J. Am. Chem. Soc.*, 1963, **85**, 2017.
27. M. A. Cooper and S. L. Manatt, *Org. Magn. Reson.*, 1970, **2**, 511.
28. J. B. Lambert, A. P. Iovanovich, and W. I. Oliver, *J. Phys. Chem.* 1970, **74**, 2221.
29. E. A. Hill and J. D. Roberts, *J. Am. Chem. Soc.*, 1967, **89**, 2047.
30. H. Günther and D. Cremer, *Justus Liebigs Ann. Chem.*, 1972, **763**, 87.
31. R. Pariser and R. G. Parr, *J. Chem. Phys.*, 1953, **21**, 466.
32. J. A. Pople, *Trans. Faraday Soc.*, 1953, **49**, 1375.
33. S. W. Staley and A. W. Orvedal, *J. Am. Chem. Soc.*, 1973, **95**, 3384.
34. H. Günther, M.-E. Günther, D. Mondeshka, H. Schmickler, F. Sondheimer, N. Darby, and T. M. Cresp, *Chem. Ber.*, 1979, **112**, 71.
35. S. Castellano and C. Sun, *J. Am. Chem. Soc.*, 1966, **88**, 4741.
36. J. F. M. Oth, *Pure Appl. Chem.*, 1971, **25**, 573.
37. R. C. Haddon, V. R. Haddon, and L. M. Jackman, *Topics Curr. Chem.*, 1971, **16**, 103.
38. H. Günther, *Z. Naturforsch.*, 1969, **24B**, 680.
39. H. Günther and H.-H. Hinrichs, *Tetrahedron*, 1968, **24**, 7033.
40. A. Alscher, W. Bremser, D. Cremer, H. Günther, H. Schmickler, W. Sturm, and E. Vogel, *Chem. Ber.*, 1975, **108**, 640.
41. J. Kowalewski, *Prog. Nucl. Magn. Reson. Spectrosc.*, 1977, **11**, 1.

Biographical Sketch

Harald Günther, *b* 1935. Studied chemistry at the Universities of Stuttgart and Heidelberg, Ph. D., 1961, Heidelberg with G. Wittig. Research fellow at Mellon-Institute, Pittsburgh 1961–63; introduced to NMR by A. A. Bothner-By. 1963–77 Staff member at the Institute of Organic Chemistry, University of Cologne; Habilitation 1968 with E. Vogel; Associate Professor 1970; since 1977 Full Professor at the University of Siegen. 1973 Chemistry Award of the Academy of Sciences, Göttingen; 1973 Award of the Fonds der Chemischen Industrie, Frankfurt; ca. 200 publications; author of NMR textbook (German, English, Russian, Polish, French editions). Editor-in-Chief of *Magnetic Resonance in Chemistry* since 1992. Research interests include applications of high-resolution and solid state NMR in organic and organometallic chemistry.

Vicinal Coupling Constants and Conformation of Biomolecules

Cornelis Altona

Leiden University, Leiden, The Netherlands

1	Introduction	1
2	Vicinal Proton–Proton Coupling Constants ^3J(H,C,C,H)	1
3	Vicinal Coupling Constants Involving Heteroatoms	6
4	Selected Applications of ^3J in the Field of Biomolecules	8
5	Caveats	13
6	Related Articles	13
7	References	13

1 INTRODUCTION

The discovery[1] that the vicinal (three-bond) proton–proton coupling constant, ^3J(H,H), varies smoothly with the associated H–C–C–H torsion angle ϕ(HH) in ethane had a profound impact on the acceptance of NMR as an indispensable tool in stereochemistry and conformational analysis. The well-known Karplus equation,[1,2] also called the cosine-square rule [equation (1)], was derived from valence bond calculations on the unperturbed ethane molecule.

$$^3J(\mathrm{H,H}) = C_0 + C_1\cos(\phi_{\mathrm{HH}}) + C_2\cos(2\phi_{\mathrm{HH}}) \quad (1a)$$

The Fourier series embodied in equation (1) is more often written as:

$$^3J(\mathrm{H,H}) = A\cos^2(\phi_{\mathrm{HH}}) + B\cos(\phi_{\mathrm{HH}}) + C \quad (1b)$$

Of course, simple relationships exist between C_0, C_1, C_2 and A, B, C, respectively: $C_0 = 0.5A + C$, $C_1 = B$, $C_2 = 0.5A$. Karplus[2] predicted that ^3J(H,H) depends on various other molecular parameters, such as the electronegativity of the substituents, bond lengths, and bond angles. In the same paper[2] he issued a caveat against the indiscriminate application of his equation and the theoretically derived parameters [coefficients in equation (1)] to 'estimate torsion angles to an accuracy of one or two degrees'.

The general shape of the Karplus curve, large ^3J at $\phi = 0^\circ$ (eclipsed, sp) and at or near $\phi = 180^\circ$ (*trans*, *anti* or *ap*), and decreasing to a minimum value ($^3J \approx 0$ Hz) near $\phi = 90^\circ$, in the course of time was shown to be applicable to many molecular fragments, including ^3J(H,H) with heteroatoms in the coupling path and also ^3J(X,H) and ^3J(X,Y) with X,Y NMR-active heteronuclei like ^{13}C, ^{15}N, and ^{31}P, for example ^3J(H,C,O,H), ^3J(H,N,C,H), ^3J(N,C,C,H), ^3J(C,C,C,H), ^3J(H,C,O,P), ^3J(C,C,O,P). Several of these more exotic vicinal couplings are useful in the conformational analysis of bio-molecules such as peptides, proteins, nucleic acids, and polysaccharides.

In suitable cases direct (^1J) and geminal (^2J) coupling constants provide additional structural information, albeit of a more qualitative nature. Long-range couplings (^nJ, $n > 3$) are often highly useful, especially ^4J couplings (planar W path). However, the present contribution focuses entirely on vicinal (^3J) couplings.

The coupling constant ^3J(H,C,C,H) with C saturated carbon is by far the best investigated and will be treated in depth in the present article. A selection of more simple Karplus equations involving heteroatoms will be presented and briefly discussed. Familiarity with the basic tenets and methods of conformational analysis is assumed. The multitude of techniques that are currently available to measure the coupling constants of interest remain outside the scope of the present contribution (see Section 7 for related articles). Clearly, the approaches that are found useful in the conformational analysis of biomolecules are applicable to many other molecular fragments in organic chemistry. The article concludes with some applications in the field of (poly)peptides and nucleic acids, and caveats are issued. The reader is advised to consult the selection of references given for further details and for references therein.

2 VICINAL PROTON–PROTON COUPLING CONSTANTS ^3J(H,C,C,H)

2.1 General Background

In the late 1950s experiments already showed[3] that the *time-averaged* ^3J(H,H) [equation (2)] in monosubstituted ethanes CH_3CH_2X decreases more or less linearly with increasing electronegativity of the substituent X.

$$\langle ^3J(\mathrm{H,H})\rangle = [J(60) + J(180) + J(300)]/3 \quad (2)$$

Studies carried out in the early 1960s[4,5] confirmed these findings. Perhaps unfortunately, the (erroneous) notion that ^3J(H,H) in all situations decreases with increasing electronegativity became firmly lodged in the minds of NMR spectroscopists. A second, also erroneous, assumption was generally accepted and that is the linear additivity of (relative) electronegativities $\Delta\chi_1 = \chi_i - \chi_{\mathrm{H}}$. In other words, the general validity of equation (3) was accepted without question, although proper analysis of the experimental data on monosubstituted ethanes and 2-substituted propanes, already available in the early 1960s, could have shown differently.

$$^3J(\mathrm{H,H}) = \mathrm{f}(\phi) + a\Sigma_i\Delta\chi_i \quad (3a)$$

or alternatively:

$$^3J(\mathrm{H,H}) = \mathrm{f}(\phi)[1 - a(\Sigma_i\Delta\chi_i)/\mathrm{f}(\phi)] \quad (3b)$$

where f(ϕ) denotes a Karplus function of ϕ_{HH}; a/f(ϕ) is usually written as k.

In the case of coupling to the fast-rotating methyl protons, for example in substituted ethanes and 2-substituted propanes [equation (2)], the ϕ-dependent terms in equation (1a) vanish and f(ϕ) reduces to the 'constant' C_0. The following comparison is obtained (Hz):

$$CH_3CH_2X:^3\ C_0 = 7.5,\ a = -0.4$$

$$CH_3CH_2X:^4\ C_0 = 7.9,\ a = -0.7$$

$$CH_3CHXCH_3:^3\ C_0 = 7.0,\ a = -0.55$$

$$\text{Combined}:^5\ C_0 = 7.7,\ a = -0.80$$

In the remainder of this article the slope (a) will be denoted C_{01}. The 'goodness of fit' of these least-squares regressions (± 0.3 Hz) is disappointing, moreover, several workers[4,5] noted a breakdown of linearity in cases where X and Y in CH_3CHXY represent highly electronegative substituents like fluorine or oxygen. It should be noted that the measured coupling to methyl cannot yield the electronegativity dependence of the 'constants' C_1 and C_2 in equation (1); it was simply assumed that these dependences were all equal.

In 1965 Booth[6] noted that an electronegative substituent located on the C–C fragment constituting the coupling path and in antiparallel (*ap*) position relative to one of the two coupling *gauche* (*sc*) protons causes an 'extra' diminution of their mutual coupling constant (Booth's rule). In hindsight it is easy to see that this observation implies a breakdown of the symmetry inherent to a Fourier series with cosine terms only, e.g., equation (1a), but it was not so interpreted at the time. On the contrary, one might say, and for a long time the Durette–Horton equation[7] [equation (4)], was popular in the field.

$$^3J(\mathrm{H,H}) = [C_0 + C_1\cos(\phi) + C_2\cos(2\phi)](1 - k\sum_1^4 \Delta\chi_i) \qquad (4)$$

Equation (4) is simply a combination of equations (1a) and (3b), rewritten here in terms of cosine Fourier coefficients C; ϕ denotes the torsion angle between the coupling nuclei indicated in parentheses on the left-hand side of equation (4), $\Delta\chi_i$ are relative electronegativities of substituents according to either the Pauling[8] or the Huggins[9] scale.

Unfortunately, equation (4) embodies at least four questionable or even erroneous assumptions:

1. The orientation of any electronegative substituent with respect to the coupling protons is unimportant (in negation of Booth's rule).
2. Coefficients C_0, C_1, C_2 have the same electronegativity dependence.
3. Substituent effects are linearly additive.
4. The standard atomic electronegativity scales[8,9] can be applied to polyvalent substituents, regardless of the remaining atoms or groups attached.

At this point it should be mentioned that many workers in the field of stereochemistry in a way circumvented assumptions 2, 3, and 4 by the calibration of Karplus parameters for given classes of molecules of interest with the aid of model compounds with known or estimated torsion angles. Even today this approach often remains the only sensible course of action available in the case of couplings to heteronuclei, e.g., ^3J(C,H), ^3J(N,H), ^3J(P,H), ^3J(P,C), vide infra. More refined approaches are now possible in the case of ^3J(H,H) in sp^3–sp^3 H–C–C–H fragments.

2.2 Substituent-Induced Asymmetry in the Karplus Curve

The first systematic investigation into the orientational effects of substituents on ^3J(H,H) was carried out by Abraham and Gatti[10] with the aid of a series of 1,2-disubstituted ethanes CH_2X–CH_2Y. Their results are summarized in Figure 1.

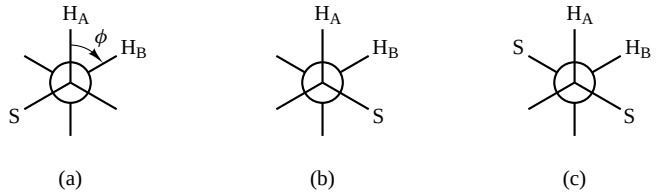

Figure 1 Newman projections along the central bond of a H_A–C–C–H_B fragment, H_A and H_B are mutually coupled. (a) Situation pertaining to Booth's rule (strong decrease of ^3J(H,H) for an electronegative substituent S); (b) situation pertaining to Abraham's rule [weak increase of ^3J(H,H)]; (c) situation where Abraham's rule applies twice. This configuration occurs, for example, in cyclohexanes with H_A, H_B diequatorial and the S substituents diaxial

For most practical purposes one needs to distinguish three different situations:

(a) *Gauche* (*sc*) protons, J_g, with X in an *anti* orientation X_t: J_g decreases strongly with increasing electronegativity of X (Booth's rule);
(b) *Gauche* (*sc*) protons, J_g, and a substituent X in a *gauche* orientation with respect to its vicinal coupling proton, X_g: J_g increases with increasing electronegativity of X (Abraham's rule);
(c) *Anti* or *trans* (*ap*) protons, J_t, with X necessarily in a *gauche* position (not shown in Figure 1): J_t decreases with increasing electronegativity of X.

For X = oxygen in conformationally rigid pyranose sugars, a statistical analysis[11] of a large set of couplings indicated the following changes of ^3J from X = H: situation (a) -1.8 Hz; (b) $+0.5$ Hz; (c) -1.45 Hz. This example clearly illustrates the fact that *gauche* (*sc*) couplings do not obey the simple cosinesquare rule. The various effects are additive to a good approximation, 24 additivity constants (eight different substituent types) gave an rms error of only 0.29 Hz for a test set consisting of 305 couplings.

Extended Hückel molecular orbital theory (EHT) calculations of ^3J(H,H), carried out by Pachler[12,13] on CH_3CH_2X(X = H, CH_3, NH_2, OH, F), CH_3CHF_2, and CH_2FCH_2F, indicated that an X substituent (or the C–X bond) induces an asymmetry in the Karplus curve. More refined EHT calculations[14,15] confirmed this important finding and showed[15] that mutual interaction between substituents cannot be neglected. Pachler[12,13] described the calculated influence of the X substituent in terms of the summation of two effects: (1) an attenuation of the Fourier coefficients, i.e., as in equation (4) but with different k values for C_0, C_1, and C_2; (2) a phase shift, assumed to be proportional to the electronegativity of the substituent (Figure 2).

A phase shift can be formulated in several ways, for example by the introduction of sine terms.[12,13] This leads to equation (5).

$$^3J(\mathrm{H,H}) = C_0 + C_1\cos(\phi) + C_2\cos(2\phi) + S_1\sin(\phi) + S_2\sin(2\phi) \qquad (5a)$$

with

$$C_m = C_{m0} + C_{m1}\Sigma_i\Delta\chi_i \quad \text{and} \quad S_m = S_{m1}\Sigma_i s_i\Delta\chi_i \qquad (5b)$$

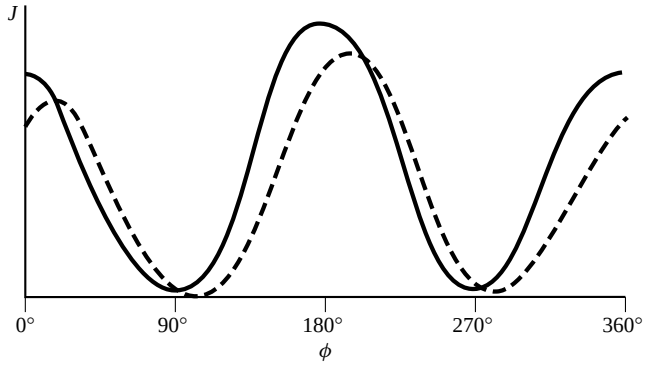

Figure 2 The calculated coupling constants (EHT method[14]) for ethane (solid line) and fluoroethane (dashed line) as a function of the HH torsion angle ϕ; the positive direction of ϕ is defined according to IUPAC,[17] the F atom occupies the S_1 substituent position shown in Figure 3 (sign factor s_i = +1). (Reproduced with permission from Elsevier Science Ltd., Kidlington, UK, from K. G. R. Pachler, *Tetrahedron*, 1971, **27**, 187)

In equation (5) the original Pachler equation[12,13] is recast into a general Fourier expression.[15] Moreover, the use of a separate and cumbersome proton-substituent torsion angle $\cdot\Phi_{HX}$[12,13] is avoided by the introduction of the 'sign' factor s_i for each substituent S_i, s_i is +1 or −1 according to the definition by Haasnoot et al.[16] (see Figure 3). (In this paper, as well as in others,[15] the sign factor S_i was denoted ξ_i.)

It is important to keep in mind that the sign factors s_i of the substituents S_1 and S_2 (*not* to be confused with the Fourier coefficients S_1 and S_2) depend exclusively upon their stereochemical position with respect to their 'own' geminal coupling proton H_A. The following recipe applies: choose a Newman projection along the coupling path in such a manner that the chosen coupling proton H_A is located on the front side (Figure 3): S_1 is found at 120° and S_2 at −120° (positive angle defined as clockwise). Repeat the procedure with H_B up front, S_3 is at 120° and S_4 at −120°. The sign factors (s_i = +1 for substituents S_1 and S_3, s_i = −1 for S_2 and S_4) are thus uniquely defined and are *independent* of the actual value of the torsion angle ϕ_{AB}. It goes without saying that in the case of a CH_2 group ($CH_{A1}H_{A2}$) one has to take care to select the proper H_A (interchange of H_{A1} and H_{A2} means a change of sign factor for the remaining substituent). Equation (6) simplifies the computer programming:

$$\Sigma_i s_i \Delta\chi_i = \Delta\chi_1 - \Delta\chi_2 + \Delta\chi_3 - \Delta\chi_4 \qquad (6)$$

It is easily appreciated that the sine terms vanish in all cases where equivalent substituents (same $\Delta\chi_i$) occupy a +1 and a −1 position at the same time, for example in $-CH_2-CHX_2$ and the +, − coupling in the $-CHX-CH_2X$ molecular fragment. The above sign factor definition is associated with the definition of the positive direction of ϕ_{AB} according to IUPAC rules:[17] positive when H_B rotates clockwise away from H_A, with the H_A,H_B eclipsed position taken as zero angle. Since the sine terms change sign at ϕ_{AB} = 0° a change of substituent position from +1 to −1 can be depicted as a mirroring of the ΔJ curve (Figure 4). Equation (5) is invariant under electronegativity scale changes,[15] aside from changes in the values of the coefficients C_m and S_m. It is a valid procedure to choose the relative electronegativity of hydrogen as zero and to fix $\Delta\chi$ of one other substituent. For practical reasons, a value λ_{OR} = 1.40 was selected, vide infra.

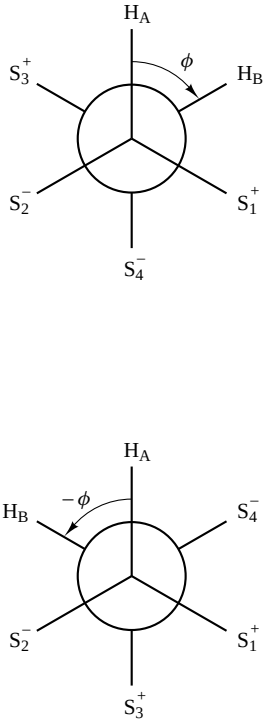

Figure 3 Definition of substituents with positive (S_1 and S_3) and negative (S_2 and S_4) sign factors s_i. Note that with each coupling nucleus in an sp^3–sp^3 fragment two geminal substituents with opposite sign factors are associated. The result of rotation of H_B with respect to H_A in the $-\phi$ direction is mathematically equivalent to the result of a $+\phi$ rotation with concomittant interchange of S_1 and S_2. (Reproduced with permission of Elsevier Science Ltd., Kidlington, UK, from C. A. G. Haasnoot, F. A. A. M. de Leeuw, and C. Altona, *Tetrahedron*, 1980, **36**, 2783)

Haasnoot et al.[16] also sought to describe the generalized Karplus equation by superimposing a phase shift upon the symmetrical ethane curve [equation (7) and Figure 4].

$$^3J(\mathrm{H,H}) = P_1\cos^2(\phi) + P_2\cos(\phi) + P_3 + \Sigma_i \Delta\chi_i[P_4 + P_5\cos^2(s_i(\phi) + P_6 \mid \Delta\chi_i \mid)] \qquad (7)$$

Comparison with equation (5) shows that C_{11} and S_{11} have been set to zero, and that in the cos(2ϕ) and sin(2ϕ) terms

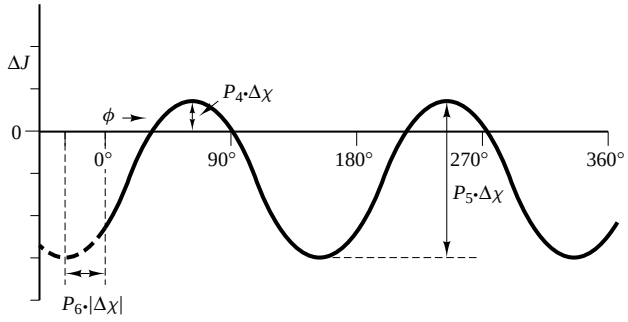

Figure 4 The calculated difference curve $\Delta J = J(CH_3CH_2S) - J(CH_3CH_3)$ for a substituent S with a positive sign factor, showing the rationale behind the phase-shift parameters P_4, P_5, and P_6 in the Haasnoot equation (7)[16]

both a constraint (through a common parameter P_5) and a nonlinear $\Delta\chi_i$ dependence have been introduced. The invariance property (vide supra) does not hold for equation (7). The parameters P_1–P_6 were empirically determined with the aid of a test set containing 315 couplings and corresponding ϕ_{HH} values.[16] Each substituent was assigned a $\Delta\chi_i$ value according to Huggins,[9] but empirically modified to account for the moderation of the electronegativity of the α substituent by attached atoms or groups (β substituents), other than hydrogen. A least-squares regression (J_{calc} versus J_{obs}) showed an rms error of 0.48 Hz and a correlation coefficient R of 0.992, in contrast to a similar regression using three parameters only, equation 1(a) (rms = 1.20 Hz, R = 0.947).[16]

2.3 Group Electronegativities and Nonadditivity Effects

Analysis[15] of the results of a systematic series of calculations of ^3J(H,H) in a variety of mono-, di-, tri-, and tetrasubstituted ethanes by means of the EHT method (1404 J values) suggested that: (a) the use of standard relative electronegativities $\Delta\chi_i$ should perhaps be abandoned in favor of 'best values' of substituent constants λ_i derived from the data set at hand; (b) the nonadditivity effect (interaction between substituents) can be well described by the introduction of cross terms involving products $\Delta\chi_i\Delta\chi_j$ or $\lambda_i\lambda_j$. Díez et al.[18] allowed the coefficients of equation (5b) to be quadratically dependent upon λ. It was shown that only certain combinations of cross terms can survive in such an expansion because of symmetry. Neglecting interactions between more than two substituents, one obtains equation (8), which is in fact an extension of equation (5).

$$C_m = C_{m0} + C_{m1}\Sigma_i\lambda_i + C_{m11}\Sigma_i\lambda_i^2 + C_{m12}(\lambda_1\lambda_2 + \lambda_3\lambda_4) + C_{m13}(\lambda_1\lambda_3 + \lambda_2\lambda_4) + C_{m14}(\lambda_1\lambda_4 + \lambda_2\lambda_3) \quad (8a)$$

$$S_m = S_{m1}\Sigma_i s_i\lambda_i + S_{m11}\Sigma_i s_i\lambda_i^2 + S_{m13}(\lambda_1\lambda_3 + \lambda_2\lambda_4) \quad (8b)$$

How can we determine the 'substituent constants' or 'group electronegativities' λ_i (which may contain other factors beside electronegativity)? Which of the cross terms in equation (8) are important and which can be neglected safely? In an attempt to answer these questions a combined empirical and theoretical approach was taken.

First, a large body of accurate (±0.02 Hz) coupling data from mono- and 1,1-disubstituted ethanes was measured and analyzed.[19] Because of torsional averaging, one isolates the 'constant' C_0 in equation (8a), m = 0. Excluding the self-quadratic term C_{011} from consideration,[15] we obtain equation (9).

$$\langle^3J(\mathrm{H,\ H})\rangle = C_{00} + C_{01}(\lambda_1 + \lambda_2) + C_{012}(\lambda_1\lambda_2) \quad (9)$$

Not only were the coefficients C_{00}, C_{01}, and C_{012} optimized, but also the λ_i values. As explained above, parameter redundancies were removed by fixing the λ values of two different substituents present in the set: λ_H = 0.00 and λ_{OR} = 1.40 (measurements in solvent $CDCl_3$). The 'best' least-squares regression[19] yielded equation (10):

$$\langle^3J(\mathrm{H,\ H})\rangle = 7.836 - 0.594(\lambda_1 + \lambda_2) - 0.423(\lambda_1 \cdot \lambda_2) \quad (10)$$

and in addition 50 λ_i values[19] from 84 couplings; rms deviation = 0.018 Hz, maximum deviation = 0.06 Hz. A similar regression with the use of Huggins's relative electronegativities yielded a 10-times larger rms deviation;[19] however, this regression also underlined the importance of the $\lambda_1\lambda_2$ cross term, at least for coupling to methyl protons.

Table 1 Substituent Parameters λ_i (Relative Group Electronegativities) Deduced from $\langle^3J\rangle$ of Various Mono- and 1,1-Disubstituted Ethanes in $CDCl_3$ and in D_2O, Equation (10). More Detailed Data are Given Elsewhere.[19,20,24] R Signifies Carbon, Usually Alkyl; Z Signifies any Substituent, Except Hydrogen and Halogens.[19] Fixed Points are Indicated by an Asterisk; 90% Confidence Limits (×100) are Shown in Parentheses. Note That Several Values Are Not Applicable to Mono-Substituted Ethanes[19,20]

Group	$\lambda_i(CDCl_3)$	$\lambda_i(D_2O)$
H	0.00*	0.00
CN	0.33(3)	0.33(3)
COOH	0.39(3)	0.33(3)
COO^-	–	0.41(4)
$COOR/CONH_2$	0.42(2)	–
Ph	0.45(4)	–
C(=O)R	0.50(3)	0.50
$C(Me)_3$	0.48	–
CHMeZ[a]	0.62	–
CH_2Z[b]	0.72	–
CH_3	0.80	–
SH	0.75(3)	0.75(3)
I	0.63(4)	–
Br	0.80(3)	–
Cl	0.94(3)	0.94(3)
F	1.37(5)	–
NRC(=O)R (*S-cis*)	0.52(4)	0.52(4)
9-Purines	0.56(2)	0.56(2)
1-Pyrimidines	0.56(2)	0.56(2)
NHC(=O)R	0.85(3)	0.81(3)
NH_3^+	–	0.82(4)
NR_2	1.12(5)	1.00(5)
NHR	1.15(5)	1.02(5)
NH_2	1.19(4)	1.09(4)
NO_2	0.77(3)	0.77(3)
OC(=O)R	1.16(3)	1.16(3)
OSO_2OR	1.19(9)	–
OPO_2OR	–	1.25(4)
$OPO(OR)_2$	1.29(4)	1.25(4)
OH	1.33(4)	1.25(4)
OR	1.40*	1.26(4)
OAr	1.42(5)	1.34(5)

[a] λ_i range 0.60–0.62; for Z = halogen: Cl 0.85, Br 0.92, I 1.02.
[b] λ_i range 0.65–0.78; for Z = halogen: F 0.65, Cl 0.82, Br 0.92, I 0.99.

Equation (10) proved to be highly useful for determining λ_i values of substituents not present in the original data set. Recently, special attention[20] was paid to solvent effects, in particular to the influence of the solvent D_2O in cases where the α substituent carries at least one nonconjugated lone pair of electrons that can readily act as a hydrogen bond acceptor. The vicinal coupling constants (and thus λ values) measured in common organic solvents (like acetone-d_6, CD_3CN, and DMSO) hardly differ from those established in $CDCl_3$. Table 1 presents a selection of λ_i values of substituents that are of particular value in the analysis of couplings measured in biomolecules.

Second, the least-squares analysis of the set of 1404 J values indicated[15] that only two more cross terms (besides C_{012}) are probably important for use in equation (8a): C_{214} and either S_{211} or S_{213}.

Table 2 Final rms Deviations Obtained for ^3J(H,H) with the Aid of the 299 J Test Set in the Various Approximations[a]

Approximations	rms($\Delta\chi_i$)[b] (Hz)	rms(λ_i)[c] (Hz)	N[d]
1. Karplus[e]	1.18	1.18	3
2. Karplus (linear)[f]	0.73	0.70	5
3. Pachler[g]	0.38	0.39	6
4. Haasnoot[h]	0.37	0.36	6
5. Díez–Donders[i]	0.38	0.33	6
6. Díez–Donders[j]	0.37	0.32	8
7. Díez–Donders[k]	0.36	0.31	7

[a]The C_{11} coefficient in equation (5b) was set to zero in all parameter optimizations. It is strongly correlated to some other coefficients.
[b]With the use of Huggins's relative electronegativity scale[9] without β substituent correction.[16]
[c]With the use of experimental 'group electronegativity' values λ_i.[19,20]
[d]Number of optimized parameters.
[e]Equation (1a).
[f]Equation (5), C coefficients only.
[g]Equation (5), S_2 added (the rms error does not change when C_{11} and S_{11} are also added).
[h]Equation (7), the coefficients (based on λ_i) are shown in equation (11).
[i]Equation (8): C_{00}, C_{01}, C_{10}, C_{20}, C_{21}, S_{211} used, the coefficients (based on λ_i) are shown in equation (12).
[j]Equation (8): C_{00}, C_{01}, C_{012}, C_{10}, C_{20}, C_{21}, C_{214}, S_{211} used.
[k]Equation (8), as in footnote [??], but C_{01} fixed on the 'ethane' value, and C_3 added (C_3 = 0.1 taken as the fixed value); the coefficients (based on λ_i) are shown in equation (13).

2.4 Parameter Optimizations

In order to test the ideas developed in the previous sections, an empirical approach was again taken. The original data set (315 J set)[16] was first reduced to 299 J values (299 J set) by the deletion of norbornane- and norbornene-like structures [equations (5) and (7) do not contain correction terms for through-space effects,[21] nor for deviations of CCH bond angles from the tetrahedral value, see Section 5]. Group electronegativities λ_i were selected for the various substituents present in the data set. The corresponding torsion angles were recalculated with the aid of the MM2-85 force field.[22]

A series of least-squares parameter optimizations were carried out (see Table 2). It is of interest to watch the successive improvement, as judged by the drop in rms deviation, as we start (entry 1) from the original three-parameter Karplus equation [equation (1a)], and successively add (entry 2) an electronegativity dependence of the C_0 and C_2 coefficients, add (entry 3) the sine terms of the modified Pachler equation [equation (5)], use (entry 4) the Haasnoot approximation [equation (7)], and finally the Díez–Donders equation [equation (8)], the latter in three forms: (1) (entry 5), all cross terms zero, except the S_{211} $\sum_u S_i$ $\lambda_i{}^2$; (2) (entry 6) as (1) but C_{012} ($\lambda_1\lambda_2$ + $\lambda_3\lambda_4$) and C_{214} ($\lambda_1\lambda_4$ + $\lambda_2\lambda_3$) cos(2ϕ) added; (3) (entry 7) as (2) plus a small threefold term C_3 cos(3ϕ) added. In the latter parameter optimization, the C_{01} parameter was kept fixed on the value obtained from the 'ethane set' [equation (10)]; C_3 was fixed at −0.10, a value close to that suggested by ab initio calculations.[23]

The current parameters are shown in equations (11)–(13), with reference to the entries in Table 2.

Entry 4, Haasnoot:

$$^3J(\mathrm{H,H}) = 14.64\cos^2(\phi) - 0.78\cos(\phi) + 0.58 + \Sigma_i\lambda_i[0.34 - 2.31\cos^2(s_i(\phi) + 18.40|\lambda_i|)] \quad (11)$$

Entry 5, Díez–Donders:

$$^3J(\mathrm{H,H}) = (7.82 - 0.79\Sigma_i\lambda_i) - 0.78\cos(\phi) + (6.54 - 0.64\Sigma_i\lambda_i)\cos(2\phi) + (0.70\Sigma_i s_i\lambda_i^2)\sin(2\phi) \quad (12)$$

Entry 7, Díez–Donders:

$$^3J(\mathrm{H,H}) = [7.41 - 0.59\Sigma_i\lambda_i - 0.27\Sigma_i(\lambda_1\lambda_2 + \lambda_3\lambda_4)] - 0.85\cos(\phi) + [6.84 - 0.87\Sigma_i\lambda_i + 0.29(\lambda_1\lambda_4 + \lambda_2\lambda_3)]\cos(2\phi) - 0.10\cos(3\phi) + (0.71\Sigma_i s_i\lambda_i^2)\sin(2\phi) \quad (13)$$

The coefficients of equation (13) differ from previous ones[24] mainly because a constraint is now laid upon the cos(3ϕ) coefficient, vide supra.

2.5 Summary of Results

1. In previous work the unsatisfactory rms deviation (0.48 Hz) obtained with the use of equation (7) and the full 315 J calibration set, prompted Haasnoot et al.[16] to propose a division of the set into three parts. In other words, separate parameters were presented for ethane-like fragments which contained two, three, and four substituents, i.e. for CH_2-CH_2, $CH-CH_2$, and $CH-CH$ moieties, respectively. In contrast, all of the parameter optimizations reported in Table 2 were carried out on the full 299 J test set and it was found that a single optimization suffices to reach an acceptable rms deviation (0.37 Hz). Presumably, the improved agreement between J_{obs} and J_{calc} is at least, in part, the result of an improvement in calculated ϕ_{HH} values in the present calibration set.
2. The extended five-parameter Karplus equation [terms up to cos(2ϕ) and linear electronegativity dependence of the Fourier coefficients C_0 and C_2] gives a 'best' rms deviation of only 0.70 Hz. Introduction of the asymmetry effect induced by a substituent diminishes the rms error in a dramatic way to less than 0.4 Hz. Systematic theoretical and experimental investigations into the effect of asymmetry on other types of vicinal couplings: ^3J(C,H), ^3J(N,H), ^3J(P,H), ^3J(P,C), unfortunately appear to be lacking, but see Section 3.2.
3. The Pachler Fourier series equation, equation (5), postulates a linear electronegativity dependence of the asymmetric part, expressed as $S_{21}\sum_i s_i\Delta\chi_i$ sin(2ϕ) or in the present work also as $S_{21}\sum S_i\lambda_i$ sin(2ϕ). The Haasnoot[16] formulation, equation (7), implicitly contains $\Delta\chi_i{}^2$ cos(2ϕ) and $\Delta\chi_i{}^2$ sin(2ϕ) terms. The Díez–Donders equation, equation (8), explicitly uses an $S_{211}\sum_i S_i\lambda_i{}^2$ sin(2ϕ) term. This term alone, in combination with the use of empirical group electronegativities λ_i, is responsible for a substantial decrease in the rms deviation compared with the linear Fourier: 0.33 Hz versus 0.39 Hz, compare entries 5 and 3 in Table 2.

4. The introduction of two more cross terms (C_{012} and C_{214}) in the Díez–Donders formulation is only slightly effective, compare entries 5 and 6. This result comes as a surprise in view of the importance of the C_{012} term in the ethane/2-propane series [equation (10)].
5. The use of a Pauling/Huggins-type electronegativity scale appears perfectly justified up to a certain level of approximation.

3 VICINAL COUPLING CONSTANTS INVOLVING HETEROATOMS

3.1 General Background

Measurement of heteronuclear coupling constants is an essential factor in the conformational analysis of biomolecules.[25–28] Over the past three decades much effort has been invested into the delineation of Karplus-type relations for couplings involving one or more heteronuclei, either as coupling partner or contained in the coupling path. Unfortunately, there exists no firmly established quantitative correlation between ^3J(H,C,C,H) and corresponding couplings to heteronuclei [^3J(X,C,C,H), X = ^{13}C, ^{15}N, ^{31}P], nor simple rules that predict the behavior of a vicinal coupling when a carbon atom in the coupling path is replaced by a heteroatom. In short, for each different combination of nuclei and coupling path, a Karplus-type equation must be parameterized from scratch, preferably on the basis of a large number of experimental couplings (calibration points). Semiempirical calculationsn of vicinal couplings cannot predict ^3J with an accuracy desired by NMR spectroscopists, but such calculations, especially when carried out for a series of related molecular fragments,[25] may reveal details that would otherwise not be considered.

Thus far, the proposed parameterizations, resulting in a set of Karplus coefficients, rarely appear to have gone beyond the level of the three-parameter equation (1b). The problem of substituent effects on the A, B, and C coefficients is usually circumvented by the use of model compounds that contain the same (or at least similar) substituents as the compounds that one is interested in. The torsion angles necessary for such a parameterization are either estimated from molecular models, calculated by means of force-field methods, or taken from X-ray studies. Thus, one may hope to work effectively on the level of the five-parameter Karplus expression. It should be remembered that in the case of ^3J(H,C,C,H) this level yields an rms deviation of 0.7 Hz (299 experimental calibration points); inclusion of an asymmetry term causes the rms deviation to drop to less than 0.4 Hz, vide supra.

A selection of coefficients for use in equation (1b) that are currently used in structural and conformational studies of proteins (Table 3) and nucleic acids (Table 4) is presented here. Some parameterizations have been carried out solely on the basis of semiempirical MO calculations in various approximations and these should perhaps be taken only as a rough guide. The coefficients for ^3J(C,C,C,H) in Table 3 were determined from measurements[33] in norbornanes and are not necessarily representative for this coupling in open-chain compounds.

The most important asset that these coefficients presently offer is *not* their overall reliability (statistically tested in a small minority of cases) but the opportunities that are provided to remove ambiguities. For example, a single coupling constant ^3J(H,H), measured along a given bond in an open-chain molecule, in the general case (single conformer assumed) corresponds to any one out of four torsion angles ϕ_{HH}. The situation is even more complex in the case of a conformational mixture. Modern NMR techniques allow us to measure accurately one or more ^3J(X,H) and sometimes ^3J(X,Y) along the same bond. The various Karplus curves are phase-shifted with respect to one another, because the X and/or Y nuclei are shifted by $\pm 120^\circ$ (sp^3) or 180° (sp^2). Thus, comparison of the various couplings often solves an assignment problem, always acute when dealing with diaster-eotopic nuclei, and/or may result in the selection of only one conformation that fits all the data.[38] Other applications are discussed in Section 4.

3.2 Vicinal Carbon–Proton Couplings ^3J(C,C,C,H)

This particular coupling constant appears to have resisted[39] all attempts to formulate satisfyingly simple and general trigonometric relationships similar to those developed for ^3J(H,C,C,H). Although early MO calculations[40] on ^3J(C,H) in substituted propanes already indicated that these couplings indeed obey a Karplus-type equation, in practice severe complications arose and progress remains slow. The present situation concerning ^3J(C,H), Figure 5, can be summarized as follows:

(a) The ratio ^3J(C,H)/^3J(H,H) in molecular fragments where C replaces a corresponding H varies from 0.50 to 0.85 (mean 0.61 ± 0.065).[27] Thus, this ratio cannot be used with confidence to scale ^3J(H,H) couplings or Karplus coefficients to fit ^3J(C,H) data.

(b) The influence of electronegative substituents on rotationally averaged $\langle ^3J(C,H)\rangle$ in t-butyl derivatives correlates well with ^3J(H,H), with the former slightly more sensitive to the electronegativity effect.[41] More recently, an analysis of ^3J(C,H) in carbohydrates[42] suggested that oxygen (and carbon) substituents require a different set of coefficients [including the sin(2ϕ) term] when moved from the β position to the γ position with respect to the coupling carbon nucleus, Figure 5. This implies that the minimum number of Karplus coefficients could be twice as large compared with the six that suffice to describe ^3J(H,H).

(c) When the coupling ^{13}C nucleus itself carries one or more substituents besides hydrogen, matters are even more complicated. It has long been known that the nature of the X substituent has a profound influence on the magnitude of the rotationally averaged ^3J(C,H) in $(CH_3)_3{}^{13}CX$ compounds.[43] Other factors besides electronegativity appear to be operative here. Moreover, MO calculations of ^3J(C,H) in 1-fluoropropane[40] (Figure 5,

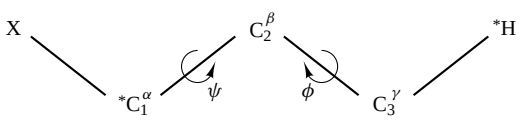

Figure 5 Torsion angles ϕ and ψ and atomic numbering for ^3J(C,C,C,H). The coupling nuclei are marked with an asterisk

Table 3 Selection of Coefficients (Hz) for Use in the Standard $\cos^2$ Karplus Equation [Equation (1b)] for Couplings Relevant to Amino Acids and Polypeptides; $^3J_{ap}$, $^3J_{sc}$ and the Rotationally Averaged Value $\langle ^3J \rangle$ are Also Given. In the Column Remarks MO Stands for Semiempirical Calculations; (Exp(N) Denotes Experimental Calibration on N Data Points. See Figures 6 and 7 for Atom Numbering and Definition of Torsion Angles. In Many Amino Acids X = C^γ

Main torsion angle	^3J monitored	A	B	C	$^3J_{ap}$	$^3J_{sc}$	$\langle ^3J \rangle$	Remarks
ϕ	$HNC^\alpha H^\alpha$	6.7	−1.3	1.5	9.5	2.5	4.8	Exp(112)[29]
		6.4	−1.4	1.9	9.7	2.8	5.1	Exp(37)[30]
		9.4	−1.1	0.4	10.9	2.2	5.1	Exp(22)[25]
ϕ	$HNC^\alpha C^\beta$	4.7	−1.5	−0.2	6.0	0.2	2.1	MO *trans*-amides[25]
ϕ	$HNC^\alpha C'$	5.7	−2.7	0.1	8.5	0.2	3.0	MO *trans*-amides[25]
ϕ	$C'NC^\alpha H^\alpha$	9.0	−4.4	−0.8	12.6	−0.8	3.7	Exp(3) tentative[25]
		4.5	−1.3	−1.2	4.6	−0.7	1.1	MO *trans*-amides[25]
		4.0	−1.8	0.8	6.6	0.9	2.8	Exp(12) *cis*-amides[31]
ϕ	$C'NC^\alpha C\beta$	1.8	−0.2	0.5	2.5	0.9	1.4	Exp(17) *cis*-amides[31]
		1.3	−0.6	−0.1	1.8	−0.1	0.5	MO *trans*-amides[25]
ϕ	$C'NC^\alpha C'$	1.4	−0.8	−0.3	1.9	−0.4	0.4	MO *trans*-amides[25]
χ	$H^\alpha C^\alpha C^\beta H^\beta$	see equation (12) and Table 5						Exp(299)
$\chi_1\chi_2$	$H^\alpha C^\alpha C^\beta C^\gamma$	10.2	−1.3	0.2	11.7	2.1	5.3	Exp(6) ornithines[32]
χ	$C'C^\alpha C^\beta H^\beta$	7.7	−0.9	0.0	8.6	1.5	3.9	Exp(10) norbornanes[33]
		–	–	–	10.0	1.0	4.0	Exp[a, 34]
		–	–	–	11.9	0.4	4.2	Exp[a, 34]
χ	$NC^\alpha C^\beta H^\beta$	–	–	–	−5.4	−1.7	−2.9	Exp[a, 36]
χ	$C'C^\alpha C^\beta C^\gamma$	1.4	−0.8	−0.3	1.9	−0.4	0.4	MO *trans*-amides[25]
ψ	$H^\alpha C^\alpha C'N$	−5.1	2.2	0.9	−6.4	0.7	−1.7	MO diamide[25]
		−5.3	2.2	0.9	−6.6	0.7	−1.7	MO N–Me acetamide[37]

[a]Assumption made that populations about χ follow from ^3J(H,C,C,H): $^3J_{ap}$ = 13.6 Hz, $^3J_{sc}$ = 2.6 Hz.

Table 4 Selection of Coefficients (Hz) for Use in the Standard $\cos^2$ Karplus Equation [Equation (1b)] for Couplings Relevant to Nucleic Acids. In the Column Remarks Exp(N) Denotes Experimental Calibration on N Data Points. See Figures [8, 10, 11] for Atom Numbering and Definition of Torsion Angles

Main torsion angle	^3J monitored	A	B	C	$^3J_{ap}$	$^3J_{sc}$	$\langle ^3J \rangle$	Remarks
χ	C(=C)NCH	6.2	−2.4	0.1	8.7	0.5	3.2	Exp(5)[47]
χ	C(=O)NCH	5.0	−2.1	0.1	7.2	0.3	2.6	Exp(4)[47]
β,ϵ	HCOP	15.3	−6.1	1.6	23.0	2.4	9.3	Exp(7)[45]
β,ϵ	CCOP	6.9	−3.4	0.7	11.0	0.7	4.1	Exp(10)[45]
γ Sugar	HCCH	see equation (12) and Table 7						Exp(299)

X = F) predicted that this coupling is substantially larger when ψ_{FC} is set at 180° than when it is set at 60°. In a recent MO study[44] on a series of 1-substituted propanes (Figure 5, X = H, CH_3, NH_2, OH, and F) both ϕ and ψ were varied from 0° to 360° in 30° steps. The rotation of ψ indeed appears to have a profound effect on ^3J(C,H). For example, for ϕ_{CH} = 180° the calculated ^3J(C,H)(X = F) varies from 8.0 Hz (ψ_{FC} = 0°) to 12.0 Hz (ψ_{FC} = 150°). These predictions were experimentally verified by measurements on *cis*- and *trans*-4-*t*-butylcyclohexanols, where the effect is even larger than predicted for X = OH.[44] In the same paper[44] the set of 340 calculated $^{13}C-H$ couplings was fitted (rms = 0.27 Hz) with the aid of a nine-coefficient Karplus-type expression. A 15-coefficient approximation was used to fit 39 experimental ^3J(C,H) values of cycloalkanols and pyranose sugars (rms = 0.30 Hz).[42]

In summary, much work has to be done before ^3J(C,H) can be used to calculate torsion angles. In the meantime, it appears safe to apply the general rule: $^3J_{ap} \gg {}^3J_{sc}$.

3.3 Vicinal Proton–Proton Couplings ^3J(H,N,C,H)

This coupling, usually denoted $^3J_{HN\alpha}$, deserves some attention because it can be measured with precision in proteins and affords important information concerning the

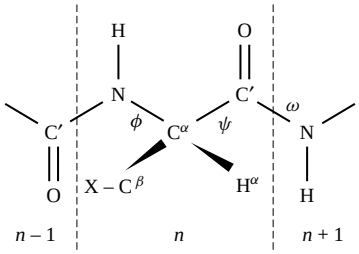

Figure 6 Schematic representation of the main-chain torsion angles ϕ, ψ, and ω in polypeptides and proteins. The χ_1 angle is defined as the torsion angle N–C^{α}–C^{β}–X; in many amino acids X = C^{γ}

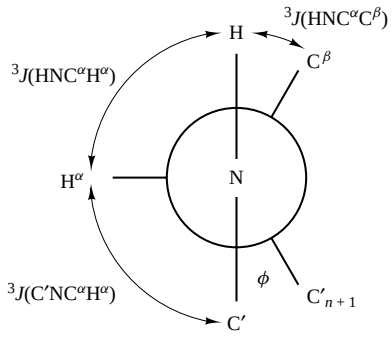

Figure 7 Newman projection along the N–C^{α} bond of a peptide backbone showing three important vicinal coupling constants that supply information about the ϕ torsion angle

local backbone geometry along the ϕ angle (Figures 6 and 7). It should be noted here that in protein chemistry the torsion angle between coupling nuclei is denoted as θ; for θ_{HNCH} one uses the relationship $\theta = \phi - 60^{\circ}$ (Figure 7).

Independent calibrations in terms of A, B, and C [equation (1b)], were carried out by Pardi et al.[30] (37 data points, rms = 0.87 Hz) and by Ludvigsen et al.[29] (112 data points, rms = 1.01 Hz), Table 3, on the basis of known X-ray structures. Inspection of the plots given suggests that corrections for differences in electronegativity of the various side chains might improve the rms deviation, especially for θ_{HNCH} near 180° and near 0°. The Karplus coefficients proposed by Bystrov[25] predict $J(180) = 10.9$ Hz and $J(0) = 8.7$ Hz, the latter value is probably too large by about 1.5–2.0 Hz.

3.4 Vicinal ^{1}H and ^{13}C Couplings to ^{31}P in Phosphate Diesters

The vicinal couplings ^{3}J(P,O,C,H) and ^{3}J(P,O,C,C), taken in combination, yield important conformational information concerning two backbone torsion angles in nucleic acids: β (angle PO5′C5′C4′) and ϵ (angle C4′C3′O3′P), (Figure 8). The Karplus coefficients that describe the angular dependence of ^{3}J(P,H) and ^{3}J(P,C) are relatively large. This fact contributed to the success of a different approach taken in the parameterization,[45] necessitated by the knowledge that phosphates (and sulfates) often display 'nonclassical' torsion angles, i.e. large deviations from 'classical' 180° and 60° angles. Moreover, it is desirable to avoid the use of crystallographic information which in individual cases can

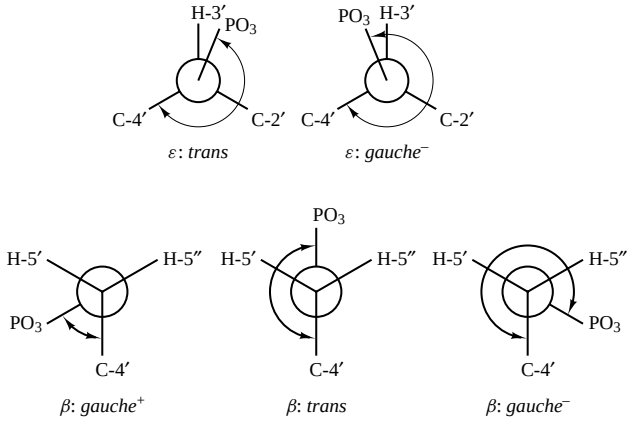

Figure 8 Newman projections along the main-chain torsion angle ϵ and β in nucleic acids. The negative charge on the phosphate group is omitted. These angles are monitored by ^{3}J(P,O,C,H) and ^{3}J(P,O,C,C). (Reproduced by permission of Adenine Press from P. P. Lankhorst, C. A. G. Haasnoot, C. Erkelens, and C. Altona, *J. Biomol. Struct. Dyn*., 1984, **1**, 1387)

be biased by crystal-packing effects. Instead, the unknown backbone angle (ϵ) can be determined simultaneously with the Karplus coefficients, provided that several different couplings along the same central bond are available and that conformational purity along this bond can be attained. In the case discussed here, six Karplus coefficients and four torsion angles were determined from 17 experimental couplings in RNA compounds (rms = 0.2 Hz). As it turned out, the *mean* NMR value of ϵ_{ap} in the RNA molecules in the stacked form (219°) corresponded well with the *mean* of crystallographic determinations in similar RNAs (218°). The same Karplus coefficients (Table 4) are transferable to DNA molecules.[46]

4 SELECTED APPLICATIONS OF ^{3}J IN THE FIELD OF BIOMOLECULES

4.1 General Remarks

For more than a decade the conformational situation ('structure') of biopolymers, such as proteins and nucleic acids, was judged from characteristic NOEs. More recently, interatomic distances or NOEs were introduced as constraints in MD (molecular dynamics calculations) trajectories. However, without additional information, it is very difficult to judge whether or not conformational homogeneity exists along each chemical bond of interest. This is especially true in cases where a given conformer predominates; minor forms may then escape detection altogether. Contradictory NOEs certainly point to the simultaneous existence of various rotamers, but these are not easily quantified from NOE information. With the advent of more powerful NMR spectrometers and techniques, investigators are becoming more and more aware that homo- and heteronuclear coupling constants offer a rich source of the additional information that is required.

An important recent application[48,49] of the Karplus coefficients involves the introduction of coupling constant restraints into molecular dynamics calculations. Defining $\Delta J = J_{\mathrm{obs}} -$

J_{calc}, one adds a penalty function in the form of a pseudoenergy term $\frac{1}{2}k_i \Delta J_i^2$ to the force field for each conformational constraint along given torsion angles, in addition to the usual distance constraints obtained from NOEs. One of the advantages of this approach, when applied to multiple couplings along a chosen bond, is that conformational equilibria, which occur on a short timescale, can be handled with more confidence. Of course, the k_i 'force constants' should be weighed according to the reliability of J_{obs} and J_{calc}, but to date such information on J_{calc} is limited to a few types of vicinal couplings, see Sections 3.2–3.5. It was also proposed to incorporate time-averaged J values[50] as constraints; this idea was succesfully tested on a cyclic peptide, antamanide ($^3J_{HN\alpha}$). Extension to multiple couplings about certain bonds undoubtedly will follow soon.

4.2 Amino Acids, Peptides, and Proteins

4.2.1 Main Chain Torsion Angles in Polypeptides and Proteins

The main chain in an amino acid sequence is characterized by three sequential torsion angles: ϕ, ψ, ω (Table 3 and Figure 6). For several reasons most attention was and still is focused on ϕ. This particular angle is correlated with the local shape of the sequence (α-helix, β-sheet, and various turns). In principle, ϕ can be monitored by the use of six different coupling constants (Table 3). Of these, $^3J(H,N,C^\alpha, H^\alpha)$ is the easiest one to measure, even in large proteins, followed by $^3J(H,N,C^\alpha, C^\beta)$.[38] Coupling to carbonyl carbon requires more effort and is difficult to obtain when the coupling is small. Nevertheless, a qualitative insight into the magnitude of two more ϕ couplings can be gained, at least in small cyclic peptides, from natural abundance NMR spectra; $^3J(C^\alpha, C',N,H)$ and $^3J(C',N,C^\alpha,H^\alpha)$.[38,51] Now that $^{13}C^{15}N$ isotopically-enriched proteins are becoming available, 3D and 4D NMR techniques offer new possibilities for measuring previously 'unmeasurable' couplings in large proteins, e.g., $^3J(H,N,C^\alpha,C')$.[52] The ψ angle remains elusive. For $^3J(H^\alpha,C^\alpha,C',N)$ and $^3J(C^\beta,C^\alpha,C',N)$ very little reference material is available at present. A similar remark applies to $^3J(C^\alpha,C',N,H)$, which coupling monitors the ω angle. In rigid domains, both ψ and ω can be determined from NOEs, however.

4.2.2 Side-Chain Conformations of Amino Acid Residues

The heteronuclear $^3J(C',C^\alpha,C^\beta,H^\beta)$ and $^3J(N,C^\alpha,C^\beta,H^\beta)$ couplings along with the two homonuclear $^3J(H^\alpha,C^\alpha,C^\beta,H^\beta)$ couplings allow the unambiguous diastereotopic assignment of the two β-methylene protons of the side chain of amino acid residues.[51,53] Given the correct assignment of H^β(pro-*R*) and H^β(pro-*S*) (Figure 9), the conformational populations of the equilibrating three rotameric species can be calculated from the two $^3J(H^\alpha,C^\alpha,C^\beta,H^\beta)$ couplings when the limiting values ($^3J_{ap}$ and $^3J_{sc}$) are known. The Pachler[54] values $^3J_{ap}$ = 13.6 Hz and $^3J_{sc}$ = 2.6 Hz are still widely used in the literature, although Abraham et al.[55] in 1977 already pointed out that differentiation according to the electronegativity of the side chain as well as the inclusion of substituent orientation was called for. In that work[55] a simple additivity scheme of substituent constants for the prediction of $^3J_{sc}$ was proposed. For example, for X = carbon, the two $^3J_{sc}$ values predicted were 3.4 Hz and 4.2 Hz, for X = oxygen, values of 2.2 Hz and 4.9 Hz were proposed. A more refined, but similar, approach is now possible through the use of equations (11), (12) or (13) in conjunction with the experimental group electronegativities λ_i. It appears best to distinguish three different groups of side chains A through C according to the respective λ_i values given in Table 1.

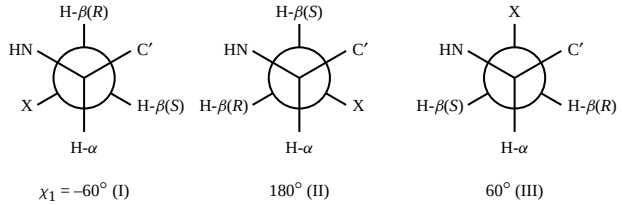

Figure 9 Newman projections of the three staggered χ_1 side-chain conformations in an amino acid with two H-β protons. The three rotamers are designated I, II, and III for $\chi_1 = -60°$, 180°, and 60°, respectively. For the sake of clarity pro-*R* and pro-*S* are abbreviated as *R* and *S*, respectively

A: λ_i = 0.42 (Asn, Asp, His, Phe, Trp, Tyr)
B: λ_i = 0.60–0.75 (Arg, Cys, Gln, Glu, Leu, Lys, Met)
C: λ_i = 1.25(Ser in D_2O),λ_i = 1.33 (Ser in $CDCl_3$)

The predicted $H^\alpha H^\beta$ limiting coupling constants for each of the three rotamers along χ_i in peptides and proteins (idealized staggered geometry assumed), differentiated according to the electronegativity of the side chain, are shown in Table 5. The nature of the solvent plays a role only in the cases of free amino acids and N-terminal residues, because $\lambda(NH_2) > \lambda(NH_3^+)$ (Table 1).

Some examples of $H^\alpha H^\beta$ coupling constants and rotamer populations are displayed in Table 6. For purposes of comparison, the populations calculated with standard values[54] are also given. The differences between the new and the old population values are usually $\leq$ 7%, except for Ser ($\leq$10%). It is concluded that the trends recorded in the literature thus far remain valid. For future work requiring high precision, the new values are recommended. It is noted in passing that application of equations (11), (12), or (13) allows us to predict safely couplings pertaining to any deviation from ideal staggered geometries. A good example of nonstaggered situations occurs in proline residues. An analysis of the 10 coupling constants of proline and of 12 model compounds[59] with the aid of the Haasnoot equation [equation (7)][16] in conjunction with the pseudorotation model for five-membered rings[60] showed that the unsubstituted proline ring occurs in a practically 1:1 conformational equilibrium between N-type and S-type forms (see Section 4.3.1 for a discussion of N- and S-conformers). Recently, Karplus and co-workers[61] successfully used the Haasnoot equation [equation (7)] to probe the motional characterisitics of the four proline residues in the cyclic decapeptide antamanide on a picosecond time scale.

4.3 Nucleic Acids

The structural properties and current nomenclature rules[17] of nucleic acid conformations have been treated by Wüthrich[28] and by Saenger.[62] The conformational analysis of oligonucleotides with the aid of coupling constants has been reviewed by Altona,[63] backbone torsion angles are shown in Figures 8, 10, and 12.

Table 5 Predicted Limiting $H^{\alpha}H^{\beta}$ Coupling Constants (Hz) [Equation (13)] for Each of the Three Rotamers Along $C^{\alpha}C^{\beta}$ in Peptides and Proteins. Idealized Staggered Models Assumed. Three Classes of Amino Acid Residues A–C (See Text) are Differentiated According to the Group Electronegativity λ_i of the Side-Chain Substituent X, Figure 9. Because $\lambda(NH_2) > \lambda(NH_3^+) \approx \lambda$[NHC(=O)R] (Table 1) N-Terminal Residues are Further Differentiated According to Solvent Conditions

	I(χ^-)		II(χ^t)		III(χ^+)	
ϕ_{HH}	pro-*R* 180°	pro-*S* −60°	pro-*R* 60°	pro-*S* 180°	pro-*R* −60°	pro-*S* 60°
D_2O (neutral or acidic: all residues) or nonaqueous solutions (except N-terminals)						
A	12.9	3.1	3.7	12.9	3.0	3.5
B	12.6	3.2	3.8	12.6	2.8	3.3
C	11.7	3.7	4.4	11.8	1.9	2.4
D_2O (basic) or nonaqueous solution: amino acids and N-terminal residues						
A	12.4	2.7	4.0	12.5	2.5	3.7
B	12.1	2.8	4.0	12.2	2.4	3.6
C	11.2	3.3	4.6	11.5	1.5	2.6

Table 6 Examples of $H^{\alpha}H^{\beta}$ Coupling Constants and χ Rotamer Populations in L-Amino Acids and Proteins.[a] The Appropriate Limiting Couplings are Given in Table 5. In Parentheses are the Populations Calculated with J_{ap} = 13.6 Hz and J_{sc} = 2.6 Hz[54]

		$^3J_{exp}$(Hz)		Rotamer populations (%)		
Residue	pH or solvent	$\alpha\beta$(pro-*R*)	$\alpha\beta$(pro-*S*)	I	II	III
Phe[56]	9.8	8.4	4.9	57(53)	20(21)	23(26)
Phe[56]	2.2	8.3	4.5	53(52)	13(17)	34(31)
AcPSer[57]	8.0	5.6	3.3	37(27)	4(6)	59(67)
AcSer[57]	7.5	6.2	3.8	42(32)	9(11)	49(57)
Cyclosporin A[58] MeLeu[4]	$CDCl_3$	12.0	4.5	91(85)	12(17)	−3(−2)
Cyclosporin A[58] MeLeu[6]	$CDCl_3$	6.0	10.5	24(31)	77(72)	−1(−3)
Cyclohexapeptide[58] Phe[7]	DMSO	4.5	9.0	11(17)	59(58)	30(25)
Cyclohexapeptide[58] Trp[8]	DMSO	10.9	4.2	79(75)	11(15)	10(10)
Cyclohexapeptide[58] Phe[11]	DMSO	11.5	3.1	86(80)	2(5)	12(15)

[a]The rotamer populations are computed from three equations with three unknowns using standard matrix methods; for the sake of clarity pro-*R* and pro-*S* are abbreviated as *R* and *S*, respectively:

$$J_{obs(R)} = p_I\, J_{I(R)} + p_{II}\, J_{II(R)} + p_{III}\, J_{III(R)}$$

$$J_{obs(S)} = p_I\, J_{I(S)} + p_{II}\, J_{II(S)} + p_{III}\, J_{III(S)}$$

$$p_I + p_{II} + p_{III} = 1$$

The computation is simpler when it is assumed that all J_{sc} values are equal.[54]

4.3.1 The Furanose Ring

The flexible five-membered sugar ring plays a pivotal role in nucleic acid structure and dynamic behavior. Structural differences between A-, B-, and Z-type duplexes are intimately correlated with specific conformational ranges of individual sugars. Within the B-DNA family each sugar responds to its surroundings (e.g., the base-stacking pattern) by an appropriate adaptation of its geometry. Careful analysis of sets of ^3J(H,H) values reveals intimate details on the 'atomic level' that cannot be obtained from NOEs.[64,65] Various reviews are available[24,63–65] and only a brief outline of the coupling constant approach is sketched here.

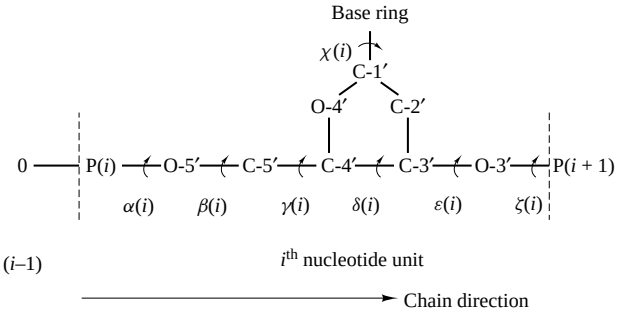

Figure 10 Conformational notation of the torsion angles of the backbone and χ of the base in nucleic acids[17]

Two distinct D-ribose conformations (better: conformational ranges) occur in nucleic acids, N-type (North, roughly C-3′-*endo*) and S-type (South, roughly C-2′-*endo*), Figure 11, which occur in fast equilibrium unless the stereochemical requirements of the helix impose restraints. For example, an RNA double helix consists of an N–N–N sequence of sugars, Z DNA of an S–N–S–N alternation. In B DNA the duplex structure allows the sugars some mobility to flip from S to N and vice versa. Pyrimidine sequences are relatively more mobile (78 ± 13% S) than are purine sequences (90 ± 7% S).[24] One always measures time-averaged couplings and shifts under 'fast-exchange' conditions. Nevertheless, it remains possible to extract quantitative information on geometry and conformational population from the couplings thanks to the fact that the five endocyclic torsion angles υ_i are mutually dependent via the two-parameter equation (14).

$$\upsilon_j = \phi_m \cos\{P + 0.8\pi(j-2)\},\ j = 0-4 \qquad (14)$$

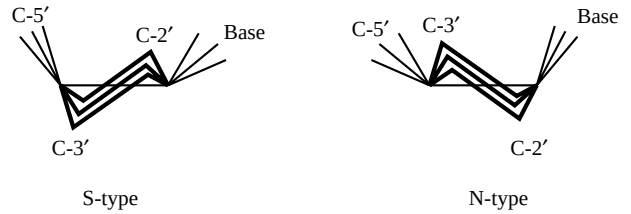

Figure 11 Schematic composite representation of the furanose conformations in nucleic acids: S-type (C-2′-*endo*/C-3′-*exo*) (left) and N-type (C-2′-*exo*/C-3′-*endo*) (right). (Reproduced by permission of Academic Press from J. van Wijk, B. D. Huckriede, J. H. Ippel, and C. Altona, *Methods Enzymol*., 1992, **211**, 286)

in which ϕ_m represents the amplitude of pucker and P the phase angle of pseudorotation.[60] The torsion angles are numbered clockwise, starting with υ_0(C4′–O4′–C1′–C2′). In D-sugars, N-type conformers are characterized by a positive sign of υ_3, S-type forms by a negative sign of υ_3. The (exocyclic) proton–proton torsion angles ϕ_{HH} are related to the υ_j-values via the pseudorotation parameters ϕ_m and P [equation (15)]:[66]

$$\phi_{HH} = a + b\phi_m \cos(P + \text{phase shift}) \tag{15}$$

where, in the idealized approximation, $b = 1$ and $a = 0^\circ$ for *cis* protons and $\pm 120^\circ$ for *trans* protons. Empirically established values for the parameters a and b in equation (15) for deoxyribose, ribose, arabinose, lyxose, and xylose are available.[66,67] Equations (14) and (15) and the extended Karplus equation [equation (13)] are employed in the iterative least-squares program PSEUROT.[68] Given a complete set of experimental proton–proton couplings $J(1',2')$, $J(2',3')$, and $J(3',4')$ for riboses and, in addition, $J(1',2'')$ and $J(2'',3')$ for deoxyriboses, the program minimizes the functional $R = \sum(J_{exp} - J_{calc})^2$ and yields the pseudorotation parameters of the two stable furanose conformers and the mole fractions. The accuracy of the procedure is greatly enhanced when the conformational equilibrium displays a strong shift with temperature. Version 4.0 of the PSEUROT program is in the public domain (*Quantum Chemistry Program Exchange No. 463*, Indiana State University, 1983); this version employs equation (7) and the original coefficients.[16] Later versions (PC, IBM compatible) 5.4 and 6.0 (see text) are available under licence from the author. Note that the PSEUROT programs are designed to yield the conformational characteristics of any saturated five-membered ring, provided that the appropriate vicinal ^{1}H–^{1}H couplings are input.

In NMR practice it is not always feasible to carry out the laborious spectral simulations that are required to obtain the individual coupling constants. Often, the sums of couplings to given protons are easily available, however, and these contain much the same information.[24,69] In the case of DNA we define:

$$\Sigma 1' = J(1',2') + J(1',2'') \tag{16a}$$

$$\Sigma 2' = J(1',2') + J(2',3') + J(2',2'') \tag{16b}$$

$$\Sigma 2'' = J(1',2'') + J(2'',3') + J(2',2'') \tag{16c}$$

$$\Sigma 3'\{^{31}\text{P}\} = J(2',3') + J(2'',3') + J(3',4) \tag{16d}$$

The $\sum 2'$ and $\sum 2''$ terms include the absolute value of $^2J(2',2'')$ (approximately 14 Hz in deoxyribofuranose). A graphical method, based on the theory employed in PSEUROT, successfully utilizes graphs of $\sum J$ versus P and $\sum J$ versus populations to solve the conformational problems.[24,69] Recently, the graphical procedure was automated in program PSEUROT, Version 6.0.[68]

4.3.2 Orientation of the Nucleic Acid Base

The glycosyl torsion angle χ (not shown) defines the orientation of the base with respect to the sugar ring.[62] Two major orientations are known: *anti* and *syn*. In the more common *anti* form, the C-8-H-8 and C-6-H-6 vectors of the purine and the pyrimidine bases point roughly in the direction of the C-1′–O-4′ bond and are antiparallel to the C-1′–H-1′ bond. From pyrimidine model compounds the Karplus coefficients for ^3J(C-6,N-1,C-1′,H-1′) and ^3J(C-2,N-1,C-1′,H-1′) were determined[47] (Table 4) and from these values one predicts the following (very approximate) characteristics:

$$anti\text{base}: {}^3J(\text{C}-6, \text{H}-1') \approx 9\text{Hz}, {}^3J(\text{C}-2, \text{H}-1') \approx 3\text{Hz}$$

$$syn\text{base}: {}^3J(\text{C}-6, \text{H}-1') \approx 4\text{Hz}, {}^3J(\text{C}-2, \text{H}-1') \approx 7\text{Hz}$$

In a regular B-DNA structure with *anti* bases, the angle χ is well defined ($\pm 10^\circ$) from three NOE contacts: H-6/H-8–H-2′, H-6/H-8–H-2″, H-6/H-8–H-3′, but in exceptional cases where the base enjoys more conformational freedom measurement of ^3J(C,H) may well supply valuable additional information.

4.3.3 Backbone Conformations of RNA and DNA

The six torsion angles along the nucleic acid backbone are denoted α–ζ, starting with P–O-5′ as the central bond for α, Figure 10. NMR spectroscopy provides no direct grip upon the important phosphate diester torsions ζ and α; these are usually determined from NOE-constrained MD trajectories. The remaining backbone angles β, γ, δ, and $\in$ are monitored by various vicinal coupling constants. Because X-ray crystallography[62] has made it clear that important deviations from pure staggered geometries (180°, 60°) in double-helical structures commonly occur, it is the task of the NMR spectroscopist to deduce at the same time values for the backbone angles as well as conformational populations. This is possible in principle because Nature has conveniently provided a sufficient number of coupling nuclei along the backbone that can be put into use.

It is often helpful to study the behavior of sums of couplings versus rotation about a given torsion angle. As an aid to the discussion, Table 7 has been prepared. The Karplus coefficients used to calculate the ^3J(P,H) and ^3J(P,C) values in Table 7 are taken from Table 4.

Torsion angle β (P–O5′–C5′–C4′), Figure 8. In 5′-mononucleotides of RNA and DNA, the $\beta^t(ap)$ rotamer is invariably preferred (>70%). In stacked oligonucleotides, the β^t angle is confined to a small range of values (176 ± 4°). Under the additional assumption that in unstacked ('melted') states an equilibrium exists between two or three rotamers (β^t, 175°; β^+, 60°; β^-, 300°), a sum rule is easily derived [equation (17)]:

$$p(\beta^t) = (25.4 - \Sigma')/20.5 \tag{17}$$

where p stands for the fractional population and $\sum' = J(5',\text{P}) + J(5'',\text{P})$. Stereospecific assignments of H-5′ and H-5″ are not

Table 7 Backbone Angles β, γ, and ϵ(°) of Nucleic Acids in the Most Populated Ranges and Corresponding Calculated Vicinal Coupling Constants (Hz) (See Text)

β^t	170	175	180	185	190
J(P,H − 5′)	4.0	3.1	2.4	1.8	1.3
J(P,H − 5″)	1.3	1.8	2.4	3.1	4.0
$\sum'$	5.3	4.9	4.8	4.9	5.3
J(P,C − 4′)	10.7	10.9	11.0	10.9	10.7
β^+	50	55	60	65	70
J(P,H − 5′)	1.3	1.8	2.4	3.1	4.0
J(P,H − 5″)	22.5	22.9	23.0	22.9	22.5
$\sum'$	23.8	24.7	25.4	26.0	26.5
J(P,C − 4′)	1.4	1.0	0.7	0.5	0.3
β^-	−50	−55	−60	−65	−70
J(P,H − 5′)	22.5	22.9	23.0	22.9	22.5
J(P,H − 5″)	1.3	1.8	2.4	3.1	4.0
$\sum'$	23.8	24.7	25.4	26.0	26.5
J(P,C − 4′)	1.4	1.0	0.7	0.5	0.3
γ^+	45	50	55	60	65
J(H − 4′,H − 5′)	1.1	1.5	2.0	2.5	3.2
J(H − 4′,H − 5″)	2.9	2.2	1.6	1.2	0.8
$\sum$	4.0	3.7	3.6	3.7	4.0
γ^t	165	170	175	180	185
J(H − 4′,H − 5′)	5.1	4.5	3.6	3.0	2.4
J(H − 4′,H − 5″)	11.0	11.0	10.9	10.6	10.2
$\sum$	16.1	15.5	14.5	13.6	12.6
γ^-	−80	−75	−70	−65	−60
J(H − 4′,H − 5′)	9.5	10.1	10.5	10.8	10.9
J(H − 4′,H − 5″)	1.9	2.4	3.1	3.8	4.6
$\sum$	11.4	12.5	13.6	14.6	15.4
ϵ^t	180	190	200	210	220
J(P,H − 3′)	2.4	4.0	5.9	7.8	9.4
J(P,C − 2′)	0.7	0.3	0.3	0.7	1.5
J(P,C − 4′)	11.0	10.7	10.0	8.8	7.4
ϵ^-	−105	−100	−95	−90	−85
J(P,H − 3′)	10.0	9.9	8.6	7.8	6.9
J(P,C − 2′)	6.6	7.4	8.1	8.8	9.5
J(P,C − 4′)	2.0	1.5	1.1	0.7	0.5

necessary at this stage. Unfortunately, we have no information concerning the true values of the β^+ and β^- angles, but it can be verified that nonclassical β_{sc} rotamers (e.g. β_{sc}, ±90°) would introduce less than 2% error in the $p(\beta^t)$ value calculated from equation (17). The C-4′,P coupling can be used as an independent check on the β^t population [equation (18)]:

$$p(\beta^t) = [^3J(\text{C-4}', \text{P}) - 0.7]/10.2 \tag{18}$$

Assuming that the H-5′ and H-5″ resonances are assigned stereospecifically from NOEs, approximate values of the minor populations $p\beta^+$ and $p\beta^-$ are derived from J(5′,P) and J(5″,P). Preference for β^+ was found to occur locally in a minihairpin loop.[70]

Torsion angle γ(O5′–C5′–C4′–C3′), Figure 12. Nucleosides and mononucleotides in the solid state display a preference for γ^+ (76%), followed by γ^t (18%) and γ^-(6%). This rotamer distribution in the crystalline state is mirrored by the distribution found in aqueous solution at ambient temperatures. Crystallographic data reveal trends toward nonclassical angles: γ^+, 53°; γ^t, 180°; γ^-, 290°. The right-handed helix requires a pure γ^+ rotamer; upon melting, conformational mobility is regained. The population γ^+ again follows from a sum rule

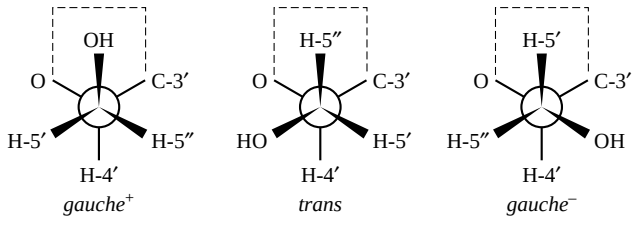

Figure 12 Newman projections of the three γ rotamers in nucleosides. In nucleotides the OH group is replaced by an O–PO_3^- group

[equation (19)]:

$$p(\gamma^+) = (13.6 - \Sigma)/10.0 \tag{19}$$

where $\sum = J_{4'5'} + J_{4'5''}$. A pure or almost pure γ^t form is adopted by dG residues in Z DNA[62] and at the 5′–3′ loop stem junction in small hairpin loops in DNA, i.e. at the position of the local sharp turn of the backbone.[70] Such a turn is revealed by a large (>9 Hz) value of $^3J_{4'5''}$.

Torsion angle δ (C5′–C4′–C3′–O3′): This torsion angle is directly related to the pseudorotation parameters P and ϕ_m of

the D-(deoxy)ribose sugar by equation (20).[63]

$$\delta = 120.6 + 1.1\phi_m \cos(P + 145.2) \quad (20)$$

Torsion angle ϵ (C4′–C3′–O3′–P), Figure 8. The study of the conformational behavior of this backbone angle is virtually impossible without the aid of vicinal $^{13}C-^{13}P$ couplings because only a single ^3J(P,H) value is measured for each residue. The ϵ^+ rotamer is sterically 'forbidden'[63] and need not be considered. The two allowed conformational ranges, ϵ^t and ϵ^-, are more or less symmetrically disposed with respect to H-3′ and, without further information, ^3J(P,H) can give few clues concerning the ϵ^t/ϵ^- rotamer population distribution. It is known, however, that ^3J(P,H-3′) of single-stranded RNA oligomers increases with increasing population of stacked (single-helical) conformer to a maximum of about 9 Hz, whereas ^3J(P,H-3′) in similar DNA compounds decreases to a minimum of about 4 Hz when fully stacked. This difference in behavior was quantitatively interpreted with the aid of ^{13}C NMR data.[45,46,71] It turned out that there exists a strong correlation between the conformation of the sugar ring and the ϵ^t angle. In RNA the stacked state strongly biases the sugar towards the N-type form [$\epsilon^t{}_N$ = 219°; ^3J(P,C-4′) ≈ 8 Hz; ^3J(P,H-3′) ≈ 9 Hz], whereas in DNA the sugar mainly occupies the S-type range [$\epsilon^t{}_S$ = 192°; ^3J(P,C-4′) ≈ 10.7 Hz; ^3J(P,H-3′) ≈ 4.5 Hz]. The $\epsilon^-{}_N$ combination appeared 'forbidden', whereas $\epsilon^-{}_S$ = 266°, corresponding with ^3J(P,C-2′) ≈ 8.3 Hz, remains allowed. The latter combination must be considered important, because X-ray crystallography has shown that it occurs in various residues throughout the double helix (BII form). We expect that the BII form will be studied in solution as soon as ^{13}C-enriched synthetic DNAs become available. Finally, it should be mentioned that $\epsilon^t{}_N$ in DNA (212°) is smaller than $\epsilon^t{}_N$ in RNA (219°).[71]

5 CAVEATS

The original optimism that arose among stereochemists when Karplus's first paper[1] on ^3J(H,H) in ethane appeared in 1959 soon gave way to grave scepticism in the course of the 1960s.[2] Nevertheless, the Karplus-type relationships are by now firmly rooted in stereochemical thinking. Perhaps unfortunately, not all the known ramifications are widely appreciated. Moreover, even in the situation of the best-known coupling, ^3J(H,C,C,H) along sp^3-sp^3 C–C bonds, some influences that affect couplings have not been taken into consideration in the present contribution. At least three of these (perhaps not unrelated) influences are known, but as yet not understood to the extent that quantitative corrections to calculated couplings can be brought into play: (a) the β effect, the orientation of a β substituent appears to affect ^3J(H,C,C,H), an increase of about 0.5 Hz is noted for $^3J_{ap}$ when a C–O bond occurs in the *ap* position with respect to one of the coupling protons;[11] (b) the through-space (Barfield) transmission effect,[72,73] first noted in norbornane-like structures but not necessarily limited to highly strained compounds; (c) bond angle deformations, semiempirical calculations[2,74] predict that vicinal couplings depend significantly on the bond angles HCC′ and CC′H′ of the HCC′H′ fragment. The effect would be maximal for $^3J_{ap}$ and $^3J_{sp}$. At this point a dilemma arises. Assuming that reliable empirical corrections for influences (a)–(c) can be established, it would be necessary to introduce much detailed structural information concerning the molecular fragment under study into play before a measured coupling can be interpreted quantitatively in terms of the same structure. Undoubtedly, in the future this will be done for selected fragments which are of vital interest to researchers. However, we may also expect that for times to come present-day knowledge will suffice to solve stereochemical problems routinely along the lines pioneered by Karplus in 1959.[1]

6 RELATED ARTICLES

Amino Acids, Peptides and Proteins: Chemical Shifts; Biological Macromolecules: Structure Determination in Solution; Biological Macromolecules: NMR Parameters; Carbohydrates and Glycoconjugates; Coupling Constants Determined by ECOSY; Coupling Through Space in Organic Chemistry; DNA: A-, B-, and Z-; DNA Triplexes, Quadruplexes, and Aptamers; Half-Filter Experiments: Proton–Carbon-13; Homonuclear Three-Dimensional NMR of Biomolecules; Indirect Coupling: Semiempirical Calculations; Nucleic Acid Structures in Solution: Sequence Dependence; Nucleic Acids: Phosphorus-31 NMR; Nucleic Acids: Spectra, Structures, and Dynamics; Quantitative Measurements; Structures of Larger Proteins, Protein-Ligand, and Protein-DNA Complexes by Multi-Dimensional Heteronuclear NMR; Three-Dimensional HMQC-NOESY, NOESY-HMQC, and NOESY-HSQC; Three- and Four-Dimensional Heteronuclear Magnetic Resonance; Two-Dimensional J-Resolved Spectroscopy; Vicinal ^1H, ^1H Coupling Constants in Cyclic π-Systems.

7 REFERENCES

1. M. Karplus, *J. Chem. Phys.*, 1959, **30**, 11.
2. M. Karplus, *J. Am. Chem. Soc.*, 1963, **85**, 2870.
3. R. E. Glick and A. A. Bothner-By, *J. Chem. Phys.*, 1956, **25**, 362.
4. C. N. Banwell and N. Sheppard, *Discuss. Faraday Soc.*, 1962, **34**, 115.
5. R. J. Abraham and K. G. R. Pachler, *Mol. Phys.*, 1964, **7**, 165.
6. H. Booth, *Tetrahedron Lett.*, 1965, 411.
7. P. L. Durette and D. Horton, *Org. Magn. Reson.*, 1971, **3**, 417.
8. L. Pauling, *The Nature of the Chemical Bond*, 3rd edn., Cornell University Press, Ithaca, NY, 1960.
9. M. L. Huggins, *J. Am. Chem. Soc.*, 1953, **75**, 4123.
10. R. J. Abraham and G. Gatti, *J. Chem. Soc. B*, 1969, 961.
11. C. Altona and C. A. G. Haasnoot, *Org. Magn. Reson.*, 1980, **13**, 417.
12. K. G. R. Pachler, *Tetrahedron*, 1971, **27**, 187.
13. K. G. R. Pachler, *J. Chem. Soc. Perkin Trans. 2*, 1972, 1935.
14. F. A. A. M. de Leeuw, C. A. G. Haasnoot, and C. Altona, *J. Am. Chem. Soc.*, 1984, **106**, 2299.
15. L. A. Donders, F. A. A. M. de Leeuw, and C. Altona, *Magn. Reson. Chem.*, 1989, **27**, 556.
16. C. A. G. Haasnoot, F. A. A. M. de Leeuw, and C. Altona, *Tetrahedron*, 1980, **36**, 2783.

17. IUPAC Tentative Rules for the Nomenclature of Organic Chemistry, *J. Org. Chem.*, 1970, **35**, 2849; for nucleic acids, see JCBN Recommendations, *Eur. J. Biochem.*, 1983, **131**, 9; *J. Biol. Chem.*, 1986, **261**, 13.
18. E. Díez, J. San-Fabián, J. Guilleme, C. Altona, and L. A. Donders, *Mol. Phys.*, 1989, **68**, 49.
19. C. Altona, J. H. Ippel, A. J. A. Westra Hoekzema, C. Erkelens, M. Groesbeek, and L. A. Donders, *Magn. Reson. Chem.*, 1989, **27**, 564.
20. C. Altona, R. Francke, R. de Haan, J. H. Ippel, G. J. Daalmans, and J. van Wijk, *Magn. Reson. Chem.*, 1994, **32**, 670.
21. F. A. A. M. de Leeuw, A. A. van Beuzekom, and C. Altona, *J. Comp. Chem.*, 1983, **4**, 438.
22. N. L. Allinger, *Quantum Chemistry Program Exchange MMP(85)*, Indiana State University, 1985.
23. J. San-Fabián, J. Guilleme, E. Díez, P. Lazzeretti, M. Malagoli, and R. Zanasi, *Chem. Phys. Lett.*, 1993, **206**, 253.
24. J. van Wijk, B. D. Huckriede, J. H. Ippel, and C. Altona, *Methods Enzymol.*, 1992, **211**, 286.
25. V. F. Bystrov, *Prog. Nucl. Magn. Reson. Spectrosc.*, 1976, **10**, 41.
26. P. E. Hansen, *Prog. Nucl. Magn. Reson. Spectrosc.*, 1981, **14**, 175.
27. J. L. Marshall, *Carbon–Carbon and Carbon–Proton NMR Couplings*, Verlag Chemie Int., Deerfield Beach, FL, 1983.
28. K. Wüthrich, *NMR of Proteins and Nucleic Acids*, Wiley, New York, 1986.
29. S. Ludvigsen, K. V. Anderson, and F. M. Poulsen, *J. Mol. Biol.*, 1991, **217**, 731.
30. A. Pardi, M. Billeter, and K. Wüthrich, *J. Mol. Biol.*, 1985, **180**, 741.
31. L.-F. Kao and M. Barfield, *J. Am. Chem. Soc.*, 1985, **107**, 2323.
32. A. de Marco and M. Llinas, *Biochemistry*, 1979, **18**, 3847.
33. R. Aydin, J. P. Loux, and H. Günther, *Angew. Chem., Int. Ed. Engl.*, 1982, **21**, 449.
34. M. C. Reddy, B. P. Nagy Reddy, K. R. Sridharan, and J. Ramakrishna, *Org. Magn. Reson.*, 1984, **22**, 464.
35. P. E. Hansen, J. Feeney, and G. C. K. Roberts, *J. Magn. Reson.*, 1975, **17**, 249.
36. D. Cowburn, D. H. Live, A. J. Fishman, and W. C. Agosta, *J. Am. Chem. Soc.*, 1983, **105**, 7435.
37. M. Barfield and H. L. Gearhart, *Mol. Phys.*, 1974, **27**, 899.
38. P. Schmieder and H. Kessler, *Biopolymers*, 1992, **32**, 435.
39. F. H. Cano, C. Foces-Foces, J. Jiménez-Barbero, A. Alemany, M. Bernabé, and M. Martin-Lomas, *J. Am. Chem. Soc.*, 1987, **52**, 3367.
40. R. Wasylishen and T. Schaefer, *Can. J. Chem.*, 1973, **51**, 961.
41. T. P. Forrest and S. Sukumar, *Can. J. Chem.*, 1977, **55**, 3686.
42. A. A. van Beuzekom, *Thesis*, Leiden University, 1989.
43. G. J. Karabatsos and C. E. Orzech, Jr., *J. Am. Chem. Soc.*, 1965, **87**, 560.
44. A. A. van Beuzekom, F. A. A. M. de Leeuw, and C. Altona, *Magn. Reson. Chem.*, 1990, **28**, 68.
45. P. P. Lankhorst, C. A. G. Haasnoot, C. Erkelens, and C. Altona, *J. Biomol. Struct. Dyn.*, 1984, **1**, 1387.
46. P. P. Lankhorst, C. A. G. Haasnoot, C. Erkelens, H. P. Westerink, G. A. van der Marel, J. H. van Boom, and C. Altona, *Nucleic Acids Res.*, 1985, **13**, 927.
47. D. B. Davies, P. Rajani, M. MacCoss, and S. Danyluk, *Magn. Reson. Chem.*, 1985, **23**, 72.
48. Y. Kim and J. H. Prestegard, *Proteins*, 1990, **8**, 377.
49. D. F. Mierke and H. Kessler, *Biopolymers*, 1993, **33**, 1003.
50. A. E. Torda, R. M. Brunne, T. Huber, H. Kessler, and W. F. van Gunsteren, *J. Biomol. NMR*, 1993, **3**, 55.
51. M. Eberstadt, D. F. Mierke, M. Köck, and H. Kessler, *Helv. Chim. Acta*, 1992, **75**, 2583.
52. G. W. Vuister and A. Bax, *J. Magn. Reson.*, 1992, **98**, 428.
53. P. Schmieder, M. Kurz, and H. Kessler, *J. Biolmol. NMR*, 1991, **1**, 403.
54. K. G. R. Pachler, *Spectrochim. Acta*, 1964, **20**, 581.
55. R. J. Abraham, P. Loftus, and W. A. Thomas, *Tetrahedron*, 1977, **33**, 1227.
56. J. Feeney, *J. Magn. Reson.*, 1976, **21**, 473.
57. L. Pogliani, D. Ziessow, and C. H. Krüger, *Tetrahedron*, 1979, **35**, 2867.
58. H. Kessler, C. Griesinger, and K. Wagner, *J. Am. Chem. Soc.*, 1987, **109**, 6927.
59. C. A. G. Haasnoot, F. A. A. M. de Leeuw, H. P. M. de Leeuw, and C. Altona, *Biopolymers*, 1981, **20**, 1211.
60. C. Altona and M. Sundaralingam, *J. Am. Chem. Soc.*, 1972, **94**, 8205.
61. J. M. Schmidt, R. Brüschweiler, R. R. Ernst, R. L. Dunbrack, Jr., D. Joseph, and M. Karplus, *J. Am. Chem. Soc.*, 1993, **125**, 8747.
62. W. Saenger, *Principles of Nucleic Acid Structure*, Springer, New York, 1984.
63. C. Altona, *Recl. Trav. Chim. Pays-Bas*, 1982, **101**, 413.
64. C. Altona, in *Theoretical Biochemistry and Molecular Biophysics*, ed. D. L. Beveridge and R. Lavery, Adenine Press, New York, 1990, p. 1.
65. F. J. M. van de Ven and C. W. Hilbers, *Eur. J. Biochem.*, 1988, **178**, 1.
66. C. A. G. Haasnoot, F. A. A. M. de Leeuw, H. P. M. de Leeuw, and C. Altona, *Org. Magn. Reson.*, 1981, **15**, 43.
67. F. A. A. M. de Leeuw and C. Altona, *J. Chem. Soc., Perkin Trans. 2*, 1982, 375.
68. F. A. A. M. de Leeuw and C. Altona, *J. Comp. Chem.*, 1983, **4**, 428.
69. L. J. Rinkel and C. Altona, *J. Biomol. Struct. Dyn.*, 1987, **4**, 621.
70. J. M. L. Pieters, E. de Vroom, G. A. van der Marel, J. H. van Boom, Th. M. G. Koning, R. Kaptein, and C. Altona, *Biochemistry*, 1990, **29**, 788.
71. P. P. Lankhorst, C. A. G. Haasnoot, C. Erkelens, and C. Altona, *Nucleic Acids Res.*, 1984, **12**, 5419.
72. M. Barfield, *J. Am. Chem. Soc.*, 1980, **102**, 1.
73. F. A. A. M. de Leeuw, A. A. van Beuzekom, and C. Altona, *J. Comp. Chem.*, 1983, **4**, 438.
74. M. Barfield and W. B. Smith, *J. Am. Chem. Soc.*, 1992, **114**, 1574.

Biographical Sketch

Cornelis Altona. *b* 1931. Ph.D., 1964, Leiden University. Introduced to NMR by E. Havinga and L. J. Oosterhoff. Visiting lecturer, Case Western University, 1967–69. Faculty of Chemistry, Leiden University, 1964—present. Approximately 185 publications. Research interests include: stereoelectronic effects (anomeric effect, *gauche* effect); conformational analysis (of five-membered rings in particular); generalized Karplus-type equations for vicinal spin—spin coupling constants; conformation, structure and dynamics of oligonucleotides (DNA, RNA) in aqueous solution, including hairpin loops and four-way junctions; force-field calculations and charge distributions; application of ab initio methods.

Cryogenic NMR Probes: Applications

Gary E. Martin

Global Pharmaceutical Sciences, Pharmacia Corporation, Kalamazoo, MI, USA

1 References 1

Conceptually, cryogenic NMR probes are not a new idea. Early work demonstrated that considerable gains in sensitivity could be obtained by cooling the probe rf coils and associated electronics.[1–4] More recently, there have been poster presentations at various NMR meetings showing applications of cryogenic NMR probe technology.[5–9] Reports in the primary literature have begun to appear dealing with applications to both proteins[10,11] and small molecules.[12–15]

For small molecules, cryogenic NMR probes open the possibility of acquiring both direct and long-range heteronuclear shift correlation data for a variety of scarce samples, e.g., rare natural products and impurities, degradation products, and metabolites of pharmaceuticals. Cryogenic NMR probe technology should also make it feasible to characterize unstable compounds prior to their degradation, which have heretofore been difficult to characterize.[16] This technology will have an impact on the application of relatively insensitive NMR experiments in structure characterization studies. Examples will likely include the acquisition of long-range heteronuclear shift correlation data on very small samples that are beyond the detection limits with conventional 3 or 1.7 mm NMR probes; the more routine acquisition of $^{13}C-^{13}C$ INADEQUATE spectra;[13] and the acquisition of HSQC-TOCSY data. It is also likely that cryogenic NMR probes will make the utilization of long-range $^{1}H-^{15}N$ two-dimensional NMR experiments, which have recently been reviewed,[17] a routine tool in structural characterization studies.

To illustrate the significant improvement in performance offered by cryogenic NMR probe technology relative to conventional NMR probes, comparative long-range $^{1}H-^{15}N$ 2D NMR spectra of a 2 mg sample of the oxazolidinone antibiotic eperezolid **(1)** in 150 μL d_3-acetonitrile in a 3-mm NMR tube are shown in Figure 1.[15] The cryogenic NMR probe data were acquired using a Varian INOVA 500 MHz NMR spectrometer equipped with a 5 mm gradient triple resonance Chili-probe™ in which the 3 mm sample tube was run coaxially. The data acquired conventionally employed a Varian INOVA 500 MHz NMR spectrometer equipped with a Nalorac 3-mm gradient triple resonance micro NMR probe. The cryogenic NMR probe data shown in Figure 1(a) were recorded in a total of 26 min and gave a S/N ratio in the projection of 101 : 1. To acquire comparable S/N data (112 : 1) using a conventional 3-mm NMR probe required >17 h (Figure 1b).

The considerable sensitivity advantage offered by cryogenic NMR probe technology can be expected to open numerous new avenues of structural chemistry investigation in the areas of small or unstable samples, and in the application of relatively insensitive NMR experiments on a routine basis. Comparable gains will undoubtedly be enjoyed for hyphenated techniques such as LC-NMR when cryogenic probe technology is applied in this area.

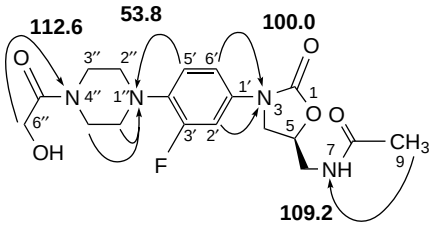

(1)

1 REFERENCES

1. P. Styles, N. F. Soffe, C. A. Scott, D. A. Cragg, F. Row, D. White, and P. C. J. White, *J. Magn. Reson.*, 1983, **60**, 397–404.
2. P. Styles, N. F. Soffe, and C. A. Scott, *J. Magn. Reson.*, **84**, 376–378.
3. W. A. Anderson, W. W. Brey, A. L. Brooke, B. Cole, K. A. Delin, L. H. Fuks, H. D. W. Hill, M. E. Johanson, V. Y. Kotsubo, R. Nast, R. S. Withers, and W. H. Wong, *Bull. Magn. Reson.*, 1995, **17**, 98–102.
4. H. D. W. Hill, *IEEE Trans. Appl. Superconduct.*, 1997, **7**, 3750–3755.
5. R. Triebe, R. Nast, D. Marek, R. Withers, L. Baselikgia, M. Haeberli, T. Gerfin, and P. Calderon, 'A User-Friendly System for the Routine Application of Cryogenic NMR Probes: Technology and Results', 40th Experimental NMR Conference, Orlando FL, Feb 28–Mar 5, 1999, Abst. W&Th, p. 201.
6. J. Pease, R. Withers, R. Nast, A. Deese, P. Calderon, M. Saumil, T. Kelly, and F. Laukein, 'Application of a 2.5-mm CryoProbe to Metabolite Studies', 40th Experimental NMR Conference, Orlando FL, Feb 28–Mar 5, 1999, Abst. W&Th, p. 202.
7. M. Goger, J. McDonnell, and D. Cowburn, 'Using CryoProbe to Decrease the Amount of Instrument Time Required for Protein Assignment', 41st Experimental NMR Conference, Asilomar, CA, April 9–14, 2000, Abstr. W&Th, p. 152.
8. C. Richter, D. Marek, M. Haebeli, L. Baseligia, O. Schett, R. Triebe, and D. Moskau, 'New Applications for Triple Resonance Cryogenic High-Resolution NMR Probes', 41st Experimental NMR Conference, Asilomar, CA, April 9–14, 2000, Abstr. W&Th, p. 153.
9. Y. Liu, J. Pease, B. Potts, A. Deese, Y. D. Liu, M. O'Neil-Johnson, R. Withers, and R. Nast, 'SMASH 2000–Small Molecule NMR Conference', Chicago, IL, July 16–19, 2000, Abst., p. 21.
10. Z. Serber, C. Richter, D. Moskau, J.-M. Böhlen, T. Gerfin, D. Marek, M. Häberli, L. Baslgia, F. Laukein, A. S. Stern, J. C. Hoch, and V. Dötsch, *J. Am. Chem. Soc.*, 2000, **122**, 3554–3555.
11. P. F. Flynn, D. Mattiello, H. D. W. Hill, and A. J. Wand, *J. Am. Chem. Soc.*, 2000, **122**, 4823–4824.
12. T. M. Logan, N. Mural, G. Wang, and C. Jolivet, *Magn. Reson. Chem.*, 1999, **37**, 762–765.
13. G. Bringmann, M. Wohlfarth, H. Rischer, M. Grüne, and J. Schlauer, *Angew. Chem., Intl. Edn., Engl.*, 2000, **35**, 1464–1466.

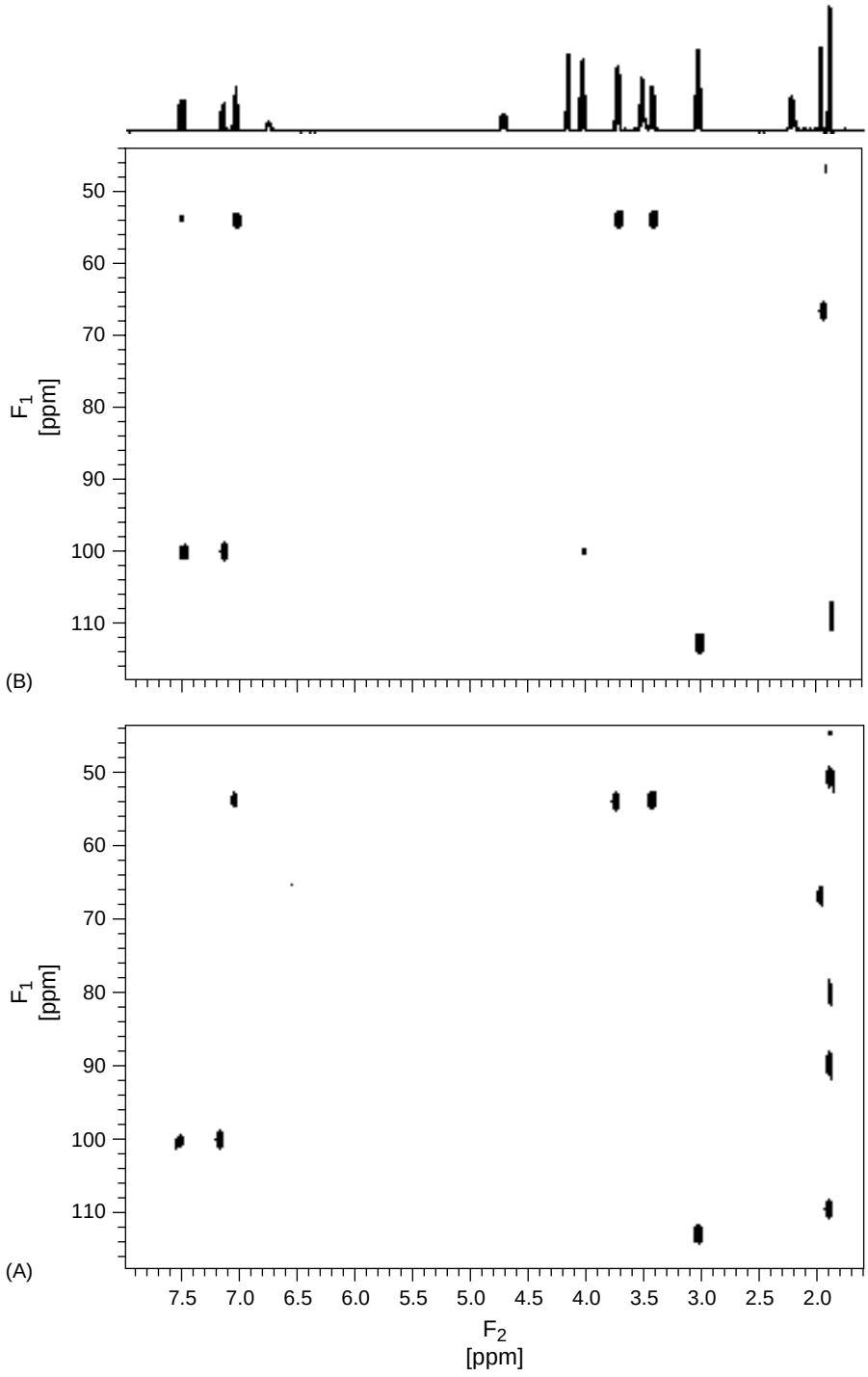

Figure 1 Comparison long-range $^{1}H-^{15}N$ GHMBC spectra of a 2 mg sample of the oxazolidinone antibiotic eperezolid **(1)** dissolved in 150 μL d_3-acetonitrile in a 3-mm NMR tube.[15] The data shown in panel A were acquired in 26 min using a Varian INOVA 500 MHz NMR spectrometer equipped with a Varian 5-mm gradient inverse triple resonance cryogenic Chili-probe™. Data shown in panel (B) were acquired in >17 h using a Varian INOVA 500 MHz NMR spectrometer equipped with a Nalorac MIDTG-500-3 3 mm gradient inverse triple resonance micro NMR probe. Both spectra were acquired using a CIGAR-HMBC experiment optimized for 5–10 Hz.[18,19] Both data sets were taken using 64 increments of the evolution time. Spectral widths were 4248 Hz in F_2 and 4561 Hz in F_1 in both experiments. For the Cryo-Q probe, 90° pulse lengths were 9 μs for ^{1}H at a power of 3 watts and 18 μs for ^{15}N at a power of 140 watts. Wurst-8 shaped gradients were employed with the Cryo-Q probe pulses applied in the ratio of 5 : 5 : 1 (12 : 12 : 2.43 G cm^{-1}) with an eight-step phase cycle. A total of eight transients were accumulated/t_1 increment. In comparison, the data acquired in the conventional 3-mm NMR probe required 1024 transients/t_1 increment to achieve comparable S/N

15. D. J. Russell, C. E. Hadden, G. E. Martin, A. A. Gibson, A. P. Zens, and J. L. Carolan, *J. Nat. Prod.*, 2000, **63**, 1047–1049.
16. R. C. Crouch, W. Llanos, K. Mehr, C. E. Hadden, D. R. Russell, and G. E. Martin, *Magn. Reson. Chem.*, 2001, **39**, 555–557.
17. G. E. Martin, B. A. Perlman, R. H. Robins, F. W. Crow, W. K. Duholke, J. E. Guido, C. E. Hadden, B. D. Kaluzny, and T. J. Thamann, *J. Heterocycl. Chem.*, 1999, **36**, 1107–1114.
18. G. E. Martin and C. E. Hadden, *J. Nat. Prod.*, 2001, **64**, 543–585.
19. C. E. Hadden, G. E. Martin, and V. V. Krishnamurthy, *Magn. Reson. Chem.*, 2000, **38**, 143–147.
20. G. E. Martin and C. E. Hadden, *Magn. Reson. Chem.*, 2000, **38**, 251–256.

Biographical Sketch

Gary Edwin Martin, *b* 1949. Ph.D. 1972 Pharmaceutical Sciences, University of Kentucky. Professor, University of Houston, 1975–89. Principal Scientist Burroughs Wellcome Co., Research Triangle Park, NC 1989–1995. Senior Fellow, Pharmacia Corp. 1996–present. Approx. 250 publications. Current research interests: high sensitivity, small volume and cryogenic NMR probe development and applications; development of new long-range heteronuclear shift correlation experiments; application of long-range ^{1}H–^{15}N heteronuclear shift correlation at natural abundance.

Field Gradients and Their Application

Ralph E. Hurd
GE Medical Systems, Fremont, CA, USA

1	Introduction	1
2	Early Applications	1
3	Gradient Hardware Considerations	1
4	The Effect of Magnetic Field Gradients	2
5	Coherence Pathway Selection	2
6	Homonuclear Applications	4
7	Proton Detected Heteronuclear Applications	6
8	Water Elimination	8
9	Phase Sensitive Methods	9
10	Spatial Tools	13
11	Summary	14
12	Related Articles	15
13	References	15

1 INTRODUCTION

Pulsed magnetic field gradients can be used in NMR to suppress unwanted magnetization, or to encode space, motion, and coherence order. These applications, which are central elements of in vivo magnetic resonance, can also be used to enhance high-resolution NMR spectroscopy. There are several ways in which a conventional NMR experiment can benefit from pulsed field gradients. Coherence pathway selection using field gradient pulses instead of phase cycling can minimize data collection time, reduce artifacts, and avoid signal loss associated with traditional water elimination methods. Differences in the rates of molecular motion between solvent and macromolecules can be exploited to achieve linewidth and lineshape independent water suppression. The consequences of poor homogeneity can be reduced using spatially selective excitation, and spoiler gradients can be used to selectively eliminate unwanted magnetization. The present article describes the development and application of $\boldsymbol{B}_0$ pulse field gradients in high resolution NMR spectroscopy. For a description of $\boldsymbol{B}_1$ gradient applications see ***Radiofrequency Gradient Pulses*** .

2 EARLY APPLICATIONS

The first report of using pulsed field gradients was published in 1955 and described the potential of magnetic resonance for information storage.[1] This work detailed the use of gradient pulses in multipulse, multiecho NMR to eliminate selectively unwanted signal. In this paper, bracketing a 180° refocusing pulse with a symmetric gradient pair was introduced as an efficient way to avoid spurious echoes. Further, the application of a gradient pulse during a z axis storage interval was introduced as a way to select for stimulated echoes. These early pulsed gradient applications are still used in contemporary NMR, especially in imaging and localized spectroscopy, where they have taken on names such as primer−crusher pairs, crushers, and spoiler gradients. These concepts are also important for the application of pulsed gradients in high-resolution NMR spectroscopy.

The use of pulsed field gradients to measure molecular diffusion was introduced in 1965 by Stejskal and Tanner.[2] This approach overcame severe bandwidth limitations associated with earlier static gradient measurements. In this method, transverse magnetization is encoded with spatially dependent phase by application of an initial gradient pulse, allowed to stay encoded for a fixed period of time, and then rephased by a second gradient pulse. The loss of recoverable signal due to the movement of spins is related to the diffusion coefficient by the Stejskal−Tanner equation:

$$\ln(S/S_0) = -\gamma^2 g^2 \tau^2 (\Delta - 1/3\tau) D \qquad (1)$$

where γ is the magnetogyric ratio, g is the strength and τ the duration of the gradient pulse pair, Δ is the time between gradient pulses, and D is the diffusion coefficient (see also ***Diffusion Measurements by Magnetic Field Gradient Methods***). The large difference in D for macromolecules relative to solvent water provides the basis for the use of diffusion gradients in spectroscopy.

In 1968, Vold and co-workers[3] used a spoiler gradient to overcome imperfect 180° inversion in a T_1 recovery sequence. Shortly thereafter, the benefits of using spoiler gradients, or homospoil pulses, as they sometimes became to be known, were reported by a number of groups. One of the best known applications has been as a mix time spoiler in the NOESY experiment (see also ***NOESY***).

Even spatial resolution has shown potential value in high-resolution spectroscopy. As will be discussed later in this article, slice selection can be used to reduce end effects from sample and coil, and field maps may provide a way to optimize homogeneity. For a description of the development of spatial applications of pulsed field gradients see ***Magnetic Resonance Imaging: A Historical Overview*** .

In 1977, Wokaun and Ernst[4] described the relationship between coherence order and the effect of a gradient pulse. The idea of using gradients for coherence pathway selection was further developed by the studies of several groups.[5–8]

3 GRADIENT HARDWARE CONSIDERATIONS

3.1 Eddy Current Compensation

In early studies, potential benefits of using pulsed gradients were often overshadowed by drawbacks such as long gradient recovery times, increased phase instability, peak shape distortion, and, for high-resolution applications, disturbance of the field/frequency lock system. The problem is with the induced eddy currents generated in conductive materials by the switched gradient field. This may include such items as the magnet cryoshields, the bore tube, and the coil itself. The transient fields generated by eddy currents have a variety of decay times which may be of the order of milliseconds, or can persist for seconds. To reduce this problem, the gradient

amplifier can be overdriven to compensate for these undesirable fields. This approach, referred to as preemphasis, is in common use on almost all modern gradient systems, but does not completely overcome the problem (***Eddy Currents and Their Control***).

3.2 Gradient Amplifier Noise

With the incorporation of strong ($>200\,\mathrm{mT\ m^{-1}}$) pulsed gradient systems into the NMR experiment, it is important to consider the dynamic range of the gradient amplifier. For example, a $1\,\mathrm{T\ m^{-1}}$ gradient is capable of producing 425 800 2π radians $\mathrm{s^{-1}}$ gradient across a 1 cm sample. The tolerance of most experiments requires that any variation of the amplifier quiescent state (the noise floor) be significantly less than 10^{-7} of this peak value. For many experiments, especially those in which a nonrectangular gradient wave form is used, 16-bit control of the gradient amplitude is also desirable.

3.3 Actively Shielded Gradients

One of the most important improvements in gradient technology for NMR has been the introduction of actively shielded gradients (see ***Gradient Coil Systems***). The basic idea is to provide a second coil of opposite polarity outside the primary gradient coil, which is then driven to buck the stray field generated outside the primary coil. In practice the combination of active shielding and preemphasis gives the best performance.

Phase error can also come from movement of the coil during sharp gradient transitions. This is the source of the characteristic sound made by gradient pulses, sometimes referred to as the speaker-coil effect. It is often desirable to attenuate the amplitude and ring down time of this vibration. Reduced mechanical noise from the gradients is usually accomplished by potting the coils in a nonconductive material such as concrete or epoxy. These coils must also be designed to dissipate the significant heat that can be generated by gradient experiments.

3.4 Single-Axis versus Three-Axis Gradients

In any experiment which consists of multiple rf and multiple gradient pulses, care must be taken to avoid recovering unwanted signal dephased earlier in the pulse sequence. This is relatively straightforward, and can be achieved by prudent choice of sign, amplitudes, or durations of the gradient pulses. If multiple axes are available, gradient cycling has been shown to be effective.[9] In practice, single z axis gradient coils have been more widely available for high-resolution applications, and have proven sufficient to provide improvements over conventional phase cycled methods. Unfortunately, in some cases the static gradients generated by the homogeneity shims can create a problem. Although weak in comparison to the applied gradient pulses, these static gradients may have over 1 s (e.g. acquisition time) to rephase the effect of a 1 ms or shorter gradient interval.

In 1971, Redfield and Gupta[10] commented on the formation of unwanted gradient echoes when using spoiler gradients. The misadjustment of shims, in the same direction as the applied gradient, is suggested as a way to prevent this accidental rephasing by the static shim gradients during acquisition. Misadjustment of shims, however, is rarely desirable. Further, in the case of high order z shims, the rephased signal may be from a small part of the NMR sample. An effective approach to reducing this problem is to avoid application of a pure z pulsed gradient, using additional x and/or y gradients to provide an off z axis distribution of phase.[11]

3.5 Sample Spinning and Field Frequency Locking

Although the effect of a gradient pulse on a deuterium field/frequency lock system is reduced relative to protons by γ_D/γ_H, lock blanking during the gradient pulse can be valuable. Recovery of the steady-state lock signal is determined primarily by the sensitivity of the lock as reflected in the M_{xy}/M_z of the deuterium spins, and by the T_2 relaxation rates of the deuterium solvent. Lock recovery rates can be very favorable for strong lock solvents such as the 5–10% D_2O commonly used for biochemical studies.

Sample spinning is only compatible with z axis gradient application, and even there care must be taken to avoid vortexing of the sample. Any increased mixing leads to signal loss in both diffusion weighted and in gradient coherence selection methods. Also, in practice, sample spinning has been observed to reintroduce t_1 noise, partially negating one of the benefits of using gradients in the first place. Fortunately, full performance can be achieved nonspin for most biochemical samples.

4 THE EFFECT OF MAGNETIC FIELD GRADIENTS

4.1 Dephasing

The application of a pulsed field gradient generates a reversible distribution of phase

$$\phi_r = \gamma(g\tau)rp \tag{2}$$

where γ is the magnetogyric ratio, g is the gradient strength, τ is the gradient duration, r is the distance from gradient isocenter, and p is the coherence order. This effect can be visualized by mapping the effect of gradient pulse on a phase sensitive proton image as shown in Figure 1. As expected the application of a rectangular, $10\,\mathrm{mT\ m^{-1}}$ gradient of 1 ms in duration generates approximately three 2π cycles of phase along the z axis of a 1.5 cm long water sample. If not resolved in space, the signal from the volume of spins self-cancels. The effectiveness of cancellation increases with gradient integral $g\tau$.

The amount of gradient needed for complete signal dephasing is variable and depends strongly on factors such as $\boldsymbol{B}_1$ homogeneity and bulk magnetic susceptibility shifts. Although these would appear to be well controlled in a typical high-resolution NMR experiment, small deviations can make a significant difference when the amount of unwanted signal is large, as it is for most dilute biochemical samples in 90–95% H_2O. The largest variations in $\boldsymbol{B}_1$ are in the transition bands, at the ends of the rf coil, where $\boldsymbol{B}_1$ goes from maximum to zero. Short samples and bubbles can lead to localized frequency shifts, which also lead to inefficiency in self-cancellation.

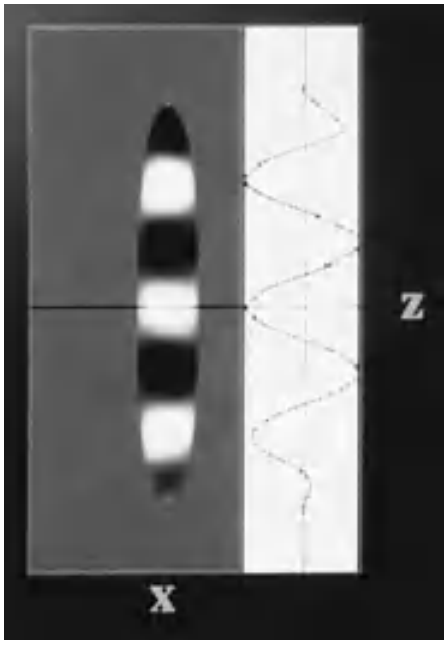

Figure 1 Phase sensitive image of a water sample in a standard 5 mm NMR tube. The effect of a 1 ms 10 mT m^{-1} rectangular z gradient pulse is recorded. The height of the detected volume is about 1.5 cm. As illustrated by the image and accompanying profile, the expected phase distribution is encoded by the applied gradient pulse. The curvature at the ends of the sample is the fall-off of x gradient strength as a function of z

5 COHERENCE PATHWAY SELECTION

Coherence selection using gradients takes advantage of the field dependence of coherence order. This dependence is described in terms of the phase generated by an applied gradient as shown in equation (2). In its simplest form, a sequence of rf pulses and delays generate multiple coherence pathways. A particular pathway can be selected, for example, by application of a gradient pulse to coherence order label the spins during an evolution or mixing delay interval, followed by the application of a read gradient just prior to data acquisition to rephase the desired pathway. This assumes that the chosen pathway will have zero net phase gradient and that the unwanted pathways will have a net distribution of phase, and therefore self-cancel. In general, signal will only be observed from pathways in which

$$\sum_i G_i p_i = 0 \tag{3}$$

where G_i represents the integral ($g\tau$, for a rectangular gradient pulse) of each gradient interval, i, and p_i is the coherence order during each interval, i.

5.1 Density Operator Description

The effect of a pulsed magnetic field gradient on the nuclear spin can be understood by describing the state of the spin system in terms of density operators. Many different formalisms express the density operator in matrix elements of appropriate sets of operators in a Cartesian or spherical basis. A detailed description of the effect of magnetic field gradients on the magnetization or coherence component is given by Counsell et al.[8]

For the purpose of describing the effects of magnetic field gradients, it is convenient to classify the density operator $\rho(t)$ of the spin system at any time t according to its various coherence orders or components:

$$\rho(t) = \sum_p \rho^p(t) \tag{4}$$

where p and ρ^p represent a particular coherence order and the density operator component corresponding to that coherence order. The spin coherences undergo precession during a gradient pulse, and the extent of precession depends on the spatial coordinate r of the spin, and the coherence order p of that particular component. Hence the Hamiltonian of the spin system during the gradient pulse is predominantly from Zeeman contributions. The Zeeman fields experienced by the various spins in the sample vary according to their spatial coordinates. The precession or rotation can be represented by $\exp\{-i\omega_z(r)F_z\tau\}$, where $\omega_z(r)$ is the precession frequency at a spatial position r, and τ is the duration of the field gradient pulse, and F_z is the z component of the total angular momentum. Classification of the density operator into the various coherence order components is convenient, since the effect of the field gradient pulse can be written as

$$\rho^p(t-) \xrightarrow{\exp\{i\omega_z(r)F_z\tau\}} \exp\{-ip\omega_z(r)\tau\}\rho^p(t+) \tag{5}$$

which describes the transformation of the pth component of the density operator ρ. $\rho(t-)$ and $\rho(t+)$ are used to label the density operator before and after the gradient pulse. As the right hand side shows, the effect of the gradient pulse is to modulate the density operator component by a complex phase factor. This phase factor depends on the coherence order of the component and on the integral of the gradient pulse. In other words, the phase of each magnetization component is modified by a factor which depends on the coherence order of the component, spatial position of that particular spin and also on the duration and amplitude of the applied field gradient. If we consider heteronuclear spins, the phase factor would also take into account the magnetogyric ratio of the nuclear spin. Essentially, the effect of the gradient pulse is to defocus the coherence by a controlled amount. Each of the coherence pathways can be thought to be coherence order labeled by the gradient pulse. Selection of a particular pathway or decoding is then accomplished by applying a rephasing gradient pulse with amplitude and duration $\omega_z^{\mathrm{R}}(r)\tau^{\mathrm{R}}$, which transforms the density operator described by

$$\sum_k C_k \rho^{(-1)} \exp\{-i\phi_k\} \tag{6}$$

where k is the index for a particular coherence pathway in the experiment, ϕ_k is the cumulative phase dispersal for that particular pathway, C_k denotes all of the time dependence and $\rho^{(-1)}$ denotes the observable component of the density operator, corresponding to coherence order $p = -1$. This can

be written as

$$\sum_k C_k \rho^{(-1)} \xrightarrow{\exp\{-\mathrm{i}\omega_z^{\mathrm{R}}(r)F_z\tau^{\mathrm{R}}\}} C_1\rho^{(-1)} + \sum_{k\neq 1} C_k\rho^{(-1)}\exp\{-\mathrm{i}(\phi_k + \omega_z^{\mathrm{R}}(r)\tau^{\mathrm{R}})\} \tag{7}$$

where 1 denotes the desired coherence pathway in the experiment. The first term on the right hand side $k = 1$, corresponds to the pathway which has been exactly decoded, and hence observed since

$$\phi_k = -\omega_z^{\mathrm{R}}(r)\tau^{\mathrm{R}} \tag{8}$$

The second term denotes all the other pathways which are still defocused and are not observable. Equation (5) describes the most important feature of all coherence transfer selection schemes, including rf phase cycling, $\boldsymbol{B}_0$ and $\boldsymbol{B}_1$ gradient methods. In conventional rf phase cycling methods, each coherence component accumulates phase factors during the various cycles of the phase cycle. The receiver phase cycle is then determined such that only the desired pathways yield a signal (see also ***Phase Cycling***). In the case of pulsed field gradients, each of the gradient pulses contributes to the cumulative phase factors of the various coherence components. The desired pathway is then selected by choosing the appropriate rephasing gradient integral (the product of amplitude and duration for rectangular gradient pulses) prior to data acquisition. A major feature of gradient selection of coherence pathways is that the selection is accomplished in a single acquisition, unlike rf phase cycling, where multiple acquisitions are required. It can be thought of as phase cycling in space rather than time. Also, the major limitation of gradient pathway selection has been the loss of all but a single pathway, resulting in lower sensitivity.

5.2 Coherence Pathway Diagrams

Coherence pathway diagrams[12,13] are a convenient way to visualize the use of gradients. This is illustrated with the homonuclear correlation experiment, COSY, in Figure 2. The spin system starts at thermal equilibrium with $p = 0$ and is detected in quadrature with $p = -1$. For this rf sequence there are two coherence pathways, $p = (0, -1, -1)$ and $p = (0, +1, -1)$. According to equation (3), a pathway will be selected only if $p_1G_1 + p_2G_2 = 0$. For the first pathway, where p_1 and p_2 are of the same sign, the gradient integral G_2 must be the negative of G_1. For the second pathway, where $p_2 = -p_1$, G_1 and G_2 must be identical. In a similar way, a pair of identical gradient pulses eliminates spurious signals in a spin echo experiment by selecting for a sign change in coherence order (e.g. $p = +1$ to -1 and $p = -1$ to $+1$). Unwanted signal excited by an imperfect 180° pulse will be dephased, $p_2G_2 \neq 0$.

For the multiple quantum experiments a third rf pulse adds another coherence transfer interval, and adds the possibility of using DQ coherence levels $p = \pm 2$. For the double quantum filtered correlations (DQF) COSY sequence illustrated in Figure 3, a gradient ratio, G_1:G_2:G_3 of 1:1:3, selects for one of the four DQ coherence pathways (0, +1, +2, −1).

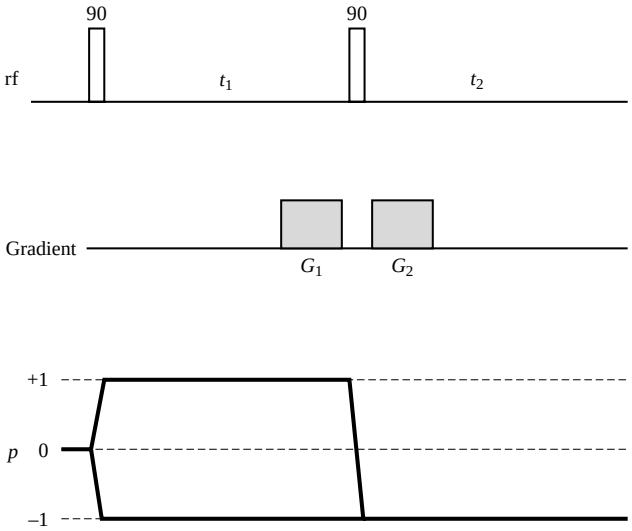

Figure 2 Pulse sequence and coherence pathway diagrams for the incorporation of pulse field gradients in COSY. P type (0, −1, −1) COSY is selected when $G_2 = G_1$ and N type (0, +1, −1) is selected when $G_2 = -G_1$

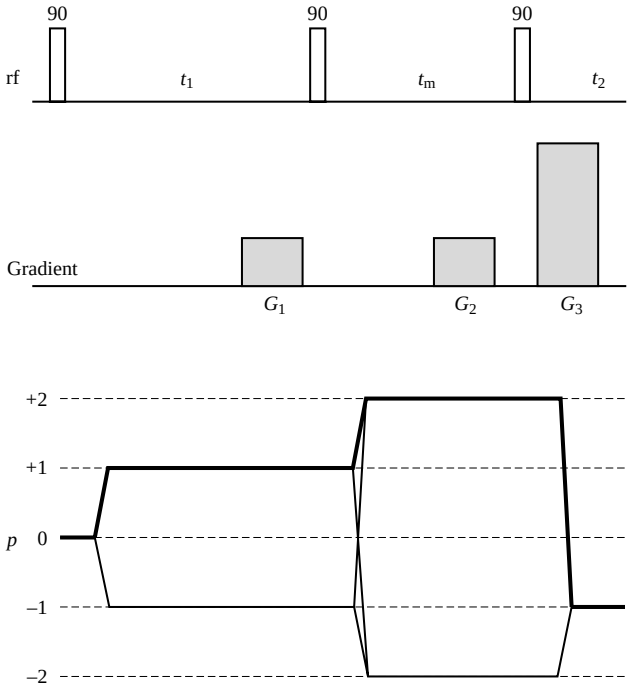

Figure 3 Pulse sequence and coherence pathway diagram for gradient enhanced DQF COSY. One of the four possible DQ pathways is selected

6 HOMONUCLEAR APPLICATIONS

For small organic molecule NMR, the major use of pulse field gradients is speed and reduction of artifacts in simple 2D NMR. For aqueous based proton NMR, gradient selection of multiple quantum pathways to discriminate against water, is an important application.

The uncoupled spins of water cannot generate $p = \pm 2$ coherence order, and can easily be left dephased during the detection period. This has been an advantage for in

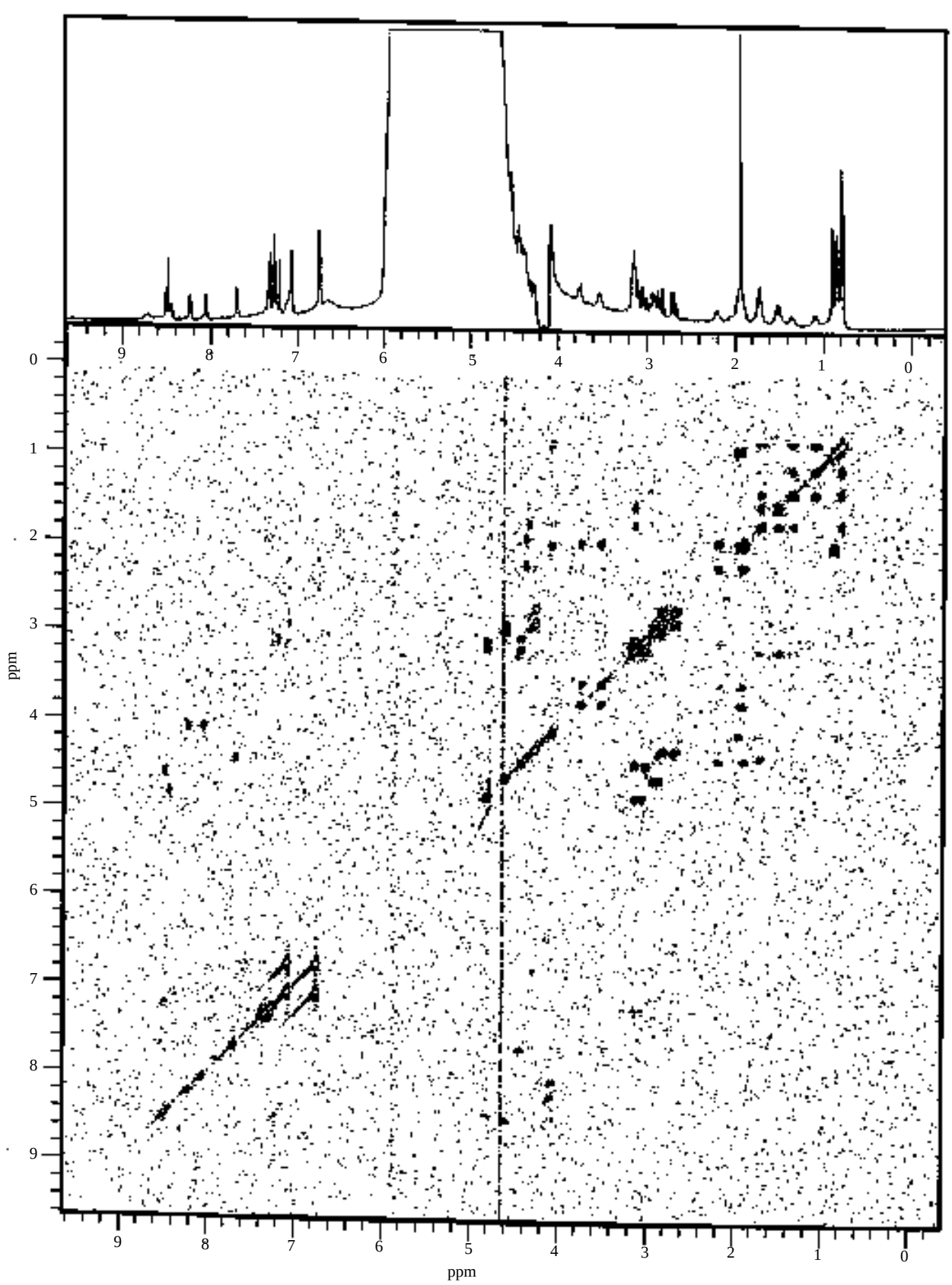

Figure 4 Noise floor contour plot of 400 MHz GE DQF COSY spectrum of 8 mM angiotensin II in H_2O. An 800-fold vertical expansion of the reference one-pulse spectrum is shown above the contour plot. 2D data were collected at 4 Hz resolution in ω_1 and ω_2 without phase cycling. A transmitter zero-frequency artifact, not residual water, is responsible for the intensity at 4.6 ppm. (Adapted by permission of Academic Press from Hurd[15])

vivo detection of lactate.[14] The single-shot selection process avoids the motion related subtraction errors that can be a problem in vivo. The further addition of rf selective coherence transfer provides extraordinary discrimination between the lactate methyl signal and the overlapping lipid CH_2 in a 2D DQ sequence.[11] Success of the in vivo results obtained using actively shielded gradients led to experiments with this technology on high-resolution NMR systems. Not surprisingly, one of the first experiments was gradient enhanced GE DQF COSY.[15] As illustrated by the noise floor contour plot shown in Figure 4, this approach to solvent suppression does not perturb signals close to or at the water chemical shift. It is also apparent that the nonsubtractive nature of gradient coherence pathway selection reduces the problem of t_1 noise.

7 PROTON DETECTED HETERONUCLEAR APPLICATIONS

7.1 GE HMQC

Proton detection of low γ nuclei is a good example of a method in which the desired signal is but a small part of the overall proton magnetization. As such, this type of experiment lends itself well to the application of gradients. The pulse sequence and modified coherence pathway diagram for a gradient enhanced version of a heteronuclear correlation experiment GE HMQC[16] are shown in Figure 5. In this diagram, shared coherence levels are drawn using a γ_H normalized coherence order

$$p' = p(^1\mathrm{H}) + p(\mathrm{X})\gamma_X/\gamma_H \tag{9}$$

Since phase distribution is proportional to the product of p' and gradient integral G, signal will only be observed for transverse magnetization from pathways for which the sum of the effects from all of the individual gradient pulses goes to zero:

$$\sum p'[i]G[i] = 0 \tag{10}$$

For $^1H/^{13}C$ experiments, $\gamma_X/\gamma_H = 0.25$. This means, for example, that $^1H[+1]^{13}C[-1]$ zero-quantum coherence will have a normalized order $p' = 0.75$. A gradient, G_1, applied during such an interval will cause a coherence pathway through this zero quantum level to be encoded with a distribution of phase, $\phi = 0.75G_1$. To select for this pathway, a read ($p' = -1$) gradient, G_3 must be set to $0.75G_1$. This pathway, H[0]C[0] $\rightarrow$ H[+1]C[0] $\rightarrow$ H[+1]C[-1] $\rightarrow$ H[-1]C[-1] $\rightarrow$ H[-1], can also be selected using alternate ratios of gradients G_1:G_2:G_3. These sequences can be optimized for best use of available gradient strength for dephasing (2:2:1) or can be optimized to avoid certain artifacts.[17]

In natural-abundance carbon experiments, more than 99% of the signal must be subtracted out to reveal the protons attached to the 1% abundant ^{13}C nuclei. With gradient selection, protons attached to ^{12}C and from solvents such as water are not detected, thus avoiding subtraction and dynamic range limitations. The effectiveness of this suppression is illustrated in Figure 6 by a noise floor contour plot of a single acquisition

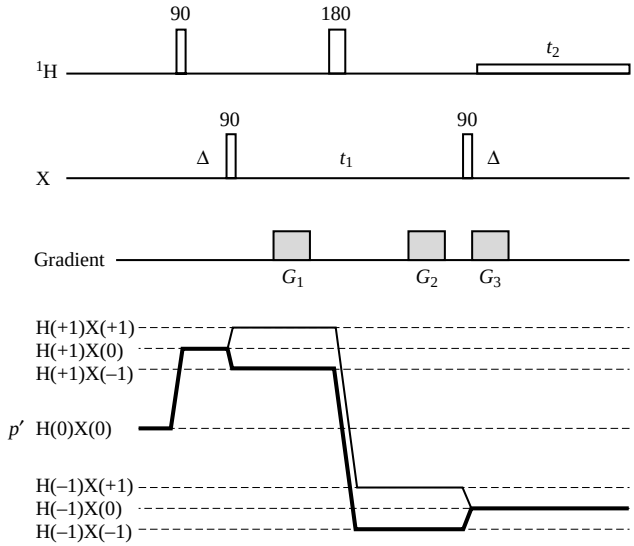

Figure 5 Pulse sequence and coherence pathway diagram for GE HMQC

per block ^1H[natural abundance ^{13}C] GE HMQC spectrum of sucrose in water. In this example, without broadband ^{13}C decoupling, the correlations are observed as ^{13}CH doublets. The absence of signal at the ^{12}C proton chemical shifts and at the water chemical shift in this spectrum demonstrate the complete cancellation of signal from protons not attached to ^{13}C. Another good application is in the long range heteronuclear multiple bond correlation (HMBC) experiment where t_1 noise from the uncoupled protons may obscure weak long range $^{13}C-^1H$ correlations in a conventional experiment.

7.2 3D and 4D Applications

It was recognized from early on that the reduction in the phase cycle requirement and the concomitant reduction in total data collection time would be a significant reason to use pulse field gradients in 3D and 4D applications. These experiments usually require large numbers of acquisitions just to achieve adequate resolution in the evolution domains. In fact, in some cases, it is the phase cycle and not the signal-to-noise ratio (S/N) which dictates the length of data collection time. A number of multidimensional methods have been developed to take advantage of the reduced data collection time, water suppression characteristics, and fewer artifacts.[18–23] Others have taken advantage of reduced phase cycle to increase resolution in the evolution dimensions.[24]

One of the first 3D gradient sequences was a modification of HMQC–COSY. The GE HMQC–COSY sequence[18] is a combination of a gradient-enhanced HMQC experiment, in which heteronuclear zero quantum magnetization is coherence order labeled and then selectively rephased via a 4:$-$3 gradient pair surrounding the final carbon 90° pulse, and a gradient-enhanced COSY experiment in which quadrature in the COSY dimension is selected with a 1:1 gradient pair around the final 90° pulse. The resulting gradient integrals are 4:$-$2:1. The asymmetry of this gradient pulse scheme leaves protons which are not at least indirectly connected to ^{13}C dephased and unobserved. This method provides editing, simple pattern

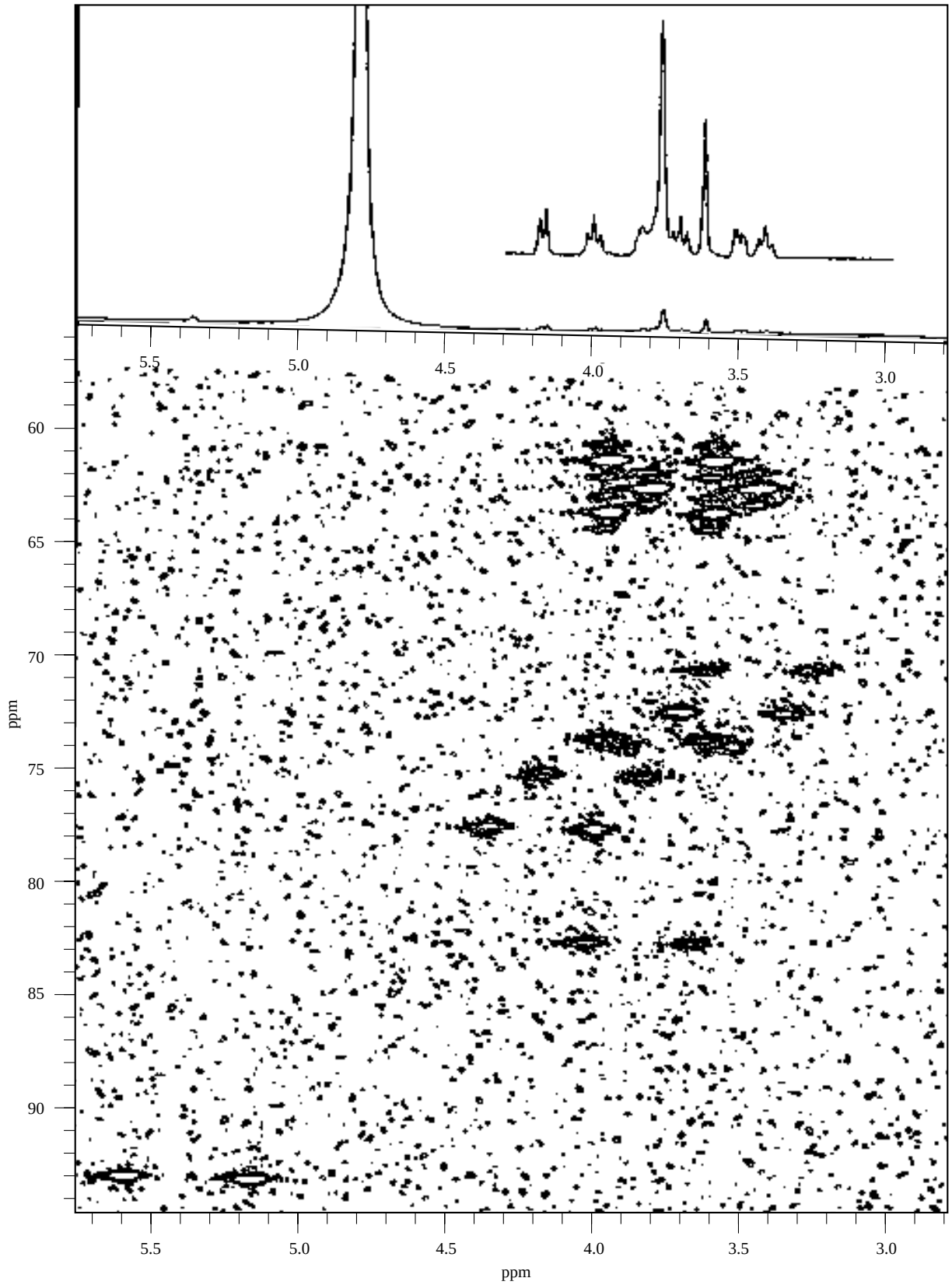

Figure 6 Noise floor contour plot of a 2 min total acquisition time $^{1}H[^{13}C$ natural abundance] GE HMQC spectrum of sucrose in water shows complete elimination of ^{12}C protons and solvent water

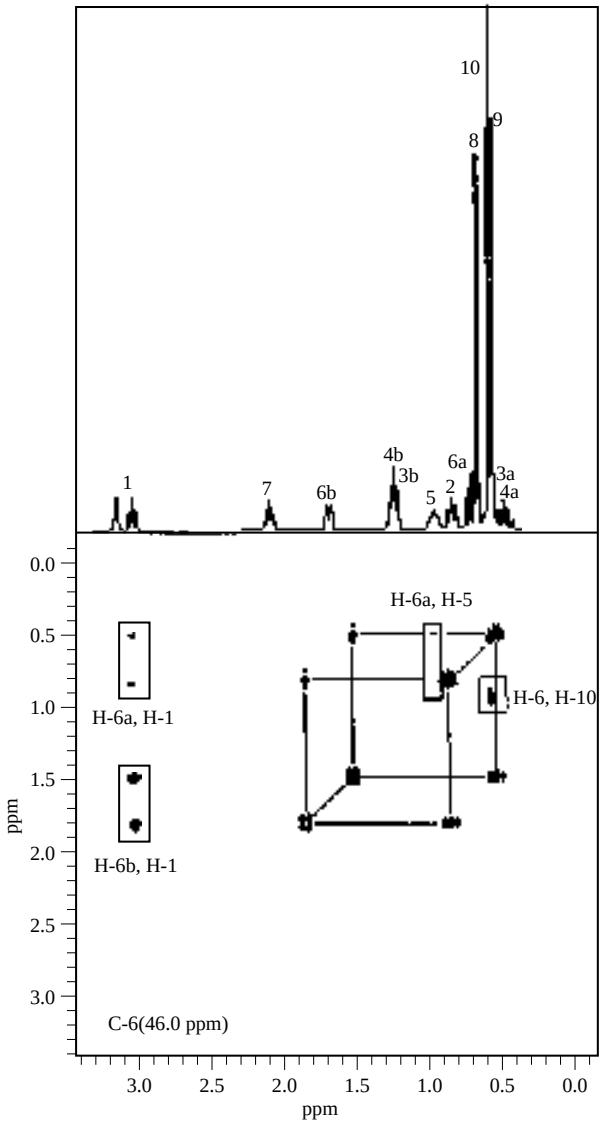

Figure 7 C-6 plane from a 512 × 128 × 128 GE HMQC–COSY spectrum of menthol collected in less than 7 h. Simple correlation patterns are observed for direct and remotely coupled protons. (Reproduced by permission of Academic Press from Hurd and John[18])

recognition features, and in some cases additional resolution. Without the need for phase cycling, a moderate resolution 512 × 128 × 128 spectrum can be obtained in just a few hours. As illustrated by the C-6 plane of menthol, shown in Figure 7, protons directly attached to carbon are observed as J(C,H) doublets along the $\omega_3 = \omega_2$ diagonal. A proton attached to a directly adjacent carbon (^{12}C) is observed at its ^{12}C proton chemical shift in ω_3, and at the frequencies of the directly (^{13}C) attached proton in ω_2 (see, for example, the H-6b,H-1 correlation). Proton connectivities from two carbon bonds away are observed as single correlations at the ^{12}C proton chemical shift in ω_3 and at the ^{12}C proton chemical shift of the intermediary proton in ω_2 (see, for example, H-6,H-10). The inequivalent CH_2 protons of C-6 (H-a,H-b and H-b,H-a correlations) remain coupled in both ω_2 and ω_3 to give a parallel squares pattern. This occurs because both protons are attached to the same ^{13}C nuclei.

Proton detected 3D SQ–DQ COSY of ^{13}C enriched sugars has been reported to be more useful with the incorporation of pulse field gradients, yielding 'unsurpassed' resolution plus better overall artifact suppression.[24]

7.3 Protein NMR Applications

The analysis of protein structure by NMR has been a driving force in the development of proton-detected multidimensional methods. The success of these applications often depends on the ability to identify, assign, and obtain distance information from C-α,H resonances. The proximity of these signals to the water chemical shift can be a problem in some cases. Traditional methods of water suppression often exhibit an inherent disadvantage. Selective excitation often results in the loss or attenuation of desired signals near the water resonance and, when presaturation is used, magnetization transfer and proton exchange can lead to a loss of signal intensity throughout the spectrum. Although these issues can be managed, in part, by compromises in solvent conditions and temperature, gradient based coherence selection offers an alternative. GE HMQC–TOCSY and GE HMQC–NOESY give full unobscured C-α,H correlations at water chemical shift.[19] These experiments were also among the first gradient coherence selection experiments run using a field/frequency lock and variable temperature; these are key requirements for routine use of gradients.

8 WATER ELIMINATION

Removal of the large unwanted water signal without perturbing the desired signal has been one of the great technical challenges of biomolecular proton NMR. Potential difficulties include exchangeable protons, a crowded water chemical shift region, and correlation times which allow signal loss via magnetization transfer. Gradients have had an increasingly important role in this area. The advantage relative to presaturation has been quantitatively measured using gradient versions of the heteronuclear single quantum correlation (HSQC) experiment.[25,26] As illustrated in Figure 8, the retention of signal is most significant for proteins in the physiologically important pH range of 6.5–7.5.[26] Elimination of the presaturation effect reveals the smaller loss of signal due to a 'short' recycle delay. This second effect is presumably due to an increased rate of exchange with long T_1 water protons at higher pH. In addition to multiple quantum coherence pathway selection, there are several other gradient based methods which can be used for water suppression. Spoiler gradients can be used in combination with selective rf excitation as an effective replacement of conventional presaturation, gradient pairs can be used to improve selective spin echo methods, and diffusion weighted methods can provide lineshape independent water reduction (***Water Signal Suppression in NMR of Biomolecules***).

8.1 CHESS

In a method sometimes referred to as a *che*mical *s*hift *s*elective (CHESS)[27] pulse, water is selectively excited and

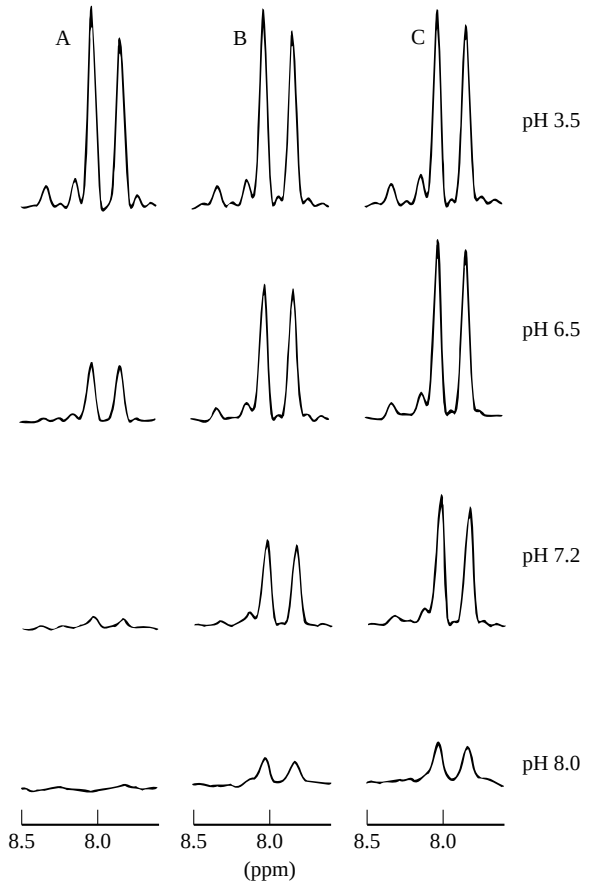

Figure 8 1D $^{15}N-^{1}H$ PFG HSQC spectra showing saturation transfer between solvent H_2O and the ^{15}N-labeled amide protons of 0.8 mM Ac–L-Asn–L-Pro–L-[^{15}N]Tyr–NHMe at various pH values and a temperature of 30 °C. (A) PGF HSQC spectra recorded with 1.3 s of water presaturation and total recycle time of 3.3 s. (B) PFG HSQC spectra recorded without presaturation and with a total recycle time of 3.3 s. (C) PFG HSQC spectra recorded without presaturation and with a total recycle time of 15.3 s. (Reproduced by permission of Academic Press from Li and Montelione[26])

then spoiled by application of a pulsed field gradient. For optimum elimination the tip angle of the excitation pulse must be adjusted for water T_1 relaxation which occurs during the excitation–dephase intervals. For high-resolution applications, this delay period can be increased to allow for recovery of shorter T_1 signals of interest at the water chemical shift.[28] When used for in vivo applications, where the volume of interest usually has multiple water T_1 values, a series of intervals (usually three) is used to provide the optimum water elimination. In practice, multiple CHESS pulses also improve water elimination in high-resolution NMR applications. This is likely due to $\boldsymbol{B}_1$ rather than T_1 heterogeneity. In the case of multiple CHESS pulses, care must be taken to avoid the rephasing of water. This can be accomplished by using spoiler gradients with different intensities, durations, or axes. This method is not only dependent on gradient performance, but also on selective rf pulse design. Desirable features of these rf pulses are minimum out-of-band excitation and sharp transition bands. Since the water signal is to be dephased anyway, the phase in the excitation band is unimportant and can be sacrificed in pulse design.[28]

8.2 Spin Echoes and Gradient Pairs

Elimination of the unwanted signals generated by the non-π character of selective time reversal pulses is an important application of pulse field gradients. A pair of gradients placed on either side of a 180° pulse to avoid spurious signal, one of the first applications of pulse field gradients, can provide significant improvement in modern high-resolution NMR. Placed on either side of a nonselective 180° refocusing pulse, a gradient pair eliminates unwanted signal from imperfections in $\boldsymbol{B}_1$ that would ordinarily have to be eliminated by phase cycling. This effect can be even more dramatic with frequency selective π pulse methods. Figure 9 illustrates the benefit of a gradient pair in the performance of *g*radient *e*nhanced *s*pin *e*cho *w*ater *s*uppression (GE SEWS), a selective 1–1 spin echo experiment.

8.2.1 WATERGATE

In a related experiment dubbed WATERGATE,[29] *water* suppression by *gra*dient-*t*ailored *e*xcitation is also accomplished using a gradient pair to improve a frequency selective spin echo. In this case, the frequency selectivity is achieved using a nonselective 180° pulse/water selective 180°($-x$) pulse combination. This has the advantage that peaks away from the water signal see only a nonselective spin echo. The disadvantage of these frequency selective methods is that they give up the chemical shift region near water.

8.3 Diffusion Weighted Water Suppression

The difference between the translational diffusion of a large solute molecule such as a protein and that of solvent water is the basis of the DRYCLEAN water suppression method.[30] DRYCLEAN comes from *d*iffusion-*r*educed water signals in spectroscopy of molec*u*les moving s*l*ow*e*r th*an* water. The idea is that water will move far enough in the time between the encode and the decode gradient pulses to remain dephased, while the large solute molecule will not move very far and will be largely rephased. According to equation (1), for a modest 20-fold difference in diffusion constant, D, a gradient pair could be selected to preserve over 70% of solute signal, while suppressing water by 1000-fold.

9 PHASE SENSITIVE METHODS

Modern multidimensional spectra are almost always recorded in pure absorption mode. The primary reasons are improved resolution and lineshape, and an increase of root-2 (about 40%) in S/N compared with magnitude mode. Absorption mode spectra are also phase sensitive.

Typically, pure absorption phase is obtained by amplitude modulation of the signal as a function of the evolution period t_1, in contrast to phase modulation in the magnitude methods. Amplitude modulation yields separable phases (separable to absorption and dispersion), but loses the ability to discriminate between positive and negative frequencies. Frequency discrimination can be obtained by independent collection of the real and imaginary parts in t_1 (quadrature

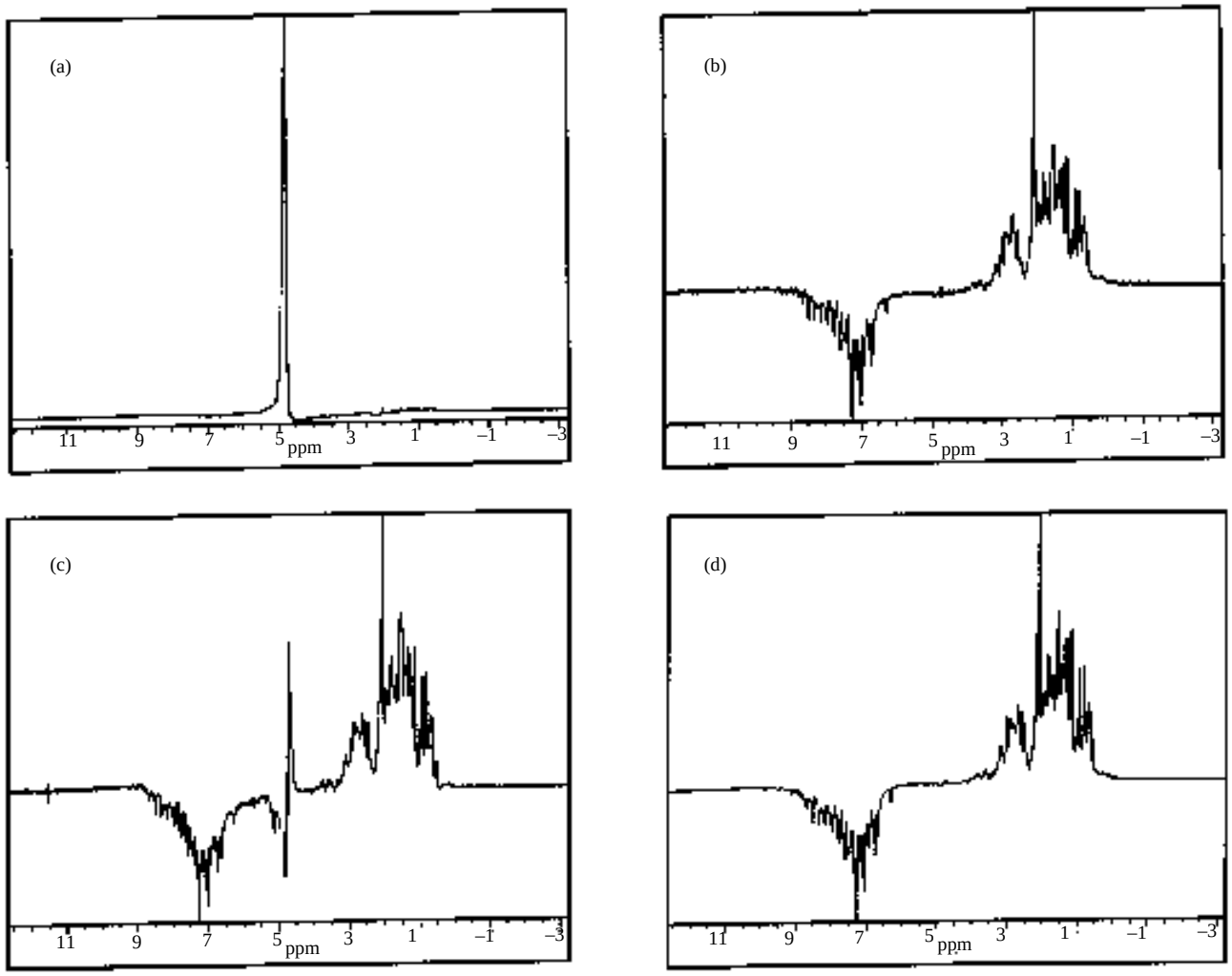

Figure 9 GE SEWS: comparison of spin echo water suppression (a, c) without and (b, d) with a gradient pair bracketing the semiselective 1–1 refocusing pulse. Suppression is shown for the 90% H_2O in a 2.6 mM sample of ^{15}N-enriched bovine pancreas trypsin inhibitor (BPTI). A single acquisition without gradient pair shown in (a) reduces water only by a factor of 50 and thereby limits optimization of receiver gain and ultimate SNR. In (b) complete suppression is obtained in a single acquisition using the gradient method allowing optimum setting of receiver gain. Although phase cycling improves the water suppression in the method without gradients (c), neither suppression or S/N matches the level achieved using the gradient pair (d). (Reproduced by permission of GE NMR Instruments)

data in t_1). Complex Fourier transformation of these data in t_1 produces spectra with quadrature detection in ω_1. By acquiring mirror image pathways (+1) and (−1) in t_1, this approach provides pure absorption shapes for the correlation peaks, and quadrature detection in the evolution dimension(s).

In the case of phase sensitive detection in gradient spectroscopy, there can exist a fundamental limitation. The single-shot selection of a unique coherence pathway precludes the acquisition of the mirror image pathways of (+1) and (−1). If both pathways are not acquired, mixed phase (absorption and dispersion components mixed in an inseparable manner) results for the correlation peaks. Hence the earlier gradient spectroscopy experiments were carried out in the magnitude mode. The requirement for selection of mirror image pathways for pure absorption mode can be at odds with that for improved dynamic range performance which requires selection of a unique pathway in a single acquisition.

The methods developed for pure absorption spectra in gradient spectroscopy adopted a compromise approach. The techniques can be broadly classed as: (a) those which acquire both the mirror image coherence pathways simultaneously by not applying a field gradient during the evolution dimension, albeit, using gradients elsewhere in the pulse sequence; (b) those which acquire both mirror image coherence pathways (+1) and (−1) in the evolution dimension, independently, and then combine both of these signal components in the time domain or in the frequency domain, to yield pure absorption spectra; (c) methods which use gradients as spoilers only and not for coherence pathway selection; and (d) methods which switch between the signals from the two mirror image pathways during the acquisition time.

9.1 Phase Sensitive GE DQF COSY

The DQF COSY experiment proposed by Davis et al.[31] falls into category (a). In this experiment, gradients are used to select DQ coherence transfer. However, gradients are not

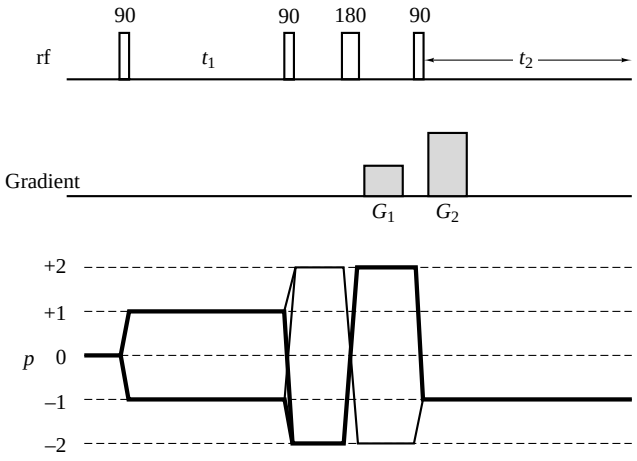

Figure 10 Pulse sequence and coherence pathway diagram for phase sensitive GE DQF COSY as described by Davis and co-workers[31]

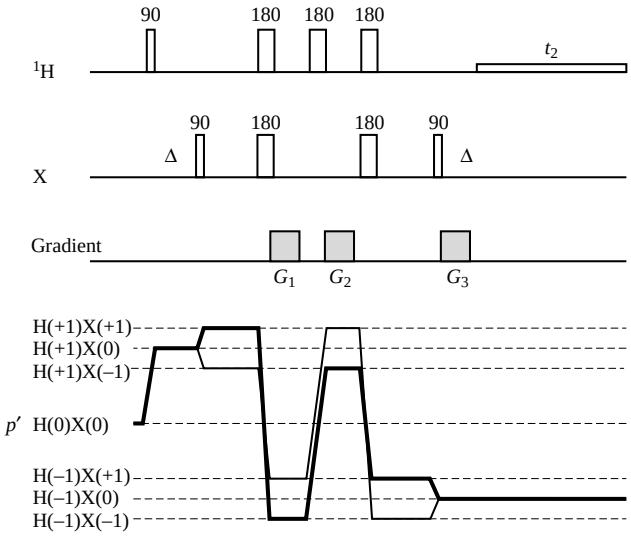

Figure 11 Pulse sequence and modified coherence pathway diagram for phase sensitive pulse field gradient HMQC described by Tolman et al.[33]

applied during the evolution period. With this modification, both mirror image coherence pathways are allowed during t_1 and pure absorption lineshapes can be obtained in the 2D spectrum. This work also addresses the problem of time dependent phase errors associated with chemical shift precession during the gradient pulse. In this pulse sequence as shown in Figure 10, these phase errors are refocused by the addition of a 180° rf pulse. The DQ selection is made using a pair of gradients G_1 and G_2 about the read pulse with a ratio of 1:2. The gradient sequence selects two of the four possible DQ pathways and hence the S/N of the experiments is root-2 (40%) lower than that of conventional phase cycled DQF COSY. Some of the loss can be avoided by use of an optimized tip angle for the read pulse. Frequency discrimination in t_1 is obtained in the normal manner.

The addition of a CHESS pulse (water selective excitation–gradient dephase interval), as described in the previous section, allows reduced gradient coherence selection intervals, and makes this an attractive approach for the study of biomolecules in water.

9.2 Phase Sensitive GE HMQC and GE HSQC

There are a variety of methods which belong in category (b), where the mirror image components corresponding to (+1) and (−1) coherence orders are acquired separately and then recombined in the time or frequency domain. Most of the proposed methods for gradient enhanced proton detected heteronuclear correlation[32–36] fall into this category. One example is the phase sensitive ^{1}H–^{13}C HMQC experiment described by Tolman et al.[33] The sequence consists of a HMQC sequence with three gradients G_1, G_2, and G_3, as shown in Figure 11. G_1 and G_2 are applied during the multiple quantum period on either side of the central proton 180. Additional 180° pulses on both ^{1}H and ^{13}C are applied to refocus chemical shift precession that has occurred during the gradient intervals. The final gradient G_3 is applied after the last ^{13}C 90. The sign of the final gradient is changed to retrieve the mirror image pathway. These two pathways correspond to mirror images in t_1, and are collected separately and subtracted to produce the real part of t_1 and are added to produce the imaginary part of

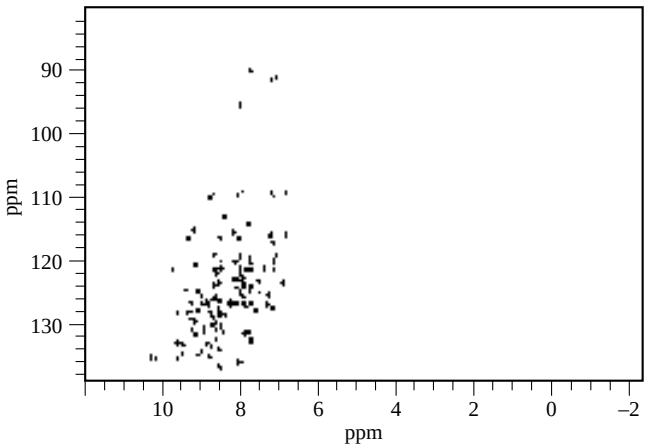

Figure 12 Phase sensitive ^{15}N–^{1}H GE HMQC spectrum of 100 μM ketosteroid isomerase (KSI) (27 kDa dimer) in 90% H_2O at 37 °C obtained at 500 MHz. (Sample provided by courtesy of M. Summers, University of Maryland)

t_1. Ross et al.[36] avoid the use of additional refocusing pulses by back-prediction of the t_1 domain. The method described by Tolman et al.[33] was used to collect the phase sensitive GE HMQC spectrum of the dilute (100 μM in 90% H_2O) protein sample shown in Figure 12. Here again, the addition of a CHESS pulse interval allows the use of shorter coherence selection intervals and allows for the study of larger, more dilute molecules. The unmatched level of water suppression is characteristic of the coherence selective $\boldsymbol{B}_0$ gradient methods.

9.3 Heteronuclear *zz* Filters

The most compelling benefit arising from the use of gradient coherence pathway selection in proton detected heteronuclear correlation experiments is the nearly complete elimination of signal from protons not attached to the

heteronuclear spins. This advantage is especially important for the suppression of water protons since conventional methods such as presaturation and most of the selective excitation methods can lead to loss of desired signal. Unfortunately, some of the benefits of these experiments are offset by the loss of a factor of root-2 in the S/N that results from the selection of a single or limited number of coherence pathways. On the other hand, the suppression of protons not attached to the X nucleus, and of the solvent proton resonance, can be a challenging task in the conventional, phase cycled methods. One approach to reduce this problem, which belongs in category (c) above, was described by Brühwiler and Wagner.[37] This approach takes advantage of the heteronuclear longitudinal spin order (described by the density operator I_zS_z, and also termed heteronuclear *zz* magnetization) which is formed by the sequence fragment $90_x(^1\text{H})-\tau-180_x(^1\text{H, X})-\tau-90_y(^1\text{H})$ where τ is $1/4J(\text{X,H})$. In this method, referred to here as the heteronuclear *zz* filter, protons not attached to the X spins remain in the transverse plane following this interval and are eliminated by application of a spoiler gradient. Although this method maintains full sensitivity, it is not overly effective at eliminating magnetization from protons that are not attached to the X nucleus, and especially those for H_2O solvent.

This approach has been successfully applied in combination with other suppression schemes.[38–43] The symmetry of the HSQC sequence allows for incorporation of two *zz* filters.[40] This approach maintains full sensitivity and pure absorption peak shapes, since all the necessary coherence pathways are selected. A HSQC sequence with gradient *zz* filters is shown in Figure 13. The gradient G_3 dephases the transverse magnetization while the desired components are stored along the *z* axis. As in the conventional HSQC experiment, X chemical shift labeling occurs in the evolution time, t_1, between the two 90°(X) pulses, and the application of the 180°(^{1}H) pulse in the center of the evolution time removes the J(X,H) coupling from the evolution dimension. The frequency labeled magnetization is transferred back into heteronuclear longitudinal *zz* order by the second 90°(X) pulse, and the spoiler gradient G_4 is applied further to eliminate unwanted signals. To improve the suppression of the water signal, a pair of CHESS pulses can be applied at the beginning of the sequence. As described previously, the water resonance can be partially inverted allowing for recovery of desired signal at the water chemical shift. In the implementation shown here, spoiler gradients, G_1 and G_2, are applied along the *x* and *y* axes, respectively, while the G_3 and G_4 gradients are applied along the *x*, *y*, and *z* axes simultaneously to minimize any residual water signal that may arise from accidental gradient rephasing.

This approach provides an optimum S/N and peak shapes but is inferior in performance to gradient coherence selection techniques for water elimination.

9.4 Gradient-Enhanced *z* Filter

To improve on the HSQC with *zz* filters, a gradient form of the *z* filter was developed and added to the sequence as shown in Figure 13.[40] This filter consists of two 90°(^{1}H) pulses with a gradient in between. The first pulse of the filter, $90°_y(^1\text{H})$, rotates the in-phase magnetization (i.e. protons coupled to X) to the *z* axis. The unwanted magnetization is left in the transverse plane, which is then dephased by the spoiler gradient G_5. The desirable component of the magnetization, which is aligned along the *z* axes is then read by the final 90°(^{1}H) pulse. This filter resembles a conventional *z* filter,[45] but has the advantage of full sensitivity, since the desired magnetization that enters the filter is completely aligned along a single axis. Unlike conventional *z* filters which use multiple delays and hence require multiple acquisitions, the gradient *z* filter accomplishes the filtering in a single acquisition. As illustrated in Figure 14, this method yields full sensitivity, pure absorption peak shapes, and good elimination of water. Furthermore, loss of signal associated with conventional water suppression and the requirement for additional phase cycling to improve suppression is avoided. This method, applied without the CHESS pulse and with *z* axis only gradients, was found to outperform nongradient methods in terms of solvent and artifact suppression, based on a comparable recording time.[42]

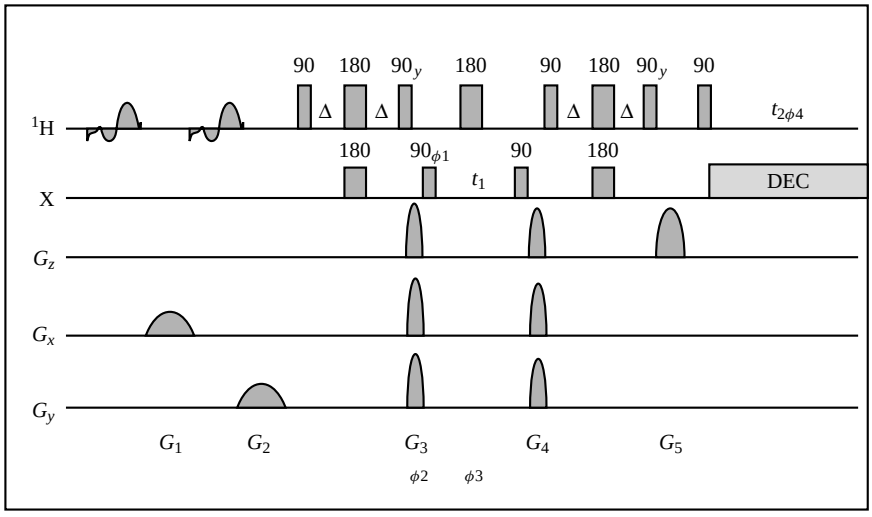

Figure 13 Pulse sequence for gradient-enhanced *z*-filtered (GEZ) HSQC. This sequence contains two gradient zz filters G_3 and G_4 and one gradient-enhanced *z* filter G_5. Additional water elimination can be achieved via the two CHESS pulses (G_1 and G_2) which precede the sequence. (Reproduced by permission of Academic Press from John et al.[40])

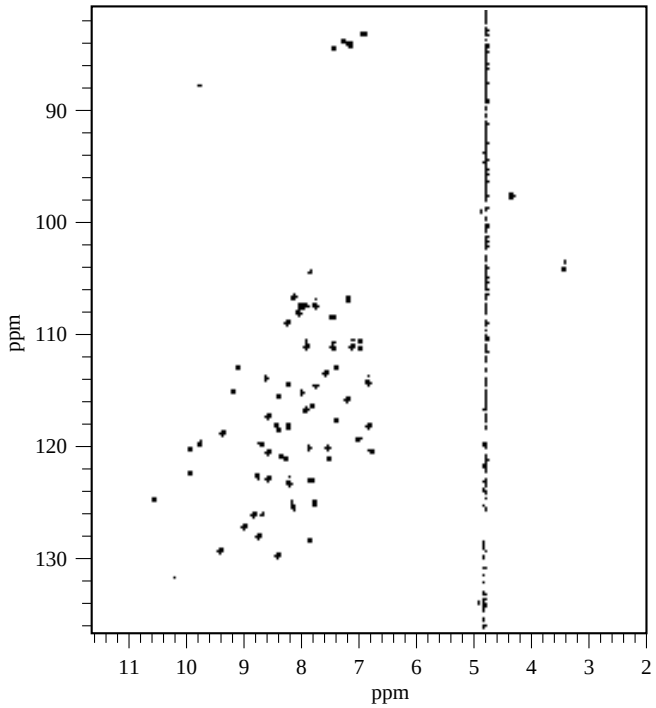

Figure 14 $^{15}N-^{1}H$ GEZ HSQC spectrum of 2.6 mM BPTI in 90% H_2O. (Reproduced by permission of Academic Press from John et al.[40])

Gradient *z* and *zz* units have also been used to improve ^{13}C resolution in an HSQC–NOESY experiment.[44]

9.5 SWAT Gradients

In the *sw*itched *a*cquisition *t*ime (SWAT) gradient method,[45] the N type (0, +1, . . . , −1) and P type (0, −1, . . . , −1) coherence pathway signals are alternately and individually acquired on alternate sampling points of the digitizer. Since the signals from the N type and P type pathways are in an easily separable format, pure phase 2D spectra with quadrature detection in both dimensions can be reconstructed from a single acquisition. The basic idea of the SWAT gradient method is to sample at twice the Nyquist frequency, inserting appropriate gradient pulses between digitizer sampling points, to rephase alternatively the desired coherence. Ordinarily, in a gradient COSY spectrum, either the N type or the P type coherence pathway would remain dephased and unobserved during the acquisition period. The data can be processed to yield pure absorption lineshapes in a number of ways. Although, the SWAT method is quite demanding on gradient switching time, it is the only method which achieves pure phase fully quadrature multidimensional data in a single acquisition per t_1 frame.

10 SPATIAL TOOLS

The rf coils used in high resolution NMR are designed to produce a homogeneous $\boldsymbol{B}_1$ magnetic field. In practice, homogeneous $\boldsymbol{B}_1$ fields are achievable in the transverse plane of sample volume and over most the detectable volume along the *z* axis. Normally, the transition band, the region of sample volume in which the $\boldsymbol{B}_1$ field strength goes from its maximum value to zero, is responsible for the $\boldsymbol{B}_1$ inhomogeneity that can lead to artifacts in multiple pulse NMR experiments. A separate problem that can occur at the coil extremes is that the lineshape of the NMR signal can be distorted by bulk magnetic susceptibility effects from the ends of the sample volume and the end of the NMR sample tube. Like $\boldsymbol{B}_1$ inhomogeneity, this lineshape distortion can be a problem, especially for observation of protons in aqueous solutions where the water signal must be eliminated or reduced. The principle of slice selection can be applied to eliminate this $\boldsymbol{B}_1$ inhomogeneous signal in high-resolution NMR.

10.1 $\boldsymbol{B}_1$ Inhomogeneity and Transition Band Suppression

Gross rf coil inhomogeneity can be visualized via spatial projections along the *z* axis (so-called *z* profiles). A *z* profile of a 180° pulse generated by a typical rf coil is shown in Figure 15(a). Comparison with the 90° pulse *z* profile from the same coil [Figure 15(b)] illustrates the gradient of $\boldsymbol{B}_1$ field (transition bands) that occurs at the top and bottom of the coil. In the 180° pulse profile, signal is not detected where a 180° rotation of

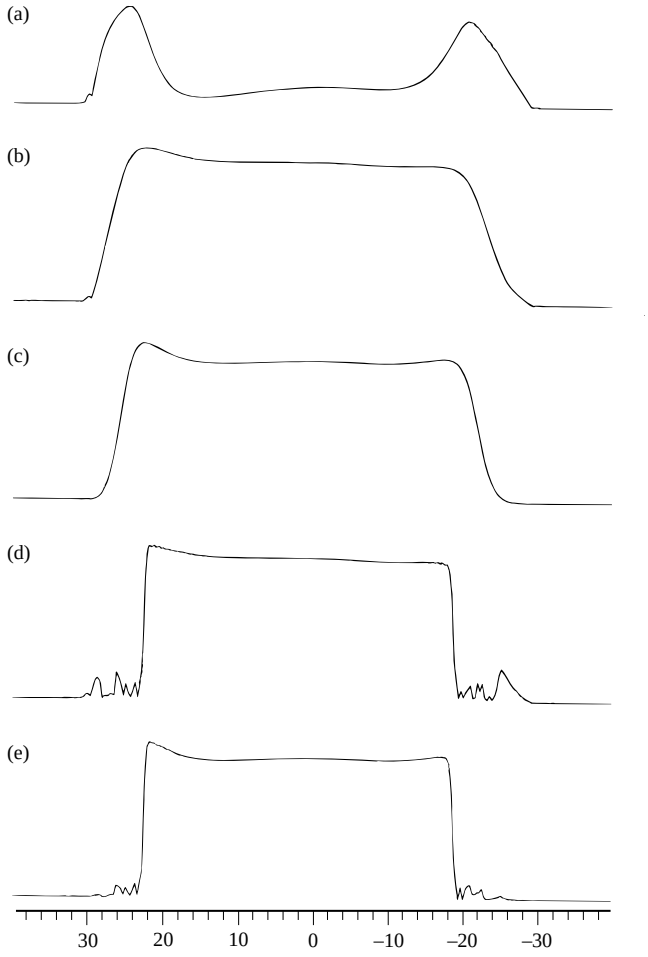

Figure 15 *z* profiles of an (a) 180° rf pulse, (b) 90° rf pulse, (c) composite 90° rf pulse, (d) 90° rf pulse following transition band suppression (TBS), and (e) composite 90° rf pulse following TBS

spins has occurred, but is detected in the sample volume which does not experience a 180° flip. These transition band regions can be reduced slightly by employing a composite 90° pulse as illustrated by the z profile in Figure 15(c). In the transition band suppression (TBS) method,[46] signals from these regions of coil volume are selectively excited and then eliminated by gradient dephasing. Slice selection is achieved by application of one or more frequency selective pulses during a constant z gradient. In practice, multiple pulses work better because of the differences in $\boldsymbol{B}_1$ of the region to be suppressed. While this effectively eliminates signal from these unwanted regions of the coil volume, care must be exercised in choice of pulse design to avoid excitation of the spins within the region of homogeneous $\boldsymbol{B}_1$. Figure 15(d) shows a 90° pulse profile of the sample following application of TBS, and Figure 15(e) shows the combined effect of TBS and a composite 90° pulse.

10.2 Improvements in WEFT and Reduction of Susceptibility Artifacts

One application of TBS is the reduction in the susceptibility water hump which is often observed in a very short samples. In essence, this is the slice selective version of a matched susceptibility plug.

Spatial differences in both $\boldsymbol{B}_0$ and $\boldsymbol{B}_1$ homogeneity also limit the effectiveness of water suppression by T_1 inversion recovery methods such as WEFT. A water elimination technique was described earlier using gradient dephasing in which the duration of the relaxation delay is used to recover the biopolymer spins at the water chemical shift. The TBS approach can be used to limit the effects of $\boldsymbol{B}_1$ inhomogeneity and significantly reduce the amount of signal left at the water 'null'.

The first practical test of TBS was its incorporation into the phase sensitive version of gradient enhanced DQF COSY. The pulse sequence is shown in Figure 16. Water is first selectively excited using a crafted rf pulse and dephased by application of an x gradient. The residual water spins are then partially inverted and transverse magnetization dephased by application of a y gradient pulse. This is followed by a recovery period during which the inverted water spins relax to a 'null'. During this recovery period, typically 200 ms, the transition band slices are excited and dephased using a z slice gradient. The water elimination is followed by a phase sensitive gradient enhanced DQF COSY sequence. Coherence is selected using a $1{:}-2$ ratio of gradients applied simultaneously along the x, y, and z axes. The careful choice of gradient axes during the water elimination period and for coherence selection is important to avoid unwanted rephasing of water signal. This approach was tested on a 1 mM sample of ubiquitin in 90% H_2O. As demonstrated by the contour plots of these data shown in Figure 17, water is nearly eliminated and correlations are observed unperturbed, even at or near the water chemical shift.

10.3 Field Maps and Shimming

One advantage of gradients is that you can make images with them. 3D phase or frequency maps are in effect images of the inhomogeneity experienced by the sample. Shim coil fields can also be directly characterized by measurement of a set of field maps with known shim current offsets. The foregoing information should be sufficient to determine in a noniterative way, the optimum corrected field. This approach to shimming, common to in vivo NMR, may become a significant advantage for three-axis gradient systems in high resolution NMR (***Shimming of Superconducting Magnets***).

11 SUMMARY

By effectively replacing the functions of phase cycling with a single-step, pulse field gradients are used to suppress artifacts, extend resolution in the evolution domains of multidimensional NMR and, where S/N allows, reduce total data collection time. Further, $\boldsymbol{B}_0$ field gradients provide unmatched levels of water elimination, with reduced dependence on the effects of lineshape, magnetization transfer, and dynamic range. With continued improvements in performance and availability, gradients are likely to become a routine part of high-resolution NMR.

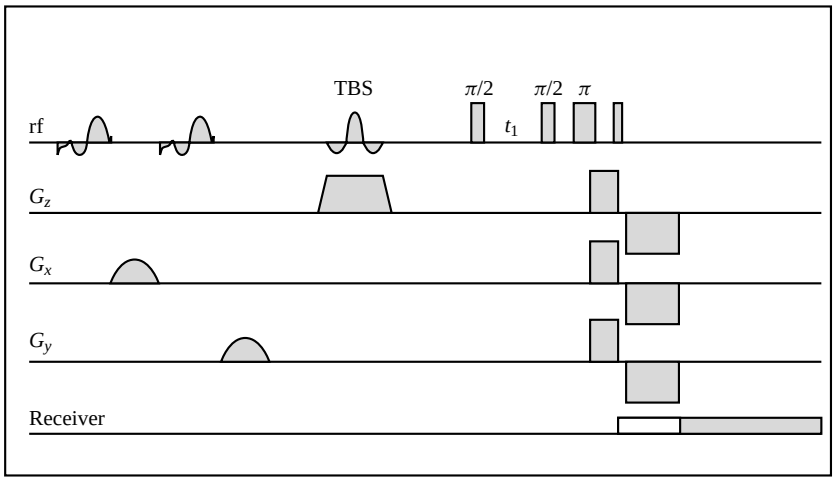

Figure 16 Pulse sequence for phase sensitive GE DQF COSY incorporating crafted rf CHESS pulses and TBS. (Reproduced by permission of Academic Press from Hurd et al.[47])

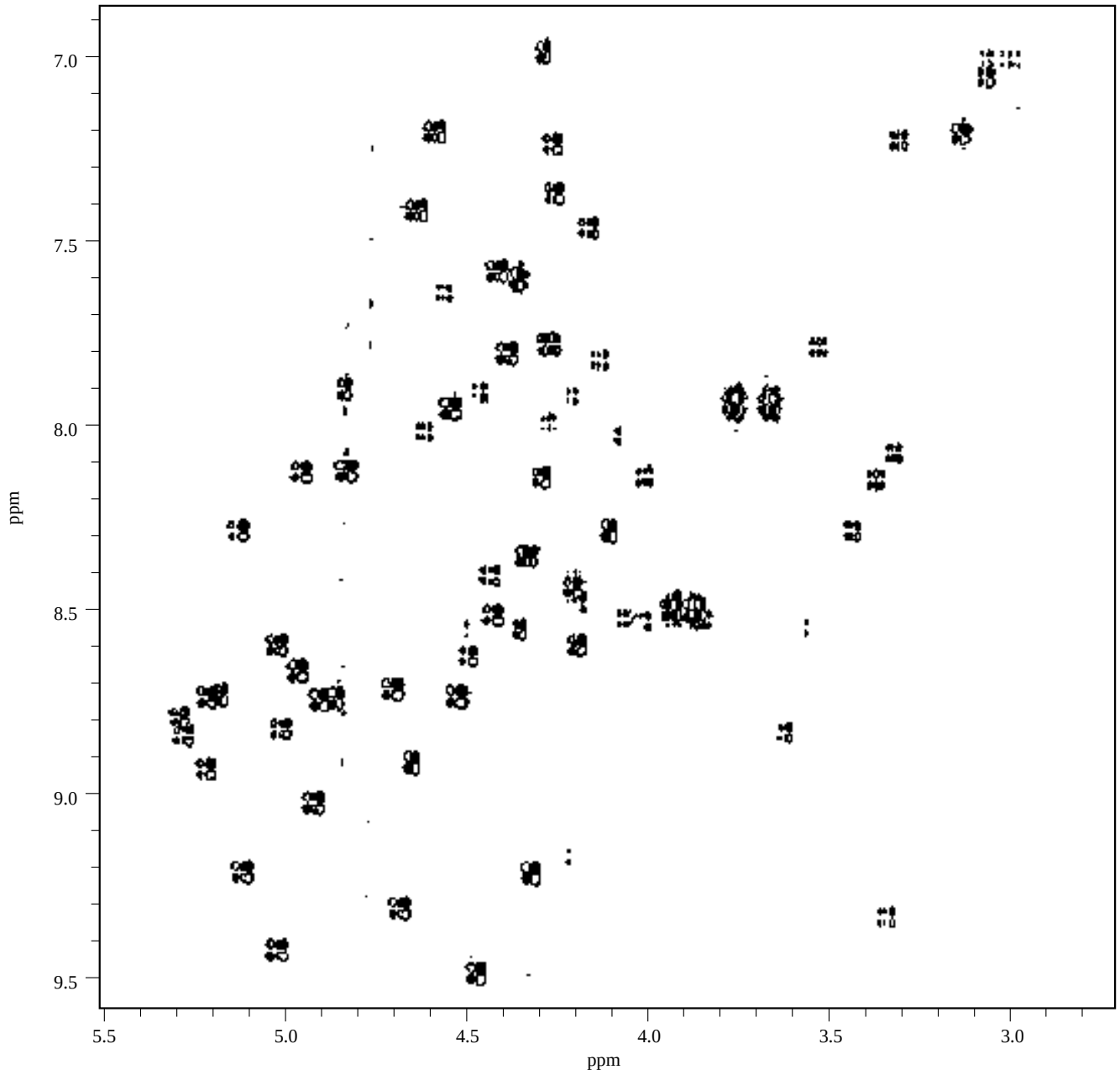

Figure 17 Phase sensitive GE DQF COSY contour plot of a 1 mM ubiquitin sample in 90% H_2O. Expansion of the fingerprint region shows nearly complete suppression of water at 4.7 ppm in ω_2 and unreduced correlations at that chemical shift. (Reproduced by permission of Academic Press from Hurd et al.[47])

12 RELATED ARTICLES

Diffusion Measurements by Magnetic Field Gradient Methods; Double Quantum Coherence; Eddy Currents and Their Control; Gradient Coil Systems; Heteronuclear Shift Correlation Spectroscopy; Magnetic Resonance Imaging: A Historical Overview; Multiple Quantum Coherence Imaging; Multiple Quantum Spectroscopy of Liquid Samples; NOESY; Phase Cycling; Radiofrequency Gradient Pulses; Shimming of Superconducting Magnets; Three- and Four-Dimensional Heteronuclear Magnetic Resonance; Water Signal Suppression in NMR of Biomolecules; Water Suppression in Proton MRS of Humans and Animals.

13 REFERENCES

1. A. G. Anderson, R. L. Garwin, E. L. Hahn, J. W. Horton, G. L. Tucker and R. M. Walker, *J. Appl. Phys.*, 1955, **26**, 1324.
2. E. O. Stejskal and J. E. Tanner, *J. Chem. Phys.* 1965, **42**, 288.
3. R. L. Vold, J. S. Waugh, M. P. Klein, and D. E. Phelps, *J. Chem. Phys.*, 1968, **48**, 3831.
4. A. Wokaun and R. R. Ernst, *Chem. Phys. Lett.*, 1977, **52**, 407.
5. A. A. Maudsley, A. Wokaun, and R. R. Ernst, *Chem. Phys. Lett.*, 1978, **55**, 9.
6. A. Bax, P. G. deJong, A. F. Mehlkopf, and J. Smidt, *Chem. Phys. Lett.*, 1980, **69**, 567.
7. P. Barker and R. Freeman, *J. Magn. Reson.*, 1985, **64**, 334.

8. C. J. R. Counsell, M. H. Levitt, and R. R. Ernst, *J. Magn. Reson.*, 1985, **64**, 470.
9. D. M. Doddrell, G. J. Galloway, W. M. Brooks, J. Field, J. M. Bulsing, M. G. Irving and H. Baddeley, *J. Magn Reson.*, 1986, **70**, 176.
10. A. G. Redfield and R. K. Gupta, *Adv. Magn. Reson.*, 1971, **5**, 81.
11. R. E. Hurd and D. M. Freeman, *Proc. Natl. Acad. Sci. U.S.A.*, 1989, **86**, 4402.
12. A. D. Bain, *J. Magn. Reson.*, 1984, **56**, 418.
13. G. Bodenhausen, H. Kogler, and R. R. Ernst, *J. Magn. Reson.*, 1984, **58**, 370.
14. D. M. Freeman and R. E. Hurd, *NMR: Basic Princ. Prog.*, 1992, **27**, 200.
15. R. E. Hurd, *J. Magn. Reson.*, 1990, **87**, 422.
16. R. E. Hurd and B. K. John, *J. Magn. Reson.*, 1991, **91**, 648.
17. J. Ruiz-Cabello, G. W. Vuister, C. T. W. Moonen, P. van Gelderen, J. S. Cohen and P. C. M. van Zijl, *J. Magn. Reson.*, 1992, **100**, 282.
18. R. E. Hurd and B. K. John, *J. Magn. Reson.*, 1991, **92**, 658.
19. B. K. John, D. Plant, S. Heald, and R. E. Hurd, *J. Magn. Reson.*, 1991, **94**, 664.
20. G. W. Vuister, R. Boelens, R. Kaptein, R. E. Hurd, B. John, and P. C. M. van Zijl, *J. Am. Chem. Soc.*, 1991, **113**, 9688.
21. A. L. Davis, R. Boelens, and R. Kaptein, *J. Biomol. NMR*, 1992, **2**, 395.
22. L. E. Kay, *J. Am. Chem. Soc.*, 1993, **115**, 2055.
23. G. W. Vuister, G. M. Clore, A. M. Gronenborn, R. Powers, D. S. Garrett, R. Tschudin, and A. Bax, *J. Magn. Reson., Ser. B*, 1993, **101**, 210.
24. J. Chung, J. R. Tolman, K. P. Howard, and J. H. Prestegard, *J. Magn. Reson., Ser. B*, 1993, **102**, 137.
25. L. E. Kay, P. Keifer, and Tim Saarinen, *J. Am. Chem. Soc.*, 1992, **114**, 10 663.
26. Y.-C. Li and G. T. Montelione, *J. Magn. Reson., Ser. B*, 1993, **101**, 315.
27. A. Haase, J. Frahm, W. Hanicke, and D. Matthaie, *Phys. Med. Biol.*, 1985, **30**, 341.
28. B. K. John, D. Plant, P. Webb, and R. E. Hurd, *J. Magn. Reson.*, 1992, **98**, 200.
29. M. Piotto, V. Saudek, and V. Sklenár, *J. Biomol. NMR*, 1992, **2**, 661.
30. P. C. M. van Zijl and C. T. W. Moonen, *J. Magn. Reson.*, 1990, **87**, 18.
31. A. L. Davis, E. D. Laue, J. Keeler, D. Moskau, and J. Lohman, *J. Magn. Reson.*, 1991, **94**, 637.
32. A. L. Davis, J. Keeler, E. D. Laue, and D. Moskau, *J. Magn. Reson.*, 1992, **98**, 207.
33. J. R. Tolman, J. Chung, and J. H. Prestegard, *J. Magn. Reson.*, 1992, **98**, 462.
34. J. Boyd, N. Soffe, B. K. John, D. Plant, and R. E. Hurd, *J. Magn. Reson.*, 1992, **98**, 660.
35. G. W. Vuister, J. Ruiz-Cabello, and P. C. M. van Zijl, *J. Magn. Reson.*, 1992, **100**, 215.
36. A. Ross, M. Czisch, C. Ciesslar, and T. A. Holak, *J. Biomol. NMR*, 1993, **3**, 215.
37. D. Brühwiler and G. Wagner, *J. Magn. Reson.*, 1986, **69**, 546.
38. E. R. P. Zuiderweg, *J. Magn. Reson.*, 1987, **71**, 283.
39. A. Bax and S. S. Pochapsky, *J. Magn. Reson.*, 1992, **99**, 638.
40. B. K. John, D. Plant, and R. E. Hurd, *J. Magn. Reson., Ser. A*, 1993, **101**, 113.
41. L. E. Kay, G.-Y. Xu, A. U. Singer, D. R. Muhandiram, and J. D. Forman-Kay, *J. Magn. Reson., Ser. B*, 1993, **101**, 333.
42. G. Wider and K. Wütrich, *J. Magn. Reson. B*, 1993, **102**, 239.
43. V. Sklenár, M. Piotto, R. Leppik, and V. Saudek, *J. Magn. Reson., Ser. A*, 1993, **102**, 241.
44. A. Majumdar and E. R. P. Zuiderweg, *J. Magn. Reson., Ser. B*, 1993, **102**, 242.
45. O. W. Sorensen, M. Rance, and R. R. Ernst, *J. Magn. Reson.*, 1984, **56**, 527.
46. R. E. Hurd, B. K. John, and D. Plant, *J. Magn. Reson.*, 1991, **93**, 666.
47. R. E. Hurd, B. K. John, P. Webb, and D. Plant, *J. Magn. Reson.*, 1991, **99**, 632.

Biographical Sketch

Ralph E. Hurd. *b* 1950. B.A., 1973, Chemistry, CSUSB, Ph.D., 1977, Biochemistry, University of California, Riverside (advisor Brian R. Reid). Joined Nicolet Magnetics in 1980 (working with LeRoy Johnson on HR applications of NMR); 1983, manager CSI Applications, GE Medical Systems (formerly Nicolet Magnetics); 1989, manager Combined CSI and HR Applications; since 1990, manager Spectroscopy Research and Development. Approx. 60 publications, 4 patents. Current research: clinical MR spectroscopy.

Instrumentation for the Home Builder

Robert M. Pearson
Tri-Valley Research, Pleasanton, CA, USA

and

Constantin Job
University of Arizona, Tucson, AZ, USA

1 Introduction 1
2 Getting Started 1
3 A Home Built NMR Spectrometer 2
4 Some Applications of a Home Built Spectrometer 6
5 References 7

1 INTRODUCTION

NMR spectrometers have been commercially available for just over 40 years. The first spectrometers were based on the CW NMR method, and spectrometer design did not change dramatically until the late 1960s, when pulsed spectrometers were introduced. After superconducting magnets became the norm in high resolution NMR, commercial instrument makers engaged in competition, which has resulted in NMR spectrometers becoming ever more complex and expensive. Now, only the most well funded laboratories can afford to purchase a state-of-the-art NMR spectrometer at the highest frequencies available.

This would seem to lock the young NMR spectroscopist into a situation where he or she has to work at a large, well funded institution in order to practise his or her technology. However, the advent of the microprocessor based personal computer has provided the possibility for anyone to build a near state-of-the-art, and relatively inexpensive, NMR spectrometer, mostly from commercial components. The sources of the components used in the spectrometer described below are referenced as an aid to the reader.

There are only a few components of a modern pulsed NMR spectrometer that are not commercially available at a cost within the budget limitations of most small companies or even individuals. The first thing one must realize is that NMR was originally developed at frequencies of 60 MHz and lower, so a lot of good NMR was done at lower frequencies. If one can find an old CW system with a good magnet, and there are hundreds around universities and other large institutions, one can follow the simple procedures outlined in this article and construct a good pulsed NMR spectrometer at a reasonable cost.

The home built spectrometers described below are pulsed wideline instruments. But there is no reason why one could not obtain a used high-resolution magnet and add the features needed for high-resolution work such as a field/frequency lock and a decoupler.

With the availability of the new pulse programmer/modulator system discussed here, one need not be an electronics engineer or a computer programmer to build an NMR spectrometer. Most of the components needed for an NMR spectrometer are commercially available at reasonable cost if one is willing to stay at relatively low fields, i.e. 60 MHz or less. This includes powerful software packages that can act as both the operating and data reduction systems for an NMR spectrometer. We discuss two of these, the Asyst software, and that sold by National Instruments.

In many ways the pulse programmer/modulator is the heart of a pulsed NMR spectrometer. Until now this has been the hardest component part of an NMR spectrometer to either make or buy at a price an individual or small company can afford. The pulse programmer/modulator described here can be purchased either as a kit, or assembled, at reasonable cost. (Tri-Valley Research, 3590 Churchill Court, Pleasanton, CA 94588). This system fits in two expansion slots of an IBM-compatible personal computer (PC). It will deliver a 1 V peak-to-peak (p−p) rf pulse, of any pulse sequence desired, into a 50 Ω load. The pulse programmer portion of this system is based on logic cell arrays (LCAs) (Xilinx, Santa Clara, CA) that can be programmed to produce any pulse sequence needed for NMR. The modulator contains a direct digital synthesizer (DDS) that can produce a wide range of rf frequencies.

One can purchase rf amplifiers that will amplify this signal up to any level needed for NMR from a number of companies. This pulse then goes to the probe, which can be home built.[1] The NMR signal then goes to the receiver, which is commercially available (Tri-Valley Research, 3590 Churchill Court, Pleasanton, CA 94588) or can be made from any number of designs published in the literature.

The receiver delivers the detected NMR signal to a commercial analog-to-digital (A/D) converter located in the PC. The spectrum ends up on the computer hard drive ready for data reduction by a commercial software package. The whole system less the magnet can be built at a cost of below $20 000.

2 GETTING STARTED

Before starting to build an NMR spectrometer it is advisable to obtain a few books. One possibility is ‘Experimental Pulse NMR, A Nuts and Bolts Approach’, written by Fukushima and Roeder and published by Addison-Wesley in 1981. Also, it is recommended that a copy of ‘The AARL Handbook’ is obtained.[2] You will also need some test equipment. Besides an inexpensive multimeter, you will need an oscilloscope, both of which can now be purchased, at reasonable cost, from any good electronics store. For the spectrometer described here, a 20 MHz scope is adequate. One possibility is a BK Precision model 2120 made by the Dynascan Corp.

An important aspect of the fabrication of a home built NMR spectrometer is the knowledge of how to make a quarter-wavelength coaxial cable tuned to the frequency of the spectrometer. A quarter-wavelength coaxial cable at a given frequency behaves as an infinite resistance when shorted to ground. A practical way to fabricate a quarter-wavelength cable is by using a frequency sweep generator. The Wavetek Model 1062 (5808 Churchman, PO Box 190, Beech Grove, IN 46107) will work well. You will also need either a

reflection bridge, such as those furnished by Bruker (based in Germany) to people who purchase their spectrometers, or a three-port coupler, such as made by Mini-Circuits. A Mini-Circuits coupler model ZDC-10-1 serves this purpose, and can be purchased at an electronics supply house. By grounding one side of the quarter-wavelength cable and comparing the other side to an infinite resistance one can observe on the oscilloscope the quarter-wavelength frequency for a specific cable length.

Several rf attenuators will be needed, which can be built from plans in 'The ARRL Handbook'. Both a step low-power resistive attenuator[3] covering a range of attenuation, and two heavier 20 db π network attenuators[4] can be built by placing 10 W resistors in a small die cast box which can be purchased at any electronics store. These attenuators are used to measure the output of the high power transmitter and its driver.

Most people who will want to build an NMR spectrometer at home will have some experience in this field and will know how to use this test equipment or will have access to an NMR laboratory that employs people who will know the technology. A detailed set of instructions on the use of this equipment can also be obtained (Tri-Valley Research, 3590 Churchill Court, Pleasanton, CA 94588).

3 A HOME BUILT NMR SPECTROMETER

Figure 1 is a photograph of the NMR spectrometer built by the authors in Pleasanton, CA. This spectrometer was built under a contract from the Strategic Highway Research Program to study the use of NMR spectroscopy to measure the amount of asphalt in hot mix as it is prepared and used in the field.

Space does not permit a detailed description of how this spectrometer was built or the NMR studies conducted with it. However, an outline of this work is given below, and the details are available on request (Tri-Valley Research, 3590 Churchill Court, Pleasanton, CA 94588). There were two basic design concepts used in the development of this spectrometer. The first was to place as much of the digital electronics as possible on the bus of a personal computer. The second was to use as many commercially available components as possible. The latter concept makes it possible to buy much of the spectrometer from large companies with well developed and supported products. This is especially true for the high power

Figure 1 Home built NMR spectrometer

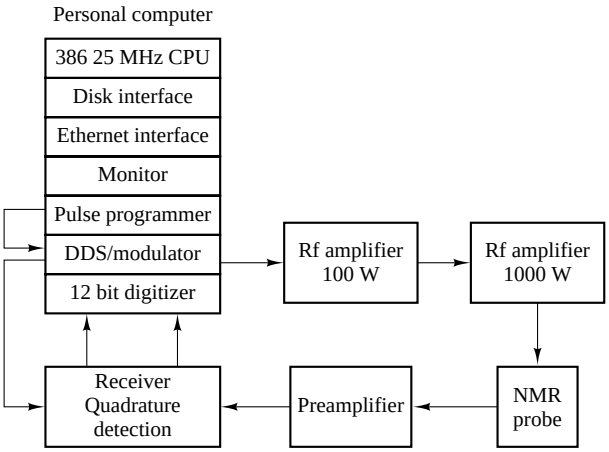

Figure 2 Block diagram of the home built NMR spectrometer. (Reproduced from Job et al.[5])

rf amplifier and the data reduction software. Figure 2 shows a block diagram of this spectrometer.

The system described here is flexible enough to accommodate a wide variety of NMR experiments. For example, the block diagram shows the pulse programmer/modulator boards and the A/D board all in one computer. This is the normal configuration. Examination of Figure 1 shows the system contains two computers, the small Everex 286 placed under the oscilloscope on the middle Tuffy cart, and the large 486 under the keyboard and monitor on the right-hand Tuffy cart (purchased from K-Log Education Division, PO Box 5, Zion, IL 60099-0005). The small Everex 286 contains the pulse programmer/modulator system, and the 486 contains the A/D board and does the data reduction. The use of one computer for spectrometer control and another for data reduction is common practice for large NMR systems. This makes it easier to accommodate the special software requirements of some of the components of the spectrometer. This is discussed in the software section later in this article.

3.1 The Pulse Programmer/Modulator System

This is the most difficult component part of the NMR spectrometer to obtain commercially. Both National Instruments (6504 Bridge Point Parkway, Austin, TX 78730) and Keithley/Metrabyte Instruments (12440 Myles Standish Boulevard, Tauton, MA 02780) sell boards which could in theory produce trains of dc pulses, or at least square waves. The system described here is modestly priced and fits into two expansion slots of a PC and produces any desired sequence of rf pulses at any frequency or phase relationship between pulses. This system has been used in computers ranging from a 10 MHz XT to a 33 MHz 486 with an ESIA bus. This system is shown in Figure 3.

Block diagrams of the pulse programmer and modulator boards are shown in Figures 4 and 5, the working details of which have been published.[5]

3.2 The High Power rf Amplifier

The pulse programmer/modulator system in the PC produces a 1 V rf pulse into a 50 Ω load. This pulse sequence is sent to a

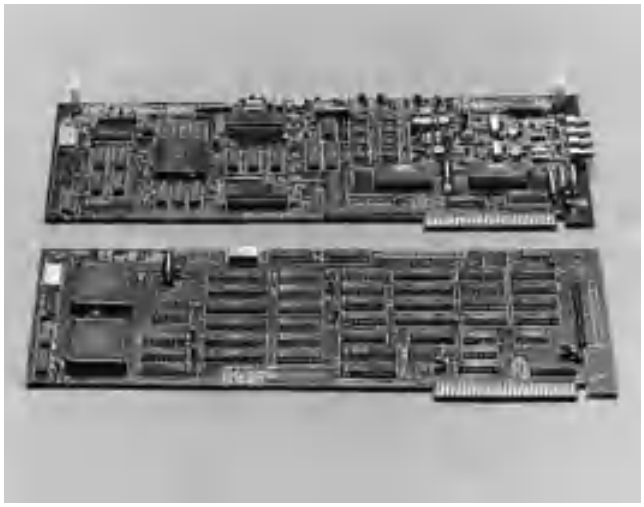

Figure 3 Pulse programmer/modulator system. These two boards hook together with a flat band cable and occupy two slots on the PC bus. (Reproduced from Job et al.[5])

driver for the high power amplifier that amplifies the rf pulses to about 200 V p−p (100 W). (Table 35−37 in 'The ARRL Handbook' lists the conversion of p−p voltages to power for a 50 Ω system. This conversion can also be made by dividing the square of the p−p voltage by 400.)

A Henry KD Standard Amplifier (Henry Radio, 2050 South Bundy Drive, Los Angeles, CA 90025) is driven with this signal. The output of this amplifier delivers about 1 kW to the probe. This system appears to function well, being almost trouble free. Henry Radio makes a range of reasonably priced amplifiers for the amateur radio market.

3.3 The Probe

The probes used in both the 10 MHz Halbach magnet and the 20 MHz H magnet all have the same general configuration as shown in Figure 6. A general treatment of probe design is available.[2]

The inductor coils are usually wound from magnet wire. Almost any weight wire can be used. In fact, some constructors prefer to use ordinary copper tubing purchased at a hardware store for larger sized probes. Copper tubing of $\frac{1}{8}''$ (3 mm) diameter works well. Simply wrap the wire or tubing around the glass tube to be used as an insert in the probe to hold the coil. Care must be used in wrapping coils of copper tubing or noninsulated wire to make sure that there is enough space between the coils so that arcing does not occur. Arcing is not so much a problem between the wraps of the coils as it is between the leads or between the leads and the probe body.

The position of the coil is at the point where, when the probe is in the magnet, the coil will be in the area of highest homogeneity of the magnetic field. The number of turns needed depends on the frequency of the system being built. One needs to balance the circuit using a sweep generator and reflection bridge or coupler. With the Mini-Circuits coupler the output of the probe is hooked to the BNC connector marked 'in' on the coupler, the rf output of the sweeper is connected to the 'out' BNC connector of the coupler, and the 'Demod in' connector of the sweeper is connected to the BNC connector marked 'CPL' of the coupler. The sweeper is then hooked up to the scope in the XY mode and a proper swept signal applied to the system. A dip will be seen on the scope display. This will be at the frequency the probe balances to 50 Ω. The capacitance of the probe circuit or the inductance of the coil must then be adjusted so that the probe balances to 50 Ω at the required frequency. In the spectrometer described, 1000 V ceramic disk capacitors were used. Obtain a collection of these capacitors in the low picofarad range, take an afternoon off, and learn how to balance a probe. You will find that after a few attempts it becomes easy. Any good machine shop can make the probe body. Thin wall aluminum tubing is available in a wide range of sizes, so this type of probe can be made for almost any magnet.

3.4 The Magnet

The spectrometer built for the Strategic Highway Research Program, shown in Figure 1, was designed to determine the proton NMR wideline spectrum of a 4″ (100 mm) highway core. The magnet required for this large a sample needed to have at least a 5″ (125 mm) free bore in order to hold an NMR probe large enough to accommodate this sample. A standard H-type permanent magnet would have been large and very heavy. Therefore, a Halbach dipole was used for this application.

Halbach dipoles[6] were first proposed as focusing magnets for particle accelerators. A Halbach dipole is essentially a tube of magnetic material which has been segmented in such a way so as to create a dipole magnet with the axis of the magnetic material transverse to the bore of the magnet. This is ideal for NMR use because it allows one to use a solenoid as the NMR coil rather than a saddle coil. It is essentially a permanent magnet that uses its own magnetic material, in this case neodymium−iron−boron (NdFeB), as a carrier for the flux return lines. This eliminates a heavy steel yoke. The magnet used in the spectrometer described here has a 5.5″ (140 mm) free bore and weighs 300 lb (136 kg). We also have a standard H magnet that was part of an IBM NR-02 NMR spectrometer.

Although the Halbach dipole functioned well in the asphalt application, its use is not recommended for any but the most experienced NMR spectroscopist. It needs more work before it should be considered for use on a routine basis. A number of magnet makers can furnish excellent H-type dipole magnets for low field NMR work.

Any magnet used in an NMR spectrometer needs field stabilization. Permanent magnet materials change field strength with temperature, and NdFeB is particularly difficult in this regard. This has always been a problem with commercially available small NMR spectrometers. We have solved this problem by placing the magnet in an aluminum tank and circulating a temperature controlled antifreeze solution through the tank. The temperature of the solution in our spectrometer is controlled by a Cole-Parmer Circulator Bath (catalog number L-10267-62; Cole-Parmer Instrument Company, 7425 North Oak Park Avenue, Chicago, IL 60648).

3.5 The Receiver

Figure 7 is a block diagram of the commercially available[1] receiver used for the system described herein.

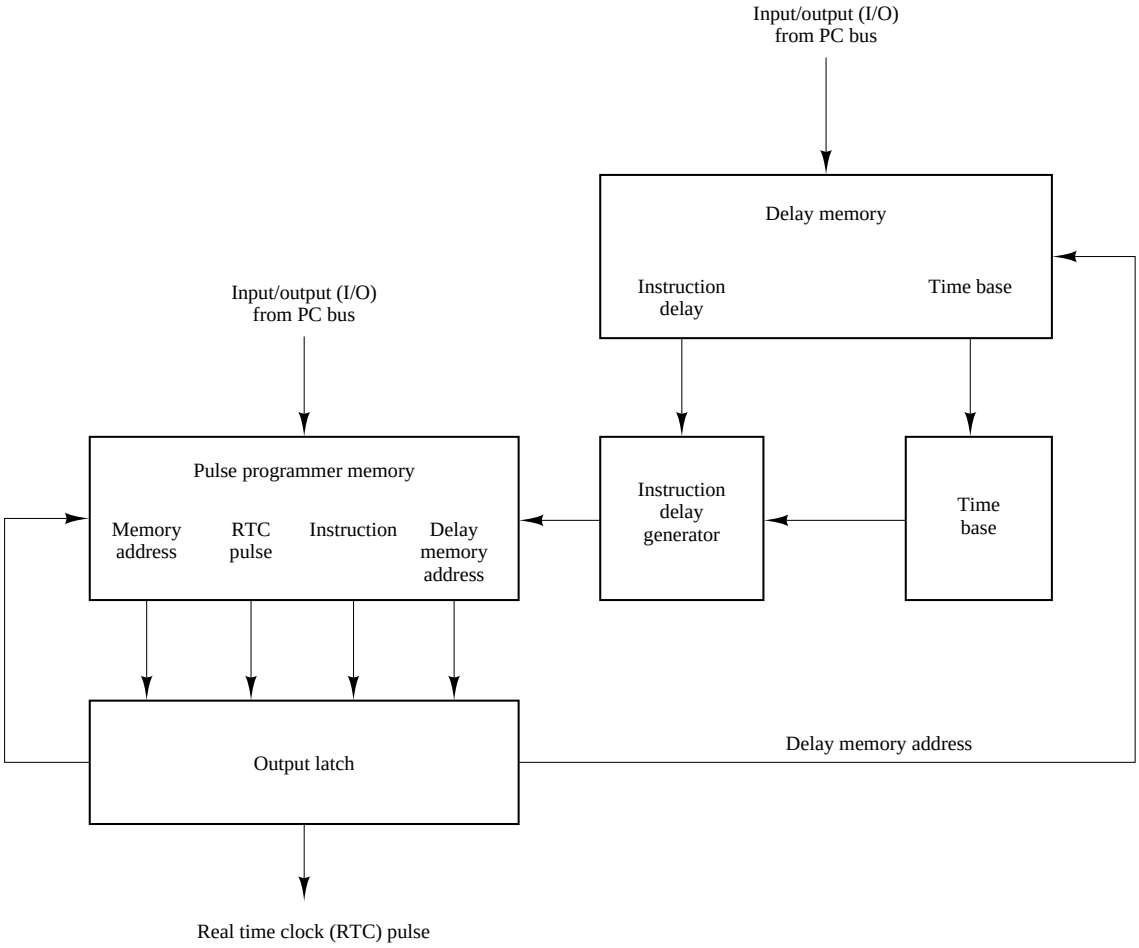

Figure 4 Block diagram of the pulse programmer board. (Reproduced from Job et al.[5])

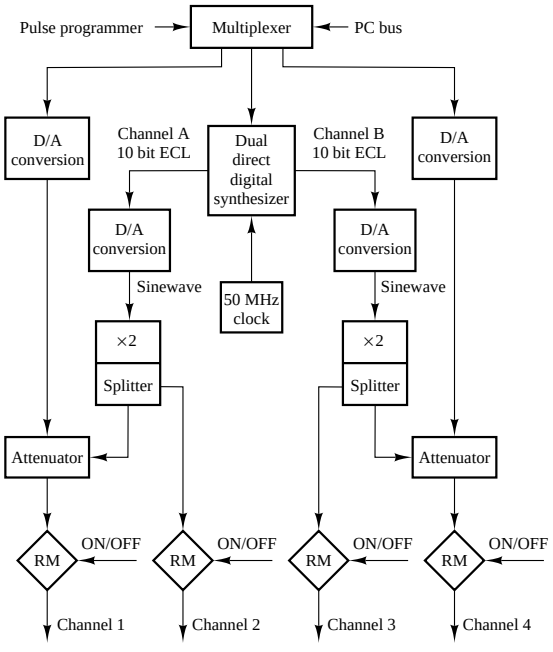

Figure 5 Block diagram of the modulator board. (Reproduced from Job et al.[5])

The preamplifier is protected from the high power rf pulse by placing a pair of 914A crossed diodes between the input and ground. The output of the probe is connected to the preamplifier with a quarter-wavelength coaxial cable. Such a cable shorted to ground is an infinite resistance in an rf circuit. The rf pulse will open the diodes at the input of the preamplifier and create a shorted quarter-wavelength cable to ground. This protects the preamplifier. You can also place a T connector on the input to the probe and place the transmitter line to one side of the connector, with a grounded quarter-wavelength cable on the other side. The quarter-wavelength cable will pass all rf frequencies other than the transmitter frequency to ground, i.e. act as a filter.

3.6 The Analog-to-Digital Converter

Good analog-to-digital (A/D) converters suitable for use in an NMR spectrometer are now available. There are several A/D converters on the market that can be used in an NMR spectrometer. However, an A/D converter must be chosen which is compatible with the data reduction software to be used. There must either be a driver written to allow the software to communicate with the A/D board in the computer, or the A/D board must be able to place the data on the computer hard drive so that the software can address it. The simplest

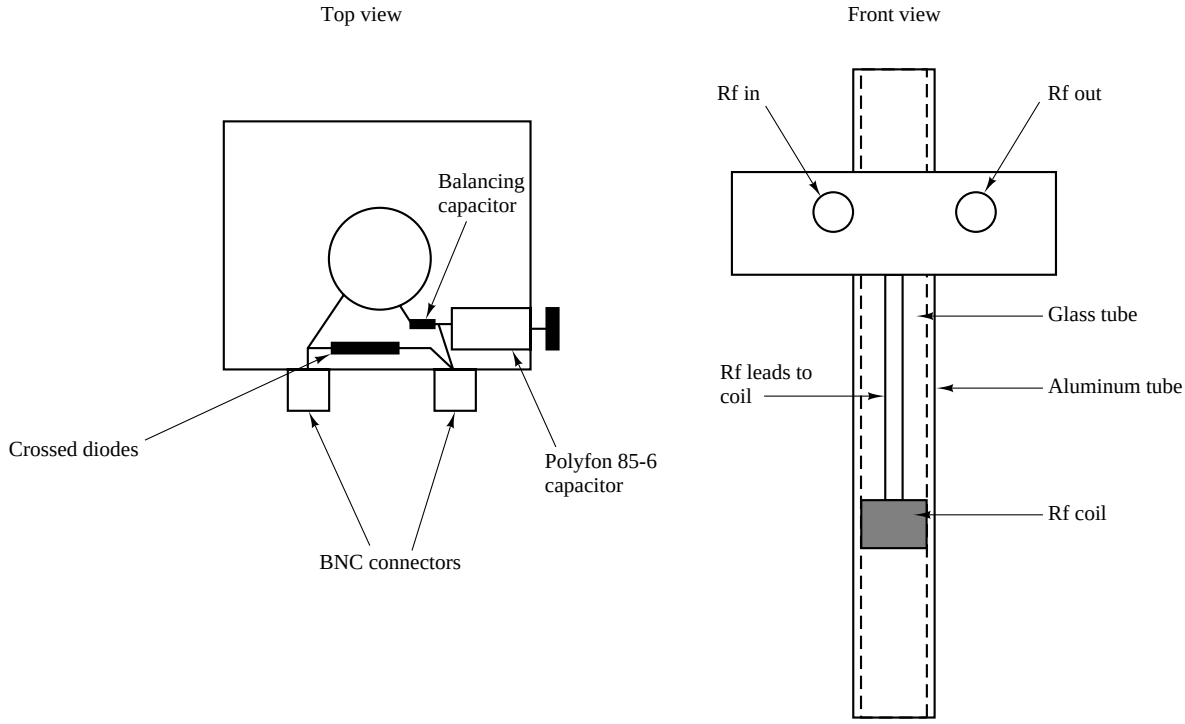

Figure 6 NMR probe. (Reproduced from Job et al.[5])

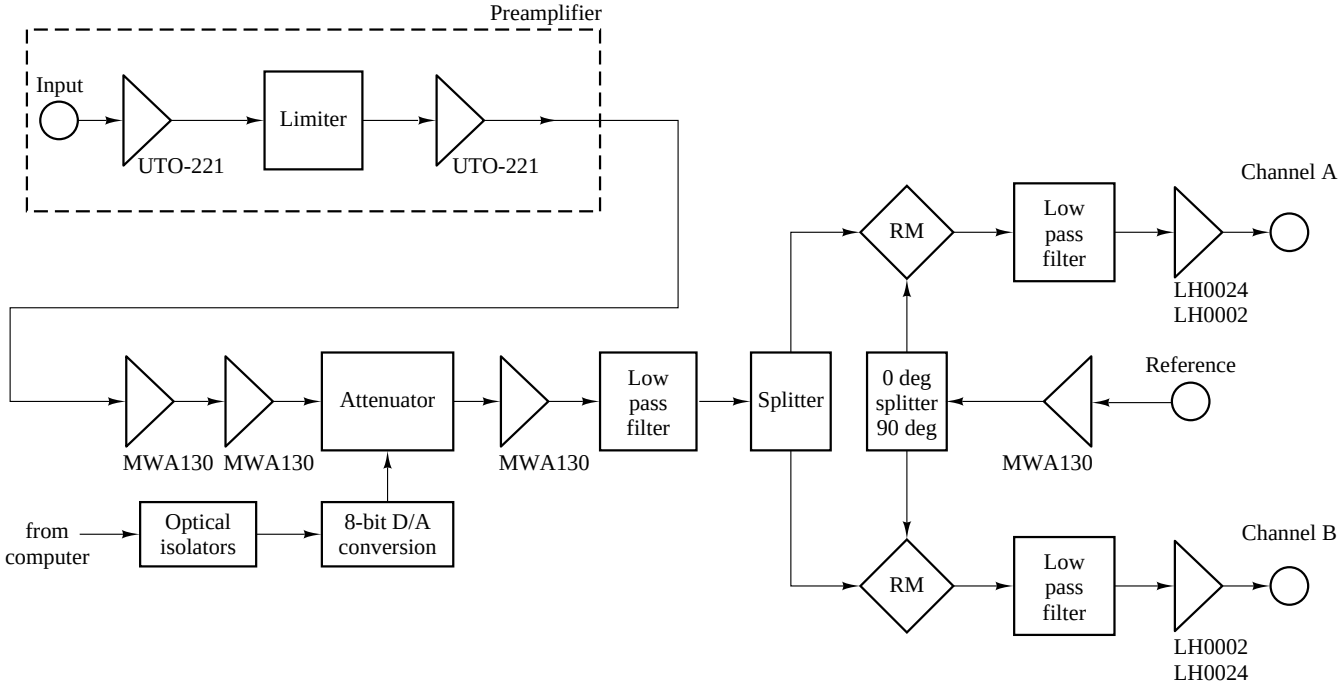

Figure 7 Block diagram of the receiver

solution to this problem is to use an A/D board compatible with the software, i.e. one that has a software driver.

There are at least two companies that furnish 1 MHz, 12-bit A/D converters and software suitable for use in data reduction on an NMR spectrometer. These are Keithley Instruments and National Instruments (addresses given above). Keithley Instruments has also written a driver for a Markenrich (Markenrich Corp., 1812 Flower Avenue, Duarte, CA 91010) Waag I A/D board. This board has only 8-bit resolution, but it has conversion rates of up to 20 MHz. Both boards have been found to function well with the Keithley software.

The National Instruments A/D board has been designed for an EISA bus computer and does not have on-board memory. The National Instruments software system will work with a

PC, Apple Macintosh, or work station. It is also operates under Windows.

3.7 The Data Reduction Software

Our own experience has been limited to the Keithley 'Asyst' package. The complete Asyst is a large software package designed to allow an end user to write an overlay program that will work with the underlying Asyst software to perform any experiment the end user would like to carry out. Two problems with this package are that it requires almost the whole of the computer memory under 640 kilobytes to load, and that it is made to work with expanded memory rather than extended memory. Expanded memory presents a problem in that it requires a page swapping segment in the PC memory above 640 kilobytes and below 1 megabyte. The Markenrich A/D board requires segment E000 of this memory. The pulse programmer software is written for a VGA monitor, which takes the first three memory segments above 640 kilobytes. When the driver for the Markenrich board is loaded and a VGA monitor used, there is no memory left for an expanded memory page swapping segment, as required by the Asyst software. This is not a problem if one uses both a control computer and a data reduction computer in the system as shown in Figure 1.

The overlay program needed for data reduction of NMR spectra is not difficult to write. Although there is a 'C' compiler with Asyst, we prepared our overlay in 'Fourth', which is the usual language used with Asyst. Fourth is not hard to learn and is a good language for instrument control and data reduction software. The Asyst software was found to be very flexible and powerful.

4 SOME APPLICATIONS OF A HOME BUILT SPECTROMETER

Beside the asphalt application for Strategic Highway Research Program our work has mostly been in the development of quantitative methods for moisture determination

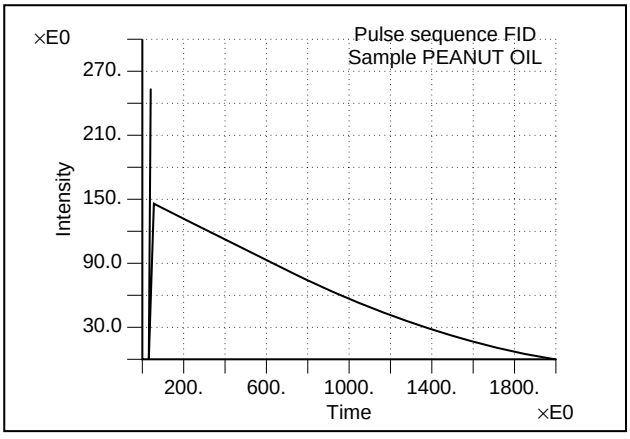

File Name 11311.fid | No. of scans 100 | Detector PSD
Attenuation 48 | DATE 05/08/91
RD (sec) = 2 | TIME 19:46:55:90
Tau (μ secs) is | Band Width MED

PRESS ANY FUNCTION KEY TO PRINT/ANY OTHER FOR MAIN MENU

Figure 8 FID of peanut oil

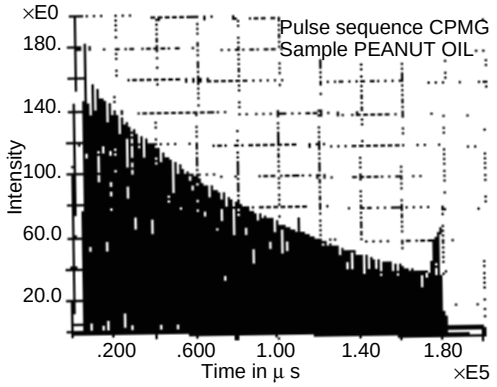

File Name 11311.cpm | No. of scans 100 | Detector PSD
Attenuation 48 | DATE 05/08/91
RD (sec) = 2 | TIME 19:55:17:97
Tau (μ secs) is | Band Width MED

PRESS ANY FUNCTION KEY TO PRINT/ANY OTHER FOR MAIN MENU

Figure 9 CPMG data of peanut oil

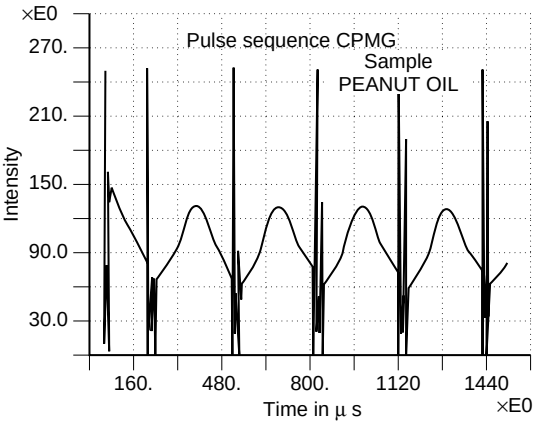

File Name 2P106L4.CPM | No. of scans 100 | Detector PSD
Attenuation 52 | DATE 11/25/90
RD (sec) = 2 | TIME 18:26:54:31

Figure 10 Expanded CPMG data

in the agricultural/food processing industries. These methods use free induction decays, Carr–Purcell–Meiboom–Gill (CPMG) relaxation time measurements, and off-resonance FIDs with subsequent Fourier transformation to obtain a frequency domain spectrum.

Recently we have developed, in addition to the asphalt in hot mix method, qualitative methods to determine the concentration of solids in whole onions and the solids/fat ratio in edible oils. These methods were all developed on the system described in this article. These methods all used our large Halbach magnet and CPMG pulse sequences to determine changes in relaxation times which are related to the parameters of interest. These methods, and others, are available on request (Tri-Valley Research, 3590 Churchill Court, Pleasanton, CA 94588).

Figure 8 illustrates a typical NMR FID obtained with our spectrometer. This spectrum was plotted on a standard printer connected to the data reduction computer. It was done with

the Asyst software. Figure 9 shows the data from a CPMG experiment and illustrates the ability of this pulse sequence to average out magnet inhomogeneities. Figure 10 shows the expanded spectrum of the first few echoes and illustrates one of the features of the Asyst software. The use of this spectrometer in the agricultural field has been described.[7]

5 REFERENCES

1. P. D. Murphy and B. C. Gerstein, *Analysis and Computerized Design of NMR Probe Circuits*, IS-4436, UC-3, Ames Laboratory of the US Department of Energy, Iowa State University, Ames
2. ARRL, *The ARRL Handbook*, The American Radio Relay League, Newington, CT, 1989.
3. ARRL, *The ARRL Handbook*, The American Radio Relay League, Newington, CT, 1989, p. 25.
4. ARRL, *The ARRL Handbook*, The American Radio Relay League, Newington, CT, 1989, p. 25, Table 2.
5. C. Job, R. M. Pearson, and F. M. Brown, *Rev. Sci. Instrum.*, 1994, **65**, 11.
6. K. Halbach, *Nucl. Instrum. Methods*, 1980, **169**, 1.
7. R. M. Pearson and C. Job, *Food Processing Automation II, Proceedings of the 1992 Conference, Food and Process Engineering Institute, St. Joseph, Michigan, 1992*, p. 40.

Biographical Sketches

Robert M. Pearson. *b* 1930. B.S., 1957, M.S., 1959, University of Nevada. Ph.D., 1965, University of California-Davis. NMR spectroscopist, Kaiser Aluminum & Chemical Corp., 1967–86. Owner, Tri-Valley Research, 1987–present. Approximately 20 publications. Research interests include wideline NMR of solid oxides, especially catalytic materials, and application of NMR to online industrial process control.

Constantin Job. *b* 1948. Electrical Engineering Diploma, 1972, College of Technology, Winterthur, Switzerland. Engineer, Bruker Instruments, 1973–83. Research engineer, Kaiser Aluminum & Chemical Corp., 1983–85. Research scientist, University of Arizona, Tucson, 1985–present. Approximately 10 publications. Interests include NMR spectroscopy, NMR instrumentation, and computer software.

Microprobes and Methodologies for Spectral Assignments: Applications

Gary E. Martin

Global Pharmaceutical Sciences, Pharmacia Corporation, Kalamazoo, MI, USA

1	Introduction	1
2	High Sensitivity, Small Volume Probe Performance Comparisons	6
3	Applications of Small Volume NMR Probes in the Solution of Chemical Structure Problems	9
4	Conclusions	12
5	References	12

1 INTRODUCTION

Nuclear magnetic resonance or NMR has become the cornerstone of modern chemical structure elucidation. The technique is unparalleled in its ability to determine chemical structures by tracking atom-to-atom connectivity. Experiments are now available that allow one to determine homonuclear (^{1}H–^{1}H and ^{13}C–^{13}C) and heteronuclear (^{1}H–X where X = ^{13}C, ^{15}N, ^{19}F and ^{31}P among other heteronuclear pairs) connectivity information that is invaluable in assembling unknown chemical structures. Despite the considerable power of NMR methods, the technique unfortunately suffers from inherently low sensitivity when compared to other analytical spectroscopic methods such as mass spectrometry. This rather stringent limitation has prompted very considerable effort in the development of small volume, high sensitivity NMR probe designs. In part, these efforts have been necessary as it is not always possible to isolate additional sample for analysis.

The earliest detailed description of NMR spectroscopy using small rf coils that the author is aware of is found in the work of Odelblad in 1966.[1] In this study, solenoidal microcoils were used in conjunction with continuous wave (CW) NMR methods to study human cervical mucous secretions. The study examined ^{1}H chemical shifts and spin-lattice (T_1) relaxation behavior of the secretions. From that study, there was a gap of more than a decade before the pioneering work of Shoolery in 1979.[2] Shoolery's work focused on the use of 1.7 mm capillary NMR probes for direct observe ^{13}C NMR measurements. Shoolery demonstrated that it was possible to substantially reduce data acquisition times, acquiring decoupled ^{13}C NMR spectra for samples as small as 1 mg of cholesterol in 16 h. Corresponding gains were reported for ^{1}H spectra, with data acquired for a 1 μg sample of cortisone acetate.

These early studies set the stage for the development of 3 mm micro NMR probes that started in 1991 in a collaboration between the author, colleagues and staff at Nalorac Corporation. The first report utilizing 3 mm micro NMR probe technology appeared in 1992.[3] Using the simple indoloquinoline alkaloid cryptolepine **(1)** as a model compound for the study, the authors reported the acquisition of inverse-detected direct heteronuclear shift correlation HMQC data[4] using a 12 μg (0.05 μMole) sample of the alkaloid dissolved in 145 μl of d_6-DMSO in 16 h. These data are shown in Figure 1. Long-range heteronuclear correlations were measured using the substantially less sensitive HMBC experiment[5] on a 35 μg sample (0.15 μmole) of the alkaloid in 145 μl of d_6-DMSO in 21 h. These studies ushered in new capabilities for the characterization of small samples by NMR spectroscopy. It would have been necessary to isolate substantially larger samples than those reported for characterization using conventional 5 mm NMR probeheads.

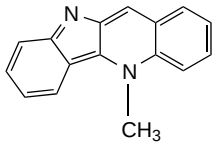

(1)

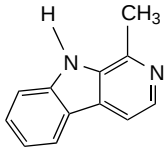

(2)

Later in 1992, a direct comparison of the performance of 3 mm and 5 mm inverse-detection NMR probes for the acquisition of heteronuclear shift correlation data was reported.[6] Using 1 μMole samples of the alkaloid harmane **(2)** prepared in appropriate volumes for the two probe formats, HMQC spectra were acquired with identical s/n (signal-to-noise) ratios. It took four times as long to acquire comparable s/n data in a 5 mm probe with an identical quantity of sample as for the same data in a 3 mm micro inverse NMR probe design (Figure 2). Clearly, for structural characterization problems when limited quantities of sample are available, there is a significant time advantage to acquiring the data using a 3 mm rather than 5 mm probehead.

Several years after the introduction of the 3 mm micro NMR probes, another innovation appeared in the form of the Varian Nano-probe™.[7–9] Shoolery, the driving force behind this probe technology, had the vision of having 100% of the sample within the confines of the rf coils of the probe. Obviously, however, this would result in considerable inhomogeneity over the sample due to the discontinuity of the magnetic susceptibility at the cell boundary. To circumvent this problem, the sample cell was oriented at the magic angle, 54.7°, and spun at high speed (>1 kHz) to average all of the magnetic dipoles to zero. The small volume of the nano-cell, 40 μl, makes it well suited to small samples. Nano-probe technology has made it possible to acquire ^{1}H spectra on samples of an aromatic alkaloid, **1**, as small as 75 ng (32 picomoles)

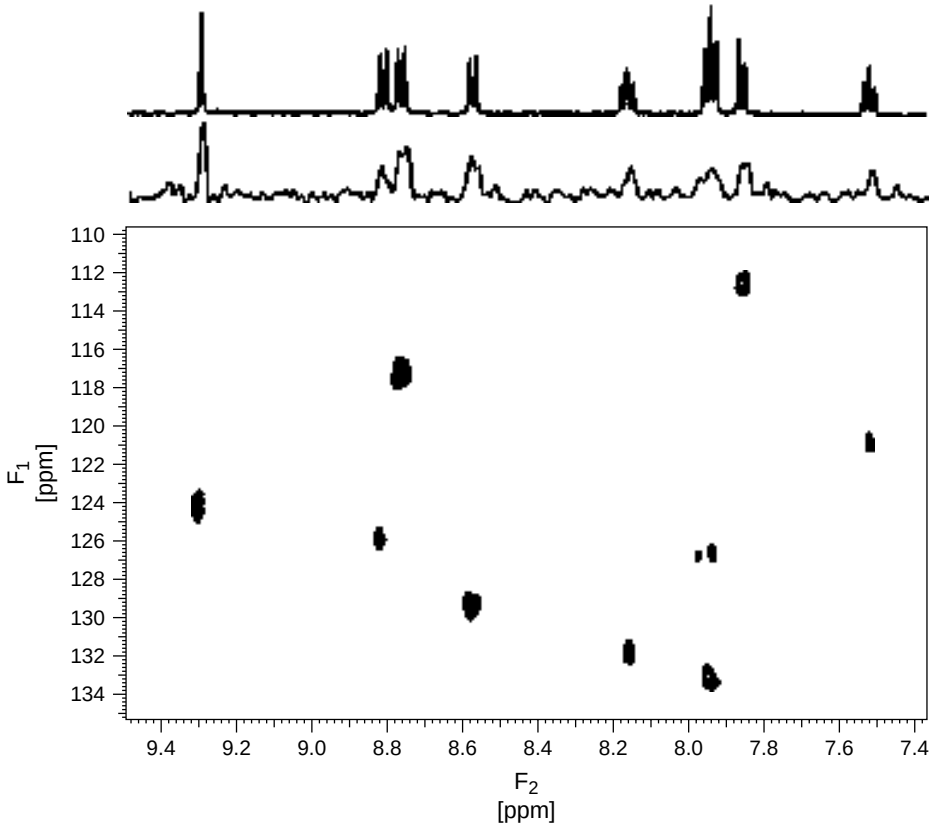

Figure 1 HMQC spectrum of a 12 μg (0.05 μmole) sample of the alkaloid cryptolepine **(1)** acquired overnight using a 3 mm micro inverse-detection NMR probe. The projection of the 2D data matrix through the proton frequency domain (F_2) is shown immediately above the contour plot; the ^{1}H reference spectrum is shown at the top

and COSY spectra overnight on an 85 picomole (200 ng) sample of the same model alkaloid.[10] The ^{1}H spectrum of an 32 picomole sample of cryptolepine **(1)** in shown in Figure 3; the corresponding COSY spectrum is shown in Figure 4. Using a heteronuclear version of the probe in conjunction with specialized processing software, Shoolery demonstrated that an INADEQUATE spectrum of a 3.8 mg sample of sucrose could be acquired in 62 h.[8] Since the initial development of the Nano-probe, a gradient inverse-detection version of the probe has also been developed yielding impressive results.[11] Applications of the Nano-probe for the characterization of small samples are discussed below.

The next step in the development of high-sensitivity, small volume NMR probes was the initial report of the μ-coil NMR probe by Sweedler and co-workers in 1995, which essentially overlapped the development of the nano-probe.[12] Unlike conventional NMR probes or the nano-probe described above, the μ-coil probe was instead a flow probe design, with the rf coil wrapped around a polyimide-coated fused-silica capillary. To obtain usable lineshape, it was necessary to immerse the coil in Fluorinert FC-43 when in use. While a linewidth of 0.6 Hz was initially reported, lineshape, based on visual inspection of figures in the initial report, was evidently not well optimized. Nevertheless, the authors reported a detection limit, defined as a s/n = 3 : 1, for a 19 ng sample of sucrose (56 picomoles) using a 1 min acquisition. It is also worth noting that since the μ-coil probe was a flow probe design that a smaller percentage of the actual sample, <20%, was calculated to be contained within the rf coil of the probe.

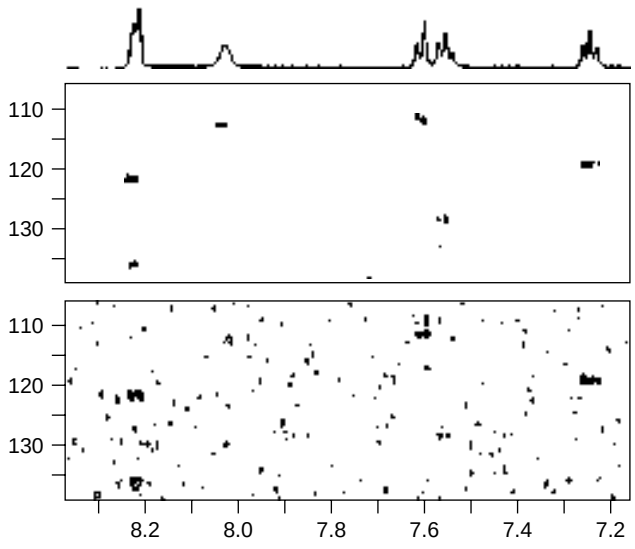

Figure 2 Comparison HMQC spectra of 1 μmole samples of the simple alkaloid harmane **(2)**. The spectrum shown in the bottom panel was acquired with a sample dissolved in 600 of d_6-DMSO using a 5 mm inverse detection probe. The data were acquired in 23 min. The same quantity of material was dissolved in 160 μl of d_6-DMSO and the data were acquired using a 3 mm micro inverse probe in 12 min to afford the spectrum shown in the top panel. To achieve comparable signal-to-noise using the 5 mm probe required ∼70 of data acquisition

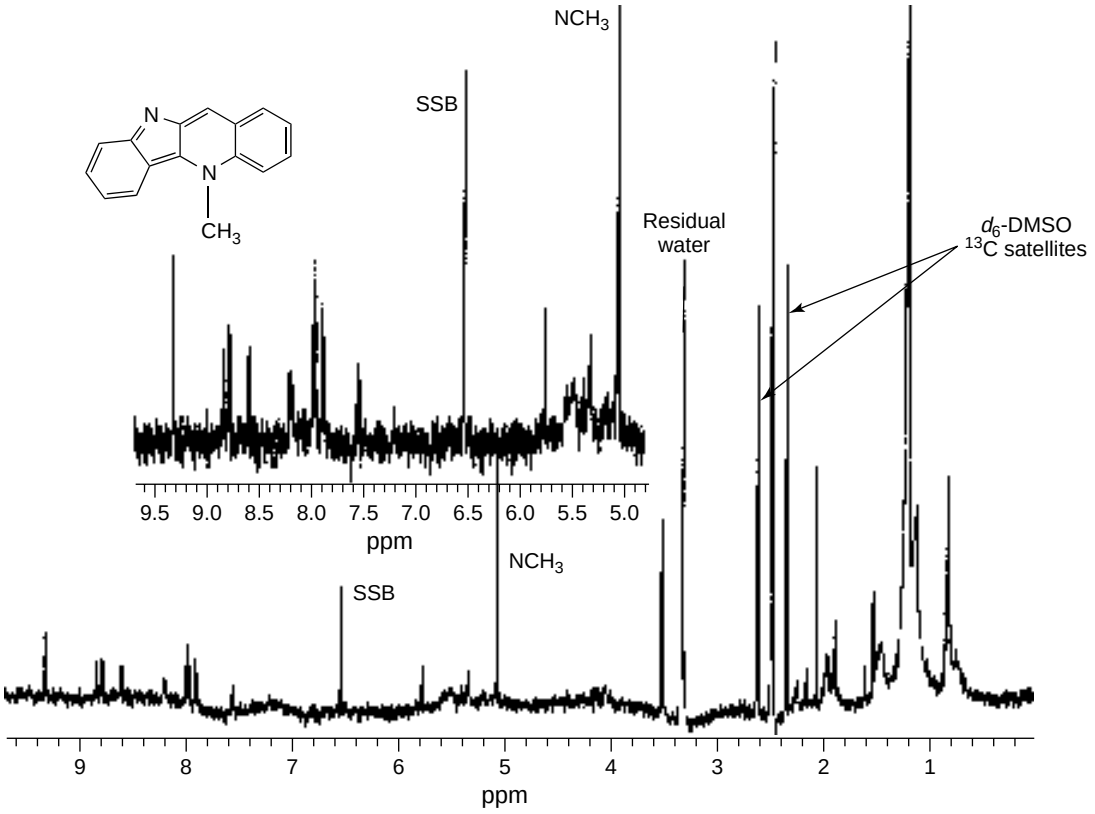

Figure 3 Proton NMR spectrum of a 75 ng (32 picomoles) sample of the indoloquinoline alkaloid cryptolepine (**1**, inset structure) acquired overnight using a Varian Nano-probe™. Both the residual water and the protio DMSO signals were suppressed in the experiment. Note the intensity of the ^{13}C satellite lines of the solvent relative to the intensity of the N-methyl group (~5.05 ppm) of cryptolepine

In contrast, conventional NMR probe designs can load up to ~80% of the sample within the confines of the rf coils in conventional NMR tubes and >95% of the sample when Shigemi micro cells are employed, or 100% with a nano-cell.

Following the initial report, refinements of the μ-coil NMR probe design have been reported. Designs have included probes for ^{13}C detection, although only labeled samples have thus far been studied.[13] Multiple solenoidal microcoil probes for possible applications to high-throughput screening have been developed.[14] Susceptibility matching plugs used in conjunction with microcoils have also been described for limited sample applications.[15] Using this approach it was possible to position ~43% of the sample within the coil volume, a substantial improvement over initial flow designs. Perhaps the most interesting report has been a probe design for inverse-detection experiments.[16] In the latter study, the authors reported the acquisition of a ^{13}C decoupled HMQC spectrum of a 13 μg sample of chloroquine diphosphate dissolved in 745 nl of D_2O. These data were acquired by accumulating 32 transients for each of 2048 × 128 increments of the 2D NMR data matrix. The few applications of the μ-coil probe that have appeared thus far have all be contained in papers reporting the development of these probes and are discussed below.

Following in 1998, the development of 1.7 mm gradient submicro inverse-detection or SMIDG NMR probes was reported.[17,18] This probe design returned to the 1.7 mm format pioneered in the 1970's by Shoolery.[2] The SMIDG probe design employs a conventional 1.7 mm NMR tube format that can be inserted pneumatically as with 5 mm or 3 mm micro NMR probes. Sample volumes range from 22–30 μl depending on the coil dimensions and allow ~78% of the sample to be located within the coil volume when careful sample positioning and shimming are done. In one of the original reports, an 8% cryptolepinone impurity contained in a 0.55 μmole sample of cryptolepine was fully characterized by a combination of GHMQC and GHMBC experiments despite the dynamic range problems inherent to the sample.[18] The SMIDG probe has also been used for a number of low-level, long-range $^{1}H-^{15}N$ 2D NMR studies at natural abundance, dramatically lowering sample requirements for this very insensitive experiment.[19,20] A number of applications of 1.7 mm SMIDG NMR probe technology for natural product and pharmaceutical impurity characterization have been reported and are discussed below.

In 2001, the development of a 1 mm gradient inverse NMR probe was reported.[21] Using this probe technology, it was possible to record the HMQC spectrum of a 1 μg sample of ibuprofen **(3)** overnight. To date, there have not been any reported applications of this probe technology to the best of the author's knowledge.

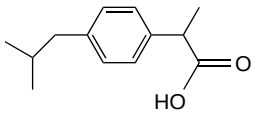

(3)

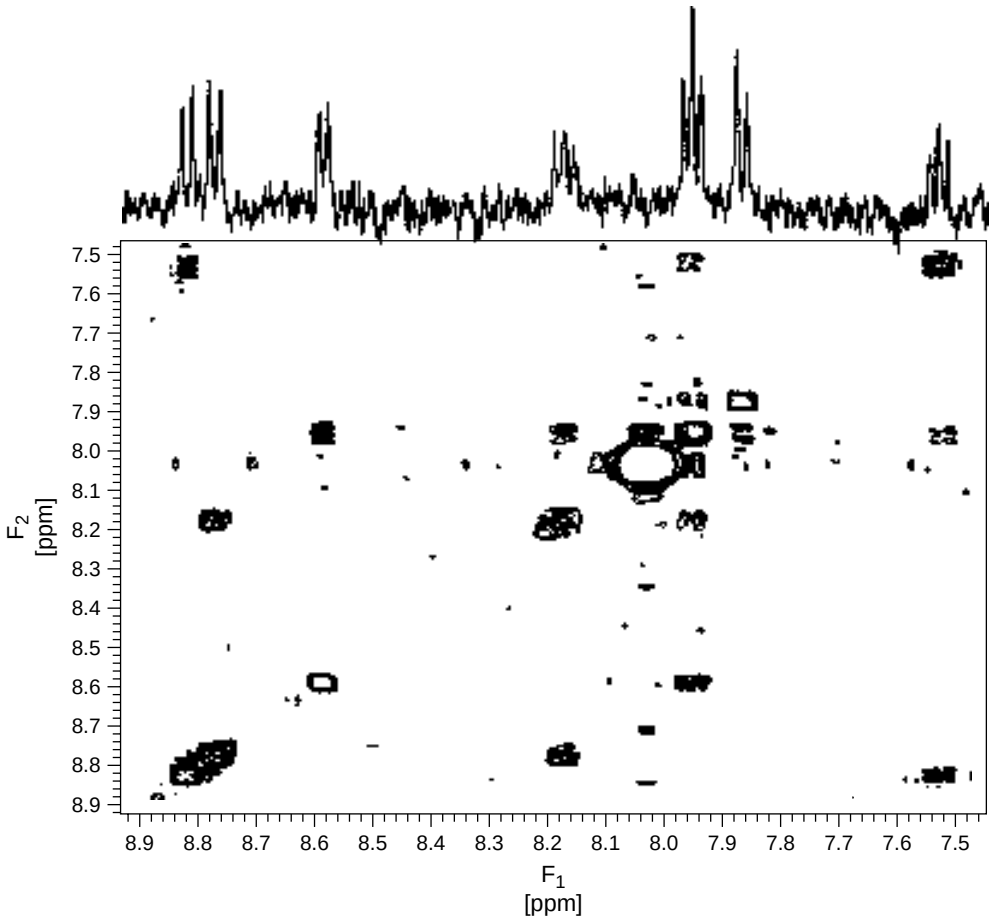

Figure 4 Overnight COSY spectrum obtained using a 200 ng sample of the simple alkaloid cryptolepine **(1)** dissolved in 40 μl d_6-DMSO and acquired using a Varian Nano-probe™

More recently, intensive effort has been directed toward the development of cryogenic NMR probes. Thus far, 5 and 3 mm designs have been reported by various manufacturers. Several studies using prototype cryogenic 3 mm probes have been presented as posters[22–24] and several reports have appeared in the published literature.[25,26] Cryogenic NMR probes operate by cooling the rf coils to temperatures in the range of 10–25 K to reduce noise; preamplifiers used in conjunction with these probes are also frequently cooled to temperatures in the range of from 40–60 K. Considerable sensitivity gains are obtained by using this complex and technologically demanding design strategy. Early versions of the 3 mm cryogenic NMR probe tested in the author's laboratory gave s/n ratios for the anomeric proton of a 2 mM sucrose sample in the range of ~180 : 1. More recent designs have given s/n ratios as high as 242 : 1. In comparison, a conventional 3 mm probe can be expected to give s/n ratios in the range of 62–67 : 1 for the same sample tube. The extremely high sensitivity of the cryogenic NMR probes translates to very considerable time savings to achieve identical s/n ratios when compared to conventional NMR probeheads. In the initial report from the author's laboratory using a prototype Nalorac 3 mm CryoSPEC™ (CryoM{H}C500-3) probe[25] a 40 μg sample of strychnine **(4)** was employed as a model compound and HSQC data were acquired. All of the responses were observable in 45 min albeit with noise still present in the spectrum; an essentially noise-free spectrum was recorded in 90 min. In comparison, to achieve a comparable s/n ratio using a conventional 3 mm micro NMR probe, the sample had to be run for 17.5 h, which is a factor of 12.5 in time. These comparative spectra are shown in Figure 5. Although not performed in a small volume probe, still more impressive results have been obtained for long-range $^{1}H-^{15}N$ experiments run on a 2 mg sample of the antibiotic eperezolid **(5)** in 160 μl of solvent in a 3 mm NMR tube run coaxially in

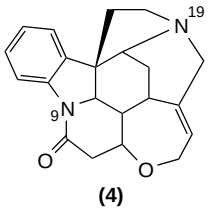

(4)

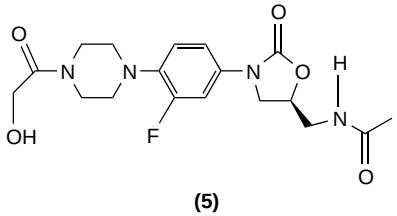

(5)

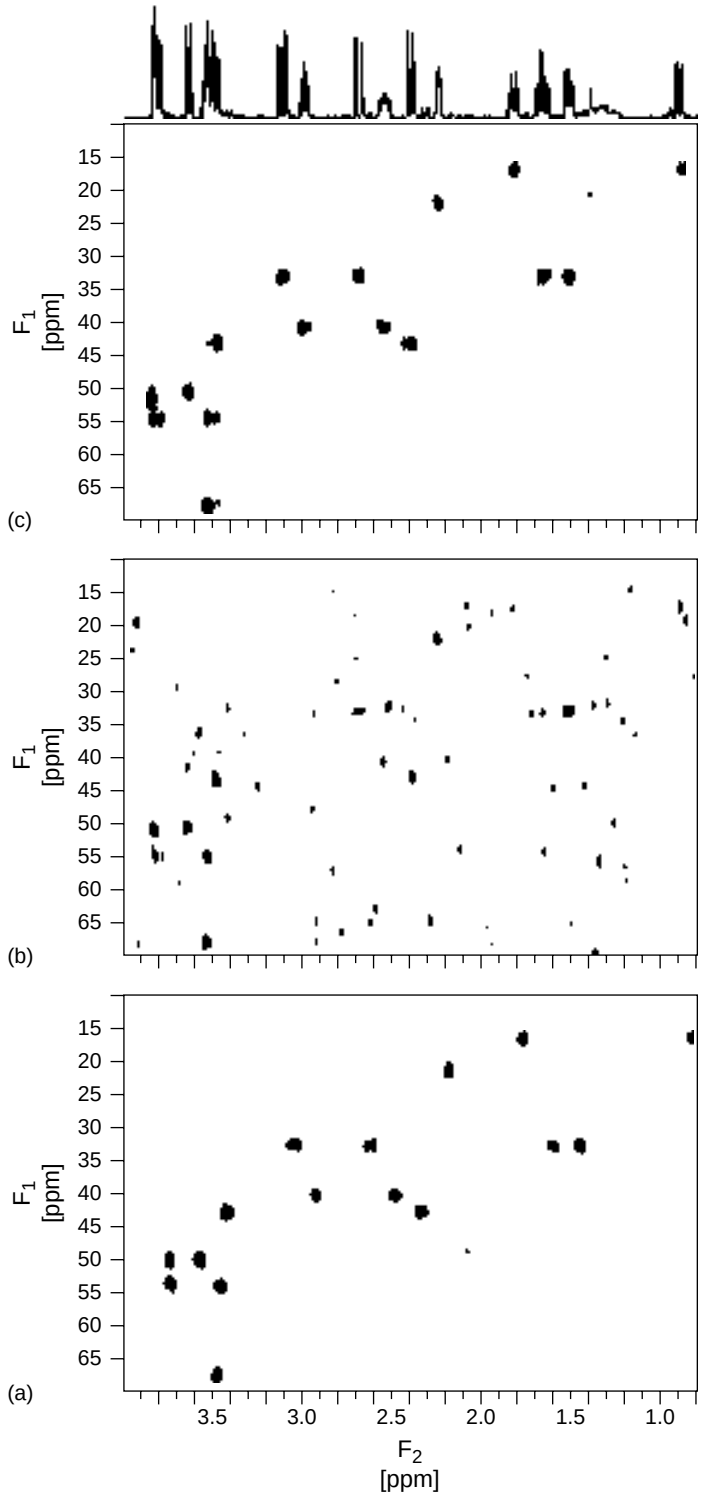

Figure 5 Comparison of 3 mm gradient inverse triple resonance and 3 mm cryoprobe performance comparison using a 40 μg (120 nanomole) sample of strychnine **(4)**. The same sample, prepared by serial dilution, was used for the acquisition of the HSQC spectra (non-gradient) shown in all three panels. The data shown in (a) were acquired by accumulating 32 transients/t_1 increment as 2048 × 48 (hypercomplex files × 2) data points, which were linear predicted to 192 points in the second frequency domain and zero-filled to 256 points during Fourier transformation using a Nalorac CryoSPEC 3 mm cryogenic micro inverse NMR probe. The data acquisition time was 90 min. Data shown in (b) were acquired identically except that a conventional Nalorac MIDTG-500-3 gradient inverse 3 mm triple resonance NMR probe was employed. Processing and scaling were identical to the data presented in (a), obviously lower in quality since these data were acquired using a conventional NMR probe. Data shown in (c) were again acquired using the Nalorac MIDTG-500-3 gradient inverse triple resonance probe except that 352 transients were accumulated/t_1 increment giving an acquisition time of 17.5 h. Processing and scaling were identical to that used to prepare panel (a). S/n ratios in panels (a) (90 min) and (c) (17.5 h) are comparable

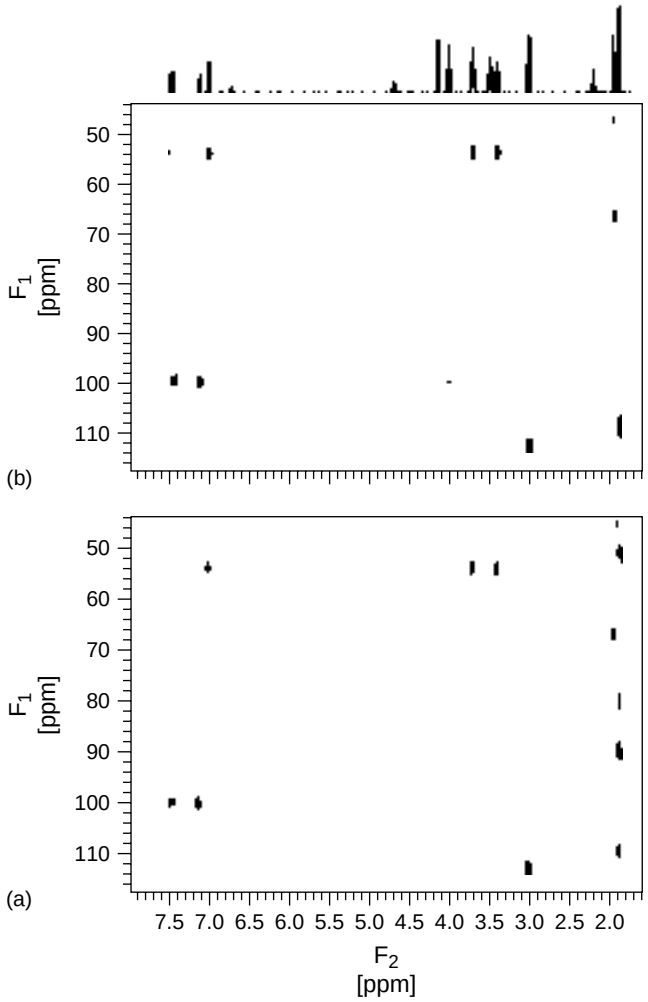

Figure 6 Comparison $^{1}H-^{15}N$ CIGAR-HMBC[27] 5–10 Hz optimized long-range heteronuclear shift correlation data for the oxazolidinone antibiotic eperezolid **(5)** at natural abundance ^{15}N. The data shown in (a) were acquired using a Varian Cryo-Q 500 MHz HN gradient cryogenic NMR probe in 26 min with a s/n ratio of 101 : 1. To acquire comparable s/n data using a conventional Nalorac MIDTG-500-3 gradient inverse triple resonance probe using the same sample required 17 h 40 min (b)

a 5 mm Varian Cryo-Q 500 MHz HN probe.[26] A CIGAR-HMBC[27] spectrum in which all of the anticipated long-range $^{1}H-^{15}N$ 2D NMR responses were observed was recorded in 26 min. To achieve comparable s/n ratio in a conventional 3 mm gradient inverse triple resonance probe required 17 h 40 min, corresponding to a factor of 38 in time. These results are shown in Figure 6.

2 HIGH SENSITIVITY, SMALL VOLUME PROBE PERFORMANCE COMPARISONS

One question that immediately comes to the mind of an investigator when faced with the problem of acquiring NMR data for a small sample is what probe should be used? This question has prompted a number of comparisons of various probe formats since the introduction of the 3 mm micro NMR probes in 1992. A complete set of all possible comparisons is unfortunately not available. Indeed, there are no direct comparisons at all between any of the formats discussed in the contribution vs. any of the μ-coil NMR probes. Nevertheless, those comparisons that have been reported are summarized below.

2.1 3 mm Micro Inverse vs. 5 mm Inverse NMR Probe Performance Comparison

The first comparison of a small volume NMR probe to the standard 5 mm probe was reported in late 1992 following the introduction of the 3 mm micro NMR probes.[6] Using a 1 μmole sample of the simple alkaloid harmane **(2)** dissolved in appropriate volumes of d_6-DMSO for 3 and 5 mm NMR probes, comparison HMQC spectra were recorded. When data were acquired for identical times, the pair of spectra shown in Figure 2 were obtained. The advantage of the 3 mm micro probe over the conventional 5 mm probe when dealing with the 167 μg (1 μmole) sample of harmane **(2)** is obvious. When data were acquired in 12 min (4 transients/t_1 increment, 2048 × (2 × 32) hypercomplex files) using the 3 mm micro inverse probe, it was necessary to acquire data for 69 min (32 transients/t_1 increment 2048 × (2 × 32) hypercomplex files) to achieve comparable performance with a conventional 5 mm inverse-detection probe. These data heralded the beginning of renewed interest in the utilization of high-sensitivity, small volume NMR probes.

2.2 3 mm Micro Dual vs. Heteronuclear Nano-probe Performance Comparison

A rigorous comparison of these probe formats has not been reported. There are, however, several examples in the literature where both probe formats were used to acquire ^{13}C reference spectra. One example is contained in a paper describing the elucidation of the structure of the alkaloid cryptolepicarboline **(6)** from the Ghanaian plant *Cryptolepus sanguinolenta*.[28] The total available sample of the alkaloid was ∼100 μg (∼0.25 μmole). The acquisition of a ^{13}C reference spectrum of the alkaloid sample in 40 μl of d_6-DMSO using a heteronuclear nano-probe was accomplished overnight giving a spectrum with a s/n ratio of 9 : 1. In comparison, the same sample of alkaloid, after transfer to a 3 mm micro NMR probe in the process of which the sample was diluted to 140 μl gave a spectrum with 9 : 1 s/n over a weekend. A similar non-rigorous comparison of the performance of the 3 mm micro dual and heteronuclear nano-probes is found in a report of the characterization of an N-acetyl keto derivative of fumonisin-B_1 **(7)**.[29] An overnight acquisition of a ^{13}C reference spectrum of an ∼200 μg sample of the material gave a carbon spectrum with a s/n ratio of 5.5 : 1 when a 3 mm micro dual probe was employed. Curiously, a ketone carbonyl resonance expected on the basis of mass spectrometric fragmentation data was not observed in the spectrum. The acquisition of the ^{13}C reference spectrum was repeated with the same sample after concentration to 40 μl to allow the use of a heteronuclear nano-probe. The overnight nano-probe acquisition gave a spectrum with a s/n ratio of 11 : 1 and the carbonyl resonance at 219.5 ppm was observed in the spectrum. These data are presented in Figure 7. There is no obvious reason why carbonyl resonance wasn't observed in the spectrum recorded using the 3 mm micro dual probe;

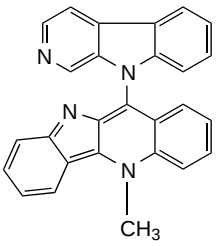

(6)

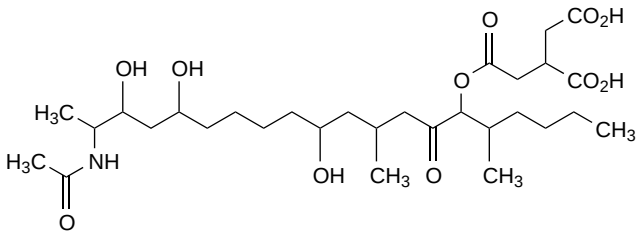

(7)

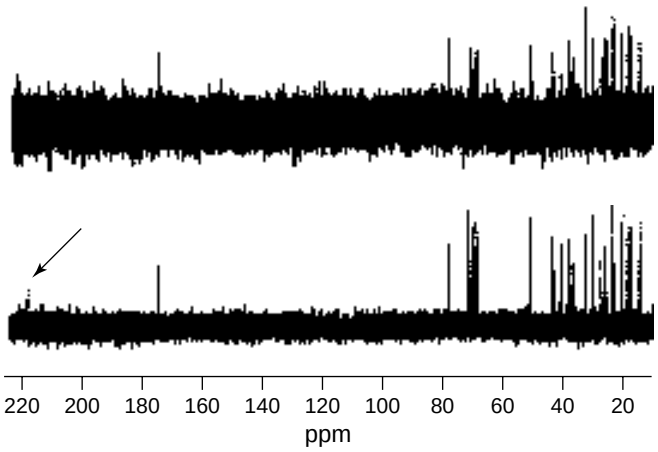

Figure 7 Overnight ^{13}C reference spectra of an ~200 μg sample of a secondary fungal metabolite, fumonisin-B_1 **(7)**, in D_2O. The data shown in the top panel were acquired using a 3 mm micro dual NMR probe in 145 μl of solvent and gave a signal-to-noise ratio of 5.5 : 1. A ketone carbonyl resonance expected on the basis of mass spectrometric fragmentation data was not observed in the spectrum. Following the concentration of the sample to 40 μl to allow the use of a heteronuclear Nano-probe™, the data shown in the bottom panel were acquired. The overnight Nano-probe™ acquisition gave a spectrum with a s/n ratio of 11 : 1 and the carbonyl resonance at 219.5 ppm was observed in the spectrum

the relaxation delay between transients was identical. From these data, however, it can be concluded that the per transient efficiency of the conventional micro dual probe is somewhat better than that of the nano-probe. This conclusion derives from the nearly four-fold concentration of the sample for acquisition of the nano-probe data. If probe efficiencies were identical, a s/n ratio for the nano-probe approaching 22 : 1 should have been obtained on the basis of the concentration factors.

2.3 1.7 mm SMIDG vs. 3 mm Micro Inverse Probe Performance Comparison

A rigorous comparison of the 1.7 mm submicro gradient inverse or SMIDG and a 3 mm micro inverse detection NMR probes has been reported for both $^{1}H-^{13}C$ direct and long-range and $^{1}H-^{15}N$ long-range heteronuclear shift correlation experiments.[30] In addition, the results obtainable by running a 1.7 mm sample coaxially in a 3 mm micro probe were also reported in this study. Using an 0.5 μmole sample of the non-steroidal anti-inflammatory agent ibuprofen **(3)** in either 30 or 150 μl of d_6-DMSO, gradient $^{1}H-^{13}C$ HSQC spectra were acquired using both probes. Data accumulation for the three experiments performed was 48 min for each spectrum. Using the 1.7 mm SMIDG probe, a s/n ratio of 148 : 1 was obtained. All of the expected responses were observed in the spectrum, including that of the relatively weak *sec*-butyl methine resonance. When the 1.7 mm sample was run in the 3 mm micro inverse probe, again all of the responses were observed; the s/n ratio was 75 : 1. When the GHSQC data were acquired using the 3 mm micro inverse probe, the *sec*-butyl methine resonance was absent from the spectrum; the s/n ratio was 62 : 1. Similar results were obtained for the same series of $^{1}H-^{13}C$ GHSQC experiments using a 1 μmole sample of strychnine **(4)**. These comparison GHSQC spectra are presented and described in Figure 8.

Using a 1 mg sample of strychnine **(4)**, long-range $^{1}H-^{15}N$ GHMBC experiments were also performed using both the 1.7 mm SMIDG and the 3 mm micro inverse probes; these data are presented in Figure 9. The 1.7 mm SMIDG data gave all of the expected long-range $^{1}H-^{15}N$ responses;[30–33] all responses were well above the noise floor of the spectrum. When the 1 mg sample in the 1.7 mm tube was run coaxially in the 3 mm micro inverse probe, again, all of the expected long-range responses to the two strychnine nitrogen resonances were observed although there were some noise spikes contained in the spectrum with comparable intensity to the desired, long-range responses. For the 3 mm sample, all but one of the expected long-range responses was observed. However, there were substantial numbers of spurious peaks with greater intensity than the desired long-range responses. It was concluded that a sample containing ~3 μmoles (~1 mg in the case of strychnine) was borderline for an overnight long-range $^{1}H-^{15}N$ 2D NMR experiment at natural abundance in a 3 mm probe.

2.4 Conventional vs. Cryogenic NMR Probe Performance Comparison

To date there are two studies in the literature that report comparisons of conventional and cryogenic NMR probe performance. The first is a direct comparison of 3 mm cryogenic inverse and conventional 3 mm inverse-detection probes.[25] Using a 40 μg (120 nanomoles) sample of strychnine dissolved in 150 μl d_6-benzene, identical HSQC spectra were recorded using a Nalorac 3 mm CryoSPEC inverse probe and a conventional Nalorac Z•SPEC™ MIDTG-500-3 gradient inverse-detection probe. With the cryogenic probe, all of the aliphatic direct correlation responses were observable within 45 min and a noise-free spectrum was obtained in 90 min. To achieve a comparable s/n ratio using the conventional probe required 17 h of data acquisition. With the initial prototype

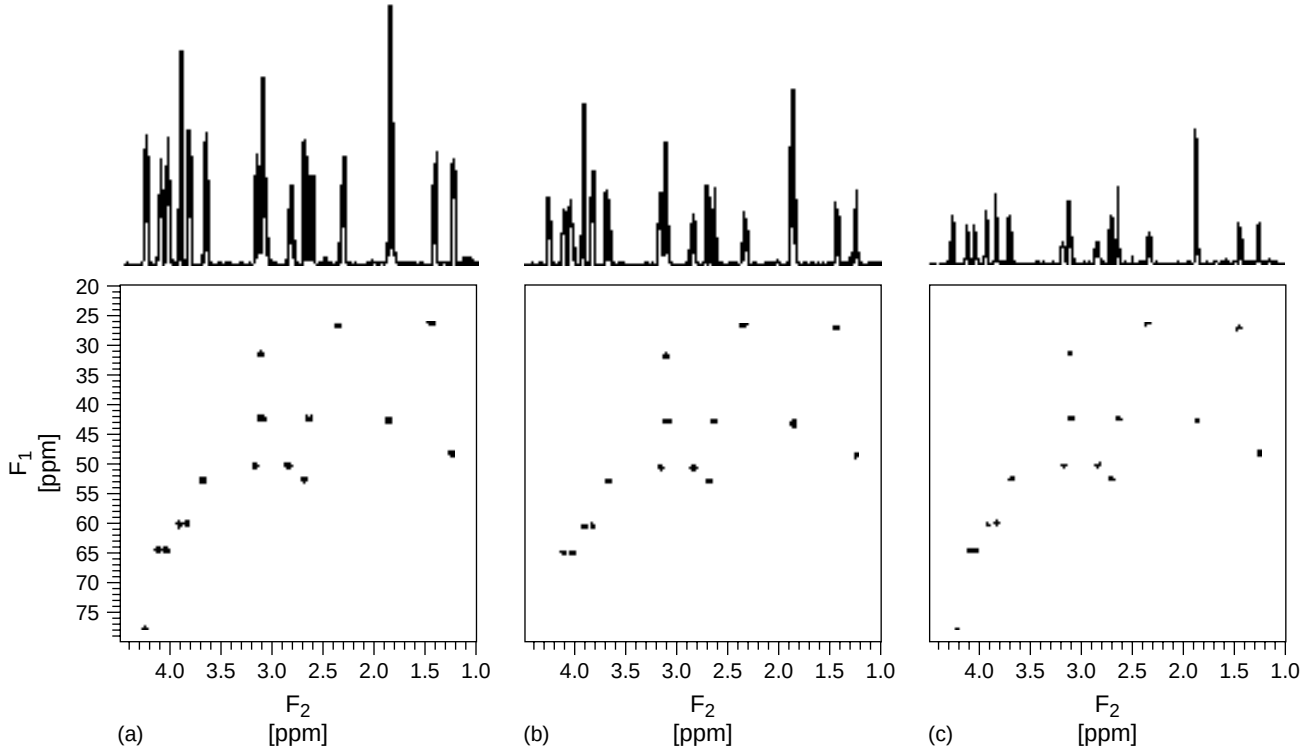

Figure 8 Comparison 600 MHz $^{1}H-^{13}C$ GHSQC spectra acquired for a 1 μmol sample of strychnine **(4)** in $CDCl_3$ in either a 1.7 or 3 mm NMR tube in a volume appropriate to the tube format. All data were acquired by accumulating four transients at each of 64 increments of the evolution time, t_1, giving identical data acquisition times. All data were processed and scaled identically to prepare the three panels shown. Data shown in (a) were acquired using a 1.7 mm sample in a Nalorac SMIDG-600-1.7 submicro gradient inverse detection NMR probe; using the region from 5.5 to 4.5 ppm as representative noise, the s/n ratio for this spectrum was 112 : 1. The data shown in (b) were acquired by running the 1.7 mm sample coaxially in a conventional Nalorac MIDTG-600-3 gradient triple resonance micro inverse NMR probe. The s/n ratio for these data was 75 : 1. Finally, the data shown in (c) were acquired using a 1 μmol sample in a 3 mm tube, the data again acquired using the conventional Nalorac MIDTG-600-3 probe. The s/n ratio for this experiment was 62 : 1. Projections through the F_2 frequency domain are plotted above each of the contour plots to provide a more effective portrayal of the relative s/n ratio in the three experiments

cryoprobe used for this comparison, a 3.5 × improvement in signal-to-noise was afforded by the cryoprobe, which corresponds to a 12.5-fold time advantage to equivalent signal-to-noise. The comparison 90 min HSQC spectra are shown in Figure 5.

More recently, a comparison was drawn for the acquisition of long-range $^{1}H-^{15}N$ 2D experiments at natural abundance.[26] Using a 2 mg sample of the oxazolidinone antibiotic eperezolid **(5)** dissolved in 160 μl d_3-acetonitrile in a 3 mm NMR, $^{1}H-^{15}N$ CIGAR-HMBC 2D NMR spectra optimized for a long-range coupling range of from 5 to 10 Hz[34–36] were acquired using a Varian 5 mm Cryo-Q HN probe (because of the considerable variability of long-range $^{1}H-^{15}N$ couplings, it is advisable to use an accordion-optimized long-range 2D NMR experiment such as IMPEACH-MBC or CIGAR-HMBC to record long-range $^{1}H-^{15}N$ 2D NMR spectra at natural abundance. See Ref.[34]). In less than 10 min, most of the anticipated long-range $^{1}H-^{15}N$ responses were observed. A second experiment run in 26 min afforded a spectrum with 101 : 1 (projecting through the F_1 or ^{15}N frequency domain) s/n in which even the weakest response had ∼40 : 1 s/n. Acquisition of a 26 min data set using a conventional Nalorac Z•SPEC MIDTG-500-3 gradient inverse probe gave only the N7-9CH_3 response. A longer 4 h experiment gave all of the expected long-range responses albeit with <50 : 1 s/n. To attain a s/n ratio comparable to that of the 26 min cryoprobe experiment, it was necessary to acquire data with the conventional 3 mm probe for 17 h 40 min (112 : 1 s/n). A comparison of the 26 min 5 mm cryoprobe data with the 17 h 40 min 3 mm $^{1}H-^{15}N$ CIGAR-HMBC spectra optimized over the range of 5–10 Hz is shown in Figure 6. Thus, for long-range $^{1}H-^{15}N$ experiments, the cryogenic NMR probe afforded a >38× time advantage relative to a conventional 3 mm micro probe despite potential losses of signal due to filling factor associated with running a 3 mm tube coaxially in the 5 mm probe. Unfortunately, at present, it is not possible to make a direct comparison of 3 mm NMR probes for long-range $^{1}H-^{15}N$ 2D NMR experiments at natural abundance as a 3 mm cryogenic NMR probe with an X-coil tunable to ^{15}N or doubly tuned to ^{13}C and ^{15}N has yet to be developed.

While 5 mm cryogenic NMR probes are not in the category of small volume NMR probes by any means, the extremely high sensitivity which they offer makes them competitive when dealing with small samples, particularly when 3 mm tubes are run coaxially or specialized micro cells are employed to restrict sample volume. To date, there have not been any reports of tubes smaller than 3 mm in diameter being run coaxially in a cryogenic probe; it is likely that filling factor losses would substantially offset the gains in sensitivity offered by the probe if a small tube such as 1.7 mm were run coaxially in a 5 mm cryogenic probe. Thus, it is likely that as cryogenic probes

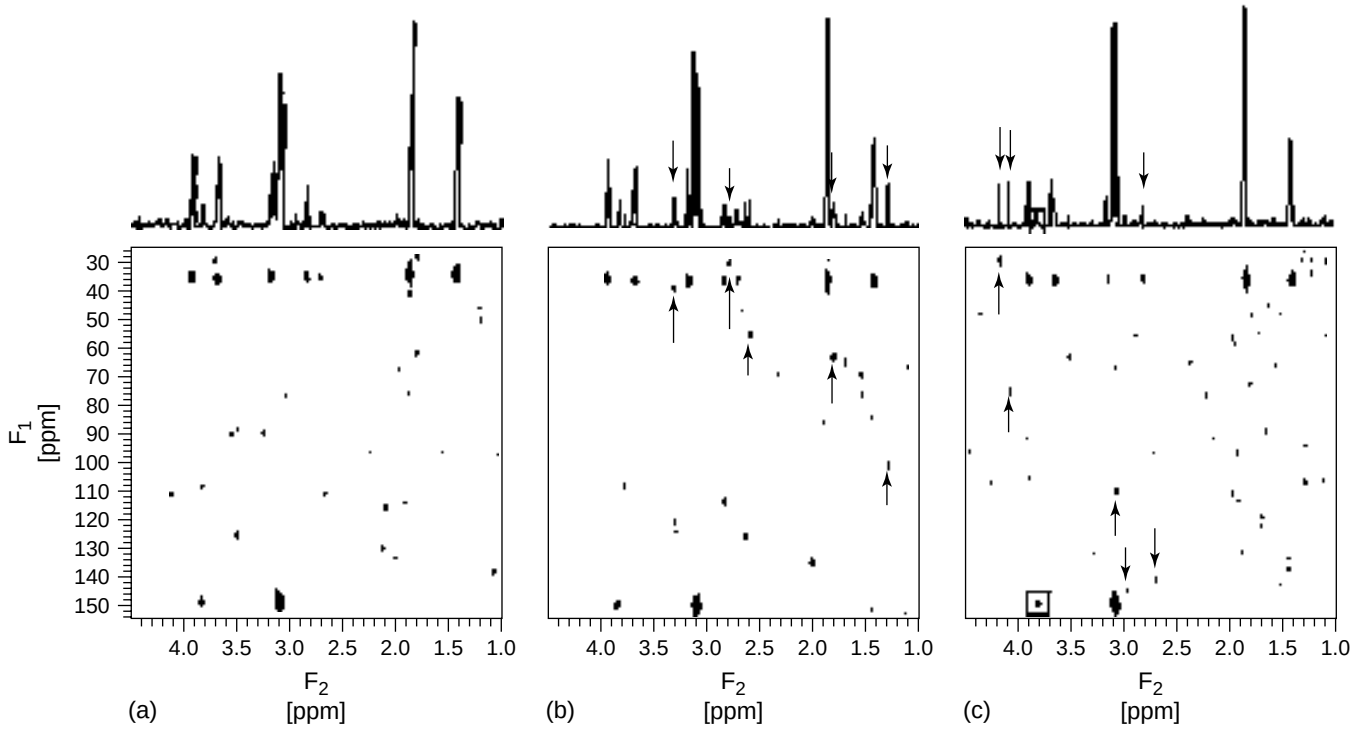

Figure 9 Comparison $^{1}H-^{15}N$ 8 Hz optimized GHMBC spectra of 3 μmole samples of strychnine **(4)** at natural abundance prepared in either a 1.7 or 3 mm NMR tube in a volume appropriate to the tube format. All spectra were recorded at 600 MHz, accumulating 4096 transients for each of 40 increments of the evolution time, t_1, giving identical 18 h data acquisitions. The data shown in (a) were acquired using a 1.7 mm sample in a Nalorac SMIDG-600-3 gradient inverse submicro NMR probe. Again using the region of the proton spectrum from 5.5 to 4.5 ppm for representative noise, the SMIDG data gave a s/n ratio of 60 : 1. All anticipated responses were observed either directly in the contour plot or readily in the traces from the N9 amide or N19 aliphatic nitrogen resonances. When the 1.7 mm sample was run coaxially in a Nalorac MIDTG-600-3 gradient inverse triple resonance probe, the data shown in (b) were obtained, giving a s/n ratio of 41 : 1. Some spurious responses are observed in the projection through F_2 as well as in the contour plot. Finally, when a 3 mm sample was used in a 3 mm probe, the result shown in (c) was obtained. In this case, spurious responses in the projection are of greater intensity than some legitimate responses, suggesting that either a longer data acquisition or larger sample would be desirable with this probe technology to obtain reliable data. The s/n ratio of the spectrum shown in (c) was 26 : 1

become more widely available that 5 mm versions of this probe technology will be used to deal with small NMR samples in those labs not equipped with more specialized probeheads.

2.5 Conventional NMR Tubes vs. Specialized Sample Cells

One alternative available to researchers without access to any of the specialized NMR probeheads described in this contribution is to use a specialized sample cell to restrict overall sample volume, thereby keeping a greater percentage of a scarce sample within the confines of the rf coils of the probe being used. Various tactics have been employed to achieve this goal. Approaches have included the development of plastic NMR tube inserts, the properties of which are matched as closely as possible to those of the solvent being employed. Shigemi, using a more novel approach, has employed specialized glass that matches the magnetic susceptibility of several NMR solvents, to make both the NMR tube and a precision bore 'plunger'. Tubes have been manufactured thus far for use with $CDCl_3$, CD_3OD, D_2O and d_6-DMSO. With a conventional 5 mm NMR tube, sample volumes can be reduced from ~500 μl to roughly 225–250 μl. The resulting two-fold increase in sample concentration will correspondingly quarter acquisition time to a given s/n ratio.

To date, two studies have appeared in the literature that compare the results obtainable with normal NMR tubes vs. specialized NMR cells. The earliest report was a study of Caribbean ciguatoxin.[37] A substantial improvement in the HMQC data that could be recorded for an ~0.95 μmole sample of Caribbean ciguatoxin was noted when the data were acquired in 67 μl d_5-pyridine when the sample was run in a 3 mm Shigemi D_2O-matched micro NMR cell (despite the mismatch of the solvent to the optimization of the micro cell) vs. data acquired in 120 μl in a conventional 3 mm NMR tube. No quantitative comparison was drawn. A similar improvement was noted by Reynolds, Yu and Enriquez[38] for ^{13}C-detected 2D heteronuclear NMR experiments when run in Shigemi micro NMR cells vs. data acquired in normal 3 mm NMR tubes. Although 1.7 mm Shigemi cells have been developed, there have not been any reported applications of this type of tube in the literature.

3 APPLICATIONS OF SMALL VOLUME NMR PROBES IN THE SOLUTION OF CHEMICAL STRUCTURE PROBLEMS

There is a wide range of potential applicability of specialized NMR probe technology in the solution of structural

problems, not all of which have yet been reported. Some research areas where specialized NMR probe heads can be highly advantageous include: characterization of scarce natural product samples; identification of metabolites of pharmaceuticals; characterization of forensic samples; protein characterization; and the identification of chemically unstable species. Given that the first of the new generation of small volume specialized probes to be described were the 3 mm micro inverse and dual probes, applications utilizing these probeheads will be surveyed first, followed by applications utilizing Nano-probe technology. To date, there have not been any applications of μ-coil probes in the solution of structural problems of which the author is aware. The examples that have been reported in conjunction with the development of this probe technology will be summarized next. Examples of potential applications and structural problems solved using 1.7 mm SMIDG probes, and then cryogenic probe applications will complete this section.

3.1 Existing Reviews

Several reviews have been published that deal with either probe-specific or the general topic of small sample NMR spectroscopy.[39–44] Various aspects of dealing with small samples by NMR have also been discussed in reviews of specific classes of molecules, which include alkaloids,[45] carbohydrates,[46] and a recent review of long-range $^{1}H-^{15}N$ 2D NMR applications.[47]

3.2 Applications of 3 mm Micro Probes

Following the initial reports on the development of 3 mm micro NMR probe technology in the authors laboratories, then at Burroughs Wellcome, Co., the first reported 'real world' application of this technology was in the characterization of a 30 μg (0.07 μmoles) metabolite sample through the use of a combination of 3 mm micro and heteronuclear nano-nmr probe technology.[48] A heteronuclear nano-nmr probe was used to record a ^{13}C reference spectrum and a homonuclear nano-nmr probe was used to record a COSY spectrum. Following transfer of the sample and dilution to 120 μl, heteronuclear shift correlation spectra were recorded using a 3 mm micro inverse NMR probe. In 1995, the structure of an N-acetyl keto derivative of fumonisin-B_1 **(7)** was determined, again using a combination of probeheads. Two-dimensional NMR spectra were recorded using a 3 mm micro probe while a ^{13}C reference spectrum was recorded using both a 3 mm micro dual and heteronuclear nano-nmr probe. Interestingly, the keto resonance at 219 ppm was not observed in the data from the 3 mm micro dual probe while it was readily observed in the data recorded with the nano-nmr probe.[28] Later in 1995, the structure of the complex indoloquinoline alkaloid cryptolepicarboline was reported.[27] The homo- and heteronuclear 2D NMR data were recorded using a 3 mm micro inverse nmr probe. A comparison of the ^{13}C spectra recorded using a 3 mm micro dual and heteronuclear nano-nmr probe were also contained in the report.[27] Later in 1995, in a report by the author and co-workers[37] the benefits of using reduced volume Shigemi micro nmr cells was reported in the context of a study of Caribbean ciguatoxin. In a related study, the proton and carbon NMR spectra of the marine toxin brevetoxin-2 were fully assigned on less than 1 μmole of material through the use of 3 mm micro nmr probe technology.[49]

Late in 1995, the structure of the indolobenzazepine alkaloid homocryptolepinone, which serves as a structural component of the complex spiro nonacyclic alkaloid cryptospirolepine, was reported.[50] Continuing in the indoloquinoline series of alkaloids in 1996, two new members of this series with novel ring fusion between the indole and quinoline portions of the molecule were reported.[51] Cryptosanguinolentine was based on an indolo[3,2*c*]quinoline ring fusion rather than the more common [3,2-*b*] ring fusion. Cryptotakiine was based on a indolo[2,3-*b*]quinoline ring system which placed both annular nitrogens on the same side of the molecule. Later in 1996 the structure of the novel, dimeric alkaloid cryptomisrine was reported.[52]

In 1997, Reynolds and co-workers,[38] as noted above, examined the limits of ^{13}C detected heteronuclear shift correlation experiments through the combined usage of 3 mm micro probes and Shigemi micro nmr cells. Although the sensitivity of ^{13}C-detected heteronuclear 2D nmr methods is inarguably lower than that of newer, proton-detected methods, there are still occasions when high digitization requirements in the ^{13}C frequency domain are better addressed by direct ^{13}C detection, provided that sufficient sample is available.[53]

3.3 Applications of Nano-nmr Probes

Magic angle spinning (MAS) liquid NMR probes, or nano-nmr probes as they are frequently referred to *in lieu* of Varian's trademarked Nano-probe™ nomenclature, have been applied in the study of a diverse range of chemical structure problems. A very useful subdivision of these applications is suggested in the review by Keifer.[39] For discussion, it is convenient to separate applications into heterogeneous and homogeneous sample types. The former encompasses samples as diverse as whole cells, tissue samples and solid phase synthesis (SPS) supports used for combinatorial chemistry and related applications. Homogeneous samples, as the name implies, refers to solutions in the usual NMR sense.

3.3.1 Heterogeneous Samples

Nano-nmr probes, which spin at the magic angle (54.7°) at speeds of up to several KHz, are quite useful for the study of heterogeneous samples. The earliest such application, of which the author is aware, is a 1994 report dealing with SPS beads on which the synthetic chemistry was being carried out. The first report, which employed ^{1}H NMR, used a Varian homonuclear Nano-probe.[54] Results that can be obtained with various SPS resins using various types of probes were reported in 1996 by Keifer and co-workers.[55] The effect of tether length between the resin and the synthetic site has been examined[56] as has the use of MAS liquids probes to monitor the extent of reaction completion on SPS supports.[57,58] More recently, Seffler and Gerritz[59] have used 1D and 2D NMR methods to characterize reaction products bound to Chiron SynPhase crowns used in the elaboration of combinatorial chemical libraries. Finally, although not chemically bound, Mohri and co-workers[60] have studied the mobility of surface-adsorbed molecules on insoluble pigment particles using ^{1}H T_1 relaxation measurements in a nano-nmr probe. Reviews on the analysis of materials on solid supports include those of Keifer[39] and Gallop and Fitch.[61]

Another interesting heterogeneous nano-nmr probe application has been used in an attempt to biochemically classify kidney carcinoma biopsy samples.[62] While by no means a rapid analytical or screening tool, this study does provide a glimpse of where the probe technology may be applied in the future.

3.3.2 Homogeneous Samples

Numerous reports of applications of nano-nmr probes to homogeneous solution samples have been reported. Broadly, these applications can be further subgrouped into natural products or small molecules and biomacromolecule studies. One of the first reported small molecule applications was a combined 3 mm micro NMR probe/nano-nmr probe study of a metabolite structure.[48] The 3 mm micro probe was used to record the heteronuclear 2D nmr data on a 30 μg sample of a low molecular weight metabolite while a heteronuclear nano-nmr probe was used to record the ^{13}C reference spectrum. Combined 3 mm micro probe/nano-nmr probe applications have also been reported in the elucidation of a complex indoloquinoline alkaloid structure[27] and a fumonisin-B_1 fungal metabolite structure.[28] In both of these studies, comparative ^{13}C NMR spectra acquired in a 3 mm micro dual probe and a heteronuclear nano-nmr probe are presented. Another combined 3 mm micro probe/nano-nmr probe application is found in the structural characterization of laingolide, a novel 15-membered macrolide from a blue green alga.[63] In this study, the direct and long-range heteronuclear chemical shift correlation experiments were performed in a 3 mm micro probe while the ^{13}C reference spectrum was recorded using a heteronuclear nano-nmr probe.

The sensitivity of heteronuclear nano-nmr probes, combined with the small volume of a nano cell (40 μl) has led to the application of this probe technology for the characterization of a novel steroid skeleton[64] through the use of the INADEQUATE[65,66] experiment.

More recently, several additional applications of nano-nmr probe technology have been reported in the characterization of natural product samples. Bierer and co-workers[67] reported using a nano-nmr probe in the characterization of the indoloquinoline alkaloid cryptolepinone, which was independently characterized by Martin and co-workers[68] using 3 mm micro probe hardware. A modified tetrapeptide, lyngbyapeptin A, has been characterized, in part, using nano-nmr to acquire a ^{13}C reference spectrum.[69] Lyngbapeptin A was described as being produced by a cyanobacterium in 'trace' amounts and thus it is likely that the heteronuclear shift correlation data were recorded using a 3 mm micro NMR probe although this was not specified in the report. Most recently, the structure of a new macrocyclic trichotehcene produced by a marine-derived fungus has been reported.[70] In this case, a Varian Nano-probe was used for the acquisition of all of the NMR data reported, including the heteronuclear shift correlation spectra.

The first reported application of nano-nmr probes in the study of biomacro-molecules is found in the report of Manzi et al.[71] on the identification of a novel glycosaminoglycan core-like molecule. Delepierre and co-workers[72] next reported studies of the structure of a potassium channel blocking toxin (peptide) from the scorpion *Pandinua imperator* using a homonuclear nano-nmr probe. That report was followed by another from the same laboratory that examined the kinetics of secondary structure recovery during the refolding of reduced hen egg white lysozyme.[73] Further work on potassium channel blocking peptide toxins was also reported later in 1997 by Delepierre and co-workers.[74] Delepierre and colleagues[75] next reported the results of a study of renatured lysozyme using nano-nmr techniques. In 1999, Delepierre, et al.,[76] reported the analysis of the structure of Pi7, an orphan peptide from the scorpion *Pandinus imperator* using ^1H nano-nmr methods. Van Halbeek and co-workers[77] initiated studies of glycan classes and their analysis by nano-nmr methods that were first reported in 2000. Finally, the biosynthesis of ganglioside mimics of *Campylobacter jejuni* has been studied at the nanomole level through the use of nano-nmr methods.[78]

Most recently, Kupce et al.[79] have examined the issue of adiabatic TOCSY MAS in liquids, demonstrating that adiabatic mixing sequences are less susceptible to modulation effects due to both rf and magnetic field homogeneities than are conventional mixing sequences.

3.4 Applications of Small Volume Cryoprobes

To date, only a scant few reports on the use of small volume cryogenic NMR probes have been reported. Withers and co-workers[22–24] have presented several posters describing the utilization of a 2.5 or 3 mm cryogenic probes for the acquisition of heteronuclear shift correlation data needed for metabolite characterization. The author and colleagues[25] have reported a comparison of conventional and cryogenic 3 mm NMR probes using a 40 μg (120 nanomoles) sample of strychnine **(4)** shown in Figure 5. Finally, although not using a small volume cryogenic probe, the author and co-workers[26] have reported a comparison of long-range $^1H-^{15}N$ heteronuclear shift correlation data (shown in Figure 6) acquired using a 3 mm sample in both a 5 mm cryogenic and conventional 3 mm NMR probes. Undoubtedly more applications of small volume cryogenic probes will appear given the substantial sensitivity advantage which these probes afford.

3.5 Phase Cycled vs. Gradient NMR Experiments When Dealing with Very Small Samples

Work in the author's laboratories at Pharmacia, directed to the characterization of very small samples of isolated and impurities of potential drug candidates, has shown that at very low concentrations the use of gradient NMR experiments is disadvantageous. Reynolds and Enriquez[80] after a discussion of this observation have gone on to report a rigorous experimental verification of this observation. They demonstrated that at high concentrations, the t_1 ridges due to incomplete suppression of $^1H-^{12}C$ components of magnetization (or that from protons bound to heteroatoms) constitutes the main source of noise in phase-cycled 2D NMR spectra. Gradient NMR pulse sequences strongly suppress this noise, as would be expected. This observation is consistent with the generally accepted advantage of gradient-based NMR experiments when only a few transients/t_1 increment will be accumulated. However, as also reported by Reynolds and Enriquez, the intensity of the t_1 ridges appears to be directly proportional to the signal strength and consequently, for very dilute samples, t_1 ridges contribute to the total noise in an HMBC experiment to only a minor extent. When sufficient numbers of transients are accumulated

per t_1 increment, the intrinsically higher sensitivity of phase-cycled experiments vs. gradient-based experiments makes the former preferable.

To illustrate this observation rather dramatically, Russell[81] has recorded gradient and phase-cycled HMBC data for a 20 μg sample of retrorscine **(8)**. These data are shown in Figure 10 compared to data from a 700 μg sample of the same molecule. The 700 μg data were acquired overnight at 500 MHz using a conventional Nalorac MIDTG-500-3 gradient micro inverse 3 mm NMR probe and provide a references for the responses expected to be observed in the spectrum.

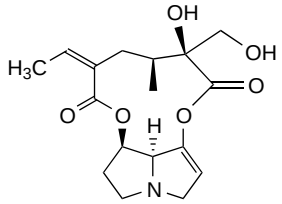

(8)

The reference gradient HMBC spectrum acquired overnight using the 700 μg sample of the alkaloid is shown in Figure 10 Panel a and contains all of the responses expected for the molecule. The phase-cycled, non-gradient HMBC spectrum acquired using a 20 μg sample of the alkaloid in 160 h is shown in Panel b. A significant percentage of the possible responses are observed in the spectrum, particularly when traces for the individual carbons are extracted from the data matrix. In contrast, the gradient HMBC spectrum on the same 20 μg sample after an identical data acquisition, shown in Panel c, shows only the most intense responses in the spectrum. This result is consistent with the work of Reynolds and Enriquez[80] which was done with substantially larger samples.

4 CONCLUSIONS

Small volume, high sensitivity NMR probes have had a significant impact on the conduct of research in many areas of chemistry and biochemistry that depends on NMR methods since the first reports on the contemporary versions of these probes appeared about a decade ago. Probes have been developed in a number of formats for conventional tube configurations including 3, 2.5, 1.7 and 1 mm. New probe technologies such as Varian's Nano-probe and the μ-Coil probes have also been reported. The development of small volume, cryogenic NMR probes is now on-going. With the continuing developments and refinements in this rapidly advancing field of NMR research, sample requirements have concomitantly decreased. COSY spectra on samples as small as 200 ng of cryptolepine **(1)**, HMQC spectra on 1 μg of ibuprofen **(3)**, and HMBC spectra on 6 μg of cryptolepinone, an oxidative degradation product contained in a sample of cryptolepine **(1)** have been discussed in this report. While it is difficult to foresee how much further sample requirements will diminish in the coming years, it is assured that with the advent of small volume, cryogenic NMR probes that the frequency of studies with very small samples will increase in the near future.

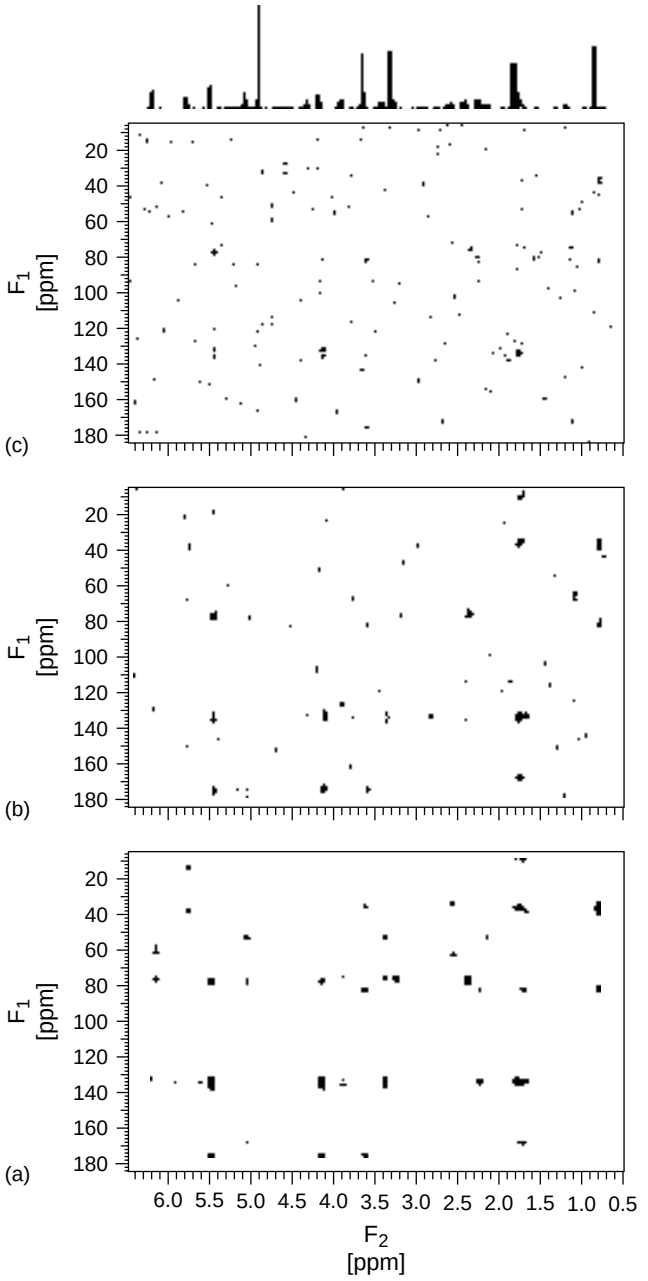

Figure 10 Comparison HMBC spectra of retrorscine **(8)**.[81] The 8 Hz optimized gradient HMBC reference spectrum shown in panel (a) was acquired overnight using a 700 μg sample of the alkaloid dissolved in 150 μl of d_4-methanol. The data shown in panels (b) and (c) were accumulated using a 20 μg sample of the alkaloid dissolved in 150 μl of d_4-methanol. The data shown in panel (b) were acquired using a conventional phase-cycled, non-gradient HMBC pulse sequence. In comparison, the data shown in panel (c) were obtained using the more contemporary gradient HMBC experiment. The superior performance at these low levels of the phase-cycled non-gradient HMBC experiment is consistent with the recent report of Reynolds and Enriquez[80]

5 REFERENCES

1. E. Odelblad, 'Nordisk Forening for Obsterik och Gyynekologi', Karolinska Institute: Stockholm, 1966.
2. J. N. Shoolery, 'Topics in Carbon-13 NMR Spectroscopy', ed G. C. Levy, Wiley: New York, 1979, Vol. 3, p 28.

3. R. C. Crouch and G. E. Martin, *J. Nat. Prod.*, 1992, **55**, 1343.
4. A. Bax and S. Subramanian, *J. Magn. Reson.*, 1986, **67**, 565.
5. A. Bax and M. F. Summers, *J. Magn. Reson.*, 1986, **108**, 2093.
6. R. C. Crouch and G. E. Martin, *Magn. Reson. Chem.*, 1992, **30**, S66.
7. T. Barbara, *J. Magn. Reson.*, 1994, **109A**, 265.
8. J. N. Shoolery, *Prog. NMR Spectrosc.*, 1995, **28**, 37.
9. P. A. Kifer, L. Baltusis, D. M. Rice, A. A. Tymiak, and J. N. Shoolery, *J. Magn. Reson.*, 1996, **119A**, 65.
10. G. E. Martin, unpublished results, 1995.
11. V. V. Krishnamurthy, unpublished results, 1998.
12. D. L. Olson, T. L. Peck, A. G. Webb, R. L. Magin, and J. V. Sweedler, *Science*, 1995, **270**, 1967.
13. R. Subramanian and A. G. Webb, *Anal. Chem.*, 1998, **70**, 2454.
14. Y. Li, A. M. Wolters, P. V. Malawey, J. V. Sweedler, and A. G. Webb, *Anal. Chem.*, 1999, **71**, 4815.
15. B. Behnia and A. G. Webb, *Anal. Chem.*, 1998, **70**, 5326.
16. R. Subramanian, J. V. Sweedler, and A. G. Webb, *J. Am. Chem. Soc.*, 1999, **121**, 2333.
17. G. E. Martin, R. C. Crouch, and A. P. Zens, *Magn. Reson. Chem.*, 1998, **36**, 551.
18. G. E. Martin, J. E. Guido, R. H. Robins, M. H. M. Sharaf, A. N. Tackie, and P. L. Schiff, Jr., *J. Nat. Prod.*, 1998, **61**, 555.
19. C. E. Hadden and G. E. Martin, *J. Nat. Prod.*, 1998, **61**, 969.
20. C. E. Hadden and G. E. Martin, *Magn. Reson. Chem.*, 1999, **37**, 385.
21. G. Schlotterbeck, A. Ross, H. Senn, R. Hochstrasser, H. Tschirky, R. Seydoux, D. Marek, T. Kühn, O. Schett, and M. Warden, *42nd Experimental Nuclear Magnetic Resonance Conference*, Orlando, FL, March 11–16, 2001, Abst. W&Th, p 143.
22. J. Pease, R. Withers, R. Nast, A. Deese, P. Calderon, M. Saumil, T. Kelly, and F. Laukein, *40th Experimental Nuclear Magnetic Resonance Conference*, Orlando, FL, February 28–March 5, 1999, Abst. W&Th, p 202.
23. Y. Liu, J. Pease, B. Potts, A. Deese, Y. D. Liu, M. O'Neil-Johnson, R. Withers, and R. Nast, *SMASH 2000 – Small Molecule NMR Conference*, Argonne, IL, July 16–19, Abstr. 21.
24. M. A. O'Neil-Johnson, J. Pease, Y. Liu, B. Potts, A. Deese, R. Withers, and R. Nast, *42nd Experimental Nuclear Magnetic Resonance Conference*, Orlando, FL, March 11–16, 2001, Abst. W&Th, p 162.
25. D. J. Russell, C. E. Hadden, G. E. Martin, A. A. Gibson, A. P. Zens, and J. L. Carolan, *J. Nat. Prod.*, 2000, **63**, 1047.
26. R. C. Crouch, W. Llanos, K. G. Mehr, Chad E. Hadden, D. J. Russell, and G. E. Martin, *Magn. Reson. Chem.*, 2001, **39**, 555.
27. For a review of accordion-optimized long-range heteronuclear 2D NMR experiments, see G. E. Martin, in *Annu. Rep. NMR Spectrosc.*, ed G. A. Webb, Academic Press: New York, 2000, Vol. H6, pp. 37–100.
28. M. H. M. Sharaf, P. L. Schiff, Jr., A. N. Tackie, C. H. Phoebe, Jr., L. Howard, C. Meyers, C. E. Hadden, S. K. Wrenn, A. O. Davis, C. W. Andrews, D. Minick, R. L. Johnson, J. P. Shockcor, R. C. Crouch, and G. E. Martin, *Magn. Reson. Chem.*, 1995, **33**, 767.
29. S. M. Musser, R. M. Eppley, E. P. Mazzola, C. E. Hadden, J. P. Shockcor, R. C. Crouch, and G. E. Martin, *J. Nat. Prod.*, 1995, **58**, 1392.
30. G. E. Martin and C. E. Hadden, *Magn. Reson. Chem.*, 1999, **37**, 721.
31. G. E. Martin, R. C. Crouch, and C. W. Andrews, *J. Heterocyclic Chem.*, 1995, **32**, 1759.
32. H. Koshino and J. Uzawa, *Kagaku to Seibutsu*, 1995, **33**, 252.
33. C. E. Hadden and G. E. Martin, *J. Nat. Prod.*, 1998, **61**, 969.
34. G. E. Martin and C. E. Hadden, *Magn. Reson. Chem.*, 2000, **38**, 251.
35. C. E. Hadden, G. E. Martin, and V. V. Krishnamurthy, *J. Magn. Reson.*, 1999, **140**, 274.
36. C. E. Hadden, G. E. Martin, and V. V. Krishnamurthy, *Magn. Reson. Chem.*, 2000, **38**, 143.
37. R. C. Crouch, G. E. Martin, S. M. Musser, H. R. Grenade, and R. W. Dickey, *Tetrahedron Lett.*, 1995, **38**, 6827.
38. W. F. Reynolds, M. Yu, and R. G. Enriquez, *Magn. Reson. Chem.*, 1997, **35**, 614.
39. P. A. Keifer, *Drug Discovery Today*, 1997, **2**, 468.
40. P. A. Keifer, *Curr. Opin. Biotech.*, 1997, **10**, 34.
41. N. Wu, T. L. Peck, A. G. Webb, R. L. Magin, and J. V. Sweedler, *Anal. Chem.*, 1994, **66**, 3849.
42. D. L. Olson, M. E. Lacey, and J. V. Sweedler, *Anal. Chem.*, 1998, **70**, A257.
43. M. E. Lacey, R. Subramanian, D. L. Olson, A. G. Webb, and J. V. Sweedler, *Chem. Rev.*, 1999, **99**, 3133.
44. M. Delepierre, *J. Chim. Phys.*, 1998, **95**, 235.
45. G. E. Martin and R. C. Crouch, in 'Modern Methods of Plant Analysis', eds H. F. Linskens and J. F. Jackson, Springer-Verlag: Berlin, 1994, Vol. 15, pp. 25–89.
46. J. Ø. Duus, C. H. Gotfredsen, and K. Bock, *Chem. Rev.*, 2000, **100**, 4589.
47. G. E. Martin and C. E. Hadden, *J. Nat. Prod.*, 2000, **63**, 543.
48. J. P. Shockcor, R. M. Wurm, I. S. Silver, R. C. Crouch, and G. E. Martin, *Tetrahedron Lett.*, 1994, **35**, 4919.
49. R. C. Crouch, G. E. Martin, R. W. Dickey, D. G. Baden, R. E. Gawley, K. S. Rein, and E. P. Mazzola, *Tetrahedron*, 1995, **51**, 8409.
50. M. H. M. Sharaf, P. L. Schiff, Jr., A. N. Tackie, C. H. Phoebe, Jr., A. O. Davis, C. W. Andrews, R. C. Crouch, and G. E. Martin, *J. Heterocyclic Chem.*, 1995, **32**, 1631.
51. M. H. M. Sharaf, P. L. Schiff, Jr., A. N. Tackie, C. H. Phoebe, Jr., and G. E. Martin, *J. Heterocyclic Chem.*, 1996, **33**, 239.
52. M. H. M. Sharaf, P. L. Schiff, Jr., A. N. Tackie, C. H. Phoebe, Jr., R. L. Johnson, D. Minick, C. W. Andres, R. C. Crouch, and G. E. Martin, *J. Heterocyclic Chem.*, 1996, **33**, 789.
53. W. F. Reynolds, S. McLean, H. Jacobs, and W. W. Harding, *Can. J. Chem.*, 1999, **77**, 1922.
54. W. L. Fitch, G. Detre, C. P. Homes, J. N. Shoolery, and P. A. Keifer, *J. Org. Chem.*, 1994, **59**, 7955.
55. P. A. Keifer, L. Baltusis, D. M. Rice, A. A. Tymiak, and J. N. Shoolery, *J. Magn. Reson.*, 1996, **199A**, 65.
56. P. A. Keifer, *J. Org. Chem.*, 1996, **61**, 1558.
57. T. Wehler and J. Westman, *Tetrahedron Lett.*, 1996, **37**, 4771.
58. M. Pursch, G. Schlotterbeck. L.-H. Tseng, K. Albert, and W. Rapp, *Angew. Chem., Intl. Ed., Engl.*, 1996, **35**, 2867.
59. A. M. Seffler and S. W. Gerritz, *J. Comb. Chem.*, 2000, **2**, 127.
60. T. Mohri, Y. Nakahara, W. Zhang, Y. Nakatsuji, T. Murreishi, Y. Miyoji, and I. Ikeda, *Chem. Lett.*, 2000, 998.
61. M. A. Gallop and W. L. Fitch, *Curr. Opin. Chem. Biol.*, 1997, **1**, 94.
62. D. Moka, R. Vorreuther, H. Schicha, M. Spraul, E. Humpfer, M. Lipinski, P. J. D. Foxall, J. K. Nicolson, and J. C. Lindon, *J. Pharm. Biomed. Anal.*, 1998, **17**, 125.
63. D. Klein, J.-C. Braekman, D. Daloze, L. Hoffmann, and V. Demoulin, *Tetrahedron Lett.*, 1996, **37**, 7519.
64. D. C. Chauret, T. Durst, J. T. Amason, P. Sanchez-Vindas, L. San Roman, L. Poveda, and P. A. Keifer, *Tetrahedron Lett.*, 1996, **44**, 7575.
65. A. Bax, R. Freeman, and T. A. Frenkiel, *J. Am. Chem. Soc.*, 1981, **103**, 2102.
66. A. Bax, R. Freeman, and T. A. Frenkiel, *J. Magn. Reson.*, 1981, **43**, 478.
67. D. M. Fort, J. Vlitvak, J. L. Chm. Q. Lu, P.-W. Phuan, R. Cooper, and D. E. Bierer, *J. Nat. Prod.*, 1998, **61**, 1528.
68. M. H. M. Sharaf, P. L. Schiff, Jr., A. N. Tackie, and G. E. Martin, *J. Heterocyclic Chem.*, 1998, **35**, 1365.
69. D. Klein, J.-C. Brakeman, D. Daloze, L. Hoffmann, G. Castillo, and V. Demoulin, *Tetrahedron Lett.*, 1999, **40**, 695.
70. M. Namikoshi, K. Akano, S. Meguro, I. Kasuga, Y. Mine, T. Takahashi, and H. Bobayashi, *J. Nat. Prod.*, 2001, **64**, 396.
71. A. Manzi, P. V. Salimath, R. C. Spiro, P. A. Keifer, and H. H. Freeze, *J. Biol. Chem.*, 1995, **270**, 9154.

72. M. Delpierre, A. Prochnicka-Chalufour, and L. D. Possani, *Biochemistry*, 1997, **36**, 2649.
73. P. Roux, M. Delepierre, M. E. Goldberg, and A.-F. Chaffotte, *J. Biol. Chem.*, 1997, **272**, 24 843.
74. M. Delepierre, A. Prochnicka-Chalufour, and L. D. Possani, *Toxicon*, 1997, **36**, 1599.
75. M. Delepierre, P. Roux, A.-F. Chaffotte, and M. E. Goldberg, *Magn. Reson. Chem.*, 1998, **36**, 645.
76. M. Delepierre, A. Prochnicka Chalufour, J. Boisbouvier, and L. D. Possani, *Biochemistry*, 1999, **38**, 16 756.
77. A. E. Manzi, K. Norgard-Sumnicht, S. Argade, J. D. Marth, H. van Halbeek, and A. Varki, *Glycobiology*, 2000, **10**, 669.
78. M. Bilgert, J.-R. Brisson, M.-F. Karwaski, J. Michniewicz, A.-M. Cunningham, Y. Wu, N. M. Young, and W. W. Wakarchuk, *J. Biol. Chem.*, 2000, **I275**, 3896.
79. E. Kupce, P. A. Keifer, and M. DelPiere, *J. Magn. Reson.*, 2001, **148**, 115.
80. W. F. Reynolds and R. G. Enriquez, *Magn. Reson. Chem.*, 2001, **39**, 531.
81. D. J. Russell, unpublished data.

Acknowledgements

The author would like to acknowledge the assistance of his colleagues, C.E. Hadden and D.J. Russell at Pharmacia Corp., K. Krishnamurthy at Eli Lily and R.C. Crouch at Varian, Inc. for discussions pertaining to the Nano-probe. Thanks also go to Professor W.F. Reynolds of the University of Toronto for many stimulating discussions on the topic of small sample NMR probes and to Professor P.L. Schiff, Jr. of the University of Pittsburgh for providing many of the natural product samples that have been studied and used as model compounds during the development of small volume NMR probe technology over the past decade.

Biographical Sketch

Gary Edwin Martin, *b* 1949. Ph.D. 1975 Pharmaceutical Sciences, University of Kentucky. Professor, University of Houston, 1975–89. Principal Scientist Burroughs Wellcome Co., Research Triangle Park, NC 1989–1995. Senior Fellow, Pharmacia Corp. 1996–present. Approx. 250 publications. Current research interests: high sensitivity, small volume and cryogenic NMR probe development and applications; development of new long-range heteronuclear shift correlation experiments; application of long-range $^{1}H-^{15}N$ heteronuclear shift correlation at natural abundance.

Probe Design and Construction

F. David Doty
Doty Scientific Inc., Columbia, SC, USA

1	Introduction	1
2	General Classes of NMR Probes	1
3	Historical Perspective on NMR Probes	2
4	Radiofrequency Engineering—Basics	2
5	Signal-to-Noise Ratio and B_1	4
6	Double Resonance	6
7	Construction Materials and Techniques	7
8	Thermal Engineering	8
9	Gradient NMR Probes	8
10	Related Articles	9
11	References	9

1 INTRODUCTION

From the early days of NMR, the word probe (or probehead) has been used to refer to the complete piece of equipment intimately associated with the sample (except the sample tube). For the simplest experiments, the probe consists of the mechanical structure required to hold the sample in the 'sweet spot' of the magnet, a coil surrounding the sample, a tuning capacitor, and an rf transmission line. However, most chemical problems of interest require control over the sample environment (temperature, electromagnetic irradiation, pressure, orientation, and re-orientation), and apparatus associated therewith becomes a part of the NMR probe.

The modern NMR probe is a complex piece of apparatus designed to accommodate all of the environmental requirements of the NMR experiment. The radiofrequency (rf) portion often includes (a) an rf 'observe' channel optimized for highest signal-to-noise-ratio (SNR, or S/N, also called sensitivity) at the X nucleus frequency, (b) a less efficient rf channel for heteronuclear decoupling (usually ^{1}H, except for indirect detection), and (c) another low-efficiency channel for magnetic field lock (usually ^{2}H). Variable temperature (VT) control is achieved with a resistive heater in a gas stream that flows over the sample. In high-resolution liquids probes, slow sample spinning (10–200 revolutions per second, Hz) about the $\boldsymbol{B}_0$ axis to average out azimuthal inhomogeneity in $\boldsymbol{B}_0$ is usually accomplished with a pneumatic system external to the probe, but high-speed sample spinning apparatus (200–26 000 Hz) for solids averaging techniques is an integral part of a solids probe.

One of the most demanding technical aspects of liquids probes is the requirement of extremely high $\boldsymbol{B}_0$ field homogeneity (as high as several parts per billion), but sometimes it is advantageous to be able deliberately to spoil the field homogeneity over precise time periods by applying field gradients. When very high gradients and fast switching are required, as in diffusion measurements or solids microscopy magnetic resonance imaging (MRI), the gradient coils must be as small as possible and incorporated into the probe. However, for most MRI work with samples larger than 40 mm, the gradient coils are external to the probe.

Another challenging technical requirement is often that of minimizing NMR background signals from construction materials that contain trace amounts of the nuclide of interest—particularly for highly sensitive proton (^{1}H) experiments. Other technical complications may stem from provisions for optical or microwave irradiation and operation at extreme temperatures.

Addressing the often conflicting requirements of high sensitivity, high resolution, large spectral bandwidth, low background signals, wide VT range, high-speed sample spinning, intense irradiation, and uniform field gradients requires careful attention to a number of problems in materials science, physics, electrical engineering, and mechanical engineering. The engineering effort often makes the price of a probe comparable to the price of a new sports car.

2 GENERAL CLASSES OF NMR PROBES

2.1 Liquids Probes

Approximately 80% of NMR experiments are performed on high-resolution liquids probes designed for samples in axially aligned glass tubes in superconducting magnets using saddle-shaped rf coils or slotted resonators for signal reception. They are often required to achieve a spectral resolution of several parts per billion on slowly spinning samples. A small fraction of their usage has been for in vivo experiments on small living animals or ex vivo or in vitro experiments on surgically removed tissues kept alive for short periods of time by perfusion with nutrients in saline solutions furnished by a flow system in the probe. Most multinuclear liquids probes have provided proton decoupling with multinuclear observe and deuterium lock, but recently many have been designed for inverse experiments (proton detection with X-nucleus decoupling). At present, high-resolution liquids probes are commercially available for experiments from $-180\,^\circ$C to $380\,^\circ$C.

2.2 Gradient Probes

Pulsed field gradient (PFG) and microscopy MRI probes are usually similar to conventional liquids probes with the addition of gradient coils for one or three axes respectively. PFG probes are used for the measurement of diffusion coefficients, solvent suppression, or selection of specific coherences. Their usage has grown very rapidly in the past several years because of the time savings they provide in two-dimensional NMR. Microscopy in vivo probes may include surface coils for improved localized signal reception.

2.3 Solids Probes

The original (and simplest) probe for NMR of solid samples is the wideline probe, which is normally characterized as being able to generate 90° pulse lengths less than $3\,\mu$s (spectral excitation bandwidths greater than 80 kHz) by withstanding

peak rf coil voltages in excess of 3 kV. Often they are double tuned (DT) to permit cross polarization (CP) with high-power decoupling for increased sensitivity and resolution. High-speed magic angle spinning (MAS) of the sample is added in the CP MAS probe for line narrowing of spin-$\frac{1}{2}$ nuclei, and dynamic angle spinning (DAS) and double rotation (DOR) may be provided for quadrupolar nuclei. When sufficiently large single crystals of the sample can be grown, high-resolution spectra and the chemical shift tensor can be obtained using a single crystal probe that includes a suitable goniometer and crystal orientation mechanism.

3 HISTORICAL PERSPECTIVE ON NMR PROBES

Through the late 1960s 'NMR' implied 'proton NMR of liquids' unless specifically stated otherwise, and multinuclear probes were unheard of. There was a rather widespread misconception that sensitivity increased linearly with coil inductance, even though the early classic treatments[1,2] were sound. High-inductance solenoids (1–50 μH, compared with 40–200 nH for modern probes) wound around the sample tube could be used for efficient reception in the transverse field of the electromagnet, but audio field-modulation coils were needed to shift the detection frequency above the $1/\nu$ noise region of the phase-sensitive video detector. The orthogonal Helmholtz transmit coils could be driven with low-power (milliwatt) oscillators for most continuous wave (CW) techniques, and the transmit/receive coils were carefully isolated using Faraday shields and tuning paddles. Since low-impedance preamplifiers with low noise figures were not available, it was best to include the first stage of the preamplifier in the probe and match it (usually 300–2000 Ω) directly to the receive coil.

Although many time domain pulsed NMR experiments were performed in the first two decades of NMR for relaxation studies, the explosion of NMR techniques awaited the application of Fourier transform (FT) by Richard Ernst in 1966 to the time domain data to obtain the complete frequency domain spectra in a single free induction decay (FID). The increase in sensitivity was comparable to the ratio of the total spectral width to the narrowest line in the spectrum—often two or three orders of magnitude.[3,4] (See also ***Fourier Transform Spectroscopy***.)

Field shimming (homogenizing) was extremely crude and tedious prior to Golay's development of the theory and practice of orthogonal shim coils.[5] With the advent of FT NMR came more incentive to obtain higher resolution because of its dramatic impact on sensitivity. Ultrahigh purity (99.9995%) copper receive coils with precision magnetic compensation and Varian's sample spinner mounted on top of the probe quickly became standard. An external lock employing a sealed sample and separate coil (usually tuned to ^{19}F or ^{2}H) beside the sample coil was used to stabilize the field.[6]

The probe rf circuitry was also quickly impacted by FT NMR. To excite the entire spectral width with large Helmholtz coils at 60 MHz required 10–100 W and generated several kV across the coil, so impedance matching to the transmit circuit became important. The increase in sensitivity from FT NMR opened up the field of multinuclear MR—especially ^{13}C and ^{31}P.[7] The advantages in resolution and sensitivity provided by proton decoupling required double resonance circuits, which made it more difficult to use separate transmit/receive coils, and double-tuned single-coil circuits with transmit/receive duplexers began to appear.[8,9] It is fair to say that modern NMR probe technology was ushered in by David Hoult in 1976 with his transparent analysis of S/N based on the obscure concept of reciprocity.[10] Today, separate transmit/receive coils survive only in single resonance MRI where the high rf homogeneity afforded by a large transmit coil is beneficial and small surface coils are optimum for reception.

Probe technology has matured over the past two decades, and major advances in most probe specifications are not expected. Nonetheless, probe technology will retain its pivotal role in NMR progress because even small improvements can contribute a lot to total system performance.

4 RADIOFREQUENCY ENGINEERING—BASICS

Basic rf engineering has been treated in a number of elementary texts[11,12] and introductory review articles,[13,14] but the probe engineer also needs a working understanding of some of the more advanced concepts in electromagnetic field theory.[15,16] NMR signal reception is different from (and simpler than) antenna theory, in that antennas are designed to receive electromagnetic waves in the far-field limit whereas NMR probes are designed to sense magnetic fields in the near-field limit.[17] While the rf circuits in NMR probes can usually be approximated with simple circuits and analyses, the critical importance of the probe to the total spectrometer performance justifies a level of detailed field and efficiency analysis seldom encountered outside of NMR probes. A number of articles[10,18–25] and a textbook[26] have presented excellent treatments of general NMR probe design problems over the past two decades. A summary of basic NMR probe electronics follows.

4.1 Capacitance

Capacitance (farads) is defined as electric charge per volt (Q/V), and capacitive energy storage is equal to $CV^2/2$. Stray capacitance can often be estimated to sufficient accuracy from the expression for the parallel plate capacitor C_p of area A (m^2), separation distance d (m), and dielectric constant k_d,

$$C_\mathrm{p} = \frac{k_\mathrm{d}\varepsilon_0 A}{d} \tag{1}$$

or from the expression for the low-frequency capacitance of a coaxial capacitor[21] of length h, dielectric o.d. d_o, and dielectric i.d. d_i,

$$C_\mathrm{c} = \frac{2\pi k_\mathrm{d}\varepsilon_0(h + d_\mathrm{o})}{\ln(d_\mathrm{o}/d_\mathrm{i})} \tag{2}$$

where ε_0 is the permittivity of free space, 8.84 pF m^{-1}. Parallel capacitors add algebraically, ($C_\mathrm{T} = C_1 + C_2 + \ldots$), while series capacitors add reciprocally ($C_\mathrm{T}^{-1} = C_1^{-1} + C_2^{-1} + \ldots$).

4.2 Inductance

The simplest definition of inductance L (henrys) comes from Faraday's law of induction—the induced voltage divided

by the rate of change in current di/dt. For inductance calculations, the most practical 'definition' follows from the energy equation

$$U = i_T^2 L/2 \tag{3}$$

where U is the total energy in the magnetic field (the integral of $B^2/2\mu\mu_0$ over all space) and i_T is the current *at the pair of terminals* generating the magnetic field $\boldsymbol{B}$. [We follow popular usage of denoting the magnetic flux density or induction field $\boldsymbol{B}$ (T) as the 'magnetic field' and $\boldsymbol{H} = \boldsymbol{B}/\mu\mu_0$ as the field intensity (A m^{-1}) where μ is the relative permeability of the material.] For all NMR probes, μ is always unity. The permeability of free space μ_0 equals $4\pi \times 10^{-7}$ H m^{-1}.

The inductance of the finite, multiturn, single layer rf solenoid of Figure 1 with a constant pitch, an integral number of turns, and a high surface coverage is given in nH, for dimensions in mm, by the following expression:

$$L_S = \frac{4n^2r^2(1 - 0.2/n)}{h + 1.2r^{0.9}} \quad \text{[mixed]} \tag{4}$$

where n is the number of turns (Figure 1 has five turns), h is the *overall* axial length, and r is the effective inside radius, which for round wire is approximately equal to the inside coil radius plus 20% of the wire radius. The last term in the numerator corrects for the fact that the helix makes the effective coil length a little less than the overall length. The above expression is correct to within several per cent for $h/r > 0.2$. For the loop-gap resonator[27,28] (a single-turn solenoid, also called a split ring), the helix correction term is dropped, and the coefficient changes to 3.9 to correct for current concentrating at the ends of the ring. Higher order corrections for multiturn coils with low surface coverage can be added.

Lead (parasitic) inductance is usually best estimated by calculating the inductance of a loop-gap resonator having a length equal to the diameter of the lead wire and $r^2 = A_C/\pi$, where A_C is the area enclosed by the loop formed by the leads. Sometimes lead inductance is better estimated from the expression for the inductance L_C of a coaxial transmission line:

$$L_C = \frac{\mu_0 h}{2\pi} \ln\left(\frac{d_o}{d_i}\right) \tag{5}$$

Clearly from equation (5), series inductors add like resistors ($L_T = L_1 + L_2 + \ldots$); likewise, parallel inductors add reciprocally ($L_T^{-1} = L_1^{-1} + L_2^{-1} + \ldots$).

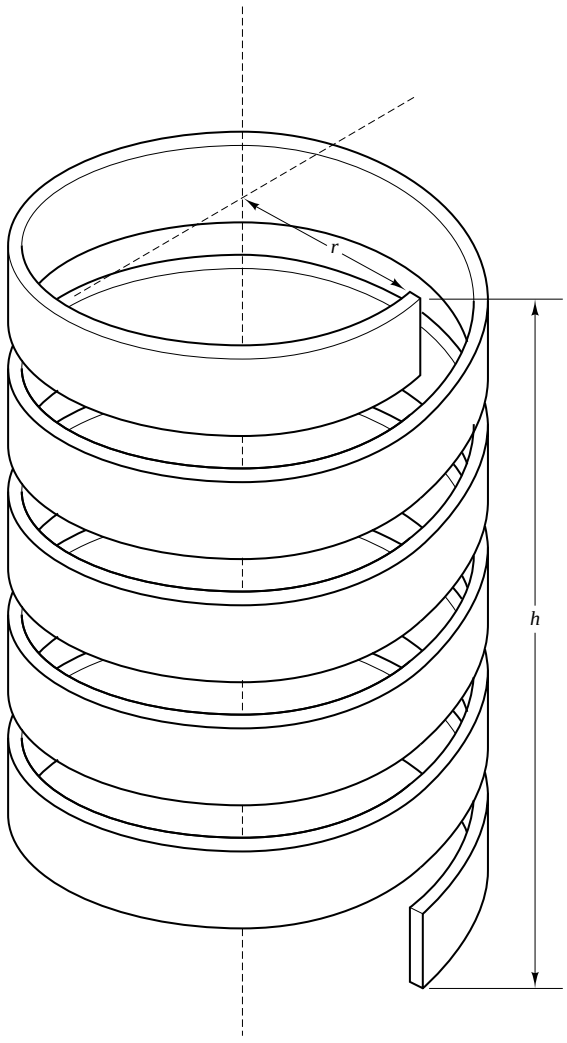

Figure 1 A five-turn solenoid

4.3 Single Resonance Circuits

4.3.1 Power

Figures 2 and 3 illustrate the basic *RLC* series and parallel circuits, respectively. The losses in the series *RLC* circuit of Figure 2 are best represented by the total effective series resistance R_s (from the coil, capacitor, leads, etc.). For the parallel circuit of Figure 3, the losses may be represented more conveniently by a total effective parallel resistor R_p. In both cases, the basic equations from ac circuits apply for rms power P and peak power P_P. (Power is assumed to be rms unless denoted otherwise.)

$$P = \frac{P_P}{2} = \frac{i_P^2 R_s}{2} = \frac{V_P^2}{2R_p} \tag{6}$$

Power ratios are often expressed in dB, $10 \log(P_2/P_1)$, and power is often expressed in dBm—defined as dB relative to a milliwatt:

$$\text{dBm} \equiv 10 \log(1000P) \tag{7}$$

In practice, peak-to-peak voltages ($2V_P$) are usually measured on an oscilloscope, and the measurements are significantly influenced by harmonic distortion, VSWR (Voltage

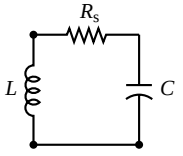

Figure 2 Series *RLC* circuit

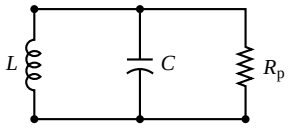

Figure 3 Parallel *RLC* circuit

Standing Wave Ratio), loading, and oscilloscope bandwidth. Most conventional liquids probes are excited with 100 W pulses of 10–80 μs at the observe frequency (usually the low frequency, LF) at duty cycles below 0.1% while they are driven with 10 W at the decouple frequency (usually ^{1}H, the high frequency, HF) at duty cycles below 50%. Solids probes typically see LF pulses of 200–400 W with duty cycles up to 1% while irradiating with HF power of 50–200 W at duty cycles below 30%. Whole body MRI probes are usually driven with 1–10 kW at duty cycles below 0.5%.

4.3.2 Resonance

Since charge (q) equals CV and $i = \mathrm{d}q/\mathrm{d}t$, a capacitor reaches a steady-state (monochromatic) reactance X_C (analogous to resistance, V/i) of $1/\mathrm{i}\omega C$ after several RC time-constants, where i is the imaginary unit, $\sqrt{-1}$. Likewise, since $V = -L\ \mathrm{d}i/\mathrm{d}t$, an inductor has reactance $X_L = \mathrm{i}\omega L$ and time constant L/R. For the normal high-Q condition ($Q = \omega_0/\Delta\omega_{\frac{1}{2}}$), resonance occurs when the inductive reactance X_L plus the capacitive reactance X_C equals zero. (Often the phase is omitted for convenience, but it must be remembered that the voltage phase in the inductor leads by 90° while in the capacitor it lags by 90° relative to that in the resistor.) Hence,

$$\omega_0 = \frac{1}{\sqrt{LC}} \tag{8}$$

At resonance, the series impedance of the series RLC circuit is R_s (since $X_L + X_C = 0$) and the parallel impedance of the parallel RLC circuit is R_p [since $(X_L X_C)/(X_L + X_C) = \infty$]. The 3 dB width $\Delta\omega_{1/2}$ of the resonance defines the quality factor of the unloaded (and unmatched) RLC circuit, and the following relationships are readily derived:

$$R_\mathrm{p} = QX_L \tag{9}$$

$$R_\mathrm{s} = X_L/Q = R_\mathrm{p}/Q^2 \tag{10}$$

4.3.3 Matching

Since X_L is typically 20–200 Ω, R_s is usually less than 1 Ω and R_p is greater than 2000 Ω. For efficient coupling to the transmitter and preamplifier, the resonant circuit, transmission lines, preamplifier, and transmitter must all be matched to approximately the same impedance, although mismatches of up to a factor of two are often unimportant. The international standard is 50 Ω (except in the television industry, where it is 75 Ω). Figures 4 and 5 illustrate the two basic methods of impedance matching: shunt inductor and series capacitor.

The inductive matching technique has the advantage of not requiring a second high-voltage capacitor, but the matching range is limited by the difficulty of adjusting very small inductors. The required shunt inductor (for $R_\mathrm{p} \gg Z_0$) is

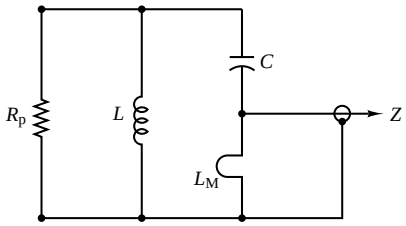

Figure 4 Shunt inductive matching circuit

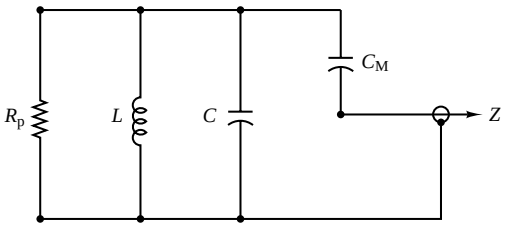

Figure 5 Series capacitive matching circuit

$$L_\mathrm{M} = L_\mathrm{T}\sqrt{Z_0/R_\mathrm{p}} \tag{11}$$

where L_T is the total series inductance ($L_\mathrm{s} + L_\mathrm{M}$ + leads) and Z_0 is the transmission line characteristic impedance—normally 50 Ω. The resonant frequency is calculated from L_T and C.

The capacitive matching circuit simplifies multinuclear (broadband) tuning requirements as high-voltage (HV) variable capacitors are readily available. The required match capacitance (again, for $R_\mathrm{p} \gg Z_0$) has reactance X_{CM} given by

$$X_{CM} = \sqrt{R_\mathrm{p} Z_0} \tag{12}$$

and rms current equal to that in the transmission line, $\sqrt{P/Z_0}$. In practice, some combination of capacitive and inductive matching is often used, and capacitive voltage division is often employed to reduce the demands on the matching variable capacitor.[29] Properly 'pruned' transmission lines can also be used to transform impedance (see ***Probes for Special Purposes***).

5 SIGNAL-TO-NOISE RATIO AND B_1

5.1 Magnetization and the NMR Signal

The NMR voltage signal S from a sample with susceptibility χ, with nuclear spins precessing at angle ϕ in magnetic field $\boldsymbol{B}_0$ at angular frequency ω, detected by a coil that generates a circularly polarized (rotating) transverse field $\boldsymbol{B}_1(\boldsymbol{r})$, over the sample volume V_S for current i, may be shown from the principle of reciprocity[10,26] to be

$$S = \frac{\chi B_0 \omega}{\mu_0 i} \int_S \sin\phi\, B_1(\boldsymbol{r})\, \mathrm{d}V \tag{13}$$

Simply put, the receiver coil need only be analyzed as a $\boldsymbol{B}_1$ transmitter. For a uniform $\boldsymbol{B}_1$ generated by a current i,

immediately following a 90° pulse,

$$S = \frac{\chi B_0 \omega B_1 V_S}{\mu_0 i} \tag{14}$$

The equilibrium magnetization $\boldsymbol{M}_0$ is given by[1,6]

$$\boldsymbol{M}_0 = \frac{\chi \boldsymbol{B}_0}{\mu_0} = \frac{n_s \gamma^2 \hbar^2 I_x (I_x + 1) \boldsymbol{B}_0}{3 k_B T_S} \tag{15}$$

where n_s is the number of spins at resonance per unit volume, γ is the magnetogyric ratio, I_x is the spin quantum number, k_B is Boltzmann's constant, T_S is the sample temperature, and $\hbar = h/2\pi$, where h is Planck's constant.

5.2 Thermal Noise

The Johnson (thermal) rms noise N from a resistor R_E for filter bandwidth $\Delta\nu$ (not ν/Q) is[1,2]

$$N = (4 R_E k_B T_R \Delta\nu)^{1/2} \tag{16}$$

where T_R is the temperature of the resistor. (For R_E = 50 Ω, N = −168 dBm $Hz^{-1/2}$.) The effective series resistance (X_L/Q) of the loaded circuit is best determined by measuring Q. Other noise sources (interference, triboelectric, spurious, shot, microphonic, preamplifier) can usually be made negligibly small with careful engineering.[23]

5.3 B_1 in the Rotating Frame

A linearly polarized oscillating magnetic field $2B_1$ (as in a solenoid) may be decomposed into the sum of two oppositely rotating circularly polarized fields, each of magnitude B_1. One of these components can be used to drive NMR precession within a bandwidth approximately equal to its magnitude (in Hz) if it is transverse to $\boldsymbol{B}_0$; the other has no effect on NMR precession, as its frequency in the rotating frame is -2ω. From the Biot–Savart law,[15] B_1 at the center of a solenoid is given by

$$B_1 = \frac{\mu_0 n i}{2h\sqrt{1 + 4(r/h)^2}} \tag{17}$$

Using equations (3), (6), and (10), it may be shown that $U = PQ/\omega$, and B_1 may be expressed as follows for the infinite solenoid:

$$B_1 = \left[\frac{\mu_0 P Q}{2\omega V_C}\right]^{1/2} \tag{18}$$

where V_C is the coil volume. [Adding the term $1 + 4(r/h)^2$ in the denominator inside the brackets of equation (18) improves the accuracy for typical solenoids.]

The unloaded Q_0 of the typical multiturn solenoid (well below self-resonance and with high surface coverage) is, in mixed units, approximately

$$Q_0 \approx 6\sqrt{hrf} \quad [\mathrm{MHz}^{1/2}\ \mathrm{mm}^{-1}] \tag{19}$$

Saddle coils (commonly, but incorrectly, called Helmholtz coils;[15] more properly they could be called Ginsberg[30] or Golay[5] coils) and slotted resonators[19,25] are better suited for liquids NMR in superconducting magnets, as they generate a transverse $\boldsymbol{B}_1$ while allowing axial access. Moreover, their axial symmetry makes it easier to obtain high $\boldsymbol{B}_0$ homogeneity. The coefficient in equation (19) is reduced to a value of 2 for saddle coils with medium surface coverage, as is necessary for orthogonal double resonance operation.

The loaded circuit quality factor Q_L will be lower than that of the coil because of losses in capacitors, shields, and sample. A convenient method of measuring Q_L is with a reflectance bridge, where the appropriate Δf value is measured at −7 dB return loss, which may be calibrated with a 21 Ω or 119 Ω load on a 50 Ω line.[23] (Q_L is not lowered much by 'matching' to the preamplifier if its noise figure is less than ∼1 dB.)

For *any* coil, *average* B_1 in gauss over the usable volume may be expressed in mixed units by the following:

$$\langle B_1 \rangle = \beta \left[\frac{\eta_E P Q_L}{f V_C}\right]^{1/2} \quad \text{[mixed]} \tag{20}$$

where β is a dimensionless function of coil geometry, f is in MHz, V_C is in mL, and η_E is the rf efficiency—the fraction of the power delivered to the rf coil and sample.[21] The rf efficiency η_E is usually greater than 0.9 for single resonance circuits at low fields, but it may be less than 0.2 for double resonance at high fields. In practice, it is always necessary to measure rather than calculate Q_L, which then includes the capacitor losses. The above equation is still valid if η_E is then defined as $1 - \eta_L$, where η_L is the fraction of the power dissipated in inductors not generating B_1 (leads and coils added for multiple resonances).

For special high-resolution applications of solenoidal rf coils, the optimum h/r value is 2, and $\beta \approx 2.4$. For very lossy samples, the optimum h/r is the largest permitted by space constraints, and $\beta = \sqrt{10}$ for the infinite solenoid. For MAS, the optimum h/r is 3, and β = 2.1 when the coil is at the magic angle. For saddle coils and slotted resonators, β ranges from 0.8 to 1.4, depending on surface coverage, subtended angle, and the ratio of height to diameter.

A magnetic filling factor η_f may be defined by

$$\eta_f = \frac{\int B_1^2 \, dV}{\mu_0 U} \tag{21}$$

where the integration is over the sample volume V_S. From equations (3), (10), (20), and (21) comes a very practical (and exact) definition of the filling factor:

$$\eta_f = \frac{\beta^2}{20} \frac{V_S}{V_C} \tag{22}$$

5.4 S/N

From the above, the S/N from a single 90° pulse with an optimum filter [$1/(\pi\Delta\nu) = T_2$, the spin–spin relaxation time, and $\Delta\nu < \omega/2\pi Q_L$] can be written as follows:

$$\text{S/N} = \frac{S}{2N} = \left[\frac{\hbar^2\sqrt{\pi\mu_0}}{12k_B^{3/2}}\right]\left[\frac{n_s\gamma I_x(I_x+1)\sqrt{T_2}}{T_S\sqrt{T_R}}\right](\eta_E\eta_f Q_L V_S)^{1/2}\omega^{3/2} \tag{23}$$

The extra factor of 2 in the denominator arises because S is the initial peak signal voltage that decays with time-constant T_2 and N is the rms noise voltage. The product of the two bracketed terms is $1.65 \times 10^{-5}\,\text{s}^{3/2}\,\text{m}^{-3/2}$ for protons in water with $T_2 = 0.1$ s and $T_S = T_R = 300$ K.

A useful simplification of equation (23) is the following for given NMR conditions (sample, γ, $\boldsymbol{B}_0$, T_S, T_2, technique):

$$\text{S/N} \propto \frac{V_S}{\tau_{90}\sqrt{P}} \tag{24}$$

where τ_{90} is the mean 90° pulse width obtained over sample volume V_S with power P.

5.5 Minimizing Losses

For small samples, the Q_L is usually dominated by coil resistance. However, above 400 MHz it may be dominated by capacitor losses unless extreme care is taken in their selection, and it may be necessary to parallel a number of low-value capacitors for sufficiently low capacitor losses. For large, lossy samples, Q_L and T_R are dominated by sample losses. Dielectric losses from electric fields in the sample may be reduced by decreasing the coil inductance and increasing the capacitance.[20,31] Usually, the only ways to reduce power P_S deposited by the inductive mechanism in a sample of uniform resistivity by a rotating $\boldsymbol{B}_1$ are to maximize the $\boldsymbol{B}_1$ homogeneity and to maximize the rms flux path length ξ for a given volume, but sometimes it is possible to use insulating films to suppress currents in the sample.[32] The presence of skin, fat, and bones in MRI can make the estimate of P_S as much as an order of magnitude too large when using a worst-case tissue resistivity ρ_S of 1.2 Ω m.

$$P_S \approx \frac{B_1^2\omega^2 V_S^2}{16\pi\rho_S\xi} \tag{25}$$

Equation (25) is equivalent to the low-frequency limit given by Carlson[24] for a sphere, but the inclusion of ξ improves loss predictions for nonspherical samples. The loaded Q_L may be estimated from the unloaded Q_0 and the sample Q_S:

$$Q_L = \frac{Q_0 Q_S}{(Q_0 + Q_S)} \tag{26}$$

For reasonably uniform, *linear* B_1, Q_S is approximately

$$Q_S \approx \frac{32\pi\rho_S\xi V_C}{\mu_0\eta_E\beta^2\omega V_S^2} \tag{27}$$

The numerical coefficient in equation (27) is increased to 64 for circular polarization.

The ratio Q_0/Q_L has frequently been used as a figure-of-merit for coils in MRI, but this does not properly consider the dielectric losses nor the major effects of $\boldsymbol{B}_1$ inhomogeneity in surface coils.[33] equation (24) provides a better figure-of-merit, but it still does not adequately evaluate homogeneity.

The 'birdcage' resonator of Edelstein et al. made quadrature coils practical for generating a single rotating $\boldsymbol{B}_1$.[22,34] Liquids and solids NMR find few applications for quadrature rf coils, as coil losses usually dominate. However, in MRI, when inductive sample losses dominate, quadrature coils offer up to a 40% improvement in S/N. For an advanced treatment of the birdcage resonator, the reader is referred to the article by Tropp.[35] (See also ***Birdcage Resonators: Highly Homogeneous Radiofrequency Coils for Magnetic Resonance***.)

A proper calculation of L, B_1, and Q_0 requires a knowledge of the surface current distribution in the conductors—especially in single-turn resonators.[25] The so-called 'proximity effect' is ambiguous. A better method of determining current distribution in large conductors is to iterate on Biot–Savart integration, letting the currents move around in the conductors to a minimum inductance ($2U/i_T^2$) configuration. The current usually prefers to take the shorter paths (inside surface) and tends to concentrate near regions of high flux curvature (end edges) and high flux density (nearby shields). The normal component of the rf magnetic field always vanishes near the surface of conductors, and the current penetrates only to a depth given by the classical skin depth:

$$\delta = \left(\frac{2}{\omega\mu_0\sigma}\right)^{1/2} \tag{28}$$

where σ is the electrical conductivity. For copper at 300 K, δ = 6.4 μm at 100 MHz. Nonuniform surface current density is responsible for Q_0 being lower by a factor of 3–8 than would occur for uniform surface current density. In some cases, Q_0 may be improved by the use of Litz wire (woven wire, using individually enameled strands as fine as 0.03 mm).

6 DOUBLE RESONANCE

Two saddle coils, rotated 90° about the $\boldsymbol{B}_0$ axis provide a convenient method of doing double resonance NMR with good isolation. However, only the innermost coil can have the optimum filling factor, and sometimes it is beneficial to have the same spatial distribution of the two rf fields, $\boldsymbol{B}_1$ and $\boldsymbol{B}_2$. Also, triple- or quadruple-resonance NMR experiments are often useful. Thus, it is often desirable to double-tune or triple-tune a single sample coil, although Anderson described in 1973 a clever method of using three orthogonal, single-tuned coils.[36]

The number of modes in a resonant circuit will generally be equal to the number of unique inductors or capacitors, whichever is fewer. (Resonant transmission lines may count as either.) It is sometimes necessary to add additional inductors or capacitors (producing extraneous modes) to improve isolation or to achieve balance at the frequencies of interest, although this can complicate tuning.[37,38] The most common double-tuned circuit, shown in Figure 6, has been analyzed by several authors.[21,23,39] It has an HF parallel mode and an LF series mode. The efficiency at the HF is increased by *decreasing* L_S/L_H, where L_S is the sample coil inductance and L_H is the HF tuning coil inductance. On the other hand, efficiency

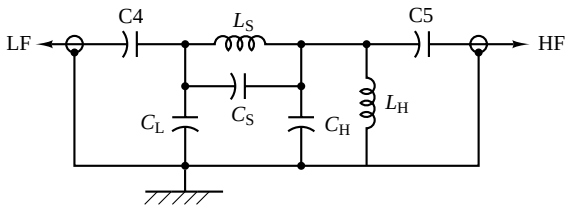

Figure 6 Double resonance circuit

at the LF is increased by *increasing* L_S/L_H. In principle, if the losses in L_H and the tuning capacitors can be made vanishingly small compared with sample losses, the efficiency can approach 100% at both frequencies.[40] Rise time, however, will be degraded (because the total Q_L must increase), but this is seldom significant for in vivo experiments. For 8-mm sample coils, efficiencies at HF and LF are typically 40% and 75% respectively (when Q_L includes capacitor losses, as in the referenced analyses). From equations (20) and (23), B_1 and S/N are degraded only as the square root of the efficiency.

7 CONSTRUCTION MATERIALS AND TECHNIQUES

Although $\boldsymbol{B}_0$ homogeneity specifications sound frighteningly stringent, the capability of orthogonal shim systems is such that only in the immediate vicinity of the sample is magnetic susceptibility critical. Austenetic stainless steels (with SI volume susceptibility $\chi_V = \mu - 1 \approx 0.02$) can often be used for thin-walled Dewars surrounding the sample region and for Dewared transfer lines, although glass is preferred if space permits. It is, of course, desirable to minimize the amount of shimming effort required when the probe is changed, so low-susceptibility construction materials and thin sections are preferred. The magnetic susceptibilities of the components immediately above and below the sample region (in the B_z direction) are more significant, and axial and azimuthal symmetry are both important.[41,42]

The common aluminum alloys[43] 6063-T6 (0.7% Mg, 0.4% Si, up to 0.3% Fe) and 6061-T6 (1% Mg, 0.6% Si, 0.3% Cu, 0.3% Cr, up to 0.7% Fe) are usually acceptable for thin shield cylinders and support structure since the iron is usually in a nonmagnetic phase ($FeAl_3$ or Fe_2Al_7),[44] but they often present acoustic ringing problems below 15 MHz.[45] Jewelry bronze [copper alloy C22600, 87.5% Cu, 12.5% Zn, 0.005% (max.) Fe] is usually a better choice for shields and support structure because of its lower magnetism, much higher acoustic absorption, good electrical conductivity, high strength, and excellent finishing and joining properties. Iron content is also rather carefully controlled in the more readily available phosphor–tin bronzes, such as C51000 [94.8% Cu, 5% Sn, 0.2% P, 0.1% Fe (max.)]. Aluminum, silicon, and zinc bronzes (or brasses) have to be checked carefully if they are to be used within $r_b/3$ of the sample, where r_b is the bore radius, as iron contents can exceed 0.5%. Copper-rich iron compounds are not stable, and the solubility of iron in copper at 200 °C is only 13 ppm,[44] thus copper alloys are likely to be ferromagnetic unless the iron is bound up in iron-poor compounds (such as $FeAl_3$ or $FeSi_2$), in which case it is still strongly paramagnetic ($\chi_V \sim 2$ for Fe_2O_3). For B_0 above 2.16 T, the ferromagnetic components saturate with a high-field χ_V of 2.16 T/B_0.

The critical importance of high-integrity ground connections throughout multiple resonance probes cannot be overemphasized, especially as the wavelength becomes comparable to or shorter than four times the maximum dimension of the electronics region. Welding, press-fits, and solder joints are preferred over silver-filled epoxy and silver paint.[23] The external shield cylinders are often anodized for an aesthetically pleasing finish that also helps eliminate variability in grounds. Figure 7 illustrates three typical NMR probes: a high-resolution liquids narrow bore probe, a CP MAS wide bore probe, and a single crystal probe with a goniometer.

Quartz is usually selected for coil forms in high-field magnets because of its lower dielectric loss, even though its magnetic, mechanical, and acoustic properties are inferior to those of Pyrex. Acoustic ringing in quartz, Macor, and ceramic capacitors may cause problems at frequencies up to 50 MHz. Zirconia has often been used in MAS probes for solids because of its superior mechanical properties.

One of the best engineering thermoplastics is polyether ketone (PEK) because of its low dielectric loss and excellent chemical, thermal, and dimensional stability at modest cost, but other insulating materials (Kel-f, Teflon, Macor, Vespel, zirconia) are often chosen for specific background or thermal considerations. Fiberglass reinforced composites are also widely used, but they must be cleaned well after machining to

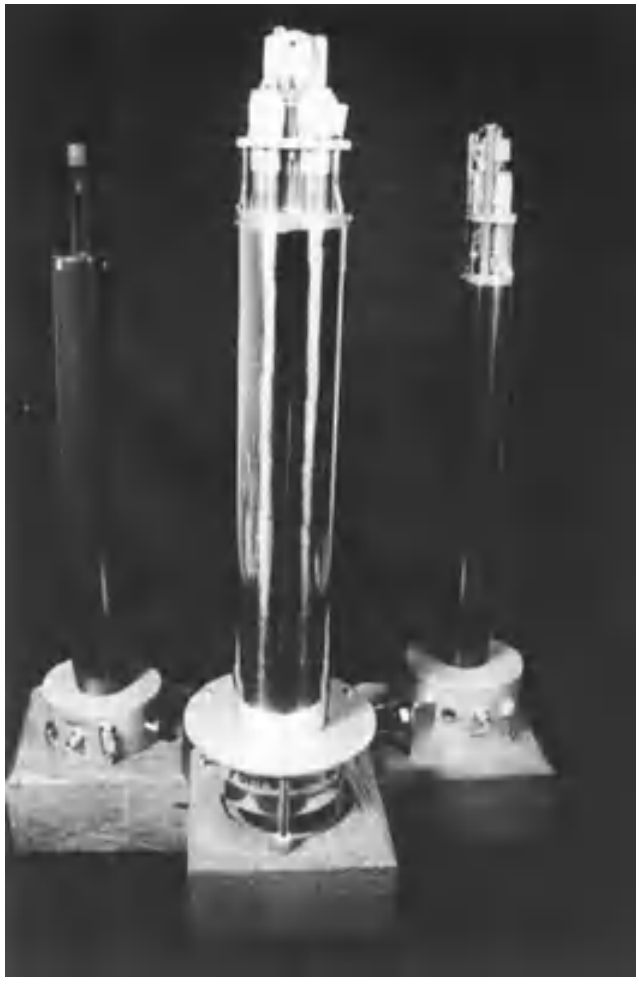

Figure 7 Three typical NMR probes

remove traces of steel from the tools, and the glass fibers may produce aluminum and silicon background signals. Excellent epoxies are available for securing components and mounting coils—such as Epo-Tek 354, 360, and 377 from Epoxy Technology, Inc., Billerica, MA, USA. Several brands of Kel-f and heat-shrink Teflon have sufficiently low hydrogenous content for critical proton applications, but experimentation and careful control are necessary.

8 THERMAL ENGINEERING

Linewidth and lineshape are often critically dependent on temperature control and stability.[46] Most commercial probes are intended to operate from −100 °C to +120 °C, but special liquids probes are commercially available for operation from −170 °C to +380 °C, and solids probes are available to cover the range 35–900 K. Temperatures are usually regulated by using a dc resistive heater (designed for minimal magnetic interaction) to heat a stream that is directed past the sample.

First-order heat-transfer calculations and simple power balance analysis are generally sufficient in the probe design. The heater power P_H required to increase the temperature of the gas by δT with specific heat C_p (1000 J kg^{-1} K^{-1} for N_2) and flow rate G (typically 1–2 g s^{-1} for MAS probes) is

$$P_H = GC_p\delta T \tag{29}$$

The gas temperature is usually measured with a copper–constantan thermocouple shortly before it reaches the sample, but optical sensors have also been used.[47] Platinum resistors (RTDs) are best in the range from 20–75 K and above 700 K, but in the intermediate range they are not as accurate as a thermocouple unless small magnetic-field-dependent corrections are made. They are often used to sense the heater temperature for protection in the event of inadvertent loss of gas flow. The control problems are more difficult than usually encountered elsewhere because of the requirement for precision temperature control of a stream of low specific heat that may encounter large fluctuations in flow rate. Standard PID (proportional-integral-derivative) control algorithms have been incorporated within the past several years by all manufacturers with vast improvements over the simple PI algorithms used previously. Dynamic control stability can be further improved by adding a power estimate that is a function of temperature and flow rate, and fuzzy logic may have advantages. Lead shot has occasionally been used for a thermal ballast because of its high volumetric specific heat and low Debye temperature (105 K).

Heat-transfer calculations are often limited to simple conduction calculations through thin sheets:

$$P_T = k_T A\delta T/d \tag{30}$$

where P_T is the thermal conduction power (W), k_T the thermal conductivity (W m^{-1}) of the material, A the area perpendicular to the direction of heat transfer, δT the temperature difference between the two surfaces, and d the thickness in the direction of heat transfer. The other common conduction problem is through a thick-walled tube with i.d. d_i, o.d. d_o, and length h:

$$P_T = \frac{2\pi k_T h\delta T}{\ln(d_o/d_i)} \tag{31}$$

The high Reynolds numbers (often greater than 10^5) that are seen in Dewared transfer lines result in a very high heat transfer through the bare glass or metal joints unless they are lined internally with plastic tubing, in which case the above equation can be used to estimate the losses.

The extreme temperatures that are often desired[48–50] can make differential thermal expansion responsible for stresses that exceed the rupture limit of one of the components in the probe if not properly designed. However, most of the materials used in NMR probes have high strength. The exceptions, Macor and glasses, tolerate high compressive stresses. Hence, even these materials can often be used with plastics in properly designed situations even though their thermal expansions differ widely. Macor is the only commonly used material that is likely to rupture from internal steady-state thermal stresses, as its maximum thermal stress temperature ($T_T = S/b_T E$, where S is tensile strength, b_T thermal expansion coefficient, and E the Young's modulus of elasticity) and thermal conductivity are both very low.

9 GRADIENT NMR PROBES

By applying magnetic field gradients in three orthogonal directions ($\delta B_z/\delta x$, $\delta B_z/\delta y$, $\delta B_z/\delta z$), it is possible to use NMR to image macroscopic structures, and indeed this has made clinical magnetic resonance imaging (MRI) an important medical diagnostic technique.[51,52] Obtaining spatial resolution below 1 mm on liquid-like samples requires gradients above the 10 m T m^{-1} available in most clinical MR machines. Higher gradients are easily obtained by reducing the size of the gradient coils or improving their efficiency. MR microscopy generally involves incorporating the gradient coils into wide-bore or narrow-bore probes along with small rf coils so that spatial resolution down to 10 μm can be obtained on liquid-like samples. Limited imaging experiments are also then possible on solid samples.[53]

Single axis gradients ($\delta B_z/\delta z$) based on Maxwell pairs (sometimes called anti-Helmholtz coils) are much easier to implement in small spaces and are very useful for diffusion experiments using pulsed field gradients (PFG).[54] Similar probes (with lower gradient coefficients, to keep digital-to-analog convertor and amplifier drift requirements more manageable) have recently become very popular for gradient enhanced spectroscopy (GES), as the run time is often dramatically reduced for 2D NMR.

Rapid switching of large gradient coils requires high-power audio amplifiers (up to 500 kW). Hence, the switching efficiency η_s is very important:

$$\eta_s = \frac{\alpha^2 d_S^4 h_S}{\mu_0 L} \tag{32}$$

where α is the gradient coefficient (T A^{-1} m^{-1}), d_S the sample diameter, h_S the sample length, and L the gradient coil inductance. (The gradient coefficient is sometimes called the 'efficiency', but the above dimensionless definition is more consistent with other efficiency definitions.) The 'fingerprint'

design of Schenck et al.[55] achieves much higher η_s values than earlier Golay coils, but new proprietary designs achieve even higher efficiency.

Image linearity has often been described in terms of field linearity—the relative difference between the gradient field and a linear field at the edge of the sample. A better definition of image linearity is rms local deviation of the gradient from its mean value throughout the sample volume. This has also been called differential linearity. It is sometimes desirable to use highly nonlinear local gradients (more than 40% local deviation) and image distortion correction software so that higher gradients can be achieved,[56] but local deviation below 10% is usually preferred.

When the gradients are switched, eddy currents are induced in the cold radiation shield of the magnet that have long decay times because of the ultralow resistivity of copper below 40 K. Active shielding of the gradients greatly reduces the external fields generated by the gradients and permits rapid pulse techniques without excessive cryogen boiling or high-order compensation techniques.[57,58] Acoustic resonances in the gradient coils are then likely to limit gradient decay time, particularly at very high fields, but novel coil geometries are becoming available that greatly reduce this electromechanical or acoustic efficiency.

10 RELATED ARTICLES

Gradient Coil Systems; Instrumentation for the Home Builder; Probes for High Resolution; Radiofrequency Systems and Coils for MRI and MRS; Sensitivity of Whole Body MRI Experiments; Solid State Probe Design; Spectrometers: A General Overview; SQUIDs; Surface Coil NMR: Detection with Inhomogeneous Radiofrequency Field Antennas.

11 REFERENCES

1. A. Abragam, *The Principles of Nuclear Magnetism*, Oxford University Press, Oxford, UK, 1961.
2. W. G. Clark, *Rev. Sci. Instrum.*, 1964, **35**, 316.
3. R. R. Ernst and W. A. Anderson, *Rev. Sci. Instrum.*, 1966, **37**, 93.
4. R. R. Ernst, in *Advances in Magnetic Resonance*, ed. J. S. Waugh, Academic Press, New York, 1966, Vol. 2, pp. 1–135.
5. M. J. E. Golay and N. J. Rumson, US Pat. 3 569 823, 1971.
6. H. D. W. Hill and R. E. Richards, *J. Phys. E, Ser. 2*, 1968, **1**, 977.
7. D. G. Gillies, in *Nuclear Magnetic Resonance*, ed. R. K. Harris, Chemical Society, London, 1972, Vol. 1, pp. 176–180.
8. J. D. Ellett, M. G. Gibby, U. Haeberlen, L. M. Huber, M. Mehring, A. Pines, and J. S. Waugh, in *Advances in Magnetic Resonance*, ed. J. S. Waugh, Academic Press, New York, 1971, Vol. 5, pp. 117–176.
9. D. D. Traficante, J. A. Simms, and M. Mulcay, *J. Magn. Reson.*, 1974, **15**, 484.
10. D. I. Hoult and R. E. Richards, *J. Magn. Reson.*, 1976, **24**, 71.
11. M. J. Wilson, *The ARRL Handbook for the Radio Amateur*, ARRL, Newington, CT, USA, 1987.
12. *Basic Electronics*, US Navy Bureau of Naval Personnel, Dover, NY, 1973.
13. R. E. Gordon, *Phys. Med. Biol.*, 1985, **30**, 8, 741.
14. D. D. Traficante, *Concepts Magn. Reson.*, 1989, **1**, 73.
15. J. R. Reitz and F. J. Milford, *Foundations of Electromagnetic Theory*, Addison-Wesley, Palo Alto, 1967.
16. J. D. Jackson, *Classical Electrodynamics*, 2nd edn., Wiley, New York, 1975.
17. D. I. Hoult, *Concepts Magn. Reson.*, 1989, **1**, 1.
18. D. I. Hoult, *Prog. NMR Spectrosc.*, 1978, **12**, 41.
19. H. J. Schneider and P. Dullenkopf, *Rev. Sci. Instrum.*, 1977, **48**, 68.
20. D. I. Hoult and P. Lauterbur, *J. Magn. Reson.*, 1979, **34**, 425.
21. F. D. Doty, R. R. Inners, and P. D. Ellis, *J. Magn. Reson.*, 1981, **43**, 399.
22. C. Hayes, W. Edelstein, J. Schenck, O. M. Mueller, and M. Eash, *J. Magn. Reson.*, 1985, **63**, 622.
23. F. D. Doty, T. J. Connick, X. Z. Ni, and M. N. Clingan, *J. Magn. Reson.*, 1988, **77**, 536.
24. J. W. Carlson, *J. Magn. Reson.*, 1988, **78**, 563.
25. G. J. Kost, S. E. Anderson, G. B. Matson, and C. B. Conboy, *J. Magn. Reson.*, 1989, **82**, 238. (Improved methods of treating nonuniform surface current distributions have recently been developed: S. Crozier, K. Luescher, L. K. Forbes, and D. M. Doddrell, *J. Magn. Reson., Ser. B*, 1995, **109**, 1.)
26. C.-N. Chen and D. I. Hoult, *Biomedical Magnetic Resonance Technology*, Adam Hilgar, New York, 1989.
27. W. N. Hardy and L. A. Whitehead, *Rev. Sci. Instrum.*, 1981, **52**, 213.
28. M. F. Koskinen and K. R. Metz, *J. Magn. Reson.*, 1992, **98**, 576.
29. F. D. Doty, US Pat. 4 710 719, 1987.
30. D. M. Ginsberg and M. J. Melchner, *Rev. Sci. Instrum.*, 1970, **41**, 122.
31. D. W. Alderman and D. M. Grant, *J. Magn. Reson.*, 1979, **36**, 447.
32. H. Kugel, *J. Magn. Reson.*, 1991, **91**, 179.
33. J. J. H. Ackerman, *Concepts Magn. Reson.*, 1990, **2**, 23.
34. W. A. Edelstein, J. F. Schenck, O. M. Mueller, and C. E. Hayes, US Pat. 4680548, 1987.
35. J. Tropp, *J. Magn. Reson.*, 1989, **82**, 51.
36. W. A. Anderson, US Pat. 3 771 055, 1973.
37. S. M. Holl, R. A. McKay, T. Gullion, and J. Schaefer, *J. Magn. Reson.*, 1990, **89**, 620.
38. F. D. Doty, US Pat. 5 162 739, 1992.
39. E. Najim and J.-P. Grivet, *J. Magn. Reson.*, 1991, **93**, 27.
40. J. R. Fitzsimmons, H. R. Brooker, and B. Beck, *Magn. Reson. Med.*, 1989, **10**, 302.
41. H. D. Hill and A. P. Zens, US Pat. 4 517 516, 1985.
42. H. D. Hill, US Pat. 4 563 648, 1986.
43. J. R. Davis (ed.), *Metals Handbook*, 10th edn., ASM International, New York, 1990, Vol. 2.
44. M. Hansen (ed.), *Constitution of Binary Alloys*, 2nd. edn., McGraw-Hill, New York, 1989.
45. M. L. Buess and G. L. Petersen, *Rev. Sci. Instrum.*, 1978, **49**, 1151.
46. A. Allerhand and S. R. Maple, *J. Magn. Reson.*, 1988, **76**, 375.
47. H. J. Williams, Y. Gao, A. I. Scott, M. H. Gross, and M. H. Sun, *J. Magn. Reson.*, 1988, **78**, 338.
48. F. D. Doty, J. B. Spitzmesser, and D. G. Wilson, US Pat. 5 202 633, 1993.
49. M. S. Conradi, *Concepts Magn. Reson.*, 1993, **5**, 243.

50. J. F. Stebbins, E. Schneider, J. B. Murdoch, A. Pines, and I. S. E. Carmichael, *Rev. Sci. Instrum.*, 1986, **57**, 39.
51. P. Mansfield and P. G. Morris, in *Advances in Magnetic Resonance*, ed. J. S. Waugh, Academic Press, New York, 1982, Vol. 12, Suppl. 2.
52. D. G. Taylor, R. Inamdar, and M.-C. Bushell, *Phys. Med. Biol.*, 1988, **33**, 6, 635.
53. D. G. Cory, J. W. M. van Os, and W. S. Veeman, *J. Magn. Reson.*, 1988, **76**, 543.
54. P. T. Callaghan and Y. Xia, *J. Magn. Reson.*, 1991, **91**, 326. (Important improvements in the original technique have recently been developed: D. Wu, A. Chen, and C. S. Johnson, *J. Magn. Reson., Ser. A*, 1995, **115**, 260.)
55. J. F. Schenck, M. A. Hussain, and W. A. Edelstein, US Pat. 4 646 024, 1987.
56. P. Roemer, US Pat. 4 926 125, 1990.
57. P. Mansfield and B. Chapman, *J. Magn. Reson.*, 1986, **66**, 573. (Force cancellation has recently been described: R. Bowtell and P. Mansfield, *Magn. Reson. Med.*, 1995, **34**, 494.)
58. J. J. Van Vaals and A. H. Bergman, *J. Magn. Reson.*, 1990, **90**, 52.

Biographical Sketch

F. David Doty. *b* 1950. B.A., Physics, 1972, Anderson University, IN, USA, Ph.D., 1983, Physics, University of South Carolina. Began work in NMR under Paul Ellis, 1979. President of Doty Scientific, Inc., 1982–present. Approx. 20 publications and 15 patents. Research interests include rf electronics, NMR probe technology, electromagnetism, manufacturing, turbomachinery, energy conversion cycles, ceramics engineering, acoustics, economics, and religions.

Probes for High Resolution

Howard D. W. Hill

Varian Associates, Palo Alto, CA, USA

1 Introduction 1
2 Historical Review 1
3 Modern Probe Technology 2
4 Conclusions 5
5 Related Articles 6
6 References 6

1 INTRODUCTION

The NMR probe provides the coupling between the nuclear spins of the sample and the spectrometer electronics. As such, it must provide a rotating radiofrequency (rf) field perpendicular to the polarizing magnetic field to excite the spins and, similarly, detect the rotating magnetization of the spins. While these considerations apply to any NMR probe, a particularly important requirement for high-resolution NMR probes is to minimize the perturbation of the polarizing magnetic field so as to maintain the inherent resolution of the signals. This has become more important as the proton resonance frequency of high-resolution spectrometers has increased from the earliest values of 30 MHz to 750 MHz or more.

For a given magnetic field strength, the probe is a primary determinant in the *sensitivity* of a *spectrometer*. Sensitivity can be improved by using a larger sample, thereby including more spins, provided that the field homogeneity can be maintained over the sample volume. Larger volumes are typically used to observe the resonances of low-γ nuclei for which the inherent sensitivity is lower, and the resolution requirements are less severe, than for proton NMR.

The excitation and detection of a single nuclear species can be accomplished with a fairly simple probe structure. However, as the techniques of high-resolution spectroscopy have developed, it has become increasingly common to excite and perhaps detect the response from more than one nuclear species simultaneously.

The probe structure must also provide the required environment for the sample. This usually means the provision of an accurate and stable temperature control. For more sophisticated experiments, it may also be necessary to provide pulsed magnetic *field gradients*, optical excitation, or high sample pressure.

2 HISTORICAL REVIEW

The earliest high-resolution spectrometers operated in the continuous wave (CW) mode and were designed to excite and observe a single nuclear species, usually protons. Two different types of probe systems were used for the detection of the weak NMR response in the presence of the strong rf excitation. In the single coil system, derived from the work of Purcell,[1,2] one coil was used for excitation and detection, while isolation of the transmitter and receiver was achieved by including the probe in one arm of a bridge circuit. The bridge was adjusted close to a complete balance in the absence of an NMR absorption. A nuclear resonance changed the balance to produce a detectable signal. In the crossed-coil system, first used by Bloch and his co-workers,[3,4] two separate coils were used for transmission and reception. By arranging the coils to be geometrically orthogonal to minimize the magnetic coupling, and by including an electrostatic screen between the two coils to minimize capacitive coupling, the direct interaction could be kept to a low value. An NMR response induced a signal in the receiver coil. With both coil systems, it was possible to detect either an absorption or a dispersion signal by detecting the NMR response as a change of a deliberately introduced 'leakage' signal. The bridge circuit included two adjustments to control the in-phase and quadrature phase imbalance. The crossed-coil probe included two 'paddles'[5,6] to control in-phase and quadrature phase leakage between the transmitter and receiver coils.

The magnetic field was typically generated between the poles of an electromagnet or permanent magnet with the sample arranged perpendicular to the axis of the magnet poles. A solenoidal coil around the sample provided the appropriate orientation of the rf field for the detection of the nuclear magnetization. In a crossed-coil probe, a second coil system, arranged in the form of a large Helmholtz pair, with its axis perpendicular to the polarizing field, was used as the transmitter. The use of a separate transmitter coil provided a very uniform rf excitation although it did require a larger transmitter power. For CW experiments, this additional transmitter power was not a serious problem.

Sample spinning[7,8] was introduced to average transverse gradients and thereby improve resolution. Consequently, from an early date, a high-resolution NMR probe included a mechanism to provide for spinning the sample at a few tens of revolutions per second. An air bearing and drive was the preferred method, since this was the only way to provide a sufficiently smooth rotation.

The influence of the probe design on the spectrometer resolution was recognized early on. Symmetry of materials around the active sample volume was vital, as was the choice of probe material itself. It was particularly important to use materials which were uniform in composition and free from ferromagnetic impurities. The receiver coil, which was, of necessity, very close to the sample, was a particular concern. Low susceptibility materials were selected or specially manufactured[9] to minimize the magnetic perturbations introduced by the coil.

The use of modulation[10,11] and the phase-sensitive detection of modulation sideband signals helped to improve the isolation of the transmitter and received signals. Magnetic field modulation, at frequencies typically in the range of a few kHz, was provided by coils built into the probe. Field modulation allowed the generation of multiple effective rf fields by the addition of different modulation frequencies. Thus, the use of homonuclear decoupling[12,13] or of a homonuclear field/frequency lock[14] did not change the rf configuration of the probe.

The introduction of pulsed *Fourier transform* (FT) methods[15,16] required much higher rf excitation fields and, to keep transmitter powers to reasonable levels, the use of separate

transmitter and receiver coils for a single nucleus quickly died out. Since the transmitter and receiver functions occupied separate time intervals, a single coil could be switched between transmission and reception using techniques which were well established in pulsed NMR methods.[17,18]

Superconducting magnets for high-resolution NMR were introduced at about the same time as FT methods.[19] The configuration of the superconducting magnet was different from that of existing electromagnets and permanent magnets; it was in the form of a solenoid with the magnetic field generated along the axis of the solenoid. This required a significantly different probe geometry.

3 MODERN PROBE TECHNOLOGY

3.1 Introduction

Since the majority of modern high-resolution probes are designed for use in superconducting magnets with pulsed FT spectrometers, the most common configuration is one in which the sample is parallel to the axis of the magnet and one or more saddle-shaped rf coils are arranged around the sample. Solenoidal coils are somewhat more efficient than saddle coils[20,21] but their use would require the sample to be placed perpendicular or at an angle to the magnet axis. The added inconvenience in sample handling and the implications for resolution are only warranted for special applications.

The transmit and receive functions for the nuclear species being observed are handled on a single coil. However, most high-resolution experiments require the probe to support more than one nuclear resonance frequency. In the simplest configuration, this may be only a single observe nucleus (for example, protons) and a field/frequency lock nucleus (for example, deuterium). In this case, the most common practice is to 'double tune' a single coil[22] to support both frequencies.

In addition, many experiments demand the irradiation of other nuclear species, either to provide coupling information by *multidimensional methods*[16,23,24] or to remove couplings during acquisition, for example by broadband *decoupling*.[25,26] While it is possible to multiply tune a single coil, by an extension of the double tuning scheme, it is more common to provide a second coil, arranged geometrically orthogonal to the first, to support the additional frequency or frequencies. Coupling between the two coils can be reduced to about -20 dB or -30 dB from geometry alone. Greater isolation is required to prevent overloading of the receiver electronics and is provided by frequency-selective filters (either internal to the probe, or external).

3.2 Probe Tuning

The probe coil is tuned and matched, usually to 50 Ω, to provide efficient coupling to the rest of the circuit. A common circuit for a single tuned coil is shown in Figure 1(a) and for a double tuned circuit in Figure 1(b). The resonant frequency of the singly tuned circuit is given by

$$\omega = \frac{1}{\sqrt{L(C_1 + C_2)}} \tag{1}$$

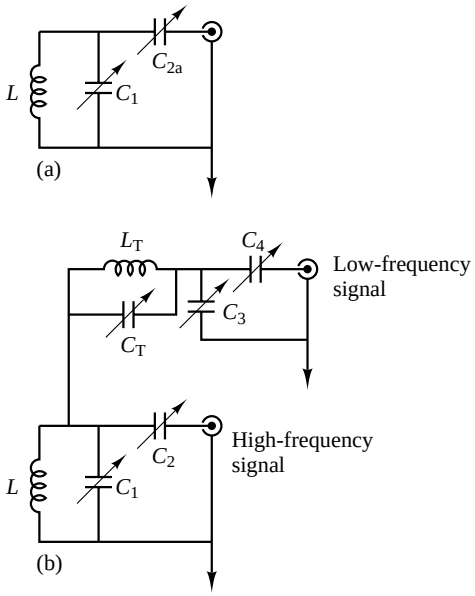

Figure 1 (a) A two capacitor network to tune and match a sample coil, L, to a resistive impedance. (b) A double tuned circuit providing separate inputs for the high- and low-frequency signals. The trap circuit formed by L_T and C_T is tuned to approximately the same frequency as the high-frequency circuit. Capacitors C_3 and C_4 provide tuning and matching for the low-frequency signal

and the input resistance at resonance by

$$R_{in} = \frac{1}{\omega^3 L Q C_2^2} \tag{2}$$

For a high-Q circuit, $C_1 \gg C_2$, and C_1 primarily affects the tuning and C_2 the impedance match. By providing a wide range of variability in the values of these capacitors, a probe may be made to tune over a wide frequency range to allow excitation and/or detection of many nuclear species. It is normally not feasible to provide a very wide tuning range with a variable capacitor alone. Instead, a range of fixed capacitors is switched in parallel with a variable capacitor of more limited range. In this way the physical size of the circuits and the associated inductance can be kept small.

3.3 Sensitivity

For a given operating magnetic field strength, the NMR probe is the primary factor governing the sensitivity of a spectrometer. Both the signal voltage and the major noise source originate in the probe.

The factors affecting the sensitivity of a signal excited by a single pulse can be understood by considering the equivalent circuit of a receiver coil shown in Figure 2. The voltage source e_s represents the signal voltage induced in the coil by the precessing magnetization, while e_n represents the rms thermal noise voltage generated in the resistance r of the circuit. The resistance may be due to losses in the coil and capacitors of the probe, or to conductive losses in the sample itself.

The signal voltage is best calculated by invoking the principle of reciprocity as described by Hoult and Richards.[20] If a coil carrying a unit current produces a transverse magnetic

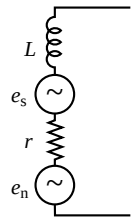

Figure 2 The equivalent circuit of a receiver coil

field $\boldsymbol{B}_t$ at a given point in space, then a magnetic dipole $\boldsymbol{m}$ at that point will induce an emf in the coil given by

$$e_s = -(d/dt)(\boldsymbol{B}_t \cdot \boldsymbol{m}) \tag{3}$$

For an extended sample, this expression must be integrated over the sample volume, V_s. In terms of the probe parameters and its operating frequency, ω, the signal voltage may be written as

$$e_s \propto N\lambda\omega^2 B_t V_s \tag{4}$$

where N is the concentration of spins and λ has been introduced as an 'inhomogeneity factor' to reflect the variation of B_t over the sample volume. This may be calculated analytically for some geometries and numerically in more complex cases. The induced voltage is expressed in terms of the coil inductance by introducing a 'filling factor' defined by

$$\xi = \frac{\int_{\text{sample}} B_t^2 \, dV}{\int_{\text{all space}} B^2 \, dV} \tag{5}$$

and representing the fact that only a portion of the total magnetic energy of the coil is effective in exciting magnetic resonance. The inductance of the coil is given by

$$L = \frac{1}{\mu_o} \int_{\text{all space}} B^2 \, dV \tag{6}$$

since B has been defined for a unit current in the coil. We may then write

$$\xi' = \frac{B_t^2 V_s}{\mu_o L} \tag{7}$$

where ξ' represents a modification of the filling factor to account for the inhomogeneity of the rf field over the sample volume. The induced signal is thus

$$e_s \propto N\lambda\omega^2(\xi' L V_s)^{1/2} \tag{8}$$

The signal is coupled to the spectrometer by a tuning and matching network, for example that shown in Figure 1(a).

The rms thermal noise voltage generated in the resistance r of the coil is

$$e_n = (4kTr\Delta f)^{1/2} \tag{9}$$

where k is Boltzmann's constant, T is the temperature of the resistance (normally equal to the sample temperature), and Δf is the bandwidth of the measurement. The noise voltage is transformed by the matching network exactly as the signal voltage, but additional noise power, characterized by the noise factor F, is introduced by the spectrometer electronics. The receiver bandwidth appears in the expression for the noise voltage in the time domain but drops out of the corresponding expression for noise voltage in the frequency domain when the correct antialiasing filter is utilized before digitization and Fourier transformation. In terms of probe and spectrometer parameters, the sensitivity, as given by the signal-to-noise ratio in the frequency domain, is then

$$\frac{e_s}{e_n} \propto N\lambda\omega^{3/2}\left[\frac{\xi' V_s Q}{F}\right]^{1/2} \tag{10}$$

where Q, the quality factor of the resonant circuit, is defined by

$$Q = \frac{\omega L}{r} \tag{11}$$

The expression for sensitivity highlights a number of important considerations for probe design. There is a strong dependence on operating frequency, hence the continued emphasis on spectrometers with higher field magnets. Since coil Q values generally increase as $\omega^{1/2}$, the frequency dependence is slightly greater than the explicit function included in equation (10). The selection of the sample volume is governed to a large extent by the sample and the application. For a fixed *concentration* of spins, the sensitivity increases with increasing sample volume. However, for a fixed *number* of spins, the sensitivity can be increased by concentrating them into a smaller volume and adjusting the coil dimensions to maximize the filling factor. The volume, V_s, is that volume from which signal is detected while for homogeneity reasons, discussed below, the total sample volume must be somewhat greater. Typical total sample volumes are approximately 400 μL to 500 μL in 5 mm diameter sample tubes and 2.5 mL in 10 mm diameter sample tubes.

The filling factor and the coil Q value are parameters which the probe designer can control by careful choice of probe layout and materials. The filling factor is increased by coupling the coil as tightly as possible to the sample (by reducing the coil diameter relative to that of the sample) and by minimizing the fraction of inductive energy stored outside the sample volume, for example in that part of the circuit associated with the tuning elements. This suggests the use of a coil with as large an inductance as possible. However, this limits the upper frequency of the coil and requires the use of higher voltages to generate a given rf field strength. This, in turn, results in higher electric fields within the sample. The use of a low inductance coil to minimize these problems requires keeping the tuning elements as close as possible to the coil.

The coil Q value is influenced both by the conductor of the coil itself and also by the insulating materials which are used to support the coil. Naturally the coil should be constructed from the best possible conductor, e.g. copper or silver, and also be constructed in such a way as to minimize the concentration of currents in small volumes of the conductor. For this reason, sharp corners and edges should be avoided. Insulating materials close to conductors should be very low loss. Most plastic materials do not satisfy this requirement.

Epoxies are particularly poor and should be avoided if at all possible. Losses in the capacitors of the tuned circuit also contribute to a reduction in the overall circuit Q value. While such losses are generally small, they are not negligible and the best quality capacitors are required for high-sensitivity probe circuits.

In many cases, particularly for biological applications, the sample can be a significant contributor to the losses in an NMR probe. Both inductive losses, from currents induced in a conductive sample by the rf magnetic field, and dielectric losses, associated with the rf electric field from the distributed capacitance of the coil, contribute to the overall loss.[27,28] The electric fields can be reduced by balancing the coil with respect to ground[29] and by including electrostatic shields within the probe structure. Typical circuit configurations for balanced coils are shown in Figure 3.

If the coil resistance is the primary source of noise, the noise voltage may be reduced by cooling the coil. To provide thermal isolation from the sample, the filling factor is sacrificed but, by cooling a standard coil to approximately 20 K, significant sensitivity advantages have been achieved.[30,31] The use of high-temperature superconducting materials for probe coils may also prove advantageous for sensitivity improvement.

3.4 Resolution

A probe and a sample can cause significant distortions of the polarizing magnetic field due to differences in the magnetic susceptibility of materials.[32] A major aspect of high-resolution probe design is the control and correction of those distortions. Materials commonly used in probe construction have diamagnetic volume susceptibilities of several ppm. Therefore, abrupt changes in susceptibility near the sensitive volume of the probe can cause serious degradation of the field uniformity. Probe designs use two important methods to minimize such perturbations: (a) the geometry and symmetry; and (b) a careful choice of materials.

The use of cylindrically symmetric components and material boundaries well removed from the sample region ensures that perturbations within the sample volume are minimized or are at least correctable by adjustment of the magnet shim coils. The most critical element is the sample coil, since it is closest to the active volume of the sample and inevitably includes some susceptibility discontinuities in its geometry. Sometimes the geometry can be modified to minimize the effect of these discontinuities, but the main strategy employed to minimize perturbations is to construct the coil from a material which is specially designed to have a very low magnetic susceptibility. This is accomplished by making the coil from a composite material with diamagnetic and paramagnetic components, either by electroplating or by some other method of making a sandwich structure, while maintaining a high conductivity. Diamagnetic materials which can be used are copper, silver, and gold. Suitable paramagnetic materials are aluminum, rhodium, and platinum. For a good quality coil, it is necessary to reduce the effective volume susceptibility to less than one-tenth that of copper.

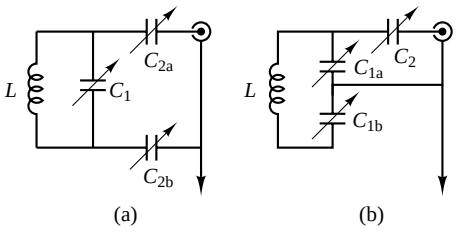

Figure 3 Two configurations for balancing a coil with respect to ground. For optimum performance $C_{1a} \approx C_{1b}$ and $C_{2a} \approx C_{2b}$. In (a) the tuning capacitor, C_1, must support the full voltage across the coil, while the voltage across the matching capacitors is approximately one-half the coil voltage. In (b) the voltage across all capacitors is approximately one-half the coil voltage, but tuning over a wide frequency range is more difficult since C_{1a} and C_{1b} are twice the value of C_1 in configuration (a)

The ends of the sample itself are a major source of perturbation and must be kept at some distance from the active sample region if their effects are to be corrected by shim coils. Some reduction in the sample volume can be realized if the sample is restricted by a container with a volume susceptibility which closely matches that of the sample.[33]

As operating field strengths have increased, the requirements for absolute resolution have remained fixed or even tightened. Thus the demands on the probe performance with respect to resolution have increased. In addition, many experiments are performed with static rather than spinning samples because of undesirable artifacts caused by sample spinning.

3.5 Radiofrequency Excitation

Both the intensity and the uniformity of the rf excitation are important parameters. The rf field strength must be sufficient to excite all the spins of interest. This has become more of a technical challenge as spectrometer frequencies have increased.

The relationship between the various factors contributing to the rf field strength may be understood by considering the fundamental definition of the quality factor, Q, of a resonant circuit:

$$Q = \frac{\omega U}{P} \tag{12}$$

where U is the energy stored and P is the power dissipated in the circuit. Now,

$$U \propto B_1^2 V_c \tag{13}$$

where V_c is the volume of the coil. For a given coil, operating in the range where $Q \propto \omega^{1/2}$, the strength of the rf field, expressed in frequency units is

$$\omega_1 \propto \gamma P^{1/2} \omega^{-1/4} V_c^{-1/2} \tag{14}$$

Thus, for a given nuclear species and a fixed coil volume, the power required to generate a given rf field strength increases as $\omega^{1/2}$. However, to provide an equivalent frequency range of excitation, the rf field should increase in proportion to the resonance frequency. Therefore, to maintain the same effective spectral excitation, the power increases as $\omega^{5/2}$. This strong dependence represents a significant challenge in the design of probes for high-field spectrometers. The power dissipation becomes an important factor in the generation of

long pulses or continuous rf excitation as in spin locking pulses or decoupling. For the generation of short excitation pulses, the major design consideration is the voltage handling capability of the tuning capacitors of the circuit.

Because of the increased size of the outer coil of a multicoil probe, correspondingly higher powers are required to generate the required rf fields. In a high-frequency probe of this type, designed to observe protons on an inner coil and to irradiate ^{13}C and/or ^{15}N with an outer coil, several hundreds watts of power are needed for the ^{13}C and ^{15}N channels. This requires the use of capacitors which can handle many thousands of volts. These are values which are more traditionally associated with probes for solids applications.

Uniformity of the excitation is important in a number of different types of measurements. In a simple pulsed FT experiment with a spinning sample, nonuniformity in the rf field distribution can cause spinning sidebands. These arise from phase and amplitude modulation of the detected signal and, unlike sidebands arising from inhomogeneity of the polarizing magnetic field, have an amplitude which is independent of the spinning frequency. Positive and negative sidebands may be of different intensity and may not always be in phase with the parent peak.

In many multidimensional experiments, rf pulses are used to transfer magnetization from one spin system to another. The efficiency of the transfer depends on the effective rotation induced by the pulse. Many such transfers may occur[34,35] before a spin response is detected. Variation of rf intensity over the sample volume results in a variation of the magnetization transfer and a loss of sensitivity.

The uniformity of the excitation can be improved by careful attention to the design of the coil shapes and the arrangement of multiple coil systems. Electromagnetic modeling programs are useful in this regard for the calculation of field distributions.

3.6 Probe Artifacts

Precautions must be taken to eliminate a number of possible signal artifacts which can originate in the probe.

3.6.1 Spurious rf Signals

An NMR probe is a very sensitive antenna and must be shielded from external sources of rf such as other electronic equipment or radio stations. Special attention must be paid to the grounding of all electrical connections into the probe. It is difficult to provide complete shielding since access must be provided for the sample. In exceptional cases, it may be necessary to adjust the spectrometer frequency to avoid external interference.

3.6.2 NMR Background Signals

NMR background signals from probe materials can be troublesome. Very small amounts of proton-bearing material may give rise to a detectable signal. Some relief is achieved from the fact that most of the signals are from solid probe construction materials and hence are very broad. Probe surfaces should be clean to avoid picking up signals from fingerprints. Moisture in gases in the probe will also give strong signals.

3.6.3 Acoustic Ringing

Acoustic ringing[36] can be a very serious problem, particularly for probes designed to detect low-γ nuclei. The probe coil and other metal parts of the probe may be excited into mechanical oscillation at the rf frequency by Lorentz forces during the rf excitation pulse. These oscillations often have a very high mechanical Q value and persist long after the pulse. The oscillating metal in the magnetic field induces an rf field which can be picked up by the probe coil. The signal may persist for several hundred microseconds and be transformed into serious baseline distortion of spectra. Acoustic resonance signals can be distinguished from NMR signals by the use of special pulse sequences,[37] but are best eliminated by changing the materials of the probe.

3.7 Other Requirements

3.7.1 Variable Temperature

Sample temperature is normally controlled by passing a temperature controlled gas stream past the sample. The probe structure is designed to minimize thermal losses and to provide a uniform temperature distribution over the sample itself. A temperature sensor (thermocouple or resistance thermometer) is located as close as possible to the sample and used to regulate the gas temperature via a heater in the gas stream.

3.7.2 Pulsed Field Gradients

An increasingly useful technique is the application of pulsed field gradients,[38–40] either to suppress strong solvent signals or to provide selective detection of coherence transfers. To provide rapid switching and to minimize the generation of eddy currents, these gradients are best provided by a set of shielded coils[41] built into the probe itself. The gradient coils have sufficient symmetry and are far enough removed from the sample that they cause little problem with resolution, but may be close enough to some of the rf coils to degrade their electrical performance.

3.7.3 Optical Excitation

High-resolution experiments are combined with optical excitation in the method of chemically induced dynamic polarization (CIDNP).[42,43] Here, pulses from a laser are typically coupled via a light pipe from the base of the probe and a mirror or prism to the active sample volume. This usually results in an asymmetric structure close to the sample and may cause some loss in resolution.

4 CONCLUSIONS

The range of applications for high-resolution probes continues to develop. It seems likely that the field strengths

used for NMR will continue to increase, placing additional demands on the performance of the probes.

Sensitivity remains the major disadvantage of NMR spectroscopy. As a result, efforts will continue to improve the performance. In addition to the possible use of high-temperature superconductors for probe coils, the use of these new superconducting materials also offers the possibility of building magnets to generate still higher magnetic fields. Already high-resolution magnets at greater than 20 T are being developed. If history is any guide, the requirements for absolute resolution will remain constant, or even increase, and the demands on the probe will be even more stringent.

As improvements are made, it is likely that new applications for high-resolution NMR will be opened up, perhaps necessitating the development of different probe configurations.

5 RELATED ARTICLES

Chemically Induced Dynamic Nuclear Polarization; Decoupling Methods; Double Resonance; Field Gradients and Their Application; Fourier Transform Spectroscopy; High- Pressure NMR; Magnetic Susceptibility and High Resolution NMR of Liquids and Solids; Multidimensional Spectroscopy: Concepts; Probe Design and Construction; Probes for Special Purposes; Radiofrequency Pulses: Response of Nuclear Spins; Sensitivity of the NMR Experiment; Shimming of Superconducting Magnets; Spectrometers: A General Overview.

6 REFERENCES

1. E. M. Purcell, H. C. Torrey, and R. V. Pound, *Phys. Rev*, 1948, **69**, 37.
2. N. Bloembergen, *Nuclear Magnetic Relaxation* W. A. Benjamin, Inc, New York, 1961.
3. F. Bloch, W. W. Hansen, and M. Packard, *Phys. Rev.*, 1946, **69**, 127.
4. F. Bloch, *Phys. Rev.*, 1946, **70**, 460.
5. F. Bloch, W. W. Hansen, and M. Packard, *Phys. Rev.*, 1946, **70**, 474.
6. F. A. Nelson, in *NMR and EPR Spectroscopy*, Pergamon Press, Oxford, UK, 1960, Chap. 6
7. F. Bloch, *Phys. Rev.*, 1956, **94**, 496.
8. W. A. Anderson and J. T. Arnold, *Phys. Rev.*, 1956, **94**, 497.
9. W. A. Anderson and J. N. Shoolery, US Pat. 3 091 732, 1963.
10. W. A. Anderson, in *NMR and EPR Spectroscopy*, Pergamon Press, Oxford, UK, 1960, Chap. 14
11. O. Haworth and R. E. Richards, *Prog. NMR Spectrosc.* 1966, **1**, 1.
12. R. Freeman and W. A. Anderson, *J. Chem. Phys.*, 1962, **37**, 85.
13. R. A. Hoffman and S. Forsen, *Prog. NMR Spectrosc.*, 1966, **1**, 15.
14. R. Freeman and D. H. Whiffen, *Proc. R. Soc. London, Ser. A*, 1962, **79**, 794.
15. R. R. Ernst and W. A. Anderson, *Rev. Sci. Instrum.*, 1966, **37**, 93.
16. R. R. Ernst, G. Bodenhausen, and A. Wokaun, *Principles of Nuclear Magnetic Resonance in One and Two Dimensions*, Clarendon Press, Oxford, UK, 1987.
17. I. J. Lowe and C. E. Tarr, *J. Phys. E, Sci. Instrum.*, 1968, **1**, 320.
18. J. D. Ellett, M. G. Gibby, U. Haeberlen, L. M. Huber, M. Mehring, A. Pines, and J. S. Waugh, *Adv. Magn. Reson.*, 1971, **5**, 117.
19. H. L. Marshall and H. E. Weaver, *J. Appl. Phys.*, 1963, **34**, 3175.
20. D. I. Hoult and R. E. Richards, *J. Magn. Reson.*, 1976, **24**, 71.
21. H. D. W. Hill and A. P. Zens, *24th Exp. NMR Conf., Asilomar, CA, USA, 1983*.
22. D. I. Hoult, *Prog. NMR Spectrosc.*, 1978, **12**, 41.
23. J. Jeener, AMPERE Summer School, Basko Polje, Yugoslavia, 1971.
24. W. P. Aue, E. Bartholdi, and R. R. Ernst, *J. Chem. Phys.*, 1976, **64**, 2229.
25. R. R. Ernst, *J. Chem. Phys.*, 1966, **45**, 3845.
26. M. H. Levitt, R. Freeman, and T. Frenkiel, *Adv. Magn. Reson.*, 1983, **11**, 47.
27. D. I. Hoult and P. C. Lauterbur, *J. Magn. Reson.*, 1979, **34**, 425.
28. D. G. Gadian and F. N. H. Robinson, *J. Magn. Reson.*, 1979, **34**, 449.
29. J. Murphy-Boesch and A. P. Koretsky, *J. Magn. Reson.*, 1983, **54**, 526.
30. P. Styles, N. F. Soffe, C. A. Scott, D. A. Cragg, F. Row, D. J. White, and P. C. J. White, *J. Magn. Reson.*, 1984, **60**, 397.
31. P. Styles, N. F. Soffe, and C. A. Scott, *J. Magn. Reson.*, 1989, **84**, 376.
32. L. F. Fuks, F. S. C. Huang, C. M. Carter, W. A. Edelsein, and P. B. Roemer, *J. Magn. Reson.*, 1992, **100**, 229.
33. A. P. Zens, US Pat. 4 549 136, 1985.
34. B. T. Farmer, II, *J. Magn. Reson.*, 1991, **94**, 413.
35. H. B. Olsen, S. Ludvigsen, and O. W. Sorensen, *J. Magn. Reson., Ser. A*, 1993, **105**, 321.
36. J. P. Gerothanasis, *Prog. NMR Spectrosc.*, 1987, **19**, 267.
37. S. L. Patt, *J. Magn. Reson.*, 1984, **49**, 161.
38. A. Bax, P. G. de Jong, A. F. Mehlkopf, and J. Smidt, *Chem. Phys. Lett.*, 1980, **69**, 567.
39. P. Barker and R. Freeman, *J. Magn. Reson.*, 1985, **64**, 334.
40. R. Hurd, *J. Magn. Reson.*, 1990, **87**, 422.
41. P. Mansfield and B. Chapman, *J. Magn. Reson.*, 1987, **72**, 211.
42. R. Kaptein, in *Biological Magnetic Resonance*, eds. L. J. Berliner and J. Reuben, Plenum Press, New York, 1982, Vol. 4, p. 145.
43. P. J. Hoare and R. W. Broadhurst, *Prog. NMR Spectrosc.*, 1993, **25**, 345.

Biographical Sketch

Howard D. W. Hill. *b*. 1938. B.A. (physics), 1961, D. Phil. (physics), Oxford University, 1965. Research assistant with Professor R. E. Richards, Physical Chemistry Laboratory, Oxford, 1965–68. Postdoctoral Fellow, Varian Associates, Palo Alto, CA, 1968–69. Member of R&D staff, Varian NMR Instruments, 1969–present. Varian Fellow, 1988. Current interests include the improvement of sensitivity and resolution of NMR systems.

Probes for Special Purposes

Robert A. McKay
Washington University, St. Louis, MO, USA

1	Introduction	1
2	Transmission Line Theory	1
3	Two- and Three-Frequency Probes	2
4	Traps	3
5	Summary	3
6	Related Articles	3
7	References	4

1 INTRODUCTION

With the development of CP MAS solid state NMR experiments in the 1970s using dipolar decoupling and with the recent development of REDOR and TEDOR type experiments, the need for multiple tuned probes has evolved. This article describes the use of transmission lines in designing these types of probes. There have been several probes for doing two frequency, i.e. ^{1}H and ^{13}C CP MAS, described in the literature.[1–4] (See also ***Probe Design and Construction*** and ***Solid State Probe Design***). Some of these use transmission lines in their design, but all have some tuning elements at the sample coil. The probes described in this article will not, in general, have any tuning elements at the sample coil but may have a fixed capacitance in series with the sample coil in the magnet. All other tuning elements are remote from the magnet. The advantages of this type of design are (1) good frequency discrimination, (2) the use of more rugged tuning elements, and (3) the sample can be in a hostile environment.

2 TRANSMISSION LINE THEORY

The theory of rf transmission lines, and coaxial lines in particular, are covered in many texts, and the reader is referred to them for additional help. Smith charts will not be used, but understanding them can make visualizing these designs easier.

Two fundamental equations regarding transmission lines are

$$Z_{\text{in}} = Z_0[Z_{\text{r}}\cosh(\gamma l) + Z_0\sinh(\gamma l)]/[Z_0\cosh(\gamma l) + Z_{\text{r}}\sinh(\gamma l)] \quad (1)$$

$$V_x = V_{\text{s}}[\cosh(\gamma x) - Z_0/Z_{\text{s}}\sinh(\gamma x)] \quad (2)$$

where Z_{in} is the impedance looking into a section of transmission line of length l terminated with an impedance Z_{r}, Z_0 is the characteristic impedance of the transmission line, Z_{s} is the Z_{in} for a particular line looking into the line from the sending end, x is the distance measured from the input to the point of calculation, V_{s} is the applied voltage, and γ is the propagation constant and is equal to $\alpha + \text{i}\beta$ where α is the attenuation constant in nepers/meter and β is the phase constant equal to $2\pi/\lambda$, where λ is the wavelength of the frequency of measurement. All units are SI.

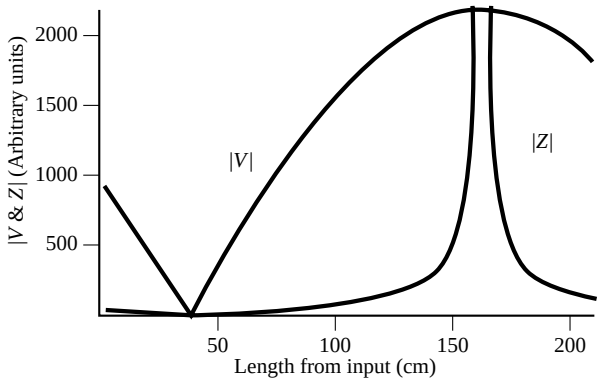

Figure 1 Magnitude of voltage and impedance along a mismatched transmission line

The voltage and impedance along a section of transmission line terminated with an impedance of a typical sample coil have a similar dependence, i.e. they both have a minimum at a common point. A magnitude plot for both is shown in Figure 1. This point will be referred to as the null point. The impedance to the left of the null point is inductive and to the right capacitive for lengths less than a quarter wavelength. This can be verified from equation (1) by noting the phase angle of Z_{in}. Therefore, a single-frequency probe can be made by using standard tuning and matching capacitors at the left or sending end of the line since it looks inductive. This should be the highest frequency channel in a multifrequency probe. At this frequency the impedance at the null point is very low and is insensitive to other circuit elements being connected there. Therefore it is a good point to connect the tuning elements of lower frequency channel(s). Using the null point in this manner achieves a high degree of isolation between the high-frequency channel, usually proton, used for CP and dipolar decoupling, and the lower frequency channel(s) used for observation, dephasing, or coherence transfer. The length of the transmission line used to the left of the null point is just sufficient so that reasonable values of capacitance can be used. (1) can be used to calculate the inductive reactance and hence the value of capacitance to use.

The isolation is very good, but there is a price to pay, and it is efficiency. When transmission lines are terminated in an impedance other than their Z_0, the efficiency is reduced. The impedance of a typical sample coil will be considerably different from Z_0 mainly by the fact that it will have a large imaginary part and a small real part where Z_0 is purely real. The efficiency of a transmission line (Eff) with a high SWR (Standing Wave Ratio) is given by[5]

$$Eff = 1/(1 + SWR \cdot \alpha \cdot l) \quad (3)$$

where SWR is the ratio of the maximum voltage to the minimum voltage in Figure 1 and l is the length of line. The quantities SWR and α can be minimized with respect to Z_0 and α can also be reduced by increasing the diameter of the coaxial conductors. The quantity SWR is optimized when the magnitude of reactance of the load (sample coil) is equal to Z_0[6] and α is minimized when the ratio of the outer to inner radii of the transmission line is 3.59.[7] The optimization

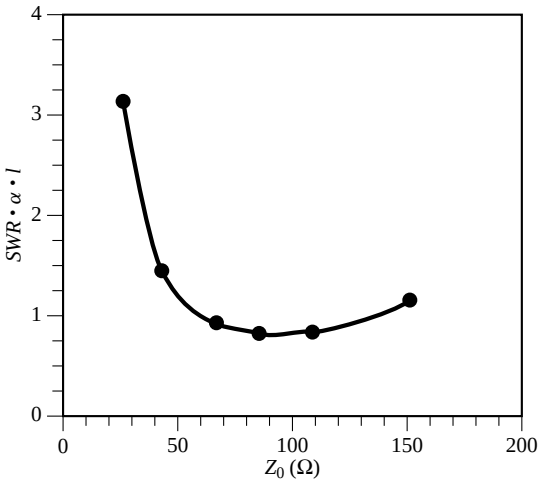

Figure 2 Efficiency parameter of transmission line as a function of its characteristic impedance

for *SWR* should be done for the highest frequency since α decreases with decreasing frequency. Figure 2 shows a plot of the product $SWR \cdot \alpha \cdot l$ for a typical transmission line and sample coil with the $|Z_r|$ ca. 50% higher than Z_0. It shows that there is a broad minimum from about 65 Ω to 125 Ω that gives low loss.

3 TWO- AND THREE-FREQUENCY PROBES

Figure 3 shows a general schematic diagram for a two- or three-frequency probe. TL1 is the main transmission line connecting the sample coil L3 to the tuning elements remote from the magnet. Point A is the null point on the transmission line as discussed above and is the tie-in point for the lower frequency channel(s).

Depending on the proton frequency $F1$, point A may or may not be outside the bore of the magnet. If $F1$ is below 175 MHz, point A will most likely be outside the bore, and the low-frequency tuning elements can be placed in a separate box connected to TL1 at point A. If the value of $F1$ is above 175 MHz, point A will be in the bore of the magnet and a second transmission line TL2 can be used to connect the low-frequency tuning elements into TL1. Since the overall length

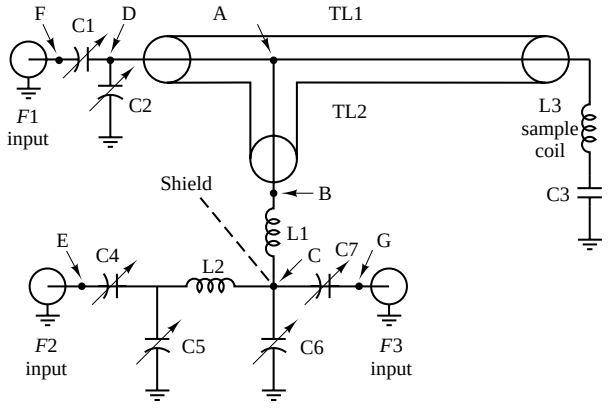

Figure 3 Two- or three-frequency transmission line probe

of TL1 will not be too long, it is very convenient to put the tuning elements for all channels in one box and terminate both TL1 and TL2 in that box. In this case the sizes of TL1 and TL2 must be selected so that both, plus a shield, can fit inside the bore of the magnet. This requires a wide bore (89 mm) magnet for a good low loss design. If point A is just inside the bore, three things can be done to gain a little extra length. The inductance of the sample coil can be reduced by removing turns, the Z_0 of TL1 can be increased by increasing the ratio of outer to inner radii of the conductors, and a capacitor C3 can be used in series with the sample coil. Using C3 can cause problems with the low-frequency channels and will be discussed later. As shown above, there is broad latitude in choosing Z_0 for minimum loss. Also, lowering the inductance will generally help meet the criteria for $|X\text{L3}|$ to equal Z_0. Hoult and Richards[8] have shown that the sensitivity of the NMR experiment is not critically dependent on the Q of the sample coil if proper winding parameters are used. Therefore reducing the number of turns, which will lower the value of Q, will not degrade the sensitivity.

Making the outer diameter of TL1 as large as possible is important since it is used for the highest frequency. If this criterion is to be met, a wide bore magnet is necessary. In this laboratory using 89 mm bore magnets, transmission lines using 3.81 cm (1.5 in) outer diameter and both 0.953 cm (0.375 in) and 0.635 cm (0.25 in) inner diameters have been used. TL2 has an outer diameter of 1.0 cm (0.4 in) and an inner diameter of 0.441 cm (0.173 in). Standard rigid copper plumbing pipe has been used to make the TL1 transmission lines and TL2 is a commercial 50 Ω rigid coaxial cable with these dimensions. They are essentially air dielectric since the center conductor is supported at a few points with Teflon® discs.

To locate point A, a narrow slot can be cut in the outer conductor of TL1 in its approximate location. This point can be calculated from equation (1) by knowing Z_r for the sample coil and letting $\alpha = 0$. The hyperbolic functions reduce to trigonometric functions, and by solving for several values of x, the crossover point between inductive and capacitive can be located. By driving point D (C1 and C2 not in place) with a sweep generator and using an oscilloscope probe to detect the voltage along TL1 in the region of the slot, a point of minimum voltage will be found. This is the null point. Care should be taken in making this measurement, since the isolation between the proton and the low-frequency channels depends on the location of this point. Good rf practices and test equipment designed for the frequencies needed must be used. Once this point is located, a connection must be made and brought out through the outer conductor to make a connection to TL2, or in the case of lower frequency systems tuning elements in a box. This must be a well-insulated connection capable of carrying large values of rf current and withstanding high rf voltage, since this is part of a resonant circuit. A conductor size of 0.318 cm (0.125 in) insulated with Teflon® can be used.

After TL1 and TL2 are in place, C1 and C2 (a conventional tuning network) can be used to tune and match the circuit at $F1$. It is important that this is done before the low-frequency channels are constructed because their tuning will depend on C1 and C2.

A two-channel probe will be described first. The highest frequency for the low channel that has been designed in this laboratory is for ^{31}P, except for some special probes where ^{19}F was the next lowest frequency. These require special

considerations, and space does not allow their discussion here. For a two-channel probe, L1 is replaced by a short circuit, and C4, C5, and L2 are not used.

After TL1 and TL2 are in place and C1 and C2 are tuned and matched to $F1$, the impedance at point C is measured at the frequency $F3$. In most cases it will be inductive, and C6 and C7 are used to tune and match to 50 Ω at $F3$. If the impedance at point C is capacitive, then a capacitor C3 must be added in series with the sample coil L3. The reactance of C3 at $F3$ should be sufficient such that the impedance at point C is inductive and its real part less than 50 Ω, preferably 20 Ω or less. For networks such as C1 and C2 and C6 and C7, the real part of the inductive circuit that is being tuned must be less than 50 Ω.

For a three-channel probe, $F3$ should be no more than 65% of $F2$ or some of the power at $F3$ will be absorbed in the $F2$ circuit. All elements in Figure 3 are used in a three-channel probe.

The first requirement for this probe is that the impedance at point B looking into TL2 must be capacitive so C3 will not be needed. If it is still inductive, a capacitor can be added from point A and/or point B to ground or TL2 can be lengthened. Once point B is capacitive, it has a negative imaginary part ($-iX$), and a value of L1 is selected such that its imaginary part is ($+iX$) making the impedance at point C a small real part (losses in L1, and TL1 and TL2). This is essentially a series resonant circuit and has created an impedance null at point C for $F2$, similiar to point A for $F1$. A value for L2 is now chosen such that reasonable values of C5 and C4 can be used to tune and match point E at frequency $F2$ to 50 Ω. L1 and L2 should be made with as high a Q value as possible (i.e. low loss) to keep the efficiency up. A convenient material to use is 0.3175 cm (1/8 in) copper tubing.

Now that the $F2$ circuit is completed, the impedance at point C is measured at frequency $F3$; if $F3$ is 65% of $F2$ or lower, it should be inductive, and C6 and C7 can be chosen to tune and match point G to 50 Ω. Inductor L1 must be shielded from L2 or there will be inductive coupling between them. Since they would not be independent, the circuit will not work properly. A compartmentalized tuning box that gives good rf shielding should separate the tuning elements for all three channels and is recommended.

4 TRAPS

Figure 4 shows two types of traps that are used with the probes described in this article. Type 1 makes a particular channel less dependent on what is connected to the other input ports. Type 2 traps are used to attenuate proton ($F1$) frequencies at the low-frequency input ports to help prevent pre-amplifier overload in the observe channel.

Type 1 traps work as follows. The transmission line TL is a shorted 1/4λ line at the frequency of the port where it is used. This will always be a port at a higher frequency than the frequency it is used to trap, i.e. a ^{13}C trap used on the proton port. This constraint means that the impedance at point A, looking into the TL, will be inductive, and the circuit can be made series resonant with C at the frequency of the trap. This will cause the input impedance to be very low and create a virtual ground at the frequency of the trap. If too large a value of C is required, an inductor L1 can be added in series

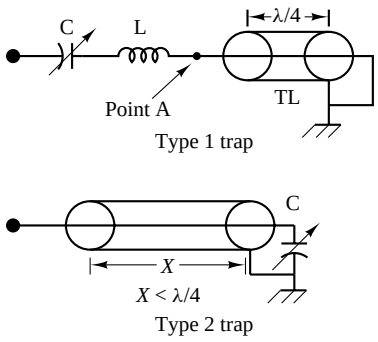

Figure 4 Traps for multifrequency probes

to reduce the value of C required. Since the impedance of TL is infinite at the frequency of the port where it is connected, and it is in series with C and L1, the whole trap will have a very high impedance and will not load the port at its own frequency. There will be two traps of type 1 at the proton input port, one for $F2$ and one for $F3$. The inputs of these traps are connected from the proton ($F1$) input port (point F in Figure 3) to ground. There will be one type 1 trap at the $F2$ input port tuned for $F3$ and connected from point E in Figure 3 to ground. These traps make the tuning of the $F2$ and $F3$ circuits insensitive to what is connected to the other ports. An $F2$ frequency trap is not needed at the $F3$ port since the $F2$ frequency is already highly attenuated at point C in Figure 3 due to the null point there.

Type 2 traps create a low impedance at their input and hence short to ground any $F1$ frequency signal that gets to input ports of the observe channels. This is very important when observing resonances while decoupling protons at $F1$.

An open circuited 1/4λ line is a short circuit, but cutting a piece of the coaxial exactly is difficult. If the TL is made shorter than 1/4λ, then a variable capacitor can be used to trim the circuit to the exact value necessary to create a short at its input at $F1$. There needs to be one of these traps at the input of the $F2$ and $F3$ ports.

The coaxial cable used for these traps is RG-58A/U, and the capacitors are rated for 400 V.

5 SUMMARY

Probes using the design in this article have been built in this laboratory at proton frequencies of 60, 90, 127, 150, 200, and 300 MHz, some for two frequencies, some for three frequencies and some for four frequencies using the same ideas described here. All of these probes are made for high power (300–1000 W) and are capable of proton decoupling in the 100 kHz range. High-voltage vacuum or Teflon® variable capacitors are used in the high-voltage areas, but since all tuning elements are remote from the magnet, large and, if necessary, magnetic ones can be used. Since the sample coil is the only component in the magnet, the circuit is insensitive to first order to the environment of the sample.

6 RELATED ARTICLES

Probe Design and Construction; Solid State Probe Design.

7 REFERENCES

1. M. E. Stoll, A. J. Vega, and R. W. Vaughn, *Rev. Sci. Instrum.*, 1977, **48**, 800.
2. V. R. Cross, R. K. Hester, and J. S. Waugh, *Rev. Sci. Instrum.*, 1976, **47**, 1486.
3. V. J. Bartuska and G. E. Maciel, *J. Magn. Reson.*, 1981, **42**, 312.
4. F. D. Doty, R. R. Inners, and P. D. Ellis, *J. Magn. Reson.*, 1981, **43**, 399.
5. E. C. Jordan (ed.), *Reference Data for Engineers: Radio, Electronics, Computer, and Communications*, 7th edn., Sams, Indianapolis, IN, 1985, p. 29–10.
6. D. E. MacLaughlin, *Rev. Sci. Instrum.*, 1989, **10**, 3242.
7. F. E. Terman, *Electronic and Radio Engineering*, 4th edn., McGraw-Hill, New York, 1955, p. 106.
8. D. I. Hoult and R. E. Richards, *J. Magn. Reson.*, 1976, **24**, 71.

Biographical Sketch

Robert A. McKay. *b* 1933. B.E., 1955, Vanderbilt University, M.S., 1965, Southern Methodist University. Introduced to NMR at Mobil Oil research laboratories by Don Woessner and John Zimmerman, 1960–75. Worked with Jake Schaefer in CP MAS at Washington University and Monsanto Co. since 1975. Research specialty: developing NMR instrumentation.

Rapid Scan Correlation Spectroscopy

Raj K. Gupta
Albert Einstein College of Medicine, Bronx, NY, USA

and

James A. Ferretti and Edwin D. Becker
National Institutes of Health, Bethesda, MD, USA

1	Introduction	1
2	Description of the Technique	2
3	Selected Applications	4
4	Future Prospects	5
5	Related Articles	5
6	References	5

1 INTRODUCTION

During the late 1960s and early 1970s, fairly extensive searches were carried out to find new methods for obtaining the highest sensitivity in NMR experiments. These searches were primarily applied to optimization of high-resolution NMR spectra. It was recognized at a very early stage in the development of modern NMR that the original continuous wave (CW) method was usually inefficient in terms of both the time required to obtain a single NMR scan and the magnitude of the signal produced per scan. In CW experiments, the magnetization vector is tipped only slightly from its equilibrium value, thus producing a relatively weak signal. The necessity of maintaining a small tip or effective flip angle arises because nuclear spin systems become nonlinear in their response at high applied rf field. To record CW spectra properly, it was necessary to approximate slow passage conditions to produce spectral lines that were undistorted by such effects as frequency oscillations in the tails of the spectral lines (ringing), relaxation, and the inability of the detector to respond to the 'ringing'. Because of the necessity of obeying these slow passage conditions, attempts to tip the magnetization vector by a significant amount resulted in a reduction of the total intensity or 'saturation' of the resonance lines. These limitations provided the driving force behind attempts to develop alternative techniques to maximize the sensitivity of the NMR experiment.

Several alternative methods were proposed and developed that allowed rapid acquisition of an entire spectrum as well as the use of a large nutation angle, thus reducing the time required to obtain a single scan while also producing an enhanced signal per scan. The most popular of these methods is the pulse Fourier transform technique, on which almost all modern NMR spectrometers are based. A second method involves stochastic excitation, for which there have been several recent developments that appear quite promising. These two methods rely on simultaneous excitation of the different resonance transitions of a nuclear spin system. A third method is the rapid scan correlation technique, in which the entire spectrum is traversed under fast passage conditions where typical circumstances involve tipping the magnetization vector into the (x,y) plane. Here each transition is excited successively in a fast sequence. If the field or the frequency is swept rapidly enough, constructive and destructive oscillations characteristic of the spectrum occur. The origin of these frequency oscillations was understood 30 years ago. It was recognized then that all of the available spectral information is in the frequency oscillations found in the tails of resonance lines obtained by rapidly scanning the spectrum. However, the proper analysis procedure for extracting the corresponding undistorted spectra remained elusive for many years. Several papers were published about 20 years ago describing the mathematical procedures for obtaining the undistorted spectrum, and pointing out that this rapid scan technique is capable of producing spectra with sensitivity comparable to the pulse Fourier transform technique. The technique was initially referred to both as rapid scan Fourier transform NMR spectroscopy and correlation NMR spectroscopy, because of the nature of the experiment and because the procedure for obtaining the undistorted spectrum may involve cross correlation. Ultimately, it was named rapid scan correlation spectroscopy. The purpose here is to examine the historical development of the method, review some applications of the technique, and speculate on future developments. Interestingly, the original discovery of NMR by Bloch was a rapid scan experiment where the signal was observed when the field was rapidly changing as the magnet was turned off, after a frustrating failed slow passage search for an NMR signal.

Dadok originally pointed out at the 1972 Experimental NMR Conference in Asilomar, CA that the true undistorted high-resolution NMR spectrum can be obtained from a rapidly scanned response by cross correlation with the response obtained under identical sweep conditions from a single 'reference' line.[1a] The quality of the spectra was quite good, but suffered from several inherent disadvantages. First of all, the correlated spectra showed broadened lines with widths that were the sums of the inherent linewidths and the width of the single reference line used in the cross-correlation operation. Secondly, any additional spectral lines (e.g., from impurities) present in the reference sample produced additional spectral lines in the correlated spectra. Subsequently, the theoretical basis of this method was examined, and it was shown that the undistorted spectra could be obtained with no added linewidth by Fourier transforming the fast passage response and multiplying it with an analytical function of the form $\exp(-\frac{1}{2}ibT^2)$, where b is the sweep rate and T is the running variable in the time domain.[1b,2] It was also shown that the data are easily obtained using a spectrometer–computer interface, just as all modern FT spectra are acquired and processed. It was shown that rapid scan correlation FT NMR offers an alternative to pulse methods for rapid acquisition of NMR spectral information. The sensitivity of the rapid scan method was shown to be comparable to that of the pulse Fourier transform method. However, two potential advantages of rapid scan FT over the pulse technique were recognized:

1. the ease with which a portion of the spectrum can be scanned without recording large peaks such as H_2O or

HDO, which cause dynamic range problems and severely limit the sensitivity of pulse FT NMR;
2. the ability to study selectively in a multiline spectrum the spectral properties of some spins without perturbing others, thus avoiding complications due to cross relaxation or chemical exchange.

At that time, another distinct advantage appeared to be that no new spectrometer hardware was required and no high-power pulse equipment was needed. Furthermore, for heteronuclei with large chemical shift dispersion, or for protons in paramagnetic systems, the rapid scan technique offered a simple straightforward procedure to obtain spectra of a chemical shift region of particular interest. The typical problems associated with foldover that are often encountered in pulse FT were avoided.

2 DESCRIPTION OF THE TECHNIQUE

2.1 Slow Passage Spectrum from the Rapid Scan Response

In the rapid scan technique,[1,2] the entire spectrum is traversed under fast passage conditions such that the magnetization corresponding to each line produces pronounced ringing (wiggles), which persists a time of the order of $3T_2$*, and results in badly distorted spectral lines. The true spectrum is then obtained from such a fast scan response by cross correlating the response with that obtained from a reference consisting of only a single sharp NMR line scanned under identical conditions, or alternatively by applying to the Fourier-transformed response an analytical function $\exp(\frac{1}{2}\mathrm{i}bT^2)$. Unlike pulse FT NMR, where the different resonance conditions of a complex spin system are satisfied simultaneously, in rapid scan correlation NMR, as in CW NMR, the resonance conditions are met sequentially.

Cross correlation of two complex functions G and H defined mathematically as

$$\int_{-\infty}^{\infty} H^*(\tau)G(t+\tau)\,\mathrm{d}\tau \tag{1}$$

where H* is the complex conjugate of H, has the physical meaning of one function searching for itself in another function, and is useful in picking out hidden periodicities. The property that cross correlation in one domain is equivalent to complex conjugate multiplication in the Fourier domain is used to simplify data handling considerably.

The detailed theory of rapid scan correlation NMR treats the spins as a linear time-independent system. The frequency response function $Y(\omega)$ of such a system and the corresponding impulse response $h(T)$ form a Fourier transform pair. In rapid passage experiments, the frequency ω is scanned rapidly ($\omega_t = bt$) and the response $Y(\omega_t)$ is observed as a function of time (frequency), giving rise to the well-known transient effects as wiggles or ringing following passage through a resonance. The linear response $R(t)$ of the spins to a swept rf field $E(t) = \exp(\frac{1}{2}\mathrm{i}bt^2)$ is given by the convolution integral

$$R(t) = \int_{-\infty}^{\infty} h(\tau)E(t-\tau)\,\mathrm{d}\tau \tag{2}$$

so that the detected NMR signal $Y(\omega_t)$, which is the component of the response in phase with the rf field, is given by

$$\begin{aligned} Y(\omega_t) &= R(t)\exp(-\tfrac{1}{2}\mathrm{i}bt^2) \\ &= \int_{-\infty}^{\infty} h(\tau)\exp[\tfrac{1}{2}\mathrm{i}b(\tau^2 - 2t\tau)]\,\mathrm{d}\tau \end{aligned} \tag{3}$$

It is straightforward to show that the inverse Fourier transform $F(T)$ of this response is given by

$$F(T) = h(T)\exp(\tfrac{1}{2}\mathrm{i}bT^2) \tag{4}$$

where T is the running variable of the time domain. This result for the Fourier transform of the rapid scan signal can also be obtained from the usual Bloch equations,[2] as well as the Bloch equations modified to include chemical exchange,[3] provided that spin saturation is avoided. However, nonlinearities due to spin–spin couplings can modify the observed response.[4]

It is clear from the expression for the inverse Fourier transform $F(T)$ of the rapid scan response that multiplication of $F(T)$ by $\exp(-\frac{1}{2}\mathrm{i}bT^2)$ gives the impulse response of the system $h(T)$, from which the slow passage spectrum is readily obtained by another (forward) Fourier transformation (Figure 1). Because of the extensive use of Fourier transformations for rapid data processing, we suggested that the technique be named rapid scan FT NMR, despite the fact that the resulting slow passage spectrum and the initial rapid scan response are in the same Fourier domain.

Use of an experimental reference involves cross correlation of an unknown rapid scan response with the rapid scan response of a single narrow reference resonance. Cross correlation is carried out most efficiently by Fourier transforming both the reference and the unknown responses and then multiplying the Fourier transform of the unknown response, $h(T)\exp(\frac{1}{2}\mathrm{i}bT^2)$, with the complex conjugate of the Fourier

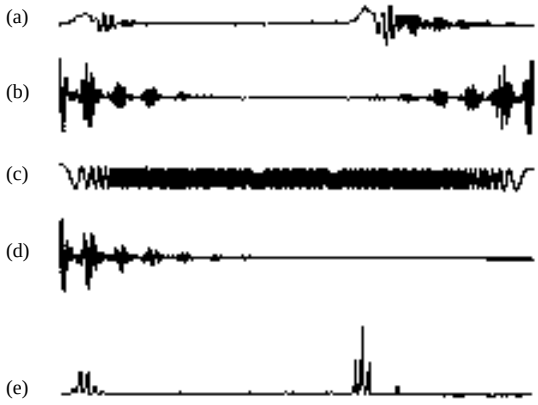

Figure 1 Signals at various stages of analysis in rapid scan correlation NMR. (a) Rapid scan data, showing the proton resonances of the CH_2 and CH_3 groups of ethylbenzene at a scan rate of 200 Hz s^{-1}. (b) Inverse cosine Fourier transform of (a). (c) The real part of the function $\exp(-\frac{1}{2}\mathrm{i}bT^2)$ for $b/2\pi$ = 200 Hz s^{-1}. (d) The result of multiplying (b) and (c), followed by zeroing of half of the data points. (e) The Fourier transform of (d), with phase correction applied if necessary.

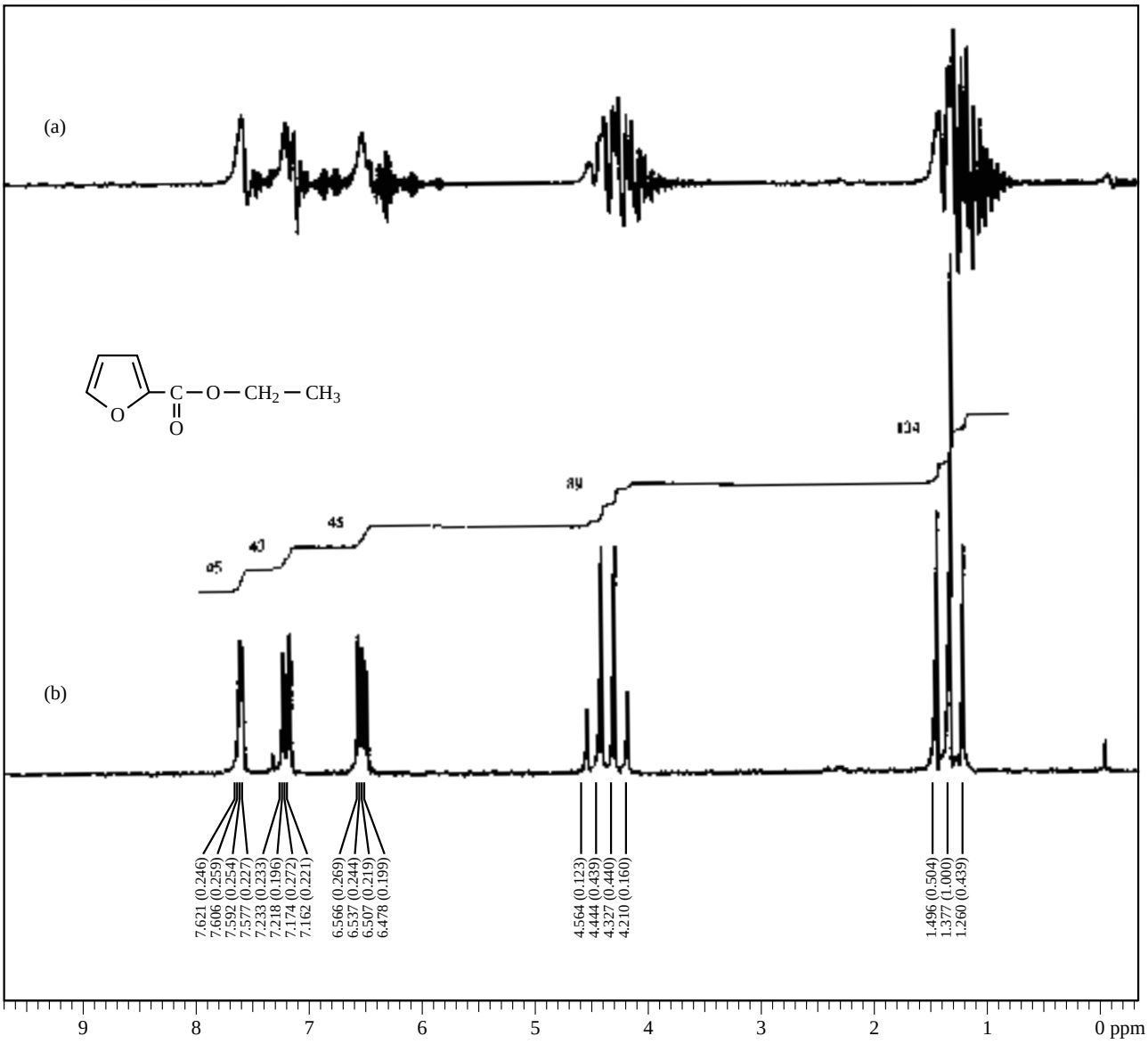

Figure 2 Rapid scan (a) and correlated spectrum (b) obtained at 60 MHz on a Hitachi Instruments, Inc. Model R-1200 rapid scan NMR spectrometer

transform of the reference response, $h_{\text{ref}}^*(T)\exp(-\frac{1}{2}ibT^2)$, to obtain $h_{\text{ref}}^*(T)h(T)$. The Fourier transform of this product is then taken as an approximation to the slow passage spectrum (Figure 2). The linewidths of the resulting spectrum in this case will be the sums of the true linewidths and the width of the reference line. When using the reference line approach, the final slow passage spectrum is properly phased, provided that the same phase setting is used for both the reference and the unknown. Also, the frequency axis of the final spectrum is shifted so as to set the reference line to zero frequency. In using the theoretical function approach, an adjustment of the spectral phase may be needed to produce a pure absorption signal, if the initial rapid scan response was not properly phased. However, when the theoretical function is used, the resonance positions remain unchanged with respect to their original positions in the rapid scan response. Cross correlation using the experimental reference results in slightly broader resonances, but this broadening could be minimized by choosing a very narrow reference line such that the broadening effect will be negligible for lines whose widths are greater than 1–2 Hz. With a strong reference signal, the additional noise introduced by cross correlation is normally very small, and the decay constant inherent in h_{ref} leads in effect to exponential filtering, which improves the signal-to-noise ratio. It was noted that TMS is not the most suitable reference since its NMR response shows observable ^{29}Si satellites. It was suggested that a sample of degassed benzene or cyclohexane would be better.[2]

It is interesting to note that just before the final Fourier transformation, the data in the rapid scan technique are analogous to a simple free induction decay (see Figure 1). Thus, digital filtering techniques (e.g., resolution and sensitivity enhancement) to manipulate the quality of the final spectrum can be used just as in pulse FT NMR. The maximum intensity of the absorption signal in the rapid scan mode has been shown to be equal to the equilibrium magnetization, and it has been shown that the sensitivity of the rapid scan technique is comparable to that of the pulse FT technique. However, a necessary condition to be satisfied for the spin

system to be driven into the rapid passage region is that the sweep rate be greater than $1/2\pi T_2^{*2}$.

2.2 Nonlinear Effects in Rapid Scan Correlation Spectroscopy of Coupled Spin Systems

The existence of spectral distortions due to nonlinear effects in rapid scan correlation NMR of coupled spin systems has been described in the literature.[4] These distortions depend strongly on the applied sweep rate and the rf power level where the effective flip angle may be close to 90°. The resultant spectra can show serious variations in resonance lineshapes (both phase and intensity), which depend upon the sweep rate, power level, and the initial state of the spin system, although the resonance frequencies remain essentially unaltered. These effects occur when the spin system does not completely recover in the time between passage through adjacent resonance lines owing to incomplete transverse and/or longitudinal relaxation. Under rapid passage conditions, the transverse magnetization components of the first scanned lines will be mixed by later passage through any connected resonance transitions, causing distortion of the resonances traversed first, while the later lines show normal behavior (e.g., for certain sweep rates in Figure 3, the first two lines are badly distorted). Maximum distortion of the spectrum of a weakly coupled two-spin system was found to occur for values of the sweep rate (in radians per second squared) $b = 2J(\omega_1 - \omega_2)$ where J is the coupling constant (in hertz), and $(\omega_1 - \omega_2)$ is the chemical shift difference (in radians per second). Effects of incomplete longitudinal relaxation manifest themselves as flip angle dependent anomalies in the intensities of the spectral lines that are observed when the spin system is initially in a nonequilibrium state. The above nonlinear effects should be kept in mind in interpreting the results of rapid scan correlation experiments with coupled spin systems.

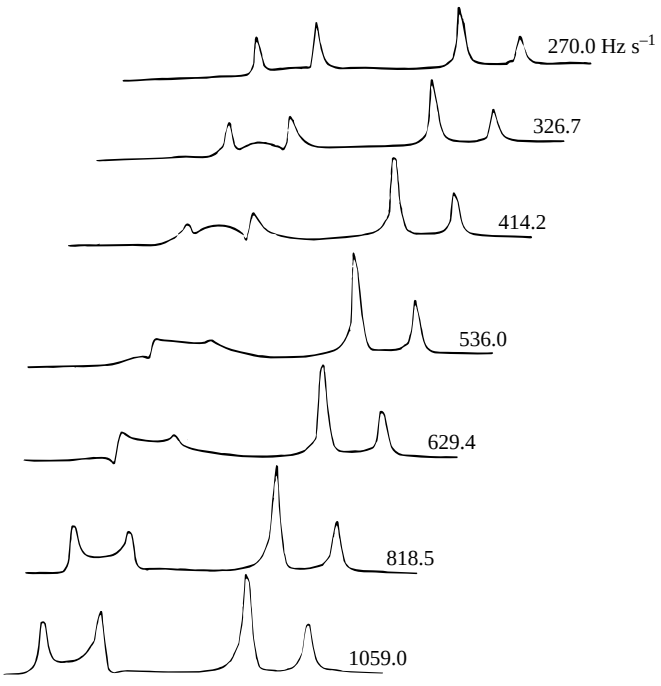

Figure 3 Rapid scan correlation spectra of 2,3,4-trichloronitrobenzene at different scan rates.

2.3 Spin–Lattice Relaxation Measurements

An analog of the progressive saturation experiment well known in CW and pulsed FT works well in rapid scan spectroscopy.[2] The entire spectrum or a part of it is repetitively scanned and a steady state is established where there is a dynamic balance between the passages through the resonances. It is important to make optimum adjustments such that the spin magnetization following passage through a resonance ends up in the (x, y) plane. This requires careful adjustment of rf power and sweep rate. Further, this technique is limited to relatively long T_1 values.

A different approach, somewhat analogous to the saturation recovery pulse method, is applicable for measurement of both long and short T_1s using rapid scan FT NMR.[5] Here, the initial state of the spin system is established by applying a saturating rf field to the spectral lines to be studied. Such an rf field causes essentially complete demagnetization of the spins in a time of the order of a few times $T_{1\rho}$. The saturating rf is then turned off, and, after a variable delay time, the partially relaxed spins are rapidly scanned under fast passage conditions with another rf field of appropriate strength. The fast passage response thus obtained is cross correlated or treated with an analytical function to yield a partially relaxed slow passage spectrum. Repetition of saturation and observation sequence permits the determination of T_1 for each saturated line from its exponential recovery. In a multiline spectrum, T_1 values in the range 0.7–10 s were easily measured by this technique.[5]

3 SELECTED APPLICATIONS

3.1 Observation of Hyperfine Shifted Resonances in Hemoproteins

Ho and co-workers[6] used rapid scan correlation spectroscopy at 250 MHz to obtain proton nuclear magnetic resonance spectra of human deoxyhemoglobin in D_2O in the region from 6 to 20 ppm downfield from the proton resonance of residual water, showing a number of hyperfine shifted resonances due to groups on or near the α- and β-hemes. They showed, by the use of correlation spectroscopy, that at least two resonances, one at about 18 ppm downfield from HDO due to the β chain and the other at about 12 ppm downfield due to the α chain, can be used to study the binding of oxygen to the α and β chains of hemoglobin. They also used rapid scan correlation proton NMR in H_2O to investigate the conformations of proximal histidyl residues in human deoxyhemoglobin and its mutants.[7] Two resonances sensitive to the quaternary state of hemoglobin that occur between 58 and 76 ppm, far downfield from the water proton signal, could be readily observed and assigned to the hyperfine-shifted proximal histidyl NH-exchangeable protons of the α and β chains of deoxyhemoglobin. The biochemical information derived from these hyperfine-shifted proximal histidyl NH-exchangeable proton resonances complemented that obtained from the other hyperfine-shifted exchangeable and nonexchangeable proton resonances of deoxyhemoglobin in the spectral region from 5 to 20 ppm downfield from H_2O.

These studies made use of the ability of the rapid scan correlation technique to observe selected spectral regions, in the

presence of a large chemical shift dispersion, without perturbing other regions of the proton spectrum. No presaturation of the water resonance was necessary.

3.2 Transfer of Saturation from Water and 'Underwater' Decoupling

In several studies of biologically important peptides,[8–12] the rapid scan correlation technique provided well-resolved proton NMR spectra with signal-to-noise ratios significantly better than those obtainable using the CW but comparable to those obtained with the pulse FT technique. Furthermore, when protonated solvents were used, rapid scan correlation spectroscopy provided distinct advantages over the short pulse method because of its ability to avoid interference from the overwhelmingly large solvent signal. Peptide NH resonances of individual amino acids could be assigned by the correlation method using 'underwater decoupling' (i.e., decoupling from the corresponding C-α proton resonances, which are buried beneath the intense water peak). These experiments could be done maintaining good signal-to-noise ratio and resolution. Solvent exposure of specific hydrogens and exchangeability of NH protons could be studied by comparing peptide proton spectra in H_2O, with and without rf saturation of the large water resonance. Such experiments would have been difficult to perform using the pulse FT technique, since the latter requires saturation of water as a precondition for spectral data acquisition. Underwater decoupling experiments are useful for assignment of peptide NH resonances, while transfer of saturation from water measures solvent exposure of specific nuclei in the biomolecule.

As an example of the above, peptide NH resonances in the 250 MHz NMR spectrum of oxytocin in H_2O were assigned to specific amino acid residues by the 'underwater decoupling' technique.[12] Exposure to solvent of specific hydrogens of oxytocin in H_2O could be studied by monitoring intensity changes of peptide resonances when the solvent peak was saturated. Positive nuclear Overhauser effects (NOEs) of sizeable magnitude were observed for the Tyr *ortho*-CH and *meta*-CH resonances, indicating intimate contact between water and the aromatic CH hydrogens of the Tyr side chain. Transfer of saturation from water to NH protons reflected acid–base catalysis of the proton exchange reaction. There was no indication that any NH protons were substantially shielded from the solvent, which pointed to the need for avoiding solvent saturation to observe true resonance intensities.

3.3 Nonexchangeable Protons in Proteins

The rapid scan correlation technique has also been used for routine observation of one-dimensional protein proton NMR spectra as an alternative to pulse techniques with comparable signal-to-noise ratio and resolution.[13–15] For example, Markley and co-workers[14] used the technique at 250 MHz to measure titration curves of the three histidine residues of staphylococcal protease, while Arata and co-workers[13] applied it to lysozyme. Bothner-By and co-workers[15] used rapid scan correlation at 600 MHz to study glucocerbrosidase activator protein from Gaucher spleen. The upfield ring current shifted aliphatic region and the downfield aromatic region were examined using NOE methods in the correlation mode.

3.4 Applications in Food Chemistry

Since the rapid scan correlation NMR technique combines the sensitivity advantage of pulse FT NMR with the dynamic range advantage of the CW method, it has found recent applications in the analysis of food products.[16] Results of qualitative as well as quantitative studies from a variety of foods and food-related systems have been reported. The rapidity and noninvasiveness of the technique are important considerations in such applications. A quantitative analysis of the ethanol content of various wines has also been carried out with this technique.[17]

4 FUTURE PROSPECTS

Even though rapid scan correlation spectroscopy showed significant promise in 1970s, it was soon overtaken by the rapid developments in the pulse FT method. With the advent of the new generation of pulse Fourier transform spectrometers, the advantage of not requiring new instrumental hardware for the rapid scan method disappeared. Eventually, most NMR manufacturers discontinued producing spectrometers capable of performing swept field or frequency experiments. Also, it is quite difficult to envision numerous heteronuclear and homonuclear multidimensional applications, now known for pulse FT NMR. Nevertheless, Hitachi Instruments, Inc. manufactures a spectrometer operating at 60 MHz that functions exclusively in the rapid scan correlation mode. Recent applications of the technique seem to have been in the area of quality control in food chemistry and in the study of biomolecules in H_2O solution. The ability to avoid overdriving the dynamic range of the spectrometer, which is still problematical on modern NMR spectrometers, implies that the rapid scan correlation technique is still a useful complement to pulse FT NMR. Also, one can envision applications in magnetic resonance imaging that might be advantageous in terms of rf power requirements. One purpose of this review is to remind the NMR community of the existence of this potentially powerful alternative to pulse techniques.

While we do not envision any widespread resurgence in the use of the rapid scan method, the technique is likely to continue to be useful for routine one-dimensional NMR analyses and for specific applications in the study of biomolecule–water interactions. Possible applications of the rapid scan technique in imaging and in vivo proton spectroscopy may still result in the future.

5 RELATED ARTICLES

Biological Macromolecules; Fourier Transform Spectroscopy; Selective Pulses; Stochastic Excitation; Water Signal Suppression in NMR of Biomolecules.

6 REFERENCES

1. (a) J. Dadok, R. F. Sprecher, and A. A. Bothner-By, *13th Experimental NMR Conference, Asilomar, Pacific Grove, California, 1972*. (b) J. Dadok and R. F. Sprecher, *J. Magn. Reson.*, 1974, **13**, 243.

2. R. K. Gupta, J. A. Ferretti, and E. D. Becker, *J. Magn. Reson.*, 1974, **13**, 275.
3. J. Jen, *J. Magn. Reson.*, 1981, **45**, 257.
4. J. A. Ferretti and R. R. Ernst, *J. Chem. Phys.*, 1976, **65**, 4283.
5. R. K. Gupta, J. A. Ferretti, and E. D. Becker, *J. Magn. Reson.*, 1974, **16**, 505.
6. G. Viggiano, N. T. Ho, and C. Ho, *Biochemistry*, 1979, **18**, 5238.
7. S. Takahashi, A. K. Lin, and C. Ho, *Biophys. J.* 1982, **39**, 33.
8. J. D. Glickson, J. Dadok, and G. R. Marshall, *Biochemistry*, 1974, **13**, 11.
9. T. P. Pitner, J. D. Glickson, J. Dadok, and G. R. Marshall, *Nature (London)*, 1974, **250**, 582.
10. J. D. Glickson, J. Dadok, and G. R. Marshall, *Biochemistry*, 1974, **13**, 11.
11. W. A. Gibbons, C. F. Beyer, J. Dadok, R. F. Sprecher, and H. R. Wyssbrod, *Biochemistry*, 1975, **14**, 420.
12. J. D. Glickson, R. Rowan, T. P. Pitner, J. Dadok, A. A. Bothner-By, and R. Walter, *Biochemistry*, 1976, **15**, 1111.
13. Y. Arata, H. Ogawa, T. Ogino, and S. Fujiwara, *Pure Appl. Chem.*, 1978, **50**, 1273.
14. J. L. Markley, W. R. Finkenstadt, H. Dugas, P. Leduc, and G. R. Drapeau, *Biochemistry*, 1975, **14**, 998.
15. L. Sheh, R. H. Glew, A. A. Bothner-By, and P. K. Mishra, 1985, **24**, 6645.
16. H. Barjat, P. S. Belton, and B. J. Goodfellow, *Food Chem.*, 1993, **48**, 307.
17. H. Barjat, P. S. Belton, and B. J. Goodfellow, *Analyst (Cambridge, UK)*, 1993, **118**, 73.

Biographical Sketches

Raj K. Gupta. *b* 1943. Ph.D., 1969, Indian Institute of Technology, Kanpur. Introduced to NMR by A. G. Redfield. Professor of Physiology & Biophysics, and of Biochemistry, Albert Einstein College of Medicine, NYC, 1982–present. Approx. 200 publications. Research interests include applications of NMR in physiology and biochemistry, especially in the measurement of intracellular ions.

James. A. Ferretti. *b* 1939. Ph.D., 1965, University of California at Berkeley. NIH, 1966–present, currently Chief of the Structural Biophysics Section, Laboratory of Biophysical Chemistry, National Heart, Lung & Blood Institute, Bethesda, MD. Approx. 100 publications. Research interests include 3D solution structures of peptides and proteins.

Edwin D. Becker. *b* 1930. B.S., 1952, University of Rochester, Ph.D., 1955, chemistry, University of California, Berkeley, USA. National Institutes of Health, 1955–present; Laboratory Chief (1972–80, 1988–present); Associate Director for Research Services (1980–88). Concurrent position on Faculty, Georgetown University, 1959–present. Books on NMR. Research interests and publications: hydrogen bonding, molecular structure elucidation, technique development in NMR and other areas of molecular spectroscopy.

Sensitivity of the NMR Experiment

David I. Hoult

Institute for Biodiagnostics, National Research Council Canada, Winnipeg, MB, Canada

1 INTRODUCTION

With any spectroscopic technique, there is a lower limit to the amount of material that yields a detectable signal, and NMR is no exception in this regard. Indeed, in comparison with other methods such as mass spectroscopy or electron spin resonance, NMR is a very insensitive tool. As such, it is therefore a tribute to its versatility that it occupies such an important position in the analytical armory, be it in chemistry, biochemistry, or medicine. However, it is almost an axiom that the desired detection sensitivity is always a little greater than that available, and in repeated efforts to prise more from the technique, the limits thereof have been explored in great detail. This article therefore seeks to explain those limits, and to give an account of the origins of the NMR signal and the unwanted voltages that tend to mask it.

The NMR phenomenon is detected overwhelmingly nowadays by its transient response to a 'pulse'—a brief burst of oscillating magnetic field of suitable duration, orientation, and frequency. In the simplest of experiments that pulse leaves in its wake an ensemble of nuclei that, for our purposes, can be considered to constitute a small magnet that rotates at the Larmor frequency about a direction parallel to the main applied magnetic field. However, as Michael Faraday was well aware as long ago as 1830, a rotating magnet creates an electromotive force (EMF) in a nearby conductor—the phenomenon of electromagnetic induction. Thus, at its simplest, detection of the NMR phenomenon is accomplished by placing a coil of wire (the 'receiving coil') round the sample, be it a human being or in a test tube, and, after the pulse, recording the voltage induced in the coil by the rotating nuclear magnetism. The principle is the same as that employed to generate current with a bicycle dynamo or car alternator. However, the induced signal voltage is usually at least seven orders of magnitude less than in these well-known generators, and therefore rather difficult to measure. Thus, the receiving coil is part of a special circuit (the probe) that aids in passing the signal without degradation to the electronics of the NMR receiver. Regrettably, in many elementary descriptions of NMR, particularly in the medical literature, it is wrongly stated that radio waves are emitted from the NMR system and then received by an antenna rather than a probe. It cannot be stressed too strongly that this is a wrong (and needlessly complex) description.[1,2] Only at field strengths considerably higher than those normally in use, when the sample dimensions approach the wavelength of any radio waves, does the emission of such waves begin to contribute appreciably (constructively or destructively) to the received signal.[3]

Unfortunately, in addition to the NMR signal, there are many potential sources of unwanted voltage that may obscure the desired signal—so-called noise. Some of them are, at the time of writing, unavoidable, but others can enter through bad design of the NMR instrument, or through some usage that the manufacturer did not envisage. Unavoidable noise, which we shall consider in detail, is associated with Brownian motion: firstly, of the electrons in the receiving coil (the coil's resistance is a measure thereof) and, secondly, of electrolytes in the sample. Noise in the electronics of the receiving system can also not be completely eliminated. Avoidable noise sources tend to be of human origin away from the immediate vicinity of the NMR magnet. (An exception is dielectric loss in the sample.) Chief offenders are television and radio stations, cellular telephones and radio paging systems, fluorescent lights, computers (including the NMR computer and pulse programmer), electric motors, etc. When badly constructed or modified, an NMR spectrometer or imager can function only too well as a radio receiver. Thus, we shall also examine briefly how these sources can interfere with the NMR signal and degrade the signal-to-noise ratio, and how such interference can be avoided. In accord with the earlier statement concerning radio waves, the design goal is to minimize this far-field receptive ability while maximizing the ability to detect near-field induced voltages. We begin, then, with a description of signal reception.

2 SIGNAL RECEPTION

2.1 The Principle of Reciprocity

Once a sample has been in the main magnetic field $\boldsymbol{B}_0$ for a time greater than a few longitudinal relaxation times T_1, the ensemble of nuclear spins has become magnetized: there is a net alignment (typically tens of ppm) of nuclear magnets with the field, which, following convention, we assume to be in the z direction. The magnitude of the magnetic moment per unit volume (or magnetization M_0) so created is given by

$$M_0 = \mathcal{N}\gamma^2 B_0 \hbar^2 I(I+1)/3k_{\mathrm{B}}T \tag{1}$$

where $\mathcal{N}$ is the number of nuclei of interest per unit volume, γ is their gyromagnetic ratio, and I is their spin. T is the absolute temperature of the sample, $\hbar$ is Planck's constant h divided by 2π, and k_{B} is Boltzmann's constant. Table 1 shows the magnetization of a 1 M solution for several common nuclei at 20 °C in a field of 1 T.

Thus, in an elementary volume dV, there is a magnetic moment d$\boldsymbol{m}$ given by

$$\mathrm{d}\boldsymbol{m} = M_0 \mathrm{d}V\boldsymbol{z} \tag{2}$$

where $\boldsymbol{z}$ is the unit vector in the z direction. Application of a pulse realigns the magnetic moment, placing it in a new direction with declination θ relative to z (the pulse is said to have a 'flip angle' of θ), so that there is a component

$$\mathrm{d}m_{xy} = \mathrm{d}m \sin\theta \tag{3}$$

parallel to the (x,y) plane. The component then precesses (rotates) about the z direction with frequency ν_0 (the 'Larmor frequency') and suffers transverse relaxation.

A full calculation of the voltage induced in a neighboring conductor is not difficult,[2] but valuable insight may be gained as follows: consider the form of the magnetic field that *would* be created by the conductor *if* 1 A of current at the Larmor frequency were to be passed through it. This is shown in Figure 1(a). Now it is intuitively obvious that if the rotating nuclear magnetic moment is close to the coil at, say, point P, a much larger voltage will be induced than if the moment is far away at, say, point Q. Equally, it may be seen that the magnetic field created by a hypothetical current is much stronger close to the coil than far away. This behavioral correspondence suggests that the induced voltage is proportional to the field, a hypothesis supported by calculation and measurement,[2] and the variation of both quantities with distance along the x axis is shown in Figure 1(a). Mathematically, this example of the near-field principle of reciprocity is expressed by[4]

$$d\xi = -\frac{d(\tilde{\boldsymbol{B}}_1 \cdot d\boldsymbol{m})}{dt} \tag{4}$$

where $d\xi$ is the induced electromotive force or voltage. The tilde above the magnetic field $\tilde{\boldsymbol{B}}_1$ indicates that the field is hypothetical—it is the field that would be created by unit current. As the magnetic moment rotates at the Larmor frequency, the scalar product in equation (4) is constantly changing, and the more rapid the rotation, the greater the time derivative and the induced voltage. However, note that if the field $\tilde{\boldsymbol{B}}_1$ were in the z direction, the scalar product would always be zero. This is illustrated in Figure 1(b), where there is no change of magnetic flux through the receiving coil as the magnet rotates. It follows that the primary design criterion for any receiving coil

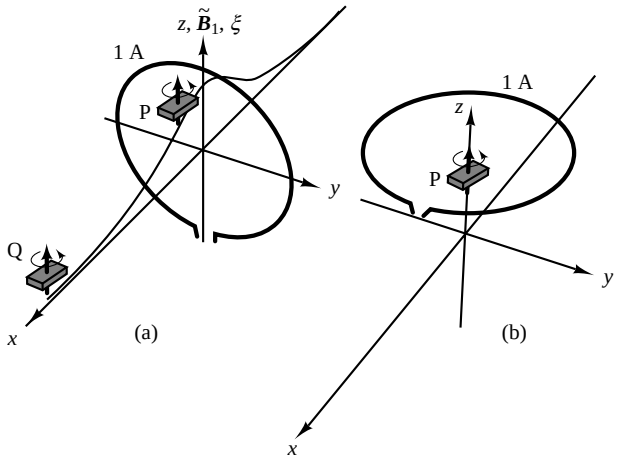

Figure 1 The principle of reciprocity. Following a pulse, the nuclear magnetic moment of a sample can be considered to be a small magnet rotating about the z axis. (a) Close to the loop of conductor at point P, the rotating magnet induces therein a much larger voltage than if it were at point Q. Similarly, if a current of 1 A at the Larmor frequency were passed through the loop, the magnetic field $\tilde{\boldsymbol{B}}_1$ produced (a graph of the field along the x axis is shown) at point P would be much larger than that at point Q. Thus, there would appear to be a correspondence between field strength and induced voltage, and this is borne out by a full calculation. (The graph therefore represents both signal ξ and field $\tilde{\boldsymbol{B}}_1$.) However, if the hypothetical $\tilde{\boldsymbol{B}}_1$ field produced by the loop is in the z direction at the sample, as shown in (b), there is no change in flux linkage through the loop as the nuclear magnet rotates, and therefore no induced voltage. We therefore conclude that, to receive an NMR signal, a receiving coil must generate a $\tilde{\boldsymbol{B}}_1$ field with a component in the (x,y) plane

Table 1 Nuclear Magnetization of a 1 M Solution at 20 °C

Nucleus and atomic weight	Natural % abundance	Spin I	Frequency (MHz T^{-1})	Magnetization (μA m^{-1} T^{-1})
^{1}H	99.98	$\frac{1}{2}$	42.5749	29.62
^{2}H	0.015	1	6.5357	1.861
^{10}B	19.58	3	4.5751	5.473
^{11}B	80.42	$\frac{3}{2}$	13.6597	15.25
^{13}C	1.108	$\frac{1}{2}$	10.7050	1.873
^{14}N	99.63	1	3.0756	0.4122
^{15}N	0.37	$\frac{1}{2}$	4.3141	0.3041
^{17}O	0.037	$\frac{5}{2}$	5.7719	6.351
^{19}F	100	$\frac{1}{2}$	40.0535	26.22
^{23}Na	100	$\frac{3}{2}$	11.2615	10.36
^{29}Si	4.7	$-\frac{1}{2}$	8.4575	1.169
^{31}P	100	$\frac{1}{2}$	17.2348	4.854
^{33}S	0.76	$\frac{3}{2}$	3.2651	0.8711
^{35}Cl	75.53	$\frac{3}{2}$	4.1715	1.422
^{37}Cl	24.47	$\frac{3}{2}$	3.4724	0.9852
^{39}K	93.10	$\frac{3}{2}$	1.9870	0.3226
^{41}K	6.88	$\frac{3}{2}$	1.0903	0.09713
^{43}Ca	0.145	$\frac{7}{2}$	2.8644	2.816
^{57}Fe	2.19	$\frac{1}{2}$	1.3756	0.03092
^{63}Cu	69.09	$\frac{3}{2}$	11.2849	10.41
^{65}Cu	30.91	$\frac{3}{2}$	12.0887	11.19

is that its field $\tilde{\boldsymbol{B}}_1$ must have a substantive component in the (x,y) plane. Hence, allowing for the transverse relaxation that takes place once magnetization is unaligned with the z direction, we have, from equations (2)–(4)

$$\mathrm{d}\xi = 2\pi\nu_0(\tilde{B}_{1xy}M_0 \sin\theta\, \mathrm{d}V)\exp(-t/T_2)\cos(2\pi\nu_0 t + \phi) \qquad (5)$$

where ν_0 is the Larmor frequency (in Hz), $\tilde{B}_{1xy}$ is the component of $\tilde{\boldsymbol{B}}_1$ at the sample parallel to the (x,y) plane, T_2 is the sample's transverse relaxation time, and ϕ is a phase constant determined by the relative orientations of the $\tilde{\boldsymbol{B}}_1$ field and the magnetic moment $\mathrm{d}\boldsymbol{m}$ at time $t = 0$. Equation (5) is the master equation for the signal from an NMR experiment in which the emission of radio waves is negligible, and is directly applicable to, say, a small volume element in an imaging experiment.

Equations (1) and (5) contain one of the main reasons for the drive in NMR to ever higher magnetic field strengths. (The other main reason is improved spectral resolution.) From equation (1), the magnetization M_0 may be seen to be proportional to B_0, while in equation (5), the frequency is also proportional to B_0 via the Larmor relation $2\pi\nu_0 = -\gamma B_0$. Thus, the induced EMF $\mathrm{d}\xi$ is proportional to the square of B_0. As the time taken for many NMR experiments diminishes as the square of the signal strength, equation (5) holds the promise (albeit not fully realized, see later) that even a modest increase in field will be richly rewarded in time saved. However, there are other factors in equations (1) and (5) that merit attention with a view to increasing the signal strength as much as possible. Apart from the obvious strategy, where feasible, of increasing the effective concentration of the sample, we note that both a reduction of temperature and an increase in $\tilde{B}_{1xy}$ increase the induced EMF. Assuming that the temperature is minimized whenever necessary and possible, let us therefore turn our attention to the hypothetical field created by unit current at the Larmor frequency in the receiving coil.

2.2 Receiving Coil Geometry

Viewing the receiving coil of Figure 1(a), it would appear that it should tightly surround the sample to receive the largest induced EMF, for it may be shown that the field at the center of a current loop varies inversely with its size (any good text on electromagnetic theory deals with the fields created by simple conductors—see, e.g., that by Bleaney and Bleaney[5]). (We ignore for the moment the question of whether the homogeneity of the $\tilde{\boldsymbol{B}}_1$ field is of import.) It would also appear that if we place more turns of wire on the coil, the field for unit current, and hence the signal strength, can be increased at will. We must remember, however, that the hypothetical field $\tilde{\boldsymbol{B}}_1$ is for unit current *at the Larmor frequency*. Thus, consider a coil, short in comparison to its diameter, that has many turns but whose conductor length is effectively one wavelength λ (a 'helical resonator'). As current at different points on the coil therefore has different phases (thanks to the finite speed of light and the presence of distributed capacitance between turns), the alternating field produced at the coil center (but not elsewhere) is almost zero. It follows that an NMR sample placed at the middle of the coil will give negligible signal—a phenomenon not predictable from measurements of bulk parameters such as coil inductance or quality factor. The corollary of this observation is that the length of conductor may not be increased ad infinitum to boost signal strength. Indeed, there is an optimal length for receiving coil use, and experience shows that this length is usually less than about $\frac{1}{20}\lambda$.[2] Put another way, the optimal number of turns on a coil diminishes as its operating frequency increases, and it is interesting to note that a single turn can exceed $\frac{1}{20}\lambda$ at 600 MHz with 10 mm sample tubes, and can approach λ in whole body applications at 170 MHz. It follows that designing good coils for these applications is both nontrivial and very difficult.

A further practical problem is that the loop geometry of Figure 1(a) may be unsuitable for use with most superconducting magnets, since the sample is usually inserted therein down the z axis. While such loops are sometimes employed to give a strong signal from a limited region on the side of an extensive sample (so-called 'surface coils', see ***Surface and Other Local Coils for In Vivo Studies***),[2] if signal from a complete section of a long, cylindrical sample is desired, the latter must be encompassed by a receiving coil having a geometry of the form shown in Figure 2. (Surface coils have been used throughout the history of NMR. The first use specifically to obtain better signal-to-noise ratio is probably that by Abe et al.[6] See also Ackerman et al.[7])

Once a coil has been designed to take account of the above factors, we may calculate with confidence, with the aid of equation (5), the induced EMF from an elementary volume of sample. The total signal can then be found by integration (usually numerical) over the complete sample volume. This calculation is simplest when the receiver coil is also used for transmission with a genuine current I at the Larmor frequency. The phase is then invariant with spatial position, while the flip angle for a rectangular pulse of duration τ, is given by

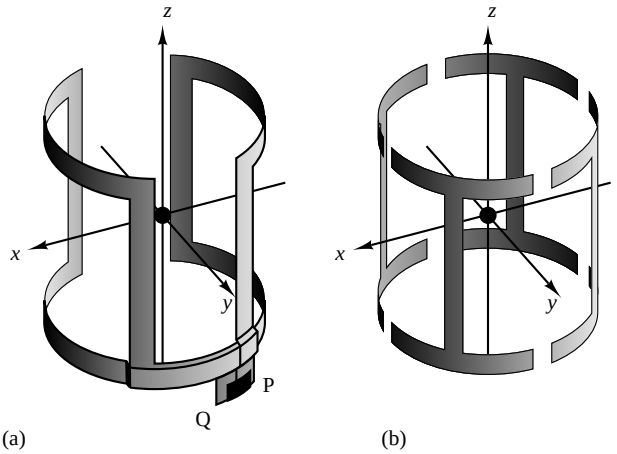

Figure 2 Two geometries for producing $\tilde{\boldsymbol{B}}_1$ fields predominantly in the (x,y) plane, while allowing sample insertion down the z axis—the preferred direction when employing a superconducting magnet. In (a), a traditional 'saddle coil' is shown. Alternating current entering at P and leaving at Q generates at the coil center a $\tilde{\boldsymbol{B}}_1$ field in the x direction. In (b), circuits are completed with the aid of capacitors (not shown for clarity) across the eight gaps. Current flowing round the various circuits can create fields in any direction, but, in particular, two $\tilde{\boldsymbol{B}}_1$ fields (in the x and y directions) with a 90° phase difference between them can be made. In some circumstances, the second field can increase the available sensitivity by 40%.[2] With both designs, the 'active volume' (see the text) is roughly that of the enclosed cylinder

$$\theta = \tfrac{1}{2}\gamma I \tilde{B}_{1xy}\tau \tag{6}$$

(the factor of 2 in this equation arises because it is the magnetic field in the rotating frame, rather than the laboratory frame, that determines the flip angle). The signal is then

$$\xi = 2\pi\nu_0 \left\{ \int_{\text{all space}} \tilde{B}_{1xy}(\boldsymbol{r}) M_0(\boldsymbol{r}) \sin[\tfrac{1}{2}\gamma I B_{1xy}(\boldsymbol{r})\tau]\, \mathrm{d}V \right\} \times \exp\left(-\frac{t}{T_2}\right) \cos(2\pi\nu_0 t + \phi_0) \tag{7}$$

The dependence of the variables on spatial position $\boldsymbol{r}$ has been included for clarity, though the main field $\boldsymbol{B}_0$ has been assumed to be homogeneous so that the Larmor frequency ν_0 is spatially invariant. Of course, for most liquid samples in a test tube, $M_0(\boldsymbol{r})$ is a constant within and zero without. Equation (7) is then often dispensed with, and, using equation (5) again, an approximate value of ξ is found by taking the values of $\tilde{B}_{1xy}$ and θ to be those pertaining to the center of the receiving coil. An effective volume ΔV [the 'active volume', the volume encompassed by the receiving coil of Figure 2(a)], is then substituted for $\mathrm{d}V$.

2.3 Orders of Magnitude

We shall briefly discuss coil geometry further when we consider noise sources, but, at this juncture, it is instructive to put numbers in equation (5) for two common samples that experience shows are easily detectable. We consider proton signals from first, 0.1% ethylbenzene at 500 MHz (14 T) and 20 °C in a 5 mm tube with a receiving coil having the geometry of Figure 2, and second, from 1 μl of water at 64 MHz (1.5 T) and 37 °C in a biological sample using a surface coil. Ethylbenzene is routinely used as a standard for checking the sensitivity of high-resolution NMR spectrometers, and it is the signal-to-noise ratio of a central peak in the spectral quartet from the CH_2 group that is usually measured (Figure 3). Thus, signal effectively comes from 0.75 atoms of hydrogen per molecule. We first calculate the magnetic moment of the sample. Taking a specific gravity of 0.867 for ethylbenzene (molecular weight 106.2) and the active volume of sample to be about 150 μl (Figure 2), the latter contains 130 μg, or 1.22 μM, of ethylbenzene. Thus, the magnetic moment of the hydrogen contributing to the measured line is, from equation (1) or Table 1, 3.2×10^{-13} A m^2. Now the magnetic field created by unit current in a saddle coil of diameter 7 mm and length 15 mm [Figure 2(a)], is approximately 210 μT,[4] and so, following a 90° pulse, from equation (5), the tiny voltage induced in the coil is about 210 nV.

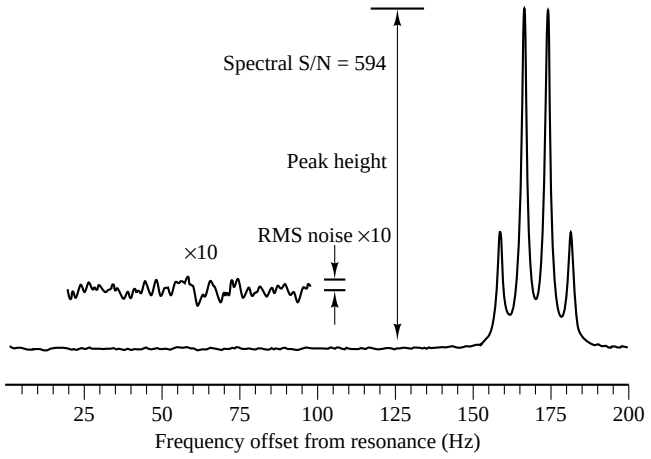

Figure 3 A typical NMR spectrum. To be strictly accurate, the spectral sensitivity (or signal-to-noise ratio, S/N) of such a spectrum should be assessed by measurement, in each of a large set of spectra, of the height of the peak of interest. The mean and standard deviation of the peak height may then be found, and the ratio of these two quantities is the S/N. However, provided the instrument is in all respects stable, the same result may often be obtained in far less time by comparing, as shown, the peak height and the root mean square deviation of the spectral baseline ('baseline noise') in some flat region adjacent to the peak. It is stressed that this short cut is only valid with linear data processing techniques such as Fourier transformation, and when there is no phase noise in the NMR signal caused, for example, by sample spinning or an unstable magnetic field. Measurement of baseline noise can also be used in the test of receiver performance discussed later in the article

Following a similar path, since the molecular weight of H_2O is 18 and its specific gravity to good accuracy is 1, one liter contains approximately 111 mol of hydrogen. Thus, from Table 1, and allowing for the temperature, the proton magnetization is 4.67×10^{-3} A m^{-1}, and the magnetic moment in 1 μl is 4.67×10^{-12} A m^2. Consider the signal received at 64 MHz by a single turn surface coil of radius a = 5 cm from the sample an axial distance x = 5 cm away. If the permeability of free space is μ_0, the magnetic field created by unit current at this point is[5]

$$B_{1xy} = \frac{0.5\mu_0 a^2}{(a^2 + x^2)^{3/2}} = 4.44\mu\mathrm{T} \tag{8}$$

Thus, following a 90° pulse, the induced EMF at 64 MHz has an initial amplitude of 8.3 nV. From these examples, we see that the signals received by an NMR spectrometer are truly small. However, let us now see how they compare with the unavoidable noise.

3 UNAVOIDABLE NOISE

3.1 Receiving Coil Resistance

The primary unavoidable source of noise when the sample is an electrical insulator is Brownian motion of the electrons in the receiving coil. The atoms in the coil conductor (usually copper or silver) have vibrational thermal energy, and interact with conduction electrons in the valence band. Thus, when current is passed and the electrons are given kinetic energy, the interaction transfers that energy to the atoms, and the conductor becomes hot. The usual measure of this interaction is the resistivity ρ of the conductor: a superconductor with zero resistivity generates no heat when current is passed. It was Einstein, in his famous paper on Brownian motion, who pointed out that where there is dissipation of energy by such interactions, there must also be energy fluctuations, and when this 'fluctuation–dissipation' theorem is applied to an electrical conductor,[8] the 'Nyquist formula'

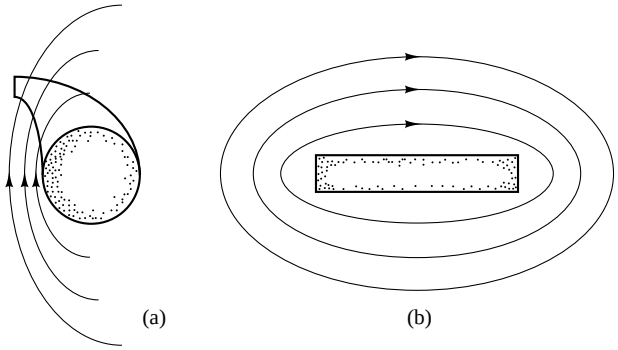

Figure 4 Proximity effect. When radiofrequency alternating current flows in adjacent conductors, their combined alternating magnetic fields induce EMFs in the conductors that constrain the current flow in such a way as to minimize the stored energy. Thus, in (a), which shows a greatly enlarged section of a circular loop (Figure 1), current flows preferentially on the inner radius, owing to the influence of the fields from the rest of the loop. In (b), similar constraints influence the distribution of current on the surface of a rectangular conductor. This 'proximity effect' renders difficult any calculation of conductor resistance

$$N_R = (4k_B TR\Delta\nu)^{1/2} \tag{9}$$

is obtained. Equation (9) states that the voltage measured between the ends of a conductor of resistance R fluctuates with a standard deviation (root mean square value) of N_R. (The distribution of the noise is Gaussian.) Note that the effective bandwidth $\Delta\nu$ of the measuring apparatus affects the measurement. The fluctuations are sometimes called 'Johnson noise', and it is clear that a major goal of receiving coil design is to minimize them, by reducing the coil's resistance.

It might be thought that theoretical prediction of the noise is a simple task. However, this is not the case, because we are concerned with measurements (and therefore fluctuations) in the radiofrequency range. If we consider once again the simple loop of Figure 1(a), a hypothetical current of 1 A at the Larmor frequency generates an alternating magnetic field. While it is well known that this field creates a voltage across the ends of the loop—the phenomenon of self-induction—it is less well known that the electromotive forces it induces also cause the distribution of current in the conductor to become inhomogeneous and asymmetric, as shown in Figure 4. With a (fictitious) infinitely long wire of circular section of radius r_0, the current flows uniformly in a 'skin' over the surface, and its density J decreases exponentially with penetration into the wire as

$$J = J_0 \exp\left(\frac{r - r_0}{\delta}\right), \quad \delta = \left(\frac{\rho}{\pi\nu_0\mu\mu_0}\right)^{1/2}, \quad r_0 \gg \delta \tag{10}$$

where r is the radius within the wire, μ is the permeability of the wire, and δ is known as the 'skin depth'. For copper at 100 MHz, $\delta = 6.6\,\mu$m. However, when one conductor is in close proximity to another, the field created by the one alters (via the mechanism of induced EMFs) the distribution of current in the other, and vice versa, in such a manner as to minimize the energy stored in the magnetic field. Thus, in Figure 4(a), we see the effects of the current in the rest of the ring on the current distribution in one short segment. There is more current on the inside bend than elsewhere. This 'proximity effect' can effectively increase the resistance of the conductor by a factor ζ of up to an order of magnitude, since the current cannot fully utilize the available surface. It bedevils any calculation of resistance. Figure 4 also shows the effect when the conductor is rectangular. Current flows mainly in the corners of the conductor, illustrating the axiom that where the alternating field is strongest, there the current is.

It follows that, without a very tedious finite element computation, we may only estimate the resistance of a receiving coil, and hence its noise. Once the thickness of a conductor is very much larger than the skin depth (and this is usually so at the frequencies employed in NMR), we may write the resistance R_c as

$$R_c = \frac{\zeta\rho l}{s\delta} = \frac{\zeta l}{s}(\pi\nu\mu\mu_0\rho)^{1/2} \tag{11}$$

where l is the length of the conductor and s is its circumference. However, increasing s to reduce R_c can also reduce the $\boldsymbol{B}_1$ field created by the coil, and much of the art of receiving coil manufacture lies in optimization of the ratio $\tilde{B}_1/R_c^{1/2}$. Thus, a well-designed saddle coil of the previous section might have a resistance of roughly 1 Ω at 500 MHz, while the surface coil might have a resistance of about 0.1 Ω at 64 MHz.

3.2 Sample Losses and Effective Resistance

When the sample is an electrical conductor, as is often the case in biological NMR experiments, our hypothetical alternating magnetic field $\tilde{\boldsymbol{B}}_1$ induces eddy currents which hypothetically heat the sample. (The transmitter $\boldsymbol{B}_1$ field really does heat the sample, and is potentially dangerous. See ***Sensitivity of Whole Body MRI Experiments***.) This dissipation of energy must be interpreted electrically as an extra resistance R_m in series with the coil, for in electrical theory, only resistance can produce heat from current. Conversely, by the fluctuation–dissipation theorem, there must be noise associated with the resistance, as per equation (9), where T is now the temperature of the sample.[2,9] In general, calculation of R_m is difficult, and if a measure of it is needed, it is best sought experimentally.[2] However, in one or two simple cases, it may be deduced—and one of these is where a circular coil sits on the surface of a semi-infinite sample. If the skin depth and wavelength in the conductor are very much greater than the radius of the coil, the resistance R_m is

$$R_m = \tfrac{4}{3}\sigma\pi^2\mu_0^2\nu_0^2 a^3 \tag{12}$$

where a is the coil radius and σ is the conductivity of the sample.[2] Thus, for $a = 5$ cm and a conductivity of 0.3 S m^{-1} (a typical average value for animal tissue), the effective resistance at 64 MHz is 3.2 Ω. In practice, measured values tend to be smaller than this, since surface coils are usually lifted a little from the surface.[2] However, it is clear that inductive losses in the sample can be a major source of noise for most biological NMR experiments, since R_m is often very much greater than R_c. (See also ***Sensitivity of Whole Body MRI Experiments***.) The origin of the noise in such experiments is the Brownian

motion of the electrolytes. The random motions of the charges induce random electromotive forces in the receiving coil, and employing the concept of an effective resistance is simply a convenient way of quantifying such random voltages.

3.3 Receiver Noise

No NMR receiver is noiseless, and there are always small contributions to the noise from various parts of the circuitry, notably from the mixers and the audiofrequency amplifiers.[2,10] However, with a well-designed system, the receiver noise should come overwhelmingly from the first stage of preamplification and be small in comparison to the two sources of noise already discussed. Unfortunately, this desirable situation can easily be abrogated by the user, the most common mistake being the insertion of an attenuator between the preamplifier and the rest of the receiver. This error can easily result in the noise from the receiving coil being so attenuated that the noise from, for example, the first mixer in the receiver, can predominate. The result is inevitably a reduction of sensitivity. An attenuator should only be used as a last resort in the presence of huge signal strength, when the maintenance of an optimal signal-to-noise ratio is of no concern. Another common mistake concerns the matching (see later) of the probe. The preamplifier manufacturer designs the first stage of the device so that it gives its best performance from a signal source of a specific impedance—usually 50 Ω resistance for NMR purposes. However, this does *not* mean that the input impedance Z_{in} of the preamplifier is 50 Ω, and so matching the probe to the input impedance, for example by maximizing the receiver output, can destroy the conditions for optimal noise performance. It should not be attempted—the signal may be increased, but the noise will increase more rapidly!

The additional noise added by the NMR receiver can be found from the 'noise figure' F of the device—a number usually quoted by the manufacturer in decibels. In general, if noise βN_a is added by an amplifier of gain β, to the noise βN_s from a 50 Ω source, the total noise delivered by the device is $\beta(N_a^2 + N_s^2)^{1/2}$ (random numbers add quadratically). However, if the device were perfect, N_a would be zero and the output would be βN_s. The ratio of the imperfect to perfect outputs is the 'noise factor' F', and, converted to decibels, this is the noise figure

$$F = 20\log_{10} F' = 10\log_{10}\left(1 + \frac{N_a^2}{N_s^2}\right) \tag{13}$$

A good NMR receiver has a noise figure of less than 2 dB; in other words, the noise it adds degrades the inherent sensitivity of the receiving coil by less than 25%.

A devastating test of receiver performance can easily be made with the aid of hot and cold noise sources that temporarily replace the probe on the preamplifier input. The sources are two identical, well-shielded resistances, one 50 Ω at room temperature and the other 50 Ω in liquid nitrogen at 77 K both resistances being on the ends of identical short lengths of 50 Ω cable and both being specified at the Larmor frequency. From equation (9), the noise from the source in liquid nitrogen is about half that from the source at room temperature T, and so we should expect the noise from the spectrometer to change significantly when the two sources are interchanged. If the measured ratio of the 'cold' to 'hot' receiver outputs is α, the noise figure is, to fair accuracy[2]

$$F = 10\log_{10}\left(1 - \frac{77}{T}\right) - 10\log_{10}(1 - \alpha^2) \tag{14}$$

For example, if T = 293 K and α = 0.64, F = 1 dB, and the system has good noise performance. As many NMR computing systems have software available to measure RMS noise (see, e.g., Figure 3), it is a relatively simple matter to compute the noise figure. The only trap of which to beware is that a shielded resistance that is accurately 50 Ω at room temperature will almost certainly not be 50 Ω when plunged into liquid nitrogen! This simple procedure has further value when one remembers that an NMR probe should give the same noise output as the room temperature 50 Ω resistance. If it does not, the probe is either unmatched or is receiving interference.

4 SIGNAL-TO-NOISE RATIO

4.1 Filtered Fourier Transformation

We have seen that quite a good estimate of the signal induced in a receiving coil can be obtained, while the resistance R_c or effective resistance $R = R_c + R_m$ of the coil can sometimes also be estimated tolerably well. Thus, a reasonable knowledge of signal and noise is available, and both are passed to the preamplifier and thence to the NMR receiver. However, it is not normally the initial amplitude of a free induction decay and its accompanying noise that is observed in an NMR experiment, but rather some function of these voltages obtained by computational manipulation—for example, by a filtered Fourier transform. The purpose of such a transform is to find how much signal is present at a number of discrete frequencies covering a limited spectral width about the Larmor frequency. For simplicity, assume that the spectrometer frequency is such that one of the central peaks of the ethylbenzene quartet of Figure 3 mentioned earlier is exactly on resonance. As the on-resonance FID issues from the NMR receiver, let it be integrated (this mathematical device is equivalent to picking the peak out of the many frequencies present in a Fourier transform). Employing equation (5) with a 90° pulse, and, for simplicity, setting the gain of the receiver to 1, the signal is then

$$\begin{aligned}\xi &= \int_{t'=0}^{t} 2\pi\nu_0 \tilde{B}_{1xy} M_0 \,\mathrm{d}V \exp\left(-\frac{t'}{T_2}\right) \mathrm{d}t' \\ &= 2\pi\nu_0 \tilde{B}_{1xy} M_0 T_2 \,\mathrm{d}V \left[1 - \exp\left(-\frac{t}{T_2}\right)\right]\end{aligned} \tag{15}$$

and in the limit as $t \to \infty$, $\xi \to 2\pi\nu_0\ {}_{1xy}\ M_0\ T_2\,\mathrm{d}V$. This value represents the height of the spectral peak, and is dependent upon the relaxation time T_2. (We assume the main magnetic field is homogeneous.

Next, examine the effects of the integration on the noise. It may be shown that integration is equivalent to applying a filter of width $\Delta\nu = 1/t$ (in Hz) and gain t. Thus the RMS noise on the spectral baseline is

$$N_R = F'(4k_BTRt)^{1/2} \tag{16}$$

and as t increases, so does the noise. Thus, the signal-to-noise ratio (S/N) $\Psi = \xi/N_R$ passes through a maximum when data are gathered for a time $t = 1.255T_2$, and is

$$\Psi_{\text{truncated}} = \frac{0.638}{F'} 2\pi\nu_0 \tilde{B}_{1xy} M_0 \, \mathrm{d}V \left(\frac{T_2}{4k_BTR}\right)^{1/2} \tag{17}$$

In low-field imaging experiments, the signal and noise from the receiver may well only be collected for this length of time, but in spectroscopic experiments, the resulting lineshape is unsatisfactory, and, further, a slightly better S/N can be obtained. Thus, it is common practice *not* to truncate the signal and noise, but to multiply both by an exponential filter $G = \exp(-t'/T_2)$ until the signal has decayed to a negligible value. Following Fourier transformation, a broader Lorentzian line, of width $2/\pi T_2$ (in Hz) and of height 22% *less* than previously, is obtained. However, the effect on the noise of such filtering followed by integration is to limit it to

$$N_G = F'(2k_BTRT_2)^{1/2} \tag{18}$$

and when we calculate the S/N under these conditions, it becomes [cf. equation (17)]

$$\Psi_{\text{filtered}} = \frac{0.707}{F'} 2\pi\nu_0 \tilde{B}_{1xy} M_0 \, \mathrm{d}V \left(\frac{T_2}{4k_BTR}\right)^{1/2} \tag{19}$$

In Section 2.3, we calculated the amplitude of the FID for the largest line in the quartet of ethylbenzene to be about 210 nV, while in Section 3.1, an estimate of the probe resistance was $R = R_c = 1\,\Omega$. Setting T_2 to a typical value of 300 ms and F′ = 1.26 (F = 2 dB), we obtain a value of 510:1 for the S/N in equation (19). Considering the uncertainties in our estimation of probe resistance, this is in good agreement with the typical experimental value of 594:1 at 500 MHz shown in Figure 3. It may be noticed in equation (11) that the probe resistance is proportional to the frequency to the quarter power. From equation (19) we may then conclude that the S/N increases not as the square of field strength as mentioned earlier, but roughly as the Larmor frequency to the power of $\frac{7}{4}$, provided T_2 does not change with frequency. There is a strong dependence of equation (19) on temperature (roughly as $T^{-7/4}$), since, in addition to M_0, the resistance of the receiving coil is strongly temperature-dependent, and attempts have been made to fabricate probes where the receiving coil is at very low temperature.[11] The challenge is not to freeze the sample while keeping the receiving coil tightly wrapped about it.

When we consider the S/N of an experiment involving a conducting sample, the dependences are very different. If the effective resistance R_m is very much bigger than the intrinsic resistance R_c, we may substitute equations (8) and (12) into equation (19) to obtain the maximum S/N available from an elementary volume dV a distance x below a surface coil of radius a. We then have

$$\Psi_{\text{filtered}} = \frac{M_0 \, \mathrm{d}V}{F'} \left[\frac{3aT_2}{32k_BT\sigma(a^2 + x^2)^3}\right]^{1/2} \tag{20}$$

Provided the conductivity σ (the reciprocal of the sample's resistivity) and the transverse relaxation time T_2 of the sample do not vary with frequency, the S/N only increases linearly with field strength via the magnetization M_0. This is because the noise, being an induced voltage, also has a linear dependence on frequency. Further, note the very strong dependence of Ψ upon the size of the surface coil. (See ***Sensitivity of Whole Body MRI Experiments***.) Thus, we may expect a S/N of about 11 from the example given earlier of 1 μl of water, at 64 MHz, 5 cm below a surface coil of radius 5 cm (T_2 was set to 300 ms and $F' = 1.26$). While we have chosen an illustrative example of a surface coil, the demonstrated dependences hold for most experiments where the noise from the sample is dominant, regardless of the shape of the coil.

4.2 Data Accumulation

Of course, many experiments will be performed repetitively, and the results summed to increase the S/N. This strategy is possible because the signal, being deterministic, adds linearly, whereas the noise, being random, adds as the square root of the number of repetitions. Thus, the S/N also increases as the square root of the number of repetitions—and of time. Conversely, the time taken for an experiment to acquire a desired S/N will depend on field strength between $B_0^{-7/2}$ and B_0^{-2}, depending on the sample's conductivity and size. However, to repeat the NMR experiment, we must wait for magnetization to relax longitudinally before attempting a repetition. Suppose that during a cumulative experiment and just prior to a pulse of flip angle θ, no vestige of transverse magnetization remains from the effects of the previous pulse that was applied a time T_R earlier. In other words, $T_R >> T_2$. If the longitudinal magnetization at this time is M_1, immediately after the pulse, the longitudinal magnetization has become $M_1 \cos\theta$, while the transverse magnetization is $M_1 \sin\theta$. The latter determines the voltage induced in the receiving coil, but a repetition period T_R later, the longitudinal magnetization M_z has recovered somewhat to become once again M_1:

$$M_z = M_0 - (M_0 - M_1\cos\theta)\exp(-T_R/T_1) = M_1 \tag{21}$$

Thus,

$$M_1 = M_0 \frac{1 - \exp(-T_R/T_1)}{1 - \cos\theta\exp(-T_R/T_1)} \tag{22}$$

Now, in a time T_n, there can be $n = T_n/T_R$ repetitions, which, notwithstanding the type of experiment (spectroscopic, imaging, etc.), increases the S/N Ψ by a factor of $n^{1/2}$. Thus, at the end of data accumulation, at time T_n,

$$\Psi \propto n^{1/2} M_1 \sin\theta = M_0 \left(\frac{T_n}{T_R}\right)^{1/2} \sin\theta \times \frac{1 - \exp(-T_R/T_1)}{1 - \cos\theta\exp(-T_R/T_1)} \tag{23}$$

A normalized contour plot of this function is shown in Figure 5, but, by simple differentiation, it is easy to show that for constant T_R, it passes through a maximum when $\theta = \arccos[\exp(-T_R/T_1)]$, the so-called 'Ernst angle'. Substituting this value into equation (23), we find that

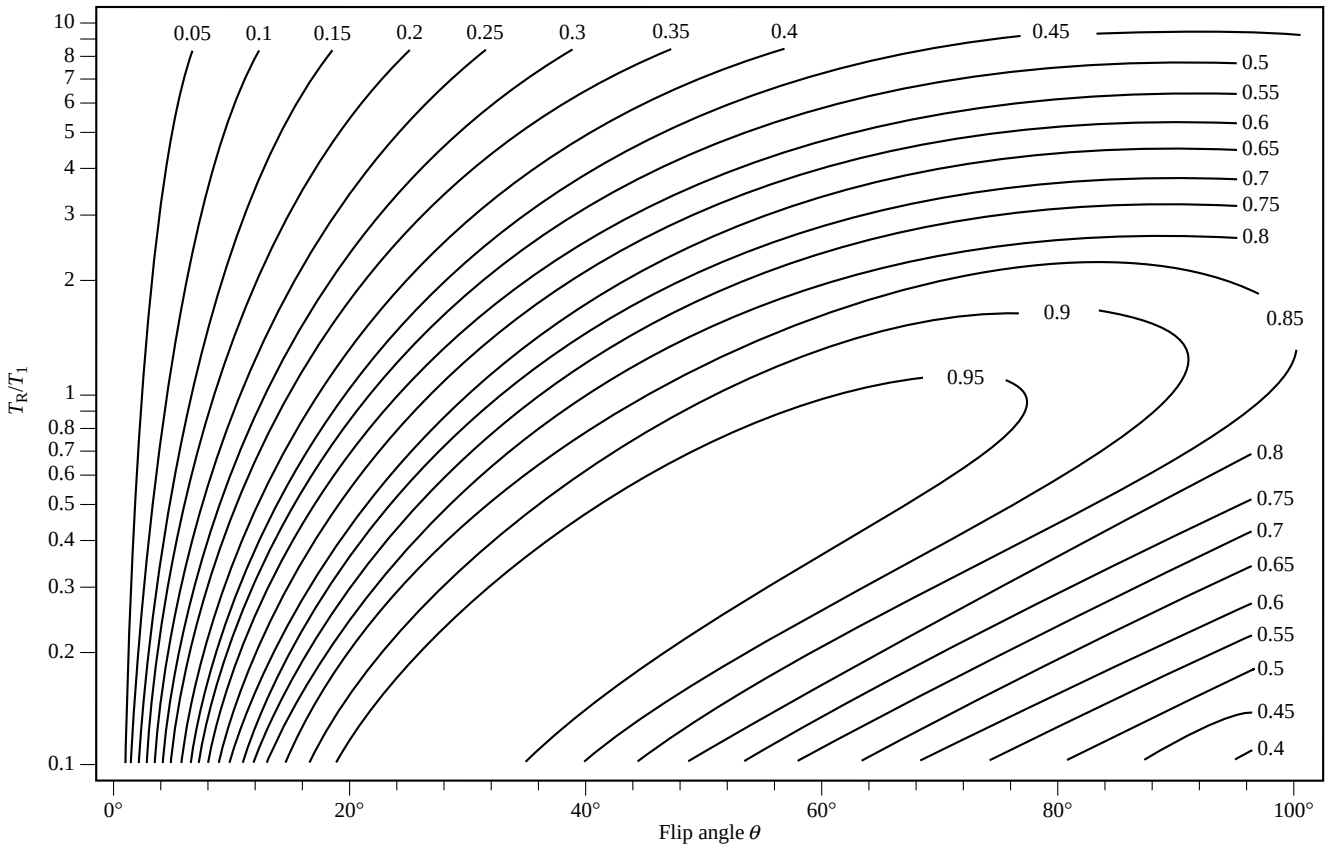

Figure 5 The signal-to-noise ratio in a spectrum accumulated for a given fixed time as a function of the pulse flip angle, and the ratio T_R/T_1 of the repetition period T_R and longitudinal relaxation time T_1. The plot is normalized to unity, since it takes no account of vagaries such as spectral filtering and transverse relaxation time. Note that the y axis is logarithmic. (For a plot of the dependence of signal strength on variations in T_1, see ***Sensitivity of Whole Body MRI Experiments***, Figure 1)

$$\Psi_{\max} \propto M_0 \left[\frac{T_n}{T_R} \frac{1-\exp(-T_R/T_1)}{1+\exp(-T_R/T_1)}\right]^{1/2} \tag{24}$$

and a global maximum is obtained when T_R is as small as possible, say $2.5T_2$. Thus, in a spectroscopic experiment, from equations (19) and (24), when $2.5T_2 = T_R << T_1$, $\Psi_{\max} \propto M_0(T_n T_2/T_1)^{1/2}$, and, not surprisingly, we see that it is the ratio of the relaxation times that governs the accumulated S/N. However, we can see from Figure 5 that the sensitivity is excessively dependent upon the flip angle under such conditions, and so it is often better to sacrifice a little sensitivity and use, say, a 50° pulse with a repetition time T_R of about $0.4\ T_1$.

5 ELECTRIC FIELDS AND EXTRANEOUS NOISE

Almost nothing has been said so far concerning matching of the probe. The calculations above assume that this task has been performed correctly and that the additional components required have negligible effect upon the sensitivity of the instrument. However, we now turn to it as a possible conduit for noise. It has been mentioned that the preamplifier is designed to give its best noise performance from a source of impedance 50 Ω resistive, this value being chosen by the manufacturer to be compatible with a common value of coaxial cable characteristic impedance. It follows that the predominantly reactive impedance of the receiving coil, $Z_L = R_c + R_m + i2\pi\nu_0 L$ (typically, 0.5 + i70, ± 50%), where L is the coil inductance and $i = \sqrt{-1}$, must be transformed to 50 Ω resistive. This statement implies the use of capacitors (capacitance C), with their negative reactance $Z_C = -i/2\pi\nu_0 C$. The capacitors should have a resistance that is much less than $R_c + R_m$ so that they introduce negligible extra noise—they should have a high quality factor. The theory of impedance transformation in *LCR* circuits is outside the scope of this article.[2] (Any good electronics text deals with the subject of impedence transformation—a 'classic' is that by Terman.[12]) However, we note that as soon as capacitance is deemed to be an important circuit component, we must take cognizance not only of magnetic fields but also of electric fields. This aspect of probe design, often neglected, is of crucial importance whenever the size of the probe is not very much less than wavelength $\lambda = c/\nu_0$ where c is the speed of light in free space or the sample. The ideal probe has no electric fields running through the sample, no fields escaping from its confines into the outside world, and an average potential that is equal to that of its surroundings. The corollary of these statements is that (i) dielectric properties of the sample or its holder neither generate noise nor modulate the impedance transformation, and (ii) no interference is received from the outside world. Thus, for example, a dielectrically lossy sample such as a human does not produce noise by

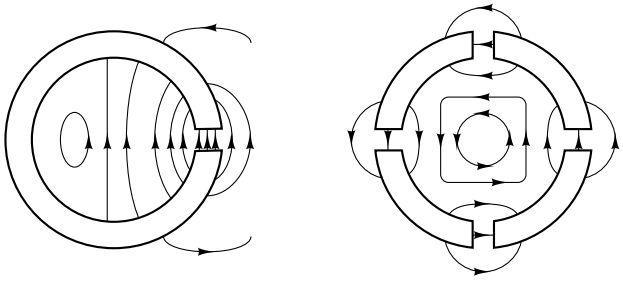

(a) (b)

Figure 6 Electric fields. In (a) are shown the fields (conservative and nonconservative) of the Hertzian loop of Figure 1. Because there is only a single gap in the loop (across which is placed the sole tuning capacitor), a considerable dipolar field is created. The direct consequence is that the tuning and Q factor are dependent upon the dielectric properties of the sample. Concomitantly, the loop acts as an excellent antenna for reception of electromagnetic interference (EMI) propagated by electric fields. In (b), the four gaps and tuning capacitors (not shown) create an octapolar conservative field that reduces substantially both the sample dependence of the loop's characteristics and the sensitivity to interference. However, the principle of distributed capacitance is not a sinecure, and each probe design should be individually assessed with regard to its electric field properties and suitable placement of capacitors

the Brownian motion of electric charges capacitively coupling to the probe, nor does a spinning sample modulate the probe tuning, producing so-called 't_1 noise'. Neither does a sample of high dielectric constant such as water appreciably change the probe tuning when inserted. Equally, grasping the leads entering a probe (a useful test) makes no difference to the probe matching to $50\,\Omega$, and does not change the noise emanating from the receiver.

It is sometimes claimed that the ideal situation outlined above is completely unattainable, since Maxwell's equations dictate that whenever there is an alternating magnetic field, such as the hypothetical $\tilde{\boldsymbol{B}}_1$ field, there must also be an alternating electric field—the fields are linked. This is correct, but the operative word is 'whenever' not 'wherever'. A standing wave on a transmission line is a simple example of the linking of magnetic and electric fields: however, where the former is greatest, the latter is least. The deleterious effects of conservative electric fields in probes have been known for many years—mainly as a heating mechanism when samples are dielectrically lossy.[13] The key to rendering such effects negligible is to ensure that the fields' order is as high as possible, and each probe design has to be assessed individually in this regard. However, a simple example is afforded by the Hertzian loop, as shown in Figure 6(a). Commonly used as a surface coil in biomedical experiments, Hertz demonstrated the existence of radio waves with it—it is an excellent antenna and a poor probe. The figure shows that there is a strong dipolar electric field across the gap, which can produce localized heating in a sample beneath, and excessive dependence of resonant frequency on sample position and composition. However, in Figure 6(b), distributing the tuning capacitance symmetrically about the loop creates an octapolar field that reduces dramatically resonant frequency variation, heating and concomitant noise.[13] It also ensures that any external electric fields (with up to eighth-order variation with distance) cannot couple to the probe. Such fields can be created by a variety of sources, as mentioned in Section 1—for example, when radio waves impinge on the magnet, or on surrounding objects and cables. Thus, using distributed capacitance also helps reject interference in this instance. It should be stressed that discretely distributed capacitance does not automatically kill dipolar fields—each situation must be analyzed individually. For example, despite a surfeit of capacitors, the well-known birdcage design (see also ***Birdcage Resonators: Highly Homogeneous Radiofrequency Coils for Magnetic Resonance***) has a dipolar field across its mouth if a guard ring is not employed.

The manner in which a tuned and matched probe is connected to the preamplifier can also generate conservative dipolar electric fields—not this time in the confines of the probe, but rather between the cabling and surrounding conductor (e.g., the magnet). In other words, current can spill out of the probe and flow over the outer surface of the coaxial cable linking the probe and the preamplifier. Thus, a large antenna is created that may radiate quite efficiently during transmission and may also receive interference. This situation is far more difficult to analyze, but one approach is shown in Figure 7. Consider the matched probe of Figure 7(a) connected to a preamplifier of input impedance Z_{in}. There is also present a source of electromagnetic interference (EMI) that has capacitance to the probe. For simplicity, only two capacitances are shown, but it is obvious that interference current flows through the coaxial cable and into impedance Z_{in}: the preamplifier receives interference. Now consider the so-called 'balanced' circuit of Figure 7(b). By virtue of the halfwave cable and symmetry, points P and Q must be at the same potential as the braiding of the coaxial cable at point R. Thus, no current can flow into the preamplifier, and there is no interference. Concomitantly, during transmission, no dipolar fields are created between the cabling and the magnet. In practice, there is rarely perfect symmetry, and a balance can never be totally attained, but a reduction in interference of a factor of 50 or 100 can often be garnered with this technique.

Finally, where possible, the probe should be shielded. This is normally not a difficult matter in a high-resolution spectrometer, where the length of the magnet bore is much greater than its diameter. A metal tube of diameter D attenuates radiation as $\exp(-3.68z/D)$. Thus, if the probe is in the middle of a tube whose length is greater than eight diameters, negligible interference can be received, while physical access is still possible. Of course, the efficacy of such a tube shield is easily ruined by having a conductor running through it. A large coaxial cable is then created, which acts as a conduit to transport interference. Thus $50\,\Omega$ cable running to the probe should always go up the inside tube wall (or even through it) and have its outer conductor electrically attached at numerous places. Any other cabling (for sensors, stimulators, etc.) should be fitted with stringent low-pass filters at the tube entrance; it should also run up the wall and always be 'decoupled' with capacitors to the tube at several positions. When the bore of the magnet is not long in comparison with the diameter, shielding is much more difficult, and it is sometimes necessary, in noisy environments (e.g., close to a radio transmitter), to shield the magnet room and spectrometer or imager. This is an expensive and difficult task, since every electrical conductor entering the

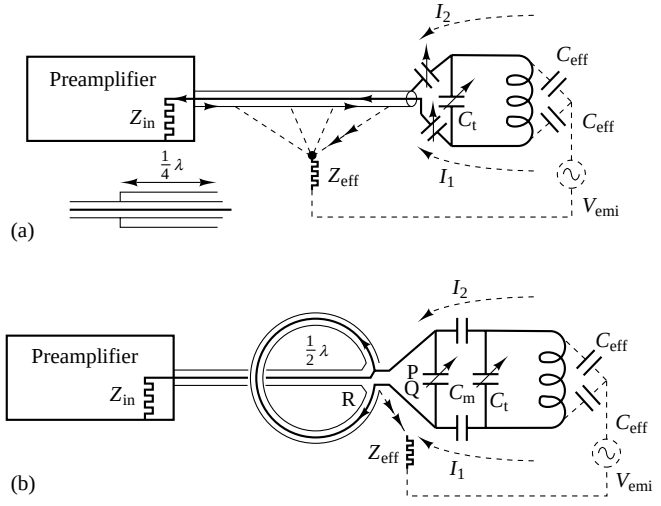

Figure 7 The reduction of electromagnetic interference (EMI) by good total probe design. In both figures, a model circuit for EMI reception is shown. The interference is represented as a voltage source V_{emi} that has distributed capacitance to the probe. For simplicity, this is shown by two small capacitors C_{eff} (say of order 1 fF). The current return path, which typically involves capacitive coupling to the braid of the coaxial cable running to the preamplifier, and to the exterior of the latter, is shown as comprising an arbitrary effective impedance Z_{eff}. In (a), it may be seen that, despite the use of two matching capacitors (which need to be adjusted in tandem), a current I_1 flows into the preamplifier where it generates an interfering voltage across Z_{in}. The current may be reduced by ensuring that Z_{eff} is large, and one way of doing this is to mount a 'quarter-wave balun' at the end of the coaxial cable, as shown in the inset. The sleeve on the cable, being $\frac{1}{4}\lambda$ long, creates an impedance of a few kΩ between the inside and the outside of the coaxial braiding and thereby hinders the flow of current I_1 somewhat, depending on the impedance of C_{eff}. However, in (b), the half-wave cable ensures that any potential common to both points P and Q is shorted to point R. To the extent that the model for interference has electrical symmetry, it therefore follows that no voltage is present across the end of the coaxial cable and no interference is received by the preamplifier. This design of 'half-wave balun' may also be applied to the probe of (a), but the circuit of (b) has the advantage of needing only a single variable matching capacitor C_m while maintaining electrical symmetry

room must then pass through an excellent low-pass filter. Nor must it be forgotten that rectification of rf interference can take place in circuitry, thus rendering audiofrequency devices noisy too. For example, the currents in shims or gradients may alter in the presence of interference, and it is not unknown for a local radio station to be clearly audible near a magnet as the gradient coils act as a loudspeaker. The S/N is then degraded by changes of the Larmor frequency and/or main field homogeneity during data accumulation—'phase noise' appears on the spectrum.

6 CONCLUSION

This article has attempted to provide an introduction to questions of sensitivity in the NMR experiment. However, since there are so many variants of the basic 'pulse and collect' experiment, the reader should be aware that no work of this type can be comprehensive. Thus, for example, there has been negligible discussion of phase noise and receiver gain, and the effects of field drift, temperature variation, distortion, etc. have not been considered. In addition, when the Larmor frequency is sufficiently high that the wavelength $\lambda = c/\nu_0$ in the sample approaches the sample dimensions, the theory given above needs modification; notwithstanding excellent probe design, the $\tilde{\boldsymbol{B}}_1$ field in the sample can become highly inhomogeneous in amplitude and phase. In an imaging experiment, the root mean square S/N will be approximately that predicted by the theory above, but in an experiment that collects signal from the entire sample, there may well be destructive interference between signals from different spatial positions. However, such ramifications affect only the highest sensitivity field imaging experiments and are of little concern to the vast majority of NMR practitioners. Finally, a major extension of the ideas presented concerns the sensitivity of the human NMR imaging experiment. This topic is sufficiently important and complex that it is treated separately under the heading of ***Sensitivity of Whole Body MRI Experiments***.

7 RELATED ARTICLES

Birdcage Resonators: Highly Homogeneous Radiofrequency Coils for Magnetic Resonance; Sensitivity of Whole Body MRI Experiments; Surface and Other Local Coils for In Vivo Studies.

8 REFERENCES

1. D. I. Hoult, *Concepts Magn. Reson.*, 1989, **1**, 1.
2. C.-N. Chen and D. I. Hoult, 'Biomedical Magnetic Resonance Technology', Adam Hilger, Bristol, 1989.
3. D. I. Hoult and B. Bhakar, *Concept Magn. Reson.*, 1997, **9**, 277.
4. D. I. Hoult and R. E. Richards, *J. Magn. Reson.*, 1976, **24**, 71.
5. B. I. Bleaney and B. Bleaney, 'Electricity and Magnetism', 3rd edn., Oxford University Press, London, 1976.
6. Z. Abe, K. Tanneka, M. Hotta, and M. Imai, 'Method of obtaining internal information of a measuring Target from the outside by the application of a nuclear magnetic resonance phenomenon', US Patent 3 932 805, 1976.
7. J. J. H. Ackerman, T. H. Grove, G. G. Wong, D. G. Gadian, and G. K. Radda, *Nature*, 1980, **283**, 167.
8. C. W. Helstrom, 'Probability and Stochastic Processes for Engineers', 2nd edn., Macmillan, New York, 1991.
9. D. I. Hoult and P. C. Lauterbur, *J. Magn. Reson.*, 1979, **34**, 425.
10. D. I. Hoult, in 'Progress in Nuclear Magnetic Resonance Spectroscopy', eds. J. W. Emsley, J. Feeney, and L. H. Sutcliffe, Pergamon Press, Oxford, 1978, Vol. 12, p. 41.
11. P. Styles, N. F. Soffe, and C. A. Scott, *J. Magn. Reson.*, 1989, **84**, 376.
12. F. E. Terman, 'Electronic and Radio Engineering', 4th edn., McGraw-Hill, New York, 1955.
13. D. W. Alderman and D. M. Grant, *J. Magn. Reson.*, 1979, **36**, 447.

Acknowledgements

The author gratefully acknowledges the assistance of Dr. G. N. Chmurny, and the hospitality of the In Vivo NMR Center, University of Utrecht.

Biographical Sketch

David I. Hoult. *b*. 1945; B.A. (physics) 1968, D. Phil (supervisor Sir Rex Richards F.R.S.) 1974 University of Oxford, UK. Biochemistry Department, Oxford University, 1974–1977. National Institutes of Health, Bethesda, MD, 1977–1982. Head, NMR Instrumentation Group, NIH, Bethesda, MD, 1982–1991. University of Utrecht, The Netherlands, 1991–1994. Institute for Biodiagnostics, NRC, Winnipeg, 1994–present. Approx. 70 publications, and with C-N. Chen, the book 'Biomedical Magnetic Resonance Technology'. 7 awards including Gold Medal, Society of Magnetic Resonance in Medicine, 1985. Research interests: all aspects of instrumentation (mainly NMR), mostly in the biological and medical fields.

Shimming of Superconducting Magnets

Virginia W. Miner and Woodrow W. Conover
Acorn NMR, Fremont, CA, USA

1	Introduction	1
2	History of Shimming	1
3	The Problem	2
4	Sample Spinning	2
5	The Basics of Shimming	3
6	A New Magnet	5
7	A Shimming Procedure	7
8	Symptoms of Inhomogeneity	8
9	The **Z**1 Profile	8
10	The Sample and Shimming	12
11	Probes and Shimming	13
12	Computer Shimming	16
13	Related Articles	17
14	References	17

1 INTRODUCTION

In its basic form, nuclear magnetic resonance (NMR) spectroscopy requires a very uniform magnetic field over the region of the sample under observation. Magnets used for NMR do not provide sufficient magnetic field homogeneity for use in high-resolution NMR experiments. The magnet's intrinsic inhomogeneities are further degraded by the magnetic susceptibilities of the NMR instrument's transducer (probe), the NMR sample's container (tube), and the NMR sample itself. The process of correcting the magnetic field to be as uniform as possible is called shimming.

The process of shimming has been one of the least understood aspects of operating an NMR instrument. The process is sometimes very frustrating and shrouded in mysticism. Many different 'procedures' for shimming have developed over time and more continue to evolve. However, most NMR operators do not need a theoretical understanding of shimming, but they all need an empirical approach to the process with some practical tools to use in the process. This article is an attempt to provide an empirical approach to shimming with some tools to use to make the process less magical and more logical.

2 HISTORY OF SHIMMING

Magnetic field homogeneity has always been critical in high-resolution NMR, and is becoming more so as NMR technology advances. In the history of NMR, there have been many different ways to do the adjustment of the magnetic field homogeneity. The methods and techniques for shimming continue to develop and improve today.

Among the first magnets used for NMR were large electromagnets whose field homogeneity was adjusted by purely mechanical means. The magnet's pole faces were precision ground to be very smooth and flat. As long as the magnet's pole faces were very flat, the more parallel the pole faces, the more homogeneous the magnetic field. The first step in adjusting magnetic homogeneity was to adjust the tilt of the pole faces by turning three large bolts to make the magnet's pole faces as parallel as possible. When the bolts ran out of range, coarse adjustment was done by placing thin pieces of brass between the magnet yoke and the back of the pole pieces. These thin pieces of brass were also placed in other strategic locations to make the pole faces parallel in a manner not addressed by the three adjustment bolts. The metal pieces were called shim stock and the seemingly endless process of placing and removing pieces of shim stock acquired the name 'shimming'. Because the NMR signal is more sensitive to the magnetic homogeneity than any other means of testing either the value of the magnetic field at different positions in the NMR sample area or the precision of the mechanical alignment of the pole faces, the signal from the NMR sample became the only means to adjust the magnetic field homogeneity. Because tons of pressure from the magnetic field existed on the pole faces of an energized magnet, the magnet had to be turned off to add or move pieces of shim stock. The final step in adjusting magnetic homogeneity with these systems was to adjust a bolt with a large ratchet. This pulled together or pushed apart the tops of the magnet pole pieces to give a fine adjustment of the Y gradient.

While these mechanical adjustments seem crude, these instruments were typically capable of giving better than 0.2 Hz resolution. This is rather impressive considering that 0.2 Hz out of 60 MHz represents 3 parts per billion field homogeneity over the volume of the sample. To improve the level of performance and reduce the difficulty of adjusting the magnetic homogeneity, an electrical 'shimming' process, consisting of a set of small electromagnets placed around the sample, was developed to supplement the mechanical process.[1] The magnetic field homogeneity could be adjusted by varying the current in each of these small electromagnets. This process retained the name shimming and the small electromagnetic coils assumed the name 'shims'. With the advent of superconducting NMR magnets, the electrical shims became the only adjustment available to the NMR operator. Each small electromagnet can be used to 'shape' the field to compensate for existing magnetic gradients.

At first only a few low-order (X, Y, and Z) electrical shims were used. As the fields became higher and magnet production became more difficult, more and higher-order electrical shims were added to maintain the same level of performance. The process becomes more difficult as the number of these electrical shims increases, not only because there are more adjustments to make, but because each shim does not generate 100% pure gradients. There are interactions with shims of a similar nature (e.g. ZX creates some Z gradient and X gradient in addition to the intended ZX gradient). Because of these interactions, the number of adjustments necessary to shim the magnet increases geometrically with the number of shims, not just linearly. In addition, the raw field encountered in superconducting magnets is usually worse than in electromagnets, so larger corrections are required. These two facts make the process of shimming superconducting magnets more difficult and the shimming process correspondingly more important to obtain useful NMR spectra.

Obtaining 0.2 Hz resolution requires 10 times greater magnetic field homogeneity at 600 MHz than at 60 MHz, so shimming becomes more important to achieve the same results as the magnetic fields increase. Other aspects of instrument performance are also dependent on shimming, such as solvent suppression, which requires good lineshape very far down at the base of the peak.

3 THE PROBLEM

An organized and logical approach to shimming is the key if the process is to be both fast and effective. Each shim or shim type generates symptoms in the NMR instrument's performance indicative of its misadjustment. An understanding of the relationship of each shim and the corresponding instrumental performance is essential to achieve good results in a reasonable amount of time.

Shimming has some generalized procedures to be used when certain clues are observed. In addition to these procedures, there are tools available for use in the shimming process. Each tool is called upon as the conditions warrant, and each works in some cases, but not all.

The most common method of adjusting the homogeneity of an NMR magnet is the observation of an NMR signal. Since the natural linewidth of an NMR signal may be less than 0.1 Hz, then even for a 100 MHz NMR instrument a field homogeneity of one part per billion would be required to measure this linewidth. Very few test instruments have this precision. This means that the NMR instrument becomes the test instrument used to adjust itself.

An additional problem with the shimming process is that the observed NMR signal arises from the integrated signal from the total volume of the observed sample, which may have many different resonant frequencies with different degrees of excitation arising from different positions in the sample. Visualize the NMR sample as a collection of isolated minisamples, each of which is infinitesimally small. Each minisample then generates a signal whose linewidth is determined by the T_2 relaxation time of the sample and whose frequency results from the field value at that point. The intensity of the signal generated by each minisample would reflect the amount of excitation at that point. The observed signal is the total integrated signal over the entire sample volume times each area's degree of excitation. It is the integration of the NMR signal response which leads to a major difficulty in the shimming process. Any knowledge as to which part of the NMR sample is experiencing which magnetic inhomogeneity is lost in this integration process.

The NMR operator adjusts the field homogeneity for the NMR instrument with a set of electrical shims, each of which has its effects over a complex geometry. If positional information for each of the mini-samples were not lost in the integration process discussed above, the NMR operator would have much better clues as to which shim to adjust. This is why many NMR magnets are initially set up using a special field plotting probe. This is a tedious process of moving a small NMR sample to different and known positions in the magnet's field, and so retains the positional relationship for each frequency measurement. Automated field mapping equipment has been developed which maps the field, calculates the optimum currents for all shims, applies them and then iterates,[2] clearly a more efficient and effective approach. After magnet installation and in general use there are, however, clues from the NMR signal which allow the NMR operator to narrow the selection of shims which probably need adjustment. These clues will be discussed below in Section 8.

Table 1 Room Temperature Shims

Common shim name	Function	Interaction order
$Z0$	1	0
$Z1$	z	0
$Z2$	$2z^2 - (x^2 + y^2)$	1
$Z3$	$z[2z^2 - 3(x^2 + y^2)]$	2
$Z4$	$8z^2[z^2 - 3(x^2 + y^2)] + 3(x^2 + y^2)^2$	2
$Z5$	$48z^3[z^2 - 5(x^2 + y^2)] + 90z(x^2 + y^2)^2$	2
X	x	0
Y	y	0
ZX	zx	2
ZY	zy	2
XY	xy	1
$X2 - Y2$	$x^2 - y^2$	1
$Z2X$	$x[4z^2 - (x^2 + y^2)]$	2
$Z2Y$	$y[4z^2 - (x^2 + y^2)]$	2
ZXY	zxy	2
$Z(X2 - Y2)$	$z(x^2 - y^2)$	2
$X3$	$x(x^2 - 3y^2)$	1
$Y3$	$y(3x^2 - y^2)$	1

The shim gradients used to adjust the magnetic field homogeneity in superconducting magnets have common names which reflect their geometry. However, these shims have more complicated expanded equations describing their actions as indicated in Table 1.[3] Although every different type of shim set has a slightly different set of expanded equations, the expanded equations for the shim gradients shown in Table 1 are reasonable examples of the full gradient created by each shim coil. The equations are shown for interest and are not used in the shimming process to be described.

4 SAMPLE SPINNING

In the early days of NMR, Bloch suggested that the effective homogeneity of the magnetic field could be improved in a simple way by creating motion of the molecules within the sample.[4] The rate of molecular motion necessary to accomplish this task is on the order of 4 Hz, a speed easily obtainable by mechanical spinning of the sample tube. Anderson and Arnold[5] demonstrated the improvement by spinning a water sample about an axis coincident with the axis of the receiver coil. At rotational speeds in excess of 10 Hz, they reduced the halfwidth of the NMR signal by a factor of 17 and increased the amplitude by a factor of seven. The size of the improvement is proportional to the size of the field inhomogeneity in the plane averaged by the spinning process. As the magnetic field homogeneity increases, the improvement obtained by sample spinning decreases. Spinning the sample also has some undesirable effects, some of which are discussed in Section 4.1 below.

If the magnetic field had no field inhomogeneities which could be averaged by spinning, spinning would not produce better apparent resolution and would not be necessary.

Throughout the development of NMR, more and higher order shims have been added to produce better field homogeneity. This process continues with some advanced shim sets having as many as 38 different shim gradients.[6] The ability of these expanded shim sets to correct magnet gradients is calculated to be improved by a factor of two to five. Careful adjustment of all these shims while not spinning the sample leads to a field homogeneity approaching that of the spinning sample without the negative effects of spinning. As the trend in the direction of better nonspin homogeneity continues, spinning the NMR sample may not be a common practice in future NMR instruments.

The practice of spinning the sample separates the set of shims into two categories: on-axis shims, which are not averaged by spinning, and off-axis shims, which are averaged by spinning. The process of adjusting the on-axis shims while spinning and the off-axis shims while not spinning 'decouples' the two sets of shims to a first approximation and the overall process is divided into two processes of smaller scope. Usually this decoupling process is less than perfect, but with some iteration between spinning and nonspinning shimming processes, spinning becomes a useful tool in simplifying the shimming procedure.

Spinning the NMR sample tube averages the field inhomogeneities in the plane perpendicular to the spinning axis, but not along the axis. If the NMR operator could make a spherical sample and spin about the X, Y, and Z axes simultaneously, shimming might become a lot easier. However, no simple mechanical means of preparing and spinning the sample to average all three axes has yet been devised. The effect of spinning in all three axes simultaneously can be seen when starting and stopping spinning on large diameter tubes. The turbulence created by starting and stopping causes sample mixing along the spinning axis. If the NMR operator watches the lock level of a spinning sample and suddenly turns off the spinner, the lock level will actually rise while the sample is mixing from the turbulence. The same effect can be seen when starting to spin where the lock level goes up to a higher level and fades back down to a final value between the nonspin value and its highest level. This is because turbulence when the spinner starts causes vertical mixing of the sample. As the sample moves around with spinning and up and down with turbulence it is effectively being 'spun' in all axes simultaneously. The effect is most visible on large diameter tubes.

4.1 Artifacts of Sample Spinning

An undesirable effect of spinning the sample is the creation of spinning sidebands. Field inhomogeneity modulates the NMR signal at the spinning rate and produces small peaks on either side of the resonance signal. There are actually several types of spinning sidebands. Each type has some observable different characteristics, but they have a common characteristic of occurring at integer multiples of the spinning rate with a tendency to become smaller as the spinning rate is increased. These properties can be used to help identify these spurious signals. Spinning sidebands (SSB) can be of three general types as discussed below.

Off-Axis Inhomogeneity Sidebands: These are first- and second-order (sometimes more) sidebands (SSBs) which are in phase with, and usually present on both sides of, the main peak. These signals average with the main peak and so do not tend to decrease with the acquisition of more scans. This type of SSB arises from off-axis gradients in the magnetic field and can be decreased or eliminated with shimming. Whether the sideband is first- or second-order depends on the geometry of the magnetic field inhomogeneity. In a conceptually simple model, if the sample is spinning through a linear off-axis gradient, it will produce first-order SSBs, offset from the main peak by the spinning rate. Examples of gradients of this type are X, Y, ZX, and ZY. If the sample is spinning through a second-order off-axis gradient, it will produce second-order SSBs, appearing at twice the spinning rate. Examples of gradients of this type are XY and $X^2 - Y^2$.

Phase-Modulation Sidebands: Another kind of SSB is a first-order (sometimes second) SSB present on both sides of the main peak and out of phase with the main peak. These do not have the same phase with each scan (not phase coherent with the main peak) and so tend to average out with multiple scans. They arise when the sample tube wobbles as it spins, which perturbs the probe's tuning, and creates a phase modulation of the NMR signal. The resulting SSBs are sometimes referred to as 'Q-modulation' sidebands, and are more apparent with higher Q probes. These SSBs have a phase relationship to the main peak related to the instantaneous position of the spinning tube. Because the spinning position is not usually related to the signal acquisition, the SSBs appear to have a random phase. Because signal acquisition from scan to scan is not synchronized with the spin rate, these SSBs have a different phase with each scan and do not average with the main peak. These SSBs are not improved by shimming. Improving these requires either much better symmetry while spinning, better sample tubes, or balancing the probe's electrical circuit to reduce dielectric and capacitive effects. Another problem caused by tube wobbling while spinning is poorer scan-to-scan reproducibility, which is critical in many difference experiments such as inverse detection. These experiments are performed without sample spinning.

$\boldsymbol{B}_1$ *Inhomogeneity Sidebands*: Another kind of SSB occurs on one side only at either twice or four times the spin rate. This SSB is in phase with the main peak and signal averages with the main peak. Since this type of SSB is worse in probes with poor $\boldsymbol{B}_1$ homogeneity, they are believed to arise from the rf inhomogeneity of the probe. If the probe coil has two vertical bands, the SSB will be of second order (at twice the spin rate). If the probe coil has four vertical bands, the SSB will be a fourth-order SSB. Which side of the main peak the offending SSB appears on is determined by the sign of the magnetogyric ratio of the NMR nucleus, its spinning direction, and the direction the main field is polarized. This SSB arises from the sample spinning through areas of stronger and weaker rf pickup by the coil, which takes place near the coil's bands when rf homogeneity is poor. Larger coils in both length and diameter tend to have lower rf homogeneity. These SSBs are not improved by shimming.

5 THE BASICS OF SHIMMING

5.1 Criteria For Shimming

Progress during shimming can be monitored in various ways, the most common being a swept NMR resonance, lock level,

and free induction decay (FID). Choice of the most useful method depends on the instrument and its current condition and need not remain constant throughout the shimming process.

Swept Signal: The swept NMR resonance is most commonly deuterium from the lock solvent which is swept by either field sweep or frequency sweep, but could be any NMR-active nucleus. To be used for shimming, the signal should have sufficient signal-to-noise ratio that the height and ringing pattern can be observed. The sweep repetition rate should be fast enough to give a real-time response as the shims are adjusted. One of the best uses for this method of homogeneity measurement is the initial adjustment of the shims from a raw magnetic field. It is also commonly used when the spectrometer has no internal lock. The swept response should be adjusted for pure absorption phase and the rf power adjusted to avoid saturation of the signal. The height of the initial signal response is used to determine the best response while shimming. The ringdown pattern can be used for the final adjustment of $Z1$ and $Z2$, but should not be overemphasized in the initial stages of shimming because varying lineshapes can produce better ringing, but less desirable lineshape and resolution.

Lock Level: The lock level is probably the most common method of adjusting homogeneity. The lock level can be displayed by an analog meter on the NMR spectrometer or digitized and displayed as a number or level on a computer display. The NMR lock nucleus must not be partially saturated with rf power and the phase of the NMR signal adjusted carefully. Care should be taken if the lock phase is adjusted by maximizing the lock level. An asymmetric NMR lineshape leads to a lock maximum at a phase that is not at pure absorption. Improper lock phase can lead to an asymmetric lineshape, or an asymmetric lineshape can lead to an improper lock phase. Care should be taken that whenever an even-order axial shim is significantly changed the lock phase is checked and possibly readjusted.

Another problem with using a deuterium lock level for homogeneity adjustment is the relative sensitivity to field inhomogeneities of the NMR lock signal and the signal under observation. If the nuclei under observation are protons, then the lock signal's sensitivity to inhomogeneities is one-sixth that of a proton (the ratio of the magnetogyric ratios of the nuclei). This is further complicated by a deuterium resonance usually being broader than its proton counterpart. In general, good shimming results can be obtained by using a lock solvent with a sharp lock signal to do shimming for basic lineshape and minimum spinning sidebands followed by a touch-up adjustment of $Z1$ and $Z2$ on the FID signal.

FID Shimming: Using the FID response is probably the most difficult method of shimming and is usually left for the final touch-up of $Z1$ and $Z2$. The shape of the FID reveals more information about the lineshape and resolution than a lock level, similar to the ringdown pattern from a swept signal. Some excellent examples of FID shape and resulting lineshape are given in an article by Chmurny and Hoult.[7] Briefly, the longer the FID rings, the better the resolution. The closer the FID's shape to a perfect exponential decay, the better the lineshape. A FID that falls sharply to another level and then decays more slowly either has a poor lineshape displaying a substantial hump at its base or contains the resonances from two or more signals with different linewidths. Some NMR computer systems can integrate the total area of the FID and yield a number indicative of the resolution similar to the lock level. FID shimming is the most sensitive method for shimming and has the advantage of using the observed nucleus as the shimming criterion. It removes all doubt that what the lock system 'sees' is not what the observe system 'sees'.

All three of the above methods for monitoring field homogeneity can be used successfully. The shimming sequences described later refer only to response. Except where otherwise indicated, the operator should choose his/her own method. It is probably best to use all of them in some combination during the shimming process.

5.2 Procedures for Shimming

If the shimming operation were a simple maximization of each shim gradient, then shimming would be quick and easy. However, several things prohibit this.

Shims have, by nature of their design, levels of interactions with other shims (see Table 1). Some shims generate some gradients of other shims. An example of this is that $Z4$ is expected to generate some $Z2$ and $Z0$. Because the construction of the shim sets does not meet the theoretical design perfectly, each shim also has the impurities of other shims. For example, when the $Z4$ gradient current is adjusted it not only generates a $Z4$ gradient and the expected $Z0$ and $Z2$ discussed above, but some unexpected $Z3$ and $Z1$ gradients.

As the shimming process progresses, the response being used to adjust the shims becomes more sensitive. As an oversimplified example, if the magnetic field has a 20% $Z2$ gradient and an 80% $Z4$ gradient, the adjustment of $Z2$ first will be insensitive (feel 'mushy' or unresponsive). Then after $Z4$ is adjusted, $Z2$ will be more sensitive and might adjust to a different value.

The shimming process can be caught at a local maximum. To avoid this the NMR operator needs to explore shim changes large enough to step over a local maximum and explore the next maximum before further progress can be obtained. Shimming N number of shims can be represented as an $N + 1$ dimensional surface. While it is not easy to visualize such a surface, it is easy to think of shimming any two shims as moving over a two-dimensional surface. The third dimension would be the response of the shimming criterion, such as the lock level. The goal is to find the highest spot on the entire surface.

5.3 Shim Interactions

Each pair or set of shims has an interaction relationship. This relationship determines how the respective shims need to be adjusted to minimize the possibility of being caught on a local maximum which is not the overall best maximum for the set of shims.

Zero-Order Interactions: Shims having no interactions (zero-order interaction) can be adjusted for best homogeneity by one simple adjustment. However, most shims have interactions that complicate the process. The other two types of shim interaction are called first-order and second-order interactions.

First-Order Interactions: First-order interactions are the type that allow a true optimization of magnetic homogeneity

by repeated optimization of the individual shims. After the complete set of shims is adjusted, readjustment of the first shim of the set leads to a different optimum. Successive iterations then lead to less and less change on readjustment until finally no further change is observed. The $Z1$ and $Z2$ shims have a first-order interaction. The iterative process can often be accomplished faster by noting the direction the $Z1$ shim is changing and moving slightly too far on the early corrections. The ability to make educated guesses based on a knowledge of the shims leads to a much faster shimming process.

Second-Order Interactions: In a second-order interaction, a given shim must first be moved and then others adjusted before any determination of improvement can be evaluated. Simply adjusting these shims successively does not necessarily lead to the best homogeneity. The process employed for second-order interactions is usually to change the shim a measured amount and reoptimize the set of related shims. If this leads to a better response, then the shim is changed further and the process repeated until the response starts to decline. If the initial response is worse, the other direction is tried.

A classification of each shim as to the type of interactions to be expected is shown in Table 1. The interaction order assigned to each shim is a general description of the expected type of response. It can often be noted that shims displaying a complex type of interaction in the early stages of the shimming process display a much simpler type of interaction as the homogeneity improves. This simplification process often yields zero-order interactions for most shims in the later stages of shimming. Under these conditions, the shims appear to 'drive' directly to their final positions with almost no interactions.

6 A NEW MAGNET

When an NMR instrument is first installed, the setup is usually done by a trained service engineer. The installation engineer has one of the most important roles in determining the instrument's future performance. If the superconducting magnet is properly set up and shim values determined for all the probes, routine operation of the instrument can be very easy. A list of these shim values should be stored in a safe place, so that they can be used as a known starting point in the event that problems develop in the future.

Making sure the room temperature shim assembly is installed in the correct position in the magnet is very important. Usually, the best position for the room temperature shim assembly is with its center aligned with the center of the superconducting shims, determined from the magnet manufacturer's data. This can be confirmed with a technique similar to that used to establish the center of the room temperature (RT) shims, described below. There are conditions where the center of the rt shims should not be coincident with the center of the superconducting shims. In general, these arise when a different area of the magnet has a better overall field shape (on- and off-axis) than the area around the center of the superconducting shims. However, when the center of the rt shims is not the center of the superconducting shims it is more often than not a mistake.

6.1 Field Centering

The interaction of different shims makes shimming a tedious process requiring many repetitive passes through the shimming sequence. Shim interactions become much greater when the center of the shim set and the center of the sample are not coincident. Since the $Z1$ gradient has zero contribution to the field at its center ($z = 0$), it can be used to locate the center of the shim set. One or both of the processes described below can be used to ensure the probe and shim alignment. If the sample and shim alignment is unknown and the alignment process is not followed, the shimming sequences described later still optimize the field homogeneity, but there are considerably more shim interactions. These interactions make the shimming process more difficult than is necessary.

Most NMR systems do not allow the probe position and the room temperature shim assembly position to move independently. For this reason, if one of the following tests indicates that the probe center and the room temperature shim center are not the same, the problem probably resides in the placement of the probe coil in the probe. This is not usually an NMR operator adjustable parameter. If any of the tests reveal a misalignment, check several different probes and see if they are all misaligned. If the problem exists in only one probe, consider having the probe manufacturer check the coil placement. If all the probes are misaligned, something fundamental in the spectrometer installation or design is wrong.

Swept Lock: If the NMR spectrometer can display a swept lock signal, the easiest method of checking the probe and room temperature assembly alignment is to observe the swept lock display while adjusting the $Z1$ shim control. The first step is to display the swept lock signal. Then while noting the lock signal display position, adjust the $Z1$ shim current in one direction and then the other. If the probe is in alignment with the room temperature shim assembly, the lock signal should not move, but should become wider and shorter while staying in the same position. If it does move while becoming broader and shorter, the direction should change as $Z1$ is moved in different directions. If the peak moves then there is some degree of misalignment between the probe position and the room temperature shim alignment.

A value judgment is called for if the lock signal does change position with $Z1$ current. In general, if the peak moves less than it broadens then the misalignment is small and is usually best ignored. If the peak moves more than it broadens then corrective action, if possible, would make shimming easier.

6.2 Probe Coil Plot

If a swept lock signal is not available, an alternative, albeit slightly more involved, technique for determining the relative probe position and room temperature shim alignment is the effect of the $Z1$ current on a plot of probe coil response. While being more involved, this technique also gives more information which is useful for understanding the overall NMR instrument's operation. Place a drop of water in the bottom of an NMR tube, the smaller the drop the better. Also be careful to keep water from the sides of the NMR tube. Put this sample in the NMR spinner at a depth such that the drop of water is in the center of the probe's coil and insert the sample into the spectrometer. The sample should not be spinning. Set up the spectrometer for proton observation and acquire a spectrum with a sweep width appropriate for the experiment. What is appropriate comes with experience and you will know more

about how large a sweep width to use when the experiment is over, but for now use something like +/−2000 Hz. After doing the experiment you may want to go back and collect the data again using a different sweep width.

Process the spectrum using a magnitude calculation and whatever processing parameters are necessary to keep the computer scaling constant for the duration of this experiment (e.g. Bruker or Nicolet AI command). Take an integral of the entire sweep width and set up whatever integral corrections are necessary. If possible set this integral value to 100 and record all future integrals relative to this one. Record the integral value and the frequency position at halfheight on the integral line. An eyeball guess at the frequency position is usually more than good enough for this experiment. Now adjust the $Z1$ current in the positive direction by an appropriate amount. What is appropriate again comes with experience, but it needs to be a large amount and you should note that you are going to change the $Z1$ current the same amount in the negative direction next, so do not change the current more than you have available in the opposite direction. Now record the integral value and the frequency position of the halfheight of the integral with the $Z1$ current change in the positive direction and again with the same $Z1$ current change in the negative direction. You should now have three sets of two values:

Z Position	$Z1 = +$		$Z1 = 0$		$Z1 = -$	
	Freq.	Integral	Freq.	Integral	Freq.	Integral
0mm	0Hz	100	0Hz	100	0Hz	100

Do not be concerned at this stage if the frequencies or integral values are changing by small amounts. If they are changing by large amounts, make sure you have undertaken the measurements correctly by reproducing the values, but if they are changing by small amounts complete the data collection.

Now move the position of the water drop up 5 mm in the spinner and repeat the above experiment. Record the data and move the water drop position up in 5 mm steps until the water signal can no longer be observed. Then move the water drop 5 mm below the original position. Record the data and move the water drop position down in 5 mm steps until the water signal can no longer be observed. Plot the frequency versus Z position of the water drop for the three values of $Z1$ current.

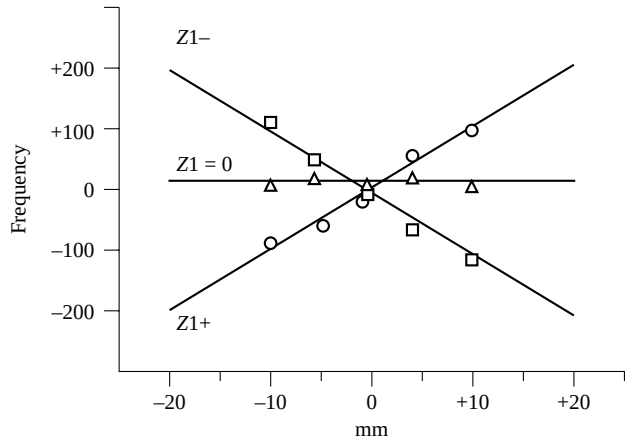

Figure 1 NMR frequency versus position in the probe for different values of $Z1$

You should get a graph something like that shown in Figure 1. The three lines should cross at one point, but usually you get a small triangle. For this purpose, the center of the triangle is the center of the room temperature shim assembly.

Now plot the integral versus Z position when the water drop is at $Z1 = 0$. Note that the $Z1 = 0$ current value is not zero current but the starting value for $Z0$ on the shimmed instrument. You should get a graph something like that shown in Figure 2.

The plot of NMR signal versus water drop position allows one to see over what height of sample the probe coil is active. This should describe roughly a rectangular region. The center of this rectangular region should be the region on the previous graph where the $Z1$ current lines crossed. This method tells the NMR operator where the active coil region is located relative to the room temperature shim assembly. In addition, it tells the NMR operator how long the probe coil is, which is useful for determining how tall a sample is required for shimming in a particular NMR instrument. Techniques for shimming different sample lengths will be discussed later in Section 10. Another very important piece of information which can be seen from this plot is any possible probe coil lead pickup which can make shimming more difficult. If the plot is similar to that shown in Figure 2 with the ends approaching zero but with increased intensity further out, then coil lead pickup has been detected. This phenomenon comes from the probe coil's leads being at a high voltage potential and not being shielded from the sample. If this occurs, it is often the case that the lead pickup is occurring at a region of the rt shims that is not very homogeneous, which leads to lineshape problems.

The unshielded lead problem often reveals itself in another way. For a normal single resonance close to the carrier frequency, as the pulse length is increased past a 90° flip to a 180° flip, the signal should pass through a null. With lead pickup, most of the signal goes through a null but a small portion of it remains positive even when the rest of the signal is becoming negative with increasing pulse length. The small positive portion of the signal is coming from lead pickup. The sample seen by the leads is outside the main coil region and is seeing a much smaller effective field than the main region of the sample. The effective 180° flip for this region can be many times that for sample in the main coil region. Often, since this sample can be in a region of different field homogeneity and therefore have a different field value, the small peak which remains positive will be to one side or another of the main peak which is going through a null with a 180° pulse.

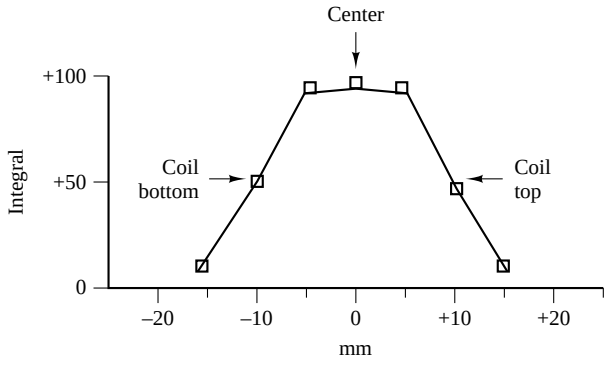

Figure 2 NMR signal integral versus position in probe

If either of these symptoms of probe coil lead pickup are observed, the probe should be modified to have a lead shield. This will lead to better lineshapes, pulse homogeneity, and solvent suppression.

7 A SHIMMING PROCEDURE

A shimming procedure[8] follows. It should not be taken as a Gospel truth, but as a suggestion of where to start the learning process about the relationship of shimming procedures, your samples, your instrument, and the NMR data acquisition process in general as it relates to your laboratory. Not every instrument will shim the same, nor will every sample. Later discussions will talk about what to look for and do when this process is done. For this procedure the optimization processes are:

1. *Zero order*: This is a straightforward process of adjusting the control for the best response.
2. *First order*: Adjust one control, then the next control, then the next until all controls in the set have been adjusted. Repeat the process until no further response improvement can be obtained.
3. *Second order*: Note the current response level. Adjust a shim control from the current value by a defined amount (a rule of thumb would be enough to change the response to between 50% and 75% of the original value) to a new value. Optimize all other shims in the set with a first-order process. If the new response is better than the previous response, note the new response level and adjust the shim to a new value in the same direction and repeat the process. If the new response is less than the original response, adjust the shim control a defined amount in the opposite direction and repeat the process. Continue until the best value is clearly determined. This means it is necessary to go too far to make sure no further improvement can be made and then return to the optimum value. It is often useful in this process to plot the results of the shim of interest and the response value after the other shims have been optimized. The operator can then make sure that the changes being observed are real and significant and can better determine the optimum shim value. A typical plot for $Z4$ is shown in Figure 3.

7.1 First Stage

If the NMR spectrometer is in a state of unknown homogeneity or is known to have poor homogeneity, a simple optimization of certain shims is the first step in the shimming sequence. A swept NMR signal is the recommended method of judging the response for this operation:

1. Spin the sample (20–30 Hz) and adjust the $Z1$ and the $Z2$ shims interactively to produce the tallest swept signal response (first-order process).
2. Stop the spinner and adjust X and Y for the tallest swept signal response (first-order process).
3. Adjust X and ZX for the tallest swept signal response (second-order process).
4. Adjust Y and ZY for the tallest swept signal response (second-order process).
5. Adjust XY and $X2 - Y2$ for the tallest swept signal response (first-order process).
6. If any large shim changes were observed in the above process then the process should be repeated from step 1.

After the above procedure, the NMR instrument should be capable of a field/frequency lock. Any one of the three methods described above for measuring homogeneity can be used in the following sequence steps.

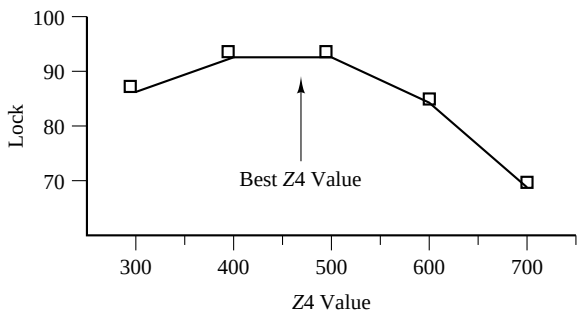

Figure 3 $Z4$ plot technique

7.2 Spinning Shims

The adjustment procedure for the spinning shims should be conducted with the sample spinning at more than 10 Hz. Care should be taken to avoid a vortex, which leads to a false shim optimum, usually with $Z2$ being the most misadjusted. If the lock signal is being used for shimming, then ensure that the lock signal is not being partially saturated with rf power and that the lock phase is correctly adjusted. The lock phase should be checked and adjusted each time a large change is made in an even-order Z shim.

For second-order adjustments of $Z3$, $Z4$, and $Z5$ described below, it is best to make a plot of the response level versus shim setting. Start by noting the shim value and response level, then change the shim. Obtain data points far enough on both sides of the maximum to clearly define the optimum setting.

1. Use the first-order process to optimize $Z1$ and $Z2$.
2. Use the second-order process to optimize $Z3$. Change $Z3$ enough to degrade the response by 20–30%. Repeat the process in step 1.
3. Use the second-order process to optimize $Z4$. Change $Z4$ enough to change the response by 30–40%. Repeat the process in step 1, then adjust $Z3$ to give maximum response. If the $Z3$ shim changes considerably, then repeat step 1 again and readjust $Z3$ again for maximum response. If, after optimizing $Z3$, $Z2$, and $Z1$, the new response is better than the previous response, then continue in the same direction; otherwise, try the other direction.
4. The $Z5$ shim is difficult to adjust because it often has substantial $Z1$, $Z2$, $Z3$, and $Z4$ components. It therefore becomes a tedious iterative process involving adjusting all five shims. See Section 9 for a different approach to adjusting high-order shims.

7.3 Nonspinning Shims

Shims with X and Y components should be adjusted while the sample is not spinning. Changing the nonspin shims which have Z components causes changes in the spinning shim set.

If any of these shims change significantly, then the spinning shim sequence should be repeated after completion of the nonspinning sequence. With all shims involving a second-order process, the technique described under the spinning shim sequence of plotting the result and interpolating the shim position should be followed either on paper or mentally.

1. Adjust X and Y interactively using the first-order process for maximum response.
2. Use a second-order process to adjust ZX. Change ZX by an amount sufficient to lower the response by 10% and then adjust X for a maximum response. If the new response is better, continue in the same direction with ZX. If the response is less, try the opposite direction with ZX.
3. Repeat step 2 but using the Y and ZY shims.
4. Adjust XY and $X2 - Y2$ interactively using the first-order process for maximum response. If either XY or $X2 - Y2$ change significantly, then repeat steps 2 and 3.
5. Use a second-order process to adjust $Z2X$. Change $Z2X$ by an amount sufficient to decrease the response 30%, then maximize the response with ZX and then with X. If the new response is larger than the initial response, then continue with $Z2X$ in the same direction. If the response is less, then try the opposite direction.
6. Repeat step 5 but using $Z2Y$, ZY, and Y.
7. Use a second-order process to adjust ZXY. Change ZXY by enough to decrease the response by 20%, then maximize the response with XY. If the new response is larger than the initial response, continue with ZXY in the same direction. If the response is less, try the other direction.
8. Repeat step 7 but using $Z(X2 - Y2)$ and $X2 - Y2$.
9. Adjust $X3$ and X interactively for maximum response (first-order process).
10. Adjust $Y3$ and Y interactively for maximum response (first-order process).
11. If the nonspin shim settings have significantly changed, then the spinning shim sequence should be repeated. If there are significant changes in the spin set after optimization, repeat the nonspin set also.

7.4 Final Stage

After the spinning and nonspinning sequences have been conducted, the NMR instrument should be delivering less than 0.5 Hz linewidth with good lineshape and minimum spinning sidebands. This is all that is required for most NMR experiments. If better resolution is desired, then a first-order adjustment of $Z1$ and $Z2$ using the FID can be helpful. Maximize the response by adjusting $Z1$ and $Z2$ for maximum ringout of the FID. If the FID is not observable, then the swept lock signal ringout is the best second choice. The ringout of the FID or the lock signal is a very sensitive measure of resolution. Adjusting only $Z1$ and $Z2$ prevents changes in the lineshape.

8 SYMPTOMS OF INHOMOGENEITY

An examination of the NMR signal lineshape can often reveal which shim needs the most attention. In general, even-order spinning shims ($Z2$ and $Z4$) create asymmetric lineshapes when misadjusted. The odd-order spinning shims ($Z1$, $Z3$, and $Z5$) create symmetrical lineshape symptoms when misadjusted. Also, in general, the higher the order the shim causing the problem, the further down the peak the symptom will appear. The lineshape problems to be expected are summarized in Figure 4.

Spinning sidebands were discussed in Section 4.1. The third-order nonspin shims, $Z2X$, $Z2Y$, ZXY, $Z(X2 - Y2)$, $X3$, and $Y3$, can create both spinning sideband problems and lineshape problems, usually very low at the base of the peak. An especially interesting symptom from two of these shims can be seen while adjusting the spinning shims. When the adjustment of $Z3$ changes the observed NMR signal from a broad-based signal with no spinning sidebands to a narrow-based signal with spinning sidebands, then the responsible shim is most likely $Z2X$ or $Z2Y$.

In the endless search for greater sensitivity, one approach has historically been to use longer coils in the NMR probe. As the active sample length increases, it becomes more difficult to optimize the field over the entire length of the coil. Also, the higher-order shim gradients become much more important with longer coils, making shimming more complex. Usually some degradation of lineshape is inevitable when longer coils are used.

The probe coil also contributes to resolution and lineshape problems by means of the magnetic susceptibility of the materials used in probe construction. This magnetic susceptibility has a tendency to bend the magnetic field, distorting the observed lineshape. The effect is greatest close to the source of the magnetic susceptibility. As the probe filling factors become better, the coil parts move closer to the sample, and the coil's magnetic susceptibility has a greater effect on lineshape and resolution. A typical probe induces magnetic gradients on the sample which look a lot like a $Z4$ inhomogeneity symptom. The process of creating these gradients and how to shim them is discussed in depth in Section 11.

9 THE $Z1$ PROFILE

One tool which can be used to help the NMR operator in the shimming process is the '$Z1$ profile'. This can be thought of as an axial image of the sample in the probe. To obtain a $Z1$ profile, a large $Z1$ gradient, offset from its optimum value, is applied and the resulting lineshape examined. If the probe had no magnetic susceptibility and the magnet's field were perfect, then when a large $Z1$ gradient is applied the resulting lineshape resembles a rectangle as shown in Figure 4(a).

While this may seem a very uninteresting and undesired lineshape, it contains a lot of useful information. Imagine the NMR sample being composed of many discrete minisamples located along the axis of the NMR tube. When a $Z1$ gradient is applied to the sample, each of these minisamples has a slightly different frequency due to the slightly different $Z1$ gradient value at each position. There is no standard for NMR instruments as to which direction of $Z1$ gradient is generated with a positive current in the $Z1$ coil, so we cannot tell whether the left end arises from the top or the bottom of the sample. However, this image of the sample provides some positional information to work with.

The $Z1$ profile can also be used to see if the center of the probe's receiver coil is at the center of the room temperature shims. Take a $Z1$ profile with a positive $Z1$ offset value. Take another $Z1$ profile with a negative $Z1$ offset of the same size,

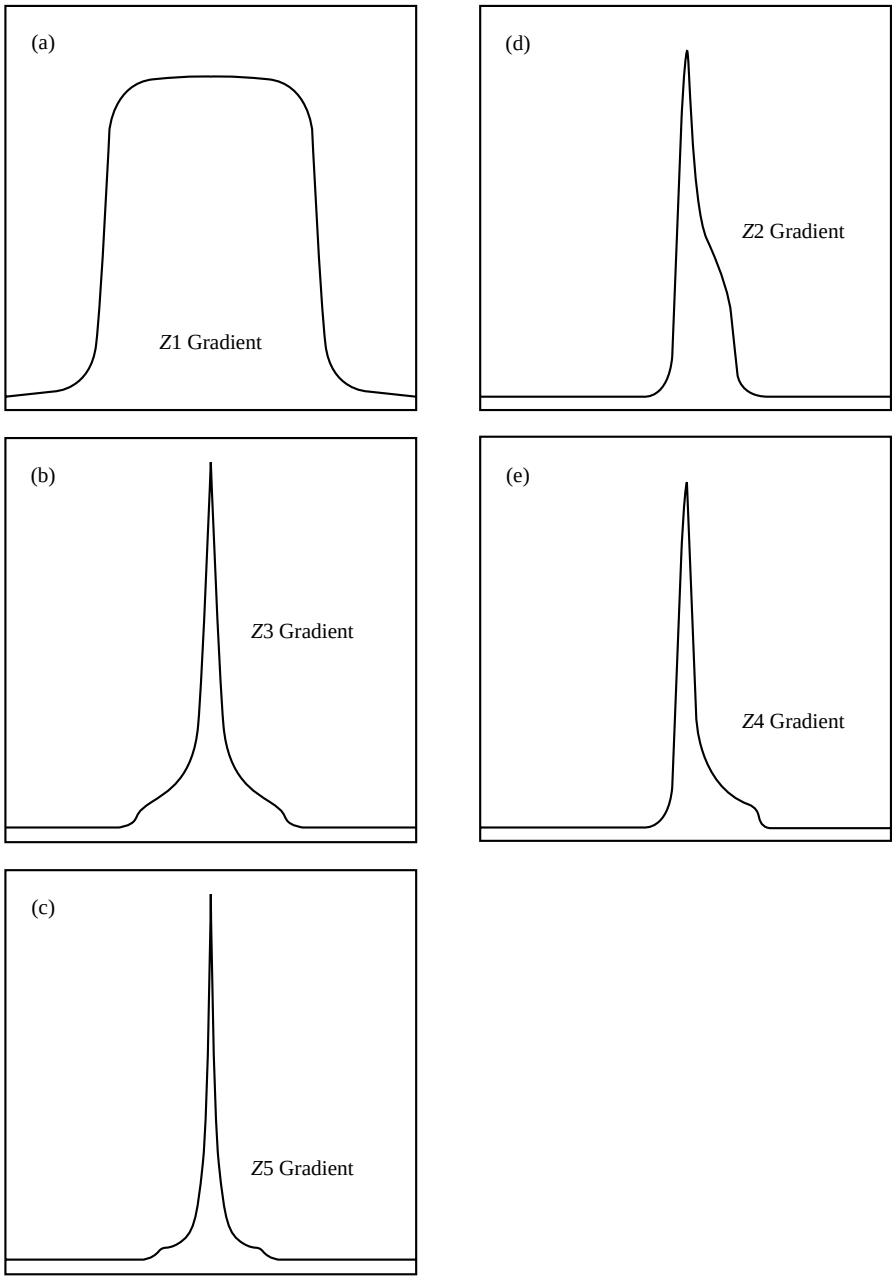

Figure 4 Lineshapes resulting from Z gradients

but in the opposite direction. Overlay the two $Z1$ profiles plotted on the same scale. If the two profiles are offset relative to each other, then the center of the probe's receiver coil and the center of the room temperature shims are not coincident. For NMR operators familiar with the $Z1$ profile technique, this method of determining the center of the room temperature shims is faster and easier than the plotting method discussed in Section 6.

The $Z1$ profile can also give information about other gradients present in the magnetic field. If the magnetic field has a $Z2$ gradient and a $Z1$ profile is taken, lineshapes as shown in Figure 5(a) would be obtained. Note that the shape is asymmetrical and that the top of the $Z1$ profile is a curve with the order Z^2. With practice and when comparing with later examples of gradients, it is apparent that as the gradient order increases, the outside edges of the $Z1$ profile are affected more than the center. In fact, with the higher-order gradients, the center of the $Z1$ profile is relatively unaffected. If a positive $Z1$ profile and a negative $Z1$ profile were taken with a $Z2$ gradient in the magnetic field, they would look identical. This is because the even-order Z gradients are symmetrical about the center of the room temperature shims.

If the magnetic field has a $Z3$ gradient and a $Z1$ profile is obtained, the result would resemble Figure 5(b). Here it is easy to note that the $Z1$ profile changed shape symmetrically. Note the drooping edges when $Z3$ is changed in one direction and the peaked edges when $Z3$ is changed in the opposite direction. Also note how far from the center the effects start taking place and that the two lineshapes have different widths.

As we move to higher-order gradients, it will be easy to see that the effect takes place farther to the outside edges.

With this example of a $Z3$ gradient with a $Z1$ profile, if the direction of the $Z1$ profile is changed then the positive and negative $Z3$ gradient lineshapes would interchange. This is different from even-order gradients which stay the same as the opposite $Z1$ profile polarity is taken. The fact that the $Z1$ profiles of $Z3$ gradients interchange with opposite $Z1$ profile polarity can be used to adjust the $Z3$ value to its correct position. The process would be to change $Z3$ until the plus and minus $Z1$ profile had about the same width. On many NMR systems obtaining the proper $Z3$ and $Z4$ values is a large part of the battle in the shimming process, and this technique makes finding the proper $Z3$ value relatively easy.

If the magnetic field has a $Z4$ gradient and a $Z1$ profile is taken, the results would resemble Figure 5(c). It can be seen that the change in the $Z1$ profile is again asymmetrical, but now there is a flat region near the center that is relatively unaffected compared to the ends of the $Z1$ profile.

If the magnetic field has a $Z5$ gradient and a $Z1$ profile is taken, the results would resemble Figure 5(d). It can be seen that the change in the $Z1$ profile is symmetrical. Again there is a flat region near the center that is relatively unaffected compared to the sides of the $Z1$ profile.

Continuing the process with $Z6$, $Z7$, and $Z8$ gradients would give a set of profiles as shown in Figure 5(e)–(g). A pattern emerges from the complete set of $Z1$ profiles:

1. Even-order gradients ($Z2$, $Z4$, $Z6$, and $Z8$) produce asymmetrical changes in the $Z1$ profile.
2. Odd-order gradients ($Z1$, $Z3$, $Z5$, and $Z7$) produce symmetrical changes in the $Z1$ profile.
3. The higher the order of shim gradient applied, the farther from the center the significant effects are observed in the $Z1$ profile.
4. Odd-order gradients, in particular $Z3$, give different width profiles with opposite polarity $Z1$ profiles, while even-order gradients are unchanged with opposite polarity $Z1$ profiles.

There are similar effects that can be observed when shimming while looking at normal lineshapes instead of the $Z1$ profile:

1. An asymmetrical change in lineshape is seen when even-order Z shims are adjusted.
2. A symmetrical change in lineshape is seen when odd-order Z shims are adjusted.

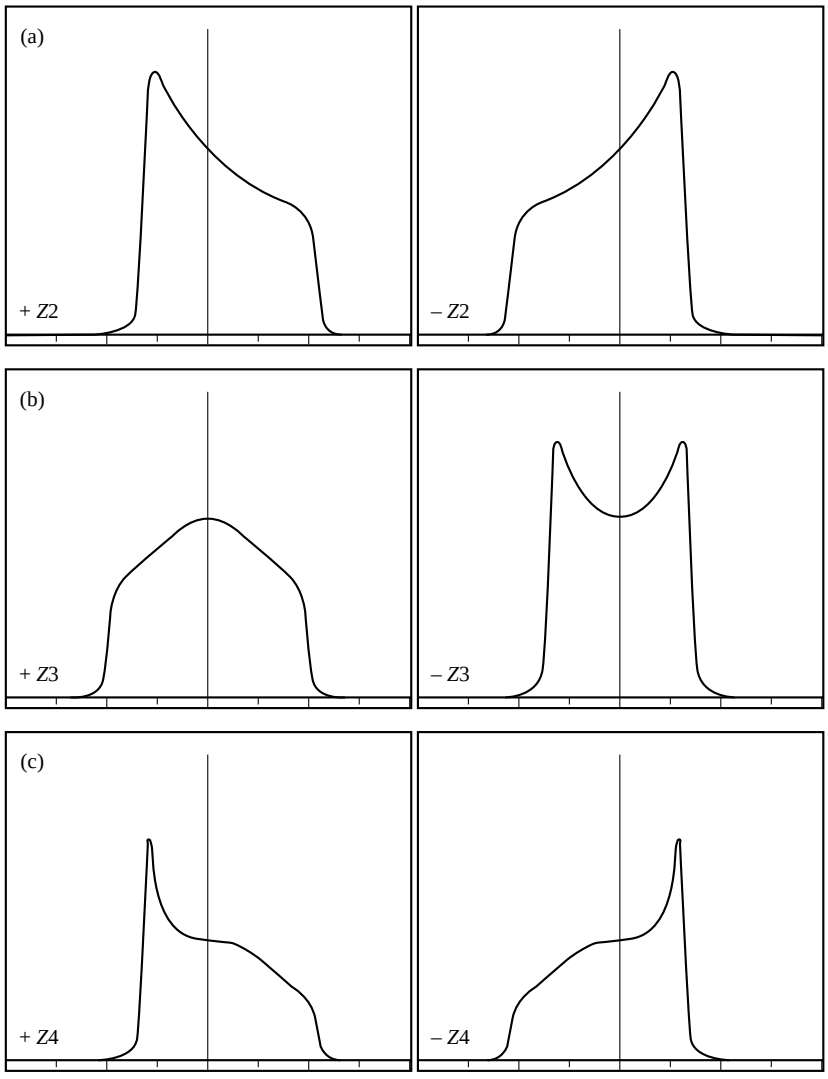

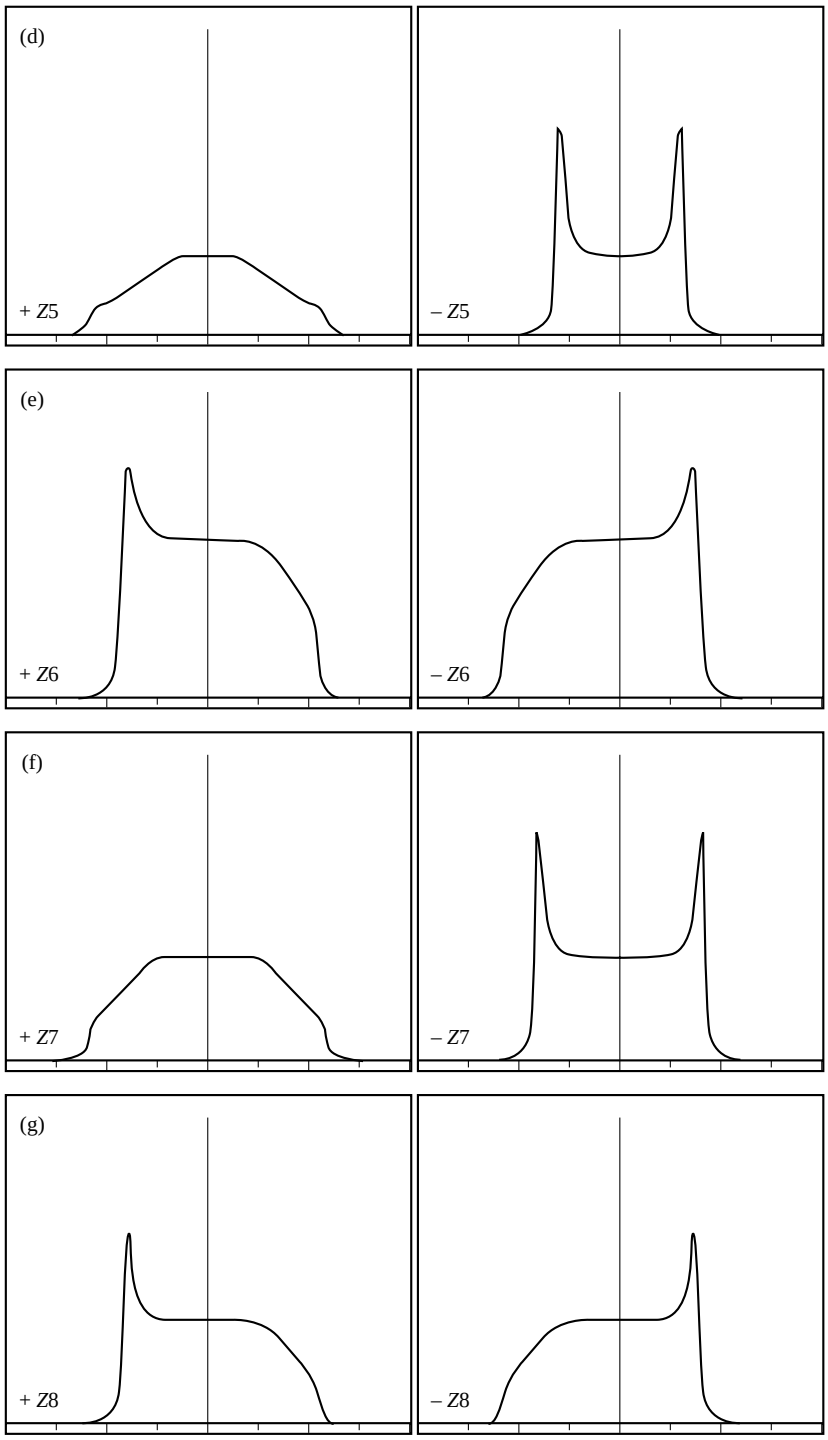

Figure 5 $Z1$ Profiles with positive and negative Z gradients. For (a)–(g), see text

3. The higher the order of shim gradient adjusted, the lower down the peak the lineshape distortion is noticed.

From this study of $Z1$ profiles, another procedure of shim optimization emerges as a new shim tool. Normally the lowest order gradients ($Z1$, $Z2$, and $Z3$) are adjusted first, then based on lineshape criteria, the higher order gradients are adjusted. The low-order gradients are readjusted as necessary in this process. However, if the NMR operator applies a $Z1$ gradient to get a $Z1$ profile of the sample, the highest order gradients are adjusted *first* to get the most square and symmetrical ends on the $Z1$ profile, then the center region is flattened with the lower order gradients. During the entire process, odd-order gradients are adjusted when a symmetrical change is desired. Even-order gradients are adjusted when an asymmetrical change is desired.

In general, when trying to shim using this technique, the goal is to make the squarest and flattest $Z1$ profile possible which does not change width with opposite polarity $Z1$ profiles. This applies even when the NMR probe has magnetic susceptibility problems. When you shim for the squarest and flattest $Z1$ profile, you will get the best lineshape when the

$Z1$ gradient is removed. If the NMR probe has very severe magnetic susceptibility problems (discussed further in Section 11), the $Z1$ profile will not be very flat at all. With probe magnetic susceptibility problems localized to specific regions of the probe's coil, the $Z1$ profile may have many peaks and valleys where it should be flat. Probes that have several regions of deep peaks and valleys will be very difficult to shim and will probably not produce a good lineshape when shimming has been completed.

The $Z1$ profile technique is not the one and only best way to shim, but is a useful tool which can be used as appropriate. It does seem to offer some advantages when trying to adjust the higher order gradients.

The $Z1$ profile can also be used to visualize the probe's $\boldsymbol{B}_1$ homogeneity. After shimming is complete, apply a $Z1$ gradient. Take a spectrum with a 90° pulse and plot out the rectangular lineshape. This represents the probe coil's excitation picture. Now take another spectrum with a 180° pulse and plot it out with the same scale and position as above. This plot will have a region near the center of the initial rectangular region which is near zero intensity. This shows the area of the sample which is experiencing the 180° tip angle. The ends of the initial rectangular region represent the ends of the probe's coil. These regions will not be near zero because the ends of the coil receive less than a 180° tip angle. In probes with a good $\boldsymbol{B}_1$ homogeneity, the region near zero will be a significant portion of the initial rectangular region. In probes with poor $\boldsymbol{B}_1$ homogeneity, the center region will dip slightly below zero intensity with little or no flat region near zero. This is a picture of the sample receiving a 180° tip angle versus position in the probe's coil.

10 THE SAMPLE AND SHIMMING

The NMR sample and its preparation have tremendous influence on the quality of the spectra and the shimming process. These areas include end effects (magnetic susceptibility) of the sample, particulate materials in the sample, dissolved materials in the sample, and radiation damping.

End Effects: An often overlooked parameter in the shimming process is the magnetic susceptibility effect caused by the ends of the sample. The solvent–air interface generates field gradients which can create lineshape distortions if it occurs close to the 'active' region of the probe coil (the part of the sample which lies within the coil window). An empirical method of determining the active region of the probe's receiver coil is discussed in Section 6.2. The key question in this discussion is how far from the active area of the probe must the solvent interface be to avoid distortions. The answer depends on many variables, a few important ones being the height of the receiver coil, the diameter of the receiver coil, and the magnetic susceptibility of the solvent. The larger the diameter of the tube, the further away the effect from the solvent ends is detectable. For a 5 mm tube, the effects are easy to measure when the sample extends 1 cm above and below the active region of the probe's coil. The effects are difficult to measure when the sample extends 2 cm above and below the active region of the coil. This is more sample length than most NMR operators want to use. The shorter the sample used, the more difficult the shimming process will be, but less sample is required.

As a general rule, if the sample length used in the 5 mm probes is going to be longer than 2 cm above and below the active region of the probe's coil, the sample-to-sample variations of the shim values derived from the end effects of the solvent will be negligible. If the typical sample to be run on the NMR spectrometer is going to be within 1.5 cm above and below the active region of the coil, then the sample length should be tightly controlled and maintained the same for all samples. Then if the sample tube's position in the spinner is kept the same, a set of shim values can be developed and reused from sample to sample.

When a spectrum of a limited amount of sample is necessary, one can use a microsample probe or constrain the sample in a micro-cell. When the microcell is inserted in a 5 mm NMR tube, it is usually best to surround the microcell by the same solvent as used in the microcell such that the ends of the surrounding solvent extend more than 2 cm above and below the coil's active area.

Since deuterochloroform is a common NMR solvent, another trick which has been used by many NMR laboratories is to take advantage of the fact that Teflon has about the same magnetic susceptibility as chloroform. The sample is then placed between two Teflon plugs. The total length of the sample and Teflon plugs is then maintained to be 2 cm above and below the probe's active region. This technique also minimizes the effects from the end of the solvent and makes shimming small samples easier.

Particulates: When an NMR sample is examined under a magnifying glass, one can often see little extraneous bits floating around. These particulates often have a very different magnetic susceptibility from the NMR sample. These perturbations on the magnetic homogeneity over the active volume of the probe cannot be compensated for by shimming because the particulates are moving about while the sample is spinning. The particles need to be removed by filtering the sample.

As surprising as it sounds, it is not at all uncommon for the particulates to be iron. Holding a small magnet to the side of the NMR sample can cause these iron particles to move to one side of the sample tube, as seen by examining the sample under a magnifying glass. Some samples with iron particles can be examined before putting them into the NMR spectrometer and appear clean. After shimming for a while with unsatisfactory results, the sample can be removed and examined under a magnifying glass and big particles can be seen. This comes about because the original sample had some very fine iron particles that could not be seen, but which coagulated after being magnetized in the magnet. It is often a good idea to look at the sample under a magnifying glass before expending a lot of time on a sample which seems difficult to shim.

Dissolved Material: In addition to having macroscopic particles in the sample, it is possible to have dissolved paramagnetic material in the sample. This will not be visible to the eye, but can cause dramatic broadening of NMR lines due to paramagnetic relaxation, which is a very efficient mechanism of T_2 relaxation. Even dissolved oxygen in the sample will cause broadening, which is why NMR resolution standard samples are always supplied degassed in sealed tubes.

Viscosity is also a cause of broadening of NMR lines because of the reduced correlation times for molecular tumbling. Slower motions are a more efficient mechanism of T_2 relaxation.

Radiation Damping: Another broadening phenomenon which can be observed under some conditions is called 'radiation damping'. When used in conjunction with NMR, this phenomenon is different from radiation damping when discussed by an electronics engineer. When discussed in relation to NMR, it is an additional relaxation mechanism arising from energy in the NMR sample being coupled into the probe's coil. Losses in the probe's circuit then provide a means for removing energy from the nuclei. This relaxation process is proportional to the strength and frequency of the nuclear signal, the sample coil filling factor, and the Q value of the probe's tuned circuit. This means that it is most likely to be observed on high-field instruments when observing protons in water solutions. The phenomenon can be seen with other samples such as $CHCl_3$ on 500 MHz and 600 MHz systems if the $CHCl_3$ sample is very concentrated ($>5\%$).

The presence of radiation damping is easy to detect. Run a spectrum of the sample under conditions where you suspect radiation damping and measure the linewidth of the signal. Then de-tune the probe off-resonance and run the same spectrum again. You will of course have a reduced signal intensity, but if the line becomes narrower, then radiation damping was present. Because the degree of relaxation the nucleus experiences by this mechanism is directly related to the strength of the NMR signal, it is possible that only the intense peaks in the spectrum show broadening.

11 PROBES AND SHIMMING

Ideally, probes should have little or no influence on the shimming process. However, many probes have one or more characteristics that make them nonideal. In general, the better the probe, the easier the shimming process. Major areas where probes can influence shimming are the materials used in probe construction, size (length and diameter) of the probe coil, and the rf homogeneity generated by the probe coil.

Each of these areas produces constraints and/or influences on the shimming process. An understanding of these influences and what the NMR operator can and cannot do makes shimming less frustrating.

Materials: The basic way probe materials can influence the shimming process is via the magnetic susceptibility of the probe materials. The area of the probe of major concern is the probe's coil because it is closest to the active region of the probe, the volume of sample which contributes to the observed signal. Other parts of the probe can influence the shimming process, but they are usually further away from the probe's active region and, because the effects fall off with distance, they have less influence. Because of the distance from the sample, the effect that these probe parts produce is a low-order gradient. Low-order gradients can cause the shim values of particular gradients to change, but they are usually straightforward to shim. The coil, however, is much closer to the probe's active region and has a complex geometric arrangement relative to the sample. Any magnetic susceptibility of the probe's coil changes the magnetic field profile in the active region in a complex manner related to the complex geometric pattern. The NMR operator is then faced with the prospect of trying to correct this influence with the shims.

As an example for discussion, consider a simple probe coil often referred to as a single-turn Helmholtz or coaxial cavity

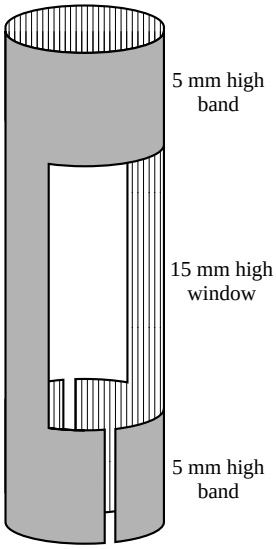

Figure 6 Simplified drawing of a single-turn Helmholtz or coaxial cavity probe coil

as shown in Figure 6. If the coil material has a magnetic susceptibility, it perturbs the magnetic field producing a gradient whose geometry is related to the geometry of the coil. If the coil described were made of a material with nonzero magnetic susceptibility such as copper, the gradient profile generated along the Z axis through the center of the sample can be calculated and would look like the graph on the right of Figure 7. The vertical axis in this figure represents the position along the sample. Gradients are displayed as horizontal deviations from zero at the center. A perfect field would have a profile which is a straight, vertical line at the center of the plot, showing no gradient over the active region of the probe, which is the area between the top and bottom edges of the window. The deviation from ideality of the gradient profile shown would result in a distorted lineshape.

If it is assumed that only the sample within the window generates a signal, the calculated values of $Z0$ through $Z4$ gradients best able to correct this coil-induced gradient are shown in the upper right corner of Figure 7. If we apply these gradients to the induced field to correct them by shimming, then the result is shown on the graph on the left of Figure 7. Notice that there are residual field gradients not correctable with $Z0$–$Z4$. In this example, there are strong $Z0$, $Z2$, and $Z4$ gradients induced. When using such a probe, the NMR operator would adjust these shim gradients to correct the coil-induced gradients. However, there are residual gradients that are not correctable by $Z0$ through $Z4$. These residual gradients oscillate between a slightly positive and a slightly negative field value. This would result in a split field lineshape where the peaks would either be broader than necessary or split into a doublet. This type of lineshape would even result from perfectly compensating for the coil-induced gradients up to fourth order. The NMR operator would be very unhappy with a resulting lineshape where every peak is a doublet and might continue to shim, probably concentrating on the even-order shims. In general, the operator would probably move $Z2$ a little one way and $Z4$ a little the other way and then adjust $Z1$ for the best lineshape. This process consists of misadjusting the shims to smear out the lineshape so

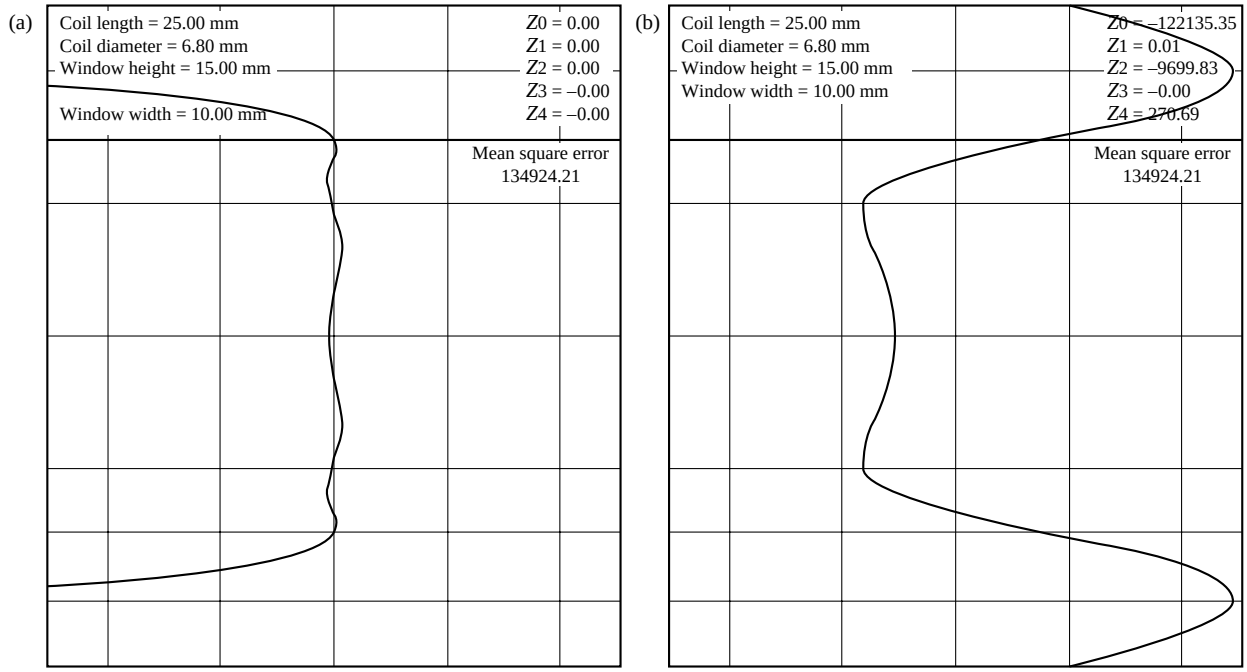

Figure 7 Magnetic field gradient induced by material with magnetic susceptibility of pure copper for a probe made from a single-turn Helmholtz or coaxial cavity probe coil: (left) after correction with $Z0$–$Z4$; (right) before correction

that it is not a doublet, but a more acceptable fat singlet. This results in shimming symptoms that many operators may have noticed: the resolution gets better while the lineshape distortions get worse. In extreme cases of this phenomenon, the NMR operator observes a very frustrating symptom. When the NMR instrument is shimmed the lines in the spectrum tend to split. About the only cure for such a problem is to deshim the system to spread out the doublet to a broad singlet or use a different probe.

The actual shimming process to correct for the probe coil's magnetic susceptibility influence is more complicated from the NMR operator's point of view. Using the example of the typical single-turn Helmholtz coil made from a material with magnetic susceptibility one-fifth that of pure copper in a perfect magnetic field, the magnetic gradients induced by the probe on the sample would generate a lineshape as shown in the first frame of Figure 8. The user would look at this and try to correct the lineshape problem using $Z4$. Using only pure $Z4$, the user would get the result shown in step 2. This generates a lineshape which looks like $Z2$ needs adjustment.

Correcting with pure $Z2$ would give the result shown in frame 3 of Figure 8. This again looks like $Z4$ needs adjustment, but less than at the start shown in frame 1. Iterating back and forth between $Z2$ and $Z4$ would correct the lineshape with the final result shown in frame 4 of Figure 8.

While the result looks like an acceptable lineshape, its low-order lineshape, width at halfheight, and peak amplitude are all poorer than what would have been obtained with the same probe and sample in a probe with zero magnetic susceptibility components.

In the absence of magnetic susceptibility problems, as the operator changes the value of $Z4$, the hump in the base of the lineshape peak moves through the peak and appears on the opposite side. The time when the hump is totally under the peak results in the best resolution. In cases where the probe's magnetic susceptibility is a problem, the lineshape hump looks like a $Z4$ problem, but is a magnetic susceptibility problem. The gradients induced in the sample by magnetic susceptibility of the probe coil perturb the sample near the ends of the coil more than in the center of the coil. This creates a gradient profile that looks like $Z4$. The actual profile is a much more complex function which, in its simplest form, contains $Z2$, $Z4$, $Z6$, $Z8$, etc. Since most NMR spectrometers do not have these as shimmable gradients, the best the operator can do is overcorrect the sample near the ends of the coil with $Z4$ and try to back-correct the sample near the middle of the coil with $Z2$. In the process of doing this, when the small hump starts to move under the peak, the resolution degrades. It is impossible to get the best resolution and no $Z4$ hump in these cases.

The susceptibility phenomenon is usually present more in lower-frequency probes than high-frequency probes. This is because the lower frequency probes usually have more inductance in the probe, meaning that the probe coil has more turns of wire and therefore larger amounts of the magnetically imperfect material. The lower frequency probes are also more likely to have a separate decoupler coil which also adds more material to the probe. However, the same ppm of magnetic susceptibility effects creates greater perturbation at high frequency. For this reason, lineshape problems produced by probe coil magnetic susceptibility are usually observed more with higher frequency probes such as proton. The addition of more probe coils, and therefore more materials in reverse probes and dual probes where one of the nuclei is proton, is one of the reasons that good lineshape performance in these probes is more difficult.

Today, all NMR probe manufacturers correct the probe coil's magnetic susceptibility to some degree. It is interesting to note that glass has a much greater magnetic susceptibility than the copper from which coils are commonly made. The insert and sample tube are effectively infinitely long uniform

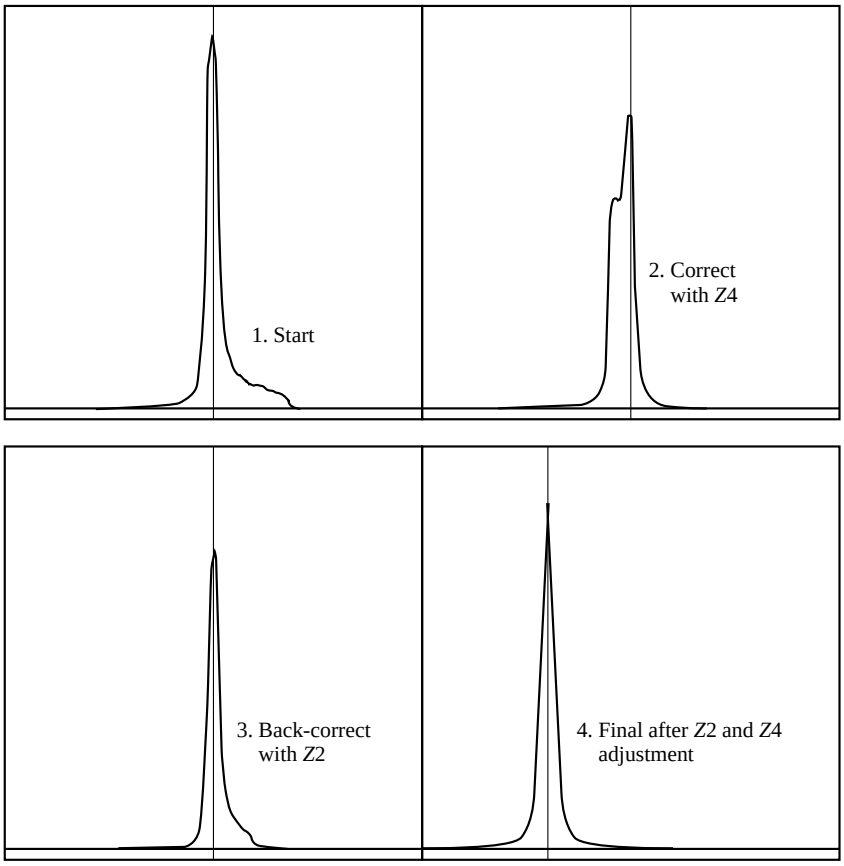

Figure 8 Four steps in shimming a probe with magnetic field gradients induced by a probe coil with the geometry of a single-turn Helmholtz or a coaxial cavity probe coil with material of the magnetic susceptibility of pure copper

cylinders and, by virtue of this symmetry, generate no field gradients at the sample. When a hole is drilled in the center of an NMR probe insert (as in a CIDNP probe), this symmetry is lost and results in substantially degraded resolution. A cracked insert can also perturb lineshape. Poor quality NMR tubes which have nonsymmetrical wall thickness can create gradients to the degree that they deviate from being perfectly cylindrical. Because the resolution requirements become more stringent at higher fields, better quality tubes are necessary to obtain optimum resolution and lineshape. When no other reason can be found for poor resolution or lineshape, try transferring the sample to a different tube.

11.1 Magnetic Susceptibility Correction

There are several techniques used by probe builders to reduce problems with gradients induced by probe coil materials. One way is to correct the magnetic susceptibility of the probe material. A common way to do this is to use a copper–aluminum sandwich.[9] Good, oxygen-free copper is diamagnetic (negative magnetic susceptibility) and aluminum is paramagnetic (positive magnetic susceptibility). The goal is to make a composite with close to zero magnetic susceptibility by adjusting the amounts of the component materials. Other plating techniques are also commonly used. The difficulty is that the magnetic susceptibility varies greatly with purity and measuring the magnetic susceptibility accurately for these materials is difficult.

Very few techniques can measure magnetic susceptibility at the absolute levels which cause very strong gradients in an NMR probe. A common way is to measure a large amount of the probe coil material in a very strong, very inhomogeneous magnetic field either by a change in weight or by a change in deflection as a function of field strength. To have the necessary sensitivity, a large sample of the probe coil material is necessary. This presents the additional problem that small point-to-point fluctuations in the magnetic susceptibility within the large sample of material are not detected. When these materials are used in a probe, point-to-point susceptibility fluctuations can be present all along the probe coil leading to field gradients and lineshape distortions.

Another method is to use the NMR spectrometer itself to measure the materials. This is usually done by placing a piece of the material to be tested at the top of a shimmed NMR system's probe coil.[9] This will create a lineshape distortion which resembles a solids powder pattern. If the material is diamagnetic, the powder pattern is sloped in one direction and if the material is paramagnetic, the powder pattern is sloped in the opposite direction. If the material has no magnetic susceptibility, there is no lineshape distortion. This technique has the ability to test smaller samples more resembling the probe coil itself and in fact can be used on an actual probe coil. A limitation of the technique is that a good lineshape is needed to do the test well. The better a lineshape is to start with, the more sensitive the technique becomes. This technique ends up being a bootstrapping technique where

a good probe is used to make better materials, which are used to make better probes which allows one to make better materials.

Another technique to improve the situation of gradients induced by probe coil magnetic susceptibility is to change the shape of the coil window. Depending on several parameters such as the length of the coil and the height and width of the window, the shape of the window can change the type and magnitude of the gradients induced. Thus improvement in lineshape can be obtained just by changing the window shape, even if the materials in the probe coil are not magnetically compensated. In the previous discussion of the single-turn Helmholtz coil, the coil window was rectangular in shape. As the bands of copper at the coil ends become small compared to window height, the minimum influence from the coil's magnetic susceptibility will be observed with this rectangular shape. As the bands of copper at the coil ends become large compared to the coil window height, an ellipsoid window shape becomes better. The best shape depends on the ratio of the height and width of the window as well as the size of the bands at the top and bottom of the coil.

Another common problem which comes from probe coil magnetic susceptibility arises when the susceptibility at the top and the bottom of the coil are different. In this situation, a high-order even gradient, typically $Z4$, is used to correct the asymmetrical lineshape induced by the probe's materials. But the amount of correction required for the top region and the bottom region are different. Typically what happens is that, as the asymmetry is improved with the change of $Z4$, a different asymmetry is produced on the other side of the lineshape. With probes of this type, the 'best' lineshape does not occur at the settings which give the best width at halfheight. This produces a situation where shimming for the best response produces an asymmetrical lineshape. The NMR operator is then forced to use $Z4$ to produce the best lineshape and the remaining controls to produce the best width at halfheight. Shimming for the best response with $Z4$ does produce the best width at halfheight but not the best lineshape. This is a case that many NMR operators will recognize and makes shimming $Z4$ very difficult. It is also a case where automatic computer shimming will lead to the 'wrong' answer. What is happening is that $Z4$ is being used to destroy the field in the center of the probe's active region, but make the field values at the ends of the coil acceptable for lineshape. The NMR operator then tries to make the field in the center of the probe's active region as good as possible with lower order gradients. Here is an example of a situation where the use of a $Z6$ or $Z8$ shim would provide better results.

Size of the Probe Coil: The size of the probe coil, or its length and diameter, can affect the shimming process in three ways. The first is via the magnetic susceptibility of the probe materials and the induced, noncorrectable gradients as just discussed. As the coil length becomes larger at a constant window width, the NMR lineshape tends to split. This aspect ratio of the coil is very important when shimming with probes which have less than perfect magnetic susceptibility compensation for their materials. Having a longer receiver coil is also something many probe manufacturers try to do, since longer coils 'see' more sample and therefore have greater sensitivity.

If the probe's materials were perfect, then longer coils and larger diameter coils would still be more difficult to shim, but only because it is always more difficult to make a magnetic field perfect over a larger volume than a smaller volume. The case of longer and larger diameter probes is a situation where a 'good' magnet is easier than a 'bad' magnet to shim. This also means that wide bore magnets are better than narrow bore magnets at a given sample volume. As the amount of sample decreases relative to the probe materials, the probe materials become more important to the shimming process than good or bad magnets. This is one reason why microsample probes are difficult to shim and not commonly used. As probe material compensation becomes better, microsample probes will probably become more useful.

12 COMPUTER SHIMMING

Many instruments provide automated shimming, commonly using computer-driven digital to analog converters (DAC) as one input to the shim power supply and a Simplex computer optimization routine to adjust the shim settings. Automating the shimming process can save wear and tear on the operator, provided a few precautions are taken.

1. Each shim should have equal control of the homogeneity. This is best done by setting the voltage from the DACs to the shim power supply such that an equal DAC step for each shim produces an equal depression of the lock level.
2. The initial step size for the Simplex search should be large enough to include the best value for each shim to be optimized by the Simplex routine.
3. The lock phase must be correctly adjusted if the Simplex routine is using the lock signal for measuring homogeneity.
4. The waiting period between measurements of homogeneity must be long enough to allow the NMR system time to respond. This is especially true if the lock signal is being used as a measure of homogeneity. The response time for a lock with deuteroacetone as a lock solvent can be several seconds as the homogeneity improves.
5. When the FID is used as a measure of magnetic homogeneity, a steady state must be established and maintained between the rf pulses before the FID can provide a valid measurement of the homogeneity. Because the time between adjustments may not be constant as the Simplex optimization proceeds, the best way to meet this condition is to avoid saturation.
6. The most sensitive method for adjusting the final values for $Z1$ and $Z2$ is by using the FID as the measurement of homogeneity.

In theory, the Simplex routines should be able to optimize the homogeneity regardless of the shim interactions. However, experience has shown that with second-order shim interactions, Simplex often fails to find the best values. In these cases, slower and less elegant computer routines following a shimming sequence similar to the manual one described can give better results. Also, the initial shimming steps must be large enough to ensure that the computer algorithm is not caught at a local maximum.

Some other algorithms for computer shimming have been explored. One called 'hypershim'[10] searches in a circle to fully define where the valleys are before optimizing. The goal is to provide a more robust algorithm which does not get caught at a local maximum.

13 RELATED ARTICLES

Birdcage Resonators: Highly Homogeneous Radiofrequency Coils for Magnetic Resonance; Coils for Insertion into the Human Body; Instrumentation for the Home Builder; Probes for High Resolution; Probes for Special Purposes; Refrigerated and Superconducting Receiver Coils in Whole Body Magnetic Resonance; Solid State Probe Design; Water Signal Suppression in NMR of Biomolecules

14 REFERENCES

1. W. A. Anderson, *Rev. Sci. Instr.*, 1961, **32**, 241; J. Taquin, *Methodes Phys. Anal.*, 1971, **7**, 3.
2. P. M. Starewicz (Resonance Research Inc.), personal communication (1993).
3. N. D. Sauzade and S. K. Kan, *Adv. Electron. Electron Phys.*, 1973, **34**, 1.
4. F. Bloch, *Phys. Rev.*, 1954, **94**, 496.
5. W. A. Anderson and J. T. Arnold, *Phys. Rev.*, 1954, **94**, 497.
6. P. Jastrzebski, D. F. Hildebrand, and P. M. Starewicz, poster at *34th Exp. NMR Conf.*, 1993.
7. G. N. Chmurny and D. I. Hoult, *Concept. Magn. Reson.*, 1990, **2**, 131.
8. W. W. Conover, in *Topics in Carbon-13 NMR Spectroscopy*, ed. G. C. Levy, Wiley, New York, 1984, Chap. 2
9. L. F. Fuks, F. S. C. Huang, C. M. Carter, W. A. Edelstein, and P. B. Roemer, *J. Magn. Reson.*, 1992, **100**, 229.
10. D. E. Brown (Eastman Kodak Co.), private communication (1993).

Biographical Sketches

Woodrow W. Conover. *b* 1947. B.S., 1969, Rose−Hulman Polytechnic Institute, Ph.D., 1973, Indiana State University. Postdoctoral studies, The University of Chicago, 1973−75. Operation Manager, Stanford Magnetic Resonance Labortories, 1975−78; NMR instrument design, Nicolet/GE, 1978−88. Acorn NMR, 1988−present, providing NMR spectroscopy services and NMR utility software.

Virginia W. Miner. *b* 1956. B.A., 1978, Smith College, Ph.D., 1984, Yale University. NMR spectroscopist for Dow Chemical Co., 1983−91. Acorn NMR, 1991−present, providing NMR spectroscopy services and NMR utility software.

Solid State Probe Design

F. David Doty

Doty Scientific Inc., Columbia, SC, USA

1	Introduction	1
2	High-Power Capacitors	1
3	Sample Coils for Solids	3
4	WideLine	5
5	Magic Angle Spinning	5
6	Goniometers and Slow MAS	7
7	Variable Temperature (VT)	8
8	Dynamic Angle Spinning (DAS)	9
9	Double Rotation (DOR)	9
10	Related Articles	10
11	References	10

1 INTRODUCTION

Obtaining detailed structural information from NMR of solid samples is more complex than for liquids because of the absence of molecular tumbling in solids to average line-broadening interactions; hence, much greater probe bandwidths are required.[1–4] The wideline probe usually has spectral excitation bandwidth greater than 80 kHz (i.e., able to generate 90° pulses less than 3 μs). To do this, it normally must withstand peak rf voltages in excess of 3 kV. Often wideline probes are double-tuned (DT) to permit cross polarization (CP) and high-power decoupling for increased sensitivity and resolution. If $\pi/2$ pulse lengths below 2 μs can be generated, multiple pulse line-narrowing techniques may be used to remove dipolar broadening,[3] but this is generally possible only in single resonance probes where low inductance coils can be used effectively.

The most common solids probe is the cross polarization/magic angle spinning (CP MAS) probe, which adds high-speed sample spinning at the magic angle to the other capabilities of the DT wideline probe for effective averaging of the chemical shift anisotropy (and perhaps dipolar broadening at very high speeds), thereby greatly improving resolution for spin-$\frac{1}{2}$ nuclei.[5] Single resonance MAS probes can generate the short pulses needed for the combined rotation and multiple pulse spectroscopy (CRAMPS) line-narrowing technique for ^{1}H or ^{19}F. Large volume MAS rotors can achieve the rotational spin rate stability needed for slow MAS, where pulses are applied at precise rotor orientations to average out the anisotropic chemical shift broadening as with high-speed MAS, although sensitivity may be reduced. Commercially available extended variable temperature (X-VT) CP MAS probes permit experiments from 35 K to 650 °C.

When sufficiently large single crystals of the sample can be grown, high-resolution spectra and the chemical shift tensor can be obtained using a single crystal probe,[6] which is similar to a wideline probe but includes a goniometer and crystal orientation mechanism for rotating the sample about three perpendicular axes.

Table 1 Dielectric Properties

Dielectric	k_d	tan δ[a]
Teflon, PE, PP	2.0–2.2	0.0002+
Kel-F	2.5	0.001
PMMA	2.8	0.03
PEK	3.4	0.003
Vespel	3.5	0.004
Epoxy	3.6	0.03
Quartz	3.8	0.0001
Macor	5.5	0.005
Porcelains	5–8	0.0002+
Si_3N_4[b]	8	0.001+
MgO	9.65	0.0005
Al_2O_3 (sapphire)	9.9	0.0002
PSZ (ZrO_2–MgO)	22	0.005+
BaO	34	0.001
COG	65–95	0.001
TiO_2	90	0.001
$SrTiO_3$	330	0.002+

[a]Loss tangent is approximate at 300 K, 30 MHz, and increases with temperature and frequency, especially in plastics and high-k dielectrics.
[b]High purity, high density, with minor Y–Al–Mg–O glass phase.

Quadrupolar interactions require more complex motions for effective averaging.[7] The dynamic angle spinning (DAS) probe allows the spinning axis to be changed rapidly while spinning the sample at high speeds. In another approach, known as double rotation (DOR), the sample is placed in a small spinner inside a larger spinner and spun about two intersecting axes simultaneously.

The short T_2 values (and often long T_1 values) in solids make sensitivity much lower than in liquids, and the requirement for high-power decoupling requires attention to efficiency at the proton frequency. In liquids probes, it is the sample coil that is most critical. For solids, it is the capacitors.

2 HIGH-POWER CAPACITORS

The special requirements of capacitors for NMR probes include the following: ultra-low magnetic susceptibility, high Q, high voltage, high current, ultra-low piezoelectric effects, and dielectrics devoid of unwanted NMR background signals. Losses in rf capacitors at a given frequency may be indicated by a capacitor quality factor Q_c, an effective series resistance [ESR = $(\omega C Q_c)^{-1}$], a loss tangent (tan $\delta \cong \pi/Q_c$), or a loss factor, k_d tan δ, where k_d is the dielectric constant (relative permittivity). Direct current losses may be specified by a leakage resistance, but this usually has no relationship to R_P (the effective parallel resistance of a tuned circuit) above 1 MHz. Table 1 lists typical permittivity and loss properties of dielectrics frequently encountered in NMR probes.[8–12]

Solids probes are usually designed for peak voltages of 2.5–4 kV, compared with ~1 kV for most liquids probes. Voltage breakdown strengths often tabulated for dielectrics are best ignored unless two important parameters are also specified: test material thickness and frequency. The frequency dependence is not easily characterized, but dc ratings of rf capacitors are typically four times the short-pulse rf ratings at 100 MHz. For very short pulses where heating is not much of a factor, the voltage rating at 10 MHz is typically only twice that

Table 2 Typical Dielectric Breakdown Voltages

Thickness (mm)	V_B, $k_d > 30$ (V)	V_B, $k_d < 10$ (V)
0.1	500	1000
0.5	1200	2200
3.0	3000	5400

at 500 MHz, but with long pulses the voltage derates at least as the $\frac{3}{2}$ power of the frequency above a cutoff that is a function of Q_c/C. Table 2 shows typical rf breakdown voltages, V_B, for several thicknesses of low-k and high-k dielectrics at 30 MHz. Above 50–100 V, V_B is a square root function of thickness and shows relatively little variation within the two classes of rf dielectrics listed.[11] Dry air has an ionization V_B comparable to that of high-k dielectrics, but arc voltage in monatomic gases (He, Ne, Ar) is less by a factor of at least five (more for large gaps) because of the absence of low-energy rotational and vibrational relaxation modes.[13] The additional rotational modes in polyatomic gases usually increase the breakdown voltage, except in the case of ionic gases such as H_2O.

2.1 Ceramic Capacitors

The standard COG (ceramic oxide glass) rf capacitor specification (formerly type NPO) requires a temperature coefficient of less than ± 30 ppm and tan δ below 0.001 for the range $-55\,^{\circ}$C to $125\,^{\circ}$C. For moderate-power applications up to 300 MHz, the COG formulation usually consists of fine-grained baria–neodymia–titania systems or magnesium titanate prefired with 6 mol% calcium titanate, but they are also made from mixtures of neodymium carbonate, titania, and barium titanate. A two-stage firing is generally required for multilayer capacitors so that the final firing temperature can be kept below $1150\,^{\circ}$C to allow the use of Pd–Ag electrodes. The ceramic precursors are prefired at a high temperature, then reground and mixed with a powdered glass binder with matched thermal expansion such as 36% CdO, 23% Bi_2O_3, 25% PbO, 5% ZnO, 5% B_2O_3, 5% SiO_2, 1% Al_2O_3.[9] Alternate layers of ceramic/glass and metallization slurry are built up by a screening or spraying process.

Porcelains (magnesium–aluminum–silicates) are often used in the UHF range for high-power capacitors below 15 pF. Corning Pyroceram 9606 consists mostly of cordierite ($2MgO–2Al_2O_3–5SiO_2$), with lesser amounts of cristobalite and various magnesium titanates. Its low thermal expansion can cause problems with the metallization. Forsterite ($2MgO \cdot SiO_2$) is electrically almost as good as Pyroceram, easier to produce, and easy to metallize, but has poor thermal shock resistance.

UHF high-power capacitors above 30 pF are usually based on strontium titanate, which is not piezoelectric but may contain piezoelectric barium titanate impurities. High-power rf capacitors are often coated with a sealing glass such as $2PbO \cdot SiO_2$ ($550\,^{\circ}$C) to keep out moisture,[8] as it facilitates silver migration in the presence of an electric field.

The magnetic properties of ceramic capacitors are unpredictable, as most ceramics are slightly diamagnetic (bismuth compounds are very diamagnetic), palladium is extremely paramagnetic, and ferromagnetic nickel barriers are sometimes used in the terminations. A number of manufacturers are by now quite familiar with the stringent requirements of NMR/MRI capacitors and offer 'nonmagnetic' chip capacitors with 500–1000 V rating (a 2.5–3 mm cube), but it is always necessary to screen them for magnetism using a small magnet (a 2-mm cube of high-energy neodymium–boron–iron) suspended from a string. Also, nearly 1% of new capacitors may be noisy in a double resonance circuit as a result of microgaps between the electrodes or terminations and the dielectric.[14] Premature breakdown may be initiated by surface tracking and moisture in solder rosin.

At least four manufacturers (JFD, ATC, Murata Erie, and Tansitor Electronics) offer 3-kV multilayer ceramic rf capacitors in roughly a $3.5 \times 10 \times 11\,mm^3$ package. The JFD capacitors have generally been found to have the highest Q, but the difference is often not important. Some of the best NMR ceramic capacitors (when available, but once discontinued) are the 2-kV UV10 and UV17 series ($3.3 \times 6 \times 8\,mm^3$) by Murata Erie, as they have very low magnetic susceptibilities and a 2-kV rating in a small package. Moreover, for typical circuit values (reactance above 100 Ω), Q_c is usually greater than 3000 for capacitance below 150 pF at frequencies at least up to 50 MHz, and Q_c is usually greater than 1000 up to 500 MHz.

2.2 Piezoelectric Acoustic Ringing

While acoustic ringing is seldom a problem in liquids probes because of the longer T_2s and the effectiveness of the Patt acoustic suppression sequence,[15] piezoelectric-induced acoustic ringing[16] of capacitors can obscure signals in solids probes requiring short recovery times. Subjecting a capacitor with ferroelectric impurities to a dc electric field in excess of $1\,kV\,mm^{-1}$, as may occur in a voltage withstanding test or from asymmetric rf breakdown, causes domain alignment and imparts a net crystallographic piezoelectric orientation to the ceramic. The ferroelectric is said be 'poled', and may exhibit acoustic ringing. The polarization of ferroelectrics can be annealed out by heating above the Curie temperature ($130\,^{\circ}$C for $BaTiO_3$; 180–$300\,^{\circ}$C for lead–magnesium–niobates), but they can easily become poled again.

Grain size is usually under $4\,\mu$m for rf power COG capacitors in the 10–30 pF range, in which case Rayleigh scattering will normally keep acoustic decay times under a few μs above 30 MHz. However, grain size may exceed $100\,\mu$m in high-voltage (HV) capacitors above 150 pF and occasionally in low-valued capacitors, resulting in reduced acoustic absorption and acoustic decay times greater than $10\,\mu$s at frequencies as high as 45 MHz. On the other hand, acoustic ringing in bulk metals from the Lorentz interaction is seldom a problem above 15 MHz.[17]

2.3 Variable Capacitors

The double rotation (DOR) probe shown in Figure 1 illustrates the use of three common types of variable capacitors (air, quartz, and pressurized gas) and 3-kV ceramic chip capacitors (attached to the left of the quartz variable near the center of the photo). The Johanson 5000-series nonmagnetic, air-dielectric, trimmer capacitor (one is mounted on the upper circuit board near the center of Figure 1, just to the right of the central support post) is typical of that used in most liquids NMR probes and the high-frequency (HF) channel in solids probes with capacitive voltage division. It consists

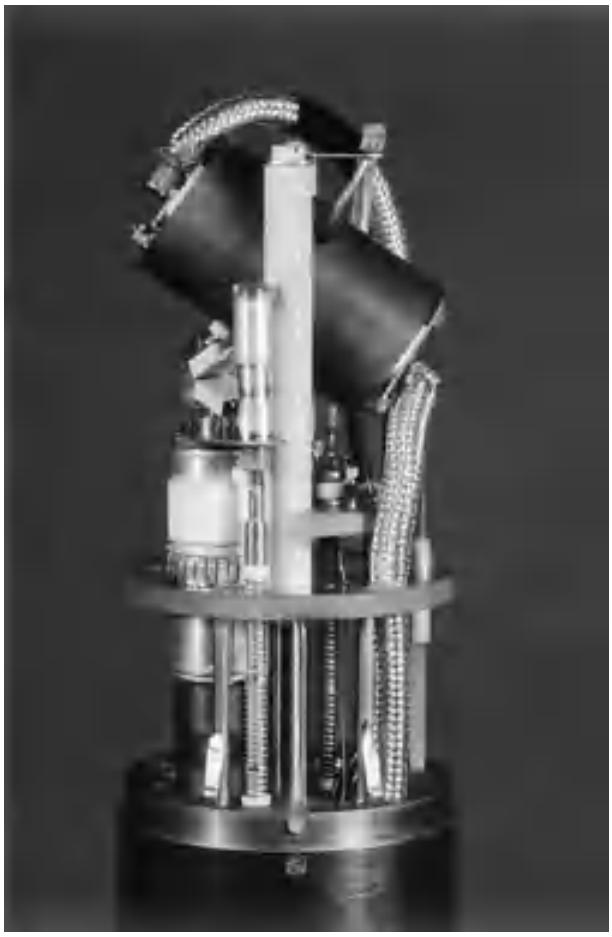

Figure 1 DOR WB probe (Doty Scientific, Inc.)

of an alumina ceramic housing supporting several concentric, silver plated brass cylinders at the 'hot' end; a precision screw mechanism adjusts a similar intermeshing arrangement at the mount end. The minimum radial air gap is under 0.1 mm, and breakdown occurs at 500–700 V when new. With use, alignment deteriorates, and the voltage rating decreases. Care must be taken to avoid dissolving the internal lubricants (which are essential for an acceptable lifetime) with cleaning solvents. The capacitors may be sealed, but this is inconvenient; hence, their voltage rating also decreases with altitude and humidity or high concentrations of monatomic gases. These variable capacitors are manufactured using 300 °C Pb–Ag solder between the alumina and brass body parts, and they tolerate repeated overvoltages.

Also shown in Figure 1 (near the center, on top of a gas variable capacitor, just left of the central support post) is the JMC 7584, quartz-dielectric, 0.8–10 pF, variable capacitor. Its 2.5-kV rf capability allows five-times the tuning range of the above air variables, as tuning range is generally proportional to $(CV^2)^{\frac{1}{2}}$. Defective silver plating on the piston or sleeve has occasionally been found to produce noise at lower voltages in double resonance circuits.[14] Impurities in the brass base and piston of the JMC capacitor are not controlled as carefully as in a similar capacitor by Voltronics, but the JMC capacitor is more robust which simplifies certain capacitive voltage division arrangements,[18] and the magnetism is acceptable unless it must be very close to the sample. These capacitors have been used successfully up to 400 MHz. They may lock up at high temperatures from the piston expanding or at low temperatures from the lubricants freezing.

The single component most synonymous with solids NMR probes is the Jennings CHV1 N-45 gas variable capacitor—the 22-mm diameter ceramic cylinder on the left side of the main circuit board in Figure 1. It is pressurized with about six atmospheres of CO_2 and SO_2 in its minimum capacitance position and may be adjusted from 1.5 pF to 45 pF using a pushrod mechanism. It has a peak breakdown voltage V_B of about 3.5 kV near the low end of its range (∼10 pF) but V_B increases to about 5 kV near the high end as the gas becomes more compressed. The ceramic-to-metal seals are slightly magnetic, but this is seldom a problem as they are normally more than 20 mm from the sample. These variables have been used successfully for tuning purposes up to 220 MHz. With proper layout, they are usable on the low-frequency (LF) channels of multituned circuits with 500 MHz HF. These capacitors tolerate repeated overvoltages and are usable from −20 °C to 100 °C. If the external mechanical stop is not set properly, they may be easily damaged by pushing the adjustment rod beyond the specified limit.

Teflon variables with very low magnetism are available from Polyflon and Voltronics in a variety of sizes and ratings similar to the three described above, but Teflon does not tolerate the brief, inadvertent overvoltages which are unavoidable in most laboratories.

3 SAMPLE COILS FOR SOLIDS

Almost all solids probes use solenoidal rf coils for higher filling factor and Q than saddle coils. Standard oxygen-free, high-conductivity (OFHC) electronic-grade copper wire (C10100, 99.99%) has acceptably low iron content (less than 25 ppm, typically 4 ppm) for most solids coils at high fields. Optimum space between wires is half the wire diameter[19] or perhaps a little less. An enamel coating does not usually cause a background problem with carbon experiments, but it should be removed using warm sulfuric acid if proton experiments are planned.

High-Q circuits are usually preferred—except perhaps for wideline. Coil length-to-diameter ratio is not critical, but values between 1.0 and 1.4 (depending on available wire sizes) are usually best, except for MAS. Larger ratios (1.4–3.0) give better S/N for MAS (more sample for a given speed and lower dielectric losses), but some manufacturers use short coils to achieve shorter pulse lengths and higher decoupling fields. Coil forms help stabilize tuning but reduce both filling factor and maximum voltage before the onset of arcing. If used, they should be of low-permittivity dielectrics for minimal electric field gradients and arcing.

Special or custom wire may be obtained from MWS Wire Industries, Westlake Village, CA. Gold flash (0.3-μm plating) is often applied to prevent copper sulfates and chlorides (which have a large positive susceptibility due to antiferromagnetism) from forming on the wire surface, but it is critical to specify that the common practice of first applying a nickel strike (to minimize diffusion into the copper) be omitted or the wire will be very magnetic. The gold flash degrades the Q by about 1%. Silver plating does not improve Q (because of unavoidable defects) and does not provide the same degree of

Table 3 Properties of NMR Probe Materials at 300 K

(a) Conductors

Material	Density	Young's modulus	Poisson ratio	Yield strength	Electrical conductivity	Thermal conductivity	Thermal expansion	Specific heat	Magnetic susceptibility
Symbol	d	E	r	S	σ	k_T	b_T	C_p	χ_v
Units	kg m^{-3}	GPa		MPa	(MWm)$^{-1}$	W mK^{-1}	10^6 K^{-1}	J (kg K)$^{-1}$	10^{-6}
Aluminum	2700	69	0.33	30	36.6	230	22	900	21
Copper	8950	122	0.34	150	58.0	400	16.5	490	−9.8
Gold	19 300	78	0.42	20	44.0	315	14.2	128	−34
Hafnium	13 090	110	0.34	300	2.9	22	5.9	145	69
Iridium	22 500	440	0.27	1200	19.8	147	6.8	130	38
Molybdenum	10 200	320	0.3	300	18.1	138	5.2	276	120
Palladium	12 020	115	0.38	250	9.3	76	11.8	245	840
Rhodium	12 440	330	0.29	800	20.9	150	8.3	247	168
Silver	10 500	78	0.38	100	61.4	428	19	235	−24
Tungsten	19 250	410	0.28	1000	18.4	173	3.8	133	80
Zirconium[a]	6506	99	0.35	200	2.3	21	5.85	295	160
Al-6061T6[b]	2700	69	0.33	214	25	180	23.6	896	20
H. C-22[c]	8690	206	0.3	400	0.9	10	12.4	414	650
J-bronze[d]	8780	115	0.34	200	23.5	173	18.6	380	−10
P-bronze[e]	8860	110	0.35	200	11.5	84	17.8	380	−9.2
60/40PbSn	9700	30	0.4	40	6.3	45	24	176	∼5
SS304[f]	8000	193	0.31	300	1.4	16	17	500	∼3000

(b) Insulators

Material	Density	Young's modulus	Poisson ratio	Yield strength	Electrical conductivity	Thermal conductivity	Thermal expansion	Specific heat	Magnetic susceptibility
Symbol	d	E	r	S	k_d	k_T	b_T	C_p	χ_v
Units	kg m^{-3}	GPa		MPa	(MΩm)$^{-1}$	W mK^{-1}	10^6 K^{-1}	J (kg K)$^{-1}$	10^{-6}
99.5Al_2O_3	3950	390	0.22	240	9.9	35	8	780	−18
A-JGN3030[g]	1560	10	0.35	130	3.7	0.3	∼35	960	−5
HIPd-Si_3N_4[h]	3250	310	0.26	710	7	25	3.2	740	−20
Kel-f	2100	1.3	∼0.45	20	2.5	0.21	60	800	−10.6
Macor[i]	2520	64	0.28	80	5.9	1.7	9	750	∼−15
99.5%MgO	3400	250	0.2	100	9.6	20	13.5	955	
PEK	1300	3.8	∼0.4	70	3.3	0.24	54	1500	∼−8
PSZ[j]	5700	200	0.25	500	23	3	9.5	490	−8
Pyrex-7070	2500	70	0.2	60	4.0	1.3	3.3	800	−11
Quartz[k]	2250	74	0.16	50	3.8	1.4	0.5	700	−16
Silica foam[l]	770	∼20	–	∼5	∼1.5	∼0.1	0.5	700	−3.5
Teflon	2200	0.4	∼0.45	12	2–2.2	0.25	120	750	−9.8
Vespel[m]	1430	3.1	0.41	86	3.5	0.33	54	1130	−9
Water	997	0	–	0	80	0.6	–	4182	−9.06

Note: Volume susceptibility χ_v in SI is related to cgs molar susceptibility χ_m by: $\chi_v = 4\pi d\chi_m/(\text{M.wt.})$.
[a]Commercially pure zirconium, grade 702: 96Zr, 3Hf, 0.1Cr, 0.1Fe.
[b]97Al, 1Mg, 0.6Si, 0.4Fe.
[c]Haynes C-22: 60Ni, 22Cr, 13Mo, 5W + Co.
[d]C22600: 88Cu, 12Zn, 0.005Fe.
[e]C51000: 95Cu, 5Sn, 0.1Fe.
[f]68Fe, 19Cr, 9Ni, 2Mn, 1Si.
[g]Aurum PI resin, 30% glass fiber.
[h]98Si_3N_4, 2Y_2O_3, HIPd.
[i]Al–B–Si–Mg–F ceramic glass, Corning.
[j]94ZrO_2, 3HfO_2, 3MgO.
[k]Fused silica, electronic grade.
[l]Fused silica foam, industrial grade.
[m]Dupont polyimide SP-1.

protection against corrosion—even when the plating thickness is increased to 3 μm. Silver and its compounds are quite diamagnetic but often contain paramagnetic impurities.

High-purity copper coils for high resolution are often plated with the proper thickness of iridium or rhodium to cancel the diamagnetism of copper.[20] Palladium can also be used for this purpose if it is plated only on the side that will be the external surface of the coil (where there is little current flow) so that the Q is not spoiled. Table 3 lists various properties, including volumetric magnetic susceptibility χ_v, for materials commonly

found in NMR probes. The desired plating thickness for foil is that for which the algebraic sum of the product of thickness and χ_v for the different layers is zero.

4 WIDELINE

The initial instrumentation for solids NMR borrowed extensively from radar and UHF transmitter technology, using fixed-frequency transmission lines as circulators and magic-Ts to isolate the multikilowatt transmitter from the low-noise preamplifier.[2,3] However, it was soon determined that it was not difficult to deal with the phase transients from Qs of 50–200—an order of magnitude higher than initially thought. Pulse rise times could be as much as one-third the pulse length without serious difficulties.[21] Hence, several hundred watts were sufficient except perhaps for low-γ nuclei. The cost savings of moderate power transmitters and the shift from transmission line traps to lumped elements facilitated the commercial solids probe,[22] which is usually required to be multinuclear and reasonably user friendly.

For proton NMR it is still beneficial to damp the Q to about 100 by coating the coil with tin–lead solder (as proton linewidths are large and sensitivity is enormous) but care must be taken not to trap rosin in the coating, or backgrounds will be seen. Also, experiments on other nuclides with very broad lines may benefit from moderate Q-damping if samples larger than 0.1 mL are being used, since the increased bandwidth simplifies data collection. A number of accelerated ringdown schemes have been proposed,[2,23] but the method seeing more use today appears to be overcoupling[24,25] because of noise, reliability, and magnetism problems associated with other methods. Moreover, the recent availability of linear prediction often obviates the need for active damping (see ***Fourier Transform and Linear Prediction Methods***).

The unbalanced, capacitively matched DT circuit (see ***Probe Design and Construction***, Figure 6) is usually used for wideline probes to simplify multinuclear tuning. The HF tuning coil L_H (which may be a capacitively shortened $\lambda/4$ coaxial transmission line) is chosen to have an inductance such that its untuned reactance would be between 25 Ω and 60 Ω at the HF. Lead inductance is minimized subject to VT, high voltage, and multinuclear constraints. The total series lead inductance is then typically 25–40 nH.[14] Maximum B_1/V_T, where V_T is the maximum total circuit voltage, is obtained for coil inductance L_S half of the total circuit inductance, but a somewhat higher value is usually selected for improved LF sensitivity with some sacrifice in HF efficiency and a slight reduction in maximum B_1.

Minimum 90° pulse lengths have typically been 3 μs, but recent successful demonstrations of wideline ^{2}H Hadamard NMR[26] may have a major impact on single resonance solids NMR. In Hadamard NMR, the spin system response to the application of a large number of pseudorandom pulses with flip angles as small as 0.1° (mW, μs pulses) at periods on the order of tens of microseconds can be transformed into the equivalent NMR response from a single high-power pulse. A Hadamard wideline probe should benefit from a low-Q (∼5) saddle excitation coil in combination with a moderate-Q (∼100) solenoid receive coil. SNR for Hadamard appears comparable to Fourier transform (FT). (See also ***Stochastic Excitation***.)

5 MAGIC ANGLE SPINNING

In 1958, Raymond Andrew[27] and co-workers showed that high-speed sample spinning at the 'magic' angle of 54.7° could be an effective tool in averaging out dipolar broadening. However, the required rotational rates for abundant dipolar nuclei (35 kHz for ^{1}H) appeared impossible, and the technique was largely ignored[28] for nearly two decades until Stejskal and Schaefer[4,5] showed that more realistic rotational rates (3–5 kHz), capable of averaging chemical shift anisotropy, combined with high-power decoupling to remove the ^{1}H dipolar broadening, could be extremely effective in obtaining high-resolution ^{13}C spectra from solid samples.

Andrew used a conical bearing/drive surface which eventually achieved speeds in excess of 10 kHz using helium gas.[29] This spinner was based on the classic ultracentrifuge work by Beams[30] and depended on the Bernoulli effect to hold the sample spinner close to the drive jets. The stiffness of such a bearing is extremely low, which results in low-frequency oscillations, precession, and instabilities. Moreover, angular accuracy of 0.3° is sometimes required in MAS, which is an order of magnitude beyond the capability of the conical Bernoulli–Beams bearing. Lippmaa,[31] Veeman, Pines, Eckman, and others introduced the double bearing cylindrical rotor to circumvent these problems, and Doty and Ellis presented an approximate analysis of the cylindrical air bearing optimization.[32] [Note that typographical errors resulted in equations (9) and (12) in the referenced article[32] appearing twice. The second equation in each case is correct. The first should be deleted.]

The high-strength ceramics[8] that have recently become available are required to obtain high sensitivity (from high filling factor) and high spinning speeds simultaneously. Silicon nitride[33] has the highest strength-to-mass ratio of any available ceramic, which allows the highest surface speeds with low-density samples; but zirconia has higher strength, better toughness, and fewer defects, making it the preferred material for heavier samples—except perhaps at very high fields or high temperatures. Most commercial MAS rotors and stators are ground and lapped (using precision diamond tooling) from partially stabilized zirconia (PSZ) or hot isostatic pressed (HIPd) Si_3N_4. As a consequence, these items are rather expensive. The press-fit turbine caps are usually machined from Vespel, as polyether ether ketone (PEEK) has poor wear resistance despite its other desirable properties. Zirconia turbines may be attached to a zirconia rotor by thermal interference fit. Other high-strength plastics and ceramics as listed in Table 3 are also used for special thermal or background considerations. Fiber-optics spin-rate detection is normally provided to allow precise, synchronous pulsing for the total suppression of sidebands (TOSS) technique.[34]

5.1 High-Speed Air Bearings

The high mass of ceramic rotors requires more attention to rotor resonances than was required in the earlier designs using plastic rotors.[35] For stability throughout a wide speed range, it is advantageous to have the high bearing stiffness that comes from tight radial clearances. However, as the clearance is reduced, bearing frictional heating becomes more severe; moreover, the possibility of a 'crash' increases. A crash may

occur in a hydrostatic bearing when the rotor moves close enough to the stator to cause extreme choking around the perimeter of the bearing nozzles on the proximal side, at which point the stiffness changes sign and the rotor is driven into the stator. Pockets or recesses at the orifice exit may eliminate this crash mechanism,[36] but the reduced response time adversely affects stability at very high speeds unless the pockets are very small.[37]

Highest spinning speeds have been obtained with the design illustrated in Figure 2, which has achieved surface speeds in excess of the speed of sound at room temperature for rotor diameters from 5–14 mm. Half of the bearing gas exits over the ends of the rotor forming an axial thrust bearing at each end, while half exits out the center of the stator. Allowing the gas to flow axially inward as well as outward (nearly) doubles the bearing stiffness (by nearly doubling effective area) and was probably the most significant innovation in the spinner by Langer et al.[38] which achieved a 40% increase in surface speed over previous designs.

Optimum bearing radial clearance for controlling Taylor vortices[39] in the air bearing at moderate speeds is proportional to $(\mu^2 d/c^2\rho^2)^{\frac{1}{3}}$, where μ is the gas viscosity, d is the rotor diameter, c is the velocity of sound, and ρ is the gas density. Optimum clearance r_c for the control of whirl instabilities with minimum friction at high speeds fits the following empirical equation for typical NMR spinners:

$$r_c \cong kT^{0.25}d^{0.4} \text{ (mixed units)} \quad (1)$$

where T is the gas temperature (K), d is the rotor diameter in mm, and k has an approximate numerical value of 0.0027 for nitrogen and 0.0035 for helium with units of $K^{-0.25}$ $mm^{0.6}$; it is necessary to take into account the strain that will occur even in ceramic rotors at top speeds: 0.1% and 0.15% for silicon nitride and zirconia, respectively. Smaller clearances than given by equation (1) may be used if the additional heating can be tolerated, and larger clearances may be used with large rotors if other measures are taken to control whirl instabilities. Optimum bearing hole size is such that bearing

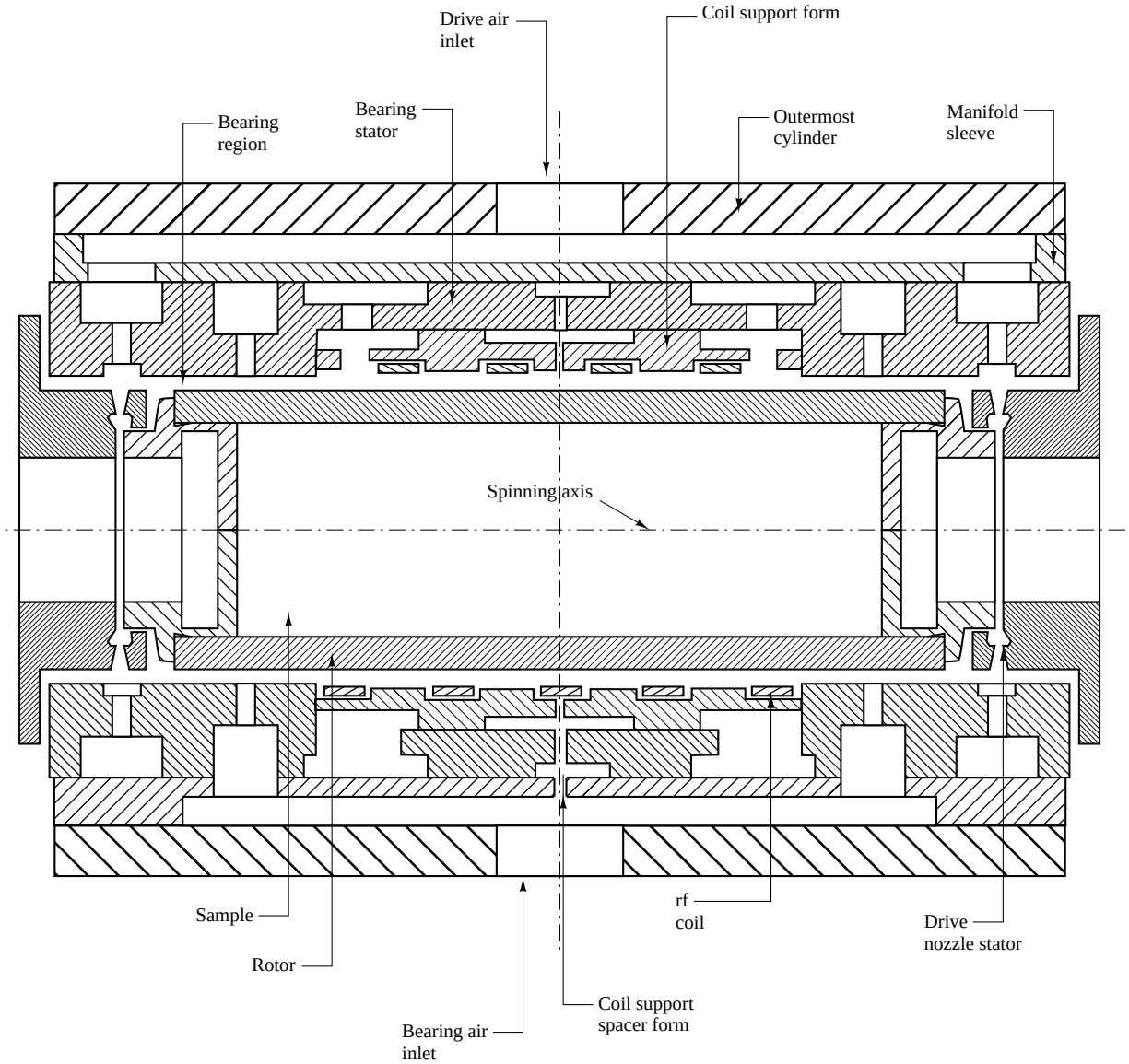

Figure 2 Supersonic sample spinner (Doty Scientific, Inc.)

mass flow at 0.3 MPa with the rotor in place is 60%–85% of the mass flow with the rotor removed. Short bearing hole sizes normally range from 0.13 mm for 3.5-mm rotors to 0.28 mm for 14-mm rotors, but slightly larger long bearing holes work better for VT.

With very small rotors, the bearing clearance becomes extremely critical—partly for manufacturing reasons and partly for fundamental reasons. To appreciate the fundamental limitation, consider the conical resonance frequency,[32] which is approximately proportional to the square root of the quotient of the bearing stiffness and the rotor mass near the end of the rotor. In order for this resonance to scale as $1/d$, the stiffness must be linear with diameter (since the mass is cubic with diameter), which requires the radial clearance to be proportional to the diameter if the pressure is constant. But clearance cannot be linear with diameter or frictional power density on the rotor surface becomes unmanageable with small rotors. Hence, Nature does not like small rotors, and it is in fact fortuitous that 5-mm rotors can achieve supersonic surface speeds (21 kHz) under optimum conditions with nitrogen bearing pressures of 0.5 MPa. While 3.5-mm Si_3N_4 rotors have occasionally reached 27 kHz, they are fraught with instabilities above 24 kHz which are exacerbated by the large, axial Bernoulli effects from poor turbine efficiency.

5.2 Radial-Inflow Microturbines

To achieve surface speeds above 240 m s^{-1} it is necessary to use microturbines in a symmetrical fashion so that axial reaction forces are precisely balanced at all speeds (unless helium drive gas is used), since the load capacity of the axial thrust bearings is quite limited.[40] The reduced-diameter radial-inflow microturbines used in Figure 2 achieve order-of-magnitude higher isentropic efficiency that the earlier Peltier microturbines by (a) controlling flow separation over the blades, (b) operating at lower tip speed, and (c) reducing exhaust swirl.[41] Inlet and exit angles are not particularly critical, but axial clearance over the blades is—unless the turbine is designed for a very low reaction ratio. A vaneless radial-inflow supersonic diffuser may be used with the larger sizes to obtain supersonic, nonseparated flow at the rotor entrance. The microturbines on a 14-mm rotor have 28 blades with 10-mm tip o.d. and produce 25 W shaft power each at 40% isentropic efficiency at 6 kHz. The 2.5-mm o.d. microturbines on the 3.5-mm rotor have only 12 blades and achieve approximately 10% efficiency at 22 kHz. Unlike large turbines, substantial efficiency losses occur in the nozzles (even with the 14-mm spinners) because of boundary layer effects. For an excellent treatment of turbine theory and design, the reader is referred to the text by Wilson.[42]

5.3 Radiofrequency Circuits

Most MAS work requires CP and/or high-power decoupling. Hence, the circuit is essentially identical to that described earlier for the DT wideline probe except that lead inductance may be a little larger,[14] necessitating somewhat higher sample coil inductance for high sensitivity. Maximum $\boldsymbol{B}_1$ is usually 30% less than expected of a similar DT wideline probe, but many wideline experiments are still possible with an MAS probe. For large samples at high fields, it can be beneficial to balance the HF channel for more efficient decoupling—especially at high temperatures. A modified form of the standard ^1H–^2H high-resolution balanced decoupler/lock circuit may be adapted to the high-power requirements of solids.[43]

Wu and Zilm[44] showed that high rf homogeneity is much more important than originally recognized for efficient CP at high speeds and that variable amplitude proton $\boldsymbol{B}_2$ can greatly improve CP efficiency in the presence of large rf inhomogeneity. Leifer[45] recently presented an elegant method of optimizing rf homogeneity for six- and 10-turn solenoids. Many software packages using numerical methods are now available for general field calculations and optimizations, and a few are capable of properly handling nonuniform surface current distributions.[46]

Single resonance circuits can efficiently use very low inductance coils (e.g., two-turn, 6-mm, 18-nH coils) to achieve the short $\pi/2$ pulse lengths (1.5 μs) needed for multiple pulse techniques to average dipolar interactions of abundant ^1H or ^{19}F nuclei.[4] When combined with sample spinning at several kHz to average chemical shift anisotropy, the technique is called combined rotation and multiple pulse spectroscopy (CRAMPS). High resolution in CRAMPS requires extremely high $\boldsymbol{B}_1$ homogeneity. Since wide conductors and leads are required with low-inductance coils (to limit lead voltage, if not losses), the current locations are not known and the method of Leifer and related analytical methods cannot be used to homogenize the field. However, the most difficult technical problem in making CRAMPS probes is usually that of eliminating proton background signals from hydrogenous contaminants in Teflon and even Kel-F.

Triple resonance circuits have been used occasionally for more than a decade,[47] but the development of the powerful rotational echo double resonance (REDOR) technique[48] for accurate distance determinations from weak dipolar couplings has recently resulted in a large demand for triple resonance MAS probes. The circuit shown in Figure 3 uses an inductively coupled HF tank to permit multinuclear tuning at both the middle and the low frequency with high efficiency and excellent isolation on all ports.[49] It has been used successfully for ^1H up to 500 MHz, and can easily be extended to quad resonance experiments such as RETRO.[50] Fixed frequency triple resonance MAS probes for REDOR experiments are expected to be available soon at 750 MHz.

6 GONIOMETERS AND SLOW MAS

The earliest applications of NMR to solids involved the study of single crystals, as relatively narrow lines are observed without multiple pulse or high-speed spinning techniques. These studies are necessarily limited to materials that can be obtained in single crystals of sufficient size (usually several mm^3) for acceptable S/N. The method requires the ability to slowly and precisely rotate the crystal about three orthogonal axes while observing the anisotropic chemical shift. The standard method for the past two decades has involved gluing a small crystal into a three-sided, 4-mm 'semicube'.[6] (Similar probes with larger coils have rotated sealed tubes to study oriented liquid crystals.) The sample may then be inserted into a precision holder inside the sample coil for 360° rotation

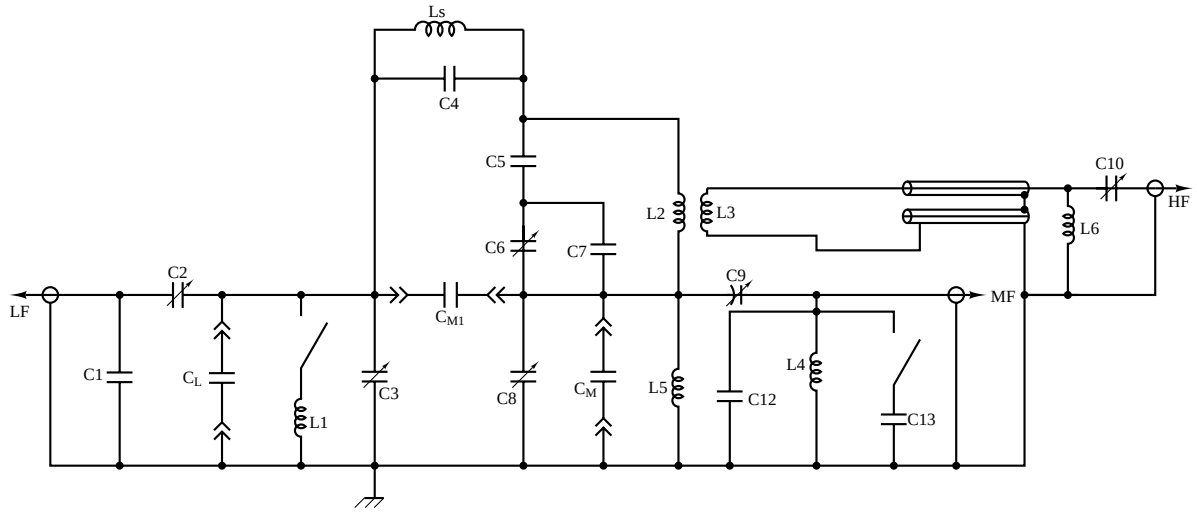

Figure 3 Doubly broadband, triple resonance circuit (Doty Scientific, Inc.)

about an axis perpendicular to $\boldsymbol{B}_0$ in small increments at which spectra are collected. The semicube is then removed and reinserted for rotation about a second axis, and the process is repeated again for the third axis. The crystal orientation with respect to the semicube holder is determined using X-ray crystallographic techniques.

The sample holder axis may be inclined at the magic angle to permit slow MAS, which is a method of addressing the spinning sideband problem by applying pulses precisely at 0°, 120°, and 240°. There is renewed interest in this technique for obtaining high-resolution spectra from large samples of dilute systems. (See ***Magic Angle Turning and Hopping***.)

Rotation has usually been accomplished using precision aluminum or brass bevel gears, but worm gears, belts, and flexible shafts have also been used. The early versions used a manual goniometer, but a stepper motor under computer control is now common. A DT multi-X circuit is usually used.

7 VARIABLE TEMPERATURE (VT)

Most CP MAS probes operate from −120 °C to +160 °C, but XVT CP MAS probes are available for wider temperature ranges, and several methods[51] have been used to cool the drive gas and circumvent liquefaction problems in pressurized nitrogen. Gay[52] optimized the conventional high-resolution sample tube spinner to obtain rotational rates sufficient for many MAS applications (over 3 kHz for 5-mm tubes) with the advantages of greater independence of the sample temperature and spinning characteristics and the ability to spin long, sealed glass tubes at the magic angle. The MAS design of Bartuska et al.[53] also provides clear separation between the VT and the bearing gas.

One manufacturer (Doty Scientific) uses a low-temperature and a high-temperature CP MAS probe, as pictured in Figure 4 along with a standard CP MAS probe, to cover the range from 35 K to over 900 K. In these probes, the electronics are maintained near room temperature and positioned close to the sample to allow multinuclear tuning without excessive lead losses, although lead inductance is increased by about 30 nH over the standard probes. Another manufacturer (Bruker) offers a gas-levitated, laser-heated wideline probe for experiments to 1200 °C.[54] Attempts to provide CP MAS down to 6 K have proven too difficult for commercial success thus far, but a number of research groups[55,56] have performed wideline NMR experiments in the 0.03−3 K range.

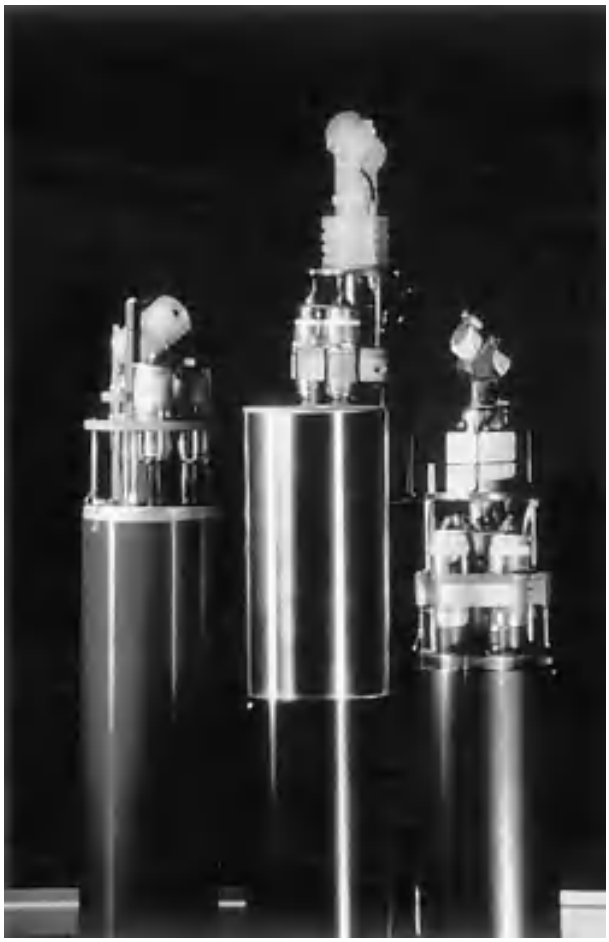

Figure 4 VT CP MAS, low-temperature CP MAS, and high-temperature CP MAS probes

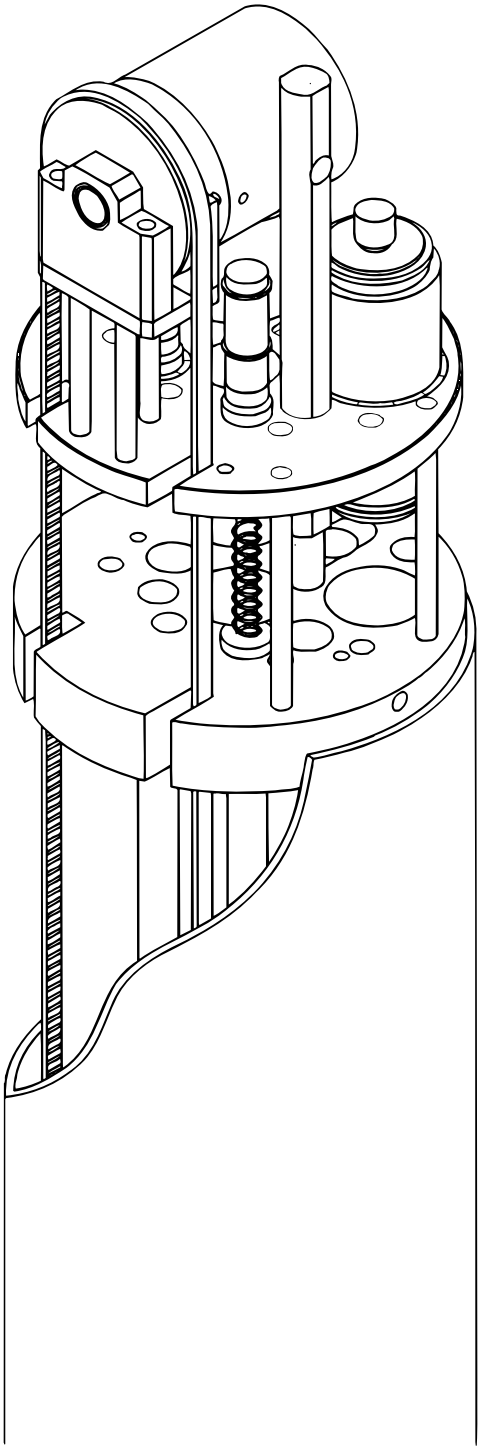

Figure 5 DAS probe with fixed coil and belt-drive spinner reorientation

8 DYNAMIC ANGLE SPINNING (DAS)

High-resolution NMR spectra can be obtained from quadrupolar nuclei if the sample spinning axis can be dynamically reoriented such that the time average of the second and fourth spherical harmonic functions vanishes.[7] The dynamic angle spinning (DAS) probe allows the spinning axis to be rapidly changed while spinning the sample at high speeds to accomplish the required averaging. One early design used a pneumatic system to switch between two fixed angles, but a high-performance servo motor and precision encoder are now standard, as programming flexibility is needed to experiment with the various 'magic angle pairs' such as [0°, 63.43°], [30.56°, 70.12°], and [37.38°, 79.19°].[57]

Two basic approaches have been used: moving coil and fixed coil. The moving coil design has the rf coil mounted on the spinner stator and attached with flexible leads or sliding contacts.[58] The fixed coil design uses a small spinner assembly that can be rotated perpendicular to its spinning axis inside a large rf coil that is perpendicular to the external field and coaxial with the reorientation axis.[59] The first commercial DAS probes used a moving coil, but it was abandoned in favor of the fixed coil because of lead failures, as most DAS experiments are two-dimensional and require millions of flips. The fixed-coil design has inherently poor filling factor, but special spinners and coils are being developed to minimize this drawback.

High-torque, low-inertia servo motors with optimized linkage should permit axis reorientation under 5 ms if the air bearings supporting the sample rotor have sufficient stiffness and load capacity; but control limitations, linkage compliance, and structure vibrations have often resulted in settling times of 25 ms or more.[59] The currently available commercial DAS probe shown in Figure 5 uses a 21-mm diameter rf coil, 8 mm long, and offers a choice of three interchangeable sample spinners: 8.6-mm diameter by 12 mm; 7-mm diameter by 13 mm; and 5-mm diameter by 14 mm. The shortest reorientation times thus far with 8.6-mm rotors are about 15 ms. Half that time may be possible with the 5-mm rotors, but the filling factor is very small. One of the factors contributing to the engineering difficulties is that the motor must be positioned well below the magnet to operate properly, which requires a rather long drive linkage that still must allow easy insertion of the probe into the magnet. The other major technical problem is that rotors with small aspect ratio (length-to-diameter ratio) are required for good filling factor, but a large aspect ratio is needed for bearing stability during rapid reorientation.

9 DOUBLE ROTATION (DOR)

In the DOR technique, the sample is placed in a small spinner inside a larger spinner and spun about two intersecting axes simultaneously to accomplish the time averaging needed to remove dipolar and quadrupolar interactions. It usually comes as a surprise to the uninitiated that such a feat would be possible at high speeds, even though most have observed a football traveling through the air executing free precession—spinning about two axes simultaneously with no significant external torques acting upon it.

The requirement for no net torques on the inner rotor is given by the following:

$$f_1 = \frac{f_2(I_T - I_A)\cos\theta_2}{I_A} \tag{2}$$

where f_1 is the frequency of the inner rotor, f_2 the frequency of the outer rotor, I_A the *axial* moment of inertia of the inner spinner (rotor, sample, caps), I_T the *transverse* moment of inertia of the inner spinner, and θ_2 is the angle of the inner rotor with respect to the axis of the outer rotor.[60]

In practice, the outer rotor is always inclined at the dipolar magic angle, 54.7°, and θ_2 is 30.56°. For stability, (a) f_1 must be a few per cent larger than given by the above, (b) the center of mass of the inner rotor must lie precisely on the axis of the outer rotor, and (c) the outer rotor must be dynamically balanced when the inner rotor is removed. The highest double rotation rates thus far are approximately 1800 Hz outer and 7000 Hz inner for 0.1-mL samples. The outer spinner assembly of a DOR spinner is shown in Figure 1, inclined at 54.7°. (The braid-reinforced lines entering each end of the assembly supply air to the inner spinner.)

10 RELATED ARTICLES

Ceramics Imaging; CRAMPS; Double Rotation; Dynamic Angle Spinning; Magic Angle Spinning; Probe Design and Construction; Probes for Special Purposes

11 REFERENCES

1. S. R. Hartmann and E. L. Hahn, *Phys. Rev.*, 1962, **128**, 2042.
2. P. Mansfield and J. G. Powles, *J. Sci. Instrum.*, 1963, **40**, 232.
3. J. S. Waugh, US Pat. 3 530 373, 1970.
4. R. W. Vaughan, *Annu. Rev. Phys. Chem.*, 1978, **29**, 397.
5. E. O. Stejskal, J. Schaefer, and J. S. Waugh, *J. Magn. Reson.*, 1977, **28**, 105.
6. R. S. Honkonen, F. D. Doty, and P. D. Ellis, *J. Am. Chem. Soc.*, 1983, **105**, 4163.
7. B. F. Chmelka and A. Pines, *Science*, 1989, **246**, 71.
8. S. J. Schneider (ed.), *Engineered Materials Handbook*, *Vol. 4, Ceramics and Glasses*, ASM International, Novelty, OH, 1991.
9. R. C. Buchanan (ed.), *Ceramic Materials for Electronics*, Marcel Dekker, New York, 1991.
10. J. Agranoff (ed.), *Modern Plastics Encyclopedia*, McGraw-Hill, New York, 1982.
11. J. J. O'Dwyer, *The Theory of Electrical Conduction and Breakdown in Solids Dielectrics*, Oxford University Press (Clarendon), London/New York, 1973.
12. D. R. Lide (ed.), *CRC Handbook of Chemistry and Physics*, 73rd edn., CRC Press, Boca Raton, FL, 1992.
13. J. D. Swift, in *The Encyclopedia of Physics*, 2nd edn., ed. R. M. Besancon, Van Nostrand Reinhold, New York, 1974, pp. 249–253.
14. F. D. Doty, T. J. Connick, X. Z. Ni, and M. N. Clingan, *J. Magn. Reson.*, 1988, **77**, 536.
15. S. L. Patt, US Pat. 4 438 400, 1984.
16. D. G. Hughes and L. Pandey, *J. Magn. Reson.*, 1984, **56**, 428.
17. M. L. Buess and G. L. Petersen, *Rev. Sci. Instrum.*, 1978, **49**, 1151.
18. F. D. Doty, US Pat. 4 710 719, 1987.
19. D. I. Hoult and R. E. Richards, *J. Magn. Reson.*, 1976, **24**, 71.
20. D. I. Hoult, *Prog. Nucl. Magn. Reson., Spectrosc.*, 1978, **12**, 41.
21. R. W. Vaughan, D. D. Elleman, L. M. Stacey, W. K. Rhim, and J. W. Lee, *Rev. Sci. Instrum.*, 1972, **43**, 1356.
22. F. D. Doty, R. R. Inners, and P. D. Ellis, *J. Magn. Reson.*, 1981, **43**, 399.
23. W. G. Clark and J. A. McNeil, *Rev. Sci. Instrum.*, 1973, **44**, 844.
24. G. C. Chingas, *J. Magn. Reson.*, 1983, **54**, 153.
25. D. I. Hoult, *J. Magn. Reson.*, 1984, **57**, 394.
26. M. Greferath, B. Blumich, W. M. Griffith, and G. L. Hoatson, *J. Magn. Reson., Ser. A*, 1993, **102**, 73.
27. E. R. Andrew, A. Bradbury, and R. G. Eades, *Nature (London)*, 1958, **182**, 1659.
28. J. D. Ellett, M. G. Gibby, U. Haeberlen, L. M. Huber, M. Mehring, A. Pines, and J. S. Waugh, in *Advances in Magnetic Resonance*, ed. J. S. Waugh, Academic Press, New York, 1971, Vol. 5, pp. 117–176.
29. E. Andrew, L. Farnell, M. Firth, T. Gladhill, and I. Roberts, *J. Magn. Reson.*, 1969, **1**, 27.
30. J. W. Beams, *J. Appl. Phys.*, 1937, **8**, 795.
31. E. T. Lippmaa, M. A. Alla, A. A. Salumyae, and T. A. Tukherm, US Pat. 4 254 373, 1981.
32. F. D. Doty and P. D. Ellis, *Rev. Sci. Instrum.*, 1981, **52**, 1868.
33. J. Adlerborn, M. Burstrom, L. Hermansson, and H. T. Larker, *Mater. Design*, 1987, **8**, 229.
34. W. T. Dixon, J. Schaefer, M. D. Sefcik, E. O. Stejskal, and R. A. McKay, *J. Magn. Reson.*, 1982, **49**, 341.
35. V. J. Bartuska and G. E. Maciel, *J. Magn. Reson.*, 1981, **42**, 312.
36. W. B. Rowe, *Hydrostatic and Hybrid Bearing Design*, Butterworths, London, 1983.
37. F. D. Doty, US Pat. 4 456 882, 1984.
38. V. Langer, P. Daugaard, and H. J. Jakobsen, *J. Magn. Reson.*, 1986, **70**, 472
39. D. Dowson (ed.), *Superlaminar Flow in Bearings*, MEP, London, 1975.
40. F. D. Doty, J. B. Spitzmesser, and D. G. Wilson, US Pat. 5 202 633, 1993.
41. F. D. Doty, B. L. Miller, G. S. Hosford, D. G. Wilson, W. Huanbo, and J. D. Jones, *Proc. IECEC-91*, 1991, Vol. 2, SAE, Warrendale, PA, p. 436.
42. D. G. Wilson, *The Design of High-Efficiency Turbomachinery and Gas Turbines*, MIT Press, Cambridge, 1984.
43. F. D. Doty, US Pat. 5 162 739, 1992.
44. X. Wu and K. Zilm, *J. Magn. Reson., Ser. A*, 1993, **104**, 154.
45. M. C. Leifer, *J. Magn. Reson., Ser. A*, 1993, **105**, 1.
46. G. J. Kost, S. E. Anderson, G. B. Matson, and C. B. Conboy, *J. Magn. Reson.*, 1989, **82**, 238.
47. S. Kan, M. Fan, and J. Courtieu, *Rev. Sci. Instrum.*, 1980, **51**, 887.
48. T. Gullion and J. Schaefer, in *Advances in Magnetic Resonance*, ed. W. S. Warren, Academic Press, San Diego, CA, 1989, Vol. 13, pp. 57–83.
49. F. D. Doty, 'Doubly Broadband Triple Resonance Circuit', US Pat. 5 424 645, 1995.
50. S. M. Holl, R. A. McKay, T. Gullion, and J. Schaefer, *J. Magn. Reson.*, 1990, **89**, 620.
51. R. D. Kendrick, S. Friedrich, B. Wehrle, H. H. Limbach, and C. S. Yannoni, *J. Magn. Reson.*, 1985, **65**, 159.
52. I. D. Gay, *J. Magn. Reson.*, 1984, **58**, 413.
53. V. J. Bartuska, D. H. Lewis, R. B. Lewis, and D. G. Dalbow, US Pat. 4 511 841, 1985.
54. D. Massiot, C. Bessada, P. Exchegut, J. P. Coutures, and F. Taulelle, *Solid State Ionics*, 1990, **37**, 223.
55. K. Carduner, M. Villa, and D. White, *Rev. Sci. Instrum.*, 1984, **55**, 68.
56. J. L. Weil, S. L. Tan, J. S. Waugh, and D. D. Osheroff, *J. Magn. Reson.*, 1987, **66**, 264.
57. B. Q. Sun, J. H. Baltisberger, Y. Wu, A. Samoson, and A. Pines, *Solid State NMR*, 1992, **1**, 267.
58. K. T. Mueller, B. Q. Sun, G. C. Chingas, J. W. Zwanziger, T. Terao, and A. Pines, *J. Magn. Reson.*, 1990, **86**, 470.
59. K. T. Mueller, G. C. Chingas, and A. Pines, *Rev. Sci. Instrum.*, 1991, **62**, 1445.
60. Y. Wu, B. Q. Sun, A. Pines, A. Samoson, and E. Lippmaa, *J. Magn. Reson.*, 1990, **89**, 297.

Biographical Sketch

F. David Doty. *b* 1950. B.A., 1972, physics, Anderson University, IN, USA, Ph.D., 1983, Physics, University of South Carolina. Began work in NMR under Paul Ellis, 1979. President of Doty Scientific, Inc., 1982–present. Approx. 20 publications and 15 patents. Research interests include rf electronics, NMR probe technology, electromagnetism, manufacturing, turbomachinery, energy conversion cycles, ceramics engineering, acoustics, economics, and religions.

Spectrometers: A General Overview

Howard D. W. Hill

Varian Associates, Palo Alto, CA, USA

1	Introduction	1
2	Historical Background	1
3	Magnets for NMR Spectrometers	3
4	Probes	6
5	Spectrometer Electronics	7
6	Auxiliary Systems	12
7	Conclusion	12
8	Related Articles	12
9	References	13

1 INTRODUCTION

In the most general sense, any instrument for recording a nuclear magnetic resonance signal may be regarded as an NMR spectrometer. As such it can include devices as diverse as magnetometers used for the measurement of magnetic fields, instruments to measure *relaxation* times (either for fundamental physical studies or for applications to process analysis), instruments to study the details of the nuclear spin response in the frequency domain, and magnetic resonance *imaging* systems in which the frequency of the NMR response is associated with position within an object. As NMR spectroscopy developed, some of these applications required quite different instrumentation. In recent years, a number of the instrumental requirements for many of these applications have tended to converge. The aim of this article is to provide an overview of the components and operation of NMR spectrometers. The emphasis will be on spectrometers used for analytical applications, although differences for other applications will be indicated.

Since the function of any NMR spectrometer is to excite and detect nuclear spin responses, it must include certain components. This minimum set is: a magnetic field to polarize the spins, an rf system to generate the excitation, a coil or coils to couple the excitation to the spins and to receive the NMR response, a detection system to amplify and detect the spin response, and an output device for displaying the spin response. In addition, some form of control mechanism is required for these various components. For many applications, further components and features are included to condition the sample in some way, e.g. temperature control or sample spinning, to provide the information of interest.

A constant theme in the development of NMR spectrometers and the practice of NMR spectroscopy for analytical applications has been the quest for improving the *sensitivity* of the method. The nuclear magnetization, which is the origin of the NMR signal, is proportional to $\exp(-h\omega/kT)$. Thus, two parameters can be manipulated to control the available signal, namely the resonance frequency (expressed in radian s^{-1}), ω, and the sample temperature, T. The operating temperature is usually dictated by the nature of the problem to be investigated, so the operating frequency is often the only fundamental parameter which can be varied to improve the available signal. An important aspect of the development of NMR spectrometers has been the continuing trend toward the use of higher magnetic field strengths to provide a higher resonance frequency for a given nuclear species. The available signal is proportional to both the nuclear magnetization and the resonance frequency. Thus for a given nuclear species, the available signal varies as the square of the NMR frequency. Noise considerations reduce the overall sensitivity slightly to $\omega^{\frac{7}{4}}$.[1] The gains from operating at higher frequencies are clearly very significant.

A further facet of spectrometer development for a number of applications has been to increase the resolution of spectral information. The use of higher magnetic fields has contributed here also and, in addition, experimental techniques have been extended to involve multiple irradiation, the study of a wide range of nuclear species and the use of multidimensional Fourier transform methods. For solid samples, which normally have very broad lines, a number of techniques have been developed to remove some of the interactions leading to that broadening. The development of NMR spectrometers has been intimately related to the development in techniques.

2 HISTORICAL BACKGROUND

2.1 Early Spectrometers

The earliest investigators[2,3] used a continuous radiofrequency source to excite the spin response and a variable magnetic field to sweep through the resonance lines. This is the essence of the continuous wave (CW) NMR spectrometers. An equivalent operation of maintaining a constant field while sweeping the frequency was used a little later. In these methods the steady-state response of the spins to an rf excitation is recorded. Torrey[4] and Hahn[5] introduced alternative methods for recording the transient response to a pulsed excitation. The response was detected following the pulse as the spins relaxed towards equilibrium. The two methods evolved independently, with the CW methods focusing on the details of the resonance lineshapes while the pulse methods focused on the study of relaxation times

The observation of chemically shifted resonances in nitrogen spectra by Proctor and Yu[6] stimulated efforts to improve the homogeneity and stability of the magnets used in the experiments and led to the observation of chemically shifted resonances in proton spectra.[7] This was the basis for the development of NMR spectroscopy as an analytical tool for chemistry and initiated a rapid growth in the development of CW NMR spectrometers. Pulse spectrometers developed less rapidly as their applications were much more limited.

In general, the nuclear spin response is very weak in comparison with the rf excitation. An important consideration for an NMR spectrometer is the isolation of these two signals so that the receiver is not overwhelmed by the excitation signal.

The design of the probe was an important factor. Purcell and his co-workers developed a bridge circuit[2,8] to buck out

the majority of the transmitter signal. Bloch and his colleagues developed a crossed coil probe[3,9] in which the direct coupling of the transmitter signal into the receiver was minimized by the orthogonal arrangement of two coils. Pulse methods originally used one of these two designs but, later, switching schemes which exploited the fact that the transmitter and receiver were active sequentially were developed.

A further important development was the use of modulation coupled with phase-sensitive detection at the modulation frequency.[10–12] Modulation is usually applied to the magnetic field, although frequency modulation is also possible. For broad resonance lines, for which the linewidth is greater than the amplitude of the modulation, the output signal is proportional to the derivative of the resonance line. However, when the amplitude of the modulation is greater than the width of the resonance line, the response is more complicated. When the modulation frequency is much greater than the resonance linewidth, distinct sideband responses are generated. Excitation can then occur at a frequency

$$\omega_0 = \omega_t \pm n\omega_m = \gamma B_0 \tag{1}$$

where ω_0 is the resonance frequency at a magnetic field B_0, ω_t is the transmitter frequency, ω_m is the modulation frequency, n is an integer, and γ is the magnetogyric ratio of the nuclear spins.

Several important features derive from this relationship. First, the transmitter and receiver frequencies can be separated by the modulation frequency. When field modulation is used, there is no radiofrequency signal at the receiver frequency in the absence of an NMR response. Separating the weak NMR response from the strong excitation then becomes much simpler. Second, narrow band detection methods may be used by phase detecting the signal at the modulation frequency, Third, the effective frequency of the excitation can be changed by changing the modulation frequency and the excitation amplitude by changing the modulation amplitude. Since the modulation frequency is usually a few kHz, this represents a much more convenient method of sweeping the excitation frequency than by variation of the radiofrequency itself.

An alternative to field or frequency modulation is pulse modulation, first proposed by Arnold in 1955,[11,13,14] in which the spin response is detected in the periods between pulses used for excitation. A sequence of pulses of width t separated by an interval T has a frequency spectrum with components at frequencies

$$\omega_n = \omega_0 \pm 2\pi n/T \tag{2}$$

and amplitudes

$$A_n = \sin(n\pi t/T)/(n\pi t/T) \tag{3}$$

This method was not widely adopted for CW spectrometers but is used in some cases in more modern spectrometers, for example, in the field/frequency lock channel and for homonuclear decoupling in a high-resolution Fourier transform spectrometer.

2.2 Requirements for Resolution and Stability

The natural linewidths in liquid samples can be extremely small, so that an important instrumental development was the improvement of magnet homogeneity and stability. Any variation of the magnetic field strength over the volume of the sample causes a smearing of the resonance lines and a consequent degradation of resolution. In addition to the improvement of the basic magnet performance, resolution was improved by spinning the sample[15,16] and by the use of electric shims.[17,18] Stability was enhanced by the introduction of flux stabilizers[19] and field/frequency lock systems.[20,21]

2.3 Double Resonance Methods

Double resonance methods were first introduced in the study of the interaction of electron and nuclear spins,[22] and theoretically analyzed by Overhauser.[23] The first use of double resonance methods for purely nuclear spectroscopy was by Royden[24] for the detection of a weak resonance through its coupling to a strong resonance. Such 'indirect detection' techniques have become very important in modern high-field spectroscopy. Shortly after Royden's experiments, the use of a second irradiation frequency within the spectral range of the observed nucleus was introduced[25,26] as a method to aid in the analysis of spectra. An additional frequency could be added relatively easily to a spectrometer operating in the CW mode with modulation sidebands by the use of an additional modulation frequency. When the coupling of a different nuclear species was to be removed, a second radiofrequency channel was required. The concept of broadband decoupling was introduced in 1966 by Ernst[27] to remove all the couplings of one nuclear species from another.

2.4 Improvements in Sensitivity

Since NMR is an inherently insensitive technique, there has been a continual quest to improve the sensitivity of spectrometers. Methods employed have been to improve the signal, reduce the noise, and improve the signal processing methods.

Signal intensity has been improved by increasing the spin polarization or by using a larger sample. The use of a larger sample places a more stringent requirement on the uniformity of the magnetic field and has been rather limited. The sample volumes used for analytical applications have not changed dramatically from the earliest NMR spectrometers. Improvements in magnet technology, on the other hand, have occurred and NMR spectrometers now operate with superconducting magnets at field strengths up to 18 T.

Spectrometers have been built to exploit the sensitivity advantage available through coupling to electron spins in the sample.[28,29] In some cases, the sensitivity can be improved by saturation of electron spin resonance transitions but the method lacks generality to be widely useful. By contrast, the sensitivity to be gained through the nuclear Overhauser effect in the study of nuclei such as ^{13}C and ^{15}N is extensively exploited.

Reduction in the noise associated with the detection of NMR signals has occurred through a number of factors. The introduction of modulation was a contributor in that it allowed the use of phase-sensitive detection at the modulation frequency and the avoidance of some of the low-frequency contributions to the noise. These gains more than offset a

reduction of the basic sensitivity by $\sqrt{2}$ because the signal was only present at one sideband while the noise was present at two. Ernst[30] recognized that this loss could be recovered by the use of quadrature detection. Improvements in probe circuits and receivers have had continual small effects on the overall noise performance.

A number of signal processing techniques have had a profound impact on the overall sensitivity of spectrometers. The advent of digital techniques allowed the easy summation of a number of separate recordings of the resonance signal. This technique, known as time averaging,[31] allowed the possibility of much longer recording times without the introduction of noise due to very low-frequency phenomena, such as spectrometer drift. Since coherent signals add directly and random noise adds as the square root of the number of additions, the improvement in sensitivity provided by time averaging is proportional to the square root of the number of additions.

2.5 Fourier Transform Methods

A major improvement for high-resolution spectroscopy was the introduction of *Fourier transform* methods. The CW method of spectroscopy requires a sequential sweep through the resonance lines of a spectrum. For a complex spectrum containing many resonance lines, the total time to record the spectrum is therefore many times the time needed to sweep through a single resonance line. If all the lines could be excited and their responses recorded simultaneously, a significant saving in spectrometer time would be possible. The significance of this was recognized by Varian[32] but the practical realization was made by Ernst and Anderson.[33] They used a short pulse to excite a wide range of chemically shifted resonances and digitized the subsequent free induction response of the spins. Fourier transformation of the response provided the spectral response. The time taken to record the free induction signal is independent of the number of distinct resonance frequencies and is approximately equal to the time required to sweep through a single resonance line. The time reduction afforded by this method compared with the CW technique is the ratio of the total range of the spectrum to the width of an individual resonance line. For a typical proton spectrum at 60 MHz (the frequency of the original experiments), this ratio is about 600. The time averaging method was immediately applicable so that the response could be summed 600-times in the time taken for a single spectral sweep.

At the time of the pioneering experiments of Anderson and Ernst, the data handling necessary for the Fourier transformation and the subsequent spectral display was a very time-consuming process, so that the potential benefits of the technique were not immediately realized. However, small computer systems were developing rapidly and it was soon practical to add a computer to a spectrometer. The introduction of improved algorithms[34] for the calculation of Fourier transforms also had a significant impact on the practicality of the Fourier transform method. Initially, the spectrometers were capable of operating in both the CW and pulsed Fourier transform mode, but by about 1974 instruments operating solely in the Fourier transform mode were available and, soon afterwards, dual mode instruments ceased to be built. Detailed descriptions of spectrometers for liquids[35] and solids[36] applications were published in *Advances in Magnetic Resonance*.

The pulsed mode of operation meant that instruments designed for high-resolution applications now shared some similarities with instruments designed for solids applications. Initially the timing and pulse power requirements were very different but, over time, these differences have gradually diminished. Now it is common for a single instrument to be capable of a wide range of different experiments for both solids and liquids applications.

Spectrometers designed to study nuclei other than protons were relatively uncommon before the introduction of Fourier transform methods. With the Fourier transform technique, the study of insensitive nuclei, such as ^{13}C, became very practical and instruments were designed specifically to study ^{13}C NMR.

A number of alternative schemes for simultaneous, or near simultaneous, excitation of a spectrum were proposed shortly after the introduction of the pulsed FT method. *Stochastic excitation*[37,38] used a pseudorandom noise source as the excitation. By correlating the spin response with the excitation, the spectral response could be calculated. It offered the advantage of lower peak power excitation but more complexity in data handling, and has received only minor attention. A second method involves a very rapid sweep through the spectrum. It was observed in the early days of CW spectroscopy that sweeping too rapidly through a resonance line caused 'wiggles' following the line. These were an annoyance in conventional CW spectroscopy but could be exploited, again by making a cross correlation between excitation and response, to produce a spectrum. This technique was dubbed 'correlation spectroscopy'[39] and is in use in a few laboratories and in some low-cost commercial spectrometers.

2.6 Additional Developments

In 1974, Jeener[40] introduced the idea of *two-dimensional* spectroscopy. This was exploited by Ernst and his coworkers[41,42] and has extended the applications of NMR spectroscopy enormously. As computers have developed, NMR spectrometers have incorporated more computing power to provide control for the pulse sequences required for multidimensional spectroscopy, and also for the analysis of the data. The method has further been extended to three and four dimensions to provide even greater resolving power.

A different application of spectroscopy was spawned by the idea of Lauterbur[43] to introduce magnetic field gradients to the sample region. The concept was to couple the resonance frequency to spatial position within the sample by the imposition of one or more field gradients, and hence to be able to provide a spin density map of the sample. Ernst and coworkers[44] applied the ideas of multidimensional spectroscopy to the method and this has led to the development of magnetic resonance imaging systems. Such instruments share a great deal in common with a pulsed Fourier transform spectrometer for analytical applications. Coils to provide to provide linear gradients along three orthogonal axes are provided and large magnets have been developed to allow the study of larger samples, in particular the human body.

3 MAGNETS FOR NMR SPECTROMETERS

3.1 Introduction

Except for magnetometers, which are used to measure an available magnetic field, the magnet is a key element of the spectrometer. For most NMR applications, the major considerations for magnets are field strength, field uniformity, and stability. The uniformity and stability must be sufficiently high that the inherent properties of the NMR responses can be observed. In liquid samples, the relaxation times can be many seconds, so that natural linewidths may be much less than 1 Hz. In solid samples, resonance lines are broadened to tens or hundreds of kHz by static dipole or quadrupole interactions, or chemical shift anisotropies. Even for the study of these broad resonances, the magnetic field should be uniform to about 1 part in 10^4 over the volume of the sample, whereas for high-resolution liquids applications the uniformity should be up to 1 part in 10^9 or better. For imaging applications the uniformity requirement is typically about 1 part in 10^7. Stability must be commensurate with these values to avoid degrading the resonance signals over the duration of a measurement which, in some cases, may extend to many hours or even several days. For the most demanding applications, the basic uniformity of the magnet is improved by a number of means including shimming and sample spinning and the stability is improved by the use of field/frequency lock systems and the use of persistent superconducting magnets.

3.2 Magnet Types

For laboratory applications, three main types of magnets have been used for spectrometers. These are permanent magnets, electromagnets, and superconducting magnets. The basic configuration of these three types of magnet is shown in Figure 1.

3.2.1 Permanent Magnets and Electromagnets

Permanent and electromagnets typically produce the magnetic field between two parallel pole faces. These are mounted on cylindrical pole pieces which are in turn connected by an iron yoke to complete the magnetic circuit. In the permanent magnet, the pole pieces are made from a material with a high remanence which is magnetized by passing a high charging current through energizing coils wound around them. A typical magnetic field for a permanent magnet for NMR applications is 1.4 T corresponding to a proton resonance frequency of 60 MHz. In an electromagnet the magnetizing force is provided by passing current continuously through coils around the pole pieces. Again, an iron yoke completes the magnetic circuit. Magnetic fields up to about 2.3 T, corresponding to a proton resonance frequency of 100 MHz, can be produced by an electromagnet. The limit on the attainable field is the magnetic saturation of the pole piece and the pole cap. In order to provide the field homogeneity necessary for NMR, the ratio of pole diameter to pole gap is fairly high (greater than 10) and the pole caps are carefully shaped.[45,46] A typical 2.3 T electromagnet for NMR applications has a pole diameter of 12 in. and weighs about 2 tons. The electric power consumption is several kilowatts and water cooling is required for the magnet coils.

Electromagnets have also been used for imaging applications but in the form of multiple solenoid windings with no

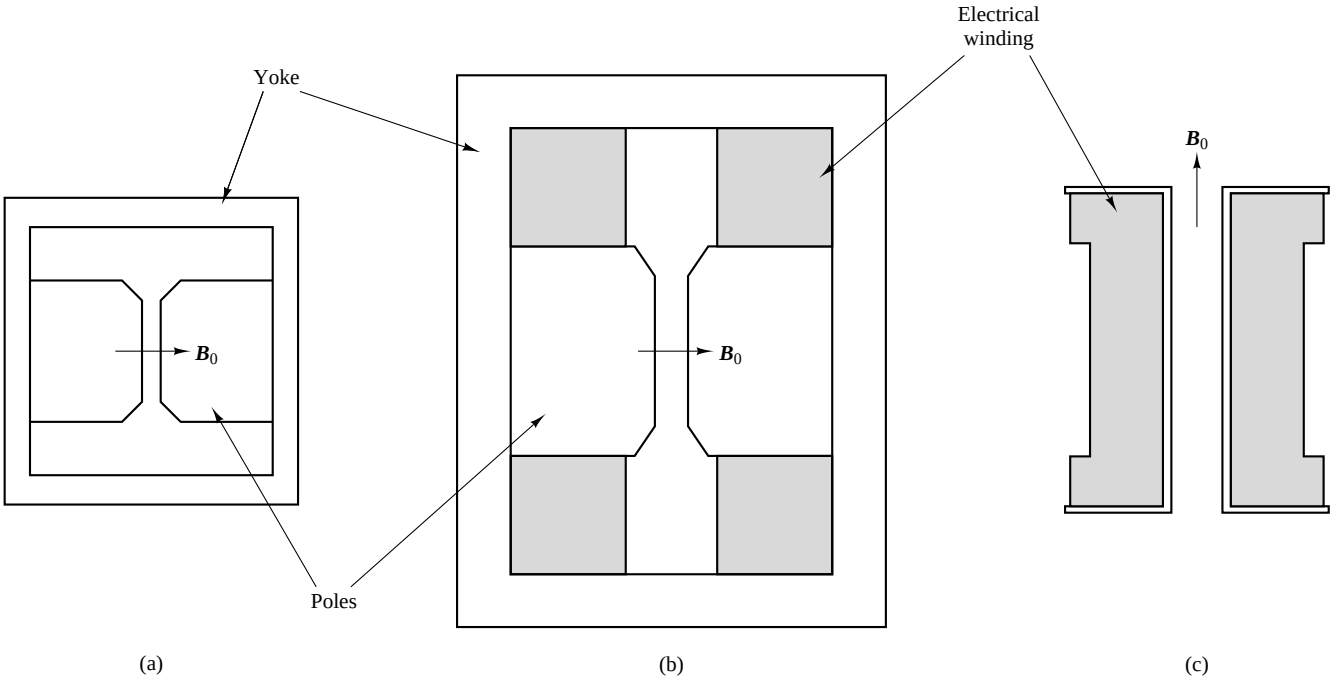

Figure 1 Cross-sections of (a) permanent magnet, (b) electromagnet, and (c) superconducting magnet. For high-resolution applications, a permanent magnet is usually enclosed in a temperature controlled and magnetically shielded enclosure. An electromagnet usually requires water cooling of the coils and a superconducting magnet must be cooled in a bath of liquid helium

iron yoke. They are limited to the generation of a magnetic field of about 0.3 T.

3.2.2 Superconducting Magnets

Because of the high power consumption and limited magnetic field capability, the use of electromagnets, for most applications, has been superseded by superconducting magnets. Their configuration is generally in the form of a multilayer solenoid wound with a superconducting wire and maintained in a bath of liquid helium. Since the majority of NMR experiments are performed with the sample at or near room temperature, the cryostat for the liquid helium is designed with a room temperature access to the bore of the magnet. For spectroscopic applications, the bore diameter is between 50 and 100 mm. For imaging applications, the bore diameter is up to 1 m. Most cryostats also include a liquid nitrogen reservoir and thermal shields to provide cooling to minimize the loss of liquid helium.

To provide the homogeneity needed for NMR applications the superconducting solenoid is wound with additional turns toward the ends.[47,48] The design of these windings is critical to the performance of the magnet. The type of wire used for a superconducting magnet depends on the field strength required. For fields up to 9.4 T (400 MHz for protons), niobium–titanium is used as the superconductor. The superconducting alloy is arranged as one or more filaments in a copper sheath. This type of wire is very ductile and can be readily wound into a solenoid. For higher magnetic fields, niobium–tin is used as the superconductor. This is a very brittle material and cannot usually be manipulated to wind a solenoid. Consequently the magnet solenoid is wound with a wire containing niobium and bronze and is subsequently heat-treated to form the niobium–tin superconductor. Only the inner portions of the magnet need be made in this way. The outer sections of the solenoid which experience lower fields can be wound with niobium–titanium. Magnets using niobium–tin can produce fields in excess of 20 T. The highest field magnet suitable for high-resolution NMR applications is currently 17.6 T (750 MHz for protons). Higher field high-resolution magnets are being designed.

The use of high-temperature superconductors has not yet had an impact on magnets for NMR spectrometers. However, it does appear that these materials offer the possibility of still higher magnetic field strengths when operated at liquid helium temperatures, or the possibility of intermediate field strengths when operated at higher temperatures with simplified cryogenic requirements.

Electromagnets and superconducting magnets can operate at different magnetic fields simply by changing the current through them. However, because of the stability and homogeneity requirements, most NMR spectrometers operate with a fixed magnetic field. Superconducting magnets are nearly always designed to operate in the persistent mode in which the terminals of the solenoid are connected by a superconducting link. The current leads used to energize the magnets can then be removed to minimize thermal losses into the helium bath. The superconducting magnet is effectively a permanent magnet as long as the cryogens are maintained. Operated in the persistent mode, a superconducting magnet may be sufficiently stable for some NMR applications (e.g. solids and imaging) without any additional stabilization. For high-resolution liquids applications, it is still necessary to provide additional stabilization against long term drift and environmental fluctuations.

3.3 Shimming and Homogeneity Improvement

Magnet uniformity can be improved by '*shimming*', a term which derives from the use of thin metallic shims placed between the pole pieces and the yoke of a magnet to adjust the alignment of the pole faces.

The magnetic field can be expressed as a uniform field plus a series expansion of orthogonal field gradients. Expressed in spherical coordinates, the field at a point (r,θ,φ) may be written as

$$B_0 = \sum_{l=1}^{\infty} \sum_{m=1}^{l-1} r^{l-1} P_{l-1}^{m}(\cos\theta)[a_l^m \cos(m\varphi) + b_l^m \sin(m\varphi)] \qquad (4)$$

where $P_l{}^m(\cos\theta)$ are associated Legendre functions of order l and degree m. A significant improvement in magnetic field homogeneity was made by the introduction of 'electric shims'.[17,18,49] These consist of a set of coils, each one of which is designed to produce a particular field gradient. Gradients inherent in the magnet, either from the design or construction, can then be canceled by the appropriate adjustment of currents in the shim coils. The shim coil currents are adjusted by the operator, or by a computer, to optimize a parameter of the spectrum.

Superconducting magnets include a number of superconducting shim coils for correction of the lower order gradients. In addition, magnets designed for high-resolution applications also include a more extensive set of shim coils in the room temperature bore of the magnet.

An alternative to current shims is the use of passive shims,[50,51] pieces of magnetizable material positioned within the magnet bore to modify the field distribution. This type of shimming is used extensively in imaging magnets where, once corrected, there is no further need to adjust the field homogeneity.

An early technique to improve resolution was to spin the sample about its axis.[15,16] If the spinning speed is fast compared with the spread of resonance frequencies across the sample, field inhomogeneities perpendicular to the spinning axis are averaged. The inhomogeneities cause a field modulation in the spinning sample and modulation sideband signals (spinning sidebands) are generated. Sidebands arising from this mechanism can easily be reduced to less than 1% of the intensity of their parent peak, but are still an unwelcome annoyance in spectra. Spinning sidebands are also produced by inhomogeneities in the radiofrequency field of the probe and by small eccentricities in the spinning axis caused by imperfections in the sample tube and spinning mechanism. It is sometimes difficult to reduce these sidebands below 1%. With the introduction of multiple dimensional methods and techniques which rely on the cancellation of signals, the effects of sample spinning have become intolerable. To maintain field uniformity without the averaging effects of sample spinning, more extensive shim coil systems, which correct for many more field gradients, have been introduced. It is quite common for a shim system to include more than 20 gradient coils and up to 40. Fortunately, most of these only need to be adjusted

once at the installation of the magnet. In normal operation, only a few of the gradients require optimization.

To improve the resolution of an NMR spectrometer by operating at higher magnetic fields, the relative homogeneity of the magnet system must improve. This has proved to be possible by careful attention to construction details and by improved shim coil systems. The specified resolution of a commercial high-resolution spectrometer operating at a proton frequency of 600 MHz is approximately the same as that of a 60 MHz spectrometer of 30 years ago.

3.4 Magnetic Field Gradients

While improvement of the magnetic field homogeneity is an important aspect of the operation of NMR spectrometers, a number of important applications exploit the presence of field inhomogeneities. If a spin echo experiment[52,53] is performed in the presence of a known linear field gradient, the self-*diffusion* coefficients of the sample can be measured. The measurement was first made with a static field gradient[54] but later with pulsed *field gradients*.[55–57]

Magnetic resonance imaging relies on the use of magnetic field gradients to couple the resonance frequency with the spatial position within the sample. In the earliest experiments,[43,44] the shim coils were used to provide the gradients. These are generally too weak to provide adequate gradient strengths, so additional coils are included to provide linear gradients dB_0/dx, dB_0/dy, and dB_0/dz. Most applications require rapid switching of the field gradients and eddy current effects must be avoided. This is done by shaping the current driving pulse to compensate for eddy currents or by the use of shielded gradients[58] which minimize the generation of eddy currents in surrounding structures.

In high-resolution experiments, a pulsed field gradient was first introduced to suppress undesirable transverse magnetization in a spin–lattice relaxation time measurement.[59] For this application, the 'homospoil' pulses were provided by pulsing the current to one of the magnet shim coils. More recently, the use of field gradients has become very important for the selection of coherence pathways[60–62] and it is usual to include gradient coils as part of the probe assembly to allow more rapid gradient switching and to keep the coil physically as small as possible for the greatest efficiency.

4 PROBES

The *probe* is a critical component of an NMR spectrometer. It provides the coupling between the nuclear spins and the spectrometer by generating and responding to a radiofrequency magnetic field perpendicular to the polarizing magnetic field.

For a given field strength and sample size, the performance of the probe defines the sensitivity of the spectrometer.[1] The efficiency of the coupling of the probe coil to the sample determines the signal induced by the spin system while Johnson noise in the probe coil, and sometimes in the sample itself, is the major source of noise in a spectrometer. Two key probe parameters are the filling factor and quality factor (Q). The filling factor is a measure of the energy stored in the transverse magnetic field coupling to the sample, compared with the total magnetic energy stored in the resonant circuit. The Q of the probe circuit is proportional to the ratio of the energy stored in the resonant circuit to the power dissipated through resistive losses. Thus, both filling factor and Q should be as high as possible for the maximum sensitivity. Other parameters of importance in the probe are the uniformity of the rf field and the ability to recover rapidly following a strong rf pulse. For some measurements, the probe may have to generate very high rf fields which require very high voltages across the coil; in others the rf may be applied for long periods, resulting in high power dissipation in the probe coil. In addition to the rf characteristics, the probe must also provide the required environment for the sample, for example, temperature control or mechanical rotation of the sample, or other special conditions. Some of these parameters and requirements are in conflict and hence many different probe designs have been developed to support the wide variety of NMR experiments.

For observation of a single nuclear species, the probe can be as simple as a single coil tuned to the resonance frequency by a capacitor and matched to a transmission line (usually 50 Ω) by capacitive or inductive coupling. However, many NMR experiments require the irradiation of the sample with more than one frequency. Unless the frequencies are very close together (for example, exciting different spectral regions of a single nuclear species), the probe coil must be multiply tuned to resonate at a number of different frequencies. Double tuning,[63] or even triple tuning, of coils is quite common. There is inevitably some degradation of performance compared with a singly tuned probe because inductive elements are used to provide the frequency separation, and energy stored in these inductances effectively reduces the filling factor. It is also common to use two orthogonal coils to generate fields which are each perpendicular to the polarizing field and yet have little mutual interaction. By combining the use of multiple tuning and orthogonal coils, a single probe can be designed to provide rf excitation and/or detection at four or five different frequencies.

In almost all modern spectrometers, the same coil is used for transmission of energy to the spins and reception of signal from the spins. In a pulse spectrometer, these two functions are separated in time, and switching between the two functions is accomplished external to the probe. In a CW spectrometer, where transmission and reception occur simultaneously, transmitter coupling into the receiver is minimized by the use of a bridge[8] or a directional coupler. An alternative form of probe for CW measurements used two orthogonal coils, one for transmission and one for reception.[9] The coupling between the coils was minimized by careful mechanical alignment of the coils and by manipulating the residual coupling with 'paddles',[64,65] movable pieces of metal designed to modify the magnetic flux distribution in the probe.

For liquids applications, the sample is commonly contained in a thin-walled test tube. Typical diameters are 5 mm or 10 mm. In a permanent magnet or an electromagnet the axis of the sample is perpendicular to the magnetic field between the pole faces, and the probe coil can be a simple solenoid around the sample. In a superconducting magnet, the sample tube is parallel to the field and the probe coil must be split to provide a transverse field. Figure 2 shows these two configurations.

A vital consideration for liquids applications is the maintenance of field uniformity. The requirements for magnetic field homogeneity have already been discussed in connection with

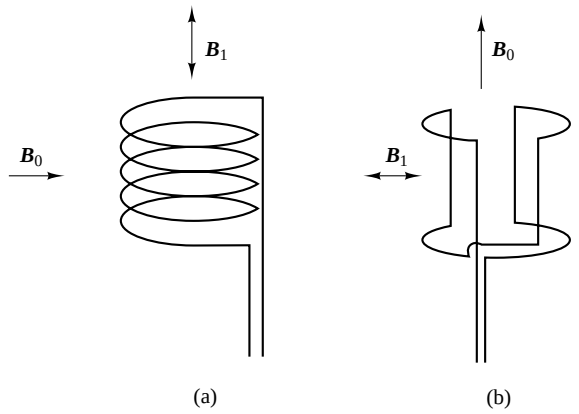

Figure 2 Two common types of probe rf coils for high-resolution liquids applications: (a) solenoid coil used with permanent and electromagnets; and (b) saddle coil used with superconducting magnets

the magnet. However, without due care, the probe and the sample itself will distort the magnetic field and destroy the resolution of the spectrometer.[66] The problem arises from the magnetic susceptibilities of the sample and its container, and of the materials used in the construction of the probe. Volume susceptibilities of many diamagnetic materials are approximately 10^{-6} so that discontinuities in susceptibility can cause field variations of this magnitude. Such effects can be minimized by keeping any discontinuities away from the active sample volume and by maintaining cylindrical symmetry as much as possible in the design of the probe. For this reason, the NMR sample tubes are filled with sample to a depth greater than the active region of the probe. This, of course, requires an excess of sample and compromises the uniformity of the rf excitation and detection. Special attention must be paid to the probe coil itself. Its geometry is not simple and, if a high filling factor is to be maintained, it must be close to the sample. The magnetic susceptibility of normal metals, such as copper or silver, are sufficiently high to cause intolerable distortions of the magnetic field in the sensitive volume of the sample. Coils are therefore manufactured from special composite materials specifically designed to have very low susceptibilities.

For solids applications, rf field homogeneity and efficiency are much more significant than the perturbation of the $\boldsymbol{B}_0$ homogeneity. Therefore, it is usual to use a solenoidal coil with the sample limited to a portion of its total volume. For some applications, e.g. CP MAS[67] and CRAMPS,[68] the sample must be rotated at a very high speed (many kHz) about an axis inclined at 54.7° with respect to the polarizing field.

A single coil generates an oscillating magnetic field, while the nuclear spins respond to and generate a rotating magnetic field. An oscillating field, which may be regarded as two counter rotating fields, is therefore wasteful of transmitter power and signal reception is less efficient. Probes can be built to produce a rotating field and regain this efficiency (a factor of two in reduction in transmitter power and a factor of $\sqrt{2}$ in sensitivity) by using two orthogonal coils driven by rf signals in relative phase quadrature.[69] They are used extensively in whole body imaging systems where high power must be used to generate fields over a very large volume and where, often, only a single frequency must be supported. In spectroscopic applications, where multiple frequency excitation is common, quadrature coils have not found widespread use.

5 SPECTROMETER ELECTRONICS

5.1 Introduction

The electronic portion of the spectrometer includes the radiofrequency section for the excitation and detection of the spin response, control systems for the rf and for the magnet, and digital electronics to manipulate the data. A block diagram of a typical pulse spectrometer for high-resolution liquids applications is shown in Figure 3. A spectrometer for solids applications would not require the lock system or the gradient coils. An imaging system would not require the lock system and would not usually have a second transmitter channel.

The elements of the rf system are: frequency synthesis; transmitter system; power amplification; coupling to probe; receiver system; and signal detection.

5.2 Frequency Generation and Transmitter System

The transmitter provides the rf signals to excite the spins. In a simple spectrometer designed to observe a single nuclear species, this can be a fixed frequency source with a fixed amplitude. In a CW spectrometer, variation in the excitation intensity can be achieved by varying the amplitude of the field modulation signal, and scanning through the spectrum is provided by sweeping the magnetic field or the modulation frequency. In a pulse spectrometer, the effective excitation of the spins is controlled by the amplitude and duration of the rf pulse.

A modern pulse spectrometer designed to satisfy a wide range of applications and to observe a wide range of nuclear species requires a more complex frequency generation scheme. It is common to use a crystal oscillator operating at a standard frequency, such as 10 MHz, to provide a stable source of rf from which all other spectrometer frequencies can be derived. The transmitter may include a general purpose frequency synthesizer so that the output frequency can be set to correspond to a wide range of nuclear resonance frequencies. It is also quite common to generate the transmitter frequency by mixing one or more frequencies. This offers several advantages. First, the gating efficiency in the transmitter can be improved by providing gates before the mixing which generates the final transmitter frequency. This is important to minimize leakage of the transmitter signal into the receiver. Second, one of the intermediate frequencies can be constant for all transmitter frequencies and can be used to control the characteristics (e.g. phase or amplitude) of the transmitter output. Third, the receiver often operates on the heterodyning principle with a portion of the gain at an intermediate frequency. Frequency generation for the transmitter and receiver can then share some common frequencies. A disadvantage is that each mixing stage introduces multiple frequency components, only one of which is required. Careful filtering or suppression of the unwanted frequencies is therefore necessary to maintain the required spectral purity of the transmitter output. A block diagram for a transmitter using frequency mixing is shown in Figure 4.

In almost all pulse spectrometers, some control of the rf phase is used. For the simplest applications, this may only require the phase to be controlled in 90° increments. The first

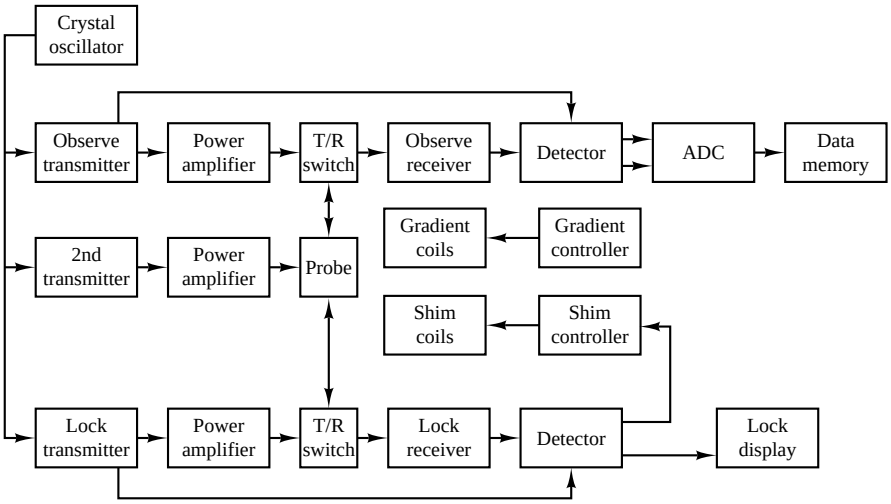

Figure 3 Block diagram of a typical two channel high-resolution NMR spectrometer

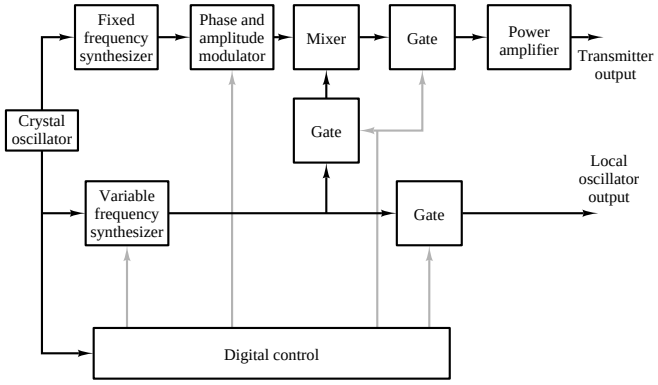

Figure 4 Simplified block diagram of a typical spectrometer transmitter

pulse experiment to require phase shifts was the modification to the Carr–Purcell *spin echo* experiment[53] proposed by Meiboom and Gill.[70] Now, many experimental methods have been developed to exploit the use of transmitter phase shifts. In some, the behavior of the spin system is modified; in others, spectrometer imperfections can be controlled. It is important to realize that the absolute phase of the rf in a pulse is usually not constant from pulse to pulse. That would require the pulse interval to be a multiple of the rf period. What is important is that the pulses have a fixed phase relative to a continuous rf source at the same frequency. Many experimental methods have been developed in recent years which require a variety of rf phase shifts. Therefore many modern spectrometers include a general purpose phase shift capability to provide any rf phase between 0° and 360° with a phase shift resolution of less than 1°. This is most easily provided by controlling the phase of a fixed frequency section of the transmitter. Phase changes are transferred to the transmitter frequency through the subsequent mixing stages.

Short pulses provide an excitation of a wide range of spectral frequencies. This was the prime motivation for the development of the pulsed FT method. However, there are many instances when selective excitation of less than the full spectral width may be required. A number of methods were developed to provide selective excitation by pulse modulation.[71,72] These experiments can also be performed by modulating the amplitude of the rf. These methods first found widespread use for imaging applications but have become common in spectroscopic applications. The use of amplitude modulation requires that the frequency generation scheme is linear, or that it can be linearized by calibration. Again, the use of a fixed frequency section of the transmitter provides a convenient place to provide amplitude control for the rf.

The inclusion of a flexible phase and amplitude control means that complex modulation of the rf may be employed to generate a variety of excitation profiles for a wide range of experiments.[73–76]

5.3 Power Amplification

The rf signals provided in the transmitter are amplified to the appropriate level before coupling into the probe. In a CW spectrometer, the power required is quite low. The use of modulation reduces the effective field strength in the probe but, even so, a few watts is all that is required.

In a pulse spectrometer, the output power required varies greatly with the application, the nuclei being observed, the sample size, and the operating field strength. For the observation of proton spectra in liquids, a few tens of watts is often sufficient, while the observation of nuclei with lower magnetogyric ratios often requires several hundred watt pulses. Solids applications usually require pulses to be short compared with relaxation times and pulse powers of a kilowatt may be needed. In whole body imaging applications, the probe coils can be very large so that, again, kilowatts of pulse power may be needed to generate only a modest rf field.

For applications in which a constant amplitude is sufficient, the use of a nonlinear class C amplifier offers a number of advantages. In the absence of an rf input, there will be no output from a class C amplifier, so the effective gating of the rf source is improved. Further, there is no noise generated by such an amplifier when there is no input signal. Class C amplifiers are often inexpensive to build. Disadvantages are the difficulty of building a broadband amplifier and the difficulty of controlling the gain.

For well-controlled broadband amplification and for use with variable amplitude drive, a linear amplifier is used. These amplifiers are more expensive than class C amplifiers and have the disadvantage that they do generate noise output with no input signal. To overcome this difficulty, amplifiers must be actively blanked off by switching the bias of the output stage until an output pulse is needed.

5.4 Multiple Irradiation

In a modern spectrometer, the need for a second irradiation frequency is so prevalent and varied that a second transmitter channel is added. This channel usually has all the attributes of the first transmitter, namely the ability to adjust the frequency and to control the amplitude and phase of the rf source. A number of experiments have been developed which require the excitation of several nuclear species either simultaneously or sequentially. Therefore a spectrometer may be equipped with three or four transmitters to provide the necessary excitation frequencies.

Care must be exercised if irradiation from a second or third irradiation channel is used during the acquisition of an NMR response. If the irradiation is within the spectral range of the receiver, as in the case of homonuclear decoupling, time-share modulation is used. In a manner similar to an earlier scheme of CW spectrometers,[13,14] the irradiation is pulse modulated with the receiver being gated off during the pulses and turned on during the interval between pulses. If the irradiation frequency is at a significantly different frequency, as in heteronuclear decoupling, frequency selective filters are used to prevent any overload of the receiver by strong rf signals.

5.5 Transmit–Receive Switch

Transmitter energy must be coupled into the probe and received signals must be coupled out. In a pulsed spectrometer these events occur sequentially and a switching circuit is used to direct the signals correctly. A simple, commonly used circuit[77] makes use of crossed diodes and quarter-wavelength lines (Figure 5) to effect the switching by the application of the rf itself. High voltages during the rf pulse excitation cause the diodes to conduct and act as short circuits. Those to ground in front of the preamplifier protect the amplifier from overload and also reflect energy so that all the transmitter power is delivered to the probe. During the receive cycle, voltages are so low that the diodes effectively act as open circuits. The transmitter is effectively isolated and all the signal energy is coupled to the preamplifier. Such a circuit is nonlinear in that a threshold pulse amplitude is required to switch the diodes into a conducting state. For applications requiring linear control of the rf level in the probe, a linear version of the same circuit can be built using PIN diodes,[78] which can be switched from a conducting state to a nonconducting state by the application of a dc control voltage.

5.6 Receiver and Detector

The receiver system[63] provides the amplification of the weak NMR signal with the minimum degradation and distortion, and detection of the rf signals for display and measurement.

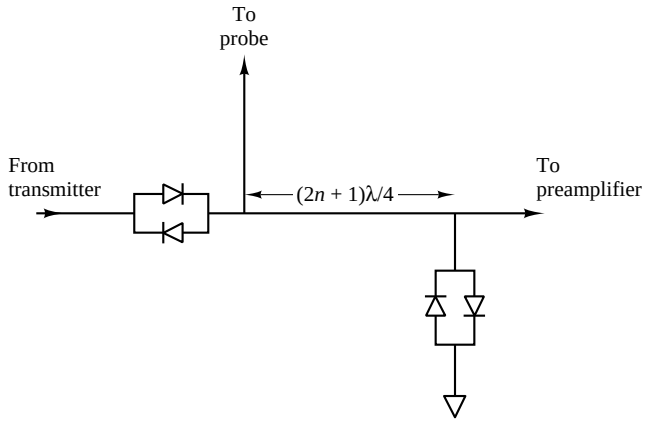

Figure 5 A simple transmit–receive switch using passive diodes. The interconnections are transmission lines and λ is the wavelength at the radiofrequency of interest. Errors in choice of line length affect the efficiency of power transmission to the probe, not that of reception. A single length of line can therefore be used to cover a factor of two in operating frequencies

The total gain required in an NMR receiver system is typically between 60–100 dB. In a few applications this might all be provided at the NMR frequency. More commonly, the NMR signal frequency is amplified by about 20–30 dB and then converted to a fixed intermediate frequency (IF) by mixing with a local oscillator frequency derived from the transmitter. This provides a more stable receiver and allows most of the amplification to be at a fixed frequency. In some cases more than one intermediate frequency might be used. Phase detection at the final intermediate frequency provides the output signal or signals of the spectrometer. A block diagram of a receiver employing a single intermediate frequency and quadrature phase detection is shown in Figure 6.

For pulse applications, it is necessary to deactivate the receiver during transmitter pulses to prevent overload and subsequent slow recovery to optimum performance. In a receiver using an intermediate frequency, very effective disabling can be achieved by gating off the local oscillator signal. Additional gating of the preamplifier is also sometimes used but is not always necessary.

The output of a mixer contains both sum and difference frequencies of the two inputs, only one of which is at the desired frequency. The unwanted frequency is easily rejected by limiting the bandwidth of the following receiver stages. A more difficult problem is that of rejecting the so-called image frequency. For example, in the first mixer of the receiver, signals at two frequencies are converted to the IF, namely

$$\omega_1 = \omega_{LO} - \omega_{IF} \tag{5}$$

and

$$\omega_1 = \omega_{LO} + \omega_{IF} \tag{6}$$

While only one of these frequencies corresponds to the NMR frequency, ω_0, any noise at the second frequency will be converted to the IF to the detriment of the overall signal-to-noise ratio. The image frequency must therefore be rejected, either by including a filter to eliminate it before the mixer or by the use of a single sideband mixer[79] which rejects signals at the image frequency by cancellation. In a spectrometer designed

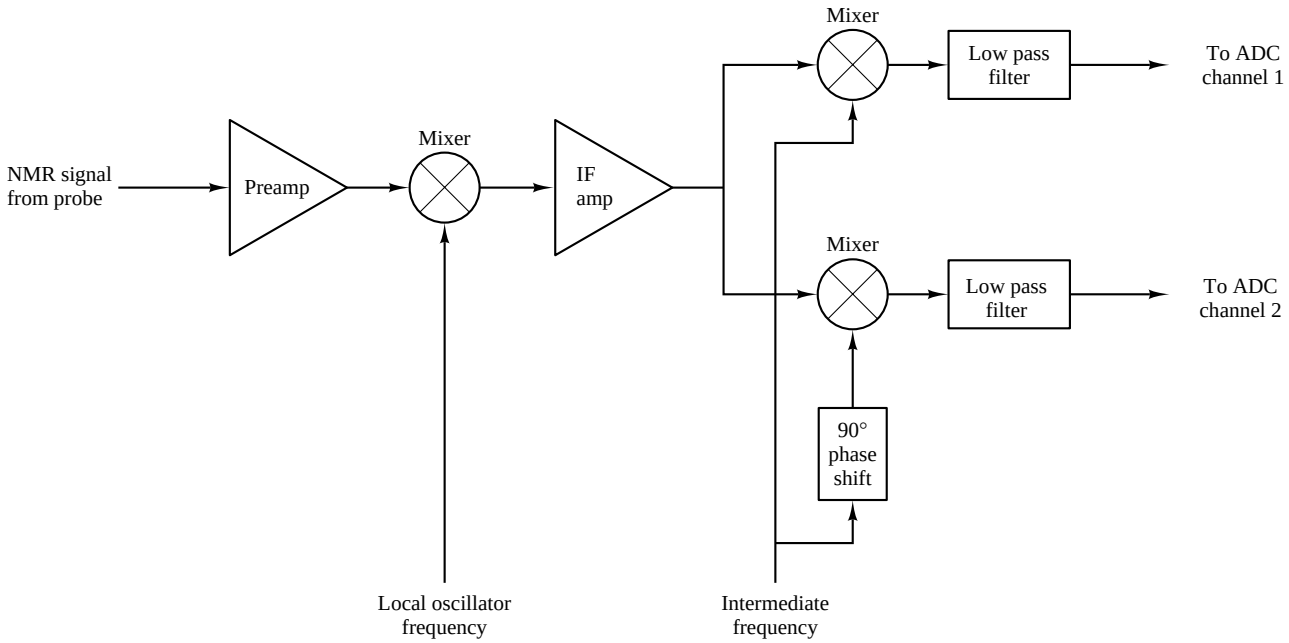

Figure 6 Block diagram of a quadrature detection receiver using a single intermediate frequency

to operate over a wide range of NMR frequencies, a broadband single sideband mixer can be used whereas the use of a simple mixer may require the switching of several filters. At the final mixers of Figure 6, the image frequency is twice the IF and is simply rejected by limiting the bandwidth of the IF section of the receiver.

The bandwidth of the receiver must be sufficient to amplify all the signal components generated in the probe. The rf and IF sections of the receiver have relatively large bandwidths and the low pass filter following the final detector determines the overall frequency response. In a CW spectrometer, this is a very narrow band since the signal is the response at the excitation frequency. In a pulse spectrometer, the bandwidth must be sufficient to record the transient response. Many individual signal components might be included in that response.

The output of the final mixers is at a frequency, ω_s, equal to the difference between the NMR frequency and the transmitter frequency. As such it is equal to the precession frequency in a reference frame rotating at the frequency of the spectrometer transmitter. The output of a single detector corresponds to the projection of the rotating magnetization vector onto an axis in the rotating frame. By using two phase detectors driven by reference signals in quadrature, as shown in Figure 6, two outputs are provided representing the projections onto two orthogonal axes in the rotating frame. The two axes may not correspond to the x- and y-axes as defined by the transmitter excitation, but can be brought into correspondence, if necessary, by phase rotation of the reference signals relative to the phase of the transmitter. In applications where the signals are subsequently digitized, the phase rotation can be effected by manipulating the digital data.

The sense of rotation of the signals in the rotating reference frame can be distinguished by the phase relationship between these two detected signals. Hence, NMR signals at frequencies above and below the transmitter frequency can be distinguished. For accurate separation, the outputs of the two channels must be exactly in quadrature and equal in amplitude. Imperfections can be canceled by accumulating multiple spectra excited with differing transmitter phases and by suitably combining the resultant responses.[80,81]

Noise at frequencies above and below the transmitter frequency is similarly distinguished. With only a single detector, the noise components from either side of the transmitter frequency both contribute to the noise in the output, and the signal-to-noise ratio is degraded by $\sqrt{2}$. The use of quadrature detection in NMR receivers was first proposed by Ernst[30] for the improvement of the sensitivity of spectrometers then in use.

For all types of NMR spectrometer, the noise performance of the receiver is an important consideration. Signals may be degraded by the addition of noise or by the introduction of spurious signals. Any circuit element can be characterized by its noise factor[82] which is the ratio of the signal-to-noise power at the output compared with the signal-to-noise power at the input. Noise factors are usually expressed in dB as noise figures although, in cases where the noise source and the receiver may be at different temperatures, the use of noise temperatures is more appropriate. A noise factor of 2 is equivalent to a noise figure of 3 dB and results in a loss of signal-to-noise ratio (which is normally defined in terms of voltage) by $\sqrt{2}$. Typical noise figures for a modern NMR receiver are between 1 and 2 dB. Any lossy components between the probe and the receiver degrade the noise figure by a factor equal to its loss. Special care is therefore taken to use low loss cables and to minimize any loss in filters and the transmit–receive switch.

In FT spectrometers, where a number of signals over a band of frequencies are amplified simultaneously by the receiver, linearity and dynamic range are other important parameters. Any nonlinearity in the receiver response can give rise to harmonic or intermodulation distortion which can result in spurious signals which fall within the pass band of the receiver and hence can be confused with real signals. Dynamic range is

important because the receiver must be able to handle the sum of all signals excited by a pulse at the start of a free induction decay and yet also record faithfully the response of individual components, which may be very weak, as the signals dephase.

5.7 Analog-to-Digital Converter

In most modern NMR spectrometers, the analog signal following detection is converted to a digital form for time averaging or other signal processing. The analog-to-digital converter (ADC) must have sufficient resolution and accuracy to make a faithful representation of the signal in the digital domain.[83] Linearity must be maintained by adjusting the receiver gain to limit the maximum signal intensity to less than the full scale response of the ADC. At this gain, the resolution of the ADC (number of bits) should ideally be sufficient such that the quantization steps are less than the noise associated with the signal. This may not always be possible to achieve for all types of signal but, typically, 16-bit ADCs are used in a pulsed FT spectrometer.

The sampling rate of an ADC must be twice the maximum signal frequency to prevent aliasing of signals. In a quadrature receiver system, each channel must be sampled at a frequency equal to the total spectral width. The filter bandwidth in each channel is set close to one-half the total spectral width.

Since noise voltage increases with the square root of noise bandwidth, there are advantages of operating with as large a bandwidth as possible, even if signals only occupy a relatively small bandwidth. The time domain signal-to-noise ratio is reduced so that, for an ADC of a given amplitude resolution, it is possible to reduce the spectrometer gain, and hence handle larger signals, without running into the quantization noise limit of the ADC. The large amounts of data generated by high speed sampling can be reduced by digital filtering following the digitizer.

5.8 Field/Frequency Lock System

For high-resolution applications in liquids NMR, the inherent stability of the magnet is often not sufficient to ensure accurate results. Therefore it is common to stabilize the field by making use of an auxiliary magnetic resonance signal from the sample. This concept of an internal lock was introduced in 1961.[20,21] An error signal is generated from the dispersion mode signal of this second resonance signal.

In a CW spectrometer using field modulation techniques, the resonance used for stabilization can be a resonance in the spectrum itself, excited by a second modulation frequency. Spectrometers designed for proton spectroscopy used the signal of tetramethylsilane (TMS) as a reference and as a 'lock' for the field/frequency control. For spectrometers designed to study a variety of nuclear species, and for systems which operate in the pulsed mode, it has become common to use a deuterium resonance as the 'lock' signal. A deuterium compound is included in the solvent of the high-resolution sample and the spectrometer is equipped with a separate deuterium spectrometer for the excitation and detection of the deuterium resonance. This is essentially a simple CW spectrometer operating at a fixed frequency with an output which controls the magnetic field. The probe includes a coil tuned to the deuterium resonance frequency. Sometimes this is a separate coil, orthogonal to the observe coil, but more usually one of the coils in the probe is doubly tuned to the deuterium frequency and another operating frequency.

In a pulsed spectrometer, the lock system usually operates with pulsed modulation in the time-shared mode, since this is very compatible with the rest of the control circuits of the spectrometer. Pulse repetition frequencies of between 10 Hz and 10 kHz have been used. The transmitter power is quite low (less than 1 W) since it is normal to operate the lock system below saturation to maintain the linearity of the control loop. The output of the lock channel is phase detected and the dispersion signal is used as the control signal feedback to the field offset coil of the shim coil system. The output is zero exactly at resonance and an error signal is generated if the field/frequency relationship changes. From the dispersion response, the sign of the signal depends on the sign of the deviation from resonance and hence provides the required control for a feedback loop.

When the field variation over the sample volume is greater than the natural linewidth of the resonance, the amplitude of the absorption signal will vary with field homogeneity. Thus the amplitude of the lock signal can be used as an indicator for the quality of the magnet shimming.

A drawback of the use of deuterium is its low magnetogyric ratio. This results in a relatively low signal sensitivity and a lower sensitivity to changes in field homogeneity. For these reasons, and when deuterium is to be observed, lock systems are sometimes used with other nuclei. Good candidates are ^{19}F and ^{7}Li.

5.9 Digital System

The majority of spectrometers include a digital subsystem to provide control of the spectrometer and processing of signals. In a modern spectrometer, this system may consist of one or more powerful computers with some specialized hardware for specific functions. The use of a computer as an integral part of a spectrometer became essential with the introduction of FT techniques. Prior to that, spectrometer functions were controlled by manual knobs. In a modern spectrometer, interaction with the spectrometer variables is via a computer interface. This provides greater flexibility and lower cost than manual control.

The functions of the digital system may be divided into several parts: instrument control; data acquisition; and data processing.

5.9.1 Instrument Control

The control system provides the interface between the user and the spectrometer variables.

Some of these functions are time-critical whereas others are not. The non-time-critical functions are generally handled by a general purpose computer whereas the time-critical functions require some dedicated hardware and possibly a dedicated computer system.

An increasingly important aspect is the control of pulse sequences. Much of the flexibility in a modern spectrometer has come about by the ability to implement a wide range of experiments through a versatile pulse sequence programmer.

This provides the control of all of the relevant parameters used in the excitation of the spin system, e.g. rf level, pulse durations, pulse intervals, phase of transmitter and receiver, field gradient pulses, and timing of data acquisition. In multidimensional experiments, one or more of the timing durations is incremented for successive elements in an array of acquisitions. The control system must provide this control and keep track of the data associated with each increment.

The increasing use of pulses modulated in phase and amplitude has led to the use of distributed control in which the modulation information is stored in a memory buffer and recalled when required as part of a pulse sequence.

5.9.2 Data Acquisition

Since data acquisition is intimately connected with pulse sequence control, the same computer system or timing circuitry provides control for each. Time averaging is usually performed in the time domain as an integral part of the data acquisition process. The time domain data can then be transferred to disk from whence it can be accessed for further processing. If a separate computer system is used for data processing, acquisition of new data can continue while previously accumulated data are being processed.

Increasing use is being made of sampling data at a high fixed bandwidth. Bandwidth is then adjusted by digital filtering and the number of data points reduced, commensurate with the final bandwidth, before storing to disk.

5.9.3 Data Processing

The stored free induction signal or array of signals can be manipulated in a number of ways. The data may be weighted as a function of time to provide improved sensitivity or resolution. Data points may be modified or added, for example by *linear prediction* methods,[84] to overcome instrumental deficiencies or to correct for truncated data. Fourier transformation is most commonly used to generate the frequency spectrum although other methods are also used.[85,86] Following transformation, the phase of the data is adjusted prior to display. It is usual to display the data on a video terminal to allow convenient selection of scales and displayed regions before finally plotting the data.

6 AUXILIARY SYSTEMS

6.1 Variable Temperature System

Sample temperature is a critical parameter for many experiments, so that control of the temperature is often included as part of the spectrometer function. The most common form of control for temperatures between about $-100\,^{\circ}C$ and $+200\,^{\circ}C$ is to use a flow of controlled temperature gas (usually dry nitrogen or air) over the sample. A heater and temperature sensor in the gas stream are connected to a temperature control unit in the spectrometer. For extremely low temperature operation, more sophisticated systems using liquid helium are used. For high temperatures, furnace systems have been employed.

6.2 Pneumatics System

Gas bearings and drive are used for sample spinning. For high-resolution applications, the NMR sample tube is mounted in a turbine which can be rotated by a jet of gas. The turbine walls can also provide the gas bearing surfaces or, sometimes, the sample tube itself can provide the bearing surface. While sample spinning has lost favor for most multidimensional experiments, it is still used for simple high-resolution applications as a means for improving resolution. An optical detector is used to detect and measure the rotation rate. For many applications, the precise control of the spinning speed is not important and an open loop system is used. More sophisticated spectrometers provide closed loop control of the spinning speed using the spin rate detector to generate a feedback signal to control the flow of gas to the spinner.

For solids applications requiring magic angle spinning, the sample is packed into a small rotor which is supported by gas bearings and rotated at high speed (up to 20 kHz).

In a superconducting magnet, the sample is located in the center of the long, narrow magnet bore. It is quite common to use a pneumatic lift mechanism to eject the sample and to provide a gentle lowering of the sample into the probe.

6.3 Automation

Many applications of NMR require the measurement of a large number of samples on a continuous basis. Therefore, the integration of automatic sample-changing mechanisms has become important for these applications. Such systems include a holder (tray or carousel) for a large number of samples and a mechanism to move the samples individually to and from the magnet. Coupled with sophisticated software, the required experimental parameters can be established for each individual sample and a large number of samples can be analyzed completely unattended.

7 CONCLUSION

The basic structure of a pulsed NMR spectrometer is well suited to a wide range of applications. Future developments are most likely to be in the greater accuracy and convenience of implementing more complex pulse sequences and other aspects of spectrometer control through improvements in digital technology and software. Developments in magnet technology may lead to still higher magnetic field strengths or simplified cryogenic requirements through the use of new superconducting materials. Some of these improvements may open new applications for nuclear magnetic resonance. The probe will be one aspect of the spectrometer which will continue to develop specifically for a particular application.

8 RELATED ARTICLES

CRAMPS; Cross Polarization in Solids; Diffusion and Flow in Fluids; Double Resonance; Field Gradients and Their Application; Fourier Transform and Linear Prediction Methods; Fourier Transform Spectroscopy; Magnetic

Resonance Imaging: A Historical Overview; Magic Angle Spinning; Multidimensional Spectroscopy: Concepts; Phase Cycling; Probe Design and Construction; Probes for High Resolution; Probes for Special Purposes; Radiofrequency Pulses: Response of Nuclear Spins; Relaxation: An Introduction; Sensitivity of the NMR Experiment; Shaped Pulses; Shimming of Superconducting Magnets; Spin Echo Spectroscopy of Liquid Samples; Stochastic Excitation.

9 REFERENCES

1. D. I. Hoult and R. E. Richards, *J. Magn. Reson.*, 1976, **24**, 71.
2. E. M. Purcell, H. C. Torrey, and R. V. Pound, *Phys. Rev.*, 1946, **69**, 37.
3. F. Bloch, W. W. Hansen, and M. Packard, *Phys. Rev.*, 1946, **69**, 127.
4. H. C. Torrey, *Phys. Rev.*, 1949, **75**, 1326.
5. E. L. Hahn, *Phys. Rev.*, 1949, **76**, 461.
6. W. G. Proctor and F. C. Yu, *Phys. Rev.*, 1950, **77**, 717.
7. J. T. Arnold, S. S. Dharmatti, and M. E. Packard, *J. Chem. Phys.*, 1951, **19**, 1608.
8. N. Bloembergen, *Nuclear Magnetic Relaxation*, W. A. Benjamin, Inc., New York, 1961.
9. F. Bloch, *Phys. Rev.*, 1946, **70**, 460.
10. W. A. Anderson, *NMR and EPR Spectroscopy*, Pergamon Press, Oxford, UK, 1960, Chap. 14
11. W. A. Anderson, *Rev. Sci. Instrum.*, 1962, **33**, 1160.
12. O. W. Haworth and R. E. Richards, *Prog. Nucl. Magn. Reson. Spectrosc.*, 1966, **1**, 1.
13. E. Grunwald, C. F. Jumper, and S. Meiboom, *J. Am. Chem. Soc.*, 1962, **84**, 4664.
14. E. B. Baker, L. W. Burd, and G. N. Root, *Rev. Sci. Instrum.*, 1965, **36**, 1495.
15. F. Bloch, *Phys. Rev.*, 1956, **94**, 496.
16. W. A. Anderson and J. T. Arnold, *Phys. Rev.*, 1956, **94**, 497.
17. M. J. E. Golay, *Rev. Sci. Instrum.*, 1958, **29**, 313.
18. W. A. Anderson, *Rev. Sci. Instrum.*, 1961, **32**, 241.
19. F. A. Nelson, *NMR and EPR Spectroscopy*, Pergamon Press, Oxford, UK, 1960, Chap. 6
20. H. Primas and H. H. Gunthard, *Rev. Sci. Instrum.*, 1957, **28**, 510.
21. R. Freeman and D. H. Whiffen, *Proc. Phys. Soc., London*, 1962, **79**, 794.
22. T. R. Carver and C. P. Slichter, *Phys. Rev.*, 1953, **92**, 212.
23. A. W. Overhauser, *Phys. Rev.*, 1953, **92**, 411.
24. V. Royden, *Phys. Rev.*, 1954, **96**, 543.
25. A. L. Bloom and J. N. Shoolery, *Phys. Rev.*, 1955, **97**, 1261.
26. R. Freeman and W. A. Anderson, *J. Chem. Phys.*, 1962, **37**, 85.
27. R. R. Ernst, *J. Chem. Phys.*, 1966, **45**, 3845.
28. K. H. Hauser and D. Stehlik, *Adv. Magn. Reson.*, 1968, **3**, 70.
29. J. G. Kenworthy and R. E. Richards, *J. Sci. Instrum.*, 1965, **42**, 675.
30. R. R. Ernst, US Pat. 3 501 691, 1970.
31. M. P. Klein and G. W. Barton, *Rev. Sci. Instrum.*, 1963, **34**, 754.
32. R. Varian, US Pat. 3 287 629, 1968.
33. R. R. Ernst and W. A. Anderson, *Rev. Sci. Instrum.*, 1966, **37**, 93.
34. J. W. Cooley and J. W. Tukey, *Math. Comput.*, 1965, **19**, 297.
35. A. G. Redfield and R. K. Gupta, *Adv. Magn. Reson.*, 1971, **5**, 81.
36. J. D. Ellett, Jr., M. G. Gibby, U. Haeberlen, L. M. Huber, M. Mehring, A. Pines, and J. S. Waugh, *Adv. Magn. Reson.*, 1971, **5**, 117.
37. R. R. Ernst, *J. Magn. Reson.*, 1970, **3**, 10.
38. R. Kaiser, *J. Magn. Reson.*, 1970, **3**, 28.
39. J. Dadok and R. F. Sprecher, *J. Magn. Reson.*, 1974, **13**, 243.
40. J. Jeener, *AMPERE Int. Summer School*, Basko Polje, Yugoslavia, 1971.
41. W. P. Aue, E. Bartholdi, and R. R. Ernst, *J. Chem. Phys.*, 1976, **64**, 2229.
42. R. R. Ernst, G. Bodenhausen, and A. Wokaun, *Principles of Nuclear Magnetic Resonance in One and Two Dimensions*, Clarendon Press, Oxford UK, 1987.
43. P. Lauterbur, *Nature (London)*, 1973, **242**, 190.
44. A. Kumar, D. Welti, and R. R. Ernst, *J. Magn. Reson.*, 1975, **18**, 69.
45. A. Huber and H. Primas, *Nucl. Instrum. Methods*, 1965, **33**, 125.
46. R. E. Gang, US Pat. 3 434 085, 1969.
47. H. L. Marshall and H. E. Weaver, *J. Appl. Phys.*, 1963, **34**, 3175.
48. M. D. Sauzade and S. K. Kan, *Adv. Electron. Electron Phys.*, 1973, **34**, 1.
49. F. Roméo and D. I. Hoult, *Magn. Reson. Med.*, 1994, **1**, 44.
50. D. I. Hoult and D. Lee, *Rev. Sci. Instrum.*, 1985, **56**, 131.
51. R. Vadovic, *IEEE Trans. Magn.*, 1989, **25**, 3133.
52. E. L. Hahn, *Phys. Rev.*, 1950, **80**, 580.
53. H. Y. Carr and E. M. Purcell, *Phys. Rev.*, 1954, **94**, 630.
54. D. E. Woessner, *J. Chem. Phys.*, 1961, **34**, 2057.
55. E. O. Stejskal and J. E. Tanner, *J. Chem. Phys.*, 1965, **42**, 288.
56. J. E. Tanner, *Rev. Sci. Instrum.*, 1965, **36**, 1086.
57. P. Stilbs, *Prog. Nucl. Magn. Reson. Spectrosc.*, 1987, **19**, 1.
58. P. Mansfield and B. Chapman, *J. Magn. Reson.*, 1987, **72**, 211.
59. R. R. Vold, J. S. Waugh, M. P. Klein, and D. E. Phelps, *J. Chem. Phys.*, 1968, **43**, 3831.
60. A. Bax, P. G. de Jong, A. F. Mehlkopf, and J. Smidt, *Chem. Phys. Lett.*, 1980, **69**, 567.
61. P. Barker and R. Freeman, *J. Magn. Reson.*, 1985, **64**, 334.
62. R. Hurd, *J. Magn. Reson.*, 1990, **87**, 422.
63. D. I. Hoult, *Prog. Nucl. Magn. Reson. Spectrosc.*, 1978, **12**, 41.
64. F. Bloch, W. W. Hansen, and M. Packard, *Phys. Rev.*, 1946, **70**, 474.
65. F. A. Nelson, *NMR and EPR Spectroscopy*, Pergamon Press, Oxford UK, 1960, Chap. 6
66. L. F. Fuks, F. S. C. Huang, C. M. Carter, W. A. Edelstein, and P. B. Roemer, *J. Magn. Reson.*, 1992, **100**, 229.
67. J. Schafer, E. O. Stejskal, and R. Buchdahl, *Macromolecules*, 1977, **10**, 384.
68. B. C. Gerstein, R. G. Pembleton, R. C. Wilson, and L. M. Ryan, *J. Chem. Phys.*, 1977, **66**, 361.
69. D. I. Hoult, C.-N. Chen, and V. J. Shank, *Magn. Reson. Med.*, 1984, **1**, 339.
70. S. Meiboom and D. Gill, *Rev. Sci. Instrum.*, 1958, **29**, 688.
71. B. L. Tomlinson and H. D. W. Hill, *J. Chem. Phys.*, 1973, **59**, 1775.
72. G. A. Morris and R. Freeman, *J. Magn. Reson.*, 1978, **29**, 433.
73. H. Geen and R. Freeman, *J. Magn. Reson.*, 1991, **93**, 93.
74. S. L. Patt, *J. Magn. Reson.*, 1992, **96**, 94.
75. E. Kupce and R. Freeman, *J. Magn. Reson., Ser. A*, 1993, **105**, 314.
76. R. Freeman, *Chem. Rev.*, 1991, **91**, 1397.
77. I. J. Lowe and C. E. Tarr, *J. Phys. E, Sci. Instrum.*, 1969, **1**, 320.

78. See, for example, I. Bahl and P. Bhartia, *Microwave Solid State Circuit Design*, Wiley, New York, 1988, p. 409.
79. See, for example, F. E. Terman, *Electronic and Radio Engineering*, 4th edn., McGraw-Hill, New York, 1955, p. 541.
80. E. O. Stejskal and J. Schafer, *J. Magn. Reson.*, 1974, **14**, 160.
81. D. I. Hoult and R. E. Richards, *Proc. R. Soc. London, Ser. A*, 1975, **344**, 311.
82. See, for example, J. Minkoff, *Signals, Noise and Active Sensors*, Wiley, New York, 1992, p. 48.
83. J. C. Lindon and A. G. Ferrige, *Prog. Nucl. Magn. Reson. Spectrosc.*, 1980, **14**, 27.
84. D. S. Stephenson, *Prog. Nucl. Magn. Reson. Spectrosc.*, 1988, **20**, 515.
85. P. J. Hore, *J. Magn. Reson.*, 1985, **62**, 561.
86. G. L. Bretthorst, *J. Magn. Reson.*, 1992, **98**, 501.

Biographical Sketch

Howard D. W. Hill. *b* 1938. B.A., 1961, D.Phil., 1965, Oxford. Research assistant with Professor R. E. Richards, Physical Chemistry Laboratory, Oxford, 1965–68; Postdoctoral fellow, Varian Associates, Palo Alto, CA, 1968–69; Member of R&D staff, Varian NMR Instruments, 1969–present; Varian Fellow, 1988. Current interests include the improvement of sensitivity and resolution of NMR systems.

SQUIDs

Ulrike Werner-Zwanziger
Indiana University, Bloomington, IN, USA

1	Introduction	1
2	How a SQUID Works	1
3	Design of a SQUID Spectrometer	1
4	Applications	2
5	Conclusion	3
6	Related Articles	4
7	References	4

1 INTRODUCTION

Superconducting quantum interference devices (abbreviated SQUIDs) can be used as sensitive magnetic flux-to-voltage converters. In this mode they can detect NMR signals, replacing the tuned coil in a conventional NMR probe. Their primary applications include low frequency studies (below a few megahertz), observation of large spectral widths (several megahertz), and measurements at ultralow temperatures (millikelvin regime).

In conventional detection of NMR, the signal is observed as a voltage induced in a tuned coil by a changing magnetization $\mathrm{d}M/\mathrm{d}t$ (Faraday's law). This method is inefficient at low frequencies, where $\mathrm{d}M/\mathrm{d}t$ is small. The SQUID, on the other hand, directly transforms changes in the magnetization ΔM, induced by spin transitions, into voltages. Thus, SQUID detection works sensitively down to very low frequencies.[1]

SQUIDs can detect changes in both the longitudinal and transverse magnetization. SQUID measurements of the longitudinal magnetization have been used to obtain NMR,[2,3] NQR,[3,4] and EPR[5] spectra and relaxation times. There are no restrictions on the methods used to excite the transitions: techniques employed include CW excitation,[3,6,7] rf pulses,[8] and acoustic fields.[9] Applications of SQUID NMR spectrometers range from structural studies of solids[4] to thermometry,[1,10] study of enhanced nuclear moments,[11] and properties of superfluid ^{3}He.[8,12,13]

Changes in the transverse magnetization, that is, in the FID following an rf pulse, have been observed with SQUIDs both at high frequencies (30 MHz)[14] and in the low frequency regime ($<$200 kHz).[15–17] This application has great potential in that it could make use of the multitude of pulse sequences developed for high field NMR.

After sketching the principles of operation of a SQUID and the design of a SQUID spectrometer, we outline some applications of SQUID detection in NMR. We conclude with a summary of areas of future potential progress for the field.

2 HOW A SQUID WORKS

Here we briefly describe the principles of operation of SQUIDs. For a more detailed description of both operation and noise characteristics, see Meredith et al.[1] and Clarke.[18]

By combining the phenomena of fluxoid quantization in a superconducting ring and Josephson tunneling, SQUIDs convert changes in magnetic field into voltages that can be detected by conventional semiconducting electronics.[19] Fluxoid quantization in a superconducting ring restricts the magnetic flux threading the ring to $n\Phi_0$, a multiple of the flux quantum $\Phi_0 \sum h/2e \approx 2 \times 10^{-15}$ Wb. Application of an arbitrary flux Φ causes the ring to generate a supercurrent of Cooper pairs such that the self-generated flux exactly cancels Φ. To detect these flux-induced changes the superconducting ring is interrupted by one or two Josephson junctions. A Josephson tunnel junction consists of two superconducting films separated by a thin insulating layer. When a current I is passed through the junction, the Cooper pairs tunnel through the barrier. No voltage V is developed by this supercurrent until I exceeds the maximum supercurrent I_0 that the junction can sustain. Depending on whether one or two Josephson junctions interrupt the superconducting ring, one distinguishes between rf and dc SQUIDs, respectively. Direct current SQUIDs are normally operated by fixing the dc bias current across the SQUID at a constant value larger than the supercurrent I_0. Since the amount of current that travels as supercurrent through the ring depends on the flux threading the SQUID, the voltage changes periodically as a function of the applied flux with a period Φ_0. To obtain an output voltage that is proportional to the input flux even when the applied flux is less than Φ_0 or corresponds to many Φ_0, one uses a feedback circuit in which the SQUID acts as a null-flux detector.

The rf SQUID, on the other hand, consists of a superconducting loop interrupted by a single Josephson junction. The prefix 'rf' implies that the device is biased with a radiofrequency modulated flux. Both types of SQUID have been incorporated into NMR and NQR spectrometers.

3 DESIGN OF A SQUID SPECTROMETER

Despite the multitude of applications and experimental techniques exploiting the high sensitivity of a SQUID, the basic features of the spectrometers and their problems are similar. We therefore describe in some detail a particular spectrometer which uses a dc SQUID to detect the changes of the longitudinal magnetization.[3,20]

The probehead of this spectrometer is shown in Figure 1. The commercial dc SQUID (Model DBS, Biomagnetic Technologies, Inc.) operates in the flux-locked mode as a linear flux-to-voltage converter. To protect the SQUID from direct rf irradiation, the SQUID is embedded in a superconducting niobium tube (shown on the left-hand side of Figure 1), and is spatially separated from the sample environment (shown on the right-hand side of Figure 1). A superconducting flux transformer transfers the changes of magnetic flux from the sample into the SQUID. The transformer consists of two coils of equal inductance, and shunt resistors. The pickup coil holds the sample, which has a volume of roughly 100 mm^3. The second coil, the coupling coil close to the SQUID, feeds the flux change of the pickup coil into the SQUID itself. The shunt resistors in parallel with the coils at the bottom of the probehead act as a low pass filter to prevent rf from being transferred directly into the SQUID.

Changes of magnetic flux in the sample are induced by rf excitation of spin transitions. In this spectrometer, two

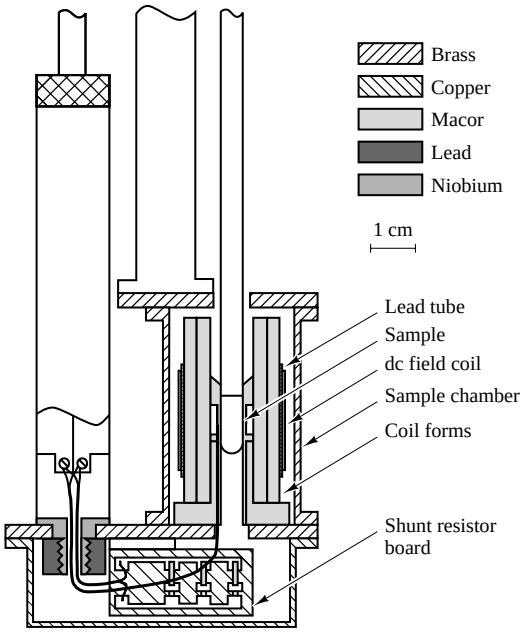

Figure 1 Cross section of the low-temperature part of the SQUID spectrometer. (Reproduced by permission of the American Institute of Physics from C. Conner, J. Chang, and A. Pines, *Rev. Sci. Instrum.*, 1990, **61**, 1059)

Helmholtz saddle coils wound orthogonally to the pickup coil emit a linearly or circularly polarized rf field to the sample (of microtesla magnitude). The exact orientation of these coils with respect to the pickup coil is one of the main factors in minimizing rf influence on the SQUID. The rf circuit is not tuned to a specific frequency, thus allowing a wide range of frequencies to be observed. Also, since the SQUID detects the slowly changing magnetization of the sample parallel to the static magnetic field, the resonance frequencies do not determine directly the sensitivity of detection. A small static magnetic field (up to about 10 mT) can be trapped in a lead tube surrounding the rf coils, the pickup coil, and the sample.

In this apparatus the probehead is immersed completely in liquid helium, giving a constant temperature of 4.2 K. The SQUID feedback circuit rests on top of the cryostat; this circuit, the cryostat, and the probehead are placed inside a cage made of copper mesh to shield them from external rf fields. The rest of the spectrometer, consisting of the rf transmitter, the remaining SQUID electronics, and the receiver is situated outside the copper cage. The rf irradiation is generated by a computer-controlled frequency synthesizer. The signal obtained from the SQUID is passed through the feedback unit to the SQUID controller (BTi Model 40). The signal is amplified, filtered, digitized, and finally transferred to a computer for storage and analysis.

4 APPLICATIONS

Early experiments using SQUIDs as part of NMR spectrometers concentrated mainly on studying the physical properties of systems. For example, Meredith et al. took advantage of the low excitation powers needed for the SQUID-based spectrometer to measure temperatures in the millikelvin regime, by determining relaxation times T_1 of a bundle of copper wires and using the Korringa relation T_1T = Constant.[1,10] Similarly, the low power requirements of the SQUID, together with the wider accessible frequency range (10 kHz to 1 GHz) allowed NMR and EPR relaxation studies of Ce^{3+} in cerium magnesium nitrate at temperatures down to 10 mK with the same spectrometer.[5] The wide available frequency range was also important for studies of the hyperfine-enhanced nuclear moment in $TmPO_4$,[11] for which an effective field 77.9 times stronger than the applied magnetic field was found. Pickens et al. presented NQR spectra and the first measurements of magnetic-field-dependent nuclear spin relaxation rates in a bulk metal (^{121}Sb and ^{123}Sb).[9] These experiments were performed using a SQUID spectrometer to detect the change of static susceptibility caused by transitions driven by acoustic energy. Webb studied the difference between the static and dynamic susceptibilities of superfluid ^{3}He–B at ultralow temperatures (1.2 K to 2 mK) and various pressures.[12,13]

Besides investigating the physical problems outlined above, SQUID spectrometers are valuable tools for obtaining answers to a wide range of chemical questions. Examples discussed below include studies of rotational tunneling in methyl groups to characterize local environments, and various quadrupole resonance experiments.

4.1 Rotational Tunneling of Methyl Groups

The tunneling frequencies of methyl groups have been used to characterize the local methyl group environments and correlate them with macroscopic properties.[2] The ground state rotation eigenfunctions of hindered methyl groups split into A and E symmetry states. The energy difference between the A and the E levels, denoted as the tunnel splitting $h\nu_T$, depends on the hindering potential given by the environment. The Pauli principle dictates that transitions between the rotational states are coupled to changes in the spin states. Unfortunately, transitions between the pure A and E states, which contain information about the environment, are symmetry forbidden in both high and zero magnetic fields. The SQUID experiments detect these transitions by applying a small magnetic field, resulting in Larmor frequencies of only a few hundred kilohertz. For methyl groups attached to sp^3 hybridized carbon, the similar size of the proton Larmor frequency, the dipole–dipole coupling constant between the protons, and the tunneling frequencies render transitions between the A and E symmetry species observable. The spectra (an example is shown in Figure 2) show maxima at the proton Larmor frequency ν_0 and twice the Larmor frequency $2\nu_0$, with their tunneling sidebands $\nu_0 \pm \nu_T$ and $2\nu_0 \pm \nu_T$. A systematic study of the dependence of the tunneling frequencies on the chain length of a series of carboxylic acids, and comparison to macroscopic properties like the heat of fusion, has led to a deeper understanding of subtle differences in crystal packing and its consequences for physical properties.[2]

4.2 NQR: Longitudinal Magnetization

NQR transitions provide chemical and structural information about the environment of the nuclei studied. In pure NQR the transition frequencies are sharply defined by the local electric

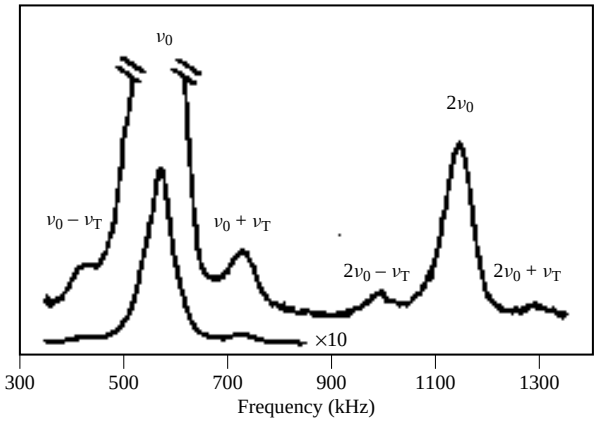

Figure 2 The proton SQUID NMR spectrum of solid hexanol in a magnetic field of 13.5 mT at 4.2 K. One frequency sweep each, from low to high frequencies and in opposite directions, were added. The insert shows the resonance at the Larmor frequency (reduced by 1/10th). The transitions at the Larmor frequencies ν_0 = 574 kHz and $2\nu_0$ = 1147 kHz are flanked by the tunneling sidebands $\nu_0 \pm \nu_T$ for a tunneling frequency ν_T = 145 ± 3 kHz. (Shown at the 33rd ENC, Asilomar, 1992, by B. Black, G. Majer, U. Werner, and A. Pines, reproduced in part by B. Black, Ph.D. Thesis, University of California, Berkeley, CA, 1993)

field gradients at the nucleus studied. However, low signal intensities due to low quadrupole transition frequencies, which can differ by several megahertz in the same sample, pose problems. These difficulties have been addressed by using a SQUID based spectrometer, both by detecting the longitudinal and transverse magnetization.

Studying NQR through the change in static susceptibility differs significantly from NQR experiments that observe the transverse magnetization either with a SQUID or a conventional detection scheme. The difference arises from the quenching of the magnetic moment of the quadrupolar eigenstates in zero field. This quenching is the result of time reversal symmetry of the quadrupole Hamiltonian.[21] For half-integer spins, the eigenstates with magnetic quantum numbers m and $-m$ ($m \neq 0$) are degenerate. For integer spins the eigenstates are either degenerate (for $\eta = 0$, where η is the asymmetry of the quadrupole interaction) or a superposition of equal contributions of the states with magnetic quantum numbers m and $-m$. In either case, exciting a transition between the pure quadrupole eigenstates with linearly polarized rf does not change the static susceptibility, and therefore no signal is induced in the SQUID. Any magnetization induced by a circularly polarized radiation is rapidly quenched by cross relaxation between the $\pm m$ manifolds. These difficulties are avoided by applying a small magnetic field to lift the degeneracy of the eigenstates and suppress cross relaxation. A frequency sweep using linearly polarized radiation through one of the resonances first excites one manifold at its resonance frequency, thereby creating a signal in the SQUID. Upon further increase of the frequency, the resonance of the corresponding negative manifold inverts the magnetization change again. Thus, the spectra resemble a square shape, possibly distorted by relaxation effects between the two resonance transitions.[4,22] This technique has been applied to a number of ^{27}Al, ^{10}B, and ^{11}B containing compounds in single crystals, and in polycrystalline and amorphous samples.[4,22]

Using circularly polarized radiation selectively excites transitions among either the $+m$ or the $-m$ manifold, depending on the sense of polarization.[22] The spectra show the sharp change of magnetization followed by the relaxation decay back to the equilibrium value. One peculiarity of this technique and other NQR measurements with a SQUID is that the sign of the observed changes in magnetization depends on the sign change of the magnetic quantum number of the transitions induced, an effect not observable by non-SQUID NMR.[9]

For integer spins, the application of a magnetic field either splits degenerate eigenstates or redistributes the weights in the superpositions of Zeeman states making up the quadrupolar eigenstates. These effects may still not be sufficient to create an observable signal in the SQUID. A study of the NQR of ^{14}N interacting with the weak electric field gradients in amino acids and small peptides[23,24] shows that the NQR transitions can be observed via cross relaxation of the ^{14}N polarization to adjacent proton spins. Properties of this technique such as the magnetic field dependence, additional signal enhancement by double irradiation, as well as application to studies of the changes of the nitrogen environment by mixing optical isomers and by combining amino acids into small peptides, are given in Werner et al.[23,24]

4.3 NQR: Transverse Magnetization

Pure NQR transitions can be detected with a SQUID by observing the FID after a rf pulse, or a spin echo created by a two-pulse sequence. The echo and a spectrum obtained by Fourier transformation for ^{14}N in NH_4ClO_4 at 1.5 K are shown in Figure 3.[16,17] The signal, a sum of 16 000 transients, shows an FID after the second pulse and the formation of a spin echo after 5 ms. For display, the echo signal was demodulated with a frequency of 35 kHz. The spectrum shows the FT of the echo obtained with a pulse spacing reduced to 4 ms. The sharp peaks at 17.4, 38.8, and 56.2 kHz are the lowest directly detected ^{14}N NQR transition frequencies. Note that these are the absolute frequencies, not those demodulated from a Larmor frequency as is done in high field NMR. The peak at 10.6 kHz was attributed to magnetoacoustic resonance of the input circuit. The three transitions allow determination of the ^{14}N NQCC $|e^2qQ/h| = \chi$ = 63.3 kHz and an asymmetry parameter η = 0.550. The absence of proton zero field NMR lines and of splittings of the ^{14}N NQR in the experimental results suggest motional averaging.

Finally, a SQUID acting as a tuned rf low noise amplifier at liquid helium temperatures was used to detect pulsed NQR at 30.686 MHz of ^{35}Cl in $NaClO_3$.[14,25] The long ring-down times after an rf pulse of the circuit, due to the high quality factor Q = 2500, was reduced using a Q spoiler consisting of a series array of Josephson tunnel junctions.

5 CONCLUSION

Detection of NMR and NQR signals using a SQUID has proven advantageous for studies at low frequencies, over large spectral widths, and at ultralow temperatures. Further technical developments should make these techniques even more widely applicable. For example, current SQUID spectrometers that

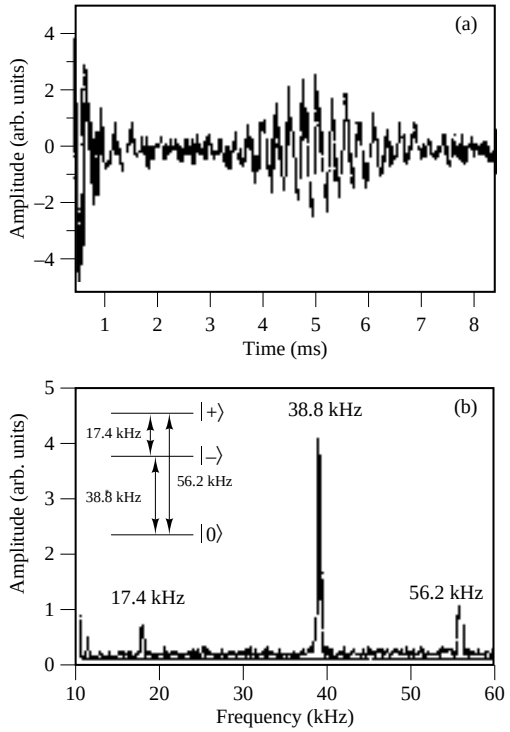

Figure 3 (a) FID after second pulse and spin echo of NH_4ClO_4 at 1.5 K. For display purposes, the real-time signal has been demodulated with 35 kHz. (b) FT of the spin echo. The inset shows the energy level diagram of ^{14}N in the presence of the electric field gradient of NH_4ClO_4. (Reproduced by permission of The American Physical Society from M. D. Hürlimann, C. H. Pennington, N. Q. Fan, J. Clarke, A. Pines, and E. L. Hahn, *Phys. Rev. Lett.*, 1992, **69**, 684)

detect the FID following an rf pulse with untuned circuits are limited by the feedback electronics to frequencies below 200 kHz. An increase in the spectral width and improved stability against rf pulses would open up the possibility for a variety of otherwise very difficult, if not impossible, single- and multi-dimensional NMR and NQR experiments at low magnetic fields using multipulse sequences. Whether detecting longitudinal or transverse magnetization, recent results show that SQUID spectrometers are becoming valuable tools for obtaining answers to a wide range of chemical and physical questions.

6 RELATED ARTICLES

Boron NMR; Cross Polarization in Solids; Field Cycling Experiments; Nitrogen NMR; Quadrupolar Interactions; Quadrupolar Nuclei in Solids; Quantum Tunneling Spectroscopy; Zero Field NMR.

7 REFERENCES

1. D. J. Meredith, G. R. Pickett, and O. G. Symko, *J. Low. Temp. Phys.*, 1973, **13**, 607.
2. B. Black, G. Majer, and A. Pines, *Chem. Phys. Lett.*, 1993, **201**, 550.
3. C. Conner, J. Chang, and A. Pines, *Rev. Sci. Instrum.*, 1990, **61**, 1059.
4. C. Conner, J. Chang, and A. Pines, *J. Chem. Phys.*, 1990, **93**, 7639.
5. R. V. Chamberlin, L. A. Moberly, and O. G. Symko, *J. Low Temp. Phys.*, 1979, **35**, 337.
6. E. P. Day, *Phys. Rev. Lett.*, 1972, **29**, 540.
7. E. P. Day, *Low Temp. Phys.-LT13, 'Proceedings, International Conference on Low Temperature Physics, 13th Meeting', Plenum Press, New York, 1972*, Vol. 4, p. 550.
8. Y. Kondo, T. Mizusaki, A. Hirai, Y. Hirayoshi, and K. Eguchi, *J. Low Temp. Phys.*, 1989, **75**, 289.
9. K. S. Pickens, D. I. Bolef, M. R. Holland, and R. K. Sundfors, *Phys. Rev. B: Condens. Matter*, 1984, **30**, 3644.
10. D. J. Meredith, G. R. Pickett, and O. G. Symko, *Phys. Lett. A*, 1972, **42**, 13.
11. H. Suzuki, Y. Higashino, and T. Ohtsuka, *J. Low Temp. Phys.*, 1980, **41**, 449.
12. R. A. Webb, *Phys. Rev. Lett.*, 1977, **38**, 1151.
13. R. A. Webb, *Rev. Sci. Instrum.*, 1977, **48**, 1585.
14. N. Q. Fan, M. B. Heaney, J. Clarke, D. Newitt, L. L. Wald, E. L. Hahn, A. Bielecki, and A. Pines, *IEEE Trans. Magn. Reson.*, 1989, **25**, 1193.
15. G. J. Ehnholm, J. P. Ekström, M. T. Loponen, and J. K. Soini, *Cryogenics*, 1979, **19**, 673.
16. N. Q. Fan and J. Clarke, *Rev. Sci. Instrum.*, 1991, **62**, 1453.
17. M. D. Hürlimann, C. H. Pennington, N. Q. Fan, J. Clarke, A. Pines, and E. L. Hahn, *Phys. Rev. Lett.*, 1992, **69**, 684.
18. J. Clarke, in *Superconducting Devices*, ed. S. T. Ruggiero and D. A. Rudman, 1st edn, Academic, San Diego, 1990, p. 51.
19. J. Clarke and R. H. Koch, *Science*, 1988, **242**, 217.
20. C. Conner, Ph.D. Thesis, University of California, Berkeley, CA, 1989.
21. G. W. Leppelmeier and E. L. Hahn, *Phys. Rev.*, 1966, **141**, 724.
22. J. Chang, C. Connor, E. L. Hahn, H. Huber, and A. Pines, *J. Magn. Reson.*, 1989, **82**, 387.
23. U. Werner, B. Black, M. Ziegeweid, and A. Pines, *Chem. Phys. Lett.*, 1993, **209**, 17.
24. U. Werner-Zwanziger, M. Ziegeweid, B. Black, and A. Pines, *Z. Naturforsch.*, 1994, **49a**, 1188.
25. C. Hilbert, J. Clarke, T. Sleator, and E. L. Hahn, *Appl. Phys. Lett.*, 1985, **47**, 637.

Biographical Sketch

Ulrike Werner-Zwanziger. *b* 1961. Diplom, 1988, Dr.rer.nat., 1991, Westfälische Wilhelms Universität Münster, Germany. DAAD fellow, 1987–88, Feodor Lynen fellow, 1991–93, with Professor A. Pines. Presently postdoctoral associate at Indiana University, Bloomington, IN, USA. 12 publications. Research interests: the structure of crystalline and disordered materials, and classical and quantum mechanical dynamics in solids.

Knight Shift

Walter D. Knight
University of California, Berkeley, CA, USA

and

Shun-Ichi Kobayashi
University of Tokyo, Tokyo, Japan

1	Introduction—NMR and Structure of Metals	1
2	Lattice Structure and Dynamics	1
3	Orbital and Core Polarization Shifts, Spin Relaxation	2
4	Structures of Alloys	3
5	Electronic Structure of Mesoscopic Particles[20]	3
6	Knight Shift in Superconductors	5
7	Related Articles	6
8	References	6

1 INTRODUCTION—NMR AND STRUCTURE OF METALS

The Knight shift refers to the relative shift K in NMR frequency for atoms in a metal (e.g. sodium) compared with the same atoms in a nonmetallic environment (e.g. sodium chloride). The observed shift reflects the local magnetic field produced at the sodium nucleus by the magnetization of the conduction electrons. The average local field in sodium augments the applied resonance field by approximately one part per 1000. In nonmetallic sodium chloride the local field is negligible in comparison.

Conduction electrons[1] in a metal are delocalized, meaning that no electron is uniquely associated with any particular atom more than another but all exist in eigenstates within an energy band, whose highest occupied state lies at an energy E_F, the Fermi energy. At lower energies the electron wave functions tend to be mainly s states, while at higher energies there are increasing admixtures of higher (p, d, ...) states. For s states the probability density at the nucleus ($R = 0$) is high, and since each electron carries a spin and magnetic moment μ_B, the contact interaction momentarily produces a local magnetic field at the nuclei, as the electron moves through the lattice.

The local hyperfine field in atomic sodium is approximately 39 T. This is an atomic property, independent of external fields. The average contact hyperfine field in a metal is zero, in zero applied field, because the nucleus is exposed to equal numbers of spin-up and spin-down electrons. In an externally applied magnetic field the conduction electron system acquires a magnetization proportional to the magnetic susceptibility of the conduction electron system. The appropriate susceptibility χ_p is the temperature independent Pauli paramagnetism. Because the electron magnetic moments parallel to the applied field have the lower energies, the parallel orientation is more favorable than the antiparallel, and consequently the number of parallel moments is greater, hence the paramagnetism. The fractional change in field, or observed resonance frequency, is[2]

$$K = \Delta B/B = \Delta\nu/\nu = (8\pi/3)\chi_p V_0 P_F \qquad (1)$$

where χ_p is the Pauli susceptibility per unit volume, V_0 is the volume per atom in the metal, P_F is the average value of the s electron probability density at $R = 0$, B is the applied magnetic field, and ν is the observed resonance frequency. The average P_F is taken for electrons at the Fermi energy E_F. The local field of p electrons is usually 10% or less of the contact interaction, and produces small anisotropic shifts in noncubic metals (c.f. Section 2.3). The anisotropic effects vanish in cubic metals. In noncubic metals the effects are relatively small, but yield valuable information concerning electronic and crystal structures.

To summarize some typical parameters: the hyperfine field per electron in a free sodium atom is 39 T; the corresponding contact hyperfine field in metallic sodium is smaller, ~30 T, mainly because of p admixtures in the wave functions at the Fermi surface; the small Pauli susceptibility reflects the small number of unpaired spins; the average local field is 1.1×10^{-3} T for an applied field of 1 T; and equation (1) gives $K = 0.11\%$.

Values of K have been measured for most of the metallic elements, and recorded results range approximately from $K = 0.026\%$ (Li) to 2.7% (Hg). The measurement of K is a sensitive means for probing, noninvasively, electronic and geometric structures of metallic systems in solids and liquids, and has been of value in studying phase transitions in metals, alloys, intermetallic compounds, and superconductors.[3]

2 LATTICE STRUCTURE AND DYNAMICS

2.1 Effects of Pressure, Volume, and Temperature

It is evident from equation (1) that insofar as the parameters χ_p, V_0, and P_F depend on pressure, volume, or temperature, K is affected by, and is a measure of, these variables. Compressing a specimen effectively changes the volume per atom and P_F, while heating affects the volume, the lattice dynamics, and electron–phonon interactions as well. Although the Pauli susceptibility is essentially independent of temperature, other contributions to the susceptibility are temperature dependent, and NMR shifts have corresponding temperature dependences (c.f. Sections 3.1 and 3.2).

In order to find the intrinsic temperature dependence, one can measure K versus T at constant P, and K versus V at constant T, also knowing the thermal expansion coefficient and compressibility. With so many variables, the end results are useful, but may not be as precise as one would wish. Bloembergen has pointed out[4] that P_F is nonlinear with respect to volume, and χ_p depends on lattice vibration frequency via spin–lattice relaxation.

Recently, Götz and Winter[5] have considered the volume dependence of K for the alkali metals lithium and sodium, for which many experimental data exist. They pointed out that the theoretical analysis requires the inclusion of orbital plus exchange and correlation terms (c.f. Sections 3.1 and 3.2). While they were able to arrive at good agreement with the experimental results for lithium, the result for sodium is less clear. The work serves to illustrate the fact that the theoretical problems are more elaborate than was believed at first.

2.2 Anisotropic Shift

For noncubic crystals K becomes a function of crystal orientation with respect to the applied field.[6] We can perform and analyze NMR shift experiments in crystals with axial symmetry, for example, introducing the axial shift K_{ax}, which depends on hyperfine magnetic fields at the nucleus generated by p electrons. These fields are generally 10% or less of the contact hyperfine fields, but valuable structural information may be obtained.[6]

For crystals of axial symmetry, the anisotropic part of the NMR shift is a function of the angle θ between the principal symmetry axis and the applied magnetic field.

$$K_{ax} = q_F \chi_p (3\cos^2\theta - 1) \tag{2}$$

The shape of the p electron charge distribution and its dipole field at $R = 0$ are included in the function q_F in equation (2). For an axially symmetric crystal the total NMR shift is the sum of equations (1) and (2).

For a single crystal specimen the NMR appears at frequencies varying between extremes at $\theta = 0^\circ$ and 90°. A polycrystalline sample shows a broadened lineshape between the above extremes, with the largest intensity near $\theta = 90^\circ$, and the frequency of minimum intensity appears at higher frequency for positive q_F. For nonaxial symmetry, the corresponding extended analysis is straightforward.[6] Experimental results are also interpreted in terms of crystal structure and electronic band structure (s–p admixture).

2.3 Quadrupole Coupling

An analysis similar to the above can be made for nuclei with the quadrupole moment Q in a noncubic environment. The first-order quadrupole interaction frequency is

$$\nu = e^2 q Q / h \tag{3}$$

where q is the local electric field gradient at the nucleus, which depends on crystal structure ($q = 0$ in cubic symmetry). For a first-order interaction in a specimen with nuclear $spin - \frac{3}{2}$ the spectrum consists of a pair of satellites astride the central NMR resonance and split by $\pm e^2 qQ/4h$. More complete discussions, including second-order quadrupole effects, are available.[6]

3 ORBITAL AND CORE POLARIZATION SHIFTS, SPIN RELAXATION

3.1 Orbital Paramagnetism

Several other factors contribute to the total NMR shift in metals. Beyond the Pauli term in equation (1), there is the orbital (Van Vleck) paramagnetism, and also the core polarization by d electrons. Each of the above effects is associated with a respective magnetic susceptibility, and may be summed as follows:

$$\chi = \chi_p + \chi_v + \chi_d \tag{4}$$

The Pauli term χ_p predominates in light monovalent metals, while the second and third terms generally make large contributions in heavy and transition metals. The first two are nearly independent of temperature in the normal state. The last tends to be paramagnetic and temperature dependent for transition metals with narrow d bands and low Fermi temperatures.

The orbital paramagnetism χ_v is a second-order effect in solids analogous to the Van Vleck temperature independent paramagnetism in molecules.[7,8] It arises because of the mixing of filled and unfilled orbitals in the same band. It appears that the contact term χ_p for vanadium is approximately cancelled by the negative χ_d term, and small compared with the orbital χ_v term.[9] This conclusion is consistent with the fact that the NMR shift in vanadium is minimally affected by the transition to the superconducting state (the predominant orbital hyperfine field is not related to electron spin pairing—see Sections 3.2, 4.3, and 6.1).

The orbital susceptibility can be estimated[8] in several ways, one of which can be expressed as

$$\chi_v \sim 2\mu_B^2 N/E \tag{5}$$

where N is the number of d electrons per unit volume, and E is the average energy separation of the mixed states.

3.2 Core Polarization

The third term in equation (4) represents the temperature dependent paramagnetic d states. Although the direct hyperfine interaction of d electrons is small, s electrons (either in a filled shell or in an s band) couple[10] with the paramagnetic d electrons and produce hyperfine fields which can be comparable (or of opposite sign) to the direct s electron contact interaction. For example, in platinum the predominant contribution[11] to K derives from core polarization, which is calculated to be negative, resulting in a large observed negative shift, $K_{Pt} = -3.5\%$.

A recent band structure Green's function analysis[12] points out that equation (4) implies independence among the several terms, while in fact the terms are not strictly independent, and it is in principle necessary to include spin–orbit and exchange correlation effects in the calculations. It is also clear from their results and comparison of several calculations with equation (5) that the latter provides useful but imprecise estimates for susceptibilities and shifts. The theoretical results support the previous interpretations for the observed shifts in vanadium[9] and platinum.[11]

3.3 Diamagnetism of Conduction Electrons

In addition to the terms in equations (1) and (4), the contribution of the Landau diamagnetism by the conduction electrons is significant. When a magnetic field is applied to the conduction electron system, the levels split so that the average energy of the system increases, corresponding to a diamagnetism of one-third χ_p,[13] with a correction factor involving the electron effective mass:

$$\chi_L = -(\chi_p/3)(m/m^*)^2 \tag{6}$$

This χ_L term appears to be significant but relatively small in most metals, and is believed to be mainly responsible for the large negative $K = -1.25\%$ in solid bismuth, which is characterized by a very small effective mass. By contrast, liquid bismuth behaves more like an ordinary metal, since $K = +1.4\%$ in the liquid. A further interesting observation is the oscillation of K as a function of applied magnetic field, in analogy to the de Haas–van Alphen effect.

3.4 Korringa Relation

An important means of directly relating metallic properties to NMR experiments depends on the Korringa relation,[4] which is based on the fact that the nuclear spin relaxation rate $1/T_1$ varies directly as temperature T and the square of the density of states $[N(E_F)]^2$ at the Fermi surface, while K is simply proportional to $N(E_F)$. In abbreviated form the Korringa relation is expressed

$$K^2 T_1 T \sim S \tag{7}$$

The Korringa product factor S on the right-hand side of equation (7) includes the magnetogyric ratios of the electron and nucleus. Equation (7) permits an independent evaluation of K in cases where χ is uncertain. The order of magnitude of S is generally unity when K is dominated by the contact interaction, as is true for the alkali and simple metals. For transition metals, where $S \gg 1$, equation (7) must be used with caution, noting also that the measured T_1 may include a contribution produced by fluctuating nuclear quadrupole interactions. The orbital paramagnetism χ_v depends on the average density of states over the conduction band and should not be included in a calculation involving equation (7), since χ_p and K depend simply on $N(E_F)$.

3.5 Overhauser Effect

The contact hyperfine interaction which produces the Knight shift, as well as relaxing the nuclear spins, acts reciprocally to produce a magnetic field on the conduction electrons because of the large nuclear polarization. This interaction produces a shift in the ESR, and a large enhancement of the NMR intensity, the Overhauser effect.[14] The magnitude of the intensity enhancement is easily a factor of 10 or more. Under conditions of maximum NMR intensity enhancement, the ESR is saturated, and the frequency of the ESR is shifted (the Day shift).

4 STRUCTURES OF ALLOYS

4.1 Metallurgical Phases in Simple Binary Alloys

The classical treatment of alloys was based on thermodynamic analysis, crystal structures, and the average electron–atom ratios. Further local information is obtained by measurements of the Knight shift. Alloys of cadmium in silver include an α phase (face-centered cubic) with up to ~40% cadmium, followed by a mixed α and β phase (41–49% cadmium), then a β phase (body-centered cubic) (49–51% cadmium), followed by the phases γ, ϵ, η (pure Cd). The mixed phases are characterized by two NMR lines with K values appropriate to the respective adjacent pure phases.[6,15]

In the α phase of silver–cadmium alloy, K_{Cd} decreases linearly from 0.59 to 0.53% at the β phase boundary. The silver shift drops linearly from 0.52 to 0.46% in the α phase, as predicted,[16] but was not observed at higher concentrations because of low signal strength.

Analysis of the local electronic structure, as seen by the solute atom in the alpha phase may proceed on the basis of equation (1), using χ_p (solvent), and P_F (solute, modified to include s–p character of the solvent).

The average electron density is reduced by long range charge density oscillations in space, which are induced by the perturbing solute atoms.[16] The net result is a decreasing average charge density at solvent atoms with increasing solute concentration. Since the charge density oscillates with relative positions of solute and solvent atoms, the average reduction of the K shift is accompanied by a resonance line broadening.

4.2 Intermetallic Compounds

These are alloys with definite stoichiometries. Depending on the constituents and temperature, intermetallic compounds may be metallic conductors, semiconductors, or superconductors (c.f. Section 6). It was found[9] that K for vanadium is strongly dependent on temperature in the superconducting intermetallic compound V_3Ga. Just above the transition temperature T_c the vanadium shift $K_V = +0.45\%$, changing to +0.65% for $T \ll T_c$. Correspondingly, the gallium shift K_{Ga} changes from -0.8 to -0.2%. In both cases the average hyperfine field becomes more positive as the negative core polarization shift decreases. These results raise a number of interesting questions, such as what are the charge density patterns of the band electrons.

4.3 Alloys with Dilute Magnetic Impurities

The scattering of conduction electrons by impurity atoms is considered in Sections 4.1 and 5.3. Long range spatial charge oscillations and indirect spin couplings[17] between distant electrons and nuclei result in long-range variations in local fields, and polarizations which couple with host atoms as well as other impurities. NMR shifts and line broadenings are observed, in addition to resolved satellites for the NMR resonance lines.[18]

4.4 Muon Spin Resonance

Just as the conduction electrons probe the atom cores, the muon spin rotations, prior to their decay, provide signals measuring the local magnetic fields near the decay sites.[19] Knight shifts of from 10 to 100 ppm are observed for $\mu+$ at frequencies of a few megahertz in fields of a few kilogauss. Muon spin resonance techniques have the advantages of fast timescales and no complications by quadrupole interactions.

5 ELECTRONIC STRUCTURE OF MESOSCOPIC PARTICLES

5.1 Energy Levels

The energy spectrum of electrons confined in a finite volume is, in principle, discrete. In macroscopic metals, however, the spacing of the energy levels is very much smaller than the lifetime broadening of the levels, and, therefore, the continuous energy spectrum is a good approximation. The broadening caused by electron–phonon interactions and/or electron–electron interactions diminishes as the temperature is lowered, and typically becomes of the same order as thermal energy at 1 K. Thus, in small particles with an energy spacing larger than 1 K we would expect anomalies in electronic properties at temperatures below 1 K. The spacing is evaluated as

$$\delta = [N(E_F)\Omega]^{-1} \tag{8}$$

where $N(E_F)$ is the density of states at the Fermi level and Ω is the sample volume. In ordinary metals, Ω is $(10^4\ \text{pm})^3$ for δ to be 1 K.

Fröhlich was the first to point out anomalies in the thermodynamic properties in particles, assuming that the levels are equally spaced.[21] Kubo took a more realistic level distribution, i.e. a random distribution. Kubo also put emphasis on the charge neutrality of particles because a single electron imbalance brings a large charging energy.[22] Shortly after, Gorkov and Eliashberg suggested that the level distribution is not random but has statistical correlations, in analogy to the level distribution in heavy nuclei.[23] These correlations are the results of the symmetries of Hamiltonians governing the system.

Let $P(E)\ \mathrm{d}E$ be the probability of finding the next level between E and E + dE. It can be shown that, in the limit of small E,

$$P(E) = E^{n-1}/\delta^n \tag{9}$$

where n is the number of random variables. Four cases are possible:

1. case 1, n = 2: elements of the Hamiltonian matrix are real.
2. case 2, n = 3: in high magnetic fields where the elements are complex.
3. case 3, n = 5: with a strong spin–orbit interaction, where spin and orbital states are not separable.
4. case 4, n = 1: with a large Zeeman energy, where the levels of up and down spins are no longer correlated.

These discrete and correlated levels modify the electronic quantities such as spin paramagnetism, nuclear spin–lattice relaxation time, orbital diamagnetism, and specific heat. So far, the first two have been investigated both theoretically and experimentally. The specific heat is very difficult to measure accurately. There is a prediction that the orbital magnetization can be both positive and negative, and will fluctuate with a large amplitude when a magnetic field is swept,[24] but no experiment has been reported.

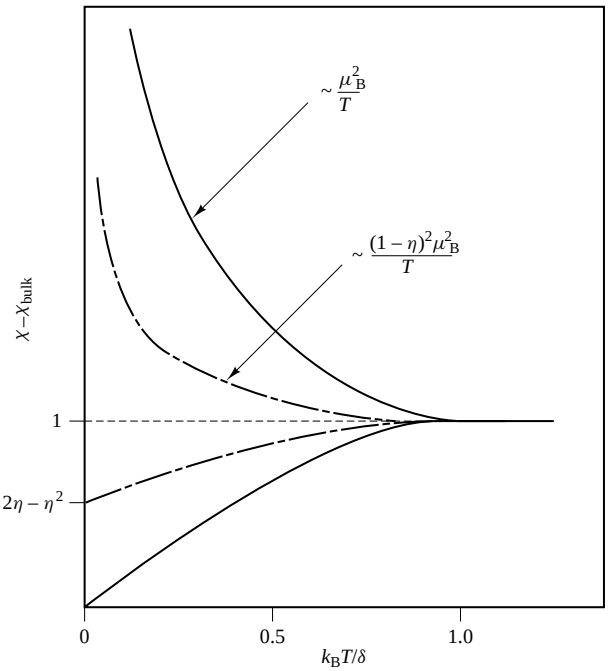

Figure 1 Temperature dependence of χ_{even} and χ_{odd}, with $\eta = (h/\tau_{so})$[27]

5.2 Magnetism

The spin paramagnetism of small particles shows characteristic behaviors. For case 1, the spin susceptibility of a particle with an odd number of electrons, χ_{odd}, is Curie-like as $T \to 0$ because there is an electron that has no partner with opposite spin. The susceptibility of a particle with an even number of electrons, χ_{even}, tends to zero as $T \to 0$, as all the spins are paired with opposite ones. In case 2, χ_{even} revives because of the mixing of up- and down-spin states. The behaviors of χ_{even} and χ_{odd} are calculated with a finite strength of the spin–orbit interaction. The results are shown schematically in Figure 1. All anomalies in susceptibility vanish when $k_B T > \delta$.

The spin magnetization is nonlinear when the magnetic field is as high as $2\mu_B H \geq \delta$, because the level correlation is diminished.[25] Thus, when $2\mu_B H \geq \delta$, the spin magnetization will take a normal Pauli value.

Nuclear spin–lattice relaxation in metals is governed by the Korringa process, the relaxation time, T_1, being inversely proportional to the temperature, reflecting the continuous energy spectrum of electrons. In small particles this process is strongly suppressed, because it is not always possible to conserve the energy through the process which involves a mutual flip of electron and nuclear spins and a change in electron orbital state.

5.3 Small Particles and Alloys

The first quantitative experiment of the Knight shift in small copper particles was reported by Yee and Knight.[26] The samples were particles that are formed on substrates at early stages of vacuum deposition. This method has been used for all the experiments described in this article. The distribution width of linear sizes of particles in each sample is about 20%

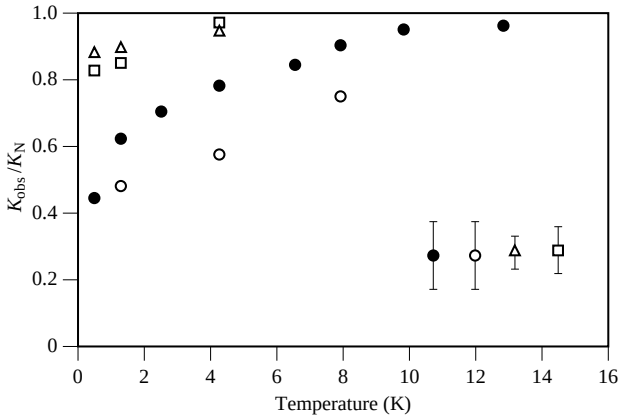

Figure 2 Temperature dependence of shifts in copper particles.[26] Particle diameters: ○, 2.5 nm; ●, 4.0 nm; □, 10.0 nm; △, 11.0 nm

of its mean value. In Figure 2 the results of the Knight shift are shown for several samples. The temperature dependence and the size dependence of the residual shifts at $T = 0$ agree quantitatively with theory.[27]

The spin–lattice relaxation time in copper particles was measured, and extraordinarily enhanced T_1 values were observed, as expected.[28]

The suppression of the Knight shift anomaly in high magnetic fields (case 4) was confirmed in 10.0 and 6.0 nm copper particles.[29] The suppression was observed when $2\mu_B H \geq \delta$.

The spin scattering by magnetic impurities destroys the effects of level discreteness. To establish a kinetic energy level in a particle, an electron has to 'see' all the boundary conditions, i.e. it has to 'sweep' the whole volume of the particle. It can be shown that the time necessary for this travel is $\tau = \Omega/\pi v_F \lambda_F{}^2$, where v_F and λ_F are the Fermi velocity and the Fermi wavelength, respectively. If an inelastic scattering takes place before τ, the level cannot be sharp. The above expression for τ is equivalent to $\tau\delta = h$. This consideration can help interpret the results of the Knight shift of ^{63}Cu in particles of copper–manganese alloys.[30] The suppression of spin paramagnetic susceptibility disappeared when the manganese concentration was increased so that the spin scattering time is shorter than h/δ. The anomaly in T_1 also vanished.[31]

The strength of the spin–orbit interaction can be modified by alloying a heavy element in particles. The Knight shift was measured in copper particles alloyed with gold.[32] As the concentration of gold increased, the Knight shift recovered the bulk value. Although this change is the same as that in copper–manganese, a substantial difference was observed in T_1. The value of T_1 stayed very long even after the shift was completely recovered. This is because the spin scattering is inelastic while the spin–orbit scattering is elastic, the phase memory being retained in the latter.[31]

6 KNIGHT SHIFT IN SUPERCONDUCTORS

6.1 Spin Pairing

According to the BCS theory of superconductivity, the Knight shift quickly vanishes below the transition temperature, because of spin–singlet pairing.[33] NMR experiments were intensively carried out to check the validity of the theory. However, in some superconductors of heavy metals the shift did not vanish but stayed finite when $T \to 0$. Soon after, it was recognized that this was a size effect. To measure the shift, samples of reduced dimension (thin films or fine powders) were used, in order to increase critical fields of superconductors of the first kind and to let the rf field penetrate the samples. The reduced dimension makes the mean free path shorter, and enhances mixing of up- and down-spin states due to spin–orbit interactions. Thus, for the same reason as for the residual Knight shift in normal heavy metal particles, the shift remains finite even when $T \to 0$.[34]

6.2 Contributions to Shift

In transition metal superconductors the Knight shift consists of three contributions: the s band spin polarization, the orbital (Van Vleck) polarization, and the core polarization induced by non-s spin polarization. The first two are positive in sign, and the last is experimentally negative, although it can take both signs in principle. The three contributions can be resolved by observing the temperature dependence of the shift in the normal state. What is suppressed in the superconducting state is the first and the last polarization, while the orbital part does not change (cf. Section 3). A great deal of data has been accumulated for various superconductors.[35]

6.3 How Small is a Superconductor

In the 1970s, the order parameter fluctuation in superconductors with reduced dimensions was exhaustively studied. Measured Knight shifts in aluminum particles smaller than the coherence length and penetration depth[36] agreed with microscopic theories for the critical region of temperature.[37] The result for aluminum particles is shown in Figure 3.[36] The theories were based on a grand canonical treatment, which is hardly applicable to small particles with a large charging energy, and does not take the discreteness of energy levels into account. As expected, substantial deviation takes place when the particles are smaller than 10.0 nm, in which δ is larger than the superconducting energy gap, Δ.[38]

The residual Knight shift in tin particles as a function of particle size demonstrates the competition among three energy parameters, i.e. δ, Δ, and h/τ_{so}, where τ_{so} is the time within which the spin direction diffuses by an angle π due to spin–orbit interactions.[39] These energies are proportional to d^{-3}, d^0 and d^{-1}, respectively, d being a linear size. Therefore, Δ dominates in the bulk, and the shift vanishes. As the size is reduced, h/τ_{so} surpasses δ, and the shift (of particles with even number electrons) revives. With a further reduction, δ becomes the largest, and the shift disappears again. The experiment in tin particles with d ranging from 2.5 to 60.0 nm[38] clearly demonstrates this competition (Figure 4). The shift exhibits a peak at around 10.0 nm which corresponds to $\delta \sim \Delta$.

It is interesting to know how many atoms are necessary in small particles for superconductivity. Unfortunately, the level discreteness and the superconductivity modify the Knight shift (in particles with an even number of electrons) and T_1 in the same direction. A reliable way to judge the superconductivity

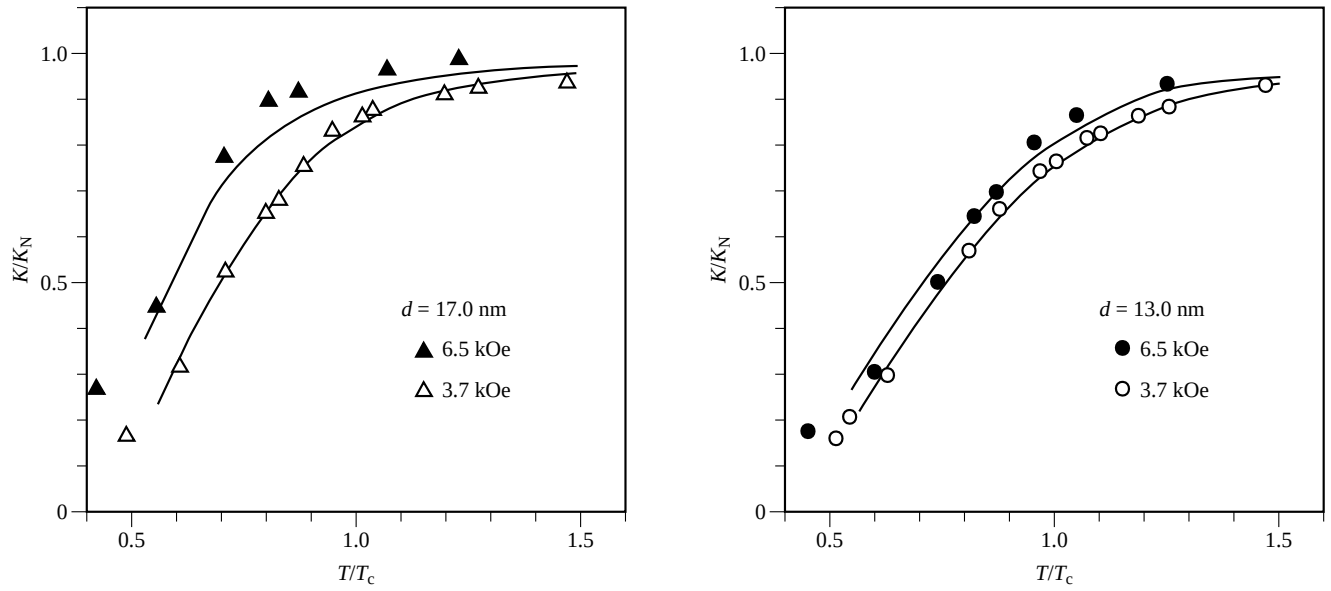

Figure 3 Temperature dependence of shifts in aluminum particles[36]

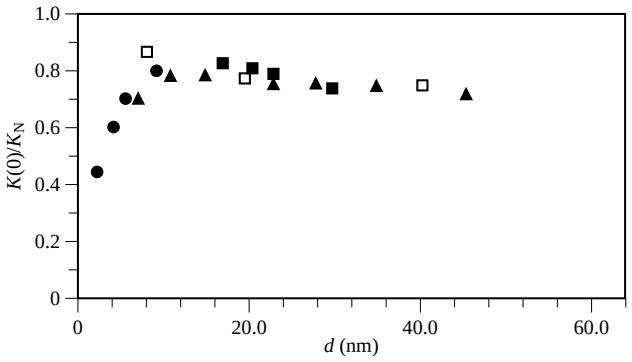

Figure 4 Size dependence of residual shifts in tin particles[38]

is to see if there is a sharp decrease in T_1 at an expected critical magnetic field for superconductivity. The results show that particles are superconductive even when $\delta \geq \Delta$. The observed critical fields support microscopic theories of pair breaking.[39,40] Much smaller particles of aluminum with $\delta \sim 65\,\mathrm{K}$ still exhibit superconducting features as long as T_1 is involved.[41]

6.4 High T_c

Since the discovery of high-T_c oxide superconductors, NMR has been used extensively to clarify the mechanism. The Knight shifts and relaxation times were measured for most of the constituent elements, such as ^{89}Y, ^{137}Ba, ^{63}Cu, and ^{17}O, in 'YBCO', yttrium barium copper oxide.

The main interest is to identify the nature of pairing, i.e. s wave or d wave pairing.[42] Recently, there has been considerable debate on this question, which appears not to be settled as of March 1994. A complete understanding of the mechanisms operating in high-T_c materials still seems remote.

7 RELATED ARTICLES

Electron–Nuclear Hyperfine Interactions; High Temperature Superconductors; Nuclear Overhauser Effect; Quadrupolar Nuclei in Solids; Relaxation of Quadrupolar Nuclei Measured via Multiple Quantum Filtration.

8 REFERENCES

1. C. Kittel, *Introduction to Solid State Physics*, Wiley, New York, Chap. 18
2. C. H. Townes, C. Herring, and W. D. Knight, *Phys. Rev.*, 1950, **77**, 852.
3. G. C. Carter, L. H. Bennett, and D. J. Kahan, *Metallic Shifts in NMR*, Part I, Pergamon Press, Oxford, 1977.
4. N. Bloembergen, *Can. J. Phys.*, 1956, **34**, 1299.
5. W. Götz and H. Winter, *J. Phys. F.*, 1991, **3**, 8931.
6. T. J. Rowland., *Progr. Metal Phys.*, 1961, **9**.
7. N. F. Ramsey, *Nuclear Moments*, Wiley, New York, 1953.
8. R. Kubo and Y. Obata, *J. Phys. Soc. Jpn.*, 1956, **11**, 547.
9. A. M. Clogston, A. C. Gossard, V. Jaccarino, and Y. Yafet, *Phys. Rev. Lett.*, 1966, **9**, 262.
10. M. H. Cohen, D. A. Goodings, and V. Heine, *Proc. Phys. Soc. (London)*, 1959, **A73**, 811.
11. A. M. Clogston, V. Jaccarino, and Y. Yafet, *Phys. Rev.*, 1964, **134**, A650.
12. H. Ebert, H. Winter, and J. Voitländer, *J. Phys F.*, 1986, **16**, 1133.
13. R. E. Peierls, *Quantum Theory of Solids*, Oxford University Press, Oxford, 1955, p. 144.
14. A. W. Overhauser, *Phys. Rev.*, 1953, **92**, 411.
15. L. E. Drain, *Phil. Mag.*, 1959, **4**, 444.
16. J. Friedel, *Phil. Mag.*, 1952, **43**, 153.
17. C. Kittel, *Quantum Theory of Solids*, Wiley, New York, 1963.
18. J. B. Boyce and C. P. Slichter, *Phys. Rev.*, 1976, **13**, 379.
19. A. Schenk, *μSR Spectroscopy, Principles and Applications in Solid State Physics*, Adam Hilger, Bristol, 1985.

20. W. P. Halperin, *Rev. Mod. Phys.*, 1986, **58**, 533; S. Kobayashi, *Phase Transitions*, 1990, **24**, 463.
21. H. Fröhlich, *Physica*, 1937, **6**, 406.
22. R. Kubo, *J. Phys. Soc. Jpn.*, 1962, **17**, 975.
23. L. P. Gorkov and G. M. Eliashberg, *JETP*, 1965, **21**, 940.
24. D. Yoshioka and H. Fukuyama, *J. Phys. Soc. Jpn.*, 1992, **61**, 2368.
25. K. B. Efetov, *JETP*, 1982, **56**, 467.
26. P. Yee and W. D. Knight, *Phys. Rev. B*, 1975, **11**, 3261.
27. J. Sone, *J. Phys. Soc. Jpn.*, 1977, **42**, 1457.
28. T. Goto, F. Komori, and S. Kobayashi, *J. Phys. Soc. Jpn.*, 1989, **58**, 3788.
29. S. Kobayashi and S. Katsumoto, *J. Phys. Soc. Jpn.*, 1987, **56**, 2256.
30. S. Kobayashi, H. Goto, and S. Katsumoto, *J. Phys. Soc. Jpn.*, 1992, **61**, 762.
31. H. Goto, S. Katsumoto, and S. Kobayashi, *J. Phys. Soc. Jpn.*, 1993, **62**, 1439.
32. S. Kobayashi, H. Goto, and S. Katsumoto, *J. Phys. Soc. Jpn.*, 1992, **61**, 1856.
33. K. Yosida, *Phys. Rev.*, 1958, **110**, 769.
34. R. A. Ferrell, *Phys. Rev.*, 1959, **3**, 262; P. W. Anderson, *Phys. Rev. Lett.*, 1959, **3**, 325; F. Reif., *Phys. Rev.*, 1957, **61**, 208; F. Wright, Jr., W. A. Hines, and W. D. Knight, *Phys. Rev. Lett.*, 1967, **18**, 115.
35. D. E. MacLaughlin, in *Solid State Physics*, ed. F. Seitz, D. Turnbull, and H. Ehrenreich, Academic Press, New York, 1976, pp. 1–69.
36. S. Kobayashi, T. Takahashi, and W. Sasaki, *J. Phys. Soc. Jpn.*, 1975, **38**, 559; M. Ido and R. Hoshino, *J. Phys. Soc. Jpn.*, 1975, **38**, 897.
37. H. Shiba, *J. Low Temp. Phys.*, 1976, **22**, 105; J. Sone, *J. Low Temp. Phys.*, 1976, **23**, 699.
38. Y. Fukagawa, S. Kobayashi, and W. Sasaki, *J. Phys. Soc. Jpn.*, 1982, **51**, 1095.
39. J. Sone, *J. Phys. Soc. Jpn.*, 1977, **41**, 1457.
40. K. Nomura, S. Kobayashi, and W. Sasaki, *J. Phys. Soc. Jpn.*, 1980, **48**, 37.
41. F. Komori, T. Goto, K. Wago, and S. Kobayashi, *J. Phys. Soc. Jpn.*, 1988, **57**, 3868.
42. C. P. Slichter, S. E. Barrett, J. A. Martindale, D. J. Durand, C. H. Pennington, C. A. Klug, K. E. O'Hara, S. M. DeSoto, T. Imai, J. P. Rice, T. A. Friedman, and D. M. Ginsberg, *Appl. Magn. Res.*, 1992, **3**, 423.

Biographical Sketches

Walter D. Knight. *b* 1919. A.B., 1941, Physics, Middlebury College, M.A., 1943, Ph.D., 1950, Physics, Duke University, NC (informal supervisor, Charles H. Townes). Instructor in physics, Trinity College, Hartford, 1946–50. Assistant, associate, and professor, Physics Department, University of California, Berkeley, 1950–90, Dean, College of Letters and Science, 1967–72, Professor Emeritus, 1990–present. Member, National Academy of Sciences, American Academy of Arts and Sciences. Approx. 90 publications. Research specialties: NMR in metals, properties of metal clusters.

Shun-ichi Kobayashi. *b* 1938. B.S., 1962, Ph.D., 1967, Physics, Osaka University, Japan; introduced to NMR by Junkichi Itoh. Postdoctoral work at Orsay, Université de Paris, 1967–68. Successively research associate, lecturer, associate professor, and professor, University of Tokyo, Japan, 1968–present. Approx. 120 publications. Research specialties: NMR in small particles of metals, the Anderson localization, quantum transport in mesoscopic systems.

Metals: Pure and Alloyed

Theodore J. Rowland
University of Illinois, Urbana, IL, USA

1	Introduction and Background	1
2	Experimental Details	2
3	Principal Theoretical Concepts	3
4	Pure Metals with Nonzero μ_I	5
5	Alloys	6
6	Nuclear Relaxation and Atomic Diffusion: Nuclear Relaxation in $I = 1/2$ Systems	7
7	Related Articles	8
8	References	8

1 INTRODUCTION AND BACKGROUND

1.1 The Beginning of NMR in Metals: Investigators and Material

The discovery of the resonance of nuclei is so recent that the number of subspecialties that have developed is astounding. In large part it represents the number of working scientists during the intervening years. In addition, the time period is one during which solid state physics, polymer physics, and more recently the biological sciences have seen unprecedented advance.

The discovery of the fact that proton resonance could be observed with relative ease if the required conditions were understood led two independent groups to construct apparatus to search for, and to find, the phenomenon in the same year. Fortunately, nuclear physics had a long history of research culminating in a burst of activity in the early 1940s. Tables of nuclear moments were available and there was an immediate spread of NMR to a host of elements in the Periodic Table. Pound saw the Cu metal resonance from the wire of his rf spectrometer[1] and Knight[2] soon after found that Cu metal and the corresponding isotopes in CuCl were at different frequencies in the same external magnetic field. Nuclear magnetic resonance in metals was thus launched only two years after the first nuclear resonance observation of hydrogen. The latter required the knowledge and skill of brilliant scientists, each of whom received a (shared) Nobel prize. Reading the Nobel prize acceptance speeches is rewarding, as is the study of the papers of Purcell et al. and Bloch et al. published in *Physical Review* in 1946.

Workers in the field of NMR in metals require an interdisciplinary background strong in physics, especially the theory of the solid state, and also well-developed in metallurgy. The latter subject remains one in which few phenomena are derived a priori, and the words 'experience' and 'art' are sometimes necessary to describe the methods successfully used in specimen preparation. Complex studies that purport to demonstrate a correlation between an NMR result and a particular aspect of the behavior of a metal or alloy should assume from the outset that the physical property under investigation must be measured on a batch of material prepared for the study, and that the NMR must be conducted on samples from the same batch. An example study might be the rate of internal oxidation measured using resistivity or susceptibility together with NMR absorption line parameters. Correlation of NMR results with mechanical properties (rather than electrical) is usually more difficult.

1.2 Metals and Nuclei

The metallic state has several familiar but different characteristic mechanical and electrical properties when compared with other solid types. If we consider the four classic types of solids, metallic, ionic, covalent, and molecular (or van der Waals),[3] the metals are known to be highly ductile, good electrical and thermal conductors, and different in their magnetic properties from ionic and covalent solids. The underlying reasons for the physical properties of metals lies almost entirely in their electronic structure. In solids which are primarily ionic or covalent the bonding potentials are largely central or directional, respectively. Metals by contrast are held together by nondirectional atomic potentials. Nearly all metals have one atom per lattice site, and thus have structures in which the atoms lie on the points of a Bravais lattice.[4] Not surprisingly most metals have lattice structures in which the atoms are arranged as closely packed spheres [face centered cubic (fcc) and hexagonal close packed (hcp)]. The next most common structure among metals is body centered cubic (bcc). Of the roughly 50 metals in the Periodic Table about 36 are close packed and 14 bcc. Nearly *all* of these metals have at least one isotope which is useful for NMR, i.e., it has nonzero nuclear spin I, and thus a nonzero nuclear magnetic moment $\mu = \gamma_I \hbar I$, where γ_I is the nuclear gyromagnetic ratio and $\hbar$ = Planck's constant divided by 2π. The majority of metals have more than one isotope of $I > 0$ (i.e., from among $I = \frac{1}{2}, 1, \frac{3}{2}, 2, \ldots$). Isotopic abundance is a crucial factor in considering the feasibility of observing the nuclear resonance of a particular metal.

In addition to a magnetic dipole moment μ, a majority of nuclei have an observable electric quadrupole moment Q. In brief form there are two restrictions that limit the observability of electrical multipole moments:[5] (a) No odd (l odd) electrical multipole (2^l-pole) moments can exist, and (b) for a nuclear spin I, it is impossible to observe a nuclear multipole moment of order 2^l greater than that corresponding to $l = 2I$. (The result of these restrictions is that we can expect to observe no dipole, octupole, ... electrical moments; and that for $I = \frac{1}{2}$ we can observe no multipole greater than dipole, for $I = 1$ we can observe no multipole greater than quadrupole, for $I = \frac{3}{2}$ we can observe no multipole greater than octupole, for $I = 2$ we can observe no multipole greater than hexadecapole, and so on.) We distill from these statements that $Q = 0$ when $I = \frac{1}{2}$ and that for $I \geq 1$, Q may be and usually is nonzero. The hexadecapole and higher existing moments have not been observed, probably because of their minute interaction energies. These conditions apply to all nuclei; however we enumerate them here because, since metals constitute over half of the Periodic Table, it is prudent as a first step for the experimentalist to ensure that a suitable isotope is available for any projected study. Usually tables list all relevant data.[6] An additional useful fact is that the nuclear spin I is half integral

if the nuclear mass number is odd, and integral if its mass number is even.[5]

The above fundamental nuclear properties must be known if a metal is to be usefully probed. The observed magnetic dipole and electric quadrupole interaction energies are vector and tensor products, respectively, of the moments and the corresponding interaction parameters.

2 EXPERIMENTAL DETAILS

2.1 Specimen Preparation

Sample preparation is unquestionably one of the most important steps in any experimental study of metals or alloys. The metallurgical techniques necessary to prepare an alloy in a well-known state must be known and used. The characterization of metallic specimens after they are made is literally impossible. The only hope of understanding the NMR results is to have complete knowledge of the history of the alloy. The final step in preparation is usually reducing at least one and sometimes two or three dimensions of the sample to a size smaller than the skin-depth of the rf field in the specimen. At this point the metal is usually heavily cold worked and to some extent oxidized. A protective oxide layer may be very thin; a nonprotective oxide layer continues to grow if oxygen is present. The quantity of specimen in one powder particle of the total specimen is small (approx. $10-100\,\mu$g). The question of whether to anneal the specimen or not depends on having knowledge of the consequences of each alternative; there is no general answer and the choice depends upon the nuclear resonance and the materials aspects of the situation. Even the considerations involved are too numerous to introduce here. The nuclear spin, the annealing temperature of the metal or alloy, and the diffusivity of oxygen (or nitrogen, ...) at a proposed temperature are usually dominant factors.

The need to subdivide the metal was understood from the beginning; the *skin depth* or *depth of penetration* δ of the rf field into the metal depends on the frequency ν, and the resistivity ρ of the metal. The quantity δ plays a dual role in the experimental results; not only is it the distance into the metal at which the rf field strength falls to e^{-1} of its value at the surface, but a phase shift is introduced which mixes the absorption (imaginary or χ'') and dispersion (real or χ') components of the nuclear susceptibility χ.[7] If the rf field does not penetrate the metal then it is the outer layer only (measured by δ) that contributes to the magnitude of χ. The *filling factor*, which is the ratio of the volume of sample in which the rf field energy is stored, to the total volume in which the rf field energy is stored, can also be greatly decreased. The ideal situation for nonspinning samples is to have the detector (receiver) coil just full of subdivided specimen, no particles of which are in electrical contact with any other and all of which are roughly of dimension $\delta \approx 5 \times 10^{-3}(\rho/\nu)^{\frac{1}{2}}$ where δ is in centimeters, ρ is in microhm centimeters, and ν is the frequency in megahertz.

The method of separation of the particles of specimen is chosen entirely on the basis of appropriateness. The temperature, state of the sample, and composition of sample often suggest materials such as mineral oil, any inert inorganic compound containing no active nuclei, e.g. Al_2O_3 when NMR of V is observed, sheet mica, and so on. A minimum of 'filler' should be used to accomplish the particle separation; beyond that there is simply a loss of sample, filling factor, and signal.

The specimen may be either a pure metal or alloy. It is exceedingly difficult to handle metals of 99.9999% purity (usually called 'six 9s pure') or greater, without decreasing their purity. Fortunately the impurity is often on the surface only and it can be tolerated, or in some circumstances and with some risk, etched away. If during the preparation, a mechanical process such as filing, rolling, drawing, or swaging is used, the sample will be work hardened (cold worked) in addition to being contaminated. Work hardening is caused by mechanical imperfections in the lattice, primarily high densities of dislocations that comprise a three-dimensional 'forest'. The effects of mechanical and chemical imperfections will be discussed below.

2.2 Sample Containment and Conditions Used

Preparation of specimens for use at low temperature depends upon the detection technique being employed. Commonly a small thin-walled glass vial will be used to confine the specimen. For various reasons it is advisable to seal (tip off) the vial leaving the specimen under vacuum or an inert gas. Some of the same considerations apply to high-temperature NMR. A large number of experiments have been done on liquid metals.[8] The separation of particles (spheres) and the choice of filler material is more difficult because of the likelihood of increased reactivity of sample with filler.

Finally it is interesting to note that many studies of the temperature dependence of the Knight shift were done in the solid state with the thought that the results would be approximations to volume-dependence measurements. Certainly the change in volume with temperature is a straightforward concept, but the intrinsic temperature dependence is less easily measured. The exact equation,

$$\left.\frac{\partial \ln K}{\partial T}\right|_p = \left(\frac{\partial \ln K}{\partial \ln V}\right)_T \left(\frac{\partial \ln V}{\partial T}\right)_p + \left.\frac{\partial \ln K}{\partial T}\right|_V \qquad (1)$$

shows that obtaining the explicit temperature dependence of K on T at constant V requires use of the first term on the right, obtained from the pressure dependence of K at constant T and the compressibility $(\partial \ln V/\partial p)_T$, together with the coefficient of thermal expansion $(\partial \ln V/\partial T)_p$.[9]

2.3 Experimental Apparatus and Data

Early workers in the field usually used one of two or three types of nuclear resonance detection. A single-coil technique introduced by Pound[10] was used almost exclusively by those working with or near him. Bloch used a cross-coil apparatus; students and others in his laboratory favored it. The 'Pound box' (a marginal oscillator) detected only the nuclear absorption χ'', and was capable of sweeping over wide frequency regions with ease. The crossed coils, transmitter, and receiver, were constructed and adjusted in a way that made frequency change infeasible. An rf bridge technique was favored by many for its single coil capability and ease of use. For each method mentioned the rf field was applied

continuously so these were all used for steady-state NMR detection.[11] Audiofrequency modulation of the magnetic field B_0 and phase sensitive detection of the demodulated rf were commonly used to detect and display the derivative of χ'' or, for crossed coils, of a mixed χ'',χ' signal. For metals the separation of χ'' and χ' into pure components of χ is not straightforward. A bulk (1.27 cm × 1.9 cm) Al single crystal study illustrates the procedure under ideal circumstances.[12]

Pulsed nuclear resonance apparatus[13] has proved to be almost universally superior to the steady-state methods. There remain pitfalls when the samples are metallic, and these are compounded if sample spinning is introduced. The skin effect and classical Eddy currents[14] must be taken into account, or conversely, the sample prepared so as to make their effects negligible.

The data obtained from most magnetic resonance experiments eventually emerge in the form of absorption lineshape, width, amplitude (relative to a reference), and position (with respect to a reference). These are the quantities from which physical information, the goal of the work, is extracted. The interaction between the conduction electrons and the nuclei allows us to use the nuclear resonance as a probe of the charge density distribution. The association is not easy because of the complexity of the electron–nuclear, and electron–electron interactions; however problems with the theory are revealed as concepts of the electronic structure of the metal are refined. The number of locations in the lattice that can be probed are few, but when NMR is compared with other experimental approaches used to obtain data on this scale it has achieved a very impressive record.

2.4 NMR Lineshape in Powdered Metal Samples

In view of the fact that most NMR in metals is done on particles (or filings, foils, thin wires) with individual external dimensions of about 0.001″ (0.0025 cm) it is clear that the sample comprises crystallites of at most that size or smaller. The results obtained from algebraic solutions of nuclear interactions are for single crystals and include the crystal orientation, as necessary, in keeping with the crystal symmetry. A number of such averaging calculations can be handled using no more than cylindrical symmetry and an average over all angles θ of the symmetry axis with respect to the magnetic field. This procedure is sufficient to treat hexagonal and tetragonal metal lattice structures as well as a large number of cubic, hexagonal, and tetragonal alloys. The absorption distribution $I(\nu)$ for an isotropic orientation distribution of crystals having axial symmetry is obtained by a transformation from crystallite orientation density to resonance amplitude at frequency ν (B_0 = constant). The calculation entails deriving $I(\nu)$ using $I(\nu)\,\mathrm{d}\nu = \sin\theta\,\mathrm{d}\theta$,[15] and thus $I(\nu) \propto \sin\theta\,(\partial\nu/\partial\theta)^{-1}$. Derivations of NMR lineshapes (powder patterns) and the phenomena associated with structures of lower symmetry or causing low symmetry have been published.[6,15]

2.5 Some Sources of Line Broadening in Stationary Samples

The implicit assumption has been made that the NMR resembles a Dirac δ function $\delta(\nu - \nu_0)$. There are at least three sources of broadening in a stationary sample that contribute to the *linewidth* independently of its definition. The applied magnetic field is always inhomogeneous; the sample has nuclear dipoles and in the absence of atomic diffusion nuclear dipole–dipole interactions are a source of broadening; an internal field of totally classical origin is present because each metal particle has an internal field $B_{\mathrm{int}} = \chi_{\mathrm{m}}B_0$, where χ_{m} is the magnetic susceptibility of the metal. (This source can be significant in transition elements with large χ_{m}.) Lifetime or T_1 broadening is seldom a contributing factor to the linewidth of metals. T_1 and T_2 are the longitudinal and transverse relaxation times, respectively of the vector nuclear magnetization $\boldsymbol{M}$ in the stationary reference frame. M_z approaches its maximum equilibrium value in the direction of the external polarizing field; M_x and M_y decay toward zero through dephasing. These relaxation times appeared in Bloch's phenomenological equations describing the behavior of steady-state nuclear magnetization. The Bloch equations do not apply to solids in general, but the nomenclature has been carried over to the parallel quantities describing the behavior of $\boldsymbol{M}$. A brief, qualitative discussion of this topic appears in Schumacher.[11]

3 PRINCIPAL THEORETICAL CONCEPTS

3.1 Introduction

The theory of NMR per se is presented in many books and papers. The interpretation of NMR in metals has been an especially active field because of the continuing interest in understanding the electron–electron interactions, which ultimately determine our understanding of the metallic state. Although high-temperature superconductors now attract much research (including NMR), for decades metals displayed properties and posed puzzles that were unique. Both type I and type II superconductivity and ferromagnetism have been thought to have their origin in the electron–electron and electron–phonon interactions in metals.

One of the tools that confirmed the Bardeen–Cooper–Schrieffer theory of superconductivity was NMR,[6] and repeatedly it has shown its ability to reveal, on the atomic scale, electron distributions that cannot be otherwise obtained or can be obtained only with greater difficulty using another technique.

3.2 Electron–Nucleus Interactions

The topic of NMR in metals is one that can appear to lead to such complexity that it is intractable. Fortunately, however, all of the electron–nuclear interactions encountered can be formulated within the framework of quantum mechanics. It is helpful to understand the elements of the problem and the barriers to obtaining solutions in agreement with observation. Many of the difficulties can be identified in one statement: the potentials are not accurately known. The dense electron plasma is not completely understood; the chemical and other point imperfections (e.g. substitutional solutes, foreign atoms, vacancies and interstitial solutes) distort the lattice so that the positions of the surrounding atoms are not accurately known, and the potentials of the imperfections themselves are

perturbed self-consistently; higher dimensional imperfections such as dislocations (one-dimensional, 1D), grain boundaries, twin planes, and stacking faults (two-dimensional, 2D) are difficult to characterize in the metal and have received less attention than impurities and vacancies.

The above group of chemical and mechanical imperfections scatter conduction electrons and generate charge density fluctuations $\rho(\boldsymbol{r})$, which produce or perturb the following interactions: (a) hyperfine, (b) the electron–dipole nuclear–dipole, (c) indirect nuclear-spin exchange coupling via the conduction electrons, and (d) nuclear quadrupole. The magnitudes of the energy level shifts to which these give rise are usually related to the magnitudes of the nuclear dipole and/or electric quadrupole moments, and the external magnetic field. The derivation of all of the concepts to be included below and many more are explained in rigorous and elegant form by Slichter.[14] A brief introduction to the application of NMR to pure metals and to alloys follows. Examples are offered of the way such studies are approached in terms of the information it is reasonable to expect. They are presented as models to help associate the atomic structure of a metal to the fundamental properties of a nucleus, which make it useful as a probe of that structure. Atomic structure includes lattice structure with imperfections and the total electronic structure. Nuclear properties include γ, I and Q as well as the mass and charge. Such quantities as isotopic abundance, and the bulk properties of the metal, both liquid and solid, are known.

3.3 Conduction Electrons and Scattering

The electronic structure of metals in its most exact form is responsible for the distinctive character of their NMR spectra. The electron energy levels of agglomerated metal atoms resemble those of any other solid when there is no overlap between wavefunctions, i.e. the inner levels are atomic in nature. The outer (conduction) electron orbitals of metals have significant overlap and the free atom energy levels are broadened into bands that may be 1–10 eV wide. Since each atom of a pure metal is identical to each other atom, and is neutral, no shift of charge from one atomic cell to another is expected. Rather, all conduction-electron wavefunctions are delocalized and exist over the volume of the bulk metal. For the alkali metals, which have highly s-like outer electrons; the valence bands are half-full. All metals in fact have only partially filled conduction (valence) bands and thus at T = 0 K have empty states within about 10^{-21} eV of the topmost filled energy level. Presentations of band theory (i.e. the energy distribution of electrons in solids and metals in particular) appear in the solid state literature.[16] Of special interest are the transition metals in which s–d interactions are prominent; the s- and d-bands at the Fermi surface overlap and are partially full. Throughout the Periodic Table admixed orbitals can be expected for the conduction band. The greatest opportunity for systematic study is within the rows.

The s wavefunctions ψ_s play a crucial role in one of the useful applications of NMR in metals. The outer s radial wavefunctions $\psi_s(r)$ have the form $R_{n,s}(r)\,e^{-Zr/n\sigma}$, where $R_{n,s}$ is a polynomial in r, n is the principle quantum number ($n \geq 1$), Z is the screened nuclear charge,[17] r is the distance from the center of the nucleus, and σ is the screening radius. Since $\psi_s(r)$ is finite at the nucleus there is a magnetic interaction between the nuclear magnetic dipole moment μ_I and the electrons in the metal. The magnetic field at the nucleus is $B = B_0 + \Delta B$, where B_0 is the field that would exist at the site of the nucleus in the absence of the metal (the 'external' or 'applied' field) and ΔB is the difference found by measuring $B - B_0$. The quantity of interest $\Delta B/B$ is known as the Knight shift K.[2] The quantity B_0 is usually obtained by using identical nuclei in an insulating diamagnetic solid, from a solution containing the isotope of interest, or the application of any other method by which it can be accurately measured. The medium used becomes the *reference*. The Fermi contact interaction in an atom has the form $E_a = a\,\boldsymbol{I}\cdot\boldsymbol{S}$ where a, the hyperfine coupling constant, is $(16\pi/3)\gamma_I\hbar\mu_B|\psi_s(0)|^2$. Here γ_I is the nuclear gyromagnetic ratio, μ_B is the Bohr magneton, and $|\psi_s(0)|^2$ is the outer s-electron concentration at the nucleus. In a simplified discussion[4] it is found that $\Delta B = (a\chi_s M/g\mu_B\hbar\gamma_1)B_0$. A form more often used is

$$K = \Delta B/B = (8\pi/3)\chi_s\langle|\psi_A(0)|^2\rangle_{FS}M \qquad (2)$$

where χ_s is the conduction-electron spin susceptibility per unit mass (also called the Pauli paramagnetism), M is the mass of the atom, and $\langle|\psi_A(0)|^2\rangle_{FS}$ is the probability density at the nucleus of the metal A atom of those electrons at the Fermi surface (FS) averaged over the FS. Earlier in this paragraph it was shown that $|\psi_s(0)|^2 \approx R_{nl}^2(0)$. The Knight shift can, in principle, be used to measure the conduction-electron density for FS electrons at the nucleus, but the value of the s conduction-electron susceptibility χ_s is extremely difficult to measure accurately, and the experiment has been accomplished only rarely.[18] The experimental determination of $\langle|\psi_A(0)|^2\rangle_{FS}$ and its comparison with calculated values is of fundamental interest; however, many applications of NMR to metals do not require knowledge of χ_s. There are experiments in which it can be made to 'cancel out' or in which relative differences in ΔB are important in themselves.

The conduction electron component χ_s of the magnetic susceptibility is assumed to be a bulk electronic property. According to equation (2) the Knight shift at the solvent lattice sites *around* an isolated solute atom at the origin will be different from the Knight shift K_0 of the pure solvent if the charge density is changed by the solute. The value of the quantity $\langle|\psi_A(0)|^2\rangle_{FS}$ is different in pure A than it is if a B atom is in a neighboring site. The perturbation caused by B of the charge density in A is effective over several lattice spacings and is spherical; consequently the n_i atoms in shell i at distance r_i from the B nucleus all experience the same change. The word 'shell' is used in the sense that the ith shell contains n_i atoms all at r_i. (Note that the solute atoms in a dilute alloy are often referred to as 'impurity' or 'foreign' atoms.)

The above physical description of a solute atom B located on a lattice site of the solvent A suggests treating the system from the point of view of scattering on an atomic scale. Conduction electrons with velocities ranging from near zero to the Fermi velocity v_F at the top of the band impinge on the B atom and are scattered by it. The scattering potential $V_B(r)$ can be computed using atomic wavefunctions, but a simple approach that demonstrates the effect is to use the spherical square well. Electrons in states below the Fermi surface cannot be scattered because all nearby momentum states are filled. Only electrons at the FS can be scattered: an integral of the scattered charge

over all states in the band shows that the only contribution is from electrons at the FS, and that the scattered electrons produce an oscillatory charge-density wave $\delta\rho(r_i)$ around the solute.[19]

The conduction-electron density at nuclei surrounding the scattering center is $\rho(r_i)$, the sum of ρ_0 ($\langle|\psi_A(0)|^2\rangle_{FS}$ for the pure solvent) and the spherical wave $\delta\rho(r_i)$. An expression for $\delta\rho(r_i)$ is derived using the method of partial waves found in most standard texts on quantum mechanics.[20] Since $\delta\rho(r_i)$ is oscillatory and has a complicated dependence on r at short distances (several lattice spacings) expressions for it must be evaluated using the complete solution without simplification.[21] An asymptotic approximation valid as $r \to \infty$ is $\delta\rho(r) \propto r^{-3}$ $\cos(2k_F r + \theta)$, where θ is a function of the phase shifts η_l determined by the scattering potential. The asymptotic value for $\delta\rho(r)$ is never of use because: (a) even for a low solute concentration ($C_B \approx 0.01$) there is significant overlap among the charge density waves from the randomly distributed solutes and (b) the value of $\delta\rho(r)$ at large r is very small compared with other sources of linewidth. In summary, the effect of foreign atoms in a solvent matrix when the solvent nuclear spin I is $\frac{1}{2}$ is to cause a spectrum of resonance lines. Each line derives from the n_i solvent atoms in shell i. An example of such a study employing silver as the solvent and Group I, II, III, IV and V solute atoms demonstrated the presence of charge density waves.[22]

4 PURE METALS WITH NONZERO μ_I

4.1 Initial Considerations: Lattice Symmetry and Nuclear Properties of Isotope(s)

The primary concern is the point symmetry at each lattice site, assuming an imperfection-free lattice. Of the 14 space lattices only three are cubic (yet these include many metals), four (trigonal, tetragonal and hcp) have three, four and sixfold axial symmetry respectively, and the balance have lower symmetry. There are thus three possible types of lattice symmetry to be combined with the nuclear and electron moments and the electron charge distribution; this is a closed set of possible combinations.

4.2 Pure Metals with I = 1/2

For nuclei of spin $I = \frac{1}{2}$ energy level changes are caused by the contact interaction and the nuclear–dipole electron–dipole interaction at a distance.[15,23] The former has been discussed above (Section 3.3), the latter results from the non-s spin distribution in lattices with axial or lower symmetry. If for example a p_z orbital in a tetragonal lattice contained more charge than the $p_x = p_y$, then in the presence of a magnetic field the electrons near the top of the Fermi sea would produce a magnetic field at the nucleus with the axial symmetry of the spatial electron distribution. This *anisotropic Knight shift* has been observed in several metals with noncubic symmetry.[6] The resulting powder pattern lineshape (because of the polycrystalline sample) is peaked by an integrable infinity at one end and falls off abruptly at the other, since the range of symmetry axis orientation (with respect to $\boldsymbol{B}_0$) is from 0 to 180°, with the usual weighting factor of $\sin\theta$ for an isotropic orientation distribution. The number of crystallite orientations near $\theta = 90°$ is infinitely greater than those near zero degrees. Since this anisotropy gives rise to a broadening mechanism proportional to the external field it is clearly linked to the electron polarization via the Pauli susceptibility; equation (3) gives the shift for a single crystal orientation θ; it is

$$\frac{\Delta B}{B} = \mu_B^2 V_0 N(E_F) Q_K (3\cos^2\theta - 1) \tag{3}$$

where

$$Q_K = \int \psi (3\cos^2\theta - 1) r^{-3} \psi \, dV \tag{4}$$

The distribution of electron dipoles is contained in the conduction band wavefunctions ψ and the band structure determines $N(E_F)$. An s wavefunction would cause the integral to vanish so we have secondary evidence for the mixing of orbitals at the FS. Other factors important in pure metals with nuclei of $I = \frac{1}{2}$ are the *core polarization* (the polarization of inner s electrons simply because of the necessity of orthogonalizing all electrons in the atomic cell) and the *orbital* contribution.[23] The average value of the orbital magnetic moments is nonzero because currents are produced in the inner shells by the static magnetic field.

Another interaction depends upon the conduction-electron spins to couple nuclei. *Indirect coupling* describes the indirect spin–spin interaction between two nuclei i, j via the electron gas.[23] The wavefunction is in contact with both nuclei through their hyperfine interactions. This indirect exchange would be zero in the absence of s electrons; however it can be a dominant source of line broadening (and is expected to be if the hyperfine interaction is large). Large hyperfine interactions accompany large (massive) nuclei, and it is roughly true that the Knight shift and indirect nuclear coupling increase with increasing nuclear mass. The relationship is only approximate because of the many other contributing factors, not the least being the fraction of $\langle|\psi_A(0)|^2\rangle_{FS}$, which is s-like.

Pure metals with $I = \frac{1}{2}$ but which are highly paramagnetic, may exhibit nuclear linewidths reflecting (i.e. increased by) the inhomogeneity δB_0 of the static field B_0 within the particle (unless the particles are all shaped and oriented so as to ensure that the demagnetizing factor is identical in each). The additional field is of the order of $\chi_m B_0$, where χ_m is the bulk measured volume magnetic susceptibility of the metal.[6] A further contribution to the susceptibility, small in the simple metals but significant in transition metals, is the Van Vleck contribution χ_{VV}.[23] Shifts and linewidths found under the conditions of this section are of the order 0.1–1 mT.

4.3 Pure Metals with $I \geq 1$

The magnitudes of shifts and contributions to the absorption linewidth considered in Section 4.2 are likely to be totally overwhelmed by quadrupole splitting of the magnetic resonance if the lattice symmetry is other than cubic. The nuclear electric quadrupole moment Q is a measure of the shape of the nucleus and thus its charge distribution. Since magnetic resonance is the topic of interest we assume a high (1–10 T) magnetic field is present and the quadrupole perturbation is said

to take place in the high-field regime; the electric quadrupole interaction energy is much smaller than the nuclear magnetic dipole resonance energy $h\nu_0$. The magnitudes of the electric field gradient, the quadrupole moment, and $h\nu_0$ can vary over a sufficiently large range for both first- and second-order quadrupole perturbation to be frequently required in analyzing data. A comprehensive and authoritative monograph on this topic has been published.[24] In addition, the subject is covered in all works on NMR in metals and in the 'high-resolution' literature.[25] The information gained is interesting and useful, and there are more nuclei with $I \geq 1$ than with $I = \frac{1}{2}$ by almost a factor of 3. A concise yet moderately transparent expression for the quadrupole energy is the Hamiltonian,

$$\hat{\mathcal{H}}_{\mathrm{Q}} = \frac{1}{6} \sum_{j,k} V_{jk} Q_{jk} \tag{5}$$

The way in which the field gradients $V_{jk} = (\partial^2 V/\partial x_j \partial x_k)$ multiply the second rank tensor components Q_{jk} is reminiscent of other stress tensor–matter tensor interactions. The quantity Q, a scalar, is defined as the quadrupole moment of the nucleus, and is determined in the standard way of evaluating n-pole moments through knowledge of the charge distribution. By convention, the charge e is not included, and $Q = \frac{1}{2}\int(3z^2 - r^2)\rho(\boldsymbol{r})\mathrm{d}^3\boldsymbol{r}$, where $\rho(\boldsymbol{r})$ is the expectation value of the nuclear charge density for the state $m = I$. The expression requires knowledge of the probability density of the protons in the nucleus: Q is in fact a measured quantity, tabulated for many nuclei. (The accuracy to which Q is known is generally much lower than for the nuclear gyromagnetic ratio γ; however, it should also be admitted that the reason nuclear scientists began to study shieldings, electron–nuclear interactions, and so on, was because they were a nuisance in accurately determining γ.) An extensive literature has developed in the pure metal, $I \geq 1$ subset;[26] there is opportunity for systematic study because so many transition and rare earth (f shell) metals are hcp.

Early in the work on quadrupole interactions it was pointed out by Sternheimer (cf. Ref.[24] p. 341) that a factor contributing to V_{ij} is $-\gamma_\infty V^*_{ij}$. The charge distribution of an atom is distorted by the quadrupolar field of its nucleus and by the electric field gradient caused by the other atoms in the lattice. Surrounding atomic cells appear to be ionic because the mobile charge tends to distribute uniformly over the lattice; the remaining ionic lattice should be summed to derive the $V^l_{ij} \rightarrow q_{\mathrm{latt}}$ contribution to q from the lattice. The literature frequently uses a standard notation that incorporates these and other factors into the expression for the total field gradient q, given by

$$q = q_{\mathrm{latt}}(1 - \gamma_\infty) + q_{\mathrm{loc}}(1 - R_{\mathrm{Q}}) \tag{6}$$

Here q_{latt} is discussed above, $-\gamma_\infty$ is the Sternheimer factor (which may be as large as 100 in heavy atoms) required to correct for the charge redistribution in the atoms caused by q_{latt}. The local field gradient from sources inside the atomic cell q_{loc} is also a sum of terms. Schumacher[27] provides a particularly good introductory treatment of the basic features of this topic.

4.4 Pure Metals with $I \geq 1$, and Mechanical Imperfections

The majority of the strain in a metallic lattice is the result of dislocations. An early experiment[15] in which the resonance intensity of the untreated filings of Cu was compared with the intensity of annealed filings showed the effect of lattice distortion dramatically, since the satellite lines from the first order broadening were almost totally removed from the region of the central $I = \frac{1}{2} \rightarrow -\frac{1}{2}$ line; the intensity of the latter was decreased to about one-half of the absorption intensity in annealed Cu. A more careful analysis showed the slight narrowing of the Cu absorption line caused by the elimination of the contribution of the group of 'like' spins in regions of high lattice distortion. Dislocation pinning is very strongly dependent upon other imperfections, including grain boundaries and dislocations on other slip systems which cross the primary. When we use the concept of 'annealing temperature', for which there is a clear definition, the impurity content is the greatest unknown. By producing fine filings or heavily rolled or drawn Cu the dislocation density may be as high as $10^{12}\,\mathrm{cm}^{-2}$. This may be reduced to 10^6–$10^8\,\mathrm{cm}^{-2}$ upon annealing. Even at $10^{12}\,\mathrm{cm}^{-2}$ the majority of nuclei are not within several lattice spacings of a dislocation core.

5 ALLOYS

5.1 Solvent Nuclear Spin $I = 1/2$

5.1.1 Alloy Types and NMR

An alloy ordinarily is assumed to be any number of metals put into a perfectly inert container and melted under a vacuum or inert gas, then solidified under equilibrium conditions. The alloy specimens used for NMR should be very thoughtfully made; if called 'dilute' they usually consist of at most one or two elements present in minor concentration (0.1–10 at.%) in addition to the solvent. These are called binary or ternary alloys and may or may not be single phase.

Several compilations of phase (or equilibrium, or constitution) diagrams exist, and journals publish newly determined diagrams, updates, and extended work.[28] For elements and compounds of more than passing commercial or academic interest, individual monographs are devoted to the binary alloys of a single element. A four-volume work published by ASM characterizes intermetallic compounds, classifies them by structure type, and incorporates all dimensions and atom locations within the unit cell.[29] Similar collections of the literature of ternary alloys are available.

There are instances of the application of NMR to concentrated binary alloys with compositions ranging from 0 to 100 at.%B in an A–B alloy. Over this composition range, at room temperature, one can expect to encounter several solid solutions and/or intermetallic compounds with two phase regions separating them.[6] The results obtained resemble those of an X-ray study of a binary system. It is seen, however, that X-ray diffraction studies are better in almost every way, when they are feasible. (For metals this means essentially always.) However, NMR is not a universal approach, but is useful

only for special felicitous choices of nuclei. Important factors include the spin and the magnitude of the dipole moment.

5.1.2 Solvent NMR in Dilute Substitutional Random Solid Solution (DSRSS)

This subject has been discussed above in the context of Section 3.3 for simple metal A–B alloys. The substitution of a paramagnetic species causes very long range spin density waves around the magnetic site acting as a scatterer.

5.1.3 Solute NMR in DSRSS

Many references have been made to the charge density waves scattered from a solute atom. If the solute B nucleus has spin $\frac{1}{2}$ it is possible (other conditions being favorable) that the solute resonance absorption will be observable. The B site is a center of symmetry, and it is possible to evaluate $\langle|\psi_s(0)|^2\rangle_{B,FS}$ with the wavefunctions, theoretical techniques, and computing capabilities available.

5.2 Solvent Nuclear Spin $I \geq 1$

5.2.1 Solvent NMR in DSRSS

For DSRSS the scattering of electrons from solute atoms is unchanged from the foregoing description. Each impurity atom is imagined to be isolated and, by definition, *on* a site of the solvent crystal lattice. The solvent band structure and scattering process are unchanged. Here the similarity in treatment ends. Surrounding the solute are spherical charge density waves; these cause potential waves and electric field gradients that ripple out from the solute. Consider the $n_1 = 8$ nearest neighbors of a solute in a bcc lattice: Over the volume of a near neighbor (nn) cell the electric field changes and the quantity $V_{ij}^s(r_1)$ results at the nucleus. In addition, because of the presence of $V_{ij}^s(r_1)$, the electron orbitals in the nn cell are polarized. Crudely, this latter effect is the Sternheimer factor introduced earlier.

If the magnitude of V_{ij} at $r_1 = \sqrt{3}\,a_0/2$, where a_0 is the bcc lattice constant, is such that the quadrupole interaction energy, $\chi = e^2qQ/h$, is roughly equal to or within an order of magnitude greater than the unperturbed ($q = 0$) linewidth, a set of first-order satellite lines would in principle appear in the powder pattern of the NMR of the powdered DSRSS alloy.[6] In practice, the distribution of both shifts and symmetries leads to a broad distribution of absorption at the solute concentrations used. A large number of measurements of q_i at several r_i have been done using more dilute solutions.

Because of the number of energy levels associated with the nuclear spin I, for integral I (i.e., $I = 1, 2, \ldots$) there is no $m = \frac{1}{2} \leftrightarrow -\frac{1}{2}$ transition. For half-integral spin ($I = \frac{3}{2}, \frac{5}{2}, \ldots$) the $m = \frac{1}{2} \leftrightarrow -\frac{1}{2}$ transition is unperturbed and becomes the *central* $m = \frac{1}{2} \leftrightarrow -\frac{1}{2}$ line of the first order quadrupole split line structure. Carter et al.[6] illustrate the various patterns.

In second-order perturbation the remaining central ($m = \frac{1}{2} \leftrightarrow -\frac{1}{2}$) transition is shifted with respect to the unperturbed ($q = 0$) absorption. (Since first-order perturbation theory is no longer valid, but the higher $m \leftrightarrow m - 1$, $m \neq \frac{1}{2}$ transitions are very far removed, there are no longer observable satellites.)

The digression into high-field quadrupole perturbation was necessary to complete even a brief description of the many experiments in which q is the primary quantitative information obtained. A rather sweeping summation of the topic would state that in a large majority of DSRSS studies, the NMR absorption of an $I \geq 1$ solvent is either broadened, decreased in magnitude to an asymptotic limit, or decreased in magnitude to a very small value near zero. There is so little absorption left in the region of the original line that it can no longer be detected.

5.2.2 Solute Nuclei of $I \geq 1$ in DSRSS

Although many such studies exist, the principal interest in the results and the way in which the electronic structure interacts with the nuclei have been described. A study that involves the combined effects of nuclear quadrupole interaction, anisotropic Knight shift, dipolar broadening, and an inhomogeneous Knight shift distribution at the solute sites,[30] can serve as an example of a more complex system; the solutes Al and V were dissolved in hcp Ti in concentrations of 1 at.% and 2 at.%. A semiquantitative analysis of the Ti lattice wavefunction as it joins the localized orbitals in the Al and V cells is carried out. The substitution of Al on an hcp Ti site decreases the Knight shift of Al to near zero. The $3s^2$ orbitals probably lie below the Fermi surface of Ti.

5.2.3 Further Considerations

Very large segments of material have been omitted from this entry. Each is as significant as the material included, and the choice of topics presented is merely slanted toward the most basic considerations of nuclear interaction and the simplest aspects of metals and alloys, stressing their electronic structure in real space. It is clear that other electronic properties are very closely related to this area. For example, the electronic specific heat is directly proportional to $N(E_F)$, a factor in $(\Delta B/B)$. The residual resistivity (that part related to solutes in DSRSS) involves electron scattering processes, one aspect of which invokes the same phase shifts as appear in the evaluation of the solvent Knight shift in DSRSS using the method of partial waves.

6 NUCLEAR RELAXATION AND ATOMIC DIFFUSION: NUCLEAR RELAXATION IN I = 1/2 SYSTEMS

The discoverers of NMR worried about this topic. It is easy to see that in order to absorb net energy, a spin in a lower level must be excited into an upper level. How long can this go on? Experience shows that if the incoming photon density is not too large, it can go on forever, but if the magnitude goes beyond some critical level, the net photon absorption decreases, the populations of the upper and lower level approach equality and net absorption approaches zero. The strong implication is that there exists a mechanism by which nuclei in the upper energy state return to the lower state and lose the required energy to the lattice, a passing electron, a paramagnetic impurity, or by another process that can absorb the required energy $h\nu_0$. The spontaneous loss of energy to a large reservoir is described by

the relaxation time T_1. In metals T_1 is determined most often by collisions with passing conduction electrons; the calculation of T_1 was done by Korringa who found that the temperature $\times$ T_1 product is a constant in this case. Since nuclei relax via the contact interaction, T_1 is found to be directly related to the Knight shift.[23]

Another type of relaxation occurs because of the static dipole–dipole interactions among the nuclei. The transverse dipolar relaxation time T_2'' is calculated from the nuclear moments and their lattice locations in terms of the second moment of the dipolar field.[31] (If all lattice sites are occupied by nuclei with magnetic dipole moments then a field caused by all of the other dipoles is present at each site.) If the nuclei move through the lattice the average field at any nucleus will decrease and the more rapid the motion the narrower the resonance line. Accurate measurement of the linewidth as a function of temperature measures the activation energy of diffusion for this motional narrowing.[14] The mean time between atomic jumps has also been measured for Al using a pulse technique.[32]

7 RELATED ARTICLES

Chemical Exchange on Solid Metal Surfaces; Germanium, Tin, and Lead NMR; Hydrogen–Metal Systems; Lithium NMR; Metallic Superconductors; Quadrupolar Transition Metal and Lanthanide Nuclei; Supported Metal Catalysts; Thallium NMR.

8 REFERENCES

1. R. V. Pound, *Phys. Rev.*, 1948, **73**, 1112.
2. W. D. Knight, *Phys. Rev.*, 1949, **76**, 1259.
3. For simplicity models that represent the 'pure' elementary bond types will be used. Solids generally have charge distribution, which can be represented by a mixture of these types.
4. C. Kittel, *Introduction to Solid State Physics*, 5th edn., Wiley, New York, 1976, Chap. 1 (Also, any book on Solid State Physics which includes metals.)
5. N. Ramsey, *Nuclear Moments*, Wiley, New York, 1953.
6. G. C. Carter, L. H. Bennett, and D. J. Kahan, *Prog. Mater. Sci.*, 1977, **20**, Part 1, 123.
7. N. Bloembergen, *J. Appl. Phys.*, 1952, **23**, 1383.
8. R. Dupree and E. F. W. Seymour, in *Liquid Metals*, ed. S. Z. Beer, Marcel Dekker, New York, 1972, Chap. 11, p. 461; M. Shimoji, *Liquid Metals*, Academic Press, New York, 1977.
9. G. B. Benedek, *Magnetic Resonance at High Pressure*, Interscience, New York, 1963.
10. R. V. Pound and W. D. Knight, *Rev. Sci. Instrum.*, 1950, **21**, 219.
11. R. T. Schumacher, *Introduction to Magnetic Resonance*, Benjamin, New York, 1970, p. 43.
12. P. L. Sagalyn and A. Hofmann, *Phys. Rev.*, 1962, **127**, 68.
13. E. L. Hahn, *Phys. Rev.*, 1950, **80**, 580; ed. D. M. S. Bagguley, *Pulsed Magnetic Resonance: NMR, ESR and Optics*, Clarendon, Oxford, 1992.
14. C. P. Slichter, *Principles of Magnetic Resonance*, 3rd edn., Springer, New York, 1989.
15. N. Bloembergen and T. J. Rowland, *Acta Metall.*, 1953, **1**, 731.
16. M. A. Omar, *Elementary Solid State Physics*, Addison-Wesley, Reading, MA, 1975, Chaps. 4 and 5; C. Kittel, *op. cit.*, Chaps. 7 and 9.
17. W. A. Harrison, *Solid State Theory*, McGraw-Hill, New York, 1970, Chap. 3, Sect. 4.
18. R. T. Schumacher and C. P. Slichter, *Phys. Rev.*, 1956, **101**, 58.
19. A. Blandin and E. Daniel, *J. Phys. Chem. Solids*, 1959, **10**, 126.
20. A. Messiah, *Quantum Mechanics*, Wiley, New York, 1962; L. I. Schiff, *Quantum Mechanics*, McGraw-Hill, New York, 1949.
21. L. E. Drain, *Metall. Rev.*, 1967, **119**, 195; A. Blandin and E. Daniel, *J. Phys. Chem. Solids*, 1959, **10**, 126.
22. T. J. Rowland, *Phys. Rev.*, 1962, **125**, 459.
23. J. Winter, *Magnetic Resonance in Metals*, Clarendon, Oxford, 1971.
24. M. H. Cohen and F. Reif, *Solid State Phys.*, 1957, **5**, 321.
25. B. C. Gerstein and C. R. Dybowski, *Transient Techniques in NMR of Solids*, Academic Press, Orlando, FL, 1985, p. 121. (Highly recommended: proper presentation of many interactions included in this article.)
26. A. Maio, L. Hermans, M. Rots, G. N. Rao, and R. Coussement, *Hyperfine Interactions*, 1981, **11**, 239.
27. R. T. Schumacher, *Introduction to Magnetic Resonance*, Benjamin, New York, 1970, p. 110.
28. The Journal of Phase Equilibrium (formerly *Bulletin of Alloy Phase Digrams*), American Society for Metals, Materials Park, OH.
29. *Pearson's Handbook of Crystallographic Data for Intermetallic Phases*, 2nd edn., American Society for Metals, Materials Park, OH, 1991.
30. L. H. Chou and T. J. Rowland, *Phys. Rev. B.*, 1992, **45**, 11580.
31. T. J. Rowland, *Prog. Mater. Sci.*, 1961, **9**, 1.
32. F. Y. Fradin and T. J. Rowland, *Appl. Phys. Lett.*, 1967, **11**, 207.

Biographical Sketch

Theodore J. Rowland. *b* 1927. B.S., 1948, Western Reserve University; A.M., Ph.D., Applied Physics, Harvard University, USA. First student of Nicolaas Bloembergen (also vividly recalls R. V. Pound, J. H. Van Vleck, Leon Brillouin, E. M. Purcell). Research physicist, Metallurgical Laboratory, Union Carbide Corp., 1954–61; Professor of Physical Metallurgy, Metallurgy Department (now Materials Science and Engineering), University of Illinois (Urbana-Champaign) 1961–92. Research interests: NMR in metals, physics of solids, electrical and mechanical properties of metals.

Paramagnetic Relaxation in Solution

Jozef Kowalewski
Stockholm University, Sweden

1	Introduction	1
2	Theory	1
3	Experimental Methods	4
4	Related Articles	6
5	References	6

1 INTRODUCTION

Paramagnetic systems are materials with positive magnetic susceptibility, normally associated with unpaired electrons. Chemically, paramagnetic systems of relevance for this article are dilute aqueous or organic solutions of free radicals and transition metal ions or their complexes, including metalloproteins. The presence of unpaired electron spins has a profound influence on the NMR spectra of such solutions. The origin of the effects is to be found in the large value of the electronic magnetic moment, about 650 times that of the proton.

The influence of the paramagnetic species on NMR spectra of liquids may be two-fold. First, the nuclear spin relaxation rates are enhanced. The paramagnetic relaxation enhancement (PRE) is caused by random variation of the electron spin–nuclear spin interactions, which opens new pathways for longitudinal as well as transverse relaxation. The PRE is most often studied for $I = \frac{1}{2}$ nuclei, but oxygen-17 applications are not uncommon. Second, the NMR signals may be shifted, provided the relevant electron spin–nuclear spin interaction has a nonzero average. Paramagnetic complexes in solution often contain exchangeable ligands, and the exchange phenomena (see***Chemical Exchange Effects in Biological Macromolecules***), together with the intrinsic relaxation rates and shifts, contribute to the observed lineshapes and line positions. The paramagnetic effects have been used for several decades by chemists and biochemists as a source of structural, thermodynamic, and dynamic information. Applications of this type have been described in numerous books, recently by Bertini and Luchinat[1] and by Banci et al.[2] A more recent application of PRE is the use of paramagnetic compounds as contrast agents in MRI (see ***Contrast Agents in Whole Body Magnetic Resonance: An Overview*** and ***Contrast Agents in Magnetic Resonance: Operating Mechanisms***).

2 THEORY

The theory of nuclear relaxation in paramagnetic systems contains many intricate points, described some years ago in a review article.[3] Here, we concentrate on the most important issues and begin by formulating the relationships between the measured macroscopic PRE and the microscopic quantities. We then proceed with the theory for relaxation times for nuclei residing in the ligands in paramagnetic complexes and conclude the theory section by a brief discussion of intermolecular relaxation.

2.1 The Macroscopic and Microscopic Quantities

The PRE experiments are often performed with a considerable excess of a ligand (e.g. solvent) over the paramagnetic centers (e.g. transition metal ions). The type of information obtainable from PRE measurements in solution depends on the relative magnitudes of the exchange rates, the intrinsic relaxation rates, and shifts. The set of equations relating the relaxation, shift, and lifetime properties of the nuclei in paramagnetic complexes to the observables of the NMR experiments has been derived by Swift and Connick[4] and by Luz and Meiboom:[5]

$$T_{1\mathrm{P}}^{-1} = \frac{P_\mathrm{M}}{\tau_\mathrm{M} + T_{1\mathrm{M}}} \tag{1}$$

$$T_{2\mathrm{P}}^{-1} = \frac{P_\mathrm{M}}{\tau_\mathrm{M}} \left[\frac{T_{2\mathrm{M}}^{-2} + (T_{2\mathrm{M}}\tau_\mathrm{M})^{-1} + \Delta\omega_\mathrm{M}^2}{(T_{2\mathrm{M}}^{-1} + \tau_\mathrm{M}^{-1})^2 + \Delta\omega_\mathrm{M}^2} \right] \tag{2}$$

$$\Delta\omega_\mathrm{P} = \frac{P_\mathrm{M}\Delta\omega_\mathrm{M}}{(\tau_\mathrm{M}/T_{2\mathrm{M}} + 1)^2 + \tau_\mathrm{M}^2\Delta\omega_\mathrm{M}^2} \tag{3}$$

$T_{1\mathrm{P}}{}^{-1}$, $T_{2\mathrm{P}}{}^{-1}$, and $\Delta\omega_\mathrm{P}$ are the excess (see Section 3) spin–lattice relaxation rate, spin–spin relaxation rate and shift measured for the ligand in solution, while the properties with index M refer to the ligand in the paramagnetic complex. τ_M is the lifetime of the ligand in the complex and P_M is the mole fraction of ligand nuclei in bound positions.

2.2 The Modified Solomon–Bloembergen Equations

The nuclear spin relaxation in a paramagnetic complex arises through the electron–nucleus hyperfine interaction (see ***Electron-Nuclear Interactions***) between the nuclear spin I and the electron spin S. The hyperfine interaction consists of two parts. The first term is the dipole–dipole interaction between the nuclear magnetic moment and the electron spin of the electron outside of the nucleus; the second term is the scalar interaction or Fermi contact coupling between the nuclear magnetic moment and the spin of s electrons at the site of the nucleus. Each of these terms can be modulated by random processes and can contribute to the nuclear relaxation rates. The dipole–dipole part of the hyperfine interaction is modulated by reorientation of the spin–spin axis, by changes in the orientation of the electron spin (electron spin relaxation) and by ligand exchange. The scalar interaction part remains unaffected by reorientation of the molecule and is only modulated by electron relaxation and ligand exchange.

These qualitative ideas are reflected in the set of equations for nuclear relaxation rates in paramagnetic complexes, known as the ‘modified Solomon–Bloembergen equations’:

$$T_{1M}^{-1} = (T_{1M}^{SC})^{-1} + (T_{1M}^{DD})^{-1}$$
$$= \frac{2}{3}\left(\frac{A}{\hbar}\right)^2 S(S+1)\frac{\tau_{e2}}{1+(\omega_S-\omega_I)^2\tau_{e2}^2}$$
$$+\frac{2}{15}\left(\frac{\mu_0}{4\pi}\right)^2 S(S+1)\hbar^2\gamma_I^2\gamma_S^2 R^{-6}$$
$$\times\left[\frac{\tau_{c2}}{1+(\omega_S-\omega_I)^2\tau_{c2}^2}+\frac{3\tau_{c1}}{1+\omega_I^2\tau_{c1}^2}\right.$$
$$\left.+\frac{6\tau_{c2}}{1+(\omega_S+\omega_I)^2\tau_{c2}^2}\right] \quad (4)$$

and

$$T_{2M}^{-1} = (T_{2M}^{SC})^{-1} + (T_{2M}^{DD})^{-1} = \frac{1}{3}\left(\frac{A}{\hbar}\right)^2 S(S+1)$$
$$\times\left(\tau_{e1}+\frac{\tau_{e2}}{1+(\omega_S-\omega_I)^2\tau_{e2}^2}\right)$$
$$+\frac{1}{15}\left(\frac{\mu_0}{4\pi}\right)^2 S(S+1)\hbar^2\gamma_I^2\gamma_S^2 R^{-6}$$
$$\times\left[4\tau_{c1}+\frac{3\tau_{c1}}{1+\omega_I^2\tau_{c1}^2}+\frac{\tau_{c2}}{1+(\omega_S-\omega_I)^2\tau_{c2}^2}\right.$$
$$\left.+\frac{6\tau_{c2}}{1+\omega_S^2\tau_{c2}^2}+\frac{6\tau_{c2}}{1+(\omega_S+\omega_I)^2\tau_{c2}^2}\right] \quad (5)$$

where

$$\tau_{ci}^{-1} = \tau_R^{-1} + \tau_M^{-1} + T_{ie}^{-1} \quad (i = 1, 2) \quad (6)$$

$$\tau_{ei}^{-1} = \tau_M^{-1} + T_{ie}^{-1} \quad (7)$$

τ_R is an isotropic rotational correlation time of the complex, T_{ie} (i = 1 or 2) is the electron spin relaxation time, and S is the electron spin quantum number, $A/\hbar$ is the isotropic scalar coupling constant, μ_0 is the permeability of vacuum, R is the distance between the nuclear spin and the electron spin (considered as a point dipole), and γ_S equals $g_{eff}\beta/\hbar$, where g_{eff} is the effective g factor of the electron in the complex under consideration and β is the Bohr magneton. ω_S and ω_I are the electronic and nuclear Larmor frequencies. The electronic Larmor frequency is so much larger than the nuclear Larmor frequency that the latter can be neglected in the terms involving the sum and difference frequencies, and some of the terms in the dipole–dipole parts of equations (4) and (5) can be brought together. Note the peculiar dual role that the exchange can play in the PRE: in equations (4)–(7) the τ_M acts as a correlation time, while its role in equations (1)–(3) is that of a relaxation time.

The modified Solomon–Bloembergen equations were first presented in the papers by Connick and Fiat[6] and by Reuben et al.[7] The formal derivation of the equations is fairly complicated and was in fact published much later.[8] It is based on the Redfield relaxation theory for the nuclear spin and involves two critical assumptions. The first one is that the electron relaxation (which is a motion in the electron spin space) is uncorrelated with molecular reorientation (which is a spatial motion influencing the dipole coupling). The second assumption is concerned with the description of the dynamics in the electron spin space. It is assumed that the electron spin system is dominated by the electronic Zeeman interaction. Other interactions lead to relaxation, which can be described in terms of the longitudinal and transverse relaxation times T_{1e} and T_{2e}. This point is elaborated on in Section 2.3. In this sense, one can call the modified Solomon–Bloembergen equations a 'Zeeman-limit theory'. If the second assumption is fulfilled, then the scalar interaction parts in equations (4) and (5) become analogous to the equations describing scalar relaxation originating from the modulation of the nuclear spin–spin coupling, with the hyperfine coupling constant $A/\hbar$ replacing the J coupling constant. The first assumption does not directly influence the scalar interaction term, but the failure to fulfil it will lead to an additional interference (cross correlation) term between the dipole–dipole and the scalar interactions. The validity of both the above assumptions is questionable in many cases of practical importance.

Apart from these two main assumptions, equations (4) and (5) contain several additional approximations, the most important of which are the following:

1. The electron spin is assumed to be a point dipole centered at the metal ion. The validity of this assumption can be tested by ab initio quantum-chemical calculations, which indicate that it is reasonable for protons but may cause errors for heavier nuclei, in particular if the atoms where they reside are involved in bonding with the paramagnetic metal center.[9]
2. The electron g tensor is assumed to be isotropic. The effects of deviations from this assumption were first investigated by Sternlicht.[10]
3. It is assumed that the reorientation of the nuclear–electron spin vector can be described by a single correlation time, τ_R. This amounts to neglecting the effects of internal motion and anisotropic reorientation.
4. It is assumed that chemical exchange is uncorrelated with the remaining motions in the lattice. This assumption seems to be easy to fulfil. We return to the exchange effects in Section 3.1.

2.3 The Bloembergen–Morgan Theory for Electron Spin Relaxation

As one can see in equations (4) and (5), the magnitude of the PRE for the ligand nuclei depends on the energy level splittings and the relaxation behavior of the electron spin system of the transition metal ion in the magnetic field. For discussing the splittings, the spin Hamiltonian formalism, developed originally for the interpretation of ESR spectra,[11] normally constitutes an appropriate framework. The spin Hamiltonian is an operator involving only nuclear and electron spin operators and parameters characterizing the spin system under consideration. Neglecting the terms containing only nuclear spins and the hyperfine coupling to the ligand nuclei, the spin Hamiltonian can be written:

$$\hat{\mathcal{H}}_S = \hat{\boldsymbol{S}}\cdot\boldsymbol{g}\cdot\hat{\boldsymbol{B}}_0\cdot + \hat{\boldsymbol{S}}\cdot\boldsymbol{D}\cdot\hat{\boldsymbol{S}} + \hat{\boldsymbol{S}}\cdot\boldsymbol{A}\cdot\hat{\boldsymbol{I}}_M \quad (8)$$

$\hat{\boldsymbol{S}}$ is the electron spin operator. The first term describes the electron Zeeman interaction and the second the zero-field splitting (ZFS) interaction, which only has to be considered for systems with electron spin quantum number $S \geq 1$. The last term corresponds to the hyperfine interaction with the metal nucleus, if it has nonzero spin ($\hat{\boldsymbol{I}}_{\mathrm{M}}$ is the nuclear spin operator for the metal). The molecular parameters are the three second-rank tensors: the g tensor $\boldsymbol{g}$, the ZFS tensor $\boldsymbol{D}$ and the hyperfine coupling tensor $\boldsymbol{A}$. The combined effect of the electrostatic interactions and spin–orbit coupling renders the Zeeman interaction anisotropic and makes the average effective g value (equal to one-third of the trace of the g tensor) different from the free electron value of 2.0023. The effect of the g tensor on ESR spectra is similar to the effect of the shielding tensor in NMR.

The zero-field splitting tensor also has its origin in the intermingling of the electrostatic and spin–orbit interactions. In addition, the dipolar coupling between the electron spins can contribute to the ZFS, but this contribution is believed to be minor for transition metal complexes.[12] The ZFS tensor is traceless and can be characterized, in its principal axis system, by two constants:

$$D = D_{zz} - \tfrac{1}{2}(D_{xx} + D_{yy}) \tag{9a}$$

$$E = \tfrac{1}{2}(D_{xx} - D_{yy}) \tag{9b}$$

The ZFS interaction has a form similar to the quadrupolar interaction in NMR.

The modulation of various terms in equation (8) by random processes in liquids leads to electron spin relaxation. The rotational modulation of the anisotropies of the g and hyperfine tensors are important sources of electron relaxation for $S = \frac{1}{2}$ systems. Still another relaxation mechanism for $S = \frac{1}{2}$ systems, in analogy with the case of nuclear relaxation, is the spin–rotation coupling. The electron relaxation in $S = \frac{1}{2}$ systems is discussed at length in the book by Muus and Atkins[13] and is summarized in the book by Banci et al.[2]

For systems with $S \geq 1$, the electron spin relaxation is usually so fast (often on the picosecond timescale) that it competes effectively with complex reorientation as the main modulation mechanism for the dipole–dipole part of the modified Solomon–Bloembergen equations, even in small complexes. Bloembergen and Morgan[14] presented, as early as the early 1960s, a Redfield-type theory (see ***Relaxation Theory: Density Matrix Formulation***) where they related this efficient electronic relaxation in hexaaquo complexes of transition metal ions to the modulation of the ZFS by the distortion of the hydration shell. The Bloembergen–Morgan equations for $T_{1\mathrm{e}}$ and $T_{2\mathrm{e}}$ are often written as

$$T_{1\mathrm{e}}^{-1} = \frac{\Delta^2}{25}[4S(S+1) - 3]\left(\frac{\tau_v}{1 + \tau_v^2\omega_S^2} + \frac{4\tau_v}{1 + 4\tau_v^2\omega_S^2}\right) \tag{10}$$

$$T_{2\mathrm{e}}^{-1} = \frac{\Delta^2}{50}[4S(S+1) - 3] \times \left(3\tau_v + \frac{5\tau_v}{1 + \tau_v^2\omega_S^2} + \frac{2\tau_v}{1 + 4\tau_v^2\omega_S^2}\right) \tag{11}$$

where τ_v is the correlation time for the collision-related modulation of the ZFS, and Δ^2 is the trace of the square of the transient ZFS tensor:

$$\Delta^2 = D_{xx}^2 + D_{yy}^2 + D_{zz}^2 = \tfrac{2}{3}D^2 + 2E^2 \tag{12}$$

The combination of the modified Solomon–Bloembergen equations with the Bloembergen and Morgan theory for electron spin relaxation rates provides a complete theory for the magnetic field dependence of the PRE, known in the literature as the Solomon–Bloembergen–Morgan (SBM) theory.

The Bloembergen–Morgan theory has rather severe validity conditions, very clearly stated in the original paper. The most important limitation is the validity requirement for the Redfield-type or perturbative approach, which can generally be formulated as $\tau_v{}^2\Delta^2 \ll 1$. It is unfortunately rather common in the literature to use equations (10) and (11) uncritically, also beyond the limits of their validity. Analogous equations have also been derived for the case of rotational modulation of a static ZFS.[15] This case should be handled with care in the context of PRE, because it violates the requirement of no correlation between rotation and electron relaxation. An improvement of the SBM theory, within the same general framework and with the same validity limits, has been proposed by Rubinstein et al.[16] They noted that for systems with $S \geq \frac{3}{2}$ one may have more than one electronic T_1 or T_2, and they elegantly described the collision modulation of the ZFS as a pseudorotation process.

The issue of the electron spin relaxation for $S \geq 1$ in solution is not really settled, on the fundamental level of the applicability of the spin Hamiltonian formalism. An interesting line of thought, which still awaits a quantitative formulation, is that the electronic relaxation in liquids might in fact be similar to that in solids, where one talks about mechanisms involving interactions between the electron spin and phonons, mediated by the spin–orbit coupling.[2]

2.4 Beyond the Solomon–Bloembergen–Morgan Theory

During the last decade, significant effort has been invested into moving the paramagnetic relaxation theory beyond the limitations of the SBM theory. Two main approaches can be discerned. One of them can be referred to as 'low-field theories'. These are designed to handle cases when the electron Zeeman interaction does not dominate the energy level structure, either because the slow reorientation does not average out the anisotropic term in equation (8) or because another interaction (in the first place the ZFS interaction) simply is stronger and determines the quantization direction of the electron spin. This approach was originally proposed by Lindner[17] and was subsequently developed by Bertini and co-workers[1,2] and by Sharp.[18] The form of the resulting equation for $T_{1\mathrm{M}}{}^{-1}$ is similar to equation (4), in the sense that it consists of a sum of terms containing spectral density functions at the transition frequencies in the combined nuclear spin–electron spin system. The coefficients of the various spectral densities depend on the angle between the two molecule–fixed axis systems: the dipole–dipole axis and the principal axis of the anisotropic interaction. The electron spin relaxation enters the theories of this type in the simple form of 'electron relaxation

time', $\tau_S = T_{1e} = T_{2e}$, i.e. the electron spin is assumed to be in the Redfield limit. In addition, a frequency dependence of τ_S, similar to that given by the Bloembergen–Morgan theory, is sometimes used.

The other approach tries to solve the problem using more general, and more cumbersome, methods[3,8,19,20] based on the stochastic Liouville equation (see ***Liouville Equation of Motion***).[13] This formulation is often referred to as the 'slow-motion approach'. The nuclear spin is considered to be weakly coupled (in the sense that the Redfield formalism is valid) to a composite lattice, containing the electron spin degree of freedom as well as rotations and possibly other classical degrees of freedom. The electron spin and the classical degrees of freedom are coupled through the ZFS interaction of arbitary strength. The dynamics in the composite lattice can be described in terms of a spectral density function, and the nuclear T_1 is determined by the value of the spectral density at the nuclear Larmor frequency, while the nuclear T_2 depends on the spectral density at the nuclear Larmor frequency and at zero frequency. There is no need to invoke the concept of electronic relaxation time, even though the result of numerical calculations becomes identical to the SBM theory under appropriate limiting conditions. The disadvantage of the approach is its complexity: the composite lattice spectral density is obtained by the inversion of a complex matrix, in principle of infinite dimensions.

The magnetic field dependences of the nuclear spin–lattice relaxation rate, calculated using the methods of Bertini et al.[2] and of Benetis et al.,[8] have been compared with each other, imposing on the latter model the additional assumption of exponential electron spin relaxation.[2] For the case of large ZFS, the results of the two methods are identical and very different from the predictions of the SBM theory (Figure 1).

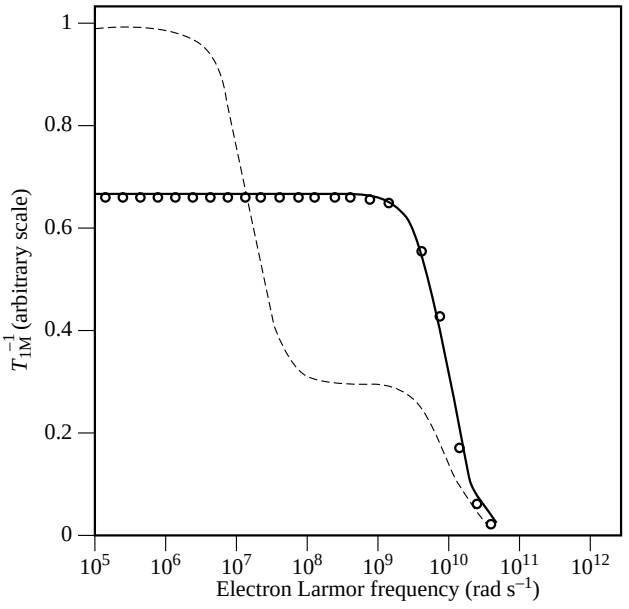

Figure 1 Calculated magnetic field dependence of proton $T_{1M}{}^{-1}$ in an $S = 1$ system according to the modified Solomon–Bloembergen equations (----), a low-field theory (—), and the slow-motion approach (○). (Reproduced by permission of VCH from L. Banci, I. Bertini, and C. Luchinat, 'Nuclear and Electron Relaxation', Weinheim, 1991)

2.5 The Curie Spin Relaxation

Gueron, Fiat, and Vega[21] have proposed an additional mechanism for the PRE, due to dipolar coupling of the nuclear spin with the thermally averaged electron magnetic moment. This average 'Curie spin' is aligned along the external magnetic field and is proportional to its magnitude. The interaction between the nuclear spin and the Curie spin is modulated by reorientation and exchange, but not by the electron spin relaxation. If the electron relaxation is much faster than the reorientation and exchange, and if the magnetic field is high, the Curie spin relaxation can become important (in particular for T_{2M}) in spite of the fact that the average electronic magnetic moment is of course much smaller than the real, rapidly oscillating one.

2.6 Intermolecular Relaxation

The above-mentioned theories of intramolecular nuclear spin relaxation due to dipole–dipole interaction assume that the distance R between the I and S spins is constant. The chemical exchange can be thought of as an extremely crude way of incorporating possible intermolecular effects or modulation of the dipole–dipole interaction by the variation of the interspin distance; it is allowed to be given a value of either R or infinity. For many transition metal complexes, this essentially intramolecular approach is sufficient. For other systems, where the paramagnetic centers in solution are either transition metal complexes with a nonlabile coordination sphere, or stable organic radicals, the relaxation of the solvent nuclei is predominantly intermolecular in nature (the concept of outer sphere relaxation is also used), and a more refined approach to the modulation of the spin–spin distance by translational diffusion is required. The problem can be solved at different levels of sophistication. The earlier development has been reviewed by Kowalewski et al.[3] Among more recent contributions, one should mention the work of Bayburt and Sharp[22] dealing with the limiting case of ZFS dominating over the electron Zeeman interaction.

3 EXPERIMENTAL METHODS

Most experimental work on PRE is technically very simple. Basically, one measures the nuclear spin–lattice or spin–spin relaxation rate (the latter is commonly estimated from the linewidth) for ligand nuclei in the presence and in the absence of the paramagnetic reagent, and one obtains the PRE by subtraction. The experiments are often performed to yield the result as a function of concentration of the paramagnetic species, temperature, pressure, or magnetic field. Variable concentration work can provide information on complexation equilibria. Variable temperature measurements can be used to clarify the relationships between the relaxation and exchange processes. Variable pressure experiments provide mechanistic information on the exchange processes (see ***Kinetics at High Pressure***). Variable field measurements are PRE experiments *par excellence*, if one is interested in verifying theoretical models. The variable temperature and variable field measurements are discussed in the following two sections, and the experimental section is concluded by a brief presentation of

the paramagnetic relaxation effects in certain two-dimensional experiments.

3.1 Variable Temperature: Fast and Slow Exchange

As can be seen from equations (1)–(3), the relationship between relaxation and exchange is simplest for the spin–lattice relaxation, where one can easily define two limiting conditions: fast exchange, $\tau_M \ll T_{1M}$; and slow exchange, $\tau_M \gg T_{1M}$. Assume a simple case of a small complex in low viscosity solution, with T_{1M} dominated by the dipole–dipole interaction and with the reorientation of the complex determining τ_{c1} and τ_{c2}. For such a case, we are likely to have $(\tau_{c1}\ \omega_I)^2 \ll 1$ and $[\tau_{c2}\ (\omega_S \pm \omega_I)]^2 \ll 1$ and, as the rate of reorientation increases with increasing temperature, the nuclear relaxation rate decreases. The opposite is true for the ligand exchange—the rate is going to increase with increasing temperature. The measurements of the PRE in the slow exchange regime give directly the exchange lifetime and its temperature dependence/activation parameters. Measurements in the fast exchange limit provide the relaxation rate in the paramagnetic complex which, given a suitable theoretical model, can yield information on structural as well as dynamic parameters. The slow and fast exchange conditions can also be formulated for paramagnetic line broadening, a quantity commonly measured in variable temperature studies. An example of variable temperature ^{17}O line-broadening data, taken from the work of Hugi et al.,[23] is shown in Figure 2.

3.2 Variable Field: Physics of Relaxation

When one wishes to reach a deeper understanding of the details of the relaxation mechanism, a variable field [nuclear magnetic relaxation dispersion (NMRD)] study is a very powerful tool. Changing the magnetic field provides a direct way of measuring the frequency dependence of the relevant spectral densities.

Figure 2 gives an example of a variable field T_2 study. More commonly, the variable field studies are concentrated on T_1 measurements. Besides performing the regular inversion–recovery experiments at as many high-field spectrometers as possible, it is useful to apply field cycling experiments (see ***Field Cycling Experiments***) to obtain the PRE also at very low magnetic fields. An illustrative example of the use of NMRD over a very wide range of magnetic fields is provided by the water proton relaxation in an aqueous solution of Mn(II) ions. The first field cycling experiments for this system were reported as early as the 1960s.[24] More recent data, as a function of solution viscosity varied by means of adding glycerol, are shown in Figure 3, taken from Bertini et al.[25] The Mn(II) ion is characterized by very small ZFS and slow electron spin relaxation; the data in Figure 3 can be interpreted successfully using the SBM theory. The scalar relaxation is observed at low field, because the electron relaxation is slow. In pure water, the scalar contribution disperses at ω_I of about 0.1 MHz, where $(T_{2e}\omega_S)^2$ becomes larger than unity. At higher fields, the dipolar relaxation dominates, and the second dispersion at ω_I of about 10 MHz corresponds to the condition $\omega_S\tau_R = 1$. Upon increasing the glycerol content, the viscosity increases, and both τ_R and τ_v increase with it, which changes the NMRD profiles.

A different case is presented by the PRE of water protons in an aqueous solution of another divalent first-row transition metal ion, Ni(II). An NMRD curve for this system, taken from work by Kowalewski et al.,[26] is shown in Figure 4. Here, the field dependence of the PRE is much weaker. The origin of this different behavior is to be sought in the electron relaxation in Ni(II), much faster than in the case of Mn(II). In fact, the nuclear and electron relaxation in aqueous Ni(II) is beyond the validity region of the SBM theory, and the details of the analysis of the data in Figure 4 are still not

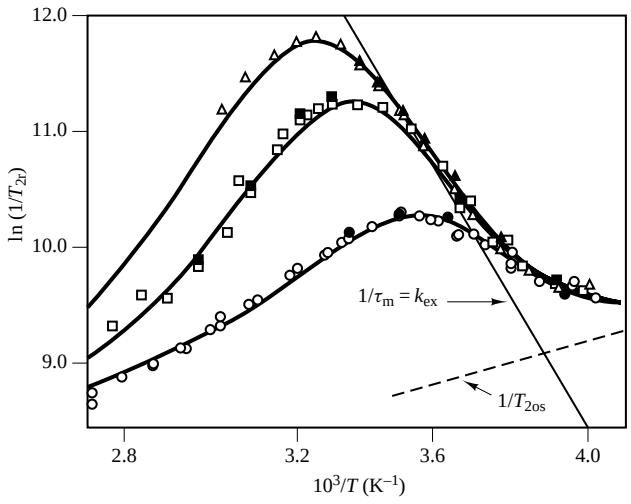

Figure 2 Oxygen-17 T_{2r}^{-1} in aqueous solution of a Ti(III) salt as a function of reciprocal temperature. Measurements were made at: (△, ▲) 8.4 T, (□, ■) 4.7 T, and (○, ●) 1.4 T. Open and filled symbols refer to different pH values. (Reproduced by permission of the American Chemical Society from A. D. Hugi, L. Helm, and A. E. Merbach, *Inorg. Chem.*, 1987, **26**, 1763)

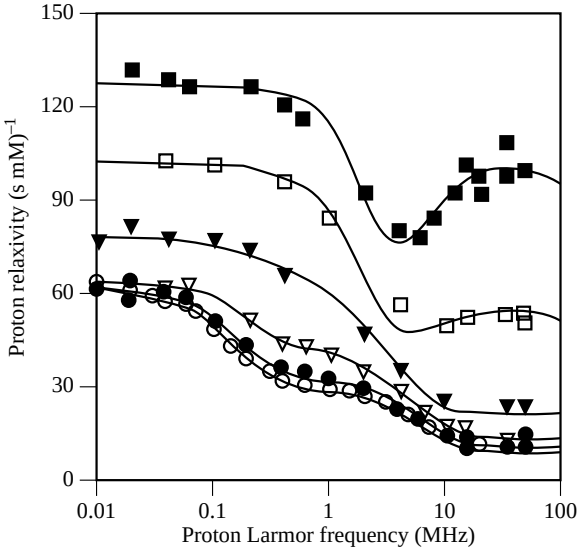

Figure 3 Water ^1H NMRD profiles of Mn(II) solutions in pure water (○) and with increasing amounts of deuterated glycerol [(●) 10%, (▼) 20%, (▼) 35%, (□) 55%, (■) 65%]. (Reproduced by permission of Academic Press from I. Bertini, F. Briganti, Z. C. Xia, and C. Luchinat, *J. Magn. Reson., Ser. A*, 1993, **101**, 198)

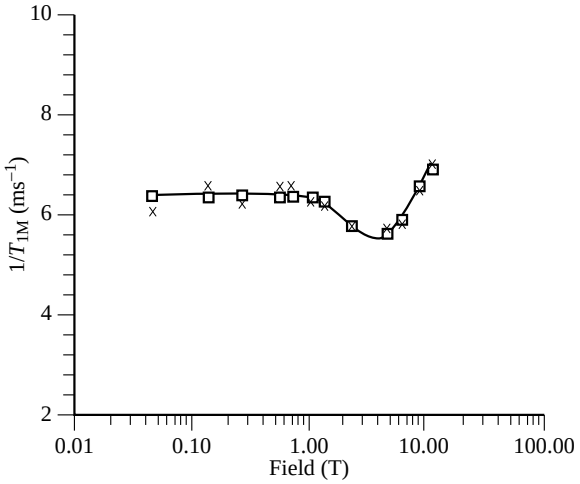

Figure 4 Water ^{1}H NMRD profile in aqueous Ni(II) solution [(×) experimental points, (□) slow-motion calculations, (—) SBM theory]. (Reproduced by permission of Academic Press from J. Kowalewski, T. Larsson, and P.-O. Westlund, *J. Magn. Reson.*, 1987, **74**, 56)

completely settled.[18,20,26] The flatness of the NMRD curve is caused by the rapid electron relaxation, which makes the scalar contribution negligible and reduces the efficiency of the dipole–dipole contribution. The weak increase of PRE at high field can be related to the onset of the dispersion of the electron relaxation.

The NMRD measurements are by no means limited to low-molecular-weight paramagnetic systems. A large number of data for metalloproteins in solutions can be found in the book by Banci et al.[2] and in a review by Koenig and Brown.[27]

3.3 Novel Experiments

The last few decades have seen a tremendous growth in the number of available NMR experiments. In many of these experiments the paramagnetic relaxation effects are a nuisance, and are carefully avoided by removing oxygen and paramagnetic impurities from the samples. In some cases, however, paramagnetic systems can be studied, and special features introduced into common two-dimensional techniques (NOESY and COSY) by the paramagnetic relaxation are worth mentioning.

The NOESY experiment suffers from the PRE in the sense that the cross-relaxation rates involving nuclei close to paramagnetic centers become much smaller than the leakage rates, which reduces the intensity of the cross peaks. As demonstrated, by Emerson and La Mar[28] among others, it is nevertheless possible to perform NOESY studies of the active site regions of fairly large paramagnetic proteins. The COSY experiments suffer from the PRE because of rapid relaxation and excessive signal cancellation when the linewidth is much larger than the J coupling. COSY cross peaks have nevertheless been reported in paramagnetic proteins. The results may, however, require a reevaluation in the light of the recent work by Bertini et al.,[29] who have demonstrated that the cross peaks may actually arise through relaxation-allowed coherence transfer, originating from cross correlation of the dipole–dipole and Curie relaxation mechanisms, rather than through J couplings.

4 RELATED ARTICLES

Chemical Exchange Effects on Spectra; Cobalt(II)- and Nickel(II)-Substituted Proteins; Contrast Agents in Whole Body Magnetic Resonance: An Overview; Contrast Agents in Magnetic Resonance: Operating Mechanisms; Copper Proteins; Electron–Nuclear Hyperfine Interactions; Electron–Nuclear Multiple Resonance Spectroscopy; Field Cycling Experiments; Iron—Sulfur Proteins; Kinetics at High Pressure; Liouville Equation of Motion; Myoglobin; Nonheme Iron Proteins; Relaxation Theory: Density Matrix Formulation; Transferrins.

5 REFERENCES

1. I. Bertini and C. Luchinat, *NMR of Paramagnetic Molecules in Biological Systems*, Benjamin/Cummings, Menlo Park, 1986.
2. L. Banci, I. Bertini, and C. Luchinat, *Nuclear and Electron Relaxation*, VCH, Weinheim, 1991.
3. J. Kowalewski, L. Nordenskiöld, N. Benetis, and P.-O. Westlund, *Progr. NMR Spectrosc.*, 1985, **17**, 141.
4. T. J. Swift and R. E. Connick, *J. Chem. Phys.*, 1962, **37**, 307.
5. Z. Luz and S. Meiboom, *J. Chem. Phys.*, 1964, **40**, 2686.
6. R. E. Connick and D. Fiat, *J. Chem. Phys.*, 1966, **44**, 4103.
7. J. Reuben, G. H. Reed, and M. Cohn, *J. Chem. Phys.*, 1970, **52**, 1617.
8. N. Benetis, J. Kowalewski, L. Nordenskiöld, H. Wennerström, and P.-O. Westlund, *Mol. Phys.*, 1983, **48**, 329.
9. D. Waysbort and G. Navon, *J. Chem. Phys.*, 1975, **62**, 1021; L. Nordenskiöld, A. Laaksonen, and J. Kowalewski, *J. Am. Chem. Soc.*, 1982, **104**, 379; N. Sahoo and T. P. Das, *J. Chem. Phys.*, 1989, **91**, 7740.
10. H. Sternlicht, *J. Chem. Phys.*, 1965, **42**, 2250.
11. A. Abragam and B. Bleaney, *Electron Paramagnetic Resonance of Transition Ions*, Clarendon, Oxford, 1970.
12. J. S. Griffith, *The Theory of Transition-Metal Ions*, Cambridge University, Cambridge, 1961.
13. L. T. Muus and P. W. Atkins (eds), *Electron Spin Relaxation in Liquids*, Plenum, New York, 1972.
14. N. Bloembergen and L. O. Morgan, *J. Chem. Phys.*, 1961, **34**, 842.
15. A. Carrington and G. R. Luckhurst, *Mol. Phys.*, 1964, **8**, 125; A. D. McLachlan, *Proc. R. Soc. London, Ser. A*, 1964, **280**, 271.
16. M. Rubinstein, A. Baram, and Z. Luz, *Mol. Phys.*, 1971, **20**, 67.
17. U. Lindner, *Ann. Phys. (Leipzig)*, 1965, **16**, 319 (Chem. Abstr., **64**: 14973c).
18. R. R. Sharp, *J. Chem. Phys.*, 1993, **98**, 912.
19. L.-P. Hwang and C.-Y. Ju, *J. Chem. Phys.*, 1985, **83**, 3775.
20. P.-O. Westlund, T. P. Larsson, and O. Teleman, *Mol. Phys.*, 1993, **78**, 1365.
21. M. Gueron, *J. Magn. Reson.*, 1975, **19**, 58; A. J. Vega and D. Fiat, *Mol. Phys.*, 1976, **31**, 347.
22. T. Bayburt and R. R. Sharp, *J. Chem. Phys.*, 1990, **92**, 5892.
23. A. D. Hugi, L. Helm, and A. E. Merbach, *Inorg. Chem.*, 1987, **26**, 1763.
24. R. Hausser and F. Noack, *Z. Phys.*, 1964, **182**, 93.
25. I. Bertini, F. Briganti, Z. C. Xia, and C. Luchinat, *J. Magn. Reson., Ser. A.*, 1993, **101**, 198.
26. J. Kowalewski, T. Larsson, and P.-O. Westlund, *J. Magn. Reson.*, 1987, **74**, 56.

27. S. H. Koenig and R. D. Brown, *Progr. NMR Spectrosc.*, 1990, **22**, 487.
28. S. D. Emerson and G. N. La Mar, *Biochemistry*, 1990, **29**, 1545.
29. I. Bertini, C. Luchinat, and D. Tarchi, *Chem. Phys. Lett.*, 1993, **203**, 445.

Biographical Sketch

Jozef Kowalewski. *b* 1947. B.Sc., 1969, Ph.D. (supervisors Ragnar Vestin and Björn Roos), 1975, Stockholm University. Postdoctoral work, Florida State University (with George Levy). Faculty, Stockholm University, 1977–present; Professor of Physical Chemistry, 1986–present. Approx. 100 publications. Research specialties: spin relaxation and molecular dynamics, cross-correlation effects, and paramagnetic systems.

Quasicrystalline Compounds: Metallic Glasses

Xiaoping Tang and Yue Wu

University of North Carolina, Chapel Hill, NC, USA

1 Introduction 1
2 Basic NMR Characteristics in Quasicrystalline Alloys 1
3 Probing Electronic Structures of Quasicrystalline Alloys by NMR 2
4 The Alignment Echo Technique for $I \geq 1$ 5
5 Detection of Slow Atomic Motion in Bulk Metallic Glasses by NMR of ^{9}Be 7
6 Related Articles in Volumes 1–8 8
7 References 8

1 INTRODUCTION

Two recent important developments of metallic alloys are the discoveries of quasicrystalline (QC) alloys and bulk metallic glasses (BMGs). In both cases, NMR studies have obtained crucial information that is important for the understanding of the novel properties of these systems. Discovered in 1984, QC alloys possess long-range translational and orientational orders, which lead to sharp Bragg diffraction peaks.[1] However, the diffraction patterns display point-group symmetry, such as icosahedral (i) symmetry, incompatible with periodicity.[1] Thus, QC alloys belong to a new class of solids unlike crystalline and glassy materials. In addition to their fascinating structure, QC alloys also possess novel physical properties such as the extremely low electric conductivity.[2] In this article we will focus on how NMR provides crucial information on the electronic structures of these QC alloys. Unlike crystalline and QC solids, glasses lack both long-range translational and orientational orders. Conventional metallic glasses are produced by rapid quenching of melts at cooling rates larger than $10^5\,\mathrm{K\,s^{-1}}$. In contrast, the newly discovered BMGs can be produced at a typical cooling rate of $1\,\mathrm{K\,s^{-1}}$ such that large pieces of glassy materials can be obtained. Examples of such BMGs are the Zr-based and Pd-based quaternary and quintary alloys.[3,4] Such BMGs exhibit excellent thermal stability making it experimentally possible to access the metallic supercooled liquid state down to the glass transition temperature (T_g). Clearly, BMGs possess unique thermodynamic and kinetic properties that hinder nucleation and growth in the supercooled liquid state. We will show how NMR can be used to obtain crucial information on the nature of atomic motions in the glassy and the supercooled liquid state of BMGs. Despite their different long-range orders, metallic glasses and QC alloys could share some similarities in local structures. For instance, icosahedral clusters were proposed to be the local structure in some metallic glasses and supercooled liquids. Experimentally, upon thermal annealing BMGs were observed to form QC phases prior to crystallization.[5]

2 BASIC NMR CHARACTERISTICS IN QUASICRYSTALLINE ALLOYS

NMR studies of QC alloys were carried out immediately after the initial discovery.[6] Structure, atomic motion, and electronic structures are the three main themes of most NMR studies of QC alloys. Lacking periodicity, the local environments in QC alloys are highly diversified despite the long-range translational and orientational orders. There exist a large number of nonequivalent atomic sites in QC alloys. As a result, the ^{27}Al NMR and NQR spectra measured in icosahedral Al-based QC alloys are broad and featureless. Based on ^{27}Al NQR spectra of i-$Al_{65}Cu_{23}Fe_{12}$ and i-$Al_{70}Cu_{15}Ru_{15}$ it was inferred that there exists a broad distribution of the magnitude of the EFG tensors associated with chemically nonequivalent Al sites.[7,8] On single-grain i-AlPdMn samples, the angular dependence of ^{27}Al NMR spectra was investigated.[8,9] In i-$Al_{70}Pd_{21.5}Mn_{8.5}$, the ^{27}Al NMR spectrum was found to be independent of the relative orientation between the static magnetic field (B_0) and the twofold rotation axis of the sample indicating a quasi-continuous distribution of structural environments.[8] In i-$Al_{72.4}Pd_{20.5}Mn_{7.1}$, the ^{27}Al NMR spectrum was found to be slightly different at parallel and perpendicular orientations between B_0 and the five-fold rotation axis suggesting a large but finite number of physically nonequivalent atomic sites.[9] A typical ^{27}Al NMR spectrum of Al-based QC alloys measured by the Hahn echo pulse sequence is shown in Figure 1. Powder pattern simulation of the $1/2 \leftrightarrow -1/2$ central transition at $B_0 = 9.4\,\mathrm{T}$ shows that the quadrupole frequency $\nu_Q = 3\chi/2I(2I-1)$ is on the order of 1.7 MHz in i-$Al_{65}Cu_{20}Ru_{15}$ (Figure 1),[10] consistent with the NQR measurements.[8] The isotropic shift is on the order of 150 ppm. Since the estimated second-order isotropic quadrupole shift $\delta_{\mathrm{iso}}^{(2)}$ is around –70 ppm and the typical ^{27}Al chemical shift is between 0 and 200 ppm, the Knight shift K is on the order of 200 ppm or less which is much smaller than $K^{^{27}\mathrm{Al}}$ of 1600 ppm observed in Al metal.

NMR was used to study atomic motion in QC alloys. In i-$Al_{65}Cu_{20}Ru_{15}$, a sharp increase of $1/T_1^{^{27}\mathrm{Al}}$ was measured above 673 K due to motion-induced quadrupole relaxation.[10] The Arrhenius plot indicated a thermally activated process with activation energy of 0.48 eV. It is about three times smaller than that in corresponding crystalline alloys where vacancy-assisted diffusion dominates. This suggests that a different atomic transport process is at work in QC alloys at high temperature. ^{27}Al two-dimensional exchange NMR has been employed to measure atomic motion in i-$Al_{70}Pd_{21.4}Re_{8.6}$ below 130 K.[11] The mixing time dependence of the two-dimensional exchange spectrum suggests that the detected atomic motion is spatially confined in this temperature range, extending over only several inter-atomic distances and is attributed to a mode of local motion specifically related to quasicrystallinity.[11]

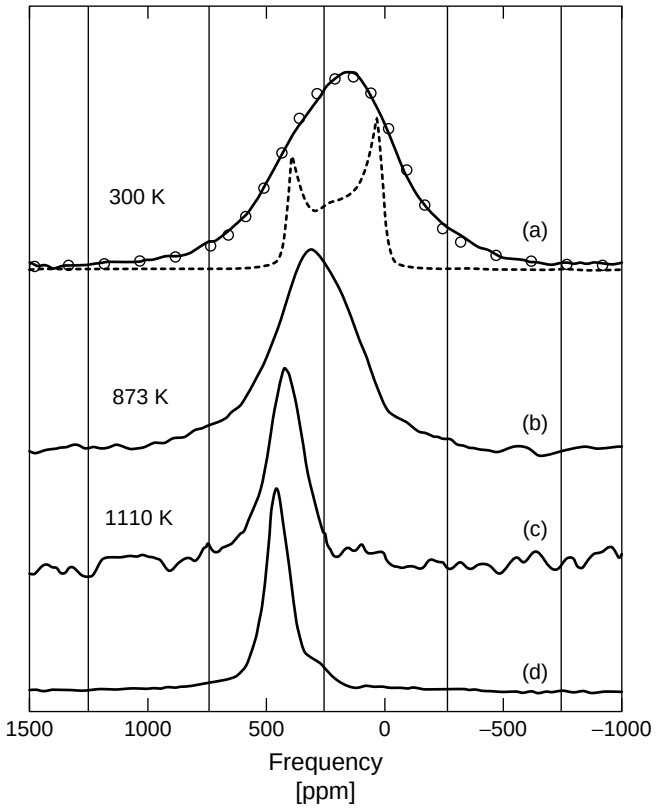

Figure 1 (a), (b), and (c) are the ^{27}Al spectra of i-$Al_{65}Cu_{20}Ru_{15}$ at various temperatures. The circles are the simulated spectrum of a powder-pattern of the anisotropic second-order quadrupole interaction convoluted with linewidth broadening. The dashed line is the quadrupole powder pattern ($\nu_Q = 1.7$ MHz, $\eta = 0$). (d) ^{27}Al spectrum of crystalline Al_7Cu_2Fe at 973 K

3 PROBING ELECTRONIC STRUCTURES OF QUASICRYSTALLINE ALLOYS BY NMR

High-quality QC alloys exhibit remarkably different physical properties than typical metals, with poor electric and thermal conductivity and very small electric heat capacity.[2] The electric resistivity of a QC alloy increases as structural order increases in contrast to typical metals.[2] Furthermore, the electric resistivity increases with decreasing temperature.[2] In fact, some of the high-quality QC alloys were found to be in the proximity of metal-insulator transition.[12] These unusual physical properties are related to novel structures of the electronic density-of-states (DOS). It is well-established both theoretically and experimentally that a broad DOS pseudogap at E_F of about 0.5–1 eV in width exists in QC alloys caused by electron scattering at the almost spherical pseudo-Brillouin zone at the Fermi surface. The pseudogap was predicted to be enhanced[13] by sp-d hybridization in Al-based QC alloys containing intermediate transition metals and plays a crucial role in the thermodynamic stability of QC phases. In addition, it was also predicted theoretically that a set of spiky DOS peaks of about 10 meV in width exist within the pseudogap as a result of strong hybridization between atomic orbits in the presence of high local symmetry[14] and hierarchical packing of icosahedral clusters.[1] The presence of such sharp feature at E_F will have a strong influence on the electric and thermal properties of QC alloys. We will show how NMR can be used to detect and characterize such sharp DOS features at E_F.

3.1 Unusual Temperature Dependence of Nuclear Spin-Lattice Relaxation

Unlike in typical metallic alloys, the measured K and $1/T_1$ in QC alloys are very small. It indicates that the DOS at E_F, $g(E_F)$, of QC alloys is small compared to the calculated value based on free-electron model. However, some earlier NMR studies did not find evidence of sharp DOS features.[15,16] Sharp features become noticeable as the quality of QC alloys improves. The NMR evidence of sharp DOS features is the unusual temperature dependence of $1/T_1$ that deviates substantially from the relation $1/T_1 \propto T$ observed in typical metallic systems. Figure 2 shows the nuclear spin-lattice relaxation (NSLR) curves of ^{27}Al measured in i-$Al_{70}Pd_{20}Re_{10}$.[17] Here, $M^*(t) = [M_0 - M(t)]/[M_0 - M(0)]$ is plotted[17] as a function of the recovery time t scaled by T^2. The NSLR curves measured between 100 and 600 K collapse into a single curve indicating that $1/T_1 \propto T^2$ (Figure 2). As discussed later, this novel temperature dependence is the signature of the sharp DOS valley at E_F. Similar temperature dependence of $1/T_1$ was also observed in other QC alloys including i-$Al_{65}Cu_{20}Ru_{15}$ and i-$Al_{62.5}Cu_{24.5}Fe_{13}$,[17] i-$Al_{70}Pd_{8.6}Re_{21.4}$,[18] i-$Al_{70.5}Pd_{21}Re_{8.5}$, i-$Al_{62}Cu_{25.5}Fe_{12.5}$ and i-$Al_{72.4}Pd_{20.5}Mn_{7.1}$.[19] At higher temperature above 600 K, $1/T_1$ is dominated by atomic motion-induced quadrupole relaxation.[10] At low temperature below 20 K, $1/T_1^{^{27}\mathrm{Al}}T \propto T^{-0.69}$ was observed in i-$Al_{70}Pd_{8.6}Re_{21.4}$.[18] This power law was described as a result of gradual real-space localization of the itinerant charge carriers. Similar low-temperature $1/T_1$ behaviors were also observed in i-$Al_{70.5}Pd_{21}Re_{8.5}$, i-$Al_{62}Cu_{25.5}Fe_{12.5}$, and i-$Al_{72.4}Pd_{20.5}Mn_{7.1}$.[19] The low-temperature NMR results, consistent with the low-temperature electric conductivity, magnetoresistivity,[12] and magnetic susceptibility[20] measurements, indicate a strong effect of the weak localization and electron-electron interaction in high-quality QC alloys at low temperature.

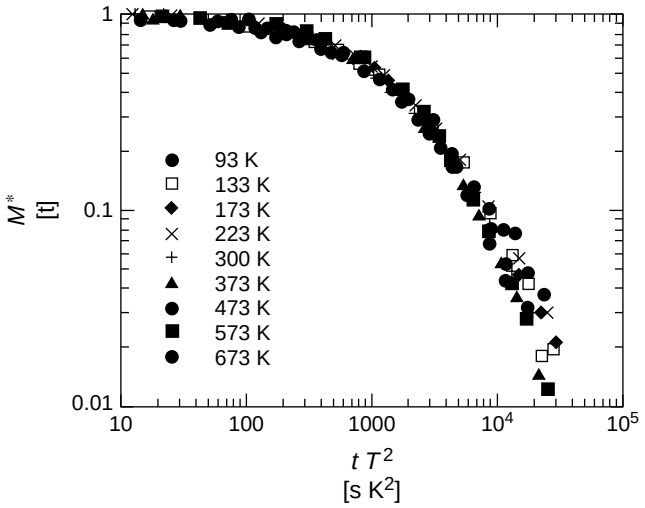

Figure 2 The inversion recovery curves of the ^{27}Al nuclear magnetization M versus τ which is scaled by T^2 in i-$Al_{70}Pd_{20}Re_{10}$. It shows that $1/T_1 \propto T^2$

3.2 The Mechanism of the Nuclear Spin-lattice Relaxation

In NMR studies of QC alloys, ^{27}Al, ^{63}Cu, and ^{63}Cu are the most frequently used isotopes. Two mechanisms can induce NSLR for these quadrupolar nuclei. One mechanism is the coupling between the nuclear spin and the unpaired conduction electron spins (magnetic relaxation). The second mechanism is the coupling of the nuclear electric quadrupole moment with the fluctuating EFG induced by atomic motions (quadrupolar relaxation). For magnetic relaxation, $1/T_1 \propto \gamma_n^2$; for quadrupolar relaxation, $1/T_1 \propto Q^2$. The relative contributions of the two mechanisms can be determined by measuring $1/T_1$ of a pair of proper isotopes. For i-AlCuRu and i-AlCuFe, ^{63}Cu and ^{65}Cu is such an excellent pair:[17] $T_1^{^{65}\mathrm{Cu}}/T_1^{^{63}\mathrm{Cu}} = (\gamma_{^{63}\mathrm{Cu}}/\gamma_{^{65}\mathrm{Cu}})^2 = 0.87$ for magnetic relaxation and $T_1^{^{65}\mathrm{Cu}}/T_1^{^{63}\mathrm{Cu}} = (Q_{^{63}\mathrm{Cu}}/Q_{^{65}\mathrm{Cu}})^2 = 1.14$ for quadrupole relaxation. Figure 3 shows the ^{63}Cu and ^{65}Cu NSLR curves measured in i-$Al_{65}Cu_{20}Ru_{15}$ at 300 K and 9.4 T where $T_1^{^{65}\mathrm{Cu}}/T_1^{^{63}\mathrm{Cu}}$ was measured to be 0.83–0.90. In i-$Al_{62.5}Cu_{24.5}Fe_{13}$ $T_1^{^{65}\mathrm{Cu}}/T_1^{^{63}\mathrm{Cu}}$ was also measured to be 0.80–0.87.[17] Thus, $1/T_1^{^{63}\mathrm{Cu}}$ and $1/T_1^{^{65}\mathrm{Cu}}$ in i-$Al_{65}Cu_{20}Ru_{15}$ and i-$Al_{62.5}Cu_{24.5}Fe_{13}$ are dominated by magnetic relaxation.[17] In i-$Al_{65}Cu_{20}Ru_{15}$ $1/T_1^{^{27}\mathrm{Al}}$ was found[17] to follow almost the same temperature dependence as $1/T_1^{^{63}\mathrm{Cu}}$. It suggests that the observed unusual temperature dependences of $1/T_1^{^{27}\mathrm{Al}}$, $1/T_1^{^{63}\mathrm{Cu}}$, and $1/T_1^{^{65}\mathrm{Cu}}$ are originated from the same mechanism through the coupling between the nuclear spins and unpaired conduction electron spins.

A strong field dependence of $1/T_1^{^{27}\mathrm{Al}}$ was observed in i-$Al_{72.4}Pd_{20.5}Mn_{7.1}$.[21] The measured $1/T_1^{^{27}\mathrm{Al}}$ was ascribed to two components; one is independent of B_0 dominating at low temperature while the other is inversely proportional to B_0 dominating at high temperature.[21] The origin of the second component remains unexplained.[21] The nature of $1/T_1^{^{27}\mathrm{Al}}$ in other QCs were shown to be different. In i-$Al_{70}Pd_{20}Re_{10}$ and i-$Al_{65}Cu_{20}Ru_{15}$, $1/T_1^{^{27}\mathrm{Al}}$ was measured to be field independent;[20] in i-$Al_{70}Pd_{21.4}Re_{8.6}$ $1/T_1^{^{27}\mathrm{Al}}$ was measured to be field independent as well.[18] Thus, the observed field dependence of $1/T_1^{^{27}\mathrm{Al}}$ in i-$Al_{72.4}Pd_{20.5}Mn_{7.1}$ is not intrinsic to QC alloys. In Al-based QC alloys with intermediate transition metals, NMR results could be complicated by possible localized magnetic moments at the atomic sites of the transition metals. Thus, the field dependence of $1/T_1^{^{27}\mathrm{Al}}$ in i-AlPdMn might be related to localized magnetic moments since the magnetic moment concentration in i-AlPdMn is several orders of magnitude larger than in i-AlPdRe and i-AlCuRu according to magnetic susceptibility measurement.[20] In view of this, i-AlPdRe and i-AlCuRu are more appropriate systems for NMR study of the intrinsic electronic properties of QC alloys.

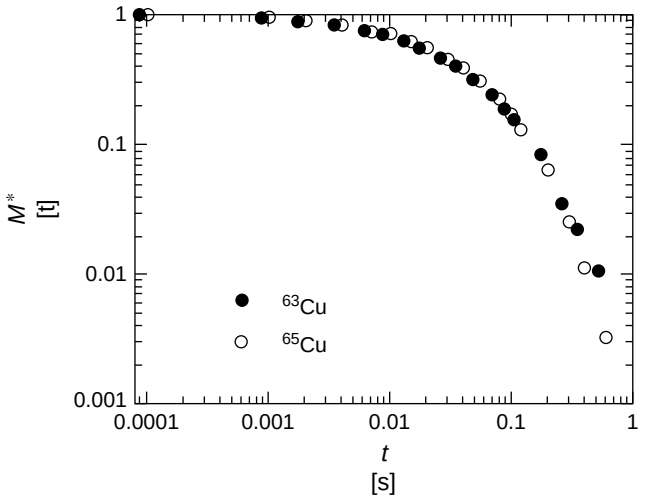

Figure 3 The ^{63}Cu and ^{65}Cu NSLR curves in i-$Al_{65}Cu_{20}Ru_{15}$ at 300 K and 9.4 T. The curve for ^{63}Cu is plotted as $M^*(0.87\,\mathrm{t})$. It shows that $T_1^{^{65}\mathrm{Cu}}/T_1^{^{63}\mathrm{Cu}}$ is 0.83–0.90

3.3 The Sharp DOS Feature

As discussed in Section 3.1, below 20 K the measured T_1 in i-$Al_{70}Pd_{8.6}Re_{21.4}$ are found to be associated with the electron-electron interaction and weak localization. Above 600 K, T_1 is dominated by the contribution of atomic motion. Therefore, only T_1 measured in the intermediate temperature range, which is governed by the coupling between the nuclear spins and the unpaired independent conduction electron spins, will be used to extract the sharp DOS feature at E_F. In this section, we discuss the derivation of the sharp DOS feature by analyzing the NMR results measured in this temperature range.

In Al-based QCs with intermediate transition metals such as i-AlPdRe and i-AlCuRu, the Al 3s and 3p-bands are strongly hybridized with the Re 5d-band and the Ru 4d-band, respectively. The K and $1/T_1$ of ^{27}Al, ^{63}Cu and ^{65}Cu are dominated by the Fermi-contact interaction with the conduction 3s-electron spins and the core-polarization induced by the conduction d electron spins. Denoting the partial DOS of the 3s and d-bands as $g_s(E)$ and $g_d(E)$, respectively, K is described by

$$K = \frac{1}{k_B T}\int [\alpha_s g_s(E) + \alpha_d g_d(E)] f(E)[1 - f(E)]\mathrm{d}E, \qquad (1)$$

where $f(E)$ is the Fermi-Dirac distribution function, $\alpha_s = \frac{4\pi}{3}\hbar^2\gamma_e^2\langle|u_k^2(0)|\rangle_{E_F}$ where γ_e is the electronic gyromagnetic ratio and $\langle|u_k^2(0)|\rangle_{E_F}$ is the density of the 3s-band wave function at the Al nucleus averaged over the Fermi surface, α_d is associated with the core-polarization by the d-bands and is negative. $1/T_1$ is described by

$$\frac{1}{T_1} = \int [\beta_s g_s^2(E) + \beta_d g_d^2(E)] f(E)[1 - f(E)]\mathrm{d}E, \qquad (2)$$

where $\beta_s = 4\pi\hbar\gamma_n^2\alpha_s^2$ and $\beta_d = 4\pi p\hbar\gamma_n^2\alpha_d^2$ (p is a factor related to the local symmetry and degeneration of the d-bands).[22]

Since $f(E)[1 - f(E)]$ vanishes quickly as E deviates from E_F by a few $k_B T$, the temperature dependence of K and $1/T_1$ are determined by DOS near E_F. In typical metallic systems, since the DOS variation over several $k_B T$ is small near E_F, K is temperature independent and $1/T_1 \propto T$. In high quality QC alloys, however, novel temperature dependences of K and $1/T_1$ were observed inferring a sharp DOS feature near E_F. For Al-based QC alloys containing intermediate transition metals,

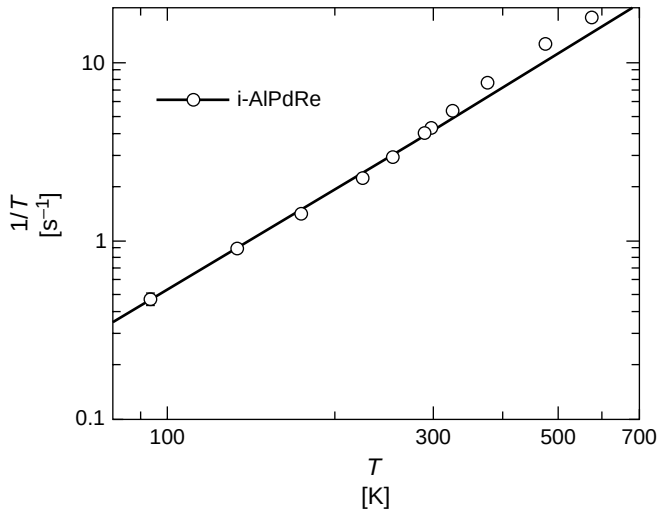

Figure 4 $1/T_1^{^{27}\mathrm{Al}}$ versus T in i-$Al_{70}Pd_{20}Re_{10}$. The solid line is a fit with equation (5)

the theoretical calculations indicated[13] an enhanced pseudogap at E_F by sp-d hybridization leading to a sharp DOS valley. The structures of the partial DOS $g_s(E)$ and $g_d(E)$ within the sharp DOS valley near E_F can be assumed as

$$g_s(E) = g_{0s} + g_{1s}|E - E_F|^{\varepsilon},$$
$$g_d(E) = g_{0d} + g_{1d}|E - E_F|^{\varepsilon} \tag{3}$$

with g_{0s} and g_{0d} as the residual DOS at E_F for 3s-band and d-bands, respectively.

K is obtained from equations (1) and (3) as

$$K = (\alpha_s g_{0s} + \alpha_d g_{0d}) + 2C(\varepsilon)(\alpha_s g_{1s} + \alpha_d g_{1d})(k_B T)^{\varepsilon}, \tag{4}$$

where $C(\varepsilon) = \int_0^{\infty} x^{\varepsilon} e^x/(1+e^x)^2 dx$. Using equations (2) and (3), $1/T_1$ is obtained as

$$\frac{1}{T_1} = k_B T[(\beta_s g_{0s}^2 + \beta_{ds} g_{0d}^2) + 4C(\varepsilon)(\beta_s g_{0s} g_{1s} + \beta_d g_{0d} g_{1d})(k_B T)^{\varepsilon}$$
$$+ 2C(2\varepsilon)(\beta_s g_{1s}^2 + \beta_{ds} g_{1d}^2)(k_B T)^{2\varepsilon}]. \tag{5}$$

At low temperature, equations (4) and (5) lead to the conventional temperature dependences where K is temperature independent and $1/T_1 \propto T$. As discussed above, however, equations (4) and (5) are not suitable for analyzing the low temperature K and $1/T_1$ data in QC alloys since the electron – electron interaction and weak localization are not included. At higher temperatures, equations (4) and (5) lead to $K \propto T^{\varepsilon}$ and $1/T_1 \propto T^{1+2\varepsilon}$. The power law $1/T_1 \propto T^2$ was observed in i-$Al_{70}Pd_{20}Re_{10}$ and i-$Al_{65}Cu_{20}Ru_{15}$ above 100 K suggesting that $\varepsilon = 1/2$.[17] Indeed, the fit of $1/T_1^{^{27}\mathrm{Al}}$ by equation (5) shows that $\varepsilon \approx 1/2$ (Figure 4). Since $1/T_1 \propto T^2$ is induced by the sharp DOS valley and is clearly obeyed up to 400 K, the width of the $\varepsilon = 1/2$ region in the sharp DOS valley should be at least as large as 25 meV.[17] The measured small residual $g(E)$ at E_F in i-$Al_{70}Pd_{20}Re_{10}$ and i-$Al_{65}Cu_{20}Ru_{15}$ agrees with the heat capacity measurements.[17] Since the NMR results at much higher temperature are complicated by atomic motion,[10] the DOS shape further away from E_F cannot be determined by NMR.

For $\varepsilon = 1/2$, equation (4) leads to a weak temperature dependence of K at high temperature. Indeed, $K^{^{27}\mathrm{Al}}$ was measured to follow such a weak temperature dependence in i-$Al_{70}Pd_{20}Re_{10}$ and i-$Al_{65}Cu_{20}Ru_{15}$.[10,17] Moreover, the measured temperature dependence of $K^{^{27}\mathrm{Al}}$ was found[17] to be correlated with that of $1/T_1^{^{27}\mathrm{Al}}$ as described by equations (4) and (5). The analysis of the temperature dependences of $K^{^{27}\mathrm{Al}}$ and $1/T_1^{^{27}\mathrm{Al}}$ indicate a strong effect of the core-polarization at Al sites that is consistent with the theoretical prediction of the strong sp-d hybridization in Al-based QC alloys containing intermediate transition metals.[12]

3.4 Comments on the Approximation Method Based on Taylor Expansion

An approximation method was used to describe the DOS variation near E_F for narrow d-bands and analyze the nonlinear temperature dependence of $1/T_1$ and the temperature dependence of K such as in Pt metal.[22] A similar approximation was used to analyze the nonlinear temperature dependence of $1/T_1$ in QC alloys.[10,19,21] Here we show that such approximation can often be insufficient and misleading in analyzing the effect of the DOS variation near E_F.

The approximation is based on the Taylor expansion of $g(E)$ at E_F^0 (E_F at $T = 0$) as

$$g(E) = g(E_F^0) + (E - E_F^0)g'(E_F^0) + \tfrac{1}{2}(E - E_F^0)^2 g''(E_F^0), \tag{6}$$

with $g'(E_F^0)$ and $g''(E_F^0)$ as the first and second derivatives of $g(E)$ to E at E_F^0, respectively. Because of the second term in equation (6), E_F could be temperature dependent if $g(E)$ is not symmetric about E_F^0. Define $\Delta E_F = E_F - E_F^0$, equation (6) can be rewritten as

$$g(E) = [g(E_F^0) + \Delta E_F g'(E_F^0) + \tfrac{1}{2}(\Delta E_F)^2 g''(E_F^0)] + (E - E_F)[g'(E_F^0) + \Delta E_F g''(E_F^0)] + \tfrac{1}{2}(E - E_F)^2 g''(E_F^0). \tag{7}$$

Using equation (7) and the conservation of electron density described by $\frac{d}{dT}[\int g(E) f(E) dE] = 0$, it is straightforward to obtain

$$\frac{d(\Delta E_F)}{dT}\left[g(E_F^0) + \Delta E_F g'(E_F^0) + \frac{1}{2}(\Delta E_F)^2 g''(E_F^0) + \frac{\pi^2}{6} g''(E_F^0)(k_B T)^2\right] = -\frac{\pi^2}{3}[g'(E_F^0) + \Delta E_F g''(E_F^0)]k_B^2\, T. \tag{8}$$

The derivatives of ΔE_F with T can be derived from equation (8) and the Taylor expansion of E_F can be calculated at $T = 0$ as

$$E_F = E_F^0 - \frac{\pi^2}{6}(k_B T)^2 \frac{g'(E_F^0)}{g(E_F^0)} + \frac{\pi^4}{72}(k_B T)^4 \frac{g'(E_F^0)}{g(E_F^0)} \times \left[2\frac{g''(E_F^0)}{g(E_F^0)} - \left(\frac{g'(E_F^0)}{g(E_F^0)}\right)^2\right] + 0(T^6). \tag{9}$$

For a symmetric $g(E)$ about $E = E_F^0$, $g'(E_F^0) = 0$ and E_F is temperature independent.

Using equations (1), (7), and (9), K can be calculated to the order of T^5 as

$$K \propto g(E_F^0)\left\{1 + \frac{\pi^2}{6}(k_BT)^2\left[\frac{g''(E_F^0)}{g(E_F^0)} - \left(\frac{g'(E_F^0)}{g(E_F^0)}\right)^2\right] + \frac{\pi^6}{60}(k_BT)^4\left(\frac{g'(E_F^0)}{g(E_F^0)}\right)^2\left[3\frac{g''(E_F^0)}{g(E_F^0)} - \left(\frac{g'(E_F^0)}{g(E_F^0)}\right)^2\right]\right\} + 0(T^6). \tag{10}$$

Using equations (2), (7), and (9), the calculated $1/T_1$ is given by

$$\frac{1}{T_1} \propto g^2(E_F^0)\left\{k_BT + \frac{\pi^2}{3}(k_BT)^3\frac{g''(E_F^0)}{g(E_F^0)} + \frac{\pi^6}{60}(k_BT)^5\frac{g''(E_F^0)}{g(E_F^0)}\left[7\frac{g''(E_F^0)}{g(E_F^0)} - 5\left(\frac{g'(E_F^0)}{g(E_F^0)}\right)^2\right]\right\} + 0(T^7). \tag{11}$$

As an approximation, equations (9), (10), and (11) are valid only if the second terms on the right hand side of these equations are much smaller than the corresponding first terms. This is exactly what was assumed in Refs.[10,19,21,22] in which only the first and second terms of these equations were included in the approximation. There, the measured $1/T_1$ in QC alloys were fitted with only the T and T^3 terms.[10,19,21] However, the fits of the $1/T_1$ data indicated that the contribution of the T^3 term is comparable or even larger than that of the T term within the investigated temperature range. In this case, equation (11) shows that the contribution of the T^5 term cannot be neglected and the expansion itself may not converge. Moreover, K should be dominated by the contribution of the T^2 and T^4 terms. Thus, the approximation implies a strong temperature dependence of K, in contrast to the observation of a weak temperature dependence of K.[10,17] Thus, the approximation is not valid for analyzing the measured $1/T_1$ in QC alloys. In general, it is not valid to use this approximation method to analyze $1/T_1$ that deviates significantly from $1/T_1 \propto T$.

4 THE ALIGNMENT ECHO TECHNIQUE FOR $I \geq 1$

NMR has made important contributions to the study of atomic and molecular motion in amorphous systems. However, NMR was rarely used to measure atomic motion in metallic glasses and metallic supercooled liquids, especially slow atomic motion. The reasons are twofold. First, the fast rate of crystallization upon heating in conventional metallic glasses and supercooled liquids does not allow sufficient time for most experimental approaches including NMR. Secondly, the longest timescale of atomic motion detectable by NMR is intrinsically limited by T_1 that is very short in typical metallic systems. Since BMGs exhibit excellent glass formability and remarkable thermal stability, a large temperature range becomes accessible for NMR up to temperatures significantly above T_g. This allows the experimental studies of the nature of glass transition and the nature of atomic motion in the supercooled liquid state near T_g. It was fortunate for NMR studies that the representative BMGs, $Zr_{41.5}Ti_{22.5}Cu_{22.5}Ni_{10}Be_{22.5}$ (vit1) and $Zr_{41.5}Ti_{22.5}Cu_{22.5}Ni_{10}$ $Be_{27.5}$ (vit4), contain Be where $T_1^{^9Be}$ is very long. This makes NMR detection of slow atomic motion feasible in both the glassy and deeply supercooled liquid states.[23–25]

The nuclear spin alignment echo technique (SAE) of ^{2}H ($I = 1$) has been used extensively for studying motion in polymers.[26] This technique was extended to the case of $I = 3/2$ in the study of translational atomic motion in BMGs using ^{9}Be NMR.[23–25] Later, ^{7}Li SAE was used in measuring ionic motion in electrolyte materials.[27] The ^{2}H SAE technique was described extensively in the literature.[26] A general treatment was given recently for $I = 1$ to 9/2.[23] Following the latter, assume that the truncated Hamiltonian of a nuclear spin system in the rotating frame consists of the Zeeman interaction (due to resonance off-set) and first-order electric quadrupole interaction given by

$$\hat{H} = \beta\hat{I}_z + \alpha\ (3\hat{I}_z^2 - \hat{I}^2) \tag{12}$$

where β is the shift relative to the rf frequency, α is proportional to the quadrupole resonance frequency.

The pulse sequence of SAE, $90^0 - \tau_1 - \theta_\phi - t - \theta'_{\phi'} - \tau_2-$, is applied with nonselective RF pulses with the time parameters chosen such that $\tau_1 < T_2 < t$. θ and θ' are the flipping angles of the second and third pulses, respectively, with ϕ and ϕ' as the corresponding phases with respect to the first pulse. Since atomic motion could occur during the diffusion time t, the values of α and β associated with a given nuclear spin during the time interval τ_1 are denoted as α_1 and β_1, respectively, and as α_2 and β_2, respectively, during the time interval τ_2. Since $t > T_2$, the spin density operator during t evolves into a diagonal density operator ($\hat{\rho}(t)$) represented by a linear combination of various nuclear spin orders (from the Zeeman order to $2I$th-rank spin order). The kth-rank spin order is proportional to the kth-rank zeroth-order irreducible tensor $A^{(k,0)}$ (see Table 1 in Ref.[23] for the explicit expressions of $A^{(k,0)}$ for $I = 1/2$ to 9/2). The signal appearing after the third pulse is given by[23]

$$S(\tau) = -\cos\phi_{\text{eff1}}e^{i\phi_{\text{eff2}}}\sum_{\text{odd}k} f_k(\theta, \alpha_1\tau_1)\, f_k(\theta', -\alpha_2\tau_2) + i\sin\phi_{\text{eff1}}e^{i\phi_{\text{eff2}}}\sum_{\text{even}k} f_k(\theta, \alpha_1\tau_1)\, f_k(\theta', -\alpha_2\tau_2), \tag{13}$$

where $\phi_{\text{eff1}} = \phi + \beta_1\tau_1$, $\phi_{\text{eff2}} = \phi' + \beta_2\tau_2$, and $f_k(\theta, \alpha\tau)$ is the coefficient given by

$$f_k(\theta, \alpha\tau) = \text{Trace}(e^{-i\theta I_y}e^{-3i\alpha I_z^2\tau}\hat{I}_x e^{3i\alpha I_z^2\tau}e^{i\theta I_y}A^{(k,0)}) \quad (\text{odd } k)$$
$$f_k(\theta, \alpha\tau) = \text{Trace}(e^{-i\theta I_y}e^{-3i\alpha I_z^2\tau}\hat{I}_y e^{3i\alpha I_z^2\tau}e^{i\theta I_y}A^{(k,0)}) \quad (\text{even } k). \tag{14}$$

Thus, $f_k(\theta, \alpha_1\tau_1)$ is the coefficient of the kth-rank nuclear spin order during t. For example, $f_1(\theta, \alpha_1\tau_1)$ and $f_2(\theta, \alpha_1\tau_1)$ correspond to the Zeeman and quadrupole order, respectively. It is of note that $\cos\phi_{\text{eff1}}e^{i\phi_{\text{eff2}}}f_k(\theta, \alpha_1\tau_1)\, f_k(\theta', -\alpha_2\tau_2)$ (odd k) and $\sin\phi_{\text{eff1}}e^{i\phi_{\text{eff2}}}f_k(\theta, \alpha_1\tau_1)\, f_k(\theta', -\alpha_2\tau_2)$ (even k) are single-particle correlation functions connecting the local environments experienced by a nuclear spin during τ_1 and τ_2.

For an ensemble of nuclear spins, an alignment echo forms at $\tau_2 = \tau_1$ if no motion occurs during t. On the other hand, atomic motion may induce the change of the local environments and destroy the single-particle correlation leading to the alignment echo decay. The kth-rank nuclear spin order created during t could decay as well during t with a decay rate of W_k induced by the NSLR mechanisms. Thus, following equation (13) the SAE echo height is described by

$$S_{\text{echo}}(t) = -\sum_{\text{odd}k} \mathrm{e}^{-W_k t}\langle \cos\phi_{\text{eff1}} \mathrm{e}^{i\phi_{\text{eff2}}} f_k(\theta, \alpha_1\tau_1) f_k(\theta', -\alpha_2\tau_2)\rangle + i\sum_{\text{even}k} \mathrm{e}^{-W_k t}\langle \sin\phi_{\text{eff1}} \mathrm{e}^{i\phi_{\text{eff2}}} f_k(\theta, \alpha_1\tau_1) f_k(\theta', -\alpha_2\tau_2)\rangle \tag{15}$$

with $\langle\rangle$ denoting the ensemble average. In metallic glasses, NSLR is usually dominated by the coupling between the nuclear spins and unpaired conduction electron spins. In this case, the evolution of $\hat{\rho}(t)$ can be described by:

$$\frac{d\hat{\rho}(t)}{dt} = J_1[[\hat{\rho}(t) - \hat{\rho}_0, \hat{I}_+], \hat{I}_-], \tag{16}$$

with J_1 as a constant related to the magnetic properties of the spin system and $\hat{\rho}_0$ as the density operator at thermal equilibrium. Using the following identity

$$[[A^{(k,0)}, \hat{I}_+], \hat{I}_-] = k(k+1)A^{(k,0)}, \tag{17}$$

it is straightforward to obtain $\hat{\rho}(t)$ as

$$\hat{\rho}(t) = \hat{\rho}_0 + \sum_{k=0}^{2I} C_k \mathrm{e}^{-k(k+1)t/2T_1} A^{(k,0)} \tag{18}$$

with C_k as the coefficients. Thus, $W_k = k(k+1)/2T_1$ which is true for other magnetic relaxation mechanisms as well. Since W_k varies with k, it is easier to extract the information about motion when only singular rank of nuclear spin order is created during t. In this case the $\mathrm{e}^{-W_k t}$ factor of the chosen rank can be easily separated from the motion-related single-particle correlation functions by measuring T_1.

In the presence of both a α distribution $\delta\alpha$ and a β distribution $\delta\beta$, it is in general difficult to produce a singular rank of spin order. If $\delta\beta \ll \delta\alpha$, τ_1 can be chosen such that $\delta\beta\tau_1 \ll \pi/2 \ll \delta\alpha\tau_1$. Then, odd-ranked spin orders can be created separately from even-ranked spin orders by choosing $\phi = 0°$ (180°) for creating odd-ranked spin orders and $\phi = 90°$ (270°) for creating even-ranked spin orders. Therefore, by selecting proper ϕ it is possible to produce pure Zeeman order or quadrupole order for $I = 1$. For $I = 3/2$, pure quadrupole order can be produced by choosing $\phi = 90°$ (270°). On the other hand, the Zeeman order and octupole order cannot be separated. Equation (15) shows that the contribution of certain undesired nuclear spin orders can be suppressed also by the choice of the θ or θ' values based on the value of $f_k(\theta, \alpha\tau)$.

In Ref.[23] $f_k(\theta, \alpha\tau)(k = 1, 2, \ldots, 2I)$ were derived explicitly based on the equation

$$\begin{aligned}\mathrm{e}^{-i\alpha\hat{I}_z^2}\hat{I}_\pm \mathrm{e}^{i\alpha\hat{I}_z^2} = \hat{I}_\pm[1 \quad \cos 2\alpha \quad \cdots \quad \cos(2I-1)\alpha] \\ \times \begin{bmatrix} 1 & 1 & \cdots & 1 \\ 0 & 2^2 & \cdots & (2I-1)^2 \\ \vdots & \vdots & \vdots & \vdots \\ 0 & 2^{2I-1} & \cdots & (2I-1)^{2I-1} \end{bmatrix} \begin{bmatrix} 1 \\ (1 \pm 2\hat{I}_z)^2 \\ \vdots \\ (1 \pm 2\hat{I}_z)^{2I-1} \end{bmatrix} \\ - i\hat{I}_\pm[\sin 2\alpha \quad \sin 4\alpha \quad \cdots \quad \sin\ (2I-1)\alpha] \\ \times \begin{bmatrix} 2 & 4 & \cdots & (2I-1) \\ 2^3 & 4^3 & \cdots & (2I-1)^3 \\ \vdots & \vdots & \vdots & \vdots \\ 2^{2I-2} & 4^{2I-2} & \cdots & (2I-1)^{2I-2} \end{bmatrix} \begin{bmatrix} (1 \pm 2\hat{I}_z) \\ (1 \pm 2\hat{I}_z)^3 \\ \vdots \\ (1 \pm 2\hat{I}_z)^{2I-2} \end{bmatrix}\end{aligned} \tag{19}$$

for half-integer I ($I = 3/2$, 5/2, 7/2, 9/2) and on the equation

$$\begin{aligned}\mathrm{e}^{-i\alpha\hat{I}_z^2}\hat{I}_\pm \mathrm{e}^{i\alpha\hat{I}_z^2} = \hat{I}_\pm[\cos\alpha \quad \cos 3\alpha \quad \cdots \quad \cos\ (2I-1)\alpha] \\ \times \begin{bmatrix} 1 & 1 & \cdots & 1 \\ 1 & 3^2 & \cdots & (2I-1)^2 \\ \vdots & \vdots & \vdots & \vdots \\ 1 & 3^{2I-2} & \cdots & (2I-1)^{2I-2} \end{bmatrix} \\ \times \begin{bmatrix} 1 \\ (1 \pm 2\hat{I}_z)^2 \\ \vdots \\ (1 \pm 2\hat{I}_z)^{2I-2} \end{bmatrix} \\ - i\hat{I}_\pm[\sin\alpha \quad \sin 3\alpha \quad \cdots \quad \sin\ (2I-1)\alpha] \\ \times \begin{bmatrix} 1 & 3 & \cdots & (2I-1) \\ 1 & 3^3 & \cdots & (2I-1)^3 \\ \vdots & \vdots & \vdots & \vdots \\ 1 & 3^{2I-1} & \cdots & (2I-1)^{2I-1} \end{bmatrix} \begin{bmatrix} (1 \pm 2\hat{I}_z) \\ (1 \pm 2\hat{I}_z)^3 \\ \vdots \\ (1 \pm 2\hat{I}_z)^{2I-1} \end{bmatrix}\end{aligned} \tag{20}$$

for integer I ($I = 1$, 3). It is interesting to note that by using

$$\mathrm{e}^{-i\alpha\hat{I}_z^2}\hat{I}_\pm^n \mathrm{e}^{i\alpha\hat{I}_z^2} = \mathrm{e}^{-in(n-1)\alpha} I_\pm^{n-1}(\mathrm{e}^{-in\alpha\hat{I}_z^2}\hat{I}_\pm \mathrm{e}^{in\alpha\hat{I}_z^2}) \tag{21}$$

and equations (19) and (20), a general formula for $\mathrm{e}^{-i\alpha\hat{I}_z^2}\hat{I}_\pm^n \mathrm{e}^{i\alpha\hat{I}_z^2}$ can be easily obtained.

For $I = 1$, $f_k(\theta, \alpha\tau)$ are given by

$$\begin{aligned} f_1(\theta, \alpha\tau) &= -\sqrt{2}\sin\theta\cos 3\alpha\tau; \\ f_2(\theta, \alpha\tau) &= \sqrt{\frac{3}{2}}\sin 2\theta \sin 3\alpha\tau. \end{aligned} \tag{22}$$

Both $f_1(\theta, \alpha\tau)$ and $f_2(\theta, \alpha\tau)$ are suitable for detecting motion, although the maximized signal from $f_1(\theta, \alpha\tau)$ (Zeeman order) is larger. For $I = 3/2$,

$$\begin{aligned} f_1(\theta, \alpha\tau) &= -\frac{1}{\sqrt{5}}\sin\theta(2 + 3\cos 6\alpha\tau); \\ f_2(\theta, \alpha\tau) &= -\frac{3}{2}\sin 2\theta \sin 6\alpha\tau; \\ f_3(\theta, \alpha\tau) &= -\frac{3}{2\sqrt{5}}\sin\theta\ (5\cos^2\theta - 1)(1 - \cos 6\alpha\tau). \end{aligned} \tag{23}$$

It is possible to create a pure Zeeman order by choosing $\phi = 0°$ (180°) and $5\cos^2\theta = 1$ or $5\cos^2\theta' = 1$. In this case

$$S_{\text{echo}}(t) \propto \mathrm{e}^{-t/T_1}\langle f_1(\theta, \alpha_1\tau_1) f_1(\theta', -\alpha_2\tau_2)\rangle \propto 4\mathrm{e}^{-t/T_1} + \frac{9}{2}\mathrm{e}^{-t/T_1}\langle\cos 6(\alpha_1 - \alpha_2)\tau_1\rangle \quad (24)$$

Since motion affects the second term but not the first, almost half the resonance signal does not change after motion. Thus, the existence of two terms with different decay rates complicates the analysis. On the other hand, a pure quadrupole order can be created by choosing $\phi = 90°$ (270°). Then, the SAE echo height is given by

$$S_{\text{echo}}(t) \propto \frac{9}{8}\mathrm{e}^{i\phi'}\mathrm{e}^{-W_2 t}\sin 2\theta \sin 2\theta' \langle\cos 6(\alpha_1 - \alpha_2)\tau_1\rangle. \quad (25)$$

The signal is maximized at $\theta = \theta' = 45°$. For $I = 5/2$,

$$f_1(\theta, \alpha\tau) = -\frac{1}{\sqrt{70}}(9 + 16\cos 6\alpha\tau + 10\cos 12\alpha\tau)\sin\theta;$$

$$f_2(\theta, \alpha\tau) = \frac{\sqrt{3}}{2\sqrt{7}}(4\sin 6\alpha\tau + 5\sin 12\alpha\tau)\sin 2\theta;$$

$$f_3(\theta, \alpha\tau) = -\frac{1}{2\sqrt{5}}(-3 - 2\cos 6\alpha\tau + 5\cos 12\alpha\tau) \times \sin\theta\ (5\cos^2\theta - 1);$$

$$f_4(\theta, \alpha\tau) = \frac{5}{8\sqrt{7}}(-2\sin 6\alpha\tau + \sin 12\alpha\tau)\sin 2\theta\ (1 + 7\cos 2\theta);$$

$$f_5(\theta, \alpha\tau) = -\frac{5}{64\sqrt{7}}(3 - 4\cos 6\alpha\tau + 12\cos 12\alpha\tau) \times \sin\theta(15 + 28\cos\theta + 21\cos 4\theta). \quad (26)$$

All $f_k(\theta, \alpha\tau)$ associated with odd-ranked nuclear spin orders contain a constant term as well as motion-related terms. As discussed above, this complicates the analysis when measuring the single-particle correlation functions of these spin orders. On the other hand, by choosing $\phi = 90°$ (270°) and $1 + 7\cos 2\theta = 0$ or $1 + 7\cos 2\theta' = 0$, a pure quadrupole order can be created. The SAE echo height is then given by

$$S_{\text{echo}}(t) \propto \frac{6}{7}\mathrm{e}^{i\phi'}\mathrm{e}^{-W_2 t}\sin 2\theta' \sin 2\theta' \times \left\langle\cos 6(\alpha_1 - \alpha_2)\tau_1 + \frac{25}{16}\cos 12(\alpha_1 - \alpha_2)\tau_1\right\rangle \quad (27)$$

5 DETECTION OF SLOW ATOMIC MOTION IN BULK METALLIC GLASSES BY NMR OF ^{9}BE

The ^{9}Be spectra of vit1 and vit4 consist of a narrow central line and a broad line (Figure 5). The broad line, with a field-independent $\Delta\nu_{1/2}$ of (100 ± 10) kHz, is associated with the satellite transitions ($3/2 \leftrightarrow 1/2$ and $-1/2 \leftrightarrow -3/2$) broadened by the first order quadrupole interaction. The central line, with $\Delta\nu_{1/2}$ as (6.1 ± 0.2) kHz at 9.4 T and (3.6 ± 0.1) kHz at 4.7 T, is associated with the central transition ($1/2 \leftrightarrow -1/2$) broadened by the Zeeman interaction distribution. The $K^{^9\text{Be}}$ is negligible and $T_2^{^9\text{Be}}$ about 1.5 ms.[24] Dominated by Korringa relaxation, $1/T_1^{^9\text{Be}}$ is[24] proportional to T with

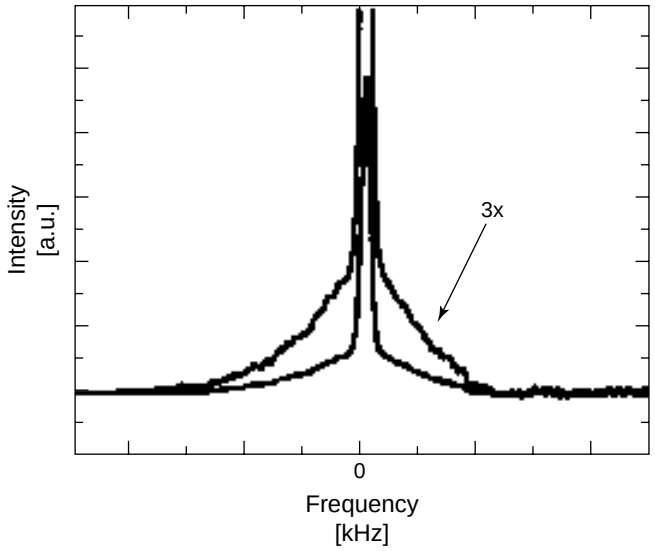

Figure 5 The ^{9}Be spectra of vit1 at 9.4 T. The broad line is shown more clearly by expanding the vertical scale by a factor of 3

$(TT_1)^{-1} = 0.00105\,\text{K}^{-1}\,\text{s}^{-1}$. According to equation (18), the decay rate of the ^{9}Be quadrupole order is $3/T_1$ as demonstrated experimentally.[23]

The ^{9}Be SAE pulse sequence is: $90^0_x - \tau_1 - 45^0_{\pm y} - t - 45^0_{\phi'} - \tau_2 -$ with a short τ_1 $(6 - 15\,\mu\text{s})$ to create a pure quadrupole order. Following equation (26), the SAE echo height is proportional to $f(t) =< \cos(\omega_1 - \omega_2)\tau_1 > \mathrm{e}^{-3t/T_1}$. $\omega_1 = 6\alpha_1$ and $\omega_2 = 6\alpha_2$, varying over a range of $2\pi \times 100$ kHz in vit1 and vit4, are determined by the truncated quadrupole interactions experienced by the spin during τ_1 and τ_2, respectively. The featureless broad line shown in Figure 5 indicates that the characteristic powder pattern of the observed ^{9}Be spectrum in Be metal is smeared out in vit1 and vit4. It suggests a random distribution of quadrupole interaction, which is crucial for SAE to be effective in detecting motion. In glasses and supercooled liquids, the quadrupole interaction with respect to B_0 differs from site to site because of the disordered structure. Thus, single-atom jumps are expected to change ω randomly within its range which induces a reduction of $f(t)$. On the other hand, SAE is not sensitive to collective motion since the quadrupole interactions at Be sites change very little under collective translational motion involving Be atoms and most of their nearest neighbors. Also, SAE is not sensitive to restricted collective rotational motion with small rotation angle because $|(\omega_1 - \omega_2)|\tau_1 \ll 1$.

Fast data acquisition is crucial for studying thermal dynamics in metastable materials such as metallic supercooled liquids. In Refs.[24,25] the pulse-spin locking technique was used to improve S/N. Following the ^{9}Be SAE pulse sequence, a train of 90° pulses are applied; the full sequence is $90^0_x - \tau_1 - 45^0_{\pm y} - t - 45^0_{\phi'} - 2\tau_1 - 90^0_{\phi'} - 2\tau_1 - 90^0_{\phi'} - \cdots - 90^0_{\phi'} -$. Here, a train of echoes with the same origin and feature as the first alignment echo are detected and all echoes are accordingly summed up. The full sequence for measuring $1/T_1$, using the saturation recovery method with a comb and quadrupole echo detection sequence, is '*comb*' $- t - 90^0_x - \tau - 90^0_{\pm y} - 2\tau - 90^0_{\pm y} - 2\tau - 90^0_{\pm y} \cdots - 90^0_{\pm y} -$. Using pulse-spin locking,

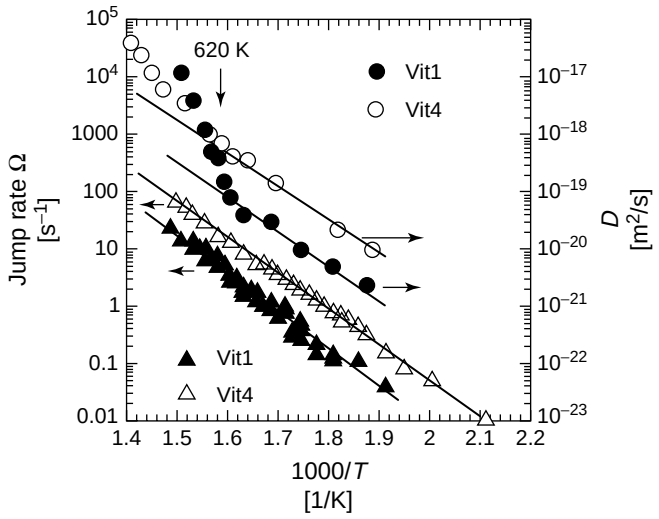

Figure 6 The temperature dependence of the atomic jump rate Ω and the diffusivity D in vit1 and vit4. D (scale on the right) and Ω (scale on the left) are plotted versus $1000/T$. A kink at 620 K, which is around T_g, is observed in the $D(T)$ curves in both vit1 and vit4. This kink is absent in the $\Omega(T)$ curves that follow the same Arrhenius behavior in both the supercooled liquid and glassy state

each ^{9}Be SAE decay curve and $1/T_1$ can be measured in several minutes. This enables the isothermal annealing study and the first NMR study in supercooled metallic liquids.

The ^{9}Be SAE echo decay curve measured at 620 K is shown in Figure 6 that is fitted by a single-exponential function $f(t) = e^{-t/T_{QE}}$. Such behavior is expected for atomic motion causing random changes of ω, where $1/T_{QE} = 3/T_1 + \Omega$ with Ω as the atomic jump rate. The observed single-exponential decay is inconsistent with constrained jumps between neighboring sites such as double-well potentials. It is consistent with unconstrained Be hopping assisted by thermal fluctuation of spread-out free volume.[24] In vit1 and vit4, the measured Ω follows Arrhenius behavior $\Omega(T) = \Omega_0 e^{-E_a/k_B T}$ with the fitted activation energy $E_a = (1.2 \pm 0.15)$ eV. Below 620 K, no annealing-time dependence of Ω is observed by SAE indicating that the measured Ω is intrinsic for the glassy state. The SAE measurements inferred that the Be diffusion process is via single-atom hopping.[24] In deeply supercooled liquids, the combine SAE and diffusion measurements indicated that two diffusion processes contribute to the long-range Be transport.[25] One is single-atom hopping. The other process is collective motion involving most of the nearest neighbors of Be atoms.

6 RELATED ARTICLES IN VOLUMES 1–8

Amorphous Materials, Volume 2; Deuterium NMR in Solids, Volume 3; Diffusion in Solids, Volume 3; Incommensurate Systems, Volume 4; Metals: Pure & Alloyed, Volume 5; Quadrupolar Nuclei in Glasses, Volume 6; Quadrupolar Nuclei in Solids, Volume 6; Quadrupolar Transition Metal & Lanthanide Nuclei, Volume 6; Relaxation Theory for Quadrupolar Nuclei, Volume 6; Slow & Ultraslow Motions in Biology, Volume 7; Ultraslow Motions in Solids, Volume 8.

7 REFERENCES

1. C. Janot, 'Quasicrystals: A Primer', 2nd edn., University Press: Oxford, 1994.
2. S. J. Poon, *Adv. Phys.*, 1992, **41**, 303.
3. A. L. Greer, *Science*, 1995, **267**, 1974.
4. W. L. Johnson, *Mat. Sci. Forum*, 1996, **225**, 35.
5. C. Li, J. Saida, M. Matsushita, and A. Inoue, *Phil. Mag. Lett.*, 2000, **80**, 621.
6. W. W. Warren, Jr., H. S. Chen, and J. J. Hauser, *Phys. Rev. B*, 1985, **32**, 7614.
7. A. Shastri, F. Borsa, D. R. Torgeson, J. E. Shield, and A. I. Goldman, *Phys. Rev. B*, 1994, **50**, 4224.
8. A. Shastri, F. Borsa, D. R. Torgeson, and A. I. Goldman, *Phys. Rev. B*, 1994, **50**, 15 651.
9. J. Apih, M. Klanjšek, D. Rau, and J. Dolinšek, *Phys. Rev. B*, 2000, **61**, 11 213.
10. E. A. Hill, T. C. Chang, Y. Wu, S. J. Poon, F. S. Pierce, and Z. M. Stadnik, *Phys. Rev. B*, 1994, **49**, 8615.
11. J. Dolinšek, B. Ambrosini, P. Vonlanthen, J. L. Gavilano, M. A. Chernikov, and R. Ott, *Phys. Rev. Lett.*, 1998, **81**, 3671.
12. J. Delahaye, J. P. Brison, and C. Berger, *Phys. Rev. Lett.*, 1998, **81**, 4204.
13. G. T. de Laissardière, D. Mayou, and D. N. Manh, *Europhys. Lett.*, 1993, **21**, 25.
14. G. T. de Laissardière and T. Fujiwara, *Phys. Rev. B*, 1994, **50**, 5999.
15. F. Hippert, L. Kandel, Y. Calvayrac, and B. Dubost, *Phys. Rev. Lett.*, 1992, **69**, 2086.
16. A. Shastri, D. B. Baker, M. S. Conradi, F. Borsa, and D. R. Torgeson, *Phys. Rev. B*, 1995, **52**, 12 681.
17. X.-P. Tang, E. A. Hill, S. K. Wonnell, S. J. Poon, and Y. Wu, *Phys. Rev. Lett.*, 1997, **79**, 1070.
18. J. L. Gavilano, B. Ambrosini, P. Vonlanthen, M. A. Chernikov, and H. R. Ott, *Phys. Rev. Lett.*, 1997, **79**, 3058.
19. J. Dolinšek, M. Klanjšek, J. Apih, A. Smontara, J. C. Lasjaunias, J. M. Dubois, and S. J. Poon, *Phys. Rev. B*, 2000, **62**, 8862.
20. X.-P. Tang, L. Wu, P. Ryan, F. Tsui, and Y. Wu, *Phys. Rev. B.*, submitted.
21. J. Apih, O. Plyushch, M. Klanjšek, and J. Dolinšek, *Phys. Rev. B*, 1999, **60**, 14 695.
22. Y. Yafet and V. Jaccarino, *Phys. Rev. A*, 1964, **133**, 1630.
23. X.-P. Tang and Y. Wu, *J. Magn. Reson.*, 1998, **133**, 155.
24. X.-P. Tang, R. Busch, W. L. Johnson, and Y. Wu, *Phys. Rev. Lett.*, 1998, **81**, 5358.
25. X.-P. Tang, U. Geyer, R. Busch, W. L. Johnson, and Y. Wu, *Nature*, 1999, **402**, 160.
26. H. W. Spiess, *J. Chem. Phys.*, 1980, **72**, 6755.
27. R. Bohmer, T. Jorg, F. Qi, and A. Titze, *Chem. Phys. Lett.*, 2000, **316**, 419.

Biographical Sketches

Xiaoping Tang, *b* 1966. B.Sc., Beijing University, PRC, 1987, Ph.D., 1996, Physics, Northwestern University, USA. Introduced to NMR by William P. Halperin studying vortex dynamics of high-T_c superconductors and ferroelectricity. Since 1996, worked on quasicrystals, metallic glasses, and carbon nanotubes with Yue Wu at UNC-Chapel Hill.

Yue Wu, *b* 1959. B.Sc., 1983, Ph.D., 1987, Physics, University of Leuven, Belgium. Postdoctoral research with Alexander Pines at Berkeley 1988–l991. Faculty in the Department of Physics and Astronomy at University of North Carolina in Chapel Hill 1991-present. Research interests: carbon nanotubes, metallic glasses, quasicrystals, and amorphous silicon.

High Speed MAS of Half-Integer Quadrupolar Nuclei in Solids

Hans J. Jakobsen

University of Aarhus, Aarhus C, Denmark

1	Introduction	1
2	Hamiltonian for Quadrupolar Nuclei in MAS NMR	2
3	Applications of High-Speed MAS NMR to Quadrupolar Nuclei	4
4	Other Sample Rotation Techniques	8
5	Related Articles	9
6	References	9

1 INTRODUCTION

Recourse to the NMR periodic table of spin isotopes reveals that about 75% of these nuclei possess a spin $I > \frac{1}{2}$, i.e., the spin isotopes known as the quadrupolar nuclei. Most quadrupolar nuclei (approximately 90%) have half-integer spin ($I = \frac{3}{2}, \frac{5}{2}, \frac{7}{2}, \ldots$), and it is therefore not surprising that by far the largest number of solid state NMR studies of quadrupolar nuclei have involved half-integer spins, maybe with the exception of ^{2}H ($I = 1$). Magic angle spinning (MAS) NMR of quadrupolar nuclei made its breakthrough in the early 1980s, first of all thanks to the exploratory ^{27}Al and ^{23}Na MAS investigations by Müller et al.,[1] Oldfield et al.,[2] and Samoson and Lippmaa.[3] Perhaps the best known MAS NMR spectrum for a half-integer quadrupolar nucleus is that of ^{79}Br in a KBr sample, which is used by almost every MAS NMR spectroscopist for adjustment of the magic angle.[4] Since that time, MAS NMR studies of $I = \frac{3}{2}, \frac{5}{2}, \frac{7}{2}, \ldots$ quadrupolar nuclei have constituted an increasingly important tool in solid state chemistry and materials research. In particular, ^{23}Na ($I = \frac{3}{2}$) and ^{27}Al ($I = \frac{5}{2}$) MAS NMR have played a significant role in studies of minerals, zeolites, catalysts, cements, and ceramics as evidenced by the numerous investigations in these fields.

For most half-integer quadrupolar nuclei (e.g., ^{23}Na and ^{27}Al), the quadrupolar coupling interaction is the predominant mechanism leading to strong line broadening in the solid state NMR spectra of powders. For a few other less commonly studied nuclei (e.g., ^{51}V, ^{59}Co, ^{85}Rb, ^{87}Rb, and ^{133}Cs), additional line broadening from chemical shielding anisotropy (CSA) becomes important, and may influence the appearance of their spectra.[5] The line broadening of the individual transitions ($I \leftrightarrow I - 1, \ldots, +\frac{1}{2} \leftrightarrow -\frac{1}{2}, \ldots, -I + 1 \leftrightarrow -I$) from the quadrupolar interaction can be quantified in terms of the quadrupolar coupling constant $\chi = e^2qQ/h$ (i.e., the magnitude of the interaction) and the asymmetry parameter η ($0 \leq \eta \leq 1$), which characterizes the symmetry of the electric field gradients around the nucleus. For example, for an axially symmetric electric field gradient tensor ($\eta = 0$), the *satellite* transitions (i.e., transitions other than $m = \frac{1}{2} \leftrightarrow m = -\frac{1}{2}$) give rise to characteristic quadrupolar splittings

$$\nu_Q = \frac{\chi}{4I(2I-1)}(6|m| - 3) \qquad (1)$$

between the 'horns' for the different symmetric $\pm m \leftrightarrow \pm (m - 1)$ transitions. From equation (1), it also follows that the maximum width of the spectrum for a spin-I quadrupolar nucleus, given approximately by $2\nu_Q$ for $|m| = I$, equals $3\chi/2I$.[6] Therefore, for the complete spectrum of all transitions not to extend beyond a spectral width of, for example, 2 MHz it is required that $\chi \leq 2$ MHz for $I = \frac{3}{2}$ and $\chi \leq 3.3$ MHz for $I = \frac{5}{2}$, i.e. rather small quadrupolar couplings. On the other hand, the *central* ($+\frac{1}{2}, -\frac{1}{2}$) transition, which is not affected by the first-order quadrupolar splitting, has a much smaller linewidth than any satellite transition. Thus, this has been the most commonly observed transition in static and MAS NMR studies of half-integer quadrupolar nuclei.

The line-narrowing effect of MAS will split the satellite transitions into numerous spinning sidebands (ssbs; cf. the ^{79}Br MAS spectrum of KBr[4]) and *reduce* the width for the central transition by a factor of about 2.5–3 as compared with the static spectrum. Provided the spinning speed ($\nu_r = \omega_r/2\pi$) is larger than the CSA and dipolar interactions, MAS will greatly improve both resolution and sensitivity (S/N ratio) for the observed spectrum. In high-field NMR, the quadrupolar interaction is much smaller than the Zeeman splitting, and can be described by average Hamiltonian theory in the secular approximation.[6,7] In this approximation, the central transition is perturbed only to second order by the quadrupolar interaction (see below).[6,7] For polycrystalline powders, this leads to a characteristic lineshape, which is unaffected (or cannot be further narrowed) by increasing ν_r beyond the width of the lineshape.[8] Provided ν_r is larger than this width, χ, η, and δ (the isotropic chemical shift) can easily be determined with good accuracy by computer fitting of the observed lineshape.[6] As an example of the characteristic lineshapes that may be observed for the central transition at sufficiently high spinning speeds, Figure 1 shows a series of computer simulations for a spin $I = \frac{5}{2}$ nucleus (e.g., ^{27}Al) using χ = 5.0 MHz, ν_L = 104.2 MHz, and various η values ($0 \leq \eta \leq 1$). For comparison, the corresponding lineshapes for the static case are also shown. It should be noted that the total width of the MAS lineshape between the outermost shoulders/edges increases only slightly on increasing η, whereas the positions of the singularities, shoulders, and edges depend strongly on η. Furthermore, the widths of the lineshapes are proportional to χ^2 and inversely proportional to the Larmor frequency $\nu_L = \omega_L/2\pi$, i.e. to the magnetic field strength for a particular nucleus (see below).

From the above considerations one may draw the following qualitative conclusions.

1. For small quadrupolar couplings, the second-order contribution may be too small for the lineshape of the central transition to be resolved in the MAS spectrum. This would prevent determination of χ and η from this transition, which is usually the case for $\chi/[4I(2I-1)] \lesssim 75$ kHz at ν_L = 100 MHz, i.e., $\chi \lesssim 0.9$ MHz for ^{23}Na and $\chi \lesssim 3.0$ MHz for ^{27}Al at 9.4 T. In such cases, the manifold of ssbs for the satellite transitions may be taken into full advantage, since it has been shown that accurate χ and η values may

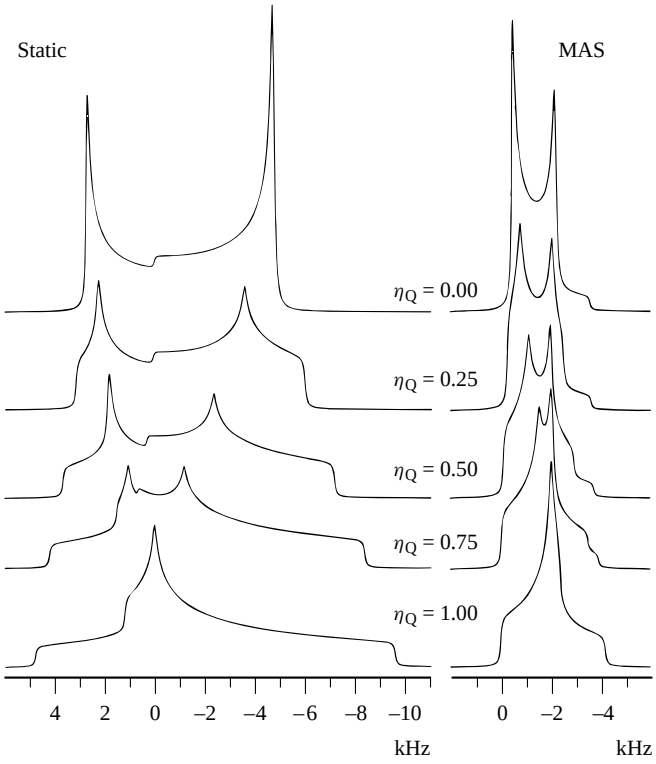

Figure 1 Simulated static (left) and MAS (right) lineshapes for the central transition of a spin $I = \frac{5}{2}$ nucleus for various values of η and assuming $\nu_r = \infty$. All simulated spectra employed χ = 5.0 MHz, ν_L = 104.2 MHz (i.e., ^{27}Al at 9.4 T), and a Lorentzian line broadening of 100 Hz

be determined from computer fitting of the ssb intensity pattern observed on modern spectrometers equipped with fast receivers.[6,9]

2. For much larger χ values than discussed in (1), the manifold of ssbs for the satellite transition may extend far beyond the maximum spectral width of the spectrometer and appear with heavily reduced intensities as compared with (1). In such cases, χ and η are most conveniently determined by computer fitting of the second-order quadrupolar lineshape observed for the central transition. Obviously, the availability of the maximum magnetic field strength and spinning speed will set the limit for the maximum χ value that can readily be determined for each nuclei by MAS NMR. This will be discussed further below.
3. For cases of intermediate χ values between (1) and (2), it may be possible to determine χ and η from computer analysis of both the manifold ssbs (1) and the lineshape for the central transition (2). In such cases, it turns out that the more accurate values are obtained from analysis of the ssb pattern (2).

Since the methods (1)–(3) outlined above for determination of χ and η all involve computer fitting of lineshapes and/or intensities from experimental MAS spectra, this puts high demands on the quality of the MAS probes, especially on the spinning performance. Thus, for the sample spinner systems the following requirements are important:

(a) the highest possible spinning frequency ν_r for the largest possible sample volume of the rotor; ν_r values up to about 24 kHz have been achieved for small cylindrical (3.5 mm outer diameter) rotors during recent years (see ***Jakobsen, Hans J.: A Retrospect on the Development of High-Speed Sample Spinners for Solids since 1980*** and ***Doty, F. David: A Random Walk Toward High-Speed Sample Spinning***);
(b) long term stability in ν_r ($\Delta\nu_r$ within a few hertz) at any spinning speed for a particular rotor size; this can be achieved by stabilizing the air-drive pressure mechanically (however, computer controlled rotor-speed stabilizers with $\Delta\nu_r \lesssim 1$ Hz are also available);
(c) adjustability and long term stability of the magic angle (54.736°) to within about 0.001°; this is of special importance when second-order lineshapes for the ssbs of the satellite transitions are subjected to computer simulations.

During the past decade, our laboratory has been intensively engaged in design/construction of spinner assemblies and CP MAS probes with special emphasis on fulfilling the requirements for studies of quadrupolar nuclei.[10–12] In particular, the recent progress and positive development around real supersonic spinning systems (see ***Jakobsen, Hans J.: A Retrospect on the Development of High-Speed Sample Spinners for Solids since 1980***) will have further impact on quadrupolar nuclei.

2 HAMILTONIAN FOR QUADRUPOLAR NUCLEI IN MAS NMR

The underlying theory and development of a software package for simulation/fitting of MAS NMR spectra to different approximations under different experimental conditions have been described in detail in recent papers from our laboratory.[5,6,9] In this description, the general Hamiltonian for a quadrupolar nucleus in a strong magnetic field $\boldsymbol{B}_0$ and subjected to an rf field $\boldsymbol{B}_1$,

$$\hat{\mathcal{H}} = \hat{\mathcal{H}}_Z + \hat{\mathcal{H}}_Q + \hat{\mathcal{H}}_{CSA} + \hat{\mathcal{H}}_{DD} + \hat{\mathcal{H}}_{rf} \tag{2}$$

is approximated by the second-order average Hamiltonian for a Larmor period,

$$\hat{\tilde{\mathcal{H}}}(t) = \hat{\tilde{\mathcal{H}}}_Q^{(1)}(t) + \hat{\tilde{\mathcal{H}}}_Q^{(2)}(t) + \hat{\tilde{\mathcal{H}}}_{rf}(t) \tag{3}$$

where the Zeeman interaction representation (high-field NMR, $\hat{\mathcal{H}}_Z \gg \hat{\mathcal{H}}_Q$) is employed and $\hat{\mathcal{H}}_{CSA} + \hat{\mathcal{H}}_{DD}$ have been neglected (this is acceptable for most quadrupolar nuclei under MAS conditions).

Under MAS and in the second-order approximation, the first- and second-order terms of the quadrupolar interaction take the forms

$$\hat{\tilde{\mathcal{H}}}_Q^{(1)}(t) = \omega_Q^{(1)}(t)[3\hat{I}_z^2 - I(I+1)] \tag{4}$$

$$\hat{\tilde{\mathcal{H}}}_Q^{(2)}(t) = \omega_Q^{(21)}(t)[-8\hat{I}_z^2 + 4I(I+1) - 1]\hat{I}_z + \omega_Q^{(22)}(t)[-2\hat{I}_z^2 + 2I(I+1) - 1]\hat{I}_z \tag{5}$$

where the factors $\omega_{\mathrm{Q}}^{(1)}(t)$ and $\omega_{\mathrm{Q}}^{(2q)}(t)$ are time-dependent because of MAS, and are given by

$$\omega_{\mathrm{Q}}^{(1)}(t) = \frac{2\pi\chi}{4I(2I-1)} \times \sum_{n=1}^{2}[P_n^{(0)}\cos(n\gamma + n\omega_{\mathrm{r}}t) + R_n^{(0)}\sin(n\gamma + n\omega_{\mathrm{r}}t)] \quad (6)$$

$$\omega_{\mathrm{Q}}^{(2q)}(t) = \frac{1}{2\omega_{\mathrm{L}}}\left(\frac{2\pi\chi}{4I(2I-1)}\right)^2 \times \left\{C^{(q)} + \sum_{n=1}^{4}[P_n^{(q)}\cos(n\gamma + n\omega_{\mathrm{r}}t) + R_n^{(q)}\sin(n\gamma + n\omega_{\mathrm{r}}t)]\right\} \quad (7)$$

The time-independent coefficients $C^{(q)}$, $P_n^{(q)}$, and $R_n^{(q)}$ are functions of the asymmetry parameter η ($0 \le \eta \le 1$) and the Euler angles α and β; expressions for these coefficients are given in Table 1 of Skibsted et al.[6] The Euler angles (α,β,γ) relate the principal axis frame of the quadrupolar coupling tensor to the rotor fixed frame, and are defined according to the conventions of Spiess.[13] Finally, for on-resonance excitation (X phase), the rf term is given by

$$\hat{\tilde{\mathcal{H}}}_{\mathrm{rf}} = \gamma B_1 \hat{I}_x \quad (8)$$

and for an infinitely short (ideal) rf pulse, the expression for the total FID for a quadrupolar nucleus in a powder undergoing MAS has been derived:[6]

$$s(t) = \sum_{\alpha\beta\gamma}\sum_{m} p_m \exp[\mathrm{i}\Phi_m(\alpha,\beta,\gamma;t)] \quad (9)$$

From equations (4)–(7), we note that the first- and second-order terms for the quadrupolar interaction can be written as

$$\hat{\tilde{\mathcal{H}}}_{\mathrm{Q}}^{(1)}(t) + \hat{\tilde{\mathcal{H}}}_{\mathrm{Q}}^{(2)}(t) = [\hat{\tilde{\mathcal{H}}}_{\mathrm{Q}}^{(1)}(t)]_{\text{time-dependent}} + [\hat{\tilde{\mathcal{H}}}_{\mathrm{Q}}^{(2)}(t)]_{\text{time-dependent}} + [\hat{\tilde{\mathcal{H}}}_{\mathrm{Q}}^{(2)}(t)]_{\text{time-independent}} \quad (10)$$

since the two coefficients $C^{(1)}$ and $C^{(2)}$ in equation (7) are time-independent, i.e., independent of the spinning frequency. These time-independent second-order terms describe small frequency shifts depending on the Euler angles α and β, whereas the time-dependent second-order terms describe the distribution of intensity from the individual crystallites over the ssbs. It is the combination of these two second-order effects that introduces a unique lineshape not only for the central transition (and any possible ssbs) but also a unique and different lineshape for each ssb of the satellite transitions.

As mentioned above, we see from equations (6) and (7) that the first-order contribution $\hat{\tilde{\mathcal{H}}}_{\mathrm{Q}}^{(1)}(t)$, which determines the width of the satellite transitions, is proportional to χ, while the second-order contributions are proportional to χ^2 and inversely proportional to ν_{L}.

2.1 Central Transition

The central ($+\frac{1}{2}$, $-\frac{1}{2}$) transition for half-integer quadrupolar nuclei has the largest transition probability,[6,14] and is independent of the quadrupolar interaction to first order [$\hat{\mathcal{H}}_{\mathrm{Q}}^{(1)}(t)$]. Therefore, it has the largest intensity and exhibits the most narrow spectral width of all transitions for a powder. However, provided χ is large enough, the linewidth will broaden and eventually give rise to the unique lineshape discussed above, because of the contribution from $\hat{\mathcal{H}}_{\mathrm{Q}}^{(2)}(t)$. In addition to the ratio χ^2/ν_{L} for a particular I spin, the experimental observation of a well-defined second-order lineshape is very much dependent on the presence of other line-broadening mechanisms such as relaxation, crystallinity, a distribution of χ and η values within the powder, or paramagnetic impurities. Provided ν_{r} is greater than the width of the central transition, the ssbs from this transition are usually small. In such cases, there are only negligible differences between the lineshape of the observed centerband and the simulated (optimized) lineshape employing only the time-independent terms $C^{(1)}$ and $C^{(2)}$ of equation (7), i.e., simulations assuming infinite ν_{r} and displayed in Figure 1. Calculations in this approximation reduce to an expression that is equivalent to that originally derived by Samoson et al.[8] These authors also produced graphs for the positions of the singularities (relative to the isotropic chemical shift)[8] for the lineshapes (Figure 1). Good estimates of χ, η, and δ may be derived from these graphs for an observed spectrum (e.g., for starting parameters in a computer fitting of the experimental lineshape). When ν_{r} becomes similar to or smaller than the width of the central transition, decent simulations for comparison with the experimental spectra can only be performed by including all terms of equation (7) (both time-independent and time-dependent). This makes the simulations/fitting more difficult and time-consuming. Obviously, a straightforward determination of large χ values from MAS NMR of the central transition becomes very much dependent on the maximum spinning speed for the MAS probe employed, combined with the available magnetic field strength[15] (see below).

2.2 Satellite Transitions

As opposed to the central transition, the appearance of the satellite transitions in MAS NMR first of all reflects the first-order [$\hat{\mathcal{H}}_{\mathrm{Q}}^{(1)}(t)$] quadrupolar interaction. The MAS NMR spectrum of these transitions consists of a manifold of ssbs with a maximum width approximately equal to $3\chi/2I$. The shape of the envelope for this symmetrical ssb pattern reflects the value of η.[6,9] On modern spectrometers with maximum spectral widths of 2–4 MHz, the observation of this ssb pattern constitutes a very accurate method for the determination of small χ values ($\lesssim$4 MHz). The effect of the second-order [$\hat{\mathcal{H}}_{\mathrm{Q}}^{(2)}(t)$] interaction is to introduce a unique

lineshape or (if unresolved) line broadening for each ssb. This lineshape (or broadening) differs for each ssb throughout the spectrum, and the shape of the nth sideband from the centerband also varies, depending upon ν_r. However, since the ratio of the second-order to first-order coefficients is proportional to $\chi/[4I(2I-1)\nu_L]$ [equations (6) and (7)], and usually small (of order 10^{-3} for $\chi < 4$ MHz and $\nu_L \approx 100$ MHz, i.e., ^{23}Na and ^{27}Al at 9.4 T), the effect of the second-order terms on the integrated intensities for each ssb can be neglected. This is illustrated in Figure 2, which shows simulations of the ssb manifold for the satellite transitions of a spin $I = \frac{3}{2}$ nucleus with χ = 2.0 MHz, η = 0.0, and ν_L = 105.8 MHz (^{23}Na and 9.4 T) based on equation (9) with an infinite short (ideal) rf pulse. The simulation in Figure 2(a), which includes $\omega_Q^{(1)}(t)$ and all terms of $\omega_Q^{(2q)}(t)$, shows different peak heights for the symmetrical ($\pm n$th) ssbs because of the lineshape for the individual ssbs induced by the time-dependent terms of $\omega_Q^{(2q)}(t)$. Examples of the lineshapes are apparent from the expansions in Figure 2(a). The simulation in Figure 2(b) uses $\omega_Q^{(1)}(t)$ and only the time-dependent terms of $\omega_Q^{(2q)}(t)$ (i.e., no lineshape but 'true' intensities for the ssbs), while the calculated spectrum in Figure 2(c) is based on the first-order terms $[\omega_Q^{(1)}(t)]$ only. Comparison of the spectra in Figures 2(b) and 2(c) demonstrates that the first-order terms alone yield an excellent approximation for the ssb intensities. Thus, employing integrated intensities for each ssb in the experimental spectrum, it is unnecessary to include any second-order terms for determination of even quite large χ values by fitting of simulated to experimentally integrated ssb intensities. This not only greatly reduces computing time, but is also quite fortunate, since often the lineshapes of the ssbs are unresolved or distorted compared with the real MAS lineshape because of different line-broadening mechanism, small variations in spinning speed, or slight misadjustment of the magic angle. In particular, it should be noted that an incorrect setting of the magic angle (off by 0.01° or less) can have a dramatic effect on the lineshape of the ssbs[16] as opposed to the effect on the lineshape for the central transition. Finally, it should be mentioned that in certain cases it may be of interest to perform the full simulations as in Figure 2(a) for comparison of experimental and simulated second-order lineshapes for the ssbs. Examples of the different types of simulated ssb patterns for comparison with experimental spectra may be found in Skibsted et al.[6,9,17]

In view of the large spectral widths (megahertz range) generally required for the observation of all ssbs for the satellite transitions, it is expected that the assumption of ideal rf excitation and detection used in the simulations above (e.g., Figure 2) does not hold for the experimental ssb intensities. The reason is that maximum achievable rf field strengths are usually in the range $\gamma B_1/2\pi \approx 50-100$ kHz and that MAS probes are usually high-Q probes ($Q \approx 200$). However, as is apparent from our first simulations employing ideal rf excitation of experimental MAS satellite spectra,[9] the effects of nonideal rf pulse excitation are not as serious as would have been expected based on earlier experiences of nonuniform rf excitation in static solid state NMR. The reason is that pulse imperfections (i.e., both phase and intensity errors) experienced by a particular crystallite and pulse perfections for another crystallite are transmitted to a large part of ssbs across the spectrum because of the time dependence of the quadrupolar interaction due to the sample rotation during acquisition. Our later work[6] has evaluated the impact of nonuniform rf excitation on the first-order ssb intensities in MAS NMR of satellite transitions and also the effect of the Q factor of the probe during detection. Both effects tend to reduce the ssb intensities in the outer wings of the spectrum, and have been incorporated into the simulation software. For simulations including these effects and their excellent agreement with experimental ssb intensities, the reader is referred to the figures in Skibsted et al.[6] (in particular Figures 2 and 6). From these results, it may be summarized that the main experimental implications to reduce phase and intensity errors are

1. on-resonance rf conditions for the center of the spectrum;
2. $\gamma B_1/2\pi \geq 40$ kHz;
3. a small pulse length ($\tau_p \lesssim 1\ \mu$s), ensuring that $\tau_p \ll (1/\nu_r)$ and that the spectrum can be phased to positive absorption across the full spectral width ($1/\Delta$t) using a linear phase correction of $-360° \times \tau_p/(2\ \Delta$t).

It should be noted that the discrepancy between the ideal and finite pulse spectra increases markedly on increasing τ_p, which is partly ascribed to transfer of magnetization into multiple quantum coherences.[18] On the other hand, at least simulations indicate that the spectra are less sensitive to increases in the rf field strength in the normal range of 40 kHz $\leq \gamma B_1/2\pi \leq$ 100 kHz. Finally, it is our experience that the observation of a perfect symmetry of the ssb intensities for the satellite transitions around the center of the spectrum can be quite sensitive to the complete probe tuning circuitry (including filters, cable lengths, and the MAS probe itself). For example, changing lengths of the coaxial cables may slightly influence and can be used to improve the symmetry of the ssb intensities for the satellite transitions at different nuclear resonance frequencies.

3 APPLICATIONS OF HIGH-SPEED MAS NMR TO QUADRUPOLAR NUCLEI

From the theoretical considerations and aspects discussed above, it is obvious that stable and high speed spinning performance for the MAS probe constitute a most important entity of the complete spectrometer system in determinations of quadrupolar coupling parameters employing MAS NMR. In addition these probe properties also play a decisive role in many applications of MAS NMR to quadrupolar nuclei in inorganic chemistry, geology, and materials research. In this section, we shall consider selected examples of the applications of high-speed MAS NMR; those of a straightforward, routine nature will be presented first, and will be followed by some examples of determination of large χ values.

3.1 Clay Minerals

The mixed-layer illite/smectite clay minerals constitute an important class of minerals that have been studied intensively by ^{27}Al MAS NMR since the early days of this technique. These minerals exhibit two central transitions in their ^{27}Al MAS NMR spectra: one each for octahedrally and tetrahedrally coordinated aluminum, Al(VI) and Al(IV); respectively. Generally, these studies aimed at a determination

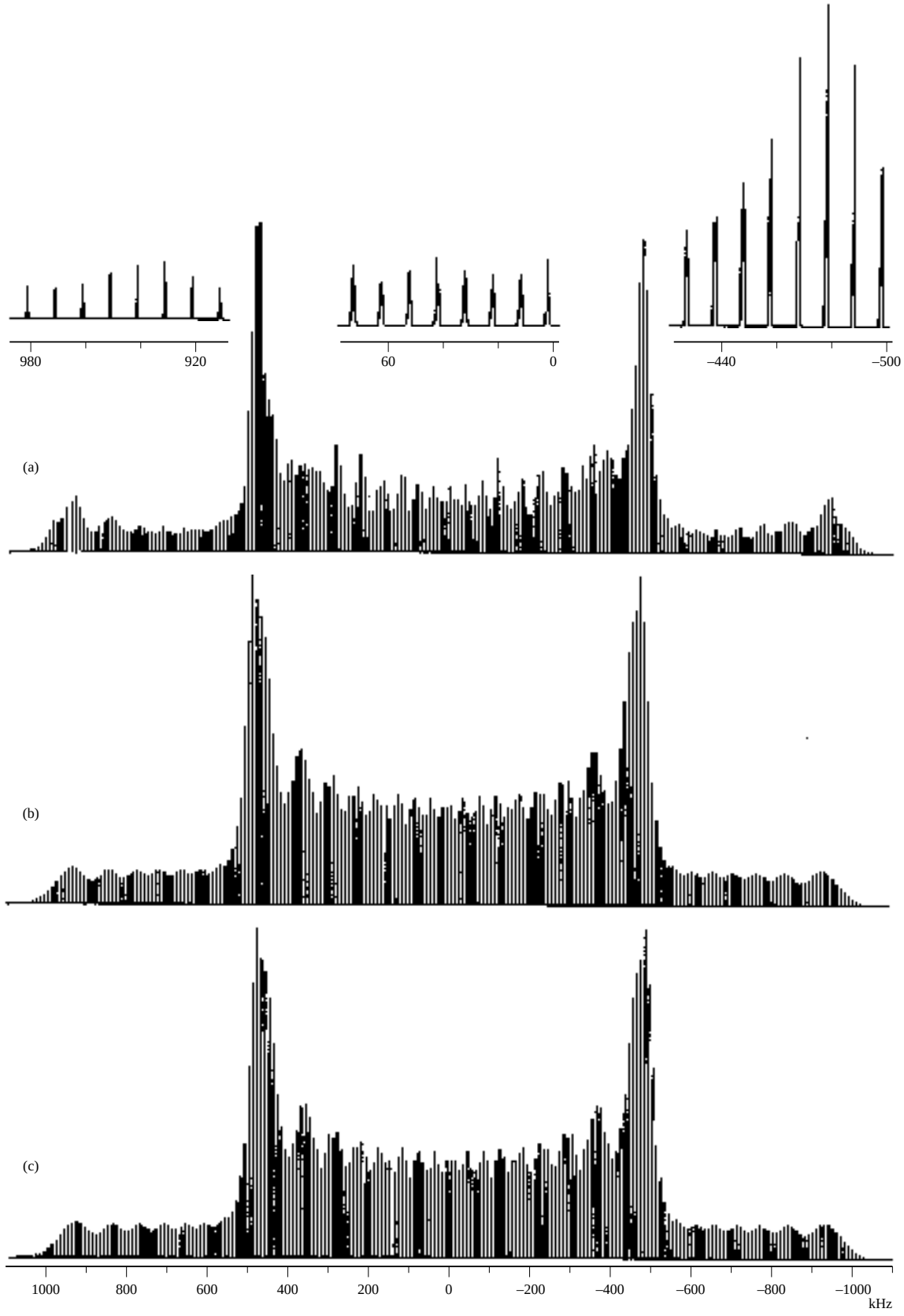

Figure 2 Simulated MAS NMR spectra of the satellite transitions for a spin $I = \frac{3}{2}$ nucleus using χ = 2.0 MHz, η = 0.0, ν_r = 10 kHz, and ν_L = 105.8 MHz (^{23}Na at 9.4 T). The calculations include (a) $\omega_Q^{(1)}(t)$ and all terms for $\omega_Q^{(2q)}(t)$, (b) $\omega_Q^{(1)}(t)$ and the time-dependent terms of $\omega_Q^{(2q)}(t)$, and (c) $\omega_Q^{(1)}(t)$ only. The second-order lineshape of the individual ssbs in (a), caused by the time-independent terms of $\omega_Q^{(2q)}(t)$, is clarified in the expansions

of the Al(IV)/Al(VI) ratios of the samples. However, the early determinations were severely hampered by the large number of ssbs for the central transitions (and therefore overlapping resonances) in the region of interest (0−70 ppm) because of the maximum $\nu_r \approx 4$ kHz employed prior to 1987. Furthermore, the intensities of these ssbs increase markedly with increasing content of paramagnetic impurities (especially Fe) of the samples.[19,20] The advent of high-speed spinning ($\nu_r \approx 10$ kHz) caused a dramatic improvement in the simplicity for the spectra since the ssbs could now be significantly suppressed,[21] and most importantly can be placed outside the region for the two centerband signals, even at the highest magnetic field strengths employed today. Provided the sample is excited by proper rf field strength and pulse length (i.e., a short and 'hard' pulse with flip angle $<15^\circ$),[3] the resulting spectra allow quantitative assessment of the Al(IV)/Al(VI) ratios in a simple and accurate manner. Such determinations have been of particular interest in examining clays sampled from a depth of about 4000 m in the oilfields of the North Sea.[21]

3.2 Ultrastable Y Zeolites

Ultrastable Y (USY) zeolites represent an important class of catalytic materials, which are usually prepared by hydrothermal dealumination of Y zeolites with a framework Si/Al ratio of about 2.5. The structural changes accompanying this treatment have been intensively studied by ^{29}Si and ^{27}Al MAS NMR. ^{29}Si MAS NMR shows that the framework Si/Al ratio, F(Si/Al), a quantity strongly related to the degree of stabilization and catalytic properties, increases as a function of steaming temperature and time. On the other hand, the total bulk Si/Al ratio, as measured by X-ray fluorescence (XRF), remains virtually constant, even for highly dealuminated samples. Therefore, large quantities of nonframework aluminum (NFA) must be present in USY zeolites, and numerous studies have employed ^{27}Al MAS NMR in attempts to characterize and quantify the Al species in these materials.[22] ^{27}Al MAS NMR spectra of USY zeolites are generally described as consisting of three signals: one at approximately 60 ppm, assigned to framework aluminum (FA), and one each at about 30 and 0 ppm attributed to NFA. In addition, the spectra exhibit a very broad hump below the three more distinct resonances—a feature that is especially pronounced in spectra of highly dealuminated samples. Quantification of the three ^{27}Al resonances in terms of the NFA% of the total Al content has consistently given too low values for the Al^{NFA}/Al^{total} % in all attempts of such determinations. This led to the concept of 'NMR-invisible Al', which flourished in the literature for some time and has been associated in particular with NFA sites having large quadrupolar interactions.

It was not until recently, when we applied high-speed spinning, $\nu_r \approx 18$ kHz, to USY zeolites in a study at 9.4 T,[22] that good consistency between the quantitative results (Al^{NFA}/Al^{total} %) obtained by ^{27}Al MAS NMR and a combination of other methods (XRF and ^{29}Si MAS NMR) could be achieved. The effect of high-speed spinning on the ^{27}Al MAS NMR spectra of strongly dealuminated USY zeolites is to increase the intensities of all three resonances (0, 30, and 60 ppm) by different percentages. This intensity increase occurs at the expense of the broad hump, which is completely eliminated ('spun out') only for $\nu_r \approx 18$ kHz at 9.4 T (see Figure 3 of Kellberg et al.[22]). Thus, the results of high-speed spinning show that the NFA residing within the hump contributes to all three narrow resonances. This is consistent with a ^{27} Al−{^{1}H} cross polarization MAS study of the same zeolites, which shows that the NFA in USY zeolites consists of Al species possessing all three types of Al coordination: Al(IV), Al(V), and Al(VI). Further details on the nature of the NFA can be found in Kellberg et al.[22] Thus, this technique appears a prerequisite and the most straightforward method for obtaining quantitative results of the different Al species in these catalysts.

3.3 Determination of 'Large' χ Values from the Central Transition at High Spinning Speeds

Perhaps the most important implication of high-speed spinning involves the determination of 'large' quadrupolar coupling constants χ from simulations of 'undistorted' second-order lineshapes for the central transition of half-integer quadrupolar nuclei. In this sense of the word, 'undistorted' means that ν_r is sufficiently large to place the first-order ssbs for the central transition just outside the region for the centerband. In such cases, the analysis/simulation of the experimental spectrum in terms of χ, η, and δ is usually straightforward. At lower spinning speeds, the central transition splits into complicated lineshapes, which are generally unamenable to spectral simulation and quantification—at least if χ and η are unknown. Obviously, a high-performance, high-speed spinning probe can be an economical alternative to a high-field spectrometer in such studies.[15] In general, the condition for the observation of a distortionless centerband for a spin-I half-integer quadrupolar nucleus can be expressed as[15]

$$\chi^2(1+\tfrac{1}{6}\eta)^2 \lesssim \frac{112\nu_L\nu_r I^2(2I-1)}{9(I+\tfrac{3}{2})} \qquad (11)$$

Thus, employing ν_r = 20 kHz and the highest magnetic field strength presently available (17.6 T), undistorted lineshapes for the central transition may be observed in ^{23}Na ($I = \frac{3}{2}$, ν_L = 198.4 MHz) and ^{27}Al ($I = \frac{5}{2}$, ν_L = 195.4 MHz) MAS NMR for χ values up to 7.8 and 15.8 MHz, respectively (assuming an intermediate value of η = 0.60).

As an illustrative example of the advantages of high-speed spinning in MAS NMR of quadrupolar nuclei at intermediate magnetic field strengths, we reinvestigated the ^{27}Al MAS NMR spectrum of $3CaO{\cdot}Al_2O_3$ (C_3A) at 7.1 and 9.4 T for ν_r up to 19 kHz.[15] An earlier reported ^{27}Al MAS spectrum of C_3A, recorded at 11.7 T and $\nu_r \approx 7$ kHz, showed a poorly resolved and distorted spectrum for the central transition.[23] However, this spectrum was analyzed in terms of just one set of quadrupolar coupling parameters,[23] despite the fact that the unit cell of C_3A contains two nonequivalent AlO_4 groups according to XRD. In the early days (1987), with a maximum spinning speed $\nu_r \approx 10$ kHz for our MAS probes, we recorded the ^{27}Al MAS spectrum of C_3A [Figure 3(a)] at 7.1 T, using ν_r = 8.0 kHz. At that time, this spectrum was far too distorted and complex for us to analyze. Following our development of a high-speed 4 mm rotor system,[12] we later recorded the 18−19 kHz ^{27}Al spectra shown in Figures 3(c) and 3(e) (on-

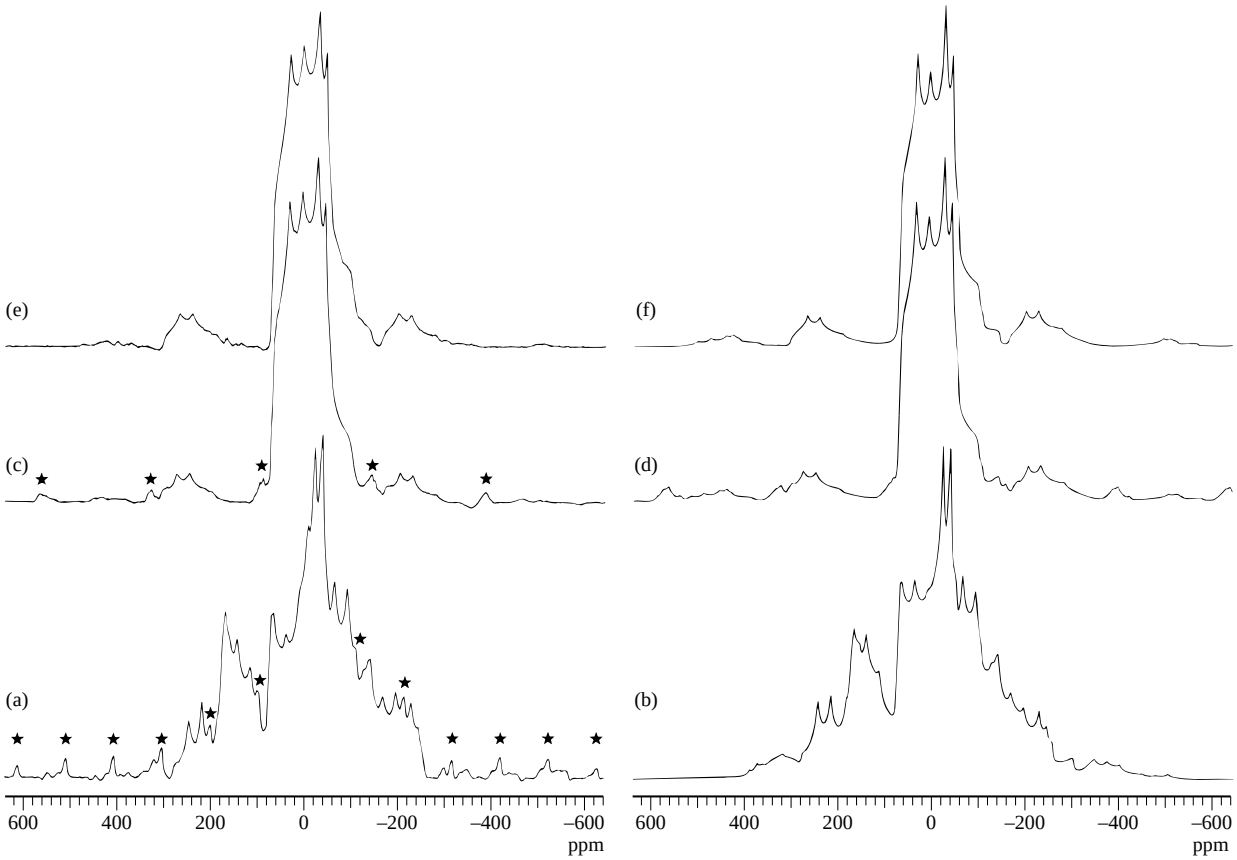

Figure 3 Experimental (a), (c), (e) and simulated (b), (d), (f) 78.2 MHz (7.1 T) ^{27}Al MAS NMR spectra of the central transition (including spinning sidebands) for C_3A obtained at different spinning speeds. For (a) and (b), ν_r = 8.0 kHz, with the spectrum in (a) recorded in 1987 using a 7 mm rotor. For (c) and (d), ν_r = 18.7 kHz (4 mm rotor), where resonances from the $(\pm\frac{3}{2}, \pm\frac{1}{2})$ satellite transitions have been included in the simulated spectrum (d). For (e) and (f), ν_r = 18.2 kHz, obtained under a slightly off-MAS (about 0.2°) condition to suppress resonances from the $(\pm\frac{3}{2}, \pm\frac{1}{2})$ satellite transitions; these transitions are not included in the simulation (f). The parameters used for the simulated spectra are given in Skibsted et al.[15] Positions of spinning sidebands and centerbands for the satellite transitions in the experimental spectra are indicated by asterisks (*)

and slightly off-angle, respectively). These spectra are easily analyzed in terms of two sets of χ, η, and δ values, as shown by the simulated spectra in Figures 3(d) and (f), which result from addition of two second-order lineshapes in a 1:1 ratio.[15] With these parameters at hand, the simulated spectrum for ν_r = 8.0 kHz in Figure 3(b) shows an excellent agreement with the originally recorded 'low-speed' spectrum in Figure 3(a).

Other research groups have similarly taken advantage of the combination of especially high magnetic field strengths with high-speed spinning for determination of 'large' χ values from observed second-order lineshapes of the central transition in ^{27}Al MAS NMR.[24–26] Examples include the extensively studied mineral andalusite, which has been investigated at 11.7 T employing ν_r = 15 kHz[24] and 18.4 kHz,[25] respectively, and at 14.1 T for ν_r = 14.8–19.5 kHz.[26]

Another aspect of high-speed spinning in MAS NMR for the central transition(s) may be found in the important area of quantitative analysis. Examples include accurate determinations of (i) the relative number of multiple sites within the asymmetric unit of synthetic or natural minerals[16,27] and (ii) the composition/identification of individual phases in phase mixtures.[17] Such analysis may be greatly assisted by the information that can be gained from the observation of the ssb pattern for the satellite transitions.[16,17,27]

3.4 Exactly On- and Slightly Off-MAS NMR of the Satellite Transitions

As pointed out and demonstrated for our first probe design with $\nu_r \approx 15$ kHz,[11] the possibility of high-speed spinning is important not only for the observation of the central transition but especially also in MAS NMR of the satellite transitions. The obvious reason is the increased sensitivity with which the individual ssbs for these transitions can be observed by increasing ν_r. Maybe just as important is the ability to adjust the magic angle accurately, because the correct second-order MAS lineshape (if observable) for each ssb is extremely dependent on an exact setting of the magic angle (see above). Thus, we have designed an adjustment device that allows very fine increments and stability in the angle adjustment.[28] Furthermore, ^{23}Na MAS NMR of the satellite transitions for $NaNO_3$ was proposed as a much more sensitive sample, as compared with ^{79}Br MAS NMR of KBr,[4] for accurately setting the magic angle.[28] In the ^{23}Na MAS NMR spectrum of $NaNO_3$, no second-order lineshapes are observed for the ssbs[6,9] and the linewidth of the individual ssbs can be narrowed down to between 0.7 and 0.8 ppm at the magic angle. Actually, the linewidth varies slightly throughout the ssbs of the manifold; the narrowest ssbs (approx. 0.7 ppm) are observed for

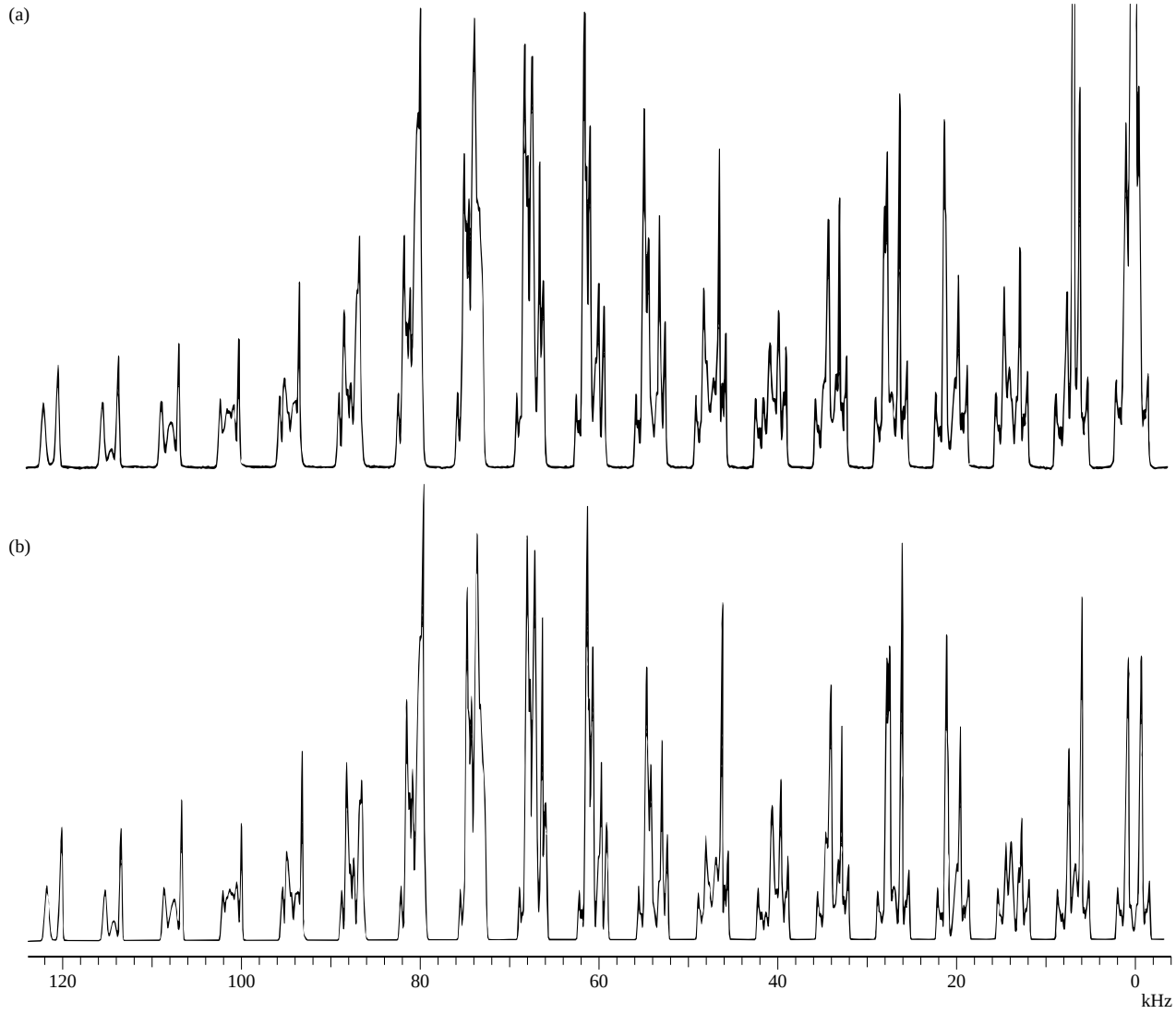

Figure 4 Expansion of part of the complex spinning sideband lineshapes observed for the ^{23}Na satellite transitions in $NaNO_3$ using slightly off MAS ($\Delta\theta = -0.44^\circ$) at 105.8 MHz (9.4 T): (a) experimental spectrum; (b) simulated spectrum calculated using ν_r = 6730 Hz, $\Delta\theta = -0.44^\circ$, χ = 337 kHz, and η = 0.0. Distortions from the central transition and its first few ssbs are observed near 0 kHz

the two 'horns' about ±80 kHz from the center of the spectrum, whereas the broader ssbs (approx. 0.8 ppm) and the most sensitive to angle adjustment are found close to the central transition. Using these linewidths as a probe, it is our experience that the magic angle can be adjusted to better than 0.001°. Slightly off-MAS (i.e., with variable angle spinning VAS), the individual ssbs start splitting into complex lineshapes. For example, for an offset $\Delta\theta = -0.44^\circ$ in the angle adjustment, the very broad and complex lineshapes observed for the ssbs are shown for some of these as the expansion in Figure 4(a). These lineshapes depend on χ, η (χ = 337 kHz, η = 0.00 for $NaNO_3$[6,9]), ν_r, and the offset $\Delta\theta$, and can be simulated based on the first-order Hamiltonian alone, employing the correct angle for the spinning axis ($54.736^\circ + \Delta\theta$), as shown in Figure 4(b). Note that the width of the ssb lineshapes mainly reflects the degree of offset $\Delta\theta$, while the lineshapes themselves are determined by χ and η for the sample.

The observation and simulation of the slightly off MAS ^{23}Na NMR spectrum of $NaNO_3$ in Figure 4 suggest an alternative method for the determination of χ and η that can be useful in certain situations. For 'small' χ values that do not give rise to an observable second-order lineshape for the central transition, χ and η are usually determined from analysis of the manifold of ssbs observed on large spectral widths (1–4 MHz), as discussed earlier. However, if a spectrometer with a fast receiver is not available, the observation of a limited number of ssbs (e.g., employing a 100 kHz spectral width) slightly off-MAS may allow determination of χ and η from lineshape analysis as illustrated in Figure 4.

4 OTHER SAMPLE ROTATION TECHNIQUES

In addition to the development and straightforward applications of high speed MAS for half-integer quadrupolar nuclei, the past decade has also witnessed the appearance and applications of several other sample rotation techniques for studies of such nuclei. These methods include double rotation (DOR)

(see ***Double Rotation***) dynamic angle spinning (DAS) (see ***Dynamic Angle Spinning***) (MAS) nutation NMR (see ***Nutation Spectroscopy of Quadrupolar Nuclei***) and variable angle spinning (VAS) (see ***Variable Angle Sample Spinning***). DOR NMR (see ***Double Rotation***) especially appears a very promising method, particularly when combined with high speed MAS, in studies of multiple sites leading to overlapping MAS lineshapes for the central transitions.

5 RELATED ARTICLES

Average Hamiltonian Theory; Double Rotation; Dynamic Angle Spinning; Geological Applications; Inorganic Solids; Magic Angle Spinning; Multiple Quantum NMR in Solids; Quadrupolar Interactions; Quadrupolar Nuclei in Solids; Variable Angle Sample Spinning.

6 REFERENCES

1. D. Müller, W. Gessner, H.-J. Behrens, and G. Scheler, *Chem. Phys. Lett.*, 1981, **79**, 59.
2. M. D. Meadows, K. A. Smith, R. A. Kinsey, T. M. Rothgeb, R. P. Skarjune, and E. Oldfield, *Proc. Natl. Acad. Sci. USA*, 1982, **79**, 1351.
3. A. Samoson and E. Lippmaa, *Phys. Rev. B*, 1983, **28**, 6567.
4. J. S. Frye and G. E. Maciel, *J. Magn. Reson.*, 1982, **48**, 125.
5. J. Skibsted, N. C. Nielsen, H. Bildsøe, and H. J. Jakobsen, *Chem. Phys. Lett.*, 1992, **188**, 405.
6. J. Skibsted, N. C. Nielsen, H. Bildsøe, and H. J. Jakobsen, *J. Magn. Reson.*, 1991, **95**, 88.
7. M. M. Maricq and J. S. Waugh, *J. Chem. Phys.*, 1979, **70**, 3300.
8. A. Samoson, E. Kundla, and E. Lippmaa, *J. Magn. Reson.*, 1982, **49**, 350.
9. H. J. Jakobsen, J. Skibsted, H. Bildsøe, and N. C. Nielsen, *J. Magn. Reson.*, 1989, **85**, 173.
10. V. Langer, P. Daugaard, and H. J. Jakobsen, *J. Magn. Reson.*, 1986, **70**, 472; US Patent 4 739 270, April 19, 1988.
11. H. J. Jakobsen, P. Daugaard, and V. Langer, *J. Magn. Reson.*, 1988, **76**, 162.
12. P. Daugaard, V. Langer, and H. J. Jakobsen, *Design of a high-speed 4, 5, 7, and 12 mm spinner system in zirconia ceramics for MAS/VAS NMR of solids, Poster WP 20, 31st Experimental NMR Conference, Asilomar, CA, April 1–5, 1990*.
13. H. W. Spiess, in *NMR Basic Principles and Progress*, eds. P. Diehl, E. Fluck, and E. Kosfeld, Springer-Verlag, Berlin, 1978, Vol. 15, p. 55.
14. A. Samoson, *Chem. Phys. Lett.*, 1985, **119**, 29.
15. J. Skibsted, H. Bildsøe, and H. J. Jakobsen, *J. Magn. Reson.*, 1991, **92**, 669.
16. J. Skibsted, E. Henderson, and H. J. Jakobsen, *Inorg. Chem.*, 1993, **32**, 1013.
17. J. Skibsted and H. J. Jakobsen, *Solid State Nucl. Magn. Reson.*, 1994, **3**, 29.
18. N. C. Nielsen, H. Bildsøe, and H. J. Jakobsen, *Chem. Phys. Lett.*, 1992, **191**, 205.
19. B. A. Goodman and J. W. Stucki, *Clay Miner.*, 1984, **19**, 663.
20. E. Oldfield, R. A. Kinsey, K. A. Smith, J. A. Nichols, and R. J. Kirkpatrick, *J. Magn. Reson.*, 1983, **51**, 3215.
21. H. J. Jakobsen, H. Jacobsen, and H. Lindgreen, *Fuel*, 1988, **67**, 727.
22. L. Kellberg, M. Linsten, and H. J. Jakobsen, *Chem. Phys. Lett.*, 1991, **182**, 120, and references cited therein.
23. D. Müller, W. Gessner, A. Samoson, E. Lippmaa, and G. Scheler, *Polyhedron*, 1986, **5**, 779.
24. L. B. Alemany, H. K. C. Timken, and I. D. Johnson, *J. Magn. Reson.*, 1988, **80**, 427.
25. L. B. Alemany, D. Massiot, B. L. Sheriff, M. E. Smith, and F. Taulelle, *Chem. Phys. Lett.*, 1991, **177**, 301.
26. S. F. Dec, J. J. Fitzgerald, J. S. Frye, M. P. Shatlock, and G. E. Maciel, *J. Magn. Reson.*, 1991, **93**, 403.
27. D. Massiot, C. Bessada, J. P. Coutures, and F. Taulelle, *J. Magn. Reson.*, 1990, **90**, 231.
28. H. J. Jakobsen, V. Langer, P. Daugaard, and H. Bildsøe, *A device and method for magic angle adjustment with millidegree accuracy using MAS of quadrupolar nuclei, Poster WP 19, 31st Experimental NMR Conference, Asilomar, CA, April 1–5, 1990*.

Biographical Sketch

Hans J. Jakobsen. *b* 1940. B.S., 1961, Ph.D., University of Aarhus, 1964. Introduced to NMR by K. Schaumburg, 1962. Faculty in Dept. of Chemistry, Univ. of Aarhus 1964–present. Approximately 135 publications. Research interests include the practice and theory of high-resolution solid state NMR with applications to chemistry and materials research.

Magic Angle Spinning Carbon-13 Lineshapes: Effect of Nitrogen-14

Charles A. McDowell

University of British Columbia, Vancouver, Canada

1	Introduction	1
2	Magic Angle Spinning	1
3	Effects of an Axially Symmetric Electric Field Gradient	2
4	^{14}N Effects of an Asymmetric Electric Field Gradient	3
5	Influence of J Coupling	6
6	Other Spin-$\frac{1}{2}$ Nuclei Bonded to ^{14}N: ^{1}H CRAMPS	6
7	Related Articles	8
8	References	8

1 INTRODUCTION

The introduction of the Hartmann–Hahn[1] technique of cross polarization into solid state nuclear magnetic resonance spectroscopy, particularly when combined with multiple pulse methods[2] to remove homo- and heteronuclear, dipolar broadening, was a significant addition to the methods available for the study of solid compounds by NMR. When cross polarization and proton decoupling were incorporated into the magic angle spinning technique,[3] there was produced a significant enlargement of the repertoire of sensitive NMR spectrometric procedures available for obtaining high-resolution spectra of solid state compounds and materials.[4] This important new spectroscopic method became known as cross polarization magic angle spinning (CP MAS) NMR. When the ^{13}C spectra of compounds containing nitrogen were studied by CP MAS some lines appeared as broadened asymmetric doublets. It was soon realized that this characteristic lineshape resulted from the ^{14}N nuclear quadrupole moment interfering with the ability of the magic angle spinning to average out the ^{13}C–^{14}N dipolar interactions. This interpretation was based on earlier observations of the ^{13}C lineshapes of carbon nuclei bonded to nitrogen in the NMR of single crystals. We shall now briefly describe the main features of such high-resolution NMR spectra of single crystals to provide a suitable background for understanding the theoretical interpretation of the asymmetrical ^{13}C–^{14}N lineshapes in CP MAS spectra.

1.1 Single Crystal NMR Spectra

Within a short time after their introduction, the new NMR spectroscopic techniques were applied to obtain ^{13}C chemical shielding data on a wide range of organic compounds. It was soon found in compounds containing a nitrogen nucleus adjacent to the carbon nucleus being studied that splittings from ^{13}C–^{14}N dipolar couplings were observed. Griffin et al.[5] found that the NMR spectrum of a single crystal of glycine at a certain orientation with respect to the magnetic field exhibited three lines from the methylene carbons split by adjacent ^{14}N nuclei. In measurements of the ^{13}C chemical shielding tensor in the metal complex $K_2Pt(CN)_4Br_{0.3}\cdot 3H_2O$, Stoll et al.[6] observed large effects clearly shown to be caused by ^{14}N quadrupolar interactions. In that compound, the electric quadrupolar interactions are of comparable size to the ^{13}C–^{14}N dipolar interaction; consequently, mixing with the pure Zeeman eigenfunctions occurs. These required eigenfunctions were obtained by the application of first-order perturbation theory and subsequent diagonalization of the combined Zeeman-quadrupole Hamiltonian. Stoll et al. assumed an axially symmetric electric field gradient tensor with its symmetry axis along the C–N bond. Good quantitative agreement was found between the theoretical and experimental spectral lineshapes for all the angular variations studied.

Because amino acids are of great biological importance, the observations of ^{13}C–^{14}N dipolar–quadrupolar interactions clearly meant that single crystal NMR spectra of amino acids would soon be investigated. Thus simultaneously there were reported such detailed studies of alanine[7] and glycine.[8] Though these two detailed single crystal studies cover similar ground, we shall give details about the more complete studies of alanine and use some of the theoretical ideas later in our discussion of the effects of ^{14}N quadrupolar interactions causing asymmetry in certain magic angle spectral lineshapes of compounds with C–N bonds.

The proton-enhanced proton-decoupled ^{13}C NMR spectra of a single crystal of L-alanine were studied by Naito et al.[7] The C-α line showed a triplet pattern arising from dipolar coupling with the ^{14}N ($S = 1$) nuclei (Figure 1). These splittings were asymmetric, especially in the a-axis orientation. The dipolar interactions in the presence of the ^{14}N quadrupolar interaction were calculated by applying ideas first employed by VanderHart et al.[9] to provide a theoretical analysis of the static proton resonance spectra of polycrystalline $HMn(CO)_5$ and $HCo(CO)_4$. The appropriate Hamiltonian for the case where the quadrupole asymmetry parameter η is zero is written in the following form for later convenience:

$$\mathcal{H} = -\gamma_N \hbar B_0 S_z + \frac{\chi h}{4S(2S-1)}[3S_z^2\cos^2\theta + 3S_x^2\sin^2\theta + 3(S_zS_x + S_xS_z)\sin\theta\cos\theta - S^2] \quad (1)$$

where the quadrupolar coupling constant is $\chi = e^2qQ/h$ This Hamiltonian was used to determine the required eigenfunctions of the ^{14}N nucleus, and these in turn employed to calculate the eigenfunctions of the ^{13}C–^{14}N dipolar interaction as a function of θ, the angle between the direction of the external magnetic field and the symmetry axis of the electric field gradient tensor, i.e., the C_θ–N bond direction. It was thus possible to calculate the three ^{13}C resonances predicted (and observed experimentally for the C-α nucleus) which correspond to the nitrogen Zeeman states $|+1\rangle$, $|0\rangle$, and $|-1\rangle$, respectively. When the sign of the quadrupole coupling constant was assumed to be positive, good agreement was found between the calculated and experimental data for all the angles studied. The experimental results thus give the sign of the quadrupole coupling constant.

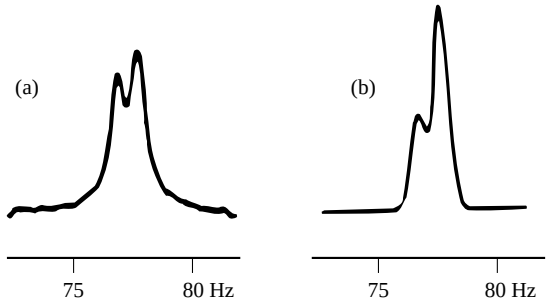

Figure 1 Lineshape of the C-α nucleus in the ^{13}C CP MAS spectrum of polycrystalline L-alanine taken at a field of 4.6 T. (a) Experimental spectrum; (b) computer-simulated spectrum assuming an axially symmetric quadrupolar parameter. (Reproduced by permission of the American Institute of Physics from Naito et al.[14])

2 MAGIC ANGLE SPINNING

As is well known, MAS tends to average out anisotropic interactions to their corresponding isotropic values when they are very weak as compared with their Zeeman interactions. Theoretical consideration of the effect of the ^{14}N quadrupolar interaction on the ^{13}C MAS spectra based on the above ideas, show that for ^{13}C nuclei bonded to ^{14}N an asymmetric doublet pattern is expected. Lippmaa et al.[10] reported that a high-resolution rotational-synchronized proton-enhanced magic angle spinning ^{13}C NMR spectrum of the polycrystalline solid of the one-dimensional compound tetrathiofulvalene–tetracyanoquinodimethane (TTF–TCQN) exhibited a three-line spectrum, one line of which consisted of an asymmetric doublet which they attributed to the C–N group. The splitting was found to be field-dependent and identified as arising from dipole–dipole interaction with the ^{14}N nuclei having a quadrupole interaction of comparable magnitude to their Zeeman interaction. This was the first observation of an asymmetric lineshape in a ^{13}C magic angle spinning NMR spectrum of a compound containing a ^{13}C–^{14}N bond.

3 EFFECTS OF AN AXIALLY SYMMETRIC ELECTRIC FIELD GRADIENT

The influence of spinning on the solid state NMR spectrum of a molecular system consisting of spin pairs in which one of the two spins has a quadrupole moment was first treated theoretically by Kundla and Alla.[11] The quadrupolar interaction fixes the spin moment at a definite orientation in the principal axis system (PAS) of the molecule. Rotation of the sample causes a rotational synchronized movement of the spin moment which does not permit the complete averaging of the dipole–dipole interaction between the spin-$\frac{1}{2}$ nucleus I and the quadrupole nucleus $S = 1$. The degree of the averaging depends on the ratio of the quadrupolar and Zeeman energies of the S nucleus.

The Hamiltonian may be written as

$$\mathcal{H} = \mathcal{H}_{\mathrm{Z}}^{I} + \mathcal{H}^{S} + \mathcal{H}_{\mathrm{D}}^{IS} \tag{2}$$

Here $\hat{\mathcal{H}}_{\mathrm{Z}}^{I}$ is the Zeeman term of the I nucleus, $\mathcal{H}^{S}$ is the quadrupolar Hamiltonian, and $\mathcal{H}_{\mathrm{D}}^{IS}$ the dipolar interaction Hamiltonian between the I and S spins. It is assumed that $\mathcal{H}_{\mathrm{D}}^{IS}$ is small so that first-order perturbation theory may be applied to calculate the resonance frequencies of the I-spin spectral lines. Because of the rotation of the sample at frequency ω_{r}, the eigenfunctions and eigenvalues of the unperturbed system become time-dependent. These were calculated for the case where the quadrupole coupling is symmetric. The energy levels were expressed in terms of parameters such as $k = \omega_{\mathrm{Q}}/\omega_{\mathrm{Z}}^{S}$; θ, the angle between the rotation axis and the magnetic field; the Euler angles α, β, and γ of the sample-fixed coordinate system, in which the α axis coincided with the rotational axis; and the PAS. When $\theta = 0$, the eigenvalue equations became the same as those giving the dependences of the spectral lines on the orientation of the nonrotating single crystal as described by Stoll et al.[6] To obtain the lineshapes and resonances of the polycrystalline sample at high spinning speeds, the average positions, $\overline{\Delta_n^{\mathrm{D}}}$, were obtained by averaging over all orientations represented by the angle β. Numerical calculations for the magic angle case showed that the line splittings and total widths depend strongly on the relative strengths of the Zeeman and quadrupolar interactions. Moreover, it was shown that in a strong magnetic field, the I-spin spectrum is an asymmetric doublet, one of the lines being the sum of two components, the full width of the single line being twice as large as that of the composite line. The splitting increased with increasing k leading to a regular triplet. The isotropic spin–spin interaction between the I and S nuclei was predicted to shift the I-spin spectral lines, the effect decreasing with increasing values of k.

Apparently unaware of the above work of the Estonian scientists, several groups reported CP MAS spectra of polycrystalline organic compounds containing C–N bonds such as amino acids, peptides, and proteins in which significant differences were observed between the solid state spectra and those in solution.[12,13] Most of the resonances from carbons bonded to nitrogens were split into broadened doublets, and some of the resonances from more distant carbons were also affected.

A classical and much studied example is the CP MAS spectrum of polycrystalline alanine.[14] The observed splittings of the asymmetric doublet of the C-α resonance was 45 Hz with a 200 MHz magnet and $\sim$ 100 Hz when measured at 90 MHz. The spectra can be fully interpreted and quantitatively explained by the following theoretical treatment.[14] First, the ^{14}N quadrupolar interaction is of comparable magnitude to the Zeeman interaction, so the ^{14}N spin eigenfunctions must be determined by diagonalizing the nitrogen Zeeman quadrupole Hamiltonian, and those eigenfunctions used in the calculation of the ^{13}C–^{14}N dipolar interactions. At the outset it should be understood that in this problem it is important to be mindful of the timescale of the magic angle spinning. In the experiments described by Naito et al.[14] the spinning frequency was 4.5 kHz, which is small compared with the ^{14}N quadrupolar interaction in L-alanine for which $\chi = 1.205$ MHz; the adiabatic approximation can therefore be employed to determine the nitrogen spin functions at time t from the following equation

$$\mathcal{H}_{\mathrm{ZQ}}\psi_{\mathrm{N}}(t) = E(t)\psi_{\mathrm{N}}(t) \tag{3}$$

Here, $\mathcal{H}_{\mathrm{ZQ}}(t)$ is the Zeeman quadrupole Hamiltonian of the nitrogen nuclei at time t. For the amino nitrogen in amino

acids and the cyano nitrogen in nitriles, one may assume with a high degree of accuracy that the electric field gradient tensor is axially symmetric, i.e., $\eta = 0$. Thus for the MAS spectrum of L-alanine we can write the Zeeman quadrupole Hamiltonian as

$$\mathcal{H}_{ZQ}(t) = -\gamma_N \hbar S_z B_0 + \frac{\chi h}{4S(2S-1)}[3S_z^2 \cos^2\theta(t) + 3S_x^2 \sin^2\theta(t) + 3(S_z S_x + S_x S_z)\sin\theta(t) \times \cos\theta(t) - S^2] \quad (4)$$

Here, $\theta(t)$ is the periodic value of the angle between the field direction $\boldsymbol{B}_0$ and the internuclear vector $\boldsymbol{r}_{CN}$. Under MAS, when a rigid array of nuclei is rotated with an angular velocity ω_r about an axis inclined at an angle β to the direction of the external magnetic field $\boldsymbol{B}_0$, and at an angle β' to $\boldsymbol{r}_{CN}$, we may write that $\theta(t)$ can vary as follows:

$$\cos\theta(t) = \cos\beta\cos\beta' + \sin\beta\sin\beta'\cos(\omega t + \psi) \quad (5)$$

where ψ is the azimuthal angle of $\boldsymbol{r}_{CN}$ at time $t = 0$.

In this case the $^{13}C-^{14}N$ dipolar interaction is very small compared with the Zeeman interaction, so first-order perturbation theory can be used to calculate the $^{13}C-^{14}N$ dipolar interaction at time t. The dipolar splitting of the ^{13}C resonance resulting from that calculation using the Hamiltonian $\mathcal{H}_{ZQ}$ represented by equation (3) yields

$$\Delta E_i(t) = -\gamma_C \gamma_N \hbar^2 / r_{CN}^3 \{[a_i(t)^2 - c_i(t)^3 2][1 - 3\cos^2\theta(t)] - (9/2)^{1/2}[a_i(t) + c_i(t)]b_i(t)\sin 2\theta(t)\} \quad (6)$$

Here, $a_i(t)$, $b_i(t)$, and $c_i(t)$ (i = 1, 2, and 3) are the coefficients at time t of the Zeeman quantized spin functions of the nitrogen nuclei, namely, $|1\rangle$, $|0\rangle$, and $|-1\rangle$, respectively. In L-alanine the $^{13}C-^{14}N$ dipolar interaction, 0.6636 kHz, is small compared with the spinning frequency 4.5 kHz, so in such cases the $\Delta E_i(t)$ have to be averaged from $t = 0$ to $t = \infty$ to obtain the $^{13}C-^{14}N$ dipolar energy of the spinning sample. The values of $\Delta E_i(t)$ were calculated for each 5° of $\omega t + \psi$ in the range 0° to 360° with constant β', and these values were then averaged to yield $\overline{\Delta E_{i\beta'}(t)}$. The theoretical lineshapes for polycrystalline samples rotating at the magic angle $\beta = 54.7°$ are obtained by calculating the numerical values of $\overline{\Delta E_{i\beta'}(t)}$ when β' is varied in steps of 2° in the interval 0° to 90°, each $\overline{\Delta E_{i\beta'}(t)}$ being weighted by its probability $\sin\beta'$. Finally, convoluting the theoretical lineshapes with a Gaussian function gave the actual lineshape. The linewidth of the Gaussian function is an adjustable parameter which takes into account any instrumental line broadening, such as effects arising from improper decoupling setting, any slight misalignment of the magic angle, and any magnetic field inhomogeneities, etc.

As shown in Figure 1, the calculated and experimental spectra agreed well. Clearly the calculated lineshape is an asymmetric doublet with a splitting of 48 Hz for a ^{13}C resonance frequency of 50.3 MHz and 108 Hz for a resonance frequency of 22.6 MHz, both values in good agreement with experimental observations.[12,14] This field-dependence of the asymmetric doublet splitting arises because a weak field causes a relative increase in the contributions from the off-diagonal elements of the matrix representation of the Hamiltonian $\hat{\mathcal{H}}_{ZQ}(t)$. Noteworthy also was the finding that when the sign of the term χh in the lineshape calculation was chosen as negative, the shape was reversed, i.e., the intensity of the high-frequency (low-field) peak was now stronger than the other one. This observation thus presents a means of determining the sign of the quadrupole coupling constant of ^{14}N bonded to ^{13}C by lineshape analysis of the CP MAS ^{13}C NMR spectra.

When the spectrum of cyanoacetamide was studied the same theoretical treatment was applicable because here also the $^{13}C-^{14}N$ dipolar interaction, 1.46 kHz, was smaller than the rotor spinning frequency. The lineshape exhibited a reversal of the intensities of the doublet components. When the value of χh was taken to be negative, the simulated lineshape was in good agreement with that observed experimentally. The splitting of the asymmetric doublet for the nitrile was 338 Hz in the simulated spectrum, in good agreement with the experimentally measured splittings of 305 Hz to 356 Hz for different cyano compounds.

The above theoretical treatment and the simulated MAS lineshapes were based on the important assumption that the rotor spinning speed was very small in comparison with the size of the quadrupole interaction of the ^{14}N nucleus in the molecule. It was, however, shown that if the spinning speeds were as large as the ^{14}N quadrupolar interaction (i.e., in the MHz range), which seems highly unlikely, the lineshape predicted is quite different from those obtained at low spinning frequencies. For the extremely high spinning frequency case, a truncated Zeeman quadrupole Hamiltonian $\overline{\mathcal{H}_{ZQ}(t)}$ (the time-dependent part is truncated) can be used for the MAS lineshape calculation. Using the same parameters as employed in the simulation of the spectra of nitrile compounds with a value of χ = 3.87 MHz and 24 Hz for the halfwidth of the Gaussian broadening function, it was found that the predicted splitting is less than one-third of the slow-spinning case, giving a broad powder pattern as the expected lineshape.

Contemporaneously with the above work, Zumbulyadis et al.[15] presented an extensive analysis of the influence of quadrupole nuclei on the magic angle spinning spectra of spin-$\frac{1}{2}$ nuclei. Here also, as above, the treatment was restricted to the case with an axially symmetric quadrupolar tensor. The formal theory described was similar to that described above; it also made use of the adiabatic approximation, in which a time-dependent wavefunction is approximated by an eigenfunction of the instantaneous Hamiltonian multiplied by a time-dependent phase factor. Theoretical powder patterns were calculated for a range of values of parameters typical of ^{13}C coupled to ^{14}N, the results being given as a function of ratio of the spin-1 Zeeman frequency Z to the quadrupole coupling constant χ. Each spectrum consisted of double-peaked bands with an intensity ratio of 1:2; the ratio of the S-spin Zeeman to the quadrupolar interaction (Z/χ) determined the widths of the bands and the splittings between them. This was also implicit in the theories of Naito et al.[14,16] as was the finding that both the widths and splittings of the bands decrease at higher magnetic fields where the quadrupolar interaction induces less mixing of the S-spin Zeeman eigenstates. It was also shown that the appearance of the bands depended critically on the mutual orientations of the unique principal axes of the dipolar and quadrupolar interaction tensors, the doublet splitting going through a minimum when the two principal axes were oriented at the magic angle *with respect to each other*.

4 ^{14}N EFFECTS OF AN ASYMMETRIC ELECTRIC FIELD GRADIENT

Though the above theoretical treatments[14,15] were successful in providing an interpretation of the CP MAS ^{13}C spectra of a number of nitrogen-containing compounds and, in particular, explaining the asymmetric lineshapes associated with C–N bonds, the restriction to cases with symmetric ^{14}N quadrupolar tensors was limiting. When the quadrupole coupling parameter $\eta \neq 0$, the C–N bond direction may not be parallel to the principal axis of the quadrupolar tensor. In this situation the off-diagonal elements in the matrix representation of the Hamiltonian $\mathcal{H}_{ZQ}$ will contain η, and hence a large value of the quadrupolar asymmetry parameter will be quite effective in determining the resulting MAS lineshape.

To extend the theory to include the ^{13}C CP MAS spectra of important organic molecules such as nitroanilines, and biomolecules like imidazoles, polypeptides, and proteins in which the influence of asymmetry of the ^{14}N quadrupole coupling tensor may play an important role in determining the lineshapes of the spectra, it was necessary to extend the theoretical formulation though the basic ideas were still sufficient to permit the required extension to encompass a wider range of molecular environments.[16]

The adiabatic approximation represented by equation (2) is still used but the Zeeman quadrupole Hamiltonian for ^{14}N must be modified to reflect the asymmetry of η, the nitrogen asymmetry parameter. The Hamiltonian is now written as

$$\mathcal{H}_{ZQ}(t) = -\gamma_N \hbar B_0 S_{z'} + \frac{eQq_{zz}}{4S(2S-1)} \times\{(3S_z^2(t) - S^2) + \eta[S_x^2(t) - S_y^2(t)]\} \qquad (7)$$

where $\eta = (q_{xx} - q_{yy})/q_{zz}$; eq_{ii} are the principal values of the electric field gradient tensor at the ^{14}N nucleus in the compound. They obey the convention that $|q_{zz}| \geq |q_{yy}| \geq |q_{xx}|$. The quantity e^2Qq_{ii} ($i = x, y, z$) is one of the principal values of the quadrupole coupling tensor and e^2Qq_{zz} is the quadrupole coupling constant. In this case there are two different coordinate systems to be considered. The Zeeman coordinate system is specified by (x', y', z'), and the principal axis system coordinates of the ^{14}N electric field gradient tensor of the compound by (x, y, z). The Euler angles of the spinner rotation axes (x^R, y^R, z^R) are written as β', θ, and ψ. The magic angle spinning axis, z^R, is inclined at an angle β' with the z axis, and at the magic angle β to the static magnetic field (Z'). The angle ψ is time-dependent and given by $\psi = \omega_r t + \psi_0$, where ψ_0 is the initial angle when $t = 0$ and ω_r is the angular velocity of spinning. Transformations of the coordinate systems (see Figure 2) give the ^{14}N Zeeman quadrupole Hamiltonian in the Zeeman coordinate system, and the resulting eigenstates are used to calculate the ^{13}C–^{14}N dipolar energy. Since, in general, the internuclear vector $\boldsymbol{r}_{CN}$ is not collinear with the z axis of the electric field gradient tensor, its direction is defined by the polar angles (θ, ψ) in the principal axis system of the electric field gradient tensor. First order perturbation theory can again be used to calculate the ^{13}C–^{14}N dipolar energy of the ^{13}C resonance of a certain

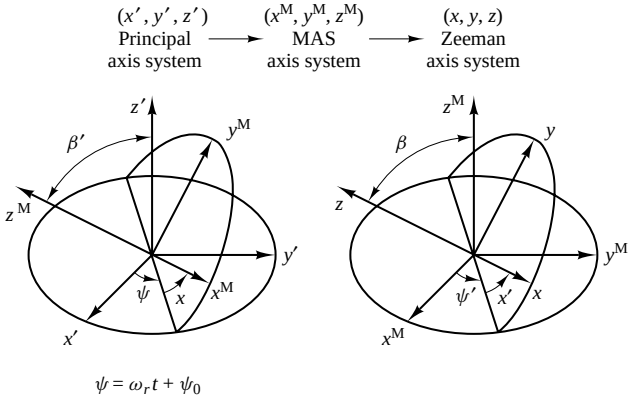

Figure 2 Diagrammatic representation of the coordinate transformations required to calculate the ^{13}C lineshapes when the quadrupolar parameter η is asymmetric. They can be summarized as follows:

x, y, z	x^R, y^R, z^R	x', y', z'
Principal $\xrightarrow{(\beta',\phi,\psi)}$	Rotating $\xrightarrow{(\beta,0,0)}$	Zeeman
axis system	axis system	axis system

molecular orientation at time t and is given by

$$\Delta E_{i\beta'\Phi}(t) = \langle\beta\psi_N(t)|\mathcal{H}_D(t)|\beta\psi_N(t)\rangle - \langle\alpha\psi_N(t)|\mathcal{H}_D(t)|\alpha\psi_N(t)\rangle \qquad (8)$$

Here, $|\alpha\rangle$ and $|\beta\rangle$ are the ^{13}C Zeeman spin functions. As before, the ^{13}C–^{14}N dipolar interaction is smaller than the spinning frequency, so $\Delta E_{i\beta'\Phi}(t)$ must be averaged over one rotor cycle, i.e., from $t = 0$ to $t = \infty$, to give the ^{13}C–^{14}N dipolar energy in the spinning sample, namely

$$\overline{\Delta E_{i\beta'\Phi}(t)} = (1/2\pi)\int_0^{2\pi} \Delta E_{i\beta'\Phi}(\psi)\,d\psi \qquad (9)$$

The values of $\overline{\Delta E_{i\beta'\Phi}(t)}$ were calculated numerically for small increments of the appropriate angles and the resulting values averaged. The resulting theoretical averaged line positions for the spinning sample were weighted by their probability, sin β', and then convoluted with a suitable lineshape function to yield the actual lineshape.

One of the first compounds chosen to test the above theory for calculating the MAS lineshapes of molecules containing ^{14}N nuclei with nonasymmetric quadrupolar tensors, i.e., with $\eta \neq 0$, was polycrystalline 2,6-dimethyl-3-nitroaniline. This molecule has two different types of ^{14}N nuclei. The ^{13}C MAS NMR spectrum showed that the resonances for both the nitro and amino carbon nuclei exhibited asymmetric doublet patterns (Figure 3). The high-frequency line in the nitro doublet was more intense than the other component, whereas the reverse was the case for the amino peak. Clearly the differences in the lineshapes arose from the different signs, orientations, and magnitudes of the respective electric field gradient tensors for the two ^{14}N nuclei. Calculations of the theoretical lineshapes by the method outlined above using the appropriate molecular parameters and a reasonable assignment for the orientation of the ^{14}N electric field gradient tensor based on that of *p*-nitrotoluene yielded lineshapes similar to those observed

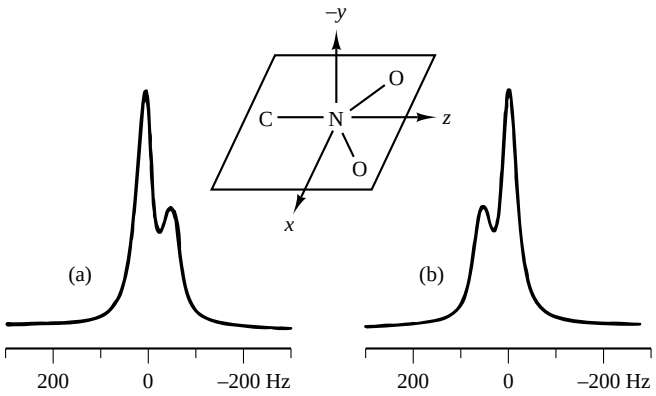

Figure 3 Lineshape of the resonance of the carbon nucleus adjacent to the NO_2 group in the ^{13}C CP MAS spectrum of 2,6-dimethyl-3-nitroaniline. Computer-simulated spectrum calculated with a quadrupolar asymmetry parameter $\eta = 0.408$ and (a) the ^{14}N quadrupolar coupling constant $e^2Qq_{zz}/h = -1.340$ MHz; (b) the quadrupolar coupling assumed to be positive. (Reproduced by permission of Academic Press from Naito et al.[16])

experimentally. With the value of χ being 1.340 MHz and η = 0.408 for ^{14}N of the $-NO_2$ group, good agreement was found with the experimental lineshape only when the sign of the quadrupole coupling constant was taken as negative. The simulation of the lineshape of the amino peak required more insight. Values for χ, η, and $\gamma_C\gamma_N\hbar/(2\pi r_{CN}^3)$, based on literature information, were chosen to be 3.977 MHz, 0.263, and 0.8466 kHz, respectively. In the case where the z axis of the quadrupole coupling constant was chosen to lie normal to the plane of the NH_2 group and the y axis assumed to be tilted 40° from the C–N bond direction, with the sign of the quadrupole coupling constant negative the resulting simulated lineshape was in excellent agreement with that observed experimentally. Also, the calculated value for the doublet splitting was 110 Hz, in good agreement with the observed value of 102 Hz.

It proved more difficult to provide an unambiguous interpretation of the lineshapes of the ^{13}C CP MAS NMR spectrum of polycrystalline glycylglycine and glycyl-L-alanine. Here again the orientation of the principal axes of the ^{14}N quadrupole coupling tensor was unknown. Proceeding as before, the calculated lineshapes for the case where the z axis was assumed to lie along the direction of the N–H bond led to a narrow singlet pattern not in agreement with the experimental spectrum. When the z axis was chosen to be normal to the C–N–C plane and the y axis along the N–H bond, the simulated lineshapes again did not agree with the observed lineshape. Several possible orientations of the axes were tried, but only when the z axis of the quadrupole tensor of the amino nitrogen was assumed to lie along the C–N bond direction and the sign of the quadrupole coupling constant taken as positive, together with acceptable values of the other constants, was a satisfactory lineshape simulation obtained. Moreover, the calculated doublet splitting for the C-α carbon in glycylglycine was 49 Hz, which was in good agreement with the experimental value of 41 Hz.

Given the satisfactory simulations of the observed lineshapes from the theory for amino acids and polypeptides, attention was then turned to a more sophisticated molecule of biological interest, namely, trimethylimidazole. This molecule has two different types of nitrogen nuclei. The quadrupole coupling constants and asymmetry constants of the two nitrogen nuclei are for N-1, χ = 1.424 MHz and η = 0.980, and for N-2 χ = 3.267 MHz and η = 0.129. The large difference in the two quadrupolar tensors for the two nitrogen nuclei is obviously mainly the cause of the notable difference between the lineshapes observed for the C-4 and C-5 carbon atoms in the CP MAS spectrum of ^{13}C in this compound. Nevertheless, it was only possibly to simulate the experimental lineshapes successfully after a judicious choice of the orientations with respect to the molecular axes of the respective quadrupolar tensor axes.

Furthermore, this work clearly showed that in nitrogen-containing organic compounds, if the correct quadrupole coupling tensor and the relative orientations of the principal axes with respect to the molecular axes are known for a particular nitrogen nucleus, it is possible to calculate the theoretical lineshape for the carbon nucleus bonded to the nitrogen. That the sign of the quadrupole coupling constant for the nitro and amino nitrogen atom in organic compounds differed was new. Since each group containing a nitrogen atom has a characteristic quadrupole coupling tensor, it follows that the ^{13}C resonances in the CP MAS NMR spectra of the carbon atoms in such groups, e.g., $-NO_2, -NH_2, \equiv N, -NH_3^+$, and −CN, all exhibit characteristic lineshapes. This information is obviously of considerable practical importance for the assignment of the solid state ^{13}C CP NMR spectra of organic compounds, particularly those of biological importance and heterocyclic compounds, pharmaceuticals, dyestuffs, etc.

Another approach to calculating the lineshapes of the ^{13}C MAS spectra of nitrogen-containing organic compounds was put forward by Hexem et al.[17] This was based on writing the Hamiltonian of the spin system in terms of irreducible spherical tensor operators, namely

$$\mathcal{H} = \sum_{\lambda} \sum_{l} \sum_{m=-l}^{l} (-1)^m R_{l-m}^{\lambda} T_{lm}^{\lambda} \qquad (10)$$

In this equation, λ represents the type of interaction, including the Zeeman interactions for the carbon, Z_C, and nitrogen spins, Z_N; the quadrupole interaction of the nitrogen spin, Q; D, the $^{13}C-^{14}N$ dipolar interaction; and CS, the chemical shielding of the carbon spins. The quantity J, the indirect spin–spin interaction, is ignored because it was assumed to be negligible. The rotational properties of the irreducible spherical tensors were used to obtain the Hamiltonian in a more convenient form. The time-dependence of the resulting Hamiltonian was removed by applying average Hamiltonian theory. The part of the average Hamiltonian representing the dominant interactions of the carbon atoms and which commutes with the appropriate Zeeman Hamiltonian can be written as

$$\mathcal{H}^C(\phi) = C^Z \rho_{00}^Z T_{00}^Z + C^{CS} \rho_{00}^{CS} T_{00}^{CS} + \sum_{m=-2}^{2} C^D (-1)^m R_2^D - (\phi) T^D 3_{2m} \qquad (11)$$

where $C^Z = \gamma_C\hbar$, $C^{CS} = \gamma_C$, $\rho_{00}^{CS} = \sigma_{iso}$, $T_{00}^Z = B_{00}I_z$, $C^D = -2\gamma_C\gamma_N\hbar^2$, and σ_{iso} is the isotropic chemical shift. Making use of Wigner rotation matrices, one set of Euler angles transforms the principal axis system of the dipolar interaction

to the principal axis system of the electric field tensor, while the angles (0, θ_M, ψ) transforms further the spatial components to the axis system of the spinning rotor. In this last transformation, θ_M is the magic angle (54.7°) and ψ is the azimuthal angle of rotation about the rotor axis.

The shifts in the energy levels of ^{13}C were calculated using zero-order average Hamiltonian theory, which is equivalent to first-order perturbation theory, this procedure being possible because the small size of the dipolar coupling means that it can be treated as a perturbation. Because of the relative orders of magnitude of the ^{14}N quadrupole coupling constant and the lower achievable spinning rates, one cannot use zero-order average Hamiltonian theory to average $\hat{\mathcal{H}}^D_{CN}$, the heteronuclear Hamiltonian over one rotational period. The ^{14}N matrix was diagonalized and the induced carbon shifts calculated. The carbon shifts were calculated for a sufficient number of points as described in the earlier theoretical treatments. These dipolar shifts were averaged over one rotation period $\overline{\omega_n^C}$ by numerical integration over the azimuthal angle of rotation, ϕ. This is equivalent to assuming the adiabatic approximation for calculating the change of the nitrogen states over the rotational period described in detail earlier by Naito et al.[14,16] and by Zumbulyadis et al.[15]

As a preliminary test of theory, and to compare the results from diagonalizing the nitrogen Hamiltonian matrix with those obtained by using first-order perturbation theory to obtain the coefficients in the eigenfunction $\Phi_n^N(\phi)$ representing a linear combination of the Zeeman spin states, Hexem et al.[17] calculated the expected powder ^{13}C spectrum for a C–N bond. Typical values of the parameters were used and the quadrupole coupling tensor was assumed to be axially symmetric with η = 0. When these theoretical predictions for the lineshapes were compared with the experimental observations for polycrystalline alanine, it was clear that the spectra lacked the resolution to show the fine structure predicted by the powder pattern. The calculated spectrum obtained using a value of 0.26 for the quadrupole asymmetry parameter, η, and taking its sign as positive was in good agreement with the experimental spectrum, in general accord with the findings of Naito et al.[16]

Explaining the ^{13}C lineshape of the α-carbon in *N*-acetylvaline was more challenging. In this case η = 0.31 and in the case of the polypeptide bond study of Naito et al.[16] it was necessary to consider carefully the relative orientations of the principal axes of the electric field gradient tensor with respect to the molecular axes. Consideration of several orientations soon yielded a set of parameters which produced good agreement between the computer simulated lineshape and that observed experimentally.

The extensive studies of Hexem et al.[17] and Naito et al.[16] showed clearly that comparing the experimental and computer-calculated spectra provides a ready method for obtaining information concerning the relative orientations of the dipolar and electric field gradient tensors from the manifestations of the influences of those parameters on the ^{13}C NMR lineshapes. Moreover, such studies also enable the sign of the asymmetry parameter of the ^{14}N nucleus bonded to the carbon to be established. Also, as is clearly apparent from the theoretical treatments outlined earlier in this article, the extent of the splitting between the doublet peaks characteristic of the ^{13}C resonance of a C–N bond depends on the magnitude and the asymmetry parameter of the ^{14}N quadrupole tensor, the internuclear distance, the strength of the applied magnetic field, and the orientation of the internuclear vector $\boldsymbol{r}_{CN}$ in the principal axis system of the electric field gradient tensor.[18]

Kundla and Alla[11] had earlier shown that the line splittings and total widths depended on the relative strengths of the Zeeman and quadrupolar interactions. The magnitude of the splitting is directly dependent on the dipolar interaction and the asymmetry parameter, which is different for differing values of the Euler angles defining its spatial orientation, with the Zeeman frequency of the ^{14}N nucleus being Z_N, the dipolar coupling $D = \gamma_C\gamma_N\hbar/4\pi^2 r_{CN}^3$, and the polar and azimuthal angles as β^D and α^D, the doublet splitting S is given by:

$$S = \tfrac{9}{20}(D\chi/Z_N)(3\cos^2\beta^D - 1 + \eta\sin^2\beta^D\cos 2\alpha^D) \quad (12)$$

which is in terms of all the geometric ($\boldsymbol{r}$, α^D, β^D) and energy variables (χ, Z_N, η) up to first order in (χ/Z_N). As a test of equation (13) the values of the splitting S predicted by that equation were plotted against the experimentally observed splittings for more than 20 compounds containing different types of C–N bonds.[19] An excellent linear relationship was found which may, at first sight, seem surprising because of the wide range of different molecular species involved.

5 INFLUENCE OF *J* COUPLING

In the Hamiltonians used in all the theoretical treatments described, the term $\mathcal{H}_J$ representing the indirect J coupling was ignored. This was because the value of J_{iso} was expected to be so small that it would have little, or no effect, on the CP MAS lineshapes of ^{13}C–^{14}N-containing compounds. The excellent agreements found between the experimental and theoretical lineshapes shows that this was usually an easily justifiable assumption. The inclusion of J coupling leads to the introduction of the term:[20]

$$[-(\Delta J/3)(3\cos^2\beta^J - 1 + \eta\sin^2\beta^J\cos 2\alpha^J)] \quad (13)$$

where β^J and α^J give the orientation of the unique z axis of the $\boldsymbol{J}$ tensor in the PAS of the quadrupole tensor. To illustrate the effect of the J coupling, Figure 4 shows how the normal two-peak powder spectrum becomes a three-peak spectrum for the case of ^{14}N. The theoretical spectra were calculated from the computer program of Naito et al.,[14,16] modified to include the term $\mathcal{H}_J$ in the Hamiltonian. The introduction of the indirect spin–spin coupling results in a splitting of the $m_{^{14}N} = -1$ and +1 levels, while the $m_{^{14}N} = 0$ peak is unaffected. In the calculations, the ^{14}N electric field gradient tensor was assumed to be axially symmetric with the largest principal component parallel to the ^{13}C–^{14}N dipolar vector. A similar procedure was employed by Eichele and Wasylishen,[21] though they used a different computer program based on the perturbation method to interpret and simulate the spectrum demonstrating the first observation of the indirect spin–spin coupling $^1J(^{14}N,^{13}C)$ effect which they discovered in the ^{13}C CP MAS NMR spectrum of [(*n*-$C_3H_7)_4N$][$Cd(SCN)_3$]. Because of the excellent agreement found between the simulated and the experimental spectra they estimated the value of $^1J(^{14}N,^{13}C)$ = 11 ± 3 Hz.

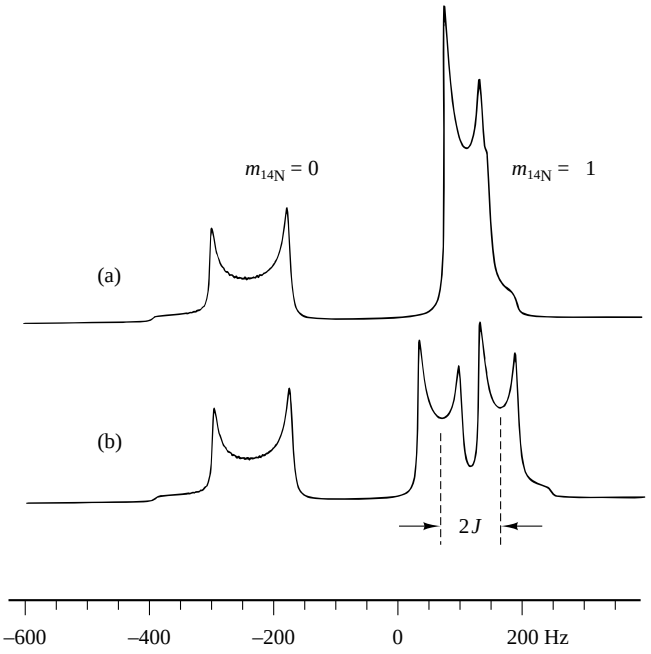

Figure 4 Diagrammatic representation of the effect of including the term $\mathcal{H}_J$ in the Hamiltonian before calculating the lineshape

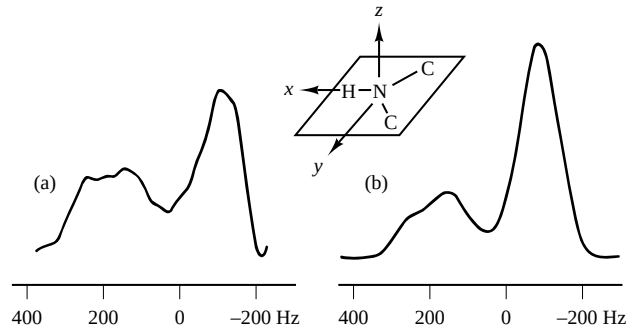

Figure 5 Lineshape of the CP MAS spectrum of a proton bonded to the peptide nitrogen nucleus in *N*-acetylglycine. (a) Experimental spectrum obtained by using CRAMPS with the MREV-8 pulse sequence. (b) Computer-simulated spectrum obtained using a quadrupolar asymmetry parameter $\eta = 0.32$ and $e^2Qq_{zz}/h = -3.21$ MHz. (Reproduced by permission of the American Chemical Society from Naito et al.[23])

6 OTHER SPIN-$\frac{1}{2}$ NUCLEI BONDED TO ^{14}N: ^{1}H CRAMPS

Protons are ubiquitous in nature and bond to many different types of nuclei. Of these the bonding to ^{14}N is important because N–H bonds are fundamental in the molecular composition of amino acids, polypeptides, and proteins. Unfortunately, the ^{1}H CP MAS spectra of such compounds were generally found to be lacking in structure because of the dipolar broadening caused by homonuclear interactions and magnetic shielding anisotropies. The introduction of the technique of combining sample rotation and multiple pulse NMR spectroscopy, the so-called CRAMPS procedure pioneered by Gerstein et al.,[22] was a major innovative addition to the CP MAS methodology which considerably enlarged its range of applications, making it possible to obtain high-resolution proton spectra of hydrogen-containing solids many of which are of great industrial importance. When applied to solid amino acids the CRAMPS technique yielded proton CP MAS spectra in which there were identified[23] asymmetric peaks clearly arising from the ^{1}H–^{14}N dipolar interaction and the ^{14}N quadrupole interaction not being averaged out, as earlier described for the analogous ^{13}C–^{14}N case. The resolution of the characteristic asymmetric lineshapes varied with the type of multiple pulse sequence used. This was presumably because a faster spinning frequency was required to reduce the N–H dipolar interactions. In all cases, characteristic asymmetric doublets were observed for the ^{1}H–^{14}N bonds, with the exception of the N-2 and N-3 nuclei in the imidazole ring of L-histidine hydrochloride monohydrate. Those two bonds exhibited broad asymmetric peaks, possibly being the result of strong hydrogen bonding.

The asymmetric peaks in the CRAMPS MAS spectra of amino acids were simulated by Naito et al.[23] using the computer programs based on the theoretical treatments described earlier.[14,16] In addition, it was necessary to multiply the quadrupole and Zeeman terms in the Hamiltonian by the scaling factors $S_m S_r$. The term S_m is the scaling factor for the multiple pulse scheme used, and $S_r = \frac{1}{2}(3\cos^2\theta - 1)$ is the scaling factor caused by a group rotation where θ is the angle between the rotation axis and the N–H direction. The lineshapes were simulated successfully. That of the peptide proton was well simulated (see Figure 5) using the ^{14}N coupling constant of -3.2 MHz and $\eta = 0.31$, the parameters having been determined in a single crystal ^{14}N NMR study on *N*-acetylvaline though the sign of the quadrupole coupling constant had been established previously from a comparison of the experimental and computer-simulated peptide carbon nuclei.[16] In addition, it was necessary to interchange the assigned axes of the electric field gradient tensor so that the *x* axis was parallel to the N–H bond direction. The spectral peaks for the proton bonded to the imidazole nitrogen N nuclei were simulated using the ^{14}N coupling constants earlier determined from ^{14}N NMR single crystal studies. The simulated spectra showed that broad lines were to be expected and that a clear asymmetric doublet was not to be anticipated in this case. It was also to be expected that the proton bonded to the N-2 nucleus should have a broader lineshape than that for the N-3 nucleus. These predicted lineshapes were in good agreement with those observed experimentally.

The interesting ^{14}N-containing spin-pairs ^{14}N≡^{15}N^{+}–and ^{15}N≡^{14}N^{+}–yield unusual lineshapes.[24] It should also be mentioned that the ^{13}C MAS lineshapes of the parent compounds 5-methyl-2-[α-^{15}N]diazobenzenesulfonic acid and its isotopomer with [β-^{15}N] exhibit characteristic novel lineshapes. It was, however, possible to obtain approximate lineshape simulations for the ^{13}C–^{14}N residual dipolar couplings even though the resulting ragged appearances of the simulations were clearly caused by the use of insufficient increments of the orientations of the angles β^Q and γ^Q in the calculations. Convolution of the two simulated spectra yielded a lineshape which was a good reproduction of the spectrum resulting from convoluting the observed ^{13}C MAS spectra of the two isotopomers. An apparent triplet lineshape was observed for the carbon nucleus bonded to the α- and β-^{14}N nuclei of the diazo group, which arises from two different residual ^{13}C–^{14}N dipolar couplings acting on the same carbon nucleus. It proved possible to simulate that feature.

Mention should be made of related studies of the lineshapes found for off-magic angle, or variable-angle, ^{13}C NMR spectra of compounds which exhibit $^{13}C-^{14}N$ dipolar–quadrupolar interaction effects.[25] Though to some extent peripheral to the main thrust of this article, the phenomena described in those studies are of considerable interest.

7 RELATED ARTICLES

Average Hamiltonian Theory; CRAMPS; Cross Polarization in Solids; Magic Angle Spinning; Quadrupolar Interactions; Quadrupolar Nuclei in Solids; Rotating Solids.

8 REFERENCES

1. S. R. Hartmann and E. L. Hahn, *Phys. Rev.*, 1962, **128**, 2042.
2. A. Pines, M. G. Gibby, and J. S. Waugh, *J. Chem. Phys.*, 1973, **59**, 569.
3. E. R. Andrew, A. Bradbury, and R. G. Eades, *Nature*, **182**, 1639; I. J. Lowe, *Phys. Rev. Lett.*, 1959, **2**, 285.
4. J. Schaefer, E. O. Stejskal, and R. Buchdahl, *Macromolecules*, 1975, **8**, 291.
5. R. G. Griffin, A. Pines, and J. S. Waugh, *J. Chem. Phys.*, 1975, **63**, 3676.
6. M. E. Stoll, R. W. Vaughan, R. B. Saillant, and T. Cole, *J. Chem. Phys.*, 1974, **61**, 2896.
7. A. Naito, S. Ganapathy, K. Akasaka, and C. A. McDowell, *J. Chem. Phys.*, 1981, **74**, 3190.
8. R. A. Haberkorn, R. E. Stark, H. van Willigen, and R. G. Griffin, *J. Am. Chem. Soc.*, 1981, **103**, 2534.
9. D. L. VanderHart, H. S. Gutowsky, and T. C. Farrar, *J. Am. Chem. Soc.*, 1967, **89**, 5056.
10. E. Lippmaa, M. Alla, H. Raude, R. Teeäär, I. Heinmaa, and E. Kundla, *Proc. 20th Congr. AMPERE, Tallin*, eds. E. Kundle, E. Lipmaa, and T. Saluvere, Springer-Verlag, Berlin, 1987, p. 87.
11. E. Kundla and M. Alla, *Proc. 20th Congr. AMPERE, Tallin*, eds. E. Kundle, E. Lipmaa, and T. Saluvere, Springer-Verlag, Berlin, 1987, p. 92.
12. C. J. Groombridge, R. K. Harris, K. J. Packer, B. J. Say, and S. F. Tanner, *J. Chem. Soc., Chem. Commun.*, 1980, 174.
13. M. H. Frey and S. J. Opella, *J. Chem. Soc., Chem. Commun.*, 1980, 474.
14. A. Naito, S. Ganapathy, and C. A. McDowell, *J. Chem. Phys.*, 1981, **74**, 5393.
15. N. Zumbulyadis, P. M. Hendricks, and R. L. Young, *J. Chem. Phys.*, 1981, **75**, 1603.
16. A. Naito, S. Ganapathy, and C. A. McDowell, *J. Magn. Reson.*, 1982, **48**, 367.
17. J. G. Hexem, M. H. Frey, and S. J. Opella, *J. Chem. Phys.*, 1982, **77**, 3847.
18. Z. Gan and D. M. Grant, *J. Magn. Reson.*, 1990, **90**, 522.
19. A. C. Olivieri, L. Frydman, and L. E. Diaz, *J. Magn. Reson.*, 1987, **75**, 50.
20. A. C. Olivieri, *J. Magn. Reson.*, 1988, **81**, 201.
21. K. Eichele and R. E. Wasylishen, *Solid State NMR*, 1992, **1**, 159.
22. B. C. Gerstein, R. G. Pembleton, R. C. Wilson, and L. M. Ryan, *J. Chem. Phys.*, 1977, **66**, 361.
23. A. Naito, A. Root, and C. A. McDowell, *J. Phys. Chem.*, 1991, **95**, 3578.
24. R. K. Harris, P. Jonsen, and K. J. Packer, *Magn. Reson. Chem.*, 1985, **23**, 565.
25. N. K. Sethi, D. W. Alderman, and D. M. Grant, *Mol. Phys.*, 1990, **71**, 217.

Biographical Sketch

Charles A. McDowell. *b* 1918. B.Sc., 1941, M.Sc., 1942, D.Sc., 1955, Queen's University of Belfast, UK; D.Sc., 1984, honoris causa, University of British Columbia, Canada. National service, UK, 1941–45; lecturer, University of Liverpool, UK, 1945–55; Professor and Head, Department of Chemistry, University of Liverpool, 1955–81; University Professor, 1981–84. Currently University Professor Emeritus, Department of Chemistry, University of British Columbia, Canada. Approx. 360 publications. Current research specialties; mainly in solid state NMR.

Magic Angle Spinning: Effects of Quadrupolar Nuclei on Spin-1/2 Spectra

Robin K. Harris
University of Durham, UK

1	Introduction	1
2	Theoretical Background	1
3	Consequences of Perturbation Theory	2
4	Results and Discussion	3
5	Departure from Perturbation Theory	4
6	Quadrupolar Coupling Dominant	5
7	Related Articles	6
8	References	6

1 INTRODUCTION

As explained in detail in ***Magic Angle Spinning Carbon-13 Lineshapes: Effect of Nitrogen-14***, magic angle spinning does not always eliminate from spin-$\frac{1}{2}$ spectra the influence of dipolar coupling to quadrupolar nuclei. In particular, when quadrupolar energies are not negligible compared with Zeeman energies, spin-$\frac{1}{2}$ spectra may show splittings and/or lineshapes which arise from residual dipolar coupling to quadrupolar nuclei. This phenomenon was first discovered and thoroughly investigated for the (^{13}C, ^{14}N) nuclear pair, but it soon became apparent that the effect was more widespread, indeed ubiquitous. The present article will discuss a wide range of examples and will place particular emphasis on the perturbation approach, which is adequate to explain many cases. The discussion will be limited to the centers of gravity of what are, strictly speaking, powder bandshapes. The reader is referred to ***Magic Angle Spinning Carbon-13 Lineshapes: Effect of Nitrogen-14*** for details of more exact theory, for questions of powder bandshapes, and for all examples involving ^{14}N. The whole subject has received attention in a review article[1] which summarizes the theoretical approaches and also lists cases for many different nuclear spin pairs.

2 THEORETICAL BACKGROUND

Consider a pair of nuclei I and S, where the former has the spin quantum number $\frac{1}{2}$ and the latter is quadrupolar. For simplicity in this discussion, it will be assumed that the electric field gradient at S is axially symmetric, but the reader must be careful not to infer that the results below apply to the general case of $\mu \neq 0$. The phenomenon mentioned above can be traced to the influence of terms in the quadrupolar Hamiltonian involving nuclear spin operators other than $\hat{S}_z$. When Zeeman terms dominate, the energy levels of quadrupolar nuclei are properly characterised by the spin component quantum number m_S, associated with $\hat{S}_z$. Since the relevant Hamiltonian terms have angular dependences $\frac{1}{2}(3\cos^2\theta_Q - 1)$, where θ_Q is the angle between the major principal axis of the quadrupolar tensor and the applied magnetic field ($\boldsymbol{B}_0$), their effects are averaged to zero by magic angle spinning at a fast enough rate. Moreover, in such circumstances, the only terms in the dipolar Hamiltonian connecting the quadrupolar nucleus with the spin-$\frac{1}{2}$ nucleus which are secular involve similar angular dependence $\frac{1}{2}(3\cos^2\theta_D - 1)$ where θ_D is the angle between $\boldsymbol{B}_0$ and the internuclear distance between the spin $\frac{1}{2}$ and the quadrupolar nuclei. Thus, magic angle spinning at a sufficiently high rate is enough to eliminate these dipolar interactions. Therefore, resonance frequencies in spin-$\frac{1}{2}$ MAS spectra are unaffected by dipolar interactions to quadrupolar nuclei in such circumstances. Similar considerations apply to anisotropy and asymmetry in the indirect ('scalar') coupling between a spin-$\frac{1}{2}$ nucleus and a quadrupolar nucleus: MAS suffices to remove the influence of such coupling components on the frequencies in the spin-$\frac{1}{2}$ spectrum, though the isotropic part of the coupling is retained.

However, when quadrupolar and Zeeman terms in the Hamiltonian become comparable, the situation is drastically changed. The detailed theoretical treatment using the full Hamiltonian is discussed in ***Magic Angle Spinning Carbon-13 Lineshapes: Effect of Nitrogen-14***. Here, the perturbation treatment, which is frequently applicable, will be presented. The use of perturbation theory was pioneered by Olivieri and co-workers[2] for the (^{13}C, ^{14}N) case (though it was implicit in earlier treatments), and rapidly extended[3] to situations involving higher-spin quadrupolar nuclei.

The spin-$\frac{3}{2}$ case is chosen here for illustration purposes. Consider the so-called 'alphabet expansion' of the dipolar and axially-symmetric quadrupolar interactions (Table 1). In the high-field approximation the Zeeman levels may be designated as $|m_S\rangle$, where $m_S = \frac{3}{2}, \frac{1}{2}, -\frac{1}{2}$ or $-\frac{3}{2}$. Under the influence of terms C, D, E, and F of the 'quadrupolar alphabet', these wavefunctions are mixed to become

$$|(-\tfrac{3}{2})'\rangle = \quad |-\tfrac{3}{2}\rangle + a_1^*|-\tfrac{1}{2}\rangle - a_2^*|\tfrac{1}{2}\rangle \tag{1a}$$

$$|(-\tfrac{1}{2})'\rangle = -a_1|-\tfrac{3}{2}\rangle + \quad |-\tfrac{1}{2}\rangle + a_3^*|\tfrac{1}{2}\rangle - a_2^*|\tfrac{3}{2}\rangle \tag{1b}$$

$$|(\tfrac{1}{2})'\rangle \quad = \quad a_2|-\tfrac{3}{2}\rangle - a_3|-\tfrac{1}{2}\rangle + \quad |\tfrac{1}{2}\rangle - a_1^*|\tfrac{3}{2}\rangle \tag{1c}$$

$$|(\tfrac{3}{2})'\rangle \quad = \quad +a_2|-\tfrac{1}{2}\rangle + a_1|\tfrac{1}{2}\rangle + \quad |\tfrac{3}{2}\rangle \tag{1d}$$

where, in the perturbation approach, $a_1 = \langle\frac{1}{2}|\hat{\mathcal{H}}_Q|\frac{3}{2}\rangle/\gamma_s\hbar B_0$, $a_2 = \langle-\frac{1}{2}|\hat{\mathcal{H}}_Q|-\frac{3}{2}\rangle/2\gamma_s\hbar B_0$ and $a_3 = \langle-\frac{1}{2}|\hat{\mathcal{H}}_Q|\frac{1}{2}\rangle/\gamma_s\hbar B_0$, etc.

The alphabet terms C and D are relevant for a_1 and a_3 whereas terms E and F are effective for a_2. However, it can be shown that $a_3 = 0$ and that a_2 cannot affect the I spectrum. Now, because of the mixed nature of the Zeeman levels, terms C and D of the (I, S) 'dipolar alphabet' become secular, the additional energy contributions being

$$\langle(-\tfrac{3}{2})'m_I|\hat{\mathcal{H}}_D|(-\tfrac{3}{2})'m_I\rangle = \langle(\tfrac{3}{2})'m_I|\hat{\mathcal{H}}_D|(\tfrac{3}{2})'m_I\rangle \propto -a_1 D m_I \tag{2a}$$

$$\langle(-\tfrac{1}{2})'m_I|\hat{\mathcal{H}}_D|(-\tfrac{1}{2})'m_I\rangle = \langle(\tfrac{1}{2})'m_I|\hat{\mathcal{H}}_D|(\tfrac{1}{2})'m_I\rangle \propto +a_1 D m_I \tag{2b}$$

Table 1 The NMR Internal Hamiltonian: The Alphabet Expansion

Term	Geometric factor[c]	Spin factors[a] Dipolar	Quadrupolar[b]	Connectivity
A	$1 - 3\cos^2\theta$	$I_z S_z$	$(I_z)^2$	Secular
B	$-\frac{1}{4}(1 - 3\cos^2\theta)$	$I_+S_- + I_-S_+$	$I_+I_- + I_-I_+$	Flip-flop[a]
C	$-\frac{1}{2}\sin\theta\cos\theta\exp(-i\phi)$	$I_zS_+ + I_+S_z$	$I_zI_+ + I_+I_z$	Single quantum
D	$-\frac{1}{2}\sin\theta\cos\theta\exp(i\phi)$	$I_zS_- + I_-S_z$	$I_zI_- + I_-I_z$	Single quantum
E	$-\frac{1}{4}\sin^2\theta\exp(-2i\phi)$	I_+S_+	$(I_+)^2$	Double quantum
F	$-\frac{1}{4}\sin^2\theta\exp(2i\phi)$	I_-S_-	$(I_-)^2$	Double quantum

[a] Secular for the quadrupolar and homonuclear dipolar interactions, but nonsecular for heteronuclear dipolar interactions.
[b] For the axially symmetric case ($\eta = 0$).
[c] There are also constant numerical factors (hD for the dipolar case and $h\chi/2S(2S-1)$ for the quadrupolar case).

where D is the dipolar coupling constant, $\gamma_I\gamma_S(\mu_0/4\pi)(\hbar/2\pi){r_{IS}}^{-3}$ (to be distinguished from the alphabet term D!). Therefore the energy levels are modified as shown in Figure 1, and the outer lines of the I multiplet will be shifted in one direction, while the inner lines will shift to the same extent but in the opposite direction. Of course the terms in the Hamiltonian also involve geometric factors which depend on the Euler angles connecting the dipolar and quadrupolar tensors with the magnetic field $\boldsymbol{B}_0$. Since these are *not* of the form $(3\cos^2\theta - 1)$, they are not eliminated by MAS although they are reduced. Thus each of the multiplet components in the I spectrum will be powder patterns under MAS. However, the structure of these powder patterns is not usually observed, and consequently the useful information normally comes from consideration of the centers of gravity of the bands. Of course the indirect coupling tensor $\boldsymbol{J}$ has some common features with $\boldsymbol{D}$, and therefore it will in principle also need to be considered.

Full evaluation for the general case results[1] in the following perturbation expression for the shift induced in the center of gravity of the spin-$\frac{1}{2}$ transition frequency associated with quadrupolar basis state m_S

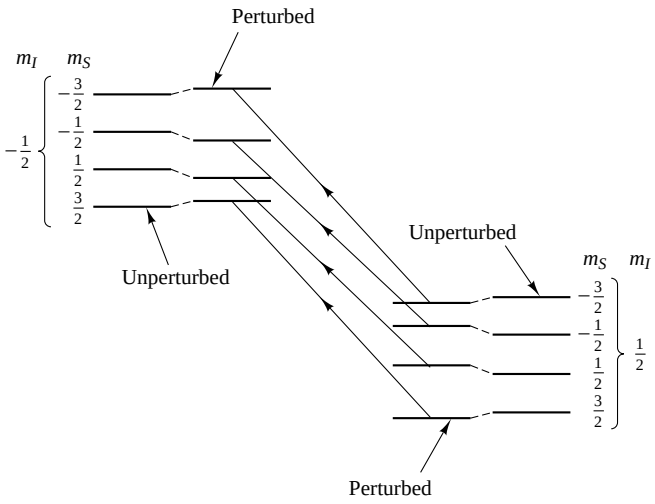

Figure 1 Energy-level diagram for an IS nuclear spin pair with $I = \frac{1}{2}$, $S = \frac{3}{2}$ to show the perturbations induced by quadrupolar and dipolar interactions. The extent of the perturbations is greatly exaggerated. It is assumed that γ_I, γ_S, and J_{iso} are all positive

$$ {}^2\Delta\nu(m_S) = \frac{3\chi}{20\nu_S}\left[\frac{S(S+1) - 3m_S^2}{S(2S-1)}\right] \times \left[Df(\alpha^D, \beta^D, \eta) - \frac{\Delta J}{3} f(\alpha^J, \beta^J, \eta)\right] \quad (3) $$

where $f(\alpha, \beta, \eta) = 3\cos^2\beta - 1 + \eta\sin^2\beta\cos 2\alpha$, α and β are the relevant Euler angles (see Harris and Olivieri[1]), η is the asymmetry in the electric field gradient, χ is the quadrupole coupling constant, ν_S is the Larmor frequency of the quadrupolar nucleus and ΔJ is the anisotropy in $\boldsymbol{J}$. The above equation assumes that $\boldsymbol{J}$ is an axially symmetric tensor. Simplifications result if there are further assumptions. In particular, if $\boldsymbol{J}$ and $\boldsymbol{D}$ are co-axial, and if η is ignored, the complete equation for the spin-$\frac{1}{2}$ transition frequency is

$$ \nu(m_S) = \nu_I - m_S J_{\text{iso}} + \frac{3D'\chi}{20\nu_S}\left[\frac{S(S+1) - 3m_S^2}{S(2S-1)}\right] \quad (4) $$

where ν_I is the Larmor frequency of the spin-$\frac{1}{2}$ nucleus, J_{iso} is the isotropic part of $\boldsymbol{J}$, and D' is an effective dipolar coupling constant, incorporating the anisotropy in J

$$ D' = D - \frac{\Delta J}{3} \quad (5) $$

The second-order shift itself, $\nu(m_S) - \nu_I + m_S J_{\text{iso}}$, depends only on the square of m_S, and for $m_S = \pm S$ it is independent of S. It is therefore convenient to normalize effects to the shift of the 'outermost' lines, defined as

$$ \Delta = -\frac{3}{10}\frac{\chi D'}{\nu_S} \quad (6) $$

This enables the second-order shifts of all lines to be written as

$$ {}^2\Delta\nu(m_S) = -\left[\frac{S(S+1) - 3m_S^2}{S(2S-1)}\right]\Delta \quad (7) $$

Table 2 lists the shifts of all lines, for various half-integral values of S, in terms of Δ.

Table 2 Second-Order Shifts in the Spectra of Spin-$\frac{1}{2}$ Nuclei Arising from Coupling to a Half-Integral Quadrupolar Nucleus S[a]

	m_S				
S	$\pm\frac{1}{2}$	$\pm\frac{3}{2}$	$\pm\frac{5}{2}$	$\pm\frac{7}{2}$	$\pm\frac{9}{2}$
$\frac{3}{2}$	-1	1			
$\frac{5}{2}$	$-\frac{4}{5}$	$-\frac{1}{5}$	1		
$\frac{7}{2}$	$-\frac{5}{7}$	$-\frac{3}{7}$	$\frac{1}{7}$	1	
$\frac{9}{2}$	$-\frac{2}{3}$	$-\frac{1}{2}$	$-\frac{1}{6}$	$\frac{1}{3}$	1

[a]Note: The values are normalized to the shift of the outermost lines as expressed in equation (6).

3 CONSEQUENCES OF PERTURBATION THEORY

A number of significant features can be understood from equations (3)–(7).

1. While perturbation theory holds, second-order shifts are inversely proportional to $\boldsymbol{B}_0$, so that no new information is obtained by using several spectrometers. However, such experiments can be used to check that the origin of splittings in the spectra does indeed involve second-order effects, since the behavior with $\boldsymbol{B}_0$ differs from that of splittings caused by either J_{iso} or differences in chemical shifts.
2. Since second-order shifts depend on m_S^2, their values occur in pairs, with the outermost multiplet lines moving most. Figure 2 illustrates the situation as a function of $\chi D/\nu_S$ when $\Delta J = 0$.
3. The average second-order shift is zero, so the isotropic chemical shift is simply obtained by averaging the frequencies of all the lines.
4. The isotropic coupling constant, $|J_{\text{iso}}|$, is also readily obtained as the average spacing between lines, though care must be taken if there is any crossover of frequencies. The value of $|J_{\text{iso}}|$ is also available from the central spacing $|\nu(m_S = \frac{1}{2}) - \nu(m_S = -\frac{1}{2})|$.
5. Since the innermost lines shift in the opposite direction to the effect on the outermost lines, there is a 'bunching' of lines at one end of the spectrum. The extent of coalescence is more apparent for lower values of S for a given $\chi D/\nu_S$. The sense depends on the sign of Δ, and in favorable cases it gives important information on relative signs.
6. In particular, if $\boldsymbol{J}$ and $\boldsymbol{D}$ are co-axial the following general rule results: 'bunching' occurs to low frequency (i.e. Δ is positive) if *either* χ is negative (with D and D' of the same sign) *or* χ is positive (with D and D' of opposite signs). An analogous statement can be made if Δ is negative. This rule takes into account the effects of signs of magnetogyric ratios. Thus, if the magnitude and sign of χ is known, together with r_{IS}, and if η is ignored, then ΔJ can be derived unambiguously. However, if only r_{IS} and $|\chi|$ are available, two possible values of ΔJ can be calculated but they cannot be distinguished.
7. When perturbation theory holds, neither the magnitude nor the sign of J_{iso} influences Δ.
8. If the value of $|J_{\text{iso}}|$ is negligible compared to linewidths, then there will be $S + \frac{1}{2}$ lines. The relative frequencies at which 'bunching' takes place will give the sign of χ. The magnitude of Δ will enable r_{IS} to be determined if $|\chi|$ is known, and vice versa. However, $S = \frac{3}{2}$ is a special case, since a 1:1 doublet will be seen [Figure 3(a)], of spacing $\frac{3}{10}(\chi D/\nu_S)(3\cos^2\beta^D - 1 + \eta\sin^2\beta^D\cos 2\alpha^D)$ in the general case, and information on the sign of χ is lost.
9. Since the denominator in equation (7) reflects the fact that the validity of the perturbation approach depends on $\chi/2S(2S-1)\nu_S$, higher spins are more accurately treated than lower spins for equivalent values of χ.

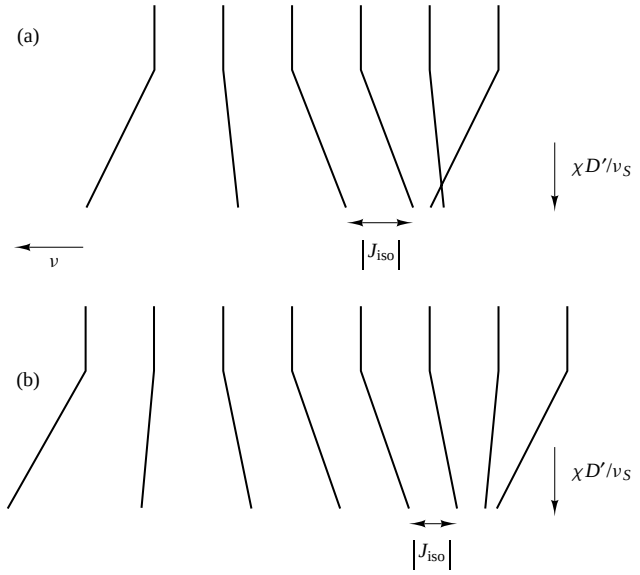

Figure 2 Second-order shifts in spin-$\frac{1}{2}$ MAS spectra arising from coupling to a quadrupolar nucleus S, as a function of the parameter $\chi D'/\nu_S$ under a perturbation approach according to equation (7): (a) $S = \frac{5}{2}$; (b) $S = \frac{7}{2}$. A positive value of Δ is assumed

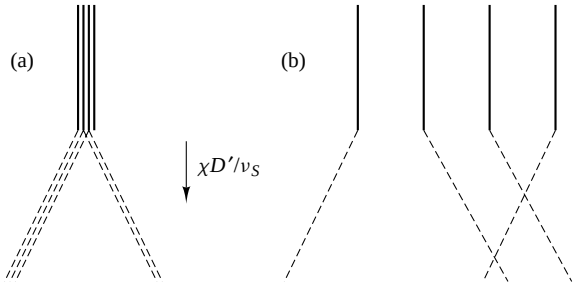

Figure 3 Second-order shifts in spin-$\frac{1}{2}$ MAS spectra arising from coupling to a quadrupolar nucleus $S = \frac{3}{2}$ as a function of the parameter $\chi D'/\nu_S$ under a perturbation approach according to equation (7): (a) $J_{\text{iso}} = 0$; (b) $-J_{\text{iso}}- > 0$. A positive value of Δ is assumed

4 RESULTS AND DISCUSSION

Many examples are now known where perturbation theory is reasonably applicable. In particular, the (^{119}Sn, $^{35/37}$Cl) situation is appropriate[3,4] since in such cases $|\chi|$ is generally modest (~35 MHz). Thus even for a 4.7 T spectrometer, the perturbation parameter $\chi/2S(2S-1)\nu_S$ is only in the region of 0.30. The splitting arising from $|J_{\text{iso}}|$ cannot be ignored. However, since chlorine is monovalent, coaxiality of $\boldsymbol{J}$ and $\boldsymbol{D}$ is a reasonable approximation for directly-bonded Sn–Cl groups except when chlorine is in a bridging situation. In fact,

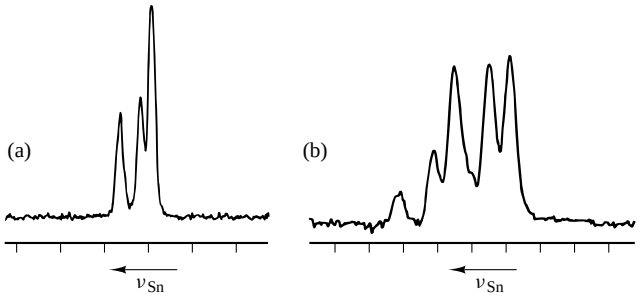

Figure 4 Tin-119 CP MAS NMR spectra at 74.63 MHz for (a) $(PhCH_2)_3SnCl$ and (b) Et_2SnCl_2, showing the second-order effects of coupling to the chlorine nuclei.[4] The markers are at 1 kHz and 0.5 kHz intervals for (a) and (b), respectively

a typical spectral pattern is a 1:1:2 triplet with relative spacings 2:1 [Figure 4(a)], which is strictly the case only when $|J_{iso}| = 2\Delta$. Values of $|J(\text{Sn,Cl})|$ have therefore been derived, as have approximate data for ΔJ. When more than one chlorine is coupled to the same Sn, simple convolution suffices to predict the spectral appearance. If the chlorines are equivalent, then $|J_{iso}| = 2\Delta$ leads to a 1:2:4:1:4:4 multiplet (with the first spacing twice the others), such as has been observed [Figure 4(b)] for Et_2SnCl_2.[4]

Cases involving ^{31}P coupled to metal nuclei are also common, and have been shown[5,6] to occur for a range of S-spin metals, e.g. $^{63/65}$Cu ($S = \frac{3}{2}$), ^{55}Mn ($S = \frac{5}{2}$), ^{59}Co ($S = \frac{7}{2}$), and ^{93}Nb ($S = \frac{9}{2}$). Figure 5 shows an example where the second-order effects are relatively small. In a number of such cases perturbation theory is not appropriate, and in others questions of nonaxiality reduce the usefulness of the observed second-order effects. However, the case of $Mn_2(CO)_9PPh_3$ proved[6] to be appropriate, since the molecular symmetry has axiality and spinning sideband analysis indicates that this is retained in the solid state. Such an analysis also gives a value for $|D'|$, so that $|\chi|$ can be derived (42 MHz). The value of $\chi/2S(2S-1)\nu_S$ for a spectrometer operating at 7.1 T is thus 0.028, which confirms that perturbation theory is applicable. Several (^{31}P, $^{63/65}$Cu) examples have been analyzed[7] using perturbation theory to yield data for $\Delta J \sim 0.6$ kHz.

Numerous other examples of residual dipolar coupling have been reported, some of which come into the category of a perturbation treatment. In particular, examples of (^{13}C, ^{2}H) have been given.[1,8,9] Although ^{2}H has a low value of χ, the residual effects of dipolar coupling are appreciable because r_{CH} is small and hence D is relatively large. With rigid molecules,[1,8] there is a nice contrast to the (^{13}C, ^{14}N) case since, although 2:1 doublets are observed in both instances, the origins differ. For the (^{13}C, ^{14}N) pair J_{iso} can usually be ignored, so there is overlap for the lines connected to states $|+1\rangle$ and $|-1\rangle$ for ^{14}N, whereas for (^{13}C, ^{2}H), the overlap is of transitions involving $|0\rangle$ and $|-1\rangle$ for ^{2}H. The latter situation arises coincidentally because $|J_{iso}(^{13}\text{C}, ^{2}\text{H})|$ is approximately equal to $\frac{9}{10}D\chi/\nu_S$. The spectra have a different appearance[9] for inclusion compounds of urea and thiourea with deuterated guest molecules, such as straight-chain alkanes and corresponding carboxylic acids. The guest molecules are relatively mobile, so that values of $\chi(^{2}\text{H})$ are substantially reduced (to ca. 50–70 kHz for CD_2 groups) by averaging. Second-order effects on the ^{13}C spectra are therefore relatively modest, simply resulting in a small asymmetry in the splittings

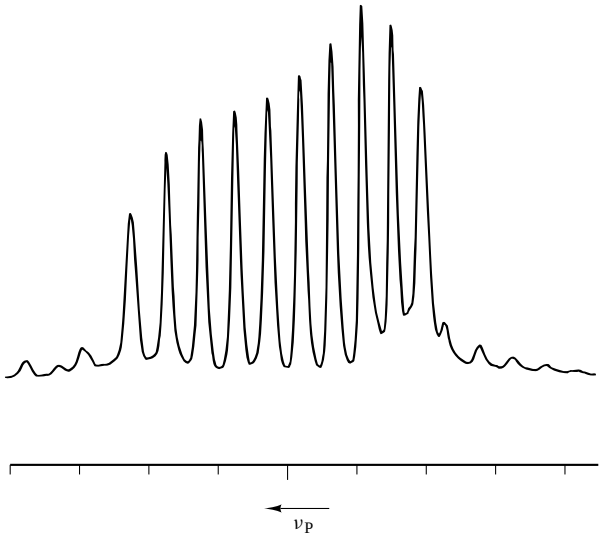

Figure 5 Phosphorus-31 CP MAS NMR spectra at 81.0 MHz for $(C_5H_5)(Me_3P)Cl_2Nb{=}N(o\text{-}tBuC_6H_4)$, showing the second-order effects of coupling to the niobium nucleus: the multiplet spacing decreases slightly from high to low frequency. The lines outside the main decet are spinning sidebands. The markers are at 1 kHz intervals

of the 1:2:3:2:1 quintet patterns. The spectra can be used to determine, at least qualitatively, the relative values of χ at different positions in a chain, which in turn depend on variations in local molecular mobility.

Of course, the appearance of splittings arising from either dipolar coupling, whether residual or full, or indirect coupling is contingent upon the lifetimes of the quadrupolar spin states being long compared with the frequency separations in the spin-$\frac{1}{2}$ spectra. If spin–lattice relaxation times of the quadrupolar nuclei become sufficiently short, the result is 'self-decoupling' (such as is frequently observed in solution state situations). In such cases a single line will be seen in the spin-$\frac{1}{2}$ spectrum. This is the situation[10] for the ^{31}P spectrum of PCl_5 where sharp singlets are observed for the PCl_4^+ and PCl_6^- ions at room temperature but multiplets at low temperature. Of course, molecular motion (e.g. rotation of ions, as for PCl_5) may affect residual dipolar splittings both directly (by averaging $\boldsymbol{D}$) and indirectly (by relaxing the S nucleus). 'Self-decoupling' can in principle also occur because of chemical exchange involving I–S bond breaking.

5 DEPARTURE FROM PERTURBATION THEORY

The first clear case of effects of dipolar coupling residual which did not involve the (^{13}C, ^{14}N) nuclear pair concerned the (^{31}P, ^{63}Cu) nuclei in bis(triphenylphosphine)copper(I) and related complexes, presented by Menger and Veeman.[5] These authors published detailed theory, but the situation was beyond the validity of perturbation theory. Many examples involving the (^{31}P, ^{63}Cu) pair have since come to light, though some are susceptible to the perturbation approach.

The (^{13}C, $^{35/37}$Cl) case is interesting.[11,12] Although there are simplifying features, since chlorine is univalent (and hence coaxiality of $\boldsymbol{J}$ and $\boldsymbol{D}$ can be assumed) and J(C, Cl) is negligibly small, the value of $|\chi|$ is sufficiently large (ca.

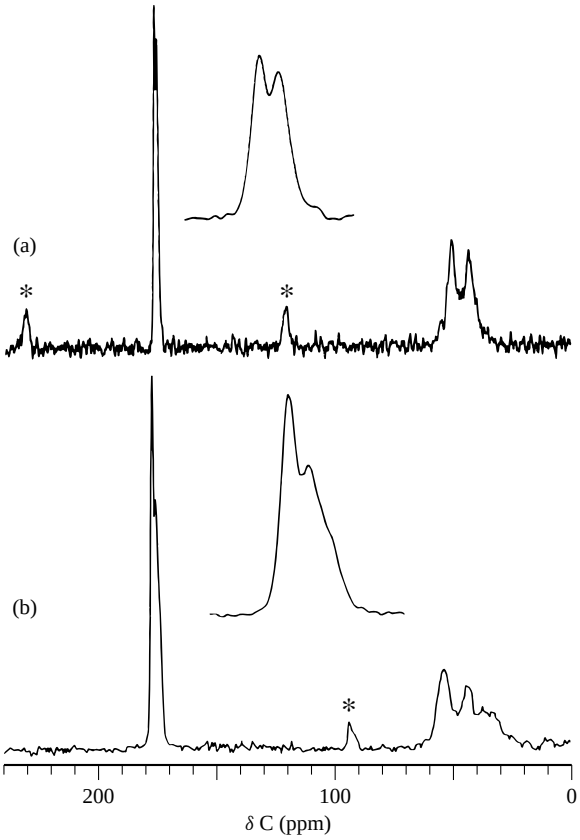

Figure 6 Carbon-13 CP MAS NMR spectra of sodium monochloroacetate: (a) 75.4 MHz; (b) 50.3 MHz, showing the second-order effects of coupling to chlorine.[12] The insets show expansions of the carboxyl region. The asterisks denote spinning sidebands

−70 MHz) that departures from perturbation theory can be observed. At modest magnetic fields (7.1 T and above), the 1:1 doublet predicted by perturbation theory is indeed observed [Figure 6(a)], but the splitting is smaller than predicted and is not inversely proportional to $\boldsymbol{B}_0$. However, it has been shown[13] by simulation using exact theory that for the case $S = \frac{3}{2}$ the doublet splitting, s, can be adequately represented in the range $0.8 < R = |\chi/\nu_S| < 3.0$ by the cubic polynomial

$$s = D(0.581R + 0.033R^2 - 0.021R^3) \tag{8}$$

A cubic equation for s has also been derived for the $S = \frac{3}{2}$ case in which J_{iso} cannot be ignored.

For the (^{13}C, $^{35/37}$Cl) case, even equation (8) is inadequate at 4.7 T, since a broad 2:1:1 triplet is both predicted and observed[11,12] [Figure 6(b)]. Figure 7 shows the theoretical line positions (centers of gravity) as a function of R for the case $I = \frac{1}{2}$, $S = \frac{3}{2}$ for positive χ and in the absence of $\boldsymbol{J}$. At high values of R, four lines are expected, and this links up with the expectation from inverse perturbation theory discussed below.

Molecular-level motion has a drastic effect on the ^{13}C spectra of sodium chloroacetates.[12] For the monochloro compound a clear doublet is seen for both the CH_2Cl and carbonyl carbons at 7.1 T and above, with the expected 2:1:1 triplet at 4.7 T. However sodium trichloroacetate shows a sharp line for each carbon at 7.1 T, not only at room temperature but also down to 163 K. The reason for this behavior undoubtedly lies in the facile internal rotation of the $C-CCl_3$ group.

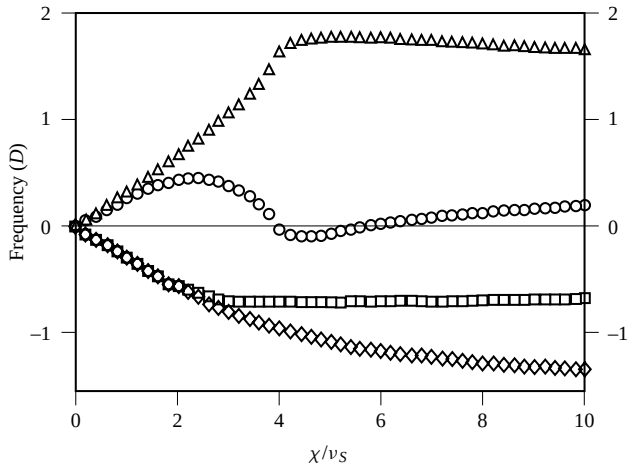

Figure 7 Line positions (centers of gravity, units of D) for a spin-1/2 nucleus coupled to a spin-3/2 nucleus as a function of $R = \chi/\nu_S$ as obtained[13] by the full theory for positive χ and assuming $J_{\text{iso}} = \Delta J = \eta = \beta^D = 0$

When J_{iso} needs to be taken into consideration and perturbation theory is inadequate, it has been shown[13] that the sign of J_{iso} can be obtained from the spectrum (if the sign of χ is known). Thence $J(^{63}\text{Cu}, ^{31}\text{P})$ has been found[13] to be negative.

6 QUADRUPOLAR COUPLING DOMINANT

Olivieri has considered[14,15] the case where the quadrupole coupling constant is very large. The dipolar and indirect couplings will still transfer the quadrupole information to the spin-$\frac{1}{2}$ nucleus under MAS conditions, giving rise to splittings in the spectra. For the case where $\boldsymbol{J}$ is axially symmetric and the three tensors $\boldsymbol{D}$, $\boldsymbol{q}$, and $\boldsymbol{J}$ are all co-axial, Olivieri showed[14] that a quartet results when $S = \frac{3}{2}$. Each component is a powder pattern, with the centers of gravity forming two doublets with splittings, independent of the applied magnetic field, given by

$$s(\pm\tfrac{1}{2}) = |1.709J_{\text{iso}} + D'| \tag{9a}$$

$$s(\pm\tfrac{3}{2}) = \tfrac{3}{2}|2D' - J_{\text{iso}}| \tag{9b}$$

When the Zeeman S term begins to be significant with respect to the quadrupolar interaction, an inverse perturbation approach ('inverse' when compared to the considerations of Section [2] above) may be used.[14] In this case equations (9a) and (9b) need to be modified, and the four centers of gravity are

$$\langle \Delta\nu(\pm\tfrac{1}{2})\rangle = \mp(0.8546J_{\text{iso}} + 0.5D') - 2(J_{\text{iso}} + D')\frac{\nu_S}{\chi} \tag{10a}$$

$$\langle \Delta\nu(\pm\tfrac{3}{2})\rangle = \pm\tfrac{3}{4}(2D' - J_{\text{iso}}) + 2(J_{\text{iso}} + D')\frac{\nu_S}{\chi} \tag{10b}$$

The spectrum is no longer symmetric, and the sense of the asymmetry depends on the relative signs of $J_{\text{iso}} + D'$, ν_S, and χ. Olivieri has also extended calculations[15] of this type to

situations where $\boldsymbol{q}$ is not axially symmetric and for arbitrary relative orientations of $\boldsymbol{q}$ and $\boldsymbol{D}$.

Frequently, large χ implies the likelihood of rapid spin–lattice relaxation and therefore self-decoupling of S from the spin-$\frac{1}{2}$ nucleus in question. However, (^{13}C, $^{79/81}$Br) systems have been shown[16] to approach the inverse perturbation case, and an example of a (^{31}P, ^{201}Hg) spin pair (with $D \ll J_{\mathrm{iso}}$ in magnitude) even nearer the low-field limit has been reported.[15,17]

7 RELATED ARTICLES

Magic Angle Spinning Carbon-13 Lineshapes: Effect of Nitrogen-14; Quadrupolar Interactions; Quadrupolar Nuclei in Solids.

8 REFERENCES

1. R. K. Harris and A. C. Olivieri, *Prog. NMR Spectrosc.*, 1992, **24**, 435.
2. A. C. Olivieri, L. Frydman, and L. E. Diaz, *J. Magn. Reson.*, 1987, **75**, 50; A. C. Olivieri, *J. Magn. Reson.*, 1989, **81**, 201.
3. R. K. Harris, *J. Magn. Reson.*, 1988, **78**, 389; D. C. Apperley, H. Bai, and R. K. Harris, *Mol. Phys.*, 1989, **68**, 1277.
4. R. K. Harris, A. Sebald, D. Furlani, and G. Tagliavini, *Organometallics* 1988, **7**, 388.
5. E. M. Menger and W. S. Veeman, *J. Magn. Reson.*, 1982, **46**, 257.
6. R. Gobetto, R. K. Harris, and D. C. Apperley, *J. Magn. Reson.*, 1992, **96**, 119.
7. A. C. Olivieri, *J. Am. Chem. Soc.*, 1992, **114**, 5758.
8. P. Jonsen, S. F. Tanner, and A. H. Haines, *Chem. Phys. Lett.*, 1989, **164**, 325; S. D. Swanson, S. Ganapathy, and R. G. Bryant, *J. Magn. Reson.*, 1987, **73**, 239.
9. A. E. Aliev, K. D. M. Harris, D. C. Apperley, R. K. Harris, and M. M. Sünnetçioglu, *J., Chem. Soc., Faraday Trans. 1*, 1993, **89**, 3791.
10. R. K. Harris and A. Root, *Mol. Phys.*, 1989, **66**, 993.
11. R. M. Cravero, M. González-Sierra, C. Fernández, and A. C. Olivieri, *J. Chem. Soc., Chem. Commun.*, 1993, 1253; R. K. Harris, M. M. Sünnetçioglu, K. S. Cameron, and F. G. Riddell, *Magn. Reson. Chem.*, 1993, **31**, 963.
12. S. H. Alarcón, A. C. Olivieri, S. A. Carss, and R. K. Harris, *J. Magn. Reson.*, 1995, in press..
13. S. H. Alarcón, A. C. Olivieri, and R. K. Harris, *Solid State NMR*, 1993, **2**, 325.
14. A. C. Olivieri, *J. Magn. Reson. Ser. A*, 1993, **101**, 313.
15. A. C. Olivieri, *Solid State NMR*, 1992, **1**, 345.
16. S. H. Alarcón, A. C. Olivieri, S. A. Carss, and R. K. Harris, *Magn. Reson. Chem.*, 1995, **33**, 603.
17. L.-J. Baker, G. A. Bowmaker, P. C. Healy, B. W. Skelton, and A. H. White, *J. Chem. Soc., Dalton Trans.*, 1992, 989.

Acknowledgments

The author is grateful to Professor A. C. Olivieri for fruitful collaborative research on the topic in question, and for valuable comments on the text of this article.

Biographical Sketch

Robin K. Harris. *b* 1936. B.A. (Nat.Sci.), Ph.D., (supervisor Norman Sheppard), Sc.D., University of Cambridge, UK. Postdoctoral work at Mellon Institute, Pittsburgh, PA (with Aksel Bothner-By). Successively lecturer, senior lecturer, and professor, University of East Anglia, UK. Currently Professor of Chemistry, University of Durham, UK. Secretary-General of ISMAR, 1986–92. Approx. 350 publications. Current research specialty: solid state NMR and its applications in materials chemistry.

Magnetic Field Induced Alignment of Molecules

Aksel A. Bothner-By

Carnegie Mellon University, Pittsburgh, PA, USA

1	Introduction	1
2	Energetics of a Rigid Molecule in Isotropic Solution in a Magnetic Field	1
3	Effects of Alignment on High-Resolution NMR Spectra	2
4	Applications	4
5	Related Articles	6
6	References	6

1 INTRODUCTION

If a sample of liquid benzene is exposed to the Earth's magnetic field passing through it along a north–south direction, there will be a slight tendency for the molecules to turn their faces east–west (or up–down) and away from north–south. The original meaning of 'orient' was to face the east, so one might describe the benzene as slightly oriented, or aligned. The normal thermal motions of the molecules largely overcome this tendency, and one can calculate that at any instant the excess of east–west facing molecules over north–south facing molecules is approximately 1 in 10^{15}. In the study of NMR, this tendency to align in the magnetic induction $\boldsymbol{B}_0$ has been ignored until recently, since the effects on the NMR spectra have been too small to observe. However, the degree of alignment increases as the square of $\boldsymbol{B}_0$, and in today's spectrometers with $\boldsymbol{B}_0$ values of 10^5 or more times the Earth's field, the alignment is sufficient that perturbations of the NMR spectrum are often readily observed. This article gives an outline of the origin of the alignment, the nature of the changes produced in the spectrum, and some applications of these to the structure determination of molecules in solution, to molecular angular correlation, to ions, and to paramagnetic species.

2 ENERGETICS OF A RIGID MOLECULE IN ISOTROPIC SOLUTION IN A MAGNETIC FIELD

All objects, molecules, men, or galaxies, possess the property called magnetic susceptibility,[1] usually denoted by χ. When the object is placed in a magnetic field $\boldsymbol{H}_0$, a magnetic dipole $\boldsymbol{m}$ is induced in it, according to the equation

$$\boldsymbol{m} = \chi \boldsymbol{H}_0 \tag{1}$$

For diamagnetic molecules or ions, χ is negative and small, for paramagnetic species, it is usually positive and larger.

The act of putting a molecule in the magnetic field results in a change in energy of the system:

$$\Delta E = -\chi \boldsymbol{H}_0 \cdot \boldsymbol{B}_0/2 \tag{2}$$

$\boldsymbol{B}_0$ is related to $\boldsymbol{H}_0$ by the fundamental relationship

$$\boldsymbol{B}_0 = \mu \boldsymbol{H}_0 \tag{3}$$

where μ is the permeability. In all cases discussed here, μ differs insignificantly from μ_0, the permeability of free space, so that one can rewrite equation (3) as

$$\Delta E = -\chi B_0^2/2\mu_0 \tag{4}$$

In the SI system, standardized in this Encyclopedia, the units of ΔE are joules, those of χ are m^3 per molecule, those of $\boldsymbol{B}_0$ are tesla, and those of μ_0 are $4\pi \times 10^{-7}$ tesla^2 m^3 joule^{-1}. Much of the experimental work performed on magnetic alignment has been reported using cgs units, in which $\mu_0 = 1$ and χ is in cm^3 per molecule. These literature values of χ can be converted into the SI system by multiplying by $4\pi \times 10^{-6}$. A few papers give χ in units of joule tesla^{-2}, collapsing μ_0 into χ.

For molecules which are not of tetrahedral or higher symmetry, χ is expected to be anisotropic, that is to differ when measured parallel to the x, y, and z axes of a molecule-fixed coordinate frame.[2] χ is then represented as a second-rank tensor, which, if the correct axes are chosen, will be diagonal:

$$\boldsymbol{\chi} = \begin{bmatrix} \chi_{xx} & 0 & 0 \\ 0 & \chi_{yy} & 0 \\ 0 & 0 & \chi_{zz} \end{bmatrix} \tag{5}$$

Equation (4) must then be written in tensor notation:

$$\Delta E = -\boldsymbol{B}_0 \cdot \boldsymbol{\chi} \cdot \boldsymbol{B}_0/2\mu_0 \tag{6}$$

In the absence of a magnetic induction, the molecules in solution undergo a random tumbling motion as a result of collisions with solvent molecules. However, in the presence of $\boldsymbol{B}_0$ there will be a torque tending to turn the molecule into its minimum energy position. Taking benzene as an example, we note that the susceptibility is most negative when measured along the six-fold axis, so the energy is highest when the six-fold axis is parallel to $\boldsymbol{B}_0$, and the alignment of benzene molecules with their planes parallel to $\boldsymbol{B}_0$ is preferred.

The degree of alignment of a particular axis i relative to $\boldsymbol{B}_0$ in the molecule is specified by the parameter S_{iB}, defined by[3]

$$S_{iB} = \langle \tfrac{3}{2} \cos^2 \theta_{iB} - \tfrac{1}{2} \rangle \tag{7}$$

where θ_{iB} is the angle between the axis i and $\boldsymbol{B}_0$, and the angle brackets indicate the expectation value of the enclosed expression. If $S_{iB} = 1$, the axis i is perfectly aligned parallel to $\boldsymbol{B}_0$, while if $S_{iB} = -\frac{1}{2}$ the axis i is always perpendicular to $\boldsymbol{B}_0$. $S_{iB} = 0$ implies completely random tumbling. S_{iB} may be evaluated assuming a Boltzmann distribution in the energies.[4] Then

$$S_{iB} = \frac{\int_0^{2\pi} \int_0^{\pi} \left(\frac{3}{2} \cos^2 \theta_{iB} - \frac{1}{2}\right) \mathrm{e}^{-\Delta E/kT} \sin \theta_{iB} \, \mathrm{d}\theta_{iB} \, \mathrm{d}\phi}{\int_0^{2\pi} \int_0^{\pi} \mathrm{e}^{-\Delta E/kT} \sin \theta_{iB} \, \mathrm{d}\theta_{iB} \, \mathrm{d}\phi} \tag{8}$$

Since ΔE is very small, the exponential can be approximated by $1 - \Delta E/kT$, and explicit integration of equation (8) gives

$$S_{iB} = \Delta\chi_{ii} B_0^2/15kT\mu_0 \tag{9}$$

with $\Delta\chi_{ii}$ equal to $\chi_{ii} - (\chi_{jj} + \chi_{kk})/2$. It is obvious that $S_{xB} + S_{yB} + S_{zB} = 0$. The degree of alignment increases as the square of the magnetic induction and is inversely proportional to the temperature. Taking benzene as an example, with a value of $\Delta\chi_{zz}$ of $-1.27 \times 10^{-33}\,\mathrm{m}^3$, and assuming B_0 = 14.1 T (600 MHz magnet), S_{zB} at 300 K is calculated to be -3.2×10^{-6}.

3 EFFECTS OF ALIGNMENT ON HIGH-RESOLUTION NMR SPECTRA

Two types of nuclear interaction have been observed to give rise to new or additional splittings in high-resolution spectra of samples in which the molecules are partially aligned by the magnetic induction: magnetic dipole interaction,[5] and electric quadrupole interaction.[6] Completely random tumbling averages these interactions to zero, so no splitting is observed. The rapidly fluctuating torques resulting from these interactions are evidenced, however, by the relaxation. However, if the tumbling is nonrandom, such that a small alignment occurs, these interactions are not completely averaged to zero, and effects on line positions and splittings are observed.

3.1 Magnetic Dipolar Interaction

An (oversimplified) model may be used. Two magnetic nuclei A and B are attached to the framework of a molecule, which is undergoing rapid tumbling. The magnetic moment of nucleus A is taken as parallel to the magnetic induction. The component of the magnetic field parallel to $\boldsymbol{B}_0$ generated by nucleus A at nucleus B is then given by[1]

$$H_\mathrm{B} = m_\mathrm{A}(3\cos^2\theta_{nB} - 1)/r_\mathrm{AB}^3 \tag{10}$$

where θ_{nB} is the angle between the internuclear axis and $\boldsymbol{B}_0$. If all orientations of the internuclear axis are equiprobable, equation (10) integrates to give $\langle H_\mathrm{B}\rangle = 0$. On the other hand, if the internuclear axis has a degree of alignment S_{nB}, then

$$\langle H_\mathrm{B}\rangle = 2m_\mathrm{A}S_{nB}/r_\mathrm{AB}^3 \tag{11}$$

This field would add to $\boldsymbol{H}_0$ causing a shift in the frequency of the NMR signal from nucleus B. If the moment of A were antiparallel to $\boldsymbol{B}_0$, the opposite shift would be observed. Thus a doublet would be produced. In the quantum mechanical formulation, the strength of the interaction is represented by D_AB, which is given by

$$D_\mathrm{AB} = -\gamma_\mathrm{A}\gamma_\mathrm{B}hS_{nB}/2\pi^2 r_\mathrm{AB}^3 \tag{12}$$

The observable splittings are directly related to D_AB. It is now necessary only to relate S_{nB} to χ:[4]

$$S_{nB} = \frac{2}{3}\sum_{i=x,y,z}\Delta\chi_{ii}(\tfrac{3}{2}\cos^2\theta_{in} - \tfrac{1}{2})B_0^2/15kT\mu_0 \tag{13}$$

where θ_{in} is the angle between the ith axis of the susceptibility tensor and the internuclear axis. Combining equations (12) and (13), and noting that the spectrometer frequency ν_A is equal to $\gamma_\mathrm{A}B_0/2\pi$, the practical formula is obtained:

$$D_\mathrm{AB} = -5.10 \times 10^{15}\nu_\mathrm{A}\nu_\mathrm{B} \times \sum_{i=x,y,z}\chi_{ii}(\tfrac{3}{2}\cos^2\theta_{in} - \tfrac{1}{2})/T a_\mathrm{AB}^3 \tag{14}$$

where a_AB is the internuclear distance (in nanometers).

The effect of D_AB on the spectrum has been thoroughly explored in studies of molecules partially aligned by solution in liquid crystal solvents.[7] For two spins with identical Larmor frequencies, the spectrum is a doublet with splitting $3D_\mathrm{AB}/2$. An example of such a splitting is shown in Figure 1. The signal arises from two methylene protons attached to a porphyrin ring in the zinc vinylphylloerythrin–pyridine complex (**1**), with the internuclear axis parallel to the four-fold symmetry axis of the ring. The observed doublet splitting of 1.98 Hz observed at 600 MHz, implies D_HH = 1.32 Hz. Taking a as 0.178 nm, T as 296 K, θ_{zn} = 0, and $\chi_{xx} = \chi_{yy}$, gives $\Delta\chi_{zz} = -11.9 \times 10^{-33}\,\mathrm{m}^3$. The $\Delta\chi_{zz}$ of the complex is the sum of $\Delta\chi_{zz}$ for the porphyrin ($-12.5 \times 10^{-33}\,\mathrm{m}^3$) and $-(\frac{1}{2})\Delta\chi_{zz}$ for the pyridine ligand ($-1.19 \times 10^{-33}\,\mathrm{m}^3$), in agreement with values obtained by other methods.[8]

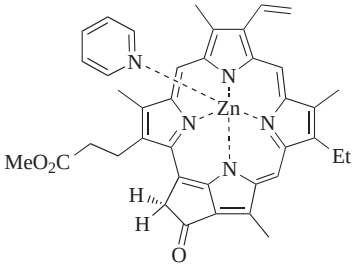

(1)

If the Larmor frequencies of the two nuclei differ by much more than D_AB and J_AB, the observed doublet spacing is simply $J_\mathrm{AB} + D_\mathrm{AB}$. The addition is algebraic,[7] so if the sign and magnitude of J_AB are known from other studies, the sign and magnitude of D_AB can be determined. As an example of this, a second porphyrin containing a similarly situated methylene group was studied in methyl pyropheophorbide A (**2**). The pyrrole ring adjacent to the methylene was reduced, rendering the methylene protons inequivalent. They now gave rise to AX type doublets, with a splitting $J_\mathrm{HH} + D_\mathrm{HH}$ of 20.17 Hz at 5.87 T, 19.95 Hz at 7.05 T, 19.51 Hz at 11.75 T, and 19.25 Hz at 14.09 T. The plot of these splittings versus B_0^2 is a straight line with intercept $J_\mathrm{HH} = -20.25$ Hz, and D_HH = +1.00 Hz at 14.09 T. Application of equation (14) yields $\Delta\chi = -10.1 \times 10^{-33}\,\mathrm{m}^3$. The reduction of the pyrrole ring has partially interrupted the circuit of π electrons responsible for the ring current and for the large anisotropic susceptibility of porphyrins.

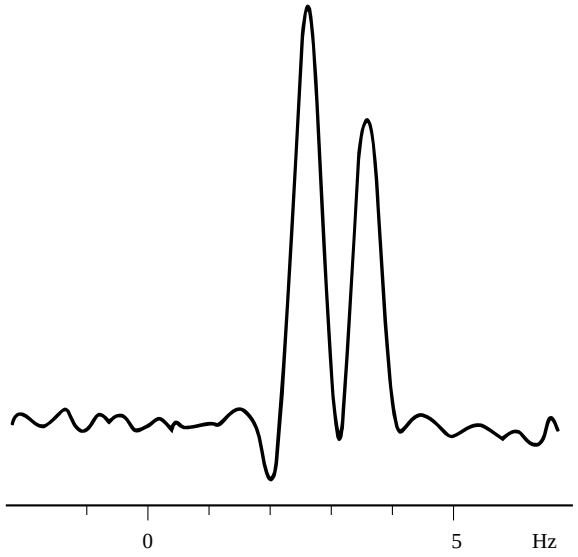

Figure 1 The doublet arising from the direct magnetic dipole interaction in zinc vinylphylloerythrin–pyridine complex

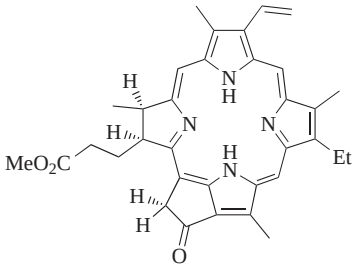

(2)

Finally, if the Larmor frequency difference between A and B and $J_{AB} \pm D_{AB}$ is of comparable magnitude, second-order effects are expected. The exact calculation of J_{AB} and D_{AB} from such spectra has been worked out in detail, in connection with the spectroscopy of solutes in liquid crystal solvents.[7] It has been shown[9] that the observation of the second order effects in suitable cases provides a sensitive method for detecting and measuring very small values of D_{AB}.

3.2 Electric Quadrupole Interaction

For most quadrupolar nuclei, the relaxation induced by the interaction of the nuclear quadrupole moment with the electric field gradient at the nucleus broadens the signals sufficiently to obscure the effects produced by molecular alignment. However, the quadrupole coupling constant for deuterium in a large variety of molecules is small, lying in the range 100–300 kHz, and the broadening is small enough that splittings arising from the quadrupole interaction can be seen in the ^{2}H NMR spectrum.

For a single deuterium atom, if molecular tumbling is not random, the signal consists of a doublet: the transitions correspond to the changes $m(-1 \rightarrow 0)$ and $m(0 \rightarrow 1)$. The frequency separation of the doublet $\Delta\nu_Q$ is given by

$$\Delta\nu_Q = 3eQ\langle V_{\boldsymbol{B}_0}\rangle/2h \qquad (15)$$

where eQ is the nuclear electric quadrupole moment, and $\langle V_{\boldsymbol{B}_0}\rangle$ is the expectation value of the electric field gradient along the direction of $\boldsymbol{B}_0$. It is convenient to establish a second molecule-fixed coordinate frame, x', y', z', in which the electric field gradient tensor is diagonal, and to define $\nu_{x'}$, $\nu_{y'}$, and $\nu_{z'}$ as the quadrupole splittings which would be observed if the molecule were fixed with the x', y', and z' axes parallel to $\boldsymbol{B}_0$, respectively. Then,[7]

$$\Delta\nu_Q = \frac{2}{3}\sum_{i=x',y',z'} \nu_i \sum_{j=x,y,z} \cos^2\theta_{ij}\, S_{jj} \qquad (16)$$

The electric field gradient tensor is traceless, implying $\nu_{x'} + \nu_{y'} + \nu_{z'} = 0$. Quadrupole coupling constants for carbon-bound deuterium have been measured by NMR relaxation methods, Zeeman microwave spectroscopy, NMR studies of deuterated molecules in liquid crystal solvents, and nuclear quadrupole resonance spectroscopy of solids.[10] The maximum splittings, $\nu_{z'}$ range from 225 to 300 kHz, with ^{2}H in similar chemical environments clustered together: ^{2}H attached to a benzene ring has $\nu_{z'}$ equal to 275 ± 5 kHz. Returning once again to benzene as an example, with $\nu_{z'} = 279$ kHz, $\nu_{x'} \approx \nu_{y'} = -139.5$ kHz, $\Delta\chi = -1.27 \times 10^{-33}\,\mathrm{m}^3$, $B_0 = 14.09$ T, $T = 300$ K, and $\theta_{zz'} = 90^\circ$, ν_Q is calculated using equation (16) to be 0.45 Hz. Figure 2 shows a ^{2}H NMR spectrum of monodeuterobenzene; the spectrum is resolution enhanced, with proton decoupling. The observed splitting (0.46 Hz) agrees well with the expected value.

Second-order effects are observed in the spectra when chemical shifts are zero or of comparable magnitude to J_{AB} and ν_{QA} or ν_{QB}. This complication prevents the direct observation of ν_Q in hexadeuterobenzene, which gives rise to a spectrum with numerous overlapping transitions.[11]

3.3 Anisotropic Chemical Shift

If the sample molecules possess anisotropic magnetic susceptibilities and also contain nuclei with anisotropic

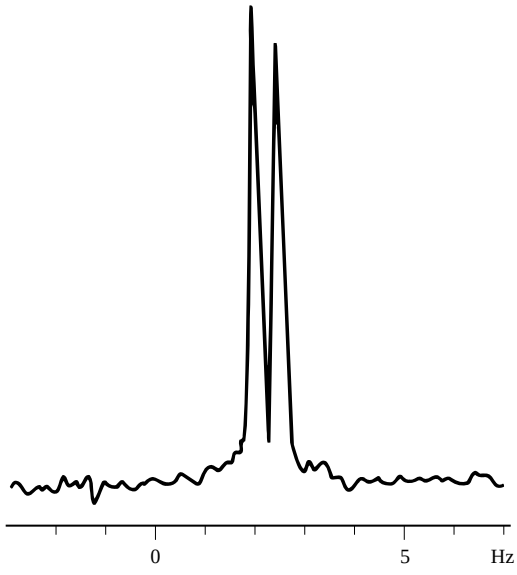

Figure 2 Deuteron quadrupole splitting of the deuteron signal from benzene-d_1, with proton decoupling

chemical shieldings, it is expected that the shift will not be linearly related to $\boldsymbol{B}_0$. The reason for this is clear: if the molecule is tumbling randomly, the average chemical shift $(\sigma_{xx} + \sigma_{yy} + \sigma_{zz})B_0/3$ will be observed; if the molecules are partly aligned, with alignment parameters S_{xB}, S_{yB}, and S_{zB}, the observed shift will be

$$2 \sum_{i=x,\,y,\,z} S_{iB}\sigma_{ii} B_0/3$$

Despite concerted effort, no such nonlinear shifts have been demonstrated to date. The difficulty is that the expected effects are very small, and easily masked by shifts arising from extraneous factors such as temperature.

4 APPLICATIONS

From the above, it can be seen that the dipolar splitting observed between two nuclei in a molecule in a high $\boldsymbol{B}_0$ relates the length and direction of the internuclear vector to $\boldsymbol{\chi}$. Similarly, the observed quadrupole splitting relates the electric field gradient tensor $\boldsymbol{V}$ and $\boldsymbol{\chi}$. If $\boldsymbol{\chi}$ is known, or can be estimated accurately, then information is obtained on the internuclear vector or on $\boldsymbol{V}$, i.e. structural information. On the other hand, if the structure is known (the length and direction of the internuclear vector relative to the principal axes, or direction and the strength of the electric field gradient), $\boldsymbol{\chi}$ may be determined. For organically bound ^{2}H, the largest component of $\boldsymbol{V}$ (V_{zz}) is directed along the C–^{2}H (or N–^{2}H, O–^{2}H, etc.) bond, and the asymmetry, $V_{xx} - V_{yy}$ is negligible. Even for ^{2}H attached to trigonal carbon, the asymmetry is normally less than 5% of V_{zz}.

4.1 $\boldsymbol{\chi}$, Systematics and Determination

In addition to the high-field NMR method, there are several methods for determining $\boldsymbol{\chi}$. In the crystal flip angle method,[2] a single crystal of the sample is suspended by a quartz fiber in a transverse magnetic induction and the torque required to cause the crystal to turn from its lowest energy state through its highest energy state is measured. In the Cotton–Mouton method,[12] the partial alignment of molecules in the liquid or gaseous state by $\boldsymbol{B}_0$ is measured by observing the optical birefringence. In the Zeeman microwave method,[13] the Zeeman effect on rotational spectra is observed. Extensive measurements have been made using all these methods, often on the same molecule; the results are generally in good agreement.[14] For example, for benzene, single crystal measurements yielded a value for $\Delta\chi$ of $-1.24 \times 10^{-33}\,\mathrm{m}^3$, three independent measurements by the Cotton–Mouton method gave -1.31, -1.32, and $-1.33 \times 10^{-33}\,\mathrm{m}^3$, and measurements by high-field NMR gave $-1.27 \times 10^{-33}\,\mathrm{m}^3$. With no electric dipole moment, benzene could not be studied directly by rotational spectroscopy.

All these measurements have demonstrated that Pascal's additivity scheme[15] for the isotropic diamagnetic susceptibility can be extended to $\boldsymbol{\chi}$, the molecular susceptibility tensor, i.e. that $\boldsymbol{\chi}$ can be expressed as the sum of bond susceptibility tensors $\boldsymbol{\chi}_\mathrm{b}$, or of atom susceptibilty tensors $\boldsymbol{\chi}_\mathrm{a}$, with the addition of $\boldsymbol{\chi}_\mathrm{e}$ (a susceptibility tensor ascribable to the delocalized circulation of electrons).[13] There is a considerable amount of literature covering $\boldsymbol{\chi}_\mathrm{e}$ in aromatic and antiaromatic compounds; an alternative name for this delocalized circulation is 'ring current'. In early studies the existence of the ring current and its magnitude were inferred from measurements of 'exaltation',[15] the amount by which χ exceeds $\Sigma\chi_\mathrm{b}$ or $\Sigma\chi_\mathrm{a}$. The circulation is in the plane of the aromatic or antiaromatic systems, so $\boldsymbol{\chi}_\mathrm{e}$ has zero elements for χ_{xx} and χ_{yy}; χ_{zz} is negative if the molecule is aromatic, and positive if it is antiaromatic.[16]

Acyclic compounds do not exhibit exaltations, and fit the additive scheme well, although multiple heavy atom substitution on carbon causes deviations. Single and triple bond susceptibility tensors are axial, that is $\chi_{xx} = \chi_{yy}$. If only single and triple bonds are present, S_{nB} for any axis can be determined using

$$S_{NB} = \sum_{\text{bonds}} (\tfrac{3}{2}\cos^2\theta_{nB} - \tfrac{1}{2})\Delta\chi_\mathrm{b} B_0^2/15kT\mu_0 \qquad (17)$$

Double bond susceptibility tensors have three different components, so the full version of equation (9) is required. Cyclic compounds, even saturated small ring compounds, such as cyclopropane, cyclobutane, and cyclopentane, show significant contributions from $\boldsymbol{\chi}_\mathrm{e}$. The exact nature of the delocalization is uncertain, but three- and five-membered rings have negative $\boldsymbol{\chi}_\mathrm{e}$, while four-membered rings have positive $\boldsymbol{\chi}_\mathrm{e}$.

The susceptibility tensor for most rigid molecules is a hard property, i.e. it is not affected appreciably by the environment. $\boldsymbol{\chi}$ is the same, within experimental error, whether measured in the gas, liquid, or solid phase. If the molecular electronic or geometrical structure is actually changed by the environment, $\boldsymbol{\chi}$ will change. For example, different solvents which produce a different weighting of the polar and nonpolar resonance forms in *N*-methyl-2-pyridone cause different quadrupole splittings to be observed for the deuterated compound.

Extensive analyses of bond susceptibility additivity schemes have been presented in articles by Flygare[13] and Haberditzl.[17]

4.2 Determination of Structure: Rigid Molecules

As an example of structural elucidation, we consider the study of the dihydrogen complex of the bridged bis(ruthenium porphyrin) · H_2 complex (**3**).[18] The structure of the $B(RuP)_2$ framework is well established. The structural question to be answered is: What is the arrangement of the H_2? How far apart are the hydrogen atoms, and what angle does the H–H axis make with the molecular *z* axis (Ru–Ru axis)?

The susceptibility tensor for the complex can be estimated within a few per cent by adding the known tensors for the two porphyrins, the phenylimidazolyl groups, and the biphenylene bridging group, using the summation

$$\Delta\chi_{zz} = \sum_{\text{groups}} (\tfrac{3}{2}\cos^2\theta_{zz} - \tfrac{1}{2})\Delta\chi_\mathrm{g} \qquad (18)$$

with $\theta_{zz'}$ being the angle between the molecular *z* axis and the normals to the ring planes of the individual groups. The anisotropy of the C–C bonds joining the biphenylene and porphyrin groups and of H_2 are less than $0.1 \times 10^{-33}\,\mathrm{m}^3$ and do not contribute significantly to the sum, which gives

$\Delta\chi_{zz} = -24.0 \times 10^{-33}\,\mathrm{m}^3$. Measurements of the H–H magnetic dipolar splitting were made at 620 MHz (14.56 T). S_{zB} is calculated to be -6.61×10^{-5} at this $\boldsymbol{B}_0$.

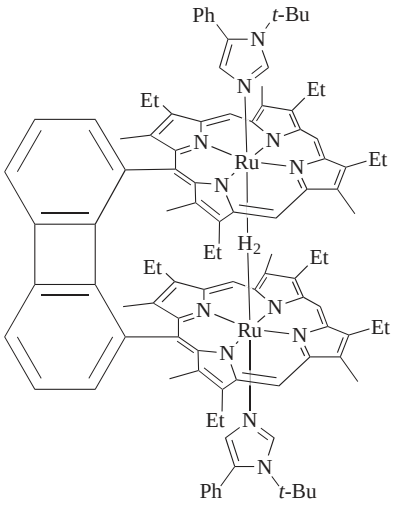

(3)

The H_2 signal at 620 MHz is a doublet with a splitting of $\pm 7.37 \pm 0.05$ Hz. D_{HH} is thus $\pm 4.91 \pm 0.03$ Hz. Using equation (14), one finds:

$$\langle \tfrac{3}{2}\cos^2\theta_{zn} - \tfrac{1}{2}\rangle / r_{HH}^3 = \pm 0.309 \times 10^{24} \tag{19}$$

The sign of D_{HH} was not known, but was determined by observing the field dependence of the splitting $J_{HD} + D_{HD}$ for the complex with HD. The sign of J_{HD} is known to be positive, so the decreasing magnitude of the splitting with increasing $\boldsymbol{B}_0$ means that D_{HD} and thus D_{HH} are negative. The internuclear distance was deduced by relaxation time measurements to be 0.121 ± 0.009 nm. This yields $\langle(3/2)\cos^2\theta_{zn} - (1/2)\rangle = -0.54 \pm 0.05$. Since $\langle(3/2)\cos^2\theta_{zn} - (1/2)\rangle$ cannot be more negative than $-\frac{1}{2}$, it appears that θ_{zn} must be very close to 90°; the H–H axis is perpendicular to the molecular z axis.

4.3 Study of Molecules with Internal Motion

As an example, a study of styrene and 1- and 2-vinylnaphthalene is outlined.[19] The motion of interest is the rotation of the vinyl group about the single bond joining it to the aromatic ring. The parameter measurable by high field studies is the expectation value, $\langle\sin^2\alpha\rangle$, where α is the dihedral angle between the planes of the vinyl group and the ring. In the study, the quadrupole splittings of the deuteron signals were measured for styrene with deuterium substituted in all positions of the vinyl and phenyl groups.

Addition of the known group susceptibility tensors for vinyl and phenyl groups suggests that the principal axis z of styrene is very nearly perpendicular to the phenyl ring, regardless of α, and that $\chi_{xx} \approx \chi_{yy}$. The equality of the observed splittings for the *ortho*, *meta*, and *para* deuterons in the phenyl group is consistent with this, and their magnitude at 14.57 T indicates a value of $\Delta\chi_{zz} = -1.45 \times 10^{-33}\,\mathrm{m}^3$. The determination of $\langle\sin^2\alpha\rangle$ is then an exercise in solid trigonometry: one has to calculate $\langle\cos^2\theta_{zz'}\rangle$ relating the molecular z axis to the z' axis of the electric field gradient tensor (the C–D bond axis) for the α and *trans*-β deuterons in the vinyl group. These are related by

$$\langle\cos^2\theta_{zz'}\rangle = \langle\sin^2\alpha\rangle\langle\sin^2\beta\rangle \tag{20}$$

where β is the angle between the C–D bond and the C–C bond joining the vinyl and phenyl groups. For the deuteron in the *cis*-β position, $\beta \approx 0°$, the C–D axis is parallel to that of the *para*-deuteron, regardless of internal rotation of the vinyl group. The ratio of the splittings is thus a measure of the ratio of the quadrupole couplings for the phenyl–D and vinyl–D nuclei (185 and 181 kHz, respectively), which is in agreement with previous measurements. For the α and *trans*-β deuterons, β is taken as 71°. From the observed splittings, it is then found that $\langle\sin^2\alpha\rangle$ is 0.081 and $\sin^{-1}\langle\sin^2\alpha\rangle^{1/2}$ is 16.5°. If the splitting were negative rather than positive, one would obtain $\langle\sin^2\alpha\rangle = 0.666$ and $\sin^{-1}\langle\sin^2\alpha\rangle^{\frac{1}{2}} = 55°$, but this can be eliminated, because the value of $\Delta\chi_{zz}$ obtained would be $-1.31 \times 10^{-33}\,\mathrm{m}^3$, which is a much smaller value than that indicated by the phenyl–D splittings. Similar measurements on 2-vinylnaphthalene indicated $\langle\sin^2\alpha\rangle$ gave values the same as those for styrene, within experimental error, while for 1-vinylnaphthalene, $\sin^{-1}\langle\sin^2\alpha\rangle^{-1/2} \approx 40°$, suggesting steric interference between the vinyl group and the *peri*-hydrogen atom in the planar arrangement.

4.4 Angular Correlation in the Liquid State

Even in the absence of a magnetic flux, a molecule (A) which is not isotropic interacts with neighboring anisotropic molecules (B) in such a way that they do not tumble randomly, but adopt preferred orientations with respect to A. A strong limiting case of this is association; if molecule A binds to molecule B, for example with a hydrogen bond or by ionic attraction, then A and B do not move independently, but tumble together synchronously. More subtle interactions can also induce molecular correlation: the electric polarizability, electric dipole moment, quadrupole moment, or higher moments, may interact with any of these of the B molecules; the shapes of molecules A and B may be conducive to better packing in particular mutual orientations. Molecule A may influence several molecules of molecule B, and vice versa. Finally, A and B may be different species (solute and solvent), or the same (neat liquids). Angular correlations may also be characterized by ordering parameters $S_{ij'} = \langle(3/2)\cos^2\theta_{ij'} - (1/2)\rangle$, where $\theta_{ij'}$ is the angle between the ith axis of A and the jth axis of B. If molecules A and B are identical, one may define Kirkwood's[20] parameter $g_{ii'}$ as

$$g_{ii'} = 1 + \sum_n S_{ii'} \tag{21}$$

The summation is taken over all neighboring B molecules, and the unity term represents the angular correlation of A with itself. For example, if $g_{zz'}$ were found to be 2.00 for neat benzene, a conceivable (though incorrect) explanation would be that neat benzene consists entirely of face-to-face dimers, with parallel z axes. For neat samples,

$$S_{iB}^{A} = g_{ii'}\Delta\chi_{ii}B_0^2/15kT\mu_0 \tag{22}$$

while for solute A in solvent B

$$S_{iB}^{A} = \left(\Delta\chi_{ii}^{A} + \frac{2}{3} \sum_{n} \sum_{j'=x',y',z'} (S_{ij'} \Delta\chi_{jj'}) \right) B_0^2 / 15kT\mu_0 \quad (23)$$

In order to measure the degree of molecular alignment caused by the induction, free of solvent angular correlation effects, it is customary to employ dilute solutions in solvents which are themselves exactly or nearly magnetically isotropic. Ideal solvents would include CCl_4, $SiMe_4$, CMe_4, and SF_6. Good, though not perfect, solvents include water, liquid ammonia, diethyl ether, and cyclohexane. The angular correlation in a number of neat liquids has been studied by comparing the alignments observed in dilute solution in isotropic solvents, and in the neat liquid. The value of $g_{zz'}$ found for benzene was 0.86, which implies a negative value for $S_{zz'}$. The rings of neighboring benzene molecules tend to form angles greater than 54.7°, rather than stack, pancake fashion.[10]

4.5 Paramagnetic and/or Charged Species

Paramagnetic or charged species are partially aligned in a magnetic field in the same way as neutral diamagnetic molecules. Since paramagnetic susceptibilities are usually much larger than diamagnetic susceptibilities, it is not surprising that the anisotropies of the paramagnetic susceptibilities are also much larger, and the degree of alignment correspondingly greater. Thus the first observation[5] of a dipolar splitting in isotropic solution was made on the paramagnetic cobalt complex bis[*p*-tolyl-tris(pyrazolyl)borato]cobalt(II) (**4**). Lanthanide shift reagents exert their effects by virtue of their large anisotropic susceptibilities; consequently, molecules complexed with shift reagents exhibit large dipolar and quadrupolar splittings of the type described here, even at moderate field strengths. A very interesting study of the susceptibility tensor for a ferric porphyrin has been reported.[21]

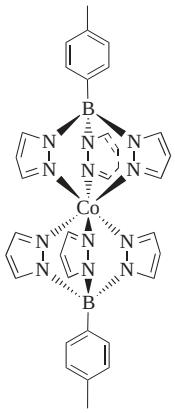

(4)

Studies of organic cations and anions have also been made.[22] Ion pairing probably occurs in the cases studied, although the counterions are expected to be nearly isotropic and thus correlation effects would be negligible. Of course the electronic structure of the organic ion itself may be strongly affected by the counterion. Values of χ_e have been deduced and related to the electronic structure of the ions.

5 RELATED ARTICLES

Anisotropy of Shielding and Coupling in Liquid Crystalline Solutions; Chemical Shift Tensors; Dipolar and Indirect Coupling Tensors in Solids; Liquid Crystalline Samples: Spectral Analysis; Quadrupolar Transition Metal and Lanthanide Nuclei.

6 REFERENCES

1. J. A. Stratton, *Electromagnetic Theory*, McGraw-Hill, New York, 1941, p. 10
2. C. V. Raman and K. S. Krishnan, *Proc. R. Soc. (London), Ser. A*, 1927, **A113**, 511.
3. A. Saupe and G. Englert, *Phys. Rev. Lett.*, 1963, **11**, 462.
4. P. C. M. Van Zijl, B. H. Ruessink, J. Bulthuis, and C. MacLean, *Acc. Chem. Res.*, 1984, **17**, 172.
5. A. A. Bothner-By, P. J. Domaille, and C. Gayathri, *J. Am. Chem. Soc.*, 1981, **103**, 5602.
6. J. A. B. Lohman and C. MacLean, *Chem. Phys.*, 1978, **35**, 269.
7. J. W. Emsley and J. C. Lindon, *NMR Spectroscopy in Liquid Crystal Solvents*, Pergamon, Oxford, 1975.
8. R. Havemann, W. Haberditzl, and P. Grzegorzewski, *Z. Phys. Chem.*, 1961, **217**, 91.
9. F. A. L. Anet, *J. Am. Chem. Soc.*, 1986, **108**, 1354.
10. A. Loewenstein, *Advances in Nuclear Quadrupole Resonance*, ed. J. A. S. Smith, Wiley, New York, 1983, Vol. 5, p. 53.
11. P. C. M. Van Zijl, C. MacLean, C. Gayathri, and A. A. Bothner-By, *J. Magn. Reson.*, 1984, **56**, 456.
12. H. Geschke, S. Pferrer, H. Haeussler, and W. Huettner, *Ber. Bunsenges. Phys. Chem.*, 1982, **86**, 790.
13. W. H. Flygare, *Chem. Rev.*, 1974, **74**, 653.
14. *Landolt-Börnstein, NSII*, eds. K.-H. Hellwege and O. Madelung, Springer-Verlag, Berlin, Vol. 16, p. 403.
15. P. Pascal, *Chemie General*, Masson, Paris, 1949.
16. H. J. Dauben, Jr., J. D. Wilson, and J. L. Laity, *Non-Benzenoid Aromatics*, ed. L. Snyder, Academic, New York, 1969, p. 167.
17. W. Haberditzl, *Angew. Chem., Int. Ed. Engl.*, 1966, 288.
18. J. P. Collman, P. S. Wagenknecht, A. A. Bothner-By, J. E. Hutchinson, N. S. Lewis, M. A. Lopez, R. Guilard, M. Lher, and P. K. Mishra, *J. Am. Chem. Soc.*, 1992, **114**, 5654.
19. K. Facchine, S. W. Staley, P. C. M. Van Zijl, P. K. Mishra, and A. A. Bothner-By, *J. Am. Chem. Soc.*, 1988, **110**, 4900.
20. J. G. Kirkwood, *J. Chem. Phys.*, 1939, **7**, 911.
21. S. H. Strauss, K. M. Long, M. Magerstaedt, and O. A. Gansow, *Inorg. Chem.*, 1987, **26**, 1185.
22. E. W. Bastiaan, P. C. M. Van Zijl, C. MacLean, and A. A. Bothner-By, *Annu. Rep. NMR Spectrosc.*, 1987, **19**, 35.

Biographical Sketch

Aksel A. Bothner-By. *b*. 1921. B.Chem., 1943, Ph.D., 1949 (with R. B. Woodward, Harvard), Brookhaven Natl. Lab. 1949–52. E.T.H. Zürich, 1952–53. Harvard, 1953–58. Mellon Institute, then Carnegie Mellon U. 1958–92. Began study of NMR in 1954. ~ 150 publications. Research specialties: molecular geometry by high-resolution NMR; Overhauser effects, longitudinal and transverse; molecular orientation by high magnetic field.

MQMAS Advances

Jean-Paul Amoureux

Université de Lille, Villeneuve d'Ascq, France

&

Marek Pruski

Iowa State University, Ames, IA, USA

1	Introduction	1
2	Theoretical Background	3
3	Detection of Pure-phase Spectra	4
4	Processing and Interpretation of MQMAS Spectra	9
5	Measurements of Dipolar Connectivities	17
6	Sensitivity Enhancement via CPMG Method	23
7	Conclusion	24
8	Related Articles in this Volume	24
9	Related Articles in Volumes 1–8	24
10	References	24

1 INTRODUCTION

NMR's ability to probe the structure of materials strongly depends upon the availability of high-resolution spectra, which serve as fingerprints of the physico-chemical surroundings of the studied nuclei. In powdered solids, the nuclear spins experience various anisotropic interactions, which broaden their spectra and render NMR more difficult for structural determinations. For spin-1/2 nuclei these interactions include dipole-dipole coupling between spins, chemical shift anisotropy (CSA), indirect spin–spin coupling and interaction with unpaired electrons.[1] The resolution and sensitivity gaps between liquid and solid state NMR began to decrease in the 1960s and 1970s with the introduction of radio frequency (RF) decoupling, magic angle spinning (MAS) and cross polarization (CP) methods.[2–5] These developments, in concert with the continuing advances in NMR hardware and software allowed for increasingly precise measurement of the spin interactions in solid samples, including the isotropic chemical shifts of spin-1/2 nuclei.

Until recently, however, these techniques could not overcome the line broadening in NMR spectra of the quadrupolar nuclei with spin greater than 1/2. This broadening arises from the coupling of the non-spherical charge distribution of such nuclei with the gradient of the electric field created by the surrounding electrons. The quadrupolar broadening is 'more anisotropic' than the first order interactions (CSA and dipolar coupling), in the sense that it contains higher order orientational terms of significant magnitude. Thus, more complex motions of the sample, or of the spin magnetization, are needed in order to achieve the highest possible resolution.[6–8] This article will focus on some of the concepts and experiments associated with the acquisition of isotropic solid state spectra of the quadrupolar nuclei by combining the multiple quantum (MQ) NMR with MAS.[8,9] In the last years MQMAS has revolutionized solid state NMR of the so-called half-integer quadrupolar spins. The most prominent nuclei that are amenable to this technique include ^{11}B (S = 3/2), ^{17}O (S = 5/2), ^{23}Na (S = 3/2) and ^{27}Al (S = 5/2).

The theory necessary for understanding of the quadrupolar interaction has been described before in numerous textbooks, monographs and reviews.[1,10–13] We first note that the size of the quadrupolar interaction can be described by the quadrupolar frequency ν_Q, which is proportional to the quadrupole moment Q of a nucleus and the electric field gradient (EFG). Depending upon the size of Q and the local electronic environment, the values of ν_Q can range from zero to several hundred of MHz. In NMR, we generally consider the strong field case, $\nu_0 > \nu_Q$, where ν_0 is the Larmor frequency in the static field $\mathbf{B}_0$. In this approximation, the first- and second-order quadrupolar energies can be easily calculated using the perturbation theory. For half-integer spins, the first-order quadrupolar effect on the satellite transition frequencies ($m - 1 \leftrightarrow m$, $m \neq 1/2$) is of the order of ν_Q. Thus, in a powdered sample, the NMR spectrum is spread over a frequency range that for most nuclei exceeds the range of chemical shifts and the bandwidth of the spectrometer under pulse excitation. However, the central transition ($-1/2 \leftrightarrow 1/2$) is not affected to first order. In the absence of additional line broadenings from chemical shift and/or dipolar interaction, the width of the powder spectrum for the central transition is determined only by the second order quadrupolar terms. Since this contribution is typically 10^2 to 10^3 times smaller than ν_Q, the central transition yields a narrower and more intense spectrum, which is the subject of most studies on half-integer quadrupolar nuclei. We note that in this approximation the width of the central transition spectrum is inversely proportional to the magnitude of magnetic field $\mathbf{B}_0$.

The detection of broad quadrupolar lineshapes can rarely be accomplished with single pulse excitation because of the loss of magnetization within the dead time of the receiver. This necessitates the use of multi-pulse excitation, with the two-pulse spin-echo sequences being the most common.[14,15] In case of sufficiently broad lines, the acquisition of spectra can be accomplished by scanning the frequency, or the magnetic field $\mathbf{B}_0$, and via point by point acquisition of the echo intensity.[16] While the static, spin-echo experiments continue to be used in the case of strong quadrupolar interactions, most studies of quadrupolar nuclei in the last two decades utilized the line-narrowing effect of spinning the sample under MAS or variable angle (VASS) conditions.[17,18] MAS eliminates the first order broadening completely and reduces the quadrupolar contribution to the central transition line width by a factor of approximately three. Consequently, the experimental strategies applied in the MAS experiments depend on the size of quadrupolar coupling. For ν_Qs not exceeding few hundred kHz, it is often possible to observe the whole spectrum, which appears as a wide manifold of spinning sidebands. The spacing between sidebands is equal to the spinning speed ν_R, whereas their individual widths and shapes are governed both by ν_R and the second order quadrupolar interaction. The width

and the shape of the entire manifold allow one to determine ν_Q and the asymmetry parameter of the EFG tensor η_Q.[17,19] The accuracy of such measurements strongly depends on the uniformity of the RF excitation, precise setting of the magic angle, probe bandwidth and tuning of the spectrometer. For large values of ν_Q, the spinning sidebands for the satellite transitions are often distorted, overlapping and embedded in background noise. Consequently, it becomes advantageous to use the MAS lineshape corresponding to the central transition for determination of the NMR parameters. While this strategy often relies upon the availability of high magnetic fields and high spinning speeds, trustworthy values of ν_Q, η_Q and the isotropic chemical shift δ_{CS} can be obtained from the computer simulations of the observed lineshapes.[20] In favorable cases, several distinct resonances can be fully characterized in a single MAS spectrum.

Several other strategies have been developed for improving the resolution of quadrupolar NMR spectra. These include static and MAS two-dimensional (2D) nutation experiments that utilize the correlation between the quadrupolar parameters and the precession frequencies induced by RF pulses of different lengths and intensities.[21–23] For moderate values of ν_Q not exceeding 1 MHz, SATRAS (satellite transition spectroscopy) can be used to determine the quadrupole and chemical shift parameters.[24,25] The problem of overlapping spinning sidebands in the MAS spectra of quadrupolar nuclei can be overcome using the recently proposed QPASS (quadrupolar phase alternated sideband suppression) sequence.[26] Finally, several techniques combined with MAS have been developed that allow for studies of dipolar interactions between the quadrupolar and spin-1/2 nuclei. These include the CP experiment, REDOR (rotational echo double resonance), TEDOR (transferred echo double resonance), TRAPDOR (transfer of populations double resonance) and REAPDOR (rotational echo adiabatic passage double resonance).[27–35]

As mentioned above, the second order quadrupolar interaction is not averaged to zero by MAS alone. However, remarkable developments have been made recently in this area of solid state NMR. The theoretical foundations and two different experimental realizations of complete spatial averaging of the second order broadening of the central transition were published in the late 1980s by the groups of Pines and Virlet.[6,7,36] It was shown that such spatial averaging requires mechanical rotation of the sample around an axis that has time dependent orientations. In the one-dimensional DOR (double rotation) experiment, the sample is spun in a small inner rotor, which is rotating inside an outer rotor.[6] The rotation axis of the outer rotor is set at the magic angle ($\chi_m = 54.74°$ with respect to $\mathbf{B}_0$), while the rotation axis of the inner rotor moves continuously on a cone of an aperture of 61.12°. In contrast with DOR, the DAS (dynamic angle spinning) technique uses two discrete rotational orientations (commonly tilted 37.38° and 79.19° away from $\mathbf{B}_0$) and correlates the corresponding resonance frequencies in a 2D experiment.[7] In general, DOR results in better averaging of the dipolar interactions and allows for studying of samples with fast relaxation times. DAS, on the other hand, provides a better filling factor and separates the anisotropic lineshapes associated with each isotropic resonance. The line narrowing abilities of DOR and DAS are best demonstrated in crystalline materials, where resolution enhancement by one or two orders of magnitude has been reported.[37] Most recently, it has been proposed and demonstrated by Frydman et al. that the line narrowing of the central transition can be obtained without changing the orientation of the spinning axis, as long as the motion of this axis in space is replaced by changing the coherence state of the observed spins.[8,9] This experiment is referred to as multiple quantum magic angle spinning (MQMAS) NMR. Similar to DAS, MQMAS is a two-dimensional method, which correlates the phase evolutions of the MQ and single quantum (1Q) coherences and allows for observation of a purely isotropic echo. The change of the coherence state of half-integer quadrupolar spins can be effectively accomplished by strong RF irradiation.[38,39] The MQMAS method precludes most of the shortcomings of DOR (presence of closely spaced spinning sidebands) and DAS (loss of magnetization during the reorientation of the spinner axis) and, being technically straightforward, has found enthusiastic approval in the NMR community. The resolution enhancement that this technique can provide is demonstrated in Figure 1, which compares static, MAS and MQMAS spectra of ^{87}Rb in well-crystallized $LiRbSO_4$.[40] The observed line width in $LiRbSO_4$ changed from approximately 400 ppm in a static spectrum to 150 ppm under MAS and 1.5 ppm in MQMAS. Hundreds of applications of this technique in the studies of catalysts, glasses and other amorphous and crystalline inorganic solids have been published.

In the six years since its inception, a great body of work has been reported that extended the efficiency and the analytical capabilities of the MQMAS method. Extensive

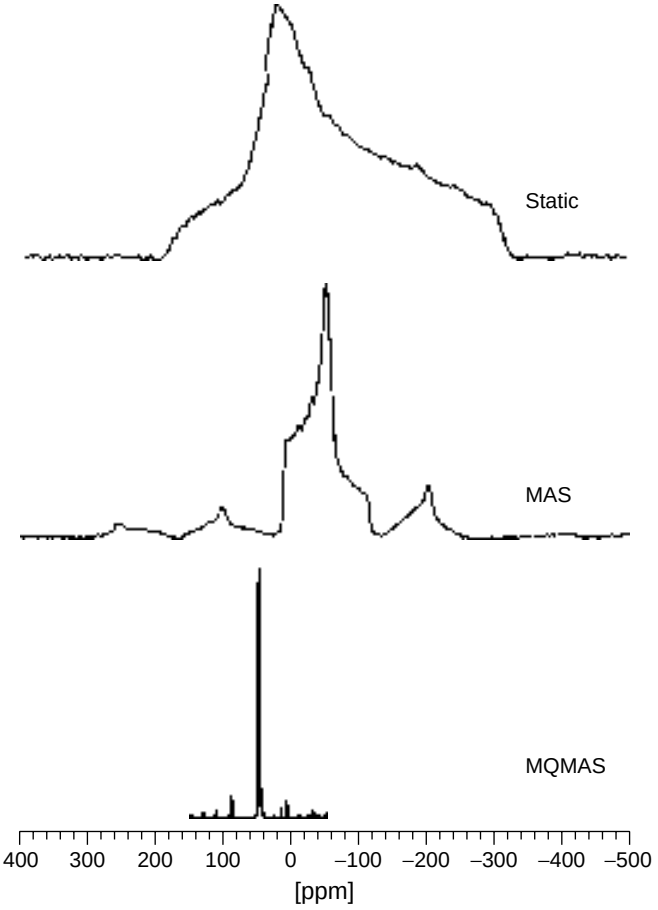

Figure 1 Static, MAS and MQMAS (isotropic projection) spectra of ^{87}Rb in polycrystalline $LiRbSO_4$ taken at 130.88 MHz

theoretical background and explanation of spin manipulations involved in MQMAS, including excitation, conversion and selection of transfer pathways for MQ coherences, is given by L. Frydman (see **Multiple-quantum Magic-angle Spinning Experiments on Half-integer Nuclei: Fundamentals**). In this article, only a brief description of the fundamental principles of the MQMAS experiment is presented. Subsequently, we review the schemes for detection of pure-phase spectra, the data processing methods (including referencing, quantitative analysis and interpretation of MQMAS spectra) and the MQMAS-based double resonance experiments.

2 THEORETICAL BACKGROUND

We consider an ensemble of nuclei with half-integer spin quantum number $S > 1/2$ in a strong magnetic field. There are $2S + 1$ Zeeman energy levels associated with such spins that can be labeled with their magnetic quantum number m. The existence of a non-vanishing (m, m′) element in the density matrix shows that there is a p-quantum coherent superposition of the states $|m\rangle$ and $|m'\rangle$ with multiplicity defined by $p = m - m'$. Thus, the diagonal elements of the density matrix (m, m), which represent the relative populations of the Zeeman states $|m\rangle$, correspond to zero-quantum coherences. It can be shown that these are the only coherences present in the density matrix of a system at thermal equilibrium. Under the conditions normally encountered in NMR the reduced density matrix can be used, which describes the relative deviations from a completely uniform distribution. The reduced density matrix at thermal equilibrium is proportional to S_z (the z component of the total spin angular momentum operator S).

In the frame of the Zeeman interaction, i.e., the 'rotating frame', the secular second order Hamiltonian governing the S spin system can be written as

$$H = H_{Q1} + H_{Q2} + [\nu_0\Delta\delta + m_I J + F(\alpha_s, \beta_s)]S_z \quad (1)$$

where

$$H_{Q1} = \overline{\nu}_Q(\alpha_s, \beta_s, \eta_Q)[S_z^2 - S^2/3] \quad (2)$$

$$H_{Q2} = -\frac{\nu_Q^2}{2\nu_0}[V_1V_{-1}(4S^2 - 8S_z^2 - 1) + V_2V_{-2}(2S^2 - 2S_z^2 - 1)]S_z$$
$$= B(\alpha_s, \beta_s, \eta_Q)S_z + D(\alpha_s, \beta_s, \eta_Q)S_z^3 \quad (3)$$

with

$$\overline{\nu}_Q(\alpha_s, \beta_s, \eta_Q) = 1.5\nu_Q[3\cos^2\beta_s - 1 + \eta_Q\sin^2\beta_s\cos 2\alpha_s] \quad (4)$$

and

$$\nu_Q = \frac{e^2qQ}{4S(2S-1)h} = \frac{C_Q}{4S(2S-1)} \quad (5)$$

In the above equations H_{Q1} and H_{Q2} represent the first and second order perturbation terms for the quadrupole interaction, $\Delta\delta$ is the resonance offset (in ppm), J is the scalar coupling constant between spin S and another spin I with magnetic number m_I, eq is the largest principal axis value of the EFG tensor, C_Q is the quadrupole coupling constant, while ν_0 and h have their usual meaning. The last term in equation (1) accounts for CSA, the anisotropy of J coupling and heteronuclear dipolar couplings, $\overline{\nu}_Q$ is the quadrupole splitting, and V_1, V_{-1}, V_2 and V_{-2} are the eigenvalues of the quadrupolar tensor in the laboratory frame. The orientation dependencies of F, $\overline{\nu}_Q$, V_1, V_{-1}, V_2 and V_{-2} can be described in terms of two polar angles α_s and β_s orienting the direction of $\mathbf{B}_0$ in the principal axis system (PAS) of the EFG tensor. Implicit in F is the dependence of the non-quadrupolar anisotropic interactions on their orientation with respect to the quadrupolar tensor, which can be described using additional sets of Euler angles.

The MQ transitions are induced using RF pulses. Following these excitations, coherences freely precess during the evolution periods. We first consider the free evolution of phase Φ^{stat} associated with the coherence (m, m′) in a single crystallite within a static sample under the Hamiltonian H described in equation (1). In the absence of RF magnetic field and relaxation processes this evolution can be written as

$$\Phi^{stat}(m, m') = [\overline{\nu}_Q(m + m') + \nu_0\Delta\delta + m_I J + F(\alpha_s, \beta_s)$$
$$+ B(\alpha_s, \beta_s, \eta_Q) + D(\alpha_s, \beta_s, \eta_Q)$$
$$\times (m^2 + mm' + m'^2)](m - m')t \quad (6)$$

It is clear that none of the internal Hamiltonians in equation (1) has an effect on the zero-quantum coherences (m, m). In nuclei with moderate or large ν_Q values, the first term in equation (6) is dominant. As a result, all non-diagonal elements ($m \neq \pm m'$) are quickly dephased, which prevents their further detection. For the anti-symmetric p-quantum coherences (p/2, −p/2), the evolution phase can be written as

$$\Phi^{stat}(p/2, -p/2) = \left\{p[\nu_0\Delta\delta + m_I J + F(\alpha_s, \beta_s)] + \sum_{k=0,2,4} A_k^Q(\alpha_s, \beta_s, \eta_Q)C_k(S, p)\right\}t \quad (7)$$

Explicit expressions for $A_k^Q(\alpha_s, \beta_s, \eta_Q)$ and $C_k(S, p)$ can be found in Amoureux.[41]

Under high-speed sample spinning at an angle χ with respect to $\mathbf{B}_0$, the evolution phase changes to

$$\Phi^{\chi}(p/2, -p/2) = \{p[\nu_0\Delta\delta + m_I J] + A_0^Q(\eta_Q)C_0(S, p)$$
$$+ [pF(\alpha_R, \beta_R) + A_2^Q(\alpha_R, \beta_R, \eta_Q)C_2(S, p)]P_2(\cos\chi)$$
$$+ A_4^Q(\alpha_R, \beta_R, \eta_Q)C_4(S, p)P_4(\cos\chi)\}t \quad (8)$$

where the polar angles α_R, β_R describe the orientation of the rotor axis with respect to the EFG tensor, and equation (9) shows the second and fourth order Legendre polynomials

$$P_2(\cos\chi) = \frac{1}{2}(3\cos^2\chi - 1)$$
$$P_4(\cos\chi) = \frac{1}{8}(35\cos^4\chi - 30\cos^2\chi + 3) \quad (9)$$

Equation (8) illustrates the challenge associated with observing high resolution spectra of half-integer quadrupolar spins: in a standard, single pulse experiment with a fixed rotation axis, the anisotropic broadening cannot be completely removed because no value of χ can simultaneously satisfy the condition $P_2(\cos\chi) = P_4(\cos\chi) = 0$. Consequently, the efficient line

narrowing methods must utilize more complex motions of the sample, or the spin magnetization. MQMAS technique achieves high resolution by involving both spatial and spin manipulations of the broadening interactions.[8] Under fast MAS rotation ($\chi_m = 54.74°$), the simplified evolution phase can be written as

$$\Phi^{MAS}(\frac{p}{2}, -\frac{p}{2}) = \{p[\nu_0\Delta\delta + m_I J] + A_0^Q(\eta_Q)C_0(S, p) + A_4^Q(\alpha_R, \beta_R, \eta_Q)C_4(S, p)P_4(\cos\chi_m)\}t \quad (10)$$

The remaining anisotropic broadening originates from the last term in equation (10), which is scaled with respect to a static case, but not eliminated by MAS alone. The unconventional aspect of the MQMAS approach is that the selective averaging of second-order quadrupolar broadening is completed by forcing the spin system to evolve outside of the 'allowed' central transition coherence, i.e., by transferring it into the multiple quantum coherences ($\mp p/2$, $\pm p/2$) with $p > 1$. After letting the spins evolve during time t_1, the spin system is transferred back to the ($-1/2$, $1/2$) coherence and allowed to freely evolve again during time t_2. The evolution phases in t_1 and t_2 are then correlated in a 2D experiment. The isotropic echo is observed as shown in equation (11), where R(S, p) is

$$t_{2e} = -[C_4(S, p)/C_4(S, -1)]t_1 = R(S, p)t_1 \quad (11)$$

$$R(S, p) = \frac{p[36S(S+1) - 17p^2 - 10]}{36S(S+1) - 27} \quad (12)$$

As the sign of $C_4(S, p)$ is reversed when changing that of p, it is always possible to obtain a positive ratio for R(S, p), which leads to a detectable echo at positive time t_{2e}. This echo signal corresponds to the selection of $p < 0$ for $|p| = 2S$ and $p > 0$ for $|p| < 2S$. Therefore, the echo pathway for spin $S = 3/2$ nuclei can be described using the notation $0 \rightarrow p = -3 \rightarrow -1$. Correspondingly, the correlation of $p = 3$ and $p = -1$ coherences ($0 \rightarrow 3 \rightarrow -1$ pathway) represents the so-called antiecho pathway, where the anisotropic quadrupolar broadening refocuses at negative values of the acquisition time t_2. The concept of antiecho will be later used in describing the experiments that allow for the acquisition of pure absorption spectra (Section 3).

A 2D Fourier transformation of the time domain signal provides a correlation spectrum, which consists of narrow resonance bands with ridges extended along the direction given by

$$F_1 = R(S, p)F_2 \quad (13)$$

where F_2 and F_1 represent frequencies in the single and multiple quantum dimensions, respectively. It is convenient to apply a shearing transformation in order to align these ridges with the F_2 direction. The shearing process transforms F_1 into a new isotropic dimension, which will be denoted F_{ISO} (see Section 4.2).

The basic MQMAS experiment consists of four steps:

(i) RF excitation of MQ coherences
(ii) evolution of these coherences under the internal Hamiltonian H during time t_1

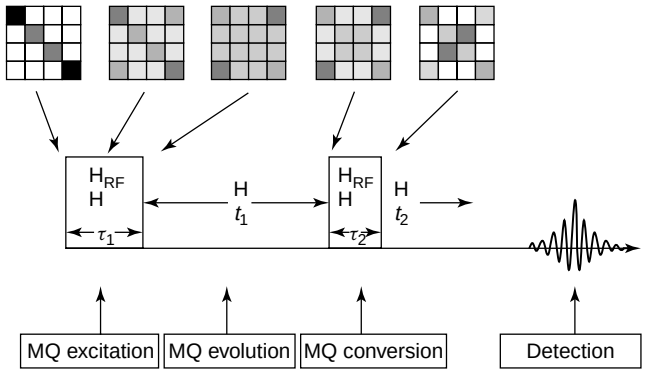

Figure 2 Schematic diagram of the original MQMAS experiment.[8] Time evolution of the reduced density matrix of spin-3/2 nuclei is also shown, with darker squares representing the increased amount of (m, m′) coherence

(iii) reconversion of the MQ coherences into the observable single quantum coherence, again using suitable RF sequence, and
(iv) detection of the signal as a function of time t_2.[8]

The pulse sequence used in the original MQMAS experiment contains two strong continuous wave (CW) RF pulses of duration τ_i and phase ϕ_i, used for preparation (MQ excitation) and mixing (MQ $\rightarrow -1$Q conversion): $H_1(\tau_1)_{\phi 1} - t_1 - H_2(\tau_2)_{\phi 2} - t_2$, as shown in Figure 2. The role of the excitation pulse (or sequence) is to create the largest possible amount of p-quantum coherence along the anti-diagonal of the density matrix (($\pm p/2$, $\mp p/2$), $3 \leq |p| \leq 2S$), as shown schematically on top of the figure for $S = 3/2$. The dephasing that this coherence acquires during the evolution time t_1 is then selectively transferred to the observable -1Q central transition by the second pulse (or sequence) where it refocuses according to equation (11).

Considerable research effort targeted two main weaknesses of MQMAS, namely the limited efficiency of excitation and reconversion, and sensitivity to the magnitude of C_Q. The efficiency could be significantly increased by using the highest possible RF magnetic field ν_{RF} (the so-called hard pulses), fast amplitude modulation (FAM), double frequency sweeps (DFS), rotary resonance excitation and rotation-induced adiabatic coherence transfer method (RIACT).[42–47] FAM, DFS and RIACT are least sensitive to C_Q and thus extend the range of quadrupolar couplings that are accessible to MQMAS to larger values. The most commonly used coherence pathways and acquisition schemes include the split-t_1 scheme with shifted (whole) echo and the z-filter method.[48–51] Several studies were reported that reviewed these schemes and evaluated their performance using standard samples.[40,52,53] At present, it appears that the split-t_1 whole echo scheme with FAM conversion could become a method of choice in MQMAS NMR, as it combines high efficiency with quantitative accuracy and is easy to implement in standard NMR spectrometers.

3 DETECTION OF PURE-PHASE SPECTRA

In general, the time domain signal corresponding to a single resonance in a given crystallite is given by a phase-modulated

function

$$s(t_1, t_2) = s_p \exp(2\pi i \nu_p t_1) \exp(2\pi i \nu_{-1} t_2) \exp[-(\lambda_p t_1 + \lambda_1 t_2)] \quad (14)$$

where s_p represents the amplitude of signal derived via the $0 \rightarrow p \rightarrow -1$ pathway, ν_p and ν_{-1} are the resonance frequencies of the symmetric coherences in p-quantum (p/2, −p/2) and single quantum (−1/2, 1/2) dimensions, and λ's represent the respective transverse relaxation rates (note that $\lambda_p = \lambda_{-p}$). Phase modulation of the detected signal is invariably encountered in 2D spectroscopy while using a single coherence transfer pathway.[54] A complex 2D Fourier transformation of $s(t_1, t_2)$ yields the frequency spectrum

$$S(F_1, F_2) = s_p[a(F_1, \nu_p) + id(F_1, \nu_p)][a(F_2, \nu_{-1}) + id(F_2, \nu_{-1})] \quad (15)$$

where $a(F_i, \nu_j)$ and $d(F_i, \nu_j)$, with i = 1,2 and j = p, −1, are the absorptive (real) and dispersive (imaginary) parts of the spectrum along the multiple and single quantum dimensions

$$a(F_i, \nu_j) = \frac{\lambda_j}{\lambda_j^2 + (F_i - \nu_j)^2}$$

$$d(F_i, \nu_j) = \frac{F_i - \nu_j}{\lambda_j^2 + (F_i - \nu_j)^2} \quad (16)$$

The absorptive and dispersive components are superimposed in equation (15), giving rise to phase-twisted lineshapes. This problem cannot be avoided simply by the adjustment of the phase sensitive detector. Although such a procedure allows the selection of the real part of $S(F_1, F_2)$

$$S^R(F_1, F_2) = s_p[a(F_1, \nu_p)a(F_2, \nu_{-1}) - d(F_1, \nu_p)d(F_2, \nu_{-1})] \quad (17)$$

the absorptive and dispersive components remain mixed in the spectrum. Such mixed-phase spectra were observed in the first MQMAS experiments that used the selection of a single coherence pathway, sometimes referred to as simple echo or simple antiecho (see Figure 3a). This is a major shortcoming, especially in cases where the observation of undistorted lineshapes in the anisotropic dimension is of significant interest or when two resonances are located in close proximity in a 2D spectrum (compare spectrum (a) with a properly acquired and phased spectrum (b) in Figure 3). The basic concepts of phase separation were first developed to facilitate the analysis of 2D correlation spectra in solutions.[54] Since the inception of MQMAS, several strategies for the collection and processing of the data have been proposed, which in essence allow for the 2D phase-adjustment. These strategies can be classified into two categories, based on the appearance of the maximum echo signal in the first row (i.e., $t_1 = 0$) of the 2D data set. The first involves a phase modulated procedure in which the maximum signal (echo) is delayed to $t_{2e} > 0$ by applying one or several $\pm 1Q \rightarrow \mp 1Q$ Hahn echoes.[14] The second category includes amplitude modulated experiments in which $t_{2e} = 0$ for $t_1 = 0$. The performance of various approaches has been thoroughly examined and compared by Brown and Wimperis.[52] We will review these methods briefly in Sections 3.1 and 3.2. Sections 3.3 and 3.4 will describe the methods that allow determination of the sign

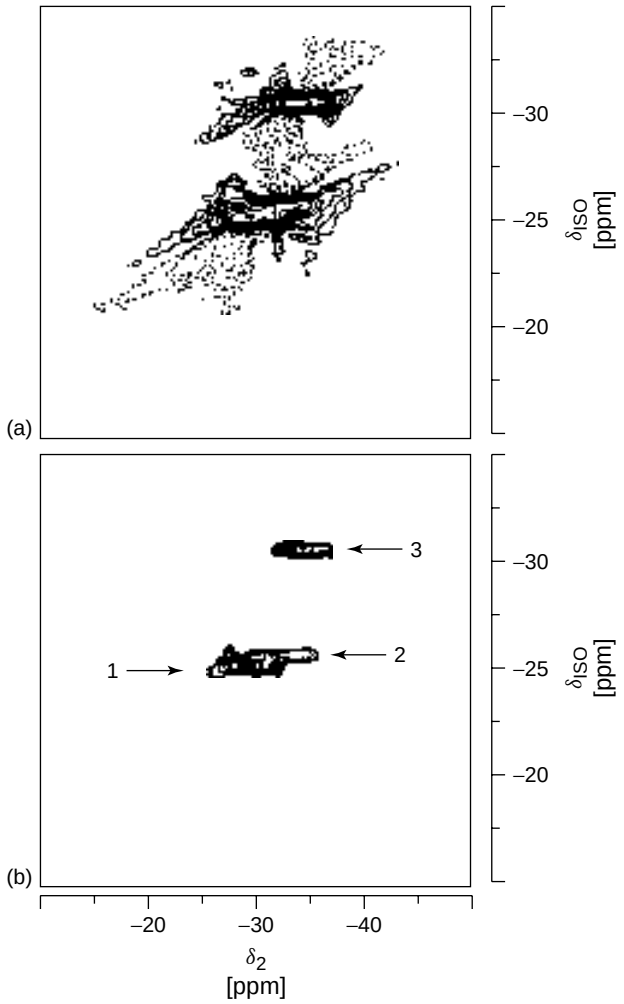

Figure 3 Sheared 3QMAS spectra measured for ^{87}Rb in $RbNO_3$. The following experimental conditions were used: $\nu_0 = 196.4$ MHz, $\nu_{RF} = 70$ kHz, $\nu_R = 10$ kHz. Positive and negative levels are represented on the contour plots by solid and dashed lines, respectively. Spectrum (a) results from acquisition of an echo coherence transfer pathway ($0 \rightarrow -3 \rightarrow -1$). When both echo and antiecho pathways ($0 \rightarrow \pm 3 \rightarrow -1$) are properly used, see spectrum (b), the dispersive parts disappear and all three Rb species present in this compound can be distinguished

of frequency in the F_1 dimension for experiments involving amplitude modulation.

3.1 Phase Modulation during t_1; Shifted Echo and Antiecho

The method of shifting the echo (and/or antiecho) eliminates the dispersive components from the spectrum by utilizing the symmetry properties of the time domain signals and their complex Fourier transforms. The complex Fourier transform of the two halves of a suitably phased symmetrical NMR echo is real. Each half yields the absorption components with the same phase and the dispersion components with opposite phases, which thus cancel. In MQMAS, the shifted echo (antiecho) approach relies upon the introduction of a refocusing π pulse at the end of the pulse sequence in order to delay the formation of an echo (antiecho) in the t_2 domain by a time interval τ.[50,52]

The time domain signals, the pulse sequence and the corresponding coherence transfer pathways for these experiments are schematically shown in Figure 4. As mentioned earlier, the 2D data set that results from the use of a single coherence pathway exhibits phase modulation. In such case, the 2D time-domain signal can be written as shown in equations (18) and (19)

$$s(t_1, t_2, \tau) = s_p \exp(2\pi i \nu_p t_1) \exp(2\pi i \nu_1 \tau) \exp(2\pi i \nu_{-1} t_2) \times \exp[-(\lambda_p t_1 + \lambda_1 \tau + \lambda_1 t_2)] \quad (18)$$

Since $\nu_1 = -\nu_{-1}$,

$$s(t_1, t_2, \tau) = s(t_1, t_2, 0) \exp[-(2\pi i \nu_{-1} + \lambda_1)\tau] \quad (19)$$

In the time domain, the signal first appears at $t_2 < \tau + t_{2e}$, where t_{2e} is given by equation (11) for echo and antiecho. The signal then rises until reaching a maximum at $t_2 = \tau + t_{2e}$, and decays to zero at $t_2 > \tau + t_{2e}$. The echo and antiecho signals (Figures 4a and 4b) shift forward and backward, respectively, as the time t_1 increases. It is important that the delay time τ be long enough to avoid truncation of the signal at any value of t_1. In this case, the shifted echo and shifted antiecho methods are referred to as whole echo experiments.[50] Clearly, the delay τ has to be longer in the case of the shifted antiecho, which can result in noticeable loss of signal due to transverse relaxation. A complex 2D Fourier transformation of $s(t_1, t_2, \tau)$, followed by a first-order phase correction of $2\pi \nu_{-1} \tau$ in the F_2 dimension, yields a spectrum described by

$$S(F_1, F_2) = 2s_p[a(F_1, \nu_p) + id(F_1, \nu_p)]a(F_2, \nu_{-1}) \exp(-2\lambda_1 \tau) \quad (20)$$

Hence, a pure phase spectrum is obtained in spite of the fact that the time domain signal given by equation (18) is phase modulated. The signal to noise (S/N) ratio is multiplied by $\sqrt{2}\exp(-2\lambda_1\tau)$, compared to the standard (non-shifted) method, and thus can be increased when the transverse losses are minor. An added advantage here is that phase modulation in itself yields sign discrimination in the F_1 domain. It is important to note that the success of these techniques in obtaining pure-phase spectra relies upon the ability of obtaining a symmetric function in the time domain for each value of t_1. Thus, it is essential that inhomogeneous second order quadrupolar broadening dominates the homogeneous effect due to, for example, the homonuclear dipolar interaction (see also Section 4.3). However, there appears to be no difference in resolution between the techniques leading to the shifted echo or antiecho.[52]

While the above method utilizes sequences for acquisition of signals via the echo or antiecho pathways in separate experiments, the shifted echo and shifted antiecho can be detected simultaneously (Figure 4c). By using the schemes that yield equal intensities of these two signals, an amplitude modulated spectrum can be obtained as described in the next section.[50]

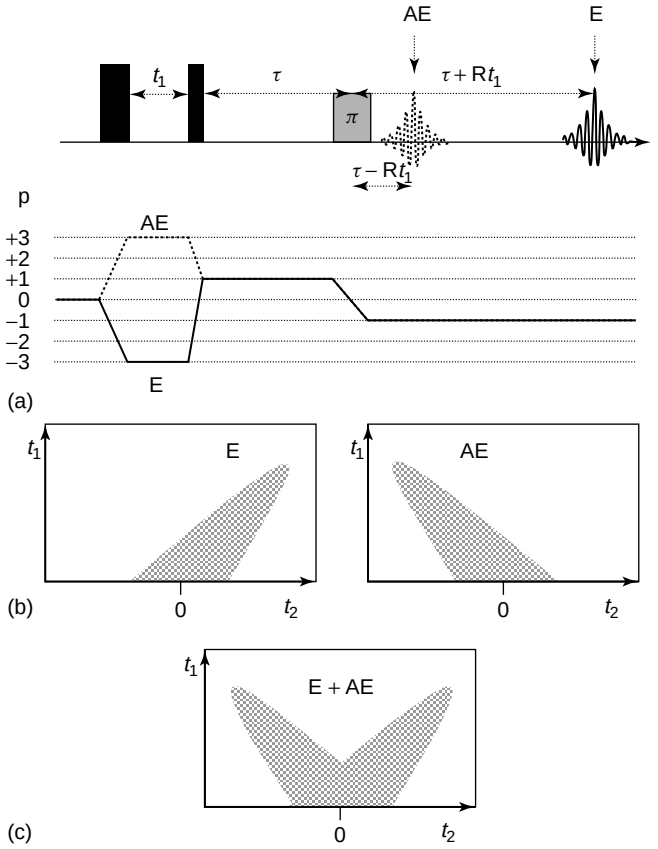

Figure 4 (a) Pulse sequence and coherence transfer pathways for the whole echo (antiecho) experiments, with $S = 3/2$ nuclei. Nonselective (hard) and selective (soft) pulses are represented by black and gray rectangles, respectively. (b) Time domain signals for shifted echo (E) and shifted antiecho (AE) phase modulated experiments. The signal is observed after the third pulse at $t_{2e} = \tau + Rt_1$ for the echo and at $t_{2e} = \tau - Rt_1$ for the antiecho. (c) Similar representation of the whole echo experiment in which shifted echo and shifted antiecho signals are acquired simultaneously

3.2 Amplitude Modulation during t_1; Z-filter Method

A frequently used approach for phase separation is to produce a time domain signal with amplitude modulation. In MQMAS this can be easily accomplished by using a linear combination of the signals from echo and antiecho coherence pathways. In general, this signal can be written as

$$s(t_1, t_2) = [s_p \exp(2\pi i \nu_p t_1) + s_{-p} \exp(2\pi i \nu_{-p} t_1)] \times \exp(2\pi i \nu_{-1} - \lambda_1) t_2 \exp(-\lambda_p t_1) \quad (21)$$

where $\nu_p = -\nu_{-p}$. When $s_p = s_{-p}$, the evolution during t_1 can be described by a cosine amplitude-modulated function

$$s(t_1, t_2) = 2s_p \cos(2\pi \nu_p t_1) \exp(2\pi i \nu_{-1} t_2) \exp[-(\lambda_1 t_2 + \lambda_p t_1)] \quad (22)$$

A 2D Fourier transform of this signal (complex in t_2 and complex in t_1 of the real part of $S(t_1, F_2)$) yields the spectrum $S(F_1, F_2)$ with a purely absorptive real part

$$S(F_1, F_2) = s_p\{[a(F_1, \nu_p) + a(F_1, -\nu_p)] + i[d(F_1, \nu_p) - d(F_1, -\nu_p)]\}a(F_2, \nu_{-1}) \quad (23)$$

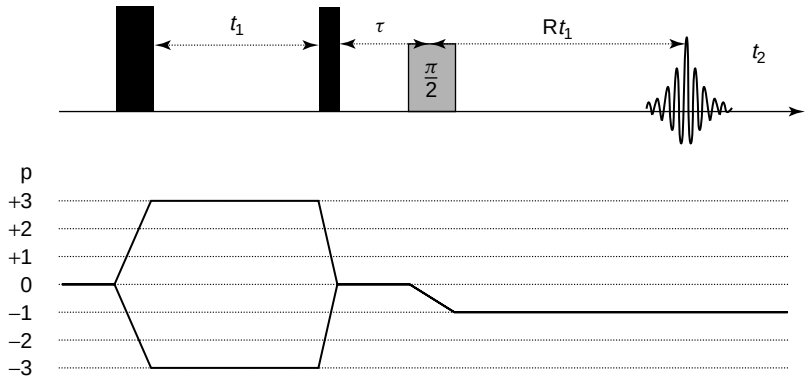

Figure 5 Pulse sequence and coherence transfer pathway for z-filter MQMAS

Note that the same purely absorptive real part can also be obtained by a 2D Fourier transform that is complex in t_2 and real (cosine) in t_1

$$S(F_1, F_2) = s_p[a(F_1, \nu_p) + a(F_1, -\nu_p)][a(F_2, \nu_{-1}) + id(F_2, \nu_{-1})] \quad (24)$$

When $s_p = -s_{-p}$, the evolution during t_1 becomes a sine amplitude-modulated function

$$s(t_1, t_2) = 2is_p \sin(2\pi\nu_p t_1) \exp(2\pi i\nu_{-1} t_2) \exp[-(\lambda_1 t_2 + \lambda_p t_1)] \quad (25)$$

and the same purely absorptive spectrum can be obtained in similar ways.

Although the acquisition of signals from the coherence transfer pathways leading to echo and antiecho can be done in two consecutive experiments, e.g., by proper selection of $0 \rightarrow +p \rightarrow -1$ and $0 \rightarrow -p \rightarrow -1$ pathways, it is more suitable to acquire these signals simultaneously.[42] For spin-3/2 nuclei, by choosing the length of the conversion pulse such that the corresponding flip-angle is approximately 90° and by using a 6-phase cycling scheme, one can acquire a single, sine amplitude-modulated free induction decay (FID) from these two pathways. The equalization $s_p = -s_{-p}$ does not merely reflect an average over the powdered sample, but occurs for each crystallite regardless of its orientation, at least for moderate values of H_{Q2}. It has been shown, that such acquisition can be also applied in concert with RIACT method.[47,55] In this technique, the efficiencies of both pathways $0 \rightarrow \pm 3 \rightarrow -1$ are essentially the same when a sufficiently large RF magnetic field is used.

However, the simultaneous balancing of the echo and antiecho intensities in 3QMAS becomes increasingly difficult for higher spin quantum numbers. Under no conditions can the echo and antiecho intensities be equalized for all individual crystallites, and only a powder-averaged matching of intensities is possible when $S > 3/2$. Although this matching can be obtained with relatively good efficiency, the resulting spectra invariably exhibit a dispersive phase. The difficulties are further increased for MQ experiments of higher order, where this equalization procedure causes a significant loss of signal.

The shortcomings of the above method can be quite easily overcome by using a so-called 'z-filter'.[48,51] This approach to eliminate phase distortions has been used earlier in 1D and 2D liquid state NMR and in DAS experiments.[54,56] The implementation of the z-filter into the 3QMAS experiment utilizing two hard pulses and the corresponding coherence transfer pathways are shown in Figure 5.[51] The z-filter consists of a short delay τ during which all magnetizations are stored along $\mathbf{B}_0$ (z-axis of the laboratory frame) as zero quantum coherences, and then transferred back to the observable single quantum coherences using a 'soft' pulse with selective $\pi/2$ flip angle. Thus, the sequence utilizes the $(0 \rightarrow \pm p \rightarrow 0 \rightarrow -1)$ coherence pathway, which results in the contributions of the echoes and anti-echoes being completely symmetric in terms of coherence transfers during the first and second hard pulses. Consequently, the efficiencies of both pathways are equal for all crystallites, leading to cosine amplitude-modulation of the 2D signal (Figure 6). An added advantage of this method is that it is robust and easy to optimize. The first pulse is adjusted to generate the maximum amount of the desired MQ coherences, and the second pulse maximizes their transfer to the zero quantum level. The delay τ must be long enough to eliminate the 'undesired' coherences that may be present due to incomplete MQ filtering, and short enough to prevent the line broadening and signal loss due to homogeneous dipolar effects and chemical exchange processes. A delay equivalent to few rotor periods is usually a good trade-off. This delay can be extended and used as a mixing time in the measurement of relative orientation of quadrupole tensors in well crystallized compounds.[57] The choice of a suitable ν_{RF} level for the soft z-filter pulse is also a compromise, in this case between selectivity and completeness of irradiation of the central transition. This is illustrated in Figure 7, which shows the relative intensities of z-filter MQMAS signals as a function of ν_{RF} applied to generate the soft pulse. This figure shows that although only a part of the signal is generated at very low values of ν_{RF} (i.e., when ν_{RF} is smaller than the MAS line width divided by $(S + 1/2)$), the use of very high strength of RF field diminishes the signal due to excitation of the undesired coherences. Setting ν_{RF} at 10–20 kHz is usually a good choice for the selective pulses in these types of experiments.

The amplitude modulated signals can be also obtained by simultaneous acquisition of the shifted echo and shifted antiecho signals, as shown schematically in Figure 4c.[50] A complete amplitude modulation is only observed when the contributions of the shifted echo and shifted antiecho are equal and, as was the case in the phase modulated whole echo experiments, when the inhomogeneous broadening dominates the lineshape. However, even when the contributions from

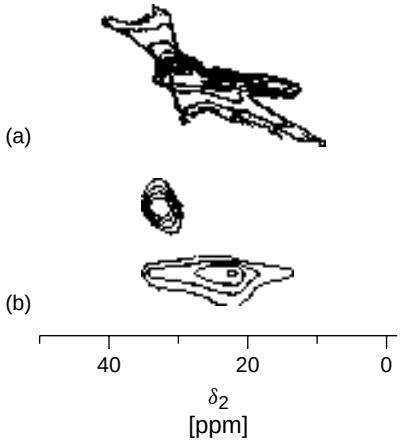

Figure 6 Two matching sections of ^{27}Al 3QMAS spectra in $AlPO_4$-14 recorded using two hard RF pulses: (a) phase modulated spectrum obtained without the z-filter (pathway $0 \rightarrow \pm 3 \rightarrow -1$) and (b) amplitude modulated spectrum measured using the z-filter (pathway $0 \rightarrow \pm 3 \rightarrow 0 \rightarrow -1$)

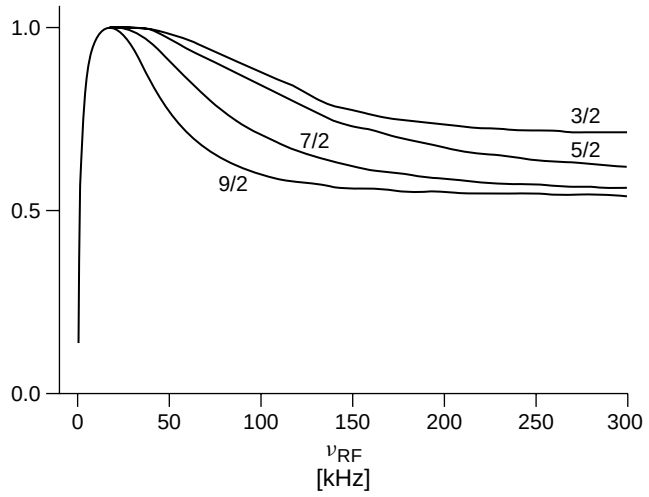

Figure 7 Evolution of the signal detected with the standard z-filter MQMAS experiment, as a function of ν_{RF} for the soft pulse. The following assumptions were made: the length of the soft pulse (in μs) is equal to $250\,000/(S + 1/2)\nu_{RF}$, the hard pulses use $\nu_{RF} = 300$ kHz, the irradiation is made on resonance at $\nu_o = 100$ MHz, $\nu_R = 15$ kHz and $\eta_Q = 0$. The full MAS line width is 19.3 kHz and the C_Q values are 6, 12.2, 18.8, and 25.5 MHz for $S = 3/2$, 5/2, 7/2 and 9/2, respectively. All curves are normalized to the maximum intensity value obtained with $\nu_{RF} = 20$ kHz

these two pathways are not equal, the 2D Fourier transform performed as described earlier in this section yields pure phase lineshapes.

The disadvantage of amplitude-modulated methods is that the resulting spectrum, described by equations (23) and (24), is fully symmetric with respect to $F_1 = 0$, i.e., the signals appearing at $F_1 = \nu_p$ and $F_1 = -\nu_p$ are indistinguishable. Thus, folding of frequencies in F_1 domain occurs in the 2D spectra obtained with such methods of acquisition. In principle, the problem of foldover can be avoided by locating the carrier frequency to one side of all spectral lines. Since this simple method causes loss of signal due to off-resonance irradiation and is often inconvenient, the so-called time-proportional phase increments (TPPI) approach or the hypercomplex data acquisition is often used to restore sign discrimination in F_1.

3.3 TPPI

In TPPI,[58] the phase ϕ^{prep} of the RF preparation pulse (or sequence) is incremented linearly with t_1

$$\phi^{prep} = \frac{\pi t_1}{2p\Delta t_1} \tag{26}$$

where Δt_1 is the time increment in t_1. The amplitude-modulated time domain signal, equation (22), then becomes

$$\begin{aligned} s(t_1, t_2) &= 2s_p \cos\left[2\pi\left(\nu_p t_1 + \frac{p\phi^{prep}}{2\pi}\right)\right] \\ &\quad \times \exp(2\pi i \nu_{-1} t_2) \exp[-(\lambda_1 t_2 + \lambda_p t_1)] \\ &= 2s_p \cos\left[2\pi\left(\nu_p + \frac{1}{4\Delta t_1}\right) t_1\right] \\ &\quad \times \exp(2\pi i \nu_{-1} t_2) \exp[-(\lambda_1 t_2 + \lambda_p t_1)] \end{aligned} \tag{27}$$

After Fourier transformation, the spectrum is as described by equations (23) and (24). Its real part is purely absorptive and equal to

$$\begin{aligned} S^R(F_1, F_2) = s_p \Bigg[& a\left(F_1, \nu_p + \frac{1}{4\Delta t_1}\right) \\ & + a\left(F_1, -\nu_p - \frac{1}{4\Delta t_1}\right)\Bigg] a(F_2, \nu_{-1}) \end{aligned} \tag{28}$$

i.e., the resulting spectrum is shifted along F_1 by $+1/4\Delta t_1$ for ν_p and by $-1/4\Delta t_1$ for its folded resonance. Thus, it becomes possible to place the carrier frequency in the center of the spectral region and discriminate between positive and negative offsets as if the signal were acquired in quadrature mode. It is advisable to decrease Δt_1 (increase the Nyquist frequency) by a factor of two with respect to an experiment done without TPPI, in order to avoid the frequency foldover between $a(F_1, \nu_p)$ and $a(F_1, -\nu_p)$.

3.4 Hypercomplex Data Acquisition (States Method)

The hypercomplex approach, also known as the States method, relies upon acquisition of signals from two complementary experiments, which provide the distinction of real and imaginary parts in t_1 in the same way as the classical quadrature detection does in t_2.[59] Both echo and antiecho signals in MQMAS are acquired simultaneously in this method. For each increment in t_1, two time domain signals s_X and s_Y are created and measured with the phases ϕ^{prep} of the preparation sequence equal to 0 and $\pi/2p$, respectively (see equations (29) and (30)).[50]

$$\begin{aligned} s_X(t_1, t_2) &= 2s_p \cos(2\pi \nu_p t_1) \exp(2\pi i \nu_{-1} t_2) \\ &\quad \times \exp[-(\lambda_1 t_2 + \lambda_p t_1)] \end{aligned} \tag{29}$$

$$\begin{aligned} s_Y(t_1, t_2) &= 2s_p \cos(2\pi \nu_p t_1 + p\phi^{prep}) \exp(2\pi i \nu_{-1} t_2) \\ &\quad \times \exp[-(\lambda_1 t_2 + \lambda_p t_1)] \\ &= -2s_p \sin(2\pi \nu_p t_1) \exp(2\pi i \nu_{-1} t_2) \\ &\quad \times \exp[-(\lambda_1 t_2 + \lambda_p t_1)] \end{aligned} \tag{30}$$

We assume here that the echo and antiecho contribute equally to the observed signal, i.e., that the condition $s_p = s_{-p}$ holds for s_X and s_Y. This can be accomplished using the methods described in Section 3.2. The complex Fourier transformation in t_2 yields equations (31) and (32)

$$s_X(t_1, F_2) = 2s_p \cos(2\pi \nu_p t_1)[a(F_2, \nu_{-1}) + id(F_2, \nu_{-1})] \exp(-\lambda_p t_1) \quad (31)$$

$$s_Y(t_1, F_2) = -2s_p \sin(2\pi \nu_p t_1)[a(F_2, \nu_{-1}) + id(F_2, \nu_{-1})] \exp(-\lambda_p t_1) \quad (32)$$

The real parts of s_X and s_Y are then combined to produce a new complex signal

$$s(t_1, F_2) = s_X^R(t_1, F_2) - is_Y^R(t_1, F_2) = 2s_p a(F_2, \nu_{-1}) \times \exp(2\pi i \nu_p t_1) \exp(-\lambda_p t_1) \quad (33)$$

A complex Fourier transformation of $s(t_1, F_2)$ with respect to t_1 then produces, for the real part, a pure-phase spectrum

$$S(F_1, F_2) = 2s_p a(F_2, \nu_{-1})[a(F_1, \nu_p) + id(F_1, \nu_p)] \quad (34)$$

with a single resonance located at $(F_1, F_2) = (\nu_p, \nu_{-1})$.

The TPPI and hypercomplex methods result in the same S/N ratio per unit of experimental time. However, the hypercomplex method allows for separating of the echo and antiecho signals according to

$$s_E(t_1, t_2) = s_X(t_1, t_2) - is_Y(t_1, t_2)$$
$$s_A(t_1, t_2) = s_X(t_1, t_2) + is_Y(t_1, t_2) \quad (35)$$

which can be independently processed (e.g., apodized).

4 PROCESSING AND INTERPRETATION OF MQMAS SPECTRA

One of the primary benefits of MQMAS is that it allows for separation and measurement of the isotropic chemical and quadrupolar-induced shifts by analyzing a single 2D spectrum.[9] However, proper assignment of the resonance shifts along the F_1 and F_2 dimensions in such an analysis is not immediately obvious. In this section, we examine the distribution of resonances in MQMAS spectra and discuss the interpretation of resonance shifts that result from processing the data with and without the shearing transformation.

4.1 Unsheared Spectrum

A typical MQMAS spectrum, resulting from a standard 2D Fourier transformation of a temporal data set obtained with the methods described in the previous sections, consists of several extended bands similar to those depicted in Figure 8a. Analysis and interpretation of such an unsheared spectrum is facilitated by introducing the chemical shift (CS) axis, the anisotropic (A) axis and the quadrupolar induced shift (QIS) axis. In a hypothetical spectrum with negligible quadrupolar interactions, the resonances would be sharp and located on the CS axis at $-p\nu_0\Delta\delta$ and $\nu_0\Delta\delta$ in the multiple and single quantum dimensions, respectively. The slope of the CS axis

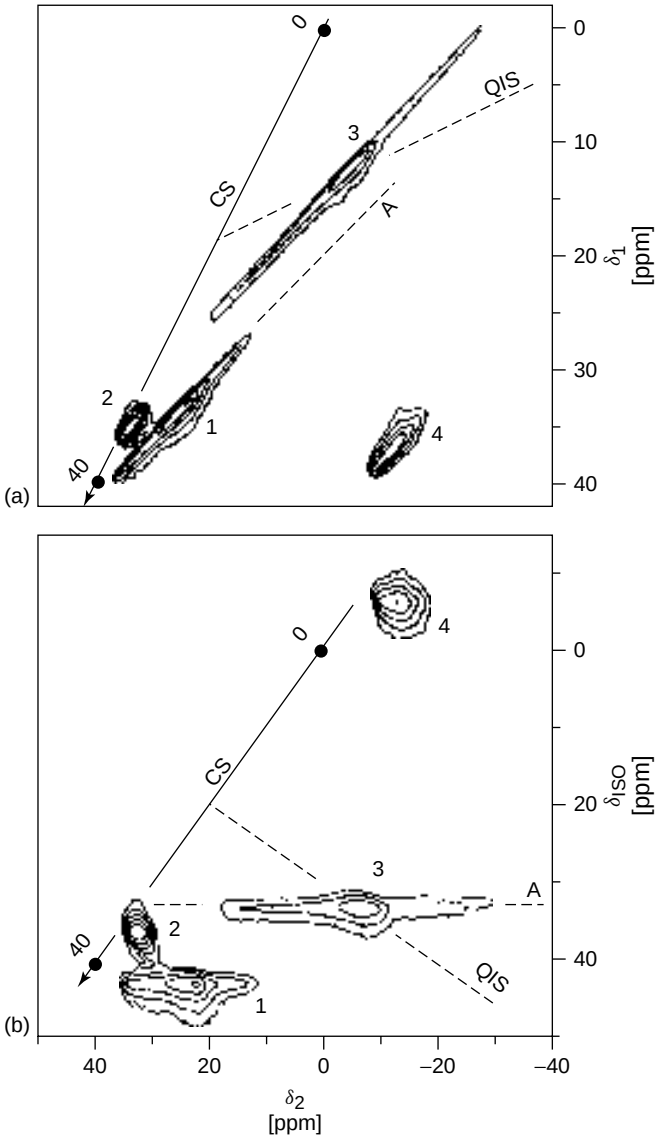

Figure 8 (a) Unsheared and (b) sheared 3QMAS spectra of ^{27}Al in $AlPO_4$-14 acquired at $\nu_0 = 104.2$ MHz using the z-filter sequence with rotor synchronization, $\nu_R = 14.5$ kHz, and $\nu_{RF} = 200$ kHz. The CS, A and QIS axes are plotted, as described in the text. Two tetrahedral sites (1 and 2), one fivefold coordinated site (3) and one sixfold coordinated site (4) are resolved, in agreement with crystallographic data. Note that resonance 4 is folded over in (a) due to the limited spectral width in rotor-synchronized spectra

is either $-p$ when resonances are expressed in Hz or 1 when ppm scales are used instead (vide infra). The A axis is defined by the orientation of anisotropic ridges in MQMAS spectra (see equation (13)) and has a slope R(S, p) given by equation (12). In the MQMAS experiment, which detects only species with a non-zero quadrupolar interaction, the center of gravity of a given resonance is displaced from the CS axis, in both dimensions, by the quadrupolar-induced shift. Assuming that the efficiency of MQMAS is constant for all crystallite orientations, this shift [see equation (10)] can be expressed (in Hz) as

$$\nu_{QIS}(S, p) = A_0^Q(\eta_Q)C_0(S, p) \quad (36)$$

The direction in which this displacement occurs defines the QIS axis, which has a slope ξ given by

$$\xi(S, p) = \frac{\nu_{QIS}(S, p)}{\nu_{QIS}(S, -1)} = \frac{-p[4S(S+1) - 3p^2]}{[4S(S+1) - 3]} \quad (37)$$

Since for a given pair (S, p) the quadrupolar induced shifts have a unique sign, all observed resonances (except for the spinning sidebands) must appear on the same side of the CS axis, as seen in Figure 8. The factors R and ξ have been given in Amoureux and Fernandez for all experimentally accessible values of S and p.[60] With the help of these parameters, both the chemical shift and quadrupolar parameters can be extracted from the unsheared spectra in a straightforward manner. The isotropic chemical shift of a given resonance is simply found by projecting its center of gravity on the CS axis along the QIS direction. Similarly, the displacement of this resonance from the CS axis measured along F_1 and F_2 and given (in Hz) by

$$\nu_{QIS}(S, p) = \frac{3p}{10\nu_0} \frac{[4S(S+1) - 3p^2]}{[4S(2S-1)]^2} P_Q^2 \quad (38)$$

can be used to evaluate the second-order quadrupolar effect parameter P_Q

$$P_Q = C_Q \sqrt{1 + \eta_Q^2/3} \quad (39)$$

From equation (39), the quadrupolar coupling constant C_Q can be determined accurately, provided the asymmetry parameter η_Q is known, e.g., from simulation of MAS lineshape.

4.2 Shearing Transformation; Referencing of MQMAS Spectra

MQMAS spectra can be most conveniently analyzed by applying a shearing transformation, which places the A axis parallel to the F_2 axis (Figure 8b) and creates a new dimension labeled F_{ISO} (or δ_{ISO}). The direct advantage of such an approach is that the orthogonal projection of MQMAS spectrum onto the F_{ISO} axis does not include the anisotropic quadrupolar and chemical shift contributions. A similar projection onto the F_2 axis yields the pQ-filtered anisotropic MAS powder pattern. This pattern should not be generally used for the accurate determination of C_Q and η_Q due to the distortions of the observed intensities, which can be severe for large values of C_Q. In addition, for a given value of C_Q these distortions increase with increasing |p| (Figure 9a). More reliable values of C_Q and η_Q can be obtained from the simulation of the MAS spectra acquired using a short RF pulse.

In the sheared spectrum, the frequency F_{ISO} can be conveniently expressed as a linear combination of F_1 and F_2

$$F_{ISO} = F_1 + RF_2 \quad (40)$$

where R is given by equation (12). This convention allows for direct determination of the sample rotation rate from the sheared spectrum when it is plotted in Hz.[60] In order to introduce the referencing in ppm, let us first consider a single resonance that is not affected by the quadrupole interaction, located at coordinates $(-p\nu_0\Delta\delta,\ \nu_0\Delta\delta)$ on the CS axis of an unsheared spectrum. After the shearing transformation, its coordinate F_{ISO} in the isotropic dimension is given in

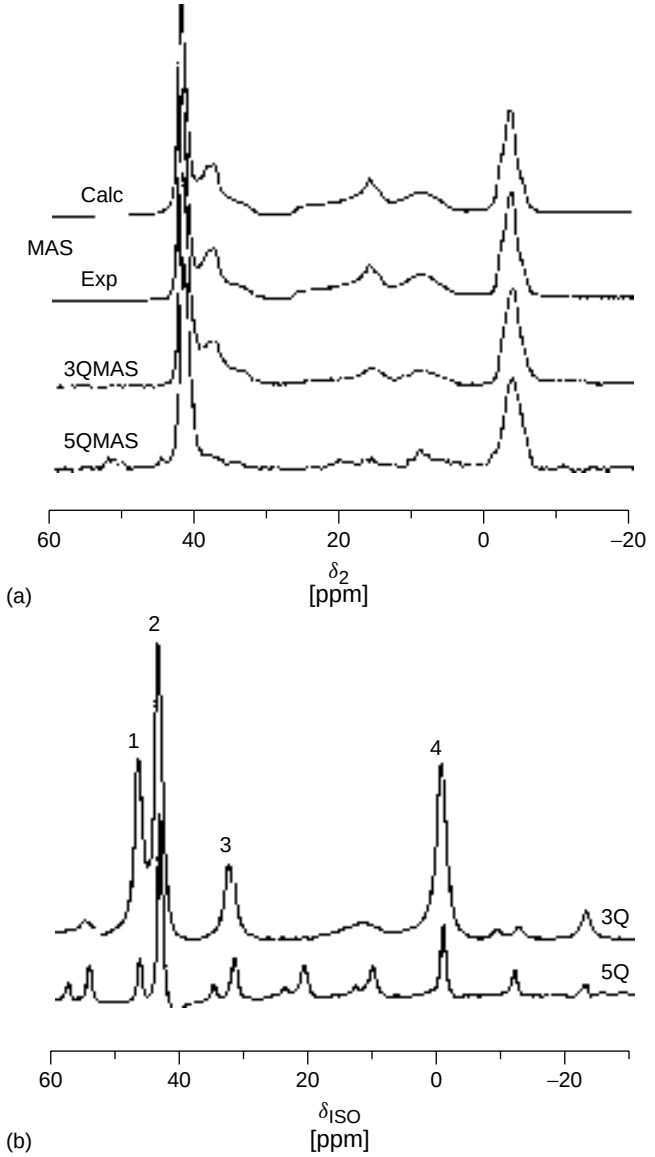

Figure 9 ^{27}Al NMR spectra of $AlPO_4$-14 obtained at 156.4 MHz: (a) simulated and experimental MAS spectrum obtained using a $\pi/12$ flip angle, compared with the anisotropic projections of 3QMAS and 5QMAS spectra; (b) isotropic projections of ^{27}Al MQMAS spectra. The isotropic resonances are labeled following Figure 8, the remaining peaks represent spinning sidebands

$$F_{ISO} = (R - p)\nu_0\Delta\delta \quad (41)$$

The ppm scales δ_1, δ_2 and δ_{ISO} use the apparent Larmor frequencies, which are equal to ν_0, $-p\nu_0$, and $(R - p)\nu_0$ along F_2, F_1 and F_{ISO}, respectively. In the absence of the quadrupole interaction, this convention results in the shifts being identical and equal to $\Delta\delta$ along the three axes.

We have seen above (equation (38)), that the quadrupole interaction shifts the resonance away from the CS axis in both dimensions. In an unsheared spectrum, this shift can be

expressed in ppm as equation (42) with equation (43)

$$\delta_{\mathrm{QIS}}(\mathrm{S,\,p}) = -\frac{\nu_{\mathrm{QIS}}(\mathrm{S,\,p})}{\mathrm{p}\nu_0}10^6 = -\frac{3}{10}\frac{[4\mathrm{S}(\mathrm{S}+1)-3\mathrm{p}^2]}{[4\mathrm{S}(2\mathrm{S}-1)]^2}\frac{\mathrm{P_Q^2}}{\nu_0^2}10^6 = \mathrm{k}_{|\mathrm{p}|}\mathrm{P_Q^2} \quad (42)$$

$$\mathrm{k}_{|\mathrm{p}|} = -\frac{3}{10}\frac{[4\mathrm{S}(\mathrm{S}+1)-3\mathrm{p}^2]}{[4\mathrm{S}(2\mathrm{S}-1)\nu_0]^2}10^6 \quad (43)$$

Clearly, $\delta_{\mathrm{QIS}}(\mathrm{S,\,p})$ is always negative along the δ_2 dimension ($\mathrm{k}_1 < 0$), but can be positive or negative along δ_1, depending on S and |p|. After the shearing transformation, the quadrupolar-induced shift in the $\mathrm{F_{ISO}}$ dimension becomes always positive and independent of p

$$\delta_{\mathrm{QIS,ISO}} = \frac{\nu_{\mathrm{QIS,ISO}}(\mathrm{S,\,p})}{(\mathrm{R}-\mathrm{p})\nu_0}10^6 = -\frac{10}{17}\delta_{\mathrm{QIS}}(\mathrm{S},-1) = -\frac{10}{17}\mathrm{k}_1\mathrm{P_Q^2} \quad (44)$$

Thus, the QIS direction in the 2D sheared spectrum expressed in ppm has a constant slope of $-10/17$, regardless of the values of S and p. Since the CS axis of such a spectrum has a constant slope of 1, the MQMAS sheared spectra displayed using these ppm scales are independent of p for a given spin system. To illustrate this point, the isotropic projections of 3QMAS and 5QMAS spectra of ^{27}Al in aluminophosphate $AlPO_4$-14 are compared in Figure 9b.[61]

Finally, it is interesting to note that MQMAS can be also useful in determination of the indirect scalar spin–spin coupling.[62] Indeed, while the J values are often small with the common quadrupolar nuclei, the J dephasing is proportional to p in the multiple quantum dimension [equation (10)] thus increasing the corresponding splitting in this dimension. Along the isotropic axis of the sheared spectrum, this splitting becomes independent of p when expressed in ppm

$$\delta_{\mathrm{ISO}} = \Delta\delta + \delta_{\mathrm{QIS,ISO}} + 10^6\mathrm{m_I}\mathrm{J}/\nu_0 \quad (45)$$

and therefore should preferentially be observed in 3QMAS for best sensitivity. Thus, in well crystallized samples, the presence of scalar coupling multiplets can be detected by recording the MQMAS spectra at different fields.

It should be noted that the above referencing scheme is directly applicable to the spectra obtained using satellite transitions and magic angle spinning (STMAS) NMR.[63] Again, the QIS slope of $-10/17$ is observed provided that the appropriate values of R are used. The apparent Larmor frequencies used to calculate the normalized shifts along the δ_{ISO} axis [see equation (41)] are half of those calculated for 3QMAS.

4.3 Split-t_1 Method

The split-t_1 method of data acquisition relies upon the splitting of time t_1 into single and multiple quantum evolution periods in proportion to the ratio R(S, p).[48] By doing so, the fourth-order anisotropic term given in equation (10) can be always refocused at the end of the t_1 period. After 2D Fourier transformation, the inhomogeneously broadened ridges appear parallel to the F_2 axis, which eliminates the need for the shearing transformation. As is shown below, the split-t_1 method has been combined with the whole echo experiment to provide a very efficient scheme for MQMAS. Another advantage of an echo being stationary within the acquisition period is that the time domain signal is easier to apodize by using t_1-independent weighting functions. This split-t_1 mode of data acquisition can be conveniently used in MQMAS-based heteronuclear correlation spectroscopy (MQ-HETCOR) experiments and in the Carr–Purcell–Meiboom–Gill (CPMG) MQMAS experiments (see Sections 5.1 and 6).

In the split-t_1 amplitude modulated methods, for each crystallite, the echo and antiecho coherence pathways must contribute to the processed signal with equal amplitude in order to obtain a pure absorption lineshape (see Section 3.2). For spin-3/2 nuclei, this can be achieved by using the coherence transfer pathway with the z-filter, $0 \rightarrow \pm3 \rightarrow \pm1 \rightarrow 0 \rightarrow -1$, as shown in Figure 10a.[52,64] The efficiency of this four-pulse method can be improved by using FAM, DFS or RIACT methods for the ±3Q to ±1Q conversion.[43–45,47,55,65,66] This scheme

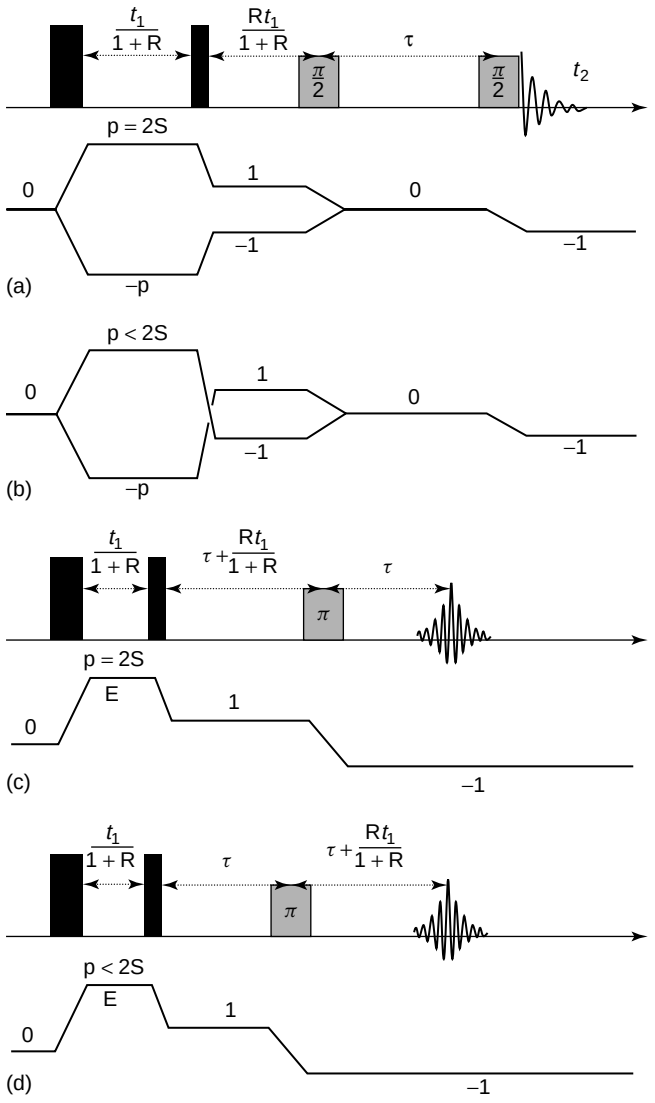

Figure 10 (a) Amplitude modulated split-t_1 pulse sequence and coherence pathway for $\mathrm{p} = 2\mathrm{S}$. For $\mathrm{p} < 2\mathrm{S}$, the experiment can be performed using the same pulse sequence and the coherence pathway as shown in figure (b). (c) and (d) Phase modulated split-t_1 pulse sequences and coherence pathways for $\mathrm{p} = 2\mathrm{S}$ and $\mathrm{p} < 2\mathrm{S}$

can easily be extended to 5-, 7-, and 9 QMAS experiments with spin-5/2, -7/2 and -9/2 nuclei. The symmetric split-t_1 pathways $0 \rightarrow \pm 3 \rightarrow \mp 1 \rightarrow 0 \rightarrow -1$ were also proposed for 3QMAS experiments with spins $S > 3/2$ (see Figure 10b). However, such experiments are relatively inefficient, as they involve the coherence change of $|\Delta p| = 4$ during $\pm 3 \rightarrow \mp 1$ conversion.

The split-t_1 method can be also used in phase modulated (shifted echo) experiments, which generate pure phase spectra through the acquisition of the whole echo. The coherence pathway displayed in Figure 10c ($0 \rightarrow 3 \rightarrow 1 \rightarrow -1$), uses $|\Delta p| = 2$ and requires a short spin echo interval.[52] For spin-3/2 systems in which the loss of magnetization due to T_2 effects is not significant, this MQMAS scheme has been recommended as the most efficient, especially when used with the FAM or DFS conversion.[40,52] This scheme works equally well in 5-, 7- and 9 QMAS experiments for spins 5/2, 7/2 and 9/2, respectively. For the MQMAS experiments with $|p| < 2S$, this scheme can be modified, as shown in Figure 10d. The referencing of split-t_1 spectra can be performed using the same method as described in Section 4.2.

4.4 Resolution of MQMAS Spectra

The timing of the echo formation, as described by equation (11), is independent on the size of quadrupolar and CSA interactions, the orientation of crystallites, and the experimental conditions (ν_{RF} and ν_R). Thus, isotropic resolution should be consistently achieved by the MQMAS method, at least in the absence of strong dipolar broadening. The isotropic line width has been analyzed in several 3QMAS spectra of $RbNO_3$ and $LiRbSO_4$, which were obtained using various schemes for coherence transfer with CW nutation, RIACT and FAM pulses.[40] $LiRbSO_4$ was particularly useful in these tests due to exceptionally narrow line observed in this compound (see Figure 1). Indeed, no significant changes in resolution were observed while switching between different coherence transfer schemes, ν_{RF} frequencies and conversion methods.

However, several authors have reported an enhancement of resolution upon increasing the MQ order p from three to five (and seven) both in crystalline and amorphous samples (see Figure 9b and Figure 11).[61,67,68] It should be noted that due to the presence of p-dependent scaling factors (see Section 4.2), non-uniform RF excitation, dipolar effects, and spinning

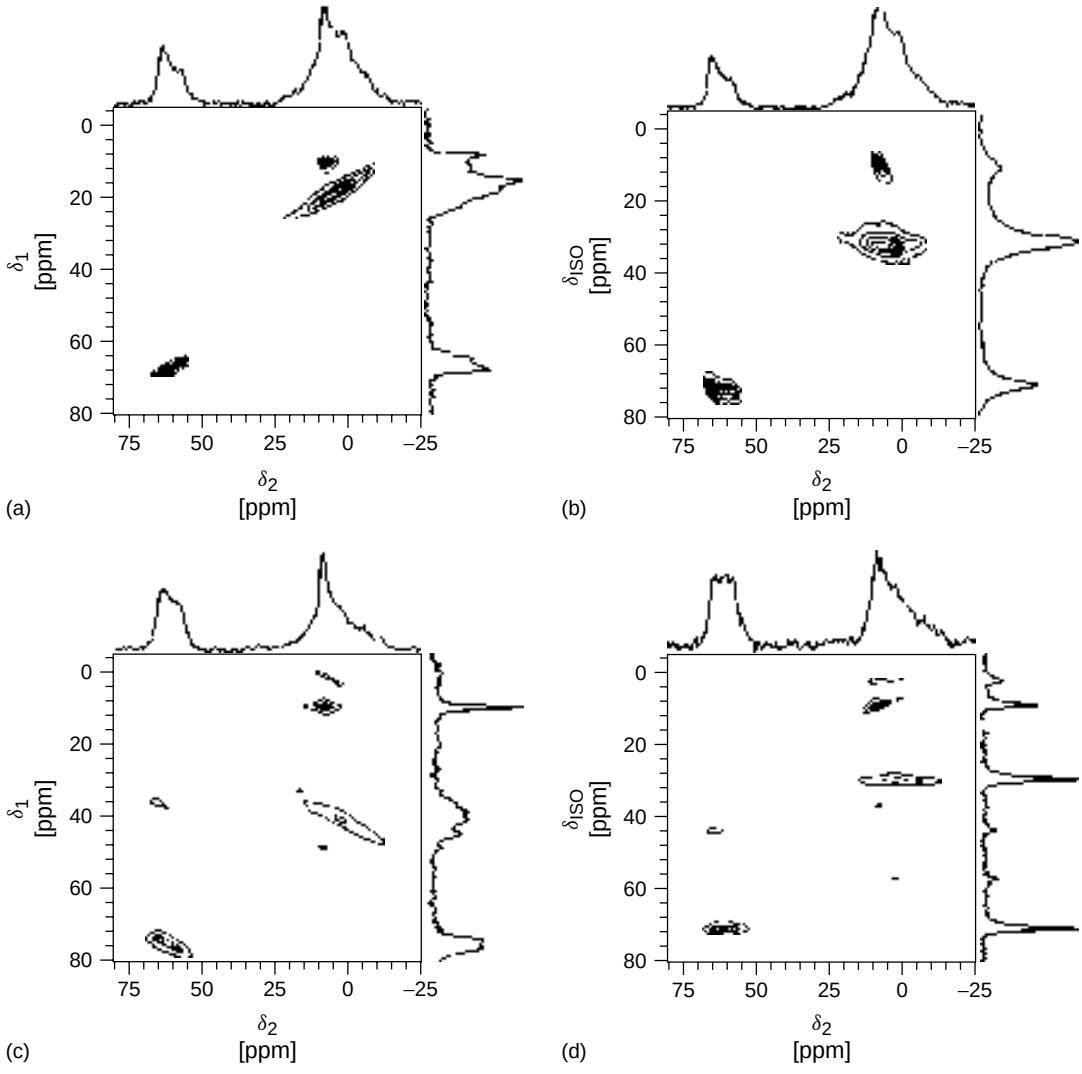

Figure 11 ^{27}Al MQMAS spectra of $SrAl_{12}O_{19}$: (a) unsheared 3QMAS, (b) sheared 3QMAS, (c) unsheared 5QMAS, and (d) sheared 5QMAS. Note the different appearance of spectral features in the Figures (a) and (c) due to the relocation of A and QIS axes

sidebands, a comparison between MQMAS experiments of different order is not straightforward. The improvement of resolution between 3QMAS and higher-order MQMAS spectra cannot be easily determined from the line width in ppm (which is arbitrary), or from the line width in Hz (due to different scaling factors involved). Instead, the dispersion of shifts relative to the observed line width along the isotropic dimension should be used when comparing these experiments.

However, it has also been noticed that this increase in the apparent resolution is not uniform among different spin systems. Recent investigations have attributed these effects to the interplay between inhomogeneous and homogeneous contributions to the isotropic line width.[67,68] In the case of well-crystallized samples, the inhomogeneous contributions may be due to inhomogeneity of the static magnetic field, changes in magnetic susceptibility, incomplete heteronuclear decoupling and second-order quadrupolar-dipolar couplings.[69,70] Since the Hamiltonians associated with these interactions are linear in S_z, under the p-quantum evolution the corresponding inhomogeneous broadening scales in the same way as the dispersion of isotropic shifts. Consequently, no apparent increase in resolution should be observed in higher-order MQMAS spectra.[60,68] The homogeneous contribution, however, is not expected to increase with p.[68] Therefore, in crystalline samples with strong homogeneous contribution to the line broadening, considerable enhancement of the isotropic resolution may be observed by moving to higher-order MQMAS schemes. This enhancement is less evident in amorphous samples, where the distribution of isotropic shifts dominates the spectra. In such cases, the more sensitive 3QMAS experiments are recommended.

Interestingly, the presence of dipolar interactions may have an opposite effect on the resolution. Since in a static sample the dipolar dephasing is proportional to p [F term in equation (7)], MAS averaging becomes less efficient in higher order multiple quantum experiments.[71] In the presence of strong dipolar interactions, continuous wave decoupling may be insufficient during t_1, and composite decoupling may be necessary to obtain a well resolved spectrum.[72,73] In the majority of applications, however, the most practical way to achieve efficient homo- and hetero-nuclear decoupling in MQMAS experiments is to use the highest possible spinning speed. The added advantage of using high spinning speed is the increased spectral width along F_1 in the experiments performed with rotor synchronization. The rotor-synchronized spectra have improved S/N ratio, although their spectral width is limited along the F1 dimension.[74]

Finally, the resolution enhancement in MQMAS can be also due to the narrowing in the MQMAS efficiency curves that is observed for higher values of p. Therefore, for each species, the relative intensities of various parts of the 2D spectra may become distorted in such a way that they appear narrower when |p| increases, especially in highly disordered samples with wide distributions of quadrupolar and/or chemical shift parameters. Most likely, this effect is negligible when using transfer methods that are less sensitive to the quadrupole splitting (FAM, DFS, or RIACT).

4.5 Quantification of MQMAS Intensities

The great advantage of MQMAS over the standard MAS experiment is the high resolution that it provides. However, MQMAS skews the spectral intensities, due to the strong dependence of the multiple quantum excitation and conversion on the quadrupole splitting $\overline{\nu}_Q$, which, in turn, is a function of C_Q, η_Q and the crystallite orientation [see equations (4) and (5)]. The resulting spectra are not quantitative in the isotropic dimension and have distorted lineshapes in the MAS dimension. Examples of such effects are shown in Figures 9 and 11. In order to minimize these distortions it is always advisable to use the aforementioned FAM, DFS and RIACT schemes for excitation and conversion. We now describe additional strategies to retrieve quantitative intensities from the MQMAS spectra.

One of these strategies relies upon combining the information given by MQMAS and MAS. In short, MQMAS can be used to obtain highly resolved spectra and to determine the isotropic chemical shifts and the quadrupolar parameters for different sites. This provides a starting set of parameters for simulation of the MAS spectra in order to obtain accurate intensities. Special care must be taken to assure the quantitative accuracy of the MAS spectra by using short RF pulses (small tip angles) for excitation. We note that this method is suitable for analysis of spectra that are not significantly broadened due to dipolar interactions and/or distribution of chemical shift and quadrupolar parameters.

Secondly, quantitative information can be obtained by calculating the theoretical powder-averaged efficiency curves for MQMAS experiments as a function of P_Q. The efficiency curves for 3QMAS and 5QMAS experiments performed using an RF magnetic field of 70 kHz are depicted in Figure 12.[61] Since the parameter P_Q can be easily derived from analysis of the first moment of the MQMAS spectrum, these curves can be used to offset the quantitative distortions. Indeed, in case of $AlPO_4$-14 this method yielded correct concentrations of various aluminum species.[61] This technique is suitable for

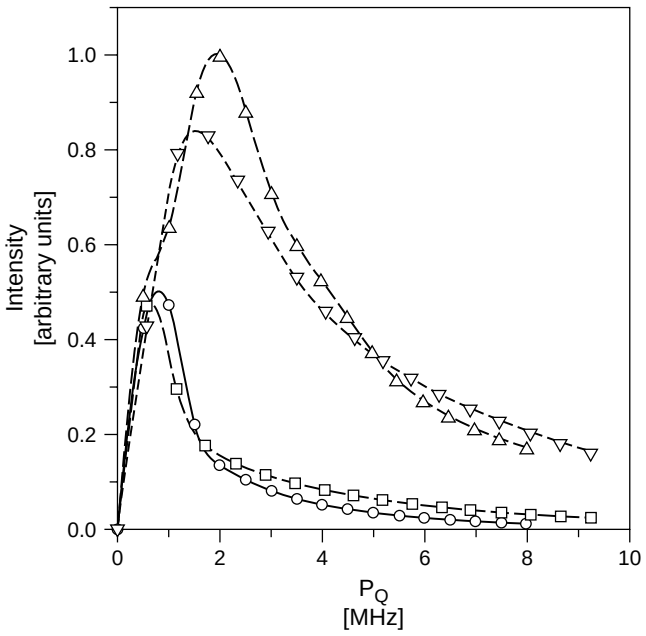

Figure 12 Relative intensities of 3QMAS (dashed lines) and 5QMAS (solid lines) spectra versus P_Q, calculated for $\nu_{RF} = 70$ kHz (Δ, O: $\eta_Q = 0$, $\nabla\square$: $\eta_Q = 1$)

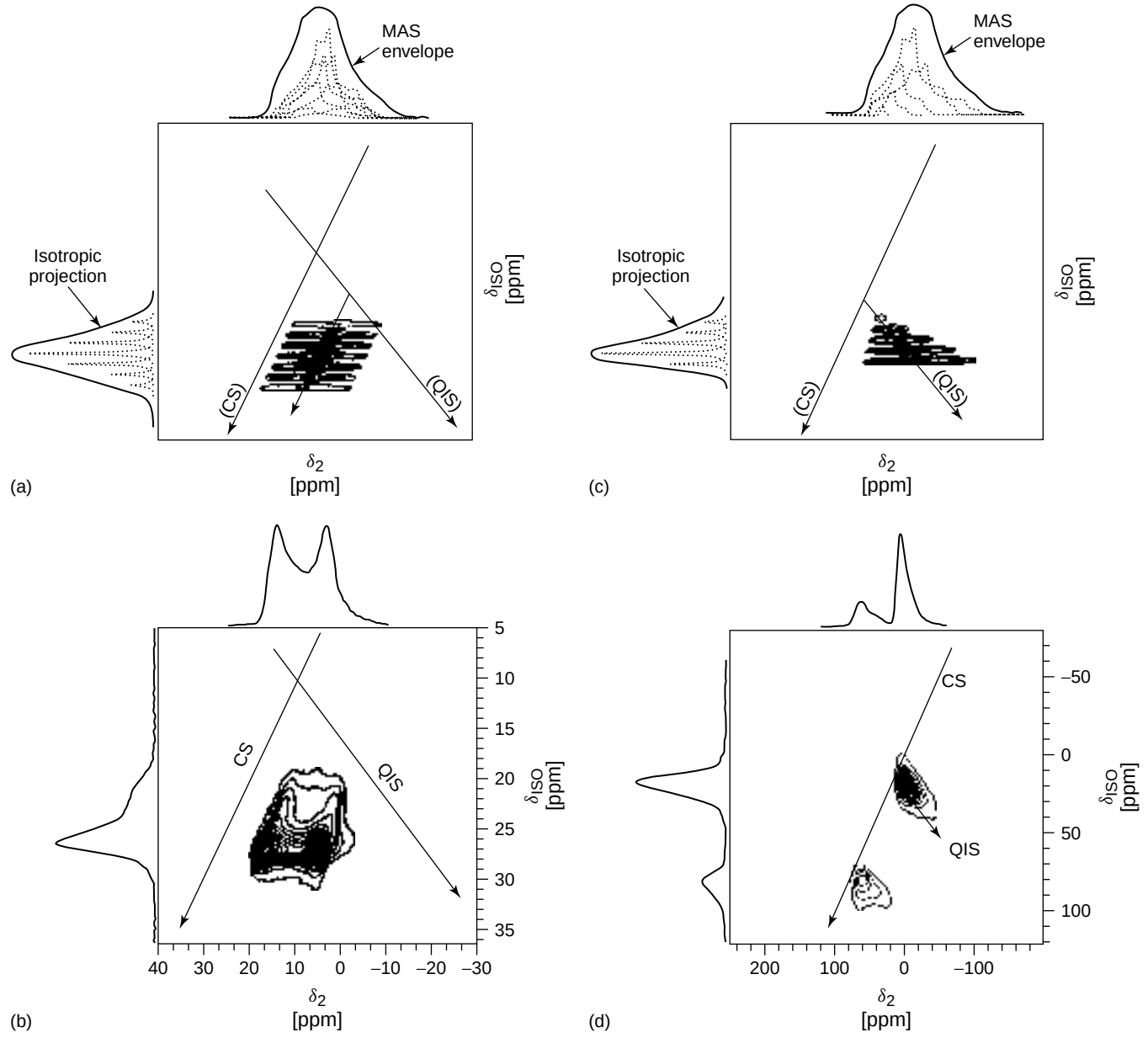

Figure 13 Schematic representations of a Gaussian distribution of (a) δcs and (c) P_Q. The individual slices add up to form the isotropic and anisotropic projections of the 2D spectra. (b) and (d) show the experimental examples of such distributions found in amorphous B_2O_3 and γ-alumina, respectively

the analysis of spectra with substantial broadening, e.g., due to amorphous nature of the sample.

4.6 Analysis of Distribution of Quadrupolar and Chemical Shift Parameters

Many samples of interest in chemistry and materials science do not have a well-organized structure with long range order. In such systems, the resonances cannot be described with a unique set of quadrupolar and chemical shift parameters. Instead, the distributions of these parameters must be considered to properly interpret the spectra. However, the numerical analysis of MQMAS spectra can provide a complete quantitative determination of the distribution of the isotropic chemical shifts δ_{CS} and the quadrupolar parameters (P_Q or C_Q and η_Q). In partly disordered or amorphous materials, this information can be used to assess the degree of disorder and can be further utilized to evaluate other properties, such as inter-nuclei distances or bond angle distributions. For example, ^{27}Al distributions can be interpreted using relationship between δ_{CS} and the T–O–T angle, or between C_Q and the O–T–O angle, where t = Al, Si. In the same way, the distribution of ^{17}O parameters can be used to analyze the Si–O–Si and Al–O–Si angles.[75–78]

To illustrate how these distributions are manifested in the MQMAS spectrum, let us first consider a single site that is characterized by a unique set of parameters δ_{CS}, C_Q and η_Q. Let us further assume that the residual line broadening due to dipolar interactions with other spins can be ignored. This leads to a second-order quadrupolar pattern with a well-defined

lineshape in an MAS spectrum and a narrow pattern in the corresponding MQMAS spectrum. In the sheared MQMAS spectrum, the center of gravity of this pattern is given by

$$\delta_2^{\mathrm{g}} = \delta_{\mathrm{CS}} + \mathrm{k}_{|1|}\mathrm{P}_{\mathrm{Q}}^2 \tag{46}$$

$$\delta_{\mathrm{ISO}}^{\mathrm{g}} = \delta_{\mathrm{CS}} - \frac{10}{17}\mathrm{k}_{|1|}\mathrm{P}_{\mathrm{Q}}^2 \tag{47}$$

where $\mathrm{k}_{|1|}$ is given by equation (43) and $\mathrm{P_Q}$ is given by equation (39). As explained in Section 4.2, any changes of δ_{CS} or $\mathrm{P_Q}$ cause shifts of the spectrum along the CS or QIS directions, respectively. Consequently, a distribution of these parameters broadens the observed 2D patterns. The numerically generated illustrations of the spectral changes due to the distribution of chemical shift and $\mathrm{P_Q}$ are shown in Figures 13a and 13c, respectively. The corresponding examples of experimental distributions are shown in Figures 13b and 13d. We note that a Gaussian distribution of chemical shifts results in a Gaussian broadening along the isotropic and anisotropic projections. However, since the intensities and widths of the individual spectra depend on the quadrupolar parameters, an asymmetrical broadening of the projections occurs in the case of a Gaussian distribution of $\mathrm{P_Q}$. In most practical applications, the distributions of δ_{CS} and $\mathrm{P_Q}$ are encountered simultaneously, which makes the spectral analysis more complex. Nevertheless, these distributions can be separated because the directions of CS and QIS axes differ by approximately 75°.

The sheared MQMAS spectrum $\mathrm{S_e}$ measured experimentally is described by an integral of the individual two-dimensional MQMAS spectra over all possible combinations of chemical shift and quadrupolar parameters

$$\mathrm{S_e}(\delta_2, \delta_{\mathrm{ISO}}) = \int_{-\infty}^{+\infty} \mathrm{d}\delta_{\mathrm{CS}} \int_0^{+\infty} \mathrm{dC_Q} \int_0^1 \mathrm{S_c}(\delta_2, \delta_{\mathrm{ISO}}; \delta_{\mathrm{CS}}, \mathrm{C_Q}, \eta_{\mathrm{Q}}) \times \Pi(\delta_{\mathrm{CS}}, \mathrm{C_Q}, \eta_{\mathrm{Q}})\mathrm{d}\eta_{\mathrm{Q}} \tag{48}$$

In equation (48), $\mathrm{S_c}$ is the calculated MQMAS spectrum corresponding to a single set of lineshape parameters δ_{CS}, $\mathrm{C_Q}$ and η_{Q}, based on the evolution of the spin density matrix during the entire MQMAS experiment. The probability function $\Pi(\delta_{\mathrm{CS}}, \mathrm{C_Q}, \eta_{\mathrm{Q}})$ characterizes the distribution of δ_{CS}, $\mathrm{C_Q}$ and η_{Q}. The propagation of the density matrix results from the first ($\mathrm{H_{Q1}}$) and second ($\mathrm{H_{Q2}}$) order quadrupole interactions, as well as the RF Hamiltonians during the pulses. As a result of sample spinning, all these interactions are rendered time-dependent, which requires the use of sophisticated routines, such as MQSIM, PULSAR, SIMPSON, or GAMMA.[55,60,79,80]

Two different strategies can be used for solving equation (48) to obtain $\Pi(\delta_{\mathrm{CS}}, \mathrm{C_Q}, \eta_{\mathrm{Q}})$. The so-called direct method relies upon iterative fit of $\Pi(\delta_{\mathrm{CS}}, \mathrm{C_Q}, \eta_{\mathrm{Q}})$ using, e.g., linear least square procedure to minimize the deviation between the experimental and simulated spectra. The second method directly computes the distribution from the experimental MQMAS spectrum by performing the so-called inversion of the 2D spectrum.[81]

In the direct method, it is assumed that the chemical shift and quadrupolar parameters are statistically independent, i.e.,

$$\Pi(\delta_{\mathrm{CS}}, \mathrm{C_Q}, \eta_{\mathrm{Q}}) = \Pi_{\mathrm{CS}}(\delta_{\mathrm{CS}})\Pi_{\mathrm{Q}}(\mathrm{C_Q}, \eta_{\mathrm{Q}}) \tag{49}$$

It is further assumed that the distribution of δ_{CS} may be described by a Gaussian distribution

$$\Pi_{\mathrm{CS}}(\delta_{\mathrm{CS}}) = \frac{1}{\sqrt{2\pi}\sigma_{\mathrm{CS}}} \exp\left[-\frac{(\delta_{\mathrm{CS}} - \langle\delta_{\mathrm{CS}}\rangle)^2}{2\sigma_{\mathrm{CS}}^2}\right] \tag{50}$$

where σ_{CS} is the variance of the chemical shift distribution around its average value $\langle\delta_{\mathrm{CS}}\rangle$. This assumption is applicable to various distributed systems (e.g., glasses), in which bond angles are randomly distributed around an average value, and for which a linear correlation exists between the bond angles and the isotropic chemical shifts of nuclei involved in these bonds.[75]

When considering the quadrupole interaction, it has been shown that the distributions of $\mathrm{C_Q}$ and η_{Q} can be fitted by a two dimensional probability function[82]

$$\Pi_{\mathrm{Q}}(\mathrm{C_Q}, \eta_{\mathrm{Q}}) = \frac{\mathrm{C_Q^4}\eta_{\mathrm{Q}}}{\sqrt{2\pi}\sigma_{\mathrm{Q}}^5}\left(1 - \frac{\eta_{\mathrm{Q}}^9}{9}\right) \exp\left[-\frac{\mathrm{C_Q^2}\left(1 + \frac{\eta_{\mathrm{Q}}^2}{3}\right)}{2\sigma_{\mathrm{Q}}^2}\right] \tag{51}$$

In this model, the quadrupolar probability function only depends on a single parameter σ_{Q}, and the marginal distribution profiles are given by[82]

$$\Pi_{\mathrm{Q}}(\mathrm{C_Q}) = \int_0^1 \Pi_{\mathrm{Q}}(\mathrm{C_Q}, \eta_{\mathrm{Q}})\mathrm{d}\eta_{\mathrm{Q}} \tag{52a}$$

$$\Pi_{\mathrm{Q}}(\eta_{\mathrm{Q}}) = \int_0^{\infty} \Pi_{\mathrm{Q}}(\mathrm{C_Q}, \eta_{\mathrm{Q}})\mathrm{dC_Q} \tag{52b}$$

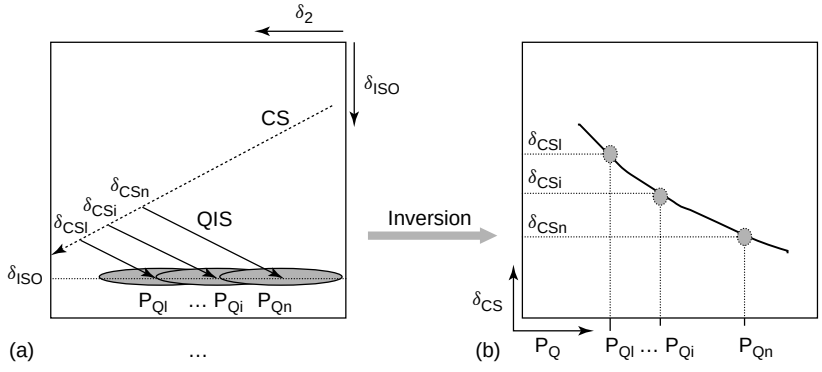

Figure 14 (a) Schematic representation of an experimental slice at position δ_{ISO}, composed of narrow bands defined by a large number of sets (δ_{CSi}, $\mathrm{P_{Qi}}$) that fulfill equation (47). (b) Representation of the quadrupolar parameter $\mathrm{P_{Qi}}$ versus the chemical shift δ_{CSi}. Each isotropic slice on the spectrum (a) provides, after inversion, a specific curve in this 2D representation

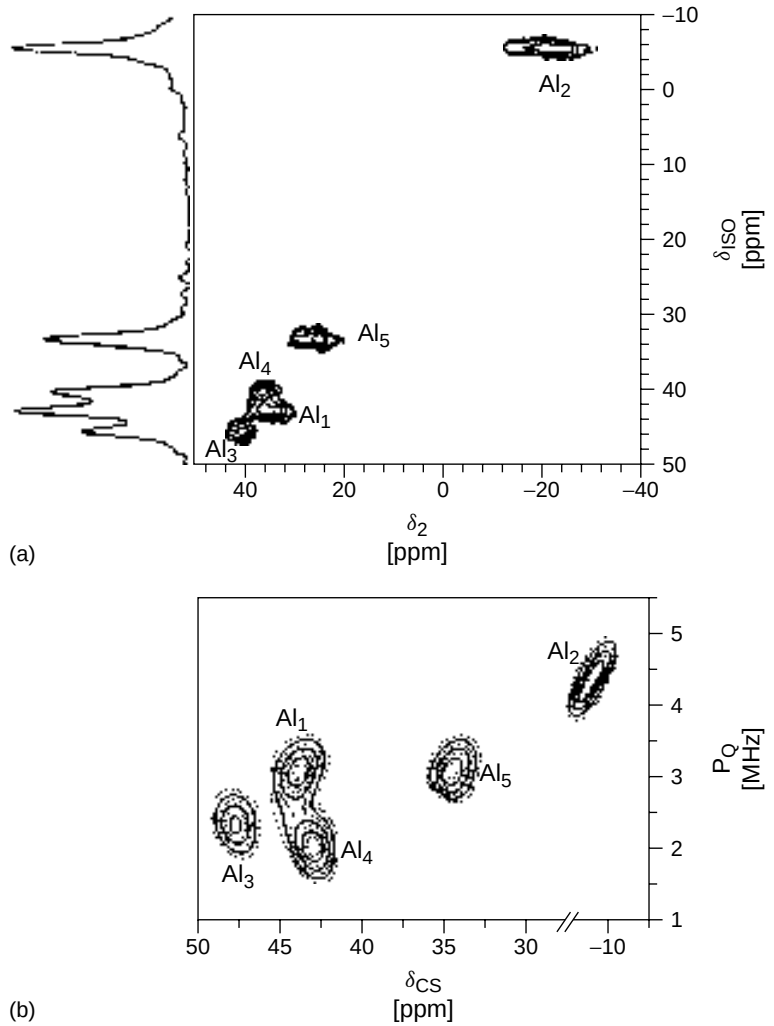

Figure 15 (a) ^{27}Al 3QMAS spectrum of the calcined and fully rehydrated $AlPO_4$-11.[85] The spectrum was acquired at $\nu_0 = 104.2$ MHz using ^{1}H decoupling, $\nu_R = 14$ kHz and $\nu_{RF} = 300$ kHz. (b) Distributions of δ_{CS} and P_Q obtained from the inversion of spectrum (a)

The average values $\langle C_Q \rangle$ and $\langle \eta_Q \rangle$ can be easily obtained from these equations (52). Thus only three parameters ($\langle \delta_{CS} \rangle$, σ_{CS}, σ_Q) are used to fit the MQMAS spectrum when using the direct method.

In the inverse method, the simulations can be simplified by assuming that the spectra are governed by a distribution of chemical shift and second order quadrupolar parameter P_Q, thus reducing the number of unknown functions to two. In cases when an approximate value of η_Q is unknown, a value of η_Q of approximately 0.5 is used in order to calculate S_c for a given value of P_Q. In a distributed resonance, a slice located at δ_{ISO} in the sheared spectrum results from a superposition of all one-dimensional MQ-filtered spectra that satisfy the condition given by equation (47) for δ_{CS} and P_Q. Thus, the two-dimensional integral of equation (48) can be reduced to a single integral with respect to P_Q

$$S_e(\delta_2)_{\delta_{ISO}} = \int_0^\infty S_c(\delta_2; \delta_{CS}(P_Q), P_Q)\Pi(\delta_{CS}(P_Q), P_Q)dP_Q \quad (53)$$

with δ_{CS} given by equation (47). Solving equation (53) to obtain $\Pi(\delta_{CS}(P_Q), P_Q)$ corresponds to inversion of the 2D spectrum. The solution can be drawn for different slices δ_{ISO} of the 2D spectrum. For each slice, the distribution function Π is evaluated versus the P_Q parameter, and for each P_Q value the corresponding δ_{CS} value is determined from equation (47). This corresponds to the determination of a particular curve in the complete two-dimensional parameter space (see Figure 14). The superposition of the curves obtained for all slices yields the final two-dimensional distribution function $\Pi(\delta_{CS}, P_Q)$. As previously noticed, solving this integral equation is not straightforward and requires the use of regularization methods.[81,83,84]

The inversion method was initially applied to analyze the 3QMAS spectra of ^{27}Al in crystalline aluminophosphate $AlPO_4$-11.[85] The 3QMAS spectrum of a crystalline aluminophosphate $AlPO_4$-11 is displayed in Figure 15a, which shows the five crystallographic sites resolved by this technique. The distribution analysis based on this spectrum leads to the canonical representation displayed in Figure 15b. As expected, the intensities of the five Al species are equal and the average values of δ_{CS} and P_Q agree very well with the literature data. A study that compares the quality of the direct and inverse approaches is yet to be reported.

5 MEASUREMENTS OF DIPOLAR CONNECTIVITIES

As a rule, the development of new high-resolution methods in NMR inspires progress in measurements of interactions between the observed nuclei and their neighbors. Such measurements provide means for analyzing the intermediate range ordering in these spin systems. The development of DOR, DAS and MQMAS offered no exception. Several methods that measure the dipolar connectivities between quadrupolar and spin-1/2 nuclei under high-resolution followed the inception of these techniques. Most of these methods utilize indirect excitation via cross polarization for spectral editing of the DOR and MQMAS spectra or for the DAS-based and MQMAS-based HETCOR experiments.[86–91] As the spin dynamics of the CP transfer that involves quadrupolar nuclei is very complex, CP-based methods may suffer from quantitative uncertainties. However, analysis of internuclear interactions between spin-1/2 and quadrupolar nuclei can also be made by reintroducing the heteronuclear dipolar dephasing between these spins using RF pulses that are synchronized with the MAS rotor. One of such methods, REDOR, capable of measurement of dipolar interactions and internuclear distances, has been combined with MQMAS.[30,31,92,93] An attempt has been also made to replace cross polarization with the coherence transfer via TEDOR.[94]

5.1 Cross Polarization and MQMAS

The dipolar coupling between two spins can be used to indirectly produce nuclear magnetization of the observed spins via CP transfer from another spin system. The standard spin-1/2 → spin-1/2 CP experiments are usually performed between abundant and rare spins to enhance the nuclear magnetization of the latter.[95] The polarization transfer in such systems is well understood, and obtaining quantitative spectra

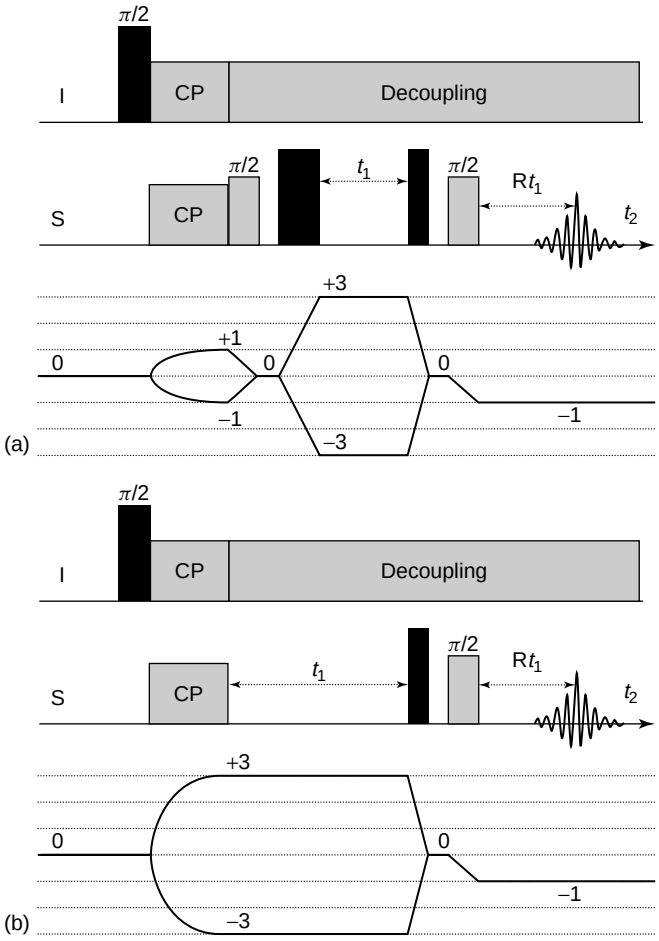

Figure 16 Pulse sequences and coherence transfer pathways for (a) 1QCP-3QMAS and (b) 3QCP-3QMAS experiments with z-filter. The phase cycling used in these experiments must include spin temperature inversion, to avoid direct observation of spins S

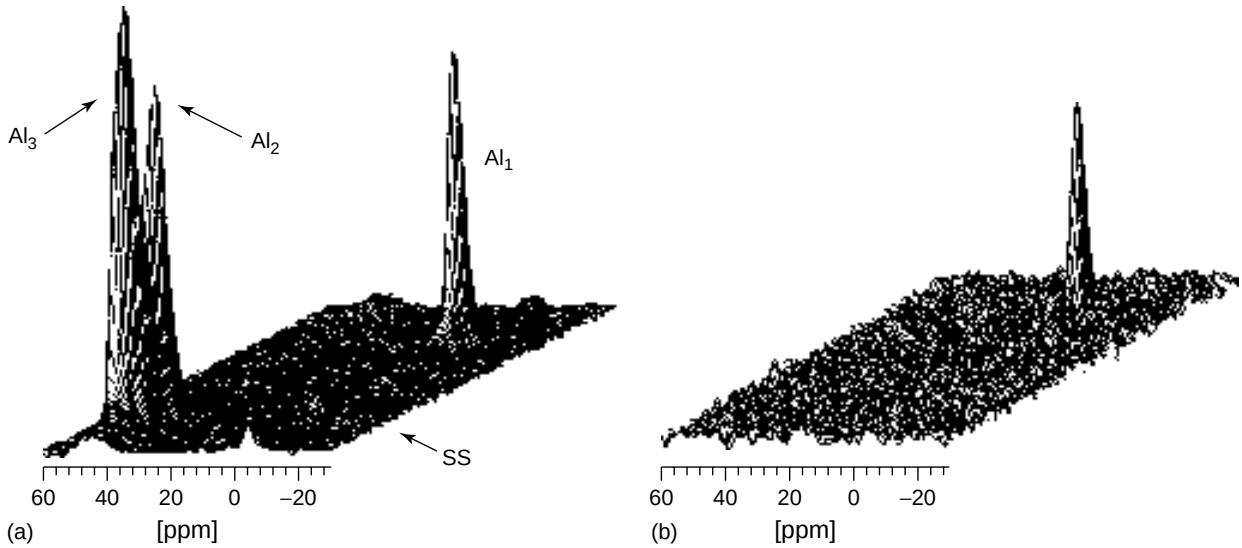

Figure 17 2D NMR spectra of ^{27}Al in $AlPO_4$-CHA obtained using (a) 3QMAS and (b) $^{19}F \rightarrow {}^{27}Al$ 1QCP-3QMAS.[87] The experiment was performed using $\nu_0 = 104.2$ MHz, $\nu_R = 20$ kHz, CP contact time of 0.3 ms and ν_{RF}^S field strengths of approximately 250 kHz, 20 kHz and 5 kHz during hard pulses, soft pulses and CP transfer, respectively. ^{19}F decoupling was applied during evolution and acquisition times using $\nu_{RF}^I \approx 80$ kHz. SS denotes the spinning sideboard

is relatively easy. For reasons to be discussed later, CP between spin-1/2 and quadrupolar nuclei does not generally lead to enhanced sensitivity. However, it is of interest as method for spectral editing. When appropriate line narrowing methods are applied to both spins, the CP transfer can be further employed to obtain high-resolution HETCOR spectra.

It has been shown that the use of cross polarization can be coupled with the MQMAS experiment. The 1QCP-MQMAS experiment shown in Figure 16a, transfers the magnetization of spins I into the ± 1Q central transition of spins S. The resulting single quantum coherence is converted into a population inversion between the states with $m = \pm 1/2$ by a selective $\pi/2$ pulse. After a short delay, a standard MQMAS is performed, e.g., using the scheme with z-filter.[85,87] More direct approaches, relying on polarization transfer to multiple quantum coherences (MQCP-MQMAS), have been successfully implemented by several authors.[96–99] The possibility of CP transfer directly to MQ coherences has been demonstrated earlier for $^{1}H \rightarrow {}^{23}Na$ system under static conditions.[100] One of the pulse sequences and coherence transfer schemes proposed for the MQCP-MQMAS experiment is shown in Figure 16b.[99] Theoretical analysis of multiple quantum cross polarization of quadrupolar nuclei has been reported under static and MAS conditions.[97,98,100]

The 1QCP-3QMAS experiment has been carried out between ^{19}F and ^{27}Al nuclei in fluorinated triclinic chabazite-like $AlPO_4$ aluminophosphate, which contains one octahedral site Al_1 coordinated to fluorine, and two sites labeled Al_2 and Al_3 representing aluminum in AlO_4 tetrahedra. The octahedral aluminum site Al_1 that is bonded to fluorine can be easily distinguished by this method (Figure 17).[87] A $^{1}H \rightarrow {}^{27}Al$ 1QCP-3QMAS experiment was applied for probing the interaction of water with the framework aluminum of fully rehydrated $AlPO_4$-11 aluminophosphate, where it allowed for distinguishing the Al sites that are most and least susceptible to hydration.[85] Such distinction would not be possible without the separation of ^{27}Al resonances under high-resolution conditions. Figure 18 shows the 5QMAS and 5QCP-5QMAS spectra of ^{45}Sc ($S = 7/2$) in scandium sulfate pentahydrate, where CP to all sites is observed.[99] The 3QMAS experiments did not allow for complete resolution of sites 1 and 2. Cross polarization to seven quantum coherences has been also demonstrated for the same sample (not shown). It has been noted that the matching parameters differed for different coherence orders and should be determined separately in each experiment.

The first high-resolution HETCOR NMR spectroscopy involving quadrupolar nuclei used DAS to average the second-order quadrupolar interaction.[89] Experimental schemes of Figure 16 can be easily modified to achieve a 3D high-resolution HETCOR-MQMAS experiment by inserting an additional evolution period between the initial ($\pi/2$) pulse on spins I and the CP transfer. However, due to unfavorable relaxation rates such experiments would require very long acquisition times. Therefore, it is advantageous to use the 2D MQMAS-HETCOR schemes shown in Figure 19, which utilize the $S \rightarrow I$ polarization transfer from fast relaxing quadrupolar nuclei.[90] The experiment can be designed for $S = 3/2$ (Figure 19a) or $S > 3/2$ (Figure 19b), and is performed by spin-locking the isotropic echo that forms at time Rt_1 after the second pulse, followed by CP transfer and acquisition of spins I signal in the t_2 domain.

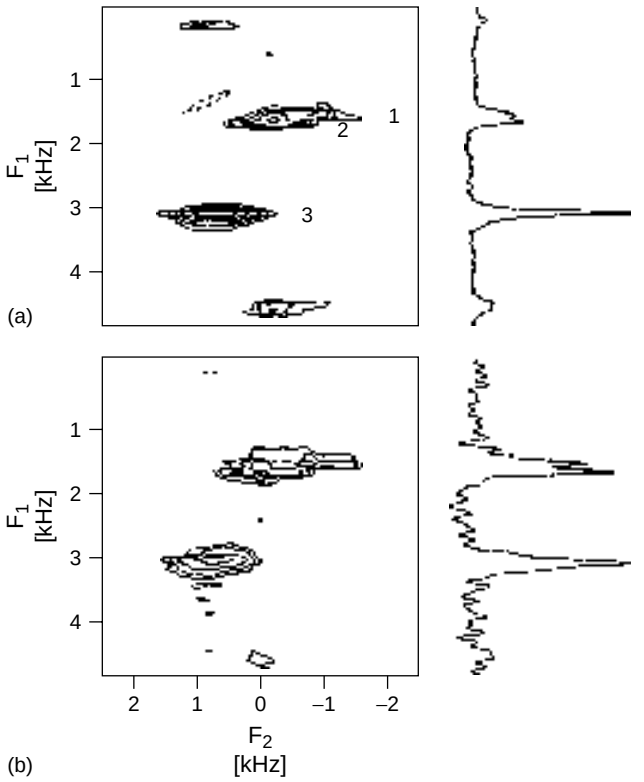

Figure 18 2D NMR spectra of ^{45}Sc in $Sc_2(SO_4)_3 \cdot 5H_2O$ obtained using (a) 5QMAS and (b) $^{1}H \rightarrow {}^{45}Sc$ 5QCP-5QMAS.[99] The experiment was performed at $\nu_0 = 97.2$ MHz with $\nu_R = 6.5$ kHz. The CP transfer used $\nu_{RF}^{S} \approx 100$ kHz, $\nu_{RF}^{I} \approx 50$ kHz and a contact time of 1 ms. ^{1}H decoupling was applied during evolution and acquisition times

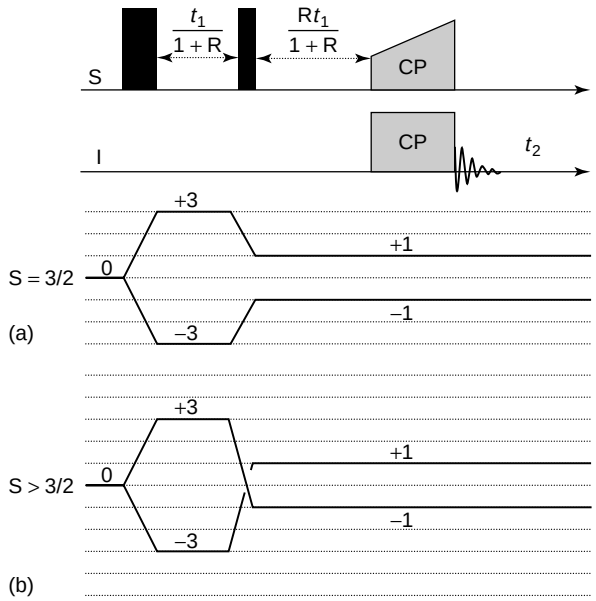

Figure 19 Pulse sequence and coherence transfer pathways used in 3QMAS-HETCOR experiment for (a) $S = 3/2$ and (b) $S > 3/2$

The 3QMAS-HETCOR method has been first used to obtain the spectrum shown in Figure 20a, which correlates the isotropic resonances of ^{23}Na and ^{31}P in $Na_3P_3O_9$.[90] Figure 20b

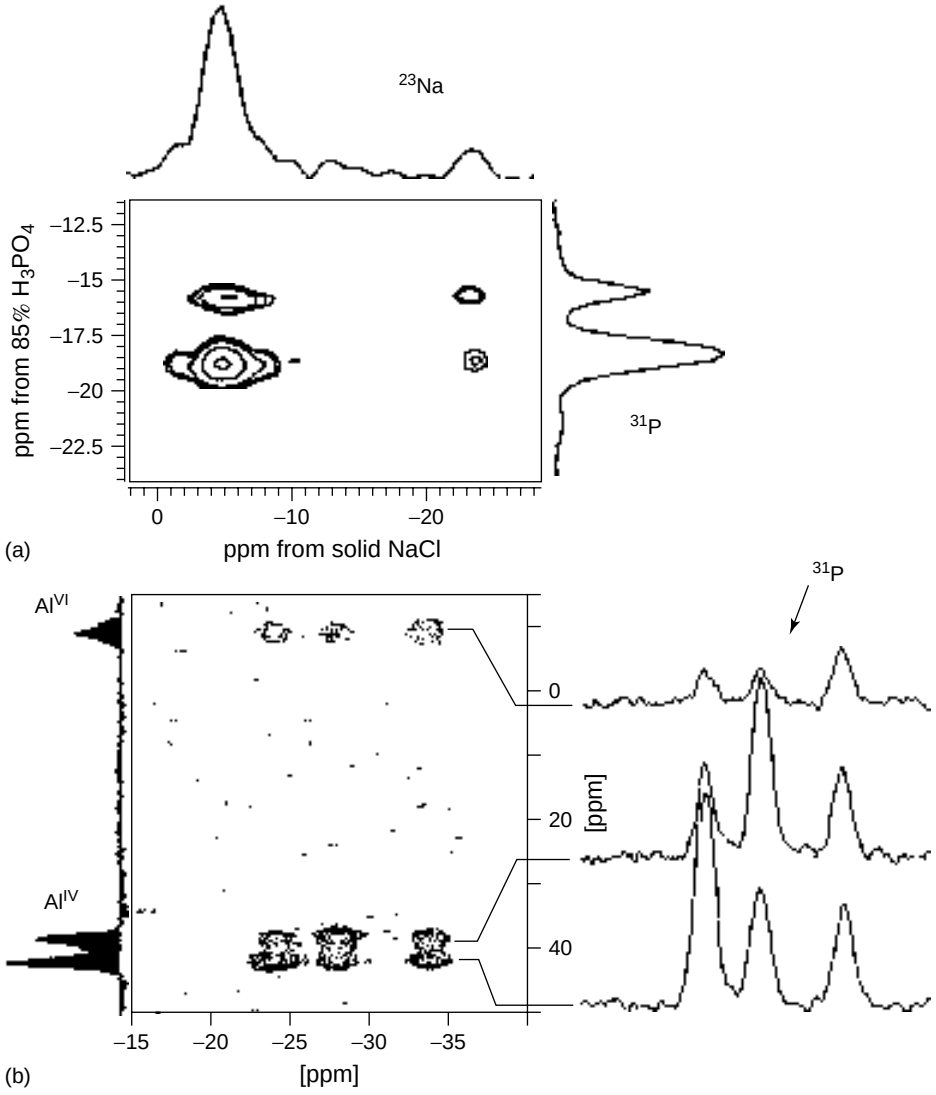

Figure 20 (a) $^{23}Na \rightarrow {}^{31}P$ 3QMAS-HETCOR spectrum of $Na_3P_3O_9$.[90] (b) $^{27}Al \rightarrow {}^{31}P$ HETCOR spectrum of VPI-5[91]

depicts the $^{27}Al \rightarrow {}^{31}P$ 3QMAS-HETCOR spectrum of the large-pore aluminophosphate molecular sieve VPI-5 in a fully hydrated state.[91] In both spectra, significant increase of resolution has been achieved with respect to a standard (CPMAS) version of the HETCOR experiment.

5.2 MQMAS with TEDOR and REDOR

The application of CP transfer to half-integer quadrupolar nuclei is difficult due to the complicated spin dynamics involved in both the spin locking and the cross polarization processes under MAS. These dynamics are strongly anisotropic with respect to crystallite orientation and depend on the relative size of the quadrupole frequency ν_Q, the amplitudes of the RF magnetic field applied to the I and S spins (ν^I_{RF} and ν^S_{RF}), the spinning speed ν_R and the resonance offsets $\delta\nu_{0I}$ and $\delta\nu_{0S}$. Significant progress in understanding of these processes has been made recently due to several excellent contributions.[28,29,86,96–99] Some of the challenges involved in such experiments are briefly reviewed below.

The Hartmann-Hahn matching condition for CP requires that $\nu^I_{RF} = \nu_{nut}$, where ν_{nut} is one of the nutation frequencies associated with the cross polarized coherence of the S spin.[101] In case of static CP between spin-1/2 nuclei and the single quantum central transition coherence of quadrupolar nuclei under on-resonance irradiation, this translates to

$$\nu^I_{RF} = \nu^S_{RF}, \quad |\overline{\nu}_Q| \ll \nu^S_{RF} \tag{54}$$

$$\nu^I_{RF} = (S + 1/2)\nu^S_{RF}, \quad |\overline{\nu}_Q| \gg \nu^S_{RF} \tag{55}$$

where $\overline{\nu}_Q$ is given by equation (4).[29]

The Hartmann-Hahn condition for CP of the (±3/2, ∓3/2) 3Q transitions cannot be well defined in a polycrystalline sample, as it depends on the crystallite orientation

$$\nu^I_{RF} = A_{nut}(\nu^S_{RF})^3/(\overline{\nu}_Q)^2, \quad |\overline{\nu}_Q| \gg \nu^S_{RF} \tag{56}$$

where, again, the conditions $\nu_R = \delta\nu_{0I} = \delta\nu_{0S} = 0$ are assumed, and $A_{nut} = 1.5$, 6, 15, and 30 for $S = 3/2$, 5/2, 7/2 and 9/2, respectively.[99,100]

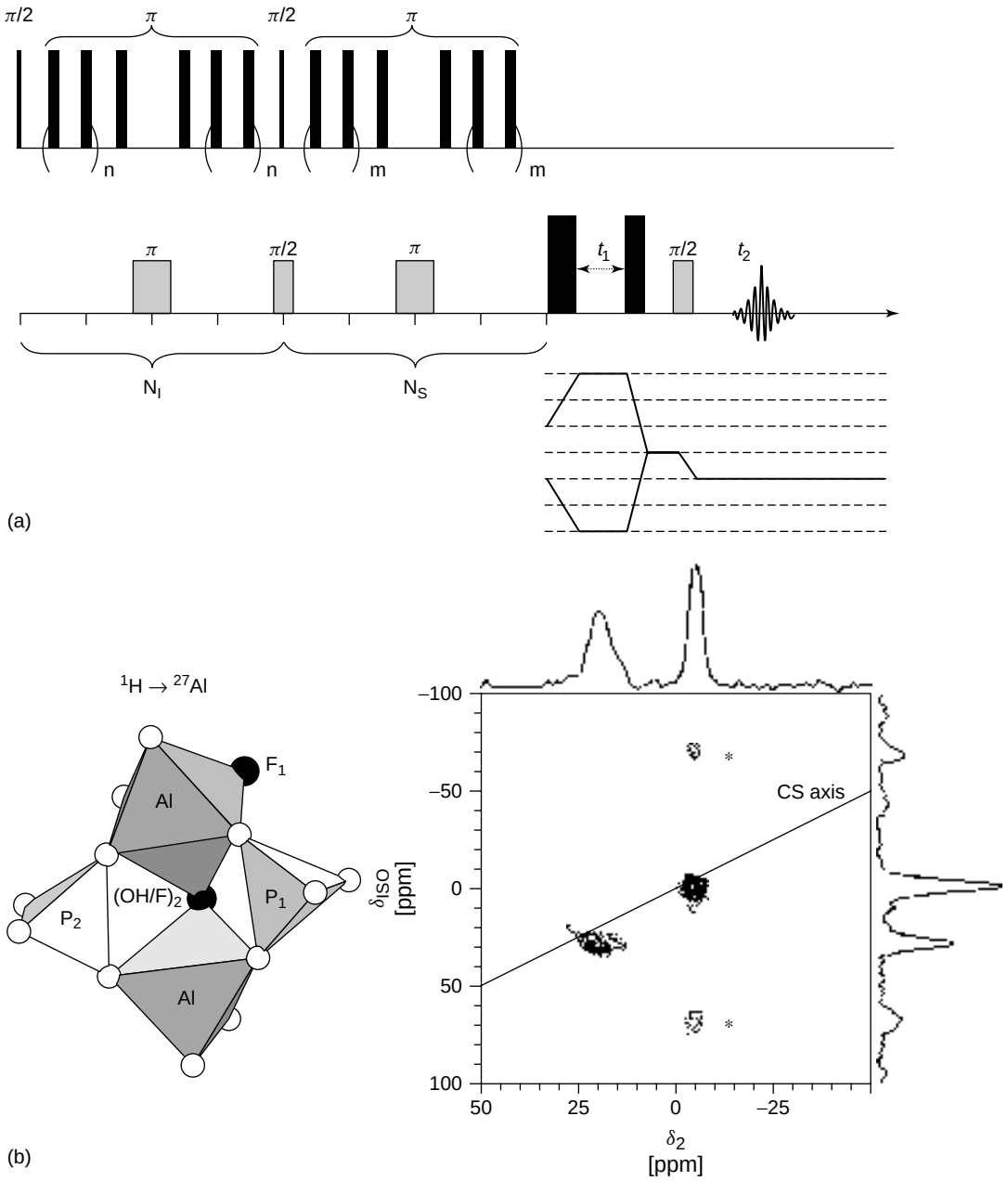

Figure 21 (a) Pulse sequence and coherence transfer pathways used in TEDOR-3QMAS experiment. (b) $^{1}H \rightarrow {}^{27}Al$ TEDOR-3QMAS spectrum of aluminophosphate $AlPO_4$-CJ2

Sample spinning makes $\overline{\nu}_Q$ time dependent and thus complicates both spin locking and polarization transfer.[28,29] The effect of MAS can be described by using the parameter $\alpha_{ad} = (\nu_{RF}^S)^2/\nu_Q\nu_R$ that is related to the speed with which $\overline{\nu}_Q$ crosses zero during sample spinning.[28] It has been shown that efficient spin-locking can be maintained when $\alpha_{ad} \ll 1$ (sudden passage) or when $\alpha_{ad} \gg 1$ (adiabatic passage), whereas the intermediate case $\alpha_{ad} \cong 1$ results in a loss of the spin-locked state. In addition, rotational modulation of the I–S dipolar interaction has profound effect on the CP process itself.[29,102]

The sudden regime ($\alpha_{ad} \ll 1$) implies the use of low RF magnetic fields, such that $\nu_{RF}^S \ll |\overline{\nu}_Q|$ for most crystallites. Under such conditions, the polarization is transferred predominantly to the single quantum central transition coherence of the S spins. The corresponding Hartmann-Hahn matching condition is

$$\nu_{RF}^I = \pm\left(S + \frac{1}{2}\right)\nu_{RF}^S \pm n\nu_R, \quad n = 1, 2 \tag{57}$$

Optimization of the Hartmann-Hahn match becomes very ambiguous in this regime due to the extreme sensitivity to off-resonance effects. Inhomogeneities of the RF magnetic field in doubly tuned probes further complicate the situation. As a result, the absence of a resonance in the CP spectrum should not be used as evidence for the lack of $I \leftrightarrow S$ connectivity without some careful experimentation.

The spin dynamics under adiabatic passage condition ($\alpha_{ad} \gg 1$) is also complex. Experimentally, this regime can be

approached by reducing the spinning speed and/or increasing the strength of RF field. Since there are significant benefits of using the highest available ν_R in MQMAS, we consider only the latter option.[74,103] Under typical conditions of $\nu_R \geq 10$ kHz and $\nu_Q = 1$ MHz, this translates to ν_{RF}^S being much greater than 100 kHz. In this case, the condition $|\overline{\nu}_Q| \gg \nu_{RF}^S$ is no longer satisfied for most of the crystallites and the nutation behavior of the S spins varies strongly with changing orientation. Consequently, no simple Hartmann-Hahn formula can be derived for 1Q and MQCP transfers. Numerical simulations show that such CP transfer is not strongly affected by the interference from ν_R, $\delta\nu_{0I}$ and $\delta\nu_{0S}$, but depends on the quadrupolar parameters, the dipolar coupling D between I and S, and the RF magnetic fields ν_{RF}^I and ν_{RF}^S.[96–99] In general, 1QCP transfer with strong RF fields ($\alpha_{ad} \gg 1$), is less efficient than with weak RF fields ($\alpha_{ad} \ll 1$), except for samples with relatively low values of C_Q and large dipolar couplings. Under fast MAS, there is a striking similarity between the 1Q, 3Q and 5Q intensities obtained with each set of C_Q and D values. A detailed analysis shows that two processes are involved here: a slow CP transfer (with the time constant of the order of 1/D) to all (p/2, −p/2) coherences followed by equilibration of these coherences via a RIACT-like mechanism, which generates fast $1Q \leftrightarrow 3Q \leftrightarrow 5Q$ transfers (with the time constant of $\sim 1/4\nu_R$) in cross polarized nuclei.

The quantitative uncertainties associated with the complex dynamics of spin-locking and CP transfer could be avoided by using TEDOR NMR. This technique has been successfully used in the studies of HETCOR spectra and dipolar couplings in spin systems involving spin-1/2 and quadrupolar nuclei under MAS.[31,32] In the TEDOR method, the magnetization is transferred in a way that is similar to an INEPT experiment in liquids. The dipolar interaction between spins I and S, which is refocused every rotor period in the standard MAS experiments, can be reintroduced by using properly spaced rotor-synchronized RF pulses. It has recently been shown that TEDOR can be used in concert with MQMAS by replacing the Hartmann-Hahn CP transfer in the scheme of Figure 16a, as shown in Figure 21a.[94] The TEDOR pulses must be selective for the central transition of S spins, and thus of weak amplitude. The TEDOR-MQMAS method has been tested on borax and $AlPO_4$−CJ2 aluminophosphate, where $^1H \rightarrow {}^{11}B$, $^1H \rightarrow {}^{27}Al$ and $^{19}F \rightarrow {}^{27}Al$ spectra were acquired (see Figure 21b). A reverse experiment, similar to that used in the MQMAS-HETCOR scheme can be also considered. According to the numerical simulations, TEDOR-MQMAS appears to be less sensitive to off-resonance effects than CP-MQMAS. However the applicability of this technique to nuclei with strong quadrupole interactions has yet to be tried.

Another version of an approach without the use of CP has been proposed, which combines the high-resolution capabilities of MQMAS with the direct determination of hetero-nuclear dipolar couplings via REDOR. Figure 22 shows the schematic diagrams of two MQ-REDOR experiments, referred to as MQ-t_1-REDOR and MQ-t_2-REDOR. The MQ-t_2-REDOR technique (Figure 22a), employs two strong and two selective RF pulses at the Larmor frequency ν_{0S} with phases cycled to select the $0 \rightarrow \pm p \rightarrow 0 \rightarrow +1 \rightarrow -1$ coherence pathway.[92] When spaced by an integer number of rotor periods nt_R, the selective pulses create two windows in which the sequences of π pulses can be applied to the spin-1/2 nuclei. Similar to the standard REDOR experiment, the role of the π pulses is to prevent MAS from refocusing the dephasing due to the dipolar interaction between spins I and S.[30]

The spectral editing capabilities of MQ-t_2-REDOR method are illustrated in Figure 23, which shows several ^{27}Al NMR spectra of $AlPO_4$-CHA aluminophosphate (see also Figure 17).[92] The tetrahedral sites Al_2 and Al_3 are not well resolved by MAS alone (spectrum (a)), but are easily distinguished by using the MQMAS method (spectrum (b)). The so-called REDOR difference spectra, obtained by subtracting the MQMAS spectra obtained without and with the dephasing pulses are shown in Figures 23c−d. As expected, only the resonance from fluorinated site (Al_1) remains strong in the spectrum of Figure 23c. However, the capabilities of the MQ-t_2-REDOR method extend beyond spectral editing. By changing the number of rotor cycles, one can measure the REDOR curves for all three Al species and estimate their distances from the nearest fluorine.[30] The results (see Figure 24) are in good agreement with the results inferred from synchrotron radiation experiments. The MQ-t_1-REDOR experiment (see Figure 22b), employs the REDOR sequence during multiple rather than single quantum evolution.[93] Because the dipolar effect is enhanced by a factor of p during the p-quantum evolution (see F term in equation (7)), this technique has potential for improved sensitivity toward weak dipolar interactions. Indeed, the results of Figure 24 show

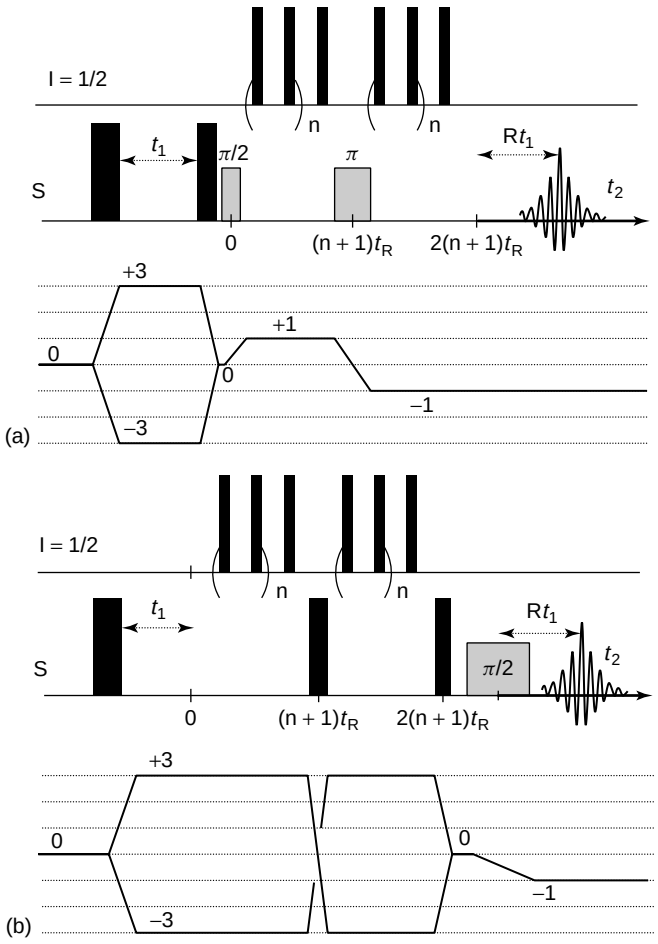

Figure 22 Pulse sequences and coherence transfer pathways used in (a) MQ-t_2-REDOR and (b) MQ-t_1-REDOR experiments

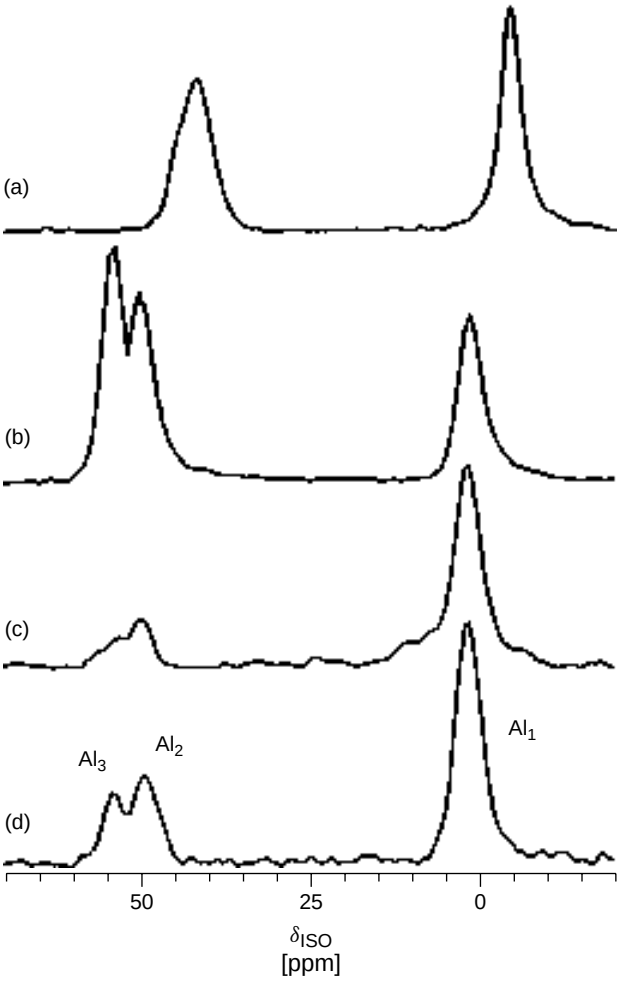

Figure 23 ^{27}Al NMR spectra of fluorinated $AlPO_4$-CHA aluminophosphate: (a) MAS, (b) 3QMAS, (c) 3Q-t_2-REDOR difference for $n = 5$, and (d) 3Q-t_2-REDOR difference for $n = 29$

that in $AlPO_4$-CHA the apparent size of ^{19}F-^{27}Al coupling measured using 3Q-t_1-REDOR was higher by a factor of 3 when compared with the data obtained with 3Q-t_2-REDOR.[93]

Although the concept of dipolar recoupling during MQ evolution is attractive, the 3Q-t_1-REDOR experiment has potential limitations. First, the more complex coherence pathway employed by this method causes a loss of sensitivity of approximately 2–8, depending on the C_Q and S spin values. Another potential drawback of both MQ-REDOR experiments stems from non-uniform response of the quadrupolar spins to the RF pulses used in the MQMAS experiment. One may expect the effect that the orientational anisotropy of MQ excitation has on the MQ-t_1-REDOR curves to be enhanced, especially in samples with significant C_Q values. However, both experimental and theoretical results show that the experiment is surprisingly robust. Indeed, the initial slope of the REDOR curve is nearly independent of C_Q for small or moderate quadrupolar interactions, and the quality of the fit improves markedly when the strength of RF field is increased, even for large C_Q values.[93] REDOR recoupling during triple quantum evolution has been recently used to determine the relative orientations of the quadrupolar and dipolar principal axis systems.[104] In this

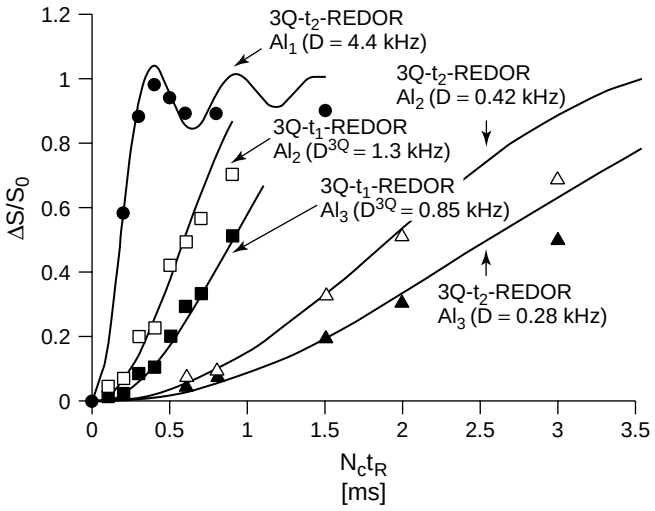

Figure 24 Experimental and simulated MQ-t_1-REDOR and MQ-t_2-REDOR curves for $ALPO_4$-CHA.[93] The values of dipolar coupling D between ^{19}F and ^{27}Al corresponding to the simulated curves are given in parentheses

experiment, the REDOR recoupling immediately follows the excitation of 3Q coherences. After the $\pm 3Q \rightarrow \mp 3Q$ inversion, a $\pi/2$ pulse is applied to spins I to create a mixture of heteronuclear 2Q and 4Q coherences, which are subsequently allowed to precess during evolution period t_1. The t_1 period is followed by a similar REDOR recoupling period to recover the 3Q coherences, which are then converted into the observable – 1Q coherence. The resulting spectrum exhibits patterns of spinning sidebands along the MQ dimension, which depend on the dipolar coupling, the quadrupolar parameters and the relative orientation of the quadrupolar and dipolar PAS.

Another experiment, referred to as MQMAS with dipolar dephasing (DD-MQMAS) is shown in Figure 25. It uses the standard z-filtered MQMAS scheme for spins S, while the dipolar recoupling with spins I is accomplished using a series of π pulses applied synchronously with the rotor frequency to the I spins during the multiple quantum evolution.[105] The simple $0 \rightarrow \pm p \rightarrow 0 \rightarrow -1$ coherence pathway that is used here results in line broadening, but allows for fast,

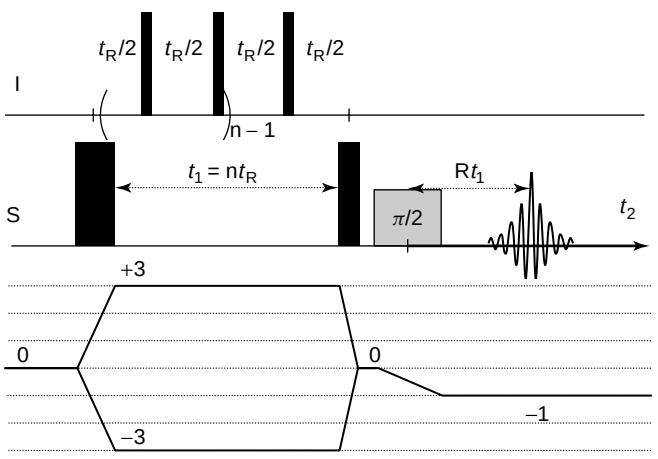

Figure 25 DD-MQMAS experiment: pulse sequence and coherence transfer pathway

yet only semi-quantitative, determination of the internuclear connectivities in well crystallized compounds.

6 SENSITIVITY ENHANCEMENT VIA CPMG METHOD

Advances in manipulating the MQ coherences considerably improved the sensitivity of the MQMAS experiment. Additional gain in the S/N ratio can be accomplished by applying a CPMG train of rotor-synchronized, selective π pulses during the acquisition of data in t_2.[106–108] The resulting CPMG-MQMAS spectrum is split into periodic combs of spin-echo sidebands that spread along the anisotropic dimension. Since the integrated spectral intensity is not affected by this procedure, the apparent S/N ratio for individual spikes can be significantly enhanced. The gain in S/N ratio is governed by periodicity τ_a of the CPMG train and the homogeneous spin–spin relaxation time T_2. The truncation effects require that τ_a exceeds the net dephasing time of transverse magnetization T_2^*, which determines the maximum gain available by this method.

An example of the experimental scheme for CPMG-MQMAS experiment with spin-3/2 nuclei, based on the split-t_1 method, is shown in Figure 26.[108] In this experiment the excitation of MQ coherences and their reconversion to the single quantum coherence is achieved following the usual rules. The CPMG sequence uses selective π pulses of the same strength of RF field as the soft pulse in the z-filter method. The phase cycling of each sequence follows the standard procedures, and the phases of the CPMG train are adjusted according to the Meiboom-Gill scheme. The sequence in Figure 26 utilizes contributions from the echo and antiecho coherence pathways, which leads to cosine modulated FIDs. Approaches suitable for spin-5/2 nuclei have been also proposed.[109]

The appearance of CPMG spectrum is determined by the sampling conditions: smaller separation τ_a between the echoes in time domain increases the S/N ratio in frequency domain at the expense of anisotropic line shape, which is determined by a reduced number of sidebands. Although the spin-echo sidebands are regularly spaced with respect to the carrier frequency, the sideband manifolds corresponding to different sites are usually well separated along the isotropic dimension. This is manifested in Figure 27, which shows a series of

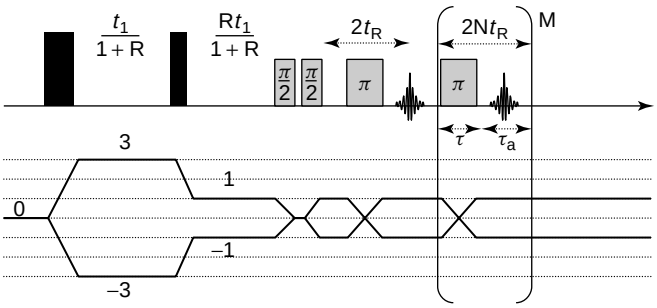

Figure 26 CPMG-3QMAS pulse sequence and coherence transfer pathway for spin-3/2 nuclei.[108] The part of the sequence shown in parenthesis is rotor-synchronized according to $2Nt_R = \tau + \tau_a$, where τ is the duration of the selective π pulse (including the transient effects) and τ_a is the echo sampling period

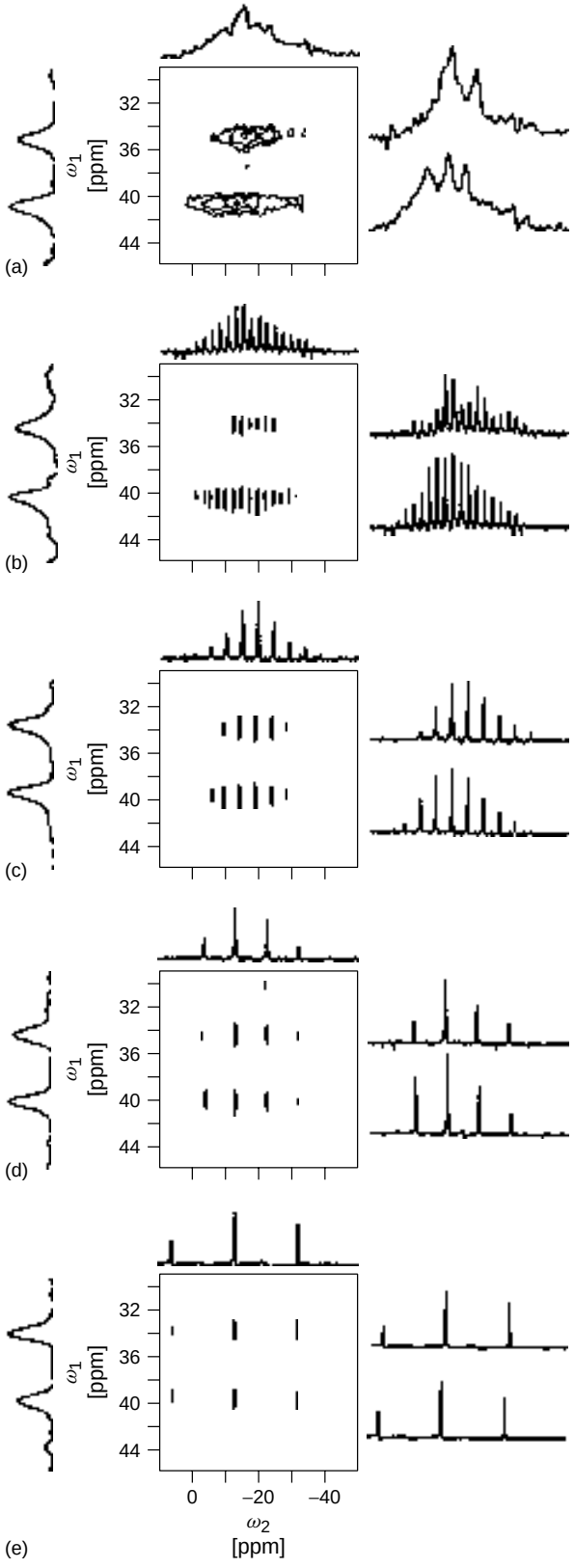

Figure 27 ^{23}Na MQMAS (a) and CPMG-MQMAS (b–e) spectra of an equimolar mixture of Na_2SO_4 and $Na_2C_2O_4$ recorded at $\nu_0 =$ 105.8 MHz using ν_R rates between 10 and 11 kHz and $\nu_{RF} = 58$ kHz for all pulses.[108] All CPMG-MQMAS spectra used $\tau = 150\,\mu$s and the following values of τ_a and M: (b) 4 ms, 9; (c) 2 ms, 19; (d) 1 ms, 39, and (e) 0.5 ms, 80

^{23}Na MQMAS and CPMG-3QMAS spectra of an equimolar mixture of Na_2SO_4 and $Na_2C_2O_4$.[108] Although each spectrum has been recorded with the same number of scans, spectra b-e corresponded to S/N gain factors of 5, 8, 12 and 20, respectively.

It has been shown that accurate parameters for quadrupole and chemical shift interactions can be extracted from the CPMG-MQMAS spectra via numerical simulation that accounts for the time-modulation of quadrupolar interaction in the course of RF pulses.[110] In addition, several methods for the numerical treatment of the CPMG spectra have been proposed, which further improve the S/N ratio and allow for full recovery of the echo envelope. These include modification of the sideband envelope through echo shifting, reconstruction of the full spectrum by superimposing the echoes, and various schemes for noise filtering via apodization.[109] Additional improvement of the numerical analysis is possible by the use of data processing techniques that are alternative to discrete Fourier transform. Recently, a simple processing technique, referred to as ANAFOR, has been proposed based on the least squares method used in linear prediction and the TIGER routines.[111,112] These methods allow for precise determination of intensities in truncated multidimensional spectra based on outside information about the line shape parameters. ANAFOR can be especially useful in the CPMG-MQMAS experiments, where the positions of sidebands are known in advance and other line shape parameters can be obtained using, e.g., one-dimensional methods. By using truncated time-domain data sets, ANAFOR offered further significant gain in sensitivity. For example, this method has been applied to ^{1}H-^{27}Al MQ-t_2-REDOR measurements in $AlPO_4$-ZON where the experimental time has been decreased by a factor of six.[111]

7 CONCLUSION

Since its development, MQMAS has matured to become a powerful investigative tool that benefits various areas of chemistry and materials science. Many research groups have applied this method to the studies of catalytic materials, glasses, numerous other crystalline and amorphous inorganic compounds and even biological samples. A wide-ranging description of these applications would warrant a separate review.

In spite of recent advances, the MQMAS method itself continues to evolve. Most of the recent effort targets the improvement of sensitivity, which may offer new perspectives for high resolution studies of inherently challenging nuclei, such as ^{17}O. New types of correlation schemes are being considered in order to increase the sensitivity and/or resolution. For example, the recently proposed schemes that use two different MQ coherences during t_1 may have the potential of improved resolution over the standard MQMAS experiment.[113] Also recently, a technique referred to as satellite transition MAS (STMAS) has been proposed, which provides isotropic spectra of half-integer quadrupolar nuclei by correlating the evolution of single quantum inner-satellite transitions in t_1 with that observed during t_2 for the $(-1/2,1/2)$ central transition (see 'Satellite Transition NMR Spectroscopy of Half-Integer Quadrupolar Nuclei under Magic Angle Spinning').[63] This is also the case for the CESAME (central satellite MAS experiment) which has been proposed most recently.[114]

8 RELATED ARTICLES IN THIS VOLUME

Adiabatic Polarization-Transfer Methods in MAS Spectroscopy; Multiple-quantum Magic-angle Spinning Experiments on Half-integer Nuclei: Fundamentals; Satellite Transition NMR Spectroscopy of Half-Integer Quadrupolar Nuclei under Magic-Angle Spinning.

9 RELATED ARTICLES IN VOLUMES 1–8

Cross Polarization in Solids, Volume 3; Double Rotation, Volume 3; Dynamic Angle Spinning, Volume 3; Line Narrowing Methods in Solids, Volume 4; Multidimensional Spectroscopy: Concepts, Volume 5; Quadrupolar Interactions, Volume 6; Quadrupolar Nuclei in Solids, Volume 6.

10 REFERENCES

1. A. Abragam, 'Principles of Nuclear Magnetism', Oxford University Press: London, 1961.
2. E. R. Andrew, A. Bradbury, and R. G. Eades, *Nature*, 1958, **182**, 1659.
3. J. S. Waugh, L. M. Huber, and U. Haeberlen, *Phys. Lett.*, 1968, **20**, 180.
4. A. Pines, M. G. Gibby, and J. S. Waugh, *J. Chem. Phys.*, 1972, **56**, 1776.
5. B. C. Gerstein, R. G. Pembelton, R. C. Wilson, and L. M. Ryan, *J. Chem. Phys.*, 1977, **66**, 362.
6. A. Samoson, E. Lipmaa, and A. Pines, *Mol. Phys.*, 1988, **65**, 1013.
7. K. T. Mueller, B. Q. Sun, G. C. Chingas, J. W. Zwanziger, T. Terao, and A. Pines, *J. Magn. Reson.*, 1990, **86**, 470.
8. L. Frydman and J. S. Harwood, *J. Am. Chem. Soc.*, 1995, **117**, 5367.
9. A. Medek, J. S. Harwood, and L. Frydman, *J. Am. Chem. Soc.*, 1995, **117**, 12 779.
10. C. P. Slichter, 'Principles of Magnetic Resonance', 3rd edn., Springer-Verlag: Berlin, 1990.
11. M. H. Cohen and F. Rief, in 'Solid State Physics', eds F. Seitz and D. Turnbull, Academic Press: New York, 1958, Vol. 5, p. 321.
12. D. Freude and J. Haase, in 'NMR Basic Principles and Progress', eds P. Diehl, E. Fluck, and R. Kosfeld, Springer-Verlag: Berlin, 1993, Vol. 29, p. 1.
13. A. Vega, in 'Encyclopedia of Magnetic Resonance', eds D. M. Grant and R. K. Harris, John Wiley & Sons: Chichester, Vol. 6, p. 3869, 1996.
14. E. L. Hahn, *Phys. Rev.*, 1950, **80**, 580.
15. E. Oldfield, H. K. C. Timken, B. Montez, and R. Ramachandran, *Nature*, 1985, **318**, 163.
16. T. Bastow, *Solid State NMR*, 1994, **3**, 17.
17. H. J. Jakobsen, in 'Encyclopedia of Magnetic Resonance', eds D. M. Grant and R. K. Harris, John Wiley & Sons: Chichester, 1996, Vol. 4, p. 2370.
18. S. Ganapathy, S. Schramm, and E. Oldfield, *J. Chem. Phys.*, 1982, **77**, 4360.
19. J. Skibsted, N. C. Nielsen, H. Bildsoe, and H. J. Jakobsen, *J. Magn. Reson.*, 1991, **95**, 88.

20. E. Kundla, A. Samoson, and E. Lipmaa, *Chem. Phys. Lett.*, 1981, **83**, 229.
21. A. Samoson and E. Lipmaa, *J. Magn. Reson.*, 1988, **79**, 255.
22. N. C. Nielsen, H. Bildsoe, and H. J. Jakobsen, *J. Magn. Reson.*, 1992, **97**, 149.
23. A. P. M. Kentgens, *J. Magn. Reson.*, 1993, **A104**, 302.
24. A. Samoson, *Chem. Phys. Lett.*, 1985, **119**, 29.
25. C. Jager, *J. Magn. Reson.*, 1992, **99**, 353.
26. D. Massiot, V. Montouillout, F. Fayon, P. Florian, and C. Bessada, *Chem. Phys. Lett.*, 1997, **272**, 295.
27. C. S. Blackwell and R. L. Patton, *J. Phys. Chem.*, 1984, **88**, 6135.
28. A. J. Vega, *J. Magn. Reson.*, 1992, **96**, 50.
29. A. J. Vega, *Solid State NMR*, 1992, **1**, 17.
30. T. Gullion and J. Schaefer, *J. Magn. Reson.*, 1989, **81**, 196.
31. A. W. Hing, S. Vega, and J. Schaefer, *J. Magn. Reson.*, 1992, **96**, 205.
32. C. A. Fyfe, K. T. Mueller, H. Grodney, and K. C. Wong-Moon, *Chem. Phys. Lett.*, 1992, **199**, 198.
33. E. R. H. van Eck, R. Jansen, W. E. J. R. Maas, and W. S. Veeman, *Chem. Phys. Lett.*, 1990, **174**, 428.
34. C. P. Grey and A. J. Vega, *J. Am. Chem. Soc.*, 1995, **117**, 8232.
35. T. Gullion, *J. Magn. Reson.*, 1995, **A117**, 326.
36. A. Llor and J. Virlet, *Chem. Phys. Lett.*, 1988, **152**, 248.
37. K. T. Mueller, Y. Wu, B. F. Chmelka, J. Stebbins, and A. Pines, *J. Am. Chem. Soc.*, 1991, **113**, 32.
38. S. Vega and Y. Naor, *J. Chem. Phys.*, 1981, **75**, 75.
39. N. C. Nielsen, H. Bildsoe, and H. J. Jakobsen, *Chem. Phys. Lett.*, 1992, **191**, 205.
40. M. Pruski, J. W. Wiench, and J.-P. Amoureux, *J. Magn. Reson.*, 2000, **147**, 286.
41. J.-P. Amoureux, *Solid State NMR*, 1993, **2**, 83.
42. J.-P. Amoureux, C. Fernandez, and L. Frydman, *Chem. Phys. Lett.*, 1996, **259**, 347.
43. P. K. Madhu, A. Goldbourt, L. Frydman, and S. Vega, *Chem. Phys. Lett.*, 1999, **307**, 41.
44. P. K. Madhu, A. Goldbourt, L. Frydman, and S. Vega; *J. Chem. Phys.*, 2000, **112**, 2377.
45. A. P. M. Kentgens and R. Verhagen, *Chem. Phys. Lett.*, 1999, **300**, 435.
46. T. Vosegaard, P. Florian, D. Massiot, and P. J. Grandinetti, *J. Chem. Phys.*, 2001, **114**, 4618.
47. G. Wu, D. Rovnyak, and R. G. Griffin, *J. Am. Chem. Soc.*, **118**, 9326, 1996.
48. S. P. Brown, S. J. Heyes, and S. Wimperis, *J. Magn. Reson.*, 1996, **A119**, 280.
49. P. J. Grandinetti, J. H. Baltisberger, A. Llor, Y. K. Lee, U. Werner, M. A. Eastman, and A. Pines, *J. Magn. Reson.*, 1993, **A103**, 72.
50. D. Massiot, B. Touzo, D. Trumeau, J. P. Coutures, J. Virlet, P. Florian, and P. J. Grandinetti, *Solid State NMR*, 1996, **6**, 73.
51. J.-P. Amoureux, C. Fernandez, and S. Steuernagel, *J. Magn. Reson.*, 1996, **A123**, 116.
52. S. P. Brown and S. Wimperis, *J. Magn. Reson.*, 1997, **128**, 42.
53. T. Vosegaard, P. Florian, P. J. Grandinetti, and D. Massiot, *J. Magn. Reson.*, 2000, **143**, 217.
54. R. R. Ernst, G. Bodenhausen, and A. Wokaun, 'Principles of Nuclear Magnetic Resonance in One and Two Dimensions', Clarendon: Oxford, 1987.
55. T. Charpentier, Ph.D. Thesis, University of Paris XI, France, 1998.
56. K. T. Mueller, E. W. Wooten, and A. Pines, *J. Magn. Reson.*, 1991, **92**, 620.
57. N. G. Dowell, S. E. Ashbrook, J. McManus, and S. Wimperis, *J. Am. Chem. Soc.*, 2001, **123**, 8135.
58. A. Bax, R. Freeman, and S. P. Kempsell, *J. Magn. Reson.*, 1980, **41**, 349.
59. D. J. States, R. A. Haberkorn, and D. J. Ruben, *J. Magn. Reson.*, 1982, **48**, 286.
60. J.-P. Amoureux and C. Fernandez, *Solid State NMR*, 1998, **10**, 211.
61. C. Fernandez, J.-P. Amoureux, J. M. Chezeau, L. Delmotte, and H. Kessler, *Microporous Materials*, 1996, **6**, 331.
62. G. Wu, S. Kroeker, R. E. Wasylishen, and R. G. Griffin, *J. Magn. Reson.*, 1997, **A124**, 237.
63. Z. Gan, *J. Am. Chem. Soc.*, 2000, **122**, 3242.
64. S. P. Brown and S. Wimperis, *J. Magn. Reson.*, 1997, **124**, 279.
65. D. Iuga, H. Schafer, R. Verhagen, and A. P. M. Kentgens, *J. Magn. Reson.*, 2000, **147**, 192.
66. K. H. Lim and C. P. Grey, *Solid State NMR*, 1998, **13**, 101.
67. S. H. Wang, Z. Xu, J. H. Baltisberger, L. M. Bull, J. F. Stebbins, and A. Pines, *Solid State NMR*, 1997, **8**, 1.
68. K. J. Pike, R. P. Malde, S. E. Ashbrook, J. McManus, and S. Wimperis, *Solid State NMR*, 2000, **16**, 203.
69. J. McManus, R. Kemp-Harper, and S. Wimperis, *Chem. Phys. Lett.*, 1999, **311**, 292.
70. S. Wi and L. Frydman, *J. Chem. Phys.*, 2000, **112**, 3248.
71. M. Hanaya and R. K. Harris, *Solid State NMR*, 1997, **8**, 147.
72. V. Lacassagne, P. Florian, V. Montouillout, C. Gervais, F. Babonneau, and D. Massiot, *Magn. Reson. Chem.*, 1998, **36**, 956.
73. A. E. Bennett, C. M. Rienstra, M. Auger, K. V. Lakshmi, and R. G. Griffin, *J. Chem. Phys.*, 1995, **103**, 6951.
74. D. Massiot, *J. Magn. Reson.*, 1996, **A122**, 240.
75. J. L. Baltisberger, Z. Xu, J. F. Stebbins, S. H. Wang, and A. Pines, *J. Am. Chem. Soc.*, 1996, **118**, 7209.
76. H. Hunger and T. Horvath, *J. Am. Chem. Soc.*, 1996, **118**, 12 302.
77. H. Maekawa, P. Florian, D. Massiot, H. Kiyono, and M. Nakamura, *J. Phys. Chem.*, 1996, **100**, 5525.
78. U. T. Pingel, J.-P. Amoureux, T. Anupold, F. Bauer, H. Ernst, C. Fernandez, D. Freude, and A. Samoson, *Chem. Phys. Lett.*, 1998, **294**, 345.
79. M. Bak, J. T. Rasmussen, and N. C. Nielsen, *J. Magn. Reson.*, 2000, **147**, 296.
80. S. A. Smith, T. O. Levante, B. H. Meier, and R. R. Ernst, *J. Magn. Reson.*, 1994, **106**, 75.
81. J. Zwanziger, *Solid State NMR*, 1994, **3**, 219.
82. G. Czjzek, J. Fink, F. Gotz, H. Schmidt, J. M. D. Coey, J. P. Rebouillat, and A. Lienard, *Phys. Rev.*, 1981, **B23**, 2513.
83. F. Angeli, T. Charpentier, P. Faucon, and J. C. Petit, *J. Phys. Chem.*, 1999, **B103**, 10 356.
84. F. Angeli, J. M. Delaye, T. Charpentier, J. C. Petit, D. Ghaleb, and P. Faucon, *J. Non-Cryst. Solids*, 2000, **276**, 132.
85. C. Fernandez, L. Delevoye, J.-P. Amoureux, D. P. Lang, and M. Pruski, *J. Am. Chem. Soc.*, 1997, **119**, 6858.
86. W. Sun, J. T. Stephen, L. D. Porter, and Y. Wu, *J. Magn. Reson.*, 1995, **A116**, 181.
87. M. Pruski, D. P. Lang, C. Fernandez, and J.-P. Amoureux, *Solid State NMR*, 1997, **7**, 327.
88. S. E. Ashbrook, S. P. Brown, and S. Wimperis, *Chem. Phys. Lett.*, 1998, **288**, 509.
89. T. P. Jarvie, R. M. Wenslow, and K. T. Mueller, *J. Am. Chem. Soc.*, 1995, **117**, 570.
90. S. H. Wang, S. M. De Paul, and L. M. Bull, *J. Magn. Reson.*, 1997, **125**, 364.
91. C. Fernandez, C. Morais, and M. Pruski, *Solid State NMR*, 2002, **21**, 61.
92. C. Fernandez, D. P. Lang, J.-P. Amoureux, and M. Pruski, *J. Am. Chem. Soc.*, 1998, **120**, 2672.
93. M. Pruski, A. Bailly, D. P. Lang, J.-P. Amoureux, and C. Fernandez, *Chem. Phys. Lett.*, 1999, **307**, 35.
94. J.-P. Amoureux and M. Pruski, in preparation.
95. A. Pines, M. G. Gibby, and J. S. Waugh, *J. Chem. Phys.*, 1973, **59**, 569.
96. D. Rovnyak, M. Baldus, and R. G. Griffin, *J. Magn. Reson.*, 2000, **142**, 145.
97. K. H. Lim and C. P. Grey, *J. Chem. Phys.*, 2000, **112**, 7490.
98. S. E. Ashbrook and S. Wimperis, *Mol. Phys.*, 2000, **98**, 1.

99. S. E. Ashbrook and S. Wimperis, *J. Magn. Reson*, 2000, **147**, 238.
100. S. Vega, *Phys. Rev.*, 1981, **23**, 3152.
101. S. R. Hartmann and E. L. Hahn, *Phys. Rev.*, 1962, **128**, 2042.
102. E. O. Stjeskal, J. Schaefer, and J. S. Waugh, *J. Magn. Reson.*, 1977, **28**, 105.
103. J.-P. Amoureux, M. Pruski, D. P. Lang, and C. Fernandez, *J. Magn. Reson.*, 1998, **131**, 170.
104. A. Lupulescu, S. P. Brown, and H. W. Spiess, in preparation.
105. M. Pruski, C. Fernandez, D. Lang, J.-P. Amoureux, *Catalysis Today*, 1999, **49**, 401.
106. H. Y. Carr and E. M. Purcell, *Phys. Rev.*, 1954, **94**, 630.
107. S. Meiboom and D. Gill, *Rev. Sci. Inst.*, 1958, **29**, 688.
108. T. Vosegaard, F. H. Larsen, H. J. Jakobsen, P. D. Ellis, and N. C. Nielsen, *J. Am. Chem. Soc.*, 1997, **119**, 9055.
109. R. Lefort, J. W. Wiench, M. Pruski, and J.-P. Amoureux, *J. Chem. Phys.*, 2002, **116**, 2493.
110. F. H. Larsen and N. C. Nielsen, *J. Phys. Chem. A*, 1999, **103**, 10 825.
111. P. Bodart, J.-P. Amoureux, and F. Taulelle, *Solid State NMR*, 2002, **21**, 1.
112. G. McGeorge, J. Z. Hu, C. Mayne, D. W. Alderman, R. J. Pugmire, and D. M. Grant, *J. Magn. Reson.*, 1997, **129**, 134.
113. A. Jerschow, J. W. Logan, and A. Pines, *J. Magn. Reson.*, 2001, **149**, 268.
114. J.-P. Amoureux, C. Morais, J. Trebosc, J. Rocha, and C. Fernandez, *J. Am. Chem. Soc.*, submitted.

Biographical Sketches

Jean-Paul Amoureux, *b* 1946. Eng., 1970, Paris, Ph.D., 1976, University of Lille, France. Approx. 140 publications. His interest in solid state NMR started in 1985, after assuming a position of professor in the Laboratoire de Dynamique et Structure des Materiaux Moleculaires (CNRS) at the University of Lille. Current research includes the development of new solid state NMR methods with emphasis on half-integer quadrupolar nuclei.

Marek Pruski, *b* 1954. M.S., 1977, Ph.D., 1981, N. Copernicus University, Torun, Poland. Introduced to NMR in 1982 at the N. Copernicus University and Universität Leipzig. Postdoctoral fellow at the Iowa State University (with B. C. Gerstein), 1985–88, scientist and head of solid state NMR group, Ames Laboratory, Iowa State University 1988–present. Approx. 90 publications. Current research specialty: solid state NMR and its applications to surface and material sciences, high resolution methods for half-integer quadrupolar nuclei.

Nutation Spectroscopy of Quadrupolar Nuclei

Bernard C. Gerstein

Ames Laboratory of Iowa State University, Des Moines, IA, USA

1	Introduction	1
2	General Considerations: Hamiltonians	1
3	The Nutation Spectrum	3
4	Experimental Considerations	3
5	Phasing of the Spectra	4
6	Line Broadening	4
7	Effect of Recycle Delay	4
8	An Example: ^{45}Sc in $Sc_2(SO_4)_3$	4
9	Related Articles	4
10	References	4

1 INTRODUCTION

As pointed out in the article ***Rudimentary NMR: The Classical Picture***, the natural motion of a magnetic moment in a field is a precession, or nutation, of the moment $\boldsymbol{M} = \gamma \boldsymbol{I}$ about the field $\boldsymbol{B}$ with nutation frequency $\omega = \gamma B$. It is this nutation in the rotating frame of the Zeeman interaction, as applied to the NMR spectra of nuclei with quadrupolar moments $I \geq 1$ that is the subject of this discussion. The main difference between the case discussed here and NMR of spin-$\frac{1}{2}$ nuclei is that in general the condition $\hat{\mathcal{H}}_{\rm rf} > \hat{\mathcal{H}}_{\rm int}$ is not met, so the condition for assuming that the rf pulses take place in an infinitely short time compared with the effects of internal Hamiltonians is violated.

In this case, we must consider the time development of the system when both the quadrupolar Hamiltonian and the rf Hamiltonian are of the same order of magnitude, or even when $\hat{\mathcal{H}}_{\rm Q} > \hat{\mathcal{H}}_{\rm rf}$. It was realized[1] that even in this case quite useful information could be extracted if the experiment was made into a two-dimensional situation, where the system evolves in time under $\hat{\mathcal{H}}_{\rm rf} + \hat{\mathcal{H}}_{\rm Q}$ for a time t_1, and then evolves under just $\hat{\mathcal{H}}^{\rm Q}$ for a time period t_2. The double Fourier transform on both times then yields the nutation spectrum, e.g. in Figure 1, from which may be inferred the number of different chemical species in the sample under investigation, and the relative values of the quadrupole versus the rf interactions, as discussed below.

2 GENERAL CONSIDERATIONS: HAMILTONIANS

As discussed by Mehring in ***Internal Spin Interactions and Rotations in Solids***, the form of the rf Hamiltonian for, e.g. a pulse with x phase, is

$$\hat{\mathcal{H}}_{\rm rf} = -\omega_1 \hat{I}_x \equiv -\omega_{\rm rf} \hat{I}_x \tag{1}$$

The pertinent Hamiltonian for a static sample during the evolution period under the influence of an rf pulse turned on for a time t_1, with x phase and a quadrupolar interaction not small compared with the pulse strength Ω_1, including and offset from resonance is

$$\begin{aligned}\hat{\mathcal{H}}^1(t_1) &= [\hat{\mathcal{H}}_{\rm off} + \hat{\mathcal{H}}_{\rm rf} + \hat{\mathcal{H}}^1_{\rm Q}] \\ &= \delta \hat{I}_z - \omega_1 \hat{I}_x + \omega^*_{\rm Q}[3\hat{\boldsymbol{I}}^2 - I(I+1)]\end{aligned} \tag{2}$$

where $\omega_{\rm Q}{}^* = \omega_{\rm Q}(3\cos^2\theta - 1 + \eta \sin^2\theta \cos 2\phi)$, and $\omega_{\rm Q} = 2\pi e^2 qQ/8hI(I+1) \equiv 2\pi\chi/8I(I+1)$, and θ, ϕ are the polar angles orienting the electric field gradient (EFG) tensor with respect to the static field axis, taken to be the z axis in the laboratory, and η is the asymmetry of the EFG tensor. Dipolar interactions and nonsecular quadrupolar interactions (second-order terms) have been neglected.

After the rf pulse, assumed to be strong compared with the magnitude of the shielding Hamiltonian, the system evolves for time t_2 under shielding, chemical shift, and the nonsecular quadrupolar terms (taking into account only the central $\frac{1}{2}-\frac{1}{2}$ transition),

$$\hat{\mathcal{H}}^2(t_2) = \hat{\mathcal{H}}_{\rm Z} + \hat{\mathcal{H}}_{\rm CS} + \hat{\mathcal{H}}^2_{\rm Q} \tag{3}$$

where Z stands for Zeeman, CS is chemical shift, and the superior 2 means the nonsecular second-order terms which have the major effect on the central transition. Using the density matrix formalism,[2] with the equilibrium density operator in the high temperature form, in the frame of detection of the signal which is the rotating frame (the Zeeman interaction disappears from the description), the evolution during time t_1 is

$$\hat{\rho}(t_1) = \exp\{-{\rm i}\hat{\mathcal{H}}_1 t_1\}\hat{\rho}\exp\{{\rm i}\hat{\mathcal{H}}_1 t_1\} \tag{4}$$

While the Zeeman states $|I, m\rangle$ are not exact eigenfunctions of the first- and second-order quadrupolar Hamiltonians, their linear combinations will be and can be found by diagonalization of the total Hamiltonian. If $\mathbf{T}$ is the orthogonal transformation which diagonalizes the Hamiltonian, then we may express the density operator at time t_1 in matrix form as

$$\boldsymbol{\rho}(t_1) = \mathbf{T}\cdot\exp\{-{\rm i}\mathbf{D}t_1\}\mathbf{T}^+\boldsymbol{\rho}(0)\mathbf{T}\exp\{{\rm i}\mathbf{D}t_1\}\mathbf{T}^+ \tag{5}$$

$\mathbf{D}$ represents the diagonalized matrix of the Hamiltonian $\hat{\mathcal{H}}^1$ with eigenvalues

$$E_j = \sum_p T^*_{pj} H^1_{pq} T_{qj} \tag{6}$$

and eigenfunctions

$$|j\rangle = \sum_k T^*_{kj}|I, m_k\rangle \tag{7}$$

Assuming that only coherence between states $|\frac{1}{2}\rangle$ and $|-\frac{1}{2}\rangle$ is detected during time t_2, so only the elements $\rho_{1/2,-1/2}$ need

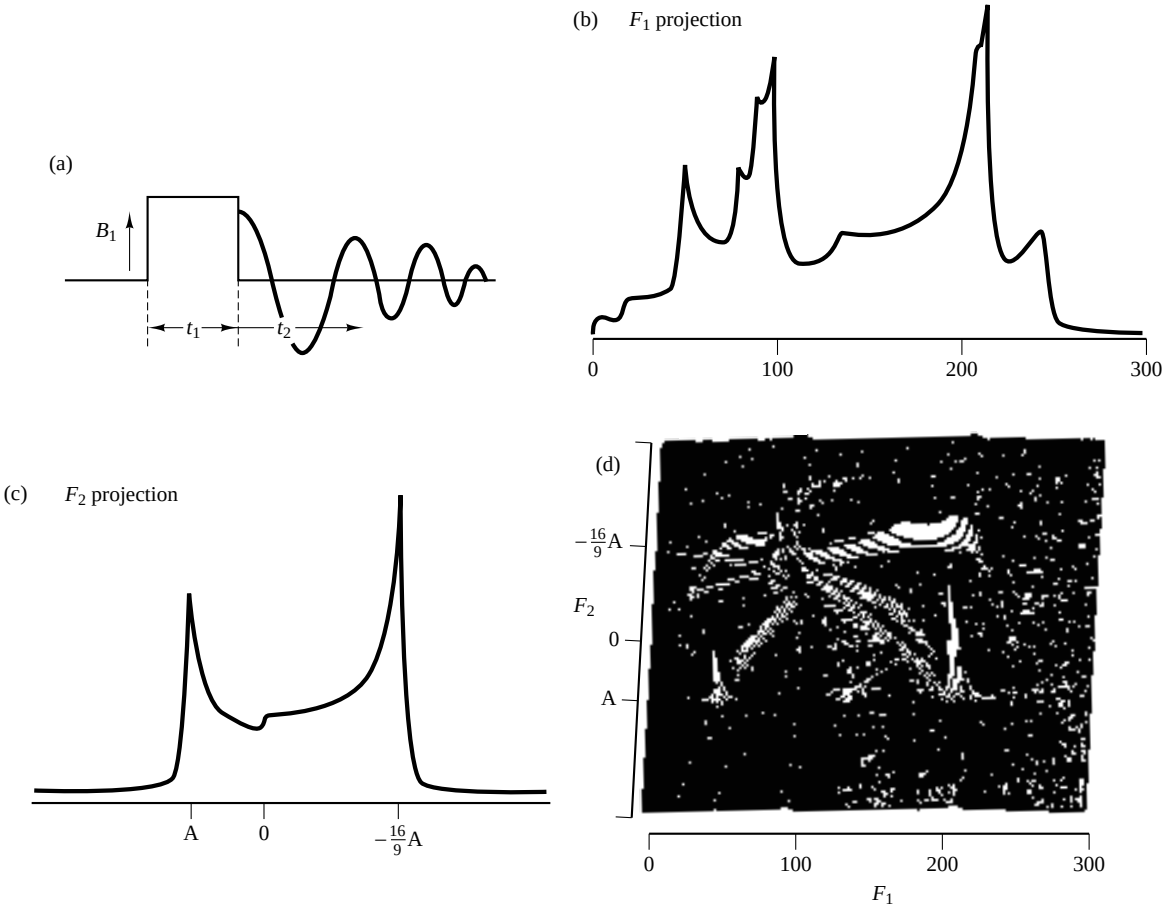

Figure 1 (a) Pulse scheme of the experiment; a free induction decay is acquired during t_2 as a function of the pulse length t_1. Subsequent Fourier transformation of the signals obtained yields a typical 2D powder pattern as shown in (d). This spectrum was calculated for $I = \frac{5}{2}$ with a ratio $\omega_Q/\omega_{rf} = 0.45$ and $\eta = 0$. The F_2 projection of this pattern (c) gives the second-order quadrupole powder pattern, and the F_1 projection (b) is a characteristic nutation spectrum for the ratio ω_Q/ω_{rf}

be evaluated, the signal from the central transition $S(t_1, t_2)$ can then be evaluated as follows:

$$S(t_1, t_2) = \mathrm{Tr}\{\hat{\rho}(t_1, t_2)(\hat{I}_x + \mathrm{i}\hat{I}_y)\} \propto \hat{\rho}(t_1)_{1/2,-1/2} \exp\{-\mathrm{i}\omega_2 t_2\}$$
$$= \sum_{k,j} (R_{-1/2,1/2})_{k,j} \exp\{\mathrm{i}\omega_{k,j} t_1\} \exp\{-\mathrm{i}\omega_2 t_2\} \quad (8)$$

Here, ω_2 represents the Larmor precession of the spins during the time t_2 and ω_{kj} is the transition frequency in the rotating frame between states $|k\rangle$ and $|j\rangle$. The coefficients $(R_{-1/2,1/2})_{kj}$ represent the contributions from coherence between states $|k\rangle$ and $|j\rangle$ in the rotating frame during t_1 to the $\frac{1}{2}$, $-\frac{1}{2}$ coherence detected during t_2:

$$(R_{-\frac{1}{2},\frac{1}{2}})_{k,j} = T_{\frac{1}{2},k} T^*_{-\frac{1}{2},j} \sum_m T^*_{m,k} T_{m,j} \rho(0)_{m,m} \quad (9)$$

The states of an isolated spin-$\frac{7}{2}$ in the presence of magnetic field B, with quadrupole coupling constant $2\pi\chi = 1$ MHz and asymmetry $\eta = 0$, are shown in Figure 2.

In summary, during time t_1 the system develops in time with eigenfunctions and eigenvalues which depend upon the ratio of ω^*_Q and ω_{rf}. The coherences between these levels, with frequency ω_{kj}, develop during time t_1 and contribute to the coherence detected between the state $|\frac{1}{2}\rangle$, $|-\frac{1}{2}\rangle$ detected during time t_2. Therefore, a 2D Fourier transform of the acquired signal will give a characteristic powder pattern [Figure 1(d)], with projection on the F_2 axis shown in Figure 1(c) being the normal powder pattern of the $\frac{1}{2}-\frac{1}{2}$ transition associated with

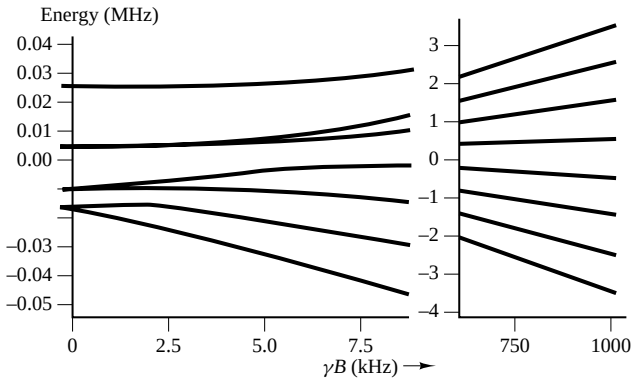

Figure 2 Energy diagram of an isolated spin $I = \frac{7}{2}$ in the presence of a magnetic field B with quadrupole parameters $e^2qQ/h = 1$ MHz and $\eta = 0$. On the left is the low field situation $\mathcal{H}_Z < \mathcal{H}_Q$ and on the right is the situation $\mathcal{H}_Z \gg \mathcal{H}_Q$, where $\mathcal{H}_Q$ appears to be negligible

shielding anisotropy and second-order quadrupole broadening. Projection onto the F_1 axis [Figure 1(b)] gives the nutation spectrum which depends upon the quadrupole parameters χ and η, the spin quantum number I, and the rf field strength ω_1, and is independent of chemical shift.

3 THE NUTATION SPECTRUM

As an example, the calculated nutation spectra as a function of ω_Q/ω_{rf} is shown in Figure 3.

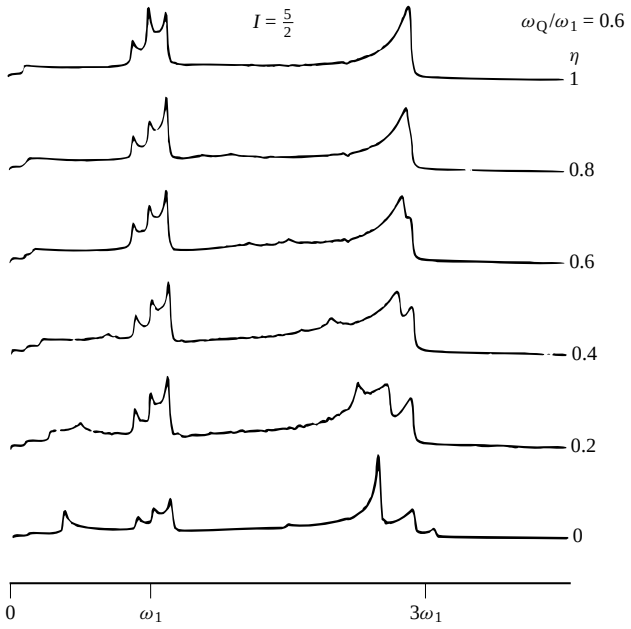

Figure 3 Calculated nutation spectra as a function of ω_Q/ω_{rf} ($\eta = 0$)

When there is only one site for the species under study, a 1D nutation spectrum suffices to characterize this species. When nuclei of a given spin are present in more than a single environment, it is advantageous to study the entire 2D powder pattern.

4 EXPERIMENTAL CONSIDERATIONS

To obtain experimental nutation spectra which can be compared with the calculated spectra, it is important to keep several experimental conditions in mind.

The first of these is the resonance offset. Thus, when the system is irradiated on-resonance ($\omega = \omega_0$) then the matrix of H_1 in equation (10) becomes symmetric with respect to both diagonals of the matrix. As a result of this

$$\left.\begin{aligned} (R_{-1/2,1/2})_{i,j} &= -(R_{-1/2,1/2})_{j,i}, \quad i \neq j \\ &\text{and} \\ (R_{-1/2,1/2})_{i,j} &= 0, \qquad\qquad i = j \end{aligned}\right\} \tag{10}$$

Substitution in equation (8) shows that the signal then becomes

$$S(t_1, t_2) = \sum_{i<j} (R_{-1/2,1/2})_{i,j} \sin\{\omega_{ij} t_1\} \exp\{-i\omega_2 t_2\} \tag{11}$$

The amplitude of the signal detected during t_2 is sine-modulated, which allows us to obtain pure absorption spectra. The presence of an off-resonance term in B_1 lowers the symmetry of its matrix and the modulation now becomes a phase modulation, which cannot be changed to amplitude modulation by phase cycling. Thus there will be dispersive contributions to the lineshapes which can easily distort powder patterns.

Another effect of off-resonance irradiation is the appearance of a dispersive line at $\omega_1 = 0$. This is due to the magnetization component along the $\boldsymbol{B}_{eff}$ field in the rotating frame which does not evolve during t_1. Both effects of off-resonance irradiation can even be observed for spins with $I = \frac{1}{2}$ for which the signal in such a case can be written as:

$$\begin{aligned} S(t_1, t_2) \sim [&A(1 - \cos(\omega_{eff} t_1) + iB \sin(\omega_{eff} t_1)] \\ &\times \exp\{-i\omega_2 t_2\} \end{aligned} \tag{12}$$

where $A = \omega_{rf}\Delta\omega/2(\omega_{rf}^2 + \Delta\omega^2)$ and $B = \omega_{rf}/2\sqrt{(\omega_{rf}^2 + \Delta\omega^2)}$. When $\Delta\omega = \omega - \omega_0 \neq 0$, then $A \neq 0$ and thus a constant and a $\cos(\omega_{eff} t_1)$ term is introduced, causing respectively the $\omega_1 = 0$ signal and the phase modulation. To avoid complications it is clearly recommendable to irradiate on-resonance, i.e. with the excitation frequency ω equal to the Larmor frequency γB_0. That on-resonance in this case does not mean equal to the $\frac{1}{2}$, $-\frac{1}{2}$ transition frequency is shown by the following magic angle spinning (MAS) experiment. Here the Larmor frequency lies outside the quadrupole lineshape and Figure 4 shows the nutation spectra of $NaNO_2$ ($e^2qQ/h = 1.1$ MHz, $\eta = 0.1$) as a function of the excitation frequency. In this case we are in the extreme situation $\omega_Q \gg \omega_{rf}$ and MAS does not influence the nutation spectrum. It is clear that the line at $\omega_1 = 0$ increases relative to the line at $2\omega_{rf}$. The line at $\omega_1 = 0$ is

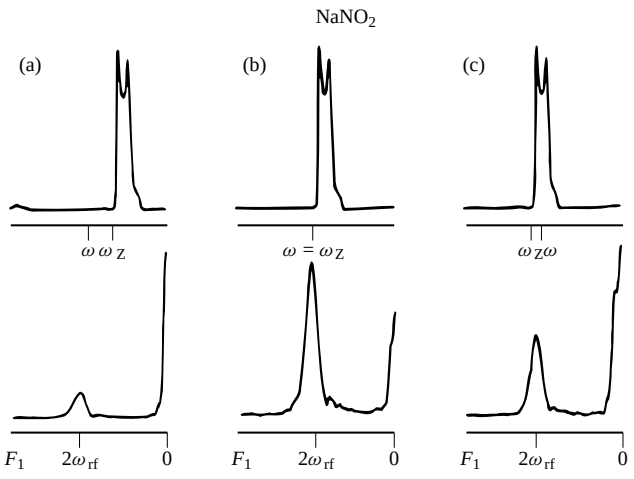

Figure 4 MAS spectra of $NaNO_2$ together with their nutation spectra as a function of the excitation frequency ω. (a) Off-resonance irradiation; in the nutation spectrum we see a large line at $\omega_1 = 0$. (b) Irradiation close to the Larmor frequency (outside the powder pattern) gives the best nutation spectrum. (c) With the carrier frequency equal to the average $\frac{1}{2}$, $-\frac{1}{2}$ transition frequency (in the middle of the powder pattern), the line at $\omega_1 = 0$ increases again

minimal when we irradiate outside the powder pattern near the Larmor frequency. An easy method to reduce the line at $\omega_1 = 0$ is to subtract the last (longest t_1 value) experiment in the 2D experiment from all the previous experiments. When enough t_1 experiments are performed, the quadrupolar modulation has damped out, and the only signal emerging after a long rf pulse is that of the magnetization causing the zero frequency signal in the F_1 direction. Because the magnetization component along $\boldsymbol{B}_{\text{eff}}$ has the same magnitude in every experiment (assuming no relaxation), subtraction of the last experiment reduces its influence on the spectrum.

5 PHASING OF THE SPECTRA

It is important to obtain pure absorption spectra when one wants to obtain 2D powder patterns which can be analyzed in a straightforward way. Because we want no dispersion signals to appear in the spectrum, it is not possible to perform an absolute value calculation. Therefore, the spectra have to be phased manually. As we have seen in the preceding paragraph, off-resonance irradiation introduces phase modulation and thus dispersive lineshapes are introduced in the spectra. This makes it very difficult to phase the spectra properly. This is so difficult because when phasing a 2D spectrum one has to set the phase correction on one slice (row or column) of the spectrum and it is not possible to inspect the effect of such a phase correction on the total spectrum. It would be desirable to have a program that shows the phase corrections of the whole spectrum directly on the display. As modern NMR spectrometers are equipped with minicomputers using array processors, it should be possible to do so because nutation spectra are generally of small size.

When one is only interested in the 1D nutation spectrum (the F_1 projection) of a sample, there is a way to avoid phasing the whole 2D spectrum. In this case we can take the first point of every FID emerging directly after the pulse of length t_1. If we arrange these points as a function of t_1, we have the amplitude modulation of the detected t_2 signal as a 1D interferogram. A straightforward 1D Fourier transform of this interferogram will give us the nutation spectrum which can be phased easily.

6 LINE BROADENING

An important cause of line broadening in the F_1 dimension is the inhomogeneity of the rf magnetic field. The effect of rf inhomogeneity cannot simply be described with a Lorentzian broadening $\exp(-t_1/\tau_1)$ because a spread in ω_{rf} will also cause a spread in the ratio $\omega_{\text{Q}}/\omega_{\text{rf}}$, and will thus change the whole nutation spectrum. Furthermore the lineshapes due to rf inhomogeneity will not be Lorentzian but asymmetric. Only in the extreme case $\omega_{\text{rf}} \gg \omega_{\text{Q}}$ do we get a line at nutation frequency ω_{rf} with a linewidth directly determined by the rf inhomogeneity. In the other extreme case $\omega_{\text{rf}} \ll \omega_{\text{Q}}$, there will be a line at $(I + \frac{1}{2})\omega_{\text{rf}}$, so the linewidth will be $(I + \frac{1}{2})\gamma$-times the rf inhomogeneity. It is therefore important to use a probe with an accurately formed rf coil to reduce rf inhomogeneity as much as possible, and care should be taken that the whole sample is in the coil.

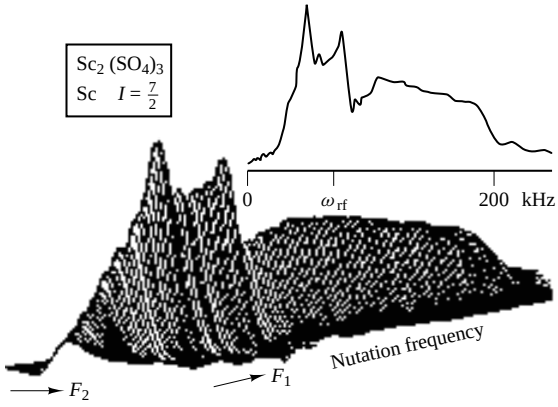

Figure 5 Two-dimensional nutation spectrum of ^{45}Sc in $Sc_2(SO_4)_3$ recorded on a Bruker WM-500 instrument, together with its F_1 projection (256 t_1 increments of 1.5 μs with a 70 kHz rf field)

7 EFFECT OF RECYCLE DELAY

Another important experimental aspect in the nutation experiment is that one has to ensure that the recycle delay or relaxation delay is long enough for the system to return to equilibrium before the next pulse arrives. If the recycle delay is short with respect to T_1 then the build up of magnetization along the z axis is incomplete. This will distort the pure sine amplitude modulation of the FID. Fourier transformation of a distorted sin $\omega_1 t$ wave will give a line at frequency ω_1 plus a number of harmonics at $2\omega_1$, $3\omega_1$, ... The number and amplitude of these harmonics depend on the distortion of the sine wave, and they can easily be mistaken for components with a large quadrupole frequency.

8 AN EXAMPLE: ^{45}Sc IN $Sc_2(SO_4)_3$

An example is the ^{45}Sc ($I = \frac{7}{2}$) nutation spectrum of $Sc_2(SO_4)_3$ (Figure 5). The spectrum of the central transition measured at 121.5 MHz is 2.6 kHz wide and shows no structure; MAS narrows the spectrum to 600 Hz. The MAS spectrum recorded at 43.8 MHz does show some structure from which it becomes clear that there must be sites with different quadrupole parameters but the same chemical shift. The 2D nutation spectrum is well structured. Comparing its projection to our set of calculated spectra reveals that the major constituent has $e^2qQ/h \sim 2$ MHz with a low asymmetry parameter ($\eta \sim 0.2$).

9 RELATED ARTICLES

Inorganic Solids; Internal Spin Interactions and Rotations in Solids; Quadrupolar Interactions; Quadrupolar Nuclei in Glasses; Quadrupolar Nuclei in Solids.

10 REFERENCES

1. E. Kundla, A. Samoson, and E. Lippmaa, *Chem. Phys. Lett.*, 1981, **83**, 229.

2. T. Farrar and J. E. Harriman, *Density Matrix Theory and its Applications in NMR Spectroscopy*, The Farragut Press, Madison, WI, 1992.

Acknowledgments

Most of the material in this treatment came from the Ph.D. Thesis of A. P. M. Kentgens, under the direction of Wiebren Veeman at The Katholieke Universiteit te Nijmegen, The Netherlands, with the permission of Wiebren Veeman.

Biographical Sketch

Bernard C. Gerstein. *b* 1932. B.S., 1953, Purdue, USA; Ph.D., 1960, Iowa State University. Introduced to NMR by R. W. Vaughan. Faculty in Chemistry, Iowa State University, 1962–present. Approx. 150 publications. Research interests include the theory and practice of learning, and applications of solid state NMR to problems in the physics and chemistry of materials, fossil fuels, and heterogeneous catalysis.

Overtone Spectroscopy of Quadrupolar Nuclei

Robert Tycko

National Institutes of Health, Bethesda, MD, USA

1	Introduction	1
2	Theory	1
3	Experiments	2
4	Conclusions	4
5	Related Articles	5
6	References	5

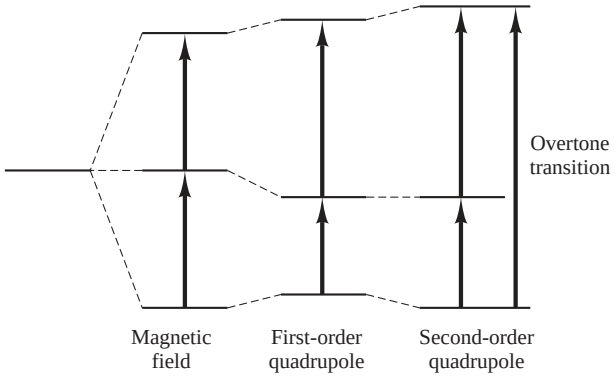

Figure 1 Spin energy levels for a spin-1 nucleus. The splitting of the energy levels due to a strong magnetic field and the first-order and second-order perturbations of the energy levels due to a quadrupole coupling are shown. (Adapted by permission of the American Chemical Society from R. Tycko and S. J. Opella, *J. Am. Chem. Soc.*, 1986, **108**, 3531)

1 INTRODUCTION

In the context of NMR, 'overtone spectroscopy' refers to the direct excitation of nuclear spin transitions and coherences and the direct detection of NMR signals at frequencies that are nearly multiples of the Larmor frequency ν_0. Overtone spectroscopy depends on the excitation and detection of 'forbidden' transitions, i.e. transitions that cannot be excited or detected directly in the limit of very strong external dc magnetic fields but that become excitable or detectable directly when the interactions of nuclear spins with the dc field are not very much stronger than the internal nuclear spin couplings. Recent interest in overtone spectroscopy grew out of the work of Bloom and LeGros,[1] who showed that overtone transitions have sufficient intensity in practice to be of experimental utility. Subsequent work[2,3] showed that overtone spectroscopy has real advantages when applied to solid state NMR measurements of integer-spin nuclei with large quadrupole couplings. Since ^{14}N is the most important nucleus of this type from the standpoint of chemistry and biochemistry, recent work has focused on ^{14}N overtone NMR.

Overtone spectroscopy should be distinguished from multiple quantum spectroscopy. In multiple quantum spectroscopy, one typically applies rf pulses with a carrier frequency close to ν_0 in order to excite nuclear spin coherences with oscillation frequencies that are nearly multiples of ν_0. The oscillation of these coherences is then detected indirectly through its effect on the single quantum signals near ν_0. In overtone spectroscopy, the rf carrier frequency is about equal to the oscillation frequency of the coherences, and the oscillation of the coherences is detected directly. Conceptually speaking, overtone spectroscopy can be thought of as a single photon spectroscopy, while multiple quantum spectroscopy can be thought of as a multiple photon spectroscopy. In some cases, the same coherences may be excited and detected either by overtone NMR or by multiple quantum NMR. As a general rule, overtone methods are probably more effective than multiple quantum methods when the nuclear quadrupole splittings exceed 1 MHz.

Figure 1 shows a spin energy level diagram for a spin-1 nucleus such as ^{14}N. A spin-1 nucleus has three possible eigenstates. In the absence of all spin interactions, the three states are degenerate. The interaction with an external dc field produces three equally spaced energy levels and two allowed, single quantum transitions at frequency ν_0. A nuclear quadrupole coupling that is weaker than the interaction with the external field perturbs the energy levels. To first order, a quadrupole coupling with coupling constant ν_Q shifts the middle ($m = 0$) level relative to the upper and lower ($m = \pm 1$) levels by an amount $\nu_Q^{(1)}$ proportional to ν_Q. This produces the first-order quadrupole splitting, with single quantum transitions at $\nu_0 \pm \nu_Q^{(1)}$. To second order, the quadrupole coupling additionally shifts the upper and lower levels by amounts $\pm\nu_Q^{(2)}$ proportional to ν_Q^2/ν_0. This is the second-order quadrupole shift. The single quantum transitions are then at $\nu_0 \pm \nu_Q^{(1)} + \nu_Q^{(2)}$. In addition, the overtone transition at frequency $2\nu_0 + 2\nu_Q^{(2)}$ becomes weakly allowed, producing signals and nutation frequencies proportional to ν_Q/ν_0 in pulsed NMR experiments. Although the overtone signals are intrinsically weaker than the allowed single quantum (or 'fundamental') signals, the fact that the overtone spectrum spans a frequency range that is narrower than the single quantum spectrum by a factor of the order of ν_Q/ν_0 makes measurement of the overtone signals substantially more tractable, especially in polycrystalline and noncrystalline solids (where the resonance lines are inhomogeneously broadened powder patterns) and in single crystals with several inequivalent sites. Thus, particularly in ^{14}N NMR, overtone spectroscopy allows NMR signals to be obtained and nuclear relaxation rates to be measured in systems where NMR experiments would otherwise be extremely difficult or impossible. Overtone spectra also contain structural information that is absent in single quantum spectroscopy, through the dependence of the overtone transition moment on the molecular or crystal orientation and on the direction of the applied rf field.

Overtone NMR spectroscopy of spin-1 nuclei is analogous to earlier 'half-field' electron paramagnetic resonance (EPR) studies of triplet states,[4,5] with the nuclear quadrupole coupling taking the place of the electronic spin–spin coupling or zero field splitting. Calculations of lineshapes and transition probabilities carried out for half-field EPR[6,7] are therefore applicable to overtone NMR of spin-1 nuclei.

2 THEORY

A detailed description of the theory and the implementation of overtone spectroscopy has been given by Tycko and Opella.[3] The essential theoretical points follow from consideration of the spin Hamiltonian $\hat{\mathcal{H}}$ for a quadrupolar nucleus with spin $\hat{S}$:

$$\hat{\mathcal{H}} = \hat{\mathcal{H}}_{\mathrm{S}} + \hat{\mathcal{H}}_{\mathrm{rf}} \tag{1}$$

$$\hat{\mathcal{H}}_{\mathrm{S}} = -h\nu_0\hat{S}_z + h\nu_{\mathrm{Q}}[3\hat{S}^2_{z'} - \hat{S}^2 + \eta(\hat{S}^2_{x'} - \hat{S}^2_{y'})] \tag{2}$$

$$\hat{\mathcal{H}}_{\mathrm{rf}} = 2\hbar\gamma_S B_1(\hat{S}_x\cos\theta + \hat{S}_z\sin\theta)\cos(2\pi\nu t + \phi) \tag{3}$$

$\hat{\mathcal{H}}_{\mathrm{S}}$ includes the interaction with the external dc field along z (the Zeeman interaction) and the quadrupole coupling. The principal axes of the quadrupole coupling tensor are $x'y'z'$. ν_{Q} is defined as $(e^2qQ)/[4S(2S-1)]$. $\hat{\mathcal{H}}_{\mathrm{rf}}$ is the interaction with an rf field with amplitude $\boldsymbol{B}_1$, frequency ν, phase ϕ, and direction in the xz plane at angle θ to x. γ_S is the nuclear gyromagnetic ratio. In the limit $\nu_0 \gg \nu_{\mathrm{Q}}$, the eigenstates of $\hat{\mathcal{H}}_{\mathrm{S}}$ are simply the eigenstates of S_z, i.e. $\{|m\rangle\}$. When this limit does not apply, but $\nu_0 > \nu_{\mathrm{Q}}$, the eigenstates are $\{|\psi_m\rangle\}$, given by

$$|\psi_m\rangle = |m\rangle + \sum_{m'\neq m} C_{mm'}|m'\rangle \tag{4}$$

If the laboratory axes (xyz) and quadrupole principal axes ($x'y'z'$) are related by Euler angles α, β, and γ, the coefficients $C_{mm'}$ are given to first order in ν_{Q}/ν_0 by

$$\begin{aligned} C_{mm'} = \frac{\nu_{\mathrm{Q}}}{2(m'-m)\nu_0}\{&-\delta_{m',\,m+1}[S(S+1) \\ &-m(m+1)]^{\frac{1}{2}}(2m+1)F(\alpha,\beta,\gamma) - \delta_{m',\,m-1} \\ &\times[S(S+1)-m(m-1)]^{\frac{1}{2}}(2m-1)F^*(\alpha,\beta,\gamma) \\ &+\delta_{m',\,m+2}\{[S(S+1)-m(m+1)][S(S+1) \\ &-(m+1)(m+2)]\}^{\frac{1}{2}}G(\alpha,\beta,\gamma) \\ &+\delta_{m',\,m-2}\{[S(S+1)-m(m-1)][S(S+1) \\ &-(m-1)(m-2)]\}^{\frac{1}{2}}G^*(\alpha,\beta,\gamma)\} \end{aligned} \tag{5a}$$

$$\begin{aligned} F(\alpha,\beta,\gamma) = e^{i\gamma}[&3\sin\beta\cos\beta - \eta(\cos 2\alpha\sin\beta\cos\beta \\ &+ i\sin 2\alpha\sin\beta)] \end{aligned} \tag{5b}$$

$$\begin{aligned} G(\alpha,\beta,\gamma) = e^{2i\gamma}\Bigg\{&\frac{3}{2}\sin^2\beta \\ &+\eta\left[\frac{1}{2}\cos 2\alpha(1+\cos^2\beta) + i\sin 2\alpha\cos\beta\right]\Bigg\} \end{aligned} \tag{5c}$$

To second order in ν_{Q}/ν_0, the energy E_m of the state $|\psi_m\rangle$ is

$$\begin{aligned} E_m = h\nu_0\Bigg\{&-m + \frac{\nu_{\mathrm{Q}}}{2\nu_0}[3m^2 - S(S+1)][(3\cos^2\beta - 1) \\ &+\eta\cos 2\alpha\sin^2\beta] + \sum_{m'\neq m}(m'-m)|C_{mm'}|^2\Bigg\} \end{aligned} \tag{6}$$

The orientation-dependent frequency of the overtone transition in a spin-1 nucleus is then

$$\nu_{1,\,-1}(\alpha,\beta,\gamma) = 2\nu_0 + \frac{\nu_{\mathrm{Q}}^2}{\nu_0}(|F(\alpha,\beta,\gamma)|^2 + |G(\alpha,\beta,\gamma)|^2) \tag{7}$$

and the orientation-dependent transition moment is

$$\begin{aligned} M_{1,\,-1}(\alpha,\beta,\gamma) &\equiv \langle\psi_1|S_x\cos\theta + S_z\sin|\psi_{-1}\rangle \\ &= \frac{\nu_{\mathrm{Q}}}{\nu_0}[\sin\theta F(\alpha,\beta,\gamma) + \cos\theta G(\alpha,\beta,\gamma)] \end{aligned} \tag{8}$$

The nutation frequency (i.e. the inverse of the 2π pulse length) for excitation of the overtone transition is given by $\gamma_S B_1|M_{1,-1}|/\pi$. The overtone signal amplitude is proportional to $|\rho_{1,-1}M_{1,-1}|$, where $|\rho_{1,-1}|$ is the amplitude of the overtone coherence excited by rf pulses. Thus, equation (8) displays the unusual features of overtone spectroscopy that the nutation frequency depends on the orientation of the quadrupole tensor principal axis system, that overtone transitions can be excited by rf fields applied parallel to the external dc field ($\theta = \pi/2$), and that signals can be detected by rf solenoid coils wound parallel to the dc field. Overtone powder pattern lineshapes in polycrystalline and noncrystalline solids are determined by the orientation-dependent overtone frequency in equation (7) weighted by an orientation-dependent function related to $M_{1,-1}$. The precise details of the weighting function depend on the excitation method. In the linear (i.e. small flip-angle pulse) regime, the weighting function is $|M_{1,-1}|^2$. Equation (8) shows that the weighting function, and hence the observed lineshape, depends on θ.

Since the coefficients $C_{mm'}$ are nonzero only for $|m - m'| = 1$ or 2, only the first ($\nu \approx 2\nu_0$) and second ($\nu \approx 3\nu_0$) overtone transitions have transition moments proportional to ν_{Q}/ν_0, and only the first overtone transition has a transition moment proportional to ν_{Q}/ν_0 when $\theta = \pi/2$. Higher overtone transitions are weaker, with transition moments proportional to higher powers of ν_{Q}/ν_0.

3 EXPERIMENTS

3.1 Detection of ^{14}N Overtone Transitions by CW NMR

Creel et al.[8] have reported the detection of the ^{14}N spectrum of hexamethylenetetramine by CW NMR methods in fields up to 2.2 T, where ν_0 = 6.6 MHz. The quadrupole coupling frequency $\nu_{\mathrm{Q}} = (e^2qQ)/4h$ is roughly 1.1 MHz in hexamethylenetetramine. Although the fields in these experiments were low by modern standards, they were high enough that the highest frequency ^{14}N signals can be considered to be overtones of the lower frequency signals.

3.2 Indirect Detection of ^{14}N Overtone Transitions

Blinc et al.[9] measured the ^{14}N NMR spectrum of triglycine sulfate by means of the Hartmann–Hahn double resonance, indirect detection technique.[10] Working in a 0.42 T field, they determined the ^{14}N resonant frequencies by observing proton NMR signals following an adiabatic demagnetization–adiabatic remagnetization cycle, with rf irradiation of the ^{14}N nuclei during a delay period between the demagnetization and remagnetization steps. In such an experiment, the proton NMR signals are destroyed or attenuated whenever the rf frequency is close to a ^{14}N resonance. In the work of Blinc et al., three resonances were observed for a single ^{14}N site, but the dc field was so low that it would be improper to call one resonance an overtone of the others. Essentially the same method was later applied to overtone spectroscopy at considerably higher fields by Tycko and Opella and by Garroway and Miller.[11] Related experiments, but involving double quantum rather than overtone excitation, were carried out by Schnur et al.[12] The indirect detection method is a comparatively simple way to locate overtone resonances in organic compounds, with high sensitivity (in favorable cases, on a single transient) but with low resolution. Figure 2 shows double resonance rf pulse sequences for the indirect detection of overtone signals.

3.3 Direct Detection of ^{14}N Overtone Signals Following Double Quantum Excitation

Bloom and LeGros[1] showed that the ^{14}N overtone signals from a single crystal of $NaNO_2$, with ν_Q = 1.4 MHz, could be detected directly with adequate sensitivity in a 5.4 T field

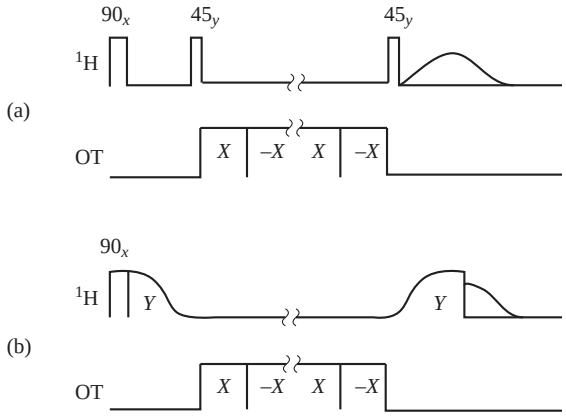

Figure 2 Sequences of rf pulses applied to proton (^{1}H) spins and to an overtone (OT) transition for the indirect detection of overtone transitions in organic solids. (a) Proton dipolar order is created by a two pulse Jeener–Broekaert sequence. A train of OT pulses, with alternating rf phases, destroys part of the dipolar order when the OT carrier frequency is close to a nuclear resonance. Proton NMR signals, proportional to the remaining dipolar order, are detected after the final proton pulse. In a typical application, one scans the OT carrier frequency and looks for a reduction in the proton signal at the OT resonance. (b) Same procedure as (a), but with dipolar order created by adiabatic demagnetization in the rotating frame (ADRF) and proton signals detected after adiabatic remagnetization in the rotating frame (ARRF). A signal enhancement by a factor of 4 over the Jeener–Broekaert method is possible

(ν_0 = 16.6 MHz). In the experiments of Bloom and LeGros, rf pulses were not applied at the overtone resonant frequency. Instead, the overtone coherence was excited by the double quantum excitation technique of Vega and Pines,[13] in which a rf pulse at frequency $\nu_0 + \nu_Q^{(2)}$, with amplitude less than ν_Q/γ_S, is applied for a time about equal to $3\pi\nu_Q/2(\gamma_S B_1)^2$. Thus, signals were detected at twice the frequency of the applied pulses. So far, this method of exciting overtone transitions has been of interest primarily from the standpoint of pure spectroscopy. Excitation near the overtone resonant frequency itself has proven to be a more practical approach.

3.4 Direct Detection and Direct Excitation of ^{14}N Overtone Transitions

Tycko and Opella[2,3] carried out a series of experiments that demonstrated the feasibility of the direct excitation and direct detection of ^{14}N overtone spectra in single crystal and polycrystalline organic solids. They showed that overtone coherences could be excited both by direct pulsed excitation of the overtone transition and by cross polarization from proton magnetization. They demonstrated the high resolution inherent in overtone spectroscopy when high-power proton decoupling is employed (overtone resonances in single crystals subject to small strains and small degrees of disorder are broadened by second-order rather than first-order quadrupole effects). They showed that quadrupole coupling constants and asymmetry parameters could be determined from overtone lineshapes of polycrystalline samples and that the powder pattern lineshapes depend on the direction of the rf coil used for excitation and detection. They also demonstrated two-dimensional overtone nutation spectroscopy, for measuring overtone nutation frequencies, and two-dimensional overtone separated-local-field spectroscopy, for measuring ^{14}N–^{1}H dipole–dipole couplings. Radiofrequency pulse sequences for the acquisition of one-dimensional ^{14}N overtone spectra of organic solids are shown in Figure 3. Examples of one-dimensional ^{14}N overtone spectra are shown in Figures 4 and 5.

Tycko and Opella[3] have discussed the comparative sensitivities of ^{14}N overtone spectroscopy and single quantum spectroscopy. Because of the reduced spectral widths and linewidths in typical overtone spectra, overtone spectroscopy has sensitivity at least comparable to that of single quantum spectroscopy despite the weakly allowed nature of overtone transitions.

Tycko and Opella[3] have also carried out preliminary experimental investigations of the effects of rapid sample spinning on ^{14}N overtone spectra of polycrystalline solids. They found that spinning about a single axis changed, but did not narrow, the overtone powder pattern lineshape. Takegoshi and Hikichi[14] performed calculations of overtone lineshapes under sample spinning that supported the experimental results. They have also discussed the use of double rotation (DOR) and dynamic angle spinning (DAS) methods as a means of narrowing the second-order quadrupole shift powder patterns observed in ^{14}N overtone spectroscopy.[14] Although this approach to line narrowing has not been demonstrated in experiments, it may turn out to be a valuable one. In principle, either the DOR or the DAS technique, or some suitable variant of these techniques, may allow one to obtain resolved ^{14}N

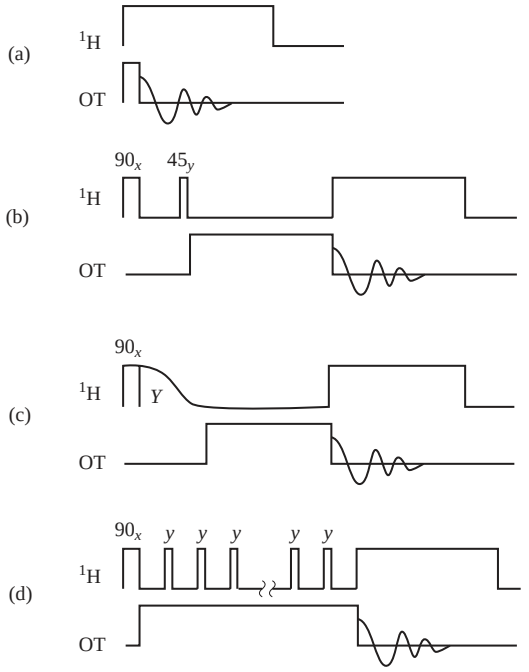

Figure 3 Pulse sequences for the direct detection of overtone spectra in organic solids. (a) Direct excitation of overtone coherences with a single OT pulse. High-power proton decoupling is applied during the acquisition of the overtone signals. (b) A Jeener–Broekaert sequence is used to create proton dipolar order. Overtone coherences are generated by cross polarization from dipolar order. (c) Adiabatic demagnetization in the rotating frame is used to create proton dipolar order. Overtone coherences are generated by cross polarization from dipolar order. (d) Overtone coherences are generated by cross polarization from transverse proton magnetization, prepared by pulsed spin locking. Pulsed, rather than continuous, spin locking reduces the effective proton rf field, allowing a Hartmann–Hahn match to be achieved despite the relatively weak effective OT rf field (due to the weakly allowed nature of the overtone transitions). (Adapted by permission of the American Institute of Physics from Tycko and Opella, *J. Chem. Phys.*, 1987, **86**, 1761)

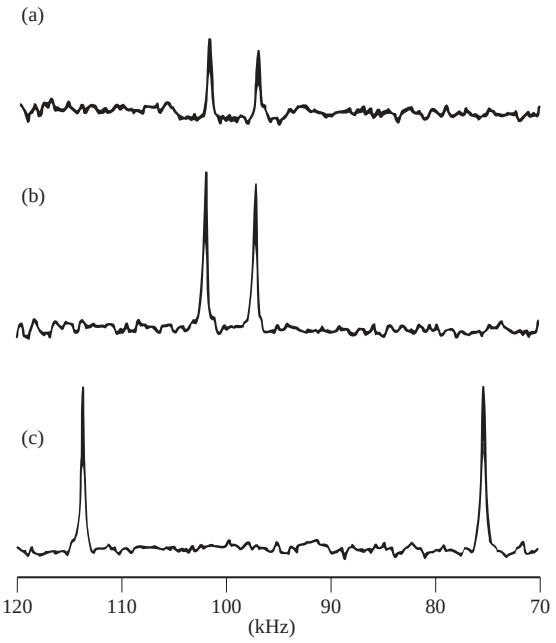

Figure 4 ^{14}N overtone NMR spectra of a 50 mg single crystal of *N*-acetyl-D,L-valine, obtained at 5.89 T ($2\nu_0$ = 36.118 MHz). The two lines result from the two magnetically inequivalent molecules in the unit cell. All spectra result from the acquisition of 1024 transients. (a) Direct excitation, using the pulse sequence in Figure 3(a). (b) Cross polarization, using the pulse sequence in Figure 3(b). (c) Cross polarization, using the pulse sequence in Figure 3(b), after an arbitrary 10° rotation of the crystal. The change in the overtone resonant frequencies is due to the orientation dependence of the second-order quadrupole shifts. (Adapted by permission of the American Chemical Society from Tycko and Opella, *J. Am. Chem. Soc.*, 1968, **108**, 3531)

overtone NMR lines from chemically inequivalent nitrogen sites in a complex polycrystalline solid (i.e. a polycrystalline peptide or oligonucleotide). The resonant frequencies in such an experiment would be determined by the isotropic parts of the chemical shift and the second-order quadrupole shift. In addition, one expects a small contribution to the overtone lineshapes from a spinning sample due to Berry's phase, as observed in pure NQR spectra of spinning samples.[15] The effects of Berry's phase, which arise because the nuclear spin eigenstates are functions of orientation when the quadrupole coupling is large, are expected to be of the order of $|C_{mm'}|^2\nu_R$, where ν_R is the sample spinning frequency, which is less than 100 Hz for typical experimental conditions.

Takegoshi and Hikichi[16] have also carried out a rotation study of a single crystal of L-alanine to determine the ^{14}N quadrupole coupling constant and asymmetry parameter in this compound. The observed angular dependences of the overtone frequency and intensity were well described by the expressions derived by perturbation theory.

Ramanathan and Opella[17] have investigated the effects of irradiation of ^{14}N overtone resonances on the ^{13}C NMR spectrum of a single crystal of *N*-acetyl-D,L-valine. The ^{13}C NMR lineshapes at 3.52 T are asymmetric triplets for carbon atoms that are coupled to ^{14}N nuclei in this crystal, with asymmetry due to the large ^{14}N quadrupole coupling (ν_Q = 0.8 MHz). Irradiation of the ^{14}N overtone resonances caused the triplet ^{13}C lineshapes to collapse into unresolved doublets. Ramanathan and Opella showed that this 'overtone decoupling' could be carried out selectively, allowing particular ^{14}N overtone resonances to be correlated with particular ^{13}C resonances. Selective overtone decoupling may be useful in the assignment of resonances in single crystal NMR studies.

4 CONCLUSIONS

Overtone spectroscopy is a useful addition to the techniques of solid state NMR. The reduced spectral widths and linewidths of ^{14}N overtone spectra compared with traditional single quantum spectra clearly make overtone spectroscopy the preferred means of applying ^{14}N NMR to the study of many classes of solids. In many cases, overtone spectroscopy is the only practical way to observe ^{14}N NMR signals. At the very least, this allows measurements of spin relaxation rates and approximate quadrupole coupling constants to be performed. Such measurements can probe the chemical, structural, dynamical, and electronic properties of solids.

Extensions of overtone spectroscopy to NMR of nuclei with spins greater than one are possible, but have not yet been

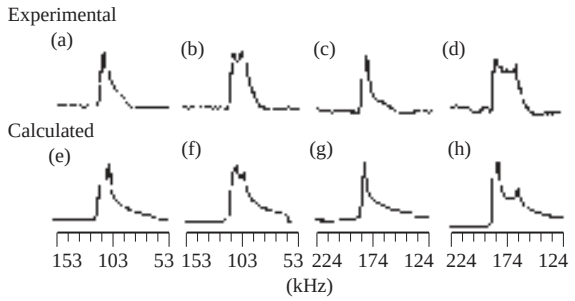

Figure 5 Experimental (a–d) and (e–h) calculated ^{14}N overtone NMR spectra of *N*-acetyl-D,L-valine powder, obtained at 5.89 T (a,b,e,f) and 3.54 T (c,d,g,h) with the pulse sequence in Figure 3(c). The rf solenoid coil used for excitation and detection of overtone signals is perpendicular to the external magnetic field in (a), (c), (e), and (g), and parallel to the external magnetic field in (b), (d), (f), and (h). Each experimental spectrum is the result of approximately 20 000 transients on a 200 mg sample. In the calculations, signal contributions from the various possible molecular orientations are weighted by $|M_{1,-1}|$ (see text), and effects of the ^{14}N chemical shift anisotropy are included. (Adapted by permission of the American Institute of Physics from Tycko and Opella, *J. Chem. Phys.*, 1987, **86**, 1761)

investigated in detail. For most quadrupolar nuclei, with non-integer spins, the 'central transition' (i.e. the $m = \frac{1}{2} \leftrightarrow m = -\frac{1}{2}$ transition) is already unaffected by first-order quadrupole splittings and is fully allowed. The arguments in favor of overtone spectroscopy are therefore less compelling. Nonetheless, one expects the observation of overtone signals in conjunction with single quantum signals to afford spectral simplification, contribute to the determination of quadrupole coupling parameters, and facilitate the assignment of resonances. The measurement of overtone relaxation rates may also add to the information available from relaxation measurements on the central transition.

5 RELATED ARTICLES

Cross Polarization in Solids; Double Rotation; Dynamic Angle Spinning; Geometric Phases; Quadrupolar Nuclei in Glasses; Quadrupolar Nuclei in Solids.

6 REFERENCES

1. M. Bloom and M. A. LeGros, *Can. J. Phys.*, 1982, **64**, 1522.
2. R. Tycko and S. J. Opella, *J. Am. Chem. Soc.*, 1986, **108**, 3531.
3. R. Tycko and S. J. Opella, *J. Chem. Phys.*, 1987, **86**, 1761.
4. J. H. van der Waals and M. S. deGroot, *Mol. Phys.*, 1959, **2**, 333.
5. M. S. deGroot and J. H. van der Waals, *Mol. Phys.*, 1960, **3**, 190.
6. P. Kottis and R. Lefebvre, *J. Chem. Phys.*, 1963, **39**, 393.
7. P. Kottis and R. Lefebvre, *J. Chem. Phys.*, 1964, **41**, 379.
8. R. B. Creel, E. D. von Meerwall, and R. G. Barnes, *Chem. Phys. Lett.*, 1977, **49**, 501.
9. R. Blinc, M. Mali, R. Osredkar, A. Prelesnik, I. Zupancic, and L. Ehrenberg, *J. Chem. Phys.*, 1971, **55**, 4843.
10. S. R. Hartmann and E. L. Hahn, *Phys. Rev.*, 1962, **128**, 2042.
11. A. N. Garroway and J. B. Miller, *J. Magn. Reson.*, 1989, **82**, 591.
12. G. Schnur, R. Kimmich, and F. Winter, *J. Magn. Reson.*, 1986, **66**, 295.
13. S. Vega and A. Pines, *J. Chem. Phys.*, 1977, **66**, 5624.
14. K. Takegoshi and K. Hikichi, *Chem. Phys. Lett.*, 1992, **194**, 359.
15. R. Tycko, *Phys. Rev. Lett.*, 1987, **58**, 2281.
16. K. Takegoshi and K. Hikichi, *Chem. Phys. Lett.*, 1993, **206**, 450.
17. K. V. Ramanathan and S. J. Opella, *J. Magn. Reson.*, 1988, **78**, 367.

Biographical Sketch

Robert Tycko. *b* 1959. A.B., 1980, Princeton University; Ph.D., 1984, University of California at Berkeley. Postdoctoral fellow, University of Pennsylvania, 1984–86. Member of the Technical Staff, AT&T Bell Laboratories, Murray Hill, NJ, 1986–94. Investigator, National Institutes of Health, Bethesda, MD, 1994–present. Approx. 50 publications on magnetic resonance. Research specialties: fundamental principles of magnetic resonance spectroscopy, development of new NMR techniques, characterization of the structural, dynamical, and electronic properties of chemical systems, materials, and biochemical systems.

Quadrupolar Interactions

Pascal P. Man

Université Pierre et Marie Curie, Paris, France

1	Introduction	1
2	Quadrupolar Hamiltonian in a Uniform Space	1
3	Spherical Tensor Representation for the Quadrupolar Hamiltonian	2
4	Quadrupolar Interaction as a Perturbation of Zeeman Interaction	2
5	Energy Levels and the Spectrum of a Single Crystal	3
6	Powder Spectrum	6
7	Appendix	8
8	Related Articles	9
9	References	9

1 INTRODUCTION

Nuclei are characterized by an atomic number Z, a mass number A, and a nuclear spin I. The value of I depends on those of A and Z (Table 1). Nuclei with spin $I > \frac{1}{2}$ are multiple energy level systems and are called quadrupolar nuclei. They represent more than 70% of those in the Periodic Table. However, they are not as frequently investigated in NMR as other elements, because of their quadrupole moments Q, which interact with the electric field gradient (EFG) generated by their surroundings. This coupling, called the quadrupolar interaction and denoted by $\mathcal{H}_Q$, may be much stronger than the amplitude of the rf excitation pulse. As a result, it affects the line intensity and alters the lineshape. These effects make the interpretation of spectra more difficult. Usually, only the first two expansion terms of $\mathcal{H}_Q$ are considered: the first-order, ($H_Q^{[1]}$), and second-order, ($H_Q^{[2]}$), quadrupolar interactions, in the vocabulary of standard perturbation theory. $H_Q^{[1]}$ splits the spectrum of a half-integer quadrupole spin system in a single crystal into $2I - 1$ satellite lines, but the central line remains at the Larmor frequency ω_0. The additional effect of $H_Q^{[2]}$ is to shift further all the lines, including the central line.

When the sample is in powder form, as it usually is, it is mainly the central line that is observed. Moreover, its lineshape becomes nonsymmetrical when $H_Q^{[2]}$ is large. In favorable cases, the powder pattern of the satellite spinning sidebands is detected using the popular MAS technique (see ***Magic Angle Spinning*** and ***Rotating Solids***). The powder pattern of the central line is characterized by three parameters: the quadrupolar coupling constant $\chi = e^2qQ/\hbar$, which is the product of a nuclear property (eQ) and a crystal property (eq), the asymmetry parameter η and the center of gravity of the experimental line, δ_{CG}^{exp} (in ppm). χ is a measure of the strength of the quadrupolar interaction and η a measure of the deviation of the EFG from axial symmetry. The true chemical shift δ_{CS} of the central line is related to these three parameters:[1,2]

$$\delta_{CS} = \delta_{CG}^{exp} + \tfrac{1}{30}(1 + \tfrac{1}{3}\eta^2)[I(I+1) - \tfrac{3}{4}]\left[\frac{3\chi}{2I(2I-1)\omega_0}\right]^2 \qquad (1)$$

A precise determination of δ_{CS} is required if its value has to be correlated with bond lengths and bond angles. Several methods are available for determining χ and η. They can be grouped into two categories:

1. there is a series of techniques, especially the mechanical spinning of the sample,[1–5] based on the frequency domain response of the spin system (see ***Variable Angle Sample Spinning***);
2. the second series deals with the time domain response of the spin system to rf excitation[6–8] (see ***Nutation Spectroscopy of Quadrupolar Nuclei***).

The experimental center of gravity δ_{CG}^{exp} is determined by spectral simulation. However, spectra acquired with DAS or DOR probes provide this value directly[5] (see ***Double Rotation*** and ***Dynamic Angle Spinning***). Books dealing with these modern techniques are available.[9–11]

In the present article, we focus on the frequency domain response of half-integer quadrupolar spin larger than 1. (Jellison and co-workers[12] calculated perturbation terms up to third order for integer spins $I = 1$ and 3.) The first part is devoted to a derivation of the Hamiltonians corresponding to first- and second-order perturbations, with the emphasis on the different conventions used in the literature, namely, the asymmetry parameter, the components of spherical tensors in their principal axis system, the Larmor frequency, transitions, and the transition frequency. With this in mind, the Magnus expansion is applied instead of standard perturbation theory. For simplicity, Hamiltonians are expressed in angular velocity units and relaxation phenomena are not taken into account. In the second part, NMR parameters related to single crystal spectra (see ***High- Pressure NMR***, ***Incommensurate Systems***, and ***Phase Transitions and Critical Phenomena in Solids***) and powder patterns in static and MAS measurements are presented (see ***Amorphous Materials***, ***Quadrupolar Nuclei in Glasses***, ***Quadrupolar Nuclei in Solids***, and ***Vanadium Catalysts: Solid State NMR***), in particular, the second-order quadrupolar shift, the critical points and the lineshapes of the powder patterns for various values of η, and the second-order quadrupolar shift for the center of gravity of a powder pattern. In the appendix, the commonly used Euler angles as well as those used by Baugher and co-workers[13–15] are given in graphical form. The Wigner rotation matrix, expressing the components of the same spherical tensor in two different coordinate frames, is also given.

Table 1 Value of Nuclear Spin I as a Function of Atomic Number Z and Mass Number A

	Z	
A	Odd	Even
Odd	Half-integer I	Half-integer I
Even	Integer I	$I = 0$

2 QUADRUPOLAR HAMILTONIAN IN A UNIFORM SPACE

Slichter[16] and others[17,18] introduce the quadrupolar interaction from the classical concept of the charge density for a nucleus in a space where the three coordinate axes x, y, and z are equivalent. Then, the quantum mechanical form

of this interaction is obtained using operators. Thanks to the Wigner–Eckart theorem, the Hamiltonian representing the quadrupolar interaction independently of the Cartesian coordinate frame is defined:

$$\hbar\hat{\mathcal{H}}_{\mathrm{Q}} = \frac{eQ}{6I(2I-1)} \sum_{\alpha,\beta=x,y,z} V_{\alpha\beta}[\tfrac{3}{2}(\hat{I}_\alpha \hat{I}_\beta + \hat{I}_\beta \hat{I}_\alpha) - \delta_{\alpha\beta} I(I+1)] \quad (2a)$$

with

$$V_{\alpha\beta} = \left.\frac{\partial^2 U}{\partial\alpha\,\partial\beta}\right|_{r=0} \quad (2b)$$

$\delta_{\alpha\beta}$ is the Kronecker delta symbol, U is the electrostatic potential at the origin (inside the nucleus) generated by external charges, and $V_{\alpha\beta}$ are the Cartesian components of the EFG at the origin, $\boldsymbol{V}$, which is a second-rank symmetrical tensor (see ***Deuterium NMR in Solids*** and ***Liquid Crystalline Samples: Deuterium NMR***). In the principal axis system Σ^{PAS} of the EFG, $\boldsymbol{V}$ is diagonal:

$$\boldsymbol{V} = \begin{bmatrix} V_{XX} & 0 & 0 \\ 0 & V_{YY} & 0 \\ 0 & 0 & V_{ZZ} \end{bmatrix} \quad (3)$$

with the convention $|V_{ZZ}| \geq |V_{YY}| \geq |V_{XX}|$. Furthermore, the Laplace equation $V_{XX} + V_{YY} + V_{ZZ} = 0$ holds for $\boldsymbol{V}$. Thus, only two independent parameters are required:

$$eq = V_{ZZ} \quad (4a)$$

$$\eta = \frac{V_{XX} - V_{YY}}{V_{ZZ}} \quad (4b)$$

the largest component and the asymmetry parameter, respectively, with $1 \geq \eta \geq 0$.

In the coordinate frame Σ^{PAS}, the Cartesian tensor representation of the quadrupolar interaction [equation (2a)] takes the form

$$\hbar\hat{\mathcal{H}}_{\mathrm{Q}} = \frac{e^2qQ}{4I(2I-1)}[3\hat{I}_Z^2 - I(I+1) + \eta(\hat{I}_X^2 - \hat{I}_Y^2)] \quad (5a)$$

In terms of the operators

$$\hat{I}_+ = \hat{I}_X + \mathrm{i}\hat{I}_Y, \quad \hat{I}_- = \hat{I}_X - \mathrm{i}\hat{I}_Y \quad (5b)$$

equation (5a) becomes

$$\hbar\hat{\mathcal{H}}_{\mathrm{Q}} = \frac{e^2qQ}{4I(2I-1)}[3\hat{I}_Z^2 - I(I+1) + \tfrac{1}{2}\eta(\hat{I}_+^2 + \hat{I}_-^2)] \quad (5c)$$

Sometimes, the opposite convention is adopted for η:

$$\eta = \frac{V_{YY} - V_{XX}}{V_{ZZ}} \quad (6)$$

which is associated with the condition $|V_{ZZ}| \geq |V_{XX}| \geq |V_{YY}|$.[19,20] As a result, a negative sign appears in front of η in equations (5a) and (5c) and in subsequent expressions containing η.

3 SPHERICAL TENSOR REPRESENTATION FOR THE QUADRUPOLAR HAMILTONIAN

The passage from one coordinate frame to another is more conveniently realized if the quadrupolar interaction is expressed as a second-rank irreducible spherical tensor (see ***Internal Spin Interactions and Rotations in Solids***), according to Mehring:[21]

$$\hbar\hat{\mathcal{H}}_{\mathrm{Q}} = \frac{eQ}{4I(2I-1)} \sum_{q=-2}^{2} (-1)^q V^{(2,q)} T^{(2,-q)}$$

$$= \frac{eQ}{4I(2I-1)} \sum_{q=-2}^{2} (-1)^q V^{(2,-q)} T^{(2,q)} \quad (7)$$

In any Cartesian coordinate frame Σ, the spherical tensor and Cartesian tensor components of $\boldsymbol{V}$ are related by

$$\left.\begin{aligned} V^{(2,0)} &\equiv V_0 = 3\sqrt{\tfrac{1}{6}}V_{zz} \\ V^{(2,1)} &\equiv V_1 = -V_{xz} - \mathrm{i}V_{yz} \\ V^{(2,-1)} &\equiv V_{-1} = V_{xz} - \mathrm{i}V_{yz} \\ V^{(2,2)} &\equiv V_2 = \tfrac{1}{2}(V_{xx} - V_{yy}) + \mathrm{i}V_{xy} \\ V^{(2,-2)} &\equiv V_{-2} = \tfrac{1}{2}(V_{xx} - V_{yy}) - \mathrm{i}V_{xy} \end{aligned}\right\} \quad (8)$$

and those of $\boldsymbol{T}$ as

$$\left.\begin{aligned} T^{(2,0)} &= \tfrac{1}{3}\sqrt{6}[3\hat{I}_z^2 - I(I+1)], \quad T^{(2,1)} = -\hat{I}_z\hat{I}_+ - \hat{I}_+\hat{I}_z \\ T^{(2,-1)} &= \hat{I}_z\hat{I}_- + \hat{I}_-\hat{I}_z, \quad T^{(2,2)} = \hat{I}_+\hat{I}_+, \quad T^{(2,-2)} = \hat{I}_-\hat{I}_- \end{aligned}\right\} \quad (9)$$

with $\hat{I}_+ = \hat{I}_x + \mathrm{i}\hat{I}_y$ and $\hat{I}_- = \hat{I}_x - \mathrm{i}\hat{I}_y$. These two operators are different from those of equation (5b) despite the same notation. It is worth noting that the numerical factors in the components of $\boldsymbol{V}$ and $\boldsymbol{T}$ [equations (8) and (9)] differ from author to author.

Using equations (7)–(9), the spherical tensor representation of the quadrupolar interaction in the coordinate frame Σ becomes

$$\hbar\hat{\mathcal{H}}_{\mathrm{Q}} = \frac{eQ}{4I(2I-1)}\{\tfrac{1}{3}\sqrt{6}[3\hat{I}_z^2 - I(I+1)]V_0 + (\hat{I}_z\hat{I}_+ + \hat{I}_+\hat{I}_z)V_{-1}$$
$$-(\hat{I}_z\hat{I}_- + \hat{I}_-\hat{I}_z)V_1 + \hat{I}_+^2 V_{-2} + \hat{I}_-^2 V_2\} \quad (10)$$

Slichter[16] uses nearly the same relationship, apart from a negative sign due to another choice of V_1. From equations (4a), (4b), and (8), the spherical tensor components of $\boldsymbol{V}$ in Σ^{PAS} are obtained:

$$V_0^{\mathrm{PAS}} = \sqrt{\tfrac{3}{2}}eq, \quad V_1^{\mathrm{PAS}} = V_{-1}^{\mathrm{PAS}} = 0, \quad V_2^{\mathrm{PAS}} = V_{-2}^{\mathrm{PAS}} = \tfrac{1}{2}eq\eta \quad (11a)$$

If the other convention for η, namely, equation (6) is used then the spherical tensor components of $\boldsymbol{V}$ in Σ^{PAS} are[20]

$$V_0^{\mathrm{PAS}} = \sqrt{\tfrac{3}{2}}eq, \quad V_1^{\mathrm{PAS}} = V_{-1}^{\mathrm{PAS}} = 0, \quad V_2^{\mathrm{PAS}} = V_{-2}^{\mathrm{PAS}} = -\tfrac{1}{2}eq\eta \quad (11b)$$

4 QUADRUPOLAR INTERACTION AS A PERTURBATION OF ZEEMAN INTERACTION

A nuclear spin possesses a magnetic moment $\boldsymbol{\mu}$ and an angular momentum $\hbar\boldsymbol{I}$, which are related by the gyromagnetic ratio γ:

$$\boldsymbol{\mu} = \gamma\hbar\boldsymbol{I} \quad (12)$$

In the laboratory frame Σ^{lab}, the direction of the strong static magnetic field $\boldsymbol{B}_0$ is taken as the z axis. The coupling of the magnetic moment with $\boldsymbol{B}_0$ is the Zeeman interaction $\hat{\mathcal{H}}_{\text{Z}}$:

$$\hbar\hat{\mathcal{H}}_{\text{Z}} = -\boldsymbol{\mu}\cdot\boldsymbol{B}_0 = -\hbar\omega_0\hat{I}_z \tag{13a}$$

$$\omega_0 = \gamma B_0 \tag{13b}$$

where $\omega_0/2\pi$ is the Larmor frequency. Sometimes this frequency is defined as $\omega_0/2\pi = -\gamma B_0/2\pi$. As a result, the Zeeman interaction takes the form $\hbar\hat{\mathcal{H}}_Z = \hbar\omega_0\hat{I}_z$. As with η, the choice of ω_0 changes the sign of some expressions below.

We deal with the case where $\mathcal{H}_{\text{Q}}$ can be treated as a weak perturbation of the Zeeman interaction. It is then more convenient to express interactions in the frame Σ^{obs} rotating relative to Σ^{lab} with an angular velocity ω_0 so that the spherical tensor representation of the quadrupolar interaction expressed by equation (10) becomes time-dependent:[22]

$$\begin{aligned}\hbar\hat{\mathcal{H}}_{\text{Q}}(t) &= \exp(\text{i}\hat{\mathcal{H}}_{\text{Z}}t)\hbar\hat{\mathcal{H}}_{\text{Q}}\exp(-\text{i}\hat{\mathcal{H}}_{\text{Z}}t)\\ &= \frac{eQ}{4I(2I-1)}\{\tfrac{1}{3}\sqrt{6}[3\hat{I}_z^2 - I(I+1)]V_0\\ &\quad +\hat{I}_+(2\hat{I}_z+1)V_{-1}\exp(-\text{i}\omega_0 t) - \hat{I}_-(2\hat{I}_z-1)V_1\exp(\text{i}\omega_0 t)\\ &\quad +\hat{I}_+^2 V_{-2}\exp(-\text{i}2\omega_0 t) + \hat{I}_-^2 V_2\exp(\text{i}2\omega_0 t)\}\end{aligned} \tag{14}$$

However, the first term in the curly brackets (i.e., the secular term) remains time-independent. In order to make the quadrupolar interaction completely time-independent, $\mathcal{H}_{\text{Q}}(\text{t})$ is averaged over one Larmor period $2\pi/\omega_0$ up to first-order (see ***Average Hamiltonian Theory***), using the Magnus expansion:[23]

$$\begin{aligned}\langle\hat{\mathcal{H}}_{\text{Q}}(t)\rangle &= \frac{\omega_0}{2\pi}\int_0^{2\pi/\omega_0}\text{d}t\;\hat{\mathcal{H}}_{\text{Q}}(t) - \frac{\text{i}\omega_0}{4\pi}\int_0^{2\pi/\omega_0}\text{d}t\int_0^t\text{d}t'\,[\hat{\mathcal{H}}_{\text{Q}}(t),\hat{\mathcal{H}}_{\text{Q}}(t')]\\ &= H_{\text{Q}}^{(0)} + H_{\text{Q}}^{(1)}\end{aligned} \tag{15}$$

with

$$H_{\text{Q}}^{(0)} = \frac{eQ}{4I(2I-1)\hbar}\frac{\sqrt{6}}{3}[3\hat{I}_z^2 - I(I+1)]V_0 \tag{16}$$

$$\begin{aligned}H_{\text{Q}}^{(1)} = -\frac{1}{\omega_0}\left[\frac{eQ}{4I(2I-1)\hbar}\right]^2\{&\sqrt{6}V_0V_{-1}\hat{I}_+(2\hat{I}_z+1)^2\\ &-\sqrt{6}V_0V_1\hat{I}_-(2\hat{I}_z-1)^2 + 2\sqrt{6}V_0V_{-2}\hat{I}_+^2(\hat{I}_z+1)\\ &+2\sqrt{6}V_0V_2\hat{I}_-^2(\hat{I}_z-1)\\ &+2V_{-1}V_1\hat{I}_z[4I(I+1) - 8\hat{I}_z^2 - 1]\\ &+2V_{-2}V_2\hat{I}_z[2I(I+1) - 2\hat{I}_z^2 - 1]\}\end{aligned} \tag{17}$$

Usually, only the secular terms that commute with $\hat{I}_z$ (i.e., the last two terms in the curly brackets of $H_{\text{Q}}^{(1)}$ are considered. With this simplification, $H_{\text{Q}}^{(0)}$ and $H_{\text{Q}}^{(1)}$ are equivalent to the first-order, $H_{\text{Q}}^{[1]}$, and second-order, $H_{\text{Q}}^{[2]}$, terms in standard perturbation theory,[24] i.e.,

$$H_{\text{Q}}^{[1]} = H_{\text{Q}}^{(0)} = \frac{eQ}{4I(2I-1)\hbar}\frac{\sqrt{6}}{3}[3\hat{I}_z^2 - I(I+1)]V_0 \tag{18}$$

$$\begin{aligned}H_{\text{Q}}^{[2]} = H_{\text{Q}}^{(1)} = -\frac{1}{\omega_0}\left[\frac{eQ}{4I(2I-1)\hbar}\right]^2&\\ \times\{2V_{-1}V_1\hat{I}_z[4I(I+1) - 8\hat{I}_z^2 - 1]&\\ +2V_{-2}V_2\hat{I}_z[2I(I+1) - 2\hat{I}_z^2 - 1]\}&\end{aligned} \tag{19}$$

respectively. Equations (18) and (19), derived in the rotating frame Σ^{obs}, are unchanged in the laboratory frame Σ^{lab}. This is because they commute with the Zeeman interaction. In other words, they commute with the operator $\hat{I}_z$. From now on, we shall use the language of standard perturbation theory. The first-order quadrupolar interaction $H_{\text{Q}}^{[1]}$ is independent of ω_0, whereas the second-order quadrupolar interaction $H_{\text{Q}}^{[2]}$ is inversely proportional to ω_0. Therefore, a strong static magnetic field is required to reduce the effects of $H_{\text{Q}}^{[2]}$.

5 ENERGY LEVELS AND THE SPECTRUM OF A SINGLE CRYSTAL

When a free spin I is introduced into a strong static magnetic field, the Zeeman interaction splits its $2I + 1$ energy levels $|m\rangle$, whose energy is defined by

$$\langle m|\hat{\mathcal{H}}_{\text{Z}}|m\rangle = -m\omega_0 \tag{20}$$

and the difference between two consecutive energy levels ($m - 1$, m), expressed in angular velocity units, is

$$\omega_{m-1,m}^{(\text{Z})} = \langle m-1|\hat{\mathcal{H}}_{\text{Z}}|m-1\rangle - \langle m|\hat{\mathcal{H}}_{\text{Z}}|m\rangle = \omega_0 \tag{21a}$$

We choose the same convention as Abragam[18] for the pair ($m - 1$, m) and equation (21a) to represent the transition and the transition frequency, respectively, but other authors choose (m, $m - 1$), (m, $m + 1$), ($m + 1$, m), equation (21a) or its negative

$$\omega_{m-1,m}^{(\text{Z})} = \langle m|\hat{\mathcal{H}}_{\text{Z}}|m\rangle - \langle m-1|\hat{\mathcal{H}}_{\text{Z}}|m-1\rangle \tag{21b}$$

Of course, these choices affect some later relationships dealing with transitions and transition frequencies. Equation (21a) implies that the energy levels $|m\rangle$ of a free spin in a strong static magnetic field $\boldsymbol{B}_0$ are equally spaced. The separation between two adjacent levels is ω_0. In the spectrum, a single line is located at ω_0. However, these energy levels may be shifted by other interactions, including the quadrupolar interaction discussed in this article.

The first-order quadrupolar interaction $H_{\text{Q}}^{[1]}$ shifts the energy levels $|m\rangle$ by an amount

$$\langle m|H_{\text{Q}}^{[1]}|m\rangle = \frac{eQ}{4I(2I-1)\hbar}\frac{\sqrt{6}}{3}[3m^2 - I(I+1)]V_0 \tag{22}$$

and in the spectrum, its contribution to the line position, i.e., the first-order quadrupolar shift $\omega_{m-1,m}^{(1)}$ of the line position associated with the transition ($m - 1$, m), is

$$\begin{aligned}\omega_{m-1,m}^{(1)} &= \langle m-1|H_{\text{Q}}^{[1]}|m-1\rangle - \langle m|H_{\text{Q}}^{[1]}|m\rangle\\ &= \frac{3eQ}{4I(2I-1)\hbar}\frac{\sqrt{6}}{3}(1-2m)V_0\end{aligned} \tag{23}$$

The spectrum consists of $2I$ lines, the central one of which, associated with the transition $(-\frac{1}{2}, \frac{1}{2})$, is still located at ω_0. The other $2I - 1$ lines are called satellite lines.

When the second-order quadrupolar interaction $H_Q^{[2]}$ is taken into account, the energy levels $|m\rangle$ are shifted further:[25]

$$\begin{aligned}\langle m|H_Q^{[2]}|m\rangle = &-\frac{1}{\omega_0}\left[\frac{eQ}{4I(2I-1)\hbar}\right]^2 \\ &\times\{2V_{-1}V_1 m[4I(I+1)-8m^2-1] \\ &+2V_{-2}V_2 m[2I(I+1)-2m^2-1]\} \end{aligned} \tag{24}$$

and its contribution $\omega_{m-1,m}^{(2)}$ to the line position, i.e., the second-order quadrupolar shift of the line, is[26]

$$\begin{aligned}\omega_{m-1,m}^{(2)} &= \langle m-1|H_Q^{[2]}|m-1\rangle - \langle m|H_Q^{[2]}|m\rangle \\ &= -\frac{2}{\omega_0}\left[\frac{eQ}{4I(2I-1)\hbar}\right]^2 \\ &\quad\times\{V_{-1}V_1[24m(m-1)-4I(I+1)+9] \\ &\quad+\tfrac{1}{2}V_{-2}V_2[12m(m-1)-4I(I+1)+6]\} \end{aligned} \tag{25}$$

Therefore, the line associated with the transition $(m - 1, m)$ is located in the spectrum at

$$\omega_{m-1,m} = \omega_0 + \omega_{m-1,m}^{(1)} + \omega_{m-1,m}^{(2)} \tag{26}$$

In the following two subsections, we apply equation (26) to two experiments, in which the single crystal is either static or is spinning at the magic angle.

5.1 Spectrum of a Static Single Crystal

We have to express V_0 in equation (23), and V_1, V_{-1}, V_2, and V_{-2} in equation (25) in terms of the components of $\boldsymbol{V}$ in Σ^{PAS}, equation (11a). For this purpose, the following relationship is used:

$$V_i = \sum_{j=-2}^{2} \mathcal{D}_{j,i}^{(2)}(\alpha, \beta, \gamma) V_j^{PAS} \tag{27}$$

where the Euler angles α, β, and γ describe the direction of the strong static magnetic field in Σ^{PAS} (Figure 1) and $\mathcal{D}_{j,i}^{(2)}$ (α, β, γ) is the Wigner rotation matrix defined in the appendix. For example,

$$V_0 = \sqrt{\tfrac{3}{2}}\, eq\left[\tfrac{1}{2}(3\cos^2\beta - 1) + \tfrac{1}{2}\eta\sin^2\beta\cos 2\alpha\right] \tag{28}$$

Its substitution into equation (18) yields

$$H_Q^{[1]} = \tfrac{1}{3}\omega_Q[3\hat{I}_z^2 - I(I+1)] \tag{29}$$

with

$$\omega_Q = \frac{3\chi}{4I(2I-1)}\left[\tfrac{1}{2}(3\cos^2\beta - 1) + \tfrac{1}{2}\eta\sin^2\beta\cos 2\alpha\right] \tag{30}$$

A negative sign will appear in front of η if the other convention for η, equation (6), is chosen or the Euler angles used by Baugher and co-workers[13–15] are used. The definitions of $H_Q^{[1]}$ by equation (29) or of ω_Q by equation (30) are not unique.

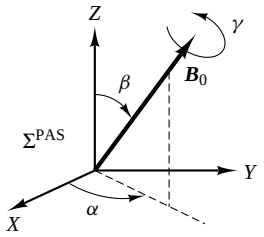

Figure 1 Euler angles defining the direction of $\boldsymbol{B}_0$ in the principal axis system Σ^{PAS} of the EFG during a static experiment

Other definitions can be found in the literature. The first-order quadrupolar shift of the lines $(m - 1, m)$, equation (23), becomes

$$\omega_{m-1,m}^{(1)static} = (1 - 2m)\omega_Q \tag{31}$$

The lines in the spectrum are separated by the same quantity $2\omega_Q$, but the central line is not shifted.

The other two factors V_1V_{-1} and V_2V_{-2} in equation (25) are

$$\begin{aligned}2V_1V_{-1} = &-\tfrac{3}{2}e^2q^2[(-\tfrac{1}{3}\eta^2\cos^2 2\alpha + 2\eta\cos 2\alpha - 3)\cos^4\beta \\ &+(\tfrac{2}{3}\eta^2\cos^2 2\alpha - 2\eta\cos 2\alpha - \tfrac{1}{3}\eta^2 + 3)\cos^2\beta \\ &+\tfrac{1}{3}\eta^2(1 - \cos^2 2\alpha)] \end{aligned} \tag{32a}$$

$$\begin{aligned}V_2V_{-2} = &\tfrac{3}{2}e^2q^2[(\tfrac{1}{24}\eta^2\cos^2 2\alpha - \tfrac{1}{4}\eta\cos 2\alpha + \tfrac{3}{8})\cos^4\beta \\ &+(-\tfrac{1}{12}\eta^2\cos^2 2\alpha + \tfrac{1}{6}\eta^2 - \tfrac{3}{4})\cos^2\beta \\ &+\tfrac{1}{24}\eta^2\cos^2 2\alpha + \tfrac{1}{4}\eta\cos 2\alpha + \tfrac{3}{8}] \end{aligned} \tag{32b}$$

The second-order quadrupolar shift of the central line, using equation (25), is given by

$$\begin{aligned}\omega_{-1/2,1/2}^{(2)static} = &-\frac{1}{6\omega_0}\left[\frac{3\chi}{2I(2I-1)}\right]^2[I(I+1) - \tfrac{3}{4}] \\ &\times[A(\alpha,\eta)\cos^4\beta + B(\alpha,\eta)\cos^2\beta + C(\alpha,\eta)] \end{aligned} \tag{33}$$

with

$$\left.\begin{aligned}A(\alpha,\eta) &= -\tfrac{27}{8} + \tfrac{9}{4}\eta\cos 2\alpha - \tfrac{3}{8}(\eta\cos 2\alpha)^2 \\ B(\alpha,\eta) &= \tfrac{30}{8} - \tfrac{1}{2}\eta^2 - 2\eta\cos 2\alpha + \tfrac{3}{4}(\eta\cos 2\alpha)^2 \\ C(\alpha,\eta) &= -\tfrac{3}{8} + \tfrac{1}{3}\eta^2 - \tfrac{1}{4}\eta\cos 2\alpha - \tfrac{3}{8}(\eta\cos 2\alpha)^2\end{aligned}\right\} \tag{34}$$

When the EFG has axial symmetry ($\eta = 0$), equation (33) becomes simply

$$\begin{aligned}\omega_{-1/2,1/2}^{(2)static} = &-\frac{1}{16\omega_0}\left[\frac{3\chi}{2I(2I-1)}\right]^2[I(I+1) - \tfrac{3}{4}] \\ &\times(1 - \cos^2\beta)(9\cos^2\beta - 1) \end{aligned} \tag{35}$$

It is worth noting that the third Euler angle γ does not appear in equations (30), (33), and (34); this is because $\boldsymbol{B}_0$ is a symmetry axis for the spins. Our results are identical to those of Narita and co-workers[27] [note that their paper contains a typographical error concerning the expression of cos 2α in $C(\alpha, \eta)$]. Subsequently, Baugher and co-workers[15] obtained expressions similar to equation (34), except that their terms containing η have the opposite sign. Their comment 23, concerning the sign in front of all the terms in cos 2α,

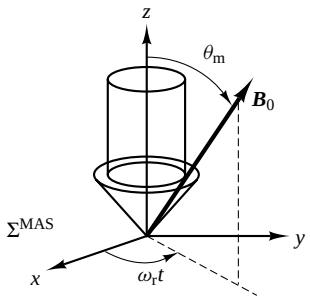

Figure 2 Euler angles defining the direction of $\boldsymbol{B}_0$ in the rotor coordinate frame Σ^{MAS} during a MAS experiment. In Σ^{MAS}, $\boldsymbol{B}_0$ rotates around the rotor with the angular velocity ω_r; θ_m is the magic angle; the third angle is $\gamma = 0$

is explained in our appendix using the Euler angles (Figure 10) defined by Goldstein.[14] Another way to obtain the same results as those of Baugher and co-workers[15] is to employ the usual Euler angles (Figure 9) and to replace η by $-\eta$ (the other convention for η). This point is confirmed by Hirshinger and co-workers[28] and by Chu and Gerstein.[29] Wolf and co-workers[30] have determined the third-order perturbation term, and shown that it is proportional to $(2m-1)/\omega_0^2$. Therefore, the position of the central line is not shifted further by this new term.

5.2 Spectrum of a Rotating Single Crystal

First of all, the expressions for V_0, V_1, V_{-1}, V_2, and V_{-2} must be expressed in terms of the components of $\boldsymbol{V}$ in the coordinate frame Σ^{MAS} of the rotor. To do this, the Wigner rotation matrix is applied once more:

$$V_i = \sum_{j=-2}^{2} \mathcal{D}^{(2)}_{j,i}(\omega_r t, \theta_m, 0) V_j^{MAS} \tag{36}$$

where ω_r is the angular velocity of the rotor and $\theta_m = 54.73^\circ$ is the magic angle (Figure 2). Then, V_j^{MAS} must be expressed in terms of the components of $\boldsymbol{V}$ in Σ^{PAS}:

$$V_j^{MAS} = \sum_{k=-2}^{2} \mathcal{D}^{(2)}_{k,j}(\alpha, \beta, \gamma) V_k^{PAS} \tag{37}$$

where the Euler angles α, β, and γ describe the direction of the rotor in Σ^{PAS} (Figure 3).

The first step, equation (36), yields

$$\omega^{(1)MAS}_{m-1,m} = \sqrt{\tfrac{2}{3}}(1-2m)\frac{3eQ}{8I(2I-1)\hbar} V_0^{MAS}(3\cos^2\theta_m - 1) \tag{38}$$

The second step, equation (37), yields the first-order quadrupolar shift:

$$\omega^{(1)MAS}_{m-1,m} = \tfrac{1}{2}(1-2m)\omega_Q(3\cos^2\theta_m - 1) \tag{39}$$

This shift is zero when the crystal rotates at the magic angle. In other words, all the energy levels become equally spaced. Therefore, a single line instead of $2I$ lines appears in the spectrum at ω_0.

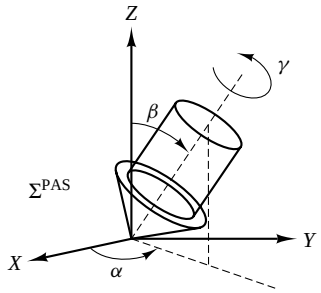

Figure 3 Euler angles defining the direction of the rotor in the principal axis system Σ^{PAS} of the EFG during a MAS experiment. In Σ^{PAS}, the rotor containing the sample appears static

For the second-order quadrupolar shift, the first step, equation (36), yields

$$\begin{aligned}\omega^{(2)MAS}_{m-1,m} = &-\frac{2}{\omega_0}\left[\frac{eQ}{4I(2I-1)\hbar}\right]^2 \\ &\times\{-\tfrac{1}{6}V_2^{MAS}V_{-2}^{MAS}[50m(m-1) - 6I(I+1) + 17] \\ &+\tfrac{1}{3}V_1^{MAS}V_{-1}^{MAS}[8m(m-1)+2] \\ &-\tfrac{1}{2}V_0^{MAS}V_0^{MAS}[14m(m-1) - 2I(I+1) + 5]\}\end{aligned} \tag{40}$$

The second step, equation (37), yields, in the fast rotation regime,[1]

$$\begin{aligned}\omega^{(2)MAS}_{m-1,m} = &-\frac{3}{32\omega_0}\left[\frac{\chi}{I(2I-1)}\right]^2(1+\tfrac{1}{3}\eta^2) \\ &\times[2I(I+1) - 14m(m-1) - 5] \\ &+\frac{3}{128\omega_0}\left[\frac{\chi}{I(2I-1)}\right]^2 \\ &\times[6I(I+1) - 34m(m-1) - 13]g(\alpha,\beta,\eta)\end{aligned} \tag{41}$$

with

$$\begin{aligned}g(\alpha,\beta,\eta) = &\tfrac{1}{2}(1 + 6\cos^2\beta - 7\cos^4\beta) \\ &+\tfrac{1}{3}\eta(1 - 8\cos^2\beta + 7\cos^4\beta)\cos 2\alpha \\ &+\tfrac{1}{18}\eta^2[-7(1-\cos^2\beta)^2\cos^2 2\alpha + 8 - 4\cos^2\beta]\end{aligned} \tag{42}$$

For the central line, the second-order quadrupolar shift is[31]

$$\begin{aligned}\omega^{(2)MAS}_{-1/2,1/2} = &-\frac{1}{6\omega_0}\left[\frac{3\chi}{2I(2I-1)}\right]^2[I(I+1) - \tfrac{3}{4}] \\ &\times[D(\alpha,\eta)\cos^4\beta + E(\alpha,\eta)\cos^2\beta + F(\alpha,\eta)]\end{aligned} \tag{43}$$

with

$$\left.\begin{aligned}D(\alpha,\eta) &= \tfrac{21}{16} - \tfrac{7}{8}\eta\cos 2\alpha + \tfrac{7}{48}(\eta\cos 2\alpha)^2 \\ E(\alpha,\eta) &= -\tfrac{9}{8} + \tfrac{1}{12}\eta^2 + \eta\cos 2\alpha - \tfrac{7}{24}(\eta\cos 2\alpha)^2 \\ F(\alpha,\eta) &= \tfrac{5}{16} - \tfrac{1}{8}\eta\cos 2\alpha + \tfrac{7}{48}(\eta\cos 2\alpha)^2\end{aligned}\right\} \tag{44}$$

As in the case of a static sample, the Euler angle γ does not appear in equations (43) and (44). This is because the experimental conditions correspond to the fast rotation regime. However, this angle does appear in the intermediate regime where the angular velocity of the rotor is of the same order of magnitude as the linewidth. As a result, spinning sidebands appear in the spectrum. Samoson and co-workers[23] established

a general expression for $\Omega_{m-1,m}^{(2)\mathrm{MAS}}$ that clearly shows the presence of modulations due to the rotation of the rotor:

$$\Omega_{m-1,m}^{(2)\mathrm{MAS}} = \omega_{m-1,m}^{(2)\mathrm{MAS}} + \sum_{n=1}^{4}[A_n \cos(n\omega_r t) + B_n \sin(n\omega_r t)] \tag{45}$$

Two typographical errors appear in the *annexe* of their paper:[23] the expressions for A_1^λ and A_2^λ should be

$$\left.\begin{aligned} A_1^\lambda &= -\tfrac{1}{2}\sqrt{2}\sin 2\beta^\lambda \rho_{20}^\lambda + \tfrac{1}{3}\sqrt{3}\cos 2\alpha^\lambda \sin 2\beta^\lambda \rho_{22}^\lambda \\ A_2^\lambda &= \tfrac{1}{2}\sin^2\beta^\lambda \rho_{20}^\lambda + \tfrac{1}{6}\sqrt{6}\cos 2\alpha^\lambda (1+\cos^2\beta^\lambda)\rho_{22}^\lambda \end{aligned}\right\} \tag{46}$$

Equation (45) allows us to investigate the spinning sidebands (see ***High Speed MAS of Half-Integer Quadrupolar Nuclei in Solids*** and ***Sideband Analysis in Magic Angle Spinning NMR of Solids***).

6 POWDER SPECTRUM

In most cases, the sample is in powder form, because the growth of single crystals of significant size is not always possible. As a result, only the central line is detected in NMR (see ***Fast Ion Conductors***, ***Geological Applications***, ***High Temperature Superconductors***, ***Intercalation Compounds*** and ***Molecular Sieves: Crystalline Systems***). However, satellite lines can be detected without spinning the sample if $\chi/2\pi < 300\,\mathrm{kHz}$; for example, for ^{23}Na ($I = \frac{3}{2}$) in $NaNO_3$ or ^{7}Li ($I = \frac{3}{2}$) in $LiNbO_3$. When the MAS technique is applied, the spinning sidebands of the satellite lines are detected; for example, for iodine ^{127}I ($I = \frac{5}{2}$) in KI or the two isotopes of bromine ($I = \frac{3}{2}$) in KBr. These two compounds are used for setting the magic angle of the MAS probe in the vicinity of ^{29}Si and ^{27}Al frequencies, respectively.

In a powder sample, the principal axes of the EFG associated with each crystallite are randomly oriented with respect to $\boldsymbol{B}_0$. The transition frequencies are not unique, but depend on the distribution of the Euler angles α and β describing the direction of the rotor in the coordinate frame Σ^{PAS} in a MAS experiment at high spinning rate, or the direction of $\boldsymbol{B}_0$ in the coordinate frame Σ^{PAS} in an experiment without spinning.

The resonance condition $\omega(\alpha, \cos\beta)$ represents a surface in a three-dimensional space described by the parameters ω, α, and $\cos\beta$. The critical points of this surface define divergences and shoulders in the spectrum. They are roots of the two coupled equations[12, 13]

$$\left.\begin{aligned} \frac{\partial}{\partial\alpha}\omega(\alpha,\cos\beta)\Big|_{\alpha=r,\cos\beta=s} &= 0 \\ \frac{\partial}{\partial\cos\beta}\omega(\alpha,\cos\beta)\Big|_{\alpha=r,\cos\beta=s} &= 0 \end{aligned}\right\} \tag{47}$$

The nature of the critical point (r, s) is related to the sign of the Wronskian determinant D_{W}:

$$D_{\mathrm{W}} = \left[\left(\frac{\partial^2\omega}{\partial\alpha\,\partial\cos\beta}\right)^2 - \left(\frac{\partial^2\omega}{\partial\alpha^2}\right)\left(\frac{\partial^2\omega}{\partial^2\cos\beta}\right)\right]_{\alpha=r,\cos\beta=s} \tag{48}$$

If D_{W} is positive then the critical point (r, s) represents a divergence; if D_{W} is negative then the critical point represents a shoulder. Unfortunately, this method does not allow us to determine the lineshape. Therefore, numerical calculations are required.

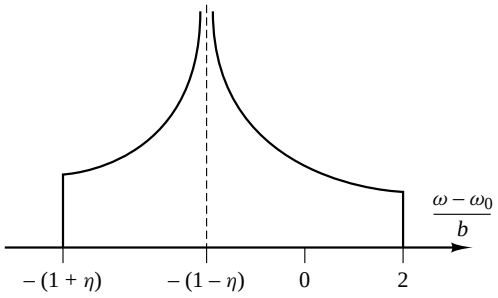

Figure 4 Critical points[13] of a satellite powder pattern associated with the transition $(m-1, m)$; $b = 3\chi(1-2m)/8I(2I-1)$

6.1 Powder Pattern for a Pair of Satellite Lines

For static samples,[27] numerical calculations are based on the summation of signals for the direction of each crystallite. The two Euler angles are redefined by $\alpha = 2\pi p/300$ and $\cos\beta = p/300$, where $p = 0, \ldots, 300$. For each value of η, the summation is performed on

$$\omega_{m-1,m}^{(1)\mathrm{static}} \Big/ \frac{3\chi(1-2m)}{8I(2I-1)} = 3\cos^2\beta - 1 + \eta\sin^2\beta\cos 2\alpha \tag{49}$$

A satellite lineshape is shown in Figure 4. The positions of the shoulder and divergence[13] are derived from equations (47) and (48). The powder pattern of a pair of satellite lines for several values of η is plotted in Figure 5.

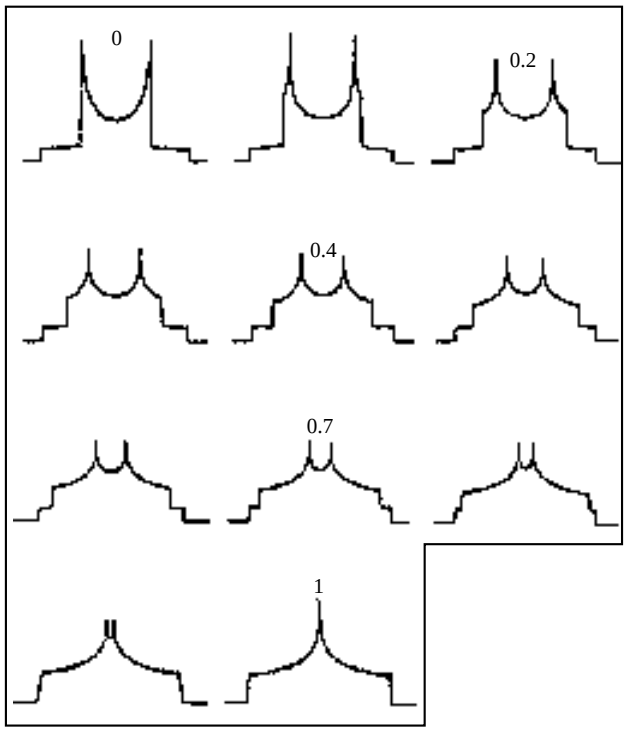

Figure 5 Simulated powder pattern of a pair of satellite lines for increasing values of the asymmetry parameter η from 0 to 1 in steps of 0.1

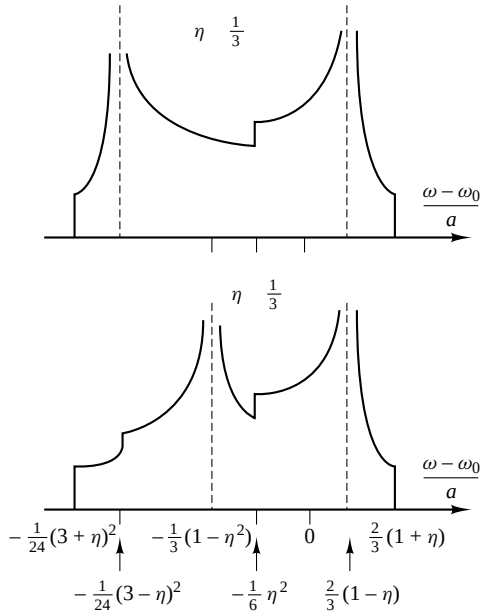

Figure 6 Critical points determined by Stauss.[32] They are associated with the powder pattern of the central line in a static experiment;

$$a = -\frac{1}{6\omega_0}\left[\frac{3\chi}{2I(2I-1)}\right]^2\left[I(I+1)-\frac{3}{4}\right]$$

6.2 Powder Pattern for the Central Line

The critical points in the powder pattern of the central line have been determined for the two experiments. For a static sample, they have been determined by Stauss.[32] Two patterns (Figure 6) appear according to the value of η compared with $\frac{1}{3}$; for example, for ^{39}K in inorganic potassium salts[33] or ^{139}La in lanthanum salts.[34] It is worth noting that these critical points depend neither on the convention for η nor on the choice of Euler angles: changing η to $-\eta$ yields the same set of critical points. For a rotating sample, these points have been determined by Müller.[31] As previously, two powder patterns (Figure 7) appear, depending on the value of η compared with $\frac{\omega}{7}$. These patterns are clearly observed in ^{27}Al compounds.[35]

The powder pattern of the central line is obtained as in the previous case using equation (33) for a static sample or equation (43) for a rapidly rotating sample. To facilitate the comparison, the two sets of spectra are superposed as shown in Figure 8. We can see that the linewidth is reduced by a factor ranging from 2 to 4, depending on the value of η when a MAS experiment is performed (see ***Line Narrowing Methods in Solids***). From a practical point of view, the asymmetry parameter of an experimental spectrum can be estimated by comparing the lineshape with those in Figure 8. Then the quadrupolar coupling constant can be calculated using the positions of the experimental critical points and those represented in Figures 6 and 7. Other simple procedures are also defined for extracting quadrupolar parameters from the spectra of static[36] or rotating[37] samples.

The second-order quadrupolar shift of the center of gravity $\omega_{iso}(m-1, m)$ of the powder pattern is determined as

Table 2 Wigner Rotation Matrix $\mathcal{D}^{(2)}_{p,q}(\alpha, \beta, \gamma)$, Identical to That Used by Spiess,[20] Mehring,[21] and Doane,[38] but the Transposed and Complex Conjugate of That Used by Haeberlen,[19] Equal to $\mathcal{D}^{(2)}_{p,q}(-\alpha, -\beta, -\gamma)$ Used by Freude and Haase[9]

p \ q	2	1	0	−1	−2
2	$\frac{1}{4}(1+\cos\beta)^2\,e^{-2i(\alpha+\gamma)}$	$-\frac{1}{2}(1+\cos\beta)\sin\beta\,e^{-i(2\alpha+\gamma)}$	$\sqrt{\frac{3}{8}}\sin^2\beta\,e^{-2i\alpha}$	$-\frac{1}{2}(1-\cos\beta)\sin\beta\,e^{i(-2\alpha+\gamma)}$	$\frac{1}{4}(1-\cos\beta)^2\,e^{-2i(\alpha-\gamma)}$
1	$\frac{1}{2}(1+\cos\beta)\sin\beta\,e^{-i(\alpha+2\gamma)}$	$[\cos^2\beta-\frac{1}{2}(1-\cos\beta)]\,e^{-i(\alpha+\gamma)}$	$-\sqrt{\frac{3}{8}}\sin 2\beta\,e^{-i\alpha}$	$[\frac{1}{2}(1+\cos\beta)-\cos^2\beta]\,e^{i(-\alpha+\gamma)}$	$-\frac{1}{2}(1-\cos\beta)\sin\beta\,e^{-i(\alpha-2\gamma)}$
0	$\sqrt{\frac{3}{8}}\sin^2\beta\,e^{-2i\gamma}$	$\sqrt{\frac{3}{8}}\sin 2\beta\,e^{-i\gamma}$	$\frac{1}{2}(3\cos^2\beta-1)$	$-\sqrt{\frac{3}{8}}\sin 2\beta\,e^{i\gamma}$	$\sqrt{\frac{3}{8}}\sin^2\beta\,e^{2i\gamma}$
−1	$\frac{1}{2}(1-\cos\beta)\sin\beta\,e^{i(\alpha-2\gamma)}$	$[\frac{1}{2}(1+\cos\beta)-\cos^2\beta]\,e^{i(\alpha-\gamma)}$	$\sqrt{\frac{3}{8}}\sin 2\beta\,e^{i\alpha}$	$[\cos^2\beta-\frac{1}{2}(1-\cos\beta)]\,e^{i(\alpha+\gamma)}$	$-\frac{1}{2}(1+\cos\beta)\sin\beta\,e^{i(\alpha+2\gamma)}$
−2	$\frac{1}{4}(1-\cos\beta)^2\,e^{2i(\alpha-\gamma)}$	$\frac{1}{2}(1-\cos\beta)\sin\beta\,e^{i(2\alpha-\gamma)}$	$\sqrt{\frac{3}{8}}\sin^2\beta\,e^{2i\alpha}$	$\frac{1}{2}(1+\cos\beta)\sin\beta\,e^{i(2\alpha+\gamma)}$	$\frac{1}{4}(1+\cos\beta)^2\,e^{2i(\alpha+\gamma)}$

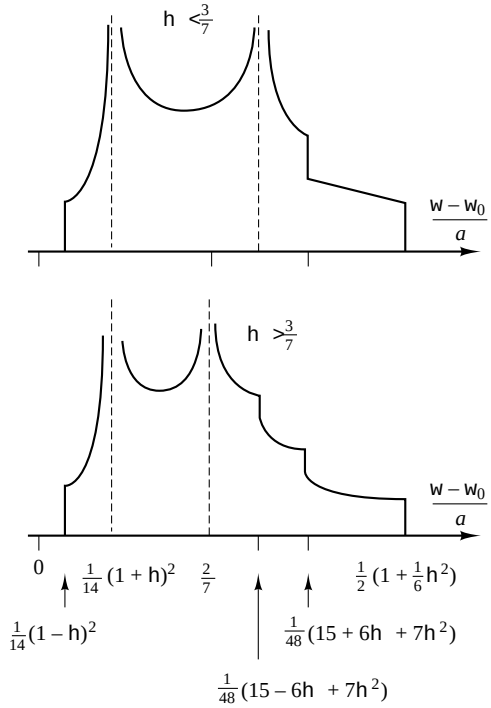

Figure 7 Corrected critical points[9,11] determined by Müller.[31] They are associated with the powder pattern of the central line in a MAS experiment;

$$a = -\frac{1}{6\omega_0}\left[\frac{3\chi}{2I(2I-1)}\right]^2\left[I(I+1)-\frac{3}{4}\right]$$

follows:[1]

$$\omega_{\text{iso}}(m-1,m) = \frac{1}{4\pi}\int_0^{\pi} \mathrm{d}\beta \sin\beta \int_0^{2\pi} \mathrm{d}\alpha\, \omega^{(2)\text{MAS}}_{m-1,m}$$
$$= -\frac{3}{40\omega_0}\left[\frac{\chi}{I(2I-1)}\right]^2 (1+\tfrac{1}{3}\eta^2)$$
$$\times[I(I+1) - 9m(m-1) - 3] \qquad (50)$$

From a practical point of view, the experimental chemical shift of the center of gravity associated with the transition $(m-1, m)$, $\delta^{\text{exp}}_{\text{CG}}(m-1,m)$, consists of two terms: the true chemical shift $\delta_{\text{CS}}(m-1,m)$ and the contribution from the second-order quadrupolar shift $\omega_{\text{iso}}(m-1,m)/\omega_0$. Thus,

$$\delta_{\text{CS}}(m-1,m) = \delta^{\text{exp}}_{\text{CG}}(m-1,m) - \omega_{\text{iso}}(m-1,m)/\omega_0 \qquad (51)$$

For the central line, equation (51) becomes equation (1).

7 APPENDIX

The Euler angles are extensively used in the study of the quadrupolar interaction, especially in MAS, VAS, DAS, and DOR. They are defined as three successive positive angles of rotation for the coordinate frame (c.f.) as described in Figure 9. First [(Figure 9a)], the starting c.f. (x, y, z), called the old c.f., in which we know the components V_k^{OLD} of the spherical tensor $\boldsymbol{V}$, is rotated counterclockwise around the z axis by an angle α. This rotation generates a new c.f. (X, Y, z). Then [(Figure 9b)] the counterclockwise rotation of this intermediate c.f. around the Y axis by an angle β generates a second intermediate c.f. (X', Y, z'). Finally [(Figure 9c)], this second intermediate c.f. is rotated counterclockwise by an angle γ around the z' axis, resulting in a c.f. (x', y', z'), called the new c.f., in which we wish to know the components V_j^{NEW} of the spherical tensor $\boldsymbol{V}$. It is worth noting that, in this definition of the Euler angles, β and α also represent the polar angles of the z' axis in the old coordinate frame.

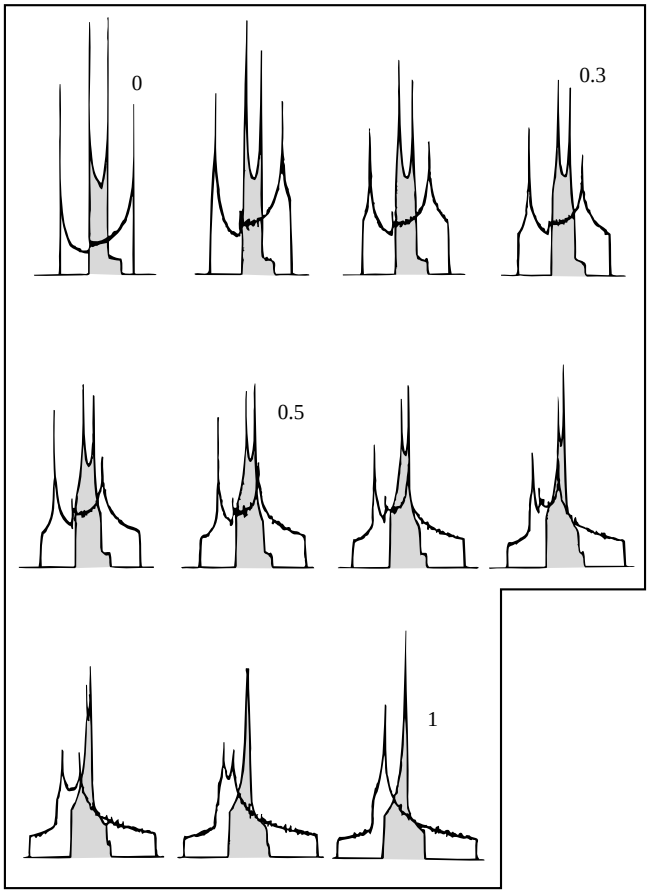

Figure 8 Superposition of simulated powder patterns of the central line during static and MAS (shaded spectra) experiments for increasing values of the asymmetry parameter η from 0 to 1 in steps of 0.1

As explained by Spiess,[20] the mathematical tool for expressing the components of the same spherical tensor $\boldsymbol{V}$ in two different coordinate frames, where the new c.f. is obtained by three positive angles of rotation (α, β, γ) of the old one, is the Wigner rotation matrix $\mathcal{D}^{(2)}_{p,q}(\alpha, \beta, \gamma)$ reported in Table 2. This matrix relates the components V_j^{NEW} of the spherical tensor in the new c.f. to the known components V_k^{OLD} of the same tensor in the old one by the relationships[20,21,38,39]

$$V_j^{\text{NEW}} = \sum_{k=-2}^{2} \mathcal{D}^{(2)}_{k,j}(\alpha,\beta,\gamma) V_k^{\text{OLD}} \qquad (52)$$

with the summation over the first subscript.

Figure 10 shows the Euler angles used by Baugher and coworkers.[13,15] First [(Figure 10a)], as in the previous definition,

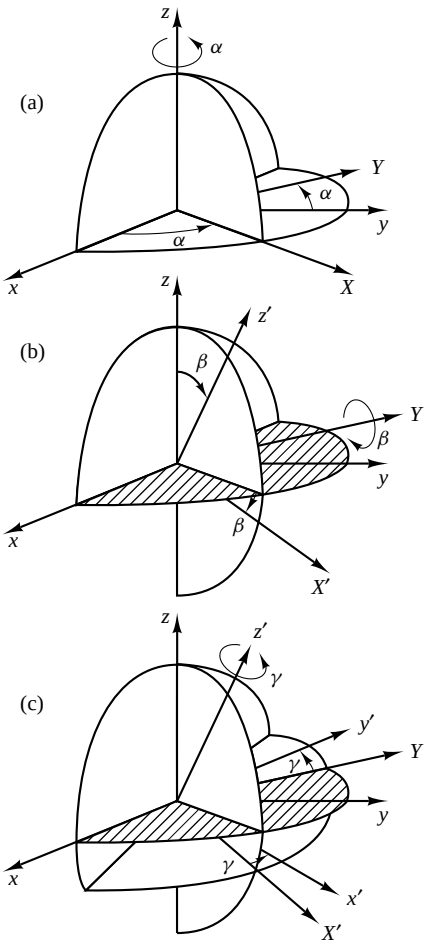

Figure 9 Euler angles defining positive rotation of the coordinate frame (x, y, z). They are used by Narita and co-workers,[27] Spiess,[20] Doane,[38] and Freude and Haase.[9] The angles β and α are the polar angles of the z' axis in (x, y, z)

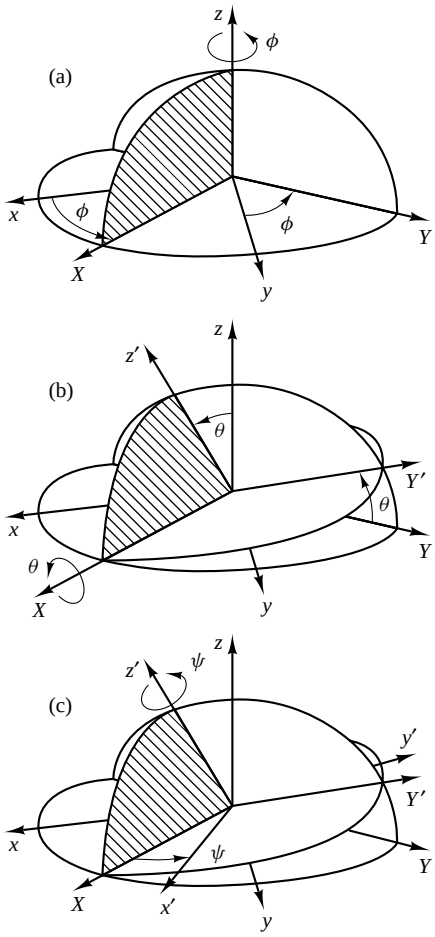

Figure 10 Euler angles used by Baugher and co-workers[13,15] and Stauss,[32] and defined by Goldstein.[14] The angles θ and ϕ are not the polar angles of the z' axis in (x, y, z)

the old c.f. (x, y, z) is rotated counterclockwise by an angle ϕ around the z axis, generating an intermediate c.f. (X, Y, z). Then [(Figure 10b)] this intermediate c.f. is rotated counterclockwise, this time around the X axis, by an angle θ, generating a second intermediate c.f. (X, Y', z'). Finally [(Figure 10c)], a counterclockwise rotation of this second intermediate c.f. around the z' axis by an angle ψ produces the new c.f. (x', y', z'). In contrast to the previous definition, θ and ϕ are not the polar angles of the z' axis in the old coordinate frame. In Figure 9, α is the angle relating the y axis and the line of nodes Y, whereas in Figure 10, ϕ is the angle relating the x axis and the line of nodes X. These two angles are related by $\alpha + \frac{1}{2}\pi = \phi$. In other words, $\alpha + \frac{1}{2}\pi$ and ϕ correspond to the angle connecting the x axis with the line of nodes. As a result, $\cos 2\phi = -\cos 2\alpha$. This explains the change of sign for the terms containing η in equations (30) and (34), as in the paper of Baugher and co-workers.[15]

8 RELATED ARTICLES

Biological Systems: Spin-3/2 Nuclei; Boron NMR; Dynamic Frequency Shift; Germanium, Tin, and Lead NMR; Lithium NMR; Overtone Spectroscopy of Quadrupolar Nuclei; Oxygen-17 NMR; Oxygen-17 NMR: Applications in Biochemistry; Quadrupolar Nuclei in Liquid Samples; Quadrupolar Transition Metal and Lanthanide Nuclei; Shielding Calculations: Perturbation Methods; Sodium-23 NMR; Sulfur, Selenium, and Tellurium NMR.

9 REFERENCES

1. A. Samoson, *Chem. Phys. Lett.*, 1985, **119**, 29.
2. E. Lippmaa, A. Samoson, and M. Mägi, *J. Am. Chem. Soc.*, 1986, **108**, 1730.
3. F. Lefebvre, J. P. Amoureux, C. Fernandez, and E. G. Derouane, *J. Chem. Phys.*, 1987, **86**, 6070.
4. D. Massiot, A. Kahn-Harari, D. Michel, D. Müller, and F. Taulelle, *Magn. Reson. Chem.*, 1990, **28**, S82.
5. B. Q. Sun, J. H. Baltisberger, Y. Wu, A. Samoson, and A. Pines, *Solid State Nucl. Magn. Reson.*, 1992, **1**, 267.
6. P. P. Man, *Chem. Phys. Lett.*, 1990, **168**, 227.
7. B. C. Sanctuary and T. K. Halstead, in *Advances in Magnetic and Optical Resonance*, ed. W. S. Warren, Academic Press, San Diego, 1990, Vol. 15, p. 79.
8. A. P. M. Kentgens, *J. Magn. Reson. A*, 1993, **104**, 302.

9. D. Freude and J. Haase, in *NMR Basic Principles and Progress*, eds. P. Diehl, E. Fluck, H. Günter, R. Kosfeld, and J. Seelig, Springer-Verlag, Berlin, 1993, Vol. 29.
10. J. L. Dye, A. S. Ellaboudy, and J. Kim, in *Modern NMR Techniques and their Application in Chemistry*, eds. A. I. Popov and K. Hallenge, Marcel Dekker, New York, 1991.
11. G. Engelhardt and D. Michel, *High-Resolution Solid-State NMR of Silicates and Zeolites*, Wiley, Chichester, 1987.
12. G. E. Jellison, Jr., S. A. Feller, and P. J. Bray, *J. Magn. Reson.*, 1977, **27**, 121.
13. P. C. Taylor, J. F. Baugher, and H. M. Kriz, *Chem. Rev.*, 1975, **75**, 203.
14. H. Goldstein, *Classical Mechanics*, 2nd edn., Addison-Wesley, Reading, MA, 1980.
15. J. F. Baugher, P. C. Taylor, T. Oja, and P. J. Bray, *J. Chem. Phys.*, 1969, **50**, 4914.
16. C. P. Slichter, *Principles of Magnetic Resonance*, 3rd edn., Springer-Verlag, New York, 1990.
17. M. H. Cohen and F. Reif, in *Solid State Physics*, eds. F. Seitz and D. Turnbull, Academic Press, New York, 1957, Vol. 5.
18. A. Abragam, *The Principles of Nuclear Magnetism*, Oxford University Press, Oxford, 1961.
19. U. Haeberlen, *High Resolution NMR in Solids. Selective Averaging*, Academic Press, New York, 1976.
20. H. W. Spiess, in *NMR Basic Principles and Progress*, eds. P. Diehl, E. Fluck, and R. Kosfeld, Springer-Verlag, Berlin, 1978, Vol. 15.
21. M. Mehring, *Principles of High Resolution NMR in Solids*, 2nd edn., Springer-Verlag, Berlin, 1983.
22. A. Samoson and E. Lippmaa, *Phys. Rev. B*, 1983, **28**, 6567.
23. A. Samoson, E. Kundla, and E. Lippmaa, *J. Magn. Reson.*, 1982, **49**, 350.
24. H. J. Behrens and B. Schnabel, *Physica B*, 1982, **114**, 185.
25. P. P. Man, H. Théveneau, and P. Papon, *J. Magn. Reson.*, 1985, **64**, 271.
26. B. A. Huggins and P. D. Ellis, *J. Am. Chem. Soc.*, 1992, **114**, 2098.
27. K. Narita, J. Umeda, and H. Kusumoto, *J. Chem. Phys.*, 1966, **44**, 2719.
28. J. Hirschinger, P. Granger, and J. Rosé, *J. Phys. Chem.*, 1992, **96**, 4815.
29. P. J. Chu and B. C. Gerstein, *J. Chem. Phys.*, 1989, **91**, 2081.
30. F. Wolf, D. Kline, and H. S. Story, *J. Chem. Phys.*, 1970, **53**, 3538.
31. D. Müller, *Ann. Phys. (Leipzig)*, 1982, **39**, 451.
32. G. H. Stauss, *J. Chem. Phys.*, 1964, **40**, 1988.
33. T. J. Bastow, *J. Chem. Soc., Faraday Trans.*, 1991, **87**, 2453.
34. B. Herreros, P. P. Man, J. M. Manoli, and J. Fraissard, *J. Chem. Soc., Chem. Commun.*, 1992, 464.
35. J. Skibsted, E. Henderson, and H. J. Jakobsen, *Inorg. Chem.*, 1993, **32**, 1013.
36. P. Granger, *Magn. Reson. Chem.*, 1990, **28**, 156.
37. G. Engelhardt and H. Koller, *Magn. Reson. Chem.*, 1991, **29**, 941.
38. J. W. Doane, in *Magnetic Resonance of Phase Transitions*, eds. F. J. Owens, C. P. Poole, Jr., and H. A. Farach, Academic Press, New York, 1979.
39. D. M. Brink and G. R. Satchler, *Angular Momentum*, 2nd edn., Clarendon Press, Oxford, 1968, p. 51.

Biographical Sketch

Pascal P. Man. *b* 1952. Ph.D., 1982, Materials Science, Sc.D., 1986, physics, Université Pierre et Marie Curie, Paris, France. Introduced to NMR by H. Zanni. Postdoctoral work at University of Cambridge (with J. Klinowski). Université Pierre et Marie Curie, 1988–present. Approx. 45 publications. Current research speciality: solid state NMR on quadrupolar nuclei and its applications in heterogeneous catalysts.

Quadrupolar Nuclei in Glasses

Philip J. Bray
Brown University, Providence, RI, USA

1	Introduction	1
2	NMR With a Quadrupolar Perturbation	1
3	Pure Nuclear Quadrupole Resonance (NQR) Studies	5
4	NQR With a Zeeman Perturbation	8
5	Related Articles	10
6	References	10

1 INTRODUCTION

The first use of nuclear magnetic resonance (NMR) to study glass structure using nuclei having electric quadrupole moments was reported by Silver and Bray in 1958.[1] In that work, the interaction between the nuclear electrical quadrupole moment (possessed by all nuclei having a spin $I > \frac{1}{2}$) and the electric field gradient at the nuclear site is small in comparison with the Zeeman interaction of the nuclear magnetic dipole moment with an externally applied magnetic field. The energy levels and transition frequencies can be calculated[2] using the quadrupolar interaction as a perturbation of the Zeeman interaction.

It is this case that is discussed and illustrated with specific examples in the following section. Extensive studies of this type have been summarized and referenced in a number of reviews of NMR studies of glasses.[3–7] (Note that the review by Eckert[3] contains, on p. 163, a table of 39 earlier reviews, listing their main topics.) Succeeding sections of this article contain discussions of the cases in which the magnetic field is absent [i.e., pure nuclear quadrupole resonance (NQR) studies], and cases in which the Zeeman interaction is present but sufficiently small to be treated as a perturbation of the quadrupolar interaction.

There will necessarily be some overlap between the material presented in this article and in other portions of the Encyclopedia. Cross references to pertinent subjects are given at the end of the article.

2 NMR WITH A QUADRUPOLAR PERTURBATION

Figure 1 displays the energy levels for the case of the pure Zeeman interaction (i.e. no quadrupolar interaction present), and the shifting of those levels when a relatively small quadrupolar interaction is present. The shifts depend on the coupling of the nuclear electrical quadrupole moment eQ with the components of the electric field gradient (EFG) tensor at the nuclear site. These are V_{xx}, V_{yy}, and V_{zz} in the system of principal axes for the EFG. Here V is the electrical potential at the nuclear site arising from charges outside the nucleus, and $V_{xx} = \partial^2 V/\partial x^2$, etc. The shifts also depend on the angles θ and ϕ that specify the orientation of the magnetic field $\boldsymbol{B}$ with respect to the principal axes of the EFG. Since all angles θ and ϕ are equally probable in a finely divided polycrystalline powder or a glass, the NMR spectra for those cases will be the envelope of responses observed for a single crystal as it is placed in all possible orientations in the magnetic field. The resulting theoretical 'powder pattern' for a quadrupolar interaction that is sufficiently small to be treated with first-order perturbation theory is displayed in Figure 2 for the case of a nuclear spin $I = \frac{3}{2}$. (No dipolar or other broadening mechanisms have been taken into account.) Here $\chi = e^2qQ = e^2V_{zz}Q$ is the quadrupole coupling constant that measures the strength of the quadrupolar interaction, and $\eta = (V_{xx} - V_{yy})/V_{zz}$ is the asymmetry parameter that measures the departure of the EFG from axial symmetry. (With $|V_{zz}| \geq |V_{yy}| \geq |V_{xx}|$, one finds that $0 \leq \eta \leq 1$.) Note that the 'central' transition ($m = +\frac{1}{2} \leftrightarrow -\frac{1}{2}$) is unaffected at first-order, and remains at the Larmor frequency ν_0, while the 'satellite' transitions ($m = +\frac{3}{2} \leftrightarrow +\frac{1}{2}$ and $m = -\frac{3}{2} \leftrightarrow -\frac{1}{2}$) are spread out into the 'powder patterns'.

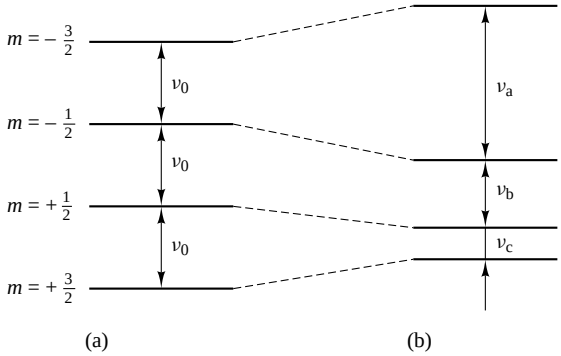

Figure 1 Energy levels arising from the interaction of the nuclear magnetic dipole moment with a magnetic field: (a) no electrical quadrupolar interaction; (b) small quadrupolar interaction present (the levels shown are appropriate for the ^{11}B nucleus)

Broadening mechanisms (e.g., dipolar interactions, and distributions in the EFG components) smooth the divergences in the theoretical powder pattern, and give breadth to the central transition peak. This is exemplified in Figure 3 for the particular case of $\eta = 0$. When use is made of older

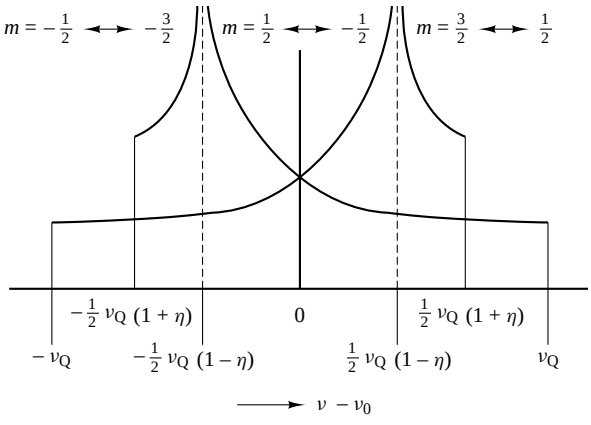

Figure 2 First-order quadrupolar spectrum for $I = \frac{3}{2}$ nuclei in a powder or glass. Here $\nu_Q = 3\chi/2I(2I - 1)$

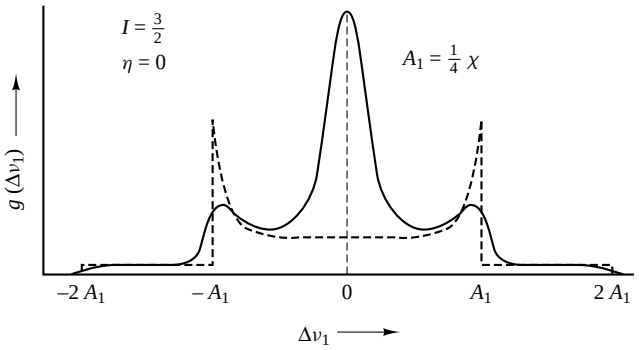

Figure 3 Resonance lineshape (solid curve) predicted for a nucleus such as ^{11}B with a small quadrupolar interaction in a glass or polycrystalline powder. This is the $\eta = 0$ case

CW NMR spectrometers, the recorded resonance is usually the first derivative of the absorption curve. This is displayed in Figure 4 for the ^{11}B ($I = \frac{3}{2}$) response in polycrystalline boron phosphate (BPO_4), for which the value of $\chi = 50.4$ kHz if η is assumed to be zero.[8] (The boron atom is at the center of a BO_4 tetrahedron that is only slightly distorted, so the components of the EFG are quite small. The EFG vanishes for perfect tetrahedral and octahedral symmetry.)

Figure 5 displays[9] the derivative response for ^7Li ($I = \frac{3}{2}$) in a glass containing 25 mol% Li_2O and 75 mol% B_2O_3. If $\eta = 0$ then $\chi \approx 185$ kHz. (The electrical quadrupole moment Q for ^7Li is relatively small.) The partial 'smearing' of the divergences in the powder pattern arises from the distribution in the EFG components caused by the disorder of the vitreous state. See Krämer et al.[10] for other examples of ^7Li NMR spectra for glasses.

When the quadrupolar interaction is larger (but still treatable as a perturbation of the Zeeman interaction), the central ($m = \frac{1}{2} \leftrightarrow -\frac{1}{2}$) transition is affected at second order. Figure 6 displays the theoretical pattern for this case, both for $\eta < \frac{1}{3}$ and $\eta > \frac{1}{3}$. The particular case of small or zero η is illustrated in Figure 7

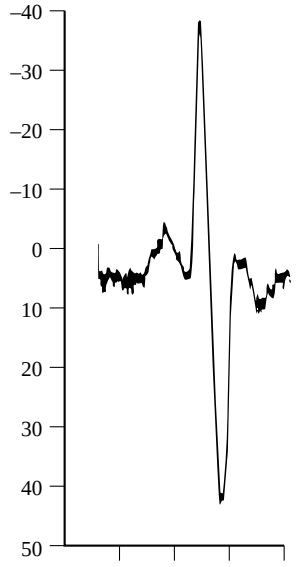

Figure 4 ^{11}B NMR spectrum in boron phosphate (BPO_4); $\nu_0 = 7.177$ MHz

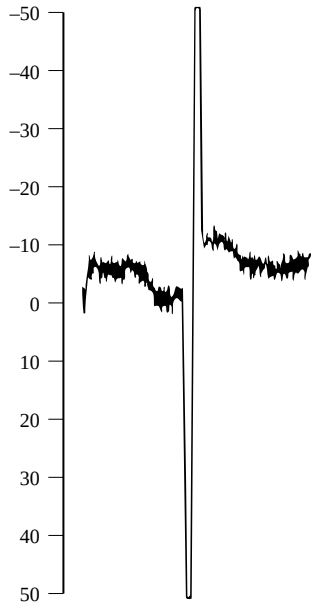

Figure 5 ^7Li NMR spectrum of glass of composition $Li_2O{\cdot}3B_2O_3$

where the dashed lines indicate the theoretical pattern without broadening and the solid line indicates the expected lineshape when broadening is included.

This transition[11a] for ^{11}B in vitreous boron oxide (B_2O_3) is displayed in Figure 8. In this case, in which all of the boron atoms are at the center of planar triangles of oxygens (i.e., BO_3 units) and all of the oxygens are bridging (i.e., bonded to two borons), one finds $\chi = 2.76$ MHz and $\eta = 0.10$. The departure from perfect trigonal symmetry about the axis perpendicular to the BO_3 units and passing through the boron is small or moderate. One finds for such BO_3 units

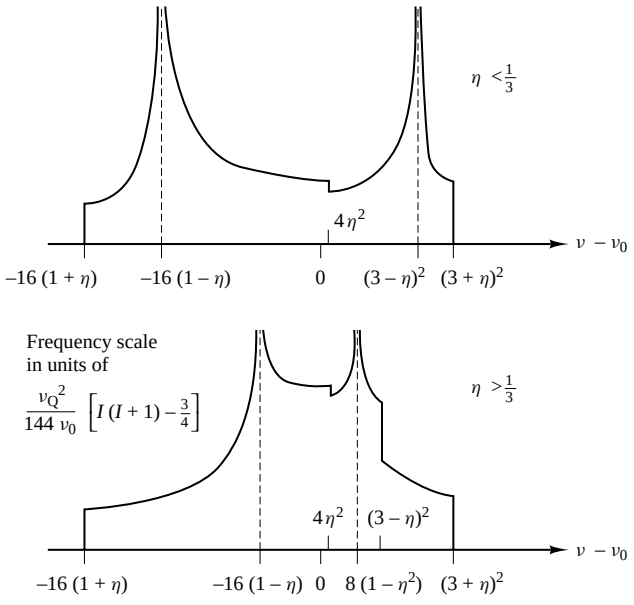

Figure 6 Powder patterns for the central transition ($m = -\frac{1}{2} \leftrightarrow m = +\frac{1}{2}$) of half-integer spin nuclei in the presence of second-order quadrupolar interactions for two regimes: $\eta < \frac{1}{3}$ and $\eta > \frac{1}{3}$. Here $\nu_Q = 3\chi/2I(2I-1)$ and ν_0 is the Larmor frequency

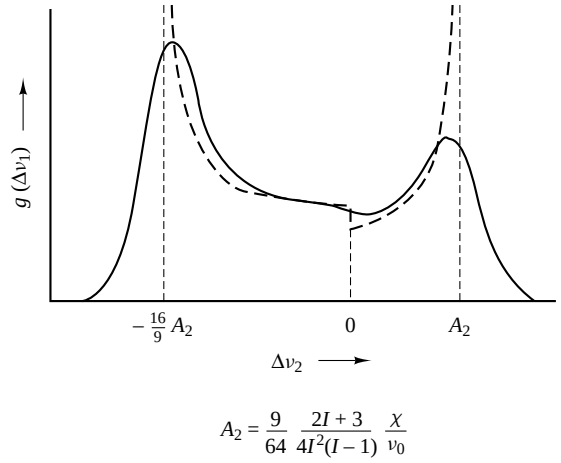

Figure 7 Resonance lineshape (solid curve) for a nucleus with a large quadrupole interaction in a glass or polycrystalline powder. This is the $\eta = 0$ case

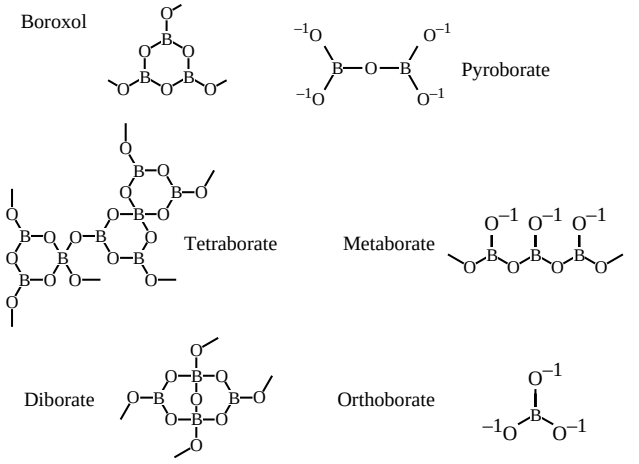

Figure 9 Structural groupings found in alkali borate compounds and glasses

that 2.4 MHz $\leq \chi \leq$ 2.9 MHz and $0 \leq \eta \leq 0.2$. (In the case of vitreous B_2O_3, the BO_3 units are portions of the boroxol structural groupings depicted in Figure 9, but they occur also in other borate structural groupings shown there.)

In alkali borate compounds of 50 mol% or more of alkali oxide, one finds BO_3 units that have one or more nonbridging oxygens (NBO) (i.e., the oxygen is bonded to only one boron and is negatively charged). If the BO_3 unit has one or two of these, the trigonal symmetry noted above is lost, and the asymmetry parameter has been found from NMR spectra to rise into the range $0.4 \leq \eta \leq 0.9$. An example is calcium metaborate ($CaO{\cdot}B_2O_3$), whose chain structure is depicted in Figure 9. The NMR spectrum[11a] of this material is displayed in Figure 10. These asymmetric BO_3 units, and the BO_4 and symmetric BO_3 units, are all present in many borate glasses. Responses from all three units are present in the ^{11}B NMR spectrum[11a] displayed in Figure 11, where the narrow structureless line from BO_4 units is off scale and the symmetric BO_3 units give rise to the middle positive peak on the left and part of one of the negative peaks on the right. The fraction of each type of unit present in the glass can be obtained from the intensity of the corresponding NMR responses, as illustrated in Figure 12 for a low-alkali glass where N_4 is the fraction of four-coordinated borons (i.e. in BO_4 tetrahedra). Figure 13 displays N_4 as a function of the molar fraction x of alkali oxide in alkali borate glasses.[12] With the composition $x\,Na_2O(1 - x)B_2O_3$, N_4 is $x/(1 - x)$ if each oxygen added as Na_2O converts two borons from three- to four-coordination.

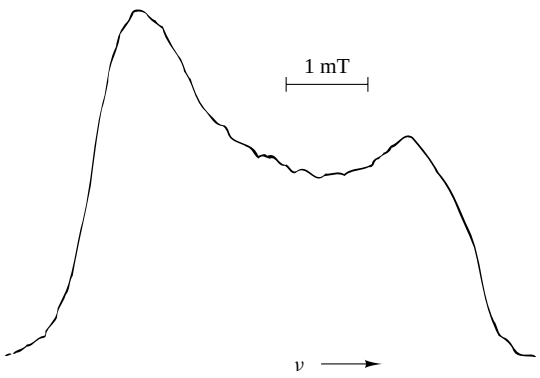

Figure 8 ^{11}B NMR spectrum of vitreous B_2O_3 at 16 MHz[11b]

Kirkpatrick and Oldfield and co-workers[13] have demonstrated that the ^{11}B NMR responses from BO_3 and BO_4 configurations can be separated using magic angle sample spinning (MAS) with high spinning speeds at high magnetic fields. Figure 14 displays the BO_3 and BO_4 responses for polycrystalline $Li_2O{\cdot}2B_2O_3$ and Pyrex glass. (For the Pyrex glass, they conclude that two BO_3 and two BO_4 sites are present. χ for the BO_3 units can be determined to perhaps two significant figures if η is assumed to be zero.)

Quadrupolar effects, then, clearly identify the various boron–oxygen bonding configurations in glasses. That information makes possible the development and validation of structural models for binary,[14] ternary,[15] and more complex glasses containing boron oxide.

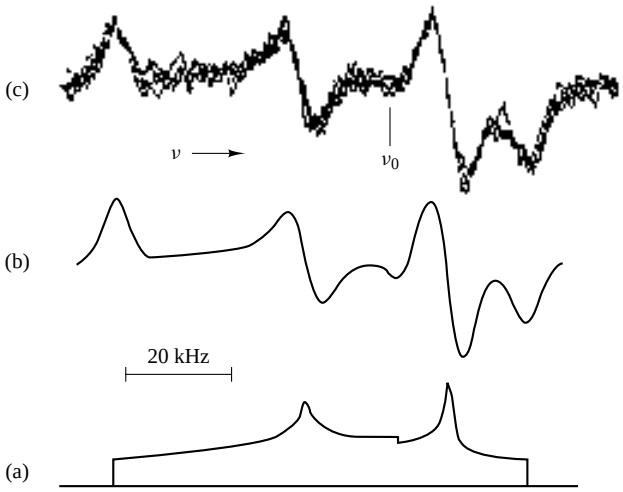

Figure 10 (a) Theoretical powder pattern for the transition ($m = +\frac{1}{2} \leftrightarrow m = -\frac{1}{2}$), with $I = \frac{3}{2}$, $\nu_0 = 16$ MHz, $\chi = 2.56$ MHz, and $\eta = 0.54$. (b) First derivative of the theoretical powder pattern after convolution with a Gaussian curve of linewidth $2\sigma = 5$ kHz. (c) Superposition of four experimental traces for ^{11}B in polycrystalline calcium metaborate, at a resonant frequency of 16 MHz[11b]

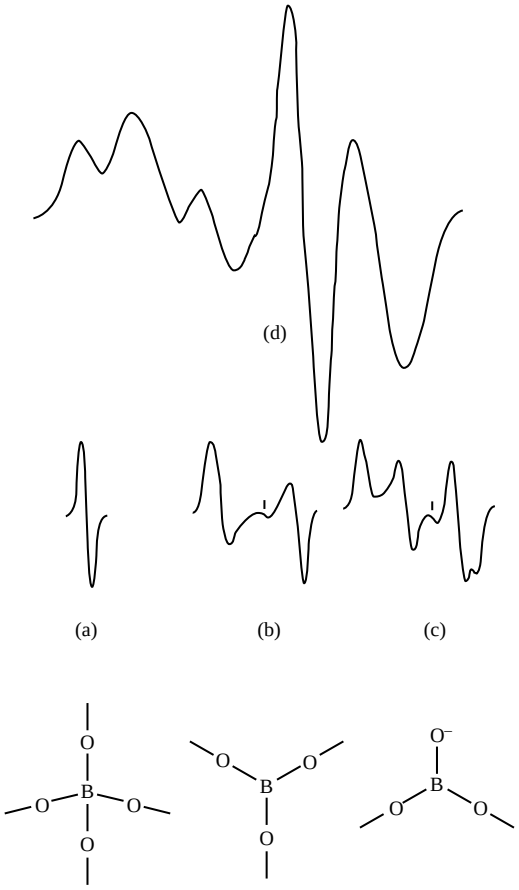

Figure 11 ^{11}B NMR spectrum of (a) a BO_4 unit, (b) a BO_3 unit, (c) a BO_3^- unit (with one NBO), and (d) a sample containing all three units[11b]

Müller-Warmuth and colleagues[16] have improved the resolution and accuracy, and obtained values of χ for the BO_4 units, using very high speed (e.g. 15 kHz) spinning rates and satellite transition spectroscopy (SATRAS). Very short excitation pulses (e.g., 0.5 μs) are used to excite large spectral ranges. Figure 15 displays ^{11}B spectra for a glass of composition (mol%) $33Li_2O{-}67B_2O_3$. Values of χ can be determined from the extent of the spinning sidebands or locations of the centers of gravity of the central and satellite transitions, and (for BO_3) computer simulation of the central transition lineshape as narrowed by the MAS procedure.[17] For the glass of Figure 15, the values of quadrupolar parameters found are 2.6 MHz and 0.3 for BO_3, and 0.80 MHz for BO_4. (The isotropic chemical shifts for BO_3 and BO_4 can also be determined.)

^{27}Al NMR has been extensively employed to study glass structure. Static NMR investigations have generally revealed only structureless, but asymmetric, lines. But utilization of MAS MMR spectroscopy by D. Müller,[18] Samoson and Lippmaa,[19] Kirkpatrick,[20] and Dupree[21] and their colleagues has yielded separation of Al responses from different sites in glasses due to different chemical shifts (and quadrupolar parameters). Kirkpatrick and co-workers[20] clearly identified four-, five-, and six-coordinated aluminum sites in $SiO_2{-}Al_2O_3$ glasses. Those studies have generally been focused on the chemical shifts, but Müller-Warmuth

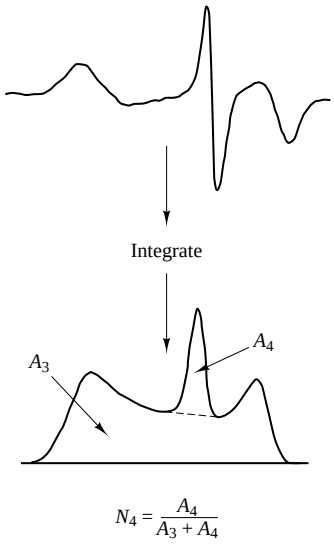

Figure 12 Method for determining N_4 in a ^{11}B NMR spectrum. The experimental spectrum at the top is the first derivative of the absorption curve

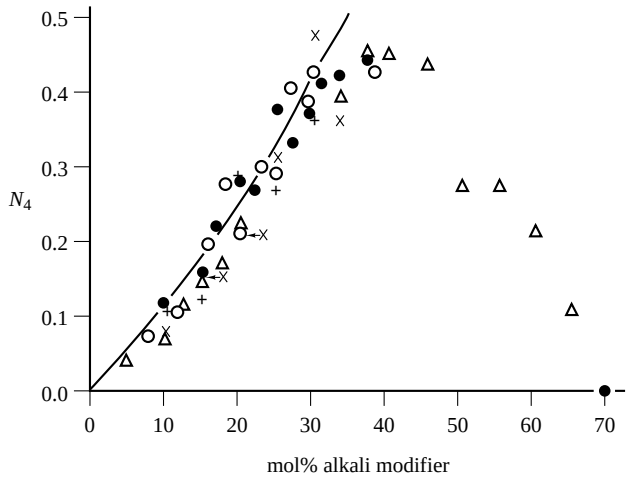

Figure 13 The fraction N_4 of boron atoms in BO_4 configurations in alkali borate glasses plotted against the molar percentage of alkali oxide: •, Na_2O; ○, K_2O; Δ, Li_2O; +, Rb_2O; ×, Cs_2O

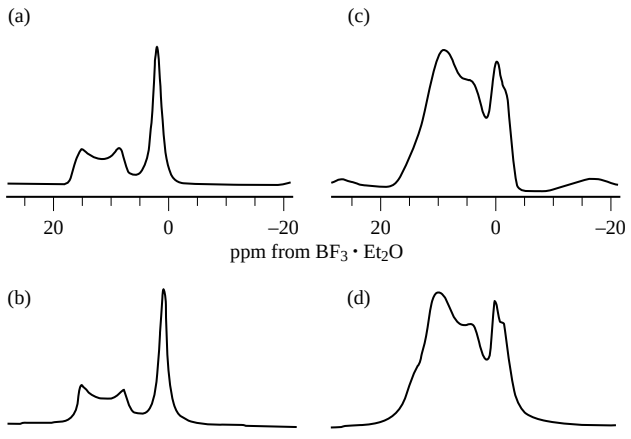

Figure 14 ^{11}B NMR spectra at 11.7 T: (a) $Li_2O{\cdot}2B_2O_3$ at a 6 kHz spinning rate; (c) commercial Pyrex glass at a 4.2 kHz spinning rate; (b) and (d) are the respective computer simulations (see Turner et al.[13])

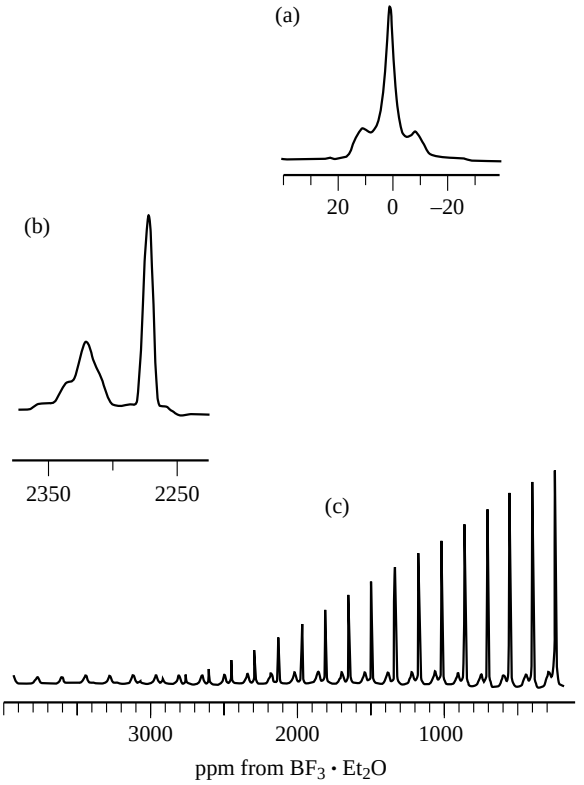

Figure 15 ^{11}B MAS–SATRAS spectrum of glass of composition (mol%) $33Li_2O–67B_2O_3$: (a) central transition; (b) 13th sideband of the satellite transition (ST); (c) part of the ST rotational sideband spectrum. The frequency of rotation is 15 kHz (see van Wüllen and Müller-Warmuth[16])

and associates[22] have used the high-field, high-spinning-rate SATRAS procedure to obtain both the isotropic chemical shifts and the values of χ for a number of ternary glasses. The value of η was not determined, and χ values are therefore limited to an accuracy of about 14%.

Oxygen bonding in vitreous SiO_2 [23] and B_2O_3 [24] has been studied using samples substantially enriched in the ^{17}O ($I = \frac{5}{2}$) isotope from the natural abundance of 0.037%. The ^{17}O spectrum in SiO_2 was simulated by only one oxygen site using the parameters χ = 5.17 MHz and η = 0.2. Changing the value of η or the width of the distributions in χ and η by as much as 30% still yielded an acceptable fit to the experimental spectrum, but the central value (5.17 MHz) of χ could be changed by only 1%. These results can be related to a distribution in the Si–O–Si bond angle between 130° and 180°, which is consistent with an earlier X-ray investigation of SiO_2 glass.

The ^{17}O NMR spectrum for vitreous B_2O_3, shown in Figure 16, required a two-site fit. Quadrupolar parameters for the two sites are χ = 4.69 MHz, η = 0.58 and 5.75 MHz, 0.40. The first site has only small distributions in χ and η, and is assigned to an oxygen in the boroxol ring (see Figure 9). The second site also has a small distribution of χ but a broad distribution in η, and arises from the oxygens connecting boroxol rings. About 83% of the borons in the glass are in boroxol rings. Kirkpatrick and co-workers[25] have extended ^{17}O NMR studies to high fields, and have succeeded in assigning features of the quadrupolar induced structure

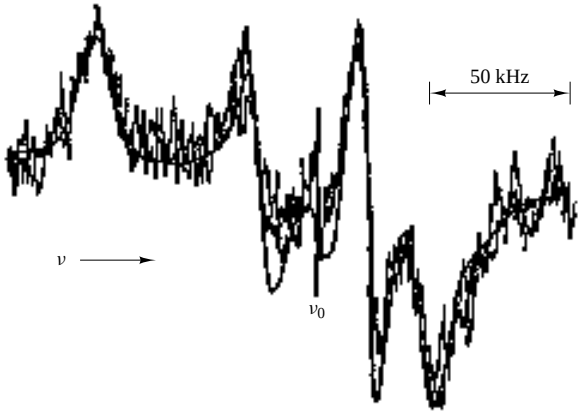

Figure 16 Two superimposed ^{17}O spectra from B_2O_3 glass and a computer simulation using the quadrupolar parameters given in the text

to oxygens in various bonding arrangements (e.g., Si–O–Si, Na–O–Si, and B–O–B).

Segel and Creel[26] prepared vitreous potassium metavanadate and found that the ^{51}V NMR response is the typical ($m = +\frac{1}{2} \leftrightarrow -\frac{1}{2}$) transaction displaying second-order quadrupolar effects. The quadrupolar parameters at 300 K are approximately 3.35 MHz and 0.47. These values are in line with those for the crystalline metavanadates,[26,27] in which each vanadium is enclosed in a tetrahedron of oxygens. In vanadium phosphate glasses[28] and crystalline V_2O_5,[29] in which the vanadiums are five-coordinated to oxygens in VO_5 units, the values of χ are found by NMR to be lower. The value[29] in crystalline V_2O_5 is 805 kHz (with η = 0.04), and rough estimates of χ for the vanadium phosphate glasses are in the 1.0–1.5 MHz range.[28]

The reader is directed to the review by Eckert[3] for summaries of, and references for, similar works on boron-doped amorphous silicon, boron in metal–metalloid glasses, gallium and arsenic studies of GaAs and GaP amorphous semiconductors, deuteron studies of 'water' in glasses, glasses based on B_2S_3, B_2Se_3, Ga_2O_3, and BeF_2, glasses containing Na_2O and Cs_2O, and other quadrupolar nuclei in glasses.

3 PURE NUCLEAR QUADRUPOLE RESONANCE (NQR) STUDIES

Since the quadrupolar interaction generates a set of energy levels in the absence of a magnetic field, transitions between these levels will yield resonance spectra if the spectrometers employed are sufficiently sensitive in the relevant frequency regions. These zero field NMR studies are labeled pure nuclear quadrupole resonance (NQR) spectroscopy.

Pure NQR spectra in solids were first detected by Dehmelt and Kruger in 1950.[30] A large body of NQR studies of chemical bonding and atomic arrangements in crystalline solids, using quadrupolar nuclei, has followed from that discovery and continues to expand (see, e.g., the summaries by Lucken,[31] Schempp and Bray,[32] Semin et al.,[33] and Rubenstein and Taylor[34,35]). The following sections summarize the application of NQR to glass studies employing particular nuclei.

3.1 ^{75}As NQR

The first detection of NQR in a glass was reported by Rubenstein and Taylor in 1972[34] and extended by Taylor and colleagues.[35,36] Rubenstein and Taylor[34] employed the spin $I = \frac{3}{2}$ nucleus ^{75}As in vitreous arsenic trisulfide (As_2S_3). The extended studies[35,36] also encompassed vitreous arsenic telluride and elemental arsenic.

The Hamiltonian for the pure quadrupolar interaction is[37]

$$\hat{\mathcal{H}} = \frac{\chi}{4I(2I-1)}[3\hat{I}_z^2 - I(I+1) + \tfrac{1}{2}\eta(\hat{I}_+^2 + \hat{I}_-^2)] \qquad (1)$$

where $\hat{I}_\pm = \hat{I}_z \pm \hat{I}_y$. When $I = \frac{3}{2}$, the secular equation (with E in units of $\frac{1}{4}\chi$) is

$$E^2 - (1 + \tfrac{1}{3}\eta^2) = 0 \qquad (2)$$

and the frequency ν_0 of the single allowed transition between the m $= \pm\frac{3}{2}$ and m $= \pm\frac{1}{2}$ states, both of which are degenerate in the absence of a magnetic field, is

$$\nu_0 = \tfrac{1}{2}\chi\sqrt{1 + \tfrac{1}{3}\eta^2} \qquad (3)$$

(Clearly, the values of χ and η cannot be independently extracted from this one transition. Methods to determine η, and thus χ, independently are discussed later in this article.)

The transition at frequency ν_0 given in equation (3) was observed by Rubenstein and Taylor[34] for crystalline (orpiment) and vitreous As_2S_3 at 4.2 K using a variable frequency pulsed NQR/NMR spectrometer and observing the frequency dependence of the spin echo amplitude. Figure 17 displays the data points and fitted Gaussian curve for the glass; the two narrower lines in the 70–73 MHz region are data for crystalline As_2S_3. The latter resonances occur at 70.38 and 72.86 MHz with respective halfwidths at half-maximum amplitude (HWHM) of 87 and 44 kHz. (There are two inequivalent As sites in the known structure of orpiment.)

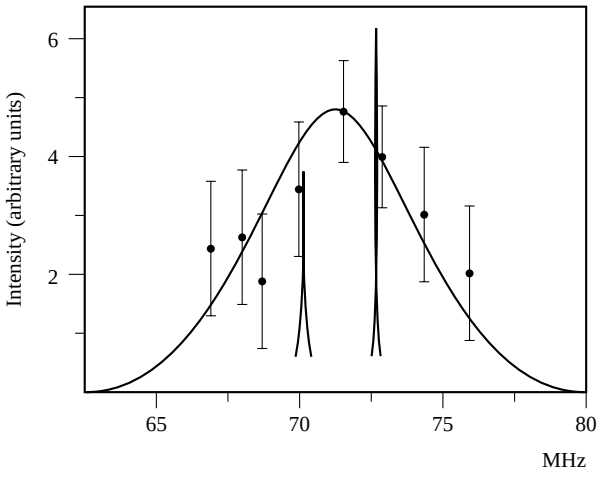

Figure 17 ^{75}As NQR in glassy and crystalline As_2S_3 at 4.2 K. The solid circles are experimental points for the glass through which a Gaussian curve has been drawn. The two narrow lines are data for crystalline As_2S_3 (see Rubenstein and Taylor[34])

But the glass yields only one very broad response centered at 71.6 MHz and having an HWHM of 3.5 MHz.

Orpiment has a layer structure in which each As atom is bonded to three S atoms in a triangular pyramidal arrangement with an As atom at the apex and three S atoms at the base. Rubenstein and Taylor[34] assumed that the large breadth of the lineshape in the As_2S_3 glasses arises from a distribution of distortions in the apex angles α. Since a difference of 1.3° between the α values for the two sites in orpiment produces a difference of 3.48 MHz between the NQR responses, a distribution of apex bonding angles α with a halfwidth of 2° will produce a distribution of frequencies with the observed halfwidth of 3.5 MHz for the glass. (The analysis assumes that the sites present in orpiment, and yielding the observed NQR frequencies, are present in the As_2S_3 glass. This has been placed in question by the work of Szeftel and Alloul that is discussed later in this article.)

In a later study, Rubenstein and Taylor[35] detected and analyzed the pure NQR spectra for crystalline and vitreous As_2Se_3 and obtained a better-resolved spectrum for vitreous As_2S_3. They also measured the spin–lattice relaxation time T_1 at various temperatures. From the near equality of the As_2S_3 crystalline and amorphous initial relaxation behavior, they concluded that the near-neighbor environments of As atoms in the crystal and the glass are quite similar (i.e., the two sites in orpiment, and two-dimensional correlations between As_2S_3 pyramidal units in the layer-structured crystalline phase, are retained in the glass).

Application of a small magnetic field at a series of orientations of an orpiment single crystal yielded data that, based on calculations by Bersohn[37] and Dean,[38] yielded values of the asymmetry parameter for the two sites in the crystal that Rubenstein and Taylor concluded are also present in the glass. This case of a Zeeman perturbation of an NQR spectrum is discussed in the next section. The values of η for the two sites are 0.343 and 0.374.

Jellison, Petersen, and Taylor[36] reported in 1980 an NQR study of amorphous, orthorhombic, and rhombohedral arsenic. Figure 18 displays the highly asymmetric response for the arsenic glass, and the much narrower line for orthorhombic arsenic. Jellison et al. found that the asymmetric pattern obtained for the glass could be reproduced in a calculation by varying the dihedral angle using distributions in the angle

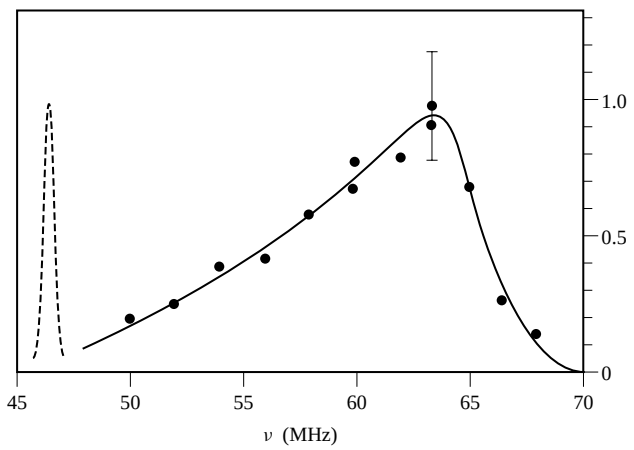

Figure 18 NQR absorption in amorphous As (circles and solid line) and orthorhombic As (dashed line) at 4.2 K (see Jellison et al.[36])

suggested in the literature. (The dihedral angle is the angle of rotation along the As–As bond required to bring the pair into an eclipsed position.) The temperature dependence of the NQR frequencies for the crystalline forms of arsenic were obtained, and could be well fitted by the customary Bayer model,[39] but the NQR lineshape for the arsenic glass is too broad for observation of shifts in the peak frequency with temperature.

In more recent studies,[40] Taylor and colleagues have used ^{75}As NQR and ^{63}Cu NMR spectroscopy to study chalcogenide glasses in the systems Cu–As–S and Cu–As–Se.

3.2 ^{11}B and ^{10}B NQR

The NQR resonance frequencies, predicted from the quadrupolar effects observed in NMR studies, for many other quadrupolar nuclei in glasses (e.g., ^{7}Li, ^{10}B, ^{11}B, ^{14}N, ^{17}O, ^{23}Na, ^{27}Al, ^{39}K, and ^{51}V) lie below 10 MHz and even below 1 MHz. Sufficient signal-to-noise (S/N) values for detection of those responses can be very difficult to achieve. However, a modified Robinson circuit,[41] placing the entire inductive-capacitive tank circuit at 77 K and utilizing state-of-the-art solid state components and Zeeman modulation, has achieved high S/N at low frequencies. Figure 19 from Gravina and Bray,[42] displays the ^{11}B NQR spectrum for crystalline boron oxide (B_2O_3). (^{11}B has spin $I = \frac{3}{2}$, and equation (3) predicts the NQR frequency.) A S/N value between 100 and 200 is easily obtained at this frequency of 1.358 MHz. Figure 20 displays a vertically expanded version of Figure 19 in which the highest frequency of 13 allowed ^{10}B transitions is seen in full detail. (^{10}B is 18.8% and ^{11}B 81.2% abundant in nature.)

In light of the extreme width of the ^{75}As NQR spectra in amorphous As and vitreous As_2S_3 and As_2Se_3, one might anticipate failure in seeking the ^{11}B NQR spectrum in borate glasses near 1.35 MHz. But, if those widths of some megahertz are caused by distributions in the EFG components, they will scale with the resonance frequency. Figure 21 displays the ^{11}B NQR spectrum for vitreous B_2O_3. The full width at half-maximum (FWHM) is 21 kHz. This is only a moderate increase in width from the FWHM of 15 kHz, arising from dipolar broadening, in crystalline B_2O_3. The larger response in Figure 21 must arise from borons in the boroxol groups that predominate[24] in the glass (see Figure 9). The site for the borons yielding the lower-frequency response in Figure 21 has not yet been identified.

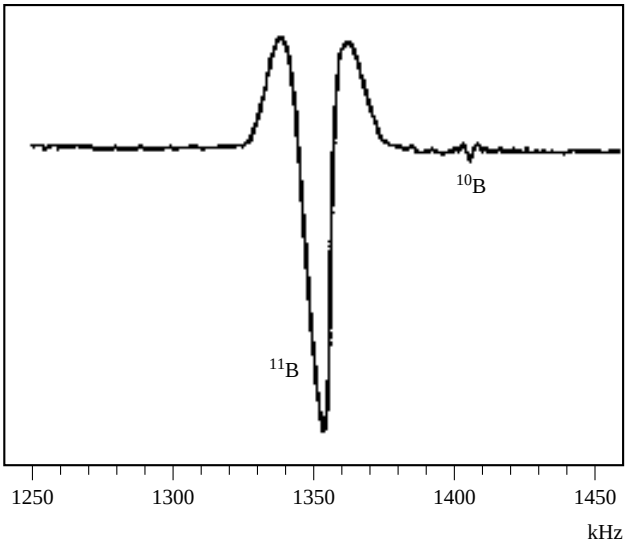

Figure 19 Boron NQR spectrum of crystalline B_2O_3

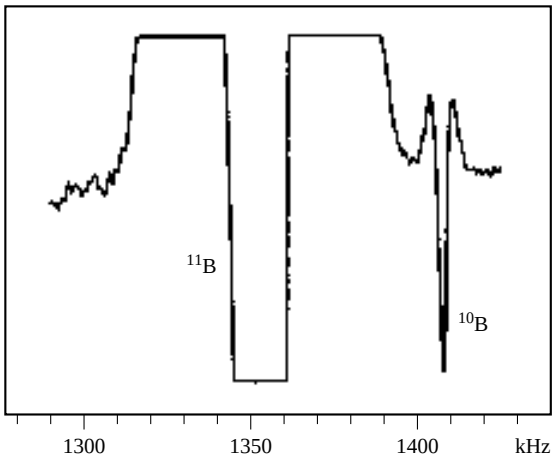

Figure 20 The features of Figure 19 displayed with a greatly expanded vertical scale

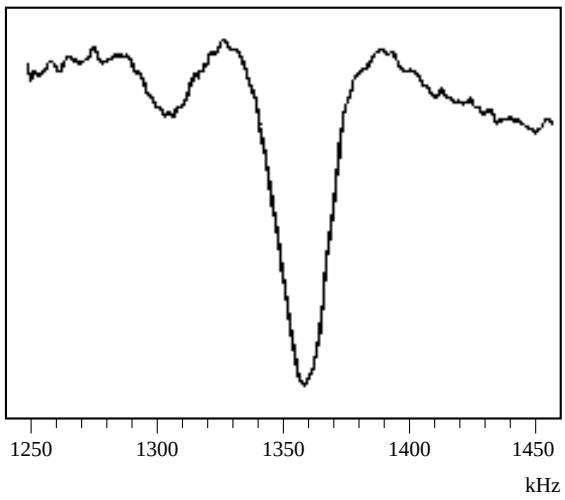

Figure 21 ^{11}B responses from vitreous B_2O_3

Some work has been completed in ^{11}B NQR studies of structural arrangements and chemical bondings in alkali borate glasses. According to the model proposed by Krogh-Moe[43] and supported (but not proved) by the ^{11}B and ^{10}B NMR studies of Bray and co-workers,[44] those glasses should be composed of mixtures of the structural groupings presented in Figure 9. As an indication of the sensitivity of the ^{11}B NQR resonance frequency to the particular structural grouping in which the BO_3 or BO_4 units are located, it is instructive to study Figure 22. The sample under study was prepared as polycrystalline sodium tetraborate ($Na_2O{\cdot}4B_2O_3$), but X-ray diffraction showed the material to be a mixture of sodium borate compounds. ^{11}B NQR responses from at least six sites are resolved in the spectrum displayed in Figure 22, and they span a range of some 150 kHz. There is hope, then, of identifying the particular structural groupings present in any

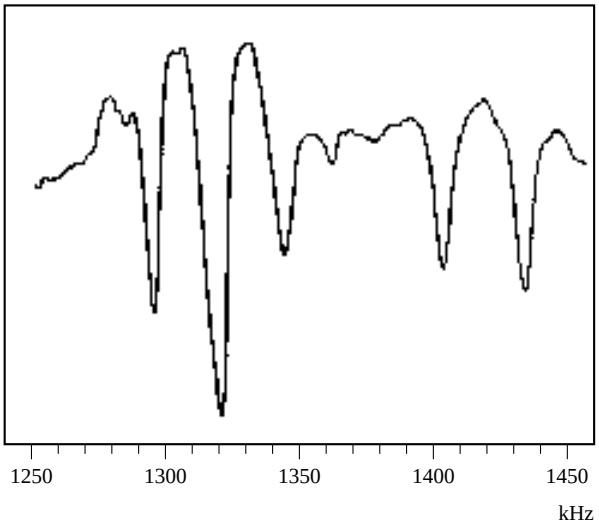

Figure 22 ^{11}B responses from a polycrystalline sample having the sodium tetraborate composition ($Na_2O{\cdot}4B_2O_3$)

borate glass, and even gaining a measure of the amount of each grouping present.

An example of the degree of correspondence between the ^{11}B NQR spectra for crystal and glass is displayed in Figure 23. The spectrum in (a) is for polycrystalline sodium diborate ($Na_2O{\cdot}2B_2O_3$), and the spectrum for the glass is in (b). The crystal is known from X-ray diffraction studies to consist of sodium ions and diborate groupings (see Figure 9). Figure 24 shows the ^{11}B NQR spectrum for a glass of molar composition $0.15\,Na_2O{-}0.85B_2O_3$, with the spectrum for vitreous B_2O_3 superposed. It is clear that there are at least three different structural groupings present in the sodium borate glass, and that one of them is probably the boroxol unit found in vitreous B_2O_3. On the basis that the structural groupings from the crystalline compounds nearest in composition to the glass should predominate, the other responses may arise from the tetraborate group or the pentaborate and triborate groups that can join to form the tetraborate structural grouping (see Figure 9).

3.3 ^{27}Al NQR

The Robinson-type CW spectrometer has been used successfully[45] to detect ^{27}Al NQR spectra in polycrystalline powders and glasses at relatively low frequencies. ^{27}Al has spin $I = \frac{5}{2}$, and the secular equation for the energy values E (with E in units of $\frac{1}{20}\chi$) is

$$E^3 - 7(3 + \eta^2)E - 20(1 - \eta^2) = 0 \qquad (4)$$

Numerical solution via a computer program yields the values of E and the transition frequencies for any set of values of χ and η.

Figure 25 displays the two NQR responses for ^{27}Al in a glass of composition (mol%) of $16.8Al_2O_3{-}83.2TeO_2$ at 77 K. The frequencies are 490.1 and 853.3 kHz and the widths (FWHM) are approximately 15 kHz. Values of χ = 2.909 ± 0.014 MHz and η = 0.346 ± 0.014 were obtained from the

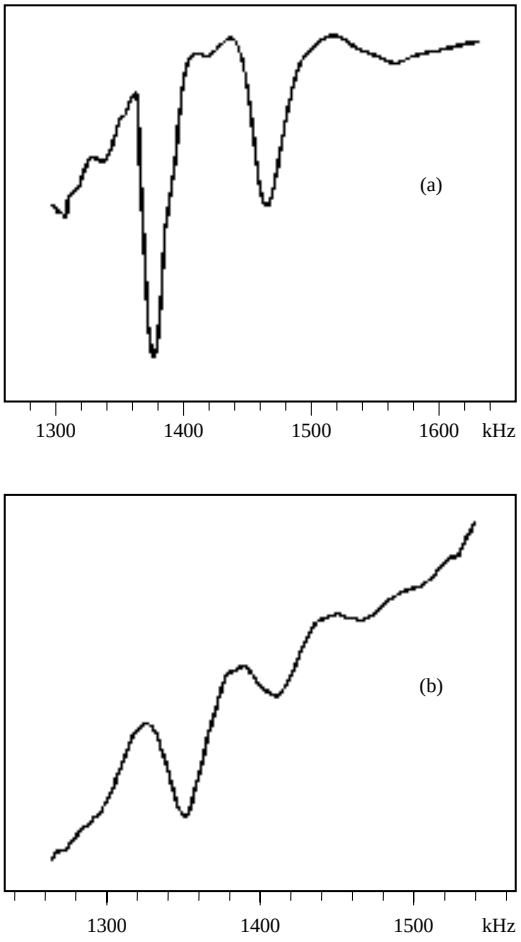

Figure 23 ^{11}B NQR spectra of (a) crystalline and (b) vitreous $Na_2O{\cdot}2B_2O_3$

data. An NMR measurement yielded an isotropic chemical shift of 36.7 ppm, which identifies a pentahedrally coordinated aluminum site.

It is clear that NQR studies of aluminum in four-, five-, and six-coordination in glasses are feasible and very accurate in measurements of the quadrupolar parameters.

4 NQR WITH A ZEEMAN PERTURBATION

We now survey the case in which a small magnetic field is present during the NQR experiment. This Zeeman splitting of a pure NQR spectrum was first treated by Bersohn[37] using a perturbation procedure. Dean[38] subsequently treated the theory of Zeeman splitting rigorously, and discussed the case of nuclear spin $I = \frac{3}{2}$ in detail. The applied field lifts the degeneracy of the $m = \pm\frac{3}{2}$ and $m = \pm\frac{1}{2}$ states, yielding the energies[46] and transition frequencies displayed in Figure 26.

Rubenstein and Taylor[35] applied the expressions for the four transition frequencies $\omega_i = \nu_i$, i = 1, ... , 4 to rotations about the a, b, and c axes of a single crystal (orpiment) of As_2S_3, using a magnetic field of about 87.5 mT. (The Zeeman interaction in this field would be 638 kHz, whereas the NQR frequencies are in the 70–72 MHz range. A first-order perturbation treatment of the Zeeman interaction is adequate.)

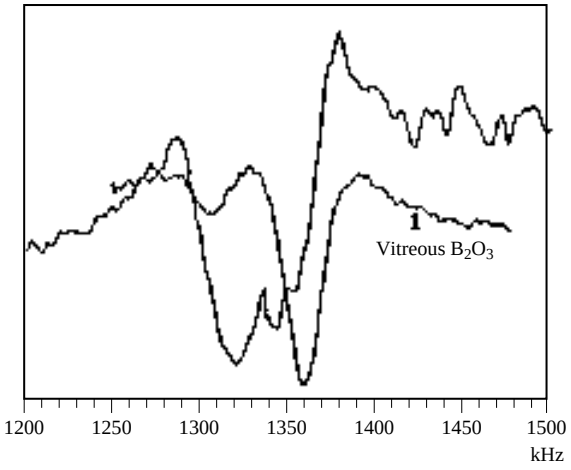

Figure 24 ^{11}B NQR spectrum of a glass of composition $0.15\,Na_2O{-}0.85B_2O_3$ referenced to vitreous B_2O_3

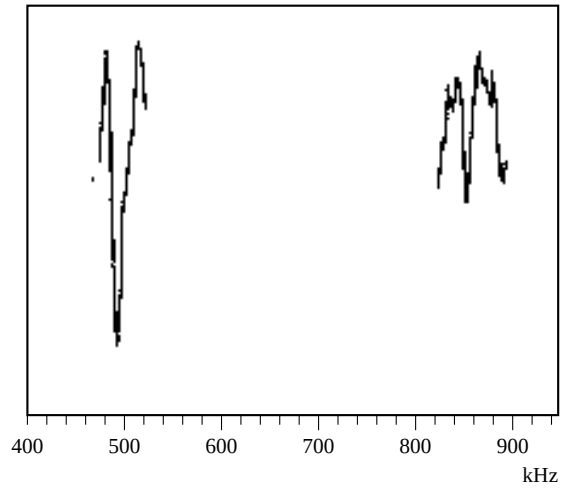

Figure 25 The two ^{27}Al NQR responses for vitreous $16.8Al_2O_3{-}83.2TeO_2$ (mol%)

The values of η extracted for the two inequivalent As sites in orpiment are 0.343 and 0.374.

Szeftel and Alloul[47] employed the frequency Ω_1 in Figure 26 to determine the value of the asymmetry parameter for ^{75}As in several vitreous chalcogenides. (In theory, Ω_3 could also be used, but the transition probability is lower than for Ω_1. No response was detected[47] at Ω_3.) The frequency Ω_1 is given by

$$\Omega_1 = \Omega\left[\left(1-\frac{2}{\rho}\right)^2\cos^2\theta + \left[\left(1+\frac{1}{\rho}\right)^2 + \frac{\eta^2}{\rho^2} - 2\frac{\eta}{\rho}\left(1+\frac{1}{\rho}\right)\cos 2\phi\right]\sin^2\theta\right]^{1/2} \quad (5)$$

where $\Omega = \gamma B$, γ is the gyromagnetic ratio, and $\rho = 1 + \frac{1}{3}\eta^2$. Since equation (4) does not include the quadrupolar coupling constant χ, this transition can be used to obtain the value of η quite decoupled from that of χ.

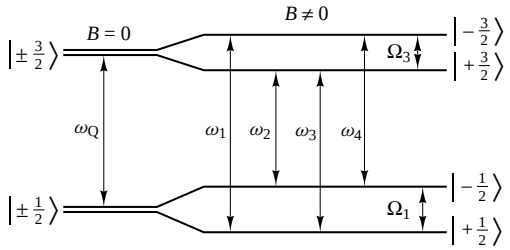

Figure 26 Energy level diagram for a nuclear spin $I = \frac{3}{2}$ in the presence of a strong quadrupolar coupling and, respectively, zero and nonzero Zeeman perturbation (see Szeftel and Alloul[47])

Prediction of the observable lineshape for a polycrystalline powder or glass requires averaging over all θ and ϕ, including the dependence of the state functions and transition probabilities on those angles. Figure 27 displays the calculated lineshapes for two values of η. The parameter $r = \Omega/\nu = \gamma H_0/\nu$, where ν is the frequency of the spectrometer, has the limits $r_m \leq r \leq r_M$, and a logarithmic divergence occurs at r_p, where

$$\left.\begin{aligned} r_m &= \left[1+\frac{1+\eta}{\rho}\right]^{-1}, \quad r_M = \left(\frac{2}{\rho}-1\right)^{-1} \\ r_p &= \left[1+\frac{1-\eta}{\rho}\right]^{-1} \end{aligned}\right\} \quad (6)$$

The ^{75}As spectra obtained at 4.2 K for four vitreous chalcogenides are displayed in Figure 28. Analysis of the spectra was carried out using Gaussian distributions in η about the value determined at the logarithmic divergence (τ_p). For vitreous As_2S_3 and As_2Se_3, it was found necessary to include the contributions from two As sites with distinctly different values of η. These were determined as 0.12 and 0.36 for vitreous As_2S_3, whereas the values for crystalline orpiment found by Rubenstein and Taylor[35] using a single crystal are 0.343 and 0.374. The site with $\eta = 0.12$ is clearly not present in orpiment, and is a site not considered by Rubenstein and Taylor[35] in their discussions of the ^{75}As NQR spectrum for vitreous As_2S_3. For vitreous As_2Se_3, the values of η were determined by Szeftel and Alloul[47] to be 0.14 ± 0.02 and 0.45.

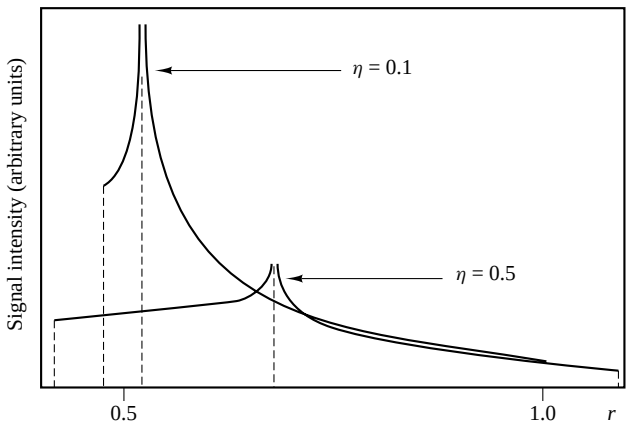

Figure 27 Spectra (solid lines) calculated for two values of η (see Szeftel and Alloul[47])

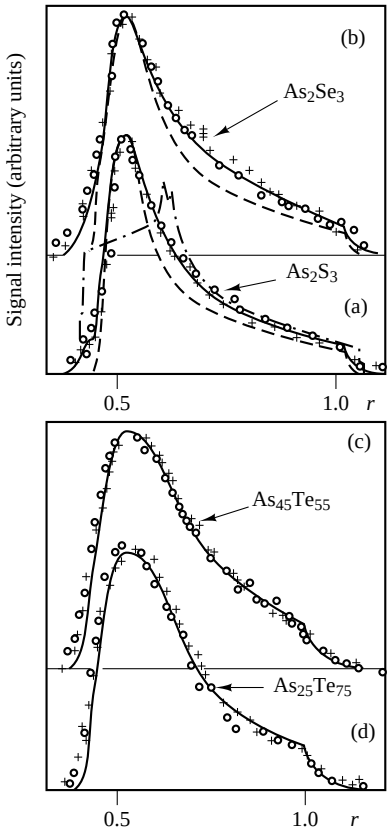

Figure 28 ^{75}As spectra recorded in four vitreous chalcogenides at 5.9 MHz (circles) and 10.3 MHz (crosses). The powder spectrum calculated with the η values of orpiment is plotted as dash-dotted lines. Solid lines indicate the best fit. When two Gaussian distributions are needed to obtain the best fit, the contribution of the distribution of higher weight is plotted as a dashed line (see Szeftel and Alloul[47])

5 RELATED ARTICLES

Amorphous Materials; Boron NMR; Ceramics; Deuterium NMR in Solids; High Speed MAS of Half-Integer Quadrupolar Nuclei in Solids; Lithium NMR; Oxygen-17 NMR; Quadrupolar Interactions; Quadrupolar Nuclei in Solids; Relaxation Theory for Quadrupolar Nuclei; Sodium-23 NMR; SQUIDs; Zero Field NMR.

6 REFERENCES

1. A. H. Silver and P. J. Bray, *J. Chem. Phys.*, 1958, **29**, 984.
2. M. H. Cohen and F. Reif, in *Solid State Physics*, eds. F. Seitz and D. Turnbull, Academic Press, New York, 1958, Vol. 5, p. 321.
3. H. Eckert, in *Progress in Nuclear Magnetic Resonance Spectroscopy*, eds. J. W. Emsley, J. Feeney, and L. N. Sutcliffe, Pergamon Press, Oxford, 1992, Vol. 24, p. 159.
4. P. E. Stallworth and P. J. Bray, *Glass Sci. Technol.*, 1990, **4**, 77.
5. A. R. Grimmer, *Exp. Tech. Phys.*, 1988, **36**, 81.
6. P. J. Bray, S. J. Gravina, D. H. Hintenlang, and R. V. Mulkern, *Magn. Reson. Rev.*, 1988, **13**, 263.
7. P. J. Bray, *J. Non-Cryst. Solids*, 1987, **95/96**, 45.
8. P. J. Bray, J. O. Edwards, J. G. O'Keefe, V. F. Ross, and I. Tatsuzaki, *J. Chem. Phys.*, 1961, **35**, 435.
9. P. J. Bray, *Classe des Mémoirs, de l'Académie Royale de Belgique, Sciences XXXIII*, 1961, **3**, 37.
10. F. Krämer, W. Müller-Warmuth, J. Scheerer, and H. Dutz, *Z. Naturforsch. A.*, 1973, **28**, 1338.
11. (a) P. J. Bray, in *Interaction of Radiation with Solids*, ed. A. Bishay, Plenum Press, New York, 1970, p. 11; (b) S. G. Bishop, Ph.D. Thesis, Brown University, 1969.
12. P. J. Bray and J. G. O'Keefe, *Phys, Chem. Glasses*, 1963, **4**, 37; J. Zhong and P. J. Bray, *J. Non-Cryst. Solids*, 1989, **111**, 67.
13. G. L. Turner, K. A. Smith, R. J. Kirkpatrick, and E. Oldfield, *J. Magn. Reson.*, 1986, **67**, 544; G. L. Turner, R. J. Kirkpatrick, S. H. Risbud, and E. Oldfield, *Am. Ceram. Soc. Bull.*, 1987, **66**, 656.
14. G. E. Jellison, Jr., and P. J. Bray, *Solid State Commun.*, 1976, **29**, 517; *J. Non-Cryst. Solids*, 1978, **29**, 187.
15. P. J. Bray and W. J. Dell, *J. Phys. (Orsay, Fr.)*, 1982, **43**, C9-131; W. J. Dell, P. J. Bray, and X. Z. Xiao, *J. Non-Cryst. Solids*, 1983, **58**, 1.
16. L. van Wüllen and W. Müller-Warmuth, *Solid State Nucl. Magn. Reson.*, 1993, **2**, 279.
17. D. Müller, *Ann. Phys. (Leipzig)*, 1982, **39**, 451.
18. D. Müller, G. Berger, I. Grunze, G. Ludwig, E. Hallas, and V. Haubenreisser, *Phys. Chem. Glasses*, 1983, **24**, 37.
19. G. Engelhardt, M. Nofz, K. Forkel, F. G. Wihsmann, M. Mägi, A. Samoson, and E. Lippmaa, *Phys. Chem. Glasses*, 1985, **26**, 157.
20. S. H. Risbud, R. J. Kirkpatrick, A. P. Taglialavore, and B. Montez, *J. Am. Ceram. Soc.*, 1987, **70**, C-10.
21. R. K. Sato, P. F. McMillan, P. Dennison, and R. Dupree, *J. Phys. Chem.*, 1991, **95**, 4483.
22. W. Müller-Warmuth, C. Mundus, and L. van Wüllen, *J. Non.-Cryst. Solids*, 1992, **149**, 209.
23. A. E. Geissberger and P. J. Bray, *J. Non-Cryst. Solids*, 1983, **54**, 121.
24. G. E. Jellison, Jr., L. W. Panek, P. J. Bray, and G. B. Rouse, Jr., *J. Chem. Phys.*, 1977, **66**, 802.
25. B. C. Bunker, D. R. Tallant, R. J. Kirkpatrick, and G. L. Turner, *Phys. Chem. Glasses*, 1990, **31**, 30.
26. S. L. Segel and R. B. Creel, *Can. J. Phys.*, 1970, **48**, 2673.
27. D. Mao, P. J. Bray, and G. L. Petersen, *J. Am. Chem. Soc.*, 1991, **113**, 6812.
28. F. R. Landsberger and P. J. Bray, *J. Chem. Phys.*, 1970, **53**, 2757.
29. S. D. Gornostansky and C. V. Stager, *J. Chem. Phys.*, 1967, **46**, 4959.
30. H. G. Dehmelt and H. Kruger, *Naturwissenschaften*, 1950, **37**, 111; 1951, **38**, 921.
31. E. A. C. Lucken, *Nuclear Quadrupole Coupling Constants*, Academic Press, New York, 1969.
32. E. Schempp and P. J. Bray, in *Physical Chemistry, an Advanced Treatise*, eds. H. Eyring, D. Henderson, and W. Jost, Academic Press, New York, 1970, Vol. 4, p. 521.
33. G. K. Semin, T. A. Babushkina, and G. G. Yakobson, *Nuclear Quadrupole Resonance in Chemistry*, Wiley, New York, 1975.
34. M. Rubenstein and P. C. Taylor, *Phys. Rev. Lett.*, 1972, **29**, 119.
35. M. Rubenstein and P. C. Taylor, *Phys. Rev. B*, 1974, **9**, 4258.
36. G. E. Jellison, Jr., G. L. Petersen, and P. C. Taylor, *Phys. Rev. B*, 1980, **22**, 3903.
37. R. Bersohn, *J. Chem. Phys.*, 1952, **20**, 1505.
38. C. Dean, *Phys., Rev.*, 1952, **96**, 1053.
39. H. Bayer, *Z. Phys.*, 1951, **130**, 227.
40. Z. M. Saleh, G. A. Williams, and P. C. Taylor, *Phys. Rev. B*, 1989, **46**, 10 557.

41. F. N. H. Robinson, *J. Phys. E: Sci. Instrum.*, 1980, **13**, 861; 1982, **15**, 814.
42. S. J. Gravina and P. J. Bray, *J. Magn. Reson.*, 1990, **89**, 515.
43. J. Krogh-Moe, *Phys. Chem. Glasses*, 1962, **3**, 101.
44. P. J. Bray, *J. Non-Cryst. Solids*, 1985, **75**, 29, and references therein.
45. D. Lee and P. J. Bray, *J. Magn. Reson.*, 1991, **94**, 51.
46. T. P. Das and E. L. Hahn, in *Solid State Physics*, eds. F. Seitz and D. Turnbull, Academic Press, New York, 1958, Suppl. 1.
47. J. Szeftel and H. Alloul, *Phys. Rev. Lett.*, 1979, **42**, 1691.

Biographical Sketch

Philip J. Bray. *b* 1925. B.S., 1948, Brown University, U.S.A.; Ph D. (supervisor Norman Ramsey), 1953, physics, Harvard University. Currently Hazard Professor of Physics, Emeritus, Brown University. Approx. 270 publications. Current research specialties: NMR and NQR studies of glass structure, and NQR of organic compounds and glasses.

Quadrupolar Nuclei in Liquid Samples

Pierre Laszlo
Université de Liège, Liège, Belgium and Ecole Polytechnique, 91128, Palaiseau, France

1	Introduction	1
2	Microdynamics From Deuterons	2
3	Organolithium Compounds: Electronic Structure, Geometry, and Degree of Aggregation	2
4	Nitrogen-14	3
5	Oxygen-17	4
6	The Sodium Anion	4
7	Coordination of Aluminum-27	5
8	Microenvironment of the Chloride Ion	6
9	How Does Cobalt-59 Relax in Octahedral Complexes?	7
10	A Note on the Sternheimer Antishielding Factor	8
11	Conclusions	8
12	Related Articles	8
13	References	8

1 INTRODUCTION

Nuclei with a spin quantum number equal to or greater than unity have an electric quadrupole moment Q, prolate or oblate. The quadrupolar coupling is the interaction between such an electric quadrupole—stemming from the nonspherical distribution of the proton charges within the nucleus—and the electric field gradient due to the rest of the molecule. This field arises entirely from charges external to the nucleus: the other nuclei and the electrons both contribute. Thus, the electrostatic field gradient (EFG) is a traceless tensor. In its principal axis system (α,β,γ), it is represented by two observables, for example,

$$eq = V_{\alpha\alpha}, \quad \eta = \frac{V_{\beta\beta} - V_{\gamma\gamma}}{V_{\alpha\alpha}} \tag{1}$$

The axes are chosen so as to rank the components of the EFG in the alphabetical sequence $|V_{\alpha\alpha}| > |V_{\beta\beta}| > |V_{\gamma\gamma}|$. η is called the asymmetry parameter, and $\chi = e^2qQ/h$ is known as the quadrupolar coupling constant. In general, quadrupolar coupling constants range between a few tens of kilohertz and a few megahertz.

A majority of the nuclides in the Periodic Table are quadrupolar. Yet, so far, the historical development of NMR has given a privileged position to spin-$\frac{1}{2}$ nuclei such as ^{1}H, ^{13}C, ^{15}N, ^{19}F, ^{29}Si, ^{31}P, and ^{131}Xe. The objective reasons are the very high sensitivity of protons, the fact that the composition of organic molecules is predominantly carbon, hydrogen, oxygen, and nitrogen, and the ease with which both scalar and dipolar couplings can be used to provide rich structural information. The former reveal coupling patterns (multiplets) uniquely diagnostic of the number and type of neighboring nuclei, and thus indicate the local connectivity. The latter, as manifested especially through nuclear Overhauser effects, gives complementary information about internuclear distances.

The efficiency of quadrupolar relaxation makes it, in general, rather difficult to extract these two types of structural information from the magnetic resonance of a quadrupolar nucleus. One should perhaps add to these objective reasons the innate conservatism of chemists—and indeed of paradigmatic science in general.

Yet quadrupolar nuclei have themselves so much to give to their observer. Even though chemists have tended to neglect it, the quadrupolar coupling constant holds comparable intrinsic interest to the electric dipole moment. It is one of the few measures we have of the electronic distribution in molecules, which in turn determines so many of their ground state properties, and can also be astutely used to make predictions of reactivity.

As is well known, any NMR relaxation mechanism gives a relaxation rate proportional to the square of the relevant interaction energy, multiplied by a spectral density. In the extreme narrowing limit, the spectral density at zero frequency is a correlation time, as defined from the appropriate correlation function. With the quadrupolar interaction energy into the megahertz range, this means that its fluctuations on a picosecond timescale, i.e., one characteristic of reorientation of organic molecules in solution, will be readily amenable to measurement. The attendant relaxation rates will be of the order of a few hertz. Thus, another major application of quadrupolar NMR is to the study of dynamics and microdynamics.

It is impossible within the space available here to give a thorough overview of the field. Probably, even a list of references for the past decade would more than fill the available space. Thus, a decision has been made not even to attempt comprehensiveness—because this would actually lead to its very opposite, superficiality. This is the reason why we have opted for a personal selection.

What are the main characteristics of this selection? It will emphasize contributions to science rather than technology. Good science is something like a convolution product between an important problem, a good idea to solve it, and an adequate technique—probably in that order. This review will also attempt to lay the groundwork for future historians by backtracking to the original seminal contributions. Scientists tend to downplay their predecessors in order to put their own contributions in the best possible light—sometimes even at the extent of mutilating their bibliography of highly relevant references. Perhaps, the length of time that this reviewer has invested in NMR will give a more balanced overview.

Yet another characteristic is the limitation to isotropic environments. This is apparently a severe limitation drastically curtailing applications of quadrupolar NMR: the transitions being made degenerate, the spectra are apparently devoid of the quadrupolar interaction, in the form of an observed splitting. Nevertheless, as already stated, even though there may be a single resonance to record, its relaxation behavior is determined by the magnitude of the quadrupolar interaction. Hence, while other articles are devoted to quadrupolar nuclei in the presence of local order, as in solids or liquid crystals (see ***Liquid Crystals: General Considerations***), this review confines itself to quadrupolar nuclei in isotropic media.

Two more constraints on this article should be mentioned briefly. Obviously, the author's own work will not be mentioned. More cruel yet is the taboo on individual areas that could have had their natural niche within this review—such as the lovely ^{43}Ca study of calciproteins by the Lund group—but which are covered elsewhere in the Encyclopedia.

2 MICRODYNAMICS FROM DEUTERONS

Deuterium is rather easy to substitute for hydrogen in organic molecules. Such a move is attractive for NMR studies. Since scalar couplings are reduced by the ratio of the gyromagnetic ratios, the spectrum is simplified—and the chemical shifts in ppm to first approximation remain the same. Furthermore, replacement of a proton with a deuteron makes interpretation of relaxation measurements much simpler. In the absence of electronic relaxation by paramagnetic species, deuteron relaxation is exclusively quadrupolar.

The electrostatic field gradient at deuterium arises from imperfect (but near-perfect) cancellation of nuclear and electronic contributions. Accordingly, the quadrupolar coupling constant χ associated with a carbon–deuterium C–^{2}H bond usually has values of about 160–180 kHz, depending upon carbon hybridization and substitution.[1] Deuterium quadrupolar coupling constants have been obtained from ab initio SCF calculations. These yield coupling constants accurate to about 5% (10 kHz). A plot of the calculated versus the experimental values has unit slope, a standard deviation of 10 kHz and a correlation coefficient of 0.989 for 24 data points. The confidence limits (P = 0.95) of the slope and the intercept include 1 and 0, respectively. Examination of the calculated values reveals an empirical proportionality to one another of the electronic and nuclear parts of the quadrupolar coupling constant. This observation is turned into a model that yields electrostatic field gradients at deuterium, q, of equal quality to the SCF calculations.[2]

The history of chemistry shows an empirical law not unlike Haeckel's Law ('ontogeny recapitulates phylogeny'), namely, whatever organic chemistry has achieved, organometallic chemistry strives to emulate. An instance is the quadrupolar coupling constant of deuterium in metal hydrides. It ranges from 55 to 158 kHz, as obtained from T_1 relaxation data in solution, and provides useful information on the ionicity of the metal–deuterium bond.[3]

After this aside, we return to deuterium-labeled organic molecules. Under extreme narrowing conditions, the longitudinal and transverse relaxation rates are equal and given by $R_{1,2} = \frac{3}{2}\pi^2\chi^2(1 + \frac{1}{3}\eta^2)\tau_c$, where η is the asymmetry parameter, which vanishes only when the C–D bond is coaxial, with a threefold or higher molecular symmetry axis. Thus, longitudinal relaxation times in the range of 17 ms to 17 s are measured under these conditions. Knowledge of both the quadrupolar coupling constant χ and the asymmetry parameter η, combined with measurement of the relaxation rates, thus yields the effective reorientational correlation time τ_c. For instance, methylenephenanthrene tumbles about in deuteriochloroform solution with τ_c = 13.6 ps. The anisotropy of the reorientation can be probed simply by monitoring C–D bonds variously located with respect to the inertial axes around which the molecule rotates: the fastest reorientational motion is associated with the highest symmetry axis.

Whenever the C–D bond, instead of being attached to a rigid skeleton, is part of a rotor, at least two correlation times are needed for the description of its motion: τ_i for the internal rotation and τ_M for the overall motion. For instance, a $-CH_2D$ group in an isotropically reorienting molecule corresponds to

$$\tau_\chi = 0.11\tau_M + 0.89(\tau_M^{-1} + \tau_i^{-1}) \qquad (2)$$

A number of substituted aromatic molecules have been examined in this way.[4]

Consider now a molecule A that incorporates the telltale C–D bond and that is involved in a dynamic equilibrium process A + B = AB. Let us denote by k_a and k_d the rate constants for association and dissociation. Since the system bears its own internal clocks ('To choose time is to save time'—Francis Bacon[5]), with τ_f and τ_g the correlation times of the free A molecule and of the complex AB, it becomes possible to measure k_a and k_d.[6] Brevard and Lehn achieved such a truly lovely application. They studied the charge-transfer complexes between trinitrobenzene as the electron acceptor and fluorene, methylfluorene, and methylenephenanthrene as the electron donors. The results showed that each of the CT complexes amounted to a collision complex.[7] During the last two decades, there have been numerous applications of deuterium nuclear relaxation to organic and biomolecules.[8]

To give but one example of the sophistication that has been achieved, a study has examined the intercalates formed by dimethyl sulfoxide in the interstitial space of a kaolinite clay, using DMSO-d_6. The results show the coexistence of two DMSO sites. In one of these sites, with χ = 67 kHz, the methyl group rotors hop through angular steps of 140°. In the other site, with χ = 59 kHz, the methyl groups hop through 110°. The former is a site in which one methyl group is anchored in a hexagonal hole within the honeycombed silicate layer, and the DMSO molecule is able to rotate around this sulfur–carbon axis. The latter has the DMSO pyramid with its symmetry plane, through the S–O bond and bisecting the C–S–C angle, orthogonal to the parallel layers of the clay.[9]

3 ORGANOLITHIUM COMPOUNDS: ELECTRONIC STRUCTURE, GEOMETRY, AND DEGREE OF AGGREGATION

The two lithium nuclides are ^{6}Li and ^{7}Li, with natural abundances of 7.42% and 92.58%, respectively. The spin quantum numbers are 1 and $\frac{3}{2}$, respectively. Nevertheless, ^{6}Li has a tiny quadrupole moment of -0.0008×10^{-28} m^2 making it an honorary spin-$\frac{1}{2}$ nucleus.[10]

An elegant use of the two isotopes is Jackman's study of the structure of phenyllithium in diethyl ether–cyclohexane (1:2) and in tetramethylethylenediamine (TMEDA)–cyclohexane (1:9) stable solutions. The idea stems from the contrasted abilities of the two lithium nuclides at dipole–dipole relaxation. Lithium-7 has 70% of the ^{1}H effectiveness while ^{6}Li has only 8%.[11,12] In the solid state, the diethyl ether solvate is a tetramer by X-ray evidence. Hence, if this cubic tetramer endures in solution, it should undergo isotropic reorientation. Describing its motion with a single correlation time is thus legitimate. This correlation time is obtained independently from the T_1 of C-4,

which arises from exclusive dipolar relaxation by the proton attached 110.7 pm away. The difference in relaxation rate R_1 of the neighboring ^{13}C nucleus at C-1 with the two lithium isotopes provides the carbon–lithium distance, with excellent accuracy. Use of [2,3,5,6-$^2H_4$]phenyllithium eliminates contributions to T_1 of C-1 from the *ortho* protons. It is necessary to measure T_1 values at 2.35 T to make relaxation by chemical shift anisotropy negligible. In this manner, the Li–C-1 distance is measured as 227 ± 5 pm in diethyl ether–cyclohexane (tetramer) and as 218.8 ± 2.2 pm in TMEDA–cyclohexane (dimer). Confirmation of the two oligomers comes from monitoring relaxation of H-2 by its two adjacent lithium nuclei in both the dimer and the tetramer. The observed values are 262 ± 2 pm in ether–cyclohexane, uniquely consistent with the tetrameric structure.[13]

Brown pioneered the use of lithium NMR to elucidate structures of alkyllithiums. The first lithium NMR showed ethyllithium to consist of a single hexameric species,[14] bound strongly enough for the exchange rate constant to be less than $10\,s^{-1}$.[15] In 1965, Lucken showed the quadrupolar coupling constant in methyllithium to be smaller than 16 kHz.[16] Brown translated the absence of $^6Li–^7Li$ scalar coupling in the methyllithium tetramer into a negligible metal–metal bond order.[17] A group at Dow Chemical made the first observation of $^7Li–^{13}C$ scalar coupling in methyllithium,[18] in various solvents.[19] The finding of a statistical distribution in ^{13}C-enriched methyllithium was consistent only with a cubic tetramer in which each lithium had three adjacent methyl groups, in accord with the local environment hypothesis of Seitz and Brown,[20] which had enabled Brown not only to confirm a cubic tetrameric structure in solution but also to measure an activation energy of approximately 100 kJ mol^{-1} for dissociation.[21,22] Subsequent work showed that the degree of oligomerization of alkyllithiums is solvent-dependent, *n*-butyllithium going from the tetramer in ether to the hexamer in hydrocarbon solutions,[23] and that, furthermore, the bonding changes from an ion pair to a covalent carbon–lithium bond as a function of the solvent.[24] Several alkyllithium compounds are converted by small amounts of bases from hexamers to solvated tetramers.[25]

The stylistic feature characteristic of the school of Brown is the use of scalar couplings to ^6Li as structural evidence. Lithium diisopropylamide (LDA) generates kinetic enolates from carbonyls. Its use in organic synthesis has become widespread in recent years.[26] The solution structure of lithium enolates is therefore of central importance. It determines their solubility, the effect of cosolvents, and addition to aldehydes and acid chlorides. Mixed aggregates determine the diastereo- and enantioselectivities.[27,28] X-ray structures in the solid state do not necessarily extend to solution structures, and the latter determine the chemistry. Hence NMR has unique value in ascertaining those. A pioneering study is that by Grutzner of the solution in tetrahydrofuran of the simplest enolate, namely, that from acetaldehyde. Carbon-13 relaxation rates indicate aggregation—the cluster is significantly bigger than a THF molecule. These data also indicate anisotropic reorientation, with fast (slow) rotation of the C-1–H (C-2–H) dipole. With an effective radius of 580 pm, the aggregated species is identified as the cubic $(CH_2{=}CHOLi)_4$ tetramer. It includes lithiums with a quadrupolar coupling constant of 65 kHz. The enolate rotates more rapidly about its C–O axis than the aggregate reorients in solution.[29] Such cubic tetramers are involved in highly selective formation of such products as result from alkylation of the lithium enolate of norbonenone, whose structure[30] was established at the same time as others of the same ilk.[31]

The solution structure of lithium isopropylcyclohexylamide (LICA) was characterized by Collum at Cornell, as an equimolar mixture of the *cis* and *trans* lithium-bridged dimers: $^6Li–^{15}N$ double labeling[32–34] shows N–Li–N and Li–N–Li connectivity. LDA exists also as the cyclic dimer. In THF solution, each lithium is coordinated to the two amide nitrogens and to a single THF. This conclusion results unambiguously from ^6Li detection of ^{15}N homonuclear zero quantum coherence[35]—the technique devised by Müller[36] and Bodenhausen and Ruben.[37] As hexamethylphosphoric triamide (HMPA) is added, HMPA sequentially displaces each of the two THF solvates in the dimer, as proved by both $^6Li–^{15}N$ and $^6Li–^{31}P$ coupling patterns.[38] Mixed dimers can form in the presence of other enolates; for instance, one LDA is replaced in the cyclic dimer by one pinacolate, as shown by the ^6Li coupled to a single ^{15}N.[39] In hydrocarbon (hexane) solution, LDA exists as an equilibrium mixture of at least three cyclic oligomers.[40]

It is worth making explicit the above statement about the virtue of inverse-detected ^{15}N homonuclear zero quantum spectroscopy, and reproduce here Collum's explanation. It provides a rigorous distinction of D_{2h} cyclic dimers from D_{nh} higher oligomers. In the ^{15}N zero quantum experiment, homonuclear ^{15}N two-spin coherence is prepared from the two ^{15}N spins neighboring a ^6Li atom in a $^6Li–^{15}N$ doubly labeled lithium dialkylamide cyclic oligomer. During the evolution period, the zero quantum coherence will evolve under scalar coupling only to ^6Li spins that couple to one, but not both, ^{15}N spins. For a lithium amide dimer, all ^6Li spins coupled to ^{15}N spins involved in the two-spin coherence couple to both ^{15}N spins. Consequently, the coupling pattern will be a singlet along the f_1 dimension of the 2D spectrum. In higher cyclic oligomers, there exist two ^6Li spins that couple to one, but not both, ^{15}N spins. The zero quantum coherence will develop scalar coupling to the two nonshared ^6Li spins, resulting in a 1:2:3:2:1 pattern along the f_1 dimension. As a result of a refocusing delay employed prior to detection, all oligomers will show a 1:2:1 pattern along the f_2 dimension.[41]

4 NITROGEN-14

With an isotopic abundance of 99.7% and a spin quantum number I of unity, ^{14}N suffers from a low gyromagnetic ratio and from long longitudinal relaxation times (see ***Nitrogen NMR***). Its relaxation is dominated by the quadrupolar mechanism—even in the most unfavorable situations. The tiny ammonium ion NH_4^+ relaxes exclusively by the quadrupolar mechanism, despite the zero electrostatic field gradient at nitrogen in the full T_d symmetry.[42] Even in the paramagnetic hexacyanide complexes of chromium, manganese, and iron, the ^{14}N linewidths are determined solely by quadrupolar relaxation.[43] Resonances are usually very broad, with linewidths greater than 500 Hz. Bypassing these experimental difficulties calls either for astute experiments or for a cop-out. Many have chosen the latter, resorting to ^{15}N enrichment, in particular for investigating biomolecules such as proteins

and nucleic acids. Nevertheless, there have been a few studies of the ^{14}N chemical shift in relation to structure. For instance, the extent of $d_\pi - p_\pi$ bonding has been determined in *N*-trimethylsilylaminoboranes[44] and in trimethylsilylamines.[45] Likewise, σ and π contributions from fluorine are sorted out in fluoronitrogen cations.[46] The nitrogen chemical shift gives a rather direct estimate of the atomic charge.[47] But there have been some rather smart solutions to circumvent the ^{14}N limitations. Indirect measurement of ^{14}N relaxation rates is feasible through attached protons in amino groups by measurement of the ^{1}H longitudinal rate in the rotating frame. In this manner, ^{14}N relaxation has been studied in a variety of biomolecules, such as nucleotide bases.[48,49] Another elegant experiment—also indirect and also taking advantage of the sensitivity of ^{1}H NMR—is observation of ^{14}N double quantum (DQ) coherence in isotropic solution. The usual recipe with two $\frac{1}{2}\pi$ pulses on the *S* spins (^{14}N) during the preparation sequence fails. Augmentation of this sequence by spin tickling of *I* spins ($I = \frac{1}{2}$) mixes *S*-spin DQ coherence into the *S*-spin magnetization.[50] An alternative solution is to excite and detect the *S* DQ coherence by using only the *I* magnetization and applying single hard pulses at both *I* and *S* frequencies. This is an example of heteronuclear coherence transfer taking advantage of the signal enhancement accruing from using only proton magnetization for both the initial and the final conditions. The method was tested on ammonium nitrate 8 M (!) in water acidified to pH 1 to slow down proton exchange. The DQ ^{14}N coherence is observed, with a splitting $2J = 105$ Hz. The multiplet resonance is a quintet with a vanishing central line. Using the composite particle method and replacing the two $I = 1$ spins with four $I = \frac{1}{2}$ spins and evaluating the matrix elements does indeed give the line amplitudes for the five transitions $m^I = \pm 2, \pm 1$, and 0: this last one has zero amplitude.[51] Determination of the quadrupolar coupling constant and of the asymmetry parameter for ^{15}N even approximately and for some general category such as cyano group, nitro group, or secondary amine, would seem to demand recourse to a method such as microwave spectroscopy, or NMR in a single crystal, or even pure quadrupole resonance. A smart manner of obtaining these required parameters in the liquid state is applicable to polar groups: alignment by a strong external electric field. Thus, the principal components of the quadrupolar coupling tensors were determined in the ^{14}N NMR of nitrobenzene.[52]

Nitrogen-14 NMR gives a handle onto relaxation, especially of highly symmetrical nitrogen-containing solutes having a vanishingly small electrostatic field gradient at nitrogen. The azide anion N_3^- shows a strong dependence of the T_1 values for both nitrogen types upon concentration. The ratio T_1(end)/T_1(central) is 0.25, reflecting a ratio of the corresponding χ values of 0.50.[53] The transverse relaxation rates for the azide ion nitrogens are extremely sensitive to the presence of an associating counterion. Observed values in aqueous solution are 500 Hz with Zn(II), 1000 Hz with Cd(II), 5×10^6 Hz with Cu(II), 2.5×10^6 Hz with Mn(II), and 6×10^5 Hz with Fe(III).[54] In an early piece of work, as handsome as it turned out to be useful, Pople had calculated the lineshapes for a spin $I = 1$ (^{14}N) resonance scalar-coupled with a spin $I = \frac{1}{2}$ (^{1}H) for various values of the ^{14}N relaxation rate. In this manner, one may obtain the ^{14}N relaxation rate indirectly from the proton resonance lineshape.[55] More than 30 years later, the method is still very useful. For instance, the ^{14}N linewidth in methyl-substituted ammonium ions increases from less than 0.2 Hz in NH_4^+ to 32.1, 80.7, and 96.4 Hz with the successive introduction of one, two, and three methyl groups; the activation energy for molecular reorientation remains relatively invariant at about 10.6 kJ mol^{-1}.[56]

5 OXYGEN-17

Townes and Dailey pioneered the interpretation of quadrupolar coupling constants to analyze chemical bonding. They did it on bonds involving halogens.[57] Brown made use of similar tactics to gain insight into the details of the carbonyl group, using ^{17}O NMR. A representative carbonyl has the α, β, and γ axes of the quadrupolar interaction tensor (see Section 1) oriented along the carbon–oxygen internuclear axis, perpendicular to the carbonyl plane, and in that plane, respectively. In 28 carbonyl-containing compounds, Cheng and Brown found a π population ranging from 1.366 for *p*-benzoquinone to 1.742 for sodium bicarbonate. The less polarizable σ bond has a narrower range, as expected. The formal electronic charge on oxygen is rather large, of the order of one electron.[58,59] Following the pioneering work of Kintzinger,[60,61] numerous authors have obtained chemical shifts and quadrupolar coupling constants in organic molecules.[62] Likewise, after Lauterwein gave a similar impulse for applications to biomolecules,[63,64] these have thrived, and have presently reached studies of hemoglobin and myoglobin.[65] Also, ^{17}O NMR is a nice biochemical labeling technique.[66] Organometallic applications have developed in parallel, to the structures of species such as metal carbonyls[67] and oxo–peroxo complexes,[68] and to mechanistic studies.[69] With the new techniques of dynamic angle spinning and double rotation,[70] ^{17}O NMR has penetrated into the solid state, and is helping to elucidate the structure of silicates.[71]

To end this section, we single out studies of molecular microdynamics based on ^{17}O relaxation to a large extent. They include, of course, water, for which the isotropic motional model was shown to be an adequate description in the picosecond timescale.[72] The motion of tetrahedral oxo anions is a natural for the technique,[73] and correlation times in heavy water at 28 °C are 0.80 ps for perchlorate, 2.8 ps for sulfate, and 14–16 ps for phosphate, reduced to 0.73 ps (perchlorate) and 1.1 ps (sulfate) in methanol-d_4.[74]

6 THE SODIUM ANION

The preamble to this story took place in London, at the Royal Institution in 1808, when Humphry Davy, after he had isolated sodium and potassium, heated the latter in ammonia and obtained potassamide.[75,76] Weyl proceeded to study the blue solutions formed when alkali metals dissolve in dry ammonia.[77] Mendeleev pointed out the quantitative resemblance between the alkali metals and the halogens.[78] Thus, alkali metal anions ought to be capable of existence. In the early 1960s, Dye used optical spectra in support of the postulated existence of alkali metal anions when the alkali metals are dissolved in primary amines and in some polyethers.[79]

In 1974, Ceraso and Dye obtained a ^{23}Na NMR spectrum with distinct, well-separated resonances for the cryptated

sodium cation and the sodium anion, after they had co-dissolved metallic sodium and the [2.2.2]cryptand in an organic solvent, ethylamine. The signal of the sodium anion is found 63 ppm to low frequency of the aqueous sodium chloride reference, and is solvent-independent when measured in THF, methylamine, and ethylamine.[80,81] Clearly, Dye had been following very carefully the new developments in polyether and cryptate chemistry, and realized the versatility of their utilizations.

The NMR spectrum published in 1974 truly demonstrated the structure of the sodium anion, Na^-. The paramagnetic part of the shielding constant of the sodium nucleus in the sodium cation arises from the introduction of orbital angular momentum by interaction of the filled outer p shell with electron pairs from neighboring solvent donor molecules.[82] The sodium anion, with a more diffuse electronic distribution, and with only a weaker interaction with external electronic pairs, should have much less of a paramagnetic shift. The two spin-paired electrons in the 3s orbital shield the 2p electrons from the influence of the solvent. Indeed, its chemical shift, with reference to external saturated aqueous NaCl, is invariant at -57 to -63 ppm[83,84] and the same within experimental error as that of -63.8 ppm calculated for the isolated anion in a gas.[85] Thus, the system studied consisted of Na^+C222.Na^-, where C222 denotes the cryptand.

Edwards's group in Cambridge then showed that it was not mandatory to hide away the sodium cation in a crown ether or cryptand in order to dismutate sodium metal into the +1 and -1 oxidation states. When they dissolved sodium in anhydrous hexamethylphosphoric triamide (HMPA), they recorded the ^{23}Na spectrum of the naked anion at -62 ppm with a linewidth of 10 Hz.[86] They were unable to observe any resonance from the sodium cation, presumably because of its extreme width in the paramagnetic (solvated electrons) solution. The Cambridge group proceeded to make a similar series of observations in 12-crown-4[87] and in various amide solutions, *N*,*N*-diethylacetamide, *N*,*N*-di-*n*-propylacetamide, *N*,*N*-dimethylpropanamide, and tetramethylurea: the chemical shift of the sodide ion is both solvent- and temperature-independent, at -62.3 ± 0.3 ppm. The linewidth is very narrow, 8–13 Hz from 233 to 200 K, in contrast to Na^+, for which the linewidth trebles in going from 279 to 250 K, in diethylacetamide solution.[88] Again, Edwards and co-workers were unable to detect the signals of the solvated cations. Direct measurements of the longitudinal relaxation rate for Na^- in solutions containing an alkali countercation in 12-crown-4 showed independence with respect to the nature of the alkali counterion. Relaxation occurs by a predominant, although rather inefficient, quadrupolar relaxation mechanism via the reorientational–vibrational motion of the surrounding 12-crown-4 molecules in the liquid. Furthermore, solvation of the sodium anion by the crown ether is very weak: there is neither a preferential orientation of the crown ether nor a clearly identifiable first solvation shell around the sodide anion. An RMS value of 0.03 MHz is deduced for the quadrupolar coupling constant χ in 12-crown-4 solutions: Na^- is a gas-like entity in solution.[89,90]

The ^{23}Na NMR of both Na^+C222 and Na^- in polycrystalline Na^+C222.Na^- was monitored from the $(+\frac{1}{2}, -\frac{1}{2})$ transition, as a function of the Larmor frequency (at 4.7, 8.5, and 11.7 T): second-order perturbation theory gives the shift of this central transition with frequency as

$$\nu - \nu_L = -\chi^2[I(I+1) - \tfrac{3}{4}](1 + \tfrac{1}{3}\eta^2)/30\nu_L \qquad (3)$$

where ν_L is the Larmor frequency and η the asymmetry parameter. For the cryptated sodium cation, the authors determined χ = 1.2 MHz and an isotropic chemical shift of -6.5 ppm, essentially the same as that for Na^+C222 in solution in various solvents. The quadrupolar contribution to the static linewidth of the complexed cation in Na^+C222.Na^- is 320 Hz whereas the observed linewidth is 3700 ± 300 Hz—a difference ascribable to dipolar couplings with the protons in the methylene groups of the [2.2.2] cryptand. Conversely, the sodium anion has a quadrupolar coupling constant χ of 0.26 MHz and a calculated (van Vleck expression) dipolar broadening from $^1H\cdots Na^-$ interactions of 2860 Hz in excellent agreement with the observed linewidth of 2800 Hz.[91] More recently, Dye has provided a more accurate determination of the quadrupolar coupling constant for the sodium anion from a single crystal ^{23}Na NMR study of the same Na^+C222.Na^- system. Values for χ of 1.268 and 0.1763 MHz were determined for Na^+ and Na^-, respectively. Isotropic chemical shifts of -5.5 and -61.8 ppm were obtained for the cation and the anion, respectively.[92] At the time of writing (December 1993), Dye is studying mixed systems such as $Cs^+(18C6)_2Na^-$, in which the ^{23}Na chemical shift of about -61 ppm is diagnostic of the sodium anion.[93]

7 COORDINATION OF ALUMINUM-27

Many applications reflect the natural state of aluminum, which constitutes 9% of the Earth's crust. They concern aluminates and aluminosilicates. In the latter category, it is not so much layered clays (phyllosilicates), but rather microporous aluminosilicates, zeolites, that have been extensively studied as industrially important catalysts. Especially since the discovery of the Mobil process for conversion of methanol into gasoline on the HZSM-5 zeolites, there has been a flurry of high-resolution ^{27}Al NMR studies of these solids. Nevertheless, the field of ^{27}Al NMR is wider. At the time when Delpuech wrote his useful review, most data pertained to tetra- or hexacoordinate compounds.[94] A fuller picture can now be given. Benn pointed out that the chemical shift characterized organoaluminum compounds in classes, depending on coordination of the metal. Tricoordinate aluminum has a chemical shift of about 250 ppm, tetracoordinate aluminum about 150 ppm, pentacoordinate aluminum about 120 ppm, and hexacoordinate aluminum 0 ppm with respect to an external reference of $Al(acac)_3$.[95] A word is in order here about the ^{27}Al reference. Usually, the hexaaquoaluminum(III) cation, $[Al(H_2O)_6]^{3+}$, is chosen.[96] It is sensitive to second-sphere effects.[97] Another candidate, with the merit of better invariance to solvation and concentration, is the AlH_4^- anion, with δ = 101 ppm with respect to the aluminum(III) hydrate.[98] A caveat on the use of ^{27}Al NMR for characterization of organometallics was issued.[99] Distinction between tricoordinate and tetracoordinate aluminum in alkylaluminum phenoxides was made.[100] In the gauge-independent decomposition,[101] the diamagnetic part of the shielding constant is invariant within a few ppm. Variations arise from the paramagnetic contribution, itself dominated by

the HOMO–LUMO gap. Low-valent aluminum compounds have been made in recent years. The chemical shift of aluminum(I) compounds has been studied experimentally and theoretically.[102] The latter are SCF calculations[103–105] using the gauge-including atomic orbital (GIAO) method.[106] The surprise is that, rather than settling into a niche of their own next to the others for aluminum(III) compounds, aluminum(I) compounds are anarchists, roaming through the whole range of ^{27}Al chemical shifts. The calculated values include one of the most shielded (AlCp, −170 ppm) and one of the most deshielded (AlSi(t-Bu)$_3$, 854 ppm). The actual, quite different, chemical shifts, are −111 and 64.5 ppm, respectively. They point to the existence of AlCp as the tetramer Al_4Cp_4 and to the importance of solvation effects in determining the chemical shift of AlSi(t-Bu)$_3$. The calculations confirm the correlation between the calculated shielding constants and the HOMO–LUMO energy gap.

A seminal finding for solid state studies of aluminosilicates has been the sensitivity of the ^{27}Al chemical shift to the composition of the second coordination sphere. Thus, studies of aluminosilicate solutions showing that the chemical shift for Si–O–Al units depended on the structural unit (Q^0, Q^1, Q^2, or Q^3) with incremental changes[107] launched this very active field. Aluminum-27 NMR can serve to characterize synthetic and natural zeolites.[108] Owing to the strong industrial interest already referred to, increased technical sophistication was brought to bear on structural studies of zeolites. Klinowski in Cambridge resorted to quadrupolar nutation ^{27}Al NMR to study isomorphous substitutions in the zeolite Y framework.[109] Already in 1988, one could start reading reviews of MAS studies in zeolites.[110] The advantages of very high fields $\boldsymbol{B}_0$ and ultrafast spinning became clear,[111] and were applied to samples such as USY zeolites[112] or dealuminate Y zeolite.[113] Another big experimental breakthrough was the development of double rotation and of dynamic angle spinning to average out both the first- and second-order anisotropic broadenings in solids. In this manner, it has been possible to characterize both tetrahedral environments and heavily distorted pentacoordinate aluminum in zeolites of the $AlPO_4$-21 and $AlPO_4$-25 types.[114] The ^{27}Al longitudinal relaxation was related to the organic molecules and exchangeable cations present within the channels and supercages of the zeolites.[115] A fine multinuclear study paid attention to satellite transitions,[116] which have been receiving increased attention.[117] The analytical aspects were not neglected, and quantitation of aluminum in zeolites was perfected.[118] A study was made of β-zeolites in relation to their catalytic prowess.[119] Of course, the acidic HZSM-5 received star treatment.[120] Aluminophosphate zeolites[121] such as VPI-5[122] and $AlPO_4$-11[123,124] were also studied. Aluminum-27 NMR was the test used to distinguish between various models of ionic solvation.[125] The quadrupolar coupling constant was determined for aqueous Al(III) in solutions of perchloric acid.[126] Other aluminosilicates got the studies that they deserved. The mechanism of kaolinite dehydroxylation was scrutinized,[127] and likewise its thermal transformation[128] and activated layered aluminosilicates were examined.[129] Adsorption of chlorine on γ-alumina was monitored.[130] Cross polarization focused on surface aluminum atoms on alumina.[131] Iron-bearing montmorillonites—outstanding catalysts for quite a few organic reactions—were examined.[132] A related study examined Friedel–Crafts catalysts formed by adsorption of divalent fluorides on the K-10 montmorillonite, a partly amorphized 2:1 clay used as a cracking catalyst in the petrochemical industry.[133] The structure of pumice was examined.[134] In the bio-inorganic realm, aluminum porphyrins were studied.[135] Dimerization of tricoordinate aluminum(III) Lewis acids such as trimethylaluminum deserved some attention.[136] Preferential solvation of aluminum(III) perchlorate in binary mixtures of urea and DMF was studied.[137]

8 MICROENVIRONMENT OF THE CHLORIDE ION

Chlorine-35 NMR was given an early and outstanding review, which continues to be extremely valuable.[138] We shall focus here on a few more recent contributions that in various guises examine the immediate environment of the chloride anion, probed by ^{35}Cl NMR. An interesting question is that of the proximity of the countercation, in the presence of a complexant that encapsulates this cation. Thus, the ^{35}Cl linewidths were determined for the KCl–18-crown-6 complex in various solvents. The chloride anion exists in acetonitrile in a completely dissociated state, approximating the proverbial and elusive 'naked anion'. The ^{35}Cl linewidth due to the Cl-ion-paired with the crown ether is 90 ± 20 Hz in aqueous solutions. The contact ion pair is that in which Cl^- and K^+ are nearest neighbors. It would have a significantly greater linewidth, of about 550 Hz. Thus, because the crown ether grabs the potassium cation with a pseudoequatorial arrangement of its coordinated oxygens, while the apical positions are occupied by water molecules, the chloride anion is unable to coordinate the potassium cation. What is observed instead is a loose, solvent-separated ion pair.[139] Another interesting question is competition between two different counterions. For instance, lithium chloride and lithium perchlorate were studied in acetone solution in the presence of various phosphates. The ^{35}Cl linewidth is monitored as a function of concentration. It shoots up in the presence of triphenyl phosphate $O{=}P(OC_6H_5)_3$. The observation is consistent only with dissymmetric penetration of the perchlorate anion coordination shell by the Li–O–P fragment, with this particular phosphate only.[140] Conceptually similar experiments can be carried out in yet more exotic environments. Sodalites are aluminosilicates with a nanoporous structure that makes them of interest in quantum electronics, nonlinear optics, information storage and processing, and so on. A recent study focused on sodalite semiconductors. The chloride anions are distributed within the cavities of $Na_{8-n-p}Ag_nX_{2-p}$ lattices. Narrow ^{35}Cl resonances are, nevertheless, observed. They stem from the presence of highly symmetrical species. A sharp peak at −122 ppm (0.1 M NaCl external reference) is ascribed to Na_4Cl tetrahedra encapsulated within the sodalite cavities. A substantially low-frequency-shifted peak at −310 ppm in the fully Ag^+-exchanged system corresponds likewise to encapsulated Ag_4Cl clusters. These symmetrical environments around the halide anion give rise to narrow resonances in the ^{35}Cl MAS spectra.[141]

Hydrophobic effects leading to asymmetric solvation and/or aggregation have been reported by many authors. Let us start with water–dimethyl sulfoxide binary mixtures. The relaxation rates at intermediate solvent compositions are higher than those in either pure solvent by more than one order of magnitude. This pronounced deviation from ideality contrasts with that of

the chemical shift: the ^{35}Cl chemical shift varies linearly with composition.[142,143] Useful applications from such observations need not resort to sophisticated analyses. Even at an empirical level, they can be turned into extremely useful consequences. A case at hand is the study by the Martins in Nantes of chloride ion reactivity. They examined the variation in the transverse relaxation of ^{35}Cl as a function of temperature for 13 chloride salts in acetonitrile solutions. When two ammonium species, such as tetrabutyl- and benzyltributylammonium chlorides, are mixed at a fixed concentration, the ^{35}Cl linewidths do not vary linearly between the values characteristic of each species. A broadening occurs, and the maximum linewidth is reached at equimolar concentrations of the two salts. From its magnitude, both types of ammonium cations must coexist in the chloride ion coordination shell. Likewise, the ^{35}Cl linewidth is very sensitive to the presence of phenols in the solution, and depends in a simple way on the pK_a of the phenol added. This behavior makes it feasible to define a linewidth $\Delta\nu^0_{\frac{1}{2}}$ characteristic of the chloride anion in various organic salts. This parameter, with an observed range of 45–450 Hz, appears to measure the reactivity of the chloride anion as displayed in reactions under phase transfer catalysis, or in the catalytic phosgenation of phenol.[144]

Paradoxically, we have kept for the end of this section the apparently much simpler behavior of a chloride salt in aqueous solution. Consider magnesium chloride. The limiting behavior at infinite dilution has been described with a so-called dynamically oriented solvation model, specifying both the structure and the internal dynamics of the hydration spheres of Mg^{2+} and Cl^-. The ^{35}Cl relaxation rate gives a value of 0.43 for water–water correlation effects, i.e., the influence of water from outer hydration layers on the hydration water molecules.[145] Turning to chloride ion relaxation for $MgCl_2$ at finite concentrations, this shows contributions from ion–ion interaction, ion-hydration water, and in-bulk water. At low salt concentrations, below 1 M, the main contribution (75%) arises from bulk water. With increasing $MgCl_2$ concentration, the contribution from the magnesium hydration water molecules becomes more important, and at 5.5 M is responsible in turn for about 75% of the total ion–water contribution. This is very likely due to encounter between the chloride anions and the hexaaquomagnesium(II) cations, with temporary distortion of the hydration shell during the encounter.[146]

9 HOW DOES COBALT-59 RELAX IN OCTAHEDRAL COMPLEXES?

Cobalt-59 NMR has the attraction of 100% isotopic abundance, high sensitivity, and an enormous range of chemical shifts. In hexacoordinate octahedral cobalt(III) complexes, the chemical shifts are correlated to electronic excitation energies, owing to magnetic-field-induced mixing of the $^1T_{1g}$ excited state with the $^1A_{1g}$ ground state, leading to a paramagnetic contribution to the ^{59}Co shielding. A quadrupolar mechanism appears to serve as the dominant mode of relaxation in cobalt(III) complexes devoid of full octahedral symmetry. Indeed, linewidths become very large in the presence of permanent electrostatic field gradients at cobalt.[147] The quadrupolar coupling constant has a value of 2.7 MHz in $[Co(NH_3)_6]^{3+}$, is multiplied about 20-fold on replacement of one ammonia by one water ligand (inner sphere perturbation),[148] but increases only slightly to 3.5 MHz in the $[Co(NH_3)_6]^{3+}$–ClO_4^- ion pair (outer sphere perturbation).[149]

The question remains of the origin of the linewidth in fully symmetric octahedral cobalt(III) complexes. Spin–rotation relaxation has been invoked. For hexamminecobalt(III), $[Co(NH_3)_6]^{3+}$, the longitudinal relaxation rate extrapolated to infinite dilution shows a temperature invariance suggestive of operation of a spin–rotation mechanism with the opposite temperature dependence to that of quadrupolar relaxation. The results were consistent with a quadrupolar coupling constant of about 3 MHz and a spin–rotation coupling constant of 72 kHz.[149] Scalar relaxation of the second kind[150] is another potential contributor. Take the same example of hexamminecobalt: the cobalt nucleus is scalar-coupled to the ^{14}N nucleus, which relaxes efficiently by a nucleus–electric quadrupole mechanism. Such an interaction makes the transverse ^{59}Co relaxation rate proportional to the product of the square of the interaction energy J and the correlation time τ_N descriptive of reorientation of the nitrogen spin. Thus, differences between T_1 and T_2 in some CoN_6 complexes have been ascribed to unresolved scalar couplings with nitrogen, of the order of magnitude of 50 Hz.[151,152] And, of course, there is the problem of explaining the intervention of quadrupolar relaxation in a complex with strict O_h symmetry, in which the electrostatic field gradient at the central nucleus has to vanish. The origin of the fluctuating EFG must be found either in instantaneous distortions with respect to the ideal O_h geometry or in deviations from this perfect symmetry due, for instance, to the proximity of a counterion. When, indeed, a charged anion was placed in the outer sphere of $[Co(en)_3]^{3+}$ and $[Co(pn)_3]^{3+}$ complexes, its contribution was reported as insignificant.[151] The remaining explanation—that of excitation of the vibrational modes of the octahedron[153]—was scrutinized in the case of tris(tropolonato)cobalt(III), and appears as a likely candidate.[152]

Potassium hexacyanocobaltate(III) $K_3Co(CN)_6$ was examined by monitoring the relaxation rates of all the nuclei in the anion. Although the ^{59}Co relaxation rate decreases with increasing temperature, the slope is half that for ^{13}C. Again, this uncoupling of ^{59}Co relaxation from rotational reorientation is suggestive of modulation of the EFG by solvent-assisted molecular vibrations.[154]

In order to proceed further the ^{59}Co chemical shift and its relationship to the linewidth enters as another piece of evidence. The context is Deverell's electronic distortion theory.[155,156] The valence atomic orbitals distort upon each collision with a solvent molecule. A paramagnetic contribution to shielding σ_p stems from injection of electrons into atomic orbitals with the appropriate symmetry. This also sets up a fluctuating electrostatic field gradient at the nucleus monitored. The relaxation rate R_1 is predicted to be proportional to the product of the reorientational correlation time with the square of a term $\sigma_p\ \Delta E$, where ΔE is the average electron excitation energy. Thus, the square root of the linewidth is predicted to be proportional to the chemical shift. After normalization to unit viscosity, the ^{23}Na linewidths for a series of sodium cation solvates[157] and for sodium cryptates[158] obey this prediction with impressive discipline. In like manner, three octahedral cobalt(III) complexes were studied in a number of solvents: $Co(en)_3Cl_3$ and *cis*- and *trans*-$Co(en)_2(N_3)_2NO_3$. Attempts to correlate linewidths and viscosity-normalized linewidths with

the solvent electric dipole moment failed to provide convincing support for the Hertz electrostatic model.[159–162] The square root of the viscosity-normalized linewidths, after correction for scalar relaxation of the second kind [a 45 Hz contribution to the linewidth for $Co(en)_3Cl_3$], produces excellent linear correlations with the ^{59}Co chemical shift.[163] A related study examined cobalt(III) porphyrin complexes—cobalt(III) is an excellent isomorphous substituent for iron(III), and ^{59}Co NMR is more amenable than ^{57}Fe NMR. The contribution of scalar relaxation of the second kind amounted to about 5% of the excess linewidth only. Arbitrary subtraction from the linewidth of a 100 Hz increment led to a quite decent linear relationship between the square root of the linewidth and the chemical shift.[164] This makes for an incisive tool, as an example will show. Two types of cobalt(III) tetraphenylporphyrin complexes are studied: unhindered or hindered, the latter bearing *ortho*-chloro or methyl substituents sterically interfering with the *meso* phenyl rings. A corrected linewidth F is defined by subtraction of a 81 Hz contribution for relaxation by scalar coupling, and by normalization to unit viscosity. Then $F^{1/2}$ correlates handsomely with the chemical shift only if the electrostatic field gradient q changes sign for the hindered complexes compared with the unhindered ones. This is a unique piece of information. It means that the electron density in the hindered complexes migrates from the axial d orbitals d_{xz}, d_{yz}, and d_{z^2} to the equatorial d orbitals $d_{x^2-y^2}$ and d_{xy}. This amounts, for the molecule as a whole, to a build-up of σ electron density at the expense of π electron density, due to steric inhibition of resonance.[165] Once again, quadrupolar NMR shows its mettle in matters of electronic distribution!

10 A NOTE ON THE STERNHEIMER ANTISHIELDING FACTOR

This is a magnifying factor that increases the effective interaction between an electrostatic field gradient q at the nucleus, and the quadrupole moment of the nucleus Q.[166–168] The reason is that the mere presence of an electrostatic quadrupole (the nucleus) distorts (slightly) the spherical electronic distribution around it, consisting of the core electrons. There is a radial part in which electrons close to the positive (negative) poles of the quadrupole are pulled in (out). There is an angular part in which s electrons acquire a d-orbital-like polarization: these distortions are conveniently referred to as, for example, 2s $\rightarrow$ d excitations. Shielding corresponds to values of the Sternheimer factor γ between 0 and 1, and antishielding corresponds to negative values of γ. Access to γ is, in general, by calculation. For instance, while the sodium cation has a Sternheimer γ of -5.073 computed at the Hartree–Fock level, the sodium anion has values of -14.98 and -15.69, depending on the method used for incorporating electron correlation.[169]

The problem is more severe yet: which value to choose from those available in the literature? For instance, in the series of halide anions, the spread between the lowest and the highest value of γ is a factor of about 2.[170–172]

11 CONCLUSIONS

In closing, this reviewer begs to be allowed the privilege of editorializing—of expressing a few sincere opinions, and submitting a few concluding observations. At the risk of belaboring the obvious, we cannot help stating that quadrupolar nuclei, at the time of writing, remain outside the mainstream of NMR studies. There are objective reasons: experimental difficulty first and foremost. For instance, ^{57}Fe is a rather discouraging nucleus, in spite of the importance of iron as an element. However, now that indirect methods of detection—we did mention earlier the example of ^{14}N—are becoming routine, we may hope for more and more forays into the quadrupolar jungle.

It became clear while preparing this survey that there are shockingly few studies of molecular electronic distributions from NMR of quadrupolar nuclei. The weak explanation is the need for determination of the full shielding tensor and of the full quadrupolar interaction tensor from high-resolution solid state studies. But here again technical solutions exist. One must conclude that the main problem is the sociological (or psychological?) issue of the necessary collaboration between theoreticians and experimentalists.

Relaxation studies are another underdeveloped area. Scientists shy away from it for a basic reason: they are being confronted with only one observable, namely the linewidth or the transverse relaxation rate. And this single observable is determined by the product of at least two parameters: the correlation time and the quadrupolar coupling constant. The obvious solution is to get at the correlation time (or the spectral density) with other nuclei—which a number of people have done, to splendid avail unfailingly.

Quite a few very handsome physicochemical studies have addressed themselves to ionic relaxation, in order to probe solutions of electrolytes. In that area, electrostatic models have been perhaps unduly popular. They have served as a red rag, to lure physical chemists into their intricacies, their (too) large number of (in fact) adjustable parameters. The relevance of electrostatic models to the systems studied from hindsight does not strike one as self-evident.

My last point is that the science-historical law asserting that the real advances to significant progress are contributed by outsiders to a field is once again vindicated. Brilliant work by Jean-Marie Lehn (^2H, ^{14}N), Jim Dye (^{23}Na), and Ted Brown ($^{6,7}Li$, ^{17}O) has thus been at the forefront of both chemical science and NMR science.

12 RELATED ARTICLES

Liquid Crystals: General Considerations; Nitrogen NMR.

13 REFERENCES

1. C. Brevard and J.-P. Kintzinger, in *NMR and the Periodic Table*, ed. R. K. Harris and B. E. Mann, Academic Press, New York, 1978, Chap. 5
2. H. Huber, *J. Chem. Phys.*, 1985, **83**, 4591.
3. D. Nietlispach, V. I. Bakhmutov, and H. Berke, *J. Am. Chem. Soc.*, 1993, **115**, 9191.
4. C. Brevard, J.-P. Kintzinger, and J.-M. Lehn, *Tetrahedron*, 1972, **28**, 2447.
5. Francis Bacon, *Of Dispatch*.

6. P. Laszlo, in *Progress in Nuclear Magnetic Resonance Spectroscopy*, ed. J. W. Emsley, J. Feeney, and L. H. Sutcliffe, Pergamon Press, Oxford, 1979, Vol. 13, p. 257.
7. C. Brevard and J.-M. Lehn, *J. Am. Chem. Soc.*, 1970, **92**, 4987.
8. H. H. Mantsch, H. Saitô, and I. C. P. Smith, in *Progress in Nuclear Magnetic Resonance Spectroscopy*, ed. J. W. Emsley, J. Feeney, and L. H. Sutcliffe, Pergamon Press, Oxford, 1977, Vol. 11, p. 211.
9. M. J. Duer and J. Rocha, *J. Magn. Reson.*, 1992, **98**, 524.
10. H. Günther, D. Moskau, P. Bast, and D. Schmalz, *Angew. Chem., Int. Ed. Engl.*, 1987, **26**, 1212.
11. L. M. Jackman and J. C. Trewella, *J. Am. Chem. Soc.*, 1976, **98**, 5712.
12. L. M. Jackman and J. C. Trewella, *J. Am. Chem. Soc.*, 1979, **101**, 6428.
13. L. M. Jackman and L. M. Scarmoutzos, *J. Am. Chem. Soc.*, 1984, **106**, 4627.
14. T. L. Brown, D. W. Dickerhoof, and D. A. Bafus, *J. Am. Chem. Soc.*, 1962, **84**, 1371.
15. T. L. Brown and J. A. Ladd, *J. Organomet. Chem.*, 1964, **2**, 373.
16. E. A. C. Lucken, *J. Organomet. Chem.*, 1965, **4**, 252.
17. T. L. Brown, L. M. Seitz, and B. Y. Kimura, *J. Am. Chem. Soc.*, 1968, **90**, 3245.
18. L. D. McKeever, R. Waack, M. A. Doran, and E. B. Baker, *J. Am. Chem. Soc.*, 1968, **90**, 3244.
19. L. D. McKeever, R. Waack, M. A. Doran, and E. B. Baker, *J. Am. Chem. Soc.*, 1969, **91**, 1057.
20. L. M. Seitz and T. L. Brown, *J. Am. Chem. Soc.*, 1966, **88**, 2174.
21. T. L. Brown, *Acc. Chem. Res.*, 1968, **1**, 23.
22. T. L. Brown, *Pure Appl. Chem.*, 1970, **23**, 447.
23. L. D. McKeever and R. Waack, *J. Chem. Soc., Chem. Commun.*, 1969, 750.
24. R. Waack, L. D. McKeever, and M. A. Doran, *J. Chem. Soc., Chem. Commun.*, 1969, 117.
25. H. L. Lewis and T. L. Brown, *J. Am. Chem. Soc.*, 1970, **92**, 4664.
26. K. Smith, *Chem. Brit.*, 1982, **13**, 29.
27. R. Amstutz, W. B. Schweizer, D. Seebach, and J. D. Dunitz, *Helv. Chim. Acta*, 1981, **64**, 2617.
28. D. Seebach, R. Amstutz, and J. D. Dunitz, *Helv. Chim. Acta*, 1981, **64**, 2622.
29. J. Q. Wen and J. B. Grutzner, *J. Org. Chem.*, 1986, **51**, 4220.
30. J. H. Horner, M. Vera, and J. B. Grutzner, *J. Org. Chem.*, 1986, **51**, 4212.
31. D. Hoell, J. Lex, and K. Müllen, *J. Am. Chem. Soc.*, 1986, **108**, 5983.
32. L. M. Jackman and L. M. Scarmoutzos, *J. Am. Chem. Soc.*, 1987, **109**, 5348.
33. L. M. Jackman, L. M. Scarmoutzos, and W. Porter, *J. Am. Chem. Soc.*, 1987, **109**, 6524.
34. N. Kallman and D. B. Collum, *J. Am. Chem. Soc.*, 1987, **109**, 7466.
35. J. H. Gilchrist and D. B. Collum, *J. Am. Chem. Soc.*, 1992, **114**, 794.
36. L. Müller, *J. Am. Chem. Soc.*, 1979, **101**, 4481.
37. G. Bodenhausen and D. J. Ruben, *Chem. Phys. Lett.*, 1980, **69**, 185.
38. F. E. Romesberg, J. H. Gilchrist, A. T. Harrison, D. J. Fuller, and D. B. Collum, *J. Am. Chem. Soc.*, 1991, **113**, 5751.
39. A. S. Galiano-Roth, Y.-J. Kim, J. H. Gilchrist, A. T. Harrison, D. J. Fuller, and D. B. Collum, *J. Am. Chem. Soc.*, 1991, **113**, 5053.
40. Y.-J. Kim, M. P. Bernstein, A. S. G. Roth, F. E. Romesberg, P. G. Williard, D. J. Fuller, A. T. Harrison, and D. B. Collum, *J. Org. Chem.*, 1991, **56**, 4435.
41. D. B. Collum, *Acc. Chem. Res.*, 1993, **26**, 227.
42. J. Mason, *Chem. Rev.*, 1981, **81**, 205.
43. M. Shporer, G. Ron, A. Loewenstein, and G. Navon, *Inorg. Chem.*, 1965, **4**, 358.
44. H. Nöth, W. Tinhof, and B. Wrackmeyer, *Chem. Ber.*, 1974, **107**, 518.
45. K. Barlos, G. Hübler, H. Nöth, P. Wanninger, N. Wiberg, and B. Wrackmeyer, *J. Magn. Reson.*, 1978, **31**, 363.
46. J. Mason and K. O. Christe, *Inorg. Chem.*, 1983, **22**, 1849.
47. M. Comeau, M.-T. Béraldin, E. C. Vauthier, and S. Fliszar, *Can. J. Chem.*, 1985, **63**, 3226.
48. M. E. Moseley and P. Stilbs, *Can. J. Chem.*, 1978, **56**, 1302.
49. M. E. Moseley and P. Stilbs, *Can. J. Chem.*, 1979, **57**, 1075.
50. V. W. Miner and J. H. Prestegard, *J. Am. Chem. Soc.*, 1981, **103**, 5979.
51. Y. S. Yen and D. P. Weitekamp, *J. Magn. Reson.*, 1982, **47**, 476.
52. T. M. Plantenga, H. Bulsink, F. J. deKanter, and C. Maclean, *Chem. Phys.*, 1982, **65**, 71.
53. A. Loewenstein, *J. Magn. Reson.*, 1982, **49**, 332.
54. T. Raj and R. G. Bryant, *J. Magn. Reson.*, 1979, **34**, 537.
55. J. Pople, *Mol. Phys.*, 1958, **1**, 168.
56. J. D. Halliday, P. E. Bindner, and S. Padamshi, *Can. J. Chem.*, 1985, **63**, 2975.
57. C. H. Townes and B. P. Dailey, *J. Chem. Phys.*, 1949, **17**, 782.
58. T. L. Brown and C. P. Cheng, *Symp. Faraday Soc.*, 1978, **13**, 75.
59. C. P. Cheng and T. L. Brown, *J. Am. Chem. Soc.*, 1980, **102**, 6418.
60. C. Delseth and J.-P. Kintzinger, *Helv. Chim. Acta*, 1982, **65**, 2273.
61. J.-P. Kintzinger, in *NMR of Newly Accessible Nuclei*, ed. P. Laszlo, Academic Press, New York, 1983, Vol. 2, Chap. 4
62. D. W. Boykin, ed., *^{17}O NMR Spectroscopy in Organic Chemistry*, CRC Press, Boca Raton, FL, 1991.
63. I. P. Gerothanassis, R. Hunston, and J. Lauterwein, *Helv. Chim. Acta*, 1982, **65**, 1764.
64. I. P. Gerothanassis, R. Hunston, and J. Lauterwein, *Helv. Chim. Acta*, 1982, **65**, 1774.
65. E. Oldfield, H. C. Lee, C. Coretsopoulos, F. Adebodun, K. D. Park, S. Yang, J. Chung, and B. Phillips, *J. Am. Chem. Soc.*, 1991, **113**, 8680.
66. A. Marker and A. B. Roy, *Biochim. Biophys. Acta*, 1983, **742**, 446.
67. R. T. C. Brownlee and B. P. Shehan, *J. Magn. Reson.*, 1986, **66**, 503.
68. M. Postel, C. Brevard, H. Arzoumanian, and J. G. Riess, *J. Am. Chem. Soc.*, 1983, **105**, 4922.
69. S. Aygen, H. Hanssum, and R. van Eldik, *Inorg. Chem.*, 1985, **24**, 2853.
70. E. W. Wooten, K. T. Mueller, and A. Pines, *Acc. Chem. Res.*, 1992, **25**, 209.
71. K. T. Mueller, Y. Wu, B. F. Chmelka, J. Stebbins, and A. Pines, *J. Am. Chem. Soc.*, 1991, **113**, 32.
72. J. R. C. van der Maarel, D. Lankhorst, J. de Bleijser, and J. C. Leyte, *Chem. Phys. Lett.*, 1985, **122**, 541.

73. Y. Masuda, M. Sano, and H. Yamatera, *J. Chem. Soc., Faraday Trans. 1*, 1985, **81**, 127.
74. Y. Masuda, M. Sano, and H. Yamatera, *J. Phys. Chem.*, 1985, **89**, 3086.
75. T. E. Thorpe, *Humphry Davy: Poet and Philosopher*, Cassell, London, 1896, p. 129.
76. Sir H. Hartley, *Humphry Davy*, EP Publishing, East Ardsley, 1972, Chap. 6
77. W. Weyl, *Ann. Phys. (Leipzig)*, 1864, **121**, 601.
78. D. I. Mendeleev, *The Principles of Chemistry*, 3rd edn., Longman, London, 1905.
79. R. R. Dewald and J. L. Dye, *J. Phys. Chem.*, 1964, **68**, 1321.
80. J. M. Ceraso and J. L. Dye, *J. Chem. Phys.*, 1974, **61**, 1585.
81. J. L. Dye, C. W. Andrews, and J. M. Ceraso, *J. Phys. Chem.*, 1975, **79**, 3076.
82. P. Laszlo, *Angew. Chem., Int. Ed. Engl.*, 1978, **17**, 254.
83. J. L. Dye and M. G. DeBacker, *Annu. Rev. Phys. Chem.*, 1987, **38**, 271.
84. A. Ellaboudy, M. L. Tinkham, B. VanEck, J. L. Dye, and P. B. Smith, *J. Phys. Chem.*, 1984, **88**, 3852.
85. G. Malli and S. Fraga, *Theor. Chim. Acta*, 1966, **5**, 275.
86. P. P. Edwards, S. C. Guy, D. M. Holton, and W. McFarlane, *J. Chem. Soc., Chem. Commun.*, 1981, 1185.
87. D. M. Holton, P. P. Edwards, D. C. Johnson, C. J. Page, W. McFarlane, and B. Wood, *J. Chem. Soc., Chem. Commun.*, 1984, 740.
88. D. M. Holton, P. P. Edwards, D. C. Johnson, C. J. Page, W. McFarlane, and B. Wood, *J. Am. Chem. Soc.*, 1985, **107**, 6499.
89. D. M. Holton, A. Ellaboudy, N. C. Pyper, and P. P. Edwards, *J. Chem. Phys.*, 1986, **84**, 1089.
90. N. C. Pyper and P. P. Edwards, *J. Am. Chem. Soc.*, 1986, **108**, 78.
91. A. Ellaboudy and J. L. Dye, *J. Magn. Reson.*, 1986, **66**, 491.
92. J. Kim and J. L. Dye, *J. Phys. Chem.*, 1990, **94**, 5399.
93. R. H. Huang, J. L. Eglin, S. Z. Huang, L. E. H. McMills, and J. L. Dye, *J. Am. Chem. Soc.*, 1993, **115**, 9542.
94. J.-J. Delpuech, in *NMR of Newly Accessible Nuclei*, ed. P. Laszlo, Academic Press, New York, 1983, Vol. 2, Chap. 6
95. R. Benn, A. Rufinska, H. Lehmkuhl, E. Janssen, and C. Krüger, *Angew. Chem., Int. Ed. Engl.*, 1983, **22**, 779.
96. R. Benn and A. Rufinska, *Angew. Chem., Int. Ed. Engl.*, 1986, **25**, 861.
97. J. W. Akitt and J. M. Elders, *J. Magn. Reson.*, 1985, **63**, 587.
98. H. Nöth, *Z. Naturforsch. B*, 1980, **35**, 119.
99. R. Benn, A. Rufinska, E. Janssen, and H. Lehmkuhl, *Organometallics*, 1986, **5**, 825.
100. R. Benn, E. Janssen, H. Lehmkuhl, A. Rufinska, K. Angermund, P. Betz, R. Goddard, and C. Kruger, *J. Organomet. Chem.*, 1991, **411**, 37.
101. R. Ditchfield, *Mol. Phys.*, 1974, **27**, 789.
102. J. Gauss, U. Schneider, R. Ahlrichs, C. Dohmeier, and H. Schnöckel, *J. Am. Chem. Soc.*, 1993, **115**, 2402.
103. J. Almlöf, K. Faegri, and K. Korsell, *J. Comput. Chem.*, 1982, **3**, 385.
104. D. Cremer and J. Gauss, *J. Comput. Chem.*, 1986, **7**, 274.
105. M. Häser and R. Ahlrichs, *J. Comput. Chem.*, 1989, **10**, 104.
106. M. Häser, R. Ahlrichs, H. P. Baron, P. Weis, and H. Horn, *Theor. Chim. Acta*, 1992, **83**, 455.
107. D. Mueller, D. Hoebbel, and W. Gessner, *Chem. Phys. Lett.*, 1981, **84**, 25.
108. J. B. Nagy, Z. Gabelica, G. Debras, E. G. Derouane, J. P. Gilson, and P. A. Jacobs, *Zeolites*, 1984, **4**, 133.
109. P. P. Man and J. Klinowski, *Chem. Phys. Lett.*, 1988, **147**, 581.
110. P. S. Iyer, J. Scherzer, and Z. C. Mester, *ACS Symposium Series 368*, American Chemical Society, Washington, DC, 1988, p. 48.
111. L. B. Alemany, H. K. C. Timken, and I. D. Johnson, *J. Magn. Reson.*, 1988, **80**, 427.
112. L. Kellberg, M. Linsten, and H. J. Jakobsen, *Chem. Phys. Lett.*, 1991, **182**, 120.
113. J. Rocha, S. W. Carr, and J. Klinowski, in *Abstracts of Papers, 202nd National Meeting of the American Chemical Society, American Chemical Society, Washington, DC, 1991*, p. 6.
114. R. Jelinek, B. F. Chmelka, Y. Wu, P. J. Grandinetti, A. Pines, P. J. Barrie, and J. Klinowski, *J. Am. Chem. Soc.*, 1991, **113**, 4097.
115. J. Haase, H. Pfeifer, W. Oehme, and J. Klinowski, *J. Chem. Soc., Chem. Commun.*, 1988, 1142.
116. N. C. Nielsen, H. Bildsoe, H. J. Jakobsen, and P. Norby, *Zeolites*, 1991, **11**, 622.
117. C. Jager, *J. Magn. Reson.*, 1992, **99**, 353.
118. P. P. Man and J. Klinowski, *J. Chem. Soc., Chem. Commun.*, 1988, 1291.
119. J. Perezpariente, J. Sanz, V. Fornes, and A. Corma, *J. Catal.*, 1990, **124**, 217.
120. R. H. Meinhold and D. M. Bibby, *Zeolites*, 1990, **10**, 74.
121. R. Jelinek, B. F. Chmelka, Y. Wu, M. E. Davis, J. G. Ulan, R. Gronsky, and A. Pines, *Catal. Lett.*, 1992, **15**, 65.
122. Y. Wu, B. F. Chmelka, A. Pines, M. E. Davis, P. J. Grobet, and P. A. Jacobs, *Nature (London)*, 1990, **346**, 550.
123. P. J. Barrie, M. E. Smith, and J. Klinowski, *Chem. Phys. Lett.*, 1991, **180**, 6.
124. S. Prabakar, K. J. Rao, and C. N. R. Rao, *Mater. Res. Bull.*, 1991, 805.
125. J. B. Sloan, S. A. Cannon, E. C. Delionback, and J. J. Dechter, *Inorg. Chem.*, 1985, **24**, 883.
126. J. M. Garrison and A. L. Crumbliss, *Inorg. Chem.*, 1988, **27**, 3058.
127. R. C. T. Slade and T. W. Davies, *Coll. Surf.*, 1989, **36**, 119.
128. J. Rocha and J. Klinowski, *Phys. Chem. Miner.*, 1990, **17**, 179.
129. B. Y. Kornilovich and A. T. Pilipenko, *Inorg. Mater.*, 1989, **25**, 693.
130. M. C. Rohner, V. K. Sharma, and W. Richarz, *Can. J. Chem. Eng.*, 1989, **67**, 513.
131. H. D. Morris and P. D. Ellis, *J. Am. Chem. Soc.*, 1989, **111**, 6045.
132. H. D. Morris, S. Bank, and P. D. Ellis, *J. Phys. Chem.*, 1990, **94**, 3121.
133. F. M. Asseid, J. M. Miller, and J. H. Clark, *Can. J. Chem.*, 1992, **70**, 2398.
134. A. M. Venezia, M. A. Floriano, G. Deganello, and A. Rossi, *Surf. Interf. Anal.*, 1992, **18**, 532.
135. J. M. Desimone, M. Staengle, J. S. Riffle, and J. E. McGrath, in *Abstracts of Papers, 199th National Meeting of the American Chemical Society, American Chemical Society, Washington, DC, 1990*, p. 375.
136. Z. Cerny, J. Fusek, O. Kriz, S. Hermanek, M. Solc, and B. Casensky, *J. Organomet. Chem.*, 1990, **386**, 157.
137. A. Fratiello, V. Kubo-Anderson, S. Azimi, C. Fowler, E. Marinez, R. Perrigan, S. Shayegan, and B. Yao, *Magn. Reson. Chem.*, 1992, **30**, 280.

138. B. Lindman and S. Forsén, *Chlorine, Bromine and Iodine NMR. Physico-Chemical and Biological Applications*, Springer-Verlag, Berlin, 1976.
139. T. Sugawara, M. Yudasaka, Y. Yokoyama, T. Fujiyama, and H. Iwamura, *J. Phys. Chem.*, 1982, **86**, 2705.
140. J. J. C. van Lier, L. J. M. van de Ven, J. W. de Haan, and H. M. Buck, *J. Phys. Chem.*, 1983, **87**, 3501.
141. R. Jelinek, A. Stein, and G. A. Ozin, *J. Am. Chem. Soc.*, 1993, **115**, 2390.
142. M. Yudasaka, T. Sugawara, H. Iwamura, and T. Fujiyama, *Bull. Chem. Soc. Jpn.*, 1982, **55**, 311.
143. B. Lindman, in *NMR of Newly Accessible Nuclei*, ed. P. Laszlo, Academic Press, New York, 1983, Vol. 1, p. 233.
144. G. Remaud, G. J. Martin, and M. L. Martin, *J. Phys. Chem.*, 1985, **89**, 2082.
145. R. P. W. J. Struis, J. de Bleijser, and J. C. Leyte, *J. Phys. Chem.*, 1989, **93**, 7932.
146. R. P. W. J. Struis, J. de Bleijser, and J. C. Leyte, *J. Phys. Chem.*, 1989, **93**, 7943.
147. P. Laszlo, in *Cobalt-59*, ed P. Laszlo, Academic Press, New York, 1983, Vol. 2, Chap. 9
148. H. Hartmann and H. Sillescu, *Theor. Chim. Acta*, 1964, **2**, 371.
149. R. B. Jordan, *J. Magn. Reson.*, 1980, **38**, 267.
150. A. Abragam, *Principles of Nuclear Magnetism*, Clarendon Press, Oxford, 1961, p. 309.
151. K. Rose and R. G. Bryant, *J. Magn. Reson.*, 1979, **35**, 223.
152. D. M. Doddrell et al., *Aust. J. Chem.*, 1979, **32**, 1219.
153. K. A. Valiev, *Soviet Phys. JETP*, 1960, **37**, 77.
154. V. P. Chacko and R. G. Bryant, *J. Magn. Reson.*, 1984, **57**, 79.
155. C. Deverell, *Mol. Phys.*, 1969, **16**, 491.
156. C. Deverell, in *Progress in Nuclear Magnetic Resonance Spectroscopy*, ed. J. W. Emsley, J. Feeney, and L. H. Sutcliffe, Pergamon Press, Oxford, 1969, Vol. 4, p. 235.
157. A. Delville, C. Detellier, A. Gerstmans, and P. Laszlo, *J. Magn. Reson.*, 1981, **42**, 14.
158. J.-P. Kintzinger and J.-M. Lehn, *J. Am. Chem. Soc.*, 1974, **96**, 3313.
159. H. G. Hertz, *Ber. Bunsenges. Phys. Chem.*, 1973, **77**, 531.
160. H. G. Hertz, *Ber. Bunsenges. Phys. Chem.*, 1973, **77**, 688.
161. H. G. Hertz, M. Holz, G. Keller, H. Versmold, and C. Yoon, *Ber. Bunsenges. Phys. Chem.*, 1974, **78**, 493.
162. C. A. Melendres and H. G. Hertz, *J. Chem. Phys.*, 1974, **61**, 4156.
163. K. K. W. Ho, W. Y. Choy, C. Yu-Xin, and S. C. F. Au-Yeung, *J. Magn. Reson.*, submitted.
164. K. I. Hagen, C. M. Schwab, J. O. Edwards, J. G. Jones, R. G. Lawler, and D. A. Sweigart, *J. Am. Chem. Soc.*, 1988, **110**, 7024.
165. H. Bang, J. O. Edwards, J. Kim, R. G. Lawler, K. Reynolds, W. J. Ryan, and D. A. Sweigart, *J. Am. Chem. Soc.*, 1992, **114**, 2843.
166. R. Sternheimer, *Phys. Rev.*, 1950, **80**, 102.
167. R. M. Sternheimer, *Phys. Rev.*, 1966, **146**, 140.
168. R. M. Sternheimer, *Z. Naturforsch. A*, 1986, **41**, 24.
169. D. M. Holton, A. Ellaboudy, N. C. Pyper, and P. P. Edwards, *J. Chem. Phys.*, 1986, **84**, 1089.
170. E. A. C. Lucken, *Nuclear Quadrupole Coupling Constants*, Academic Press, London, 1969.
171. K. D. Sen and P. T. Narasimhan, *Advances in Nuclear Quadrupole Resonance*, ed. Smith Heyden, London, 1974, Vol. 1.
172. P. C. Schmidt, K. D. Sen, T. P. Das, and A. Weiss, *Phys. Rev. B*, 1980, **22**, 4167.

Biographical Sketch

Pierre Laszlo. *b* 1938; B.S., 1961, D.Sc., 1965, Sorbonne, Paris. Research Associate, Princeton University, 1962–63. Assistant professor, Princeton University, 1966–70. Professor of chemistry, University of Liège, 1970–present. Professor of chemistry, École polytechnique, 1986–present. Over 200 publications, 14 books. With a gut repugnance for mere data collection, takes price in extracting good quantitative information about hidden variables. Will chew on a phenomenon and lay it aside with isolation of the predominant factor. Benchmark date is 1974, first foray into sodium NMR. His heroes include Anatole Abragam, Frank Anet, Richard Ernst and Ray Freeman, Erwin Hahn, Jean Jeener, Paul Lauterbur, Alex Pines, John Pople, John Waugh, and Don Woessner

Relaxation Theory for Quadrupolar Nuclei

Lawrence G. Werbelow
New Mexico Tech, Socono, NM, USA

1	Introduction	1
2	The Electric Quadrupolar Interaction	1
3	Electric Quadrupolar Relaxation of Athermal Spin Polarizations	2
4	Electric Quadrupolar Relaxation of Nuclear Spin Coherence	4
5	Electric Quadrupolar Relaxation in the Rotating Frame	6
6	The Electric Quadrupolar Interaction and Dynamic Frequency Shifts	6
7	Effects of Alternative Sources of Relaxation for Quadrupolar Nuclei	7
8	Impact of Quadrupolar Relaxation on Spin-$\frac{1}{2}$ Nuclei	8
9	Summary	9
10	Related Articles	9
11	References	9

1 INTRODUCTION

Inasmuch as three-fourths of all NMR-receptive nuclei have measurable quadrupole moments, the electric quadrupolar interaction, and its ability to effect nuclear spin relaxation, necessarily plays a central role in both the theory and practice of nuclear magnetic resonance. Furthermore, in addition to the importance on relaxing high-spin nuclei, quadrupolar interactions impact upon the relaxation features of scalar-coupled spin-$\frac{1}{2}$ nuclei.

Except for nuclei occupying molecular sites of cubic electronic symmetry, the interaction strength of the quadrupolar coupling typically is on the order of 10^6–$10^8\ \mathrm{s}^{-1}$, whereas comparable dipolar, spin rotation and anisotropic shielding interaction strengths are on the order of 10^4–$10^5\ \mathrm{s}^{-1}$. Hence, electric quadrupolar interactions usually result in extremely efficient *dissipation* of nuclear spin coherence and restoration of thermal polarization for all $I > 1$ (quadrupolar and multipolar) nuclei. However, weaker relaxation pathways, often neglected in the discussion of the relaxation of quadrupolar nuclei, are responsible for relaxation-induced polarization and coherence *transfer*.

In the context of high-resolution and multidimensional NMR, homogeneous line broadenings associated with the efficiency of quadrupolar relaxation present a number of challenging obstacles. In contrast, the general dominance of quadrupolar relaxation generally facilitates its application in the study of molecular dynamics. For applications involving spin-$\frac{1}{2}$ nuclei, it often proves difficult to isolate and identify competitive relaxation pathways. Furthermore, for spin-$\frac{1}{2}$ nuclei, inter- and intramolecular effects must be differentiated, whereas quadrupolar relaxation is purely intramolecular in nature.

Finally, from a theoretical vantage, a discussion of quadrupolar relaxation can be utilized to illustrate numerous symmetries and characteristics common to spin relaxation in any multistate system.

2 THE ELECTRIC QUADRUPOLAR INTERACTION

The electric quadrupolar interaction between a nuclear spin $\hat{\boldsymbol{I}}$ and a nonzero electric field gradient can be written compactly in tensor notation, $\hat{\mathcal{F}}^{\mathrm{Q}I} \propto \hat{\boldsymbol{I}} \cdot \boldsymbol{Q} \cdot \hat{\boldsymbol{I}}$. When written in this manner, the functional similarity between a quadrupolar interaction and an electron zero field splitting or a dipole–dipole coupling between equivalent nuclei is apparent. Since the coupling tensor $\boldsymbol{Q}$ is both symmetric and traceless, only two of the three principal components are independent. Although various conventions exist, this coupling is usually characterized by a principal value $q_{zz} \sum q_I$ and asymmetry $\eta = (q_{yy} - q_{xx})/q_{zz}$, with $|q_{zz}| > |q_{xx}| > |q_{yy}|$.

Application of the Wigner–Eckart theorem demonstrates that the quadrupolar interaction vanishes unless $I \geq 1$. Some of the more important members of the set of nuclei subject to the quadrupolar interaction are ^{2}H and ^{14}N ($I = 1$), ^{7}Li and ^{23}Na ($I = \frac{3}{2}$), ^{17}O and ^{27}Al ($I = \frac{5}{2}$), and ^{43}Ca and ^{59}Co ($I = \frac{7}{2}$).

If the electric field gradient tensor is axially symmetric ($\eta = 0$), the quadrupolar coupling can be written simply as

$$\hat{\mathcal{F}}^{\mathrm{Q}I} = \frac{e^2 q_I Q_I}{4I(2I-1)\hbar}(3\hat{I}^2_{z\mathrm{mol}} - \hat{I}^2) \tag{1}$$

Additional parameters appearing in equation (1) include the charge q_I and the nuclear electric quadrupole moment eQ_I. Occasionally, the quadrupolar coupling is written in terms of a gradient anisotropy $\Delta Q = \frac{3}{2}q_I = \frac{3}{2}q_{zz} = q_{zz} - \frac{1}{2}(q_{xx} + q_{yy})$. A subscript is attached to the operator $\hat{I}_z$ to emphasize that this interaction is defined in the molecular frame. In the presence of an applied external magnetic field $\boldsymbol{B}_0$, where $|\gamma_I B_0 \sum \omega_I| \gg |e^2 q_I Q_I/\hbar|$, the spins are effectively quantized in the laboratory frame. In all subsequent discussion, this form of the high-field approximation will be implicit. For arbitrary relative orientations of these two frames, $\hat{\mathcal{F}}^{\mathrm{Q}I}$ can be written as a scalar product of spin and spatial coordinates:

$$\hat{\mathcal{F}}^{\mathrm{Q}I} = \xi_{\mathrm{Q}I} \sum_n (-1)^n \hat{T}^n_{\mathrm{Q}}(I) V^{-n}_{\mathrm{Q}}(\theta, \phi) \tag{2a}$$

The spin operators are defined as

$$T^{\pm 2}_{\mathrm{Q}} = \frac{\hat{I}^2_{\pm}}{I(2I-1)}, \quad \hat{T}^{\pm 1}_{\mathrm{Q}} = \mp\frac{\hat{I}_{\pm}(2\hat{I}_z + 1)}{I(2I-1)}$$
$$\hat{T}^0_{\mathrm{Q}} = \left(\frac{2}{3}\right)^{1/2} \frac{3\hat{I}^2_z - \hat{I}^2}{I(2I-1)} \tag{2b}$$

The lattice or orientation functions $V^n_Q(\theta, \phi)$ are normalized rank-2 spherical harmonics. The angular arguments position the unique axis of the diagonalized electric field gradient tensor in the laboratory frame. The interaction constant is defined as $\xi_{\mathrm{Q}I} = (\frac{3}{40}\pi)^{1/2} e^2 q_I Q_I/\hbar$.

Hence, in a rigid system such as a solid, the energy level spacings for quadrupolar nuclei depend on the molecular orientation relative to the direction of the external field. These

levels do not vary in time, and a rigid lattice powder pattern results. However, in the presence of molecular motions, the energy levels appear time-dependent and act as a source of magnetic relaxation.

For a nonaxially symmetric field gradient, the electric quadrupolar interaction takes the form

$$\hat{\mathcal{F}}^{\mathrm{Q}I} = \frac{e^2 q_I Q_I}{4I(2I-1)\hbar}[(3\hat{I}^2_{z\mathrm{mol}} - \hat{I}^2) + \tfrac{1}{2}\eta(\hat{I}^2_+ + \hat{I}^2_-)] \tag{3}$$

Unfortunately, the analog of equation (2a) is cumbersome, and the separation of spin and spatial coordinates from the interaction constants proves impossible. However, it is possible to rewrite any traceless rank-2 tensor $\boldsymbol{Q}$ as the sum of two, axially symmetric composites:

$$\begin{bmatrix} q_{xx} & \vdots & \vdots \\ \cdots & \cdots & \cdots \\ \vdots & q_{yy} & \vdots \\ \cdots & \cdots & \cdots \\ \vdots & \vdots & q_{zz} \end{bmatrix} = \Delta Q^+ \begin{bmatrix} \frac{2}{3} & \vdots & \vdots \\ \cdots & \cdots & \cdots \\ \vdots & -\frac{1}{3} & \vdots \\ \cdots & \cdots & \cdots \\ \vdots & \vdots & -\frac{1}{3} \end{bmatrix} + \Delta Q^- \begin{bmatrix} -\frac{1}{3} & \vdots & \vdots \\ \cdots & \cdots & \cdots \\ \vdots & \frac{2}{3} & \vdots \\ \cdots & \cdots & \cdots \\ \vdots & \vdots & -\frac{1}{3} \end{bmatrix} \tag{4a}$$

where

$$\left.\begin{aligned} \Delta Q^+ &= q_{xx} - q_{zz} = -\Delta Q(1 + \tfrac{1}{3}\eta) \\ \Delta Q^- &= q_{yy} - q_{zz} = -\Delta Q(1 - \tfrac{1}{3}\eta) \\ \Delta Q &= q_{zz} - \tfrac{1}{2}(q_{xx} + q_{yy}) \\ \eta &= \frac{3(q_{yy} - q_{xx})}{2\Delta Q} \end{aligned}\right\} \tag{4b}$$

An important equivalence between the $(\Delta Q, \eta)$ and the $(\Delta Q^+, \Delta Q^-)$ representations is

$$\begin{aligned} &\tfrac{1}{2}[(q_{xx} - q_{yy})^2 + (q_{xx} - q_{zz})^2 + (q_{yy} - q_{zz})^2] \\ &\quad = (\Delta Q)^2\left(1 + \tfrac{1}{3}\eta^2\right) \\ &\quad = (\Delta Q^+)^2 + (\Delta Q^-)^2 - (\Delta Q^+)(\Delta Q^-) \end{aligned} \tag{5}$$

The two resultant anisotropies $\Delta Q^{\pm}$ are axially symmetric and mutually orthogonal. This alternative description enables the separation of the interaction constants from the lattice variables as implied by equation (2a). However, with respect to relaxation considerations, these two composite interactions are temporally correlated, and this correlation must not be neglected.

3 ELECTRIC QUADRUPOLAR RELAXATION OF ATHERMAL SPIN POLARIZATIONS

Spin–lattice or longitudinal relaxation in the $(2I + 1)$-level system associated with a collection of isolated spin-I nuclei can be described in master equation form:[1]

$$-\frac{\mathrm{d}}{\mathrm{d}t}P_n = \sum_{m \neq n} W_{nm}(\Delta P_m - \Delta P_n) \tag{6}$$

P_n is the population of the nth state, ΔP_n denotes the deviation of this population from the associated thermal equilibrium value, $\Delta P_n = P_n - P_n(\mathrm{eq})$, and W_{nm} $(=W_{mn})$ is the appropriate transition probability per unit time. Because of the nature of the quadrupolar interaction, W_{nm} vanishes unless $m = n \pm 1$ or $m = n \pm 2$. Values for these two transition probabilities can be written in concise form as

$$\begin{aligned} W_{n,n-1} &= W_{-n+1,-n} \\ &= \frac{2(2n-1)^2(I-n+1)(I+n)}{I^2(2I-1)^2} J_1^{\mathrm{Q}}(\omega_I) \end{aligned} \tag{7}$$

$$\begin{aligned} W_{n,n-2} &= W_{-n+2,-n} \\ &= \frac{2(I-n+2)(I-n+1)(I+n-1)(I+n)}{I^2(2I-1)^2} J_2^{\mathrm{Q}}(2\omega_I) \end{aligned} \tag{8}$$

The spectral density function[2] for an *axially symmetric quadrupolar* coupling is defined as

$$\begin{aligned} J_k^{\mathrm{Q}}(\omega) &= (4\pi)^{-1}(\xi_{\mathrm{Q}I})^2 \\ &\quad \times \mathrm{Re}\left[\int_0^\infty \langle Y_2^k(\theta(t), \phi(t)) Y_2^{-k}(\theta(0), \phi(0))\rangle \right. \\ &\quad \left. \times \exp(-\mathrm{i}\omega t)\,\mathrm{d}t\right] \end{aligned} \tag{9}$$

For isotropic media ($\langle \hat{\mathcal{F}}^{\mathrm{Q}I}(t)\rangle = 0$), the k dependence of the spectral density is superfluous.[3] In subsequent developments, *unless this index is explicitly shown*, the limit $J_k^{\mathrm{Q}}(\omega) = J_{k'}^{\mathrm{Q}}(\omega)$ $\sum$ $J^{\mathrm{Q}}(\omega)$ is assumed.

For *isotropic, diffusional reorientation* of the molecular frame relative to the laboratory frame, equation (9) reduces to

$$J^{\mathrm{Q}}(\omega) = \frac{3}{160}\left(\frac{e^2 q_I Q_I}{\hbar}\right)^2 \frac{\tau_2}{1 + \omega^2\tau_2^2} \tag{10}$$

The correlation time $\tau_2 = \frac{1}{6}D$, where D is the rotational diffusion constant.

For *symmetric-top reorientation* characterized by an axially symmetric diffusion tensor with principal components D_{zz} and $D_{xx} = D_{yy}$,

$$\begin{aligned} J^{\mathrm{Q}}(\omega) &= \frac{3}{640}\left(\frac{e^2 q_I Q_I}{\hbar}\right)^2 \left[\frac{(3\cos^2\theta - 1)^2\tau_{20}}{1 + (\omega\tau_{20})^2}\right. \\ &\quad \left. + \frac{12\cos^2\theta\sin^2\theta\,\tau_{21}}{1 + (\omega\tau_{21})^2} + \frac{3\sin^4\theta\,\tau_{22}}{1 + (\omega\tau_{22})^2}\right] \end{aligned} \tag{11}$$

Here θ is the angle between the principal axes of the diffusion and electric quadrupole tensors. The three correlation times are defined as $1/\tau_{2n} = 6D_{zz} + n^2(D_{zz} - D_{xx})$. In general, the molecular coordinate frames that diagonalize the diffusion and the electric field gradient tensors are not coincident.

The spectral density function, for an *asymmetric quadrupolar* coupling, assuming symmetric-top diffusional reorientation, can be described with either one of the two alternative

representations discussed earlier:

$$\begin{aligned} J^{\mathrm{Q}}(\omega) = (16\pi)^{-1}\Bigg\{ & \frac{[\xi_{\mathrm{Q}Ix}(3\cos^2\theta_x - 1)^2 + \xi_{\mathrm{Q}Iy}(3\cos^2\theta_y - 1)]^2\tau_{20}}{1+(\omega\tau_{20})^2} \\ & + 3(\xi_{\mathrm{Q}Ix})^2\left[\frac{4\cos^2\theta_x \sin^2\theta_x \tau_{21}}{1+(\omega\tau_{21})^2} + \frac{\sin^4\theta_x\tau_{22}}{1+(\omega\tau_{22})^2}\right] \\ & + 3(\xi_{\mathrm{Q}Iy})^2\left[\frac{4\cos^2\theta_y \sin^2\theta_y \tau_{21}}{1+(\omega\tau_{21})^2} + \frac{\sin^4\theta\tau_{22}}{1+(\omega\tau_{22})^2}\right] \\ & + 6\xi_{\mathrm{Q}Ix}\xi_{\mathrm{Q}Iy}\left[\frac{4\cos\theta_x\cos\theta_y\sin\theta_x\sin\theta_y\cos(\phi_x-\phi_y)\tau_{21}}{1+(\omega\tau_{21})^2}\right. \\ & \left. + \frac{\sin^2\theta_x\sin^2\theta_y\cos(2\phi_x-2\phi_y)\tau_{22}}{1+(\omega\tau_{22})^2}\right]\Bigg\} \end{aligned} \tag{12}$$

or

$$\begin{aligned} J^{\mathrm{Q}}(\omega) = \frac{3}{640}\left(\frac{e^2qQ}{\hbar}\right)^2\Bigg\{ & \frac{(3\cos^2\theta - 1 - \eta\sin^2\theta\cos 2\phi)^2\tau_{20}}{1+(\omega\tau_{20})^2} \\ & + \{12\sin^2\theta\,[\cos^2\theta\,(1+2\eta\cos 2\phi) \\ & + (\tfrac{1}{3}\eta)^2(1-\cos^2 2\phi\sin^2\theta)]\tau_{21}\}[1+(\omega\tau_{21})^2]^{-1} \\ & + [3\sin^4\theta - 2\eta\sin^2\theta\,(\cos^2\theta+1)\cos 2\phi \\ & + \tfrac{1}{3}\eta^2(\cos^2 2\phi\sin^4\theta + 4\cos^2\theta)]\frac{\tau_{22}}{1+(\omega\tau_{22})^2}\Bigg\} \end{aligned} \tag{13}$$

The parameters $\xi_{\mathrm{Q}Ix}$ and $\xi_{\mathrm{Q}Iy}$ are defined as $(q_{xx} - q_{zz})(\frac{1}{30}\pi)^{1/2}e^2Q_I/\hbar$ and $(q_{yy} - q_{zz})(\frac{1}{30}\pi)^{1/2}e^2Q_I/\hbar$, respectively. Utilizing equation (5), it can be seen that for isotropic reorientation, equation (12) or equation (13) reduces to

$$\begin{aligned} J^{\mathrm{Q}}(\omega) &= (1+\tfrac{1}{3}\eta^2)\frac{3}{160}\left(\frac{e^2qQ}{\hbar}\right)^2\frac{\tau_2}{1+\omega^2\tau_2^2} \\ &= [(q_{xx}-q_{yy})^2 + (q_{xx}-q_{zz})^2 + (q_{yy}-q_{zz})^2] \\ &\quad \times \frac{1}{240}\left(\frac{e^2Q}{\hbar}\right)^2\frac{\tau_2}{1+\omega^2\tau_2^2} \end{aligned} \tag{14}$$

Although equation (6) implies that the spin–lattice relaxation is described by $2I + 1$ coupled equations, transformation to an appropriate operator basis, which results in both a conceptual and mathematical simplification, proves otherwise. Using the irreducible spherical tensor basis consisting of the operators

$$\left.\begin{aligned} \hat{T}_1^0 &\propto \langle \hat{I}_z\rangle \\ \hat{T}_2^0 &\propto \langle 3\hat{I}_z^2 - \hat{I}^2\rangle \\ \hat{T}_3^0 &\propto \langle 5\hat{I}_z^3 - \hat{I}_z(3\hat{I}^2 - 1)\rangle \\ \hat{T}_4^0 &\propto \langle 35\hat{I}_z^4 - 5\hat{I}_z^2(6\hat{I}^2 - 5) + 3\hat{I}^2(\hat{I}^2 - 2)\rangle \\ \hat{T}_5^0 &\propto \langle 63\hat{I}_z^5 - 35\hat{I}_z^3(2\hat{I}^2 - 3) + (15\hat{I}^4 - 50\hat{I}^2 + 12)\hat{I}_z\rangle \\ \hat{T}_6^0 &\propto \langle 231\hat{I}_z^6 - 105\hat{I}_z^4(3\hat{I}^2 - 7) + 21\hat{I}_z^2(5\hat{I}^4 - 25\hat{I}^2 + 14) \\ &\quad - 5(\hat{I}^6 - 8\hat{I}^4 + 12\hat{I}^2)\rangle \\ &\vdots \end{aligned}\right\} \tag{15}$$

the longitudinal relaxation is described by the concise expression

$$-\frac{\mathrm{d}}{\mathrm{d}t}\hat{T}_L^0 = \sum_{L'} R_{L,L'}^{0,I}(\Delta\hat{T}_{L'}^0) \tag{16}$$

If extreme narrowing $[J_k^{\mathrm{Q}}(0) = J_k^{\mathrm{Q}}(\omega_0) = J_k^{\mathrm{Q}}(2\omega_0) \sum J_k^{\mathrm{Q}}]$ and spatial isotropy $[(J_k^{\mathrm{Q}}(\omega) = J_{k'}^{\mathrm{Q}}(\omega)]$ obtain then[4]

$$R_{L,L'}^{0,I} = \delta_{LL'}\{2L(L+1)[4I(I+1) - L(L+1) - 1](2I^2 - I)^{-2}\}J^{\mathrm{Q}} \tag{17}$$

For various situations of practical importance, the spectral density J^{Q} is given by equations (10)–(13). Table 1 provides a listing of $R_{L,L}^{0,I}J^{\mathrm{Q}}$ for various ranks L and spins I.

If conditions of extreme narrowing and spatial isotropy are not realized, additional couplings of the form $R_{L,L'}^{0,I} = \delta_{LL\pm2}C_{L,L\mp2}^{0,I}[J_1^{\mathrm{Q}}(\omega_I) - J_2^{\mathrm{Q}}(2\omega_I)]$ arise. Specific values of the proportionality constant $C_{L,L\mp2}^{0,I}$ for various spins I and ranks L can be found in the literature.[5,6] Thus, monoexponential relaxation of the Zeeman magnetization ($\propto \hat{T}_1^0$) quantified by a well-defined spin–lattice relaxation rate $R_{11}^{0,I} = 1/T_1$ occurs for arbitrary I if and only if extreme narrowing and spatial isotropy obtain. In this limit, $1/T_1 = 4(2I+3)(2I^3 - I^2)^{-1}J^{\mathrm{Q}}$.

The parity of each member of the operator basis introduced in equation (15) with respect to spin inversion is defined by

$$\exp(-\mathrm{i}\pi\hat{I}_y)\,\hat{T}_L^0\exp(+\mathrm{i}\pi\hat{I}_y) = (-1)^L\hat{T}_L^0 \tag{18}$$

Relaxation effected via the quadrupolar interaction does not couple operators of different parity.[7] If I is an integer then $\hat{T}_1^0$ couples into $I - 1$ additional polarizations of similar parity. An additional manifold comprising I polarizations, including 'quadrupolar order' ($\hat{T}_2^0$), also couple together. These latter polarizations are consequential only in anisotropic environments, where residual quadrupolar couplings lift the spectral degeneracy of various transitions. Similarly, if I is a half-integer then $\hat{T}_1^0$ couples into $\frac{1}{2}(2I+1)$ additional polarizations of similar parity. The remaining $\frac{1}{2}(2I-1)$ polarizations of opposite parity also couple together. Obviously, if $I = 1$ then there is monoexponential relaxation of the Zeeman polarization $\hat{T}_1^0$, characterized by the relaxation rate

$$R_{1,1}^{0,1} = 1/T_1 = 4[J_1^{\mathrm{Q}}(\omega_I) + 4J_2^{\mathrm{Q}}(2\omega_I)] \tag{19}$$

and quadrupolar order, characterized by the relaxation rate

$$R_{2,2}^{0,1} = 12J_1^{\mathrm{Q}}(\omega_I) \tag{20}$$

regardless of whether or not extreme narrowing obtains.

Although the relaxation characteristics of $I = 1$ are exceptionally simple, the behavior of $I = \frac{3}{2}$ is only slightly more complex.[8] Quadrupolar polarization or alignment decays exponentially with rate

$$R_{2,2}^{0,3/2} = \tfrac{16}{3}[J_1^{\mathrm{Q}}(\omega_I) + J_2^{\mathrm{Q}}(2\omega_I)] \tag{21}$$

Zeeman and octupolar ($\hat{T}_3^0$) order each evolve biexponentially. For an initial spin preparation (perturbation) that only disturbs Zeeman order, it can be shown that

$$\left.\begin{aligned} \frac{\Delta\langle\hat{I}_z(t)\rangle}{\Delta\langle\hat{I}_z(0)\rangle} &= \tfrac{1}{5}\exp[-\tfrac{16}{3}tJ_1^{\mathrm{Q}}(\omega_I)] \\ &\quad + \tfrac{4}{5}\exp[-\tfrac{16}{3}tJ_2^{\mathrm{Q}}(2\omega_I)] \\ \frac{\langle\hat{I}_z(0)\rangle - \langle\hat{I}_z(t\to 0)\rangle}{\Delta\langle\hat{I}_z(0)\rangle} &\approx R_{1,1}^{0,3/2}t \\ &= \tfrac{16}{15}t[J_1^{\mathrm{Q}}(\omega_I) + 4J_2^{\mathrm{Q}}(2\omega_I)] \end{aligned}\right\} \tag{22}$$

Table 1 The Electric Quadrupolar Relaxation Rates $R^{0,I}_{L,L}$ for Various Spins I and Spin Orders L

	$I = 1$	$I = \frac{3}{2}$	$I = 2$	$I = \frac{5}{2}$	$I = 3$	$I = \frac{7}{2}$	$I = 4$	$I = \frac{9}{2}$
$L = 1$	$20J^{\mathrm{Q}}$	$\frac{16}{3}J^{\mathrm{Q}}$	$\frac{7}{3}J^{\mathrm{Q}}$	$\frac{32}{25}J^{\mathrm{Q}}$	$\frac{4}{5}J^{\mathrm{Q}}$	$\frac{80}{147}J^{\mathrm{Q}}$	$\frac{11}{28}J^{\mathrm{Q}}$	$\frac{8}{27}J^{\mathrm{Q}}$
$L = 2$	$12J^{\mathrm{Q}}$	$\frac{32}{3}J^{\mathrm{Q}}$	$\frac{17}{3}J^{\mathrm{Q}}$	$\frac{84}{25}J^{\mathrm{Q}}$	$\frac{164}{75}J^{\mathrm{Q}}$	$\frac{32}{21}J^{\mathrm{Q}}$	$\frac{219}{196}J^{\mathrm{Q}}$	$\frac{23}{27}J^{\mathrm{Q}}$
$L = 3$		$\frac{16}{3}J^{\mathrm{Q}}$	$\frac{22}{3}J^{\mathrm{Q}}$	$\frac{132}{25}J^{\mathrm{Q}}$	$\frac{56}{15}J^{\mathrm{Q}}$	$\frac{400}{147}J^{\mathrm{Q}}$	$\frac{201}{98}J^{\mathrm{Q}}$	$\frac{43}{27}J^{\mathrm{Q}}$
$L = 4$			$\frac{10}{3}J^{\mathrm{Q}}$	$\frac{28}{5}J^{\mathrm{Q}}$	$\frac{72}{15}J^{\mathrm{Q}}$	$\frac{80}{21}J^{\mathrm{Q}}$	$\frac{295}{98}J^{\mathrm{Q}}$	$\frac{65}{27}J^{\mathrm{Q}}$
$L = 5$				$\frac{12}{5}J^{\mathrm{Q}}$	$\frac{68}{15}J^{\mathrm{Q}}$	$\frac{640}{147}J^{\mathrm{Q}}$	$\frac{15}{4}J^{\mathrm{Q}}$	$\frac{85}{27}J^{\mathrm{Q}}$
$L = 6$					$\frac{28}{15}J^{\mathrm{Q}}$	$\frac{80}{21}J^{\mathrm{Q}}$	$\frac{111}{28}J^{\mathrm{Q}}$	$\frac{98}{27}J^{\mathrm{Q}}$
$L = 7$						$\frac{32}{21}J^{\mathrm{Q}}$	$\frac{23}{7}J^{\mathrm{Q}}$	$\frac{98}{27}J^{\mathrm{Q}}$
$L = 8$							$\frac{9}{7}J^{\mathrm{Q}}$	$\frac{26}{9}J^{\mathrm{Q}}$
$L = 9$								$\frac{10}{9}J^{\mathrm{Q}}$

$$\left.\begin{aligned}\frac{\langle 5\hat{I}_z^3 - \hat{I}_z(3\hat{I}^2-1)(t)\rangle}{\Delta\langle \hat{I}_z(0)\rangle} &= \tfrac{6}{5}\{\exp[-\tfrac{16}{3}tJ_1^{\mathrm{Q}}(\omega_I)] \\ &\quad - \exp[-\tfrac{16}{3}tJ_2^{\mathrm{Q}}(2\omega_I)]\} \\ \frac{\langle 5\hat{I}_z^3 - \hat{I}_z(3\hat{I}^2-1)(t\to 0)\rangle}{\Delta\langle \hat{I}_z(0)\rangle} &\approx -R_{3,1}^{0,3/2}t \\ &= -\tfrac{32}{5}t[J_1^{\mathrm{Q}}(\omega_I) - J_2^{\mathrm{Q}}(2\omega_I)]\end{aligned}\right\} \quad (23)$$

For spin $I = \frac{3}{2}$, it is illustrative to define two fictitious spin operators,[9] $\langle \hat{I}_z^{\mathrm{b}}\rangle = \frac{3}{2}[(P_{3/2} - P_{1/2}) + (P_{-1/2} - P_{-3/2})]$ and $\langle \hat{I}_z^{\mathrm{n}}\rangle = 2(P_{1/2} - P_{-1/2})$. Thus, $\langle \hat{I}_z\rangle = \langle \hat{I}_z^{\mathrm{b}}\rangle + \langle \hat{I}_z^{\mathrm{n}}\rangle$ and $\langle 5\hat{I}_z^3 - \hat{I}_z(3\hat{I}^2-1)\rangle = \langle \hat{I}_z^{\mathrm{b}}\rangle - \frac{3}{2}\langle \hat{I}_z^{\mathrm{n}}\rangle$. These identifications permit the following transformation of the kinetic equations for $I = \frac{3}{2}$:

$$\frac{5}{2}\frac{\langle \hat{I}_z^{\mathrm{n}}(t)\rangle - \frac{2}{5}\langle \hat{I}_z(\mathrm{eq})\rangle}{\Delta\langle \hat{I}_z(0)\rangle} = 2\exp[-\tfrac{16}{3}tJ_2^{\mathrm{Q}}(2\omega_I)] - \exp[-\tfrac{16}{3}tJ_1^{\mathrm{Q}}(\omega_I)] \quad (24)$$

$$\frac{5}{3}\frac{\langle \hat{I}_z^{\mathrm{b}}(t)\rangle - \frac{3}{5}\langle \hat{I}_z(\mathrm{eq})\rangle}{\Delta\langle \hat{I}_z(0)\rangle} = \exp[-\tfrac{16}{3}tJ_1^{\mathrm{Q}}(\omega_I)] \quad (25)$$

For $I = \frac{3}{2}$, one has the highly unusual situation where a specific population difference ($P_{3/2} - P_{1/2}$ or $P_{-1/2} - P_{-3/2}$) is characterized by simple exponential relaxation. Furthermore, if $J_2^{\mathrm{Q}}(2\omega_I) < \frac{1}{2}J_1^{\mathrm{Q}}(\omega_I)$, the deviation population difference $\Delta(P_{1/2} - P_{-1/2})$ initially grows rather than decays!

Although integrated forms of equation (16) cannot be written in tractable form, for higher spin nuclei, the *initial* response to any perturbation of $\hat{I}_z$ is always described by

$$\frac{\langle \hat{I}_z(0)\rangle - \langle \hat{I}_z(t\to 0)\rangle}{\Delta\langle \hat{I}_z(0)\rangle} \approx R_{1,1}^{0,I}t \quad (26)$$

where

$$R_{1,1}^{0,I} = 1/T_1 = \tfrac{4}{5}(2I+3)I^{-2}(2I-1)^{-1}[J_1^{\mathrm{Q}}(\omega_I) + 4J_2^{\mathrm{Q}}(2\omega_I)] \quad (27)$$

4 ELECTRIC QUADRUPOLAR RELAXATION OF NUCLEAR SPIN COHERENCE

Because of the efficiency of the quadrupolar interaction in effecting nuclear spin relaxation, usually inhomogenous line broadening can be assumed negligible, and spin–spin or transverse relaxation rates can be abstracted directly from measurement of linewidths.

In addition to the aforementioned $2I + 1$ populations, a collection of isolated spin-I nuclei is characterized by $2I$ single quantum coherences (1QCs), $2I - 1$ double quantum coherences (2QCs), ... , two $(2I - 1)$QCs and one $(2I)$QC. At thermal equilibrium, all coherence vanishes. Generalized 'spin–spin' relaxation in a multilevel system can be described in a manner analogous to equation (6):

$$-\frac{\mathrm{d}}{\mathrm{d}t}\chi_{nn'} = \mathrm{i}(\omega_{nn'} + \Omega_{nn'})\chi_{nn'} + \left[Z_{nn'} + \tfrac{1}{2}\sum_j (W_{nj} + W_{n'j})\right]\chi_{nn'} + \sum_{m,m'}\delta(\omega_{nn'} - \omega_{mm'})(W_{nm}W_{n'm'})^{1/2}\chi_{mm'} \quad (28)$$

In the absence of applied rf fields, the evolution of coherence between states $|n\rangle$ and $|n'\rangle$, $\chi_{nn'}$, is characterized by an intrinsic frequency $\omega_{nn'}$, a dynamic frequency shift, $\Omega_{nn'}$, an adiabatic term or zero frequency contribution $Z_{nn'}$, lifetime terms $W_{nn'}$, which were defined earlier, and a secular coupling term $(W_{nm}W_{n'm'})^{1/2}$, which vanishes unless the coherences $\chi_{nn'}$ and $\chi_{mm'}$ are degenerate or overlapping (the secular approximation). The validity of equation (28) is restricted to the motionally narrowed, perturbative regime, $1/\tau_2 \rangle Z_{nn'}, |\hat{\mathcal{F}}^{\mathrm{Q}I}|$.

In the absence of multiplet structure attributed to a residual quadrupolar interaction, each set of $2I + 1 - n$, nQCs are degenerate. With the additional stipulation of extreme narrowing, the perturbation–response characteristics of these coherences are remarkably simple. Once again, this is revealed by transformation to an irreducible spherical tensor operator basis:

$$\left.\begin{aligned}\hat{T}_1^{\pm 1} &\propto \langle \hat{I}_\pm\rangle \\ \hat{T}_2^{\pm 1} &\propto \langle \hat{I}_\pm(2\hat{I}_z \pm 1)\rangle \\ \hat{T}_2^{\pm 2} &\propto \langle \hat{I}_\pm^2\rangle \\ \hat{T}_3^{\pm 1} &\propto \langle \hat{I}_\pm[5\hat{I}_z^2 \pm 5\hat{I}_z + (2 - \hat{I}^2)]\rangle \\ \hat{T}_3^{\pm 2} &\propto \langle \hat{I}_\pm^2(\hat{I}_z \pm 1)\rangle \\ \hat{T}_3^{\pm 3} &\propto \langle \hat{I}_\pm^3\rangle \\ &\vdots \\ \hat{T}_{2I}^{\pm(2I-1)} &\propto \langle \hat{I}_\pm^{(2I-1)}[2\hat{I}_z \pm (2I-1)]\rangle \\ \hat{T}_{2I}^{\pm 2I} &\propto \langle \hat{I}_\pm^{2I}\rangle\end{aligned}\right\} \quad (29)$$

The relaxation behavior of these coherences can be cast in a form identical to equation (16):

$$-\frac{\mathrm{d}}{\mathrm{d}t}\hat{T}_L^{\pm k} = \pm \mathrm{i}k\omega_I + \sum_{L'} R_{L,L'}^{k,I}\hat{T}_L^{\pm k} \tag{30}$$

For the moment, the dynamic frequency shift is ignored.

The validity of the secular approximation ensures that only coherences of similar precessional frequency couple together. In the limit of extreme narrowing,

$$R_{L,L'}^{k,I} = R_{L,L'}^{0,I} = \delta_{LL'}\{2L(L+1) \times [4I(I+1) - L(L+1) - 1](2I^2 - I)^{-2}\}J^{\mathrm{Q}} \tag{31}$$

When extreme narrowing fails, additional couplings of the form $R_{L,L'}^{k,I} = \delta_{LL\pm 2}\,\Sigma_{n=0}^{2} C_{L,L\mp 2}^{k,n,I} J_n^{\mathrm{Q}}(n\omega_I)$ arise. Selected values of $C_{L,L\mp 2}^{1,n,I}$ for various spins I and ranks L can be found in the literature.[6] Again, monoexponential relaxation of single quantum coherence or 'transverse' magnetization ($\propto \hat{T}_1^{\pm 1}$), quantified by a well-defined spin–spin relaxation rate $R_{1,l}^{1,I} = 1/T_2$, results for arbitrary I if and only if extreme narrowing obtains: $1/T_2 = 1/T_1 = 4(2I+3)(2I^3 - I^2)^{-1}\,J^{\mathrm{Q}}$.

However, there are other interesting decay rates that can be expressed in closed analytic form. For example, the dissipation of $(2I)$QC ($\hat{T}_{2I}^{2I}$) and in-phase ($\hat{T}_{2I-1}^{2I-1}$) and antiphase ($\hat{T}_{2I}^{2I-1}$) $2I-1$ multiple quantum coherences are determined by the respective rates

$$R_{2I,2I}^{2I,I} = (4I^{-1})J_1^{\mathrm{Q}}(\omega_I) + 8I^{-1}(2I-1)^{-1}J_2^{\mathrm{Q}}(2\omega_I) \tag{32}$$

$$R_{2I-1,2I-1}^{2I-1,I} = 2I^{-2}(2I-1)^{-1}\{3(2I-1)J_0^{\mathrm{Q}}(0) + [4I(2I-1) + (2I-3)^2]J_1^{\mathrm{Q}}(\omega_I) + 2(4I-3)J_2^{\mathrm{Q}}(2\omega_I)\} \tag{33}$$

$$R_{2I,2I}^{2I-1,I} = 2I^{-2}(2I-1)^{-1}[3(2I-1)J_0^{\mathrm{Q}}(0) + (2I-3)^2 J_1^{\mathrm{Q}}(\omega_I) + 2(4I-3)J_2^{\mathrm{Q}}(2\omega_I)] \tag{34}$$

These expressions demonstrate that for $I = 1$, not only do Zeeman and quadrupolar polarizations relax exponentially, so do both forms of single quantum coherence and the unique double quantum coherence:

$$R_{2,2}^{1,1} = 2[3J_0^{\mathrm{Q}}(0) + J_1^{\mathrm{Q}}(\omega_I) + 2J_2^{\mathrm{Q}}(2\omega_I)] \tag{35}$$

$$R_{1,1}^{1,1} = 1/T_2 = 2[3J_0^{\mathrm{Q}}(0) + 5J_1^{\mathrm{Q}}(\omega_I) + 2J_2^{\mathrm{Q}}(2\omega_I)] \tag{36}$$

$$R_{2,2}^{2,1} = 4J_1^{\mathrm{Q}}(\omega_I) + 8J_2^{\mathrm{Q}}(2\omega_I) \tag{37}$$

Equations (19), (20), and (35)–(37) summarize completely the relaxation characteristics for $I = 1$. Similarly, the description for $I = \frac{3}{2}$, initiated with equations (21)–(25), can now be completed. For $I = \frac{3}{2}$, forms of spin order associated with $\hat{T}_3^{\pm 3}$, $\hat{T}_3^{\pm 2}$, $\hat{T}_2^{\pm 2}$, and $\hat{T}_2^{\pm 1}$ dissipate in time exponentially with the following relaxation rates:

$$R_{3,3}^{3,3/2} = \tfrac{8}{3}J_1^{\mathrm{Q}}(\omega_I) + \tfrac{8}{3}J_2^{\mathrm{Q}}(2\omega_I) \tag{38}$$

$$R_{3,3}^{2,3/2} = \tfrac{8}{3}J_0^{\mathrm{Q}}(0) + \tfrac{8}{3}J_2^{\mathrm{Q}}(2\omega_I) \tag{39}$$

$$R_{2,2}^{2,3/2} = \tfrac{8}{3}J_0^{\mathrm{Q}}(0) + \tfrac{16}{3}J_1^{\mathrm{Q}}(\omega_I) + \tfrac{8}{3}J_2^{\mathrm{Q}}(2\omega_I) \tag{40}$$

$$R_{2,2}^{1,3/2} = \tfrac{8}{3}J_0^{\mathrm{Q}}(0) + \tfrac{8}{3}J_1^{\mathrm{Q}}(\omega_I) + \tfrac{16}{3}J_2^{\mathrm{Q}}(2\omega_I) \tag{41}$$

In-phase and doubly antiphase 1QC, $\hat{T}_1^{\pm 1}$ and $\hat{T}_3^{\pm 1}$, couple together, and each evolves biexponentially. For an initial spin preparation (perturbation) that selectively disturbs one-spin order, $\langle \hat{\mathrm{I}}_{\pm}(0)\rangle \neq 0$, it can be shown that

$$\left.\begin{aligned} \frac{\langle \hat{I}_{\pm}(t)\rangle}{\langle \hat{I}_{\pm}(0)\rangle} &= \tfrac{1}{5}\exp[-\tfrac{8}{3}tJ_1^{\mathrm{Q}}(\omega_I)] \\ &\quad \times \{3\exp[-\tfrac{8}{3}tJ_0^{\mathrm{Q}}(0)] + 2\exp[-\tfrac{8}{3}tJ_2^{\mathrm{Q}}(2\omega_I)]\} \\ -\frac{\langle I_{\pm}(t\to 0)\rangle - \langle \hat{I}_{\pm}(0)\rangle}{\langle \hat{I}_{\pm}(0)\rangle t} &\approx R_{1,1}^{1,3/2} = 1/T_2 \\ &= \tfrac{8}{15}[3J_0^{\mathrm{Q}}(0) + 5J_1^{\mathrm{Q}}(\omega_I) + 2J_2^{\mathrm{Q}}(2\omega_I)] \end{aligned}\right\} \tag{42}$$

$$\left.\begin{aligned} \frac{\langle \hat{I}_{\pm}[5\hat{I}_z^2 \pm 5\hat{I}_z(2-\hat{I}^2)](t)\rangle}{\langle \hat{I}_{\pm}(0)\rangle} &= \tfrac{6}{5}\exp[-\tfrac{8}{3}tJ_1^{\mathrm{Q}}(\omega_I)]\{\exp[-\tfrac{8}{3}tJ_0^{\mathrm{Q}}(0)] \\ &\quad - \exp[-\tfrac{8}{3}tJ_2^{\mathrm{Q}}(2\omega_I)]\} \\ -\frac{\langle \hat{I}_{\pm}[5\hat{I}_z^2 \pm 5\hat{I}_z + (2-\hat{I}^2)](t\to 0)\rangle}{\langle \hat{I}_{\pm}(0)\rangle t} &\approx R_{3,1}^{1,3/2} \\ &= \tfrac{16}{5}[J_0^{\mathrm{Q}}(0) - J_2^{\mathrm{Q}}(2\omega_I)] \end{aligned}\right\} \tag{43}$$

Introducing two fictitious spin operators $\langle \hat{I}_{\pm}^{\mathrm{b}}\rangle = \sqrt{3}\,(\chi_{3/2,\ 1/2} + \chi_{-1/2,\ -3/2})$ and $\langle \hat{I}_{\pm}^{\mathrm{n}}\rangle = 2\chi_{1/2,-1/2}$ {with $\langle \hat{I}_{\pm}\rangle = \langle \hat{I}_{\pm}^{\mathrm{b}}\rangle + \langle \hat{I}_{\pm}^{\mathrm{n}}\rangle$ and $\langle \hat{I}_{\pm}[5\hat{I}_z^2 \pm 5\hat{I}_{\mathrm{z}} + (2-\hat{I}^2)]\rangle$}} results in the following transformation of the kinetic equations for $I = \frac{3}{2}$:

$$\frac{5}{2}\frac{\langle \hat{I}_{\pm}^{\mathrm{n}}(t)\rangle}{\langle \hat{I}_{\pm}(0)\rangle} = \exp[-\tfrac{8}{3}tJ_2^{\mathrm{Q}}(2\omega_I) - \tfrac{8}{3}tJ_1^{\mathrm{Q}}(\omega_I)] \tag{44}$$

$$\frac{5}{3}\frac{\langle \hat{I}_{\pm}^{\mathrm{b}}(t)\rangle}{\langle \hat{I}_{\pm}(0)\rangle} = \exp[-\tfrac{8}{3}tJ_0^{\mathrm{Q}}(0) - \tfrac{8}{3}tJ_1^{\mathrm{Q}}(\omega_I)] \tag{45}$$

For $I = \frac{3}{2}$ both of the coherences $\langle \hat{I}_{\pm}^{\mathrm{b}}\rangle$ and $\langle \hat{I}_{\pm}^{\mathrm{n}}\rangle$ are characterized by simple exponential relaxation. This representation clearly illustrates one of the most interesting and useful feature of electric quadrupolar relaxation. The decay of coherence between the states $|\frac{1}{2}\rangle$ and $|-\frac{1}{2}\rangle$ is determined by a rate free from adiabatic contributions.

In numerous practical situations, a partially averaged quadrupole coupling of residual amplitude $\langle \hat{\mathcal{F}}^{\mathrm{Q}I}(t)\rangle = \omega_{\mathrm{Q}}(3\hat{I}_z^2 - \hat{I}^2)$ removes spectral degeneracies and eliminates all secular couplings from equation (28). In this limit, the free decay of nQC between states $|m\rangle$ and $|m-n\rangle$ is characterized by a unique, well-defined relaxation rate, which can be written in closed form as

$$\begin{aligned} (1/T_2)_{m,m-n} = [I(2I-1)]^{-2}\Big\{&[6n^2(2m-n)^2]J_0^{\mathrm{Q}}(0) \\ &+\{4(4m^2+1)[I(I+1)-m^2] - 16m^2 \\ &-2n(2m-n)[4I(I+1) - 8m^2 - 5 \\ &+4n(2m-n)]\}J_1^{\mathrm{Q}}(\omega_I) \\ &+\{4(I^2-m^2-1)[I(I+2)-m^2] + 16m^2 \\ &+2n(2m-n)[2I(I+1) - 2m^2 - 5 \\ &+n(2m-n)]\}J_2^{\mathrm{Q}}(2\omega_I)\Big\} \end{aligned} \tag{46}$$

Once again, it is emphasized that the coherence between states $|m\rangle$ and $|-m\rangle$ has no adiabatic $[J_0^{\mathrm{Q}}(0)]$ contribution. In the slow motion limit $[\omega_0\tau_2 \gg 1$, or, equivalently, $J_0^{\mathrm{Q}}(0) \gg J_1^{\mathrm{Q}}(\omega I)$, $J_2^{\mathrm{Q}}(2\omega_I)]$, all transitions except the $|m\rangle \leftrightarrow |-m\rangle$ n-quantum transition are dramatically broadened leaving behind a solitary, narrowed component, which contributes a fractional intensity

$$\left[\prod_{i=1}^{n+1}(2i-1)\right]\left[\prod_{i=1}^{n}(2I+2i-n)\right]\left[\prod_{i=1}^{n}(2i)\right]^{-1}\left[\prod_{i=1}^{n+1}(2I+2i-n-1)\right]^{-1} \quad (47)$$

to the overall intensity of the nQC. For half-integral spin, the 1QC is the transition that attracts most interest. The relaxation rate for this unique 1QC is defined as

$$\begin{aligned}(1/T_2)_{1/2,-1/2} = {} & (2I+3)I^{-2}(2I-1)^{-1}\{2J_1^{\mathrm{Q}}(\omega_I) \\ & +[(I+\tfrac{3}{2})(I-\tfrac{1}{2})-1]J_2^{\mathrm{Q}}(2\omega_I)\}\end{aligned} \quad (48)$$

Equation (48) is more general than suggested, and obtains in isotropic media for those situations where $J^{\mathrm{Q}}(0)$ dominates, thereby quenching the secular coupling. Equations (46) and (48) assume that $J_k^{\mathrm{Q}}(k\omega_I \pm 3k(2I-k)\omega_{\mathrm{Q}}) = J_k^{\mathrm{Q}}(k\omega_I)$. In the unlikely situation where this assumption fails, equation (46) becomes much more complex. For example, the specific relaxation rate $(1/T_2)_{1/2,-1/2}$ is given by

$$\begin{aligned}(1/T_2)_{1/2,-1/2} = {} & [I(2I-1)]^{-2}\Big\{[4I(I+1)-3][J_1^{\mathrm{Q}}(\omega_I+6\omega_{\mathrm{Q}}) \\ & +J_1^{\mathrm{Q}}(\omega_I-6\omega_{\mathrm{Q}})] \\ & +(I+\tfrac{3}{2})(I-\tfrac{1}{2})\{(I-\tfrac{3}{2})(I+\tfrac{5}{2}) \\ & \times[J_2^{\mathrm{Q}}(2\omega_I+18\omega_{\mathrm{Q}})+J_2^{\mathrm{Q}}(2\omega_I-18\omega_{\mathrm{Q}})] \\ & +(I+\tfrac{1}{2})^2[J_2^{\mathrm{Q}}(2\omega_I+6\omega_{\mathrm{Q}})+J_2^{\mathrm{Q}}(2\omega_I-6\omega_{\mathrm{Q}})]\}\Big\}\end{aligned} \quad (49)$$

5 ELECTRIC QUADRUPOLAR RELAXATION IN THE ROTATING FRAME

The preceding sections have summarized nuclear spin relaxation induced by the electric quadrupolar interaction in the absence of applied rf fields. However, sometimes it is advantagous and more informative to perform relaxation studies in the presence of a resonant or 'spin locking' field. The resultant measurement of relaxation in 'the rotating frame', provides the researcher with the opportunity to examine certain spectral densities while selectively suppressing other contributions.

It has been shown that expressions for rotating frame relaxation can be obtained very simply by replacing spectral density functions in the laboratory frame by new linear combinations of spectral density functions $J_{k\rho}^{\mathrm{Q}}$.[10] If it is assumed that a spin lock field of amplitude B_{sl} ($\gamma_I B_{\mathrm{sl}} = \omega_{\mathrm{sl}} \ll \omega_I/\gamma_I$) is applied on resonance then

$$J_{0\rho}^{\mathrm{Q}}(0) = \tfrac{1}{4}J_0^{\mathrm{Q}}(0) + \tfrac{3}{4}J_2^{\mathrm{Q}}(2\omega_I) \quad (50)$$

$$J_{1\rho}^{\mathrm{Q}}(\omega_I) = \tfrac{1}{2}J_1^{\mathrm{Q}}(\omega_I) + \tfrac{1}{2}J_2^{\mathrm{Q}}(2\omega_I) \quad (51)$$

$$J_{2\rho}^{\mathrm{Q}}(2\omega_I) = \tfrac{3}{8}J_0^{\mathrm{Q}}(2\omega_{\mathrm{sl}}) + \tfrac{1}{2}J_1^{\mathrm{Q}}(\omega_I) + \tfrac{1}{8}J_2^{\mathrm{Q}}(2\omega_I) \quad (52)$$

Thus, equation (27) becomes

$$\begin{aligned}R_{1,1}^{0,I\rho} = 1/T_{1\rho} = {} & \tfrac{2}{5}(2I+3)I^{-2}(2I-1)^{-1} \\ & \times[3J_0^{\mathrm{Q}}(2\omega_{\mathrm{sl}})+5J_1^{\mathrm{Q}}(\omega_I)+2J_2^{\mathrm{Q}}(2\omega_I)]\end{aligned} \quad (53)$$

and the analogous expression for $R_{1,1}^{1,I}$,

$$\begin{aligned}R_{1,1}^{1,I} = 1/T_2 = {} & \tfrac{2}{5}(2I+3)I^{-2}(2I-1)^{-1} \\ & \times[3J_0^{\mathrm{Q}}(0)+5J_1^{\mathrm{Q}}(\omega_I)+2J_2^{\mathrm{Q}}(2\omega_I)]\end{aligned} \quad (54)$$

reduces to

$$\begin{aligned}R_{1,1}^{1,I\rho} = 1/T_{2\rho} = {} & \tfrac{1}{10}(2I+3)I^{-2}(2I-I)^{-1} \\ & \times[3J_0^{\mathrm{Q}}(2\omega_{\mathrm{sl}})+3J_0^{\mathrm{Q}}(0) \\ & +14J_1^{\mathrm{Q}}(\omega_I)+20J_2^{\mathrm{Q}}(2\omega_I)]\end{aligned} \quad (55)$$

All expressions previously introduced can be transcribed in a similar fashion.

6 THE ELECTRIC QUADRUPOLAR INTERACTION AND DYNAMIC FREQUENCY SHIFTS

The dynamic frequency shift is associated with the imaginary part of the spectral density function introduced in equation (9):

$$\begin{aligned}L_k^{\mathrm{Q}}(\omega) = {} & (\xi_{\mathrm{QI}})^2\mathrm{Im}\Big[\int_0^\infty \langle Y_2^k(\theta(t),\phi(t))Y_2^{-k}(\theta(0),\phi(0))\rangle \\ & \times\exp(-\mathrm{i}\omega t)\,\mathrm{d}t\Big]\end{aligned} \quad (56)$$

For *isotropic*, *diffusional reorientation* of the molecular frame relative to the laboratory frame, equation (56) reduces to

$$L^{\mathrm{Q}}(\omega) = \frac{3}{160}\left(\frac{e^2qQ_I}{\hbar}\right)^2\frac{\omega\tau_2^2}{1+\omega^2\tau_2^2} = \omega\tau_2 J^{\mathrm{Q}}(\omega) \quad (57)$$

Because the dynamic frequency shift is negligible in extreme narrowing and has no adiabatic component, often this term is dismissed. However, it has been shown previously that the relaxations of numerous coherences also have no adiabatic contribution, and, in the slow motion regime, the dynamic shift can be a dominating effect.[11] The maximum dynamic frequency shift is on the order of $|\hat{\mathcal{F}}^{\mathrm{QI}}|^2/\omega_I$ and can easily exceed several kilohertz.

To illustrate the effect of the dynamic shift, consider the coherence between states $|m\rangle$ and $|m-n\rangle$ in the limit where each transition is well resolved. The dynamic frequency shift of this coherence is described by the expression

$$\begin{aligned}\Omega_{m,m-n} = {} & 2n[I(2I-1)]^{-2}\{[-4I(I+1)+24m(m-n) \\ & +8n^2+1]L_1^{\mathrm{Q}}(\omega_I)+[4I(I+1)-12m(m-n) \\ & -4n^2-2]L_2^{\mathrm{Q}}(2\omega_I)\}\end{aligned} \quad (58)$$

Of special importance are expressions for those coherences where the adiabatic contribution to the linewidth vanishes:

$$\begin{aligned}\Omega_{m,-m} = {} & 4m[I(2I-1)]^{-2}\{[-4I(I+1)+8m^2+1]L_1^{\mathrm{Q}}(\omega_I) \\ & +[4I(I+1)-4m^2-2]L_2^{\mathrm{Q}}(2\omega_I)\}\end{aligned} \quad (59)$$

The relative shift of any two components of the nQC is given by the expression

$$\Omega_{m,m-n} - \Omega_{m',m'-n} = 24n[I(2I-1)]^{-2}(m-m')(m+m'-n) \times[2L_1^{\mathrm{Q}}(\omega_I) - L_2^{\mathrm{Q}}(2\omega_I)] \quad (60)$$

Except for the case where $m = I$ and $n = 2I$, equation (58) differs dramatically from equation (46). Consequently, there is no simple relationship between the dynamic shift and linewidth (relaxation rate) for any given spectral component.

The effects of the dynamic frequency shift on the various forms of spin order, $\hat{T}_L^{\pm k}$, can be written in a manner analogous to equation (30):

$$-\frac{\mathrm{d}}{\mathrm{d}t}\hat{T}_L^{\pm k} = \sum_{L'} S_{L,L'}^{k,I}\hat{T}_{L'}^{\pm k} \quad (61)$$

Like other relaxation parameters introduced previously, $S_{L,L'}^{k,I}$ vanishes unless $L = L'$, $L' \pm 2$. In extreme narrowing, the term $S_{1,3}^{1,I}$ is proportional to $2L_1^{\mathrm{Q}}(\omega_I) - L_2^{\mathrm{Q}}(2\omega_I)$ and scales as $(\omega_I\tau_2)^3\ J^{\mathrm{Q}}(\omega_I)$, thus ensuring the insignificance of the dynamic frequency shift in this limit. The intrinsic shift of the transverse 'magnetization', $S1,1^{1,I}$, can be written as

$$S_{1,1}^{1,I} = -\tfrac{2}{5}(2I+3)I^{-2}(2I-1)^{-1}[L_1^{\mathrm{Q}}(\omega_I) + 2L_2^{\mathrm{Q}}(2\omega_I)] \quad (62)$$

Figure 1 summarizes the frequency dependence of the various relaxation rates introduced thus far. Rates applicable for $I = 1$ are shown explicitly. Note that the second-order dynamic frequency shift associated with the 2QC exceeds the relaxation rate in the slow motion limit ($\omega_I\tau_2 \gg 1$).

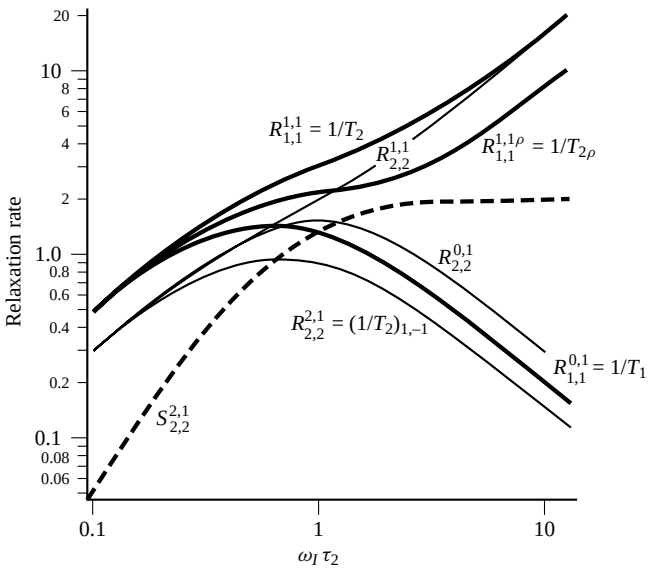

Figure 1 A plot of the various quadrupolar relaxation rates for an $I = 1$ nuclear spin versus isotropic rotational correlation time, measured in units of the reciprocal Larmor frequency. Conventional rates, $1/T_1$, $1/T_2$ (= $1/T_{1\rho}$ in the limit shown), and $1/T_{2\rho}$ are represented by the heavy full curves. Rates associated with relaxation of the three forms of two-spin order are shown as lighter full curves. The dynamic frequency shift of the double quantum coherence is shown as a dotted curve

7 EFFECTS OF ALTERNATIVE SOURCES OF RELAXATION FOR QUADRUPOLAR NUCLEI

Although $I \geq 1$ nuclei generally are driven towards equilibrium by electric quadrupolar relaxation, other sources of relaxation play important roles in relaxation-induced polarization and coherence transfer.[12] For example, as resonance experiments are performed at higher and higher magnetic field strengths, anisotropic shielding will continue to play an increasingly important role in magnetic relaxation of quadrupolar nuclei.

Utilizing the spin operators and notation introduced earlier, the relaxation of a nuclear spin I by an axially symmetric anisotropic shielding ($\Delta\sigma = \sigma_{zz} - \sigma_{xx} = \sigma_{zz} - \sigma_{yy}$) is described by the concise, general expression:

$$R_{L,L'}^{k,I} = R_{L,L'}^{k,I'} = \delta_{LL'}\{2L(L+1)J_1^{\mathrm{SA}}(\omega_I) + k^2[\tfrac{8}{3}J_0^{\mathrm{SA}}(0) - 2J_1^{\mathrm{SA}}(\omega_I)]\} \quad (63)$$

For isotropic reorientation,

$$J^{\mathrm{SA}}(\omega) = \frac{1}{30}\frac{(\gamma_I B_0 \Delta\sigma_I)^2\tau_2}{1+\omega^2\tau_2^2} \quad (64)$$

This expression, when compared with equation (31), indicates that higher forms of spin order are relaxed with increasing efficiency by shielding anisotropy.

Of special interest are the adiabatic contributions, which dominate the decay of coherence when extreme narrowing fails. In the limit where residual couplings result in well-resolved structure, the adiabatic contribution associated with the coherence between states $|m\rangle$ and $|m-n\rangle$ is simply $\frac{8}{3}n^2\ J_0^{\mathrm{SA}}(0)$. This result is independent of I or m, and only depends on the coherence order n. Meanwhile, the quadrupolar adiabatic contribution, given by equation (46), is $[I(2I-1)]^{-2}6n^2(2m-n)^2J_0^{\mathrm{Q}}(0)$. Once again, it is noted that this contribution vanishes when $n = 2m$. It should be clear that there are numerous situations where the electric quadrupolar contribution will be selectively suppressed and the relaxation characteristics of high-spin nuclei can be determined by alternative, intrinsically less efficient, relaxation pathways.

The preceding arguments implicitly presume that relaxation rates for quadrupolar and anisotropic shieldings are additive. Since both interactions are molecule-fixed and transform identically under molecular reorientation, these interactions are temporally correlated, and interference effects between these interactions must be considered. The contribution of this interference to the adiabatic portion of $(1/T_2)_{m,m-n}$ is given by the expression

$$(1/T_2)_{m,m-n}^{\text{adiabatic}} = \tfrac{1}{5}\zeta n^2(2m-n)(2I^2-I)^{-1} \times(e^2q_IQ_I/\hbar)\gamma_I B_0\Delta\sigma_I\tau_2 \quad (65)$$

where ζ is the relevant correlation factor. Unlike other relaxation parameters mentioned thus far, this interference distinguishes between the decay rates of the spin-inverted coherences, $\chi_{nn'}$ and $\chi_{-n'-n}$.

To illustrate the significance of equation (65), consider the situation where the unique axis of the quadrupole and anisotropic shielding interactions are coincident ($\zeta = 1$) and the slow motion limit obtains. Assuming the quadrupole interaction is significantly stronger than the anisotropic

shielding interaction, the differential linebroadening can be written as

$$\frac{(1/T_2)_{m,m-n} - (1/T_2)_{-m,n-m}}{(1/T_2)_{m,m-n} + (1/T_2)_{-m,n-m}} = \frac{\frac{16}{9}I(2I-1)(2m-n)\xi}{[\frac{8}{9}I(2I-1)\xi]^2 + (2m-n)^2} \approx \frac{16I(2I-1)}{9(2m-n)}\xi \quad (66)$$

where $\xi = \gamma_I B_0 \Delta\sigma_I/(e^2 q_I Q_I/\hbar)$. For example, if $I = \frac{5}{2}$, the asymmetry in the relaxation rates (linewidths) of the two 1QCs, $\chi_{3/2,1/2}$ and $\chi_{-1/2,-3/2}$, is $\frac{80}{9}\xi$. Assuming that ξ^{-1} is on the order of 100, the anisotropic shielding interaction is 1000 times less effective than the quadrupolar interaction at relaxing 1QC directly [$\frac{8}{3}J_0^{\mathrm{SA}}(0) : \frac{6}{25}J_0^{\mathrm{Q}}(0)$]. However, this same set of parameters will result in a 10% relaxation asymmetry between these two components!

Another source of relaxation that may play an increasingly important role in the relaxation of quadrupolar nuclei is the electron–nuclear anisotropic hyperfine interaction. Although the hyperfine interaction can effect nuclear spin relaxation in numerous ways, in this discussion, only relaxation effects attributed to the coupling of a nuclear spin to the thermal average of electron spin, $\langle \hat{S}_z(\mathrm{eq})\rangle = g_e\beta S(S+1)B_0/3kT$, modulated by molecular reorientation, are considered. In appropriate limits, this interaction, which is formally equivalent to an anisotropic shielding, results in 'Curie' relaxation of nuclear spin.[13] The effect of 'Curie' relaxation on the various spin operators introduced earlier can be summarized by the expression

$$R^{k,I}_{L,L'} = R^{k,I'}_{L,L'} = \delta_{LL'}\{2L(L+1)J_1^{\mathrm{CR}}(\omega_I) + k^2[\tfrac{8}{3}J_0^{\mathrm{CR}}(0) - 2J_1^{\mathrm{CR}}(\omega_I)]\} \quad (67)$$

For isotropic reorientation,

$$J^{\mathrm{CR}}(\omega) = \frac{3}{10}\left(\frac{g_e\beta S(S+1)B_0}{3kT}\right)^2 (\gamma_I g_e\beta\langle r^{-3}\rangle)^2 \frac{\tau_2}{1+\omega^2\tau_2^2} \quad (68)$$

Like anisotropic chemical shielding, this interaction can interfere with the quadrupolar interaction. The contribution of this interference to the adiabatic portion of $(1/T_2)_{m,m-n}$ is given by

$$(1/T_2)^{\mathrm{adiabatic}}_{m,m-n} = \tfrac{3}{5}\zeta n^2(2m-n)(2I^2-I)^{-1}\frac{e^2 q_I Q_I}{\hbar} \times \left[\frac{g_e\beta S(S+1)B_0}{3kT}\right]^2 (\gamma_I g_e\beta\langle r^{-3}\rangle)^2\tau_2 \quad (69)$$

where ζ is the relevant correlation factor.

In general, interference (dipole–quadrupole, anisotropic shielding–quadrupole, 'Curie spin'–quadrupole, or quadrupole–quadrupole) retards the relaxation process and results in polarization/coherence transfer. In a spherical tensor description of relaxation, interference (cross correlation) between anisotropic shieldings or 'Curie spin' and the electric quadrupolar interaction results in terms such as $R^{k,I}_{L,L\mp1}$ being nonzero. Hence, various forms of spin order of differing parity are coupled together by these interference terms. This coupling persists in all motional limits. As noted earlier, the magnitudes of these couplings scale as the geometric mean of the two competitive interactions, and can be significant even in the limit where one interaction dominates conventional relaxation parameters.[14]

8 IMPACT OF QUADRUPOLAR RELAXATION ON SPIN-$\frac{1}{2}$ NUCLEI

In multispin systems containing both quadrupolar ($I \geq 1$) and dipolar ($I = \frac{1}{2}$) nuclei, the high-spin nuclei generally are relaxed efficiently by quadrupolar interactions whereas spin-$\frac{1}{2}$ nuclei relax on a slower timescale. Thus, from the perspective of a spin-$\frac{1}{2}$ nucleus (S), the scalar coupling to a quadrupolar nucleus (I), $J\hat{\boldsymbol{S}}\cdot\hat{\boldsymbol{I}}(t)$, appears time-dependent, and, on the average, vanishes. Although the quadrupolar nucleus provides a source of relaxation (scalar relaxation of the second kind) for spin-$\frac{1}{2}$ nuclei, multiplet structure disappears as these spins are decoupled by the relaxation process.[15]

Nevertheless, there are an increasing number of studies demonstrating that various quadrupolar nuclei often exhibit narrowed lines and multiplet structure in solution state NMR studies. Such situations commonly characterize studies involving important isotopes of hydrogen, nitrogen and oxygen. In the limit where the spectrum of spin S consists of $2I + 1$ evenly spaced multiplet components, quadrupolar relaxation of spin I generally provides the dominant relaxation sink for dissipation of S-spin 1QC. However, neither I-spin adiabatic terms nor I-spin dynamic frequency shifts will influence the behavior of spin S. If it is assumed that all $2I + 1$, 1QC components are well resolved then a well-defined relaxation rate $1/T_2$ can be assigned to each coherence associated with the S-spin transition $|\frac{1}{2}, m\rangle \leftrightarrow |-\frac{1}{2}, m\rangle$:

$$(1/T_2)_{I,m} = 4(2I^2-I)^{-2}\{[I(I+1)(4m^2+1) - m^2(4m^2+5)]J_1^{\mathrm{Q}}(\omega_I) + [I^2(I+1)^2 - 2I(I+1)(m^2+1) + m^2(m^2+5)]J_2^{\mathrm{Q}}(2\omega_I)\} \quad (70)$$

A listing of these relaxation rates for half-integer spin is given in Table 2.

Also, quadrupolar–anisotropic shielding interference—for spin I!—can dramatically effect linewidths in the S spectrum,

Table 2 The Electric Quadrupolar Contribution to the Relaxation Rate $(1/T_2)_{I,m}$ for each Single Quantum Coherence Identified with the Specific Transition $|S = \frac{1}{2}, S_z = \frac{1}{2}; I, m\rangle \leftrightarrow |S = \frac{1}{2}, S_z = -\frac{1}{2}; I, m\rangle$

	$I = \frac{3}{2}$	$I = \frac{5}{2}$	$I = \frac{7}{2}$	$I = \frac{9}{2}$
$m = \pm\frac{1}{2}$	$\frac{8}{3}(J_1^{\mathrm{Q}} + J_2^{\mathrm{Q}})$	$\frac{16}{25}(J_1^{\mathrm{Q}} + \frac{7}{2}J_2^{\mathrm{Q}})$	$\frac{40}{147}(J_1^{\mathrm{Q}} + 7J_2^{\mathrm{Q}})$	$\frac{4}{27}(J_1^{\mathrm{Q}} + \frac{23}{2}J_2^{\mathrm{Q}})$
$m = \pm\frac{3}{2}$	$\frac{8}{3}(J_1^{\mathrm{Q}} + J_2^{\mathrm{Q}})$	$\frac{36}{25}(\frac{14}{9}J_1^{\mathrm{Q}} + J_2^{\mathrm{Q}})$	$\frac{8}{7}(J_1^{\mathrm{Q}} + \frac{9}{7}J_2^{\mathrm{Q}})$	$\frac{2}{3}(J_1^{\mathrm{Q}} + \frac{13}{6}J_2^{\mathrm{Q}})$
$m = \pm\frac{5}{2}$		$\frac{4}{5}(2J_1^{\mathrm{Q}} + J_2^{\mathrm{Q}})$	$\frac{120}{147}(\frac{37}{15}J_1^{\mathrm{Q}} + J_2^{\mathrm{Q}})$	$\frac{38}{27}(J_1^{\mathrm{Q}} + J_2^{\mathrm{Q}})$
$m = \pm\frac{7}{2}$			$\frac{8}{21}(3J_1^{\mathrm{Q}} + J_2^{\mathrm{Q}})$	$\frac{14}{27}(\frac{24}{7}J_1^{\mathrm{Q}} + J_2^{\mathrm{Q}})$
$m = \pm\frac{9}{2}$				$\frac{2}{9}(4J_1^{\mathrm{Q}} + J_2^{\mathrm{Q}})$

as shown by the following expression:

$$(1/T_2)_{I,m} = 4m(2I^2 - I)^{-1}[2I(I+1) - 2m^2 - 1] \times \frac{\zeta}{5} \frac{e^2 q_I Q_I}{\hbar} \frac{\gamma_I B_0 \Delta\sigma_I \tau_2}{1 + \omega_I^2 \tau_2^2} \quad (71)$$

Finally, quadrupolar–dipolar interferences can induce significant dynamic frequency shifts of individual spin-$\frac{1}{2}$ multiplet components and serve as a novel source of scalar relaxation.[16]

9 SUMMARY

In this article, the essential perturbation–response characteristics of quadrupolar (multipolar) nuclei have been introduced. For electric quadrupolar relaxation in the limit where the spectral density is neither projection- (k) nor frequency-dependent, exceptionally simple behavior is predicted [cf. equation (31)]. Likewise, when residual splittings suppress transverse cross relaxation, elementary expressions adequately describe the decay of all forms of spin coherence [cf. equation (46)]. In the slow motion limit, where adiabatic terms generally dominate the decay of coherence, it is recognized that various coherences, which lack an adiabatic contribution, decay on the timescale of the longitudinal magnetization. For these coherences, the dynamic frequency shift can prove important. Although quadrupolar interactions efficiently dissipate coherence and thermalize polarization, transfer of polarization is driven by interference effects and, necessarily, by weaker interactions that generally play only a very minor role in conventional relaxation studies.

10 RELATED ARTICLES

Brownian Motion and Correlation Times; Dynamic Frequency Shift; Quadrupolar Interactions; Quadrupolar Nuclei in Liquid Samples; Relaxation: An Introduction; Relaxation of Quadrupolar Nuclei Measured via Multiple Quantum Filtration; Relaxation Theory: Density Matrix Formulation.

11 REFERENCES

1. N. E. Ainbinder and I. G. Shaposhnikov, *Adv. Nucl. Quad. Reson.*, 1976, **3**, 67.
2. W. T. Huntress, in *Advances in Magnetic Resonance*, ed. J. S. Waugh, Academic Press, New York, 1970, Vol. 4, p. 1.
3. P. S. Hubbard, *Phys. Rev.*, 1969, **180**, 319.
4. E. Matthias, B. Olsen, D. A. Shirley, and J. E. Templeton, *Phys. Rev. A*, 1971, **4**, 1626.
5. L. G. Werbelow, D. A. Ikenberry, and G. Pouzard, *J. Magn. Reson.*, 1983, **51**, 409.
6. L. Einarsson and P. O. Westlund, *J. Magn. Reson.*, 1988, **79**, 30.
7. N. C. Pyper, *Mol. Phys.*, 1971, **21**, 1.
8. P. S. Hubbard, *J. Chem. Phys.*, 1970, **53**, 985.
9. L. G. Werbelow and A. G. Marshall, *J. Magn. Reson.*, 1981, **43**, 443.
10. J. R. C. Van der Maarel, *J. Chem. Phys.*, 1991, **91**, 1446; S. W. Kelly and C. A. Sholl, *J. Phys.: Condens. Matter*, 1992, **4**, 3317.
11. L. Werbelow and G. Pouzard, *J. Phys. Chem.*, 1981, **85**, 3887.
12. L. G. Werbelow, in *Nuclear Magnetic Resonance Probes of Molecular Dynamics*, ed. R. Tycko, Plenum, Press, New York, 1994, p. 223.
13. M. Gueron, *J. Magn. Reson.*, 1975, **19**, 58; I. Bertini, C. Luchinat, and D. Tarchi, *Chem. Phys. Lett.*, 1993, **203**, 445; D. Petit, J.-P. Korb, A. Delville, J. Grandjean, and P. Laszlo, *J. Magn. Reson.*, 1992, **96**, 252.
14. L. G. Werbelow, *J. Magn. Reson.*, 1986, **67**, 66; L. G. Werbelow, A. Allouche, and G. Pouzard, *J. Chem. Soc., Faraday Trans. 2*, 1987, **83**, 871; L. Werbelow and A. Thevand, *J. Magn. Reson., Ser. A*, 1993, **105**, 88.
15. J. Pople, *Mol. Phys.*, 1958, **1**, 168.
16. R. E. London, D. M. LeMaster, and L. G. Werbelow, *J. Am. Chem. Soc.*, 1994, **116**, 8400; S. Grzesiek and A. Bax, *J. Am. Chem. Soc.*, 1994, **116**, 10196; L. G. Werbelow and R. E. London, *J. Chem. Phys.*, 1995, **102**, 5181.

Biographical Sketch

Lawrence G. Werbelow. *b* 1948. B.S., 1970, Humboldt State University, U.S.A. Ph.D., 1974, University of British Columbia, (thesis advisor A. G. Marshall). Research Associate (with D. M. Grant) and Instructor, University of Utah, 1974–78; D.Sc., Université de Provence, 1979. Professor, New Mexico Tech, 1980–present. Professor, Université d'Aix Marseille I, 1990–95.Approx. 70 publications in the field of magnetic resonance. Current research interests include the study of relaxation-induced polarization/coherence transfer and the development of methods for isolation/identification of ultrafine interactions involving nuclear spin.

Satellite Transition NMR Spectroscopy of Half-Integer Quadrupolar Nuclei under Magic-Angle Spinning

Zhehong Gan

Center of Interdisciplinary Magnetic Resonance (CIMAR), National High Magnetic Field Laboratory (NHMFL), Tallahassee, FL, USA

1 Introduction 1
2 Quadrupolar Effects 2
3 1D Satellite Transition Magic-Angle Spinning Spectra 3
4 2D Satellite Transition Magic-Angle Spinning Experiment 6
5 Conclusions 9
6 References 9

1 INTRODUCTION

Most of the magnetically active nuclei in the Periodic Table possess spins with $S > 1/2$ that are known as quadrupolar nuclei because of the quadrupolar moment of nuclei interacting with surrounding electric field gradient.[1] Quadrupolar interactions, typically in the order of MHz, often dominate over other spin interactions such as dipolar coupling and chemical shift anisotropy and make NMR spectra of powder samples very broad. When the quadrupolar splitting is small compared to the Zeeman energy differences, perturbation theory may be used to express the quadrupolar coupling Hamiltonian to first order.[1]

$$H_Q^{(1)} = \frac{c_q}{4S(2S-1)}(3S_z^2 - S^2)\left(\frac{3\cos^2\beta - 1}{2} - \frac{\eta}{2}\sin^2\beta\cos 2\alpha\right) \quad (1)$$

The S_z^2 dependence immediately leads to a vanished first-order effect to the single-quantum $m_z = -1/2 \leftrightarrow 1/2$ transition of half-integer quadrupolar nuclei. Absence of a first-order effect reduces the central transition line width to the order of kHz. Magic-angle sample spinning narrows the central transition line further by suppressing chemical shift anisotropy and dipolar interactions. The improvement on spectral resolution has made NMR spectroscopy of half-integer quadrupolar nuclei a powerful tool for structural characterization of a variety of solid materials despite of the large quadrupolar interactions.[2–5]

There are multiple transitions among the $2S + 1$ energy-level manifolds of spins with $S > 1/2$. This article focuses on pairs of single-quantum transitions on two sides of the central transition known as satellite transitions. Satellite transitions are affected by quadrupolar interaction to first order and their static NMR spectra are usually very broad. It is not surprising that there are fewer NMR studies on satellite transitions than on central transitions. However, the advent of magic-angle spinning technology has made the acquisition of satellite transition spectra easier than ever.[6–9] Fast sample spinning can average the first-order quadrupolar effect to zero with spinning axis precisely at the magic-angle, yielding sharp resonance lines and spinning sidebands.[7–9] Perhaps the best-known satellite transition spectrum is that of KBr. The small quadrupolar coupling from lattice distortion of the nominally cubic KBr ($\sim$100 kHz) makes the ^{79}Br satellite transitions easily detectable. The sensitivity of satellite transition spinning sidebands on magic-angle setting and the convenience of the Larmor frequency very close to ^{13}C have made KBr an ideal sample for magic-angle calibration.[10]

For large quadrupolar couplings, spinning sidebands in MAS satellite transition spectra are broadened by the second-order quadrupolar effect similar to central transition peaks.[7,9] Averaging the second-order quadrupolar effect has been a long-standing issue in high-resolution NMR of half-integer quadrupolar nuclei. Unlike dipolar coupling and chemical shift anisotropy, the second-order effect contains high-rank anisotropic terms that cannot be averaged by MAS.[4,5] Residual second-order effects broaden resonance lines and may prevent resolution among nonequivalent sites. Observing satellite transitions can be advantageous in better spectral resolution over the commonly observed central transition. Samoson has discovered that the second-order effect to $\pm 3/2 \leftrightarrow \pm 1/2$ satellite transitions is 24/7 times smaller than the central transition for $S = 5/2$ spins and the relative position between satellite and central transition peaks can be used to separate the contribution from the isotropic second-order quadrupolar shift for chemical shift measurements.[6] Results at high magnetic fields and with fast spinning speed have clearly demonstrated these advantages.[9] Jakobsen et al. have studied the intensities of satellite transition spinning sidebands for measuring quadrupolar coupling parameters in analogy to the analysis of chemical shift spinning sidebands by Maricq and Waugh and by Herzfeld and Berger.[11,12] Satellite transitions are directly affected by the first-order quadrupolar interactions and the spinning sideband analysis is mostly suitable for small quadrupolar couplings with powder patterns up to 1 MHz wide.[7] Satellite transitions also play an important role in spin dynamics of central transitions such as in nutation and spin-lock experiments. The central transition matrix element of spin operator S_x equals to $(S + 1/2)$ therefore the nutation frequency of the central transition is $(S + 1/2)$ times faster than a $S = 1/2$ spin with the assumption of an isolated two-level system for the central transition. The presence of satellite transitions causes the central transition coherence to nutate at multiple frequencies that can affect the excitation and the quantitative nature of central transition spectra.[13] Spin-lock is important in cross-polarization and coherence transfer and can be easily achieved by a continuous-wave RF field for $S = 1/2$ spins. For half-integer quadrupolar nuclei, however, the presence of satellite transitions makes spin-lock of central transitions a non-trivial matter under magic-angle spinning.

The central transition coherence can leak through satellite transitions during repeated zero-crossings induced by the sample rotation.[14]

The second-order quadrupolar effect remains even under MAS and broadens resonance lines. Although high magnetic fields can reduce the second-order effect, ideally it is the best to average all anisotropic terms for so-called isotropic NMR spectra. This goal was first achieved by double rotation (DOR). The first rotation at the magic-angle averages the $l = 2$ anisotropic terms and the second rotation inside the MAS rotor at an angle that $P_4(\cos 30.56^\circ) = 0$ averages the residual high-rank $l = 4$ anisotropic terms.[15] A two-dimensional experiment with flipping spinning axis, namely dynamic angle spinning (DAS), was also proposed to refocus the signal decay caused by the anisotropic second-order effect.[16] Both DOR and DAS techniques lead to isotropic NMR spectra of half-integer quadrupolar nuclei; nevertheless the implementation of non-fixed axes sample spinning is technically difficult.[17,18] The invention of multiple-quantum magic-angle spinning (MQMAS) by Frydman et al. opened a new avenue toward isotropic NMR spectra.[19,20] Correlation between $-m_q/2 \leftrightarrow m_q/2$ multiple-quantum and central transitions refocuses the signal decay caused by the second-order effect and results in isotropic spectra. Transition-correlated experiments can be performed with commercially available MAS probes and it has gained a widespread use. However, low sensitivities and the poor quantitative nature of the MQ experiment remain as the major obstacles to its applications and a number of excitation and conversion schemes have been developed to improve the efficiencies of manipulating MQ coherence.[21–32] Recently, a different approach was proposed to dramatically improve the efficiency of transition-correlated experiments.[33] The satellite transition magic-angle spinning (STMAS) experiment correlates single-quantum satellite transitions that can be directly excited and efficiently converted to central transitions.[34] The high efficiencies of the satellite transition experiment have been demonstrated. It has also been shown that accurate magic-angle setting and stable sample spinning are required to average out the first-order quadrupolar interactions to satellite transitions for generating isotropic NMR spectra of half-integer quadrupolar nuclei.[34]

The scope of this article focuses on recent developments on satellite transition NMR spectroscopy particularly the STMAS experiment. The first half presents the theory of satellite transition NMR. The second-order quadrupolar effect to satellite transitions is expanded in rotation matrix elements. The expansion and the comparison with central transitions reveal important features of satellite transition NMR spectra. These features are demonstrated experimentally with model samples of various spins. The second half describes the STMAS experiment. The principle of the experiment to obtain isotropic NMR spectra is explained and the excitation and conversion of satellite transitions are studied. The experiment is demonstrated with various pulse sequences and model samples and the strict requirements on magic-angle setting and sample spinning stability are discussed.

2 QUADRUPOLAR EFFECTS

When the Zeeman splitting is sufficiently large compared to the effect of electric field gradients, the magnetization quantum number $m_z = S, S-1, \ldots, -S$ may be used to describe

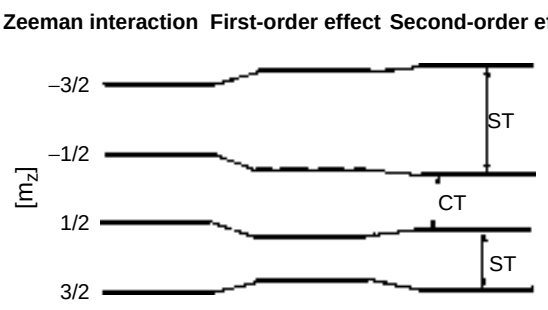

Figure 1 Energy level diagram of a $S = 3/2$ spin

the system to the first order. The energy levels of a nuclear spin S are split into a $2S + 1$ manifold separated by Larmor frequency. The first-order quadrupolar interaction shifts the energy levels by $\omega_q\ [3m_z^2 - S(S+1)]$ and has no effect on $-m_z \leftrightarrow m_z$ transition (see Figure 1). For half-integer spins, the $-1/2 \leftrightarrow 1/2$ central transition is a single-quantum transition that can be observed directly. For integer spins, all single-quantum transitions are affected by the first-order quadrupolar interaction and double-quantum transitions may have a vanished first-order effect. High-resolution double-quantum spectroscopy has been explored with indirect detection for ^{2}H nuclei and with overtone detection for ^{14}N nuclei.[35–37] The topics on integer-spins can be found in these references and will not be discussed further here. A number of review articles are also recommended for general aspect of central transition NMR and early works on satellite transition spectroscopy.[38–41]

The second-order quadrupolar effect is derived using Average Hamiltonian theory.[42] The full quadrupolar Hamiltonian can be expressed in terms of irreducible second-rank spin operators

$$H_Q = \omega_q \sum_{m=-2}^{2} (-1)^m Q_{2,-m} T_{2,m}, \quad \omega_q = \frac{2\pi e^2 q_{zz} Q}{2S(2S-1)h} \tag{2}$$

$$T_{2,0} = \frac{(3S_z^2 - S^2)}{\sqrt{6}}$$

$$T_{2,\pm 1} = \frac{\mp(S_\pm S_z + S_z S_\pm)}{2} \tag{3}$$

$$T_{2,\pm 2} = \frac{S_\pm^2}{2}, \quad S_\pm = S_x \pm i S_y$$

The quadrupolar coupling tensor components $Q_{2,m}$ can be obtained from the components in the principal axis system (PAS) frame through a rotation to the laboratory frame (α, β, γ)

$$Q_{2,m} = \sum_{m'=-2}^{2} \rho_{2,m'} D^2_{m',m}(\alpha, \beta, \gamma) \tag{4}$$

$$\rho_{2,0} = \sqrt{\frac{3}{2}}, \quad \rho_{2,\pm 1} = 0, \quad \rho_{2,\pm 2} = -\frac{\eta}{2} \tag{5}$$

$\eta = (q_{yy} - q_{xx})/q_{zz}$ is the asymmetry factor of the EFG tensor. The $T_{2,0}$ term in the quadrupolar Hamiltonian commutes with Zeeman interaction and affects the transitions in the first-order.

The second-order effect can be obtained by applying Average Hamiltonian theory in the NMR rotating frame:[43]

$$H_Q^{(2)} = -\left\{ Q_{2,-1}Q_{2,1}[T_{2,-1}, T_{2,1}] + \frac{Q_{2,-2}Q_{2,2}[T_{2,-2}, T_{2,2}]}{2} \right\} \frac{\omega_q^2}{\omega_0} \quad (6)$$

where $\omega_0 = -\gamma B_0$ is Larmor frequency. The commutators in the second-order Hamiltonian can be derived explicitly

$$[T_{2,-1}, T_{2,1}] = -\left(4S^2 - 8S_z^2 - 1\right) S_z / 2$$
$$[T_{2,-2}, T_{2,2}] = -\left(2S^2 - 2S_z^2 - 1\right) S_z \quad (7)$$

and the product of spatial parameters

$$Q_{2,-m}Q_{2,m} = \sum_{m',m''=-2}^{2} \rho_{2,m'}\rho_{2,m''} D^2_{m',m}(\alpha,\beta,\gamma) \times D^2_{m'',-m}(\alpha,\beta,\gamma) \quad (8)$$

can be expanded using the Clebsch-Gordon series[44,45]

$$D^2_{m',m} D^2_{m'',-m} = \sum_{l=0}^{4} \sum_{m'+m''=-l}^{l} c(22l, m'm'') \times c(22l, m-m) D^l_{m'+m'',0} \quad (9)$$

Equations (6)–(9) lead to the second-order quadrupolar Hamiltonian expanded in rotation matrix elements

$$H_Q^{(2)} = \frac{\omega_q^2}{\omega_0} \sum_{l=0,2,4} C_l(S, S_z) \sum_{m=-l}^{l} a^{(2)}_{l,m} D^l_{m,0}(\alpha,\beta,\gamma) \quad (10)$$

$$C_l(S, S_z) = c(22l; 1-1)\left(4S^2 - 8S_z^2 - 1\right) S_z + c(22l; 2-2)\left(2S^2 - 2S_z^2 - 1\right) S_z \quad (11)$$

$$a^{(2)}_{l,m} = \sum_{m'+m''=m} c(22l; m'm'')\rho_{2,m'}\rho_{2,m''} / 2 \quad (12)$$

The expansion coefficients $a^{(2)}_{l,m}$ vanish for $l = 1$ and 3 because of the relation $c(l_1l_2l; m_1m_2) = (-1)^{l_1+l_2+l} c(l_2l_1l; m_2m_1)$ of Clebsch-Gordon coefficients.[43,44] Thus, the second-order quadrupolar Hamiltonian contains an $l = 0$ isotropic term, the $l = 2$ terms and the high-rank $l = 4$ anisotropic terms.

The shift to transition frequencies by the second-order effect can be calculated from the expectation values of the $C_l(S, S_z)$ in $H_Q^{(2)}$. For central transitions $m_z = -1/2 \leftrightarrow 1/2$

$$\omega_{CT} = \sum_{l=0,2,4} C_l(\alpha,\beta,\gamma)$$

$$C_l = \frac{\omega_q^2[S(S+1) - 3/4]}{\omega_0} \sum_{m=-l}^{l} c_{l,m} D^l_{m,0}(\alpha,\beta,\gamma) \quad (13)$$

$$c_{l,m} = -[2c(22l; 1-1) + c(22l; 2-2)] \times \sum_{m'+m''=m} c(22l; m'm'')\rho_{2,m'}\rho_{2,m''} \quad (14)$$

Table 1 Expansion Coefficients c_{lm} of the Second-Order Quadrupolar Effect to Central Transitions

	$m = 0$	$m = \pm 2$	$m = \pm 4$
$l = 0$	$\frac{3}{10}\left(1 + \frac{\eta^2}{3}\right)$		
$l = 2$	$\frac{6}{7}\left(1 - \frac{\eta^2}{3}\right)$	$\frac{2\sqrt{6}}{7}\eta$	
$l = 4$	$-\frac{81}{70}\left(1 + \frac{\eta^2}{18}\right)$	$\frac{27\sqrt{10}}{140}\eta$	$-\frac{9\sqrt{70}}{280}\eta^2$

The explicit expressions of $c_{l,m}$ are listed in Table 1.

The second-order quadrupolar Hamiltonian in equation (10) implies that the second-order effect varies among transitions only through the expectation values of $C_l(S, S_z)$. For $m_S - 1/2 \leftrightarrow m_S + 1/2$ satellite transition, the frequency shift from the second-order effect can be expressed in terms of the expansion coefficients of the central transitions and corresponding scaling factors

$$\omega_{ST} = \sum_{l=0,2,4} R^l_{S,m_S} C_l(\alpha,\beta,\gamma) \quad (15)$$

$$R^l_{S,m_S} = 1 - \frac{12m_s^2[4c(22l; 1-1) + c(22l; 2-2)]}{[4S(S+1) - 3] \cdot [2c(22l; 1-1) + c(22l; 2-2)]} \quad (16)$$

The explicit expressions of the scaling factors for $l = 0$, 2 and 4 are

$$R^0_{S,m_S} = 1 - \frac{36m_s^2}{4S(S+1) - 3}, \quad l = 0 \quad (17)$$
$$R^2_{S,m_S} = 1 - \frac{18m_s^2}{4S(S+1) - 3}, \quad l = 2$$
$$R^4_{S,m_S} = 1 - \frac{68m_s^2}{3[4S(S+1) - 3]}, \quad l = 4$$

Table 2 lists the scaling factors for all satellite transitions with spins S up to 9/2.

3 1D SATELLITE TRANSITION MAGIC-ANGLE SPINNING SPECTRA

The previous section derived the first and second-order quadrupolar effect to central and satellite transitions. For

Table 2 Scaling Factors of Expansion Coefficients between Satellite and Central Transitions

		$l = 0$	$l = 2$	$l = 4$
$S = 3/2$,	$m_S = \pm 1$	−2	−1/2	−8/9
$S = 5/2$,	$m_S = \pm 1$	−1/8	7/16	7/24
	$m_S = \pm 2$	−7/2	−5/4	−11/6
$S = 7/2$,	$m_S = \pm 1$	2/5	7/10	28/45
	$m_S = \pm 2$	−7/5	−1/5	−23/45
	$m_S = \pm 3$	−22/5	−17/10	−12/5
$S = 9/2$,	$m_S = \pm 1$	5/8	13/16	55/72
	$m_S = \pm 2$	−1/2	1/4	1/18
	$m_S = \pm 3$	−19/8	−11/16	−9/8
	$m_S = \pm 4$	−5	−2	−50/18

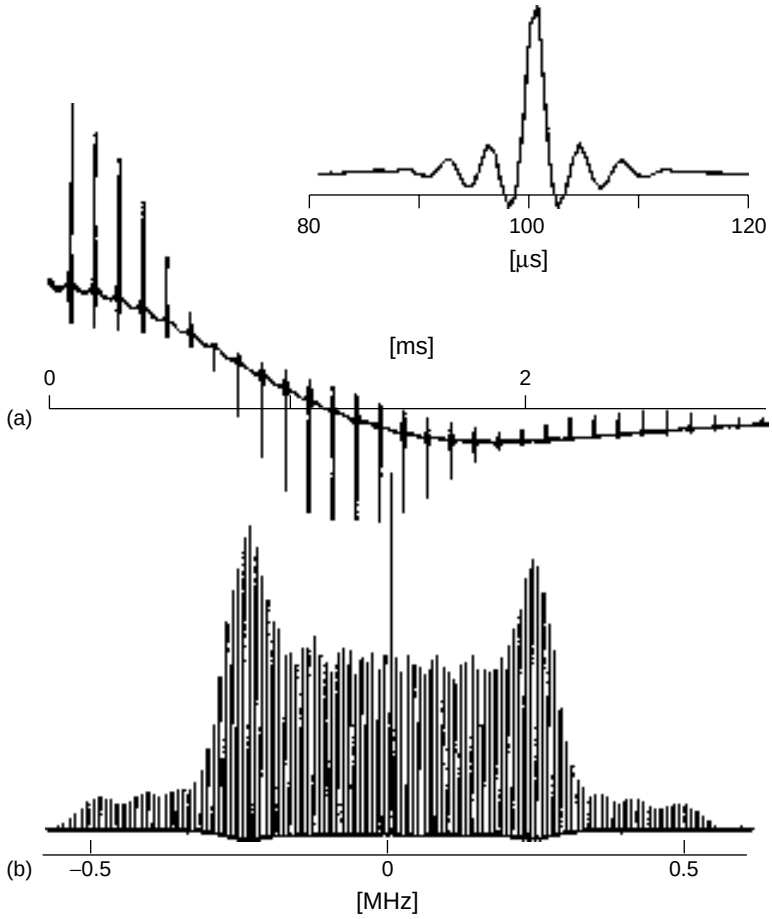

Figure 2 ^{23}Na free-induction-decay (a) and MAS spectrum (b) of $NaNO_2$ with 10 kHz spinning frequency. The insert shows the expansion to one of the rotational echoes

samples spinning at the magic-angle, the quadrupolar effects are modulated by the sample rotation. The expansion of quadrupolar effects in rotation matrix elements is advantageous because the rotation from the PAS frame to laboratory frame can be expressed as

$$D^l_{m',m}(\alpha,\beta,\gamma) = \sum_{m''=-l}^{l} D^l_{m'',m}(-\omega_r t, -\theta_M, 0) D^l_{m',m''}(\alpha_r,\beta_r,\gamma_r) = \sum_{m''=-l}^{l} d^l_{m'',m}(\theta_M) e^{im''\omega_r t} D^l_{m',m''}(\alpha_r,\beta_r,\gamma_r) \quad (18)$$

where $(\alpha_r, \beta_r, \gamma_r)$ is the rotation from the PAS frame to the rotor frame and $(-\omega_r t, -\theta_M, 0)$ describes the sample rotation with frequency ω_r and angle θ_M. Under fast sample spinning, various expansion terms of quadrupolar effects are scaled accordingly by $d^l_{0,0}(\theta_M) = P_l(\cos\theta_M)$. With the spinning axis at the magic-angle, the first-order quadrupolar effect and the $l = 2$ terms of the second-order effect are averaged. The high-rank $l = 4$ terms, however, still remain under MAS and the anisotropic second-order effect, scaled by $P_4(\cos\theta_M)$, broadens both central and satellite lines.

With finite spinning frequencies, modulation of the large first-order quadrupolar interaction yields rotational echoes in the time-domain signals and spinning sidebands in the frequency-domain spectra. Figure 2 shows a train of rotational echoes and an array of spinning sidebands as a result of averaging the first-order quadrupolar effect with spinning frequencies much lower than the quadrupolar coupling constant. The complete average of the large first-order effect occurs very briefly at the exact rotor cycles. The matching of evolution time to rotor cycles and the setting of magic-angle are the most important factors in averaging the first-order quadrupolar interactions.

The intensities of spinning sidebands show a line shape very similar to the static powder pattern. The first-order quadrupolar effect shifts satellite transition frequencies and splits the $\pm m_S - 1/2 \leftrightarrow \pm m_S + 1/2$ pair as

$$\Delta\nu^{(1)}_{m_S} = \frac{3 m_S c_q}{S(2S-1)}\left(\frac{3\cos^2\beta - 1}{2} - \frac{\eta}{2}\sin^2\beta\cos 2\alpha\right) \quad (19)$$

The maximum splitting occurs at $\beta = 0$ and leads to the full width of the powder pattern $3c_q/S(2S-1)$ for the inner pair of satellite transitions. The width increases linearly with $|m_S|$ for outer pairs of satellite transitions.

The second-order quadrupolar effect is responsible for the line shape of both central and satellite peaks under MAS. Among the expansion terms, the isotropic term $l = 0$ merely shifts the resonance frequency from the isotropic chemical shift and causes no additional line broadening. For the central

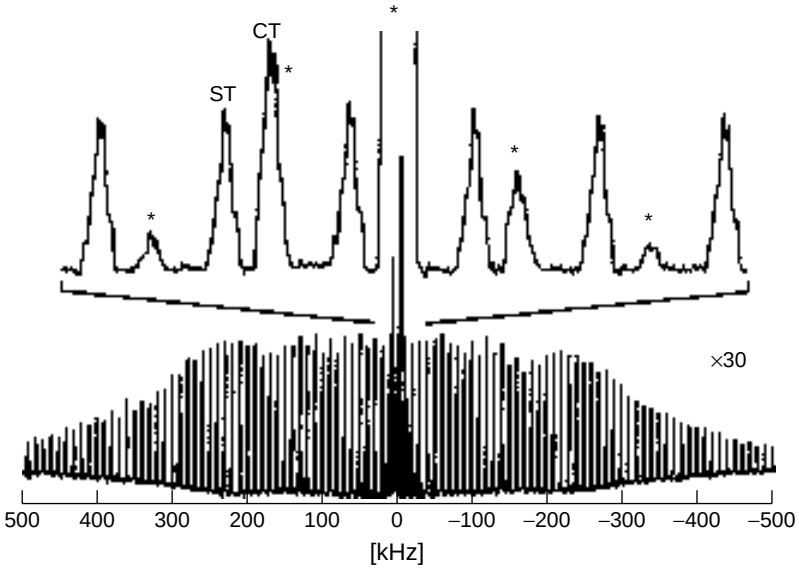

Figure 3 Satellite transition spectra of Na_2SO_4 under 10 kHz MAS

transition, the isotropic second-order quadrupolar shift is upfield (note the negative sign in $\omega_0 = -\gamma B_0$)

$$\omega_{CT}^0 = \frac{3[S(S+1) - 3/4]\omega_q^2}{10\omega_0}\left(1 + \frac{\eta^2}{3}\right) \qquad (20)$$

The terms $l = 2$ are averaged by MAS and the terms $l = 4$ become the only remaining anisotropic terms that broaden resonance lines. Because all transitions are shifted by the same anisotropic terms, $C_4(\alpha, \beta, \gamma)$, different only by the scaling factor R^4_{S,m_S}, the line shape for satellite transitions should be the same as the central transition except only the relative width determined by the scaling factors R^4_{S,m_S}. A negative R^4_{S,m_S} represents a reversed line shape.

The scaling factors R^4_{S,m_S} with explicit values listed in Table 2 are important when comparing spectral features between satellite and central transitions. Figure 3 shows the satellite transition spectra of Na_2SO_4 with spinning axis carefully calibrated to the magic-angle. The line shape of the satellite transition spinning sidebands is close to a mirror image of the central transition peak, in agreement with the scaling factor $R^4_{S,\pm1} = -8/9$ for the $S = 3/2$ spin.

Figure 4 displays the ^{27}Al satellite and central transition spectra of $9Al_2O_3 + 2B_2O_3$, a model system for spins $S = 5/2$. The sample has four non-equivalent ^{27}Al sites with quadrupolar coupling constants ranging from 6–9 MHz and the central transition lines are partially overlapped due to the line broadening by the second-order quadrupolar effects. The comparison between satellite and central transition spectra shows much narrower line width for satellite transition lines because the scaling factor of inner satellite transitions over the central transition is less than 30% ($R^4_{5/2,\pm1} = 7/24$). The outer satellite transitions in comparison are nearly twice as broad as the central transitions, $R^4_{5/2,\pm2} = -11/6$. Most of the outer satellite transition intensities are immersed in the baseline because of the broad line width and the poor excitation of outer satellite transitions. Only the relatively narrow Al_{VI} site shows a visible outer satellite transition peak. Checking

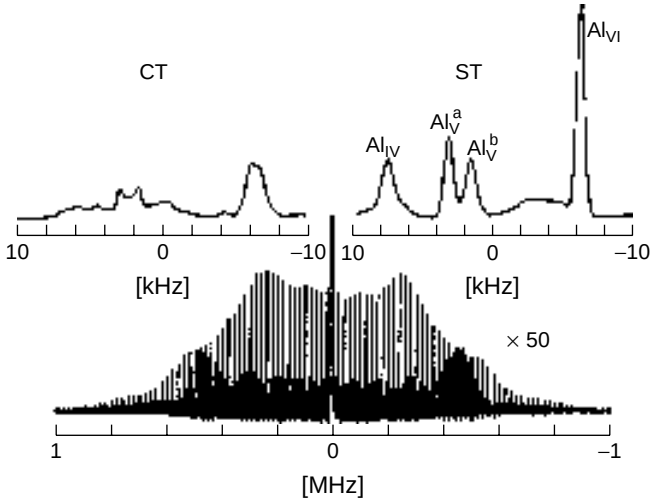

Figure 4 ^{27}Al MAS (20 kHz) spectrum of $9Al_2O_3 + 2B_2O_3$. The two inserts show the central (CT) and the satellite (ST) transition spectra within 20 kHz spectral window

through Table 2, it is interesting to find that the $\pm5/2 \leftrightarrow \pm3/2$ satellite transitions of $S = 9/2$ spins have a second-order effect 18 times smaller than the central transition that could provide much higher resolution.

The isotropic $l = 0$ term contributes no additional line broadening; however, it can change the relative peak position and affect the resolution among nonequivalent sites. In amorphous or disordered systems, the isotropic terms can become a factor in the line width. Distribution on quadrupolar couplings leads to a spread of the isotropic second-order quadrupolar shift to broaden spectral lines. For $S = 5/2$ spins, the isotropic second-order shift to the inner pair ($m_S = \pm1$) satellite transitions is 8 times smaller than the central transition and is expected to causes less line broadening by the mentioned mechanism in disordered systems.[6] In any case, satellite transition spectra compliment central transition spectra to find the best spectral resolution.

4 2D SATELLITE TRANSITION MAGIC-ANGLE SPINNING EXPERIMENT

The two-dimensional satellite transition MAS experiment correlates satellite (ω_1) with central (ω_2) transitions under magic-angle spinning.[33] The timing of the evolution period t_1 is synchronized with the rotor cycles such that the first-order quadrupolar effects to the satellite transitions are averaged by sample spinning precisely at the magic-angle. The resonance frequencies along the two dimensions are contributions from the isotropic chemical shift, the isotropic and the anisotropic $l = 4$ second-order effects

$$\omega_1 = \omega_\delta + R^0_{S,m_S}\,\omega^0_{CT} + R^4_{S,m_S}\,C_4(\Omega_r)\,P_4(\cos\theta_M)$$
$$\omega_2 = \omega_\delta + \omega^0_{CT} + C_4(\Omega_r)\,P_4(\cos\theta_M) \qquad (21)$$

For powder samples, superposition over Ω_r yields a ridge-shaped peak in the 2D STMAS spectra. The peak centers at $(\omega_\delta + \omega^0_{CT} R^0_{S,m_S}, \omega_\delta + \omega^0_{CT})$ and tilts at slope R^4_{S,m_S}. A shear of the 2D spectrum along ω_1 can make the peak parallel with the ω_2 axis and a projection to the ω_1 axis yields an isotropic peak at the position

$$\omega_{iso} = (1 - R^4_{S,m_S})\omega_\delta + (R^0_{S,m_S} - R^4_{S,m_S})\omega^0_{CT} \qquad (22)$$

In the time-domain, the signal from the correlation between satellite and central transitions can be written as

$$S(t_1, t_2) = \sum_{p_1,p_2=\pm1}\sum_{\Omega_r} E_{p_1}(\Omega_r)C_{p_1,p_2}(\Omega_r) \times e^{ip_1[\omega_\delta + R^0_{S,m_S}\omega^0_{CT} + R^4_{S,m_S}C_4(\Omega_r)]t_1} e^{ip_2[\omega_\delta + \omega^0_{CT} + C_4(\Omega_r)]t_2} \qquad (23)$$

where the factors $E_{p_1}(\Omega_r)$ and $C_{p_1,p_2}(\Omega_r)$ represent the excitation and coherence transfer of satellite transitions; p_1, $p_2 = \pm1$ are coherence orders of the single-quantum satellite and central transitions during the t_1 and t_2 periods, respectively. Superposition over Ω_r causes the signal to decay rapidly except at $t_2 = -(p_2/p_1)R^4_{S,m_S}t_1$ where coherence transfer echoes are formed. For coherence orders with $R^4_{S,m_S}p_2/p_1 > 0$, the echoes are outside the $t_1, t_2 > 0$ quadrant of the 2D time coordinate and are known as antiechoes.[45] For coherence orders with $R^4_{S,m_S}p_2/p_1 < 0$, coherence transfer echoes occur inside the $t_1, t_2 > 0$ quadrant and can be acquired directly. The signal intensities along the echo ridge $t_2 = -(p_2/p_1)R^4_{S,m_S}t_1$ oscillate at the frequency $\omega_{iso} = (1 - R^4_{S,m_S})\omega_\delta + (R^0_{S,m_S} - R^4_{S,m_S})\omega^0_{CT}$, the same expression as equation (22), and yield an isotropic NMR spectrum with a Fourier transformation.

Excitation and conversion of satellite transition coherence are critical to the efficiency of the 2D STMAS experiment. Satellite transitions are single-quantum transitions that can be excited directly. Short and strong pulses can cover the large frequency offsets caused by the first-order quadrupolar effect on the satellite transition. In Figure 4, the satellite and central transition spectra are plotted on the same intensity scale and the relative intensities indicate the efficiency of satellite transition excitation. Although individual spinning sidebands that span more than 1 MHz wide are low, the total spectral intensities from all spinning sidebands are actually higher than the CT peaks. The ratio between ST and CT intensities approaches the value $Tr(S_x^{ST}S_x) : Tr(S_x^{CT}S_x) = 16 : 9$ for the $S = 5/2$ spin assuming a uniformly excited coherence $\sigma = S_x$.

A single mixing pulse can transfer satellite transition coherence directly to central transitions. Figure 5 displays simulations and experimental results of the coherence transfer. The simulations show that the transfer is in-phase, i.e., $S_x^{(ST)} \rightarrow S_x^{(CT)}$ and $S_y^{(ST)} \rightarrow S_y^{(CT)}$ regardless of the pulse phase. Out-phase pulses, e.g., S_y pulse for $S_x^{(ST)} \rightarrow S_x^{(CT)}$ transfer, are more efficient than in-phase pulses. Simulations also show that a 180° phase shift to RF pulses has no effect on the single-pulse coherence transfer. These results suggest that a phase cycle $+x, +y, -x, -y$ to the mixing pulse balances the difference on transfer amplitude between in-phase and out-phase pulses and consequently selects the $p = -1 \rightarrow -1$ coherence transfer pathway. This pathway generates coherence transfer echoes for negative $R^4_{S,m}$ such as $S = 3/2$ spins ($R^4_{3/2,\pm1} = -8/9$) but yields coherence transfer antiechoes for spins with positive $R^4_{S,m}$. A selective π-pulse to the central transition prior to signal acquisition can convert the coherence transfer antiechoes to echoes for isotropic spectra of $S = 5/2$ spins and other spins with negative $R^4_{S,m}$. The simulations for $S = 5/2$ spins show much higher transfer amplitudes from inner satellite transitions than from outer satellite transitions. This difference can be interpreted qualitatively as the follows. Mixing of spin states by a RF pulse can be described as $|i\rangle \rightarrow \sum_j p_{ij}|j\rangle$ with $p_{ii} \rightarrow 1$ and $p_{i\neq j} \rightarrow \varepsilon$ for short pulses. For satellite transitions that share energy levels with central transition, e.g., $|1/2\rangle\langle 3/2|$, the coherence transfer $|1/2\rangle\langle 3/2| \rightarrow |1/2\rangle\langle -1/2|$ is in the order of ε. The transfer becomes second-order ε^2 for any transitions not sharing energy levels with the targeted transition. In Figure 5, the experimental optimization illustrates the high efficiency of the single-pulse mixing of inner satellite transition coherence. The optimized peak height from coherence transfer is close to 50% of peak height in the conventional central transition spectrum acquired under the same experimental conditions.

A pair of mixing-pulses sandwiched with a z-filter can also be used for the coherence transfer. The first mixing-pulse transfers satellite transition coherence to the polarization of central transitions. The second mixing-pulse flips the stored polarization for detection after the z-filter. The pulse sequence with two-pulse mixing is identical to the sequence used for 2D exchange experiments and selects both $p_1 = \pm1$ coherence-orders during the evolution period. Half of the transferred coherence contributes to the coherence transfer echoes and the other half goes to the anti-echoes. The two-pulse mixing has an advantage of pure-absorptive line shape irrespective to the signs of $R^4_{S,m}$.[33,34]

Figure 6 shows the 2D STMAS spectra of a mixed sample of Na_2SO_4 and $Na_2C_2O_4$. The correlation of satellite and central transitions yields ridge-shaped peaks that clearly resolve the overlap between two components. The peaks tilt at the slope $R^4_{3/2,\pm1} = -8/9$. A shear of the 2D spectrum corrects the tilt and results in an *isotropic* versus *anisotropic* spectrum where the projection to the isotropic-dimension shows two resolved isotropic peaks. The pulse sequence with two-pulse mixing is the same as the sequence used for 2D exchange experiments and the peak along the diagonal resulting from the central transition to central transition (CT-CT) peak is not affected by the frequency offset of satellite transitions. Thus, the relative intensities between diagonal and cross peaks

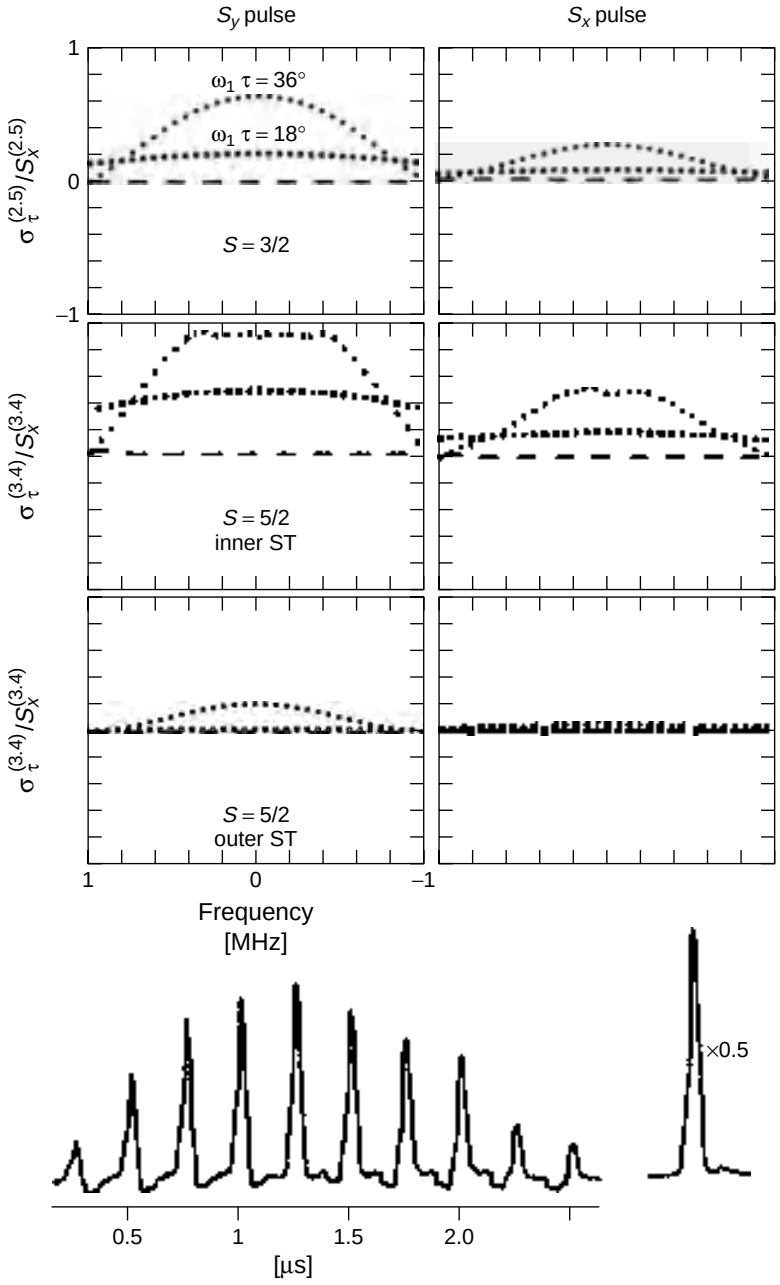

Figure 5 Coherence transfer from satellite to central transition by a single mixing pulse with RF field strength $\omega_1/2\pi = 100\,\text{kHz}$ and pulse length $\omega_1\tau = 18°$ (circles) and 36° (stars). The coherence transfer was calculated as a function of satellite transition frequency of an $S = 3/2$ and an $S = 5/2$ spins including both inner and outer satellite transitions. The two columns show the transfer by out-phase (left) and in-phase (right) pulses relative to the satellite transition coherence $S_x^{(ST)}$. The array of spectra in the bottom shows the optimization for the mixing pulse length with $\omega_1/2\pi = 60\,\text{kHz}$ for Na_2SO_4 along with a conventional central transition spectrum acquired under the same experimental conditions

are good indicators to measure the efficiencies experimentally. The two-pulse mixing yields ST-CT peaks about 30% of the diagonal peak. When the diagonal peak is compared with the ST-CT peaks (see Figure 5) obtained by the one-pulse mixing sequence under the same experimental conditions the ratio rises to nearly 80%.

Figure 7 illustrates the 2D STMAS spectrum of $9Al_2O_3 + 2B_2O_3$ for $S = 5/2$ spins. The spectrum was obtained with one-pulse mixing and a selective π-pulse before the data acquisition. The spin-echo sequence converts coherence transfer anti-echoes to echoes. The resulting spectrum is similar to $S = 3/2$ spins except that the ridge-shape peaks tilt at the opposite direction because of the sign change to the scaling factor $R^4_{5/2,\pm1} = 7/24$.

Magic-angle setting is the most critical factor in satellite transition NMR experiments. Deviations of the spinning axis from magic-angle reintroduce the first-order quadrupolar effects. Residual first-order effects can distort the satellite transition line shape and cause line broadening in 2D STMAS spectra. The line broadening can be estimated by the full width

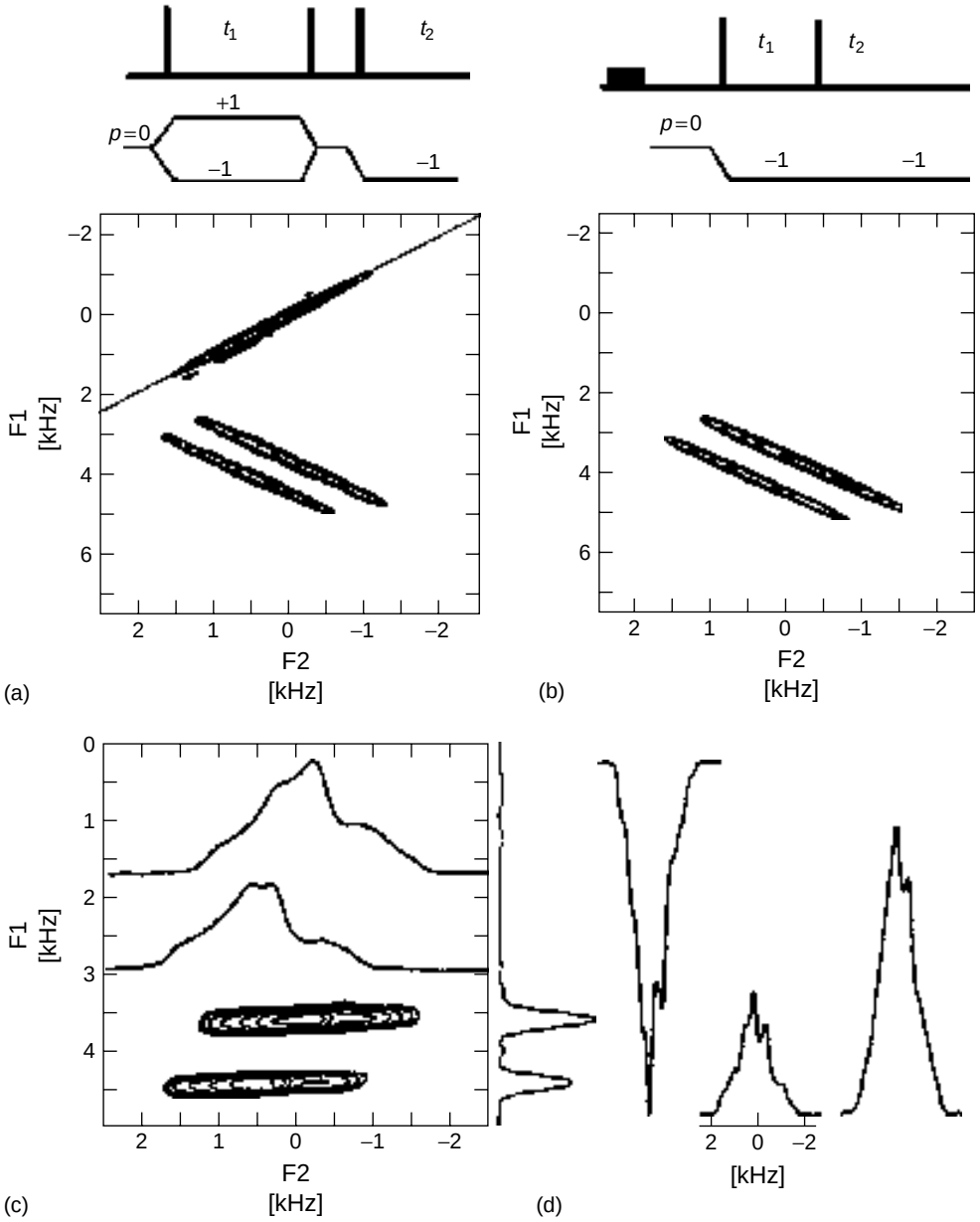

Figure 6 2D ^{23}Na STMAS spectra of a mixture of Na_2SO_4 and $Na_2C_2O_4$ acquired with (a) two-pulse mixing and (b) one-pulse mixing. The spectrum in (c) is obtained by a spectral tilt of (b) to correct the slope of ridge-shaped peaks. The projection to the isotropic dimension and the line shape along the anisotropic dimension are also plotted. The three projections in (d), from left to right, are obtained from the diagonal peak in (a) along the thin line, the cross peaks in (a), and the cross peaks in (b). The pulse sequence in (a) is identical to the sequence used for 2D exchange experiments. The phase cycle for the one-pulse mixing in (b) can be found in the text and the soft pulse is used for presaturation of the central transitions

of satellite transition powder pattern, $3c_q/S(2S-1)$, and the scaling factor $P_2(\cos\theta_S)$ by MAS

$$\Delta\nu_1 = \frac{3c_q}{S(2S-1)} P_2(\cos\theta_S) \tag{24}$$

A scaling factor $< 10^{-4}$ (0.004° in magic-angle setting) is required to reduce typical quadrupolar interactions from a few MHz to less than a few hundred Hz. Stable sample spinning is also critical to synchronize the evolution time with the rotor cycles for complete average of the first-order quadrupolar effect. A drift $\Delta\nu_r$ on spinning frequency causes a mismatch $t_1\Delta\nu_r/\nu_r$ to the synchronization condition. The mismatch at $t_1 \approx T_2^*$ should be small compared the width of the satellite transition rotational echoes Δt_1 (see Figure 1)

$$\Delta\nu_r < \nu_r \cdot \Delta t_1/T_2^* \tag{25}$$

With typical values $\nu_r \approx 10\,\text{kHz}$, $1/T_2^* \approx 300\,\text{Hz}$ and $\Delta t_1 \approx 1\,\mu s$, the stability on spinning frequency required for the STMAS experiment can be estimated about $\pm 3\,\text{Hz}$.

Finally, a comparison between MQMAS and STMAS experiments is summarized as follows. Both experiments correlate transitions of half-integer quadrupolar nuclei to obtain

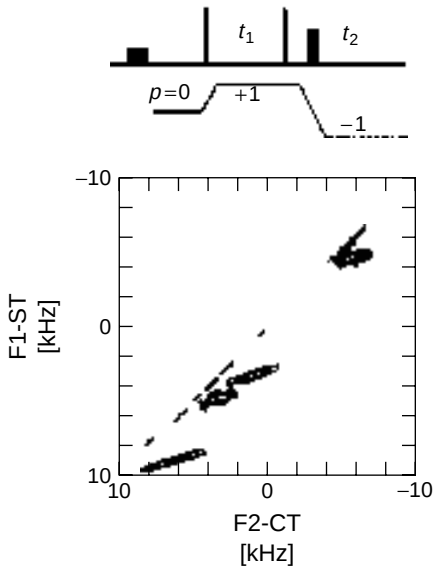

Figure 7 2D STMAS pulse sequence and spectrum of $9Al_2O_3 + 2B_2O_3$ with 20 kHz MAS. The pulse sequence uses a single pulse for mixing and the central transition selective π-pulse after the mixing generates coherence transfer echoes for $S = 5/2$ spins. The soft pulse in the beginning presaturates central transition coherence

isotropic NMR spectra under MAS. The satellite transition experiment requires accurate magic-angle setting and stable sample spinning to average out the first-order quadrupolar interactions whereas the multiple-quantum experiment correlates two transitions, both with vanished first-order effect. The excitation and the conversion of the single-quantum satellite transitions are much more efficient than that of multiple-quantum transitions. The relatively higher efficiencies allow rapid acquisition of high-resolution isotropic NMR spectra of half-integer quadrupolar nuclei (note the spectra in Figures 6 and 7 were acquired in just a few minutes).

5 CONCLUSIONS

Theoretical analysis and experimental results display the attractive features and technical requirements of satellite transition MAS NMR spectroscopy. Correlation between satellite and central transitions yields isotropic NMR spectra of half-integer quadrupolar nuclei. The transition-correlated experiment takes the advantage of efficient excitation and conversion of single-quantum satellite transitions for high-resolution NMR spectra of half-integer quadrupolar nuclei. In order to average out large first-order quadrupolar interactions, satellite transition experiment requires accurate setting of magic-angle and stable sample spinning.

6 REFERENCES

1. A. Abragam, 'Principles of Nuclear Magnetism', Clarendon Press: Oxford, 1961.
2. G. E. Maciel, *Science*, 1984, **226**, 282.
3. E. Oldfield and R. J. Kirkpatrick, *Science*, 1985, **227**, 1537.
4. E. Kundla, A. Samoson, and E. Lippmaa, *Chem. Phys. Lett.*, 1981, **83**, 229.
5. S. Ganapathy, S. Schramm, and E. Oldfield, *J. Chem. Phys.*, 1982, **77**, 4360.
6. A. Samoson, *Chem. Phys. Lett.*, 1985, **119**, 29.
7. H.J. Jakobsen, J. Skibsted, H. Bildsoe, and N.C. Nielsen, *J. Magn. Reson.*, 1989, **85**, 173.
8. L. B. Almany, D. Massiot, B. L. Sherriff, M. E. Smith, and F. Taullele, *Chem. Phys. Lett.*, 1991, **177**, 301.
9. C. Jäger, *J. Magn. Reson.*, 1992, **99**, 353.
10. J. S. Frye and G. E. Maciel, *J. Magn. Reson.*, 1982, **48**, 125.
11. M. Maricq and J. S. Waugh, *J. Chem. Phys.*, 1979, **70**, 3300.
12. J. Herzfeld and A. Berger, *J. Chem. Phys.*, 1980, **73**, 6021.
13. A. Samoson and E. Lippmaa, *J. Magn. Reson.*, 1988, **79**, 255.
14. A. Vega, *J. Magn. Reson.*, 1992, **96**, 50.
15. A. Samoson, E. Lippmaa, and A. Pines, *Mol. Phys.*, 1988, **65**, 1013.
16. A. Llor and J. Virlet, *J. Chem. Phys. Lett.*, 1988, **152**, 248.
17. B. F. Chmelka, K. T. Mueller, A. Pines, J. Stebbins, Y. Wu, and J. W. Zwanziger, *Nature*, 1989, **339**, 42.
18. K. T. Mueller, B. Q. Sun, G. C. Chingas, J. W. Zwanziger, T. Terao, and A. Pines, *J. Magn. Reson.*, 1990, **86**, 470.
19. L. Frydman and J. S. Harwood, *J. Am. Chem. Soc.*, 1995, **117**, 5367.
20. A. Medek, J. S. Harwood, and L. Frydman, *J. Am. Chem. Soc.*, 1995, **117**, 12 779.
21. C. Fernandez and J. P. Amoureux, *Chem. Phys. Lett.*, 1995, **242**, 449.
22. G. Wu, D. Rovnyank, B. Q. Sun, and R. G. Griffin, *Chem. Phys. Lett.*, 1996, **249**, 210.
23. G. Wu, D. Rovnyank, and R. G. Griffin, *J. Am. Chem. Soc.*, 1996, **118**, 9326.
24. D. Massiot, B. Tonzo, D. Trumean, J. P. Coutures, J. Virlet, P. Florian, and P. J. Grandinetti, *Solid State NMR*, 1996, **6**, 73.
25. M. J. Duer and C. Stourton, *J. Magn. Reson.*, 1997, **124**, 189.
26. C. Fernandez and P. J. Amoureux, *Solid State NMR*, 1998, **10**, 211.
27. J. P. Amoureux, C. Fernandez, and S. Steuernagel, *J. Magn. Reson. A*, 1996, **119**, 280.
28. S. P. Brown, S. J. Heyes, and S. Wimperis, *J. Magn. Reson. A*, 1996, **119**, 280.
29. D. Massiot, *J. Magn. Reson. A*, 1996, **122**, 240.
30. S. Ding and C. A. McDowell, *Chem. Phys. Lett.*, 1997, **270**, 81.
31. L. Marinelli, A. Medek, and L. Frydman, *J. Magn. Reson.*, 1998, **132**, 88.
32. S. Ding and C. A. McDowell, *J. Magn. Reson.*, 1998, **135**, 61.
33. Z. Gan, *J. Am. Chem. Soc.*, 2000, **122**, 324.
34. Z. Gan, *J. Chem. Phys.*, 2001, **114**, 10 845.
35. S. Vega, T. W. Shattuck, and A. Pines, *Phys. Rev. Lett.*, 1976, **37**, 43.
36. R. Tycko and S. J. Opella, *J. Am. Chem. Soc.*, 1986, **108**, 3551.
37. R. Tycko and S. J. Opella, *J. Phys. Chem.*, 1987, **86**, 1761.
38. M. Smith and E.R.H. van Eck, *Prog. NMR Spectrosc.*, 1999, **34**, 159.
39. J. Zwanziger and B. F. Chmelka, 'NMR Basic Principles and Progress', Springer-Verlag: Berlin, 1994, Vol. 31, p 202.
40. C. Jaeger, 'NMR Basic Principles and Progress', Springer-Verlag: Berlin, 1994, Vol. 31, p 135.
41. H. J. Jokobsen, in 'Encyclopedia of NMR', eds D. M. Grant and R. K. Harris, Wiley: Chichester, 1996.
42. M. Goldman, P. J. Grandinetti, A. Llor, Z. Olejniczak, J. R. Sachleben, and J. W. Zwanziger, *J. Chem. Phys.*, 1992, **97**, 8947.
43. J. J. Sukurai, 'Modern Quantum Mechanics', Addison-Wesley: New York, 1994.
44. M. E. Rose, 'Elementary Theory of Angular Momentum', Wiley: New York, 1951.
45. R. R. Ernst, G. Bodenhausen, and A. Wokaun, 'Principles of Nuclear Magnetic Resonance in One and Two Dimensions', Clarendon Press: Oxford, 1987.

Biographical Sketch

Zhehong Gan, *b* 1964. Ph.D. 1990, Chemical Physics, University of Utah (supervisor David M. Grant). NMR Spectroscopist, University of Illinois at Champaign-Urbana, 1990–93; Research Associate with R. R. Ernst, Eidgenössische Technische Hochschule (ETH), Switzerland, 1994–1998; Scientist, National High Magnetic Field Laboratory, USA, 1998–present. Approx. 40 publications. Current research interests: solid state NMR methodology and theory.

Concentrated Solution Effects

Warren S. Warren and Wolfgang Richter
Princeton University, NJ, USA

1	Introduction	1
2	Radiation Damping	1
3	Magnetization Anisotropy	3
4	Note Added In Proof	6
5	Related Articles	7
6	References	7

1 INTRODUCTION

The earliest NMR experiments required samples with significant bulk magnetization, and thus it is not surprising that some concentration-dependent effects were first characterized more than 40 years ago.[1] However, improvements in instrumental sensitivity, coupled with the advent of Fourier transform techniques, dramatically reduced the number of spins needed for an observable signal. As a result, most routine applications, such as determining the structure of small organic molecules, take place in moderately dilute solution (<1% concentration). Much of the solvent magnetization can be removed by deuteration. Even if the solvent peak is intense, it is often true that bulk effects contribute at most an additional effective inhomogeneity that can be shimmed away.

In recent years, magnetically concentrated samples have once again become important, in large part because of the quest for ever-greater sensitivity in biomolecular applications. This sensitivity is achieved by increasing sample volumes, redesigning probes to increase responsivity, and strengthening the static magnetic field. In addition, the solvent is typically water, and deuteration is often undesirable because exchangeable protons are lost. As a result, the bulk magnetization can be far larger than in the earliest NMR experiments. The last few years have seen a significant resurgence of interest in these effects, which have been shown to profoundly alter molecular spectra.

In this article, the two most important phenomena stemming from a large bulk magnetization will be described in detail. Either of these effects can generate additional peaks, particularly in the indirectly detected dimensions of multidimensional experiments. *Radiation damping* occurs because the bulk magnetization induces a current in the probe coil, which in turn acts like a weak pulse back on the sample; this field causes the system to return to equilibrium faster than through relaxation alone. Radiation damping is generally a nuisance, partly because the already very large water signal in a spectrum is broadened and obscures signals in its vicinity, and partly because this 'weak pulse' makes the solvent peak effectively see a different pulse sequence than does the solute. *Magnetization anisotropy* is most dramatic when magnetic field gradients are employed in the pulse sequence (see ***Field Gradients and Their Application***), although some effects can be seen with any nonspherical sample. It causes additional signals that can falsify a spectral analysis, or, when properly interpreted, *enhance* the information content of a spectrum. This leads to a new type of pulse sequence using gradient pulses to elucidate intermolecular correlations.

2 RADIATION DAMPING

2.1 The Physical Picture

Radiation damping was observed and described[1] in the first decade of NMR. The time-dependent transverse magnetization of the system (the observable signal) is always detected via the electric current which it induces in the coil. This current, in turn, generates an *additional magnetic field* at the sample. According to elementary classical physics (Lenz's law), a current that is induced by a time-varying magnetic field creates a magnetic field that acts to oppose the original one. This is also obvious from the principle of conservation of energy; the energy stored in a magnetic field is partially converted into the energy of the current that is induced. Energy is coupled out of the spins in a time comparable to the probe risetime (microseconds) and, since the energy of the spins in the magnetic field is $E = -\boldsymbol{\mu} \cdot \boldsymbol{B}$, the net effect must tend to rotate the spins back towards equilibrium.

2.2 Experimental Consequences

In dilute solutions, typical relaxation times for protons in small molecules at room temperature are of the order of 1 s, giving a linewidth [half width at half maximum (HWHM)] of 0.3 Hz. Radiation damping changes this drastically. In pure water the decay after a $\pi/2$ pulse becomes nonexponential, and can be approximately 100 times shorter. After a near-π pulse, the magnetization actually grows (Figure 1). Since the water peak is very intense, the width of the line at the base is yet much larger, and neighboring peaks will be disturbed or obscured altogether.

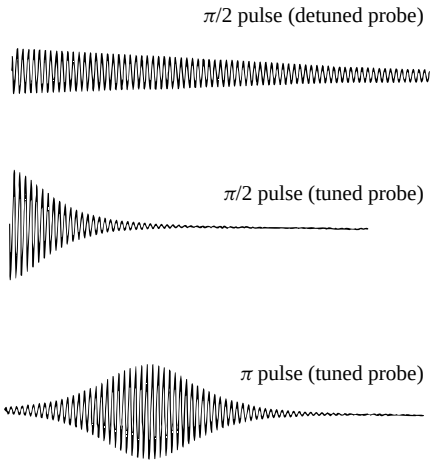

Figure 1 Free induction decays in a water sample. Note that the behavior is grossly different from the Bloch equation prediction unless the probe is detuned. (Reproduced by permission from Q. He, W. Richter, S. Vathyam, and W. S. Warren, *J. Chem. Phys.*, 1993, **98**, 6779)

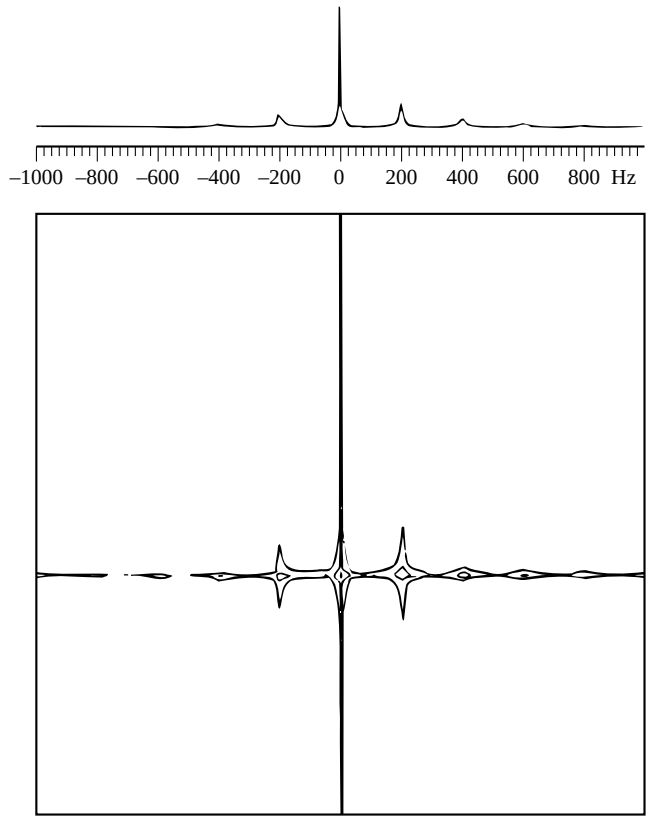

Figure 2 Two-dimensional spectrum obtained from the simple two-pulse sequence $(\pi/2)_x - t_1 - (\pi/2)_x - t_2$ on a sample of 80% H_2O in D_2O. Note that additional resonances are still seen in the ω_1 dimension, despite the normal expectation that a two-pulse sequence cannot generate and detect multiple quantum coherences. (Reproduced by permission of AIP from Q. He, W. Richter, S. Vathyam, and W. S. Warren *J. Chem. Phys.*, 1993, **98**, 6779)

In a two-dimensional spectrum, for example in a COSY experiment, radiation damping can lead to harmonic peaks (at integral multiples of the resonance offset) in the indirectly detected dimension (Figure 2). The reason for these peaks is the nonlinearity of the radiation damped signal.[2]

2.3 Theoretical Description

For most practical purposes, a mathematical description based on the classical physical picture given above is sufficient if we deal with isolated spins $\frac{1}{2}$, as in water; it is possible to write a field-quantized version of these equations, which gives some additional insight, but which has not yet been shown to predict any new phenomena.[1,3,4] Neglecting relaxation for the moment, the transverse component of the magnetization after a pulse with flip angle θ has magnitude $M_0 \sin\theta$, and precesses about the z axis at the Larmor frequency ω_0. The voltage induced in the coil by the precessing magnetization is given by

$$V = -nA\eta\mu_0 \frac{\mathrm{d}M_x}{\mathrm{d}t} = Rl\left(\frac{Q}{n}\right)\eta M_0 \sin\theta \cos(\omega_0 t) \qquad (1)$$

where n is the number of turns in the coil, A its cross-section, η the filling factor, R the electrical resistance, l the length of the coil, M_x the component of the magnetization in the x direction, and ω the precession frequency. $Q = (\mu_0 \omega n^2 A)/Rl$ is the quality factor of the probe circuit. The filling factor η is the fraction of the coil volume occupied by the sample, weighted by the product of the magnetic field that a unit current in the coil produces at each point in the sample (B_c), and the magnetization at that point:

$$\eta = \frac{\int_V M B_c \mathrm{d}V}{M_0 \int_V B_c \mathrm{d}V} \qquad (2)$$

where M is the magnetization per unit volume, and M_0 its average value. If the coil were fully immersed in the sample, the filling factor would be 1.

This voltage produces a current, and hence a field

$$B_x = \frac{\mu_0 In}{l} = \mu_0 \eta Q M_0 \sin\theta \cos(\omega t) \qquad (3)$$

This field, in turn, exerts a torque on the magnetization. The expression for the evolution of the magnetization vector is simplest in polar coordinates ($|\mathbf{M}|$, θ, ϕ):

$$\frac{\mathrm{d}\theta}{\mathrm{d}t} = -\frac{\mu_0 \eta M_0 Q \gamma \sin\theta}{2} = -\sin\tau_r, \quad \frac{\mathrm{d}\phi}{\mathrm{d}t} = 0,$$
$$\frac{\mathrm{d}|\boldsymbol{M}|}{\mathrm{d}t} = 0 \qquad (4)$$

Following Bloembergen and Pound,[1] we have defined a 'radiation damping time'

$$\tau_r = \frac{2}{\mu_0 \eta M_0 Q \gamma} \qquad (5)$$

Unlike relaxation, radiation damping does not change the *length* of the magnetization vector, but only its angle with the static magnetic field. No dephasing, either reversible or irreversible, takes place. These terms are added to the phenomenological Bloch equations, giving

$$\frac{\mathrm{d}M_x}{\mathrm{d}t} = \Delta\omega M_y + \omega_{1,y} M_z - \frac{M_x}{T_2} - \frac{M_x M_z}{\tau_r M_0} \qquad (6a)$$

$$\frac{\mathrm{d}M_y}{\mathrm{d}t} = -\Delta\omega M_x - \omega_{1,x} M_z - \frac{M_y}{T_2} - \frac{M_y M_z}{\tau_r M_0} \qquad (6b)$$

$$\frac{\mathrm{d}M_z}{\mathrm{d}t} = -\omega_{1,y} M_x + \omega_{1,x} M_y - \frac{M_z - M_0}{T_1} + \frac{M_0^2 - M_z^2}{\tau_r M_0} \qquad (6c)$$

For 80% water in a 750 MHz spectrometer, probe Q of 500 and η = 0.1, τ_r = 2.7 ms. Since both the transverse and the longitudinal relaxation times are of the order of 1 s, the decay of transverse magnetization is dominated by radiation damping, and the evolution after a pulse with flip angle θ is given by:

$$S(t) = M_x + \mathrm{i}M_y = M_0 \,\mathrm{sech}\left(\frac{t - t_0}{\tau_r}\right)\exp(\mathrm{i}\omega_0 t) \qquad (7)$$

This is a universal solution if $\omega_1 = 0$ and relaxation can be neglected.[5] The effects of radiation damping when the externally applied rf does not vanish are explored extensively in Warren et al.[3] In that case, the dynamics can be quite different from what the unmodified Bloch equations would have predicted; for example, if ω_1 is constant, the magnetization vector spirals towards a 'fixed point' the position of which is determined by $\Delta\omega$, ω_1, and τ_r.[3]

Fourier transformation of equation (7) gives the lineshape in the frequency domain, which is particularly simple for a $\pi/2$ or near-π pulse.[6] After a $\pi/2$ pulse the lineshape is

$$S(\omega) = \frac{\pi M_0 \tau_r}{2} \operatorname{sech}\left[\frac{\pi \tau_r}{2}(\omega - \omega_0)\right] \tag{8}$$

Suppose the radiation damping time of a given sample is 2.7 ms. If the concentration of the molecule of interest is 1 mM and the solvent is pure water, the tails of the water peak have the same intensity as a singlet of one proton of the dilute molecule at a resonance offset frequency of 250 Hz, assuming a Lorentzian lineshape for the solute.

The extra peaks in Figure 2 are highly nonintuitive. A rigorous density matrix treatment readily shows that the indirectly detected dimension of a COSY experiment is expected to contain only the peaks in the normal spectrum. In fact, however, even the modified Bloch equations [equation (6)] predict these peaks. As shown by He et al.,[7] this occurs because these modified Bloch equations grossly violate quantum mechanics; they generate a propagator for the time evolution which depends explicitly on the initial direction of the magnetization. A fully quantum mechanical treatment must reveal that frequencies in the indirectly detected dimension reflect actual energy differences between eigenstates (in the rotating frame); but such a treatment requires field quantization, is quite complex and does not appear to be necessary for quantitative interpretation.

2.4 Remedies

There are two general approaches to eliminating the adverse effects of radiation damping. The most obvious way is for the experimenter to choose the conditions such that radiation damping does not occur at all. For a given sample, this can be achieved by decreasing the quality factor of the circuit (for instance, by detuning), or by decreasing the filling factor (for instance, by using a capillary tube). In both cases, sensitivity will be greatly reduced, which is unacceptable in many applications. Alternatively, the sample can be magnetically diluted, in the case of an aqueous solution by the addition of D_2O. Often, though, exchangeable protons are present in the molecule under investigation, necessitating the use of H_2O. Work in progress in several laboratories aims at suppressing radiation damping with active probe design.

Alternatively, radiation damping can be put to advantage. As shown above, a magnetization vector evolves differently in the presence of radiation damping. This difference in evolution can, in principle, be used to suppress the unwanted solvent resonance by a suitably tailored pulse sequence, or by a *shaped pulse*[3] (see also ***Shaped Pulses***).

3 MAGNETIZATION ANISOTROPY

3.1 Boundary Effects

Perhaps the most visible effect in concentrated samples is that the lineshape deteriorates considerably. The reasons for this are the large magnetic susceptibility of the liquid and the resulting discontinuity at the walls of the sample tube. This effect has recently been investigated mathematically by Vlassenbroek[8] for a few cases. For most practical applications, this magnetic field inhomogeneity can be compensated for by shimming.

3.2 Reintroduction of Dipolar Couplings in Solution

3.2.1 The Physical Picture

The magnitude of the dipolar coupling between two spins has an angular dependence of $3\cos^2\theta - 1$, where θ is the angle between the interspin vector and the static magnetic field. These couplings are easily seen in solid state NMR. The spectrum of a liquid sample is considerably sharper and simpler than that of a solid because dipolar (and higher order) couplings are invisible.

The reason for sharp lines in liquids is more subtle than has been commonly appreciated. For a spin pair separated by a short distance R, the direction of the interspin vector will change rapidly in a liquid because of diffusion. The average value of $3\cos^2\theta - 1$ then becomes zero, and the dipolar couplings vanish. However, for a spin pair separated by a large distance, not all angles are sampled by the interspin vector. The couplings fall off as R^{-3}, but the number of spins a distance R from a given spin is proportional to R^2, so the net effect of couplings from one spin to 10^{20} others in a typical sample can be considerable. However, under ordinary circumstances (in the absence of gradient pulses) *the orientation of the magnetization vector is uniform throughout the sample*, and angular averaging over all the spins at distance R makes the net magnetic field vanish.

If the magnetization direction in a liquid is made anisotropic (for example, because of gradient pulses), the averaging of long range couplings might no longer hold, and dipolar couplings reappear. Spatial correlations can be established between different molecules, generating extra peaks and distorting intensities of expected peaks.

3.2.2 Experimental Consequences

Dipolar couplings in liquids were first invoked to explain multiple echoes in experiments involving magnetic field gradients. If a pulse sequence consisting of two $\pi/2$ pulses separated by a time τ is applied to a sample, an echo appears in the free induction decay at $t_2 = \tau$ (the 'Hahn spin echo').[9] In the presence of a magnetic field gradient, however, multiple echoes after $t_2 = n\tau$ are also observed.[10,11] For a typical set of experimental parameters (80% H_2O in D_2O, $\boldsymbol{B}_0 = 7$ T, G $= 5 \times 10^{-3}$ T m^{-1}), the second echo has about 10% of the intensity of the first one. These echoes are not caused by radiation damping—the ratio of the second to first echo is independent of Q or η, but is reduced by diluting the sample.

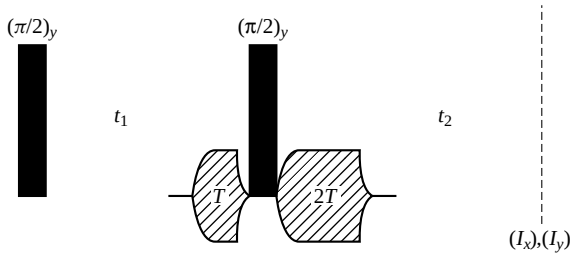

Figure 3 CRAZED pulse sequence. This sequence can be viewed as a two-pulse COSY sequence modified to include a pair of gradient pulses as a coherence transfer echo. The observable magnetization (I_y or I_x) comes entirely from one-quantum operators. The 1:2 length ratio of the two gradient pulses guarantees that only coherences that evolved as two-quantum operators during t_1 will be refocused. (Reproduced by permission of AAAS from W. S. Warren, W. Richter, A. H. Andreotti, and B. T. Farmer II, *Science*, 1993, **262**, 2005)

A simple sequence which shows the potential of these couplings to generate extra peaks in two-dimensional experiments is the CRAZED sequence (COSY revamped by asymmetric z gradient echo detection) (Figure 3).[7,12] The CRAZED experiment serves as a prototype for a whole class of experiments using magnetization anisotropy, the theoretical description for all of which is similar.

This two-dimensional pulse sequence consists of two $\pi/2$ rf pulses and two magnetic field gradient pulses along the direction of the static magnetic field. The gradient pulses have a strength of typically 0.01–0.1 T m^{-1} and are applied through a z shim coil, unless a special gradient probe is used.

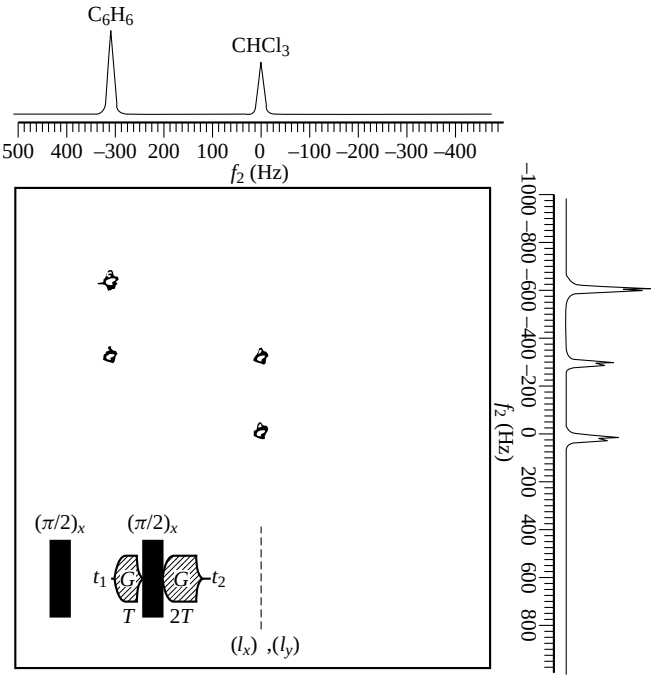

Figure 4 CRAZED spectrum of a mixture of benzene and chloroform in C_6D_6. The transmitter frequency is on resonance with chloroform. The cross-correlation resonance pairs appear at the sum of resonances of the two protons in different molecules. (Reproduced by permission of AIP from Q. He, W. Richter, S. Vathyam, and W. S. Warren, *J. Chem. Phys.*, 1993, **98**, 6779)

If the areas of the gradient pulses are in an integer ratio, peaks in the indirectly detected dimension at the frequencies of *intermolecular multiple quantum coherences* are created and detected by this pulse sequence.[7,12] Figure 4 presents a two-pulse experiment with a 1:2 ratio of gradient pulse lengths (making the gradient pulses act as a double quantum filter) on a mixture of benzene and chloroform.[7] Note that the f_2 dimension (horizontal) contains only the two expected resonances. The gradients eliminate all but two-quantum coherences in the ω_1 dimension (vertical); the nature of these resonances (two benzene spins flipping, two chloroform spins flipping, or one of each) is easily determined by peak position. Figure 4 shows intermolecular coherence transfer (cross peaks) between these independent molecules, but not all possible peaks are present—for example, the one-quantum chloroform resonance correlates only with two-quantum resonances which include at least one chloroform resonance. These peaks are huge—typically 10–20% of the amplitude of the diagonal peaks in a gradient-free COSY experiment on the same sample. Three-component mixtures (e.g. benzene/acetone/chloroform) show exactly the same pattern.[7] For example, the benzene resonance (ν_{benzene}) in f_2 is correlated with peaks at f_1 = $2\nu_{\text{benzene}}$, ν_{benzene} + ν_{acetone}, or ν_{benzene} + $\nu_{\text{chloroform}}$, but not with f_1 = ν_{acetone} + $\nu_{\text{chloroform}}$.

He et al.[7] showed that the cross peaks are not due to radiation damping by taking CRAZED spectra with coaxially separated samples within the same coil. This should not modify radiation damping effects, since they are macroscopic, but it eliminates the cross peaks.

A similar spectrum of a peptide molecule in water is shown in Figure 5.[12] There are the peptide resonances (and the water resonance) in f_1, and peaks at the sum of a peptide proton frequency and the water frequency in f_1. These are intermolecular double quantum resonances between water and the peptide molecule.

3.2.3 Theoretical Description

Modified Bloch equations (including the 'dipolar demagnetizing field', which is a mean field approximation to the full dipolar interaction) can be used to give an approximate description of multiple echoes and the CRAZED experiment. For simplicity, we will describe the experiment for a sample with only one spin species, e.g. pure water. The secular part of $\boldsymbol{B}_{\text{d}}(\boldsymbol{r})$ is given by

$$\boldsymbol{B}_{\text{d}}(\boldsymbol{r}) = \frac{\mu_0}{4\pi}\int_V \text{d}^3r' \frac{1-3\cos^2\theta_{rr'}}{2|\boldsymbol{r}-\boldsymbol{r}'|^3}[3M_z(\boldsymbol{r}')\boldsymbol{e}_z - \boldsymbol{M}(\boldsymbol{r}')] \quad (9)$$

(where $\boldsymbol{e}_z$ is the unit vector in the z direction) which is just the continuous version of the usual expression (summed over all spins) for the local magnetic field generated by the direct dipole–dipole interaction. The difficulty in calculating $\boldsymbol{B}_{\text{d}}(\boldsymbol{r})$ stems from the nonlocal nature of the interaction—even edge effects in the sample can play a significant role. However, a spatial Fourier transform simplifies the relation between $\boldsymbol{B}_{\text{d}}(\boldsymbol{r})$ and $\boldsymbol{M}(\boldsymbol{r})$ if the magnetization $\boldsymbol{M}(\boldsymbol{r})$ varies only in a single direction s. In that case[10]

$$\boldsymbol{B}_{\text{d}}(s) = C_k\boldsymbol{M}(s) = \mu_0[\Delta M_z(s)\boldsymbol{e}_z - \tfrac{1}{3}\Delta\boldsymbol{M}(s)] \quad (10)$$

$$\Delta \equiv [3(\boldsymbol{e}_s\cdot\boldsymbol{e}_z)^2 - 1]/2 \quad (11)$$

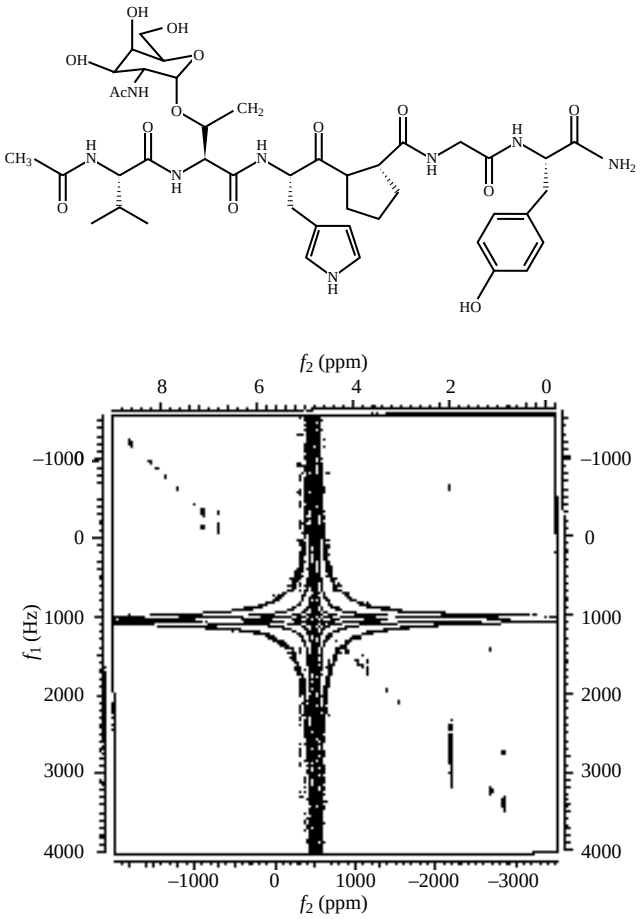

Figure 5 CRAZED spectrum of a 20 mM solution of a fibronectin fragment in water. The first gradient pulse was 1 ms long, with amplitude 0.06 T m^{-1}. Joint solute–solvent two-quantum coherences are seen from most of the glycopeptide peaks. (Reproduced by permission of AAAS from W. S. Warren, W. Richter, A. M. Andreotti, and B. T. Farmer II, *Science*, 1993, **262**, 2005)

The field $\boldsymbol{B}_\mathrm{d}(\boldsymbol{r})$ is then added into the usual form of the Bloch equations, giving an additional contribution $[\boldsymbol{M} \times \gamma \boldsymbol{B}_\mathrm{d}(\boldsymbol{r})]$ to $\mathrm{d}\boldsymbol{M}/\mathrm{d}t$. The magnitude (in angular frequency units) of the field generated by equation (10) is approximately $\Delta\gamma\mu_0 M_0$; in He et al.,[7] the quantity $(\Delta\gamma\mu_0 M_0)^{-1}$ is defined as the 'dipolar demagnetizing time' τ_d. For pure water at 750 MHz and Δ = 1, $\tau_\mathrm{d} \approx 50$ ms.

In the CRAZED experiment, the first rf pulse rotates all magnetization into the horizontal plane. In t_1, the magnetization rotates about the z axis. During the first gradient pulse, the static magnetic field and hence the resonance frequency (or rate of rotation) become position dependent. The individual magnetic moments are wound up into a helix about the z axis, and the magnetization becomes anisotropic. The second rf pulse transforms this anisotropy in the horizontal magnetization component into an anisotropy in the vertical component. Now the local static magnetic field at each spin depends on its position in the sample. The spins then evolve under this new magnetic field during t_2.

This approach qualitatively yields the observed spectrum for a sample of pure water. However, the peak intensities are not predicted correctly. Furthermore, classical calculations fail as soon as slightly more complicated pulse sequences are employed. This is not surprising, in view of the fact that a classical picture, replacing nuclear spins by tiny bar magnets and predicting their behavior by classical dynamics, neglects the correlations which are at the very heart of signals evolving at the sum of the resonance frequencies of two different spins.

A density matrix treatment is much more general. At the beginning of the pulse sequence, the spins are in thermal equilibrium. There is a slightly higher probability for a spin to point parallel to the magnetic field ('up') than antiparallel. Therefore, spins are (formally) correlated, independent of distance. The strongest such correlation is between any two spins. We will therefore focus on spin pairs. That means that we will expand the equilibrium density operator

$$\hat{\rho}_\mathrm{eq} = \frac{\exp(-\beta\hat{\mathcal{H}})}{\mathrm{Tr}\,[\exp(-\beta\hat{\mathcal{H}})]} \quad \beta \equiv \frac{1}{kT} \quad \hat{\mathcal{H}} = \hbar\omega_0 \sum_{i=1}^{N} \hat{I}_{zi} \qquad (12)$$

up to the term quadratic in β:

$$\hat{\rho}_\mathrm{eq} \approx (2^{-N})\left[1 - \beta\hbar\omega_0 \sum_{i=1}^{N} \hat{I}_{zi} + \frac{1}{2}(\beta\hbar\omega_0)^2 \sum_{i=1}^{N}\sum_{j=1}^{N} \hat{I}_{zi}\hat{I}_{zj}\right] \qquad (13)$$

Usually, this expansion is terminated after the linear term (the so-called 'high-temperature approximation'). It is commonly argued that the term quadratic in $\beta\hbar\omega_0$ is small; indeed, $\beta\hbar\omega_0 \approx 10^{-4}$ for a 17.6 T spectrometer. However, there are of the order of 10^{44} spin pairs $\hat{I}_{zi}\,\hat{I}_{zj}$ in a typical sample. It turns out that the quadratic term gives rise to a signal approximately 10% as large as the signal stemming from the linear term. In fact, the term proportional to $(\beta\hbar\omega_0)^3$ generates observable three-quantum signals if the ratio of gradient pulse lengths is set at 1:3, and effects of the $(\beta\hbar\omega_0)^4$ term have been observed as well.

From the equilibrium two-spin correlation, the first $\pi/2$ pulse creates a *two-spin, two-quantum coherence* which evolves during t_1. At the end of t_1, the first gradient pulse causes a variation of the static magnetic field along the z direction, and therefore a z-dependent resonance frequency. The coherences are wound into a helix about the z direction. The second rf pulse converts the two-spin, two-quantum coherences into two-spin, one-quantum coherences that evolve with approximately half the frequency of the two-quantum coherences. Since the second gradient pulse is twice as long as the first one, the helix is unwound, and the coherences refocus.

As described above, the magnetization anisotropy created by the gradient pulses causes the reintroduction of observable effects from dipolar couplings. The time evolution of the density operator after the second gradient pulse is such that the dipolar couplings transform the two-spin, one-quantum operators into observable one-spin, one-quantum operators which evolve during t_2. The expected signals agree quantitatively with the experiments. Figure 6 shows schematically the evolution of coherences of different order during the pulse sequence.

3.2.4 Remedies and Applications

It has been shown both theoretically and experimentally that magic angle gradients remove the extra peaks, at least for

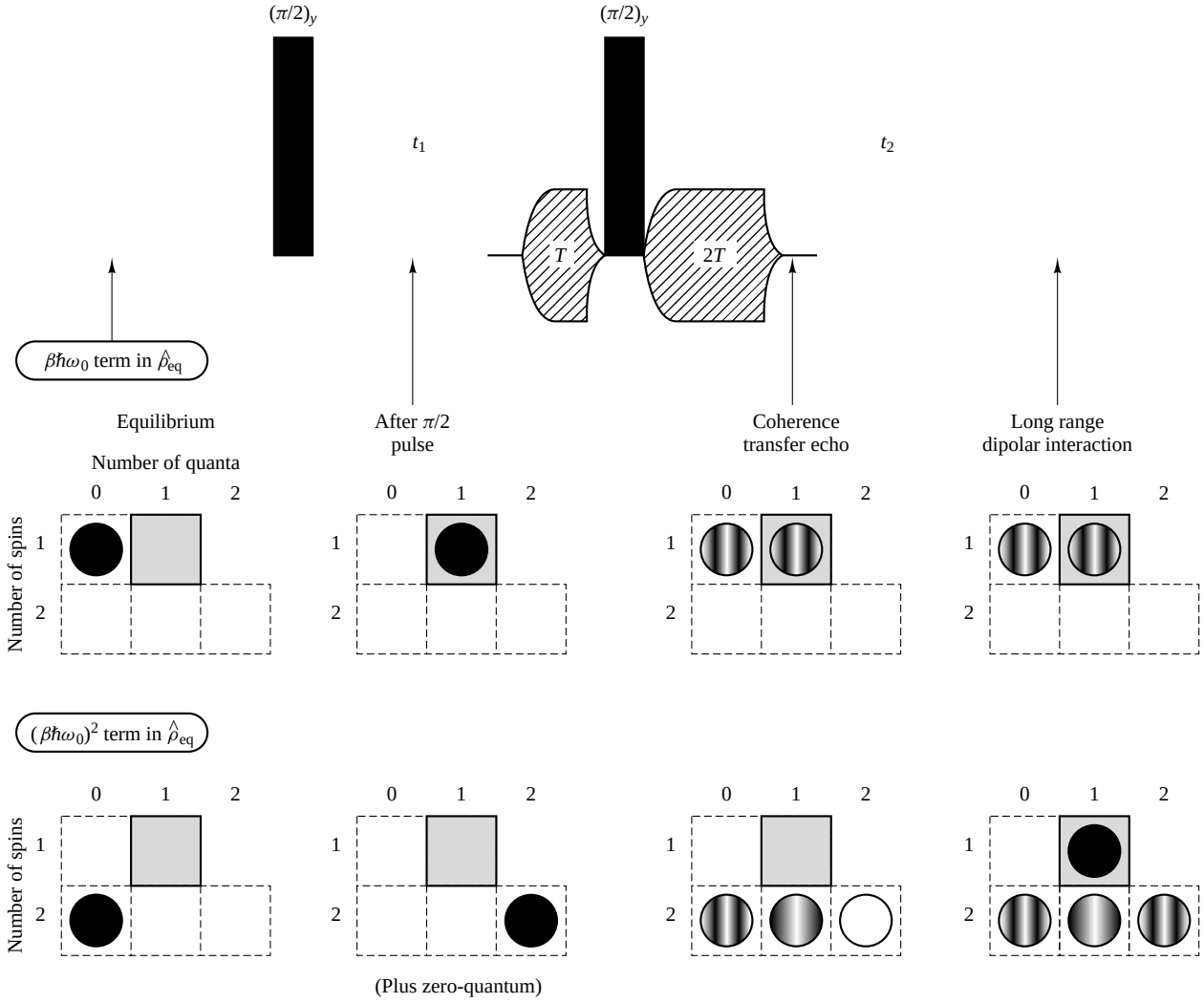

Figure 6 Schematic illustration of the dominant pathway for generating observable signals from a CRAZED sequence. Black dots illustrate operators that are not spatially modulated. The black square represents the one-spin, one-quantum operators $\hat{I}_{xi}$ and $\hat{I}_{yi}$, which are observable. The $\beta\hbar\omega_0\hat{I}_z$ term in the equilibrium density matrix is a sum of one-spin, zero-quantum operators, which are turned into an observable signal during t_2 by the first pulse. However, the coherence transfer echo imposes a strong spatial modulation on these operators, and they do not generate an observable signal during t_2. The $(\beta\hbar\omega_0\hat{I}_z)^2$ term, on the other hand, gives a two-quantum operator during t_1 (plus a zero-quantum operator which is omitted here for clarity). The fraction of this two-quantum, two-spin operator which is transferred to one-quantum, two-spin operators by the coherence transfer echo is only mildly modulated. The dipolar couplings can then act to create an unmodulated, one-spin, one-quantum operator (observable magnetization). The quantitative calculation shows that very large signals are possible. (Reproduced by permission of AAAS from W. S. Warren, W. Richter, A. H. Andreotti, and B. T. Farmer II, *Science*, 1993, **262**, 2005)

simple sequences[12] (Figure 7). In addition, the density matrix treatment described by Warren et al.[12] suggests a variety of applications which are currently under development. The most obvious ones are in imaging, and based on the fact that correlations between different molecules at a fixed distance can be measured and that the correlation distance can be selected by the strength of the gradient.

4 NOTE ADDED IN PROOF

Recent papers[13–15] have dramatically extended and clarified the theoretical picture of concentrated solution effects presented here, and have provided further applications.[16,17] Warren et al.[13] present a corrected version of the classical dipolar demagnetizing field treatment[7,10] which gives quantitative agreement with experiment. Lee et al.[14] extend the density matrix picture to provide exact calculations for expected signals from simple sequences, such as the CRAZED sequence, and show that the corrected classical picture of reference[13] is equivalent to the density matrix picture under assumptions usually met in liquids. The relationship between the quantum and classical pictures is also explored by Jeener et al.[15] All three of these papers show that extra resonances can be observed with gradient-free sequences as well, although gradient pulses dramatically enhance the signal. Richter et al.[16] demonstrate imaging with intermolecule multiple-quantum coherences, and Vathyam et al.[17] show that intermolecular zero-quantum coherences can be used to suppress inhomogeneous broadening

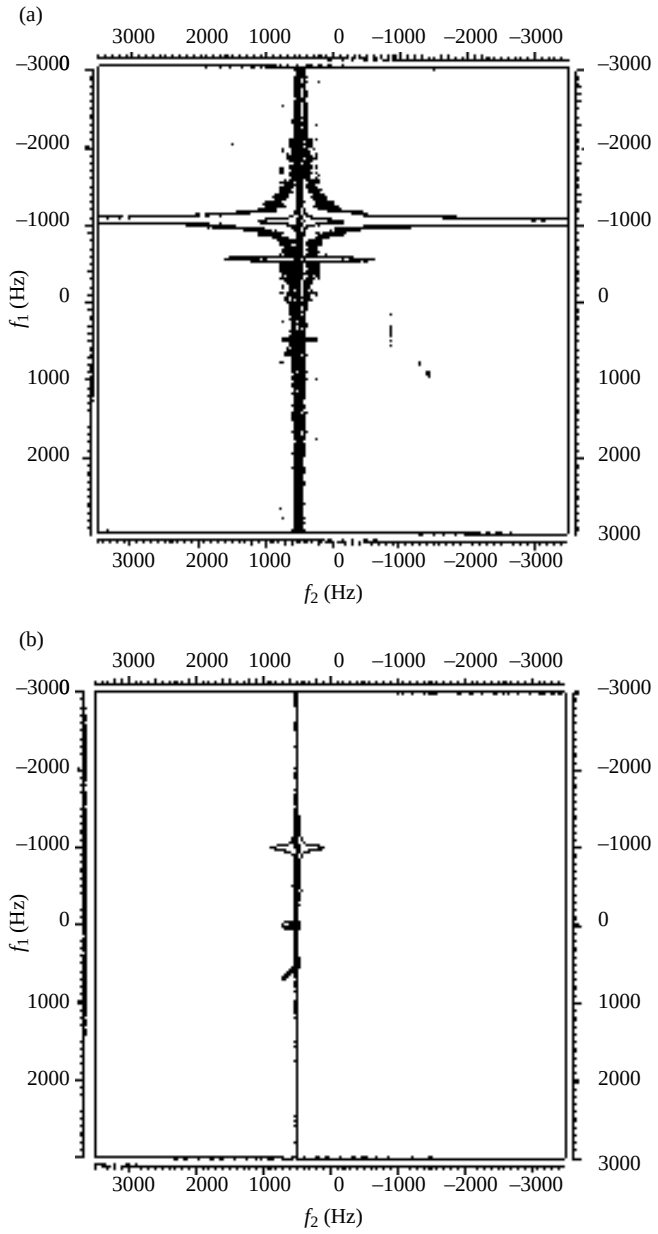

Figure 7 Comparison of two CRAZED experiments with different gradient directions. (a) An experiment on the same sample as in Figure 5, with the gradient pointed along the *z* direction. (b) The same experiment, with the gradient pointed along the magic angle; as expected, the two-quantum peaks are substantially reduced, here by a factor of 15. In order to compare the two spectra, a very low contour level was used for both

without suppressing chemical shifts or *J* couplings. References to other recent developments can be found in those papers.[13–17]

5 RELATED ARTICLES

Spinning Liquid Crystalline Samples.

6 REFERENCES

1. N. Bloembergen and R. V. Pound, *Phys. Rev.*, 1954, **95**, 8.
2. J. Jeener, presented at the *Waterloo Workshop on NMR Spectroscopy, July 1991*.
3. W. S. Warren, S. L. Hammes, and J. L. Bates, *J. Chem. Phys.*, 1989, **91**, 5895.
4. M. McCoy and W. S. Warren, *J. Chem. Phys.*, 1990, **93**, 858.
5. S. Bloom, *J. Appl. Phys.*, 1957, **28**, 800.
6. X. Mao and C. Ye, *J. Chem. Phys.*, 1993, **99**, 7455
7. Q. He, W. Richter, S. Vathyam, and W. S. Warren, *J. Chem. Phys.*, 1993, **98**, 6779, and references therein.
8. A. Vlassenbroek, Ph.D. Thesis, Université Libre de Bruxelles, Bruxelles, 1993.
9. E. Hahn, *Phys. Rev.*, 1950, **80**, 580.
10. G. Deville, M. Bernier, and J. M. Delrieux, *Phys. Rev., Ser. B*, 1979, **19**, 5666.
11. R. Bowtell, R. M. Bowley, and P. Glover, *J. Magn. Reson.*, 1990, **88**, 643.
12. W. S. Warren, W. Richter, A. H. Andreotti, and B. T. Farmer II, *Science*, 1993, **262**, 2005.
13. W. S. Warren, S. Lee, W. Richter, and S. Vathyam, *Chem. Phys. Lett.*, 1996, in press.
14. S. Lee, W. Richter, S. Vathyam, and W. S. Warren, *J. Chem. Phys.*, 1996, submitted.
15. J. Jeener, A. Vlassonbroek, and P. Brockaert, *J. Chem. Phys.*, 1995, **103**, 1309.
16. W. Richter, S. Lee, W. S. Warren, and Q. He, *Science*, 1995, **267**, 654.
17. S. Vathyam, S. Lee, and W. S. Warren, *Science*, 1966, submitted.

Biographical Sketches

Warren S. Warren. *b* 1955. A.B., 1977, Harvard University; M.S., 1979, Ph.D., 1980, University of California, Berkeley, USA. Professor of Chemistry, Princeton University, NJ, USA. Editor, *Advances in Magnetic and Optical Resonance* (Academic Press). Approx. 100 publications. Research specialties: NMR with shaped pulses, multiple quantum NMR, NMR concentrated solution effects, and coherent laser spectroscopy.

Wolfgang Richter. *b* 1966. M.S., 1989, University of Oklahoma, USA (advisor B. M. Fung). Diplom., 1990, Technische Universität Berlin, Germany. M.A., 1992, Princeton University, NJ, USA. Ph.D. candidate at Princeton University, 1990–present (advisor W. S. Warren). Six publications. Current research area: dipolar interactions in liquids.

Dipolar Field and Radiation Damping: Collective Effects in Liquid-state NMR

Jean Jeener

Université Libre de Bruxelles, Brussels, Belgium

1 Introduction 1
2 Generalities 3
2.1 NMR Without Collective Effects 3
2.2 NMR with Collective Effects 4
2.3 The Status of the Equations of Motion 5
2.3.1 In the Absence of Collective Effects 5
2.3.2 In the Presence of Collective Effects 6
2.4 Incorporating Molecular Diffusion in the Kinetic Equations 7
2.5 The High Temperature Approximation, Validity and 'Breakdown' 8
3 Radiation Damping 9
3.1 A Simple Example 9
3.2 Electronic Control of Radiation Damping 10
3.2.1 Introduction 10
3.2.2 A Digression about Electrical Engineering 10
3.2.3 The 'Brussels' Feedback Scheme 11
3.2.4 The 'École Polytechnique' Neutralization Scheme 12
3.2.5 Miscellaneous Schemes (Q-switch, etc.) 13
4 Dipolar Field Effects, the 'Classical' Presentation 13
4.1 The Classical Average Dipolar Field 13
4.2 Secular Coupling with the Dipolar Field, Various Truncations 14
4.2.1 Removing the Counter-rotating Terms and the Oscillating Z terms 15
4.2.2 Secular Couplings and Further Truncation 15
4.3 Simple Examples: Homogeneous and Helical Spatial Distributions of Magnetization ('Classical' Discussion) 16
4.3.1 Multiple Spin Echoes (Equivalent Spins) 16
4.3.2 Multiple Spin Echoes (Two Spin Species) 19
4.3.3 The CRAZED and HOMOGENIZED Experiments 20
4.3.4 The COSY Experiment 22
4.3.5 The Goldman–Desvaux Effect 23
4.4 Quantum Calculations for all Spins and all Couplings Together 24
4.4.1 Derivation of the Bloch–Redfield Equations 25
4.4.2 A Rough but 'Exactly Soluble' Model 26
4.5 Suppression of Dipolar Field Effects 26
4.6 Numerical Simulation Techniques 27
5 Dipolar Field Effects, the 'Warren' Presentation 28
5.1 Formal Introduction, Coherences, Interaction Representation 28
5.2 Intermolecular Multiple-quantum Coherences 29
5.3 Equivalence Between the 'Classical' and 'Warren' Predictions 32
6 Spectral Clustering and Dynamic Instability 33
6.1 Spectral Clustering 33
6.2 Dynamic Instabilities Caused by the Dipolar Field 33
6.3 Dynamic Instabilities Caused by Radiation Damping and the Dipolar Field 36
7 Related Articles in this Volume 36
8 Related Articles in Volumes 1–8 36
9 References 36

1 INTRODUCTION

In the usual presentation of pulsed NMR spectroscopy, the spins are initially in equilibrium in a large constant external magnetic field. Then, a short pulse of rf current in the coil surrounding the sample tips the nuclear magnetization into a state where it precesses freely around the direction of the large field. This precession induces a small emf in the coil, which excites the resonance of the tuned sample circuit, and the resulting rf voltage is fed into the acquisition circuit of the spectrometer (after suitable amplification). However, this description ignores the 'small' effects which are the topic of the present article: (i) the rf current induced in the coil generates a (small) transverse magnetic field which acts back on the spins and (ii), independently of the coil, the bulk nuclear magnetization of the sample directly generates a (weak) magnetic field which also acts back on the spins.

With the rough technology of the early days of NMR, these back effects could be discarded on the ground that they were too small to observe, with the exception of the slow tipping of the spins by the additional rf field generated by the (observed) rf current in the tuned sample circuit. This phenomenon was described in 1954 by Bloembergen and Pound[1] under the name of 'radiation damping'. It is typical of the often counter-intuitive behavior of these back effects that the original authors unwillingly chose an unrealistic model for discussing radiation damping effects in CW spectroscopy, hence reaching some flawed conclusions; this was corrected two years later.[2]

As a consequence of the continuous improvement of NMR technology (higher fields, improved homogeneity, better electronics, computer controlled experiments, ...), radiation damping has become an important issue whenever a large transverse spin magnetization is present, typically that of abundant solvent nuclei with a large $|\gamma|$ (^{1}H, ^{19}F,...). In structural studies by NMR, radiation damping is routinely exploited as a component of solvent suppression strategies; otherwise it appears as a nuisance, complicating selective excitation of solvent resonances and generating misleading

spectral features in 2D experiments (see, for instance, the multiple peaks in Figure 1). The surprise caused by the first observations of these additional peaks was such that it was suggested that quantification of the rf field was necessary for a consistent prediction of the effect.[3] It soon became clear that this quantification is much more difficult to treat than originally anticipated and that, after all, it is not required.[4,5]

In the present article, the main emphasis about radiation damping is on electronic schemes for its control and suppression, leaving out important issues like the prediction of the various spectral artifacts indicated by Figure 1, and the role of radiation damping in equilibrium fluctuations.

An important contribution to relaxation in liquids comes from the fast random modulation of the dipolar couplings between nearby spins by the Brownian motion. Dipolar couplings between distant spins remain approximately constant and their effect on each spin can be described as that of a classical average dipolar field (also called 'demagnetizing field' and 'distant dipole field') generated by the bulk magnetization in the whole sample. This field was explicitly (and rightfully) 'neglected' by Torrey in 1956 (sentence before equation (5) in Ref.[6]). In single pulse experiments, the dipolar field causes

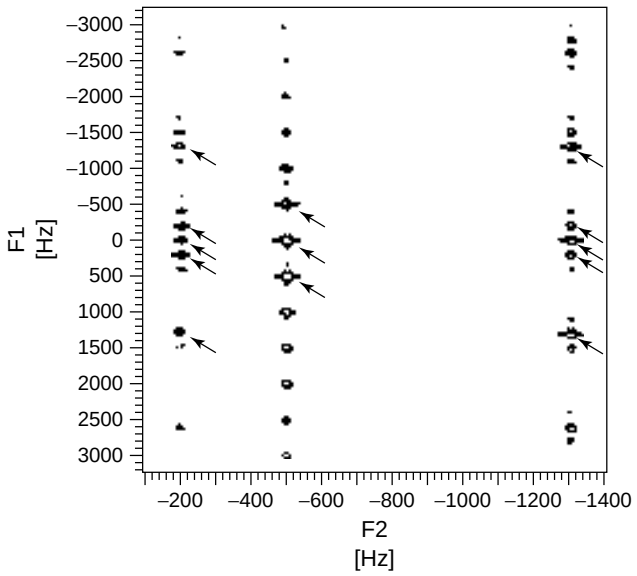

Figure 1 This is adapted from Figure 1(b) of Ahn et al.,[24] showing a radiation damped 600 MHz ^{1}H COSY spectrum of a 2 : 1 mixture of 1,1,2–trichloroethane (CH protons at −200 Hz, CH_2 protons at −1300 Hz) and methylene chloride (−500 Hz). In the absence of collective effects, COSY peaks are expected only at the positions marked by arrows. At the methylene chloride acquisition frequency F2, the strong additional harmonic peaks in the indirectly detected direction F1 are due to the radiation damping signal at the methylene chloride frequency, and the satellites caused by trichloroethylene are much weaker due to the large differences in chemical shift. At the trichloroethylene acquisition frequencies, much richer patterns of satellite peaks appear, combining the CH and CH_2 offsets. As shown by Ahn et al.,[24] these features are due to the combined effects of radiation damping and the J-coupling between CH and CH_2 protons (this J-coupling is too weak to be observed directly in the above spectrum). Under the conditions of this experiment (short evolution and acquisition times), dipolar field effects are very small. (Reproduced by permission of Taylor and Francis from S. Ahn, S. Lee, and W. S. Warren, *Mol. Phys.*, 1998, **95**, 769; http://www.tandf.co.uk/journals)

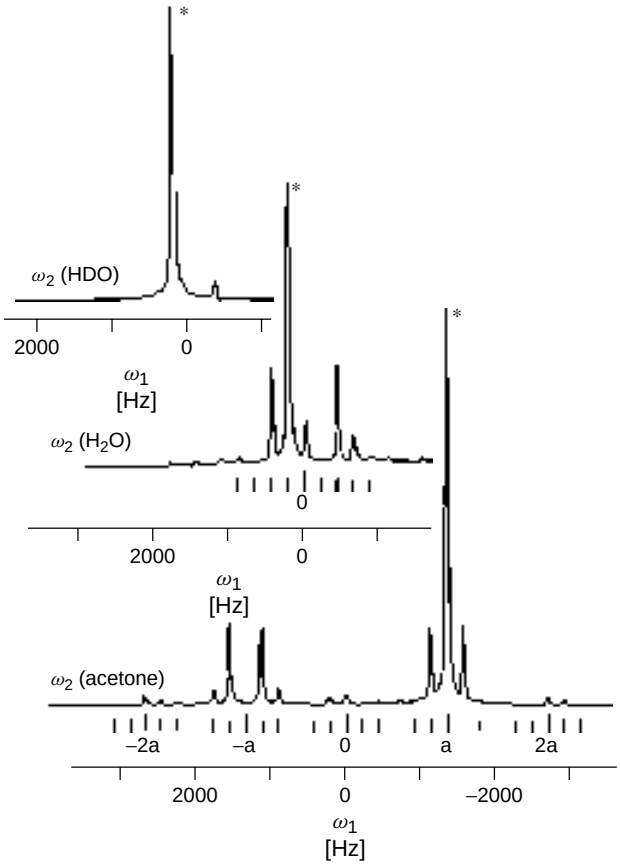

Figure 2 This is adapted from Figure 2 in Broekaert et al.,[23] showing cross sections along the indirectly detected direction ω_1, taken at acquisition offsets ω_2 as indicated, through a simple absolute value 600 MHz ^{1}H COSY spectrum acquired with standard phase cycling. Without collective effects, only the three peaks marked with a * would be observed. The vertical scale is larger for acetone to improve the visibility of the peaks. The offset of acetone is denoted a and the other ticks under the cross sections are separated by the water offset. In order to avoid strong radiation damping, the composite sample contains only a thin cylindrical core of a solution of 10% (by volume) acetone in 90% water (H_2O). This core is parallel to the external field, and it is surrounded by a larger volume filled with D_2O containing about 0.6% HDO. Deuterium lock was active throughout the experiment. Realistic numerical simulations (see Section 4.3.4), which include the calculated dipolar field, measured rates of relaxation, together with the phase cycling and apodisation actually used, faithfully reproduce the complex structure of the water and acetone cross sections. The small additional peak on the HDO cross section is due to weak radiation damping. (Reproduced by permission of Academic Press from P. Broekaert, A. Vlassenbroek, J. Jeener, G. Lippens, and J.-M. Wieruszeski, *J. Magn. Reson.* A, 1996, **120**, 97)

small shifts in the frequency of each line, which are a function of the components of the bulk nuclear magnetization and shape of the sample. As a result, the observed frequencies vary with the tipping angle and evolve due to relaxation.[7] These effects were first observed in 1979 in echo experiments, in which they generate multiple echoes.[8] The same improvements in NMR technology which made radiation damping an important issue, also made the effects of the dipolar field conspicuous whenever a large nuclear magnetization is affected by rf pulses. In 2D experiments, the dipolar field shifts modulate the acquisition

frequency as a function of the duration of the evolution delay, causing the appearance of a multiplicity of additional peaks in the indirectly detected direction, as illustrated in Figures 2 and 3.

Without the interpretation in terms of radiation damping or dipolar field, the strong additional satellite peaks shown by Figures 1 and 2 might suggest the existence of long lived molecular aggregates in many liquids. This flawed interpretation would even seem to be 'confirmed' by observing that the satellite peaks have exactly the same phase relation with the excitation pulses as the usual *intramolecular* multiple quantum coherences. The 'Warren' procedure (see Section 5.2) reconciles many of these observations by showing that dipolar field effects can be described as manifestations of *intermolecular* multiple quantum coherences, which are appreciable only for concentrated samples but do not require the participating spins to be close together. For radiation damping, the predictions still rest on a combination of analytical work and numerical simulations.

New applications and new phenomena are uncovered at a high rate: medical imaging,[9,10] high-resolution spectra in high fields of poor homogeneity and stability,[11,12] spectral clustering and dynamical instability,[13,14] all due to dipolar field effects.

In spite of the repeated success of the interpretation of multiple echoes in terms of a classical average dipolar field,[8,15–18] the surprise caused by the observation of the corresponding additional peaks in COSY experiments also led the Warren group to question the validity of the 'classical' interpretation and to propose an alternative in which all spins in the sample are treated as a single quantum system.[19–21] This proved to be an extremely fruitful move, which introduced the important new concept of *intermolecular* multiple quantum coherence and the idea that, in the new context, the 'high-temperature' approximation had to be completely re-examined. However, the earliest papers describing the new formalism also contain, besides the actual calculations and discussions, a number of provocative and questionable statements about general theoretical issues. This triggered a fierce controversy which is now progressively cooling down. Fortunately, the two approaches systematically led to the same predictions for all observable effects, and their equivalence was progressively established (see Section 5.3).[21,22]

In the present article, the emphasis concerning dipolar field effects is mainly on issues of principle (the status of the equations of motion, the high temperature approximation, 'secular' versus 'non-secular', coherences versus correlations, the incorporation of molecular diffusion in the equations of motion, the equivalence between the 'Warren' and the 'classical' formalisms, spectral clustering and dynamical instability), with simple examples in which the classical calculations are performed carefully and in detail.

Most of the ideas and results presented here are taken from the published literature, but no attempt has been made to offer a complete survey. The discussions in Sections 2.4, 2.5, 4.6, 5.2, 5.3, and 6.2 are partly new. The final version of the present article was accepted in early February, 2001. A few recent references have been added subsequently.

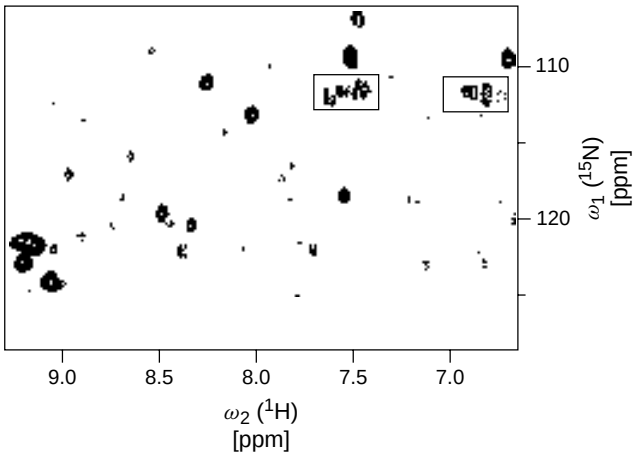

Figure 3 This is Figure 4B from Sobol et al.,[25] showing contour plots of a (600 MHz ^{1}H) 2D {^{15}N^{1}H}-HSQC-relayed NOE difference experiment used to study macromolecular hydration. The two small rectangles show subtraction artifacts originating from dipolar field effects. (Reproduced by permission of Academic Press from A. G. Sobol, G. Wider, H. Iwai, and K. Wüthrich, *J. Magn. Reson.*, 1998, **130**, 262)

2 GENERALITIES

2.1 NMR Without Collective Effects

The standard presentation and interpretation of NMR spectroscopy completely ignores the possibility that the individual spins may be influenced, directly or indirectly, by the bulk nuclear magnetization of the whole sample. For pulse experiments in liquids, this general scheme is sketched in Figure 4 with, at the top, the Bloch–Redfield equation of motion for the density operator $\hat{\rho}_p(t)$ for the spins in molecule p. $\widehat{H}_0$ is the spin Hamiltonian for molecule p (averaged over the molecular Brownian motion, and including chemical shifts, spin–spin couplings,...), the relaxation term is symbolically indicated as $\hat{\hat{\mathcal{R}}}\hat{\rho}_p(t)$, and $\hat{\boldsymbol{m}}_p = \sum_{j \text{ in } p} \gamma_j \hbar \hat{\boldsymbol{I}}_j$ is the total nuclear magnetic moment operator for molecule p. Of course, the equation of motion is different for different molecular species in the liquid, and further enhancements of the description have to be introduced to incorporate inhomogeneous fields, molecular diffusion, and intermolecular nuclear Overhauser effect (NOE). In all cases, the operator in the curly braces in the Bloch–Redfield

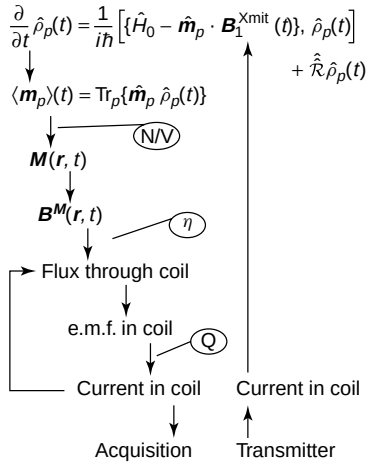

Figure 4 Sketch of the standard theory for NMR in liquids (ignoring collective effects)

equations on top of Figure 4 is independent of the state $\hat{\rho}_p(t)$ of the spins, hence, these equations are linear in the $\hat{\rho}_p(t)$s (except for minor complications originating from spin lattice relaxation towards the correct equilibrium situation). Furthermore, these equations have the form of the bona fide von Neumann equations of standard quantum mechanics when one neglects the relaxation terms.

On the right-hand side of Figure 4, the pulse transmitter causes rf current to circulate in the sample coil, and this generates the rf field $\boldsymbol{B}_1^{\text{Xmit}}(t)$ which is assumed to be the only field seen by the sample (besides the large external field $\boldsymbol{B}_0$ and the fast fluctuations causing relaxation).

The left-hand side of Figure 4 shows a step-wise description of the processes involved in the actual observation of the nuclear response. The collective effect of the average nuclear magnetic moment $\langle \boldsymbol{m}_p \rangle(t)$ of all molecules p in the sample is described by the nuclear magnetization density $\boldsymbol{M}(\boldsymbol{r}, t)$ (i.e., the nuclear magnetic moment per unit volume), which is proportional to the number density N/V of the molecules. The magnetic field $\boldsymbol{B}^{\boldsymbol{M}}(\boldsymbol{r}, t)$ is the direct contribution of $\boldsymbol{M}(\boldsymbol{r}, t)$ to the magnetic field in the sample and in the surrounding space. The time derivative of the flux of $\boldsymbol{B}^{\boldsymbol{M}}(\boldsymbol{r}, t)$ through the sample coil, which is proportional to the filling factor η, gives an induced emf which excites the resonance of the sample circuit, leading to rf currents and voltages which are further proportional to the quality factor Q of the circuit. This finally provides the input to the acquisition electronics.

It is easy to verify that, for a single spin 1/2,

$$\hat{\rho}(t) = \frac{1}{2}(\hat{1}_{\text{op}} + 4\langle \boldsymbol{I} \rangle(t) \cdot \hat{\boldsymbol{I}}) \tag{1}$$

where $\hat{\boldsymbol{m}} = \gamma\hbar\hat{\boldsymbol{I}}$ and $\langle \boldsymbol{m} \rangle(t) = \gamma\hbar\langle \boldsymbol{I} \rangle(t) = \text{Tr}\{\hat{\rho}(t)\gamma\hbar\hat{\boldsymbol{I}}\}$, hence, in this case, the classical vector $\langle \boldsymbol{m} \rangle(t)$ carries exactly the same information as the density operator. For a system of equivalent spins 1/2, equation (1) can be used to cast the equation of motion at the top of Figure 4 as the familiar Bloch equation

$$\frac{\partial}{\partial t}\langle \boldsymbol{m} \rangle(t) = \langle \boldsymbol{m} \rangle(t) \times \gamma\{\boldsymbol{B}_0 + \boldsymbol{B}_1^{\text{Xmit}}(t)\} + \mathcal{R}\text{elax} \tag{2}$$

and vice versa.

The equations of motion on top of Figure 4 [also equation (2)] and the processes shown on the left of this figure are all linear in the state of the nuclear spins. Modern acquisition electronics is also (very close to) linear, hence, the convenient and efficient tools of linear mathematics are directly applicable to the design and analysis of actual experiments. In particular, the spectral properties of the spin Hamiltonians $\widehat{H}_0$ and relaxation superoperators $\widehat{\widehat{\mathcal{R}}}$ are clearly displayed by the Fourier transforms (often multiple transforms) of suitable experiments (or computer organized sets of such experiments). These powerful and general methods are at the root of the impressive success of modern NMR.

2.2 NMR with Collective Effects

However, the provocative layout of Figure 4 clearly suggests that there is no general justification for neglecting the effect on each spin of the magnetic field $\boldsymbol{B}^{\boldsymbol{M}}(\boldsymbol{r}, t)$ generated directly by the collectivity of all spins in the sample, and the effect of the magnetic field generated by the rf current induced in the coil by the collective precession of these spins, except perhaps for the fact that these additional couplings would be too small to show up in actual experiments. If we stick to the 'hydrodynamic' description of the collective couplings as mediated by additional macroscopic magnetic fields generated by the bulk nuclear magnetization, the resulting improved scheme for the theory of NMR in liquids is sketched in Figure 5, where $\boldsymbol{B}_1^{\text{coil}}(t)$ stands for the rf field generated by the actual current in the coil, and the subtle difference between the dipolar field $\boldsymbol{B}_d(\boldsymbol{r}, t)$ 'seen' by the spins, and the Maxwell B-field $\boldsymbol{B}^{\boldsymbol{M}}(\boldsymbol{r}, t)$ generated by the bulk nuclear magnetization, will be discussed later [see e.g., equation (29)]. Obviously, the additional macroscopic magnetic fields have components oscillating at the various NMR frequencies of the spin system; hence these will react resonantly on the spins. The dipolar field also has Z-components near zero frequency, which have a significant influence on the motion of all spins in the sample, whatever their kind.

In the simple case of equivalent spins 1/2, the equation of motion on top of Figure 5 can be written as a generalized Bloch equation [see derivation of equation (2)],

$$\frac{\partial}{\partial t}\langle \boldsymbol{m}_p \rangle(t) = \langle \boldsymbol{m}_p \rangle(t) \times \gamma\{\boldsymbol{B}_0 + \boldsymbol{B}_d(r_p, t) + \boldsymbol{B}_1^{\text{coil}}(t)\} + \mathcal{R}\text{elax} \tag{3}$$

In the scheme of Figure 5, the fields $\boldsymbol{B}_d(\boldsymbol{r}, t)$ and $\boldsymbol{B}_1^{\text{coil}}(t)$ depend explicitly upon the state of the spins as described by the set of $\hat{\rho}_p(t)$s for all molecules in the sample, hence the equation of motion for $\hat{\rho}_p(t)$ shown on top of Figure 5 is no longer a linear equation of motion and the general features of spin dynamics can no longer be discussed safely in the convenient and powerful framework of linear mathematics. Of course, weak collective effects can be discussed by perturbative techniques starting from the well understood situation without collective effects, but the range of validity of such techniques is often difficult to assess. For strong collective effects, analytical solutions have been found for a few particular problems but

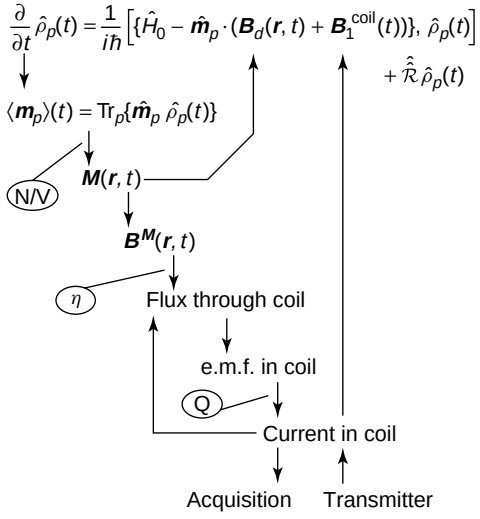

Figure 5 Sketch of the theory for NMR in liquids (including collective effects)

one usually has to resort to numerical solutions of sets of non-linear differential equations.

The effects of the contributions of $\boldsymbol{B}_1^{\text{coil}}(t)$ from the spins themselves have been called (rather inappropriately) 'radiation damping' by Bloembergen and Pound[1] in the early days of NMR, and the field $\boldsymbol{B}_d(\boldsymbol{r}, t)$ is called 'dipolar field', 'distant dipolar field', or (rather inappropriately) 'demagnetizing field', and its effects are occasionally given the misleading name of 'susceptibility effects'.

The magnitude of the observed collective effects is proportional to the magnitude of the nuclear magnetization which is present during the experiment. In the early days of proton resonance at 30 MHz or 60 MHz and poor $\boldsymbol{B}_0$ homogeneity (by present standards), for room temperature experiments, dipolar field effects were too small to be disturbing and radiation damping appeared as just a nasty contribution to the line width for very strong lines such as those of protons in pure organic liquids or water. Nowadays, with the development of high field superconducting magnets with excellent homogeneity, the impressive improvement in performance of the spectrometers, and the widespread use of fancy multiple pulse sequences, collective effects are an essential feature of many experiments.

Taking the example of the proton resonance in water (i.e., H_2O) at room temperature at 600 MHz, the equilibrium proton magnetization generates a dipolar field which shifts the proton NMR frequency by about 1 Hz (depending upon the shape of the sample), and radiation damping rotates the proton magnetization back towards its equilibrium direction with a characteristic time which can be as short as a few milliseconds for a large sample and a typical large product ηQ. Clearly, under these circumstances, radiation damping dominates the spin dynamics of the water protons and it is essential to regain control over these protons. One way to do this is to apply a pulsed field gradient which essentially suppresses the total transverse magnetization, and hence the fid signal and the radiation damping (see, however, Refs.[14,78]). Some freedom in the design of experiments would be recovered by the use of electronic suppression of radiation damping, but suitable circuitry for this is not yet available from the manufacturers. One should also not forget that weak radiation damping of lines of moderate intensity generates correspondingly weak stray additional peaks in 2D experiments.[23] The radiation damping signal emitted by the excitation of one spectral line is a weak rf field at the exact frequency of that line, hence, it directly affects lines only in a correspondingly narrow spectral range centered on the emitting line (see, however, Refs.[24,25]).

Dipolar field effects are much more insidious because, superficially, they seem to just cause minor changes of the NMR frequencies. However, the dipolar field follows the motion of the spins by which it is generated, hence, in 2D experiments, the frequency of each 'line' during the acquisition period (τ_2) will be modulated according to the duration (τ_1) of the corresponding evolution period. As a result, the Fourier transform with respect to τ_1 will have each expected peak 'decorated' by sidebands separated by multiples of the offset of the 'lines' affecting the dipolar field. For pure water, more than 10 such sidebands are easily visible where a single line would be expected. The Z-component of the dipolar field is 'seen' by all spins in the sample, hence, sidebands on one spin species can be generated by strong lines of another spin species, possibly located on different molecules. Clearly, all this threatens to play havoc if these new effects are not well understood and, preferably, suppressed. Fortunately, these unwanted peaks were usually discarded as irrelevant by NMR users, who understood their origin or thought they were due to non-linearity in the acquisition channel of the spectrometer.

For obvious reasons of simplicity, most predictions and experiments on the collective effects have been performed in spatially uniform situations for the magnetization and the dipolar field, or with the simple spatial distributions created by pulsed field gradients. However, it has been predicted that small spatial inhomogeneities, or small deviations from the simple distributions often tend to grow exponentially due to the inhomogeneities in the dipolar field, leading to 'spin turbulence'[13] and irrecoverable loss of the NMR signal. In the case of pure water discussed above, after a $\pi/2$ pulse starting from equilibrium, the inhomogeneities are expected to double for every 0.1 s time interval. If radiation damping is also present, this doubling time is significantly shortened,[14,78] particularly for helical distributions of magnetization created by field gradient pulses. This, again, stresses the importance of understanding, controlling, and preferably suppressing the collective effects.

As a counter-weight to the above catastrophic enumeration, we also mention a number of constructive uses of the collective effects. Radiation damping, undisturbed or controlled, is a useful ingredient of some of the 'water suppression' schemes,[26] and of a technique for the study of slow proton exchange between water and solute molecules,[27] and may lead to sensitive detection of very weak resonances.[28] The dipolar field effect can also be the basis of sensitive detection schemes for low-γ nuclei[17] and, remarkably, to imaging techniques with new selectivities,[29] and to the observation of high resolution spectra in high magnetic fields of moderate homogeneity and stability.[11]

2.3 The Status of the Equations of Motion

2.3.1 In the Absence of Collective Effects

The standard formulation of orthodox quantum dynamics uses the Schrödinger equation of motion

$$\frac{\partial}{\partial t}|t\rangle = \frac{1}{i\hbar}\widehat{H}(t)|t\rangle \tag{4}$$

where the ket $|t\rangle$ gives the most precise quantum mechanical description of the state of the dynamical system under discussion, and the Hermitian operator $\widehat{H}(t)$ is the observable associated with the energy of the system. This equation holds for any ket $|t\rangle$, and $\widehat{H}(t)$ is *independent* of the state of the system. A general formal solution of this equation of motion can be written under the form

$$|t\rangle = \widehat{U}(t, t_0)|t_0\rangle$$

with

$$\frac{\partial}{\partial t}\widehat{U}(t, t_0) = \frac{1}{i\hbar}\widehat{H}(t)\,\widehat{U}(t, t_0) \quad \text{and} \quad \widehat{U}(t_0, t_0) = \hat{1}_{\text{op}} \tag{5}$$

where the unitary evolution operator $\widehat{U}(t, t_0)$, also called propagator, is *independent* of the state of the system. When the state of the system is known only in a statistical sense,

as in most NMR situations, it is more convenient to describe this (average) state by the density operator $\hat{\rho}(t)$ which is the average projector on all possible kets $|t, k\rangle$ weighted by the probability p_k of the ket $|t, k\rangle$,

$$\hat{\rho}(t) = \sum_k p_k |t, k\rangle\langle t, k| \tag{6}$$

By this definition, $\hat{\rho}(t)$ is a Hermitian operator with eigenvalues in the interval between 0 and 1, and $\mathrm{Tr}\left\{\hat{\rho}(t)\right\} = 1$. When $\hat{\rho}(t)$ is known, the quantum and statistical average value $\langle A\rangle(t)$ of any observable $\hat{A}$ can be evaluated as

$$\langle A\rangle(t) = \mathrm{Tr}\{\hat{A}^\dagger\,\hat{\rho}(t)\} \tag{7}$$

where the adjoint (†) transformation is relevant when average values are evaluated for non-Hermitian operators like $\hat{I}_+$ or $\hat{I}_-$ (see Section 5.2). Corresponding to the Schrödinger equation of motion for kets, we have the von Neumann equation of motion for the density operator

$$\frac{\partial}{\partial t}\hat{\rho}(t) = \frac{1}{i\hbar}\left[\widehat{H}(t), \hat{\rho}(t)\right]$$

hence

$$\hat{\rho}(t) = \widehat{U}(t, t_0)\hat{\rho}(t_0)\widehat{U}(t_0, t) = \hat{\hat{\mathcal{U}}}(t, t_0)\hat{\rho}(t_0) \tag{8}$$

where the unitary superoperator $\hat{\hat{\mathcal{U}}}(t, t_0)$, defined by equation (8), is *independent* of the state of the system. The Schrödinger equation is linear in the ket $|t\rangle$ and the von Neumann equation is linear in the density operator $\hat{\rho}(t)$.

When relaxation is taken into account, the simplest situation arises for the spins on a single molecule, ignoring couplings with other molecules and assuming that the rotational Brownian motion which causes the relaxation has a very short autocorrelation time. In this case, one can derive a Bloch–Redfield equation of motion of the form

$$\frac{\partial}{\partial t}\overline{\hat{\rho}(t)} = \frac{1}{i\hbar}\left[\overline{\widehat{H}(t)}, \overline{\hat{\rho}(t)}\right] + \hat{\hat{\mathcal{R}}}\overline{\hat{\rho}(t)} \tag{9}$$

where the overline indicates averaging over all realizations of the molecular Brownian motion, $\hat{\hat{\mathcal{R}}}$ is the linear relaxation superoperator, and any time dependence of $\overline{\widehat{H}(t)}$ arises from the time dependence of the macroscopic magnetic field (rf field, gradients,...). $\overline{\hat{\rho}(t)}$ has all the desirable properties mentioned after equation (6) and $\overline{\widehat{H}(t)}$ is an acceptable Hamiltonian. Hence, if relaxation is ignored, equation (9) has the status of a von Neumann equation. However, it loses this status when relaxation is taken into account. For instance, it is no longer possible to write the general solution of equation (9) under the form $\overline{\hat{\rho}(t)} = \widehat{U}(t, t_0)\,\overline{\hat{\rho}(t_0)}\widehat{U}(t_0, t)$, whatever the choice made for $\widehat{U}(t, t_0)$.[30] This does not prevent equation (9) from being an acceptable and useful 'kinetic' equation of motion. In the present case, the equation remains linear in $\overline{\hat{\rho}(t)}$, hence linear mathematics are still applicable for its solution. The overlines used here are traditionally not shown explicitly, but we shall keep them in the present subsection for clarity.

2.3.2 *In the Presence of Collective Effects*

When collective effects are taken into account following the 'classical' approach, which uses density operators for the spins in single molecules, the kinetic equations of motion are of the type shown in Figure 5, namely

$$\frac{\partial}{\partial t}\overline{\hat{\rho}_p(t)} = \frac{1}{i\hbar}\left[\{\widehat{H}_0 - \hat{\boldsymbol{m}}_p \cdot (\boldsymbol{B}_d(r, t) + \boldsymbol{B}_1^{\mathrm{coil}}(t))\}, \overline{\hat{\rho}_p(t)}\right] + \hat{\hat{\mathcal{R}}}\overline{\hat{\rho}_p(t)} \tag{10}$$

where the fields $\boldsymbol{B}_d(\boldsymbol{r}, t)$ and $\boldsymbol{B}_1^{\mathrm{coil}}(t)$ depend explicitly upon the states $\left\{\overline{\hat{\rho}_p(t)}\right\}$ of all the spins in the sample, making the equation non-linear. This dependence also prevents equation (10) from recovering the von Neumann status when relaxation is ignored. A third major change in status caused by the collective effects is that the problem becomes non-local in space: whatever happens at one location depends upon the spin state at all locations in the sample.

These differences in status and their consequences have not always been fully appreciated in the recent literature, and the unorthodox notion of a state-dependent propagator, used for solving equation (10) with collective effects, has led to some unjustified conclusions. However, the following idea may help in this context. Consider an experiment in which collective effects are important, involving a given (unique) sequence of pulses at times $t > t_0$, and an *exactly specified initial condition at* $t = t_0$ for all $\overline{\hat{\rho}_p(t_0)}$s. Under these precise conditions, the complete evolution, including the fields $\boldsymbol{B}(\boldsymbol{r}, t)$ and $\boldsymbol{B}_1^{\mathrm{coil}}(t)$ in equation (10), is completely determined by this set of equations supplemented by the expressions for the collective fields in terms of the density operators $\hat{\rho}_p(t)$ indicated in Figure 5. At this point, we may (i) consider the collective fields as *known* functions of $\boldsymbol{r}$ and t, (ii) change the interpretation of the collective fields in equation (10) from 'depending upon the $\overline{\hat{\rho}_p(t)}$s' to 'known functions of $\boldsymbol{r}$ and t', and (iii) solve the new version of equation (10) with the initial condition $\left\{\overline{\hat{\rho}_p(t_0)}\right\}$ used above. The new version of equation (10) is linear in the $\overline{\hat{\rho}_p(t)}$s, the solution obtained under (iii) above can be expressed in terms of an evolution operator [see equation (8)] if relaxation is neglected, and it coincides with the 'exact' solution. However, these desirable properties are just an illusion in the present context because the 'new version' of equation (10) is valid only for a single initial condition (the collective fields change for different initial conditions), hence linearity is useless here because it cannot be used to combine evolutions with different initial conditions. Also, the collective fields are known only if the complete non-linear problem has been solved in the first place.

The issue of relaxation deserves special attention in the context of collective effects. 'Spin–spin' and 'spin–lattice' relaxation in fluids result from random processes which take place independently in each molecule (or in each pair of close by molecules if one considers intermolecular relaxation and NOE effects). In contrast, the radiation damping field and the dipolar field are macroscopic fields which act in the same way on all molecules in each small macroscopic region of the sample. Hence, for each of these macroscopic regions, the collective effects do not provide a relaxation mechanism any more than the usual rf irradiations or field inhomogeneities. This still holds when the dipolar field effects are 'suppressed' by rf irradiation[23] or by magic angle spinning (MAS),[31] and when radiation damping is controlled electronically in any way.[32–34]

The dipolar field describes dipolar interactions among spins (in different molecules), so that its contribution to the motion conserves total spin energy (i.e., for all molecules in the

sample). This does not prevent the dipolar field from possibly increasing $\langle \boldsymbol{m}_p \rangle_Z$ in some regions of the sample with a compensating decrease in other regions.

2.4 Incorporating Molecular Diffusion in the Kinetic Equations

At the microscopic level, the translational diffusion of molecules manifests itself as an important source of spin relaxation by the fast modulation of the large intermolecular spin–spin couplings at short distances. At the macroscopic level, the same translational diffusion is a major source of damping of spin echoes and pulsed field gradient responses. In these experiments, large position-dependent NMR phase shifts are created by macroscopically inhomogeneous fields and, subsequently, the phase shifts are refocused, hence producing a maximum fid if the molecules are immobile. Molecular diffusion disturbs this refocusing by randomly moving the molecules through locations with significantly different fields over the duration of the experiment. Equivalently, molecular diffusion can also be viewed as a mechanism for the spatial transport of the average spin properties, analogous to heat transport or ordinary diffusion.

This macroscopic mechanism was well understood very early and still provides the most accurate and general technique for measuring molecular diffusion in liquids. In the simple case of a single line spectrum, experiments can be adequately discussed in terms of a nuclear spin magnetization density $\boldsymbol{M}(\boldsymbol{r}, t)$ moving according to Bloch's equations complemented by a suitable molecular diffusion term and, if appropriate, by collective contributions. A very detailed and illuminating derivation of this diffusion term was given by Torrey[6] in 1956.

For more complicated situations, involving polyatomic molecules with non-trivial NMR spectra and multiple pulse preparation of intramolecular N-quantum coherences, a density operator description of the spin state of each individual molecule is, of course, required. Somewhat surprisingly, the role of molecular diffusion in this context is traditionally discussed separately for each order N of coherence, and only for particular experiments.[35–38] This limitation has the drawback of hiding the general features of spin dynamics, and constitutes an undesirable weakness when this dynamics is further complicated by dipolar field effects.

This section presents a method[39] for incorporating the effects of molecular diffusion (and also bulk flow) in the equation of motion of the density operator for the spins in a single molecule. The derivation follows Torrey's original discussion,[6] using concepts similar to the 'stochastic Liouville equation' as presented, for instance, by Schneider and Freed.[40]

The position $\boldsymbol{r}_p$ of molecule p is an important parameter whenever the initial condition or the magnetic field are not spatially uniform. When these non-uniformities are very small over the average distance between first neighbors and over the mean free path, a hydrodynamic type of description is more appropriate than one which focuses on the fate of individual molecules. The essential ingredients of such a description are that (i) each molecule carries its spin state in bulk flow and Brownian motion, and that (ii), over the relevant scales of distance and duration, the probability distribution for the future position of any molecule depends only upon its present position (and, usually very weakly, upon its present spin state), and not upon its past motion. For simplicity, the following detailed discussion is pursued for molecules all of the same kind.

A satisfactory hydrodynamic description of the spin state of the molecules in a liquid can be given in terms of the generic density operator $\hat{\rho}(\boldsymbol{r}, t)$, defined as the average density operator for all molecules which are very close to $\boldsymbol{r}$ at time t. $\hat{\rho}(\boldsymbol{r}, t)$ has the general static properties of a density operator (Hermitian, $\mathrm{Tr}\left\{\hat{\rho}(\boldsymbol{r}, t)\right\} = 1$, all eigenvalues between 0 and 1), and provides the complete information required to evaluate any average spin property for the molecules close to $\boldsymbol{r}$ at time t. As an example, the nuclear magnetization density is given by $\boldsymbol{M}(\boldsymbol{r}, t) = n\mathrm{Tr}\left\{\hat{\boldsymbol{m}}_p \hat{\rho}(\boldsymbol{r}, t)\right\}$, where n is the number of molecules per unit volume (which is taken as constant and uniform), and the magnetic moment operator $\hat{\boldsymbol{m}}_p$ is the same as in Section 2.1.

If diffusion and flow are absent, the molecules which are close to position $\boldsymbol{r}$ are always the same, they 'see' the same macroscopic fields, hence their $\hat{\rho}(t)$s evolve according to the same equation of motion (10), and this also holds for the generic density operator at position $\boldsymbol{r}$,

$$\left(\frac{\partial}{\partial t}\right)_{\substack{\text{no diff} \\ \text{no flow}}} \hat{\rho}(\boldsymbol{r}, t) = \hat{\hat{\mathcal{R}}}\hat{\rho}(\boldsymbol{r}, t) + \frac{1}{i\hbar}\left[\{\hat{H}_0 - \hat{\boldsymbol{m}}_p \cdot (\boldsymbol{B}_d(\boldsymbol{r}, t) + \boldsymbol{B}_1^{\mathrm{coil}}(t))\}, \hat{\rho}(\boldsymbol{r}, t)\right] \quad (11)$$

where the collective fields are generated by $\boldsymbol{M}(\boldsymbol{r}, t)$ defined just above.

In order to enhance the analogy with the standard discussion of heat transport or diffusion, it is useful to introduce the notion of a (generic) density operator per unit volume $n\hat{\rho}(\boldsymbol{r}, t)$, such that the sum of the density operators for all molecules in a small volume ΔV can be expressed as $n\hat{\rho}(\boldsymbol{r}, t)\Delta V$. If we now take molecular diffusion and flow into account, $n\hat{\rho}(\boldsymbol{r}, t)\Delta V$ will evolve by two mechanisms, (i) the usual spin dynamics given by equation (11) for the molecules inside ΔV, and (ii) the difference between the $\hat{\rho}$ of the molecules which enter and leave ΔV through its boundary, given by the divergence of the flux density $\hat{\boldsymbol{J}}_{n\hat{\rho}}(\boldsymbol{r}, t)$ of the quantity $n\hat{\rho}(\boldsymbol{r}, t)$. The flux density $\hat{\boldsymbol{J}}_{n\hat{\rho}}(\boldsymbol{r}, t)$ is the sum of three contributions: (i) a flow term $\boldsymbol{v}(\boldsymbol{r}, t)n\hat{\rho}(\boldsymbol{r}, t)$, (ii) an 'unbiased diffusion term' $-D\nabla_{\boldsymbol{r}}\left\{n\hat{\rho}(\boldsymbol{r}, t)\right\}$, and (iii) a small drift term $\hat{\boldsymbol{J}}_{\mathrm{drift}}(\boldsymbol{r}, t)$ arising from the force exerted by the magnetic field *gradient* on each molecule depending upon its actual spin state (the same force which operates in the Stern–Gerlach experiment), hence

$$\hat{\boldsymbol{J}}_{n\hat{\rho}}(\boldsymbol{r}, t) = \boldsymbol{v}(\boldsymbol{r}, t)n\hat{\rho}(\boldsymbol{r}, t) - D\nabla_{\boldsymbol{r}}\{n\hat{\rho}(\boldsymbol{r}, t)\} + \hat{\boldsymbol{J}}_{\mathrm{drift}}(\boldsymbol{r}, t) \quad (12)$$

where $\boldsymbol{v}(\boldsymbol{r}, t)$ is the bulk velocity of the liquid at position $\boldsymbol{r}$ and time t, and D is the coefficient of self diffusion of the relevant molecules (which may be a tensor in anisotropic fluids like liquid crystals). The drift term is easily evaluated by considering the situation of complete thermal equilibrium in the absence of bulk flow. In this case, all net flows vanish, but the equilibrium density operator $\hat{\rho}^{\mathrm{eq}}(\boldsymbol{r}, t)$ is not uniform if the magnetic field is not uniform, hence equation (12) takes the form

$$0 = -D\nabla_{\boldsymbol{r}}\{n\hat{\rho}^{\mathrm{eq}}(\boldsymbol{r}, t)\} + \hat{\boldsymbol{J}}_{\mathrm{drift}}(\boldsymbol{r}, t) \quad (13)$$

which gives an explicit expression for $\hat{\boldsymbol{J}}_{\mathrm{drift}}(\boldsymbol{r}, t)$ in equilibrium. For all standard NMR situations, which are very close to complete spin disorder ('high spin temperature'), equation (13)

remains a good approximation out of equilibrium, hence, equation (12) can be written as

$$\hat{\boldsymbol{J}}_{n\hat{\rho}}(\boldsymbol{r},t) = \boldsymbol{v}(\boldsymbol{r},t)n\hat{\rho}(\boldsymbol{r},t) - D\nabla_{\boldsymbol{r}}\{n\hat{\rho}(\boldsymbol{r},t) - n\hat{\rho}^{\mathrm{eq}}(\boldsymbol{r},t)\} \quad (14)$$

We can now combine the effects of local spin dynamics ('no diffusion, no flow') with those of diffusion and flow to obtain a continuity equation for $n\hat{\rho}^{\mathrm{eq}}(\boldsymbol{r},t)$,

$$\left(\frac{\partial}{\partial t}\right) n\hat{\rho}(\boldsymbol{r},t) = \left(\frac{\partial}{\partial t}\right)_{\substack{\text{no diff}\\ \text{no flow}}} n\hat{\rho}(\boldsymbol{r},t) - \nabla_{\boldsymbol{r}} \cdot \hat{\boldsymbol{J}}_{n\hat{\rho}}(\boldsymbol{r},t) \quad (15)$$

Combining now equations (11), (14), and (15), and taking account that $\nabla_{\boldsymbol{r}} \cdot \boldsymbol{v}(\boldsymbol{r},t)$ vanishes for an incompressible fluid, we obtain finally

$$\begin{aligned}\left(\frac{\partial}{\partial t}\right)\hat{\rho}(\boldsymbol{r},t) &= \hat{\hat{\mathcal{R}}}\hat{\rho}(\boldsymbol{r},t)\\ &+ \frac{1}{i\hbar}\left[\{\widehat{H}_0 - \hat{\boldsymbol{m}}_p \cdot (\boldsymbol{B}_d(\boldsymbol{r},t) + \boldsymbol{B}_1^{\mathrm{coil}}(t))\}, \hat{\rho}(\boldsymbol{r},t)\right]\\ &- \boldsymbol{v}(\boldsymbol{r},t)\cdot\nabla_{\boldsymbol{r}}\hat{\rho}(\boldsymbol{r},t) + \nabla_{\boldsymbol{r}} D\nabla_{\boldsymbol{r}}\{\hat{\rho}(\boldsymbol{r},t) - \hat{\rho}^{\mathrm{eq}}(\boldsymbol{r},t)\} \quad (16)\end{aligned}$$

where the drift term involving $D\nabla_{\boldsymbol{r}}\hat{\rho}^{\mathrm{eq}}(\boldsymbol{r},t)$ can be neglected in all practical situations, as discussed by Torrey.[6] Equation (16) leads directly to the usual expressions for the effects of molecular diffusion on intramolecular N-quantum coherences.[35–38] For mixtures of molecules of different types, a different generic density operator is introduced for each type of molecule, as usual (and also a different coefficient of self diffusion D and a different number density n).

In the simple case of a single line NMR spectrum (strictly speaking, similar molecules bearing a single spin 1/2), equation (16) can be simplified considerably by using equation (1), and the result no longer involves quantum operators,

$$\begin{aligned}\frac{\partial}{\partial t}\boldsymbol{M}(\boldsymbol{r},t) &= \boldsymbol{M}(\boldsymbol{r},t)\times\gamma\{\boldsymbol{B}_0 + \boldsymbol{B}_d(\boldsymbol{r},t) + \boldsymbol{B}_1^{\mathrm{coil}}(t)\}\\ &- \boldsymbol{v}(\boldsymbol{r},t)\cdot\{\nabla_{\boldsymbol{r}}\boldsymbol{M}(\boldsymbol{r},t)\}\\ &+ \nabla_{\boldsymbol{r}}\cdot(D\nabla_{\boldsymbol{r}}\{\boldsymbol{M}(\boldsymbol{r},t) - \boldsymbol{M}^{\mathrm{eq}}(\boldsymbol{r},t)\}) + \mathcal{R}\mathrm{elax} \quad (17)\end{aligned}$$

This is the usual Bloch equation, with additional terms describing radiation damping and dipolar field effects (see equation (3)), and Torrey's term[6] to account for molecular diffusion. In order to avoid ambiguities, note that the meaning of the vectorial notation used in equation (17) is $\boldsymbol{A}\cdot\{\nabla_{\boldsymbol{r}}\boldsymbol{M}(\boldsymbol{r})\} = \sum_{u=x,y,z}\mathbf{1}_{\boldsymbol{u}}\{\boldsymbol{A}\cdot(\nabla_{\boldsymbol{r}}M_u(\boldsymbol{r},t))\}$, where $\boldsymbol{A}$ can be $\boldsymbol{v}(\boldsymbol{r},t)$ or $\nabla_{\boldsymbol{r}}$, and $\mathbf{1}_{\boldsymbol{u}}$ is a unit vector pointing in the direction u.

A different line of reasoning has been proposed, in which one solves the Bloch equation for a spin undergoing Brownian motion, taking into account the changing macroscopic magnetic field encountered during this random walk.[41,42] Of course, averages have to be evaluated at the end over all initial positions and over all realizations of the Brownian random walk.

Both methods should lead to the same conclusions (and, indeed, they do) so that the choice should be a matter of taste or convenience. However, in the presence of a position dependent magnetic field, the averaging over all realizations of the Brownian motion is tricky and proved to be prone to errors,[41,42] particularly in the presence of a dipolar field caused by the spins themselves.[43]

2.5 The High Temperature Approximation, Validity and 'Breakdown'

In the absence of collective effects, the high temperature approximation is a perfectly clear concept in liquid NMR: for non-cryogenic experiments starting from thermal equilibrium, and for any given pulse sequence, all observable NMR signals $\mathrm{fid}(t, T_S)$ are proportional to the inverse of the initial spin temperature T_S,

$$\mathrm{fid}(t, T_S) = \left(\frac{1}{T_S}\right)\mathrm{fid}_1(t) \quad (18)$$

where $\mathrm{fid}_1(t)$ is independent of T_S, and the dependence of the rates of relaxation upon the temperature of the liquid has been ignored. Starting from the equation on top of Figure 4, it is easy to verify that all contributions neglected in the high temperature approximation are too small to be observed.

In the presence of collective effects, the concept of the 'high temperature approximation' can be interpreted in different ways, and this caused some confusion and a flurry of fierce controversy in liquid NMR for the last 10 years. Two of these interpretations will now be illustrated on a simple example in which the dipolar field has observable effects, radiation damping is neglected, all magnetic fields are homogeneous throughout the sample, and all spins are equivalent (for instance, a thin cylinder of water parallel to the direction Z of the large external field). With the notation of Figures 4 and 5, the average equilibrium magnetic moment per spin $\langle\boldsymbol{m}\rangle_{\mathrm{equil}}$ is proportional to the inverse temperature $1/T$, hence $\langle\boldsymbol{m}\rangle_{\mathrm{equil}} = (1/T)W\mathbf{1}_{\boldsymbol{Z}}$, where W is a constant and $\mathbf{1}_{\boldsymbol{Z}}$ is the unit vector along Z. For this simple configuration and a uniform magnetization throughout the sample, the relevant part of the dipolar field is given by $\boldsymbol{B}_d^{\mathrm{homoI}}(t) = q\langle m_Z\rangle(t)\mathbf{1}_{\boldsymbol{Z}}$ [see equation (38)], and this will just cause a shift of the NMR frequency by $\Delta\omega_d(t) = K\langle m_Z\rangle(t)$, where q and K are constants. For simplicity, relaxation will be ignored.

The response to a pulse of angle θ in the Y direction, occurring at $t = t_0$, is given by

$$\begin{aligned}&\langle m_X\rangle(t) + i\langle m_Y\rangle(t) = \mathrm{fid}(t,T)\\ &= (1/T)W\sin\theta\exp(i\{\omega_0 + \Delta\omega_d\}\{t - t_0\})\\ &= (1/T)W\sin\theta\exp(i\{\omega_0 + K(1/T)W\cos\theta\}\{t - t_0\})\\ &\quad\text{and}\quad \langle m_Z\rangle(t) = (1/T)W\cos\theta \quad (19)\end{aligned}$$

where ω_0 is the NMR frequency in the absence of collective effects. Clearly, the predicted NMR frequency depends upon the pulse angle and the initial spin temperature or spin magnetization. The results of this simple and direct experiment were reported by Edzes,[7] with excellent quantitative agreement between predictions and measurements.

In the derivation of equation (19), the high temperature approximation is invoked in two different contexts, each time with single molecules in mind: the absolute magnitude of the fid, and the dipolar shift in NMR frequency. In each case, the term in $(1/T)$ is sufficient. However, the discussion of more complex, multiple pulse experiments is often clarified by the use of a different implementation of the 'high temperature approximation' concept, in which properties of the whole spin system, like the fid or the density operator for all spins, are

expressed as a 'systematic' series expansion in powers of $(1/T)$. In the case of equation (19), this gives

$$\begin{aligned} \mathrm{fid}(t,T) &= \left(\frac{1}{T}\right)\mathrm{fid}_1(t) + \left(\frac{1}{T}\right)^2 \mathrm{fid}_2(t) + \cdots \\ \mathrm{fid}_1(t) &= W \sin\theta \exp(i\omega_0\{t-t_0\}) \\ \mathrm{fid}_2(t) &= \mathrm{fid}_1(t) i K W \cos\theta\{t-t_0\}, \ldots \end{aligned} \tag{20}$$

where the functions $\mathrm{fid}_n(t)$ are independent of T. Admittedly, the 'systematic' series expansion does not seem particularly illuminating for this simple, single pulse experiment. However, if one performs an elementary COSY experiment on the same sample and analyzes the signals by the usual double Fourier transform, the traditional peaks are 'decorated' by a number of satellites in the ω_1 direction, separated by integer multiples of the offset of ω_0. In this case, and for most other multiple pulse experiments, the 'systematic' series expansion in powers of $(1/T)$ nicely separates the satellite peaks in small groups with similar phase properties with respect to the phase difference between the two excitation pulses. The Warren group has shown[19–21] that this separation can be understood in an illuminating way by first performing a 'systematic' series expansion in powers of $(1/T)$ on the equilibrium density operator *for the quantum system of all spins in the sample* (see Section 5.2). Unfortunately the expression 'spectacular breakdown of the high temperature approximation', which they used in announcing their results, was not well understood at the time.

3 RADIATION DAMPING

3.1 A Simple Example

By way of introduction,[1,44] consider a sample of equivalent spins, subjected to homogeneous fields $\boldsymbol{B}_0$ and $\boldsymbol{B}_1^{\mathrm{coil}}(t)$, and neglect relaxation and dipolar field effects. The relevant equation of motion is equation (3). In equilibrium, $\langle \boldsymbol{m} \rangle_{\mathrm{eq}}$ points in the same direction as $\boldsymbol{B}_0$, which we choose as the Z-direction. Now consider a situation with $\langle \boldsymbol{m} \rangle(t)$ tilted from $\boldsymbol{B}_0$ by an angle $\theta(t)$. To a first approximation (neglecting radiation damping), $\langle \boldsymbol{m} \rangle(t)$ precesses around Z at the large angular velocity $\omega_0 = -\gamma \boldsymbol{B}_{0Z}$, hence $\langle m_X \rangle(t) = |\langle \boldsymbol{m} \rangle| \sin(\theta(t)) \cos(\omega_0 t + \phi_x)$, and the emf induced in the coil (with its axis in the X-direction) is proportional to the time derivative of $\langle m_X \rangle(t)$, hence $\mathrm{emf}(t) = K\omega_0 |\langle \boldsymbol{m} \rangle| \sin(\theta(t)) \sin(\omega_0 t + \phi_x)$, where K is proportional to (N/V), η, the cross-section of the coil, and the number of turns. In all practical NMR situations, the time dependence of the amplitude and phase ϕ_x of $\mathrm{emf}(t)$ is very much slower than the damping of the tuned sample circuit, hence steady state AC circuit theory applies and the current $i(t)$ in the coil is proportional to $\mathrm{emf}(t)$ (with an appropriate phase shift), $i(t) = kK\omega_0 |\langle \boldsymbol{m} \rangle| \sin(\theta(t)) \cos(\omega_0 t + \phi_i)$, where k is proportional to the quality factor Q of the sample circuit divided by its characteristic impedance.

This current $i(t)$ flows through the series resistance R_s of the circuit and generates an average Joule power (averaged over one period at frequency $\omega_0/2\pi$) $\mathcal{P}(t) = \frac{1}{2} R_s (i_{\max})^2$ as heat in R_s,

$$\mathcal{P}(t) = \frac{R_s}{2} [kK\omega_0 |\langle \boldsymbol{m} \rangle|]^2 [\sin(\theta(t))]^2 \tag{21}$$

In the present model without relaxation, this power can originate only from a corresponding rate of decrease of the total spin energy

$$E_S(t) = -N \langle \boldsymbol{m} \rangle(t) \cdot \boldsymbol{B}_0 = -N |\langle \boldsymbol{m} \rangle| |\boldsymbol{B}_0| \cos(\theta(t)) \tag{22}$$

where N is the number of spins in the sample. This is a plausible scenario, because the rf field generated by the rf current $i(t)$ in the coil can, indeed, affect the spin energy by rotating $\langle \boldsymbol{m} \rangle(t)$. Combining the above relations as $\mathrm{d}E_S(t)/\mathrm{d}t = -\mathcal{P}(t)$, we obtain

$$\frac{\mathrm{d}}{\mathrm{d}t}\theta(t) = -\frac{1}{\tau_r} \sin(\theta(t)) \tag{23}$$

where the characteristic rate of radiation damping $(1/\tau_r)$ is given by

$$\frac{1}{\tau_r} = 2\pi Q \eta |\gamma| \frac{N |\langle \boldsymbol{m} \rangle|}{V} \tag{24}$$

for a circuit tuned exactly at the NMR frequency of the spins, and decreases for increasing mistuning (never changing sign). It is easy to check that, for this simple example with a perfectly tuned sample circuit, radiation damping rotates $\langle \boldsymbol{m} \rangle(t)$ in a fixed vertical plane in a frame rotating around Z at the 'unperturbed' NMR angular velocity of the spins $\omega_0 \mathbf{1}_Z$.

Of course, the same conclusions can be reached by following the more detailed reasoning indicated in Figure 5, with the advantage of lifting the restrictions of perfect tuning,[45] single line, homogeneous fields,[46] neglect of relaxation,. . .. However, the detailed calculations involve a number of issues of sign which have been too often treated with contempt. The energy argument used above has the advantage of showing unambiguously that radiation damping rotates the nuclear magnetization towards the direction of $\boldsymbol{B}_0$, and not the opposite which would imply an absorption of heat by the resistance R_s (contrary to the second law of thermodynamics). Note that this argument breaks down when additional sources of organized energy participate in the process, as happens in active electronic control of radiation damping.[32,33]

The solution of equation (23) for $\theta(t_0)$ known at time t_0 is

$$\theta(t) = 2 \arctan\left[\tan\left(\frac{\theta(t_0)}{2}\right) \exp\left(\frac{-(t-t_0)}{\tau_r}\right)\right] \tag{25}$$

Figure 6 shows this solution for the usual range of θ, between 0 and π.

Assuming perfect tuning (and no relaxation) for simplicity, the response to a hard rf y-pulse of angle θ_0 applied at $t = t_0$ is easily evaluated with the help of equation (25),

$$\langle m_x \rangle(t) + i \langle m_y \rangle(t) = \sin(\theta(t)) \exp(i\delta\omega\{t-t_0\}) \tag{26}$$

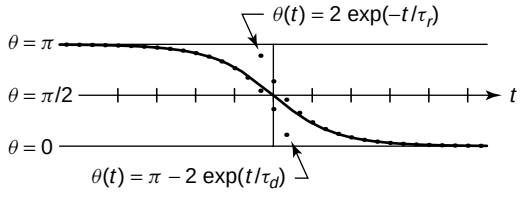

Figure 6 The solid line shows equation (25) for $t_0 = 0$ and $\theta(t_0) = \pi/2$. The dots show, respectively, approximations for θ close to 0 and close to π. The tick marks on the t scale are at τ_r intervals

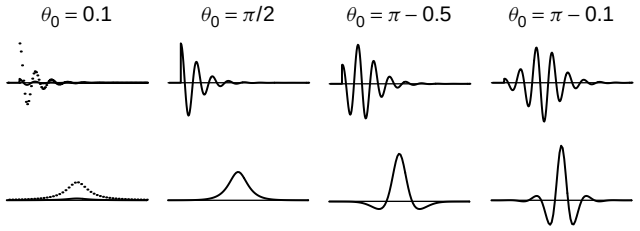

Figure 7 The effects of radiation damping on the response to a θ_0 hard pulse, for a single line spectrum (same conditions as for equation (24)). Top row: the x-component of the spin magnetization after a y-pulse, as a function of time (in the rotating frame, with a small offset of the spectral line). Lower row: the 'absorption component' of the Fourier transform of the upper row, as a function of frequency. For $\theta_0 = 0.1$, the dotted graphs are enlarged vertically by a factor of 10 for visibility

where the subscripts x and y indicate rotating frame components, and $\delta\omega$ is the offset of the nuclear spin Larmor frequency from the reference frequency of the transmitter and rotating frame. As illustrated in Figure 7, the response to a pulse of (very) small angle is damped exponentially with the characteristic time τ_r, in complete analogy with the usual damping by 'spin–spin' relaxation with $T_2 = \tau_r$ and no radiation damping. The Fourier transform of this response has the usual Lorentzian line shape (with the role of T_2 played by τ_r). For larger pulse angles, the response in not damped exponentially any more, and the Fourier transform is visibly non-Lorentzian.[47] A particularly striking situation occurs after a pulse with an angle very close to π, where the magnetization first points very close to the direction opposite to that of $\boldsymbol{B}_0$, with a very small transverse magnetization generating a very weak radiation damping. However, this radiation damping will rotate the magnetization towards the direction of $\boldsymbol{B}_0$, i.e., away from the opposite direction, hence, the transverse magnetization will increase together with its rate of increase, and θ will soon decrease through $\pi/2$ and tend to its steady state value 0, as shown also by Figure 6. For such a pulse close to π, the Fourier transform of the fid is qualitatively very different from a Lorentzian line shape.

The general properties of Fourier transforms imply that the integral over frequency of the (complex) line shapes is equal (with proper normalization) to the initial value of the (complex) transverse magnetization, irrespective of the mechanism causing the eventual decay of the nuclear response. This is the basis of the important general relation between the area under an absorption line and the number of spins participating in the line. However, in the case of radiation damped signals, a small initial transverse magnetization, hence a small area under the absorption component of the Fourier transform, does not necessarily imply that the Fourier transform itself is small (in absolute value), as shown by the examples on the left and right of Figure 7. A number of other unexpected features are discussed in a review article by Mao and Ye[48] (attention should be paid to the non-standard definitions given and used by these authors, see also Ref.[49]).

It has already been pointed out that radiation damping is not a relaxation mechanism for the spins, hence, the 'line shapes' obtained by Fourier transform of radiation damped signals cannot (and should not) be interpreted as absorption-dispersion spectra. However, radiation damping affects the transverse and longitudinal components of the spin magnetization in ways which are quite similar to relaxation effects, and this is a major problem for the measurement of long relaxation times T_1 and T_2 of spins which are not very diluted.[50]

In 2D and more sophisticated experiments, radiation damping causes the appearance of stray peaks after Fourier transforms.[45] The main culprit is, typically, the water signal. However, this very large signal is usually not the interesting one, and its taming is the purpose of the many 'water suppression' schemes.

3.2 Electronic Control of Radiation Damping

3.2.1 Introduction

Radiation damping is mediated by the electrical current flowing through the sample coil. This is a physical quantity *completely external* to the sample, hence under the direct control of the experimenter (hopefully, at least); different schemes have been proposed and demonstrated to achieve this control. An *ideal* scheme should not interfere with the normal operation of the spectrometer in any way, and retain high efficiency in all cases. For instance, it should operate during acquisition without degradation of signal to noise ratio or generation of spurious signals, and allow the use of 'digital quadrature' and other refinements. It should also provide suppression of radiation damping during 'soft pulses', hence allowing the use of very selective 'soft pulses' weaker than the radiation damping signal generated by the relevant spins.

3.2.2 A Digression about Electrical Engineering

The more ambitious and promising schemes use some simple notions of the electrical engineering of coaxial cables, which are usually not familiar to the users of NMR. For the convenience of the reader, some of these notions are now briefly reviewed, without providing detailed proofs or derivations.

Our model of coaxial cable ignores losses in the cable (electrical resistance of the conductors, dielectric losses in the insulator), and uses approximations valid for wavelengths of the signal much longer than the diameter of the cable. The only situations examined are the desirable ones in which the signal is entirely inside the cable and does not extend outside, as shown in Figure 8(a). The relevant variables are the position x along the cable, the time t, the intensity $i(x,t)$ of the current in the inner conductor, and the difference in electrical potential $V(x,t)$ between inner and outer conductor, both at every position x and every time t.

Any distribution of intensity $i(x,t)$ and voltage $V(x,t)$ in the cable can be decomposed uniquely as a sum of two 'running waves' propagating in opposite directions at the velocity v of light in the cable dielectric,

$$\begin{aligned}
&\text{(a) } i(x,t) = i_p(x - vt) + i_m(x + vt) \quad \text{and} \\
&\text{(b) } V(x,t) = V_p(x - vt) + V_m(x + vt); \quad \text{with} \\
&\text{(c) } V_p(x - vt) = +Z_c i_p(x - vt) \quad \text{and} \\
&\text{(d) } V_m(x + vt) = -Z_c i_m(x + vt)
\end{aligned} \tag{27}$$

where the (real, positive) characteristic impedance Z_c depends upon the log of the ratio of the inner and outer diameters of the conductors of the cable. A typical value for Z_c is 50 ohms.

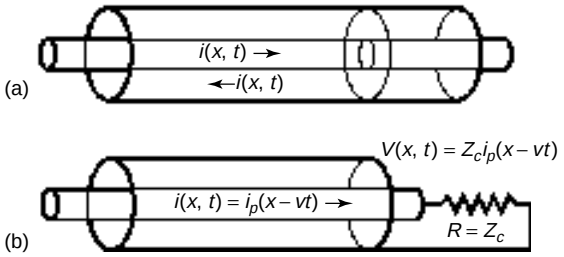

Figure 8 (a) Exactly opposite currents circulate, respectively in the inner and the outer conductor, at any position x and date t. This cancels all magnetic fields generated by these currents, except in the cable dielectric. The convention of sign used is that the arrow points in the direction of transport of conventional positive charges when the associated symbol, e.g., $i(x,t)$, has a positive value. (b) A running wave is completely absorbed when the cable is terminated by a resistance equal to its characteristic impedance Z_c

The subscript p stands for propagation in the positive direction (i.e., increasing x), and m for the negative direction.

In order to discuss realistic situations, we still have to supplement equations (27), which describe the propagation in the cable, with information about the electrical circuits connected at both ends of the cable. Only a few very simple situations will be examined here. First, assume that the cable is cut at $x = x_0$, and that each half cable remains open-circuited. This will prevent electrical current from circulating at $x = x_0$, hence, $i(x_0, t) = 0$ at all t, hence, $i_p(x_0 - vt) = -i_m(x_0 + vt)$. The running waves are reflected by an open-circuited end, with a change in sign of the 'running' i's, hence no change in sign of the 'running' Vs. This holds independently for each half cable. The situation is similar for a short-circuited end, on which reflection also takes place, but with a change of sign of the 'running' Vs. A more interesting termination would not reflect incoming signals at all, like a 'black' surface in optics. For this, consider a signal propagating *only* to the right, hence, $i_m = 0$, $V_m = 0$, $i(x,t) = i_p(x - vt)$, and $V(x,t) = V_p(x - vt)$. Equation (27c) shows that, in this case, the relation between $i(x,t)$ and $V(x,t)$ in the cable is exactly the same as it would be in a resistance $R = Z_c$, hence, if we remove the right-hand side. of the cable and replace it by this resistance, as shown in Figure 8(b), the p-signal in the cable, which hits the resistor, is not reflected at all (all its energy appears as heat in the resistor). Conversely, a generator connected to the left end of the cable of Figure 8(b) will have the same relation between current and voltage as if it were connected to a resistance $R = Z_c$.

Figure 9 describes the directional coupler, a very useful circuit element which offers the possibility of interacting separately with each of the two 'running wave' components of any signal in a cable. Figure 10 shows how a directional coupler can be used in a configuration in which, for small signals, the current in the coil (hence, the rf field in the coil) is the sum of the currents caused separately by the spins and by the 'soft pulse' generator, whereas the input to the preamplifier originates only from the spins (this last property is exact only for perfect tuning and matching, and for an ideal directional coupler perfectly terminated at B).

3.2.3 The 'Brussels' Feedback Scheme

This scheme follows the standard idea of active control by negative feedback in linear servo-systems. The quantity to be

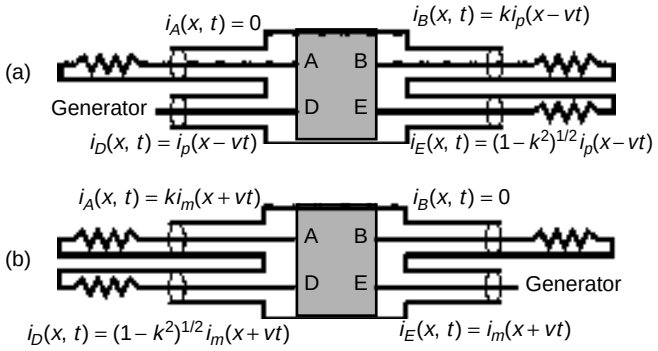

Figure 9 An idealized model of directional coupler, a passive linear device with four connecting cables. A running wave signal which enters through one of the cables (D in (a)) exits with small attenuation through the 'continuation' cable (E in (a)), an attenuated version exits through the 'diagonally opposite' cable (B in (a)), and no signal exits through the fourth cable (A in (a)) or the input cable. The coupling coefficient k is a positive number smaller than 1, typically of the order of 0.1. The position variable x is the same for the whole figure and increases from left to right. Terminating resistances $R = Z_c$ have been drawn on every free cable end to avoid ambiguities arising from reflected signals. (b) illustrates the idea that the properties discussed above in the context of (a) are unchanged by permutation of AD with BE or permutation of AB with DE

controlled here is the total rf current in the sample coil. In the absence of rf irradiation, 'hard' or 'soft', the target value of this rf current is zero, and this 'zero' is easily monitored by looking for a 'zero' at the output of the preamplifier under the conditions shown on the right-hand side of Figure 10, in which the 'generator' must be inactive. The desired control can be implemented by (weakly) coupling a suitably amplified version of the preamplifier output directly to the sample coil in such a way that the rf current caused by feedback subtracts from that present in the coil. Figure 11(a) shows the principles of a successful circuit of this type,[32] in which an additional coaxial cable is required to carry the feedback signal, and the small loop at the end of this cable induces a rf emf in the coil which subtracts from that generated by the precessing nuclear magnetization.

A rough quantitative understanding of the performance of such a scheme is easily obtained by first looking at the favorable perspective in which the feedback loop is stable and radiation damping is suppressed to a large extent. In all steady state situations we have $i_{\text{coil}}(t) = i_{\text{fid}}(t) - i_{\text{feedback}}(t)$, where $i_{\text{coil}}(t)$ is the total current in the coil, $i_{\text{fid}}(t)$ is the current originating from the spins alone, and $i_{\text{feedback}}(t)$ originating from the feedback signal alone. Note that strong suppression of radiation damping requires that $i_{\text{coil}}(t)$ should be very small compared to $i_{\text{fid}}(t)$, hence, $i_{\text{feedback}}(t)$ very close to $i_{\text{fid}}(t)$. The feedback signal $i_{\text{feedback}}(t)$ is an amplified version of $i_{\text{coil}}(t)$, hence, $i_{\text{feedback}}(t) = G i_{\text{coil}}(t)$, where G is the gain around the feedback loop (in a complete discussion, G must include rf phase shifts, and retardation around the loop). Combining the above relations, one obtains $i_{\text{coil}}(t) = i_{\text{fid}}(t)/(G+1)$, hence radiation damping is decreased by a factor $(G+1)$, and $i_{\text{feedback}}(t) = i_{\text{fid}}(t)[G/(G+1)]$, hence, $i_{\text{feedback}}(t)$ is very close to the quantity $i_{\text{fid}}(t)$ which we are directly interested in, at least for any large gain G.

A detailed discussion[32] confirms these conclusions, and shows that the circuit is stable over a range of phase shifts

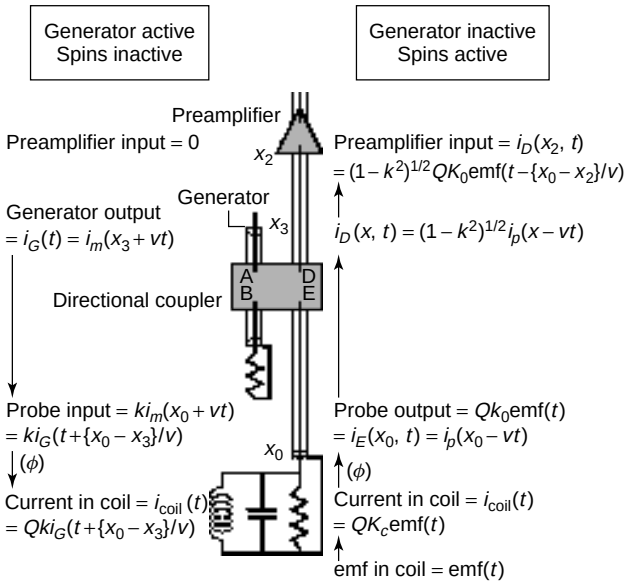

Figure 10 'Small signal' equivalent circuit, from probehead to preamplifier. The sample resonant circuit is perfectly tuned, and matched to the cable, hence, the equivalent internal damping resistance shown is equal to Z_c. Cable B is terminated in its characteristic impedance Z_c to avoid undesired reflections, the 'soft pulse' generator and the preamplifier also have impedances equal to Z_c. (ϕ) indicates that a rf phase factor has been ignored for simplicity of notation. The position variable x increases from bottom to top of the figure. The constants K_0 and K_c are properties of the probehead, k is the coupling coefficient of the directional coupler. The relation between current and voltage at the connection between cable E and probehead is $V_E(x_0, t) = -Z_c i_E(x_0, t)$ for signals originating only in the generator, and $V_E(x_0, t) = +Z_c i_E(x_0, t)$ for signals originating only in the probehead. When spins and generator are both active, the current in the coil (hence, the rf field in the coil) is the sum of the currents caused separately by the spins and by the generator, whereas the input to the preamplifier originates only from the spins

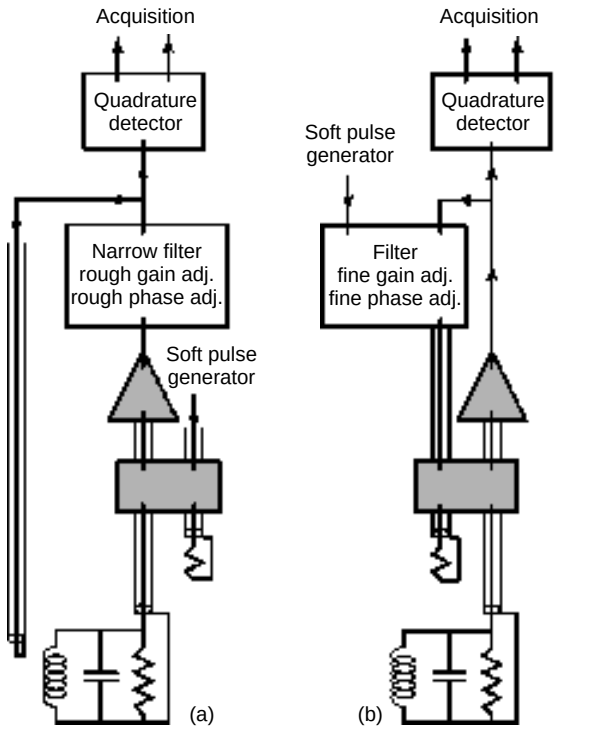

Figure 11 Two ways of using essentially the same additional electronic hardware for active electronic control of radiation damping. (a) The 'Brussels' scheme provides robust suppression of radiation damping by a large factor, but requires an additional coaxial connection to the probehead. (b) The 'École Polytechnique' scheme provides enhancement, inversion and suppression of radiation damping without modification of the probehead. Efficient suppression requires a precise and delicate adjustment of phase and gain of the signal sent back to the probehead; enhancement and inversion are robust

of $\pi/2$ or more around the loop, and for gains up to, at least, a few hundred at the NMR frequency of the relevant spins. Satisfactory performance does not require any fine adjustment of these two parameters. When the scheme is used in the configuration of Figure 11(a), suppression of radiation damping does not deteriorate the signal to noise ratio for the observed NMR signals in spite of the fact that the remaining signal in the coil, $i_{\text{coil}}(t)$, is very small.

As shown by Figure 11(a), 'soft pulses' can by applied to the spins while radiation damping is being suppressed. The 'soft pulse' signal reaches the spins without interfering with the feedback system, as explained in Figure 10(left part).

In Ref.[32] the 'narrow filter' is implemented by quadrature detection, followed by single stage RC filtering and balanced remodulation, and some hardware is saved by using these RC filtered signals also as input for acquisition. Suppression of radiation damping would be more independent of all other aspects of NMR experiments with the design of Figure 11(a), in which the acquisition circuit contains its own low pass filter (optimized for acquisition, not shown on the figure).

3.2.4 The 'École Polytechnique' Neutralization Scheme

This scheme[33] is sketched in Figure 11(b), and Figure 10 illustrates the discussion. It is useful to visualize the current $i_{\text{coil}}(t)$ in the coil (also the rf field generated by this current) as a sum of two distinct components, $i_{\text{spins}}(t)$ which arises from the precession of the spins and propagates to the input of the preamplifier, and $i_{\text{neut}}(t)$ which is generated by the additional electronics as a transformed version of $i_{\text{spins}}(t)$ and does not propagate towards the preamplifier. Hence, $i_{\text{coil}}(t) = i_{\text{spins}}(t) + i_{\text{neut}}(t)$.

A first interesting situation is reached by adjusting the gain and phase along the neutralization path in such a way that $i_{\text{neut}}(t) = -i_{\text{spins}}(t)$, hence $i_{\text{coil}}(t) = 0$, hence radiation damping is suppressed. The criterion for satisfactory adjustment here is that the spins, as observed via the preamplifier, behave in the way predicted without radiation damping. A rough adjustment is not difficult to reach in this way, but fine tuning is a delicate and time consuming process which is fragile for any small change in the sample or the probehead.

A robust use of the neutralization scheme is to increase the rate of radiation damping by making adjustments such that $i_{\text{neut}}(t) \approx ki_{\text{coil}}(t)$, hence $i_{\text{coil}}(t) \approx (k+1)i_{\text{spins}}(t)$. For positive k, this makes radiation damping faster by a factor $(k+1)$, which may be useful in water suppression schemes[26] to suppress residual water signals rapidly before acquisition.

Another robust and useful situation is obtained by changing the sign of k in the above example so as to make $(k+1)$ negative. In this 'inversion' mode, radiation damping rotates the total magnetization of the relevant spins towards the direction opposite to that of thermal equilibrium, hence stabilizing the

direction which is made unstable by 'direct' radiation damping. This can be useful for measuring weak NOE's with abundant solvent spins.[27] Note that the 'inversion' of radiation damping has no influence on spin-lattice relaxation which still progressively brings back the spin magnetization towards its usual value in thermal equilibrium.

As shown by Figure 11(b), 'soft pulses' can be applied to the spins while radiation damping is being controlled. The 'soft pulse' signal just has to be added to the neutralization signal sent towards the directional coupler.

Part of the features described above are implemented in a preliminary circuit offered by Bruker for some of their spectrometers (Radiation Damping Control Unit, Bruker France, 1999).

3.2.5 Miscellaneous Schemes (Q-switch, etc.)

A simple and safe way for suppressing radiation damping is to strongly reduce the quality factor Q of the sample circuit by connecting a low resistance in parallel with it. Of course, this resistance has to be disconnected or strongly increased during 'hard pulses' and acquisition. A 'Q-switch' of this type is offered by Bruker and has been successfully used in realistic demonstration experiments.[51,52] Unfortunately, this scheme requires a major modification of each probehead and lacks some of the versatility of the more ambitious techniques.

One of the difficulties caused by radiation damping is that it interferes with 'soft pulses' applied to abundant spins. A number of techniques have been proposed to solve this problem by designing a new class of 'soft pulses' which take radiation damping into account[53,54] or, more ambitiously, generate a final rotation independent of radiation damping.[55] An obvious advantage of this approach is that it does not require any modification of the spectrometer or probehead. A tempting idea would be to replace the analog filter and adjustments used in the feedback and neutralization schemes described above by fast digital processing of the signals, with the corresponding increase in flexibility. The fast converters between analog and digital signals, and the necessary computational power, are already present in the spectrometers. Optimistically, all that would be needed is fast, low level access to the digital side of the converters and to an internal computer. A first successful, although modest, step in this direction has already been made.[34]

4 DIPOLAR FIELD EFFECTS, THE 'CLASSICAL' PRESENTATION

4.1 The Classical Average Dipolar Field

In the standard presentation of NMR in liquids, quantum mechanics is used to describe the nuclear spin system of each individual molecule, carefully taking into account all intramolecular spin−spin couplings and all other effects of the molecule on its own spins (e.g., chemical shifts, spin-rotation coupling). At this point, one can take into account the fast molecular Brownian motion by using the average spin Hamiltonian as 'unperturbed' Hamiltonian, and the deviations from average as perturbations. In the usual case of 'short correlation times' (i.e., perturbations which have little effect over the correlation delay), this leads to a Bloch−Redfield kinetic equation of the type of equation (9), in which the Hamiltonian $\overline{\widehat{H}(t)}$ is essentially the average Hamiltonian, and the relaxation term arises from the fast random perturbations. Small effects of the immediately neighboring molecules are also routinely taken into account (e.g., intermolecular NOEs, solvent effects on the chemical shifts). Couplings with the spins in more distant molecules have been ignored for a long time because these couplings are essentially dipolar, hence they average out to zero for isotropic distributions, and one argues that the fast molecular Brownian motion maintains such a spherically symmetrical average distribution in the neighborhood of each spin; more distant spins are then neglected without detailed discussion 'because the coupling decreases rapidly for increasing distances.' However, this last argument ignores that 'distant spins' are more numerous, and that this compensates for the smaller influence of individual distant spins. Rough numerical estimates, in agreement with experiment, indicate that the *average* influence of distant spins is easily observable in standard high-field NMR of 'concentrated spins' (e.g., protons in water).

The first idea which came to mind to describe this average influence in liquid NMR is to introduce an additional magnetic field $\boldsymbol{B}_d(\boldsymbol{r}_e, t)$ acting on each spin e of molecule P, which is evaluated as the sum of the fields which are generated by the average magnetic moment of all spins g of the other molecules (all spins of the same molecule have been taken into account already),[8,56]

$$\boldsymbol{B}_d(\boldsymbol{r}_e) = \frac{\mu_0}{4\pi} \sum_{Q \neq P} \sum_{g \in Q} \gamma_g \hbar \frac{\overline{3(\langle \boldsymbol{I}_g \rangle \cdot \mathbf{1_{e,g}})\mathbf{1_{e,g}} - \langle \boldsymbol{I}_g \rangle}}{|\boldsymbol{r}_e - \boldsymbol{r}_g|^3} \qquad (28)$$

where $\mathbf{1}_{e,g} = (\boldsymbol{r}_e - \boldsymbol{r}_g)/|\boldsymbol{r}_e - \boldsymbol{r}_g|$, and the overline indicates an average over molecular positions. We shall neglect the effects of propagation of the field on the ground that the samples of interest are much smaller than the wavelength at NMR frequencies, hence all positions and averages in equation (28) are at the same time t.

Evaluation of $\boldsymbol{B}_d(\boldsymbol{r}_e)$, as given by equation (28), can be performed in most practical situations with the help of the standard techniques of macroscopic magnetostatics. A similar problem arises in permanent magnets, in which $\boldsymbol{B}_d(\boldsymbol{r}_e)$ tends to destabilize the parallel orientation of the ferromagnetic domains and is called 'demagnetizing field'. This problem is also present in the microscopic theory of (electronic) magnetic susceptibility, where it is often called 'susceptibility effects'. 'Demagnetizing field' and 'susceptibility effects' refer to particular situations of thermal equilibrium or steady state of weak irradiation. Many new features appear in the NMR case, where the relevant nuclear spin magnetization follows the rich dynamics typical of multiple pulse experiments, hence making the older denominations inappropriate (and possibly misleading). More satisfactory names are 'dipolar field' (used here) or 'distant dipole field'.

The average macroscopic aspects of the nuclear magnetization are adequately described by the magnetization density $\boldsymbol{M}(\boldsymbol{r}, t)$, averaged over volumes large enough to smooth out the molecular structure. From this, one can evaluate the usual macroscopic fields $\boldsymbol{H}(\boldsymbol{r}, t)$ and $\boldsymbol{B}(\boldsymbol{r}, t) = \mu_0\{\boldsymbol{H}(\boldsymbol{r}, t) + \boldsymbol{M}(\boldsymbol{r}, t)\}$ *due to the nuclear magnetization*. We still have to go over from these macroscopic quantities to the microscopic field $\boldsymbol{B}_d(\boldsymbol{r}_e, t)$ 'seen' by the spin at position $\boldsymbol{r}_e$. Only a brief outline of this discussion will be given here, referring the reader to the literature for details.[57–61]

The first (conceptual) step is to remove the spin at $\boldsymbol{r}_e$ and all other spins in a sphere of radius R centered on $\boldsymbol{r}_e$. For large enough R, this creates a macroscopic empty sphere at the center of which the field $\boldsymbol{B}^R$ is easily evaluated by the standard macroscopic techniques as $\boldsymbol{B}^R(\boldsymbol{r}_e) = \boldsymbol{B}(\boldsymbol{r}_e) - (2/3)\boldsymbol{M}(\boldsymbol{r}_e)$, where $\boldsymbol{B}$ and $\boldsymbol{M}$ describe the situation before removing the molecules. Note that $\boldsymbol{B}^R(\boldsymbol{r}_e)$ is the field which would be 'seen' by a spin which would be put back in the middle of the empty sphere. We can now put the removed spins back in the sphere, except for the spin at $\boldsymbol{r}_e$ and the other spins of molecule P. If we assume that, on average, the molecules are uniformly distributed in position and randomly oriented, then the nuclear magnetization of the 'spins being put back' is distributed as spherical shells of uniform magnetization centered on $\boldsymbol{r}_e$. The field generated by such a shell is exactly zero at $\boldsymbol{r}_e$. No difficulty arises from a non-zero magnetization at position $\boldsymbol{r}_e$ or in its immediate vicinity because the molecular structure prevents nuclei from approaching each other too closely. As a consequence, the 'spins being put back' give a zero contribution at $\boldsymbol{r}_e$, hence

$$\boldsymbol{B}_d(\boldsymbol{r}_e) = \boldsymbol{B}(\boldsymbol{r}_e) - \frac{2}{3}\mu_0 \boldsymbol{M}(\boldsymbol{r}_e) \tag{29}$$

Equation (29) shows that, for isotropic and uniform distributions of molecules, the classical (average) dipolar field $\boldsymbol{B}_d(\boldsymbol{r}_e)$ is a very smooth function of position, essentially the same for all spins in the same molecule. If the macroscopic quantities $\boldsymbol{B}(\boldsymbol{r})$ and $\boldsymbol{M}(\boldsymbol{r})$ are not uniform in space, the above result still holds, provided that one can neglect the changes of $\boldsymbol{M}(\boldsymbol{r})$ over the volume of the macroscopic cavity.

The actual calculation of $\boldsymbol{B}_d(r)$ for a known $\boldsymbol{M}(\boldsymbol{r})$ (i.e., the step $\boldsymbol{M}(\boldsymbol{r}, t) \rightarrow \boldsymbol{B}_d(\boldsymbol{r}, t)$ in Figure 5) is in general a rather nasty problem because numerical evaluations are often slow and inconvenient, and analytical solutions are known only for the very particular situations of (i) an ellipsoidal sample with uniform magnetization, and (ii) a spatially periodic distribution of magnetization with zero (spatial) average value, and superpositions of such distributions.

For an ellipsoidal sample with uniform magnetization $\boldsymbol{M}$, the dipolar field $\boldsymbol{B}_d$ is also uniform *inside* the sample,[58,61] and the linear relation between $\boldsymbol{M}$ and $\boldsymbol{B}_d$ is conveniently expressed with reference to the directions of the axes U, V, and W of the ellipsoid as

$$\boldsymbol{B}_d = \sum_{\alpha=U,V,W} k_{\alpha\alpha}(\boldsymbol{M} \cdot \mathbf{1}_{\boldsymbol{\alpha}})\mathbf{1}_{\boldsymbol{\alpha}},$$

where

$$\sum_{\alpha=U,V,W} k_{\alpha\alpha} = 0 \tag{30}$$

Values of $k_{\alpha\alpha}$ for some simple shapes are given below.

	$k_{\alpha\alpha}$
sphere, any direction	0
very long cylinder, $\parallel$ axis	$(1/3)\mu_0$
very long cylinder, $\perp$ axis	$-(1/6)\mu_0$
very flat pancake, $\perp$ plane	$-(2/3)\mu_0$
very flat pancake, in plane	$(1/3)\mu_0$

A convenient starting point for spatially periodic distributions of $\boldsymbol{M}$ is the simple 'plane wave' distribution $\boldsymbol{M}(\boldsymbol{r}) = \boldsymbol{F}(\boldsymbol{r} \cdot \mathbf{1}_{\boldsymbol{S}})$, where $\mathbf{1}_{\boldsymbol{S}}$ is a unit vector pointing in the reference direction S hence $\boldsymbol{M}(\boldsymbol{r})$ is uniform in any plane perpendicular to S, and $\boldsymbol{F}(\boldsymbol{r} \cdot \mathbf{1}_{\boldsymbol{S}}) = \boldsymbol{F}(\boldsymbol{r} \cdot \mathbf{1}_{\boldsymbol{S}} + \xi)$, where ξ is the spatial period. Without further specification of the function $\boldsymbol{F}$, evaluations of the dipolar field $\boldsymbol{B}(\boldsymbol{r})$ are still hampered by large contributions arising from $\boldsymbol{M}$ at distances *much* larger than $|\xi|$, reflecting the fact that no boundary has been associated with the periodic distribution $\boldsymbol{F}$. In the perspective of a boundary at distances much larger than ξ, this difficulty disappears for magnetization distributions with a spatial average of zero, $\int_0^\xi \boldsymbol{F}(s)ds = 0$, for which one ends up with the simple answer expected for a stack of very flat pancakes perpendicular to S, namely

$$\begin{aligned}\boldsymbol{B}_d(\boldsymbol{r}) &= \mu_0 \left\{ -\frac{2}{3}(\boldsymbol{M}(\boldsymbol{r}) \cdot \mathbf{1}_{\boldsymbol{S}})\mathbf{1}_{\boldsymbol{S}} \right. \\ &\qquad \left. + \frac{1}{3}(\boldsymbol{M}(\boldsymbol{r}) - (\boldsymbol{M}(\boldsymbol{r}) \cdot \mathbf{1}_{\boldsymbol{S}}))\mathbf{1}_{\boldsymbol{S}} \right\} \\ &= -\frac{\mu_0}{3}\{3(\boldsymbol{M}(\boldsymbol{r}) \cdot \mathbf{1}_{\boldsymbol{S}})\mathbf{1}_{\boldsymbol{S}} - \boldsymbol{M}(\boldsymbol{r})\}\end{aligned} \tag{31}$$

The derivation of equation (31) still does not take into account the presence of a boundary at a distance comparable to ξ or smaller, hence, for a realistic sample (of finite size), equation (31) is not necessarily a good approximation in a skin of thickness $\approx \xi$ at the surface of the sample.

The dipolar field $\boldsymbol{B}_d(\boldsymbol{r})$ at position $\boldsymbol{r}$ is very conveniently expressed by equation (31) in terms of the magnetization $\boldsymbol{M}(\boldsymbol{r})$ *at the same position*. However, this does not reflect any general change in the relation between $\boldsymbol{B}$ and $\boldsymbol{M}$ from 'global' to 'local', but is an almost fortuitous consequence of the simple spatial periodicity and zero average value assumed in this first example. If $\boldsymbol{M}(\boldsymbol{r})$ is the sum of two simple periodic distributions with different reference directions S_1 and S_2, then the contribution of each simple distribution to $\boldsymbol{B}_d(\boldsymbol{r})$ is still given by equation (31), but the total $\boldsymbol{B}_d(\boldsymbol{r})$ can no longer be expressed directly in terms of the total $\boldsymbol{M}(\boldsymbol{r})$ at the same position.

Equation (31) is obviously well suited for the discussion of spin-echo experiments, in which the spatial periodicity is created on purpose with the help of field gradients. This equation was already used by the first investigators of dipolar field effects, Deville et al.,[8,56] who also give a very careful discussion of the role of the overall shape and size of the sample, and of the average magnetization. Later, many investigators overlooked these problems, occasionally running into persistent disagreement between predictions and observations[19] until the error was subsequently corrected.[62]

4.2 Secular Coupling with the Dipolar Field, Various Truncations

The static relation between the *complete* classical average dipolar field $\boldsymbol{B}_d(\boldsymbol{r})$ and its source $\boldsymbol{M}(\boldsymbol{r})$, as discussed in Section 4.1, is independent of the presence (or not) of the large external magnetic field $\boldsymbol{B}_0$ in which all standard NMR experiments are performed. On the contrary, the dynamic effect of $\boldsymbol{B}_d(\boldsymbol{r}, t)$ on the evolution of the spin state, hence also of $\boldsymbol{M}(\boldsymbol{r}, t)$, is strongly dependent upon $\boldsymbol{B}_0$ because the

coupling of the spins with $\boldsymbol{B}_d(\boldsymbol{r},t)$ is only a small perturbation on the much larger 'unperturbed' coupling with $\boldsymbol{B}_0$. The standard procedure in such circumstances is to separate the perturbation in a 'secular' and a 'non-secular' part with respect to the unperturbed coupling, and to retain only the secular part in a first approximation. This procedure holds for a description of the spin magnetization by classical mechanics (e.g., equations (3) and (17)) or quantum mechanics (e.g., equations (10), (11) and (16)).

In the recent literature about dipolar field effects, the 'secular part of the coupling of the spins with the dipolar field' (i.e., the appropriate concept) has often been discussed in terms of a 'secular dipolar field', which has proved to be a highly misleading concept. For instance, a given part of the dipolar field may give a secular coupling with one type of spins and non-secular couplings with other spins. My attempt at avoiding these semantic problems leads to some clumsiness and repetitions in the present text.

4.2.1 *Removing the Counter-rotating Terms and the Oscillating Z terms*

If we take into account only the interaction of each spin with the large external field $\boldsymbol{B}_0$, the motion of any spin is a precession around the direction of $\boldsymbol{B}_0$ at an angular velocity $-\gamma_j\boldsymbol{B}_0$ which depends upon the spin species j. In this 'unperturbed' approximation, the nuclear magnetization is a sum of terms $\boldsymbol{M}(\boldsymbol{r},t)=\sum_j \boldsymbol{M}_j(\boldsymbol{r},t)$ precessing at the angular velocities $-\gamma_j\boldsymbol{B}_0$ of the relevant spin species, always around the same direction $\boldsymbol{B}_0$ which we shall choose as the Z direction for convenience. The Z component of $\boldsymbol{M}_j(\boldsymbol{r},t)$ is constant (in the unperturbed approximation), and the transverse component rotates at $-\gamma_j\boldsymbol{B}_0$. Each term in the magnetization generates its contribution to the dipolar field, hence $\boldsymbol{B}_d(\boldsymbol{r},t)=\sum_j \boldsymbol{B}_{d,j}(\boldsymbol{r},t)$. Due to the orientation dependence of the dipolar coupling, the motion of each term $\boldsymbol{B}_{d,j}(\boldsymbol{r},t)$ is slightly more complicated than that of the corresponding $\boldsymbol{M}_j(\boldsymbol{r},t)$: The Z component of $\boldsymbol{B}_{d,j}(\boldsymbol{r},t)$ has a constant part and one oscillating at frequency $|\gamma_j B_0|$, and the transverse component of $\boldsymbol{B}_{d,j}(\boldsymbol{r},t)$ is the sum of a 'co-rotating' part, rotating at the same angular velocity as $\boldsymbol{M}_j(\boldsymbol{r},t)$, and a 'counter-rotating' part, rotating in the opposite sense.

The constant Z component has a persistent effect on all spins, whatever their species, the oscillating Z component has no persistent effect on any spin because it just causes a minute back and forth azimuthal oscillation. The 'co-rotating' part of $\boldsymbol{B}_{d,j}(\boldsymbol{r},t)$ has a persistent resonant effect on the spins of species j and has no persistent effect on other spins, for which it is not resonant; for the same reason, the 'counter-rotating' part has no persistent effect on any spin. As a conclusion, we shall not lose any dynamical effect of $\boldsymbol{B}_{d,j}(\boldsymbol{r},t)$ (to first order) by performing a truncation which removes the oscillating Z component and the 'counter-rotating part', leaving only $\boldsymbol{B}_{d,j}^{\text{no crp}}(\boldsymbol{r},t)$. Of course, the final selection of the secular part of the coupling with the dipolar field will require further discussion.

The truncation which gives $\boldsymbol{B}_{d,j}^{\text{no crp}}(\boldsymbol{r},t)$ is easy to perform in a frame of coordinates which rotates around $\boldsymbol{B}_0$ at the same angular velocity as $\boldsymbol{M}_j$ because, in this frame, $\boldsymbol{B}_{d,j}^{\text{no crp}}(\boldsymbol{r},t)$ is not time-dependent whereas the other parts of $\boldsymbol{B}_{d,j}(\boldsymbol{r},t)$ oscillate at the frequencies $|\gamma_j B_0|$ and $2|\gamma_j B_0|$. Hence averaging over one period at the frequency $|\gamma_j B_0|$ leaves only $\boldsymbol{B}_{d,j}^{\text{no crp}}(\boldsymbol{r},t)$.

As a first example of this truncation, consider the contribution $\delta\boldsymbol{B}_{d,g}(\boldsymbol{r}_e)$ arising from spin g in equation (28), assuming $\boldsymbol{r}_e$ and $\boldsymbol{r}_g$ to be fixed positions,

$$\delta\boldsymbol{B}_{d,g}(r_e)=\frac{\mu_0\gamma_g\hbar}{4\pi|\boldsymbol{r}_e-\boldsymbol{r}_g|^3}[3(\langle\boldsymbol{I}_g\rangle\cdot\mathbf{1}_{\boldsymbol{e},\boldsymbol{g}})\mathbf{1}_{\boldsymbol{e},\boldsymbol{g}}-\langle\boldsymbol{I}_g\rangle] \tag{32}$$

In the inertial 'laboratory' frame, the only time dependent quantity in equation (32) is the vector $\langle\boldsymbol{I}_g\rangle$; conversely, in a frame rotating at the angular velocity $-\gamma_g\boldsymbol{B}_0$, only the unit vector $\mathbf{1}_{\boldsymbol{e},\boldsymbol{g}}$ is time dependent (it rotates at the angular velocity $+\gamma_g\boldsymbol{B}_0$). We can now express the vectors $\langle\boldsymbol{I}_g\rangle$ and $\mathbf{1}_{\boldsymbol{e},\boldsymbol{g}}$ in terms of the basic unit vectors $\mathbf{1}_{\tilde{X}}$, $\mathbf{1}_{\tilde{Y}}$, and $\mathbf{1}_{\boldsymbol{Z}}$ of the rotating frame, noting that $\mathbf{1}_{\boldsymbol{e},\boldsymbol{g}}\cdot\mathbf{1}_{\tilde{X}}=\cos\phi\sin\theta$, $\mathbf{1}_{\boldsymbol{e},\boldsymbol{g}}\cdot\mathbf{1}_{\tilde{Y}}=\sin\phi\sin\theta$, and $\mathbf{1}_{\boldsymbol{e},\boldsymbol{g}}\cdot\mathbf{1}_{\boldsymbol{Z}}=\cos\theta$, where θ and ϕ are the polar angles of $\mathbf{1}_{\boldsymbol{e},\boldsymbol{g}}$ in the rotating frame. θ is constant and ϕ increases at the rate $\gamma_g B_0$. After a little algebra, and averaging over a variation of ϕ by 2π, one is left with the desired truncated part of $\delta\boldsymbol{B}_{d,g}^{\text{no crp}}(\boldsymbol{r}_e)$,

$$\delta\boldsymbol{B}_{d,g}^{\text{no crp}}(\boldsymbol{r}_e)=\frac{\mu_0\gamma_g\hbar}{4\pi|\boldsymbol{r}_e-\boldsymbol{r}_g|^3}\left[\frac{3(\cos\theta)^2-1}{2}\right][3(\langle\boldsymbol{I}_g\rangle\cdot\mathbf{1}_{\boldsymbol{Z}})\mathbf{1}_{\boldsymbol{Z}}-\langle\boldsymbol{I}_g\rangle] \tag{33}$$

Equation (33) already has the usual features of the secular part of dipolar couplings: the projection direction Z is that of $\boldsymbol{B}_0$, and $\delta\boldsymbol{B}_{d,g}^{\text{no crp}}(\boldsymbol{r}_e)$ goes through zero at the 'magic angle' such that $3(\cos\theta_{\text{magic}})^2=1$.

The same calculation can be performed in the case of an ellipsoidal sample with uniform magnetization $\boldsymbol{M}$, and equation (30) for $\boldsymbol{B}_d$ leads to

$$\boldsymbol{B}_d^{\text{no crp}}=\frac{1}{2}\left[\sum_{\alpha=U,V,W}k_{\alpha\alpha}(\mathbf{1}_{\boldsymbol{\alpha}}\cdot\mathbf{1}_{\boldsymbol{Z}})^2\right][3(\boldsymbol{M}\cdot\mathbf{1}_{\boldsymbol{Z}})\mathbf{1}_{\boldsymbol{Z}}-\boldsymbol{M}] \tag{34}$$

In the case of a long cylinder, this gives

$$\boldsymbol{B}_d^{\text{no crp}}=\frac{\mu_0}{6}\left[\frac{3(\cos\theta)^2-1}{2}\right][3(\boldsymbol{M}\cdot\mathbf{1}_{\boldsymbol{Z}})\mathbf{1}_{\boldsymbol{Z}}-\boldsymbol{M}] \tag{35}$$

where θ is the angle between the cylinder axis and Z, and for a simple periodic distribution with zero average magnetization, equation (31) leads to

$$\boldsymbol{B}_d^{\text{no crp}}(\boldsymbol{r})=-\frac{\mu_0}{3}\left[\frac{3(\cos\theta)^2-1}{2}\right][3(\boldsymbol{M}(\boldsymbol{r})\cdot\mathbf{1}_{\boldsymbol{Z}})\mathbf{1}_{\boldsymbol{Z}}-\boldsymbol{M}(\boldsymbol{r})] \tag{36}$$

where θ is the angle between the reference direction S and Z.

Equations like (35) and (36) are often used in the literature with a different global sign. Presumably, this reflects the widespread contempt, in NMR, of issues of sign which seem to have no major qualitative influence on the predictions or conclusions.[63,64]

4.2.2 *Secular Couplings and Further Truncation*

In the quantum mechanical kinetic equation for the spins in a single molecule (see, for instance, equations (10) or

(16)), the dipolar field appears in a coupling term $-\hat{\boldsymbol{m}}_p \cdot \boldsymbol{B}_d(\boldsymbol{r},t)$ which adds to the usual spin Hamiltonian H_0; in the corresponding classical Bloch equation (see, for instance, equations (3) or (17)), the dipolar field contributes a coupling term $-\langle \boldsymbol{m}\rangle(t) \cdot \boldsymbol{B}_d(\boldsymbol{r},t)$, hence an additional term $\gamma \langle \boldsymbol{m}\rangle(t) \times \boldsymbol{B}_d(\boldsymbol{r},t)$ in the time derivative $\partial\langle \boldsymbol{m}\rangle(t)/\partial t$.

If all spins in the sample belong to the same species, the secular approximation consists in replacing $\boldsymbol{B}_d(\boldsymbol{r},t)$ by $\boldsymbol{B}_d^{\text{no crp}}(\boldsymbol{r},t)$ in the coupling terms and in the contributions to time derivatives mentioned just above.

In the presence of multiple spin species, the appropriate procedure is to first decompose $\hat{\boldsymbol{m}}_p$ and $\boldsymbol{B}_d(\boldsymbol{r},t)$ as sums of separated terms for the different spin species, $\hat{\boldsymbol{m}}_p = \sum_j \hat{\boldsymbol{m}}_{p,j}$ and $\boldsymbol{B}_d(\boldsymbol{r},t) = \sum_k \boldsymbol{B}_{d,k}(\boldsymbol{r},t)$, and then to express the coupling term as a double sum over j and k. For the 'homonuclear' couplings, the secular approximation is the same as for a single spin species: replace $-\hat{\boldsymbol{m}}_{p,j} \cdot \boldsymbol{B}_{d,j}(\boldsymbol{r},t)$ by the corresponding $-\hat{\boldsymbol{m}}_{p,j} \cdot \boldsymbol{B}_{d,j}^{\text{no crp}}(\boldsymbol{r},t)$. The 'heteronuclear case' (i.e., $j \neq k$) requires some further truncation because the co-rotating part of the dipolar field is no longer resonant for different spins, hence only the constant Z component remains, which we shall denote $\boldsymbol{B}_{d,j}^{Z\,\text{only}}(\boldsymbol{r},t)$. As an example, equation (35) for a long cylinder with uniform magnetization $\boldsymbol{M}_j$ of the j spins leads to

$$\boldsymbol{B}_{d,j}^{Z\,\text{only}} = \frac{\mu_0}{6}\left[\frac{3(\cos\theta)^2 - 1}{2}\right][2(\boldsymbol{M}_j \cdot \mathbf{1_Z})\mathbf{1_Z}] \tag{37}$$

For the 'heteronuclear' terms, the secular approximation consists in replacing each term $-\hat{\boldsymbol{m}}_{p,k} \cdot \boldsymbol{B}_{d,j}(\boldsymbol{r},t)$ by the corresponding $-\hat{\boldsymbol{m}}_{p,k} \cdot \boldsymbol{B}_{d,j}^{Z\,\text{only}}(\boldsymbol{r},t)$.

In the first run of exploration of the dipolar field effects, which is presently underway, much attention has been devoted to the simplest idealized situations: single spin species with a single NMR line, combined with a simple geometry and distribution of magnetization, such that the total effective dipolar field at any point $\boldsymbol{r}$ can be expressed in terms of the total nuclear magnetization at the same point $\boldsymbol{r}$ by a relation of the type of equations (34)–(36). For this type of relation, the classical equation of motion (3) or (17) clearly shows that the term $-\boldsymbol{M}$ in the second square bracket has no effect on the motion because $\boldsymbol{M}(\boldsymbol{r},t) \times \boldsymbol{M}(\boldsymbol{r},t) = 0$, hence it may be dropped, leaving a truncated dipolar field which we shall denote $\boldsymbol{B}_d^{\text{homoI}}(\boldsymbol{r},t)$ where 'homoI' stands for 'homonuclear idealized'. Of course, it is also perfectly legitimate to keep the term $-\boldsymbol{M}$, and this does not lead to any error or any additional complication in the calculations. As an example, equation (35) for a long cylinder with uniform magnetization $\boldsymbol{M}$ leads to

$$\boldsymbol{B}_{d,j}^{\text{homoI}} = \frac{\mu_0}{6}\left[\frac{3(\cos\theta)^2 - 1}{2}\right][3(\boldsymbol{M} \cdot \mathbf{1_Z})\mathbf{1_Z}] \tag{38}$$

However, it is important to note that the validity of this truncation is strictly limited to the very particular situations specified above. Once the truncation is made, one is no longer in a position to discuss the effects of 'non-idealities' like inhomogeneities in $\boldsymbol{B}_0$ or $\boldsymbol{B}_1$, imperfect shape of the sample, non-zero total magnetization, dynamical instabilities,.... As a conclusion, my recommendation is to avoid this unnecessary and misleading truncation.

4.3 Simple Examples: Homogeneous and Helical Spatial Distributions of Magnetization ('Classical' Discussion)

We shall now examine some typical examples of pulsed NMR experiments in which the dipolar field effects do not cause major changes in the spatial symmetry of the distribution of magnetization. The discussion given in this section will follow the 'classical' presentation, deferring the 'Warren' interpretation of the same effects to the section on intermolecular multiple-quantum coherences. Finally, spectral clustering and dynamic instability will be discussed in Section 6.

4.3.1 Multiple Spin Echoes (Equivalent Spins)

In the absence of collective effects, a sequence of two hard pulses, applied to the equilibrium spin state, generates a single echo in a constant field gradient;[41] an additional echo of order n may also appear for each order of intramolecular n-quantum coherence which has been prepared in the initial spin state.[65] Radiation damping[45] and the dipolar field[8] can also cause the appearance of multiple spin echoes, even for molecules bearing a single spin 1/2, which cannot support *intramolecular* n-quantum coherence for $|n| > 1$.

This first example, multiple echoes caused by the dipolar field alone in a liquid in which all spins are equivalent, has been discussed in great detail by the first investigators, Deville et al.,[8] in a study on solid ^{3}He. In the simplified version of their derivation presented here, relaxation, molecular diffusion (and flow) will be ignored. Radiation damping is usually not a major problem in spin echo experiments, because the fid signal is large only during the short echoes (see, however, Section 6.3); this problem will also be ignored here without further discussion.

A last delicate issue is the role of the shape and size of the sample on the relation between $\boldsymbol{M}(\boldsymbol{r},t)$ and the relevant part $\boldsymbol{B}_d^{\text{no crp}}(\boldsymbol{r},t)$ of the dipolar field, as discussed already in connection with equation (31). Deville et al.[8] discuss the problem for realistic sample shapes; here, the problem will be avoided by considering a sample in the shape of a cylindrical pancake perpendicular to the direction S of the field gradient, so that equation (31) applies for the 'plane wave' modulated component $\boldsymbol{M}_{\boldsymbol{S}}(\boldsymbol{r},t) = \boldsymbol{F}_{\boldsymbol{S}}(\boldsymbol{r} \cdot \mathbf{1_S})$ of $\boldsymbol{M}(\boldsymbol{r},t)$ as well as for its average value, except for a small (neglected) region along the cylindrical edge with a width comparable to the thickness of the pancake. If the direction S is changed, equation (36) shows that the relevant part of the dipolar field changes as $(3\cos^2\theta - 1)/2$, hence dipolar field effects are maximum for $\theta = 0$ and disappear when the field gradient is at the magic angle. The overall shape of the sample is not a very important issue whenever the pitch of the magnetization helix is much larger than the size of the sample.

For simplicity in the present section, the direction S will be chosen parallel to Z, so that the external magnetic field $\boldsymbol{B}_0$ will be given by $\boldsymbol{B}_0(z) = \boldsymbol{B}_0(0) + Gz\mathbf{1_Z}$ and the relevant part of the dipolar field by (see equation (36)) $\boldsymbol{B}_d^{\text{no crp}}(z,t) = -\mu_0[(\boldsymbol{M}(z,t) \cdot \mathbf{1_Z})\,\mathbf{1_Z} - (1/3)\boldsymbol{M}(z,t)]$. With the above simplifications and notations, and ignoring non-secular terms, the equation of motion (17) for $\boldsymbol{M}(z,t)$ becomes

$$\left(\frac{\partial}{\partial t}\right)_{\text{lab}} \boldsymbol{M}(z,t) = \boldsymbol{M}(z,t) \times \gamma\{\boldsymbol{B}_0(0) + Gz\mathbf{1_Z} - \mu_0(\boldsymbol{M}(z,t) \cdot \mathbf{1_Z})\mathbf{1_Z} + \boldsymbol{B}_1^{\text{co rot}}(t)\} \tag{39}$$

where $\boldsymbol{B}_1^{\text{co rot}}(t)$ is the co-rotating part of the pulsed rf field. Further discussions are simplified by rewriting this equation of motion in a frame of coordinates $(\tilde{X}, \tilde{Y}, Z)$ which rotates with respect to the 'lab' frame (X, Y, Z) at the 'unperturbed' angular velocity $-\gamma \boldsymbol{B}_0(0)$,

$$\left(\frac{\partial}{\partial t}\right)_{\text{rot}} \boldsymbol{M}(z,t) = \boldsymbol{M}(z,t) \times \gamma\{(Gz - \mu_0 M_Z(z,t))\mathbf{1}_{\boldsymbol{Z}} + \boldsymbol{B}_1^{\text{co rot}}(t)\} \tag{40}$$

In the absence of rf pulse, this gives the convenient relations

$$\frac{\partial}{\partial t} M_{\mp}(z,t) = -i\gamma(Gz - \mu_0 M_Z(z,t)) M_{\mp}(z,t)$$
$$\frac{\partial}{\partial t} M_Z(z,t) = 0 \tag{41}$$

where $M_{\mp}(z,t) = M_{\tilde{X}}(z,t) + iM_{\tilde{Y}}(z,t)$.

It is easy to check that, if one starts with the uniform equilibrium distribution $\boldsymbol{M}^{\text{eq}}$ and assumes homogeneous rf fields $\boldsymbol{B}_1(t)$, then equations (39)–(41) lead to distributions $\boldsymbol{M}(\boldsymbol{r}, t)$ which are 'plane wave' modulated only in the Z-direction, in agreement with the assumption on which these equations are based. This is a necessary condition for the self consistency of the derivation. However, in any real experiment, there will be (hopefully small) deviations from the ideal conditions described above, and most of these deviations do not have the simple symmetries assumed in equations (39)–(41), hence these simplified equations are not suitable to discuss the consequences of the deviations on the observed signals. If the perturbations are 'stable', their presence is not very disturbing, but it has been shown[13] that, in a number of dynamic situations, 'unstable' perturbations grow exponentially in time and eventually lead to 'spin turbulence' with rather sudden loss of NMR signal (see Section 6). These difficulties show up only together with very strong dipolar field effects, so that many realistic NMR experiments can still be discussed safely in terms of equations (39)–(41).

The initial spin state is the uniform equilibrium magnetization $\boldsymbol{M}^{\text{eq}} = M^{\text{eq}}\mathbf{1}_{\boldsymbol{Z}}$. At time t_0, a first hard rf pulse is applied (see Figure 12), of tipping angle $\pi/2$ and phase ϕ (ϕ is the angle from $\tilde{\boldsymbol{X}}$ to $\boldsymbol{B}_1^{\text{co rot}}$), resulting in a spin state

$$M_{\mp}(z, t_{0+}) = -M^{\text{eq}} i e^{i\phi}, \quad M_Z(z, t_{0+}) = 0 \tag{42}$$

Thereafter, the spin state evolves according to equation (41) and, after a delay τ_1 without rf pulse we have

$$M_{\mp}(z, t_0 + \tau_{1-}) = -M^{\text{eq}} i e^{i\phi} e^{-i\gamma G z \tau_1}$$
$$M_Z(z, t_0 + \tau_{1-}) = 0 \tag{43}$$

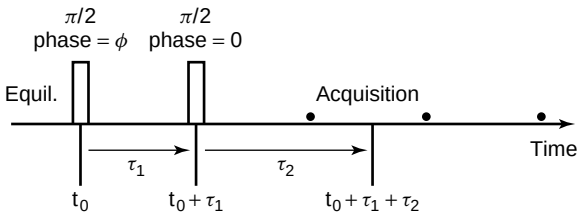

Figure 12 Timing of the hard rf pulses for equations (42)–(47), and (49). The dots show the timing of the echoes

At this point, the second $\pi/2$ pulse is applied, with phase 0, which transforms the spin state into

$$M_{\mp}(z, t_0 + \tau_{1+}) = -M^{\text{eq}} \text{Re}[i e^{i\phi} e^{-i\gamma G z \tau_1}]$$
$$= -\frac{1}{2} M^{\text{eq}}[i e^{i\phi} e^{-i\gamma G z \tau_1} - i e^{-i\phi} e^{i\gamma G z \tau_1}]$$
$$M_Z(z, t_0 + \tau_{1+}) = -M^{\text{eq}}\ \text{Im}[i e^{i\phi} e^{-i\gamma G z \tau_1}]$$
$$= -M^{\text{eq}} \cos[\phi - \gamma G z \tau_1] \tag{44}$$

From now on, $M_{\mp}$ rotates at the angular velocity $-\gamma(Gz + \mu_0 M^{\text{eq}} \cos[\phi - \gamma G z \tau_1])$, hence

$$M_{\mp}(z, t_0 + \tau_1 + \tau_2) = M_{\mp}(z, t_0 + \tau_{1+}) e^{-i\gamma G z \tau_2} \times e^{-i\gamma\mu_0 M^{\text{eq}} \tau_2 \cos[\phi - \gamma G z \tau_1]} \tag{45}$$

At this point, one may choose to simplify the discussion by restricting it to small dipolar field effects, specifically to small values of $|\gamma\mu_0 M^{\text{eq}}\tau_2|$, by expanding the factor $e^{-i\gamma\mu_0 M^{\text{eq}} \cos[\phi - \gamma G z \tau_1]\tau_2}$ in equation (45) as a power series in $\gamma\mu_0 M^{\text{eq}}\tau_2$ and keeping only the first few terms, which are easy to manipulate analytically even in a derivation which includes relaxation and molecular diffusion.[15] Here, we shall deal with this factor by expanding it in terms of Bessel functions,[8] using the relation

$$\exp(ia\cos b) = \sum_{p=-\infty}^{+\infty} i^p J_p(a) \exp(ipb) \tag{46}$$

where a and b are real, and the summation extends over all integer values of p. Some other properties of the Bessel functions, which will be used here, are given in Figure 13. With these relations, and after some algebra, equation (45) can be written as

$$M_{\mp}(z, t_0 + \tau_1 + \tau_2)$$
$$= -\frac{1}{2} M^{\text{eq}} \sum_{n=-\infty}^{+\infty} i^{-n} e^{-in\phi} e^{-i\gamma G z(\tau_2 - n\tau_1)} \{J_{n-1}(\omega_d \tau_2) + J_{n+1}(\omega_d \tau_2)\}$$
$$= -\frac{1}{2} M^{\text{eq}} \sum_{n=-\infty}^{+\infty} i^{-n} e^{-in\phi} e^{-i\gamma G z(\tau_2 - n\tau_1)} \frac{2n J_n(\omega_d \tau_2)}{\omega_d \tau_2} \tag{47}$$

where $\omega_d = \gamma\mu_0 M^{\text{eq}}$ is the 'dipolar angular velocity', which is the inverse of the 'dipolar demagnetizing time' τ_d used by the Warren group.

In order to evaluate the observed fid signal, we still have to integrate over the whole sample, i.e., to perform a z integral of equation (47) over the thickness d of the flat disk. The typical echo situation occurs when the transverse magnetization is wound in a helix with a large number of turns $|\gamma G d \tau_1/2\pi|$ during the delay between the two pulses. In this case, the z integral of $e^{-i\gamma G z(\tau_2 - n\tau_1)}$, when considered as a function of τ_2, has a sharp maximum for $\tau_2 = n\tau_1$, and this associates a well defined echo with each positive value of n in equation (47), as shown in Figure 14.

The above calculations may seem less formal with the help of the following pictorial, and hopefully intuitive, presentation: (i) during the delay between the two rf pulses, the field gradient G progressively creates a simple helical distribution of transverse magnetization $M_{\mp}$ with the spatial

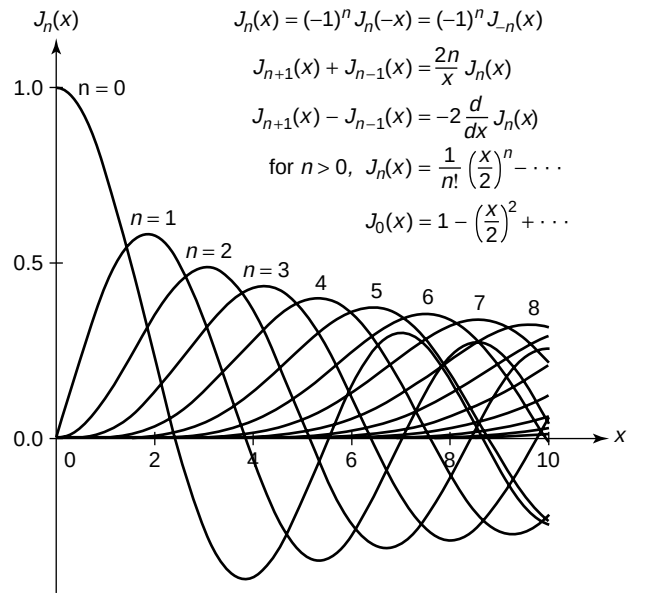

Figure 13 Some properties of the Bessel functions $J_n(x)$ for real x and integer n

period $|2\pi/\gamma G\tau_1|$ (see equation (43), the dipolar field plays no important role here); (ii) the second pulse transforms this simple helical distribution into a superposition of a grating of M_Z and a related grating of $M_{\mp}$, both with the same spatial period $|2\pi/\gamma G\tau_1|$; it is convenient to see the grating of $M_{\mp}$ as a superposition of two simple helical distributions twisted in opposite directions (see equation (44)); (iii) after the second rf pulse, the grating of dipolar field created by the grating of M_Z progressively distorts the helical distributions of $M_{\mp}$, and parts of the distorted distributions are refocused by the field gradient G into multiple echoes (see equation (47)). The complex process just described under (iii) also operates in many related experiments (heteronuclear echoes, CRAZED sequence,...).

A very convenient feature of echo experiments of the type discussed here is that some meaningful results can already be obtained without careful shimming of the field, or precise adjustment of offsets and phases (for pulses and acquisition). The clear separation in time of the echoes of different orders n, and the absolute value of the peak of each echo do not depend upon these details. The magnitude of the nth echo, as given by equation (47), is $V|M^{\mathrm{eq}}nJ_n(\omega_d\tau_2)/\omega_d\tau_2|$, where V is the volume of the sample. It is instructive to examine the limit of very weak dipolar field effects, characterized here by a small value of the dimensionless parameter $|\omega_d\tau_1| = |\gamma\mu_0 M^{\mathrm{eq}}\tau_1|$, by performing a power series expansion of the magnitude of the echoes. At positive orders n, we have

$$V|M^{\mathrm{eq}}nJ_n(\omega_d\tau_2)/\omega_d\tau_2| = V|M^{\mathrm{eq}}|\left|\frac{(\omega_d n\tau_1)^{n-1}}{(n-1)!2^n} + \cdots\right| \quad (48)$$

where $\cdots$ stands for terms in $(\omega_d\tau_1)^{n+1}$ and higher powers. This shows clearly how the echo amplitude rapidly decreases for increasing order n in the case of a small parameter $|\omega_d\tau_1|$. Equations (47)–(48) also suggest that large echoes could be observed up to large orders n in any situation in which $|\omega_d| \neq 0$, by just choosing a long enough delay τ_1 between the excitation pulses. However, this possibility is limited in real experiments by the processes of relaxation and molecular diffusion which have been ignored in the simplified model discussed above. Relaxation alone will strongly damp the echoes whenever τ_1 or τ_2 become significantly longer than the transverse relaxation time T_2, so that the largest dipolar field effects can be expected for $\tau_1 \approx T_2$. As an example, it is not uncommon to have $\omega_d T_2 \approx 10$ for the water protons in

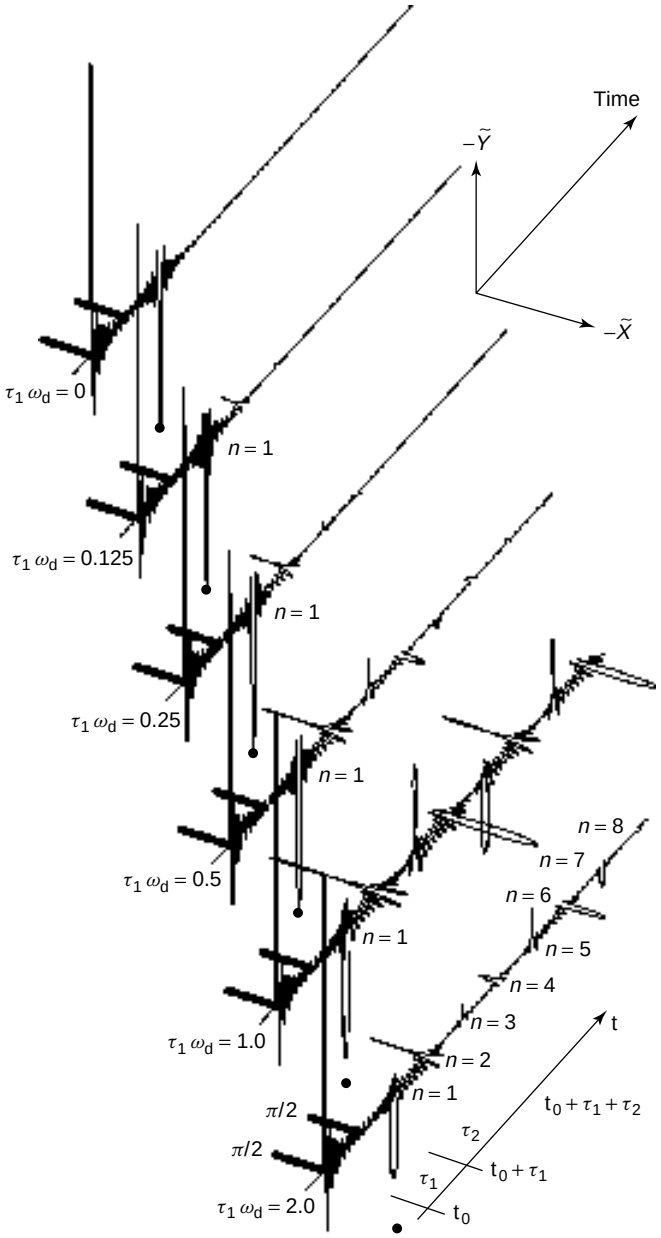

Figure 14 Multiple echoes due to the dipolar field after a $[(\pi/2, \tilde{X}) - \tau_1 - (\pi/2, \tilde{X}) - \tau_2 - \mathrm{acq.}]$ sequence, in a constant field gradient. The simulations are based on the extended Bloch equation (3) or (17), and on equation (36) for the dipolar field. Relaxation, molecular diffusion and radiation damping have been ignored for simplicity. The 'sample' is a wide slice perpendicular to Z, with a thickness such that the field gradient creates a 16-turn helix of transverse magnetization over the delay τ_1 between the two pulses. $\omega_d = \gamma\mu_0 M^{\mathrm{eq}}$ is the 'dipolar angular velocity'. The dot below each $n = 1$ echo shows the magnitude of this echo when $\omega_d = 0$, for reference

aqueous solutions in a standard high field magnet, and this can lead to very conspicuous echoes of order up to 10 or more.

Molecular diffusion is also a source of damping of spin echoes whenever the pitch of the magnetization helix is not much greater than the characteristic molecular displacements $(D\tau_1)^{1/2}$ and $(D\tau_2)^{1/2}$ during the experiment. This effect has been understood quantitatively (including the usual relaxation processes) very early in the development of NMR, and has ever since been the method of choice for the study of molecular diffusion in fluids. The Bloch equation, complemented with a suitable diffusion term as shown by Torrey[6] (see also Section 2.4), provides a safe and convenient starting point for the quantitative interpretation of experimental results. Deville et al.[8,56] have shown how this quantitative discussion can be extended to take into account dipolar field effects.

Equation (48) is almost in the form of a 'systematic' power series expansion in terms of the inverse of the initial spin temperature T (see Section 2.5), because M^{eq} and ω_d are both proportional to $(1/T)$, at least to a very good first approximation. Seen in this way, the amplitude of the echo of order n has a leading contribution proportional to $(1/T)^n$, which dominates for weak dipolar field effects.

An even simpler general property of dipolar field effects illustrated by equation (47) is the dependence upon the phase difference ϕ between the two excitation pulses: ϕ appears in the expression of the response of order n as a single multiplicative factor $e^{-in\phi}$. This opens the possibility of separating the components of the response according to the order n by phase cycling.[66] In this context, it is useful to examine the situation in which the reference frequency $|\omega_{\mathrm{ref}}/2\pi|$ of the coherent spectrometer is (slightly) different from the unperturbed resonance frequency $|\gamma B_{0Z}(0)/2\pi|$ of the spins. The usual definition of phases, for pulses and for acquisition, is given in the spectrometer rotating frame, hence we shall also write the equation of motion for the spin magnetization in this rotating frame. In the case of equation (40), this just adds a contribution $\boldsymbol{M}(\boldsymbol{r},t)\times(-\delta\omega\mathbf{1}_{\boldsymbol{Z}})$ to the right-hand side of the equation, where the small offset $\delta\omega=[-\gamma B_{0Z}(0)-\omega_{\mathrm{ref}}]$, and ω_{ref} has been given the same sign as that of $-\gamma B_{0Z}(0)$. For the first line of equation (41), the corresponding additional term is $i\delta\omega\, M_{\mp}(z,t)$. When these additional terms are taken into account, equation (47) for the z-distribution of magnetization at acquisition time becomes

$$M_{\mp}(z,t_0+\tau_1+\tau_2)=-\frac{1}{2}M^{\mathrm{eq}}\sum_{n=-\infty}^{+\infty}\left\{\frac{2nJ_n(\omega_d\tau_2)}{\omega_d\tau_2}\times i^{-n}e^{-in\phi}e^{-in\delta\omega\tau_1}e^{i\delta\omega\tau_2}e^{-i\gamma Gz(\tau_2-n\tau_1)}\right\} \tag{49}$$

In simple echo experiments, each echo is labeled by the corresponding order n so that, for well separated echoes, no additional separation procedure is needed and the various phase factors in equation (49) may seem almost pedantic details. However, in more complex spectral situations or as a check about the general interpretation of the data, one can use the $e^{-in\phi}$ phase dependence of the terms in equations (47) and (49) to achieve a systematic separation according to n, by Fourier transform of the data with respect to ϕ, as discussed at the end of Section 4.3.4.

4.3.2 *Multiple Spin Echoes (Two Spin Species)*

As an example of the extension of the techniques discussed above to multiple spin species, we shall now briefly discuss the very simple multiple echo experiment sketched by Figure 15, on a homogeneous mixture of spins of two different species, labeled a and b. For simplicity, the sample will still be a wide slab perpendicular to Z, and we shall ignore relaxation, molecular diffusion, and radiation damping. Different rotating frames will be used for the different spins: the frame denoted by 'rot, a', rotating at the angular velocity $-\gamma_a\boldsymbol{B}_0(0)$ for spins a, and a corresponding frame for spins b. As discussed in Section 4.2.2, the magnetization and the dipolar field are decomposed according to the spin species, $\boldsymbol{M}(\boldsymbol{r},t)=\boldsymbol{M}_a(\boldsymbol{r},t)+\boldsymbol{M}_b(\boldsymbol{r},t)$, and $\boldsymbol{B}_d(\boldsymbol{r},t)=\boldsymbol{B}_{d,a}(\boldsymbol{r},t)+\boldsymbol{B}_{d,b}(\boldsymbol{r},t)$, where $\boldsymbol{M}_a(\boldsymbol{r},t)$ is the source of $\boldsymbol{B}_{d,a}(\boldsymbol{r},t)$ and $\boldsymbol{M}_b(\boldsymbol{r},t)$ that of $\boldsymbol{B}_{d,b}(\boldsymbol{r},t)$. With the same simplifications as for equations (39) to (40), the equations of motion are

$$\left(\frac{\partial}{\partial t}\right)_{\mathrm{rot,a}}\boldsymbol{M}_a(z,t)=\boldsymbol{M}_a(z,t)\times\gamma_a\left\{\left(Gz-\mu_0\left[M_{aZ}(z,t)+\frac{2}{3}M_{bZ}(z,t)\right]\right)\mathbf{1}_{\boldsymbol{Z}}+\boldsymbol{B}_{1,a}^{\mathrm{co\,rot}}(t)\right\} \tag{50}$$

and the analogous equation obtained by permuting the labels a and b. The factor 2/3 is for the heteronuclear secular coupling between a and b.

Starting from equilibrium for a and b spins, the Z components of the spin magnetization between t_0 and $t_0+\tau_1$ (see Figure 15) is $M_{aZ}(t,z)=0$ and $M_{bZ}(z,t)=M_b^{\mathrm{eq}}$, hence the transverse magnetization of the a spins immediately before $t_0+\tau_1$ is

$$M_{a\mp}(z,t_0+\tau_{1-})=-M_a^{\mathrm{eq}}ie^{i\phi}e^{i\gamma_a\frac{2}{3}\mu_0M_b^{\mathrm{eq}}z\tau_1}e^{-i\gamma_aGz\tau_1} \tag{51}$$

hence the magnetizations immediately after $t_0+\tau_1$ are

$$\begin{aligned}M_{a\mp}(z,t_0+\tau_{1+})&=-M_a^{\mathrm{eq}}\mathrm{Re}[ie^{i\left(\phi+\gamma_a\frac{2}{3}\mu_0M_b^{\mathrm{eq}}\tau_1\right)}e^{-i\gamma_aGz\tau_1}]\\ M_{aZ}(z,t_0+\tau_{1+})&=-M_a^{\mathrm{eq}}\cos\left[\left(\phi+\gamma_a\frac{2}{3}\mu_0M_b^{\mathrm{eq}}\tau_1\right)-\gamma_aGz\tau_1\right]\\ M_{b\mp}(z,t_0+\tau_{1+})&=-M_b^{\mathrm{eq}}i,\quad M_{bZ}(z,t_0+\tau_{1+})=0\end{aligned} \tag{52}$$

During acquisition, the a spins behave essentially as if the b spins were absent, leading to the same echoes as in

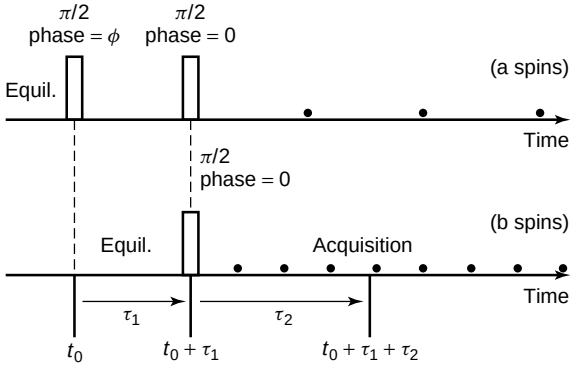

Figure 15 Timing of the hard rf pulses for equations (51)–(53). The dots show the timing of the echoes for $\gamma_b=2.5\gamma_a$

Section 4.3.1, at $\tau_2 = n\tau_1$ for all positive integers n. For the b spins, similar calculations lead to

$$M_{b\dot{+}}(z, t_0 + \tau_{1+}) = -M_b^{\text{eq}} i e^{-i\gamma_b G z \tau_2} \times e^{-i\gamma_b \frac{2}{3}\mu_0 M_a^{\text{eq}} \tau_2 \cos\left[\left(\phi + \gamma_a \frac{2}{3}\mu_0 M_b^{\text{eq}} \tau_1\right) - \gamma_a G z \tau_1\right]}$$
$$= -M_b^{\text{eq}} i \sum_{p=-\infty}^{+\infty} \left\{ i^{-p} e^{-ip\phi} e^{-ip\frac{2}{3}\gamma_a \mu_0 M_{bZ}^{\text{eq}} \tau_1} \times e^{-iGz(\gamma_b \tau_2 - p\gamma_a \tau_1)} J_p\left(\gamma_b \frac{2}{3}\mu_0 M_a^{\text{eq}} \tau_2\right)\right\} \quad (53)$$

In typical echo situations, the integral over z of the factor $e^{-iGz(\gamma_b\tau_2 - p\gamma_a\tau_1)}$, considered as a function of τ_2, has a sharp maximum for $\tau_2 = p(\gamma_a/\gamma_b)\tau_1$, and this, again, associates a well defined echo with each *positive* value of the integer p in equation (53). The new feature is the delay $(\gamma_a/\gamma_b)\tau_1$ between successive echoes.

These indirect echoes have been observed by Bowtell,[17] who gives a detailed discussion including relaxation and molecular diffusion, and shows that rare spins a with a small $|\gamma_a|$ can be observed with favorable sensitivity on the first indirect echo of abundant (solvent) spins b with a much larger $|\gamma_b|$.

In a more complete spin echo experiment, a rf pulse would also be applied to the b spins at time t_0, and a slight extension of the above calculation shows that multiple echoes are expected for all integers p, q, r, and s (positive and negative), such that $\tau_2 = [s + r(\gamma_b/\gamma_a)]\tau_1 > 0$, for a spins, and, $\tau_2 = [q + p(\gamma_a/\gamma_b)]\tau_1 > 0$ for b spins.

4.3.3 The CRAZED and HOMOGENIZED Experiments

Figure 16 shows the timing of the sequence introduced by the Warren group under the acronym CRAZED,[19,21] which can be seen as a variant of the echo sequence, in which (see 'pictorial presentation' in Section 4.3.1) τ_1-evolution, winding by the gradient, unwinding by the gradient, and distortion of the helix during τ_2-acquisition, take place in separated time intervals. This offers increased freedom in the design of experiments, notably access to the $n = 0$ echo, and provides a glimpse at the interplay between pulsed field gradients and the dipolar field in more complex situations.

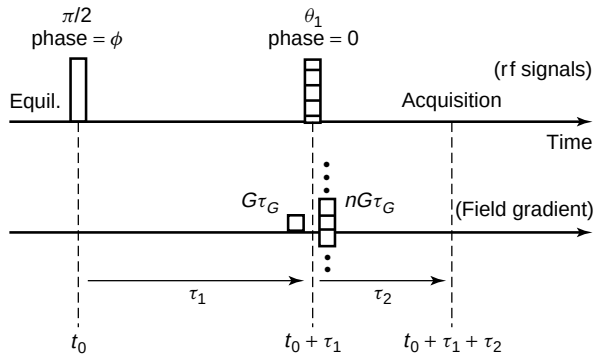

Figure 16 Timing for the basic CRAZED experiment. The field gradient pulses are characterized by the product ($G\tau_G$ or $nG\tau_G$) of the (strong) gradient and its (short) duration. n can be positive, negative or zero. For the simplified HOMOGENIZED experiment, $n = 0$. For the COSY experiment, $G\tau_G = 0$

In this introductory discussion, we shall make the same drastic simplifications as in Section 4.3.1: all spins equivalent, neglect of relaxation, molecular diffusion, and radiation damping, flat sample perpendicular to Z, spectrometer reference frequency exactly on resonance. A discussion which includes relaxation and diffusion for $n = 2$, for weak dipolar field effects, is given by Ardelean et al.[67]

Immediately after the first rf pulse, $M_Z(t_{0+}) = 0$ and $M_{\dot{+}}(t_{0+}) = -M^{\text{eq}} i e^{i\phi}$, and this holds until the beginning of the first gradient pulse, which transforms the magnetization into $m_Z(t_0 + \tau_{1-}) = 0$ and $M_{\dot{+}}(t_0 + \tau_{1-}) = -M^{\text{eq}} i e^{i\phi} e^{-i\gamma G \tau_G z}$. With the present simplifications, the position of the first field gradient pulse in the τ_1 interval is immaterial. Immediately after the second rf pulse, the magnetization is given by

$$M_{\dot{+}}(t_0 + \tau_{1+}) = -M^{\text{eq}}\{\text{Re}[i e^{i\phi} e^{-i\gamma G \tau_G z}] + i \cos\theta_1 \text{Im}[i e^{i\phi} e^{-i\gamma G \tau_G z}]\}$$
$$= -\frac{1}{2} M^{\text{eq}}\{(1 + \cos\theta_1) i e^{i\phi} e^{-i\gamma G \tau_G z} - (1 - \cos\theta_1) i e^{-i\phi} e^{i\gamma G \tau_G z}\}$$
$$M_Z(t_0 + \tau_{1+}) = -M^{\text{eq}} \sin\theta_1 \cos[\phi - \gamma G \tau_G z] \quad (54)$$

Subsequently, the second gradient pulse multiplies $M_{\dot{+}}$ by $e^{-in\gamma G\tau_G z}$, and the evolution under the dipolar field during the delay τ_2 by $e^{-i\gamma\mu_0 M^{\text{eq}}\tau_2 \cos[\phi - \gamma G \tau_G z]}$. Again, with the present simplifications, the position of the second gradient pulse in the τ_2 interval is immaterial. At acquisition time, which must be after the second gradient pulse if $n \neq 0$, $M_{\dot{+}}$ is given by

$$M_{\dot{+}}(t_0 + \tau_1 + \tau_2) = -\frac{1}{2} M^{\text{eq}} \sum_{q=-\infty}^{+\infty} i^{-q} e^{-iq\phi} e^{-i\gamma G \tau_G z(n-q)} \times \{[J_{q+1}(\omega_d \tau_2 \sin\theta_1) + J_{q-1}(\omega_d \tau_2 \sin\theta_1)] + \cos\theta_1 [J_{q+1}(\omega_d \tau_2 \sin\theta_1) - J_{q-1}(\omega_d \tau_2 \sin\theta_1)]\} \quad (55)$$

where $\omega_d = \gamma\mu_0 M^{\text{eq}}$, and the summation is over all integers q (note that n is not necessarily an integer). The last step in the calculation of the observed fid is an integral over the whole sample, i.e., a z integral over the thickness d of the flat disk. In a typical CRAZED situation, in which the first pulsed gradient winds the magnetization in a helix with a large number of turns $|\gamma G \tau_G d/2\pi|$, the z integral of $e^{-i\gamma G\tau_G z(n-q)}$, when considered as a function of n, has a sharp maximum for $n = q$. This allows separate observation of each term in the summation over q in equation (55) by an appropriate choice of n in successive experiments. As shown by combining Figure 13 and equation (55), these signals are large and last for long times (provided that relaxation, molecular diffusion, and radiation damping are not too strong). The term $q = 0$, $n = 0$ (no second gradient pulse) in equation (55) is observable only if the second pulse is different from $\theta_1 = \pi/2$ because $J_1(u) + J_{-1}(u) = 0$. This term is particularly interesting because it does not depend upon the phase ϕ of the first rf pulse, hence it is also independent of any offset between the spectrometer frequency and the unperturbed spin NMR frequency (see, e.g., equation (49)). This behavior is strongly reminiscent of *intramolecular* zero-quantum coherences (which cannot exist in the present case of molecules bearing a single spin); in the 'Warren' formalism, the $n = 0 = q$ terms clearly originate from *intermolecular* zero-quantum coherences, and this concept was at the origin of the interest for such signals, and for important applications in imaging[9,29] (not discussed

here) and in obtaining very high resolution spectra in external fields of moderate homogeneity.[11,12]

We shall now discuss a simplified version of the HOMOGENIZED experiment proposed by the Warren group for this purpose. This requires extending the above calculations for the case of a mixture of two molecular species,[79] a and b, each bearing a single spin with different offsets $\delta\omega_a$ and $\delta\omega_b$ from the spectrometer reference frequency ω_{ref}. The discussion will be limited to the case where the difference between offsets is much larger than any dipolar frequency ω_d appearing in the problem, $|\delta\omega_a - \delta\omega_b| \gg |\omega_d|$, so that the spins a and b can be treated as 'heteronuclear' in the 'secular' simplification of the equations of motion (see Section 4.2.2; for the opposite case see Section 4.3.5).

Combining the notations and discussions in the paragraph ending in equation (49) with those of Section 4.3.2, and with the timing shown in Figure 16, the a and b magnetizations after the first gradient pulse but before the rf pulse at $t_0 + \tau_1$, are given by

$$\begin{aligned} M_{a\mp}(t_0+\tau_{1-}) &= -M_a^{\text{eq}} i e^{i\phi} e^{i\delta\omega_a\tau_1} e^{-i\gamma G\tau_G z} \\ M_{b\mp}(t_0+\tau_{1-}) &= -M_b^{\text{eq}} i e^{i\phi} e^{i\delta\omega_b\tau_1} e^{-i\gamma G\tau_G z} \\ M_{aZ}(t_0+\tau_{1-}) &= 0, \quad M_{bZ}(t_0+\tau_{1-}) = 0 \end{aligned} \tag{56}$$

and immediately after the rf pulse at $t_0 + \tau_1$, by

$$\begin{aligned} M_{a\mp}(t_0+\tau_{1+}) &= -\frac{1}{2}M_a^{\text{eq}}\{(1+\cos\theta_1) i e^{i\phi} \\ &\quad \times e^{i\delta\omega_a\tau_1} e^{-i\gamma G\tau_G z} - (1-\cos\theta_1) i e^{-i\phi} e^{-i\delta\omega_a\tau_1} e^{i\gamma G\tau_G z}\} \\ M_{aZ}(t_0+\tau_{1+}) &= -M_a^{\text{eq}} \sin\theta_1 \cos[\phi - \gamma G\tau_G z + \delta\omega_a\tau_1] \end{aligned} \tag{57}$$

and similar relations for M_b obtained by permutation of the subscripts a and b. After the rf pulse at $t_0 + \tau_1$, and with the present drastic simplifications, M_{aZ} and M_{bZ} remain constant, the evolution of $M_{a\mp}$ is given by the product of three factors: (i) a factor $e^{-in\gamma G\tau_G z}$ from the second gradient pulse, (ii) a factor $e^{i\delta\omega_a\tau_2}$ from the offset, and (iii) a factor $e^{-i\gamma\mu_0\tau_2\sin\theta_1\left\{-M_{aZ}(t_0+t_{1+})-\frac{2}{3}M_{bZ}(t_0+t_{1+})\right\}}$ from the dipolar fields created by the a and b spins. The evolution of $M_{b\mp}$ is given by similar factors with permutation of a and b. With some algebra, one obtains, for acquisition times after the second gradient pulse,

$$\begin{aligned} M_{a\mp}(t_0+\tau_1+\tau_2) &= -\frac{1}{2}M_a^{\text{eq}} e^{i\delta\omega_a\tau_2} \sum_{p,q}\Bigg\{ i^{p+q} e^{i\phi(p+q)} \\ &\quad \times e^{-i\gamma G\tau_G z(n+p+q)} e^{i(p\delta\omega_a+q\delta\omega_b)\tau_1} \\ &\quad \times \Bigg(\Bigg[(1+\cos\theta_1) J_{p-1}(-\gamma\mu_0\sin\theta_1 M_a^{\text{eq}}\tau_2) \\ &\quad \times J_q\left(-\gamma\mu_0\sin\theta_1\frac{2}{3}M_b^{\text{eq}}\tau_2\right)\Bigg] \\ &\quad + \Bigg[(1-\cos\theta_1) J_{p+1}(-\gamma\mu_0\sin\theta_1 M_a^{\text{eq}}\tau_2) \\ &\quad \times J_q\left(-\gamma\mu_0\sin\theta_1\frac{2}{3}M_b^{\text{eq}}\tau_2\right)\Bigg]\Bigg)\Bigg\} \end{aligned} \tag{58}$$

and a similar relation for $M_{b\mp}$, where the summations over p and q range over all integers from $-\infty$ to $+\infty$.

In the perspective of high resolution spectra in fields of moderate homogeneity, the factor $e^{i(p\delta\omega_a+q\delta\omega_b)\tau_1}$ in equation (58) is very interesting in the cases $p = -q \neq 0$, for which it oscillates (as a function of τ_1) at the frequency *difference* between the a and b NMR lines (or multiples thereof). This difference is unaffected by small changes in external field. Of course, a 2D experiment (ω_1 associated with τ_1, and ω_2 with τ_2, both seen from the frame rotating at $\omega_{\text{ref}}\mathbf{1}_Z$) is required to study the τ_1 dependence of the signal, and the goal is to observe 2D peaks with very small width in the indirectly detected ω_1 direction.

For a pulsed gradient $G\tau_G$ which creates a magnetization helix with a large number of turns over the thickness of the sample, the $p = -q$ terms of equation (58) are efficiently selected by the choice of $n = 0$ (no gradient pulse after $t_0 + \tau_1$), and it is convenient to rewrite equation (58) in this particular case as

$$\begin{aligned} M_{a\mp}(t_0+\tau_1+\tau_2) &= -\frac{1}{2}M_a^{\text{eq}} e^{i\delta\omega_a\tau_2} \sum_{q=-\infty}^{+\infty}\Bigg\{ e^{i\tau_1 q(\delta\omega_a-\delta\omega_b)} \\ &\quad \times J_q\left(-\gamma\mu_0\sin\theta_1\frac{2}{3}M_b^{\text{eq}}\tau_2\right)[(1+\cos\theta_1) J_{-q-1}(-\gamma\mu_0\sin\theta_1 M_a^{\text{eq}}\tau_2) \\ &\quad + (1-\cos\theta_1) J_{-q+1}(-\gamma\mu_0\sin\theta_1 M_a^{\text{eq}}\tau_2)]\Bigg\} \end{aligned} \tag{59}$$

$$\begin{aligned} M_{b\mp}(t_0+\tau_1+\tau_2) &= -\frac{1}{2}M_b^{\text{eq}} e^{i\delta\omega_b\tau_2} \sum_{q=-\infty}^{+\infty}\Bigg\{ e^{i\tau_1 q(\delta\omega_b-\delta\omega_a)} \\ &\quad \times J_q\left(-\gamma\mu_0\sin\theta_1\frac{2}{3}M_a^{\text{eq}}\tau_2\right)[(1+\cos\theta_1) J_{-q-1}(-\gamma\mu_0\sin\theta_1 M_b^{\text{eq}}\tau_2) \\ &\quad + (1-\cos\theta_1) J_{-q+1}(-\gamma\mu_0\sin\theta_1 M_b^{\text{eq}}\tau_2)]\Bigg\} \end{aligned} \tag{60}$$

A simple and useful situation occurs when the a spins are abundant, hence cause large dipolar field effects, and the b spins are dilute. In this case, the Bessel function arguments involving $M_b^{\text{eq}}\tau_2$ remain much smaller than 1 (in absolute value) for any relevant value of τ_2 (i.e., for $\tau_2 < T_2$ where T_2 is the spin–spin relaxation time), hence the corresponding Bessel functions are well approximated by the first non-zero term of their power series expansion (see Figure 13).

The response due to $M_{b\mp}$ is proportional to M_b^{eq} and has a fast τ_2 dependence in $e^{i\delta\omega_b\tau_2}$, as expected. For this response, the term $q = 0$ is not interesting because it is independent of τ_1, hence it gives a narrow but uninformative spectral contribution at $\omega_1 = 0$.

The term $q = 1$ has an interesting τ_1 dependence in $e^{i\tau_1(\delta\omega_b-\delta\omega_a)}$, a contribution of $(1-\cos\theta_1)$ arising from the Bessel function J_0 in the last term in equation (60), and an additional τ_2 dependence in $J_1(-\sin\theta_1(2/3)\omega_{da}\tau_2)$ where $\omega_{da} = \gamma\mu_0 M_a^{\text{eq}}$ is the dipolar frequency of the abundant spins a alone. The contribution in J_{-2} is negligible for dilute spins b. All this generates a 2D peak at $\omega_1 = (\delta\omega_b - \delta\omega_a)$ and $\omega_2 = \delta\omega_b$, very narrow in the ω_1 direction and usually much broader in the ω_2 direction due to field inhomogeneities. The term $q = -1$ in $M_{b\mp}$ gives a similar peak at $\omega_1 = -(\delta\omega_b - \delta\omega_a)$ and $\omega_2 = \delta\omega_b$, with a magnitude proportional to $(1+\cos\theta_1)$. The terms $|q| > 1$ give much smaller contributions when the spins b are diluted. The Warren group has shown that these remarkable peaks are very conspicuous under normal circumstances,[79] and can still be observed in

fields of rather poor homogeneity,[11,12] provided that additional spin manipulations overcome the undesired effects of radiation damping, molecular diffusion, and field inhomogeneities during acquisition.

Also as expected, the response due to $M_{a\mp}$ has a fast τ_2 dependence in $e^{i\delta\omega_a\tau_2}$, and it is typically much larger because of the factor M_a^{eq} in equation (59). For this part of the response, the term $q = 0$ is equal to 0 when the rf pulses are both $\pi/2$ (see discussion after equation (55)), perhaps a favorable situation for actual experiments because large solvent signals are absent during acquisition while the relevant signals are close to maximum amplitude. The terms $|q| > 0$ no longer cancel for $\theta_1 = \pi/2$, but they give small contributions when the spins b are diluted.

By inspection of the above calculations, one can check that, for diluted b spins, the relevant signals during acquisition (the $q = \pm 1$ term in $M_{b\mp}$) arise from the b component of the $M_{\mp}$ transverse magnetization helices, progressively phase modulated by the dipolar field generated by the longitudinal magnetization grating of the abundant spins a. This process has strong analogies with the usual electronic demodulation of the (weak) fid signal by the (strong) reference signal at frequency $\omega_{\text{ref}}/2\pi$ of a coherent spectrometer, with the role of $\omega_{\text{ref}}/2\pi$ played, in the HOMOGENIZED experiment, by the NMR frequency $(\omega_{\text{ref}} + \delta\omega_a)/2\pi$ of the abundant spins in *exactly the same external field* in which the NMR frequency of the dilute spins is $(\omega_{\text{ref}} + \delta\omega_b)/2\pi$. With the above analogy, one immediately predicts that a mixture of various *diluted* spins generates a HOMOGENIZED spectrum which is the sum of the spectra for the separated diluted spins. More generally, the analogy indicates that for diluted polyatomic molecules with a complex NMR spectrum of the spins of the same species as the a spins, the HOMOGENIZED spectrum is quite similar to a standard COSY spectrum of the same molecules, with local demodulation using the frequency $(\omega_{\text{ref}} + \delta\omega_a)/2\pi$ and very narrow peaks in the ω_1 direction, and standard electronic demodulation using the frequency $\omega_{\text{ref}}/2\pi$ and broader peaks in the ω_2 direction.

4.3.4 The COSY Experiment

In echo experiments, the timing is set by the delay between the two pulses, and the main visible effect of relaxation is its influence on the magnitude of the various echoes. In COSY experiments, all delays contribute to the 2D spectra, and relaxation manifests itself not only in the size of the peaks, but also in their precise shape and position, as shown by Figures 17 and 18. As a preparation for the discussion of these features, we shall now briefly sketch the corresponding theory on the spin system already used at the end of Section 4.3.3: a mixture of spins a and b of the same species, bound on different molecules, with offsets $\delta\omega_a$ and $\delta\omega_b$ from the spectrometer reference frequency ω_{ref} such that $|\delta\omega_a - \delta\omega_b|$ is much larger than any dipolar field shift in the system.

All fields and magnetizations will be assumed to be uniform, and the shape and orientation of the ellipsoidal sample will be described by the parameter α_s (see equation (111)), which ranges from 1 for a pancake perpendicular to Z to $-(1/2)$ for a cylinder parallel to Z, through 0 for a sphere or a pancake at the magic angle. Radiation damping will be ignored and the a and b spins will be assumed to relax independently, with relaxation times T_{1a}, T_{2a}, T_{1b}, and T_{2b}. Under these

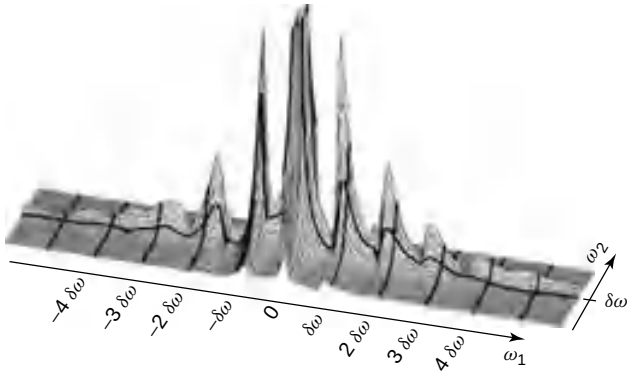

Figure 17 Absolute value COSY spectrum for a single NMR line with dipolar field effects, calculated for the sequence equil. $-[\pi/2, 0]$-τ_1-$[\pi/2, 0]$-τ_2-acq. The simulation takes into account relaxation (with $T_1 = T_2$), a homogeneous dipolar field such that $T_2\delta\omega_d = 5.25$ (where $\delta\omega_d/2\pi$ is the frequency shift caused by the equilibrium magnetization) and an offset $\delta\omega$ of the NMR line chosen such that $T_2\delta\omega = 20$. Radiation damping has been ignored. In simplified models, the 2D peaks are expected at $\omega_2 = \delta\omega$ and $\omega_1 = n\delta\omega$, where n ranges over the integers; these frequencies are shown by the thick lines in the spectral plot

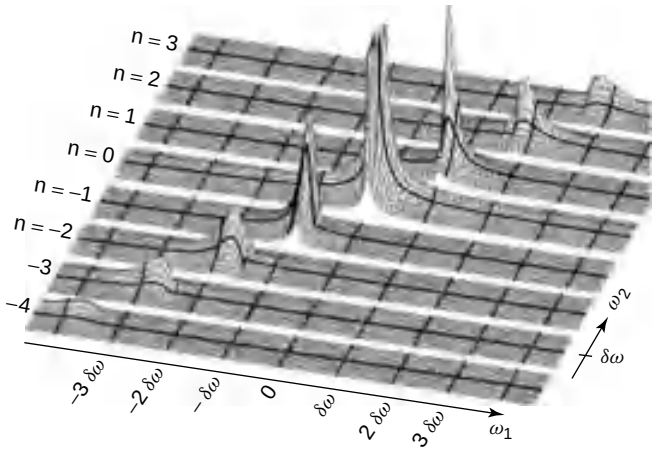

Figure 18 The same simulation as in Figure 17 is repeated 12 times for the sequence equil. $-[\pi/2, \phi]$-τ_1-$[\pi/2, 0]$-τ_2-acq., with successive incrementations of ϕ by $2\pi/12$. A Fourier transform with respect to ϕ is performed on the set of data, separating the components of the COSY response according to their dependence in $e^{in\phi}$. The plots show the absolute value of these components

conditions, the equations of motion *between* the pulses are

$$\frac{\partial}{\partial t}M_{aZ}(t) = -\frac{1}{T_{1a}}[M_{aZ}(t) - M_{aZ}^{\text{eq}}]$$

$$\frac{\partial}{\partial t}M_{a\mp}(t) = -\frac{1}{T_{2a}}M_{a\mp}(t) + i\delta\omega_a M_{a\mp}(t) + i\gamma\mu_0\alpha_s \times \left[M_{aZ}(t) + \frac{2}{3}M_{bZ}(t)\right]M_{a\mp}(t) \tag{61}$$

and analogous equations for the b spins obtained by interchanging the subscripts a and b. In the absence of pulse

between t and $t+\tau$, the solution of these equations is

$$M_{aZ}(t+\tau) = M_{aZ}^{\mathrm{eq}} + [M_{aZ}(t) - M_{aZ}^{\mathrm{eq}}]e^{-\tau/T_{2a}}$$
$$M_{a\tilde{+}}(t+\tau) = M_{a\tilde{+}}(t)e^{-\tau/T_{2a}}e^{i\delta\omega_a\tau}e^{iK_a(t+\tau,t)}$$

where

$$K_a(t+\tau,t) = \gamma\mu_0\alpha_s\int_{t'=t}^{t+\tau}\left[M_{aZ}(t') + \frac{2}{3}M_{bZ}(t')\right]dt' \qquad (62)$$

and analogous equations for the b spins.

The timing of Figure 16 is suitable for an elementary COSY experiment. By combining the known action of the hard rf pulses with equation (62), one can derive an analytical expression for the measured quantity $M_{a\tilde{+}}(t+\tau_1+\tau_2) + M_{b\tilde{+}}(t+\tau_1+\tau_2)$ at acquisition time, including a complete decomposition in terms depending upon ϕ as $e^{in\phi}$ for integer values of n (see Deville et al.[8]). This complicated expression is difficult to use directly, and it does not seem amenable to analytical Fourier or Laplace transform. The results shown in Figures 2 and 17 were obtained by numerical FFT of simulated data matrices.

Less accurate but directly usable analytical results can be obtained by ignoring relaxation. The derivation is almost the same as for equation (58), and the result for two $\pi/2$ pulses (i.e., $\theta_1 = \pi/2$) is

$$M_{a\tilde{+}}(t+\tau_1+\tau_2) = -\frac{1}{2}M_a^{\mathrm{eq}}e^{i\delta\omega_a\tau_2} \times \sum_{p,q}\left\{i^{p+q}e^{i(p+q)\phi}e^{i(p\delta\omega_a+q\delta\omega_b)\tau_1}[J_{p-1}(-\delta\omega_{d,a}\tau_2) + J_{p+1}(-\delta\omega_{d,a}\tau_2)]J_q\left(-\frac{2}{3}\delta\omega_{d,b}\tau_2\right)\right\}$$

where

$$\delta\omega_{d,a} = \gamma\mu_0\alpha_s M_a^{\mathrm{eq}} \quad \text{and} \quad \delta\omega_{d,b} = \gamma\mu_0\alpha_s M_b^{\mathrm{eq}} \qquad (63)$$

and analogous expressions for the b spins. A rough estimate of the relative magnitude of the various peaks can be obtained by replacing τ_2 by T_2 in the arguments of the Bessel functions in equation (63).

As an example, consider the situation illustrated by Figure 2, with dilute (interesting) a spins and abundant (solvent) b spins, such that the argument $-\delta\omega_{d,a}\tau_2$ of J_{p-1} and J_{p+1} is always very small in equation (63), whereas the argument $-\delta\omega_{d,b}\,\tau_2$ of J_q has relevant absolute values up to 2 or more. The response at the acquisition frequency $\omega_2 = \delta\omega_a$ of the dilute spins, shown by equation (63), has large contributions only for $p+1=0$ and $p-1=0$ (see Figure 13), but over a range of values of q centered around 0. The terms $(p=\pm1, q=0)$ are the expected peaks in the absence of dipolar field effects, other values of q give the conspicuous satellites shown in Figure 2, and other values of p give much weaker satellites, always in the indirectly detected ω_1 direction. The calculations can be extended for dilute molecules with multiple spins and a complex spectrum; in this case also, the main dipolar field effect is a decoration of each COSY peak of the dilute molecule by satellites in the ω_1 direction, separated by the b spins offset $\delta\omega_b$. Great care should be exercised in the interpretation of such spectra if conventional phase cycling is used in the acquisition (or processing): the particular phase ϕ properties of the contributions for different orders $n = p+q$ often result in unexpected cancellations for some values of n. Any phase cycling used in data acquisition should also be incorporated in the corresponding simulations.

The multitude of additional 2D peaks caused by dipolar field effects is prone to ambiguity in assignment, hence a clear separation based on the $e^{i(p+q)\phi}$ factor in equation (63) is welcome. An efficient implementation of this separation is to perform each basic experiment (i.e., acquisition of a (τ_1, τ_2) matrix at constant ϕ in the present COSY case) for a succession of K equally spaced ϕ phases, $\phi(k) = k2\pi/K$, where the integer k ranges from 0 to $(K-1)$, taking care to save all the data separately in computer memory. At this point, a Fourier transform with respect to the integer k separates the data in contributions from the individual values of $n = p+q$, provided that the number K of repetitions around the phase cycle is larger than the range of n over which appreciable contributions are present (otherwise, one encounters the usual folding problem). This procedure is much more efficient than the standard coaddition procedures because it provides a *complete* picture of the ϕ dependence of the data after a single phase cycle, a particularly important feature in exploratory experiments or in the presence of peaks of doubtful origin. The larger requirements of computer memory for this procedure are no longer a problem; modern software for 3D analysis makes the whole procedure quite simple to implement.[80]

4.3.5 *The Goldman–Desvaux Effect*

The Goldman–Desvaux effect,[68] illustrated by Figure 19, is a dynamical manifestation of the *precessing* component of the dipolar field, which appears already in the simplest single rf pulse experiment (in homogeneous fields) when two (or more) NMR lines are so close together that their separation is not much larger than the total dipolar field shifts associated with both lines. We shall now briefly discuss this effect, using the notation and many simplifications of Sections 4.3.3 and 4.3.4, assuming homogeneous fields and two types of spins with almost the same NMR frequency.

The nuclear magnetization is a sum of components for the a and b spins, $\boldsymbol{M}(t) = \boldsymbol{M}_a(t) + \boldsymbol{M}_b(t)$, and the relevant part of the dipolar field is given by $\boldsymbol{B}_d^{\text{no crp}} = -\mu_0\left[M_Z(t)\mathbf{1}_{\boldsymbol{Z}} - \frac{1}{3}\boldsymbol{M}(t)\right]$ for a flat sample perpendicular to Z [see equation (36)]. Ignoring relaxation, radiation damping, and rf fields, the equations of motion are

$$\left(\frac{\mathrm{d}}{\mathrm{d}t}\right)_{\mathrm{rot}}\boldsymbol{M}_a(t) = \boldsymbol{M}_a(t) \times [\gamma\boldsymbol{B}_d^{\text{no crp}} - \delta\omega_a\mathbf{1}_{\boldsymbol{Z}}] \qquad (64)$$

and a similar equation for $\boldsymbol{M}_b(t)$ obtained by permutation of the labels a and b. Qualitative discussions will be simplified by writing these equations in terms of rotating frame components (and performing obvious simplifications),

$$\frac{\mathrm{d}}{\mathrm{d}t}M_{a\tilde{X}}(t) = -\frac{\mu_0\gamma}{3}M_{aZ}(t)M_{b\tilde{Y}}(t) - M_{a\tilde{Y}}(t) \times \left\{\delta\omega_a + \mu_0\gamma\left[M_{aZ}(t) + \frac{2}{3}M_{bZ}(t)\right]\right\} \qquad (65)$$

$$\frac{\mathrm{d}}{\mathrm{d}t}M_{a\tilde{Y}}(t) = \frac{\mu_0\gamma}{3}M_{aZ}(t)M_{b\tilde{X}}(t) + M_{a\tilde{X}}(t) \times \left\{\delta\omega_a + \mu_0\gamma\left[M_{aZ}(t) + \frac{2}{3}M_{bZ}(t)\right]\right\} \qquad (66)$$

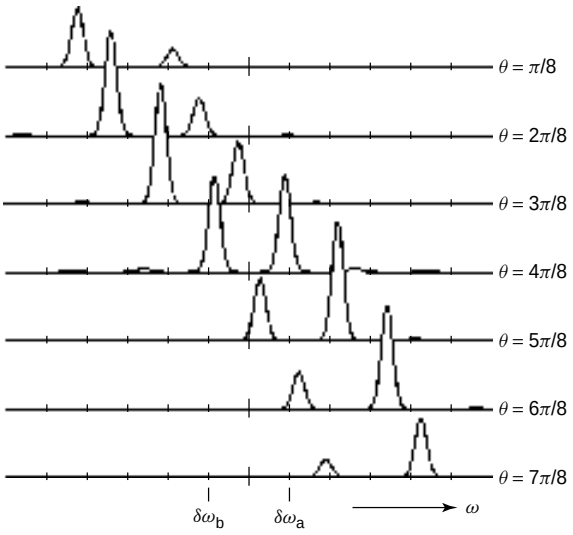

Figure 19 The Goldman–Desvaux effect[68] for a mixture of independent a and b spins of equal concentrations. $\delta\omega_a$ and $\delta\omega_b$ are the offsets with respect to the spectrometer reference frequency. The spectra shown have been calculated as the 'absorption' part of the Fourier transform of the fid after a hard θ pulse applied to the equilibrium situation, for a dipolar field shift of each separate species ($|\gamma\mu_0 M_a^{\mathrm{eq}}|$ for a flat sample perpendicular to Z) equal to the difference $|\delta\omega_b - \delta\omega_a|$ between the two unperturbed NMR frequencies. Relaxation and radiation damping were not included in the simulations, and the line widths result from a Gaussian apodisation. The overall shift of the spectrum as a function of θ is the effect demonstrated by Edzes[7] on a single spin species. The Goldman–Desvaux effect is the θ-dependence of the difference in intensity and separation of the two lines, and the presence of (weak) satellites

$$\frac{\mathrm{d}}{\mathrm{d}t}M_{aZ}(t) = \frac{\mu_0\gamma}{3}\left[M_{a\tilde{X}}(t)M_{b\tilde{Y}}(t) - M_{a\tilde{Y}}(t)M_{b\tilde{X}}(t)\right] \qquad (67)$$

and similar equations for the components of $\boldsymbol{M}_b(t)$. The unconventional spectral features shown by Figure 19 in addition to the overall θ-dependent shift, arise from the action, on each type of spin, of the precessing component of the dipolar field caused by the other type of spins.

Equation (67) shows that the longitudinal a magnetization is affected in this way whenever the transverse components of the a and b magnetizations are not parallel (this process is approximately periodic at the difference between the unperturbed NMR frequencies). Inspection confirms that the time derivatives of $M_{aZ}(t)$ and $M_{bZ}(t)$, due to the dipolar field, cancel exactly (as required by energy conservation). However, the oscillating magnetizations $M_{aZ}(t)$ and $M_{bZ}(t)$ appear separately in equations (65) and (66), where they cause a periodic phase modulation of $M_{a\tilde{\mp}}(t)$ which generates for example, the sidebands shown in Figure 19. This mechanism acts also on the b spins, and is particularly active when the magnetization is mainly transverse. Another source of periodic phase modulation of $M_{a\tilde{\mp}}(t)$ at the same frequency is the presence of a factor $M_{b\tilde{Y}}(t)$ in equation (65) for the evolution of $M_{a\tilde{X}}(t)$, which causes, for example, the appearance of a Fourier component of the a spins response at the b spins NMR frequency (and conversely for the b spins, with different sign and magnitude). This mechanism causes the differences in amplitude of the two main 'absorption' lines of the a, b mixture, and is particularly active when the magnetization is mainly longitudinal. Of course, the responses originating from the a and b spins cannot be separated experimentally, but it is important to remember, in qualitative discussions of dipolar field effects, that each individual line reflects one aspect of the collective motion of the macroscopic a, b spin system and not the motion of a single type of spins. A similar situation occurs in 'spectral clustering' (see Section 6).

Goldman and Desvaux[68] have obtained a very useful analytical solution of equation (64) for the single pulse experiment, using approximations appropriate for weak (realistic) dipolar field effects. They have also demonstrated excellent quantitative agreement (without any adjustable parameter) between predictions and experimental results.

Realistic relaxation terms are easy to incorporate in equation (64), but this will not help finding 'exact' analytical solutions of the conventional type. Fortunately, it is very easy to generate numerical solutions of such a simple set of differential equations, for instance with a tool like *Mathematica*.

4.4 Quantum Calculations for all Spins and all Couplings Together

The 'classical' discussion of dipolar field effects in liquids can be presented quite convincingly in terms of a hydrodynamic description involving an independent spin system for each molecule in the sample and a classical average dipolar field generated by the average bulk nuclear magnetization (see Sections 2.2 and 4.1). However, when these effects were first observed in the perspective of multidimensional high resolution NMR, the surprise caused by the additional 2D peaks was such that some investigators felt that the classical formalism was unsuitable for their interpretation (or possibly wrong). Part of these initial worries could be settled by additional care in the use of the classical formalism (see, for example, Sections 2.3, 2.5 and last paragraph of 4.1), but others were more fundamental. For instance, it may seems strange to ignore correlations between distant spins for which the dipolar coupling manifests itself in dipolar field effects. Also, dipolar couplings at short distances cause relaxation, those at large distances are taken into account in the dipolar field; are some couplings at 'moderate' distance not forgotten or counted twice?

A first step towards improved understanding is to choose a more general presentation of the whole problem, in which all the spins in the sample are treated as a single quantum system of coupled objects. To avoid dissuasive complications, we shall continue to use a classical description for the electromagnetic field and for the positions of the atoms. In this introductory discussion, we shall examine the simplest system which exhibits dipolar field effects: an ensemble of equivalent spins, with a single spin on each molecule.

The individual spins will be labeled by lower case subscripts, $\boldsymbol{r}_j(t)$ is the position of spin j at time t, and the dipolar magnetic interaction between spins j and k is described by the Hamiltonian

$$\widehat{H}_{jk}^{\mathrm{dip}}(t) = -\frac{\mu_0}{4\pi}\frac{\gamma\hbar\{3[\hat{\boldsymbol{I}}_j\cdot\mathbf{1}_{j,k}(t)]\mathbf{1}_{j,k}(t) - \hat{\boldsymbol{I}}_j\}}{|\boldsymbol{r}_j(t) - \boldsymbol{r}_k(t)|^3}\cdot\gamma\hbar\hat{\boldsymbol{I}}_k \qquad (68)$$

where $\mathbf{1}_{j,k}(t)$ is a unit vector pointing in the direction from j to k, the last dot product stands for a dot product in position space and a tensorial product of operators acting in the quantum state spaces of spins j and k, and $\widehat{H}_{jk}^{\mathrm{dip}}(t) = \widehat{H}_{kj}^{\mathrm{dip}}(t)$. The total

dipolar coupling between all spins in the sample is obtained by summing over all pairs,

$$\widehat{H}_S^{\mathrm{dip}}(t) = \sum_{j=1}^{N-1} \sum_{k=j+1}^{N} \widehat{H}_{jk}^{\mathrm{dip}}(t) \otimes \hat{1}_{S/jk} \tag{69}$$

where N is the total number of spins in the sample. The tensorial product with the unit operator $\hat{1}_{S/jk}$ for the state space of all spins except j and k is written explicitly in equation (69) to emphasize the fact that a sum of operators has a meaning only if the operators act in the same state space (the state space S for all spins in the sample, in this case). When no confusion seems possible, we shall follow the tradition by which the tensorial multiplication by the suitable unit operator is tacitly understood. To avoid ambiguities which are frequent in the literature, notably between density operators for a single spin or for the whole system, we shall systematically decorate every quantum operator with a subscript showing the smallest state space in which it is meaningful.

Ignoring the rf magnetic fields generated by the rf current in the sample coil, the Hamiltonian $\widehat{H}_S(t)$ for the whole spin system is

$$\widehat{H}_S(t) = \sum_{j=1}^{N} \{-\gamma\hbar \hat{\boldsymbol{I}}_j \cdot \boldsymbol{B}_0(\boldsymbol{r}_j, t)\} + \widehat{H}_S^{\mathrm{dip}}(t) \tag{70}$$

where $\boldsymbol{B}_0(\boldsymbol{r}, t)$ is the external magnetic field at position $\boldsymbol{r}$ and time t, and the von Neumann equation of motion for the density operator $\hat{\rho}_S(t)$ for the whole spin system is

$$i\hbar \frac{\partial}{\partial t} \hat{\rho}_S(t) = [\widehat{H}_S(t) \hat{\rho}_S(t)] \tag{71}$$

Before discussing various methods which have been proposed to predict dipolar field effects on the basis of this equation of motion of formidable complexity, we shall briefly review some concepts which are useful for relating density operators for all spins in the sample with the more usual density operators for the spins of a single molecule.

The observables of direct interest are sums of terms involving very few spins (one spin for the total nuclear magnetic moment, two spins for the total coupling energy). The total nuclear magnetic moment is

$$\gamma \hat{\boldsymbol{I}}_S = \sum_{j=1}^{N} \gamma \hat{\boldsymbol{I}}_j \otimes \hat{1}_{S/j} \tag{72}$$

and the (quantum and statistical) average value of one of its terms is

$$\langle \gamma \hat{\boldsymbol{I}}_j \otimes \hat{1}_{S/j} \rangle(t) = \mathrm{Tr}_S\{(\gamma \hat{\boldsymbol{I}}_j \otimes \hat{1}_{S/j}) \hat{\rho}_S(t)\} \tag{73}$$

where Tr_S is the trace over the state space S for all spins. One can take advantage of the particular properties of such observables by evaluating the trace over S in two successive steps: (i) first evaluate the partial trace $\mathrm{Tr}_{S/j}$ over the states of all spins *except* j (this does not affect $\hat{\boldsymbol{I}}_j$, which acts only on the spin j), and (ii) finally evaluate the trace Tr_j over the states of spin j alone,

$$\begin{aligned} \mathrm{Tr}_S\{(\gamma \hat{\boldsymbol{I}}_j \otimes \hat{1}_{S/j}) \hat{\rho}_S(t)\} &= \mathrm{Tr}_j\{\mathrm{Tr}_{S/j}\{(\gamma \hat{\boldsymbol{I}}_j \otimes \hat{1}_{S/j}) \hat{\rho}_S(t)\}\} \\ &= \mathrm{Tr}_j\{\gamma \hat{\boldsymbol{I}}_j \mathrm{Tr}_{S/j}\{\hat{\rho}_S(t)\}\} = \mathrm{Tr}_j\{\gamma \hat{\boldsymbol{I}}_j \hat{\rho}_j(t)\} \end{aligned}$$

where

$$\hat{\rho}_j(t) = \mathrm{Tr}_{S/j}\{\hat{\rho}_S(t)\} \tag{74}$$

The reduced density operator $\hat{\rho}_j(t)$ acts in the state space j only, it has all the desirable properties of a density operator (Hermitian, $\mathrm{Tr}_j\{\hat{\rho}_j(t)\} = 1$, all eigenvalues between 0 and 1), and it provides the complete information for evaluating the average value of any operator acting in the state space j. However, predicting the time evolution of $\hat{\rho}_j(t)$ from the equation of motion (71) for $\hat{\rho}_S(t)$ remains a formidable task. The formal manipulation of partial traces requires special care, as discussed in Appendix D of Ref.[69].

Another important issue is that of 'correlations', which will be used here in its usual meaning in statistical physics and probability theory (for more details, in the perspective of liquid NMR, see Appendix B of Ref.[69]). If the two objects j and k are not correlated, then all joined distribution functions for properties of j and k are given by the product of the corresponding individual distribution functions, for instance,

$$\hat{\rho}_{jk}(t) = \hat{\rho}_j(t) \otimes \hat{\rho}_k(t) \quad \text{for } j \text{ and } k \text{ not correlated} \tag{75}$$

In general, objects which interact become correlated, and the correlation σ_{jk} is defined by the general relation

$$\hat{\rho}_{jk}(t) = \hat{\rho}_j(t) \otimes \hat{\rho}_k(t) + \sigma_{jk}(t) \tag{76}$$

in which the (reduced) density operators for the objects j and k are obtained from $\hat{\rho}_{jk}(t)$ by partial traces. These definitions are easily extended for any number of objects or spins. Hard pulses do not create or destroy correlations, they just 'rotate' the correlations in operator space.

4.4.1 Derivation of the Bloch–Redfield Equations

The Bloch–Redfield equations are obtained 'from first principles' (e.g., from equation (71)) by taking the fast molecular Brownian motion explicitly into account, and deriving an approximate kinetic equation of motion for the reduced density operator for the spins in a single molecule, averaged over all realizations of the Brownian motion. The derivation is usually presented with a single molecule in mind,[44] in the approximation of short correlation times for the molecular motion. With such an approach, dipolar field effects can only be introduced in the kinetic equation as an afterthought, as indicated in Section 2.2. However, it is also possible to start with a description including all spins in the sample and all dipolar couplings (see equation (70)). The main additional approximation which makes this more complete model tractable is to neglect any systematic buildup of correlations between spins on different molecules.[70] It is easy to support this approximation with heuristic arguments and heavily simplified models,[69] but its limits of validity have not been investigated in detail. When the model with all spins in the sample is treated carefully, the result is a kinetic equation of the Bloch–Redfield type,

with a dipolar field term which is exactly the term previously added 'as an afterthought'. The derivation presented in Ref.[69] is explicitly extended to molecules carrying multiple spins and mixtures thereof, and does not use any approximation of high spin temperature or weak order, except in the last step leading to rates of relaxation *independent* of the average spin state. This reference assumes spatial homogeneity over the whole sample, for simplicity; Section 2.4 of the present article provides the necessary extension to spatially inhomogeneous situations, taking into account molecular diffusion and bulk flow.

4.4.2 A Rough but 'Exactly Soluble' Model

We shall now briefly discuss a rough model for which the calculations can be performed exactly on the density operator $\hat{\rho}_S(t)$ for N equivalent spins on different molecules, with dipolar interaction between every pair. This model sheds some light on the issue of correlations between spins on different molecules, and provides a pedagogical example of a mechanism by which a state-dependent NMR frequency can be derived from exact quantum mechanics with a time-independent Hamiltonian.

In a compact sample, each molecule 'explores' all regions of the sample, on average, over any duration larger than (d^2/D), where d is the largest distance in the sample and D is the molecular diffusion coefficient; the relative position of two spins also 'explores' all possible values in the sample over the same duration. For water at room temperature and a maximum sample size of $d = 10\,\mu\text{m}$, the characteristic duration (d^2/D) is less than 0.1 s and the number of protons N is still very large (on the order of 10^{13}, depending upon the shape). In this case, for simple experiments lasting on the order of 1 s, and in the absence of strong sources of spatial inhomogeneity (such as field gradients), a tempting approximation is to start the discussion by averaging the spin Hamiltonian of equation (70) over all positions in the sample. Of course, this throws away the fast fluctuations which cause relaxation, but the slow processes related to the dipolar field should survive.

The averaging of equation (70) is easy to perform for samples of ellipsoidal shape, with the same techniques as for the dipolar field. Not surprisingly, the average coupling vanishes for a spherical sample. For a flat sample perpendicular to Z, the averaged Hamiltonian is

$$\widehat{H}_S = \sum_{j=1}^{N} \hbar\omega_0 \hat{\boldsymbol{I}}_{jZ} + \widehat{H}_S^{\text{av dip sec}}$$

where

$$\widehat{H}_S^{\text{av dip sec}} = \sum_{j=1}^{N-1} \sum_{k=j+1}^{N} \frac{\mu_0(\gamma\hbar)^2}{N} \frac{N}{V} \frac{1}{3} \times \left\{ 2\hat{\boldsymbol{I}}_{jZ}\hat{\boldsymbol{I}}_{kZ} - \frac{1}{2}(\hat{\boldsymbol{I}}_{j+}\hat{\boldsymbol{I}}_{k-} + \hat{\boldsymbol{I}}_{j-}\hat{\boldsymbol{I}}_{k+}) \right\} \qquad (77)$$

where Z points in the direction of $\boldsymbol{B}_0$, non-secular terms have been ignored in the coupling, and $\omega_0 = -\gamma \boldsymbol{B}_{0Z}$. As a result of this averaging, the Hamiltonian is time-independent, the positions of the spins are irrelevant, and each spin has the same weak coupling (proportional to $1/N$ if one keeps the concentration N/V constant while changing the number of spins N) with every other spin. For arbitrary sample shapes, the averaged coupling has the same structure, with the factor 1/3 replaced by a shape-dependent number.

In Appendix C of Ref.[69], the response of this model to a hard pulse is evaluated directly from an exact solution of the equation of motion for $\hat{\rho}_S(t)$, without the high temperature approximation. Many aspects of the spin dynamics are discussed in detail, including the issue of correlations between different spins. All conclusions confirm the results of the 'classical' approach, and the corresponding assumptions and approximations. It should be noted that Ref.[69] makes the further approximations of keeping only the terms in $\hat{\boldsymbol{I}}_{jZ}\hat{\boldsymbol{I}}_{kZ}$ in the coupling, and of neglecting the couplings in the expression of the initial thermal equilibrium. F. Henin has shown that these two approximations can be lifted without altering the general conclusions of the discussion (personal communication).

4.5 Suppression of Dipolar Field Effects

In many experiments, dipolar field effects appear as a nuisance and it would be desirable to suppress them, preferably without creating new artifacts or limitations. Various techniques have been proposed for this suppression, but none has been demonstrated, yet, in a realistic setting of high-resolution structural NMR.

A simple idea, with obvious limitations, is to avoid tipping any large nuclear magnetization during the experiment, e.g., by the use of deuterated solvents. This has the additional merit of solving the 'solvent suppression' problem.

In experiments without field gradients, one can use an ellipsoidal sample shape which gives a zero relevant dipolar field for a uniform nuclear magnetization. Examples of such shapes are the sphere, a long cylinder oriented at the magic angle, and a flat sample with a normal at the magic angle. The efficiency of this solution is very dependent upon a perfect sample shape and perfectly homogeneous fields $\boldsymbol{B}_0$ and $\boldsymbol{B}_1$.

In experiments involving field gradients, the gradients can be oriented at the magic angle so that the 'modulated' part of the magnetization generates a zero relevant dipolar field (except in a surface layer of thickness of the order of the wavelength of the modulation). The shape of the sample still has to be chosen carefully (see just above) to avoid the dipolar field generated by the average ('unmodulated') part of the magnetization.

Whenever a standard deuterium field-frequency lock is active during the experiment, the lock 'tries' to compensate for the longitudinal component of the dipolar field, at a rate limited by the averaging time constant of the lock system.[25] This scheme does not compensate for the transverse component of the dipolar field, which is particularly active on the solvent itself. It is also not active on the 'modulated' part of the dipolar field (generated by field gradients) or on any other spatial inhomogeneity.

Broekaert et al.[23] have demonstrated an active decoupling technique in which the strong offending solvent line is selectively irradiated on resonance, hence causing a precession of the large solvent magnetization around a fixed transverse direction in the appropriate rotating frame. For a fast enough precession, this effectively averages out the Z component of the dipolar field which is the important component for spins other than the solvent spins. In the experiment reported in

Ref.[23], the satellite lines of the acetone cross section shown in Figure 2 were effectively eliminated by a weak permanent DANTE irradiation of the water line, with acquisition during the 'windows' of the DANTE sequence. An advantage of this technique is that it acts locally on the solvent spins, irrespective of the homogeneity (or not) of the distribution of nuclear magnetization.

An even more radical scheme was proposed, also by Broekaert et al.,[31] in which the whole sample is continuously rotated at the magic angle. The rate of rotation has to be large enough to average out to zero only that part of the dipolar couplings which has survived averaging by the molecular Brownian motion. As a result, MAS rotation at 100 Hz (or faster) would probably be satisfactory. Of course, this scheme limits the usable field gradients to being along the direction of the axis of rotation, presumably not a severe constraint.

4.6 Numerical Simulation Techniques

The analytical solutions, which are derived as an illustration for a number of examples in this article, should not create the illusion that many realistic problems in spin dynamics with collective effects can be handled completely in this way. Numerical calculations are usually required to obtain final predictions comparable to experiment, even in strongly simplified models. However, simulation techniques for position-dependent problems involving the dipolar field are still in a very primitive state of development.

The simplest problems arise for spatially homogeneous situations, in which one is confronted with sets of a small number of non-linear ordinary differential equations, even if dipolar field, relaxation, and radiation damping are taken into account. Powerful and convenient software packages, such as *Mathematica*, are available to solve such sets of equations (analytically or, if that fails, numerically) and to display the result in useful ways.

The next step concerns simple experiments using pulsed field gradients, in which a simple periodic distribution of magnetization with wave vector $\boldsymbol{q}$ is first created by the experimenter. If the overall shape of the sample is ellipsoidal, and edge effects can be neglected, the equations of motion can be Fourier transformed and the only wave vectors involved are given by $n\boldsymbol{q}$, where n is any integer (including 0).[71] For dipolar field effects of moderate strength, it is sufficient to retain a very limited range of values of n, and this leads to a correspondingly limited set of non-linear differential equations. During the calculation, it is easy to check that the magnetization terms at the ends of the n range remain silent as expected.[39]

The Warren group has proposed a new numerical method suitable for the study of general, bulk, three-dimensional phenomena involving the dipolar field.[72] Their model describes the actual, continuous, distribution of magnetization by a set of discrete magnetic moments localized at each point of a three-dimensional, simple cubic, discretization lattice, inside a cubic basic cell (see lower part of Figure 20). Alternatively, a rectangular parallelepipedic lattice can be used, and also a rectangular parallelepipedic basic cell.

In setting up the equation of motion for the magnetization at each lattice point, no difficulty arises from local properties like relaxation and field offset, and radiation damping depends only on the total magnetization. The main problem is the evaluation of the dipolar field at each lattice point for each

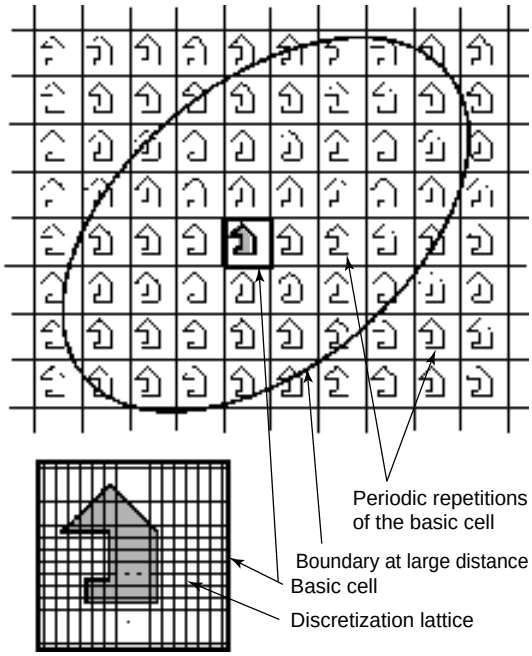

Figure 20 2-dimensional sketch of the tacit implications of the 3-dimensional model used in the numerical simulation method of Enss et al.[72] The greyed polygon in the basic cell symbolizes any spatial inhomogeneity (magnetization, offset, relaxation, coefficient of diffusion, ...)

different distribution of magnetization in the whole basic cell. A direct summation of the effects, on each localized moment, of all other localized moments, would require a prohibitive amount of calculation for any number of lattice points beyond a few hundred. If one limits the interactions to the pairs of localized moments actually in the basic cell, this procedure generates strong edge effects in the vicinity of the surface of the basic cell whenever a significant magnetization is present there. This is an undesirable feature when the basic cell is meant to describe the effects of local inhomogeneities in an otherwise larger object (as suggested by the upper part of Figure 20).

The very efficient solution proposed by Enss et al.[72] is to use the simple relation in equation (36) between the magnetization $\boldsymbol{M}(\boldsymbol{r}, t)$ and the relevant part $\boldsymbol{B}_d^{\text{no crp}}(\boldsymbol{r}, t)$ of the dipolar field for simple periodic distributions of magnetization with zero average value. A fast Fourier transform (FFT) of the discrete description of the magnetization in the basic cell generates a description of this magnetization in terms of simple plane waves, equation (36) transforms this into the corresponding plane wave description of $\boldsymbol{B}_d^{\text{no crp}}(\boldsymbol{r}, t)$, and a final inverse FFT generates the desired $\boldsymbol{B}_d^{\text{no crp}}(\boldsymbol{r}, t)$, except for the contribution of the average magnetization (the $\boldsymbol{q} = 0$ component of the FFT of $\boldsymbol{M}(\boldsymbol{r}, t)$).

Let us temporarily ignore the problems at $\boldsymbol{q} = 0$ to concentrate on the fact that equation (36) is valid for periodic distributions in unbound space, and that the FFT algorithm implies a similar extension. As a consequence, the dipolar field evaluated by the above procedure is not that due to the magnetization in the basic cell only, but that generated by an infinite 3-dimensional repetition of the contents of the basic cell, as indicated in the top part of Figure 20. This situation should not cause further worries because the $\boldsymbol{q} \neq 0$ components of

$\boldsymbol{M}(\boldsymbol{r}, t)$ do not have the long distance influence typical of the $\boldsymbol{q} = 0$ component. However, one should keep in mind that the persistence in time of the (virtual) periodic array of similar basic cells implies that all relevant parameters of spin dynamics also must have this long range spatial periodicity. This may cause trouble in attempts to model 'exactly' the effects of persistent homogeneous field gradients.

Whenever the average (or total) magnetization in the basic cell is different from zero, this average magnetization is (virtually) extended to large distances by the periodic repetition discussed above. The overall self consistency of the model requires that the dipolar field, generated by this large scale uniform magnetization, should also be uniform. This, in turn, implies that the large scale shape of the NMR object should be an ellipsoid, as sketched in the top part of Figure 20, hence the $\boldsymbol{q} = 0$ component of the dipolar field can be evaluated from the corresponding component of the magnetization using equations (34)–(36) or (106), for instance. The uniform component of the dipolar field may be an irrelevant detail, for instance in studies of contrast in imaging, or an essential feature, as for dynamic stability.

When the concentration of spins and their coefficient of molecular diffusion are uniform throughout the basic cell, and diffusion proceeds freely between adjacent periodic repetitions of the basic cell, the diffusion contribution to the equations of motion is easily obtained in reciprocal space (see, for instance, equation (111)), and transformed back to configuration space by inverse FFT.[72] For non-uniform situations, molecular diffusion can be modeled directly in configuration space as causing exchanges of magnetization between each pair of first neighbor localized magnetizations. Great care must be taken, in the case of non-uniform concentrations, to ensure a realistic description of molecular diffusion. With the algorithm of Ref.[72], problems can be treated very easily on a desktop computer for spatial resolutions of $32 \times 32 \times 32$, and even significantly better. This scheme seems appropriate for spatial features (appreciably) larger than the pitch of the discretization lattice; for smaller features, the combined effects of multiple discretization artifacts should be carefully examined.

Unfortunately, the techniques described above do not (yet) offer satisfactory tools for situations in which the boundary of the sample plays an important role: spatial inhomogeneities on the scale of the size of the sample, non-ellipsoidal samples, unusual sample shapes (e.g., the $\cup$ shape mentioned in Section 6),....

5 DIPOLAR FIELD EFFECTS, THE 'WARREN' PRESENTATION

In this introductory text, specific examples will be limited to the simplest case which manifests dipolar field effects: a single type of spins 1/2, one spin per molecule.

5.1 Formal Introduction, Coherences, Interaction Representation

Let $\hat{A}$ be a Hermitian operator (whose role will be played later by $\hat{\boldsymbol{I}}_Z$ or by the Hamiltonian) which is diagonalized by the orthonormal basis $\{|a_q\rangle\}$,

$$\hat{A}|a_q\rangle = a_q|a_q\rangle$$

where

$$\langle a_q|a_r\rangle = \delta_{q,r} \quad \text{and} \quad \sum_q |a_q\rangle\langle a_q| = \hat{1} \tag{78}$$

Now, we take any operator $\widehat{B}$ (whose role will be played later by the density operator or parts of it), multiply it to the left and to the right by the closure relation for $\{|a_q\rangle\}$, and re-arrange terms,

$$\widehat{B} = \hat{1}\widehat{B}\hat{1} = \left(\sum_q |a_q\rangle\langle a_q|\right)\widehat{B}\left(\sum_r |a_r\rangle\langle a_r|\right)$$
$$= \sum_{q,r}\langle a_q|B|a_r\rangle|a_q\rangle\langle a_r| \tag{79}$$

This expresses $\widehat{B}$ as a linear combination of operators $|a_q\rangle\langle a_r|$ which have simple and convenient relations with $\hat{A}$. Indeed, inspection shows that

$$[\hat{A}, |a_q\rangle\langle a_r|] = (a_q - a_r)|a_q\rangle\langle a_r|$$

hence

$$e^{-i\xi\hat{A}}|a_q\rangle\langle a_r|e^{i\xi\hat{A}} = e^{-i\xi(a_q - a_r)}|a_q\rangle\langle a_r| \tag{80}$$

where ξ is any real constant such that $\xi\hat{A}$ is dimensionless. The operators $|a_q\rangle\langle a_r|$ also have the convenient properties of

$$\text{orthogonality: } \mathrm{Tr}\{(|a_q\rangle\langle a_r|)^\dagger(|a_s\rangle\langle a_t|)\} = 0 \tag{81}$$

whenever $(q, r) \neq (s, t)$, and

$$\text{normalization: } \mathrm{Tr}\{(|a_q\rangle\langle a_r|)^\dagger(|a_q\rangle\langle a_r|)\} = 1 \tag{82}$$

In the particular case of a single spin 1/2 labeled j, with the role of $\hat{A}$ played by $\hat{I}_{jZ}$ and the notation $\hat{I}_{jZ}|\pm\rangle_j = \pm 1/2|\pm\rangle_j$, we have, obviously, $|+\rangle_{jj}\langle -| = \hat{I}_{j+}$ and $|-\rangle_{jj}\langle +| = \hat{I}_{j-}$. In further calculations, it will be convenient to replace the two other operators, $|+\rangle_{jj}\langle +|$ and $|-\rangle_{jj}\langle -|$, which both commute with $\hat{I}_{jZ}$, with their more familiar combinations $\hat{1}_j = |+\rangle_{jj}\langle +| + |-\rangle_{jj}\langle -|$ and $\hat{I}_{jZ} = 1/2|+\rangle_{jj}\langle +| - 1/2|-\rangle_{jj}\langle -|$, in spite of the fact that $\hat{1}_j$ and $\hat{I}_{jZ}$ are not properly normalized. With this notation, the first line of equation (80) becomes

$$[\hat{I}_{jZ}, \hat{I}_{j\pm}] = \pm\hat{I}_{j\pm}, \quad [\hat{I}_{jZ}, \hat{I}_{jZ}] = 0 = [\hat{I}_{jZ}, \hat{1}_j] \tag{83}$$

and equation (1) for $\hat{\rho}_j(t)$ takes the form

$$\hat{\rho}_j(t) = \frac{1}{2}\{\hat{1}_j + 2\langle I_{j+}\rangle(t)\hat{I}_{j+} + 2\langle I_{j-}\rangle(t)\hat{I}_{j-} + 4\langle I_{jZ}\rangle(t)\hat{I}_{jZ}\} \tag{84}$$

where the average values are evaluated according to equation (7) and $\langle I_{j+}\rangle(t)$ is the complex conjugate of $\langle I_{j-}\rangle(t)$.

Similarly, the density operator $\hat{\rho}_{jk}$, for the two spins j and k, can be expressed as a linear combination of the 16 operators obtained successively by multiplication of each operator of the

list $\{\hat{1}_j, \hat{I}_{j+}, \hat{I}_{j-}, \hat{I}_{jZ}\}$ by each operator of the corresponding list for spin k,

$$\begin{aligned}\hat{\rho}_{jk}(t) = \frac{1}{4}\{&\hat{1}_{jk} + 2\langle I_{j+}1_k\rangle(t)\hat{I}_{j+}\hat{1}_k + \cdots \\ &+ 2\langle 1_j I_{k+}\rangle(t)\hat{1}_j\hat{I}_{k+} + 4\langle I_{j+}I_{k+}\rangle(t)\hat{I}_{j+}\hat{I}_{k+} + \cdots \\ &+ 2\langle 1_j I_{k-}\rangle(t)\hat{1}_j\hat{I}_{k-} + 4\langle I_{j+}I_{k-}\rangle(t)\hat{I}_{j+}\hat{I}_{k-} + \cdots \\ &+ 4\langle 1_j I_{kZ}\rangle(t)\hat{1}_j\hat{I}_{kZ} + 8\langle I_{j+}I_{kZ}\rangle(t)\hat{I}_{j+}\hat{I}_{kZ} + \cdots \\ &+ 16\langle I_{jZ}I_{kZ}\rangle(t)\hat{I}_{jZ}\hat{I}_{kZ}\}\end{aligned} \tag{85}$$

This procedure is easily extended for any number of spins.

A more conventional procedure for this type of decomposition of density operators for systems of spins 1/2 uses the (also not properly normalized) basis $\{\hat{1}_j, \hat{I}_{jX}, \hat{I}_{jY}, \hat{I}_{jZ}\}$ for each spin j, as indicated by equation (1). However, this basis contains the operators $\hat{I}_{jX}$ and $\hat{I}_{jY}$, each of which combines the coherence orders $+1$ and -1 (see below). The use of the basis $\{\hat{1}_j, \hat{I}_{j+}, \hat{I}_{j-}, \hat{I}_{jZ}\}$ avoids this mixture of coherence orders, and simplifies discussions in which the coherence order is a key feature.

Coherences are usually defined as off-diagonal elements of the density operator, and the corresponding diagonal elements are called populations. With this definition, coherences depend upon the basis used for their evaluation. The simplest situation arises when the motion of the system is governed by a time independent Hamiltonian $\widehat{H}$ for which the eigenvalues and eigenstates are known, and one uses the eigenbasis of $\widehat{H}$ to define the coherences. Equations (78)–(80) then lead to

$$\widehat{H}|h_q\rangle = h_q|h_q\rangle\,,\ \hat{\rho}(t) = \sum_{q,r}\langle h_q|\hat{\rho}(t)|h_r\rangle|h_q\rangle\langle h_r|$$

hence

$$\langle h_q|\hat{\rho}(t)|h_r\rangle = \langle h_q|\hat{\rho}(t_0)|h_r\rangle e^{i(t-t_0)(h_q-h_r)/\hbar} \tag{86}$$

where the subscripts q and r label the eigenvalues and eigenvectors of $\widehat{H}$. During time evolution under $\widehat{H}$, each coherence just oscillates at the corresponding Bohr frequency. However, time-dependent perturbations, like rf pulses, usually cause a major reorganization of the coherences.

In typical NMR situations (with spins of a single species), the Hamiltonian $\widehat{H}$ for the spins in a single molecule can be decomposed as $\widehat{H} = \hbar\omega_0\sum_j \hat{I}_{jZ} + \widehat{V}$, where the small term $\widehat{V}$ describes chemical shifts and spin–spin couplings (suitably averaged over the molecular Brownian motion). For such small $\widehat{V}$, it is sufficient to retain the part of $\widehat{V}$ which is secular with respect to $\sum_j \hat{I}_{jZ}$, so that the eigenstates of $\widehat{H}$ are also eigenstates of $\sum_j \hat{I}_{jZ}$,

$$\left(\sum_j \hat{I}_{jZ}\right)|h_q\rangle = n_q\,|h_q\rangle \tag{87}$$

where the n_q are integers (or half-integers for an odd number of half-integer spins). For any coherence $\langle h_q|\hat{\rho}(t)|h_r\rangle$, the integer $(n_q - n_r)$ is an essential parameter because it governs the behavior of the coherence with respect to the phase of rf pulses, and to changes in external magnetic field; it also gives the zero-th order approximation of the energy difference between states q and r. The integer $(n_q - n_r)$ is the 'order of coherence' and the c-number $\langle h_q|\hat{\rho}(t)|h_r\rangle$ is called an '$(n_q - n_r)$-quantum coherence.' The operators $|h_q\rangle\langle h_r|$ and $\langle h_q|\hat{\rho}(t)|h_r\rangle|h_q\rangle\langle h_r|$ are also called '$(n_q - n_r)$-quantum coherences.' All these ideas are easily extended to the case of multiple spin species.

The present discussion of the 'Warren' presentation of the dipolar field effects will be based on a spin Hamiltonian of the type often used for solids,

$$\widehat{H}_S = \sum_{j=1}^{N}\hbar(\omega_0 + \delta\omega_j)\hat{I}_{jZ} + \widehat{H}_S^{\text{dip sec}} + \hat{P}_S(t)$$

where

$$\begin{aligned}\widehat{H}_S^{\text{dip sec}} &= \sum_{i=1}^{N}\sum_{j=1(j\neq i)}^{N}\hbar D_{ij}\{3\hat{I}_{iZ}\hat{I}_{jZ} - \hat{\mathbf{I}}_i\cdot\hat{\mathbf{I}}_j\} \\ D_{ij} &= -\frac{1}{2}\frac{\mu_0}{4\pi}\frac{\gamma^2\hbar}{|\boldsymbol{r}_i - \boldsymbol{r}_j|^3}\frac{3(\cos\theta_{ij})^2 - 1}{2}\end{aligned} \tag{88}$$

$\delta\omega_j$ is a small frequency offset, the non-secular part of the dipolar coupling has been ignored, $\hat{P}_S(t)$ describes rf pulses, and the D_{ij} are the same as in Ref.[21]. Discussions of spin dynamics will be simplified by the usual interaction representation based on the unitary transformation

$$\widehat{W}_S(t) = \prod_{j=1}^{N} e^{-i\omega_0\hat{I}_{jZ}(t-t_*)} \tag{89}$$

where t_* is an arbitrary reference date. The transformed versions of operators $\hat{A}_S(t)$ and evolution operators $\widehat{U}_S(t_1, t_0)$ are given by

$$\begin{aligned}\hat{\tilde{A}}_S(t) &= \widehat{W}_S^{\dagger}(t)\hat{A}_S(t)\widehat{W}_S(t) \\ \widehat{\tilde{U}}_S(t_1, t_0) &= \widehat{W}_S^{\dagger}(t_1)\widehat{U}_S(t_1, t_0)\widehat{W}_S(t_0)\end{aligned} \tag{90}$$

the von Neumann equation of motion for $\hat{\tilde{\rho}}(t)$ is

$$i\hbar\frac{\partial}{\partial t}\hat{\tilde{\rho}}_S(t) = \left[\left(\sum_{j=1}^{N}\hbar\delta\omega_j\hat{I}_{jZ} + \widehat{H}_S^{\text{dip sec}} + \hat{\tilde{P}}_S(t)\right), \hat{\tilde{\rho}}_S(t)\right] \tag{91}$$

and the average values of the components of the spin magnetization, as seen from the rotating frame of coordinates, are given by

$$\langle I_{j\tilde{+}}\rangle(t) = \text{Tr}_S\{(\hat{I}_{j+})^{\dagger}\hat{\tilde{\rho}}(t)\}, \ldots \tag{92}$$

Assuming that we can neglect the dipolar couplings (and the offsets) in the expression of the equilibrium density operator, $\hat{\rho}_S^{\text{eq}}$ is factorized in equilibrium density operators for the individual spins

$$\hat{\tilde{\rho}}_S^{\text{eq}} = \hat{\rho}_S^{\text{eq}} = \prod_{j=1}^{N}\hat{\rho}_j^{\text{eq}} = \prod_{j=1}^{N}\left\{\frac{1}{2}\left(\hat{1}_j - \mathcal{J}\hat{I}_{jZ}\right)\right\}$$

where

$$\mathcal{J} = 2\tanh\left(\frac{\hbar\omega_0}{2kT}\right) \approx \frac{\hbar\omega_0}{kT} \tag{93}$$

5.2 Intermolecular Multiple-quantum Coherences

Following the example of equation (85), the density operator $\hat{\tilde{\rho}}_S(t)$ for the system of N spins 1/2 can always be decomposed as[22]

$$\hat{\tilde{\rho}}_S(t) = \sum_{\xi=1}^{4^N} k^{(\xi)} \langle A^{(\xi)} \rangle(t) \hat{A}^{(\xi)}$$

where

$$\langle A^{(\xi)} \rangle(t) = \mathrm{Tr}_S\{\hat{A}^{(\xi)\dagger} \hat{\tilde{\rho}}_S(t)\}$$
$$k^{(\xi)} = 1/\mathrm{Tr}_S\{\hat{A}^{(\xi)\dagger} \hat{A}^{(\xi)}\}$$

and (orthogonality)

$$\mathrm{Tr}_S\{\hat{A}^{(\xi)\dagger} \hat{A}^{(\eta)}\} = (1/k^{(\xi)})\, \delta_{\xi,\eta} \tag{94}$$

The $\hat{A}^{(\xi)}$ are products of one operator of the list $\{\hat{1}_j, \hat{I}_{j+}, \hat{I}_{j-}, \hat{I}_{jZ}\}$ for each spin j in the system, and the $k^{(\xi)}$ are not all unity because the operators $\hat{1}_j$ and $\hat{I}_{jZ}$ are not properly normalized. Each $\hat{A}^{(\xi)}$ has a well defined coherence order, equal to the number of single spin $\hat{I}_+$ minus that of $\hat{I}_-$ used to build $\hat{A}^{(\xi)}$. In the procedure proposed by the Warren group,[19,21] the time evolution of the relevant observables is studied by solving the set of linear equations of motion of coherences involving progressively increasing numbers of spins (i.e., increasing numbers of spins contributing an operator other than $\hat{1}$ to the coherence),

$$\frac{\partial}{\partial t}\langle A^{(\xi)} \rangle(t) = \mathrm{Tr}_S\left\{\hat{A}^{(\xi)\dagger} \frac{\partial}{\partial t} \hat{\tilde{\rho}}_S(t)\right\}$$
$$= -\frac{i}{\hbar}\mathrm{Tr}_S\left\{\hat{A}^{(\xi)\dagger}\left[\left(\sum_{j=1}^{N} \hbar\delta\omega_j \hat{I}_{jZ} + \widehat{H}_S^{\mathrm{dip\,sec}}\right), \hat{\tilde{\rho}}_S(t)\right]\right\} \tag{95}$$

where rf pulses have been ignored for simplicity. Due to the orthogonality of the coherences, the evaluation of the trace in equation (95) becomes trivial if one knows the coefficient of $\hat{A}^{(\xi)}$ in the expansion of the commutator in terms of coherences. The following simple relations, valid for spins 1/2, will be useful in further discussions,

$$[\widehat{B}_q \widehat{C}_r, \widehat{D}_q \widehat{E}_r] = \widehat{B}_q \widehat{D}_q [\widehat{C}_r, \widehat{E}_r] + [\widehat{B}_q, \widehat{D}_q] \widehat{E}_r \widehat{C}_r$$
$$\hat{I}_{q\pm}\hat{I}_{qZ} = \pm\frac{1}{2}\hat{I}_{q\pm}\,,\ \hat{I}_{qZ}\hat{I}_{q\pm} = \mp\frac{1}{2}\hat{I}_{q\pm}$$
$$\hat{I}_{q+}\hat{I}_{q-} = \frac{1}{2}\hat{1}_q + \hat{I}_{qZ}\,,\ \hat{I}_{q-}\hat{I}_{q+} = \frac{1}{2}\hat{1}_q - \hat{I}_{qZ}$$
$$\left[\sum_{i,j} D_{ij}\hat{I}_{iZ}\hat{I}_{jZ}, \hat{I}_{q+}\right] = 2\sum_{i\neq q} D_{iq}\hat{I}_{iZ}\hat{I}_{q+}$$
$$\left[\sum_{i,j} D_{ij}\hat{\mathbf{I}}_i \cdot \hat{\mathbf{I}}_j, \hat{I}_{q+}\right] = 2\sum_{i\neq q} D_{iq}(\hat{I}_{iZ}, \hat{I}_{q+} - \hat{I}_{i+}\hat{I}_{qZ})$$
$$\left[\sum_{i,j} D_{ij}\hat{\mathbf{I}}_i \cdot \hat{\mathbf{I}}_j, \hat{I}_{qZ}\right] = \sum_{i\neq q} D_{iq}(\hat{I}_{i+}\hat{I}_{q-} - \hat{I}_{i-}\hat{I}_{q+})$$
$$\left[\sum_{i,j} D_{ij}\hat{\mathbf{I}}_i \cdot \hat{\mathbf{I}}_j, \hat{I}_{qZ}\hat{I}_{rZ}\right] = D_{qr}(\hat{I}_{q+}\hat{I}_{r-} - \hat{I}_{q-}\hat{I}_{r+}) + [3]$$
$$\left[\sum_{i,j} D_{ij}\hat{I}_{iZ}\hat{I}_{jZ}, \hat{I}_{q+}\hat{I}_{rZ}\right] = \frac{1}{2}D_{qr}\hat{I}_{q+} + [3]$$
$$\left[\sum_{i,j} D_{ij}\hat{\mathbf{I}}_i \cdot \hat{\mathbf{I}}_j, \hat{I}_{q+}\hat{I}_{rZ}\right] = \frac{1}{2}D_{qr}(\hat{I}_{q+} - \hat{I}_{r+}) + [3]$$
$$\left[\sum_{i,j} D_{ij}\hat{I}_{iZ}\hat{I}_{jZ}, \hat{I}_{q+}\hat{I}_{r-}\right] = [3]$$
$$\left[\sum_{i,j} D_{ij}\hat{\mathbf{I}}_i \cdot \hat{\mathbf{I}}_j, \hat{I}_{q+}\hat{I}_{r-}\right] = D_{qr}(\hat{I}_{rZ} - \hat{I}_{qZ}) + [3]$$
$$\left[\sum_{i,j} D_{ij}\hat{I}_{iZ}\hat{I}_{jZ}, \hat{I}_{q+}\hat{I}_{r+}\right] = [3]$$
$$\left[\sum_{i,j} D_{ij}\hat{\mathbf{I}}_i \cdot \hat{\mathbf{I}}_j, \hat{I}_{q+}\hat{I}_{r+}\right] = [3]$$
$$\left[\sum_{i,j} D_{ij}\hat{I}_{iZ}\hat{I}_{jZ}, \hat{I}_{q+}\hat{I}_{rZ}\hat{I}_{pZ}\right] = \frac{1}{2}D_{qr}\hat{I}_{q+}\hat{I}_{pZ}$$
$$+ \frac{1}{2}D_{qp}\hat{I}_{q+}\hat{I}_{rZ} + [4]$$
$$\left[\sum_{i,j} D_{ij}\hat{\mathbf{I}}_i \cdot \hat{\mathbf{I}}_j, \hat{I}_{q+}\hat{I}_{rZ}\hat{I}_{pZ}\right] = \frac{1}{2}D_{qr}(\hat{I}_{q+} - \hat{I}_{r+})\hat{I}_{pZ}$$
$$+ \frac{1}{2}D_{qp}(\hat{I}_{q+} - \hat{I}_{p+})\hat{I}_{rZ} + [3]$$
$$\left[\sum_{i,j} D_{ij}\hat{I}_{iZ}\hat{I}_{jZ}, \hat{I}_{q+}\hat{I}_{r-}\hat{I}_{p+}\right] = [3]$$
$$\left[\sum_{i,j} D_{ij}\hat{\mathbf{I}}_i \cdot \hat{\mathbf{I}}_j, \hat{I}_{q+}\hat{I}_{r-}\hat{I}_{p+}\right] = D_{rq}\hat{I}_{p+}(\hat{I}_{rZ} - \hat{I}_{qZ})$$
$$+ D_{rp}\hat{I}_{q+}(\hat{I}_{rZ} - \hat{I}_{pZ}) + [3] \tag{96}$$

where $[n]$ stands for additional terms involving at least n different spins. Two general features of such commutators of $\widehat{H}_S^{\mathrm{dip\,sec}}$ with any operator $\hat{A}$ are that (i) the order of coherence of the commutator is the same as that of $\hat{A}$, and (ii) the list of spins involved in the various terms of the commutator can be the same as that of $\hat{A}$, that of $\hat{A}$ with one spin removed, or that of $\hat{A}$ with one spin added.

Another set of useful relations describes the action of a hard rf pulse of tipping angle θ and phase ϕ on the single spin operators,

$$\widehat{\tilde{R}}_j(\theta,\phi)\hat{I}_{jZ}\widehat{\tilde{R}}_j^{\dagger}(\theta,\phi) = i\frac{\sin\theta}{2}e^{-i\phi}\hat{I}_{j+} - i\frac{\sin\theta}{2}e^{i\phi}\hat{I}_{j-} + \cos\theta\hat{I}_{jZ},$$
$$\widehat{\tilde{R}}_j(\theta,\phi)\hat{I}_{j+}\widehat{\tilde{R}}_j^{\dagger}(\theta,\phi) = \frac{\cos\theta}{2}\hat{I}_{j+} - \frac{\cos\theta}{2}e^{2i\phi}\hat{I}_{j-} + \sin\theta e^{i\phi}\hat{I}_{jZ},$$
$$\widehat{\tilde{R}}_j(\theta,\phi)\hat{I}_{j-}\widehat{\tilde{R}}_j^{\dagger}(\theta,\phi) = -\frac{\cos\theta}{2}e^{-2i\phi}\hat{I}_{j+} + \frac{\cos\theta}{2}\hat{I}_{j-} + \sin\theta e^{-i\phi}\hat{I}_{jZ} \tag{97}$$

where $\widehat{\tilde{R}}_j(\theta,\phi) = e^{-i\phi\hat{I}_{jZ}}e^{-i\theta\hat{I}_{jx}}e^{i\phi\hat{I}_{jZ}}$ is the pulse operator for spin j in the interaction representation.

As a starting point for the discussion of the Warren procedure, consider the response to a hard θ pulse, in the X-direction of the rotating frame, applied to the equilibrium state given by equation (93). Immediately after the pulse, the density operator is still factorized, and is given by

$$\hat{\tilde{\rho}}_S(t_{0+}) = \prod_{j=1}^{N} \frac{1}{2}\left(\hat{1}_j - \frac{i}{2}\mathcal{J}\sin\theta(\hat{I}_{j+} - \hat{I}_{j-}) - \mathcal{J}\cos\theta\,\hat{I}_{jZ}\right) \quad (98)$$

Neglecting all offsets in a first round of discussion, we evaluate the time derivatives of $\langle I_{q\mp}\rangle(t)$ and $\langle I_{qZ}\rangle(t)$ at $t = t_{0+}$, using equations (95) and (96). The commutators with $\sum_{i,j} D_{ij}\hat{\boldsymbol{I}}_i \cdot \hat{\boldsymbol{I}}_j$ are antisymmetric for permutations of spin labels, hence they give total contributions of zero in the state given by equation (98) which is symmetric for these permutations. The commutators with $\sum_{i,j} D_{ij}\hat{I}_{iZ}\hat{I}_{jZ}$ give no contribution in $\hat{I}_{qZ}$, hence $d\langle I_{qZ}\rangle(t)/dt = 0$ at $t = t_{0+}$, and give a contribution in I_{q+} arising from the terms $(1/2)^N 8\langle I_{q\mp}\rangle(t_{0+})\langle I_{rZ}\rangle(t_{0+})\hat{I}_{q+}\hat{I}_{rZ}$ in $\hat{\tilde{\rho}}_S(t_{0+})$, where $\langle I_{q\mp}\rangle(t_{0+}) = -\frac{i}{4}\mathcal{J}\sin\theta$ and $\langle I_{qZ}\rangle(t_{0+}) = -\frac{1}{4}\mathcal{J}\cos\theta$, hence

$$\left.\frac{\partial}{\partial t}\langle I_{q\mp}\rangle(t)\right|_{t=t_0} = -i\langle I_{q\mp}\rangle(t_{0+})\sum_{r\neq q} 6D_{qr}\langle I_{rZ}\rangle(t_{0+}) \quad (99)$$

This is the time derivative which is expected at $t = t_{0+}$ if spin q precesses (in the rotating frame) *exactly* at the angular velocity caused by the average classical dipolar field, as given by equation (28) without averaging over molecular motion. The sum in equation (99) is relatively small because the large individual contributions from near-by spins tend to cancel on average, and one is left with distant contributions (depending upon the shape of the sample).

Note that the same dipolar field shift, which is predicted from a set of non-linear equations of motion for individual spins in the 'classical' presentation, is predicted here from a linear equation of motion for the system of all spins in the sample. In both cases, this effect appears at order 2 in a 'systematic' series expansion in powers of $(1/T)$ or $\mathcal{J}$.

At this point, it is instructive to evaluate the second time derivative of $\langle I_{q\mp}\rangle(t)$, still at $t = t_{0+}$, under the same conditions,

$$\left.\frac{\partial^2}{\partial t^2}\langle I_{q\mp}\rangle(t)\right|_{t=t_0} = \left(\frac{i}{\hbar}\right)^2 \mathrm{Tr}_S\{(\hat{I}_{q+})^\dagger[\widehat{H}_S^{\mathrm{dip\,sec}}, [\widehat{H}_S^{\mathrm{dip\,sec}}, \hat{\tilde{\rho}}_S(t_0)]]\} \quad (100)$$

Inspection of equation (96) show that terms $\hat{I}_{q+}$ in the double commutator originate from two types of terms in $\hat{\tilde{\rho}}_S(t_0)$: terms in $\hat{I}_{q+}$ and terms in $\hat{I}_{q+}\hat{I}_{rZ}\hat{I}_{pZ}$. The result is

$$\left.\frac{\partial^2}{\partial t^2}\langle I_{q\mp}\rangle(t)\right|_{t=t_0} = -\langle I_{q\mp}\rangle(t_{0+})\left\{9\sum_{r\neq q} D_{qr}^2 + 72\sum_{r\neq q}\sum_{\substack{p\neq q\\ p>r}} D_{qr}D_{qp}\langle I_{rZ}\rangle(t_{0+})\langle I_{pZ}\rangle(t_{0+})\right\} \quad (101)$$

$$= -\langle I_{q\mp}\rangle(t_{0+})\left\{9\sum_{r\neq q} D_{qr}^2\left(1 - 4\{\langle I_{rZ}\rangle(t_{0+})\}^2\right) + \sum_{r\neq q} 6D_{qr}\langle I_{rZ}\rangle(t_{0+})\sum_{p\neq q} 6D_{qp}\langle I_{pZ}\rangle(t_{0+})\right\} \quad (102)$$

The product of two (equal) sums in equation (102) gives the acceleration expected for the precession indicated by equation (99). The much larger single sum in equation (102) is dominated by the positive contributions D_{qr}^2 for spins r in the immediate vicinity of spin q, and the contributions from distant spins are negligible because they are proportional to $|r_q - r_r|^{-6}$. This single sum is essentially the Van Vleck second moment for the rigid lattice, not a surprise for a model of immobile spins with dipolar couplings. However, the fid of such a model of a 'frozen' liquid usually lasts for less than 100 μs, an intolerable feature for a model of liquids. In a liquid, the molecular Brownian motion very efficiently averages out to zero the effects of the strong couplings between near-by spins, hence suppressing the fast decay of the fid typical of solids. However, this motional averaging has negligible effects on distant couplings, hence it does not affect the dipolar field effects.

All this provides a strong motivation for the solution proposed by the Warren group in the first publication[20] on the quantum model described here: ignore the dipolar couplings between near-by spins by setting $D_{ij} = 0$ for all pairs for which $|\boldsymbol{r}_i - \boldsymbol{r}_j| < r_0$, with r_0 chosen large enough to avoid visible solid-like broadening of the lines, and smaller than the distance scale of the spatial inhomogeneity of the average spin magnetization during the experiment. As shown by the Warren group, this usually leaves a lot of leeway for the choice of r_0, and the predictions are independent of the value of r_0 chosen. In some publications,[21] the cutoff distance r_0 is discussed in terms of a 'coherent interaction time' for each pair of molecules in the liquid. The use of this heuristic notion is not necessary, and I feel that it undermines the overall soundness of the model without leading to new conclusions.

Let us now come back to the mechanism which causes the fast decay of the fid when all D_{ij} are taken into account. At $t = t_{0+}$, the density operator $\hat{\tilde{\rho}}_S(t_{0+})$ is factorized and we have $\langle I_{q\mp}\rangle(t_{0+}) \sim \mathcal{J}$ and $\langle I_{q\mp}I_{rZ}\rangle(t_{0+}) \sim \mathcal{J}^2$. The first step, described by the inner commutator in equation (100), acts on $\hat{I}_{q+}$ to generate coherences $\langle I_{q\mp}I_{rZ}\rangle \sim D_{qr}\mathcal{J}$. The second step, described by the outer commutator, acts on these coherences to generate a coherence $\langle I_{q\mp}\rangle \sim \sum_{r\neq q} D_{qr}^2\mathcal{J}$ which describes the fast decay. The intermediate coherence $\langle I_{q\mp}I_{rZ}\rangle$ is obviously not factorized because it does not have the same $\mathcal{J}$ and D dependences as the product of $\langle I_{q\mp}\rangle \sim \mathcal{J}$ and $\langle I_{rZ}\rangle \sim \mathcal{J}$, hence this corresponds to the growth of two-spin *correlations* involving spin q and all other spins r. If we ignore couplings at short distances, the remaining correlations are small and, to a very good approximation, have no effect whatsoever on the evolution of the observed quantities $\langle I_{q\mp}\rangle$ and $\langle I_{rZ}\rangle$.

In summary, in this particular case, the neglect of couplings at short distances makes quantities of the type $\sum_{r\neq q} D_{qr}^2$ completely negligible, and avoids the generation of *intermolecular correlations* in $\hat{\tilde{\rho}}_S$ which would cause observable effects. Warren and co-workers[21] have shown that this conclusion is

general. Hence, the factorized part of $\hat{\tilde{\rho}}_S$ is sufficient for all practical purposes of NMR, quantities of the type $\sum_{r\neq q} D_{qr}^2$ can safely be ignored in detailed calculations, and this implies that one can also ignore all contributions arising from terms in the expansion of commutators with $\widehat{H}_S^{\text{dip sec}}$ which 'add' one spin. These properties simplify the calculations enough to make them tractable and confirm the validity of the factorization approximation for $\hat{\tilde{\rho}}_S(t)$ used in the derivation of the 'classical' procedure. In this way, the two methods appear as strictly equivalent for all situations in which the molecular Brownian motion is not an active participant (causing relaxation and macroscopic molecular diffusion).

A less formal, but more detailed discussion of intermolecular multiple quantum coherences in liquids, together with a complete calculation for the CRAZED experiment, can be found in Ref.[73].

5.3 Equivalence Between the 'Classical' and 'Warren' Predictions

This equivalence can be seen in a particularly useful way by coming back to the evaluation of the time derivatives of the average values $\langle I_{q\tilde{+}}\rangle(t)$ and $\langle I_{qZ}\rangle(t)$ at any time t, taking into account only the factorized part of $\hat{\tilde{\rho}}_S(t)$. The calculation will be carried out for a single type of spins 1/2, but it will include offsets and spatial inhomogeneities. By combining equations (83), (88), (91), (95), and (96), without the simplifications used for equation (99) we obtain

$$\frac{\partial}{\partial t}\langle I_{q\tilde{+}}\rangle(t) = -i\,\delta\omega_q\langle I_{q\tilde{+}}\rangle(t) - i\langle I_{q\tilde{+}}\rangle(t)\sum_{r\neq q} 6D_{qr}\langle I_{rZ}\rangle(t) + i\left\{\langle I_{q\tilde{+}}\rangle(t)\sum_{r\neq q} 2D_{qr}\langle I_{rZ}\rangle(t) - \langle I_{qZ}\rangle(t)\sum_{r\neq q} 2D_{qr}\langle I_{r\tilde{+}}\rangle(t)\right\} \tag{103}$$

$$\frac{\partial}{\partial t}\langle I_{qZ}\rangle(t) = -i\langle I_{q\tilde{-}}\rangle(t)\sum_{r\neq q} 2D_{qr}\langle I_{r\tilde{+}}\rangle(t) + i\langle I_{q\tilde{+}}\rangle(t)\sum_{r\neq q} 2D_{qr}\langle I_{r\tilde{-}}\rangle(t) \tag{104}$$

In spite of a different notation, this is exactly the generalized Bloch equation (3) for spin q seen in the rotating frame, with an offset $\delta\omega_q$ and a dipolar field given by equation (33), but without relaxation and without rf current in the coil.

In the classical procedure, one considers the Bloch equations as a set of coupled nonlinear differential equations for the three components of the average magnetic moment of each individual spin, i.e., the functions of time explicitly written in equation (103) and (104), a total of $3N$ real variables (here, N real and N complex variables). When a solution has been worked out, all coherences involving a single spin are known as a function of time, hence all higher order coherences can be easily evaluated from the factorization property of $\hat{\tilde{\rho}}_S(t)$. However, there is usually little incentive to do this.

In the Warren procedure, one starts from the same set of equations (103) and (104) for the time derivatives of the average components of the magnetic moments of individual spins, but one considers it as a (small) subset of the much larger set of equations of motion (95) for all coherences in the spin system. With this viewpoint, the equations are linear, but the number of equations and (real) unknowns has grown to $4^N - 1$. In the approximations appropriate for liquid NMR, all relevant multiple spin coherences remain factorized in the corresponding single spin coherences. Hence, if one should choose to describe the spin state in terms of single spin coherences only, the multiple spin coherences would be expressed as products of single spin coherences, and this would introduces the non-linearities which are directly visible in the classical procedure. The Warren procedure takes the other tack, and starts from an initial situation (at time t_{ini}) for which all coherences are known: immediately after a hard rf pulse applied to the thermal equilibrium situation (for instance, equation (98)), or after some tractable evolution after which all coherences are still known. The next step is to express the observable quantities like $\langle I_{q\tilde{+}}\rangle(t)$ as a series expansion in powers of the delay $t - t_{\text{ini}}$,

$$\langle I_{q\tilde{+}}\rangle(t) = \langle I_{q\tilde{+}}\rangle(t_{\text{ini}}) + \sum_{v=1}^{\infty}\frac{1}{v!}(t-t_{\text{ini}})^v\frac{\partial^v}{\partial t^v}\langle I_{q\tilde{+}}\rangle(t)\bigg|_{t=t_{\text{ini}}}$$

where

$$\frac{\partial^v}{\partial t^v}\langle I_{q\tilde{+}}\rangle(t)\bigg|_{t=t_{\text{ini}}} = \text{Tr}_S\left\{(\hat{I}_{q+})^\dagger\left[\overbrace{\widehat{K}_S,\ldots,[\widehat{K}_S}^{v},\hat{\tilde{\rho}}_S(t_{\text{ini}})]\ldots\right]\right\}$$

and

$$\widehat{K}_S = \sum_{j=1}^{N}\hbar\delta\omega_j\hat{I}_{jZ} + \widehat{H}_S^{\text{dip sec}} \tag{105}$$

The 'Warren' procedure is particularly useful in the frequent case of weak dipolar field effects, for which $\mathcal{J}$ is a small parameter, because the initial coherences involving n spins are proportional to $\mathcal{J}^n$ and decrease rapidly for increasing n. The analogy with the usual discussion of *intramolecular* q-quantum coherences in terms of product operators indicates that the observed effects of order q in multiple spin echoes, CRAZED experiments, COSY spectra, ..., arise from the evolution of intermolecular q-quantum coherences during the delay τ_1 between the two rf pulses. Hence, when these effects are small, they arise essentially from q-quantum coherences involving the smallest possible number of spins (which is also $|q|$, except when $q = 0$). These $|q|$-spins, q-quantum coherences are transformed by the second rf pulse into combinations of various $|q|$-spins coherences, of which only $|q|$-spins, 1-quantum coherences contribute to the time derivative of order $|q|$ after $|q|$ commutations with $\widehat{H}_S^{\text{dip sec}}$. A wide choice of detailed calculations of this type can be found in publications of the Warren group[21] and others.[66] For strong dipolar field effects, many more coherences have to be taken into account and the Warren procedure becomes extremely clumsy, unfortunately.

Most quantitative predictions of dipolar field effects are strongly dependent upon relaxation, and relaxation is not a built-in feature of the original 'Warren' procedure, so that it has to be introduced 'by hand' as an afterthought. This is easily justified by using the equivalence with the classical procedure

which automatically includes relaxation.[69] Molecular diffusion is much more difficult to handle, and no reliable method has been proposed yet for its incorporation in the Warren procedure.

6 SPECTRAL CLUSTERING AND DYNAMIC INSTABILITY

For obvious reasons of simplicity and efficiency, many NMR experiments are planned and modeled with homogeneous fields, homogeneous distributions of nuclear magnetization (and a sample shape leading to a homogeneous dipolar field). In experiments using field gradients (usually pulsed), homogeneous distributions of magnetization and dipolar field are replaced by multiple turn helical and grating-like distributions with direction and pitch under the direct control of the experimenter. The calculations show that such *perfectly* regular situations remain perfectly regular in the presence of dipolar field effects.

In this section, we shall discuss two types of unexpected consequences of small deviations from these 'well controlled' distributions, both due to the dynamical effects of the rotating component of the dipolar field:[13] spectral clustering and dynamical instabilities.

6.1 Spectral Clustering

Spectral clustering was first observed in cryogenic experiments, which offer the favorable combination of slow relaxation and large dipolar fields due to large nuclear polarizations. Particularly clear results were obtained by the Nacher group on dilute solutions of hyperpolarized ^{3}He in ^{4}He at lattice temperatures of the order of 0.2 K,[74–76] and later on hyperpolarized liquid ^{129}Xe.[77] In these experiments, the sample is contained in a capillary tube in the shape of a ∪, with a constant external magnetic field parallel to the straight arms of the ∪. With this geometry, the 'equilibrium' dipolar field varies continuously from $+2B_d$ in the vertical arms to $-B_d$ at the bottom of the ∪; hence one naively expects an absorption spectrum (i.e., the Fourier transform of the response to a small pulse of transverse magnetic field) with the corresponding continuous shape, resembling a powder pattern in solids. What is actually observed is a set of very sharp and well separated lines in a pattern for which the naive expectation looks like an envelope. As shown by the Nacher group, this set of sharp lines, which they associate with the 'magnetic modes' of the sample, is predicted whenever one takes into account the dipolar couplings between the slices along the capillary. Semi-quantitative agreement is even obtained with such a simplistic model as a regular necklace of 48 equal classical spins, in the shape of a ∪ or a circle, with dipolar couplings between first neighbors or between all spins.

Figure 21 shows the result of a numerical simulation of spectral clustering under circumstances more familiar in high-resolution NMR: a compact sample and a small B_0 inhomogeneity. If the nuclei on which a small rf pulse is applied generate a small dipolar field (e.g., dilute nuclei), the Fourier transform of the fid will faithfully show the overall inhomogeneity over the sample, and this may serve as indicator for further shimming. In contradistinction, for abundant nuclei generating maximum dipolar field shifts comparable to the inhomogeneity over the sample, the response to a small pulse is dominated by a single sharp line and does not clearly reflect the inhomogeneity any more. This should not be mistaken for an actual elimination or compensation of the inhomogeneity, it is a dynamic mechanism acting only on the strong (usually solvent) line and not on the weak (usually interesting) lines from dilute molecules in the same sample.

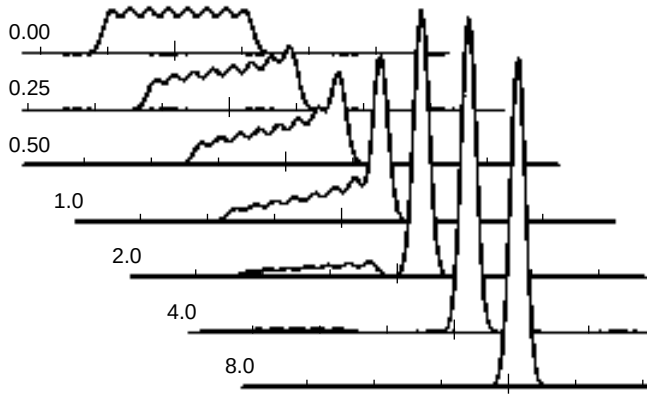

Figure 21 The usual expectation is that a $\boldsymbol{B}_0$ inhomogeneity causes a corresponding line broadening (top spectrum). Spectral clustering is the process by which, for small pulses, this broadening is suppressed by the dynamic effect of the dipolar field (bottom spectra). The figure shows the absorption component of the Fourier transform of the response to a very small rf pulse, as a function of frequency, for a 'single NMR line'. The spectra are marked by the ratio $\omega_d/\omega_{\text{inhom width}}$, where $\omega_d = \gamma\mu_0 M^{\text{eq}}$ is the typical maximum dipolar field shift and $\omega_{\text{inhom width}}$ is the line width due to the external field inhomogeneity. The large tick is at the same frequency in all seven spectra. For this numerical simulation, the $\boldsymbol{B}_0$ field inhomogeneity is a ∧∧∧-function of the Z-coordinate and the overall shape of the sample is spherical. Eight layers of spins are present over each region of increase or decrease of the external field (changing this number to 16 or 32 does not significantly alter the result), the width of individual lines is artificial. Relaxation and radiation damping have been ignored

In the numerical simulations, the situation shown by Figure 21 persists for tipping angles up to about 0.2 radian; for larger tipping angles and ratios $|\omega_d/\omega_{\text{inhom width}}|$ above 1 or 2, the 'spectra' become broad and complex, and dynamic instabilities set in for tipping angles larger than about 0.7 radian. The corresponding effects have been observed in cryogenic experiments,[77] but the lack of satisfactory equipment for the elimination of radiation damping has prevented clear observations under ordinary NMR conditions (as far as I know).

6.2 Dynamic Instabilities Caused by the Dipolar Field

Even in the best spectrometer, the regular 'well controlled' distributions of magnetization which are the aim of the experimenter and the starting point of standard NMR predictions, are approximations which ignore such 'imperfections' as edge effects, minor field inhomogeneities, equilibrium fluctuations, etc. Common sense suggests that, if the imperfections are small, their overall influence on the experimental outcomes will also be small. Fortunately, this is what happens whenever collective effects are negligible. However, the dipolar field mediates interactions between the bulk nuclear magnetizations at different places in the sample, and this raises the question of the fate of (even small) deviations from the perfectly regular

distribution of magnetization. In the case of a helical distribution of magnetization, for which the fid signal is ideally zero, a similar question arises about the effects of radiation damping; this part of the discussion will be deferred to Section 6.3.

In general, after a small pulse applied to the equilibrium situation, the very small deviations just oscillate as a function of time, hence they are harmless. On the contrary, after a large pulse (typically between about $\pi/4$ and $3\pi/4$), some of the deviations grow exponentially with time, with characteristic doubling delay as short as $1/\omega_d$. Such instabilities rapidly cause major spin turbulence and an irrecoverable loss of NMR signal.

We shall now discuss a slightly extended version of an example presented in Ref.[13], in which the issue of stability is easy to treat analytically. In this model, all spins are equivalent, all external fields are homogeneous, radiation damping is ignored, and the shape of the sample is such that a homogeneous magnetization $\boldsymbol{M}_{\rm av}(t)$ generates a dipolar field $\boldsymbol{B}_{\rm d,av}(t)$ which is also homogeneous inside the sample. After removal of the counter-rotating parts, the relevant part of this dipolar field is given by [see equations (34) to (36)]

$$\boldsymbol{B}_{\rm d,av}^{\rm no\ crp}(t) = -\frac{\mu_0}{3}\left[\frac{3(\cos\theta_s)^2-1}{2}\right][3M_{{\rm av}Z}(t)\mathbf{1}_Z - \boldsymbol{M}_{\rm av}(t)] \quad (106)$$

where θ_s is the angle between Z and the normal to the plane for a flat sample, and suitably chosen values of θ_s can simulate other shapes and orientations (for instance $\theta_s = \arccos(1/\sqrt{3})$ simulates a sphere). The deviations from $M_{\rm av}(t)$ will be described as a superposition of plane wave distributions of magnetization of the type $\boldsymbol{m}_{\boldsymbol{q}}(t)e^{i\boldsymbol{q}\cdot\boldsymbol{r}}$. If the distribution of magnetization $\boldsymbol{m}_{\boldsymbol{q}}(t)e^{i\boldsymbol{q}\cdot\boldsymbol{r}}$ should extend over all space, it would generate a dipolar field with a relevant part given by

$$\boldsymbol{B}_{{\rm d},\boldsymbol{q}}^{\rm no\ crp}(\boldsymbol{r},t) = -\frac{\mu_0}{3}\left[\frac{3(\cos\theta_{\boldsymbol{q}})^2-1}{2}\right]e^{i\boldsymbol{q}\cdot\boldsymbol{r}}[3m_{\boldsymbol{q}Z}(t)\mathbf{1}_Z - \boldsymbol{m}_{\boldsymbol{q}}(t)] \quad (107)$$

For large vectors $\boldsymbol{q}$, for which the spatial wavelength $2\pi/|q|$ is much shorter than the smaller axis of the sample, equation (107) remains a good approximation for the positions $\boldsymbol{r}$ inside the sample at distances from the surface (much) larger than $2\pi/|q|$. We shall limit the discussion to such large vectors $\boldsymbol{q}$, and neglect the surface layer.

If the magnetization is exactly homogeneous, the equation of motion, written in the frame of coordinates rotating at the angular velocity $-\gamma\boldsymbol{B}_0$ is

$$\left(\frac{\rm d}{{\rm d}t}\right)_{\rm rot}\boldsymbol{M}_{\rm av}(t) = \boldsymbol{M}_{\rm av}(t)\times\gamma\boldsymbol{B}_{\rm d,av}^{\rm no\ crp}(t) = \boldsymbol{M}_{\rm av}(t)\times(-\boldsymbol{\omega}_{\rm d,av})$$

where

$$\boldsymbol{\omega}_{\rm d,av} = \frac{\gamma\mu_0}{3}\left[\frac{3(\cos\theta_s)^2-1}{2}\right]3M_{{\rm av}Z}(t)\mathbf{1}_Z \quad (108)$$

This describes an additional (slow) rotation, also around Z, due to the dipolar field generated by the average magnetization $\boldsymbol{M}_{\rm av}(t)$. If relaxation is neglected, $\boldsymbol{\omega}_{\rm d,av}$ is constant.

We can now express the total magnetization $\boldsymbol{M}(\boldsymbol{r},t)$ as a spatial Fourier series (perhaps with periodic boundary conditions over a parallelepiped surrounding the sample),

$$\boldsymbol{M}(\boldsymbol{r},t) = \boldsymbol{M}_{\rm av}(t) + \sum_{\boldsymbol{q}\neq 0}\boldsymbol{m}_{\boldsymbol{q}}(t)e^{i\boldsymbol{q}\cdot\boldsymbol{r}} \quad (109)$$

where $\boldsymbol{m}_{\boldsymbol{q}}(t) = (\boldsymbol{m}_{-\boldsymbol{q}}(t))^*$ to satisfy the reality condition for $\boldsymbol{M}(\boldsymbol{r},t)$. The equation of motion for $\boldsymbol{M}(\boldsymbol{r},t)$ is

$$\left(\frac{\rm d}{{\rm d}t}\right)_{\rm rot}\boldsymbol{M}(\boldsymbol{r},t) = \boldsymbol{M}(\boldsymbol{r},t)\times\left\{\boldsymbol{B}_{\rm d,av}^{\rm no\ crp}(t) + \sum_{\boldsymbol{q}\neq 0}\boldsymbol{B}_{{\rm d},\boldsymbol{q}}^{\rm no\ crp}(\boldsymbol{r},t)\right\} - \sum_{\boldsymbol{q}\neq 0}Dq^2\boldsymbol{m}_{\boldsymbol{q}}(t)e^{i\boldsymbol{q}\cdot\boldsymbol{r}} \quad (110)$$

where D is the coefficient of molecular diffusion, and relaxation has been ignored. As a first step in the discussion of linear stability, equations (106), (107), and (109) are substituted in equation (110) and only the terms of order 0 and 1 in the small quantities $\boldsymbol{m}_{\boldsymbol{q}}(t)$ are retained. The terms of order 0 just reproduce equation (108). It is worth noting that this is no longer true when one retains the terms of order 2 in the small quantities, which provide the mechanism by which large irregularities strongly attenuate the observed fid. The only position dependences left in the terms of order 1 are then a single factor $e^{i\boldsymbol{q}\cdot\boldsymbol{r}}$ in the summation over $\boldsymbol{q}$ in the left-hand side, and a single term $e^{i\boldsymbol{q}'\cdot\boldsymbol{r}}$ in the summations over $\boldsymbol{q}'$ in the right-hand side; hence, a single equality results for each separate wave vector $\boldsymbol{q}$,

$$\left(\frac{\rm d}{{\rm d}t}\right)_{\rm rot}\boldsymbol{m}_{\boldsymbol{q}}(t) = \boldsymbol{m}_{\boldsymbol{q}}(t)\times\left(\frac{-\gamma\mu_0}{3}\right)\alpha_s 3M_{{\rm av}Z}(t)\mathbf{1}_Z + \boldsymbol{M}_{\rm av}(t)\times\left(\frac{-\gamma\mu_0}{3}\right)\{\alpha_{\boldsymbol{q}}3m_{\boldsymbol{q}Z}(t)\mathbf{1}_Z + [\alpha_s-\alpha_{\boldsymbol{q}}]\boldsymbol{m}_{\boldsymbol{q}}(t)\} - Dq^2\boldsymbol{m}_{\boldsymbol{q}}(t)$$

where

$$\alpha_s = \left[\frac{3(\cos\theta_s)^2-1}{2}\right] \quad \text{and} \quad \alpha_{\boldsymbol{q}} = \left[\frac{3(\cos\theta_{\boldsymbol{q}})^2-1}{2}\right] \quad (111)$$

The systematic rotation of all magnetization vectors at the 'additional' angular velocity $\boldsymbol{\omega}_{\rm d,av}$ is conveniently taken into account by using an appropriate frame of coordinates ${}_{\rm rotA}$ rotating at the angular velocity $\boldsymbol{\omega}_{\rm d,av}$ with respect to the frame ${}_{\rm rot}$. Taking into account the effects of molecular diffusion, we can re-write equation (111) as

$$\left(\frac{\rm d}{{\rm d}t}\right)_{\rm rotA}\{\boldsymbol{m}_{\boldsymbol{q}}(t)e^{Dq^2(t-t_0)}\} = \boldsymbol{M}_{\rm av}(t)\times\left(\frac{-\gamma\mu_0}{3}\right) \times\{\alpha_{\boldsymbol{q}}3m_{\boldsymbol{q}Z}(t)\mathbf{1}_Z + [\alpha_s-\alpha_{\boldsymbol{q}}]\boldsymbol{m}_{\boldsymbol{q}}(t)\} \quad (112)$$

This leads to an eigenvalue problem involving the 3-dimensional vector $\boldsymbol{m}_{\boldsymbol{q}}(t)$. The solution is of the form

$$\boldsymbol{m}_{\boldsymbol{q}}(t) = \sum_{g=1}^{3}k_{\boldsymbol{q},g}(t_0)\tilde{m}_{\boldsymbol{q},g}(t)e^{\lambda_{q,g}(t-t_0)}e^{-Dq^2(t-t_0)} \quad (113)$$

where g labels the eigenvectors, the $k_{\boldsymbol{q},g}(t_0)$ are complex constants depending upon the state at time t_0, the eigenvectors $\tilde{\boldsymbol{m}}_{\boldsymbol{q},g}(t)$ are immobile in the rotating frame $_{\text{rotA}}$ (and normalized if convenient), and the $\lambda_{\boldsymbol{q},g}$ are the eigenvalues in the absence of diffusion. If we now substitute one of the terms of the summation of equation (113) in equation (112), we obtain a standard eigenvector problem for the Cartesian components of $\tilde{\boldsymbol{m}}_{\boldsymbol{q},g}$,

$$\lambda_{\boldsymbol{q},g}\tilde{\boldsymbol{m}}_{\boldsymbol{q},g} = \boldsymbol{M}_{\text{av}} \times \left(\frac{-\gamma\mu_0}{3}\right)\{\alpha_{\boldsymbol{q}} 3\tilde{\boldsymbol{m}}_{\boldsymbol{q},gZ}\mathbf{1}_{\boldsymbol{Z}} + [\alpha_s - \alpha_{\boldsymbol{q}}]\tilde{\boldsymbol{m}}_{\boldsymbol{q},g}\} \quad (114)$$

If we choose X and Y coordinates such that $\boldsymbol{M}_{\text{av}}$ is in the XZ-plane, the eigenvectors of equation (114) are given by

eigenvalue $\lambda_{\boldsymbol{q}}$	eigenvector $\{\tilde{m}_{\boldsymbol{q}X}, \tilde{m}_{\boldsymbol{q}Y}, \tilde{m}_{\boldsymbol{q}Z}\}$,
0	$\left\{-\dfrac{2\alpha_{\boldsymbol{q}}+\alpha_s}{\alpha_{\boldsymbol{q}}-\alpha_s}\dfrac{M_{\text{av}X}}{M_{\text{av}Z}}, 0, 1\right\}$
$\sqrt{\Delta}\dfrac{\gamma\mu_0}{3}$	$\left\{-\dfrac{M_{\text{av}Z}}{M_{\text{av}X}}, \dfrac{\sqrt{\Delta}}{(\alpha_{\boldsymbol{q}}-\alpha_s)M_{\text{av}X}}, 1\right\}$
$-\sqrt{\Delta}\dfrac{\gamma\mu_0}{3}$	$\left\{-\dfrac{M_{\text{av}Z}}{M_{\text{av}X}}, \dfrac{-\sqrt{\Delta}}{(\alpha_{\boldsymbol{q}}-\alpha_s)M_{\text{av}X}}, 1\right\}$

where

$$\Delta = (\alpha_{\boldsymbol{q}} - \alpha_s)(2\alpha_{\boldsymbol{q}} + \alpha_s)M_{\text{av}X}^2 - (\alpha_{\boldsymbol{q}} - \alpha_s)^2 M_{\text{av}Z}^2 \quad (115)$$

Equation (113) shows that the time evolution of the components of the actual spin magnetization $\boldsymbol{m}_{\boldsymbol{q}}(t)$ is governed by eigenvalues $\lambda_{\boldsymbol{q},g} - Dq^2$, in which molecular diffusion contributes an additional damping proportional to q^2. In a first round of discussion, we shall ignore diffusion effects. Under these conditions, the eigenvalue 0 corresponds to a constant, hence harmless, component of the small deviations from uniformity, and the general behavior of the two other components is governed by the sign of Δ. For $\Delta < 0$, these two components oscillate as a function of time, hence they are also harmless. On the contrary, for $\Delta > 0$, one of the components grows exponentially with time and will soon contribute to spin turbulence (provided that it is not damped by relaxation and diffusion). A necessary condition for $\Delta > 0$, independent of the ratio $M_{\text{av}X}/M_{\text{av}Z}$, is that $(\alpha_{\boldsymbol{q}} - \alpha_s)(2\alpha_{\boldsymbol{q}} + \alpha_s) > 0$. Figure 22 shows the region in which this condition holds.

An important property of the instability eigenvectors (see equation (115)) is that they have non-zero components in the transverse direction and in the Z-direction. As a result, instability creates a very complicated spatial distribution of transverse and longitudinal magnetization, and this situation persists when spin turbulence sets in.

For a spherical sample, $\alpha_s = 0$, instability is present for all orientations of $\boldsymbol{q}$ (except the magic angle), and equation (115) shows that this instability sets in whenever the angle between $\boldsymbol{M}_{\text{av}}$ and the transverse plane is smaller than the magic angle. More details about this case are given in Ref.[13], where it is also shown that, for water at 298 K and a proton NMR frequency of 600 MHz, the maximum growth rate of instabilities is about $7.2\,\text{s}^{-1}$ and all instabilities are suppressed by diffusion for wavelengths $2\pi/q$ shorter than about 0.11 mm.

A particular situation occurs for a flat sample perpendicular to Z (i.e., $\alpha_s = 1$), for which no instability is predicted. As soon as the sample is slightly tilted, α_s decreases below 1,

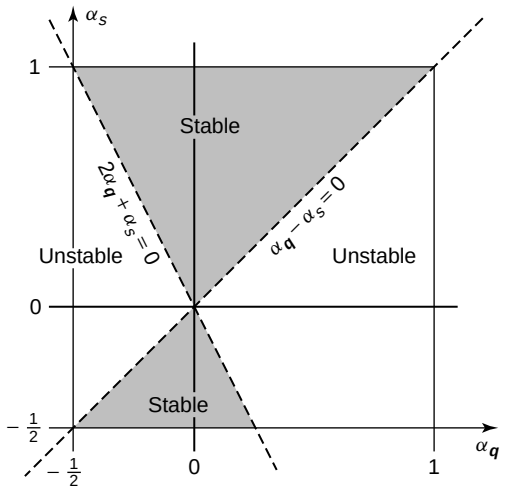

Figure 22 Stability (or not) of small magnetization inhomogeneities of wave vector q in a homogeneous background. The quantities α_s and $\alpha_{\boldsymbol{q}}$ are defined under equation (111). When the direction of q varies between Z and transverse, $\alpha_{\boldsymbol{q}}$ varies from 1 to $-1/2$ ($\alpha_{\boldsymbol{q}} = 0$ for q at the magic angle). For flat samples, α_s similarly depends upon the orientation of the pancake; for any ellipsoidal shape, α_s is also between 1 and $-1/2$, with $\alpha_s = 0$ for a sphere. The situation is unconditionally stable in the gray region; for every point in the white region, there is a range of orientations of the average (background) magnetization M_{av} for which instability occurs

hence instabilities occur (over a wide range of orientations of $\boldsymbol{M}_{\text{av}}$ for $\boldsymbol{q}$ pointing close to Z, and only for $\boldsymbol{M}_{\text{av}}$ close to the transverse plane for $\boldsymbol{q}$ close to the transverse plane). For such a slight tilt, the predicted rates of growth of the instabilities are quite small.

All the detailed analytical predictions presented here derive from equation (111), which is a linear approximation valid for small deviations from the uniform distribution $\boldsymbol{M}_{\text{av}}(t)$. In the present model, these small deviations have a zero total magnetization over the whole sample, hence they do not contribute to the fid signal. As a result, the dynamic instabilities give rise to directly observable effects only when they have grown enough to violate the linear approximation and cause non-linear effects. No convenient analytical methods are available to treat these non-linearities, so that one has to solve equation (110) numerically with initial conditions simulating small inhomogeneities. The numerical solutions show that (i) the fid is unaffected during an initial induction delay, while the growing inhomogeneities are still small (as expected from the analytical results), (ii) when the fastest growing inhomogeneities become comparable to the initial magnetization, the fid is abruptly affected and rapidly decays, usually after some large oscillations. Due to the difficulty of performing realistic numerical simulations, it is not yet clear which details of part (ii) of the above scenario are intrinsic properties of the non-linear spin dynamics, and which may be numerical artifacts.

Presumably, the analytical method used above for homogeneous situations can be extended to the helical distributions of magnetization created, e.g., by a pulsed field gradient applied soon after the initial rf pulse in an otherwise homogeneous case. In the mean time, numerical simulations have indicated that helical distributions behave much in the same way as their homogeneous counterparts, with the angle between the pulsed

field gradient and Z playing the role of θ_s in the homogeneous case (see equation (111)). For instance, a pulsed field gradient in the Z direction protects against instability, whereas a pulsed field gradient at the magic angle does not.[78]

I have performed numerical investigations of the issue of dynamical stability on a variety of other models. The conclusion is that instability is a general feature of spin dynamics with dipolar field effects, at least when the bulk magnetization points closer to the transverse plane than to the Z direction. Exceptions (like the flat sample perpendicular to Z) are very rare (the suggestion made in Ref.[13] that instability would be restricted to three-dimensional models was the result of looking at oversimplified cases).

6.3 Dynamic Instabilities Caused by Radiation Damping and the Dipolar Field

Recently, the Warren group[14] has discovered an important new type of instability, caused by the joint action of radiation damping and the dipolar field. The example studied by these authors involves a single NMR line, homogeneous external fields (except for a pulsed field gradient), and an initial situation created from equilibrium by a hard $\pi/2$ pulse followed by a pulsed field gradient in the Z direction, chosen such as to create a magnetization helix with a large number of turns in the sample, hence a very small fid signal immediately after this preparation.

The discussion at the end of Section 6.2 indicates that this initial situation is stable (although marginally) in the presence of *only* dipolar field effects. In the presence of *only* radiation damping, this situation is also 'marginally stable' in the sense that any small (total) transverse magnetization will cause a correspondingly slow tipping of the local magnetization at every point in the sample. The outcome of this motion strongly depends upon the small (total) Z magnetization.

The new result, demonstrated by numerical simulations as well as in actual experiments, is that the simultaneous action of radiation damping and the dipolar field turns the combination of marginal stabilities described above into strong instability. Some extensions of these results are given in Ref.[78] As an example, the total transverse magnetization grows exponentially, at a rate intermediate between the characteristic rate for maximum radiation damping and that for maximum dipolar field effects. In typical experiments on water, the transverse magnetization reached a value close to 10 % of the equilibrium magnetization in less than half a second. The experiments have also shown that the results are exceedingly sensitive to details such as weak temperature gradients and delay since a magnet fill.

The Warren group notes that the new results may provide a clear explanation for the unexpected failure of a number of tempting water suppression schemes. This should give additional motivation for the spectrometer manufacturers to provide efficient and versatile instrumentation for the electronic control of radiation damping.

7 RELATED ARTICLES IN THIS VOLUME

Nuclear Spin Superradiance; Rheo-NMR: A New Window on the Rheology of Complex Fluids.

8 RELATED ARTICLES IN VOLUMES 1–8

Concentrated Solution Effects, Volume 3; Diffusion Measurements by Magnetic Field Gradient Methods, Volume 3; Liouville Equation of Motion, Volume 4; Low Spin Temperature NMR, Volume 5; Magnetic Susceptibility & High Resolution NMR of Liquids & Solids, Volume 5; Optically Enhanced Magnetic Resonance, Volume 5; Polarization Transfer Experiments via Scalar Coupling in Liquids, Volume 6; Quantum Optics: Concepts of NMR, Volume 6; Water Signal Suppression in NMR of Biomolecules, Volume 8.

9 REFERENCES

1. N. Bloembergen and R. V. Pound, *Phys. Rev.*, 1954, **95**, 8–12.
2. C. R. Bruce, R. E. Norberg, and G. E. Pake, *Phys. Rev.*, 1956, **104**, 419–420.
3. M. A. McCoy and W. S. Warren, *J. Chem. Phys.*, 1990, **93**, 858–860.
4. D. Abergel, M. A. Delsuc, and J.-Y. Lallemand, *J. Chem. Phys.*, 1992, **96**, 1657–1658.
5. W. S. Warren, M. M. Q. He, and F. C. Spano, *J. Chem. Phys.*, 1992, **96**, 1659–1661.
6. H. C. Torrey, *Phys. Rev.*, 1956, **104**, 563–565.
7. H. T. Edzes, *J. Magn. Reson.*, 1990, **86**, 293–303.
8. G. Deville, M. Bernier, and J. M. Delrieux, *Phys. Rev. B*, 1979, **19**, 5666–5688.
9. R. Bowtell and P. Robyr, *Phys. Rev. Lett.*, 1996, **76**, 4971–4974.
10. W. S. Warren, S. Ahn, M. Mescher, M. Garwood, K. Ugurbil, W. Richter, R. R. Rizi, J. Hopkins, and J. S. Leigh, *Science*, 1998, **281**, 247–251.
11. S. Vathyam, S. Lee, and W. S. Warren, *Science*, 1996, **272**, 92–96.
12. Y.-Y. Lin, S. Ahn, N. Murali, W. Brey, C. R. Bowers, and W. S. Warren, *Phys. Rev. Lett.*, 2000, **85**, 3732–3735.
13. J. Jeener, *Phys. Rev. Lett.*, 1999, **82**, 1772–1775 (beware of some inconsistencies of notation in the discussion of equation (8) of this reference).
14. Y.-Y. Lin, N. Lisitza, S. Ahn, and W. S. Warren, *Science*, 2000, **290**, 118–121.
15. R. Bowtell, R. M. Bowley, and P. Glover, *J. Magn. Reson.*, 1990, **88**, 643–651.
16. A. S. Bedford, R. Bowley, and R. M. Bowley, *J. Magn. Reson.*, 1991, **93**, 516–532.
17. R. Bowtell, *J. Magn. Reson.*, 1992, **100**, 1–17.
18. M. H. Levitt, *Concepts Magn. Reson.*, 1995, **8**, 77–103.
19. Q. He, W. Richter, S. Vathyam, and W. S. Warren, *J. Chem. Phys.*, 1993, **98**, 6779–6800.
20. W. S. Warren, W. Richter, A. H. Andreotti, and B. T. Farmer II, *Science*, 1993, **262**, 2005–2009.
21. S. Lee, W. Richter, S. Vathyam, and W. S. Warren, *J. Chem. Phys.*, 1996, **105**, 874–900.
22. J. Jeener, *J. Chem. Phys.*, 2000, **112**, 5091–5094.
23. P. Broekaert, A. Vlassenbroek, J. Jeener, G. Lippens, and J.-M. Wieruszeski, *J. Magn. Reson. A*, 1996, **120**, 97–104.
24. S. Ahn, N. Lisitza, and W. S. Warren, *Mol. Phys.*, 1998, **95**, 266–272.
25. A. G. Sobol, G. Wider, H. Iwai, and K. Wüthrich, *J. Magn. Reson.*, 1998, **130**, 262–271.
26. G. Lippens, C. Dhalluin, and J.-M. Wieruszeski, *J. Biomol. NMR*, 1995, **5**, 327–331.
27. D. Abergel, A. Louis-Joseph, and J.-Y. Lallemand, *Chem. Phys. Lett.*, 1996, **262**, 465–469.
28. M. P. Augustine and E. L. Hahn, *J. Chem. Phys.*, 1997, **107**, 3324–3328.

29. W. Richter, S. Lee, W. S. Warren, and Q. He, *Science*, 1995, **267**, 654–657.
30. J. Jeener, *Adv. Magn. Reson.*, 1982, **10**, 1–51.
31. P. Broekaert, J. Jeener, G. Lippens, and J.-M. Wieruszeski, *J. Magn. Reson.*, 2000, **145**, 259–261.
32. P. Broekaert and J. Jeener, *J. Magn. Reson. A*, 1995, **113**, 60–64.
33. A. Louis-Joseph, D. Abergel, and J.-Y. Lallemand, *J. Biomol. NMR*, 1995, **5**, 212–216.
34. H. Barjat, D. L. Mattiello, and R. Freeman, *J. Magn. Reson.*, **136**, 1999, 114–117.
35. G. Bodenhausen, R. L. Vold, and R. R. Vold, *J. Magn. Reson.*, 1980, **37**, 93–106.
36. J. F. Martin, L. S. Selwyn, R. R. Vold, and R. L. Vold, *J. Chem. Phys.*, 1982, **76**, 2632–2634.
37. D. Zax and A. Pines, *J. Chem. Phys.*, 1983, **78**, 6333–6334.
38. R. R. Ernst, G. Bodenhausen, and A. Wokaun, 'Principles of Nuclear Magnetic Resonance in One and Two Dimensions', Clarendon Press: Oxford, 1987.
39. J. Jeener, *Concepts Magn. Reson.*, 2002, **14**, 79–88.
40. D. J. Schneider and J. H. Freed, *Adv. Chem. Phys.*, 1989, **73**, 387–527.
41. E. L. Hahn, *Phys. Rev.*, 1950, **80**, 580–594.
42. H. Y. Carr and E. M. Purcell, *Phys. Rev.*, 1954, **94**, 630–638.
43. J. Jeener, *J. Chem. Phys.*, 2002, **116**, 1204–1205.
44. A. Abragam, 'The Principles of Nuclear Magnetism', Oxford University Press: Oxford, 1961.
45. A. Vlassenbroek, J. Jeener, and P. Broekaert, *J. Chem. Phys.*, 1995, **103**, 5886–5897.
46. E. L. Hahn, *Concepts Magn. Reson.*, 1997, **9**, 65–67.
47. X. Mao and C. Ye, *J. Chem. Phys.*, 1993, **99**, 7455–7462.
48. X.-A. Mao and C.-H. Ye, *Concepts Magn. Reson.*, 1997, **9**, 173–187.
49. M. P. Augustine and E. L. Hahn, *Concepts Magn. Reson.*, 2001, **13**, 1–7.
50. D. Wu and C. S. Johnson, *J. Magn. Reson. A*, 1994, **110**, 113–117.
51. C. Anklin, M. Rindlisbacher, G. Otting, and F. H. Laukien, *J. Magn. Reson. B*, 1995, **106**, 99–201.
52. W. E. Maas, F. H. Laukien, and D. G. Cory, *J. Magn. Reson. A*, 1995, **113**, 274–277.
53. W. S. Warren, S. L. Hammes, and J. L. Bates, *J. Chem. Phys.*, 1989, **91**, 5895–5904.
54. J.-H. Chen, A. Jerschow, and G. Bodenhausen, *Chem. Phys. Lett.*, 1999, **308**, 397–402.
55. D. E. Rourke and M. P. Augustine, *Phys. Rev. Lett.*, 2000, **84**, 1685–1688.
56. A. Abragam and M. Goldman, 'Nuclear Magnetism: Order and Disorder', Clarendon Press: Oxford, 1982.
57. J. R. Reitz and F. J. Milford, 'Foundations of Electromagnetic Theory', Addison-Wesley: Reading, MA, 1960.
58. L. D. Landau and E. M. Lifshitz, 'Electrodynamics of Continuous Media', Pergamon Press: 1960.
59. C. Kittel, 'Introduction to Solid State Physics', John Wiley & Sons: New York, 1968 (see chapter on dielectric properties).
60. M. H. Levitt, *Concepts Magn. Reson.*, 1996, **8**, 77–103.
61. A. Vlassenbroek, J. Jeener, and P. Broekaert, *J. Magn. Reson. A*, 1996, **118**, 234–246.
62. W. S. Warren, S. Lee, W. Richter, and S. Vathyam, *Chem. Phys. Lett.*, 1995, **247**, 207–214.
63. M. H. Levitt, *J. Magn. Reson.*, 1997, **126**, 164–182.
64. M. H. Levitt and O. G. Johannessen, *J. Magn. Reson.*, 2000, **142**, 190–194.
65. A. A. Maudsley, A. Wokaun, and R. R. Ernst, *Chem. Phys. Lett.*, 1978, **55**, 9–14.
66. E. D. Minot, P. T. Callaghan, and N. Kaplan, *J. Magn. Reson.*, 1999, **140**, 200–205.
67. I. Ardelean, E. Kossel, and R. Kimmich, *J. Chem. Phys.*, 2001, **114**, 8520–8529 (to correct a misprint, a factor $\exp(-D(\gamma G)^2\delta^2\Delta_2)$ must be inserted in the right hand side of Equation (14) and in the left hand side of Equation (17)).
68. M. Goldman and H. Desvaux, *Chem. Phys. Lett.*, 1996, **256**, 497–501.
69. J. Jeener, A. Vlassenbroek, and P. Broekaert, *J. Chem. Phys.*, 1995, **103**, 1309–1332.
70. V. Sinivee, *J. Magn. Reson.*, 1972, **7**, 127–136.
71. D. Einzel, G. Eska, Y. Hirayoshi, T. Kopp, and P. Wölfle, *Phys. Rev. Lett.*, 1984, **53**, 2312–2315.
72. T. Enss, S. Ahn, and W. S. Warren, *Chem. Phys. Lett.*, 1999, **305**, 101–108.
73. W. Richter and W. S. Warren, *Concepts Magn. Reson.*, 2000, **12**, 396–409.
74. D. Candela, M. E. Hayden, and P.-J. Nacher, *Phys. Rev. Lett.*, 1994, **73**, 2587–2590.
75. E. Stoltz, J. Tannenhauser, and P.-J. Nacher, *J. Low Temp. Phys.*, 1995, **101**, 839–844.
76. P.-J. Nacher and E. Stoltz, *J. Low Temp. Phys.*, 1995, **101**, 311–316.
77. K. L. Sauer, F. Marion, P.-J. Nacher, and G. Tastevin, *Phys. Rev. B*, 2001, **63**, 184427-1-4.
78. J. Jeener, *J. Chem. Phys.*, 2002, **116**, 8439–8446.
79. S. Ahn, N. Lisitza, and W. S. Warren, *J. Magn. Reson.*, 1998, **133**, 266–272.
80. R. T. Syvitski, N. Burlinson, E. E. Burnell, and J. Jeener, *J. Magn. Reson.*, 2002, **155**, in press.

Acknowledgements

This article owes much to the collaboration of Paul Broekaert and Alain Vlassenbroek over the last ten years. It is a pleasure to thank Warren Warren for having drawn my attention to the topic of this article, for illuminating discussions, and for advance communication of many important results. Fruitful discussions are also acknowledged with Malcolm Levitt and Pierre-Jean Nacher. Paul Broekaert, William Stone and Warren Warren were helpful in the preparation of the manuscript.

Biographical Sketch

Jean L. Jeener, *b* 1931. Ph.D., 1958, Université Libre de Bruxelles (ULB), Postdoctoral studies with N. Bloembergen at Harvard University, Professor at ULB 1960–1996, now Professor Emeritus. About 40 publications. Research interests include spin thermodynamics in solids (including the 'Jeener–Broekaert' pulse sequence), relaxation of dipolar energy in solids by quasi-adiabatic transformations, initiation of 2D spectroscopy (COSY and NOESY), superoperators and study of chemical reactions by 2D peak shape analysis, formulation of coherent pulse spectroscopy with complete quantification of the field, collective effects in liquid NMR (issues of principle and dynamic instability).

Brownian Motion and Correlation Times

Donald E. Woessner
The University of Texas Southwestern Medical Center at Dallas and Department of Radiology, The Mary Nell and Ralph B. Rogers Magnetic Resonance Center, Dallas, TX, USA

1	Introduction	1
2	Remarks on Models of Molecular Reorientation	2
3	Correlation Functions for a Rigid, Completely Asymmetric Ellipsoid	3
4	Correlation Functions for Axially Symmetric Ellipsoids with Internal Motion	5
5	Correlation Functions for InterGroup Magnetic Dipolar Relaxation with Internal Motion	7
6	'Model-Free' Correlation Functions for Flexible Macromolecules	9
7	Correlation Functions for Intermolecular Magnetic Dipolar Relaxation	10
8	Experimental and Theoretical Correlation Times of Rigid Molecules	10
9	Correlation Functions for a 'Nearly-Free' Rotor Attached to an Ellipsoid	16
10	Scrutiny of the Mathematical Form of Correlation Functions	16
11	Related Articles	17
12	References	17

1 INTRODUCTION

In nuclear magnetic resonance (NMR), the magnetic interaction between the nuclear magnetic dipole moment and the magnetic field $\boldsymbol{B}_0$ determines the nuclear spin energy levels. Nuclear spin interactions with the chemical structures in the local environment cause small shifts of the energy levels. Brownian molecular motions cause this local structure to fluctuate and as a result cause the energy levels to be time dependent. The frequency component of energy level fluctuation at the frequency difference between two energy levels induces nuclear spin transitions between the energy levels. The rate of such transitions depends on the intensity of the nuclear spin energy at the nuclear spin transition frequency. These transitions couple the spin system to the kinetic energy of the molecular system, enabling the spin system to reach thermal equilibrium (i.e. to relax). The relaxation times are inversely proportional to the transition rates. Therefore, we can use NMR relaxation time measurements to study molecular motions in liquids.

In the case of spin-$\frac{1}{2}$ nuclei, the spin interactions include magnetic interactions of the nuclear magnetic moment with the local magnetic field. The local magnetic field depends on the distance and position relative to neighboring nuclear spins and unpaired electrons, and on the effective local fields generated by the chemical shielding due to the surrounding electrons. Nuclei of spin $> \frac{1}{2}$ have an additional interaction, the electric interaction between the nuclear quadrupole moment and the surrounding electric changes. Both interactions depend on the length of the vector that joins the nucleus to the interacting entity and on the orientation of this interaction vector in the magnetic field $\boldsymbol{B}_0$. Such interactions are the mechanism by which the energy of the nuclear spins is coupled to the molecular system.

To illustrate the relationship between Brownian motion and NMR relaxation, we consider the cases of magnetic dipolar interaction between two identical spin-$\frac{1}{2}$ nuclei and of electric quadrupolar interaction of a spin 1 nucleus with an electric charge ze. In both instances, the relaxation times are given[1] by the expressions:

$$1/T_1 = H[J_1(\omega_0) + J_2(2\omega_0)] \tag{1}$$

$$1/T_2 = \tfrac{1}{4}H[J_0(0) + 10J_1(\omega_0) + J_2(2\omega_0)] \tag{2}$$

where T_1 is the spin–lattice relaxation time, T_2 is the transverse of spin–spin relaxation time, and ω_0 is the angular Larmor frequency. These equations apply in the motionally narrowed limit (see ***Relaxation Theory: Density Matrix Formulation***) which is appropriate for liquids.

In deriving these relationships, we express the time dependencies of the nuclear spin interactions $\mathcal{H}(t)$ in terms of the interaction constants H and the time correlation functions $\langle F_\mathrm{h}(t)F_\mathrm{h}^*(t+\tau)\rangle$ in which the $F_\mathrm{h}(t)$ terms are the spatial parts of the time-dependent nuclear spin interactions and the $\langle\ \rangle$ brackets denote ensemble average. The $J_\mathrm{h}(\omega)$ terms are Fourier intensities (or spectral densities) of the time correlation functions at the angular frequency ω as given by

$$J_h(\omega) = \int_{-\infty}^{+\infty} \langle F_\mathrm{h}(t)F_\mathrm{h}^*(t+\tau)\rangle \exp(\mathrm{i}\omega\tau)\,\mathrm{d}\tau \tag{3}$$

where $\mathrm{i} = (-1)^{\frac{1}{2}}$ and the asterisk denotes the complex conjugate. The interaction constants are $H = (9/8)\gamma^4\hbar^2$ for magnetic dipole–dipole interaction between two identical atomic nuclei and $H = (9/8)e^4Q^2z^2\hbar^2$ for the electric quadrupolar interaction. The physical quantities are: γ, the nuclear magnetogyric ratio; $\hbar$, Planck's constant divided by 2π; e, the unit electric charge; z, the number of unit charges in the electric charge; and Q, the nuclear quadrupole moment. For both interactions, the $F_\mathrm{h}(t)$ terms are related to the second-order spherical harmonics as given by:

$$F_0(t) = r(t)^{-3}[3\cos^2\theta(t) - 1] \tag{4a}$$

$$F_1(t) = r(t)^{-3}\{\sin\theta(t)\cos\theta(t)\exp[\mathrm{i}\phi(t)]\} \tag{4b}$$

$$F_2(t) = r(t)^{-3}\{\sin^2\theta(t)\exp[2\mathrm{i}\phi(t)]\} \tag{4c}$$

in which $r(t)$ is the length of the vector connecting the nucleus with the interacting unit, and $\theta(t)$ and $\phi(t)$ are the polar and azimuthal angles that describe the orientation of this vector in the laboratory rectangular coordinate system S (magnetic field $\boldsymbol{B}_0$ of the NMR spectrometer).

Different motions of molecules in liquids cause r, θ, and ϕ to be time dependent. We classify them as rotational and translational. The translational motions cause the molecules to move in three-dimensional space. The rotational motions cause

an axis in the molecule to change in orientation with respect to the axes of the fixed three-dimensional laboratory rectangular coordinate system. Many molecules contain chemical groups that can rotate with respect to the rest of the molecule. Methyl groups that reorient about the methyl threefold symmetry axis comprise a common example of molecular internal motion.

We commonly designate relaxation interactions as *intramolecular* or *intermolecular*, depending on whether the entity that interacts with the nucleus is part of the same molecule. This designation is related to the above classification of molecular motions. For a completely rigid molecule (Section 3), the intramolecular relaxation results only from the time dependences of θ and ϕ because r is constant. Then, we may remove r from equations (3) and (4) absorb it into a redefined H (i.e. H'), and redefine the $F_{\mathrm{h}}(t)$:

$$F_0(t) = 3\cos^2\theta(t) - 1 \tag{5a}$$

$$F_1(t) = \sin\theta(t)\cos\theta(t)\exp[\mathrm{i}\phi(t)] \tag{5b}$$

$$F_2(t) = \sin^2\theta(t)\exp[2\mathrm{i}\phi(t)] \tag{5c}$$

For magnetic dipolar relaxation of two identical nuclei with spin-$\frac{1}{2}$, $H' = (9/8)\gamma^4\hbar^2 r^{-6}$. For quadrupolar relaxation of a nucleus with spin 1, $H' = (9/8)e^4Q^2z^2\hbar^2r^{-6}$. Here, if all the electric charges result in a nuclear quadrupolar interaction with zero asymmetry parameter, $H' = (9/8)\pi^2\chi^2$. The same statement applies to intragroup relaxation of nuclei in a rigid group that rotates within an otherwise rigid ellipsoid (Section 4), such as a methyl group that rotates about its threefold symmetry axis that is fixed to the ellipsoid. However, intramolecular magnetic dipolar relaxation between a nucleus of such a rotating group and a nucleus on the remainder of the ellipsoid (Section 5) is more complex. Besides θ and ϕ, r also is time dependent. For intermolecular magnetic dipolar relaxation (Section 7), r, θ, and ϕ are all time dependent. A mathematical description of the correlation function is especially complex. It depends on the translational diffusion of the molecules and on the rotational motions of the molecule. We emphasize intramolecular NMR relaxation in this article and briefly treat intermolecular relaxation in Section 7.

As the NMR relaxation times are related to the molecular motions through the correlation function and the spectral densities, we need relationships between these quantities to analyze the relaxation times of liquids in terms of molecular motions. It is customary to invoke specific models of molecular motions and formulate correlation functions from these models. There are many different models that are based on different starting points and perturbations from them. Some are based on a quantum mechanical formulation and some are treated from the viewpoint of classical mechanics. No single, tractable model that describes all liquids has been found.

2 REMARKS ON MODELS OF MOLECULAR REORIENTATION

Molecules in the gaseous state undergo vibrational and rotational motions and exist in discrete vibrational–rotation energy levels with discrete frequencies. Molecular collisions cause transitions between the energy states and broaden the energy levels. In a condensed phase, such as a liquid or a solid, the 'collisions' between molecules occur much more frequently and the kinetic and potential energies of the different molecules are much more closely coupled. Consequently, we cannot calculate the correlation functions that are effective in NMR relaxation from the motions of isolated, noninteracting molecules. Rothschild[2] has presented a comprehensive, detailed account of the theoretical and experimental knowledge of the rotational and vibrational motions of small, nearly spherical molecules in liquids.

Many different models of molecular reorientation have been discussed. It is beyond the scope of this article to review these models in detail because the literature is extensive (see ***Spin–Rotation Relaxation Theory***). One approach is to start from an assembly of freely rotating molecules, as in a dilute gas. There are different ways of introducing the effects of the surrounding molecules. One way is to have collisions that introduce sudden or instantaneous changes in molecular angular momentum. Another way is to examine the potential energy of the molecule as a function of orientation. If the potential energy is independent of orientation, the molecule experiences no torques and rotates freely. The correlation function is that for an assembly of freely rotating molecules. If the potential energy does depend on orientation, the molecule experiences torques that depend on the molecular shape and on the shape, configuration, motions ('collisions'), and distances of the neighboring molecules. These torques quench or change the molecular rotation. The effective molecular shape could be that of a spherical top, a symmetric top, or a completely asymmetric rotor. The molecule might experience a constant torque or a torque that is significant only when the neighboring molecules attain specific configurations. In such approaches, the rotational inertia of the molecule is important in deciding the mathematical form of the correlation function.

Another approach is to assume that the environment of the molecule sets up an energy barrier that the molecule must surmount to rotate into an orientation in which its interaction energy with its neighbors is the next minimum. While in this potential well, the molecule undergoes low-amplitude rotational oscillations. A 'large' change in orientation occurs when a transition from one potential well to another takes place. The molecule is stationary except for occasional jumps to a different orientation. Some consider the jump to be instantaneous and others consider the jump velocity to be the rms average molecular rotational velocity obtained from kinetic energy considerations.

Clearly the rotational motion of molecules in liquids is a many-body problem and, to calculate the correlation functions, we must introduce approximate methods. We can view Brownian rotational motion as a random walk in coordinate space in which the molecular orientations are defined relative to a motionless laboratory coordinate system. Diffusion-type equations correctly describe the observed rms displacements after many random steps have taken place. The length of the step is an important parameter if solutions of diffusion-type equations are to be used to calculate the correlation functions. The average length of the step must be small compared with the correlation distance of the orientational function. Because the orientational functions undergo large changes with a one-radian change in orientation, the step must be much smaller than one radian.

The Debye theory[3] is a widely used model of molecular reorientation. The molecule is assumed to be a rigid sphere that

undergoes isotropic reorientations by infinitestimal rotations caused by thermal collisions with other molecules. Because the reorientation occurs by infinitesimal rotations, isotropic rotational diffusion motion is obtained. The rotational diffusion coefficient is related through Stokes's law to the viscosity of the fluid. This approach was used by Bloembergen, Purcell, and Pound[4] in their pioneering work on NMR relaxation.

Perrin[5] has developed an anisotropic model of molecular reorientation. The molecule reorients like a rigid ellipsoid that undergoes rotational diffusion by infinitesimal rotations about the different ellipsoid axes at different rates. Although the diffusion approximation may not be an exact model and molecules are not completely rigid, it does provide a reasonably reliable model for many liquids. Also, use of it yields equations that are well suited for straightforward data reduction. In the following sections, we assume that molecules are rigid bodies that follow the Perrin model and that internal motion is described by rigid groups that rotate about an axis that is fixed to the rigid body. This internal rotation is independent of the ellipsoid reorientation. Some consequences of vibrations and oscillations of the otherwise rigid bodies are noted in Section 8.1.

3 CORRELATION FUNCTIONS FOR A RIGID, COMPLETELY ASYMMETRIC ELLIPSOID

In formulating the spatial orientational correlation functions of nuclei in a completely asymmetric ellipsoid, it is convenient to express the $F_h(t)$ in terms of the direction cosines l, m, and n of the nuclear interaction vector with respect to the X, Y, and Z axes, respectively, of the laboratory coordinate system S. Rotational Brownian motions cause these direction cosines to fluctuate. The coordinate system S is fixed in space with its Z axis in the direction of $\boldsymbol{B}_0$. Using the definitions $l = \sin\theta\cos\phi$, $m = \sin\theta\sin\phi$, and $n = \cos\theta$, the $F_h(t)$ terms, as given by equation (5) in which r is constant, are:

$$F_0(t) = 1 - 3n^2 \tag{6a}$$

$$F_1(t) = (l + \mathrm{i}m)n \tag{6b}$$

$$F_2(t) = (l + \mathrm{i}m)^2 \tag{6c}$$

To include the fluctuations of these direction cosines, we use two additional rectangular coordinate systems. The first is S_0, a stationary reference frame, to describe the rotational motion of the ellipsoid. The other coordinate system is S' which is fixed to the ellipsoid and oriented such that the X', Y', and Z' axes of S' always coincide with the three major axes of the ellipsoid. We reference the direction cosines of the relaxation interaction vector in the ellipsoid directly to S'. At time t, these direction cosines are denoted by l', m', and n'. When there is no internal motion, the direction cosines always have these values. However, to allow for internal motion in later equations, we let l'', m'', and n'' be the respective direction cosines at the later time $t + \tau$.

We assume that all of the ellipsoids are equivalent. Since we are dealing with liquids, at any instant t there is a random orientation distribution of ellipsoids. Let us choose a particular ellipsoid. We orient S_0 of this ellipsoid so that, at time t, S_0 coincides with S' and the Euler angles (ϕ_0, θ_0, ψ_0) that describe the orientation of S' in S_0 are all zero. Since S_0 is stationary and S' is fixed to the ellipsoid, rotational Brownian motion of the ellipsoid causes ϕ_0, θ_0, and ψ_0 to become nonzero. The direction cosines of the relaxation interaction vector in S_0 at $t + \tau \geq 0$ are given by the following transformation that involves the change in the Euler angles of S' in S_0:

$$\begin{pmatrix} l_0 \\ m_0 \\ n_0 \end{pmatrix} = \begin{pmatrix} c_{11} & c_{12} & c_{13} \\ c_{21} & c_{22} & c_{23} \\ c_{31} & c_{32} & c_{33} \end{pmatrix} \begin{pmatrix} l'' \\ m'' \\ n'' \end{pmatrix} \tag{7}$$

where

$$\left.\begin{aligned} c_{11} &= \cos\psi\cos\phi - \cos\theta\sin\phi\sin\psi \\ c_{12} &= -\sin\psi\cos\phi - \cos\theta\sin\phi\cos\psi \\ c_{13} &= \sin\theta\sin\phi \\ c_{21} &= \cos\psi\sin\phi + \cos\theta\cos\phi\sin\psi \\ c_{22} &= -\sin\psi\sin\phi + \cos\theta\cos\phi\sin\psi \\ c_{23} &= -\sin\theta\cos\phi \\ c_{13} &= \sin\theta\sin\psi \\ c_{32} &= \sin\theta\cos\psi \\ c_{33} &= \cos\theta \end{aligned}\right\} \tag{8}$$

In this definition of the transformation matrix elements, the subscript of the Euler angles has been omitted for simplicity. Finally, the direction cosines of the interaction vector in S are given by the following transformation in Euler angles (ϕ, θ, ψ) that describe the orientation of S_0 in S:

$$\begin{pmatrix} l \\ m \\ n \end{pmatrix} = \begin{pmatrix} a_{11} & a_{12} & a_{13} \\ a_{21} & a_{22} & a_{23} \\ a_{31} & a_{32} & a_{33} \end{pmatrix} \begin{pmatrix} l_0 \\ m_0 \\ n_0 \end{pmatrix} \tag{9}$$

where the definitions of the a_{ij} are analogous to those of the c_{ij} in equation (8). We use the transformations shown in equations (7) and (9) to evaluate the functions $F_h(t + \tau)$ for $\tau \geq 0$. The initial conditions imply that $c_{ij}(t) = \delta_{ij}$ (the delta function). Consequently, the initial values at time t are:

$$F_0(t) = 1 - 3(a_{31}l' + a_{32}m' + a_{33}n')^2 \tag{10a}$$

$$F_1(t) = (A_1l' + A_2m' + A_3n')(a_{31}l' + a_{32}m' + a_{33}n') \tag{10b}$$

$$F_2(t) = (A_1l' + A_2m' + A_3n')^2 \tag{10c}$$

where

$$A_1 = a_{11} + \mathrm{i}a_{21} \tag{11a}$$

$$A_2 = a_{12} + \mathrm{i}a_{22} \tag{11b}$$

$$A_3 = a_{13} + \mathrm{i}a_{23} \tag{11c}$$

Because molecular orientations in a liquid are random, there is a random distribution of orientations of S_0 in S. The c_{ij} in all the S_0 are equivalent at all times $t + \tau \geq t$. The rotational Brownian motion of the ellipsoid causes the c_{ij} to be time dependent. Suppose $\Delta\alpha$, $\Delta\beta$, and $\Delta\gamma$ are the angular displacements of the ellipsoid about the X', Y', and Z', axes, respectively, of S' due to the Brownian motion. We assume that the elementary angular displacments are sufficiently small (see Section 8.2) so that the angular displacements during time τ are given by rotational diffusion relationships that involve rotational diffusion coefficients R_i as:

$$\langle(\Delta\alpha)^2\rangle = 2R_1\tau \tag{12a}$$

$$\langle(\Delta\beta)^2\rangle = 2R_2\tau \tag{12b}$$

$$\langle(\Delta\gamma)^2\rangle = 2R_3\tau \tag{12c}$$

and the motions are statistically independent, e.g., $\langle\Delta\alpha\Delta\beta\rangle = 0$. Internal motion within the ellipsoids, when it occurs, causes the direction cosines l'', m'', and n'' to be time dependent. Because we assume that the internal motion is statistically independent of the Brownian motion of the ellipsoid, we average separately over the two types of motion to obtain the final correlation functions. For each S_0, and for a given set of intramolecular parameters, the $F_{\rm h}(t)$ in the correlation function is a time independent multiplication factor and the autocorrelation function becomes:

$$\langle F_{\rm h}(t)F_{\rm h}^*(t+\tau)\rangle_{S_0} = F_{\rm h}(t)\langle F_{\rm h}^*(t+\tau)\rangle_{S_0} \tag{13}$$

In the calculation of the rotational Brownian motion parts of $\langle F_h^*(t+\tau)\rangle_{s_a}$, we find for each S_0 a sum of terms that are proportional to squares and products of the c_{ij} that appear in the transformation shown in equation (8). To calculate these terms, we use the time dependent probability density $P(\phi_0, \theta_0, \psi_0; \tau)$ for S' to be in orientation $(\phi_0, \theta_0, \psi_0)$ in S_0 at time $t + \tau$. This probability density is described[6] by the partial differential equation:

$$\partial P(\phi_0, \theta_0, \psi_0; \tau)/\partial\tau = \Lambda P(\phi_0, \theta_0, \psi_0; \tau) \tag{14}$$

where the operator Λ is given by:

$$\begin{aligned}\Lambda = {} & (R_1\cos^2\psi_0 + R_2\sin^2\psi_0)\left(\frac{\partial^2}{\partial\theta_0^2}\right) \\ & +(R_1\sin^2\psi_0 + R_2\cos^2\psi_0)\left(\cot\theta_0\frac{\partial}{\partial\theta_0} + \frac{1}{\sin^2\theta_0}\frac{\partial^2}{\partial\phi_0^2}\right. \\ & \left.+\cot^2\theta_0\frac{\partial^2}{\partial\psi_0^2} - \frac{2\cot\theta_0}{\sin\theta_0}\frac{\partial^2}{\partial\phi_0\partial\psi_0}\right) \\ & +2(R_1 - R_2)\frac{\cos\psi_0\sin\psi_0}{\sin\theta_0}\left(\frac{\partial^2}{\partial\theta_0\partial\phi_0} - \cos\phi_0\frac{\partial^2}{\partial\theta_0\partial\psi_0}\right. \\ & \left.+\frac{1+\cos^2\theta_0}{2\sin\theta_0}\frac{\partial}{\partial\psi_0} - \cot\theta_0\frac{\partial}{\partial\phi_0}\right) \\ & +R_3\frac{\partial^2}{\partial\psi_0^2}\end{aligned} \tag{15}$$

The properties of Λ are such that the time differential $\langle f\rangle$, the average value of any function f of the orientation of the ellipsoid, is given by the relationship

$$\mathrm{d}\langle f\rangle/\mathrm{d}\tau = \langle\Lambda f\rangle \tag{16}$$

The application of equation (15) yields:

$$\Lambda(c_{jj}c_{kk} + c_{jk}c_{kj}) = -(4R_i + R_j + R_k)(c_{jj}c_{kk} + c_{jk}c_{kj}) \tag{17}$$

$$\Lambda c_{ri}^2 = -2(R_j + R_k)c_{ri}^2 + 2R_j c_{rk}^2 + 2R_k c_{rj}^2 \tag{18}$$

where the indices i, j, and k are all different. With the condition $c_{ij} = \delta_{ij}$ (i.e. the delta function) when $\tau = 0$, the application of equations (16) yields the average values:

$$\langle c_{jj}c_{kk} + c_{jk}c_{kj}\rangle = \exp[-(4R_i + R_j + R_k)\tau] \tag{19}$$

The application of equations (16) and (18) in deriving the average values of the c_{ri}^2 yields three first-order linear differential equations that are related because $\sum_i C_{ri}^2 = 1$. The average values are:

$$\begin{aligned}\langle c_{ii}^2\rangle = {} & (\tfrac{1}{3}) + (\tfrac{1}{6})(2+\delta_i)\exp(-\tau/\tau_-) \\ & +(\tfrac{1}{6})(2-\delta_i)\exp(-\tau/\tau_+)\end{aligned} \tag{20}$$

$$\begin{aligned}\langle c_{jk}^2\rangle = {} & (\tfrac{1}{3}) - (\tfrac{1}{6})(1-\delta_i)\exp(-\tau/\tau_-) \\ & -(\tfrac{1}{6})(1+\delta_i)\exp(-\tau/\tau_+)\end{aligned} \tag{21}$$

where

$$\delta_i = (R_i - R)/(R^2 - L^2)^{1/2} \tag{22}$$

$$1/\tau_\pm = 6[R \pm (R^2 - L^2)^{1/2}] \tag{23}$$

in which

$$R = (\tfrac{1}{3})(R_1 + R_2 + R_3) \tag{24}$$

$$L^2 = (\tfrac{1}{3})(R_1R_2 + R_1R_3 + R_2R_3) \tag{25}$$

The final result, after averaging over all S_0, is[7]

$$\begin{aligned}\langle F_{\rm h}(t)F_{\rm h}^*(t+\tau)\rangle = {} & (\tfrac{1}{2})K_{\rm h}\langle C_+\exp(-|\tau|/\tau_+) + C_-\exp(-|\tau|/\tau_-) \\ & +C_1\exp(-|\tau|/\tau_1) + C_2\exp(-|\tau|/\tau_2) \\ & +C_3\exp(-|\tau|/\tau_3)\rangle_{\rm av}\end{aligned} \tag{26}$$

in which

$$K_0 = \tfrac{4}{5} \tag{27a}$$

$$K_1 = \tfrac{2}{1} \tag{27b}$$

$$K_2 = \tfrac{8}{15} \tag{27c}$$

$$1/\tau_1 = 4R_1 + R_2 + R_3 \tag{28a}$$

$$1/\tau_2 = 4R_2 + R_1 + R_3 \tag{28b}$$

$$1/\tau_3 = 4R_3 + R_1 + R_2 \tag{28c}$$

$$C_+ = d - e \tag{29a}$$

$$C_- = d + e \tag{29b}$$

$$C_1 = 6m'n'm''n'' \tag{29c}$$

$$C_2 = 6l'n'l''n'' \tag{29d}$$

$$C_3 = 6l'm'l''m'' \tag{29e}$$

in which

$$d = (\tfrac{1}{2})[3(l'^2 l''^2 + m'^2 m''^2 + n'^2 n''^2) - 1] \tag{30a}$$

$$\begin{aligned} e = (\tfrac{1}{2})[&\delta_1(l'^2 l''^2 + m'^2 n''^2 + n'^2 m''^2) \\ &+\delta_2(m'^2 m''^2 + l'^2 n''^2 + n'^2 l''^2) \\ &+\delta_3(n'^2 n''^2 + l'^2 m''^2 + m'^2 l''^2)] \end{aligned} \tag{30b}$$

Frequently, the shape of a molecule approximates an axially symmetric ellipsoid. In this case, given by $R_1 = R_2$, the correlation function in equation (26) is simplified to

$$\begin{aligned} \langle F_h(t) F_h^*(t+\tau)\rangle = (\tfrac{1}{2})K_h\langle &C_A \exp(-|\tau|/\tau_A) \\ &+C_B \exp(-|\tau|/\tau_B) + C_C \exp(-|\tau|/\tau_C)\rangle_{av} \end{aligned} \tag{31}$$

where

$$1/\tau_A = 6R_2 \tag{32a}$$

$$1/\tau_B = 5R_2 + R_3 \tag{32b}$$

$$1/\tau_C = 2R_2 + 4R_3 \tag{32c}$$

$$C_A = C_+ = (\tfrac{1}{2})(1 - 3n'^2)(1 - 3n''^2) \tag{33a}$$

$$C_B = C_1 + C_2 = 6n'n''(m'm'' + l'l'') \tag{33b}$$

$$C_C = C_- + C_3 = (\tfrac{3}{2})(l'^2 - m'^2)(l''^2 - m''^2) + 6l'l''m'm'' \tag{33c}$$

The operation $\langle\cdots\rangle_{av}$ on the right-hand side of equations (26) and (31) signifies the final average over molecular internal motions that introduce additional time dependencies into the correlation function. If there are no internal motions and the ellipsoid is rigid, this final averaging procedure is unnecessary. In this case, l'', m'', n'' are equal to l', m', n', respectively.

The correlation functions for a rigid, completely asymmetric ellipsoid are then

$$\begin{aligned} \langle F_h(t) F_h^*(t+\tau)\rangle = (\tfrac{1}{2})K_h[&C_+ \exp(-|\tau|/\tau_+) + C_- \exp(-|\tau|/\tau_-) \\ &+C_1 \exp(-|\tau|/\tau_1) + C_2 \exp(-|\tau|/\tau_2) \\ &+C_3 \exp(-|\tau|/\tau_3)] \end{aligned} \tag{34}$$

It is useful to note that $C_+ + C_- + C_1 + C_2 + C_3 = 2$. For a sphere, $R_1 = R_2 = R_3 = R_s$, where R_s is the rotational diffusion constant for the sphere and all of the correlation times are equal to the well-known result $\tau_c = 1/6R_s$.

Similarly, the correlation functions for a rigid, axially symmetric ellipsoid are

$$\begin{aligned} \langle F_h(t) F_h^*(t+\tau)\rangle = \ &(\tfrac{1}{2})K_h[C_A \exp(-|\tau|/\tau_A) \\ &+C_B \exp(-|\tau|/\tau_B) + C_C \exp(-|\tau|\tau_C)] \end{aligned} \tag{35}$$

In this case, the C_i simplify to:

$$C_A = (\tfrac{1}{2})(1 - 3n'^2)^2 \tag{36a}$$

$$C_B = 6n'^2(1 - n'^2) \tag{36b}$$

$$C_C = (\tfrac{3}{2})(1 - n'^2)^2 \tag{36c}$$

Note that the correlation functions are independent of l' and m'. The $J_h(\omega)$ depend only on the angle between the nuclear interaction vector and the motional symmetry axis.

The rotational correlation function is a sum of five (or three) simple exponential decay functions. This functional form is a consequence of the assumption of rotational diffusion that involves only infinitesimally small rotational steps.

4 CORRELATION FUNCTIONS FOR AXIALLY SYMMETRIC ELLIPSOIDS WITH INTERNAL MOTION

When the nuclear interaction vector reorients independently inside the ellipsoid, the direction cosines l', m', and n' of the interaction vector with respect to the rectangular coordinate system S' of the ellipsoid are time dependent and time dependent averaging on the right-hand side of equation (31)

must be performed to obtain the correlation functions. Because the internal rotational motion is independent of the rotational motions of the ellipsoid, we must evaluate the separate correlation functions (i.e. the C_i) in equation (33). To do this, it is convenient to express the internal motion in terms of spherical polar coordinates in S'. The relaxation vector rotates about the z' axis with a constant polar angle Δ and a time dependent azimuthal angle $\phi'(t)$. In the case of a methyl group, the z' axis is the threefold symmetry axis. The z' axis makes a constant angle α with the Z' symmetry axis of the ellipsoid. In the coordinate system of the ellipsoid,

$$C_{\mathrm{A}} = (\tfrac{1}{2})\langle[1 - 3\cos^2\theta(t)][1 - 3\cos^2\theta(t+\tau)]\rangle \tag{37a}$$

$$C_{\mathrm{B}} = (\tfrac{3}{2})\langle\sin 2\theta(t)\exp[\mathrm{i}\phi(t)]\sin 2\theta(t+\tau) \times \exp[-\mathrm{i}\phi(t+\tau)]\rangle \tag{37b}$$

$$C_{\mathrm{C}} = (\tfrac{3}{2})\langle\sin^2\theta(t)\exp[2\mathrm{i}\phi(t)]\sin^2\theta(t+\tau) \times \exp[-2\mathrm{i}\phi(t+\tau)]\rangle \tag{37c}$$

where $\theta(t)$ and $\phi(t)$ are the time dependent polar and azimuthal angles of the interaction vector in S'.

The quantities in brackets are products of spherical harmonics; the C_i can be expressed in terms of the constant angles α and Δ and of the time dependent angle $\phi'(t)$ by using the transformation formulas for spherical harmonics. The result of setting $\phi''(\tau) = \phi'(t + \tau) - \phi'(t)$ and averaging over the random distribution at time t is[8]

$$C_{\mathrm{A}} = C_{\mathrm{A1}} + C_{\mathrm{A2}}\langle\cos\phi''(\tau)\rangle + C_{\mathrm{A3}}\langle\cos 2\phi''(\tau)\rangle \tag{38a}$$

$$C_{\mathrm{A1}} = (\tfrac{1}{8})(1 - 3\cos^2\alpha)^2(1 - 3\cos^2\Delta)^2 \tag{38b}$$

$$C_{\mathrm{A2}} = (\tfrac{9}{16})\sin^2 2\alpha\sin^2 2\Delta \tag{38c}$$

$$C_{\mathrm{A3}} = (\tfrac{9}{16})\sin^4\Delta\sin^4\alpha \tag{38d}$$

$$C_{\mathrm{B}} = C_{\mathrm{B1}} + C_{\mathrm{B2}}\langle\cos\phi''(\tau)\rangle + C_{\mathrm{B3}}\langle\cos 2\phi''(\tau)\rangle \tag{39a}$$

$$C_{\mathrm{B1}} = (\tfrac{3}{8})\sin^2 2\alpha(3\cos^2\Delta - 1)^2 \tag{39b}$$

$$C_{\mathrm{B2}} = (\tfrac{3}{4})(\cos^2 2\alpha + \cos^2\alpha)\sin^2 2\Delta \tag{39c}$$

$$C_{\mathrm{B3}} = (\tfrac{3}{4})[\sin^2\alpha + (\tfrac{1}{4})\sin^2 2\alpha]\sin^4\Delta \tag{39d}$$

$$C_{\mathrm{C}} = C_{\mathrm{C1}} + C_{\mathrm{C2}}\langle\cos\phi''(\tau)\rangle + C_{\mathrm{C3}}\langle\cos 2\phi''(\tau)\rangle \tag{40a}$$

$$C_{\mathrm{C1}} = (\tfrac{3}{8})\sin^4\alpha(3\cos^2\Delta - 1)^2 \tag{40b}$$

$$C_{\mathrm{C2}} = (\tfrac{3}{4})[\sin^2\alpha + (\tfrac{1}{4})\sin^2 2\alpha]\sin^2 2\Delta \tag{40c}$$

$$C_{\mathrm{C3}} = (\tfrac{3}{16})[(1 + \cos^2\alpha)^2 + 4\cos^2\alpha]\sin^4\Delta \tag{40d}$$

Each of the three coefficients C_{A}, C_{B}, and C_{C} consists of a time-independent term (subscripted 1) and two terms that are time dependent because of the internal motion.

The internal motion determines the time dependence of $\phi''(\tau)$. One model for the time dependence is that of a terminal methyl group in an *n*-paraffin molecule in the *s-trans* configuration. Because there are three equivalent positions of the methyl group, the allowed values of $\phi''(\tau)$ are 0°, 120°, and 240°. Here, the internal motion occurs by random jumping of the methyl group from any of these equivalent positions to either of the two adjacent positions at an average rate of $(3\tau_{\mathrm{ci}})^{-1}$. With this type of motion,[9] we have

$$\langle\cos\phi''(\tau)\rangle = \langle\cos 2\phi''(\tau)\rangle = \exp(-|\tau|/\tau_{\mathrm{ci}}) \tag{41}$$

so that

$$C_{\mathrm{A}} = C_{\mathrm{A1}} + (C_{\mathrm{A2}} + C_{\mathrm{A3}})\exp(-|\tau|/\tau_{\mathrm{ci}}) \tag{42a}$$

$$C_{\mathrm{B}} = C_{\mathrm{B1}} + (C_{\mathrm{B2}} + C_{\mathrm{B3}})\exp(-|\tau|/\tau_{\mathrm{ci}}) \tag{42b}$$

$$C_{\mathrm{C}} = C_{\mathrm{C1}} + (C_{\mathrm{C2}} + C_{\mathrm{C3}})\exp(-|\tau|/\tau_{\mathrm{ci}}) \tag{42c}$$

As a result of this type of internal motion, the correlation function contains the three additional correlation times

$$1/\tau_{\mathrm{A23}} = 6R_2 + 1/\tau_{\mathrm{ci}} \tag{43a}$$

$$1/\tau_{\mathrm{B23}} = 5R_2 + R_3 + 1/\tau_{\mathrm{ci}} \tag{43b}$$

$$1/\tau_{\mathrm{C23}} = 2R_2 + 4R_3 + 1/\tau_{\mathrm{ci}} \tag{43c}$$

Another model of internal motion is a stochastic diffusion process among a very large number of equilibrium positions that are uniformly distributed from $\phi' = 0$ to 2π such that $\langle\phi''^2\rangle = 2R_{\mathrm{i}}\tau$, where R_{i} is the internal rotational diffusion coefficient. With this model[9] of internal motion,

$$\langle\cos\phi''(\tau)\rangle = \exp(-R_{\mathrm{i}}|\tau|) \tag{44a}$$

$$\langle\cos 2\phi''(\tau)\rangle = \exp(-4R_{\mathrm{i}}|\tau|) \tag{44b}$$

so that

$$C_{\mathrm{A}} = C_{\mathrm{A1}} + C_{\mathrm{A2}}\exp(-R_{\mathrm{i}}|\tau|) + C_{\mathrm{A3}}\exp(-4R_{\mathrm{i}}|\tau|) \tag{45a}$$

$$C_{\mathrm{B}} = C_{\mathrm{B1}} + C_{\mathrm{B2}}\exp(-R_{\mathrm{i}}|\tau|) + C_{\mathrm{B3}}\exp(-4R_{\mathrm{i}}|\tau|) \tag{45b}$$

$$C_{\mathrm{C}} = C_{\mathrm{C1}} + C_{\mathrm{C2}}\exp(-R_{\mathrm{i}}|\tau|) + C_{\mathrm{C3}}\exp(-4R_{\mathrm{i}}|\tau|) \tag{45c}$$

giving the six new correlation times

$$1/\tau_{\mathrm{A2}} = 6R_2 + R_{\mathrm{i}} \tag{46a}$$

$$1/\tau_{\mathrm{A3}} = 6R_2 + 4R_{\mathrm{i}} \tag{46b}$$

$$1/\tau_{B2} = 5R_2 + R_3 + R_i \tag{46c}$$

$$1/\tau_{B3} = 5R_2 + R_3 + 4R_i \tag{46d}$$

$$1/\tau_{C2} = 2R_2 + 4R_3 + R_i \tag{46e}$$

$$1/\tau_{C3} = 2R_2 + 4R_3 + 4R_i \tag{46f}$$

Frequently, the internal rotation axis lies along the symmetry axis of the ellipsoid so that $\alpha = 0$ in equations (38)–(40). Consequently, the value of many of these equations is zero and the correlation function is[7]

$$\langle F_h(t)F_h^*(t+\tau)\rangle = (\tfrac{1}{2})K_h[A\exp(-|\tau|/\tau'_A) + B\exp(-|\tau|/\tau'_B) + C\exp(-|\tau|/\tau'_C)] \tag{47}$$

in which

$$A = (\tfrac{1}{2})(1 - 3\cos^2\Delta)^2 \tag{48a}$$

$$B = (\tfrac{3}{2})\sin^2 2\Delta \tag{48b}$$

$$C = (\tfrac{3}{2})\sin^4\Delta \tag{48c}$$

For the internal jump model,

$$1/\tau'_A = 1/\tau_A = 6R_2 \tag{49a}$$

$$1/\tau'_B = 5R_2 + R_3 + \tau_{ci} \tag{49b}$$

$$1/\tau'_C = 2R_2 + 4R_3 + \tau_{ci} \tag{49c}$$

For the internal rotational diffusion model,

$$1/\tau'_A = 1/\tau_A = 6R_2 \tag{50a}$$

$$1/\tau'_B = 5R_2 + R_3 + R_i \tag{50b}$$

$$1/\tau'_C = 2R_2 + 4R_3 + 4R_i \tag{50c}$$

Generally, the correlation function of a nonspherical molecule that reorients at different rates about different molecular axes depends on many external and internal molecular motions. We can use NMR relaxation time measurements on nuclei that have different nuclear interaction vector orientations in the molecule to give information on the internal and external molecular motions.

5 CORRELATION FUNCTIONS FOR INTERGROUP MAGNETIC DIPOLAR RELAXATION WITH INTERNAL MOTION

In intramolecular magnetic dipolar relaxation between a nucleus of a rotating group and a nucleus on the remainder of the molecule, the length as well as the orientation of the nuclear interaction vector is time dependent. Consequently, we use the $F_h(t)$ as defined in equation (4). To restrict the calculation of the correlation function to simple but useful cases, we assume the following geometry.[10] The two nuclei rotate in parallel planes about the same perpendicular axis. The planes are separated by the distance b and the radii of rotation are a and c. This geometry describes the magnetic dipolar interaction between protons in different methyl groups in ethane, protons on neighboring carbon atoms in n-paraffins, methyl and ring protons in toluene, fluorine nuclei and protons in benzotrifluoride, etc.

Let us assume that the molecule is an axially symmetric ellipsoid and that the internal rotation axis is parallel to the ellipsoid symmetry axis. Because the internal motion causes simultaneous changes in the orientation and length of the internuclear vector, the correlation function is an extension of equations (31)–(33) to include a time dependent r.

$$\langle F_h(t)F_h^*(t+\tau)\rangle = (\tfrac{1}{2})K_h\langle C_{Ar}\exp(-|\tau|/\tau_A) + C_{Br}(-|\tau|/\tau_B) + C_{Cr}\exp(-|\tau|/\tau_C)\rangle_{av} \tag{51}$$

where

$$1/\tau_A = 6R_2 \tag{52a}$$

$$1/\tau_B = 5R_2 + R_3 \tag{52b}$$

$$1/\tau_C = 2R_2 + 4R_3 \tag{52c}$$

$$C_{Ar} = (\tfrac{1}{2})(1 - 3n'^2)(1 - 3n''^2)r'^{-3}r''^{-3} \tag{53a}$$

$$C_{Br} = 6n'n''(m'm'' + l'l'')r'^{-3}r''^{-3} \tag{53b}$$

$$C_{Cr} = [(\tfrac{3}{2})(l'^2 - m'^2)(l''^2 - m''^2) + 6l'l''m'm'']r'^{-3}r''^{-3} \tag{53c}$$

The operation $\langle\cdots\rangle_{av}$ on the right-hand side of equation (51) signifies the final average over the internal motions. These motions are statistically independent from the rotational motions of the ellipsoid. The values at time t are l', m', n', and r', and those at the later time $t + \tau$ are l'', m'', n'', and

r''. In terms of the geometry of the problem, the C quantities are:

$$C_{\mathrm{Ar}} = (\tfrac{1}{2})r'^{-5}r''^{-5}\{(a^2+c^2-2b^2)^2 - 2(a^3c+ac^3-2ab^2c) \times[\cos(\phi_1'-\phi_2') + \cos(\phi_1''-\phi_2'')] +4a^2c^2\cos(\phi_1'-\phi_2')\cos(\phi_1''-\phi_2'')]\} \tag{54a}$$

$$C_{\mathrm{Br}} = 6r'^{-5}r''^{-5}b^2\{c^2\cos(\phi_1'-\phi_1'') + a^2\cos(\phi_2'-\phi_2'') -ac[\cos(\phi_1'-\phi_2'') + \cos(\phi_2'-\phi_1'')]\} \tag{54b}$$

$$C_{\mathrm{Cr}} = (\tfrac{3}{2})r'^{-5}r''^{-5}\{c^4\cos(2\phi_1'-2\phi_1'') + a^4\cos(2\phi_2'-2\phi_2'') +4a^2c^2\cos(\phi_1'+\phi_2'-\phi_1''-\phi_2'') +a^2c^2[\cos(2\phi_1'-2\phi_2'') + \cos(2\phi_2'-2\phi_1'')] -2ac^3[\cos(2\phi_1'-\phi_1''-\phi_2'') + \cos(\phi_1'+\phi_2'-2\phi_1'')] -2a^3c[\cos(2\phi_2'-\phi_1''-\phi_2'') + \cos(\phi_1'+\phi_2'-2\phi_2'')]\} \tag{54c}$$

in which ϕ_1' and ϕ_2' are the azimuthal angles of the nuclei at time t and ϕ_1'' and ϕ_2'' are the angles at time $t+\tau$.

Calculating the time dependent average values $\langle C_{\mathrm{ir}}\rangle$ involves integrals of functions that approach the complete elliptic integrals at long τ values if $(\phi_1' - \phi_1'')$ and $(\phi_2' - \phi_2'')$ are allowed to have all values from 0 to 2π. The calculation is greatly simplified with the model in which one nucleus occupies three positions 120° apart and the other nucleus occupies three similar positions that are staggered with respect to those of the former nucleus. Here, there are only two different values of r, as given by the expressions:

$$r_{\mathrm{l}}^2 = a^2+b^2+c^2+2ac \tag{55a}$$

$$r_{\mathrm{s}}^2 = a^2+b^2+c^2-ac \tag{55b}$$

If each nucleus independently and randomly jumps among its three positions, the $\langle C_{\mathrm{ir}}\rangle$ are

$$\langle C_{\mathrm{Ar}}\rangle = C_{\mathrm{a1}} + C_{\mathrm{a2}}\exp[-|\tau|(1/\tau_1+1/\tau_2)] \tag{56a}$$

$$\langle C_{\mathrm{Br}}\rangle = C_{\mathrm{b1}}\exp[-|\tau|/\tau_1] + C_{\mathrm{b2}}\exp[-|\tau|/\tau_2] +C_{\mathrm{b3}}\exp[-|\tau|(1/\tau_1+1/\tau_2)] \tag{56b}$$

$$\langle C_{\mathrm{Cr}}\rangle = C_{\mathrm{c1}}\exp[-|\tau|/\tau_1] + C_{\mathrm{c2}}\exp[-|\tau|/\tau_2] +C_{\mathrm{c3}}\exp[-|\tau|(1/\tau_1+1/\tau_2)] \tag{56c}$$

where

$$C_{\mathrm{a1}} = (\tfrac{1}{18})[(a^2+c^2-2b^2)^2Q_1 + 4a^2c^2Q_2 -4(a^3c+ac^3-2ab^2c)Q_3] \tag{57a}$$

$$C_{\mathrm{a2}} = (\tfrac{1}{9})[(a^2+c^2-2b^2)^2Q_2 + a^2c^2Q_5 -2(a^3c+ac^3-2ab^2c)Q_4] \tag{57b}$$

$$C_{\mathrm{b1}} = (\tfrac{2}{3})b^2(c^2Q_1 + a^2Q_2 - 2acQ_3) \tag{57c}$$

$$C_{\mathrm{b2}} = (\tfrac{2}{3})b^2(c^2Q_2 + a^2Q_1 - 2acQ_3) \tag{57d}$$

$$C_{\mathrm{b3}} = (\tfrac{2}{3})b^2(a+c)^2Q_2 \tag{57e}$$

$$C_{\mathrm{c1}} = (\tfrac{1}{6})(c^4Q_1 + a^4Q_2 + 6a^2c^2Q_6 - 4ac^3Q_3 + 4a^3cQ_2) \tag{57f}$$

$$C_{\mathrm{c2}} = (\tfrac{1}{6})(c^4Q_2 + a^4Q_1 + 6a^2c^2Q_6 + 4ac^3Q_2 - 4a^3cQ_3) \tag{57g}$$

$$C_{\mathrm{c3}} = (\tfrac{1}{6})(c^4Q_2 + a^4Q_2 + 6a^2c^2Q_7 - 4ac^3Q_3 - 4a^3cQ_3) \tag{57h}$$

in which

$$Q_1 = 4r_{\mathrm{s}}^{-10} + r_{\mathrm{l}}^{-10} + 4r_{\mathrm{s}}^{-5}r_{\mathrm{l}}^{-5} \tag{58a}$$

$$Q_2 = r_{\mathrm{s}}^{-10} + r_{\mathrm{l}}^{-10} - 2r_{\mathrm{s}}^{-5}r_{\mathrm{l}}^{-5} \tag{58b}$$

$$Q_3 = 2r_{\mathrm{s}}^{-10} - r_{\mathrm{l}}^{-10} - r_{\mathrm{s}}^{-5}r_{\mathrm{l}}^{-5} \tag{58c}$$

$$Q_4 = r_{\mathrm{s}}^{-10} - 2r_{\mathrm{l}}^{-10} + r_{\mathrm{s}}^{-5}r_{\mathrm{l}}^{-5} \tag{58d}$$

$$Q_5 = r_{\mathrm{s}}^{-10} + 4r_{\mathrm{l}}^{-10} + 4r_{\mathrm{s}}^{-5}r_{\mathrm{l}}^{-5} \tag{58e}$$

$$Q_6 = r_{\mathrm{l}}^{-10} - r_{\mathrm{s}}^{-5}r_{\mathrm{l}}^{-5} \tag{58f}$$

$$Q_7 = 3r_{\mathrm{s}}^{-10} + r_{\mathrm{l}}^{-10} + 2r_{\mathrm{s}}^{-5}r_{\mathrm{l}}^{-5} \tag{58g}$$

The correlation time of internal motion of the nucleus associated with ϕ_1 and c is τ_1 and that of the nucleus associated with ϕ_2 and a is τ_2.

The final correlation times are given by:

$$1/\tau_{\mathrm{a1}} = 1/\tau_{\mathrm{A}} = 6R_2 \tag{59a}$$

$$1/\tau_{\mathrm{a2}} = 6R_2 + 1/\tau_1 + 1/\tau_2 \tag{59b}$$

$$1/\tau_{\mathrm{b1}} = 5R_2 + R_3 + 1/\tau_1 \tag{59c}$$

$$1/\tau_{b2} = 5R_2 + R_3 + 1/\tau_2 \tag{59d}$$

$$1/\tau_{b3} = 5R_2 + R_3 + 1/\tau_1 + 1/\tau_2 \tag{59e}$$

$$1/\tau_{c1} = 2R_2 + 4R_3 + 1/\tau_1 \tag{59f}$$

$$1/\tau_{c2} = 2R_2 + 4R_3 + 1/\tau_2 \tag{59g}$$

$$1/\tau_{c3} = 2R_2 + 4R_3 + 1/\tau_1 + 1/\tau_2 \tag{59h}$$

Use of this simple model of internal motion with magnetic dipolar relaxation interaction increases the number of correlation times for the axially symmetric ellipsoid from three to eight. If the internal rotational axis were not parallel to the ellipsoid symmetry axis, then more than eight correlation times would result. Even in this simple case, many simplifications occur if the molecule rotates with spherical symmetry, if $\tau_1 = \tau_2$, or if either of the two nuclei does not rotate internally.

Examination of the sum of the eight coefficients given by equation (57) reveals insight into the effects of internal motion. This sum is $(4/3)r_s^{-6} + (2/3)r_1^{-6}$, which is twice the weighted average of r^{-6}. The corresponding sum for a rigid molecule, obtained from the sum of equation (53) when the single-primed and double primed quantities are equal, is $2r^{-6}$. The effect of the internal motion, then, is to split r^{-6} into several terms. Most of these terms have shorter correlation times than for a rigid molecule. One of the terms is independent of the internal motion and it gives rise to the 'order parameter' that represents a kind of order in a large, flexible molecule.

6 'MODEL-FREE' CORRELATION FUNCTIONS FOR FLEXIBLE MACROMOLECULES

Modern applications of NMR include the use of relaxation time measurements to investigate the dynamics of flexible macromolecules, such as polymers, lipids, and proteins (see ***Protein Dynamics from NMR Relaxation***), in solution. Clearly, the correlation function for such systems is extremely complex because many different correlation times and associated preexponential factors are involved in its formulation. In addition, we must assume structural and dynamical models to make the formulation. Even with such a formulation, the typical NMR relaxation time measurement does not allow for the experimental evaluation of all the parameters that are in the assumed models.

We can use the expressions presented in this article with various assumed dynamics and structures to formulate the correlation functions for a complex flexible molecule and compute values of relaxation times. We can use these values to validate simplified expressions for the spectral density to figure out (a) what is the unique information in a set of relaxation time data and (b) how can we extract this information from the data?

Such simplified expressions are called[11–13] 'model-free' because the analysis of relaxation time data using these expressions does not require the adoption of a physical model. However, the derivation and productive use of these expressions do require the assumption of certain limiting cases. The description of the motion of the flexible macromolecule is that of overall reorientation of the molecular framework and internal motions within this framework that are independent of the reorientation of the framework. To illustrate this approach, we factor equation (47) as

$$\langle F_h(t)F_h^*(t+\tau)\rangle = (\tfrac{1}{2})K_h[\exp(-|\tau|/\tau_{ov})] \times[A + B\exp(-|\tau|/\tau_{i1}) + C\exp(-|\tau|/\tau_{i2})] \tag{60}$$

in which $A + B + C = 2$. When the internal motion is rotational diffusion, for example, the correlation times are:

$$1/\tau_{ov} = 1/\tau_A = 6R_2 \tag{61a}$$

$$1/\tau_{i1} = -R_2 + R_3 + R_i \tag{61b}$$

$$1/\tau_{i2} = -4R_2 + 4R_3 + 4R_i \tag{61c}$$

We can view equation (60) as the product of a correlation function $C_{ov}(\tau)$ that depends only on overall motion, and a correlation function $C_{in}(\tau)$ that contains a constant term and terms that involve the internal motion, so that

$$\langle F_h(t)F_h^*(t+\tau)\rangle = K_h C_{ov}(\tau)C_{in}(\tau) \tag{62}$$

where

$$C_{ov}(\tau) = \exp(-|\tau|/\tau_{ov}) \tag{63a}$$

$$C_{in}(\tau) = (\tfrac{1}{2})[A + B\exp(-|\tau|/\tau_{i1}) + C\exp(-|\tau|/\tau_{i2})] \tag{63b}$$

The model-free approach is to approximate $C_{in}(\tau)$ as

$$C_{in}(\tau) = \zeta^2 + (1-\zeta^2)\exp(-|\tau|/\tau_{eff}) \tag{64}$$

where ζ is called an order parameter, equal to $(A/2)^{\frac{1}{2}}$ in the present example, and τ_{eff} is an effective correlation time as given by the definition:

$$\tau_{eff} = (1-\zeta^2)^{-1}\int_0^\infty [C_{in}(\tau) - \zeta^2]\,d\tau \tag{65}$$

When the internal motions are rapid so that $2\omega_0/R_i \ll 1$, use of this definition in the spectral density function provides an excellent approximation.

In considering the consequences of the fluctuations of internuclear separation on magnetic dipolar relaxation that are

caused by the internal motion, we can use equations (56)–(59) to factor equation (51) as

$$\begin{aligned}\langle F_{\rm h}(t)F_{\rm h}^*(t+\tau)\rangle &= (\tfrac{1}{2})K_{\rm h}[\exp(-|\tau|/\tau_{\rm ov})]\\ &\times[C_{\rm a1}+C_{\rm a2}\exp(-|\tau|/\tau_{\rm i1})\\ &+C_{\rm b1}\exp(-|\tau|/\tau_{\rm i2})+C_{\rm b2}\exp(-|\tau|/\tau_{\rm i3})\\ &+C_{\rm b3}\exp(-|\tau|/\tau_{\rm i4})+C_{\rm c1}\exp(-|\tau|/\tau_{\rm i5})\\ &+C_{\rm c2}\exp(-|\tau|/\tau_{\rm i6})+C_{\rm c3}\exp(-|\tau|/\tau_{\rm i7})]\end{aligned} \tag{66}$$

in which

$$1/\tau_{\rm ov} = 6R_2 \tag{67a}$$

$$1/\tau_{\rm i1} = 1/\tau_1 + 1/\tau_2 \tag{67b}$$

$$1/\tau_{\rm i2} = -R_2 + R_3 + 1/\tau_1 \tag{67c}$$

$$1/\tau_{\rm i3} = -R_2 + R_3 + 1/\tau_2 \tag{67d}$$

$$1/\tau_{\rm i4} = -R_2 + R_3 + 1/\tau_1 + 1/\tau_2 \tag{67e}$$

$$1/\tau_{\rm i5} = -4R_2 + 4R_3 + 1/\tau_1 \tag{67f}$$

$$1/\tau_{\rm i6} = -4R_2 + 4R_3 + 1/\tau_2 \tag{67g}$$

$$1/\tau_{\rm i7} = -4R_2 + 4R_3 + 1/\tau_1 + 1/\tau_2 \tag{67h}$$

The analogous order parameter $\zeta_{\rm r}$ for internal motion with equation (62) is similarly defined by:

$$C_{\rm in}(\tau) = \zeta_{\rm r}^2 + (1-\zeta_{\rm r}^2)\exp(-|\tau|/\tau_{\rm er}) \tag{68}$$

in which $\zeta_{\rm r}$ is equal to $(C_{\rm a1}/2)^{\frac{1}{2}}$ and $\tau_{\rm er}$ is the effective correlation time that is defined in the same fashion as $\tau_{\rm eff}$.

When the internal motions are rapid compared with the overall molecular reorientation rate and obey the condition $2\omega_0/R_{\rm i} \ll 1$, the correlation function is the sum of two terms. One of these terms involves the overall correlation time and the other term involves the effective correlation time that depends on the internal motions. The term that is dependent on the overall molecular motion is weighted by the order parameter.

7 CORRELATION FUNCTIONS FOR INTERMOLECULAR MAGNETIC DIPOLAR RELAXATION

Magnetic dipolar NMR relaxation between nuclei of different molecules is an important relaxation mechanism that depends on Brownian motion. The values of r, θ, and ϕ are time dependent because of translational diffusion of the molecular centers and rotation of the molecules about their centers. If the interacting nuclei are at the centers of spherical molecules, the correlation functions can be calculated[1] from classical diffusion theory. The correlation function is[1]

$$\langle F_{\rm h}(t)F_{\rm h}^*(t+\tau)\rangle = \frac{\alpha_{\rm h}N}{d^3} \times \int_0^\infty [J_{3/2}(u)]^2 \exp\left[-\left(\frac{2D}{d^2}u^2\tau\right)\right]\frac{{\rm d}u}{u} \tag{69}$$

where N is the number of nuclear spins per cm^3, D is the translational diffusion coefficient, d is the minimum distance of approach between nuclei on different molecules, $J_{3/2}$ is a Bessel function, $\alpha_{\rm h}$ is a numerical factor that depends on h, and u is a dummy integration parameter. The spectral energy densities are then

$$J_{\rm h}(\omega) = \frac{\alpha_{\rm h}N}{dD}\int_0^\infty [J_{3/2}(u)]^2 \frac{u\,{\rm d}u}{u^4+\omega^2\tau^2} \tag{70}$$

where $\tau = d^2/2D$. The effects on $J_{\rm h}(\omega)$ in the case of off-center nuclei[14] depend on the ratio $\tau/\tau_{\rm c}$ and they are not insignificant.

8 EXPERIMENTAL AND THEORETICAL CORRELATION TIMES OF RIGID MOLECULES

8.1 Evaluation of Correlation Times from NMR Relaxation Data

We can express the correlation functions in the preceding sections of this article (except for Section 7) as the following sum of exponential functions:

$$\langle F_{\rm h}(t)F_{\rm h}^*(t+\tau)\rangle = (\tfrac{1}{2})\langle F_{\rm h}(t)F_{\rm h}^*(t)\rangle \sum_j C_j \exp(-|\tau|/\tau_{cj}) \tag{71}$$

in which $\Sigma_j C_j = 2$. The values of the correlation times τ_{cj} depend on the rates of molecular motions, and the number and values of the C_j depend on the details of molecular structure and motion. Because equation (71) is a sum of exponential functions, the spectral densities $J_{\rm h}(\omega)$ in equation (3) are given by the sum of Lorentzian functions

$$J_{\rm h}(\omega) = \langle F_{\rm h}(t)F_{\rm h}^*(t)\rangle \sum_j C_j[\tau_{cj}/(1+\omega^2\tau_{cj}^2)] \tag{72}$$

Note that the spectral densities for intermolecular magnetic dipolar relaxation in Section 7 are not sums of Lorentzian functions because equation (69) is not a sum of exponential functions.

The models presented in the preceding sections do not explicity include various motions, such as high frequency, small amplitude bond stretching vibrations, as well as torsional oscillations about temporary equilibrium positions that change because of Brownian motion. The inclusion of such motions would increase the number of terms in equations (71) and (72) and could decrease the spectral density. If the decrease in spectral density is significant, the application of the preceding models to relaxation time data could lead to inconsistencies of interpretation. In the case of magnetic dipolar relaxation of CH_3 groups, the predicted decrease due to torsional ocillations agrees[15] with experiment.

The study of Brownian motions by means of NMR relaxation time measurements involves the evaluation of the τ_{cj} from $J_h(\omega)$ values that are obtained from the measured relaxation times. These relaxation times should be from different nuclei that have different orientations of relaxation interaction vector with respect to the various axes of the ellipsoidal molecule.

There can be an ambiguity in evaluating correlation times from relaxation data, especially for large molecules with relatively small R_i values. Because the function $\tau_{cj}/(1 + \omega^2\tau_{cj}^2)$ is at its maximum value $1/\omega$ at $\omega\tau_{cj} = 1$, there is an ambiguity of τ_{cj} values when the 'experimental' value of $\tau_{cj}/(1 + \omega^2\tau_{cj}^2)$ is less than $1/\omega$. This ambiguity does not occur if, for example, all of the τ_{cj} values are small compared to $1/\omega$. In ordinary NMR spectrometers, this condition is met for nonviscous liquids. For example, $2\omega_0\tau_c \approx 0.05$ for protons in liquid water at 0 °C in a 750 MHz NMR spectrometer. Clearly, the simplest circumstance is a rigid, spherical molecule of a nonviscous liquid so that there is only one correlation time. We can compare the correlation time obtained from the analysis of the NMR relaxation time to the value that is predicted from liquid properties and molecular parameters.

8.2 Relationship of Rotational Correlation Times to Brownian Motion

In the preceding sections of this article, the correlation functions for a rigid ellipsoid are expressed in terms of the rotational diffusion coefficients R_i. The R_i values can be determined from the analysis of the proper relaxation time measurements. The next step is to relate the R_i to Brownian motion in the liquid. Molecules in the liquid undergo random collisions with other molecules. Perrin's exquisitely detailed description of the translational and rotational motion of an ellipsoid that is immersed in a liquid and experiencing collisions with the liquid molecules[5] is useful in establishing this relationship.

It is assumed that the average action of molecular collisions on the ellipsoid gives rise to the friction of viscosity. Fluctuations of these collisions produce impulses of torque that affect the rotation of the ellipsoid. These impulses couple the rotational kinetic energy of the ellipsoid to the kinetic energy of its surroundings so that thermodynamic equilibrium obtains and the average kinetic energy for each degree of freedom is equal to $kT/2$, where T is the absolute temperature of the fluid and k is Boltzmann's constant.

Let ω_1, ω_2, and ω_3 be the angular velocities of the ellipsoid about the X, Y, and Z axes and I_1, I_2 and I_3 be the moments of inertia about these axes, respectively. Similarly, let α_1, α_2, and α_3 be small rotation angles about these axes. In the following discussion, designate the subscripts 1, 2, and 3 as the subscript i. If K is the kinetic energy of the particle, the angular momenta λ_i are the partial derivatives of K with respect to the angular velocities ω_i:

$$\lambda_i = \partial K/\partial\omega_i \tag{73}$$

At each instant, the collisions with the surrounding molecules produce a torque L_i about the respective ellipsoid axes. Each L_i is the sum of the frictional torque $-\mathcal{C}_i\omega_i$ that results from viscosity and a variable torque Γ_i that is caused by fluctuations of the collisions. This torque causes changes in angular momenta as given by

$$d\lambda_i/dt = -\mathcal{C}_i\omega_i + \Gamma_i \tag{74}$$

We take time intervals Δt that are sufficiently great so that there is almost complete statistical independence of the angular displacements that are produced by torque Γ_i during two consecutive time intervals, and nevertheless, sufficiently small so that the rotation during each interval is very small. If α_i are the very small angles that are needed to describe the changes in orientation from its initial position to its orientation at the end of time interval Δt, to a first approximation the angular velocities are

$$\omega_i = d\alpha_i/dt \tag{75}$$

Under these conditions, the angular displacements that result from successive impulses due to the thermal motions of the liquid are independent and simply additive. If we divide the time interval Δt into very small successive intervals δt, the variable couple Γ_i communicates to the ellipsoid an impulse $\mathcal{L}_i$ that is the integral of Γ_i over the interval δt,

$$\mathcal{L}_i = \int_0^{\delta t} \Gamma_i\, dt \tag{76}$$

Also, to calculate the net angular displacement that results from these impulses, it suffices to calculate the displacement that results from each impulse, assuming action on the initially immobile particle, and take the sum of these small displacements as if they are not superposed in time.

Because $\omega_i = d\alpha_i/dt$ and $d\lambda_i/dt = -\mathcal{C}_i\omega_i + \Gamma_i$

$$d\lambda_i/dt = -\mathcal{C}_i(d\alpha_i/dt) + \Gamma_i \tag{77}$$

Integration between the initial time t_0 and the final time t gives:

$$\lambda_i - \lambda_{i0} = -\mathcal{C}_i(\alpha_i - \alpha_{i0}) + \int_{t_0}^{t} \Gamma_i\, dt \tag{78}$$

The ellipsoid is assumed to be immobile at time t_0 so that $\lambda_0 = 0$. If the torque Γ_i acts on the particle only during the time interval δt,

$$\lambda_i = -\mathcal{C}_i(\alpha_i - \alpha_{i0}) + \mathcal{L}_i \tag{79}$$

If t is large enough so that the particle is now practically stopped due to the friction, the rotational displacement of the particle that results from the total of the angular impulses $\mathcal{L}$ is

$$\delta\alpha_i = \mathcal{L}_i/\mathcal{C}_i \tag{80}$$

The displacement does not depend on the moments of inertia, I_i; it depends only on the coefficients of friction $\mathcal{C}_i$. However, this result is true only if the preceding approximations are justified by the smallness of the angular displacements.

If the time interval Δt is sufficiently great, the displacement is that which results from the n successive intervals δt that compose it. If the intervals δt are not too small, the successive corresponding impulses are nearly statistically independent, and the net angular displacement $\Delta\alpha_i$ over time Δt is given by:

$$\langle\Delta\alpha_i^2\rangle = (1/\mathcal{C}_i^2)\sum_k\langle\mathcal{L}_{ik}^2\rangle = n\langle\mathcal{L}_i^2\rangle/\mathcal{C}_i^2 \tag{81}$$

because the average values for time intervals of the same duration δt are equal. Also, the average values of cross terms $\Delta\alpha_i\Delta\alpha_j$ are zero.

The average values of the $\Delta\alpha_i{}^2$ quantities can be found by noting that the impulses received by the particle maintain statistically a state of agitation that corresponds to the average kinetic energy that, from the equipartition theorem of statistical mechanics, is given by:

$$\langle\lambda_i\omega_i\rangle = kT \tag{82}$$

If the time interval δt is sufficiently small so that the rotational velocity ω_i is nearly constant, integration of equation (74) over δt gives:

$$\lambda_i' = \lambda_i - \mathcal{C}_i\omega_i\delta t + \mathcal{L}_i \tag{83}$$

where λ_i and λ_i' are angular momenta at the beginning and end of the interval δt. After squaring and taking the average,

$$\begin{aligned}\langle\lambda_i'^2\rangle = {} & \langle\lambda_i^2\rangle + \mathcal{C}_i^2\langle\omega_i^2\rangle\delta t^2 + \langle\mathcal{L}_i^2\rangle \\ & -2\mathcal{C}_i\langle\lambda_i\omega_i\rangle\delta t + 2\langle\lambda_i\mathcal{L}_i\rangle - 2\mathcal{C}_i\langle\omega_i\mathcal{L}_i\rangle\delta t\end{aligned} \tag{84}$$

Several characteristics allow us to simplify this expression. Since the system is in steady-state conditions, $\langle\lambda_i'^2\rangle = \langle\lambda_i^2\rangle$. The impulses $\mathcal{L}_i$ do not depend directly on the angular velocities, and the intervals δt are assumed to be sufficiently long in order than the impulses may be independent of the previous impulses that have influenced the angular velocities. Therefore, the average values of products of impulses and angular velocities and of products of impulses and angular momenta are null. Finally, the terms in δt^2 are negligible. Equation (84) then reduces to:

$$\langle\mathcal{L}_i^2\rangle = 2\mathcal{C}_i\langle\lambda_i\omega_i\rangle\delta t \tag{85}$$

and use of equation (82) gives the relation:

$$\langle\mathcal{L}_i^2\rangle = 2\mathcal{C}_i kT\delta t \tag{86}$$

Then, because $n\delta t = \Delta t$ equation (81) gives:

$$\langle\Delta\alpha_i^2\rangle = 2(kT/\mathcal{C}_i)\Delta t \tag{87}$$

and $\Delta\alpha_i$ changes with time as described by the rotational diffusion coefficient

$$R_i = kT/\mathcal{C}_i \tag{88}$$

In an analogous fashion, Einstein[16] considered the translational Brownian motion of colloidal particles and showed that the translational diffusion coefficient D in an infinitely dilute solution is given by the equation:

$$D = kT/f \tag{89}$$

where f is the frictional coefficient of the particle.

8.3 Relationships between Friction Coefficients and Properties of Molecules and Liquids

8.3.1 Hydrodynamic Models

The strategy to evaluate the $\mathcal{C}_i$ and f friction coefficients for *molecules* in ordinary liquids is not completely straightforward. Usually, the results of classical hydrodynamics are used. Stokes[17] considered the special case of the motion of a macroscopic spherical particle of radius a moving with uniform velocity in a continuous fluid (i.e. infinitesimally small particles) of viscosity η. He assumed that the moving sphere carries along with it, *with no slippage*, the layer of fluid in contact with it (i.e. the surface of the sphere is 'wetted' by the fluid medium). Parenthetically, using this assumption avoids the problems of evaluating the friction coefficient between two different materials, the surface of the smooth sphere and the adjacent surface of the fluid medium. Using classical hydrodynamical principles, such as perfect streamline flow, etc., he showed that the translational movement of the sphere is impeded by the sum of two forces: (1) the force ($=4\pi\eta a$) due to pressure built up in front of it, and (2) a frictional force ($=2\pi\eta a$) parallel to its surface. Then, the friction coefficient f_0 is given by

$$f_0 = 6\pi\eta a \tag{90}$$

Einstein[16] noted that *if* one can assume that this equation applies to spherical *molecules* of radius a, the resulting value of the molecular diffusion coefficient is given by the equation

$$D = kT/6\pi\eta a \tag{91}$$

which is known as the Stokes–Einstein equation. This relationship has been experimentally verified many times for particles whose size can be measured directly, including latex particles of only 1300 Å radius in water. The increase in size

due to the monolayer of water molecules is negligible for spheres of such size.

For the case of a sphere rotating uniformly in the continuous medium, the Stokes approach gives the rotational friction coefficient

$$\mathcal{C}_i = 8\pi\eta a^3 \tag{92}$$

Following Einstein's lead in assuming that the translational friction coefficient of a molecule obeys the classical hydrodynamic formulation, Debye[3] made the analogous assumption that the rotational motion of a spherical molecule is described by rotational diffusion with the classical rotational friction coefficient given above.

Edwardes extended Stokes's calculation of the single rotational friction coefficient of a rotating sphere to evaluate the three friction coefficients for an asymmetric ellipsoid rotating in a continuous fluid. The results, as corrected by Perrin,[5] are:

$$\mathcal{C}_1 = 16\pi\eta(b^2 + c^2)/[3(b^2Q + c^2R)] \tag{93a}$$

$$\mathcal{C}_2 = 16\pi\eta(c^2 + a^2)/[3(c^2R + a^2P)] \tag{93b}$$

$$\mathcal{C}_3 = 16\pi\eta(a^2 + b^2)/[3(a^2P + b^2Q)] \tag{93c}$$

where a, b, and c are the X', Y', and Z' semiaxes of the ellipsoid, and P, Q and R are the elliptic integrals

$$P = \int_0^\infty (a^2 + s)^{-3/2}(b^2 + s)^{-1/2}(c^2 + s)^{-1/2}\,\mathrm{d}s \tag{94a}$$

$$Q = \int_0^\infty (b^2 + s)^{-3/2}(a^2 + s)^{-1/2}(c^2 + s)^{-1/2}\,\mathrm{d}s \tag{94b}$$

$$R = \int_0^\infty (c^2 + s)^{-3/2}(a^2 + s)^{-1/2}(b^2 + s)^{-1/2}\,\mathrm{d}s \tag{94c}$$

These quantities are related by the equations:

$$P + Q + R = 2/(abc) \tag{95}$$

$$a^2P + b^2Q + c^2R = S \tag{96}$$

where

$$S = \int_0^\infty [(a^2 + s)(b^2 + s)(c^2 + s)]^{-1/2}\,\mathrm{d}s \tag{97}$$

For the axially symmetric ellipsoid, with $a = b$ so that $R_1 = R_2$, the $\mathcal{C}_i$ simplify to

$$\mathcal{C}_1 = \mathcal{C}_2 = 32\pi\eta(c^4 - b^4)/\{3[(2c^2 - b^2)S - 2c]\} \tag{98a}$$

$$\mathcal{C}_3 = 32\pi\eta b^2(c^2 - b^2)/[3(2c - b^2S)] \tag{98b}$$

Also, for $b > c$,

$$S = 2(b^2 - c^2)^{-1/2}\tan^{-1}[(b^2 - c^2)^{1/2}/c] \tag{99a}$$

and for $b < c$,

$$S = 2(c^2 - b^2)^{-1/2}\ln\{[c + (c^2 - b^2)^{1/2}]/b\} \tag{99b}$$

For a sphere, where $a = b = c$, all the the $\mathcal{C}_i$ are equal to $8\pi\eta a^3$.

The relationships given above can be used to calculate the NMR correlation times for rigid molecules of a variety of shapes. Generally, for pure liquids and for solutes in solutions in which the solute molecules are not large compared to the solvent molecules, the calculated correlation times are approximately an order of magnitude greater than the values obtained from analysis of NMR relaxation time data. The discrepancy is especially great for small, nearly spherical molecules. Also, the calculated translational diffusion coefficients for such systems are significantly smaller than measured D values.[18]

8.3.2 Gierer–Wirtz Microviscosity Factor

Two difficulties will arise from use of these hydrodynamic friction coefficients. One difficulty is uncertainty of the size of small molecules. Because of the free space between molecules in a liquid, it is not sufficient to equate the molecular volume to the molar volume divided by Avogadro's number. For example, a crystal made up of closely packed spheres is 26% empty volume. Accordingly, 74% of the above molecular volume is commonly used in calculating the molecular radius for rotational correlation time estimates. Several other methods are described[18] for use in the Stokes–Einstein equation. However, using any realistic method of calculating molecular size does not solve the problem. The inclusion of a 'wetting' or 'sticking' layer of molecules would make the situation worse, because even smaller molecular volumes are generally needed to fit the experimental results to equations (91) and (92).

Another problem is that the molecule of interest is surrounded by particles of comparable size instead of a continuous fluid of infinitesimally small particles. Gierer and Wirtz[19] estimated the rotational and translational friction coefficients of a 'solute' sphere surrounded by 'solvent' spheres by formulating the liquid viscosity in terms of the kinetics of the spheres. They regard the given molecule of interest to be a sphere of radius r and the surrounding molecules to be spheres of radius r_1. The surrounding molecules form spherical layers, each of thickness $2r_1$, around the given molecule. If this central molecule is set rotating about the z axis with angular velocity ω, each layer will eventually acquire an angular velocity because of the friction between layers. In the steady state, the mth layer will have angular velocity ω_m. At equilibrium the total torque acting on the mth layer will be equal to the resistive torque on the central molecule, which is zero. The rotational friction coefficient for the central molecule is given by

$$\mathcal{C}_\mathrm{s} = 8\pi\eta r^3 f_\mathrm{r} \tag{100}$$

where

$$f_r = \frac{\rho}{6}\left[\sum_m (1+2m\rho)^{-4}\right]^{-1} \approx \left[6\rho + \frac{1}{(1+\rho)^3}\right]^{-1} \quad (101)$$

in which f_r is the rotational 'microviscosity factor', the summation is from $m = 0$ to $m = \infty$, and $\rho = r_1/r$. For translational motion, the Stokes–Einstein friction coefficient is multiplied by the microviscosity factor

$$f_t = [(3/2)\rho + 1/(1+\rho)]^{-1} \quad (102)$$

The value for pure liquids is $f_r = 0.164$. Use of these microviscosity correction factors gives correlation times and diffusion coefficients that are generally close to experimental values when the assumed molecular volume is 0.74 times the molar volume divided by Avogadro's number. However, when ρ differs from unity, the experimental f_r depends more strongly on ρ than equation (101) predicts. Generally, $\rho \neq 1$ for molecules in solutions.

8.3.3 Mutual Viscosity Formulation

The preceding calculations of the friction coefficient $\mathcal{C}_i$ use the viscosity of the fluid. This usage represents a deficiency of approach. As discussed by Hill,[20] every molecule in a pure liquid is surrounded by molecules of the same kind and the interactions between these like molecules determine both the liquid viscosity η and the friction coefficient $\mathcal{C}_i$. Despite the particular argument by which η and $\mathcal{C}_i$ are related, it is expected that they will vary in a similar manner from one substance to another. But in a dilute solution, η is determined almost entirely by the interactions between the solvent molecules while $\mathcal{C}_i$ is determined almost entirely by interactions between the solute and solvent molecules. Therefore, there is no reason to expect a general, simple relationship between η and $\mathcal{C}_i$ for solutions of different substances. To obtain an improved relationship, it is necessary to consider more closely the interactions that determine these quantities.

In the Andrade theory of liquid viscosity, the molecules in a liquid are regarded as vibrating with a frequency ν about equilibrium positions that change slowly with time. The transfer of momentum that occurs in a viscous liquid between layers moving with different velocities is due to temporary unions or collisions of adjacent molecules. These unions occur at the extremes of each vibrational swing so that, for an infinitesimal time, the two molecules move as one. Hill[20] applied this approach to a mixture of two liquids and found that the viscosity η_m of the mixture is:

$$\eta_m = f_A^2 \eta_A \sigma_A/\sigma_m + f_B^2 \eta_B \sigma_B/\sigma_m + 2 f_A f_B \eta_{AB} \sigma_{AB}/\sigma_m \quad (103)$$

where η_A and η_B are the viscosities of the pure liquids A and B, η_{AB} is the 'mutual viscosity', σ_A and σ_B are the average distances between molecules in the liquids A and B, σ_m is the average distance between molecules in the mixture, and σ_{AB} is the mean distance between a molecule of type A and an adjacent molecule of type B in the mixture. The resultant value of $\mathcal{C}_s$ for a molecule of type B is:

$$\begin{aligned}\mathcal{C}_s = {} & 6 f_A \{[(I_{AB} I_B)/(I_{AB} + I_B)] \\ & \times [(m_A + m_B)/(m_A m_B)]\} \eta_{AB} \sigma_{AB} \\ & + 3(3 - \sqrt{2})\, f_B \{[(I_{BB} I_B)/(I_{BB} + I_B)] \\ & \times [(m_B + m_B)/(m_B m_B)]\} \eta_B \sigma_B\end{aligned} \quad (104)$$

where I_B is the moment of inertia of a type B molecule, m is the mass of a molecule, and I_{AB} is the moment of inertia of molecule A about the center of mass of molecule B at the instant of collision. For a pure liquid ($f_B = 1$), the results are nearly the same as the Gierer and Wirtz approach, but for an infinitely dilute solution ($f_A = 1$), the viscosity is the mutual viscosity η_{AB} instead of the solvent viscosity. This approach explains[20] the different correlation times, found from dielectric relaxation measurements, for one solute in a variety of solvents having the same viscosity and for the relatively short correlation times found for solutes in high viscosity solvents.

In studies of the dielectric relaxation times of molecules of a wide range of size in solution, the use of equation (92) gives friction coefficients that agree[21] with experiment when the molecular volume is at least three times that of the solvent molecule. Furthermore, the Hill theory is inferior for large solute molecules but it is superior for small solute molecules. Therefore, use of the rotational friction coefficients that are given in equations (92)–(99) to evaluate the correlation times for rotational diffusion of ellipsoids should provide a good approximation for large molecules in a solvent of small molecules.

8.4 Deficiencies of Viscosity/Rotational Diffusion Models

Since the earliest studies on molecular reorientational phenomena by nuclear magnetic relaxation, many have attempted to find a fundamental connection between orientational correlation times and macroscopic viscosity. Macroscopic viscosity, or shear viscosity, is defined as the resistance to shear if a thin liquid layer is moved ('sheared') between parallel plates. The physical dimension of viscosity is force times time divided by area. This tells us that we deal with momentum transfer. The momentum transfer tries to equalize the velocities of the moving layers. As indicated in Section 8.3.1, the hydrodynamic boundary conditions for the viscosity dependence of the orientational function of a spherical molecule have been defined in terms of a 'rough sphere'; the surface of the reorienting molecule entrains its neighbors. A perfectly slipping sphere would have zero viscosity. On the other hand, we know that, on the molecular level, interactions take place through impulsive collisions between only a few neighbors. It is therefore not surprising that such a macroscopic rough sphere model overestimates $\mathcal{C}_s$. The microviscosity and mutual viscosity approaches are different attempts to formulate relationships that retain the idea of smooth spheres that, nevertheless, have surface friction. The situation is simpler for systems of small molecules of ellipsoidal shape since their reorientational motion displaces their neighbors; the rotational motion of a perfectly slipping ellipsoid would show a viscosity dependence.

The NMR relaxation behavior of several pure liquids of small molecules provides instructive cases. When the

molecules are rigid, all of the rotational diffusion models described above predict that the correlation times are directly proportional to the quantity η/T. However, this relationship is not always obeyed. Perdeuterobenzene provides a good example of this behavior. The temperature dependence of the deuteron T_1 value obeys[22] an Arrhenius equation with an apparent activation energy E_a = 7.78 kJ mol^{-1}. On the other hand, the temperature dependence of η/T is much greater; an Arrhenius equation is obeyed, but with E_a = 13.05 kJ mol^{-1}. Besides varying temperature, the viscosity can be adjusted by changing the pressure on the liquid. The pressure dependence of the benzene viscosity[23] is described by an activation volume of 20.5 cm^3 mol^{-1}. The pressure dependence of the deuteron T_1 of perdeuterobenzene is much less,[24] described by an activation volume of only 0.44 cm^3 mol^{-1}. On the other hand, the pressure dependence of the translational diffusion coefficient of benzene[25] obeys an activation volume of 20.0 cm^3 mol^{-1}, nearly identical to that of the viscosity. This means that the translational frictional coefficient is directly coupled to the viscosity, but the effective rotational friction coefficient is largely decoupled from the viscosity.

Acetonitrile, CH_3CN,[26] is another instructive case. In the temperature range from 20 °C to 50 °C, the temperature dependence of η/T obeys an Arrhenius equation with E_a = 8.66 kJ mol^{-1}. This molecule has an electric dipole moment that is parallel to the C–N axis of the molecule and the ^{14}N nucleus experiences an electric quadrupole interaction in the same direction. The temperature dependence of the dielectric relaxation time (E_a = 8.28 kJ mol^{-1}) and of the ^{14}N T_1 (7.9 kJ mol^{-1}) are nearly equal to the above value for η/T. This shows that the rotational friction coefficient for reorientation of the C–N molecular axis at a given temperature is directly proportional to the viscosity. Also, the microviscosity model of Gierer and Wirtz,

$$\tau_c \equiv V\eta/6kT \tag{105}$$

where V is the molecular volume, yields at room temperature τ_c = 0.89 × 10^{-2} s. This value is close (81%) to the value found from the ^{14}N measurements of T_1. The deuteron T_1 values of CD_3CN, however, have a smaller temperature dependence with E_a = 5.73 kJ mol^{-1}. This temperature dependence behavior shows that the rotational friction coefficient of the C–N axis of the molecule is directly proportional to the viscosity but that of the other molecular axes is relatively uncoupled from the viscosity. Also, at 25 °C, the effective deuteron correlation time is 0.340 × 10^{-12} s, which is much smaller than the value 1.104 × 10^{-12} s for ^{14}N. Evidently, the molecular reorientation rate about the C–N axis is much greater than that about an axis that is perpendicular to the C–N direction. If the molecule reorients like a rigid axially symmetric ellipsoid, use of equations (32) and (34)–(36) gives R_3 = 10.35 × R_2. Also, the temperature dependence of R_3 is small, described by an Arrhenius equation with E_a = 3.05 kJ mol^{-1}.

Toluene provides another informative case[27] of motions of small molecules. The temperature dependence of η/T is well described by an Arrhenius equation with E_a = 11.51 kJ mol^{-1}. This value is larger than that of the T_1 of the ring deuterons of perdeuterotoluene (8.20 kJ mol^{-1}) and that of the methyl group deuterons of perdeuterotoluene (5.77 kJ mol^{-1}). Toluene has a small electric dipole moment (0.3–0.4 D) that is parallel to the methyl group symmetry axis. The dielectric relaxation time is approximately three times the NMR correlation time of the ring deuterons and its temperature dependence is essentially the same as that of this correlation time. Also, the T_1 values of the *ortho* and *para* ring deuterons are apparently equal. These dielectric and NMR relaxation results indicate that the ring of the toluene molecule reorients approximately like a sphere with $R_1 = R_2 = R_3$. However, the observation that the activation energy for the dielectric and NMR relaxation times is significantly smaller than that of η/T suggests that the molecular rotational friction coefficients of the ring are not directly related to the liquid viscosity.

Another significant observation is that the methyl deuterons have a much longer T_1 than the ring deuterons (4.88 s compared with 0.943 s). This longer T_1 and the smaller activation energy mean that the methyl group of the toluene molecule is internally reorienting rapidly about its symmetry axis. The intramolecular energy barrier to internal rotation of the methyl group in molecules such as toluene is very small, only 0.059 kJ mol^{-1},[28] especially in comparison with the hinderance from interactions with neighboring molecules. Here, reorientation of the methyl group about its symmetry axis is completely independent from the reorientation of the remainder of the molecule, and the terms involving R_3 in equations (49) and (50) are omitted. Analysis[27] of the data using the 'internal' rotational diffusion model gives an apparent activation energy of 3.47 kJ mol^{-1}. Use of the 'internal' 120° jump model gives a similar value, 3.89 kJ mol^{-1}. Many other molecules have rapid internal reorientation of the methyl group, including methanol, acetone, acetic anhydride, ethanol, acetic acid, *t*-butanol, *p*-xylene, and acetophenone.

The rapid reorientation of the methyl group about its symmetry axis, the low values of apparent activation energy of this motion, and the decoupling of the rotational friction coefficient of benzene from the liquid viscosity may show that the model of rotational diffusion of a rigid ellipsoid may provide an incomplete description of molecular rotation of small molecules.

Relationships among viscosity, molecular reorientational motions, and molecular translational diffusion depend on the physical model that is assumed in the derivation. The Stokes–Einstein–Debye–Perrin model is based on the idea of particles surrounded by a continuous medium that is characterized by viscosity. The Gierer–Wirtz and Hill methods assume that the molecule of interest is surrounded by other particles and use specific physical models of interactions of spheres to interrelate the quantities. In all models, the system is at thermal equilibrium and subject to the general laws of thermodynamics and statistical mechanics. Different models may be appropriate for different molecular liquids. Steric considerations and the NMR observation[29] that benzene molecules rotate in the solid state suggest that liquid benzene molecules could rotate much faster about the C_6 molecular symmetry axis than about a C_2 axis. Such C_6 rotation requires less accommodation of the surrounding molecules than is required by a C_2 rotation. Similarly, for such molecules as toluene and acetonitrile, the rotation of a methyl group about its C_3 symmetry axis requires less accommodation by the surroundings than the rotation of the symmetry axis itself. Because the viscosity is likely to reflect the motions

that experience the greatest hindrances, the above C_6 and C_3 rotations could be largely uncoupled from the liquid viscosity. However, these rotations need not be completely free or frictionless. For example, the electric dipole moments of the individual C–H or C–D bonds could interact with the fluctuating local electric dipole fields due to the nearby molecules and hinder this motion.

9 CORRELATION FUNCTIONS FOR A 'NEARLY-FREE' ROTOR ATTACHED TO AN ELLIPSOID

The rotational diffusion model is a limiting case of the Langevin model. The internally reorienting part of the molecule may be treated as a classical rigid rotor that rotates about one axis. This rotational problem is analogous[30] to the case of translational motion.[31] The distribution of rotational angular velocities follows the Boltzmann energy distribution law. The angular frequency ω of a rotor changes in time as described by

$$\mathrm{d}\omega/\mathrm{d}t = -[\xi\omega + F(t)]/I \tag{106}$$

where ξ is a rotational friction coefficient, I is the moment of inertia, and $F(t)$ is a randomly fluctuating torque. The fluctuating part is an instantaneous angular velocity independent, statistically defined force (its autocorrelation function decays much faster than that of the angular frequency) that causes random changes in the angular frequency. The value of the rotational angle $\phi''(\tau)$ of a rotor with initial angular velocity ω_i obeys a normal Gaussian distribution with a mean value

$$\langle\phi''(\tau)\rangle = \omega_\mathrm{i}(I/\xi)\{1 - \exp[-(\xi/I)\tau]\} \tag{107}$$

When ξ is small, the value of $\langle\phi''(\tau)\rangle$ is $\omega_\mathrm{i}\tau$. The averages $\langle\cos\phi''(\tau)\rangle$ and $\langle\cos 2\phi''(\tau)\rangle$ that appear in equations (38)–(40), obtained by a final averaging over the distribution of ω_i values, are:

$$\langle\cos\phi''(\tau)\rangle = \exp\{-(IkT/\xi^2)[\xi\tau/I + \exp(-\xi\tau/I) - 1]\} \tag{108a}$$

$$\langle\cos 2\phi''(\tau)\rangle = \exp\{-4(IkT/\xi^2)[\xi\tau/I + \exp(-\xi\tau/I) - 1]\} \tag{108b}$$

When the rotational friction coefficient is sufficiently great, we obtain an exponentially decaying function in τ as given in equation (44) with $R_\mathrm{i} = kT/\xi$. This is the rotational diffusion limit. However, when the friction coefficient is sufficiently small, at short τ values we obtain exponentially decaying functions in τ^2 as given by

$$\langle\cos\phi''(\tau)\rangle = \exp[-(kT/2I)\tau^2] \tag{109a}$$

$$\langle\cos 2\phi''(\tau)\rangle = \exp[-(2kT/I)\tau^2] \tag{109b}$$

In this limit, the average values are independent of the friction coefficient and inertial effects dominate. The rotational motions are decoupled from the viscosity of the liquid. The temperature dependencies predicted for these limiting cases are greatly different. Because the friction coefficient is likely to decrease with an increase in temperature, the temperature dependence in the rotational diffusion limit is expected to be much greater than in the inertial limit.

Although the temperature dependence may be used as a criterion between the applicability of these models, the value of R_i obtained from data analysis with the average angular velocity $(kT/I)^{\frac{1}{2}}$ provides another criterion. The rotational diffusion case may apply when the time required for the internal orientation to change by one radian calculated from the value of R_i obtained from data analysis, $(1/2R_\mathrm{i})$, is large compared to the time required by free rotation, $(I/kT)^{\frac{1}{2}}$. The motion of of the methyl groups (CD_3) at room temperature falls between these two limits.[27] Further information about methyl group reorientation is available as follows. Equation (108) shows that I/ξ is the time constant for frictional changes in the rotational velocity of the CD_3 rotor. The quantity $(kT/I)^{\frac{1}{2}}$ is the average rotational angular velocity. The product of these two quantities, $(IkT/\xi^2)^{\frac{1}{2}}$, is the number of radians through which the CD_3 group rotates before its angular velocity changes appreciably. For the CD_3 groups of perdeuterotoluene at 298 K, this angle is 16°. This value is too large for rigorous application of the rotational diffusion model. Nevertheless, it is sufficiently small so that this model provides a convenient mathematical form for data analysis.

The experimental correlation times for many small rigid molecules in pure liquids and solutions obey a linear relationship with the liquid viscosity but have a nonzero intercept at zero viscosity. The intercept yields a correlation time[2] that appears to equal the time interval $(2\pi/9)(I/kT)^{\frac{1}{2}}$. This is the time required for a freely rotating molecule to turn through an angle of 41°, the angle for the correlation function of a second-order Legendre polynomial to drop to 1/e of its original (at $\tau = 0$) value. This result, which also shows that the correlation time is not directly proportional to viscosity at constant temperature, provides another indication that rotational diffusion may not accurately describe the motions of small molecules and the inertial effects are important in the rotational motions of small liquid molecules.

10 SCRUTINY OF THE MATHEMATICAL FORM OF CORRELATION FUNCTIONS

Realistically, at short enough times molecular collisions have not yet occurred and, consequently, molecular motion is purely kinetic. Because of this, the real correlation function has no first-order term in τ(it has zero slope at $\tau = 0$). Consequently, the rotational diffusion model fails with the first-order term and the spectral density derived from it is in error. We cannot use it to give a credible description of the details of molecular motion, especially for small molecules, since it is invalid for initial time intervals where the correlation function is least 'scrambled' by complicated orientation–collision events. This is dramatically shown by the nonexponential infrared and Raman spectral correlation functions[2] obtained in measurements on small molecules. NMR relaxation measurements made over a range

of frequencies do not reveal this dramatic behavior because the spectral density at ordinary Larmor frequencies is merely the integral of the correlation function. However, at sufficiently 'high' Larmor frequencies, the Lorentzian spectral density equation would not be obeyed. When this happens, and if the Larmor frequency is varied on both sides of the 'T_1 minimum', serious errors could occur if we interpret the relaxation data by use of the Lorentzian spectral density equation.

When the angle of free rotation is very large, the correlation functions derived for rotational diffusion of an asymmetric ellipsoid are no longer a reasonable approximation. In the spirit of Brownian rotational motion that is based on the Langevin equation in Section 9, the correlation functions for a rotating sphere with three degrees of rotational freedom are given by:

$$\langle F_{\mathrm{h}}(t)F_{\mathrm{h}}^{*}(t+\tau)\rangle = \langle F_{\mathrm{h}}(t)F_{\mathrm{h}}^{*}(t)\rangle \exp\{-6(IkT/\mathcal{C}_{\mathrm{s}}^{2}) \times[\mathcal{C}_{\mathrm{s}}\tau/I + \exp(-\mathcal{C}_{\mathrm{s}}\tau/I) - 1]\} \quad (110)$$

At long times, this function decays exponentially with time. At very short times, the results for a freely rotating sphere are obtained. At 'low' frequencies a plot of spectral density vs. friction coefficient $\mathcal{C}_{\mathrm{s}}$ has a nonzero intercept equal to $(\pi/12)^{\frac{1}{2}}(I/kT)^{\frac{1}{2}}$. The spectral density function at high frequencies would deviate significantly from a Lorentzian function. When the friction is very large so that $\mathcal{C}_{\mathrm{s}}\tau/I \gg 1$, we obtain from equation (110) the results for rotational diffusion of a sphere.

There is a wide variety of correlations between NMR spectral densities of liquid molecules and macroscopic liquid properties such as viscosity. These correlations are sensitive to molecular size and intermolecular interactions. The spectral densities of large molecules appear to obey rotational diffusion equations with friction coefficients calculated with hydrodynamic models. Those for small molecules may be approximated by microviscosity and mutual viscosity formulations. Experiments that include NMR relaxation measurements at very high B_0 values and wide temperature ranges may yield more information on the rotational motions of molecules in liquids.

11 RELATED ARTICLES

Coupled Spin Relaxation in Polymers; Molecular Motions: T_1 Frequency Dispersion in Biological Systems; Polymers: Relaxation and Dynamics of Synthetic Polymers in Solution; Protein Dynamics from NMR Relaxation; Protein Structures: Relaxation Matrix Refinement; Relaxation: An Introduction; Relaxation of Coupled Spins from Rotational Diffusion; Relaxation Processes: Cross Correlation and Interference Terms; Relaxation Theory: Density Matrix Formulation; Relaxation Theory for Quadrupolar Nuclei; Relaxation of Transverse Magnetization for Coupled Spins; Relaxometry of Tissue; Spin–Rotation Relaxation Theory

12 REFERENCES

1. A. Abragam, *The Principles of Nuclear Magnetism*, Clarendon Press, Oxford, 1961.
2. W. G. Rothschild, *Dynamics of Molecular Liquids*, John Wiley & Sons, New York, 1984.
3. P. Debye, *Polar Molecules*, Dover Publications, New York, 1945.
4. N. Bloembergen, E. M. Purcell, and R. V. Pound, *Phys. Rev.*, 1948, **73**, 679.
5. F. Perrin, *J. Phys. Radium*, 1934, **5**, 497.
6. F. Perrin, *J. Phys. Radium*, 1936, **7**, 1.
7. D. E. Woessner, *J. Chem. Phys.*, 1962, **37**, 647.
8. D. E. Woessner, B. S. Snowden, Jr., and G. H. Meyer, *J. Chem. Phys.*, 1969, **50**, 719.
9. D. E. Woessner, *J. Chem. Phys.*, 1962, **36**, 1.
10. D. E. Woessner, *J. Chem. Phys.*, 1965, **42**, 1855.
11. G. Lipari and A. Szabo, *J. Am. Chem. Soc.*, 1982, **104**, 4546.
12. G. Lipari and A. Szabo, *J. Am. Chem. Soc.*, 1982, **104**, 4559.
13. M. Dellwo and A. J. Wand, *J. Am. Chem. Soc.*, 1993, **115**, 1886.
14. J. F. Harmon, *J. Magn. Reson.*, 1978, **31**, 411.
15. C. S. Johnson, Jr., *J. Magn. Reson.*, 1976, **24**, 63.
16. A. Einstein, *Ann. Phys.*, 1905, **17**, 549.
17. G. Stokes, *Trans. Cambridge Philos. Soc.*, 1856, **9**, 5.
18. J. T. Edward, *J. Chem. Educ.*, 1970, **47**, 261.
19. A. Gierer and K. Wirtz, *Z. Naturforsch.*, 1953, **8a**, 532.
20. N. E. Hill, *Proc. Phys. Soc. London*, 1954, **B67**, 149.
21. R. J. Meakins, *Trans Faraday Soc.*, 1958, **54**, 1160.
22. D. E. Woessner, *J. Chem. Phys.*, 1964, **40**, 2341.
23. P. W. Bridgman, *Proc. Am. Acad. Arts Sci.*, 1926, **61**, 57.
24. D. E. Woessner and B. S. Snowden, Jr., *J. Chem. Phys.*, 1970, **52**, 1621.
25. D. W. McCall, D. C. Douglass, and E. W. Anderson, *J. Chem. Phys.*, 1959, **31**, 1555.
26. D. E. Woessner, B. S. Snowden, Jr., and E. Thomas Strom, *Mol. Phys.*, 1958, **14**, 265.
27. D. E. Woessner and B. S. Snowden, Jr., *Adv. Mol. Relaxation Processes*, 1972, **3**, 181.
28. H. D. Rudolph, H. Breizler, A. Jaeschke, and P. Wendling, *Z. Naturforsch.*, 1967, **22a**, 940.
29. E. R. Andrew and R. G. Eades, *Proc. R. Soc. London*, 1953, **A218**, 537.
30. W. A. Steele, *J. Chem. Phys.*, 1963, **38**, 2404.
31. G. Uhlenbeck and L. S. Ornstein, *Phys. Rev.*, 1930, **36**, 823.

Biographical Sketches

Donald E. Woessner. *b* 1930. A.B., 1952, Ph.D. (supervisor Herbert Gutowsky), 1957, Chemistry, University of Illinois, USA. Postdoctoral work at University of Illinois (with Herbert Gutowsky). Successively senior research chemist, research associate, senior research associate, Mobil Research and Development Corporation, Dallas, Texas, USA. Currently Adjunct Assistant Professor of Radiology, The University of Texas Southwestern Medical Center at Dallas, 1992–present. Approx. 72 publications. Research specialties: NMR relaxation and molecular motions in liquids, relationships of NMR relaxation of hydrogen and ionic nuclei to motions, structure, and order in aqueous heterogeneous systems and biological tissue.

Liouville Equation of Motion

Charles L. Mayne
University of Utah, Salt Lake City, UT, USA

1	Introduction	1
2	Operators and Operator Bases	1
3	Some Commonly Used Bases	7
4	The Density Operator	10
5	Superoperators	13
6	Related Article	14
7	References	14

1 INTRODUCTION

Nuclear magnetic resonance is uniquely capable of revealing structure and dynamics on a molecular level. An understanding of nuclear spin relaxation is fundamental to an understanding of nuclear magnetic resonance in general. The theoretical framework needed to promote this understanding is conveniently constructed in terms of the time evolution of the density operator under the influence of some Hamiltonian as expressed by the Liouville–von Neuman equation. The emphasis here will be on molecules in liquids, though many of the principles presented are applicable to solids and gases. The experimental observables of NMR are oscillatory magnetizations induced in a sample as a consequence of subjecting it to various static and time-varying magnetic fields. The quantum mechanical operators corresponding to these observables act only on the nuclear spin degrees of freedom of the system. Furthermore, these operators are proportional to the spin angular momentum operators or products thereof, and, hence, can be dealt with using finite basis sets of states or operators. Relaxation, however, is a consequence of interactions between the nuclear spins and the rest of the system, referred to as the 'lattice'. In most cases, the lattice cannot be treated exactly using quantum mechanics, because the density operator and the Hamiltonian cannot be defined exactly. The strategy generally employed, then, is to treat the effects of the lattice classically as a random time-dependent modulation of the nuclear spin operators while retaining a quantum mechanical description of the nuclear spins themselves. All externally applied magnetic fields are likewise treated classically. Our goal is to derive equations that correctly describe the observed temporal behavior of the experimental observables. This is done by proposing a Hamiltonian for the system under study, solving the Liouville–von Neuman equation for the time evolution of the density operator, computing the expected time evolution of the experimental observables, and comparing the result with measured values of these observables. Secondly, one wants to extract from this temporal behavior of the observables information about the fundamental nature of the system under investigation. For example, internuclear distances and rates of molecular reorientation due to Brownian motion can dramatically affect the results of an NMR experiment. How can this kind of information be extracted from the behavior of the magnetization in a sample as a function of time? This article will lay out the theoretical framework of NMR experiments, with emphasis on an understanding of nuclear spin relaxation in liquids.

This article presumes a basic knowledge of the nuclear magnetic resonance phenomenon, including nuclear spin polarization in an external static magnetic field and interaction of nuclear spins with applied radiofrequency fields. For those not acquainted with these concepts, several basic texts may be consulted.[1–3] The reader is assumed to have some grasp of basic quantum mechanics and angular momentum theory at the level generally taught in undergraduate physical chemistry courses. Some command of linear algebra and integral and differential calculus is also assumed. All abbreviations and symbols are either defined in the endpapers or are defined in context. Vectors and matrices will be distinguished by bold italic and bold roman type, respectively, and the same symbol in normal weight type will denote the magnitude of a vector or, with appropriate subscripts, components of a vector or elements of a matrix. Quantum mechanical operators will have a hat, for example, $\hat{\mathcal{H}}$. Liouville space operators will have a double hat, for example $\hat{\hat{\mathcal{L}}}$.

It is a familiar concept that the wavefunction embodies all that can be known about a quantum mechanical system and that any wavefunction can be expressed as a linear combination of the members of a complete set of eigenfunctions of the Hamiltonian of the system. However, in NMR, the density operator has proven to be a more convenient vehicle for this information, and the density operator, the Hamiltonian, and all other operators associated with the system can be cast as linear combinations of a complete set of orthonormal operators. These two descriptions are completely equivalent, and each can be formulated from the general concepts embodied in the bracket notation introduced by Dirac[4] to describe abstract vector spaces. For nuclear spin systems in liquids, it is often possible to focus on a small number of spins (all the spins in one molecule, for example) and to consider the macroscopic sample as an ensemble of such systems, identical in their dependence on quantum mechanical operators but sampling the distribution of random classical variables. Since each nuclear spin has only a small number of eigenstates and the number of eigenstates for the whole system is the product of the numbers for each of the component spins, the necessary mathematics reduces, by means of an ensemble average, to a problem in linear algebra of reasonable dimension. In the following sections, the mathematics needed to discuss most of the experiments done on liquid samples will be formulated. Space limitations make it impossible to give a completely detailed exposition; for this, the reader may consult several excellent texts.[5–9]

2 OPERATORS AND OPERATOR BASES

When a quantum mechanical system has a finite number of discrete energy levels (suppose there are n of them), the operators and states of the system can be represented as matrices and vectors in an n-dimensional vector space. Thus, the algebra of abstract n-dimensional vector spaces is essential to the theory we wish to develop. Dirac developed a convenient notation for describing these concepts.

2.1 Dirac Bracket Notation

For now, let us develop the bracket notation in a very abstract sense. It is important to realize that the bracket notation is just a formalism and can be applied to represent any desired vector space. Later, we shall apply it to both Hilbert and Liouville representations of the density operator. In the following equation is defined something called a *bra* and something called a *ket*:

$$\langle bra|(c)|ket\rangle \tag{1}$$

Bras and kets may have any kind of label inside to distinguish one from another. A ket may be converted into the corresponding bra by taking the Hermitian conjugate or adjoint, i.e., the complex conjugate transpose, and, of course, a bra can be converted into a ket in the same manner:

$$\langle bra| = [(|ket\rangle)^*]^{\mathrm{T}} = (|ket\rangle)^\dagger \tag{2}$$

Multiplication of a bra and a ket in that order yields a number that can be real, imaginary, or complex:

$$\langle bra|ket\rangle = \mathrm{c} \tag{3}$$

Note that this *scalar product* is not commutative, as we shall see in equation (9). Equation (3) is a key concept. In what follows, one must be able to recognize the $\langle\ |\ \rangle$ construct as a number that commutes with operators, bras, and kets. The scalar product is linear:

$$\left.\begin{aligned}\langle \mathrm{bra}|(|\mathrm{ket}_1\rangle + |\mathrm{ket}_2\rangle) &= \langle \mathrm{bra}|\mathrm{ket}_1\rangle + \langle \mathrm{bra}|\mathrm{ket}_2\rangle \\ (\langle \mathrm{bra}_1| + \langle \mathrm{bra}_2|)|\mathrm{ket}\rangle &= \langle \mathrm{bra}_1|\mathrm{ket}\rangle + \langle \mathrm{bra}_2|\mathrm{ket}\rangle\end{aligned}\right\} \tag{4}$$

Next we define something called an *operator* that converts a ket into some other ket:

$$\widehat{Op}|\mathrm{ket}\rangle = |\mathrm{new\ ket}\rangle \tag{5}$$

Operators will be distinguished by a hat (circumflex). Operators do not, in general, commute. The identity operator $\hat{E}$ just leaves a ket unaltered:

$$\hat{E}|\mathrm{ket}\rangle = |\mathrm{ket}\rangle \tag{6}$$

The identity operator does commute with all other operators.

Taking the adjoint of both sides of equation (5) yields the following relationship, which shows how an operator can act to the left on a bra:

$$(\widehat{Op}|\mathrm{ket}\rangle)^\dagger = \langle \mathrm{bra}|\widehat{Op}^\dagger = \langle \mathrm{new\ bra}| \tag{7}$$

If $\widehat{Op}^\dagger = \widehat{Op}$, the operator is said to be *Hermitian* or *self-adjoint*.

If an operator acting on a ket yields the same ket multiplied by a number c (perhaps complex), the ket is said to be an *eigenket* of the operator, and c is the *eigenvalue*:

$$\widehat{Op}|\mathrm{ket}\rangle = c|\mathrm{ket}\rangle \tag{8}$$

As mentioned above, multiplication of bras and kets is not commutative, so the question arises of the meaning of the following product of a ket with a bra:

$$|\mathrm{ket}\rangle\langle \mathrm{bra}| = \mathrm{operator} \tag{9}$$

This is called the *outer product* or *tensor product* of the bra and ket. Equation (9) asserts that this combination is an operator. This assertion can be easily proven by operating on some ket:

$$|a\rangle\langle b\|c\rangle = |a\rangle\langle b|c\rangle = |a\rangle n_{bc} = n_{bc}|a\rangle \tag{10}$$

Remember that $\langle b|c\rangle$ is just a number, by equation (3), and a number will commute with a ket. Thus, $|a\rangle\langle b|$ satisfies the definition of an operator as in equation (5), because it produces a new ket $|a\rangle$ from $|c\rangle$. The numerical coefficient involved is not a problem, because a number times a ket is still a ket. The fact that one can reinterpret or regroup bras and kets in this way is a key concept of the formalism. In Section 2.2 it will become more obvious why these alternative interpretations are possible. We shall not put a hat over these operators, since there is no possibility of confusion; expressions of the type $|\ \rangle\langle\ |$ will always be interpretable as operators.

If we have a set of kets $\{|i\rangle,\ i = 1, 2, 3, \ldots, n\}$ such that

$$\langle i|\ j\rangle = \delta_{ij} \quad \text{for all} \quad i, j = 1, 2, 3, \ldots, n \tag{11}$$

then the set is said to be an *orthonormal* (orthogonal and normalized) basis. The Kronecker delta function is defined by

$$\delta_{ij} = \begin{cases} 1 & (i = j) \\ 0 & (i \neq j) \end{cases} \tag{12}$$

If for some member of the set $\langle i|i\rangle \neq 1$ then we simply define a new ket $|i'\rangle = |i\rangle/\langle i|i\rangle^{\frac{1}{2}}$ to replace $|i\rangle$ until all members of the set are normalized.

With just these simple rules for manipulating operators, bras, and kets as postulates, one can develop the mathematics necessary to treat nuclear spin dynamics.

2.2 Representations

Suppose we have some system in a state that corresponds to an abstract vector or ket designated as $|\psi(t)\rangle$. The indicated time dependence shows that the system may be evolving in time. We attempt to expand this state in the stationary orthonormal set of equation (11) as follows, and we want to know the form of the coefficients $c_i(t)$:

$$|\psi(t)\rangle = \sum_{i=1}^{n} c_i(t)|i\rangle \tag{13}$$

Multiplying from the left by $\langle i|$, a bra corresponding to one of the members of the basis set, and using equation (11) yields

$$\begin{aligned}\langle i|\psi(t)\rangle &= \langle i|\sum_{j=1}^{n} c_j(t)|\ j\rangle \\ &= \sum_{j=1}^{n} c_j(t)\langle i|\ j\rangle \\ &= \sum_{j=1}^{n} c_j(t)\delta_{ij} = c_i(t)\end{aligned} \tag{14}$$

The last step follows because, by equation (12), only the ith term survives in the sum. This is a formal prescription for computing the expansion coefficients; later, we shall see how it is implemented in real cases. The question of whether the set $\{|i\rangle\}$ is complete, i.e., contains all the basis vectors necessary to represent $|\psi(t)\rangle$, will not be addressed here. It will simply be asserted that such a set can be found. Taking the adjoint of both sides of equation (14) yields the analogous equation for bras:

$$\langle\psi(t)|i\rangle = c_i^*(t) \tag{15}$$

Having chosen a basis set, we can compute all the coefficients needed for equation (14) or equation (15). If these coefficients are arranged in a column or a row vector then we have the Hilbert space representation of the state (bra or ket) in the basis:

$$|\psi\rangle \xrightarrow{|i\rangle} \begin{bmatrix} \langle 1|\psi\rangle \\ \langle 2|\psi\rangle \\ \langle 3|\psi\rangle \\ \vdots \\ \langle n|\psi\rangle \end{bmatrix} = \begin{bmatrix} c_1 \\ c_2 \\ c_3 \\ \vdots \\ c_n \end{bmatrix} \tag{16a}$$

$$\begin{aligned} \langle\psi| \xrightarrow{|i\rangle} & [\langle\psi|1\rangle \quad \langle\psi|2\rangle \quad \langle\psi|3\rangle \quad \dots \quad \langle\psi|n\rangle] \\ & = [c_1^* \quad c_2^* \quad c_3^* \quad \dots \quad c_n^*] \end{aligned} \tag{16b}$$

A mapping of this sort is sometimes written with an equals sign in the literature. This is not consistent with the notation we have developed, because the state $|\psi\rangle$ is an abstraction implying no particular basis, whereas the vector representing $|\psi\rangle$ requires that a particular basis be chosen. It is also inconsistent to equate a wavefunction to a ket, because a wavefunction is a representation of the ket in a continuous rather than a discrete basis. The result is a function rather than a vector with discrete elements; that is why it is called a wave*function*. In this article, mappings of this sort will be indicated by an arrow as in equation (16). The basis used will be indicated as shown or will be obvious from the context.

Of course, the members of the basis set can themselves be represented in the basis. If the jth member of the basis is represented then all the elements of the vector will be zero except the jth, which is one:

$$|\,j\rangle \xrightarrow{|i\rangle} \begin{bmatrix} \langle 1|\,j\rangle \\ \langle 2|\,j\rangle \\ \vdots \\ \langle\,j|\,j\rangle \\ \vdots \\ \langle n|\,j\rangle \end{bmatrix} = \begin{bmatrix} 0 \\ 0 \\ \vdots \\ 1 \\ \vdots \\ 0 \end{bmatrix} \tag{17a}$$

$$\begin{aligned} \langle\,j| \xrightarrow{|i\rangle} & [\langle\,j|1\rangle \quad \langle\,j|2\rangle \quad \dots \quad \langle\,j|\,j\rangle \quad \dots \quad \langle\,j|n\rangle] \\ & = [0 \quad 0 \quad \dots \quad 1 \quad \dots \quad 0] \end{aligned} \tag{17b}$$

If we rewrite equation (13) using the result in equation (14) and commute the number with the ket on the right, we have

$$\begin{aligned} |\psi(t)\rangle &= \sum_{i=1}^{n} \langle i|\psi(t)\rangle|i\rangle \\ &= \sum_{i=1}^{n} |i\rangle\langle i|\psi(t)\rangle \\ &= \left(\sum_{i=1}^{n} |i\rangle\langle i|\right)|\psi(t)\rangle \end{aligned} \tag{18}$$

Written this way, the implication is

$$\sum_{i=1}^{n} |i\rangle\langle i| = \hat{E} \tag{19}$$

Rearranging and reinterpreting the brackets in this way may seem quite strange at first, but the examples given below should clarify the formalism. The operators $|i\rangle\langle i|$ are called *projection operators* because they project from any state the part that projects on the ith basis state. Summing over all the projection operators then just gives the unit operator.

Suppose we have two alternative sets of basis states, $\{|a,i\rangle\}$ and $\{|b,i\rangle\}$, spanning the same vector space; then we can effect a transformation between the bases using projection operators as in equation (19). Projecting the b basis onto the a basis, we have

$$\begin{aligned} |b,i\rangle &= \left(\sum_{j=1}^{n} |a,j\rangle\langle a,j|\right)|b,i\rangle \\ &= \sum_{j=1}^{n} |a,j\rangle\langle a,j|b,i\rangle \\ &= \sum_{j=1}^{n} \langle a,j|b,i\rangle|a,j\rangle \end{aligned} \tag{20}$$

If we have an arbitrary state represented in the b basis, it can be transformed to the a basis as follows:

$$\begin{aligned} \psi\rangle &= \sum_{i=1}^{n} \langle b,i|\psi\rangle|b,i\rangle \\ &= \sum_{i=1}^{n} \langle b,i|\psi\rangle \sum_{j=1}^{n} \langle a,j|b,i\rangle|a,j\rangle \\ &= \sum_{i,j=1}^{n} \langle a,j|b,i\rangle\langle b,i|\psi\rangle|a,j\rangle \end{aligned} \tag{21a}$$

$$\begin{aligned} \langle\psi| &= \sum_{i=1}^{n} \langle\psi|b,i\rangle\langle b,i| \\ &= \sum_{i=1}^{n} \langle\psi|b,i\rangle \sum_{j=1}^{n} \langle b,i|a,j\rangle\langle a,j| \\ &= \sum_{i,j=1}^{n} \langle\psi|b,i\rangle\langle b,i|a,j\rangle\langle a,j| \end{aligned} \tag{21b}$$

Comparing these results with equations (16a) and (16b), it is apparent that equations (21a) and (21b) can be represented as follows:

$$\begin{bmatrix} \langle a,1|\psi\rangle \\ \langle a,2|\psi\rangle \\ \langle a,3|\psi\rangle \\ \vdots \\ \langle a,n|\psi\rangle \end{bmatrix}$$

$$= \begin{bmatrix} \langle a,1|b,1\rangle & \langle a,1|b,2\rangle & \langle a,1|b,3\rangle & \dots & \langle a,1|b,n\rangle \\ \langle a,2|b,1\rangle & \langle a,2|b,2\rangle & \langle a,2|b,3\rangle & \dots & \langle a,2|b,n\rangle \\ \langle a,3|b,1\rangle & \langle a,3|b,2\rangle & \langle a,3|b,3\rangle & \dots & \langle a,3|b,n\rangle \\ \vdots & \vdots & \vdots & \ddots & \vdots \\ \langle a,n|b,1\rangle & \langle a,n|b,2\rangle & \langle a,n|b,3\rangle & \dots & \langle a,n|b,n\rangle \end{bmatrix}$$

$$\times \begin{bmatrix} \langle b,1|\psi\rangle \\ \langle b,2|\psi\rangle \\ \langle b,3|\psi\rangle \\ \vdots \\ \langle b,n|\psi\rangle \end{bmatrix} \tag{22a}$$

$$[\langle\psi|a,1\rangle \quad \langle\psi|a,2\rangle \quad \langle\psi|a,3\rangle \quad \dots \quad \langle\psi|a,n\rangle]$$

$$= [\langle\psi|b,1\rangle \quad \langle\psi|b,2\rangle \quad \langle\psi|b,3\rangle \quad \dots \quad \langle\psi|b,n\rangle]$$

$$\times \begin{bmatrix} \langle b,1|a,1\rangle & \langle b,1|a,2\rangle & \langle b,1|a,3\rangle & \dots & \langle b,1|a,n\rangle \\ \langle b,2|a,1\rangle & \langle b,2|a,2\rangle & \langle b,2|a,3\rangle & \dots & \langle b,2|a,n\rangle \\ \langle b,3|a,1\rangle & \langle b,3|a,2\rangle & \langle b,3|a,3\rangle & \dots & \langle b,3|a,n\rangle \\ \vdots & \vdots & \vdots & \ddots & \vdots \\ \langle b,n|a,1\rangle & \langle b,n|a,2\rangle & \langle b,n|a,3\rangle & \dots & \langle b,n|a,n\rangle \end{bmatrix} \tag{22b}$$

Note that the columns of the first transformation matrix are merely the representation of the b basis kets in the a basis, while the rows are the representation of the a bras in the b basis. The second transformation matrix is the adjoint (complex conjugate transpose) of the first. If the two matrices are multiplied in either order, the result is a unit matrix, because the basis states are normalized. But this is just the definition of a unitary matrix. In compact matrix notation, we have

$$\boldsymbol{\psi}_a = \mathbf{T}\boldsymbol{\psi}_b, \quad \boldsymbol{\psi}_a^\dagger = \boldsymbol{\psi}_b^\dagger \mathbf{T}^\dagger \tag{23}$$

The unitary nature of the transformation is expressed as

$$\mathbf{T}\mathbf{T}^\dagger = \mathbf{T}^\dagger\mathbf{T} = \mathbf{E} = \mathbf{T}\mathbf{T}^{-1} = \mathbf{T}^{-1}\mathbf{T} \tag{24}$$

From these two equations, it is evident that the normalization of the state is preserved, regardless of the representation used:

$$\boldsymbol{\psi}_a^\dagger\boldsymbol{\psi}_a = \boldsymbol{\psi}_b^\dagger\mathbf{T}^\dagger\mathbf{T}\boldsymbol{\psi}_b = \boldsymbol{\psi}_b^\dagger\boldsymbol{\psi}_b \tag{25}$$

The inverse transformation can easily be derived. If $\boldsymbol{\psi}_\mathrm{a} = \mathbf{T}\boldsymbol{\psi}_\mathrm{b}$ then we have

$$\mathbf{T}^{-1}\mathbf{T}\boldsymbol{\psi}_b = \mathbf{T}^{-1}\boldsymbol{\psi}_a, \quad \boldsymbol{\psi}_b = \mathbf{T}^{-1}\boldsymbol{\psi}_a \tag{26}$$

But the inverse transformation is

$$\begin{aligned} |\psi\rangle &= \sum_{i=1}^{n} \langle a,i|\psi\rangle |a,i\rangle \\ &= \sum_{i=1}^{n} \langle a,i|\psi\rangle \sum_{j=1}^{n} \langle b,j|a,i\rangle |b,j\rangle \\ &= \sum_{i,j=1}^{n} \langle b,j|a,i\rangle\langle a,i|\psi\rangle |b,j\rangle \end{aligned} \tag{27}$$

Comparing equations (21a) and (27), the relationship between the a to b and b to a transforms is found to be

$$T_{ji}^* = \langle b,i|a,j\rangle^* = \langle a,j|b,i\rangle = T_{ij}^\dagger \tag{28}$$

which shows that the inverse transformation matrix $\mathbf{T}^{-1}$ is just the adjoint of the original matrix—but this is again just the definition of a unitary matrix. Examining equations (22a) and (22b), it is clear that the complex conjugate transpose of the transformation matrix is, indeed, the desired inverse transformation. This may be shown more easily by noting from equation (24) that $\mathbf{T}^\dagger = \mathbf{T}^{-1}$. Then, from equation (23), we have

$$\left.\begin{aligned} \mathbf{T}^\dagger\boldsymbol{\psi}_a = \mathbf{T}^\dagger\mathbf{T}\boldsymbol{\psi}_b = \boldsymbol{\psi}_b \\ \boldsymbol{\psi}_a^\dagger\mathbf{T} = \boldsymbol{\psi}_b^\dagger\mathbf{T}^\dagger\mathbf{T} = \boldsymbol{\psi}_b^\dagger \end{aligned}\right\} \tag{29}$$

We now turn to some relationships involving operators. Suppose one has some arbitrary operator $\hat{\mathrm{O}}$. Using equation (19), we can write

$$\begin{aligned} \hat{O} &= \left(\sum_{i=1}^{n} |i\rangle\langle i|\right)\hat{O}\left(\sum_{j=1}^{n} |\,j\rangle\langle\,j|\right) \\ &= \sum_{i,j=1}^{n} |i\rangle\langle i|\hat{O}|\,j\rangle\langle\,j| \\ &= \sum_{i,j=1}^{n} \langle i|\hat{O}|\,j\rangle |i\rangle\langle\,j| \\ &= \sum_{i,j=1}^{n} c_{ij}|i\rangle\langle\,j| \end{aligned} \tag{30}$$

A unit operator can be inserted anywhere without affecting the equality. This equation is a prescription for writing any operator as a sum of operators $|i\rangle\langle\,j|$. Clearly, if there are n basis states $|i\rangle$ then there are n^2 basis operators $|i\rangle\langle\,j|$. If we multiply this equation from the left and right by a basis state, the result is a prescription for the coefficients c_{ij}:

$$\begin{aligned} \langle k|\hat{O}|l\rangle &= \langle k|\left(\sum_{i,j=1}^{n} c_{ij}|i\rangle\langle\,j|\right)|l\rangle \\ &= \sum_{i,j=1}^{n} c_{ij}\langle k|i\rangle\langle\,j|l\rangle \\ &= \sum_{i,j=1}^{n} c_{ij}\delta_{ki}\delta_{jl} = c_{kl} \end{aligned} \tag{31}$$

These coefficients are commonly called the *matrix elements* of the operator, and can be arranged in a matrix to form a Hilbert space representation of the operator:

$$\hat{O} \xrightarrow{|i\rangle} \mathbf{O} = \begin{bmatrix} \langle 1|\hat{O}|1\rangle & \langle 1|\hat{O}|2\rangle & \langle 1|\hat{O}|3\rangle & \dots & \langle 1|\hat{O}|n\rangle \\ \langle 2|\hat{O}|1\rangle & \langle 2|\hat{O}|2\rangle & \langle 2|\hat{O}|3\rangle & \dots & \langle 2|\hat{O}|n\rangle \\ \langle 3|\hat{O}|1\rangle & \langle 3|\hat{O}|2\rangle & \langle 3|\hat{O}|3\rangle & \dots & \langle 3|\hat{O}|n\rangle \\ \vdots & \vdots & \vdots & \ddots & \vdots \\ \langle n|\hat{O}|1\rangle & \langle n|\hat{O}|2\rangle & \langle n|\hat{O}|3\rangle & \dots & \langle n|\hat{O}|n\rangle \end{bmatrix} \tag{32}$$

Proceeding as in equation (25), we can write

$$\boldsymbol{\psi}_a^\dagger \mathbf{O}_a \boldsymbol{\psi}_a = \boldsymbol{\psi}_b^\dagger \mathbf{T}^\dagger \mathbf{T} \mathbf{O}_a \mathbf{T}^\dagger \mathbf{T} \boldsymbol{\psi}_b = \boldsymbol{\psi}_b^\dagger \mathbf{O}_b \boldsymbol{\psi}_b \tag{33}$$

where we have defined the operator in the b basis as

$$\mathbf{O}_b = \mathbf{T} \mathbf{O}_a \mathbf{T}^\dagger \tag{34}$$

Analogously, the basis operators themselves can be represented as follows to yield a matrix of all zero elements except the ijth:

$$|i\rangle\langle j| \xrightarrow{|i\rangle} \begin{bmatrix} \langle 1|i\rangle\langle j|1\rangle & \langle 1|i\rangle\langle j|2\rangle & \dots & \langle 1|i\rangle\langle j|j\rangle & \dots & \langle 1|i\rangle\langle j|n\rangle \\ \langle 2|i\rangle\langle j|1\rangle & \langle 2|i\rangle\langle j|2\rangle & \dots & \langle 2|i\rangle\langle j|j\rangle & \dots & \langle 2|i\rangle\langle j|n\rangle \\ \vdots & \vdots & \ddots & \vdots & & \vdots \\ \langle i|i\rangle\langle j|1\rangle & \langle i|i\rangle\langle j|2\rangle & \dots & \langle i|i\rangle\langle j|j\rangle & \dots & \langle i|i\rangle\langle j|n\rangle \\ \vdots & \vdots & & \vdots & \ddots & \vdots \\ \langle n|i\rangle\langle j|1\rangle & \langle n|i\rangle\langle j|2\rangle & \dots & \langle n|i\rangle\langle j|j\rangle & \dots & \langle n|i\rangle\langle j|n\rangle \end{bmatrix}$$

$$= \begin{bmatrix} 0 & 0 & \dots & 0 & \dots & 0 \\ 0 & 0 & \dots & 0 & \dots & 0 \\ \vdots & \vdots & \ddots & \vdots & & \vdots \\ 0 & 0 & \dots & 1 & \dots & 0 \\ \vdots & \vdots & & \vdots & \ddots & \vdots \\ 0 & 0 & \dots & 0 & \dots & 0 \end{bmatrix} \tag{35}$$

This result can also be obtained from equations (17a) and (17b) by writing

$$\begin{bmatrix} \langle 1|i\rangle \\ \langle 2|i\rangle \\ \vdots \\ \langle j|i\rangle \\ \vdots \\ \langle n|i\rangle \end{bmatrix} \begin{bmatrix} \langle j|1\rangle & \langle j|2\rangle & \dots & \langle j|j\rangle & \dots & \langle j|n\rangle \end{bmatrix}$$

$$= \begin{bmatrix} \langle 1|i\rangle\langle j|1\rangle & \langle 1|i\rangle\langle j|2\rangle & \dots & \langle 1|i\rangle\langle j|j\rangle & \dots & \langle 1|i\rangle\langle j|n\rangle \\ \langle 2|i\rangle\langle j|1\rangle & \langle 2|i\rangle\langle j|2\rangle & \dots & \langle 2|i\rangle\langle j|j\rangle & \dots & \langle 2|i\rangle\langle j|n\rangle \\ \vdots & \vdots & \ddots & \vdots & & \vdots \\ \langle i|i\rangle\langle j|1\rangle & \langle i|i\rangle\langle j|2\rangle & \dots & \langle i|i\rangle\langle j|j\rangle & \dots & \langle i|i\rangle\langle j|n\rangle \\ \vdots & \vdots & & \vdots & \ddots & \vdots \\ \langle n|i\rangle\langle j|1\rangle & \langle n|i\rangle\langle j|2\rangle & \dots & \langle n|i\rangle\langle j|j\rangle & \dots & \langle n|i\rangle\langle j|n\rangle \end{bmatrix} \tag{36}$$

The basis operators are orthogonal, just as the basis states are; however, the inner product exemplified by equation (11) must be replaced by the trace operation:

$$\begin{aligned} \mathrm{Tr}(|\,j\rangle\langle k|l\rangle\langle m|) &= \sum_{i=1}^{n} \langle i|\,j\rangle\langle k|l\rangle\langle m|i\rangle \\ &= \langle k|l\rangle\langle m|\,j\rangle \\ &= \delta_{kl}\delta_{mj} \end{aligned} \tag{37}$$

In equation (37), the right-hand side will be nonzero if and only if $j = m$ and $k = l$; then

$$|\,j\rangle\langle k|k\rangle\langle\,j| = |\,j\rangle\langle k|(|\,j\rangle\langle k|)^\dagger \tag{38}$$

In order to simplify notation, we now make a mapping of the indices j and k of $|j\rangle\langle k|$ onto a single index i of $\hat{U}_i$. This is simply a relabeling of the basis operators. The exact nature of the mapping is arbitrary, except that there must be a one-to-one correspondence between the pair of indices j, k and the index i. The expression corresponding to equation (37) is then

$$\mathrm{Tr}(\hat{U}_i \hat{U}_j^\dagger) = \delta_{ij} \tag{39}$$

This equation is the normalization condition for basis operators analogous to equation (11). Note that if the basis states used in equation (37) are normalized then these basis operators will also be normalized.

If we expand the generic operator $\hat{O}$ in terms of this basis set, the result is

$$\hat{O} = \sum_{i=1}^{n^2} c_i \hat{U}_i \tag{40}$$

Now, if this equation is multiplied by ${\hat{U}_j}^\dagger$ and the trace taken, a prescription is obtained for the expansion coefficients c_i:

$$\begin{aligned} \mathrm{Tr}(\hat{O}\hat{U}_j^\dagger) &= \mathrm{Tr}\left(\sum_{i=1}^{n^2} c_i \hat{U}_i \hat{U}_j^\dagger \right) \\ &= \sum_{i=1}^{n^2} c_i \mathrm{Tr}(\hat{U}_i \hat{U}_j^\dagger) = \sum_{i=1}^{n^2} c_i \delta_{ij} = c_j \end{aligned} \tag{41}$$

Equation (40) may then be rewritten as

$$\hat{O} = \sum_{i=1}^{n^2} \mathrm{Tr}(\hat{O}\hat{U}_i^\dagger)\hat{U}_i \tag{42}$$

The coefficients in this equation can be arranged in a vector to form the Liouville space representation of the operator:

$$\hat{O} \xrightarrow{\hat{U}_i} \begin{bmatrix} \mathrm{Tr}(\hat{O}\hat{U}_1^\dagger) \\ \mathrm{Tr}(\hat{O}\hat{U}_2^\dagger) \\ \mathrm{Tr}(\hat{O}\hat{U}_3^\dagger) \\ \vdots \\ \mathrm{Tr}(\hat{O}\hat{U}_{n^2}^\dagger) \end{bmatrix} \tag{43}$$

Note that this space is n^2-dimensional.

As was done with basis states, it is possible to transform among alternative sets of basis operators. Consider a new operator basis $\{\hat{V}_i, i = 1, 2, 3, \ldots, n^2\}$. These operators can be expressed in the original basis as

$$\hat{V}_i = \sum_{j=1}^{n^2} \mathrm{Tr}(\hat{V}_i \hat{U}_j^\dagger)\hat{U}_j \tag{44}$$

Equation (42) can be written in terms of the $\hat{V}_i$; then equation (44) can be substituted:

$$\begin{aligned}\hat{O} &= \sum_{j=1}^{n^2} \mathrm{Tr}(\hat{O}\hat{V}_j^\dagger)\hat{V}_j \\ &= \sum_{j=1}^{n^2} \mathrm{Tr}(\hat{O}\hat{V}_j^\dagger) \sum_{i=1}^{n^2} \mathrm{Tr}(\hat{V}_j \hat{U}_i^\dagger)\hat{U}_i \\ &= \sum_{i,j=1}^{n^2} \mathrm{Tr}(\hat{V}_j \hat{U}_i^\dagger)\mathrm{Tr}(\hat{O}\hat{V}_j^\dagger)\hat{U}_i \end{aligned} \tag{45}$$

Comparing equations (42) and (45), it is evident that the conversion of operator bases is accomplished as follows:

$$\mathrm{Tr}(\hat{O}\hat{U}_i^\dagger) = \sum_{j=1}^{n^2} \mathrm{Tr}(\hat{V}_j \hat{U}_i^\dagger)\mathrm{Tr}(\hat{O}\hat{V}_j^\dagger) \tag{46}$$

In terms of the Liouville space representation, this can be written as

$$\begin{bmatrix} \mathrm{Tr}(\hat{O}\hat{U}_1^\dagger) \\ \mathrm{Tr}(\hat{O}\hat{U}_2^\dagger) \\ \mathrm{Tr}(\hat{O}\hat{U}_3^\dagger) \\ \vdots \\ \mathrm{Tr}(\hat{O}\hat{U}_{n^2}^\dagger) \end{bmatrix} = \begin{bmatrix} \mathrm{Tr}(\hat{V}_1\hat{U}_1^\dagger) & \mathrm{Tr}(\hat{V}_2\hat{U}_1^\dagger) & \mathrm{Tr}(\hat{V}_3\hat{U}_1^\dagger) & \ldots & \mathrm{Tr}(\hat{V}_{n^2}\hat{U}_1^\dagger) \\ \mathrm{Tr}(\hat{V}_1\hat{U}_2^\dagger) & \mathrm{Tr}(\hat{V}_2\hat{U}_2^\dagger) & \mathrm{Tr}(\hat{V}_3\hat{U}_2^\dagger) & \ldots & \mathrm{Tr}(\hat{V}_{n^2}\hat{U}_2^\dagger) \\ \mathrm{Tr}(\hat{V}_1\hat{U}_3^\dagger) & \mathrm{Tr}(\hat{V}_2\hat{U}_3^\dagger) & \mathrm{Tr}(\hat{V}_3\hat{U}_3^\dagger) & \ldots & \mathrm{Tr}(\hat{V}_{n^2}\hat{U}_3^\dagger) \\ \vdots & \vdots & \vdots & \ddots & \vdots \\ \mathrm{Tr}(\hat{V}_1\hat{U}_{n^2}^\dagger) & \mathrm{Tr}(\hat{V}_2\hat{U}_{n^2}^\dagger) & \mathrm{Tr}(\hat{V}_3\hat{U}_{n^2}^\dagger) & \ldots & \mathrm{Tr}(\hat{V}_{n^2}\hat{U}_{n^2}^\dagger) \end{bmatrix} \times \begin{bmatrix} \mathrm{Tr}(\hat{O}\hat{V}_1^\dagger) \\ \mathrm{Tr}(\hat{O}\hat{V}_2^\dagger) \\ \mathrm{Tr}(\hat{O}\hat{V}_3^\dagger) \\ \vdots \\ \mathrm{Tr}(\hat{O}\hat{V}_{n^2}^\dagger) \end{bmatrix} \tag{47}$$

2.3 Direct Product Bases

It is quite common that one is able to derive a basis for two or more parts of a system using the techniques described in the previous section, but it is then desired to represent the whole system so that interactions among the parts can be considered. For example, a molecule might contain two spins, say a ^{13}C nucleus and a ^{1}H nucleus. For this purpose, we introduce the *direct* or *outer product* of the subspaces to form the space appropriate for the whole system. One can form the direct products in either Hilbert space or Liouville space. The only new definitions needed are as follows. For vectors (states),

$$|\psi_1\rangle|\psi_2\rangle = |\psi\rangle \tag{48a}$$

$$\begin{bmatrix} \langle 1,1|\psi_1\rangle \\ \langle 1,2|\psi_1\rangle \\ \langle 1,3|\psi_1\rangle \\ \vdots \\ \langle 1,n|\psi_1\rangle \end{bmatrix} \otimes \begin{bmatrix} \langle 2,1|\psi_2\rangle \\ \langle 2,2|\psi_2\rangle \\ \langle 2,3|\psi_2\rangle \\ \vdots \\ \langle 2,m|\psi_2\rangle \end{bmatrix} = \begin{bmatrix} \langle 1,1|\psi_1\rangle \begin{bmatrix} \langle 2,1|\psi_2\rangle \\ \langle 2,2|\psi_2\rangle \\ \langle 2,3|\psi_2\rangle \\ \vdots \\ \langle 2,m|\psi_2\rangle \end{bmatrix} \\ \langle 1,2|\psi_1\rangle \begin{bmatrix} \langle 2,1|\psi_2\rangle \\ \langle 2,2|\psi_2\rangle \\ \langle 2,3|\psi_2\rangle \\ \vdots \\ \langle 2,m|\psi_2\rangle \end{bmatrix} \\ \langle 1,3|\psi_1\rangle \begin{bmatrix} \langle 2,1|\psi_2\rangle \\ \langle 2,2|\psi_2\rangle \\ \langle 2,3|\psi_2\rangle \\ \vdots \\ \langle 2,m|\psi_2\rangle \end{bmatrix} \\ \vdots \\ \langle 1,n|\psi_1\rangle \begin{bmatrix} \langle 2,1|\psi_2\rangle \\ \langle 2,2|\psi_2\rangle \\ \langle 2,3|\psi_2\rangle \\ \vdots \\ \langle 2,m|\psi_2\rangle \end{bmatrix} \end{bmatrix} \tag{48b}$$

A slightly more condensed notation is required to make the corresponding definition for matrices (operators) manageable:

$$\hat{O} = \hat{O}^{(1)} \otimes \hat{O}^{(2)} \tag{49a}$$

$$\mathbf{O} = \begin{bmatrix} O_{1,1}^{(1)}\mathbf{O}^{(2)} & O_{1,2}^{(1)}\mathbf{O}^{(2)} & O_{1,3}^{(1)}\mathbf{O}^{(2)} & \ldots & O_{1,n}^{(1)}\mathbf{O}^{(2)} \\ O_{2,1}^{(1)}\mathbf{O}^{(2)} & O_{2,2}^{(1)}\mathbf{O}^{(2)} & O_{2,3}^{(1)}\mathbf{O}^{(2)} & \ldots & O_{2,n}^{(1)}\mathbf{O}^{(2)} \\ O_{3,1}^{(1)}\mathbf{O}^{(2)} & O_{3,2}^{(1)}\mathbf{O}^{(2)} & O_{3,3}^{(1)}\mathbf{O}^{(2)} & \ldots & O_{3,n}^{(1)}\mathbf{O}^{(2)} \\ \vdots & \vdots & \vdots & \ddots & \vdots \\ O_{n,1}^{(1)}\mathbf{O}^{(2)} & O_{n,2}^{(1)}\mathbf{O}^{(2)} & O_{n,3}^{(1)}\mathbf{O}^{(2)} & \ldots & O_{n,n}^{(1)}\mathbf{O}^{(2)} \end{bmatrix} \tag{49b}$$

$$\mathbf{O}^{(2)} = \begin{bmatrix} O_{1,1}^{(2)} & O_{1,2}^{(2)} & O_{1,3}^{(2)} & \ldots & O_{1,m}^{(2)} \\ O_{2,1}^{(2)} & O_{2,2}^{(2)} & O_{2,3}^{(2)} & \ldots & O_{2,m}^{(2)} \\ O_{3,1}^{(2)} & O_{3,2}^{(2)} & O_{3,3}^{(2)} & \ldots & O_{3,m}^{(2)} \\ \vdots & \vdots & \vdots & \ddots & \vdots \\ O_{m,1}^{(2)} & O_{m,2}^{(2)} & O_{m,3}^{(2)} & \ldots & O_{m,m}^{(2)} \end{bmatrix} \tag{49c}$$

Note that the dimension of the product space is always the product of the dimensions of the subspaces.

In equation (43) the Liouville space was introduced. With the introduction of the concept of direct products, it is possible to give a more satisfying explanation of the mapping from Hilbert space to Liouville space. The Hilbert space operators $|i\rangle\langle j|$ can be mapped onto a Liouville space with the following basis states:

$$|i\rangle|\ j\rangle = |ij\rangle \tag{50}$$

Clearly, a one-to-one mapping is possible. In Section 5, the use of Liouville space representations will be explored further with the introduction of superoperators.

It is common in the NMR literature to have implied direct products. For example, one might write $\hat{I}_z{}^{(1)} + \hat{I}_z{}^{(2)}$, where (1) and (2) refer to different spins. This is meant to imply $\hat{I}_z{}^{(1)} \otimes \hat{E}^{(2)} + \hat{E}^{(1)} \otimes \hat{I}_z{}^{(2)}$. Alternatively, one might encounter $\hat{I}_z\hat{I}_+$, where no direct product is implied, or $\hat{I}_+{}^{(1)}\hat{I}_-{}^{(2)}$, where we are to understand that this means $\hat{I}_+{}^{(1)} \otimes \hat{I}_-{}^{(2)}$. It is necessary to understand from the context and notation what is really meant.

3 SOME COMMONLY USED BASES

Next let us consider some examples of bases commonly used in NMR, using simple spin systems to illustrate how this formalism can be applied to nuclear spins.

3.1 The Single Spin Eigenstate Basis

A single isolated spin-$\frac{1}{2}$ nucleus has two energy eigenstates. They are commonly represented as $|\alpha\rangle$ and $|\beta\rangle$; however, since this notation is applicable only for spin-$\frac{1}{2}$, we shall also use the notation $|\frac{1}{2}\rangle$ and $|-\frac{1}{2}\rangle$, respectively, where each state is labelled by its $\hat{I}_z$ eigenvalue (this will be discussed in more detail below). It is assumed that these states are orthonormal. Using equation (17a), we can write the Hilbert space representation of the basis states as

$$\left.\begin{aligned} |\alpha\rangle = |\tfrac{1}{2}\rangle \rightarrow \begin{bmatrix}\langle\alpha|\alpha\rangle\\ \langle\beta|\alpha\rangle\end{bmatrix} = \begin{bmatrix}1\\0\end{bmatrix} \\ |\beta\rangle = |-\tfrac{1}{2}\rangle \rightarrow \begin{bmatrix}\langle\alpha|\beta\rangle\\ \langle\beta|\beta\rangle\end{bmatrix} = \begin{bmatrix}0\\1\end{bmatrix} \end{aligned}\right\} \tag{51}$$

The corresponding Hilbert space representation of the basis operators can be obtained most easily using equation (36) to write

$$\left.\begin{aligned} \hat{U}_1 = |\alpha\rangle\langle\alpha| \rightarrow \begin{bmatrix}1\\0\end{bmatrix}[1\quad 0] = \begin{bmatrix}1&0\\0&0\end{bmatrix} \\ \hat{U}_2 = |\alpha\rangle\langle\beta| \rightarrow \begin{bmatrix}1\\0\end{bmatrix}[0\quad 1] = \begin{bmatrix}0&1\\0&0\end{bmatrix} \\ \hat{U}_3 = |\beta\rangle\langle\alpha| \rightarrow \begin{bmatrix}0\\1\end{bmatrix}[1\quad 0] = \begin{bmatrix}0&0\\1&0\end{bmatrix} \\ \hat{U}_4 = |\beta\rangle\langle\beta| \rightarrow \begin{bmatrix}0\\1\end{bmatrix}[0\quad 1] = \begin{bmatrix}0&0\\0&1\end{bmatrix} \end{aligned}\right\} \tag{52}$$

It is easily verified that these matrices satisfy the orthonormality conditions by comparing with equation (39) for all pairs.

For spins with a higher angular momentum quantum number, the bases are similar but with higher dimension. For example, a spin-1 nucleus, like ^{2}H, has three eigenstates and nine basis operators. Representations of basis states and operators for any nucleus can be obtained just as above knowing only the number of eigenstates and assuming that they are orthonormal.

3.2 The Basis Derived from Direct Products of Single Spin Bases

When the system of interest includes more than one spin, a direct product of single spin bases described in the previous section (one set corresponding to the correct spin for each nucleus) yields a basis for the combined system. The first state and the first operator for two spin-$\frac{1}{2}$ nuclei, for example, would be

$$\left.\begin{aligned} |\alpha\rangle \otimes |\alpha\rangle = |\alpha\alpha\rangle \rightarrow \begin{bmatrix}1\\0\end{bmatrix} \otimes \begin{bmatrix}1\\0\end{bmatrix} \\ = \begin{bmatrix}1\begin{bmatrix}1\\0\end{bmatrix}\\ 0\begin{bmatrix}1\\0\end{bmatrix}\end{bmatrix} = \begin{bmatrix}1\\0\\0\\0\end{bmatrix} \\ \hat{U}_1 \otimes \hat{V}_1 \rightarrow \begin{bmatrix}1&0\\0&0\end{bmatrix} \otimes \begin{bmatrix}1&0\\0&0\end{bmatrix} = \begin{bmatrix}1\begin{bmatrix}1&0\\0&0\end{bmatrix} & 0\begin{bmatrix}1&0\\0&0\end{bmatrix}\\ 0\begin{bmatrix}1&0\\0&0\end{bmatrix} & 0\begin{bmatrix}1&0\\0&0\end{bmatrix}\end{bmatrix} \\ = \begin{bmatrix}1&0&0&0\\0&0&0&0\\0&0&0&0\\0&0&0&0\end{bmatrix} \end{aligned}\right\} \tag{53}$$

The other 3 basis states and 15 operators are composed in the same fashion using all the pairs of single spin matrices.

3.3 The Basis Derived from the Eigenstates of the Hamiltonian

The states given in equation (51) for a single spin $\frac{1}{2}$ are the eigenstates of the Hamiltonian, but for two identical spin-$\frac{1}{2}$ nuclei (an A_2 spin system), the eigenstates are

$$\left.\begin{aligned} |\mathrm{A}_2, 1\rangle = |\alpha\alpha\rangle \rightarrow \begin{bmatrix}1\\0\\0\\0\end{bmatrix} \\ |\mathrm{A}_2, 2\rangle = \sqrt{\tfrac{1}{2}}(|\alpha\beta\rangle + |\beta\alpha\rangle) \rightarrow \begin{bmatrix}0\\\sqrt{\frac{1}{2}}\\\sqrt{\frac{1}{2}}\\0\end{bmatrix} \\ |\mathrm{A}_2, 3\rangle = \sqrt{\tfrac{1}{2}}(|\alpha\beta\rangle - |\beta\alpha\rangle) \rightarrow \begin{bmatrix}0\\\sqrt{\frac{1}{2}}\\-\sqrt{\frac{1}{2}}\\0\end{bmatrix} \\ |\mathrm{A}_2, 4\rangle = |\beta\beta\rangle \rightarrow \begin{bmatrix}0\\0\\0\\1\end{bmatrix} \end{aligned}\right\} \tag{54}$$

These equations show a representation of the eigenstates in the basis of the spin product states. Assembling these vectors into a unitary matrix according to equation (22a) gives the following transformation matrix from the spin product basis to the eigenbasis:

$$\mathbf{U} = \begin{bmatrix} 1 & 0 & 0 & 0 \\ 0 & \sqrt{\frac{1}{2}} & \sqrt{\frac{1}{2}} & 0 \\ 0 & \sqrt{\frac{1}{2}} & -\sqrt{\frac{1}{2}} & 0 \\ 0 & 0 & 0 & 1 \end{bmatrix} \tag{55}$$

It is easily verified that $\mathbf{U}\mathbf{U}^{\dagger} = \mathbf{U}\mathbf{U}^{-1} = \mathbf{E}$. Applying this transformation to the spin product states or operators yields the desired eigenstate basis for the Hilbert space representation or the Liouville space representation, respectively.

3.4 The Angular Momentum Operator Basis

For a single spin-$\frac{1}{2}$ nucleus, the components of the angular momentum vector operator $\hat{\boldsymbol{I}} = \{\hat{I}_x, \hat{I}_y, \hat{I}_z\}$ augmented by the identity operator $\hat{E}$ are a complete basis. For a development of the angular momentum operators from first principles, the reader is referred to the standard texts.[6,7,10] We shall be content to define them according to their effect on the basis states as in equation (5). For any spin-I nucleus there are $2I + 1$ quantum states $|m\rangle$ such that

$$\left.\begin{aligned} \hat{I}_x|m\rangle &= \tfrac{1}{2}\{[I(I+1) - m(m+1)]^{1/2}|m+1\rangle \\ &\quad + [I(I+1) - m(m-1)]^{1/2}|m-1\rangle\} \\ \hat{I}_y|m\rangle &= \tfrac{1}{2\mathrm{i}}\{[I(I+1) - m(m+1)]^{1/2}|m+1\rangle \\ &\quad - [I(I+1) - m(m-1)]^{1/2}|m-1\rangle\} \\ \hat{I}_z|m\rangle &= m|m\rangle \end{aligned}\right\} \tag{56}$$

The eigenvalue m ranges in integer steps such that $-I \leq m \leq I$. For spin-$\frac{1}{2}$, using the $\{|\frac{1}{2}\rangle, |-\frac{1}{2}\rangle\}$ basis, the angular momentum operators and their representations are

$$\begin{aligned} \hat{I}_x &\rightarrow \tfrac{1}{2}\begin{bmatrix} 0 & 1 \\ 1 & 0 \end{bmatrix}, \quad \hat{I}_y \rightarrow \tfrac{1}{2\mathrm{i}}\begin{bmatrix} 0 & 1 \\ -1 & 0 \end{bmatrix} \\ \hat{I}_z &\rightarrow \tfrac{1}{2}\begin{bmatrix} 1 & 0 \\ 0 & -1 \end{bmatrix}, \quad \hat{E} \rightarrow \begin{bmatrix} 1 & 0 \\ 0 & 1 \end{bmatrix} \end{aligned} \tag{57}$$

It is easily verified that these operators are orthogonal but not normalized using equation (39). Normalization can easily be achieved by multiplying by the appropriate constants to satisfy equation (39); this yields the desired basis for spin-$\frac{1}{2}$:

$$\left.\begin{aligned} \hat{U}_1 &= \frac{1}{\sqrt{2}}\hat{E} \rightarrow \frac{1}{\sqrt{2}}\begin{bmatrix} 1 & 0 \\ 0 & 1 \end{bmatrix} \\ \hat{U}_2 &= \sqrt{2}\hat{I}_z \rightarrow \frac{\sqrt{2}}{2}\begin{bmatrix} 1 & 0 \\ 0 & -1 \end{bmatrix} \\ \hat{U}_3 &= \sqrt{2}\hat{I}_x \rightarrow \frac{\sqrt{2}}{2}\begin{bmatrix} 0 & 1 \\ 1 & 0 \end{bmatrix} \\ \hat{U}_4 &= \sqrt{2}\hat{I}_y \rightarrow \frac{\sqrt{2}}{2\mathrm{i}}\begin{bmatrix} 0 & 1 \\ -1 & 0 \end{bmatrix} \end{aligned}\right\} \tag{58}$$

For a spin-1 nucleus, using equation (56), the angular momentum operators are

$$\left.\begin{aligned} \hat{I}_x &\rightarrow \tfrac{1}{\sqrt{2}}\begin{bmatrix} 0 & 1 & 0 \\ 1 & 0 & 1 \\ 0 & 1 & 0 \end{bmatrix}, \quad \hat{I}_y \rightarrow \tfrac{1}{\mathrm{i}\sqrt{2}}\begin{bmatrix} 0 & 1 & 0 \\ -1 & 0 & 1 \\ 0 & -1 & 0 \end{bmatrix} \\ \hat{I}_z &\rightarrow \begin{bmatrix} 1 & 0 & 0 \\ 0 & 0 & 0 \\ 0 & 0 & -1 \end{bmatrix} \end{aligned}\right\} \tag{59}$$

However, since nine basis operators are required for spin 1, augmenting this set with $\hat{E}$ would clearly not be sufficient to produce a complete basis. However, we shall defer enumerating the other members of this basis until the next section, because the task becomes much easier once the spherical tensor operators have been introduced.

3.5 The Spherical Tensor Operator Basis

Examination of equation (56) rapidly leads one to conclude that a simpler basis might be composed including the following operators:

$$\left.\begin{aligned} \hat{I}_+|m\rangle &= [I(I+1) - m(m+1)]^{1/2}|m+1\rangle \\ \hat{I}_-|m\rangle &= [I(I+1) - m(m-1)]^{1/2}|m-1\rangle \end{aligned}\right\} \tag{60}$$

These operators are commonly called the *raising* or *step-up* and *lowering* or *step-down* operators, because they convert a given eigenket of $\hat{I}_z$ into one with the eigenvalue increased or decreased, respectively, by one. In terms of these operators, we have

$$\hat{I}_x = \tfrac{1}{2}(\hat{I}_+ + \hat{I}_-), \quad \hat{I}_y = \tfrac{1}{2\mathrm{i}}(\hat{I}_+ - \hat{I}_-) \tag{61}$$

The inverse relationship is

$$\hat{I}_+ = \hat{I}_x + \mathrm{i}\hat{I}_y, \quad \hat{I}_- = \hat{I}_x - \mathrm{i}\hat{I}_y \tag{62}$$

Applying these relations to equation (57) leads to a new basis:

$$\left.\begin{aligned} \hat{I}_+ &\rightarrow \begin{bmatrix} 0 & 1 \\ 0 & 0 \end{bmatrix}, \quad \hat{I}_- \rightarrow \begin{bmatrix} 0 & 0 \\ 1 & 0 \end{bmatrix} \\ \hat{I}_z &\rightarrow \tfrac{1}{2}\begin{bmatrix} 1 & 0 \\ 0 & -1 \end{bmatrix}, \quad \hat{E} \rightarrow \begin{bmatrix} 1 & 0 \\ 0 & 1 \end{bmatrix} \end{aligned}\right\} \tag{63}$$

The orthonormal basis corresponding to equation (58) is given by

$$\left.\begin{aligned} \hat{U}_1 &= \hat{T}^{(0)}_{0,0} = \frac{1}{\sqrt{2}}\hat{E} \rightarrow \frac{1}{\sqrt{2}}\begin{bmatrix} 1 & 0 \\ 0 & 1 \end{bmatrix} \\ \hat{U}_2 &= \hat{T}^{(1)}_{0,0} = \sqrt{2}\hat{I}_z \rightarrow \frac{\sqrt{2}}{2}\begin{bmatrix} 1 & 0 \\ 0 & -1 \end{bmatrix} \\ \hat{U}_3 &= \hat{T}^{(1)}_{1,0} = -\hat{I}_+ \rightarrow \begin{bmatrix} 0 & -1 \\ 0 & 0 \end{bmatrix} \\ \hat{U}_4 &= \hat{T}^{(1)}_{-1,0} = \hat{I}_- \rightarrow \begin{bmatrix} 0 & 0 \\ 1 & 0 \end{bmatrix} \end{aligned}\right\} \tag{64}$$

The $\hat{T}^{(k)}_{q,j}$ designation for these operators is that characterizing the *irreducible spherical tensor operators*. There will be

$2k + 1$ members in a set of operators of rank k with projection q ranging from $-k$ to k in integer steps. Note that the index j is not needed here, but will come into play when more complicated spin systems are considered with more than one set of operators of a given k. In what follows, the index j will be suppressed when it is not needed. It is easily verified that this basis is orthonormal. The minus sign associated with $\hat{U}_3$ does not affect the orthonormality of the set. It is common practice to choose this 'phase factor' to correspond to that of the spherical harmonic functions, i.e., such that

$$\hat{T}_q^{(k)\dagger} = (-1)^q \hat{T}_{-q}^{(k)} \tag{65}$$

The operators then satisfy equation (39) in the form

$$\mathrm{Tr}(\hat{T}_q^{(k)} \hat{T}_{q'}^{(k)\dagger}) = (-1)^q \mathrm{Tr}(\hat{T}_q^{(k)} \hat{T}_{-q'}^{(k')}) = \delta_{kk'}\delta_{q-q'} \tag{66}$$

The defining characteristic of the irreducible spherical tensor operators is that when they are subjected to a rotation of the coordinate system, they behave like the spherical harmonic functions, i.e., they transform to linear combinations of the set such that operators of differing k or j never mix:

$$\hat{R}(\phi, \theta, \chi)\hat{T}_{q,j}^{(k)}\hat{R}^{-1}(\phi, \theta, \chi) = \sum_{q'=-k}^{k} D_{q'q}^{(k)}(\phi, \theta, \chi)\hat{T}_{q',j}^{(k)} \tag{67}$$

The rotation operator $\hat{R}(\phi, \theta, \chi)$ and its inverse (defined by equation (68)) transform any operator from the original coordinate system $\{x,y,z\}$ into a new one $\{x',y',z'\}$:

$$\left.\begin{aligned} \hat{R}(\phi, \theta, \chi) &= \exp(-\mathrm{i}\phi\hat{I}_z)\exp(-\mathrm{i}\theta\hat{I}_y)\exp(-\mathrm{i}\chi\hat{I}_z) \\ \hat{R}^{-1}(\phi, \theta, \chi) &= \exp(\mathrm{i}\phi\hat{I}_z)\exp(\mathrm{i}\theta\hat{I}_y)\exp(\mathrm{i}\chi\hat{I}_z) \end{aligned}\right\} \tag{68}$$

The Euler angles $\{\phi,\theta,\chi\}$ define rotations about the z, then y, then z again axes of the original coordinate system, which rotations carry the original coordinate system to coincide with the new one. The $D_{q'q}^{(k)}(\phi, \theta, \chi)$ are called the *Wigner rotation matrix elements*. The definition of these coefficients is rather involved, and will not be given here. They are defined and tabulated in numerous texts, such as the excellent one by Zare.[10] Exponential operators like those in equation (68) as generators of rotations play a central role in the theoretical development of NMR. They, too, are discussed in great detail in Zare's text.

It was noted in Section 2.1 that operators do not necessarily commute. A special shorthand notation is commonly used for *commutators* of operators, defined as follows:

$$\hat{A}\hat{B} - \hat{B}\hat{A} \equiv [\hat{A}, \hat{B}] \tag{69}$$

Using this notation, an equivalent, though perhaps less intuitive, definition of irreducible spherical tensor operators is provided by the following commutation relations:

$$\left.\begin{aligned} [\hat{I}_\pm, \hat{T}_{q,j}^{(k)}] &= \{(k \mp q)(k \pm q + 1)\}^{1/2}\hat{T}_{q\pm1,j}^{(k)} \\ [\hat{I}_z, \hat{T}_{q,j}^{(k)}] &= q\hat{T}_{q,j}^{(k)} \end{aligned}\right\} \tag{70}$$

Note that one is free to choose either the positive or the negative square root in the coefficient in equation (70), and the result will still satisfy both commutation relations. Thus, we choose the one that satisfies equation (65). The following commutators are easily verified for spin-$\frac{1}{2}$ from equation (63):

$$[\hat{I}_z, \hat{I}_\pm] = \pm\hat{I}_\pm, \quad [\hat{I}_\pm, \hat{I}_\mp] = \pm 2\hat{I}_z \tag{71}$$

From equation (59), using equation (62), one can generate the following operators and verify that equation (71) holds for spin 1 also:

$$\left.\begin{aligned} \hat{I}_+ \to \sqrt{2}\begin{bmatrix} 0 & 1 & 0 \\ 0 & 0 & 1 \\ 0 & 0 & 0 \end{bmatrix}, \quad \hat{I}_- \to \sqrt{2}\begin{bmatrix} 0 & 0 & 0 \\ 1 & 0 & 0 \\ 0 & 1 & 0 \end{bmatrix} \\ \hat{I}_z \to \begin{bmatrix} 1 & 0 & 0 \\ 0 & 0 & 0 \\ 0 & 0 & -1 \end{bmatrix} \end{aligned}\right\} \tag{72}$$

It can be shown[6] that these commutation relations are true in general. These three matrices represent an irreducible spherical tensor operator of rank one just as was the case for spin-$\frac{1}{2}$ in equation (64), and the zeroth-order operator can be written as well. Note, however, that the required normalization factors are different:

$$\left.\begin{aligned} \hat{T}_0^{(0)} &= \frac{1}{\sqrt{3}}\hat{E} \to \frac{1}{\sqrt{3}}\begin{bmatrix} 1 & 0 & 0 \\ 0 & 1 & 0 \\ 0 & 0 & 1 \end{bmatrix} \\ \hat{T}_1^{(1)} &= -\tfrac{1}{2}\hat{I}_+ \to -\frac{1}{\sqrt{2}}\begin{bmatrix} 0 & 1 & 0 \\ 0 & 0 & 1 \\ 0 & 0 & 0 \end{bmatrix} \\ \hat{T}_{-1}^{(1)} &= \tfrac{1}{2}\hat{I}_- \to \frac{1}{\sqrt{2}}\begin{bmatrix} 0 & 0 & 0 \\ 1 & 0 & 0 \\ 0 & 1 & 0 \end{bmatrix} \\ \hat{T}_0^{(1)} &= \frac{1}{\sqrt{2}}\hat{I}_z \to \frac{1}{\sqrt{2}}\begin{bmatrix} 1 & 0 & 0 \\ 0 & 0 & 0 \\ 0 & 0 & -1 \end{bmatrix} \end{aligned}\right\} \tag{73}$$

It is easily verified that these operators are orthonormal and satisfy equation (70).

Using these four operators as a starting point, the problem of finding the other five basis operators for spin 1 can now be addressed. The required operators must be mutually orthogonal and orthogonal to the four already proposed. A logical extension of what has been done so far would be the five elements of an irreducible spherical tensor operator of rank two. For spin 1, the step-up operator can be applied twice to the eigenstate $|-1\rangle$ to produce first the $|0\rangle$ then the $|1\rangle$ eigenstate. The corresponding second-rank operator is $\hat{I}_+\hat{I}_+$. The representation of this operator can be obtained in several ways according to what we have learned so far. Perhaps the easiest way is to square the matrix given in equation (72) and normalize the result to give

$$\hat{T}_2^{(2)} = \tfrac{1}{2}\hat{I}_+\hat{I}_+ \to \begin{bmatrix} 0 & 0 & 1 \\ 0 & 0 & 0 \\ 0 & 0 & 0 \end{bmatrix} \tag{74}$$

which is easily shown to satisfy equation (70). Equation (70) can now be used to successively generate the other members of the set as follows:

$$[\hat{I}_-, \hat{T}_2^{(2)}] = \{(2 + 2)(2 - 2 + 1)\}^{1/2}\hat{T}_1^{(2)} = -2\hat{T}_1^{(2)} \tag{75}$$

The negative square root is chosen so as to satisfy equation (65). Hence, we have

$$\begin{aligned}\hat{T}_1^{(2)} &= -\tfrac{1}{2}[\hat{I}_-, \tfrac{1}{2}\hat{I}_+\hat{I}_+] = -\tfrac{1}{4}[\hat{I}_-, \hat{I}_+\hat{I}_+] \\ &= -\tfrac{1}{4}(\hat{I}_-\hat{I}_+\hat{I}_+ - \hat{I}_+\hat{I}_+\hat{I}_-)\end{aligned} \tag{76}$$

Then substituting from equation (71) yields

$$\begin{aligned}\hat{T}_1^{(2)} &= -\tfrac{1}{4}\{\hat{I}_-\hat{I}_+\hat{I}_+ - \hat{I}_+(2\hat{I}_z + \hat{I}_-\hat{I}_+)\} \\ &= -\tfrac{1}{4}\{(\hat{I}_-\hat{I}_+ - \hat{I}_+\hat{I}_-)\hat{I}_+ - 2\hat{I}_+\hat{I}_z\} \\ &= -\tfrac{1}{4}(-[\hat{I}_+, \hat{I}_-]\hat{I}_+ - 2\hat{I}_+\hat{I}_z)\end{aligned} \tag{77}$$

Using equation (71) again gives the desired operator, and substitution from equation (72), gives the representation:

$$\hat{T}_1^{(2)} = \tfrac{1}{2}(\hat{I}_z\hat{I}_+ + \hat{I}_+\hat{I}_z) \rightarrow \frac{1}{\sqrt{2}}\begin{bmatrix}0 & 1 & 0\\ 0 & 0 & -1\\ 0 & 0 & 0\end{bmatrix} \tag{78}$$

Applying the same procedure successively generates the other three operators. The $q = 0$ component is

$$\begin{aligned}\hat{T}_0^{(2)} &= -\sqrt{\tfrac{1}{6}}[\hat{I}_-, \hat{T}_1^{(2)}] \\ &= -\tfrac{1}{2}\sqrt{\tfrac{1}{6}}[\hat{I}_-, (\hat{I}_z\hat{I}_+ + \hat{I}_+\hat{I}_z)] \\ &= -\tfrac{1}{2}\sqrt{\tfrac{1}{6}}(\hat{I}_-\hat{I}_z\hat{I}_+ - \hat{I}_z\hat{I}_+\hat{I}_- + \hat{I}_-\hat{I}_+\hat{I}_z - \hat{I}_+\hat{I}_z\hat{I}_-) \\ &= -\tfrac{1}{2}\sqrt{\tfrac{1}{6}}\{(\hat{I}_- + \hat{I}_z\hat{I}_-)\hat{I}_+ - \hat{I}_z\hat{I}_+\hat{I}_- + \hat{I}_-\hat{I}_+\hat{I}_z \\ &\quad -\hat{I}_+(-\hat{I}_- + \hat{I}_-\hat{I}_z)\} \\ &= -\tfrac{1}{2}\sqrt{\tfrac{1}{6}}(\hat{I}_+\hat{I}_- + \hat{I}_-\hat{I}_+ + \hat{I}_z[\hat{I}_-, \hat{I}_+] + [\hat{I}_-, \hat{I}_+]\hat{I}_z) \\ &= \sqrt{\tfrac{1}{6}}\{2\hat{I}_z^2 - \tfrac{1}{2}(\hat{I}_+\hat{I}_- + \hat{I}_-\hat{I}_+)\} \rightarrow \frac{1}{\sqrt{6}}\begin{bmatrix}1 & 0 & 0\\ 0 & -2 & 0\\ 0 & 0 & 1\end{bmatrix}\end{aligned} \tag{79}$$

In this case, the negative phase is chosen arbitrarily, because equation (65) places no constraint on the phase of this operator. The $q = -1$ component is

$$\begin{aligned}\hat{T}_{-1}^{(2)} &= \sqrt{\tfrac{1}{6}}[\hat{I}_-, \hat{T}_0^{(2)}] \\ &= \tfrac{1}{6}[\hat{I}_-, \{2\hat{I}_z^2 - \tfrac{1}{2}(\hat{I}_+\hat{I}_- + \hat{I}_-\hat{I}_+)\}] \\ &= \tfrac{1}{6}(2\hat{I}_-\hat{I}_z^2 - 2\hat{I}_z^2\hat{I}_- + \tfrac{1}{2}\hat{I}_+\hat{I}_-\hat{I}_- - \tfrac{1}{2}\hat{I}_-\hat{I}_-\hat{I}_+) \\ &= \tfrac{1}{6}\{2(\hat{I}_- + \hat{I}_z\hat{I}_-)\hat{I}_z - 2\hat{I}_z(-\hat{I}_- + \hat{I}_-\hat{I}_z) \\ &\quad +\tfrac{1}{2}(2\hat{I}_z + \hat{I}_-\hat{I}_+)\hat{I}_- - \tfrac{1}{2}\hat{I}_-(-2\hat{I}_z + \hat{I}_+\hat{I}_-)\} \\ &= \tfrac{1}{2}(\hat{I}_z\hat{I}_- + \hat{I}_-\hat{I}_z) \rightarrow \frac{1}{\sqrt{2}}\begin{bmatrix}0 & 0 & 0\\ 1 & 0 & 0\\ 0 & -1 & 0\end{bmatrix}\end{aligned} \tag{80}$$

Here the positive phase has been chosen to satisfy equation (65). The $q = -2$ component is

$$\begin{aligned}\hat{T}_{-2}^{(2)} &= \tfrac{1}{2}[\hat{I}_-, \hat{T}_{-1}^{(2)}] \\ &= \tfrac{1}{4}[\hat{I}_-, (\hat{I}_z\hat{I}_- + \hat{I}_-\hat{I}_z)] \\ &= \tfrac{1}{4}(-\hat{I}_z\hat{I}_-\hat{I}_- + \hat{I}_-\hat{I}_-\hat{I}_z) \\ &= \tfrac{1}{4}\{-(-\hat{I}_- + \hat{I}_-\hat{I}_z)\hat{I}_- + \hat{I}_-(\hat{I}_- + \hat{I}_z\hat{I}_-)\} \\ &= \tfrac{1}{2}\hat{I}_-\hat{I}_- \rightarrow \begin{bmatrix}0 & 0 & 0\\ 0 & 0 & 0\\ 1 & 0 & 0\end{bmatrix}\end{aligned} \tag{81}$$

The positive phase has been chosen here, again arbitrarily. The same result could also be obtained by starting from $T_{-2}{}^{(2)}$ and stepping it up with I_+. These nine operators given by equations (73), (74), and (78)–(81) form a complete basis set for spin 1. Of course, higher spin bases can be constructed in the same way; spin I will require irreducible spherical tensors of rank $k = 0, 1, 2, \ldots, 2I$.

4 THE DENSITY OPERATOR

It is a familiar concept[7] that an experimental measurement will yield a value corresponding to the bracket of the state of the system under study with the operator corresponding to the observable:

$$\langle\hat{O}(t)\rangle = \langle\psi(t)|\hat{O}|\psi(t)\rangle \tag{82}$$

The notation on the left-hand side carries some connotation that the operator is time-dependent, which need not be the case; the time dependence in this case is carried entirely in the state. Some authors use the notation $\langle\hat{O}\rangle(t)$ or some other variant to avoid possible ambiguity. We shall retain the notation of equation (82), trusting the reader to realize the subtle difference implied. This leads to a discussion of Schrödinger versus Heisenberg versus interaction pictures of quantum mechanics, which will be addressed in Section 4.1. Of course, this result is independent of the 'picture' employed or the basis chosen. Inserting twice the sum on projection operators for some basis as in equation (19) and rearranging yields

$$\begin{aligned}\langle\hat{O}(t)\rangle &= \langle\psi(t)|\sum_{i=1}^{n}|i\rangle\langle i|\hat{O}\sum_{j=1}^{n}|\,j\rangle\langle\,j|\psi(t)\rangle \\ &= \sum_{i,j=1}^{n}\langle\psi(t)|i\rangle\langle i|\hat{O}|\,j\rangle\langle\,j|\psi(t)\rangle \\ &= \sum_{i,j=1}^{n}\langle\,j|\psi(t)\rangle\langle\psi(t)|i\rangle\langle i|\hat{O}|\,j\rangle\end{aligned} \tag{83}$$

As in equation (9), the quantity $|\psi(t)\rangle\langle\psi(t)|$ can be regarded as an operator, which is known as the density operator $\hat{\rho}(t)$:

$$\hat{\rho}(t) = |\psi(t)\rangle\langle\psi(t)| \tag{84}$$

Continuing from equation (83), we can write

$$\begin{aligned}\langle \hat{O}(t)\rangle &= \sum_{i,j=1}^{n} \langle\, j|\hat{\rho}(t)|i\rangle\langle i|\hat{O}|\, j\rangle \\ &= \sum_{j=1}^{n} \langle\, j|\hat{\rho}(t)\hat{O}|\, j\rangle \\ &= \mathrm{Tr}(\hat{\rho}(t)\hat{O}) \end{aligned} \tag{85}$$

This is an important relationship showing that the expected value of any operator can be computed by taking the trace of its product with the density operator. This form is completely equivalent to equation (82), and is the form commonly used for discussion of magnetic resonance phenomena. Just as the state $|\psi(t)\rangle$ contains all that can be known about the state of a system, so does the density operator.

According to equation (42), using an appropriate operator basis, we can write

$$\begin{aligned}\hat{\rho}(t) &= \sum_{i=1}^{n^2} \mathrm{Tr}\{\hat{\rho}(t)\hat{U}_i^{\dagger}\}\hat{U}_i \\ &= \sum_{i=1}^{n^2} \langle \hat{U}_i^{\dagger}(t)\rangle \hat{U}_i \end{aligned} \tag{86}$$

Thus, the expected values of all the basis operators provide the coefficients needed to represent the density operator in any basis, and these values provide a Liouville space representation of the density operator according to equation (43). Extensive use of this concept will be made later in developing the equations needed to explain spin relaxation.

The development so far has implied that the system of interest can be characterized by a state $|\psi(t)\rangle$. Liquid samples can never be so characterized, but can often be viewed as an ensemble of such isolated systems. Thus, it is desirable to take an ensemble average of equation (84). Since all the variation among the members of the ensemble resides in the operator $|\psi(t)\rangle\langle\psi(t)|$, the averaging process commutes with the sums over basis states, and we can write

$$\begin{aligned}\overline{\langle \hat{O}(t)\rangle} &= \sum_{i,j=1}^{n} \overline{\langle\, j|\psi(t)\rangle\langle\psi(t)|i\rangle}\langle i|\hat{O}|\, j\rangle \\ &= \sum_{i,j=1}^{n} \overline{\langle\, j|\hat{\rho}(t)|i\rangle}\langle i|\hat{O}|\, j\rangle \\ &= \sum_{j=1}^{n} \langle\, j|\bar{\hat{\rho}}(t)\hat{O}|\, j\rangle \\ &= \mathrm{Tr}\{\bar{\hat{\rho}}(t)\hat{O}\} \end{aligned} \tag{87}$$

Clearly, $\hat{\rho}(t)$ can be replaced by $\bar{\hat{\rho}}(t)$ in the above equations, leaving the form of the equations the same. In what follows, we shall not retain the overbar notation, but the density operator should be assumed to be averaged over an ensemble.

4.1 Time Evolution of the Density Operator

The time-dependent Schrödinger equation

$$\mathrm{i}\hbar\frac{\mathrm{d}}{\mathrm{d}t}|\psi(t)\rangle = \hat{\mathcal{H}}(t)|\psi(t)\rangle \tag{88}$$

can easily be converted to our density operator formalism. Beginning from equation (84) and using equation (88) and its complex conjugate obtained using equations (2) and (7), we can write

$$\begin{aligned}\frac{\mathrm{d}\hat{\rho}(t)}{\mathrm{d}t} &= \frac{\mathrm{d}}{\mathrm{d}t}\{|\psi(t)\rangle\langle\psi(t)|\} \\ &= \frac{\mathrm{d}}{\mathrm{d}t}\{|\psi(t)\rangle\}\langle\psi(t)| + |\psi(t)\rangle\frac{\mathrm{d}}{\mathrm{d}t}\{\langle\psi(t)|\} \\ &= -\frac{\mathrm{i}}{\hbar}\hat{\mathcal{H}}(t)|\psi(t)\rangle\langle\psi(t)| + \frac{\mathrm{i}}{\hbar}|\psi(t)\rangle\langle\psi(t)|\hat{\mathcal{H}}(t) \\ &= -\frac{\mathrm{i}}{\hbar}\{\hat{\mathcal{H}}(t)\hat{\rho}(t) - \hat{\rho}(t)\hat{\mathcal{H}}(t)\} \\ &= -\frac{\mathrm{i}}{\hbar}[\hat{\mathcal{H}}(t), \hat{\rho}(t)] \end{aligned} \tag{89}$$

Note that the Hamiltonian is Hermitian. The commutator of the Hamiltonian with the density operator determines the time development of the density operator. This relation is referred to as the *Liouville–von Neuman equation*, and will play a central role in what follows. Our goal, generally stated, will be to find solutions of this equation using a Hamiltonian corresponding to various experimental situations. The density operator at some particular time will generally be known—at least parametrically—and equation (89) must then be integrated to obtain the time development of the density operator.

The solution of this equation of motion is fairly simple if the Hamiltonian is not time-dependent. If we suppose that the density operator has the value $\hat{\rho}(0)$ at $t = 0$ then

$$\hat{\rho}(t) = \exp\left(-\frac{\mathrm{i}}{\hbar}\hat{\mathcal{H}}t\right)\hat{\rho}(0)\exp\left(\frac{\mathrm{i}}{\hbar}\hat{\mathcal{H}}t\right) \tag{90}$$

is a solution, as can be verified by differentiation:

$$\begin{aligned}\frac{\mathrm{d}\hat{\rho}(t)}{\mathrm{d}t} &= \left(-\frac{\mathrm{i}}{\hbar}\hat{\mathcal{H}}\right)\exp\left(-\frac{\mathrm{i}}{\hbar}\hat{\mathcal{H}}t\right)\hat{\rho}(0)\exp\left(\frac{\mathrm{i}}{\hbar}\hat{\mathcal{H}}t\right) \\ &\quad + \exp\left(-\frac{\mathrm{i}}{\hbar}\hat{\mathcal{H}}t\right)\hat{\rho}(0)\left(\frac{\mathrm{i}}{\hbar}\hat{\mathcal{H}}\right)\exp\left(\frac{\mathrm{i}}{\hbar}\hat{\mathcal{H}}t\right) \\ &= -\frac{\mathrm{i}}{\hbar}\left\{\hat{\mathcal{H}}\exp\left(-\frac{\mathrm{i}}{\hbar}\hat{\mathcal{H}}t\right)\hat{\rho}(0)\exp\left(\frac{\mathrm{i}}{\hbar}\hat{\mathcal{H}}t\right)\right. \\ &\quad \left. - \exp\left(-\frac{\mathrm{i}}{\hbar}\hat{\mathcal{H}}t\right)\hat{\rho}(0)\exp\left(\frac{\mathrm{i}}{\hbar}\hat{\mathcal{H}}t\right)\hat{\mathcal{H}}\right\} \\ &= -\frac{\mathrm{i}}{\hbar}\{\hat{\mathcal{H}}\hat{\rho}(t) - \hat{\rho}(t)\hat{\mathcal{H}}\} = -\frac{\mathrm{i}}{\hbar}[\hat{\mathcal{H}}, \hat{\rho}(t)] \end{aligned} \tag{91}$$

We have used the fact that an operator commutes with a function of itself.

Now let us examine the expected value of a generic operator with this solution. Substituting equation (90) into equation (87) yields

$$\begin{aligned}\langle \hat{O}(t)\rangle &= \mathrm{Tr}\{\hat{\rho}(t)\hat{O}\} = \mathrm{Tr}\left\{\exp\left(-\frac{\mathrm{i}}{\hbar}\hat{\mathcal{H}}t\right)\hat{\rho}(0)\exp\left(\frac{\mathrm{i}}{\hbar}\hat{\mathcal{H}}t\right)\hat{O}\right\} \\ &= \mathrm{Tr}\left\{\hat{\rho}(0)\exp\left(\frac{\mathrm{i}}{\hbar}\hat{\mathcal{H}}t\right)\hat{O}\exp\left(-\frac{\mathrm{i}}{\hbar}\hat{\mathcal{H}}t\right)\right\} \\ &= \mathrm{Tr}\{\hat{\rho}(0)\hat{O}(t)\} \end{aligned} \tag{92}$$

The fact that the trace operation is invariant under cyclic permutation of the factors has been used, and the time-dependent operator $\hat{O}(t)$ has been introduced according to

$$\hat{O}(t) = \exp\left(\frac{\mathrm{i}}{\hbar}\hat{\mathcal{H}}t\right)\hat{O}\exp\left(-\frac{\mathrm{i}}{\hbar}\hat{\mathcal{H}}t\right) \tag{93}$$

Equation (87) expresses the Schrödinger picture of quantum mechanics, whereas equation (92) transforms into the Heisenberg picture. Clearly, the two forms are equivalent.

Differentiating equation (93) yields the equation of motion for the time-dependent operators of the Heisenberg picture, corresponding to equation (89) for the Schrödinger picture:

$$\frac{\mathrm{d}\hat{O}(t)}{\mathrm{d}t} = \frac{\mathrm{i}}{\hbar}[\hat{\mathcal{H}}, \hat{O}(t)] \tag{94}$$

The derivation proceeds like that of equation (91). The equations for the Schrödinger and the Heisenberg pictures are similar in form, but the sign differences in the various terms should be noted.

When the Hamiltonian is time-dependent, the situation is considerably more complex, and no attempt will be made here to discuss this case in general terms. However, suppose the Hamiltonian can be separated into a term that is time-dependent and another that is not:

$$\hat{\mathcal{H}}(t) = \hat{\mathcal{H}}_0 + \hat{\mathcal{H}}_1(t) \tag{95}$$

Equation (89) may then be rewritten as

$$\begin{aligned}\frac{\mathrm{d}\hat{\rho}(t)}{\mathrm{d}t} &= -\frac{\mathrm{i}}{\hbar}[\hat{\mathcal{H}}_0 + \hat{\mathcal{H}}_1(t), \hat{\rho}(t)] \\ &= -\frac{\mathrm{i}}{\hbar}\{[\hat{\mathcal{H}}_0, \hat{\rho}(t)] + [\hat{\mathcal{H}}_1(t), \hat{\rho}(t)]\}\end{aligned} \tag{96}$$

If $\hat{\mathcal{H}}_1(t) = 0$ then the solution is as in equation (90). By analogy with equation (90), let us define the transformed operators

$$\hat{\rho}'(t) = \exp\left(\frac{\mathrm{i}}{\hbar}\hat{\mathcal{H}}_0 t\right)\hat{\rho}(t)\exp\left(-\frac{\mathrm{i}}{\hbar}\hat{\mathcal{H}}_0 t\right) \tag{97}$$

$$\hat{\mathcal{H}}_1'(t) = \exp\left(\frac{\mathrm{i}}{\hbar}\hat{\mathcal{H}}_0 t\right)\hat{\mathcal{H}}_1(t)\exp\left(-\frac{\mathrm{i}}{\hbar}\hat{\mathcal{H}}_0 t\right) \tag{98}$$

Differentiating equation (97) and substituting from equations (96) and (98) then gives

$$\begin{aligned}\frac{\mathrm{d}\hat{\rho}'(t)}{\mathrm{d}t} &= \frac{\mathrm{i}}{\hbar}\hat{\mathcal{H}}_0\exp\left(\frac{\mathrm{i}}{\hbar}\hat{\mathcal{H}}_0 t\right)\hat{\rho}(t)\exp\left(-\frac{\mathrm{i}}{\hbar}\hat{\mathcal{H}}_0 t\right) \\ &\quad + \exp\left(\frac{\mathrm{i}}{\hbar}\hat{\mathcal{H}}_0 t\right)\frac{\mathrm{d}\hat{\rho}(t)}{\mathrm{d}t}\exp\left(-\frac{\mathrm{i}}{\hbar}\hat{\mathcal{H}}_0 t\right) \\ &\quad + \exp\left(\frac{\mathrm{i}}{\hbar}\hat{\mathcal{H}}_0 t\right)\hat{\rho}(t)\exp\left(-\frac{\mathrm{i}}{\hbar}\hat{\mathcal{H}}_0 t\right)\left(-\frac{\mathrm{i}}{\hbar}\hat{\mathcal{H}}_0\right) \\ &= \frac{\mathrm{i}}{\hbar}[\hat{\mathcal{H}}_0, \hat{\rho}'(t)] + \exp\left(\frac{\mathrm{i}}{\hbar}\hat{\mathcal{H}}_0 t\right)\left(-\frac{\mathrm{i}}{\hbar}\{[\hat{\mathcal{H}}_0, \hat{\rho}(t)]\right. \\ &\quad \left. + [\hat{\mathcal{H}}_1(t), \hat{\rho}(t)]\}\right)\exp\left(-\frac{\mathrm{i}}{\hbar}\hat{\mathcal{H}}_0 t\right) \\ &= -\frac{\mathrm{i}}{\hbar}[\hat{\mathcal{H}}_1'(t), \hat{\rho}'(t)]\end{aligned} \tag{99}$$

Thus, in this 'interaction picture', part of the time dependence is placed in the operators and part remains in the density operator. The effect of $\hat{\mathcal{H}}_0$ appears only implicitly in the exponential transformation operator. Of course, this is not a solution of the equation of motion, but it will prove to be a useful technique to be applied later on.

4.2 The Reduced Density Operator

In NMR experiments, it is usually the case that the nuclear spins interact weakly with the other degrees of freedom of the sample of interest. For the moment, let us assume that they do not interact at all. The state of the system can be written as a direct product, as in equation (48a), of a ket corresponding to the spin degrees of freedom with one corresponding to the rest of the system, the lattice:

$$|S\rangle|L\rangle = |SL\rangle \tag{100}$$

The number of degrees of freedom, i.e., the number of basis states, necessary to span the spins is modest, while that necessary to span the lattice is very large—effectively infinite.

Consider the expected value of an operator that acts only on the spin degrees of freedom. If $\{|sl\rangle\}$ is a basis set spanning both the spins and the lattice, we can write

$$\begin{aligned}\langle\hat{O}\rangle &= \mathrm{Tr}(\hat{\rho}\hat{O}) = \mathrm{Tr}(|SL\rangle\langle SL|\hat{O}) \\ &= \sum_{sl}\langle sl|SL\rangle\langle SL|\hat{O}|sl\rangle\end{aligned} \tag{101}$$

Since $\hat{O}$ commutes with the lattice operators, this can be rearranged to yield

$$\begin{aligned}\langle\hat{O}\rangle &= \sum_s\langle s|S\rangle\langle S|\hat{O}|s\rangle\sum_l\langle l|L\rangle\langle L|l\rangle \\ &= \sum_s\langle s|S\rangle\left(\sum_l\langle l|L\rangle\langle L|l\rangle\right)\langle S|\hat{O}|s\rangle\end{aligned} \tag{102}$$

We can now define the reduced density operator by

$$\hat{\sigma} = |S\rangle\left(\sum_l\langle l|L\rangle\langle L|l\rangle\right)\langle S| = \mathrm{Tr}_l(\hat{\rho}) \tag{103}$$

The expected value of $\hat{O}$ can then be written as

$$\langle\hat{O}\rangle = \mathrm{Tr}_s(\hat{\sigma}\hat{O}) \tag{104}$$

Thus, observing experimental quantities corresponding to spin operators requires only a knowledge of this reduced density operator, and the problem has, at least in principle, only the small dimensionality of the spin degrees of freedom and not the very large dimensionality of the spins and the lattice. In particular, the Liouville equation, equation (99), can be cast in this form. However, if there were, indeed, no interaction of the spins with the lattice, as was assumed above, there would be no relaxation. Of course, this is observed not to be the case, but the interaction is sufficiently weak that it can be treated by perturbation methods, and the very large number of

degrees of freedom in the lattice permits treating the lattice classically to achieve excellent correspondence of theory to experiment. In what follows, then, solutions will be sought of the Liouville–von Neuman equation for the reduced density operator:

$$\frac{\mathrm{d}\hat{\sigma}(t)}{\mathrm{d}t} = -\frac{\mathrm{i}}{\hbar}[\hat{\mathcal{H}}(t), \hat{\sigma}(t)] \tag{105}$$

5 SUPEROPERATORS

The representation of operators in Liouville space has been discussed in Section 2.2. In this section, we shall introduce superoperators that act on operators in Liouville space in much the same way as operators act on states in Hilbert space, i.e., superoperators transform one operator into another.

Consider the operator product

$$\hat{C} = \hat{B}_1 \hat{A} \hat{B}_2 \tag{106}$$

Let us attempt to cast $\hat{A}$ in a Liouville space representation and then find a superoperator $\hat{\hat{B}}$ such that $|\hat{C}\rangle = \hat{\hat{B}}|\hat{A}\rangle$. The operator product can be written as follows and rearranged as shown by applying equations (7) and (15):

$$\begin{aligned}\langle i|\hat{C}|\ j\rangle &= \sum_{k,l=1}^{n} \langle i|\hat{B}_1|k\rangle\langle k|\hat{A}|l\rangle\langle l|\hat{B}_2|\ j\rangle \\ &= \sum_{k,l=1}^{n} \langle i|\hat{B}_1|k\rangle\langle\ j|\hat{B}_2^{\dagger}|l\rangle\langle k|\hat{A}|l\rangle \end{aligned} \tag{107}$$

The superoperator matrix elements can now be defined by

$$\langle ij|\hat{\hat{B}}|kl\rangle = \langle i|\hat{B}_1|k\rangle\langle\ j|\hat{B}_2^{\dagger}|l\rangle \tag{108}$$

This expression can be viewed as the matrix elements of a direct product in a space with basis $|i\rangle|j\rangle = |ij\rangle$, the direct product of two identical Hilbert space bases as in equation (50):

$$\hat{\hat{B}} = \hat{B}_1 \otimes \hat{B}_2^{\dagger} \tag{109}$$

The matrix elements of $\hat{A}$ may be mapped into a vector in this same space just as in equation (43). In fact, the operator basis $\{\hat{U}_i\}$ introduced in equation (43) is equivalent to the basis $\{|ij\rangle\}$. The matrix elements of $\hat{A}$ may be written as

$$\langle ij|\hat{A}\rangle = \langle i|\hat{A}|\ j\rangle \tag{110}$$

Then equation (107) can be written as

$$|\hat{C}\rangle = \hat{\hat{B}}|\hat{A}\rangle \tag{111}$$

The utility of this formalism is evident from several examples.

5.1 Unitary Transformations

Unitary transformations like $\hat{U}\hat{A}\hat{U}^{\dagger}$ in Hilbert space can easily be translated to Liouville space using equation (109) to define the relevant superoperator

$$\hat{\hat{U}} = \hat{U} \otimes \hat{U} \tag{112}$$

Note that $(\hat{U}^{\dagger})^{\dagger} = \hat{U}$. Then the unitary transformation becomes

$$\hat{\hat{U}}|\hat{A}\rangle \tag{113}$$

The superoperator $\hat{\hat{U}}$ is unitary. To show this, we can write

$$\hat{A} = \hat{U}^{\dagger}\hat{U}\hat{A}\hat{U}^{\dagger}\hat{U} \tag{114}$$

But this implies

$$|\hat{A}\rangle = (\hat{U}^{\dagger} \otimes \hat{U}^{\dagger})(\hat{U} \otimes \hat{U})|\hat{A}\rangle = \hat{\hat{U}}^{\dagger}\hat{\hat{U}}|\hat{A}\rangle \tag{115}$$

where the second equality in equation (115) follows immediately by considering the adjoint of equation (108). Thus, it must be that

$$\hat{\hat{U}}^{\dagger}\hat{\hat{U}} = \hat{\hat{E}} \tag{116}$$

5.2 Commutators

Consider the commutator $[\hat{A}, \hat{B}]$ as the action of something denoted by $[\hat{A}, \ ]$ on the operator $\hat{B}$ to produce a new operator $\hat{C}$. This relationship can be written as

$$[\hat{A}, \hat{B}] = \hat{A}\hat{B} - \hat{B}\hat{A} = \hat{A}\hat{B}\hat{E} - \hat{E}\hat{B}\hat{A} \tag{117}$$

Applying equation (109) then yields

$$\hat{\hat{A}} = \hat{A} \otimes \hat{E} - \hat{E} \otimes \hat{A}^{\dagger} \tag{118}$$

5.3 The Liouvillian

Using equation (118), the equation of motion for the density operator equation (89) can be re-written as

$$\frac{\mathrm{d}|\hat{\rho}(t)\rangle}{\mathrm{d}t} = -\frac{\mathrm{i}}{\hbar}\hat{\hat{\mathcal{L}}}(t)|\hat{\rho}(t)\rangle \tag{119}$$

The Liouvillian superoperator corresponding to the commutator with the Hamiltonian is defined as

$$\hat{\hat{\mathcal{L}}}(t) = \hat{\mathcal{H}}(t) \otimes \hat{E} - \hat{E} \otimes \hat{\mathcal{H}}(t) \tag{120}$$

Note that the Hamiltonian is Hermitian, so that $\hat{\mathcal{H}}(t) = \hat{\mathcal{H}}(t)^{\dagger}$.

6 RELATED ARTICLES

Rudimentary NMR: The Classical Picture.

7 REFERENCES

1. T. C. Farrar, and E. D. Becker, *Pulse and Fourier Transform NMR: Introduction to Theory and Methods*, Academic Press, New York, 1971.
2. H. Friebolin, *Basic One- and Two-Dimensional NMR Spectroscopy*, VCH, New York, 1991.
3. A. E. Derome, *Modern NMR Techniques for Chemistry Research*, Pergamon Press, Oxford, 1987.
4. P. A. M. Dirac, *The Principles of Quantum Mechanics*, 4th edn., Oxford University Press, Oxford, 1958.
5. T. C. Farrar and J. E. Harriman, *Density Matrix Theory and its Applications in NMR Spectroscopy*, 2nd edn., The Farragut Press, Madison, WI, 1992.
6. M. Goldman, *Quantum Description of High-Resolution NMR in Liquids*, Oxford University Press, Oxford, 1988.
7. C. P. Slichter, *Principles of Magnetic Resonance*, 3rd edn., Springer-Verlag, Berlin, 1990.
8. R. R. Ernst, G. Bodenhausen, and A. Wokaum, *Principles of Nuclear Magnetic Resonance in One and Two Dimensions*, Oxford University Press, Oxford, 1987.
9. A. Abragam, *The Principles of Nuclear Magnetism*, Oxford University Press, Oxford, 1961.
10. R. N. Zare, *Angular Momentum*, Wiley, New York, 1988.

Biographical Sketch

Charles L. Mayne. *b* 1942. B.S., 1970, New Mexico State University, U.S.A., Ph.D., 1976, University of Utah. Introduced to NMR by George A. Gray and subsequently tutored by David M. Grant. Manager of NMR Laboratories, University of Utah, Department of Chemistry, 1973–present. Academic appointment as Adjunct Associate Professor of Chemistry, University of Utah. Approx. 40 publications in NMR. Research interests include nuclear-spin relaxation, NMR at high pressure, structure elucidation of natural products, various aspects of multidimensional NMR, and computerized analysis of NMR data.

Nuclear Overhauser Effect

David Neuhaus

MRC Laboratory of Molecular Biology, Cambridge, UK

1	Introduction	1
2	Cross Relaxation and the Origin of the NOE	1
3	Multispin Systems	4
4	Steady-State NOE Experiments with Small Molecules	4
5	Kinetic NOE Experiments with Large Molecules	6
6	The Rotating Frame NOE	9
7	The Heteronuclear NOE	9
8	Exchanging Systems and the Transferred NOE	10
9	Related Articles	11
10	References	11

1 INTRODUCTION

The nuclear Overhauser effect is defined as the change in the overall intensity of one resonance that occurs when another resonance is saturated. Generally it is expressed as the fractional enhancement:

$$f_I\{S\} = \frac{I - I^0}{I^0} \tag{1}$$

where I is the intensity of the observed resonance when the spin S is saturated and I^0 is the equilibrium intensity of the I resonance. Conventionally, the observed spin is called I and the saturated spin is called S. However, particularly for heteronuclear cases, the NOE is often also expressed as the enhancement ratio:

$$\eta = \frac{I}{I^0} = f_I\{S\} + 1 \tag{2}$$

Detection of an appreciable NOE between two spins indicates that there is a relatively short internuclear distance between them, generally less than about 4 or 5 Å. It is this through-space dependence, which is completely independent of the nature of the covalent bonding network between the two interacting spins, that makes the NOE extremely powerful for characterizing molecular stereochemistry and conformation. However, the dependence on the internuclear separation between I and S is complicated by a dependence on several other factors, particularly the rates of molecular motions. For this reason, a truly quantitative interpretation of NOE enhancements is difficult, and the effect is usually interpreted at a semiquantitative level when deriving structural information, as will be discussed below.

The original prediction by Overhauser concerning the enhancement of nuclear spin polarization in metals upon saturation of the electron spins was published in 1953,[1] and the nuclear analog was described by Solomon in 1955.[2] The first applications to structure determination were by Anet and Bourne in 1965,[3] and for 10 years or so the method found applications mainly in organic chemistry.[4] Detection of NOE enhancements using repeated integration of CW-detected one-dimensional spectra imposed a detection limit in the region of 5%, but the introduction of new measurement techniques together with high-field, computer-assisted Fourier transform NMR spectrometers in the mid-1970s revolutionized the whole area. Now two experiments in particular, NOE difference spectroscopy and NOESY, have greatly improved sensitivity and allow very much more extensive use to be made of the NOE in structure determination than was possible previously. The technique is very widely used to determine stereo- and regiochemical isomerism in small and medium-sized natural and synthetic molecules, and more recently it has become the basis for a whole area of NMR, namely the structure determination of biological macromolecules, particularly proteins, in solution.[5]

2 CROSS RELAXATION AND THE ORIGIN OF THE NOE

The origin of the NOE lies in population changes caused by a particular form of longitudinal relaxation, namely dipole–dipole cross relaxation (see also ***Relaxation Processes in Coupled-Spin Systems***). Longitudinal relaxation involves energy exchange events between the nuclear spin states and the 'lattice', which term is used to depict the continuum of translational and rotational energy levels of the system as a whole. If the population of the high-energy state of a particular nuclear spin transition is larger than its equilibrium value, it will relax back towards equilibrium through events in which individual nuclei flip from high-energy to low-energy spin state while the lattice accepts the energy released, for instance by accelerating either the overall rotation or some internal motion of the molecule in which the nuclear spin transition occurred. Similarly, if the population of the high-energy state were smaller than its equilibrium value, then corresponding decelerations of molecular motions would provide energy to promote spins to the high-energy state.

However, such relaxation events can only occur if there exists a mechanism to couple the motions of the molecule to the nuclear spin states. In practice this means that the motion must itself cause a varying transverse magnetic field at the site of the nucleus it is to relax, and that this magnetic field variation must have an appreciable frequency component corresponding to the frequency of the nuclear spin transition. In the case of dipole–dipole relaxation, this 'local field' originates from the magnetic dipoles of other neighboring spins. Because in this case the local field itself originates from a spin, this opens the possibility for cooperative relaxation events in which *both* spins simultaneously flip, while the lattice accepts or provides energy corresponding to the net change. This is dipole–dipole cross relaxation. The various possible transitions for the simplest case of a two-spin system are summarized in Figure 1.

Two types of cross relaxation event are possible. In one, characterized by the transition probability W_2, both spins flip in the same sense, and the energy change accommodated by the lattice corresponds to the *sum* of the energies of the individual spin transitions. For these 'W_2 transitions' to occur, the local field resulting from lattice motions must contain fluctuations

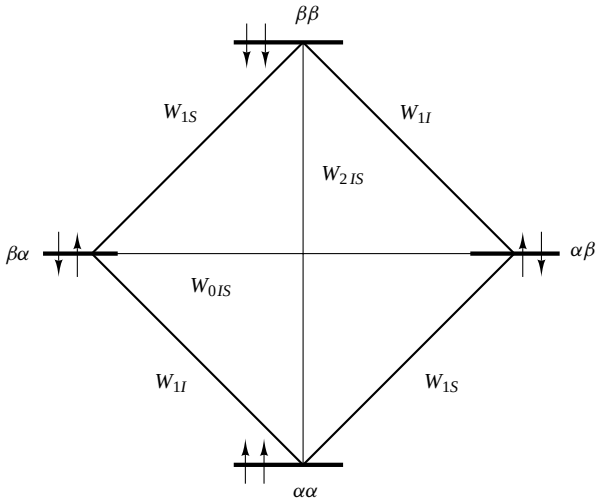

Figure 1 Energy level for a two-spin system, showing the definitions of transition probabilities (W_0, W_1, and W_2) and spin states ($\alpha\alpha$, $\alpha\beta$, $\beta\alpha$, and $\beta\beta$). Spin states are written with the state of I first and that of S second, i.e. $\alpha\beta$ means spin I is in the α state, and spin S in the β

at the sum frequency ($\omega_I + \omega_S$). In the other type of transition, characterized by the transition probability W_0, the spins flip in opposite senses. In the homonuclear case, this implies that a very much smaller energy change is accommodated by the lattice, corresponding to the *difference* between the energies of the individual transitions. For 'W_0 transitions', the local field must contain fluctuations at the difference frequency ($\omega_I - \omega_S$).

These two types of cross relaxation event are crucially different in their influence on the NOE. Suppose that spin S is saturated, thereby equalizing the populations of states $\alpha\alpha$ and $\alpha\beta$, and (separately) equalizing the populations of the states $\beta\alpha$ and $\beta\beta$. For all of the relaxation transitions involving S there will now be an excess of downward transitions (i.e. high $\rightarrow$ low energy), since there are more spins in the high-energy state than would be the case at equilibrium. The excess of downward single spin flips of S (W_1 transitions) has no effect on the intensity of I. However, if spin S flips downwards during a W_2 transition, spin I also flips downwards, thereby *increasing* the population difference across the I spin transition. Thus when W_2 transitions predominate over W_0 transitions, saturation of S causes the intensity of I to increase, which corresponds to a positive NOE enhancement. Conversely, for a W_0 transition, if spin S flips downwards then spin I must flip upwards, thereby *decreasing* the population difference across the I spin transitions. Therefore if W_0 transitions predominate over W_2 transitions, saturation of S causes the intensity of I to decrease, implying a negative NOE enhancement. If there are equal numbers of W_2 and W_0 transitions, the opposing effects cancel and there is no NOE at all.

2.1 The NOE for an Isolated Two-Spin System

These points may be expressed more formally using the Solomon equations, which form the basis for the theory of the NOE. For a system of two isolated spins $\frac{1}{2}$, the equation of motion for the longitudinal component of I spin magnetization is given by[2,6]

$$\frac{dI_z}{dt} = -(I_z - I_z^0)(W_{0IS} + 2W_{1I} + W_{2IS}) - (S_z - S_z^0)(W_{2IS} - W_{0IS}) \quad (3)$$

If S is saturated until steady state is reached, then dI_z/dt and S_z may both be set to zero, whereupon rearrangement and substituting $I_z^0 = (\gamma_I/\gamma_S)S_z^0$ gives

$$f_I\{S\} = \frac{I_z - I_z^0}{I_z} = \frac{\gamma_S}{\gamma_I}\frac{W_{2IS} - W_{0IS}}{W_{0IS} + 2W_{1I} + W_{2IS}} \quad \text{(two-spin)} \quad (4)$$

where $f_I\{S\}$ is the fractional steady state NOE enhancement measured at I upon completely saturating S. For the case of two spins $\frac{1}{2}$ relaxing exclusively via their mutual dipole–dipole interaction, the values of the various transition probabilities can be shown to be[7]

$$\left.\begin{aligned} W_{0IS} &= \tfrac{1}{20}K^2J(\omega_I - \omega_S) \\ W_{1I} &= \tfrac{3}{40}K^2J(\omega_I) \\ W_{2IS} &= \tfrac{3}{10}K^2J(\omega_I + \omega_S) \end{aligned}\right\} \quad \left(\begin{array}{c}\text{dipole}\\ \text{only,}\\ \text{extreme}\\ \text{narrowing}\end{array}\right) \quad (5)$$

where $K = (\mu_0/4\pi)\hbar\gamma_I\gamma_S r_{IS}^{-3}$. Given that K always appears as its square, this shows that all of these intramolecular dipole–dipole transition probabilities depend linearly on the minus sixth power of the internuclear distance r_{IS}. The various spectral density functions $J(\omega_x)$ each describe the power available at the corresponding frequency ω_x from molecular motions to stimulate relaxation. These spectral density functions provide the vital link between transition probabilities and molecular tumbling properties. If it is assumed that molecular tumbling is isotropic, and that it can be described by a correlation function that is a simple exponential decay with a rate constant τ_c, then the spectral density functions are given by

$$J(\omega_X) = \frac{2\tau_c}{(1 + \omega_X^2\tau_c^2)} \quad (6)$$

For small molecules molecular tumbling is very rapid, τ_c is very short and $\omega_X\tau_c < 1$. This is called the 'extreme narrowing' condition, and in this limit the denominators of the various spectral density expressions can all be set to unity, leading to much simpler expressions for the transition probabilities in equation (5). When these are substituted into equation (4), we have

$$f_I\{S\} = \frac{\gamma_S}{\gamma_I}\frac{\frac{3}{5}K^2\tau_c - \frac{1}{10}K^2\tau_c}{\frac{1}{10}K^2\tau_c + \frac{3}{10}K^2\tau_c + \frac{3}{5}K^2\tau_c} = \frac{\gamma_S}{2\gamma_I} \quad \left(\begin{array}{c}\text{two-spin}\\ \text{dipole only,}\\ \text{extreme}\\ \text{narrowing}\end{array}\right) \quad (7)$$

which, in the homonuclear case, is just +50%.

As molecular weight increases and tumbling becomes slower, the spectrum of rates of molecular motions becomes

more and more concentrated at low frequencies. The spectral densities $J(\omega_I + \omega_S)$ and $J(\omega_I)$ thus become progressively smaller until they cease to make any significant contribution to relaxation; in other words, the local field produced by motions of neighboring dipoles in large molecules has no frequency component high enough to stimulate W_2 or W_1 transitions. In heteronuclear systems, the same fate eventually overtakes $J(\omega_I - \omega_S)$ also [indeed, if γ_S and γ_I have opposite signs, $J(\omega_I + \omega_S)$ will diminish before $J(\omega_I - \omega_S)$, and for $S = {}^1\mathrm{H}$, ω_I is generally smaller than $(\omega_I - \omega_S)$ or $(\omega_I + \omega_S)$], but in homonuclear cases the difference frequency $(\omega_I - \omega_S)$ is so low (being just a difference of chemical shifts in this case) that $J(\omega_I - \omega_S)$ always remains large.

Thus, although in the extreme narrowing limit there are six times as many W_2 transitions as W_0 transitions, where $\omega\tau_c \approx 1$ (for a homonuclear system) the numbers of W_2 and W_0 transitions are nearly equal, resulting in small or zero NOE enhancements irrespective of the internuclear distances involved. For homonuclear systems in still larger molecules where $\omega\tau_c \gg 1$, all the spectral densities other than $J(\omega_I - \omega_S)$ become insignificant, dipolar relaxation is completely dominated by W_0 transitions and NOE enhancements are all negative. This limit is known as the 'spin diffusion' limit, for reasons that will become apparent shortly.

The overall dependence of the NOE on $\omega_I\tau_c$ for an ideal two-spin system relaxing exclusively through mutual dipole–dipole interactions can be calculated from equations (4)–(6). This function, often called η_{max}, is actually *independent* of the internuclear distance r, since all of the terms in equation (4) have an identical dependence on r^{-6} that cancels out. Conceptually, η_{max} represents the theoretical maximum NOE enhancement observable between two spins in the absence of other spins and external relaxation. Figure 2 shows η_{max} for a homonuclear system.

To simplify later equations, it is convenient to introduce here the cross-relaxation rate σ_{IS} and the direct relaxation rate ρ_{IS}, defined by

$$\sigma_{IS} = W_{2IS} - W_{0IS}; \quad \rho_{IS} = W_{0IS} + 2W_{1I} + W_{2IS} \qquad (8)$$

In this way, η_{max} can be reexpressed as

$$\eta_{max} = \frac{\gamma_S}{\gamma_I}\frac{\sigma_{IS}}{\rho_{IS}} \qquad (9)$$

2.2 Competition from Other Relaxation Mechanisms

Of course, in real situations, there will be relaxation mechanisms other than intramolecular dipole–dipole operating, and there will generally be more than two spins in the system. Almost without exception, other relaxation mechanisms do not contribute to cross relaxation at all, so their only influence is to dilute the contribution of dipolar relaxation to the whole. Such additional relaxation is often referred to as 'leakage', and in the equations the 'leakage rate' ρ^*_I is introduced as a *purely empirical* correction factor to allow for it; the subscript I is required since, in principle, every spin could have a different leakage rate.

$$f_I\{S\} = \frac{\gamma_S}{\gamma_I}\frac{\sigma_{IS}}{\rho_{IS} + \rho^*_I} \quad \text{(two-spin)} \qquad (10)$$

Significantly, for most systems leakage is much more important for small molecules than for large. This is because dipolar relaxation becomes steadily more efficient as tumbling rates diminish, whereas the leakage rate is often not greatly affected by solute tumbling rate. For instance, in many cases the dominant source of leakage is intermolecular dipole–dipole interactions between spins on the solute and unpaired electrons of dissolved oxygen molecules (see also ***Paramagnetic Relaxation in Solution***). This interaction is likely to be largely independent of solute tumbling rate, since the relative positions of the electron and nuclear spins will always vary rapidly as the oxygen molecule tumbles. Figure 3 shows how the ideal homonuclear two-spin NOE η_{max} is reduced more severely for small molecules than for large, assuming various constant leakage rates.

For spin systems involving nuclei with $I > \frac{1}{2}$, efficient quadrupolar relaxation usually leads to very high leakage rates,

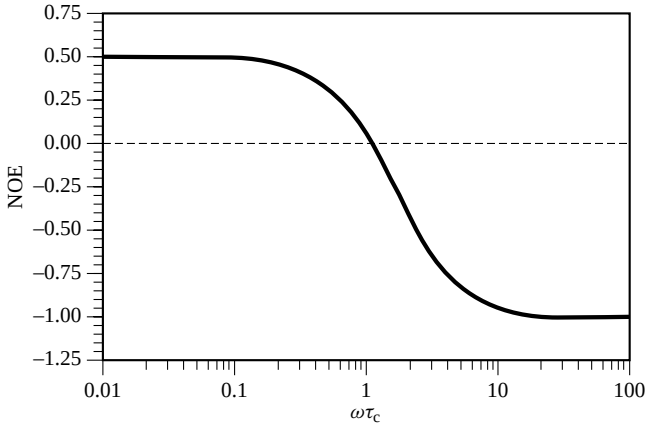

Figure 2 Maximum theoretical homonuclear NOE enhancement (η_{max}) for a two-spin system relaxing exclusively via dipolar interaction, as a function of $\omega\tau_c$. For small rapidly tumbling molecules where $\omega\tau_c \ll 1$, the maximum NOE enhancement is +50%, while for large, slowly tumbling molecules where $\omega\tau_c \gg 1$, the maximum enhancement is −100%

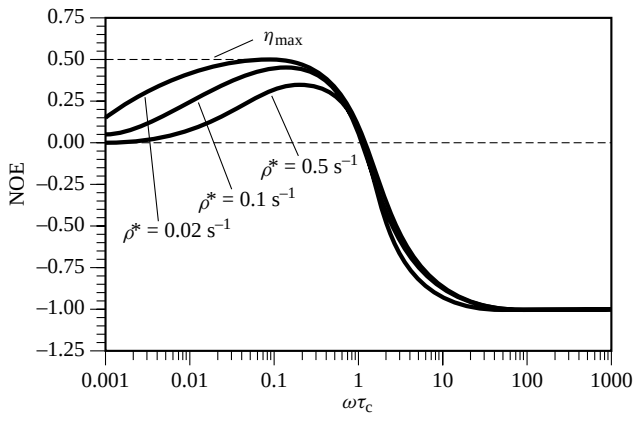

Figure 3 Reduction in η_{max} resulting from leakage, e.g. due to intermolecular relaxation by dissolved oxygen. The different curves are calculated according to equation (10) using the indicated values for ρ^*_I, assumed to remain constant as a function of solute tumbling rate, and taking an internuclear distance r_{IS} of 2 Å and a spectrometer frequency of 300 MHz

so that little or no NOE is detectable (see also ***Relaxation of Quadrupolar Nuclei Measured via Multiple Quantum Filtration***).

3 MULTISPIN SYSTEMS

In multispin systems, two further points need to be considered. Firstly, spin I will be relaxed not only by spin S but also potentially by all the other spins in the system (here collectively denoted X), depending on their distances from I. This adds further terms to the direct relaxation rate of I, diluting the NOE in much the same way as does ρ_I*. Thus, the total relaxation rate of I becomes

$$R_I = \rho_{IS} + \sum_X \rho_{IX} + \rho_I^* \tag{11}$$

Note that there is an implicit assumption made in equation (11) and in all the theory for multispin NOE enhancements that follows, namely that the total relaxation behavior of the system can be obtained by a simple summation over all possible pairwise interactions. This amounts to neglecting the cross correlation that must exist between the random motions of one spin pair and another within the same molecule. This assumption is almost universally made throughout applications of the NOE, and various authors have shown that it actually introduces little error into conventional interpretations (see also ***Relaxation Processes: Cross Correlation and Interference Terms***).[8]

Note also that the inclusion of ρ^*_I in this definition implies that R_I corresponds to the reciprocal of the *experimentally measured* selective T_1. In all the equations involving R_I that follow, one may in principle either include or exclude ρ^*_I. If it is included, the equations relate directly to measured results, but they require that measured values or at least estimates of leakage rates are available. If ρ^*_I is excluded, the equations relate to a hypothetical spin system with no leakage, allowing idealized NOE properties to be calculated provided only that the relevant internuclear distances are known.

The second important point for the NOE in multispin systems is the possibility of indirect enhancements. Once spins close to S have themselves received NOE enhancements, their own populations are no longer at equilibrium. This in turn disturbs the balance of their cross relaxation with their own neighboring spins, thereby creating additional NOE enhancements often called *indirect* enhancements. Such indirect enhancements can themselves cause further enhancements, and so on, until at steady state the original population disturbance at S may cause intensity changes to a greater or lesser extent throughout the spin system. For a multispin system, the relevant Solomon equation is

$$\begin{aligned}\frac{\mathrm{d}I_z}{\mathrm{d}t} = &-(I_z - I_z^0)(W_{0IS} + 2W_{1I} + W_{2IS}) - (S_z - S_z^0) \\ &\times (W_{2IS} - W_{0IS}) - \sum_X (X_z - X_z^0) \\ &\times (W_{2IX} - W_{0IX})\end{aligned} \tag{12}$$

Setting $\mathrm{d}I_z/\mathrm{d}t$ and S_z to zero as before, then rearranging and substituting $I_z^0 = (\gamma_I/\gamma_S)S_z^0 = (\gamma_I/\gamma_X)X_z^0$ gives the steady state enhancement as

$$f_I\{S\} = \frac{\gamma_S}{\gamma_I}\frac{1}{R_I}\left[\sigma_{IS} - \sum_X \frac{\gamma_X}{\gamma_S} f_X\{S\}\sigma_{IX}\right] \tag{13}$$

where all the indirect contributions to $f_I\{S\}$ are represented by the summation over the other spins X. Thus, in general, the theoretical steady state enhancements (i.e. assuming no leakage) upon saturating S in an N-spin system where the distances are all known can be calculated from a set of $(N - 1)$ linear simultaneous equations of the form of equation (12).[9] Note particularly that steady state enhancements are not controlled only by the internuclear distance between I and S, but are a function of many (potentially all) of the internuclear distances in the system. This crucially important point is all too often ignored in naïve interpretations of NOE experiments, particularly those involving small molecules.

The significance of indirect enhancements depends very much on the tumbling rate of the molecule under study, as will be illustrated in the following sections.

4 STEADY-STATE NOE EXPERIMENTS WITH SMALL MOLECULES

For homonuclear systems in small molecules, direct enhancements are positive, so that a directly enhanced signal can itself be thought of as being 'negatively saturated'. Spins that are significantly closer to such a directly enhanced spin than they are to the saturated spin therefore receive a *negative* enhancement from the directly enhanced spin, often called a 'three-spin effect'. However, at extreme narrowing, σ is significantly smaller than R_I, so that the transmission of enhancements down a chain of spins is a relatively inefficient process, even in the absence of leakage. In practice, efficient leakage reduces the transmission of indirect effects still further, and effects transmitted over more than one intermediate spin are almost never observed in small molecules. Given the sign distinction between direct and three-spin effects, this makes distinguishing indirect effects a relatively trivial matter.

Clearly, the geometry of a spin system is crucial in determining what effects will actually be seen. Substantial three-spin effects are generally associated with spins in a nearly linear arrangement, and it also follows that for some arrangements of spins, appreciable direct and indirect effects cancel leaving a small or zero net enhancement despite a short *IS* internuclear distance. These points are illustrated by the theoretical enhancements shown for some particular geometries in Figure 4.

4.1 NOE Difference Spectroscopy

The experiment that is now most widely used to measure steady state enhancements in small molecules is the NOE difference experiment, the pulse sequence for which is summarized in Figure 5. Two datasets are acquired, in one of which selective, low-power preirradiation is applied to the target resonance S. In the other experiment (the control), all details are identical to the first except that the preirradiation is applied in a blank area of the spectrum. Subtraction of

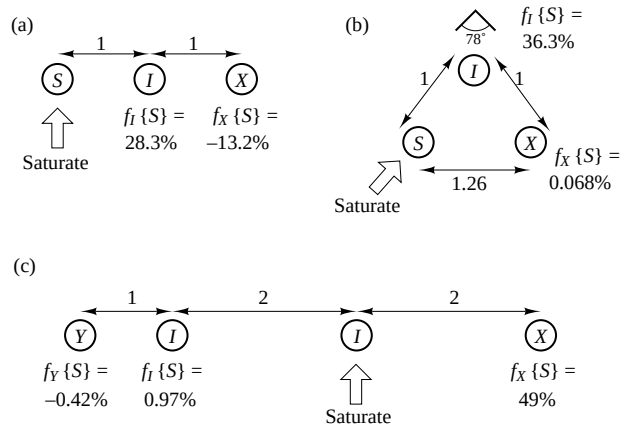

Figure 4 Theoretical NOE intensities ($\rho^*_I = 0$) for various simple multispin systems at the extreme narrowing limit ($\omega\tau_c \ll 1$). (a) Illustration of the transmission of a three-spin effect (here $f_X\{S\}$) in a linear spin system. (b) Illustration of how substantial direct and indirect contributions can cancel, leaving a very small net enhancement ($f_X\{S\}$) despite short distances. (c) Illustration as to how two direct effects corresponding to the same distance can differ drastically when one enhanced spin is rapidly relaxed by another near neighbor, and the other enhanced spin is not

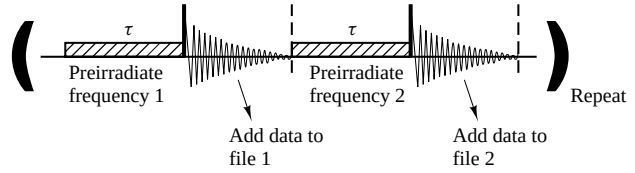

Figure 5 Pulse sequence for the one-dimensional NOE difference experiment

the control spectrum from that in which S is preirradiated yields a difference spectrum containing only those signals that changed intensity upon preirradiation of S. Note that, since the saturating field is switched off during acquisition of the FID, no coherent decoupling effects are present to complicate the data, and (ideally) only population effects can contribute to the difference spectrum.

In order to minimize unwanted differences between the datasets arising from instrumental instabilities, acquisition of the two datasets is usually carried out in an interleaved manner. If, as is usual, a series of experiments is to be carried out, a list is constructed of frequencies corresponding to the various preirradiation targets. Since, in principle, the control data are identical for all the different preirradiation targets, generally only one or two control entries are included in this list. The spectrometer then cycles repeatedly through the whole list, typically acquiring two or four dummy scans followed by eight or 16 transients at each frequency on each pass, until the available experimental time has been filled. A separate dataset is maintained for each preirradiation frequency, and incoming data are always added to data acquired at the same frequency on previous cycles. Careful attention to temperature equilibration and stability are also crucial to obtaining high-quality data. Long preirradiation periods (5–10 s or more) are often useful in NOE difference experiments, since then informative three-spin effects are allowed to become significant. However, when sensitivity for measuring relatively strong direct effects is the only issue, somewhat shorter preirradiation periods of $(1-3)T_1$ are often used in conjunction with an increased number of scans. Note also that there is no need whatsoever for a relaxation delay between acquisition and the start of the next preirradiation.

Preirradiation power is generally set extremely low, in order to avoid unwanted saturation of neighboring resonances. This can result in the target resonance being only partially saturated, which leads to NOE enhancements being only partially excited in direct proportion. However, this is of little real consequence since the absolute size of the enhancement rarely needs to be interpreted quantitatively in steady state experiments, the only real loss being one of sensitivity. Various techniques are available for saturating multiplets evenly without using high powers, for instance by cycling the preirradiation frequency around the multiplet components during each preirradiation period. These methods help to minimize the unwanted effects of selective population transfer (SPT) that arise at scalar coupling partners of the irradiated signal if the multiplet components of S are unevenly saturated (e.g. see Figure 6); these appear as intense antiphase signals at the coupled signals, and are completely unrelated to the NOE. Further suppression of SPT effects can be achieved by using a composite 90° pulse to excite the spectrum.

With care and long acquisition periods, enhancements well below the 1% level may now be quite routinely detected using

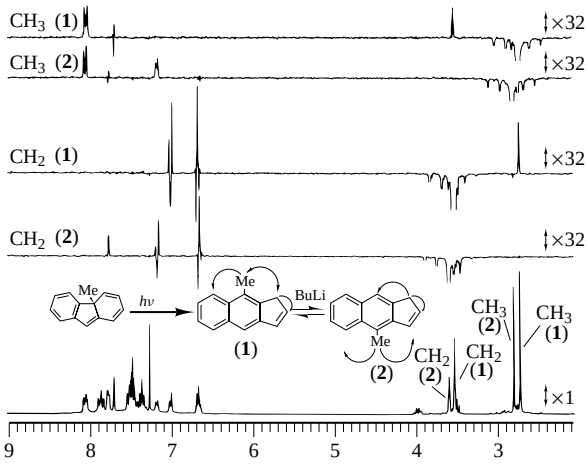

Figure 6 NOE difference and control spectra of a mixture of 4- and 9-methylcyclopenta[*b*]naphthalenes [compounds (**1**) and (**2**), obtained by photolysis of 4a-methyl-4a*H*-fluorene followed by treatment with butyllithium] in $CDCl_3$ solution, recorded at ambient temperature and 250 MHz (preirradiation period 5 s).[11] For each NOE difference trace, the preirradiation target is indicated on the left, and the relative vertical scaling on the right. The enhancements between the CH_2 and CH_3 signals in compound (**1**), and the enhancements $H_9\{CH_2\}$ and $H_3\{CH_3\}$ in compound (**2**), established the relative assignment of signals from the two isomers, thereby allowing compound (**1**) to be identified as the one that was initially formed in the photolysis step (the small peaks near 2.9 ppm and 3.9 ppm are due to impurities). This example also demonstrates the use of NOE difference experiments in analyzing mixtures in cases where spectral overlap is not too severe, and the appearance of SPT artifacts at coupling partners of the preirradiated signals (these spectra were recorded before the methods of SPT suppression referred to in the text had been introduced). Adapted with permission from Neuhaus[11]

the NOE difference technique (but such experiments are a particularly demanding test of instrumental stability).[10]

4.2 Applications to Small Molecules

One-dimensional NOE difference spectroscopy has now become an essential and routine tool for the determination of regio- and stereochemical isomerism in small and medium-sized molecules. However, a major and unavoidable limitation to the approach is imposed by molecular flexibility. The NOE can only distinguish between two or more possible structures or conformations if there is some significant and *consistently maintained* difference between internuclear distances corresponding to measurable NOE enhancements in the various cases. In this context, it is largely irrelevant whether the formal difference between the possibilities is one of covalently bonded structure or one of noncovalently stabilized conformation, provided that the relative spatial arrangement of protons is preserved.

Some of the simplest applications of the NOE involve the determination of aromatic ring and olefinic double-bond substitution patterns. Interpretation of the NOE enhancements in these essentially flat molecules is particularly simple, since the differences between internuclear distances in various possible structures are usually extremely clear cut. Aromatic ring fusion patterns are also usually quite straightforward to establish, provided, as in the case of substitution patterns, that there are strategically located protons at or near the sites that differ between the structures needing be distinguished (e.g. on each side of ring junctions). A simple example is shown in Figure 6.

Saturated systems often require a somewhat more sophisticated analysis, since differences between internuclear distances in various structures may be more subtle, and the importance of relaxation from other nearby protons in determining the relative sizes of enhancements may be less obvious. Substitution positions and ring fusion patterns are more likely to be available from coupling connectivities in such cases, so it is more often *stereochemical* information that is required from the interpretation of the NOE results. Applications to five-membered rings are perhaps more common than to six-membered rings, presumably due to the relative difficulty of using coupling constant magnitudes to distinguish whether protons are *cis* or *trans* in a five-membered ring. Rigidity is again crucial to the successful application of the technique, so applications to medium-sized or larger ring systems are more difficult, unless flexibility is limited, e.g. by fusion to another ring.

In larger systems, rigidity may be maintained in more complicated ways, e.g. by a specific, intramolecular network of hydrogen bonds that may, in effect, convert an acyclic portion of a molecule into a cyclic one. In combination with other NMR techniques, the NOE has been used to define largely or completely the stereochemistry and conformation of many complicated natural products, including steroids and other terpenoids, alkaloids, saccharides, small cyclic peptides, and various other types of natural macrocycles (see also ***Carbohydrates and Glycoconjugates***).[15]

Applications to characterizing conformational equilibria have been much less common. Accurate quantitation and very careful analysis are essential, and several unavoidable assumptions render analysis of even the simplest systems extremely approximate. In particular, if averaged NOE data from a rapidly exchanging system are to be fitted to try to find the relative proportions of two or more conformers, then the r^{-6} dependence of enhancements implies that the fit will be critically dependent on having very accurate internuclear distances available from models of the contributing conformers. The outlook for improvement in this situation remains bleak.

A few representative examples of applications of the NOE to problems of structure determination in small and medium-sized molecules are summarized in Figure 7.

5 KINETIC NOE EXPERIMENTS WITH LARGE MOLECULES

In complete contrast to the situation for small molecules, for homonuclear experiments with large molecules direct and

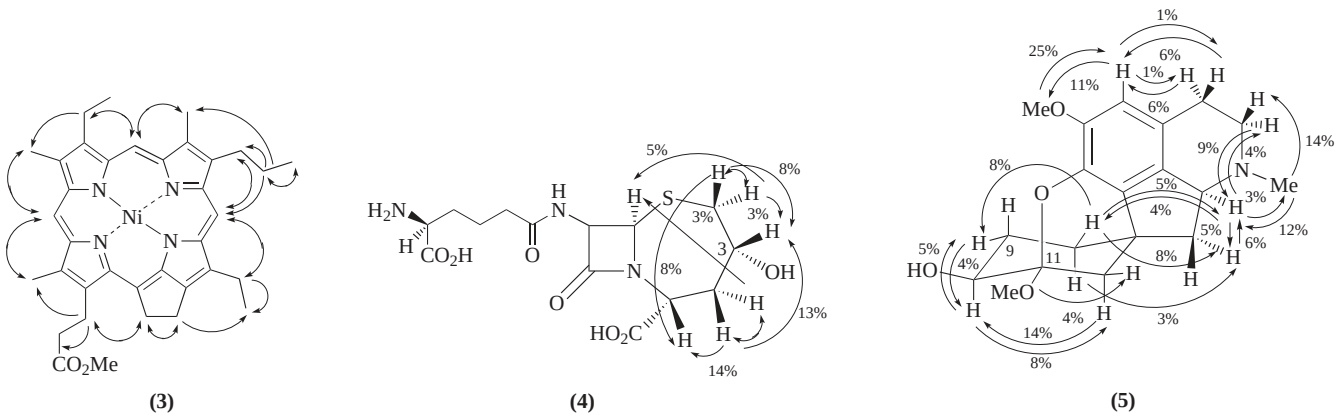

(3) (4) (5)

Figure 7 A few representative examples of structural applications of the NOE in small molecules. Compound (**3**) is a petroporphyrin whose substitution pattern was determined by the NOE enhancements shown.[12] Compound (**4**) is a hydroxyhomocepham isolated during work on penicillin biosynthesis, in which the stereochemistry at C-3 was established by the enhancements shown.[13] Compound (**5**) is a benzylisoquinoline alkaloid called misramine, the structure of which was established by a combination of spectroscopic techniques, and including the NOE enhancements shown.[14] In this case the enhancement data helped to link together partial ^{1}H spin systems determined by decoupling experiments, to determine the stereochemistry, and to determine that the site of the acetal function was C-11 rather than C-9

indirect enhancements are all negative, and the predominance of W_0 transitions over all others means that indirect enhancements can be transmitted efficiently down a chain of spins. In the limit of slow tumbling, saturation of any spin in a homonuclear multispin system will, at steady state, cause a -100% enhancement of every other spin; in other words, the entire spectrum will become saturated and disappear. This is the ultimate demonstration of the process known as 'spin diffusion', whereby enhancements in large molecules lose their specificity by dissipating onto other nearby spins.

Spin diffusion renders steady state homonuclear experiments on large molecules completely useless in terms of determining structures. Even limited spin diffusion poses a severe problem for interpretation, since direct and indirect enhancements cannot be distinguished a priori, being all negative, making it impossible to equate a given strength of enhancement with a given distance even approximately. In order to overcome this problem, NOE enhancements for such molecules are measured not at steady state but rather during the early stages of their build up.

Two types of simple kinetic experiment are possible. In the first, generally called the truncated driven Overhauser experiment or TOE, the NOE is driven by continuous saturation of the S signal throughout a short, variable period of NOE evolution. This experiment is essentially identical to the NOE difference experiment, except that the period of preirradiation during which the NOE evolves is kept much shorter. In the second type of kinetic experiment, perturbation of the S spin populations is achieved effectively instantaneously using pulses, and the NOE is then allowed to evolve for a short variable period in the absence of saturation. Experiments in this latter category include the two-dimensional NOESY experiment (see ***NOESY***) and all its variants (see also ***Homonuclear Three-Dimensional NMR of Biomolecules***), and also various transient one-dimensional experiments based on allowing the NOE to evolve after a selective inversion pulse to the signal corresponding to S (note, however, that there can be no true two-dimensional analog of the steady state or TOE experiments).

The period of NOE evolution in any kinetic experiment is generally called the mixing time, or τ_{m}. Provided that τ_{m} is sufficiently short, direct enhancements never become large enough to cause substantial indirect enhancements, and the process of spin diffusion has no chance to begin. This limit is known as the 'initial rate approximation'. The limiting form of equation (12) at short times may be found by substituting $S_z = 0$, $I_z = I_z^0$, and $X_z = X_z^0$, leaving

$$\left.\frac{\mathrm{d}I_z}{\mathrm{d}t}\right|_{t=0} = \sigma_{IS} S_z^0 \tag{14}$$

(for experiments where S is selectively inverted rather than saturated, the appropriate initial condition is $S_z = -S_z^0$, leading to an initial rate of $2\sigma_{IS}S_z^0$).

Thus the initial rate of NOE buildup is directly proportional to σ_{IS}, and therefore also to r^{-6}. It is this simple proportionality that forms the basis for most uses of the NOE in the structure determination of large molecules. At later times, once an appreciable enhancement has built up at I, then relaxation of the I spins at a rate determined by R_I starts significantly to oppose the buildup of the enhancement, and the steady state represents the balance that is eventually reached between these processes and also the influence of indirect enhancements. This also shows that the period of validity of the initial rate approximation depends on R_I, and may thus be different for different spins. However, broadly speaking, it is the molecular tumbling rate that is the main factor that determines how short mixing times must be if the direct proportionality between NOE intensity and r^{-6} is to be at least approximately preserved; the more slowly the solute tumbles, the faster longitudinal relaxation will occur and the shorter the validity of the initial rate approximation will last.

Although most interpretation of NOESY data and other kinetic NOE experiments is based on the assumption (or hope) that the initial rate approximation is still valid at the particular values of τ_{m} used, it is also possible to calculate the whole time-course for the evolution of NOE enhancements in multispin systems of known geometry. The relaxation behavior of a multispin system can be fully described in terms of the relaxation matrix $\mathbf{R}$, defined by

$$\mathbf{R} = \begin{bmatrix} R_1 & \sigma_{12} & \sigma_{13} & \cdots & \sigma_{1N} \\ \sigma_{21} & R_2 & \sigma_{23} & \cdots & \sigma_{2N} \\ \sigma_{31} & \sigma_{32} & R_3 & \cdots & \sigma_{3N} \\ \vdots & \vdots & \vdots & \ddots & \\ \sigma_{N1} & \sigma_{N2} & \sigma_{N3} & & R_N \end{bmatrix} \tag{15}$$

The intensities of the NOESY cross peaks at time τ_{m} are then given by:

$$\mathbf{a}(\tau_{\mathrm{m}}) = \exp(-\mathbf{R}\tau_{\mathrm{m}})\,\mathbf{a}(0) = \mathbf{T}\exp(-\mathbf{D}\tau_{\mathrm{m}})\,\mathbf{T}^{-1}\,\mathbf{a}(0) \tag{16}$$

where $\mathbf{a}(\tau_{\mathrm{m}})$ is the matrix of cross peak intensities at mixing time τ_{m}, $\mathbf{a}(0)$ is the corresponding matrix at zero mixing time, $\mathbf{D}$ is the diagonal matrix comprised of the eigenvalues of $\mathbf{R}$, and $\mathbf{T}$ is the matrix comprised of the eigenvectors of $\mathbf{R}$. The matrix $\mathbf{a}(0)$ is of course diagonal, and is needed only for normalization. Figure 8 shows how the intensities of the cross peaks and diagonal peaks in the NOESY spectrum vary as a function of τ_{m}, for a two-spin system in the extreme narrowing limit, and for one near the spin diffusion limit.

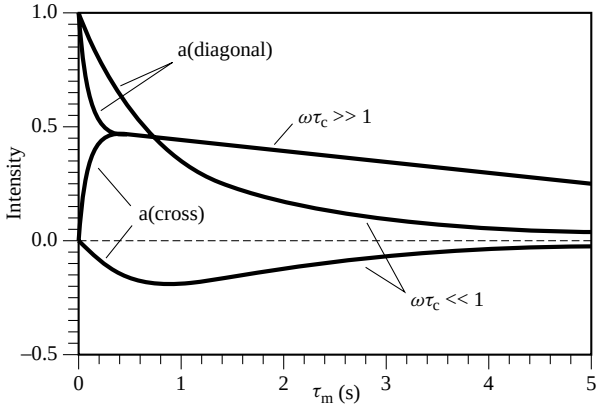

Figure 8 Simulated time course for cross-peak and diagonal peak intensity in a NOESY experiment for an isolated two-spin homonuclear system, as a function of mixing time (τ_{m}) for two different motional regimes. In a rapidly tumbling molecule ($\omega\tau_{\mathrm{c}} \ll 1$) the cross peak is negative relative to the diagonal, and builds up and decays slowly, whereas for a slowly tumbling molecule ($\omega\tau_{\mathrm{c}} \gg 1$) the cross peak is positive and builds up rapidly before decaying slowly

A slightly more complicated matrix equation also exists for describing the time-course of TOE experiments:

$$\mathbf{f} = [\mathbf{R}'^{-1}\,\boldsymbol{\sigma}] - [\mathbf{T}'\exp(-\mathbf{D}'\tau_{\mathrm{m}})\,\mathbf{T}'^{-1}\,\mathbf{R}'^{-1}\,\boldsymbol{\sigma}] \qquad (17)$$

where $\mathbf{f}$ is the column matrix of enhancements $f_I\{S\}$, σ is the column matrix of cross-relaxation rates involving S, and $\mathbf{R}'$, $\mathbf{T}'$, and $\mathbf{D}'$ are matrices analogous to $\mathbf{R}$, $\mathbf{T}$, and $\mathbf{D}$ in equation (16), but reduced by the elimination of all entries involving spin S. In addition to these matrix formulations, there are iterative numerical approaches to calculating the time course of NOESY and TOE experiments.[16,17]

At a practical level, if quantitative intensities are required for estimating internuclear distances, it is important that the spin populations be at equilibrium at the start of each pass through the pulse sequence. This is one reason why such kinetic experiments are used mainly for large molecules; for small molecules, this condition implies that long relaxation delays (tens of seconds) are required, making overall experiment times very long.

5.1 Applications to Biological Macromolecules

Generally, structure determinations of biological macromolecules rely on the assignment and classification of a large number of NOESY cross peaks linking individual spin pairs, followed by the calculation of a family of structures consistent with these data. Methods for assigning such spectra are discussed elsewhere.[18] The simple interpretation of data derived from NOESY spectra is usually based on an assumed validity of the initial rate approximation, so that the intensities of individual cross peaks are identified exclusively with the corresponding internuclear distance. In this context, this approximation is often known as the 'isolated spin-pair approximation', or ISPA. Cross peaks are classified semiquantitatively into groups such as 'strong', 'medium', and 'weak', and each category is interpreted as corresponding to a particular range of internuclear distances, following calibration by comparison with cross peaks corresponding to known distances. Usually, only the upper bound of each distance range is defined by the NOE intensity, in order to allow for the possibility that enhancements due to spins that are actually close together are made weaker by internal motions.

Various types of computer program are then used to generate a structure from the NMR data in conjunction with the known covalent connectivity and ideal covalent geometry. Although the bulk of the NMR data comprise NOE-derived distance constraints, it is common also to use torsion angle constraints derived from scalar coupling constant measurements and hydrogen bonding constraints derived from identification of slowly exchanging NH protons. Methods used for calculating biological macromolecular structures include distance-geometry, simulated annealing, and restrained molecular dynamics calculations, and also probabilistic model-building approaches; details may be found elsewhere (see also ***Distance Geometry***).[19] Normally an ensemble of calculations is run with each member starting from a randomly different set of initial conditions. Comparing the structures by superposition identifies which regions are well defined by the data, since only such regions are conserved across the ensemble.

Full matrix calculations of the NOE intensities can also be used to refine structures based on ISPA calculations, since they allow at least limited spin-diffusion to be accounted for explicitly (see ***Protein Structures: Relaxation Matrix Refinement***). Although equation (16) allows the prediction of NOE intensities at any point during their evolution for a known structure, the reverse process, calculation of all the internuclear distances directly from the NOE intensities, would require that the *complete* NOESY intensity matrix be known, including all of the diagonal elements. Given that, in practice, such complete information is never available for complicated spectra of macromolecules, various iterative approaches have been developed that improve the fit of a starting structure to the available NOE data, either by progressively modifying the structure (e.g. the program IRMA[20]), or by iterating on the internuclear distances themselves (e.g. the program MARDIGRAS[21]).

The whole field of application of the NOE to macromolecules has seen a huge growth since the first three-dimensional protein structure derived from NMR (that of BUSI-IIA) was published by Williamson et al. in 1986.[22] The size of proteins that can be tackled is limited principally by the assignment problem, both in terms of assigning all the ^{1}H chemical shifts within the protein, and in terms of assigning each individual NOE cross peak; the latter becomes a severe problem in its own right for proteins that exhibit extensive chemical shift degeneracy. The homonuclear experiments used for making assignments in unlabeled proteins begin to fail when ^{1}H linewidths become significantly greater than the values of typical (^{1}H,^{1}H) coupling constants, implying that for nonaggregated globular proteins this methodology is usually applicable up to polypeptide chain lengths of a little over 100 residues (see also ***Structures of Larger Proteins, Protein-Ligand, and Protein-DNA Complexes by Multi-Dimensional Heteronuclear NMR***).[18]

More recently, it has become practical to obtain protein samples in which all (<98%) carbon atoms are isotopically substituted with ^{13}C, and all nitrogens with ^{15}N; this is achieved by overexpression of the protein in a bacterial system growing in an appropriately isotopically enriched medium. This has opened the door to a whole barrage of new NMR techniques for the assignment of signals and NOE cross peaks, the details of which may be found elsewhere (see also ***Half-Filter Experiments: Proton–Carbon-13***; ***Three- and Four-Dimensional Heteronuclear Magnetic Resonance***; ***Three-Dimensional HMQC-NOESY, NOESY-HMQC, and NOESY-HSQC***).[23] These make use of the much larger one-bond heteronuclear and (^{13}C,^{13}C) couplings to detect through-bond connectivities and disperse crowded spectra in three or four frequency dimensions. It is not really clear yet what the upper size limit is for studying such isotopically enriched proteins, but systems approaching 200 residues have already been solved and it seems likely that larger ones will follow.

Although perhaps the most spectacular results have been obtained with proteins, related studies for DNA oligonucleotides have yielded much structural information,[24] although reliable identification of sequence-dependent conformation of double-helical DNA has proved somewhat elusive due to the essentially linear nature of the DNA molecule (see ***DNA Triplexes, Quadruplexes, and Aptamers***; ***DNA: A-, B-, and Z-***; ***Nucleic Acid Structures in Solution: Sequence Dependence***; ***Nucleic Acids: Spectra, Structures, and Dynamics***). Very

recently, NOE-based structure determinations of small RNA molecules have been reported, some making use of global isotopic labeling in a similar fashion to that used for proteins,[25] and the first solution structures of protein–nucleic acid complexes are now beginning to appear.[26]

6 THE ROTATING FRAME NOE

As Figure 2 makes clear, for homonuclear spin systems where $\omega\tau_c \approx 1$, all conventional NOE enhancements are small or zero, irrespective of the internuclear distances involved, representing a severe problem for studies of intermediate-sized molecules. However, this problem can be avoided by carrying out a different type of NOE experiment, in which NOE enhancements evolve not between elements of longitudinal magnetization as in the conventional experiment, but rather between elements of transverse magnetization during a period of spin locking.

Spin locking suppresses the *relative* precession of chemically shifted resonances within the spectrum; in other words, while the spin locking field is switched on, all the transverse magnetization components from the different signals in the spectrum precess *together*, with a constant relative phase. The simplest spin locking sequence comprises a hard 90° pulse followed by application of a spin locking field 90° out of phase with the pulse. If, prior to the 90° pulse, the system is prepared by inverting a particular signal S, then transverse cross relaxation during the spin locking period will lead to a transient rotating frame Overhauser effect, accumulating at signals corresponding to the cross-relaxation partners of S. This is exactly analogous to a conventional one-dimensional transient NOE experiment, in which the S signal is inverted prior to a period for evolution of longitudinal NOE enhancements. The role of the spin locking field is perhaps best viewed as maintaining a constant phase relationship between the inverted signal and the others; had the spin locking field been absent, relative precession due to chemical shifts would have prevented any *net* accumulation of enhancement. Most commonly, ROE enhancements are measured using the two-dimensional ROESY experiment, which is the ROE analog of NOESY (see ***ROESY***). Note that since there is no frequency difference between any of the spins while the ROE enhancements are evolving during the spin locking period, it is not possible to saturate selectively any of them separately during this time. There can therefore be no ROE analog of the conventional steady-state experiment.

The reason why ROE experiments differ fundamentally from longitudinal ones is that the transition probabilities for spin locked dipolar relaxation are based on different spectral densities. The transverse cross-relaxation rate σ_2 and transverse direct relaxation rate ρ_2 are given by[27]

$$\sigma_2 = \tfrac{1}{40}K^2[\tfrac{9}{2}J(2\omega_1) - \tfrac{1}{2}J(0) + 6J(\omega_0)] \quad (18)$$

$$\rho_2 = \tfrac{1}{40}K^2[\tfrac{9}{2}J(2\omega_1) + \tfrac{1}{2}J(0) + 9J(\omega_0) + 6J(2\omega_0)] \quad (19)$$

where ω_0 is the Larmor frequency and ω_1 is the frequency of precession about the $\boldsymbol{B}_1$ field. For comparison, the equivalent expressions for their longitudinal counterparts, obtained by substituting into equation (8), are

$$\sigma_1 = \tfrac{1}{20}K^2[-J(\omega_I - \omega_S) + 6J(2\omega_0)] \quad (20)$$

$$\rho_1 = \tfrac{1}{20}K^2[J(\omega_I - \omega_S) + 3J(\omega_0) + 6J(2\omega_0)] \quad (21)$$

Note that for slowly tumbling molecules where terms in $J(\omega_0)$ and $J(2\omega_0)$ are insignificant, σ_2 is twice σ_1. If NOESY and ROESY data are to be compared directly in such cases, τ_m should therefore be set twice as long in the NOESY experiment as in the ROESY.

The key difference between these expressions is that, unlike σ_1, σ_2 cannot become negative unless the extreme narrowing approximation breaks down *with respect to* ω_1. Typical spin locking field strengths in ROE experiments are between about $\omega_1 = 2$ kHz and $\omega_1 = 10$ kHz, implying that molecular motions in liquid samples will never be significantly slower than this so that direct ROE enhancements are always positive. Another key difference to the conventional experiment concerns spin diffusion. In effect, any size of molecule behaves in an ROE experiment as though it were a small molecule in a conventional NOE experiment (hence the original acronym CAMELSPIN for the experiment;[28] this stands for cross relaxation appropriate for mini-molecules emulated by spin locking). Thus, there is an alternation of sign for each intermediate spin over which an indirect enhancement is transmitted, and the transmission of indirect effects is relatively inefficient due to the loss that occurs at each step. For a large molecule, the influence of spin diffusion is markedly reduced in an ROE experiment relative to the corresponding NOE experiment, and what spin diffusion there is can usually readily be identified from the relative sign of the corresponding cross peaks.

Against these advantages, there are some difficulties that arise from the application of the spin locking field. Significant resonance offset effects are inevitable at the relatively low spin locking field strengths that can be applied in practice, implying that the cross relaxation controlling cross-peak intensities will, in general, be a composite of longitudinal and transverse contributions. Also, for coupled spins that are symmetrically disposed about the spin lock frequency, or are both close to it, a net transfer of magnetization may occur through the scalar coupling via the homonuclear Hartmann–Hahn (HOHAHA) interaction. Multistep mechanisms involving both HOHAHA transfer and ROE transfer may also occur, making the interpretation of ROESY data potentially quite complicated (see also ***TOCSY in ROESY and ROESY in TOCSY***).[29]

Nonetheless, there have been many applications of the ROE in the decade or so since its discovery. Mainly, these have been to intermediate-sized molecules, such as small peptides, that often give very poor NOESY spectra. However, it may also be worthwhile running a series of conventional steady state NOE difference spectra, since these are often significantly more sensitive than NOESY for such systems. For macromolecules, although clearly ROESY does not supplant NOESY for obtaining internuclear distance constraints, it can be very useful to compare NOESY and ROESY data in order to help identify spin diffusion pathways in the former.

7 THE HETERONUCLEAR NOE

Figure 9 shows the maximum theoretical steady-state heteronuclear two-spin NOE enhancement (η_{max}) for the

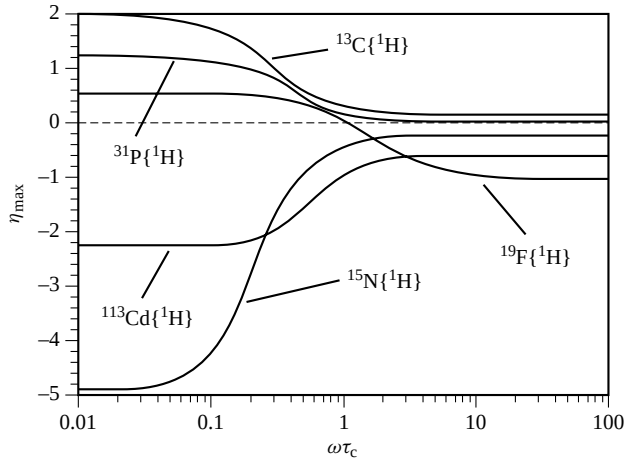

Figure 9 Maximum theoretical two-spin NOE enhancements (η_{max}) for various heteronuclear systems relaxing exclusively via dipolar interaction, as a function of $\omega\tau_c$. Note that for ^{15}N, the NOE can be negative, and that for ^{13}C and ^{31}P the NOE becomes very small for large molecules

more important heteronuclei and hydrogen, calculated using equations (4)–(6). The commonest application of these heteronuclear NOE enhancements is for sensitivity improvement during direct observation of heteronuclear signals, e.g. the application of ^1H decoupling when acquiring ^{13}C spectra of small molecules (at the extreme narrowing limit, η_{max} for the $^{13}C\{^1H\}$ NOE is 199%, corresponding to a threefold gain in signal). Note that η_{max} also corresponds to the theoretical NOE ($\rho^* = 0$) seen in a multispin system when all spins but one are saturated (provided all the saturated spins have the same γ).[5] However, any value of η_{max} between 0% and −200% means that saturation of the protons causes a *reduced* intensity for the X resonances, and a value of −100% means they are destroyed altogether. Inspection of the curves in Figure 9 shows that such circumstances do occur in some cases where γ_X is negative, e.g. for $^{15}N\{^1H\}$ with $\omega_N\tau_c \approx 0.5$. In such cases, if proton decoupling is to be used to collapse the X resonance multiplet structures, it should be applied in a gated fashion during the acquisition time only, and be switched off during the relaxation delay. In several other cases, the heteronuclear NOE becomes very small for slowly tumbling molecules, e.g. at the spin diffusion limit η_{max} for the $^{13}C\{^1H\}$ NOE is 15.4%, and for the $^{31}P\{^1H\}$ NOE it is only 2.2%. For these cases, there is of course virtually no sensitivity gain to be had from the heteronuclear NOE.

Measurements of specific heteronuclear enhancements to aid in structure determination are much less common than homonuclear applications because the sensitivity of the experiments is much lower, but several applications to small molecules have appeared.[30] Although the NOE observed on protons is a lot smaller than that observed on the X resonance, it is still often preferable to use proton observation as the sensitivity gain from detecting the higher frequency nucleus more than compensates; however, such ^1H-detected (inverse) NOE experiments may be compromised by inferior subtraction quality if the X nucleus is a dilute spin. Another factor that makes heteronuclear NOE experiments difficult is that the buildup rate σ_{XH} is slower than the corresponding interproton rate by a factor of $(\gamma_H/\gamma_X)^2$, for the same internuclear separation. Thus specific steady-state heteronuclear NOE difference experiments with small molecules can be extremely time-consuming, while experiments with macromolecules are usually precluded by the small values of η_{max}. Even in cases where η_{max} appears to behave quite similarly to that for the interproton NOE (e.g. for $^{19}F\{^1H\}$), one must remember that in the spin diffusion limit W_0 transitions will always be more efficient for the homonuclear case, since for sufficiently large molecules the tumbling rate will always be slower than the heteronuclear frequency difference ($\omega_I - \omega_S$). Thus, for example, in a $^1H\{^{19}F\}$ NOE experiment where a single fluorine resonance is saturated in a macromolecule, the buildup of heteronuclear enhancements at the nearest protons will be much slower than the dissipation of those enhancements onto other protons via homonuclear spin diffusion.

Recently, one of the more significant uses for heteronuclear NOE measurements (in conjunction with X nucleus T_1 and T_2 values) has been in the determination of local flexibility in macromolecules (see ***Protein Dynamics from NMR Relaxation***). Typically, for each ^{15}N resonance in a ^{15}N-labeled protein, the corresponding T_1, T_2, and $^{15}N\{^1H\}$ steady-state NOE would be measured, and these data analyzed using a suitable formalism, most commonly the 'model-free' formalism of Lipari and Szabo.[31] For internal motions of the ^{15}N–^1H vector that are faster than the overall molecular tumbling, this approach yields an 'order parameter' S^2 that describes the geometric extent of the internal motion relative to the molecular frame; $S^2 = 1$ implies complete rigidity, while $S^2 = 0$ implies the internal motion is isotropic relative to the molecular frame.

8 EXCHANGING SYSTEMS AND THE TRANSFERRED NOE

There are many types of exchange that can affect NMR spectra, including chemical exchange of labile protons (OH, NH, etc.) in protic solvents, conformational equilibria, and exchange of a solute between free and bound states. The effects that these processes have on NOE experiments depends mainly on their rate, relative both to the T_1 timescale and to the chemical shift timescale (see also ***Relaxation Effects of Chemical Exchange***). If exchange is slow relative to T_1, then NOE enhancements will evolve largely unaffected by the exchange process. However, if exchange is fast relative to T_1, then many exchange events will occur during NOE evolution, causing the various relaxation rates themselves to be averaged, and it will be as though the NOE had evolved in an 'averaged molecule'. Thus, if two resonances are linked by exchange that is faster than T_1, irradiation of one will result in saturation of both (saturation transfer), and if one resonance receives an NOE enhancement, exchange will transfer the enhancement onto the second resonance also. Under these circumstances, NOE enhancements will reflect so-called '$\langle r^{-6}\rangle$ average' distances, defined as

$$\langle r_{IS}^{-6}\rangle = \left[\frac{1}{N}[(r_{IS}^{A})^{-6} + (r_{IS}^{B})^{-6} + \cdots (r_{IS}^{N})^{-6}]\right]^{-1/6} \quad (22)$$

where r_{IS}^{A}, r_{IS}^{B}, etc. represent the IS internuclear distance in each of the N exchanging forms of the system. For internal

motions faster than overall molecular tumbling, it transpires that $\langle r^{-3} \rangle$ averaging of distances is appropriate, and that in addition there is a geometry-dependent reduction of NOE enhancements caused by the anisotropy of the internal motion with respect to the molecular frame; this situation usually applies for methyl group rotations.[32]

Note that the rate of exchange relative to $\Delta\delta$ (the chemical shift difference for the same spin in its two environments, for the case of two-site exchange) does not directly affect the NOE intensities at all; however, it does affect the number of separate resonances in the spectrum, and thereby dictates what NOE interactions can be measured separately. In cases of exchange which is slow relative to $\Delta\delta$, where separate signals are seen for each exchanging species, exchange can provide an additional mechanism for magnetization transfer in NOE experiments. For large molecules in conventional NOE experiments, exchange that is fast on the T_1 timescale causes saturation transfer signals that have the same sign as the NOE-enhanced signals; a distinction between the two types of signal can generally only be made on grounds of intensity or buildup rate. Conversely, for conventional NOE experiments with small molecules, and for ROE experiments with any size of solute, exchange will lead to signals of opposite sign to direct enhancements. Although this implies that they have the same sign as indirect enhancements transmitted over one intermediate spin, in the context of a general interpretation of all the cross peaks, the distinction between these two types of signal is usually quite straightforward.

More insidious than the signals due to exchange itself, however, is the possibility that conformational averaging affects the NOE intensities, giving results that reflect an 'averaged structure'. This can lead to data that are inconsistent with any single structure. In the case of slow exchange on the chemical shift timescale there is likely to be warning of the danger since multiple resonances are observed, but in the case of fast exchange on the chemical shift timescale there may be no indication of conformational exchange other than mutual inconsistencies amongst the NOE intensities. If models of the separate exchanging conformers are available from some other source, then in principle it is possible to fit the NOE data, using the relative proportions of the conformers as one of the fitting variables; however, this process is difficult and, given the r^{-6} dependence of the NOE, very heavily dependent upon the accuracy of the initial models. In large molecules, the main issue concerning conformational exchange is usually how to allow for relatively small-scale local motions when interpreting NOE data. These have two principal effects: they reduce the size of the enhancements, by making the effective τ_c shorter, and they change relative intensities by altering the values of $\langle r^{-6} \rangle$. For small-scale motions, these effects are both taken into account, at least approximately, by specifying NOE-derived distance constraints as ranges rather than specific distances, as mentioned earlier.

A particularly significant case of the influence of exchange is in the transferred NOE, or TRNOE experiment. Suppose a small ligand binds to a large molecule, and that exchange between the free and bound states is fast both on the T_1 and chemical shift timescales. The ligand resonances and also its intramolecular NOE enhancements will be averaged over the free and bound states by such an exchange. If the ligand is present in moderate excess, then the averaged ligand resonances will largely retain the narrow linewidths associated with the free ligand. However, because the tumbling rate of the ligand when bound to the large molecule is very much slower than in the free state, dipolar relaxation rates will be very much faster for the bound ligand than for the free [equations (4)–(6)]. Therefore, the observed NOE interactions will be dominated by the bound state, and thus reflect the bound conformation of the ligand, even though the free ligand concentration is higher than the bound. Although the first applications involved one-dimensional experiments, TRNOE experiments are now usually carried out using either NOESY or ROESY. Typical applications include studies of inhibitors bound to enzymes and small peptides bound to immunoglobulins; however, the generality of the technique is somewhat limited by the requirements for suitable exchange rates for the ligand–macromolecule interaction.[33] More recently, related experiments have been used to investigate protein hydration using intermolecular NOE enhancements between the protein surface and water protons (see ***Protein Hydration***).

9 RELATED ARTICLES

Biological Macromolecules: Structure Determination in Solution; Biological Macromolecules; Carbohydrates and Glycoconjugates; NOESY; Nucleic Acid Structures in Solution: Sequence Dependence; Relaxation Processes in Coupled-Spin Systems; ROESY; Selective NOESY; Structures of Larger Proteins, Protein-Ligand, and Protein-DNA Complexes by Multi-Dimensional Heteronuclear NMR.

10 REFERENCES

1. A. W. Overhauser, *Phys. Rev.*, 1953, **89**, 689.
2. I. Solomon, *Phys. Rev.*, 1955, **99**, 559.
3. F. A. L. Anet and A. J. R. Bourne, *J. Am. Chem. Soc.*, 1965, **87**, 5250.
4. J. H. Noggle and R. E. Schirmer, *The Nuclear Overhauser Effect; Chemical Applications*, Academic Press, New York, 1971.
5. D. Neuhaus and M. P. Williamson, *The Nuclear Overhauser Effect in Structural and Conformational Analysis*, VCH, New York, 1989.
6. Ref. 5, pp. 27–29.
7. Ref. 5, Appendix II.
8. T. E. Bull, *J. Magn. Reson.*, 1987, **72**, 379, and references therein.
9. Ref. 5, p. 76.
10. Further practical details concerning NOE difference spectroscopy may be found in Ref. 5, Chap. 7
11. D. Neuhaus, Ph. D. Thesis, University of London, 1982; see also D. Neuhaus and C. W. Rees, *J. Chem. Soc., Chem. Commun.*, 1983, 318.
12. R. Ocampo, H. J. Callot, and P. Albrecht, *J. Chem. Soc., Chem. Commun.*, 1985, 200.
13. A. E. Derome, *Modern NMR Techniques for Chemistry Research*, Pergamon Press, Oxford, 1987, pp. 124–127.
14. S. El-Masry, Z. Mahmoud, M. Amer, A. J. Freyer, E. Valencia, A. Patra, and M. Shamma, *J. Org. Chem.*, 1985, **50**, 729.
15. Ref. 5, Chap. 10
16. M. P. Williamson, *Magn. Reson. Chem.*, 1987, **25**, 356.

17. M. J. Forster, *J. Comput. Chem.*, 1991, **12**, 292.
18. K. Wüthrich, *NMR of Proteins and Nucleic Acids*, Wiley, New York, 1986.
19. M. J. Sutcliffe, in *NMR of Macromolecules; A Practical Approach*, ed. G. C. K. Roberts, IRL Press at Oxford University Press, Oxford, 1993, Chap. 11
20. R. Boelens, T. M. G. Konig, and R. Kaptein, *J. Mol. Struct.*, 1988, **173**, 299.
21. B. A. Borgias and T. L. James, *J. Magn. Reson.*, 1990, **87**, 475.
22. M. P. Williamson, T. F. Havel, and K. Wüthrich, *J. Mol. Biol.*, 1985, **182**, 295.
23. G. M. Clore and A. M. Gronenborn, *Prog. NMR Spectrosc.*, 1991, **23**, 43.
24. F. J. N. Van De Wen. and C W. Hilbers, *Eur. J. Biochem.*, 1988, **178**, 1.
25. G. Varani and I. Tinoco, Jr., *Q. Rev. Biophys.*, 1991, **24**, 479.
26. J. G. Omichinski, G. M. Clore, O. Schaad, G. Felsenfeld, C. Trainor, E. Appella, S. J. Stahl, and A. M. Gronenborn, *Science*, 1993, **261**, 438.
27. Ref. 5, p. 316.
28. A. A. Bothner-By, R. L. Stephens, J.-M. Lee, C. D. Warren, and R. W. Jeanloz, *J. Am. Chem. Soc.*, 1984, **106**, 811.
29. Ref. 5, pp. 312–327.
30. M. F. Aldersley, F. M. Dean, and B. E. Mann, *J. Chem. Soc., Chem. Commun.*, 1983, 107.
31. G. Lipari and A. Szabo, *J. Am. Chem. Soc.*, 1982, **104**, 4546, and following paper.
32. J. Tropp, *J. Chem. Phys.*, 1980, **72**, 6035.
33. For a recent review, see B. D. Sykes and A. P. Campbell, *Biophys. Biomol. Struct.*, 1993, **22**, 99.

Biographical Sketch

David Neuhaus. *b* 1956. B.A., 1978, Oxford University, Ph.D., 1982, Imperial College of Science and Technology, London (supervisor Prof. Charles Rees). Postdoctoral visits to Professor Kurt Wüthrich, ETH Hönggerberg, Zürich, Switzerland (1983) and Dr. Ray Freeman, Physical Chemistry Laboratory, Oxford University (1984). NMR spectroscopist for Parke Davis Research Centre, Cambridge, 1985–88; staff scientist and NMR facility manager for MRC Laboratory of Molecular Biology, Cambridge, 1988–present. Approx. 40 publications. Research interests: structure determination of proteins and protein–nucleic acid complexes using NMR.

Relaxation: An Introduction

Daniel D. Traficante

The University of Rhode Island, Kingston, RI, USA

1	Introduction	1
2	Phenomenological Observations of Relaxation	1
3	Physicochemical Origin of Relaxation	3
4	Spin–Spin Relaxation, T_2	4
5	Measurements of T_1 and T_2	5
6	PhysiCochemical Mechanisms of Relaxation	8
7	Relaxation Due to Radiation Damping	11
8	Relationship Between T_1 and T_2 Relaxation Times	12
9	Related Articles	14
10	References	14

1 INTRODUCTION

A knowledge of nuclear magnetic relaxation processes is important for a variety of reasons. For example, the proper operation of a Fourier transform spectrometer requires the precise settings of pulse widths and time delays to optimize the sensitivity, resolution, integral accuracy, and nuclear Overhauser enhancements. Measurements of relaxation times are extremely useful for calculating diffusion constants and overall molecular motion, as well as segmental motion. They are also useful for making line assignments, determining internuclear distances, and establishing molecular structure. Finally, knowledge of relaxation times are important for understanding T_1- and T_2-weighted images in MRI, and for the synthesis of new contrast agents.

There are a host of excellent books, reviews and articles[1–6] that cover all aspects of relaxation, from both practical and theoretical viewpoints. Two recent and particularly interesting articles by Hahn[7] and Bloembergen[8] describe the historical development of the concepts underlying relaxation, and the experiments they used to measure relaxation phenomena. It is not the intent of this article to review previously published material. Instead, the approach given here is one that is not easily found elsewhere, and is meant to complement the articles already published. In addition, this article will focus only on the introductory aspects of relaxation.

2 PHENOMENOLOGICAL OBSERVATIONS OF RELAXATION

Consider the simple case of delivering a pulse to a single type of nucleus that is not coupled to any other nucleus; for example, the proton in 100% $H^{12}CCl_3$. Before an rf pulse is given, the net magnetization $\boldsymbol{M}_0$ is aligned along the $\boldsymbol{B}_0$ lines of force. After the pulse, two observations can be made. First, a rather large signal will be obtained initially, but the intensity of the signal will gradually decay as a function of time. Second, if enough time is allowed to elapse after the pulse, the experiment can be repeated with exactly the same results. From these observations and others, several conclusions can be drawn. First, because the signal is induced in a receiver coil that is wound along the y axis, the pulse must tip $\boldsymbol{M}_0$ away from the longitudinal z axis and into the (x, y) transverse plane. Second, because it is a magnetization ($\boldsymbol{M}_{xy}$) that generates the signal in a receiver coil that is wound with its axis in the (x, y) plane, the decay of the signal means that $\boldsymbol{M}_{xy}$ gradually vanishes from the transverse plane. Finally, the fact that the experiment can be repeated means that, between the pulses, the component of $\boldsymbol{M}_0$ along the z axis (M_z) must be growing back up along the z axis. The decay of the signal and the recovery of M_z back to M_0 are both called 'relaxation processes', even though one is a decay and the other is a growth. More specifically, the growth along the z axis is called a 'T_1 process', and the decay in the (x, y) plane is called a 'T_2 process'. Sometimes these two processes are linked, in the sense that one influences the other, and sometimes they are not, as explained later in this article.

If the chloroform sample is placed in the field $\boldsymbol{B}_0$, the magnetic moment $\boldsymbol{\mu}$ of the nuclei will take up two orientations: parallel to (in the same direction as) the field, and antiparallel to (in the opposite direction as) the field. These two states have different energies, and are called the α (low-energy) and β (high-energy) states, respectively. The energies of these states depend upon the magnitudes of the two interacting fields, $\boldsymbol{\mu}$ and $\boldsymbol{B}_0$. Hence, the energy of the β state is $+\mu B_0$ and that of the α state is $-\mu B_0$. The difference between these two energies, ΔE, is $2\mu B_0$. Initially, the number of nuclei will be equal in these two states, i.e., the states will be equally populated. However, this is not the lowest energy state for this system. The lowest energy is attained when the populations equal those that are given by the Boltzmann factor:

$$\frac{N_\beta}{N_\alpha} = \exp\left(-\frac{\Delta E}{kT}\right) = \exp\left(-\frac{2\mu B_0}{kT}\right) \qquad (1)$$

where N_α and N_β represent the number of nuclei in the low- and high-energy states, respectively, ΔE is the difference in energy between these states, k is Boltzmann's constant, and T is the absolute temperature. Hence, the nuclei will attempt to reorient themselves to achieve this new distribution. The length of time that it takes for this reorientation to occur is characterized by a constant, T_1. It is extremely important to note that T_1 *is not the time that is takes for this reorientation to be complete*—it will be shown later that it takes at least five times this long.

When the sample is first placed in the magnet, the difference between the two populations will be zero, i.e., $\Delta N = N_\alpha - N_\beta = 0$. As time progresses, nuclei will drop from the high-energy state into the lower, and ΔN will become increasingly more positive until the ratio given by equation (1) is established. For protons at room temperature in a 7.05 T field (300 MHz for protons), the ratio is approximately 0.999 95. Because the ratio is so close to unity, ΔN is a relatively small number for most sample sizes. Note that the limits of the ratio given by equation (1) are zero and one, as the temperature approaches absolute zero and infinity, respectively. The magnitude of the macroscopic magnetization vector, M_z, is directly proportional to ΔN at any time. Figure 1 shows how M_z grows immediately after the sample is inserted. The growth is exponential, and M_z asymptotically approaches the value M_0. Theoretically, it takes an infinite length of time to reach the Boltzmann ratio,

but, in practice, the ratio is considered to be reached when M_z has grown to 99% of M_0.

To gain some physical insight into the growth of M_z, two related phenomena with identical underlying principles will be described below. The first will be the recovery of an ideal spring after it has been stretched, and the second will be the first-order return to equilibrium for a unimolecular chemical system that has been displaced from its equilibrium position.

2.1 Spring Analogy

Consider the case of an ideal spring with one end attached to the ceiling and the other hanging free. The free end is at its *equilibrium* position, i.e., it is neither stretched nor compressed. This ideal spring has three properties that are analogous to a nuclear magnetization vector. Specifically,

1. the spring is weightless, and will have no momentum while moving;
2. while stretching or contracting, it will not lose energy because of internal friction;
3. it can be considered to be a point source.

Suppose the spring is stretched only a short distance toward the floor. When released, its instantaneous velocity will not be very high, because it has not been stretched very far; it has not been displaced very far from its equilibrium position. If stretched further before releasing then its instantaneous velocity will be higher. This property is the basic principle embodied in Hooke's law, which states that 'the stress is proportional to the strain' for an equilibrium system. If snapshots are taken of a series of these stretch-and-release experiments, joined together, and then run backwards, the end of the spring would appear to move very rapidly at first, but then move more and more slowly as it approaches its initial position of equilibrium. A plot of the position of the end of the spring versus time will be identical to that shown in Figure 1. In this figure, the slope at any point on the line

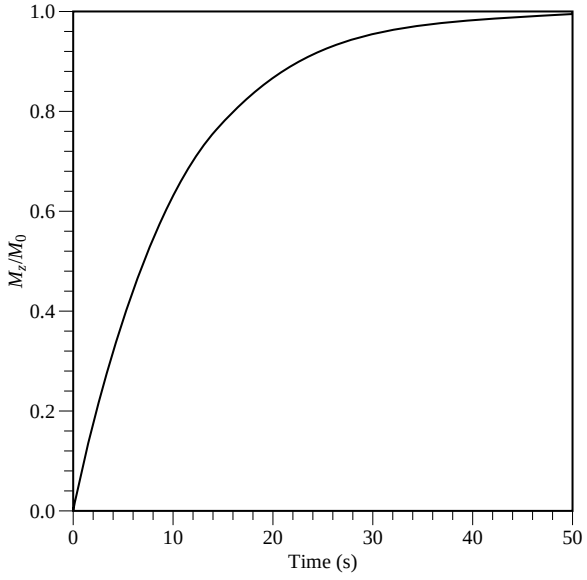

Figure 1 The growth of a magnetization vector along the z axis as a function of time for the case when $T_1 = 10\,\mathrm{s}$

gives the instantaneous rate of change, which is greatest at the beginning. It will be shown later that this rate of change is directly proportional to the displacement from equilibrium. If several springs manufactured from different sizes of wire were subjected to these stretch-and-release experiments, the ends of each spring would return exponentially to its equilibrium position, but at a rate determined by the force constant of the spring.

Hooke's law can be applied to a spin system because the nuclei that populate the two energy levels are in equilibrium. The ratio of N_α to N_β can be a constant without the nuclei permanently residing in any one state—this would be a *static* equilibrium. For the nuclear system, the ratio given by equation (1) remains constant because the total number of nuclei moving from the α state up to the β state is equal to the number moving from the β state down to the α state—this is a *dynamic* equilibrium. Hence, the end of an ideal spring may be imagined to be connected to the tip of the net magnetization vector $\boldsymbol{M}_0$. After a pulse, the component remaining along the z axis, M_z, will be less than M_0, and the spring will stretch. During relaxation, the spring will return exponentially back to its equilibrium position, pulling M_z up with it. Thus, the force constant for a spring is analogous to the T_1 for a nuclear spin system.

2.2 Chemical Analogy

A first-order, unimolecular equilibrium may be written as $\mathrm{A} \leftrightharpoons \mathrm{B}$. This is a dynamic equilibrium, and is not chemically the same as a static mixture of A + B. In the latter system, a molecule of A never becomes a molecule of B, whereas in the former case, a molecule of A becomes a molecule of B. However, to maintain a constant A/B ratio, for each molecule of A that becomes a B, a molecule of B must become an A. Again, this chemical equilibrium is analogous to the nuclear system, and we may apply the same mathematical treatment to both.

If A is added to the equilibrium mixture of A and B, or if B is removed, the system will attempt to return to its equilibrium concentrations, given by K_{eq}. The application of Hooke's law here states that 'the instantaneous rate of return to equilibrium is directly proportional to its displacement from equilibrium'. For a nuclear system that has been displaced from equilibrium,

$$\frac{\mathrm{d}M_z}{\mathrm{d}t} \propto M_0 - M_z \tag{2}$$

where $\mathrm{d}M_z/\mathrm{d}t$ is the rate of change of M_z, and $M_0 - M_z$ is the displacement from equilibrium, i.e., its equilibrium position (M_0) minus its present position (M_z). The proportionality symbol $\propto$ can be replaced by an equals sign and a constant of proportionality, k:

$$\frac{\mathrm{d}M_z}{\mathrm{d}t} = k(M_0 - M_z) \tag{3}$$

After collecting variables, the indefinite integral can be written as

$$\int \frac{\mathrm{d}M_z}{M_0 - M_z} = k \int \mathrm{d}t \tag{4}$$

At $t = 0$, when the sample is first placed in the field, $\Delta N = 0$ and $M_z = 0$. After some period of time t, the magnetization

will grow to some new value, M_z. Hence, the limits of the integration are as follows:

$$\int_0^{M_z} \frac{\mathrm{d}M_z}{M_0 - M_z} = k \int_0^t \mathrm{d}t \tag{5}$$

The solution of this equation is easily obtained by standard mathematical manipulations:

$$\ln \frac{M_0 - M_z}{M_0} = -\frac{t}{T_1} \tag{6}$$

where, in order to make the right-hand side dimensionless, like the left, k has been set equal to T_1^{-1}, with T_1 having dimensions of time. Equation (6) can be written equivalently as

$$M_z = M_0(1 - \mathrm{e}^{-t/T_1}) \tag{7}$$

Equation (6) has the form of a straight line $y = mx + b$ and a semilogarithmic plot of $M_0 - M_z$ versus t will give an intercept equal to M_0 and a slope equal to $-1/T_1$. Figure 1 was prepared from equation (7), using a value of 10 s for T_1. Table 1 was also prepared from equation (7).

As stated previously, M_z asymptotically approaches M_0, and would take infinitely long to reach its maximum value. However, the recovery is normally considered to be complete when it has reached 99%. Hence, relaxation delays of $5T_1$ are commonly used in pulse sequences.

2.3 The Meaning of T_1

As explained earlier in this section, T_1 is a *measure* of how fast M_z grows back to M_0—it is *not* how long it takes to grow back to M_0. In this sense, it is analogous to the force constant of a spring, and not to the length of time it takes the end of a stretched spring to return to its relaxed position when released. After a 90° pulse, T_1 is the time it takes for M_z to grow back to $1 - \mathrm{e}^{-1}$ of the original value that it had immediately before the pulse. Figure 2 shows that if the initial slope is extended until it intersects the M_0 line, the intersection occurs at a time equal to T_1. *If* —repeat—*if* the magnetization grew at a constant rate equal to the initial rate then the relaxation would be complete in a time equal to T_1, which is 10 s in this case.

Table 1 Percentage Recovery of M_z as a Function of Time, in Units of T_1

Time/T_1	Recovery (%)
0.0	0.00
0.5	39.3
1.0	63.2
1.5	77.7
2.0	86.5
3.0	95.0
4.0	98.2
5.0	99.3

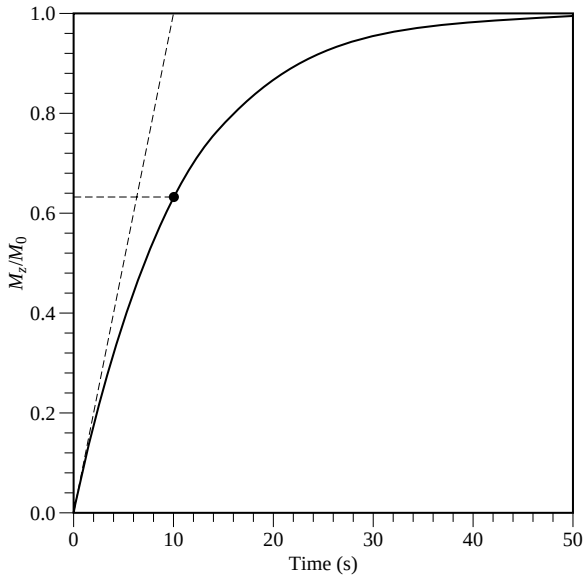

Figure 2 A plot (dashed line) of the *initial* rate of growth of a magnetization vector with T_1 = 10 s. This dashed line intersects the M_0 line at a time equal to T_1, which is the time that the relaxation would be complete *if* it continued at the *initial* rate. At this time, however, the vector *actually* grows to only 63.2% of its maximum value, as shown by the dotted line

3 PHYSICOCHEMICAL ORIGIN OF RELAXATION

Equation (1) shows that at 0 K the N_β/N_α population ratio is zero, and that all of the nuclei will be in the lower energy state, but at room temperature the ratio is approximately 0.999 95, and almost half are in the higher energy state. Based simply on the population ratios, the spin system at room temperature has a higher energy than the one at 0 K. Furthermore, the nuclei must jump back and forth between the α and β states if the nuclear system is to remain in dynamic equilibrium at room temperature. To induce an upward transition requires an input of energy. The only source of this energy is the sample itself, which is called the 'lattice'. Conversely, a downward transition requires dissipation of energy, whose only sink is again the lattice. This dissipation of spin energy into the lattice is called 'spin–lattice relaxation'. Any relaxation that alters the population ratio will also alter ΔN, and in turn M_z, which represents the magnetization along the $\boldsymbol{B}_0$ lines of force. Hence, it is also called 'longitudinal relaxation', or 'T_1 relaxation'.

3.1 Molecular Motion

The foundations of the quantum theory of nuclear magnetic relaxation were laid in 1948 by the classic work of Bloembergen, Purcell and Pound.[9] This theory has been extensively developed and has found widespread applications. Redfield[10] and Abragam[2] have also described relaxation using the density matrix formalism, but these theories are outside the scope of this article(for further details, see ***Relaxation Theory: Density Matrix Formulation***). The treatment presented here is based largely on the perturbation theory applied by Solomon,[11] who assumed that the Brownian motion of molecules in a sample is random and isotropic. Barring chemical changes effected by

higher temperatures, one main difference between a sample at two different temperatures is increased translational and rotational motion. It is this motion that plays an important role in both the absorption and the dissipation of lattice energy described above. The absorption of energy will be described first, and then, by using reverse arguments, the dissipation will be described.

The motion of a molecule does not directly affect the orientation of the nuclear spin with respect to the $\boldsymbol{B}_0$ field. The alignment of a spin parallel to the field cannot change as a result of a physical rotation of the molecule. To reorient the spin so that it is antiparallel to the field requires the absorption of an amount of energy equal to the difference in energies between the two possible orientations. One source of this energy is provided by the random motions of other magnetic dipoles, especially other protons in the molecule. Another source is the randomly fluctuating magnetic fields that are generated from the randomly moving electric dipoles in a tumbling molecule. When these magnetic fields change at a rate equal to the Larmor frequency, they act on the spins in the same way as does a $\boldsymbol{B}_1$ field. Hence, they induce transitions from the lower energy state to the higher one. It is somewhat more difficult to see how this motion can be involved in the dissipation of energy, but Newton's third law can be employed to show that the same mechanisms can operate in reverse. For example, a fluctuating magnetic field from a β-to-α transition produces a fluctuating electric field, which can attract or repel another electric dipole and cause motion. Analogously, a randomly fluctuating electric field can attract or repel a magnetic dipole through the Oersted effect, i.e., the movement of a magnet placed near a wire carrying an electric current (a moving electric field). Hence, the dissipated energy is converted into rotational and translational energy.

3.2 Spin Temperature

An alternative explanation for the dissipation involves the concept of spin temperature, which is valuable in this context. The concept has been thoroughly examined by Abragam and Proctor.[12] For spin-$\frac{1}{2}$ nuclei, the spin temperature T_s may be defined as the temperature that satisfies equation (1) for any given population ratio. It is important to note that the concept of spin temperature is not well defined for nuclei with spin greater than $\frac{1}{2}$. For these nuclei, there will be more than two states, and the populations between adjacent energy levels may not give a unique value for T_s.

For protons at room temperature (293 K) in a field strength of 7.05 T, the ratio is 0.999 95. If an rf pulse between 90° and 270° is given to a proton spin system that is initially in thermal equilibrium with the lattice at 293 K then, immediately after the pulse, the ratio inverts and becomes greater than 1.

At that instant, T_s is negative. Purcell and Pound[13] were able to achieve this with a crystal of lithium fluoride. For tip angles between 0° and 90°, the ratio remains between 0 and 1, but becomes more positive. Then, the spin temperature is hotter than the lattice. Spin–lattice relaxation then corresponds to the tendency of two thermodynamic systems to approach the same temperature when in contact with each other. Thus, T_1 is a measure of the rate at which the spin system comes into thermal equilibrium with the other degrees of freedom. This concept is frequently used to explain the growth of a ^{13}C magnetization vector during the 'contact time' employed in a solid state NMR experiment. During this period, the 'hot' carbon spins transfer their energy to the 'cooler' proton spins. It is instructive to note that if a sample is allowed to reach equilibrium in a 1.41 T magnet (60 MHz), and then instantly placed in a field strength of 7.05 T (300 MHz), the spins initially will be 'hotter' than the lattice by only 3×10^{-4} K.

For a sample at equilibrium, transitions are continuously being induced from the α state to the β state by the absorption of energy from the lattice, while transitions from the β to the α state dissipate energy into the lattice. Because these energy differences are equal and opposite, and because there must be as many upward as downward transitions to maintain a population at equilibrium, the net change in energy is zero and the temperature of the sample remains constant.

3.3 Nonexponential Relaxation

It must be emphasized here that nonexponential relaxation may take place even if the spin system consists of identical nuclei. Although it is more common in solids, such behavior is not rare in liquids. This has been predicted theoretically[14] for a group of three protons that are dipolar-coupled. The various mechanisms that contribute to relaxation will be discussed later, but it suffices to say here that if two or more mechanisms contribute significantly to relaxation then non-exponential behavior may be observed. For example, at the higher magnetic field strengths used today, chemical shift anisotropy (CSA) and dipole–dipole (DD) relaxation mechanisms may both be important and may not be purely additive. This effect, which is known as the 'interference of interactions', was predicted theoretically[15,16] and has been confirmed experimentally.[17] Detailed accounts have been given by Farrar and colleagues,[18,19] Shimizu,[20] Redfield,[21] Mackor and MacLean,[22,23] Vold and Vold,[24] Noggle and Schirrer,[25] and Werbelow and Grant.[26] For further details, see ***Relaxation Processes: Cross Correlation and Interference Terms***.

4 SPIN–SPIN RELAXATION, T_2

When T_1 longitudinal relaxation is complete, all of the magnetization is aligned along the z axis. At this point, there cannot be any magnetization left in the (x, y) transverse plane; otherwise the magnitude of the vector sum would exceed the original value, M_0. Hence, T_1 relaxation contributes to T_2, but even if T_1 is very long, the magnetization vector would still shrink in the (x, y) plane. For high-resolution proton and carbon spectra of liquids, the main cause of shrinking is typically the inhomogeneity of the $\boldsymbol{B}_0$ field: but even in a perfectly homogeneous field, the vector will still shrink, albeit more slowly, owing to an exchange of energy between two spins. These two mechanisms will be discussed separately.

4.1 Effect of Field Inhomogeneity

This effect is not a true relaxation, in the sense that the nuclei do not drop from a high-energy state to a lower one by a transfer of energy. Nevertheless, inhomogeneous fields cause

the magnetization vector to decay in the (x, y) plane. In this sense, it may be called a relaxation mechanism.

The net magnetization along the z axis is generally pictured as a single, distinct vector. However, it should be remembered that it is a vector sum of many smaller ones. For protons and other spin-$\frac{1}{2}$ nuclei, it can be imagined to be formed from the microscopic nuclear magnetic moments $\boldsymbol{\mu}$ by first subtracting the number in the high-energy state from those in the lower, and then, from the remaining moments, vectorially adding their maximum observable components $\mu_z \boldsymbol{k}$ (where $\boldsymbol{k}$ is the unit vector along the z axis):

$$\boldsymbol{M}_0 = (N_\alpha - N_\beta)\mu_z \boldsymbol{k} \tag{8}$$

If a 90° pulse is given to this vector, its magnitude may be considered to be held constant during the pulse, because the duration of the pulse is usually orders of magnitude shorter than the time constants for the relaxation processes that generally cause the vector to shrink. However, once the vector reaches the (x, y) plane, the inhomogeneous field will act on the individual vector components, which are called 'isochromats'. This inhomogeneity acts in a way that causes the vector sum to decrease. The individual μ_z components will be located in different positions throughout the sample, and, because the field is inhomogeneous, they will experience different field strengths. Hence, there will be a distribution of Larmor frequencies even though the shielding constants for all the nuclei are the same. These isochromats will then precess at different rates, and will begin to separate from each other. This fanning, which is frequently called a 'dephasing', produces a smaller vector sum, and $\boldsymbol{M}_{xy}$ shrinks in the (x, y) plane, as shown in Figure 3. In this figure, and throughout this chapter, the 'right-hand rule' will be used to be consistent with the product operator formalism. Using this rule, a 90° pulse on the $+x$ axis tips $\boldsymbol{M}_0$ to the $-y$ axis, and not to the $+y$ axis, as is the case with the 'left-hand rule'. Then, vectors moving faster than the rotating frame (positive frequency) move counterclockwise (ccw), and those moving slower (negative frequency) move clockwise (cw). With the right-hand rule, the definition of positive and negative frequencies is consistent with the rules of mathematics, i.e., a rotation of a vector from the $+x$ axis to the $+y$ axis (ccw) is a positive angle, whereas a rotation from the $+x$ axis to the $-y$ axis (cw) is a negative angle.

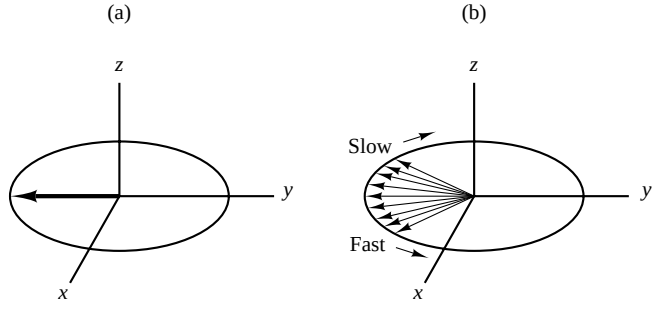

Figure 3 After a 90° pulse (a), the isochromats begin to fan, or dephase in the (x, y) plane (b). In this figure, the right-hand rule is used. Hence, a pulse delivered on the $+x$ axis rotates the magnetization vector onto the $-y$ axis. Isochromats whose Larmor frequencies are greater than that of the rotating frame will move counterclockwise, while slower ones will move clockwise

4.2 Spin–Spin Relaxation

Any process that causes a dephasing will cause the resultant vector to shrink. It has been explained above that an inhomogeneous field can cause a dephasing, but even if the field were perfectly homogeneous, a dephasing would still take place by a 'natural process'. Immediately after the pulse, all of the microscopic vector components of $\boldsymbol{M}_{xy}$ are aligned with each other, and the angle between them is 0°, i.e., they are 'in-phase'. Protons that are in the high-energy state as a result of the pulse can be relaxed by nearby low-energy protons in the same molecule by an exchange of energy between the β and α states. A nucleus that drops to the α state may reabsorb energy and return to the β state. This is a random process, and it is unlikely that it would return with the same phase, i.e., 0°. It is very probable that it would acquire a random phase upon its return, and lose its phase memory. Hence, the isochromats that were originally aligned with each other will scatter in the (x, y) plane as a result of random phase changes. As this scattering occurs, the isochromats will begin to fan out, and the vector sum will decrease toward zero. The decay of M_{xy} is exponential, with a time constant of T_2, which is frequently called the 'natural T_2'.

The overall rate at which $\boldsymbol{M}_{xy}$ shrinks will be equal to sum of the rates for the two processes described above:

$$\text{overall rate} = \text{rate from field inhomogeneity} + \text{natural rate} \tag{9}$$

It is this rate that causes the decay of the FID collected from the spectrometer. In a $\boldsymbol{B}_0$ field that has been well shimmed, this is also an exponential decay, and the time constant assigned to it is T_2*. Because rates and times are the reciprocals of each other, the overall rate in equation (9) is given by

$$\frac{1}{T_2^*} = \frac{1}{T_2'} + \frac{1}{T_2} \tag{10}$$

where T_2' is the rate constant due to field inhomogeneity.

4.3 The Meaning of T_2*

An FID decays because $\boldsymbol{M}_{xy}$ shrinks in the (x, y) plane. Both processes are exponential, and T_2* is a *measure* of how fast the FID decays. It is analogous to the halflife of a radioactive element. After one halflife, the amount of the material remaining is one-half of the original amount at time zero. But there is nothing magical about the number 2: in fact, the number e (= 2.71828 ...) is very special in the sense that it appears much more often in Nature than the number 2. Hence, spectroscopists do not speak of the rate of decay of an FID in terms of its halflife; instead, they speak of its 1/e-life, that is, how long it takes for the FID to decay to a value that equals 1/e of its original value at time zero. Figure 4(a) depicts a situation in which T_2* = 1.5 s for an FID. Note that after 1.5 s have elapsed, the amplitude is A_0/e, where A_0 is the original amplitude at time zero. Figure 4(b) shows that if the initial slope is extended until it intersects the M_{xy} axis then the intersection occurs at a time equal to T_2*. *If* —repeat—*if* the FID decayed at a constant rate equal to the initial rate then the FID would be completely decayed in a time equal to T_2*, which is 1.5 s in this case.

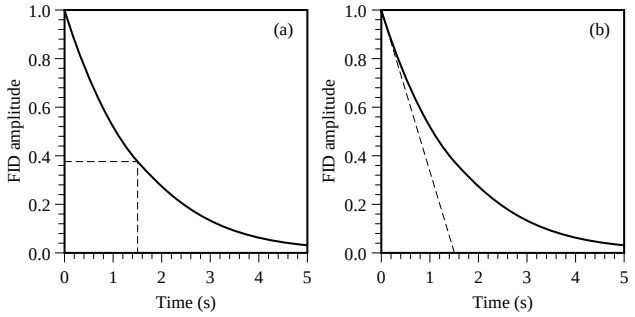

Figure 4 A plot of the decay of an FID as a function of time, for the case in which T_2* = 1.5 s. In (a), the dotted lines show that after 1.5 s have elapsed, the FID has decayed to 36.8%, or 1/e, of its initial value. In (b), the dashed line shows the *initial* rate of decay. This line intersects the M_{xy} axis at 1.5 s, which is the time that the decay would be compete *if* it continued at the initial rate

5 MEASUREMENTS OF T_1 AND T_2

There are numerous excellent descriptions of the methods that can be used to measure the T_1 and T_2 time constants in the laboratory (see, e.g., Frye[27] and Farrar,[5] respectively). Hence, only very brief summaries will be given here, and the reader is referred to those articles for further details.

5.1 Measurement of T_1

One of the earliest methods is called the 'inversion–recovery', or the '180°–tau–90°' method. A 180° pulse is first delivered to $\boldsymbol{M}_0$, causing it to invert and align along the negative z axis. After waiting a period of time, τ, $\boldsymbol{M}_0$ exponentially recovers along the z axis, as shown by equation (3). The limits of the integration shown in equation (5) must then be from $-M_0$ to M_z on the left-hand side, and from 0 to τ on the right. Equation (7) then becomes

$$M_z = M_0(1 - 2\,\mathrm{e}^{-\tau/T_1}) \tag{11}$$

After time τ, a 90° pulse is given that has the same phase as the first one. If $\boldsymbol{M}_0$ has not yet reached the origin and is still aligned along the negative z axis, then M_z will rotate into the (x, y) plane to give a negative signal after Fourier transformation. On the other hand, if it recovers fast enough to have grown through the origin to the positive z axis then a positive signal will be obtained, as shown in Figure 5. A special case occurs when T_1 has a value such that $\tau = (\ln 2)T_1$. Then, $\boldsymbol{M}_0$ will have grown exactly to the origin, and no signal results. T_1 is experimentally determined by measuring M_z at various values of τ. The article by Frye[27] gives an excellent comparison of the various methods for measuring T_1.

5.2 Measurement of T_2

5.2.1 Spin Echo Experiments

Perhaps the most common method is the Carr–Purcell–Meiboom–Gill (CPMG) modification of the Hahn '90°–tau–180°' echo experiment. This modification reduces the effects of the errors in the 180° pulses. In the original Carr–Purcell train of 180° pulses, these errors accumulate, but not in the CPMG sequence. This is well described by Farrar.[5]

After a pulse, M_{xy} begins to shrink because of T_2* relaxation, which is a combination of the effects of field inhomogeneity and natural relaxation. The decay from T_2' is predictable, at least in the sense that the inhomogeneity will not change during the course of the experiment. It should therefore be possible to reverse this decay. However, the decay from T_2 is a random process—randomness is not predictable, by definition, and no pulse sequence can reverse its effects.

After a 90° pulse is applied on the x axis, $\boldsymbol{M}_{xy}$ shrinks in the rotating frame because some of the isochromats will move clockwise (cw), and others will move counterclockwise (ccw), as shown in Figure 3(a) and (b). They will move in opposite directions and separate from each other because some have a higher Larmor frequency than the frame, while others have a lower one. After some time τ, if a 180° pulse is given along the $\pm y$ axis, as in the CPMG sequence, then the isochromats that were on one side of the $-y$ axis will precess about the axis and move to the other side, i.e., those on one side will exchange places with those on the other, as shown in Figure 6(b). If the nuclei have not diffused through the sample to a location very far from their original positions, then the strength of the $\boldsymbol{B}_0$ field that they experience will be essentially the same after time τ as it was at the start of the experiment. This is the predictable part. Then, the isochromats that were initially moving cw will continue to move in that same direction, because their Larmor frequencies will still be the same as they were before. Similarly, those that were initially moving ccw also continue to move in that same direction. Hence, the isochromats will begin to move back toward the $-y$ axis. After a time τ, most of the isochromats will be realigned along the $-y$ axis, because the angle that they traverse before the 180° pulse will be equal to the angle they traverse after the pulse—their frequencies remain unchanged. During the time that they are moving back toward the y axis, $\boldsymbol{M}_{xy}$ grows. This process is frequently called 'refocusing', because the fanning, or 'defocusing', is being reversed. The point at which refocusing is complete is called the 'echo' (see Figure 6). After this point, the isochromats continue to move and cross over to the other side of the $-y$ axis, and the FID begins again. Then, if a series of 180° pulses is continually delivered along the $\pm y$ axis, a series of echoes will be produced. If a Fourier transform is performed on the FIDs collected after each echo, the intensity of the line in the spectrum will be proportional to the magnitude of $\boldsymbol{M}_{xy}$ at the echo.

An important question to answer here is 'At the echoes, how do the magnitudes of M_{xy} compare with each other, and to the initial magnitude of $\boldsymbol{M}_{xy}$?' The answer is that each echo will have a smaller amplitude than its predecessor. The $\boldsymbol{M}_{xy}$ vector formed at the first echo consists of the vector sum of only those isochromats that retained their sense of motion in the rotating frame. However, from the first pulse to the echo, the natural T_2 process is randomly dephasing some of the isochromats. This part is not predictable, and the randomization process cannot be reversed by applying a 180° pulse. If it were possible then, in principle, one could obtain infinitely good S/N in an NMR spectrum by collecting first one FID, and then adding to it another FID obtained by removing the sample and applying a 180° pulse to invert only the noise. Obviously, this experiment

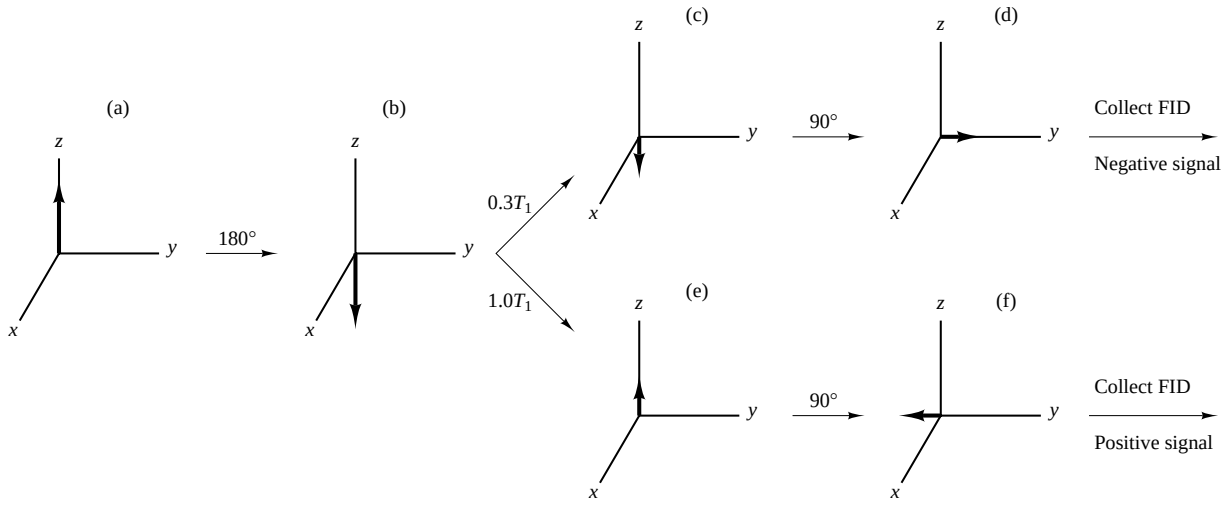

Figure 5 The sequence involved in measuring T_1 by the inversion–recovery method. A magnetization vector (a), is inverted (b), and allowed to recover (c) and (e). A 90° pulse is then given and a signal collected. If the vector has not yet grown up to the origin, the collected signal will be negative (d), whereas if the vector has grown up past the origin, the signal will be positive (f)

would not work. Randomness ignores 180° pulses and remains random.

If $\boldsymbol{M}_{xy}$ is measured at the time of the first echo, its magnitude will be exactly the same as the magnitude that would be measured if a single 90° pulse is applied to a sample placed in a perfectly homogeneous field, and the magnitude measured after the same length of time. The randomization process would have the same length of time to operate and shrink the vector. Hence, the amplitudes of the echoes show how $\boldsymbol{M}_{xy}$ would shrink in a perfect $\boldsymbol{B}_0$ field, and from these data, T_2 can be obtained.

5.2.2 $T_{1\rho}$ Experiments

For the CPMG experiment described above, it was stated that the predictable part depends, at least partially, on the molecules not diffusing out of their local environments. If this restriction does not hold then a useful alternative is the $T_{1\rho}$ experiment, or 'T_1 in the rotating frame'. In this experiment, a 90° pulse on the x axis is immediately followed by the application of a continuous wave $\boldsymbol{B}_2$ field that is phase-shifted to the $\pm y$ axis. As soon as the isochromats begin to fan, they will precess around the strong $\boldsymbol{B}_2$ field, which keeps them 'spin locked' along the $-y$ axis (see Figure 7). Here again, however, because of the natural T_2 randomization, the isochromats that are dephasing will not remain spin locked. As long as they keep a given phase, they will precess around $\boldsymbol{B}_2$, but at some random time they will change their phases and 'jump' to another location in the rotating frame. The overall result is a shrinking due only to random dephasing, a pure T_2 process.

Relaxation in this frame of reference is called $T_{1\rho}$ because it is a type of T_1 relaxation, in the sense that the magnetization vector shrinks longitudinally along the $\boldsymbol{B}_2$ lines of force. When $\boldsymbol{M}_0$ is first tipped into the (x, y) plane, it has the same length that it had immediately before the pulse, when it was aligned along the z axis. If the $\boldsymbol{B}_2$ field is applied 'on resonance', i.e., at a frequency equal to the Larmor frequency of the nucleus, then $\boldsymbol{M}_{xy}$ will not precess about the z axis in the rotating frame. Because $\boldsymbol{B}_0$ vanishes in this rotating frame, the 'fictitious field', $\Delta\boldsymbol{B}_0$ is equal to zero. Hence, $\boldsymbol{M}_{xy}$ will stay aligned along the $-y$ axis. However, because $\boldsymbol{B}_0$ is no longer present in this frame, $\boldsymbol{M}_{xy}$ experiences only the $\boldsymbol{B}_2$ field, which is stationary in this frame and is very much smaller than $\boldsymbol{B}_0$. In this field, $\boldsymbol{M}_{xy}$ is much too long immediately after the 90° pulse; its length is a result of polarization in the field $\boldsymbol{B}_0$, not $\boldsymbol{B}_2$. Hence, the

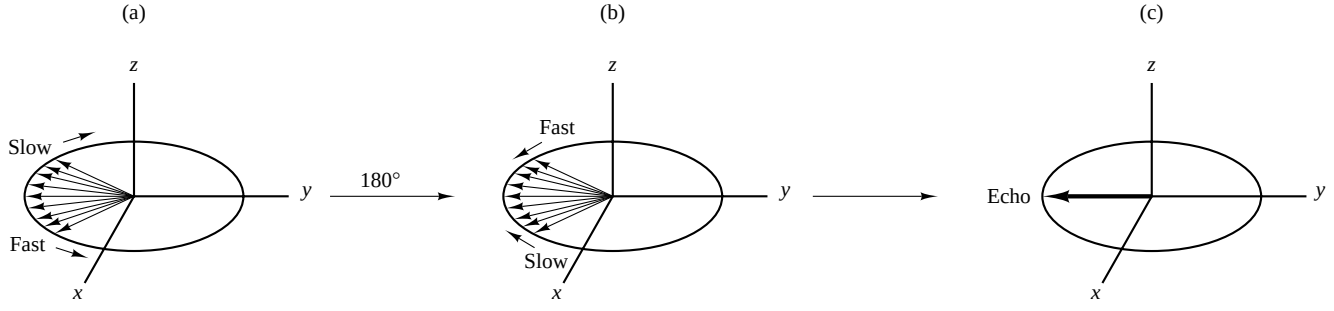

Figure 6 The Carr–Purcell–Meiboom–Gill sequence for measuring T_2. In (a), the isochromats have dephased as shown in Figure 3. A 180° pulse applied along the $\pm y$ axis rotates the dephased isochromats to the opposite side of the y axis (b). If the nuclei have not diffused very far from their original locations in the sample, they will retain their Larmor frequencies and sense of rotation in the rotating frame, and will refocus to form an echo (c)

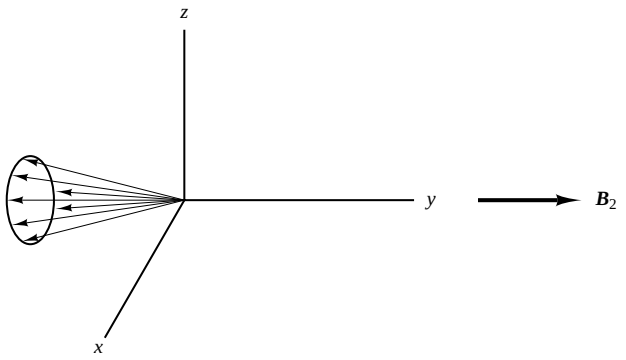

Figure 7 Spin locking of the isochromats in the measurement of T_2 by a $T_{1\rho}$ experiment. The $\boldsymbol{B}_2$ field applied along the $\pm y$ axis causes the isochromats to precess around the y axis. After a period of time has elapsed, the resultant shrinks because of T_2 relaxation, and can be measured by turning off the $\boldsymbol{B}_2$ field and collecting the signal

N_β/N_α ratio is too small, and the spin temperature is too low. The $\boldsymbol{B}_2$ field is a continuous field and is applied for seconds; it is not pulsed for microseconds, as is a $\boldsymbol{B}_1$ field. Hence, there is sufficient time for the nuclei to re-establish a new N_β/N_α ratio consistent with that given by equation (1) where ΔE normally equals $2\mu B_0$, but must now be replaced by $2\mu B_2$. This new value of ΔE is very much smaller, and $\boldsymbol{M}_{xy}$ shrinks to near zero. If $\gamma B_2 \tau_c \ll 1$ (τ_c is the molecular correlation time), a condition usually satisfied for small molecules in nonviscous solvents, then $T_{1\rho} = T_2$.

The decay of the vector is observed by first applying $\boldsymbol{B}_2$ for some time τ, turning it off, and then collecting an FID. After Fourier transformation, the intensity of the signal in the spectrum will be proportional to the length of $\boldsymbol{M}_{xy}$ at time τ. Then, the experiment is repeated using a longer period of time for τ, during which time the vector shrinks further. When $\boldsymbol{B}_2$ is turned off and the FID collected, the spectrum will show the same signal as before, but with a smaller intensity. From a series of such experiments, $T_{1\rho}$ may be calculated. However, a word of caution is appropriate here. The above description of the shrinking in the rotating frame is accurate only when 'on resonance'. For lines 'off resonance', analysis of the $T_{1\rho}$ data may be difficult.[28–32] For further details, see ***Rotating Frame Spin–Lattice Relaxation Off-Resonance***.

5.3 Pulsed Field Gradient Spin Echo Experiments

As explained earlier, the $T_{1\rho}$ experiment eliminates the effects of diffusion when measuring T_2. However, if one is interested in measuring the translational diffusion rate of molecules then the pulsed field gradient spin echo experiment (PFGSE) can be used.[5]

6 PHYSICOCHEMICAL MECHANISMS OF RELAXATION

6.1 Randomly Fluctuating Magnetic Fields

It was stated previously that spin–lattice (T_1) relaxation involves an energy exchange between the spin system and the lattice, via molecular motion. Random Brownian movements in the liquid create small fluctuating fields in the vicinity of the spin. Listed below are six sources for these magnetic fields. For typical organic molecules at field strengths near 7.05 T (300 MHz), only the first two are effective relaxation 'mechanisms'.

1. *Magnetic dipole-dipole interaction* is due to a 'through-space' interaction of magnetic moments of other nuclei.
2. *Spin–rotation interaction* is due to the distribution of electrons in the rotating molecule, or to portions of the molecule (segmental motion).
3. *Chemical shift anisotropy* is due to the variability of the nuclear shielding (chemical shift) as a function of the orientation of the molecule with respect to the $\boldsymbol{B}_0$ lines of force, (*tropic*, space; *iso*, same; *an*, not—the chemical shift is not the same in all orientations of the $\boldsymbol{B}_0$ space).
4. *Quadrupolar interaction* (for nuclei with $I > \frac{1}{2}$), is due to the changing direction of the electric field gradient at the nucleus.
5. *Scalar interaction* is due to fluctuations of the coupling constant (J), 'first kind', or fluctuations of the spin state of the coupled nucleus, 'second kind'. This is a 'through-bond' interaction, rather than the dipole–dipole 'through-space' interaction described above. Scalar relaxation of the 'third kind' has been described.[33,34]
6. *Electron–nuclear* or *paramagnetic interaction* is due to the presence of unpaired electrons, which have a magnetic moment 685 times larger than that of a proton.

If these fields have a fluctional component at the Larmor frequency ω_0 then they can induce transitions in a manner similar to the pulsed rf field $\boldsymbol{B}_1$. Although it is not obvious, motional frequencies at $2\omega_0$ also provide a relaxation mechanism.[8,35] Hence, T_1 will depend upon the magnitude and the rate of fluctuation of the local fields. Because the macroscopic viscosity and the temperature of the sample affect molecular motion, these will in turn also affect T_1.

Under these circumstances, a basic condition for the theory of Brownian motion to be valid is that the molecule makes many collisions with other molecules before it turns around, or moves through a distance characteristic of one molecular spacing. This is a reasonable approximation for many liquids, but not for gases, where a molecule may rotate many times between collisions. This Brownian motion is not a single frequency—it is composed of many frequencies. Just as the Fourier transform of an FID produces a plot (spectrum) of the amplitudes of the frequencies present in the FID, the amplitudes of the frequency components $J(\omega)$ in the Brownian motion can also be plotted. The relationship between $J(\omega)$ and ω is[4]

$$J(\omega) \propto \frac{\tau_c}{1 + \omega^2 \tau_c^2} \tag{12}$$

where τ_c is the 'correlation time', which is analogous to the period of a frequency. It is a time that is characteristic of the random motion, and is approximately equal to the average time needed for the molecule to change its orientation. It is a measure of the time it takes for the field to 'lose memory' of a previous value. For a very comprehensive treatment of Brownian motion and correlation times, see ***Brownian Motion and Correlation Times***. Table 2 shows the approximate correlation times for some typical molecules of various sizes.

Table 2 Correlation Times for Some Typical Molecules

Compound	Correlation time τ_c (s)
Methyl iodide	10^{-13}
Toluene	10^{-12}
Naphthalene	10^{-11}
Cholestane	10^{-10}
Vitamin B_{12}	5×10^{-9}
Ribonuclease A	10^{-8}
tRNA	10^{-8}

Figure 8 is a plot of $J(\omega)$ versus ω for three values of τ_c. The intermediate value was chosen to be the reciprocal of the Larmor frequency for protons at a field strength of 11.75 T. Thus, ω_0 = 500 MHz, or 3.14×10^7 rad s^{-1}, and $\tau_c = 2 \times 10^{-9}$ s. When a molecule tumbles at a rate equal to its Larmor frequency, the product $\omega_0\tau_c = 1$.

For large molecules, the overall motion is slow, and the lower frequencies have higher amplitudes than the higher frequencies. For small molecules, the reverse is true; i.e., there are more higher frequency components than lower ones. When a molecule tumbles at the intermediate rate chosen here, $J(\omega)$ at 1.0 has a higher value (indicated by a closed circle in Figure 8) than at slower or faster tumbling rates (indicated by open circles). In other words, protons in these molecules will experience stronger local fields fluctuating at 500 MHz than protons in smaller or larger molecules. Because the rate of relaxation is a function of the strength of the fluctuating field at that frequency, protons in intermediate size molecules will relax faster at this field strength.

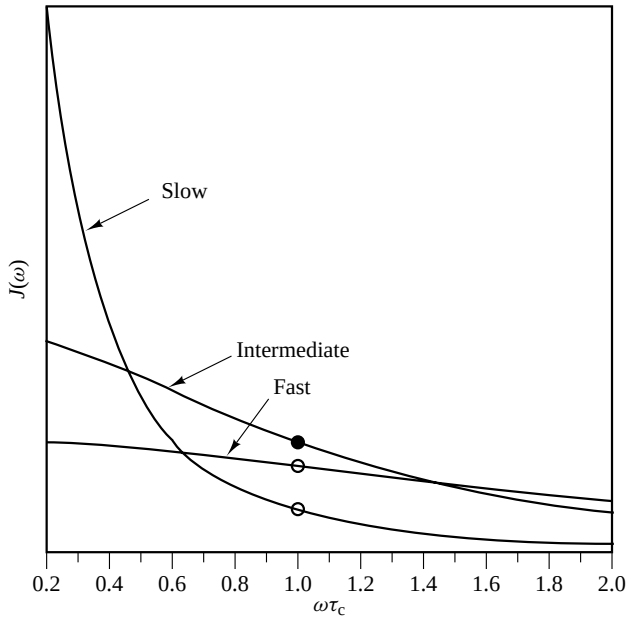

Figure 8 A plot of the amplitudes of the frequency components, $J(\omega)$, for randomly tumbling molecules whose overall rate of motion is slow, intermediate, and fast. The horizontal axis is the product of ω times τ_c. This product equals 1 when the molecule tumbles as fast as the Larmor frequency. For the condition specified in the text, $J(\omega)$ has a higher value when the molecule tumbles at an intermediate rate (indicated by a closed circle), than at slower or faster rates (indicated by open circles)

6.2 Dipolar-Coupled Nuclei

A proton that is directly bonded to a ^{13}C atom is coupled to it in two ways: the proton is both scalar- and dipolar-coupled to it. Scalar coupling is transmitted through bonds, and produces the J splitting usually observed in spectra. Dipolar coupling is a 'through-space' interaction. It does not produce a splitting, but it is responsible for the NOE effects observed in proton-decoupled ^{13}C spectra. However, these effects are not the result of the removal of the J splitting by decoupling. Instead, they arise from saturating the protons with irradiation from the proton decoupler. When a proton is directly bonded to ^{13}C, the internuclear distance is short. It is this closeness in space, and not the sigma bond, that leads to dipolar coupling and the NOE effects. For details of the NOE, see ***Nuclear Overhauser Effect***.

When two different nuclei, such as a proton and a ^{13}C nucleus, are coupled to each other, they are frequently referred to as an AX system. Both the A and X nuclei in the same molecule may be in either the α or in the β state, with approximately the same probability—recall that the N_β/N_α ratio is nearly 1. Hence, four types of molecules will exist in the sample: those in which the AX nuclei are in the $\alpha\alpha$, $\alpha\beta$, $\beta\alpha$, and $\beta\beta$ states. These four combinations have different energies, as shown in Figure 9. In this figure, the $\alpha\alpha$ and the $\beta\beta$ states are the lowest and highest energy states, respectively. The $\alpha\beta$ and $\beta\alpha$ states are in between, but these two intermediate states are not at the same level. The symbol ω_1 represents the frequency required to elevate a proton from the α to the β state, while that proton is coupled to a carbon that is in the α state. Similarly, the ω_2 symbol represents the frequency required to elevate a carbon from the α to the β state, while that carbon is coupled to a proton that is in the α state. Hence, ω_1 is four times greater than ω_2, because an $\alpha\alpha \rightarrow \alpha\beta$ transition represents a ^{13}C transition, which requires 75 MHz at a 7.05 T field, whereas an $\alpha\alpha \rightarrow \beta\alpha$ transition represents a proton transition at 300 MHz, four times as much energy. In Figure 9, ω_1' and ω_2' respectively represent proton and carbon transitions for these nuclei coupled to their partners in the β state. When a single bond connects the proton and the carbon, scalar coupling is also present, and ω_1' will be larger than ω_1 by an amount J, and ω_2' will be larger than ω_2 by the same amount. W_1 and W_1' represent the probabilities of

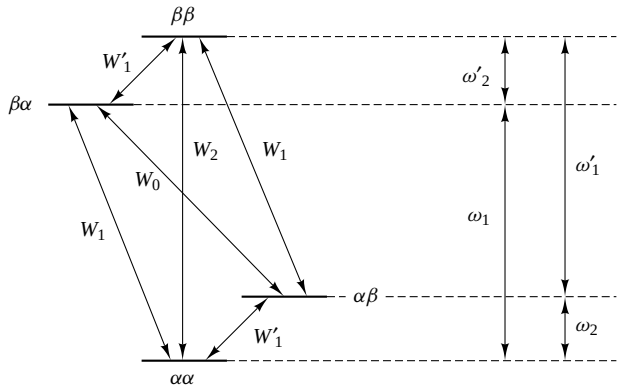

Figure 9 A diagram indicating the probabilities (W_1, W_2, and W_0) and corresponding frequencies (ω_1, ω_2, and ω_0) required for single, double, and zero quantum transitions, respectively, for the case of a proton dipolar-coupled to a carbon-13 nucleus

these four single quantum transitions. W_2 and W_0 represent the probabilities of the double quantum and zero quantum transitions, respectively.

The rate of change of the component of the proton spin along the z axis, $\langle I_z^{\mathrm{A}}\rangle$, will depend upon the three possible proton transitions W_0, W_1, and W_2. However, because the $\alpha\beta \rightarrow \beta\alpha$ and the $\alpha\alpha \rightarrow \beta\beta$ proton transitions are both accompanied by carbon transitions, the rate of change will also depend upon the component of the carbon spin along the z axis, $\langle I_z^{\mathrm{X}}\rangle$. For the double quantum transition, energy must be added, because the concomitant carbon transition is from an α to a β state. For the zero quantum transition, energy must be subtracted, because the carbon transition is from a β to an α state. Hence,

$$\frac{\mathrm{d}(I_z^{\mathrm{A}})}{\mathrm{d}t} = (2W_1 + W_0 + W_2)\langle I_0^{\mathrm{A}} - I_z^{\mathrm{A}}\rangle + (W_2 - W_0)\langle I_0^{\mathrm{X}} - I_z^{\mathrm{X}}\rangle \tag{13}$$

where I_0^{A} and I_0^{X} are the Boltzmann equilibrium values for the A and X spins, respectively, as given by equation (1). If proton transitions are induced without any irradiation of the ^{13}C nuclei then I_0^{A} will change to some new value, I_z^{A}, but, because ^{13}C transitions were not induced by the proton pulse, I_z^{X} will equal I_0^{X}. Then, equation (13) reduces to

$$\frac{\mathrm{d}(I_z^{\mathrm{A}})}{\mathrm{d}t} = (2W_1 + W_0 + W_2)\langle I_0^{\mathrm{A}} - I_z^{\mathrm{A}}\rangle \tag{14}$$

For the homonuclear case, X and A are the same, and equation (13) then becomes

$$\frac{\mathrm{d}(I_z^{\mathrm{A}})}{\mathrm{d}t} = 2(W_1 + W_2)\langle I_0^{\mathrm{A}} - I_z^{\mathrm{A}}\rangle \tag{15}$$

It was explained earlier in this article that a transition can take place, either upward or downward, only when a frequency is available whose energy matches that of the transition energy. Hence, the probabilities shown in Figure 9 depend upon the spectral density function, $J(\omega)$, i.e., the frequency components in the Brownian motion. This figure shows that the probabilities for the three possible proton transitions, W_0, W_1, and W_2, require the frequencies $\omega_1 - \omega_2$, ω_1, and $\omega_1 + \omega_2$, respectively. Hence, these three probabilities are proportional to $J(\omega)$, given in equation (12):

$$W_0 = k_0 \frac{\tau_{\mathrm{c}}}{1 + (\omega_1 - \omega_2)^2\tau_{\mathrm{c}}^2} \tag{16}$$

$$W_1 = k_1 \frac{\tau_{\mathrm{c}}}{1 + \omega_1^2\tau_{\mathrm{c}}^2} \tag{17}$$

$$W_2 = k_2 \frac{\tau_{\mathrm{c}}}{1 + (\omega_1 + \omega_2)^2\tau_{\mathrm{c}}^2} \tag{18}$$

The proportionality constants k_0, k_1, and k_2, are[6]

$$k_0 = \frac{d^2}{10\hbar^2} \tag{19}$$

$$k_1 = \frac{3d^2}{20\hbar^2} \tag{20}$$

$$k_2 = \frac{3d^2}{5\hbar^2} \tag{21}$$

where $d = \gamma_{\mathrm{A}}\gamma_{\mathrm{X}}\hbar^2/r^3$ is the 'dipolar coupling constant' and r is the distance between nuclei A and X.

The dipole–dipole relaxation rate $1/T_1^{\mathrm{DDU}}$ for unlike nuclei (heteronuclear), is obtained from equations (14) and (16)–(21):

$$\frac{1}{T_1^{\mathrm{DDU}}} = \tfrac{2}{15}\gamma_{\mathrm{X}}^2\gamma_{\mathrm{A}}^2\hbar^2 I_{\mathrm{A}}(I_{\mathrm{A}} + 1)\sum_i r_i^{-6} Y\tau_{\mathrm{c}} \tag{22a}$$

where

$$Y = \frac{1}{1 + (\omega_{\mathrm{A}} - \omega_{\mathrm{X}})^2\tau_{\mathrm{c}}^2} + \frac{3}{1 + \omega_{\mathrm{X}}^2\tau_{\mathrm{c}}^2} + \frac{6}{1 + (\omega_{\mathrm{A}} + \omega_{\mathrm{X}})^2\tau_{\mathrm{c}}^2} \tag{22b}$$

$$I_{\mathrm{A}} = \tfrac{1}{2} \quad \text{for protons} \tag{22c}$$

and the summation sign indicates the total contribution if more than one nucleus is involved in the relaxation process.

For like nuclei (homonuclear), $1/T_1^{\mathrm{DDL}}$ is obtained from equations (15), (17), (18), (20), and (21):

$$\frac{1}{T_1^{\mathrm{DDL}}} = \tfrac{2}{5}\gamma^4\hbar^2 I(I + 1)\sum_i r_i^{-6}\left(\frac{1}{1 + \omega^2\tau_{\mathrm{c}}^2} + \frac{4}{1 + 4\omega^2\tau_{\mathrm{c}}^2}\right)\tau_{\mathrm{c}} \tag{23}$$

For protons and other spin-$\frac{1}{2}$ nuclei, equation (23) becomes

$$\frac{1}{T_1^{\mathrm{DDL}}} = \tfrac{3}{10}\gamma^4\hbar^2\sum_i r_i^{-6}\left(\frac{1}{1 + \omega^2\tau_{\mathrm{c}}^2} + \frac{4}{1 + 4\omega^2\tau_{\mathrm{c}}^2}\right)\tau_{\mathrm{c}} \tag{24}$$

Similar derivations for transverse relaxation times lead to

$$\frac{1}{T_2^{\mathrm{DDU}}} = \tfrac{1}{15}\gamma_{\mathrm{X}}^2\gamma_{\mathrm{A}}^2\hbar I_{\mathrm{A}}(I_{\mathrm{A}} + 1)\sum_i r_i^{-6} Z\tau_{\mathrm{c}} \tag{25a}$$

where

$$Z = 4 + \frac{1}{1 + (\omega_{\mathrm{A}} - \omega_{\mathrm{X}})^2\tau_{\mathrm{c}}^2} + \frac{3}{1 + \omega_{\mathrm{X}}^2\tau_{\mathrm{c}}^2} + \frac{6}{1 + (\omega_{\mathrm{A}} + \omega_{\mathrm{X}})^2\tau_{\mathrm{c}}^2 y} + \frac{6}{1 + \omega_{\mathrm{A}}^2\tau_{\mathrm{c}}^2} \tag{25b}$$

and

$$\frac{1}{T_2^{\mathrm{DDL}}} = \tfrac{1}{5}\gamma^4\hbar^2 I(I + 1) \times \sum_i r_i^{-6}\left(3 + \frac{5}{1 + \omega^2\tau_{\mathrm{c}}^2} + \frac{2}{1 + 4\omega^2\tau_{\mathrm{c}}^2}\right)\tau_{\mathrm{c}} \tag{26}$$

$$\frac{1}{T_2^{\mathrm{DDL}}} = \tfrac{3}{20}\gamma^4\hbar^2\sum_i r_i^{-6}\left(3 + \frac{5}{1 + \omega^2\tau_{\mathrm{c}}^2} + \frac{2}{1 + 4\omega^2\tau_{\mathrm{c}}^2}\right)\tau_{\mathrm{c}} \tag{27}$$

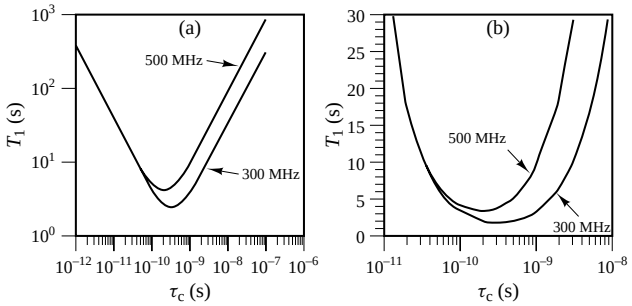

Figure 10 Plots of dipole–dipole relaxation time T_1 versus correlation time τ_c for two protons separated by 0.26 nm, at two different field strengths. In (a), the vertical axis is logarithmic, whereas in (b) the scale is linear and covers a narrower range

For low molecular weight compounds in mobile liquids, τ_c is very small. Hence, $\omega\tau_c \ll 1$, which is referred to as the 'extreme narrowing condition'. Then, equations (22)–(27) reduce to

$$\frac{1}{T_1^{\mathrm{DDU}}} = \frac{1}{T_2^{\mathrm{DDU}}} = \tfrac{4}{3}\gamma_X^2\gamma_A^2\hbar^2 I_A(I_A+1)\sum_i r_i^{-6}\tau_c \quad (28)$$

$$\frac{1}{T_1^{\mathrm{DDL}}} = \frac{1}{T_2^{\mathrm{DDL}}} = 2\gamma^4\hbar^2 I(I+1)\sum_i r_i^{-6}\tau_c \quad (29)$$

$$\frac{1}{T_1^{\mathrm{DDL}}} = \frac{1}{T_2^{\mathrm{DDL}}} = \tfrac{3}{2}\gamma^4\hbar^2\sum_i r_i^{-6}\tau_c \quad (30)$$

Figure 10(a) is a plot of equation (24) for two different field strengths, 7.05 and 11.75 T, and for an average proton–proton distance of 0.26 nm. Note that the relaxation time reaches a minimum when $\tau_c = \omega_0{}^{-1}$. Although Brownian motion is random, on average the overall motion can still be slower or faster than ω_0. If this is the case, the component of the overall motion that is at ω_0 will be small, and will not be effective in inducing transitions. Hence, the relaxation time will be longer. Also note that the minimum for the 11.75 T plot is to the left of the minimum for the 7.05 T plot. At the higher field strength, ω_0 is higher; hence, the τ_c required for effective relaxation is smaller. This figure depicts the relaxation times in the same manner as in most articles and books, i.e., in the form of a log–log plot. However, it may be more instructive to visualize the relaxation in the form of a semilogarithmic plot, i.e., one that is linear with respect to the relaxation time, as shown in Figure 10(b).

Figure 11 was prepared from equations (24) and (27), and shows how both T_1^{DDL} and T_2^{DDL} vary as a function of τ_c for a field strength of 7.05 T. The plot shows that in the extreme narrowing condition, when $\omega\tau_c \ll 1$, $T_1^{\mathrm{DDL}} = T_2^{\mathrm{DDL}}$, as shown by equation (30). To the right of the minimum in this plot, the motion is too slow to cause an effective T_1 relaxation. However, as described earlier in this article, there are several mechanisms that give rise to T_2 relaxation. If τ_c is long, as in solids and highly viscous liquids, or at very low temperatures, then the nuclei remain in the same relative positions for a long time. The nuclei will then experience a variety of local magnetic fields due to neighboring dipoles. This variation can be quite large—for example, the magnetic field at a distance of 0.1 nm from a proton is of the order of 10^{-3} T, which will

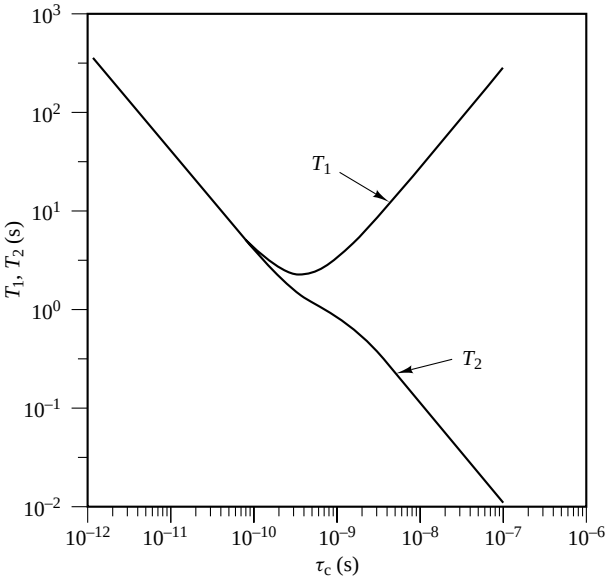

Figure 11 Plots of dipole–dipole relaxation times T_1 and T_2 versus correlation time, for two protons separated by 2.6 Å, and at a field strength of 7.05 T (300 MHz)

lead to substantial line broadening. The distribution of Larmor frequencies will cause a rapid fanning of the isochromats, as explained earlier in this article, resulting in a short T_2. Conversely, when τ_c is short, as in gases and mobile liquids, or at higher temperatures, the molecules tumble fast enough to average all of the local fields that might cause line broadening. Under these conditions, T_1 and T_2 become approximately equal and the line narrows—hence the expression 'extreme narrowing condition'. For a full theoretical treatment of the relaxation times throughout the whole range, see Kubo and Tomita.[36]

Equations (22a)–(30) were developed specifically for the dipole–dipole relaxation mechanism. Analogous equations and detailed calculations can be found for spin rotation, chemical shift anisotropy, quadrupolar, scalar, and electron–nuclear relaxation mechanisms.[37] For decoupled systems, the overall rate of relaxation is simply the sum of the contributions from all of the mechanisms. Because rates and times are reciprocals of each other

$$\left.\begin{array}{l}\text{overall rate} = \text{sum of rates}\\ \dfrac{1}{T_1} = \dfrac{1}{T_1^{\mathrm{DD}}} + \dfrac{1}{T_1^{\mathrm{SR}}} + \dfrac{1}{T_1^{\mathrm{CSA}}} + \dfrac{1}{T_1^{\mathrm{Q}}} + \dfrac{1}{T_1^{\mathrm{SC}}} + \dfrac{1}{T_1^{\mathrm{EN}}}\end{array}\right\} \quad (31)$$

However, for coupled systems at high fields, this additivity relationship may no longer hold.[18–24]

7 RELAXATION DUE TO RADIATION DAMPING

For most chemical samples, relaxation from radiation damping is not a significant mechanism. However, when proton spectra are obtained from samples containing primarily H_2O as the solvent, especially at high field strengths, the NMR signal can be relatively large. The relatively large currents induced in the receiver coil create a magnetic field in the same

way that the pulsed radiofrequency currents produce the initial $\boldsymbol{B}_1$ field. However, this induced field has a phase that acts oppositely to that of the $\boldsymbol{B}_1$ field. This process is analogous to the actions that take place in an electrical transformer. In a transformer, fluctuating magnetic lines of force from the primary coil induce a current in the secondary coil. These currents create another fluctuating field, whose lines of force cut back through the turns of the primary, inducing a back electromotive force (back-emf). A common statement used to describe this is: 'The impedance of the secondary is reflected back into the primary'. This process also explains why a motor can 'burn out' if the shaft locks, or 'freezes', and why some powerful equipment containing transformers should not be operated without a load connected to the output of the transformer. When a load is not connected, current will not flow through the load from the secondary coil, and a back-emf will not be produced in the primary. The impedance of the primary then drops to a lower value. The current in this coil will then be higher, and could 'burn out' the transformer. In an NMR probe, the sample and the receiver coil are analogous to the primary and secondary windings of a transformer, respectively. The magnetic field created by the current induced in the receiver coil applies a reverse torque to the macroscopic magnetization vector, causing it to precess from the transverse (x, y) plane back to the longitudinal z axis (see Figure 12). When this mechanism is effective, relaxation is faster than usual and results in broader lines in the spectrum.

8 RELATIONSHIP BETWEEN T_1 AND T_2 RELAXATION TIMES

This discussion will be limited to systems in which no mechanisms, except simple relaxation, are available for increasing the magnitude of a net magnetization vector; i.e., it will be limited to systems in which cross polarization, polarization transfer, radiation damping, etc., are either nonexistent or have a negligibly small effect on the relaxation process. However, even with all these restrictions imposed, this discussion will be applicable to the vast majority of proton and ^{13}C high-resolution samples run under typical conditions.

In Figure 12(a), $\boldsymbol{M}_0$ is shown tipped onto the (x, y) plane while maintaining a constant magnitude. The time elapsed during this period is on the order of 10 μs, and is equal to the pulse width. This time is very short compared with most relaxation processes in liquids and gases; hence, the vector is correctly depicted as one that is not changing during this time. However, in the typical high-resolution case, the relaxation processes that tip the vector back take much longer, and are of the order of seconds. Hence, in the absence of radiation damping, the vector does not maintain a constant magnitude as shown in Figure 12(b). Instead, it changes its length while returning to the z axis.[38] This can be shown by a simple analysis of the parameters typically used during the acquisition of ^{13}C signals. It is not unusual to acquire such signals for 1–3 s, and to employ a relaxation delay of 5–10 s between the end of the acquisition time and the beginning of the next pulse. This is especially true if a rather large tip angle is used (e.g., 60°). An acquisition time of 1–3 s is generally used, because the typical T_2* encountered for ^{13}C signals is such that almost all (95%) of the signal has disappeared after that time. This means that if Figure 12(b) correctly depicts the relaxation of $\boldsymbol{M}_0$ then in 1–3 s, when the component of $\boldsymbol{M}_0$ in the (x, y) plane ($\boldsymbol{M}_{xy}$) and the signal have decayed to zero, $\boldsymbol{M}_0$ is completely realigned along the z axis. If that were true, there would be no need for a relaxation delay, because relaxation would already be complete, and another rf pulse could be given immediately after the signal has disappeared.

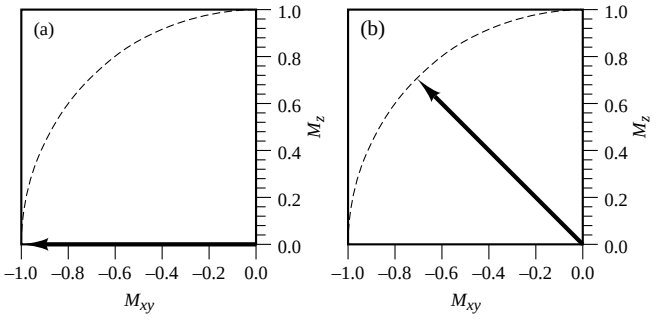

Figure 12 An illustration of a magnetization vector relaxing solely because of radiation damping. After a 90° pulse (a), the vector returns back to the z axis without changing its length, and its tip traces a circle (dashed line) whose radius is unity (b)

8.1 T_2/T_1 Ratio Under Typical Conditions

From the solutions of the Bloch equations, the magnitudes of $\boldsymbol{M}_{xy}$ and M_z at any time are given by

$$M_{xy} = M_0 \, \mathrm{e}^{-t/T_2^*} \tag{32}$$

$$M_z = M_0(1 - \mathrm{e}^{-t/T_1}) \tag{33}$$

From these equations, the vector sum of $\boldsymbol{M}_{xy}$ and $M_z\boldsymbol{k}$ (where $\boldsymbol{k}$ is the unit vector in the z direction) can be calculated at any time. In ^{13}C NMR spectroscopy, it is not unusual for the linewidth to be 0.2 Hz. From $\Delta\upsilon = 1/\pi T_2$*, T_2* can be estimated to be 1.6 s. For ^{13}C, a T_1 of 5 s is not abnormally long. Thus, a T_1/T_2* ratio of at least 5 is common. Figure 13 is a plot of the magnitude of the resultant as relaxation takes place. Table 3 lists the magnitudes at 10° increments from the (x, y) plane. The figure clearly shows that the tip of the resultant *does not trace a quarter-circle*, which is shown by the dashed line, on its way back to the z axis. Instead, it first shrinks from its maximum length, reaches a minimum, and then grows back to its maximum length after at least $5T_1$.

8.2 T_2/T_1 Ratio in a Perfectly Homogeneous Field

The shrinking of the resultant, as described above, is not a consequence of using T_2* instead of T_2 in equation (32). Even in a perfectly homogeneous field, and in the extreme narrowing region, where $T_2 \approx T_1$, the resultant would still shrink. If T_2* in equation (32) is replaced by T_1 then it can be combined with equation (33) to give

$$M_z = M_0 \left(1 - \frac{M_{xy}}{M_0}\right) = M_0 - M_{xy} \tag{34}$$

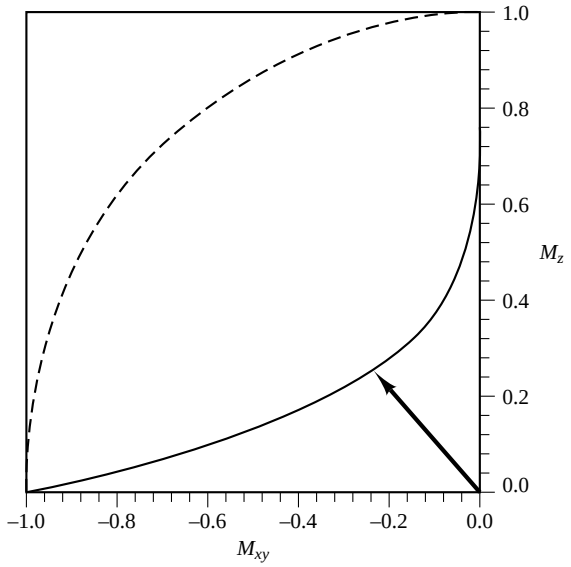

Figure 13 An illustration of a magnetization vector relaxing because of a variety of relaxation mechanisms occurring simultaneously, a much more general case than that depicted in Figure 12. For this example, $T_1 = 5T_2$*, and the vector first shrinks and then grows as it returns

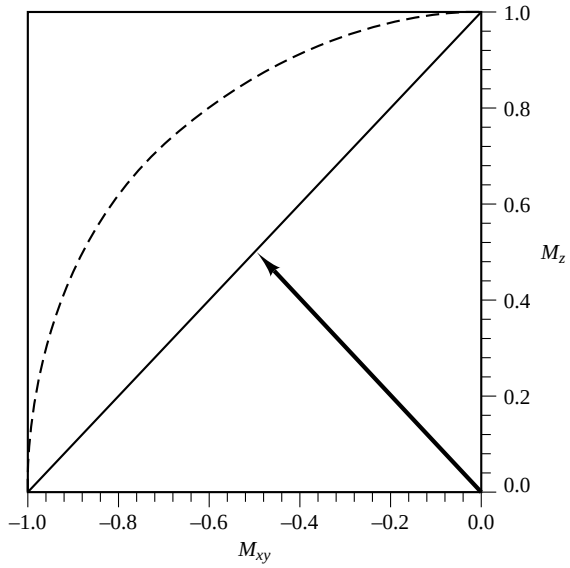

Figure 14 An illustration of a magnetization vector relaxing, as in Figure 13, but with $T_1 = T_2$. The vector still shrinks and then grows, with its tip following a straight line

Table 3 Magnitudes of the Resultants for Figure 13

Angle	Magnitude	Time (s)
0°	1.000	0.00
10°	0.372	1.00
20°	0.261	1.40
30°	0.213	1.69
40°	0.188	1.94
50°	0.176	2.18
60°	0.174	2.44
70°	0.180	2.79
80°	0.203	3.35
90°	1.000	∞

Equation (34) has the form of a straight line $y = b + mx$, where M_0 is the intercept and -1 is the slope of the line in a plot of M_z versus M_{xy}. Figure 14 and Table 4 show that the tip of the resultant follows a straight line back to M_0 on the z axis.

Table 4 Magnitudes of the Resultants for Figure 14

Angle	Magnitude	Time (s)
0°	1.000	0.000
10°	0.864	0.162
20°	0.780	0.310
30°	0.732	0.456
40°	0.710	0.609
50°	0.710	0.785
60°	0.732	1.01
70°	0.780	1.32
80°	0.863	1.90
90°	1.000	∞

8.3 Maximum T_2/T_1 Ratio

A comparison of Figures 13 and 14 shows that the tip of the vector is closer to the dashed quarter-circle line as the T_2/T_1 ratio increases from $\frac{1}{5}$ to $\frac{1}{1}$. If the ratio is increased even further, to 2.0, the trajectory of the tip becomes even closer to the quarter-circle, as shown by Figure 15 and Table 5. Even for this case, the resultant still shrinks immediately after the 90° pulse, reaches a minimum, and then grows back to its maximum value. However, note that the magnitude of the resultant does not exceed 1.0 at any time. According to this treatment, T_2 can be twice as long as T_1. Similar tables and plots show that if $T_2 > 2T_1$ then at some time the magnitude does exceed 1.0. Figure 16 and Table 6 show the case when T_2 is three times as long as T_1. Here, the magnitude of the resultant exceeds 1.0, and this is clearly a situation that seems to contradict our present understanding of the laws of physics, although theories to the contrary have been reported.[39,40] But, at or below the threshold $T_2 = 2T_1$, the mathematical treatment presented above will allow for $T_2 > T_1$. In fact, the T_2/T_1 ratio is 1.16 for the olefinic carbons of tetrachlorocyclopropene in toluene-d_8 at $-89\,^{\circ}$C.[41] Anet has

Table 5 Magnitudes of the Resultants for Figure 15

Angle	Magnitude	Time (s)
0°	1.000	0.000
10°	0.929	0.088
20°	0.888	0.181
30°	0.869	0.285
40°	0.868	0.408
50°	0.884	0.565
60°	0.914	0.783
70°	0.952	1.12
80°	0.986	1.77
90°	1.000	∞

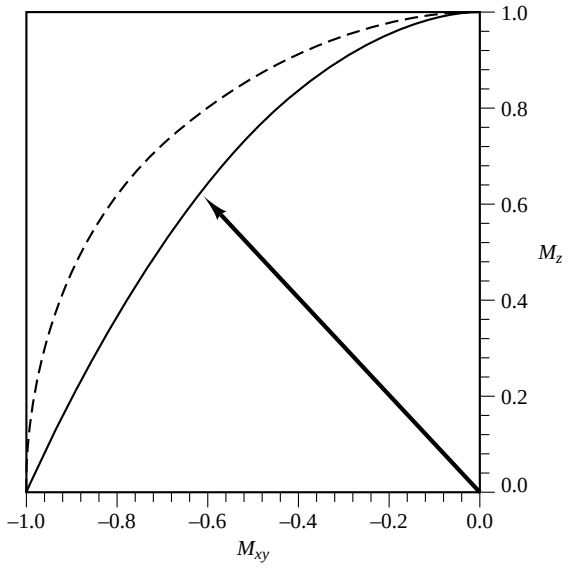

Figure 15 An illustration of a magnetization vector relaxing, as in Figure 13, but with $T_1 = \frac{1}{2}T_2$, i.e., T_2 is twice as long as T_1. The vector still shrinks, but at its shortest length the tip is closer to the dashed line than in Figure 13 or Figure 14. At no time does the length exceed 1 and extend beyond the dashed line

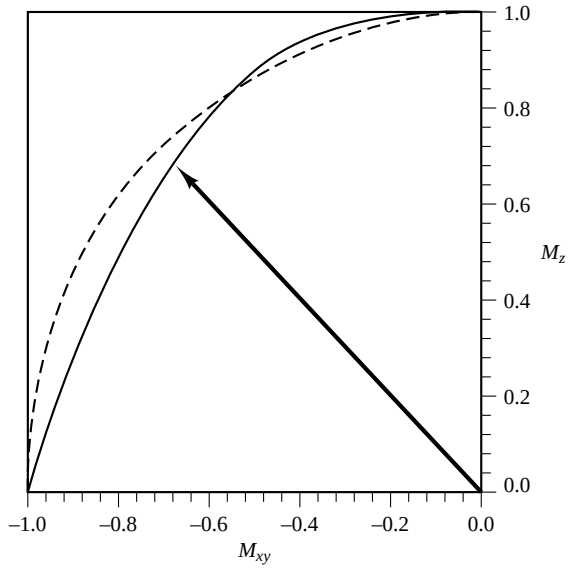

Figure 16 An illustration of a magnetization vector relaxing, as in Figure 13, but with $T_1 = \frac{1}{3}T_2$, i.e., T_2 is three times as long as T_1. The vector still shrinks at first, but later its length will exceed 1 and extend beyond the dashed line. Outside this line, the vector is longer than it was before the pulse, which is a case that is generally considered to be impossible

Table 6 Magnitudes of the Resultants for Figure 16

Angle	Magnitude	Time (s)
0°	1.000	0.000
10°	0.956	0.060
20°	0.936	0.129
30°	0.936	0.210
40°	0.952	0.316
50°	0.980	0.463
60°	1.01	0.686
70°	1.02	1.05
80°	1.01	1.74
90°	1.000	∞

presented a detailed description of this experiment, as well as a very comprehensive paper on the T_2/T_1 ratio.[42,43]

9 RELATED ARTICLES

Carbon-13 Relaxation Measurements: Organic Chemistry Applications; Contrast Agents in MRI: Superparamagnetic Iron Oxide; Molecular Motions: T_1 Frequency Dispersion in Biological Systems; Polymers: Relaxation and Dynamics of Synthetic Polymers in Solution; Protein Dynamics from NMR Relaxation; Protein Structures: Relaxation Matrix Refinement; Relaxation of Coupled Spins from Rotational Diffusion; Relaxation Effects of Chemical Exchange; Relaxation Matrix Refinement of Nucleic Acids; Relaxation Measurements in Imaging Studies; Relaxation Mechanisms: Magnetization Modes; Relaxation Mechanisms: Magnetization Modes; Relaxation Processes in Coupled-Spin Systems; Relaxation of Quadrupolar Nuclei Measured via Multiple Quantum Filtration; Relaxation Theory for Quadrupolar Nuclei; Relaxation of Transverse Magnetization for Coupled Spins; Relaxometry of Tissue; Selective Relaxation Techniques in Biological NMR.

10 REFERENCES

1. A. Carrington and A. D. McLachlan, *Introduction to Magnetic Resonance*, Harper & Row, New York, 1967.
2. A. Abragam, *Principles of Nuclear Magnetism*, Oxford University Press, Oxford, 1961.
3. R. E. Wasylishen, in *NMR Spectroscopy Techniques*, eds. C. Dybowski and R. L. Lichter, Marcel Dekker, New York, 1987, Chap. 2
4. J. McConnell, *The Theory of Nuclear Magnetic Relaxation in Liquids*, Cambridge University Press, Cambridge, 1987.
5. T. C. Farrar, *Introduction to Pulse NMR Spectroscopy*, Farragut Press, Madison, 1989.
6. J. W. Hennel and J. Klinowski, *Fundamentals of Nuclear Magnetic Resonance*, Longman, Harlow, UK, 1993.
7. E. L. Hahn, *Concepts Magn. Reson.*, 1994, **6**, 193.
8. N. Bloembergen, *Concepts Magn. Reson.*, 1994, **6**, 185.
9. N. Bloembergen, E. M. Purcell, and R. V. Pound, *Phys. Rev.*, 1948, **73**, 679.
10. A. G. Redfield, *IBM J. Res. Develop.*, 1957, **1**, 19.
11. I. Solomon, *Phys. Rev.*, 1955, **99**, 559.
12. A. Abragam and W. G. Proctor, *Phys. Rev.*, 1957, **106**, 160(L).
13. E. M. Purcell and R. V. Pound, *Phys. Rev.*, 1951, **81**, 279.
14. P. S. Hubbard, *Phys. Rev.*, 1958, **109**, 1153.
15. J. S. Blicharski, *Phys. Lett. A*, 1967, **24**, 608.
16. J. S. Blicharski, *Acta Phys. Polon.*, 1970, **38**, 19.
17. J. S. Blicharski and W. Nosel, *Acta Phys. Polon. A*, 1972, **42**, 223.
18. T. C. Farrar and I. C. Locker, *J. Chem. Phys.*, 1987, **87**, 3281; T. C. Farrar and M. J. Jablonsky, *J. Chem. Phys.*, 1991, **95**, 9159.

19. T. C. Farrar and R. A. Quintero-Arcaya, *J. Phys. Chem.*, 1987, **91**, 3224.
20. H. Shimizu, *J. Chem. Phys.*, 1964, **40**, 3357.
21. A. G. Redfield, in *Advances in Magnetic Resonance*, ed. J. S. Waugh, Academic Pess, New York, Vol. 1, p. 1.
22. E. L. Mackor and C. MacLean, *J. Chem. Phys.*, 1965, **42**, 4254.
23. E. L. Mackor and C. MacLean, in *Progress in Nuclear Magnetic Resonance Spectroscopy*, eds. J. W. Emsley, J. Feeney, and L. H. Sutcliffe, Pergamon Press, Oxford, 1967, Vol. 3, p. 129.
24. R. L. Vold and R. R. Vold, in *Progress in Nuclear Magnetic Resonance Spectroscopy*, eds. J. W. Emsley, J. Feeney, and L. H. Sutcliffe, Pergamon Press, Oxford, 1978, Vol. 12, p. 79.
25. J. H. Noggle and R. E. Schirmer, *The Nuclear Overhauser Effect—Chemical Applications*, Academic Press, New York, 1971.
26. L. G. Werbelow and D. M. Grant, in *Advances in Magnetic Resonance*, ed. J. S. Waugh, Academic Press, New York, 1979, Vol. 9, p. 189.
27. J. S. Frye, *Concepts Magn. Reson.*, 1989, **1**, 27.
28. T. K. Leipert, J. H. Noggle, W. J. Freeman, and D. L. Dalrymple, *J. Magn. Reson.*, 1975, **19**, 208.
29. T. L. James, G. B. Matson, I. D. Kuntz, R. W. Fisher, and D. H. Buttlaire, *J. Magn. Reson.*, 1977, **283**, 417.
30. T. L. James, G. B. Matson, and I. D. Kuntz, *J. Am. Chem. Soc.*, 1978, **100**, 3590.
31. P. Bendel, *J. Magn. Reson.*, 1981, **42**, 364.
32. P. Bendel and T. L. James, *J. Magn. Reson.*, 1982, **48**, 76.
33. F. A. L. Anet and X.-H. Ji, *Poster Number B1, 23rd Experimental NMR Conference, Asilomar, CA, 1982*.
34. F. A. L. Anet and X.-H. Ji, *Poster Number I.B. 5, 25th Experimental NMR Conference, Asilomar, CA, 1984*.
35. E. R. Andrew, *Nuclear Magnetic Resonance*, Cambridge University Press, Cambridge, 1955.
36. R. Kubo and K. Tomita, *J. Phys. Soc. Jpn.*, 1954, **9**, 935.
37. J. L. Sudmeier, S. E. Anderson, and J. S. Frye, *Concepts Magn. Reson.*, 1990, **2**, 197.
38. D. D. Traficante, *Concepts Magn. Reson.*, 1991, **3**, 171.
39. H. M. Sevian and J. L. Skinner, *J. Chem. Phys.*, 1989, **91**, 1775.
40. B. B. Laird and J. L. Skinner, *J. Chem. Phys.*, 1991, **94**, 4405.
41. F. A. L. Anet, D. J. O'Leary, C. G. Wade, and R. D. Johnson, *Chem. Phys. Lett.*, 1990, **171**, 401.
42. F. A. L. Anet and D. J. O'Leary, *Concepts Magn. Reson.*, 1991, **3**, 193.
43. F. A. L. Anet and D. J. O'Leary, *Concepts Magn. Reson.*, 1992, **4**, 35.

Biographical Sketch

Daniel D. Traficante. *b* 1933. B.S., 1955, Syracuse University, USA; Ph.D., 1962, Massachusetts Institute of Technology, in synthetic organic chemistry under the supervision of Herbert O. House. Director of the Chemical Spectrometry Laboratory, Massachusetts Institute of Technology, 1968–78. Director of the Chemical Instrumentation Center, Yale University, 1978–83. Program Director, National Science Foundation, 1983–84. Director of the Life Sciences NMR Consortium, Monsanto's World Headquarters, 1984–86. Professor of Chemistry and Director of NMR Concepts, University of Rhode Island, 1986–present. Approx. 50 publications Research interests have centered around determination of organic structures, mathematical treatment of raw NMR data, and electronics, including instrument modifications and probe design.

Relaxation Effects Involving Cross Correlation in Biomolecules

Mark Rance

Department of Molecular Genetics, Biochemistry and Microbiology, University of Cincinnati College of Medicine, Cincinnati, OH, USA

1	Introduction	1
2	Theory	1
3	Sensitivity and Resolution Enhancement via Cross-Correlation Effects	3
4	Measurement of Angles Between Bond Vectors	4
5	Studies of Molecular Dynamics via Cross-Correlated Relaxation Effects	5
6	Cross-Correlation Effects in Paramagnetic Systems	8
7	Characterization of Hydrogen Bond Lengths	8
8	Relaxation-Induced Violations of Coherence Transfer Selection Rules in Multiple Quantum NMR Spectroscopy	8
9	Additional Cross-Correlation Effects	9
10	Elimination of Cross-Correlation Effects	9
11	Summary	9
12	Related Articles in this Volume	9
13	Related Articles in Volumes 1–8	9
14	References	9

1 INTRODUCTION

Studies of nuclear spin relaxation processes can provide invaluable information regarding the structure and dynamics of biological macromolecules. Numerous methodologies have been proposed for the measurement and interpretation of various nuclear spin relaxation rate constants. In recent years the arsenal of tools available for NMR relaxation studies has expanded rapidly, due in part to the greater appreciation and subsequent exploitation of cross-correlation effects. The presence of cross-correlation, or relaxation interference, effects in nuclear spin relaxation processes has been recognized since the early days of NMR experimentation. One of the earliest reports on this subject was the proposal by McConnell[1] that relaxation interference effects could explain the observed dependence of multiplet linewidths on the nuclear spin quantum number in paramagnetic resonance spectra of solutions of ionic salts. Another pioneering study was that by Hubbard,[2,3] concerning relaxation interference effects on the spin-lattice relaxation of three- and four-spin-1/2 systems. Despite these early reports, and with some notable exceptions, the prevailing view for many years seemed to be that cross-correlation effects were more of a theoretical curiosity than a practically useful feature of nuclear spin relaxation. This sentiment was due in part to improper extrapolations of Hubbard's results to other systems.[4] Fortunately, the rigorous theoretical treatments of cross-correlation effects by several groups, especially those of Werbelow, Grant, and Lynden-Bell,[5–7] and the development of multi-dimensional and multiple quantum NMR methodologies in the 1970s lead to a renewed interest and solid foundation for the exploitation of cross-correlated relaxation phenomena. As a result, many important and very valuable NMR techniques that rely on the measurement and/or utilization of cross-correlation effects are now available and in common use for obtaining detailed information on the structure and dynamics of a variety of systems, including biological macromolecules.

The purpose of the present article is to provide an overview of the subject of cross-correlated nuclear spin relaxation effects (see also **Relaxation Processes: Cross Correlation & Interference Terms,** Volume 6, and **Relaxation Theory: Density Matrix Formulation,** Volume 6), focusing on those areas of particular importance in studies of the structure and dynamics of proteins, nucleic acids and other biological macromolecules. The basic concepts are emphasized, rather than providing a detailed theoretical description. Readers interested in the theoretical formalism of cross-correlated relaxation and/or a more complete presentation than is possible here are directed to an excellent and comprehensive review of cross-correlations in NMR that was published recently by Kumar et al.[8] A number of other review and research articles are also highly recommended for those wishing to learn more about this fascinating field.[5–14]

2 THEORY

A number of interactions can contribute to the overall relaxation behavior of a nuclear spin, including the stochastic modulation of dipole–dipole couplings, chemical shift anisotropies, and quadrupolar couplings (for spin $>1/2$). Cross-correlation effects result from the interference of two such relaxation mechanisms, under the conditions that the time-dependent modulation of the two relaxation mechanisms arises from the same source, and that the tensors that describe the time-dependence of the interactions have the same rank. To put this in more formal terms, the stochastic Hamiltonian responsible for the relaxation behavior of a nuclear spin can be written as:[15]

$$\mathbf{H}_1(t) = \sum_m \sum_{q=-k}^{k} F_{mk}^q(t)\mathbf{A}_{mk}^q \tag{1}$$

in which the summation over the index m accounts for the different relaxation mechanisms, $F_{mk}^q(t)$ is a function of spatial variables that describes the effective motional behavior and $\mathbf{A}_{mk}^q$ is a tensor spin operator. The index k gives the rank of the tensor operators for the relevant interactions. The Liouville-von Neumann equation for the density operator is given by:

$$\frac{\mathrm{d}\sigma}{\mathrm{d}t}(t) = -i[\mathbf{H}_\mathrm{o}, \sigma(t)] - \hat{\Gamma}(\sigma(t) - \sigma_\mathrm{o}) \tag{2}$$

where $\mathbf{H}_\mathrm{o}$ is the time-independent part of the nuclear spin Hamiltonian, $\sigma(t)$ is the time-dependent density operator, σ_o is the thermal equilibrium density operator, and $\hat{\Gamma}$ is the

relaxation superoperator. If the density operator σ is expanded in terms of a set of basis spin operators $\mathbf{B}_i$, the rate constant for relaxation between the operators $\mathbf{B}_r$ and $\mathbf{B}_s$ is:

$$\begin{aligned}\Gamma_{rs} &= \frac{1}{2}\sum_m\sum_q\sum_p\{\langle\mathbf{B}_r|[\mathbf{A}^{-q}_{mkp},[\mathbf{A}^{q}_{mkp},\mathbf{B}_s]]\rangle/\langle\mathbf{B}_r|\mathbf{B}_r\rangle\}j^q(\omega_p)\\ &\cdots+\frac{1}{2}\sum_{\substack{m,n\\ m\neq n}}\sum_q\sum_p\{\langle\mathbf{B}_r|[\mathbf{A}^{-q}_{mkp},[\mathbf{A}^{q}_{nkp},\mathbf{B}_s]]\rangle/\langle\mathbf{B}_r|\mathbf{B}_r\rangle\}j^q_{mn}(\omega_p)\\ &\cdots=\sum_m\Gamma^m_{rs}+\sum_{\substack{m,n\\ m\neq n}}\Gamma^{mn}_{rs}\end{aligned}\qquad(3)$$

in which the $\mathbf{A}^q_{mkp}$ are basis operators that can be summed over index p to generate the tensor operators $\mathbf{A}^q_{mk}$ appearing in equation (1), and the cross-correlation spectral density is:

$$j^q_{mn}(\omega)=\mathrm{Re}\left\{\int_{-\infty}^{\infty}\overline{F^q_{mk}(t)F^{-q}_{nk}(t+\tau)}\exp(-i\omega\tau)\mathrm{d}\tau\right\}\qquad(4)$$

The terms Γ^{mn}_{rs} represent the contributions to the relaxation between $\mathbf{B}_r$ and $\mathbf{B}_s$ that results from the interference or cross-correlation between the m^{th} and n^{th} relaxation mechanisms. From equation (4) it is clear that if the motional processes modulating relaxation mechanisms m and n are uncorrelated, there will be no cross-correlated relaxation involving these two mechanisms. Likewise, from equation (3) it can be seen that cross-correlated relaxation requires that the double commutator involving spin operators $\mathbf{A}^{-q}_{mkp}$ and $\mathbf{A}^q_{nkp}$ be non-zero. In applications to biomolecules, the most common relaxation interference effects arise from the three cross-correlation combinations involving the dipole–dipole (DD) and chemical shift anisotropy (CSA) relaxation mechanisms.

The concept of cross-correlated nuclear spin relaxation can be illustrated by considering a simple two spin-1/2 system, a ^{15}N–^{1}H spin pair in a protein backbone, and analyzing the transverse relaxation of the ^{15}N spin.[16] The relevant cross-correlation in this example is the relaxation interference between the ^{15}N chemical shift anisotropy (CSA) and the ^{15}N–^{1}H dipole–dipole (DD) interactions. Figure 1 demonstrates the basic principle of CSA/DD cross-correlated relaxation in the ^{15}N–^{1}H system. The case of a ^{15}N spin bonded to a ^{1}H spin in the $|\alpha\rangle$ state (as indicated by the upward arrow through the ^{1}H nucleus) is shown in Figure 1(A) and (B); in Figure 1(A) the ^{15}N–^{1}H bond vector is oriented parallel to the externally applied magnetic field, whereas Figure 1(B) shows the case where the bond vector is perpendicular to the applied field. Figure 1(C) and (D) show the analogous situations where the ^{1}H spin is in the $|\beta\rangle$ state. The solid lines drawn to the right of the ^{15}N nuclei indicate the direction of the local magnetic field, arising from the ^{1}H spin, at the position of the ^{15}N spin, while the dashed lines to the left of the ^{15}N nuclei show the direction of the induced magnetic field arising from the ^{15}N CSA interaction. Relaxation of the ^{15}N spin is caused by fluctuations in the net sum of these local magnetic fields as the orientation of the bond vector is randomly modulated by motional processes. The key observation in this example is that when the ^{1}H spin is in the $|\alpha\rangle$ state, the local magnetic fields arising from the CSA and DD interactions have the same sign, regardless of the bond orientation, whereas these local fields have opposite signs when the ^{1}H spin is in the $|\beta\rangle$ state. Constructive interference of the local magnetic fields arising from the CSA and dipolar interactions will therefore result in a broadening of the ^{15}N resonance associated with the ^{1}H in the $|\alpha\rangle$ state, while destructive interference of these local fields will lead to a narrowing of the ^{15}N resonance associated with the ^{1}H in the $|\beta\rangle$ state. This type of cross-correlated relaxation effect forms the basis of TROSY, or transverse relaxation-optimized spectroscopy (see **Transverse Relaxation-optimized NMR Spectroscopy with Biomacromolecular Structures in Solution**).

The measurement of cross-correlated relaxation rate constants is greatly facilitated by the fact that the relaxation behavior can be controlled in a substantial way via the design of the pulse sequences.[17] This is quite different from the situation that exists for the measurement of auto-relaxation processes, where pulse sequence elements normally do not affect relaxation. Thus, pulse sequence design has played an essential role in allowing various cross-correlated relaxation processes to be distinguished from one another and in allowing quantitative analyses to be performed. Cross-correlated relaxation rate constants are normally measured in one of two ways. The first method is to observe changes in individual multiplet intensities after an evolution period (usually a constant-time element) during which the relaxation processes of interest have been active. The second possibility is to observe and measure the cross-correlation-induced cross-relaxation of one spin operator with another. In many cases the cross-correlated relaxation rate constants of interest are rather small, and this can present significant challenges in terms of making reliable measurements. Careful attention to experimental design can reduce some sources of uncertainty and error in cross-correlated relaxation measurements.[18]

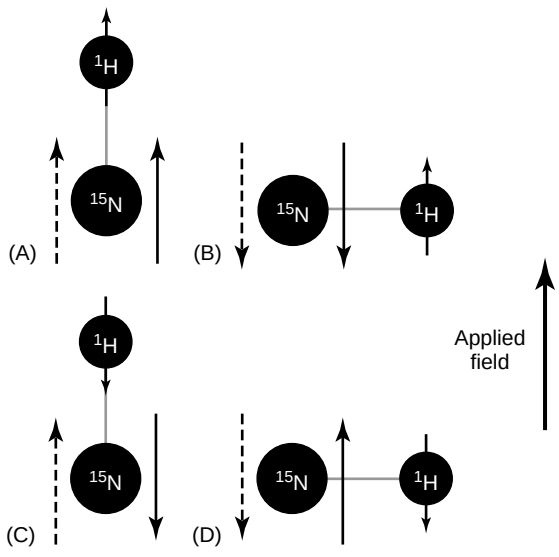

Figure 1 Schematic illustration of the origin of ^{15}N chemical shift anisotropy/^{15}N–^{1}H dipole–dipole cross-correlation effects on the relaxation of the ^{15}N spin. Arrows through the ^{1}H nuclei indicate the ^{1}H spin state $|\alpha\rangle$ (up arrow) or $|\beta\rangle$ (down arrow). Solid arrows adjacent to the ^{15}N nuclei indicate the direction of the local ^{1}H dipolar magnetic field at the site of the ^{15}N spin, while the dashed arrows indicate the direction of the induced magnetic field from the ^{15}N chemical shift interaction. In (A) and (C) the ^{15}N–^{1}H bond vector is parallel to the applied external field, while in (B) and (D) the bond vector is in the perpendicular orientation

Cross-correlation effects in nuclear spin relaxation can be exploited for a number of useful purposes in studies of biomolecules, including sensitivity and/or resolution enhancement, dynamics studies, and measurement of structural constraints. Cross-correlation contributions to relaxation can also be an undesirable feature in dynamics studies that are based on the measurement of auto-relaxation rate constants, and thus it has been necessary to devise various techniques for eliminating specific, cross-correlation-induced cross-relaxation pathways. The following sections describe examples of both the exploitation and elimination of cross-correlation effects that have been found to be of particular relevance in studies of biological macromolecules.

3 SENSITIVITY AND RESOLUTION ENHANCEMENT VIA CROSS-CORRELATION EFFECTS

3.1 TROSY

One of the most exciting and important developments in recent years in the field of solution-state NMR studies of biomolecules has been the introduction of methodologies for sensitivity and/or resolution enhancement that are based on the exploitation of cross-correlation effects. These enhancements have their origin in the differential relaxation rates of multiplet components in the presence of relaxation interference between DD and CSA interactions. Griffey and Redfield anticipated the potential advantages of DD/CSA cross-correlation, as evidenced by their statement that "In certain cases higher resolution and/or sensitivity might be achieved by operating without decoupling, perhaps using an INEPT or double-INEPT sequence".[19] Their belief was validated ten years later when Pervushin and coworkers[20] reported the development of an experimental scheme for transverse relaxation-optimized spectroscopy (TROSY). The TROSY methodology is the subject of another article in this volume, and so only a very brief discussion of the basic principles is presented here.

One of the most important and widely used NMR techniques for studies of biomolecules is the 2D HSQC experiment,[15] which provides correlation information for heteronuclear spin pairs such as ^{1}H–^{15}N or ^{1}H–^{13}C. The HSQC-type pulse scheme is an integral component in most heteronuclear, multi-dimensional NMR experiments. The sensitivity and resolution of HSQC-based experiments is dependent on the transverse relaxation rates of the spins actively involved in the coherence transfer pathway. As the molecular weight of the system under study increases, so do the transverse relaxation rate constants, and thus the sensitivity and resolution of the HSQC spectra are degraded. In the presence of significant dipole–dipole/CSA relaxation interference, the linewidths of individual spin multiplet components can be quite different. The spin decoupling normally performed during an HSQC-type experiment causes an averaging of the transverse relaxation rates of the multiplet components. However, by carefully avoiding this mixing of spin states, it is possible to take advantage of the line-narrowing of one of the multiplet components that arises due to destructive interference of the dipole–dipole and CSA interactions.[14] This forms the basis for the TROSY scheme, as was illustrated in Figure 1. In the first application reported by Pervushin et al.,[20] the TROSY scheme was incorporated into a 2D ^{1}H–^{15}N HSQC experiment. The pulse sequence was designed to select only one of the four multiplet components that would normally be observed for a ^{1}H–^{15}N spin pair correlation in an undecoupled 2D HSQC spectrum. Selecting the component with the smallest ^{15}N and ^{1}H linewidths can lead to significant improvements in sensitivity and/or resolution, under favorable conditions. Heading the list of required conditions of course is that there be a significant dipole–dipole/CSA cross-correlation effect. Thus, the TROSY scheme is most effective at ultra-high magnetic field strengths, due to the field dependence of the CSA interaction, and for heteronuclei with large chemical shift anisotropies, such as ^{15}N or aromatic ^{13}C spins. A number of other factors also affect whether the TROSY scheme will provide useful sensitivity and/or resolution enhancements. Other sources of relaxation, such as dipolar interactions with remote protons, will tend to mask the line narrowing from the DD/CSA interference, as will exchange contributions to the linewidths. Thus, TROSY-based schemes are most useful for large molecular systems that are highly deuterated and not subject to conformational exchange broadening. Even under such conditions, the maximal advantage theoretically possible for a TROSY-based pulse sequence is usually not reached, due to different data acquisition and processing parameters for TROSY and non-TROSY experiments. For example, the advantage of reduced transverse relaxation rates in the ^{15}N evolution period of a TROSY-based HSQC is most useful if relatively long evolution periods are required; such is the case for experiments used to measure small coupling constants. Implementation of the TROSY scheme is also of particular value in constant-time periods in various multi-pulse sequences to minimize relaxation-associated loss of signal intensity.

In practical applications, the TROSY scheme has been extremely useful for studies of deuterated molecules or complexes, especially those that are in excess of 50 kDa in size. The TROSY scheme has been incorporated into a large number of the standard triple resonance experiments employed for resonance assignment as well as other pulse sequences, such as those used to measure small scalar couplings across hydrogen bonds (see **Polarization Transfer Experiments via Scalar Coupling in Liquids,** Volume 6).

The TROSY scheme, as it was originally proposed, was based on the exploitation of relaxation interference between dipole–dipole and CSA interactions to achieve line narrowing of single quantum coherences. Griffey and Redfield[19] pointed out that line-narrowing could also be achieved for zero-quantum (ZQ) coherences, utilizing relaxation interference of the CSA interactions of the two spins actively involved in the ZQ coherence. Pervushin and coworkers[21] have developed a modified TROSY scheme to take advantage of this ZQ line-narrowing via the cross-correlation of ^{15}N and ^{1}H CSA interactions for ^{15}N–$^{1}H^{N}$ spin pairs. They have also incorporated this ZQ-TROSY scheme into a novel 3D ^{15}N-separated ^{1}H–^{1}H NOESY experiment. The three main features/advantages of this so-called 3D NOESY-[^{1}H, ^{15}N, ^{1}H]-ZQ-TROSY experiment are: (1) the ^{15}N CSA/$^{1}H^{N}$ CSA cross-correlation is used to reduce transverse relaxation during the ^{15}N evolution time; (2) line-narrowing is achieved in all three frequency dimensions; and (3) substantial suppression of the diagonal peaks is achieved, thereby facilitating the observation of NOESY cross-peaks that lie very close to the diagonal.

3.2 CRINEPT

Most multi-dimensional experiments applied to biomolecules employ polarization/coherence transfer steps to transfer magnetization from one nuclear species to another; in some cases this is done solely for sensitivity enhancement, and in others it is done to implement a desired coherence transfer pathway. The coherence transfer between two spins I and S normally involves the evolution of magnetization under the scalar coupling Hamiltonian according to (assuming a pulse-interrupted free precession period)

$$I_x \xrightarrow{H_J} I_x \cos(\pi J_{IS}\tau) + 2I_y S_z \sin(\pi J_{IS}\tau) \qquad (5)$$

where J_{IS} is the scalar coupling between spins I and S. Coherence is transferred from I to S by the application of 90° rf pulses to the I and S spins to convert the second term above from anti-phase I spin magnetization to anti-phase S spin magnetization. The 90° rf pulses are applied at a time τ that is chosen to optimize the efficiency of the transfer; in the absence of relaxation, exchange effects, and remote couplings to the I spin, the optimal value of τ would be $1/(2J_{IS})$. However, in the presence of significant I spin relaxation and/or exchange broadening of the I spin, the coherence transfer process is adversely affected and τ will have to be reduced in order to obtain the maximum transfer allowed by the experimental conditions. The loss of magnetization due to relaxation during the scalar coupling evolution period becomes increasingly significant as the size, and thus the rotational correlation time, of the system increases.

Another possibility exists for achieving polarization/coherence transfer between a heteronuclear spin pair. Dalvit[22] and Brüschweiler and Ernst[23] have demonstrated the possibility of employing DD/CSA cross-correlation effects to obtain a coherence transfer of the type

$$I_x \xrightarrow{\Gamma_{\mathrm{DD,CSA}}} 2I_x S_z \qquad (6)$$

In this case the relevant process is the cross-correlation of the I spin CSA and the dipolar interaction between the I and S spins. Coherence can then be transferred from the I spin to the S spin via the anti-phase term by application of 90° rf pulses to both I and S spins. Riek and coworkers[24] have coined the term CRIPT (cross relaxation-induced polarization transfer) for this process, and have discussed the sensitivity advantages achievable, relative to scalar coupling-induced coherence transfer, in applications to very large molecules. They have also developed experimental procedures for utilizing both scalar coupling-induced and cross-correlation-induced coherence transfer pathways in a methodology they have named CRINEPT. Maximum sensitivity enhancements in appropriate applications are obtained by also including the TROSY scheme in the CRINEPT pulse sequences.[25]

3.3 CSA Tensor Characterization via Cross-Correlation Effects

Accurate knowledge of CSA tensors is important for interpreting the results of many NMR experiments in order to obtain structural and motional parameters. Information concerning the magnitude and orientation of CSA tensors has most commonly been obtained from solid-state NMR studies of model compounds. However, experimental studies have demonstrated that CSA tensors are very sensitive to the local environment of a nucleus in a biomolecule, and thus the applicability of tensor parameters from small model compounds is limited. Progress has been made in the use of quantum-chemical calculations to obtain CSA tensor parameters,[26] but there clearly is still a great need to have procedures for experimentally measuring such parameters directly from the systems of interest. Such measurements are potentially a valuable source of structure and dynamics information.

Several groups have demonstrated that site-specific, quantitative information on ^{1}H, ^{13}C and ^{15}N chemical shift anisotropies can be obtained for these nuclei in biomolecules from the measurement of dipole–dipole/CSA relaxation interference effects.[8] Several related procedures have been proposed for obtaining CSA information from DD/CSA relaxation interference measurements. For a heteronuclear two spin (I, S) system, DD/CSA transverse cross-correlation rate constants can be obtained either from measurements of the differential relaxation of the individual doublet components or from measurements of the $I_x \rightarrow 2I_xS_z$ coherence transfer process. The methodology described by Kroenke and coworkers[27] also involves measurement of the longitudinal cross-correlation rate constants via the $I_z \rightarrow 2I_zS_z$ polarization transfer process. Fushman and coworkers[28] demonstrated that the magnitudes and the orientation of a CSA tensor (^{15}N in their study) can be obtained from magnetic field-dependent measurements of the ratio η/R_2, where η is the transverse DD/CSA cross-correlation rate constant and R_2 is the heteronuclear transverse relaxation rate constant. Pang and Zuiderweg[29] have proposed an elegant procedure for determining the protein backbone ^{13}C′ carbonyl CSA tensor that involves measuring the relaxation interference between the ^{13}C′ CSA transverse relaxation and three different dipole–dipole relaxation terms: ^{13}C′–^{13}C$^{\alpha}$, ^{13}C′–^{15}N, and ^{13}C′–^{1}H$^{\mathrm{N}}$.

4 MEASUREMENT OF ANGLES BETWEEN BOND VECTORS

Due to the dependence of cross-correlated relaxation effects on the relative orientation of the interaction tensors involved, the measurement of such effects can provide valuable structural information in studies of biomolecules. Considering CSA and dipolar interactions, cross-correlated relaxation can arise from the CSA of two different spins, from the CSA of spin i and the dipolar interaction between spins j and k[DD(jk)], from the CSA of spin j or k and the dipolar interaction between spins j and k affecting the relaxation of spin i, and from two pairs of dipolar interactions DD(ij) and DD(kl) with no common spin between them. In such cases the cross-correlation effects depend on the relative orientation of the relevant interaction tensors but not explicitly on distances. These types of cross-correlations are termed ‘remote’,[30] since the relaxation interference does not depend explicitly on the distance of other spins from the spin or spins of interest. For example, the CSA/CSA cross-correlation involving spins i and j does not depend explicitly on the distance between i and j. Likewise, the DD/DD cross-correlation between spin pairs i, j and k, l depends on r_{ij} (the distance between spins i and j) and

r_{kl} inter-nuclear distances but not explicitly on the distances between the spin pairs, i.e., the r_{ik}, r_{il}, r_{jk} or r_{jl} distances.

Reif and coworkers[31] introduced a strategy which utilizes remote cross-correlation effects to measure the relative orientation of bond angles; a major advantage of this strategy is the fact that there is no requirement to establish a parameterized Karplus-type relationship, as there is when scalar couplings are used to measure torsion angles. Another advantage is the fact that the cross-correlated relaxation is not limited to the analysis of local geometry, since there is no explicit distance dependence. In principle, the relative orientation of arbitrary interaction tensors within one molecule, or even between two molecules, can be measured as long as a correlation between these two can be established.[17]

An approach that has proven to be very effective for the measurement of remote cross-correlation effects is to examine the relaxation behavior of double and zero quantum coherences created between nuclei affected by the interactions of interest. In the strategy proposed by Reif et al., double quantum coherence is created involving the $^{13}C^{\alpha}$ nucleus of amino acid residue i and the backbone ^{15}N nucleus of residue $i+1$ in a protein, and the effects of relaxation interference between the $^{13}C^{\alpha}$–$^{1}H^{\alpha}$ (residue i) and the ^{15}N–$^{1}H^{N}$ (residue $i+1$) dipolar interactions on the $^{13}C^{\alpha}$–^{15}N double quantum coherence is probed. The cross-correlation effects are manifested in the differential relaxation rates of the four double quantum transitions. These rates can be determined either from the linewidths of the double quantum signals or from resonance intensities measured from a constant-time NMR experiment. For practical reasons the latter approach is normally easier to accomplish. Intensity ratios provide a measure of the desired cross-correlation relaxation rate constants. In turn, these rate constants can then be used to determine the relative orientation of the interaction tensors.[14] For the example described here, and assuming a macromolecule that tumbles slowly in solution, the cross-correlated dipolar relaxation depends on the angle θ between the $^{13}C^{\alpha}$–$^{1}H^{\alpha}$ (residue i) and ^{15}N–$^{1}H^{N}$ (residue $i+1$) bonds according to

$$\Gamma = \frac{\gamma_H \gamma_N}{(r_{NH})^3} \frac{\gamma_H \gamma_C}{(r_{CH})^3} \left(\frac{\hbar \mu_o}{4\pi}\right)^2 \frac{2}{5} (3\cos^2\theta - 1)\tau_c \qquad (7)$$

The γ_H, γ_N and γ_C are the magnetogyric ratios of the ^{1}H, ^{15}N and ^{13}C nuclei, respectively, r_{NH} and r_{CH} are the ^{15}N–$^{1}H^{N}$ and $^{13}C^{\alpha}$–$^{1}H^{\alpha}$ inter-nuclear distances, respectively, τ_c is the rotational correlation time of the molecule, and $\hbar$ and μ_o are natural constants. This expression does not take fast internal motion or anisotropic reorientation of the molecule into account. Due to the planarity of the peptide bond, the angle θ can be directly related to the dihedral angle ψ, and thus the dipole–dipole cross-correlation measurement provides information on the allowed values of ψ. Such information can provide important new structural constraints in the structure determination of proteins, due to the fact that the dihedral angle ψ is difficult to assess by other experimental means.

Since the pioneering work of Reif et al. was first reported, additional and/or improved schemes for using cross-correlation effects to assess ϕ and ψ dihedral angles in proteins and sugar puckers in nucleic acids have been proposed by several groups (see for example Kloiber and Konrat[32] and references cited therein). Almost all of these schemes have been based on the measurement of DD/DD and/or DD/CSA cross-correlation effects. However, Skrynnikov and coworkers[33] have proposed a technique for measuring CSA cross-correlated relaxation between pairs of carbonyl spins in proteins, and have demonstrated that in the case where the carbonyl spins reside on successive residues, information about the intervening (ϕ, ψ) backbone dihedral angles is obtained. They also demonstrated the possibility of observing CSA/CSA cross-correlated relaxation between carbonyl spins residing on two peptide planes linked via a hydrogen bond, which can provide information about the relative orientation of these planes. With the availability of dihedral angle information, especially for the ψ angles, from various cross-correlated relaxation measurements, it has become possible to use such structural constraints in NMR protein structure calculations. Refinement methods that have been modified to incorporate cross-correlation-based structural constraints can be used to significantly improve the quality of NMR structures and are applicable to larger proteins.[34]

5 STUDIES OF MOLECULAR DYNAMICS VIA CROSS-CORRELATED RELAXATION EFFECTS

The measurement of nuclear spin relaxation rate constants provides valuable information on motional processes occurring within biomolecules. Experiments for measuring auto-correlated relaxation rate constants for ^{1}H, ^{13}C, ^{15}N and ^{2}H are in widespread use, particularly for characterizations of the backbone dynamics and the rotational diffusion tensor of proteins and their complexes.[11] Building upon this base, there is growing interest in obtaining more detailed information on conformational dynamics within proteins. Two areas of focus are the development of more realistic models of the local motions of peptide planes in proteins and quantitative measurements of side chain dynamics. Cross-correlated relaxation experiments are proving to be particularly useful for studying the motional properties of structural elements that have a fixed geometry, such as peptide planes and CH_2, CH_3 and NH_2 groups. The motions of such moieties within proteins and similar elements within other biomolecules are expected in general to be anisotropic. Experimental NMR studies of such anisotropic motions are greatly facilitated by exploiting the sensitivity of cross-correlated relaxation rates to the direction of motion. Cross-correlated relaxation measurements are complementary to the standard auto-correlated relaxation experiments in several ways. Cross-correlation rate constants are not, or only little, affected by conformational or chemical exchange processes (see **Chemical Exchange Effects in Biological Macromolecules**), spin-rotation relaxation, or relaxation by paramagnetic oxygen;[35] such contributions can complicate the interpretation of dipolar or CSA auto-relaxation data. An additional advantage is that transverse cross-correlation effects are generally confined to subsystems containing two, three or four spins, with outside spins having little effect. On the other hand, a potential complication in the use of cross-correlation effects involving CSA interactions is that independent knowledge of the CSA tensor parameters is necessary in order to separate out the motional contributions to the cross-correlated relaxation processes. Information from other sources, such as solid-state NMR, molecular dynamics simulations, and CSA quantum chemical calculations, can be employed for characterizing the necessary CSA tensor parameters.[26,35]

A thorough description of the theory and application of cross-correlated relaxation measurements for studies of motional processes in biomolecules is beyond the scope of this article. The interested reader is directed to several excellent review articles that have appeared recently.[8–11] Instead, a very limited survey of some of the most promising uses of cross-correlation effects in biomolecular dynamics studies is presented here.

5.1 Dipole–Dipole/Dipole–Dipole Cross-Correlation Measurements

The cross-correlated relaxation measurements most commonly employed in biomolecular NMR studies involve dipole–dipole/dipole–dipole (DD/DD) and DD/CSA interactions. The measurement of DD/DD cross-correlated relaxation has the advantage that no assumptions generally need to be made about the interaction tensors, since they involve known physical constants such as the bond lengths, the orientation of the principal axis of the dipolar tensor is usually known, and the dipolar tensor is axially symmetric. There has been a long history to the use of DD/DD cross-correlated relaxation effects for characterizing molecular motions. Much of the work has focussed on the examination of relaxation effects for proton-coupled ^{13}C spins, especially for AX_2 and AX_3 groups.[7,8,10] For the ^{13}C multiplet spectra of methylene and methyl groups, the central and outer components of the multiplet exhibit different relaxation behavior as a result of DD/DD cross-correlation.[10] Differences in the high field relaxation behavior of the outer lines of the ^{13}C multiplet result from DD/CSA cross-correlation. Building upon earlier work of their own and that of other groups such as Grant, Werbelow and Bodenhausen, Daragan and Mayo have championed the use of DD/DD cross-correlated relaxation measurements for obtaining information on motional processes in biomolecules.[10,11]

A particularly useful method for measuring DD/DD cross-correlated relaxation in heteronuclear spin systems is to monitor the cross-relaxation process $S_z \rightarrow 4S_zI_{1z}I_{2z}$; this technique has been referred to as "SIIS cross relaxation".[36] This cross-relaxation process can occur only when the two heteronuclear dipolar interactions SI_1 and SI_2 are modulated in a correlated manner by the random process that causes relaxation. The SIIS-type of experiment is particularly useful for characterizing the motion of CH_2 groups about χ dihedral angles in the side chains of proteins, since the relative orientation of the two interacting dipoles is known. Measurements of scalar coupling constants can provide information concerning the relative populations of χ rotamers, but provides no information on the rate constants for the bond rotations. By measuring the cross-relaxation behavior between the S_z polarization and the three-spin order $4S_zI_{1z}I_{2z}$, Ernst and Ernst[36] demonstrated that it is possible to distinguish between equally populated three-site jump or unrestricted rotational diffusion models on the one hand and two-site or restricted rotational diffusion models on the other hand; it is often possible to make this judgement based just on the sign of the cross-relaxation peaks. The SIIS cross-relaxation process is typically measured by creating either the S_z polarization or the three-spin order $4S_zI_{1z}I_{2z}$, and then detecting the cross-relaxation partner. Due to the slow tumbling of large molecules, there is some advantage to performing the experiment in the so-called tilted rotating frame, as in the related T-ROESY experiment.[37] The reason for this is that in the laboratory frame the cross-relaxation process depends only on the spectral density function at the Larmor frequency ω_{os}, which tends towards zero as the tumbling slows. A dependence on $J(0)$ is introduced by performing the experiment in the tilted rotating frame. Yang and coworkers[38] have proposed an alternative method, using a triple resonance pulse scheme, for measuring cross-correlated dipole–dipole spin relaxation in proteins. Their experiment records $^{13}C^{\beta}$ multiplet component intensities in one of the three dimensions, and the cross-correlation relaxation rate constant for the interaction between the two ^{13}C β-methylene ^{13}C–^{1}H dipoles is obtained by taking the appropriate ratio of multiplet component intensities. Kay's group, among others, has elegantly demonstrated the usefulness of DD/DD cross-correlation measurements for assessing side-chain dynamics in folded and unfolded proteins and for selecting appropriate motional models.[10,38,39]

A number of DD/DD cross-correlations exist among the various nuclei that form the backbone of a protein, and in principle measurements of the associated cross-correlated relaxation rate constants can provide information about the dynamics of peptide planes. Carlomagno and coworkers[40] proposed a scheme for measuring the sum of the $^{13}C'$–$^{13}C^{\alpha}$/^{15}N–$^{1}H^{N}$ and $^{13}C'$–$^{1}H^{N}$/^{15}N–$^{13}C^{\alpha}$ DD/DD cross-correlated relaxation rate constants by analyzing the influence of these processes on ^{15}N–$^{13}C'$ double and zero quantum coherences. The same experiment gives access to the cross-correlated relaxation rate constants between the $^{13}C'$ CSA and the ^{15}N–$^{1}H^{N}$ or $^{13}C'$–$^{13}C^{\alpha}$ dipoles. The rate constants are very small for small proteins, and thus are difficult to interpret quantitatively. However, the rate constants are expected to increase for larger molecules, which would allow a more rigorous, quantitative analysis. Nevertheless, even a qualitative analysis of the DD/DD cross-correlation data can be helpful in identifying anisotropic motions of peptide planes. Another possible DD/DD cross-correlation involving protein backbone nuclei is the $^{1}H^{N}$–^{15}N/$^{1}H^{N}$–$^{13}C'$ dipole–dipole interaction, which has been examined by Zuiderweg's group.[41]

5.2 Dipole–Dipole/CSA Cross-Correlation Measurements

The measurement of dipole–dipole/CSA cross-correlation effects has proven to be quite valuable for studying motional processes in biomolecules. Such experiments have found important applications in characterizing motional processes occurring on both fast timescales (picosecond-nanosecond) and slower timescales (microsecond-millisecond).

Tjandra and coworkers[42] demonstrated the possibility of measuring ^{15}N–^{1}H dipolar/^{15}N CSA relaxation interference effects to obtain approximate values of the generalized order parameter S^2 that is frequently used to characterize the motional properties of bond vectors such as the backbone $^{1}H^{N}$–^{15}N amide group in proteins. They proposed a straightforward experiment for monitoring the cross-relaxation between in-phase ^{15}N coherence, S_x (or S_y), and anti-phase coherence, $2I_zS_x$ (or $2I_zS_y$), and measuring the corresponding cross-correlation rate constant η_{xy}. The theoretical expression for this transverse cross-correlation rate constant is[42,43]

$$\eta_{xy} = -\frac{\sqrt{3}}{6} cd P_2(\cos\beta)[4J(0) + 3J(\omega_N)] \qquad (8)$$

in which $d = (\mu_o h\gamma_H\gamma_N)/(8\pi^2 r_{NH}^3)$, $c = \gamma_N B_o \Delta\sigma/\sqrt{3}$, μ_o is the permeability of free space, h is Planck's constant, γ_H and γ_N are the magnetogyric ratios for ^{1}H and ^{15}N, respectively, r_{NH} is the distance between the two nuclei, B_o is the static magnetic field strength, $\Delta\sigma = \sigma_\parallel - \sigma_\perp$, the principal components of the ^{15}N CSA tensor are $\sigma_\parallel$ and $\sigma_\perp$, $P_2(x) = (3x^2 - 1)/2$, β is the angle between the symmetry axis of the ^{15}N CSA tensor and the ^{15}N–^{1}H bond vector, and $J(\omega)$ is the spectral density function. Since the cross-correlation rate constant η_{xy} is proportional to the generalized order parameter S^2 (through the dependence on the spectral density function), measurements of η_{xy} yield information on the amplitude of rapid internal motions within a biomolecule. A major advantage of utilizing measurements of η_{xy} is the fact that this cross-correlation process is not affected by line broadening caused by slow conformational exchange,[23,42] and thus the interpretation of the data is greatly simplified in that regard. A disadvantage of the method, however, is that variation in S^2 and $\Delta\sigma$ cannot be distinguished from each other in terms of their effect on η_{xy}. Thus, one must be cautious when interpreting changes in η_{xy}, due to the uncertainties there may be in knowledge of $\Delta\sigma$. On the other hand, if the generalized order parameter S^2 has been determined independently, measurement of η_{xy} can provide information on $\Delta\sigma$.[42]

Dipole–dipole/CSA cross-correlation can cause not only the transverse cross-relaxation process described above but also the longitudinal cross-relaxation process between a single spin order S_z and two-spin order $2I_zS_z$, characterized by a rate constant η_z. The theoretical expression for η_z is[43]

$$\eta_z = -\sqrt{3}cdP_2(\cos\beta)J(\omega_N) \tag{9}$$

with the various symbols having the same definitions as above in the expression for η_{xy}. Kroenke and coworkers[43] have developed a method for distinguishing the contributions of chemical exchange from the contributions due to anisotropic rotational diffusion in ^{15}N spin relaxation studies by measuring both the longitudinal and transverse relaxation interference between the ^{1}H–^{15}N dipolar and ^{15}N CSA interactions. Accurate assessment of chemical exchange contributions to transverse relaxation rate constants (R_2) is critical for a proper interpretation of both model-free and spectral density mapping results. If a biomolecule is regarded as a spherical top that rotates isotropically in solution, then the trimmed mean value of the ratio R_2/R_1 (R_1 is the spin-lattice relaxation rate constant) provides an estimate of the isotropic rotational correlation time of the molecule. Atomic sites subject to chemical or conformational exchange have significantly increased R_2/R_1 ratios. A serious complication arises if the rotational diffusion of the molecule is not isotropic. If rotational diffusion anisotropy is significant, increases in the values of R_2/R_1 for a given nucleus can result from particular orientations of the symmetry axis of the dipolar or CSA tensor in the principal axis frame of the diffusion tensor. These increases can be interpreted mistakenly as evidence of conformational exchange. At the same time, real chemical exchange contributions to R_2 interfere with measurements of the rotational diffusion anisotropy by systematically increasing the R_2/R_1 ratio for the affected nuclei. In practice, sites with large R_2/R_1 ratios are excluded from analysis, which reduces the available data and risks exclusion of data important for accurate assessment of rotational diffusion anisotropy. The basis for the methodology proposed by Kroenke et al.[43] is the fact that both η_{xy} and η_z are independent of chemical exchange and that the η_{xy}/η_z ratio is, to a good approximation, independent of the principal values and orientations of the CSA tensor, unlike the η_{xy} and η_z values separately. As a result, the η_{xy}/η_z ratio is sensitive only to internal and overall motions that contribute to dipolar and CSA relaxation mechanisms. The dependence of the η_{xy}/η_z ratio on the orientation of the ^{1}H–^{15}N bond vector in a molecular reference frame provides a robust method of determining the rotational diffusion tensor. In addition, comparison of the η_{xy}/η_z ratios to the R_2/R_1 ratios permits unequivocal identification of nuclei that are subject to chemical exchange processes, without the need for multi-field and/or rotating-frame relaxation experiments. The methodology for measuring η_z is straightforward.[43] A potential complication in the measurement of η_z is the competing cross-relaxation of the $2I_zS_z$ two-spin order ($I \equiv {}^1$H) with surrounding protons. This problem can be minimized through the use of deuteration or by more complex experimental schemes.[44,45]

Cross-correlated relaxation measurements are proving to be a rich source of information for characterizing the backbone dynamics of proteins. Such motions have commonly been studied through the use of ^{15}N, $^{13}C^\alpha$ and, more recently, ^{13}C′ carbonyl auto-correlated relaxation experiments. Several groups have demonstrated that the measurement of various relaxation interference effects, many involving the cross-correlation of dipole–dipole and CSA interactions, can provide useful insights concerning the locally anisotropic motions of peptide planes and complement the information obtained from auto-correlated relaxation experiments. A large number of relaxation interference effects are possible among the group of spin-1/2 nuclei in the protein backbone (^{13}C′, ^{15}N, $^1H^N$, $^{13}C^\alpha$, $^1H^\alpha$), and many have already been exploited. Only some of the possibilities that have been demonstrated are discussed here.

Zuiderweg's group has reported that there is a poor correlation between the generalized order parameters of the C′–C^α and the $^1H^N$–^{15}N bond vectors, as determined from auto-correlated relaxation studies.[46] They interpreted the lack of correlation as evidence of local or semi-local anisotropic motion of the peptide planes. To further their studies, they developed a new experiment to measure the relaxation interference between the carbonyl (C′) CSA and the ^{13}C′–$^{13}C^\alpha$ dipole–dipole relaxation interactions. The availability of such additional experimental data that reports on anisotropic motion is of great value for modeling such motions.[10,11,47] The Zuiderweg group has also developed a novel scheme for measuring transverse ^{13}C′–$^1H^N$ dipole–dipole/^{13}C′ CSA cross-correlated relaxation rates, using an E.COSY-type triple resonance experiment.[48] The advantage of this method for measuring the cross-correlation effects is that it by-passes the usual requirement for having a resolvable scalar coupling between, in this case, the ^{13}C′ and $^1H^N$ nuclei.

Brutscher and coworkers[49] devised a general scheme to use zero-quantum/double-quantum (ZQ/DQ) NMR experiments to measure various dipole–dipole/CSA cross-correlation rate constants. They demonstrated their methodology for the three-spin system consisting of the $^1H^N$, ^{15}N and ^{13}C′ nuclei of the peptide plane in proteins. The dipole–dipole/CSA relaxation interference effects on the zero- and double-quantum coherences formed between the ^{15}N and ^{13}C′ spins are manifested as differential relaxation in the two components of the ^{15}N–$^1H^N$ doublet. The measured relaxation rate constants include both

local and remote cross-correlation effects. There is a distinct dependence of the local and remote cross-correlation effects on internal anisotropic reorientational fluctuations of the peptide plane, providing the possibility of using such information to obtain a better understanding of local motions within a protein backbone.

5.3 CSA/CSA Cross-Correlation Measurements

Although the measurement of CSA/CSA cross-correlation effects has not yet attracted as much attention as DD/DD or DD/CSA cross-correlation measurements, the CSA/CSA-based experiments complement the other methods and can also provide valuable information for characterizing motional anisotropy within biomolecules. Vold and Vold[12] anticipated the possibility of observing CSA/CSA relaxation interference effects, which other groups subsequently have verified and elaborated upon.[8,11] In terms of applications to biomolecules, Pellecchia and coworkers[41] have demonstrated the potential usefulness of measuring the cross-correlation effects between the CSAs of the backbone amide ^{15}N and carbonyl $^{13}C'$ nuclei in proteins. Their measurement scheme is based upon the differential relaxation of double- and zero-quantum coherences formed between the backbone ^{15}N and carbonyl $^{13}C'$ spins. As it turns out, their experiment also permits the measurement of the cross-correlation between $^{1}H^{N}$–^{15}N and $^{1}H^{N}$–$^{13}C'$ dipole–dipole interactions. The ^{15}N CSA tensor is, to a good approximation, axially symmetric, which simplifies the theoretical treatment. However, the $^{13}C'$ tensor is not axially symmetric. However, it is possible to decompose the $^{13}C'$ CSA tensor into two orthogonal axially symmetric tensors and separately consider the contributions of each.[11] Interpretation of CSA/CSA cross-correlated relaxation effects is challenging since observed variations, as reported by Pellecchia et al., can depend on local internal anisotropic motion and variations of tensor parameters and of angles between tensors. However, even though much work is still required in developing a robust procedure for interpreting CSA/CSA relaxation interference effects in biomolecules, such measurements will clearly be useful in characterizing internal motional anisotropies such as that for individual peptide planes. Such studies will be greatly facilitated by developments in the understanding of structural and motional effects on CSA tensor parameters.

6 CROSS-CORRELATION EFFECTS IN PARAMAGNETIC SYSTEMS

The presence of cross-correlation effects in paramagnetic systems has been exploited for a number of useful purposes.[8] The dipolar interaction between a nucleus and the static electron magnetic moment results in the so-called Curie spin relaxation (CSR). A theoretical analysis demonstrates that, for example, the cross-correlation between the ^{1}H-Curie spin and ^{1}H–^{15}N dipolar interactions is formally identical to ^{1}H–^{15}N dipolar/^{1}H CSA cross-correlated relaxation. Boisbouvier and coworkers[50] have demonstrated that the measurement of ^{1}H–^{15}N dipole–dipole/^{1}H CSR cross-correlated relaxation rate constants can provide valuable, long-range structural constraints in NMR studies of paramagnetic molecules, due to the dependence of the rate constant on the distance between the amide proton and the electron spin and on the angle defined by the triangle ^{15}N–^{1}H–S (S is the electron spin). Madhu and coworkers[51] demonstrated that in addition to providing geometric constraints for structure refinement, the presence of cross-correlated relaxation involving the Curie spin relaxation and inter-nuclear dipolar relaxation mechanisms can also permit TROSY-type schemes to be used to obtain sensitivity and/or resolution enhancements. In this case, the enhancements can occur for any of the four components of a 2D ^{1}H–^{15}N multiplet, in contrast to the case for diamagnetic proteins and dipole–dipole/CSA cross-correlations.[8,51] Another important consequence of cross-correlation effects in paramagnetic systems is the possibility of observing 'relaxation-allowed' coherence transfer between two nuclei.[8,52]

7 CHARACTERIZATION OF HYDROGEN BOND LENGTHS

Hydrogen bond formation is an essential mechanism for the stabilization of biomolecular structures, and thus the development of experimental methods capable of directly detecting the presence of hydrogen bonds is quite valuable. Riek[53] has demonstrated that hydrogen bond lengths can be characterized by the measurement of DD/CSA cross-correlated relaxation involving the ^{1}H CSA and the dipole–dipole couplings of the ^{1}H to its hydrogen bond acceptor ^{15}N and to its hydrogen bond donor ^{15}N. The ratio of these two cross-correlation rate constants is dependent on the hydrogen bond length and on the generalized order parameter of the dipole–dipole ^{1}H–^{15}N vectors. Although the distance and motional contributions cannot be distinguished in this experiment, qualitative information is obtained concerning the characteristics of the hydrogen bond.

8 RELAXATION-INDUCED VIOLATIONS OF COHERENCE TRANSFER SELECTION RULES IN MULTIPLE QUANTUM NMR SPECTROSCOPY

Homonuclear multiple quantum and multiple quantum-filtered spectroscopy can be quite useful for resonance assignment in NMR studies of biomolecules.[54,55] The interpretation of multiple quantum and multiple quantum-filtered spectra is greatly assisted by the use of the coherence transfer selection rules given by Braunschweiler and coworkers,[56] which indicate the conditions required for transfer of multiple quantum coherence to observable single quantum transitions. While the predictions made based on these selection rules generally agree very well with experimental results, some anomalous resonances are frequently observed that violate these selection rules. In particular, multiple quantum coherence actively involving two or three methyl protons (attached to the same carbon atom) can be transferred to observable single quantum transitions of the methyl protons, in violation of the aforementioned selection rules. Such 'forbidden' peaks arise due to differential relaxation rates of degenerate single quantum transitions of magnetically equivalent nuclei.[57–59] Müller and coworkers presented a detailed analysis of the dipolar cross-correlation effects that give rise to the multi-exponential transverse relaxation of degenerate transitions. Müller has also proposed several experiments that exploit the presence of relaxation-allowed coherence transfer pathways in systems of degenerate spins.[8]

9 ADDITIONAL CROSS-CORRELATION EFFECTS

Most of the applications of cross-correlation effects in studies of biomolecules have involved the various combinations of dipole–dipole and CSA interactions and, for paramagnetic molecules, Curie spin relaxation. However, other possibilities exist as well, and a few of these are mentioned here.

Brüschweiler and Ernst[23] pointed out that cross-correlated relaxation effects can occur when a motional process simultaneously modulates a chemical shielding and a spin coupling term. For example, cross-correlated relaxation would occur for an I–S spin pair if the chemical shift of one of the spins and the isotropic scalar coupling J_{IS} were both modulated by the same motional process. Another possibility is the cross-correlation of chemical exchange effects involving multiple quantum coherences.[60] The latter effect was hypothesized to be a contributing factor in $^1H^N/^{15}N$ CSA/CSA cross-correlated relaxation measurements in proteins. Cross-correlation effects can be important in the analysis of dynamic frequency shifts.[8] For example, a dynamic frequency shift (see **Dynamic Frequency Shift,** Volume 3) can result from DD/CSA cross-correlated relaxation in a two-spin-1/2 system and is manifested as an additive contribution to the apparent scalar J coupling between the two spins.[61] This cross-correlation-induced J coupling is dependent on the motional properties of the spin system and thus can serve as a unique probe of molecular dynamics.

10 ELIMINATION OF CROSS-CORRELATION EFFECTS

The presence of cross-correlation effects can complicate the measurement of various relaxation rate constants by introducing additional terms into the rate equations that describe relaxation. In such cases it is desirable to devise methods for eliminating specific cross-correlation effects. These methods can be as simple as using non-selective 90° measuring pulses to eliminate multiplet effects in homonuclear spin systems,[8] or more elaborate procedures requiring new elements to be added to the relevant pulse sequences. Among the most common type of experiments in which the elimination of cross-correlation effects is important is the measurement of heteronuclear spin relaxation rate constants. At high magnetic fields, the magnitudes of the ^{1}H–X dipolar and X spin CSA interactions are comparable for X representing the ^{15}N in a peptide group or the aromatic ^{13}C nuclei; consequently, cross-correlation between these two relaxation mechanisms systematically affects relaxation rate constants measured using conventional experimental methods. Boyd and coworkers[62] demonstrated that unwanted dipole–dipole/CSA cross-correlation effects in ^{15}N longitudinal (T_1) relaxation measurements can be eliminated by broadband ^{1}H decoupling during the magnetization recovery period. They also proposed experimental schemes for monitoring the cross-relaxation between S_z and $2I_zS_z$ operators that results from dipole–dipole/CSA cross-correlation, and suggested that such measurements could provide information on the ^{15}N CSA tensor and on the angle θ between the principal axis of the ^{15}N CSA tensor and the ^{1}H–^{15}N inter-nuclear vector. Analogous means for suppressing dipole–dipole/CSA cross-correlation effects in CPMG experiments have been proposed,[63,64] allowing accurate measurements of spin-spin relaxation rate constants for heteronuclei with significant chemical shift anisotropies.

11 SUMMARY

Rather than being a complicating nuisance, as it was widely perceived to be in the past, cross-correlated relaxation has turned out to be extremely valuable as the basis for many new NMR tools that have been developed for probing the structure and dynamics of biomolecules. The observed effects of cross-correlated relaxation range from subtle to dramatic. The sensitivity and resolution improvements achieved in TROSY- and CRINEPT-type experiments have made it possible to study much larger systems than was previously feasible. New experiments are available for the characterization of CSA tensors, obtaining unique structural constraints, and probing motional processes within biomolecules at an unprecedented level of detail. Although much theoretical and experimental work needs to be done to fully exploit the potential of cross-correlated relaxation phenomena, the rewards are clear and undoubtedly there are many new, valuable discoveries yet to be made in this field.

12 RELATED ARTICLES IN THIS VOLUME

Chemical Exchange Effects in Biological Macromolecules; Transverse Relaxation-optimized NMR Spectroscopy with Biomacromolecular Structures in Solution.

13 RELATED ARTICLES IN VOLUMES 1–8

Dynamic Frequency Shift, Volume 3; Protein Dynamics from NMR Relaxation, Volume 6; Relaxation: An Introduction, Volume 6; Relaxation of Transverse Magnetization for Coupled Spins, Volume 6; Relaxation Processes: Cross Correlation & Interference Terms, Volume 6; Relaxation Processes in Coupled-Spin Systems, Volume 6; Relaxation Theory: Density Matrix Formulation, Volume 6.

14 REFERENCES

1. H. M. McConnell, *J. Chem. Phys.*, 1956, **25**, 709.
2. S. Hubbard, *Phys. Rev.*, 1958, **111**, 1746.
3. P. S. Hubbard, *Phys. Rev.*, 1958, **109**, 1153.
4. R. Brüschweiler, Structural Dynamics in Biomolecules Monitored by Nuclear Magnetic Resonance Relaxation, Ph.D. Diss. No. 9466, ETH Zürich, Zürich, 1991.
5. A. D. Bain and R. M. Lynden-Bell, *Mol. Phys.*, 1975, **30**, 325.
6. L. G. Werbelow and D. R. Grant, *Adv. Magn. Reson.*, 1977, **9**, 189.
7. D. M. Grant, C. L. Mayne, F. Liu, and T.-X. Xiang, *Chem. Rev.*, 1991, **91**, 1591.
8. A. Kumar, R. C. R. Grace, and P. K. Madhu, *Prog. NMR Spectrosc.*, 2000, **37**, 191.
9. B. Brutscher, *Concepts Magn. Reson.*, 2000, **12**, 207.
10. V. A. Daragan and K. H. Mayo, *Prog. NMR Spectrosc.*, 1997, **31**, 63.
11. M. W. F. Fischer, A. Majumdar, and E. R. P. Zuiderweg, *Prog. NMR Spectrosc.*, 1998, **33**, 207.

12. R. L. Vold and R. R. Vold, *Prog. NMR Spectrosc.*, 1978, **12**, 79.
13. L. G. Werbelow, in 'Nuclear Magnetic Resonance Probes of Molecular Dynamics', ed R. Tycko, Kluwer: Amsterdam, 1994, p. 223–263.
14. M. Goldman, *J. Magn. Reson.*, 1984, **60**, 437.
15. J. Cavanagh, W. J. Fairbrother, A. G. Palmer, and N. J. Skelton, 'Protein NMR Spectroscopy. Principles and Practice', Academic Press, 1996.
16. M. H. Levitt, 'Spin Dynamics. Basics of Nuclear Magnetic Resonance', Wiley, 2001.
17. B. Reif, A. Diener, M. Hennig, M. Maurer, and C. Griesinger, *J. Magn. Reson.*, 2000, **143**, 45.
18. T. Carlomagno and C. Griesinger, *J. Magn. Reson.*, 2000, **144**, 280.
19. R. H. Griffey and A. G. Redfield, *Q. Rev. Biophys.*, 1987, **19**, 51.
20. K. Pervushin, R. Riek, G. Wider, and K. Wüthrich, *Proc. Natl. Acad. Sci. USA*, 1997, **94**, 12 366.
21. K. V. Pervushin, G. Wider, R. Riek, and K. Wüthrich, *Proc. Natl. Acad. Sci. USA*, 1999, **96**, 9607.
22. C. Dalvit, *J. Magn. Reson.*, 1992, **97**, 645.
23. R. Brüschweiler and R. R. Ernst, *J. Chem. Phys.*, 1992, **96**, 1758.
24. R. Riek, G. Wider, K. Pervushin, and K. Wüthrich, *Proc. Natl. Acad. Sci. USA*, 1999, **96**, 4918.
25. R. Riek, K. Pervushin, and K. Wüthrich, *Trends Biochem. Sci.*, 2000, **25**, 462.
26. D. Sitkoff and D. A. Case, *Prog. NMR Spectrosc.*, 1998, **32**, 165.
27. C. D. Kroenke, M. Rance, and A. G. Palmer, *J. Am. Chem. Soc.*, 1999, **121**, 10 119.
28. D. Fushman, N. Tjandra, and D. Cowburn, *J. Am. Chem. Soc.*, 1998, **120**, 10 947.
29. Y. Pang and E. R. P. Zuiderweg, *J. Am. Chem. Soc.*, 2000, **122**, 4841.
30. P. Kumar and A. Kumar, *J. Magn. Reson., Ser. A*, 1996, **119**, 29.
31. B. Reif, M. Hennig, and C. Griesinger, *Science*, 1997, **276**, 1230.
32. K. Kloiber and R. Konrat, *J. Am. Chem. Soc.*, 2000, **122**, 12 033.
33. N. R. Skrynnikov, R. Konrat, D. R. Muhandiram, and L. E. Kay, *J. Am. Chem. Soc.*, 2000, **122**, 7059.
34. R. Sprangers, M. J. Bottomley, J. P. Linge, J. Schultz, M. Nilges, and M. Sattler, *J. Biomol. NMR*, 2000, **16**, 47.
35. C. Scheurer, N. R. Skrynnikov, S. F. Lienin, S. K. Straus, R. Brüschweiler, and R. R. Ernst, *J. Am. Chem. Soc.*, 1999, **121**, 4242.
36. M. Ernst and R. R. Ernst, *J. Magn. Reson. A*, 1994, **110**, 202.
37. R. Brüschweiler, C. Griesinger, and R. R. Ernst, *J. Am. Chem. Soc.*, 1989, **111**, 8034.
38. D. Yang, A. Mittermaier, Y.-K. Mok, and L. E. Kay, *J. Mol. Biol.*, 1998, **276**, 939.
39. D. Yang, Y.-K. Mok, D. R. Muhandiram, J. D. Forman-Kay, and L. E. Kay, *J. Am. Chem. Soc.*, 1999, **121**, 3555.
40. T. Carlomagno, M. Maurer, M. Hennig, and C. Griesinger, *J. Am. Chem. Soc.*, 2000, **122**, 5105.
41. M. Pellecchia, Y. Pang, L. Wang, A. V. Kurochkin, A. Kumar, and E. R. P. Zuiderweg, *J. Am. Chem. Soc.*, 1999, **121**, 9165.
42. N. Tjandra, A. Szabo, and A. Bax, *J. Am. Chem. Soc.*, 1996, **118**, 6986.
43. C. D. Kroenke, J. P. Loria, L. K. Lee, M. Rance, and A. G. Palmer, *J. Am. Chem. Soc.*, 1998, **120**, 7905.
44. I. C. Felli, H. Desvaux, and G. Bodenhausen, *J. Biomol. NMR*, 1998, **12**, 509.
45. L. Wang, A. V. Kurochkin, and E. R. P. Zuiderweg, *J. Magn. Reson.*, 2000, **144**, 175.
46. M. W. F. Fischer, L. Zeng, Y. Pang, W. Hu, A. Majumdar, and E. R. P. Zuiderweg, *J. Am. Chem. Soc.*, 1997, **119**, 12 629.
47. T. Bremi and R. Brüschweiler, *J. Am. Chem. Soc.*, 1997, **119**, 6672.
48. Y. Pang, L. Wang, M. Pellecchia, A. V. Kurochkin, and E. R. P. Zuiderweg, *J. Biomol. NMR*, 1999, **14**, 297.
49. B. Brutscher, N. R. Skrynnikov, T. Bremi, R. Brüschweiler, and R. R. Ernst, *J. Magn. Reson.*, 1998, **130**, 346.
50. J. Boisbouvier, P. Gans, M. Blackledge, B. Brutscher, and D. Marion, *J. Am. Chem. Soc.*, 1999, **121**, 7700.
51. P. K. Madhu, R. Grandori, K. Hohenthanner, P. K. Mandal, and N. Müller, *J. Biomol. NMR*, 2001, **20**, 31.
52. H. Desvaux and M. Gochin, *Mol. Phys.*, 1999, **96**, 1317.
53. R. Riek, *J. Magn. Reson.*, 2001, **149**, 149.
54. M. Rance, W. J. Chazin, C. Dalvit, and P. E. Wright, *Methods Enzymol.*, 1989, **176**, 114.
55. T. J. Norwood, *Prog. NMR Spectrosc.*, 1992, **24**, 295.
56. L. Braunschweiler, G. Bodenhausen, and R. R. Ernst, *Mol. Phys.*, 1983, **48**, 535.
57. M. Rance and P. E. Wright, *Chem. Phys. Lett.*, 1986, **124**, 572.
58. N. Müller, G. Bodenhausen, and R. R. Ernst, *J. Magn. Reson.*, 1987, **75**, 297.
59. L. E. Kay, T. A. Holak, and J. H. Prestegard, *J. Magn. Reson.*, 1988, **76**, 30.
60. M. Tessari and G. W. Vuister, *J. Biomol. NMR*, 2000, **16**, 171.
61. R. Brüschweiler, *Chem. Phys. Lett.*, 1996, **257**, 119.
62. J. Boyd, U. Hommel, and I. D. Campbell, *Chem. Phys. Lett.*, 1990, **175**, 477.
63. A. G. Palmer, N. J. Skelton, W. J. Chazin, P. E. Wright, and M. Rance, *Mol. Phys.*, 1992, **75**, 699.
64. L. E. Kay, L. K. Nicholson, F. Delaglio, A. Bax, and D. A. Torchia, *J. Magn. Reson.*, 1992, **97**, 359.

Acknowledgements

This work was supported by funding from the National Institutes of Health (GM40089).

Biographical Sketch

Mark Rance, *b* 1953. B.Sc. physics, 1976, University of Waterloo, Canada; Ph.D. physics, 1981, University of Guelph, Canada. Research associate, National Research Council of Canada, 1981–82. Postdoctoral fellow, ETH Zürich, Switzerland with Profs. Ernst and Wüthrich, 1982–84. Scripps Research Institute, La Jolla, California, 1984–95. Associate professor, University of Cincinnati, 1996–present. Principal research interests: NMR methodology development, biomolecular structure and dynamics.

Relaxation Effects of Chemical Exchange

Donald E. Woessner
The University of Texas Southwestern Medical Center at Dallas, Department of Radiology, The Mary Nell and Ralph B. Rogers Magnetic Resonance Center, Dallas, TX, USA

1	Introduction	1
2	Relaxation Under Extremely Rapid Exchange Conditions	1
3	'Two-Site'Chemical Exchange	2
4	Relaxation for the Case of Equal Larmor Frequencies	3
5	Transverse Relaxation for the Case of Unequal Larmor Frequencies	4
6	'Multiple Site'Chemical Exchange and Transverse Relaxation	6
7	Preferential Orientation, Exchange, and Order in Aqueous Heterogeneous Systems	8
8	Effects of Diffusive Exchange in Heterogeneous Systems	10
9	Related Articles	10
10	References	10

1 INTRODUCTION

The NMR properties of atomic nuclei in atoms, molecules, and ions depend mainly on short-range effects. For example, the chemical shift of a nucleus in a molecule depends mainly on the molecular structure and only slightly on whether the molecule is in a gas, a liquid, or a solid. In a solid, the chemical shift is anisotropic, depending on the orientation of the molecule in the magnetic field. In a liquid, the molecular motions are very rapid, so that the chemical shift is the weighted average over the solid 'powder pattern'. The liquid molecule moves very rapidly, or exchanges, among all orientations and local molecular associations. In this general sense, exchange is ubiquitous, and the results are readily understood in terms of the appropriate average. Multicomponent NMR relaxation behavior can occur when the nuclei under study are constrained in different regions or at different sites that are characterized by different time-averaged environmental parameters that affect the relaxation times. These parameters include any that affect the nuclear spin energy levels and the mobility or time dependences of these parameters.

The NMR relaxation times are expressed[1] in terms of the Fourier intensities or spectral densities $J_h(\omega)$ of the time correlation function $\langle F_h(t)F_h{}^*(t+\tau)\rangle$ of nuclear spin interactions $F_h(t)$ at the angular frequency ω as given by

$$J_h(\omega) = \int_{-\infty}^{\infty} \langle F_h(t) F_h^*(t+\tau)\rangle \exp(\mathrm{i}\omega\tau)\,\mathrm{d}\tau \qquad (1)$$

The interaction function $F_h(t)$ is the product of a nuclear relaxation interaction strength (r^{-3} for magnetic dipolar relaxation) and a function of orientation (second-order spherical harmonic). (The average value $\langle F_h(t)\rangle$ is zero, unless there is preferential orientation such as that imposed by a stationary interface on a nonspherical molecule.) Let us consider the case when the correlation function of a site is

$$\langle F_h(t) F_h^*(t+\tau)\rangle = \langle F_h(t) F_h^*(t)\rangle \exp(-|\tau|/\tau_c) \qquad (2)$$

in which the correlation time τ_c depends on the rate of molecular motion (see ***Brownian Motion and Correlation Times***). Because equation (2) is an exponential function, the spectral densities $J_h(\omega)$ are given by the Lorentzian functions

$$J_h(\omega) = \langle F_h(t) F_h^*(t)\rangle \frac{2\tau_c}{1+\omega^2\tau_c^2} \qquad (3)$$

To illustrate the relationship between the spectral densities and the NMR relaxation times, consider the cases of magnetic dipolar interaction between two identical spin-$\frac{1}{2}$ nuclei and of nuclear quadrupolar interaction of a spin-1 nucleus. In both instances, the relaxation times are given by the equations[1]

$$\frac{1}{T_1} = H[J_1(\omega_0) + J_2(2\omega_0)] \qquad (4a)$$

$$\frac{1}{T_2} = \tfrac{1}{4}H[J_0(0) + 10J_1(\omega_0) + J_2(2\omega_0)] \qquad (4b)$$

where T_1 is the spin–lattice relaxation time, T_2 is the transverse relaxation time, and ω_0 is the angular Larmor frequency. The interaction strength $H = \frac{9}{8}\gamma^4\hbar^2 r^{-6}$ for magnetic dipolar relaxation and $\frac{9}{8}\pi^2\chi^2$ for nuclear quadrupolar interaction with zero asymmetry parameter. These equations apply (see ***Relaxation Theory: Density Matrix Formulation***) to the motionally narrowed limit in which $H^{1/2}\tau_c < 1$. When this limit does not apply, the $J_0(0)$ term is incorrect and the transverse relaxation must be calculated differently. We can do this by replacing the $J_0(0)$ term with the time dependence of the ensemble average of $M_+ = M_x + \mathrm{i}M_y$ obtained by introducing time dependence into the Larmor frequency. This is done in Sections 5–8 of this article for the transverse relaxation in many systems that involve chemical exchange of nuclei between sites with different Larmor frequencies.

In a more general approach that includes chemical exchange between different types of sites that are designated by j, we need to look closely at the evaluation of the correlation function $\langle F_h(t)F_h{}^*(t+\tau)\rangle$ in equation (2), which is an ensemble average (see ***Relaxation Theory: Density Matrix Formulation***) to calculate NMR relaxation phenomena properly.[2] Take any given nucleus at time t in site j, evaluate the interaction function at this time to obtain $F_{hj}(t)$, evaluate the autocorrelation function for this nucleus at later times $t+\tau$, and continue to do this as τ increases from zero to 'large' values. Finally, take the sum over all the j-type sites, weighting each site by its fractional population P_j. Note that the fraction of time that a nucleus occupies a j-type site is equal to P_j. The average time that nucleus occupies a j-type site is τ_j.

2 RELAXATION UNDER EXTREMELY RAPID EXCHANGE CONDITIONS

If chemical exchange of nuclei is merely rapid so that all the lifetimes τ_j are long compared with the correlation times τ_{cj}, the relaxation times of nuclei in the different j types of sites are independent of the exchange, and the preceding treatment for calculating the $J_h(\omega)$ for the relaxation times of a given site j is valid. However, when the exchange is extremely rapid so that the lifetimes in a site are shorter than the correlation times, this condition is not met and the effective correlation time depends on the average lifetime in a site. There are several different cases, depending on whether the strength of the nuclear relaxation interaction is the same in the different types of sites.[2]

When the strength of the relaxation interaction is the same in all sites and when there is complete randomization of the interaction direction upon chemical exchange, each τ_{cj} for equation (3) is replaced by an effective correlation time

$$\tau_{\text{eff},j} = \left(\frac{1}{\tau_{cj}} + \frac{1}{\tau_j}\right)^{-1} \tag{5}$$

If the direction of interaction is retained, instead of randomized, upon exchange, the exchange process can have several different effects on relaxation.[2] When the rotational correlation time is much longer in one site than in another, exchange involving this site can give a very large contribution to the rate of relaxation. As a nucleus in this slow site moves by chemical exchange to a site with much faster motion, the effective correlation time for the slow site is shortened. Another possible effect is that the strength of the relaxation interaction may be changed. When the exchange is much faster than the molecular rotational motions, there is a single effective correlation time

$$\tau_{\text{eff}} = \left\{\sum_i \frac{p_i}{\tau_{cj}}\right\}^{-1} \tag{6}$$

Also, the ensemble interaction average $\langle F_h(t)F_h{}^*(t)\rangle$ for a single type of site in equation (3) is replaced by the square of the weighted average of $F(t)$ at a given orientation, taken over all types j of sites, and then averaged over all orientations. This type of averaging, in the case of extremely rapid motions, is important for nonspherical molecules at the interface in many aqueous heterogeneous systems (see Section 7 of this article).

3 'TWO-SITE' CHEMICAL EXCHANGE

In all the cases described above, the nuclear relaxation is single component. However, when the nuclei are constrained in the sites, the observed NMR relaxation behavior is merely the weighted sum taken over the different sites that are characterized by specific relaxation times. When the nuclei migrate among these sites at rates that are small compared with molecular motions, the observed relaxation behavior is modified even when the relaxation time of each site is unaffected by this migration or exchange. Zimmerman and Brittin[3] have treated this situation with a stochastic theory, and McConnell[4] has presented a mathematically equivalent approach of adding exchange terms to the Bloch equations. These modified Bloch equations are particularly convenient for discussing the simplest case that illustrates the main features of the effects of chemical exchange on NMR relaxation: exchange between two different types of sites under the condition that the relaxation time of a nucleus in a given site is independent of the lifetime of the nucleus in that given site.

The Bloch equations are written for a rectangular coordinate system that rotates at angular frequency ω about its Z axis, which is parallel to the direction of $\boldsymbol{B}_0$, i.e., the rotating frame of reference. The modified Bloch equations that include chemical exchange[5] between states a and b are

$$\frac{dM_{xa}}{dt} = -(\omega_a - \omega)M_{ya} - \frac{M_{xa}}{T_{2a}} - \frac{M_{xa}}{\tau_a} + \frac{M_{xb}}{\tau_b} \tag{7a}$$

$$\frac{dM_{xb}}{dt} = -(\omega_b - \omega)M_{yb} - \frac{M_{xb}}{T_{2b}} - \frac{M_{xb}}{\tau_b} + \frac{M_{xa}}{\tau_a} \tag{7b}$$

$$\frac{dM_{ya}}{dt} = (\omega_a - \omega)M_{xa} - \frac{M_{ya}}{T_{2a}} - \frac{M_{ya}}{\tau_a} + \frac{M_{yb}}{\tau_b} - \omega_1 M_{za} \tag{7c}$$

$$\frac{dM_{yb}}{dt} = (\omega_b - \omega)M_{xb} - \frac{M_{yb}}{T_{2b}} - \frac{M_{yb}}{\tau_b} + \frac{M_{ya}}{\tau_a} - \omega_1 M_{zb} \tag{7d}$$

$$\frac{dM_{za}}{dt} = -\frac{M_{za} - M_{0a}}{T_{1a}} - \frac{M_{za}}{\tau_a} + \frac{M_{zb}}{\tau_b} + \omega_1 M_{ya} \tag{7e}$$

$$\frac{dM_{zb}}{dt} = -\frac{M_{zb} - M_{0b}}{T_{1b}} - \frac{M_{zb}}{\tau_b} + \frac{M_{za}}{\tau_a} + \omega_1 M_{yb} \tag{7f}$$

where ω is the angular rf frequency and $\omega_1 = \gamma B_1$, with γ the nuclear magnetogyric ratio. Also, P_a is the fraction of nuclei that are in state a, ω_a is the Larmor frequency, τ_a is the average lifetime of a given nucleus in state a before it leaves a and enters state b, T_{1a} and T_{2a} are the longitudinal and transverse relaxation times for nuclei while in state a, and M_{0a} is the equilibrium nuclear magnetization along $\boldsymbol{B}_0$. Similar definitions apply for state b. Since we are interested in relaxation, and relaxation times are defined in terms of the time-dependent behavior of the nuclear magnetization when $\boldsymbol{B}_1 = 0$, the coupled differential equations that describe the effects of chemical exchange can be written as

$$\frac{d(M_{0a} - M_{za})}{dt} = -\alpha_{1a}(M_{0a} - M_{za}) + \frac{M_{0b} - M_{zb}}{\tau_b} \tag{8a}$$

$$\frac{d(M_{0b} - M_{zb})}{dt} = -\alpha_{1b}(M_{0b} - M_{zb}) + \frac{M_{0a} - M_{za}}{\tau_a} \tag{8b}$$

for longitudinal relaxation. For transverse relaxation, it is convenient to combine the M_x and M_y magnetizations into the transverse magnetization:

$$\frac{dM_{+a}}{dt} = -\alpha_{2a}M_{+a} + \frac{M_{+b}}{\tau_b} \tag{9a}$$

$$\frac{dM_{+b}}{dt} = -\alpha_{2b}M_{+b} + \frac{M_{+a}}{\tau_a} \tag{9b}$$

In these equations, we use the definitions

$$M_{+a} = M_{xa} + \mathrm{i}M_{ya} \tag{10a}$$

$$\alpha_{1a} = \frac{1}{T_{1a}} + \frac{1}{\tau_a} \tag{10b}$$

$$\alpha_{2a} = \frac{1}{T_{2a}} + \frac{1}{\tau_a} - \mathrm{i}(\omega_a - \omega) \tag{10c}$$

for state a. Similar definitions apply for state b. The principle of detailed balance requires that $M_{0a}/\tau_a = M_{0b}/\tau_b$.

Equations (8a,b) and (9a,b) represent two sets of two simultaneous differential equations of the form

$$\frac{\mathrm{d}m}{\mathrm{d}t} = -\alpha m + bn \tag{11a}$$

$$\frac{\mathrm{d}n}{\mathrm{d}t} = -\beta n + am \tag{11b}$$

The solutions of each of these sets of equations are[5]

$$m(t) = A_+ \,\mathrm{e}^{-\phi_+ t} + A_- \,\mathrm{e}^{-\phi_- t} \tag{12a}$$

$$n(t) = B_+ \,\mathrm{e}^{-\phi_+ t} + B_- \,\mathrm{e}^{-\phi_- t} \tag{12b}$$

where

$$2\phi_\pm = (\alpha + \beta) \pm [(\alpha - \beta)^2 + 4ab]^{1/2} \tag{13}$$

and $A_\pm$ and $B_\pm$ are related by

$$B_\pm = -(\phi_\pm - \alpha)A_\pm/b \tag{14}$$

The net magnetizations are given by the sum $m(t) + n(t)$. The integration constants $A_\pm$ and $B_\pm$ are determined by the values of m and n at time $t = 0$, with the aid of equation (13). These initial values of m and n are determined by the rf pulse flip angles and the nuclear magnetizations that exist when the pulse is applied.

These solutions to equation (11) fail[5] mathematically when

$$(\alpha - \beta)^2 + 4ab = 0 \tag{15}$$

As shown later, this condition represents a point at which there is a change in behavior of the solutions when the Larmor frequencies are unequal. The appropriate solutions are

$$m(t) = \{A'[1 - \tfrac{1}{2}(\alpha - \beta)t] + bB't\}\,\mathrm{e}^{-(\alpha+\beta)t/2} \tag{16a}$$

$$n(t) = \{B'[1 + \tfrac{1}{2}(\alpha - \beta)t] + aA't\}\,\mathrm{e}^{-(\alpha+\beta)t/2} \tag{16b}$$

The integration constants A' and B' are also determined by the initial conditions.

4 RELAXATION FOR THE CASE OF EQUAL LARMOR FREQUENCIES

4.1 General Case

Here, we apply an rf pulse and examine the subsequent behavior of the longitudinal and transverse magnetization. We define the relaxation curve as the time dependence of the deviation of the particular nuclear magnetization from its equilibrium value. When there is no chemical exchange and $\omega_a = \omega_b$, the NMR signal is the sum of signals from the 'uncoupled' sites, and the T_1 and T_2 relaxation curves are each the sum of two exponential functions whose preexponential coefficients and decay time constants are the intrinsic state populations and relaxation times, respectively. When chemical exchange occurs, we see from equations (12a) and (12b) that the NMR signal is *still* the sum of two exponential functions. For convenience, we designate state a as that with the longer relaxation time. The mathematical form of the T_1 and T_2 curves is

$$F(t) = P_a' \exp\left(-\frac{t}{T_a'}\right) + P_b' \exp\left(-\frac{t}{T_b'}\right) \tag{17}$$

where T' and P' signify the apparent relaxation times and population fractions, respectively. These quantities are related to the intrinsic values by the equations

$$\frac{1}{T_a'} = C_1 - C_2 \tag{18a}$$

$$\frac{1}{T_b'} = C_1 + C_2 \tag{18b}$$

$$P_b' = \frac{1}{2} - \frac{1}{4}\left[(P_b - P_a)\left(\frac{1}{T_a} - \frac{1}{T_b}\right) + \frac{1}{\tau_a} + \frac{1}{\tau_b}\right] \Big/ C_2 \tag{19a}$$

$$P_a' = 1 - P_b' \tag{19b}$$

in which

$$C_1 = \frac{1}{2}\left(\frac{1}{T_a} + \frac{1}{T_b} + \frac{1}{\tau_a} + \frac{1}{\tau_b}\right) \tag{20a}$$

$$C_2 = \frac{1}{2}\left[\left(\frac{1}{T_b} - \frac{1}{T_a} + \frac{1}{\tau_b} - \frac{1}{\tau_a}\right)^2 + \frac{4}{\tau_a \tau_b}\right]^{1/2} \tag{20b}$$

Under all exchange conditions, the parameters in equation (17) obey the relationship

$$\frac{P_a'}{T_a'} + \frac{P_b'}{T_b'} = \frac{P_a}{T_a} + \frac{P_b}{T_b} = \frac{1}{T_\mathrm{m}} \tag{21}$$

where T_m is defined as an effective mean relaxation time. This means that the initial slope of $F(t)$ in equation (17) is independent of the exchange rate between the two states—a consequence of the assumption that the inherent relaxation times are unaffected by chemical exchange. Other relationships that are useful in deriving simplified, approximate relationships for limiting cases are

$$P_a' + P_b' = P_a + P_b = 1 \tag{22}$$

$$P_a/\tau_a = P_b/\tau_b \tag{23}$$

4.2 Limiting Cases

Let us examine the case where $P_a \approx P_b$ and $T_a \gg T_b$ when the exchange rate is increased from small values. Initially, P_a', P_b', and T_b' are nearly equal to the inherent values, and

T_a' is decreased from T_a. With increasing exchange rate, T_a' continues to decrease, and can be completely different from T_a. When τ_b becomes of the same order of magnitude as T_b, T_b' decreases, P_b' becomes smaller than P_b, and T_a' continues to decrease. Finally, when τ_b is small compared with T_b, P_b' is very small, and the relaxation decay curve is approximately a single exponential with a relaxation time given by equation (21). Thus, exchange can cause the observed, or apparent, relaxation decay curve parameters to be completely different from the values inherent to the different types of sites.

There are several pertinent limiting cases[6] that involve the relative values of the inherent relaxation times and the residence times.

When the exchange is very slow so that

$$\frac{1}{\tau_a} + \frac{1}{\tau_b} \ll \frac{1}{T_b} - \frac{1}{T_a} \tag{24}$$

the P_a' and P_b' values are very close to P_a and P_b; however, the apparent relaxation times are decreased:

$$\frac{1}{T_a'} = \frac{1}{T_a} + \frac{1}{\tau_a} \tag{25a}$$

$$\frac{1}{T_b'} = \frac{1}{T_b} + \frac{1}{\tau_b} \tag{25b}$$

As the exchange rate increases, the values of T_a' and T_b' decrease and the value of P_a' increases. In the special case where the intrinsic relaxation times are very different and the lifetimes are intermediate,

$$T_b \ll \tau_a,\ \tau_b \ll T_a \tag{26}$$

the results are $P_a' = P_a$, $P_b' = P_b$, and

$$T_a' = \tau_a \tag{27a}$$

$$T_b' = T_b \tag{27b}$$

Clearly, this is a favorable case for the determination of lifetimes.

Finally, when the chemical exchange is very fast so that

$$\frac{1}{\tau_a} + \frac{1}{\tau_b} \gg \frac{1}{T_b} - \frac{1}{T_a} \tag{28}$$

the rapid exchange limit is obeyed in which a single average relaxation time is observed:

$$P_a' = 1 \tag{29}$$

$$T_a' = T_{\mathrm{m}} \tag{30}$$

Another special case involves very different population fractions. When $T_b \ll T_a$ and $P_a \approx 1$ (which also means that $\tau_b \ll \tau_a$), the observable relaxation is approximately a single exponential with

$$\frac{1}{T_a'} = \frac{1}{T_a} + \frac{P_b}{P_a T_b + P_b \tau_a} \tag{31}$$

The observed relaxation time may bear no obvious relationship to that of type a sites. Even by changing the exchange rates by a large factor, such as by changing the temperature, the relaxation curve will not reveal that the system is two-site. The inherent relaxation times of the site types and the value of P_b might not be available from simple relaxation time measurements. This case applies, for example, to heterogeneous systems and biological materials that may have a small concentration of strongly relaxive sites, such as strong adsorption sites or paramagnetic centers. Note that if P_b is very small so that the b sites are widely spaced, τ_a may not be single valued, because the exchange will involve translational diffusion of the molecules of state a (see Section 8 of this article).

5 TRANSVERSE RELAXATION FOR THE CASE OF UNEQUAL LARMOR FREQUENCIES

5.1 General Case for the NMR Signal Following One Pulse

The effect of unequal Larmor frequencies is nonexistent for longitudinal relaxation, but transverse relaxation can be greatly increased. The following general solution[5] of the set of equations given by equations (9a) and (9b) following the application of a pulse to a spin system at equilibrium is relatively simple because there is no transverse nuclear magnetism at the time of application of the pulse:

$$F_2(t) = \frac{M_+(t)}{M_0 \sin\theta_1} = P_{2+}\,\mathrm{e}^{-(\phi_2 + c)t} + P_{2-}\,\mathrm{e}^{-(\phi_2 - c)t} \tag{32}$$

where

$$P_{2+} = -(f + \mathrm{i}g)\,\mathrm{e}^{-\mathrm{i}dt} \tag{33}$$

$$P_{2-} = [f - \mathrm{i}(1-g)]\,\mathrm{e}^{\mathrm{i}dt} \tag{34}$$

$$\phi_2 = \frac{1}{2}\left(\frac{1}{T_{2a}} + \frac{1}{T_{2b}} + \frac{1}{\tau_a} + \frac{1}{\tau_b}\right) \tag{35}$$

$$f = -\frac{1}{4}\left\{c(P_b - P_a)(\omega_a - \omega_b) + d\left[(P_b - P_a)\left(\frac{1}{T_{2a}} - \frac{1}{T_{2b}}\right) + \frac{1}{\tau_a} + \frac{1}{\tau_b}\right]\right\}(c^2 + d^2)^{-1} \tag{36}$$

$$g = \frac{1}{2} - \frac{1}{4}\left\{c\left[(P_b - P_a)\left(\frac{1}{T_{2a}} - \frac{1}{T_{2b}}\right) + \frac{1}{\tau_a} + \frac{1}{\tau_b}\right] - d(P_b - P_a)(\omega_a - \omega_b)\right\}(c^2 + d^2)^{-1} \tag{37}$$

$$|c| = [(X^2 + Y^2)^{1/2} + X]^{1/2}/\sqrt{8} \tag{38}$$

$$|d| = [(X^2 + Y^2)^{1/2} - X]^{1/2}/\sqrt{8} \tag{39}$$

with

$$X = \left(\frac{1}{T_{2a}} - \frac{1}{T_{2b}} + \frac{1}{\tau_a} - \frac{1}{\tau_b}\right)^2 - (\omega_a - \omega_b)^2 + \frac{4}{\tau_a \tau_b} \tag{40}$$

$$Y = -2(\omega_a - \omega_b)\left(\frac{1}{T_{2a}} - \frac{1}{T_{2b}} + \frac{1}{\tau_a} - \frac{1}{\tau_b}\right) \quad (41)$$

and θ_1 is the pulse flip angle. The algebraic sign of d is always positive; the sign of c is positive except for negative Y values. The value of ω is $\frac{1}{2}(\omega_a + \omega_b)$.

This function is even more complicated than the case of equal Larmor frequencies, and examination of limiting cases is necessary to show the effects of the Larmor frequency difference on transverse relaxation. When the exchange is slow so that the term $4/\tau_a\tau_b$ in equation (40) can be neglected, $d = \frac{1}{2}|\omega_a - \omega_b|$, $f \approx 0$, $g = P_b$, and $c = \pm\frac{1}{2}(1/T_{2b} - 1/T_{2a} + 1/\tau_b - 1/\tau_a)$. The upper algebraic sign applies when $\omega_a > \omega_b$, and the lower when $\omega_a < \omega_b$. Equation (32) then becomes

$$F_2(t) \approx -\mathrm{i}\left\{P_a \exp[\tfrac{1}{2}\,\mathrm{i}(\omega_a - \omega_b)t]\exp\left[-\left(\frac{1}{T_{2a}} + \frac{1}{\tau_a}\right)t\right] + P_b \exp[-\tfrac{1}{2}\mathrm{i}(\omega_a - \omega_b)t]\exp\left[-\left(\frac{1}{T_{2b}} + \frac{1}{\tau_b}\right)t\right]\right\} \quad (42)$$

Equation (42) is the sum of the two transverse magnetizations with separate frequencies, because d is not equal to zero. The decay rate of each signal increases (see ***Chemical Exchange Effects on Spectra***) with increasing exchange rate, as in equations (25a) and (25b) for equal Larmor frequencies, but it is insensitive to the difference between the Larmor frequencies. This may be expected, since a nucleus that enters a state from the other state has a random phase because it has existed in the former state for many periods of the frequency difference $\omega_a - \omega_b$. When the exchange rate increases, the amount of dephasing per transfer becomes dependent on the Larmor frequency difference.

The terms $\mathrm{e}^{-\mathrm{i}dt}$ and $\mathrm{e}^{\mathrm{i}dt}$ in equations (33) and (34) represent two different nuclear magnetizations rotating at frequencies that differ by $2d$. At very slow exchange rates, as shown above, the frequency difference is $\omega_a - \omega_b$. With increasing exchange rates, as examination of equation (39) reveals, the value of $2d$ decreases. The peaks in the NMR spectrum approach each other (see ***Chemical Exchange Effects on Spectra***). In general, the value of d never becomes zero, even at extremely high exchange rates such that $4/\tau_a\tau_b \gg (\omega_a - \omega_b)^2$. This means that, rigorously, there is *some* splitting in the NMR spectrum and that the NMR signal following a pulse *cannot* be a simple sum of two exponential decays when there is a difference in Larmor frequencies.

The above conclusion holds even in the specific case where $d = 0$. Examination of equations (38)–(41) shows that $d = 0$ when $1/T_{2a} - 1/T_{2b} + 1/\tau_a - 1/\tau_b = 0$. When the additional condition $(\omega_a - \omega_b)^2 = 4/\tau_a\tau_b$ holds, the special case in equation (15) holds, and the relatively simple solutions in equations (16a) and (16b) describe the NMR signal. This signal is

$$F_2(t) = -\tfrac{1}{2}(P_b - P_a)(\omega_a - \omega_b)t\,\mathrm{e}^{-\phi_2 t} - \mathrm{i}\left[1 + \frac{1}{2}(P_b - P_a) \times \left(\frac{1}{T_{2a}} - \frac{1}{T_{2b}}\right)t + \frac{1}{2}\left(\frac{1}{\tau_a} + \frac{1}{\tau_b}\right)t\right]\mathrm{e}^{-\phi_2 t} \quad (43)$$

Clearly, this is not a simple exponential decay.

When the exchange rate is very large so that the conditions $1/\tau_a,\ 1/\tau_b \gg 1/T_{2a},\ 1/T_{2b},\ |(\omega_a - \omega_b)|$ and $(\omega_a - \omega_b)^2 \gg (1/T_{2a} - 1/T_{2b})^2$ prevail, $F_2(t)$ is closely approximated by

$$F_2(t) = \sin(\omega_{\mathrm{av}}t)\,\mathrm{e}^{-t/T_2} \quad (44)$$

where

$$\omega_{\mathrm{av}} = P_a\omega_a + P_b\omega_b \quad (45)$$

$$\frac{1}{T_2} = \frac{1}{T_{\mathrm{m}}} + \frac{P_a P_b \tau_a \tau_b}{\tau_a + \tau_b}(\omega_a - \omega_b)^2 \quad (46)$$

This expression shows that the difference in Larmor frequencies enhances the transverse relaxation when the chemical exchange is fast. As the exchange rate increases to extremely large values, the observed T_2 value approaches T_{m}, the relaxation time when the Larmor frequencies are equal.

5.2 General Case for the NMR Signal Following Two Pulses

As usual, the NMR signal following the second pulse, applied at time $t = \tau$, is the sum[5] of three signals. The first signal results from the M_z component of magnetization that exists at the time of application of the second pulse. It is given by

$$\frac{M_+(t\rangle\tau)}{M_0 \sin\theta_2[1 - (1 - \cos\theta_1)]} = F(T_1, \tau)F_2(t\rangle\tau) \quad (47)$$

where $F(T_1, \tau)$ is equation (17) evaluated at time τ for T_1, and $F_2(t > \tau)$ is equation (32) evaluated as a function of the time after the second pulse, $t > \tau$.

The other two signals result from the transverse magnetization that exists at the time of application of the second pulse. The first is the reduced continuation of the signal following the first pulse as follows:

$$\frac{M_+(t)}{\frac{1}{2}M_0 \sin\theta_1(1 + \cos\theta_2)} = F_2(t) \quad (48)$$

where $F_2(t)$ is given by equation (32).

The other signal is the spin echo that can be found by using the complex conjugate of the one-pulse signal evaluated at time τ as the initial condition for the signal following the second (a 180°) pulse:

$$\begin{aligned} E(t) &= \frac{M_+(t)}{-\frac{1}{2}M_0 \sin\theta_1(1 - \cos\theta_2)} \\ &= P_{\mathrm{E}+}\,\mathrm{e}^{-(\phi_2 + c)t} + P_{\mathrm{E}-}\,\mathrm{e}^{-(\phi_2 - c)t} \\ &\quad +\{2[\,f\cos dt + (g + j)\sin dt]\sinh[c(t - 2\tau)] \\ &\quad +2\mathrm{i}[\,f\sin dt - (g + j)\cos dt]\cosh[c(t - 2\tau)]\} \\ &\quad \times\mathrm{e}^{-\phi_2 t} \end{aligned} \quad (49)$$

where

$$P_{\mathrm{E}+} = \mathrm{i}j\,\mathrm{e}^{-\mathrm{i}d(t - 2\tau)} \quad (50a)$$

$$P_{\mathrm{E}-} = \mathrm{i}(2g + j - 1)\,\mathrm{e}^{\mathrm{i}d(t - 2\tau)} \quad (50b)$$

with

$$j = \frac{1}{2} - g - \frac{1}{2}\frac{c^2 + \frac{1}{4}(\omega_a - \omega_b)^2}{c^2 + d^2} \tag{51}$$

The dependences of terms in equation (49) on the quantity $t - 2\tau$ clearly show the refocusing action of the second pulse on the attenuation of the signal following the first pulse that is caused by the difference in Larmor frequencies. When the exchange rates and the Larmor frequency differences are comparable, the use of equations (16a) and (16b) shows that the spin echo signal is

$$\begin{aligned} E(t) = {} & \tfrac{1}{2}(P_b - P_a)(\omega_a - \omega_b)(t - 2\tau)\,\mathrm{e}^{-\phi_2 t} \\ & + \mathrm{i}\left[1 + \frac{1}{2}(P_b - P_a)\left(\frac{1}{T_{2a}} - \frac{1}{T_{2b}}\right)t + \frac{1}{2}\left(\frac{1}{\tau_a} + \frac{1}{\tau_b}\right)t \right. \\ & \left. + \frac{1}{2}(\omega_a - \omega_b)^2\tau(t - \tau)\right]\mathrm{e}^{-\phi_2 t} \end{aligned} \tag{52}$$

When $P_a = P_b$, comparison of equation (52) with equation (43) shows that at the time of the peak of the spin echo, $t = 2\tau$, the spin echo signal is greater than the signal from a single pulse. This refocusing phenomenon is qualitatively similar to that for the spin echoes of molecules that diffuse into different values of B_0. Aside from a different statistical problem, the main difference here is that the precession frequency is restricted to two values; in molecular diffusion, a range of values is available to each nucleus.

Transverse relaxation is easily measured from the dependence of the spin echo amplitude at time $t = 2\tau$ determined as a function of 2τ. At very small chemical exchange rates, the Larmor frequency difference has a negligible effect on the transverse relaxation. With increasing exchange rates, the nucleus alternately experiences two different precession frequencies for random periods of time, causing a contribution to transverse relaxation by dephasing of the NMR signal. This dephasing passes through a maximum when the exchange rate and the Larmor frequency difference are comparable. Then, with increasing exchange rates, the transverse relaxation contribution from the frequency difference decreases, and is given by equation (46) when the exchange rates are large compared with the frequency difference. In the intermediate range, the spin echo time dependence is significantly modulated, and is not approximated by a sum of two exponential decays. We can readily see this from the sine and cosine terms in the time dependence of the spin echo amplitude by writing equation (49) at time $t = 2\tau$:

$$\begin{aligned} E(2\tau) = {} & \mathrm{i}[\, j\,\mathrm{e}^{-ct} + (2g + j - 1)\,\mathrm{e}^{ct} + 2f\sin dt \\ & - 2(g + j)\cos dt]\,\mathrm{e}^{-\phi_2 t} \end{aligned} \tag{53}$$

For zero exchange rate, $f = 0$ and $g + j = 0$; the magnitudes of these quantities increase with increasing exchange rate, become greatest when $\frac{1}{2}\pi(1/\tau_a + 1/\tau_b) \approx |\omega_a - \omega_b|$, decrease with further increase in exchange rate, and approach zero as the exchange rates approach infinity. Also, when the exchange rate is large compared with the Larmor frequency difference, the spin echo amplitude closely approximates an exponential decay with a T_2 value given by equation (46). Calculations[5] of the decay curves show that when T_{2a}, $T_{2b} \approx \infty$, the shapes are closely approximated by exponential decays under the condition $|\omega_a - \omega_b| \ll 1/\tau_a$, $1/\tau_b$. In the intermediate range of $1/\tau_a$ and $1/\tau_b$ values, the decay curves are not exponential, and are modulated. If we define T_{2E}* as the time required for the curve to decay from its initial value at $t = 0$ to 1/e of this value, T_{2E}* passes through a minimum when $\frac{1}{2}\pi(1/\tau_a + 1/\tau_b) \approx |\omega_a - \omega_b|$.

5.3 The Spin Echo Amplitudes in Carr–Purcell Pulse Sequences

The spin echo for the special mathematical case, equation (52), when evaluated at time $t = 2\tau$ and compared with the single pulse signal, includes the extra term $(\omega_a - \omega_b)^2\tau^2$; this suggests that the contribution of the Larmor frequency difference to the transverse relaxation can be eliminated by using the Carr–Purcell sequence with sufficiently small pulse separations. The effect of each 180° pulse in the sequence can be calculated by using the complex conjugate of the transverse magnetization at the time of the pulse as the initial condition for the solutions, equations (12a) and (12b), of equations (11a) and (11b) for the time after the pulse. We might expect that the plot of the peak spin echo amplitudes is a sum of two exponential decays or, one exponential when the exchange rates are rapid. Much theoretical work has been done for various cases to obtain exchange rates from Carr–Purcell sequences,[7–9] and complete solutions for the two-site case are available.[8,9] Generally, computer-assisted calculations are needed to analyze experimental data. From the complex preexponential coefficients, we may anticipate that alternations in echo amplitudes could occur along the pulse sequence, especially in cases where the exchange rates and the Larmor frequency differences are of the same order of magnitude. The early echoes observed in Carr–Purcell sequences frequently show amplitude alternations. This behavior may be related to the alternations in consecutive spin echo amplitudes for powder pattern distributions of Larmor frequencies, calculated in Section 6.2.1 of this article. These alternations die away with a time constant that is comparable to the reciprocal of the exchange rate. The shift of the peak of the first echo, and presumably other odd-numbered echoes, to 'short' times may also be related to this.

6 'MULTIPLE SITE' CHEMICAL EXCHANGE AND TRANSVERSE RELAXATION

6.1 Gaussian Frequency Distribution

The mathematical treatment of the general multiple-site case is extremely complicated. However, the case of a continuous Gaussian distribution[10] of Larmor frequencies ω_j is tractable mathematically and computationally. The results parallel those of the two-site case and are instructive. If the nucleus exchanges among the ω_j values so that the covariance function

$$\langle \Delta\omega(t)\Delta\omega(t + \tau)\rangle = \langle \Delta\omega(t)^2\rangle\,\mathrm{e}^{-\tau/\tau_\mathrm{e}} \tag{54}$$

is obeyed then the decay curve following a single pulse is

$$F_2(t) = \exp\left[-\sigma^2\tau_\mathrm{e}^2\left(\mathrm{e}^{-t/\tau_\mathrm{e}} + \frac{t}{\tau_\mathrm{e}} - 1\right)\right] \tag{55}$$

where σ is the rms value of $\Delta\omega = \omega_j - \omega_0$ and τ_e is an exchange time. The signal following the second pulse that is applied at time $t = \tau$ is

$$F_2(t\rangle\tau) = \exp\left[-\sigma^2\tau_e^2\left(\frac{t}{\tau_e} - 3 - e^{-t/\tau_e} + 2e^{-\tau/\tau_e} + 2e^{-(t-\tau)/\tau_e}\right)\right] \quad (56)$$

and the maximum value of this signal occurs at time

$$t_m = \tau_e[\ln(2e^{\tau/\tau_e} - 1)] \quad (57)$$

Equation (57) shows that $t_m < 2\tau$. For very slow exchange, t_m is nearly equal to 2τ. However, $t_m = 1.4899\tau$ when $\tau_e = \tau$; this is a large shift from the expected value, 2τ. The conventional spin echo amplitude curve is given by equation (56) evaluated at time $t = 2\tau$:

$$E(2\tau) = \exp\left[-\sigma^2\tau_e^2\left(\frac{2\tau}{\tau_e} - 3 - e^{-2\tau/\tau_e} + 4e^{-\tau/\tau_e}\right)\right] \quad (58)$$

We can examine the time dependences of these functions by defining T_2^* as the time required for equation (55) to decay from its initial value at $t = 0$ to 1/e of this value, and T_{2E}^* as the comparable quantity for equation (58). When the exchange rate is fast (i.e., $\sigma\tau_e \ll 1$), both of the above curves approximate exponential decays with decay rates

$$\frac{1}{T_2^*} \approx \frac{1}{T_{2E}^*} = \sigma^2\tau_e \quad (59)$$

This result agrees with equation (46) for the two-site case. Also, in qualitative agreement with the two-site case, with changing exchange rate, T_{2E}^* passes through a minimum at $\sigma\tau_e \approx 1$. With decreasing exchange rate, the decay curve $E(2\tau)$ becomes

$$E(2\tau) \approx \exp\left(-\frac{2}{3}\frac{\sigma^2\tau^3}{\tau_e}\right) \quad (60)$$

below the T_{2E}^* minimum. However, equation (60) shows that T_{2E}^* becomes equal to $(12\tau_e/\sigma^2)^{1/3}$ instead of the value τ_e that is found in the two-site case. This dependence of the attenuation of the spin echo amplitude on τ^3 is analogous to that of nuclei diffusing[11] in a gradient in $\boldsymbol{B}_0$ (see ***Diffusion Measurements by Magnetic Field Gradient Methods***). When a molecule diffuses, there is a Gaussian probability distribution of changes in Larmor frequency; the width of this distribution increases in time. Also, with decreasing exchange rate, T_2^* monotonically decreases and asymptotically approaches the constant value $\sigma^{-1}\sqrt{2}$.

6.2 Powder Pattern Frequency Distribution

6.2.1 'Rotational Diffusion' Site Exchange

A logical choice for ω_j values is that which appears in NMR magnetic dipolar splitting and nuclear quadrupolar splitting:

$$\omega_j = C(3\cos^2\theta_j - 1) \quad (61)$$

in which C is the splitting constant. For a 'powder' sample, the values of P_j are directly proportional to $\sin\theta_j$ and the number of different sites is very large. The resultant mean square value of ω_j is $\frac{4}{5}C^2$.

The rotational diffusion case[12] allows direct exchanges only between sites with adjacent θ values and thus between adjacent frequencies. The signal following one pulse can be computed[12] by solving the differential equation

$$\frac{\partial A}{\partial t} = (6\tau_e)^{-1}\cot\theta\frac{\partial A}{\partial\theta} + (6\tau_e)^{-1}\frac{\partial^2 A}{\partial\theta^2} + iC(3\cos^2\theta - 1) \quad (62)$$

as a function of time using the initial condition $A_j(0, \theta_j) = P_j$. The NMR signal following the second pulse is computed by using the complex conjugate $A_j^*(\tau, \theta_j)$ as the initial condition for equation (62). As in the Gaussian case, T_2^* is the time at which the signal following one pulse has 1/e times the value at time $t = 0$; T_{2E}^* is the value of 2τ at which the NMR signal following the second pulse has 1/e times the value at $2\tau = 0$. When the exchange is fast (i.e., $C\tau_e \ll 1$), both the T_2 and T_{2E} curves approximate exponential decays with decay rates

$$\frac{1}{T_2^*} \approx \frac{1}{T_{2E}^*} = \tfrac{4}{5}C^2\tau_e \quad (63)$$

in agreement with equation (46) for the two-site case and equation (59) for the Gaussian case. Also in agreement with these cases, with decreasing exchange rate, T_{2E}^* passes through a minimum at $(\frac{4}{5})^{1/2}C\tau_e \approx 1$. With further decreases in exchange rate, the spin echo amplitude asymptotically approaches

$$E(2\tau) \approx \exp\left(-\frac{8}{15}\frac{C^2\tau^3}{\tau_e}\right) \quad (64)$$

so that T_{2E}^* becomes equal to $(15\tau_e/C^2)^{1/3}$. Simultaneously, T_2^* decreases monotonically and approaches the constant value $T_2^* = 1.46/C$.

The computed NMR signals in multiple pulse sequences[12] show several interesting features. When pulses are applied at times $t = 0$, τ, 3τ, 5τ, etc., the amplitudes calculated at times 2τ, 4τ, 6τ, etc., increase when the number of pulses per unit time increases. The result is analogous to that for liquid molecules diffusing in a magnetic field gradient.[11] In addition, the odd-numbered spin echoes in a given multipulse sequence, calculated at the above times, are of smaller amplitude than the even-numbered echoes. This amplitude alternation decreases with succeeding spin echoes. The time constant for this decay appears to be equal to τ_e. An alternation of spin echo amplitudes in multiple pulse sequences is also predicted and observed[11] for liquid molecules flowing in a magnetic field gradient (see ***Diffusion and Flow in Fluids***).

Also, as calculation of the NMR signal shapes for three pulses shows, this formalism predicts that the peak of the first spin echo, as in the Gaussian case, is shifted to times shorter than 2τ. This shift appears to be given approximately by equation (57), which was derived for the Gaussian case.

However, the peak value of the calculated second spin echo appears at the expected time, $t = 4\tau$. This predicted shift of the first echo peak but not of the second is indeed observed experimentally[12,13] in aqueous heterogeneous systems.

6.2.2 Random Site Exchange

We can predict the NMR behavior of systems with other chemical exchange dynamics[14] by generalizing equations (11a) and (11b) to allow direct exchange among many types of sites that are characterized by different frequencies. To emphasize the contribution of the Larmor frequency distribution to transverse relaxation, we set the T_2 values in equation (10c) equal to infinity.

The total transverse magnetization of a system of N types of sites is

$$M_+(t) = \mathrm{i}M_0 \sum_{j=1}^{N} P_j A_j(t, \omega) \tag{65}$$

where P_j is the occupation probability of sites of type j normalized so that

$$\sum_{j=1}^{N} P_j = 1 \tag{66}$$

We express the time dependences of the A_j by the set of N coupled differential rate equations

$$\frac{\partial A_j}{\partial t} = \mathrm{i}\omega_j - \frac{A_j}{\tau_j} + \sum_{\substack{j=1 \\ k\neq j}}^{N} \frac{A_k}{\tau_{kj}}, \quad j = 1, 2, \ldots, N \tag{67}$$

where ω_j is the difference frequency (compared with the average frequency) for j-type sites, τ_j is the average lifetime of a nucleus in j-type sites, and $1/\tau_{kj}$ is the average rate at which nuclei in k-type sites move to j-type sites.

To solve the set of N equations in equation (67), we must specify the frequencies (ω_j values), occupation probabilities (P_j values), and exchange probabilities (τ_j and τ_{kj} values). We choose the powder pattern frequencies as described by equation (61) and P_j values that are directly proportional to $\sin\theta_j$. The exchange probabilities implicit in the preceding sections of this article represent one extreme case. The opposite extreme case is to allow direct exchanges between sites of all the different frequencies. This case more closely corresponds to the two-site case in that the individual exchange events can involve large changes in Larmor frequency. To set up the exchange probabilities, we use the principle of detailed balance, which requires that the total number of exchanges per second between sites j and k is directly proportional to the product P_jP_k. Then, if we define $1/\tau_e$ as the average rate for nuclei to leave the sites that they occupy, we obtain

$$\frac{1}{\tau_j} = V \sum_{\substack{j=1 \\ k\neq j}}^{N} P_k = V(1 - P_j) \tag{68}$$

$$\frac{1}{\tau_{kj}} = V P_j \tag{69}$$

where

$$V = \left[\tau_e\left(1 - \sum_{j=1}^{N} P_j^2\right)\right]^{-1} \tag{70}$$

When N is very large, $V = 1/\tau_e$.

The signal following one pulse[14] can be calculated by solving equation (67) as a function of time using the initial condition $A_j(0, \omega_j) = P_j$. The T_{2E} curves[13] can be computed by using the complex conjugate $A_j{*}(\tau, \omega_j)$ as the initial condition after the second pulse in evaluating the signal at time τ after the second pulse. When the exchange is fast (i.e., $C\tau_e \ll 1$), both the T_2 and T_{2E} curves approximate exponential decays with decay rates

$$\frac{1}{T_2^*} \approx \frac{1}{T_{2E}^*} = \tfrac{4}{5}C^2\tau_e \tag{71}$$

in agreement with equation (46) for the two-site case and with the Gaussian and rotational diffusion cases. Also in agreement with the two-site case, with decreasing exchange rate, $T_{2E}{*}$ passes through a minimum at $(\frac{4}{5})^{1/2}C\tau_e \approx 1$ and approaches τ_e when $C\tau_e \gg 1$. This result represents a much stronger dependence of the spin echo attenuation on exchange rate than in the Gaussian and rotational diffusion cases. Simultaneously, $T_2{*}$ decreases monotonically and approaches the constant value $T_2{*} = 1.46/C$.

In calculations of the NMR signals for the three-pulse case, the peak of the first spin echo is shifted to times smaller than 2τ, while the second echo peak remains at time 4τ. The shapes of the signals and the effects of changes in exchange rates differ between the present case and the preceding cases, and measurements of them allow us to determine which case better describes the sample under consideration.

7 PREFERENTIAL ORIENTATION, EXCHANGE, AND ORDER IN AQUEOUS HETEROGENEOUS SYSTEMS

In aqueous heterogeneous systems[14,15] such as biological tissue, biopolymer gels, polyelectrolyte solutions, clay–water gels, etc., the water molecule or a hydrated ion such as sodium can be located in the bulk liquid or at the solid/liquid interface. The nonspherical bonding and electric charge distribution (electric dipole and quadrupole moments) strongly affect the motions and arrangements of water molecules at the interface. When a water molecule is at the solid surface, its motion is slowed down, and some orientations with respect to the local surface plane are more probable than others. This preferential orientation due to the nonspherical interaction causes different rotational rates about different molecular axes. The structure of the interfacial water is different from that of bulk water because this water interacts differently with the relatively immobile solid material compared to other rapidly moving water molecules. At each allowed molecular orientation at the surface, there is a different magnetic dipolar interaction of the protons (H_2O) or nuclear quadrupolar interaction of the deuterons (D_2O). The water molecules not only occupy the various site environments at the interface, but they migrate

among them and also into the bulk liquid away from the interface. This rapid chemical exchange enables all of the water molecules to experience the interfacial environment. Consequently, the spectral densities $J_h(\omega)$ that determine NMR relaxation phenomena are influenced by the effects on the correlation functions caused by the motions and local structure of the interface and the exchange between the bulk and interfacial sites.

The correlation functions of the water in such a heterogeneous system can be written[14] as the sum over the different j environments:

$$\langle F_h(t)F_h^*(t+\tau)\rangle = \sum_j P_j \langle F_{hj}(t)F_{hj}^*(t+\tau)\rangle \qquad (72)$$

where the sum of the occupation probabilities P_j is unity. We now assume, with good evidence, that all local permitted molecular reorientations and all local chemical exchange rates are rapid compared with the Larmor frequency ω_0. Then, at times τ that are long compared with $1/\omega_0$, nuclei that were in a given j at time t are now distributed among all the different j sites in accordance with P_j, and $\langle F_{hj}{}^*(t+\infty)\rangle = \langle F_h{}^*(t)\rangle$. Also, for each of these nuclei, the value of $F_{hj}{}^*(t+\infty)$ is independent of the value of the original $F_{hj}(t)$, and equation (72) can be written as

$$\begin{aligned}\langle F_h(t)F_h^*(t+\infty)\rangle &= \langle F_h(t)\langle F_h^*(t+\infty)\rangle\rangle \\ &= \langle F_h(t)\rangle\langle F_h^*(t+\infty)\rangle \\ &= \langle F_h(t)\rangle\langle F_h^*(t)\rangle \end{aligned} \qquad (73)$$

In a bulk liquid, the values of $\langle F_h(t)\rangle$ and $\langle F_h{}^*(t+\infty)\rangle$ at such long times are zero. However, preferential molecular orientation at the interface can result in nonzero values.

Let us temporarily assume that the surface is an infinite plane, so that the interface is planar. The orientation of the interface in $\boldsymbol{B}_0$ is defined by the 'director', which is normal to the surface. For simplicity, let the molecular orientation distribution be axially symmetric about the director. If the orientation of the director in $\boldsymbol{B}_0$ is given by the polar and azimuthal angles θ' and ϕ', and the orientation of the nuclear spin interaction vector with respect to the director is given by the polar and azimuthal angles θ'' and ϕ'', then $\langle F_0(t)\rangle = \langle 3\cos^2\theta - 1\rangle$ is given by

$$\langle 3\cos^2\theta - 1\rangle = \tfrac{1}{2}(3\cos^2\theta' - 1)\langle 3\cos^2\theta'' - 1\rangle \qquad (74)$$

The last term on the right-hand side of equation (74) expresses the preferential orientation. The correlation function is then given by

$$\langle F_h(t)F_h^*(t+\tau)\rangle = \langle F_h(t)F_h^*(t)\rangle \times\left(P_p\,\mathrm{e}^{-\tau/\tau_{cp}} + \sum_{j=1}^{p-1} P_j\,\mathrm{e}^{-\tau/\tau_{cj}}\right) \qquad (75)$$

where

$$P_p + \sum_{j=1}^{p-1} P_j = 1 \qquad (76a)$$

$$P_p = \frac{\tfrac{1}{4}(3\cos^2\theta' - 1)^2\langle 3\cos^2\theta'' - 1\rangle_{av}^2}{\langle F_0(t)F_0^*(t)\rangle} \qquad (76b)$$

The τ_{cj} are short correlation times that result from the rapid molecular motions, including exchange. The correlation time associated with the preferential orientation, τ_{cp}, is infinite in the present case.

When τ_{cp} is extremely long, its contributions to $J_1(\omega_0)$ and $J_2(2\omega_0)$ in the relaxation times given in equations (4a) and (4b) are extremely small and can be neglected. However, the $J_0(0)$ term in equation (4b) is incorrect, and the contribution of the terms that involve τ_{cp} to transverse relaxation must be calculated differently. The term $3\cos^2\theta - 1$ in equation (74) is $F_0(t)$, and a nonzero average value causes a residual magnetic dipolar or nuclear quadrupolar splitting in the NMR spectrum due to the preferential orientation. From equation (61), this residual splitting is

$$\omega' = \tfrac{1}{2}C(3\cos^2\theta' - 1)\langle 3\cos^2\theta'' - 1\rangle \qquad (77)$$

where C is the splitting constant for a stationary molecule. At any instant of time, a certain number of water molecules are preferentially oriented by the interface, so that these molecules have a certain nonzero value of $\langle 3\cos^2\theta'' - 1\rangle$ and the remainder of the molecules has a zero value for this quantity. We assume that the value of $\langle 3\cos^2\theta'' - 1\rangle$ for the instantaneously preferentially oriented water molecules and the number of these molecules are independent of the number of other water molecules. When rapid exchange between these two environments occurs, all of the water experiences preferential orientation, as referred to the director, for a fraction F of the time. The value of F is the fraction of the water molecules at any instant that is preferentially oriented, and the value of ω' is

$$\omega' = C'(3\cos^2\theta' - 1) \qquad (78)$$

where

$$C' = \tfrac{1}{2}FC\langle 3\cos^2\theta'' - 1\rangle \qquad (79)$$

The effective splitting constant C' depends on the surface-to-volume ratio of the water.

In addition to the surface-to-volume ratio, the value of C' depends on the geometry of the surface. If the surface is that of the circumference of a cylinder and if rapid exchange occurs over all of the surface of the cylinder, the value of C' is one-half of that for the same surface on a plane, and the direction of the director is along the axis of the cylinder.

A system that contains many parallel planes or cylinders with uniform distribution of water will have a doublet NMR spectrum with a splitting that varies as $3\cos^2\theta' - 1$. This is observed in many ordered systems such as water distributed among parallel fibers, water among parallel smectite clay platelets (smectite clay minerals are comprised of 1 nm thick aluminosilicate sheets that are many micrometers or even millimeters in length and width), and lyotropic liquid crystals.

The doublet splitting constant depends on the degree of order in the system. If the system has a large number of cylinders that are not parallel and if rapid exchange occurs among all of them, the value of C' is reduced[16] by this disorder as described by the second-rank order parameter

$$S = \tfrac{1}{2}(3\langle\cos^2\theta_{C1C2}\rangle - 1) \qquad (80)$$

where θ_{C1C2} is the angle between the axes of a pair of cylinders C1 and C2. When all the cylinders are parallel, $S = 1$ and the splitting constant is maximum. However, if the cylinders are randomly oriented (i.e., a powder), $S = 0$ and there is no spectral splitting. A similar statement applies to a system of sheets.

The above illustration describes the extreme case of rapid exchange and local disorder. Another case is local order and global disorder as occurs with a powder made of crystallites. A crystallite may be a domain in which there is perfect order. If the molecules are constrained in individual domains, the NMR signal is the superposition of the signals of all the domains, i.e., a powder pattern. This signal will be changed if molecules are exchanged among the domains with different orientations in $\boldsymbol{B}_0$. This exchange will affect the transverse relaxation, and the methods described in Section 6 of this article can be used to calculate the NMR signals for various assumed models of order/disorder. In these calculations, the ω_j values are given by equations (78) and (79). If there is less than perfect order in the domains or if the degree of order is changed, the splitting constant must be reduced by the factor in equation (80). Also, if the water content is changed, the splitting constant is changed in accordance with equation (79). The exchange lifetime τ_e will depend on the size of a domain and on the diffusion coefficient of the water. Changes in the domain size or internal order caused by purely physical treatment of the sample, without any change in chemical composition, will cause changes in the transverse NMR relaxation behavior.

These phenomena are observed in deuteron NMR measurements on aqueous biopolymer gels[17] and clay–water systems.[13,14] Values of τ_e are obtained by using the methods of Section 6 to analyze the data, and the splitting constants and the domain sizes are found. Also, when a hydrated ion such as sodium is at an interface, the distortion of the hydration atmosphere causes a nuclear quadrupolar coupling that is described by a quadrupolar coupling constant and the orientation of the director. The transverse relaxation of sodium in linear polyelectrolyte solutions is quantitatively explained[16] by the scheme described above for the NMR signals of water.

8 EFFECTS OF DIFFUSIVE EXCHANGE IN HETEROGENEOUS SYSTEMS

In the preceding sections, chemical exchange has been modeled so that all nuclei in a given site environment have the same time-independent exchange or transition probability to move to different environments. However, this picture fails to describe completely the spatial aspects of the exchange process.[18–20] For example, consider the case of water in heterogeneous and biological systems. The probability per unit time that a given molecule in the interface leaves the interface may be the same for all the interfacial molecules. An interfacial molecule exchanges places with a neighboring bulk water molecule, and the interface is only a molecular layer or two in thickness. Therefore, when the bulk water is many molecular diameters in thickness, the lifetime in the bulk for a molecule that is next to the interface can be much shorter than that of a molecule that is many molecular diameters away from the interface. In order for the latter molecule to be able to exchange with the interface, it first must diffuse to the interface, taking some time and lowering its effective exchange rate. This is not a simple diffusion problem, because the mobility of water molecules in the interface is less than that in the bulk. Also, because of proximity, a molecule that has just left the interface is likely to reenter[18] the interface before a molecule away from the interface has a chance to enter the interface. The exchange rate of such molecules is thus enhanced. This can lead to some relaxation behavior that is qualitatively different from the simple exchange picture.[18] Also, the occupation probability for a diffusing molecule to occupy a given volume of space is a sum of exponential decays. However, the major term of this probability is generally a single exponential. Thus, the simple exchange view provides a convenient framework that is adequate, in most cases, to formulate the effects of molecular migration on NMR relaxation and interpret experimental results.

9 RELATED ARTICLES

Brownian Motion and Correlation Times; Chemical Exchange Effects on Spectra; Diffusion and Flow in Fluids; Diffusion Measurements by Magnetic Field Gradient Methods; Dynamics of Water in Biological Systems: Inferences from Relaxometry; Magnetization Transfer and Cross Relaxation in Tissue; Magnetization Transfer between Water and Macromolecules in Proton MRI; Molecular Motions: T_1 Frequency Dispersion in Biological Systems; Quadrupolar Nuclei in Liquid Samples; Relaxation Theory: Density Matrix Formulation; Relaxometry of Tissue; Sodium-23 NMR; Well Logging.

10 REFERENCES

1. A. Abragam, *The Principles of Nuclear Magnetism*, Clarendon Press, Oxford, 1961.
2. H. Wennerström, *Mol. Phys.*, 1972, **24**, 69.
3. J. R. Zimmerman and W. E. Brittin, *J. Phys. Chem.*, 1957, **61**, 1328.
4. H. M. McConnell, *J. Chem. Phys.*, 1958, **28**, 430.
5. D. E. Woessner, *J. Chem. Phys.*, 1961, **35**, 41.
6. H. Winkler and D. Michel, *Adv. Colloid Interface Sci.*, 1985, **23**, 149.
7. A. Allerhand and H. S. Gutowsky, *J. Chem. Phys.*, 1964, **41**, 2115.
8. J. P. Carver and R. E. Richards, *J. Magn. Reson.*, 1972, **6**, 89.
9. W. T. Sobol, *Magn. Reson. Med.*, 1991, **21**, 2.
10. J. R. Klauder and P. W. Anderson, *Phys. Rev.*, 1962, **125**, 912.
11. H. Y. Carr and E. M. Purcell, *Phys. Rev.*, 1954, **94**, 630.
12. D. E. Woessner, B. S. Snowden, Jr., and G. H. Meyer, *J. Chem. Phys.*, 1969, **51**, 2968.
13. D. E. Woessner, B. S. Snowden, Jr., and G. H. Meyer, *J. Colloid Interface Sci.*, 1970, **34**, 43.
14. D. E. Woessner, *Mol. Phys.*, 1977, **34**, 899.
15. K. J. Packer, *Phil. Trans. R. Soc. Lond. B*, 1977, **278**, 59.
16. B. Halle, H. Wennerström, and L. Piculell, *J. Phys. Chem.*, 1984, **88**, 2482.
17. D. E. Woessner and B. S. Snowden, Jr., *Ann. N. Y. Acad. Sci.*, 1973, **204**, 113.
18. B. Halle, *Mol. Phys.*, 1984, **53**, 1427.
19. P. S. Belton and B. P. Hills, *Mol. Phys.*, 1987, **61**, 999.
20. B. Halle and P.-O. Westlund, *Mol. Phys.*, 1988, **63**, 97.

Biographical Sketch

Donald E. Woessner. *b* 1930. A.B., 1952, Ph.D. (supervisor Herbert Gutowsky), 1957, Chemistry, University of Illinois, USA. Postdoctoral work at University of Illinois (with Herbert Gutowsky). Successively senior research chemist, research associate, senior research associate, Mobil Research and Development Corporation, Dallas, TX. Adjunct Assistant Professor of Radiology, The University of Texas Southwestern Medical Center at Dallas, 1992–present. Approx. 72 publications. Research specialties: NMR relaxation and molecular motions in liquids, and relationships of NMR relaxation of hydrogen and ionic nuclei to motions, structure and order in aqueous heterogeneous systems and biological tissue.

Relaxation Mechanisms: Magnetization Modes

Daniel Canet

Université H. Poincaré, Vandoeuvre-Nancy, France

1	Introduction	1
2	The Density Operator for Treating the Evolution of a Spin System	1
3	Construction of Magnetization Modes and Their Relation to Observable Quantities	3
4	Evolution of Magnetization Modes Under Relaxation Phenomena	5
5	Related Articles	7
6	References	7

1 INTRODUCTION

The concept of magnetization modes is related to longitudinal relaxation (spin–lattice relaxation) of weakly coupled spin-$\frac{1}{2}$ systems, possibly including subsets of magnetically equivalent nuclei. They are useful in two respects:

1. they can be easily associated with observable quantities;
2. they lead to simplifications (factorization) in the kinetic equations describing the evolution of the system under longitudinal relaxation.

Magnetization modes were introduced in 1975 by Werbelow and Grant[1] in the context of ^{13}C relaxation studies of methine, methylene, and methyl moieties, and were discussed thoroughly by these authors in a review article published in 1977.[2] An attempt to rationalize the construction procedures of magnetization modes as well as their evolution and detection features was provided in an article by Canet in 1989.[3] Grant and colleagues[4] published in 1991 a review about relaxation of coupled nuclear spins and molecular motions in liquids, with emphasis on magnetization modes in the $^{13}CH_2$ grouping. Finally, magnetization modes have been generalized into 'magnetization transfer modes',[5] which are adapted to selective two-dimensional experiments of the NOESY type.

For the sake of clarity and simplicity, two simple spin-$\frac{1}{2}$ systems will be discussed here in some detail, namely the AX spin system (two weakly J-coupled spins) and the AX_2 spin system (a spin A weakly J-coupled with two magnetically equivalent spins X and X′). An isotropic medium (liquid state) will be assumed most of the time, although molecules partially oriented in liquid crystal matrices will be alluded to in some instances.[6] Let us first recall that it is a common practice to describe the evolution of the longitudinal magnetization (denoted by $\langle \hat{I}_z \rangle$, the angular brackets specifying the expectation value of the operator $\hat{I}_z$) by means of the Bloch equation

$$\frac{\mathrm{d}\langle \hat{I}_z \rangle}{\mathrm{d}t} = -R_1(\langle \hat{I}_z \rangle - I_{\mathrm{eq}}) \tag{1}$$

where R_1 is the longitudinal relaxation rate (the inverse of the longitudinal relaxation time T_1) and I_{eq} the equilibrium magnetization. Equation (1) implies a monoexponential recovery, and, although it may often represent a very good approximation, it is strictly valid for a single spin-$\frac{1}{2}$ subjected to randomly fluctuating magnetic fields (as far as spins $\frac{1}{2}$ are considered). As soon as the system includes two spin-$\frac{1}{2}$ nuclei, A and X, mutually interacting by dipolar coupling (the latter being modulated by molecular reorientation and being zero on average), the relevant longitudinal magnetizations no longer exhibit monoexponential recoveries, and their evolution is governed by the Solomon equations

$$\left.\begin{aligned} \frac{\mathrm{d}\langle \hat{I}_{\mathrm{A},z} \rangle}{\mathrm{d}t} &= -R_1^{\mathrm{A}}(\langle \hat{I}_{\mathrm{A},z} \rangle - I_{\mathrm{A,eq}}) - \sigma_{\mathrm{AX}}(\langle \hat{I}_{\mathrm{X},z} \rangle - I_{\mathrm{X,eq}}) \\ \frac{\mathrm{d}\langle \hat{I}_{\mathrm{X},z} \rangle}{\mathrm{d}t} &= -R_1^{\mathrm{X}}(\langle \hat{I}_{\mathrm{X},z} \rangle - I_{\mathrm{X,eq}}) - \sigma_{\mathrm{AX}}(\langle \hat{I}_{\mathrm{A},z} \rangle - I_{\mathrm{A,eq}}) \end{aligned}\right\} \tag{2}$$

where, in addition to the specific relaxation rates R_1^{A} and R_1^{X}, there exists a coupling term σ_{AX}, known as the cross-relaxation rate. These three rates can be expressed in terms of structural and motional parameters as explained below. Although, as will be seen later, equation (2) do not fully account for longitudinal relaxation in a two-spin system, the two quantities $\langle \hat{I}_{\mathrm{A},z} \rangle - I_{\mathrm{A,eq}}$ and $\langle \hat{I}_{\mathrm{X},z} \rangle - I_{\mathrm{X,eq}}$ are what will be called magnetization modes. This is because A and X are supposed to be weakly coupled, meaning that the observables (transitions) belong unambiguously either to A or to X and that it is possible by appropriate read pulses to monitor either $\langle \hat{I}_{\mathrm{A},z} \rangle$ or $\langle \hat{I}_{\mathrm{X},z} \rangle$.

In spite of the evident biexponential character of the evolutions implied by equation (2), a familiar exception must be mentioned, concerning the evolution of longitudinal magnetization of spin A (e.g., ^{13}C) while spin X (e.g., ^{1}H) is irradiated continuously for decoupling purposes. The second of equation (2) ceases to be valid, since the driving term of the decoupling field should be added. Anyhow, the fact that X is completely saturated can be accounted for in the first of these equations by putting $\langle \hat{I}_{\mathrm{X},z} \rangle \equiv 0$. The monoexponential behavior of $\langle \hat{I}_{\mathrm{A},z} \rangle$ becomes apparent on reformulating the relevant equation as

$$\frac{\mathrm{d}\langle \hat{I}_{\mathrm{A},z} \rangle}{\mathrm{d}t} = -R_1^{\mathrm{A}}(\langle \hat{I}_{\mathrm{A},z} \rangle - I_{\mathrm{A,stat}}) \tag{3}$$

where $I_{\mathrm{A,stat}}$ is the 'new' equilibrium value (or stationary state value) of $\langle \hat{I}_{\mathrm{A},z} \rangle$ when X transitions are continuously irradiated:

$$I_{\mathrm{A,stat}} = I_{\mathrm{A,eq}}\left(1 + \frac{\gamma_{\mathrm{X}}}{\gamma_{\mathrm{A}}}\frac{\sigma_{\mathrm{AX}}}{R_1^{\mathrm{A}}}\right) \tag{4}$$

γ_{X} and γ_{A} being the gyromagnetic ratios. It should be emphasized that this stationary magnetization, different from the equilibrium magnetization, is a manifestation of the well-known nuclear Overhauser effect.[7,8] Some caution must be exercised regarding the monoexponentiality implied by equation (3); for instance, this feature no longer strictly holds in an AX_2 system, when X transitions are irradiated, owing to the necessity of accounting for additional magnetization modes.

2 THE DENSITY OPERATOR FOR TREATING THE EVOLUTION OF A SPIN SYSTEM

The general approach for treating relaxation phenomena[9] rests on the Liouville–von Neumann equation, which indicates in a compact and formal way how the so-called reduced density operator $\hat{\sigma}$ evolves:

$$\frac{\mathrm{d}\hat{\sigma}}{\mathrm{d}t} = \mathrm{i}[\hat{\sigma}, \hat{\mathcal{H}}(t)] \tag{5}$$

where the square brackets denote the commutator. For the systems considered here, the total Hamiltonian can be decomposed according to

$$\hat{\mathcal{H}}(t) = \hat{\mathcal{H}}_0 + \hat{\mathcal{H}}'(t) \tag{6}$$

$\hat{\mathcal{H}}_0$ is the 'static' Hamiltonian containing the Zeeman term (which includes the chemical shift information) and the J coupling interaction term. $\hat{\mathcal{H}}'(t)$ embodies all time-dependent interactions responsible for relaxation phenomena. The interest of the density operator stems from the property that any quantity $\langle\hat{G}\rangle$ can be calculated at any time through the relation

$$\langle\hat{G}\rangle = \mathrm{Tr}(\hat{G}\hat{\sigma}) \tag{7}$$

where Tr stands for the trace (sum of all diagonal elements of the matrix associated with $\hat{G}\hat{\sigma}$). For instance, the Bloch equation or the Solomon equations, which relate to the evolution of magnetization modes encountered until now, could be derived in this way, provided that equation (5) has been solved. This is usually done by a perturbation calculation (whose result is outlined below), starting from the equilibrium value of $\hat{\sigma}$:

$$\hat{\sigma}_{\mathrm{eq}} = \frac{1}{2^n}\left(\hat{E} + \sum_{k=1}^{n} \Delta_k \hat{I}_{kz}\right) \tag{8}$$

Equation (8) has been written for a system of n spin-$\frac{1}{2}$ nuclei; Δ_k is a constant proportional to the gyromagnetic ratio of nucleus k and $\hat{E}$ is the identity operator. It should be recalled that the density matrix, the matrix associated with the density operator, is diagonal when it is constructed on the eigenbasis of $\hat{\mathcal{H}}_0$ and when the magnetization does not involve any transverse component; this is the case for the matrix associated with $\hat{\sigma}_{\mathrm{eq}}$. In general, the evolution of the density operator, when representative of longitudinal magnetization, can be written as[10]

$$\frac{\mathrm{d}\hat{\sigma}}{\mathrm{d}t} = -\sum_{r,r'}\sum_{m=-2}^{2} [\hat{A}_r^{m\dagger}, [\hat{A}_{r'}^{m}, \hat{\sigma} - \hat{\sigma}_{\mathrm{eq}}]]\mathcal{J}^{rr'}(m\omega_0) \tag{9}$$

where the symbol † indicates the transposed complex conjugate (adjoint). The spin operators $\hat{A}_r^m$, as well as the spectral density $\mathcal{J}^{rr'}(m\omega_0)$, originate from the Hamiltonian $\hat{\mathcal{H}}'(t)$, which, for all relaxation mechanisms involved in $\hat{\mathcal{H}}'(t)$ and labeled by the subscript r, can be expressed in the compact form

$$\hat{\mathcal{H}}'(t) = \sum_{r}\sum_{m=-2}^{2} \hat{A}_r^{m\dagger} F_r^m \tag{10}$$

F_r^m is a function of the space coordinates (in a broad sense), generally depending on molecular motions, and belongs to the class of irreducible tensors,[11] as do the spin operators $\hat{A}_r^m$ [among other things, irreducible tensors possess the property that $\hat{A}_r^{m\dagger} = (-1)^m \hat{A}_r^{-m}$]. Since an exhaustive list of these irreducible tensors, for the various relaxation mechanisms affecting spin-$\frac{1}{2}$ nuclei, has been given before,[3] only the three most common relaxation mechanisms will be considered here, the relevant $\hat{A}_r^m$ being given in Table 1.

The *intramolecular dipolar interaction* (that is, within the considered spin system) is by far the most informative, since it leads to dynamical and structural information. The F_r^m, as well as the $\hat{A}_r^m$, are of rank 2 (m actually goes from −2 to +2). Each F_r^m is simply the spherical harmonic $Y_2^m(\theta, \phi)$ multiplied by a constant and by the inverse of r_{AX}^3, where r_{AX} is the distance between the two interacting nuclei. The angles θ and ϕ involved in the spherical harmonics specify the orientation of r_{AX} with respect to a laboratory frame defined in such a way that the Z axis coincides with the direction of the static magnetic field $\boldsymbol{B}_0$. θ and ϕ are of course modulated by molecular reorientational processes.

The so-called *chemical shift anisotropy* (*CSA*) mechanism arises from the reorientation of the shielding tensor. The spin irreducible tensors $\hat{A}_r^m$ are of rank 1, so that the summation over m goes from −1 to +1. However, the 'space' irreducible tensors F_r^m are of rank 2, and, provided that the shielding tensor has axial symmetry, each can be expressed as the spherical harmonic $Y_2^m(\theta, \phi)$ multiplied by a factor involving constants and the quantity $B_0\,\Delta\sigma$. The molecular frame (x, y, z) is defined by the principal axes of the shielding tensor so that $\sigma_{xx} = \sigma_{yy}$ and $\Delta\sigma = \sigma_{zz} - \sigma_{xx}$. Again, θ and ϕ specify the orientation of the molecular z axis with respect to the laboratory frame defined above.

Table 1 Spin Operators in Irreducible Form, for the Three Essential Relaxation Mechanisms Affecting Spin-$\frac{1}{2}$ Nuclei[a]

Mechanism	$\hat{A}^{\pm 2}$	$\hat{A}^{\pm 1}$	$\hat{A}^{0}$
Random fields		$\mp\sqrt{\frac{1}{2}}\,\hat{I}_{\pm}$	$\hat{I}_z$
Chemical shift anisotropy		$\mp\sqrt{\frac{3}{8}}\,\hat{I}_{\pm}$	$\hat{I}_z$
Dipolar interaction	$\frac{1}{2}\hat{I}_{\mathrm{A},\pm}\hat{I}_{\mathrm{X},\pm}$	$\mp\frac{1}{2}(\hat{I}_{\mathrm{A},\pm}\hat{I}_{\mathrm{X},z} + \hat{I}_{\mathrm{A},z}\,\hat{I}_{\mathrm{X},\pm})$	$[4\hat{I}_{\mathrm{A},z}\hat{I}_{\mathrm{X},z} - (\hat{I}_{\mathrm{A},+}\hat{I}_{\mathrm{X},-} + \hat{I}_{\mathrm{A},-}\hat{I}_{\mathrm{X},+})]\sqrt{24}$

[a] $\hat{I}_{\pm}$ are raising and lowering operators, defined as $\hat{I}_x \pm \mathrm{i}\hat{I}_y$.

Other relaxation mechanisms (including spin–rotation, intermolecular dipolar interactions, and interactions with paramagnetic impurities) are usually gathered in the so-called *random field* mechanism, for which both $\hat{A}_r^m$ and F_r^m are of rank 1, the F_r^m including randomly fluctuating magnetic fields whose average value is zero.

The spectral densities of equation (9), for an *isotropic* medium, can be expressed as[12]

$$\mathcal{J}^{rr'}(m\omega_0) = \int_0^\infty \overline{F_r^{0*}(t)F_{r'}^0(0)} \exp(-\mathrm{i}m\omega_0 t)\,\mathrm{d}t \qquad (11)$$

where the asterisk indicates the complex conjugate. Since r and r' refer to relaxation mechanisms, $\mathcal{J}^{rr'}$ is an *autocorrelation* spectral density for $r = r'$ (same interaction; e.g., the dipolar interaction between two nuclei A and X), and is a *cross-correlation* spectral density for two different mechanisms ($r \neq r'$; e.g., with r standing for the dipolar interaction between A and X, and r' for the dipolar interaction between A and X′). This terminology comes from the correlation function $\overline{F_r^{0*}(t)F_{r'}^0(0)}$, where the overbar denotes an ensemble average. The dependence on the measurement frequency ω_0 must be understood as $m\omega_0 = \omega_{ab}$, which is the energy difference (expressed in rad s^{-1}) between two $\hat{\mathcal{H}}_0$ eigenstates $|a\rangle$ and $|b\rangle$, the latter being such that $\langle a|\hat{A}_{r'}^m|b\rangle \neq 0$. Examination of equation (11) leads to the conclusion that cross-correlation spectral densities vanish if the ranks of F_r^0 and of $F_{r'}^0$ are different. Consequently, cross correlation is possible only between (i) two different dipolar interactions sharing one spin and (ii) chemical shift anisotropy of a given spin and a dipolar interaction involving that spin.

In the case where F_r^m can be expressed as spherical harmonics of rank 2, equation (11) can be simplified to

$$\mathcal{J}^{rr'}(m\omega_0) = K^{rr'}\tilde{J}^{rr'}(m\omega_0) \qquad (12)$$

where $\tilde{J}^{rr'}$ is the so-called reduced spectral density involving the spherical harmonics $Y_2^0(\theta)$ (proportional to $3\cos^2\theta - 1$):

$$\tilde{J}^{rr'}(\omega) = \frac{5}{4}\int_{-\infty}^{\infty} \overline{[3\cos^2\theta(t) - 1][3\cos^2\theta'(0) - 1]} \times \exp(-\mathrm{i}\omega t)\,\mathrm{d}t \qquad (13)$$

The correlation function in equation (13) must be evaluated according to a motional model. As an example, for the simplest one that can be thought of (isotropic diffusional reorientation, which is characterized by a single characteristic time τ_c), the calculation of the above integral leads to

$$\tilde{J}(\omega) = \frac{2\tau_c}{1 + \omega^2\tau_c^2} \qquad (14)$$

which reduces to $2\tau_c$ under extreme narrowing conditions (fast motion; $\omega^2\tau_c^2 \ll 1$).

$K^{rr'}$ contains the constants alluded to before and the molecular quantities relevant to the considered relaxation mechanism. One has, for an autocorrelation dipolar spectral density (where μ_0 is the permeability of the vacuum and $\hbar$ Planck's constant divided by 2π)

$$K^{\mathrm{d(AX)}} = \frac{3}{5}\left(\frac{\mu_0}{4\pi}\right)^2 \frac{\gamma_A^2\gamma_X^2\hbar^2}{r_{AX}^6} \qquad (15)$$

for a cross-correlation spectral density

$$K^{\mathrm{d(AX,AX')}} = \frac{3}{5}\left(\frac{\mu_0}{4\pi}\right)^2 \frac{\gamma_A^2\gamma_X\gamma_{X'}\hbar^2}{r_{AX}^3 r_{AX'}^3} \qquad (16)$$

for an autocorrelation CSA spectral density

$$K^{\mathrm{csa(A)}} = \tfrac{2}{45}(\Delta\sigma_A)^2(\gamma_A^2 B_0^2) \qquad (17)$$

and for a CSA–dipolar cross-correlation spectral density (often dubbed an 'interference term')

$$K^{\mathrm{csa(A),d(AX)}} = -\frac{1}{5}\sqrt{\frac{2}{3}}\frac{\mu_0}{4\pi}\frac{\Delta\sigma_A B_0\gamma_A^2\gamma_X\hbar}{r_{AX}^3} \qquad (18)$$

Now, equation (9) can be recast in matrix form by means of the widely used Redfield equations,[13] which, for the case of longitudinal relaxation, amount to a set of simultaneous first-order kinetic equations governing the evolution of energy level populations:

$$\frac{\mathrm{d}P_a}{\mathrm{d}t} = \sum_b W_{ab}P_b \qquad (19)$$

where P_a is the deviation, with respect to its equilibrium value, of the population of the $\hat{\mathcal{H}}_0$ eigenstate $|a\rangle$ and where the familiar transition probabilities W_{ab} can be expressed as a function of the spectral densities introduced above:

$$\left.\begin{aligned} W_{ab}(a \neq b) &= W_{ba} \\ &= 2\sum_{r,r'}(-1)^m \mathcal{J}^{rr'}(\omega_a - \omega_b)(\hat{A}_r^{-m})_{ab}(\hat{A}_{r'}^m)_{ba} \\ W_{aa} &= -\sum_{b\neq a} W_{ab} \end{aligned}\right\} \qquad (20)$$

3 CONSTRUCTION OF MAGNETIZATION MODES AND THEIR RELATION TO OBSERVABLE QUANTITIES

3.1 General Considerations

The ultimate goal is to arrive at kinetic equations as simple as the Redfield equations [equations (19) and (20)] but involving quantities easily converted to observables by appropriate read pulses. Since one is dealing with *longitudinal* magnetization in a system of n spins $\frac{1}{2}$, there should be as many magnetization modes as there are eigenstates of $\hat{\mathcal{H}}_0$; that is, 2^n (4 for an AX system and 8 for an AX_2 system). The corresponding Hermitian operators $\hat{V}_i$ must therefore satisfy a condition of commutation with $\hat{\mathcal{H}}_0$:

$$[\hat{\mathcal{H}}_0, \hat{V}_i] = 0 \qquad (21)$$

which amounts to saying that their associated matrices must be diagonal in the eigenbasis of $\hat{\mathcal{H}}_0$ (the condition under

which they effectively represent longitudinal magnetization). In addition, conditions of orthogonality and normalization will be imposed:

$$\mathrm{Tr}(\hat{V}_i^{\dagger}\hat{V}_j) = \delta_{ij} \tag{22}$$

This ensures that the relaxation matrix (the analog of **W** in the Redfield equations) will be symmetric (see below). Thus the $\{\hat{V}_i\}$ constitute a basis, over which the part of the density operator pertaining to longitudinal magnetization (denoted by $\hat{\sigma}_{\mathrm{L}}$) can be expanded:

$$\hat{\sigma}_{\mathrm{L}}(t) - \hat{\sigma}_{\mathrm{eq}} = \sum_{i=1}^{2^n} v_i(t)\hat{V}_i \tag{23}$$

which, from equation (7), is equivalent to

$$v_i(t) = \langle \hat{V}_i - \hat{V}_{i,\mathrm{eq}} \rangle \tag{24}$$

The expectation value of $\hat{V}_i - \hat{V}_{i,\mathrm{eq}}$, $v;_i(t)$, is called a magnetization mode (although this term can be extended to the operator itself). It can be seen that equations (21) and (22) do not lead to a unique set of magnetization modes. The actual choice is in fact dictated by intuition and practical considerations relevant to the ease with which magnetization modes can be measured.

A unitary transformation necessarily exists when moving from the energy populations to the magnetization modes. Therefore, first-order kinetic equations [having the same structure as the Redfield equations, equation (19)] can be found for magnetization modes; they will be written in the form

$$\frac{\mathrm{d}v_i(t)}{\mathrm{d}t} = \sum_{j=1}^{2^n} \Gamma_{ij} v_j(t) \tag{25}$$

According to a general property of quantum mechanics, the elements Γ_{ij} constitute a $2^n \times 2^n$ symetric matrix, since the latter is constructed on an orthogonal and normalized basis of Hermitian operators. The expression for these elements can be derived from equations (9) and (23):

$$\Gamma_{ij} = \sum_{r,r'} \sum_{m=-2}^{+2} (-1)^m \mathcal{J}^{rr'}(m\omega_0)\,\mathrm{Tr}\{[\hat{A}_r^{-m}, \hat{V}_i][\hat{A}_{r'}^{m}, \hat{V}_j]\} \tag{26}$$

Factorization of equation (25) may result from the consideration of the symmetry of magnetization modes with respect to total spin inversion.[2,14,15] This operation can be seen as interchanging a spin function α into β, and vice versa; likewise, any individual operator $\hat{I}_z$ is transformed into its opposite. Of course, changing z into $-z$ must leave equation (25) globally unchanged. If i and j refer to magnetization modes of different symmetries, one mode must change sign (the antisymmetric one) and the other not (the symmetric one); if, at the same time, Γ_{ij} does not change sign, it is necessarily zero. This situation occurs most of the time, leading to the conclusion that *antisymmetric modes do not generally couple into antisymmetric modes*, and vice versa, leading to a factorization of the matrix Γ [relevant to equation (25) in matrix form] into two blocks: one corresponding to antisymmetric modes, the other to symmetric modes. The possible sign change of Γ_{ij} can arise from a sign change of $\hat{A}_r^{-m}\hat{A}_{r'}^{m}$ [see equation (26)]; examination of Table 1 shows that this can only occur through CSA–dipolar cross correlation, as discussed further in Section 4.

3.2 The AX Spin System

Regarding weakly coupled spin systems without equivalence, because of the expression of the coupling term in the static Hamiltonian ($\sum_{k<l} J_{kl}\hat{I}_{k,z}\hat{I}_{l,z}$), it is obvious that either individual spin operators $\hat{I}_z$ or any product of operators $\hat{I}_z$ pertaining to different spins do commute with $\hat{\mathcal{H}}_0$. Therefore, as far as a two-spin system is considered, the four magnetization modes satisfying equations (21) and (22) are readily obtained. As for any spin system, they include the identity, which evidently does not evolve, thus leaving three active magnetization modes, which are easily classified according to their symmetric or antisymmetric nature with respect to total spin inversion [this is indicated below by the superscript (a) or (s)]:

$$\begin{aligned} {}^{(\mathrm{a})}v_1 &= \langle \hat{I}_{\mathrm{A},z} - I_{\mathrm{A,eq}} \rangle, \quad {}^{(\mathrm{a})}v_2 = \langle \hat{I}_{\mathrm{X},z} - I_{\mathrm{X,eq}} \rangle \\ {}^{(\mathrm{s})}v_3 &= \langle 2\hat{I}_{\mathrm{A},z}\hat{I}_{\mathrm{X},z} \rangle \end{aligned} \tag{27}$$

v_1 and v_2 are simply measured by means of a semiselective read pulse applied to A or X, respectively. Concerning v_3, sometimes called the longitudinal spin order, it can be seen that the equilibrium value of $\langle 2\hat{I}_{\mathrm{A},z}\hat{I}_{\mathrm{X},z} \rangle$ is zero. It can therefore be created either by a special spin preparation involving selective pulses, or through transfers from antisymmetric modes by relaxation. A semiselective pulse $(\pi/2)_{\mathrm{A},x}$ (i.e., one acting solely on A along the x axis of the rotating frame) converts $2\hat{I}_{\mathrm{A},z}\hat{I}_{\mathrm{X},z}$ into $2\hat{I}_{\mathrm{A},y}\hat{I}_{\mathrm{X},z}$, which corresponds to an antiphase configuration of the A doublet.[16] This is shown in Figure 1, where the line A_1 includes equal contributions from v_1 and v_3, whereas the intensity of line A_2 represents the contribution of mode v_1 minus the contribution of the mode v_3. This leads to the well-known differential recovery[17] of the two lines of the doublet as long as v_3 has been activated. The contribution of the sole v_3 can be obtained by considering the same experiment, but preceded by a semiselective inverting pulse applied to X.[18]

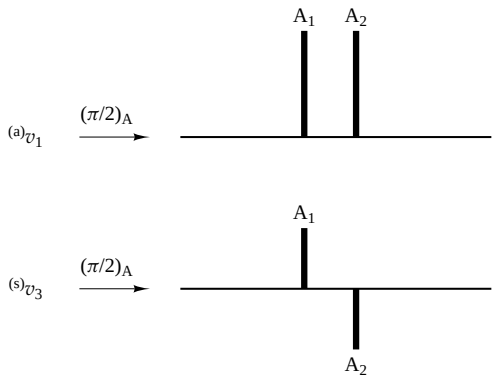

Figure 1 A semiselective $\pi/2$; pulse (acting only on A) converts the ${}^{(\mathrm{a})}v_1$ mode into the normal A doublet (of an AX spin system), and the ${}^{(\mathrm{s})}v_3$ mode into an antiphase doublet

A situation of practical interest is that of observation of A under X irradiation (e.g., observation of ^{13}C while ^{1}H transitions are irradiated for decoupling purposes). It can be shown that both $\langle \hat{I}_{X,z} \rangle$ and $\langle 2\hat{I}_{A,z}\hat{I}_{X,z} \rangle$ are identically zero. Consequently, one is left with a simple magnetization mode, namely v_1, for which equation (3) applies.

3.3 The AX_2 Spin System

The problem is here complicated by the fact that the two spins X and X′ are no longer weakly coupled (since they share the same chemical shift). The trick is to start with the Hamiltonian of an X_2 system in an anisotropic medium and to find operators that satisfy both equations (21) and (22). In addition to the identity, a possible set is

$$\tfrac{1}{2}(\hat{I}_{X,z} + \hat{I}_{X',z});\ \ 2\hat{\boldsymbol{I}}_X \cdot \hat{\boldsymbol{I}}_{X'};\ \ \sqrt{\tfrac{2}{3}}(3\hat{I}_{X,z}\hat{I}_{X',z} - \hat{\boldsymbol{I}}_X \cdot \hat{\boldsymbol{I}}_{X'}) \quad (28)$$

These operators can be shown to be suitable for an AX_2 system. Yet, four operators have still to be found. It turns out that those can be $\hat{I}_{A,z}$ itself and the operators in equation (28) multiplied by $\hat{I}_{A,z}$ (all with appropriate normalization factors). Choosing normalized combinations adapted to easily measurable quantities leads to the magnetization modes that seem at present to be widely accepted:[19]

$$\left.\begin{aligned}
&{}^{(a)}v_1 = \sqrt{\tfrac{1}{2}}\langle \hat{I}_{A,z} - I_{A,eq} \rangle \\
&{}^{(a)}v_2 = \tfrac{1}{2}\langle \hat{I}_{X,z} + \hat{I}_{X',z} - 2I_{X,eq} \rangle \\
&{}^{(a)}v_3 = \sqrt{8}\langle \hat{I}_{A,z}\hat{I}_{X,z}\hat{I}_{X',z} \rangle \\
&{}^{(a)}v_4 = 2\langle \hat{I}_{A,z}(\hat{I}_{X,x}\hat{I}_{X',x} + \hat{I}_{X,y}\hat{I}_{X',y}) \rangle \\
&{}^{(s)}v_5 = \langle \hat{I}_{A,z}(\hat{I}_{X,z} + \hat{I}_{X',z}) \rangle \\
&{}^{(s)}v_6 = \sqrt{2}\langle \hat{I}_{X,z}\hat{I}_{X',z} \rangle \\
&{}^{(s)}v_7 = \langle (\hat{I}_{X,x}\hat{I}_{X',x} + \hat{I}_{X,y}\hat{I}_{X',y}) \rangle
\end{aligned}\right\} \quad (29)$$

In the situation where X transitions are irradiated for decoupling purposes, ${}^{(a)}v_2$ does not evolve and is equal to $\hat{I}_{X,eq}$ whereas ${}^{(s)}v_5$ is zero. In order to account for other quantities that are also identically zero, ${}^{(a)}v_4$ and ${}^{(a)}v_3$ must be substituted by ${}^{(a)}v'_3 = \sqrt{\tfrac{8}{3}}\langle \hat{I}_{A,z}\hat{\boldsymbol{I}}_X \cdot \hat{\boldsymbol{I}}_{X'} \rangle$, and ${}^{(s)}v_6$ and ${}^{(s)}v_7$ by ${}^{(s)}v'_6 = \sqrt{\tfrac{2}{3}}\langle \hat{\boldsymbol{I}}_X \cdot \hat{\boldsymbol{I}}_{X'} \rangle$. One is thus left, in that case, with three active modes: ${}^{(a)}v_1$, ${}^{(a)}v'_3 = \sqrt{\tfrac{1}{3}}({}^{(a)}v_3 + \sqrt{2}\ {}^{(a)}v_4)$, and ${}^{(s)}v'_6 = \sqrt{\tfrac{1}{3}}({}^{(s)}v_6 + \sqrt{2}\ {}^{(s)}v_7)$.

Returning to the modes given by equation (29), it can be seen that the equilibrium values are zero for all modes except for the first two. Therefore, unless they have benefited by relaxation transfers originating from v_1 and v_2, or created by dedicated spin preparations, they yield no net result. In the following, it will be assumed that they exist by either means, the emphasis being put on the way in which they can be observed.

The various modes can be related to the line intensities of an AX_2 spin system, whose spectrum is shown schematically at the top of Figure 2. Also shown in Figure 2 are the effects of the two simplest read pulses that can be considered, namely a semiselective $\pi/2$ pulse acting only on A or only on X. These detection schemes deserve some comments.

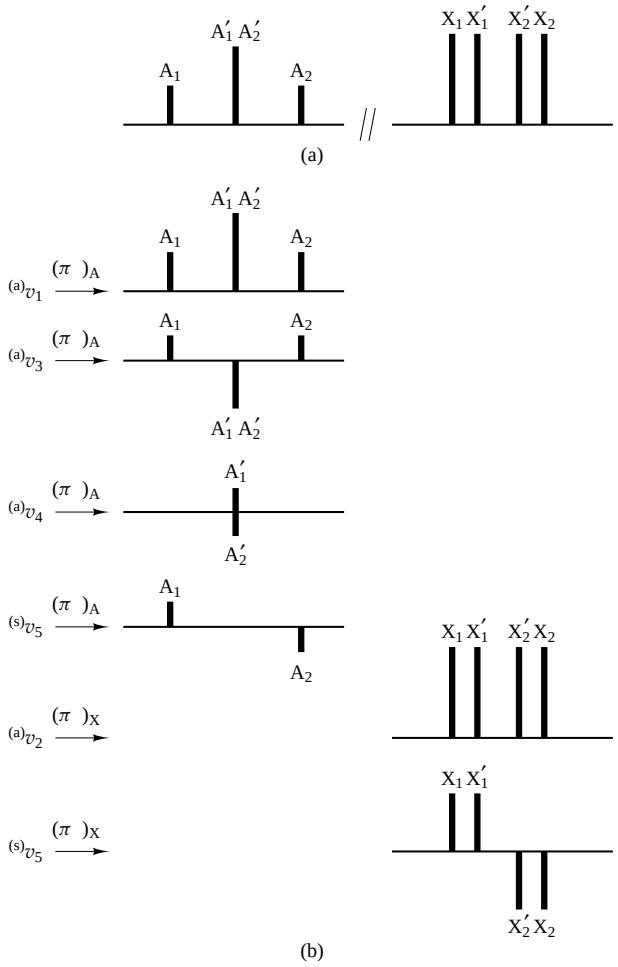

Figure 2 (a) Schematic representation of the spectrum of an AX_2 system. The lines X_1 and X'_1 on the one hand, and X'_2 and X_2 on the other, are separated only in an anisotropic medium. (b) Effects of semiselective $\pi/2$ pulses (read pulses acting only on A or only on X) on the magnetization modes of an AX_2 spin system

1. A $(\pi/2)_A$ read pulse results in a superposition of contributions from the modes ${}^{(a)}v_1$, ${}^{(a)}v_3$, and ${}^{(s)}v_5$, recognizing that the mode ${}^{(a)}v_4$ contributes nothing, since the lines A'_1 and A'_2 share exactly the same resonance frequency.
2. A $(\pi/2)_X$ read pulse allows one to detect contributions from the modes ${}^{(a)}v_2$ and ${}^{(s)}v_5$. More elaborate detection schemes[3] are available for tracing out the different modes of an AX_2 spin system. They involve multipulse experiments, sometimes combined with decoupling of one of the two considered nuclei.
3. Finally, it can be seen that modes ${}^{(s)}v_6$ and ${}^{(s)}v_7$ can only be measured in an anisotropic medium where the lines X_1, X'_1 on the one hand, and X_2, X'_2 on the other, can be separated.

4 EVOLUTION OF MAGNETIZATION MODES UNDER RELAXATION PHENOMENA

The evolution of magnetization modes rests on the relaxation matrix, which can be constructed by referring to equations

(25) and (26). It should be stressed that this matrix comprises all types of spectral densities (autocorrelation and cross correlation), in contrast with the so-called relaxation matrix used for interpretating NOESY experiments, which generally involves only autocorrelation spectral densities, giving rise to the sole specific relaxation rates and cross-relaxation rates. In this respect, the relaxation matrices given below provide all the details of relaxation pathways in AX and AX_2 spin systems.

4.1 The AX Spin System

The complete relaxation matrix is given in Table 2. As mentioned above, if CSA–dipolar cross-correlation spectral densities can be considered as negligible (matrix elements Γ_{13} and Γ_{23}), antisymmetric modes are effectively decoupled from symmetric modes, and the simple Solomon equations [equation (2)], hold because the symmetric mode ${}^{(s)}v_3$ is zero at thermal

Table 2 Relaxation Matrix for an AX Spin System[a]

$$\Gamma_{11} = -R_1^{\mathrm{A}}$$
$$\Gamma_{12} = -\sigma_{\mathrm{AX}}$$
$$\Gamma_{13} = -\sqrt{\tfrac{3}{2}}\,\mathcal{J}^{\mathrm{csa(A),d(AX)}}(\omega_{\mathrm{A}})$$
$$\Gamma_{22} = -R_1^{\mathrm{X}}$$
$$\Gamma_{23} = -\sqrt{\tfrac{3}{2}}\,\mathcal{J}^{\mathrm{csa(X),d(AX)}}(\omega_{\mathrm{X}})$$
$$\Gamma_{33} = -\tfrac{1}{4}[\mathcal{J}^{\mathrm{d(AX)}}(\omega_{\mathrm{A}}) + \mathcal{J}^{\mathrm{d(AX)}}(\omega_{\mathrm{X}})] - \tfrac{3}{2}\,[\mathcal{J}^{\mathrm{csa(A)}}(\omega_{\mathrm{A}}) + \mathcal{J}^{\mathrm{csa(X)}}(\omega_{\mathrm{X}})] - 2[\mathcal{J}^{\mathrm{rf(A)}}(\omega_{\mathrm{A}}) + \mathcal{J}^{\mathrm{rf(X)}}(\omega_{\mathrm{X}})]$$

[a]Superscripts have the following meanings: d = dipolar; csa = chemical shift anisotropy; rf = randomly fluctuating fields. The classical relaxation parameters are given by $R_1^A = \tfrac{1}{2}\mathcal{J}^{\mathrm{d(AX)}}(\omega_{\mathrm{A}} + \omega_{\mathrm{X}}) + \tfrac{1}{4}\mathcal{J}^{\mathrm{d(AX)}}(\omega_{\mathrm{A}}) + \tfrac{1}{2}\mathcal{J}^{\mathrm{d(AX)}}(\omega_{\mathrm{A}} - \omega_{\mathrm{X}}) + \tfrac{3}{2}\mathcal{J}^{\mathrm{csa(A)}}(\omega_{\mathrm{A}}) + 2\mathcal{J}^{\mathrm{rf(A)}}(\omega_{\mathrm{A}})$ (interchange A and X for R_1^X); $\sigma_{\mathrm{AX}} = \tfrac{1}{2}\mathcal{J}^{\mathrm{d(AX)}}(\omega_{\mathrm{A}} + \omega_{\mathrm{X}}) - \tfrac{1}{2}\mathcal{J}^{\mathrm{d(AX)}}(\omega_{\mathrm{A}} - \omega_{\mathrm{X}})$.

Table 3 Relaxation Matrix for an AX_2 Spin System[a]

$$\Gamma_{11} = -R_1^{\mathrm{A}'}$$
$$\Gamma_{12} = -\sqrt{2}\sigma_{\mathrm{AX}}$$
$$\Gamma_{13} = -\tfrac{1}{2}\mathcal{J}^{\mathrm{d(AX,AX')}}(\omega_{\mathrm{A}})$$
$$\Gamma_{14} = -\sqrt{\tfrac{1}{2}}\,\mathcal{J}^{\mathrm{d(AX,AX')}}(\omega_{\mathrm{A}} + \omega_{\mathrm{X}}) - \tfrac{1}{6}\sqrt{\tfrac{1}{2}}\,\mathcal{J}^{\mathrm{d(AX,AX')}}(\omega_{\mathrm{A}} - \omega_{\mathrm{X}})$$
$$\Gamma_{15} = -\sqrt{3}\mathcal{J}^{\mathrm{csa(A),d(AX)}}(\omega_{\mathrm{A}})$$
$$\Gamma_{16} = 0$$
$$\Gamma_{17} = 0$$

$$\Gamma_{22} = -R_1^{\mathrm{X}} - \mathcal{J}^{\mathrm{d(XX')}}(2\omega_{\mathrm{X}}) - \tfrac{1}{4}\mathcal{J}^{\mathrm{d(XX')}}(\omega_{\mathrm{X}})$$
$$\Gamma_{23} = -\sqrt{\tfrac{1}{2}}\,\mathcal{J}^{\mathrm{d(AX,XX')}}(\omega_{\mathrm{X}})$$
$$\Gamma_{24} = -\tfrac{1}{2}\mathcal{J}^{\mathrm{d(AX,AX')}}(\omega_{\mathrm{A}} + \omega_{\mathrm{X}}) + \tfrac{1}{2}\mathcal{J}^{\mathrm{d(AX,XX')}}(\omega_{\mathrm{X}}) + \tfrac{1}{2}\mathcal{J}^{\mathrm{d(AX,AX')}}(\omega_{\mathrm{A}} - \omega_{\mathrm{X}})$$
$$\Gamma_{25} = -\sqrt{\tfrac{3}{2}}\,\mathcal{J}^{\mathrm{csa(X),d(AX)}}(\omega_{\mathrm{X}})$$
$$\Gamma_{26} = -\sqrt{3}\mathcal{J}^{\mathrm{csa(X),d(XX')}}(\omega_{\mathrm{X}})$$
$$\Gamma_{27} = -\sqrt{\tfrac{3}{2}}\,\mathcal{J}^{\mathrm{csa(X),d(XX')}}(\omega_{\mathrm{X}})$$

$$\Gamma_{33} = -\tfrac{1}{2}[\mathcal{J}^{\mathrm{d(AX)}}(\omega_{\mathrm{A}}) + \mathcal{J}^{\mathrm{d(AX)}}(\omega_{\mathrm{X}}) + \mathcal{J}^{\mathrm{d(XX')}}(\omega_{\mathrm{X}})] - \tfrac{3}{2}[\mathcal{J}^{\mathrm{csa(A)}}(\omega_{\mathrm{A}}) + 2\mathcal{J}^{\mathrm{csa(X)}}(\omega_{\mathrm{X}})] - 2\mathcal{J}^{\mathrm{rf(A)}}(\omega_{\mathrm{A}}) - 4\mathcal{J}^{\mathrm{rf(X)}}(\omega_{\mathrm{X}})$$
$$\Gamma_{34} = \tfrac{1}{2}\sqrt{\tfrac{1}{2}}\,[\mathcal{J}^{\mathrm{d(XX')}}(\omega_{\mathrm{X}}) + \mathcal{J}^{\mathrm{d(AX,AX')}}(\omega_{\mathrm{X}})] + 3\sqrt{\tfrac{1}{2}}\mathcal{J}^{\mathrm{csa(X),csa(X')}}(\omega_{\mathrm{X}}) + 2\sqrt{2}\mathcal{J}^{\mathrm{rf(X),rf(X')}}(\omega_{\mathrm{X}})$$
$$\Gamma_{35} = -\sqrt{3}[\mathcal{J}^{\mathrm{csa(A),d(AX)}}(\omega_{\mathrm{A}}) + \mathcal{J}^{\mathrm{csa(X),d(XX')}}(\omega_{\mathrm{X}})]$$
$$\Gamma_{36} = -\sqrt{6}\mathcal{J}^{\mathrm{csa(X),d(AX)}}(\omega_{\mathrm{X}})$$
$$\Gamma_{37} = \sqrt{3}\mathcal{J}^{\mathrm{csa(X),d(AX')}}(\omega_{\mathrm{X}})$$

$$\Gamma_{44} = -R_1^X - \tfrac{1}{3}\mathcal{J}^{\mathrm{d(AX)}}(0) - \tfrac{1}{4}\mathcal{J}^{\mathrm{d(XX')}}(\omega_{\mathrm{X}}) + \tfrac{1}{3}\mathcal{J}^{\mathrm{d(AX,AX')}}(0) - \tfrac{3}{2}\,\mathcal{J}^{\mathrm{csa(A)}}(\omega_{\mathrm{A}}) - 2\mathcal{J}^{\mathrm{csa(X)}}(0) - 2\mathcal{J}^{\mathrm{rf(A)}}(\omega_{\mathrm{A}}) - 2\mathcal{J}^{\mathrm{rf(X)}}(0)$$
$$+ 2\mathcal{J}^{\mathrm{csa(X),csa(X')}}(0) + 2\mathcal{J}^{\mathrm{rf(X),rf(X')}}(0)$$
$$\Gamma_{45} = \sqrt{\tfrac{3}{2}}\,\mathcal{J}^{\mathrm{csa(X),d(XX')}}(\omega_{\mathrm{X}})$$
$$\Gamma_{46} = \sqrt{3}\mathcal{J}^{\mathrm{csa(X),d(AX')}}(\omega_{\mathrm{X}})$$
$$\Gamma_{47} = -\sqrt{\tfrac{3}{2}}\,\mathcal{J}^{\mathrm{csa(X),d(AX)}}(\omega_{\mathrm{X}}) - 2\sqrt{\tfrac{2}{3}}\mathcal{J}^{\mathrm{csa(X),d(AX)}}(0) + 2\sqrt{\tfrac{2}{3}}\mathcal{J}^{\mathrm{csa(X),d(AX')}}(0)$$

$$\Gamma_{55} = -R_1^{\mathrm{X}} - \tfrac{1}{2}\mathcal{J}^{\mathrm{d(AX)}}(\omega_{\mathrm{A}}) - \mathcal{J}^{\mathrm{d(XX')}}(2\omega_{\mathrm{X}}) - \tfrac{1}{4}\mathcal{J}^{\mathrm{d(XX')}}(\omega_{\mathrm{X}}) - \tfrac{1}{2}\mathcal{J}^{\mathrm{d(AX,AX')}}(\omega_{\mathrm{A}}) - \tfrac{3}{2}\,\mathcal{J}^{\mathrm{csa(A)}}(\omega_{\mathrm{A}}) - 2\mathcal{J}^{\mathrm{rf(A)}}(\omega_{\mathrm{A}})$$
$$\Gamma_{56} = -\sqrt{\tfrac{1}{2}}\,\mathcal{J}^{\mathrm{d(AX)}}(\omega_{\mathrm{A}} + \omega_{\mathrm{X}}) + \tfrac{1}{6}\sqrt{\tfrac{1}{2}}\mathcal{J}^{\mathrm{d(AX)}}(\omega_{\mathrm{A}} - \omega_{\mathrm{X}}) - \sqrt{\tfrac{1}{2}}\mathcal{J}^{\mathrm{d(AX,XX')}}(\omega_{\mathrm{X}})$$
$$\Gamma_{57} = \tfrac{1}{2}\mathcal{J}^{\mathrm{d(AX,XX')}}(\omega_{\mathrm{X}}) + \tfrac{1}{2}\mathcal{J}^{\mathrm{d(AX,AX')}}(\omega_{\mathrm{A}} + \omega_{\mathrm{X}}) - \tfrac{1}{2}\mathcal{J}^{\mathrm{d(AX,AX')}}\,(\omega_{\mathrm{A}} - \omega_{\mathrm{X}})$$

$$\Gamma_{66} = -2R_1^X - \tfrac{1}{2}\mathcal{J}^{\mathrm{d(XX')}}(\omega_{\mathrm{X}})$$
$$\Gamma_{67} = \tfrac{1}{2}\sqrt{\tfrac{1}{2}}\mathcal{J}^{\mathrm{d(XX')}}(\omega_{\mathrm{X}}) + \sqrt{\tfrac{1}{2}}\mathcal{J}^{\mathrm{d(AX,AX')}}(\omega_{\mathrm{A}} + \omega_{\mathrm{X}}) + \tfrac{1}{2}\sqrt{\tfrac{1}{2}}\mathcal{J}^{\mathrm{d(AX,AX')}}(\omega_{\mathrm{X}}) + \tfrac{1}{6}\sqrt{\tfrac{1}{2}}\mathcal{J}^{\mathrm{d(AX,AX')}}(\omega_{\mathrm{A}} - \omega_{\mathrm{X}}) + 3\sqrt{\tfrac{1}{2}}\mathcal{J}^{\mathrm{csa(X),csa(X')}}(\omega_{\mathrm{X}}) + 2\sqrt{2}\mathcal{J}^{\mathrm{rf(X),rf(X')}}(\omega_{\mathrm{X}})$$

$$\Gamma_{77} = -R_1^X - \tfrac{1}{2}\mathcal{J}^{\mathrm{d(AX)}}(\omega_{\mathrm{A}}) - \tfrac{1}{3}\mathcal{J}^{\mathrm{d(AX)}}(0) - \tfrac{1}{4}\mathcal{J}^{\mathrm{d(XX')}}(\omega_{\mathrm{X}}) + \tfrac{1}{2}\mathcal{J}^{\mathrm{d(AX,AX')}}(\omega_{\mathrm{A}}) + \tfrac{1}{3}\mathcal{J}^{\mathrm{d(AX,AX')}}(0) - 2\mathcal{J}^{\mathrm{csa(X)}}(0) + 2\mathcal{J}^{\mathrm{csa(X),csa(X')}}(0) - 2\mathcal{J}^{\mathrm{rf(X)}}(0)$$
$$+2\mathcal{J}^{\mathrm{rf(X),rf(X')}}(0)$$

[a]The various symbols have the same meanings as in Table 2. $R_1^{\mathrm{A}'}$ differs from R_1^{A} by a factor of 2 multiplying the dipolar spectral densities (to account for the two nuclei X and X′).

equilibrium. Conversely, with the advent of high-field NMR spectrometers, CSA contributions may become nonnegligible, and so do CSA–dipolar cross-correlation spectral densities. This somewhat complicates the evolution of this simple two-spin system under longitudinal relaxation, but, in turn, yields valuable molecular information of structural nature through the shielding tensor and also information of dynamical nature through the correlated motions of dipolar and shielding tensors. In addition to the early works of Shimizu,[20] Mackor and MacLean,[21] and Blicharsky,[22] there has been an abundant (and increasing) literature on the subject from the beginning of the 1980s based either on one-dimensional[23–34] or two-dimensional[35–39] experiments.

Invariably, the initial perturbation consists in disturbing semiselectively one longitudinal magnetization (A or X) and looking at recoveries of either A or X longitudinal magnetizations (or both). For this simple two-spin system, one may content oneself with the initial behavior, which yields the whole relaxation information. As an example, let us suppose that the perturbation consists in inverting the A magnetization. Initial behaviors of A and X longitudinal magnetizations yield respectively R_1^{A} and σ_{AX}. In the same context, converting $\langle 2\hat{I}_{\mathrm{A,z}}\hat{I}_{\mathrm{X,z}}\rangle$ into an antiphase transverse configuration makes it possible to monitor the build-up of longitudinal order through the CSA–dipolar interference term $\mathcal{J}^{\mathrm{csa(A),d(AX)}}$. Conversely, an initial perturbation applied to the X nucleus yields the interference term $\mathcal{J}^{\mathrm{csa(A),d(AX)}}$.

4.2 The AX_2 Spin System

As can be seen from the relaxation matrix given in Table 3, a wealth of molecular information can be gained through the various spectral densities that are involved. In particular, in a three-spin system, cross-correlation dipolar spectral densities show up; they carry some additional information about correlated motions of internuclear vectors. As for the AX system, antisymmetric modes are coupled into symmetric modes only via interference terms (CSA–dipolar cross-correlation spectral densities). Owing to the large number of spectral densities that have to be determined, it is almost mandatory to analyze the whole recovery curve and not to rely simply on initial behavior. In most studies carried out so far,[4] the carbon longitudinal magnetization of a $^{13}CH_2$ grouping has been monitored after an appropriate perturbation. The following perturbations have proven to be sufficient for determining most spectral densities (extreme narrowing assumed), including interference terms:[19]

1. semiselective inversion of A magnetization;
2. semiselective inversion of (X, X′) magnetizations;
3. selective inversion of one line of the (X, X′) doublet;
4. the so-called J-pulse preparation,[40] by which a nonzero initial value is obtained for the $^{(a)}\nu_3$ mode.

5 RELATED ARTICLES

Coupled Spin Relaxation in Polymers; Relaxation Processes in Coupled-Spin Systems; Relaxation Processes: Cross Correlation and Interference Terms; Relaxation Theory: Density Matrix Formulation; Selective NOESY.

6 REFERENCES

1. L. G. Werbelow and D. M. Grant, *J. Chem. Phys.*, 1975, **63**, 544.
2. L. G. Werbelow and D. M. Grant, in *Advances in Magnetic Resonance*, ed. J. S. Waugh, Academic Press, New York, 1977, Vol. 9, p. 189.
3. D. Canet, in *Progress in Nuclear Magnetic Resonance Spectroscopy*, eds. J. W. Emsley, J. Feeney, and L. H. Sutcliffe, Pergamon Press, Oxford, 1989, Vol. 21, p. 237.
4. D. M. Grant, C. L. Mayne, F. Lin, and T. X. Xiang, *Chem. Rev.*, 1991, **91**, 1591.
5. L. Di Bari, J. Kowalewski, and G. Bodenhausen, *J. Chem. Phys.*, 1990, **93**, 7698.
6. J. M. Courtieu, C. L. Mayne, and D. M. Grant, *J. Chem. Phys.*, 1977, **66**, 2669.
7. J. H. Noggle and R. E. Schirmer, *The Nuclear Overhauser Effect: Chemical Applications*, Academic Press, New York, 1971.
8. D. Neuhaus and M. Williamson, *The Nuclear Overhauser Effect*, VCH Weinheim, 1989.
9. T. C. Farrar and J. E. Harriman, *Density Matrix Theory and its Applications in NMR Spectroscopy*, 2nd edn., The Farragut Press, Madison, WI, 1989.
10. R. R. Ernst, G. Bodenhausen, and A. Wokaun, *Principles of Nuclear Magnetic Resonance in One and Two Dimensions*, Oxford University Press, Oxford, 1987, p. 50.
11. M. E. Rose, *Elementary Theory of Angular Momentum*, Wiley, New York, 1967.
12. P. S. Hubbard, *Phys. Rev.*, 1969, **180**, 319.
13. A. G. Redfield, in *Advances in Magnetic Resonance*, ed. J. S. Waugh, Academic Press, New York, 1965, Vol. 1, p. 1.
14. M. D. Zeidler, *Ber. Bunsenges. Phys. Chem.*, 1968, **72**, 48.
15. N. C. Pyper, *Mol. Phys.*, 1968, **22**, 433.
16. O. W. Sørensen, G. W. Eich, M. H. Levitt, G. Bodenhausen, and R. R. Ernst, in *Progress in Nuclear Magnetic Resonance Spectroscopy*, eds. J. W. Emsley, J. Feeney, and L. H. Sutcliffe, Pergamon Press, Oxford, 1983, Vol. 16, p. 163.
17. M. Goldman, *J. Magn. Reson.*, 1984, **60**, 437.
18. G. Jaccard, S. Wimperis, and G. Bodenhausen, *Chem. Phys. Lett.*, 1987, **138**, 601.
19. Z. Zheng, C. L. Mayne, and D. M. Grant, *J. Magn. Reson., Ser. A*, 1993, **103**, 268.
20. H. Shimizu, *J. Chem. Phys.*, 1964, **40**, 3357.
21. E. L. Mackor and C. MacLean, in *Progress in Nuclear Magnetic Resonance Spectroscopy*, eds. J. W. Emsley, J. Feeney, and L. H. Sutcliffe, Pergamon Press, Oxford, 1967, Vol. 3, p. 129.
22. J. L. Blicharsky, *Phys. Lett. A*, 1967, **24**, 608.
23. H. Néry and D. Canet, *J. Magn. Reson.*, 1981, **42**, 370.
24. T. C. Farrar and I. C. Locker, *J. Chem. Phys.*, 1981, **87**, 3281.
25. E. Konigsberger and H. Sterk, *J. Chem. Phys.*, 1985, **83**, 2723.
26. F. A. L. Anet, *J. Am. Chem. Soc.*, 1986, **108**, 7102.
27. K. Elbayed and D. Canet, *Mol. Phys.*, 1989, **68**, 1033.
28. T. C. Farrar and J. Decatur, *J. Phys. Chem.*, 1990, **94**, 7395.
29. J. A. Boyd, U. Hommel, and J. D. Campbell, *Chem. Phys. Lett.*, 1990, **175**, 477.
30. G. Kontaxis, N. Muller, and H. Sterk, *J. Magn. Reson.*, 1991, **92**, 332.
31. C. L. Tsai, W. S. Price, Y. C. Chang, B. C. Perng, and L. P. Hwang, *J. Phys. Chem.*, 1991, **95**, 7546.
32. T. C. Farrar and M. J. Jablonsky, *J. Phys. Chem.*, 1991, **95**, 9159.
33. J. Chung, E. Oldfield, A. Thevand and L. Werbelow, *J. Magn. Reson.*, 1992, **100**, 69.

34. V. A. Daragan and K. H. May, *Chem. Phys. Lett.*, 1993, **206**, 393.
35. C. Dalvit and G. Bodenhausen, *Chem. Phys. Lett.*, 1989, **161**, 554.
36. C. Dalvit, *J. Magn. Reson.*, 1991, **95**, 410.
37. I. Burghardt, R. Konrat, and G. Bodenhausen, *Mol. Phys.*, 1992, **75**, 467.
38. L. E. Kay, L. K. Nicholson, F. Delaglio, A. Bax, and D. A. Torchia, *J. Magn. Reson.*, 1992, **97**, 359.
39. C. Dalvit, *J. Magn. Reson.*, 1992, **97**, 645.
40. F. Liu, C. L. Mayne, and D. M. Grant, *J. Magn. Reson.*, 1989, **84**, 344.

Biographical Sketch

Daniel Canet. *b* 1944. B.S., 1966; Thesis, 1973, University of Nancy, France. Introduced to NMR by Pierre Granger. Postdoctoral work at UCSD with R. L. Vold and R. R. Vold. Faculty in Physical Chemistry, University of Nancy, 1973–present. Approx. 160 publications. Research specialties: spin relaxation, selectivity in NMR, and use of radiofrequency field gradients in NMR.

Relaxation of Coupled Spins from Rotational Diffusion

David M. Grant and Russell A. Brown
University of Utah, Salt Lake City, UT, USA

1	Introduction	1
2	Redfield Theory	2
3	Separation of the Nuclear Spin Hamiltonian into Spin and Spatial Terms	3
4	Motional Power Densities in the Molecular Rotational Diffusion Frame	6
5	The Favro Equation and Molecular Rotational Diffusion in Liquids	7
6	Interaction Tensors in Their Principal Axis and Molecular Diffusion Frames	10
7	Specific Expressions for Spectral Density Functions and Relaxation Rates	12
8	Related Articles	15
9	References	15

1 INTRODUCTION

Nuclear spin relaxation in liquids arises from random fluctuations of magnetic fields associated with a variety of intramolecular and intermolecular interactions that are modulated by molecular tumbling and other lattice motions. Interactions that produce such temporal magnetic oscillations include the dipole–dipole terms, chemical shift anisotropy, spin rotation, scalar coupling to a chemically exchanging nucleus or to a quadrupolar nucleus, free electrons within the sample, oscillating electrostatic fields for quadrupolar nuclei, etc. This article focuses primarily on the molecular motional aspects of the problem, and it is sufficient to select two prominent relaxation mechanisms, the dipole–dipole (dd) and the chemical shift anisotropy (csa), to illustrate both the nature and potential of nuclear relaxation for characterizing molecular motions. In particular, this article deals with the rotational diffusion of rigid molecules in an isotropic medium. Motional models for asymmetric and symmetric diffusion will be developed and compared with simple spherical diffusion.

The motional models must be developed in a principal molecular diffusion frame, which invariably differs from the laboratory measurement frame and also from the principal axis frames of the various spin interactions. This diversity of coordinate frames introduces a degree of complication in the mathematical development that need not obscure the relatively simple motional models that govern relaxation processes. The various relationships existing between the several coordinate systems are outlined in Figure 1. The laboratory and molecular frames are related to each other by a set of time-dependent Euler angles $\Omega_t \sum (\alpha_t, \beta_t, \gamma_t)$, which introduce the temporal fluctuations into the motional models. The effect of diffusional motion upon relaxation has been discussed for autocorrelated terms by Woessner[1] based on the work of Perrin,[2] but the approach of Huntress[3]

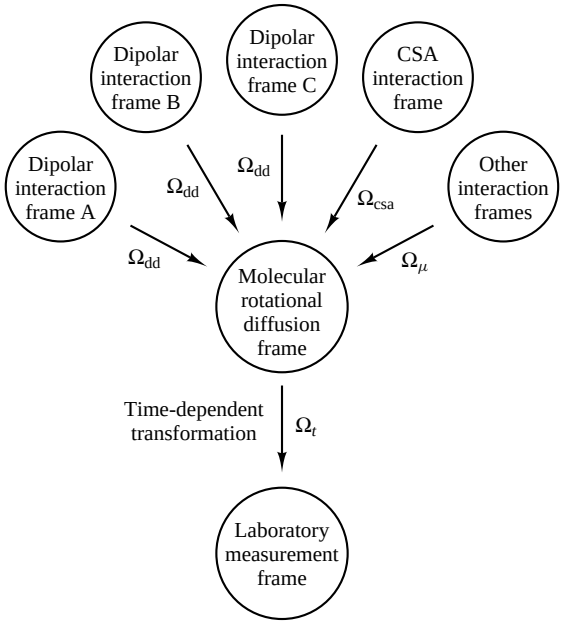

Figure 1 Coordinate frames in spin relaxation

using the Favro[4] diffusion equation provides a preferable approach for treating both autocorrelated and cross-correlated spin relaxation terms. Huntress's discussion of autocorrelated spectral densities was extended to a discussion of both auto- and cross-correlated dipolar spin relaxation.[5] Recently, Smith[6] used the Favro method to discuss the effect on relaxation of the chemical shift anisotropy interaction, including cross terms with the dipolar interaction. The Favro diffusion equation is the mathematical method used in this article to relate spin relaxation to molecular motions.

Invariably, the various principal interaction frames differ from the molecular diffusion frame, except for spherical diffusion, where the molecular motion has no unique axis system. In anisotropic diffusion, however, the geometrical relationships between the interaction frames and the molecular diffusion frame become an essential feature of the spatial geometry affecting spin relaxation. These transformations between the interaction and molecular coordinate frames are identified with the Euler angles $\Omega_\mu \sum (\alpha_\mu, \beta_\mu, \gamma_\mu)$ in Figure 1. In coupled-spin relaxation, the number of dipole–dipole interactions increases rather rapidly with the number of spins (i.e., one dipolar term for two spins, three terms for three spins, six for four spins, etc.). Thus, for even modest-size spin systems, the number of independent dipole–dipole interaction frames may become appreciable. To the several dipolar frames must be added the interaction frames for chemical shift anisotropy and other important relaxation interactions. Figure 1 portrays a minimal diversity to indicate the necessary geometric transformations required to describe relaxation in coupled-spin systems dominated by dipolar or chemical shift anisotropy mechanisms.

Recognizing that spin relaxation ensues from a time-correlated pairing of interactions, it becomes easy to understand the difference between auto- and cross-correlated spectral relaxation terms. In the autocorrelated terms, a single relaxation interaction is considered, whereas cross terms require a mixing of two interactions from Figure 1. Thus, in some cross

correlated relaxation terms, one may encounter as many as four different frames: the laboratory, the molecular diffusion, and two interaction frames. Articles on coupled-spin relaxation have appeared in the literature dating back over the past three decades. In addition, several reviews[7–11] provide important background for this article, which focuses on motional models affecting relaxation.

All discussions of coupled relaxation begin with the Redfield equation,[12] introduced in Section 2, and proceed with secular approximations and time-reversal symmetry considerations to transform the fourth-rank Redfield matrix into autocorrelated and cross-correlated terms in the Hamiltonian. Section 3 expands the Hamiltonian in spin and spatial variables. Separation of these two variables results in spin matrices that contain the spectral selection rules for relaxation and expressions for the spectral densities that measure the strength of both auto and cross terms found for various relaxation mechanisms. Section 3 contains explicit expressions for the dipolar and chemical shift anisotropy spin operators. Section 4 discusses the separation of the spectral densities into the time-dependent motional power densities associated with the molecular motion and into the various time-independent interaction tensors in the molecular frame. Section 5 provides the Favro diffusion equation and its solution in terms of the molecular rotational diffusion tensor. The motional models developed in this section assume a rigid molecule tumbling in an isotropic fluid, but treat spherical, symmetrical, and asymmetrical diffusional cases. This diffusion equation is solved with both first- and second-rank diffusion constants, and therefore information is available to treat both first- and second-rank interactions found in the Hamiltonian. Section 6 discusses the transformations between the principal interaction frames and the principal molecular diffusion frame. Finally, explicit information on the geometrical relationships between these sets of frames is presented in Section 7 for the auto- and cross-correlation spectral densities encountered in dipole–dipole and chemical shift anisotropy relaxation mechanisms.

2 REDFIELD THEORY

Coupled relaxation processes may be described using Redfield theory[12] wherein the time derivatives of the density matrix elements $\sigma_{\kappa\kappa'}{}^*(t)$ are expressed using the following set of coupled differential equations:

$$\frac{\mathrm{d}\sigma^*_{\kappa\kappa'}(t)}{\mathrm{d}t} = \sum_{\lambda\lambda'} \exp\left[\frac{\mathrm{i}}{\hbar}(E_\kappa - E_{\kappa'} - E_\lambda + E_{\lambda'})t\right] \times R_{\kappa\kappa'\lambda\lambda'}[\sigma^*_{\lambda\lambda'}(t) - \sigma^*_{\lambda\lambda'}(\infty)] \quad (1)$$

A discussion of this equation and its origin has been given by Slichter.[13] In equation (1), the terms $\sigma_{\lambda\lambda'}{}^*(\infty)$ and $\sigma_{\lambda\lambda'}{}^*(t)$ represent the thermal equilibrium and the time-dependent density matrix elements, respectively. The asterisk designates a spin density matrix in the eigenstate interaction representation. The fourth-rank relaxation matrix $R_{\kappa\kappa'\lambda\lambda'}$ is combined with an exponential oscillating term $\exp[(\mathrm{i}/\hbar)(E_\kappa - E_{\kappa'} - E_\lambda + E_{\lambda'})t]$ involving up to four different eigenvalues E_i. Equation (1) allows for significant simplifications using a so-called secular approximation. The explicit oscillatory time dependence is removed whenever $E_\kappa - E_{\kappa'} = E_\lambda - E_{\lambda'}$. In longitudinal relaxation, this is especially obvious for diagonal density matrix terms when $\kappa = \kappa'$ and $\lambda = \lambda'$. Rapid temporal oscillations, encountered in off-diagonal terms when $E_\kappa - E_{\kappa'} \neq E_\lambda - E_{\lambda'}$, eliminate the corresponding relaxation terms from consideration. The terms surviving the secular approximation form block-diagonalized relaxation matrices that can be used to discuss either longitudinal or transverse spin relaxation. The spin symmetry reduces the complexity by separating the longitudinal and transverse blocks from one another. The fit of the relaxation matrix in equation (1) to experimental data describes the time evolution of the spin system, and these spin relaxation solutions to equation (1) may be expressed either as NMR spectral densities appearing in the superoperator $R_{\kappa\kappa'\lambda\lambda'}$ or alternatively as spin interaction terms coupled with a set of molecular rotational diffusion constants.

2.1 The Hamiltonian for Spin Interactions Affecting Relaxation

The Hamiltonian contains a number of interactions, each of which contribute to a variety of spin relaxation mechanisms. These separate terms in the Hamiltonian may be expressed as

$$\begin{aligned}\hat{\mathcal{H}} &= \sum_\mu \hat{\mathcal{H}}_\mu(t) \\ &= \hat{\mathcal{H}}_{\mathrm{dd}}(t) + \hat{\mathcal{H}}_{\mathrm{csa}}(t) + \hat{\mathcal{H}}_{\mathrm{SR}}(t) + \hat{\mathcal{H}}_{\mathrm{SC}}(t) \\ &\quad + \hat{\mathcal{H}}_{\mathrm{Q}}(t) + \ldots \end{aligned} \quad (2)$$

where the index μ designates the respective spin interactions [i.e., dipole–dipole (dd), chemical shielding anisotropy (csa), spin–rotation (SR), scalar coupling (SC), quadrupolar (Q), etc.] associated with a specific relaxation mechanism contributing to $R_{\kappa\kappa'\lambda\lambda'}$. This relaxation matrix is given by

$$R_{\kappa\kappa'\lambda\lambda'} = K_{\kappa\lambda\kappa'\lambda'}(\omega_{\kappa\lambda}) + K_{\kappa\lambda\kappa'\lambda'}(\omega_{\lambda'\kappa'}) - \delta_{\kappa'\lambda'}\sum_\gamma K_{\gamma\lambda\gamma\kappa} \times(\omega_{\gamma\lambda'}) - \delta_{\kappa\lambda}\sum_\gamma K_{\gamma\kappa'\gamma\lambda'}(\omega_{\lambda\gamma}) \quad (3)$$

$\delta_{\kappa\lambda}$ are Kronecker deltas and $\omega_{\kappa\lambda} = (E_\kappa - E_\lambda)/\hbar$. The several relaxation rates $K_{\kappa\lambda\kappa'\lambda'}(\omega_{\kappa\lambda})$ are Fourier transforms of a correlation function in the Hamiltonian as follows:

$$K_{\kappa\lambda\kappa'\lambda'}(\omega_{\kappa\lambda}) = \sum_{\mu,\mu'}\frac{1}{\hbar^2}\int_0^\infty \langle\kappa|\hat{\mathcal{H}}_\mu(t)|\lambda\rangle\langle\lambda'|\hat{\mathcal{H}}_{\mu'}(t+\tau)|\kappa'\rangle \times \mathrm{e}^{-\mathrm{i}\omega_{\kappa\lambda}\tau}\,\mathrm{d}\tau \quad (4)$$

Standard matrix notation is used for the $\hat{\mathcal{H}}_\mu(t)$ elements involving eigenfunctions $\langle\kappa|$ and $|\lambda\rangle$, etc.

2.2 Time-Reversal Symmetry and Integration Limits

The two Hamiltonian matrix elements in equation (4) are real because of the Hermitian character of $\hat{\mathcal{H}}_\mu(t)$, but the imaginary terms, resulting from $\mathrm{e}^{-\mathrm{i}\omega_{\kappa\lambda}t}$, leave $K_{\kappa\lambda\kappa'\lambda'}(\omega_{\kappa\lambda})$ a complex quantity. While the imaginary part of $K_{\kappa\lambda\kappa'\lambda'}(\omega_{\kappa\lambda})$ does not

contribute directly to spin relaxation, these terms characterize a second-order dynamic frequency shift,[14] which is measurable under certain circumstances. Furthermore, the correlated functions in equation (4) arise in liquids from stationary random motions that must exhibit time-reversal symmetry.[15] Correlated properties with time-reversal symmetry render the integral in equation (4) with a range from 0 to ∞ equal to the corresponding integral from $-\infty$ to 0. Thus, focus on relaxation terms, which must be real, is consistent with a change of the integral in equation (4) to one-half of a full Fourier integral from $-\infty$ to $+\infty$. This change in the integral will be made later in this article after spin and spatial variables have been separated and after developing equation (4) to the point where relaxation and dynamic frequency shift terms are readily separated.

2.3 Autocorrelated and Cross-Correlated Relaxation Terms

The relaxation terms given in equation (4) have both autocorrelated contributions with $\mu' = \mu$ and cross-correlated terms with $\mu \neq \mu'$. In the cross terms there is an implied time ordering in $K_{\kappa\lambda\kappa'\lambda'}(\omega_{\kappa\lambda})$ since μ is identified with t and μ' is associated with $t + \tau$. Thus, to retain time-reversal symmetry in the cross-relaxation expression, it is necessary to link together the pairs of complementary cross terms in μ and μ'. These cross terms, to be appreciable, transform under the same spin symmetry and depend upon the same motional correlation functions. Thus, equation (4) may be written as a sum of autocorrelated and cross-correlated relaxation components as follows:

$$\begin{aligned} K_{\kappa\lambda\kappa'\lambda'}(\omega_{\kappa\lambda}) = {} & \frac{1}{\hbar^2}\sum_{\mu}\int_0^{\infty}\langle\kappa|\hat{\mathcal{H}}_{\mu}(t)|\lambda\rangle\langle\lambda'|\hat{\mathcal{H}}_{\mu}(t+\tau)|\kappa'\rangle e^{-i\omega_{\kappa\lambda}\tau}\,d\tau \\ & + \frac{1}{\hbar^2}\sum_{\mu\rangle\mu'}\int_0^{\infty}[\langle\kappa|\hat{\mathcal{H}}_{\mu}(t)|\lambda\rangle\langle\lambda'|\hat{\mathcal{H}}_{\mu'}(t+\tau)|\kappa'\rangle \\ & + \langle\kappa|\hat{\mathcal{H}}_{\mu'}(t)|\lambda\rangle\langle\lambda'|\hat{\mathcal{H}}_{\mu}(t+\tau)|\kappa'\rangle]e^{-i\omega_{\kappa\lambda}\tau}\,d\tau \end{aligned} \quad (5)$$

The restricted summation in $\mu > \mu'$ for the cross terms prevents double counting in equation (5).

2.4 Explicit Expressions for the Dipole–Dipole and Chemical Shift Hamiltonians

The dipolar Hamiltonian is

$$\hat{\mathcal{H}}_{dd}(t) = \hbar\hat{\boldsymbol{I}}(s)\cdot\boldsymbol{D}(t)\cdot\hat{\boldsymbol{I}}(s') \quad (6)$$

where $\hat{\boldsymbol{I}}(s) = [\hat{I}_x(s), \hat{I}_y(s), \hat{I}_z(s)]$ is the angular momentum vector and the time-dependent dipolar coupling tensor $\boldsymbol{D}(t)$ is given by

$$\begin{aligned} \boldsymbol{D}(t) &= \gamma_s\gamma_{s'}\hbar\left(\frac{\boldsymbol{1}}{r_{ss'}^3} - \frac{3\boldsymbol{r}_{ss'}(t)\boldsymbol{r}_{ss'}(t)}{r_{ss'}^5}\right) \\ &= \frac{\gamma_s\gamma_{s'}\hbar}{r_{ss'}^5}\begin{bmatrix} r_{ss'}^2 - 3x_{ss'}^2 & x_{ss'}y_{ss'} & x_{ss'}z_{ss'} \\ x_{ss'}y_{ss'} & r_{ss'}^2 - 3y_{ss'}^2 & y_{ss'}z_{ss'} \\ x_{ss'}z_{ss'} & y_{ss'}z_{ss'} & r_{ss'}^2 - 3z_{ss'}^2 \end{bmatrix} \end{aligned} \quad (7)$$

where $\boldsymbol{1}$ is the unit tensor, $x_{ss'}$, $y_{ss'}$ and $z_{ss'}$ are the x, y and z components of the vector $\boldsymbol{r}_{ss'}(t)$, between nuclei s and s', and γ_s is the magnetogyric ratio of spin s. The time dependence of this internuclear vector is explicit in most of equation (7), but is suppressed for clarity in the final term. The scalar distance between the two interacting nuclear spins is given by $r_{ss'}$.

Expressions of the type given in equation (6) may be rearranged to give an inner product of two matrices using the relationship

$$\hat{\boldsymbol{A}}\cdot\boldsymbol{M}\cdot\hat{\boldsymbol{B}} = \sum_{i,j}^{x,y,z} M_{ij}\hat{T}_{ij} \quad (8)$$

where M_{ij} are the elements of the matrix $\boldsymbol{M}$, and the elements of the composite tensor $\boldsymbol{T}$ are formed from $\hat{\boldsymbol{A}}$ and $\hat{\boldsymbol{B}}$ in accordance with $\hat{T}_{ij} = \hat{A}_i\hat{B}_j$. Thus, for the dipolar interaction,

$$\hat{\boldsymbol{T}}(s,s') = \begin{bmatrix} \hat{I}_x(s)\hat{I}_x(s') & \hat{I}_x(s)\hat{I}_y(s') & \hat{I}_x(s)\hat{I}_z(s') \\ \hat{I}_y(s)\hat{I}_x(s') & \hat{I}_y(s)\hat{I}_y(s') & \hat{I}_y(s)\hat{I}_z(s') \\ \hat{I}_z(s)\hat{I}_x(s') & \hat{I}_z(s)\hat{I}_y(s') & \hat{I}_z(s)\hat{I}_z(s') \end{bmatrix} \quad (9)$$

and the Hamiltonian for the dipole–dipole interaction becomes

$$\hat{\mathcal{H}}_{dd}(t) = \hbar\boldsymbol{D}(t)\cdot\hat{\boldsymbol{T}}(s,s') \quad (10)$$

Using a formulation analogous to that for the dipolar Hamiltonian, the chemical shift Hamiltonian is

$$\hat{\mathcal{H}}_{csa}(t) = \hbar\gamma_s\hat{\boldsymbol{I}}(s)\cdot\boldsymbol{\delta}(t)\cdot\boldsymbol{B} = \hbar\boldsymbol{\delta}(t)\cdot\hat{\boldsymbol{T}}(s,b) \quad (11)$$

where the time-dependent Cartesian chemical shift tensor $\boldsymbol{\delta}$(t) is given by

$$\boldsymbol{\delta}(t) = \gamma_s B_0\begin{bmatrix} \delta_{xx}(t) & \delta_{xy}(t) & \delta_{xz}(t) \\ \delta_{yx}(t) & \delta_{yy}(t) & \delta_{yz}(t) \\ \delta_{zx}(t) & \delta_{zy}(t) & \delta_{zz}(t) \end{bmatrix} \quad (12)$$

A composite spin field tensor $\boldsymbol{T}(a,b)$ is provided by

$$\hat{\boldsymbol{T}}(s,b) = \begin{bmatrix} \hat{I}_x(s)b_x & \hat{I}_x(s)b_y & \hat{I}_x(s)b_z \\ \hat{I}_y(s)b_x & \hat{I}_y(s)b_y & \hat{I}_y(s)b_z \\ \hat{I}_z(s)b_x & \hat{I}_z(s)b_y & \hat{I}_z(s)b_z \end{bmatrix} \quad (13)$$

where $b_q = B_q/B_0$, for $q = x$, y, and z. These reduced field variables provide a way to track the direction of the magnetic field that quantizes the nuclear spins. It is therefore appropriate that this feature be retained with the spin variables in the mathematical development of spin relaxation.

3 SEPARATION OF THE NUCLEAR SPIN HAMILTONIAN INTO SPIN AND SPATIAL TERMS

3.1 Spin Matrices and Spatial Spectral Densities

In a manner similar to equation (8), all μ mechanistic components in the Hamiltonian may also be formulated with

irreducible spherical tensors in spin, $\hat{T}^l_{-m}(s_\mu)$, and in time-dependent spatial variables, $F^l_m(\mu, t)$, as follows:

$$\hat{\mathcal{H}}_\mu = \hbar \sum_l \sum_{m=-l}^{l} (-1)^m \hat{T}^l_{-m}(s_\mu) F^l_m(\mu, t) \tag{14}$$

where the spin designator s_μ for the μth interaction represents either a single spin mechanism such as given by equation (11) for the chemical shift interaction or else the two-spin dipolar mechanism in equation (6). For convenience, s_μ is subsumed into the summation index μ. In equation (14) the indices l and m span all l ranks and corresponding m projections in the irreducible spherical operators. These tensors specified by $\hat{T}^l_{-m}(s_\mu)$ and $F^l_m(\mu, t)$ are defined in the laboratory coordinate system, with the magnetic field along the z axis. Such formulations of the Hamiltonians, defined in terms of spin and spatial spherical tensors, have been treated by Mehring[16] and by Smith et al.[17] Details of the spin, $\hat{T}^l_{-m}(s_\mu)$, and spatial, $F^l_m(\mu, t)$, tensors are provided in Section 3.2.

The Hamiltonian in equation (14) may be introduced into equation (5) to give

$$\begin{aligned} K_{\kappa\lambda\kappa'\lambda'}(\omega_{\kappa\lambda}) = \sum_{\mu,\mu'\rangle\mu} \sum_{l,l'} \sum_{m=-l}^{l} \sum_{m'=-l'}^{l'} \int_0^\infty \{ & S^\mu_{ll'mm'} \langle F^l_m(\mu, t) \\ & \times F^{l'}_{m'}(\mu, t+\tau) \rangle e^{-i\omega_{\kappa\lambda}\tau} + [S^{\mu\mu'}_{ll'mm'} \\ & \times \langle \hat{F}^l_m(\mu, t) \hat{F}^{l'}_{m'}(\mu', t+\tau) \rangle + S^{\mu'\mu}_{ll'mm'} \\ & \times \langle F^l_m(\mu', t) F^{l'}_{m'}(\mu, t+\tau) \rangle] e^{-i\omega_{\kappa\lambda}\tau} \} d\tau \end{aligned} \tag{15}$$

where the $\langle\ \rangle$ around the spatial correlation functions specifies an ensemble average, and the spin matrix $S^{\mu\mu'}_{ll'mm'}$ in equation (15) is defined by

$$S^{\mu\mu'}_{ll'mm'} = (-1)^m \langle \kappa | \hat{T}^l_{-m}(s_\mu) | \lambda \rangle \langle \lambda' | \hat{T}^{l'}_{-m'}(s_{\mu'}) | \kappa' \rangle \tag{16}$$

The autocorrelation spin function $S^\mu_{ll'mm'}$ is obtained by merely setting $\mu' = \mu$ in equation (16).

The spin matrices, embodied in $S^{\mu\mu'}_{ll'mm'}$, provide spin selection rules that impose constraints upon the relaxation process. Included in these constraints is the symmetry of the coupled spin system, which reflects the symmetry of the parent molecule. Selection rules governing the constraints upon the various l and m values, however, have several important consequences for the correlation functions given in equation (16). In order for $S^{\mu\mu'}_{ll'mm'}$ to survive under the secular approximation, i.e., $E_{\kappa'} - E_{\lambda'} = E_\kappa - E_\lambda$, it is necessary that any change in the angular momentum between eigenstates $\langle\lambda'|$ and $|\kappa'\rangle$ be equal and opposite in sign to the change in angular momentum between eigenstates $\langle\kappa|$ and $|\lambda\rangle$. This requires that the two spin tensors have conjugate angular momentum properties, i.e., $l' = l$ but $m' = -m$. Under these constraints, the summations on rank and projection indices in equation (15) are contracted to a single l and a single m index, and the respective auto- and cross-correlated spin matrices are given as follows:

$$\left.\begin{aligned} S^\mu_{lm} &= \delta_{l,l'}\delta_{m',-m} S^\mu_{ll'mm'} \\ &= (-1)^m \langle \kappa | \hat{T}^l_{-m}(s_\mu) | \lambda \rangle \langle \lambda' | \hat{T}^l_m(s_\mu) | \kappa' \rangle \\ S^{\mu\mu'}_{lm} &= \delta_{l,l'}\delta_{m',-m} S^{\mu\mu'}_{ll'mm'} \\ &= (-1)^m \langle \kappa | \hat{T}^l_{-m}(s_\mu) | \lambda \rangle \langle \lambda' | \hat{T}^l_m(s_{\mu'}) | \kappa' \rangle \end{aligned}\right\} \tag{17}$$

Using the Kronecker deltas to contract l' and m' converts equation (15) into the following simplified expressions for the auto- and cross-correlation spectral densities:

$$\begin{aligned} K_{\kappa\lambda\kappa'\lambda}(\omega_{\kappa\lambda}) = \sum_l \sum_{m=l}^{l} \Bigg[& \sum_\mu S^\mu_{lm} \mathcal{J}^\mu_{lm}(\omega_{\kappa\lambda}) \\ & + \sum_{\mu\rangle\mu'} \tfrac{1}{2}(S^{\mu\mu'}_{lm} + S^{\mu'\mu}_{lm}) \operatorname{Re} \mathcal{K}^{\mu\mu'}_{lm}(\omega_{\kappa\lambda}) \\ & + \sum_{\mu\rangle\mu'} \tfrac{1}{2}(S^{\mu\mu'}_{lm} - S^{\mu'\mu}_{lm}) \operatorname{Im} \mathcal{K}^{\mu\mu'}_{lm}(\omega_{\kappa\lambda}) \Bigg] \end{aligned} \tag{18}$$

where $S^{\mu\mu'}_{lm} + S^{\mu'\mu}_{lm}$ and $S^{\mu\mu'}_{lm} - S^{\mu'\mu}_{lm}$ are, respectively, even and odd spin matrices that select either the real, $\operatorname{Re}\mathcal{K}^{\mu\mu'}_{lm}(\omega_{\kappa\lambda})$, or imaginary, $\operatorname{Im}\mathcal{K}^{\mu\mu'}_{lm}(\omega_{\kappa\lambda})$, portions of the cross-correlated spatial terms. The factors of $\frac{1}{2}$ in the cross terms are required to avoid double counting with the symmetrizing of spin in equation (18). The following definitions hold for the spatial spectral densities:

$$\begin{aligned} \mathcal{J}^\mu_{lm}(\omega_{\kappa\lambda}) = \tfrac{1}{2}(-1)^m \int_{-\infty}^{\infty} & \langle F^l_m(\mu, t) F^l_{-m}(\mu, t+\tau) \rangle \\ & \times e^{-i\omega_{\kappa\lambda}\tau}\, d\tau \end{aligned} \tag{19}$$

$$\begin{aligned} \operatorname{Re} \mathcal{K}^{\mu\mu'}_{lm}(\omega_{\kappa\lambda}) \quad \tfrac{1}{2}(-1)^m \int_{\infty}^{\infty} & [\langle F^l_m(\mu, t) F^l_{-m}(\mu', t+\tau) \rangle \\ & + \langle F^l_m(\mu', t) F^l_{-m}(\mu, t+\tau) \rangle] e^{-i\omega_{\kappa\lambda}\tau}\, d\tau \end{aligned} \tag{20}$$

$$\begin{aligned} \operatorname{Im} \mathcal{K}^{\mu\mu'}_{lm}(\omega_{\kappa\lambda}) = (-1)^m \int_0^{\infty} & [\langle F^l_m(\mu, t) F^l_{-m}(\mu', t+\tau) \rangle \\ & - \langle F^l_m(\mu', t) F^l_{-m}(\mu, t+\tau) \rangle] e^{-i\omega_{\kappa\lambda}\tau}\, d\tau \end{aligned} \tag{21}$$

The real spectral densities, $\mathcal{J}^\mu_{lm}(\omega_{\kappa\lambda})$ and $\operatorname{Re}\mathcal{K}^{\mu\mu'}_{lm}(\omega_{\kappa\lambda})$, given in equations (19) and (20), are Fourier transforms of the spatial auto- and cross-correlation functions, respectively. Both now possess time-reversal symmetry, and the integral may be changed accordingly from $(0, \infty)$ to $(-\infty, \infty)$. The $\frac{1}{2}$ in front of each integral is associated with doubling the range of these integrals.

The imaginary spectral density $\operatorname{Im}\mathcal{K}^{\mu\mu'}_{lm}(\omega_{\kappa\lambda})$ given in equation (21) and selected by the $S^{\mu\mu'}_{lm} - S^{\mu'\mu}_{lm}$ spin matrices, is an odd function in time and must retain the $(0, \infty)$ range in its integral. The spin matrices $S^{\mu\mu'}_{lm}$ are Hermitian, and as such yield only real values, but reversing the order of the interaction labels in individual spin matrices can in some instances change the sign of $S^{\mu\mu'}_{lm}$. Under these conditions, such an alternation in

sign will quench the real terms needed for relaxation, but will introduce the imaginary component of the spatial correlation functions. This imaginary term accounts for the second-order dynamic frequency shift discussed earlier; hence, only the two real terms are considered further in this article on molecular motion and spin relaxation. The angle-bracketed correlation functions specify ensemble averages over all equivalent spins in the sample.

3.2 The General Cartesian Interaction Tensor and its Irreducible Spherical Tensor

A typical interaction tensor, in the principal rotational diffusion frame, is a 3×3 Cartesian tensor that may be separated into three individual tensors of rank zero, one, and two as follows:

$$\begin{bmatrix} \mu_{xx} & \mu_{xy} & \mu_{xz} \\ \mu_{yx} & \mu_{yy} & \mu_{yz} \\ \mu_{zx} & \mu_{zy} & \mu_{zz} \end{bmatrix} = \mu_0 \begin{bmatrix} 1 & 0 & 0 \\ 0 & 1 & 0 \\ 0 & 0 & 1 \end{bmatrix} + \begin{bmatrix} 0 & \mu_{xy}^{(a)} & \mu_{xz}^{(a)} \\ -\mu_{xy}^{(a)} & 0 & \mu_{yz}^{(a)} \\ -\mu_{xz}^{(a)} & -\mu_{yz}^{(a)} & 0 \end{bmatrix} + \begin{bmatrix} \mu_{xx}^{(s)} - \mu_0 & \mu_{xy}^{(s)} & \mu_{xz}^{(s)} \\ \mu_{xy}^{(s)} & \mu_{yy}^{(s)} - \mu_0 & \mu_{yz}^{(s)} \\ \mu_{xz}^{(s)} & \mu_{yz}^{(s)} & \mu_{zz}^{(s)} - \mu_0 \end{bmatrix} \quad (22)$$

where the isotropic scalar term $\mu_0 = \frac{1}{3}(\mu_{xx} + \mu_{yy} + \mu_{zz})$, the antisymmetric elements $\mu_{ij}^{(a)} = \frac{1}{2}(\mu_{ij} - \mu_{ji})$, and the symmetric elements $\mu_{ij}^{(s)} = \frac{1}{2}(\mu_{ij} + \mu_{ji})$ have been isolated, respectively, into zeroth-, first- and second-rank tensors.

Using the prescription of Mehring,[18] the general irreducible spherical tensors are readily obtained from equation (22) as

$$\left.\begin{aligned} \mathcal{T}_0^{(0)}(\mu) &= -\sqrt{3}\mu_0 = -\sqrt{\tfrac{1}{3}}(\mu_{xx} + \mu_{yy} + \mu_{zz}) \\ \mathcal{T}_0^{(1)}(\mu) &= -\mathrm{i}\sqrt{2}\mu_{xy}^{(a)} = -\mathrm{i}\sqrt{\tfrac{1}{2}}(\mu_{xy} - \mu_{yx}) \\ \mathcal{T}_{\pm1}^{(1)}(\mu) &= \mu_{xz}^{(a)} \pm \mathrm{i}\mu_{yz}^{(a)} = \tfrac{1}{2}[(\mu_{xz} - \mu_{zx}) \pm \mathrm{i}(\mu_{yz} - \mu_{zy})] \\ \mathcal{T}_0^{(2)}(\mu) &= \sqrt{\tfrac{1}{6}}[3\mu_{zz}^{(s)} - (\mu_{xx}^{(s)} + \mu_{yy}^{(s)} + \mu_{zz}^{(s)})] \\ &= \sqrt{\tfrac{3}{2}}(\mu_{zz} - \mu_0) \\ \mathcal{T}_{\pm1}^{(2)}(\mu) &= \mp(\mu_{xz}^{(s)} \pm \mathrm{i}\mu_{yz}^{(s)}) \\ &= \mp\tfrac{1}{2}[(\mu_{xz} + \mu_{zx}) \pm \mathrm{i}(\mu_{yz} + \mu_{zy})] \\ \mathcal{T}_{\pm2}^{(2)}(\mu) &= \left[\tfrac{1}{2}(\mu_{xx}^{(s)} - \mu_{yy}^{(s)}) \pm \mathrm{i}\mu_{xy}^{(s)}\right] \\ &= \tfrac{1}{2}[(\mu_{xx} - \mu_{yy}) \pm \mathrm{i}(\mu_{xy} + \mu_{yx})] \end{aligned}\right\} \quad (23)$$

These expressions may be used with equations (7), (9), (12), and (13) to define both the spin, $\hat{T}_{-m}^{l}(s_\mu)$, and spatial, $F_m^l(\mu, t)$, variables used in equations (14)–(21).

3.2.1 *Specific Expressions for Various Irreducible Spin Operators*

The irreducible spherical tensors defined in equation (23) may be used for the two coupled spin angular momentum operators $\hat{\boldsymbol{I}}^i$ and $\hat{\boldsymbol{I}}^j$ encountered in equation (9) for the dipole–dipole Hamiltonian; these spin tensors are given by

$$\left.\begin{aligned} \hat{T}_0^{(0)}(i,j) &= -\sqrt{\tfrac{1}{3}}\left[\hat{I}_z^i\hat{I}_z^j + \tfrac{1}{2}(\hat{I}_+^i\hat{I}_-^j + \hat{I}_-^i\hat{I}_+^j)\right] \\ \hat{T}_0^{(1)}(i,j) &= \sqrt{\tfrac{1}{8}}(\hat{I}_+^i\hat{I}_-^j - \hat{I}_-^i\hat{I}_+^j) \\ \hat{T}_{\pm1}^{(1)}(i,j) &= \tfrac{1}{2}(\hat{I}_\pm^i\hat{I}_z^j - \hat{I}_z^i\hat{I}_\pm^j) \\ \hat{T}_0^{(2)}(i,j) &= \sqrt{\tfrac{2}{3}}\left[\hat{I}_z^i\hat{I}_z^j - \tfrac{1}{4}(\hat{I}_+^i\hat{I}_-^j + \hat{I}_-^i\hat{I}_+^j)\right] \\ \hat{T}_{\pm1}^{(2)}(i,j) &= \mp\tfrac{1}{2}(\hat{I}_\pm^i\hat{I}_z^j + \hat{I}_z^i\hat{I}_\pm^j) \\ \hat{T}_{\pm2}^{(2)}(i,j) &= \tfrac{1}{2}\hat{I}_\pm^i\hat{I}_\pm^j \end{aligned}\right\} \quad (24)$$

The ladder spin operators $\hat{I}_\pm = \hat{I}_x \pm \mathrm{i}\hat{I}_y$, used extensively in NMR, have been employed here. These ladder operators should not be confused with the similar irreducible spherical angular momentum operators $\hat{I}_{+1}$ and $\hat{I}_{-1}$ used elsewhere.

The appropriate spin–field combined tensors for the anisotropic chemical shift interaction is formed by coupling the first-rank angular momentum operators, for a single spin with the first-rank magnetic field vector $\boldsymbol{B}_0$. The resulting combined irreducible spherical tensors are given by

$$\left.\begin{aligned} \hat{T}_0^{(0)}(\mathrm{csa}) &= -\sqrt{\tfrac{1}{3}}\left[\hat{I}_z b_z + \tfrac{1}{2}(\hat{I}_+ b_- + \hat{I}_- b_+)\right] \\ \hat{T}_0^{(1)}(\mathrm{csa}) &= \sqrt{\tfrac{1}{8}}(\hat{I}_+ b_- - \hat{I}_- b_+) \\ \hat{T}_{\pm1}^{(1)}(\mathrm{csa}) &= -\tfrac{1}{2}(\hat{I}_z\hat{b}_\pm - \hat{I}_\pm\hat{b}_z) \\ \hat{T}_0^{(2)}(\mathrm{csa}) &= \sqrt{\tfrac{2}{3}}\left[\hat{I}_z b_z - \tfrac{1}{4}(\hat{I}_+ b_- + \hat{I}_- b_+)\right] \\ \hat{T}_{\pm1}^{(2)}(\mathrm{csa}) &= \mp\tfrac{1}{2}(\hat{I}_\pm b_z + \hat{I}_z b_\pm) \\ T_{\pm2}^{(2)}(\mathrm{csa}) &= \tfrac{1}{2}\hat{I}_\pm\hat{b}_\pm \end{aligned}\right\} \quad (25)$$

where $\boldsymbol{b}_\pm = (B_x\boldsymbol{h} \pm \mathrm{i}B_y\boldsymbol{j})/B_0$ and $b_z = B_z/B_0$. B_x, B_y, and B_z are the components of $\boldsymbol{B}_0$ in a general coordinate frame, with unit vectors $\boldsymbol{h}$, $\boldsymbol{j}$, and $\boldsymbol{k}$ along the x, y, and z axes, respectively.

In the laboratory frame the static magnetic field is $B_z = B_0$, and $B_x = B_y = 0$. This coordinate system simplifies equation (25) considerably to yield the following combined irreducible spin–field tensors:

$$\left.\begin{aligned} &\hat{T}_0^{(0)}(\mathrm{csa}) = -\sqrt{\tfrac{1}{3}}\hat{I}_z b_z, \quad \hat{T}_0^{(2)}(\mathrm{csa}) = \sqrt{\tfrac{2}{3}}\hat{I}_z b_z \\ &\hat{T}_0^{(1)}(\mathrm{csa}) = 0, \quad \hat{T}_{\pm1}^{(2)}(\mathrm{csa}) = \mp\tfrac{1}{2}\hat{I}_\pm b_z \\ &\hat{T}_{\pm1}^{(1)}(\mathrm{csa}) = \tfrac{1}{2}\hat{I}_\pm b_z, \quad \hat{T}_{\pm2}^{(2)}(\mathrm{csa}) = 0 \end{aligned}\right\} \quad (26)$$

3.2.2 *Specific Irreducible Spatial Operators*

The time-dependent irreducible spatial terms $\boldsymbol{F}(\mu,t)$, used in equation (14) for a general second-rank interaction, include $F_0^{(1)}(\mu,t)$, $F_{\pm1}^{(1)}(\mu,t)$, $F_0^{(2)}(\mu,t)$, $F_{\pm1}^{(2)}(\mu,t)$, and $F_{\pm2}^{(2)}(\mu,t)$. The zeroth-rank member, $\hat{F}_0^{(0)}(\mu)$, is proportional to the trace of the Cartesian interaction tensor, and is therefore time-independent under molecular tumbling. Specific expressions for each of the relevant terms may be obtained for the dipolar and chemical shift anisotropy mechanisms, respectively, from

equation (7) and (12) following the prescription of equation (23). These elements of the spatial irreducible tensors characterize the temporal motions of molecular tumbling while introducing the geometry of spin interactions into the relaxation Hamiltonian.

The $F_0^{(0)}(\mu, t)$ term is invariant under molecular tumbling, and therefore cannot create magnetic field oscillations that affect spin relaxation processes; it need not be considered further. Fluctuating magnetic fields arising from first-rank terms, $\hat{F}_0^{(1)}(\mu, t)$ and $\hat{F}_{\pm 1}^{(1)}(\mu, t)$, are modulated by molecular motion and will relax the nuclear spins. These first-rank terms do not exist for the prominent dipolar interactions, but the first-rank antisymmetric chemical shift terms can relax a magnetic spin. Such chemical shift terms, however, are poorly characterized compared with the more commonly encountered second-rank terms. The first-rank chemical shift anisotropy terms are easily formulated with the methods outlined below, but theoretical studies would indicate that these interesting terms are probably restricted to fairly unusual molecular systems.[19–21] Molecules for which the antisymmetric, first-rank chemical shift anisotropy terms appear to be important include π-electron systems with sterically distorted bond arrangements. The magnitude of such first-rank chemical shift terms, supported theoretically in a few unusual molecules, is difficult to establish experimentally, since only the zeroth- and second-rank chemical shift terms may be measured in Zeeman splittings. Consequently, only the specifics of second-rank terms are developed in this article, which focuses primarily upon molecular diffusional motion. The methods are sufficiently general, however, that they may be extended to first-rank terms when needed.

In order to evaluate the second-rank dipole–dipole and chemical shift anisotropy tensors for all molecules in a sample, an ensemble average of $\boldsymbol{F}(\mu,t)$ must be obtained using standard statistical mechanical methods to describe the effects of Brownian motion in liquids.[22] Attention is therefore directed to separating the molecular motional features that are time-dependent from the specific formulations of the irreducible spatial interaction tensors. Once the time dependence has been extracted in Sections 4 and 5, the exact form of the remaining time-independent interaction tensors will be considered.

4 MOTIONAL POWER DENSITIES IN THE MOLECULAR ROTATIONAL DIFFUSION FRAME

The irreducible spatial tensor, $\boldsymbol{F}(\mu,t)$, may be obtained by a coordinate transformation from the corresponding spatial tensor in the molecular rotational diffusion frame as follows:

$$F_m^l(\mu, t) = \sum_{n=-l}^{l} \mathcal{D}_{n,m}^{(l)}(\Omega_t)\mathcal{F}_n^l(\mu) \tag{27}$$

where $F_m^l(\mu, t)$ is in the laboratory frame and $\mathcal{F}_n^l(\mu)$ is in the principal axis frame of the molecular rotational diffusion tensor. The Wigner rotation matrix elements $\mathcal{D}_{n,m}^{(l)}(\Omega_t)$ transform the diffusion frame into the laboratory coordinate frame and simultaneously absorb the explicit time dependence manifest in $F_m^l(\mu, t)$. The time-dependent Euler angles are represented by $\Omega_t \sum (\alpha_t,\beta_t,\gamma_t)$. The interaction tensor $\mathcal{F}_n^l(\mu)$, given in the principal diffusion frame, provides a time-independent spatial description of the spin interaction for the μth relaxation mechanism. This division of $F_m^l(\mu, t)$ into time-dependent and time-independent terms separates the molecular dynamics, described by $\mathcal{D}_{n,m}^{(l)}(\Omega_t)$, from the NMR spectral and geometrical parameters contained in $\mathcal{F}_n^l(\mu)$.

Substituting equation (27) into equations (19) and (20) provides expressions for the auto- and cross-correlated spectral densities as follows:

$$\mathcal{J}_{lm}^{\mu}(\omega_{\kappa\lambda}) = \tfrac{1}{2}(-1)^m \sum_{n,n'=-l}^{l} \int_{-\infty}^{\infty} \langle \mathcal{D}_{n,m}^{(l)}(\Omega_t)\mathcal{F}_n^l(\mu) \times \mathcal{D}_{n',-m}^{(l)}(\Omega_{t+\tau})\mathcal{F}_{n'}^l(\mu)\rangle \mathrm{e}^{-\mathrm{i}\omega_{k\lambda}\tau}\,\mathrm{d}\tau \tag{28a}$$

$$\mathrm{Re}\,\mathcal{K}_{lm}^{\mu\mu'}(\omega_{\kappa\lambda}) = \tfrac{1}{2}(-1)^m \sum_{n,n'=-l}^{l} \int_{-\infty}^{\infty} \{\langle \mathcal{D}_{n,m}^{(l)}(\Omega_t)\mathcal{F}_n^l(\mu) \times \mathcal{D}_{n',-m}^{(l)}(\Omega_{t+\tau})\mathcal{F}_{n'}^l(\mu')\rangle + \langle \mathcal{D}_{n,m}^{(l)}(\Omega_t)\mathcal{F}_n^l(\mu') \times \mathcal{D}_{n',-m}^{(l)}(\Omega_{t+\tau})\mathcal{F}_{n'}^l(\mu)\rangle\} \mathrm{e}^{-\mathrm{i}\omega_{\kappa\lambda}\tau}\,\mathrm{d}\tau \tag{28b}$$

Since all of the interaction tensors typified by $\mathcal{F}_n^l(\mu)$ are time-independent when defined in the principal axis frame of the molecular rotational diffusion tensor, they may be factored out of the ensemble-averaging brackets, and they also pass through the time integrals given in equation (28). The ergodic hypothesis renders both time- and sample-averaged ensembles equivalent, thereby allowing the removal also of the explicit time variable t from equation (28) while retaining the correlation time difference τ. Rearranging equation (28), the following expressions are obtained for $\mathcal{J}_{lm}^{\mu}(\omega_{\kappa\lambda})$ and $\mathrm{Re}\mathcal{K}_{lm}^{\mu\mu'}(\omega_{\kappa\lambda})$:

$$\mathcal{J}_{lm}^{\mu}(\omega_{\kappa\lambda}) = \sum_{n,n'=-l}^{l} [\mathcal{F}_n^l(\mu)\mathcal{F}_{n'}^l(\mu)]\mathcal{M}_{nn'm}^{(l)}(\omega_{\kappa\lambda}) \tag{29}$$

$$\mathrm{Re}\,\mathcal{K}_{lm}^{\mu\mu'}(\omega_{\kappa\lambda}) = \sum_{n,n'=-l}^{l} [\mathcal{F}_n^l(\mu)\mathcal{F}_{n'}^l(\mu') + \mathcal{F}_n^l(\mu')\mathcal{F}_{n'}^l(\mu)] \times \mathcal{M}_{nn'm}^{(l)}(\omega_{\kappa\lambda}) \tag{30}$$

All of the time-dependent terms in equation (28) have been collected together into a molecular motional power density $\mathcal{M}_{nn'm}^{(l)}(\omega_{\kappa\lambda})$, given by

$$\mathcal{M}_{nn'm}^{(l)}(\omega_{\kappa\lambda}) = \tfrac{1}{2}(-1)^m \int_{-\infty}^{\infty} G_{nn'm}^{(l)}(\tau)\mathrm{e}^{-\mathrm{i}\omega_{\kappa\lambda}\tau}\,\mathrm{d}\tau \tag{31}$$

The correlation function $G_{nn'm}^{(l)}(\tau)$ appearing in $\mathcal{M}_{nn'm}^{(l)}$ $(\omega_{kappa\lambda})$ is totally free from nuclear spin parameters, and it is the same function for both the autocorrelated spectral density in equation (29) and the cross-correlated spectral density in equation (30). $G_{nn'm}^{(l)}(\tau)$ characterizes only molecular motional features, and, consistently with equations (28)–(31), it has the form

$$G_{nn'm}^{(l)}(\tau) = \langle \mathcal{D}_{n,m}^{(l)}(\Omega_0)\mathcal{D}_{n',-m}^{(l)}(\Omega_\tau)\rangle = (-1)^{m-n'}\langle \mathcal{D}_{n,m}^{(l)}(\Omega_0)\mathcal{D}_{-n',m}^{(l)*}(\Omega_\tau)\rangle \tag{32}$$

The Euler angles for the molecular orientations relative to the laboratory frame are specified at $t + 0$ by Ω_0 and at $t + \tau$ by Ω_τ. As discussed above, the explicit dependence on time t found in equation (28) has been removed in this expression for $G^{(l)}_{nn'm}(\tau)$, which depends only upon the time-difference variable τ. Averaging $G^{(l)}_{nn'm}(\tau)$ with the integral ranging over $(-\infty, \infty)$ recognizes the time-reversal symmetry of correlation functions, such as $G^{(l)}_{nn'm}(\tau)$, that describe stationary random molecular motions.[15]

5 THE FAVRO EQUATION AND MOLECULAR ROTATIONAL DIFFUSION IN LIQUIDS

5.1 Conditional Probabilities for Correlation of Molecular Rotational Orientations

The correlation function in equation (32) implies an ensemble average over all possible orientational angles, and this average may be expressed by a double integral over the probabilistic weighted angles Ω_0 and Ω_τ as follows:

$$G^{(l)}_{nn'm}(\tau) = (-1)^{m-n'} \int\int \mathrm{d}\Omega_0\, \mathrm{d}\Omega_\tau \times [\mathcal{D}^{(l)}_{n,m}(\Omega_0)\mathcal{D}^{(l)*}_{-n',m}(\Omega_\tau) P(\Omega_0) P(\Omega_0|\Omega_\tau)] \quad (33)$$

where $P(\Omega_0)$ is the probability that the molecule has an orientation Ω_0 at an arbitrary time zero and $P(\Omega_0|\Omega_\tau)$ is a conditional probability that the molecule will have the orientation Ω_τ at a time τ, given that at time zero the orientation was Ω_0. Molecules dissolved in randomly ordered or isotropic fluids have no preferred orientation, and the initial probability $P(\Omega_0)$ is constant for all values of Ω_0. Thus, $P(\Omega_0)$ can be evaluated by normalizing to unity over all orientations as follows:

$$\int P(\Omega_0)\mathrm{d}\Omega_0 = P(\Omega_0) \int_0^{2\pi} \mathrm{d}\alpha \int_0^{\pi} \sin\beta\, \mathrm{d}\beta \int_0^{2\pi} \mathrm{d}\gamma = 8\pi^2 P(\Omega_0) = 1 \quad (34)$$

$$P(\Omega_0) = (8\pi^2)^{-1} \quad (35)$$

Note that the assumption of isotropic liquid ordering does not imply that the molecular tumbling is isotropic. This discussion, however, does presume a rigid molecule without internal degrees of motional freedom.

The Favro equation[4] for molecular diffusion has the same general form as the wave equation for a rigid asymmetric rotor, and characterizes the $P(\Omega_0|\Omega_\tau)$ conditional probability according to

$$\frac{\partial P(\Omega_0|\Omega_\tau)}{\partial \tau} = \sum_{p,q} \hat{\mathcal{L}}_p R'_{pq} \hat{\mathcal{L}}_q P(\Omega_0|\Omega_\tau) = -\hat{\mathcal{R}} P(\Omega_0|\Omega_\tau) \quad (36)$$

where $\hat{\mathcal{R}}$ is the rotational diffusion operator (defined by this equation), and $\hat{\mathcal{L}}_p$ and $\hat{\mathcal{L}}_q$ are the pth and qth components of the angular momentum operator. $R_{pq}{}'$ is the general pq component of the rotational diffusion tensor in an arbitrary reference frame, and is defined by

$$R'_{pq} = \tfrac{1}{2} \lim_{\Delta\tau \to 0} \frac{\langle \varphi_p \varphi_q \rangle}{\Delta\tau} \quad (37)$$

where φ_p and φ_q are the rotational angles about the pth and qth molecular axes, respectively.

Under the assumption of an isotropic fluid, $R_{pq}{}'$ is a symmetric tensor that may be diagonalized in the principal axis frame (PAF) of the molecular rotational diffusion tensor. This provides the generalized rotational diffusion operator $\hat{\mathcal{R}}$ (PAF) as follows:

$$\hat{\mathcal{R}}(\mathrm{PAF}) = \sum_{p,q} \hat{\mathcal{L}}_p R_{pq}(\mathrm{PAF}) \mathcal{L}_q = R_{xx}\hat{\mathcal{L}}_x^2 + R_{yy}\hat{\mathcal{L}}_y^2 + R_{zz}\hat{\mathcal{L}}_z^2 \quad (38)$$

where the principal components, without primes, of the rotational diffusion tensor are given by R_{xx}, R_{yy}, and R_{zz}. For convenience, equation (38) may be rewritten using irreducible angular momentum operators as

$$\hat{\mathcal{R}}(\mathrm{PAF}) = A\hat{\mathcal{L}}^2 + \tfrac{1}{2}B(\hat{\mathcal{L}}_+^2 + \hat{\mathcal{L}}_-^2) + C\hat{\mathcal{L}}_z^2 \quad (39)$$

where

$$\hat{\mathcal{L}}_+ = \hat{\mathcal{L}}_x + \mathrm{i}\hat{\mathcal{L}}_y, \quad \hat{\mathcal{L}}_- = \hat{\mathcal{L}}_x - \mathrm{i}\hat{\mathcal{L}}_y, \quad \hat{\mathcal{L}}^2 = \hat{\mathcal{L}}_x^2 + \hat{\mathcal{L}}_y^2 + \hat{\mathcal{L}}_z^2 \quad (40)$$

$$A = \tfrac{1}{2}(R_{xx} + R_{yy}) \quad B = \tfrac{1}{2}(R_{xx} - R_{yy}) \quad C = R_{zz} - \tfrac{1}{2}(R_{xx} + R_{yy}) \quad (41)$$

Equation (36) has a solution of the general form

$$P(\Omega_0|\Omega_\tau) = \sum_\nu g_\nu(\tau)\Psi_\nu(\Omega_\tau) \quad (42)$$

The explicit dependence of $P(\Omega_0|\Omega_\tau)$ upon τ is now contained in $g_\nu(\tau)$, and the $\Psi_\nu(\Omega_\tau)$ are expressed as stationary eigenfunctions of the diffusion operator $\hat{\mathcal{R}}$ with eigenvalues b_ν as follows:

$$\hat{\mathcal{R}}\Psi_\nu(\Omega_\tau) = b_\nu \Psi_\nu(\Omega_\tau) \quad (43)$$

By substituting equation (42) into equation (36) and using equation (43) the following expression is obtained:

$$\sum_\nu \Psi_\nu(\Omega_\tau) \frac{\partial g_\nu(\tau)}{\partial t} = -\sum_\nu b_\nu g_\nu(\tau)\Psi_\nu(\Omega_\tau) \quad (44)$$

Matching the corresponding coefficients of the linearly independent functions $\Psi_\nu(\Omega_\tau)$, the following differential equation for $g_\nu(\tau)$ is obtained:

$$\frac{\partial g_\nu(\tau)}{\partial t} = -b_\nu g_\nu(\tau) \quad (45)$$

which has the general solution

$$g_\nu(\tau) = g_\nu(0)\,\mathrm{e}^{-b_\nu\tau} \tag{46}$$

Standard expansion methods, such as used in equation (42), also render an expression for $g_\nu(\tau)$ as follows:

$$g_\nu(\tau) = \int \mathrm{d}\Omega\, \Psi_\nu^*(\Omega_\tau) P(\Omega_0|\Omega_\tau) \tag{47}$$

The boundary condition $P(\Omega_0|\Omega_{\tau=0}) = \delta^{(3)}_{\Omega_0,\Omega_\tau}$ for $\tau = 0$ may be used with equation (47) to evaluate $g_\nu(0)$, giving the expression

$$\begin{aligned} g_\nu(0) &= \int \mathrm{d}\Omega\, \Psi_\nu^*(\Omega_\tau) P(\Omega_0|\Omega_{\tau=0}) \\ &= \int \mathrm{d}\Omega\, \Psi_\nu^*(\Omega_\tau)\delta^{(3)}_{\Omega_0,\Omega_\tau} = \Psi_\nu^*(\Omega_0) \end{aligned} \tag{48}$$

Use has been made here of the definition of the three-dimensional Dirac delta function, i.e., $f(a) = \int \delta^{(3)}_{a,b} f(b)\mathrm{d}b$. Combining equations (42), (46), and (47) provides the following expression for $P(\Omega_0|\Omega_\tau)$:

$$P(\Omega_0|\Omega_\tau) = \sum_\nu \Psi_\nu^*(\Omega_0)\Psi_\nu(\Omega_\tau)\,\mathrm{e}^{-b_\nu\tau} \tag{49}$$

5.2 Rotational Diffusion Eigenvalues and Eigenvectors

The challenge has now been reduced to finding $\Psi_\nu(\Omega_\tau)$, the eigenfunctions of $\hat{\mathcal{R}}$(PAF) given in equation (43). The corresponding eigenvalues b_ν are obtained from the typical characteristic equation in the operator $\hat{\mathcal{R}}$(PAF). Wavefunctions[23] for the analogous asymmetric rotor problem in quantum mechanics are the Wigner rotation functions $\mathcal{D}^{(l)}_{k,m}(\Omega_t)$, and these provide an excellent basis[3,24] for expanding the eigenfunctions $\Psi_\nu(\Omega_\tau)$ associated with rotational diffusion as follows:

$$\Psi_\nu = \sum_{l,k,j} c^{(l)}_{\nu,k,j}\psi_{l,k,j} = \sum_{l,k,j} c^{(l)}_{\nu,k,j}\sqrt{\frac{2l+1}{8\pi^2}}\mathcal{D}^{(l)}_{k,j}(\Omega_\tau) \tag{50}$$

The factor $\sqrt{2l+1/8\pi^2}$ is a normalization constant for the functions $\mathcal{D}^{(l)}_{k,j}(\Omega_\tau)$ when integrated over the space of Euler angles Ω_τ. The various $c^{(l)}_{\nu,k,j}$ are the appropriate eigenvectors to be obtained along with the eigenvalues b_ν from the characteristic equation in the diffusion operator $\hat{\mathcal{R}}$(PAF). Because of the analogy with the asymmetric rigid rotor problem, it is not surprising that expansions in Wigner rotation matrices provide a natural basis for the study of rotational diffusion.

The functions $\mathcal{D}^{(l)}_{k,j}(\Omega_\tau)$ possess a number of angular momentum properties associated with the total angular momentum squared, $\hat{\mathcal{L}}^2$, and the z component of the angular momentum in the molecular diffusion frame, $\hat{\mathcal{L}}_z$. The $\mathcal{D}^{(l)}_{k,j}(\Omega_\tau)$ also manifest a third important property for the z' component of angular momentum, $\hat{\mathcal{L}}_{z'}$, in the laboratory frame. This property, however, is only used when a molecule is dissolved in ordered solvents, e.g., nematic liquid crystals. Thus,

$$\left.\begin{aligned} \hat{\mathcal{L}}^2\mathcal{D}^{(l)}_{k,j}(\Omega_\tau) &= l(l+1)\hbar^2\mathcal{D}^{(l)}_{k,j}(\Omega_\tau) \\ \hat{\mathcal{L}}_z\mathcal{D}^{(l)}_{k,j}(\Omega_\tau) &= k\hbar\mathcal{D}^{(l)}_{k,j}(\Omega_\tau) \\ \hat{\mathcal{L}}_{z'}\mathcal{D}^{(l)}_{k,j}(\Omega_\tau) &= j\hbar\mathcal{D}^{(l)}_{k,j}(\Omega_\tau) \end{aligned}\right\} \tag{51}$$

Expressions may also be obtained for the operator $\hat{\mathcal{L}}^2_+ + \hat{\mathcal{L}}^2_-$ found in equation (39) using the following:

$$\left.\begin{aligned} \hat{\mathcal{L}}_\pm\mathcal{D}^{(l)}_{k,j}(\Omega_\tau) &= \sqrt{(l\mp k)(l\pm k+1)}\,\mathcal{D}^{(l)}_{k\pm1,j}(\Omega_\tau) \\ \hat{\mathcal{L}}^2_\pm\mathcal{D}^{(l)}_{k,j}(\Omega_\tau) &= \sqrt{(l\mp k)(l\pm k+1)(l\mp k-1)(l\pm k+2)} \\ &\quad\times\mathcal{D}^{(l)}_{k\pm2,j}(\Omega_\tau) \end{aligned}\right\} \tag{52}$$

It is important to note from equations (51) and (52) that terms in $\hat{\mathcal{R}}$(PAF) mixes only functions $\mathcal{D}^{(l)}_{k,j}(\Omega_\tau)$ with k values that differ by 0 and ±2 units. A further useful property of functions $\mathcal{D}^{(l)}_{k,j}(\Omega_\tau)$ involves the orthogonality relationship

$$\int \mathrm{d}\Omega_\tau\, \mathcal{D}^{(l')*}_{k',j'}(\Omega_\tau)\mathcal{D}^{(l)}_{k,j}(\Omega_\tau) = \frac{8\pi^2}{2l+1}\delta_{l',l}\delta_{k',k}\delta_{j',j} \tag{53}$$

Using equations (51)–(53) and the definitions in equations (38)–(40) for $\hat{\mathcal{R}}$(PAF) and $\Psi_{l,k,j}(\Omega_\tau)$, respectively, the individual matrix elements $\langle\Psi^*_{l,k,j}(\Omega_\tau)\hat{\mathcal{R}}(\mathrm{PAF})\Psi_{l,k,j}(\Omega_\tau)\rangle$ of the secular determinant required to solve the eigenvalue problem are given by

$$\begin{aligned} &\langle\psi^*_{l,k,j}(\Omega_\tau)\hat{\mathcal{R}}(\mathrm{PAF})\psi_{l,k,j}(\Omega_\tau)\rangle \\ &= \delta_{j',j}\{\delta_{k',k}[l(l+1)A + k^2C] \\ &\quad +\tfrac{1}{2}B\delta_{k',k+2}\sqrt{(l-k)(l+k+1)(l-k-1)(l+k+2)} \\ &\quad +\tfrac{1}{2}B\delta_{k',k-2}\sqrt{(l+k)(l-k+1)(l+k-1)(l-k+2)}\} \end{aligned} \tag{54}$$

The characteristic equations for rank $l = 1$ and $l = 2$ are then given by

$$\begin{bmatrix} C-\epsilon^{(1)}_\nu & B & 0 \\ B & C-\epsilon^{(1)}_\nu & 0 \\ 0 & 0 & -\epsilon^{(1)}_\nu \end{bmatrix}\begin{bmatrix} c^{(1)}_{\nu,-1} \\ c^{(1)}_{\nu,+1} \\ c^{(1)}_{\nu,0} \end{bmatrix} = 0 \tag{55}$$

$$\begin{bmatrix} C-\epsilon^{(2)}_\nu & 3B & \vdots & & & \\ 3B & C-\epsilon^{(2)}_\nu & \vdots & & \mathbf{0} & \\ \cdots\cdots & \cdots\cdots & \vdots & \cdots\cdots & \cdots\cdots & \cdots\cdots \\ & & \vdots & 4C-\epsilon^{(2)}_\nu & \sqrt{6}B & 0 \\ & \mathbf{0} & \vdots & \sqrt{6}B & -\epsilon^{(2)}_\nu & \sqrt{6}B \\ & & \vdots & 0 & \sqrt{6}B & 4C-\epsilon^{(2)}_\nu \end{bmatrix} \times \begin{bmatrix} c^{(2)}_{\nu,-1} \\ c^{(2)}_{\nu,+1} \\ \cdots\cdots \\ c^{(2)}_{\nu,-2} \\ c^{(2)}_{\nu,0} \\ c^{(2)}_{\nu,+2} \end{bmatrix} = 0 \tag{56}$$

The substitution $\epsilon_\nu^{(l)} = b_\nu^{(l)} - l(l+1)A$ has been made to simplify these two characteristic equations. The eigenvalues $b_\nu^{(l)}$ and corresponding eigenvectors $c_{\nu,k}^{(l)}$ obtained from solution of equations (55) and (56) are given in Table 1. Note that the mixing coefficients in the eigenvectors are simplified with the substitutions of $\sin\frac{1}{2}\chi$ and $\cos\frac{1}{2}\chi$, where $\chi = \tan^{-1}[\sqrt{3}(R_{xx} - R_{yy})/(2R_{zz} - R_{xx} - R_{yy})]$.

Motional symmetry will factor further the characteristic equations given in equations (55) and (56). When the molecular diffusion is symmetric, i.e., $R_{xx} = R_{yy} = R_\perp$, then $B = 0$ and the $\hat{\mathcal{L}}_+^2 + \hat{\mathcal{L}}_-^2$ term is eliminated from $\hat{\mathcal{R}}$(PAF). In this limit of symmetric diffusion, the individual Wigner rotation matrices are the solutions to the characteristic equation, and the roots for $\pm k$ become doubly degenerate. The eigenvalues and eigenvectors for symmetrical diffusion are given in Table 2 along with the simpler solutions for the spherical diffusion case, i.e., $R_{xx} = R_{yy} = R_{zz} = R_0$.

5.3 Correlation Functions for Molecular Rotational Diffusion

An explicit expression for the correlation function $G_{nn'm}{}^{(l)}(\tau)$ may now be obtained by first substituting equation (50) into equation (49) and using this result along with equation (35) in equation (33). The expression becomes

$$G_{nn'm}^{(l)}(\tau) = \sum_\nu \sum_{l'l''} \sum_{kk'} \sum_{jj'} \frac{\sqrt{(2l'+1)(2l''+1)}}{(8\pi^2)^2} c_{\nu,k,j}^{(l')} c_{\nu,k',j'}^{(l'')} \times \exp(-b_\nu^{(l')}\tau)(-1)^{m-n'} \left[\int \mathrm{d}\Omega_0\, \mathcal{D}_{n,m}^{(l)}(\Omega_0) \times \mathcal{D}_{k,j}^{(l')*}(\Omega_0) \int \mathrm{d}\Omega_\tau\, \mathcal{D}_{-n',m}^{(l)*}(\Omega_t) \mathcal{D}_{k',j'}^{(l'')}(\Omega_\tau) \right] \quad (57)$$

The integrals over Ω_0 and Ω_τ are readily evaluated using the orthogonality properties of the functions $\mathcal{D}_{n,m}^{(l)}(\Omega_\tau)$ expressed by equation (53) to give

$$G_{nn'm}^{(l)}(\tau) = \sum_\nu \sum_{l'l''} \sum_{kk'} \sum_{jj'} \frac{\sqrt{(2l'+1)(2l''+1)}}{(2l+1)^2} c_{\nu,k,j}^{(l')} c_{\nu,k',j'}^{(l'')} \times \exp(-b_\nu^{(l')}\tau)\,(-1)^{m-n'} \delta_{l',l}\delta_{l'',l}\delta_{k,n}\delta_{k',-n'} \times \delta_{j',m}\delta_{j,m} \quad (58)$$

The Kronecker deltas in equation (58) provide constraints that relate l to both l' and l'', k to n, and k' to $-n'$, and force $j' = j = m$. These simplifications render $G_{nn'm}^{(l)}(\tau)$ equal to

$$G_{nn'm}^{(l)}(\tau) = \frac{(-1)^{m-n'}}{2l+1} \sum_\nu c_{\nu,n,m}^{(l)} c_{\nu,-n',m}^{(l)} \mathrm{e}^{-b_\nu^{(l)}\tau} \quad (59)$$

With this expression for $G_{nn'm}^{(l)}(\tau)$ along with the required parameters for the eigenvalues and eigenvectors contained in Tables 1 and 2, the motional power density $\mathcal{M}_{nn'm}^{(l)}(\omega_{\kappa\lambda})$, from equation (31) becomes

$$\mathcal{M}_{n,n'm}^{(l)}(\omega_{\kappa\lambda}) = \frac{(-1)^{n'}}{2l+1} \sum_\nu c_{\nu,n,m}^{(l)} c_{\nu,-n',m}^{(l)} \frac{1}{2} \int_{-\infty}^{\infty} \mathrm{e}^{-b_\nu^{(l)}}\, \tau \mathrm{e}^{-\mathrm{i}\omega_{\kappa\lambda}\tau}\, \mathrm{d}\tau = \frac{(-1)^{n'}}{2l+1} \sum_\nu c_{\nu,n,m}^{(l)} c_{\nu,-n'm}^{(l)} \frac{b_\nu^{(l)}}{b_\nu^{(l)2} + \omega_{\kappa\lambda}^2} \quad (60)$$

The integral here provides the Lorentzian form for $\mathcal{M}_{nn'm}^{(l)}(\omega_{\kappa\lambda})$.

The absence of an m index in the eigenvectors of Tables 1 and 2 results from the absence of an $\hat{\mathcal{L}}_{z'}$ term in the rotational diffusion tensor operator $\hat{\mathcal{R}}$. Hence, for the remainder of this development, we omit, for convenience, the subscript m on the eigenvectors $c_{\nu,n,m}^{(l)}$. This indicates that all interlevel relaxation transitions, expressed in the laboratory frame, are affected equally by the motional power density function. In the event that the diffusing molecule is in an anisotropic ordered solvent, the eigenvalues and eigenvectors will have a dependence upon the mth projection index. The treatment of such ordered solvents[8,25,26] goes beyond the scope of this article, but the development would follow essentially that given above to

Table 1 Eigenvalues and Eigenvectors for Asymmetric Rotational Diffusion

l	ν	$\epsilon_\nu{}^{(l)}$	$b_\nu{}^{(l)}$	Nonzero eigenvectors
	-1	$C - B$	$R_{yy} + R_{zz}$	$-c_{-1,-1}^{(1)} = c_{-1,+1}^{(1)} = \sqrt{\frac{1}{2}}$
1	0	0	$R_{xx} + R_{yy}$	$c_{0,0}^{(1)} = 1$
	1	$C + B$	$R_{xx} + R_{zz}$	$c_{1,-1}^{(1)} = c_{1,+1}^{(1)} = \sqrt{\frac{1}{2}}$
	-2	$4C$	$R_{xx} + R_{yy} + 4R_{zz}$	$-c_{-2,-2}^{(2)} = c_{-2,+2}^{(2)} = \sqrt{\frac{1}{2}}$
	-1	$C - 3B$	$R_{xx} + 4R_{yy} + R_{zz}$	$-c_{-1,-1}^{(2)} = c_{-1,+1}^{(2)} = \sqrt{\frac{1}{2}}$
2	0	$2C - \sqrt{C^2 + 3B^2}$	$6R - 6\sqrt{R^2 - L^2}$	$c_{0,-2}^{(2)} = c_{0,+2}^{(2)} = \sqrt{\frac{1}{2}}\sin\frac{1}{2}\chi$, $c_{0,0}^{(2)} = -\cos\frac{1}{2}\chi$
	1	$C + 3B$	$4R_{xx} + R_{yy} + R_{zz}$	$c_{1,-1}^{(2)} = c_{1,+1}^{(2)} = \sqrt{\frac{1}{2}}$
	2	$2C + \sqrt{C^2 + 3B^2}$	$6R + 6\sqrt{R^2 - L^2}$	$c_{2,-2}^{(2)} = c_{2,+2}^{(2)} = \sqrt{\frac{1}{2}}\cos\frac{1}{2}\chi$, $c_{2,0}^{(2)} = \sin\frac{1}{2}\chi$

Here $R = \frac{1}{3}(R_{xx} + R_{yy} + R_{zz})$, $L^2 = \frac{1}{3}(R_{xx}R_{yy} + R_{yy}R_{zz} + R_{zz}R_{xx})$, $\chi = \tan^{-1}\left[\frac{\sqrt{3}(R_{xx} - R_{yy})}{2R_{zz} - R_{xx} - R_{yy}}\right]$

Table 2 Eigenvalues and Eigenvectors for Axially Symmetric and Spherical Rotational Diffusion

l	ν	$\epsilon_\nu{}^{(l)}$	$b_\nu{}^{(l)}$	Nonzero eigenvectors
			Axially symmetric diffuser	
1	0	0	$2R_\perp$	$c^{(1)}_{0,0} = 1$
	1	C	$R_\perp + R_\parallel$	$c^{(1)}_{1,\pm1} = 1$
	0	0	$6R_\perp$	$c^{(2)}_{0,0} = 1$
2	1	C	$5R_\perp + R_\parallel$	$c^{(2)}_{1,\pm1} = 1$
	2	$4C$	$2R_\perp + 4R_\parallel$	$c^{(2)}_{2,\pm2} = 1$
			Spherical diffuser	
1	0	0	$2R_0$	$c^{(1)}_{0,0} = 1, c^{(1)}_{0,\pm1} = 1$
2	0	0	$6R_0$	$c^{(2)}_{0,0} = 1, c^{(2)}_{0,\pm1} = 1, c^{(2)}_{0,\pm2} = 1$

[a]Here $R_\perp = R_{xx} = R_{yy}$, $R_\parallel = R_{zz}$, $R_0 = R_{xx} = R_{yy} = R_{zz}$

treat isotropic liquids, except that the characteristic equation would have a dependence upon m through the operator $\hat{\mathcal{L}}_{z'}$. To introduce the effect of solvent ordering into coupled spin relaxation also requires the introduction of an ordering potential function into equation (54).

Substitution of equation (60) into equations (29) and (30) yields the following expressions for the spectral densities:

$$\mathcal{J}^{\mu}_{lm}(\omega_{\kappa\lambda}) = \frac{1}{2l+1}\sum_{\nu}\sum_{n=-l}^{l}[c^{(l)}_{\nu,n}\mathcal{F}^{l}_{n}(\mu)] \times \sum_{n'=-l}^{l}[(-1)^{n'}c^{(l)}_{\nu,-n'}\mathcal{F}^{l}_{n'}(\mu)]\frac{b^{(l)}_{\nu}}{b^{(l)2}_{\nu}+\omega^2_{\kappa\lambda}} \quad (61)$$

$$\mathrm{Re}\,\mathcal{K}^{\mu'\mu}_{lm}(\omega_{\kappa\lambda}) = \frac{1}{2l+1}\sum_{\nu}\sum_{n,n'=l}^{l}(-1)^{n'} [c^{(l)}_{\nu,n}\mathcal{F}^{l}_{n}(\mu)c^{(l)}_{\nu,-n'}\mathcal{F}^{l}_{n'}(\mu') + c^{(l)}_{\nu,n}\mathcal{F}^{l}_{n'}(\mu') \times c^{(l)}_{\nu,-n'}\mathcal{F}^{l}_{n'}(\mu)]\frac{b^{(l)}_{\nu}}{b^{(l)2}_{\nu}+\omega^2_{\kappa\lambda}} \quad (62)$$

Equation (61) and (62) are of the forms

$$\mathcal{J}^{\mu}_{lm}(\omega_{\kappa\lambda}) = \frac{1}{2l+1}\sum_{\nu}\mathcal{A}^{(l)}_{\nu}(\mu)\mathcal{A}^{(l)*}_{\nu}(\mu)\frac{b^{(l)}_{\nu}}{b^{(l)2}_{\nu}+\omega^2_{\kappa\lambda}} \quad (63)$$

$$\mathrm{Re}\,\mathcal{K}^{\mu\mu}_{lm}(\omega_{\kappa\lambda}) = \frac{1}{2l+1}\sum_{\nu}[\mathcal{A}^{(l)}_{\nu}(\mu)\mathcal{A}^{(l)*}_{\nu}(\mu') + \mathcal{A}^{*}_{\nu}(\mu')\mathcal{A}^{(l)}_{\nu}(\mu)]\frac{b^{(l)}_{\nu}}{b^{(l)2}_{\nu}+\omega^2_{\kappa\lambda}} \quad (64)$$

$\mathcal{A}_\nu{}^{(l)}(\mu)$ is given by

$$\mathcal{A}^{(l)}_{\nu}(\mu) = \sum_{n=-l}^{l}c^{(l)}_{\nu,n}\mathcal{F}^{l}_{n}(\mu) \quad (65)$$

The complex conjugate $\mathcal{A}^{(l)}_{\nu} * (\mu)$ gives an important relationship between n and n'; consider the following:

$$\begin{aligned}\mathcal{A}^{(l)*}_{\nu}(\mu) &= \left[\sum_{n=-l}^{l}c^{(l)}_{\nu,n}\mathcal{F}^{l}_{n}(\mu)\right]^{*} = \sum_{n=-l}^{l}c^{(l)}_{\nu,n}\mathcal{F}^{l*}_{n}(\mu)\\ &= \sum_{n=-l}^{l}(-1)^{n}c^{(l)}_{\nu,n}\mathcal{F}^{l}_{-n}(\mu)\\ &= \sum_{n'=l}^{-l}(-1)^{n'}c^{(l)}_{\nu,-n'}\mathcal{F}^{l}_{n'}(\mu)\end{aligned} \quad (66)$$

These relationships rely upon the vectors $c^{(l)}_{\nu,n}$ being real, the properties of complex conjugates of second-rank tensors, and finally the symmetry about zero of the arbitrary index n' as it is summed over the complete set of values allowed by the index l. Thus, the use of the relevant eigenvalues and eigenvectors encountered in molecular rotational diffusion requires that $n' = -n$. Note that the paucity of $c^{(l)}_{\nu,n}$ values given in Tables 1 and 2 considerably reduces the number of terms summed in equation (65) and explicit expressions may be readily obtained for $\mathcal{A}^{(l)}_{\nu}(\mu)$ for various mechanisms μ, once the orientations of the interaction principal axis frame (PAF) is known relative to the molecular rotational diffusion PAF. The introduction of the molecular dynamics, embodied in $\mathcal{M}^{(l)}_{nn'm}(\omega_{\kappa\lambda})$, has reduced the problem of obtaining spectral densities to that of finding explicit expressions for the interaction tensors $\mathcal{F}^{l}_{n}(\mu)$ in the molecular diffusion frame. Attention is therefore directed to the geometrical relationships that transform these tensors from their own PAF to those of the rotational diffusion PAF (e.g., consider again the relationships in Figure 1).

6 INTERACTION TENSORS IN THEIR PRINCIPAL AXIS AND MOLECULAR DIFFUSION FRAMES

The interaction tensor components, $\mathcal{F}^{l}_{n}(\mu)$, in the rotational diffusion frame may be obtained from the corresponding PAF

components $\mathcal{F}_p^l(\mu_{\mathrm{PAF}})$ as follows:

$$\mathcal{F}_n^l(\mu) = \sum_{p=-l}^{l} \mathcal{D}_{p,n}^{(l)}(\Omega_\mu)\mathcal{F}_p^l(\mu_{\mathrm{PAF}}) \tag{67}$$

where $\Omega_\mu \sum (\alpha_\mu,\beta_\mu,\gamma_\mu)$ represents the Euler angles that transform the PAF of the μth relaxation interaction into the PAF of the molecular rotational diffusion tensor (see Figure 1). The Wigner rotation matrix elements, $\mathcal{D}_{p,n}^{(l)}(\alpha_\mu, \beta_\mu, \gamma_\mu)$ provide the geometrical constants used to transform between the two coordinate frames. The following convention of Zare[27] is used for $\mathcal{D}_{p,n}^{(l)}(\alpha_\mu, \beta_\mu, \gamma_\mu)$ in this treatment:

$$\mathcal{D}_{p,n}^{(l)}(\alpha_\mu, \beta_\mu, \gamma_\mu) = \mathrm{e}^{-\mathrm{i}p\alpha_\mu} d_{p,n}^{(l)}(\beta_\mu)\mathrm{e}^{-\mathrm{i}n\gamma_\mu} \tag{68}$$

6.1 The Relaxation Interaction Tensor in Its Principal Axis Frame

In the interaction PAF, the second-rank tensor is diagonal, and only two unique values for $\mathcal{F}_p^{(2)}(\mu_{\mathrm{PAF}})$ are encountered; these are obtained from equation (23) as follows:

$$\left.\begin{aligned}
\mathcal{F}_0^{(2)}(\mu_{\mathrm{PAF}}) &= \sqrt{\tfrac{3}{2}}[\mu_{zz}(\mathrm{PAF}) - \mu_0] \\
&= \sqrt{\tfrac{2}{3}}\{\mu_{zz}(\mathrm{PAF}) \\
&\quad - \tfrac{1}{2}[\mu_{xx}(\mathrm{PAF}) + \mu_{yy}(\mathrm{PAF})]\} \\
&= \sqrt{\tfrac{2}{3}}\zeta \\
\mathcal{F}_{\pm1}^{(2)}(\mu_{\mathrm{PAF}}) &= 0 \\
\mathcal{F}_{\pm2}^{(2)}(\mu_{\mathrm{PAF}}) &= \tfrac{1}{2}[\mu_{xx}(\mathrm{PAF}) - \mu_{yy}(\mathrm{PAF})] \\
&= \tfrac{1}{2}\eta\zeta
\end{aligned}\right\} \tag{69}$$

The parameters ζ and η are the tensor's anisotropy and asymmetry parameters, respectively.

The explicit forms of $\mathcal{F}_0^{(2)}(\mu_{\mathrm{PAF}})$ and $\mathcal{F}_{\pm2}^{(2)}(\mu_{\mathrm{PAF}})$ for the dipolar and chemical shift tensors may be obtained from equations (7) and (12), respectively, and are provided for the reader's convenience in Table 3. The $\mathcal{F}_0^{(2)}(\mathrm{dd}_{\mathrm{PAF}})$ in Table 3 is given for a heteronuclear dipolar coupling constant. Note that heteronuclear and homonuclear splittings, obtained from Pake doublets in solid NMR powder patterns, exhibit a quantum mechanical degeneracy effect for dipolar coupled spins. In homonuclear A_2 spin systems, a larger Pake splitting, by a factor of 1.5, is found when compared with a heteronuclear splitting in the corresponding AX spin system. Thus, the measured heteronuclear splittings render $D_{\mathrm{hetero}} = \gamma_{\mathrm{A}}\gamma_{\mathrm{X}}\hbar/r_{\mathrm{AX}}^3$ and the homonuclear $D_{\mathrm{homo}} = 3\gamma_{\mathrm{A}}^2\hbar/2r_{\mathrm{AA'}}^3$. This feature of dipolar couplings is discussed by Harris.[28]

Table 3 Values of $\mathcal{F}_0^{(2)}(\mu_{\mathrm{PAF}})$ and $\mathcal{F}_{\pm2}^{(2)}(\mu_{\mathrm{PAF}})$ Parameters for Dipolar and Chemical Shift Anisotropy

$\mathcal{F}_p^{(l)}(\mu_{\mathrm{PAF}})$	Dipolar interaction	Chemical shift anisotropy
$\mathcal{F}_0^{(2)}(\mu_{\mathrm{PAF}})$	$-\sqrt{6}\frac{\gamma_{\mathrm{A}}\gamma_{\mathrm{X}}}{r_{\mathrm{AX}}^3} = -\sqrt{6}\mathrm{D}$	$\sqrt{\frac{3}{2}}[\delta_{zz}(\mathrm{PAF}) - \delta_0]\gamma_s B_0$
$\mathcal{F}_{-2}^{(2)}(\mu_{\mathrm{PAF}})$	0	$\frac{1}{2}[\delta_{xx}(\mathrm{PAF}) - \delta_{yy}(\mathrm{PAF})]\gamma_s B_0$

6.2 Explicit Geometrical Relationships for $\mathcal{F}_n^l(\mu)$ in the Rotational Diffusion PAF

The Wigner rotation matrices $\mathcal{D}_{p,n}^{(l)}(\Omega_\mu)$ in equation (67) contain the geometrical information implied by Figure 1 for the transformations between the interaction frames and the molecular rotational diffusion frame. The Ω_μ in the rotation matrices represents the Euler angles for the designated coordinate transformation. Using equation (67), the expressions for both axial and asymmetric tensors $\mathcal{F}_n^l(\mu)$ in the rotational diffusion frame are of the following respective forms:

$$\mathcal{F}_n^{(2)}(\mu_{\mathrm{axial}}) = \mathcal{D}_{0,n}^{(2)}(\Omega_\mu)\mathcal{F}_0^{(2)}(\mu_{\mathrm{PAF}}) \tag{70}$$

$$\begin{aligned}\mathcal{F}_n^{(2)}(\mu_{\mathrm{asym}}) = \mathcal{D}_{0,n}^{(2)}(\Omega_\mu)\mathcal{F}_0^{(2)}(\mu_{\mathrm{PAF}}) \\ +[\mathcal{D}_{2,n}^{(2)}(\Omega_\mu) + \mathcal{D}_{-2,n}^{(2)}(\Omega_\mu)]\mathcal{F}_{\pm2}^{(2)}(\mu_{\mathrm{PAF}})\end{aligned} \tag{71}$$

Equation (70) is the equation that is used for dipolar and axially symmetric chemical shift tensors, and equation (71) is for an asymmetric interaction such as encountered in a general asymmetric chemical shift tensor. Values of $\mathcal{F}_n^{(2)}(\mu_{\mathrm{axial}})$ are obtained from equation (70) or from equation (71) by setting $\mathcal{F}_{\pm2}^{(2)}(\mu_{\mathrm{PAF}}) = 0$. The $\mathcal{D}_{p,n}^{(l)}(\alpha_\mu, \beta_\mu, \gamma_\mu)$ may be obtained from equation (68) along with explicit expressions for $d_{p,n}^{(l)}(\beta_\mu)$, given in Table 4 for the reader's convenience.

Equations (70) and (71) may now be used in equation (65) to evaluate $\mathcal{A}_\nu^{(l)}(\mu, \mathrm{asym})$ and $\mathcal{A}_\nu^{(l)}(\mu, \mathrm{axial})$, and these expression are given in Table 5 in terms of the three Euler angles $(\alpha_\mu,\beta_\mu,\gamma_\mu)$ that define the transformation between the interaction and the molecular rotational diffusion frames. The designations 'axial' and 'asym' here apply to motional diffusion models, and should not be confused with similar designations of the symmetry of the interaction tensors given in equations (70) and (71).

In Table 6 corresponding expressions for $\mathcal{A}_\nu^{(l)}(\mu, \mathrm{asym})$ and $\mathcal{A}_\nu^{(l)}(\mu, \mathrm{axial})$ also are given using directional cosines to relate the interaction and diffusion frames. For axially symmetric interaction tensors, only three directional cosines (l_Z,m_Z,n_Z) are required to relate the unique z principal axis of the interaction PAF to the three principal axes in the rotational diffusion frame. For asymmetric tensors, all nine directional cosines are required to relate the interaction tensor's PAF (X,Y,Z) to the PAF (x,y,z) of the diffusion tensor. The traditional rotational transformation matrix,[29] expressed in both directional cosines and Euler angles, establishes the relationship between these two set of variables, and is

Table 4 Values of $d^{(2)}_{p,n}(\beta_\mu)$ for Various Indices p and n

n	$d^{(2)}_{-2,n}(\beta_\mu)$	$d^{(2)}_{0,n}(\beta_\mu)$	$d^{(2)}_{2,n}(\beta_\mu)$
−2	$\cos^4 \frac{1}{2}\beta_\mu$	$\sqrt{\frac{3}{8}} \sin^2 \beta_\mu$	$\sin^4 \frac{1}{2}\beta_\mu$
−1	$\frac{1}{2} \sin \beta_\mu (1 + \cos \beta_\mu)$	$-\sqrt{\frac{3}{2}} \sin \beta_\mu \cos \beta_\mu$	$\frac{1}{2} \sin \beta_\mu (\cos \beta_\mu - 1)$
0	$\sqrt{\frac{3}{8}} \sin^2 \beta_\mu$	$\frac{1}{2}(3 \cos^2 \beta_\mu - 1)$	$\sqrt{\frac{3}{8}} \sin^2 \beta_\mu$
+1	$-\frac{1}{2} \sin \beta_\mu (\cos \beta_\mu - 1)$	$\sqrt{\frac{3}{2}} \sin \beta_\mu \cos \beta_\mu$	$-\frac{1}{2} \sin \beta_\mu (1 + \cos \beta_\mu)$
+2	$\sin^4 \frac{1}{2}\beta_\mu$	$\sqrt{\frac{3}{8}} \sin^2 \beta_\mu$	$\cos^4 \frac{1}{2}\beta_\mu$

Table 5 $\mathcal{A}_\nu$ Values in Terms of Euler Angles for Asymmetric Interaction Tensors

Asymmetric diffuser

$$\mathcal{A}^{(2)}_{-2}(\mu, \text{asym}) = -\text{i}\sqrt{\tfrac{1}{2}}[cos\ 2\alpha(1 + cos^2\ \beta)sin\ 2\gamma + 2\ sin\ 2\alpha\ cos\ \beta\ cos\ 2\gamma]\mathcal{F}^{(2)}_{\pm2}(\mu_{\text{PAF}}) - \text{i}\sqrt{\tfrac{3}{4}}(\sin^2\beta \sin 2\gamma)\mathcal{F}^{(2)}_0(\mu_{\text{PAF}})$$

$$\mathcal{A}^{(2)}_{-1}(\mu, \text{asym}) = \sqrt{-\tfrac{1}{2}}(cos\ 2\alpha \sin 2\beta \cos\gamma + 2 \sin 2\alpha \sin\beta \sin\gamma)\mathcal{F}^{(2)}_{\pm2}(\mu_{\text{PAF}}) + \sqrt{\tfrac{3}{4}}(\sin 2\beta \cos\gamma)\mathcal{F}^{(2)}_0(\mu_{\text{PAF}})$$

$$\mathcal{A}^{(2)}_0(\mu, \text{asym}) = \{\sqrt{\tfrac{1}{2}}[\cos 2\alpha(1 + \cos^2\beta)\cos 2\gamma - 2 \sin 2\alpha \cos\beta \sin 2\gamma]\sin\tfrac{1}{2}\chi - \sqrt{\tfrac{3}{2}}(\sin^2\beta \cos 2\alpha)\cos\tfrac{1}{2}\chi\}\mathcal{F}^{(2)}_{\pm2}(\mu_{\text{PAF}})$$
$$+[\tfrac{1}{2}\sqrt{3}(\sin^2\beta \cos 2\gamma)\sin\tfrac{1}{2}\chi - \tfrac{1}{2}(3\cos^2\beta - 1)\cos\tfrac{1}{2}\chi]\mathcal{F}^{(2)}_0(\mu_{\text{PAF}})$$

$$\mathcal{A}^{(2)}_1(\mu, \text{asym}) = \text{i}\sqrt{\tfrac{1}{2}}(\cos 2\alpha \sin 2\beta \sin\gamma + 2 \sin 2\alpha \sin\beta \cos\gamma)\mathcal{F}^{(2)}_{\pm2}(\mu_{\text{PAF}}) - \text{i}\tfrac{1}{2}\sqrt{3}(\sin 2\beta \sin\gamma)\mathcal{F}^{(2)}_0(\mu_{\text{PAF}})$$

$$\mathcal{A}^{(2)}_2(\mu, \text{asym}) = \{\sqrt{\tfrac{1}{2}}[\cos 2\alpha(1 + \cos^2\beta)\cos 2\gamma - 2 \sin 2\alpha \cos\beta \sin 2\gamma]\cos\tfrac{1}{2}\chi + \sqrt{\tfrac{3}{2}}(sin^2\beta \cos 2\alpha)\sin\tfrac{1}{2}\chi\}\mathcal{F}^{(2)}_{\pm2}(\mu_{\text{PAF}})$$
$$+[\tfrac{1}{2}\sqrt{3}(\sin^2\beta \cos 2\gamma)\cos\tfrac{1}{2}\chi + \tfrac{1}{2}(3\cos^2\beta - 1)\sin\tfrac{1}{2}\chi]\mathcal{F}^{(2)}_0(\mu_{\text{PAF}})$$

Axially symmetric diffuser

$$\mathcal{A}^{(2)}_0(\mu, \text{axial}) = \sqrt{\tfrac{3}{2}}(\sin^2\beta \cos 2\alpha)\mathcal{F}^{(2)}_{\pm2}(\mu_{\text{PAF}}) + \tfrac{1}{2}(3\cos^2\beta - 1)\mathcal{F}^{(2)}_0(\mu_{\text{PAF}})$$

$$\mathcal{A}^{(2)}_1(\mu, \text{axial}) = [-\tfrac{1}{2}\cos 2\alpha \sin 2\beta\ (\cos\gamma - \text{i}\sin\gamma) + \sin 2\alpha \sin\beta\ (\sin\gamma + \text{i}\cos\gamma)]\mathcal{F}^{(2)}_{\pm2}(\mu_{\text{PAF}}) + \sqrt{\tfrac{3}{8}}\sin 2\beta\ (\cos\gamma - \text{i}\sin\gamma)\mathcal{F}^{(2)}_0(\mu_{\text{PAF}})$$

$$\mathcal{A}^{(2)}_2(\mu, \text{axial}) = [\tfrac{1}{2}\cos 2\alpha\ (1 + \cos^2\beta)(\cos 2\gamma - \text{i}\sin 2\gamma) - \sin 2\alpha \cos\beta\ (\sin 2\gamma + i\cos 2\gamma)]\mathcal{F}^{(2)}_{\pm2}(\mu_{\text{PAF}}) + \sqrt{\tfrac{3}{8}}\sin^2\beta\ (\cos 2\gamma - \text{i}\sin 2\gamma)\mathcal{F}^{(2)}_0(\mu_{\text{PAF}})$$

expressed as follows:

$$R = \begin{bmatrix} l_X & l_Y & l_Z \\ m_X & m_Y & m_Z \\ n_X & n_Y & n_Z \end{bmatrix} = \begin{bmatrix} c_\alpha c_\beta c_\gamma - s_\alpha s_\gamma & s_\alpha c_\beta c_\gamma + c_\alpha s_\gamma & -s_\beta c_\gamma \\ -c_\alpha c_\beta s_\gamma - s_\alpha c_\gamma & -s_\alpha c_\beta s_\gamma + c_\alpha c_\gamma & s_\beta s_\gamma \\ c_\alpha s_\beta & s_\alpha s_\beta & c_\beta \end{bmatrix} \tag{72}$$

The l, m, and n designations relate to the x, y, and z axes, respectively, in the molecular diffusion frame, and the subscripts X, Y, and Z designate the interaction principal axes. Directional cosines enjoy a certain conceptual simplicity, and the redundancy embodied in these nine cosines tends to make the notation for $\mathcal{A}^{(l)}_\nu(\mu, \text{asym})$ in Table 6 rather compact. Fortunately, the explicit expressions contained in equation (72) relate all nine directional cosines to the three unique Euler angles, thereby removing any ambiguity that could ensue from the oversubscription of directional cosine parameters for the rotational transformation.

7 SPECIFIC EXPRESSIONS FOR SPECTRAL DENSITY FUNCTIONS AND RELAXATION RATES

With equations (63)–(65) and Tables 1–3 and 5 or 6, explicit expressions for both auto- and cross-correlated relaxation spectral densities may be obtained for a variety of spin interactions. The interaction may be described with both axially symmetric or asymmetric interaction tensors. Spherically symmetric interaction tensors do not provide fluctuating magnetic fields with rotational diffusion, and cannot relax magnetic spins. The diffusion model governs the form of the relaxation expression, and explicit expressions will be presented in this section. The procedure for assembling the spectral densities for the various diffusion models is straightforward, though considerably more laborious for the more complex cases when cross-correlated spectral densities between asymmetric interactions are encountered in the asymmetric diffusional limit. This article allows only for a detailed discussion of a few of the simpler cases, but some of the more complicated cases have been discussed elsewhere.[7,11] The spherical and axial diffusion cases are common but still sufficiently complex to illustrate the procedure for assembling different spectral density expressions.

7.1 Spherical Rotational Diffusion Model

The second-rank spectral densities for the simple but important spherical diffusion case are given by

$$\left.\begin{aligned} \mathcal{J}^{\mu}_{2m}(\omega_{\kappa\lambda}, \text{spher diff}) &= A^{(2)\mu}_{\text{spher}} \frac{6R_0}{(6R_0)^2 + \omega^2_{\kappa\lambda}} \\ \mathcal{K}^{\mu\mu'}_{2m}(\omega_{\kappa\lambda}, \text{spher diff}) &= A^{(2)\mu\mu'}_{\text{spher}} \frac{6R_0}{(6R_0)^2 + \omega^2_{\kappa\lambda}} \end{aligned}\right\} \tag{73}$$

The rotational diffusion is isotropic, with diffusion constant R_0, and $A^{(2)\mu}_{\text{spher}}$ and $A^{(2)\mu\mu'}_{\text{spher}}$ become

Table 6 $\mathcal{A}_\nu$ Values in Terms of Direction Cosines for Asymmetric Interaction Tensors

Asymmetric diffuser

$$\mathcal{A}_{-2}^{(2)}(\mu,\text{asym}) = \mathrm{i}\sqrt{2}(l_X m_X - l_Y m_Y)\mathcal{F}_{\pm2}^{(2)}(\mu_{\text{PAF}}) + \mathrm{i}\sqrt{3}(l_Z m_Z)\mathcal{F}_0^{(2)}(\mu_{\text{PAF}})$$
$$\mathcal{A}_{-1}^{(2)}(\mu,\text{asym}) = -\sqrt{2}(l_X n_X - l_Y n_Y)\mathcal{F}_{\pm2}^{(2)}(\mu_{\text{PAF}}) - \sqrt{3}(l_Z n_Z)\mathcal{F}_0^{(2)}(\mu_{\text{PAF}})$$
$$\mathcal{A}_0^{(2)}(\mu,\text{asym}) = [\sqrt{\tfrac{1}{2}}(l_X^2 - l_Y^2 + m_Y^2 - m_X^2)\sin\tfrac{1}{2}\chi - \sqrt{\tfrac{3}{2}}(n_X^3 - n_Y^2)\cos\tfrac{1}{2}\chi]\mathcal{F}_{\pm2}^{(2)}(\mu_{\text{PAF}})$$
$$+[\tfrac{1}{2}\sqrt{3}(l_Z^2 - m_Z^2)\sin\tfrac{1}{2}\chi - \tfrac{1}{2}(3n_Z^2 - 1)\cos\tfrac{1}{2}\chi]\mathcal{F}_0^{(2)}(\mu_{\text{PAF}})$$
$$\mathcal{A}_1^{(2)}(\mu,\text{asym}) = -\mathrm{i}\sqrt{2}(m_X n_X - m_Y n_Y)\mathcal{F}_{\pm2}^{(2)}(\mu_{\text{PAF}}) - \mathrm{i}\sqrt{3}(m_Z n_Z)\mathcal{F}_0^{(2)}(\mu_{\text{PAF}})$$
$$\mathcal{A}_2^{(2)}(\mu,\text{asym}) = [\sqrt{\tfrac{1}{2}}(l_X^2 - l_Y^2 + m_Y^2 - m_X^2)\cos\tfrac{1}{2}\chi + \sqrt{\tfrac{3}{2}}(n_X^2 - n_Y^2)\sin\tfrac{1}{2}\chi]\mathcal{F}_{\pm2}^{(2)}(\mu_{\text{PAF}})$$
$$+[\tfrac{1}{2}\sqrt{3}(l_Z^2 - m_Z^2)\cos\tfrac{1}{2}\chi + \tfrac{1}{2}(3n_Z^2 - 1)\sin\tfrac{1}{2}\chi]\mathcal{F}_0^{(2)}(\mu_{\text{PAF}})$$

Axially symmetric diffuser

$$\mathcal{A}_0^{(2)}(\mu,\text{axial}) = \sqrt{\tfrac{3}{2}}(n_X^2 - n_Y^2)\mathcal{F}_{\pm2}^{(2)}(\mu_{\text{PAF}}) + \tfrac{1}{2}(3n_Z^2 - 1)\mathcal{F}_0^{(2)}(\mu_{\text{PAF}})$$
$$\mathcal{A}_1^{(2)}(\mu,\text{axial}) = [-n_X(l_X + \mathrm{i}m_X) + n_Y(l_Y + \mathrm{i}m_Y)]\mathcal{F}_{\pm2}^{(2)}(\mu_{\text{PAF}}) - \sqrt{\tfrac{3}{2}}n_Z(l_Z + \mathrm{i}m_Y)\mathcal{F}_0^{(2)}(\mu_{\text{PAF}})$$
$$\mathcal{A}_2^{(2)}(\mu,\text{axial}) = [\tfrac{1}{2}(l_X^2 - l_Y^2 + m_Y^2 - m_X^2) + \mathrm{i}(l_X m_X - l_Y m_Y)]\mathcal{F}_{\pm2}^{(2)}(\mu_{\text{PAF}}) + [\sqrt{\tfrac{3}{8}}(l_Z^2 - m_Z^2) + \mathrm{i}\sqrt{\tfrac{3}{2}}l_Z m_Z]\mathcal{F}_0^{(2)}(\mu_{\text{PAF}})$$

$$A_{\text{spher}}^{(2)\mu} = \tfrac{1}{5}\mathcal{F}_0^{(2)}(\mu_{\text{PAF}})^2 + \tfrac{2}{5}\mathcal{F}_{\pm2}^{(2)}(\mu_{\text{PAF}})^2 \tag{74a}$$

$$\begin{aligned} A_{\text{spher}}^{(2)\mu\mu'} &= \tfrac{1}{5}(3n_Z^2 - 1)\mathcal{F}_0^{(2)}(\mu_{\text{PAF}})\mathcal{F}_0^{(2)}(\mu'_{\text{PAF}}) \\ &+\tfrac{1}{5}\sqrt{6}(n_X^2 - n_Y^2)\mathcal{F}_0^{(2)}(\mu_{\text{PAF}})\mathcal{F}_{\pm2}^{(2)}(\mu'_{\text{PAF}}) \\ &+\tfrac{1}{5}\sqrt{6}(l_Z^2 - m_Z^2)\mathcal{F}_{\pm2}^{(2)}(\mu_{\text{PAF}})\mathcal{F}_0^{(2)}(\mu'_{\text{PAF}}) \\ &+\tfrac{2}{5}(l_X^2 - l_Y^2 + m_Y^2 - m_X^2)\mathcal{F}_{\pm2}^{(2)}(\mu_{\text{PAF}}) \\ &\times\mathcal{F}_{\pm2}^{(2)}(\mu'_{\text{PAF}}) \end{aligned} \tag{74b}$$

The above autocorrelation coefficient $A_{\text{spher}}^{(l)\mu}$ for spherical diffusion was obtained by placing the arbitrary rotational diffusion frame on the PAF of the μth interaction. The cross term, represented by $A_{\text{spher}}^{(l)\mu\mu'}$, again places the arbitrary rotational diffusion frame on the μ interaction frame, and then the μ' frame is transformed into this diffusion frame. Thus, the directional cosines in equation (74) relate the μ' interaction frame (l,m,n) to the μ interaction frame (X,Y,Z). Using equation (72), the equivalent expression in Euler angles to that given in equation (74b) becomes

$$\begin{aligned} A_{\text{spher}}^{(2)\mu\mu'} &= \tfrac{1}{5}(3\cos^2\beta - 1)\mathcal{F}_0^{(2)}(\mu_{\text{PAF}})\mathcal{F}_0^{(2)}(\mu'_{\text{PAF}}) \\ &+\tfrac{1}{5}\sqrt{6}\sin^2\beta\cos 2\alpha\,\mathcal{F}_0^{(2)}(\mu_{\text{PAF}})\mathcal{F}_{\pm2}^{(2)}(\mu'_{\text{PAF}}) \\ &+\tfrac{1}{5}\sqrt{6}\sin^2\beta\cos 2\gamma\,\mathcal{F}_{\pm2}^{(2)}(\mu_{\text{PAF}})\mathcal{F}_0^{(2)}(\mu'_{\text{PAF}}) \\ &+\tfrac{2}{5}[\cos 2\alpha\,(\cos^2\beta + 1)\cos 2\gamma \\ &-2\sin 2\alpha\cos\beta\sin 2\gamma] \\ &\times\mathcal{F}_{\pm2}^{(2)}(\mu_{\text{PAF}})\mathcal{F}_{\pm2}^{(2)}(\mu'_{\text{PAF}}) \end{aligned} \tag{75}$$

The symmetry between the two interaction frames has been preserved in equation (75), even though the μth frame was selected as the rotational diffusion frame. The Euler angle α is associated with frame μ and γ with frame μ'. The spherical diffusion expressions for the autocorrelated spectral density in an axially symmetric tensor may be obtained when $\mathcal{F}_{\pm2}^{(2)}(\mu_{\text{PAF}}) = 0$, and for centrosymmetric tensors when $\mathcal{F}_0^{(2)}(\mu_{\text{PAF}}) = 0$.

7.2 Axially Symmetric Rotational Diffusion Model

7.2.1 Autocorrelation Spectral Densities

The autocorrelated spectral densities given in equation (63) along with the values for $b_\nu^{(l)}$(axial) from Table 2 and for $\mathcal{A}_\nu^{(l)}(\mu,\text{axial})$ from Table 6 yield the following expression:

$$\begin{aligned} \mathcal{J}_{2m}^{\mu}(\omega_{\kappa\lambda},\text{axial}\ \ \text{diff}) &= A_{\text{axial}}^{(2)\mu}\frac{6R_\perp}{(6R_\perp)^2 + \omega_{\kappa\lambda}^2} \\ &+B_{\text{axial}}^{(2)\mu}\frac{5R_\perp + R_\parallel}{(5R_\perp + R_\parallel)^2 + \omega_{\kappa\lambda}^2} \\ &+C_{\text{axial}}^{(2)\mu}\frac{2R_\perp + 4R_\parallel}{(2R_\perp + 4R_\parallel)^2 + \omega_{\kappa\lambda}^2} \end{aligned} \tag{76}$$

The coefficients $A_{\text{axial}}^{(2)\mu}$, $B_{\text{axial}}^{(2)\mu}$, and $C_{\text{axial}}^{(2)\mu}$ for an autocorrelated and axially symmetric diffusion tensor are given by

$$\left.\begin{aligned} A_{\text{axial}}^{(2)\mu} &= \tfrac{1}{5}\mathcal{A}_0^{(2)*}(\mu,\text{axial})\mathcal{A}_0^{(2)}(\mu,\text{axial}) \\ B_{\text{axial}}^{(2)\mu} &= \tfrac{2}{5}\mathcal{A}_1^{(2)*}(\mu,\text{axial})\mathcal{A}_1^{(2)}(\mu,\text{axial}) \\ C_{\text{axial}}^{(2)\mu} &= \tfrac{2}{5}\mathcal{A}_2^{(2)*}(\mu,\text{axial})\mathcal{A}_2^{(2)}(\mu,\text{axial}) \end{aligned}\right\} \tag{77}$$

Note that the degenerate solutions for $\Psi_{\pm\nu}$ given in equation (50) reduce the number of unique eigenvalues for axial diffusion from five to three. Therefore, a two-fold degeneracy factor is introduced into equation (77) to address this feature. In this axial case, the degeneracy is 1 for ν = 0, and 2 for ν = 1 or 2.

7.2.1.1 Axially Symmetric Dipolar Interaction. This case was treated in the early seminal work of Woessner[1] for dipole–dipole spectral densities, and is commonly encountered in many molecular systems. Expressions for $A_{\text{axial}}^{(2)\text{dd}}$, $B_{\text{axial}}^{(2)\text{dd}}$, and $C_{\text{axial}}^{(2)\text{dd}}$ may be obtained from Table 6, and are given as follows:

$$\left.\begin{aligned} A_{\text{axial}}^{(2)\text{dd}} &= \tfrac{1}{20}(3n_Z^2 - 1)^2\mathcal{F}_0^{(2)}(\text{dd})^2 \\ B_{\text{axial}}^{(2)\text{dd}} &= \tfrac{3}{5}n_Z^2(l_Z^2 + m_Z^2)\mathcal{F}_0^{(2)}(\text{dd})^2 \\ C_{\text{axial}}^{(2)\text{dd}} &= \tfrac{3}{20}(l_Z^2 + m_Z^2)^2\mathcal{F}_0^{(2)}(\text{dd})^2 \end{aligned}\right\} \tag{78}$$

where l_Z, m_Z, and n_Z are the directional cosines relating the Z axis of the interaction PAF to the x, y, and z axes, respectively, in the rotational diffusion frame. The expressions in equation (78) are sufficiently general that they would also apply to an autocorrelated axially symmetric chemical shift anisotropy case by substituting $\mathcal{F}_0^{(2)}(\text{csa})$ for $\mathcal{F}_0^{(2)}(\text{dd})$ in equation (78). Values for these principal values are given in Table 3.

7.2.1.2 Asymmetric Chemical Shift Interaction. The autocorrelated relaxation encountered when chemical shift anisotropy affects the relaxation is covered by this example. With the use of higher magnetic fields, this type of asymmetric interaction is becoming increasingly more common. The thesis of Smith[6] provides an extensive coverage of this chemical shift anisotropy case. The expressions are

$$\begin{aligned} A_{\text{axial}}^{(2)\text{csa}} &= \tfrac{1}{20}(3n_Z^2-1)^2\mathcal{F}_0^{(2)}(\text{csa})^2 + \tfrac{3}{10}(n_X^2-n_Y^2)^2\mathcal{F}_{\pm2}^{(2)}(\text{csa})^2 \\ &\quad + \tfrac{1}{10}\sqrt{6}(3n_Z^2-1)(n_X^2-n_Y^2)\mathcal{F}_0^{(2)}(\text{csa})\mathcal{F}_{\pm2}^{(2)}(\text{csa}) \quad (79a) \\ B_{\text{axial}}^{(2)\text{csa}} &= \tfrac{3}{5}n_Z^2(l_Z^2+m_Z^2)\mathcal{F}_0^{(2)}(\text{csa})^2 \\ &\quad + \tfrac{2}{5}[(l_Xn_X-l_Yn_Y)^2+(m_Xn_X-m_Yn_Y)^2]\mathcal{F}_{\pm2}^{(2)}(\text{csa})^2 \\ &\quad + \tfrac{2}{5}\sqrt{6}n_Z[l_Z(l_Xn_X-l_Yn_Y) \\ &\quad + m_Z(m_Xn_X-m_Yn_Y)]\mathcal{F}_0^{(2)}(\text{csa})\mathcal{F}_{\pm2}^{(2)}(\text{csa}) \quad (79b) \\ C_{\text{axial}}^{(2)\text{csa}} &= \tfrac{3}{20}(l_Z^2+m_Z^2)^2\mathcal{F}_0^{(2)}(\text{csa})^2 \\ &\quad + \tfrac{1}{10}[(l_X^2-l_Y^2+m_Y^2-m_X^2)^2 \\ &\quad + 4(l_Xm_X-l_Ym_Y)^2]\mathcal{F}_{\pm2}^{(2)}(\text{csa})^2 \\ &\quad + \tfrac{1}{10}\sqrt{6}[(l_Z^2-m_Z^2)(l_X^2-l_Y^2+m_Y^2-m_X^2) \\ &\quad + 4m_Zl_Z(l_Xm_X-l_Ym_Y)]\mathcal{F}_0^{(2)}(\text{csa})\mathcal{F}_{\pm2}^{(2)}(\text{csa}) \quad (79c) \end{aligned}$$

7.2.2 Cross-Correlated Spectral Densities

This cross-correlated case retains a similar Lorentzian form to the spectral density given in equation (73):

$$\begin{aligned} \mathcal{K}_{2m}^{\mu\mu'}(\omega_{\kappa\lambda},\text{axial diff}) = A_{\text{axial}}^{(2)\mu\mu'}&\frac{6R_\perp}{(6R_\perp)^2+\omega_{\kappa\lambda}^2} \\ + B_{\text{axial}}^{(2)\mu\mu'}&\frac{5R_\perp+R_\parallel}{(5R_\perp+R_\parallel)^2+\omega_{\kappa\lambda}^2} \\ + C_{\text{axial}}^{(2)\mu\mu'}&\frac{2R_\perp+4R_\parallel}{(2R_\perp+4R_\parallel)^2+\omega_{\kappa\lambda}^2} \end{aligned} \quad (80)$$

but differs in the forms of the coefficients: $A_{\text{axial}}^{(2)\mu\mu'}$, $B_{\text{axial}}^{(2)\mu\mu'}$, and $C_{\text{axial}}^{(2)\mu\mu'}$. These are given by

$$\left.\begin{aligned} A_{\text{axial}}^{(2)\mu\mu} &= \tfrac{1}{5}[\mathcal{A}_0^{(2)*}(\mu,\text{axial})\mathcal{A}_0^{(2)}(\mu',\text{axial}) \\ &\quad + \mathcal{A}_0^{(2)*}(\mu',\text{axial})\mathcal{A}_0^{(2)}(\mu,\text{axial})] \\ B_{\text{axial}}^{(2)\mu\mu} &= \tfrac{2}{5}[\mathcal{A}_1^{(2)*}(\mu,\text{axial})\mathcal{A}_1^{(2)}(\mu',\text{axial}) \\ &\quad + \mathcal{A}_1^{(2)*}(\mu',\text{axial})\mathcal{A}_1^{(2)}(\mu,\text{axial})] \\ C_{\text{axial}}^{(2)\mu\mu} &= \tfrac{2}{5}[\mathcal{A}_2^{(2)*}(\mu,\text{axial})\mathcal{A}_2^{(2)}(\mu',\text{axial}) \\ &\quad + \mathcal{A}_2^{(2)*}(\mu',\text{axial})\mathcal{A}_2^{(2)}(\mu,\text{axial})] \end{aligned}\right\} \quad (81)$$

Cross-correlated dipolar interactions between more than two spins in coupled-relaxation studies were observed early,[30] and more recently cross terms between chemical shift and dipolar interactions have been found as relaxation work has moved to higher magnetic fields[31,32] (for a more extensive list of references, see Grant et al.[11]). Cross terms reveal a dependence upon the angles relating the principal axes of the two interacting tensors. These cross-correlated spectral densities also provides critical information on the asymmetry of motion. Without the spatial complexity of cross terms, it is more difficult to obtain information on anisotropic motional diffusion constants (i.e., R_{xx}, R_{yy}, and R_{zz}) with high sensitivity.

7.2.2.1 Two Pairs of Axial Dipolar Tensors. Again, we turn to dipolar interactions to illustrate this cross-correlation case. The dipolar $A_{\text{axial}}^{(2)\mu\mu'}$, $B_{\text{axial}}^{(2)\mu\mu'}$, and $C_{\text{axial}}^{(2)\mu\mu'}$ constants of equation (81) become

$$\left.\begin{aligned} A_{\text{axial}}^{(2)\text{d}_a\text{d}_b} &= \tfrac{1}{10}(3n_{Z,a}^2-1)(3n_{Z,b}^2-1)\mathcal{F}_0^{(2)}(\text{dd}_a)\mathcal{F}_0^{(2)}(\text{dd}_b) \\ B_{\text{axial}}^{(2)\text{d}_a\text{d}_b} &= \tfrac{6}{5}n_{Z,a}n_{Z,b}(l_{Z,a}l_{Z,b}+m_{Z,a}m_{Z,b}) \\ &\quad \times \mathcal{F}_0^{(2)}(\text{dd}_a)\mathcal{F}_0^{(2)}(\text{dd}_b) \\ C_{\text{axial}}^{(2)\text{d}_a\text{d}_b} &= \tfrac{3}{10}[(l_{Z,a}l_{Z,b}+m_{Z,a}m_{Z,b})^2 \\ &\quad - (l_{Z,a}m_{Z,b}-m_{Z,a}l_{Z,b})^2] \\ &\quad \times \mathcal{F}_0^{(2)}(\text{dd}_a)\mathcal{F}_0^{(2)}(\text{dd}_b) \end{aligned}\right\} \quad (82)$$

Two different dipolar pairs interacting in a cross term give a cross correlated spectral density that is directly proportional to the subtended angle between their associated internuclear vectors.

7.2.2.2 Asymmetric csa and Axial Dipolar Cross Term. The cross term between the axially symmetric dipolar and asymmetric chemical shift interactions is discussed briefly for this final axial diffusion case. The equations governing such cross terms are

$$\begin{aligned} A_{\text{axial}}^{(2)\text{d,csa}} &= \tfrac{1}{10}(3n_{Z,\text{d}}^2-1)(3n_{Z,\text{cs}}^2-1)\mathcal{F}_0^{(2)}(\text{dd})\mathcal{F}_0^{(2)}(\text{csa}) \\ &\quad + \tfrac{1}{10}\sqrt{6}(3n_{Z,\text{d}}^2-1)(n_{X,\text{cs}}^2-n_{Y,\text{cs}}^2)\mathcal{F}_0^{(2)}(\text{dd}) \\ &\quad \times\mathcal{F}_{\pm2}^{(2)}(\text{csa}) \quad (83a) \\ B_{\text{axial}}^{(2)\text{d,csa}} &= \tfrac{6}{5}n_{Z,\text{d}}n_{Z,\text{cs}}(l_{Z,\text{d}}l_{Z,\text{cs}}+m_{Z,\text{d}}m_{Z,\text{cs}})\mathcal{F}_0^{(2)}(\text{dd})\mathcal{F}_0^{(2)} \\ &\quad \times(\text{csa}) + \tfrac{1}{5}\sqrt{6}[l_{Z,\text{d}}n_{Z,\text{d}}(l_{X,\text{cs}}n_{X,\text{cs}}-l_{Y,\text{cs}}n_{Y,\text{cs}}) \\ &\quad + m_{Z,\text{d}}n_{Z,\text{d}}(m_{X,\text{cs}}n_{X,\text{cs}}-m_{Y,\text{cs}}n_{Y,\text{cs}})] \\ &\quad \times\mathcal{F}_0^{(2)}(\text{dd})\mathcal{F}_{\pm2}^{(2)}(\text{csa}) \quad (83b) \\ C_{\text{axial}}^{(2)\text{d,csa}} &= \tfrac{3}{10}[(l_{Z,\text{d}}l_{Z,\text{cs}}+m_{Z,\text{d}}m_{Z,\text{cs}})^2 \\ &\quad -(l_{Z,\text{d}}m_{Z,\text{cs}}-m_{Z,\text{d}}l_{Z,\text{cs}})^2]\mathcal{F}_0^{(2)}(\text{dd})\mathcal{F}_0^{(2)}(\text{csa}) \\ &\quad + \tfrac{1}{10}\sqrt{6}[(l_{Z,\text{d}}^2-m_{Z,\text{d}}^2)(l_{X,\text{cs}}^2-l_{Y,\text{cs}}^2+m_{Y,\text{cs}}^2-m_{X,\text{cs}}^2) \\ &\quad + 4l_{Z,\text{d}}m_{Z,\text{d}}(l_{X,\text{cs}}m_{X,\text{cs}}-l_{Y,\text{cs}}m_{Y,\text{cs}})]\mathcal{F}_0^{(2)}(\text{dd}) \\ &\quad \times\mathcal{F}_{\pm2}^{(2)}(\text{csa}) \quad (83c) \end{aligned}$$

This case is unique because it mixes symmetric and asymmetric interaction tensors together. The effect of this mixed

symmetry is to destroy certain symmetries in the relaxing coupled multiplet, e.g., triplets, quartets, etc. The symmetric and asymmetric transient line intensities of these multiplets are coupled during the relaxation process, indicating the presence of this cross term. While magnetic field strengths were too low to observe these types of cross-correlated spectral densities until the past decade, theoretical considerations predicted their existence over two decades ago.[33–36] Inevitably, this case will acquire greater significance in the future as magnetic fields continue to increase.

7.3 Asymmetric Rotational Diffusion Model

Using equations (63) and (64), the second-rank spectral densities arising from asymmetric rotational diffusion have five terms, with the explicit forms

$$\left.\begin{aligned}\mathcal{J}^{\mu}_{2m}(\omega_{\kappa\lambda},\text{asym diff}) &= \tfrac{1}{5}\sum_{\nu=-2}^{2}\mathcal{A}^{(2)*}_{\nu}(\mu,\text{asym})\\ &\quad\times\mathcal{A}^{(2)}_{\nu}(\mu,\text{asym})\\ &\quad\times\frac{b^{(2)}_{\nu}(\text{asym})}{b^{(2)^2}_{\nu}(\text{asym})+\omega^2_{\kappa\lambda}}\\ \mathcal{K}^{\mu\mu'}_{2m}(\omega_{\kappa\lambda},\text{asym diff}) &= \tfrac{1}{5}\sum_{\nu=-2}^{2}\left\{\begin{array}{c}\mathcal{A}^{(2)*}_{\nu}(\mu,\text{asym})\\ \mathcal{A}^{(2)}_{\nu}(\mu',\text{asym})+\\ \mathcal{A}^{(2)*}_{\nu}(\mu',\text{asym})\\ \mathcal{A}^{(2)}_{\nu}(\mu,\text{asym})\end{array}\right\}\\ &\quad\times\frac{b^{(2)}_{\nu}(\text{asym})}{b^{(2)^2}_{\nu}(\text{asym})+\omega^2_{\kappa\lambda}}\end{aligned}\right\}\quad(84)$$

Values of the asymmetric motional eigenvalues $b^{(2)}_{\nu}(\text{asym})$, are found in Table 1, and may be used with the asymmetric motional parameters $\mathcal{A}^{(2)}_{\nu}(\mu,\text{asym})$ given in either Table 5 or Table 6. Expressions for asymmetric diffusion with an axially symmetric interaction tensor has the same form as equation (84) and is easily obtained by setting $\mathcal{F}^{(2)}_{\pm2}(\mu_{\text{PAF}})=0$ in the various $\mathcal{A}^{(2)}_{\nu}(\mu,\text{asym})$ of Tables 5 and 6. Likewise, the equations for a centrosymmetric tensor may be obtained, as before, by setting $\mathcal{F}^{(2)}_{0}(\mu_{\text{PAF}})=0$. Explicit expressions for asymmetric diffusional motion are obtained in the same manner as the axial diffusion examples found in Section 7.2. These expressions are sufficiently extensive, however, that they should be constructed only as needed.

7.4 Extreme Narrowing Limit

Equations (73), (76), and (84) lend themselves to a further simplification when the so-called extreme narrowing limit, i.e., $\omega^2_{\kappa\lambda}\ll b^{(l)^2}_{0}$, obtains. The Lorentzian form then becomes

$$\frac{b^{(l)}_{\nu}}{b^{(l)2}_{\nu}+\omega^2_{\kappa\lambda}}\approx\frac{1}{b^{(l)}_{\nu}}\quad(85)$$

7.5 Use of Spectral Densities in Relaxation Rate Expressions

Equations (73)–(84) illustrate the methods used for obtaining both autocorrelated, $\mathcal{J}^{\mu}_{lm}(\omega_{\kappa\lambda})$, and cross correlated, $\mathcal{K}^{\mu'\mu}_{lm}(\omega_{\kappa\lambda})$, spectral densities. Explicit spectral densities have been expressed here for a few illustrative models, and other spectral densities may be assembled in the same manner. These spectral densities, along with the respective auto- and cross-correlated spin matrices S^{μ}_{lm} and $S^{\mu\mu'}_{lm}$ defined in equation (16) combine in equation (18) to provide expressions for the several relaxation rates $\hat{\hat{K}}_{\kappa'\lambda'\kappa\lambda}(\omega_{\kappa\lambda})$. These rates, when introduced into equation (3), yield values for the Redfield relaxation matrix $R_{\kappa'\kappa\lambda'\lambda}$, which then completes the development of the master relaxation equation given in equation (1). Fitting of these relaxation parameters with a number of different pulse experiments yields values for the rotational diffusion constants expressed in Tables 1 and 2, and approximates many of the critical constants contained in Table 3. The fitting process, as might be expected, is enhanced considerably when molecular symmetry provides independent information on the geometrical constants that relate the various interaction and motional diffusion frames outlined in Figure 1. Other NMR studies usually provide more accurate information on dipole–dipole constants and chemical shift anisotropy than can be obtained from relaxation data. This is especially beneficial in analyzing relaxation data, since these more reliable spectral parameters, when available from other sources, make it possible for the relaxation data to be used exclusively in fitting the molecular diffusion parameters.

8 RELATED ARTICLES

Coupled Spin Relaxation in Polymers; Liouville Equation of Motion; Paramagnetic Relaxation in Solution; Protein Structures: Relaxation Matrix Refinement; Relaxation: An Introduction; Relaxation Effects of Chemical Exchange; Relaxation Matrix Refinement of Nucleic Acids; Relaxation Mechanisms: Magnetization Modes; Relaxation Processes in Coupled-Spin Systems; Relaxation Processes: Cross Correlation and Interference Terms; Relaxation Theory: Density Matrix Formulation; Relaxation Theory for Quadrupolar Nuclei; Relaxation of Transverse Magnetization for Coupled Spins; Rotating Frame Spin–Lattice Relaxation Off-Resonance; Spin–Rotation Relaxation Theory.

9 REFERENCES

1. D. E. Woessner, *J. Chem. Phys.*, 1962, **37**, 647; *Mol. Phys.*, 1968, **14**, 265.
2. F. Perrin, *J. Phys. Radium*, 1934, **5**, 497; 1936, **7**, 1.
3. W. T. Huntress, *J. Chem. Phys.*, 1968, **48**, 3524; *Adv. Magn.*, 1970, **4**, 1.
4. L. D. Favro, *Phys. Rev.*, 1960, **119**, 53.
5. D. M. Grant and L. G. Werbelow, *J. Magn. Reson.*, 1976, **21**, 367.
6. S. Smith, *Simulations of pulsed nuclear magnetic resonance experiments*, PhD thesis, University of California, Santa Barbara, June 1991.
7. L. G. Werbelow and D. M. Grant, in *Advances in Magnetic Resonance*, ed. J. S. Waugh, Academic Press, New York, 1977, Vol. 9, p. 189.

8. R. R. Vold and R. L. Vold, in *Progress in Nuclear Magnetic Resonance Spectroscopy*, eds. J. W. Emsley, J. Feeney, and L. H. Sutcliffe, Pergamon Press, Oxford, 1978, Vol. 12, p. 79.
9. H. W. Spiess, in *NMR Basic Principles and Progress*, eds. P. Diehl, E. Fluck, and R. Kosfeld, Springer-Verlag, New York, 1978, Vol. 15, p. 55.
10. D. Canet, in *Progress in Nuclear Magnetic Resonance Spectroscopy*, eds. J. W. Emsley, J. Feeney, and L. H. Sutcliffe, Pergamon Press, Oxford, 1989, Vol. 21, p. 237.
11. D. M. Grant, C. L. Mayne, F. Liu, and T. X. Xiang, *Chem. Rev.*, 1991, **91**, 1591.
12. A. G. Redfield, *IBM J. Res. Dev.*, 1957, **1**, 19; in *Advances in Magnetic Resonance*, ed. J. S. Waugh, Academic Press, New York, 1965, Vol. 1, p. 1.
13. C. P. Slichter, *Principles of Magnetic Resonance*, 3rd edn., Springer-Verlag, Berlin, 1990, pp. 199–215.
14. L. G. Werbelow, *J. Chem. Phys.*, 1979, **70**, 5381.
15. J. McConnell, *The Theory of Nuclear Magnetic Relaxation in Liquids*, Cambridge University Press, Cambridge, 1987 (Chap. 2 contains an especially illuminating treatment of this subject).
16. M. Mehring, in *NMR Basic Principles and Progress*, eds. P. Diehl, E. Fluck, and R. Kosfield, Springer-Verlag, New York, 1976, Vol. 11, pp. 215–218.
17. S. A. Smith, W. E. Palke and J. T. Gerig, *Concepts Magn. Reson.*, 1992, **4**, 107, 181.
18. M. Mehring, in *NMR Basic Principles and Progress*, eds. P. Diehl, E. Fluck, and R. Kosfield, Springer-Verlag, New York, 1976, Appendix A, p. 214.
19. A. D. Buckingham and S. M. Malm, *Mol. Phys.*, 1971, **22**, 1127.
20. J. C. Facelli, A. M. Orendt, D. M. Grant, and J. Michl, *Chem. Phys. Lett.*, 1984, **112**, 147.
21. M. T. Chenon, C. Coupry, and L. G. Werbelow, *J. Phys. Chem.*, 1992, **96**, 561.
22. J. McConnell, *The Theory of Nuclear Magnetic Relaxation in Liquids*, Cambridge University Press, Cambridge, 1987, p. 99.
23. S. C. Wang, *Phys. Rev.*, 1929, **34**, 243.
24. R. N. Zare, *Angular Momentum*, Wiley, New York, 1988, pp. 318–321.
25. J. M. Bernassau, E. P. Black and D. M. Grant, *J. Chem. Phys.*, 1982, **76**, 253; E. P. Black, J. M. Bernassau, C. L. Mayne and D. M. Grant, *J. Chem. Phys.*, 1982, **76**, 265.
26. R. R. Vold, in *NMR in Liquid Crystals*, eds. J. W. Emsley and C. A. Veracini, Reidel, Dordecht, 1985, p. 253.
27. R. N. Zare, *Angular Momentum*, Wiley, New York, 1988, p. 85.
28. R. K. Harris, *Nuclear Magnetic Resonance Spectroscopy*, Longman, Harlow, UK, 1986, Chap. 6
29. R. N. Zare, *Angular Momentum*, Wiley, New York, 1988, p. 81.
30. C. L. Mayne, D. W. Alderman and D. M. Grant, *J. Chem. Phys.*, 1975, **63**, 2514; 1976, **65**, 1684.
31. H. Nery and D. Canet, *J. Magn. Reson.*, 1981, **42**, 370; H. Nery, C. Canet, F. Toma and S. Fermandjian, *J. Am. Chem. Soc.*, 1983, **105**, 1482. See ref. 11 for a more extensive list of citations.
32. T. C. Farrar and R. A. Quintero-Arcaya, *J. Phys. Chem.*, 1987, **91**, 3224; T. C. Farrar and I. C. Locker, *J. Chem. Phys.*, 1987, **87**, 3281; T. C. Farrar and J. D. Decatur, *J. Phys. Chem.*, 1990, **94**, 7395; T. C. Farrar and M. J. Jablonsky, *J. Phys. Chem.*, 1991, **95**, 9159.
33. E. L. Mackor and C. MacLean, in *Progress in Nuclear Magnetic Resonance Spectroscopy*, eds. J. W. Emsley, J. Feeney, and L. H. Sutcliffe, Pergamon Press, Oxford, 1967, Vol. 3, p. 129.
34. N. C. Pyper, *Mol. Phys.*, 1971, **21**, 1.
35. J. S. Blicharski, W. Nosel, and H. Schneider, *Ann. Phys. (Leipzig)*, 1971, **27**, 17; J. S. Blicharski, and W. Nosel, *Acta Phys. Polon. A*, 1972, **42**, 223.
36. L. G. Werbelow and D. M. Grant, *J. Magn. Reson.*, 1975, **20**, 554.

Biographical Sketches

David M. Grant. *b* 1931. B.S., 1954, Ph.D., 1957, chemistry, University of Utah, USA. DuPont Instructor, University of Illinois, 1957–58, where he was introduced to NMR by Herb Gutowsky and Martin Karplus. Faculty in Chemistry, University of Utah, 1958–present, where he is Distinguished Professor. Approx. 300 publications. Current research specialties: methods and theoretical foundations of carbon-13 NMR, coupled spin relaxation and molecular motions, chemical shifts in liquids and solids with emphasis on carbon-13 shift tensors and their origins in electronic and molecular structure.

Russell A. Brown. *b* 1952. B.A., 1975, Ph.D., 1994, chemistry, M.D., 1979, University of Utah, USA. Director of Research, Evans and Sutherland Computer Corporation, 1981–91. Faculty in Neurosurgery, University of Utah, 1991–95. Research specialties: carbon-13 NMR, coupled spin relaxation, and molecular structure and dynamics simulations.

Relaxation of Quadrupolar Nuclei Measured via Multiple Quantum Filtration

Stephen Wimperis
University of Oxford, UK

1	Introduction	1
2	Tensor Operator Description of Spin-$\frac{3}{2}$ Quadrupolar Relaxation	1
3	Multiple Quantum Filtration Experiments for Spin-$\frac{3}{2}$ Nuclei	2
4	Measurement of Spin-$\frac{3}{2}$ Relaxation Parameters	3
5	Discrimination of Intra- and Extracellular Spin-$\frac{3}{2}$ Nuclei	5
6	Residual Spin-$\frac{3}{2}$ Quadrupolar Splittings	5
7	Discussion and Summary	6
8	Related Articles	7
9	References	7

1 INTRODUCTION

Metal ions play a vital role in a large number of biological processes. For this reason, there is widespread interest in NMR of the spin-$\frac{3}{2}$ nuclei ^{7}Li, ^{23}Na, ^{39}K, and ^{87}Rb, the spin-$\frac{5}{2}$ nuclei ^{25}Mg and ^{85}Rb, and the spin-$\frac{7}{2}$ nuclei ^{43}Ca and ^{133}Cs. In particular, ^{23}Na is one of the most widely studied of all quadrupolar nuclei, especially in vivo. Even in the most heterogeneous biological tissues, however, the NMR spectra of these metal ions usually exhibit only a single resonance at a chemical shift that is characteristic of the aqueous ion. This apparent lack of structure in the spectra is compensated for by the wealth of information about the environment of the ions yielded by the spin relaxation parameters.

It has long been known that both the transverse and longitudinal relaxation of spin $S \geq \frac{3}{2}$ nuclei are multiexponential if the extreme-narrowing condition is not fulfilled.[1] For example, the transverse relaxation of spin-$\frac{3}{2}$ nuclei is described by two distinct relaxation rates, $R_{\mathrm{f}}^{(1)}$ and $R_{\mathrm{s}}^{(1)}$ [the superscript (1) denotes relaxation of single quantum coherences, $p = \pm 1$], if the product of the Larmor frequency ω_0 and correlation time τ_{c} is unity or greater, $\omega_0\tau_{\mathrm{c}} \gtrsim 1$. As a result of this biexponential relaxation, the NMR spectrum of slowly tumbling spin-$\frac{3}{2}$ nuclei is a superposition of two Lorentzian lines with full widths (in Hz) at halfheight of $R_{\mathrm{f}}^{(1)}/\pi$ and $R_{\mathrm{s}}^{(1)}/\pi$. Figure 1 shows the normal free induction decay and the corresponding spectrum of sodium ions in an agarose gel. The ^{23}Na lineshape can be seen to be bi-Lorentzian, with 60% of the total intensity in the broader component and 40% in the narrower component. Full analysis of the spectrum of a spin-$\frac{3}{2}$ nucleus requires measurement of both the fast, $R_{\mathrm{f}}^{(1)}$, and slow, $R_{\mathrm{s}}^{(1)}$, transverse relaxation rates. This is a difficult task, especially if (a) the two relaxation rates are very similar or (b) the relaxation rate $R_{\mathrm{f}}^{(1)}$ is so fast that the broader of the two lines cannot be observed.

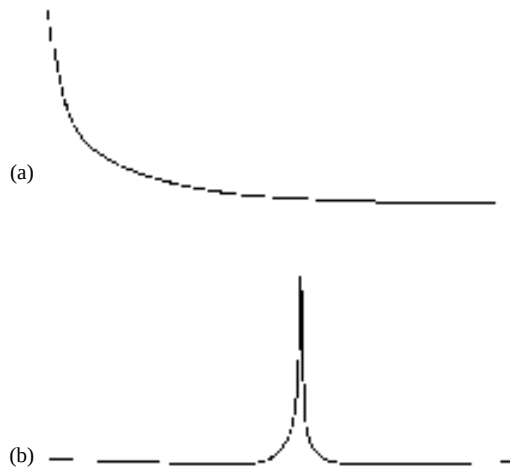

Figure 1 Magnitude mode free induction decay (a) and ^{23}Na spectrum (b) of 2 M NaCl in an agarose gel. Acquisition parameters: 2500 Hz spectral width, 48 transients coadded, 105.8 MHz Larmor frequency, 256 points in (a) zero filled to 1024 in (b)

In 1986, both Pekar and Leigh[2] and Jaccard et al.[3] showed that multiple quantum coherences could be excited in isolated spin $S \geq \frac{3}{2}$ nuclei in liquids if, but only if, their relaxation was multiexponential. This discovery helped overturn the orthodox view that excitation of multiple quantum coherence required the presence of splittings due to scalar, dipolar, or quadrupolar couplings, and so could not be achieved in a spectrum that consisted of only a single resonance. The aim of this article is to show how multiple quantum NMR is currently being used to measure the relaxation parameters of spin $S \geq \frac{3}{2}$ nuclei in liquid environments. This article will concentrate on spin-$\frac{3}{2}$ nuclei, while multiple quantum NMR of the much less important spin-$\frac{5}{2}$ and spin-$\frac{7}{2}$ nuclei will be mentioned briefly in Section 7.

2 TENSOR OPERATOR DESCRIPTION OF SPIN-$\frac{3}{2}$ QUADRUPOLAR RELAXATION

Jaccard et al.[3] have shown that a tensor operator description of multiexponential quadrupolar relaxation is particularly convenient for discussing multiple quantum NMR experiments. In this formulation, the density operator $\sigma(t)$ is expanded as a linear combination of tensor operators:

$$\sigma(t) = \sum_{l=0}^{2S} \sum_{p=-l}^{l} b_{l,p}(t) T_{l,p} \qquad (1)$$

where $T_{l,p}$ is an irreducible spherical tensor operator of rank l and order p. These two concepts have clear meanings in this usage. For example, an operator $T_{1,-1}$ represents an in-phase coherence of order $p = -1$ (i.e., one of the two components of in-phase single quantum coherence), $T_{3,+1}$ represents a doubly

antiphase coherence of order $p = +1$, $T_{3,-2}$ represents a singly antiphase coherence of order $p = -2$ (i.e., a singly antiphase double quantum coherence), and so on. The fact that the rank and coherence order of each term in the expansion of equation (1) are readily identifiable is a major asset in the description of multiple quantum NMR experiments.

A 90°_y pulse applied to a system of spin-$\frac{3}{2}$ nuclei at thermal equilibrium creates in-phase single quantum coherence. If a number of uninteresting constants are ignored, this initial state can be written in tensor form as

$$\sigma(t=0) = T_{1,-1} - T_{1,+1} \tag{2}$$

Jaccard et al.[3] have shown that if the time evolution of the density operator occurs solely as a result of biexponential transverse relaxation then the new density operator $\sigma(t)$ is given in tensor operator form by

$$\sigma(t) = f_{11}^{(1)}(t)(T_{1,-1} - T_{1,+1}) + f_{31}^{(1)}(t)(T_{3,-1} - T_{3,+1}) \tag{3}$$

where

$$f_{11}^{(1)}(t) = \tfrac{1}{5}[3\exp(-R_{\mathrm{f}}^{(1)}t) + 2\exp(-R_{\mathrm{s}}^{(1)}t)] \tag{4a}$$

$$f_{31}^{(1)}(t) = \tfrac{1}{5}\sqrt{6}[\exp(-R_{\mathrm{f}}^{(1)}t) - \exp(-R_{\mathrm{s}}^{(1)}t)] \tag{4b}$$

For pure quadrupolar relaxation in the absence of exchange, the fast and slow transverse relaxation rates can be calculated as

$$R_{\mathrm{f}}^{(1)} = C(J_0 + J_1) \tag{5a}$$

$$R_{\mathrm{s}}^{(1)} = C(J_1 + J_2) \tag{5b}$$

where the spectral densities J_n and the constant C are given by

$$J_n = \frac{2\tau_{\mathrm{c}}}{1 + n^2\omega_0^2\tau_{\mathrm{c}}^2} \tag{6}$$

$$C = \tfrac{1}{40}(e^2qQ/\hbar)^2(1 + \tfrac{1}{3}\eta^2) \tag{7}$$

In the extreme-narrowing limit, $\omega_0\tau_{\mathrm{c}} \ll 1$, the two relaxation rates are equal, $R_{\mathrm{f}}^{(1)} = R_{\mathrm{s}}^{(1)} = 4C\tau_{\mathrm{c}}$; hence, the function $f_{31}^{(1)}(t)$ is zero at all times, and spin-$\frac{3}{2}$ transverse relaxation is monoexponential. However, when the ions are tumbling slowly, $\omega_0\tau_{\mathrm{c}} \gtrsim 1$, the two rates are unequal, with $R_{\mathrm{f}}^{(1)} \rangle R_{\mathrm{s}}^{(1)}$, and both the biexponential functions $f_{11}^{(1)}(t)$ and $f_{31}^{(1)}(t)$ are needed for a full description of transverse relaxation.

The function $f_{11}^{(1)}(t)$ in equations (3), (4a), and (4b) describes the biexponential decay of in-phase single quantum coherence, $T_{1,\pm1}$, with the two components having relative intensities of 60% and 40%. As mentioned in Section 1, this behavior has been known for a long time, and the tensor operator description has here revealed nothing new. Equations (3), (4a), and (4b) also show, however, the biexponential growth and decay of doubly antiphase single quantum coherence, $T_{3,\pm1}$, according to the function $f_{31}^{(1)}(t)$. Only coherences described by the tensor operator $T_{1,-1}$ give rise to magnetization that is observable as a free induction decay, so these third-rank single quantum coherences cannot be detected directly.[3] It will be shown in the next section, however, that the function $f_{31}^{(1)}(t)$ can be measured using multiple quantum filtration.

The tensor operator description of spin-$\frac{3}{2}$ longitudinal relaxation is broadly similar to that of transverse relaxation.[3] If a 180° pulse is applied to a system of spin-$\frac{3}{2}$ nuclei at thermal equilibrium, the resulting deviation from thermal equilibrium can be written in tensor operator form [normalized to equation (2)] as

$$\sigma(t=0) - \sigma^{\mathrm{eq}} = -2\sqrt{2}\,T_{1,0} \tag{8}$$

If biexponential longitudinal relaxation occurs for a time t, then the new density operator $\sigma(t)$ is given by

$$\sigma(t) - \sigma^{\mathrm{eq}} = -2\sqrt{2}[T_{1,0}\,f_{11}^{(0)}(t) + T_{3,0}\,f_{31}^{(0)}(t)] \tag{9}$$

where

$$f_{11}^{(0)}(t) = \tfrac{1}{5}[\exp(-R_{\mathrm{f}}^{(0)}t) + 4\exp(-R_{\mathrm{s}}^{(0)}t)] \tag{10a}$$

$$f_{31}^{(0)}(t) = \tfrac{2}{5}[\exp(-R_{\mathrm{f}}^{(0)}t) - \exp(-R_{\mathrm{s}}^{(0)}t)] \tag{10b}$$

The fast and slow longitudinal relaxation rates for pure quadrupolar relaxation are given by [the superscript (0) denotes relaxation of spin populations, $p = 0$]

$$R_{\mathrm{f}}^{(0)} = 2CJ_1 \tag{11a}$$

$$R_{\mathrm{s}}^{(0)} = 2CJ_2 \tag{11b}$$

As with transverse relaxation, equations (9)–(11b) show that in the extreme-narrowing limit, $R_{\mathrm{f}}^{(0)} = R_s^{(0)} = 4C\tau_{\mathrm{c}}$, so that longitudinal relaxation is monoexponential. Outside this limit, the relaxation is again biexponential, with $R_{\mathrm{f}}^{(0)} \rangle R_{\mathrm{s}}^{(0)}$. Multiple quantum filtration experiments that allow the function $f_{31}^{(0)}(t)$ to be measured will be discussed in the next section.

3 MULTIPLE QUANTUM FILTRATION EXPERIMENTS FOR SPIN-$\frac{3}{2}$ NUCLEI

A tensor operator $T_{l,p}$ transforms under a radiofrequency pulse of flip angle β and phase ϕ according to

$$T_{l,p} \xrightarrow{\beta(\hat{I}_y\cos\phi - \hat{I}_x\sin\phi)} \sum_{p'=-l}^{l} T_{l,p'} d_{p',p}^{l}(\beta)\exp(-\mathrm{i}\Delta p\phi) \tag{12}$$

where p' is the new coherence order, and $\Delta p = p' - p$ is the change in coherence order under the pulse.[3] The amplitude of the transfer $T_{l,p} \rightarrow T_{l,p'}$ is given by the reduced rotation matrix element $d_{p',p}^{l}(\beta)$. These elements are defined to be real; hence, the phase ϕ represents a positive excursion with respect to the rotating frame y axis (i.e., $\phi = 0^\circ$ for a y pulse, $\phi = 90^\circ$ for a $-x$ pulse, and so on).

The important feature revealed by equation (12) is that a pulse cannot change the rank l of a tensor operator (or the coherence it represents), but will, in general, produce operators of all possible coherence orders p. Thus, while the $T_{1,\pm1}$ terms

in equation (3) cannot be transformed by a pulse into multiple quantum coherences ($|p| \geq 2$), the $T_{3,\pm1}$ terms that appear as a result of biexponential spin-$\frac{3}{2}$ transverse relaxation can be transformed into triple quantum coherences, $T_{3,\pm3}$, and antiphase double quantum coherences, $T_{3,\pm2}$. Therefore, it is the appearance of the third-rank terms in equations (3) and (9) that makes the excitation of multiple quantum coherence possible.

Figure 2 shows two pulse sequences for multiple quantum filtration of spin-$\frac{3}{2}$ nuclei and their corresponding coherence pathway diagrams.[4] The standard multiple quantum filtration experiment in Figure 2(a) allows the transverse relaxation function $f_{31}^{(1)}(t)$ to be measured.[2,3] At the end of the τ_e evolution interval, both $T_{1,\pm1}$ and $T_{3,\pm1}$ operators will be present as result of biexponential transverse relaxation (the 180° pulse merely refocuses any offsets). Depending on its phase ϕ', the $\beta = 90°$ pulse then converts the $T_{3,\pm1}$ coherences into either double ($T_{3,\pm2}$) or triple ($T_{3,\pm3}$) quantum coherences, which can be selected by an appropriate phase cycling of the receiver and the pulse phase ϕ. The final $\beta' = 90°$ pulse then reconverts these multiple quantum coherences into a single quantum coherence, $T_{3,\pm1}$, at the start of acquisition of the free induction decay. As mentioned

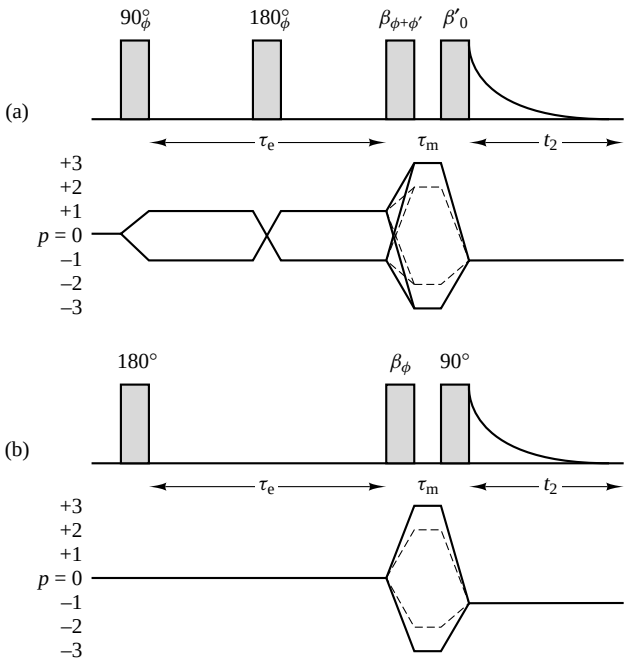

Figure 2 Pulse sequences and coherence pathway diagrams for multiple quantum filtration of spin-$\frac{3}{2}$ nuclei. Sequence (a) is used to study biexponential transverse relaxation, while sequence (b) is used to study longitudinal relaxation. The pulse phase ϕ in (a) and (b) is stepped through the values 0°, 90°, 180°, and 270° for double quantum filtration (dashed coherence pathways), and through 30°, 90°, 150°, 210°, 270°, and 330° for triple quantum filtration (solid pathways), while the receiver phase alternates between 0° and 180°. The pulse phase ϕ' in (a) is 0° for double quantum and 90° for triple quantum filtration. Maximum sensitivity is achieved with flip angles $\beta = \beta' = 90°$, except for the double quantum filtration version of (b), where $\beta = 54.7°$. The interval τ_m is a few microseconds to allow for phase shifting of the pulses, unless multiple quantum relaxation rates are being measured. The double quantum filtration version of (a) can be used selectively to observe spin-$\frac{3}{2}$ nuclei in ordered environments if $\beta = \beta' = 54.7°$

above, this third-rank single quantum coherence is not directly observable. However, further biexponential transverse relaxation during the free induction decay will convert the $T_{3,-1}$ coherence into an observable $T_{1,-1}$ coherence. The function that describes this conversion can be written as $f_{13}^{(1)}(t)$ in analogy to equation (3), and it is easily shown that $f_{13}^{(1)}(t) = f_{31}^{(1)}(t)$. Using equations (3) and (12), the observable components of the density operators produced by the double and triple quantum filters in Figure 2(a) can be calculated as[3]

$$\sigma^{DQF}(t_2) = \tfrac{10}{16}\, T_{1,-1}\, f_{31}^{(1)}(\tau_e)\, f_{31}^{(1)}(t_2) \cos 2\phi \qquad (13a)$$

$$\sigma^{TQF}(t_2) = \tfrac{15}{16}\, T_{1,-1}\, f_{31}^{(1)}(\tau_e)\, f_{31}^{(1)}(t_2) \mathrm{i} \sin 3\phi \qquad (13b)$$

where evolution solely as a result of transverse relaxation has been assumed. The dependence on the pulse phase ϕ in equations (13a) and (13b) is the basis for selection of these components by phase cycling. Note that either double or triple quantum filtration can be used to measure the function $f_{31}^{(1)}(t)$, either as a function of the evolution interval τ_e or in 'real time' as the envelope of the free induction decay. The only difference between the results of the two experiments is that the spin-$\frac{3}{2}$ triple quantum filter is 50% more sensitive than the double quantum filter.[5]

The pulse sequence in Figure 2(b) can be viewed as a multiple quantum filtered inversion–recovery experiment, and allows the longitudinal relaxation function $f_{31}^{(0)}(t)$ to be measured.[3] Again, either double (with $\beta = 54.7°$) or triple (with $\beta = 90°$) quantum filtration are possible. Using equations (9) and (12), the observable component of the density operator for each alternative can be written as

$$\sigma^{DQF}(t_2) = \tfrac{5}{6}\sqrt{2}\, T_{1,-1}\, f_{31}^{(0)}(\tau_e)\, f_{13}^{(1)}(t_2) \cos 2\phi \qquad (14a)$$

$$\sigma^{TQF}(t_2) = \tfrac{5}{8}\sqrt{6}\, T_{1,-1}\, f_{31}^{(0)}(\tau_e)\, f_{13}^{(1)}(t_2) \mathrm{i} \sin 3\phi. \qquad (14b)$$

Thus, either double or triple quantum filtration can be used to measure $f_{31}^{(0)}(t)$ as a function of the evolution interval τ_e. The envelope of the free induction decay is again described by the transverse biexponential function $f_{31}^{(1)}(t)$.

4 MEASUREMENT OF SPIN-$\frac{3}{2}$ RELAXATION PARAMETERS

The free induction decay produced by the triple quantum filter of Figure 2(a) from sodium ions in an agarose gel is shown in Figure 3(a). As predicted, the envelope of the free induction decay is the difference of two exponentials, and corresponds to the function $f_{31}^{(1)}(t_2)$. Fourier transformation of this free induction decay in the normal way yields the triple quantum filtered ^{23}Na spectrum in Figure 3(b). This spectrum corresponds to a function $F_{31}^{(1)}(\omega)$, the Fourier transform of $f_{31}^{(1)}(t)$, and is the difference of two Lorentzian lines with widths $R_f^{(1)}/\pi$ and $R_s^{(1)}/\pi$.

The experimental results in Figure 3(a) and (b) are described by exactly the same two relaxation rates, $R_f^{(1)}$ and $R_s^{(1)}$, as the results in Figure 1. However, the use of multiple quantum filtration has conferred a number of advantages. First, the very fact that a multiple quantum filtered spectrum can be recorded

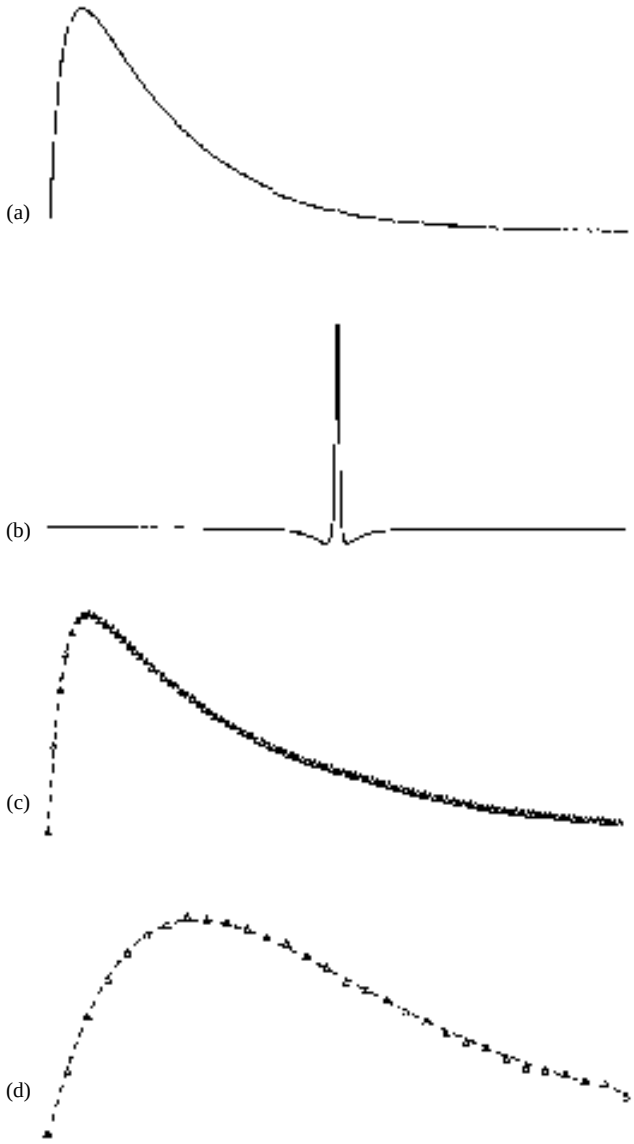

Figure 3 Magnitude mode free induction decay (a) and ^{23}Na spectrum (b) of 2 M NaCl in an agarose gel recorded with the triple quantum filter of Figure 2(a). The amplitudes of ^{23}Na spectra recorded with the triple quantum filter of Figure 2(a) are plotted in (c) as a function of the evolution interval τ_e (triangles represent 100 amplitudes between τ_e = 0 and 99 ms). Computer fitting (dashed line) of the points in (c) yielded the relaxation rates $R(1)/f = 409\,s^{-1}$ and $R(1)/s = 30.7\,s^{-1}$. Similarly, the amplitudes of ^{23}Na spectra recorded with the triple quantum filter of Figure 2(b) are plotted in (d) as a function of τ_e (triangles represent 30 amplitudes between τ_e = 0 and 116 ms). Computer fitting (dashed line) of the points in (c) yielded the relaxation rates $R(0)/f = 38.5\,s^{-1}$ and $R(0)/s = 29.7\,s^{-1}$. Acquisition parameters for all spectra: 2500 Hz spectral width, 48 transients co-added, 105.8 MHz Larmor frequency, 256 points acquired and zero filled to 1024

is significant, since it constitutes unambiguous proof that the ^{23}Na nuclei are tumbling outside the extreme-narrowing limit. Second, both the conventional and multiple quantum filtered data are now available for computer fitting, and this should result in increased accuracy. Third, it is believed that, owing to its greater number of turning points, the $F_{31}^{(1)}(\omega)$ lineshape should yield more reliable fittings than the conventional lineshape $F_{11}^{(1)}(\omega)$, especially when the two relaxation rates are similar. And finally, because the first point of the free induction decay is zero, the multiple quantum filtered spectrum shows less baseline distortion than the conventional spectrum.

The use of multiple quantum filtration is particularly favorable when the broad component of the spin-$\frac{3}{2}$ lineshape cannot be observed because it has relaxed completely in the 'dead time' between the end of the last pulse and the start of data acquisition. Clearly, this 'visibility' problem will be the same in both conventional and multiple quantum filtered spectra. Equations (13a) and (13b) show, however, that the function $f_{31}^{(1)}(t)$ can also be measured by recording the intensity of the filtered spectrum as a function of the evolution interval τ_e. This measurement suffers from no dead time problems, and, in addition, the presence of the 180° pulse means that the effects of B_0 inhomogeneity are refocused. Figure 3(c) shows the experimental function $f_{31}^{(1)}(t)$ measured in this way for the gel sample used previously. The computer fitting of these points yielded the ^{23}Na relaxation rates $R_f^{(1)} = 409\,s^{-1}$ and $R_s^{(1)} = 30.7\,s^{-1}$.

The longitudinal relaxation function $f_{31}^{(0)}(t)$ can be measured as a function of the τ_e interval in the experiment of Figure 2(b) in much the same way as the transverse function.[3] Figure 3(d) shows a computer fitting of results from the agarose gel that yielded the ^{23}Na relaxation rates $R_f^{(0)} = 38.5\,s^{-1}$ and $R_s^{(0)} = 29.7\,s^{-1}$. In general, however, the longitudinal triple quantum filter is much less sensitive and informative than the transverse experiment, and has not attained the same widespread popularity in spin-$\frac{3}{2}$ NMR.

In addition to the methods discussed so far, it is also possible to measure the spin-$\frac{3}{2}$ multiple quantum relaxation rates using a minor modification of the pulse sequence of Figure 2(a).[3,6] The decays of $T_{3,\pm2}$ and $T_{3,\pm3}$ are monoexponential and can be measured as functions of the τ_m interval (previously assumed to be of negligible duration) in the double and triple quantum filtration experiments, respectively. A 180° refocusing pulse can be inserted into the middle of the τ_m interval if required.

A full discussion of the analysis of spin-$\frac{3}{2}$ relaxation rates measured using multiple quantum filtration experiments is beyond the scope of this article, and only a brief summary can be given here. The relaxation rates given in equations (5a), (5b), (11a), and (11b) were derived on the assumption that relaxation is purely quadrupolar and is described by a single correlation time τ_c. In this case, the correlation time τ_c and the constant C can be easily extracted from the ratio of any two of the measured relaxation rates. In systems where rapid chemical exchange is occurring, however, the assumption of a single correlation time is clearly invalid. This applies to spin-$\frac{3}{2}$ ions in agarose gels, in aqueous solutions of proteins, and in both intra- and extracellular environments in cell suspensions and tissues.[7–9] In 1972, Bull[10] proposed a two-site exchange model for spin-$\frac{3}{2}$ nuclei in such systems. In this model, an observed relaxation rate is the weighted sum of the relaxation rate of ions bound to macromolecules and of those in free solution, the weights being the probabilities of the ions being found in each environment. The Bull model is attractive, since the free relaxation rates can easily be estimated and the free site probability can be taken as approximately unity. Thus, the bound relaxation rates can be easily derived and then treated according to the single correlation time model. Unfortunately,

in spite of its elegance, the Bull model does not seem to be very successful in explaining the majority of experimental data. If, using the full range of experimental techniques available, the six possible relaxation rates are measured for a spin-$\frac{3}{2}$ nucleus in, say, a protein solution then it is usually found that the value of τ_c calculated by taking the ratio of a pair of relaxation rates can differ by an order of magnitude according to which pair is chosen.[7,8] For example, using $R_{free} = 25\,s^{-1}$, a Bull analysis of the rates $R_f^{(1)}$ and $R_s^{(1)}$ measured in Figure 3(c) yields $\omega_0\tau_c = 9.1$, while the analysis of $R_f^{(0)}$ and $R_s^{(0)}$ measured in Figure 3(d) yields $\omega_0\tau_c = 1.3$. Although the error on the latter figure may be very large because of the closeness of $R_f^{(0)}$ and $R_s^{(0)}$, the failure of the two-site Bull model is clear. Attempts to extend the Bull model to include multisite exchange would seem to be futile, since (a) the number of parameters would soon become too large for any meaningful fitting, and (b) it is unlikely that monovalent metal ions bind in any discrete manner to the majority of macromolecules. In a more promising development, however, Rooney and Springer[7,8] have successfully fitted ^{23}Na relaxation data from both protein solutions and cell suspensions by using a model that allowed for a continuous distribution of correlation times.

5 DISCRIMINATION OF INTRA- AND EXTRACELLULAR SPIN-$\frac{3}{2}$ NUCLEI

As mentioned in Section 1, the ^{23}Na or ^{39}K NMR spectra of heterogeneous biological tissues or cell suspensions, either in vivo or in vitro, exhibit only a single resonance at a chemical shift characteristic of the aqueous ion. This is unfortunate, since a key aim of such studies is to determine selectively the relaxation parameters of the ions in the individual tissue compartments. One solution to this problem involves the use of lanthanide shift reagents,[11,12] such as $Dy(PPP)_2^{7-}$ or $TmDOTP^{5-}$. These are too large to cross the cell membrane, and so produce a paramagnetic shift of only the extracellular resonance. The main disadvantage of shift reagents is their toxicity. Nevertheless, they have proved popular for in vitro work and have occasionally been used in vivo, although never, of course, for studies on humans.

In 1987, Pekar et al.[13] suggested that multiple quantum filtration could be used to observe selectively the resonance from intracellular spin-$\frac{3}{2}$ metal ions. The idea was that the intracellular ions would be slowly tumbling and would thus exhibit biexponential transverse relaxation, while the extracellular ions would be in the extreme-narrowing limit. A double or triple quantum filter would, therefore, fail to excite any multiple quantum coherences in the extracellular nuclei, and only signal from the intracellular ions would appear in the spectrum. This technique has proved only a partial success, however, since it has been found that, in general, the extracellular ions also exhibit biexponential relaxation.[14,15] In spite of this, the relaxation behavior of spin-$\frac{3}{2}$ nuclei does differ widely between the various tissue compartments, and multiple quantum filters have been used to achieve partial discrimination between compartments in situations where shift reagents are not appropriate.

As an example of the degree of discrimination achieved, Figure 4(a) and (b) show the conventional and triple quantum filtered ^{23}Na NMR spectra of packed human red blood cells, while Figure 4(c) and (d) show the corresponding spectra of human red blood cells suspended in a solution containing 50 mM NaCl, 100 mM choline chloride, and 6 mM $DyTTHA^{3-}$. The triple quantum filtered lineshape of the intracellular ions in Figure 4(d) corresponds closely to that of Figure 4(b), while the intensity of the extracellular resonance relative to the intracellular resonance is clearly much reduced in Figure 4(d) compared with Figure 4(c).

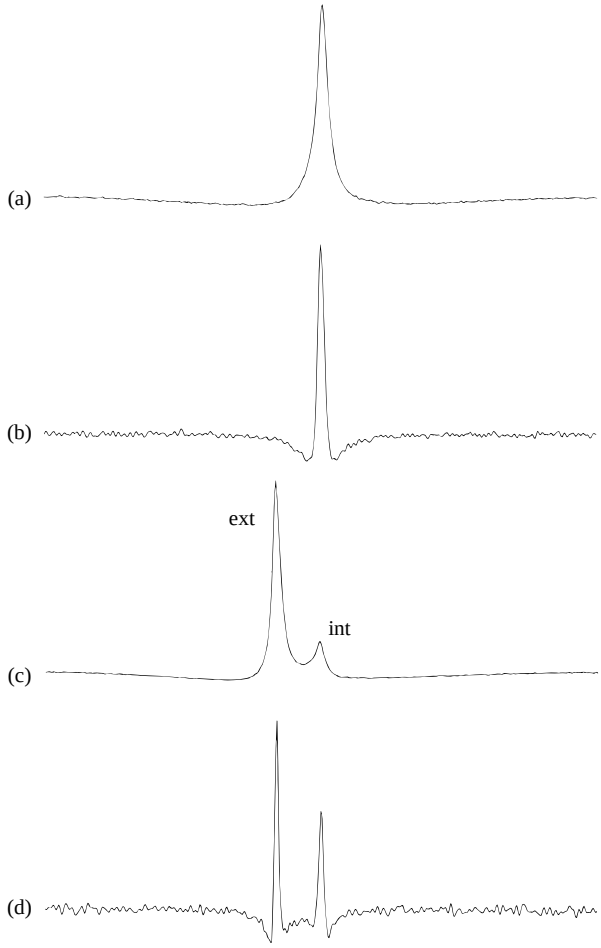

Figure 4 Conventional, (a) and (c), and triple quantum filtered, (b) and (d), ^{23}Na spectra of human red blood cells. Packed cells were used in (a) and (b), and cells suspended in a solution of 50 mM NaCl, 100 mM choline chloride, and 6 mM $DyTTHA^{3-}$ were used in (c) and (d). The pulse sequence of Figure 2(a) was used in (b) and (d). Acquisition parameters: 2500 Hz spectral width, 240 transients coadded for (a) and (c), 2400 transients coadded for (b) and (d), 105.8 MHz Larmor frequency, 128 points acquired and zero filled to 512, 5 ms evolution interval τ_e in (b) and (d). Fresh blood was drawn from the author on the day of the experiments

6 RESIDUAL SPIN-$\frac{3}{2}$ QUADRUPOLAR SPLITTINGS

The discussion in this article of the use of multiple quantum filtration in the study of spin-$\frac{3}{2}$ quadrupolar relaxation has so far assumed that the ions occur in purely isotropic, liquid-type environments; hence, their spectra exhibit no quadrupolar splittings. In 1986, however, Jaccard et al.[3] noted that if residual quadrupolar splittings were present but were

not apparent in the lineshape then these would provide an alternative pathway for the excitation of multiple quantum coherence. If, starting from the initial state of equation (2), free precession occurs solely as a result of the residual quadrupolar splitting $2\omega_Q$ for a time t then the new density operator is given by

$$\sigma(t) = g_{11}^{(1)}(t)(T_{1,-1} - T_{1,+1}) + g_{21}^{(1)}(t)(T_{2,-1} + T_{2,+1}) + g_{31}^{(1)}(t)(T_{3,-1} - T_{3,+1}) \quad (15)$$

where

$$g_{11}^{(1)}(t) = \tfrac{1}{5}(2 + 3\cos 2\omega_Q t) \quad (16a)$$

$$g_{21}^{(1)}(t) = \mathrm{i}\sqrt{\tfrac{3}{5}}\sin 2\omega_Q t \quad (16b)$$

$$g_{31}^{(1)}(t) = -\tfrac{1}{5}\sqrt{6}(1 - \cos 2\omega_Q t) \quad (16c)$$

The functions $g_{l'l}^{(1)}(t)$ in equations (15)–(16c) describe the evolution of in-phase single quantum coherence, $T_{1,\pm1}$, into antiphase single quantum coherence, $T_{2,\pm1}$, and doubly antiphase single quantum coherence, $T_{3,\pm1}$. The major difference between evolution as a result of biexponential relaxation and residual quadrupolar splittings, therefore, is that only in the latter case do singly antiphase coherences, $T_{2,\pm1}$, appear.

The appearance of the operator $T_{2,\pm1}$ as a result of a quadrupolar splitting forms the basis of a method of distinguishing this effect from biexponential relaxation. If the double quantum filter of Figure 2(a) is performed on a system that exhibits a residual quadrupolar splitting then both in-phase double quantum coherence, $T_{2,\pm2}$, and antiphase double quantum coherence, $T_{3,\pm2}$, will be selected. This does not achieve the desired discrimination, since $T_{3,\pm2}$ coherence arising as a result of pure transverse relaxation will also be selected by the filter. Jaccard et al.[3] and Eliav et al.[16] have shown, however, that if either or both of the flip angles β or β' in the double quantum filter is set to 54.7° then third-rank coherences are suppressed and only second-rank coherences will appear. Thus, the resulting spectrum will feature only those ^{23}Na nuclei that exhibit a residual quadrupolar splitting. The Jeener–Broekaert experiment can be used to achieve the same result with slightly higher sensitivity.[17]

Figure 5(a) shows the double quantum filtered ^{23}Na spectrum (with $\beta = \beta' = 90°$) of the suspension of human red blood cells used in Figure 4(c) and (d). If biexponential relaxation were solely responsible for this spectrum then equations (13a) and (13b) show that these lineshapes would be identical to those in the triple quantum filtered spectrum in Figure 4(d). Clearly, however, both intra- and extracellular lineshapes are very different, and this is because those in Figure 5(a) contain a $T_{2,-1}$ component that has arisen from residual quadrupolar splittings hidden within the linewidth. Figure 5(b) shows the result of using the double quantum filter of Figure 2(a) with $\beta = \beta' = 54.7°$ to record a spectrum arising solely from ^{23}Na nuclei that exhibit residual quadrupolar splittings (presumably those associated with the cell membrane[18,19]). The lineshapes here consist of antiphase spin-$\frac{3}{2}$ powder patterns, except that, using the same phasing parameters as in Figure 5(a), they appear in dispersive mode.[16,17]

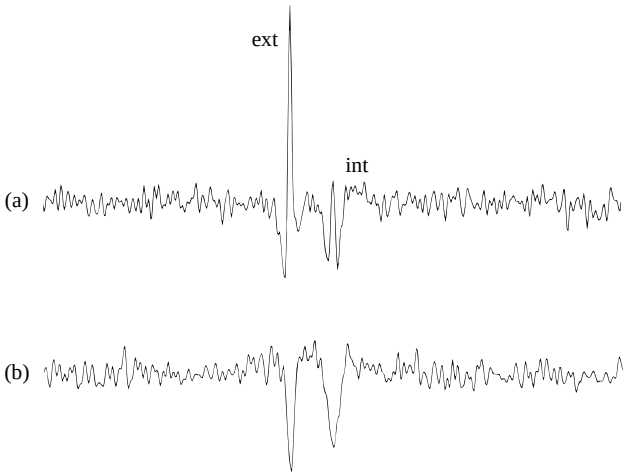

Figure 5 Double quantum filtered ^{23}Na spectra of the red blood cell suspension used in Figure 4(c) and (d). The experiment of Figure 2(a) was used with $\beta = \beta' = 90°$ (a) and $\beta = \beta' = 54.7°$ (b). Acquisition parameters: 2500 Hz spectral width, 2400 transients coadded, 105.8 MHz Larmor frequency, 128 points acquired and zero filled to 512, 5 ms evolution interval τ_e

7 DISCUSSION AND SUMMARY

This article has concentrated on spin-$\frac{3}{2}$ nuclei. This is inevitable, since nuclei such as ^{7}Li, ^{39}K, ^{87}Rb, and, in particular, ^{23}Na are studied very frequently, while higher spin nuclei such as ^{25}Mg, ^{43}Ca, ^{85}Rb, and ^{133}Cs have less favorable NMR parameters and are only rarely studied. Multiple quantum filtration has been used, however, in ^{25}Mg NMR of MgCl in bovine albumin solutions.[20,21] The relaxation of spin-$\frac{5}{2}$ nuclei is triexponential outside the extreme narrowing limit, and is described by transverse and longitudinal functions of the type $f_{11}^{(n)}(t)$, $f_{31}^{(n)}(t)$, and $f_{51}^{(n)}(t)$. Thus, excitation of multiple quantum coherences up to $p = \pm5$ is possible. The most straightforward method of determining the relaxation parameters of spin-$\frac{5}{2}$ nuclei is probably measurement of the four- and five-quantum relaxation rates in an analogous way to which the double and triple quantum relaxation rates can be measured for spin-$\frac{3}{2}$ nuclei.[21]

In summary, since being introduced only in 1986, multiple quantum filtration studies of quadrupolar relaxation have proved highly rewarding, especially in biological systems. Multiple quantum filters allow the biexponential relaxation of spin-$\frac{3}{2}$ nuclei to be measured with great accuracy, and have also been used to obtain partial discrimination of sodium and potassium ions in the various compartments of tissues and cell suspensions. A relatively new application of multiple quantum filtration has been the selective observation and study of spin-$\frac{3}{2}$ nuclei that exhibit residual quadrupolar splittings as a result of their association with ordered structures in cells and tissues. In addition to the applications discussed here, multiple quantum filters have also been used as a method of reversing contrast in ^{23}Na magnetic resonance imaging[22–24] and as a method of accurately measuring spin-$\frac{3}{2}$ dynamic shifts.[25] It seems likely that interest in all these areas will continue to grow in the next few years.

8 RELATED ARTICLES

Biological Systems: Spin-3/2 Nuclei; Cation Movements Across Cell Walls of Intact Tissues using MRS; Multiple Quantum Spectroscopy of Liquid Samples; Quadrupolar Nuclei in Liquid Samples; Relaxation Theory for Quadrupolar Nuclei; Sodium-23 Magnetic Resonance of Human Subjects; Sodium-23 NMR.

9 REFERENCES

1. P. S. Hubbard, *J. Chem. Phys.*, 1970, **53**, 985.
2. J. Pekar and J. S. Leigh, Jr., *J. Magn. Reson.*, 1986, **69**, 582.
3. G. Jaccard, S. Wimperis, and G. Bodenhausen, *J. Chem. Phys.*, 1986, **85**, 6282.
4. G. Bodenhausen, H. Kogler, and R. R. Ernst, *J. Magn. Reson.*, 1984, **58**, 370.
5. C.-W. Chung and S. Wimperis, *J. Magn. Reson.*, 1990, **88**, 440.
6. W. D. Rooney, T. M. Barbara, and C. S. Springer, Jr., *J. Am. Chem. Soc.*, 1988, **110**, 674.
7. W. D. Rooney and C. S. Springer, Jr., *NMR Biomed.*, 1991, **4**, 209.
8. W. D. Rooney and C. S. Springer, Jr., *NMR Biomed.*, 1991, **4**, 227.
9. G. S. Payne and P. Styles, *J. Magn. Reson.*, 1991, **95**, 253.
10. T. E. Bull, *J. Magn. Reson.*, 1972, **8**, 344.
11. M. M. Pike and C. S. Springer, Jr., *J. Magn. Reson.*, 1982, **46**, 348.
12. R. K. Gupta and P. Gupta, *J. Magn. Reson.*, 1982, **47**, 344.
13. J. Pekar, P. F. Renshaw, and J. S. Leigh, Jr., *J. Magn. Reson.*, 1987, **72**, 159.
14. L. A. Jelicks and R. K. Gupta, *J. Magn. Reson.*, 1989, **81**, 586.
15. L. A. Jelicks and R. K. Gupta, *J. Magn. Reson.*, 1989, **83**, 146.
16. U. Eliav, H. Shinar, and G. Navon, *J. Magn. Reson.*, 1992, **98**, 223.
17. R. Kemp-Harper and S. Wimperis, *J. Magn. Reson. B*, 1993, **102**, 326.
18. H. Shinar, T. Knubovets, U. Eliav, and G. Navon, *Biophys. J.*, 1993, **64**, 1273.
19. J. S. Tauskela and E. A. Shoubridge, *Biochim. Biophys. Acta*, 1993, **1158**, 155.
20. C.-W. Chung and S. Wimperis, *Chem. Phys. Lett.*, 1990, **172**, 94.
21. C.-W. Chung and S. Wimperis, *Mol. Phys.*, 1992, **76**, 47.
22. R. H. Griffey, B. V. Griffey, and N. A. Matwiyoff, *Magn. Reson. Med.*, 1990, **13**, 305.
23. S. Wimperis and B. Wood, *J. Magn. Reson.*, 1991, **95**, 428.
24. S. Wimperis, P. Cole, and P. Styles, *J. Magn. Reson.*, 1992, **98**, 628.
25. U. Eliav, H. Shinar, and G. Navon, *J. Magn. Reson.*, 1991, **94**, 439.

Biographical Sketch

Stephen Carl Wimperis. *b* 1962. B.A., 1984 (Chemistry), University of Oxford, UK. Doctorat ès Sciences, 1988 (supervisor Geoffrey Bodenhausen), Université de Lausanne. Research Fellow at Darwin College, Cambridge, 1988–90. Temporary lecturer at University of Manchester, 1990–91. Currently Royal Society University Research Fellow at University of Oxford and R. J. P. Williams Junior Research Fellow at Wadham College, Oxford, 1991–present. Approx. 35 publications. Current research specialties: multiple quantum NMR, spin relaxation, quadrupolar nuclei, NMR imaging, composite pulses, average Hamiltonian theory, two-dimensional NMR, selective excitation.

Relaxation of Transverse Magnetization for Coupled Spins

Thomas C. Farrar and Thomas C. Stringfellow
University of Wisconsin, Madison, WI, USA

1	Introduction	1
2	Redfield Theory and Transverse Relaxation	1
3	Application to Molecular Structure and Dynamics in Na_2PHO_3	3
4	Discussion	5
5	Summary	5
6	Related Articles	6
7	References	6

1 INTRODUCTION

Several excellent articles on Redfield relaxation theory are presented elsewhere in this Encyclopedia (see, e.g., ***Relaxation Theory: Density Matrix Formulation***), and the applications given here are based on that work. The theory is not only simple and elegant, it is also a very powerful and useful tool for the experimental NMR spectroscopist. As shown below, NMR relaxation time measurements of coupled spin systems provide a wealth of information about molecular structure and molecular dynamics in solution that is available in no other way. Such studies are especially important, since a large fraction of chemistry takes place in solution or at interfaces where molecules are still mobile.

For an isolated spin system consisting of two spins of $\frac{1}{2}$ (e.g., C–H, P–H, C–F, P–F, etc.) at low magnetic fields (2.3 T or lower) where only dipolar relaxation is important, the NMR relaxation in a nonviscous fluid sample can be characterized by a single parameter, R_1, the spin–lattice relaxation rate, since in this case the longitudinal relaxation, R_1, and the transverse relaxation, R_2, are equal. That is, all four spectral lines (two for each nucleus) have the same relaxation rate. For magnetic fields of 4.7 T (200 MHz for protons) and higher, most nuclei other than hydrogen are relaxed by both the dipolar and by the chemical shift anisotropy (CSA) mechanisms. In this event, for a coupled system, the observed relaxation rate cannot be described as the sum of the relaxation rates of the contributing mechanisms, that is, $R_{\text{total}} \neq R_{\text{dipolar}} + R_{\text{CSA}}$. Furthermore, four parameters are required to describe the transverse relaxation (each of the four lines has a different R_2 value);[1–9] and for longitudinal relaxation, each line relaxes as a triple exponential.[6–12]

A clear understanding of such relaxation processes is essential, since it has recently been shown that in coherence transfer experiments on large molecules (with long correlation times), anomalous peaks may arise in 2D multiple quantum filtered correlation spectra owing to the presence of such multiple relaxation processes.[10] Differential relaxation can also affect two-dimensional correlation (COSY) experiments.[13,14] The experiments in an aqueous solution of Na_2PHO_3 discussed below provide insight into these differential longitudinal and transverse relaxation processes.

For the general case of two coupled spins of $\frac{1}{2}$, A and K, the parameters that affect the longitudinal and the transverse relaxation are the CSA values of spin A and spin K, the A–K bond distance, the molecular correlation time, and the random field terms. The simultaneous determination of all these parameters at a given temperature presents the opportunity to measure their temperature dependence, a situation that is not possible when relaxation is due to a single relaxation mechanism[15] or when one of the two spins is decoupled. In addition, in the coupled experiments described here, the temperature dependence of the random field terms provides information about the molecular motion of those solvent molecules that are in close proximity to the spin pair.

2 REDFIELD THEORY AND TRANSVERSE RELAXATION

The theory of spin–lattice relaxation in coupled spin systems has been treated thoroughly by a number of authors,[1–12] and is not repeated in detail here. For the most general case, the time evolution of the density matrix $\boldsymbol{\sigma}$ is given by

$$\frac{\mathrm{d}\boldsymbol{\sigma}}{\mathrm{d}t} = \mathbf{R}[\boldsymbol{\sigma} - \boldsymbol{\sigma}(\infty)] \tag{1}$$

This equation can in most cases be greatly simplified. If the basis functions for the density matrix are eigenstates of the Hamiltonian then the diagonal elements σ_{ii} of the density matrix represent the populations of the energy levels, and are related to the longitudinal ('T_1') relaxation. Furthermore, in this eigenbasis representation, if the eigenstates are not degenerate, the density matrix elements σ_{ij} are not connected via the relaxation superoperator to any other matrix elements, and the time evolution of these states is given by

$$\frac{\mathrm{d}\sigma_{ij}}{\mathrm{d}t} = -R_{ijij}[\sigma_{ij} - \sigma_{ij}(\infty)] \tag{2}$$

Given the boundary condition that the transverse magnetization at time $t = 0$ is $\sigma_{ij}(\max)$, the solution of the above differential equation is

$$\sigma_{ij}(t) = \sigma_{ij}(\max)\exp(-t/T_2) \tag{3}$$

Equation (3) tells us that the free induction decay (FID) signal for the coherence σ_{ij} will decay as a single exponential with a time constant T_2. The Fourier transform of this FID is consequently a Lorentzian line with a linewidth, $\pi\Delta\nu_{1/2}(i \rightarrow j) = R_{ijij}$ (see Figure 1). The matrix elements R_{ijij} are then related in a simple fashion to the linewidths of the six transverse coherences for the two-spin system. There are four single quantum coherences: R_{1212} and R_{3434}, the low- and high-frequency lines, respectively, in the carbon spectrum (for a carbon–hydrogen spin pair), and R_{1313} and R_{2424}, the low- and high-frequency lines, respectively, in the proton spectrum (a similar situation would hold, of course, for a proton–phosphorus spin pair or a fluorine–phosphorus spin

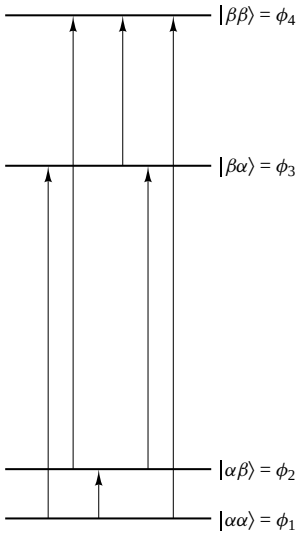

Figure 1 The energy level diagram for PHO_3^{2-}. The labeled wavefunctions correspond to the weak coupling limit. The transitions are as follows: $1 \rightarrow 3$ and $2 \rightarrow 4$ correspond to the low- and high-frequency proton peaks, $1 \rightarrow 2$ and $3 \rightarrow 4$ correspond to the low- and high-frequency phosphorus peaks, $2 \rightarrow 3$ corresponds to the zero quantum transition, and $1 \rightarrow 4$ corresponds to the double quantum transition

pair). We may indirectly measure the zero quantum coherence rate constant R_{2323} and the double quantum coherence rate constant R_{1414}. These relaxation matrix elements are related in a straightforward fashion to the dipolar parameter p, the two chemical shift anisotropies $\Delta\sigma_I = \delta_I$ and $\Delta\sigma_S = \delta_S$, the molecular correlation time, τ_c, and random field terms as indicated in Table 1.

This is, in principle, an attractive way to obtain a wealth of information about molecular structure and molecular dynamics, since it would appear that one need only measure six relaxation rates. As mentioned above, in a completely homogeneous magnetic field, the rate constant is related to the spectral linewidth:

$$R_{ijij} = (1/T_2)_{(i \rightarrow j)} = \pi \Delta\nu_{1/2}(i \rightarrow j) \tag{4}$$

where $\Delta\nu_{1/2}(i \rightarrow j)$ is the full width at halfheight of a peak with Lorentzian lineshape.

In practice, accurate values of the transverse relaxation time may be obtained using the experimental linewidth only when the relaxation time is short. In this event, the linewidth is usually very large compared with any magnetic field inhomogeneities. In principle, accurate values for the linewidth may be obtained by a spin echo experiment, which circumvents the errors arising from pulse imperfections and self-diffusion through an inhomogeneous field. One popular and often used version of the spin echo experiment is the one proposed by Meiboom and Gill.[16] This experiment uses the pulse sequence

$$90^\circ_x - (\tau - 180^\circ_y - \tau)_n \tag{5}$$

This is a variation of the Carr–Purcell pulse sequence.[17] This experiment is, in principle, quite straightforward. In practice, it is very difficult to obtain accurate, meaningful results in the laboratory. If done with great care, however, this experiment is capable of providing accurate results. Vold et al.[18] used numerical analysis of the Bloch equations to evaluate the effects of several experimental conditions. To obtain an accuracy of 1–2% in CPMG experiments, they suggested that the following conditions be satisfied.

Table 1 Relaxation Matrix Elements for a Weakly Coupled System of Two Spins of $\frac{1}{2}$ in the Population Basis; the Y_{ijij} and Z_{ijij} Random Field Terms Include the Longitudinal Random Field Terms A and B

Longitudinal

$R_{1111} = -3(p - \delta_I)^2 k_I - 3(p - \delta_S)^2 k_S - 12p^2 k_+ - \frac{1}{2}(A + B)$
$R_{1122} = 3(p - \delta_S)^2 k_S + \frac{1}{2}A$
$R_{1133} = 3(p - \delta_I)^2 k_I + \frac{1}{2}B$
$R_{1144} = 12p^2 k_+$
$R_{2222} = -3(p + \delta_I)^2 k_I - 3(p - \delta_S)^2 k_S - 2p^2 k_- - \frac{1}{2}(A + B)$
$R_{2233} = 2p^2 k_-$
$R_{2244} = 3(p + \delta_I)^2 k_I + \frac{1}{2}B$
$R_{3333} = -3(p - \delta_I)^2 k_I - 3(p + \delta_S)^2 k_S - 2p^2 k_- - \frac{1}{2}(A + B)$
$R_{3344} = 3(p + \delta_S)^2 k_S + \frac{1}{2}A$
$R_{4444} = -3(p + \delta_I)^2 k_I - 3(p + \delta_S)^2 k_S - 12p^2 k_+ - \frac{1}{2}(A + B)$

Transverse

$R_{1212} = -3(p^2 + \delta_I^2)k_I - 3(p - \delta_S)^2 k_S - 4(p - \delta_S)^2 k_0 - 6p^2 k_+ - p^2 k_- - Y_{1212}$
$R_{1313} = -3(p^2 + \delta_S^2)k_S - 3(p - \delta_I)^2 k_I - 4(p - \delta_I)^2 k_0 - 6p^2 k_+ - p^2 k_- - Z_{1313}$
$R_{2424} = -3(p^2 + \delta_S^2)k_S - 3(p + \delta_I)^2 k_I - 4(p + \delta_I)^2 k_0 - 6p^2 k_+ - p^2 k_- - Z_{2424}$
$R_{3434} = -3(p^2 + \delta_I^2)k_I - 3(p + \delta_S)^2 k_S - 4(p + \delta_S)^2 k_0 - 6p^2 k_+ - p^2 k_- - Y_{3434}$

Zero/multiple quantum

$R_{2323} = -3(p^2 + \delta_I^2)k_I - 3(p^2 + \delta_2^2)k_S - 4(\delta_I - \delta_S)^2 k_0 - 2p^2 k_- - X_{2323}$
$R_{1414} = -3(p^2 + \delta_I^2)k_I - 3(p^2 + \delta_S^2)k_S - 4(\delta_I + \delta_S)^2 k_0 - 12p^2 k_+ - X_{1414}$
$p = \gamma_I \gamma_S \mu\hbar/8\pi r_{IS}^3$
$\delta = \frac{1}{3}\gamma B_0[\sigma_{33} - \frac{1}{2}(\sigma_{11} + \sigma_{22})]$
$k_0 = \frac{1}{5}\tau_c$
$k_i = \tau_c/5(1 + \omega_i^2 \tau_c^2)$
$\omega_+ = \omega_I + \omega_S$
$\omega_- = \omega_I - \omega_S$

1. Pulse widths must be calibrated and accurate to within about 5% of ideal.
2. Data from the first part of the relaxation curve should not be used in the least-squares fit.
3. The transmitter should be as close to on resonance as possible to eliminate off-resonance effects.
4. Amplitudes of the spin echoes must be calculated relative to an experimentally determined steady-state value.
5. The sample should remain static so that the gradients in the magnetic field are not time-dependent.
6. Refocusing pulse spacings should be less than approximately 100 ms so that diffusion effects are eliminated.

Another method of measuring relaxation in the transverse plane is the spin locking experiment,[19,20] in which one employs a continuous $\boldsymbol{B}_1$ field in lieu of the sequence of 180° pulses used in spin echo experiments. This field locks the magnetization along the applied axis in the transverse plane. By varying the duration of the spin locking period, one may fit the peak intensity versus time to a decaying exponential and obtain the spin–lattice relaxation time in the rotating frame, $T_{1\rho}$. For most liquid samples, $T_{1\rho}$ is essentially equivalent to T_2.[19,21]

To obtain information about the relaxation rates for zero and multiple quantum coherences, a number of different pulse sequences have been proposed.[22] For heteronuclear spin systems, the following pulse sequence may be used to generate double quantum coherences:[23]

$$\left.\begin{array}{lllll} I: & 90^\circ_y - \frac{1}{2}\tau - & 180^\circ - \frac{1}{2}\tau - 90^\circ_x - t_1 - \text{acquire} \\ S: & & 180^\circ - \frac{1}{2}\tau - 90^\circ - t_1 \end{array}\right\} \quad (6)$$

where $\tau = \pi/2J$. The purpose of the 180° pulses is to refocus the dephasing of the magnetization due to magnetic field inhomogeneities and chemical shifts and suppress the dependence of the transmitter offset frequency. Yang et al.[24] proposed using a similar pulse sequence with explicit pulse phasings to separate the zero and double quantum coherences. This sequence is as follows:

$$\left.\begin{array}{llll} I: & 90^\circ_1 - \frac{1}{2}\tau - & 180^\circ_y - \frac{1}{2}\tau/2 & 180^\circ_x - \frac{1}{2}t_1 - 90^\circ_2 \\ S: & & 180^\circ_y - \frac{1}{2}\tau - 90^\circ_y - \frac{1}{2}t_1 - & 180^\circ_x - \frac{1}{2}t_1 - \text{acquire}_3 \end{array}\right\} \quad (7)$$

To obtain purely zero quantum coherence, the relative phasing of the pulses is

$$\left.\begin{array}{llll} (1) & x & x & -x & -x \\ (2) & x & y & x & y \\ (3) & x & y & -x & -y \end{array}\right\} \quad (8)$$

which is arranged to eliminate any magnetization from the S spin. The recovery curve may then be fit to the following equation to obtain the zero quantum relaxation time T_{ZQ}:

$$\begin{aligned} I(t_1) &= I(\infty) + B' \mathrm{e}^{-t_1/T_{\text{ZQ}}} \sin(\pi J \tau) \\ &= A + B \mathrm{e}^{-t_1/T_{\text{ZQ}}} \end{aligned} \quad (9)$$

To obtain purely double quantum coherence, the relative phasing of the pulses is

$$\left.\begin{array}{llll} (1) & x & x & -x & -x \\ (2) & x & -y & x & -y \\ (3) & x & y & -x & -y \end{array}\right\} \quad (10)$$

The recovery curve may then be fit to an equation similar to that for a zero quantum coherence to obtain the double quantum relaxation time T_{DQ}.

3 APPLICATION TO MOLECULAR STRUCTURE AND DYNAMICS IN NA_2PHO_3

It is important to test the development of a new theory by carrying out experiments on a sample for which one knows the experimental results. All of the pertinent NMR parameters for a sample of Na_2PHO_3 have been measured by a number of independent methods. We therefore decided to carry out a set of transverse relaxation experiments with a solution of sodium phosphite, Na_2PHO_3, dissolved in a 60%/40% mixture of ethylene glycol-d_6 and methanol-d_4. They were performed at −25.4°C, a temperature slightly higher than the temperature of the proton-decoupled T_1 minimum of the phosphorus nuclei at a field of 4.7 T. Figure 2 shows the ^{31}P NMR spectra of the sample in a field of 11.5 T. The upper trace was recorded at 300 K, the middle trace at 250 K, and the bottom trace at 225 K. At 225 K, the low-frequency line has become so broad that it has disappeared into the baseline noise.

Fitting the data to equation (1) produced the following best fit parameters: the P–H bond length r = 150.4 pm, the proton chemical shift anisotropy $\Delta\sigma_{\text{H}}$ = 5.3 ppm, the phosphorus chemical shift anisotropy $\Delta\sigma_{\text{P}}$ = −137.5 ppm, the rotational correlation time, assuming a Lorentzian spectral density function, τ_{c} = 818 ps, the phosphorus intermolecular term $A = 0.27\,\text{s}^{-1}$, and the proton intermolecular term $B = 0.22\,\text{s}^{-1}$. The theoretical transverse relaxation times may be calculated using these molecular parameters and the equations given in Table 1. Independent values for the P–H bond length were obtained from X-ray and neutron diffraction experiments.[25] Independent values for the phosphorus and proton chemical shift anisotropies were obtained from NMR

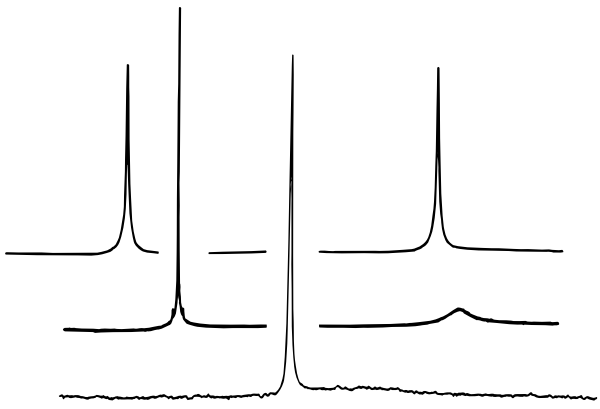

Figure 2 The ^{31}P NMR spectra of a sample of Na_2PHO_3 in a magnetic field of 11.5 T (202 MHz resonance frequency for phosphorus). The upper trace was recorded at 300 K, the middle trace at 250 K, and the bottom trace at 225 K. At 225 K, $\omega_0\tau_{\text{c}} \sim 1$, and the low-frequency line has become so broad that it has disappeared into the baseline noise

experiments on a solid sample of Na_2PHO_3 (T. C. Farrar, unpublished results).

These results show clearly that the two lines in the phosphorus spectrum will have different widths and the two lines in the proton spectrum will have different widths. The width of the $(1 \rightarrow 2)$ phosphorus line in PHO_3^{2-} must be broad, since the sign of the phosphorus CSA is negative and R_{1212} contains terms with the difference between δ_P and p. Similarly, the width of the $(3 \rightarrow 4)$ phosphorus line must be narrow, since R_{3434} contains terms with the sum of the CSA and dipolar terms. In the phosphorus spectra shown in Figure 2, the low-frequency line is broad; consequently, the sign of the phosphorus–proton coupling constant J(P,H) must be positive. The equations for R_{ijij} above also show that the greatest differential line broadening will occur at that field for which the CSA and the dipolar parameters are approximately equal, and under those sample conditions for which $\omega\tau_c \sim 1$. This is exactly what we have found experimentally.

The theory clearly tells us what to expect, but it is always a bit more satisfying if one can obtain a simple physical picture of what is happening. Consider, then, a single crystal of Na_2PHO_3 with the various orientations shown in Figure 3(a). The resonance frequency for the phosphorus nuclei that are bonded to protons will change as a function of Θ in the following manner:

$$f_\alpha = f_0 - \frac{\gamma_H \gamma_P \hbar}{r^3}(3\cos^2\Theta - 1) \tag{11}$$

$$f_\beta = f_0 + \frac{\gamma_H \gamma_P \hbar}{r^3}(3\cos^2\Theta - 1) \tag{12}$$

where f_α and f_β are the two frequencies in the phosphorus spectrum, Θ is the angle between the P–H internuclear vector and the magnetic field $\boldsymbol{B}_0$, and r is the P–H bond length. The other constants are defined in Table 1. Note that the f_α line arises from that half of the molecules in which the phosphorus is bonded to a proton nucleus in the α spin state (i.e., those proton nuclei that have their spins aligned parallel with the magnetic field $\boldsymbol{B}_0$), and the f_β line arises from that half of the molecules in which the phosphorus is bonded to a proton nucleus in the β spin state. If the chemical shift of the phosphorus is isotropic ($\delta_P = 0$), there will be a maximum splitting of $2p$ (about 15 kHz) for the two lines at a value of $\Theta = 0$. For $\Theta = 54.7^\circ$ (the 'magic angle'), the two lines will coalesce, and at $\Theta = 90^\circ$ the splitting is p (about 7.5 kHz, see the definition of p in Table 1). The spectra for these orientations are depicted in Figure 3(a). The hatched lines below the spectra show the total variation in the magnetic field at the phosphorus nuclei as Θ varies.

If the phosphorus and/or proton chemical shifts are anisotropic (which they are for PHO_3^{2-}) then the local field experienced by the phosphorus nuclei will be very different. Figure 3(b) shows the single crystal spectra for the phosphorus for the same orientations as in Figure 3(a). The frequencies of the two lines are now given by

$$f_\alpha = f_0 - \frac{\gamma_H \gamma_P \hbar}{r^3}(3\cos^2\Theta - 1) + \delta_P(3\cos^2\Theta - 1) \tag{13}$$

$$f_\beta = f_0 + \frac{\gamma_H \gamma_P \hbar}{r^3}(3\cos^2\Theta - 1) + \delta_P(3\cos^2\Theta - 1) \tag{14}$$

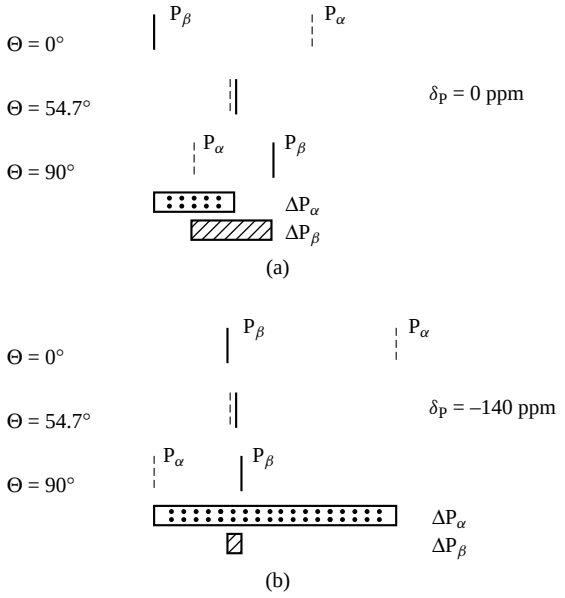

Figure 3 (a) ^{31}P NMR spectra for a single crystal of Na_2PHO_3 at three different orientations of Θ, the angle between the P–H internuclear vector and the magnetic field direction, assuming a phosphorus CSA of zero. (b) As (a), but with a phosphorus CSA value of -140 ppm

If the magnitudes of the phosphorus dipolar and CSA terms are about equal then one of the lines in the single crystal spectrum will experience almost no change in frequency as a function of Θ, since any change in the local field due to the dipolar term will be canceled by the CSA term. The other line will experience a change almost twice as great, since local fields generated by the dipolar and CSA terms add constructively. For PHO_3^{2-}, the phosphorus CSA, $\delta_P = (\sigma_\parallel - \sigma_\perp)_P = -125$ ppm.[6,7] In this case, the total range of magnetic fields experienced as a function of Θ is very small for the P_β nuclei, the phosphorus nuclei spin-coupled to proton nuclei in the β spin state. At a magnetic field of about 6.3 T, the local magnetic field for the P_β nuclei is almost independent of orientation. For the P_α nuclei, the local field changes over a range almost twice as great as that expected for the dipolar interaction. In other words, the dipolar field fluctuations at the P_β nuclei due to changes in orientation are largely canceled by field changes of the opposite sign due to the CSA. The hatched bars below the spectra in Figure 3(b) show schematically this very small range in the local field for the P_β nuclei and the twofold greater-than-normal dipolar range in the dipolar field for the P_α nuclei.

When the molecules begin to move, the magnetic fields at the P_α and P_β nuclei are modulated by the molecular motion. And it is the magnitude of this motion-induced magnetic field modulation [represented by the hatched bars in Figure 3(a) and (b)] that couples the precessional motion of the nuclear spins to the molecular motion and brings about relaxation of the nuclear spin system. When the CSA and dipolar interactions are comparable, as they are in the present case, relatively little magnetic field modulation occurs at the P_β nuclei. Consequently, they will have a very long relaxation time, even for slow molecular motions where $\omega_P\tau_c \sim 1$. The P_α nuclei, however, will experience much larger than normal magnetic field fluctuations, and as a result will have short relaxation times.

Normally, one cannot determine which of the lines in a high-resolution NMR spectrum are associated with the transitions between the various energy levels. For example, in a spectrum such as that in Figure 2, it is not usually possible to determine whether the high-frequency phosphorus line arises from the transition between energy levels 1 and 2 or between levels 3 and 4. However, when differential line broadening is present, one can easily determine which line is associated with the transitions between the energy levels. As pointed out above, since we know from solid state NMR experiments that the phosphorus CSA is negative and since we know from the spectrum that it is the low-frequency phosphorus line that is broad, by looking at the expression for R_{1212} above, we know that the broad line must be associated with the R_{1212} transition. Consequently, the absolute sign of the phosphorus–hydrogen spin coupling constant, J(P,H) must be positive; in this case, J(P,H) = +565 Hz. In a similar fashion, we have shown that the absolute sign of directly bonded carbon–hydrogen spin coupling is positive.[8]

The transverse relaxation times for all four lines were measured using the CPMG sequence [see equation (5)] and $T_{1\rho}$ experiments. The experiments were performed on resonance at the same temperature as the longitudinal relaxation experiments. The sample was static, and field/frequency locking was not used. A three-parameter fit to an equation similar to equation (9) gives the transverse relaxation time. For the $R_{1\rho}$ experiments, the spin locking fields γB_1 were 340 and 746 s^{-1}, respectively, for the proton and phosphorus nuclei. Table 2 shows a comparison of the results from these experiments.

4 DISCUSSION

Examining Table 2, one sees that the experimentally determined transverse relaxation times do not agree with the theoretical relaxation times calculated from the bond length, the two CSAs, and the correlation time obtained from the longitudinal relaxation studies. The calculated T_{ij} values are appreciably longer than the experimentally determined values. The differences are due to several factors. The largest source of the differences probably arises from the intermolecular, random field terms. These terms account for relaxation mechanisms of rank one, such as scalar relaxation, spin rotation, chemical exchange, and relaxation due to the presence of paramagnetic species. Since the experiments were done at low temperature, spin rotation can be ruled out. Very careful sample preparation allows one also to rule out paramagnetic impurities. Since the random field terms for the longitudinal relaxation also contribute to the transverse relaxation, and have been included in the Y_{ijij} and Z_{ijij} terms in the calculated values, the difference must arise from additional random field terms that are unique to the transverse relaxation. Such terms would include those due to chemical exchange and other relatively slow random dynamic processes. Neglect of these terms will result in calculated values for the transverse relaxation rates that are smaller (and calculated relaxation times that are longer) than the experimentally measured values.

If one assumes that the additional intermolecular contribution is the same for both single quantum coherences of a given nucleus, one may subtract the relaxation rates and get a relation independent of the intermolecular interactions:

$$\Delta_{\mathrm{P}} = R_{1212} - R_{3434} = 12p\delta_{\mathrm{P}}k_{\mathrm{P}} + 16p\delta_{\mathrm{P}}k_0 \qquad (15)$$

$$\Delta_{\mathrm{H}} = R_{1313} - R_{2424} = 12p\delta_{\mathrm{H}}k_{\mathrm{H}} + 16p\delta_{\mathrm{H}}k_0 \qquad (16)$$

where k_i and k_0 are defined in Table 1. Comparing the experimentally obtained values of these parameters with those calculated from T_1 data, the results still do not agree, implying either that these additional intermolecular terms are not the sole factor causing the difference or that there are still additional random field terms operating that do not equally affect the two different coherences for a given nucleus. This suggests, for example, that Y_{1212} and Y_{3434} (see Table 1) are not equal.

Another factor that may lead to the discrepancies seen between the theoretical relaxation rates and the experimentally determined rates is the form of the spectral density function. Longitudinal relaxation depends on rapidly fluctuating fields near the Larmor frequency γB_0. Transverse relaxation times depend on fluctuating fields near the Larmor frequency as well as slowly fluctuating fields described by k_0. The Lorentzian spectral density function may not be valid for this range of molecular motions. Finally, the experiments may not be measuring the true transverse or zero/multiple quantum relaxation rates.

5 SUMMARY

In principle, transverse relaxation studies, including zero and multiple quantum coherences, can provide structural and dynamic information. They complement longitudinal relaxation studies in that they provide information concerning low-frequency motions and cross-correlation functions. Preliminary work comparing longitudinal and transverse relaxation results obtained for PHO_3^{2-} in solution indicates that great caution

Table 2 Theoretical and Experimental Results of Transverse Relaxation Studies on PHO_3^{2-}

Source	T_{12} (ms)	T_{34} (ms)	T_{13} (ms)	T_{24} (ms)	T_{23} (ms)	T_{14} (ms)
Theory and T_1 study[a]	151	537	279	254	406	320
CPMG	121	386	185	165		
Zero quantum					319	
Double quantum						205
$T_{1\rho}$	125	369	215	181		

[a]The values for p, $\Delta\sigma_{\mathrm{P}}$, $\Delta\sigma_{\mathrm{H}}$, τ_{c}, and the random field terms A and B were taken from longitudinal NMR experiments, solid state NMR experiments, and neutron diffraction work, and were used in the equations for the R_{ijij} matrix elements given in Table 1.

should be used in using the transverse experiments to obtain structural and dynamic information. This is in part due to the difficulty in executing accurate, meaningful CPMG and $T_{1\rho}$ experiments. It may also be due to the fact that a single spectral density function is not a faithful representation of the molecular motions over the entire range of motion.

Given the six equations for the six different coherences and the up to 10 unknown parameters (δ_H, δ_P, p, and τ_c, and the six transverse random field terms; see Table 1), a measurement of the six coherences is not enough information to give one accurate, uniquely determined values for all of those parameters. In addition, as we have seen in the example presented above, there are experimental problems, since it is very difficult indeed to measure linewidths (coherences) accurately, especially for very narrow lines. In our experience, neither linewidth measurements nor Carr–Purcell–Meiboom–Gill spin echo experiments give highly reliable results, especially at the higher temperatures where some of the linewidths are relatively narrow. $T_{1\rho}$ experiments, if done carefully, give reasonably good results.

The most fundamental difficulty is that one has 6 equations and there are probably 10 unknown parameters. This would seem to indicate that experimental information about the transverse relaxation must be complemented by additional data from longitudinal relaxation experiments. In practice, a better way to obtain information about the molecular parameters is to carry out longitudinal relaxation time experiments. Although the data analysis is considerably more difficult, the experiments are easier to execute, and give more reliable and more reproducible results.[6–8]

6 RELATED ARTICLES

Relaxation of Coupled Spins from Rotational Diffusion; Relaxation Mechanisms: Magnetization Modes; Relaxation Processes in Coupled-Spin Systems; Relaxation Processes: Cross Correlation and Interference Terms; Relaxation Theory: Density Matrix Formulation.

7 REFERENCES

1. A. G. Redfield, in *Advances in Magnetic Resonance*, ed. J. S. Waugh, Academic Press, New York, Vol. 1, p. 1.
2. H. J. Shimizu, *J. Chem. Phys.*, 1964, **40**, 3357.
3. E. L. Mackor and C. MacLean, in *Progress in Nuclear Magnetic Resonance Spectroscopy*, eds. J. W. Emsley, J. Feeney, and L. H. Sutcliffe, Pergamon Press, Oxford, 1967, Vol. 3, p. 129.
4. L. G. Werbelow and D. M. Grant, in *Advances in Magnetic Resonance*, ed. J. S. Waugh, Academic Press, New York, 1977, Vol. 9, p. 189.
5. R. L. Vold and R. R. Vold, in *Progress in Nuclear Magnetic Resonance Spectroscopy*, eds. J. W. Emsley, J. Feeney, and L. H. Sutcliffe, Pergamon Press, Oxford, 1978, Vol. 12, p. 79.
6. T. C. Farrar and I. C. Locker, *J. Chem. Phys.*, 1987, **87**, 3281; see also *Z. Phys. Chem.*, 1987, **151**, 24.
7. T. C. Farrar and J. D. Decatur, *J. Phys. Chem.*, 1990, **94**, 7395.
8. T. C. Farrar, M. A. Jablonsky, and J. L. Schwartz, *J. Phys. Chem.*, 1994, **98**, 4780; see also T. C. Farrar, B. A. Adams, G. C. Grey, R. A. Quintero, and Q. Zuo, *J. Am. Chem. Soc.*, 1986, **108**, 8190.
9. T. C. Farrar and R. A. Quintero, *J. Phys. Chem.*, 1987, **91**, 3224.
10. N. Mueller, G. Bodenhausen, K. Wuethrich, and R. R. Ernst, *J. Magn. Reson.*, 1985, **65**, 531.
11. K. Elbayed and D. Canet, *Mol. Phys.*, 1989, **68**, 1033.
12. E. Koenigsberger and H. Sterk, *J. Chem. Phys.*, 1985, **83**, 2723.
13. S. Wimperis and G. Bodenhausen, *Chem. Phys. Lett.*, 1987, **140**, 41.
14. S. Wimperis and G. Bodenhausen, *Mol. Phys.*, 1989, **66**, 897.
15. H. G. Hertz, in *Progress in Nuclear Magnetic Resonance Spectroscopy*, eds. J. W. Emsley, J. Feeney, and L. H. Sutcliffe, Pergamon Press, Oxford, 1983, Vol. 16, p. 115; see also H. G. Hertz, ibid., 1967, Vol. **3**, p. 159.
16. S. Meiboom and D. Gill, *Rev. Sci. Instrum.*, 1958, **29**, 688.
17. H. Y. Carr and E. M. Purcell, *Phys. Rev.*, 1954, **94**, 630.
18. R. L. Vold, R. R. Vold, and H. E. Simon, *J. Magn. Reson.*, 1973, **11**, 283.
19. Farrar, T. C., *Introduction to Pulse NMR Spectroscopy*, The Farragut Press, Chicago, 1989.
20. T. K. Leipert, J. H. Noggle, W. J. Freeman, and D. L. Dalrymple, *J. Magn. Reson.*, 1975, **19**, 208.
21. J. S. Blicharski, *Z. Naturforsch. A*, 1972, **27**, 1355; *Acta Phys. Polon. A*, 1972, **41**, 223.
22. A. Wokaun and R. R. Ernst, *Mol. Phys.*, 1978, **36**, 317.
23. A. Minoretti, W. P. Aue, M. Reinhold, and R. R. Ernst, *J. Magn. Reson.*, 1980, **40**, 175.
24. J. Yang, W. Qin-yi and Y. Chao-hui, *Chin. J. Phys.*, 1987, **7**, 905.
25. T. C. Farrar, D. R. Powell, S. K. Smith, and F. K. Ross, *Acta Crystallogr., Sect. C*, 1994, **50**, 342.

Biographical Sketches

Thomas C. Farrar. *b* 1933. B.Sc. (mathematics and chemistry), 1954, Wichita State University, USA; Ph.D. (chemistry), 1959, University of Illinois, Urbana. National Science Foundation Postdoctoral fellow at Cambridge University, Department of Theoretical Chemistry, 1959–61. Introduced to NMR by H. S. Gutowsky and M. Karplus. Faculty in Chemistry, University of Oregon, 1961–63. National Bureau of Standards, Chief of Magnetism Section, 1963–71. Director of Research and Development, JEOL, 1971–75. Director of Chemical Instrumentation Program, National Science Foundation, 1975–79. Professor of Chemistry, University of Wisconsin–Madison, 1979–present. Approx. 100 publications. Current research interests: molecular structure and molecular dynamics, ab initio calculations of molecular structure and of NMR parameters, experimental and theoretical development of density matrix theory and its applications in spectroscopy, and NMR relaxation time studies of molecular structure and dynamics.

Thomas C. Stringfellow. *b* 1957. B.A. (chemistry), 1991, Indiana State University, where magnetic resonance studies were begun under the guidance of Professor Myong-Ku Ahn. Graduate student at the University of Wisconsin–Madison, in the laboratory of Professor Thomas C. Farrar, 1991–present. Current research interests include the use of NMR relaxation measurements, Raman light scattering, and ab initio calculations to obtain information about the dynamics, structure and interactions of molecules in solution.

Relaxation Processes: Cross Correlation and Interference Terms

Lawrence G. Werbelow
New Mexico Tech, Socorro, NM, USA

1	Introduction	1
2	Semiclassical Theory of Nuclear Spin Relaxation	1
3	'Magnetizations'and Coherences	2
4	The Cross-Correlation Spectral Density	2
5	Effects of Cross-Correlation in Simple, Scalar-Coupled Spin-$\frac{1}{2}$ Systems	3
6	Effects of Cross Correlation in Multiply Degenerate Spin-$\frac{1}{2}$ Systems	5
7	Cross Correlation and Relaxation in the Rotating Frame	6
8	Summary	7
9	Related Articles	7
10	References	7

1 INTRODUCTION

Whenever molecular motions effectively average the spatially anisotropic couplings between a nuclear spin and the extranuclear environment, NMR relaxation parameters can be described using standard second-order time-dependent perturbation theory.[1] Because of the quadratic relationship between interaction strength and relaxation rate, if several couplings are responsible for effecting nuclear spin relaxation, relaxation rates identified with each distinct coupling are not additive unless all bilinear cross products vanish.

Although symmetry arguments require that these cross products vanish in certain instances, generally these terms are nonzero. It is important to recognize that each cross term must be modified by a factor that describes the degree of correlated fluctuation between the competing relaxation pathways. Fundamentally different *cross* correlation and *auto*correlation times are needed to describe the perturbation response characteristics of spins influenced by competitive relaxation pathways.

The distinction between autocorrelation and cross correlation is more than arithmetic. Autocorrelation is instrumental in thermalization/dissipation processes, and can be associated with measurements of T_1, T_2, $T_{1\rho}$, or cross relaxation. In contrast, cross correlation initiates polarization and coherence transfer, and is manifest in higher forms of transient spin order. The roles played by autocorrelation and cross correlation are complementary.

The study of relaxation-induced multispin order probes temporal spin correlation in a manner similar to a multidimensional NMR probe of residual spin correlation. Indeed, most contemporary NMR techniques utilize polarization transfer, and if the relaxation process selectively dissipates certain forms of spin order then failure to consider such relaxation effects can damage the credibility of the most elementary 2D experiment. From a practitioner's perspective, utilization of cross correlation yields much finer detail of molecular structure and dynamics than conventional relaxation parameters, and should be the method of choice, whenever possible, for the contemporary molecular scientist who wishes to exploit nuclear spin relaxation to its fullest.

Two established reviews, by Werbelow and Grant[2] and by Vold and Vold[3], discuss relaxation-induced magnetization transfer and coherence transfer, respectively. Three reviews by Canet,[4] Grant et al.,[5] and Werbelow,[6] provide valuable discussions of numerous other features associated with cross correlation and nuclear spin relaxation in multispin systems.

2 SEMICLASSICAL THEORY OF NUCLEAR SPIN RELAXATION

In the absence of applied rf fields, the interaction between a nuclear spin and the extranuclear environment can be written as $\hat{\mathcal{H}}(t) = \hat{\mathcal{E}} + \hat{\mathcal{F}}(t)$ where $\hat{\mathcal{E}} = \langle\hat{\mathcal{H}}(t)\rangle$ and $\hat{\mathcal{F}}(t) = \hat{\mathcal{H}}(t) - \hat{\mathcal{E}}$. The term associated with nuclear spin relaxation, $\hat{\mathcal{F}}(t)$, can be cast in the form

$$\hat{\mathcal{F}}(t) = \sum_{\eta} \hat{\mathcal{F}}^{\eta} = \sum_{\eta} \xi_{\eta} \sum_{k} (-1)^k \hat{T}_{\eta}^{k} V_{\eta}^{-k}(t) \qquad (1)$$

The Hamiltonian $\hat{\mathcal{F}}(t)$ is composed of a number of distinct couplings or relaxation pathways (η). Each interaction has been partitioned into a symmetrized product of classical lattice functions V, characteristic interaction coupling constants ξ, and spin operators $\hat{T}$. The simple decomposition implicit in equation (1) obtains for interactions with axial symmetry.

If motional narrowing obtains, the time evolution of individual matrix elements of a thermally normed, reduced spin density operator $\hat{\chi}(t)$ are described by a simple set of linearly coupled first-order equations[1]

$$\frac{\mathrm{d}}{\mathrm{d}t}\chi_{\alpha\alpha'}(t) = -\mathrm{i}\omega_{\alpha\alpha'} + \sum_{\alpha''}\sum_{\alpha'''} \mathcal{R}_{\alpha\alpha'\alpha''\alpha'''}\chi_{\alpha''\alpha'''}(t) \times \exp[\mathrm{i}(\omega_{\alpha\alpha'} - \omega_{\alpha''\alpha'''})t] \qquad (2)$$

$$\begin{aligned}\mathcal{R}_{\alpha\alpha'\alpha''\alpha'''} = &\sum_{k}\sum_{\eta}\sum_{\eta'}[J_k^{\eta\eta'}(\omega_{\alpha\alpha''}) + J_k^{\eta\eta'}(\omega_{\alpha'''\alpha'})] \\ &\times (T_{\eta}^{k})_{\alpha\alpha''}(T_{\eta'}^{-k})_{\alpha'''\alpha'} \\ &-\delta_{\alpha\alpha''}\sum_{\beta} J_k^{\eta\eta'}(\omega_{\alpha'''\beta})(T_{\eta}^{k})_{\alpha'''\beta}(T_{\eta'}^{-k})_{\beta\alpha'} \\ &-\delta_{\alpha'''\alpha'}\sum_{\beta} J_k^{\eta\eta'}(\omega_{\beta\alpha'''})(T_{\eta}^{k})_{\alpha\beta}(T_{\eta'}^{-k})_{\beta\alpha''} \qquad (3)\end{aligned}$$

The spectral density $J_k^{\eta\eta'}$ is derived from the correlation function $\langle V_{\eta}^{-k}(t-\tau)V_{\eta'}^{k}(t)\rangle$ via a one-sided Fourier transformation:

$$J_k^{\eta\eta'}(\omega) = \xi_{\eta}\xi_{\eta'}\mathrm{Re}\int_0^{\infty}\langle V_{\eta}^{-k}(t-\tau)V_{\eta'}^{k}(t)\rangle\exp(-\mathrm{i}\omega\tau)\,\mathrm{d}\tau \qquad (4)$$

In this discussion, the imaginary component of the spectral density, identified with a second-order frequency shift, is ignored. The abbreviated matrix elements introduced in equations (2) and (3) are defined by $\chi_{\alpha\beta} = \langle\alpha|\hat{\chi}|\beta\rangle$, $(T_\eta^k)_{\alpha\beta} = \langle\alpha|\hat{T}_\eta^k|\beta\rangle$, and $\omega_{\alpha\beta} = \langle\alpha|\hat{\mathcal{E}}|\alpha\rangle - \langle\beta|\hat{\mathcal{E}}|\beta\rangle$. If appropriate caution is exercised, one may invoke the secular approximation[1] and replace $\exp[i(\omega_{\alpha\alpha'} - \omega_{\alpha''\alpha'''})t]$ with $\delta[i(\omega_{\alpha\alpha'} - \omega_{\alpha''\alpha'''})]$.

3 'MAGNETIZATIONS' AND COHERENCES

Although equation (2) provides a convenient framework for computation, it imparts little insight into the inherent kinetic symmetries of spin relaxation. Furthermore, many observables in the relaxation experiment do not identify with individual elements of the reduced density operator, and the correspondence between theory and experiment is unclear. However, certain inadequacies of equation (2) are avoided upon transformation to a more useful operator basis[2,7]

$$\hat{v}_i = \sum_j \mathcal{Q}_{ij}\chi_j \tag{5}$$

$$-\Gamma_{ij} = \sum_{m,m'} \mathcal{Q}_{im}\mathcal{R}_{mm'}\mathcal{Q}_{m'j} \tag{6}$$

where the summation indices j, m and m' designate sums over all distinct pairs of states ($\alpha\alpha'$). The negative sign is introduced as a matter of convention. Various linear combinations of diagonal elements of the density operator correspond to magnetization or polarization modes, whereas combinations of various off-diagonal elements are identified as coherence modes. In general, each mode is characterized by a well-defined order or rank L and parity (under spin inversion). Most importantly, each mode can be brought into direct correspondence with a measurable of the system. The operator basis most suitable for discussion of relaxation effects is not necessarily the most appropriate for discussion of pulse effects or evolution under $\hat{\mathcal{E}}$.

Obviously, $\hat{\chi}$ could be expanded initially in a complete set of orthogonal basis operators, $\hat{\chi} = \Sigma_i c_i \hat{v}_i$, followed by the development of an operator equivalent to equation (2):[8,9]

$$\begin{aligned}\frac{\mathrm{d}}{\mathrm{d}t}\langle\hat{v}_i(t)\rangle &= \mathrm{i}[\hat{v}_i, \hat{\mathcal{E}}] + \sum_{k,\eta,\eta'} J_k^{\eta\eta'}(\omega_k)\mathrm{Tr}\{\hat{\chi}(t)[[\hat{v}_i, \hat{T}_\eta^k], \hat{T}_{\eta'}^{-k}]\} \\ &= \mathrm{i}[\hat{v}_i, \hat{\mathcal{E}}] - \sum_j \Gamma_{ij}\langle\hat{v}_j(t)\rangle\end{aligned} \tag{7}$$

A computational framework can be built around the evaluation of spin matrix elements or an evaluation of composite spin commutators. In certain situations, utilizing equation (2) may provide certain advantages, both in terms of insight and computation, over equation (7), whereas in other situations, the opposite argument could be made.

4 THE CROSS-CORRELATION SPECTRAL DENSITY

Looking at either equation (3) or equation (7), it is apparent that the time evolutions of various coherence and magnetization modes are influenced by both autocorrelation ($\eta = \eta'$) and cross correlation ($\eta \neq \eta'$) spectral densities. Cross correlation is quenched only if the correlation function $\langle V_\eta^{-k}(t-\tau)V_{\eta'}^k(t)\rangle$ vanishes. In the context of those interactions commonly encountered, one must consider the following nonvanishing interferences: random fields operative at different nuclear sites, interferences between interactions where the lattice variables transform as first-rank spherical harmonics, and those interferences where the lattice variables transform as second-rank spherical harmonics.

The most *useful* interferences encountered in practice occur between mechanisms that probe rotational dynamics via the rank-2 spherical harmonic angular correlation function. These interactions include dipole–dipole (direct and indirect), electric quadrupolar and anisotropic shielding. Detailed formulas for rank-2 spherical harmonic angular correlation functions applicable for studies in isotropic fluids[2] and anisotropic fluids[10] are available, as are expressions applicable for nonaxially symmetric rank-2 interactions.[11] For illustrative purposes, a suitable correlation function loses little versatility if it is assumed that motions can be modeled as diffusive and the fluid is spherically symmetric (i.e., isotropic), $\langle V_\eta^k\rangle = 0$, in which instance the k dependence of the spectral density can be suppressed. However, the assumption of isotropic molecular reorientation is too restrictive, whereas equations for general asymmetric reorientation are too unwieldy. An acceptable compromise is provided by the symmetric top rotator, which encompasses the essential element of model-free reorientation. For a symmetric top rotator, the reduced spectral density $J^{\eta\eta'}(\omega)/\xi^\eta\xi^{\eta'}$ of a second-rank spherical harmonic angular correlation function is defined as

$$\begin{aligned}\frac{J^{\eta\eta'}(\omega)}{\xi^\eta\xi^{\eta'}} &= \mathrm{Re}\int_0^\infty \langle Y_2^{-k}(\Omega_\eta(t))Y_2^k(\Omega_{\eta'}(0))\rangle \exp(-\mathrm{i}\omega t)\,\mathrm{d}t \\ &= \frac{1}{16\pi}\left[\frac{(3\cos^2\theta_\eta - 1)(3\cos^2\theta_{\eta'} - 1)\tau_{20}}{1 + (\omega\tau_{20})^2}\right. \\ &\quad + \frac{12\cos\theta_\eta\cos\theta_{\eta'}\sin\theta_\eta\sin\theta_{\eta'}\cos(\phi_\eta - \phi_{\eta'})\tau_{21}}{1 + (\omega\tau_{21})^2} \\ &\quad \left. + \frac{3\sin^2\theta_\eta\sin^2\theta_{\eta'}\cos(2\phi_\eta - 2\phi_{\eta'})\tau_{22}}{1 + (\omega\tau_{22})^2}\right]\end{aligned} \tag{8}$$

where $1/\tau_{Ln} = L(L+1)D_\perp + n^2(D_\parallel - D_\perp)$. $D_\parallel$ is the unique component of the diagonalized diffusion tensor and $D_\perp$ is the doubly degenerate component.

In the limit of isotropic reorientation ($\tau_{20} = \tau_{21} = \tau_{22} \sum \tau_2$) and extreme narrowing ($\omega\tau_2 \ll 1$), this expression reduces to $\tau_2/4\pi$ for autocorrelation terms ($\eta = \eta'$) and $\tau_2(3\cos^2\Theta - 1)/8\pi$ for cross correlation terms ($\eta \neq \eta'$). The angle Θ is defined as the angle between the principal axes of the two correlated interactions. In the subsequent development, the autocorrelation spectral densities $J^{\eta,\eta'=\eta} \sum J^\eta$ are explicitly distinguished from the cross-correlation spectral densities $J^{\eta,\eta'\neq\eta} \sum K^{\eta\eta'}$.

Unlike autocorrelation spectral densities, a cross-correlation spectral density can be either positive or negative, and often the measurement of sign rather than magnitude provides crucial information. Furthermore, cross correlation is *extremely* sensitive to rotational anisotropy. In Figure 1, the angular cross correlation factor $K^{\eta\eta'}/[J^{\eta\eta}(\omega)J^{\eta'\eta'}(\omega)]^{1/2}$ is plotted as a function of $D_\parallel/D_\perp$ for various values of $\omega\tau_{20}$. This plot

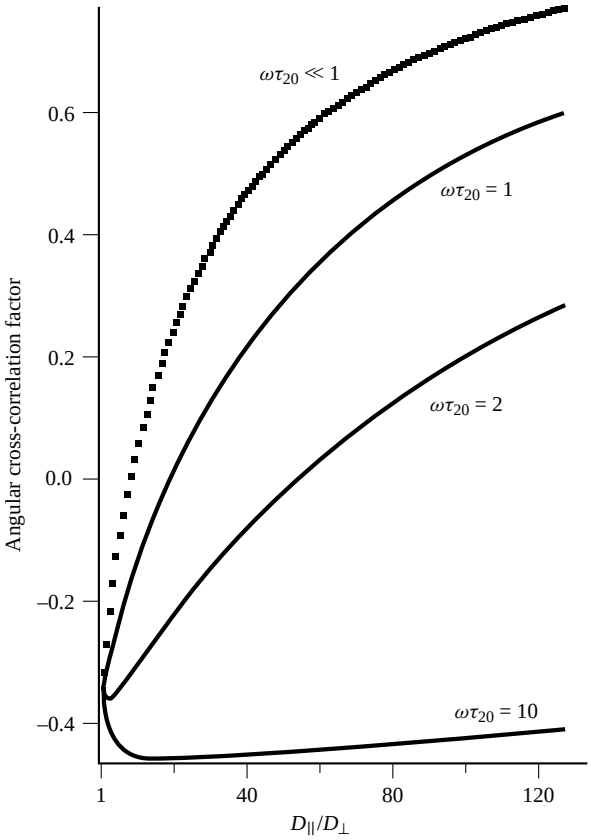

Figure 1 Plot of the angular cross correlation factor $K^{\eta\eta'}(\omega)/[J^{\eta}(\omega)J^{\eta'}(\omega)]^{1/2}$ versus motional anisotropy $D_\parallel/D_\perp$, for $\omega\tau_{20}$ = 0, 1, 2, and 10. This plot is generated from equation **8** using the geometric factors $\cos\theta_\eta = \cos\theta_{\eta'} = \frac{1}{3}$ and $\phi_\eta - \phi_{\eta'} = \frac{2}{3}\pi$. It is assumed that $\xi_\eta\xi_{\eta'} > 0$

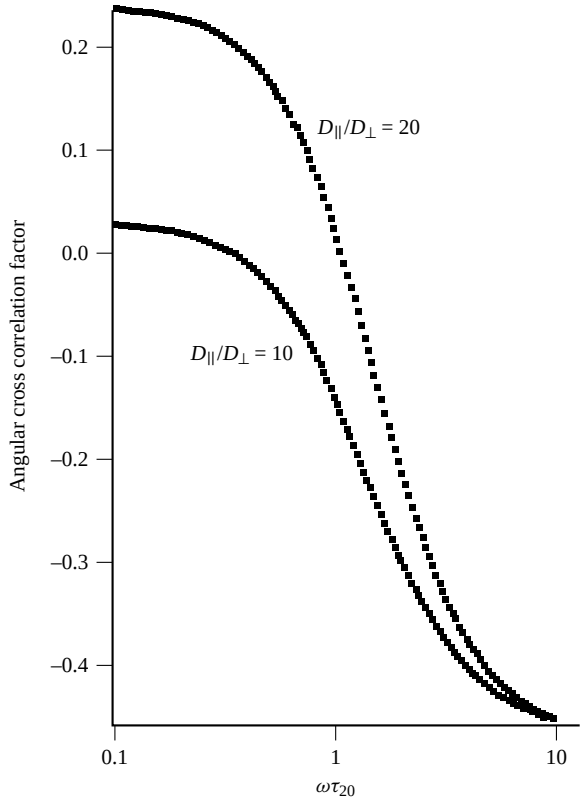

Figure 2 Plot of the angular cross-correlation factor $K^{\eta\eta'}(\omega)/[J^{\eta}(\omega)J^{\eta'}(\omega)]^{1/2}$ versus $\omega\tau_{20}$ for $D_\parallel/D_\perp$ = 10 and 20. This plot is generated from equation **8** using the geometric factors $\cos\theta_\eta = \cos\theta_{\eta'} = \frac{1}{3}$ and $\phi_\eta - \phi_{\eta'} = \frac{2}{3}\pi$. It is assumed that $\xi_\eta\xi_{\eta'} > 0$

is generated from equation (8) using a geometry relevant for methyl relaxation; $\theta_\eta = \theta_{\eta'} = \cos^{-1}\frac{1}{3}$ and $\phi_\eta - \phi_{\eta'} = \frac{2}{3}\pi$. For isotropic motions, intrinsic rank-2 spherical harmonic angular cross correlation factors reduce to the ubiquitous factor $\frac{1}{2}(3\cos^2\Theta - 1) = -\frac{1}{3}$, noted earlier. As illustrated in Figure 1, this is independent of whether or not extreme narrowing obtains.

Although cross-correlation factors for different geometric arrangements have unique dependences on motional anisotropy, representative features are portrayed in Figure 1. Obviously, large motional anisotropies do not guarantee strong cross correlation. Furthermore, interference (cross correlation) vanishes for certain motional anisotropies, and the influence of anisotropic motions on cross-correlation changes dramatically if slow motions are present. Indeed, for a given motional anisotropy, the *sign* of the cross-correlation spectral density may be opposite for high- and low-field studies. Conversely, if the degree of motional anisotropy is temperature-dependent, variable temperature studies performed at one field strength may produce similar behavior. In Figure 2, this behavior is demonstrated more clearly, with the cross-correlation factor plotted as a function of $\omega\tau_{20}$ for two fixed values of $D_\parallel/D_\perp$.

As mentioned, the cross-correlation spectral density can be positive, negative or zero for dynamical reasons. The preceding argument presumes the two interaction constants are like-signed: $\xi_\eta\xi_{\eta'} > 0$. If these interaction constants are oppositely signed then the cross-correlation spectral density is intrinsically negative in the limit of complete (positive) correlation. Generally, NMR observables are immune to relative signs of interaction strengths. Most definitely, this is not true when cross-correlation effects are the subject of discussion.

5 EFFECTS OF CROSS-CORRELATION IN SIMPLE, SCALAR-COUPLED SPIN-$\frac{1}{2}$ SYSTEMS

Many basic features of cross correlation are illustrated nicely by consideration of the spin grouping of scalar-coupled, distinguishable, spin-$\frac{1}{2}$ nuclei. The magnetization/coherence modes for all nondegenerate first-order systems composed of N spin-$\frac{1}{2}$ nuclei are provided by the direct product operators $\Pi_{i=1}^{N}(\hat{\mathcal{E}}^i + \hat{I}_z^i + \hat{I}_+^i + \hat{I}_-^i)$. Since $\chi_{\alpha\alpha'} = (\chi_{\alpha'\alpha})^*$, the unrestricted decays of $\hat{I}_x$, $\hat{I}_y$, $\hat{I}_+$, or $\hat{I}_-$ are indistinguishable. Therefore, although the dimensionality of the density matrix for this system is 2^{2N}, the decay of athermal magnetization (polarization) is characterized by $2^N - 1$ unique relaxation rates. $N(2^{N-1})$ rate constants are associated with the dissipation of single quantum coherence. The remaining $2^{N-1}(2^N - 1 - N)$ rate constants quantify the relaxation of other forms of multispin/multiquantum order. Only for $N = 1$ will two time constants (T_1 and T_2) completely describe the relaxation characteristics (in the absence of applied rf fields) of the N-spin system.

For a spin system composed of N-spin-$\frac{1}{2}$ nuclei, $\hat{I}^{(1)}$, $\hat{I}^{(2)}$, ... , $\hat{I}^{(N)}$, with each spin relaxed through anisotropic shielding (SA) and mutual dipole–dipole (D) interactions, the interconversion/dissipation rates of the various polarizations are described succinctly by the following expressions:

$$\left.\begin{aligned}
\hat{I}_z^{(i)} &\Leftarrow \sum_{j\neq i}\rho_{ij} + 4J^{\mathrm{SA}_i}(\omega_i) \Rightarrow \hat{I}_z^{(i)}\\
\hat{I}_z^{(i)} &\Leftarrow \sigma_{ij} \Rightarrow \hat{I}_z^{(j)}\\
\hat{I}_z^{(i)} &\Leftarrow -4K^{\mathrm{D}_{ij},\mathrm{SA}_i}(\omega_i) \Rightarrow 2\hat{I}_z^{(i)}\hat{I}_z^{(j)}\\
\hat{I}_z^{(i)} &\Leftarrow 2K^{\mathrm{D}_{ij},\mathrm{D}_{ik}}(\omega_i) \Rightarrow 4\hat{I}_z^{(i)}\hat{I}_z^{(j)}\hat{I}_z^{(k)}\\
2\hat{I}_z^{(i)}\hat{I}_z^{(j)} &\Leftarrow \sum_{k\neq i,j}\rho_{ik} + \sum_{k\neq i,j}\rho_{jk} + \Delta_{ij} + 4J^{\mathrm{SA}_i}(\omega_i)\\
&\quad + 4J^{\mathrm{SA}_j}(\omega_j) \Rightarrow 2\hat{I}_z^{(i)}\hat{I}_z^{(j)}\\
2\hat{I}_z^{(i)}\hat{I}_z^{(j)} &\Leftarrow \sigma_{jk} + 2K^{\mathrm{D}_{ij},\mathrm{D}_{ik}}(\omega_i) \Rightarrow 2\hat{I}_z^{(i)}\hat{I}_z^{(k)}\\
2\hat{I}_z^{(i)}\hat{I}_z^{(j)} &\Leftarrow -4K^{\mathrm{D}_{ik},\mathrm{SA}_i}(\omega_i) - 4K^{\mathrm{D}_{jk},\mathrm{SA}_j}(\omega_j)\\
&\quad \Rightarrow 4\hat{I}_z^{(i)}\hat{I}_z^{(j)}\hat{I}_z^{(k)}\\
4\hat{I}_z^{(i)}\hat{I}_z^{(j)}\hat{I}_z^{(k)} &\Leftarrow \sum_{l\neq i,j,k}\rho_{il} + \sum_{l\neq i,j,k}\rho_{jl} + \sum_{l\neq i,j,k}\rho_{kl}\\
&\quad + \Delta_{ij} + \Delta_{ik} + \Delta_{jk} + 4J^{\mathrm{SA}_i}(\omega_i)\\
&\quad + 4J^{\mathrm{SA}_j}(\omega_j) + 4J^{\mathrm{SA}_k}(\omega_k) \Rightarrow 4\hat{I}_z^{(i)}\hat{I}_z^{(j)}\hat{I}_z^{(k)}\\
4\hat{I}_z^{(i)}\hat{I}_z^{(j)}\hat{I}_z^{(k)} &\Leftarrow \sigma_{kl} + 2K^{\mathrm{D}_{ik},\mathrm{D}_{il}}(\omega_i) + 2K^{\mathrm{D}_{jk},\mathrm{D}_{jl}}(\omega_i)\\
&\quad \Rightarrow 4\hat{I}_z^{(i)}\hat{I}_z^{(j)}\hat{I}_z^{(l)}\\
2\hat{I}_z^{(i)}\hat{I}_z^{(j)} &\Leftarrow 0 \Rightarrow 2\hat{I}_z^{(k)}\hat{I}_z^{(l)}\\
\hat{I}_z^{(i)} &\Leftarrow 0 \Rightarrow 2\hat{I}_z^{(j)}\hat{I}_z^{(k)}\\
4\hat{I}_z^{(i)}\hat{I}_z^{(j)}\hat{I}_z^{(k)} &\Leftarrow 0 \Rightarrow 4\hat{I}_z^{(i)}\hat{I}_z^{(l)}\hat{I}_z^{(m)}
\end{aligned}\right\} \quad (9)$$

where

$$\left.\begin{aligned}
\rho_{ij} &= \tfrac{1}{3}J_0^{\mathrm{D}_{ij}}(\omega_i-\omega_j) + J_1^{\mathrm{D}_{ij}}(\omega_i) + 2J_2^{\mathrm{D}_{ij}}(\omega_i+\omega_j)\\
\sigma_{ij} &= -\tfrac{1}{3}J_0^{\mathrm{D}_{ij}}(\omega_i-\omega_j) + 2J_2^{\mathrm{D}_{ij}}(\omega_i+\omega_j)\\
\Delta_{ij} &= J_1^{\mathrm{D}_{ij}}(\omega_i) + J_1^{\mathrm{D}_{ij}}(\omega_j)
\end{aligned}\right\} \quad (10)$$

Of course, the individual rates introduced in equation (9) are specific elements of the (super)operator $\hat{\hat{\Gamma}}$ introduced earlier [see equation (7)]. Shielding anisotropy and dipole–dipole interactions are defined in terms of gyromagnetic ratios γ_i, internuclear distances r_{ij}, shielding anisotropies $\Delta\sigma_i$ and magnetic field strength B_0: $\xi_{\mathrm{D}_{ij}} = (\frac{6}{5}\pi)^{1/2}\gamma_i\gamma_j\hbar r_{ij}^{-3}$, $\xi_{\mathrm{SA}_i} = (\frac{2}{15}\pi)^{1/2}\Delta\sigma_i\gamma_i B_0$.

These expressions clearly demonstrate that cross correlation results in polarization transfer. Interferences between SA and dipole–dipole interconvert even and odd spin orders, whereas dipole–dipole interferences interconvert various forms of spin order with similar parity under spin inversion symmetry. Equation (9) only list mutual couplings between one- two-, and three-spin order. If higher forms of spin order are considered, the appropriate polarization transfer selection rules are summarized by the expressions

$$\left.\begin{aligned}
2^{k-1}\hat{I}_z^{(1)}\hat{I}_z^{(2)}\cdots\hat{I}_z^{(k)} &\Leftarrow \sum_{i=1}^{k} 4K^{\mathrm{D}_{i,k+1},\mathrm{SA}_{k+1}}(\omega_{k+1})\\
&\quad \Rightarrow 2^k(\hat{I}_z^{(1)}\hat{I}_z^{(2)}\cdots\hat{I}_z^{(k)})\hat{I}_z^{(k+1)}\\
2^{k-1}\hat{I}_z^{(1)}\hat{I}_z^{(2)}\cdots\hat{I}_z^{(k)} &\Leftarrow \sum_{i=1}^{k} 2K^{\mathrm{D}_{i,k+1},\mathrm{D}_{i,k+2}}(\omega_{k+1})\\
&\quad \Rightarrow 2^{k+1}(\hat{I}_z^{(1)}\hat{I}_z^{(2)}\cdots\hat{I}_z^{(k)})\hat{I}_z^{(k+1)}\hat{I}_z^{(k+2)}
\end{aligned}\right\} \quad (11)$$

These restrictions limit the overall changes in spin order to ±1 (SA–D interference) or ±2 (D–D interference) and are a direct consequence of the commutator relations embedded in equation (7). Dipole–dipole cross correlation can induce polarization transfer between spin orders of similar rank, for spin orders greater than one, the same as cross relaxation, σ_{ij}:

$$\begin{aligned}
2^{k-1}\hat{I}_z^{(1)}\hat{I}_z^{(2)}\cdots\hat{I}_z^{(k)} &\Leftarrow \sum_{i=1}^{k-1}\sigma_{k,k+1} + 2K^{\mathrm{D}_{i,k},\mathrm{D}_{i,k+1}}(\omega_i)\\
&\quad \Rightarrow 2^{k-1}(\hat{I}_z^{(1)}\hat{I}_z^{(2)}\cdots\hat{I}_z^{(k-1)}\hat{I}_z^{(k+1)})
\end{aligned} \quad (12)$$

These same considerations are equally helpful in descriptions of single quantum (1Q) or multiple quantum coherence (MQC). For example, consider the dynamic transformations of spin-'i' single quantum coherence:

$$\left.\begin{aligned}
\hat{I}_+^{(i)} &\Leftarrow (1/T_2)_i \Rightarrow \hat{I}_+^{(i)}\\
2\hat{I}_+^{(i)}\hat{I}_z^{(j)} &\Leftarrow (1/T_2)_i \Rightarrow 2\hat{I}_+^{(i)}\hat{I}_z^{(j)}\\
4\hat{I}_+^{(i)}\hat{I}_z^{(j)}\hat{I}_z^{(k)} &\Leftarrow (1/T_2)_i \Rightarrow 4\hat{I}_+^{(i)}\hat{I}_z^{(j)}\hat{I}_z^{(k)}\\
\hat{I}_+^{(i)} &\Leftarrow 0 \Rightarrow \hat{I}_+^{(j)}\\
\hat{I}_+^{(i)} &\Leftarrow -\tfrac{8}{3}K^{\mathrm{D}_{ij},\mathrm{SA}_i}(0) - 2K^{\mathrm{D}_{ij},\mathrm{SA}_i}(\omega_i)\\
&\quad \Rightarrow 2\hat{I}_+^{(i)}\hat{I}_z^{(j)}\\
2\hat{I}_+^{(i)}\hat{I}_z^{(k)} &\Leftarrow -\tfrac{8}{3}K^{\mathrm{D}_{ij},\mathrm{SA}_i}(0) - 2K^{\mathrm{D}_{ij},\mathrm{SA}_i}(\omega_i)\\
&\quad \Rightarrow 4\hat{I}_+^{(i)}\hat{I}_z^{(j)}\hat{I}_z^{(k)}\\
\hat{I}_+^{(i)} &\Leftarrow \tfrac{1}{2}\sigma_{jk} + \tfrac{4}{3}K^{\mathrm{D}_{ij},\mathrm{D}_{ik}}(0) + K^{\mathrm{D}_{ij},\mathrm{D}_{ik}}(\omega_i)\\
&\quad \Rightarrow 4\hat{I}_+^{(i)}\hat{I}_z^{(j)}\hat{I}_z^{(k)}\\
2\hat{I}_+^{(i)}\hat{I}_z^{(j)} &\Leftarrow \tfrac{1}{2}\sigma_{jk} + \tfrac{4}{3}K^{\mathrm{D}_{ij},\mathrm{D}_{ik}}(0) + K^{\mathrm{D}_{ij},\mathrm{D}_{ik}}(\omega_i)\\
&\quad \Rightarrow 2\hat{I}_+^{(i)}\hat{I}_z^{(k)}
\end{aligned}\right\} \quad (13)$$

Permutation of nuclear labels will generate expressions for the relevant 1QCs of other spins. The parameter $(1/T_2)_i$ is defined as

$$\begin{aligned}
(1/T_2)_i = \sum_{j\neq i}\tfrac{2}{3}J^{\mathrm{D}_{ij}}(0) + \tfrac{1}{2}\Big[\sum_{j<k}\rho_{jk} + J^{\mathrm{D}_{jk}}(\omega_k)\Big]\\
+\tfrac{8}{3}J^{\mathrm{SA}_i}(0) + 2J^{\mathrm{SA}_i}(\omega_i)
\end{aligned} \quad (14)$$

The subtle differences between descriptions of the evolution of populations and single quantum coherences are due to

the 'simple line' approximation, which suppresses secular couplings and transverse cross relaxation.

The informational content of these expressions is illustrated clearly by consideration of the simple AMX spin system. Each member of the A quartet can be associated with its own fictitious spin:

$$\left.\begin{aligned}
\hat{I}_z^{\alpha\alpha} &= \tfrac{1}{4}(\hat{I}_z^{(\mathrm{A})} + 2\hat{I}_z^{(\mathrm{A})}\hat{I}_z^{(\mathrm{M})} + 2\hat{I}_z^{(\mathrm{A})}\hat{I}_z^{(\mathrm{X})} + 4\hat{I}_z^{(\mathrm{A})}\hat{I}_z^{(\mathrm{M})}\hat{I}_z^{(\mathrm{X})}) \\
\hat{I}_z^{\alpha\beta} &= \tfrac{1}{4}(\hat{I}_z^{(\mathrm{A})} + 2\hat{I}_z^{(\mathrm{A})}\hat{I}_z^{(\mathrm{M})} - 2\hat{I}_z^{(\mathrm{A})}\hat{I}_z^{(\mathrm{X})} - 4\hat{I}_z^{(\mathrm{A})}\hat{I}_z^{(\mathrm{M})}\hat{I}_z^{(\mathrm{X})}) \\
\hat{I}_z^{\beta\alpha} &= \tfrac{1}{4}(\hat{I}_z^{(\mathrm{A})} - 2\hat{I}_z^{(\mathrm{A})}\hat{I}_z^{(\mathrm{M})} + 2\hat{I}_z^{(\mathrm{A})}\hat{I}_z^{(\mathrm{X})} - 4\hat{I}_z^{(\mathrm{A})}\hat{I}_z^{(\mathrm{M})}\hat{I}_z^{(\mathrm{X})}) \\
\hat{I}_z^{\beta\beta} &= \tfrac{1}{4}(\hat{I}_z^{(\mathrm{A})} - 2\hat{I}_z^{(\mathrm{A})}\hat{I}_z^{(\mathrm{M})} - 2\hat{I}_z^{(\mathrm{A})}\hat{I}_z^{(\mathrm{X})} + 4\hat{I}_z^{(\mathrm{A})}\hat{I}_z^{(\mathrm{M})}\hat{I}_z^{(\mathrm{X})})
\end{aligned}\right\} \quad (15)$$

Assuming an initial perturbation described as the nonselective inversion of the A quartet, the *initial* relaxation rates associated with each member of the quartet are given by

$$\left.\begin{aligned}
(1/T_1)_{\alpha\alpha} &= (1/T_1)_{\mathrm{A}} - 4K^{\mathrm{D_{AM},SA_A}}(\omega_{\mathrm{A}}) \\
&\quad - 4K^{\mathrm{D_{AX},SA_A}}(\omega_{\mathrm{A}}) + 2K^{\mathrm{D_{AM},D_{AX}}}(\omega_{\mathrm{A}}) \\
(1/T_1)_{\alpha\beta} &= (1/T_1)_{\mathrm{A}} - 4K^{\mathrm{D_{AM},SA_A}}(\omega_{\mathrm{A}}) \\
&\quad + 4K^{\mathrm{D_{AX},SA_A}}(\omega_{\mathrm{A}}) - 2K^{\mathrm{D_{AM},D_{AX}}}(\omega_{\mathrm{A}}) \\
(1/T_1)_{\beta\alpha} &= (1/T_1)_{\mathrm{A}} + 4K^{\mathrm{D_{AM},SA_A}}(\omega_{\mathrm{A}}) \\
&\quad - 4K^{\mathrm{D_{AX},SA_A}}(\omega_{\mathrm{A}}) - 2K^{\mathrm{D_{AM},D_{AX}}}(\omega_{\mathrm{A}}) \\
(1/T_1)_{\beta\beta} &= (1/T_1)_{\mathrm{A}} + 4K^{\mathrm{D_{AM},SA_A}}(\omega_{\mathrm{A}}) \\
&\quad + 4K^{\mathrm{D_{AX},SA_A}}(\omega_{\mathrm{A}}) + 2K^{\mathrm{D_{AM},D_{AX}}}(\omega_{\mathrm{A}})
\end{aligned}\right\} \quad (16)$$

where $(1/T_1)_{\mathrm{A}} = \rho_{\mathrm{AM}} + \rho_{\mathrm{AX}} + 4J^{\mathrm{SA_A}}(\omega_{\mathrm{A}})$.

Notice that various sums and differences of initial rates can be identified with unique spectral densities. The combinations of line intensities that isolate each of the four terms are exactly the combinations that result in the product operator description implicit in equation (9). Looking at equation (7), it is apparent that when one specific coherence or magnetization mode $\hat{v}_i$ is selectively perturbed then the initial response of an observed mode $\hat{v}_j$ is completely determined by the coupling Γ_{ij}. In virtually all circumstances, this experiment often provides definitive, accessible, qualitative information. It is equally important to recognize that the initial rate approximation, when applied to the perturbation response of one-spin order, is always independent of cross correlation.

Conversely, if all four members of the quartet are characterized by the same relaxation behavior, no multispin order is generated, and cross correlation is insignificant. Similarly, a nonselective perturbation affecting symmetrically disposed lines within a multiplet does not generate differential relaxation unless anisotropic shielding/dipole–dipole interferences are present.

A parallel description of 1QC utilizes the single transition operators

$$\left.\begin{aligned}
I_+^{\alpha\alpha} &= \tfrac{1}{4}(\hat{I}_+^{(\mathrm{A})} + 2\hat{I}_+^{(\mathrm{A})}\hat{I}_z^{(\mathrm{M})} + 2\hat{I}_+^{(\mathrm{A})}\hat{I}_z^{(\mathrm{X})} + 4\hat{I}_+^{(\mathrm{A})}\hat{I}_z^{(\mathrm{M})}\hat{I}_z^{(\mathrm{X})}) \\
I_+^{\alpha\beta} &= \tfrac{1}{4}(\hat{I}_+^{(\mathrm{A})} + 2\hat{I}_+^{(\mathrm{A})}\hat{I}_z^{(\mathrm{M})} - 2\hat{I}_+^{(\mathrm{A})}\hat{I}_z^{(\mathrm{X})} - 4\hat{I}_+^{(\mathrm{A})}\hat{I}_z^{(\mathrm{M})}\hat{I}_z^{(\mathrm{X})}) \\
I_+^{\beta\alpha} &= \tfrac{1}{4}(\hat{I}_+^{(\mathrm{A})} - 2\hat{I}_+^{(\mathrm{A})}\hat{I}_z^{(\mathrm{M})} + 2\hat{I}_+^{(\mathrm{A})}\hat{I}_z^{(\mathrm{X})} - 4\hat{I}_+^{(\mathrm{A})}\hat{I}_z^{(\mathrm{M})}\hat{I}_z^{(\mathrm{X})}) \\
I_+^{\beta\beta} &= \tfrac{1}{4}(\hat{I}_+^{(\mathrm{A})} - 2\hat{I}_+^{(\mathrm{A})}\hat{I}_z^{(\mathrm{M})} - 2\hat{I}_+^{(\mathrm{A})}\hat{I}_z^{(\mathrm{X})} + 4\hat{I}_+^{(\mathrm{A})}\hat{I}_z^{(\mathrm{M})}\hat{I}_z^{(\mathrm{X})})
\end{aligned}\right\} \quad (17)$$

with the associated linewidth parameters

$$\left.\begin{aligned}
(1/T_2)_{\alpha\alpha} &= (1/T_2)_{\mathrm{A}} - \tfrac{8}{3}K^{\mathrm{D_{AM},SA_A}}(0) - 2K^{\mathrm{D_{AM},SA_A}}(\omega_{\mathrm{A}}) \\
&\quad - \tfrac{8}{3}K^{\mathrm{D_{AX},SA_1}}(0) - 2K^{\mathrm{D_{AX},SA_A}}(\omega_{\mathrm{A}}) + \tfrac{1}{2}\sigma_{\mathrm{MX}} \\
&\quad + \tfrac{4}{3}K^{\mathrm{D_{AM},D_{AX}}}(0) + K^{\mathrm{D_{AM},D_{AX}}}(\omega_{\mathrm{A}}) \\
(1/T_2)_{\alpha\beta} &= (1/T_2)_{\mathrm{A}} - \tfrac{8}{3}K^{\mathrm{D_{AM},SA_A}}(0) - 2K^{\mathrm{D_{AM},SA_A}}(\omega_{\mathrm{A}}) \\
&\quad + \tfrac{8}{3}K^{\mathrm{D_{AX},SA_1}}(0) + 2K^{\mathrm{D_{AX},SA_A}}(\omega_{\mathrm{A}}) - \tfrac{1}{2}\sigma_{\mathrm{MX}} \\
&\quad - \tfrac{4}{3}K^{\mathrm{D_{AM},D_{AX}}}(0) - K^{\mathrm{D_{AM},D_{AX}}}(\omega_{\mathrm{A}}) \\
(1/T_2)_{\beta\alpha} &= (1/T_2)_{\mathrm{A}} + \tfrac{8}{3}K^{\mathrm{D_{AM},SA_A}}(0) + 2K^{\mathrm{D_{AM},SA_A}}(\omega_{\mathrm{A}}) \\
&\quad - \tfrac{8}{3}K^{\mathrm{D_{AX},SA_1}}(0) - 2K^{\mathrm{D_{AX},SA_A}}(\omega_{\mathrm{A}}) - \tfrac{1}{2}\sigma_{\mathrm{MX}} \\
&\quad - \tfrac{4}{3}K^{\mathrm{D_{AM},D_{AX}}}(0) - K^{\mathrm{D_{AM},D_{AX}}}(\omega_{\mathrm{A}}) \\
(1/T_2)_{\beta\beta} &= (1/T_2)_{\mathrm{A}} + \tfrac{8}{3}K^{\mathrm{D_{AM},SA_A}}(0) + 2K^{\mathrm{D_{AM},SA_A}}(\omega_{\mathrm{A}}) \\
&\quad + \tfrac{8}{3}K^{\mathrm{D_{AX},SA_1}}(0) + 2K^{\mathrm{D_{AX},SA_A}}(\omega_{\mathrm{A}}) + \tfrac{1}{2}\sigma_{\mathrm{MX}} \\
&\quad + \tfrac{4}{3}K^{\mathrm{D_{AM},D_{AX}}}(0) + K^{\mathrm{D_{AM},D_{AX}}}(\omega_{\mathrm{A}})
\end{aligned}\right\} \quad (18)$$

The various effects of cross correlation are written across each multiplet in a characteristic fashion, and if spectral linewidths accurately reflect homogeneous broadening then appropriate linear combinations of linewidth differentials can be used to isolate cross-correlation spectral densities:

$$\left.\begin{aligned}
&\tfrac{1}{4}[(1/T_2)_{\alpha\alpha} + (1/T_2)_{\alpha\beta} + (1/T_2)_{\beta\alpha} + (1/T_2)_{\beta\beta}] \\
&\quad = (1/T_2)_{\mathrm{A}} \\
&\tfrac{1}{2}[(1/T_2)_{\alpha\alpha} - (1/T_2)_{\alpha\beta} - (1/T_2)_{\beta\alpha} + (1/T_2)_{\beta\beta}] \\
&\quad = \sigma_{\mathrm{MX}} + \tfrac{8}{3}K^{\mathrm{D_{AM},D_{AX}}}(0) + 2K^{\mathrm{D_{AM},D_{AX}}}(\omega_{\mathrm{A}}) \\
&\tfrac{1}{4}[(1/T_2)_{\alpha\alpha} + (1/T_2)_{\alpha\beta} - (1/T_2)_{\beta\alpha} - (1/T_2)_{\beta\beta}] \\
&\quad = -\tfrac{8}{3}K^{\mathrm{D_{AM},SA_A}}(0) - 2K^{\mathrm{D_{AM},SA_A}}(\omega_{\mathrm{A}}) \\
&\tfrac{1}{4}[(1/T_2)_{\alpha\alpha} - (1/T_2)_{\alpha\beta} + (1/T_2)_{\beta\alpha} - (1/T_2)_{\beta\beta}] \\
&\quad = -\tfrac{8}{3}K^{\mathrm{D_{AX},SA_A}}(0) - 2K^{\mathrm{D_{AX},SA_A}}(\omega_{\mathrm{A}})
\end{aligned}\right\} \quad (19)$$

In high-field studies of adiabatically broadened lines, differential linewidths are the norm rather than the exception.

6 EFFECTS OF CROSS CORRELATION IN MULTIPLY DEGENERATE SPIN-$\frac{1}{2}$ SYSTEMS

For spin systems containing identical nuclei, the same fundamental principles introduced previously can be applied, and the A_2, A_3, AX_2, AX_3, and AMX_2 groupings[2,4,5,12,13] have been discussed extensively.

However, there are some significant differences between degenerate and nondegenerate first-order spin systems. These differences include

1. adiabatic (zero frequency) cross-correlation spectral densities play a role in polarization transfer;
2. secular couplings conflict with the simple line approximation invoked earlier, which results in lineshapes that are non-Lorentzian;
3. polarization transfer can be consumated by interferences between mechanisms that share no nucleus in common;

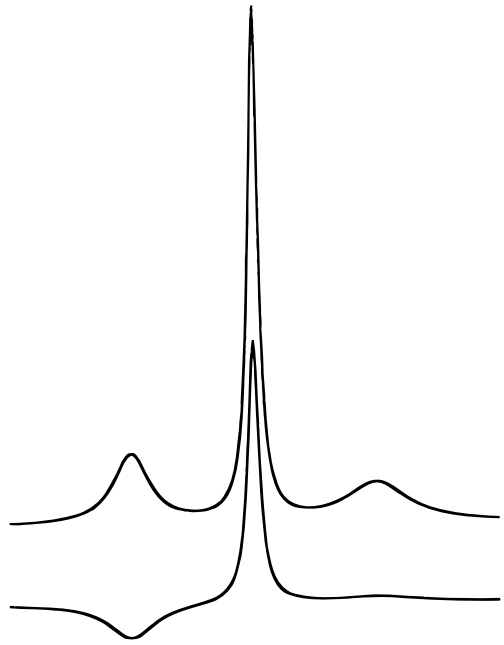

Figure 3 Theoretical inversion–recovery curves of the A triplet of an AX_2 spin grouping relaxed by dipole–dipole and anisotropic electronic shielding. The lower curve corresponds to a delay on the order of $T_1 = [2\rho_{AX} + 4J_1^{SA_A}(\omega_A)]^{-1}$ and the upper curve corresponds to the equilibrium spectrum (delay $\gg T_1$). For clarity, these two curves have been vertically displaced. Relaxation-induced polarization and coherence transfer results in strongly asymmetric spectral features. See the text for additional details

4. no longer can every mode be brought into correspondence with a conventional observable.

A brief indication of the relaxation behavior expected for a simple degenerate spin system such as AX_2 is shown in Figure 3. This figure is constructed assuming a simple inversion–recovery experiment is performed on spin A. The lower curve corresponds to a recovery time on the order of (ln 2)T_1, where $(1/T_1) = 2\rho_{AX} + 4J_1^{SA_A}(\omega_A)$ and the vertically offset upper curve corresponds to a recovery time much longer than T_1. These curves are constructed assuming complete equivalence of the two dipolar interactions, D_{AX} and $D_{AX'}$, with $\omega_A\tau_{20} = 10$, $D_\parallel/D_\perp = 100$, $\theta_{SA_A} = 0^\circ$, $\theta_{D_{AX}} = \theta_{D_{AX'}} = 71^\circ$, $\phi_{D_A} - \phi_{D_{AX'}} = 120^\circ$, and $(\Delta\sigma\gamma_A B_0)/\gamma_i\gamma_j\hbar r_{ij}^{-3} = \zeta = \frac{1}{8}$. This realistic set of parameters is chosen for illustrative purposes, and bears no special significance.

Assuming a positive scalar coupling and positive interaction constants, the homogeneous linewidths of the low-frequency, central, and high-frequency components are in the ratios

$$(1 + \kappa^{DD} + 2\zeta^2 - 4\zeta\kappa^{DSA}) : (1 - \kappa^{DD} + 2\zeta^2) : (1 + \kappa^{DD} + 2\zeta^2 + 4\zeta\kappa^{DSA}) \quad (20)$$

In this motional limit (see Figure 1), the dipole–dipole cross correlation factor κ^{DD} is $\frac{3}{4}$. In this same limit, the cross-correlation factor κ^{DSA} for dipole–anisotropic shielding interference is -1 (see equation (8)). Differential broadening of the outer lines relative to the central line indicates a positive dipole–dipole cross correlation. Broadening of the low-frequency component relative to the high-frequency component indicates dipole–shielding anisotropy cross correlation. Assuming positive scalar coupling and interaction constants, this cross-correlation spectral density is negative.

Comparison of the two curves also indicates that the athermal 'magnetization' of the central component relaxes more rapidly than the outer components. It may seem paradoxical that the component identified with the longest T_2 has the shortest T_1. However, as noted earlier, it is not uncommon for a cross-correlation spectral density to change sign when sampled at two markedly different frequencies. A detailed discussion of the wealth of molecular information implanted in Figure 3 is beyond the scope of this brief introduction, and the reader is directed to the original literature.[2,4,5]

In other spin systems containing tightly coupled nuclei (e.g., AB, ABX, ABC, etc.), well-defined relaxation selection rules and simple sets of basis operators cannot be defined so simply. The distinctive roles of cross correlation, autocorrelation, and cross relaxation become blurred.

7 CROSS CORRELATION AND RELAXATION IN THE ROTATING FRAME

As a complement to the study of polarization transfer in the laboratory frame, analogous studies can be applied to selectively spin locked magnetization in the rotating frame.

Consider the N spin-$\frac{1}{2}$ system described earlier. In the presence of a strong spin locking field ($\gamma_i B_1 = \omega_r >$ frequency offset) applied selectively to spin i, modification of equation (9) proves exceptionally simple.[14] For each relevant polarization, $\hat{I}_z^{(i)}$ is replaced by $\hat{I}_{z\rho}^{(i)}$ ($\hat{I}_z^{(i)}$ in the rotating frame, which is equivalent to $\hat{I}_+^{(i)}$ in the laboratory frame, and the various rate constants are replaced by the following modified expressions:

laboratory frame rate $\Rightarrow$ rotating frame equivalent

$$\left.\begin{aligned}
\rho_{ij} &\Rightarrow \tfrac{1}{2}\rho_{ij} + \tfrac{2}{3}J^{D_{ij}}(\omega_r \approx 0) + J^{D_{ij}}(\omega_j)\\
\sigma_{ij} &\Rightarrow 0\\
2K^{D_{ij},D_{ik}}(\omega_i) &\Rightarrow \tfrac{4}{3}K^{D_{ij},D_{ik}}(\omega_r \approx 0) + K^{D_{ij},D_{ik}}(\omega_i)\\
2K^{D_{ij},D_{jk}}(\omega_j) &\Rightarrow 0\\
\Delta_{ij} &\Rightarrow \tfrac{1}{2}\rho_{ij} + \tfrac{2}{3}J^{D_{ij}}(\omega_r \approx 0)\\
4J^{SA_i}(\omega_i) &\Rightarrow \tfrac{8}{3}J^{SA_i}(\omega_r \approx 0) + 2J^{SA_j}(\omega_i)\\
4K^{D_{ij},SA_i}(\omega_i) &\Rightarrow \tfrac{8}{3}K^{D_{ij},SA_i}(\omega_r \approx 0) + 2K^{D_{ij},SA_i}(\omega_i)\\
4K^{D_{ij},SA_j}(\omega_{ij}) &\Rightarrow 0
\end{aligned}\right\} \quad (21)$$

Except for the appearance of certain secular couplings, these couplings are identical to those first introduced in equation (13).

Equation (21) reveal some interesting traits. If the spin lock field is large compared with the frequency *offset*, cross relaxation between spins i and j is quenched. In this same limit, $\hat{I}_+^{(i)}$ and $2\hat{I}_+^{(i)}\hat{I}_z^{(j)}$ are coupled together by the term $\frac{8}{3}K^{D_{ij},SA_i}(\omega_r \approx 0) + 2K^{D_{ij},SA_i}(\omega_i)$. This expression demonstrates that when extreme narrowing fails, cross correlation can replace cross relaxation as the source of homonuclear spin diffusion. Once again, measurement of cross correlation under spin lock conditions has enormous potential, and permits one

to focus on specific elements of $\hat{\hat{\Gamma}}$ while suppressing other elements that may be an annoyance.[15]

8 SUMMARY

Cross-correlation effects, once considered little more than theoretical curiosities, have assumed a central role in contemporary NMR relaxation studies. In multispin systems, cross-correlation features are ubiquitous, and, for high applied field strengths, very modest shielding anisotropies can result in significant polarization transfer. In practice, dipole–dipole interferences have been utilized primarily in studies of molecular dynamics, whereas applications of dipole–shielding anisotropy interferences have provided details of shielding anisotropies. As shielding tensors become better characterized, these archetypal applications will change.

In addition to the most familiar interferences discussed thus far, dipole–quadrupole, quadrupole–quadrupole, and quadrupole–shielding anisotropy interferences can be important in the relaxation of quadrupolar nuclei. These interferences provide unique information, and enable the study of weak interactions in the presence of more dominant interactions. Similarly, random field interferences have received considerable attention in the context of double resonance and multiquantum studies. Recently, cross-correlation effects between rank-2 interactions and 'Curie' spin have received considerable attention, as have interference effects in scalar relaxation.

9 RELATED ARTICLES

Brownian Motion and Correlation Times; Liouville Equation of Motion; Relaxation: An Introduction; Relaxation of Coupled Spins from Rotational Diffusion; Relaxation Mechanisms: Magnetization Modes; Relaxation Processes in Coupled-Spin Systems; Relaxation Theory: Density Matrix Formulation; Relaxation of Transverse Magnetization for Coupled Spins; ROESY.

10 REFERENCES

1. A. G. Redfield, *IBM J. Res. Develop.*, 1957, **1**, 19; in *Advances in Magnetic Resonance*, ed. J. S. Waugh, Academic Press, New York, 1965, Vol. 1, p. 1
2. L. G. Werbelow and D. M. Grant, in *Advances in Magnetic Resonance*, ed. J. S. Waugh, Academic Press, New York, 1977, Vol. 9, p. 189.
3. R. L. Vold and R. R. Vold, in *Progress in Nuclear Magnetic Resonance Spectroscopy*, eds. J. W. Emsley, J. Feeney, and L. H. Sutcliffe, Pergamon Press, Oxford, 1978, Vol. 12, p. 79.
4. D. Canet, in *Progress in Nuclear Magnetic Resonance Spectroscopy*, eds. J. W. Emsley, J. Feeney, and L. H. Sutcliffe, Pergamon Press, Oxford, 1989, Vol. 21, p. 237.
5. D. M. Grant, C. L. Mayne, F. Liu, and T. -X. Xiang, *Chem. Rev.*, 1991, **91**, 1591.
6. L. G. Werbelow, in *Nuclear Magnetic Resonance Probes of Molecular Dynamics*, ed. R. Tycko, Plenum, Press, New York, 1994, p. 223.
7. N. C. Pyper, *Mol. Phys.*, 1971, **21**, 1; 1972, **22**, 433.
8. A. Abragam, *Principles of Nuclear Magnetism*, Clarendon Press, Oxford, 1961.
9. S. Szymanski, A. M. Gryff-Keller, and G. Binsch, *J. Magn. Reson.*, 1988, **68**, 399.
10. R. R. Vold and R. L. Vold, *J. Chem. Phys.*, 1988, **88**, 1443; in *Advances in Magnetic and Optical Resonance* ed. W. Warren, Academic Press, New York, 1991, Vol. 6, p. 85.
11. H. W. Spiess, in *NMR Basic Principles and Progress*, eds. P. Diehl, E. Fluck and R. Kosfeld, Springer-Verlag, Berlin, 1978, Vol. 15, p. 55.
12. L. G. Werbelow, D. Canet, and H. Nery, *J. Magn. Reson.*, 1984, **60**, 405.
13. L. G. Werbelow and D. M. Grant, *J. Chem. Phys.*, 1975, **63**, 544; A. D. Bain and R. M. Lynden-Bell, *Mol. Phys.*, 1975, **30**, 325.
14. T. E. Bull, in *Progress in Nuclear Magnetic Resonance Spectroscopy*, eds. J. W. Emsley, J. Feeney, and L. H. Sutcliffe, Pergamon Press, Oxford, 1992, Vol. 24, p. 377.
15. I. Burghardt, R. Konrat, and G. Bodenhausen, *Mol. Phys.*, 1992, **75**, 467; B. Boulat, R. Konrat, I. Burghardt, and G. Bodenhausen, *J. Am. Chem. Soc.*, 1992, **114**, 5412.

Biographical Sketch

Lawrence G. Werbelow. *b.* 1948. B.S., 1970, Humboldt State University, U.S.A. Ph.D., 1974, University of British Columbia, (thesis advisor A. G. Marshall). Research associate (with D. M. Grant) and instructor, University of Utah, 1974–78; D.Sc., Université de Provence, 1979. Professor, New Mexico Tech, 1980–present. Professor, Université d'Aix Marseille I, 1990–95. Approx. 70 publications in the field of magnetic resonance. Current research interests include the study of relaxation-induced polarization/coherence transfer and the development of methods for isolation/identification of ultrafine interactions involving nuclear spin.

Relaxation Processes in Coupled-Spin Systems

Charles L. Mayne and Scott A. Smith
University of Utah, Salt Lake City, UT, USA

1	Introduction	1
2	Time-Dependent Perturbation Theory	2
3	Relaxation Mechanisms and Cross Correlation	10
4	Some Examples	13
5	References	19

1 INTRODUCTION

Nuclear magnetic resonance is uniquely capable of revealing structure and dynamics on a molecular level. An understanding of nuclear spin relaxation is fundamental to an understanding of nuclear magnetic resonance in general. The theoretical framework needed to promote this understanding is conveniently constructed in terms of the time evolution of the density operator under the influence of some Hamiltonian as expressed by the Liouville–von Neumann equation. The basic theory needed for what follows may be found in ***Liouville Equation of Motion***. It will be presumed that the reader is familiar with the contents of this article.

The emphasis here will be on molecules in liquids, though many of the principles presented are applicable to solids and gases. The experimental observables of NMR are magnetizations induced in a sample as a consequence of subjecting it to various static and time-varying magnetic fields. The quantum mechanical operators corresponding to these observables act only on the nuclear spin degrees of freedom of the system. Furthermore, these operators are proportional to the spin angular momentum operators or products thereof and, hence, can be dealt with using finite basis sets of states or operators. Relaxation, however, is a consequence of interactions between the nuclear spins and the rest of the system, referred to as the 'lattice' or 'bath'. In most cases, the lattice cannot be treated exactly using quantum mechanics, because the density operator and the Hamiltonian cannot be defined in explicit mathematical detail. The strategy generally employed, then, is to treat the effects of the lattice classically as a random time-dependent modulation of the nuclear spin operators while retaining a quantum mechanical description of the nuclear spins themselves. All externally applied magnetic fields are likewise treated classically. Our goal is to derive equations that correctly describe the observed temporal behavior of the experimental observables. This is done by proposing a Hamiltonian for the system under study, solving the Liouville–von Neumann equation for the time evolution of the density operator, computing the expected time evolution of the experimental observables, and comparing the result with measured values of these observables. Secondly, one wants to extract from this temporal behavior of the observables information about the fundamental nature of the system under investigation. For example, bond angles and rates of molecular reorientation due to Brownian motion dramatically affect the results of an NMR experiment. How can this kind of information be extracted from the behavior of the magnetization in a sample as a function of time? This article will present the time-dependent perturbation theory methods commonly used in NMR to explain observed phenomena, discuss the various mechanisms that influence relaxation in liquids, and present some simulations exemplifying how nuclear spins behave as a consequence of these mechanisms.

This article presumes a basic knowledge of the nuclear magnetic resonance phenomenon, including nuclear spin polarization in an external static magnetic field and interaction of nuclear spins with applied radiofrequency fields. For those not acquainted with these concepts, several basic texts may be consulted.[1–3] The reader is assumed to have some grasp of basic quantum mechanics and angular momentum theory at the level generally taught in undergraduate physical chemistry courses. Some command of linear algebra and integral and differential calculus is also assumed. All abbreviations and symbols are either defined in the endpapers or are defined in context. Vectors will be distinguished by bold italic type, and the same symbol in normal weight type will denote the magnitude of a vector or, with appropriate subscripts, its components. Quantum mechanical operators will have a hat, for example $\hat{\mathcal{H}}$. Liouville space operators or superoperators will have a double hat, for example $\hat{\hat{\mathcal{L}}}$.

No experimental data will be presented in this article. The experimental literature on coupled relaxation has been recently reviewed.[4] Rather, many simulations using the GAMMA magnetic resonance simulation platform[5] will be used, so that particular aspects of the subject may be illustrated and contrasted without lengthy digressions into experimental detail. While some references to the original literature will be given, most references will be to texts where additional details of the concepts discussed can be found.

1.1 What Is Nuclear Spin Relaxation?

To begin, let us consider nuclear spin relaxation from a phenomenological viewpoint. When a sample containing nuclear spins (e.g., water, which contains ^{1}H nuclei) is placed in a strong, uniform, static magnetic field $\boldsymbol{B}_0$, the sample is observed to develop a macroscopic magnetization $\boldsymbol{M}_0$ parallel to $\boldsymbol{B}_0$. The direction of $\boldsymbol{B}_0$ is taken to be the z direction of a laboratory-fixed coordinate system. Certain nuclei, for example ^{15}N, develop magnetization antiparallel to $\boldsymbol{B}_0$. The magnetization of a sample placed suddenly in a strong field increases with time and asymptotically approaches a steady state value. The magnitude of the steady state magnetization is proportional to the number of magnetic nuclei in the sample and to the strength of $\boldsymbol{B}_0$ (it depends on temperature also, but constant temperature will be assumed for now). Each nucleus of an isotope having a nonzero nuclear spin contributes an amount of magnetization characteristic of that particular isotope. If one used deuterium oxide rather than normal water, for example, both the rate of approach to the steady state and the steady-state magnetization would be different. If the sample is left in the magnet for a long time so that it has closely approached the steady state, this condition is called *thermal equilibrium*. If the magnetization is perturbed from thermal equilibrium, by a pulse of radiofrequency

field at the appropriate frequency, it will return to thermal equilibrium—again asymptotically. This process that causes the magnetization to approach thermal equilibrium is called *nuclear spin relaxation*. The time needed for a sample to achieve thermal equilibrium is, of course, infinite, since the approach is asymptotic. However, the time needed to reasonably approximate thermal equilibrium is in the range of milliseconds to hundreds of seconds for liquids, depending on the nature of the sample and the nuclei involved.

The rest of this article will consist mainly of a detailed discussion of the behavior of the magnetization as a function of time and how measurement of this behavior can be used to determine the structural and dynamical features of the molecules bearing the magnetic nuclei.

1.2 Classical Treatment: Bloch's Equations

The first investigations of nuclear-spin relaxation were conducted soon after the discovery of NMR.[6–8] The main results of this work can be summarized by the following equations:

$$\left.\begin{aligned}\frac{dM_x}{dt} &= [M_y(\gamma B_0 - \omega) - M_z\gamma B_y] - \frac{M_x}{T_2}\\ \frac{dM_y}{dt} &= -[M_x(\gamma B_0 - \omega) - M_z\gamma B_x] - \frac{M_y}{T_2}\\ \frac{dM_z}{dt} &= [M_x\gamma B_y - M_y\gamma B_x] - \frac{M_z - M_0}{T_1}\end{aligned}\right\} \quad (1)$$

These phenomenological equations are generally referred to as the Bloch equations and are cast here in terms of a reference frame rotating at an angular frequency ω about the z axis with respect to a laboratory-fixed frame. A particularly lucid discussion of the Bloch equations may be found in the text by Slichter.[9] This system of coupled linear differential equations with constant coefficients has solutions wherein the magnetization precesses about the effective field in the rotating frame having components (B_x, B_y, $B_0 - \omega/\gamma$). In order for B_x and B_y to be stationary in the rotating frame, they must be oscillating in the laboratory frame so that their sum rotates at frequency ω. This will be discussed in mathematical detail in Section 2.7. For usual high-resolution experiments with liquids, ω will be of the order of tens or hundreds of megahertz, thus, radiofrequency technology is used to produce B_x and B_y in the laboratory frame.

However, the main interest here is in the terms involving T_1 and T_2. If $\omega = \gamma B_0$ and $B_x = B_y = 0$ then equation (1) uncouple and yield particularly simple solutions wherein M_x and M_y relax exponentially to zero governed by T_2 while M_z relaxes exponentially toward M_0 governed by T_1. Specifically, the solution of equation (1) is given by

$$\left.\begin{aligned}M_x(t) &= M_x(0)\exp(-t/T_2)\\ M_y(t) &= M_y(0)\exp(-t/T_2)\\ M_z(t) &= M_0 + [M_z(0) - M_0]\exp(-t/T_1)\end{aligned}\right\} \quad (2)$$

where $\boldsymbol{M}(0)$ is the magnetization at time zero. These equations accurately describe the evolution of the macroscopic magnetization whenever the system under study may be regarded as an ensemble of spins interacting only with the lattice and not with each other. The relaxation of a surprisingly large number of materials that have been studied is satisfactorily explained by equation (2).

The fact that the magnetization changes with time implies that the nuclei are undergoing transitions among the available quantum mechanical states. Just as the magnetization may be manipulated by inducing transitions with externally applied rf pulses, any natural phenomenon that produces a time-varying field at a nucleus can induce transitions. The effect of all of these natural phenomena is to drive the macroscopic magnetization toward the thermal equilibrium value. See Section 3 for a discussion of specific examples of natural phenomena that can be mechanisms of spin relaxation. The decay of M_x and M_y involves exchange of energy among the spins, whereas the evolution of M_z toward its steady state value involves transfer of energy between the spins and the lattice.

1.3 When There Are Two or More Coupled Spins

When two or more spins are coupled by some sort of interaction, equation (1) may not be sufficient to explain the observed evolution of the magnetization. Consider, for example, a ^{13}C–^{1}H moiety such as might be found in the formate ion.[10] In a conceptually simple experiment, the ^{1}H magnetization is inverted, and then the ^{1}H and ^{13}C magnetizations are followed as a function of time. Additional details of this experiment can be found in Section 4.1.1. If there were no interaction between ^{1}H and ^{13}C then each of the spins could be treated separately according to equation (1), and the resulting evolution would be as shown in Figure 1(a). The ^{1}H magnetization recovers to thermal equilibrium exponentially as expected, and the ^{13}C magnetization remains unperturbed; however, when one actually performs this experiment, the results are as shown in Figure 1(b). The ^{13}C magnetization grows beyond thermal equilibrium, and then decays back to thermal equilibrium. Apparently, magnetization is flowing from the ^{1}H to the ^{13}C nuclei; this behavior cannot be predicted by equation (1). The mechanism that has been introduced to produce this effect is dipole–dipole (DD) coupling between the two nuclei. This is an example of cross relaxation. The theory of which this is a simple example will be the subject of the rest of this article.

2 TIME-DEPENDENT PERTURBATION THEORY

The theoretical model generally adopted for high-resolution NMR of liquids is that of a molecule bearing the spin system of interest immersed in a solvent. The concentration of such molecules is sufficiently low that intermolecular interactions among the spins of interest need not be considered. Because of the short range and random nature of the interactions involved, this assumption is adequately met even at fairly high concentrations. The macroscopic sample may then be considered as an ensemble of isolated systems each consisting of a single spin system of interest immersed in a bath or lattice the exact state of which is of no interest. The terms 'bath' and 'lattice' will be used interchangeably to refer to all the degrees of freedom of one member of the ensemble not directly associated with the nuclear spins in which we

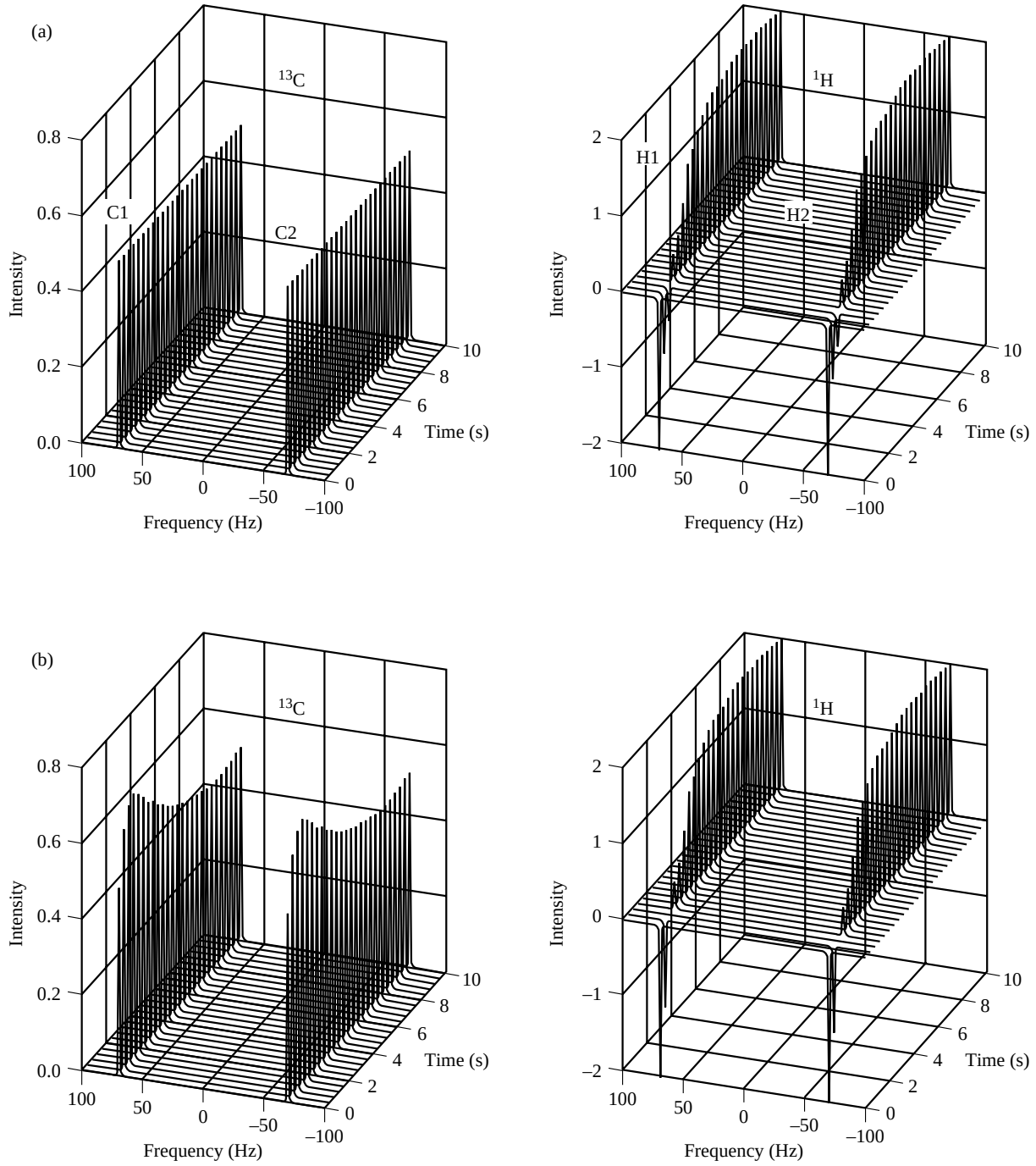

Figure 1 Simulation of relaxation of a two-spin (^{13}C–^{1}H) system after a proton π nonselective pulse: (a) relaxed only by external random fields (T_1 = 1.6 s, J = 140 Hz); (b) relaxed also by dipole–dipole coupling between the two spins (internuclear distance 0.109 nm, spherical top, correlation time 10 ps). The intensity is scaled so that the total ^{13}C magnetization at thermal equilibrium is unity, and that of ^{1}H is then greater by a factor γ_H/γ_C, or about four. See Section 4.1.1 for a more detailed discussion of the experiment

are interested. For example, the translational, rotational, and vibrational states of the molecule bearing the spin system of interest as well as the states of any nuclear or electron spins in solvent molecules would be in this category. The number of degrees of freedom of the lattice is so great as to be effectively infinite, with essentially a continuum of energy eigenstates. Using the terms somewhat loosely, the 'heat capacity' of the lattice is assumed to be so much greater than that of the nuclear spins that no interaction between the two can change the 'temperature' of the lattice. The nuclear spins also interact with externally applied magnetic fields, which are treated classically. In this discussion, the external magnetic field will be only the usual static field $\boldsymbol{B}_0$, the direction of which is taken to be the z axis of our laboratory coordinate system. Pulses will be treated as instantaneous rotations. A more general treatment of pulses and time-dependent external fields in general has been given by Smith et al.[11–13]

To begin our theoretical development, the Hamiltonian for one member of our ensemble can be expressed as a combination of terms acting on the spin system $\hat{\mathcal{H}}_s$, terms acting on the bath $\hat{\mathcal{H}}_b$, and terms for the interaction between the two $\hat{\mathcal{H}}_I$:

$$\hat{\mathcal{H}} = \hat{\mathcal{H}}_s + \hat{\mathcal{H}}_b + \hat{\mathcal{H}}_I \tag{3}$$

The density operator $\hat{\rho}(t)$ encompasses both spin system and bath. The Liouvillian $\hat{\hat{\mathcal{L}}}$ is a commutation or derivation superoperator relating to the Hamiltonian according to

$$\hat{\hat{\mathcal{L}}} = \hat{\mathcal{H}} \otimes \hat{E} - \hat{E} \otimes \hat{\mathcal{H}} \tag{4}$$

For a discussion of superoperators and their relationship to operators see Section 5 of ***Liouville Equation of Motion***. The Hamiltonian for a spin system $\hat{\mathcal{H}}_s$ interacting only with $\boldsymbol{B}_0$ contains terms from Zeeman interactions, chemical shieldings, scalar couplings, etc. A detailed discussion of high-resolution NMR Hamiltonians may be found in the first of the series of articles by Smith et al.[11] Some of these interactions involve terms that are dependent upon spin system orientation relative to $\boldsymbol{B}_0$, in which case interaction terms involving the rotational state of the molecule will be of interest. Such terms are of principal interest for spin relaxation studies in liquids, since molecules in liquids are rotating rapidly and changing rotational state frequently owing to collisions. Because of this, it is useful to express individual terms of the Hamiltonian in a general spherical tensor format. The Hamiltonian may be expressed as[11]

$$\hat{\mathcal{H}} = \sum_{\mu} \xi_{\mu} \sum_{m=-l}^{l} (-1)^m \hat{T}^{\mu}_{m} \hat{F}^{\mu}_{-m} \tag{5}$$

These tensors can be easily rotated from one coordinate system to another.[14] Here the $\hat{T}^{\mu}_{m}$ are spin operators acting on the system of interest, the $\hat{F}^{\mu}_{-m}$ are operators on the lattice states or functions relating to the externally applied magnetic fields, and ξ_{μ} are interaction constants, which will vary depending upon the nature of the interaction. The index μ is used to label a particular interaction, and each interaction has one or more associated values of the rank l. For each l, one must sum over the projection index m as shown. All of the terms in this sum can be assigned to one of the three Hamiltonians on the right-hand side of equation (3). Terms involving $l = 0$ and $m = 0$ for the spin operators are bath terms. Those involving $l = 0$ and $m = 0$ for the lattice operators as well as those depending only on the applied external field are spin terms. All others are interaction terms.

Both $\hat{T}^{\mu}_{m}$ and $\hat{F}^{\mu}_{-m}$ transform like spherical harmonics under rotations,[14] and are related to their adjoints as follows:

$$\left.\begin{aligned} (\hat{F}^{\mu}_{m})^{\dagger} &= (-1)^m \hat{F}^{\mu}_{-m} \\ (\hat{T}^{\mu}_{m})^{\dagger} &= (-1)^m \hat{T}^{\mu}_{-m} \end{aligned}\right\} \tag{6}$$

The superscript † indicates the adjoint or Hermitian conjugate of the operator. When the operator is represented in Liouville space using some operator basis, this means transpose the vector and take the complex conjugate of each element.

The Liouville equation in the Schrödinger representation is

$$\frac{\mathrm{d}|\hat{\rho}(t)\rangle}{\mathrm{d}t} = -\frac{\mathrm{i}}{\hbar}\hat{\hat{\mathcal{L}}}|\hat{\rho}(t)\rangle \tag{7}$$

(For a more detailed development of this type of equation, see Section 5 of ***Liouville Equation of Motion***). It defines the time evolution of the density operator for the entire system, spins and lattice, in terms of the Liouvillian of equation (4). In this representation, the density superket is time-dependent whereas the Liouvillian is not. This implies, as mentioned above, that no time-varying magnetic fields are applied. Unfortunately, equation (7) is completely intractable, because the lattice and interaction Hamiltonians $\hat{\mathcal{H}}_b$ and $\hat{\mathcal{H}}_I$ cannot be clearly defined and the dimension of the Liouville space of the lattice would be far too large for meaningful calculations to be performed. Hence, we are forced to seek an approximate method for solving the Liouville equation. Nuclear spins relax very slowly compared with most events on a molecular scale, so it is reasonable to suppose that the interaction $\hat{\mathcal{H}}_I$ is very weak. Further, collisions between the molecule of interest and solvent molecules should be treatable as a random process amenable to statistical methods. These two facts lead one to attempt a solution of equation (7) using perturbation theory and statistical mechanics.

2.1 The Interaction Representation

We begin the application of time-dependent perturbation theory by making use of the interaction picture of the problem to permit focusing on the small interaction terms. If we transform all the operators in the Liouville equation into an interaction representation based on the combined bath and spin system Hamiltonians, we can effectively 'remove' the pure bath and pure spin system contributions, a procedure that simplifies equation (7) and, it is to be hoped, facilitates its integration:

$$\frac{\mathrm{d}|\hat{\rho}'(t)\rangle}{\mathrm{d}t} = -\frac{\mathrm{i}}{\hbar}\hat{\hat{\mathcal{L}}}'_{\mathrm{I}}(t)|\hat{\rho}'(t)\rangle \tag{8}$$

(for a discussion of interaction representations and transformations, see Section 4.1 of ***Liouville Equation of Motion***). Operators (superkets) and superoperators in the interaction representation are indicated by a prime. These relate to the Schrödinger representation via

$$\left.\begin{aligned} \hat{\hat{\mathcal{L}}}_0 &= \hat{\hat{\mathcal{L}}}_s + \hat{\hat{\mathcal{L}}}_b \\ |\hat{\rho}'(t)\rangle &= \exp\left(\frac{\mathrm{i}}{\hbar}\hat{\hat{\mathcal{L}}}_0 t\right)|\hat{\rho}(t)\rangle \\ \hat{\hat{\mathcal{L}}}'_{\mathrm{I}}(t) &= \exp\left(\frac{\mathrm{i}}{\hbar}\hat{\hat{\mathcal{L}}}_0 t\right)\hat{\hat{\mathcal{L}}}_{\mathrm{I}}\exp\left(-\frac{\mathrm{i}}{\hbar}\hat{\hat{\mathcal{L}}}_0 t\right) \end{aligned}\right\} \tag{9}$$

2.2 Second-Order Perturbation Theory

Because of the inherently complex interaction between bath and spin system, as embodied in the superoperator $\hat{\hat{\mathcal{L}}}'_{\mathrm{I}}(t)$, the equation of motion must be solved using some sort of approximation technique. One approach is to use

a Dyson expansion of the integral. The initial steps are trivial—equation (8) is integrated formally from an arbitrary starting time t_0 to some later time t:

$$\left.\begin{aligned}\int_{t_0}^{t} \mathrm{d}|\hat{\rho}'(t_1)\rangle &= -\frac{\mathrm{i}}{\hbar}\int_{t_0}^{t} \mathrm{d}t_1\, \hat{\hat{\mathcal{L}}}'_{\mathrm{I}}(t_1)|\hat{\rho}'(t_1)\rangle \\ |\hat{\rho}'(t)\rangle &= |\hat{\rho}'(t_0)\rangle - \frac{\mathrm{i}}{\hbar}\int_{t_0}^{t} \mathrm{d}t_1\, \hat{\hat{\mathcal{L}}}'_{\mathrm{I}}(t_1)|\hat{\rho}'(t_1)\rangle\end{aligned}\right\} \tag{10}$$

We can now make a change of variable in equation (10),

$$|\hat{\rho}'(t_1)\rangle = |\hat{\rho}'(t_0)\rangle - \frac{\mathrm{i}}{\hbar}\int_{t_0}^{t_1} \mathrm{d}t_2\, \hat{\hat{\mathcal{L}}}'_{\mathrm{I}}(t_2)|\hat{\rho}'(t_2)\rangle \tag{11}$$

and substitute back into the integrand of equation (10) to produce

$$\begin{aligned}|\hat{\rho}'(t)\rangle &= |\hat{\rho}'(t_0)\rangle \\ &\quad -\frac{\mathrm{i}}{\hbar}\int_{t_0}^{t} \mathrm{d}t_1\, \hat{\hat{\mathcal{L}}}'_{\mathrm{I}}(t_1)\left[|\hat{\rho}'(t_0)\rangle - \frac{\mathrm{i}}{\hbar}\int_{t_0}^{t_1} \mathrm{d}t_2\, \hat{\hat{\mathcal{L}}}'_{\mathrm{I}}(t_2)|\hat{\rho}'(t_2)\rangle\right] \\ &= |\hat{\rho}'(t_0)\rangle - \frac{\mathrm{i}}{\hbar}\int_{t_0}^{t} \mathrm{d}t_1\, \hat{\hat{\mathcal{L}}}'_{\mathrm{I}}(t_1)|\hat{\rho}'(t_0)\rangle \\ &\quad -\frac{1}{\hbar^2}\int_{t_0}^{t} \mathrm{d}t_1 \int_{t_0}^{t_1} \mathrm{d}t_2\, \hat{\hat{\mathcal{L}}}'_{\mathrm{I}}(t_1)\, \hat{\hat{\mathcal{L}}}'_{\mathrm{I}}(t_2)|\hat{\rho}'(t_2)\rangle\end{aligned} \tag{12}$$

This process is iterated, substituting equation (11), with the appropriate change of variable for $|\hat{\rho}'(t_2)\rangle$, into equation (12). With each iteration, the lower order integrals involve only the initial density superket. Continuing the iterations and assuming that the series eventually converges so that the last term involving $|\hat{\rho}'(t_n)\rangle$ may be ignored produces the Dyson series

$$\begin{aligned}|\hat{\rho}'(t)\rangle = |\hat{\rho}'(t_0)\rangle + \sum_{n=1}^{\infty}\left(-\frac{\mathrm{i}}{\hbar}\right)^n \int_{t_0}^{t} \mathrm{d}t_1 \int_{t_0}^{t_1} \mathrm{d}t_2 \cdots \\ \times \int_{t_0}^{t_{n-1}} \mathrm{d}t_n\, \hat{\hat{\mathcal{L}}}'_{\mathrm{I}}(t_1)\, \hat{\hat{\mathcal{L}}}'_{\mathrm{I}}(t_2) \cdots \hat{\hat{\mathcal{L}}}'_{\mathrm{I}}(t_n)|\hat{\rho}'(t_0)\rangle\end{aligned} \tag{13}$$

If it could be shown that the interaction Liouvillians at different times commute then the time ordering would be inconsequential, and equation (12) would be equivalent to a Taylor series for an exponential:

$$|\hat{\rho}'(t)\rangle = \exp\left[-\frac{\mathrm{i}}{\hbar}\int_{t_0}^{t} \mathrm{d}t_1\, \hat{\hat{\mathcal{L}}}'_{\mathrm{I}}(t_1)\right]|\hat{\rho}'(t_0)\rangle \tag{14}$$

If the interaction Liouvillian (in the interaction representation) were time-independent then the integral would be trivial and the solution in the interaction representation would be

$$|\hat{\rho}'(t)\rangle = \exp\left[-\frac{\mathrm{i}}{\hbar}\,\hat{\hat{\mathcal{L}}}'_{\mathrm{I}}(t - t_0)\right]|\hat{\rho}'(t_0)\rangle \tag{15}$$

We shall assume that the Liouvillians at different times do not commute, but that terms higher than second order are negligible, i.e., that *second-order perturbation theory* is adequate to describe the system. The equation of motion is then approximated by

$$\begin{aligned}|\hat{\rho}'(t)\rangle = |\hat{\rho}'(t_0)\rangle - \frac{\mathrm{i}}{\hbar}\int_{t_0}^{t} \mathrm{d}t_1\, \hat{\hat{\mathcal{L}}}'_{\mathrm{I}}(t_1)|\hat{\rho}'(t_0)\rangle \\ -\frac{1}{\hbar^2}\int_{t_0}^{t} \mathrm{d}t_1 \int_{t_0}^{t_1} \mathrm{d}t_2\, \hat{\hat{\mathcal{L}}}'_{\mathrm{I}}(t_1)\, \hat{\hat{\mathcal{L}}}'_{\mathrm{I}}(t_2)|\hat{\rho}'(t_0)\rangle\end{aligned} \tag{16}$$

2.3 Application of the Wangsness–Bloch–Redfield Assumptions

Equation (16) is still not in a form that can be handled either analytically or numerically for useful systems. We therefore apply several additional approximations that will eventually lead to a manageable expression. Recognizing that the first integral term in equation (16) is nondissipative, it can at most add a constant term to the density matrix. Furthermore, we shall shortly deal with an ensemble of spin systems, and the average effect of the interaction Liouvillian at any point in time is zero for an isotropic liquid. This is true for a bath interacting in an essentially random fashion with the system of interest. Therefore the first integral term in equation (16) may be ignored, giving

$$|\hat{\rho}'(t)\rangle = |\hat{\rho}'(t_0)\rangle - \frac{1}{\hbar^2}\int_{t_0}^{t} \mathrm{d}t_1 \int_{t_0}^{t_1} \mathrm{d}t_2\, \hat{\hat{\mathcal{L}}}'_{\mathrm{I}}(t_1)\, \hat{\hat{\mathcal{L}}}'_{\mathrm{I}}(t_2)|\hat{\rho}'(t_0)\rangle \tag{17}$$

If the integrand is continuous over the integration range then we can differentiate equation (17) to obtain a differential equation again:

$$\frac{\mathrm{d}|\hat{\rho}'(t)\rangle}{\mathrm{d}t} = -\frac{1}{\hbar^2}\int_{t_0}^{t} \mathrm{d}t_1\, \hat{\hat{\mathcal{L}}}'_{\mathrm{I}}(t)\, \hat{\hat{\mathcal{L}}}'_{\mathrm{I}}(t_1)|\hat{\rho}'(t_0)\rangle \tag{18}$$

It is assumed that the integral really only depends upon the difference $\tau = t - t_1$, so that the variable of integration may be changed as follows:

$$\frac{\mathrm{d}|\hat{\rho}'(t)\rangle}{\mathrm{d}t} = -\frac{1}{\hbar^2}\int_{t_0}^{t} \mathrm{d}\tau\, \hat{\hat{\mathcal{L}}}'_{\mathrm{I}}(t)\, \hat{\hat{\mathcal{L}}}'_{\mathrm{I}}(t - \tau)|\hat{\rho}'(t_0)\rangle \tag{19}$$

It is further assumed that the density superket does not change rapidly over the range of the integral, so that replacing $|\hat{\rho}'(t_0)\rangle$ with $|\hat{\rho}'(t)\rangle$ does not introduce significant error. This yields

$$\frac{\mathrm{d}|\hat{\rho}'(t)\rangle}{\mathrm{d}t} = -\frac{1}{\hbar^2}\int_{0}^{t} \mathrm{d}\tau\, \hat{\hat{\mathcal{L}}}'_{\mathrm{I}}(t)\, \hat{\hat{\mathcal{L}}}'_{\mathrm{I}}(t - \tau)|\hat{\rho}'(t)\rangle \tag{20}$$

A final assumption is that t will be long enough that the integrand will have decayed to zero and no error will be introduced by extending the limit of integration to infinity. Then we have

$$\frac{\mathrm{d}|\hat{\rho}'(t)\rangle}{\mathrm{d}t} = -\frac{1}{\hbar^2}\int_{0}^{\infty} \mathrm{d}\tau\, \hat{\hat{\mathcal{L}}}'_{\mathrm{I}}(t)\, \hat{\hat{\mathcal{L}}}'_{\mathrm{I}}(t - \tau)|\hat{\rho}'(t)\rangle \tag{21}$$

2.4 The Semiclassical Liouville Equation

At this point, it is essential to depart from the treatment of the entire system of spins and bath and focus only on the smaller system of interest, namely, the spin system. The total system density operator can always be represented as a tensor product of two density operators, one spanning the spin system subspace and one spanning the lattice subspace:

$$|\hat{\rho}(t)\rangle = |\hat{\sigma}(t)\rangle|\hat{\rho}_{\mathrm{b}}(t)\rangle \tag{22}$$

Keep in mind that it is the smaller spin system represented by the reduced density operator $|\hat{\sigma}(t)\rangle$ that is of interest, not the entire system $|\hat{\rho}(t)\rangle$. The latter resides in a Liouville space of unmanageable dimensionality whereas the dimension of the former is normally small enough that its evolution in time can be mathematically detailed with some precision. One can define a superket $|\hat{\rho}_{\mathrm{s}}(t)\rangle$ that resides in the full Liouville space of the spin system and bath, and yet contains only the information regarding the spin system of interest:

$$\left.\begin{aligned} |\hat{\rho}_{\mathrm{s}}(t)\rangle &= \hat{\hat{P}}|\hat{\rho}(t)\rangle = \hat{\hat{E}}_{\mathrm{s}} \otimes (|\hat{\rho}_{\mathrm{b}}(t)\rangle \otimes \langle\hat{E}_{\mathrm{b}}|) \\ |\hat{\sigma}(t)\rangle &= (\hat{\hat{E}}_{\mathrm{s}} \otimes \langle\hat{E}_{\mathrm{b}}|)|\hat{\rho}_{\mathrm{s}}(t)\rangle = (\hat{\hat{E}}_{\mathrm{s}} \otimes \langle\hat{E}_{\mathrm{b}}|)\,\hat{\hat{P}}|\hat{\rho}(t)\rangle \\ &= (\hat{\hat{E}}_{\mathrm{s}} \otimes \langle\hat{E}_{\mathrm{b}}|)\,\hat{\hat{E}}_{\mathrm{s}} \otimes (|\hat{\rho}_{\mathrm{b}}(t)\rangle \otimes \langle\hat{E}_{\mathrm{b}}|) \end{aligned}\right\} \tag{23}$$

The equation of motion for $|\hat{\rho}_{\mathrm{s}}(t)\rangle$ is obtained by use of the projection superoperator $\hat{\hat{P}}$ in the approximate equation of motion:

$$\frac{\mathrm{d}|\hat{\rho}'_{\mathrm{s}}(t)\rangle}{\mathrm{d}t} = -\frac{1}{\hbar^2}\,\hat{\hat{P}}\int_0^\infty \mathrm{d}\tau\;\hat{\hat{\mathcal{L}}}'_1(t)\,\hat{\hat{\mathcal{L}}}'_1(t-\tau)\,\hat{\hat{P}}|\hat{\rho}'_{\mathrm{s}}(t)\rangle \tag{24}$$

Back-transformation into the Schrödinger representation produces

$$\begin{aligned} \frac{\mathrm{d}|\hat{\rho}'_{\mathrm{s}}(t)\rangle}{\mathrm{d}t} = &-\frac{\mathrm{i}}{\hbar}\,\hat{\hat{\mathcal{L}}}_{\mathrm{s}}|\hat{\rho}_{\mathrm{s}}(t)\rangle - \frac{1}{\hbar^2}\,\hat{\hat{P}}\int_0^\infty \mathrm{d}\tau\;\hat{\hat{\mathcal{L}}}'_1(t)\exp\left(-\frac{\mathrm{i}}{\hbar}\,\hat{\hat{\mathcal{L}}}_0\tau\right) \\ &\times\hat{\hat{\mathcal{L}}}'_1(t-\tau)\exp\left(\frac{\mathrm{i}}{\hbar}\,\hat{\hat{\mathcal{L}}}_0\tau\right)\hat{\hat{P}}|\hat{\rho}'_{\mathrm{s}}(t)\rangle \end{aligned} \tag{25}$$

This equation is general for any system interacting with a large bath, so long as the constraints outlined in Section 2.3 are fulfilled. The Liouvillians $\hat{\hat{\mathcal{L}}}_{\mathrm{s}}$ and $\hat{\hat{\mathcal{L}}}_{\mathrm{b}}$ commute, and $\hat{\hat{\mathcal{L}}}_{\mathrm{b}}$ cannot operate on $|\hat{\rho}_{\mathrm{s}}(t)\rangle$, so that $\exp(-\mathrm{i}\hbar^{-1}\hat{\hat{\mathcal{L}}}_0\tau)\,\hat{\hat{P}} = \exp(-\mathrm{i}\hbar^{-1}\hat{\hat{\mathcal{L}}}_{\mathrm{s}}\tau)\,\hat{\hat{P}}$. Then,

$$\begin{aligned} \frac{\mathrm{d}|\hat{\rho}_{\mathrm{s}}(t)\rangle}{\mathrm{d}t} = &-\frac{\mathrm{i}}{\hbar}\,\hat{\hat{\mathcal{L}}}_{\mathrm{s}}|\hat{\rho}_{\mathrm{s}}(t)\rangle - \frac{1}{\hbar^2}\,\hat{\hat{P}}\int_0^\infty \mathrm{d}\tau\;\hat{\hat{\mathcal{L}}}'_1(t)\exp\left(-\frac{\mathrm{i}}{\hbar}\,\hat{\hat{\mathcal{L}}}_0\tau\right) \\ &\times\hat{\hat{\mathcal{L}}}'_1(t-\tau)\exp\left(\frac{\mathrm{i}}{\hbar}\,\hat{\hat{\mathcal{L}}}_{\mathrm{s}}\tau\right)\hat{\hat{P}}|\hat{\rho}'_{\mathrm{s}}(t)\rangle \end{aligned} \tag{26}$$

It is beyond the scope of this article to show that the net result of continued manipulations produces

$$\begin{aligned} &\hat{\hat{P}}\int_0^\infty \mathrm{d}\tau\;\hat{\hat{\mathcal{L}}}'_1(t)\exp\left(-\frac{\mathrm{i}}{\hbar}\hat{\hat{\mathcal{L}}}_0\tau\right)\hat{\hat{\mathcal{L}}}'_1(t-\tau)\exp\left(\frac{\mathrm{i}}{\hbar}\hat{\hat{\mathcal{L}}}_{\mathrm{s}}\tau\right)\;\hat{\hat{P}}|\hat{\rho}'_{\mathrm{s}}(t)\rangle \\ &= \;\hat{\hat{P}}\int_0^\infty \mathrm{d}\tau\;\hat{\hat{\mathcal{L}}}'_1(t)\exp\left(-\frac{\mathrm{i}}{\hbar}\hat{\hat{\mathcal{L}}}_{\mathrm{s}}\tau\right)\hat{\hat{\mathcal{L}}}'_1(t-\tau)\exp\left(\frac{\mathrm{i}}{\hbar}\hat{\hat{\mathcal{L}}}_{\mathrm{s}}\tau\right) \\ &\quad\times\hat{\hat{P}}|\hat{\rho}'_{\mathrm{s}}(t)-\hat{\rho}'_{\mathrm{s}}(\infty)\rangle \end{aligned} \tag{27}$$

Further details of this step may be found in an article by Szymanski et al.[15] The projection operators allow us now to work exclusively with the reduced density operator and place all operators into the corresponding reduced space. Switching to the difference (reduced) density operator $\Delta\hat{\sigma}$, we now perform an ensemble average over all the spin systems in the sample to yield

$$\begin{aligned} \frac{\mathrm{d}|\hat{\sigma}(t)\rangle}{\mathrm{d}t} = &-\frac{\mathrm{i}}{\hbar}\,\overline{\hat{\hat{\mathcal{L}}}_{\mathrm{s}}}|\hat{\sigma}(t)\rangle - \frac{1}{\hbar^2}\int_0^\infty \mathrm{d}\tau\;\hat{\hat{\mathcal{L}}}'_1(t) \\ &\times\overline{\exp\left(-\frac{\mathrm{i}}{\hbar}\hat{\hat{\mathcal{L}}}_{\mathrm{s}}\tau\right)\hat{\hat{\mathcal{L}}}'_1(t-\tau)\exp\left(\frac{\mathrm{i}}{\hbar}\hat{\hat{\mathcal{L}}}_{\mathrm{s}}\tau\right)} \\ &\times|\hat{\sigma}(t)-\hat{\sigma}(\infty)\rangle \\ = &-\frac{\mathrm{i}}{\hbar}\,\overline{\hat{\hat{\mathcal{L}}}_{\mathrm{s}}}|\hat{\sigma}(t)\rangle - \frac{1}{\hbar^2}\int_0^\infty \mathrm{d}\tau\;\hat{\hat{\mathcal{L}}}'_1(t) \\ &\times\overline{\exp\left(-\frac{\mathrm{i}}{\hbar}\hat{\hat{\mathcal{L}}}_{\mathrm{s}}\tau\right)\hat{\hat{\mathcal{L}}}'_1(t-\tau)\exp\left(\frac{\mathrm{i}}{\hbar}\hat{\hat{\mathcal{L}}}_{\mathrm{s}}\tau\right)} \\ &\times|\Delta\hat{\sigma}(t)\rangle \end{aligned} \tag{28}$$

As in the Hilbert space formulation of Wangsness–Bloch–Redfield theory, it remains to isolate the time dependence in the integral function in order to formulate spectral densities.

2.5 The Spin and Interaction Hamiltonians

The lattice Hamiltonian $\hat{\mathcal{H}}_{\mathrm{b}}$ now influences the equation of motion only in that the system relaxes toward thermal equilibrium at the temperature of the bath $|\hat{\sigma}(\infty)\rangle$. We must now define in detail the form of the spin and interaction Hamiltonians. The principal influence of the lattice is to reorient the spin system. Equation (5) can then be interpreted as follows to account for both the spin system and its interaction with the lattice:

$$\hat{\mathcal{H}}_{\mathrm{s}} + \hat{\mathcal{H}}_1(t) = \sum_\mu \xi_\mu \sum_{m=-l}^{l} (-1)^m \hat{T}^\mu_m F^\mu_{-m}(t) \tag{29}$$

The lattice operators are now manifested as random functions of time that reorient the spin system. This is referred to as the *semiclassical model* for the Hamiltonian; the interaction terms of the Hamiltonian are time-dependent through the lattice functions $F^\mu_{-m}(t)$, but the operators that act on the spin system are independent of time. Invoking the ergodic hypothesis, the ensemble average can be replaced by a time average, and, if all orientations are equally probable (an isotropic liquid), many of the interactions average to zero in first order. The isotropic terms, $l = m = 0$, in equation (29) are independent of spin system orientation, and, hence, do not need to be time-averaged. These terms yield for a system of n spins the isotropic Hamiltonian commonly found in texts on high-resolution NMR:

$$\hat{\mathcal{H}}_{\mathrm{s}} = \hat{\mathcal{H}}_0 = -\sum_{i=1}^{n}\hbar\omega_i\hat{I}_{iz} + 2\pi\hbar\sum_{i=2}^{n}\sum_{j=1}^{i-1}J_{ij}\hat{\boldsymbol{I}}_i\cdot\hat{\boldsymbol{I}}_j \tag{30}$$

The symbol J is widely used in the literature for both scalar couplings and spectral densities, which will be introduced in equation (41). We prefer to retain this notation in both cases, trusting that the reader will be able to discern from the context which is meant in a given case. Other Hamiltonian components that are orientation-dependent and, therefore, time-dependent will be categorized in the interaction Hamiltonian term of equation (29):

$$\hat{\mathcal{H}}_{\mathrm{I}}(t) = \sum_{\mu} \xi_{\mu} \sum_{m=-l}^{l} (-1)^m \hat{T}^{\mu}_{m} F^{\mu}_{-m}(t) \tag{31}$$

Although it is not explicit, note that the sum over μ in equation (29) includes the rotationally invariant components, whereas the sum in equation (31) does not include them. Furthermore, since the lattice operators are now simply functions, the adjoint used in equation (6) is replaced by a complex conjugate, so that $[F^{\mu}_{m}(t)]* = (-1)^m F^{\mu}_{-m}(t)$. The equation of motion is then

$$\frac{\mathrm{d}|\hat{\sigma}(t)\rangle}{\mathrm{d}t} = -\frac{\mathrm{i}}{\hbar}\hat{\hat{\mathcal{L}}}_0|\hat{\sigma}\rangle - \frac{1}{\hbar^2}\int_0^{\infty} \mathrm{d}\tau\, \hat{\hat{\mathcal{L}}}_{\mathrm{I}} \times \overline{\exp\left(-\frac{\mathrm{i}}{\hbar}\hat{\hat{\mathcal{L}}}_0\tau\right)\hat{\hat{\mathcal{L}}}_{\mathrm{I}}\exp\left(\frac{\mathrm{i}}{\hbar}\hat{\hat{\mathcal{L}}}_0\tau\right)}|\Delta\hat{\sigma}\rangle \tag{32}$$

2.6 The Relaxation Superoperator

Making use of the semiclassical interaction model for $\hat{\mathcal{H}}_{\mathrm{I}}$ given in equation (29), the interaction Liouvillian can be constructed:

$$\begin{aligned}\hat{\hat{\mathcal{L}}}_{\mathrm{I}}(t) &= \sum_{\mu}\xi_{\mu}\sum_{m=-l}^{l}(-1)^m(\hat{T}^{\mu}_{m}\otimes\hat{E} - \hat{E}\otimes\hat{T}^{\mu}_{m})F^{\mu}_{-m}(t)\\ &= \sum_{\mu}\xi_{\mu}\sum_{m=-l}^{l}(-1)^m\hat{\hat{\Gamma}}^{\mu}_{m}F^{\mu}_{-m}(t)\end{aligned} \tag{33}$$

Substitution of this relationship into equation (32) produces

$$\begin{aligned}\frac{\mathrm{d}|\hat{\sigma}(t)\rangle}{\mathrm{d}t} = -\frac{\mathrm{i}}{\hbar}\hat{\hat{\mathcal{L}}}_0|\hat{\sigma}\rangle - \frac{1}{\hbar^2}\sum_{\mu}\sum_{\mu'}\xi_{\mu}\xi_{\mu'}\sum_{m=-l}^{l}\sum_{m'=-l'}^{l'}(-1)^{m+m'}\hat{\hat{\Gamma}}^{\mu}_{m}\\ \times\int_0^{\infty}\mathrm{d}\tau\,\overline{F^{\mu}_{-m}(t)F^{\mu'}_{-m'}(t-\tau)}\exp\left(-\frac{\mathrm{i}}{\hbar}\hat{\hat{\mathcal{L}}}_0\tau\right)\\ \times\hat{\hat{\Gamma}}^{\mu'}_{m'}\exp\left(\frac{\mathrm{i}}{\hbar}\hat{\hat{\mathcal{L}}}_0\tau\right)|\Delta\hat{\sigma}\rangle\end{aligned} \tag{34}$$

Our objective is to separate quantities that depend on the time variable τ from the spin operators, which do not. The spherical spin tensor operator components $\hat{T}^{\mu}_{m}$ generally will not commute with $\hat{\mathcal{H}}_0$ and, hence, will not commute with $\hat{\hat{\mathcal{L}}}_0$ either, so one cannot isolate the exponentials involving τ.

One can express the spherical tensor operators in a basis comprising the eigenoperators of the static Hamiltonian superoperator $\hat{\hat{\mathcal{L}}}_0$:

$$\left.\begin{aligned}|\hat{T}^{\mu}_{m}\rangle &= \sum_{p}|\hat{T}^{\mu}_{m,p}\rangle\\ |\hat{T}'^{\mu}_{m}(t)\rangle &= \exp\left(-\frac{\mathrm{i}}{\hbar}\hat{\hat{\mathcal{L}}}_0\tau\right)|\hat{T}^{\mu}_{m}\rangle\\ &= \sum_{p}\exp\left(-\frac{\mathrm{i}}{\hbar}\hat{\hat{\mathcal{L}}}_0\tau\right)|\hat{T}^{\mu}_{m,p}\rangle = \sum_{p}\mathrm{e}^{-\mathrm{i}\Omega_p\tau}|\hat{T}^{\mu}_{m,p}\rangle\end{aligned}\right\} \tag{35}$$

The Ω_p are the transition frequencies in the laboratory frame, eigenvalues of the Liouvillian $\hat{\hat{\mathcal{L}}}_0$. The range of p is from 1 to the dimension of the spin system Liouville space. For a system of n spin-$\frac{1}{2}$ nuclei, this would be 2^{2n}. Such a treatment is equivalent to expanding the spin operators in terms of a basis consisting of the eigenfunctions of the static Hamiltonian $\hat{\mathcal{H}}_0$, as is done in the usual Hilbert space development of the Redfield equation.[9,16] Using these relations, the equation of motion now becomes

$$\begin{aligned}\frac{\mathrm{d}|\hat{\sigma}(t)\rangle}{\mathrm{d}t} = -\frac{\mathrm{i}}{\hbar}\hat{\hat{\mathcal{L}}}_0|\hat{\sigma}(t)\rangle - \frac{1}{\hbar^2}\sum_{\mu}\sum_{\mu'}\xi_{\mu}\xi_{\mu'}\sum_{m=-l}^{l}\sum_{m'=-l'}^{l'}(-1)^{m+m'}\\ \times\int_0^{\infty}\mathrm{d}\tau\,\overline{F^{\mu}_{-m}(t)F^{\mu'}_{-m'}(t-\tau)}\\ \times\hat{\hat{\Gamma}}^{\mu}_{m}\sum_{p}\hat{\hat{\Gamma}}^{\mu'}_{m',p}\mathrm{e}^{-\mathrm{i}\Omega_p\tau}|\Delta\hat{\sigma}(t)\rangle\end{aligned} \tag{36}$$

This expansion uses the close relationship between a similarity transformation superoperator and the exponential of a commutation superoperator. The commutation superoperator of the isotropic spin system Hamiltonian is given by

$$\hat{\hat{\mathcal{L}}}_0 = \hat{\mathcal{H}}_0\otimes\hat{E} - \hat{E}\otimes\hat{\mathcal{H}}_0 \tag{37}$$

The similarity transformation superoperator will, in this instance, be given by

$$\begin{aligned}\hat{\hat{G}}|\hat{T}^{\mu}_{m}\rangle &= \exp\left(-\frac{\mathrm{i}}{\hbar}\hat{\mathcal{H}}_0 t\right)\otimes\exp\left(\frac{\mathrm{i}}{\hbar}\hat{\mathcal{H}}_0 t\right)|\hat{T}^{\mu}_{m}\rangle\\ &= \left|\exp\left(-\frac{\mathrm{i}}{\hbar}\hat{\mathcal{H}}_0 t\right)\hat{T}^{\mu}_{m}\exp\left(\frac{\mathrm{i}}{\hbar}\hat{\mathcal{H}}_0 t\right)\right\rangle = |\hat{T}'^{\mu}_{m}\rangle\end{aligned} \tag{38}$$

The two superoperators are related by

$$\hat{\hat{G}} = \exp\left(-\frac{\mathrm{i}}{\hbar}\hat{\hat{\mathcal{L}}}_0 t\right) \tag{39}$$

The exponential term in τ can now be grouped with the rest of the variables involving τ, and the desired separation of spin operators and τ-dependent lattice functions is thus achieved:

$$\begin{aligned}\frac{\mathrm{d}|\hat{\sigma}(t)\rangle}{\mathrm{d}t} = -\frac{\mathrm{i}}{\hbar}\hat{\hat{\mathcal{L}}}_0|\hat{\sigma}(t)\rangle - \frac{1}{\hbar^2}\sum_{\mu}\sum_{\mu'}\xi_{\mu}\xi_{\mu'}\sum_{m=-l}^{l}\sum_{m'=-l'}^{l'}(-1)^{m+m'}\\ \times\sum_{p}\hat{\hat{\Gamma}}^{\mu}_{m}\hat{\hat{\Gamma}}^{\mu'}_{m',p}\int_0^{\infty}\mathrm{d}\tau\,\overline{F^{\mu}_{-m}(t)F^{\mu'}_{-m'}(t-\tau)}\mathrm{e}^{-\mathrm{i}\Omega_p\tau}|\Delta\hat{\sigma}(t)\rangle\end{aligned} \tag{40}$$

The integral is defined as the spectral density function by

$$\mathcal{J}^{\mu\mu'}_{mm'}(\Omega) = \int_0^\infty \mathrm{d}\tau\ \overline{F^{\mu}_{-m}(t)F^{\mu'}_{-m'}(t-\tau)}\mathrm{e}^{-\mathrm{i}\Omega\tau} \qquad (41)$$

The spherical tensor properties of the $F^{\mu}_{-m}(t)$ guarantee that the integrand averaged over all orientations with equal probability will be nonzero only when $m' = -m$ and the result will be independent of m. Thus, one can write equation (41) in terms of a reduced spectral density $J^{\mu\mu'}$:

$$\mathcal{J}^{\mu\mu'}_{mm'}(\Omega) = (-1)^m \delta_{-mm'} J^{\mu\mu'}(\Omega) \qquad (42)$$

Furthermore, it is presumed that the lattice functions are stationary random variables, i.e., that the result of a time average does not depend on the time at which the averaging process is started, and we may set $t = 0$ in the integrand of equation (41). The reduced spectral density is then

$$J^{\mu\mu'}(\Omega) = \int_0^\infty \mathrm{d}\tau\ \overline{F^{\mu}_{-m}(0)F^{\mu'}_{m}(\tau)}\mathrm{e}^{-\mathrm{i}\Omega\tau} \qquad (43)$$

A detailed discussion of spectral densities and how they relate to the dynamical and geometrical parameters of the spin system is found in ***Relaxation of Coupled Spins from Rotational Diffusion***.

The relaxation superoperator is defined by

$$\hat{\hat{\Gamma}} = \sum_{\mu}\sum_{\mu'} \xi_\mu \xi_{\mu'} \sum_{m=-l}^{l} (-1)^m \sum_{p} \hat{\hat{\Gamma}}^{\mu}_{m} \hat{\hat{\Gamma}}^{\mu'}_{-m,p} J^{\mu\mu'}(\Omega_p) \qquad (44)$$

The equation of motion for the density superket may be written very compactly using these definitions:

$$\frac{\mathrm{d}|\hat{\sigma}(t)\rangle}{\mathrm{d}t} = -\frac{\mathrm{i}}{\hbar}\hat{\hat{\mathcal{L}}}_0|\hat{\sigma}(t)\rangle - \frac{1}{\hbar^2}\hat{\hat{\Gamma}}|\Delta\hat{\sigma}(t)\rangle \qquad (45)$$

The relaxation superoperator may be written as a sum of terms of the form

$$\hat{\hat{\Gamma}} = -\sum_{\mu}\sum_{\mu'} \hat{\hat{\Gamma}}^{\mu\mu'} \qquad (46)$$

with the individual terms defined by

$$\hat{\hat{\Gamma}}^{\mu\mu'} = \xi_\mu \xi_{\mu'} \sum_{m=-l}^{l} (-1)^m \sum_{p} \hat{\hat{\Gamma}}^{\mu}_{m} \hat{\hat{\Gamma}}^{\mu'}_{-m,p} J^{\mu\mu'}(\Omega_p) \qquad (47)$$

The $\hat{\hat{\Gamma}}^{\mu\mu'}$ terms express how the various interactions characterizing the spin system correlate with one another to produce relaxation. If $\mu = \mu'$, the relaxation is termed *autocorrelated*; otherwise, it is called *cross correlated*. This latter term must not be confused with *cross relaxation*, which is simply the flow of magnetization from one nucleus to another rather than from a nucleus to the lattice. Cross relaxation may involve either autocorrelated or cross-correlated relaxation mechanisms. This concept will be discussed further in Section 3.

2.7 The Rotating Frame

It is common practice in NMR to work in a rotating frame, or simultaneously in multiple rotating frames. One use of the rotating frame is to remove Zeeman contributions to the Hamiltonian by rotating about the field axis at or near the Larmor frequency of a spin. Although not of significance in rendering a formal solution to the Liouville equation in the case presented here, in numerical solutions of the equation of motion this avoids computational roundoff, which can occur in mixing frequencies on a megahertz scale (from the static magnetic field) with those on a hertz scale (from chemical shifts and scalar couplings).

Transformation into a rotating frame about the static magnetic field axis, the z axis, is accomplished using the rotation operator

$$\hat{R}_z(\theta) = \exp\left(-\frac{\mathrm{i}}{\hbar}\hat{F}_z\theta\right) \qquad (48)$$

In this case, the angle of rotation is written as $\theta = \Omega t$, where Ω is the angular frequency of the rotation. The form of the Liouville equation in the rotating frame is only a slight modification of that in the laboratory frame. In the frame rotating about the z axis at angular frequency Ω,

$$\frac{\mathrm{d}|\underline{\hat{\rho}}(t)\rangle}{\mathrm{d}t} = -\frac{\mathrm{i}}{\hbar}\left[\hat{\hat{\underline{\mathcal{L}}}}(t) + \hat{\hat{\Gamma}}_z(\Omega)\right]|\underline{\hat{\rho}}(t)\rangle \qquad (49)$$

The superoperator $\hat{\hat{\Gamma}}_z(\Omega)$ is formed as the commutator of $\Omega\hat{F}_z$. Superkets and superoperators in the rotating frame are indicated by an underscore and relate to the laboratory frame via the rotation superoperator

$$\hat{\hat{R}}_z(\Omega t) = \hat{R}_z(\Omega t) \otimes \hat{R}^*_z(\Omega t) \qquad (50)$$

The transformations have the form

$$\left.\begin{aligned} |\underline{\hat{O}}(t)\rangle &= \hat{\hat{R}}_z(\Omega t)|\hat{O}\rangle \\ \hat{\hat{\underline{\mathcal{L}}}}(t) &= \hat{\hat{R}}_z(\Omega t)\hat{\hat{\mathcal{L}}}\ \hat{\hat{R}}_z^{-1}(\Omega t) \end{aligned}\right\} \qquad (51)$$

That equations (49) and (7) are equivalent is shown by carrying out the differentiation as follows, making the indicated substitutions:

$$\begin{aligned} \frac{\mathrm{d}|\underline{\hat{\rho}}(t)\rangle}{\mathrm{d}t} &= \frac{\mathrm{d}}{\mathrm{d}t}\left[\ \hat{\hat{R}}_z(\Omega t)|\hat{\rho}(t)\rangle\right] \\ &= \frac{\mathrm{d}}{\mathrm{d}t}\left[\ \hat{\hat{R}}_z(\Omega t)\right]|\hat{\rho}(t)\rangle + \ \hat{\hat{R}}_z(\Omega t)\frac{\mathrm{d}|\hat{\rho}(t)\rangle}{\mathrm{d}t} \\ &= -\frac{\mathrm{i}}{\hbar}\hat{\hat{\Gamma}}_z(\Omega)\ \hat{\hat{R}}_z(\Omega t)|\hat{\rho}(t)\rangle + \ \hat{\hat{R}}_z(\Omega t)\frac{\mathrm{d}|\hat{\rho}(t)\rangle}{\mathrm{d}t} \\ &= -\frac{\mathrm{i}}{\hbar}\hat{\hat{\Gamma}}_z(\Omega)\ \hat{\hat{R}}_z(\Omega t)|\hat{\rho}(t)\rangle \\ &\quad -\frac{\mathrm{i}}{\hbar}\ \hat{\hat{R}}_z(\Omega t)\hat{\hat{\mathcal{L}}}\ \hat{\hat{R}}_z^{-1}(\Omega t)\ \hat{\hat{R}}_z(\Omega t)|\hat{\rho}(t)\rangle \\ &= -\frac{\mathrm{i}}{\hbar}\left[\ \hat{\hat{\underline{\mathcal{L}}}}(t) + \hat{\hat{\Gamma}}_z(\Omega)\right]|\underline{\hat{\rho}}(t)\rangle \end{aligned} \qquad (52)$$

From spherical tensor arguments, we know that the static Hamiltonian $\hat{\mathcal{H}}_0$ is isotropic and rotationally invariant. Thus, it is left unaffected by transformation into the rotating frame, as we might suspect since $[\hat{\mathcal{H}}_0, \hat{F}_z] = 0$, and from equation (30), we can write

$$\underline{\hat{\mathcal{H}}}_0 = \hat{\mathcal{H}}_0 = \sum_{i=1}^{n} \hbar\omega_i \hat{I}_{iz} + 2\pi\hbar \sum_{i=1}^{n} \sum_{j=1}^{i-1} J_{ij} \hat{\boldsymbol{I}}_i \cdot \hat{\boldsymbol{I}}_j \qquad (53)$$

The interaction Hamiltonian as given by equation (31) will become as follows in the rotating frame:

$$\hat{\mathcal{H}}_1(t) = \sum_{\mu} \xi_\mu \sum_{m=-l}^{l} (-1)^m \underline{\hat{T}}^{\mu}_{m} F^{\mu}_{-m}(t) \qquad (54)$$

The bath variables are functions of time in this semiclassical treatment, and are unaffected by the rotation operator, which acts only on spin operators.

The question now is how the solution of equation (49) differs from that already presented in the laboratory frame. The form of the rotating frame Liouville equation is very similar to that in the laboratory frame, and the approach to a solution is the same. We define an effective Hamiltonian according to

$$\hat{\mathcal{H}}_{\text{eff}} = \hat{\mathcal{H}}_0 + \Omega \hat{F}_z \qquad (55)$$

and transform into an interaction representation based on $\hat{\mathcal{H}}_{\text{eff}}$ rather than $\hat{\mathcal{H}}_0$ to remove the static components of the rotating frame Hamiltonian from our differential equation. It is of some interest to note that this particular $\hat{\mathcal{H}}_{\text{eff}}$ is time-independent both in the frame rotating about the z axis and in the laboratory frame. The new equation of motion has exactly the same form as equation (8), but all quantities have been transformed into the rotating frame:

$$\frac{\mathrm{d}|\underline{\hat{\rho}}'(t)\rangle}{\mathrm{d}t} = -\frac{\mathrm{i}}{\hbar}\, \underline{\hat{\mathcal{L}}}'_{\mathrm{I}}(t)|\underline{\hat{\rho}}'(t)\rangle \qquad (56)$$

We are still using a prime to signify the interaction representation. Equation (56) is the analog to equation (8), and a modified equation (9) is used to relate the interaction representation to the rotating frame:

$$|\underline{\hat{O}}'\rangle = \exp\left(\frac{\mathrm{i}}{\hbar}\hat{\hat{\mathcal{L}}}_{\text{eff}} t\right) \qquad (57)$$

The order in which one alters these reference frames can, in this instance, be switched, because $\hat{\mathcal{H}}_{\text{eff}}$ commutes with $\hat{R}_z$. That is to say, for the effective Hamiltonian of this treatment, the following relations hold:

$$\begin{aligned} |\underline{\hat{O}}'\rangle &= \exp\left(\frac{\mathrm{i}}{\hbar}\hat{\hat{\mathcal{L}}}_{\text{eff}} t\right)|\underline{\hat{O}}\rangle = \exp\left(\frac{\mathrm{i}}{\hbar}\hat{\hat{\mathcal{L}}}_{\text{eff}} t\right) \\ &\quad \times \exp\left(\frac{\mathrm{i}}{\hbar}\,\hat{\hat{F}}_z \Omega t\right)|\hat{O}\rangle \\ &= \exp\left(\frac{\mathrm{i}}{\hbar}\,\hat{\hat{F}}_z \Omega t\right)\exp\left(\frac{\mathrm{i}}{\hbar}\hat{\hat{\mathcal{L}}}_{\text{eff}} t\right)|\hat{O}\rangle \end{aligned} \qquad (58)$$

The steps taken towards the solution of equation (56) are virtually identical to the treatment performed in the laboratory frame, we simply write the analog to equation (34):

$$\begin{aligned} \frac{\mathrm{d}|\underline{\hat{\sigma}}\rangle}{\mathrm{d}t} &= -\frac{\mathrm{i}}{\hbar}\hat{\hat{\mathcal{L}}}_{\text{eff}}|\underline{\hat{\sigma}}\rangle - \frac{1}{\hbar^2}\sum_{\mu}\sum_{\mu'}\xi_\mu\xi_{\mu'}\sum_{m=-l}^{l}\sum_{m'=-l'}^{l'}(-1)^{m+m'}\hat{\underline{\Gamma}}^{\mu}_{m} \\ &\quad \times \int_0^\infty \mathrm{d}\tau\, \overline{F^{\mu}_{-m}(t)F^{\mu'}_{-m'}(t+\tau)} \\ &\quad \exp\left(-\frac{\mathrm{i}}{\hbar}\hat{\hat{\mathcal{L}}}_{\text{eff}}\tau\right)\hat{\underline{\Gamma}}^{\mu'}_{m'}\exp\left(\frac{\mathrm{i}}{\hbar}\hat{\hat{\mathcal{L}}}_{\text{eff}}\tau\right)|\Delta\hat{\sigma}\rangle \end{aligned} \qquad (59)$$

The difference is that now we perform the expansion in terms of eigenoperators of the effective Hamiltonian and note that these are still in the rotating frame. Analogs of equation (35) in this treatment are

$$\left.\begin{aligned} |\hat{\underline{T}}^{\mu}_{m}\rangle &= \sum_p |\hat{\underline{T}}^{\mu}_{m,p}\rangle \\ |\hat{\underline{T}}'^{\mu}_{m}(t)\rangle &= \exp\left(-\frac{\mathrm{i}}{\hbar}\hat{\hat{\mathcal{L}}}_{\text{eff}}\tau\right)|\hat{\underline{T}}^{\mu}_{m}\rangle \\ &= \sum_p \exp\left(-\frac{\mathrm{i}}{\hbar}\hat{\hat{\mathcal{L}}}_{\text{eff}}\tau\right)|\hat{\underline{T}}^{\mu}_{m,p}\rangle \\ &= \sum_p \mathrm{e}^{-\mathrm{i}\omega_p\tau}|\hat{\underline{T}}^{\mu}_{m,p}\rangle \end{aligned}\right\} \qquad (60)$$

This choice of representing the interaction Hamiltonian produces an important relationship between the spin operators and the commutator superoperator of $\hat{F}_z$:

$$\hat{\hat{F}}^{\mathrm{D}}_{z}|\hat{T}^{\mu}_{m}\rangle = m|\hat{T}^{\mu}_{m}\rangle \qquad (61)$$

Equation (59) then becomes

$$\begin{aligned} \frac{\mathrm{d}|\underline{\hat{\sigma}}(t)\rangle}{\mathrm{d}t} &= -\frac{\mathrm{i}}{\hbar}\hat{\hat{\mathcal{L}}}_{\text{eff}}|\underline{\hat{\sigma}}(t)\rangle - \frac{1}{\hbar^2}\sum_{\mu}\sum_{\mu'}\xi_\mu\xi_{\mu'}\sum_{m=-l}^{l}\sum_{m'=-l'}^{l'} \\ &\quad \times(-1)^{m+m'}\int_0^\infty \mathrm{d}\tau\, \overline{F^{\mu}_{-m}(t)F^{\mu'}_{-m'}(t+\tau)} \\ &\quad \times\hat{\underline{\Gamma}}^{\mu}_{m}\sum_p \mathrm{e}^{-\mathrm{i}m_p\omega_0\tau}\hat{\underline{\Gamma}}^{\mu'}_{m',p}\mathrm{e}^{\mathrm{i}\omega_p\tau}|\Delta\underline{\hat{\sigma}}(t)\rangle \end{aligned} \qquad (62)$$

In these equations, we are using ω_p for the transition frequencies associated with the effective Hamiltonian $\hat{\mathcal{H}}_{\text{eff}}$ in order to distinguish them from the transition frequencies Ω_p associated with the isotropic Hamiltonian $\hat{\mathcal{H}}_0$. Another, more common, viewpoint is that ω_p are the transition frequencies in the rotating frame whereas Ω_p are the transition frequencies in the laboratory frame.

When we transform the spin tensor superoperator components out of the rotating frame, the rotating frame frequencies disappear from the relaxation matrix in that the spectral densities are always evaluated at laboratory frame frequencies as

follows:

$$\frac{\mathrm{d}|\hat{\underline{\sigma}}(t)\rangle}{\mathrm{d}t} = -\frac{\mathrm{i}}{\hbar}\hat{\hat{\mathcal{L}}}_{\mathrm{eff}}|\hat{\underline{\sigma}}(t)\rangle - \frac{1}{\hbar^2}\sum_{\mu}\sum_{\mu'}\xi_\mu\xi_{\mu'}\sum_{m=-l}^{l}\sum_{m'=-l'}^{l'} \times(-1)^{m+m'}\int_0^\infty \mathrm{d}\tau\ \overline{F^{\mu}_{-m}(t)F^{\mu'}_{-m'}(t+\tau)} \times\hat{\hat{\Gamma}}^{\mu}_{m}\sum_{p}\mathrm{e}^{-\mathrm{i}m_p\Omega_0\tau}\hat{\hat{\Gamma}}^{\mu'}_{m',p}\mathrm{e}^{\mathrm{i}\omega_p\tau}|\Delta\hat{\underline{\sigma}}(t)\rangle \tag{63}$$

$$\frac{\mathrm{d}|\hat{\underline{\sigma}}(t)\rangle}{\mathrm{d}t} = -\frac{\mathrm{i}}{\hbar}\hat{\hat{\mathcal{L}}}_{\mathrm{eff}}|\hat{\underline{\sigma}}(t)\rangle - \frac{1}{\hbar^2}\sum_{\mu}\sum_{\mu'}\xi_\mu\xi_{\mu'}\sum_{m=-l}^{l}\sum_{m'=-l'}^{l'} \times(-1)^{m+m'}\int_0^\infty \mathrm{d}\tau\ \overline{F^{\mu}_{-m}(t)F^{\mu'}_{-m'}(t+\tau)} \times\hat{\hat{\Gamma}}^{\mu}_{m}\sum_{p}\hat{\hat{\Gamma}}^{\mu'}_{m',p}\mathrm{e}^{\mathrm{i}\Omega_p\tau}|\Delta\hat{\underline{\sigma}}(t)\rangle \tag{64}$$

The end result is that the relaxation matrix is unaffected by rotation about the z axis. The solution in the rotating frame—highly preferred over that in the laboratory frame in computation—is often used as is; i.e., no transformation is performed to place the density matrix back into the laboratory frame after the solution of $|\hat{\underline{\sigma}}(t)\rangle$ is obtained.

A word of caution is in order. Although the transformation into a single rotating frame about the static field axis does not affect the relaxation matrix, this is not true for a transformation into a multiple rotating frame. Multiple rotating frames are particularly useful in dealing with heteronuclear spin systems, but in such cases a secular approximation must be applied. Fortunately, the nonsecular terms will be oscillating at frequencies that are on the order of the difference between the isotope Larmor frequencies. For the vast majority of cases, these will be at least several megahertz at common field strengths. At low field strengths or in the event that two isotopes have very similar Larmor frequencies, only a single rotating frame can be used, but will typically suffice to place all transition frequencies on a reasonable scale for accurate computation.

3 RELAXATION MECHANISMS AND CROSS CORRELATION

We have shown that spin system relaxation is dictated by the superoperator $\hat{\hat{\Gamma}}$, and, according to equation (46), it is a sum over products of superoperators corresponding to the active interactions as indexed by symbols μ and μ'. Using this equation, we can proceed to formulate superoperators for individual relaxation mechanisms. To complete the formulation of $\hat{\hat{\Gamma}}$, it is only necessary to give explicit form to equation (31) for each of the relaxation mechanisms active in the spin system under study. In this section, such will be done for several of the mechanisms most frequently encountered in liquid samples.

3.1 Intramolecular Dipole–Dipole Coupling

Relaxation by dipolar interactions is the most commonly treated relaxation mechanism in NMR. As such, we shall begin our specific relaxation discussions with the dipolar interaction and the dipole–dipole relaxation mechanism. The dipolar Hamiltonian for a system of n spins is given by

$$\hat{\mathcal{H}}^{\mathrm{D}} = \sum_{i=2}^{n}\sum_{j=1}^{i-1}\xi^{\mathrm{D}}_{ij}\sum_{m=-2}^{2}(-1)^m F^{(2)}_{-m}(\mathrm{D},\theta_{ij},\phi_{ij})\hat{T}^{(2)}_{m} \times(\mathrm{D},i,j) \tag{65}$$

The index μ has been resolved into the label D and a sum over all pairs of spins in the system. The spherical polar coordinates (θ_{ij}, ϕ_{ij}) specify the orientation of the internuclear vector for each pair of spins relative to the laboratory fixed coordinate system, and are implicitly time-dependent through the rotational diffusion of the molecule. Only the $l = 2$ spherical tensor components contribute to this mechanism. The dipolar interaction is symmetric about the internuclear vector, so that only two orientational parameters are required. The two spins interact through space, so that it is immaterial whether they are proximate through chemical bonds or not. The dipolar interaction constant is given by

$$\xi^{\mathrm{D}}_{ij} = -2\sqrt{\frac{6\pi}{5}}\frac{\gamma_i\gamma_j}{r^3_{ij}} \tag{66}$$

The required rank-2 spatial functions are identical to the spherical harmonic functions as given by

$$\left.\begin{aligned} F^{(2)}_0(\mathrm{D},\theta_{ij},\phi_{ij}) &= Y^{(2)}_0(\theta_{ij},\phi_{ij}) \\ &= \sqrt{\frac{5}{16\pi}}(3\cos^2\theta_{ij}-1) \\ F^{(2)}_{\pm1}(\mathrm{D},\theta_{ij},\phi_{ij}) &= Y^{(2)}_{\pm1}(\theta_{ij},\phi_{ij}) \\ &= \mp\sqrt{\frac{15}{8\pi}}(\cos\theta_{ij}\sin\theta_{ij}\,\mathrm{e}^{\pm\mathrm{i}\phi_{ij}}) \\ F^{(2)}_{\pm2}(\mathrm{D},\theta_{ij},\phi_{ij}) &= Y^{(2)}_{\pm2}(\theta_{ij},\phi_{ij}) \\ &= \sqrt{\frac{15}{32\pi}}(\sin^2\theta_{ij}\,\mathrm{e}^{\pm2\mathrm{i}\phi_{ij}}) \end{aligned}\right\} \tag{67}$$

Since the molecule reorients in a liquid, these angles are time-dependent and contribute to the lattice spectral densities as described in Section 2.6.

The rank-2 spherical tensor operators are given by

$$\left.\begin{aligned} \hat{T}^{(2)}_0(\mathrm{D},i,j) &= \sqrt{\tfrac{1}{6}}(3\hat{I}_{iz}\hat{I}_{jz} - \hat{\boldsymbol{I}}_i\cdot\hat{\boldsymbol{I}}_j) \\ \hat{T}^{(2)}_{\pm1}(\mathrm{D},i,j) &= \mp\tfrac{1}{2}(\hat{I}_{i\pm}\hat{I}_{jz} + \hat{I}_{iz}\hat{I}_{j\pm}) \\ \hat{T}^{(2)}_{\pm2}(\mathrm{D},i,j) &= \tfrac{1}{2}\hat{I}_{i\pm}\hat{I}_{j\pm} \end{aligned}\right\} \tag{68}$$

For a system composed of two spins, both $I = \frac{1}{2}$, the spin operators take on the following matrix representations when

expressed in the product basis $\{|\alpha\alpha\rangle, |\alpha\beta\rangle, |\beta\alpha\rangle, |\beta\beta\rangle\}$:

$$\left.\begin{array}{c} \hat{T}_0^{(2)} \\ \frac{1}{2\sqrt{6}}\begin{bmatrix} 1 & 0 & 0 & 0 \\ 0 & -1 & -1 & 0 \\ 0 & -1 & -1 & 0 \\ 0 & 0 & 0 & 1 \end{bmatrix}, \end{array} \quad \begin{array}{c} \hat{T}_1^{(2)} = -(\hat{T}_{-1}^{(2)})^{\mathrm{T}} \\ \frac{1}{4}\begin{bmatrix} 0 & -1 & -1 & 0 \\ 0 & 0 & 0 & 1 \\ 0 & 0 & 0 & 1 \\ 0 & 0 & 0 & 0 \end{bmatrix} \end{array} \right\} \quad \begin{array}{c} \hat{T}_2^{(2)} = (\hat{T}_{-2}^{(2)})^{\mathrm{T}} \\ \frac{1}{2}\begin{bmatrix} 0 & 0 & 0 & 1 \\ 0 & 0 & 0 & 0 \\ 0 & 0 & 0 & 0 \\ 0 & 0 & 0 & 0 \end{bmatrix} \end{array} \right\} \tag{69}$$

The commutation superoperators required for equation (44) are formed from the spin tensor components as follows:

$$\hat{\hat{\Gamma}}_m^{\mathrm{D}ij} = \hat{T}_m^{(2)}(\mathrm{D}, i, j) \otimes \hat{E} - \hat{E} \otimes \hat{T}_m^{(2)}(\mathrm{D}, i, j) \tag{70}$$

The dipole–dipole contribution to relaxation is thus given by

$$\hat{\hat{\Gamma}}^{\mathrm{DD}} = \sum_{i=2}^{n}\sum_{j=1}^{i-1}\sum_{k=2}^{n}\sum_{l=1}^{k-1}\xi_{ij}^{\mathrm{D}}\xi_{kl}^{\mathrm{D}}\sum_{m=-2}^{2}(-1)^m \times \sum_{p}\hat{\hat{\Gamma}}_m^{\mathrm{D}ij}\hat{\hat{\Gamma}}_{-m,p}^{\mathrm{D}kl}J^{\mathrm{DD}ijkl}(\Omega_p) \tag{71}$$

3.2 Chemical Shielding Anisotropy

Another important interaction contributing to relaxation arises from the anisotropic part of the chemical shielding Hamiltonian (SA). Because the energies involved are dependent on the static magnetic field strength, this type of relaxation becomes more important as the spectrometer field strength increases. The Hamiltonian for shielding anisotropy is given by

$$\hat{\mathcal{H}}^{\mathrm{S}} = \sum_{i=1}^{n}\xi_i^{\mathrm{S}}\sum_{m=-2}^{2}(-1)^m F_{-m}^{(2)}(\mathrm{S}, \theta_i, \phi_i, \chi_i)\hat{T}_m^{(2)}(\mathrm{S}, i) \tag{72}$$

In this case, the index μ has been resolved into the label S and a sum over all the spins in the system. Only the $l = 2$ tensors are required. The set $\{\theta_i, \phi_i, \chi_i\}$ are the three Euler angles that orient the principal axes of a given shielding tensor into a common coordinate system according to

$$F_m^{(2)}(\mathrm{S}, \theta_i, \phi_i, \chi_i) = \sum_{m'=\pm 2}\mathcal{D}_{mm'}^{(2)}(\theta_i, \phi_i, \chi_i)F_{m'}^{(2)}(\mathrm{S}, \mathrm{PAS}_i) \tag{73}$$

If the shielding tensor is symmetric ($\eta = 0$) then the spherical harmonic is sufficient to describe the lattice fluctuations, and equation (73) reduces to

$$F_m^{(2)}(\mathrm{S}, \theta_i, \phi_i, \chi_i) = Y_m^{(2)}(\theta_i, \phi_i) \tag{74}$$

Here PAS is used to indicate the principal axis system in which the rank-2 irreducible tensor is diagonal, and $\mathcal{D}_{mm'}^{(2)}$ are the elements of the rank-2 Wigner rotation matrices. We have neglected the $l = 1$ component in equation (72) because it is very small in almost all cases. Although the isotropic component ($l = 0$) does not vanish for this interaction, as it does for the DD interaction in liquid systems, we have combined it with the Zeeman term in the Hamiltonian to produce the chemical shielding contribution to $\hat{\mathcal{H}}_0$, i.e., these contributions are absorbed into the ω_i of equation (30).

It is important to note that in the treatment of shielding anisotropy, the 'spin' tensors are actually 'spin–space' tensors in that they contain normalized components of the static magnetic field and are thus dependent upon its spatial orientation. Since this is stationary and oriented along the z axis in the laboratory frame, it is of no concern to the theory presented. However, using this type of formulation, one cannot rotate this tensor in spin space, as conceivably could be done for the dipolar Hamiltonian spin tensor. The shielding interaction constant, spatial functions, and 'spin–space' tensor components are given below, the latter having field components that stem from a normalized field vector $\boldsymbol{B}_{\mathrm{n}} = \boldsymbol{B}_0/|\boldsymbol{B}_0| = \boldsymbol{B}_0/B_0$. The interaction constants are given by

$$\xi_i^{\mathrm{S}} = \sqrt{\frac{6\pi}{5}}\nu_i B_0 \delta_{zz}(i) = \sqrt{\frac{6\pi}{5}}\frac{\gamma_i}{\gamma_{\mathrm{H}}}\Omega_{\mathrm{spec}}\delta_{zz}(i) \tag{75}$$

The SA tensor functions in the PAS are given by

$$\left.\begin{aligned} F_0^{(2)}(\mathrm{S}, \mathrm{PAS}) &= \sqrt{\frac{5}{4\pi}} \\ F_{\pm 1}^{(2)}(\mathrm{S}, \mathrm{PAS}) &= 0 \\ F_{\pm 2}^{(2)}(\mathrm{S}, \mathrm{PAS}) &= \sqrt{\frac{5}{24\pi}}\eta \end{aligned}\right\} \tag{76}$$

The spherical tensor operators are given by

$$\left.\begin{aligned} \hat{T}_0^{(2)}(\mathrm{S}, i) &= \sqrt{\tfrac{1}{6}}(3\hat{I}_{iz}B_z - \hat{\boldsymbol{I}}_i \cdot \boldsymbol{B}_n) \\ \hat{T}_{\pm 1}^{(2)}(\mathrm{S}, i) &= \mp\tfrac{1}{2}(\hat{I}_{i\pm}B_z + \hat{I}_{iz}B_{\pm}) \\ \hat{T}_{\pm 2}^{(2)}(\mathrm{S}, i) &= \tfrac{1}{2}\hat{I}_{i\pm}B_{\pm} \end{aligned}\right\} \tag{77}$$

For a treatment of a single spin-$\frac{1}{2}$ particle, the rank-2 shielding 'spin–space' tensor components take on the following matrix forms when expressed in the standard spin basis $\{|\alpha\rangle, |\beta\rangle\}$ in the laboratory frame, with the field axis along $+z$:

$$\begin{array}{ccccc} \hat{T}_0^{(2)} & & \hat{T}_1^{(2)} = [\hat{T}_{-1}^{(2)}]^{\mathrm{T}} & & \hat{T}_2^{(2)} = [\hat{T}_{-2}^{(2)}]^{\mathrm{T}} \\ \frac{1}{\sqrt{6}}\begin{bmatrix} 1 & 0 \\ 0 & -1 \end{bmatrix}, & & -\frac{1}{2}\begin{bmatrix} 0 & 1 \\ 0 & 0 \end{bmatrix}, & & \begin{bmatrix} 0 & 0 \\ 0 & 0 \end{bmatrix} \end{array} \tag{78}$$

Although the shielding Hamiltonian is of rank 2, the $m = 2$ component disappears, and the shift anisotropy–shift anisotropy contribution to relaxation is thus given by

$$\hat{\hat{\Gamma}}^{\mathrm{SS}} = \sum_{i=1}^{n}\sum_{j=1}^{n}\xi_i^{\mathrm{S}}\xi_j^{\mathrm{S}}\sum_{m=-1}^{1}(-1)^m\sum_{p}\hat{\hat{\Gamma}}_m^{\mathrm{S}i}\hat{\hat{\Gamma}}_{-m,p}^{\mathrm{S}j}J^{\mathrm{SS}ij}(\Omega_p) \tag{79}$$

The $\hat{\hat{\Gamma}}_m^{\mathrm{S}i}$ are commutation superoperators are formed from the spin tensor component for spin i according to

$$\hat{\hat{\Gamma}}_m^{\mathrm{S}i} = \hat{T}_m^{(2)}(\mathrm{S}, i) \otimes \hat{E} - \hat{E} \otimes \hat{T}_m^{(2)}(\mathrm{S}, i) \tag{80}$$

3.3 Quadrupolar Interactions

Spins having spin angular momentum quantum numbers larger than $\frac{1}{2}$, $I \geq 1$, may possess an appreciable electric quadrupole moment, which can provide important relaxation mechanisms. The Hamiltonian for quadrupolar interactions is given by

$$\hat{\mathcal{H}}^{\mathrm{Q}} = \sum_{i=1}^{n} \xi_i^{\mathrm{Q}} \sum_{m=-2}^{2} (-1)^m F_{-m}^{(2)}(\mathrm{Q}, \theta_i, \phi_i, \chi_i) \hat{T}_m^{(2)}(\mathrm{Q}, i) \quad (81)$$

As for the Q mechanism, the index μ has been resolved into the label Q and a sum over all the spins in the system. Only the $l = 2$ tensors are required. The set $\{\theta_i, \phi_i, \chi_i\}$ are the three Euler angles that orient the principal axes of the quadrupolar tensor into a common coordinate system according to

$$F_m^{(2)}(\mathrm{Q}, \theta_i, \phi_i, \chi_i) = \sum_{m=\pm 2} \mathcal{D}_{mm'}^{(2)}(\theta_i, \phi_i, \chi_i) F_{m'}^{(2)}(\mathrm{Q}, \mathrm{PAS}_i) \quad (82)$$

When the quadrupolar tensor is symmetric ($\eta = 0$), the spherical harmonic is sufficient to describe the lattice fluctuations and equation (82) reduces to

$$F_m^{(2)}(\mathrm{Q}, \theta_i, \phi_i, \chi_i) = Y_m^{(2)}(\theta_i, \phi_i) \quad (83)$$

As for the shielding Hamiltonian, three angles are necessary for specification of the spatial tensor orientation. For an axially symmetric quadrupolar tensor, $\eta = 0$, only two angles are necessary, and in that case the spatial functions are equivalent to the rank-2 spherical harmonics given for the dipolar interaction. The quadrupolar interaction constants are given by

$$\begin{aligned} \xi_i^{\mathrm{Q}} &= \hbar \sqrt{\frac{6\pi}{5}} \frac{\delta_{zz}(i)}{2I_i(2I_i - 1)} = \hbar \sqrt{\frac{6\pi}{5}} \frac{\mathrm{QCC}_i}{2I_i(2I_i - 1)} \\ &= \hbar \sqrt{\frac{6\pi}{5}} \frac{2\pi \nu_i^{\mathrm{Q}}}{2I_i(2I_i - 1)} \end{aligned} \quad (84)$$

where QCC is the quadrupolar coupling constant. The lattice interaction functions are given by

$$\left.\begin{aligned} F_0^{(2)}(\mathrm{PAS}) &= \sqrt{\frac{5}{4\pi}} \\ F_{\pm}^{(2)}(\mathrm{PAS}) &= 0 \\ F_{\pm 2}^{(2)}(\mathrm{PAS}) &= \sqrt{\frac{5}{24\pi}} \eta \end{aligned}\right\} \quad (85)$$

The spherical tensor operators are given by

$$\left.\begin{aligned} \hat{T}_0^{(2)}(\mathrm{Q}, i) &= \sqrt{\tfrac{1}{6}}(3\hat{I}_{iz}^2 - \hat{\boldsymbol{I}}_i^2) \\ \hat{T}_{\pm 1}^{(2)}(\mathrm{Q}, i) &= \mp \tfrac{1}{2}(\hat{I}_{i\pm}\hat{I}_{iz} + \hat{I}_{iz}\hat{I}_{i\pm}) \\ \hat{T}_{\pm 2}^{(2)}(\mathrm{Q}, i) &= \tfrac{1}{2}\hat{I}_{i\pm}^2 \end{aligned}\right\} \quad (86)$$

For treatment of a spin-1 particle, the rank-2 quadrupolar spin tensor components are expressed in their matrix form as

$$\begin{matrix} \hat{T}_0^{(2)} & \hat{T}_1^{(2)} = [\hat{T}_{-1}^{(2)}]^{\mathrm{T}} & \hat{T}_2^{(2)} = [\hat{T}_{-2}^{(2)}]^{\mathrm{T}} \end{matrix}$$

$$\frac{1}{\sqrt{6}} \begin{bmatrix} 1 & 0 & 0 \\ 0 & -2 & 0 \\ 0 & 0 & 1 \end{bmatrix}, \quad \frac{1}{\sqrt{2}} \begin{bmatrix} 0 & -1 & 0 \\ 0 & 0 & 1 \\ 0 & 0 & 0 \end{bmatrix}, \quad \begin{bmatrix} 0 & 0 & 1 \\ 0 & 0 & 0 \\ 0 & 0 & 0 \end{bmatrix} \quad (87)$$

The spin index is implicit and the matrices are in the standard single spin basis $\{|\alpha\rangle, |\beta\rangle, |\gamma\rangle\}$. The quadrupole–quadrupole contribution to relaxation is thus given by

$$\hat{\hat{\Gamma}}^{\mathrm{QQ}} = \sum_{i=1}^{n} \sum_{j=1}^{n} \xi_i^{\mathrm{Q}} \xi_j^{\mathrm{Q}} \sum_{m=-2}^{2} (-1)^m \sum_{p} \hat{\hat{\Gamma}}_m^{\mathrm{Q}i} \hat{\hat{\Gamma}}_{-m,p}^{\mathrm{Q}j} J^{\mathrm{QQ}ij}(\Omega_p) \quad (88)$$

The superoperator $\hat{\hat{\Gamma}}_m^{\mathrm{Q}i}$ is formed from the spin tensor operators as follows:

$$\hat{\hat{\Gamma}}_m^{\mathrm{Q}i} = \hat{T}_m^{(2)}(\mathrm{Q}, i) \otimes \hat{E} - \hat{E} \otimes \hat{T}_m^{(2)}(\mathrm{Q}, i) \quad (89)$$

3.4 External Random Fields

Relaxation by random fields is often used as a 'catch-all' in order to account for relaxation that cannot be attributed to other relaxation mechanisms. The origin of the random fields is not precisely specified. They could, for example, arise from DD interactions with paramagnetic species or nuclear spins of solvent molecules. Consider a random field at spin i given by $\boldsymbol{B}(\mathrm{R}, i, t)$. The time average of the field must be zero, since all constant terms have been absorbed into the static Hamiltonian. However, the time-averaged amplitude of the field irrespective of its direction is nonzero, and this quantity $\boldsymbol{B}(\mathrm{R}, i) = \overline{|\boldsymbol{B}(\mathrm{R}, i, t)|}$ will define the interaction strength according to

$$\xi_i^{\mathrm{R}} = \gamma_i B(\mathrm{R}, i) \quad (90)$$

A normalized random field with unit time-averaged amplitude can now be defined as follows:

$$\boldsymbol{b}(\mathrm{R}, i, t) = \frac{\boldsymbol{B}(\mathrm{R}, i, t)}{B(\mathrm{R}, i)} \quad (91)$$

The spherical components of this vector are

$$\left.\begin{aligned} b_0^{(1)}(\mathrm{R}, i, t) &= b_z(\mathrm{R}, i, t) \\ b_{\pm 1}^{(1)}(\mathrm{R}, i, t) &= \mp \sqrt{\tfrac{1}{2}} b_{\pm}(\mathrm{R}, i, t) \end{aligned}\right\} \quad (92)$$

These spherical components of the normalized random field may be identified with the lattice fluctuation functions as follows, and expressed in terms of the spherical harmonics and the time-dependent norm of the scaled random field:

$$F_m^{(1)}(\mathrm{R}, i, t) = b_m^{(1)}(\mathrm{R}, i, t) = |\boldsymbol{b}(\mathrm{R}, i, t)| Y_m^{(1)}(\theta_i, \phi_i) \quad (93)$$

In contrast to the other interactions we have discussed, all of which have constant amplitude but random orientation, the random field interaction must be assumed to vary randomly in both orientation and amplitude. All the time dependence of the lattice functions then cannot be vested in the spherical harmonics. The Hamiltonian for the random field interaction is

$$\hat{\mathcal{H}}^{\mathrm{R}} = \sum_{i=1}^{n} \xi_i^{\mathrm{R}} \sum_{m=-1}^{1} (-1)^m F_{-m}^{(1)}(\mathrm{R}, i, t) \hat{T}_m^{(1)}(\mathrm{R}, i) \quad (94)$$

The spherical tensor operators are given by

$$\left.\begin{aligned}\hat{T}_0^{(1)}(\mathrm{R},i) &= \hat{I}_{iz}\\ \hat{T}_{\pm1}^{(1)}(\mathrm{R},i) &= \mp\sqrt{\tfrac{1}{2}}\hat{I}_{i\pm}\end{aligned}\right\} \tag{95}$$

For a single spin-$\frac{1}{2}$ particle, the random field spin tensor components are

$$\begin{matrix}\hat{T}_0^{(1)} & \hat{T}_1^{(1)} = -[\hat{T}_{-1}^{(1)}]^{\mathrm{T}}\\ \frac{1}{2}\begin{bmatrix}1 & 0\\ 0 & -1\end{bmatrix}, & \frac{1}{\sqrt{2}}\begin{bmatrix}0 & 0\\ 1 & 0\end{bmatrix}\end{matrix} \tag{96}$$

The random field–random field contribution to relaxation is thus given by

$$\hat{\hat{\Gamma}}^{\mathrm{RR}} = \sum_{i=1}^{n}\sum_{j=1}^{n}\xi_i^{\mathrm{R}}\xi_j^{\mathrm{R}}\sum_{m=-1}^{1}(-1)^m\sum_{p}\hat{\hat{\Gamma}}_m^{\mathrm{R}i}\hat{\hat{\Gamma}}_{-m,p}^{\mathrm{R}j} J^{\mathrm{RR}ij}(\Omega_p) \tag{97}$$

3.5 Cross Correlation Effects

According to equation (47), the relaxation matrix is a sum of terms, each of which involves two interactions. The index μ implicitly contains a spin or spin pair index, the type of interaction, and the interaction rank. Since there is no restriction on the double sum, there are a great many terms involving different spins or spin pairs and different mechanisms. If the value of any of the indices associated with μ' is different from that associated with μ, the term is referred to as a cross-correlation term. Such terms can involve two different spins or spin pairs of the same mechanism, or two different mechanisms. Some of these terms are zero because the interactions involved are not correlated, so the time average over the product of lattice functions yields zero, but many of them are not negligible and contribute dramatically to relaxation, as will be demonstrated in Section 4. Consider the DD mechanism with three or more spins in the system of interest as shown in equation (71). If $i \neq k$ or $j \neq l$ (both of these inequalities can hold if there are four or more spins) then we have an example of cross correlation. Interactions of different ranks will never correlate, but dipolar and shielding anisotropy interactions are both of rank-2, and cross terms like the following will occur in addition to those enumerated previously:

$$\left.\begin{aligned}\hat{\hat{\Gamma}}^{\mathrm{DS}} &= \sum_{i=2}^{n}\sum_{j=1}^{i-1}\sum_{k=1}^{n}\xi_{ij}^{\mathrm{D}}\xi_k^{\mathrm{S}}\sum_{m=-2}^{2}(-1)^m \times\sum_{p}\hat{\hat{\Gamma}}_m^{\mathrm{D}ij}\hat{\hat{\Gamma}}_{-m,p}^{\mathrm{S}k}J^{\mathrm{DS}ijk}(\Omega_p)\\ \hat{\hat{\Gamma}}^{\mathrm{SD}} &= \sum_{i=1}^{n}\sum_{j=2}^{n}\sum_{k=1}^{j-1}\xi_i^{\mathrm{S}}\xi_{jk}^{\mathrm{D}}\sum_{m=-2}^{2}(-1)^m \times\sum_{p}\hat{\hat{\Gamma}}_m^{\mathrm{S}i}\hat{\hat{\Gamma}}_{-m,p}^{\mathrm{D}jk}J^{\mathrm{SD}ijk}(\Omega_p)\end{aligned}\right\} \tag{98}$$

Some simulations showing the effects of cross correlation may be found in Sections 4.2 and 4.4.

4 SOME EXAMPLES

Now that the mathematical tools needed are at our disposal and several relaxation mechanisms have been presented, we can explore their effects using some simple spin systems as examples. This will be done by means of simulations using the GAMMA magnetic resonance simulation platform[5] so that the various mechanisms can be turned on and off or adjusted at will to illustrate their effects. Most of our attention will be focused on longitudinal relaxation, though some transverse effects will be noted. In addition, the influence of molecular motion and geometry on the results of our 'experiments' will be examined. A growing body of experimental results[4] indicates that the theoretical framework developed above predicts the results of experiments very accurately. Thus, we can proceed with some confidence to predict the results of experiments, though they may not yet be in the literature. The complexity of the relationship between these geometrical and dynamical parameters is such that it is clearly impossible to explore every variable fully here, but selected examples will be used to exhibit the sensitivity of experimental results to various physical parameters.

4.1 Coupled Relaxation Experiments: The AX Spin System

In this section, several experiments will be described that are used for studying longitudinal relaxation in coupled spin systems. Examples of their application to a $^{13}\mathrm{C}-^{1}\mathrm{H}$ (AX) spin system will be given. Many of the basic principles of coupled relaxation can be illustrated using only this simple spin system. Some other pair of heteronuclei or a homonuclear spin system could be treated equally well.

The return to thermal equilibrium of magnetization that has been perturbed is governed by equation (45). Experiments to study spin relaxation normally consist of

1. preparing the spin system in a nonequilibrium state using rf pulses;
2. allowing the magnetization to relax for a period of time t_1;
3. projecting the magnetization of interest onto the observable single quantum coherences, again using rf pulses;
4. observing the resulting FID as a function of the time t_2;
5. Fourier transforming the FID to obtain a spectrum exhibiting the partially relaxed magnitudes of the various magnetizations.

This procedure is repeated for various values of t_1 and for various preparations of the nonequilibrium state until a sufficient body of data has been accumulated to elucidate all desired aspects of the relaxation of the system under study. Generally, one acquires enough data to overdetermine the relaxation, and then utilizes nonlinear least-squares fitting techniques to extract the values of the physical parameters of interest from the experimental data. Using the theory given above as implemented in the GAMMA platform, one can numerically simulate all of these steps. To exhibit all aspects of the relaxation behavior, it is generally necessary to perform several experiments, preparing the spin system in various ways. In each case, the relaxation during the evolution time t_1 is governed by equation (45), but the initial condition for the differential equation (i.e., the density operator at the start of the evolution period) is different in each case. Several

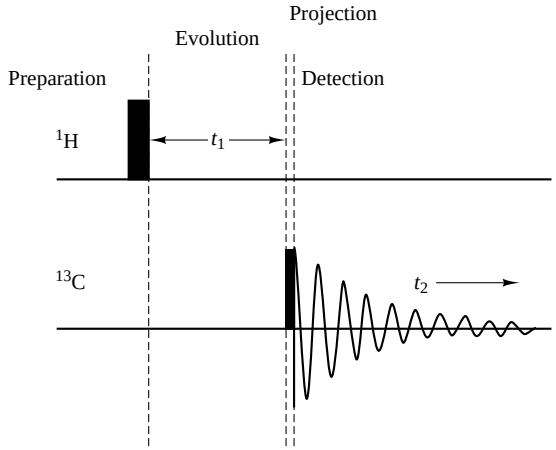

Figure 2 The proton hard pulse experiment used to create Figure 1. The wide pulse is a π pulse; the narrow one is a $\frac{1}{2}\pi$ pulse

such experiments are described below. More experimental details can be found in the review by Grant et al.[4] We shall confine ourselves to exploring the effects of several relaxation mechanisms on some simple spin systems to illustrate the kinds of physical parameters to which spin relaxation is sensitive. Using the $^{13}C-^{1}H$ (AX) spin system as a simple example, several typical experiments for studying coupled relaxation will be presented.

4.1.1 Nonselective Inversion: Hard Pulse

In the introduction (Section 1.3) the concept of cross relaxation due to dipolar coupling between the spins was introduced, and was illustrated in Figure 1. Figure 2 shows the proton hard pulse or nonselective inversion procedure used to create the simulations in Figure 1. This experiment illustrates many of the features of coupled relaxation and many of the effects of the various relaxation mechanisms. The protocol of the experiment is as follows:

1. Preparation: the system is started at thermal equilibrium, then a nonselective π pulse is applied at the proton resonance frequency. All the proton magnetization is now aligned along the negative z axis; the carbon magnetization remains at thermal equilibrium.
2. Evolution: the system is allowed to evolve for a time t_1. The proton magnetization returns toward thermal equilibrium, with cross relaxation to the carbon.
3. Projection: a $\frac{1}{2}\pi$ pulse is applied at the carbon resonance frequency to project the z components of the carbon magnetization onto the carbon single quantum coherences.
4. Detection: the carbon FID is digitized.
5. The FID is Fourier transformed.

A series of values of t_1 was chosen and the procedure repeated for each value. The resulting spectra are shown in Figure 1. The ^{1}H spectra shown there were obtained by shifting the projection and observation steps to the proton frequency. Note that the two lines in each doublet evolve identically; this leads naturally to the idea of magnetization modes. More on this subject can be found in ***Relaxation Mechanisms: Magnetization Modes***. It is generally more convenient and instructive to plot linear combinations of peak intensities corresponding to these magnetization modes. In Figure 1 note that the four lines have been designated as C1, C2, H1, and H2. The magnetization modes for this AX system are

$$\left.\begin{aligned} M_{\mathrm{C}} &= M_{\mathrm{C1}} + M_{\mathrm{C2}} \\ M_{\mathrm{H}} &= M_{\mathrm{H1}} + M_{\mathrm{H2}} \\ M_{\Delta} &= M_{\mathrm{C1}} - M_{\mathrm{C2}} = M_{\mathrm{H1}} - M_{\mathrm{H2}} \\ M_{\mathrm{T}} &= \text{sum over all state populations} \end{aligned}\right\} \tag{99}$$

The M_{T} mode is just the sum of the populations of all the states, which is assumed to be constant, since the number of spins in the sample is constant. This corresponds to using the irreducible spherical tensor operators for two nonidentical spins as basis operators. The procedure for generating these operators is discussed in detail by Wang and Grant.[17] Figure 3 shows the effect of several relaxation mechanisms on the spin system of Figure 1. The dotted line shows evolution under DD relaxation alone; random field effects have been turned off. The system relaxes much more slowly than shown in Figure 1. The addition of SA relaxation results in evolution as shown by the light line. To this point, M_{Δ} has not been perturbed at all. However, when cross correlation between DD and SA (see Section 3.5) is added, the evolution shown by the heavy lines results. Thus, only the DD–SA cross correlation relaxation couples M_{Δ} to the other modes. Figure 4 shows expanded views of the lines of the doublet at thermal equilibrium for these same cases. When DD–SA relaxation is considered, the two linewidths, i.e., the T_2 values of the lines, are no longer equal, and the doublet is not symmetric. In this case, lineheights may not be used to follow the evolution of the magnetization modes, but integrated intensities must be used. This has been done in Figure 3.

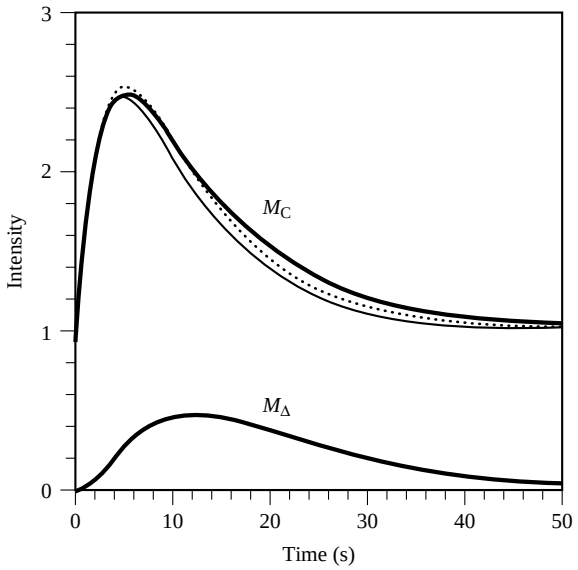

Figure 3 Magnetization mode evolution plots showing the effect on a $^{13}C-^{1}H$ spin system of DD relaxation (dotted line), the addition of SA on the ^{13}C of 100 ppm (light line), and finally with cross correlation between DD and SA (heavy lines). The spin system is as in Figure 1. The shielding tensor is axially symmetric, with the unique axis along the internuclear vector. A hard pulse perturbation as in Figure 2 is used. There is no random field relaxation. The M_{Δ} mode is shown only for the last case, since it is always zero in the first two cases

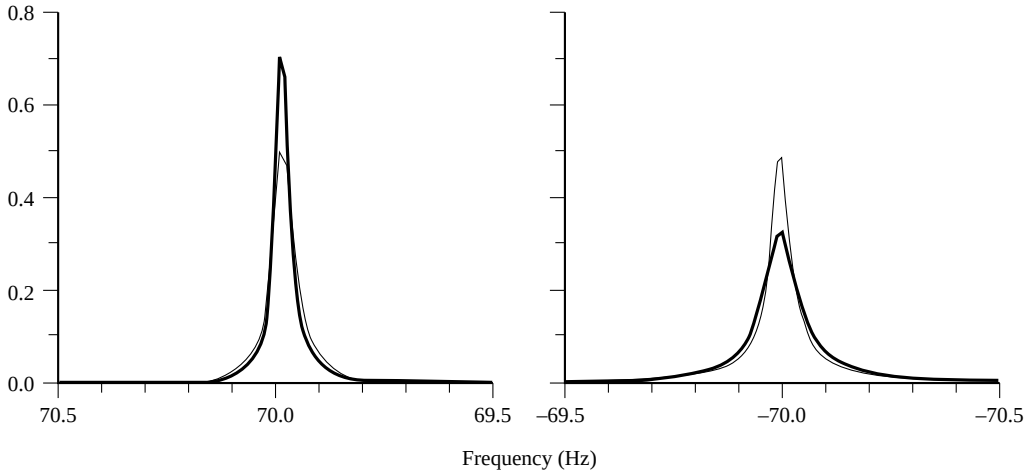

Figure 4 Expanded plots showing thermal equilibrium ^{13}C spectra from the data set of Figure 3. The light line shows only DD relaxation, while the heavy line includes DD–SA cross correlation. The doublet remains symmetric for DD relaxation, but addition of DD–SA cross correlation affects T_2 differentially for the two transitions, yielding an unsymmetrical doublet

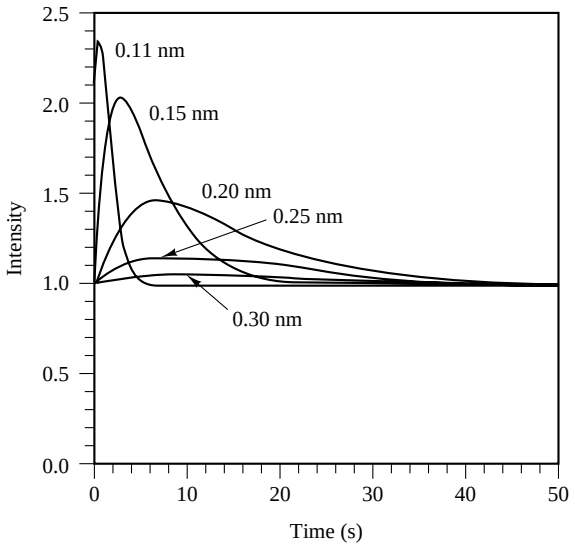

Figure 5 The effect of internuclear distance on DD cross relaxation from M_H to M_C. Random field relaxation of T_1 = 10 s is also present for both ^{13}C and ^{1}H. All other aspects of the experiment are the same as for Figure 1

In Figure 1, relaxation following a π ^{1}H pulse has already been illustrated for a nominal bond distance of 0.109 nm. The DD relaxation mechanism depends on the inverse sixth power of the internuclear separation. Suppose, now, that the proton is more remote. Figure 5 shows a plot of M_C as a function of the proton carbon distance from 0.11 to 0.30 nm. The random field mechanism has been set for a T_1 of 10 s. The internuclear distance has a dramatic effect on the cross relaxation, and one would expect to be able to measure distances quite accurately by studying cross relaxation. However, the rotational diffusion correlation time has a similar effect, as shown in Figure 6. It is only possible to determine the ratio of these two quantities. In a large molecule where a number of internuclear distances are sought, it is often possible to determine at least one internuclear distance a priori, for example, by assuming that one C–H bond has its usual value for similar hybridization of the carbon; then all other internuclear distances can be calculated. This calculation presumes that nuclei involved all reorient at the same rate, i.e., that the molecule is rigid. As the internuclear distance is increased, the DD mechanism weakens rapidly, but, even at 0.3 nm, the DD mechanism is still evident in that it produces cross relaxation. It is not the weakening of the DD mechanism that imposes this limit, but rather that it becomes weak compared to the combined effect of all other mechanisms.

So far, we have assumed that the molecule under study undergoes rotational diffusion as a spherical top, and the orientation of the internuclear vector with respect to some molecule-fixed coordinate system is irrelevant. If the molecule is diffusing as a symmetric top, this is no longer the case. Let the molecule-fixed coordinate system be that which diagonalizes the rotational diffusion tensor. Then Figure 7 shows the dependence of M_C on the angle θ between the

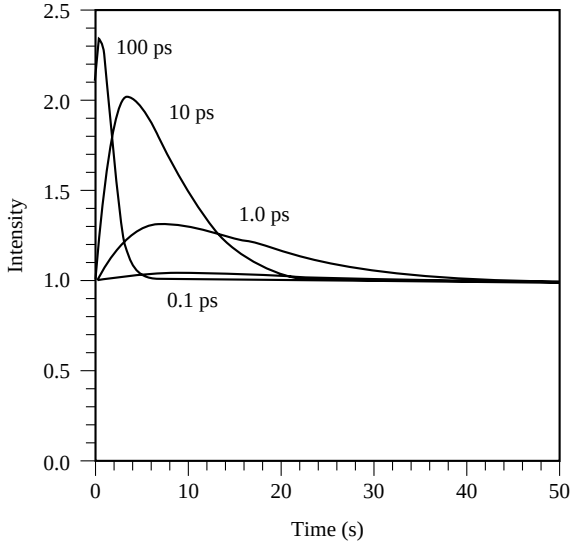

Figure 6 The effect of rotational correlation time on cross relaxation. A random field relaxation of T_1 = 10 s is present for both ^{13}C and ^{1}H. All other aspects of the experiment are the same as for Figure 5

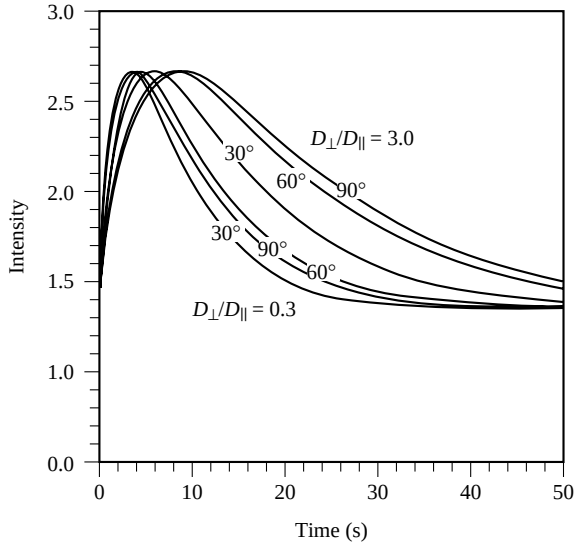

Figure 7 The effect of motional anisotropy on cross relaxation from M_H to M_C for various angles between the internuclear vector and the unique axis of the rotational diffusion tensor. Curves are given for an oblate and a prolate top as shown. All other aspects of the experiment are the same as for Figure 1

unique axis of the top and the internuclear vector for motional anisotropies $D_\perp/D_\parallel$ of 0.3 and 3.0. To effect DD relaxation, molecular motion must change the direction of the internuclear vector. Thus, if the C–H vector is oriented parallel to the direction of $D_\parallel$ then changing the value of $D_\parallel$ has no effect on the relaxation. In Figure 7, $D_\perp$ has been kept constant as in Figure 1, and $D_\parallel$ has been altered to produce the anisotropies.

4.1.2 Inversion–Recovery

Figure 8 illustrates the inversion–recovery experiment. This procedure is identical to that commonly used for measuring ^{13}C T_1 values under ^1H decoupling, but here no decoupling is applied. The protocol for the experiment is as follows:

1. Preparation: the system is started at thermal equilibrium; then a π pulse is applied at the carbon resonance frequency. All the carbon magnetization is now aligned along the negative z axis; the proton magnetization remains at thermal equilibrium.
2. Evolution: the system is allowed to evolve for a time t_1. The carbon magnetization returns to thermal equilibrium, with cross relaxation to the protons.
3. Projection: a $\frac{1}{2}\pi$ pulse is applied at the carbon resonance frequency to project the z components of the carbon magnetization onto the carbon single quantum coherences.
4. Detection: the carbon FID is digitized.
5. The FID is Fourier transformed.

Figure 9 shows the resulting simulated spectra for the AX spin system as in Figure 1. As before, the ^1H spectra shown in Figure 9 were obtained by shifting the projection and observation steps to the proton frequency. Note that magnetization flows from the ^{13}C to the ^1H in this case—the reverse of what was observed in Figure 1. For this simulation, only DD relaxation was used, to accentuate the effects of cross relaxation; thus, the relaxation times are substantially longer. Figure 10 shows a plot of M_C taken from the spectra of

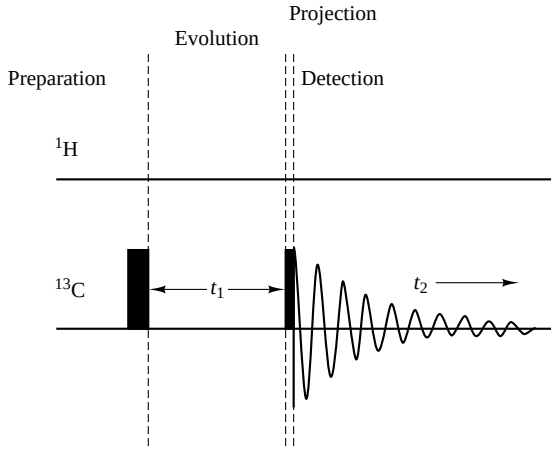

Figure 8 The inversion–recovery experiment. The wide pulse is a π pulse; the narrow one is a $\frac{1}{2}\pi$ pulse

Figure 9. The dotted line shows a single exponential with the T_1 adjusted to best fit the actual evolution. The nonexponential behavior indicates that the ^{13}C magnetization is perturbed by the presence of the ^1H, i.e., by cross relaxation to the protons. The departure is slight, and might be overlooked in a real experiment unless careful studies were done with high S/N data. Thus, the hard pulse experiment of the previous section is a much more sensitive measure of the effects of cross relaxation. Again, the M_Δ mode is unperturbed.

4.1.3 Selective Inversion: Polarization Transfer

There are several variations of the selective inversion or soft pulse experiment, depending on which of the spectral lines are to be inverted and the method to be used for inversion. A simple low-power 'soft' rectangular pulse or a shaped pulse can be used to invert a single line. One member of a doublet can be inverted by adjusting the pulse amplitude so that the on-resonance peak experiences a π nutation while the off-resonance one experiences an effective field producing a 2π precession and is thus unchanged. These methods have been used before the advent of modern spectrometers with sufficient phase agility to accomplish polarization transfer or INEPT-type procedures such as the one described in Figure 11. This latter procedure is now the preferable one in most cases. It proceeds as follows:

1. Preparation: the system is started at thermal equilibrium; then a proton $(\frac{1}{2}\pi)_x$ pulse is applied to orient the two members of the proton doublet along the y axis. Precession due to scalar coupling for a period of $\frac{1}{2}J$ produces antiphase proton magnetization along the x axis that is then rotated back onto the z axis with a $(\frac{1}{2}\pi)_y$ pulse. The simultaneous π pulses in the center of the preparation period cause the evolution due to chemical shift to refocus, but do not affect the evolution due to scalar coupling. The carbon thermal equilibrium magnetization is inverted by the π pulse, and to this is added the antiphase magnetization generated in the proton domain. This yields a $1.5 : -2.5$ doublet intensity ratio.
2. Evolution: the system is allowed to evolve for a time t_1. Both the carbon and proton magnetizations return toward thermal equilibrium.

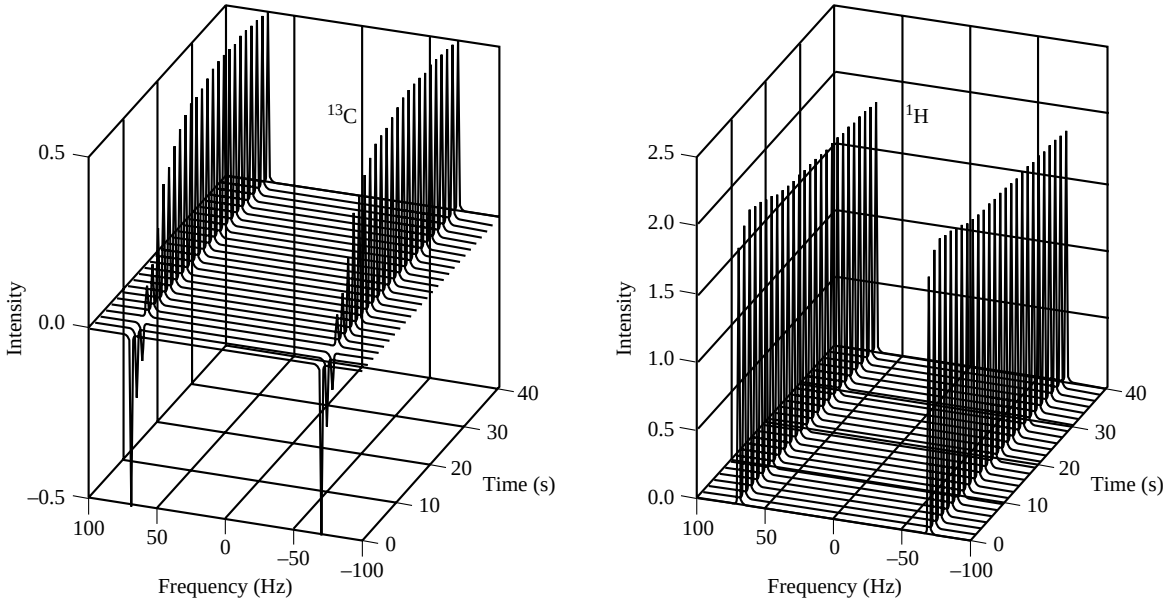

Figure 9 Simulated spectra resulting from the inversion–recovery experiment described in Figure 8. The spin system is the same as for Figure 1. Only DD relaxation is enabled

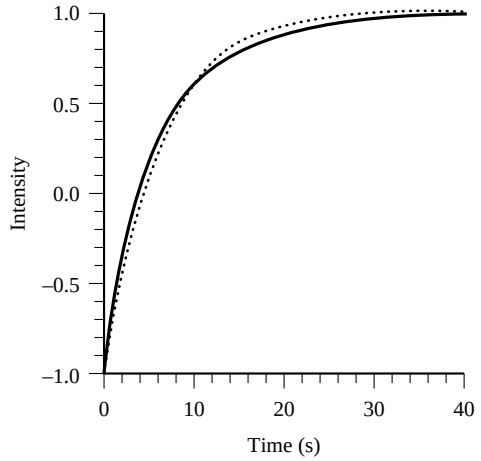

Figure 10 The M_C mode taken from the spectra of Figure 9 plotted versus time. The solid line is the actual evolution of the magnetization; the dotted line is the corresponding single exponential evolution

3. Projection: a $\frac{1}{2}\pi$ pulse is applied at the carbon or the proton resonance frequency to project the z components of the corresponding magnetization onto the single quantum coherences.
4. Detection: the carbon or proton FID is digitized.
5. The FID is Fourier transformed.

Figure 12 shows the spectra obtained by applying this sequence to the spin system of Figure 1. Note how proton magnetization is transferred to the ^{13}C in much the same way as happens in an INEPT experiment. In this case, the M_Δ mode is strongly perturbed, but, as shown in Figure 13, it is mono-exponential because this mode is not coupled to any other for an AX system with only DD relaxation. Even though the spectral lines evolve in a more complicated way and evolve differently for the ^{1}H than for the ^{13}C doublet, the difference of the two lines of the doublet M_Δ evolves identically and mono-exponentially, whether measured in the ^{1}H or the ^{13}C spectrum as stated in equation (99). This is a manifestation of the fact that the operator corresponding to M_Δ is identical whether it is measured in the proton spectrum or the carbon spectrum. These two differences of line intensities are just two different views of the same measurable, and this measurable is not coupled to any other mode.

4.2 Angles Between Internuclear Vectors: The AX_2 Spin System

In Section 4.1.3, we observed how cross correlation between DD and SA interactions can influence relaxation. The AX_2 spin system introduces the possibility to have cross correlation between two different DD interactions. There are

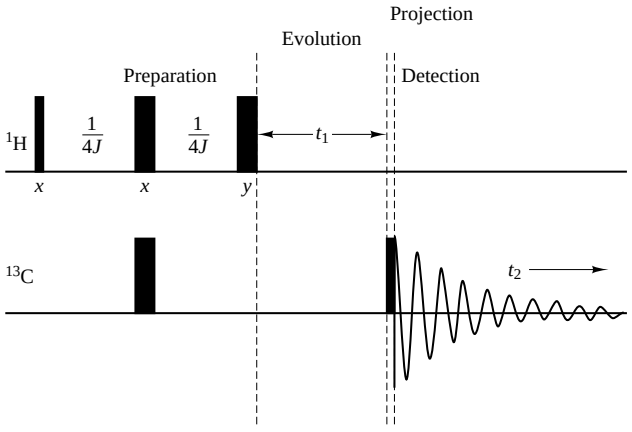

Figure 11 Selective inversion of a proton doublet using nonselective pulses. The wide pulses are π; the narrow ones are $\frac{1}{2}\pi$. The letters under the pulses indicate relative phases. If no phase is indicated, it is arbitrary

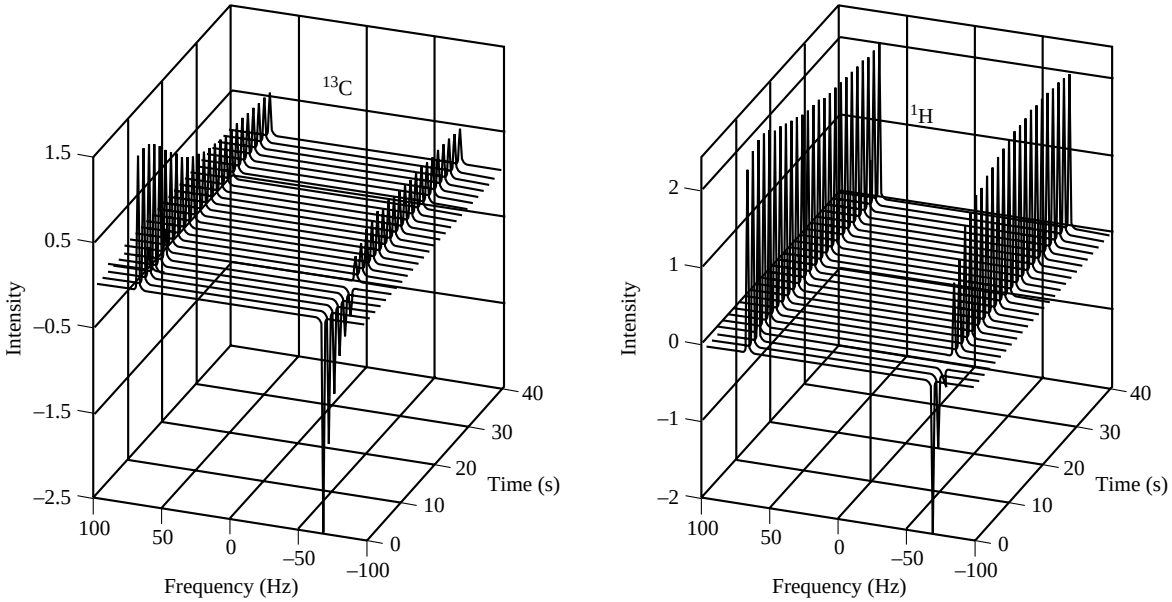

Figure 12 Spectra obtained by applying the selective inversion procedure of Figure 11 to the proton spin system described in Figure 1. Only the DD mechanism is enabled

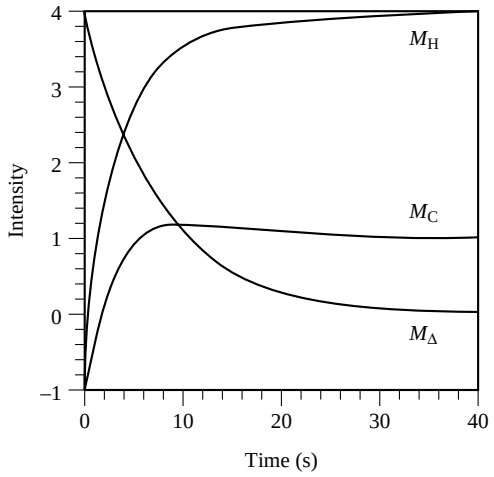

Figure 13 Magnetization modes taken from the spectra of Figure 12 plotted as a function of evolution time. Here the single exponential (dotted) line precisely superimposes on M_Δ and is not visible. Compare with Figure 10

three different spin pairs (AX, AX′, and XX′), each of which has a DD interaction, and there can be cross correlation among these various interactions (see Section 3.5). Because of the complexity of the way in which these cross correlations are folded into the elements of the relaxation superoperator, it is difficult to show how they influence relaxation in a clear way. However, the AX_2 spin system also introduces the angle between two internuclear vectors as a parameter of interest that is affected by this DD–DD cross-correlation. In Section 4.1.1, it was noted that for an AX spin system, the orientation of the internuclear vector with respect to some molecule-fixed frame is irrelevant for a spherical top. However, Figure 14 shows the influence of the angle between two internuclear vectors on the results of a proton hard pulse experiment. The magnetization modes of interest here are

$$\left.\begin{aligned} M_C &= M_{C1} + M_{C2} + M_{C3} \\ M_{+-+} &= M_{C1} - M_{C2} + M_{C3} \end{aligned}\right\} \tag{100}$$

The M_{+-+} mode was not present in the AX spin system, and is coupled to both the total proton and total carbon magnetizations. Both of these modes show dramatic sensitivity to the HCH angle for spherical top diffusion.

4.3 Rotational Anisotropy: The AX_3 Spin System

The prototypical AX_3 spin system is a ^{13}C methyl group. If a methyl is attached to a larger molecule, the free rotation

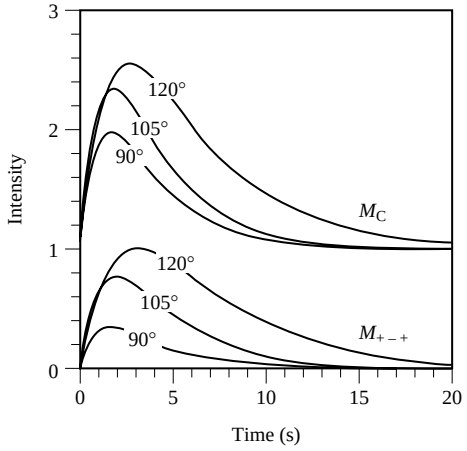

Figure 14 For a ^{1}H–^{13}C–^{1}H (AX_2) system, the effect of the HCH angle on the cross relaxation of the observable magnetization modes. Only the DD mechanism is enabled in the simulations. The perturbation is a proton hard pulse as in Figure 2. All other conditions are the same as for Figure 1

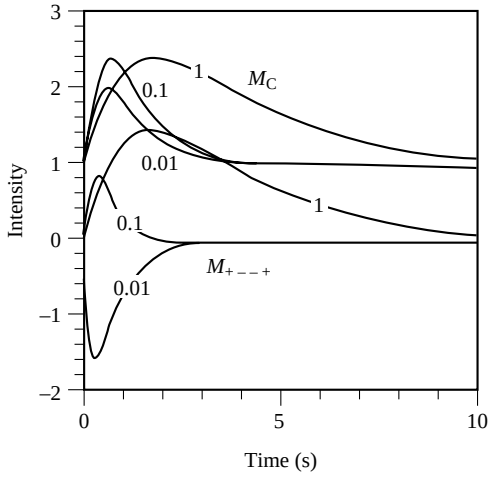

Figure 15 For a $^{13}C–^{1}H_3$ (AX_3) system, the effect of motional anisotropy (shown as $D_\perp/D_\parallel$ for the various curves) on the cross relaxation of the M_C and M_{+--+} magnetization modes. Only the DD mechanism is enabled in the simulations. The geometry is tetrahedral, with the threefold axis of the methyl collinear with $D_\parallel$. The perturbation is a proton hard pulse as in Figure 2. All other conditions are the same as for Figure 1

about the threefold axis of the methyl combined with the much slower overall tumbling of the molecule as a whole results in high motional anisotropy. This situation is a good case for exploring the effect of motional anisotropy on spin relaxation. The magnetization modes of interest in this case can be written as linear combinations of the four transitions of the carbon quartet:

$$\left.\begin{aligned} M_C &= M_{C1} + M_{C2} + M_{C3} + M_{C4} \\ M_{+--+} &= 3M_{C1} - M_{C2} - M_{C3} + 3M_{C4} \end{aligned}\right\} \quad (101)$$

Figure 15 shows these ^{13}C magnetization modes as they evolve in a proton hard pulse experiment. Beginning with a spherical top, cross relaxation is observed much as in previous cases; however, as the anisotropy of the reorientation increases, the M_{+--+} mode is very sensitive, even switching to a negative excursion rather than a positive one under highly unsymmetrical reorientation.

4.4 *o*-Dichlorobenzene

The simulation in Figure 16 uses experimental parameters as for the protons of *o*-dichlorobenzene (an AA′BB′ spin system.) The basic parameters for this simulation were taken from a paper by Stark et al.[18] The lower traces show spectra with full DD relaxation, including both autocorrelation and cross-correlation terms, whereas the upper traces have only autocorrelated DD terms. Under extreme narrowing (the two left traces), there is no apparent difference. When the correlation times are increased by a factor of 10, however, differences in maximum peak heights and linewidths are clearly visible. This simulation includes only dipolar relaxation terms, and uses a rigid asymmetric top as the motional model.

These few examples show the wealth of information available from coupled relaxation studies. Furthermore, many of the

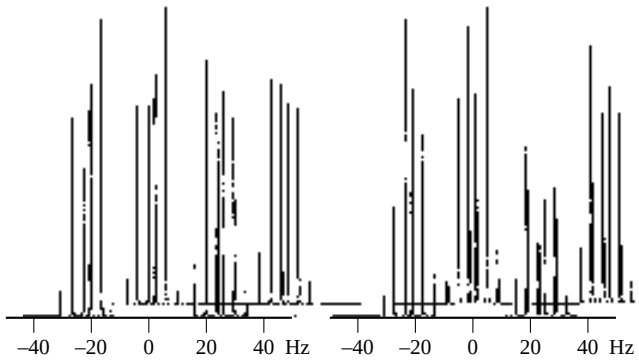

Figure 16 Simulated proton spectra at 220 MHz of *o*-dichlorobenzene with DD relaxation including both autocorrelated and cross-correlated relaxation terms (lower traces) and with only autocorrelated terms (upper traces). The motion was modeled as a rigid asymmetric top with correlation times of 3.4, 5.4, and 1.9 ps (left traces) and 34, 54, and 19 ps (right traces). Artificial line broadening of 0.05 Hz was used for the spectra on the left to suppress truncation artifacts

multidimensional experiments that have become commonplace tools for the chemist and biochemist involve placing coupled spin systems in nonequilibrium states. In many cases, the cross relaxation and cross-correlation effects illustrated here markedly influence the results of such experiments, and due consideration must be given when interpreting these experiments.

The GAMMA platform has been made available to the public by its authors. The source code of the GAMMA-based program that generated all the simulations herein, as well as online simulations of these effects, are available courtesy of the National High Magnetic Field Laboratory at **http://gamma1.magnet.fsu.edu/~gamma/**.

5 REFERENCES

1. T. C. Farrar and E. D. Becker, *Pulse and Fourier Transform NMR: Introduction to Theory and Methods*, Academic Press, New York, 1971.
2. H. Friebolin, *Basic One- and Two-Dimensional NMR Spectroscopy*, VCH, New York, 1991.
3. A. E. Derome, *Modern NMR Techniques for Chemistry Research*, Pergamon Press, Oxford, 1987.
4. D. M. Grant, C. L. Mayne, F. Liu, and T. Xiang, *Chem. Rev.*, 1991, **91**, 1591.
5. S. A. Smith, T. O. Levante, B. H. Meier, and R. R. Ernst, *J. Magn. Reson. Ser. A*, 1994, **106**, 75.
6. E. M. Purcell, H. C. Torrey, and R. V. Pound, *Phys. Rev.*, 1946, **69**, 37.
7. F. Bloch, W. W. Hansen, and M. Packard, *Phys. Rev.*, 1946, **70**, 474.
8. F. Bloch, *Phys. Rev.*, 1946, **70**, 460.
9. C. P. Slichter, *Principles of Magnetic Resonance*, 3rd edn., Springer-Verlag, Berlin, 1990.
10. C. L. Mayne, D. W. Alderman, and D. M. Grant, *J. Chem. Phys.*, 1975, **63**, 2514.
11. S. A. Smith, W. E. Palke, and J. T. Gerig, *Concepts Magn. Reson.*, 1992, **4**, 107.
12. S. A. Smith, W. E. Palke, and J. T. Gerig, *Concepts Magn. Reson.*, 1992, **4**, 181.

13. S. A. Smith, W. E. Palke, and J. T. Gerig, *Concepts Magn. Reson.*, 1993, **5**, 151.
14. R. N. Zare, *Angular Momentum*, Wiley, New York, 1988.
15. S. Szymanski, A. M. Gryff-Keller, and G. Binsch, *J. Magn. Reson.*, 1986, **68**, 399.
16. A. G. Redfield, in *Advances in Magnetic Resonance*, ed. J. S. Waugh, Academic Press, New York, 1965, Vol. 1, p. 1.
17. C. H. Wang and D. M. Grant, *J. Chem. Phys.*, 1976, **64**, 1522.
18. R. E. Stark, R. L. Vold, and R. R. Vold, *J. Magn. Reson.*, 1979, **33**, 421.

Biographical Sketch

Charles L. Mayne. *b* 1942. B.S., 1970, New Mexico State University, U.S.A.; Ph.D., 1976, University of Utah. Introduced to NMR by George A. Gray and subsequently tutored by David M. Grant. Manager of NMR Laboratories, University of Utah, Department of Chemistry, 1973–present; academic appointment as Adjunct Associate Professor of Chemistry, University of Utah. Approx. 40 publications in NMR. Research interests include nuclear-spin relaxation, NMR at high pressure, structure elucidation of natural products, various aspects of multidimensional NMR, and computerized analysis of NMR data.

Scott A. Smith. *b* 1955. B.S., 1980, San Diego State University, U.S.A.; Ph.D., 1989, University of California, Santa Barbara. Introduced to NMR by Dr Stephen B. W. Roeder. Currently working for Dr R. R. Ernst with Tilo Levante on the GAMMA project and its release to the public. 5 publications in computer simulation of NMR experiments. Research interests include nuclear-spin relaxation and computer simulation of magnetic resonance phenomena.

Relaxation Theory: Density Matrix Formulation

Alfred G. Redfield

Brandeis University, Waltham, MA, USA

1	Introduction	1
2	Review of the Literature	1
3	Strong Relaxation	2
4	Ensembles, Systems, Operators, and Representations	2
5	The Density Matrix and the Relaxation Matrix	3
6	Transition Rates	4
7	Linewidths and Off-Diagonal Elements	5
8	Effects of rf Fields: Spin Locking	5
9	Cross-Correlation Effects	5
10	Transverse Relaxation Rates and Dynamic Shifts	6
11	Derivation of the Relaxation Equation	7
12	Conclusions	7
13	Related Articles	8
14	References	8

1 INTRODUCTION

This article introduces nuclear spin relaxation primarily in the *weak limit*, by which we mean the kind of relaxation theory that is also called the perturbation limit, or the motionally narrowed limit. This is the most common form of relaxation in NMR.

Generally any theoretical treatment of relaxation divides the equations of motion of the spin system into two parts: first, a static or nearly static part consisting of the Zeeman energy, the spin–spin couplings (usually also including the dipolar energy between spins, and quadrupolar interactions, for rigid solids), and some other terms depending on the system; and second, a randomly time-varying part that produces relaxation. The latter can often be described approximately by two parameters: a size in energy units of $\hbar\omega_i$, and a time τ_c or 'correlation time', which is a characteristic time, usually the time that it takes for the random interaction to change by an amount that is unpredictable but is comparable to $\hbar\omega_i$. For example, when two nuclear spins in a molecule in solution relax mainly via the dipolar interaction between each other, ω_i is of the order of 10^5 s^{-1} for vicinal protons, decreasing as the inverse cube of the distance for further neighbors, and τ_c is of the order of the time for the interspin vector to rotationally diffuse by about one radian away from any initial direction. Neither ω_i nor τ_c can be defined precisely for every problem, although for some important problems they can be usefully defined. For large biopolymers, τ_c is of the order of 10^{-8} s, and it is roughly proportional to molecular weight.

The weak limit is almost always valid if $\omega_i\tau_c \ll 1$, but a more useful criterion is that the relaxation rate (such as ${T_1}^{-1}$ or ${T_2}^{-1}$), calculated using the weak limit formulas, be small compared to ω_i. A useful rule of thumb is that transverse relaxation times T_2 are of the order of ${\omega_i}^2\tau_c$ and longitudinal rates are of the order of ${\omega_i}^2\tau_c/(1 + \omega^2{\tau_c}^2)$, where ω is a nuclear spin frequency, or difference in nuclear spin frequencies, depending on the relaxation process under consideration. It is commonplace that $\omega\tau_c$ be greater than one for moderately large molecules, and it also can happen that $\omega_i\tau_c$ is greater than one, so that T_2 processes cannot be treated using the weak limit, whereas, in the same system, T_1 processes can be. In fact, T_1 processes can almost always be treated by the weak limit, with the exception of experiments, usually field cycling, performed at low field; and for conceptually similar experiments in the rotating frame such as studies of slow motions described in ***Ultraslow Motions in Solids***.

In the present article, we shall introduce this topic in as simple a way as possible, in the hope of demystifying it for the inexperienced reader. We do not attempt a thorough review or much discussion of the different classes of relaxation that can occur. Even setting up the main Hamiltonian and the smaller time-dependent Hamiltonian requires many assumptions and some intuition about the system. On the other hand, we shall mention a number of topics not found in general texts. We shall not discuss details of applications since these are treated elsewhere in this Encyclopedia. Fortunately, the list of relaxation interactions is not long: dipolar relaxation already mentioned; similar relaxation due to electron spin–nuclear spin interaction in paramagnetic materials; spin–rotation interaction, especially in gases but also in smaller molecules in solution; and, for nuclei other than spin-$\frac{1}{2}$, the fluctuating electric quadrupolar interaction.

The kind of theory we have been describing is called *semiclassical*, because the time dependence of the perturbing interaction is generally described by classical variables such as distances. Relaxation theories can be, and generally are, also set up completely quantum mechanically. Unfortunately, the character of the time dependences of most relaxation interactions cannot be calculated from first principles, so that most relaxation theories are semiclassical. An exception is relaxation by lattice vibrations in solids or electron spins in metals, although even in these cases theories are likely to be somewhat phenomenological. Quantum relaxation theory also helps to justify some apparently arbitrary assumptions of the semiclassical theory.

2 REVIEW OF THE LITERATURE

The original Bloch equations,[1] containing two relaxation times, hinted at the probable richness of information contained in relaxation theory. ${T_1}^{-1}$ was the rate at which energy changes would occur, and this more demanding process was expected to be slower than T_2 (line-broadening) processes, which do not require energy transfer in the absence of an rf field. The basic picture of nuclear relaxation was virtually completed with the masterful paper by Bloembergen, Purcell, and Pound (BPP), connecting transition rates between levels with spectral densities, and T_2 processes primarily with spectral densities at zero frequency.[2] By symmetry, T_1 and T_2 should be equal in the low-field limit and also, since T_2 must be a continuous function of B_0, $T_1 = T_2$ in the limit of short correlation time, $\omega_0\tau_c \ll 1$ (where ω_0 is the Zeeman frequency γB_0).

In early papers, it was assumed that the relaxation by spin–spin interactions in rigid solids would produce straightforward transverse relaxation, but this view was

incorrect. The dipolar spin–spin interaction has to be treated separately from weak relaxation mechanisms in a rigid solid, and it can participate in a wide variety of interesting phenomena.

The next important development was the introduction of the density matrix to describe the system to be relaxed, and the satisfactory calculation of T_1 and T_2 for a single spin, by Wangsness and Bloch. This treatment was then restated and generalized by various workers. Kubo and Tomita provided a theory based on the general theory of irreversible processes; Bloch treated relaxation in the rotating frame, among other things; and the present writer provided a version of the theory that may be useful to the novice reader. During this same period, Solomon was performing his important experiments on the HF molecule, providing a systematic basis for discussion of cross-relaxation theory (NOE) as treated in the papers of Solomon and Bloembergen. The topic has been treated in several texts, reviews, and monographs,[1–15] of which Abragam's may be the most lucid introduction to the operator version of the formalism.[3,6,14] In the present article, we use the notation of our own work[15] and of Slichter[4] as far as possible, while maintaining consistency with the other articles in this Encyclopedia. Excellent reviews of applications of weak and strong relaxation theories can be found in the books edited by Muus and Atkins[8] and by Tycko.[11]

A somewhat separate, more sophisticated and general approach has been developed by several theorists, based primarily on the work of Kubo and Tomita, and of Morita.[8,10,12,13] The reader should be aware that there is only one underlying theory, and that the independent formalisms of various workers mentioned are all valid, and differ only in sophistication and in suitability for different problems.

3 STRONG RELAXATION

Strong relaxation theories are not presented here, but we describe them briefly. Many such theories are generalizations of the early well-known treatment of McConnell and of Slichter in which the chemical shift of a single spin is assumed to change at a random rate between two definite values, as a model for a dynamic change between two major average conformations. Generally, weak mechanisms such as dipolar relaxation are grafted onto such a theory, and the entire spin-dynamic problem can be solved analytically, as described in ***Chemical Exchange Effects on Spectra***. Sometimes essentially the same kind of theory is set up with an infinite number of conformational states and shifts. An important example is the simulation of lineshapes for deuterium NMR in membranes and liquid crystals. The type of problem discussed in ***Ultraslow Motions in Solids*** is also in this class.

All such strong relaxation mechanisms can become weak in the limit where the correlation time becomes sufficiently short, as already implied.

Another class of strong relaxation mechanisms is that of the Orbach processes, in which excited electronic states are important.[8] This type of relaxation is not important for NMR problems, except perhaps for paramagnetic solids.

Finally we mention Anderson theory,[8] which was first used to describe the exchange narrowing[3] of electron spin resonances in solids. In NMR, it is adapted to estimate linewidths of dilute heteronuclei in solids,[3] and processes like solid state cross relaxation and magnetization (spin) diffusion for which perturbation theory is not applicable, but that are nevertheless slow.[7]

4 ENSEMBLES, SYSTEMS, OPERATORS, AND REPRESENTATIONS

We now describe the elements of models for relaxation theories. Here and throughout this article we only outline those topics that are relatively standard. The reader who is not familiar with topics mentioned is urged to refer to the literature surveyed above and to standard texts on quantum and statistical physics.

A typical relaxation theory treats the average behavior of an *ensemble* of systems. Most generally, each member of the ensemble is a replica of the NMR lab, according to Gibbs, but an almost equivalent view is that each member of the ensemble is represented by a single experiment on the same system, out of a large ensemble of experiments in which the sample is prepared as far as possible in the same way each time. A gentler version of an ensemble can be that it represents the average behavior of many pieces of a large sample of N particles ($N \approx 10^{23}$), each piece having fewer than N particles, but still a great many, say 10^{12}. Finally, it is useful sometimes, though not strictly correct, to view each member of the ensemble as one molecule out of the collection (ensemble) of molecules being studied. The latter view cannot be used for a rigorous treatment of intermolecular or collective effects such as intermolecular NOE or 'radiation damping'. In any case, it is most important to be entirely clear as to what system one is defining, before starting.

As already indicated, a starting point for any semiclassical weak relaxation theory is to write the Hamiltonian $\hat{\mathcal{H}}$ in the form

$$\hat{\mathcal{H}} = \hat{\mathcal{H}}_0 + \hat{K}(t) \tag{1}$$

where $\hat{\mathcal{H}}_0$ is the main Hamiltonian, and relaxation is produced by the randomly varying part $\hat{K}$. It is specifically assumed that $\hat{K}$ has zero value after being averaged over the ensemble: $\langle \hat{K}(t) \rangle = 0$, where the angular brackets always denote the ensemble average. It is important to remember that $\hat{K}$ is assumed to be different for each member of the ensemble.

It is useful to note explicitly that $\hat{K}$ can usually be written as the sum of more or less independent terms, each of which can be written (for one member of the ensemble) as a spin operator times a function of classical variables (usually internuclear distances, and angles defining directions of internuclear vectors):

$$\hat{K} = \sum_q H_q(t) \hat{K}^q \tag{2}$$

The H_q are ordinary real random functions of the time. They can be terms such as those of the dipolar interaction of BPP, for example $\hbar^2\gamma^2(1 - 3\cos^2\theta)/r^3$. The $\hat{K}^q$s corresponding to this H_q would be the operators $\hat{I}_{1z}\hat{I}_{2z}$ and $-\frac{1}{4}(\hat{I}_1{}^-\hat{I}_2{}^+ + \hat{I}_2{}^+\hat{I}_1{}^-)$. In this case, the classical variable H_q is random because θ and

r vary randomly, in solution. The elements of $\hat{K}^q$ may also be functions of the time for a time-dependent *representation* of the system, discussed below. For weak relaxation, it turns out that all we need to know about $\hat{K}$ are the auto- and cross-correlation of the functions $\langle H_q(t)H_{q'}(t+\tau)\rangle$. These will be discussed later.

The quantum Hamiltonian is an operator, and the thing on which it operates is a wavefunction:

$$\psi = c_n(t)u_n \tag{3}$$

where the c_n are complex numbers that generally vary with time, and the u_n are a complete set of *basis functions*. There are rules concerning how to set up such a complete set, and how they must change under transformations of various kinds. For spin problems, we mention four, out of many, ways to define them.

1. The u_n can be wavefunctions that specify the orientation (or m_z, for $S > \frac{1}{2}$) of each spin in the system. These are eigenfunctions of the Zeeman Hamiltonian and we call this the 'Zeeman' representation.
2. The u_n can be eigenfunctions of the entire main Hamiltonian $\hat{\mathcal{H}}_0$, with energy eigenvalues E_n. $\hat{\mathcal{H}}_0$ includes, in addition to the Zeeman Hamiltonian, spin–spin coupling for molecules in solution. Deriving these u_n from the Zeeman ones can be easy—or it can be very complicated—but nevertheless it is useful to talk about them. This is the 'Schrödinger' representation. The terms c_n generally depend on time in this representation, as exp (i$E_nt/\hbar$), modified by relaxation.
3. The u_n can be appropriate for a rotating frame transformation. For such a transformation, most of the Zeeman Hamiltonian is removed, and the u_n are the same as for case 1 except that the new u_n are equal to those of case 1 multiplied by exp $(-\mathrm{i}\omega_j t)$, where ω_j are the sums of, or differences between, nuclear resonance frequencies of relevant spins. This could be called the 'product operator' representation, since it is used for product operator theory.
4. The representation may be one in which the entire average Hamiltonian $\hat{\mathcal{H}}_0$ is transformed away. This is the 'Heisenberg' or 'interaction' representation. It is most convenient for setting up relaxation theory. In this representation, the c_n are time-independent except for the relaxing effect of $\hat{K}(t)$, and the new u_n are equal to those of the Schrödinger representation times exp $(-\mathrm{i}E_nt/\hbar)$. All operators such as $\hat{K}(t)$ are similar to their form in the Schrödinger representation, except that their off-diagonal elements are time-dependent.

The wavefunction ψ is completely specified by specifying the basis u_n and all the c_n. The latter set of numbers is viewed as a *vector in Hilbert space* in analogy to the set (x, y, z) of coordinates that represents the real-space position vector of a particle.

Before proceeding, we note that $\hat{\mathcal{H}}_0$ can include time-varying things such as rf pulses or field gradients. For the most part, we ignore such fields. Equation (1) also omits any semiclassical interaction that restores thermal equilibrium. The equation should include another friction term that will do so.[8,13,16] Otherwise, the energy of each system will increase continuously, toward infinite temperature. This is a consequence of the fact that $\hat{K}(T)$ does not have a temperature associated with it.

In fact, *nuclear spin relaxation theory is virtually identical to Brownian motion theory*. It deals with Brownian-like motion of vectors, in Hilbert space, that describe the spin system.[8,10] In each time of the order of the correlation time τ_c, an individual system wavefunction changes very little, in analogy to the effect of single collisions on a large particle undergoing Brownian motion. The interested reader should read the last chapter of Reif's text[17] to see how Brownian motion of relatively large particles is related to fluctuating forces of the surrounding medium—in particular to the spectral densities (see below) of these forces. The analogy to Brownian motion may reassure the novice reader that nuclear spin relaxation involves nothing really new. In particular, Brownian motion theory always contains a presumed force of friction, and Einstein showed how the friction coefficient must be related to the diffusion coefficient, which is a manifestation of the fluctuating forces of collisions. Frictional forces were not described as such in early papers.[15,16]

The statement in the above paragraph describes an *analogy*, which should not be confused with the important *applications* of NMR to the study of real diffusion. These include studies of translational diffusion, dating back to Hahn's original papers on spin echoes, and of rotational diffusion, starting with BPP (reviewed, for example, in ***Relaxation Effects of Chemical Exchange***).

5 THE DENSITY MATRIX AND THE RELAXATION MATRIX

The density matrix is defined by[4]

$$\sigma_{ij} = \langle c_i c_j^* \rangle \tag{4}$$

where * here denotes the complex conjugate. Notice that it is a matrix whose elements depend on what representation we are using, which has to be kept in mind during any discussion or calculation. The density matrix can be shown to transform in the same way as any standard quantum operator, under change of representation, so it can be thought of as an object $\hat{\sigma}$ that is represented in some particular representation by a matrix σ_{ij}. Thus $\hat{\sigma}$ is often referred to as the density operator, even though it does not seem to operate on anything.

The symbol $\hat{\rho}$ was originally used for the density matrix of an entire system, including coordinates of nonspin variables. The notation $\hat{\sigma}$ was introduced to denote a "reduced" density matrix that describes the nuclear spin system alone. Often, as for example in the product operator formalism, $\hat{\sigma}$ is written as a sum of products of spin operators; this is what we mean by an operator formalism. Use of this language implies that correlations between spin orientations and molecule or lattice variables are, on the average, not large. This assumption has to be dropped for strong relaxation theories. In the absence of relaxation, $\hat{\sigma}$ obeys the quantum version of the Liouville equation:

$$\frac{\mathrm{d}\hat{\sigma}}{\mathrm{d}t} = \frac{\mathrm{i}}{\hbar}[\hat{\sigma}, \hat{\mathcal{H}}_0] \tag{5a}$$

where $[\hat{\sigma}, \hat{\mathcal{H}}_0]$ denotes the commutator bracket $\hat{\sigma}\hat{\mathcal{H}}_0 - \hat{\mathcal{H}}_0\hat{\sigma}$.

The Schrödinger representation that we will use is not convenient for actual calculations, but is useful in developing and discussing the general theory. In this representation, the basis functions u_n are exact eigenvalues of $\hat{\mathcal{H}}_0$, as already mentioned. The diagonal element σ_{ii} of $\hat{\sigma}$ is simply the probability that the energy level E_i is occupied. As expected, the Liouville equation predicts that σ_{ii} will be time-independent, a consequence of the fact that $\hat{\mathcal{H}}_0$ is diagonal in this representation. The elements of $\hat{\sigma}$ represent the entire set of possible physical observables of the system. These are not the same things that we may observe in practice, and in NMR there is usually really only one quantity that we observe. It is the transverse magnetization in the fixed x direction, $\hat{M}_x$. Its expectation value is given by $\mathrm{Tr}(\hat{M}_x\hat{\sigma})$, where Tr means a sum over diagonal elements. It is the sum of many off-diagonal elements of $\hat{\sigma}$ in the Schrödinger representation, because $\hat{M}_x$ has many off-diagonal elements in this representation, for a system of several spins. From the Liouville equation, the time dependence of an off-diagonal element σ_{ij} is given by a constant times $\exp[\mathrm{i}(\omega_i - \omega_j)t]$. Each spectral line in a directly observed spectrum is a manifestation of a coherence represented by an off-diagonal density matrix element, damped, of course, by relaxation not included in equation (5a). However, typically $\hat{\sigma}$ has many more off-diagonal elements than are observed in this way; for a system of 10 protons, for example, it has only 1024 diagonal elements, but roughly a million off-diagonal elements. The vast majority of the latter are both uninteresting and difficult to study. Elements that are not directly observable in a simple free induction decay are called forbidden, and of these the most useful are the lower order (zero, double, triple, etc.) 'multiple quantum' coherences.[6]

As might be expected, the result of weak relaxation theory is an equation for $\hat{\sigma}$ that is a direct generalization of Bloch's equations:

$$\frac{\mathrm{d}\hat{\sigma}}{\mathrm{d}t} = \frac{\mathrm{i}}{\hbar}[\hat{\sigma}, \hat{\mathcal{H}}_0] + \hat{R}(\hat{\sigma} - \hat{\sigma}^0) \tag{5b}$$

where $\hat{\sigma}^0$ is the thermal equilibrium value of $\hat{\sigma}$, equal to a constant times $(\exp -\hat{\mathcal{H}}_0/RT)$. The extra term $\hat{R}(\hat{\sigma} - \hat{\sigma}^0)$ is shorthand for a matrix whose ij element is $\Sigma_{i'j'}R_{iji'j'}(\sigma_{i'j'} - \sigma_{i'j'}{}^0)$; thus the *relaxation matrix* $\hat{R}$ is a fourth-order matrix. We shall discuss it using the Schrödinger representation here. The elements of $\hat{\sigma}$ are analogous to the magnetizations in Bloch's equations, and the term $\mathrm{i}[\hat{\sigma}, \hat{\mathcal{H}}_0]/\hbar$ is analogous to $\gamma(\boldsymbol{B} \times \boldsymbol{H})$. The coefficients in $\hat{R}$ are extensions of Bloch's rates $T_1{}^{-1}$ and $T_2{}^{-1}$, and the term $\hat{\sigma}^0$ is similar to his M_0.

As already mentioned, frictional forces must exist that return the system to equilibrium, and the term $-\hat{R}\hat{\sigma}_0$ was arbitrarily inserted to account for these. As included in equation (5b), it ensures that $\mathrm{d}\hat{\sigma}/\mathrm{d}t$ is zero at equilibrium, when $\hat{\sigma} = \hat{\sigma}^0$. Friction forces are connected with the memory of the surroundings: for example, as a spin precesses in matter, the interaction represented as relaxation by $\hat{\mathcal{H}}_1(t)$ will slightly deform the matter to produce a small local field at the spin. The deformation is analogous to the deformation in a bed when you lie on it. As the spin moves, this deformation follows it, but not instantly. There is a small lag, and this produces a memory field that is exactly right to make the system approach equilibrium.[8] The $\hat{R}\hat{\sigma}^0$ term can also be fully justified by a quantum derivation,[16] or by taking spin interaction into account for the lattice's motion.[17]

6 TRANSITION RATES

The semidiagonal element R_{iijj} is simply the rate constant for the transition from level i to level j. The theory of these transition rates was already fully implied in BPP, not requiring a density matrix for its description. Thus we can redefine σ_{ii} as a probability p_i that level i is occupied, and R_{iijj} as a transition rate w_{ij} from level j to i, writing equations of the form

$$\frac{\mathrm{d}p_i}{\mathrm{d}t} = \sum_j w_{ij}(p_j - p_j^0) \tag{6a}$$

where $p_j{}^0$ is the thermal equilibrium value of p_j, proportional to $\exp(-E_j/kT)$. The form of equation (6a) is based on the relaxation equation, equation (5b), and the w_{ij} are symmetric: $w_{ij} = w_{ji}$, as defined in the original theory.[15] The w_{ij} are not identical to what are normally considered transition probabilities, which occur in the so-called master equation:

$$\frac{\mathrm{d}p_i}{\mathrm{d}t} = \sum_j (W_{ij}p_j - W_{ji}p_i) \tag{6b}$$

Here, detailed balance requires $W_{ij}/W_{ji} = \exp[-(E_i - E_j)/kT]$. Equation (6b) is also the equation for standard first-order chemical kinetics, if p_i is replaced by the molarity $[i]$ of systems in spin level i, and the W_{ij} are replaced with first-order rate constants usually denoted by k_{ij} or the equivalent.

Since the matrix w_{ij} is symmetric, whereas W_{ij} is not, equation (6a) is inconsistent with the more general equation, equation (6b), and with detailed balance. Apparently, the convenient form of relaxation theory described by equation (6a) *is valid only in the high-temperature approximation*, where $(E_i - E_j)/kT \ll 1$. Fortunately, this approximation is almost always obeyed for NMR experiments. In that case, it is reasonable to specify W_{ij} by

$$W_{ij} = w_{ij}\left(1 - \frac{E_i - E_j}{2kT}\right) \tag{7}$$

which preserves detailed balance within the high-temperature approximation. The problem with the semiclassical theory mentioned above can be avoided, when the high-temperature approximation is invalid, by either using the completely quantum version of the theory,[15] or by augmenting the semiclassical model of equation (1) with a memory, or friction term, as already mentioned.[13,16] A simple example of a memory effect is 'radiation damping' (see below).

For a large and important class of experiments such as NOESY, the situation is even simpler. With important exceptions such as methyl groups, there are no complicated correlations between spins, and the important evolution by relaxation is described by diffusion of magnetization among spins ('spin diffusion'). Relaxation is described by

$$\frac{\mathrm{d}m_i}{\mathrm{d}t} = \sum_j s_{ij}(m_j - m_j^0) - r_1(m_i - m_i^0) \tag{6c}$$

where m_i is the z component of magnetization of the ith spin species, m_i^0 is its thermal equilibrium value, r_i is the relaxation rate of the ith spin due to all mechanisms, and the s_{ij} are cross relaxation rates between spins. Note that s and r are often denoted by σ and ρ in the literature. Furthermore, the term 'relaxation matrix' is often used in the literature of these problems, to denote the collection of relaxation rates; it is not to be confused with the more complicated $\hat{R}$ matrix of the full theory.

An equation similar to equation (6c) can also describe the ROESY experiment, with redefinition of m_i as magnetization along the effective field of spin i. We shall briefly return to ROESY below.

All these versions of NMR kinetic theory are described by first-order differential equations, whose evolution can be described by sums of simple normal modes, each having a single relaxation time. These modes include in principle all the m_i (or possibly σ_{ii}) and are time consuming to calculate. Magnetization diffusion and relaxation viewed in terms of normal modes has been applied by T. L. James to macromolecules. However, an equivalent approach is to ask how a localized departure from equilibrium, at a single spin i, spreads to other spins as time passes. This 'Green's function' approach is perhaps more economical in computer time than the normal mode approach, and it may provide a rather direct and more intuitive model for the evolution of diagonal and cross peaks in NOESY and ROESY. Routines that can perform such a calculation are included in some NMR data analysis programs. The normal mode approach is more useful for problems having a high degree of symmetry.

7 LINEWIDTHS AND OFF-DIAGONAL ELEMENTS

In the Schrödinger representation, any element of σ_{ij} of $\hat{\sigma}$ varies as exp (i$\omega_{ij}t$), neglecting relaxation, where $\omega_{ij} = (E_i - E_j)/\hbar$. The elements of $\hat{R}$ are time-independent (only for this representation!). A *secular* term $R_{ii'jj'}$ is one for which $\omega_{ii'} = \omega_{jj'}$. All the rates in the previous section are thus secular, because all the ω_{ii} and ω_{jj} are zero. Likewise, terms of the relaxation matrix $\hat{R}$ terms R_{ijij}, which are rather direct analogs to Bloch's rate ${T_2}^{-1}$, are secular. The minimum full linewidth of a spectral transition between levels i and j is R_{ijij}/π, just as the full linewidth for Bloch's equations is $(\pi T_2)^{-1}$. Thus, if all relaxation terms of equation (5b) are ignored except R_{ijij} then σ_{ij} varies as a damped exponential, exp (i$\omega_{ij}t$ + $R_{ijij}t$). The sign of R_{ijij} is negative (see below).

Those terms of the relaxation matrix $\hat{R}$ that are not of the form R_{iijj} or R_{ijij} can mostly be ignored. That is fortunate, because $\hat{R}$ has roughly 10^{12} elements for a 10-proton problem, for example.

Specifically, any element $R_{ii'jj'}$ connecting any density matrix element $\sigma_{ii'}$ to another one $\sigma_{jj'}$ can often be ignored provided

$$|\omega_{ii'} - \omega_{jj'}| graphic |R_{ii'jj'}| \tag{8}$$

If equation (8) is strongly obeyed (if the equation is valid with $>$ replaced by $\gg$) then the element of $\hat{R}$ being considered is a time-independent relaxation term connecting two elements of $\hat{\sigma}$ that are varying rapidly compared with the element of $\hat{R}$. These terms are called 'nonsecular', and they are expected to perturb the final solution by an amount equal to the ratio of the right-hand to the left-hand side of equation (8), compared with secular terms of the same size. The name and idea of secular and nonsecular perturbations date back to classical mechanics, and were invoked by Van Vleck in truncating the dipolar Hamiltonian in order to calculate moments of resonance lines.

Terms in $\hat{R}$ for which equation (8) is only weakly obeyed, or corresponding terms in operator-based theories of relaxation,[14] should always be included in any solution of a relaxation problem. The effect of such terms can be dramatic, and can unexpectedly produce narrowing, and collapse of multiplets. A simple example is the non-observance of ^{14}N splitting of the proton resonances of NH groups, due to rapid electric quadrupole relaxation of the ^{14}N spin. The N–H J splitting is suppressed by rapid relaxation coupling of coherences of the product operator form $\hat{I}_z\hat{S}_x$, where I is ^{14}N and S is the NH proton. Of course, this example, like many, does not require density matrix relaxation theory in order to be understood. This kind of relaxation is called 'narrowing of the second kind'.[3]

8 EFFECTS OF RF FIELDS: SPIN LOCKING

The consideration of nonsecular terms in $\hat{R}$ became richer when it was realized that the elements of $\hat{\sigma}$ can have their time dependence altered by the presence of rf fields, such as in a spin lock experiment. Off-diagonal elements can be driven to have periodic variation at the rf frequency, rather than their natural frequencies, and elements of $\hat{R}$ that connect two elements of σ which have slightly different frequencies become secular. Thus, rf fields can alter the relaxation behavior, as first shown by Vold and Vold. Here it is assumed that $\hat{R}$ itself is not affected by the rf field. A commonplace example of this effect is in the ROESY (CAMELSPIN) experiment of Bothner-By. Magnetizations of different spins cross relax in this experiment because they are spin locked at the same rf frequency, and these magnetizations correspond directly to off-diagonal density matrix elements that would evolve at different frequencies, and not cross relax, in the absence of the spin lock. It must be emphasized, however, that the ROESY experiment was undoubtedly invented and analyzed independently of the theory outlined in the present article.

The phenomena described in the last paragraph are quite general. Another useful measurement can be made on systems that are expected to have dynamic, chemical, or conformational changes taking place on a timescale in the range of 10 ms or slower. Then it is of interest to study the variation in the transverse relaxation time with respect to the spin-locking rf field intensity $\omega_1 = \gamma B_1$. This relaxation time is generally called $T_{1\rho}$, since the process it describes resembles a T_1 process, but in the rotating frame. The theory of $T_{1\rho}$ can be treated using spectral densities and density matrix theory, following Bloch, or it can with equal validity be treated using the type of theory reviewed in ***Chemical Exchange Effects on Spectra***. In general, $T_{1\rho}$ starts to decrease below its value at zero B_1, (which is the same quantity as T_2) at field intensities where $\omega_1\tau_c$ approaches one. Here τ_c is the correlation time for the slow perturbation. Such a measurement yields an estimate of this correlation time, and also the general size of the shift ω_i associated with the perturbation.

9 CROSS-CORRELATION EFFECTS

An understanding of the effect of cross correlations between the random functions $H^q(t)$ in equation (2) can help to provide interesting information about a system from its linewidths or transition rates. This topic is reviewed in ***Relaxation Processes: Cross Correlation and Interference Terms***. An important example is the often-seen unequal linewidth of ^{13}C (or ^{15}N) multiplets, due to correlation and interference between the dipolar interaction and the CSA of the ^{13}C nucleus. A rough estimate of the CSA can be obtained from this effect.[5]

To understand the general usefulness of cross-correlation effects, consider the dipolar interaction in a hypothetical spin system ABC, where nuclei A, B, and C are nonequivalent protons and the distances A to B, and B to C, are assumed fixed and equal. If the angle ABC could vary randomly with equal probability for all angles then the spectrum of B would show an uninteresting multiplet due to the uncorrelated dipolar interactions between A and B, and B and C. If, instead, the system is rigid and linear, with the angle ABC equal to 180°, the dipolar interactions mentioned above are highly correlated. If spins A and C are oriented oppositely for the rigid linear case, their dipole fields at B will cancel; if spins A and C are both oriented in the same direction, the dipolar fields always add. Thus, the centerlines of B's multiplet will be narrow, and the outer lines will be four times as broad as in the uncorrelated case.

An interesting example of a correlation effect is 'radiation damping'. This is due to the rf fields, fluctuating and induced, from the probe pickup coil. The effect is misnamed, because no radiation is involved. It is a correlated effect, because the field felt at each spin is virtually the same as at every other spin. This means that these fields cannot directly change the magnitude of total nuclear magnetism, only its direction, if rf inhomogeneity of the probe coil is ignored.

10 TRANSVERSE RELAXATION RATES AND DYNAMIC SHIFTS

Let us focus on two levels i and j giving an observable signal, or a forbidden coherence, at a frequency $\omega_{ij} = (E_i - E_j)/h$, where E_i and E_j are the energies of the two levels. We shall not write down the form for the elements of $\hat{R}$ in general, which can be found in many texts, as well as in other articles in this Encyclopedia. However, it is of interest to write the expressions for elements of $\hat{R}$ that are most closely analogous to Bloch's relaxation rates as explained above. The term similar to $T_1{}^{-1}$ is R_{iijj}, given by

$$\tfrac{1}{2}\, T_1^{-1}\rangle R_{iijj} = J_{ijij}(\omega_{ij}) + J_{jiji}(\omega_{ji}) \qquad (9a)$$

Here $T_1{}^{-1}$ is the apparent rate that would be measured for the spectral line at ω_{ij} by a selective saturation–recovery experiment, and '>' indicates that the actual apparent rate could be shortened by relaxation to levels other than i and j. The factor of $\frac{1}{2}$ multiplying $T_1{}^{-1}$ is inserted because Bloch's $T_1{}^{-1}$ is twice the rate constant connecting two levels in a two-level master equation, as one can verify by writing and solving such a master equation for the recovery of M_z. The Js are Fourier transforms of correlation functions of $\hat{K}$. They are called spectral densities, and are given in general by

$$J_{iji'j'}(\omega) = \int_{-\infty}^{\infty} \mathrm{e}^{\mathrm{i}\omega\tau}\, \langle K_{ij}(t) K^*_{i'j'}(t+\tau)\rangle \,\mathrm{d}\tau \qquad (10)$$

with * here denoting the complex conjugate. The expressions within the ensemble-average brackets $\langle\ \rangle$ are cross-correlation functions, or autocorrelation functions if $i', j' = i, j$. These are assumed to be real and independent of t, and are also assumed to be even functions of τ (that is, unchanged by the substitution of τ by $-\tau$). From these assumptions, it is easy to show that the right-hand side of equation (9a) is real, as it has to be.

The term of $\hat{R}$ most closely similar to Bloch's $T_2{}^{-1}$ is

$$\begin{aligned} T_2^{-1}\rangle R_{ijij} = {} & 2J_{iijj}(0) - J_{iiii}(0) - J_{jjjj}(0) \\ & - J_{ijij}(\omega_{ji}) - J_{jiji}(\omega_{ji}) \\ & - \sum_{m\neq i,j} [J_{mimi}(\omega_{mi}) + J_{mjmj}(\omega_{mj})] \end{aligned} \qquad (9b)$$

This equation is much simpler than it appears, and can be obtained from the original equations for the $\hat{R}$ matrix given elsewhere[6] and in ***Dynamic Frequency Shift***; ***Relaxation Processes: Cross Correlation and Interference Terms*** and ***Relaxation Theory for Quadrupolar Nuclei*** by rearranging sums, and substitution of equation (9a).

The first three terms on the right-hand side of equation (9b) can be rewritten [by substitution with equation (10)] as

$$\begin{aligned} & 2J_{iijj}(0) - J_{iiii}(0) - J_{jjjj}(0) \\ & \quad = -\int_{-\infty}^{\infty} \langle \Delta_{ij}(t)\Delta_{ij}(t+\tau)\rangle \,\mathrm{d}\tau \end{aligned} \qquad (11)$$

where $\Delta_{ij}(t) = K_{ii}(t) - K_{jj}(t)$. The quantity Δ_{ij} is just the fluctuating part of the first-order extra splitting between levels i and j produced by the perturbation $\hat{K}(t)$ for a member of the ensemble, and equation (11) is the zero-frequency spectral density associated with this fluctuation, or its 'motionally averaged' relaxation rate. This *adiabatic* term usually dominates relaxation in large molecules. Equation (11) also provides an important refinement over the rule of thumb above that transverse relaxation rates are proportional to $\omega_{\mathrm{i}}{}^2\tau_{\mathrm{c}}$, where $\omega_{\mathrm{i}}{}^2$ is approximately the size of squares of elements of $\hat{K}$. For T_2 processes, it is the size of fluctuating *differences* between diagonal elements of $\hat{K}$ that matters. The adiabatic contribution to $T_2{}^{-1}$ is often denoted by $(T_2{}^*)^{-1}$ (here of course, * does not indicate the complex conjugate).

For example, in larger proteins, the dipolar interaction between ^{15}N and H, for NH groups of fully ^{15}N-labeled proteins, might be expected to dominate linewidths. However, for double quantum evolution, as in heteronuclear double quantum correlation experiments, the dominant $\hat{I}_z\hat{S}_z$ part of the dipolar interaction does not contribute to widths, because it affects the two levels connected in the zero, and the double, quantum coherences equally. Thus the double quantum transition connects levels $m_I = m_S = +\frac{1}{2}$ with levels $m_I = m_S = -\frac{1}{2}$, and the expectation value of the operator $\hat{I}_z\hat{S}_z$ is the same for both of these levels. The spacing between these two

levels does not fluctuate as the molecule tumbles, even though the energy of each level fluctuates; they fluctuate together (as far as this particular dominant interaction is concerned). Simple reasoning of this kind is often useful in thinking about linewidths.

The next two terms of equation (9b) are equal, and the sum of their real parts is identical to R_{iijj} [see equation (9a)]. The real part often dominates, and its presence in equation (9b) indicates that T_1 processes will always contribute to T_2 processes. However, comparing with equation (9a), the contribution is only half of the minimum value ${T_1}^{-1}$. The origin of the factor $\frac{1}{2}$ can be seen for a model system consisting of a single spin interacting with a fluctuating field $\boldsymbol{h}(t)$. T_1 processes (longitudinal spin flips) are produced by both of the transverse components of $\boldsymbol{h}(t)$, namely h_x and h_y. However, transverse relaxation of magnetization M_x, for example, cannot be produced by h_x, only by h_y, because h_x is along M_x. Transverse relaxation can also be produced by h_z, but this latter contribution is the adiabatic kind of relaxation discussed above, represented by the first terms in equation (9b).

The terms of equation (9b) discussed so far are often described in the older literature by the equation ${T_2}^{-1} = ({T_2}^*)^{-1} + \frac{1}{2}T_1$.

The real part of the last terms expresses the obvious fact that T_1 relaxation to other levels m, in a multispin or $S > \frac{1}{2}$ system, will also contribute to T_2. However, in contrast to equation (9a), the last five terms of equation (9b) are not arranged in pairs ensuring that their sum is real. In fact, if the magnitudes of ω_{ij}, ω_{jm} or ω_{im} are greater than τ_c, the imaginary parts of these terms can be greater than the real parts, a fact that was not properly recognized in the earlier theories of weak relaxation, and was first emphasized by Paul Hubbard.[15] These imaginary contributions to 'T_2' give rise to 'dynamic shifts' of resonances, and are reviewed in ***Dynamic Frequency Shift***.

These dynamic shifts are useful for making an estimate of the size of fluctuating parts of $\hat{K}$. They can also be derived quantum mechanically as the second-order perturbation of the spin–lattice interaction, represented above semiclassically by $\hat{K}(t)$, on the spin levels.[15] An important example of a dynamic shift is that of the resonance connecting the $\pm\frac{1}{2}$ levels of a quadrupolar spin, relaxed by a fluctuating electric field gradient. In this case, $\hat{K}$ does not connect these levels directly, and the first terms of equation (9b) are therefore small. The last terms are mainly imaginary provided $\omega_0\tau_c > 1$, where ω_0 is the Larmor frequency.

11 DERIVATION OF THE RELAXATION EQUATION

The general form of the terms of $\hat{R}$ is given in some of the other articles in this Encyclopedia. It is most easily derived in the time-dependent Heisenberg representation mentioned above, in which the time-average main Hamiltonian $\hat{\mathcal{H}}_0$ is transformed to zero, and each element of the perturbation $K_{ij}(t)$ is replaced by $e^{i\omega_{ij}t}K_{ij}(t)$. Lacking the perturbation $\hat{K}(t)$, each ensemble member would have a stationary wavefunction in this representation, and $\hat{\sigma}$ would be time-independent. Relaxation is treated by considering a time Δt that is somewhat larger than any correlation time τ_c, but shorter than any relaxation time. It is always possible to define such a Δt, by the definition of weak limit relaxation, when that limit applies. One then gets an equation of motion by calculating $\hat{\sigma}(t + \Delta t) - \hat{\sigma}(t)$ using a perturbation expansion, and dividing by Δt to get $\mathrm{d}\hat{\sigma}/\mathrm{d}t$. The evolution of the c_i is calculated to second order in the elements of $\hat{K}$, for a member of the ensemble. Then the density matrix is formed from the c_i by using equation (4), and terms that are of first order in the $K_{ij}(t)$ vanish because the $K_{ij}(t)$ are zero in the ensemble average. The lowest nonzero terms are the second-order terms, while terms of higher than second order are assumed negligible, and are dropped. Finally, the solution outlined involves double integrals of correlation functions (multiplied by oscillating $e^{i\omega t}$ terms) with limits between t and $t + \Delta t$; these limits are extended to $\pm\infty$ because the integrands are assumed nonzero over only a short range, of the order of τ_c. The mathematics is very simple for secular elements of $\hat{R}$, and the assumptions involved are explained in detail elsewhere.[4,15] For nonsecular terms, the situation is more complicated; the contribution to the change in $\hat{\sigma}$ for a given time is smaller than it is for secular terms, but this decrease in effectiveness appears to be entirely due to the fact that the elements of $\hat{\sigma}$ in the Schrödinger representation, connected by the elements of $\hat{R}$, have a different time variation. So it was proposed that these elements could be taken to be time-independent in the Schrödinger representation and have essentially the same form as the secular terms. This somewhat unsatisfactory reasoning seems to have withstood the test of time.

The spectral densities $J(\omega)$ of elements of $\hat{R}$ are usually smoothly varying functions that become small for $\omega\tau_c > 1$. If τ_c is small compared with the Larmor frequencies then all the Js can be replaced by their values at zero frequency, and the $\hat{R}\hat{\sigma}$ term can then be written as a pleasing double commutator of $\hat{K}$ with $\hat{\sigma}$. This operator expression is also applicable in a modified form for high-field NMR, where levels are grouped into collections having nearly the same energy.[3,6,14] However, it is probably prudent to avoid using approximations in these operator methods for more complicated problems.

12 CONCLUSIONS

Weak relaxation theory was born with NMR, already well developed in BPP, and mature by the 25th anniversary of NMR. It achieved a new lease on life with the advent of FT NMR and, later, multidimensional methods, providing access to relaxation phenomena that were not dreamed of when the subject was developed. It is now virtually certain that computers will have a strong impact on the field, being able to predict the behavior of complex spin systems, to analyze data, and eventually to suggest better ways to obtain data, rather than relying on complicated analysis.

Experimentally, new developments will undoubtedly come from new pulse methods. An obvious general development will be the combination of pulse methods with high-speed high-resolution field cycling in some form, to map out completely the frequency dependence of spectral densities in a way that has so far been done only for the water resonance (described in ***Dynamics of Water in Biological Systems: Inferences from Relaxometry***).

The theory we have described has had minor impact in other fields. Obviously, it is useful for electron paramagnetic

resonance. Theory equivalent to BPP has also been developed by Zusman and others to describe the nonadiabatic regime of electron transfer.[18] Other forms of spectroscopy do not have the interesting variety of phenomena that NMR does, and such a theory is not needed.

13 RELATED ARTICLES

Chemical Exchange Effects on Spectra; Coupled Spin Relaxation in Polymers; Deuterium NMR in Solids; Diffusion Measurements by Magnetic Field Gradient Methods; Diffusion in Solids; Dynamic Frequency Shift; Dynamic NMR in Liquid Crystalline Solvents; Dynamics of Water in Biological Systems: Inferences from Relaxometry; Fast Ion Conductors; Field Cycling Experiments; Gas Phase Studies of Chemical Exchange Processes; Gas Phase Studies of Intermolecular Interactions and Relaxation; Gases at High Pressure; Overhauser Effect Imaging of Free Radicals; Liquid Crystalline Samples: Relaxation Mechanisms; Magnetization Transfer and Cross Relaxation in Tissue; Magnetization Transfer between Water and Macromolecules in Proton MRI; Molecular Motions: T_1 Frequency Dispersion in Biological Systems; Motional Effects on Protein Structure: Acyl Carriers; NOESY; Nuclear Overhauser Effect; Paramagnetic Relaxation in Solution; Protein Dynamics from NMR Relaxation; Protein Dynamics from Solid State NMR; Protein Structures: Relaxation Matrix Refinement; Quantum Tunneling Spectroscopy; Relaxation: An Introduction; Relaxation of Coupled Spins from Rotational Diffusion; Relaxation Effects of Chemical Exchange; Relaxation Matrix Refinement of Nucleic Acids; Relaxation Mechanisms: Magnetization Modes; Relaxation Processes in Coupled-Spin Systems; Relaxation Processes: Cross Correlation and Interference Terms; Relaxation of Quadrupolar Nuclei Measured via Multiple Quantum Filtration; Relaxation Theory for Quadrupolar Nuclei; Relaxation of Transverse Magnetization for Coupled Spins; Relaxometry of Tissue; ROESY; Rotating Frame Spin–Lattice Relaxation Off-Resonance; Selective Relaxation Techniques in Biological NMR; Slow and Ultraslow Motions in Biology; Spin–Rotation Relaxation Theory.

14 REFERENCES

1. F. Bloch, *Phys. Rev.*, 1946, **69**, 1.
2. N. Bloembergen, E. M. Purcell, and R. V. Pound, *Phys. Rev.*, 1948, **73**, 679.
3. A. Abragam, *Principles of Nuclear Magnetic Resonance*, Oxford University Press, Oxford, 1961.
4. C. P. Slichter, *Principles of Magnetic Resonance*, 3rd edn., Springer-Verlag, Berlin, 1990.
5. M. Goldman, *Quantum Description of High-Resolution NMR in Liquids*, Oxford University Press, Oxford, 1988.
6. R. R. Ernst, G. Bodenhausen, and A. Wokaun, *Principles of Nuclear Magnetic Resonance in One and Two Dimensions*, Oxford University Press, Oxford, 1987.
7. D. Wolf, *Spin-Temperature and Nuclear-Spin Relaxation in Matter*, Oxford University Press, Oxford, 1979.
8. L. T. Muus and P. W. Atkins (eds.), *Electron Spin Relaxation in Liquids*, Plenum Press, New York, 1972.
9. J. McConnell, *The Theory of Nuclear Magnetic Relaxation in Liquids*, Cambridge University Press, Cambridge, 1987.
10. R. Lenk, *Brownian Motion and Spin Relaxation*, Elsevier, Amsterdam, 1977.
11. R. Tycko (ed.), *Nuclear Magnetic Resonance Probes of Molecular Dynamics*, Plenum Press, New York, 1994.
12. P. W. Atkins, *Adv. Molec. Relax. Processes*, 1972, **2**, 121.
13. D. Kivelson and K. Ogan, in *Advances in Magnetic Resonance*, ed. J. S. Waugh, Academic Press, New York, 1974, Vol. 7, p. 72.
14. S. Szymanski and G. Binsch, *J. Magn. Reson.*, 1989, **81**, 104.
15. A. G. Redfield, in *Advances in Magnetic Resonance*, ed. J. S. Waugh, Academic Press, New York, 1965, Vol. 1, p. 1.
16. A. G. Redfield, in *NMR Basic Principles and Progress*, eds. P. Diehl, E. Fluck, and R. Kosfeld, Springer-Verlag, Berlin, 1976, Vol. 13, p. 1.
17. F. Reif, *Fundamentals of Statistical and Thermal Physics*, McGraw-Hill, New York, 1965.
18. J. Tan, Z. Wang, and J. R. Norris, *J. Chem. Phys.*, 1993, **99**, 97.

Acknowledgments

I thank Dr. L. Werbelow for helpful suggestions and information.

Biographical Sketch

Alfred G. Redfield. *b* 1929. B.A., 1950, Harvard, USA; Ph.D., 1993, University of Illinois at Champaign-Urbana. Postdoctoral works with N. Bloembergen, 1953–55. IBM Watson Laboratory at Columbia University and Adjunct Member, Columbia Physics Department, 1955–72. Professor of Physics and Biochemistry, Brandeis University, 1972–present. Sabbatical visitor in the laboratories of A. Abragam, 1960–61, and D. Koshland, 1970–72. Principal research interests: superconductivity, transfer RNA, and small G-proteins.

Relaxation Theory for Quadrupolar Nuclei

Lawrence G. Werbelow
New Mexico Tech, Socono, NM, USA

1	Introduction	1
2	The Electric Quadrupolar Interaction	1
3	Electric Quadrupolar Relaxation of Athermal Spin Polarizations	2
4	Electric Quadrupolar Relaxation of Nuclear Spin Coherence	4
5	Electric Quadrupolar Relaxation in the Rotating Frame	6
6	The Electric Quadrupolar Interaction and Dynamic Frequency Shifts	6
7	Effects of Alternative Sources of Relaxation for Quadrupolar Nuclei	7
8	Impact of Quadrupolar Relaxation on Spin-$\frac{1}{2}$ Nuclei	8
9	Summary	9
10	Related Articles	9
11	References	9

1 INTRODUCTION

Inasmuch as three-fourths of all NMR-receptive nuclei have measurable quadrupole moments, the electric quadrupolar interaction, and its ability to effect nuclear spin relaxation, necessarily plays a central role in both the theory and practice of nuclear magnetic resonance. Furthermore, in addition to the importance on relaxing high-spin nuclei, quadrupolar interactions impact upon the relaxation features of scalar-coupled spin-$\frac{1}{2}$ nuclei.

Except for nuclei occupying molecular sites of cubic electronic symmetry, the interaction strength of the quadrupolar coupling typically is on the order of 10^6–$10^8\ \mathrm{s}^{-1}$, whereas comparable dipolar, spin rotation and anisotropic shielding interaction strengths are on the order of 10^4–$10^5\ \mathrm{s}^{-1}$. Hence, electric quadrupolar interactions usually result in extremely efficient *dissipation* of nuclear spin coherence and restoration of thermal polarization for all $I > 1$ (quadrupolar and multipolar) nuclei. However, weaker relaxation pathways, often neglected in the discussion of the relaxation of quadrupolar nuclei, are responsible for relaxation-induced polarization and coherence *transfer*.

In the context of high-resolution and multidimensional NMR, homogeneous line broadenings associated with the efficiency of quadrupolar relaxation present a number of challenging obstacles. In contrast, the general dominance of quadrupolar relaxation generally facilitates its application in the study of molecular dynamics. For applications involving spin-$\frac{1}{2}$ nuclei, it often proves difficult to isolate and identify competitive relaxation pathways. Furthermore, for spin-$\frac{1}{2}$ nuclei, inter- and intramolecular effects must be differentiated, whereas quadrupolar relaxation is purely intramolecular in nature.

Finally, from a theoretical vantage, a discussion of quadrupolar relaxation can be utilized to illustrate numerous symmetries and characteristics common to spin relaxation in any multistate system.

2 THE ELECTRIC QUADRUPOLAR INTERACTION

The electric quadrupolar interaction between a nuclear spin $\hat{\boldsymbol{I}}$ and a nonzero electric field gradient can be written compactly in tensor notation, $\hat{\mathcal{F}}^{\mathrm{Q}I} \propto \hat{\boldsymbol{I}} \cdot \boldsymbol{Q} \cdot \hat{\boldsymbol{I}}$. When written in this manner, the functional similarity between a quadrupolar interaction and an electron zero field splitting or a dipole–dipole coupling between equivalent nuclei is apparent. Since the coupling tensor $\boldsymbol{Q}$ is both symmetric and traceless, only two of the three principal components are independent. Although various conventions exist, this coupling is usually characterized by a principal value $q_{zz} \sum q_I$ and asymmetry $\eta = (q_{yy} - q_{xx})/q_{zz}$, with $|q_{zz}| > |q_{xx}| > |q_{yy}|$.

Application of the Wigner–Eckart theorem demonstrates that the quadrupolar interaction vanishes unless $I \geq 1$. Some of the more important members of the set of nuclei subject to the quadrupolar interaction are ^{2}H and ^{14}N ($I = 1$), ^{7}Li and ^{23}Na ($I = \frac{3}{2}$), ^{17}O and ^{27}Al ($I = \frac{5}{2}$), and ^{43}Ca and ^{59}Co ($I = \frac{7}{2}$).

If the electric field gradient tensor is axially symmetric ($\eta = 0$), the quadrupolar coupling can be written simply as

$$\hat{\mathcal{F}}^{\mathrm{Q}I} = \frac{e^2 q_I Q_I}{4I(2I-1)\hbar}(3\hat{I}^2_{z\mathrm{mol}} - \hat{I}^2) \tag{1}$$

Additional parameters appearing in equation (1) include the charge q_I and the nuclear electric quadrupole moment eQ_I. Occasionally, the quadrupolar coupling is written in terms of a gradient anisotropy $\Delta Q = \frac{3}{2}q_I = \frac{3}{2}q_{zz} = q_{zz} - \frac{1}{2}(q_{xx} + q_{yy})$. A subscript is attached to the operator $\hat{I}_z$ to emphasize that this interaction is defined in the molecular frame. In the presence of an applied external magnetic field $\boldsymbol{B}_0$, where $|\gamma_I B_0 \sum \omega_I| \gg |e^2 q_I Q_I/\hbar|$, the spins are effectively quantized in the laboratory frame. In all subsequent discussion, this form of the high-field approximation will be implicit. For arbitrary relative orientations of these two frames, $\hat{\mathcal{F}}^{\mathrm{Q}I}$ can be written as a scalar product of spin and spatial coordinates:

$$\hat{\mathcal{F}}^{\mathrm{Q}I} = \xi_{\mathrm{Q}I} \sum_n (-1)^n \hat{T}^n_{\mathrm{Q}}(I) V^{-n}_{\mathrm{Q}}(\theta, \phi) \tag{2a}$$

The spin operators are defined as

$$T^{\pm 2}_{\mathrm{Q}} = \frac{\hat{I}^2_{\pm}}{I(2I-1)}, \quad \hat{T}^{\pm 1}_{\mathrm{Q}} = \mp\frac{\hat{I}_{\pm}(2\hat{I}_z + 1)}{I(2I-1)}$$
$$\hat{T}^0_{\mathrm{Q}} = \left(\frac{2}{3}\right)^{1/2} \frac{3\hat{I}^2_z - \hat{I}^2}{I(2I-1)} \tag{2b}$$

The lattice or orientation functions $V^n_Q(\theta, \phi)$ are normalized rank-2 spherical harmonics. The angular arguments position the unique axis of the diagonalized electric field gradient tensor in the laboratory frame. The interaction constant is defined as $\xi_{\mathrm{Q}I} = (\frac{3}{40}\pi)^{1/2} e^2 q_I Q_I/\hbar$.

Hence, in a rigid system such as a solid, the energy level spacings for quadrupolar nuclei depend on the molecular orientation relative to the direction of the external field. These

levels do not vary in time, and a rigid lattice powder pattern results. However, in the presence of molecular motions, the energy levels appear time-dependent and act as a source of magnetic relaxation.

For a nonaxially symmetric field gradient, the electric quadrupolar interaction takes the form

$$\hat{\mathcal{F}}^{\mathrm{Q}I} = \frac{e^2 q_I Q_I}{4I(2I-1)\hbar}[(3\hat{I}^2_{z\mathrm{mol}} - \hat{I}^2) + \tfrac{1}{2}\eta(\hat{I}^2_+ + \hat{I}^2_-)] \tag{3}$$

Unfortunately, the analog of equation (2a) is cumbersome, and the separation of spin and spatial coordinates from the interaction constants proves impossible. However, it is possible to rewrite any traceless rank-2 tensor $\boldsymbol{Q}$ as the sum of two, axially symmetric composites:

$$\begin{bmatrix} q_{xx} & \vdots & \vdots \\ \cdots & \cdots & \cdots \\ \vdots & q_{yy} & \vdots \\ \cdots & \cdots & \cdots \\ \vdots & \vdots & q_{zz} \end{bmatrix} = \Delta Q^+ \begin{bmatrix} \frac{2}{3} & \vdots & \vdots \\ \cdots & \cdots & \cdots \\ \vdots & -\frac{1}{3} & \vdots \\ \cdots & \cdots & \cdots \\ \vdots & \vdots & -\frac{1}{3} \end{bmatrix} + \Delta Q^- \begin{bmatrix} -\frac{1}{3} & \vdots & \vdots \\ \cdots & \cdots & \cdots \\ \vdots & \frac{2}{3} & \vdots \\ \cdots & \cdots & \cdots \\ \vdots & \vdots & -\frac{1}{3} \end{bmatrix} \tag{4a}$$

where

$$\left.\begin{aligned} \Delta Q^+ &= q_{xx} - q_{zz} = -\Delta Q(1 + \tfrac{1}{3}\eta) \\ \Delta Q^- &= q_{yy} - q_{zz} = -\Delta Q(1 - \tfrac{1}{3}\eta) \\ \Delta Q &= q_{zz} - \tfrac{1}{2}(q_{xx} + q_{yy}) \\ \eta &= \frac{3(q_{yy} - q_{xx})}{2\Delta Q} \end{aligned}\right\} \tag{4b}$$

An important equivalence between the $(\Delta Q, \eta)$ and the $(\Delta Q^+, \Delta Q^-)$ representations is

$$\begin{aligned} &\tfrac{1}{2}[(q_{xx} - q_{yy})^2 + (q_{xx} - q_{zz})^2 + (q_{yy} - q_{zz})^2] \\ &\quad = (\Delta Q)^2\left(1 + \tfrac{1}{3}\eta^2\right) \\ &\quad = (\Delta Q^+)^2 + (\Delta Q^-)^2 - (\Delta Q^+)(\Delta Q^-) \end{aligned} \tag{5}$$

The two resultant anisotropies $\Delta Q^{\pm}$ are axially symmetric and mutually orthogonal. This alternative description enables the separation of the interaction constants from the lattice variables as implied by equation (2a). However, with respect to relaxation considerations, these two composite interactions are temporally correlated, and this correlation must not be neglected.

3 ELECTRIC QUADRUPOLAR RELAXATION OF ATHERMAL SPIN POLARIZATIONS

Spin–lattice or longitudinal relaxation in the $(2I + 1)$-level system associated with a collection of isolated spin-I nuclei can be described in master equation form:[1]

$$-\frac{\mathrm{d}}{\mathrm{d}t}P_n = \sum_{m \neq n} W_{nm}(\Delta P_m - \Delta P_n) \tag{6}$$

P_n is the population of the nth state, ΔP_n denotes the deviation of this population from the associated thermal equilibrium value, $\Delta P_n = P_n - P_n(\mathrm{eq})$, and W_{nm} $(=W_{mn})$ is the appropriate transition probability per unit time. Because of the nature of the quadrupolar interaction, W_{nm} vanishes unless $m = n \pm 1$ or $m = n \pm 2$. Values for these two transition probabilities can be written in concise form as

$$\begin{aligned} W_{n,n-1} &= W_{-n+1,-n} \\ &= \frac{2(2n-1)^2(I-n+1)(I+n)}{I^2(2I-1)^2} J_1^{\mathrm{Q}}(\omega_I) \end{aligned} \tag{7}$$

$$\begin{aligned} W_{n,n-2} &= W_{-n+2,-n} \\ &= \frac{2(I-n+2)(I-n+1)(I+n-1)(I+n)}{I^2(2I-1)^2} J_2^{\mathrm{Q}}(2\omega_I) \end{aligned} \tag{8}$$

The spectral density function[2] for an *axially symmetric quadrupolar* coupling is defined as

$$\begin{aligned} J_k^{\mathrm{Q}}(\omega) &= (4\pi)^{-1}(\xi_{\mathrm{Q}I})^2 \\ &\quad \times \mathrm{Re}\left[\int_0^\infty \langle Y_2^k(\theta(t), \phi(t)) Y_2^{-k}(\theta(0), \phi(0))\rangle \right. \\ &\quad \left. \times \exp(-\mathrm{i}\omega t)\,\mathrm{d}t\right] \end{aligned} \tag{9}$$

For isotropic media ($\langle \hat{\mathcal{F}}^{\mathrm{Q}I}(t)\rangle = 0$), the k dependence of the spectral density is superfluous.[3] In subsequent developments, *unless this index is explicitly shown*, the limit $J_k^{\mathrm{Q}}(\omega) = J_{k'}^{\mathrm{Q}}(\omega)$ $\sum$ $J^{\mathrm{Q}}(\omega)$ is assumed.

For *isotropic, diffusional reorientation* of the molecular frame relative to the laboratory frame, equation (9) reduces to

$$J^{\mathrm{Q}}(\omega) = \frac{3}{160}\left(\frac{e^2 q_I Q_I}{\hbar}\right)^2 \frac{\tau_2}{1 + \omega^2\tau_2^2} \tag{10}$$

The correlation time $\tau_2 = \frac{1}{6}D$, where D is the rotational diffusion constant.

For *symmetric-top reorientation* characterized by an axially symmetric diffusion tensor with principal components D_{zz} and $D_{xx} = D_{yy}$,

$$\begin{aligned} J^{\mathrm{Q}}(\omega) &= \frac{3}{640}\left(\frac{e^2 q_I Q_I}{\hbar}\right)^2 \left[\frac{(3\cos^2\theta - 1)^2\tau_{20}}{1 + (\omega\tau_{20})^2}\right. \\ &\quad \left. + \frac{12\cos^2\theta\sin^2\theta\,\tau_{21}}{1 + (\omega\tau_{21})^2} + \frac{3\sin^4\theta\,\tau_{22}}{1 + (\omega\tau_{22})^2}\right] \end{aligned} \tag{11}$$

Here θ is the angle between the principal axes of the diffusion and electric quadrupole tensors. The three correlation times are defined as $1/\tau_{2n} = 6D_{zz} + n^2(D_{zz} - D_{xx})$. In general, the molecular coordinate frames that diagonalize the diffusion and the electric field gradient tensors are not coincident.

The spectral density function, for an *asymmetric quadrupolar* coupling, assuming symmetric-top diffusional reorientation, can be described with either one of the two alternative

representations discussed earlier:

$$\begin{aligned} J^{\mathrm{Q}}(\omega) = (16\pi)^{-1}\Bigg\{ & \frac{[\xi_{\mathrm{Q}Ix}(3\cos^2\theta_x - 1)^2 + \xi_{\mathrm{Q}Iy}(3\cos^2\theta_y - 1)]^2\tau_{20}}{1+(\omega\tau_{20})^2} \\ & + 3(\xi_{\mathrm{Q}Ix})^2\left[\frac{4\cos^2\theta_x \sin^2\theta_x \tau_{21}}{1+(\omega\tau_{21})^2} + \frac{\sin^4\theta_x\tau_{22}}{1+(\omega\tau_{22})^2}\right] \\ & + 3(\xi_{\mathrm{Q}Iy})^2\left[\frac{4\cos^2\theta_y \sin^2\theta_y \tau_{21}}{1+(\omega\tau_{21})^2} + \frac{\sin^4\theta\tau_{22}}{1+(\omega\tau_{22})^2}\right] \\ & + 6\xi_{\mathrm{Q}Ix}\xi_{\mathrm{Q}Iy}\left[\frac{4\cos\theta_x\cos\theta_y\sin\theta_x\sin\theta_y\cos(\phi_x-\phi_y)\tau_{21}}{1+(\omega\tau_{21})^2}\right. \\ & \left. + \frac{\sin^2\theta_x\sin^2\theta_y\cos(2\phi_x-2\phi_y)\tau_{22}}{1+(\omega\tau_{22})^2}\right]\Bigg\} \end{aligned} \tag{12}$$

or

$$\begin{aligned} J^{\mathrm{Q}}(\omega) = \frac{3}{640}\left(\frac{e^2qQ}{\hbar}\right)^2\Bigg\{ & \frac{(3\cos^2\theta - 1 - \eta\sin^2\theta\cos 2\phi)^2\tau_{20}}{1+(\omega\tau_{20})^2} \\ & + \{12\sin^2\theta\,[\cos^2\theta\,(1+2\eta\cos 2\phi) \\ & + (\tfrac{1}{3}\eta)^2(1-\cos^2 2\phi\sin^2\theta)]\tau_{21}\}[1+(\omega\tau_{21})^2]^{-1} \\ & + [3\sin^4\theta - 2\eta\sin^2\theta\,(\cos^2\theta+1)\cos 2\phi \\ & + \tfrac{1}{3}\eta^2(\cos^2 2\phi\sin^4\theta + 4\cos^2\theta)]\frac{\tau_{22}}{1+(\omega\tau_{22})^2}\Bigg\} \end{aligned} \tag{13}$$

The parameters $\xi_{\mathrm{Q}Ix}$ and $\xi_{\mathrm{Q}Iy}$ are defined as $(q_{xx} - q_{zz})(\frac{1}{30}\pi)^{1/2}e^2Q_I/\hbar$ and $(q_{yy} - q_{zz})(\frac{1}{30}\pi)^{1/2}e^2Q_I/\hbar$, respectively. Utilizing equation (5), it can be seen that for isotropic reorientation, equation (12) or equation (13) reduces to

$$\begin{aligned} J^{\mathrm{Q}}(\omega) &= (1+\tfrac{1}{3}\eta^2)\frac{3}{160}\left(\frac{e^2qQ}{\hbar}\right)^2\frac{\tau_2}{1+\omega^2\tau_2^2} \\ &= [(q_{xx}-q_{yy})^2 + (q_{xx}-q_{zz})^2 + (q_{yy}-q_{zz})^2] \\ &\quad \times \frac{1}{240}\left(\frac{e^2Q}{\hbar}\right)^2\frac{\tau_2}{1+\omega^2\tau_2^2} \end{aligned} \tag{14}$$

Although equation (6) implies that the spin–lattice relaxation is described by $2I + 1$ coupled equations, transformation to an appropriate operator basis, which results in both a conceptual and mathematical simplification, proves otherwise. Using the irreducible spherical tensor basis consisting of the operators

$$\left.\begin{aligned} \hat{T}_1^0 &\propto \langle \hat{I}_z\rangle \\ \hat{T}_2^0 &\propto \langle 3\hat{I}_z^2 - \hat{I}^2\rangle \\ \hat{T}_3^0 &\propto \langle 5\hat{I}_z^3 - \hat{I}_z(3\hat{I}^2 - 1)\rangle \\ \hat{T}_4^0 &\propto \langle 35\hat{I}_z^4 - 5\hat{I}_z^2(6\hat{I}^2 - 5) + 3\hat{I}^2(\hat{I}^2 - 2)\rangle \\ \hat{T}_5^0 &\propto \langle 63\hat{I}_z^5 - 35\hat{I}_z^3(2\hat{I}^2 - 3) + (15\hat{I}^4 - 50\hat{I}^2 + 12)\hat{I}_z\rangle \\ \hat{T}_6^0 &\propto \langle 231\hat{I}_z^6 - 105\hat{I}_z^4(3\hat{I}^2 - 7) + 21\hat{I}_z^2(5\hat{I}^4 - 25\hat{I}^2 + 14) \\ &\quad - 5(\hat{I}^6 - 8\hat{I}^4 + 12\hat{I}^2)\rangle \\ &\vdots \end{aligned}\right\} \tag{15}$$

the longitudinal relaxation is described by the concise expression

$$-\frac{\mathrm{d}}{\mathrm{d}t}\hat{T}_L^0 = \sum_{L'} R_{L,L'}^{0,I}(\Delta\hat{T}_{L'}^0) \tag{16}$$

If extreme narrowing $[J_k^{\mathrm{Q}}(0) = J_k^{\mathrm{Q}}(\omega_0) = J_k^{\mathrm{Q}}(2\omega_0) \sum J_k^{\mathrm{Q}}]$ and spatial isotropy $[(J_k^{\mathrm{Q}}(\omega) = J_{k'}^{\mathrm{Q}}(\omega)]$ obtain then[4]

$$R_{L,L'}^{0,I} = \delta_{LL'}\{2L(L+1)[4I(I+1) - L(L+1) - 1](2I^2 - I)^{-2}\}J^{\mathrm{Q}} \tag{17}$$

For various situations of practical importance, the spectral density J^{Q} is given by equations (10)–(13). Table 1 provides a listing of $R_{L,L}^{0,I}J^{\mathrm{Q}}$ for various ranks L and spins I.

If conditions of extreme narrowing and spatial isotropy are not realized, additional couplings of the form $R_{L,L'}^{0,I} = \delta_{LL\pm2}C_{L,L\mp2}^{0,I}[J_1^{\mathrm{Q}}(\omega_I) - J_2^{\mathrm{Q}}(2\omega_I)]$ arise. Specific values of the proportionality constant $C_{L,L\mp2}^{0,I}$ for various spins I and ranks L can be found in the literature.[5,6] Thus, monoexponential relaxation of the Zeeman magnetization ($\propto \hat{T}_1^0$) quantified by a well-defined spin–lattice relaxation rate $R_{11}^{0,I} = 1/T_1$ occurs for arbitrary I if and only if extreme narrowing and spatial isotropy obtain. In this limit, $1/T_1 = 4(2I+3)(2I^3 - I^2)^{-1}J^{\mathrm{Q}}$.

The parity of each member of the operator basis introduced in equation (15) with respect to spin inversion is defined by

$$\exp(-\mathrm{i}\pi\hat{I}_y)\,\hat{T}_L^0\exp(+\mathrm{i}\pi\hat{I}_y) = (-1)^L\hat{T}_L^0 \tag{18}$$

Relaxation effected via the quadrupolar interaction does not couple operators of different parity.[7] If I is an integer then $\hat{T}_1^0$ couples into $I - 1$ additional polarizations of similar parity. An additional manifold comprising I polarizations, including 'quadrupolar order' ($\hat{T}_2^0$), also couple together. These latter polarizations are consequential only in anisotropic environments, where residual quadrupolar couplings lift the spectral degeneracy of various transitions. Similarly, if I is a half-integer then $\hat{T}_1^0$ couples into $\frac{1}{2}(2I+1)$ additional polarizations of similar parity. The remaining $\frac{1}{2}(2I-1)$ polarizations of opposite parity also couple together. Obviously, if $I = 1$ then there is monoexponential relaxation of the Zeeman polarization $\hat{T}_1^0$, characterized by the relaxation rate

$$R_{1,1}^{0,1} = 1/T_1 = 4[J_1^{\mathrm{Q}}(\omega_I) + 4J_2^{\mathrm{Q}}(2\omega_I)] \tag{19}$$

and quadrupolar order, characterized by the relaxation rate

$$R_{2,2}^{0,1} = 12J_1^{\mathrm{Q}}(\omega_I) \tag{20}$$

regardless of whether or not extreme narrowing obtains.

Although the relaxation characteristics of $I = 1$ are exceptionally simple, the behavior of $I = \frac{3}{2}$ is only slightly more complex.[8] Quadrupolar polarization or alignment decays exponentially with rate

$$R_{2,2}^{0,3/2} = \tfrac{16}{3}[J_1^{\mathrm{Q}}(\omega_I) + J_2^{\mathrm{Q}}(2\omega_I)] \tag{21}$$

Zeeman and octupolar ($\hat{T}_3^0$) order each evolve biexponentially. For an initial spin preparation (perturbation) that only disturbs Zeeman order, it can be shown that

$$\left.\begin{aligned} \frac{\Delta\langle\hat{I}_z(t)\rangle}{\Delta\langle\hat{I}_z(0)\rangle} &= \tfrac{1}{5}\exp[-\tfrac{16}{3}tJ_1^{\mathrm{Q}}(\omega_I)] \\ &\quad + \tfrac{4}{5}\exp[-\tfrac{16}{3}tJ_2^{\mathrm{Q}}(2\omega_I)] \\ \frac{\langle\hat{I}_z(0)\rangle - \langle\hat{I}_z(t\to 0)\rangle}{\Delta\langle\hat{I}_z(0)\rangle} &\approx R_{1,1}^{0,3/2}t \\ &= \tfrac{16}{15}t[J_1^{\mathrm{Q}}(\omega_I) + 4J_2^{\mathrm{Q}}(2\omega_I)] \end{aligned}\right\} \tag{22}$$

Table 1 The Electric Quadrupolar Relaxation Rates $R^{0,I}_{L,L}$ for Various Spins I and Spin Orders L

	$I = 1$	$I = \frac{3}{2}$	$I = 2$	$I = \frac{5}{2}$	$I = 3$	$I = \frac{7}{2}$	$I = 4$	$I = \frac{9}{2}$
$L = 1$	$20J^{\mathrm{Q}}$	$\frac{16}{3}J^{\mathrm{Q}}$	$\frac{7}{3}J^{\mathrm{Q}}$	$\frac{32}{25}J^{\mathrm{Q}}$	$\frac{4}{5}J^{\mathrm{Q}}$	$\frac{80}{147}J^{\mathrm{Q}}$	$\frac{11}{28}J^{\mathrm{Q}}$	$\frac{8}{27}J^{\mathrm{Q}}$
$L = 2$	$12J^{\mathrm{Q}}$	$\frac{32}{3}J^{\mathrm{Q}}$	$\frac{17}{3}J^{\mathrm{Q}}$	$\frac{84}{25}J^{\mathrm{Q}}$	$\frac{164}{75}J^{\mathrm{Q}}$	$\frac{32}{21}J^{\mathrm{Q}}$	$\frac{219}{196}J^{\mathrm{Q}}$	$\frac{23}{27}J^{\mathrm{Q}}$
$L = 3$		$\frac{16}{3}J^{\mathrm{Q}}$	$\frac{22}{3}J^{\mathrm{Q}}$	$\frac{132}{25}J^{\mathrm{Q}}$	$\frac{56}{15}J^{\mathrm{Q}}$	$\frac{400}{147}J^{\mathrm{Q}}$	$\frac{201}{98}J^{\mathrm{Q}}$	$\frac{43}{27}J^{\mathrm{Q}}$
$L = 4$			$\frac{10}{3}J^{\mathrm{Q}}$	$\frac{28}{5}J^{\mathrm{Q}}$	$\frac{72}{15}J^{\mathrm{Q}}$	$\frac{80}{21}J^{\mathrm{Q}}$	$\frac{295}{98}J^{\mathrm{Q}}$	$\frac{65}{27}J^{\mathrm{Q}}$
$L = 5$				$\frac{12}{5}J^{\mathrm{Q}}$	$\frac{68}{15}J^{\mathrm{Q}}$	$\frac{640}{147}J^{\mathrm{Q}}$	$\frac{15}{4}J^{\mathrm{Q}}$	$\frac{85}{27}J^{\mathrm{Q}}$
$L = 6$					$\frac{28}{15}J^{\mathrm{Q}}$	$\frac{80}{21}J^{\mathrm{Q}}$	$\frac{111}{28}J^{\mathrm{Q}}$	$\frac{98}{27}J^{\mathrm{Q}}$
$L = 7$						$\frac{32}{21}J^{\mathrm{Q}}$	$\frac{23}{7}J^{\mathrm{Q}}$	$\frac{98}{27}J^{\mathrm{Q}}$
$L = 8$							$\frac{9}{7}J^{\mathrm{Q}}$	$\frac{26}{9}J^{\mathrm{Q}}$
$L = 9$								$\frac{10}{9}J^{\mathrm{Q}}$

$$\left.\begin{aligned}\frac{\langle 5\hat{I}_z^3 - \hat{I}_z(3\hat{I}^2-1)(t)\rangle}{\Delta\langle \hat{I}_z(0)\rangle} &= \tfrac{6}{5}\{\exp[-\tfrac{16}{3}tJ_1^{\mathrm{Q}}(\omega_I)] \\ &\quad - \exp[-\tfrac{16}{3}tJ_2^{\mathrm{Q}}(2\omega_I)]\} \\ \frac{\langle 5\hat{I}_z^3 - \hat{I}_z(3\hat{I}^2-1)(t\to 0)\rangle}{\Delta\langle \hat{I}_z(0)\rangle} &\approx -R_{3,1}^{0,3/2}t \\ &= -\tfrac{32}{5}t[J_1^{\mathrm{Q}}(\omega_I) - J_2^{\mathrm{Q}}(2\omega_I)]\end{aligned}\right\} \quad (23)$$

For spin $I = \frac{3}{2}$, it is illustrative to define two fictitious spin operators,[9] $\langle \hat{I}_z^{\mathrm{b}}\rangle = \frac{3}{2}[(P_{3/2} - P_{1/2}) + (P_{-1/2} - P_{-3/2})]$ and $\langle \hat{I}_z^{\mathrm{n}}\rangle = 2(P_{1/2} - P_{-1/2})$. Thus, $\langle \hat{I}_z\rangle = \langle \hat{I}_z^{\mathrm{b}}\rangle + \langle \hat{I}_z^{\mathrm{n}}\rangle$ and $\langle 5\hat{I}_z^3 - \hat{I}_z(3\hat{I}^2-1)\rangle = \langle \hat{I}_z^{\mathrm{b}}\rangle - \frac{3}{2}\langle \hat{I}_z^{\mathrm{n}}\rangle$. These identifications permit the following transformation of the kinetic equations for $I = \frac{3}{2}$:

$$\frac{5}{2}\frac{\langle \hat{I}_z^{\mathrm{n}}(t)\rangle - \frac{2}{5}\langle \hat{I}_z(\mathrm{eq})\rangle}{\Delta\langle \hat{I}_z(0)\rangle} = 2\exp[-\tfrac{16}{3}tJ_2^{\mathrm{Q}}(2\omega_I)] - \exp[-\tfrac{16}{3}tJ_1^{\mathrm{Q}}(\omega_I)] \quad (24)$$

$$\frac{5}{3}\frac{\langle \hat{I}_z^{\mathrm{b}}(t)\rangle - \frac{3}{5}\langle \hat{I}_z(\mathrm{eq})\rangle}{\Delta\langle \hat{I}_z(0)\rangle} = \exp[-\tfrac{16}{3}tJ_1^{\mathrm{Q}}(\omega_I)] \quad (25)$$

For $I = \frac{3}{2}$, one has the highly unusual situation where a specific population difference ($P_{3/2} - P_{1/2}$ or $P_{-1/2} - P_{-3/2}$) is characterized by simple exponential relaxation. Furthermore, if $J_2^{\mathrm{Q}}(2\omega_I) < \frac{1}{2}J_1^{\mathrm{Q}}(\omega_I)$, the deviation population difference $\Delta(P_{1/2} - P_{-1/2})$ initially grows rather than decays!

Although integrated forms of equation (16) cannot be written in tractable form, for higher spin nuclei, the *initial* response to any perturbation of $\hat{I}_z$ is always described by

$$\frac{\langle \hat{I}_z(0)\rangle - \langle \hat{I}_z(t\to 0)\rangle}{\Delta\langle \hat{I}_z(0)\rangle} \approx R_{1,1}^{0,I}t \quad (26)$$

where

$$R_{1,1}^{0,I} = 1/T_1 = \tfrac{4}{5}(2I+3)I^{-2}(2I-1)^{-1}[J_1^{\mathrm{Q}}(\omega_I) + 4J_2^{\mathrm{Q}}(2\omega_I)] \quad (27)$$

4 ELECTRIC QUADRUPOLAR RELAXATION OF NUCLEAR SPIN COHERENCE

Because of the efficiency of the quadrupolar interaction in effecting nuclear spin relaxation, usually inhomogenous line broadening can be assumed negligible, and spin–spin or transverse relaxation rates can be abstracted directly from measurement of linewidths.

In addition to the aforementioned $2I + 1$ populations, a collection of isolated spin-I nuclei is characterized by $2I$ single quantum coherences (1QCs), $2I - 1$ double quantum coherences (2QCs), ... , two $(2I - 1)$QCs and one $(2I)$QC. At thermal equilibrium, all coherence vanishes. Generalized 'spin–spin' relaxation in a multilevel system can be described in a manner analogous to equation (6):

$$-\frac{\mathrm{d}}{\mathrm{d}t}\chi_{nn'} = \mathrm{i}(\omega_{nn'} + \Omega_{nn'})\chi_{nn'} + \left[Z_{nn'} + \tfrac{1}{2}\sum_j (W_{nj} + W_{n'j})\right]\chi_{nn'} + \sum_{m,m'}\delta(\omega_{nn'} - \omega_{mm'})(W_{nm}W_{n'm'})^{1/2}\chi_{mm'} \quad (28)$$

In the absence of applied rf fields, the evolution of coherence between states $|n\rangle$ and $|n'\rangle$, $\chi_{nn'}$, is characterized by an intrinsic frequency $\omega_{nn'}$, a dynamic frequency shift, $\Omega_{nn'}$, an adiabatic term or zero frequency contribution $Z_{nn'}$, lifetime terms $W_{nn'}$, which were defined earlier, and a secular coupling term $(W_{nm}W_{n'm'})^{1/2}$, which vanishes unless the coherences $\chi_{nn'}$ and $\chi_{mm'}$ are degenerate or overlapping (the secular approximation). The validity of equation (28) is restricted to the motionally narrowed, perturbative regime, $1/\tau_2 \rangle Z_{nn'}, |\hat{\mathcal{F}}^{\mathrm{Q}I}|$.

In the absence of multiplet structure attributed to a residual quadrupolar interaction, each set of $2I + 1 - n$, nQCs are degenerate. With the additional stipulation of extreme narrowing, the perturbation–response characteristics of these coherences are remarkably simple. Once again, this is revealed by transformation to an irreducible spherical tensor operator basis:

$$\left.\begin{aligned}\hat{T}_1^{\pm 1} &\propto \langle \hat{I}_\pm\rangle \\ \hat{T}_2^{\pm 1} &\propto \langle \hat{I}_\pm(2\hat{I}_z \pm 1)\rangle \\ \hat{T}_2^{\pm 2} &\propto \langle \hat{I}_\pm^2\rangle \\ \hat{T}_3^{\pm 1} &\propto \langle \hat{I}_\pm[5\hat{I}_z^2 \pm 5\hat{I}_z + (2 - \hat{I}^2)]\rangle \\ \hat{T}_3^{\pm 2} &\propto \langle \hat{I}_\pm^2(\hat{I}_z \pm 1)\rangle \\ \hat{T}_3^{\pm 3} &\propto \langle \hat{I}_\pm^3\rangle \\ &\vdots \\ \hat{T}_{2I}^{\pm(2I-1)} &\propto \langle \hat{I}_\pm^{(2I-1)}[2\hat{I}_z \pm (2I-1)]\rangle \\ \hat{T}_{2I}^{\pm 2I} &\propto \langle \hat{I}_\pm^{2I}\rangle\end{aligned}\right\} \quad (29)$$

The relaxation behavior of these coherences can be cast in a form identical to equation (16):

$$-\frac{\mathrm{d}}{\mathrm{d}t}\hat{T}_L^{\pm k} = \pm \mathrm{i}k\omega_I + \sum_{L'} R_{L,L'}^{k,I}\hat{T}_L^{\pm k} \tag{30}$$

For the moment, the dynamic frequency shift is ignored.

The validity of the secular approximation ensures that only coherences of similar precessional frequency couple together. In the limit of extreme narrowing,

$$R_{L,L'}^{k,I} = R_{L,L'}^{0,I} = \delta_{LL'}\{2L(L+1) \times [4I(I+1) - L(L+1) - 1](2I^2 - I)^{-2}\}J^{\mathrm{Q}} \tag{31}$$

When extreme narrowing fails, additional couplings of the form $R_{L,L'}^{k,I} = \delta_{LL\pm 2}\,\Sigma_{n=0}^{2} C_{L,L\mp 2}^{k,n,I} J_n^{\mathrm{Q}}(n\omega_I)$ arise. Selected values of $C_{L,L\mp 2}^{1,n,I}$ for various spins I and ranks L can be found in the literature.[6] Again, monoexponential relaxation of single quantum coherence or 'transverse' magnetization ($\propto \hat{T}_1^{\pm 1}$), quantified by a well-defined spin–spin relaxation rate $R_{1,l}^{1,I} = 1/T_2$, results for arbitrary I if and only if extreme narrowing obtains: $1/T_2 = 1/T_1 = 4(2I+3)(2I^3 - I^2)^{-1}\,J^{\mathrm{Q}}$.

However, there are other interesting decay rates that can be expressed in closed analytic form. For example, the dissipation of $(2I)$QC ($\hat{T}_{2I}^{2I}$) and in-phase ($\hat{T}_{2I-1}^{2I-1}$) and antiphase ($\hat{T}_{2I}^{2I-1}$) $2I-1$ multiple quantum coherences are determined by the respective rates

$$R_{2I,2I}^{2I,I} = (4I^{-1})J_1^{\mathrm{Q}}(\omega_I) + 8I^{-1}(2I-1)^{-1}J_2^{\mathrm{Q}}(2\omega_I) \tag{32}$$

$$R_{2I-1,2I-1}^{2I-1,I} = 2I^{-2}(2I-1)^{-1}\{3(2I-1)J_0^{\mathrm{Q}}(0) + [4I(2I-1) + (2I-3)^2]J_1^{\mathrm{Q}}(\omega_I) + 2(4I-3)J_2^{\mathrm{Q}}(2\omega_I)\} \tag{33}$$

$$R_{2I,2I}^{2I-1,I} = 2I^{-2}(2I-1)^{-1}[3(2I-1)J_0^{\mathrm{Q}}(0) + (2I-3)^2 J_1^{\mathrm{Q}}(\omega_I) + 2(4I-3)J_2^{\mathrm{Q}}(2\omega_I)] \tag{34}$$

These expressions demonstrate that for $I = 1$, not only do Zeeman and quadrupolar polarizations relax exponentially, so do both forms of single quantum coherence and the unique double quantum coherence:

$$R_{2,2}^{1,1} = 2[3J_0^{\mathrm{Q}}(0) + J_1^{\mathrm{Q}}(\omega_I) + 2J_2^{\mathrm{Q}}(2\omega_I)] \tag{35}$$

$$R_{1,1}^{1,1} = 1/T_2 = 2[3J_0^{\mathrm{Q}}(0) + 5J_1^{\mathrm{Q}}(\omega_I) + 2J_2^{\mathrm{Q}}(2\omega_I)] \tag{36}$$

$$R_{2,2}^{2,1} = 4J_1^{\mathrm{Q}}(\omega_I) + 8J_2^{\mathrm{Q}}(2\omega_I) \tag{37}$$

Equations (19), (20), and (35)–(37) summarize completely the relaxation characteristics for $I = 1$. Similarly, the description for $I = \frac{3}{2}$, initiated with equations (21)–(25), can now be completed. For $I = \frac{3}{2}$, forms of spin order associated with $\hat{T}_3^{\pm 3}$, $\hat{T}_3^{\pm 2}$, $\hat{T}_2^{\pm 2}$, and $\hat{T}_2^{\pm 1}$ dissipate in time exponentially with the following relaxation rates:

$$R_{3,3}^{3,3/2} = \tfrac{8}{3}J_1^{\mathrm{Q}}(\omega_I) + \tfrac{8}{3}J_2^{\mathrm{Q}}(2\omega_I) \tag{38}$$

$$R_{3,3}^{2,3/2} = \tfrac{8}{3}J_0^{\mathrm{Q}}(0) + \tfrac{8}{3}J_2^{\mathrm{Q}}(2\omega_I) \tag{39}$$

$$R_{2,2}^{2,3/2} = \tfrac{8}{3}J_0^{\mathrm{Q}}(0) + \tfrac{16}{3}J_1^{\mathrm{Q}}(\omega_I) + \tfrac{8}{3}J_2^{\mathrm{Q}}(2\omega_I) \tag{40}$$

$$R_{2,2}^{1,3/2} = \tfrac{8}{3}J_0^{\mathrm{Q}}(0) + \tfrac{8}{3}J_1^{\mathrm{Q}}(\omega_I) + \tfrac{16}{3}J_2^{\mathrm{Q}}(2\omega_I) \tag{41}$$

In-phase and doubly antiphase 1QC, $\hat{T}_1^{\pm 1}$ and $\hat{T}_3^{\pm 1}$, couple together, and each evolves biexponentially. For an initial spin preparation (perturbation) that selectively disturbs one-spin order, $\langle \hat{\mathrm{I}}_{\pm}(0)\rangle \neq 0$, it can be shown that

$$\left.\begin{aligned} \frac{\langle \hat{I}_{\pm}(t)\rangle}{\langle \hat{I}_{\pm}(0)\rangle} &= \tfrac{1}{5}\exp[-\tfrac{8}{3}tJ_1^{\mathrm{Q}}(\omega_I)] \\ &\quad \times \{3\exp[-\tfrac{8}{3}tJ_0^{\mathrm{Q}}(0)] + 2\exp[-\tfrac{8}{3}tJ_2^{\mathrm{Q}}(2\omega_I)]\} \\ -\frac{\langle I_{\pm}(t\to 0)\rangle - \langle \hat{I}_{\pm}(0)\rangle}{\langle \hat{I}_{\pm}(0)\rangle t} &\approx R_{1,1}^{1,3/2} = 1/T_2 \\ &= \tfrac{8}{15}[3J_0^{\mathrm{Q}}(0) + 5J_1^{\mathrm{Q}}(\omega_I) + 2J_2^{\mathrm{Q}}(2\omega_I)] \end{aligned}\right\} \tag{42}$$

$$\left.\begin{aligned} \frac{\langle \hat{I}_{\pm}[5\hat{I}_z^2 \pm 5\hat{I}_z(2-\hat{I}^2)](t)\rangle}{\langle \hat{I}_{\pm}(0)\rangle} &= \tfrac{6}{5}\exp[-\tfrac{8}{3}tJ_1^{\mathrm{Q}}(\omega_I)]\{\exp[-\tfrac{8}{3}tJ_0^{\mathrm{Q}}(0)] \\ &\quad - \exp[-\tfrac{8}{3}tJ_2^{\mathrm{Q}}(2\omega_I)]\} \\ -\frac{\langle \hat{I}_{\pm}[5\hat{I}_z^2 \pm 5\hat{I}_z + (2-\hat{I}^2)](t\to 0)\rangle}{\langle \hat{I}_{\pm}(0)\rangle t} &\approx R_{3,1}^{1,3/2} \\ &= \tfrac{16}{5}[J_0^{\mathrm{Q}}(0) - J_2^{\mathrm{Q}}(2\omega_I)] \end{aligned}\right\} \tag{43}$$

Introducing two fictitious spin operators $\langle \hat{I}_{\pm}^{\mathrm{b}}\rangle = \sqrt{3}\,(\chi_{3/2,\ 1/2} + \chi_{-1/2,\ -3/2})$ and $\langle \hat{I}_{\pm}^{\mathrm{n}}\rangle = 2\chi_{1/2,-1/2}$ {with $\langle \hat{I}_{\pm}\rangle = \langle \hat{I}_{\pm}^{\mathrm{b}}\rangle + \langle \hat{I}_{\pm}^{\mathrm{n}}\rangle$ and $\langle \hat{I}_{\pm}[5\hat{I}_z^2 \pm 5\hat{I}_{\mathrm{z}} + (2-\hat{I}^2)]\rangle$}} results in the following transformation of the kinetic equations for $I = \frac{3}{2}$:

$$\frac{5}{2}\frac{\langle \hat{I}_{\pm}^{\mathrm{n}}(t)\rangle}{\langle \hat{I}_{\pm}(0)\rangle} = \exp[-\tfrac{8}{3}tJ_2^{\mathrm{Q}}(2\omega_I) - \tfrac{8}{3}tJ_1^{\mathrm{Q}}(\omega_I)] \tag{44}$$

$$\frac{5}{3}\frac{\langle \hat{I}_{\pm}^{\mathrm{b}}(t)\rangle}{\langle \hat{I}_{\pm}(0)\rangle} = \exp[-\tfrac{8}{3}tJ_0^{\mathrm{Q}}(0) - \tfrac{8}{3}tJ_1^{\mathrm{Q}}(\omega_I)] \tag{45}$$

For $I = \frac{3}{2}$ both of the coherences $\langle \hat{I}_{\pm}^{\mathrm{b}}\rangle$ and $\langle \hat{I}_{\pm}^{\mathrm{n}}\rangle$ are characterized by simple exponential relaxation. This representation clearly illustrates one of the most interesting and useful feature of electric quadrupolar relaxation. The decay of coherence between the states $|\frac{1}{2}\rangle$ and $|-\frac{1}{2}\rangle$ is determined by a rate free from adiabatic contributions.

In numerous practical situations, a partially averaged quadrupole coupling of residual amplitude $\langle \hat{\mathcal{F}}^{\mathrm{Q}I}(t)\rangle = \omega_{\mathrm{Q}}(3\hat{I}_z^2 - \hat{I}^2)$ removes spectral degeneracies and eliminates all secular couplings from equation (28). In this limit, the free decay of nQC between states $|m\rangle$ and $|m-n\rangle$ is characterized by a unique, well-defined relaxation rate, which can be written in closed form as

$$\begin{aligned} (1/T_2)_{m,m-n} = [I(2I-1)]^{-2}\Big\{&[6n^2(2m-n)^2]J_0^{\mathrm{Q}}(0) \\ &+\{4(4m^2+1)[I(I+1)-m^2] - 16m^2 \\ &-2n(2m-n)[4I(I+1) - 8m^2 - 5 \\ &+4n(2m-n)]\}J_1^{\mathrm{Q}}(\omega_I) \\ &+\{4(I^2-m^2-1)[I(I+2)-m^2] + 16m^2 \\ &+2n(2m-n)[2I(I+1) - 2m^2 - 5 \\ &+n(2m-n)]\}J_2^{\mathrm{Q}}(2\omega_I)\Big\} \end{aligned} \tag{46}$$

Once again, it is emphasized that the coherence between states $|m\rangle$ and $|-m\rangle$ has no adiabatic $[J_0^{\mathrm{Q}}(0)]$ contribution. In the slow motion limit $[\omega_0\tau_2 \gg 1$, or, equivalently, $J_0^{\mathrm{Q}}(0) \gg J_1^{\mathrm{Q}}(\omega I)$, $J_2^{\mathrm{Q}}(2\omega_I)]$, all transitions except the $|m\rangle \leftrightarrow |-m\rangle$ n-quantum transition are dramatically broadened leaving behind a solitary, narrowed component, which contributes a fractional intensity

$$\left[\prod_{i=1}^{n+1}(2i-1)\right]\left[\prod_{i=1}^{n}(2I+2i-n)\right]\left[\prod_{i=1}^{n}(2i)\right]^{-1}\left[\prod_{i=1}^{n+1}(2I+2i-n-1)\right]^{-1} \quad (47)$$

to the overall intensity of the nQC. For half-integral spin, the 1QC is the transition that attracts most interest. The relaxation rate for this unique 1QC is defined as

$$\begin{aligned}(1/T_2)_{1/2,-1/2} = {} & (2I+3)I^{-2}(2I-1)^{-1}\{2J_1^{\mathrm{Q}}(\omega_I) \\ & +[(I+\tfrac{3}{2})(I-\tfrac{1}{2})-1]J_2^{\mathrm{Q}}(2\omega_I)\}\end{aligned} \quad (48)$$

Equation (48) is more general than suggested, and obtains in isotropic media for those situations where $J^{\mathrm{Q}}(0)$ dominates, thereby quenching the secular coupling. Equations (46) and (48) assume that $J_k^{\mathrm{Q}}(k\omega_I \pm 3k(2I-k)\omega_{\mathrm{Q}}) = J_k^{\mathrm{Q}}(k\omega_I)$. In the unlikely situation where this assumption fails, equation (46) becomes much more complex. For example, the specific relaxation rate $(1/T_2)_{1/2,-1/2}$ is given by

$$\begin{aligned}(1/T_2)_{1/2,-1/2} = {} & [I(2I-1)]^{-2}\Big\{[4I(I+1)-3][J_1^{\mathrm{Q}}(\omega_I+6\omega_{\mathrm{Q}}) \\ & +J_1^{\mathrm{Q}}(\omega_I-6\omega_{\mathrm{Q}})] \\ & +(I+\tfrac{3}{2})(I-\tfrac{1}{2})\{(I-\tfrac{3}{2})(I+\tfrac{5}{2}) \\ & \times[J_2^{\mathrm{Q}}(2\omega_I+18\omega_{\mathrm{Q}})+J_2^{\mathrm{Q}}(2\omega_I-18\omega_{\mathrm{Q}})] \\ & +(I+\tfrac{1}{2})^2[J_2^{\mathrm{Q}}(2\omega_I+6\omega_{\mathrm{Q}})+J_2^{\mathrm{Q}}(2\omega_I-6\omega_{\mathrm{Q}})]\}\Big\}\end{aligned} \quad (49)$$

5 ELECTRIC QUADRUPOLAR RELAXATION IN THE ROTATING FRAME

The preceding sections have summarized nuclear spin relaxation induced by the electric quadrupolar interaction in the absence of applied rf fields. However, sometimes it is advantagous and more informative to perform relaxation studies in the presence of a resonant or 'spin locking' field. The resultant measurement of relaxation in 'the rotating frame', provides the researcher with the opportunity to examine certain spectral densities while selectively suppressing other contributions.

It has been shown that expressions for rotating frame relaxation can be obtained very simply by replacing spectral density functions in the laboratory frame by new linear combinations of spectral density functions $J_{k\rho}^{\mathrm{Q}}$.[10] If it is assumed that a spin lock field of amplitude B_{sl} ($\gamma_I B_{\mathrm{sl}} = \omega_{\mathrm{sl}} \ll \omega_I/\gamma_I$) is applied on resonance then

$$J_{0\rho}^{\mathrm{Q}}(0) = \tfrac{1}{4}J_0^{\mathrm{Q}}(0) + \tfrac{3}{4}J_2^{\mathrm{Q}}(2\omega_I) \quad (50)$$

$$J_{1\rho}^{\mathrm{Q}}(\omega_I) = \tfrac{1}{2}J_1^{\mathrm{Q}}(\omega_I) + \tfrac{1}{2}J_2^{\mathrm{Q}}(2\omega_I) \quad (51)$$

$$J_{2\rho}^{\mathrm{Q}}(2\omega_I) = \tfrac{3}{8}J_0^{\mathrm{Q}}(2\omega_{\mathrm{sl}}) + \tfrac{1}{2}J_1^{\mathrm{Q}}(\omega_I) + \tfrac{1}{8}J_2^{\mathrm{Q}}(2\omega_I) \quad (52)$$

Thus, equation (27) becomes

$$\begin{aligned}R_{1,1}^{0,I\rho} = 1/T_{1\rho} = {} & \tfrac{2}{5}(2I+3)I^{-2}(2I-1)^{-1} \\ & \times[3J_0^{\mathrm{Q}}(2\omega_{\mathrm{sl}})+5J_1^{\mathrm{Q}}(\omega_I)+2J_2^{\mathrm{Q}}(2\omega_I)]\end{aligned} \quad (53)$$

and the analogous expression for $R_{1,1}^{1,I}$,

$$\begin{aligned}R_{1,1}^{1,I} = 1/T_2 = {} & \tfrac{2}{5}(2I+3)I^{-2}(2I-1)^{-1} \\ & \times[3J_0^{\mathrm{Q}}(0)+5J_1^{\mathrm{Q}}(\omega_I)+2J_2^{\mathrm{Q}}(2\omega_I)]\end{aligned} \quad (54)$$

reduces to

$$\begin{aligned}R_{1,1}^{1,I\rho} = 1/T_{2\rho} = {} & \tfrac{1}{10}(2I+3)I^{-2}(2I-I)^{-1} \\ & \times[3J_0^{\mathrm{Q}}(2\omega_{\mathrm{sl}})+3J_0^{\mathrm{Q}}(0) \\ & +14J_1^{\mathrm{Q}}(\omega_I)+20J_2^{\mathrm{Q}}(2\omega_I)]\end{aligned} \quad (55)$$

All expressions previously introduced can be transcribed in a similar fashion.

6 THE ELECTRIC QUADRUPOLAR INTERACTION AND DYNAMIC FREQUENCY SHIFTS

The dynamic frequency shift is associated with the imaginary part of the spectral density function introduced in equation (9):

$$\begin{aligned}L_k^{\mathrm{Q}}(\omega) = {} & (\xi_{\mathrm{QI}})^2\mathrm{Im}\Big[\int_0^\infty \langle Y_2^k(\theta(t),\phi(t))Y_2^{-k}(\theta(0),\phi(0))\rangle \\ & \times\exp(-\mathrm{i}\omega t)\,\mathrm{d}t\Big]\end{aligned} \quad (56)$$

For *isotropic*, *diffusional reorientation* of the molecular frame relative to the laboratory frame, equation (56) reduces to

$$L^{\mathrm{Q}}(\omega) = \frac{3}{160}\left(\frac{e^2qQ_I}{\hbar}\right)^2\frac{\omega\tau_2^2}{1+\omega^2\tau_2^2} = \omega\tau_2 J^{\mathrm{Q}}(\omega) \quad (57)$$

Because the dynamic frequency shift is negligible in extreme narrowing and has no adiabatic component, often this term is dismissed. However, it has been shown previously that the relaxations of numerous coherences also have no adiabatic contribution, and, in the slow motion regime, the dynamic shift can be a dominating effect.[11] The maximum dynamic frequency shift is on the order of $|\hat{\mathcal{F}}^{\mathrm{QI}}|^2/\omega_I$ and can easily exceed several kilohertz.

To illustrate the effect of the dynamic shift, consider the coherence between states $|m\rangle$ and $|m-n\rangle$ in the limit where each transition is well resolved. The dynamic frequency shift of this coherence is described by the expression

$$\begin{aligned}\Omega_{m,m-n} = {} & 2n[I(2I-1)]^{-2}\{[-4I(I+1)+24m(m-n) \\ & +8n^2+1]L_1^{\mathrm{Q}}(\omega_I)+[4I(I+1)-12m(m-n) \\ & -4n^2-2]L_2^{\mathrm{Q}}(2\omega_I)\}\end{aligned} \quad (58)$$

Of special importance are expressions for those coherences where the adiabatic contribution to the linewidth vanishes:

$$\begin{aligned}\Omega_{m,-m} = {} & 4m[I(2I-1)]^{-2}\{[-4I(I+1)+8m^2+1]L_1^{\mathrm{Q}}(\omega_I) \\ & +[4I(I+1)-4m^2-2]L_2^{\mathrm{Q}}(2\omega_I)\}\end{aligned} \quad (59)$$

The relative shift of any two components of the nQC is given by the expression

$$\Omega_{m,m-n} - \Omega_{m',m'-n} = 24n[I(2I-1)]^{-2}(m-m')(m+m'-n) \times[2L_1^{\mathrm{Q}}(\omega_I) - L_2^{\mathrm{Q}}(2\omega_I)] \quad (60)$$

Except for the case where $m = I$ and $n = 2I$, equation (58) differs dramatically from equation (46). Consequently, there is no simple relationship between the dynamic shift and linewidth (relaxation rate) for any given spectral component.

The effects of the dynamic frequency shift on the various forms of spin order, $\hat{T}_L^{\pm k}$, can be written in a manner analogous to equation (30):

$$-\frac{\mathrm{d}}{\mathrm{d}t}\hat{T}_L^{\pm k} = \sum_{L'} S_{L,L'}^{k,I}\hat{T}_{L'}^{\pm k} \quad (61)$$

Like other relaxation parameters introduced previously, $S_{L,L'}^{k,I}$ vanishes unless $L = L'$, $L' \pm 2$. In extreme narrowing, the term $S_{1,3}^{1,I}$ is proportional to $2L_1^{\mathrm{Q}}(\omega_I) - L_2^{\mathrm{Q}}(2\omega_I)$ and scales as $(\omega_I\tau_2)^3\ J^{\mathrm{Q}}(\omega_I)$, thus ensuring the insignificance of the dynamic frequency shift in this limit. The intrinsic shift of the transverse 'magnetization', $S1,1^{1,I}$, can be written as

$$S_{1,1}^{1,I} = -\tfrac{2}{5}(2I+3)I^{-2}(2I-1)^{-1}[L_1^{\mathrm{Q}}(\omega_I) + 2L_2^{\mathrm{Q}}(2\omega_I)] \quad (62)$$

Figure 1 summarizes the frequency dependence of the various relaxation rates introduced thus far. Rates applicable for $I = 1$ are shown explicitly. Note that the second-order dynamic frequency shift associated with the 2QC exceeds the relaxation rate in the slow motion limit ($\omega_I\tau_2 \gg 1$).

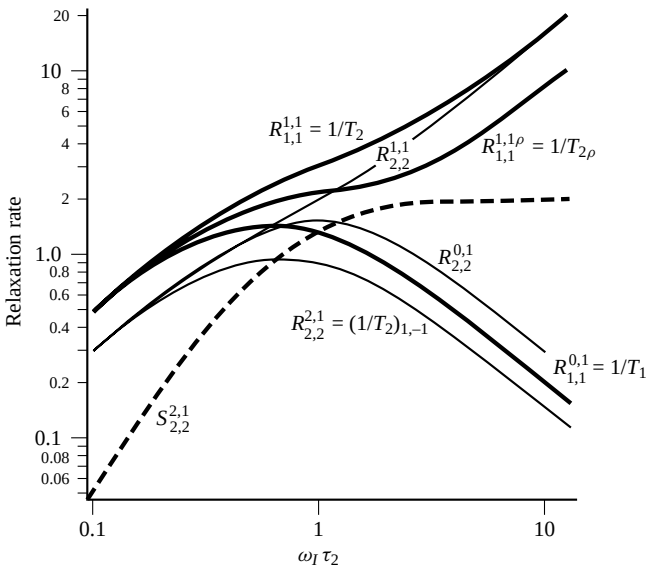

Figure 1 A plot of the various quadrupolar relaxation rates for an $I = 1$ nuclear spin versus isotropic rotational correlation time, measured in units of the reciprocal Larmor frequency. Conventional rates, $1/T_1$, $1/T_2$ (= $1/T_{1\rho}$ in the limit shown), and $1/T_{2\rho}$ are represented by the heavy full curves. Rates associated with relaxation of the three forms of two-spin order are shown as lighter full curves. The dynamic frequency shift of the double quantum coherence is shown as a dotted curve

7 EFFECTS OF ALTERNATIVE SOURCES OF RELAXATION FOR QUADRUPOLAR NUCLEI

Although $I \geq 1$ nuclei generally are driven towards equilibrium by electric quadrupolar relaxation, other sources of relaxation play important roles in relaxation-induced polarization and coherence transfer.[12] For example, as resonance experiments are performed at higher and higher magnetic field strengths, anisotropic shielding will continue to play an increasingly important role in magnetic relaxation of quadrupolar nuclei.

Utilizing the spin operators and notation introduced earlier, the relaxation of a nuclear spin I by an axially symmetric anisotropic shielding ($\Delta\sigma = \sigma_{zz} - \sigma_{xx} = \sigma_{zz} - \sigma_{yy}$) is described by the concise, general expression:

$$R_{L,L'}^{k,I} = R_{L,L'}^{k,I'} = \delta_{LL'}\{2L(L+1)J_1^{\mathrm{SA}}(\omega_I) + k^2[\tfrac{8}{3}J_0^{\mathrm{SA}}(0) - 2J_1^{\mathrm{SA}}(\omega_I)]\} \quad (63)$$

For isotropic reorientation,

$$J^{\mathrm{SA}}(\omega) = \frac{1}{30}\frac{(\gamma_I B_0 \Delta\sigma_I)^2\tau_2}{1+\omega^2\tau_2^2} \quad (64)$$

This expression, when compared with equation (31), indicates that higher forms of spin order are relaxed with increasing efficiency by shielding anisotropy.

Of special interest are the adiabatic contributions, which dominate the decay of coherence when extreme narrowing fails. In the limit where residual couplings result in well-resolved structure, the adiabatic contribution associated with the coherence between states $|m\rangle$ and $|m-n\rangle$ is simply $\frac{8}{3}n^2\ J_0^{\mathrm{SA}}(0)$. This result is independent of I or m, and only depends on the coherence order n. Meanwhile, the quadrupolar adiabatic contribution, given by equation (46), is $[I(2I-1)]^{-2}6n^2(2m-n)^2J_0^{\mathrm{Q}}(0)$. Once again, it is noted that this contribution vanishes when $n = 2m$. It should be clear that there are numerous situations where the electric quadrupolar contribution will be selectively suppressed and the relaxation characteristics of high-spin nuclei can be determined by alternative, intrinsically less efficient, relaxation pathways.

The preceding arguments implicitly presume that relaxation rates for quadrupolar and anisotropic shieldings are additive. Since both interactions are molecule-fixed and transform identically under molecular reorientation, these interactions are temporally correlated, and interference effects between these interactions must be considered. The contribution of this interference to the adiabatic portion of $(1/T_2)_{m,m-n}$ is given by the expression

$$(1/T_2)_{m,m-n}^{\text{adiabatic}} = \tfrac{1}{5}\zeta n^2(2m-n)(2I^2-I)^{-1} \times(e^2q_IQ_I/\hbar)\gamma_I B_0\Delta\sigma_I\tau_2 \quad (65)$$

where ζ is the relevant correlation factor. Unlike other relaxation parameters mentioned thus far, this interference distinguishes between the decay rates of the spin-inverted coherences, $\chi_{nn'}$ and $\chi_{-n'-n}$.

To illustrate the significance of equation (65), consider the situation where the unique axis of the quadrupole and anisotropic shielding interactions are coincident ($\zeta = 1$) and the slow motion limit obtains. Assuming the quadrupole interaction is significantly stronger than the anisotropic

shielding interaction, the differential linebroadening can be written as

$$\frac{(1/T_2)_{m,m-n} - (1/T_2)_{-m,n-m}}{(1/T_2)_{m,m-n} + (1/T_2)_{-m,n-m}} = \frac{\frac{16}{9}I(2I-1)(2m-n)\xi}{[\frac{8}{9}I(2I-1)\xi]^2 + (2m-n)^2} \approx \frac{16I(2I-1)}{9(2m-n)}\xi \quad (66)$$

where $\xi = \gamma_I B_0 \Delta\sigma_I/(e^2 q_I Q_I/\hbar)$. For example, if $I = \frac{5}{2}$, the asymmetry in the relaxation rates (linewidths) of the two 1QCs, $\chi_{3/2,1/2}$ and $\chi_{-1/2,-3/2}$, is $\frac{80}{9}\xi$. Assuming that ξ^{-1} is on the order of 100, the anisotropic shielding interaction is 1000 times less effective than the quadrupolar interaction at relaxing 1QC directly [$\frac{8}{3}J_0^{\mathrm{SA}}(0) : \frac{6}{25}J_0^{\mathrm{Q}}(0)$]. However, this same set of parameters will result in a 10% relaxation asymmetry between these two components!

Another source of relaxation that may play an increasingly important role in the relaxation of quadrupolar nuclei is the electron–nuclear anisotropic hyperfine interaction. Although the hyperfine interaction can effect nuclear spin relaxation in numerous ways, in this discussion, only relaxation effects attributed to the coupling of a nuclear spin to the thermal average of electron spin, $\langle \hat{S}_z(\mathrm{eq})\rangle = g_e\beta S(S+1)B_0/3kT$, modulated by molecular reorientation, are considered. In appropriate limits, this interaction, which is formally equivalent to an anisotropic shielding, results in 'Curie' relaxation of nuclear spin.[13] The effect of 'Curie' relaxation on the various spin operators introduced earlier can be summarized by the expression

$$R^{k,I}_{L,L'} = R^{k,I'}_{L,L'} = \delta_{LL'}\{2L(L+1)J_1^{\mathrm{CR}}(\omega_I) + k^2[\tfrac{8}{3}J_0^{\mathrm{CR}}(0) - 2J_1^{\mathrm{CR}}(\omega_I)]\} \quad (67)$$

For isotropic reorientation,

$$J^{\mathrm{CR}}(\omega) = \frac{3}{10}\left(\frac{g_e\beta S(S+1)B_0}{3kT}\right)^2 (\gamma_I g_e\beta\langle r^{-3}\rangle)^2 \frac{\tau_2}{1+\omega^2\tau_2^2} \quad (68)$$

Like anisotropic chemical shielding, this interaction can interfere with the quadrupolar interaction. The contribution of this interference to the adiabatic portion of $(1/T_2)_{m,m-n}$ is given by

$$(1/T_2)^{\mathrm{adiabatic}}_{m,m-n} = \tfrac{3}{5}\zeta n^2(2m-n)(2I^2-I)^{-1}\frac{e^2 q_I Q_I}{\hbar} \times \left[\frac{g_e\beta S(S+1)B_0}{3kT}\right]^2 (\gamma_I g_e\beta\langle r^{-3}\rangle)^2\tau_2 \quad (69)$$

where ζ is the relevant correlation factor.

In general, interference (dipole–quadrupole, anisotropic shielding–quadrupole, 'Curie spin'–quadrupole, or quadrupole–quadrupole) retards the relaxation process and results in polarization/coherence transfer. In a spherical tensor description of relaxation, interference (cross correlation) between anisotropic shieldings or 'Curie spin' and the electric quadrupolar interaction results in terms such as $R^{k,I}_{L,L\mp1}$ being nonzero. Hence, various forms of spin order of differing parity are coupled together by these interference terms. This coupling persists in all motional limits. As noted earlier, the magnitudes of these couplings scale as the geometric mean of the two competitive interactions, and can be significant even in the limit where one interaction dominates conventional relaxation parameters.[14]

8 IMPACT OF QUADRUPOLAR RELAXATION ON SPIN-$\frac{1}{2}$ NUCLEI

In multispin systems containing both quadrupolar ($I \geq 1$) and dipolar ($I = \frac{1}{2}$) nuclei, the high-spin nuclei generally are relaxed efficiently by quadrupolar interactions whereas spin-$\frac{1}{2}$ nuclei relax on a slower timescale. Thus, from the perspective of a spin-$\frac{1}{2}$ nucleus (S), the scalar coupling to a quadrupolar nucleus (I), $J\hat{\boldsymbol{S}}\cdot\hat{\boldsymbol{I}}(t)$, appears time-dependent, and, on the average, vanishes. Although the quadrupolar nucleus provides a source of relaxation (scalar relaxation of the second kind) for spin-$\frac{1}{2}$ nuclei, multiplet structure disappears as these spins are decoupled by the relaxation process.[15]

Nevertheless, there are an increasing number of studies demonstrating that various quadrupolar nuclei often exhibit narrowed lines and multiplet structure in solution state NMR studies. Such situations commonly characterize studies involving important isotopes of hydrogen, nitrogen and oxygen. In the limit where the spectrum of spin S consists of $2I + 1$ evenly spaced multiplet components, quadrupolar relaxation of spin I generally provides the dominant relaxation sink for dissipation of S-spin 1QC. However, neither I-spin adiabatic terms nor I-spin dynamic frequency shifts will influence the behavior of spin S. If it is assumed that all $2I + 1$, 1QC components are well resolved then a well-defined relaxation rate $1/T_2$ can be assigned to each coherence associated with the S-spin transition $|\frac{1}{2}, m\rangle \leftrightarrow |-\frac{1}{2}, m\rangle$:

$$(1/T_2)_{I,m} = 4(2I^2-I)^{-2}\{[I(I+1)(4m^2+1) - m^2(4m^2+5)]J_1^{\mathrm{Q}}(\omega_I) + [I^2(I+1)^2 - 2I(I+1)(m^2+1) + m^2(m^2+5)]J_2^{\mathrm{Q}}(2\omega_I)\} \quad (70)$$

A listing of these relaxation rates for half-integer spin is given in Table 2.

Also, quadrupolar–anisotropic shielding interference—for spin I!—can dramatically effect linewidths in the S spectrum,

Table 2 The Electric Quadrupolar Contribution to the Relaxation Rate $(1/T_2)_{I,m}$ for each Single Quantum Coherence Identified with the Specific Transition $|S = \frac{1}{2}, S_z = \frac{1}{2}; I, m\rangle \leftrightarrow |S = \frac{1}{2}, S_z = -\frac{1}{2}; I, m\rangle$

	$I = \frac{3}{2}$	$I = \frac{5}{2}$	$I = \frac{7}{2}$	$I = \frac{9}{2}$
$m = \pm\frac{1}{2}$	$\frac{8}{3}(J_1^{\mathrm{Q}} + J_2^{\mathrm{Q}})$	$\frac{16}{25}(J_1^{\mathrm{Q}} + \frac{7}{2}J_2^{\mathrm{Q}})$	$\frac{40}{147}(J_1^{\mathrm{Q}} + 7J_2^{\mathrm{Q}})$	$\frac{4}{27}(J_1^{\mathrm{Q}} + \frac{23}{2}J_2^{\mathrm{Q}})$
$m = \pm\frac{3}{2}$	$\frac{8}{3}(J_1^{\mathrm{Q}} + J_2^{\mathrm{Q}})$	$\frac{36}{25}(\frac{14}{9}J_1^{\mathrm{Q}} + J_2^{\mathrm{Q}})$	$\frac{8}{7}(J_1^{\mathrm{Q}} + \frac{9}{7}J_2^{\mathrm{Q}})$	$\frac{2}{3}(J_1^{\mathrm{Q}} + \frac{13}{6}J_2^{\mathrm{Q}})$
$m = \pm\frac{5}{2}$		$\frac{4}{5}(2J_1^{\mathrm{Q}} + J_2^{\mathrm{Q}})$	$\frac{120}{147}(\frac{37}{15}J_1^{\mathrm{Q}} + J_2^{\mathrm{Q}})$	$\frac{38}{27}(J_1^{\mathrm{Q}} + J_2^{\mathrm{Q}})$
$m = \pm\frac{7}{2}$			$\frac{8}{21}(3J_1^{\mathrm{Q}} + J_2^{\mathrm{Q}})$	$\frac{14}{27}(\frac{24}{7}J_1^{\mathrm{Q}} + J_2^{\mathrm{Q}})$
$m = \pm\frac{9}{2}$				$\frac{2}{9}(4J_1^{\mathrm{Q}} + J_2^{\mathrm{Q}})$

as shown by the following expression:

$$(1/T_2)_{I,m} = 4m(2I^2 - I)^{-1}[2I(I+1) - 2m^2 - 1] \times \frac{\zeta}{5} \frac{e^2 q_I Q_I}{\hbar} \frac{\gamma_I B_0 \Delta\sigma_I \tau_2}{1 + \omega_I^2 \tau_2^2} \quad (71)$$

Finally, quadrupolar–dipolar interferences can induce significant dynamic frequency shifts of individual spin-$\frac{1}{2}$ multiplet components and serve as a novel source of scalar relaxation.[16]

9 SUMMARY

In this article, the essential perturbation–response characteristics of quadrupolar (multipolar) nuclei have been introduced. For electric quadrupolar relaxation in the limit where the spectral density is neither projection- (k) nor frequency-dependent, exceptionally simple behavior is predicted [cf. equation (31)]. Likewise, when residual splittings suppress transverse cross relaxation, elementary expressions adequately describe the decay of all forms of spin coherence [cf. equation (46)]. In the slow motion limit, where adiabatic terms generally dominate the decay of coherence, it is recognized that various coherences, which lack an adiabatic contribution, decay on the timescale of the longitudinal magnetization. For these coherences, the dynamic frequency shift can prove important. Although quadrupolar interactions efficiently dissipate coherence and thermalize polarization, transfer of polarization is driven by interference effects and, necessarily, by weaker interactions that generally play only a very minor role in conventional relaxation studies.

10 RELATED ARTICLES

Brownian Motion and Correlation Times; Dynamic Frequency Shift; Quadrupolar Interactions; Quadrupolar Nuclei in Liquid Samples; Relaxation: An Introduction; Relaxation of Quadrupolar Nuclei Measured via Multiple Quantum Filtration; Relaxation Theory: Density Matrix Formulation.

11 REFERENCES

1. N. E. Ainbinder and I. G. Shaposhnikov, *Adv. Nucl. Quad. Reson.*, 1976, **3**, 67.
2. W. T. Huntress, in *Advances in Magnetic Resonance*, ed. J. S. Waugh, Academic Press, New York, 1970, Vol. 4, p. 1.
3. P. S. Hubbard, *Phys. Rev.*, 1969, **180**, 319.
4. E. Matthias, B. Olsen, D. A. Shirley, and J. E. Templeton, *Phys. Rev. A*, 1971, **4**, 1626.
5. L. G. Werbelow, D. A. Ikenberry, and G. Pouzard, *J. Magn. Reson.*, 1983, **51**, 409.
6. L. Einarsson and P. O. Westlund, *J. Magn. Reson.*, 1988, **79**, 30.
7. N. C. Pyper, *Mol. Phys.*, 1971, **21**, 1.
8. P. S. Hubbard, *J. Chem. Phys.*, 1970, **53**, 985.
9. L. G. Werbelow and A. G. Marshall, *J. Magn. Reson.*, 1981, **43**, 443.
10. J. R. C. Van der Maarel, *J. Chem. Phys.*, 1991, **91**, 1446; S. W. Kelly and C. A. Sholl, *J. Phys.: Condens. Matter*, 1992, **4**, 3317.
11. L. Werbelow and G. Pouzard, *J. Phys. Chem.*, 1981, **85**, 3887.
12. L. G. Werbelow, in *Nuclear Magnetic Resonance Probes of Molecular Dynamics*, ed. R. Tycko, Plenum, Press, New York, 1994, p. 223.
13. M. Gueron, *J. Magn. Reson.*, 1975, **19**, 58; I. Bertini, C. Luchinat, and D. Tarchi, *Chem. Phys. Lett.*, 1993, **203**, 445; D. Petit, J.-P. Korb, A. Delville, J. Grandjean, and P. Laszlo, *J. Magn. Reson.*, 1992, **96**, 252.
14. L. G. Werbelow, *J. Magn. Reson.*, 1986, **67**, 66; L. G. Werbelow, A. Allouche, and G. Pouzard, *J. Chem. Soc., Faraday Trans. 2*, 1987, **83**, 871; L. Werbelow and A. Thevand, *J. Magn. Reson., Ser. A*, 1993, **105**, 88.
15. J. Pople, *Mol. Phys.*, 1958, **1**, 168.
16. R. E. London, D. M. LeMaster, and L. G. Werbelow, *J. Am. Chem. Soc.*, 1994, **116**, 8400; S. Grzesiek and A. Bax, *J. Am. Chem. Soc.*, 1994, **116**, 10196; L. G. Werbelow and R. E. London, *J. Chem. Phys.*, 1995, **102**, 5181.

Biographical Sketch

Lawrence G. Werbelow. *b* 1948. B.S., 1970, Humboldt State University, U.S.A. Ph.D., 1974, University of British Columbia, (thesis advisor A. G. Marshall). Research Associate (with D. M. Grant) and Instructor, University of Utah, 1974–78; D.Sc., Université de Provence, 1979. Professor, New Mexico Tech, 1980–present. Professor, Université d'Aix Marseille I, 1990–95.Approx. 70 publications in the field of magnetic resonance. Current research interests include the study of relaxation-induced polarization/coherence transfer and the development of methods for isolation/identification of ultrafine interactions involving nuclear spin.

Rotating Frame Spin–Lattice Relaxation Off-Resonance

Thomas Schleich

University of California, Santa Cruz, CA, USA

1	Introduction	1
2	Theory	1
3	Experimental Implementation	5
4	Applications	5
5	Related Articles	7
6	References	7

1 INTRODUCTION

The off-resonance rotating frame spin–lattice relaxation experiment is a preeminent technique for the measurement of molecular rotational diffusion. The method relies on a ratio of relaxation expressions that are sensitive to the correlation time-dependent spectral densities, thereby obviating the need for a direct determination of relaxation times. Off-resonance rotating frame spin–lattice relaxation has been used to study rotational diffusion in aqueous solution and under in vivo conditions, and for the investigation of magnetization transfer phenomena. Off-resonance rotating frame spin–lattice relaxation considerations have also been used to create a high-resolution NMR three-dimensional off-resonance ROESY experiment, designated O-ROESY. Applications of the O-ROESY experiment include the assessment of macromolecular internal motion, internuclear distance, and the rotational correlation time for reorientational motion.

The off-resonance rotating frame spin–lattice relaxation experiment is established by the application of a low-power rf field off-resonance from a selected resonance. Thus, the essence of this experiment is simply described as a form of off-resonance saturation, in which a selected resonance is partially saturated, resulting in signal intensity diminution, in a manner explicitly dependent on molecular motion and/or magnetization transfer. Several reviews describing this experiment have appeared.[1,2]

The different guises of the off-resonance rotating frame spin–lattice relaxation experiment showing the reduction in signal intensity as a consequence of the application of a low-power off-resonance rf irradiation field are shown in Figure 1.

2 THEORY

2.1 Off-Resonance Rotating Frame Experiment

The theoretical basis of the off-resonance rotating frame spin–lattice relaxation experiment was established by Jones[3] and Blicharski[4] who derived the relevant expressions appropriate for both spin-$\frac{1}{2}$ and quadrupolar spin-1 nuclei.

In a coordinate frame rotating with angular velocity $\boldsymbol{\omega} = \omega \boldsymbol{k}$, the effective field $\boldsymbol{B}_\mathrm{e}$ is given by

$$\boldsymbol{B}_\mathrm{e} = \frac{\boldsymbol{\omega}_\mathrm{e}}{\gamma_I} = (B_0 - \omega/\gamma_I)\boldsymbol{k} + B_2\boldsymbol{i} \tag{1}$$

where $\omega_\mathrm{e} = |\boldsymbol{\omega}_\mathrm{e}|$ is the angular precessional frequency about the effective field for an ensemble of noninteracting spins with gyromagnetic ratio γ_I, $\boldsymbol{B}_0 = B_0\boldsymbol{k}$ is the static magnetic field strength, $\boldsymbol{i}$ and $\boldsymbol{k}$ are unit vectors, and B_2 is an rf field off-resonance by an amount Δ:

$$\Delta = 2\pi\nu_\mathrm{off} = -\gamma_I\left(B_0 - \frac{\omega}{\gamma_I}\right) \tag{2}$$

ν_off is the difference in frequency between the applied off-resonance rf field and the selected resonance. The effective field vector, $\boldsymbol{B}_\mathrm{e}$, is inclined to the static magnetic field, $\boldsymbol{B}_0$, at an angle Θ defined by

$$\Theta = \arctan\left(\frac{\gamma_I B_2}{\Delta}\right) \tag{3}$$

The angular precessional frequency about the effective field vector is

$$\omega_\mathrm{e} = \frac{\Delta}{\cos\Theta} \tag{4}$$

Assuming exponential relaxation of the magnetization aligned along $\boldsymbol{B}_\mathrm{e}$ ($\boldsymbol{M}_\mathrm{e}$), which is defined by the time constant $T_{1\rho}^{\mathrm{off}}$, the magnetization ratio, M_e/M_0, can be shown to be equal to $\cos\Theta\ (T_{1\rho}^{\mathrm{off}}/T_1)$ in the high temperature limit $[kT \gg \gamma_I(h/2\pi)B_0]$, with $B_0 > B_\mathrm{e}$.[5] In the conventional implementation of the experiment utilizing continuous wave rf irradiation to establish the off-resonance spin lock, the projection of M_e on the z axis of the rotating frame is measured. Thus, the signal intensity ratio, $R = M_z/M_0$ [$= \cos\Theta\ (M_\mathrm{e}/M_0)$] also equals $\cos^2\Theta\ (T_{1\rho}^{\mathrm{off}}/T_1)$. This equation is valid under the saturating condition $[(\gamma B_2)^2 T_1 T_2 \gg 1]$. M_e is obtained in the presence of, whereas M_0 is obtained in the absence of, the off-resonance rf irradiation field. For a small effective-field inclination angle, the $\cos^2\Theta$ term may be neglected.

The time constant $T_{1\rho}^{\mathrm{off}}$ may be directly measured by use of the conventional inversion–recovery pulse sequence modified to include off-resonance irradiation during the relaxation interval between the inversion and read pulses.[6]

2.2 Random Isotropic Reorientation

For random isotropic molecular reorientation involving two intramolecular dipolar coupled spin-$\frac{1}{2}$ heteronuclei, designated I and S, the following intramolecular dipole–dipole relaxation expressions for a particular spin S, in the absence of cross relaxation and under the far off-resonance condition, $|\Delta| \geq 5\gamma_S B_2$ and $\omega_\mathrm{e} \ll \omega_0$ (off-resonance irradiation experiment only), may be written[7,8]

$$\left(\frac{1}{T_1}\right)_{\mathrm{DD,rot}}^{SI} = \sum_{i=1}^{N}(K_{IS})_i[J_0(\omega_{I_i} - \omega_S) + 3J_1(\omega_S) + 6J_2(\omega_{I_i} + \omega_S)] \tag{5}$$

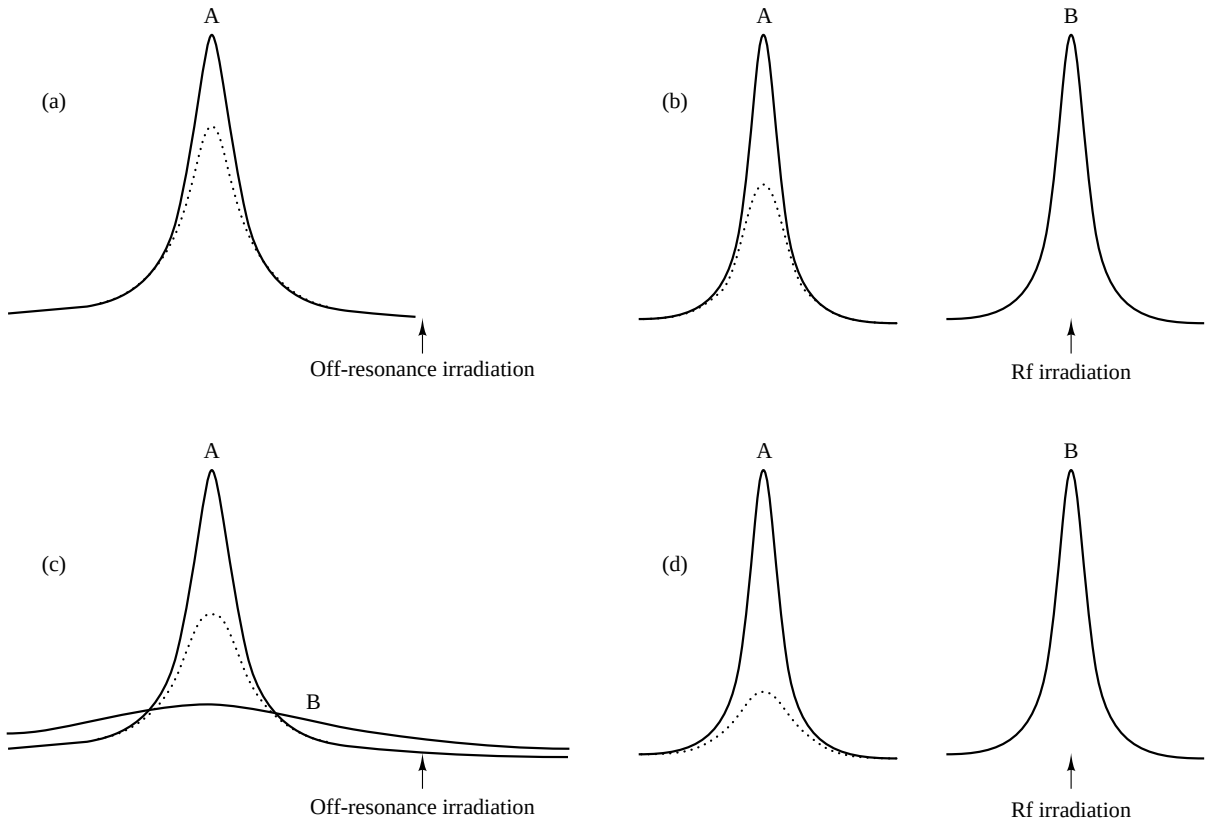

Figure 1 Schematic representation of the different forms of the off-resonance rotating frame spin–lattice relaxation experiment. Resonances A and B are assumed to be in chemical exchange equilibrium. In each case the dotted lineshape represents the response of the A resonance to the off-resonance rf irradiation. (a) Conventional representation of the off-resonance rotating frame spin–lattice relaxation technique employed for the determination of the rotational correlation time. The far off-resonance limiting value of the intensity ratio equals unity. Magnetization transfer effects are assumed to be absent. (b) Conventional representation of the saturation transfer experiment employed for the determination of kinetic rate constants. The absence of off-resonance effects on resonance A is assumed. (c) The effect of exchange on the behavior of the off-resonance rotating frame spin–lattice relaxation experiment from a very broad spectral component (NMR 'invisible') into an NMR 'visible' pool of spins. The far off-resonance limiting value of the intensity ratio is less than unity. Off-resonance and magnetization transfer effects on resonance A are assumed. (d) The effect of exchange on the behavior of the off-resonance rotating frame spin–lattice relaxation experiment when both pools of spins are NMR 'visible'. Off-resonance and magnetization transfer effects are assumed. (Reproduced by permission of Plenum Press from T. Schleich et al.[2])

$$\left(\frac{1}{T_{1\rho}^{\text{off}}}\right)_{\text{DD,rot}}^{SI} = \left(\frac{1}{T_1}\right)_{\text{DD,rot}}^{SI} + (\sin^2\Theta)\sum_{i=1}^{N}(K_{IS})_i[2J_0(\omega_e) + \tfrac{3}{2}J_1(\omega_{I_i} + \omega_e) + \tfrac{3}{2}J_1(\omega_{I_i} - \omega_e)] \quad (6)$$

where $K_{IS} = (h/2\pi)^2\gamma_I^2\gamma_S^2/20r_{IS}$. $J_n(\omega)$ is the spectral density function in which motional dynamics information is embedded, h is Planck's constant, γ_I and γ_S are the gyromagnetic ratios for the I and S spins, respectively, ω_I and ω_S are the respective angular Larmor precessional frequencies, r_{IS} is the distance between the I and S spins, and N is the number of I spins responsible for dipole–dipole IS relaxation. The summation over N is necessary when more than one I spin is responsible for relaxation, and allows for the occurrence of different spectral densities for each of the interactions. For biological applications, I and S typically represent ^{1}H, and ^{13}C or ^{31}P, respectively. Analogous relaxation expressions for $(1/T_1)_{\text{DD,rot}}^{SS}$ and $(1/T_{1\rho}^{\text{off}})_{\text{DD,rot}}^{SS}$ may be written for homonuclear two-spin systems with $S = \frac{1}{2}$ (e.g., ^{1}H, ^{31}P).[9]

In many instances the off-resonance rotating frame experiment spin–lattice relaxation experiment is performed in water, a proton-containing solvent. Under such circumstances it may be necessary to consider intermolecular contributions $[(1/T_1)_{\text{DD,trans}}^{SH}$ and $(1/T_{1\rho}^{\text{off}})_{\text{DD,trans}}^{SH}]$ to the total dipole–dipole relaxation rate from solvent (water) translational motion. The relevant expressions to enable inclusion of intermolecular relaxation effects arising from solvent diffusion have been derived.[2] CSA relaxation contributions assume significance at high magnetic field strengths for the protein peptide carbonyl carbon atom and the phosphoryl group of phosphorus metabolites. Relaxation expressions for CSA relaxation are presented elsewhere.[1,2] The total relaxation rate is obtained by summing the individual relaxation rates contributed by each of the assumed mechanisms:

$$\left(\frac{1}{T_1}\right)_{\text{total}} = \left(\frac{1}{T_1}\right)_{\text{DD,rot}}^{SI} + \left(\frac{1}{T_1}\right)_{\text{DD,rot}}^{SS} + \left(\frac{1}{T_1}\right)_{\text{DD,}trans}^{SH} + \left(\frac{1}{T_1}\right)_{\text{CSA}}^{S} \quad (7)$$

$$\left(\frac{1}{T_{1\rho}^{\text{off}}}\right)_{\text{total}} = \left(\frac{1}{T_{1\rho}^{\text{off}}}\right)_{\text{DD,rot}}^{SI} + \left(\frac{1}{T_{1\rho}^{\text{off}}}\right)_{\text{DD,rot}}^{SS} + \left(\frac{1}{T_{1\rho}^{\text{off}}}\right)_{\text{DD,}trans}^{SH} + \left(\frac{1}{T_{1\rho}^{\text{off}}}\right)_{\text{CSA}}^{S} \quad (8)$$

For random isotropic reorientational motion of an $I = 1$ spin, the quadrupolar relaxation mechanism contribution is usually dominant. The relevant expressions and their validation for the assessment of rotational diffusion by off-resonance rotating frame spin–lattice relaxation have been presented.[10]

2.3 Random Anisotropic Reorientation

Anisotropic molecular reorientation is encountered with nonspherical macromolecules, i.e., one represented hydrodynamically by an ellipsoid of revolution. The expressions appropriate for isotropic tumbling require modification to take into account differential motion about the major and minor axes of revolution. Expressions appropriate for anisotropic reorientational motion involving dipole–dipole and CSA relaxation have been derived.[1,2]

2.4 Spectral Density Functions

The rotational correlation time reflects the rapidity of reorientational motion responsible for magnetic relaxation. For an uncharged spherical rigid rotor at infinite dilution, engaged in isotropic reorientational motion, the rotational correlation time is defined by the hydrodynamic volume. Correction procedures to account for the effect of finite macromolecular concentration on the correlation time have been described.[2] In biological systems, nuclear spins are likely to be distributed among different microenvironments, thus leading to a distribution of correlation times. Many studies assume, for simplicity, a single (average) rotational correlation time for the characterization of reorientational motion.

The spectral density function for dipolar relaxation is

$$J_n(\omega) = \frac{2\tau_0}{1 + \omega^2\tau_0^2} \quad (9)$$

where τ_0 is the rotational correlation time for isotropic reorientational motion of a rigid uncharged spherical particle.[2] The spectral density functions pertinent to CSA relaxation for isotropic reorientational motion as well as the corresponding dipolar and CSA expressions appropriate for anisotropic motion are summarized elsewhere.[1,2]

2.5 Equivalence of Off-Resonance Rotating Frame Spin–Lattice Relaxation Formalism to the Bloch Equations for Off-Resonance Irradiation

Under appropriate conditions, the off-resonance rotating frame spin–lattice relaxation formalism leads to results equivalent to the steady state solution of the Bloch equation for the z magnetization. The necessary requirements were first noted by Bendel and James.[11] Manipulation of off-resonance rotating frame spin–lattice relaxation theory, assuming appropriate conditions,[2] leads to the following expression:

$$\left(\frac{M_z}{M_0}\right)_{\text{off-reson}} = \frac{1 + (\omega - \omega_0)^2 T_2^2}{1 + (\omega - \omega_0)^2 T_2^2 + T_1 T_2 (\gamma B_2)^2 \left[1 + \frac{1}{(\omega - \omega_0)^2 T_2^2}\right]} \quad (10)$$

whereas the Bloch expression for the z magnetization is

$$\left(\frac{M_z}{M_0}\right)_{\text{Bloch}} = \frac{1 + (\omega - \omega_0)^2 T_2^2}{1 + (\omega - \omega_0)^2 T_2^2 + T_1 T_2 (\gamma B_2)^2} \quad (11)$$

Equations (10) and (11) converge when

$$\frac{1}{(\omega - \omega_0)^2 T_2^2} \ll 1 \quad (12)$$

thus, both z magnetization formalisms converge under saturating conditions [$T_1 T_2 (\gamma B_2)^2 \gg 1$], and when ($\omega - \omega_0$) $\gg 1/T_2$. It should be noted that when the offset frequency comes close to the resonance of interest, the Bloch equation formalism deviates from off-resonance rotating frame spin–lattice relaxation formalism. As zero frequency is approached, $(M_z/M_0)_{\text{Bloch}}$ [equation (11)] approaches a finite spectral intensity ratio defined by $1/[1 + T_1 T_2 (\gamma B_2)^2]$, whereas $(M_z/M_0)_{\text{off-reson}}$ approaches zero.

2.6 Simulated Behavior of the Off-Resonance Rotating Frame Spin–Lattice Experiment

For illustrative purposes the off-resonance rotating frame spin–lattice relaxation behavior of the peptide chain backbone ^{13}C carbonyl carbon present in a hypothetical rigid protein engaged in isotropic reorientation is considered. For the isotropic tumbling of a rigid spherical protein each peptide bond carbonyl carbon is equivalent to all other residues in terms of its contribution to the resonance intensity, assuming that local peptide geometries and principal values of the peptide bond carbonyl carbon chemical shift tensor are identical. By contrast, for anisotropic reorientational motion, this assumption is not valid. Simulations describing anisotropic reorientational motion are considered elsewhere.[1,2] The calculation of the spectral intensity ratio for proteins takes into account intramolecular ^{13}C–^{1}H dipole–dipole interactions between the carbonyl carbon of the peptide bond and H-α, and CSA relaxation of the peptide carbonyl carbon. Intramolecular ^{13}C–^{14}N dipole–dipole contributions and intermolecular ^{13}C–^{1}H dipole–dipole interactions arising from solvent translational motion are negligible, and thus ignored.

The spectral intensity ratio, R, is typically measured in an off-resonance rotating frame spin–lattice relaxation experiment, and is defined by the ratio of $T_{1\rho}^{\text{off}}$ to T_1. The theoretical dependence of $1/T_1$ on τ_0 displays a maximum when $\omega_c^2 \tau_0^2 = 1$, and is therefore dependent on the static magnetic field strength, moving to shorter τ_0 values with increasing field strength. Figure 2 shows the dependence of $1/T_{1\rho}^{\text{off}}$ on τ_0 at three values of ν_{off} at constant B_2 field

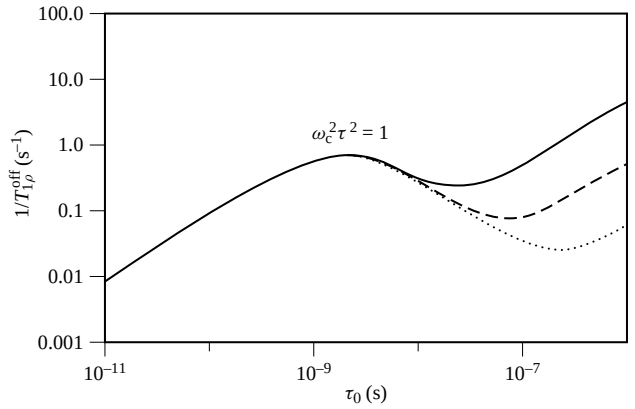

Figure 2 Theoretical dependence of the ^{13}C carbonyl carbon off-resonance rotating frame spin–lattice relaxation rate constant ($1/T_{1\rho}^{off}$) on the correlation time for random isotropic reorientation (τ_0). The computed curves assume dipolar relaxation by a proton 2.16 Å from the ^{13}C carbonyl carbon and CSA relaxation contributions at 7.05 T. Values of 81.8 ppm and −0.82 were used for the anisotropy factor and asymmetry parameter, respectively. An off-resonance field of 0.5×10^{-4} T applied 5 (——), 15 (– – –), and 45 (. . . ..) kHz off-resonance was assumed. (Reproduced by permission of Plenum Press from T. Schleich et al.[2])

strength. At values of $\omega_c^2\tau_0^2 \leq 1$, $1/T_{1\rho}^{off}$ is independent of ν_{off}, whereas for τ_0 values such that $(\omega_c\tau_0)^2 > 1$ the dependence of $1/T_{1\rho}^{off}$ becomes significant. A minimum occurs at a value of τ_0 corresponding to an R value of 0.5, i.e., an inflection point in a plot of R versus τ_0 (see Figure 3). As shown in Figure 3 the window of motional sensitivity of the off-resonance rotating frame spin–lattice relaxation experiment is approximately 1–1000 ns.

The effect of increasing ν_{off} (at constant B_2 field strength) is to shift the inflection of the R vs. τ_0 curve to longer correlation times, whereas, for the converse situation of variable B_2 field strength at constant ν_{off}, as shown in Figure 4, the inflection point of the curve moves to shorter correlation times with increasing B_2 field strength. The consequence of altering either

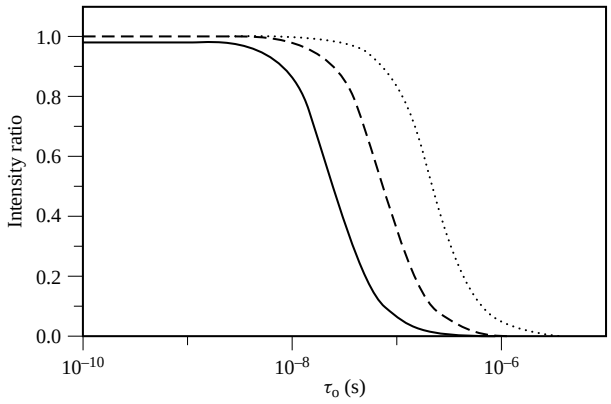

Figure 3 Simulation of the ^{13}C carbonyl carbon intensity ratio ($R = T_{1\rho}^{off}/T_1$) vs. τ_0 at 7.05 T. The computed curves assume dipolar and CSA relaxation mechanism contributions using the parameters listed in Figure 2. An off-resonance field of 0.5×10^{-4} T applied 5 (——), 15 (– – –), and 45 (. . . ..) kHz off-resonance was assumed. (Reproduced by permission of Plenum Press from T. Schleich et al.[2])

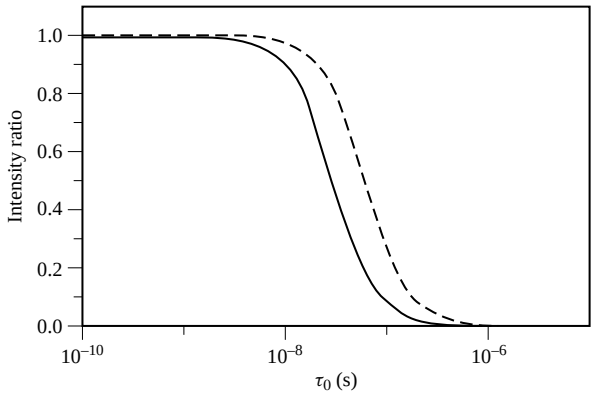

Figure 4 Simulation of the ^{13}C carbonyl carbon intensity ratio ($R = T_{1\rho}^{off}/T_1$) vs. τ_0 at 7.05 T. The computed curves assume dipolar and CSA relaxation mechanism contributions using the parameters listed in Figure 2. An off-resonance field of 0.4×10^{-4} (——), and 0.2×10^{-4} (– – –) T was applied 5 kHz off-resonance. (Reproduced by permission of Plenum Press from T. Schleich et al.[2])

ν_{off} or B_2 is to change both the angle that the effective field makes with the z axis as well as the precessional frequency (ω_e) of the nuclear spins about $\boldsymbol{B}_e$.

The intensity ratio can also be plotted versus ω_e (at constant B_2), i.e., in the form of a frequency-dependent or dispersion curve, as shown in Figure 5, for several different values of τ_0. The intensity ratio dispersion curve has the advantage that the effects of polydispersity and chemical exchange can be readily assessed. The frequency-dependent form of the experiment therefore incorporates the results of a number of different off-resonance rotating experiments performed at different values of ν_{off}, but at constant B_2.

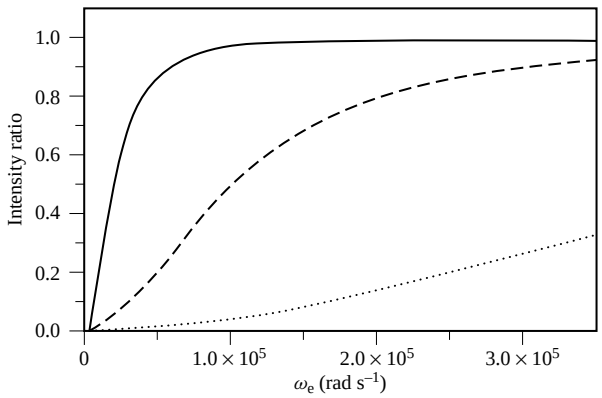

Figure 5 Simulation of the ^{13}C carbonyl carbon intensity ratio ($R = T_{1\rho}^{off}/T_1$) vs. the angular precessional frequency of the effective field (ω_e) produced by a radiofrequency field applied off-resonance at three different values of τ_0: 20 (——), 100 (– – –), and 500 (. . . ..) ns. In aqueous solution at 20 °C, assuming a protein partial specific volume of 0.73 cm^3 g^{-1}, and an average hydration value of 0.51 g of H_2O g^{-1} of protein, these correlation times represent hydrated macromolecular masses of 39.2, 196.1, and 980 kDa, respectively. The computed curves assume an off-resonance field strength of 0.4×10^{-4} T and a B_0 strength of 7.05 T. Dipolar and CSA relaxation mechanism contributions were assumed using the parameters listed in Figure 2. (Reproduced by permission of Plenum Press from T. Schleich et al.[2])

A potential source of intramolecular dipole–dipole relaxation of the peptide bond carbonyl carbon is the amide proton. However, simulations indicate this source of relaxation to be negligible.[2]

The simulated behavior of the ^{13}C off-resonance rotating frame spin–lattice relaxation experiment is also representative of the behavior of other spin-$\frac{1}{2}$ nuclei, as well as spin = 1 quadrupolar nuclei, engaged in isotropic reorientational motion.

The rotational correlation time obtained using an assumed isotropic model for the analysis of an anisotropically reorienting particle will be larger than the corresponding value for a sphere of equivalent volume. The resulting value of the correlation time is denoted $\tau_{0,\mathrm{eff}}$. The error associated with the application of an isotropic reorientational model to an anisotropically tumbling particle may be estimated by use of an empirically derived polynomial in which the rigid rotor axial ratio is the independent variable.[12]

3 EXPERIMENTAL IMPLEMENTATION

The implementation of the off-resonance rotating frame spin–lattice experiment using continuous wave irradiation is straightforward on modern spectrometers, and is described in detail elsewhere.[1,2] Calibration of the B_2 off-resonance irradiation field is of critical importance. Detailed procedures to accomplish B_2 field calibration have been described.[1,2] The experimental intensity ratio, R, as a function of offset frequency, is the ratio of the measured intensity in the presence of an off-resonance irradiation field to a reference intensity obtained with very far off-resonance irradiation. For well-separated resonances the intensity is obtained by integration, whereas for overlapping resonances lineshape deconvolution is generally required in order to provide the relevant signal intensities.

Quantitative analysis of the R vs. ω_e dispersion curve is achieved by nonlinear least-squares regression with R and ω_e the respective dependent and independent variables. Nonlinear regression is performed by incorporating the appropriate (for the specific case under consideration) off-resonance rotating frame spin–lattice relaxation formalism into a program such as NONLINWOOD.[13] The effective (average) rotational correlation time, $\tau_{0,\mathrm{eff}}$, and the intensity ratio very far off-resonance, $R(\omega_e \rightarrow \infty)$, are fit to the experimental data using a model which assumes a single correlation time for random isotropic tumbling. Saturation transfer effects are manifested by dispersion curves which plateau at R (large ω_e) values less than unity. In this case, the effective rotational correlation time and the rate constant, k_a, for exchange from site A to B (2-site exchange is assumed) can be fit to the experimental data using a modified formalism.[2] Other models may be employed which recognize anisotropic motion, or polydispersity arising from discrete mixtures or from assumed models of association.

4 APPLICATIONS

4.1 Protein Rotational Diffusion

The ^{13}C off-resonance rotating frame spin–lattice relaxation experiment has been applied to a variety of proteins in dilute aqueous solution for the purpose of determining rotational correlation times. As noted by James et al.[7] values of the protein rotational correlation time ($\tau_{0,\mathrm{eff}}$) for six monodisperse protein preparations, varying in axial ratio (a/b) from 1.2 to at least 3.5, and spanning the molecular mass range from 14.6 to 150 kDa, obtained by assuming isotropic reorientational motion, were in reasonable agreement with those evaluated by the use of well-established rotational diffusion techniques. A more recent study improved the agreement between experimentally derived and theoretically estimated rotational correlation times, and established the upper molecular mass limit to be at least 800 kDa, by including carbonyl carbon backbone segmental and side-chain internal motion in the analysis, as well as corrections for anisotropic shape and viscosity effects.[14] A comparison of the experimental τ_0 values with those expected theoretically as a function of molecular mass is shown in Figure 6. Departures from expected behavior occur at a molecular mass as low as 50 kDa, unless internal motion effects are included in the formalism.[14]

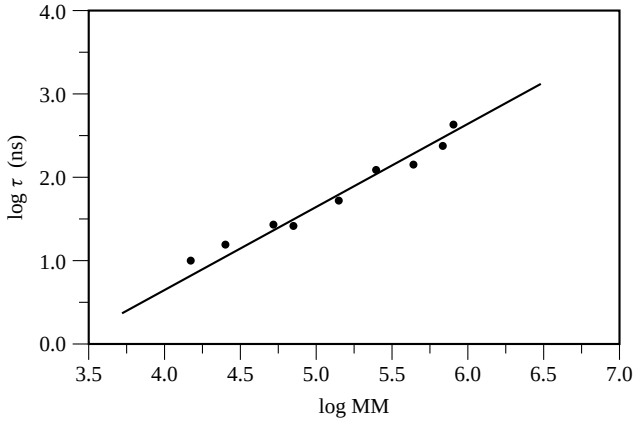

Figure 6 Log of rotational correlation time (τ_0) vs. log of protein molecular mass (MM). (——) Theoretically predicted dependence of τ_0 (Stokes–Einstein equation) on protein molecular mass. (•) Rotational correlation times determined from experimental R vs. ω_e dispersion curves by nonlinear least squares analysis (with the inclusion of carbonyl carbon backbone segmental and side-chain internal motion, and corrections for anisotropic reorientation and viscosity effects) for lysozyme (14.6 kDa, a/b = 1.7), chymotrypsinogen A (25 kDa, a/b = 2.0), concanavalin A (53 kDa, a/b = 2.1), bovine serum albumin (69 kDa, a/b = 2.9), yeast alcohol dehydrogenase (141 kDa, a/b = 2.8), β_H-crystallin (250 kDa, a/b = 1.6), apoferritin 440 kDa, a/b = 1.0), thyroglobulin (669 kDa), and α-crystallin (800 kDa). Temperature = 23 °C.[14] (Reproduced by permission of Wiley from S. X. Wang et al.[14])

Aqueous proton solvent translational diffusion does not appear to be a significant complication in the determination of native globular protein rotational correlation times. An exception may be for very high molecular mass particles, in which case it is possible to make a correction by inclusion of a solvent-derived intermolecular dipole–dipole relaxation contribution in the analysis.[2]

Polydisperse protein systems may also be analyzed if a model describing the molecular weight distribution is known or a reasonable one can be assumed.[15] Other studies involving concentration-dependent association include γ-crystallin[2,16] and the pH-dependent aggregation of lysozyme.[1,2] For γ-crystallin the observed dependence of the derived isodesmic association constant on concentration was attributed to the

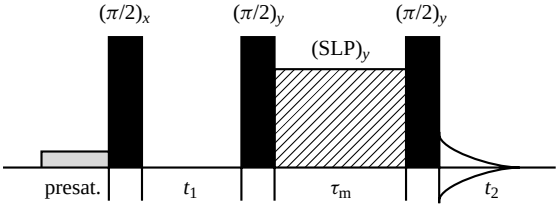

Figure 7 Pulse sequence for the O-ROESY experiment.[19] Elements of both the NOESY and ROESY experiments are incorporated in this sequence. The off-resonance spin lock is applied during the mixing time in the form of a Shifted Laminar Pulse (SLP).[20] Presaturation is used to minimize the water signal contribution

effect of 'macromolecular crowding'. Application has also been made to the aggregation of hemoglobin S aggregation in oxygenated sickle cells.[17] Other studies have examined the rotational diffusion characteristics of crystallins in ocular lens tissues homogenates.[18]

4.2 Off-Resonance ROESY Experiment

Off-resonance irradiation considerations have been included in the ROESY experiment, thereby establishing a three-dimensional off-resonance version of the two-dimensional ROESY experiment, designated O-ROESY.[19] The salient difference between the O-ROESY and ROESY experiments is that the on-resonance spin lock is replaced by an off-resonance spin lock applied at frequency ν_{off} and at field strength B_2. The O-ROESY pulse sequence is shown in Figure 7.

Experimentally the O-ROESY experiment is implemented by the use of Shifted Laminar Pulses[20] to ensure phase coherency between the off-resonance irradiation spin lock irradiation and the $(\pi/2)_y$ hard pulse. Variation of ν_{off} at constant B_2 creates a suite of two-dimensional experiments with frequency-dependent (ν_{off}) dispersion behavior in the cross-peak intensity established by the relevant interacting spin-$\frac{1}{2}$ nuclei. This stack of two-dimensional spectra contains a third frequency domain, thereby, in essence, defining a three-dimensional experiment. The cross-peak intensity dispersion curve contains a continuously increasing NOESY contribution at the expense of ROESY as the off-resonance spin lock frequency is increased. This experiment has been described in terms of product operator formalism for interacting homonuclear spin-$\frac{1}{2}$ nuclei leading to an expression for the dependence of cross-peak intensity dispersion behavior of ν_{off} (at constant B_2).[21] Analysis of experimental cross-peak intensity dispersion data permits the evaluation of the internal motion correlation time of the internuclear vector defined by the relevant nuclei, its order parameter, the internuclear separation distance, as well as the rotational correlation time for macromolecular reorientational motion. An example for lysozyme is shown in Figure 8.

The O-ROESY experiment is analogous to the heteronuclear two-dimensional off-resonance experiments proposed by Peng and Wagner.[22]

4.3 Phosphorus Metabolite Rotational Diffusion

Phosphorus-31 off-resonance rotating frame spin–lattice relaxation experiments have been used to study phosphorus metabolite rotational diffusion in tissue, as a means of exploring the issue of 'free' versus 'bound' metabolites.[22] Effective rotational correlation times for the major phosphorus metabolites present in cortical and nuclear bovine calf lens homogenates were obtained assuming isotropic reorientational motion. Intramolecular dipole–dipole ($^{31}P-^{1}H$, $^{31}P-^{31}P$), CSA, and solvent (water) translational dipole–dipole ($^{31}P-^{1}H$) relaxation contributions were included in the analysis. In several cases the limiting value of the spectral intensity ratio failed to reach unity at large offset frequency, necessitating use of a modified formalism incorporating chemical exchange-mediated saturation transfer between two sites.[24]

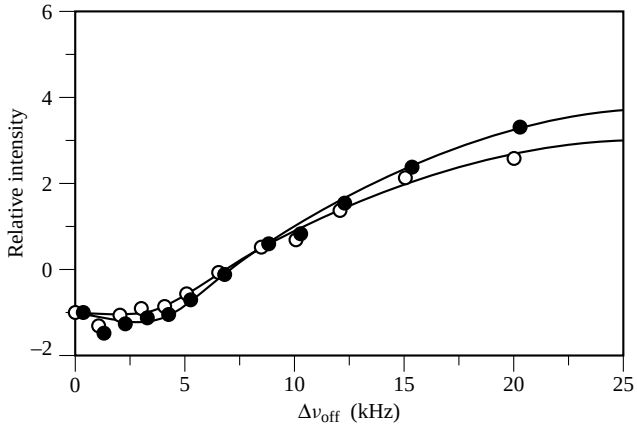

Figure 8 Normalized O-ROESY cross-peak intensity vs. off-resonance spin lock frequency (B_2 field strength = 1.2×10^{-4} T) obtained for the lysozyme C-α protons (○, $d_{\alpha\alpha}$ [45–51]; •, $d_{\alpha\alpha}$ [2–39]).[19] Normalization of off-resonance cross-peak intensity is relative to the on-resonance cross-peak intensity. The solid lines are the theoretical curves obtained by a theoretical fit to the experimental data, and are described by the following parameters for $d_{\alpha\alpha}$ [45–51] and $d_{\alpha\alpha}$ [2–39], respectively: internal correlation time, τ_i, 1.0, 1.2 ns; order parameter, S, 0.86, 0.82; correlation time for overall reorientational motion, $\tau_{o,eff}$, 6.4 and 6.3 ns (temperature = 35 °C)

4.4 Saturation Transfer

The extension of off-resonance rotating frame spin–lattice relaxation theory to include the effects of chemical exchange-mediated saturation transfer affords knowledge about the occurrence of magnetization exchange kinetic processes in addition to the usually obtained rotational diffusion behavior. Analytical expressions have been derived[24] describing the time-dependent and steady-state behavior of the exchanging nuclear magnetization experiencing off-resonance field-induced partial or complete saturation.

Specific applications of the modified formalism include the exchange of free and G-actin-bound adenosine triphosphate (ATP), creatine kinase-catalyzed phosphocreatine (PCr), and ATP γ-phosphate exchange, and phosphorus metabolite exchange between two different relaxation environments, representing mobile and relatively immobile (solid-like) pools of metabolites present in bovine calf nuclear ocular lens tissue homogenates.[2,24] The extended formalism also permits evaluation of saturation transfer experiments involving slowly tumbling or motionally restricted metabolites when nonselective, off-resonance, partial saturation effects become appreciable.

4.5 Proton Magnetization Transfer

The off-resonance rotating frame spin–lattice relaxation formalism has been extended to include the effects of magnetization occurring between 2 proton spin baths. The intensity ratios for the A and B spins are given by:[2,25]

$$R^{\mathrm{A}} = \frac{\left[R_{\mathrm{A}}\left(\frac{R_{\mathrm{T}}}{f}+R_{\mathrm{B}}+\frac{1}{T_{\mathrm{e,B}}}\right)\cos^2\Theta_{\mathrm{A}}+R_{\mathrm{B}}R_{\mathrm{T}}\cos^2\Theta_{\mathrm{B}}\right]}{D^{\mathrm{off}}} \quad (13a)$$

$$R^{\mathrm{B}} = \frac{\left[R_{\mathrm{B}}\left(R_{\mathrm{T}}+R_{\mathrm{A}}+\frac{1}{T_{\mathrm{e,A}}}\right)\cos^2\Theta_{\mathrm{B}}+R_{\mathrm{A}}\frac{R_{\mathrm{T}}}{f}\cos^2\Theta_{\mathrm{A}}\right]}{D^{\mathrm{off}}} \quad (13b)$$

where $R_{\mathrm{A,B}}$ and R_{T} are the rate constants for longitudinal relaxation of the A or B spins in the absence of cross relaxation, and the cross-relaxation rate constant for *magnetization transfer from the A to B spin systems*, respectively. By contrast, for magnetization transfer from the B to the A spin system the rate constant is equal to R_{T}/f, where f represents the ratio of the number of B spins to the number of A spins. The terms D^{off} and $1/T_{\mathrm{e,A,B}}$ are given by

$$D^{\mathrm{off}} = R_{\mathrm{A}}^{\mathrm{off}}R_{\mathrm{B}}^{\mathrm{off}} + R_{\mathrm{A}}^{\mathrm{off}}\frac{R_{\mathrm{T}}}{f} + R_{\mathrm{B}}^{\mathrm{off}}R_{\mathrm{T}} \quad (14c)$$

$$\frac{1}{T_{\mathrm{e,A,B}}} = \frac{T_2\omega_1^2}{1+4\pi^2\Delta_{\mathrm{A,B}}^2T_2^2} \quad (14d)$$

respectively, where $R_{\mathrm{A}}^{\mathrm{off}} = 1/T_{1\rho,\mathrm{A}}^{\mathrm{off}} = R_{\mathrm{A}} + 1/T_{\mathrm{e,A}}$, $R_{\mathrm{B}}^{\mathrm{off}} = 1/T_{1\rho,\mathrm{B}}^{\mathrm{off}} = R_{\mathrm{B}} + 1/T_{\mathrm{e,B}}$, $\omega_1^2 = (\gamma B_2)^2$, and Δ is the offset of the rf irradiation field from the A or B spins. The other symbols have their usual meaning. Using the expression for $1/T_{\mathrm{e,A,B}}$ given by equation (13d), equations (13a) and (13b) can be shown to be equivalent to the equations obtained by solution of the relevant six coupled Bloch equations,[25] when the value of $\cos^2\Theta$ is approx. 1. Thus, the off-resonance rotating frame spin–lattice formalism and the Bloch formalism modified to include cross relaxation are identical under the usual experimental conditions employed.

This formalism has been applied to the study of proton magnetization transfer between water and rotationally immobilized protein in a wide variety of tissues,[2] and represents a form of the saturation transfer experiment.

5 RELATED ARTICLES

Biological Macromolecules; Biological Macromolecules: NMR Parameters; Brownian Motion and Correlation Times; Enzyme-Catalyzed Exchange: Magnetization Transfer Measurements; Inversion-Recovery Pulse Sequence in MRI; Magnetization Transfer Contrast: Clinical Applications; Magnetization Transfer and Cross Relaxation in Tissue; Magnetization Transfer between Water and Macromolecules in Proton MRI; Molecular Motions: T_1 Frequency Dispersion in Biological Systems; NOESY; Nuclear Overhauser Effect; Phosphorus-31 Magnetization Transfer Studies In Vivo; Relaxation Effects of Chemical Exchange; Relaxation Processes in Coupled-Spin Systems; Relaxometry of Tissue; TOCSY in ROESY and ROESY in TOCSY.

6 REFERENCES

1. T. Schleich, C. F. Morgan, and G. H. Caines, *Methods Enzymol.*, 1989, **176**, 386.
2. T. Schleich, C. H. Caines, and J. M. Rydzewski, in *Biological Magnetic Resonance*, eds. L. J. Berliner and J. Reuben, Plenum Press, New York, 1992, Vol. 11, Chap. 3
3. G. P. Jones, *Phys. Rev.*, 1966, **148**, 332.
4. J. S. Blicharski, *Acta Phys. Pol. A*, 1972, **41**, 223.
5. J. F. Jacquinot and M. Goldman, *Phys. Rev. B*, 1973, **8**, 1944.
6. B. A. Cornell and J. M. Pope, *J. Magn. Reson.*, 1974, **16**, 172.
7. T. L. James, G. B. Matson, and I. D. Kuntz, *J. Am. Chem. Soc.*, 1978, **100**, 3590.
8. T. L. James, in *Phosphorus-31 NMR Principles and Applications*, ed. D. Gorenstein, Academic Press, New York, 1984, Chap. 12
9. T. L. James, G. B. Matson, I. D. Kuntz, and R. W. Fisher, *J. Magn. Reson.*, 1977, **28**, 417.
10. J. M. Rydzewski and T. Schleich, *J. Magn. Reson., Ser. B*, 1994, **104**, 11.
11. P. Bendel and T. L. James, *J. Magn. Reson.*, 1982, **48**, 76.
12. C. F. Morgan, T. Schleich, G. H. Caines, and D. Michael, *Biopolymers*, 1990, **29**, 469.
13. C. Daniel and F. S. Woods, *Fitting Equations to Data*, Wiley, New York, 1980.
14. S. X. Wang, A. Stevens, and T. Schleich, *Biopolymers*, 1993, **33**, 1581.
15. C. F. Morgan, T. Schleich, and G. H. Caines, *Biopolymers*, 1990, **29**, 501.
16. A. Stevens, S. X. Wang, G. H. Caines, and T. Schleich, *Biochim. Biophys. Acta*, 1995, **1265**, 1.
17. T. L. James, R. Mathews, and G. B. Matson, *Biopolymers*, 1979, **18**, 1763.
18. C. F. Morgan, T. Schleich, G. H. Caines, and P. N. Farnsworth, *Biochemistry*, 1989, **28**, 5065.
19. K. Kuwata and T. Schleich, *J. Magn. Reson., Ser. A*, 1994, **105**, 43.
20. S. L. Patt, *J. Magn. Reson.*, 1992, **96**, 94.
21. K. Kuwata and T. Schleith, *J. Magn. Reson., Ser. A*, 1995, **114**, 219.
22. J. W. Peng, V. Thanabal, and G. Wagner, *J. Magn. Reson.*, 1991, **94**, 84.
23. G. H. Caines, T. Schleich, C. F. Morgan, and P. N. Farnsworth, *Biochemistry*, 1990, **29**, 7547.
24. G. H. Caines and T. Schleich, *J. Magn. Reson.*, 1991, **95**, 457.
25. G. H. Caines, T. Schleich, and J. M. Rydzewski, *J. Magn. Reson.* 1991, **95**, 558.

Acknowledgments

T.S. wishes to acknowledge the contributions of his co-workers to the development of the material presented in this article. Special thanks are due to: D. Brooks, G. H. Caines, K. Kuwata, J. Loo, C. F. Morgan, J. M. Rydzewski, A. Stevens, S. X. Wang, and H. Yang.

Biographical Sketch

Thomas Schleich. *b* 1938. B.S., 1960, Cornell; Ph.D., 1966, Rockefeller. Helen Hay Whitney Foundation postdoctoral fellow, University of

Oregon (with P. H. von Hippel). Faculty in Chemistry University of California, (UC) Santa Cruz, 1969–present; Faculty in Pharmaceutical Chemistry, UC San Francisco, 1986–present. Approx. 90 publications. Research interests include the development and application of NMR spectroscopy to problems of biomedical relevance and protein and nucleic acid structure and dynamics.

Spin–Rotation Relaxation Theory

R. E. D. McClung

University of Alberta, Edmonton, Alberta, Canada

1	Introduction	1
2	Basic Theory of Spin–Rotation Relaxation	1
3	Spin–Rotation Relaxation in Fluids	2
4	Spin–Rotation Relaxation in Molecules with Internal Rotation	4
5	Spin–Rotation Relaxation in Solids	5
6	Related Articles	5
7	References	5

1 INTRODUCTION

When a molecule rotates, a magnetic field is generated by the rotational motion, and the magnetic moments of the nuclei in the molecule experience this magnetic field. The energies of the nuclear spins, therefore, vary with the magnitude of the rotational magnetic field, and we say that there exists a 'spin–rotation' interaction between each nuclear spin and the rotational motion of the molecule. Since the size of the rotational magnetic field at the nucleus is proportional to the magnitude of the rotational angular momentum of the molecule, the Hamiltonian operator for the spin–rotation interaction, $\hat{\mathcal{H}}_{\mathrm{SR}}$, is generally written in the form[1]

$$\hat{\mathcal{H}}_{\mathrm{SR}} = \hat{\boldsymbol{I}} \cdot \boldsymbol{C} \cdot \boldsymbol{J} \tag{1}$$

where $\hat{\boldsymbol{I}}$ is the dimensionless spin angular momentum operator of the nucleus, $\boldsymbol{J}$ is the rotational angular momentum of the molecule (in units of J s), and $\boldsymbol{C}$ is the spin–rotation interaction tensor (in units of s^{-1}). The elements of $\boldsymbol{C}$ are empirical constants that, in favorable cases, can be measured by molecular beam resonance or estimated from nuclear shielding constants.[2]

All molecules in gases, liquids and many solids are constantly in motion and undergo frequent collisions with other molecules. Since the rotational angular momentum of a molecule may change during a collision with another molecule, the magnitude of the spin–rotation interaction in the molecule varies with time. This time-dependent interaction connects the nuclear spin system to the motional degrees of freedom of the molecule and provides a pathway for the transfer of energy between the nuclear spins and the rotational motion of the molecule (see also ***Brownian Motion and Correlation Times***). This energy transfer from the nuclear spins to other degrees of freedom is just spin–lattice (or longitudinal) relaxation, so the motional modulation of spin–rotation interactions gives a contribution to nuclear relaxation that is generally referred to as spin–rotation relaxation. Spin–rotation relaxation was first proposed by Schwinger, and was established as the predominant mechanism for spin–lattice relaxation in hydrogen gas by Bloom[3] in 1957, and in several polyatomic gases by 1961 (see also ***Gas Phase Studies of Intermolecular Interactions and Relaxation***).

Spin–rotation relaxation is important for nuclei in small molecules (e.g., $^{1}H_2$, $C^{1}H_4$, $C^{19}F_4$, $^{13}C_6D_6$) in gas (see ***Gas Phase Studies of Intermolecular Interactions and Relaxation*** and ***Gases at High Pressure***) and liquid phases,[4,5] for nuclei in highly mobile environments on large molecules in liquid solution (e.g., protons in CH_3 groups of peptides and proteins), and occasionally for nuclei in highly symmetric molecules or ions in solids [e.g., $N^{1}H_4^{+}$ in $NH_4Cl_{(s)}$].

2 BASIC THEORY OF SPIN–ROTATION RELAXATION

In order to develop theoretical expressions for the spin–rotation contributions to nuclear spin relaxation rates, it is important to recognize that the nuclear spin angular momentum operator $\hat{\boldsymbol{I}}$ is quantized along the static magnetic field (i.e., in a coordinate system fixed in the laboratory), while $\boldsymbol{C}$ is best described in its principal axis coordinate system, which is fixed in the molecule. In this principal axis frame, the Cartesian form of $\boldsymbol{C}$ is diagonal and has elements C_{x}, C_{y}, and C_{z}. The description of the transformation from laboratory to molecular coordinates is most compact if we recognize that $\hat{\boldsymbol{I}}$ is a spherical tensor of rank 1, so that the molecular k component, $\hat{I}_k^{\mathrm{molec}}$, is related to the laboratory m component, $\hat{I}_{\mathrm{m}}$, by the relation

$$\hat{I}_k^{\mathrm{molec}} = \sum_{k=-1}^{1} \hat{I}_m \mathcal{D}_{mk}^{(1)}[\Omega(t)] \tag{2}$$

where $\mathcal{D}^{(1)}[\Omega(t)]$ is the Wigner rotation matrix, which describes the transformation of the components of a spherical tensor of rank 1, and $\Omega(t)$ is the set of Euler angles connecting the laboratory and molecular frames at time t. Having made these connections, we can show the time dependence of the spin–rotation interaction explicitly:

$$\hat{\mathcal{H}}_{\mathrm{SR}}(t) = \sum_{m,k,l=-1}^{1} \hat{I}_m \mathcal{D}_{mk}^{(1)}[\Omega(t)] C_{kl} J_l(t) \tag{3}$$

where $J_l(t)$ is the l spherical tensor component of the rotational angular momentum of the molecule in the molecule-fixed coordinate system at time t, and the elements of the spin–rotation interaction tensor are

$$\begin{aligned} C_{kl} = {} & C_{\mathrm{o}}\delta_{k,-l}(\delta_{k,0} - \delta_{|k|,1}) \\ & + \Delta C \delta_{k,-l}(2\delta_{k,0} + \delta_{|k|,1}) + \delta C \delta_{k,l}\delta_{|k|,1} \end{aligned} \tag{4}$$

in the spherical tensor representation. In equation (4),

$$\left.\begin{aligned} C_{\mathrm{o}} &= \tfrac{1}{3}(C_x + C_y + C_z) \\ \Delta C &= \tfrac{1}{3}[C_z - \tfrac{1}{2}(C_x + C_y)] \\ \delta C &= \tfrac{1}{2}(C_x - C_y) \end{aligned}\right\} \tag{5}$$

In the Redfield description of relaxation (see ***Relaxation Theory: Density Matrix Formulation***), it is easily shown that the rates of transverse and longitudinal relaxation, R_1 and R_2,

respectively, due to motional modulation of an interaction of the form

$$\hat{\mathcal{H}}_{\text{int}}(t) = \hbar \sum_{m=-1}^{1} \hat{I}_m V_m(t) \tag{6}$$

where $V(t)$ has a random time dependence, are given by

$$\left.\begin{aligned} R_1 = \frac{1}{T_1} &= 2\int_0^\infty \overline{V_1^*(0)V_1(t)}\exp(-\mathrm{i}\omega_0 t)\,\mathrm{d}t \\ R_2 = \frac{1}{T_2} & \\ &= \int_0^\infty \overline{V_1^*(0)V_1(t)}\exp(-\mathrm{i}\omega_0 t)\,\mathrm{d}t + \int_0^\infty \overline{V_0^*(0)V_0(t)}\,\mathrm{d}t \end{aligned}\right\} \tag{7}$$

In these equations, T_1 is the spin–lattice relaxation time, T_2 is the spin–spin relaxation time, $\overline{V^*{}_\mu(0)V_\mu(t)}$ is the time correlation function for the stationary random variable $V_\mu(t)$, and ω_0 is the nuclear resonance frequency (in s^{-1}) for nucleus I. The bar in $\overline{V^*{}_\mu(0)V_\mu(t)}$ represents an average over all the molecules in the sample (the 'ensemble').

The correlation functions arise in the expressions for the relaxation rates because the interactions between the spin and lattice systems exhibit random time dependence (see also ***Brownian Motion and Correlation Times***). A time correlation function is a quantitative measure of the time period over which a precise knowledge of the value of the random variable at time zero allows an accurate prediction of its value at some time t later. Generally, the correlation function is approximately equal to 1 at short times, and decays to zero at longer times after many changes in the random variable have occurred. The time dependence of the correlation function can be characterized by a correlation time τ_c. For a correlation function $\overline{V^*(0)V(t)}$, the correlation time is defined by

$$\tau_c = \int_0^\infty \frac{\overline{V^*(0)V(t)}}{\overline{|V(0)|^2}}\,\mathrm{d}t \tag{8}$$

Qualitatively, a correlation function is approximately unity for times $t \ll \tau_c$ and is zero for $t \gg \tau_c$. In the expressions for the relaxation rates, it is the Fourier transforms or spectral densities $\mathcal{J}(\omega)$ of the correlation functions

$$\mathcal{J}(\omega) = \int_0^\infty \overline{V^*(0)V(t)}\exp(-\mathrm{i}\omega t)\,\mathrm{d}t \tag{9}$$

that appear. Qualitatively, $\mathcal{J}(\omega)$ is large and approximately constant for $\omega \ll \tau_c^{-1}$, and is zero for $\omega \gg \tau_c^{-1}$. Note that τ_c is proportional to $\mathcal{J}(0)$.

For spin–rotation interactions, we make the connection

$$V_m(t) = \hbar^{-1} \sum_{k,l=-1}^{1} \mathcal{D}^{(1)}_{mk}[\Omega(t)]C_{kl}J_l(t) \tag{10}$$

and note that the correlation time for the correlation function $\overline{V^*{}_1(0)V_1(t)}$ is short compared with ω_0^{-1}, so that $\mathcal{J}(\omega_0) = \mathcal{J}(0)$ and we can write

$$R_{1\text{SR}} = R_{2\text{SR}} = 2\hbar^{-2} \sum_{k,l,k',l'=-1}^{1} C_{k'l'}C_{kl}\mathcal{J}_{k'l'kl} \tag{11}$$

where R_{1SR} and R_{2SR} are, respectively, the spin–rotation contributions to the rates of longitudinal and transverse nuclear relaxation, and the zero-frequency spectral density $\mathcal{J}_{k'l'kl}$ is given by

$$\mathcal{J}_{k'l'kl} = \int_0^\infty \overline{\mathcal{D}^{(1)*}_{1k'}[\Omega(t)]J^*_{l'}(t)\mathcal{D}^{(1)}_{1k}[\Omega(0)]J_l(0)}\,\mathrm{d}t \tag{12}$$

The spin–rotation correlation functions

$$G_{k'l'kl}(t) = \overline{\mathcal{D}^{(1)*}_{1k'}[\Omega(t)]J^*_{l'}(t)\mathcal{D}^{(1)}_{1k}[\Omega(0)]J_l(0)} \tag{13}$$

involve the time dependence of *both* the angular momentum and the orientation of the molecule. They are very different from the reorientational correlation functions $\overline{\mathcal{D}^{(2)*}_{mk'}[\Omega(t)]\mathcal{D}^{(2)}_{mk}[\Omega(0)]}$ involved in the relaxation contributions from rotational modulation of intramolecular dipole–dipole, anisotropic chemical shift, and electric quadrupolar interactions, since the reorientational correlation functions involve only the orientation of the molecule, not its angular momentum. The values of the spectral densities $\mathcal{J}_{k'l'kl}$, and hence the spin–rotation relaxation rates, are determined by the rotational dynamics of the molecules in the medium being studied. The general expression for the spin–rotation relaxation rate given in Equation (11) does not convey any clear and simple relationships between the relaxation rate and physical parameters that characterize the rotational dynamics of the molecules in the medium. These relationships are most clearly developed by investigating the simple physical models used to describe the rotational motion of the molecules in the medium. It is best to focus our attention on the spin–rotation relaxation and rotational dynamics of molecules in fluids, mobile species in disordered solids, and rotating methyl groups in large molecules in turn, since the models used to describe the motions in each are different.

3 SPIN–ROTATION RELAXATION IN FLUIDS

3.1 The Hubbard Model and the Hubbard Relation

In Hubbard's classic work[6] on spin–rotation relaxation of spherical top molecules in liquids, he assumed that the rotational motion of a molecule was like that of a rigid macroscopic sphere immersed in a viscous fluid and experiencing strong random torques due to the Brownian motion of other molecules, just as Bloembergen, Purcell, and Pound[7] had done in their classic description of dipolar relaxation in liquids (see ***Brownian Motion and Correlation Times***). Hubbard found that the spin–rotation relaxation rate could be written as[6]

$$R_{1\text{SR}} = R_{2\text{SR}} = \frac{2Ik_\text{B}T}{\hbar^2}(C_\text{o}^2 + 2\Delta C^2)\tau_J \tag{14}$$

where I is the moment of inertia of the spherical molecule, k_B is the Boltzmann constant, and τ_J is the correlation time for the rotational angular momentum of the molecule. In deriving this result, Hubbard assumed that the reorientation of the molecule was very slow compared with the modulation of its angular momentum by collisions with other molecules in the liquid, so that the spin–rotation correlation function in Equation (13) is approximately

$$\begin{aligned} G_{k'l'kl}(t) &\approx \overline{\mathcal{D}^{(1)*}_{1k'}[\Omega(0)]\mathcal{D}^{(1)}_{1k}[\Omega(0)]}\int_0^\infty \overline{J^*_{l'}(t)J_l(0)}\,\mathrm{d}t \\ &\approx \tfrac{1}{3}\delta_{k,k'}\int_0^\infty \overline{J^*_{l'}(t)J_l(0)}\,\mathrm{d}t \end{aligned} \tag{15}$$

In Hubbard's model, the angular momentum of a molecule is assumed to follow the rotational Langevin equation

$$\frac{\mathrm{d}\boldsymbol{J}}{\mathrm{d}t} = -\frac{\xi_{\mathrm{R}}}{I}\boldsymbol{J} + \mathcal{T}(t) \tag{16}$$

where ξ_{R} is the rotational friction coefficient describing the viscous retarding torque on the molecule and $\mathcal{T}(t)$ is the Brownian torque due to the rapid random motions of other molecules. The correlation function for the ith Cartesian component of the angular momentum is

$$\overline{J_i(t)J_i(0)} = Ik_{\mathrm{B}}T\exp(-t/\tau_J) \tag{17}$$

and the angular momentum correlation time is given by

$$\tau_J = I/\xi_{\mathrm{R}} \tag{18}$$

so there is a clear relationship between the angular momentum correlation time, which determines the rate of spin–rotation relaxation, and the rotational friction coefficient. The latter may be estimated from the Stokes relationship

$$\xi_{\mathrm{R}} = 8\pi a^3\eta \tag{19}$$

where a is the hydrodynamic radius of the spherical molecule and η is the viscosity of the fluid medium. Hubbard showed that the reorientational correlation time $\tau_\theta^{(2)}$, which characterizes the random time dependence of the orientation of the molecule (see ***Brownian Motion and Correlation Times***) within the reorientational part of the correlation function $G_{k'l'kl}(t)$ and determines the rate of intramolecular dipolar relaxation, is also related to the rotational friction coefficient by

$$\tau_\theta^{(2)} = \xi_{\mathrm{R}}/6k_{\mathrm{B}}T \tag{20}$$

The celebrated 'Hubbard relation'

$$\tau_\theta^{(2)}\tau_J = I/6k_{\mathrm{B}}T \tag{21}$$

was obtained[6] by combining equations (18) and (20). Equations (14) and (21) are valid for spherical molecules in the region where molecular rotation is slow compared with the rate of fluctuations in the angular momentum ($\tau_J \ll \tau_\theta^{(2)}$).

For nonspherical molecules, the friction coefficients describing the viscous retarding torques in the rotational Langevin equations [see equation (16)] are different for the x, y, and z components of the angular velocity, and equation (14) becomes

$$R_{1\mathrm{SR}} = R_{2\mathrm{SR}} = \frac{2k_{\mathrm{B}}T}{3\hbar^2}(I_xC_x^2\tau_{J_x} + I_yC_y^2\tau_{J_y} + I_zC_z^2\tau_{J_z}) \tag{22}$$

where τ_{J_x}, τ_{J_y}, and τ_{J_z} are the correlation times for the respective angular velocity components. In deriving this result, the precession terms in the rotational Langevin equations for the angular velocity components are ignored, so Equation (22) is valid only in the limit $\tau_{J_x}, \tau_{J_y}, \tau_{J_z} \ll \tau_\theta^{(2)}$.

Some of the important extensions of the Hubbard model will be discussed presently, but it is useful to investigate spin–rotation relaxation in dilute gases first in order to put the later extensions into a more complete perspective.

3.2 Relaxation in Dilute Fluids

In a dilute gas,[2] the molecules rotate freely and their rotational angular momenta remain constant during the long periods between collisions with other molecules (see also ***Gas Phase Studies of Intermolecular Interactions and Relaxation*** and ***Gases at High Pressure***). The orientation of the molecule $\Omega(t)$ and its angular momentum $\boldsymbol{J}$ are intimately connected since the rotational velocity for a spherical top molecule is just $\boldsymbol{J}/I$. The 'inertial' motion of the molecules in the intervals between collisions has important effects on the rate of spin–rotation relaxation. The ensemble average of each of the spin–rotation correlation functions for an ensemble of freely rotating spherical top molecules, $G_{k'l'k}^{\mathrm{free}}(t)$, can be expressed as the sum of a constant term and terms with Gaussian time dependence. If the time between collisions in the gas is long compared with the time required for a complete rotation of the molecule, the time-dependent terms in the free rotor correlation function do not contribute to the spin–rotation spectral densities, and one obtains the spin–rotation relaxation rate[8]

$$R_{1\mathrm{SR}} = R_{2\mathrm{SR}} = \frac{2Ik_{\mathrm{B}}T}{\hbar^2}(C_0^2 + \tfrac{4}{5}\Delta C^2)\tau_J \tag{23}$$

where τ_J is the time between collisions that randomize the magnitude and/or direction of the angular momentum vector of the molecule.

It is useful to compare equations (14) and (23) in order to discern the important differences in the rates of spin–rotation relaxation in dense and dilute fluids. Clearly, the time between 'collisions' in the liquid will be much shorter than in the gas, so τ_J is much longer, and hence spin–rotation relaxation is much faster, in the gas phase. The isotropic spin–rotation interactions, which are characterized by the constant C_0, give contributions to spin relaxation rates that have the same form for all fluids. This is not surprising, because the isotropic spin–rotation interactions are completely independent of molecular reorientation, so their time correlation should be characterized completely by the angular momentum correlation time τ_J. On the other hand, the spin relaxation rates due to motional modulation of the anisotropic parts of the spin–rotation interaction (characterized by ΔC) are smaller by a factor of $\frac{2}{5}$ in the dilute gas owing to the 'inertial' motion of the molecules. This inertial motion causes a loss of correlation in the anisotropic spin–rotation interactions during the long periods of free rotation, and this leads to less effective spin–rotation relaxation in the dilute gas. Inertial effects also produce dramatic changes in the reorientational correlation time $\tau_\theta^{(2)}$ and hence in the relaxation contributions from dipole–dipole and electric quadrupolar interactions.

3.3 The Extended Diffusion Model

The importance of inertial effects on the relaxation rates in gases leads one to ask about their potential importance in dense fluids. A simple model that spans the range from the dense fluid to the dilute gas is the extended diffusion model for rotational motion in fluids.[9,10] The extended diffusion model uses a rather crude idealized picture for the rotational motion of molecules in a fluid—the molecules rotate just as though they were in a very dilute gas, except that instantaneous random torques continually change the direction and possibly the speed of the rotational motion (see also ***Brownian Motion and Correlation Times***). In this model, the orientation and angular momentum of a general molecule is followed in microscopic detail. The molecules are assumed to rotate freely during a series of 'diffusive' steps, which are interrupted by random impulsive torques. These 'collisional events' (the

random torques due to the Brownian nature of the fluid) are assumed to follow a Poisson distribution with average time τ_J between collisions. The collisions are taken to be instantaneous and are assumed to randomize the orientation (M diffusion) or both the orientation and magnitude (J diffusion) of the angular momentum vector. Although the reorientational correlation times $\tau_\theta^{(2)}$ in the M- and J-diffusion limits differ significantly, the spin–rotation relaxation rates are the same in both limits. For a spherical top molecule, the spin–rotation relaxation rate is given by

$$R_{1SR} = R_{2SR} = \frac{2Ik_BT}{\hbar^2}\left\{C_0^2 + \tfrac{4}{5}\Delta C^2 F\left[\frac{1}{2^{1/2}\bar{\omega}\tau_J}\right]\right\}\tau_J \tag{24}$$

where

$$F[x] = 1 + x^2 - 2x^4[1 - \pi^{1/2}x\exp(x^2)\mathrm{erfc}(x)]$$
$$\approx \begin{cases} \frac{5}{2}\left(1 - \frac{3}{2x^2} + \frac{21}{4x^4} + \ldots\right) & \text{for large } x \\ 1 + x^2 - 2x^4 + \ldots & \text{for small } x \end{cases} \tag{25}$$

erfc (x) is the complementary error function and

$$\bar{\omega} = k_BT/I \tag{26}$$

is the average rotational velocity. When τ_J is much shorter than the time $\bar{\omega}^{-1}$ for the molecule to make a complete rotation, as it is in a dense liquid, equation (24) reduces to equation (14); and in the limit $\tau_J \gg \bar{\omega}^{-1}$, which is appropriate for a dilute gas, Equation (24) reduces to equation (23). The extended diffusion model can also be used to describe spin–rotation relaxation in linear, symmetric top[9] and asymmetric top[10] molecules. In molecules of all symmetries, the temporal behavior of all components of the angular momentum vector is characterized by a single correlation time τ_J.

3.4 The Fokker–Planck–Langevin Model

The Fokker–Planck–Langevin model[11–18] for the rotational motion of molecules in fluids is a true extension of the rotational diffusion model (see ***Brownian Motion and Correlation Times***) used by Bloembergen, Purcell, and Pound to treat dipole–dipole magnetic relaxation, and by Hubbard to describe spin–rotation relaxation. In the Hubbard model, the stochastic behavior of the angular momentum is assumed to follow a rotational Langevin equation [see Equation (16)], and the conditional probability density $P(\Omega, t|\Omega_0)$ that a molecule will have orientation between Ω and $\Omega + d\Omega$ at time t, given that it had orientation between Ω_0 and $\Omega_0 + d\Omega_0$ at time zero, follows a rotational diffusion equation. This treatment of orientational and angular velocity variables as essentially independent processes is valid only if $\tau_J \ll \tau_\theta^{(2)}$. In the Fokker–Planck–Langevin model, the angular velocity is again assumed to follow a rotational Langevin equation (including the terms describing the precession of the angular velocity components), but the orientational behavior is not treated independently. Instead, the molecular rotation is treated as a Markovian process, and the focus is on the joint conditional probability density $P(\omega, \Omega, t|\omega_0, \Omega_0)$ that a molecule will have angular velocity between ω and $\omega + d\omega$ and orientation between Ω and $\Omega + d\Omega$ at time t, given that it had angular velocity between ω_0 and $\omega_0 + d\omega_0$ and orientation between Ω_0 and $\Omega_0 + d\Omega_0$ at time zero. $P(\omega, \Omega, t|\omega_0, \Omega_0)$ follows the rotational Fokker–Planck equation. For a spherical molecule[18], the Fokker–Planck–Langevin model gives the spin–rotation relaxation rate

$$R_{1SR} = R_{2SR} = \frac{2Ik_BT}{\hbar^2}[C_0^2 + 2\Delta C^2 f(\tau_J)]\tau_J \tag{27}$$

where

$$f(\tau_J) = 1 - \tfrac{3}{2}\bar{\omega}^2\tau_J^2 + \tfrac{13}{4}\bar{\omega}^4\tau_J^4 - \tfrac{22}{3}\bar{\omega}^6\tau_J^6 + \ldots \tag{28}$$

For nonspherical molecules, the precessional motion of the angular velocity leads to a more complicated relationship between the angular velocity correlation time and the friction coefficient than that given in equation (18). This leads to an expression for the spin–rotation relaxation rate that is similar to equation (22), but contains corrections to the correlation times and additional small cross-correlation terms (e.g., terms containing C_xC_y).

4 SPIN–ROTATION RELAXATION IN MOLECULES WITH INTERNAL ROTATION

In a large molecule that tumbles very slowly in solution, the motion of the nuclei on a fragment that can undergo facile internal rotation will be dominated by the internal rotational motion, and the rate of spin–rotation relaxation should be determined by the correlation time for the velocity of this internal motion, rather than the correlation time for the angular velocity of the molecule itself. A number of models have been proposed to describe the spin–rotation relaxation rate in the presence of internal rotation.[19–22]

A phenomenological libration model[19] has been developed to describe the spin–rotation relaxation contributions to the ^{13}C-relaxation rates of carbon atoms in methyl groups (see also ***Carbon-13 Relaxation Measurements: Organic Chemistry Applications***). The basic physical assertions here are

1. if the methyl group rotates freely, the correlation time for the angular velocity of the internal rotator is just the time required for it to rotate by 1 rad;
2. when the rotator experiences a barrier to free rotation, its angular velocity correlation function will decay more rapidly and lead to a shorter angular velocity correlation time.

In this model, the potential governing the rotational motion of the methyl group has threefold symmetry with a barrier V_0 between the three potential wells, and a methyl group will spend an average time $\tau_{\text{libration}}$ in one potential well before rotating through 120° into the next well. It is usually assumed that the $I_zC_z^2\tau_z$ term dominates the other terms in equation (22), and τ_z is given by

$$\tau_z^{-1} = \tau_{\text{free}}^{-1} + \tau_{\text{libration}}^{-1} \tag{29}$$

where τ_{free} is the time required for a freely rotating (unhindered) internal rotator to rotate through 1 rad. The magnitude of $\tau_{\text{libration}}$ is governed by the height of the barrier, and is calculated from an ensemble average of the semiclassical libration frequencies over all bound states (states with energy less than V_0) of the hindered internal rotator.

More fundamental and elaborate descriptions[20–22] of the spin–rotation relaxation rates of nuclei on internal rotators have used the extended diffusion or Fokker–Planck–Langevin models for both internal rotation and overall molecular rotation. The classical equation of motion for the internal rotator, including the potential barrier to rotation, is solved

exactly, and V_0 enters the spin–rotation correlation times via the 'free rotor' internal angular velocity–orientation correlation functions. The expressions for the relaxation rates are very complicated and contain terms arising from the internal rotation and from the overall rotation of the molecule.

5 SPIN–ROTATION RELAXATION IN SOLIDS

In solids, the molecules or ions are fixed at lattice positions, but highly symmetric ions or molecules in a rotationally disordered solid may exhibit some rotational motion. The rudimentary phenomenological model[23] that has been developed to describe the spin–rotation relaxation rate for nuclei in a molecule or ion in a solid is based on the idea that molecules in a solid are rotationally restrained in a cage of other molecules, but that reorientation can occur if the cage expands or if the molecule acquires enough energy to overcome the potential barrier to rotation. (In fact, this model was first presented as a phenomenological explanation of observed spin–rotation relaxation in liquids, but was quickly supplanted by Hubbard's model). When rotation does occur, it is viewed as a random jump of short duration from one orientation to another uncorrelated orientation. In this picture, the angular velocity of the molecule is zero except during one of the random jumps. Assuming that the times between random jumps follow a Poisson distribution with mean time τ between jumps, one finds that

$$R_{1\mathrm{SR}} = R_{2\mathrm{SR}} = \tfrac{1}{3}\gamma^2\langle B_{\mathrm{SR}}^2\rangle\Delta^2\tau^{-1}, \tag{30}$$

where γ is the magnetogyric ratio for the nucleus, $\langle B_{\mathrm{SR}}^2\rangle$ is the mean square magnetic field produced by the spin–rotational interaction during a random jump, and Δ is the duration of the random jump. It is expected that $\gamma^2\langle B_{\mathrm{SR}}^2\rangle$ will be proportional to the temperature T, and to the squares of the spin–rotation constants for the molecule, and that τ will decrease with increasing temperature.

6 RELATED ARTICLES

Brownian Motion and Correlation Times; Carbon-13 Relaxation Measurements: Organic Chemistry Applications; Gas Phase Studies of Intermolecular Interactions and Relaxation; Gases at High Pressure; Relaxation Theory: Density Matrix Formulation.

7 REFERENCES

1. C. H. Townes and A. L. Schawlow, *Microwave Spectroscopy*, McGraw-Hill, New York, 1955 (reprinted by Dover, New York, 1975), Chap. 8
2. C. J. Jameson, *Chem. Rev.*, 1991, **91**, 1375.
3. M. Bloom, *Physica*, 1957, **23**, 237.
4. J. Kowalewski, in *Annual Reports on NMR Spectroscopy*, ed. G. A. Webb, Academic Press, London, 1989, Vol. 22, p. 307.
5. J. Kowalewski, in *Annual Reports on NMR Spectroscopy*, ed. G. A. Webb, Academic Press, London, 1991, Vol. 23, p. 289.
6. P. S. Hubbard, *Phys. Rev.*, 1963, **131**, 1155.
7. N. Bloembergen, E. M. Purcell, and R. V. Pound, *Phys. Rev.*, 1948, **73**, 679.
8. M. Bloom, F. Bridges, and W. N. Hardy, *Can. J. Phys.*, 1967, **45**, 3533.
9. R. E. D. McClung, *Advances in Molecular Relaxation Interaction Processes*, 1977, **10**, 83.
10. T. E. Bull, *J. Chem. Phys.*, 1984, **81**, 3181.
11. M. Fixman and K. Rider, *J. Chem. Phys.*, 1969, **51**, 2425.
12. P. S. Hubbard, *Phys. Rev. A*, 1972, **6**, 2421.
13. P. S. Hubbard, *Phys. Rev. A*, 1973, **8**, 1429.
14. P. S. Hubbard, *Phys. Rev. A*, 1974, **9**, 481.
15. R. E. D. McClung, *J. Chem. Phys.*, 1981, **75**, 5503.
16. D. H. Lee and R. E. D. McClung, *Chem. Phys.*, 1987, **112**, 23.
17. J. McConnell, *The Theory of Nuclear Magnetic Relaxation in Liquids*, Cambridge University Press, Cambridge, 1987.
18. G. Lévi, J. P. Marsault, F. Marsault-Hérail, and R. E. D. McClung, *J. Chem. Phys.*, 1980, **73**, 2443.
19. C. Mendonca, H. A. Farach, C. P. Poole, Jr., and P. D. Ellis, *J. Magn. Reson.*, 1981, **45**, 290.
20. T. E. Bull, *J. Chem. Phys.*, 1976, **65**, 4802.
21. D. S. Chung, E. M. Kim, and K. J. Shin, *Chem. Phys. Lett.* 1984, **108**, 283.
22. T. E. Bull, *Chem. Phys.*, 1988, **121**, 1.
23. R. J. C. Brown, H. S. Gutowsky, and K. Shimomura, *J. Chem. Phys.*, 1963, **38**, 76.

Biographical Sketch

R. E. D. (Ted) McClung. *b* 1941. B.Sc., 1963, chemistry, University of Alberta, Canada; Ph.D. (supervisor Daniel Kivelson), 1967, chemistry, University of California, Los Angeles. Postdoctoral work at the University of Leeds (with Peter B. Ayscough). Currently Professor of Chemistry, Department of Chemistry, University of Alberta, Edmonton, Alberta, Canada. Approx. 70 publications. Research interests: chemical exchange, multisite magnetization transfer, infrared bandshapes, molecular motion in liquids.

Ultraslow Motions in Solids

David C. Ailion

University of Utah, Salt Lake City, UT, USA

1	Introduction	1
2	Spin–Lattice Relaxation in the Rotating Frame ($T_{1\rho}$)	1
3	Dipolar Relaxation in the Laboratory Frame (T_{1D})	3
4	Dipolar Relaxation in the Rotating Frame ($T_{1D\rho}$)	5
5	Experimental Results using Ultraslow Motion Techniques	5
6	Conclusions	7
7	Related Articles	7
8	References	8

1 INTRODUCTION

The use of conventional NMR relaxation measurement techniques for studying moderately rapid atomic motions may result in observation of the following phenomena:

1. a decrease (or a minimum)[1] of the spin–lattice relation time T_1 in a plot of T_1 versus temperature;
2. motional narrowing of the resonance linewidth[2] (or motional lengthening of the free induction decay or the spin–spin relaxation time T_2);
3. a decrease[2] in the Hahn echo decay time compared to the Carr–Purcell–Meiboom–Gill (CPMG)[3] time constant (see ***Diffusion Measurements by Magnetic Field Gradient Methods***).

The term ultraslow motions[4] refers to motions that are observable by NMR but are sufficiently infrequent that they produce no motional narrowing of the resonance line and make no measurable contribution to the spin–lattice relaxation rate. Typical T_1 minima correspond to motions for which the mean atomic jump rate $1/\tau_c$ is of the order of the nuclear precession frequency Ω_0 ($\approx 10^8$ s^{-1}, typically).[1] Motions having jump frequencies one or two orders of magnitude higher or lower than that for the minimum usually still give measurable contributions to the relaxation rate. Since the condition for motional narrowing is that the atomic jump time τ_c be less than T_2, ultraslow motions are typically those for which $T_2 < \tau_c < T_1$.[4] A very wide range of atomic motions falls under this classification, since $T_2 \approx 10^{-4}$–10^{-5} s in solids, while T_1 can be as long as several seconds to hours in length.

It is clearly desirable to extend to lower frequencies the frequency range (and thus the temperature range) of motions that can be studied. One advantage of studying a wider range of atomic motions is that motions having slightly different activation energies may be distinguished if they are observed over a sufficiently wide temperature range. Also, motions associated with a particular phenomenon, like a phase transition, may occur only in a particular temperature region.

The basic idea of the ultraslow motion techniques can be understood by considering what happens to a T_1 minimum if the field B_0, and thus the resonant frequency, is greatly reduced. According to the Bloembergen, Purcell, and Pound (BPP) theory,[1] atomic diffusion or molecular reorientations will cause fluctuations in the dipolar interactions that can be treated as perturbations on the Zeeman levels, and, furthermore, these fluctuations can be described by an exponential correlation function. BPP derived for T_1 an expression of the form

$$\frac{1}{T_1} \approx \frac{\Omega_d^2 \tau_c}{1 + \Omega_0^2 \tau_c^2} \tag{1}$$

where Ω_0 is the Larmor angular frequency and Ω_d is the angular frequency corresponding to a typical dipolar splitting. (Actually, there are additional terms of similar form. For interactions involving identical spins, there is an extra term proportional to $1/(1 + 4\Omega_0^2\tau_0^2)$; for heteronuclear systems, there are also terms having $[1 + (\Omega_I - \Omega_S)^2\tau_c^2]$ and $[1 + (\Omega_I + \Omega_S)^2\tau_c^2]$ in the denominator.) Equation (1) predicts that, in a temperature plot of T_1, there will be a minimum value for T_1 at the temperature for which $\tau_c \approx \Omega_0^{-1}$, in agreement with the idea that the transition probability $1/T_1$ arises largely from frequency components in the perturbation that equal the energy level spacing divided by $\hbar$. If Ω_0 is reduced, the minimum will correspond to a longer value of τ_c, and thus to lower frequency motions. For a typical diffusion mechanism, atomic jumps become less frequent as the temperature is lowered. Thus the T_1 minimum in a low field will occur at a lower temperature than would the T_1 minimum at a higher field.

There are experimental problems associated with attempting to study relaxation in very weak fields where the NMR signal might be very small (see ***Zero Field NMR***). There are also theoretical difficulties, since the theory underlying equation (1) is a perturbation theory that treats the fluctuating dipolar Hamiltonian due to diffusion as a perturbation on the Zeeman Hamiltonian; such an assumption may not be valid in very weak applied fields. Solutions to both these problems will now be discussed. Ultraslow motion techniques have been reviewed by Ailion.[5–7]

2 SPIN–LATTICE RELAXATION IN THE ROTATING FRAME ($T_{1\rho}$)

One approach to studying relaxation in weak applied fields and yet having the strong signal strength for a large field is to use the field cycling method[8,9] (see ***Field Cycling Experiments***), in which the external magnetic field is reduced adiabatically to a small value and subsequently increased adiabatically back to the original value, where the signal is measured. If there are no irreversible processes, the entropy will be constant, and the full signal will be measured after the remagnetization. However, atomic diffusion constitutes an irreversible process, which will cause a loss of dipolar order. Thus, by plotting the signal strength versus time in the demagnetized state, the weak field relaxation can in principle be measured. One difficulty with this approach is that it may be difficult to satisfy the requirement that the demagnetization and remagnetization processes be sufficiently slow that the adiabatic condition is satisfied and yet be rapid compared with T_1.

An alternate approach is to measure $T_{1\rho}$, the spin–lattice relaxation time in the rotating frame of the rf field $\boldsymbol{B}_1$ (see ***Magnetization Transfer between Water and Macromolecules in Proton MRI***). According to Redfield,[10] a spin system

in an rf field strong enough to saturate the resonance line (i.e., $\gamma^2 B_1^2 T_1 T_2 \gg 1$) will form a canonical distribution among energy levels separated by γB_{eff} rather than γB_0, where the effective field $\boldsymbol{B}_{\text{eff}}$ in a frame rotating at angular frequency ω is given by

$$\boldsymbol{B}_{\text{eff}} = B_1 \boldsymbol{i} + (B_0 - \omega/\gamma)\boldsymbol{k} \tag{2}$$

In this case, the spins will, after equilibrium has been achieved, be characterized by a 'spin temperature in the rotating frame', which means that Curie's law will hold, but with $\boldsymbol{M}_{\text{eq}} = C\boldsymbol{H}_{\text{eff}}/T$. The significance is that, at exact resonance ($B_0 = \omega/\gamma$), the equilibrium magnetization $\boldsymbol{M}_{\text{eq}}$ will be parallel to $\boldsymbol{B}_1$ rather than to $\boldsymbol{B}_0$. The $T_{1\rho}$ minimum will then occur when $\gamma B_1 \tau_c \approx 1$, for B_0 at exact resonance. Since B_1 is typically of order 1–50 G, this minimum arises from much lower frequency motions than does the normal T_1 minimum. If B_1 is much larger than the magnetic dipolar or electric quadrupolar local fields, the dipolar and quadrupolar fluctuations can still be treated by perturbation theory (this approach is called the 'weak collision' theory).[11] If, on the other hand, B_1 is comparable to or less than the dipolar or quadrupolar local fields, perturbation theory fails, and a different theory, called the 'strong collision' theory,[12] must be used. In this article, we shall consider the case for a spin-$\frac{1}{2}$ nucleus or one in which quadrupolar interactions can be neglected; the inclusion of quadrupolar interactions in the strong collision theory has been described by Ailion.[5]

2.1 Weak Collision Theory

All of the weak collision calculations are applications of the BPP theory in which the fluctuating dipolar Hamiltonian is treated as a perturbation on the Zeeman system. The only important difference is that the basic laboratory frame Hamiltonian is replaced by a rotating frame Hamiltonian in which $\boldsymbol{B}_0$ is replaced by $\boldsymbol{B}_{\text{eff}}$, as given by equation (2). At exact resonance, this theory predicts that $T_{1\rho}$ should exhibit a low-frequency minimum of the form

$$\frac{1}{T_{1\rho}} = K \frac{\tau_c}{1 + 4\Omega_1^2 \tau_c^2} \tag{3}$$

where Ω_1 (= γB_1) is proportional to the energy level splitting in the rotating frame. Thus the $T_{1\rho}$ minimum occurs when $\tau_c \approx (2\Omega_1)^{-1}$, which may be several orders of magnitude longer than the value of τ_c at a typical T_1 minimum. Accordingly, a $T_{1\rho}$ minimum is deeper than a T_1 minimum, and corresponds to slower atomic motions occurring at lower temperatures, as shown in Figure 1.

2.2 Strong Collision Theory

In order to get even more effective relaxation so as to observe even lower frequency motions, B_1, and thus Ω_1 in equation (3), can be reduced to a value comparable to the local dipolar field, or even to zero (e.g., by adiabatic demagnetization in the rotating frame (ADRF),[13] which is discussed in Section 3.3). In this case, equation (3) would predict that the minimum would not occur unless τ_c were infinite. However, perturbation theories like BPP and the weak collision theory will not be valid, since the perturbation

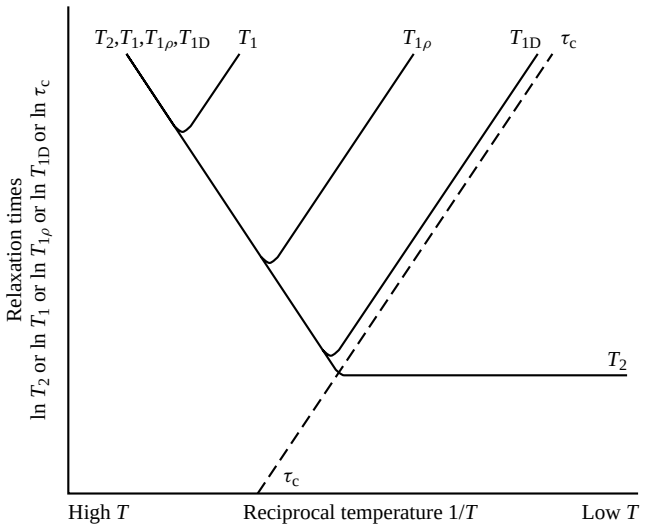

Figure 1 Temperature plot of relaxation times (T_2, T_1, $T_{1\rho}$, and T_{1D}) and atomic jump time τ_c. (Reproduced by permission of Academic Press from D. C. Ailion, in 'Methods of Experimental Physics', ed. J. N. Mundy, S. J. Rothman, M. J. Fluss, and L. C. Smedskjaer, Academic Press, Orlando, 1983, Vol. 21, Chap. 6)

(the dipolar Hamiltonian) in this case is comparable to or larger than the unperturbed Hamiltonian (the Zeeman Hamiltonian). Nevertheless, the condition for the relaxation time minimum in zero magnetic field can still be easily understood. The underlying physical basis for all relaxation time minima is that the most effective relaxation (and thus the minimum) occurs when the principal frequency components of the fluctuating Hamiltonian are comparable to the energy level splitting (in units of $\hbar$). We have seen, for Zeeman relaxation in the laboratory or rotating frames, that this requirement is equivalent to requiring that $1/\tau_c \approx \Omega_0$ or $1/\tau_c \approx \Omega_1$, respectively. For relaxation due to a fluctuating dipolar Hamiltonian in zero field, the energy level splittings $\hbar\Omega_d$ are determined by dipolar interactions. Thus the minimum in zero field occurs when $1/\tau_c \approx \Omega_d$ or $\tau_c \approx T_2$, which is at the onset of motional narrowing. The zero field relaxation time for the case in which quadrupolar interactions can be neglected is commonly called the dipolar relaxation time T_{1D},[14] and is also shown in Figure 1.

In order to study the dynamics of the atomic motions, it is desirable to obtain theoretical expressions that relate the measured relaxation time $T_{1\rho}$ or T_{1D} to the atomic jump time τ_c throughout the temperature range of observations. Experimental procedures for measuring these relaxation times are described in Sections 2.3 and 3.3, respectively. The strong collision theory, originally developed by Slichter and Ailion[12] for low-field relaxation, is not a perturbation theory, but is based on the assumption that sufficient time elapses between diffusion jumps to allow the dipolar and rotating frame Zeeman interactions to cross relax to a common spin temperature between each jump. This temperature is then disturbed by the sudden change in dipolar energy resulting from a jump, but reequilibrates in a time of order T_2 to a new value prior to the next jump. This spin temperature assumption is thus equivalent to requiring that $\tau_c \gg T_2$; hence the strong collision theory will be valid in the 'rigid lattice' below both the $T_{1\rho}$ minimum and the temperature for motional narrowing. If the

ADRF process is complete so that $\boldsymbol{B}_1$ is reduced to zero in the demagnetized state, the ADRF process will have transferred long-range Zeeman order due to spins aligned preferentially along $\boldsymbol{B}_{\text{eff}}$ to short-range dipolar order from spins aligned along their individual local fields. A single diffusion jump per spin will then have a major effect on the relaxation so that, in zero B_1, we should expect $T_{1\rho}$ (= $T_{1\text{D}}$ for zero field) to be of order τ_{c}. In the weak collision regime, much less of the order is dipolar and much more is Zeeman; accordingly, it will take many jumps to relax the magnetization, and $T_{1\rho}$ will be much larger than τ_{c}. Both these effects are shown in Figure 1.

The actual strong collision result[12] for $T_{1\rho}$ at exact resonance due to dipolar fluctuations of a homonuclear (i.e., having only one nuclear species) system in a field B_1 is

$$\frac{1}{T_{1\rho}} = \frac{1}{T_{1\text{D}}} \frac{B_{\text{D}}^2}{B_1^2 + B_{\text{D}}^2} \tag{4}$$

where B_{D} is the dipolar local field. We see that $T_{1\rho}$ reduces to $T_{1\text{D}}$ in the limit as B_1 approaches zero. Note that the local field B_{D} can be determined experimentally by measuring $T_{1\rho}$ versus B_1^2 for fixed $T_{1\text{D}}$ (i.e., at a fixed temperature).

2.3 Experimental Techniques for Measuring $T_{1\rho}$

Essentially all methods for measuring $T_{1\rho}$ start by tipping the magnetization from its original direction (the z direction) to a direction parallel to $\boldsymbol{B}_{\text{eff}}$ in the rotating frame, a procedure called spin locking. For exact resonance, the magnetization would then be aligned parallel to $\boldsymbol{B}_1$ (in contrast to the situation immediately after a $\frac{1}{2}\pi$ pulse, when the magnetization would be perpendicular to $\boldsymbol{B}_1$). $T_{1\rho}$ can then be determined by measuring the magnetization as a function of time τ in the aligned state, since $T_{1\rho}$ is given by

$$M_x = M_0 \exp(-\tau / T_{1\rho}) \tag{5}$$

where M_x is the height of the FID following the turn-off of the variable length B_1 pulse. Figure 2 shows several different pulse sequences for measuring $T_{1\rho}$.

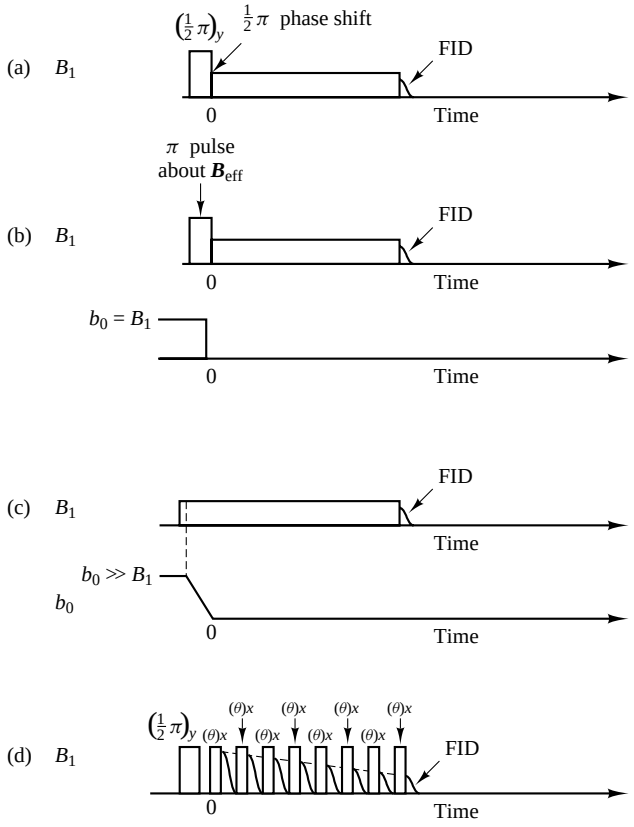

Figure 2 Pulse sequences for measuring $T_{1\rho}$. (a), (b), and (c) all have a spin locking sequence followed by a long rf pulse. The spin locking in (a) consists of a $\frac{1}{2}\pi$ pulse followed by a $\frac{1}{2}\pi$ phase shift. In (b), spin locking is achieved by a π pulse about $\boldsymbol{B}_{\text{eff}}$ (at an angle of 45° with respect to the z direction). In (c), $\boldsymbol{B}_1$ is turned on when the z field (or frequency) is far off resonance, and spin locking is achieved as a result of an adiabatic return to resonance. In (d), spin locking is achieved, as in (a), by a $\frac{1}{2}\pi$ pulse followed by a $\frac{1}{2}\pi$ phase shift; $T_{1\rho}$ is measured by monitoring the FID following short pulses of duration θ. (Reproduced with modifications by permission of Academic Press from D. C. Ailion, in 'Methods of Experimental Physics', ed. J. N. Mundy, S. J. Rothman, M. J. Fluss, and L. C. Smedskjaer, Academic Press, Orlando, 1983, Vol. 21, Chap. 6)

3 DIPOLAR RELAXATION IN THE LABORATORY FRAME ($T_{1\text{D}}$)

3.1 Homonuclear Systems

For homonuclear systems, $T_{1\text{D}}$ can be calculated by considering the fractional change in dipolar energy per jump for N jumping atoms with a time τ_{c} between jumps

$$\frac{1}{T_{1\text{D}}} = \frac{N}{\tau_{\text{c}}} \frac{E_{\text{Df}} - E_{\text{Di}}}{E_{\text{Di}}} = \frac{N}{\tau_{\text{c}}} \frac{\langle \hat{\mathcal{H}}_{\text{Df}}^{(0)} \rangle - \langle \hat{\mathcal{H}}_{\text{Di}}^{(0)} \rangle}{\langle \hat{\mathcal{H}}_{\text{Di}}^{(0)} \rangle} \tag{6}$$

where E_{Di} and E_{Df} are, respectively, the dipolar energies before and after a jump. $\hat{\mathcal{H}}_{\text{Di}}^{(0)}$ and $\hat{\mathcal{H}}_{\text{Df}}^{(0)}$ are, similarly, the secular parts of the dipolar Hamiltonian (i.e., those parts that commute with the Zeeman Hamiltonian), and the angle brackets indicate expectation values. If the system can be characterized by a spin temperature before each jump, the expectation values can be expressed as traces of the quantum mechanical operators, and the following expression is obtained in the high-temperature approximation:[2]

$$\frac{1}{T_{1\text{D}}} = \frac{N}{\tau_{\text{c}}} \frac{\text{Tr}(\hat{\mathcal{H}}_{\text{Di}}^{(0)})^2 - \text{Tr}(\hat{\mathcal{H}}_{\text{Di}}^{(0)} \hat{\mathcal{H}}_{\text{Df}}^{(0)})}{\text{Tr}(\hat{\mathcal{H}}_{\text{Di}}^{(0)})^2} \tag{7}$$

This equation can be rewritten as

$$\frac{1}{T_{1\text{D}}} = \frac{2(1-p)}{\tau_{\text{c}}} \tag{8}$$

where $1 - p$ is a calculable geometrical factor of order unity that characterizes the fractional change in energy resulting from a diffusion jump. Because of this factor, $T_{1\text{D}}$ shows a 10–20% dependence on the orientation of the field $\boldsymbol{B}_0$ relative to the crystal axes, and, furthermore, this anisotropy depends on diffusion mechanism.[15] We also note that $T_{1\text{D}}$ is of order τ_{c}, as we have seen intuitively. Diffusion can be studied by measuring either $T_{1\text{D}}$ or $T_{1\rho}$, provided the relaxation rate due to diffusion is greater than the relaxation rate due to other T_1

processes. The condition for observability of diffusion effects is then that $\tau_c < T_1$. Since T_1 values are typically 10^{-3}–10^3 s, this condition is much less stringent than the condition for motional narrowing ($\tau_c < T_2$).

We should note that the strong collision formula, equation (8), can be used to obtain τ_c from the measured relaxation time, assuming $\tau_c \gg T_2$. BPP-type theories can be used to determine τ_c in the motionally narrowed region where $\tau_c \ll T_2$. In the vicinity of the T_{1D} minimum, neither theory is valid.

3.2 Heteronuclear Systems

A problem arises in the interpretation of T_{1D} measurements for heteronuclear systems in which one nuclear species is diffusing and the others are stationary. For simplicity, consider a system containing two species of comparable abundance and gyromagnetic ratio, whose spin quantum numbers are labeled I and S. Assume further that the I and S spins are in strong contact. (A good example would be the alkali halide LiF, in which every lithium atom is surrounded by fluorines, and vice versa.) The problem is that if the I spins are irradiated and T_{1D} is measured, the result will be the same as when the S spins are irradiated and their T_{1D} measured, independent of which spin is actually diffusing.[16] Hence, from a T_{1D} measurement alone, it would not be possible in this case to determine which species is diffusing. This feature arises because there is normally strong coupling between parts of the dipolar interaction involving different species (i.e., the I–I and S–S dipolar terms are strongly coupled through the I–S interaction). So, if an S spin undergoes a jump, there will be rapid cross relaxation between I–I and S–S terms, which will result in the local heating being transferred rapidly to the entire spin system. Thus, in the strong collision limit, the entire dipolar reservoir is describable by a single temperature prior to a diffusion jump, but either spin species alone is not.

Fortunately, there is a way to determine in a T_{1D} experiment which spin species is diffusing for the case where the S spins are weakly magnetic (small γ_S) compared with the more strongly magnetic I spins (large γ_I). If the relaxation is due to the motion of S spins, T_{1D} will have an enormous anisotropy, whereas for diffusion of I spins the anisotropy will be very small [arising only from the $1 - p$ factor in equation (8)]. A more general strong collision theory,[17] appropriate for heteronuclear systems, shows that, for the case in which the strongly magnetic I spins are diffusing, only the I–I interaction terms need be kept. The resulting expression for $1/T_{1D}$ is similar to equation (8), only with p replaced by p_{II} and τ_c by τ_I:

$$\frac{1}{T_{1D}} = \frac{2(1 - p_{II})}{\tau_I} \tag{9}$$

However, if T_{1D} is due to the diffusion of weakly magnetic S spins then the diffusion produces significant changes in the I–S interaction, with the result that

$$\frac{1}{T_{1D}} = \frac{1 - p_{SI}}{\tau_S} \frac{B_{DIS}^2}{B_{DII}^2} \tag{10}$$

where B_{DIS} and B_{DII} are the I–S and I–I contributions to the dipolar local fields and τ_S is the time between jumps of the S spins. The precise definitions of these local fields and the parameters p_{II} and p_{SI} are given by Stokes and Ailion.[17] equation (10) predicts a strong anisotropy, arising from the factor B_{DIS}^2/B_{DII}^2, which is absent for motion by I atoms. The observation of this anisotropy would confirm that the diffusion arises from the motion of weakly magnetic spins. The experimental verification of this idea is shown in Figure 7 in Section 5 below.

3.3 Experimental Techniques for Measuring T_{1D}

There are basically two commonly used methods for measuring T_{1D}, and each involves transferring order to the dipolar system and then monitoring the decrease in dipolar order arising from dipolar relaxation. The first technique consists in following a spin locking sequence by an adiabatic demagnetization–remagnetization cycle of the rf field.[5] The second consists in creating a state of dipolar order by a pair of phase-shifted pulses and then using a third pulse to monitor the decrease in dipolar order due to the relaxation.[14] Both are shown in Figure 3.

3.3.1 Adiabatic Demagnetization in the Rotating Frame (ADRF)

This method, illustrated in Figure 3(a), is similar to the methods for measuring $T_{1\rho}$, shown in Figure 2(a)–(c), except that spin locking is now followed by an adiabatic demagnetization of B_1 to zero followed a variable time later by an adiabatic remagnetization, so that the NMR signal can be measured. The adiabatic demagnetization transfers order from Zeeman order in the rotating frame to dipolar order (in alignment of the spins along the local fields). The subsequent remagnetization converts the remaining dipolar order (not destroyed by the dipolar relaxation) back to Zeeman order, where it is observed in the form of an FID following the turn-off of the rf pulse. Dipolar relaxation results in a reduction in this FID.

One limitation of this technique arises from the conflicting requirements that the B_1 sweep be adiabatic yet that it also be

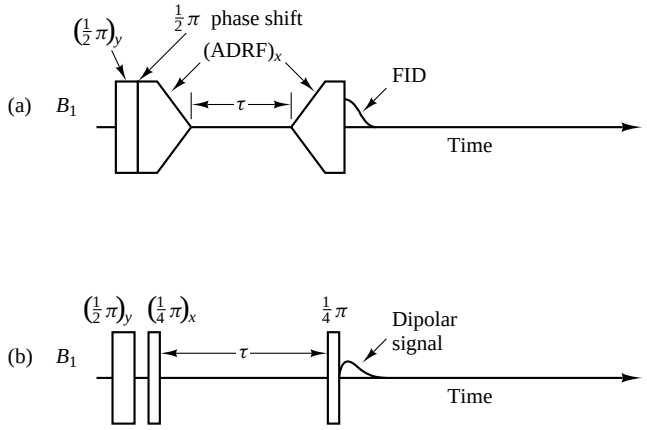

Figure 3 Pulse sequences for measuring T_{1D}. (a) The ADRF sequence showing demagnetization of B_1 following spin locking. (b) The phase-shifted pulse pair sequence. The first two pulses are separated by a time that is approximately T_2 for maximum signal. (Reproduced with modifications by permission of Academic Press from D. C. Ailion, in 'Methods of Experimental Physics', ed. J. N. Mundy, S. J. Rothman, M. J. Fluss, and L. C. Smedskjaer, Academic Press, Orlando, 1983, Vol. 21, Chap. 6)

completed in a time short compared with T_{1D}. This limitation makes it difficult to measure a T_{1D} less than about 0.1–1 ms.

3.3.2 *Phase-Shifted Pulse Pair*

This method, shown in Figure 3(b), avoids the difficulty in measuring a short T_{1D} inherent in ADRF. In this technique, a state of dipolar order is created by applying two closely spaced pulses that are 90° out of phase. The dipolar order is observed by applying a third pulse of arbitrary phase in the (x,y) plane. The dipolar signal that appears after the third pulse is proportional to the time derivative of the FID.

A major disadvantage of this technique is that the maximum efficiency for transfer of order is only about 56%, in contrast to the 100% efficiency theoretically obtainable with ADRF.

In summary, the ADRF technique is superior when measuring longer relaxation times or when $T_{1\rho}$ measurements are also desired, while the phase-shifted pulse pair method is better for very short T_{1D} measurement.

4 DIPOLAR RELAXATION IN THE ROTATING FRAME ($T_{1D\rho}$)

The last paragraph of Section 3.2 described the possibility of using a measurement of the anisotropy of T_{1D} in a single crystal to verify that a weakly magnetic spin species is diffusing. There are two disadvantages of this approach:

1. single crystals are not always available;
2. even though S spins are diffusing, they may not be dominating T_{1D} if they are sufficiently weakly magnetic or low in abundance.

This second feature can be seen in equation (10), since, for $B_{DIS} \ll B_{DII}$, we have $T_{1D} \gg \tau_S$ for weak (S) spin motion. In contrast, for strong (I) spin motion, $T_{1D} \approx \tau_I$. These results arise from the fact that the heat capacities of the terms involving S spins are much smaller than the I–I heat capacities. Accordingly, it may be very difficult, or even impossible, in many cases to study the diffusion of sufficiently weak S spins in a T_{1D} experiment.

In order to determine the diffusing species in a slow motion experiment, it is necessary to identify a parameter that is sensitive to which species is diffusing. If this parameter can be varied by the experimenter then the diffusing species can be identified and studied. Furthermore, for the case of diffusion by spins that are so weakly magnetic as to preclude their study through direct T_{1D} measurement, it is desirable to vary the parameter so as to enhance the temperature change of the entire system resulting from the weak spins' motions. A way to perform such experiments is to observe the dipolar relaxation in the rotating frame of one of the species, say, the I spins. In this frame, only part of the original dipolar Hamiltonian will be secular. The symbol $T_{1D\rho}$ is used for the relaxation time of this secular part of the rotating-frame Hamiltonian, in analogy to T_{1D}, which is the relaxation time for the secular part of the laboratory-frame dipolar Hamiltonian. $T_{1D\rho}$ may be considered to be the dipolar relaxation time in the rotating frame, whereas T_{1D} is the dipolar relaxation time in the laboratory frame. In contrast to T_{1D}, $T_{1D\rho}$ may depend on the angle θ_I between $\boldsymbol{B}_{\text{eff}}$ and $\boldsymbol{B}_0$ in the rotating reference frame. For diffusion by the strong I spins, $T_{1D\rho} = T_{1D}$ and is described by equation (9) for all θ_I except near the magic angle θ_m (defined by $\cos^2\theta_m = \frac{1}{3}$), where there is a small change.[17] However, for diffusion by weak S spins, the following expression is obtained for $T_{1D\rho}$:[17]

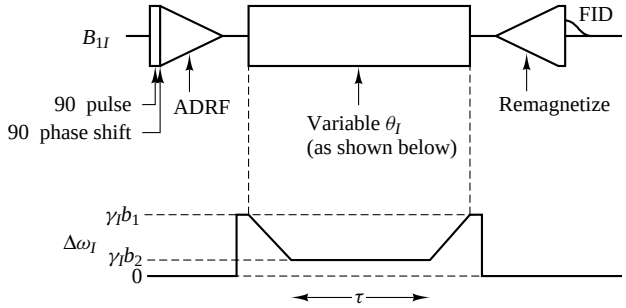

Figure 4 Pulse sequence for measuring $T_{1D\rho}$. The lower part of the figure shows the variation of $\Delta\omega_I = \gamma_I B_0 - \omega_I$, the off-resonance frequency of B_{1I}. (Reproduced with modifications by permission of the American Physical Society from H. T. Stokes and D. C. Ailion, *Phys. Rev. B*, 1978, **18**, 141)

$$\frac{1}{T_{1D\rho}(\theta_I)} = \frac{1}{\tau_S}\,\frac{\cos^2\theta_I B_{DIS}^2(1-p_{SI}) + 2B_{DSS}^2(1-p_{SS})}{[\frac{1}{2}(3\cos^2\theta_I - 1)^2]^2 B_{DII}^2 + \cos^2\theta_I B_{DIS}^2 + B_{DSS}^2} \quad (11)$$

where $1 - p_{SI}$ and $1 - p_{SS}$ are geometrical factors of order unity (analogous to p of the conventional strong collision theory). In contrast to the result obtained in the case of diffusion by the strong I spins, this expression predicts a very strong dependence of $T_{1D\rho}$ on θ_I, which can be observed experimentally, using the pulse sequence described in the next section.

4.1 Experimental Technique for Measuring $T_{1D\rho}$

Figure 4 shows a pulse sequence that can be used to measure $T_{1D\rho}$.[17] A spin locking sequence followed by an ADRF is applied on resonance to the I spins. This step transfers Zeeman order, which was originally along $\boldsymbol{B}_0$, to dipolar order. A large off-resonance pulse is then applied, which does not change the dipolar order but rather changes its reference frame from the laboratory frame to the rotating frame. After establishing a spin temperature in the rotating frame, the frequency of the rf pulse is then reduced adiabatically toward resonance, thereby reducing B_{eff} and changing θ_I. By reversing this sequence, the remaining order is transferred back to laboratory-frame Zeeman order, where it appears as an FID following the turn-off of the rf pulse. If one increases the time τ in the state at θ_I, the magnitude of the resulting FID will be reduced, owing to $T_{1D\rho}$ relaxation. A plot of magnetization versus τ on a semilogarithmic plot will yield a straight line of slope $-1/T_{1D\rho}(\theta_I)$. To vary θ_I, one merely needs to vary the frequency of the pulse (and thus b_2) in the variable time interval τ.

5 EXPERIMENTAL RESULTS USING ULTRASLOW MOTION TECHNIQUES

Ultraslow motions have been widely studied in the last 30 years, generally via $T_{1\rho}$ and T_{1D} measurements. It would be impossible in this article to summarize all the applications. Instead, just a few examples will be given to confirm various

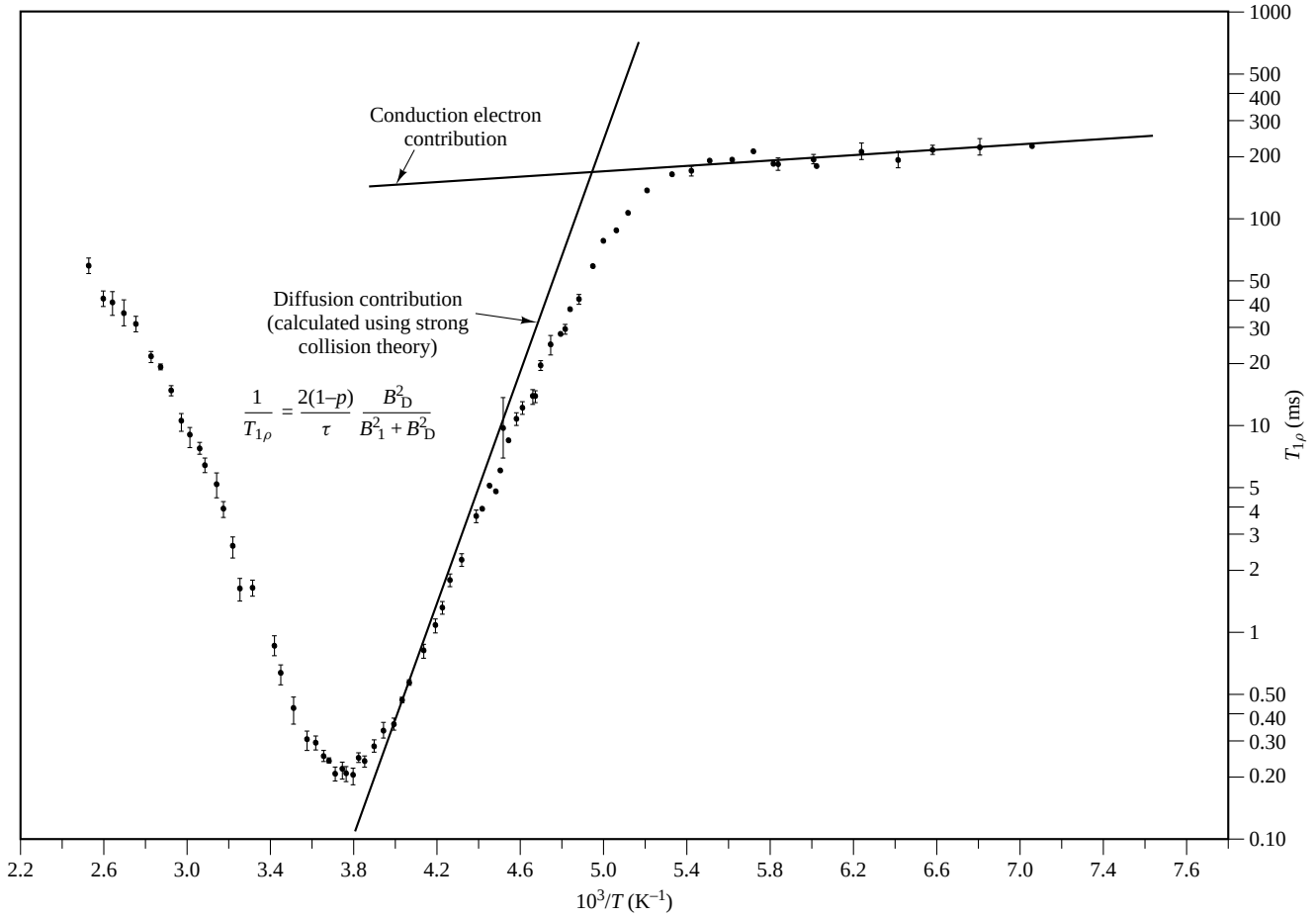

Figure 5 $T_{1\rho}$ versus reciprocal temperature in metallic lithium, with $B_1 = 1.3 \times 10^{-4}$ T. (Reproduced with modifications by permission of the American Physical Society from D. C. Ailion and, C. P. Slichter, *Phys. Rev.*, 1965, **137**, A235)

features of the previous discussion and illustrate the kinds of additional information that may be obtained from such measurements.

Figure 5 shows the original $T_{1\rho}$ data of Ailion and Slichter[18] in metallic lithium. The principal feature is that the $T_{1\rho}$ minimum is symmetric and occurs at the onset of motional narrowing. Furthermore, the minimum value of $T_{1\rho}$ is within an order of magnitude of T_2, as expected from the strong collision theory. Figure 6 shows a plot of the atomic jump time obtained from the experimental $T_{1\rho}$ values, using the strong collision theory. As can be seen, the data exhibit Arrhenius behavior over eight orders of magnitude, and correspond to extremely slow diffusion (of the order of one atomic jump per second) at the lowest temperatures.

Figure 7 shows the verification of the prediction of a very strong anisotropy in T_{1D} described in Section 3.2 for a system having diffusion dominated by weakly magnetic spins. These measurements were performed on a single crystal of KF doped with 0.1% CaF_2. In this case, mobile potassium vacancies are created to compensate for the extra charge of the Ca^{2+}. We thus have a case in which the diffusion of weak spins (potassium) dominates T_{1D} (of fluorine). The solid curve is the calculated anisotropy of the local field factor of equation (10).

Figure 8 shows experimental verification of the strong collision theory for $T_{1D\rho}$. The sample used in this experiment is the same KF:0.1% CaF_2 single crystal used for the data of Figure 7. The curve is calculated from equation (11). All the strong dependence of $T_{1D\rho}$ on θ_I (described earlier) appears, thereby indicating that the weak S spins (in this case, ^{39}K) are diffusing rather than the strong I spins (^{19}F here).

A possibly important potential application of this $T_{1D\rho}$ technique is the study of impurity diffusion. In this case, the S spins are weak because their concentration N_S is small (but γ_S may be large). As in the case of small γ_S, diffusion by the weak S spins should again be characterized by a sharp dip in $T_{1D\rho}$ at the magic angle. For this application to be fruitful, an abundant, easily observable I spin species must exist and be in good thermal contact with the S spins. However, it has been shown[19] that nonadiabatic effects will also give rise to a dip in $T_{1D\rho}$ at the magic angle, which could mask the effect of the S spins' diffusion. Nevertheless, by appropriately modifying the 'adiabatic' sweeps of Figure 4, these effects can be minimized.[19]

An interesting new application of ultraslow motion NMR has been developed[20] to study the ultraslow hopping of selenium atoms between two sites in crystalline Se having well-resolved separate NMR lines. By selective excitation, one of the lines is saturated. Then, as the ^{77}Se atoms jump between the two sites, the magnetization of the previously saturated site builds up and the magnetization of the previously unsaturated site decreases. By measuring the time constant for these decays, the jump time τ_c and the diffusion constant D can

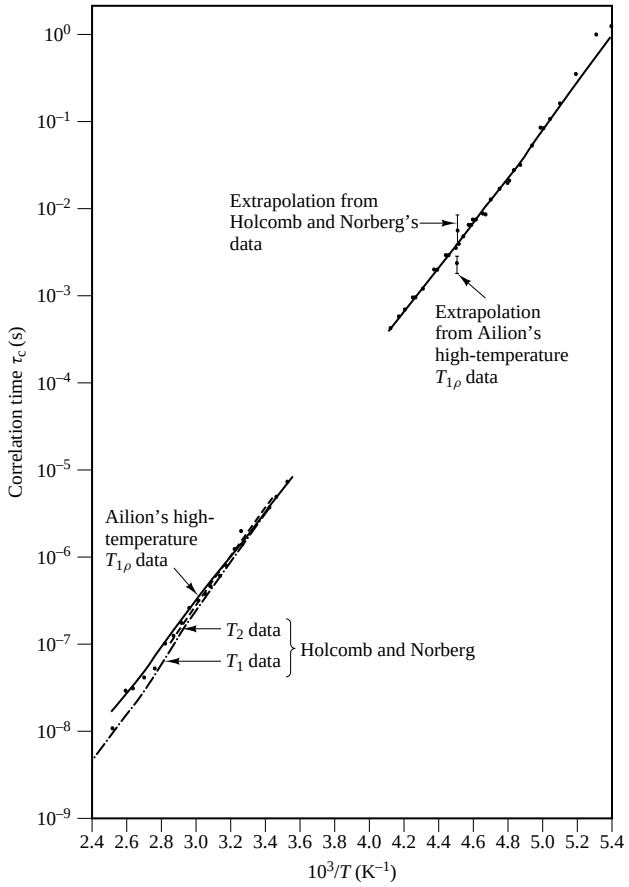

Figure 6 τ_c versus reciprocal temperature in metallic lithium. The experimental points were obtained from the data of Figure 5 using the strong collision theory in the low-temperature region and the weak collision theory in the high-temperature region. The 'gap' in the middle corresponds to the region around the $T_{1\rho}$ minimum where neither theory is valid. In the high temperature region, values of τ_c obtained from Holcomb and Norberg[21] were also plotted. (Reproduced with modifications by permission of the American Physical Society from D. C. Ailion and C. P. Slichter, *Phys. Rev.*, 1965, **137**, A235)

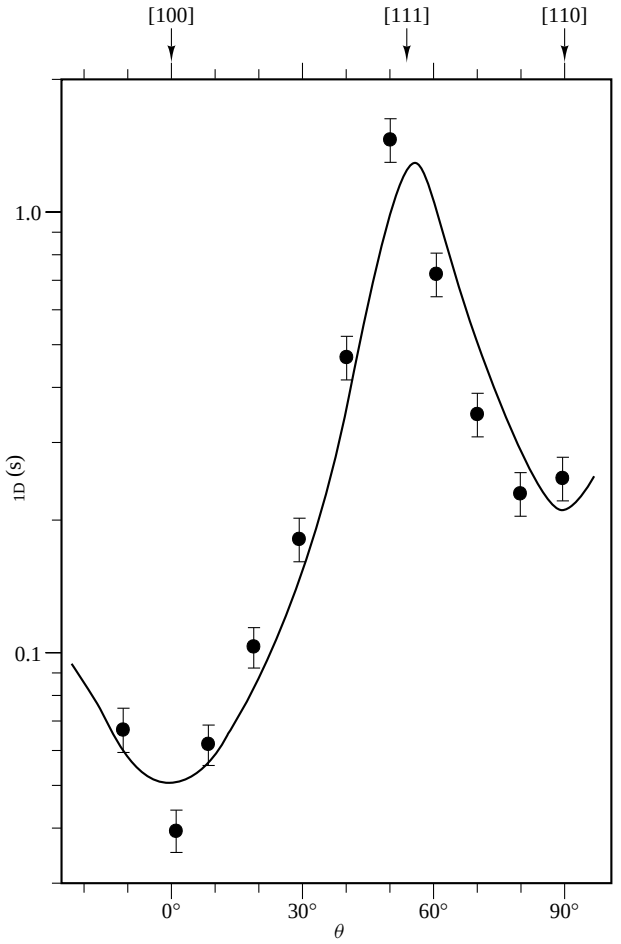

Figure 7 T_{1D} anisotropy in KF:0.1% CaF_2 at 227 °C. The crystal was rotated about its [110] axis. The curve is the calculated anisotropy of $B2/DII/B2/DIS$. (Reproduced by permission of the American Physical Society from H. T. Stokes and D. C. Ailion, *Phys. Rev. B*, 1978, **18**, 141)

both be directly determined. Excellent agreement was found between D measured by this NMR approach and D measured by radioactive tracers. As with the T_{1D} measurements, this technique will be able to observe jump times limited by T_1 for these specialized systems.

6 CONCLUSIONS

The most obvious advantage of the slow motion methods is to extend downward in temperature the range over which atomic diffusion can be studied. As a result, diffusion mechanisms occurring only at lower temperatures can be observed. Moreover, since the effect of diffusion on the dipolar relaxation time will be much greater than its effect on the spin–lattice relaxation time, going to zero field magnifies the relaxation effects, thereby making possible the observation of diffusion whose relaxation effects might otherwise be too weak to be observable. A measurement of the frequency dependence of the relaxation time can determine the relaxation mechanism and can check the validity of the theory used, such as the assumption of an exponential correlation function, underlying equation (1). $T_{1\rho}$ and T_{1D} measurements greatly increase the frequency range available, since they are effectively very low frequency measurements (of order 10^3 Hz), in contrast to typical T_1 measurements (of order 10^7 Hz). Finally, by having a wider temperature range available, it is possible to observe the onset of other diffusion mechanisms having different activation energies. $T_{1D\rho}$ measurements can be used to enhance the NMR effects arising from the ultraslow motions of weakly magnetic nuclei and, possibly, impurities.

7 RELATED ARTICLES

Brownian Motion and Correlation Times; Diffusion Measurements by Magnetic Field Gradient Methods; Diffusion in Rare Gas Solids; Diffusion in Solids; Double Resonance; Field Cycling Experiments; Low Spin Temperature NMR; Magnetization Transfer between Water and Macromolecules in Proton MRI; Relaxation Theory: Density Matrix Formulation; Rotating Frame Spin–Lattice Relaxation Off-Resonance; Slow and Ultraslow Motions in Biology; Zero Field NMR.

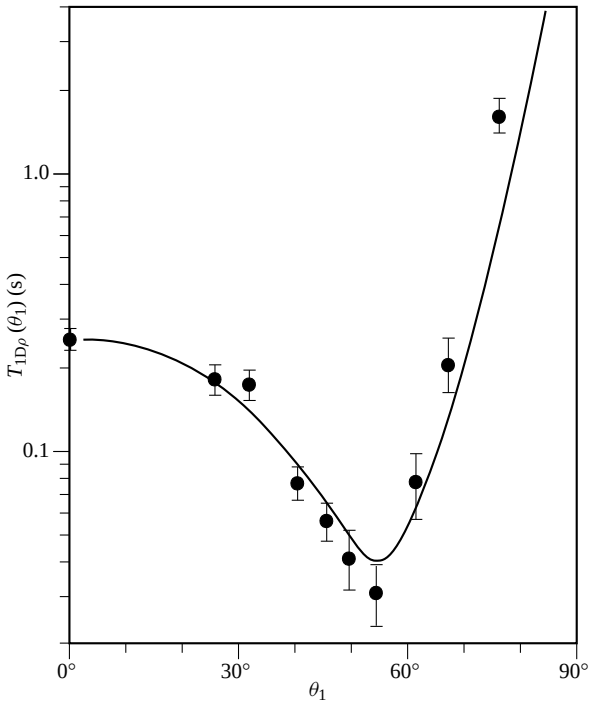

Figure 8 $T_{1D\rho}$ as a function of θ_I in KF:0.1% CaF_2 at 200 °C. The curve was calculated from equation (11). Note that the data point at $\theta_I = 0$ is T_{1D}. (Reproduced by permission of the American Physical Society from H. T. Stokes and D. C. Ailion, *Phys. Rev. B*, 1978, **18**, 141)

8 REFERENCES

1. N. Bloembergen. E. M. Purcell, and R. V. Pound, *Phys. Rev.*, 1948, **73**, 679.
2. C. P. Slichter, *Principles of Magnetic Resonance*, 3rd edn., Springer-Verlag, Berlin, 1990.
3. H. Y. Carr and E. M. Purcell, *Phys. Rev.*, 1954, **94**, 630; S. Meiboom and D. Gill, *Rev. Sci. Instrum.*, 1958, **29**, 6881.
4. D. C. Ailion and C. P. Slichter, *Phys. Rev. Lett.*, 1964, **12**, 168.
5. D. C. Ailion, in *Advances in Magnetic Resonance*, ed. J. S. Waugh, Academic Press, New York, 1971, Vol. 5, Chap. 4
6. D. C. Ailion, in *Methods of Experimental Physics*, ed. J. N. Mundy, S. J. Rothman, M. J. Fluss, and L. C. Smedskjaer, Academic Press, Orlando, 1983, Vol. 21, Chap. 6
7. D. C. Ailion, in *Proceedings of 10th Ampère Summer School and Symposium*, ed. R. Blinc, M. Vilfan, and J. Slak, J. Stefan Institute, Ljubljana, 1988, p. 47.
8. L. C. Hebel and C. P. Slichter, *Phys. Rev.*, 1959, **113**, 1504; A. G. Anderson and A. G. Redfield, *Phys. Rev.*, 1959, **116**, 583.
9. F. Noack, in *Progress in Nuclear Magnetic Resonance Spectroscopy*, ed. J. W. Emsley, J. Feeney, and L. H. Sutcliffe, Pergamon Press, Oxford, 1986, Vol. 18, p. 171.
10. A. G. Redfield, *Phys. Rev.*, 1955, **98**, 1787.
11. D. C. Look and I. J. Lowe, *J. Chem. Phys.*, 1966, **46**, 2995.
12. C. P. Slichter and D. C. Ailion, *Phys. Rev.*, 1964, **135**, A1099.
13. C. P. Slichter and W. C. Holton, *Phys. Rev.*, 1961, **122**, 1701.
14. J. Jeener and P. Broekaert, *Phys. Rev.*, 1967, **157**, 232.
15. D. C. Ailion and P. Ho, *Phys. Rev.*, 1968, **168**, 662.
16. H. T. Stokes and D. C. Ailion, *Phys. Rev. B*, 1977, **16**, 4746.
17. H. T. Stokes and D. C. Ailion, *Phys. Rev. B*, 1978, **18**, 141.
18. D. C. Ailion and C. P. Slichter, *Phys. Rev.*, 1965, **137**, A235.
19. B. Günther and D. C. Ailion, *J. Magn. Reson.*, 1985, **61**, 482.
20. B. Günther and O. Kanert, *Phys. Rev. B*, 1985, **31**, 20.
21. D. F. Holcomb and R. F. Norburg, *Phys. Rev.*, 1955, **98**, 1074.

Biographical Sketch

David C. Ailion. *b* 1937. A.B., 1956, M.S., 1958, Ph.D., 1964, Physics, University of Illinois, under supervision of C. P. Slichter. Faculty member (currently Professor of Physics) University of Utah, 1964–present. Fellow of American Physical Society, Humboldt Senior Research Award (1994–6), University of Utah Distinguished Research Award (1995), NIH Special Fellow (1971–2), Guest Member of AMPERE Committee. Approx. 130 publications. Current research specialties: magnetic resonance imaging of lungs, NMR of partially disordered systems (incommensurate insulators and glasses).

Accurate Determination of Nuclear Quadrupole Coupling Constants and other NMR Parameters in Liquids from the Combination of Molecular Dynamics Simulations and ab initio Calculations

Debra J. Searles

Griffith University, Brisbane, Australia

&

Hanspeter Huber

Institut für Physikalische Chemie der Universität Basel, Basel, Switzerland

1	Introduction	1
2	Tools for Calculation of Properties of Fluids	2
3	Results	5
4	Conclusions	10
5	References	10

1 INTRODUCTION

Quantum chemical studies are usually carried out on gases and solids where reasonable approximations can be invoked to yield accurate results. This is despite the fact that most important reactions occur in the liquid phase where both dynamics and intermolecular interactions are important. Molecular dynamics simulations are a well established technique for the study of liquids and provide a means of determining structural and dynamic properties as well as understanding the structure of the fluid and dynamics in fluids on a molecular level. Furthermore, the conditions of the system can be precisely controlled, and are not affected by experimental measurement. By combining molecular dynamics simulation with ab initio quantum chemical calculation, the range of liquid properties that can be determined is expanded. There are still limitations to the size of the system that can be studied and the timescale over which it can be investigated; however with advances in computational power these limitations will continue to be reduced.

The complexity of the structure and dynamics of liquids also presents difficulties to the experimentalist. The experimentalist must invoke various approximations to interpret the measurements made on these systems. Often it is difficult to test the accuracy of these approximations using experimental methods. Theoretical investigations using simulation and quantum chemical calculations can thus be used to obtain reliable interpretations of the experimental data.

The difference between the gas phase value and the liquid value is the 'solvent effect'. Most explanations of chemical reactions and processes are on the molecular level, without a solvent, and any unexpected behavior is often referred to as a solvent effect. A sound knowledge of the solvent effect on various properties is therefore necessary in understanding and predicting chemical behavior. Often the effects of solvents are identified by looking at trends observed in given properties and through development of models. However, because simulations are carried out at molecular level, a real understanding of the influences of the solvent can be obtained using simulations.

In this review we discuss the combined use of simulation and quantum chemical methods to determine the nuclear quadrupole coupling constants, nuclear magnetic resonance (NMR) relaxation times, chemical shifts and J-couplings in liquids. A chapter discussing nuclear quadrupole coupling constants and NMR relaxation in liquids was recently published in Volume 7 of Theoretical and Computational Chemistry.[1]

The quadrupole coupling energy is the interaction energy between the nuclear electric quadrupole moment and the electric field gradient (EFG) at the site of the nucleus that exists due to the rest of the molecule and its surroundings. The EFG is a traceless tensor, V, and in its principal axes system (α, β, γ) can be represented by two quantities, e.g., equation (1)

$$eq = V_{\alpha\alpha}$$
$$\eta = \left(\frac{V_{\beta\beta} - V_{\gamma\gamma}}{V_{\alpha\alpha}}\right) \tag{1}$$

The axes are chosen such that the components of the EFG tensor have the order $|V_{\alpha\alpha}| > |V_{\beta\beta}| > |V_{\gamma\gamma}|$. η is called the 'asymmetry parameter' and $\chi = e^2qQ/h$ is known as the nuclear quadrupole coupling constant (NQCC) where Q is the nuclear quadrupole moment. The nuclear quadrupole moment is a property of the nucleus itself. Since the EFG depends on the electric field around the nucleus, the EFG, NQCC and asymmetry parameter are sensitive to the environment of the nucleus.

Quantum mechanical calculations allow calculation of the EFG at a nucleus and therefore calculation of the NQCC and asymmetry parameter at the nucleus of a molecule is straightforward. However, since quantum mechanical calculations become more expensive in computer-time as the system size increases, the size of the molecule for which these properties can be calculated is limited. For liquid systems, this means that only the effects of a limited number of neighboring molecules (a cluster or supermolecule) can be considered or that the solvent must be treated in an approximate way. Furthermore, in the liquid state the environment of a nucleus is continually changing, and therefore an ensemble of clusters of molecules must be considered. The calculation of the NQCC for liquids using ab initio methods is discussed below.

Under extreme narrowing conditions, the spin-lattice relaxation time is given by equation (2)

$$\frac{1}{T_1} = \frac{3}{8}\frac{2I+3}{I^2(2I-1)}\left(\frac{2\pi eQ}{h}\right)^2 \int_0^\infty \mathrm{d}t \langle V_{zz}(0)V_{zz}(t)\rangle \tag{2}$$

where I is the nuclear spin, h is Planck's constant and $\langle V_{zz}(0)V_{zz}(t)\rangle$ is the correlation function of the field gradient in the laboratory coordinate system. Defining an effective correlation time, transforming to a principal axis system and using the definitions for the NQCC and asymmetry parameters above, the spin-lattice relaxation time can be expressed as equation (3)

$$\frac{1}{T_1} = \frac{3}{40}\frac{2I+3}{I^2(2I-1)}(2\pi\chi)^2\tau_{\text{eff}}\left(1+\frac{\eta^2}{3}\right) \tag{3}$$

Using this relationship, experimental values for the NQCC are often obtained from the measured T_1 and an indirect measurement or estimate of τ_{eff}. Since the value of τ_{eff} is not directly available from experiment, it is often assumed that the rotation is isotropic so that a correlation time can be estimated from the rotational correlation time along a bond or the dipole-dipole relaxation time. The asymmetry parameter cannot generally be determined directly from experiment if the NQCC is unknown, and therefore it is often assumed to be zero or is estimated from experimental or calculated gas phase or solid state values. In many cases these approximations are not justified and need to be tested. It should be noted that, in order to aid comparison between the experimental and computed NQCCs, the ensemble average NQCCs are often computed as roots of the mean square values. Calculation of various relaxation times and their equivalence is discussed in the Results section below, and compared with experimental results where available.

Recently, a new experimental method of determining the liquid state NQCC has been used by Farrar and co-workers who observed a high degree of correlation between the NQCC of a nucleus and its chemical shift.[2–4] These experimental results have been found to be in good agreement with the simulated values.

To make it feasible to carry out calculations of liquid properties and local properties of liquids, like chemical shifts, without using any empirical information some preconditions had to be fulfilled. Computers had to become fast enough for extensive simulations and quantum chemical calculations and methods had (and still have) to be developed for the calculation of these properties with the necessary accuracy. Knowledge in quantum chemistry and in simulations was developed in different groups and had to be exchanged before a combination of the two fields could occur. On the simulation side the tools were available and the computers fast enough for reasonable computations around 1980. Although quite accurate quantum chemical calculations could be performed for molecules at that time, intermolecular interactions, which are of crucial importance for liquids, could not yet be obtained with the necessary accuracy for reasonably large systems. For this purpose quite huge basis sets are usually needed with many polarization functions as well as diffuse functions, but also electron correlation has to be included on a high level in most cases. This is not only true for the interaction energy, but also for electronic properties like electric field gradients (EFGs). It was only at the end of the eighties that quantum chemistry could fulfill these preconditions. For more details on this development see Ref.[5] Some of the techniques developed are described in the next section.

2 TOOLS FOR CALCULATION OF PROPERTIES OF FLUIDS

Here we consider the tools available for calculation of solvent effects. The methods used can be grouped into three broad categories:

(1) *Macroscopic treatment of the solvent*: In this approach, the solvent is treated using continuum models or reaction fields. This is the method that is commonly incorporated in quantum chemical packages.
(2) *Microscopic cluster methods*: In these studies, the solvent molecules are explicitly treated when determining the molecular property of interest (for details see below and Figure 1). The necessary cluster size varies with the property considered as does the way in which the solvent molecule is treated. In some cases the main influence of the solvent molecules on the molecular property being determined is due to electrostatic interactions and therefore the solvent is modeled as a distribution of charges (electrostatic model), however in general the full electronic effects of the solvent should be considered.[6]
(3) *Car-Parrinello simulations*: In this case the periodic bulk fluid and its dynamics are modeled using quantum chemical calculations on the fly. Various techniques are introduced to account for the periodicity.

We will focus on microscopic cluster methods for the following reasons. Firstly we doubt that studies using the first approach can reach predictive accuracy without including increasingly more microscopic features (so that this approach becomes more like the second category; see e.g., the polarizable continuum model (PCM) by Tomasi and co-workers.[7,8]) The first approach also needs at least one empirical parameter and therefore will never be able to provide completely theoretical predictions. However, it should be noted that it is currently the only method that can be applied routinely by most scientists, and uses little additional computer time to that required for single molecule (gas phase) calculations. The third category is still very computer time intensive, and few examples of calculations of NMR related properties in liquids exist in the literature at this time. Moreover, in certain cases the density functional theory (DFT) method inherent to it might not yield the required accuracy.

2.1 Cluster Method

The cluster method involves the generation of clusters of molecules, and the treatment of each cluster as a supermolecule for which the required property of the central molecule is calculated using quantum chemistry. The fluid property is then determined from the ensemble average of its value for each of the clusters.

Liquid clusters are obtained using Monte Carlo (MC) simulations or from single configurations ('snapshots') of a classical simulation trajectory formed using molecular dynamics (MD) simulations.[9] A molecule is randomly selected from the molecules in the MC or MD liquid snapshot, and the configuration of molecules nearby the central molecule is used to form the cluster. This is illustrated in Figure 1. Periodic boundary conditions are generally used to model the bulk fluid. In MC simulations, the liquid configurations are determined by random sampling with the statistics of the ensemble required. MD

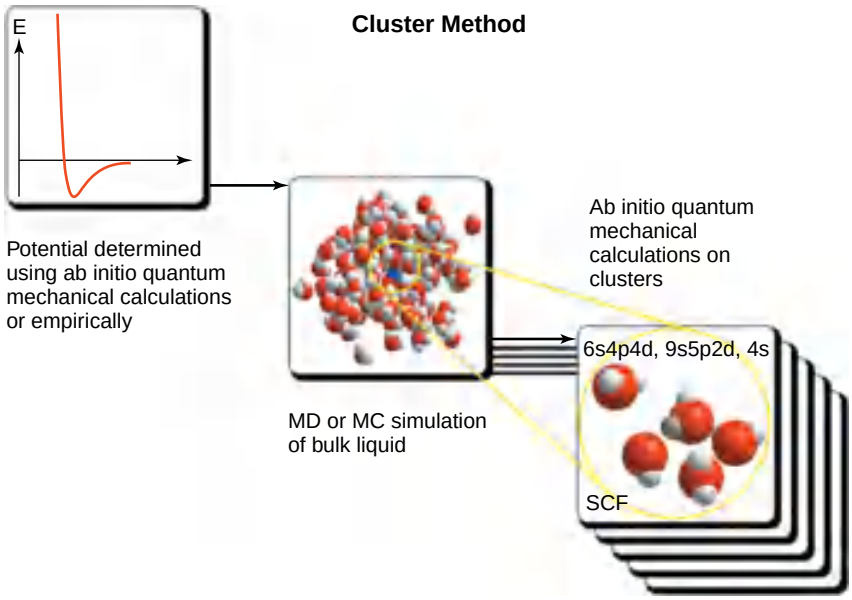

Figure 1 A schematic diagram demonstrating how the cluster method is used to determine properties in liquids. Firstly a potential energy hypersurface is determined empirically or using ab initio methods. This is then used in MD or MC calculations of the bulk liquid. Finally, 'snapshots' of the liquid are taken and clusters of molecules are used in ab initio quantum mechanical calculations to determine values for the property of interest. Averaging over many snapshots and clusters results in the liquid state value

simulations involve solution of Newton's equations of motion for each particle in the simulation box and the configurations obtained are representative of the microcanonical ensemble. Modifications to the equations of motion allow other ensembles to be sampled using MD simulations. Both MC and MD simulation techniques are thoroughly described in Allen and Tildesley.[9]

Once clusters have been generated from the snapshots, the properties of the central molecule are determined using the liquid cluster (or supermolecule) as the input structure to a quantum chemical calculation. For example, the deuterium NQCC for an atom in the central molecule is calculated quantum chemically with the cluster input as the structure for the quantum chemical calculation. This is repeated for many clusters sampled from the MC or MD simulation, and averaged to obtain the liquid state property.

Questions that must be addressed when using the cluster method are: how many snapshots of the fluid are required; how many molecules should be included in the supermolecule; how the molecules to be included in the supermolecule should be selected; and for clusters obtained from MD simulations, the time required between snapshots should be considered. Optimization of the number of surrounding molecules to be included in the cluster and the selection criteria are determined by sample calculations, and require a balance between the time taken and the accuracy required. For the properties of interest for this review, it is necessary to carry out a quantum chemical calculation to determine the property of the molecule in the liquid state cluster. The quantum chemical calculations are generally more computer time intensive than the MC or MD simulations, and therefore the number of clusters and their size are restricted. It is also important to optimize the time between snapshots so that convergence to the ensemble average property of the liquid is obtained using the minimum number of calculations.

The cluster method has been used to determine various liquid state properties. Algorithms have been developed to calculate properties including vibrations,[10] NQCCs,[11] chemical shifts,[12] J-couplings,[13] electronic spectra,[14] and EPR (electron paramagnetic resonance) hyperfine couplings.[15] In the last case the solvent is treated only in an electrostatic approximation. These algorithms have been applied extensively since these early papers and extended to study a wide range of liquids.

An approach that is related to the cluster method is the Quantum Cluster Equilibrium (QCE) method. This method has been applied to the calculation of NQCCs in fluids by Ludwig, Weinhold, Farrar and co-workers.[16–29] The QCE approach uses standard quantum statistical thermodynamics to consider the chemical equilibria existing between the clusters and thus determines the probabilities of observing clusters in the liquid state at the required temperature, pressure and composition of the fluid.[27] In contrast to the conventional cluster method discussed above, in this approach all possible clusters that might be expected to be present in the liquid are generated, and the structures of these clusters are optimized using quantum chemical calculations. A canonical ensemble is assumed, and for each cluster the energies, harmonic vibrational frequencies and moments of inertia of the cluster at its equilibrium structure are calculated using quantum mechanics. Hence partition functions for each cluster and the total partition function can be determined. The cluster populations obtained are then used to determine expectation value of the property of interest, such as the NQCC. The NQCC of nuclei in the liquid state of water,[19] formamide,[16] N-methylformamide,[17] N-methylacetamide,[18] ammonia[24] and ethanol[26] have been determined in this way. Thermodynamic and structural properties, vibrational frequencies and chemical shifts have also been calculated using the QCE method.[16,18,20,22–26,28,29] Limitations of the QCE method are discussed by Ludwig et al.[19] and include the treatment of the low-frequency intermolecular vibrational modes by a harmonic approximation, approximation of the

molecular volume, the possibility of excluding significant clusters in the ensemble and the use of a mean-field approximation to treat residual cluster-cluster interactions which requires an empirical parameter. Advantages over the cluster method where clusters are selected from a molecular dynamics simulation, are that the accuracy does not depend on the accuracy of a model potential energy function and generation of the clusters takes negligible time.

2.2 Dynamic Properties

The above cluster method is very general and can be applied to calculate most static properties at any phase point. Similarly the QCE method is very general, although it may be difficult to extend it to non-hydrogen bonded systems and some problems exist with higher order temperature derivatives.[28] However, both methods are only able to calculate static properties. This is true even if the cluster method is combined with molecular dynamics (MD) simulations, because the simulation is only used to obtain the static clusters. Hence, for relaxation times or other dynamic properties other techniques are needed.

'Mechanical' dynamic properties like transport properties can be obtained by integration of the underlying time correlation function in equilibrium simulations (Green-Kubo integrals). Relaxation times are obtained similarly (see equation (2)), the only problem is the need of additional electronic properties like field gradients (for quadrupolar relaxation, which we take as an example in the following) at each step of the simulation. The required field gradient can in principle be calculated quantum chemically at any position of the simulation cell and at each time step. However, this is not practical today. Even if one reduced the ensemble to a cluster by use of a cutoff radius, the high accuracy needed in the quantum chemical calculation would make it unfeasible to perform such a calculation at each step. The same problem would occur if one desired a quantum chemical calculation of the intermolecular potential (i.e., the forces) at each step. The usual approximation invoked in this case is to calculate pair potentials only and to assume pair additivity for the simulation. The same approximation is possible for the electronic property of interest. That means that for quadrupolar relaxation, for example, a pair EFG hypersurface is calculated firstly, e.g., in the case of Neon a one-dimensional curve of the EFG at one Neon nucleus induced by the other Neon atom as a function of the distance. This pair function, obtained pointwise from quantum chemical calculations, is fitted to an analytical function and implemented in the simulation program to obtain the property at each step of the simulation (for details see Refs.[30–32]). Another possibility would be to use Car-Parrinello types of methods[33] and to calculate the electrical property on the fly with the same density functional theory (DFT) procedure as used for the potential. To our knowledge this has not yet been done.

There are several levels of difficulty in obtaining the EFG in a liquid. The first calculations in the eighties were all for atomic ions[30–32,34] or a rare gas[35] in aqueous solutions. In these cases the EFG is completely intermolecular and can be obtained with relatively crude approximations like Hartree-Fock (HF) calculations with small basis sets or even classical electrostatic models [35]as the solvent is very polar. The next step was the treatment of the relaxation of ^{21}Ne in liquid Neon.[36] Here the solvent is also very simple, but one already needs very high-level quantum chemical calculations as we are dealing with a pure dispersion interaction. A step further leads us to molecular systems. To our knowledge the quadrupolar relaxation of a molecular nucleus has not yet been studied computationally. In our groups we are currently doing this for the system D_2O/DMSO, but with an empirical force field. For this polar system with deuterium as the nucleus of interest, a HF calculation yields a sufficiently accurate EFG. The only calculated relaxation time for a molecular system using quantum chemistry we are aware of is a dipolar relaxation, which was calculated in a slightly different manner and will be discussed in the Results section.[37]

2.3 Quantum Chemical Tools

If one is interested in obtaining completely non-empirical predictions, the interatomic potential has to be calculated quantum chemically. Except for very polar systems, dispersion energy always has a major contribution to the potential energy. This means that one has to include electron correlation on a reasonably high level and use quite large basis sets. If this is not possible one might use an empirical potential. The importance of inclusion of electron correlation for the calculation of the electric property applies equally when using a pair surface and using clusters. However, recourse to empirical approximations is usually not possible. This is the main reason why such calculations only became possible in the last decade. In the Results section we will show how improvements of the quantum chemical calculations influence the results for the example of the quadrupolar ^{21}Ne relaxation. In the cluster method one typically needs 50 to 100 quantum chemical calculations for clusters that typically consist of 5 to 15 monomers. For an electric property surface one typically needs several hundred pair calculations. This is currently only possible for reasonably small monomers, but even then it would barely be possible with the methods available two decades ago. There were two developments in the eighties that assisted these calculations greatly. One was the improvement of DFT by the introduction of the generalized gradient approximation and some additional developments, and the other was the development of special basis sets to calculate local properties in a molecule or cluster.

The latter method is based on the idea that a local property like an EFG or a chemical shift needs a very accurate basis set close to the location of interest, smaller basis sets in the next neighborhood and only small basis sets far away (note that this is a similar philosophy to that which has been applied in the so called QM/MM methods, where distant molecular parts are only treated by molecular mechanics). We developed this strategy under the name Basis sets of high local quality in the early eighties for EFG calculations and showed in many papers that it works excellently for deuterium,[38–43] but also reasonably well for other nuclei like N,[44,45] Li,[46] O[47] and S.[48,49] Chesnut et al. applied the same concept under the name Locally dense basis sets to chemical shifts,[12,50–54] whereas Hinton et al.[55] call it Attenuated basis sets. Other groups have also applied it to chemical shifts.[37,56] DiLabio et al.[57–61] and Pratt et al.[62] showed recently that the concept also works well for bond and dissociation energies, whereas Chesnut and Byrd[63] use it to get correlation energies in an additive scheme.

The DFT method, although much older, improved in the mid-eighties with the introduction of the generalized

gradient approximations and it started a triumphant advance in chemistry. Due to its lower scaling it is particularly suited to large systems such as the clusters in the cluster method. Bailey has shown recently in several papers,[64–68] that it yields excellent EFGs for nuclei like D, B, O, N, S and Ge. This new finding has not yet been applied to liquid calculations. As shown by Schwerdtfeger et al.,[69] its suitability needs to be checked for each nucleus. The sum-over-states density functional perturbation theory method is an important method for the calculation of magnetic properties that was developed by Malkin et al.[70,71] in the last decade.

3 RESULTS

3.1 Nuclear Quadrupole Coupling Constants

Some early studies of monatomic ions and atoms have been carried out with the goal of investigating quadrupole relaxation, and in these cases the NQCC was calculated assuming pair additivity (see below).

In the mid-1980s the first ab initio calculations of the NQCC and asymmetry parameter of deuterium (^{2}H or D) and oxygen (^{17}O) nuclei in water were carried out. The electric field about the isolated water molecule is not symmetric, therefore the EFG at each nucleus is non-zero and changes in the structure of the water molecule will influence the EFG. In addition, the strong intermolecular interactions in hydrogen bonded liquid water mean that the influence of neighboring molecules in the cluster will be important. Hence, liquid water is an interesting candidate for study. The first ab initio predictions of the NQCCs of liquid water did not use a cluster approach, but assumed that the water molecule was hydrogen bonded 75% of the time.[72,73] In the early 1990s the cluster approach was used to determine the D and ^{17}O NQCC and asymmetry parameters in liquid water.[11,74,75] A number of potential models were used in MD simulations to generate clusters, including the ab initio MCYL potential energy surface of Lie and Clementi.[76] The NQCC was determined at the HF level, i.e., NQCCs for liquid water were determined by purely computational methods with no empirical parameters. Furthermore, a model for the dependence of the deuterium NQCC on the structure of the water cluster was developed[11] and has been used to identify a slight temperature dependence of the deuterium NQCC43, consistent with experimental results. The HF ab initio calculations of the deuterium NQCC in single molecules indicate that a systematic error of 3% is expected due to limitations of the ab initio method used,[41] therefore the best estimate of the NQCC should be corrected by this factor. In Figure 2 the temperature dependence of the experimentally determined NQCC is compared with that obtained using the model developed in Ref.[11] and corrected by the error due to the ab initio calculations. The recent experimental results are in good agreement with the calculated values.[43,75] When the calculated value of the NQCC of ^{17}O, $\chi = 8.9 \pm 0.3$ MHz, was published in 1993 the value was somewhat higher than the best experimental results at that time. However, as is shown in Figure 3, the most recent experimental result that we are now aware of[4] is in excellent agreement with the calculated value. Rather than determine the NQCC directly from relaxation times, Ropp et al.[4] use the observed correlation between the chemical shift and the NQCC ($R^2 = 0.99$ for deuterium and $R^2 = 0.96$ for ^{17}O) for its determination and therefore do not rely on the assumptions necessary in the earlier works. For a review of the early calculations of NQCCs in the liquid state see.[43]

Alternative approaches for the computational determination of the deuterium and ^{17}O NQCC and asymmetry parameter in

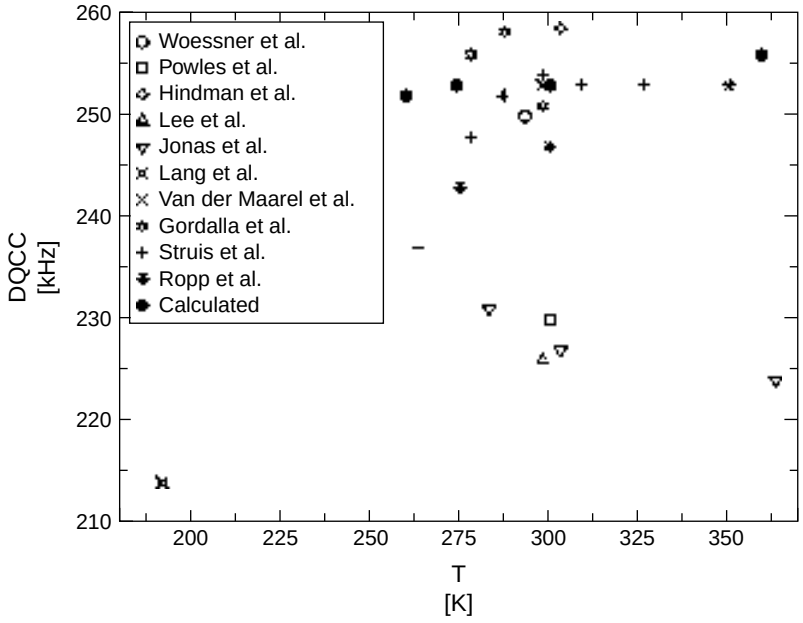

Figure 2 Experimental and calculated deuterium NQCCs. The results before 1980 have open symbols, whereas the more recent ones have crosses or star symbols. The symbol key for the experimental values is ordered by the year of publication. The calculated values are from Eggenberger et al.[11] The simulations were performed with the MCYL ab initio potential. The values were obtained from a model (see Ref.[11]) which lead to statistical errors <1 kHz and they were empirically corrected, i.e., reduced by 3% such that the gas phase value is in agreement with experiment

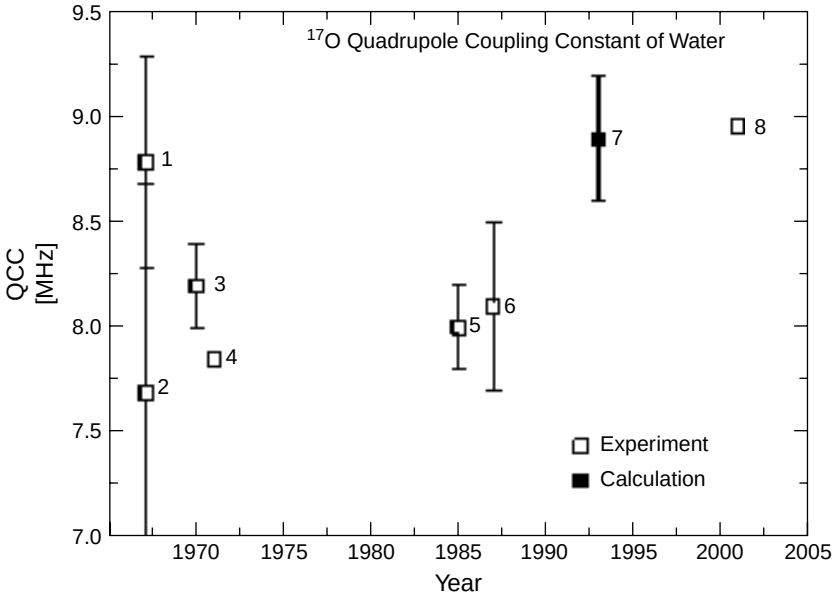

Figure 3 Experimental and calculated NQCCs for ^{17}O in water versus the year of publication. All but one result (black square) were determined experimentally (open squares). The early results of Glasel[106] (labelled 1) were criticized by later authors, although it is in good agreement with the calculated value of Eggenberger et al.[74] (labelled 7) and the newest experimental value,[4] labelled 8. The other experimental results are from the following references: 2 is from Ref.[107], 3 is from Ref.[108], 4 is from Ref.[109], 5 is from Ref.[110] and 6 is from Ref.[111]

liquid water have been taken by Moriarty et al.[77] and Ludwig et al.[19] Moriarty et al. used HF theory to treat the central water molecule within a statistical mechanical bath of water molecules. The configurations of the liquid water cluster were generated using MC simulations. Their best results include configuration interaction and a zero point energy correction, and for deuterium $\chi = 228.2\,\text{kHz}$ and $\eta = 0.1605$. For ^{17}O, $\chi = 11.04\,\text{MHz}$ and $\eta = 0.8237$. Ludwig et al.[19] used the QCE approach and for deuterium in liquid water obtained $\chi =$ 264 kHz and $\eta = 0.134$. For ^{17}O, $\chi = 8.4\,\text{MHz}$ and $\eta = 0.855$.

Experimental studies have shown an interesting and surprising behavior for the deuterium NQCC of water in a mixture of water and DMSO.[78] Recently, we have shown that this behavior is not reproduced in computational studies using the cluster approach.[79] Experimental determinations of liquid state NQCCs are not straightforward and various approximations must be employed in interpretation of the experimental results. The disagreement between experiment and computation suggests that one of these approximations is not valid, but also may be due to deficiencies in the simulations. Studies are underway to clarify the current situation.

The cluster approach has also been used to calculate ^{17}O NQCC in liquid CO_2.[80] The results were in excellent agreement with experiment and it was found that the NQCC is constant over a wide range of densities and temperatures between 298 K and 325 K, in the liquid and supercritical phase. The asymmetry parameter has a negligible contribution in equation (3). The same approach was used by Laaksonen and Wasylishen[81] to determine the ^{14}N and deuterium NQCC of liquid ammonia and their temperature dependence. The ab initio calculations of the NQCC were carried out at the MP2 level with a 6-31 G** basis set and at this level of theory the gas phase deuterium NQCC is overestimated by approximately 10% and the ^{14}N NQCC by approximately 4%. For liquid ammonia, the calculated ^{14}N NQCC at 271 K was $\chi = -3.67\,\text{MHz}$ and at 197 K $\chi = -3.43\,\text{MHz}$. For the deuterium nucleus, $\chi = 264\,\text{kHz}$ at 271 K, $\chi = 255\,\text{kHz}$ at 197 K and the asymmetry parameter is insensitive to temperature with $\eta = 0.13 \pm 0.01$ over the range of temperature studied. These values are approximately 13% higher than recent experimental results for the deuterium NQCC in liquid ammonia of Hardy and Zeidler[82] who obtained $\chi = 232\,\text{kHz}$ at 273 K. However, accounting for the 10% error due to limitations of the ab initio calculations results in excellent agreement between the computational and theoretical values. Furthermore an increase in the deuterium NQCC with temperature at a rate of $0.1\,\text{kHz}\,\text{K}^{-1}$ was observed in both the experimental and computational results. Merkling et al.[83] have calculated the deuterium NQCC of the hydroxy-deuterium of methanol in carbontetrachloride at various compositions. Experimental studies show that the NQCC decreases with an increase in the methanol mole fraction of 0.1 after a maximum at that point. Although the computed values also show a decrease with increase in the methanol mole fraction, no maximum is observed. Furthermore, the computed NQCC values are 2–20% higher than the experimental results.

Ludwig, Farrar and Weinhold have carried out QCE calculations of NQCCs for a range of liquids. As discussed above, the QCE algorithm was used to determine the deuterium and ^{17}O NQCC and asymmetry parameter in liquid water with results that are in fair agreement with experiment. Ludwig, Farrar and Weinhold use a Calibrated quadrupole moment to correct the cluster results against the single molecule value, so no correction due to inadequacies of the ab initio calculation are necessary.[19] The temperature dependencies of the NQCC and asymmetry parameter of the carbonyl deuterium, oxygen, amide trans deuterium and nitrogen nuclei in liquid formamide were also determined by Ludwig, Farrar and Weinhold.[16] The trends in the temperature dependencies are found to be in good agreement with experimental results,[3,16,84] however there are

significant discrepancies between the absolute values of the NQCCs (up to approximately 10%). The more recent experimental results for the carbonyl deuteron and the trans amide deuteron[3] show deviations of 3% from the theoretical results, while deviations of up to 13% are observed between these experimental results and the earlier results of Ludwig et al.[16,84] This indicates that the early experimental results may contain systematic errors. The new experimental results[3] are determined using the correlation between the chemical shift and NQCC whereas the earlier experimental results used relaxation data.[16,84] The differences between the two sets of experimental values highlight the difficulties in interpretation of the experimental data for determination of liquid state NQCCs. Studies on the temperature dependence of the NQCC and asymmetry parameter of nuclei in N-methylformamide[17] and N-methylacetamide[18] have also been carried out. Again, the temperature dependence of the ^{14}N and deuterium NQCC are in good agreement with the qualitative behavior of the experimental results, however the absolute values differ. NQCCs in ammonia have also been determined using the QCE method,[24] however deviations from experiment suggest that the clusters selected in the study may not be an accurate representation of the liquid.[82] Recently the QCE method has been used to determine the NQCCs of liquid ethanol[26] in the temperature range 250–350 K. The results obtained are in good agreement with experiment. In general, the temperature dependence of the NQCC that is observed in experiment can be reproduced using the QCE method. However, the absolute values of the NQCCs often differ considerably suggesting a systematic error in the experimental results or the computations. The necessity of invoking approximations in the experimental interpretations, and the variations in experimental results suggest that some of the experimental determinations are in error.

Using the cluster method accurate predictions for the NQCC of various nuclei and liquids have been obtained. The NQCC generally needs to be adjusted due to errors in the ab initio calculations of the gas phase NQCC,[43] or equivalently a Calibrated quadrupole moment needs to be used.[19] These errors can often be quantified due to the availability of accurate experimental values of the NQCC for single molecules, but suggest that improvement of the ab initio cluster calculations is an important step in obtaining NQCCs using purely computational methods. The use of DFT may alleviate these difficulties due to its ability to determine accurate values of the NQCC in an efficient manner. Bailey and co-workers have recently used DFT to calculate NQCCs of gas phase molecules with considerable success[64–68] however these are yet to be used in liquid state calculations as far as we are aware.

3.2 Relaxation Times

The history of a combined application of simulations and quantum chemical calculations for a better understanding of relaxation phenomena started just 20 years ago with an investigation on quadrupolar relaxation. In 1981 Engström and Jönsson[30] published a paper on the EFG fluctuation at the nucleus of a lithium ion in dilute aqueous solution. The results were obtained from Monte Carlo simulations on clusters of different sizes and used an EFG curve obtained from self consistent field (SCF) calculations. They used a pair approximation for the EFG, as is usually done for the potential and estimated the error due to this approximation to be smaller than 5 to 10%. The estimate was based on calculations for $Li^+ + 2H_2O$ configurations. They found interesting information that contributed to the detailed understanding of the relaxation mechanism, e.g., that the first solvation shell is the main contributor, that the lateral motion of the water molecules in this shell is much more important than the rotational motion, and that an electrostatic approximation for Li^+ is not satisfactory due to the close neighbourhood of this shell to the central ion. Although they analysed the time scale of the fluctuations, they were not yet able to calculate the relaxation time itself, as they used the static MC method rather than the dynamic MD method. This work was extended a year later to the Na^+ and Cl^- ions and for the latter case it was found that rotational motion of the water molecules has a similar influence to the translational motion.[31] In 1984 the work was further extended to MD simulations yielding, for the first time, relaxation times from first principles.[32] The dynamics clearly showed that the decay of the EFG time correlation function is not mono-exponential, and the simulated relaxation rate (experimental values in parenthesis) for Li^+ was $0.007\,s^{-1}$ ($0.027\,s^{-1}$), for Na^+ was $22\,s^{-1}$ ($16.6\,s^{-1}$) and for Cl^- was $41\,s^{-1}$ ($25\,s^{-1}$), i.e., in good agreement with the exception of Li^+. This work was recently extended by Odelius and Kowalewski.[85] They studied the dipole-dipole relaxation for Li^+ and were able to reproduce the experiment quite accurately, whereas the temperature behaviour of the quadrupolar relaxation with the EFG surface from Engström et al. showed a similar deviation as before with the deviation being a factor of 3 to 4 of the experimental value. The same system was also studied by Baumert et al.[86] by MD with an electrostatic approximation for the EFG, but in addition these authors compared the quadrupole couplings obtained from this approach and the ab initio cluster approach, finding a deviation up to a factor two and indirectly confirming the failure of the electrostatic approach for this system.

At approximately the same time that the early work of Engström et al. was performed, Schnitker and Geiger[35] used similar techniques in an MD study of the quadrupolar relaxation of ^{131}Xe in water (published for the first time in a diploma work in 1982), although they applied an empirical potential and an electrostatic approximation for the EFG. The technique applied differs from that of Engström et al. insofar as the simple electrostatic model permits calculation of the EFG 'on the fly', i.e., in each step of the simulation, rather than requiring calculation of a pair EFG surface before the simulation and use pair additivity. In many respects they came to similar conclusions, e.g., that the decay is not mono-exponential and that the first hydration shell is mainly responsible for the relaxation. In contrast to simpler theories they found agreement between simulated and experimental relaxation rates roughly within the experimental uncertainty.

With a similar method Luhmer et al.[87,88] calculated the quadrupole relaxation of ^{131}Xe dissolved in benzene. They found that no complex formation was necessary to explain the relaxation as assumed by some authors previously, but that the molecular rotation of the quadrupole of benzene around a C_2 axis can reproduce the experimental relaxation nearly quantitatively. The influence of the cross-correlation was found to be negligible and the relaxation rates between 100 and $150\,s^{-1}$ were in good agreement with experiments ($190–230\,s^{-1}$). These results are compared in a study of the dipolar relaxation of ^{129}Xe in benzene in a later paper[89]

where, in contrast to the quadrupolar relaxation, it is found that the translational motion is more important than the rotation. Additional results of similar quality were obtained with the same approach for ^{131}Xe in 1,3- and 1,4-dioxane,[90] in tetrachloride, acetonitrile, and methanol,[91,92] and in acetonitrile also for ^{21}Ne and ^{83}Kr.[93]

The only study of a relaxation time in pure water we are aware of is by Lippens et al.[94] They studied the dipolar proton relaxation of liquid water in an empirical approach with the SPC and a polarizable SPC model. The relaxation time is 75% larger than the experimental value, a detailed analysis shows however, that the intermolecular part is quite accurate.

All the simulations discussed up to now are in agreement with experiment to within approximately a factor of two. The authors of these studies usually accept this as a good agreement. There are several problems with approximations (like the difficulty in obtaining a good estimate for the Sternheimer shielding), which make it difficult to get more accurate values in this approach. Linse and Halle[34] argue that continuum-solvent theories cannot give good results. In a study of noble gases in organic solvents Vaara et al.[6] conclude that a pure electrostatic model is not good enough. These conclusions could be one reason to turn to methods that calculate the relaxation time from first principles, as performed first by Engström et al.[32] with an EFG obtained from SCF calculations. Although for more accurate values one should include electron correlation.

The quadrupolar relaxation in liquid ^{21}Ne has been treated from first principles in three papers,[36,95,96] which show the progress of the methods within a few years. This system is more difficult to handle because the EFG is completely intermolecular, but no electrostatic interaction occurs and hence electrostatic models are not possible. In addition the interaction is purely dispersive, i.e., the potential as well as the EFG has to be calculated with high-level correlation methods. In 1993 Eggenberger et al.[36] obtained values with deviations less than 20% from experiment. Although the authors discuss different error sources which might lead to fortuitous cancellations, the good agreement with experiment seduced them to assume that the error was not more than 10%, not including the error due to quantum effects at the temperatures below 33 K. Improved work in 1998 by Kirchner et al.[95] showed that the property is much more sensitive to changes in both the EFG and the potential than assumed. A better potential reduced the relaxation times by one third, whereas improving the EFG in addition increased the values by approximately 50% bringing them back close to the original results. In contrast, three-body and quantum effects were shown to induce changes of only 5 to 10% each. As a result the authors assumed that the results had, by far, not yet converged. Two years later Halkier et al.[96] were able to reach convergence (not including many-body and quantum effects) with coupled cluster calculations on the CCSD(T) level and huge basis sets for the EFG as well as for the potential. At 41 K a best estimate including quantum effects by a perturbational method is approximately 15% lower than the experimental value. Additional insights were gained by Kirchner et al.[95] from a detailed study of the self- and cross-correlation functions and a semi-quantitative model of the mechanism. There are two main effects that induce the relaxation. First an exchange between first shell and outer shell atoms with a correlation time of 5 to 0.5 ps for temperatures between 25 to 300 K and a fast process, where an outer shell atom hits a first shell atom towards the central atom with a correlation time of 200 to 50 fs for the same temperature range. The first process is a random walk process showing a linear relation with the inverse temperature, whereas the second is a linear movement (vibration), inversely proportional to the square root of the temperature.

From the experience with the quadrupolar relaxation of liquid neon, the present authors believe that most of the work on spherical symmetric systems, where the EFG is completely intermolecular, probably profited from error cancellations. For the Li^+ ions the cancellation was perhaps just not as effective as for other systems.

The most complicated system investigated by similar microscopic techniques to those discussed here was published by Scheurer et al.[37] in 1999. They studied the shielding anisotropy, dipolar relaxation and nuclear Overhauser effect values in the protein ubiquitin. MD simulations for the protein molecule in water were performed with a molecular mechanics force field. 625 snapshots of the trajectory were taken to obtain dynamic information of the magnetic properties from SOS-DFPT (sum-over-states density functional perturbation theory) calculations. Model groups or simple charges replaced part of the molecule, whereas the quantum chemical part was treated using basis sets of high local quality. They were able to reproduce experimental relaxation times and nuclear Overhauser effect values to within 10 to 20%. In our group we are currently working on the deuterium quadrupolar relaxation of the water/DMSO system, where we previously obtained the NQCC (see above).

3.3 Chemical Shieldings

Whereas in most previous sections a comparison between different results was difficult, we are here in the fortunate situation that most work on chemical shieldings up to now was performed on water at ambient conditions. A collection of results, all published between the years 1994 and 2000, is presented in Figure 4 for protons and in Figure 5 for ^{17}O. The range of the results is as large or even larger than the solvent effect itself. We will discuss the different methods here. In this section we use shift for the difference between the liquid and gas isotropic chemical shielding, i.e., no absolute shieldings are discussed here.

Method 1 is the reference interaction site model combined with self consistent field calculations (RISM-SCF approach) by Hirata and co-workers.[97] The method is in principle non-empirical and treats the solvent and the solution on an atomic level. However this first application is based on an empirical potential (TIP3P-like). The authors discuss ways to improve the method, which evidently is not yet predictive.

Method 2 is a continuum method where the water molecule is immersed in a dielectric medium. The result is again unsatisfactory with the wrong sign for the ^{17}O gas-liquid shift as above. This work by Mikkelsen et al.[98] is cited because they extended this model (Method 3) by taking a cluster with a first solvation shell which as a whole was immersed in a dielectric medium. The results improved greatly with the protons yielding a nearly perfect agreement with experiment, but for the oxygen the solvent effect is only approximately half the experimental value. The authors suggested that their somewhat accidental result (using just one fixed first solvation shell) could be improved by selection

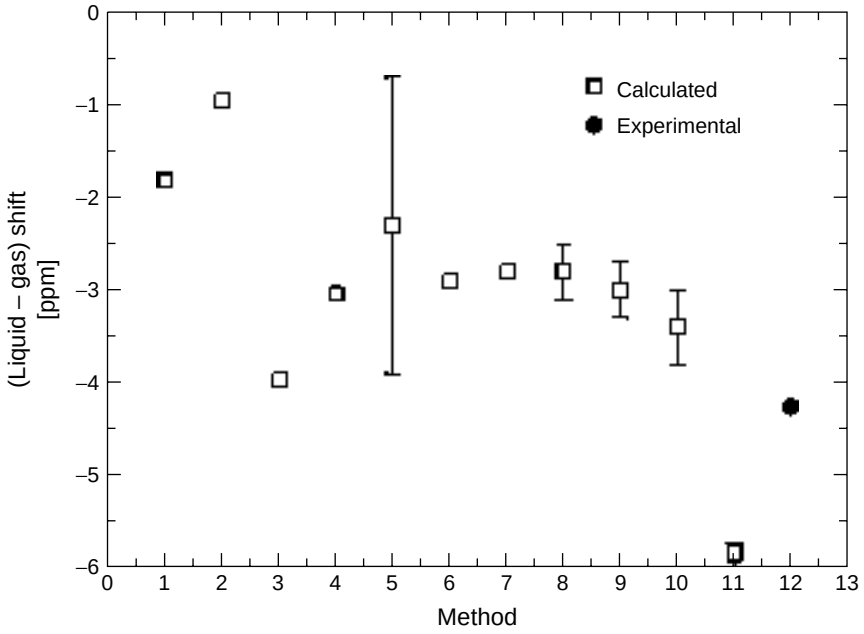

Figure 4 The solvent effect of water on the proton shift in water calculated with different methods (see text)

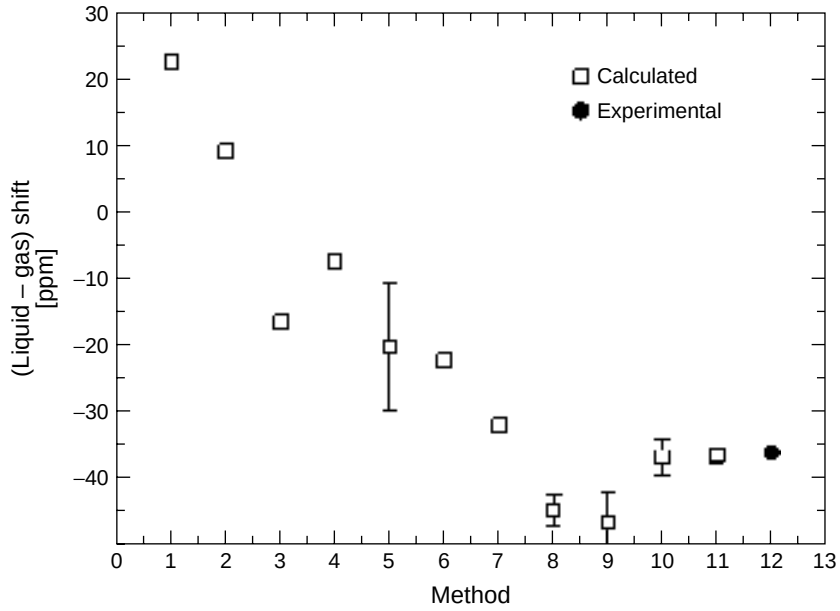

Figure 5 The solvent effect of water on the ^{17}O shift in water calculated with different methods (see text)

of clusters from simulations. This was indeed done by other authors, who also showed that the range of shifts obtained from different clusters is huge, making the method by Mikkelsen et al. not very reliable. The same authors published similar work on H_2S and HCN.[99] Method 4 by Nymand and Åstrand is a perturbational method that again does not yet give satisfying results.

Method 5 is the first work applying the cluster method. Chesnut and Rusiloski[12] used the CFF-91 force field for the simulation and the gauge including atomic orbital (GIAO) coupled HF method for the shift calculations applying locally dense basis sets. Their statistical error bars are quite large. The solvent shifts are roughly half the experimental shifts. One reason for the inadequacy of the results might be the general force field applied here in contrast to most other work where potentials calibrated for water were used. It is hard to judge whether the quality of the quantum chemical method is adequate for the intermolecular contributions.

In method 6 by Cui and Karplus[100] a QM/MM method was applied to this problem for the first time. The flexible TIP3P model by Dang and Pettitt[101] was applied in the MD simulations. DFT calculations on the B3LYP/6-311G(d,p) level were performed for 100 clusters. Their results include only the intermolecular component, which however are responsible for 90%

and 80% of the shift for protons and oxygen, respectively.[102] The results given as method 7 were obtained with a larger basis set, but for 10 clusters only.

The next three methods are by Malkin et al.[102] and apply the cluster method with different potentials. The quantum chemical method for the shift calculation is in all cases the SOS-DFPT with an IGLO-III basis set.[103] Method 8 uses the Dang and Pettitt potentials, as do methods 6 and 7. Method 9 corresponds to the potential by Bopp et al.[104] and method 10 to the MYCL potential of Lie and Clementi[76] obtained from ab initio quantum chemical calculations. Hence method 10 is the first one that uses no empirical information (with the exception of a very general empirical parameter in the SOS-DFPT method). The values presented in the figures were obtained from 10 clusters consisting of 9 water molecules. Test calculations showed that the absolute values of these shifts would increase by approximately 0.2 ppm and 1.2 ppm for H and ^{17}O, respectively, if the cluster size was increased to 13 water molecules. The small number of clusters leads to relatively large statistical errors (the bars in the figures are standard errors). In fact all three values are identical within two standard errors and two of them for oxygen and one for hydrogen, respectively, also agree with the experimental shift within two standard errors. Due to the small number of clusters it could be that the configurations do not represent the distribution of configurations in the liquid well enough. The shifts are in fair agreement with the experimental value for oxygen, the agreement is worse for protons. It would be interesting to repeat this work with today's computer power for more clusters to give a better insight into the role of the potential.

Finally, method 11 is the recent work of Pfrommer et al.[105] This is probably the first application of Car-Parrinello simulations to the calculation of magnetic properties of liquids. Their calculation of chemical shieldings with the BLYP functional is not limited to clusters of a certain size, but is performed for the ensemble consisting of 32 molecules with periodic boundary conditions. The result for oxygen is in excellent agreement with experiment, but the absolute value of the proton shift is approximately 1.6 ppm too large. The statistical errors are very small, approximately the size of the rectangle in Figure 4 and only half that size in Figure 5.

Cammi et al.[7] tested the newly developed PCM-GIAO method on the ^{13}C, ^{15}N and ^{17}O shifts for the molecules CH_3CN and CH_3NO_2 in water with good success and gave a critical evaluation of the method. Ludwig et al.[18] applied the QCE method to liquid N-methylacetamide and obtained excellent agreement with experiment for the temperature dependence of the chemical shifts of H, ^{17}O and ^{14}N and fair agreement of the shifts themselves for H and ^{17}O.

We would like to make a few concluding remarks on this comparison of calculated with experimental shifts and between different methods. The experimental error is not known, but could be sizeable. The calculations do not include rovibrational corrections in an adequate manner, but it is assumed that their classical treatment is sufficient as it will almost cancel when the difference between liquid and gas value is calculated. There are still quite a few different error sources which might cancel, like the limited quality of the potential applied in the simulation, the limited basis set and the limited treatment of correlation in the calculation of the chemical shielding, limited representation of configuration space and limited cluster size. Nevertheless the results show a great improvement in the last decade and it can be expected that such calculations will reach predictive quality in the coming decade.

3.4 J-Couplings

We are aware of only two recent papers on calculations of J-couplings in the liquid. Mikkelsen et al.[99] use a model where the solvent is represented by a dielectric medium, to study its influence on the HH^- and HS^- coupling in H_2S and the HC^-, NC^- and NH^- coupling in HCN. They find dielectric effects of more than 10% and stress the importance of geometry relaxation as they may enhance as well as oppose the direct dielectric effect. Case et al.[13] study dipeptides and ubiquitin. For the latter they apply the cluster method already applied to calculate the relaxation time of the same system[37] (see above). Their results show a reasonable scatter around an empirical Karplus curve.

4 CONCLUSIONS

Before 1990 only very few papers on the simulation of NMR properties in the liquid phase appeared. All of them were about relaxation processes for simple systems (atomic ions and rare gas atoms in polar solvents). One reason was that the computer speed and some quantum chemical tools were not yet available, but perhaps another was that simulations and quantum chemistry were completely different fields with only few people having the necessary knowledge in both fields. In the last decade the number of groups working on the subject has grown and approximately 50 papers are now available. The field is still in an experimental state, i.e., we need much more experience on the reliability of the methods. What influences do the potentials, the pair approximation in the MD cluster method or the harmonic approximations in the quantum cluster equilibrium theory have? However it has been shown that calculations of liquid properties and solvent effects have become feasible and we can see a new great area of computational chemistry evolving.

5 REFERENCES

1. M. Odelius and A. Laaksonen, in 'Molecular Dynamics. From Classical to Quantum Methods', eds P. B. Balbuena and J. M. Seminario, Amsterdam, 1999.
2. M. A. Wendt and T. C. Farrar, *Mol. Phys.*, 1998, **95**, 1077.
3. M. J. Hansen, M. A. Wendt, and T. C. Farrar, *J. Phys. Chem. A*, 2000, **104**, 5328.
4. J. A. Ropp, C. Lawrence, T. C. Farrar, and J. L. Skinner, *J. Am. Chem. Soc.*, 2001, submitted.
5. H. Huber, A. J. Dyson, and B. Kirchner, *Chem. Soc. Rev.*, 1999, **28**, 121.
6. J. Vaara, J. Jokisaari, T. T. Rantala, and J. Lounila, *Mol. Phys.*, 1994, **82**, 13.
7. R. Cammi, B. Mennucci, and J. Tomasi, *J. Chem. Phys.*, 1999, **110**, 7627.
8. C. Amovilli, V. Barone, R. Cammi, E. Cances, M. Cossi, B. Mennucci, C. S. Pomelli, and J. Tomasi, *Adv. Quant. Chem.*, 1999, **32**, 227.
9. M. P. Allen and D. J. Tildesley, in 'Computer Simulation of Liquids', Clarendon Press: Oxford, 1987.

10. K. Hermansson, S. Knuts, and J. Lindgren, *J. Chem. Phys.*, 1991, **95**, 7486.
11. R. Eggenberger, S. Gerber, H. Huber, D. Searles, and M. Welker, *J. Chem. Phys.*, 1992, **97**, 5898.
12. D. B. Chesnut and B. E. Rusiloski, *J. Mol. Struct. (Theochem)*, 1994, **314**, 19.
13. D. A. Case, C. Scheurer, and R. Brüschweiler, *J. Am. Chem. Soc.*, 2000, **122**, 10 390.
14. K. Coutinho and S. Canuto, *J. Mol. Struct. (Theochem)*, 1993, **106**, 99.
15. H. Takase and O. Kikuchi, *Chem. Phys.*, 1994, **181**, 57.
16. R. Ludwig, F. Weinhold, and T. C. Farrar, *J. Chem. Phys.*, 1995, **103**, 3636.
17. R. Ludwig, F. Weinhold, and T. C. Farrar, *J. Chem. Phys.*, 1997, **107**, 499.
18. R. Ludwig, F. Weinhod, and T. C. Farrar, *J. Phys. Chem. A*, 1997, **101**, 8861.
19. R. Ludwig, F. Weinhold, and T. C. Farrar, *J. Chem. Phys.*, 1995, **103**, 6941.
20. R. Ludwig and F. Weinhold, *J. Chem. Phys.*, 1999, **110**, 508.
21. R. Ludwig, F. Weinhold, and T. C. Farrar, *J. Chem. Phys.*, 1996, **105**, 8223.
22. R. Ludwig, O. Reis, R. Winter, F. Weinhold, and T. C. Farrar, *J. Phys. Chem. B*, 1998, **102**, 9312.
23. R. Ludwig, F. Weinhold, and T. C. Farrar, *Ber. Bunsenges. Phys. Chem.*, 1998, **102**, 197.
24. R. Ludwig, F. Weinhold, and T. C. Farrar, *Ber. Bunsenges. Phys. Chem.*, 1998, **102**, 205.
25. R. Ludwig, F. Weinhold, and T. C. Farrar, *Mol. Phys.*, 1999, **97**, 479.
26. R. Ludwig, F. Weinhold, and T. C. Farrar, *Mol. Phys.*, 1999, **97**, 465.
27. F. Weinhold, *J. Chem. Phys.*, 1998, **109**, 367.
28. F. Weinhold, *J. Chem. Phys.*, 1998, **109**, 373.
29. M. A. Wendt, F. Weinhold, and T. C. Farrar, *J. Chem. Phys.*, 1998, **109**, 5945.
30. S. Engström and B. Jönsson, *Mol. Phys.*, 1981, **43**, 1235.
31. S. Engström, B. Jönsson, and B. Jönsson, *J. Magn. Reson.*, 1982, **50**, 1.
32. S. Engström, B. Jönsson, and R. W. Impey, *J. Chem. Phys.*, 1984, **80**, 5481.
33. R. Car and M. Parrinello, *Phys. Rev. Lett.*, 1985, **55**, 2471.
34. P. Linse and B. Halle, *Mol. Phys.*, 1989, **67**, 537.
35. J. Schnitker and A. Geiger, *Z. Phys. Chem. NF*, 1987, **155**, 29.
36. R. Eggenberger, S. Gerber, H. Huber, and M. Welker, *Chem. Phys.*, 1993, **177**, 91.
37. C. Scheurer, N. R. Skrynnikov, S. F. Lienin, S. K. Straus, R. Brüschweiler, and R. R. Ernst, *J. Am. Chem. Soc.*, 1999, **121**, 4242.
38. H. Huber, *Chem. Phys. Lett.*, 1984, **112**, 133.
39. H. Huber, *J. Mol. Struct. (Theochem)*, 1985, **121**, 207.
40. H. Huber, *J. Chem. Phys.*, 1985, **83**, 4591.
41. S. Gerber and H. Huber, *J. Mol. Spectrosc.*, 1989, **134**, 168.
42. E. Fliege, H. Dreizler, S. Gerber, and H. Huber, *J. Mol. Spectrosc.*, 1989, **137**, 24.
43. H. Huber, *Z. Naturforsch.*, 1994, **49a**, 103.
44. S. Gerber and H. Huber, *Z. Naturforsch.*, 1987, **42a**, 753.
45. S. Gerber and H. Huber, *Chem. Phys.*, 1989, **134**, 279.
46. S. Gerber and H. Huber, *J. Phys. Chem.*, 1989, **93**, 545.
47. R. Eggenberger, S. Gerber, H. Huber, D. Searles, and M. Welker, *J. Mol. Spectrosc.*, 1992, **151**, 474.
48. B. Kirchner, H. Huber, G. Steinebrunner, H. Dreizler, J.-U. Grabow, and I. Merke, *Z. Naturforsch.*, 1997, **52a**, 297.
49. D. L. Fiacco, B. Kirchner, W. A. Burns, and K. R. Leopold, *J. Mol. Spectrosc.*, 1998, **191**, 389.
50. D. B. Chesnut and K. D. Moore, *J. Comp. Chem.*, 1989, **10**, 648.
51. D. B. Chesnut and C. G. Phung, *Chem. Phys. Lett.*, 1991, **183**, 505.
52. D. B. Chesnut, B. E. Rusiloski, K. D. Moore, and D. A. Egolf, *J. Comp. Chem.*, 1993, **14**, 1364.
53. D. B. Chesnut and E. F. C. Byrd, *Chem. Phys.*, 1996, **213**, 153.
54. D. B. Chesnut, *Chem. Phys.*, 1997, **214**, 73.
55. J. F. Hinton, P. Guthrie, P. Pulay, and K. Wolinski, *J. Am. Chem. Soc.*, 1992, **114**, 1604.
56. R. A. Kirby and A. E. Hansen, *Int. J. Quantum Chem.*, 1996, **57**, 199.
57. G. A. DiLabio and J. S. Wright, *Chem. Phys. Lett.*, 1998, **297**, 181.
58. G. A. DiLabio, *J. Phys. Chem. A*, 1999, **103**, 11 414.
59. G. A. DiLabio, D. A. Pratt, A. D. LoFaro, and J. S. Wright, *J. Phys. Chem. A*, 1999, **103**, 1653.
60. G. A. DiLabio, D. A. Pratt, and J. S. Wright, *Chem. Phys. Lett.*, 1999, **311**, 215.
61. G. A. DiLabio and D. A. Pratt, *J. Phys. Chem. A*, 2000, **104**, 1938.
62. D. A. Pratt, J. S. Wright, and K. U. Ingold, *J. Am. Chem. Soc.*, 1999, **121**, 4877.
63. D. B. Chesnut and E. F. C. Byrd, *J. Comp. Chem.*, 1996, **17**, 1431.
64. W. C. Bailey, *J. Mol. Spectrosc.*, 1997, **185**, 403.
65. W. C. Bailey, *J. Mol. Spectrosc.*, 1998, **190**, 318.
66. W. C. Bailey, *Chem. Phys. Lett.*, 1998, **292**, 71.
67. W. C. Bailey, *Chem. Phys.*, 2000, **252**, 57.
68. W. C. Bailey, F. M. Gonzalez, and J. Castiglione, *Chem. Phys.*, 2000, **260**, 327.
69. P. Schwerdtfeger, M. Pernpointner, and J. K. Laerdal, *J. Chem. Phys.*, 1999, **111**, 3357.
70. V. G. Malkin, O. L. Malkina, M. E. Casida, and D. R. Salahub, *J. Am. Chem. Soc.*, 1994, **116**, 5898.
71. V. G. Malkin, O. L. Malkina, L. A. Eriksson, and D. R. Salahub, in 'Modern Density Functional Theory: A Tool for Chemistry', eds J. M. Seminario and P. Politzer, Amsterdam, 1995.
72. P. L. Cummins, G. B. Bacskay, N. S. Hush, B. Halle, and S. Engström, *J. Chem. Phys.*, 1985, **82**, 2002.
73. P. L. Cummins, G. B. Bacskay, and N. S. Hush, *Mol. Phys.*, 1987, **61**, 795.
74. R. Eggenberger, S. Gerber, H. Huber, D. Searles, and M. Welker, *Mol. Phys.*, 1993, **80**, 1177.
75. R. Eggenberger, S. Gerber, H. Huber, D. Searles, and M. Welker, *J. Comp. Chem.*, 1993, **14**, 1553.
76. G. C. Lie and E. Clementi, *Phys. Rev. A*, 1986, **33**, 2679.
77. N. W. Moriarty and G. Karlström, *Chem. Phys. Lett.*, 1997, **279**, 372.
78. B. C. Gordalla and M. D. Zeidler, *Mol. Phys.*, 1986, **59**, 817.
79. B. Kirchner, D. J. Searles, A. J. Dyson, P. S. Vogt, and H. Huber, *J. Am. Chem. Soc.*, 2000, **122**, 5379.
80. M. Holz, R. Haselmeier, A. J. Dyson, and H. Huber, *Phys. Chem. Chem. Phys.*, 2000, **2**, 1717.
81. A. Laaksonen and R. E. Wasylishen, *Z. Naturforsch.*, 1995, **50a**, 137.
82. E. H. Hardy and M. D. Zeidler, *Phys. Chem. Chem. Phys.*, 2000, **2**, 1645.
83. P. J. Merkling, M. D. Zeidler, and P. A. Bopp, *J. Mol. Liq.*, 2000, **85**, 57.
84. R. Ludwig, J. Bohmann, and T. C. Farrar, *J. Phys. Chem.*, 1995, **99**, 9681.
85. M. Odelius and J. Kowalewski, *J. Chem. Soc. Faraday Trans.*, 1995, **91**, 215.
86. R. Baumert, R. Ludwig, and A. Geiger, *J. Mol. Model.*, 1996, **2**, 379.
87. A. Dejaegere, M. Luhmer, M.-L. Stien, and J. Reisse, *J. Magn. Reson.*, 1991, **91**, 362.
88. M. Luhmer, D. van Belle, J. Reisse, M. Odelius, J. Kowalewski, and A. Laaksonen, *J. Chem. Phys.*, 1993, **98**, 1566.
89. M. Luhmer, A. Moschos, and J. Reisse, *J. Magn. Reson. A*, 1995, **113**, 164.
90. M. Luhmer and J. Reisse, *J. Magn. Reson. A*, 1995, **115**, 197.

91. M. Odelius and A. Laaksonen, *Mol. Phys.*, 1994, **82**, 487.
92. M. Odelius, *J. Phys. Chem.*, 1994, **98**, 12 108.
93. M. Odelius, M. Holz, and A. Laaksonen, *J. Phys. Chem. A*, 1997, **101**, 9537.
94. G. Lippens, D. Van Belle, S. J. Wodak, and J. Jeener, *Mol. Phys.*, 1993, **80**, 1469.
95. B. Kirchner, E. Ermakova, G. Steinebrunner, A. J. Dyson, and H. Huber, *Mol. Phys.*, 1998, **94**, 257.
96. A. Halkier, B. Kirchner, H. Huber, and M. Jaszunski, *Chem. Phys.*, 2000, **253**, 183.
97. T. Yamazaki, H. Sato, and F. Hirata, *Chem. Phys. Lett.*, 2000, **325**, 668.
98. K. V. Mikkelsen, K. Ruud, and T. Helgaker, *Chem. Phys. Lett.*, 1996, **253**, 443.
99. K. V. Mikkelsen, K. Ruud, and T. Helgaker, *J. Comp. Chem.*, 1999, **20**, 1281.
100. Q. Cui and M. Karplus, *J. Phys. Chem. B*, 2000, **104**, 3721.
101. L. X. Dang and B. M. Pettitt, *J. Phys. Chem.*, 1987, **91**, 3349.
102. V. G. Malkin, O. L. Malkina, G. Steinebrunner, and H. Huber, *Chem. Eur. J.*, 1996, **2**, 452.
103. W. Kutzelnigg, U. Fleischer, and M. Schindler, in 'Deuterium and Shift Calculation', ed P. Diehl, E. Fluck, H. Günther, R. Kosfeld, and J. Seelig, Heidelberg, 1990.
104. P. Bopp, G. Jancsó, and K. Heinzinger, *Chem. Phys. Lett.*, 1983, **98**, 129.
105. B. G. Pfrommer, F. Mauri, and S. G. Louie, *J. Am. Chem. Soc.*, 2000, **122**, 123.
106. J. A. Glasel, *Proc. Natl. Acad. Sci. USA*, 1967, **58**, 27.
107. B. B. Garrett, A. B. Denison, and S. W. Rabideau, *J. Phys. Chem.*, 1967, **71**, 2606.
108. J. C. Hindman, A. Svirmickas, and M. Wood, *J. Phys. Chem.*, 1970, **74**, 1266.
109. J. C. Hindman, A. J. Zielen, A. Svirmickas, and M. Wood, *J. Chem. Phys.*, 1971, **54**, 621.
110. J. R. C. van der Maarel, D. Lankhorst, J. de Bleijser, and J. C. Leyte, *Chem. Phys. Lett.*, 1985, **122**, 541.
111. R. P. W. J. Struis, J. de Bleijser, and J. C. Leyte, *J. Phys. Chem.*, 1987, **91**, 1639.

Acknowledgements

This work is part of the project 2000-058881.99 of the Schweizerischer Nationalfonds zur Förderung der Wissenschaften. We thank the Australian Research Council for support of this work. We thank B. Kirchner and E. Hardy for reading the manuscript. We also thank those whose important contributions to the field we missed, but who are not angry with us! Our apologies – we are not perfect.

Biographical Sketches

Hanspeter Huber, *b* 1944. Diplom, 1968, ETH Zurich, Doktor, 1972, University of Basel. Postdoctoral studies with J. D. Roberts, Pasadena, (NMR) and R. Zahradnik, Prague, (quantum chemistry). Currently University Professor of Chemistry. Approx. 100 papers. Research interest: Combination of quantum chemistry and simulations to obtain bulk properties of liquids and solvent effects (mainly of NMR related properties).

Debra J. Searles, *b* 1965. BSc Hons, 1987 and PhD, 1991, University of Newcastle, Australia (quantum chemistry). Postdoctoral studies with Hanspeter Huber (bulk properties of liquids using computational chemistry) and Denis J. Evans, ANU, Australia (theoretical and computational studies of nonequilibrium liquids). Currently Chemistry Lecturer, Griffith University, Australia. Approx. 50 papers. Research interests: properties of equilibrium and nonequilibrium fluids from molecular dynamics simulations and statistical mechanics.

Anisotropy of Shielding and Coupling in Liquid Crystalline Solutions

Jukka Jokisaari

Department of Physics, University of Oulu, FIN-90570 Oulu, Finland

1	Introduction	1
2	Liquid Crystals	1
3	The Hamiltonian Operator and Observables	2
4	Shielding Anisotropy	2
5	Spin–Spin Coupling Anisotropy	7
6	Related Articles	9

1 INTRODUCTION

In the beginning of the 1960s, NMR spectroscopists started to look for means to orient molecules with a particular goal in mind, i.e. to find a situation where the intermolecular direct dipolar couplings would average out whereas the corresponding intramolecular couplings would average to a nonzero value. Various methods were tried until, in 1963, Saupe and Englert[1] proposed that the sought-after properties can be reached by using liquid crystals as solvents.

The anisotropic orientational distribution of solute molecules in liquid crystals makes it possible to use the NMR observables (anisotropic couplings including both the direct dipole–dipole couplings and a contribution from the anisotropy of the indirect spin–spin coupling tensor, chemical shifts, and nuclear quadrupole splittings) for the determination of molecular structures, the anisotropies of nuclear shielding and spin–spin couplings, and quadrupole couplings for nuclei with spin ≥ 1. In principle, the method is quite straightforward but in practice some complications may appear. In particular, the determination of molecular structures necessitates the introduction of the vibrational[2] and deformational[3–5] corrections (see ***Structure of Rigid Molecules Dissolved in Liquid Crystalline Solvents***). Since the anisotropic contribution of the spin–spin coupling tensor can only be separated from the experimental coupling when the direct dipole–dipole coupling is known, the corresponding effects have also to be considered here. To obtain reliable shielding anisotropies for protons and for nuclei with small anisotropy in general, various disturbing effects on the experimentally determined chemical shifts, such as local anisotropy due to solvent molecules, have to be taken into account.

A comprehensive review on the anisotropies of shielding and spin–spin coupling tensors determined using liquid crystalline solvents appeared in 1982.[6] Since then, however, remarkable progress has taken place. This concerns spin–spin coupling anisotropy, in particular, where the inclusion of the deformational corrections leads to unambiguous, solvent independent results.

The NMR spectra observable from the spin-$\frac{1}{2}$ nuclei in molecules dissolved in liquid crystals resemble those in isotropic liquids; relatively sharp, well resolved lines can be detected. Hence, analyses of spectra taken in the two phases are, in principle, similar (see ***Liquid Crystalline Samples: Spectral Analysis***, and ***Analysis of High-Resolution Solution State Spectra***). There are, however, also a few basic differences. Firstly, the anisotropic couplings between magnetically and chemically equivalent nuclei affect the structure of the spectrum. Thus, for example, the ^{1}H NMR spectrum of three methyl protons is a triplet and the six benzene protons give a spectrum very rich in resonance lines. Secondly, the dipole–dipole coupling constants are often large, of the order of kHz, and consequently the first-order approximation can usually be carried out only when the coupled nuclei are of different species.

2 LIQUID CRYSTALS

The liquid crystals most applicable in NMR spectroscopy are the thermotropic ones which have mesophases within certain temperature ranges.[7] In a few cases, lyotropic liquid crystals have also been used. They are formed by mixing, for example, alkyl sulfates and the corresponding alcohols, sodium sulfate, and water.[8]

Thermotropic liquid crystals which are mainly used as solvents in NMR spectroscopy, can be classified into two main categories; nematic (N) and smectic (S). In the nematic phases, the molecules have only a short range positional order. However, if the liquid crystals consist of elongated molecules, as those used in the applications described in this context usually do, they tend to align with their long axes parallel to a common axis which defines the director (often called also the optic axis), $\boldsymbol{n}$, of the liquid crystal. The nematic phases are almost in all known cases uniaxial (rotational symmetry exists around the director) and apolar (the directions $\boldsymbol{n}$ and $-\boldsymbol{n}$ are equivalent). In the smectic phases the liquid crystal molecules possess long range order. A specific feature of smectic phases is the appearance of one-dimensional density waves or, as often called, layered structures. Smectic phases are divided into subgroups of which the smectic A phase (S_A) is the one used in the present applications. In this phase, the director coincides with the normal of the layer, and $\boldsymbol{n}$ and $-\boldsymbol{n}$ are equivalent. The structures of the nematic and smectic A phases are shown in Figure 1.

When a liquid crystalline sample is placed in an external magnetic field $\boldsymbol{B}$, the sample is magnetized so that the magnetization $\boldsymbol{M}$ is given by

$$M_\alpha = \mu_0^{-1} \chi_{\alpha\beta} B_\beta \tag{1}$$

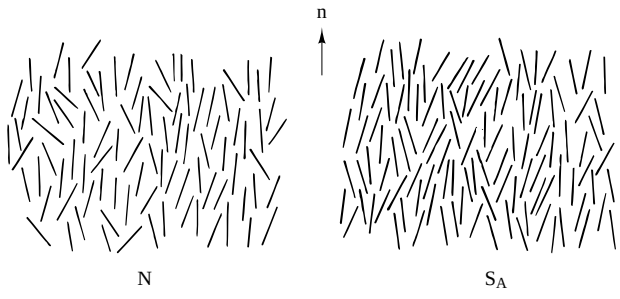

Figure 1 Structures of thermotropic nematic (N) and smectic A (S_A) liquid crystalline phases. The direction of the director is shown by **n**

where μ_0 is the permeability in vacuo and the $\chi_{\alpha\beta'}$s are elements of the diamagnetic (volume) susceptibility tensor, χ_{m}, which is diagonal in uniaxial phases.

The energy density, ρ_{B}, due to the magnetization $\boldsymbol{M}$ is:

$$\rho_B = -\int_0^B M \cdot \mathrm{d}B = -\frac{B^2}{2\mu_0}\left[\chi_{\mathrm{m}} + \frac{2}{3}\Delta\chi_{\mathrm{m}} P_2(\cos\theta)\right] \tag{2}$$

where $\chi_{\mathrm{m}} = \frac{1}{3}\,\mathrm{Tr}\chi_{\mathrm{m}}$ is the isotropic susceptibility, $\Delta\chi_{\mathrm{m}}$ is the anisotropy of the susceptibility tensor, and $P_2(\cos\theta) = \frac{1}{2}(3\cos^2\theta - 1)$ is the second Legendre polynomial (θ being the angle between $\boldsymbol{B}$ and $\boldsymbol{n}$). Considering the condition of minimum energy density, one can conclude the following:

1. When $\Delta\chi_{\mathrm{m}}$ is positive, ρ_{B} reaches a minimum with $P_2(\cos\theta) = 1$, i.e. the director is oriented parallel with the external magnetic field.
2. When $\Delta\chi_{\mathrm{m}}$ is negative, ρ_{B} reaches a minimum with $P_2(\cos\theta) = -\frac{1}{2}$, i.e. when the director is oriented perpendicular to the external field.

Both types of thermotropic liquid crystals exist and have been used in studies of the properties of solute molecules. Furthermore, proper mixtures of liquid crystals with opposite signs of diamagnetic anisotropies have been utilized. (See ***Liquid Crystals: Mixed Magnetic Susceptibility Solvents***.)

3 THE HAMILTONIAN OPERATOR AND OBSERVABLES

When considering the NMR spectra of spin-$\frac{1}{2}$ nuclei in molecules partially oriented in liquid crystals, the transition frequencies are dependent upon the nuclear shielding tensor, σ_i, the indirect spin–spin coupling tensor, $\boldsymbol{J}_{ij}$, and the direct dipole–dipole coupling tensor, $\boldsymbol{D}_{ij}$ (see ***Liquid Crystals: General Considerations***). Then the total Hamiltonian operator is (in energy units):

$$\hat{\mathcal{H}} = -\hbar\sum_i \gamma_i \hat{\boldsymbol{I}}_i \cdot (\boldsymbol{1} - \boldsymbol{\sigma}_i)\cdot B + h\sum_{i<j} \hat{\boldsymbol{I}}_i \cdot (\boldsymbol{J}_{ij} + \boldsymbol{D}_{ij})\cdot \hat{\boldsymbol{I}}_j \tag{3}$$

where $\hbar$ is Planck's constant divided by 2π, γ_{i} is the magnetogyric ratio of nucleus i, and $\boldsymbol{1}$ is the unit tensor. On the basis of perturbation theory one can conclude that the terms of the Hamiltonian operator which do not commute with the total spin component, $\hat{I}_z$,in the direction of $\boldsymbol{B}$ (defined as the z direction of the laboratory frame) can be safely neglected. Furthermore, taking the time average of the observables over the anisotropic molecular tumbling, the operator shown in equation (3) can be approximated by:

$$\begin{aligned}\hat{\mathcal{H}} = &-\hbar\sum_i \gamma_i(1-\sigma_i)B\hat{I}_{iz} \\ &+ h\sum_{i<j} J_{ij}\left[\hat{I}_{iz}\hat{I}_{jz} + \frac{1}{2}(\hat{I}_{i+}\hat{I}_{j-} + \hat{I}_{i-}\hat{I}_{j+})\right] \\ &+ h\sum_{i<j}(2D_{ij} + J_{ij}^{\mathrm{aniso}})\left[\hat{I}_{iz}\hat{I}_{jz} - \frac{1}{4}(\hat{I}_{i+}\hat{I}_{j-} + \hat{I}_{i-}\hat{I}_{j+})\right]\end{aligned} \tag{4}$$

In the operator shown in equation (4), the shielding is represented as

$$\begin{aligned}\sigma_i = \langle\sigma_{izz}\rangle &= \frac{1}{3}\sum_\alpha \sigma_{i\alpha\alpha} + \frac{2}{3}\left(\sum_{\alpha,\beta} S_{\alpha\beta}\sigma_{i\alpha\beta}\right)P_2(\cos\theta) \\ &= \sigma_i^{\mathrm{iso}} + \sigma_i^{\mathrm{aniso}}\end{aligned} \tag{5}$$

The isotropic spin–spin coupling constant, J_{ij}, and the anisotropic contribution, $J_{\mathrm{ij}}^{\mathrm{aniso}}$, are

$$J_{ij} = \frac{1}{3}\sum_\alpha J_{ij\alpha\alpha} \tag{6}$$

and

$$J_{ij}^{\mathrm{aniso}} = \left(\frac{2}{3}\sum_{\alpha,\beta} S_{\alpha\beta}J_{ij\alpha\beta}\right)P_2(\cos\theta) \tag{7}$$

In equations (5)–(7), $\sigma_{\mathrm{i}\alpha\beta}$ and $J_{\mathrm{ij}\alpha\beta}$ are the elements of the shielding and spin–spin coupling tensor, respectively, in the molecule fixed coordinate system while the $S_{\alpha\beta}$ terms in turn, are the elements of the Saupe ordering tensor[9] which are defined as

$$S_{\alpha\beta} = \frac{1}{2}\langle 3\cos\theta_{\alpha n}\cos\theta_{\beta n} - \delta_{\alpha\beta}\rangle \tag{8}$$

where $\theta_{\alpha n}$ is the angle between the director $\boldsymbol{n}$ and the α axis of the coordinate system, the $\langle\ \rangle$ brackets indicate a time average, and $\delta_{\alpha\beta}$ is the Kronecker delta. The dipole–dipole coupling constant, D_{ij}, appearing in the operator shown in equation (4) is defined (when the correlation of the molecular reorientational and vibrational motions is neglected) as

$$D_{ij} = -\frac{\mu_0\hbar\gamma_i\gamma_j}{8\pi^2 r_{ij}^3}S_{ij} \tag{9}$$

where r_{ij} is the internuclear distance, and

$$S_{ij} = \frac{1}{2}\langle 3\cos^2\theta_{ijB} - 1\rangle \tag{10}$$

is called the order parameter (with respect to the external magnetic field) of the axis passing through i and j, and θ_{ijB} is the angle between the ij direction and the magnetic field. Since the order tensor is traceless and symmetric, it consists of five independent elements which are usually chosen as S_{cc}, $(S_{\mathrm{aa}} - S_{\mathrm{bb}})$, S_{ab}, S_{ac}, and S_{bc} (a, b and c are the axes of the molecule fixed coordinate system). Utilizing the coordinate transformation equation

$$S_{ij} = \sum_{\alpha,\beta}\cos\theta_{ij\alpha}\cos\theta_{ij\beta}\ S_{\alpha\beta} \tag{11}$$

S_{ij} can be written as:

$$\begin{aligned}S_{ij} = \Big[&\frac{1}{2}S_{cc}(3\cos^2\theta_{ijc} - 1) + \frac{1}{2}(S_{aa} - S_{bb})(\cos^2\theta_{ija} - \cos^2\theta_{ijb}) \\ &+ 2S_{ab}\cos^2\theta_{ija}\cos^2\theta_{ijb} + 2S_{ac}\cos^2\theta_{ija}\cos^2\theta_{ijc} \\ &+ 2S_{bc}\cos^2\theta_{ijb}\cos^2\theta_{ijc}\Big]P_2(\cos\theta)\end{aligned} \tag{12}$$

The number of the independent elements of the order tensor can be reduced by taking into account molecular symmetry. The values of the order tensor elements are obtained from the dipole–dipole coupling constants provided that at least one internuclear distance is known.

4 SHIELDING ANISOTROPY

For a moment let us forget the complications that may occur particularly when determining small anisotropies of nuclear shieldings, and concentrate on the principles of how the shielding anisotropy is obtained from an NMR spectrum of a molecule partially oriented in a liquid crystal. Let us choose as an example a molecule possessing at least a

threefold symmetry axis, e.g. acetonitrile (CH_3CN). In such a case, the molecular orientation is completely determined by one order tensor element. Thus the experimental chemical shift, δ^{exp}, can be expressed in the form (note that δ increases to high frequency whereas σ increases to low frequency; for simplifying notations the subscript i will be omitted):

$$\begin{aligned}\delta^{exp} &= \delta^{iso} - \frac{2}{3}\left[\sigma_{zz} - \frac{1}{2}(\sigma_{xx} + \sigma_{yy})\right] SP_2(\cos\theta) \\ &\equiv \delta^{iso} - \frac{2}{3}\Delta\sigma SP_2(\cos\theta)\end{aligned} \tag{13}$$

where $\sigma_{zz} - \frac{1}{2}(\sigma_{xx} + \sigma_{yy}) \equiv \Delta\sigma$ is the anisotropy of the shielding tensor [(x, y, z) is a molecule fixed coordinate system] and S is the order parameter of the molecular symmetry axis (which in the case of acetonitrile lies along the $-C-C\equiv N$ direction). Equation (13) contains two unknown parameters δ^{iso} and $\Delta\sigma$; the order parameter S is obtained from the experimental dipole–dipole couplings [defined in equation (9)] which do not contain an anisotropic contribution, J_{ij}^{aniso}, and are corrected for harmonic vibrations and preferably also for deformational contributions. Usually couplings of the type D_{HX} with ^1H as a coupling partner (D_{HH} in CH_3CN) are a safe choice.

The shielding anisotropy can be determined by changing either S or $P_2(\cos\theta)$. There exist several possibilities for both. They are described below.

4.1 Use of Isotropic–Nematic Phase Transitions

In this method, $\delta^{iso} = \delta^{exp}$(isotropic) is determined in the liquid crystal heated to the isotropic state (when $S \equiv 0$) and assumed not to be affected by the change of phase. Then the sample is cooled to the nematic state and δ^{exp}(nem.) is measured. Consequently,

$$\Delta\sigma = -\frac{3}{2}\left[\frac{\delta^{exp}(\text{nem.}) - \delta^{exp}(\text{isotropic})}{SP_2(\cos\theta)}\right] \tag{14}$$

4.2 Gradient Method

One disadvantage of the previous method is that the experiments have to be carried out at two different phases, isotropic and nematic. This can be avoided by working exclusively in a nematic or smectic phase and changing the molecular degree of order, i.e. the order parameter S. This is achieved by changing the temperature or concentration of the sample. When δ^{exp} is expressed graphically as a function of $SP_2(\cos\theta)$, the slope of the resulting straight line gives $\Delta\sigma$ and the intercept δ^{iso}.

4.3 Use of Smectic Phases

The smectic A phases of thermotropic liquid crystals often possess the property that once oriented in a magnetic field they keep the orientation for a long time. This makes it possible to change in a very straightforward way the angle between the director $\boldsymbol{n}$ and the magnetic field $\boldsymbol{B}$, i.e. the factor $P_2(\cos\theta)$ in equation (13), while S remains unchanged.[10] The shielding anisotropy is then obtained without changing solvent properties.

When the liquid crystal is heated to the isotropic state and then cooled in the magnetic field to the smectic state, the director orients (when $\Delta\chi_m > 0$) along the magnetic field and $\theta = 0$. Thus

$$\delta^{exp}(0) = \delta^{iso} - \frac{2}{3}\Delta\sigma S \tag{15}$$

The rotation of the sample (in a conventional electromagnet) around the tube axis by 90° [generally, the rotation angle is obtained from the ratio of the dipolar couplings: $D_{ij}(\theta)/D_{ij}(0) = P_2(\cos\theta)$] gives:

$$\delta^{exp}(90) = \delta^{iso} + \frac{1}{3}\Delta\sigma\ S \tag{16}$$

and consequently,

$$\Delta\sigma = \frac{\delta^{exp}(90) - \delta^{exp}(0)}{S} \tag{17}$$

In the smectic phases the degree of solute molecular orientation is usually high, when both S and the chemical shift difference [nominator in equation (17)] are large, leading to a good relative precision in $\Delta\sigma$. Figure 2, which shows the ^{199}Hg NMR spectrum of dimethylmercury $(CH_3)_2Hg$ at the orientation described above, illustrates the method.

4.4 Use of Mixtures of Thermotropic Nematic Liquid Crystals

4.4.1 Liquid Crystals with Opposite Diamagnetic Anisotropy

This method, called NEMIX, is comparable with the one described in Section 4.3. When two thermotropic nematic liquid crystals possessing opposite anisotropies of diamagnetic susceptibility, $\Delta\chi_m$, are mixed at a certain critical concentration ratio ($\Delta\chi_m$ of the critical mixture is equal to 0), the 90°

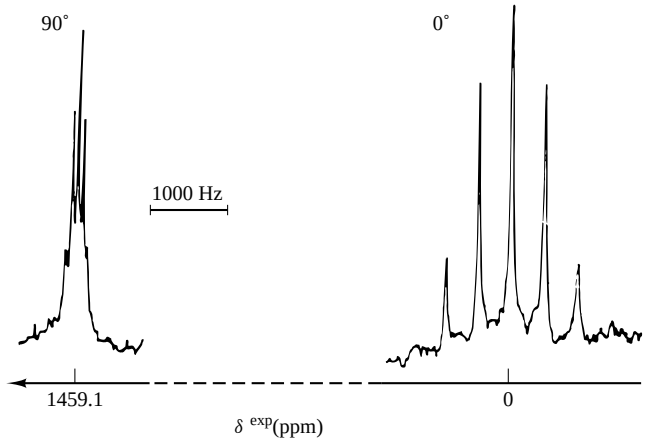

Figure 2 ^{199}Hg NMR spectrum of dimethylmercury [$(CH_3)_2Hg$] in the smectic A phase of HAB: 0°, director parallel with the external magnetic field, 90°, director perpendicular to the external magnetic field. (Reproduced with permission of Heyden & Sons from J. Jokisaari and P. Diehl[26])

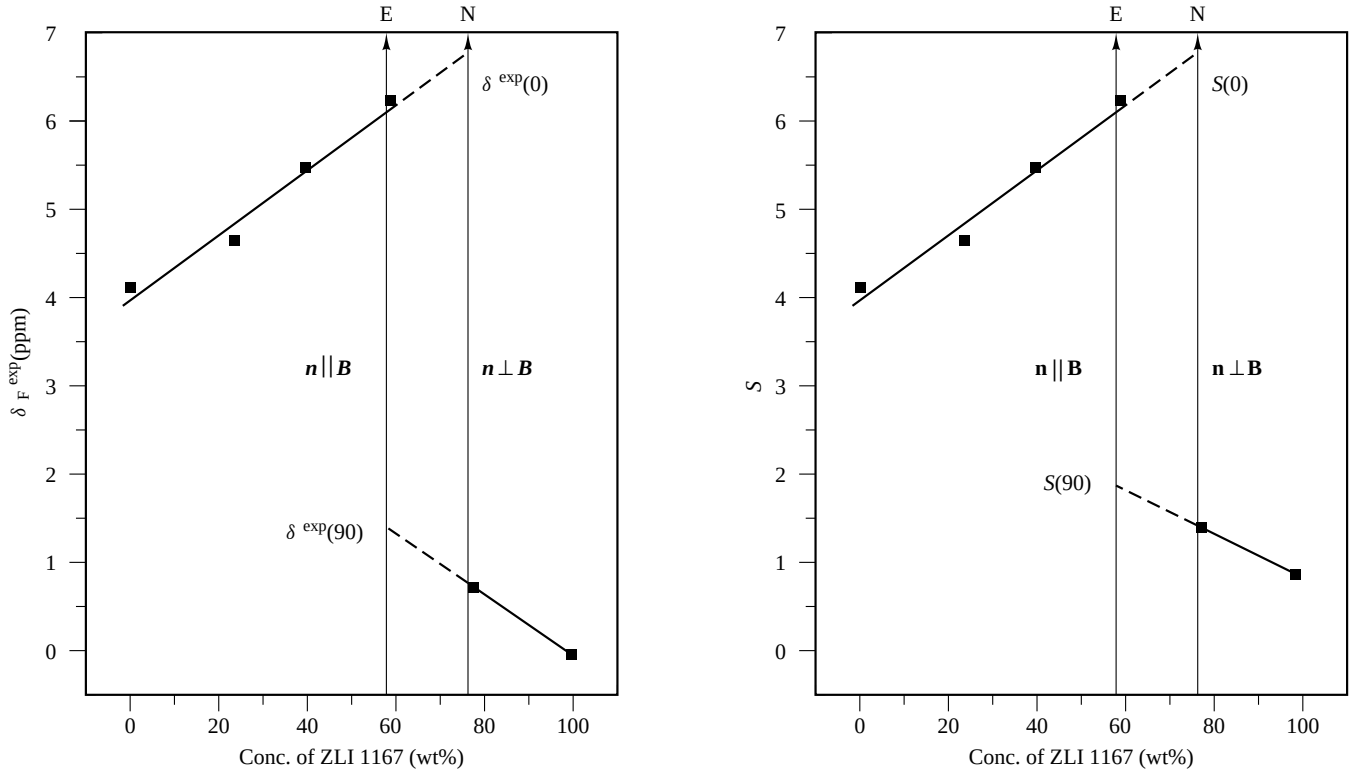

Figure 3 The experimental chemical shift, $\delta_F{}^{exp}$, of the ^{19}F nucleus and the order parameter of the C_3 symmetry axis, S, for methyl fluoride (CH_3F) as a function of the liquid crystal composition in mixtures of ZLI 1167 and EBBA. The mixtures used in the NEMIX and ENEMIX methods are indicated by N and E, respectively

rotation of the liquid crystal director is achieved by changing the sign of $\Delta\chi_m$ with the aid of a slight temperature change or a small temperature gradient over the sample volume (see ***Liquid Crystals: Mixed Magnetic Susceptibility Solvents***). In the latter case, the NMR spectra corresponding to the two director orientations can be detected simultaneously.[11,12] The shielding anisotropy can be calculated from equation (17). Figure 3 shows how the method works.

4.4.2 Liquid Crystals with Opposite Deformational Effects on Molecular Structure

The anisotropic forces that cause the orientation of solute molecules at the same time deform their structure leading to the solvent dependence of structure. It has appeared that ^{13}C-enriched methane ($^{13}CH_4$) is a convenient and practical reference, not only for chemical shifts but also for structural deformations. It has been found that in certain mixtures of thermotropic liquid crystals the methane molecule is not deformed.[13] The components of the mixture may be selected so that they possess opposite diamagnetic anisotropies and, consequently, parallel and perpendicular orientations of the director with respect to the external magnetic field can be produced in a similar way to that discussed above. Figure 3 also demonstrates this method, which is called ENEMIX. In contrast to the NEMIX method and the method based on the utilization of smectic liquid crystals, the ratio of the S parameters corresponding to the two director orientations may not exactly equal -2, whence

$$\Delta\sigma = -\frac{3}{2}\left[\frac{\delta^{exp}(0) - \delta^{exp}(90)}{S(0) - S(90)}\right] \tag{18}$$

4.5 Use of Sample Spinning

4.5.1 Sample Tube Axis Perpendicular to the Magnetic Field

As discussed above, the liquid crystals director orients either along the external magnetic field or perpendicular to it depending upon the sign of the diamagnetic anisotropy. In a conventional electromagnet, the director orients perpendicular to the tube axis (when $\Delta\chi_m > 0$; if $\Delta\chi_m < 0$ the director orients along the tube axis and no change in the orientation can be achieved by spinning the sample tube). When the sample is spinning around the tube axis the liquid crystal experiences a viscous torque

$$N_v = \lambda_1\Omega \tag{19}$$

where Ω is the angular speed and λ_1 a coefficient proportional to the viscosity of the solution. The magnetic torque opposes the viscous torque, and in equilibrium $N_B = N_v$. Thus the angle θ_0 between the magnetic field and the director is determined by

$$\sin 2\theta_0 = -\frac{2\mu_0\lambda_1}{B^2\Delta\chi_m}\Omega \tag{20}$$

The value of $SP_2(\cos\theta_0)$ can be determined from the dipolar coupling constants and the shielding anisotropy calculated as in the previous method. On the other hand, θ_0 can be varied by varying the angular speed Ω. There is, however, an upper limit for Ω, the so-called critical speed, $\Omega_c = -B_2\Delta\chi_m/2\,\mu_0\lambda_1$, above which no equilibrium state can be reached but the director rotates with the tube. When the experimental chemical shift is plotted as a function of $SP_2(\cos\theta_0)$, the shielding

anisotropy is obtained from the slope of the resulting straight line.

4.5.2 *Variable Angle Spinning*

Let us consider a general case where the spinning axis of a sample tube forms an angle β with the magnetic field. Transforming the susceptibility tensor into the principal axis system rotating around the magnetic field direction and taking a time average,[14] the magnetic energy density can be represented in the form

$$\langle \rho_B \rangle = -\frac{B^2}{2\mu_0}\left[\chi_m + \frac{2}{3}\Delta\chi_m P_2(\cos\beta)P_2(\cos\delta)\right] \quad (21)$$

where δ is the angle between the spinning axis and the liquid crystal director. From the condition of minimum energy density, one can conclude the following: (a) when $\Delta\chi_m > 0$ and $0 \leq \beta < \beta_m$ (β_m is the magic angle, 54.7°), the liquid crystal director orients parallel with the spinning axis, i.e. the angle between the director and the magnetic field equals β; (b) when $\Delta\chi_m > 0$ and $\beta_m < \beta \leq \pi/2$, the directors are equally distributed in the plane perpendicular to the spinning axis; (c) when $\Delta\chi_m < 0$ and $0 \leq \beta < \beta_m$, the situation is similar to (b); and (d) when $\Delta\chi_m < 0$ and $\beta_m < \beta \leq \pi/2$, the situation is similar to (a).

The slope of the resulting straight line obtained by plotting the experimental chemical shift as a function of $SP_2(\cos\beta)$, or as a function of a dipolar coupling constant as shown in Figure 4, gives the shielding anisotropy.

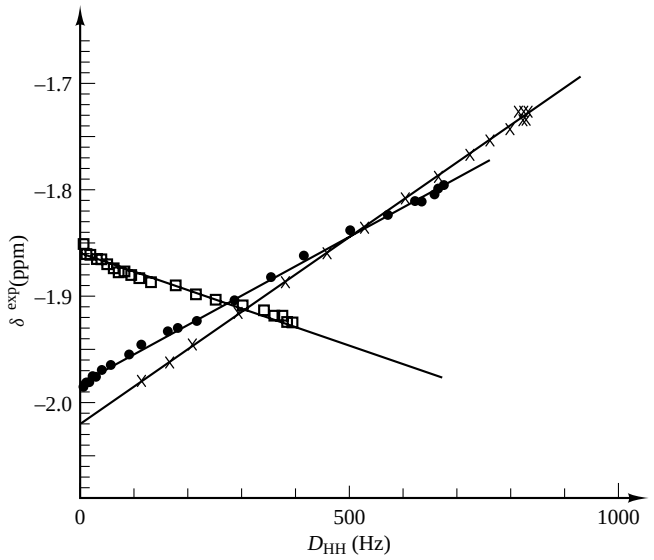

Figure 4 Plot of δ^{exp} for the ^{1}H nucleus (referenced to internal TMS) as a function of D_{HH} for methyl iodide (CH_3I) in three liquid crystals: phase 4 (□); ZLI 1167 (39.1%)/phase 4 (60.9%) (•); and ZLI 1167 (57.6%)/phase 4 (42.4%) (x). The data were produced on a VAS system by varying the angle between the spinning axis and the external magnetic field. The slope, κ, of the straight line yields the proton shielding anisotropy $\delta\sigma_H = (3/4)\,(K_{HH}/r^3_{HH})\kappa$, where $K_{HH} = \mu_0\hbar{\gamma_H}^2/8\pi^2$. (Reproduced with permission of Academic Press from T. Väänänen, J. Jokisaari, and M. Seläntaus[33]). Note: the δ scale is opposite to the one used in the present text

4.6 Examples and Reliability of Results

4.6.1 *Molecules Whose Orientation Can Be Described by One Order Parameter*

Tables (1)-(3) show $\Delta\sigma$ values determined by applying various liquid crystals and methods described above. The examples are chosen so that they cover a wide range of values, and consequently yield the weaknesses on the one hand and the reliability on the other hand of liquid crystal NMR spectroscopy as applied to the determination of shielding anisotropies. Table 1 lists the proton shielding anisotropy values measured for acetonitrile (CH_3CN). As can be seen, they vary over a relatively wide range, and both positive and negative values have been reported. The $\Delta\sigma_H$ value seems to depend upon the method used, liquid crystal solvent, and reference method and substance. This is due to the fact that the measured shielding is affected by three different anisotropic contributions:

$$\sigma^{exp} = \sigma^{mol} + \sigma^{local} + \sigma^{bulk} \quad (22)$$

where σ^{mol} (the quantity of interest) arises from the electron distribution in the molecule, σ^{local} (the local effect) from the nearest neighbor molecules, and σ^{bulk} (the bulk effect) from the other parts of the sample. The greatest problem is caused by the local effects; obviously the solute and reference molecules do not probe exactly the same local fields, leading to an erroneous $\Delta\sigma$. Local effects in a smectic liquid crystal, and in mixtures of thermotropic nematic liquid crystals with opposite diamagnetic anisotropies, have been studied by using globular solutes (which do not orient in liquid crystals, i.e. $S - 0$) and found to be from -0.2 to -0.5 ppm for protons.[15–17] These experiments and the earlier ones[18,19] mean that the anisotropic contribution of the local effects may be of the same magnitude as σ^{aniso} for protons, but also for other nuclei if their shielding anisotropy is not very large.

The first column of Table 2 shows that the shielding anisotropy of the methyl carbon, $\Delta\sigma CH_3$ in acetonitrile, being of the order of 20 ppm, also depends markedly on the applied experimental method and liquid crystal solvent. On the contrary, the shielding anisotropies measured for the $-C{\equiv}N$ carbon, $\Delta\sigma_{CN}$, in acetonitrile as well as those for the ^{199}Hg nucleus in dimethylmercury [$(CH_3)Hg$] (see Table 3) are virtually insensitive to all these factors. The small scatter arises from the internuclear distance chosen as a basis in calculating the order parameter S and from whether vibrational corrections are taken into account or not.

The experiments carried out until now and comparisons made with the values produced by other techniques or theoretical calculations provide strong support for the modified ENEMIX method giving the most reliable estimates for small $\Delta\sigma$s.[21]

4.6.2 *Molecules Whose Orientation Can Be Described by Two Order Parameters*

In cases where molecules possess two perpendicular planes of symmetry as, for example, monosubstituted benzenes and heteroatomic five-membered rings, the experimental chemical shift can be represented in the form:

$$\delta^{exp} = \delta^{iso} - \frac{2}{3}\left\{S_{zz}\left[\sigma_{zz} - \frac{1}{2}(\sigma_{xx} + \sigma_{yy})\right] + \frac{1}{2}(S_{xx} - S_{yy})(\sigma_{xx} - \sigma_{yy})\right\} P_2(\cos\theta) \quad (23)$$

Table 1 Proton Shielding Anisotropy of Acetonitrile Determined by Various Methods in Different Liquid Crystals

$\Delta\sigma_H$ (ppm)	Method	Liquid crystal	Chemical shift reference[a]
+3.9 ± 0.2	Gradient method[20]	ZLI 1167	$^{13}CH_4$
+2.3 ± 0.1	Gradient method[20]	ZLI 1167	TMS
+2.1	Modified ENEMIX[21]	ZLI 1167/Phase 4	$^{13}CH_4$
+0.30 ± 0.08 to +1.06 ± 0.8	NEMIX[20]	Various LCs mixed with ZLI 1167	TMS
−2.7 ± 0.1	Smectic phase[20]	HAB	$^{13}CH_4$
−4.5 ± 0.8	Gradient method[20]	EBBA	$^{13}CH_4$
−4.7 ± 0.1	Smectic phase[20]	HAB	TMS

[a]Internal reference.

Table 2 ^{13}C Shielding Anisotropies in Acetonitrile Determined by Various Methods in Different Liquid Crystals. For Comparison, Theoretical Values are Also Included

$\Delta\sigma CH_3$ (ppm)	$\Delta\sigma_{CN}$ (ppm)	Method	Liquid crystal	Chemical shift reference[a]
22.9	324.6	Modified ENEMIX[21]	ZLI 1167/phase 4	$^{13}CH_4$
20.5 ± 0.7	328 ± 8	Gradient[20]	ZLI 1167	$^{13}CH_4$
15.7 ± 1.5		Smectic phase[20]	HAB	$^{13}CH_4$
13.6 ± 0.6	311 ± 6	Gradient[20]	EBBA	$^{13}CH_4$
	304 ± 5	Gradient[22]	MIX	ext. $^{13}CS_2$
	307 ± 4	I–N phase transition[23]	EBBA	^{1}H reson. of CH_3CN
	299 ± 5	I–N phase transition[22]	MIX	ext. $^{13}CS_2$
21, 15	340, 348	Theory[24b]		

[a]Internal reference if not otherwise indicated.
[b]IGLO method with two different basis sets. Large basis set results on the right.

The shielding anisotropy, $\Delta\sigma = \sigma_{zz} - \frac{1}{2}(\sigma_{xx} + \sigma_{yy})$, and the difference $(\sigma_{xx} - \sigma_{yy})$ are obtained separately only if the ratio $(S_{xx} - S_{yy})/S_{zz}$ can be varied. Consequently, none of the methods described above which are based on the change of direction of the liquid crystal director with respect to the external magnetic field, i.e. the variation of the $P_2(\cos\theta)$ factor, is applicable here. The variation of the ratio $(S_{xx} - S_{yy})/S_{zz}$ may be produced by changing the sample temperature or by using different liquid crystal solvents. Then one has to assume that the shielding tensor elements are not affected by the experimental conditions.

The determination of the ^{13}C shielding anisotropies in molecules which are large in the liquid crystal NMR scale (when the number of magnetic nuclei increases, the NMR spectrum of an oriented molecule becomes very complex; in practice the upper limit for the number of active, interacting nuclei is 10–12), and contain several carbon atoms and ^{13}C in natural abundance, is usually at least very cumbersome if not impossible from the proton coupled spectra. Therefore, a method has been proposed which uses a spin echo sequence $[90^\circ - \tau - 180^\circ - 2\tau - 180^\circ - \tau - \text{acquisition}]$ and phase-alternated broadband decoupling.[30] The echo sequence cancels the possible overlap of the solute signals by the solvent signals.

Table 3 ^{199}Hg Shielding Anisotropy in Dimethylmercury Determined by Various Methods in Different Liquid Crystals. For Comparison, Results obtained from Spin–Lattice Relaxation Time Measurements are also Included

$\Delta\sigma^{199}Hg$ (ppm)	Method	Liquid crystal	Comments
7475 ± 80	Gradient[25]	EBBA	No vibr. corr.
7799 ± 55	Smectic phase[26]	HAB	No vibr. corr.
7325 ± 55	Smectic phase[26]	HAB	D_{ij}s corrected for harm. vibr.
7260 ± 90	ENEMIX[27]	ZLI 1167	D_{ij}s corrected for harm. vibr.
4600 ± 1000	T_1[28]		Saturation-recovery method
5820 ± 10%	T_1[28]		Inversion–recovery method

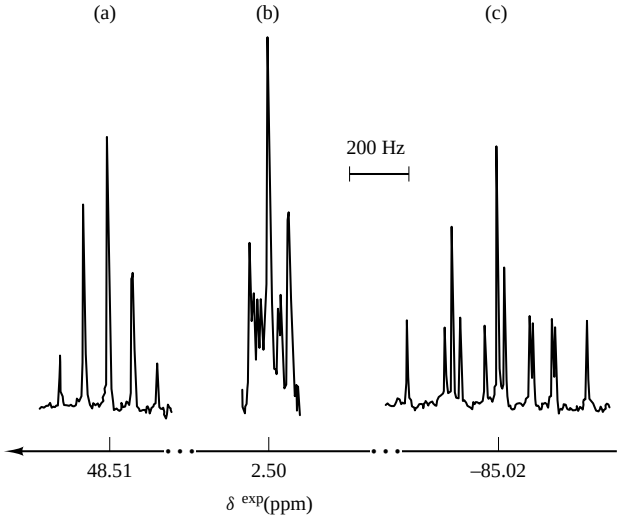

Figure 5 The ^{125}Te NMR spectrum of tellurophene (C_4H_4Te) in (a) ZLI 1167 (58%)/phase 4(42%), (b) EBBA and (c) ZLI 1167. (Reproduced with permission of Taylor & Francis from J. Jokisaari and T. Väänänen[31])

The ^{13}C NMR spectrum yields the chemical shifts whereas the order parameters appearing in equation (23) are obtained from the ^{1}H spectrum.

The NMR spectroscopy of solute molecules in liquid crystals has not been applied very much to the investigations of shielding anisotropies of the so-called heavy nuclei. Most of the studies deal with the ^{1}H, ^{13}C, ^{19}F, and ^{31}P nuclei, and highly symmetrical molecules.[6] This is somewhat surprising because the method is best when the shielding anisotropy is fairly large. There has been, however, some work carried out for ^{111}Cd, ^{113}Cd, and ^{199}Hg in molecules with C_3 symmetry, and one work for the ^{125}Te nucleus in a C_{2v} symmetric molecule, tellurophene (C_4H_4Te).[31] The ^{125}Te NMR spectra of tellurophene in three liquid crystals are shown in Figure 5.

Equation (23) can be rewritten in the form

$$-\frac{3}{2}\left[\frac{\delta^{\text{exp}}-\delta^{\text{iso}}}{S_{zz}}\right]=\left[\sigma_{zz}-\frac{1}{2}(\sigma_{xx}+\sigma_{yy})\right]+\frac{\sigma_{xx}-\sigma_{yy}}{2}\,\frac{S_{xx}-S_{yy}}{S_{zz}} \quad (24)$$

The intercept of the straight line obtained by plotting the left hand side of equation (24) as a function of $(S_{xx} - S_{yy})/S_{zz}$ yields $[\sigma_{zz} - \frac{1}{2}(\sigma_{xx} + \sigma_{yy})]$ whereas the slope gives $(\sigma_{xx} - \sigma_{yy})$. The results derived for ^{125}Te in tellurophene are collected in Table 4.

5 SPIN–SPIN COUPLING ANISOTROPY

The determination of reliable anisotropies, ΔJ_{ij}, of the spin–spin coupling tensors using NMR spectroscopy of molecules dissolved in liquid crystals may be a fairly difficult task. This is due to the fact that the experimental couplings, D_{ij}^{exp}, are dominated by the direct dipole–dipole coupling tensor elements, and moreover, in real molecules the dipole–dipole as well as spin–spin coupling tensors are averages over intramolecular motions. However, when performing proper analyses of data (sets of D_{ij}^{exp} values) preferably (often necessarily) produced in many liquid crystal solvents, most reliable and accurate ΔJ_{ij} values can be determined.

5.1 Quantitative Determination of *J* Anisotropy

The experimentally available couplings D_{ij}^{exp} can be expressed as a sum of several contributions (***Structure of Rigid Molecules Dissolved in Liquid Crystalline Solvents***):

$$D_{ij}^{\text{exp}}=D_{ij}^{\text{e}}+D_{ij}^{\text{ah}}+D_{ij}^{\text{h}}+D_{ij}^{\text{d}}+\frac{1}{2}J_{ij}^{\text{aniso}} \quad (25)$$

In equation (25), the first four terms on the right-hand side constitute the direct dipolar part of the coupling: D_{ij}^{c} is the dipole–dipole coupling corresponding to the equilibrium structure of the molecule; D_{ij}^{aff} is the contribution from the anharmonicity of the vibrational potential (the sum of these terms $D_{ij}^{\text{e}} + D_{ij}^{\text{ah}} = D_{ij}^{\alpha}$ is the dipole–dipole coupling corresponding to the so-called r_α structure of the molecule; the anharmonic force constants are often not available and thus only the r_α structure can be determined); D_{ij}^{h} is the contribution from the harmonic vibrations; and D_{ij}^{d} (the so-called deformational contribution which is responsible for the solvent dependence of structure) from the correlation between

Table 4 The Results of the ^{125}Te NMR Study of Tellurophene Dissolved in three Liquid Crystals.[31] The Signs of δ^{exp} and δ^{iso} are Opposite to those in the Original Paper due to the Different Definition of the δ scale

Liquid crystal	δ^{exp} (ppm)	δ^{iso} (ppm)[a]	$S_{xx} - S_{yy}/S_{zz}$	S_{zz}[b]
EBBA	2.41	1.55	0.5033	0.1563
ZLI 1167/phase 4	48.51	−2.18	1.7478	0.1954
ZLI 1167	−85.02	15.65	1.9992	−0.0592

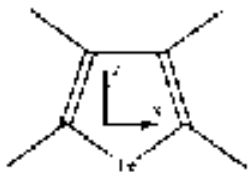

$\Delta\sigma = \sigma_{zz} - \frac{1}{2}(\sigma_{xx} + \sigma_{yy}) = 1560 \pm 21$ ppm

$\sigma_{xx} - \sigma_{yy} = 307 \pm 36$ ppm

[a] Assumed to be a simple hexagonal benzenic state.
[b] Determined from the ^{13}C–^{125}Te dipolar coupling constants assuming the corresponding J^{aniso} to be negligible.
[c] With respect to the external magnetic field.

vibrational and reorientational motions (time averages of S_{ij} and r_{ij}^{-3} appearing in the definition of the dipole–dipole coupling, equation (9), cannot be taken independently).

In order to get a reliable value for J_{ij}^{aniso} (which is normally small and in many cases comparable in magnitude with the vibrational and deformational correction terms), the molecular structure should be determined as completely as possible with the aid of the D_{ij}^{exp} values. This necessarily means a full analysis of data taking into account the interactions (the anisotropic forces that tend to orient molecules) between the solute and solvent molecules. In such an analysis the number of unknown parameters often exceeds the number of D_{ij}^{exp} values obtainable from one experiment, i.e. the problem becomes underdetermined. This increasing number of parameters is a consequence of the deformational effects. For example, in order to be able to calculate deformational corrections to J^{aniso}, one should know the derivatives of the spin–spin coupling tensor with respect to the vibrational normal coordinates. These are not available, and consequently must be used as adjustable parameters.[32] The problem of underdetermination can, however, be overcome by carrying out experiments in several liquid crystalline solvents.

Another uncertainty in the determination of J_{ij}^{aniso} may appear in cases of spin systems consisting of different nuclear species, for instance I and S spins. Thus, the NMR spectrum yields only the sum $|2D_{is}^{exp} + J_{is}|$. If the spin–spin coupling constant, J_{IS}, cannot be determined under the same experimental conditions (the same solvent, temperature, concentration, etc.) as the sum, an additional uncertainty is introduced into D_{IS}^{exp}, and consequently, also into J_{IS}^{aniso}. In principle, J_{IS} can be determined in liquid crystalline phases by performing, for instance, VAS (Variable Angle Spinning) experiments.[33]

Let us consider the determination of the anisotropy of the $^{13}C-^{19}F$ spin–spin coupling in the methyl fluoride (CH_3F) molecule. Due to the C_3 symmetry of the molecule, its orientation can be described by one order parameter, S, of the symmetry axis. Then the anisotropic contribution to the experimental coupling $D_{CF}{}^{exp}$ can be expressed in the form:

$$J_{CF}^{aniso} = \frac{2}{3}\Delta J_{CF} S P_2(\cos\theta) \tag{26}$$

where $\Delta J_{CF} = J_{CFzz} - \frac{1}{2}(J_{CFxx} + J_{CFyy})$ is the anisotropy of the coupling tensor $\boldsymbol{J}_{CF}$. When the experimental dipolar couplings are corrected for harmonic vibrations but the deformational corrections are neglected, ΔJ_{CF} appears to be solvent dependent to a very great extent, as shown in Table 5. This large scatter of results is removed when all the dipolar couplings and J_{CF}^{aniso} are corrected for deformational effects and a joint analysis of nine experiments (44 couplings, D_{CF}^{exp} in one liquid crystal could not be obtained, and 23 parameters) is carried out. This analysis results in $\Delta J_{CF} = 404 \pm 31$ Hz. The relative anisotropy, $\Delta J_{CF}/J_{CF}$, is -2.50 ± 0.20 (J_{CF} appears to be slightly dependent upon the liquid crystal solvent, its average value is -161.43 Hz) and should be compared with -2.70 obtained by Hartree–Fock theory (ab initio) and by a semiempirical finite perturbation method at the INDO MO level of approximation.[34] The first-order polarization propagator approach has led to the ΔJ_{CF} value of 296.41 Hz.[35] Consequently, the experimental results of a joint analysis and the theoretical results are in fair agreement.

Reinforcement for the workability of the method is provided by the studies on acetonitrile (CH_3CN) and methyl isocyanide (CH_3NC). Table 6 clearly shows that when the harmonic vibrational and deformational effects are taken into account in the experimental dipolar couplings, the ΔJ values are in nice accord with the theoretical ones.

Table 5 The Anisotropy ΔJ_{CF} of the $^{13}C-^{19}F$ Spin–Spin Coupling Tensor for Methyl Fluoride ($^{13}CH_3F$) in Various Liquid Crystals. The Dipolar Couplings are Corrected for Harmonic Vibrations but not for Deformational Effects. The Result of the Joint Analysis (which takes into account also the Deformational Effects) of Nine Sets of D_{ij}^{exp} Values (44 Couplings and 23 Parameters) is also given for Comparison[32]

ΔJ_{CF} (Hz)	Liquid crystal solvent[a]
690 ± 60	ZLI 1167
646 ± 46	ZLI 1167 (78.4)/EBBA (21.6)
390 ± 82	ZLI 1167 (58.7)/EBBA (41.3)
49 ± 49	ZLI 1167 (40.1)/EBBA (59.9)
-653 ± 103	ZLI 1167 (23.6)/EBBA (76.4)
-4955 ± 260	EBBA
-1365 ± 72	Phase 4
546 ± 14	Phase 1221
404 ± 31[b]	
296[c]	

[a]The figures in parentheses show the concentration (in wt.%) of the component in the mixture.
[b]Results of the joint analysis. For details, see text.
[c]Theoretical value obtained by first-order polarization propagator approach.[35]

5.2 Qualitative Revelation of J Anisotropy

Molecular symmetry can place very restrictive conditions for the ratios of dipolar coupling constants. Consequently, this can be used to reveal whether D^{exp} includes a contribution from J^{aniso} or not. If the examination of the ratios $D_{ij}{}^{exp}/D_{kl}{}^{exp}$ shows that they differ from the corresponding ratios of direct dipolar couplings ($D^{dir} = D^{exp} - \frac{1}{2}J^{aniso} = D^{e} + D^{ah} + D^{h} + D^{d}$, see equation (26)), they (or at least some of them) may be affected by J^{aniso}.

Benzene is a good example of a molecule in which symmetry completely fixes the ratios of the dipolar couplings. The order parameter of each ij direction equals $-\frac{1}{2}S$ (S is the order parameter of the sixfold symmetry axis) and consequently the following equation is valid:

$$\frac{D_{ij}^{dir}}{D_{kl}^{dir}} = \frac{\gamma_i\gamma_j}{\gamma_k\gamma_l}\left(\frac{r_{kl}}{r_{ij}}\right)^3 \tag{27}$$

It follows from the hexagonal symmetry of benzene that $r_m = \sqrt{3}r_o$ and $r_p = 2r_o$ (o = *ortho*, m = *meta*, p = *para*). Thus for the nuclei of same isotopic species, $D_o/D_m/D_p = 1 : \sqrt{3}/9 : 1/8 \sim 1 : 0.1925 : 0.1250$. It has been found that the $^1H-^1H$ couplings in benzene indeed fulfil these ratios (in particular, when the experimental couplings are corrected for harmonic vibrational and deformational effects) and thus the $J_{HH}{}^{aniso}$ values are obviously negligible.[4] In contrast, remarkable deviations have been detected for the $^{13}C-^{13}C$ couplings (corrected for harmonic vibrations).[39]

Equation (27) is not only valid for benzene but more generally. Thus, if S_{ij} for the nuclei i and j is the same as S_{kl} for the nuclei k and l, in other words the axes passing through

Table 6 Anisotropies of the $^{13}C-^{13}C$ and $^{13}C-^{15}N$ Spin–Spin Coupling Tensors in Acetonitrile (CH_3CN) and Methyl Isocyanide (CH_3NC)

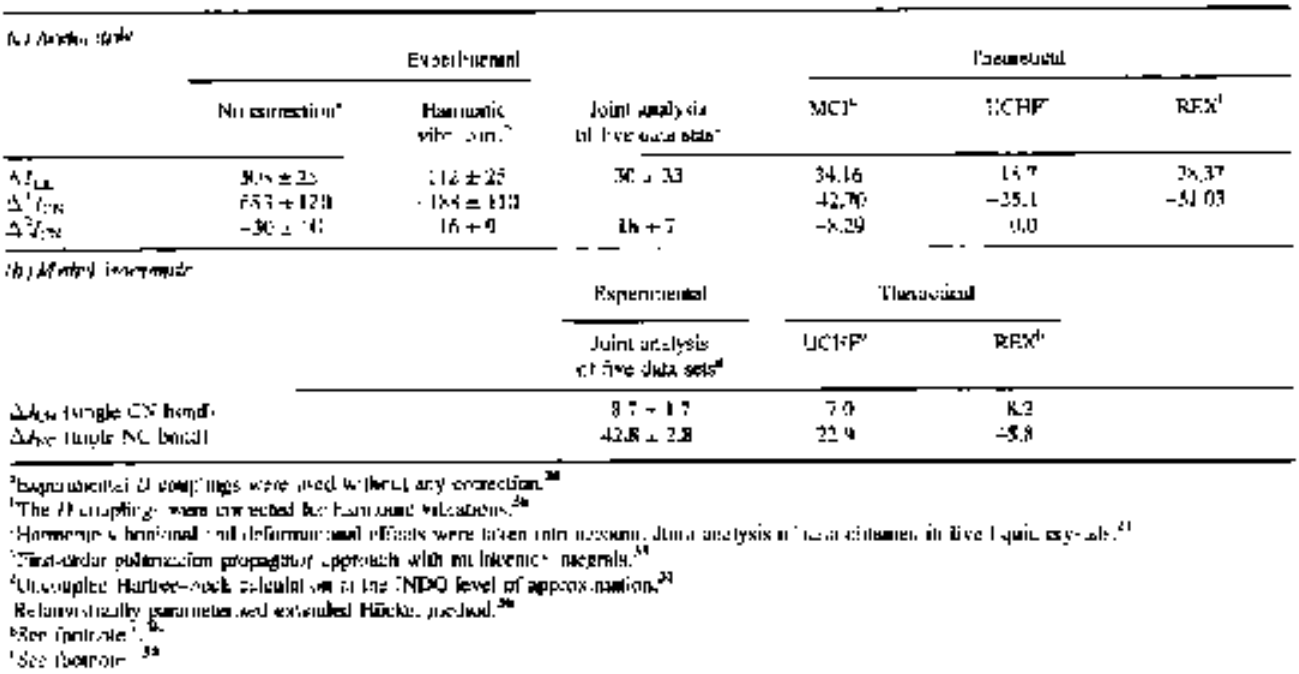

Table 7 Code Names and Compositions of the Liquid Crystals Mentioned in the Text

Code name[a]	Composition
ZLI 1167 ($\Delta\chi_m < 0$)	Mixture of 4-propyl-*trans*,*trans*-bicyclohexyl-4′-carbonitrile (36%), 4-pentyl-*trans*,*trans*-bicyclohexyl-4′-carbonitrile (34%), and 4-heptyl-*trans*,*trans*-bicyclohexyl-4′-carbonitrile (30%)
Phase 4 ($\Delta\chi_m > 0$)	Eutectic mixture of *p*-methoxy-*p*′-butylazoxybenzenes
HAB ($\Delta\chi_m > 0$)	*p*,*p*′-diheptylazoxybenzene
EBBA ($\Delta\chi_m > 0$)	(*p*-Ethoxybenzylidene)-*p*-butylaniline
ZLI 1132 ($\Delta\chi_m > 0$)	Mixture of *trans*-4-propyl-(4-cyanophenyl)cyclohexane (24%), *trans*-4-pentyl-(4-cyanophenyl)cyclohexane (36%), *trans*-4-heptyl-(4-cyanophenyl)cyclohexane (25%), and *trans*-4-pentyl-(4′-cyanobiphenyl-4)cyclohexane (15%)
Phase 1221 ($\Delta\chi_m > 0$)	Mixture of phenylcyclohexanes, biphenylcyclohexane, and phenylcyclohexane esters
MIX ($\Delta\chi_m > 0$)	Mixture of butyl-*p*-(*p*-ethoxyphenoxycarbonyl)phenyl carbonate (75%) and *p*-capronyloxy-*p*′-ethoxyazoxybenzene (25%)

[a]The sign of the anisotropy of diamagnetic susceptibility is shown below; when $\Delta\chi_m > 0$ the liquid crystal director orients along, and when $\Delta\chi_m < 0$ the director orients perpendicular to the external magnetic field.

the nuclear pairs *ij* and *kl* are parallel, the ratio $D_{ij}^{dir} : D_{kl}^{dir}$ is independent of the orientation. If the corresponding ratio of the experimental couplings is found to vary, it suggests anisotropic contribution at least in one of the couplings.[40,41] The code names and compositions of the liquid crystals mentioned above are defined in Table 7.

6 RELATED ARTICLES

Average Hamiltonian Theory; Chemical Shift Tensor Measurement in Solids; Chemical Shift Tensors; Dipolar and Indirect Coupling Tensors in Solids; Indirect Coupling: Semiempirical Calculations; Liquid Crystalline Samples: Spectral Analysis; Liquid Crystals: General Considerations; Liquid Crystals: Mixed Magnetic Susceptibility Solvents; Shielding Calculations: IGLO Method; Shielding Calculations: Perturbation Methods; Spinning Liquid Crystalline Samples; Structure of Rigid Molecules Dissolved in Liquid Crystalline Solvents.

7 REFERENCES

1. A. Saupe and G. Englert, *Phys. Rev. Lett.*, 1963, **11**, 462.
2. S. Sýkora, J. Vogt, H. Bösiger, and P. Diehl, *J. Magn. Reson.*, 1979, **36**, 53.
3. J. Lounila and P. Diehl, *J. Magn. Reson.*, 1984, **56**, 254.

4. J. Lounila and P. Diehl, *Mol. Phys.*, 1984, **52**, 827.
5. J. Lounila, *Mol. Phys.*, 1986, **58**, 897.
6. J. Lounila and J. Jokisaari, *Prog. NMR Spectrosc.*, 1982, **15**, 249.
7. A. J. Leadbetter, in *Thermotropic Liquid Crystals*, ed. G. W. Gray, John Wiley & Sons, Guildford, 1987, Chap. 1
8. C. L. Khetrapal, A. C. Kunwar, A. S. Tracey, and P. Diehl, in *NMR Basic Principles and Progress*, eds. P. Diehl, E. Fluck, and R. Kosfeld, Springer-Verlag, Heidelberg, 1975, Vol. 9.
9. A. Saupe, *Z. Naturforsch.*, 1964, **19a**, 161.
10. A. J. Montana and B. P. Dailey, *Mol. Phys.*, 1975, **30**, 1521.
11. C. L. Khetrapal and A. C. Kunwar, *Mol. Cryst. Liq. Cryst.*, 1981, **72**, 13.
12. C. L. Khetrapal and A. C. Kunwar, *Chem. Phys. Lett.*, 1981, **82**, 170.
13. J. Jokisaari and Y. Hiltunen, *Mol. Phys.*, 1983, **50**, 1013.
14. R. Teeäär, M. Alla, and E. Lippmaa, *Org. Magn. Reson.*, 1982, **19**, 134.
15. P. Diehl, J. Jokisaari, F. Moia, and J. Lounila, *Mol. Cryst. Liq. Cryst.*, 1982, **87**, 319.
16. Y. Hiltunen and J. Jokisaari, *J. Magn. Reson.*, 1987, **75**, 213.
17. E. E. Burnell and C. A. de Lange, *Chem. Phys. Lett.*, 1987, **136**, 87.
18. R. A. Bernheim and T. R. Krugh, *J. Am. Chem. Soc.*, 1967, **89**, 6784.
19. A. D. Buckingham, E. E. Burnell, and C. A. de Lange, *J. Am. Chem. Soc.*, 1968, **90**, 2972.
20. P. Diehl, J. Jokisaari, and F. Moia, *J. Magn. Reson.*, 1982, **49**, 498.
21. J. Lounila, M. Ala-Korpela, and J. Jokisaari, *J. Chem. Phys.*, 1990, **93**, 8514.
22. P. K. Bhattacharyya and B. P. Dailey, *Chem. Phys. Lett.*, 1975, **32**, 305.
23. J. D. Kennedy and W. McFarlane, *Mol. Phys.*, 1975, **29**, 593.
24. M. Schindler, *J. Am. Chem. Soc.*, 1987, **109**, 5950.
25. J. D. Kennedy and W. McFarlane, *J. Chem. Soc., Faraday Trans. 2*, 1976, **72**, 1653.
26. J. Jokisaari and P. Diehl, *Org. Magn. Reson.*, 1980, **13**, 359.
27. A. Pulkkinen, Y. Hiltunen, and J. Jokisaari, *Liq. Cryst.*, 1988, **3**, 737.
28. C. R. Lassigne and E. J. Wells, *Can. J. Chem.*, 1977, **55**, 1303.
29. R. E. Wasylishen, R. E. Lenkinski, and C. Rodger, *Can. J. Chem.*, 1982, **60**, 2113.
30. B. M. Fung, *J. Am. Chem. Soc.*, 1983, **105**, 5713.
31. J. Jokisaari and T. Väänänen, *Mol. Phys.*, 1986, **58**, 959.
32. J. Jokisaari, Y. Hiltunen, and J. Lounila, *J. Chem. Phys.*, 1986, **85**, 3198.
33. T. Väänänen, J. Jokisaari, and M. Seläntaus, *J. Magn. Reson.*, 1987, **72**, 414.
34. H. Nakatsuji, K. Hirao, H. Kato, and T. Yonezawa, *Chem. Phys. Lett.*, 1970, **6**, 541.
35. J. C. Facelli and M. Barfield, *J. Magn. Reson.*, 1984, **59**, 452.
36. P. Diehl, J. Jokisaari, J. Amrein, T. Väänänen, and P. Pyykkö, *J. Magn. Reson.*, 1982, **48**, 495.
37. H. Nakatsuji, I. Morishima, H. Kato, and T. Yonezawa, *Bull. Chem. Soc. Jpn.*, 1971, **44**, 2010.
38. Y. Hiltunen, J. Jokisaari, J. Lounila, and A. Pulkkinen, *J. Am. Chem. Soc.*, 1989, **111**, 3217.
39. P. Diehl, H. Bösiger, and J. Jokisaari, *Org. Magn. Reson.*, 1979, **12**, 282.
40. J. Gerritsen and C. MacLean, *J. Magn. Reson.*, 1971, **5**, 44.
41. J. Gerritsen and C. MacLean, *Mol. Cryst. Liq. Cryst.*, 1971, **12**, 97.

Biographical Sketches

Jukka P. Jokisaari. *b* 1944. M.S., 1968, Ph.D., 1974, University of Oulu, Finland; Postdoctoral work at University of Basel, Switzerland (with Peter Diehl). Professor of Physics (Atomic and Molecular Spectroscopy), University of Oulu, Finland. Approx. 100 publications. Current research specialty: NMR of small molecules and noble gases in liquid crystals.

Chemical Shift Scales on an Absolute Basis

Cynthia J. Jameson
University of Illinois, Chicago, IL, USA

1	Introduction	1
2	Absolute Shielding Scales Based on the Proton in Liquid Water	1
3	Absolute Shielding Information from Spin-Rotation Constants	1
4	The Connection Between Absolute Shielding Scales of Two Nuclei	5
5	Magnitudes of the Corrections Linking the Shielding in the Condensed Phase to the Isolated Molecule at its Equilibrium Geometry	6
6	Related Articles	9
7	References	9

1 INTRODUCTION

Nuclear magnetic shielding is a second-order molecular electronic property which provides a severe test of the accuracy of molecular quantum mechanical calculations. While electric dipole polarizability and hyperpolarizabilities provide tests of the wavefunction at the outer regions, nuclear shielding is very sensitive, especially to contributions from high angular momentum functions, in the regions close to a particular nucleus. Precise measurements of differences in shielding are easy to carry out. In most NMR studies the resonance frequencies are measured and a chemical shift is defined as $\delta = (\nu_i - \nu_{\text{ref}})/\nu_{\text{ref}}$. From the relationship between the resonance frequency ν_i, the external magnetic field $\boldsymbol{B}_0$, the magnetogyric ratio γ, and the nuclear shielding σ_i, i.e. $\nu_i = (\gamma/2\pi)(1 - \sigma_i) B_0$, we can write the chemical shifts in terms of the nuclear shielding as $\delta = (\sigma_{\text{ref}} - \sigma_i)/(1 - \sigma_{\text{ref}})$.

Reasonably accurate calculations are now available for nuclei in the first row of the Periodic Table in molecules with a small number of first row atoms and for hydrides of the second row, as may be seen in the articles on IGLO, LORG and SOLO and GIAO shielding calculations described by Kutzelnigg, Hansen and Pulay in this Encyclopedia (***Shielding Calculations: LORG and SOLO Approaches***, ***Shielding Calculations: IGLO Method***, ***Shielding Theory: GIAO Method***). In making a comparison of theoretical ab initio values at the equilibrium molecular geometries with experimental chemical shifts, it is necessary to have absolute quantities (absolute shielding values) to compare with rather than shielding differences or chemical shift values. Accurate chemical shift measurements can be carried out by simultaneous measurement of two frequencies in the same physical sample in the field. If we know the absolute shielding value corresponding to the first frequency, then the accurate chemical shift between the two provides the absolute shielding of the second, or indeed of any number of systems whose chemical shifts can be related to the absolute shielding of any one system. But how do we establish the absolute shielding value of the very first one?

2 ABSOLUTE SHIELDING SCALES BASED ON THE PROTON IN LIQUID WATER

The absolute proton shielding in a spherical sample of pure liquid H_2O at 34.7 °C, σ = 25.790 ± 0.014 ppm, has been established by two experiments. The first was a simultaneous measurement of the frequencies of an electronic transition and a nuclear magnetic transition in atomic hydrogen. The second was a simultaneous measurement of NMR frequencies of protons in a spherical sample of liquid water at 34.7 °C and in a spherical bulb filled with atomic hydrogen in the same magnetic field. The first experiment established the g-factor of the bare proton; the second experiment allows the determination of the absolute nuclear magnetic shielding of protons in liquid water.[1,2]

One standard technique for establishing an absolute shielding scale for a nucleus M is by combining the results of two experiments. The first is an atomic beam magnetic resonance experiment or an optical pumping experiment which measures the ratio of γ for the M nucleus to γ for the electron in the free M atom. Since the (electron) γ can be calculated from the known electron magnetic moment and electronic g-value of the atomic state, the value of γ(M, free atom) may be obtained precisely. The second is an NMR experiment which measures the ratio of the Larmor frequencies of M and ^{1}H in an infinitely dilute $M_{(aq)}{}^{n+}$ ion in aqueous solution. This provides the ratio $\gamma(^1\text{H}, H_2O, \text{liq.})/\gamma(\text{M}, M_{(aq)}{}^{n+})$. The key here is that $\gamma(^1\text{H}, H_2O, \text{liq.})$ is known precisely for pure liquid water from experiments and is assumed to be the same in the infinitely dilute aqueous solution of $M_{(aq)}{}^{n+}$ ion, so γ(M, $M_{(aq)}{}^{n+}$) can be obtained. Then, from the definition of the nuclear magnetic shielding σ relative to the bare nucleus, $\gamma = (1 - \sigma)\gamma_0$, where γ_0 is the magnetogyric ratio of the bare nucleus,

$$\frac{\sigma(\text{M, free atom}) - \sigma(\text{M}, M_{aq}{}^{n+})}{1 - \sigma(\text{M}, M_{q}{}^{n+})} = 1 - \frac{\gamma(\text{M, free atom})}{\gamma(\text{M}, M_{aq}{}^{n+})} \quad (1)$$

Since σ(M, free atom) is theoretically known[3] the absolute shielding of M in the aqueous solution of $M_{(aq)}{}^{n+}$ is thereby established.

This method is applicable when the aqueous solution of the metal ion is a convenient reference and extrapolation to infinite dilution is possible. The ratio γ(M, free atom)/γ(M, liq. ref.) has to be known to 1 part in 10^5 if the σ(M, liq. ref.) − σ(M, free atom) is to be determined to ±10 ppm. The absolute shielding scales for Li, Na, K, Rb, Cs, Zn, Cd, Ga, Hg, and Pb were determined in this way and are summarized in Table 1 in 'Multinuclear NMR' edited by Mason.[4]

3 ABSOLUTE SHIELDING INFORMATION FROM SPIN-ROTATION CONSTANTS

With the gauge origin at the nucleus in question, σ^{p} in Ramsey's expression is related to another molecular property,

Table 1 Absolute σ_0 ^{15}N Shieldings

Molecule	σ_0(^{15}N in the molecule, 300 K) (ppm)
N_2	−61.6
NNO	99.5
N**N**O	11.3
HCN	−20.4

the nuclear spin-rotation tensor. The nuclear spin-rotation tensor arises from the coupling of the magnetic moment of a nucleus with the magnetic field generated by the molecular rotation at that nucleus. Ramsey[5] and Flygare[6] have shown that

$$\sigma_{gg}^{p} = (m_p/2mg_N)C_{gg}/B_{gg}^{(e)} - (\mu_0/4\pi)(e^2/2m) \times \sum_N Z_{N'}[R_{NN'}^2 - (R_{NN'}^2)_{gg}]/R_{NN'}^3 \quad (2)$$

in which m_p and m are the masses of the proton and the electron, g_N is the g-factor for the nucleus of interest, C_{gg} and σ_{gg}^{p} are the diagonal components of the spin-rotation tensor and the paramagnetic shielding tensor in the principal axis system of the molecular moment of inertia, while $B_{gg}^{(e)}$ is the rotational constant at the equilibrium configuration.

The σ_{gg}^{p} values can be related to the components along the principal axes of the shielding tensor by a rotational transformation using the known molecular goemetry. The second term in the equation is the nuclear contribution which depends only on the coordinates and atomic number of all the other nuclei N' in the molecule. The total absolute shielding can then be determined by adding the diamagnetic contribution σ^d, which is obtained from theory, calculated at the nucleus of interest N as the gauge origin:

$$\sigma^d = (\mu_0/4\pi)(e^2/3m)\left\langle \psi^0 \left| \sum 1/r_i \right| \psi^0 \right\rangle \quad (3)$$

It is very important to calculate the nuclear terms using the same structure as that used for calculating diamagnetic terms.

Experimental values of spin-rotation constants are available from molecular beam magnetic and electric resonance experiments and also from high-resolution microwave spectroscopy. In the first two types of experiments the radiofrequency spectrum corresponding to the reorientation of the ^{15}N nuclear moment in a magnetic field, or the interaction of the electric dipole moment of the molecule with a strong external electric field, is composed of transitions from many J and M_J states which may be individually resolved. In the third type of experiment, a specific purely rotational transition is observed. Vibrationally averaged constants are obtained, usually for the ground vibrational state, occasionally for a vibrationally excited state as well. The exact relation between σ^p and C holds for a vibrationless molecule at the equilibrium nuclear configuration. Experimentally one usually obtains $\langle C \rangle_{v=0}$ components of the vibrationally averaged spin-rotation constant.

The first absolute shielding scale which was compiled in an internally consistent way is the one for ^{19}F in a small set of molecules whose chemical shifts have been measured in the limit of zero pressure at room temperature.[6] To establish the first absolute shielding for ^{19}F in a molecule,[7] Hindermann and Cornwell corrected the observed spin-rotation constant in HF to the equilibrium configuration, from which they obtained σ_e^{p}. The latter combined with the theoretical value of σ_e^{d} gave σ_e, which was then converted to σ_0 at room temperature by making the rovibrational correction. Once the absolute σ_0 for HF was known, they could then find the absolute σ_0 for their secondary reference molecule (SiF_4) by measuring the chemical shift between HF and SiF_4 at the zero-pressure limit. The absolute σ_0 for the other molecules on their scale were then determined from measured chemical shifts from SiF_4. Since all the measured chemical shifts correspond to the zero-pressure limit, Hindermann and Cornwell's scale is a list of absolute σ_0 (i.e., for the isolated molecule) at room temperature. In addition, they found the absolute shielding σ(liq., T) of $CFCl_3$. With this connection, other measurements of shifts relative to liquid $CFCl_3$ can be converted to absolute σ(liq. or soln., T) by other workers.

In general, once the absolute shielding of a primary reference molecule (in this case the HF molecule) has been established, the absolute ^{19}F shielding of a series of other molecules can be systematically determined. What is required are simultaneous accurate chemical shift measurements between the primary reference molecule and all the other molecules in the isolated molecule limit. Frequently, the primary reference molecule is not a convenient internal reference and a secondary reference molecule is used instead. In this case, the SiF_4 molecule is ideal, it is relatively inert, and has a long ^{19}F relaxation time in the gas phase so that the signal is sharp. To extend the ^{19}F absolute shielding scale, observed resonance frequencies in gas samples were reduced to the zero-density limit at 300 K using previously measured density and temperature-dependent chemical shifts for each gas. The results corresponding to a rovibrationally-averaged isolated molecule at 300 K are expressed relative to SiF_4 as a standard. The values of $[\sigma_0(300\,K) - \sigma_0^{SiF_4}(300\,K)]/[1 - \sigma_0^{SiF_4}(300\,K)]$ were obtained by dividing the frequency differences by the resonance frequency of SiF_4. The shielding differences $[\sigma_0^{A}(300\,K) - \sigma_0^{SiF_4}(300\,K)]$ were obtained for a large number of molecules[8,9] and were found to be identical to Hinderman and Cornwell's values for all of their molecules (six) which were included in the new set. Based on σ_0(HF, 300 K) = 410.0 ppm, absolute $\sigma_0(SiF_4, 300\,K)$ = 363.2 ppm. The absolute σ_0 for a large number of F-containing molecules have been determined from the ^{19}F chemical shift limit at 300 K, $[\sigma_0(A, 300\,K) - \sigma_0(SiF_4, 300\,K)]$.[8,9] Neat liquid $CFCl_3$ and C_6F_6 provide the connection for converting chemical shifts measured in other laboratories using these references into absolute shielding values; σ(^{19}F neat liq. $CFCl_3$, spherical, 300 K) = 188.7 ppm; σ(^{19}F neat liq. C_6F_6, spherical, 300 K) = 355.5 ppm.

How large can the errors be if the corrections shown in Figure 1 are not carried out, i.e. if $\langle C_{gg}\rangle_{v=0}/\langle B_{gg}\rangle_{v=0}$ are used to calculate $\langle \sigma_{gg}^{p}\rangle_{v=0}$ directly? The difference between the vibrational average of the ratios $\langle C_{gg}/B_{gg}\rangle_{v=0}$ and the ratio of the vibrational averages $\langle C_{gg}\rangle_{v=0}/\langle B_{gg}\rangle_{v=0}$ can be as much as 10% in molecules containing hydrogen. Incomplete knowledge of the first and second derivatives of C with nuclear configuration presently makes it impossible to correct for this error, as Hindermann and Cornwell had done for HF. The thermal average of σ^p can be approximated by using the spin-rotation tensor for the ground vibrational state. However, when a low-frequency vibration exists and the spin-rotation constants

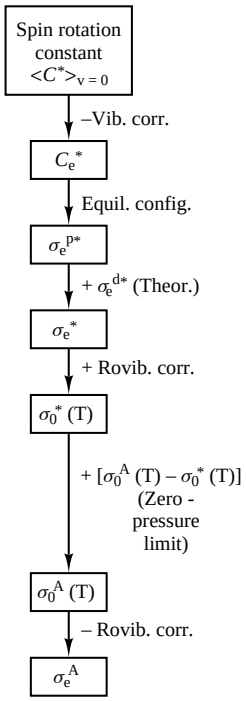

Figure 1 Building up an absolute shielding scale from the absolute shielding of one primary reference whose spin-rotation constant is accurately known. The following notations are used: * denotes the primary reference molecule, A any other compound, subscript 0 the isolated molecule, and subscript e the equilibrium configuration

for the first excited vibrational state are substantially different from those of the ground vibrational state (such as in NNO), a proper thermal average has to be carried out. There are also rotational (centrifugal distortion) corrections which have to be made.

Given the possible sources of error which we have mentioned above, some discrepancies may be observed in comparing shielding values derived from spin-rotation constants with differences in thermal averages of shielding observed in nuclear magnetic resonance spectroscopy in the zero-pressure limit. However, the precision of most available spin-rotation constants is still such that the sources of errors discussed above are not limiting.

Ab initio calculations of the diamagnetic part of the shielding are generally reliable since these depend only on the ground-state wavefunctions. The changes resulting from configuration interaction are very minor, no more than a few tenths of a ppm in σ^{d}, over the Hartree–Fock value. Where ab initio calculations are not available, it is possible to estimate σ^{d} to within 1–2 ppm even without wavefunctions. Flygare has proposed an easy method for evaluating σ^{d} which has been shown to be sufficiently reliable for evaluating the average and the components of σ from the spin-rotation tensor.[10,11] The success of this method is due to the fact that most of σ^{d} is given by the diamagnetic shielding of the free atom and the rest can then be approximately calculated by the method of atomic dipoles. It has been found that the method of Flygare and co-workers is accurate to within 1–2 ppm. Let us consider this method briefly.

By formally partitioning the sum of $1/r_j$ over all j electrons into two sums, one over electrons 'on' nucleus N and the other over all electrons 'on' all the other nuclei, N', Flygare has been able to write the average diamagnetic shielding in terms of a free atom term, a contribution of the electronic point charges centered at the other nuclei, and a third term which arises if the point charges are not centered on the N' nucleus but are displaced by a distance $\langle\rho\rangle_{N'}$:

$$\sigma_{\mathrm{av}}^{\mathrm{d}} = \sigma^{\mathrm{d}}(\text{free atom}) + (\mu_0/4\pi)(e^2/3m)\sum_{N'} Z_{N'}/R_{N'} - (\mu_0/4\pi)(e^2/3m)\sum_{N'} R_{N'}\cdot\langle\rho\rangle_{N'}/R_{N'}^3 \tag{4}$$

The second term in the above equation is identical in form and opposite in sign to the nuclear terms in equation (1) and the last term is a small correction. Thus, the absolute shielding σ can be written in the Flygare method, as

$$\sigma_{\mathrm{av}} = \sigma^{\mathrm{d}}(\text{free atom}) - (\mu_0/4\pi)(e^2/3m) \times \sum_{N'} R_{N'}\cdot\langle\rho\rangle_{N'}/R_{N'}^3 + \frac{m_{\mathrm{p}}}{2mg_N}\cdot\frac{1}{3}\sum\frac{C_{\mathrm{gg}}}{B_{\mathrm{gg}}^{(\mathrm{e})}} \tag{5}$$

This applies to the equilibrium configuration, with extension to thermal averages requiring some corrections which may be a few ppm.

Using the Flygare approximation for the diamagnetic shielding then leads to

$$\sigma_{\mathrm{av}} \simeq \frac{m_{\mathrm{p}}}{2m_{\mathrm{e}}g_N}\cdot\frac{1}{3}\sum\frac{C_{\mathrm{gg}}}{B_{\mathrm{gg}}^{(\mathrm{e})}} + \sigma^{\mathrm{d}}(\text{free atom}) \tag{6}$$

The diamagnetic shieldings of the free atoms are well known from the tabulations of Malli and Froese.[3] For a spherical top molecule,

$$\left.\begin{aligned}\sigma_{\mathrm{av}} &\simeq \frac{m_{\mathrm{p}}}{2m_{\mathrm{e}}g_N}\cdot\frac{C_{\mathrm{av}}}{B} + \sigma^{\mathrm{d}}(\text{free atom})\\ \sigma_{\parallel} - \sigma_{\perp} &\simeq \frac{m_{\mathrm{p}}}{2m_{\mathrm{e}}g_N}\cdot\frac{C_{\parallel} - C_{\perp}}{B}\end{aligned}\right\} \tag{7}$$

and for a linear molecule

$$\left.\begin{aligned}\sigma_{\perp} &\simeq \frac{m_{\mathrm{p}}}{2m_{\mathrm{e}}g_N}\cdot\frac{C_{\perp}}{B} + \sigma^{\mathrm{d}}(\text{free atom})\\ \sigma_{\parallel} &= \sigma_{\parallel}^{\mathrm{d}}\end{aligned}\right\} \tag{8}$$

since $\sigma_{\parallel}^{\mathrm{p}}$ is identically zero for a linear molecule.

The spin-rotation tensor has been used to determine the ^{15}N absolute shielding in NH_3, ^{19}F in HF, ^{13}C and ^{17}O in CO, and ^{31}P in PH_3, and these absolute shieldings have been used to establish all other absolute shieldings in various molecules containing these nuclei. Gas-phase studies provide the relative differences at the zero-density limit and these can be converted to σ_0(300 K) values absolutely. If the commonly used liquid reference is also measured relative to this one molecule, then all past and future measurements of chemical shifts relative to this liquid reference can be converted to absolute shieldings. As we have seen above, rovibrational corrections should be calculated and added to theoretical σ_{e}

before comparing with the experimental values σ_0(300 K). For some molecules this latter value is not very different from the zero-point vibrational average shielding σ_0(0 K). Similarly, the observed spin-rotation constants should be corrected for rovibrational effects before using the identity to obtain σ_e. Nevertheless, the agreement between absolute shielding values derived from spin-rotation constants and those from gas-phase measurements in the zero-pressure limit is remarkably good as shown in Figure 2, which indicates the reliability of the spin-rotation constants.

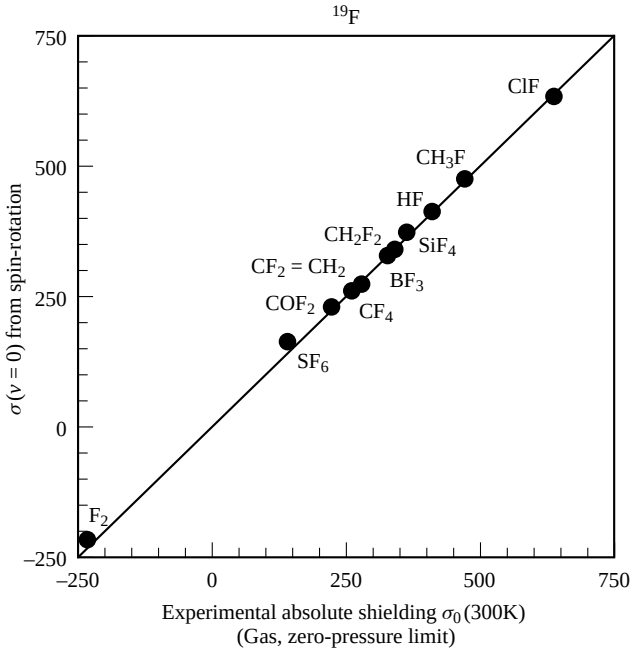

Figure 2 Experimental absolute shielding values of ^{19}F from gas-phase measurements in the zero-density limit. The gas-phase measurements are converted to absolute shielding by using HF as the primary reference molecule. These are compared with the individual absolute shielding values derived from independent measurements of the ^{19}F spin-rotation constants in various molecules

The ^{15}N absolute shielding scale is based on the spin-rotation tensor in the primary reference molecule, NH_3. The spin-rotation-derived shielding for NH_3 is 264.54 ppm.[12] Nitrogen-15 chemical shifts in the gas phase taken to the zero-pressure limit lead to absolute $\sigma_0(^{15}N)$ shieldings in the N_2, NNO, and HCN molecules,[13] see Table 1. At the same time, the absolute shielding of the liquid references were obtained: $\sigma(^{15}N, NH_3, liq., 300\,K) = 380.4$ ppm; $\sigma(^{15}N, CH_3NO_2, liq., 300\,K) = -135.8$ ppm.

The ^{17}O absolute shielding scale is based on the spin-rotation tensor in $C^{17}O$, $C_\perp = 30.4 \pm 1.2$ kHz which leads to $\sigma(^{17}O, CO) = -42.3 \pm 17.2$ ppm.[14] The gas-phase measurements of ^{17}O chemical shifts in H_2O, CO_2, NNO, OCS, OF_2, and CO lead to the absolute $\sigma_0(^{17}O)$ shielding values[14] shown in Table 2.

The ^{13}C shielding scale is based on the primary reference ^{13}C in the $^{13}C^{16}O$ molecule in which $C_\perp = 32.70 \pm 0.12$ kHz in the v = 0, J = 1 state [15] is in good agreement with the previous value of 32.59 ± 0.15 kHz. Rovibrational corrections on the spin-rotation constant to obtain $\sigma_e(^{13}C$ in $^{13}C^{16}O) = 3.0 \pm 0.9$ and then rovibrational corrections on the latter lead to $\sigma_0(^{13}C$ in $^{13}C^{16}O$, 300 K) = 1.0 ± 1.2 ppm.[16] With measurements of ^{13}C chemical shifts in the low-density gas phase under conditions such that intermolecular effects and bulk susceptibility effects are less than 0.05 ppm, the $[\sigma_0 - \sigma_0(CO)]$ have been obtained for a large number of molecules ranging from CH_4 where $\sigma_0(^{13}C, CH_4, 300\,K) = 195.1$ ppm to $CH_2{=}C{=}CH_2$ where $\sigma_0(^{13}CH_2, 300\,K) = 115.2$ ppm, $\sigma_0(={}^{13}C{=}, 300\,K) = -29.3$ ppm. The independent spin-rotation-derived absolute shieldings in $^{13}CH_4$, $D^{13}CN$, and $O^{13}CS$ are completely consistent with the values of σ_0 obtained for these molecules based on $\sigma_0(^{13}CO) = 1.0 \pm 1.2$ ppm.

The $\sigma_0(^{13}C$ in the molecule, 300 K) values for a large number of molecules have been published by Jameson[16] and Jameson (Table 16).[17] A missing value from the latter is isopentane $\cdots$ (CH)**C**H_3, for which $\sigma_0(^{13}C$ in the molecule, 300 K) = 165.0 ppm. These measurements also provide $\sigma(^{13}C$, TMS liquid, spherical, 300 K) = 184.1 ppm and $\sigma(^{13}C, C_6H_6$ liquid, spherical, 300 K) = 55.7 ppm, which are convenient references for converting chemical shift measurements to absolute shieldings.

The ^{31}P absolute shielding scale is based on the primary reference molecule PH_3, in which the spin rotation tensor $C_\perp = -114.90 \pm 0.13$ kHz and $C_\parallel = -116.38 \pm 0.32$ kHz (where the quoted errors are for 99% confidence limits),[18] leading to $\sigma_0(^{31}P, PH_3, 300\,K) = 594.45 \pm 0.63$ ppm. If the spin-rotation tensor is rovibrationally corrected, one gets[19] $\sigma_e(^{31}P$ in the PH_3 molecule) = 599.93 ppm and $(\sigma_\parallel - \sigma_\perp)_e = -64.5$ ppm.

The PF_3 molecule serves as a suitable secondary reference since its chemical shift has a smaller dependence on density. Extrapolation of gas-phase mixtures in argon to the zero-density limit provides the absolute shieldings[20] listed in Table 3. At the same time the absolute shielding of ^{31}P in convenient reference liquids has been obtained: $\sigma(^{31}P$, 85% H_3PO_4 aq., spherical, 300 K) = 328.35 ppm and $\sigma(^{31}P$, $P(OMe)_3$ liquid, spherical, 300 K) = 187.54 ppm. A ^{33}S absolute shielding scale has been derived from the spin-rotation constant $C_\perp = 870 \pm 50$ Hz in the OCS molecule, which leads to $\sigma_0(^{33}S$, OCS molecule) = 843 ± 12 ppm.[21] The ^{33}S chemical shift measurements in the gas phase lead (without full corrections for intermolecular effects) to the values shown in Table 4. A convenient liquid reference is CS_2 for which $\sigma(^{33}S, CS_2$, liquid, spherical, 300 K) = 581 ppm.

Although the proton absolute shielding for water was the first to be established, proton shifts have not been systematically measured in the gas-phase zero-pressure limit and connected to either liquid water or liquid TMS. This situation should be remedied soon as improving proton shielding calculations need some good experimental tests. There are, however, absolute shieldings that can be individually derived

Table 2 Absolute σ_0 ^{17}O Shieldings

Molecule	$\sigma_0(^{17}O$ in the molecule, 300 K) (ppm)
H_2O	344.0
CO_2	243.4
NNO	200.5
OCS	107.9
OF_2	−473.1
CO	(−42.3 ± 17.2)

Table 3 Absolute σ_0 ^{31}P Shieldings

Molecule	σ_0(^{31}P in the molecule, 300 K) (ppm)
PMe_3	391.71
OPF_3	363.43
PF_3	222.69
PCl_2Me	138.65
PCl_3	111.29
P_4	−551.5
PH_3	(594.45 ± 0.63)

Table 4 Absolute σ_0 ^{33}S Shielding Values

Molecule	σ_0(^{33}S in the molecule, 300 K) (ppm)
H_2S	752
CH_3SH	707.3
SF_6	425.6
SO_2	−125.9
OCS	(843 ± 12)

from measured spin-rotation constants by the methods already described, and these are shown in Table 5.

Table 5 Absolute σ_0 Proton Shieldings

Molecule	σ_0 (^{1}H in the molecule, 300 K) (ppm)	Other values (ppm)
CH_3F	28.27 ± 0.5	
PH_3	27.89 ± 0.15	
NH_3	32.10 ± 0.02	
H_2	26.363 ± 0.004	
CH_4	30.80 ± 0.23	30.611 ± 0.024
HCl	31.16 ± 0.09	
HF	28.64 ± 0.01	28.51 ± 0.20
H_2S	31.26 ± 0.40	
SiH_4	27.52 ± 0.44	27.63 ± 0.03

The errors quoted include only those arising from the uncertainty in the spin-rotation tensor itself. Other values reported in the last column are based on a variety of chemical shift measurements which are indirectly connected to liquid water whose absolute shielding is σ(^{1}H, H_2O, liq., spherical, 34.7 °C) = 25.790 ± 0.014 ppm.

4 THE CONNECTION BETWEEN ABSOLUTE SHIELDING SCALES OF TWO NUCLEI

Spin-rotation constants of any two nuclei in the same molecule can be related to one another provided that both nuclei relax entirely by the spin-rotation mechanism. In the gas phase, in the exchange-narrowing limit, there is a single characteristic correlation time τ which is identical for both nuclei.

The nuclear spin relaxation time characteristic of this mechanism is given by

$$(1/T_1)_{SR} = \frac{2}{3}\langle J(J+1)\rangle 4\pi^2 C_{eff}^2 \tau \qquad (9)$$

with C in units of rad s^{-1}, so that for two nuclei k and k' in the same molecule, in the same gas sample,

$$T_1(k)/T_1(k') = C_{eff}^2(k')/C_{eff}^2(k) \qquad (10)$$

For linear molecules $C_{eff}{}^2 = C_\perp{}^2$. For spherical tops

$$\begin{aligned} C_{eff}^2 &= C_{av}^2 + \frac{4}{45}(\Delta C)^2 \\ &= \left[\frac{1}{3}(2C_\perp + C_\parallel)\right]^2 + \frac{4}{45}(C_\parallel - C_\perp)^2 \end{aligned} \qquad (11)$$

A nucleus in the center of a spherical top is a favorable choice since all $C_{gg}{}^{(k)}$ are equal by symmetry and only $C_{av}{}^2$ enters into the relaxation expression. If both nuclei k and k' relax entirely by spin rotation, and if $C_{eff}{}^2$ is known for one nucleus, e.g. ^{19}F in SeF_6 or TeF_6, then C_{av} for the central nucleus (and thus the shielding) can be obtained from the measured ratio of relaxation times in the gas phase. This is supported by empirical observations for CH_4 in various buffer gases, in which the ratio of measured ^{13}C and ^{1}H relaxation times in the gas phase was found to be independent of buffer gas, temperature, or density, and was within experimental error of the inverse ratio of the $C_{eff}{}^2$ values from molecular beam data. These molecular beam data, in turn, were consistent with the ^{13}C shielding scale (based on $C_\perp$ in CO) and the ^{1}H shielding scale (based on γ of the H atom).

It is also possible to determine $C_{eff}{}^2$ from the density dependence of T_1 in the region of the minimum. However, for most systems, the minimum T_1 occurs at such low densities that appropriate measurements are feasible only for ^{1}H and ^{19}F nuclei which have the highest NMR sensitivity, and which also have well-established shielding scales based on spin-rotation constants from molecular beam and high-resolution microwave measurements.

This method was used to establish the ^{77}Se and ^{125}Te shielding scales by concurrent measurement of the ^{19}F and ^{77}Se (or ^{125}Te) spin-relaxation times in SeF_6 (or TeF_6) molecules in the dilute gas phase,[22] and also the ^{29}Si shielding scale based on both SiH_4 and SiF_4 molecules.[23] The sample was gaseous (e.g. SeF_6 or TeF_6, or an equimolar mixture of SiH_4 and SiF_4) contained in a sealed glass tube at a well-regulated temperature. Inversion–recovery experiments were set up in both the observe channel and the decoupling channel, the decoupling channel having been modified so that it could be tuned to ^{19}F as well as ^{1}H.

In one cycle, one-eighth of the total number of transients were taken and stored for each delay time for one nucleus and then the other. The next cycle went through the delay list for one nucleus and the other, acquiring the next eighth and so on. Thus the T_1 experiments were undertaken in the same molecule in the same sample essentially simultaneously. Only the magnitude of C could be obtained from the experiments. The signs were assigned on the basis of the σ values obtained. Defined with the gauge origin at the nucleus in question, σ^p is usually negative for most heavy nuclei. For SeF_6 the two possible values of σ^p which can be calculated from C are 1559.7 or −2160.7 ppm, from which we choose the latter, i.e. C(^{77}Se) is negative. For TeF_6 the two possible values of σ^p are 2570 or −3070 ppm and we choose the latter, which with a negative g(^{125}Te) implies that C(^{125}Te) is positive.

Although the relationship between σ^p and C is exact only for the rigid isolated molecule at its equilibrium configuration, we have used rovibrationally averaged values at room temperature for all quantities. The errors in σ associated with this are smaller than the rovibrational corrections to shielding (-8 and -9 ppm, respectively, for ^{77}Se and ^{125}Te in SeF_6 and TeF_6) since the vibrational corrections to C and σ^p tend to increase slightly the magnitudes of both. Hence, σ_0 (^{77}Se in SeF_6 molecule, 300 K) = 1437.8 ± 64 ppm, σ_0 (^{77}Se in H_2Se molecule, 300 K) = 2401 ± 64 ppm, and σ_0 (^{125}Te in TeF_6 molecule, 300 K) = 3790 ± 130 ppm.

These values are based on 3298 ppm and 6580 ppm for σ^d of the free Se and Te atoms, respectively, including relativistic corrections. Using the absolute shielding values for ^{77}Se in SeF_6(g) and for ^{125}Te in TeF_6(g), and the known gas-to-liquid shifts for SeF_6 and TeF_6, the absolute shielding for the reference liquids σ(^{77}Se, Me_2Se, liq.) = 2069 ppm and σ(^{125}Te, Me_2Te, liq.) = 4333 ppm are obtained. Concurrent measurement of ^{29}Si and ^{1}H spin-relaxation times in a sample of SiF_4 gas provides the ratio $C^2_{av}(^{29}Si)/C^2_{eff}$ (^{1}H), and concurrent measurement of ^{29}Si and ^{19}F spin-relaxation times in SiF_4 gas provides the ratio $C^2_{av}(^{29}Si)/C^2_{eff}(^{19}F)$. The spin-rotation tensors are independently known for ^{1}H and ^{19}F in these molecules. Using $g_{Si} = -1.1106$ and the theoretical value for the diamagnetic shielding σ^d free Si atom = 874.1 ppm, and choosing positive signs for C(^{29}Si) in both molecules, leads to$^{23}\sigma_0$(^{29}Si in SiH_4 molecule, 300 K) = 475.3 ± 10 ppm and σ_0(^{29}Si in SiF_4 molecule, 300 K) = 482.0 ± 10 ppm.

The T_1 experiments in SiH_4 and SiF_4 provide two completely independent determinations of very nearly the same point (separated by only 6.7 ppm) on the ^{29}Si shielding scale. The coincidence of these two truly independent results is remarkable. Since a large part of C^2_{eff} (^{1}H or ^{19}F) is the isotropic average C^2_{av} (^{1}H or ^{19}F) which is directly related to σ_{av} (^{1}H or ^{19}F), the values are constrained to be consistent with the absolute shielding scales of both ^{1}H and ^{19}F and also the 6.7 ppm ^{29}Si shielding difference between SiH_4 and SiF_4. All these conditions are well satisfied within realistic error estimates of ±10 ppm. The ^{19}F shielding scale is well established, with several independent determinations based on the spin-rotation constants in a number of small molecules agreeing with the chemical shifts in the zero-pressure limit. The ^{1}H shielding scale is also well established on the basis of hydrogen atomic beam data. It is satisfying to find that the Si shielding scale is consistent with these. Finally, the measured ^{29}Si chemical shifts in SiH_4 and SiF_4 gas relative to neat liquid Me_4Si lead to σ(^{29}Si, Me_4Si, liquid, spherical) = 368.5 ± 10 ppm.

In favorable systems, simultaneous measurements of T for two spin-$\frac{1}{2}$ nuclei in the same molecule in the gas phase provide a means of determining the absolute nuclear shielding scale of the second nucleus from that of the first. This method can be applied when the spin-rotation tensor of the first nucleus is independently known or can be calculated from its known shielding tensor. The latter can be obtained by measurement of the chemical shift anisotropy and the isotropic absolute shielding based on some primary reference (such as ^{1}H in the H atom, ^{13}C in CO, ^{15}N in NH_3, ^{17}O in CO, ^{19}F in HF, ^{31}P in PH_3, or ^{33}S in OCS). In a linear molecule only the isotropic shielding is necessary since $\sigma_\parallel$ is entirely diamagnetic. For spherical tops the $(\Delta C)^2$ term is 4/45-times as small as the $C^2{}_{av}$ term, so that even when $(\Delta C)^2$ and $\Delta\sigma$ are unknown an estimate may be adequate. An appropriate molecule in which two nuclei relax nearly exclusively by spin-rotation in the gas phase effectively provides a bridge between the absolute shielding scales of these nuclei.

Finally, a method of obtaining the absolute shielding directly from the measured anisotropy $\Delta\sigma \equiv (\sigma_\parallel - \sigma_\perp)$ in a linear molecule takes advantage of the symmetry requirement that the paramagnetic shielding contribution along the axis parallel to the molecular axis vanishes: $\sigma^p_{||} = 0$. A theoretically calculated diamagnetic term $\sigma^d_{||}$ provides the rest of the required information:

$$\sigma_\perp = \sigma^d_\parallel - \Delta\sigma, \qquad \sigma_\parallel = \sigma^d_\parallel \tag{12}$$

so that the absolute average shielding is

$$\sigma = \sigma^d_\parallel - \left(\frac{2}{3}\right)\Delta\sigma \tag{13}$$

albeit containing some unwanted intermolecular effects in $\Delta\sigma$ which is usually obtained from a condensed-phase measurement. One can therefore establish a shielding scale for a nucleus by choosing an appropriate linear molecule. Some examples are shown in Table 6. The absolute shieldings obtained from the anisotropy differ slightly from those obtained in the gas in the zero-pressure limit, from which we see that intermolecular effects are 1 to -8 ppm in the solid. It should be noted that the above relationships hold only for a linear molecule, not for a quasilinear or pseudolinear molecule. Any off-axis atoms break the symmetry and lead to $\sigma^p_{||} \neq 0$. For example, $CH_2{=}{}^{13}C{=}CH_2$ has $\sigma^p_{||} = -250$ ppm for the central ^{13}C. Furthermore, $\sigma^p_{||} = 0$ holds for a linear molecule only at the level of the nonrelativistic theory of shielding.

5 MAGNITUDES OF THE CORRECTIONS LINKING THE SHIELDING IN THE CONDENSED PHASE TO THE ISOLATED MOLECULE AT ITS EQUILIBRIUM GEOMETRY

The exquisite sensitivity of the shielding to the electronic environment is what makes the NMR chemical shift a very

Table 6 Absolute Shielding (ppm) Derived from the Shielding Anisotropy

Molecule/ion	$\Delta\sigma$, solid	$\sigma_\parallel = \sigma_\parallel{}^d$	$\sigma_\perp$	σ_{av}	σ_0(^{13}C in the molecule, 300 K)
OCO	335	274.1	−60.9	50.8	58.8
OCS	365	274.1	−90.9	30.8	30.0
SCS	424	276.1	−147.9	−6.6	−8.0
NCS^-	321	264.7	−56.3	50.7	
SeCSe	506	294	−212	−43.3	

powerful tool in studying structure, intermolecular effects, and dynamic averaging. For the purpose of comparing with theoretical ab initio calculations of the shielding, however, this exquisite sensitivity to the environment appears at first to be a distinct disadvantage. Nevertheless, if one knows the precise relationship between the quantities being calculated (the shielding at some specific set of nuclear coordinates) and the quantities being measured, then the appropriate comparisons against theory can still be made. In fact, a more complete comparison becomes possible when the true connection between the experimental milieu and the theoretical constructs is understood. Since it is never possible to observe a molecule as a fixed arrangement of nuclei (even in the molecular beam where no neighbor effects need to be considered, there is always at least the zero-point vibrational motion), let us consider the nature of the connection between what is measured and what can be calculated. In this respect, the NMR chemical shift is in by far a more advanced stage compared with other molecular electronic properties such as electric dipole polarizability, electric field gradient tensors, etc. It is partly a theoretical advantage, but more important an experimental advantage, that NMR spectroscopy provides. The very high resolution that is possible under the conditions of isotropic averaging in gases and solutions makes it possible to measure chemical shifts of the order of parts per billion. The more advanced temperature control of experiments in NMR spectroscopy, compared with other forms of spectroscopies, combined with the high resolution, has made it possible to measure the temperature dependence of the shielding in a nearly isolated molecule over a 200 K range almost routinely. The small chemical shifts that are the differences in shielding between two molecules differing only in the isotopic masses of some of the nuclei can be measured to a few ppb as well.

Both of these phenomena are related to the dynamic averaging of the vibrating molecule through its various nuclear configurations, each configuration having its appropriate shielding value for a particular nucleus. There are also intermolecular effects, again associated with shielding values that change with nuclear configurations, this time the configurations of supermolecules including not only the molecule bearing the NMR nucleus but all the neighboring interacting molecules. Solvent shifts are a manifestation of this, as are adsorption shifts, as well as a portion of the discrimination between different locations of the same amino acid residues in a protein. The dynamic averaging is discussed further in ***Isotope Effects on Chemical Shifts and Coupling Constants*** and some aspects of the intermolecular shifts are discussed further in the article on ***Gas Phase Studies of Intermolecular Interactions and Relaxation***. In this article, we merely take note of the mechanisms that give rise to the phase-dependent and temperature-dependent differences and how large the corrections are.

Let us first consider an isolated or nearly isolated molecule, i.e. one in which the frequency of collisions with other molecules is still enough to allow the molecule to sample its many rotational and vibrational states while being observed in the NMR spectrometer but not frequent enough to lead to a measureable intermolecular contribution. As the molecule undergoes vibrations, the distances between nuclei change in a periodic fashion, bonds being alternately compressed and expanded, bond angles being alternately enlarged and made smaller, with torsions or frustrated internal rotations possibly occuring as well. For each frozen configuration the shielding of an NMR nucleus in the molecule is different. In the context of the Born–Oppenheimer approximation, the nuclei are moving slowly enough relative to the electronic motion that it is possible to talk about a shielding surface, a highly multidimensional mathematical surface akin to the intramolecular potential energy surface, which describes the shielding at each configuration of the collection of nuclei that make up the framework of the molecule. Of course, the parts of this shielding surface that are sampled during the vibrations are those regions that correspond to the deep pockets in the intramolecular potential energy surface (PES), located at what we call the 'equilibrium' molecular geometry. Thus, it would seem that for the most part, the only interesting regions that we should concern ourselves with are those in the immediate vicinity of the single deep pocket in the PES. This may indeed be the case for the dynamic averaging in small molecules such as diatomics and methane. However, as soon as torsion angles come into the picture, the nature of the averaging changes. Wider excursions are possible, perhaps passing though *cis*-eclipsed, *gauche*, *gauche′*, *trans*-staggered, etc. Even in a simple molecule like NH_3, the umbrella inversion has to be considered in its entirety—no minor small amplitude excursions here! Thus, it becomes necessary to think in terms of not a single shielding tensor associated with a particular nucleus in a molecule, but a continuum, of such tensors changing smoothly with nuclear displacements away from the lowest energy point in the deep pocket. Some shielding surfaces are shown in the article on ***Isotope Effects on Chemical Shifts and Coupling Constants***, and the consequences of the dynamic averaging are discussed there as well.

How large are the shielding changes in going from the equilibrium geometry to the dynamically-averaged shielding? This depends on the molecule. For the ^{19}F shielding in the F_2 molecule, the difference is of the order of 40 ppm; for the ^{15}N in the N_2 molecule it is smaller, about 3 ppm, and for ^{1}H in the HF molecule it is around 0.3 ppm. Most of the dynamic averaging effects lead to a decreased shielding, but instances of increased shielding can also be found. At the time when the theoretical calculations were only good to within 50 ppm for ^{13}C in various molecules, for example, the direct comparison of the shielding calculated in a molecule rigidly fixed at its equilibrium geometry with the chemical shift measurements in solution could be excused. With the present theoretical capability discussed in the articles by Hansen and Kutzelnigg in this Encyclopedia, the real test of the quality of a calculation is really in the shape of the surface in the immediate vicinity of the equilibrium geometry, not just the value at a single one point on the surface. The rationale for determining absolute shielding scales is to be able to compare shieldings rather than differences of shieldings between two different molecules, thereby disallowing any fortuitous agreements in chemical shifts while the shieldings themselves could be far off. We go further at this point and make note not only of the absolute shielding of a nucleus in the particular molecule, but the dynamic average over a portion of the shielding surface for this nucleus; the shape of the surface itself is being tested. Typical magnitudes of the vibrational corrections that arise from this dynamic averaging are shown in Table 7.

Most of the time, we observe molecules in some medium rather than in the zero-pressure limit in the gas phase. Most of the full shielding tensor information is obtained in the solid

Table 7 Vibrational Corrections from Dynamic Averaging

	$[\sigma_0(T) - \sigma_e]$, theor. (ppm)
^{1}H in HF	−0.4
^{13}C in CH_4	−3.6
^{15}N in NH_3	−8.8
^{17}O in H_2O	−13.6
^{19}F in HF	−9.7
^{31}P in PH_3	−12.8
^{77}Se in H_2Se	−58.9

state or in liquid crystal solutions. It is therefore important to understand the ways in which that which we are measuring is affected by the surrounding molecules. We know that medium effects can be large because the gas-to-liquid shifts have been measured in pure substances. The magnitudes of some of these are shown in Table 8, where the chemical shift between the liquid and the vapor in equilibrium with it have been measured at the same temperature. We also know that intermolecular effects in physisorption can be large. Now, this is strictly an intermolecular effect, not involving a change in chemical structure. For ^{129}Xe nuclei of xenon atoms physisorbed in zeolites, the adsorption shifts are of the order of several hundred ppm! In other words, a xenon atom adsorbed in a zeolite cavity or channel has a shielding that differs from that in the gas phase by several hundred ppm. (See ***Adsorbed Species: Spectroscopy and Dynamics***.) This is strictly an intermolecular effect, not much different from the solvent effect in solution, with the only difference being that the solvent is stationary while the solute is relatively free to move. This too is a result of dynamic averaging, just as in solutions. This is clearly a many-body type of situation and the interpretation involves making some approximations.

Table 8 Gas-to-Liquid Shifts

		T(K)	$[\sigma(\text{liquid}, T) - \sigma\ (\text{vapor}, T)]$ (ppm)
^{1}H in	H_2O	298	−4.4
	NH_3	300	−1.75
	HCN	346.6	−2.0
^{13}C in	CO_2	220	−1.28
	HCN	336.6	−7.68
	C_6H_6	300	−1.5
^{15}N in	NH_3	300	−19.47
	HCN	346.7	+10.4
	CH_3CN	227.5	+11.3
^{17}O in	H_2O	488	−36.0
^{19}F in	CF_3H	280	−2.26
	CH_2F_2	280	−3.17
	CF_3Cl	280	−3.65
	CF_2Cl_2	300	−5.15
	CF_3CH_3	300	−4.65
	$CFCl_3$	340	−6.00
	CH_3F	260	−7.7
	SeF_6	300	−4.8
	TeF_6	300	−5.4
	WF_6	300	−7.4
^{31}P in	P_4	526	−77
^{77}Se in	SeF_6	300	−1.38
	H_2Se	300	−120
^{125}Te in	TeF_6	300	−2.0
^{129}Xe in	Xe	244	−200

A simpler situation is found in the gas phase. Intermolecular effects can be treated in the gas phase by the method of Buckingham and Pople by considering a virial expansion of the molecular electronic property, in this case the NMR shielding, in powers of density, i.e. $\sigma(T,\ \rho) = \sigma_0(T) + \sigma_1(T)\rho + \sigma_2(T)\rho^2 + \sigma_3(T)\rho^3 + \ldots$, where $\sigma_0(T)$ is the temperature-dependent shielding in the nearly isolated molecule. By making measurements of the shielding in gas samples of various densities at various temperatures, it is possible to obtain directly the second virial coefficient of nuclear shielding, $\sigma_1(T)$. This is a dynamic average which has a precise interpretation, as shown below.

$$\sigma_1(T) = \int_0^\infty 4\pi R^2\, \mathrm{d}R[\sigma(R) - \sigma(\infty)] \exp^{-V(R)/kT} \qquad (14)$$

In other words, the dynamic averaging occurs over an intermolecular shielding surface, $[\sigma(R) - \sigma(\infty)]$, with various weighting factors, as determined by the intermolecular potential energy, $V(R)$, surface. In a sense, this is entirely analogous to the averaging which occurs in vibration, except that the pockets are very deep in the intramolecular potential surface, whereas they are relatively shallow for intermolecular surfaces. Thus a very wide range of distances are included, and the temperature dependence is explicitly seen in the integration. The intermolecular shielding surface looks rather similar to the shielding surface of a nucleus in a diatomic molecule, except that all parts of the intermolecular surface are important other than at very very close range where the repulsive interactions dominate so strongly that such configurations are not effectively sampled.

This shielding surface is also amenable to theoretical calculations. In effect, the system under consideration is a supermolecule made up of the interacting molecules at all possible orientations and separations. A direct comparison of an intermolecular surface to an intramolecular one is not possible. However, the known differences in shielding sensitivities of nuclei across the Periodic Table allow us to scale the chemical shifts of one type of nucleus relative to another. For example, proton shifts are about 20 ppm to the fluorine shifts of about six hundred ppm. If we do this, then we can put an intramolecular shielding surface on the same plot as an intermolecular shielding surface, keeping their magnitudes in the same proportion as the well-known relative magnitudes of the ranges of their chemical shifts. One such example is shown in Figure 3, where the intramolecular shielding surface for the ^{23}Na nucleus in the NaH molecule is superimposed on the intermolecular shielding surface for the isoelectronic system, the ^{21}Ne nucleus in a Ne atom interacting with a He atom. On an absolute scale the shielding surface for ^{21}Ne in Ne–He has a much steeper change than the ^{23}Na shielding surface, but only because the nuclei on the right-hand side of the Periodic Table have much larger expectation values for the $1/r^3$ value of the electrons. When this is taken into account, it is seen that intramolecular shielding surfaces involve a much greater response of the nucleus to the changing electronic environment (bond extension or compression) than the response of the nucleus to the approach of a neighboring solvent molecule described by the intermolecular shielding surface.

If the shielding of a nucleus in a molecule surrounded by six neighbors, say, can be considered as a sum of six pairwise contributions between itself and each neighbor molecule,

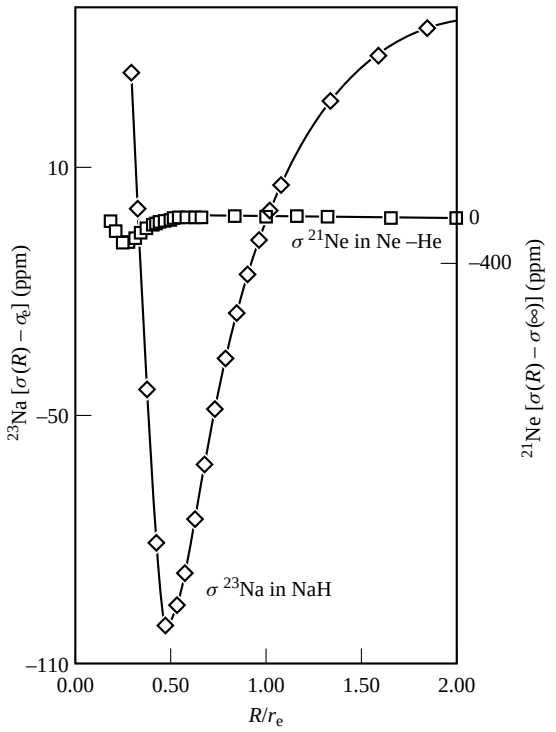

Figure 3 The intramolecular shielding surface for ^{23}Na in NaH and the intermolecular shielding surface for ^{21}Ne in NeHe

and if each pairwise intermolecular shielding function is known (similar to the ^{21}Ne shielding function for NeHe in Figure 3), then dynamic averaging amounts to sampling all such configurations of molecule and neighbors and calculating the intermolecular shielding for each configuration. This has been done for ^{129}Xe shielding in zeolite NaA. The same intermolecular shielding function that reproduces the $\sigma_1(T)$ for xenon in the gas phase reproduces the chemical shifts between the Xe, Xe_2, Xe_3, . . . , Xe_8 clusters trapped inside the cages of zeolite NaA.[24,25] In principle, chemical shifts in condensed phases can be obtained by a similar dynamic averaging.

6 RELATED ARTICLES

Shielding Calculations: LORG and SOLO Approaches; Gas Phase Studies of Intermolecular Interactions and Relaxation; Isotope Effects on Chemical Shifts and Coupling Constants; Shielding Calculations: IGLO Method; Shielding: Overview of Theoretical Methods; Shielding Theory: GIAO Method.

7 REFERENCES

1. P. F. Winkler, D. Kleppner, T. Myint, and F. G. Walther, *Phys. Rev. A.*, 1972, **5**, 83.
2. W. D. Phillips, W. E. Cooke, and D. Kleppner, *Phys. Rev. Lett.*, 1975, **35**, 1619.
3. G. Malli and C. Froese, *Int. J. Quantum Chem.*, 1967, **1S**, 95.
4. C. J. Jameson and J. Mason, in *Multinuclear NMR*, ed J. Mason, Plenum Press, London, 1987, Chap. 3
5. N. F. Ramsey, *Phys. Rev.*, 1950, **78**, 699.
6. W. H. Flygare, *J. Chem. Phys.*, 1964, **41**, 793.
7. D. K. Hindermann and C. D. Cornwell, *J. Chem. Phys.*, 1968, **48**, 4148.
8. C. J. Jameson, A. K. Jameson, and P. M. Burrell, *J. Chem. Phys.*, 1980, **73**, 6013.
9. C. J. Jameson, A. K. Jameson, and J. Honarbaksh, *J. Chem. Phys.*, 1984, **81**, 5266.
10. W. H. Flygare and J. Goodisman, *J. Chem. Phys.*, 1968, **49**, 3122.
11. T. D. Gierke and W. H. Flygare, *J. Am. Chem. Soc.*, 1972, **94**, 7277.
12. S. G. Kukolich, *J. Am. Chem. Soc.*, 1975, **97**, 5704.
13. C. J. Jameson, A. C. Jameson, D. Oppusunggu, S. Wille, P. M. Burrell, and J. Mason, *J. Chem. Phys.*, 1981, **74**, 81.
14. R. E. Wasylishen, S. Mooibroek, and J. B. Macdonald, *J. Chem. Phys.*, 1984, **81**, 1057.
15. W. L. Meerts, F. H. de Leeuw, and A. Dymanus., *Chem. Phys.*, 1977, **22**, 319.
16. A. K. Jameson and C. J. Jameson, *Chem. Phys. Lett.*, 1987, **134**, 461.
17. C. J. Jameson, in *Nuclear Magnetic Resonance*, ed. G. A. Webb, Royal Society of Chemistry, London, 1991, Vol. 20, Chap. 2
18. P. B. Davies, R. M. Neumann, S. C. Wofsy, and W. Klemperer, *J. Chem. Phys.*, 1971, **55**, 3564.
19. C. J. Jameson, A. C. de Dios, and A. K. Jameson, *J. Chem. Phys.*, 1991, **95**, 9042.
20. C. J. Jameson, A. C. de Dios, and A. K. Jameson, *Chem. Phys. Lett.*, 1990, **167**, 575.
21. R. E. Wasylishen, C. Connor, and J. O. Friedrich, *Can. J. Chem.*, 1984, **62**, 981.
22. C. J. Jameson and A. K. Jameson, *Chem. Phys. Lett.*, 1987, **135**, 254.
23. C. J. Jameson and A. K. Jameson, *Chem. Phys. Lett.*, 1988, **149**, 300.
24. C. J. Jameson and A. C. de Dios, *J. Chem. Phys.*, 1992, **97**, 417.
25. C. J. Jameson, A. K. Jameson, B. I. Baello, and H. M. Lim, *J. Chem. Phys.*, 1994, **100**, 5965.

Biographical Sketch

Cynthia J. Jameson. *b* 1937. B.S., University of the Philippines, Ph.D., 1963, University of Illinois at Urbana-Champaign. Introduced to NMR by Herb Gutowsky. Faculty in Chemistry, University of Illinois at Chicago, 1968–present. Approx. 130 publications. Research interests include theoretical and experimental studies of the chemical shift in simple systems in the gas phase and in molecules absorbed in microporous solids, with particular emphasis on intramolecular and inter-molecular shielding surfaces and averages therein; also, spin relaxation in gases and their connection with the anisotropy of intermolecular potentials and molecular dynamics.

Chemical Shift Tensor Measurement in Solids

Anita M. Orendt
University of Utah, Salt Lake City, UT, USA

1	Introduction	1
2	Magnetic Interactions	1
3	Experimental Considerations	2
4	Samples: Powders versus Single Crystals	3
5	One-Dimensional Powder Techniques	4
6	Two-Dimensional Powder Techniques	6
7	Single Crystal Techniques	12
8	Dipolar Techniques	13
9	Summary	15
10	Related Articles	15
11	References	15

1 INTRODUCTION

There are a number of methods in solid state NMR spectroscopy which can be used to obtain information about the chemical shift tensor. The method of choice is usually a function of the equipment available, the complexity of the sample, the information desired, and the state of the sample at ambient temperatures. This article serves as an overview of the various methods, and deals with the requirements and limitations in terms of both sample and instrumentation for each technique, as well as with the information that can be obtained. A more detailed description for some of these techniques can be found in other portions of the Encyclopedia, as listed in Section 10. It should be noted that no effort is made to include listings of chemical shift tensor data that have been measured. The reader is referred to compilations of this type of data, the most recent being Duncan's book.[1]

Before the description of the methods, a brief introduction concerning the Zeeman interaction, chemical shielding, dipolar coupling, and quadrupolar interactions that must be considered is presented. Again a more detailed discussion concerning these interactions is presented elsewhere in this Encyclopedia or can be obtained from a number of books.[2–5]

2 MAGNETIC INTERACTIONS

2.1 Zeeman Interaction

In the presence of a magnetic field, a nucleus possessing a spin ($I \neq 0$) will be in one of $2I + 1$ energy levels, defined by the magnetic moment of the nucleus and the strength of the static magnetic field, $\boldsymbol{B}_0$. The NMR experiment measures the transitions between these levels. The direction of the applied magnetic field is taken by convention to be along the z direction, and the difference in energy between any two of the allowed states, in frequency units (Hz), can be given as

$$\nu_0 = \gamma_I B_0 / 2\pi \tag{1}$$

This frequency ν_0 is known as the Larmor frequency, and is a function of the field strength and the magnetogyric ratio, γ, of the nucleus.

2.2 Chemical Shielding

The chemical shielding interaction separates the resonance frequencies of nuclei based on their electronic environment. The magnetic field experienced or 'seen' by the nucleus of an atom in a molecule is affected by the electrons that surround that nucleus. The chemical shift tensor is a reflection of this orientation-dependent interaction of the electronic environment of a nucleus with the external magnetic field. In general, a different value of the chemical shift will be observed for a nucleus for each orientation of that molecule in the magnetic field. The dependence of the chemical shift on the molecular orientation will be further elaborated upon in the next section.

In the most general terms this chemical shift interaction is represented by a 3×3 Cartesian matrix,

$$\delta = \begin{bmatrix} \delta_{xx} & \delta_{xy} & \delta_{xz} \\ \delta_{yx} & \delta_{yy} & \delta_{yz} \\ \delta_{zx} & \delta_{zy} & \delta_{zz} \end{bmatrix} \tag{2}$$

The interaction can be decomposed into three parts: the isotropic, the symmetric, and the antisymmetric portions,

$$\delta = \delta_{\text{iso}} + \delta_{\text{sym}} + \delta_{\text{anti}} \tag{3}$$

The isotropic matrix gives the position of the center of the spectrum, while the symmetric matrix defines the lineshape observed. The antisymmetric portion has no observable effect on the lineshape, at the current level of technology and will not be further considered in this work. Often the first two terms are combined and given as

$$\delta = \begin{bmatrix} \delta_{xx} & \delta_{xy} & \delta_{xz} \\ \delta_{xy} & \delta_{yy} & \delta_{yz} \\ \delta_{xz} & \delta_{yz} & \delta_{zz} \end{bmatrix} \tag{4}$$

The resonance frequency that is observed in high-resolution NMR spectroscopy is one-third of the trace of the matrix shown in equation (4), or $\delta_{\text{iso}} = (\delta_{xx} + \delta_{yy} + \delta_{zz})/3$.

There exists some frame in which the matrix in equation (4) is diagonal; in this case the three diagonal elements are known as the principal values of the chemical shift tensor (or tensor components), and are designated as δ_{11}, δ_{22}, and δ_{33}. Convention states that $\delta_{11} \geq \delta_{22} \geq \delta_{33}$, with δ_{11} being in the high-frequency or least shielded direction. The remaining three terms are the Euler angles which define the directions of these principal values in the molecular frame. The axis system in which the symmetric chemical shift matrix is diagonal is known as the principal axis system (PAS).

2.3 Dipolar Coupling

Interactions also exist between magnetic nuclei. The interaction of two spins through space is known as a direct or dipolar coupling. This interaction has a $1/r^3$ dependence on the separation of the two spins and a linear dependence on the γ values of the two spins involved, as shown in equation (5) for the general case of two different spin-$\frac{1}{2}$ nuclei, I and S, e.g., ^{13}C and ^{1}H.

$$D = \frac{\gamma_I \gamma_S \hbar}{r_{IS}^3} \tag{5}$$

The dipolar interaction is also orientation-dependent; in this case the tensor is axially symmetric and has a trace of zero. The fact that the dipolar tensor is traceless means that the dipolar interactions average to zero in high-resolution NMR spectra. The unique component of the dipolar tensor is along the vector connecting the two spins, generally designated as D_{zz} and is equal to $2D$, and the two identical components, D_{xx} and D_{yy}, with the value of $-D$, are in the plane perpendicular to this vector.

In the case of solid state NMR studies of organic compounds, most typically carbon is the nucleus of interest. Only 1.1% of all carbon nuclei are ^{13}C, which is the magnetic isotope of carbon. The remainder of the carbon nuclei have no magnetic moment and as such are nondetectable. For this reason, dipolar couplings between directly bonded carbons only occur in approximately one of every 10 000 pairs. Magnetic isotopes of low natural abundance, such as carbon, are said to be 'rare' or dilute spins. This is also the case for a number of other nuclei, with ^{15}N being a second important case of a rare spin. However, as more than 99% of all hydrogen nuclei are protons (^{1}H) with $I = \frac{1}{2}$, dipolar couplings both between protons and between the rare spins and the protons play an important role in organic compounds. These ^{1}H–^{1}H and ^{1}H–^{13}C dipolar interactions are very large (tens of kHz) and can completely obscure the chemical shift information. Fortunately, these interactions can be removed by a technique known as proton dipolar decoupling, which is the use of irradiation at the proton frequency during the observation period. Decoupling can be used to remove unwanted dipolar interactions in all cases where the rare spin being observed is coupled to an abundant spin system.

There are also several decoupling schemes that remove the dipolar interactions between nuclei of an abundant spin while allowing for the observation of the chemical shift information of that same spin. These techniques are grouped together as multiple pulse decoupling techniques,[6] and are most commonly used when observing ^{1}H or ^{19}F.

Finally, dipolar couplings between two (and occasionally three or more) spins can be used to obtain information about both the orientation of the PAS and the distance between the spins. A molecule can be selectively enriched with two magnetic isotopes to achieve an isolated spin pair; alternatively, compounds can be enriched in one position and the second spin of the dipolar pair can be one of high natural abundance, but uncommon (^{19}F or ^{31}P), or a spin-$\frac{1}{2}$ pair may exist naturally (^{31}P–^{31}P).

2.4 Quadrupolar Effects

For the quadrupolar nuclei, i.e. those with spins ≥ 1, the observed lineshape is typically dominated by the nuclear quadrupole interaction, given for a spin I in equation (6):

$$\boldsymbol{Q} = \frac{eQ}{2I(2I-1)h}\boldsymbol{V} \tag{6}$$

Again the interaction is anisotropic, with the factor eQ being the quadrupole moment and $\boldsymbol{V}$ the electric field gradient (EFG) tensor. The EFG tensor has a PAS just like the chemical shift tensor; the EFG tensor is traceless, and does not appear directly in liquid spectra due to rapid, isotropic molecular tumbling in solution. The quadrupole coupling constant, $\chi = e^2Qq/h$, ranges from 100 kHz to tens of MHz depending on the nuclei (i.e., ^{2}H, ^{14}N, or ^{17}O) and the symmetry about the nuclei.

Due to the fact that quadrupolar coupling terms are usually orders of magnitude larger than the span of the chemical shift values, the lineshapes obtained are typically only fitted using the isotropic chemical shift along with the quadrupolar parameters. Therefore, the principal values of the chemical shift tensor have only been obtained for a small number of quadrupolar nuclei.[1] Due to this lack of reported measurements of the principal values, no further discussion on quadrupolar nuclei will be presented in this article.

When quadrupolar nuclei are coupled to spin-$\frac{1}{2}$ nuclei, there exists a dipolar coupling; this situation will be included in the section on dipolar spectra.

3 EXPERIMENTAL CONSIDERATIONS

3.1 Cross Polarization

The first step in all the experiments that will be discussed is to take the magnetization of the spin of interest from its equilibrium position, aligned with the magnetic field, to the xy plane. This is commonly done using one of two methods: by application of a 90° pulse (also known as a Bloch decay or BD) or by cross polarization (CP).[7]

The experiment of choice is typically CP, in which the signal of the low abundance spin system is enhanced via magnetization transfer from a second magnetic nucleus which has both a higher natural abundance and a higher γ value. Again the most common nucleus used for magnetization transfer is the proton. The CP method has two advantages over BD: there is a signal enhancement of the rare spin by up to a factor of the ratio of the γ value of the high abundance spin to that of the rare, lower γ spin, and the relaxation times, which dictate how fast a repetition rate can be used in the signal averaging process, are typically faster for the more abundant spin.

In the BD experiment, a 90° pulse is used to take the magnetization of the spins directly into the xy plane, followed by an observation period during which the decay of magnetization in this plane as it returns to its equilibrium position along the magnetic field direction is recorded. The BD experiment is used in cases without an abundant spin system, i.e. systems without protons.

In order to obtain signals from only protonated carbons or signals from only nonprotonated carbons, the techniques of short CP or contact times (SCT) and dipolar dephasing (DD) can be used.[8,9] With short contact times (about 40 μs), only carbons with directly bonded protons develop magnetization, resulting in a spectrum containing only signals of these carbons. With DD, time is allowed for magnetization transfer to develop to all carbons, followed by a period during which the magnetization of the strongly coupled spins, i.e. the protonated carbons, is allowed to decay. The magnetization dephasing is much slower for the weakly dipolar-coupled (nonprotonated and mobile methyl carbons) spins. After this dephasing period a normal acquisition shows only signals from these weakly dipolar-coupled carbons.

3.2 Magic Angle Spinning

Magic angle spinning (MAS)[10,11] is a technique used in conjunction with high power decoupling to obtain high-resolution or solution-like spectra from a solid powder sample. With MAS the chemical shift interaction is averaged to its isotropic value and dipolar interactions are removed by rapid rotation of the sample at an angle of 54.7°, the magic angle, with respect to the $\boldsymbol{B}_0$. The average chemical shift δ of a given nucleus in a sample that is rotating about an angle θ with respect to the external magnetic field is given by

$$\begin{aligned}\delta = \delta_{\text{iso}} &+ \tfrac{1}{2}(3\cos^2\theta - 1) \\ &\times \left[\tfrac{1}{2}(3\cos^2\beta - 1)(\delta_{33} - \delta_{\text{iso}})\right. \\ &\left.+\tfrac{1}{2}\cos^2\beta\cos 2\alpha(\delta_{11} - \delta_{22})\right] \qquad (7)\end{aligned}$$

where α and β are two of the three Euler angles which specify the orientation of the PAS in the frame of the spinning system, and the δ quantities are the various elements of the chemical shift tensor. At θ = 54.7°, the term (3 $\cos^2\theta$ − 1) is zero, and the pattern collapses to a single line at the frequency given by the isotropic chemical shift, δ_{iso}, provided that the rotation frequency, ω_{r}, is larger than the width of the powder pattern.

4 SAMPLES: POWDERS VERSUS SINGLE CRYSTALS

4.1 Powder Samples

So-called powder techniques (both one- and two-dimensional) are performed on powdered or microcrystalline samples, or on samples that have molecules in a statistical distribution of all possible orientations with respect to the magnetic field. The principal values of the chemical shift tensor define the spectral lineshape obtained for the case of a decoupled spin-$\frac{1}{2}$ nucleus. The resultant lineshapes as shown in Figure 1 can be used to obtain the principal values of the chemical shift tensor. The change in intensity across the powder pattern can be explained by representing the chemical shift as an ellipsoid centered at the nucleus. The distance from the center to the outside of the ellipsoid represents the magnitude of the chemical shift with the static magnetic field in that direction while the three axes of the ellipsoid are the directions giving rise to the three principal values. While there are only two directions which give rise to each of the three principal values there are multiple directions that give rise to the values between the principal values.

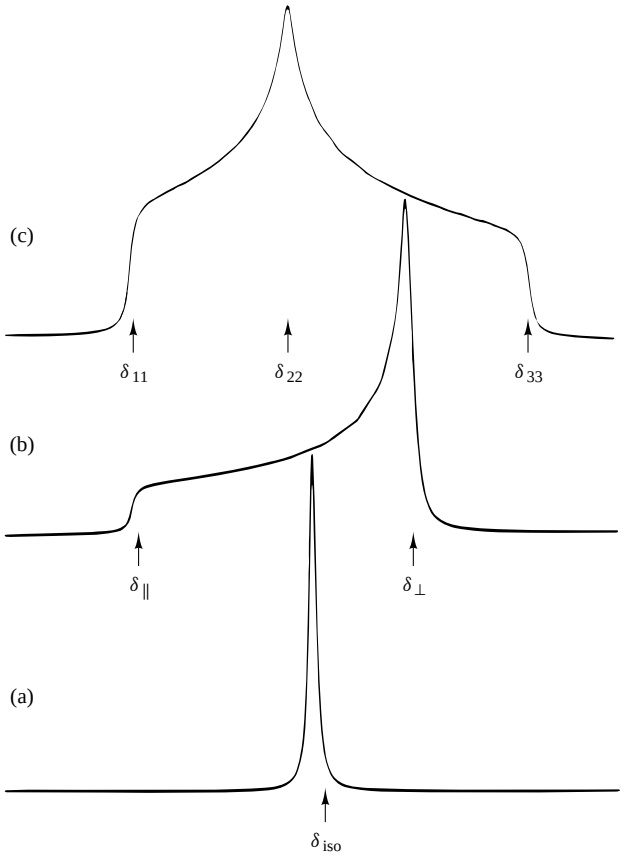

Figure 1 Examples of chemical shift powder patterns for one spin-$\frac{1}{2}$ nucleus: (a) symmetric system, (b) axially symmetric system, and (c) general asymmetric tensor. Arrows indicate the position of the principal values of the chemical shift tensor

For the case of nuclei with highly symmetric electronic environments, for example the carbon in methane, CH_4, the electronic environment does not change as a function of the orientation of the molecule in the magnetic field, and thus the chemical shift is the same in all orientations. This situation occurs when the symmetry at the nucleus is tetrahedral or greater and gives rise to an isotropic chemical shift powder pattern, shown in Figure 1(a), where the three principal values are all equivalent and equal to the value observed in high-resolution NMR spectroscopy. The entire width of the powder pattern is due to residual broadening effects.

The next case is where two of the three principal values are equivalent (known as an axially symmetric tensor) which occurs in cases where there is a threefold symmetry axis through the nucleus, e.g. N of NH_3. The unique principal value lies along the threefold axis and is designated $\delta_{\parallel}$ while the degenerate components are in the plane perpendicular to the axis and are designated $\delta_{\perp}$. These two values can be read from the extremes or breakpoints of the powder pattern, as indicated in Figure 1(b).

The most general case is when the symmetry elements present at the nucleus are all less than threefold, resulting in all three of the principal values being different, as shown in Figure 1(c). In general, only the three principal values of the

chemical shift tensor can be measured from a powder sample. However, in some cases, the symmetry of the molecule at the nuclei of interest can indicate the directions of one or more of the principal values of the tensor (but not which principal value is in that direction). The more the electronic environment varies, the broader the powder pattern.

The techniques that can be used to obtain the principal values of the chemical shift tensor for decoupled spin-$\frac{1}{2}$ nuclei using a powder sample are divided into two broad categories: the one-dimensional (1D) methods, discussed in Section 5, and the two-dimensional (2D) methods, covered in Section 6.

4.2 Single Crystals

In a single crystal there is no longer a distribution of all possible orientations with respect to the external magnetic field as in a powder sample. Instead of seeing broad powder patterns which are independent of the orientation of the powder sample in the magnetic field, the NMR signal from a single crystal placed in a magnetic field is a series of narrow lines, one for each magnetically inequivalent nucleus. When the crystal is rotated, the position of these lines change. The manner in which the position of a given line in the spectrum changes as a function of the crystal orientation in the magnetic field, again for decoupled spin-$\frac{1}{2}$ nuclei, is given by the expression

$$\delta = \delta_{11}\cos^2\alpha\sin^2\beta + \delta_{22}\sin^2\alpha\sin^2\beta + \delta_{33}\cos^2\beta \qquad (8)$$

where α and β are the Euler angles which relate the PAS to the magnetic field direction. Knowing the crystallographic orientation of the single crystal as mounted in the NMR probe, this information can be used to determine the orientation of the PAS in the molecular frame.

Aside from the advantage that the entire chemical shift tensor is determined, a second advantage is that single crystal NMR data are the most precise. The estimated errors in the principal values are in the order of 1 ppm or less, whereas the errors in the powder techniques are generally in the range of 3 ppm or more. Intermolecular interactions and/or structural distortions in crystals can lead to very small shifts in these principal values and/or orientations between two nuclei, and these effects, while immeasurable by powder techniques, can be observed by single crystal NMR.[12]

While this experimental method provides the most information, it is also the method with the most limitations. The most severe limitation is that a relatively large single crystal (several mm in all dimensions) of the compound of interest must be obtained, a feat not always possible. This automatically limits the possibilities to room temperature solids from which single crystals can be grown and transferred into the NMR probe. However, if a suitable crystal can be grown, it is the method of choice.

Single crystal studies have been completed on dilute spin systems, mainly ^{13}C, as well as on abundant spins such as ^{1}H or ^{19}F. For ^{13}C, the cross polarization method in combination with high-power proton decoupling is used; for the abundant spins, multipulse decoupling techniques are necessary.

Just as the powder techniques are divided among 1D and 2D methods, so are the single crystal methods. In Section 7, the experimental techniques for obtaining the chemical shift information from a single crystal will be presented.

5 ONE-DIMENSIONAL POWDER TECHNIQUES

5.1 Static Powder Sample

The simplest, most straightforward experimental method for obtaining the principal values of the chemical shift tensor is to record the spectrum of a static solid sample and measure the principal values from the breakpoints in the powder pattern, as indicated in Figure 1.[2] The sample can be a solid without any molecular reorientation at room temperature, or it can be a sample at a temperature low enough both to take the sample into the solid state and to stop any molecular reorientation. Most typically, the CP technique in conjunction with high-power decoupling is used to obtain the powder pattern of common, low natural-abundance spin-$\frac{1}{2}$ nuclei such as ^{13}C or ^{15}N or a high natural-abundance, but uncommon, nucleus such as ^{31}P. Powder patterns can also be obtained for common, high natural-abundance spin-$\frac{1}{2}$ nuclei (e.g., ^{1}H) with the use of multiple pulse decoupling techniques.

The use of static powder samples has one severe limitation. In molecules containing several nonmagnetically equivalent nuclei, e.g., several different carbons, overlap between the powder patterns can make the determination of the principal values impossible. This is demonstrated by the powder pattern of 1,2,3,6,7,8-hexahydropyrene, given in Figure 2 along with the best fit to the lineshape due to the aromatic carbons. In this case there are three magnetically inequivalent aromatic carbons, with the powder patterns labeled A, B, and C in the decomposed simulation. The portion of the spectral lineshape not fitted is due to the aliphatic carbons.

Even though there have been numerous techniques introduced which help to overcome this limitation concerning sample complexity, the use of a static powder sample is still very common as it is the only technique applicable for certain samples. While variable temperature probes could, in theory, be built to perform many of the experiments that will be discussed below, the majority of the probes that have been built for these techniques can only handle room-temperature solids. On the other hand, it is fairly simple to equip a NMR probe for a static sample with variable temperature capabilities to solidify a liquid and perform a static powder measurement on the sample.

NMR probes have also been constructed to interface with closed cycle cryogenic units, capable of reaching temperatures as low as 4 K.[13,14] This allows the study of not only samples that are liquids or gases at room temperature, but also molecules isolated in an inert environment. Molecules not stable under normal conditions for any reasonable length of time can be generated and quickly deposited on the cold tip of the cryogenic unit, or molecules can be generated photochemically after deposition of a precursor species. For these situations, the only option for obtaining any information on the principal values of the chemical shift tensor is to measure a static powder pattern.

5.2 Variable Angle Sample Spinning

The problem of overlapping tensor patterns can be somewhat alleviated by partially averaging the lineshape by spinning the sample at an angle other than the magic angle, a technique

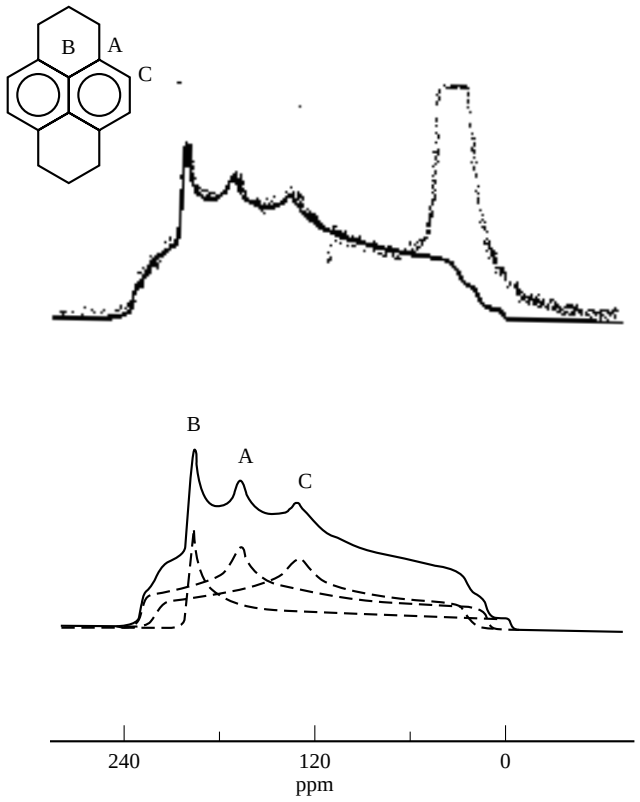

Figure 2 Static powder pattern of 1,2,3,6,7,8-hexahydropyrene with best-fit simulation of the aromatic region. Simulation is decomposed into the three components, where A is the lineshape of the substituted aromatic carbons, B is the pattern of the condensed or bridgehead aromatic carbons, and C is the pattern of the protonated aromatic carbons. (Reproduced by permission of the American Chemical Society from N. K. Sethi, R. J. Pugmire, and D. M. Grant, *Prepr. Am. Chem. Soc., Div. Fuel Chem.*, 1987, **32**, 155)

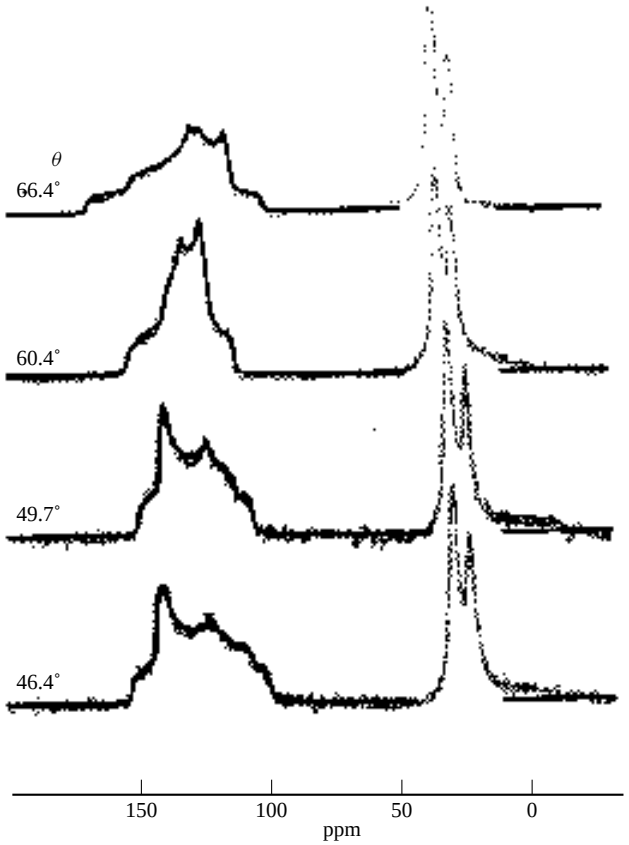

Figure 3 VASS powder patterns of 1,2,3,6,7,8-hexahydropyrene taken at specified angles θ with respect to the static magnetic field direction, along with best fit simulations of the aromatic region. (Reproduced by permission of the American Chemical Society from N. K. Sethi, R. J. Pugmire, and D. M. Grant, *Prepr. Am. Chem. Soc., Div. Fuel Chem.*, 1987, **32**, 155)

known as variable angle sample spinning or VASS.[15,16] As described in Section 3.2, if a sample is spinning at an angle of 54.7° relative to the external magnetic field, and the spinning rate is greater than the width or anisotropy of the pattern, each pattern is collapsed to a relatively narrow line at the isotropic chemical shift, according to the expression in equation (7). If the chosen angle is not the magic angle then the pattern is scaled by the $3\cos^2\theta - 1$ term, where the angle between the spinning axis and the external magnetic field is given as θ. For angles less than the magic angle the pattern is scaled, and for angles greater than the magic angle the pattern is inverted about the isotropic chemical shift as well as scaled. Representative VASS spectra of 1,2,3,6,7,8-hexahydropyrene are shown in Figure 3 for four different angles. It should be noted that the powder pattern for each individual spin is scaled differently, and therefore the resultant patterns are not just scaled versions of one another but are distinctive lineshapes. Experimentally, it has been demonstrated that recording five spectra, one at the magic angle and four at other angles, and simultaneously fitting the four off-angle spectra while locking the isotropic values to those obtained by the magic angle spectrum, gives good results.[17]

One of the major advantages of the VASS technique is that it removes the overlap that is nearly always observed between the δ_{33} component of unsaturated carbons and the aliphatic carbon signals. Also, less time is required to obtain a spectrum with the same signal-to-noise (S/N) ratio as a static powder pattern due to the scaling of the powder pattern. Because a number of different spectra can be recorded and fitted simultaneously, the number of tensors that can be fitted is slightly increased relative to the number of tensors that can be obtained from a static powder pattern.

5.3 Slow Magic Angle Spinning

Another method that can be used to alleviate the problem of overlapping powder patterns is to spin at the magic angle but at speeds less than the width of the patterns, a technique that is known as the Herzfeld–Berger method.[18,19] The resulting spectrum is a series of narrow lines spaced about isotropic chemical shift at integer multiples of the spinning speed for the width of the powder pattern, as shown in Figure 4(b) for the carbons in 1,2,3-trimethoxybenzene. Combining this spectrum with the spectrum taken at a higher speed MAS, shown in Figure 4(a) for 1,2,3-trimethoxybenzene, the center or isotropic chemical shift peaks can be identified, and the various sidebands can then be matched to the proper centerline. The intensities of these spinning sideband (ssb) patterns can

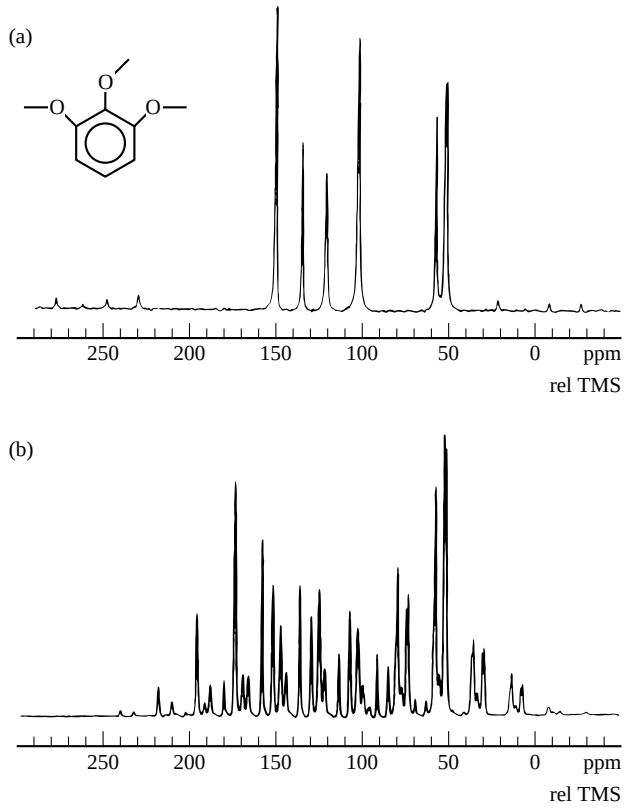

Figure 4 (a) MAS spectrum of 1,2,3-trimethoxybenzene (shown in inset) at a spinning rate of 6.0 kHz. (b) Spinning sideband pattern obtained for 1,2,3-trimethoxybenzene at a spinning rate of 1106 ± 5 Hz

then be analyzed by several methods to yield the principal values of the chemical shift tensor.

This procedure has not been used very widely as it requires a careful measurement of the integrated intensities and the use of a more complex analysis than needed for static patterns, and the errors in the principal values obtained from this technique are typically greater than those from the other methods. Experimentally, it is crucial that the spinning speed be constant (±10 Hz); however, with modern spinning speed controllers this is very feasible. The limitation in the number of magnetically inequivalent spins is determined by the width of the lines; if a compound contains several spins with similar isotropic chemical shifts, overlap can prevent accurate line intensities being obtained.

More recently, the Herzfeld–Berger method has been combined with DANTE pulse sequences[20] to saturate selectively one or more of the ssb patterns to simplify the spectra of complex compounds.[21] After the initial preparation of magnetization by a normal CP sequence, a DANTE sequence centered at the frequency of one of the peaks of the ssb pattern to be destroyed is added. This sequence leaves the magnetization of the other spins unaffected. Several DANTE sequences at different frequencies can be added, with the limitation that the spin–lattice relaxation time (T_1) be of sufficient length that the magnetization for the desired spins does not relax back to thermal equilibrium during the time it takes to apply the saturation sequences.

This concept of producing selective 1D spectra can be considered an alternative to the 2D approach of obtaining all the ssb patterns separated in 2D space, as presented in the section on 2D methods. This same approach is also used in the next section in conjunction with spinning at two different angles.

5.4 Switched Angle Spinning

A one-dimensional version of the 2D switched angle sample spinning (SASS) experiment to be discussed in the next section was introduced in 1990.[22,23] By combining the principles of switched angle spinning with some type of selective irradiation scheme, a spectrum containing only the powder pattern(s) of the selected spin(s) can be obtained. The magnetization of the selected spin is selectively prepared or inverted with the sample spinning at the magic angle using a technique such as the DANTE sequence in the case of Maciel's work[23] or selective soft rf pulses as done by Ashida et al.[22] It is necessary that spinning be conducted at the magic angle in order to be able selectively to irradiate one spin while not affecting the magnetization of the remaining spins. The spinner axis is then changed to a different angle before the detection period, resulting in a scaled powder pattern containing only the signals of the selected spin. There is, however, a limit to how selective a pulse can be; if there are two or more signals closely spaced, it is impossible selectively to irradiate only one of them.

The experiment was undertaken in a 1D manner in the belief that conducting a number of 1D experiments in such a way as to obtain the spectra of all spins may be more time-efficient than conducting a 2D experiment in some cases. This judgment is very dependent on the nature and number of the nuclei in the sample.

6 TWO-DIMENSIONAL POWDER TECHNIQUES

The various 2D techniques that have appeared in the literature are discussed in this section. However, before discussing the specifics of each technique, some comments general to 2D spectroscopy are necessary. First, all 2D spectral techniques can be described in terms of the preparation of a magnetization period, followed by an evolution time, t_1, possibly a mixing time, and then an acquisition time, t_2. The evolution time is increased by a constant time increment between successive spectra in the 2D experiment, and the signal acquired during the acquisition time is a function of both the evolution time and the acquisition time. In all the cases outlined below, the techniques were described for the observation of dilute spin-$\frac{1}{2}$ nuclei, and the preparation period consisted of a normal CP sequence to take the magnetization into the transverse plane. A general 2D pulse sequence, using CP for signal enhancement, is shown in Figure 5.

While these 2D techniques can be divided in a number of ways, in this article the techniques that obtain the isotropic dimension during the evolution time will be discussed first, followed by those which use MAS during the acquisition time to obtain the isotropic information in the second dimension.

As the spectral presentation of the individual powder patterns as ridges in a 2D contour plot, with the projection on the two axes being an isotropic spectrum and a normal powder pattern, is the same in the majority of these techniques, sample spectra are not included for each technique. Instead only one

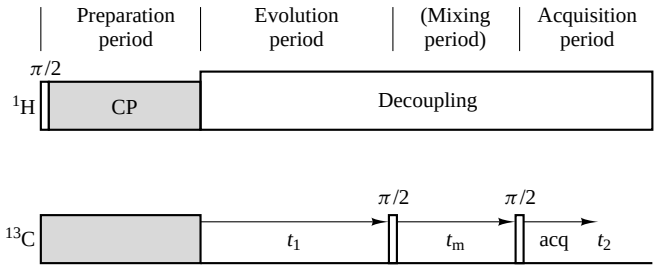

Figure 5 A schematic representation of the times in a general 2D pulse sequence, along with a typical 2D pulse sequence for both the ^{1}H (decoupler) and observe nucleus channels, using CP for the preparation of the magnetization. The pulse sequence shown is the basic 2D chemical exchange scheme. The mixing period is optional

representative spectrum of this type is included. Representative spectra obtained for the 2D methods that present the chemical shift information in a different manner are also included. Also, no information is provided on the details of the phase cycling used in the methods; the reader is referred to the original references for this information.

6.1 Magic Angle Hopping

Magic angle hopping (MAH)[24] was one of the first 2D techniques which provided isotropic chemical shifts, i.e. a normal MAS spectrum in the first dimension, with the individual powder patterns separated in the second dimension. The MAH experiment is carried out with a static sample at the magic angle with respect to the external magnetic field. The sample is successively hopped by 120° about this axis, using a computer-controlled stepping motor such that the sample spends one-third of the evolution time in each of the three orientations. Between these three periods the prepared magnetization is stored along the magnetic field direction with a 90° pulse; the sample is reoriented or hopped, followed by the return of the magnetization to the *xy* plane with a second 90° pulse. The timing of the pulses and the hopping of the sample during the evolution time are shown in Figure 6(a). As there is no spinning of the sample, the isotropic chemical shift dimension has no spinning sidebands.

The major difficulty in this experiment is the requirement of rapidly and accurately reorienting the sample during each scan. The original work reported a hopping time of 150 ms; subsequently, in a paper reporting several modifications to the original experiment,[25] the hopping time was reduced to under 60 ms with the use of a dc servo motor. The shortening of this hopping time is important as the magnetization that is prepared and subsequently stored along the magnetic field by the 90° pulse is decreased by normal $\boldsymbol{T}_1$ relaxation mechanisms. The accuracy in setting the angles is reflected in how complete the averaging process is, and it therefore affects the width of the lines observed in both the isotropic chemical shift spectrum and in the 2D space, placing a limitation of the resolution obtainable.

The reported modifications of the MAH experiment also included a larger sample volume to allow for the measurement of a 2D spectrum in under 24 h, and an increase in the signal collected in each scan by incorporating the last one-third of the evolution time into the acquisition dimension, as discussed in the next technique.

6.2 Magic Angle Turning

One of the most recent 2D techniques for the separation of the overlapping powder patterns was introduced by Gan in 1992[26] and is known as the magic angle turning (MAT) method. Gan's technique is a very simple method which can, in principle, be undertaken on a normal MAS probe without any additional equipment. The MAT method is based on the fact that continuous, very slow, spinning at the magic angle can be used in place of the three discrete 120° hops in the MAH experiment. Instead of mechanically hopping the sample by 120°, Gan proposed that the pulses in the evolution period be separated by a time equal to one-third of the rotor period, as shown in the pulse sequence in Figure 6(b).

A second modification from the previous MAH method is that the acquisition period was started immediately after the last pulse instead of waiting a time period of one-third of the evolution period. This modification of acquiring the complete echo instead of starting the acquisition at the top of the echo increases the signal intensity by nearly a factor of $\sqrt{2}$. A consequence of this modification is that the 2D space is no longer a square but has the powder patterns at an angle defined by $\tan^{-1}(1/3)$, and it must be sheared or rotated by this angle in order to obtain normal projections of the isotropic chemical shift spectrum.

This technique was subsequently refined, and the power of the method demonstrated[27] using a probe designed specifically for the experiment. The probe, designed around a large volume rotor (about 5 cm^3), has a maximum spinning rate of about 200 Hz, and is very stable at spinning rates as low as 22 Hz. Normal commercial MAS probes, on the other hand, are optimized for stable spinning at speeds in the kHz to tens of kHz range and it is usually difficult to maintain stable spinning at very low speeds. The modification of the pulse sequence, designated the triple echo MAT and shown in Figure 6(c), consists of an addition of three echo pulses to Gan's proposed pulse sequence in order to remove phase imperfections and anomalies in the 2D base plane. The lowered spinning speed also simplifies the fitting of the powder patterns obtained as slices of the 2D space, as they are identical to a static powder pattern at these speeds. It was shown that the spectral lineshape is affected at speeds as low as 44 Hz, requiring that the data be fitted instead of being able to read the break points directly from the lineshape. The large volume sample allows for a typical 2D spectrum to be obtained in less than 24 h, making it feasible for this technique to be used on a routine basis.

This paper also demonstrated that the method can be combined with the techniques of SCT to obtain spectra containing signals from only the protonated carbons, and DD for spectra containing only patterns from nonprotonated carbons. A typical 2D spectrum obtained using the triple echo MAT method, along with the individual powder patterns obtained, is shown in Figure 7 for 2,6-dimethoxynaphthalene, which has six inequivalent aromatic carbons.

6.3 5-π Pulse

The 5-π pulse experiment[28] is another method related to the MAT and MAH techniques. In this experiment, as in MAT, the sample is also spinning slowly at the magic angle. However, instead of storing the selected magnetization along

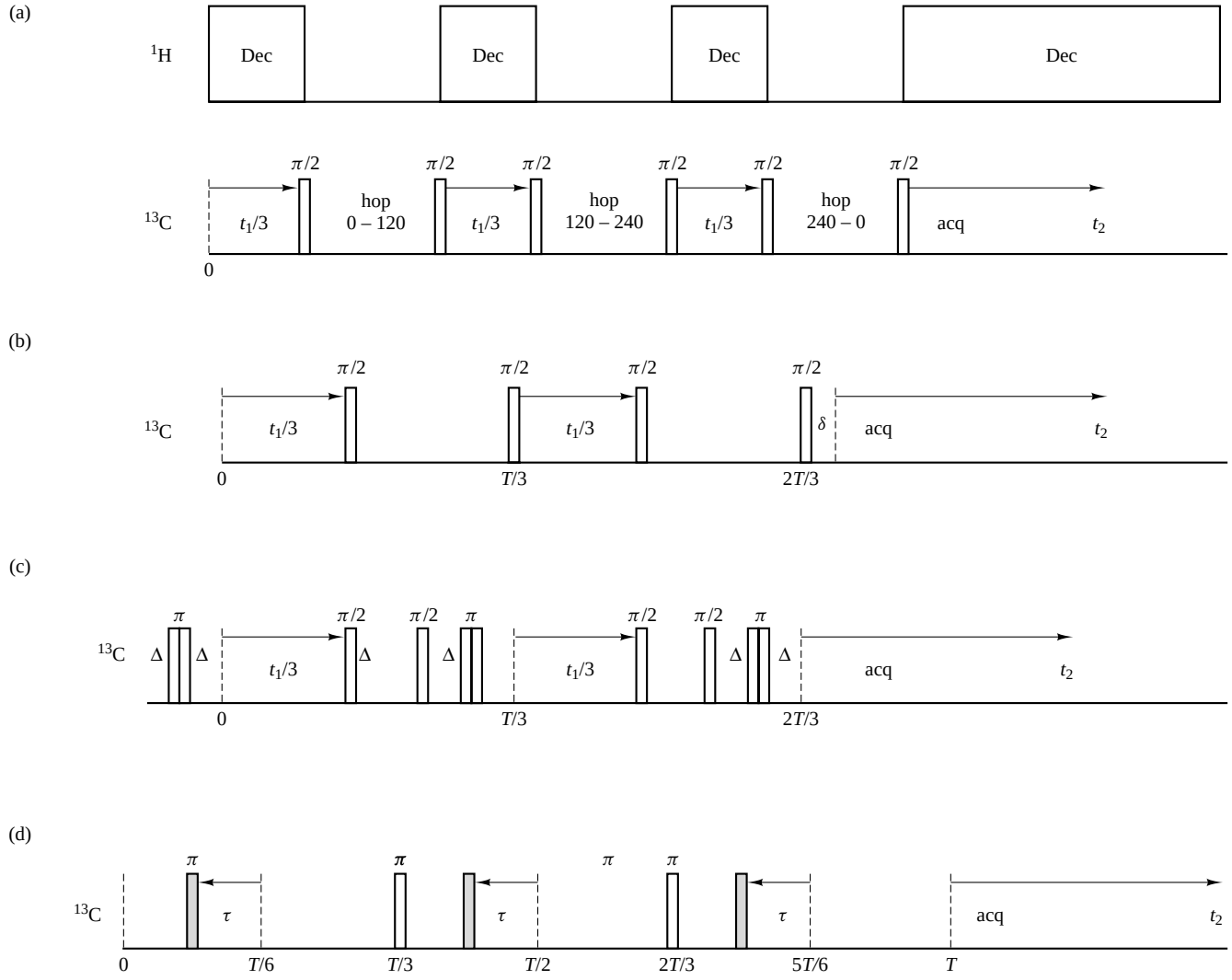

Figure 6 (a) The evolution and acquisition time of the MAH pulse sequence for both the observe and decouple channel. (b) The evolution and acquisition time of the original MAT pulse sequence. (c) The evolution and acquisition time of the triple echo MAT pulse sequence. Δ indicates the echo time. (d) The evolution and acquisition time of the 5-π pulse method. The shaded pulses are the ones which move as a function of the evolution time, τ. For (b)–(d), the decoupler remains on for the entire evolution and acquisition periods. In all cases 0 marks the start of the evolution period, T signifies the length of a rotor period, and a normal CP sequence used to prepare the magnetization

the static field direction during the course of the experiment, the magnetization is kept in the transverse plane and a series of five π pulses are used to achieve the same effect. This method can be thought of as a constant time version of the MAT experiment.

As shown in Figure 6(d), two of the five π pulses are at the fixed times of $T/3$ and $2T/3$ during the evolution period, where T must be an integral number of rotor periods. Each π pulse changes the sign of the phase angle describing the precession of the magnetization up until the application of the pulse. The position of the first, third, and fifth π pulses are set at times $T/6 - \tau$, $T/2 - \tau$, and $5T/6 - \tau$, where τ is the evolution variable which ranges from $-T/6$ to $T/6$. At $\tau = 0$, the five π pulses are evenly spaced at increments of $T/6$, such that the accumulated phase is zero, resulting in the complete suppression of the chemical shift. When $\tau \neq 0$ the pulses are no longer evenly spaced, and the phase accumulation is proportional to $\omega_{iso}\tau$. Thus, the evolution dimension displays an isotropic chemical shift spectrum. The spectrum in the acquisition dimension is either a ssb or a static powder pattern depending on the spinning speed used.

This technique has an advantage over the MAH and MAT experiments in terms of increased sensitivity by avoiding the need to project the magnetization to the longitudinal direction. However, the 5-π pulse method does suffer from a loss of signal at longer evolution times (and therefore lower rotation frequencies) if the T_2 value of the spin is short in comparison to the total time T between the preparation of the magnetization and the start of the acquisition period.

6.4 Stop and Go

In the 2D technique known as stop and go or STAG[29] the sample, at the magic angle with respect to $\boldsymbol{B}_0$, is taken from being stationary during the preparation and evolution of the magnetization to high speed spinning during the acquisition period, as shown in the pulse sequence used in Figure 8(a). The

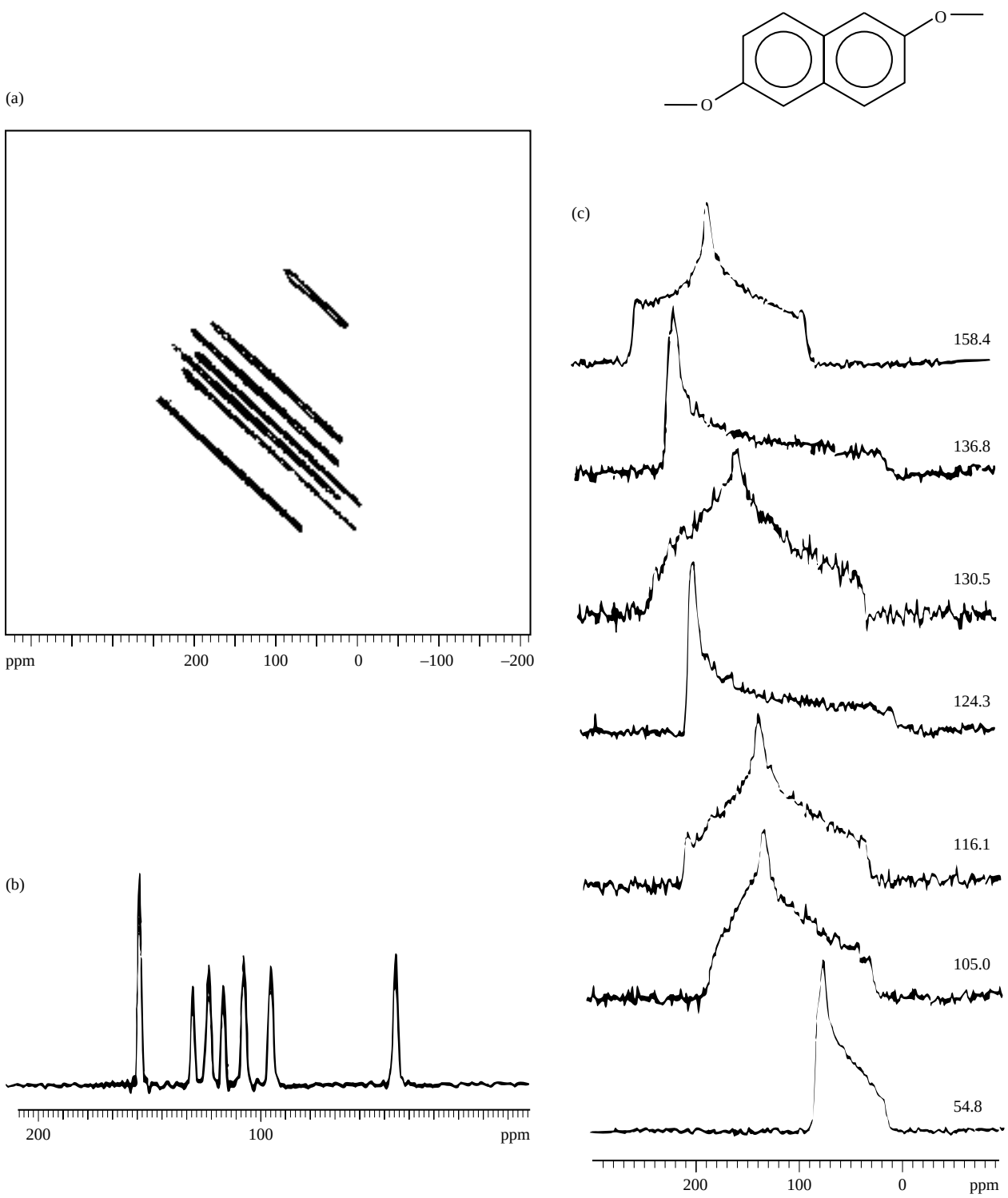

Figure 7 (a) A 2D MAT spectrum of 2,6-dimethoxynaphthalene (shown in inset). (b) The projection in the isotropic chemical shift dimension. (c) The individual powder patterns taken from the 2D spectrum in (a) at the indicated isotropic chemical shifts

air used for spinning is controlled with a solenoid valve that is electronically opened and closed by the pulse programmer controlling the NMR experiment. At the end of the evolution period the magnetization is stored along the magnetic field, in the manner discussed in the previous 2D methods, the air flow is started, and the sample is allowed to come to a relatively high spinning speed. Once the desired spinning speed has been reached, the stored magnetization is returned to the *xy* plane for detection. In the original paper the time required to start the spinner and achieve a spinning speed of 1.7 kHz was in the range of 3–5 s.

The spectra obtained are identical to those of the original MAH spectrum, with the exception that there are now spinning sidebands observed in the spectra as the sample is spinning

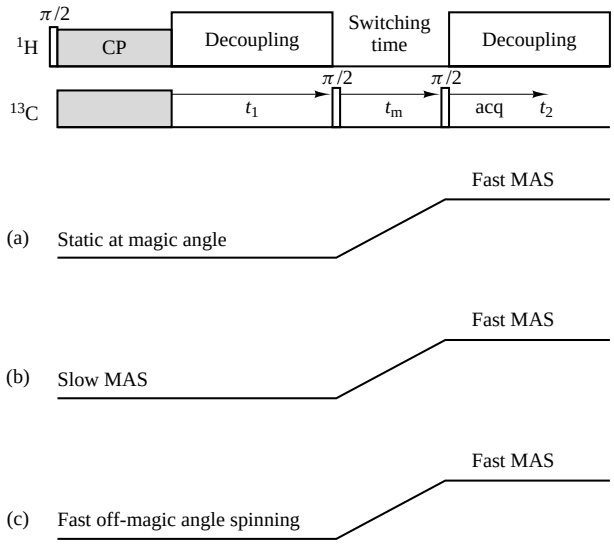

Figure 8 The 2D pulse sequence used in the STAG, S^3, and SAS 2D experiments. A normal CP preparation period was typically used. The $\pi/2$ pulses store the evolved magnetization along the field direction during the switching time and then return it to the transverse plane. (a) For STAG, the sample is stationary during the preparation and evolution periods and is spinning at the magic angle during the acquisition period. (b) In S^3, the spinning speed is increased by a factor of 5–10 during the mixing time. (c) In SAS, the spinning speed remains constant but the spinner axis changes relative to the external magnetic field. The length of time taken to accomplish these changes (the length of the switching period) is discussed in the text

during acquisition. The limitations of this method are also the same; namely this approach is only applicable to spin systems with T_1 relaxation times long compared with the time taken to bring the sample from the static condition to the maximum spinning speed.

6.5 Switched Speed Spinning

The switched speed spinning (S^3)[30] experiment is similar to that of the STAG method except that the spinning speed is only reduced by a factor of ca. 5–10 during the preparation and evolution time of the 2D experiment instead of being completely stopped, and is shown in Figure 8(b). The experiment was performed on an unmodified MAS probe using a commercially available spinning system and the spinner speed was controlled by a system which delivered a flow rate of air proportional to an applied voltage, with the change in this voltage being under the control of the NMR pulse programmer. This results in the anisotropic information being in the form of an ssb pattern instead of a static powder pattern. The fact that the spinning speed is only reduced and not completely stopped should be less demanding on the spinning system.

6.6 Switched Angle Spinning

The next technique has been discussed in the literature under two different names: dynamic angle spinning (DAS) and switched angle spinning (SASS). The method was introduced independently by two different groups shortly after the introduction of the MAH experimental technique.[31,32] This technique also requires reorientation of the sample, however this time a rapidly spinning sample is taken between the magic angle and a second angle during each scan, as shown in Figure 8(c).

In this technique the sample is held at the magic angle during the evolution period of a 2D experimental scheme. The evolved magnetization is then stored along the static magnetic field while the spinning axis is changed from the magic angle to any other angle. Following the angle switch, the stored magnetization is returned to the transverse plane for detection. The second angle used can be any other angle, resulting in patterns that are scaled by the argument $\frac{1}{2}(3\cos^2\theta - 1)$ according to equation (7).

The initial papers on this technique employed switching times on the order of 0.5–2 s. There is now a commercial probe available for SASS measurements with angle switching times on the order of 100 ms, allowing for more widespread use of this method.

Subsequent development of SASS has led to two methods which shorten the time required for the measurement of the chemical shift tensor information. The first involves a technique by which the second dimension, the dimension containing the anisotropic information, can be shortened.[33] In the initial experiment, as in all of the 2D methods discussed, one dimension contains the isotropic chemical shifts and the other contains the separated powder patterns. The projection of the 2D space onto the axis in the second dimension will result in the static powder pattern, as this dimension contains not only the anisotropic information but also the isotropic, i.e. the powder patterns are still offset from each other by the difference in their isotropic chemical shift. However this offset can be removed, resulting in all of the powder patterns being centered at the same frequency. This allows the spectral width in the second dimension to be shortened from that necessary to observe the normal static powder pattern to a spectral width set by the widest of the separated, scaled powder patterns.

The second method introduced to shorten the time necessary to obtain the chemical shift information was the use of the SASS principle in conjunction with selective irradiation or inversion in a 1D experiment,[22,23] as discussed in Section 5.4.

6.7 TOSS–Reverse TOSS

The TOSS (Total Suppression of Spinning Sidebands) sequence was originally introduced by Dixon et al.[34,35] to suppress spinning sidebands in normal MAS spectra, resulting in a spectrum containing only the centerband frequencies. The TOSS sequence consists of a series of four π pulses, applied at precise fractions of a rotor period which allow the intensities of the centerband to add while the magnetization of the sidebands are canceled. This technique improves spectral resolution and simplifies MAS spectra, especially those taken at high fields or at low spinning speeds. However, the price is that information about the anisotropic portion of the chemical shift tensor is lost.

However, the anisotropic information can be restored in a 2D experiment by following a normal TOSS sequence with an evolution time and then applying the 'mirror image' of the TOSS sequence to reverse the averaging before the start of the acquisition period. The TOSS–reverse TOSS pulse sequence[36]

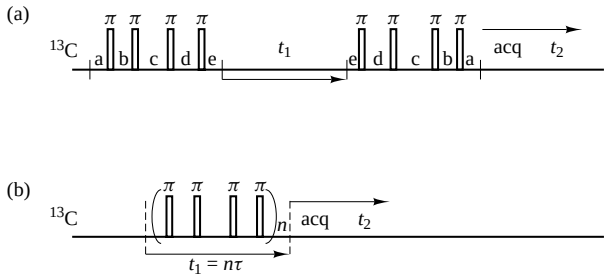

Figure 9 (a) The observe channel portion of 2D pulse sequence used in the TOSS–reverse TOSS technique. The separation between the π pulses is discussed elsewhere.[34–36] (b) The observe channel portion of 2D pulse sequence used in the synchronous application of π pulses with MAS method. The spacing of the four π pulses has been discussed by Tycko et al.[40] The rotor period is equal to τ. The decoupler remains on during the evolution and acquisition times in both sequences

is shown in Figure 9(a). The sample is spun at the magic angle at a relatively slow rotation frequency. During the evolution period, the effect of the TOSS sequence is such that the magnetization is evolving, containing only the isotropic information, without sidebands, while after the reverse TOSS sequence is applied the evolution once again contains the anisotropic information in the form of an ssb pattern. This information is then collected during the acquisition dimension.

6.8 Magic Angle Spinning with Synchronous Application of rf Pulses

The synchronous application of rf pulses during a MAS experiment in order to reconstruct the anisotropic information averaged by the spinning was first introduced by Lippmaa et al.[37] Subsequent improvement[38] led to the application of a train of six π pulses per revolution of the spinner in a 1D experimental format and the adaptation of the method to a 2D experiment utilizing four 2π pulses per rotor cycle to decrease the sensitivity of the experiment to pulse imperfections.[39] However, in none of the above do the breakpoints in the lineshapes correspond directly to the principal values of the chemical shift tensors, and the reported principal values are not in close agreement with those obtained by other techniques.

Tycko et al.[40] modified the basic method to render the intensities of the powder patterns obtained in the 2D space undistorted, making the measured principal values of the tensor more reliable, using a series of four or six π pulses as shown in Figure 9(b). The spacing of the four or six π pulses was chosen such that the isotropic scaling factor was zero.

This method, unlike many of the other 2D methods such as MAH, STAG, and SASS, is not demanding mechanically. Instead, the experiment can be performed on a normal MAS probe on a spectrometer system equipped with the ability to synchronize the application of the pulses with the spinning. However with this method it is more difficult to obtain very accurate principal values, due to the sensitivity of the technique to both the timing and quality of the rf pulses. This technique, along with the TOSS–reverse TOSS and the 5-π pulse method, also does not suffer from the loss of signals from nuclei with shorter T_1 relaxation times.

6.9 Chemical Shift–Chemical Shift Correlation

Chemical shift–chemical shift correlation (CS–CS) spectroscopy[41] is a modification of the 2D exchange NMR experiment,[42] using the basic pulse sequence shown in Figure 5 in which the stationary sample is reoriented by 90° along an axis perpendicular to the external magnetic field during the mixing time of the experiment. The projections in either dimension give the powder pattern of the sample in each of its two orientations relative to the external magnetic field. For a random powder sample, these two projections are identical. The 2D space, however, contains a unique representation of each tensor in the shape of a triangle for an axially symmetric tensor or a hexagon for a general asymmetric tensor, with the position of the corners defined by the principal values of the tensor. These shapes can be understood by considering the case of a single molecule. In the case of an axially symmetric tensor, if the molecule is in a position with respect to the external magnetic field such that its chemical shift is $\delta_{\|}$, then a 90° rotation of this molecule must gave a chemical shift of $\delta_{\perp}$. Likewise, if the signal in the first orientation is at $\delta_{\perp}$, after a 90° rotation it must be either $\delta_{\|}$ or $\delta_{\perp}$, resulting in the triangular pattern observed in the 2D space. For the case of an asymmetric tensor, a 90° rotation from an orientation which has a chemical shift of any one of the three principal values must take the molecule into an orientation that has a chemical shift of either one of the two remaining principal values, creating a hexagonal pattern in the 2D correlation space.

One of the applications of this method is in sorting out the principal values of overlapping powder patterns, as is demonstrated for coronene in Figure 10. Coronene has

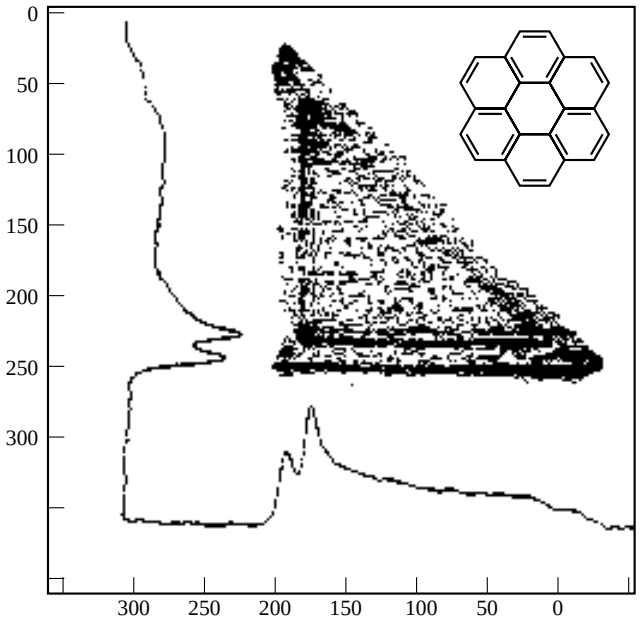

Figure 10 Contour plot of the 2D CS–CS correlation spectrum of coronene (shown in inset)

three magnetically inequivalent sets of carbons. At room temperature the molecule is rotating rapidly about an axis perpendicular to the plane of the molecule, averaging all

the three tensors to axial symmetry. From the normal 1D powder pattern (the projection on either axis) and the isotropic chemical shifts obtained from a MAS spectrum, it is difficult to determine which $\delta_{\parallel}$ and $\delta_{\perp}$ should be paired for the each of the three tensors. The patterns in the 2D space, however, clearly indicate how the six principal values are paired to obtain the three tensors.

6.10 Variable Angle Correlation Spectroscopy

In this experimental approach, known by the acronym VACSY,[43] the approach used to separate the anisotropic information is different from the above techniques. The data are not acquired as a typical 2D data set, i.e., with the evolution time being incremented between individual spectra. Instead, the experiment, performed under the conditions of high-speed spinning, involves collecting a series of VASS spectra taken at different angles. Selected intensities of the signal as a function of time and the spinning angle are then chosen to create a 2D data set for normal 2D FT processing, as shown schematically in Figure 11.

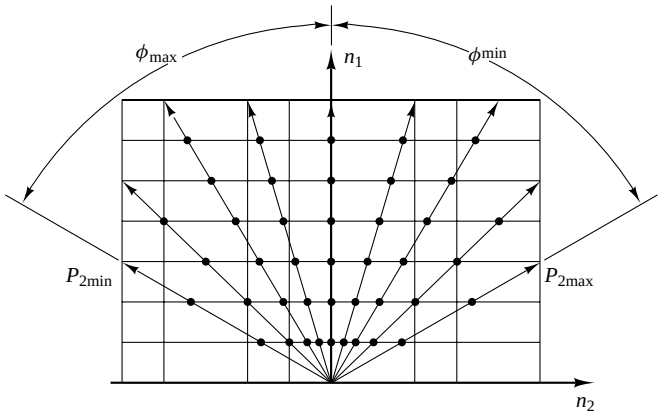

Figure 11 Representation of the strategy employed for obtaining 2D VACSY data. The arrows represent the individual FIDs recorded, each at a different spinning axis angle. The grid of points (n_a,n_i) are the points needed for the 2D FT in the acquisition and evolution dimension. Interpolation between the acquired data points is used to obtain signal intensity at all the grid points that fall inside the wedge formed by the minimum and maximum angles. (Reproduced by permission of the American Institute of Physics from L. Frydman, G. C. Chingas, Y. K. Lee, P. G. Grandinetti, M. A. Eastman, G. A. Barrall, and A. Pines, *J. Chem. Phys.* 1992, **97**, 4800)

The dwell time of the VASS spectra is chosen as the time needed in the isotropic direction for sufficient resolution in this dimension. The dwell time in the acquisition dimension is then a function of the range of angles used, and from this information the spinning angles at which spectra are obtained can be calculated. The intensities at certain points in the grid of (n_a,n_1) points shown in Figure 11 are then obtained, using interpolation as necessary; these intensities are then processed using the normal 2D FT methods. Figure 12 shows plots of the different data processing stages in the procedure of obtaining a 2D isotropic–anisotropic chemical shift spectrum of glycine.

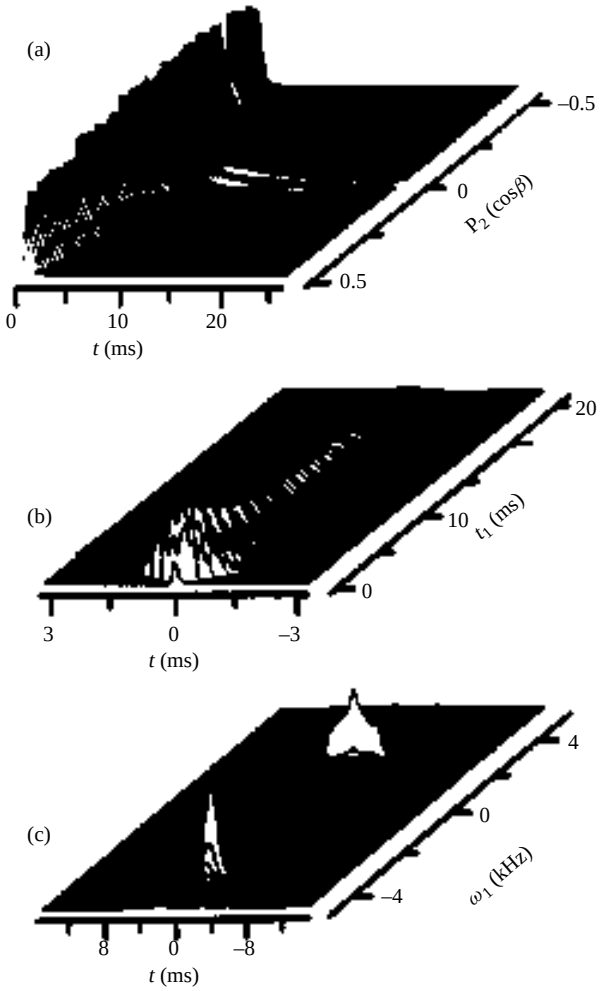

Figure 12 Plots of VACSY data for glycine (H_2NCH_2COOH). (a) Set of 75 FIDs recorded for a grid defined by the dwell time in the isotropic dimension being four times that in the anisotropic dimension. (b) 2D data set after interpolation onto the (n_a,n_i) grid. (c) Spectrum obtained after the 2D FT of data set in (b). (Reproduced by permission of the American Institute of Physics from L. Frydman, G. C. Chingas, Y. K. Lee, P. G. Grandinetti, M. A. Eastman, G. A. Barrall, and A. Pines, *J. Chem. Phys.*, 1992, **97**, 4800)

7 SINGLE CRYSTAL TECHNIQUES

7.1 Crystal Rotation Methods

All the early single crystal studies were undertaken using the 1D crystal rotation method.[2,3] In this method, the crystal is mounted in the probe on a goniometer. A succession of spectra are recorded with the crystal being rotated by a number of degrees between spectra. This rotation is continued until the sample has been rotated by 180°. The step size used depends on the number of lines and how closely they are spaced; a typical step size is on the order of 5–10°. The crystal orientation is then changed by 90° and the process is repeated. Finally the third rotation pattern is obtained for a third axis, perpendicular to the first two rotation axes. A representative rotation pattern of pyrene is shown in Figure 13.

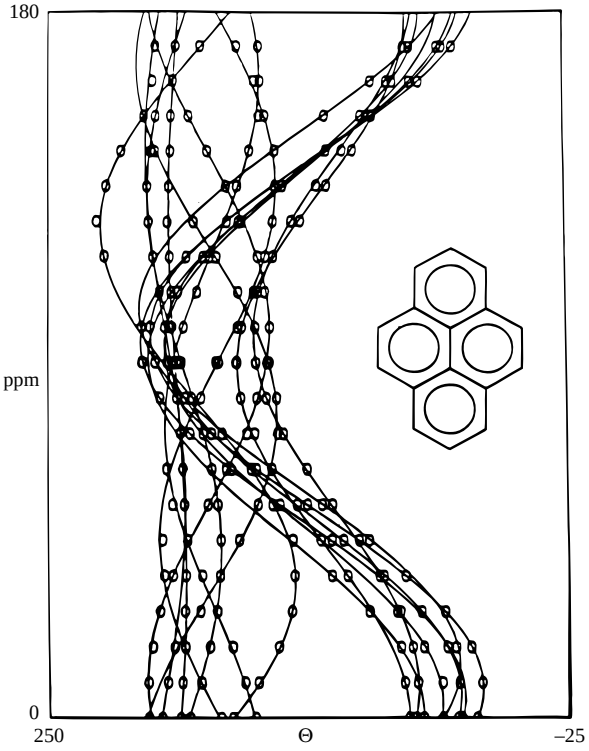

Figure 13 Rotation pattern obtained for one orientation of a single crystal of pyrene (shown in inset). One molecule in the unit cell is sampled nearly in the molecular plane by this rotation; in this case the difference between the in-plane components is small and the lines only move slightly. The other molecule is rotated in and out of the molecular plane and therefore shows a much greater range of chemical shift values as a function of the rotation angle. (Reproduced by permission of the American Chemical Society from C. M. Carter, D. W. Alderman, J. C. Facelli, and D. M. Grant, *J. Am. Chem. Soc.*, 1987, **109**, 2639)

Once the three rotation patterns are obtained, the line positions of each magnetically inequivalent spin must be followed as its position changes from one spectrum to the next, according to the expression given in equation (8). This process can be accomplished in a number of ways, one of which has been to fit the data using a least-squares Simplex fitting routine. Along with the fitting of peaks to different nuclei in one rotation pattern, a connection must be made to the lines in the other two rotation patterns.

Using this method there is a limit to the number of magnetically inequivalent nuclei in the unit cell. As there are more nuclei, the probability that the lines may not all be resolved increases and the large number of line crossings and the crowding often result in rotation patterns that cannot be interpreted, even with small step sizes. This limit has been estimated to be in the range of about 15–20 nuclei and is dependent on the width of the range of chemical shifts for the tensors. As two chemically equivalent nuclei with different orientations in the unit cell will give rise to different chemical shifts, this limitation is very restrictive especially in cases where there is more than one molecule per unit cell.

7.2 2D Crystal Correlation Methods

A 2D technique was introduced in 1985 which allowed for the study of more complex single crystals.[44,45] This method is a modification of the Jeener chemical exchange pulse sequence,[42] with the normal CP sequence for the preparation of the magnetization added. As in the CS–CS method discussed in Section 6.9, the single crystal sample is reoriented during the mixing time of the experiment. This results in a 2D spectrum where the projection onto the axis in one dimension is the spectrum obtained for the first orientation of the crystal, while the projection in the second dimension is the spectrum obtained in the second orientation. In the 2D space there are a number of peaks which correlate a given chemical shift in one dimension (or crystal orientation) with a line position in the second orientation, eliminating the need to determine the best fit in the correlation of the resonance frequencies from one spectrum to the next in a rotation pattern.

In order to obtain all the information contained in a single axis rotation pattern, it has been shown that four 2D correlation spectra are needed. In each of these spectra the two orientations are related by a 45° rotation. The four spectra are taken with the sample between 0° and 45°, 45° and 90°, 90° and 135°, and finally between 135° and 180° (which is 0°). The position of the resonance lines in these four spectra can be connected by placing the four spectra in a square, where the axes corresponding to common crystal position are placed together.

The goniometer used for obtaining rotation patterns is replaced by a device capable of being rotated between two positions using a motor-driven string. The unit has four holes for a lever arm, positioned precisely at 45° increments about the sample. However, the sample must be remounted for each of the three sets of four 2D spectra which are needed for the complete determination of the chemical shift information.

This method was modified in 1989 to include a multiple-axis sample reorientation mechanism[46] to remove the need for remounting the crystal, as this remounting process introduces errors in the data if the three mounted orientations are not exactly perpendicular. This mechanism is designed to move between any pair of six orientations (*X*, *XY*, *Y*, *YZ*, *Z*, and *ZX*) which were selected such that all the information necessary completely to characterize the chemical shift tensor can be obtained. To determine the chemical shift tensor it is necessary to record only six 2D spectra, corresponding to the *X–XY*, *XY–Y*, *Y–YZ*, *YZ–Z*, and *Z–ZX* direction pairs. A representative set of the six 2D spectra is shown in Figure 14 for a single crystal of acenaphthene,[47] which has four molecules per unit cell with two crystallographically unique molecules. The symmetry of the molecule and the crystal combine to give rise to a total of 36 resonances, which can be analyzed to give the 14 unique chemical shift tensors.

In this figure the connectivity of the peaks due to one of the 14 carbons is shown. The spectra shown in Figure 14 were analyzed to obtain all 28 chemical shift tensors, with a standard deviation of 0.52 ppm between the actual peak positions in the 2D spectra and the expected positions based on the best parameters of the chemical shift tensor. To date, the chemical shift tensors have been obtained for crystals containing up to 72 magnetically inequivalent carbons.

8 DIPOLAR TECHNIQUES

Dipolar couplings can be used to assign the orientation of the PAS to the molecular frame for the nuclei coupled, as well

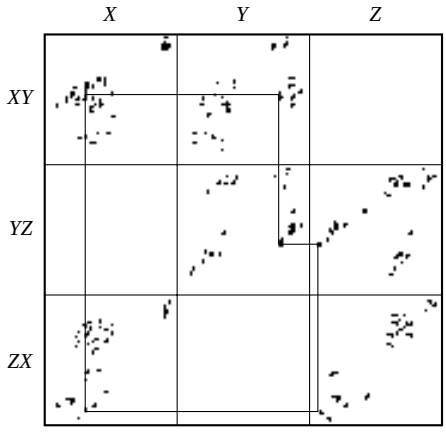

Figure 14 Set of six 2D multiple-axis reorientation spectra obtained for a single crystal of acenaphthene. The connectivity of peaks for one of the 14 magnetically inequivalent carbons is shown. The labels *X, Y, Z, XY, YZ, ZX* refer to the directions discussed in the text (Reprinted with permission from R. J. Iuluicci et al., *J. Am. Chem. Soc.*, **117**, 2336. Copyright (1995) American Chemical Society)

as to provide information on the separation of the two spins. In practice, this technique is used on compounds which have been specifically labeled in two positions, or in compounds in which there is an isolated pair of spin-$\frac{1}{2}$ nuclei, for an example a $^{31}P-^{31}P$ pair. Dipolar couplings also exist between a spin-$\frac{1}{2}$ and a quadrupolar nucleus. The lineshape obtained from a static powder sample containing such a spin pair contains not only the chemical shift information of one (for the case of a heteronuclear dipolar coupling) or both (homonuclear) spins, but also contains information on the orientation of the PAS of the chemical shift tensor with respect to the dipolar vector.

If one were to consider a single molecule in some orientation with respect to the static magnetic field, the chemical shift of a given spin in this molecule specifies the observed line position, that can be designated as ν. If this nucleus were coupled to a second spin, the result would be to see two lines spaced symmetrically about ν, with the separation dependent on D as given by the expression in equation (5) and the position of the dipolar vector. This situation is nicely shown in single crystal studies of compounds containing an isolated spin-$\frac{1}{2}$ pair.

This example can be extended to a spin-$\frac{1}{2}$ pair in a powder sample where the chemical shift of the spins involved is isotropic. In this case the dipolar coupling dominates the lineshape, and a Pake doublet, shown in Figure 15(a), is obtained. The Pake doublet consists of two axially symmetric patterns, with the central peaks being separated by D or $1.5D$ for the cases of heteronuclear and homonuclear spin pairs, respectively.

Now, if the spins have an appreciable anisotropy in their chemical shifts, the lineshape and the analysis of the dipolar pattern is more complicated. A detailed description of the mathematical treatment of the lineshape of dipolar spectra in this case is given in the literature[48] as well as in a recent review article on dipolar coupling.[49] Also, more details can be obtained in other sections of this Encyclopedia. For the purpose of this overview, however, the sensitivity of the lineshape relative to this orientation of the vector between the two spins in the PAS of the chemical shift tensor can be

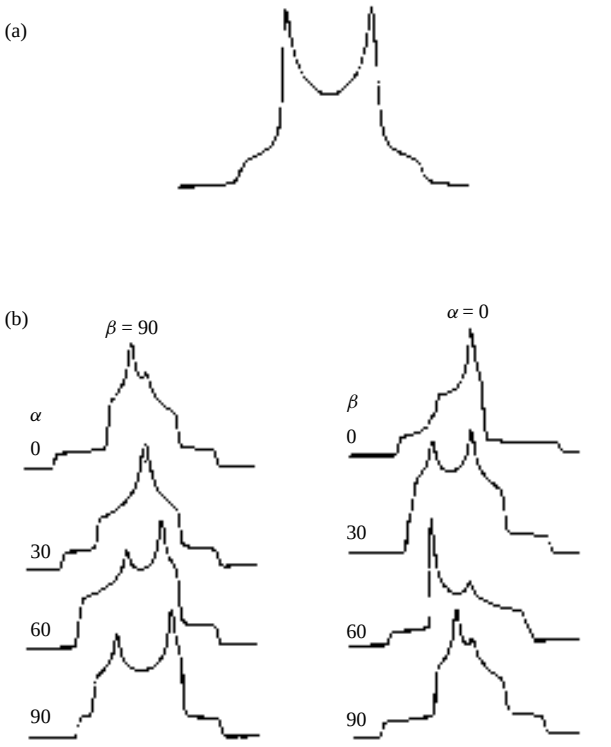

Figure 15 (a) Typical dipolar spectra resulting for the coupling of two spin-$\frac{1}{2}$ nuclei in the absence of any anisotropy in the chemical shift. (b) The dipolar pattern for two spin-$\frac{1}{2}$ nuclei with anisotropy in the chemical shift as a function of the orientation of the internuclear vector with respect to the chemical shift tensor principal axes, where α is the angle between δ_{33} and the dipolar vector, and β the angle between δ_{11} and the projection of the dipolar vector into the plane defined by δ_{11} and δ_{22}. (b) is reproduced by permission of Academic Press from W. P. Powers and R. E. Wayslishen in *Annu. Rep. NMR Spectrosc.*, 1991, **23**, 1

nicely demonstrated with the set of simulated spectra shown in Figure 15(b). The simulations in Figure 15(b) are for the same principal values and dipolar coupling, with only the two angles relating the PAS to the dipolar vector being varied.

As mentioned earlier, a dipolar coupling also exists between a spin-$\frac{1}{2}$ nucleus and a quadrupolar nucleus, and a dipolar spectrum can be obtained by observing the spin-$\frac{1}{2}$ nucleus. The complete chemical shift tensor of the spin-$\frac{1}{2}$ nucleus is obtained, along with the information of the EFG tensor of the quadrupolar nuclei.

Finally, there have been a number of 2D techniques that can be grouped together as separated local field (SLF) techniques, which can provide the chemical shift information in one dimension and information on the dipolar couplings in a second dimension. The SLF technique, first introduced in 1976,[50] can be used to orient the principal values of a rare spin based on the dipolar coupling between that rare spin (S) and an abundant spin (I), typically a ^1H. In SLF, multipulse decoupling is applied during the evolution time of the 2D experiment to decouple all ^1H-H dipolar interactions, leaving the ^1H-X interactions although they are scaled. The initial experiments were applied to single crystals and to oriented samples.

The basic ideas presented by Waugh were extended to unlabeled static powder samples,[51] with the shape of the spectra in the 2D space containing the information on the PAS; however, with powders, the patterns become very complicated if there are even two different dipolar interactions. The SLF technique has also been used with slow magic angle spinning and has been extended to the determination of the complete chemical shift of a nucleus coupled to two other spins,[52,53] as well as to being used to extend some of the 2D powder techniques into 3D techniques to gain the information on the orientation of the PAS.[54]

9 SUMMARY

As stated in the Introduction, the method of choice is primarily dependent on the sample. A single crystal study is the method of choice based solely on the amount of information obtained. The more recent 2D multiple axis reorientation method has opened up the field of single crystal studies to systems approaching 100 inequivalent nuclei. However, the limitation in obtaining a suitable sample, i.e., a large enough crystal of sufficient quality, eliminates this method as a choice for a majority of substances.

If a material is a solid at or near room temperature, but one for which a single crystal cannot be obtained, the method of choice is often determined by the equipment available. If there are more than three or four inequivalent nuclei, the experiment of choice will typically be a 2D method. In the last 12 or so years there has been an explosion of 2D and even a few 3D techniques in solid state NMR designed to obtain chemical shift information. While some of these techniques require specialized probes, several can be undertaken on any modern solid state NMR system equipped with a normal MAS probe, provided that only temperatures near ambient are needed. Though some standard MAS probes are capable of reaching temperatures down to 77 K, attaining very low temperatures at high spinning speeds for long periods of times is not easily or economically achieved.

When the sample of interest is a solid only at very low temperatures, or a sample that is stable only at very low temperatures for any reasonable time period, the choices are limited to the 1D techniques which typically take less time. However, samples that are suitable for study by 1D techniques are only the simpler compounds, i.e. those containing only three or four inequivalent nuclei. There have been efforts to use selective techniques, mainly short contact times, to look at only the protonated nuclei, or dipolar dephasing techniques to observe only the nonprotonated nuclei, but these methods have been shown to be of limited usefulness. The alternative is to use compounds selectively enriched at the nuclei of interest and study only that particular spin.

The lowest temperatures can only be achieved with the use of cryogenic equipment which does not allow for sample spinning, limiting the choice to the study of a static powder sample. It should be mentioned that there are several articles in the literature on MAS probes at temperatures in the region of 4 K, but they do not seem to be used routinely and there are no examples, to the knowledge of the author, on the use of such equipment in the study of molecules which are gases at room temperature. With the use of closed-cycle cryogenic units, it is economically feasible to achieve temperatures as low as 8–10 K on a routine basis. The static sample limits the application of the cryogenic apparatus to studies of very simple cases, or to cases where isotopic labeling has been undertaken. However, this technique is the only method available for the study of reactive species trapped in inert gas matrices, a technique known as matrix isolation. The use of matrix isolation methodology, while very limited in NMR, is more widespread in other forms of spectroscopy.

Finally, for samples where a single crystal study is not possible, but an experimental determination of the PAS orientation is desired, dipolar techniques can be employed. If two dipolar coupled spins exist, or if a sample can be made to contain such a pair using selective enrichment, the orientation of the PAS can be determined for the spins involved. Dipolar spectroscopy has been used at ambient temperatures as well as at cryogenic temperatures.

10 RELATED ARTICLES

Chemical Shift Tensors; Chemical Shift Tensors in Single Crystals; Dipolar and Indirect Coupling Tensors in Solids; Dynamic Angle Spinning; Magic Angle Turning and Hopping; Two-Dimensional Powder Correlation Methods; Variable Angle Sample Spinning.

11 REFERENCES

1. T. M. Duncan, *A Compilation of Chemical Shift Anisotropies*, Farragut Press, Chicago, 1990.
2. M. Mehring, *Principles of High Resolution NMR in Solids*, 2nd edn., Springer-Verlag, New York, 1983.
3. C. A. Fyfe, *Solid State NMR for Chemists*, C.F.C. Press, Guelph, 1983.
4. C. P. Slichter, *Principles of Magnetic Resonance*, 3rd edn., Springer-Verlag, New York, 1992.
5. R. R. Ernst, G. Bodenhausen, and A. Woukan, *Principles of Nuclear Magnetic Resonance in One and Two Dimensions*, Oxford University Press, Oxford, 1990.
6. J. S. Waugh, L. M. Huber, and U. Haeberlen, *Phys. Rev. Lett.*, 1968, **20**, 180.
7. A. Pines, M. G. Gibby, and J. S. Waugh *J. Chem. Phys.*, 1973, **59**, 569.
8. S. J. Opella and M. H. Frey, *J. Am. Chem. Soc.*, 1979, **101**, 5854.
9. L. B. Alemany, D. M. Grant, R. J. Pugmire, T. D. Alger, and K. W. Zilm, *J. Am. Chem. Soc.*, 1983, **105**, 2133.
10. E. R. Andrew and R. G. Eades, *Proc. R. Soc. London*, 1953, **A216**, 398.
11. I. J. Lowe, *Phys. Rev. Lett.*, 1959, **2**, 285.
12. J. C. Facelli and D. M. Grant, *Nature (London)*, 1993, **365**, 325.
13. K. W. Zilm, R. T. Conlin, D. M. Grant, and J. Michl, *J. Am. Chem. Soc.*, 1980, **102**, 6672.
14. J. E. Kohl, M. G. Semack, and D. White, *J. Chem. Phys.*, 1978, **69**, 5378.
15. E. O. Stejskal, J. Schaefer, and R. A. McKay, *J. Magn. Reson.*, 1977, **25**, 569.
16. N. K. Sethi., D. M. Grant, and R. J. Pugmire, *J. Magn. Reson.*, 1987, **71**, 476.
17. N. K. Sethi, R. J. Pugmire, and D. M. Grant, *Prepr. Pap. Am. Chem. Soc., Div. Fuel Chem.*, 1987, **32**, 155.

18. M. M. Maricq and J. S. Waugh, *J. Chem. Phys.*, 1979, **70**, 3300.
19. J. Herzfeld and A. E. Berger, *J. Chem. Phys.*, 1980, **73**, 6021.
20. G. A. Morris and R. Freeman, *J. Magn. Reson.*, 1978, **29**, 433.
21. J. Z. Hu, R. J. Pugmire, A. M. Orendt, D. M. Grant, and C. Ye, *Solid State NMR*, 1992, **1**, 185.
22. J. Ashida, T. Nakai, and T. Terao, *Chem. Phys. Lett.*, 1990, **168**, 523.
23. J. H. Iwamiya, M. F. Davis, and G. E. Maciel, *J. Magn. Reson.*, 1990, **88**, 199.
24. A. Bax, N. M. Szeverenyi, and G. E. Maciel, *J. Magn. Reson.*, 1983, **52**, 147.
25. J. Z. Hu, A. M. Orendt, D. W. Alderman, C. Ye, R. J. Pugmire, and D. M. Grant, *Solid State NMR*, 1993, **2**, 235.
26. Z. Gan, *J. Am. Chem. Soc.*, 1992, **114**, 8307.
27. J. Z. Hu, A. M. Orendt, D. W. Alderman, R. J. Pugmire, C. Ye, and D. M. Grant, *Solid State NMR*, 1994, **3**, 181.
28. J. Z. Hu, D. W. Alderman, C. Ye, R. J. Pugmire, and D. M. Grant, *J. Magn. Reson., Ser. A*, 1993, **105**, 82.
29. R. C. Zeigler, R. A. Wind, and G. E. Maciel, *J. Magn. Reson.*, 1988, **79**, 299.
30. A. C. Kolbert, H. J. M. DeGroot, and R. G. Griffin, *J. Magn. Reson.*, 1989, **85**, 60.
31. A. Bax, N. M. Szeverenyi, and G. E. Maciel, *J. Magn. Reson.*, 1983, **55**, 494.
32. T. Terao, T. Fujii, T. Onodera, and A. Saika, *Chem. Phys. Lett.*, 1984, **107**, 145.
33. T. Nakai and C. A. McDowell, *J. Magn. Reson.*, 1991, **93**, 618.
34. W. T. Dixon, J. Schaefer, M. D. Sefcik, E. O. Stejskal, and R. A. McKay, *J. Magn. Reson.*, 1982, **49**, 341.
35. W. T. Dixon, *J. Chem. Phys.*, 1982, **77**, 1800.
36. A. C. Kolbert and R. G. Griffin, *Chem. Phys. Lett.*, 1990, **166**, 87.
37. E. Lippmaa, M. Alla, and T. Tuherm, *Proc. 19th Congr. AMPERE, Heidelberg, 1976*, p. 113.
38. Y. Yarim-Agaev, P. N. Tutunjian, and J. S. Waugh, *J. Magn. Reson.*, 1982, **47**, 51.
39. A. Bax, N. M. Szeverenyi, and G. E. Maciel, *J. Magn. Reson.*, 1983, **51**, 400.
40. R. Tycko, G. Dabbagh, and P. A. Mirau, *J. Magn. Reson.*, 1989, **85**, 265.
41. C. D. Hughes, M. H. Sherwood, D. W. Alderman, and D. M. Grant, *J. Magn. Reson., Ser. A*, 1993, **102**, 58.
42. J. Jeener, B. H. Meier, P. Buachmann, and R. R. Ernst, *J. Chem. Phys.*, 1979, **71**, 4546.
43. L. Frydman, G. C. Chingas, Y. K. Lee, P. G. Grandinetti, M. A. Eastman, G. A. Barrall, and A. Pines, *J. Chem. Phys.*, 1992, **97**, 4800.
44. C. M. Carter, D. W. Alderman, and D. M. Grant, *J. Magn. Reson.*, 1985, **65**, 183.
45. C. M. Carter, D. W. Alderman, and D. M. Grant, *J. Magn. Reson.*, 1987, **73**, 114.
46. M. H. Sherwood, D. W. Alderman, and D. M. Grant, *J. Magn. Reson.*, 1989, **84**, 466.
47. R. J. Iuliucci, J. C. Facelli, D. W. Alderman, and D. M. Grant, *J. Am. Chem. Soc.*, 1995, **117**, 2336.
48. K. W. Zilm and D. M. Grant, *J. Am. Chem. Soc.*, 1981, **103**, 2913.
49. W. P. Powers and R. E. Wayslishen, *Annu. Rep. NMR Spectrosc.*, 1991, **23**, 1.
50. R. K. Hester, J. L. Ackerman, B. L. Neff, and J. S. Waugh, *Phys. Rev. Lett.*, 1976, **36**, 1081.
51. M. Linder, A. Hohener, and R. R. Ernst, *J. Chem. Phys.*, 1980, **73**, 4959.
52. M. Munowitz, T. -H. Huang, and R. G. Griffin, *J. Chem. Phys.*, 1987, **86**, 4362.
53. C. J. Hartzell, T. K. Pratum, and G. Drobney, *J. Chem. Phys.*, 1987, **87**, 4324.
54. T. Nakai, J. Ashida, and T. Terao, *J. Chem. Phys.*, 1988, **88**, 6049.

Biographical Sketch

Anita M. Orendt. *b* 1958. B.S., 1980, Chemistry, University of Pittsburgh, Ph.D., 1987, Physical Chemistry, University of Utah. Postdoctoral work with Professor David M. Grant, University of Utah, 1987–present. Assistant Professor of Chemistry (half-time), Westminster College of Salt Lake City, 1992–present. Research interests: measurement of chemical shift tensors, applications of solid state NMR at cryogenic temperatures and to matrix isolated species.

Chemical Shift Tensors in Single Crystals

Mark H. Sherwood

IBM Research Division, Almaden Research Center, San Jose, CA, USA

1	Introduction	1
2	Nuclear Shielding and the Chemical Shift Tensor	1
3	The Single Axis Rotation Method	3
4	Single Axis 2D Chemical Shift Tensor Correlation Spectroscopy	4
5	Multiple Axis 2D Chemical Shift Tensor Correlation Spectroscopy	6
6	Assignment Techniques	7
7	Related Articles	8
8	References	8

1 INTRODUCTION

Shortly after its first detection in condensed matter in 1945,[1,2] it became evident that NMR was an extremely sensitive probe of the local electronic environments of magnetic nuclei. Some of the first observations of NMR uncovered a chemical effect on the relative resonance frequencies of identical nuclear isotopes which has come to be known as the chemical shift, and because of this effect NMR has evolved into one of the premier spectroscopic techniques for chemical structure analysis. The primary use of NMR consists of measuring the isotropic chemical shifts of nuclei imbedded in molecules dissolved in solution; however, important information about the anisotropy of this interaction is available from the spectra of solids.[3–5]

Certain characteristics of the anisotropic chemical shift, the principal values of the chemical shift tensor for example, can be obtained from the spectra of powdered samples and, to a lesser extent, from molecules dissolved in liquid crystal solvents. Nevertheless, single crystal samples are preferred, when available, as they allow direct measurements of the complete chemical shift tensor. Single crystals are especially useful for studies of large molecules where the many overlapping powder patterns in traditional one-dimensional (1D) spectra are uninterpretable and where selectively labeling each individual site is impractical. Although progress has been made in extracting principal values from powdered samples of large molecules using two-dimensional (2D) NMR methods,[6] direct measurements of tensor orientations can be made only on single crystals.

This article is written as an introduction to the techniques that are available for measuring chemical shift tensors in single crystals. Although many aspects of the techniques are quite general, the emphasis here will be on measurements of ^{13}C chemical shift tensors in organic systems.

The first measurement of a ^{13}C chemical shift tensor was made in the very early days of ^{13}C NMR by Lauterbur[7] on the carbonate ion of single crystal calcite ($CaCO_3$). This particular sample proved to be ideal because all magnetic nuclei were at low abundance and thus the dipolar broadening was negligible. A few other systems were exploited where similar dilution occurred naturally or was introduced by substitution of ^{2}D for ^{1}H, but progress along these lines was limited. It was only after the introduction of the combined cross polarization and high-power dipolar decoupling techniques[8] that ^{13}C chemical shift tensor measurements became more generally applicable. One of the first demonstrations of these now widely used techniques was in the measurement of ^{13}C chemical shift tensors in single crystal durene (1,2,4,5-tetramethylbenzene).[9]

2 NUCLEAR SHIELDING AND THE CHEMICAL SHIFT TENSOR

The fundamental equation relating the NMR resonance frequency and the magnetic field strength is well known to all students of magnetic resonance

$$\nu_0 = |\gamma/2\pi| B_0 \tag{1}$$

For ^{13}C, this frequency corresponds to 50 MHz in a typical field of 4.7 T.

Due to the electronic circulation set up in a molecule by the applied magnetic field, the effective field experienced by a particular nucleus is not exactly equal to B_0. The electronic 'currents' induce a small shielding field $\boldsymbol{B}_s$ which must be added to $\boldsymbol{B}_0$ to obtain the effective field at the nucleus

$$\boldsymbol{B}_{\text{eff}} = \boldsymbol{B}_0 + \boldsymbol{B}_s \tag{2}$$

This vector addition is shown schematically in Figure 1.

Although $\boldsymbol{B}_s$ is called the shielding field, it does not necessarily oppose $\boldsymbol{B}_0$ and thus deshieldings or paramagnetic shifts are possible. In general, the direction of $\boldsymbol{B}_s$ is not parallel to $\boldsymbol{B}_0$ but the two are related through the shielding tensor which is represented as the 3×3 matrix $\boldsymbol{\sigma}$

$$\boldsymbol{B}_s = -\boldsymbol{\sigma} \cdot \boldsymbol{B}_0 \tag{3}$$

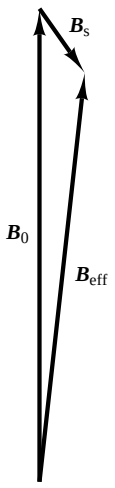

Figure 1 The relationship between the applied field $\boldsymbol{B}_0$, the shielding field $\boldsymbol{B}_s$ and the effective field $\boldsymbol{B}_{\text{eff}}$

The matrix $\boldsymbol{\sigma}$ is usually called a second rank Cartesian tensor although it also contains zeroth and first rank parts as well.

Since B_s is very small compared to B_0, equation (2) can be closely approximated by adding only the component of $\boldsymbol{B}_s$ that is either parallel or antiparallel to $\boldsymbol{B}_0$ to obtain

$$\boldsymbol{B}_{\text{eff}} = \boldsymbol{B}_0 - \frac{\boldsymbol{B}_0}{B_0} \cdot \boldsymbol{\sigma} \cdot \boldsymbol{B}_0 \tag{4}$$

The above approximation is equivalent to *truncation* or restriction to the *secular* terms of the chemical shift Hamiltonian in first-order perturbation theory. It should be pointed out that $\boldsymbol{\sigma}$ can be decomposed into a sum of second rank symmetric and first rank antisymmetric constituents

$$\boldsymbol{\sigma} = \boldsymbol{\sigma}^{\text{S}} + \boldsymbol{\sigma}^{\text{A}} \tag{5}$$

Since $\boldsymbol{\sigma}^{\text{A}}$ leads to components of $\boldsymbol{B}_s$ which are perpendicular to $\boldsymbol{B}_0$, it does not contribute to $\boldsymbol{B}_{\text{eff}}$ in first order and thus its effect on the resonance frequency of the nucleus can be ignored.

The effect of shielding is thus to change the precession frequency of the nucleus from ν_0 to the frequency given by

$$\nu = |\gamma/2\pi| B_{\text{eff}} \tag{6}$$

In practice, the frequency of the bare nucleus is not known, and measurements of the frequency ν are always made relative to a reference frequency ν_{ref}, which for ^{13}C is usually taken as the resonance of liquid tetramethylsilane (TMS). The frequency difference between sample and reference can be written as

$$\nu - \nu_{\text{ref}} = |\gamma/2\pi| \frac{\boldsymbol{B}_0}{B_0} \cdot (\boldsymbol{\sigma}^{\text{S}} - \sigma_{\text{ref}}\mathbf{1}) \cdot \boldsymbol{B}_0 \tag{7}$$

where σ_{ref} is the isotropic chemical shielding constant of the reference compound and $\mathbf{1}$ is the unit matrix. The symmetric difference matrix $(\boldsymbol{\sigma}^{\text{S}} - \sigma_{\text{ref}}\,\mathbf{1})$ is defined as the chemical shift tensor, and is assigned the symbol $\boldsymbol{\delta}$ in order to avoid its confusion with the shielding tensor $\boldsymbol{\sigma}$.

It is customary to report chemical shifts not as frequencies, since these always depend on B_0 which varies from one spectrometer to the next, but as fractions of ν_{ref}. If the chemical shift F is defined as $(\nu - \nu_{\text{ref}})/\nu_{\text{ref}}$, then

$$F = \frac{\boldsymbol{B}_0}{B_0} \cdot \boldsymbol{\delta} \cdot \frac{\boldsymbol{B}_0}{B_0} \tag{8}$$

Equation (8) is the master equation for the chemical shift in a single crystal, as it gives the observed shift in terms of the elements of $\boldsymbol{\delta}$ and the orientation of $\boldsymbol{B}_0$.

For elements with sufficiently low atomic numbers, the chemical shift tensor $\boldsymbol{\delta}$ can be represented in a Cartesian coordinate system as a 3×3 symmetric matrix

$$\boldsymbol{\delta} = \begin{bmatrix} \delta_{xx} & \delta_{xy} & \delta_{zx} \\ \delta_{xy} & \delta_{yy} & \delta_{yz} \\ \delta_{zx} & \delta_{yz} & \delta_{zz} \end{bmatrix} \tag{9}$$

The matrix $\boldsymbol{\delta}$ is called the Cartesian representation of the chemical shift tensor and is completely defined by six independent numbers. It will be seen below that other representations are possible.

The average value of $\boldsymbol{\delta}$ is known as the isotropic chemical shift

$$\delta_{\text{iso}} = \frac{1}{3}(\delta_{xx} + \delta_{yy} + \delta_{zz}) \tag{10}$$

and it is only this part of the chemical shift tensor which can be directly measured in solution samples due to rapid isotropic tumbling of the molecules. The isotropic chemical shift is also called the zeroth rank part of $\boldsymbol{\delta}$ since it transforms as a scalar quantity, i.e., it is invariant under rotation.

A Cartesian tensor can be expressed in a different coordinate system by performing a similarity transformation on the matrix $\boldsymbol{\delta}$

$$\boldsymbol{\delta}' = \mathbf{R}\boldsymbol{\delta}\mathbf{R}^{\text{T}} \tag{11}$$

where $\mathbf{R}$ is a unitary matrix. The element R_{ij} is given by the direction cosine of the ith new coordinate axis with respect to the jth old coordinate axis. For instance, $R_{12} = \cos \gamma_{x'y}$ where $\gamma_{x'y}$ is the angle between the new x axis and the old y axis.

A number of coordinate systems are necessary in single crystal work. The *laboratory frame* is a coordinate system whose z axis lies along the direction of the static magnetic field. Rather than working in the laboratory frame, it is usually more convenient to work in a coordinate system called the *sample frame* whose orientation is fixed with respect to the single crystal sample. The sample frame will always be the coordinate system in which tensors are measured. A third coordinate system is that defined by the symmetry elements of the crystal and this will be called the *crystal frame*. The orientation of the crystal frame relative to the sample frame can usually be found by diffraction methods. For molecules containing high symmetry, it is often useful to define a coordinate system based on molecule symmetry elements called the *molecular frame*. For molecules of low symmetry, coordinate systems can be defined based on the local symmetry of a particular nuclear site and these will be called *local frames*. Finally, there is an important coordinate system known as the *principal axis* system which is unique to each tensor. The principal axis system is discussed below.

The relationships between all of these reference frames, except for that between the sample frame and laboratory frame, are determined by the crystal and molecular structure, and therefore they are not under experimental control. It is clear from equation (11) that once the tensor is known in one of these reference frames, it can be expressed in any of the other frames provided the unitary matrix $\mathbf{R}$ is available.

For any symmetric second rank tensor such as the chemical shift tensor $\boldsymbol{\delta}$, there exists a unitary matrix $\mathbf{S}$ that transforms $\boldsymbol{\delta}$ into a coordinate system in which it is diagonal

$$\mathbf{S}\boldsymbol{\delta}\mathbf{S}^{\text{T}} = \boldsymbol{\Lambda} \tag{12}$$

where $\boldsymbol{\Lambda}$ is a diagonal matrix with elements λ_1, λ_2, and λ_3. This special coordinate system is called the principal axis system and the diagonal tensor elements are called the principal values. Multiplying both sides of equation (12) by $\mathbf{S}^{-1} = \mathbf{S}^{\text{T}}$ yields

$$\boldsymbol{\delta}\mathbf{S}^{\text{T}} = \mathbf{S}^{\text{T}}\boldsymbol{\Lambda} \tag{13}$$

Equation (13) is readily recognized as an algebraic eigenvalue equation and the eigenvalues (principal values) and eigenvectors (principal axes) can be found by solving the secular equation

$$|\boldsymbol{\delta} - \boldsymbol{\Lambda 1}| = \begin{vmatrix} \delta_{xx} - \lambda_1 & \delta_{xy} & \delta_{zx} \\ \delta_{xy} & \delta_{yy} - \lambda_2 & \delta_{yz} \\ \delta_{zx} & \delta_{yz} & \delta_{zz} - \lambda_3 \end{vmatrix} = 0 \qquad (14)$$

A convention for labeling the principal values is generally followed in which they are designated δ_{11}, δ_{22}, and δ_{33} in order of decreasing chemical shift. An alternative to the Cartesian representation of a chemical shift tensor is its representation as three principal values and the three Euler angles that orient the principal axis system with respect to one of the coordinate systems defined above. Other useful representations of the chemical shift tensor are described elsewhere.[10]

Recalling equation (8), the chemical shift F observed when the magnetic field is oriented with direction cosines cos γ_x, cos γ_y, and cos γ_z relative to the sample frame axes can be explicitly written as the quadratic form

$$F = [\cos(\gamma_x)\ \cos(\gamma_y)\ \cos(\gamma_z)] \begin{bmatrix} \delta_{xx} & \delta_{xy} & \delta_{zx} \\ \delta_{xy} & \delta_{yy} & \delta_{yz} \\ \delta_{zx} & \delta_{yz} & \delta_{zz} \end{bmatrix} \begin{bmatrix} \cos(\gamma_x) \\ \cos(\gamma_y) \\ \cos(\gamma_z) \end{bmatrix}$$

$$= \cos^2(\gamma_x)\,\delta_{xx} + \cos^2(\gamma_y)\,\delta_{yy} + \cos^2(\gamma_z)\,\delta_{zz} + 2\cos(\gamma_x)\ \cos,\ (\gamma_y)\delta_{xy} + 2\ \cos(\gamma_y)\ \cos(\gamma_z)\,\delta_{yz} + 2\ \cos(\gamma_z)\ \cos(\gamma_x)\,\delta_{zx} \qquad (15)$$

It is seen from equation (15) that if the chemical shift tensor $\boldsymbol{\delta}$ is known in the sample frame, the chemical shift can be calculated for any orientation of $\boldsymbol{B}_0$. Alternatively, if the chemical shift F is known for six suitably chosen directions of $\boldsymbol{B}_0$, the elements of $\boldsymbol{\delta}$ can be obtained by solving a system of linear equations.

Equation (15) takes on a particularly simple form when expressed in the principal axis system

$$F = \cos^2(\gamma_x)\delta_{11} + \cos^2(\gamma_y)\,\delta_{22} + \cos^2(\gamma_z)\,\delta_{33} \qquad (16)$$

Provided that the reference frequency is chosen such that the three principal values δ_{11}, δ_{22}, and δ_{33} are positive, a connection can be made between equation (16) and the equation of an ellipsoid with semiaxes a, b, and c

$$\frac{x^2}{a^2} + \frac{y^2}{b^2} + \frac{z^2}{c^2} = 1 \qquad (17)$$

The direction cosines of a radius vector $\boldsymbol{r}$ taken from the origin to a point on the surface of the ellipsoid are given by $\cos^2(\gamma_x) = x^2/r^2$, $\cos^2(\gamma_y) = y^2/r^2$, and $\cos^2(\gamma_z) = z^2/r^2$. Substituting these into equation (17) yields

$$\frac{r^2\cos^2(\gamma_x)}{a^2} + \frac{r^2\cos^2(\gamma_y)}{b^2} + \frac{r^2\cos^2(\gamma_z)}{c^2} = 1 \qquad (18)$$

Finally, by making the identities $a^2 = 1/\delta_{11}$, $b^2 = 1/\delta_{22}$, and $c^2 = 1/\delta_{33}$, equation (18) can be rearranged to give

$$\cos^2(\gamma_x)\,\delta_{11} + \cos^2(\gamma_y)\,\delta_{22} + \cos^2(\gamma_z)\,\delta_{33} = \frac{1}{r^2} \qquad (19)$$

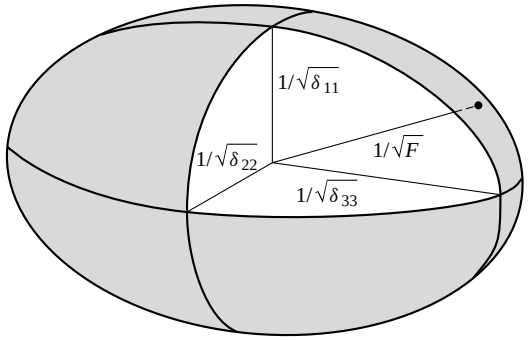

Figure 2 The chemical shift tensor representation ellipsoid

The surface described by equation (19) is called the representation ellipsoid[11] of the chemical shift tensor and is illustrated in Figure 2.

The semiaxes of the ellipsoid are given by $1/\sqrt{\delta_{11}}$, $1/\sqrt{\delta_{22}}$, and $1/\sqrt{\delta_{33}}$. Comparing equation (16) and (19), it is seen that when $\boldsymbol{B}_0$ is oriented along $\boldsymbol{r}$, the length of the radius vector is given by $r = 1/\sqrt{F}$.

The representation ellipsoid thus allows a geometrical interpretation of the chemical shift tensor, and the *mmm* (D_{2h}) symmetry of this object reflects the symmetry of the chemical shift interaction.

In order to understand the effect of crystallographic symmetry on the chemical shift, it is necessary to define some terminology. Nuclear sites related by the rotation or reflection symmetry operations of the space group of the crystal are called *crystallographically equivalent* sites. Those sites that are related by inversion or translation are called *magnetically equivalent* sites. This definition of magnetic equivalence is in contrast to that used in solution NMR where sites related by any symmetry element of the molecule are magnetically equivalent due to the rapid isotropic tumbling of the molecule. As the operations of either inversion or translation do not change the orientation of the representation ellipsoid, a set of magnetically equivalent sites gives rise to a single peak in the spectrum. On the other hand, the representation ellipsoids of crystallographically equivalent sites are oriented differently in the absence of accidental coincidence of the symmetry elements of the representation ellipsoid with those of the space group. Therefore, multiple peaks occur in the spectrum of a single crystal sample when the magnetic field is in a general orientation with respect to a lattice of crystallographically equivalent sites. Two tensors are said to be *congruent* if they are each associated with nuclear sites which are crystallographically equivalent. Congruent tensors have identical principal values, but differ in the orientations of their respective principal axes.

3 THE SINGLE AXIS ROTATION METHOD

In the case of a crystal containing only one set of magnetically equivalent nuclei, the measurement technique is straightforward since the spectrum of such a crystal contains a single peak in any orientation of the field. Six 1D spectra can be obtained with the magnetic field oriented along six different directions. The chemical shift derived from each spectrum, along with the corresponding direction cosines describing

the orientation of the magnetic field, is then substituted into equation (15) to obtain a set of six equations from which the tensor elements are extracted.

The spectrum of a sample containing multiple sets of magnetically equivalent nuclei has a corresponding multiplicity of peaks. In this case the six 1D spectra described above would be useless, since there would be no way to determine which peak in each of the spectra was from a particular set of magnetically equivalent nuclei. One solution to this problem is to acquire many 1D spectra which differ by small angle rotations of the crystal so that the paths of the lines can be traced from one spectrum to the next to form a *rotation pattern*.

Consider a rotation of the crystal about an axis that makes an angle β with the magnetic field $\boldsymbol{B}_0$. The arbitrary sample frame can be oriented such that the x axis is parallel to the rotation axis and the magnetic field $\boldsymbol{B}_0$ lies initially in the xy plane. If the crystal is rotated through an angle α, the direction cosines of the field with respect to the sample frame are given by

$$\cos(\gamma_x) = \cos(\beta) \tag{20}$$

$$\cos(\gamma_y) = \sin(\beta)\cos(\alpha) \tag{21}$$

$$\cos(\gamma_z) = \sin(\beta)\sin(\alpha) \tag{22}$$

It can easily be shown by substituting equations (20)–(22) into equation (15) that the chemical shift F is given by

$$F = A + B\cos(\alpha) + C\sin(\alpha) + D\cos(2\alpha) + E\sin(2\alpha) \tag{23}$$

where

$$A = \tfrac{1}{2}\sin^2(\beta)\,(\delta_{yy} + \delta_{zz}) + \cos^2(\beta)\,\delta_{xx} \tag{24a}$$

$$B = 2\sin(\beta)\cos(\beta)\,\delta_{xy} \tag{24b}$$

$$C = 2\sin(\beta)\cos(\beta)\,\delta_{zx} \tag{24c}$$

$$D = \tfrac{1}{2}\sin^2(\beta)\,(\delta_{yy} - \delta_{zz}) \tag{24d}$$

$$E = \sin^2(\beta)\,\delta_{yz} \tag{24e}$$

From equation (23) it is seen that if the chemical shift is observed at five different angles α, for a given angle β, the coefficients A, B, C, D, and E can be extracted. However, these five coefficients are insufficient to determine fully the six tensor elements and it is apparent that the complete chemical shift tensor cannot be measured from a single rotation pattern.

The most frequently used measurement technique is to obtain three patterns by rotating the crystal about a single axis perpendicular to $\boldsymbol{B}_0$ in the laboratory frame as depicted in Figure 3.

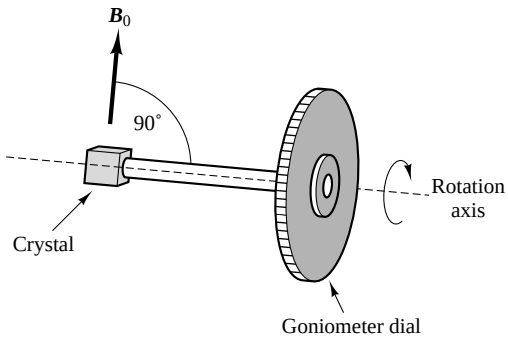

Figure 3 Schematic representation of a simple experimental set-up for obtaining single axis rotation patterns

The three rotation patterns are obtained first with the x, then the y, and finally the z sample frame axis along the rotation direction. The rotation pattern about the x axis is easily obtained from equations (23) and (24) by setting the angle β equal to $\pi/2$

$$F(\alpha_x) = \tfrac{1}{2}(\delta_{yy} + \delta_{zz}) + \tfrac{1}{2}(\delta_{yy} - \delta_{zz})\cos(2\alpha_x) + \delta_{yz}\sin(2\alpha_x) \tag{25}$$

The other two rotation patterns can be found by cyclic permutation of the sample axis labels x, y, and z

$$F(\alpha_y) = \tfrac{1}{2}(\delta_{zz} + \delta_{xx}) + \tfrac{1}{2}(\delta_{zz} - \delta_{xx})\cos(2\alpha_y) + \delta_{zx}\sin(2\alpha_y) \tag{26}$$

$$F(\alpha_z) = \tfrac{1}{2}(\delta_{xx} + \delta_{yy}) + \tfrac{1}{2}(\delta_{xx} - \delta_{yy})\cos(2\alpha_z) + \delta_{xy}\sin(2\alpha_z) \tag{27}$$

Although each rotation pattern is fully determined by measuring the chemical shift at only three different angles, the usual practice is to obtain spectra at many angles by stepping the goniometer from 0° to 180°, and to extract the tensor elements using least-squares methods. This allows a more accurate determination of the tensor and is a necessity if the spectrum of the crystal contains many peaks, since the path of a single peak can be traced only when the crystal is rotated in small angular increments. In order to obtain all six elements of the chemical shift tensor for a particular set of magnetically equivalent nuclei, the path of the corresponding peak must not only be traced within each rotation but must also be traced between rotations. This is accomplished by matching up the rotation patterns at the orientations where they intersect. Figure 4 shows three rotation patterns from which the ^{13}C chemical shift tensors of naphthalene can be obtained.

The rotation method has been successfully applied to many medium-sized molecules;[12] however, it fails when the peaks in the spectra become numerous and crowded since it becomes impossible to trace the paths of individual peaks through the three rotation patterns. Another drawback of the rotation method is the necessity of accurately mounting the crystal three times along the three orthogonal sample axes, but this problem has been overcome using a two-axis goniometer and a unique rf coil as demonstrated by Hauser et al.[13]

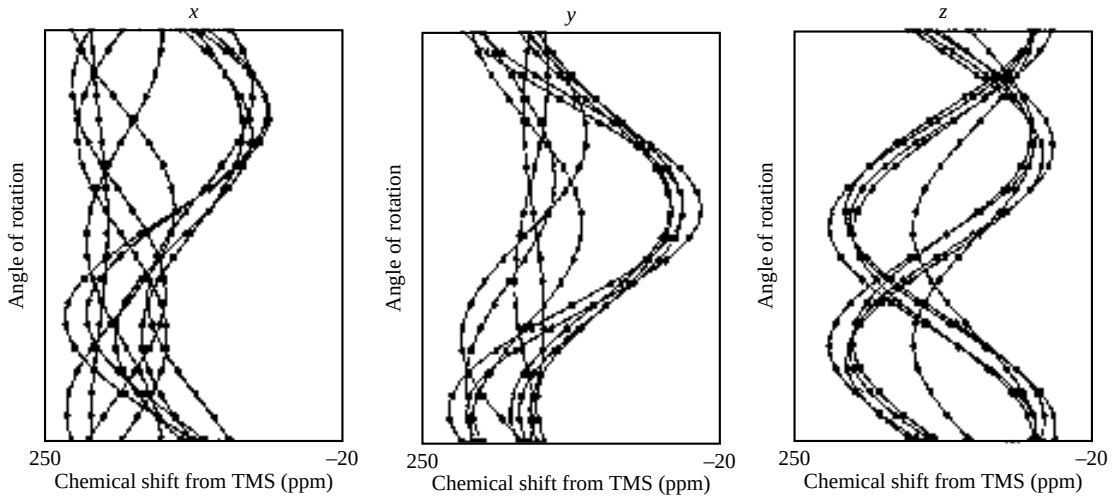

Figure 4 Rotation patterns through 180° about the x, y, and z sample axis sufficient to measure the 10 chemical shift tensors in single crystal naphthalene

4 SINGLE AXIS 2D CHEMICAL SHIFT TENSOR CORRELATION SPECTROSCOPY

The necessity of taking small angular increments in the rotation patterns can be eliminated using a 2D correlation method introduced by Carter et al.[14] This technique obtains 2D spectra in which a peak from a single set of magnetically equivalent nuclei is located by its resonant frequencies at two different orientations of the single crystal. Such spectra are obtained with the modified 2D chemical exchange[15] pulse sequence shown in Figure 5.

The preparation period of this sequence is identical to the usual cross-polarization experiment. During the evolution period, the spins precess at frequencies determined by their chemical shifts at the initial crystal orientation. The evolved magnetization is then stored along the z axis with the pulse labeled b and the crystal is reoriented during the mixing period. At the end of the mixing period, the stored magnetization is rotated back to the transverse plane with the pulse labeled a, and during the detection period the spins precess at frequencies determined by their chemical shifts at the final crystal orientation. An example of a 2D chemical shift tensor correlation spectrum is shown in Figure 6 where all 24 peaks in single crystal sucrose are resolved despite the severe crowding that exists in the corresponding 1D spectra.

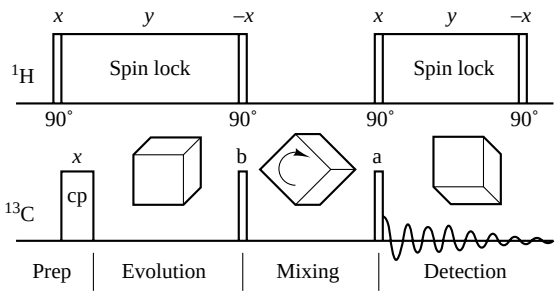

Figure 5 Modified chemical exchange sequence for 2D chemical shift tensor correlation spectroscopy. See text for details. (Reproduced by permission of Academic Press from M. H. Sherwood, D. W. Alderman, and D. M. Grant, *J. Magn. Reson.*, 1989, **84**, 466)

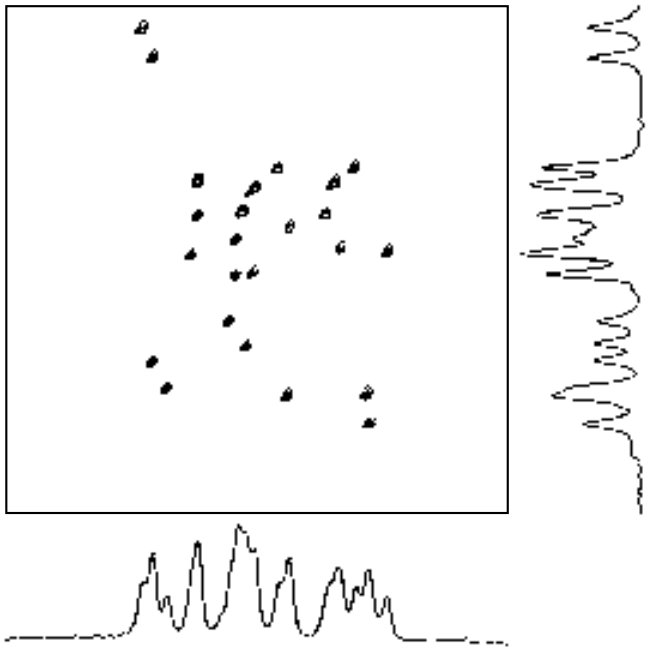

Figure 6 Two-dimensional absorption mode spectrum obtained from sucrose corresponding to a reorientation of $\boldsymbol{B}_0$ by 90° in the sample frame. The plotted spectral width is 5 kHz × 5 kHz (approximately 100 ppm × 100 ppm). The spectrum diagonal runs from upper left (high frequency) to lower right (low frequency). (Adapted by permission of Academic Press from M. H. Sherwood, D. W. Alderman, and D. M. Grant, *J. Magn. Reson.*, 1989, **84**, 466)

It has been shown that the information present in one rotation pattern can be obtained from four 2D spectra taken while stepping the sample from 0° to 45°, 45° to 90°, 90° to 135°, and 135° to 180° (equivalent to 0°).[16] The redundancy in this information permits a powerful square construction which resolves the uncertainties due to peak overlap within each rotation. However, this single axis 2D technique does

not address the problem of joining the three rotation patterns together when there are many overlapping lines in the spectra at the orientations where the patterns intersect. Thus the application of the single axis 2D method is limited to samples where the connections can be made by conventional means. As in the traditional 1D method, it is necessary to mount the sample accurately three times for the single axis 2D measurements.

5 MULTIPLE AXIS 2D CHEMICAL SHIFT TENSOR CORRELATION SPECTROSCOPY

The full power of the 2D technique can be realized by gathering data in such a way that all correlations between required crystal orientations are obtained with a single mounting of the crystal. This is accomplished with a multiple axis sample orienting mechanism which complements the 2D method to form an exceedingly powerful technique for measuring chemical shift tensors in complex single crystals.[17]

As mentioned above, the six independent elements of a chemical shift tensor, in principle, can be determined by measuring the chemical shift with the magnetic field oriented along six suitably chosen directions. Table 1 gives the orientations of six such directions in the sample frame.

Table 1 Six Magnetic Field Directions in the Sample Frame That can be Used to Measure a Chemical Shift Tensor

Magnetic field direction	$\cos(\gamma_X)$	$\cos(\gamma_Y)$	$\cos(\gamma_Z)$	Observed shift
X	1	0	0	F_X
XY	$1\sqrt{2}$	$1/\sqrt{2}$	0	F_{XY}
Y	0	1	0	F_Y
YZ	0	$1/\sqrt{2}$	$1/\sqrt{2}$	F_{YZ}
Z	0	0	1	F_Z
ZX	$1/\sqrt{2}$	0	$1/\sqrt{2}$	F_{ZX}

These directions lie on the surface of a trigonal pyramid and will be referred to here as the pyramidal directions. The observed chemical shifts F_X, F_{XY}, F_Y, F_{YZ}, F_Z, and F_{ZX} are easily calculated from equation (15), yielding the relationships

$$F_X = \delta_{xx} \tag{28a}$$

$$F_{XY} = \delta_{xy} + \delta_{xx}/2 + \delta_{yy}/2 \tag{28b}$$

$$F_Y = \delta_{yy} \tag{28c}$$

$$F_{YZ} = \delta_{yz} + \delta_{yy}/2 + \delta_{zz}/2 \tag{28d}$$

$$F_Z = \delta_{zz} \tag{28e}$$

$$F_{ZX} = \delta_{zx} + \delta_{zz}/2 + \delta_{xx}/2 \tag{28f}$$

which trivally invert to

$$\delta_{xx} = F_X \tag{29a}$$

$$\delta_{xy} = F_{XY} - F_X/2 - F_Y/2 \tag{29b}$$

$$\delta_{yy} = F_Y \tag{29c}$$

$$\delta_{yz} = F_{YZ} - F_Y/2 - F_Z/2 \tag{29d}$$

$$\delta_{zz} = F_Z \tag{29e}$$

$$\delta_{zx} = F_{ZX} - F_Z/2 - F_X/2 \tag{29f}$$

By obtaining the six 2D spectra corresponding to reorientation between the $X–XY$, $XY–Y$, $Y–YZ$, $YZ–Z$, $Z–ZX$, and $ZX–X$ direction pairs, the correlation data are sufficient to determine the complete chemical shift tensors for all of the sets of magnetically equivalent nuclei in the sample. Starting first with the $X–XY$ 2D spectrum, the chemical shifts of the X and XY directions are measured and correlated. Then the observed chemical shifts in the XY direction from the $X–XY$ spectrum are matched with those from the $XY–Y$ spectrum to advance the correlation of the chemical shift to the Y direction, and so forth through YZ, Z, ZX, and back to X. After completion of the full cycle of reorientations, the chemical shift is known for each set of magnetically equivalent nuclei at all six orientations and the tensor elements can be calculated from equations (29a)–(29f). The correlation of chemical shifts around the full cycle forms the closed path depicted in Figure 7(a).

It may be noted that the sense of the reorientation is unimportant. The same frequency information is obtained by reorienting from the X to the XY direction as is obtained by reorienting from XY to X. The only consequence is to interchange the F_1 and F_2 axes of the spectrum.

A powerful criterion, analogous to the square construction described for the single axis 2D approach, allows the correlation of peaks which have identical frequencies at one or more of the six magnetic field directions. It employs reorientations between other pairs of the six measurement directions. The full matrix of 36 possible 2D correlation spectra is shown in Figure 7(b). The 2D spectra that lie along the diagonal of this matrix correspond to trivial correlations between two identical orientations, and are thus of no experimental value. The spectra related by the transpose of this matrix differ only by the sense of the reorientation, and contain the same correlation information. Therefore, only 15 of the 36 possible spectra are necessary to obtain all of the available correlation and frequency information. The spectra matrix construction allows the chemical shifts of a single set of magnetically equivalent nuclei to be traced through all 15 possible 2D correlation spectra simply by connecting the peaks with horizontal and vertical lines as shown in Figure 7(b).

A mechanism which accomplishes the 15 flips has been described in detail elsewhere.[17] Briefly, it consists of an armature into which a glass tube containing the sample is

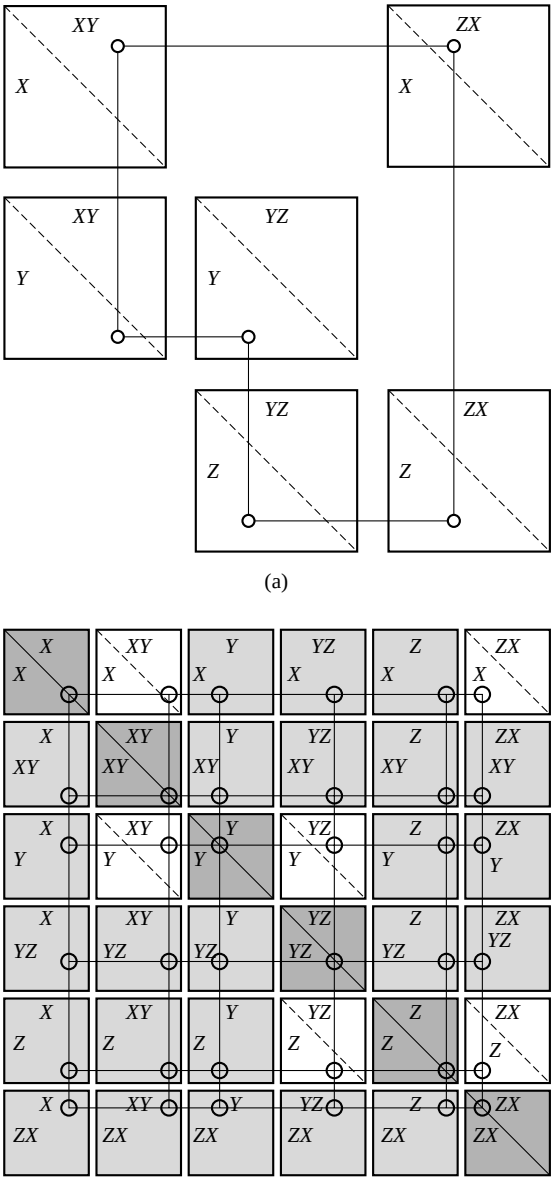

Figure 7 Matrix of 2D spectra. (a) Six 2D spectra corresponding to $XY-X$, $XY-Y$, $YZ-Y$, $YZ-Z$, $ZX-Z$, and $ZX-X$ reorientations. The relationship of the peaks in these spectra is shown for a single set of magnetically equivalent nuclei by the vertical and horizontal connecting lines. Dotted lines indicate the diagonals in the spectra. (b) All 36 possible 2D spectra. The relationship of the peaks in the spectra is shown for a single set of magnetically equivalent nuclei by the vertical and horizontal connecting lines. The six unshaded spectra with dotted diagonals correspond to those of Figure 7(a). The six darkly shaded spectra with solid diagonals are the trivial autocorrelation spectra with the peaks on the diagonals (Reproduced by permission of Academic Press from M. H. Sherwood, D. W. Alderman, and D. M. Grant, *J. Magn. Reson.*, 1989, **84**, 466)

mounted. The armature contains seven accurately drilled holes which define seven rotation axes in the sample frame. A stationary plate attached to the NMR probe contains five axle bearing holes which define five rotation axes in the laboratory frame. The mechanism is assembled by inserting an axle through one of the bearings in the stationary plate and into one of the holes in the armature. By selecting the appropriate combination of bearing and armature hole, each of the 15 possible flips can be performed. The angle of rotation is limited by a precise system of stops. One advantage of this mechanism is that the axis of the tube containing the sample changes by only 19.5° over all assemblies of the mechanism, so that a reasonably good filling factor can be achieved in the rf solenoid.

Although the pyramidal set of directions was used in the original demonstration of multiple axis 2D chemical shift tensor correlation spectroscopy, it should be realized that any set of six directions would suffice if when substituted into equation (15) they yield a system of linearly independent equations for the six chemical shifts. This restriction eliminates any set of directions that completely lie either in a plane or on the surface of a cone.

An important question that arises is how sensitive is the determination of a tensor given a particular set of measurement directions. To address this question, a variance-like figure of merit was developed[18] which quantifies the sensitivity of a given set of measurement directions. This figure of merit was evaluated for a variety of sets of measurement directions including the pyramidal set and the orthogonal rotation set. The most sensitive set of directions was found to be the six apolar directions defined by the vertices of an icosahedron. For this geometry, the figure of merit represents a significant decrease by a factor of 1.0/1.8 from that of the pyramidal directions. Therefore, it is worth considering the icosahedral direction set when designing future mechanisms. It should be noted that there is no further increase in sensitivity upon including more measurement directions than the six icosahedral directions. Another interesting result of this analysis is that the figure of merit for the orthogonal rotations set is only 1.2 times greater than that for the icosahedral directions set. This indicates that the sensitivity of the tensor measurements made using the traditional rotation method is nearly optimal.

The high symmetry of the icosahedron makes possible a very simple mechanism which rotates the crystal about a single laboratory axis inclined at an angle of 64.4° from the field. As can be seen in Figure 8, it will still be necessary to employ three rotation axes in the sample frame as specified by the three vertices labeled a, b, and c. Unfortunately the sample tube axis will reorient by 68.3° in this new mechanism, and a sacrifice in filling factor may be necessary when implementing this geometry.

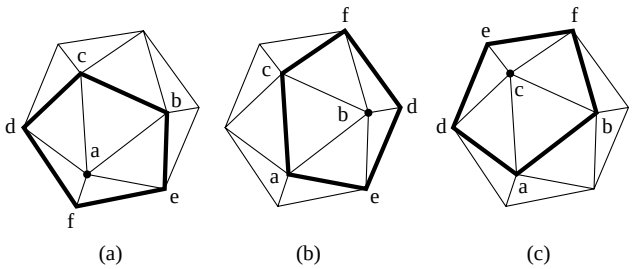

Figure 8 Icosahedra showing the vertex directions which can be aligned along the magnetic field by rotating around the a vertex (a), the b vertex (b), and the c vertex (c) (Reproduced by permission of Academic Press from D. W. Alderman, M. H. Sherwood, and D. M. Grant, *J. Magn. Reson.*, 1990, **86**, 60)

6 ASSIGNMENT TECHNIQUES

Before chemical shift tensors can be rationalized in terms of molecular structure, they must first be assigned to their respective nuclei in the unit cell. This can be a challenging step in the interpretation of the results, since the number of possible assignment permutations increases rapidly for larger molecules. The problem is compounded by the fact that most organic crystals contain two or more magnetically nonequivalent molecules in the unit cell. In order fully to exploit the power of the techniques described above, systematic methods of assignment have been developed based on local symmetry and dipolar spectroscopy. These methods have been described in detail in the literature and therefore will only be described qualitatively here.

Nearly all of the chemical shift tensor assignments made to date are based on the assumption that the symmetry elements of the representation ellipsoid should closely coincide with the actual or approximate local symmetry of its assigned nuclear site. For example, it is well established that the δ_{33} principal values of the ^{13}C chemical shift tensors orient perpendicular to the molecular plane in polycyclic aromatic hydrocarbons.[19] This fact is widely used to assign tensors to a particular molecule when there is more than one molecule in the unit cell. In more complicated molecules lacking any molecular symmetry, the approximate local symmetry established by the directly bonded atoms can be used to make assignments. For small molecules this procedure consists of manually comparing principal axis directions of the measured tensors with the approximate local symmetry elements determined from diffraction data until a reasonable match is found. As the number of measured tensors increases, it becomes more difficult to make all possible comparisons and their qualitative nature makes it difficult to distinguish between closely related assignments. In order to quantify such comparisons, the concept of a distance between two tensors was developed.[10] This distance concept has been combined with linear modeling in order to make possible an automated assignment technique which can explore all possible assignments of a reasonably large set of measured tensors to a corresponding set of chemically similar but magnetically nonequivalent nuclear sites.[10,20]

The orientational dependence of dipolar interactions has also been exploited in order to assign chemical shift tensors to specific nuclei in single crystal samples. Assignments made in this way are quite reliable since dipolar couplings can be calculated with a high degree of accuracy from the positions of the nuclei alone without resorting to molecular electronic theory. In many organic molecular crystals, the positions of all of the carbon and hydrogen nuclei in the unit cell are known from neutron diffraction studies and thus $^{13}C-^{1}H$ separated local field experiments[21,22] can be used in solving the assignment problem.

A simple extension of 2D chemical shift tensor correlation spectroscopy yields a 3D technique which allows detection of $^{13}C-^{1}H$ dipolar couplings for each of the magnetically nonequivalent sets of carbons in the sample.[20] The response of each spin is separated according to its chemical shifts at two different magnetic field orientations and a dipolar spectrum is displayed in the third dimension. This is accomplished by inserting a dipolar evolution period between the end of the mixing time and the beginning of the detection period of the previously described 2D experiment.

7 RELATED ARTICLES

Chemical Shift Tensor Measurement in Solids; Chemical Shift Tensors; Cross Polarization in Solids; Dipolar and Indirect Coupling Tensors in Solids; Multidimensional Spectroscopy: Concepts; Shielding Tensor Calculations; Two-Dimensional Powder Correlation Methods.

8 REFERENCES

1. F. Bloch, W. W. Hansen, and M. Packard, *Phys. Rev.*, 1946, **70**, 474.
2. E. M. Purcell, H. C. Torrey, and R. V. Pound, *Phys. Rev.*, 1946, **69**, 37.
3. M. Mehring, *Principles of High Resolution NMR in Solids*, Springer-Verlag, New York, 1983.
4. U. Haeberlen, *High Resolution NMR in Solids; Selective Averaging*, Academic Press, New York, 1976.
5. T. M. Duncan, *A Compilation of Chemical Shift Anisotropies*, Farragut Press, Chicago, IL, 1990.
6. J. Z. Hu, D. W. Alderman, C. Ye, R. J. Pugmire, and D. M. Grant, *J. Magn. Reson., Ser. A.* 1993, **105**, 82.
7. P. C. Lauterbur, *Phys. Rev. Lett.*, 1958, **1**, 343.
8. A. Pines, M. G. Gibbey, and J. S. Waugh, *J. Chem. Phys.*, 1973, **59**, 569.
9. S. Pausak, A. Pines, and J. S. Waugh, *J. Chem. Phys.*, 1973, **59**, 591.
10. D. W. Alderman, M. H. Sherwood, and D. M. Grant, *J. Magn. Reson. Ser. A.*, 1993, **101**, 188.
11. J. F. Nye, *Physical Properties of Crystals; Their Representation by Tensors and Matrices*, Oxford University Press, New York, 1985.
12. W. S. Veemann, *Prog. NMR Spectrosc.*, 1984, **16**, 193.
13. H. Hauser, C. Radloff, R. R. Ernst, S. Sundell, and I. Pascher, *J. Am. Chem. Soc.*, 1988, **110**, 1054.
14. C. M. Carter, D. W. Alderman, and D. M. Grant, *J. Magn. Reson.*, 1985, **65**, 183.
15. J. Jeener, B. H. Meier, P. Bachman, and R. R. Ernst, *J. Chem. Phys.*, 1979, **71**, 4546.
16. C. M. Carter, D. W. Alderman, and D. M. Grant, *J. Magn. Reson.*, 1987, **73**, 114.
17. M. H. Sherwood, D. W. Alderman, and D. M. Grant, *J. Magn. Reson.*, 1989, **84**, 466.
18. D. W. Alderman, M. H. Sherwood, and D. M. Grant, *J. Magn. Reson.*, 1990, **86**, 60.
19. M. H. Sherwood, J. C. Facelli, D. W. Alderman, and D. M. Grant, *J. Am. Chem. Soc.*, 1991, **113**, 750.
20. M. H. Sherwood, D. W. Alderman, and D. M. Grant, *J. Magn. Reson. Ser. A*, 1993, **104**, 132.
21. M. Mehring, *Principles of High Resolution NMR in Solids*, Springer-Verlag, New York, 1983, Chap. 5.
22. R. R. Ernst, G. Bodenhausen, and A. Wokaun, *Principles of Nuclear Magnetic Resonance in One and Two Dimensions*, Oxford University Press, New York, 1987, pp. 383–396.

Biographical Sketch

Mark H. Sherwood. *b* 1961. B.S., 1983, Colorado State University, where he was introduced to NMR by Gary E. Maciel, Ph.D., 1991, Chemistry, University of Utah, advisor David M. Grant. Visiting scientist, IBM Research Division, Almaden Research Center, 1991–present. Research specialties: carbon-13 and deuteron NMR in solids, NMR imaging at cryogenic temperatures.

Chemical Shift Tensors

David M. Grant

University of Utah, Salt Lake City, UT, USA

1	Introduction	1
2	The Chemical Shift	2
3	The Chemical Shift Tensor in a Variety of Reference Frames and Representations	6
4	Tensor Powder Patterns in Solids	11
5	Chemical Shift Tensors from Single Crystals	14
6	Molecular Origins of the Chemical Shift Tensor	19
7	Conclusions	23
8	Related Articles	24
9	References	24

1 INTRODUCTION

Observations of NMR signals, whose resonance positions in different compounds depend upon the chemical environment of the nucleus, were first made during 1949–50 for ^{14}N by Proctor and Yu,[1] for ^{19}F by Dickinson,[2] and for ^{1}H independently by Lindström[3] and by Thomas.[4] In 1951 Arnold, Dharmatti, and Packard[5] first published a single spectrum in which three separate ^{1}H resonance peaks were observed in a single compound, ethanol, with its three chemically different protons. This series of papers, on a chemically dependent spectral feature, launched the field of NMR into the world of chemistry. Such chemically induced shifts in the resonance positions of chemically different nuclei provide unique experimental information on the electronic structure in molecules, and these data have become the basis for innumerable chemical studies for almost half of a century. Among physical measurements in the world of chemistry the chemical shift enjoys a special distinction, and every year brings even greater and varied applications for this chemically sensitive parameter.

Dominated by the local electronic structure in the immediate vicinity of a resonating nucleus, the shift becomes a characteristic chemical signature of the atom in question and its immediate atomic neighbors. Remote structural perturbations of the chemical shift are usually restricted either to molecules in which the electronic structure is readily polarized by long-range electrostatic fields or to molecules in which distant molecular moieties have folded back upon the resonating nucleus. In this latter case, a steric perturbation of the electronic structure of the impacted atom leads to predictable chemical shifts that specify the geometry of the steric interaction.

In liquid samples, rapid molecular motions have tumbling rates sufficiently high to average the various chemical environments and the diverse orientations found in liquids. These motions narrow the resonance lines and yield sharp peaks whose frequencies provide a very sensitive way to analyze the composition of low viscosity liquids. These line positions, expressed by the chemical shifts, are highly reproducible quantities that provide a powerful set of parametric values for characterizing the molecular conformations and intermolecular interactions important in the liquid state.

Even though liquid chemical shifts may be expressed as scalar numbers, the associated shielding of a nuclear spin is a tensor quantity that depends upon the electronic environment, but also varies with the molecular orientation in the magnetic field. When the molecular orientation is locked into a solid powder sample, the nuclear resonance frequency also reflects the orientation of the sample's microcrystalline particles. The orientational diversity in a powder leads to broad resonance bands for each chemically unique nucleus. Although these tensor bands contain considerably more details on the electronic structure than found for tumbling liquid molecules, the extensive banding in powder samples with many different nuclei typically obscures the additional structural information that is available in isotropic liquid shifts.

In recent years the shift tensor's importance has increased significantly as line-narrowing methods and techniques have emerged for analyzing the overlapping spectral bands found in solids. Consequently, solid NMR shift data now rival liquid data in the study of the molecular and electronic structure of matter. For materials such as polymers, coals, and other insoluble substances, only solid state methods are available for NMR analysis. The field of solid state NMR has been treated extensively, and several excellent treatises[6–12] provide additional information on chemical shift tensors and their importance in chemistry.

This article is organized into sections with Sections 2–6 providing the main body of the work. Section 2 provides mathematical definitions of an induced magnetization vector associated with nuclear shielding and magnetic susceptibility. These magnetizations modify the static magnetic field that governs NMR frequencies, and their relative importance is discussed. The chemical shift of a resonance frequency is referenced to a designated fiducial peak, and this practice avoids the dilemma of referring chemically dependent shifts to the immeasurable resonance of a bare nucleus. The mathematical form of the chemical shift tensor is introduced in Section 2, and these expressions reflect both the chemical environment and their orientational dependence.

The transformations needed to convert shift tensors between different coordinate frames are presented in Section 3, and their importance is briefly discussed. Tensor representations (i.e., the icosahedral and irreducible spherical tensors) are discussed along with the properties that make them attractive for deriving mathematical relationships and for statistically analyzing and comparing tensor data.

Section 4 analyzes the chemical shift information contained in powder samples where the random orientations of microcrystallites produce resonance bands. These spectral bands have characteristic shapes depending upon the magnitude of the tensor components and the overall symmetry of the shift tensor. The conformal mapping approach of Bloembergen and Rowland[13] relates the intensities and frequencies found in a spectral pattern to the principal chemical shift values of the tensor expressed in its own principal axis frame (PAF).

Section 5 summarizes two single crystal methods used for obtaining complete chemical shift tensors, including both the principal shift values and the tensor's orientation in the crystal. Such crystal data provide the six parameters needed to describe a general asymmetric tensor, whereas powder patterns can provide only the three principal shift values. The

tensor's orientation, obscured in powder samples, is readily available from single crystal data. The traditional 1D single-axis goniometer method is discussed in Section 5 along with a newer 2D spatial correlation method. This 2D approach has the capacity of indexing close to an order of magnitude more peaks than the 1D single-axis goniometer method.

Section 6 briefly identifies symmetry and structural features that dominate the chemical shift tensor. Both diamagnetic and paramagnetic shielding currents are important in chemical shifts, and the magnitudes of a representative sampling of ^{13}C shifts are discussed to illustrate the governing principles. While first-order diamagnetic currents produce large shifts, arising from carbon electrons in the 1s inner shell and in the 2s, 2p valence shell, these diamagnetic currents vary less between different molecules than corresponding paramagnetic currents which arise from mixing intrinsic angular momentum components from p and d electrons into the molecule's electronic structure. Such paramagnetic shifts arise from a second-order perturbation between the nuclear magnetic moment and the static magnetic field. As these shielding currents represent very weak perturbations of the electronic structure they can vary by orders of magnitude without altering appreciably the overall electronic energy. Thus, highly variable paramagnetic currents depend upon a variety of structural factors to be discussed in Section 6.

2 THE CHEMICAL SHIFT

2.1 Chemical Shielding and Magnetic Susceptibility

Ignoring spin–spin interactions, rapidly tumbling molecules in nonviscous liquids exhibit narrow nuclear resonance lines with frequencies, f_i, given by,

$$f_i = \frac{\gamma_s}{2\pi}\boldsymbol{I}(i)\cdot\boldsymbol{B}_i = \frac{\gamma_s}{2\pi}\boldsymbol{I}(i)\cdot(\boldsymbol{M}_i + \boldsymbol{H}_0)\mu_0 = \frac{\gamma_s}{2\pi}\boldsymbol{I}(i)\cdot(1-\sigma_i-\chi_m)\mu_0\boldsymbol{H}_0 \quad (1)$$

The angular momentum of the ith spin and its corresponding gyromagnetic ratio are given, respectively, by $\boldsymbol{I}(i)$ and γ_s. The magnetic induction at the nucleus, $\boldsymbol{B}_i$, is equal to the vector sum of the static magnetic field, $\boldsymbol{H}_0$, and an induced magnetization vector, $\boldsymbol{M}_i$, arising from electronic currents that exist within the sample. This magnetization is given by $\boldsymbol{M}_i = -(\sigma_i + \chi_m)\boldsymbol{H}_0$ and is directly proportional to $\boldsymbol{H}_0$. The proportionality constant between $\boldsymbol{M}_i$ and $\boldsymbol{H}_0$, includes the chemical shielding, σ_i, and the magnetic susceptibility, χ_m, of the material surrounding the nuclear spin of interest. The magnetic permeability of free space, μ_0, equals unity in Gaussian magnetic units and $4\pi \times 10^{-7}$ in SI units.[14]

The subdivision in equation (1) of the magnetization vector into chemical shielding and magnetic susceptibility is somewhat arbitrary, unfortunately, as they both arise from the same phenomena, circular electronic currents induced in the sample by H_0. Typically, the variable shielding terms, σ_i, designate specific currents in the vicinity of the nucleus, and their variability reflects changes primarily in the electronic structure of the molecule of interest. The magnetic susceptibility term, χ_m, is usually reserved for more remote electron currents that contribute to a uniform bulk magnetic property for the sample. It is presumed that χ_m is equal for all nuclei in a given molecule, leaving variations in the nuclear resonance frequencies within the same molecule to be attributed solely to chemical shielding. It is the assignment of electron currents at intermediate distances (e.g., in neighboring molecules) which creates the challenge for separating σ_i from χ_m. In liquids, the separation of the induced magnetization into intramolecular currents for chemical shielding and into intermolecular currents for magnetic susceptibility is partially justified as molecular diffusion, both rotation and translation, averages the effect of intermolecular currents between adjacent tumbling molecules into a fairly uniform induced magnetization vector.

In solids, the absence of rapid motional averaging makes a simple division of M_i into either chemical shielding or magnetic susceptibility more difficult. It is still straightforward to assign all intramolecular currents within the parent molecule to chemical shielding and distant electronic currents to magnetic susceptibility. However, proximate intermolecular currents no longer average to uniform values across a given molecule, but depend upon the nature of the surrounding molecules and upon the irregular shape of the crystalline cavity when the parent molecule is conceptually removed from consideration. When designation of sizable intermolecular currents from neighboring molecules to χ_m fails to meet the criterion that the susceptibility should be a homogeneous bulk property, these proximate intermolecular shielding currents should appropriately be included as a part of σ_i. The lack of a precise prescription for designating a term as either shielding or susceptibility is imposed on us in part by our inability to identify experimentally or to calculate reliably the theoretical contributions to the magnetization from currents beyond the immediate molecular domain. Fortunately, the susceptibility variations in the resonance frequencies for many molecules are often less than the solid linewidths and their contributions may be ignored. When the isotropic solid and liquid shifts are very similar, then strong evidence exists that the shielding is dominated by intramolecular electronic currents.

2.2 Chemical Shifts in Liquids

As the resonance frequency of a bare nucleus cannot be measured by ordinary means, chemical shifts are typically reported relative to a fiducial resonance peak of a specified nucleus. Reference compounds are selected for their stability and chemical inertness. For example, tetramethylsilane (TMS) has become the standard for chemical shift measurements of both the ^{13}C and ^{1}H nuclides because the TMS resonance lines are relatively insensitive to solvent interactions and, in addition, this compound is chemically stable. The chemical shifts of each nuclear species in the sample are measured from their reference frequencies in accordance with the following chemical shift expression:

$$\delta_i(\text{ppm}) = \frac{f_i - f_{\text{ref}}}{f_{\text{ref}}} \times 10^6 \quad (2)$$

The f_{ref} is the resonance frequency of the reference nucleus and f_i is the corresponding frequency of the ith nucleus. Variations in f_i from f_{ref} are usually small and according to

IUPAC conventions δ_i are reported in units of parts per million (ppm). For simplicity of notation, the 10^6 factor in equation (2) is only implied henceforth in this article. By substituting equation (1) into equation (2) and rearranging the expression, one obtains

$$\delta_i = \frac{\sigma_{\text{ref}} - \sigma_i}{1 - \sigma_{\text{ref}} - \chi_{\text{m}}} \simeq \sigma_{\text{ref}} - \sigma_i \qquad (3)$$

The final expression for δ_i is obtained by neglecting the higher order infinitesimal, $\delta_i\ (\sigma_{\text{ref}} + \chi_{\text{m}})$.

The difference in the sign of δ_i versus σ_i is a consequence of δ_i applying to frequency space and σ_i designating a fractional change in the magnetic field. In NMR spectroscopy the reciprocal relationship between the magnetic field and the resonance frequency provides one of the rich legacies of this special spectroscopy, in which a variety of spectral frequencies are made possible by altering the static magnetic field. The sign anomaly in equation (3) is a modest inconvenience considering the benefits of dealing flexibly with both field and frequency variables. Unfortunately, this dual convention for reporting the position of NMR peaks introduces some perplexities in their use, especially to those approaching the field for the first time.

By substituting equation (3) in equation (1), a convenient form of the resonance frequency is given by

$$f_i = (1 + \delta_i) f_{\text{ref}} = \frac{\gamma_{\text{s}}}{2\pi} I(i)(1 + \delta_i) B_{\text{ref}} \qquad (4)$$

where the magnetic induction at the reference nucleus, B_{ref}, is given by

$$B_{\text{ref}} = (1 - \sigma_{\text{ref}} - \chi_{\text{m}})\mu_0 H_0 \qquad (5)$$

As discussed in Section 2.1, the value for χ_{m} is presumed to be the same for all nuclei in a given molecule and differences between f_i are ascribed solely to variations in δ_i. Magnetic susceptibility corrections need to be applied from time to time in the comparison of chemical shifts obtained either from different solutions or from the same material with different physical shapes. External referencing of chemical shifts in different solvents therefore should be approached with care.

Historically, NMR spectra were obtained at constant frequency while sweeping the magnetic field, and in the early days of the field it was the practice to report resonance shifts as differences in shielding constants. With the arrival of Fourier transform methods, it is now more common to record and process chemical shift data in frequency units. However, quantum mechanical calculations of nuclear shielding, by their nature, provide absolute shifts that are expressed relative to the resonance frequency of a bare nucleus. For this reason, and supported by the historical convention, most theoretical estimates of shifts are still reported as σ_i values. This can pose a problem when one wishes to compare δ_i directly to $(\sigma_{\text{ref}} - \sigma_i)$, as only theoretical methods exist for estimating the magnitude of σ_{ref} for a given reference nucleus. Jameson has related the absolute chemical shift scales of different nuclei to each other and this topic is discussed elsewhere in this Encyclopedia, (see C. J. Jameson ***Chemical Shift Scales on an Absolute Basis***).

2.3 Chemical Shifts in Solids

A variety of proton-decoupled ^{13}C spectra of methyl β-D-xylopyranoside are given in Figure 1 to illustrate the effect of immobilizing molecules in solids. The liquid spectrum is shown in Figure 1(a) with a single peak appearing for each of the six different carbons of methyl β-D-xylopyranoside. Figure 1(b) exhibits the corresponding solid spectrum using the popular cross polarization (see D. P. Burum ***Cross Polarization in Solids***) and magic angle spinning (CP MAS) techniques (see E. A. Andrew ***Magic Angle Spinning***) to suppress the orientational information. Such CP MAS spectra, obtained on powdered solids, have an appearance similar to liquid spectra. The CP MAS spectral lines are considerably broader than the very sharp liquid lines, but only relatively small chemical shifts exist between the two spectra given in Figures 1(a) and (b). These shifts reflect modest changes in the molecular conformations or intermolecular associations that exist between the liquid and solid states.

The final three spectra, given in Figures 1(c), (d), and (e), are from three mutually perpendicular orientations of a single crystal of methyl β-D-xylopyranoside. It is readily apparent in these three spectra that the shift data exhibit a high dependence on the orientation of the single crystal sample. The six lines in the liquid and CP MAS spectra are doubled to 12 lines due to the presence of two magnetically different molecules, designated as a and b, within the unit cell. Only the two C-6 peaks, 6a and 6b, are labeled in Figure 1 to illustrate the effect of magnetic nonequivalence in the unit cell, but these two lines represent the doubling found for all six carbons in methyl β-D-xylopyranoside. It should be noted that the average of the three peaks labeled 6a and the average of those labeled 6b each gives the same shift as found for the C-6 peak in the CP MAS spectrum, thereby indicating that the pair of resonances labeled 6a and 6b are chemically congruent.

The doubling of resonance lines in methyl β-D-xylopyranoside arises from two chemically equivalent but magnetically nonequivalent molecules in the crystal. The different resonance shifts between corresponding nuclei in the two molecules are due only to a difference in the orientation of the two molecules relative to the magnetic field. The chemically equivalent molecules are related by the symmetry elements in the unit cell, but in an arbitrarily oriented crystal the magnetic field usually does not comply with this symmetry. Molecules, symmetrically related but not identically oriented in the magnetic field, exhibit different resonance frequencies. Such congruent frequencies reflect the orientational dependence of the chemical shifts in solid samples and indicate the need for mathematical expressions that specify the orientational aspects of chemical shift tensors (see Section 2.4 below).

If a single crystal of methyl β-D-xylopyranoside is pulverized, broad powder patterns are observed in place of the discrete peaks found in Figures 1(c)–(e). But now these spectral bands are the same for the different a and b molecules that led to the line doubling in Figures 1(c)–(e). This loss of congruent shift information obscures the tensor's orientational information in powder samples. Excessive overlapping of powder bands also limits the chemical shift information that can be measured for multiple spins. Usually, only two, or at most three, overlapping spectral bands may be analyzed successfully from a simple 1D solid spectrum.

Figure 2 contains simulated band spectra for a variety of spectral powder patterns. Typical spectral bands for two axially

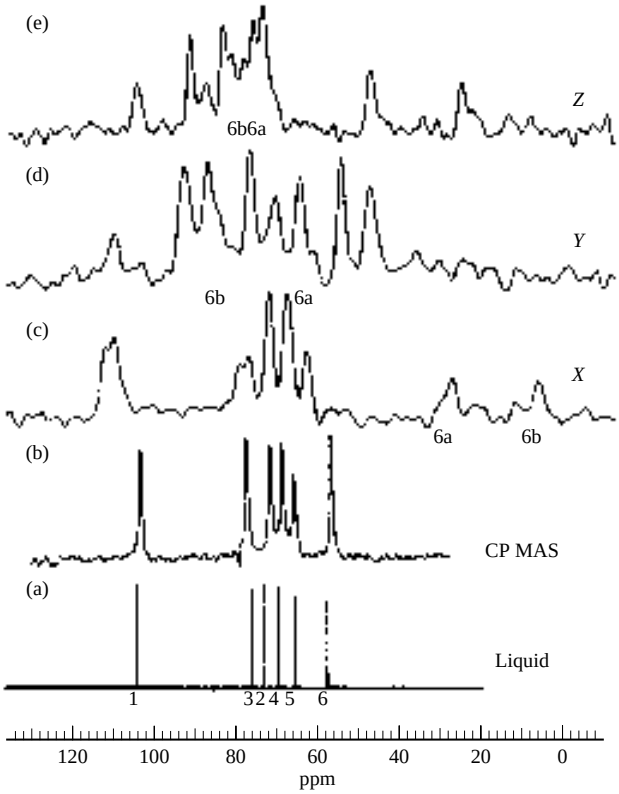

Figure 1 NMR spectra of methyl β-D-xylopyranoside obtained under various conditions: (a) typical liquid spectrum; (b) CP MAS solid spectrum; (c)–(e) single crystal spectra with magnetic field oriented along the X, Y, and Z axes, respectively. To avoid congestion in the labeling of lines, only the 6a and 6b conjugate resonance lines are illustrated. See Figure 13 for the remaining assignments. (Courtesy of Fang Liu)

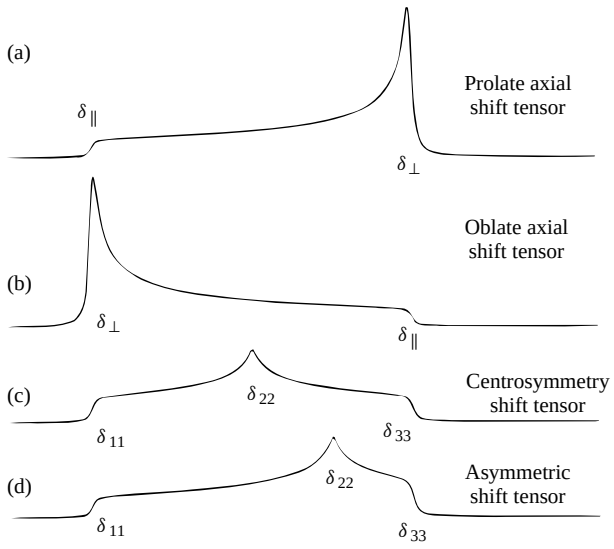

Figure 2 Spectral powder patterns for the following tensor symmetries: (a) prolate; (b) oblate; (c) centrosymmetric; and (d) general asymmetric tensors. (Courtesy of Mark S. Solum)

symmetric tensors are shown in Figures 2(a) and (b). The definition of an axial pattern requires two principal shift values, i.e. $\delta_{\parallel}$ associated with the magnetic field along the axially symmetric or unique principal axis and $\delta_{\perp}$ for the magnetic field perpendicular to the unique principal axis. Depending upon the relative magnitudes of these two principal shift frequencies, the banded spectrum consists of either a prolate ($\delta_{\parallel} > \delta_{\perp}$) or oblate ($\delta_{\perp} > \delta_{\parallel}$) powder patten. Three breakpoints are readily apparent in asymmetric powder patterns, as shown in the two remaining spectra given in Figures 2(c) and (d). These three positions correspond to the three principal values of the chemical shift tensor and may be associated with three mutually perpendicular directions in the molecule. The three directions designate the PAF of the shift tensor. The centrosymmetric tensor, illustrated in Figure 2(c), is defined by the relationship $\delta_{22} = \frac{1}{2}(\delta_{11} + \delta_{33})$, but no constraints are imposed on the values for δ_{11}, δ_{22}, and δ_{33} for the general asymmetric tensor shown in Figure 2(d).

2.4 The Quadratic Form of Chemical Shift Tensors and Their Orientational Dependence

The orientational dependence of resonance frequencies in solid samples is described by the following quadratic formulation of the chemical shift tensor:

$$f_i = \frac{\gamma_s}{2\pi} \boldsymbol{I}(i) \cdot \boldsymbol{B}_i = \frac{\gamma_s}{2\pi} \boldsymbol{I}(i) \cdot (\boldsymbol{1} + \boldsymbol{\delta}_i) \cdot \boldsymbol{B}_{\text{ref}} \qquad (6)$$

Again, the angular momentum vector and the corresponding value for the magnetic induction vector at the nucleus i are

given by $\boldsymbol{I}(i)$ and $\boldsymbol{B}_i$, respectively. The quantity $\boldsymbol{B}_i$ is related to the magnetic induction at the reference peak, $\boldsymbol{B}_{\text{ref}}$, through the unit dyadic and the chemical shift tensor given, respectively, as follows:

$$\boldsymbol{1} = \begin{bmatrix} 1 & 0 & 0 \\ 0 & 1 & 0 \\ 0 & 0 & 1 \end{bmatrix}, \quad \boldsymbol{\delta}_i = \begin{bmatrix} \delta_{xx} & \delta_{xy} & \delta_{xz} \\ \delta_{yx} & \delta_{yy} & \delta_{yz} \\ \delta_{zx} & \delta_{zy} & \delta_{zz} \end{bmatrix} \tag{7}$$

The unit dyadic, $\boldsymbol{1}$, along with γ_s characterize the effect of the nuclear Zeeman splitting and the second-rank chemical shift tensor is given by δ_i. For the sake of simplicity in notation, the nuclear index, i, has been suppressed from the individual matrix elements in equation (7).

To analyze the tensor's effect on the shift frequency, it is helpful to express the $\boldsymbol{B}_i$ found in equation (6) in matrix form using equation (7) to give

$$\begin{aligned} \boldsymbol{B}_i &= \begin{bmatrix} B_{i,x} \\ B_{i,y} \\ B_{i,z} \end{bmatrix} = \begin{bmatrix} (1+\delta_{xx}) & \delta_{xy} & \delta_{xz} \\ \delta_{yx} & (1+\delta_{yy}) & \delta_{yz} \\ \delta_{zx} & \delta_{zy} & (1+\delta_{zz}) \end{bmatrix} \\ &\times \begin{bmatrix} 0 \\ 0 \\ B_{\text{ref}} \end{bmatrix} = \begin{bmatrix} \delta_{xz} B_{\text{ref}} \\ \delta_{yz} B_{\text{ref}} \\ (1+\delta_{zz}) B_{\text{ref}} \end{bmatrix} \end{aligned} \tag{8}$$

In equation (8), the laboratory coordinate frame is defined with the z axis oriented along the magnetic field vector, $\boldsymbol{B}_{\text{ref}}$. The spatial relationships between the components of the magnetic induction, $\boldsymbol{B}_i$, and the corresponding reference field, $\boldsymbol{B}_{\text{ref}}$, may be visualized in Figure 3. Note that the contributions to $\boldsymbol{B}_i$ of the three tensor components are mutually perpendicular, but the perpendicular components fail to contribute to the measurable magnitude of $\boldsymbol{B}_i$, which is given relative to $\boldsymbol{B}_{\text{ref}}$ by the Pythagorean theorem as follows:

$$\begin{aligned} B_i &= \sqrt{(\delta_{xz} B_{\text{ref}})^2 + (\delta_{yz} B_{\text{ref}})^2 + ([1+\delta_{zz}] B_{\text{ref}})^2} \\ &\simeq (1+\delta_{zz}) B_{\text{ref}} \end{aligned} \tag{9}$$

Because $(1 + \delta_{zz})B_{z,\text{ref}}$ is several orders of magnitude larger than either $\delta_{xz}B_{\text{ref}}$ or $\delta_{yz}B_{\text{ref}}$, a root-squared sum of these components makes all contributions negligible except the one along the z axis. The expanded insert in Figure 3 attempts to indicate schematically this feature, but one must realize that the shift components are infinitesimally small compared with the magnetic field vectors even though they have been drawn out of scale to exhibit their geometrical orientations. It is the orientation of this $\boldsymbol{B}_i$ vector along the z axis which quantizes the nuclear angular momentum and makes $I_x(i) = I_y(i) = 0$ in the equilibrium description of the resonance frequency. Consequently, when the ith nuclear spin quantizes along $\boldsymbol{B}_i$, it is also quantized, within our present ability to make measurements, along $\boldsymbol{B}_{\text{ref}}$. Hence, $\boldsymbol{B}_i$ and $\boldsymbol{B}_{\text{ref}}$ are drawn parallel in Figure 3. Substituting equation (9) for B_i and $I_z(i)$ for $I(i)$ into equation (6) yields the following expression for f_i in the laboratory frame of the magnet:

$$f_i = \frac{\gamma_s}{2\pi} I_z(i)(1+\delta_{zz}) B_{\text{ref}} \tag{10}$$

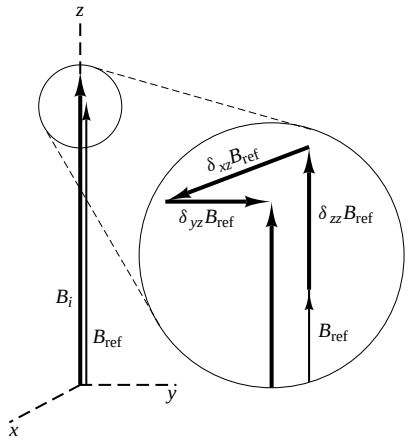

Figure 3 Chemical shift tensor components contributing to $\boldsymbol{B}_i$ in the laboratory frame. The z axis is not scaled linearly to allow the geometrical features associated with the various shift components to be portrayed. The perpendicular components have no measurable effect on the magnitude or orientation of $\boldsymbol{B}_i$ as portrayed in the expanded insert

Equation (10) correctly characterizes the resonance frequency associated with the molecular orientation in the magnetic field, and defines a single shift value, δ_{zz}, for this one measurement. The simplicity of equation (10) may be misleading, however, as a single measurement fails to provide the diversity of resonance frequencies arising from various molecular orientations that are needed to characterize a chemical shift tensor. A shift tensor can only be prescribed when a sufficient number of resonance frequencies exist to define the principal values and their orientations in space. Thus, the tensor must be formulated with equations that express explicitly the orientation of the magnetic field relative to the tensor's orientation. In the tensor's principal axis frame (PAF) the orientation of the $\boldsymbol{B}_{\text{ref}}$ field may be designated with two polar angles, θ and ϕ, as shown in Figure 4, and these two polar angles are sufficient for analyzing powder spectra. Other features in Figure 4 will be discussed in more detail in Section 3.1.2.

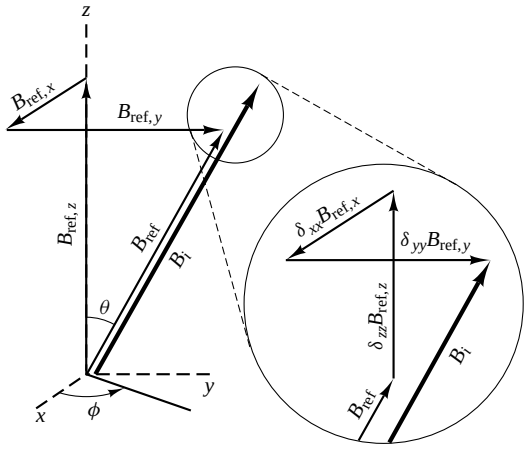

Figure 4 Chemical shift tensor components contributing to $\boldsymbol{B}_i$ in the PAF. In this frame all of the principal δ_{xx}, δ_{yy}, and δ_{zz} components contribute to $\boldsymbol{B}_i$, as indicated. Only their projections onto $\boldsymbol{B}_{\text{ref}}$, shown in the expanded insert, make measurable contributions to the resonance frequency

The spatial orientation of the PAF relative to a molecular or a unit cell frame also must be specified whenever the full chemical shift tensor is to be described. The full six-parameter tensor for chemical shielding requires not only the three principal values but also three Euler angles to describe the orientation of the PAF in a microscopic molecular frame. Only single crystal measurements can provide both principal shift values and the tensor's orientation in a molecular frame. Section 5 provides the mathematical expressions which track the resonance frequencies using the full six-parameter chemical shift tensor.

3 THE CHEMICAL SHIFT TENSOR IN A VARIETY OF REFERENCE FRAMES AND REPRESENTATIONS

3.1 The Cartesian Chemical Shift Tensor

3.1.1 Separation of the Chemical Shift Tensor into Matrices of Different Rank

The chemical shift tensor in a general reference frame may be expressed as a typical 3×3 Cartesian matrix that can be separated, respectively, into three individual tensors of rank zero, one, and two as follows:

$$\begin{bmatrix} \delta_{xx} & \delta_{xy} & \delta_{xz} \\ \delta_{yx} & \delta_{yy} & \delta_{yz} \\ \delta_{zx} & \delta_{zy} & \delta_{zz} \end{bmatrix} = \delta_{\mathrm{o}} \begin{bmatrix} 1 & 0 & 0 \\ 0 & 1 & 0 \\ 0 & 0 & 1 \end{bmatrix} + \begin{bmatrix} 0 & \delta_{xy}^{(\mathrm{a})} & \delta_{xz}^{(\mathrm{a})} \\ -\delta_{xy}^{(\mathrm{a})} & 0 & \delta_{yz}^{(\mathrm{a})} \\ -\delta_{xz}^{(\mathrm{a})} & -\delta_{yz}^{(\mathrm{a})} & 0 \end{bmatrix} + \begin{bmatrix} (\delta_{xx}^{(\mathrm{s})} - \delta_{\mathrm{o}}) & \delta_{xy}^{(\mathrm{s})} & \delta_{xz}^{(\mathrm{s})} \\ \delta_{xy}^{(\mathrm{s})} & (\delta_{yy}^{(\mathrm{s})} - \delta_{\mathrm{o}}) & \delta_{yz}^{(\mathrm{s})} \\ \delta_{xz}^{(\mathrm{s})} & \delta_{yz}^{(\mathrm{s})} & (\delta_{zz}^{(\mathrm{s})} - \delta_{\mathrm{o}}) \end{bmatrix} \tag{11}$$

where the zero, first, and second rank components appearing on the right-hand side of equation (11) are due to the scalar isotropic chemical shift, $\delta_{\mathrm{o}} = \frac{1}{3}(\delta_{xx} + \delta_{yy} + \delta_{zz})$, the antisymmetric chemical shifts, $\delta_{ij}^{(a)} = \frac{1}{2}(\delta_{ij} - \delta_{ji})$, and the symmetric chemical shifts, $\delta_{ij}^{(s)} = \frac{1}{2}(\delta_{ij} + \delta_{ji})$, respectively. Substitution of these defined quantities into equation (11) readily verifies the relationship given by this equation. In this separated form the symmetry properties of the three different ranks may be considered individually.

3.1.1.1 The Isotropic Chemical Shift, δ_{o}. The isotropic chemical shift, δ_{o}, is the trace of the Cartesian tensor and is invariant to any rotational transformation of the coordinate frame. Thus, under the rapid rotational tumbling encountered in liquid samples, the value of δ_{o} remains constant, but both the antisymmetric first-rank and the symmetric second-rank tensors vanish if the motion is isotropic. Unfortunately, this averaging process prevents access to anisotropic chemical shift information in isotropic liquids. Quite frequently, the trace of the chemical shift tensor in solids is similar to averaged shifts in isotropic liquids. The small shifts observed between solid and liquid spectra, such as shown in Figures 1(a) and (b), usually reflect minor conformational variations between solid and liquid samples. However, δ_{o} in solids may differ significantly from the liquid isotropic shift whenever the solid state affects the intermolecular associations extensively, e.g., hydrogen bonding or some similar strong electrostatic intermolecular interaction. Simple van der Waals intermolecular interactions, found in many compounds, seldom change ($\delta_{\mathrm{o}} - \delta_{\mathrm{liq}}$) beyond the experimental errors in solid shift measurements.

3.1.1.2 The Antisymmetric Chemical Shifts. The absence of diagonal elements in the first-rank antisymmetric shifts, $\delta_{ij}^{(a)}$, has significant implications as it leaves only shielding fields oriented perpendicular to the $\boldsymbol{B}_{\mathrm{ref}}$ as specified in Figure 3. Such shielding fields, as discussed in Section 2.4, are perpendicular to the strong static field, $\boldsymbol{B}_{\mathrm{ref}}$, associated with the Zeeman splitting, and the quantization of the nuclear spin angular momentum along $\boldsymbol{B}_{\mathrm{ref}}$ leaves these second-order infinitesimal shift frequencies immeasurable. While negligible in their effect on the resonance spectral frequencies, such antisymmetric shifts may provide a significant mechanism for spin relaxation with motional tumbling. Theoretical studies suggest, however, that these anomalous relaxation rates are significant only in fairly unusual molecular systems. Molecules in which the antisymmetric shifts appear to be important for spin relaxation include π-electron systems with distorted bond arrangements, such as found in cyclopropene or cyclopropenone.

3.1.1.3 The Symmetric Chemical Shifts and Shift Anisotropy. The second-rank symmetric matrix, $\delta_{ij}^{(s)}$, also develops shielding field components perpendicular to the applied magnetic field, $\boldsymbol{H}_0$, in a manner similar to antisymmetric shifts, but this second-rank tensor, while traceless, has diagonal elements that can provide first-order anisotropic shifts that add or subtract directly from the Zeeman frequencies. Even though small compared with the Zeeman splitting, the shifts associated with ($\delta_{zz} - \delta_{\mathrm{o}}$) are directly measurable in the NMR spectra of solids (see Figure 3). Because the $\delta_{ij}^{(s)}$ matrix is symmetrical, any reorientation of the magnetic field in the molecular frame will still leave anisotropic shifts along the diagonal of the transformed second-rank symmetrical matrix. Unlike the antisymmetric components, the off-diagonal shifts in the symmetric portion of the chemical shift tensor will affect the principal values under the transformations associated with matrix diagonalization. These new diagonal or principal value components will then project along $\boldsymbol{B}_{\mathrm{ref}}$ and shift the resonance frequency. Antisymmetric shifts under rotational transformations can never contribute to a diagonal element, because of symmetry considerations, and therefore are not measured in the NMR frequency.

3.1.2 Transformations Between Different Cartesian Frames

The transformation of the symmetric portion of the Cartesian tensor from one reference frame (e.g., *xyz* frame) to another (e.g., *XYZ* frame) requires the following similarity transformation:

$$\boldsymbol{\delta}(XYZ) = \mathbf{T}\boldsymbol{\delta}(xyz)\mathbf{T}^{-1} \tag{12}$$

where the rotation matrix, **T**, effects a rotational transformation, $\mathcal{R}(\alpha,\beta,\gamma)$, of the tensor from the *xyz* coordinate frame into the corresponding *XYZ* frame. The matrix, **T**, may be expressed with the nine directional cosines relating the two

frames or with an equivalent matrix using the Euler angles, α, β, and γ, as follows:[15,16]

$$\mathbf{T} = \begin{bmatrix} c_{Xx} & c_{Xy} & c_{Xz} \\ c_{Yx} & c_{Yy} & c_{Yz} \\ c_{Zx} & c_{Zy} & c_{Zz} \end{bmatrix} = \begin{bmatrix} (c_\alpha c_\beta c_\gamma - s_\alpha s_\gamma) & (s_\alpha c_\beta c_\gamma + c_\alpha s_\gamma) & (-s_\beta c_\gamma) \\ (-c_\alpha c_\beta s_\gamma - s_\alpha c_\gamma) & (-s_\alpha c_\beta s_\gamma + c_\alpha c_\gamma) & (s_\beta s_\gamma) \\ (c_\alpha s_\beta) & (s_\alpha s_\beta) & (c_\beta) \end{bmatrix} \quad (13)$$

The directional cosines, c_{Qq}, relate the two sets of Cartesian axes found in the alternative frames. The shortened notation, c = cos and s = sin, has been utilized to conserve space in equation (13) and is applied with the three Euler angles, α, β, and γ. As $\mathbf{T}$ is a real unitary matrix, its inverse matrix in equation (12) is given by the transpose (i.e., $\mathbf{T}^{-1} = \mathbf{T}^{t}$).

Typical chemical shift reference frames used in tensor studies are shown in Figure 5 and the rotational transformations, $\mathcal{R}(\alpha,\beta,\gamma)$, that link these various frames. Successive rotations may be represented by a single rotation given by $\mathcal{R}(\alpha,\beta,\gamma) = \mathcal{R}(\alpha_m,\beta_m,\gamma_m) \times \mathcal{R}(\alpha_l,\beta_l,\gamma_l)$. Successive rotations also may be represented by nested similarity transformations as follows:

$$\begin{aligned} \boldsymbol{\delta}_{PAF}(x_o, y_o, z_o) &= \mathbf{T}(\alpha_m, \beta_m, \gamma_m)\boldsymbol{\delta}_{mol}(x_m y_m z_m) \\ &\quad \times \mathbf{T}^{-1}(\alpha_m, \beta_m, \gamma_m) \\ &= \mathbf{T}(\alpha_m, \beta_m, \gamma_m)\mathbf{T}(\alpha_s, \beta_s, \gamma_s)\boldsymbol{\delta}_{samp}(x, y, z) \\ &\quad \times \mathbf{T}^{-1}(\alpha_s, \beta_s, \gamma_s)\mathbf{T}^{-1}(\alpha_m, \beta_m, \gamma_m) \end{aligned} \quad (14)$$

Consequently, there will always be a matrix $\mathbf{T}(\alpha,\beta,\gamma) = \mathbf{T}(\alpha_m,\beta_m,\gamma_m)\ \mathbf{T}(\alpha_s,\beta_s,\gamma_s)$ that will relate the experimental shift tensor, $\delta_{samp}(x,y,z)$, in the sample frame to the tensor, $\delta_{PAF}(x_o,y_o,\ z_o)$, in its own PAF. The $\mathbf{T}(\alpha,\beta,\gamma)$ matrix may be readily obtained using standard diagonalization routines from tensors measured in any reference frame; this is illustrated as follows for the sample frame tensor

$$\boldsymbol{\delta}_{PAF}(x_o y_o z_o) = \mathbf{T}(\alpha, \beta, \gamma)\boldsymbol{\delta}_{samp}(x, y, z)\mathbf{T}^{-1}(\alpha, \beta, \gamma) \quad (15)$$

Using the transformation in equation (15) along with a general expression for equations (6) and (7) provides the resonance frequency in matrix form as follows:

$$f_i = \frac{\gamma_i}{2\pi}[I_{o,x}\ \ I_{o,y}\ \ I_{o,z}] \times \begin{bmatrix} (1+\delta_{xx}^{PAF}) & 0 & 0 \\ 0 & (1+\delta_{yy}^{PAF}) & 0 \\ 0 & 0 & (1+\delta_{zz}^{PAF}) \end{bmatrix} \times \begin{bmatrix} B_{ref,x} \\ B_{ref,y} \\ B_{ref,z} \end{bmatrix} \quad (16)$$

Equation (16) may be simplified using the geometry exhibited in Figure 4 where $B_{ref,x} = lB_{ref}$, $B_{ref,y} = mB_{ref}$, and $B_{ref,z} = nB_{ref}$. The respective directional cosines (i.e., l, m, and n) of the magnetic induction vector, $\boldsymbol{B}_{ref}$, are defined in the PAF relative to the corresponding x_o, y_o, and z_o axes. Likewise, $I_{ox} = lI_o$, $I_{o,y} = mI_o$ and $I_{o,z} = nI_o$ as

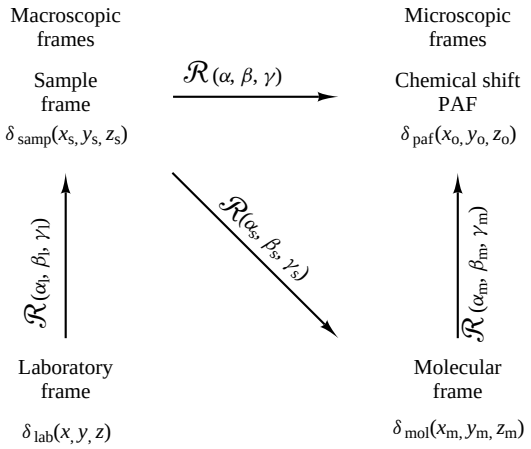

Figure 5 Representative coordinate frames for the sample, laboratory, principal axis, and molecular frames. Rotational functions with their Euler angles are given with arrows linking the various frames

the total angular momentum, given by $\boldsymbol{I}_o$, also quantizes along $\boldsymbol{B}_{ref}$. The consequence of equation (16) is visualized in Figure 4 where $\boldsymbol{B}_i$ lies along $\boldsymbol{B}_{ref}$. The contributions to $\boldsymbol{B}_i$ from components perpendicular to $\boldsymbol{B}_{ref}$ are immeasurable, and the directional cosine form of equation (16) eliminates these perpendicular components from consideration. The measurable changes in $\boldsymbol{B}_i$ arise only from the projections of the shielding components along $\boldsymbol{B}_{ref}$ as indicated in Figure 4. Using the directional cosines in the expansion of equation (16) renders the resonance frequency as follows:

$$f_i = \frac{\gamma_i}{2\pi} I_o B_{ref}(1 + l^2\delta_{xx}^{PAF} + m^2\delta_{yy}^{PAF} + n^2\delta_{zz}^{PAF}) \quad (17)$$

Note, the expression $l^2 + m^2 + n^2 = 1$ retains the simplicity of the Zeeman contribution. The spectral breakpoints observed in all of the solid powder patterns in Figure 2 correspond to the principal shift values (i.e., δ_{xx}^{PAF}, δ_{yy}^{PAF}, and δ_{zz}^{PAF}) found in equations (16) and (17). These equations contain the functional dependence of the PAF orientation necessary for analysis of spectral patterns associated with solid powder samples. The details of the powder analysis are found in Section 4.

In single crystal work, the chemical shift is tracked for various orientations of the magnetic field in the sample frame. These data are then transformed into either the frame of the unit cell or one of the molecular frames to determine the tensor's orientation in the molecule. Diffraction data provide the necessary structural relationships between the unit cell and various molecular frames. Tensors in any of these microscopic frames may be diagonalized to obtain the shift tensor in the PAF. In the process the molecular orientation of the PAF tensor is obtained. Thus, a variety of Cartesian sample frames are used in the process of measuring a shift tensor in a single crystal. The importance of such spatially correlated data, obtained from single crystals, will be discussed in Section 5. Before dealing explicitly with either powder or single crystal experiments, two alternative representations, the irreducible spherical tensor and the icosahedral representations, prove beneficial for different mathematical treatments of chemical shift tensor

data, and these are considered respectively in Sections 3.2 and 3.3.

3.2 Irreducible Spherical Representation of Chemical Shifts

Standard treatments[17,18] of the chemical shift tensor have shown that the chemical shift Hamiltonian may be expressed as an expansion of spin and spatial irreducible spherical tensors as follows:

$$\begin{aligned}\hat{\mathcal{H}} &= h\hat{f}_i = \hbar\gamma_s \hat{\boldsymbol{I}}_o(i)\cdot(\boldsymbol{1}+\boldsymbol{\delta}_i)\cdot\boldsymbol{B}_{ref} \\ &= \hbar\gamma_s\left[\hat{I}_o(i)B_{ref} + \textstyle\sum_{l,m}(-1)^m \hat{F}_m^{(l)}(i,b)\delta_{-m}^{(l)}(i)\right]\end{aligned} \tag{18}$$

The composite irreducible spin-field tensor components are given by $\hat{F}_m^{(l)}(i,b)$ and the chemical shift tensor components are given by $\delta^{(l)}{}_m$.

3.2.1 Combined Spin-Field Irreducible Spherical Tensors

The second-rank irreducible spherical form of the combined spin-field tensor is formed by coupling[17,19] the first-rank angular momentum operators for a single spin with the first-rank magnetic field vector. The resulting combined irreducible spherical tensors are given as

$$\left.\begin{aligned}\hat{F}_0^{(0)}(i,b) &= -\frac{1}{\sqrt{3}}\left[\hat{I}_z b_z + \frac{1}{2}(\hat{I}_+ b_- + \hat{I}_- b_+)\right] \\ \hat{F}_0^{(1)}(i,b) &= \frac{1}{\sqrt{8}}[\hat{I}_+ b_- - \hat{I}_- b_+] \\ \hat{F}_{\pm1}^{(1)}(i,b) &= -\frac{1}{2}[\hat{I}_z b_\pm - I_\pm b_z] \\ \hat{F}_0^{(2)}(i,b) &= \sqrt{\frac{2}{3}}\left[\hat{I}_z b_z - \frac{1}{4}(\hat{I}_+ b_- + \hat{I}_- b_+)\right] \\ \hat{F}_{\pm1}^{(2)}(i,b) &= \mp\frac{1}{2}[\hat{I}_\pm b_z + \hat{I}_z b_\pm] \\ \hat{F}_{\pm2}^{(2)}(i,b) &= \frac{1}{2}\hat{I}_\pm b_\pm\end{aligned}\right\} \tag{19}$$

where $b_\pm = (l \pm \mathrm{i}m)B_{ref}$, $b_z = nB_{ref}$, and l, m, and n are the directional cosines between the magnetic field and the x, y, and z axes, respectively. Likewise, $\hat{I}_\pm = (l \pm \mathrm{i}m)\hat{I}_o$ and $\hat{I}_z = n\hat{I}_o$.

In the laboratory frame, the z axis is defined by the static magnetic field, $\boldsymbol{B}_{ref}$; thus, $n = 1$ and $l = m = 0$. Using these values for the appropriate directional cosines leaves $\hat{I}_o$ quantized along the z axis, and with the quantization approximation the following combined spin-field irreducible spherical tensor components in the laboratory frame then become

$$\left.\begin{aligned}\hat{F}_0^{(0)}(i,b) &= -\frac{1}{\sqrt{3}}\hat{I}_z B_{ref}, \quad \hat{F}_0^{(1)}(i,b) = 0, \\ &\qquad \hat{F}_{\pm1}^{(1)}(i,b) = 0 \\ \hat{F}_0^{(2)}(i,b) &= \sqrt{\frac{2}{3}}\hat{I}_z B_{ref}, \quad \hat{F}_{\pm1}^{(2)}(i,b) = 0, \\ &\qquad \hat{F}_{\pm2}^{(2)}(i,b) = 0\end{aligned}\right\} \tag{20}$$

3.2.2 Chemical Shift Irreducible Spherical Tensors

The irreducible spherical tensor representation, $\delta_m^{(l)}(xyz)$, for the chemical shift components are given in a generalized reference frame[17] as follows:

$$\left.\begin{aligned}\delta_0^{(0)} &= -\sqrt{3}\delta_o = -\frac{1}{\sqrt{3}}(\delta_{xx}+\delta_{yy}+\delta_{zz}) \\ \delta_0^{(1)} &= -\mathrm{i}\sqrt{2}\delta_{xy}^{(a)} = \frac{-\mathrm{i}}{\sqrt{2}}(\delta_{xy}-\delta_{yx}) \\ \delta_{\pm1}^{(1)} &= [\delta_{xz}^{(a)} \pm \mathrm{i}\delta_{yz}^{(a)}] = \frac{1}{2}[(\delta_{xz}-\delta_{zx}) \pm \mathrm{i}(\delta_{yz}-\delta_{zy})] \\ \delta_0^{(2)} &= \sqrt{\frac{2}{3}}[\delta_{zz}^{(s)} - \frac{1}{2}(\delta_{xx}^{(s)}+\delta_{yy}^{(s)})] \\ &= \sqrt{\frac{2}{3}}\left[\delta_{zz} - \frac{1}{2}(\delta_{xx}+\delta_{yy})\right] \\ &= \sqrt{\frac{3}{2}}[\delta_{zz}-\delta_o] \\ \delta_{\pm1}^{(2)} &= \mp[\delta_{xz}^{(s)} \pm \mathrm{i}\delta_{yz}^{(s)}] = \mp\tfrac{1}{2}[(\delta_{xz}+\delta_{zx}) \pm \mathrm{i}(\delta_{yz}+\delta_{zy})] \\ \delta_{\pm2}^{(2)} &= \left[\frac{1}{2}(\delta_{xx}^{(s)}-\delta_{yy}^{(s)}) \pm \mathrm{i}\delta_{xy}^{(s)}\right] \\ &= \frac{1}{2}[(\delta_{xx}-\delta_{yy}) \pm \mathrm{i}(\delta_{xy}+\delta_{yx})]\end{aligned}\right\} \tag{21}$$

As the zero-rank irreducible term $\delta_0^{(0)} = \sqrt{3}\,\delta_o$ contains only the isotropic chemical shift, it also is invariant under molecular tumbling. The first-rank terms $\delta_0^{(1)}(i)$ and $\delta_{\pm1}^{(1)}(i)$ include only antisymmetric chemical shifts that are immeasurable in the frequency spectrum; they are not considered further. The remaining irreducible terms $\delta_0^{(2)}$, $\delta_{\pm1}^{(2)}$, and $\delta_{\pm2}^{(2)}$ are all second-rank symmetrical chemical shifts that can contribute to the measurable components of the tensor.

Equation (21) is simplified considerably in the PAF where off-diagonal elements are zero. The three persisting diagonal components contribute to $\delta_n^{(l)}(\mathrm{PAF})$ as follows:

$$\left.\begin{aligned}\delta_0^{(2)}(\mathrm{PAF}) &= \sqrt{\frac{2}{3}}\left[\delta_{zz}^{PAF} - \frac{1}{2}(\delta_{xx}^{PAF}+\delta_{yy}^{PAF})\right] \\ &= \sqrt{\frac{3}{2}}[\delta_{zz}^{PAF}-\delta_o] \\ \delta_{\pm1}^{(2)}(\mathrm{PAF}) &= 0 \\ \delta_{\pm2}^{(2)}(\mathrm{PAF}) &= \frac{1}{2}[\delta_{xx}^{PAF}-\delta_{yy}^{PAF}]\end{aligned}\right\} \tag{22}$$

3.2.3 Resonance Frequency Expressions in the Irreducible Representation

In the laboratory frame equation (18) may be used with the combined spin-field irreducible tensor given in equation (20) along with the general irreducible spherical form of the chemical shift tensor in equation (21) to obtain the following expression:

$$\begin{aligned}\hat{f}_i &= \frac{\gamma}{2\pi}[\hat{I}_z B_{ref} + \hat{F}_0^{(0)}(i,b)\delta_0^{(0)}(i) + \hat{F}_0^{(2)}(i,b)\delta_0^{(2)}(i)] \\ &= \frac{\gamma}{2\pi}(1+\delta_{zz})\hat{I}_z B_{ref}\end{aligned} \tag{23}$$

It is not surprising that equations (23) and (10) are equivalent for the resonance frequency expressed in the laboratory

frame, but this simple exercise illustrates the application of equation (18).

In the case of the PAF, equation (18) utilizes equation (19) for the general spin-field irreducible tensor along with equation (22) for the chemical shift tensor in the PAF to yield the following expression:

$$\begin{aligned}\hat{f}_i &= \frac{\gamma}{2\pi}[\hat{I}_o B_{\text{ref}} + \hat{F}_0^{(0)}(i,b)\delta_0^{(0)}(\text{PAF}) \\ &\quad + \hat{F}_0^{(2)}(i,b)\delta_0^{(2)}(\text{PAF}) + (\hat{F}_{+2}^{(2)}(i,b) \\ &\quad + \hat{F}_{-2}^{(2)}(i,b))\delta_{\pm 2}^{(2)}(\text{PAF})] \\ &= \frac{\gamma_i}{2\pi}\hat{I}_o B_{\text{ref}}(1 + l^2\delta_{xx}^{\text{PAF}} + m^2\delta_{yy}^{\text{PAF}} + n^2\delta_{zz}^{\text{PAF}})\end{aligned} \tag{24}$$

Once again, equation (24) gives an equivalent expression to equation (17) for the resonance frequency in the PAF and this procedure provides a second illustration for the use of equation (18). One advantage of irreducible spherical tensors is discussed in the next section dealing with their transformation properties.

3.2.4 Transformation Properties of Irreducible Spherical Tensors

The rotations associated with coordinate frame transformations, such as indicated in Figure 5, may be implemented readily for any tensor expressed in the irreducible spherical tensor representation. Wigner rotation matrices, $\mathcal{D}_{n,m}^{(l)}(\alpha, \beta, \gamma)$, may be used to convert the irreducible shift components from one frame to another in accordance with the standard formulations[20] given by

$$\delta_m^{(l)}(XYZ) = \sum_n \mathcal{D}_{n,m}^{(l)}(\alpha, \beta, \gamma)\delta_n^{(l)}(xyz) \tag{25}$$

where an explicit expression for the Wigner rotation matrix is given by

$$\mathcal{D}_{n,m}^{(l)}(\alpha, \beta, \gamma) = \mathrm{e}^{-\mathrm{i}n\alpha} d_{n,m}^{(l)}(\beta)\mathrm{e}^{-\mathrm{i}m\gamma} \tag{26}$$

and

$$\begin{aligned}d_{n,m}^{(l)} = &\sum_\nu \frac{(-1)^\nu \sqrt{(l+m)!(l-m)!(l+n)!(l-n)!}}{(l-n-\nu)!(l+m-\nu)!(\nu+m-n)!\nu!} \\ &\times \left(\cos\frac{\beta}{2}\right)^{2l+m-n-2\nu} \left(\sin\frac{\beta}{2}\right)^{n-m+2\nu}\end{aligned} \tag{27}$$

The index ν sums over all terms for which the factorial arguments are nonvanishing. It is actually the linear feature of equation (25) that empowers the Wigner rotation matrices in problems of this type and makes the irreducible spherical tensors so useful in mathematical developments of chemical shift expressions. The α, β, and γ Euler angles associated with the similarity transformations are the same as used in equation (13). The process is illustrated by transforming the irreducible spherical components from the PAF into irreducible spherical components in a generalized Cartesian frame as follows:

$$\left.\begin{aligned}\delta_0^{(2)} &= \mathcal{D}_{0,0}^{(2)}(\alpha, \beta, \gamma)\delta_0^{(2)}(\text{PAF}) \\ &\quad + [\mathcal{D}_{2,0}^{(2)}(\alpha, \beta, \gamma) + \mathcal{D}_{-2,0}^{(2)}(\alpha, \beta, \gamma)]\delta_2^{(2)}(\text{PAF}) \\ \delta_{\pm 1}^{(2)} &= \mathcal{D}_{0,\pm 1}^{(2)}(\alpha, \beta, \gamma)\delta_0^{(2)}(\text{PAF}) \\ &\quad + [\mathcal{D}_{2,\pm 1}^{(2)}(\alpha, \beta, \gamma) + \mathcal{D}_{-2,\pm 1}^{(2)}(\alpha, \beta, \gamma)]\delta_2^{(2)}(\text{PAF}) \\ \delta_{\pm 2}^{(2)} &= \mathcal{D}_{0,\pm 2}^{(2)}(\alpha, \beta, \gamma)\delta_0^{(2)}(\text{PAF}) \\ &\quad + [\mathcal{D}_{2,\pm 2}^{(2)}(\alpha, \beta, \gamma) + \mathcal{D}_{-2,\pm 2}^{(2)}(\alpha, \beta, \gamma)]\delta_2^{(2)}(\text{PAF})\end{aligned}\right\} \tag{28}$$

3.3 Icosahedral Representation of the Chemical Shift Tensor

There arises a dilemma in comparing two tensors when they are described solely by their three principal shift values. The common practice of reporting chemical shift anisotropies using only the principal values while neglecting the three orientational Euler angles, α, β, γ, given in equation (13), prevents one from determining whether two tensors are identical or merely congruent. Two tensors are considered to be identical only if the three principal values and the spatial orientations of their three principal axes agree completely. Two tensors are congruent if they have the same set of principal values but the orientations of the principal shift axes differ, a situation commonly encountered for symmetry-related molecules in the unit cell of a single crystal. Therefore, the comparison of two sets of principal values may at most indicate whether two tensors are congruent, but the information is insufficient to indicate whether the tensors are identical.

Symmetrical Cartesian shift tensors with three diagonal and three off-diagonal components contain sufficient elements for the tensor to be described completely. Similarly, three principal values and three orientational Euler angles also provide six independent quantities for fully designating a chemical shift tensor. However, comparison of two different tensors described with such mixed parameters (e.g. shift values and orientational parameters) is complicated by the necessity of relating different types of parameters, and the statistical comparison of such tensors[21] requires complex weighting metrics.

An icosahedral representation[22] of the chemical shift tensor has been proposed that employs six parameters all of the same type and has a simple metric to specify the statistical weighting factors. This representation consists of six shift components that are obtained when the magnetic field is placed along the six unique directions associated with the 12 vertices (i.e., the six diagonal pairs) of an icosahedron. The geometrical construct in Figure 6 shows the relationships between a given Cartesian frame and the corresponding icosahedron oriented in this frame. The six icosahedral directions shown in Figure 6 are numbered with single Arabic numerals and the relationship of these values to the Cartesian tensor components is given by

$$\left.\begin{aligned}&\delta_1 = a^2\delta_{xx} + b^2\delta_{yy} - 2ab\delta_{xy},\ \ \delta_2 = a^2\delta_{xx} + b^2\delta_{yy} + 2ab\delta_{xy} \\ &\delta_3 = a^2\delta_{yy} + b^2\delta_{zz} - 2ab\delta_{yz},\ \ \delta_4 = a^2\delta_{yy} + b^2\delta_{zz} + 2ab\delta_{yz} \\ &\delta_5 = a^2\delta_{zz} + b^2\delta_{xx} - 2ab\delta_{zx},\ \ \delta_6 = a^2\delta_{zz} + b^2\delta_{xx} + 2ab\delta_{zx}\end{aligned}\right\} \tag{29}$$

The geometrical constants $a = \cos(\phi/2) = 0.8507$ and $b = \sin(\phi/2) = 0.5257$ relate the shift directions to the structure of the

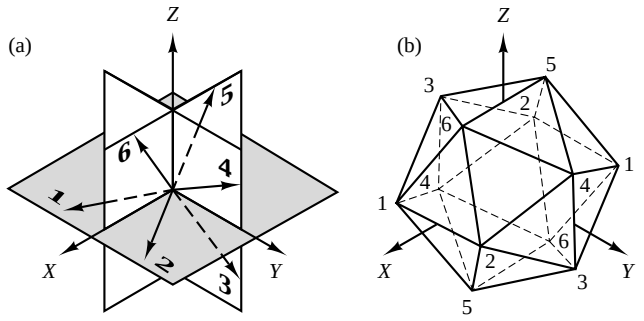

Figure 6 (a) Geometrical relationships of the six icosahedral directions to the Cartesian frame. (b) The six directions are identified with the 12 icosahedral vertices

icosahedron. The icosahedral angle, ϕ (= 63.44°), subtends the two vectors drawn from the center of the icosahedron to two adjacent icosahedral vertices.

The icosahedral representation enjoys the advantage that all six components have the same metric represented by a unit matrix, allowing a statistical comparison of two tensors to be undertaken on the same basis with equal weighting coefficients. Further, no scaling problems are encountered as the coordinate system is transformed between various chemical shift reference frames (e.g., sample, laboratory, unit cell, molecular, or principal axes frames), and the rather complicated phase factors and normalization constants found in the irreducible spherical tensors are avoided. Finally, the individual shifts in the icosahedral representation are orthogonal and linear regression methods execute optimally in this representation.

As any one vertex is equidistant from the remaining five unique icosahedral directions in this geometry, the six directions are arrayed with a maximum angular separation from each other. Consequently, the icosahedral representation optimizes the sensitivity with which a tensor can be specified with six numbers. It is anticipated that future single crystal probes will be constructed with orientational mechanisms that exploit this optimal sensitivity associated with the icosahedral symmetry. A relative figure of merit for assessing sensitivity has been reported for a variety of measurement devices,[22] and the icosahedral device has the highest sensitivity for cataloging minor deviations in shift tensor data.

3.4 Conventions for Reporting Chemical Shift Tensors

The relatively large number of coordinate frames and representations used for measuring chemical shift tensors has resulted in several chemical shift conventions for describing these tensors. This diversity of conventions, and some inconsistencies in their use, have led at times to ambiguity in reporting chemical shift tensors. Such complexities, however, may always be avoided if a full, six-parameter tensor in any representation is reported along with a molecular drawing that clearly designates the orientation of the x, y, and z reference frame. Most assignment ambiguities have been created whenever principal shift values obtained from powder spectra are reported without orientational details and without properly designated sign conventions. Three accepted conventions for reporting principal shift values are discussed below. The first involves a frequency ordered set of principal values, rank ordered from high to low frequencies, and the remaining two focus more on specific aspects of the tensor's symmetry and are cast in forms related to irreducible spherical tensor components.

3.4.1 *Frequency Ordered Principal Shift Values, δ_{11}, δ_{22}, and δ_{33}*

The simplest convention, and one that avoids confusion in discussing the three principal shifts, employs frequency ordered shifts. This convention prescribes that the principal shifts be designated as $\delta_{11} \geq \delta_{22} \geq \delta_{33}$, with the frequency ordering from high to low shifts specified with Arabic numerals as indicated These symbols were used for the two asymmetric spectra depicted in Figures 2(c) and (d). The principal values lie along three perpendicular directions in space, but no attempt is made to identify the three shifts with specific x, y, and z directions in the PAF. Only if the tensor's orientation is specifically required in a molecular reference frame is there any need for more information than contained in this set of frequency ordered values.

The motivation for using conventions more complicated than the frequency ordered set of shifts is related to the symmetry of shift tensors and to the common practice of reporting isotropic shifts, similar to those found in liquids. The isotropic shift, contained in the zero-rank component of equation (11) requires two additional second-rank components to characterize the three principal elements on the diagonal of a shift tensor. These symmetrized conventions are strongly influenced by the form of the irreducible spherical tensors.

3.4.2 *The Anisotropy, ζ, and Asymmetry, η, Parameters*

In the PAF, the chemical shift anisotropy, ζ, and the chemical shift asymmetry, η, parameters along with the isotropic shift, δ_o, are defined for the chemical shift tensor as follows:

$$\left.\begin{aligned} \delta_o &= \tfrac{1}{3}(\delta_{xx} + \delta_{yy} + \delta_{zz}) \\ \zeta &= \delta_{zz} - \tfrac{1}{2}(\delta_{xx} + \delta_{yy}) = \tfrac{3}{2}(\delta_{zz} - \delta_o) \\ \eta &= \frac{(\delta_{xx} - \delta_{yy})}{(\delta_{zz} - \delta_o)} = \frac{3(\delta_{xx} - \delta_{yy})}{2\zeta} \end{aligned}\right\} \qquad (30)$$

These parameters relate to the irreducible spherical representations given in equation (22). The z axis in the irreducible spherical basis is designated as the $m = 0$ projection, and this convention prescribes that the unique principal frequency in an axial tensor be assigned to the z axis in order to capitalize on the cylindrical symmetry found in the $\delta_0^{(2)}$ component of an irreducible spherical tensor. Thus, the ζ and η convention places the z direction along the unique tensor axis (i.e., $\delta_{zz} = \delta_{\parallel}$) in the axial tensors shown in Figures 2(a) and (b), with $\delta_{zz} = \delta_{11}$ for the prolate axial tensors and $\delta_{zz} = \delta_{33}$ for the oblate case, respectively. The remaining degenerate axial components are given by $\delta_{\perp} = \delta_{xx} = \delta_{yy}$ in both cases. For the axial case, the anisotropy is given by $\zeta = \delta_{\parallel} - \delta_{\perp}$ and $\eta = 0$, with ζ positive for a prolate axial tensor and negative for an oblate axial tensor.

In asymmetric shift tensors, the assignment of the x, y, and z axes to the three principal values uses the convention[23,24] that the x component is assigned to δ_{22} and the shift furthest

removed from δ_{22} is designated as δ_{zz} in a manner consistent with the axially symmetric case. This leaves δ_{yy} assigned to the component at the other extreme. For Figure 2(d) where $(\delta_{11} - \delta_{22}) > (\delta_{22} - \delta_{33})$, δ_{zz} is assigned to the δ_{11} shift; $\delta_{yy} = \delta_{33}$ and $\delta_{xx} = \delta_{22}$. Thus, the tensor's anisotropy, ζ, is a positive quantity for the pattern in Figure 2(d) using the definitions in equation (30). The asymmetry parameter, η, as defined in equation (30) is also a positive quantity because of the frequency order associated with the δ_{xx} and δ_{yy} labels. Conversely, if $(\delta_{11} - \delta_{22}) < (\delta_{22} - \delta_{33})$ then δ_{zz} is assigned to δ_{33}, $\delta_{yy} = \delta_{11}$ and $\delta_{xx} = \delta_{22}$. The value for ζ is now negative but η still retains its positive sign because the reversal in the order of the δ_{xx} and δ_{yy} designations compensates for the negative ζ value. As δ_{22} moves from one side of the pattern's midpoint to the opposite side, the sign of ζ changes in this convention.

Probably no better example exists to illustrate one of the awkward features confronting the ζ and η convention than the case of the centrosymmetric tensor given in Figure 2(c). Here, the selection of either $\delta_{zz} = \delta_{11}$ or $\delta_{zz} = \delta_{33}$ both comply with the convention as δ_{22} is equidistant from both δ_{11} and δ_{33}, but the sign of ζ changes with the two alternative choices even though the magnitudes of ζ and η are not altered. The centrosymmetric tensor is recognized in this convention when $\eta = 1$. This convention also suffers by not providing a readily recognized value for the overall spectral width, i.e., $(\delta_{11} - \delta_{33})$.

The indiscriminate use of anisotropy and asymmetry parameters with both nuclear shieldings, σ_i, and the chemical shift, δ_i, along with the change of signs in equation (3) has also seriously aggravated the usage of ζ and η. Some literature reports fail to indicate clearly whether the data are given in shift or shielding values, and this uncertainty leaves the sign of the anisotropy ambiguous. As most experimental shift data are now reported in frequency units, only shift parameters should be used in the definition of ζ and η unless otherwise clearly stated.

3.4.3 The Span, Ω, and Skew, κ, Chemical Shift Parameters

A recent convention[25] for principal shifts has been proposed that uses the following relationships:

$$\delta_o = \frac{1}{3}(\delta_{11} + \delta_{22} + \delta_{33}), \quad \Omega = \delta_{11} - \delta_{33},$$
$$\kappa = \frac{2\delta_{22} - (\delta_{11} + \delta_{33})}{(\delta_{11} - \delta_{33})} \tag{31}$$

The isotropic shift is the same, the chemical shift span, Ω, measures the powder pattern's width and the chemical shift skew, κ, measures the tensor's deviation from centrosymmetry. The skew is bounded by -1 for a prolate axial tensor, i.e., $\delta_{22} = \delta_{33}$ and by $+1$ for an oblate axial tensor, i.e., $\delta_{22} = \delta_{11}$. The simplicity of this convention is derived from use of frequency ordered principal shift values rather than Cartesian labels that vary when δ_{22} is either greater or less than δ_o. This convention leaves one free to select the spatial labels, i.e., xyz, to serve other purposes in the mathematical manipulation or spatial visualization of shift tensors. The centrosymmetric case, which posed a dilemma for the previous convention, is characterized by $\kappa = 0$, and the change of κ is continuous and smooth as δ_{22} moves from above to below δ_o. This span and skew convention avoids switching the label of δ_{zz} between δ_{11} and δ_{33} and claims to be both simpler and easy to remember.

The form of equations (22) and (31) suggests the use of $\delta_{xx} = \delta_{11}$, $\delta_{yy} = \delta_{33}$, and $\delta_{zz} = \delta_{22}$ for forming irreducible spherical tensor quantities, thereby making $\Omega = (\delta_{11} - \delta_{33}) = 2\delta^{(2)}_{\pm 2}$ and $\Omega\kappa = \delta_{22} - \frac{1}{2}(\delta_{11} + \delta_{33}) = \sqrt{\frac{2}{3}}\delta^{(2)}_0$. This somewhat nontraditional use for $\delta^{(2)}_{\pm 2}$ and $\delta^{(2)}_0$ still leaves in place the full benefits of the irreducible spherical tensor machinery.

4 TENSOR POWDER PATTERNS IN SOLIDS

4.1 Conformal Mapping of Principal Tensor Shifts onto Frequency Patterns

The extraction of tensor principal values from powder patterns was first discussed by Bloembergen and Rowland.[13] Using their approach, expressions describing spectral powder patterns may be obtained by conformal mapping of the chemical shift tensor, given in its own PAF, onto the frequency coordinate of a powder spectrum. Rearranging equation (17) yields the following expression in frequency space:

$$f_i = f_{xx}\sin^2\theta\cos^2\phi + f_{yy}\sin^2\theta\sin^2\phi + f_{zz}\cos^2\theta \tag{32}$$

where the directional cosines in polar angles are $l = \sin\theta\cos\phi$, $m = \sin\theta\sin\phi$, and $n = \cos\theta$. The three principal frequency values, $f_{qq} = (\gamma_i/2\pi)\, I_o B_{\text{ref}}(1 + \delta_{qq})$, for $q = x, y, z$ characterize the chemical shift tensor in its PAF.

Using conformal mapping procedures, the relationship between the integrated NMR signal, S, in the Cartesian space of the PAF and in the frequency space of the spectrum is given by

$$S = \int I(f_i)\,\mathrm{d}f_i \int_0^1 \mathrm{d}g = 8\int_0^{\pi/2}\int_0^{\pi/2} P(\theta,\phi)\sin\theta\,\mathrm{d}\theta\,\mathrm{d}\phi \tag{33}$$

where $I(f_i)$ is the intensity of the spectral band at the frequency f_i, and $P(\theta, \phi)$ is the probability that the magnetic field lies along the (θ, ϕ) direction in the PAF of the chemical shift tensor. The completion integral in $\mathrm{d}g$, with a value of unity, is required to make the dimensionality of the frequency space correspond to the dimensionality of the tensor expressions in polar angles. This integral over g maps onto a line integral in the tensor space corresponding to a constant spectral frequency. The factor of 8 on the right-hand side of equation (33) converts the PAF octant integral to a complete spherical integral. The term $P(\theta, \phi)$ is a constant for all directions in a randomly oriented powder sample; its normalized value is given by

$$S = 8\int_0^{\pi/2}\int_0^{\pi/2} P(\theta,\phi)\sin\theta\,\mathrm{d}\theta\,\mathrm{d}\phi = 1 \tag{34}$$

and therefore

$$P(\theta,\phi) = \frac{1}{8\int_0^{\pi/2}\int_0^{\pi/2}\sin\theta\,\mathrm{d}\theta\,\mathrm{d}\phi} = \frac{1}{4\pi} \tag{35}$$

A Jacobian, $J\{f_i, g—\theta, \phi\}$, is now used to convert the differentials on the right-hand side of equation (33) into frequency space as follows:

$$\mathrm{d}\theta\,\mathrm{d}\phi = \frac{\mathrm{d}f_i\,\mathrm{d}g}{J\{f_i, g \mid \theta, \phi\}} \tag{36}$$

where

$$J\{f_i, g \mid \theta, \phi\} = \begin{vmatrix} \dfrac{\partial f_i}{\partial \theta} & \dfrac{\partial f_i}{\partial \phi} \\ \dfrac{\partial g}{\partial \theta} & \dfrac{\partial g}{\partial \phi} \end{vmatrix} = \left(\frac{\partial f_i}{\partial \theta}\right)\left(\frac{\partial g}{\partial \phi}\right) - \left(\frac{\partial f_i}{\partial \phi}\right)\left(\frac{\partial g}{\partial \theta}\right) \tag{37}$$

Substituting equations (35) and (36) into equation (33) yields

$$\int I(f_i)\,\mathrm{d}f_i \int_0^1 \mathrm{d}g = \frac{2}{\pi}\int\int_{g_1}^{g_2} \frac{\sin\theta\,\mathrm{d}g\,\mathrm{d}f_i}{J\{f_i, g \mid \theta, \phi\}} \tag{38}$$

and extraction of $I(f_i)$ from the integral over f_i gives

$$I(f_i) = \frac{2}{\pi}\int_{g_1}^{g_2} \frac{\sin\theta\,\mathrm{d}g}{J\{f_i, g \mid \theta, \phi\}} \tag{39}$$

The derivation of an expression for $I(f_i)$ has thus been reduced to finding a function, g, which defines the line integral of constant resonance frequency in tensor space. It also involves solving for $\sin\theta$ and the Jacobian $J\{f_i, g—\theta, \phi\}$ in terms of f_i and g, and finally scaling the expression for g such that the limits for g_1 and g_2 are 0 and 1, respectively. The details of this procedure differ for axially symmetric and asymmetric tensors and the two cases are now treated separately.

4.2 Analytical Expressions for Powder Patterns

4.2.1 Axially Symmetric Tensors

Equation (32) in the axially symmetric limit becomes

$$f_i = f_\perp \sin^2\theta + f_\parallel \cos^2\theta = f_\perp - (f_\perp - f_\parallel)\cos^2\theta \tag{40}$$

where $f_\perp = f_{xx} = f_{yy}$ and $f_\parallel = f_{zz}$. Differentiating, equation (40) yields

$$\frac{\partial f_i}{\partial \theta} = 2(f_\perp - f_\parallel)\cos\theta\sin\theta, \quad \frac{\partial f_i}{\partial \phi} = 0 \tag{41}$$

As f_i is dependent only upon the polar angle θ and not ϕ, it may be shown by inspection that the constant frequency condition required for g, properly scaled to give the correct integral limits, yields the following expression for g:

$$g = \frac{2}{\pi}\phi \tag{42}$$

and

$$\frac{\partial g_i}{\partial \theta} = 0, \quad \frac{\partial g_i}{\partial \phi} = \frac{2}{\pi} \tag{43}$$

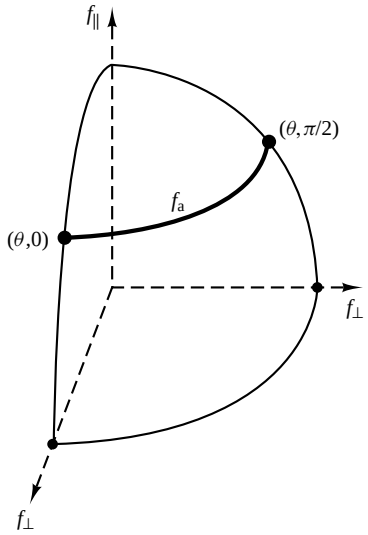

Figure 7 The ellipsoidal representation of an axial tensor in its PAF has the principal or parallel axis along the z axis and the two perpendicular principal components in the xy plane. The constant frequency path in this portrayal is indicated by f_a

Equation (42) defines the line integral in tensor space required by equation (39) for the intensity at the frequency f_i. This line integral's relationship to the tensor's orientation is illustrated graphically in Figure 7 for a prolate axially symmetric tensor. Note, the limits of 0 and $\pi/2$ for ϕ yield the values of 0 and 1 for g_1 and g_2, respectively. Using equations (37), (41), and (43), the Jacobian is evaluated as

$$\begin{aligned} J\{f_i, g \mid \theta, \phi\} &= \begin{vmatrix} 2(f_\perp - f_\parallel)\sin\theta\cos\theta & 0 \\ 0 & 2/\pi \end{vmatrix} \\ &= \frac{4}{\pi}(f_\perp - f_\parallel)\sin\theta\cos\theta \end{aligned} \tag{44}$$

Rearranging equation (40) yields

$$\cos\theta = \sqrt{\frac{f_\perp - f_i}{f_\perp - f_\parallel}} \tag{45}$$

Substituting equations (44) and (45) into equation (39) for $I(f_i)$ gives the following:

$$\begin{aligned} I(f_i) &= \frac{1}{2(f_\perp - f_\parallel)}\sqrt{\frac{f_\perp - f_\parallel}{f_\perp - f_i}}\int_0^1 \mathrm{d}g \\ &= \frac{1}{2\sqrt{(f_\perp - f_\parallel)(f_\perp - f_i)}} \end{aligned} \tag{46}$$

This equation applies to the range between $f_\parallel$ and $f_\perp$ but excludes the singular point at $f_i = f_\perp$. Outside the range from $f_\parallel$ to $f_\perp$ the spectral intensity is zero. When properly convoluted with a line-broadening function, equation (46) describes the axially symmetric patterns shown in Figures 2(a) and (b). The unique or parallel tensor value in axially symmetric tensor bands is at the lower intensity

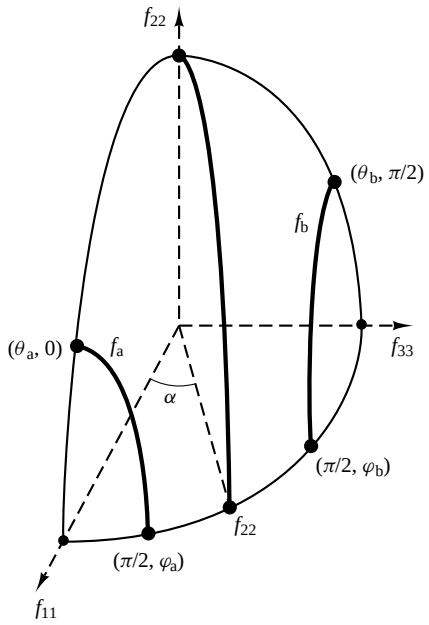

Figure 8 The ellipsoidal representation of a general asymmetric tensor has the f_{11}, f_{22}, and f_{33} principal components placed along the *x*, *z*, and *y* axes, respectively. The constant frequency paths in region a ($f_{11} > f_a > f_{22}$) and region b ($f_{22} > f_b > f_{33}$) are indicated, respectively, by f_a and f_b. The constant f_{22} frequency path at the singular point is at $\phi = \alpha$

breakpoint, while the degenerate perpendicular values are at the breakpoint of higher intensity.

4.2.2 Asymmetric Tensors

Equation (32) provides an expression for f_i in terms of the asymmetric tensor's principal shift values as follows:

$$f_i = f_{11}\sin^2\theta\cos^2\phi + f_{33}\sin^2\theta\sin^2\phi + f_{22}\cos^2\theta \quad (47)$$

where f_{11} and f_{33} correspond, respectively, to the f_{xx} and f_{yy} principal shift values given in equation (32), and f_{22} is identified with f_{zz} as indicated in Figure 8. Note, the constant frequency path for $f_i = f_{22}$ is given by $\phi = \alpha$. The derivatives required in the Jacobian for f_i relative to θ and ϕ are

$$\left.\begin{aligned}\frac{\partial f_i}{\partial\theta} &= 2(f_{11}\cos^2\phi + f_{33}\sin^2\phi - f_{22})\cos\theta\sin\theta \\ \frac{\partial f_i}{\partial\phi} &= -2\sin^2\theta\cos\phi\sin\phi(f_{11} - f_{33})\end{aligned}\right\} \quad (48)$$

An appropriate function for g, required in the conformal mapping of the shifts in tensor and frequency space, may be expressed as

$$g_a = \frac{\cos\theta}{\cos\theta_a}, \quad g_g = \frac{\cos\theta}{\cos\theta_b} \quad (49)$$

These two line integrals may be visualized in Figure 8 for the two constant frequency functions, f_a and f_b. Spectral region a spans the frequencies between f_{11} and f_{22} and region b between f_{22} and f_{33}. The expressions for cos θ_a and cos θ_b in equation (49) are obtained from equation (47) using the boundary conditions exhibited in Figure 8 for the constant frequency values f_a and f_b as follows:

$$\left.\begin{aligned}f_a &= f_i(\theta_a, 0) = f_{11}\sin^2\theta_a + f_{22}\cos^2\theta_a \\ &= f_{11} - (f_{11} - f_{22})\cos^2\theta_a \\ f_b &= f_i(\theta_b, \pi/2) = f_{33}\sin^2\theta_b + f_{22}\cos^2\theta_b \\ &= f_{33} + (f_{22} - f_{33})\cos^2\theta_b\end{aligned}\right\} \quad (50)$$

Solving for cos θ_a and cos θ_b in equation (50) yields

$$\cos\theta_a = \sqrt{\frac{f_{11} - f_a}{f_{11} - f_{22}}}, \quad \cos\theta_b = \sqrt{\frac{f_b - f_{33}}{f_{22} - f_{33}}} \quad (51)$$

Thus

$$g_a = \cos\theta\sqrt{\frac{f_{11} - f_{22}}{f_{11} - f_a}}, \quad g_b = \cos\theta\sqrt{\frac{f_{22} - f_{33}}{f_b - f_{33}}} \quad (52)$$

The angular derivatives of g needed in the Jacobian now become

$$\left.\begin{aligned}\frac{\partial g_a}{\partial\theta} &= -\sin\theta\sqrt{\frac{f_{11} - f_{22}}{f_{11} - f_a}} \\ \frac{\partial g_b}{\partial\theta} &= -\sin\theta\sqrt{\frac{f_{22} - f_{33}}{f_b - f_{33}}} \\ \frac{\partial g_a}{\partial\phi} &= \frac{\partial g_b}{\partial\phi} = 0\end{aligned}\right\} \quad (53)$$

Substituting equations (48) and (53) into equation (37) provides the asymmetric tensor expression for the Jacobians in the two spectral regions as follows:

$$\left.\begin{aligned}J\{f_a, g_a \mid \theta, \phi\} &= -2\sin^3\theta\sin\phi\cos\phi\,(f_{11} - f_{33})\sqrt{\frac{f_{11} - f_{22}}{f_{11} - f_a}} \\ J\{f_b, g_b \mid \theta, \phi\} &= -2\sin^3\theta\sin\phi\cos\phi\,(f_{11} - f_{33})\sqrt{\frac{f_{22} - f_{33}}{f_b - f_{33}}}\end{aligned}\right\} \quad (54)$$

Substitution of equation (54) into equation (39) yields the following expressions for the band intensity for regions a and b, respectively:

$$\left.\begin{aligned}I(f_a) &= -\frac{2}{\pi}\int_{g_1}^{g_2}\frac{\sin\theta\,dg}{2\sin^3\theta\sin\phi\cos\phi\,(f_{11} - f_{33})\sqrt{\frac{f_{11} - f_{22}}{f_{11} - f_a}}} \\ I(f_b) &= -\frac{2}{\pi}\int_{g_1}^{g_2}\frac{\sin\theta\,dg}{2\sin^3\theta\sin\phi\cos\phi\,(f_{11} - f_{33})\sqrt{\frac{f_{22} - f_{33}}{f_b - f_{33}}}}\end{aligned}\right\} \quad (55)$$

The dependence of the band intensity upon polar angles must now be converted into the frequency functions, f_i and g_i. This is done by rearranging equation (47) and using standard trigonometric identities to give

$$\left.\begin{aligned}\sin^2\theta\cos^2\phi(f_{11} - f_{33}) &= (f_i - f_{33}) - (f_{22} - f_{33})\cos^2\theta \\ \sin^2\theta\sin^2\phi(f_{11} - f_{33}) &= (f_{11} - f_i) - (f_{11} - f_{22})\cos^2\theta\end{aligned}\right\} \quad (56)$$

The square root of the product of the two expressions in equation (56) yields the following:

$$\sin^2\theta\cos\phi\sin\phi\,(f_{11}-f_{33}) = \sqrt{[(f_i-f_{33})-(f_{22}-f_{33})\cos^2\theta][(f_{11}-f_i)-(f_{11}-f_{22})\cos^2\theta]} \tag{57}$$

To complete the derivation of the band intensity for the asymmetric tensor, the limits of the integrals are evaluated using the boundary conditions indicated in Figure 8. With equation (49) these limits for both regions a and b are the same, i.e., $g_1 = 1$ and $g_2 = 0$. The minus sign in equation (55) may be removed, with further benefit, by reversing the integration limits. Substituting equation (57) into equation (55) and introducing the appropriate a and b labels for the ith label in equation (57) yield the following expressions:

$$\left.\begin{aligned} I(f_\mathrm{a}) &= \frac{1}{\pi}\int_0^1 \frac{\mathrm{d}g_\mathrm{a}}{\sqrt{(f_{11}-f_{22})(f_\mathrm{a}-f_{33})\left[1-\frac{(f_{22}-f_{33})}{(f_\mathrm{a}-f_{33})}\cos^2\theta\right]\left[1-\frac{(f_{11}-f_{22})}{(f_{11}-f_\mathrm{a})}\cos^2\theta\right]}} \\ I(f_\mathrm{b}) &= \frac{1}{\pi}\int_0^1 \frac{\mathrm{d}g_\mathrm{b}}{\sqrt{(f_{11}-f_\mathrm{b})(f_{22}-f_{33})\left[1-\frac{(f_{22}-f_{33})}{(f_\mathrm{b}-f_{33})}\cos^2\theta\right]\left[1-\frac{(f_{11}-f_{22})}{(f_{11}-f_\mathrm{b})}\cos^2\theta\right]}} \end{aligned}\right\} \tag{58}$$

Using equation (52) to simplify equation (58) one obtains

$$\left.\begin{aligned} I(f_\mathrm{a}) &= \frac{1}{\pi\sqrt{(f_{11}-f_{22})(f_\mathrm{a}-f_{33})}} \times \int_0^1 \frac{\mathrm{d}g_\mathrm{a}}{\sqrt{(1-m_\mathrm{a}g_\mathrm{a}^2)(1-g_\mathrm{a}^2)}} \\ I(f_\mathrm{b}) &= \frac{1}{\pi\sqrt{(f_{11}-f_\mathrm{b})(f_{22}-f_{33})}} \times \int_0^1 \frac{\mathrm{d}g_\mathrm{b}}{\sqrt{(1-g_\mathrm{b}^2)(1-m_\mathrm{b}g_\mathrm{b}^2)}} \end{aligned}\right\} \tag{59}$$

where the values for m_a and m_b are given as

$$m_\mathrm{a} = \frac{(f_{11}-f_\mathrm{a})(f_{22}-f_{33})}{(f_\mathrm{a}-f_{33})(f_{11}-f_{22})} \quad \text{and}$$
$$m_\mathrm{b} = \frac{(f_{11}-f_{22})(f_\mathrm{b}-f_{33})}{(f_{11}-f_\mathrm{b})(f_{22}-f_{33})} \tag{60}$$

The integrals found in equation (59) are complete elliptic integrals of the first kind and have a solution that is readily calculated on a computer with the following power series in m_a or m_b:

$$\int_0^1 \frac{\mathrm{d}g_i}{\sqrt{(1-m_ig_i^2)(1-g_i^2)}} = \frac{\pi}{2}\left[1+\left(\frac{1}{2}\right)^2 m_i^2 + \left(\frac{3}{2\times4}\right)^2 m_i^4 + \left(\frac{3\times5}{2\times4\times6}\right)^2 m_i^6 + \cdots\right] \tag{61}$$

4.3 Line Broadening in Spectral Powder Patterns

The calculated powder pattern described by equation (59) must be convoluted with a line-broadening function, either of a Lorentzian or Gaussian variety, to provide for the effect of transverse relaxation. Powder patterns of the type shown in Figures 2(c) and (d) include Lorentzian broadening. In the author's laboratory an equivalent numerical method, referred to as POWDER,[26] has been found to be numerically efficient for simulating such powder patterns and is especially useful in SIMPLEX fitting of multiple tensor powder patterns. In 1D powder patterns, one may seldom extract the tensor information from more than two or three overlapping ^{13}C bands if they cover wide spectral ranges. Thus, chemical shift tensors, with their highly unique spatial information, have eluded study in solid powders except for simple compounds where overlapping powder patterns can be isolated and analyzed for their principal shift values.

4.4 Resolution of Tensor Powder Patterns using 2D Spectral Methods

In recent years several 2D spectral methods have been proposed to portray powder spectra such that the principal shift values may be acquired for compounds on more than the two or three different nuclei achieved in 1D powder spectra. These include a 2D magic angle hopping experiment[27] and several modifications of the 2D magic angle slow turning experiment[28,29] (see J. Z. Hu et al. ***Magic Angle Turning and Hopping***) that slowly rotates the sample about the magic angle to obtain the isotropic shift in the evolution dimension. Also, a variety of 2D powder correlation experiments involving a mechanical flipping mechanism have been used to measure chemical shift tensors, especially in polymers.[30,31] These 2D powder methods reorient the sample during the mixing period between the evolution and detection periods. By spreading the spectral data into 2D, improved resolution is achieved for analyzing overlapping bands.

All powder spectral methods provide only shift values in the tensor's PAF, and information on the orientation of the tensor within the molecular or unit cell frames remains unavailable. Principal shift data obtained from powder samples contain up to three times more information than that found in isotropic liquid shifts, but these data are still deficient without information on the tensor's orientation in the molecular frame. A powder approach for determining ^{13}C tensor orientations involves the coupling of a dipole–dipole interaction with the shift tensor to provide the tensor's orientation.[32,33] This approach involves the analysis of composite dipolar-shift spectral patterns that arise from both the Pake dipolar splittings and the chemical shift tensor to give the orientation of the dipole–dipole vector within the PAF.

5 CHEMICAL SHIFT TENSORS FROM SINGLE CRYSTALS

5.1 Expressions for Chemical Shift Tensors in the Sample Frame

Chemical shift studies of single crystals provide both the principal tensor values and the orientations of their PAF in the sample frame. This complete tensor description involves six parameters which normally contain at least twice the information obtained from a powder pattern and up to six times the information found in the isotropic shift of a single liquid peak. The chemical shift expressions given in equations (9) and (32), and the experiments to which they relate, fail to provide for the orientation of the shift tensor in the sample frame and, therefore, have no way for delineating the orientation of tensors in their molecular frames. Thus, to describe a full chemical shift tensor, mathematical expressions are needed that correlate the resonance frequency with the orientation of the single crystal. Spatially correlated information in the sample frame allows the tensor's orientation to be projected onto one of the crystal's microscopic frames, such as the unit cell frame or the various frames at the molecular level. Because unit cells with two or more congruent molecules contain redundant shift information, the symmetry elements that take congruent tensors into one another usually identify the transformations that will convert the sample frame NMR data into the frame of the crystal's unit cell. Diffraction data may then be used to establish the structural relationships that exist between coordinates in the unit cell and the molecular frames.

The orientation of the magnetic field in a crystal's sample frame may be described by the directional cosines, l_S, m_S and n_S. In this sample frame, equations (6) and (7) become

$$f_i = \frac{\gamma_i}{2\pi} I_o B_{ref} [l_S \quad m_S \quad n_S] \times \begin{bmatrix} (1+\delta_{xx}) & \delta_{xy} & \delta_{xz} \\ \delta_{xy} & (1+\delta_{yy}) & \delta_{yz} \\ \delta_{xz} & \delta_{yz} & (1+\delta_{zz}) \end{bmatrix} \begin{bmatrix} l_S \\ m_S \\ n_S \end{bmatrix} \tag{62}$$

Equation (62) is of the same form as equation (17), deviating only in the use of a full matrix representation for the shift tensor in a non-PAF. Expansion of the matrix in equation (62) yields the following general expression:

$$f_i = f_{ref}(1 + l_S^2\delta_{xx} + m_S^2\delta_{yy} + n_S^2\delta_{zz} + 2l_S m_S\delta_{xy} + 2m_S n_S\delta_{yz} + 2l_S n_S\delta_{zx}) \tag{63}$$

where $f_{ref} = (\gamma_i/2\pi) I_o B_{ref}$. In the formulation of equation (63), use is made of the identity $(l_S^2 + m_S^2 + n_S^2) = 1$. Thus, it is the off-diagonal tensor values in equations (62) and (63) that may be used to specify the relationship between the sample frame and the tensor's PAF.

5.1.1 Single Axis Goniometer Methods

For single axis goniometer measurements, it is common to construct the data sets so they will fall in the three cardinal planes (i.e., $x = 0$, $y = 0$, and $z = 0$) of the sample frame. For example, if the data are collected for a crystal mounted with the rotation axis of the goniometer successively on the x, y, and z axis of the sample coordinate system (see Section 5.2), then the rotational dependence of these three rotation data sets in f_i become

$$\left.\begin{aligned} f_i(\xi_z) &= f_{ref}(1 + \delta_{xx}\cos^2\xi_z + \delta_{yy}\sin^2\xi_z \\ &\quad + 2\delta_{xy}\cos\xi_z\sin\xi_z) \\ f_i(\xi_y) &= f_{ref}(1 + \delta_{zz}\cos^2\xi_y + \delta_{xx}\sin^2\xi_y \\ &\quad + 2\delta_{zx}\cos\xi_y\sin\xi_y) \\ f_i(\xi_x) &= f_{ref}(1 + \delta_{yy}\cos^2\xi_x + \delta_{zz}\sin^2\xi_x \\ &\quad + 2\delta_{yz}\cos\xi_x\sin\xi_x) \end{aligned}\right\} \tag{64}$$

The angular displacements about the three different rotational axes are given by ξ_z, ξ_y, and ξ_x. The connections between the angular displacements given in equation (64) and the directional cosines found in equations (62) and (63) are given by $\cos\xi_z = \sin\xi_y = l$, $\cos\xi_x = \sin\xi_z = m$, and $\cos\xi_y = \sin\xi_x = n$. This traditional method for studying single crystals provides high-quality data except for samples with too many magnetically unique atoms per unit cell. Overlapping signals prevent the indexing of lines in spectra with more than about 15–18 peaks.

5.1.2 Two-Dimensional Single Crystal Spatial Correlation Methods

The time requirements of the single axis goniometer method and its rather restricted limits on the number of atoms in the unit cell led to the development of a more powerful 2D spatial correlation method for obtaining single crystal spectra. The greater resolution of 2D methods allows roughly an order of magnitude increase in the number of single crystal NMR peaks that may be indexed, and only six 2D spectra are required to determine the tensor. Figure 9 schematically depicts the pulse and mechanical flipping features of this 2D spatial correlation method. The ^{13}C signals of the single crystal are first cross polarized, placed in the transverse plane, and allowed to evolve in the first time dimension. During the mixing period the evolving magnetization is returned and stored along the magnetic field axis while the crystal is mechanically reoriented to a new position. In Figure 9 the sample is reoriented by 45° during the mixing period. Upon completing the mechanical reorientation, the stored magnetization is then returned to the transverse plane where the FID acquisition period constitutes the second time dimension.

Each peak in this 2D experiment exhibits the two resonance frequencies corresponding to the two directions in space. For example, a sample may be placed in the X direction during the evolution period and observed along the XY diagonal direction (i.e., $\cos\xi_z = 45°$) during the FID acquisition time. A discussion of the mechanical devices used to reorient the sample is beyond the scope of this article and may be obtained from the literature.[34] All possible pairs of cardinal (X, Y, Z) and diagonal (XY, YZ, ZX) directions may be used to compose the 2D spectrum. Such spatially correlated data, of course, are the essence of the information required to

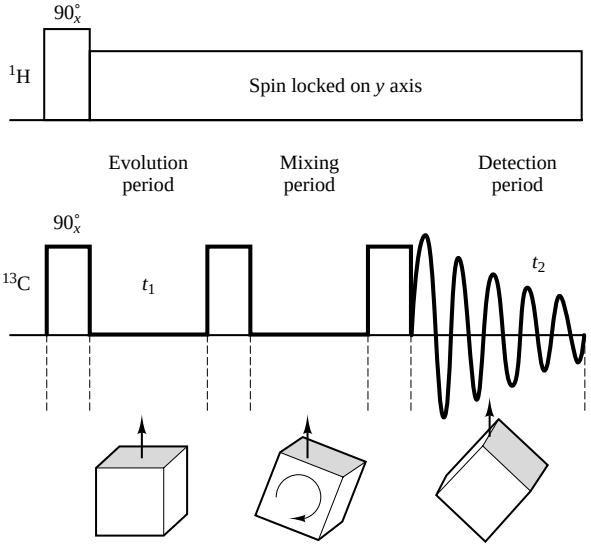

Figure 9 Mechanical and pulse relationships for the 2D spatial correlation method

characterize a chemical shift tensor. The six different sample-frame frequencies for cardinal and diagonal directions in this 2D spatial correlation experiment are given by

$$\left.\begin{aligned} f_X &= f_{\text{ref}}(1+\delta_{xx}), \qquad f_{XY} = f_{\text{ref}}\left(1+\tfrac{1}{2}\delta_{xx}+\tfrac{1}{2}\delta_{yy}+\delta_{xy}\right) \\ f_Y &= f_{\text{ref}}(1+\delta_{yy}), \qquad f_{YZ} = f_{\text{ref}}\left(1+\tfrac{1}{2}\delta_{yy}+\tfrac{1}{2}\delta_{zz}+\delta_{yz}\right) \\ f_Z &= f_{\text{ref}}(1+\delta_{zz}), \qquad f_{ZX} = f_{\text{ref}}\left(1+\tfrac{1}{2}\delta_{xx}+\tfrac{1}{2}\delta_{zz}+\delta_{zx}\right) \end{aligned}\right\} \tag{65}$$

From the six frequencies given in equation (65), the corresponding six shift parameters are obtained by inverting this set of equations.

5.2 Data from the Single Axis Goniometer Method—Naphthalene ^{13}C Tensors

The single crystal of naphthalene belongs to the $P2_1/a$ space group and has two molecules per unit cell, each chemically equivalent but oriented differently. This unit cell, first described by Bragg[35] and more recently the subject of a neutron diffraction study,[36] indicates that the inversion symmetry center of the crystal is at the center of the naphthalene molecule. The inversion symmetry makes the atoms of one naphthalene ring equivalent to those of the second ring (e.g., C-1 is equivalent to C-5, C-2 to C-6, etc.). Thus, in a single crystal of naphthalene five NMR resonance signals (four unique ring carbons and one bridgehead carbon) exist for each of the two structurally different molecules.[37] These 10 peaks constitute the single crystal spectrum of naphthalene, and a representative 1D ^{13}C spectrum is given in Figure 10. The two groupings of five peaks observed in this spectrum correspond to the two congruent naphthalene molecules in the unit cell. A twofold symmetry axis transforms the congruent molecules into each other. Pairs of tensors from corresponding atoms in the two congruent molecules have the same principal values. However, these tensors differ in their

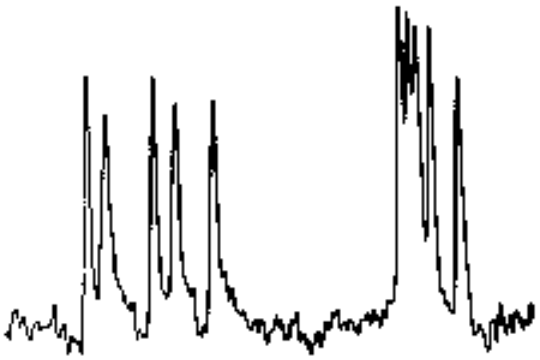

Figure 10 Single crystal spectrum of naphthalene with two groupings of five peaks from the two congruent molecules in naphthalene. (This figure is taken from Sherwood et al.[37])

relative orientations within the unit cell. The spectral patterns for a naphthalene powder sample also exhibit five different tensor bands, as congruent shifts each give the same powder patterns. Unfortunately, the five naphthalene powder bands are so similar that it is impossible to extract the very similar but slightly different principal values from the five magnetically unique atoms in naphthalene.

A single axis goniometer is used to rotate a naphthalene crystal around the x, y, and z sample axes with small angular displacements. Nineteen crystal spectra of the type shown in Figure 10 were accumulated for successive 10° angular displacements from 0° through 180°. These measurements create a dataset of 570 (i.e., 19 × 10 × 3) chemical shifts as shown in Figure 11. The sinusoidal character of the data in successive spectra, see equation (64), is apparent in this figure where each of the 19 successive spectra are plotted versus the angular rotational displacements in the goniometer. Typical data-fitting techniques allow the shift parameters of the several tensors to be extracted from the data in Figure 11 using equation (64). The full tensors for each of the 10 resonance peaks are described by six values (i.e., 60 total tensor shift parameters for the 10 peaks) in the sample frame. Thus, the acquired dataset is almost 10 times larger than the derived shift parameter set, and this redundancy improves the accuracy of the chemical shift measurements. The error in shift values, estimated from the marginal standard deviations between principal axis values in congruent tensors, is about ±0.5 ppm.

The NMR data on congruent tensors must conform to the symmetry and structural features that obtain in the unit cell. The direction of the δ_{33} principal axis for the five tensors in one of the naphthalene molecules were all found to lie, within experimental error, along the normal to the aromatic plane. Thus, NMR provides an independent measure for the angles (i.e., 63.59° for the NMR data and 63.53° for the diffraction data) between the two normal vectors of the congruent molecules and the twofold axis of the unit cell. This excellent agreement between the NMR and the diffraction data identifies the twofold symmetry axis and places the diffraction and NMR single crystal structures into direct correspondence. Using such symmetry considerations, the shift tensor is easily transformed into the unit cell frame, and consequently into the molecular frames of both congruent molecules.

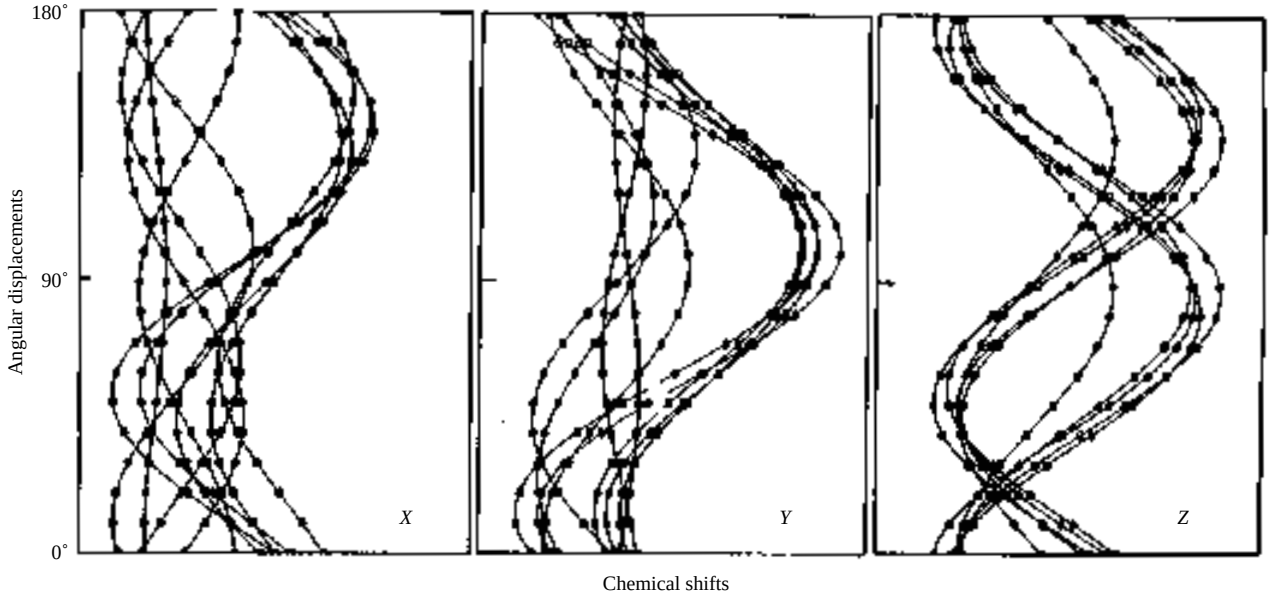

Figure 11 Three single axis goniometer patterns for naphthalene with the goniometer axis placed along the X, Y, and Z axis of the single crystal. Each rotation pattern was obtained from 19 spectra with an angular displacement of 10°. The spectral slice at each angular setting portrays up to 10 peaks as seen in Figure 10 which is taken from the Y rotational pattern with the angle in the vicinity of 120°. (Courtesy of Mark H. Sherwood)

The naphthalene shift tensor components obtained from Figure 11 are reported in Table 1. These tensor data in the molecular frame may be readily converted into the PAF using standard matrix diagonalization methods, and Table 1 also contains the naphthalene principal shift tensors. The orientations of the principal axes in the molecular frame are provided in Figure 12 which also contains theoretical bond orders obtained from quantum mechanical methods. The significance of the bond orders will be apparent in Section 6 when the relationship between tensor orientation and electronic structure is briefly discussed. The orientation of the in-plane δ_{22} component is perpendicular to the δ_{11} component and to the δ_{33} component which is oriented perpendicular to the molecular plane.

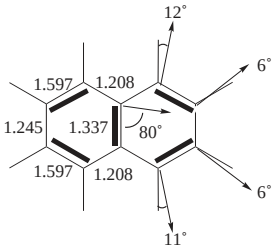

Figure 12 Orientation of the δ_{11} tensor components in naphthalene is given along with the bond orders obtained from quantum mechanical calculations. As the bridgehead tensor is nearly axially symmetric (see Table 1) its orientational error is considerably larger than the remaining directions

5.3 Data from the Single Crystal Spatial Correlation Method

The single crystal method, using a goniometer and successive small angular displacements, may be used whenever the unit cell contains about a dozen or less different nuclear resonances. The exact number depends upon the extent of spectral dispersion, linewidths, and other factors affecting spectral resolution. In Figure 11 the large chemical shift ranges associated with aromatic carbon atoms contribute significantly to the ease of indexing the 10 naphthalene peaks. Sometimes, spectra of even less nuclei cannot be spatially correlated between successive angular displacements using a single axis goniometer probe if the spectral peaks are unusually close to each other. Compacted single crystal spectra encounter assignment ambiguities whenever overlapping lines prevent the indexing of unresolved spectral lines and the preparation of the required sinusoidal spectral traces from which tensor components are extracted. Furthermore, the spectral data in Figure 11 required 19 independent experiments for each of three different crystal mountings in the single axis goniometer. These 57 different experiments represent such an extensive body of work that it is easy to understand why single crystal NMR studies have been relatively rare.

The 1D single crystal spectra in Figure 1 for methyl β-D-xylopyranoside exhibited extensive overlapping of spectral lines, and even with only 12 lines in this simple sugar

Table 1 ^{13}C Chemical Shift Tensors for Naphthalene

Shift component	C-1	C-2	C-3	C-4	C-4a
δ_{xx}	143.2	196.8	195.9	148.1	208.3
δ_{yy}	221.8	170.0	169.9	221.3	202.4
δ_{zz}	22.8	11.1	10.4	20.4	−5.9
δ_{xy}	15.5	42.0	−42.8	−13.8	1.1
δ_{yz}	−0.6	0.8	−0.1	0.5	0
δ_{zx}	−0.4	0.8	1.2	−0.8	−0.9
δ_{11}	224.7	227.6	227.6	223.9	208.5
δ_{22}	140.3	139.3	138.2	145.6	202.2
δ_{33}	22.8	11.1	10.4	20.4	−5.9
δ_{iso}	129.3	126.0	125.4	129.9	134.9

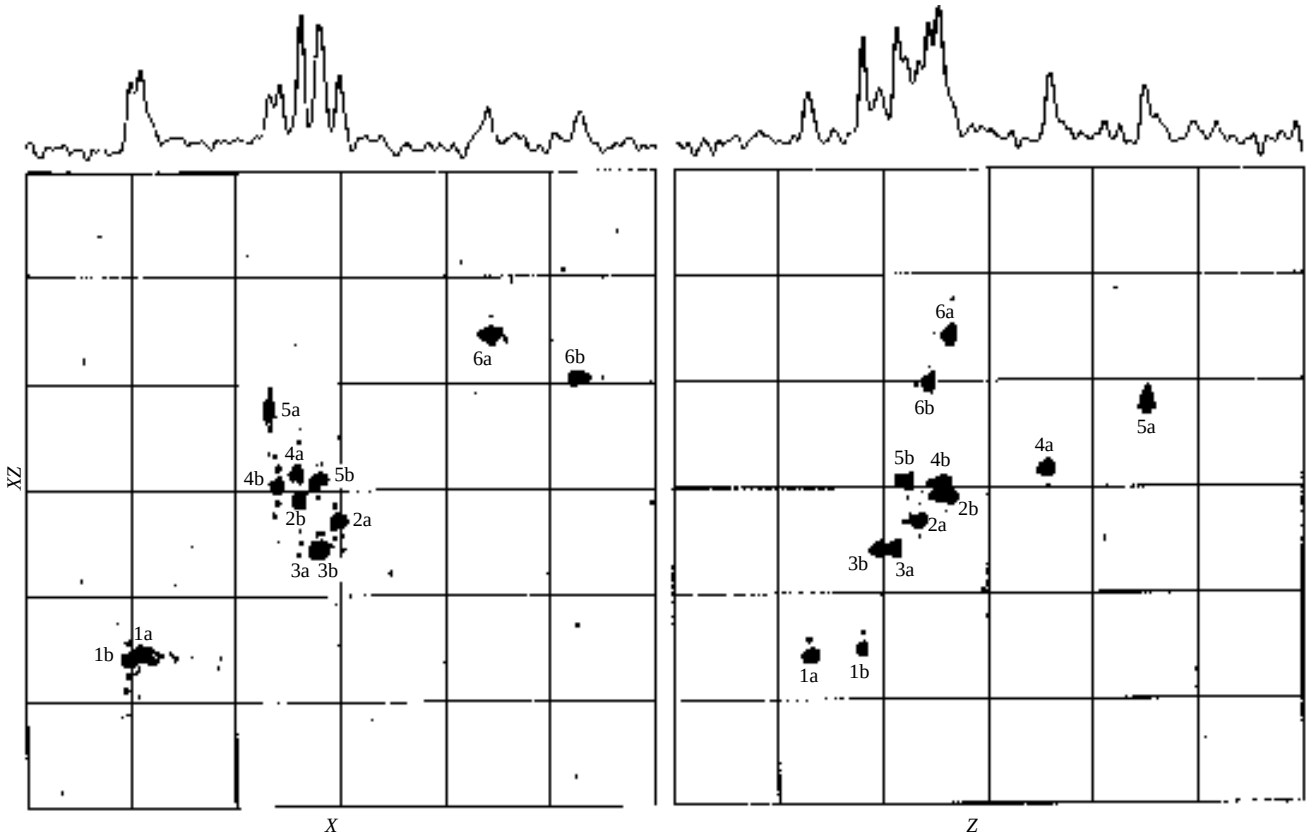

Figure 13 The 2D spatial correlation spectra of methyl β-D-xylopyranoside for the XZ versus X and XZ versus Z experiments. These 2D spectra are portrayed along with their 1D projections in the X and Z directions. Spatial correlation of shifts is given by the position of each 2D peak in these spectra. (Courtesy of Fang Liu)

it would be difficult to index the peaks using the 1D single-axis goniometer method. Figure 13 contains two 2D spectra in which the XZ orientation is given along one frequency dimension for both spectra and the second frequency dimension corresponds in the two spectra to the magnetic field along the X and Z directions, respectively. The respective spectral traces above each 2D spectrum are the same as those in Figures 1(c) and (e), and correspond to the X and Z projections of the corresponding 2D spectra. Note in Figure 13 how the position of the overlapping 1D spectral lines may be clearly established from the well-resolved peaks in the 2D spectra. These 2D spectra also illustrate how information is obtained from 2D spatially correlated spectra. Each individual spectrum provides correlated data between, respectively, the XZ and X directions and between the XZ and Z directions in the sample frame. Taken together, the pair of 2D spectra ultimately provide the correlated information between the X and Z projections. A set of six properly selected 2D spectra allow the spatial correlation to be determined for all frequencies between the three cardinal (i.e., X, Y, Z) and three diagonal (i.e., XY, YZ, ZX) directions. Such data, when used with equation (65), provide six tensor parameters for every unique spectral peak.

Figure 14 exhibits the 2D spatial correlation spectrum for 40 distinct peaks in a single crystal of perylene. This molecule exhibits the same $P2_1/a$ space group found in naphthalene, except in perylene the inversion center lies in between the four molecules per unit cell. Thus the inversion symmetry reduces the number of NMR unique molecules in the unit cell from four to two but, unlike the naphthalene case, inversion leaves all 20 atoms from each congruent molecule in unique chemical environments. The two sets of 20 peaks produce 40 distinguishable peaks in Figure 14. Only a limited number of spectral degeneracies or near-degeneracies are observed in this case, but these pose no problem to the data analysis due to the redundancy arising from the two congruent tensors. The white space remaining in the 2D spectrum of perylene suggests that single crystals of more than 100 unique carbon resonances may in certain cases be studied using the 2D spatial correlation method.

The extensive procedures required to analyze the six 2D spectra from a single crystal of a molecule as complicated as perylene (i.e., $6 \times 40 = 240$ peaks) pose assignment difficulties requiring strategies whose discussion is beyond the scope of this article. It is sufficient to indicate, however, that the perpendicular δ_{33} components for all nuclei in planar molecules are parallel to each other and provide a method of allocating sets of tensors to congruent molecules. This molecular grouping of tensors by the δ_{33} orientation causes the two sets of 20 peaks to cluster in Figure 14. The YZ direction is nearly perpendicular to the molecule with peaks designated by primes; hence the YZ shifts for this molecule lie between 0–40 ppm from TMS. Conversely, the YZ direction is nearly in the plane of the other congruent molecule and exhibits typical in-plane shifts of 130–200 ppm. Assignments of peaks within each set of 20 peaks depend in part on the orientation of the δ_{11} components and in part upon what appears to be a small

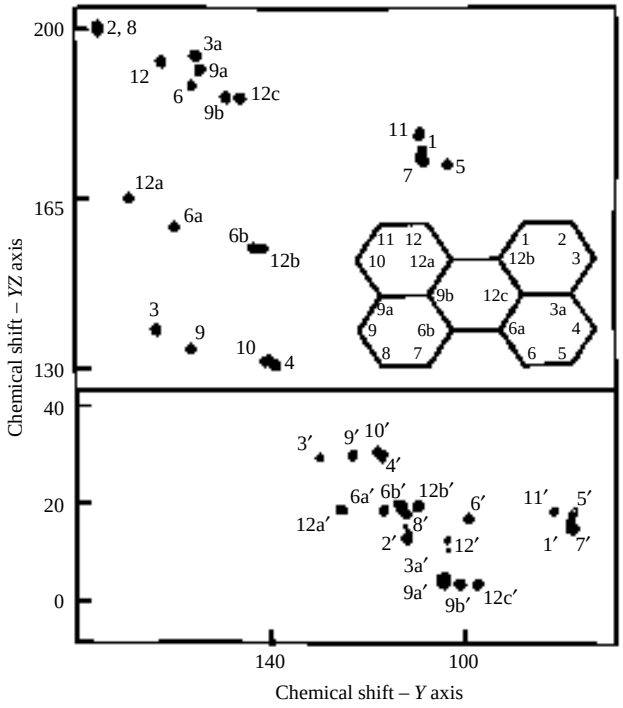

Figure 14 The 2D spatial correlation spectra of perylene appears in two spectral regions, and the 20 peak groupings in each region correspond to one of the two congruent molecules. The spectral assignments for the two molecules are compatible and transform into one another using the spatial symmetry of the unit cell of this crystal. (Courtesy of Robbie Iuliucci)

deformation from planarity along the C-3a and D-9a axis of the molecule. The assignments are also assisted by quantum mechanical calculations of the ^{13}C shifts. Predicted shift values are able in some cases to distinguish between similar tensors. The peaks from the two congruent sets of 20 tensors transform into each other under the symmetry elements in the unit cell, and this feature becomes a critical aspect of the assignment procedure.

6 MOLECULAR ORIGINS OF THE CHEMICAL SHIFT TENSOR

6.1 Effect of Molecular Symmetry and Electronic Structure on Shift Tensors

As indicated in Section 2, the chemical shift parameter has its origin in the shielding currents induced by the magnetic field in the molecular electrons. Because the magnitude of these shielding fields depends upon the inverse cubic distance of the circular current from the nucleus, it is primarily the electronic structure in the immediate vicinity of a nucleus that has the most effect on the shielding parameters. The schematic in Figure 15 summarizes the magnitudes and directions of shielding fields. Typical ranges in shift values are included for a few structural moieties to illustrate the variety of values encountered in chemical shift tensors.

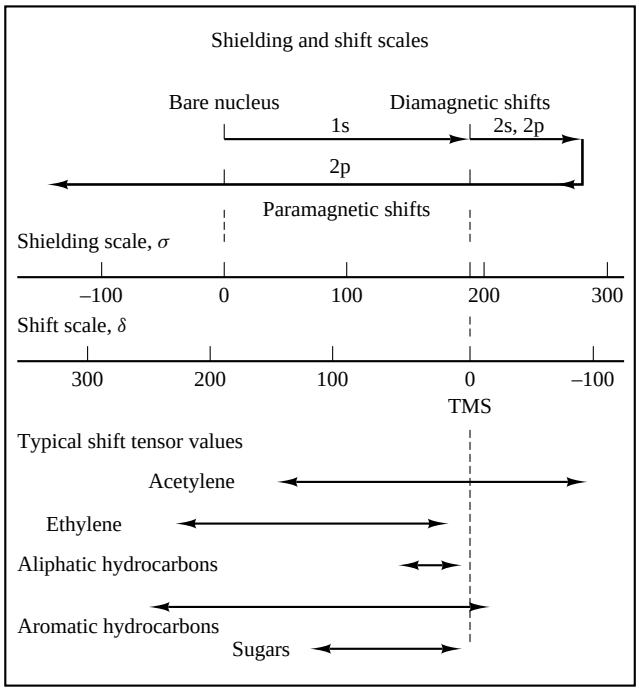

Figure 15 Carbon-13 shielding and shift scales are compared. The magnitudes of various diamagnetic and paramagnetic shift components are indicated for the 1s, 2s, and 2p electrons. Typical shift values are presented for representative molecules and classes of compounds

The shielding phenomenon arises both from diamagnetic and paramagnetic induced currents. All electrons exhibit diamagnetic currents which flow in such a manner so as to oppose the static magnetic field, $\boldsymbol{H}_0$, and thereby reduce the resonance frequency or chemical shift of the spectral line. The diamagnetic shifts result from first-order currents that depend on the density of electrons and the inverse cubic distance of the electron from the nucleus. Paramagnetic currents, also induced by the magnetic field, arise from p and d electrons that possess electron orbital angular momentum. The magnetic field induces very small admixtures of angular momentum components into the wavefunctions and these produce paramagnetic shielding currents. Intrinsic angular momentum has an associated magnetic field that enhances $\boldsymbol{H}_0$; hence, the paramagnetic fields increase the resonance frequency or chemical shift of a nucleus. These paramagnetic shifts may vary greatly between molecules and are very sensitive to electronic symmetry and molecular structural features that control the orbital mixing.

In Figure 15 it is observed that the 1s electrons in the carbon's K shell are accompanied by a very large diamagnetic shift (∼200 ppm), but the K shell is deeply embedded within the electronic structure of organic molecules and therefore is essentially insensitive to chemical variations. Thus, the 1s contribution to the chemical shift is essentially constant for all carbon atoms in different types of molecular environments and therefore will not explain the diversity of carbon-13 chemical shifts. The L shell associated with the four valence electrons of carbon (i.e., 2s and 2p electrons) also exhibits a reasonably large diamagnetic shift, ca. 80 ppm for the four valence electrons (i.e., ∼20 ppm per valence electron). Since 1s and 2s electrons in carbon possess zero orbital angular momentum, they contribute to the chemical shift only through diamagnetic

currents. While these diamagnetic shifts in ^{13}C are comparable in magnitude to the corresponding paramagnetic shifts they do not vary greatly from one molecular position to another, nor do they affect the anisotropy as much as paramagnetic currents. Thus, diamagnetic components contribute significantly to overall ^{13}C chemical shifts, but their variations and anisotropy are measured in units of 10 ppm. The low anisotropy in diamagnetic shifts supports the intuitive conclusion that the electronic structure of the carbon atom is nearly spherical in character because this diamagnetic term is proportional to the radius squared of the atom in the plane perpendicular to the magnetic field.

The large variability in the chemical shift range and the sizable chemical shift anisotropy reported for ^{13}C nuclei are due primarily to paramagnetic shielding currents, which are especially sensitive to both the symmetry and electronic structure of 2p valence electrons. For example, linear molecules with C_∞ symmetry about their long axes quench[38] the paramagnetic currents that lie in the plane perpendicular to this long axis. Conversely, the shift in the perpendicular directions is not quenched and may be sizable, leading to a large shift anisotropy for linear molecules such as acetylene. The presence of mirror symmetry in planar molecules likewise forces the δ_{33} principal shift component to lie perpendicular to the molecular plane, and this feature dominates the tensor orientation in alkenes and aromatic molecules.

The intrinsic orbital momentum of 2p electrons may contribute extensively to the paramagnetic shielding currents in organic molecules providing such orbital mixing is not symmetry-forbidden. The reason that paramagnetic components vary by several hundred ppm, more than the uniform diamagnetic currents, is explained by their second-order character. The admixture of very small angular momentum components into molecular wavefunctions can vary by several orders of magnitude for different chemical environments, and this variability has a corresponding impact on the shielding. These paramagnetic shifts are especially enhanced when multiple π-bond orbitals are present in the molecule. As π electrons are usually associated with lower promotion energies, orbital angular momentum components mix more readily into the quantum mechanical description of unsaturated molecules when placed in strong magnetic fields. The highly anisotropic nature of these paramagnetic currents reflects the π-bond structural anisotropy. Large shift ranges and anisotropies are found in acetylene and ethylene and related aromatic hydrocarbons, as shown in Figure 15. Conversely, typical aliphatic hydrocarbons exhibit chemical shift tensors that lie well within a 50 ppm range.

Sugar molecules of various types offer an important study in chemical shielding because of the high electronic polarization of the oxygen atoms in these compounds. Furthermore, hydrogen bonding strongly influences the molecular conformations in sugars. Both of these effects stamp their signature upon the sugar shift tensors. Tensor shifts for sugar molecules typically spread over a range of ca. 100 ppm, larger than aliphatic shifts but somewhat reduced from the spread in aromatic chemical shifts.

Table 2 Axial Chemical Shift Tensors in Linear or Near-Linear Molecules (Values in ppm from TMS)

Compound	$\delta_\parallel$	$\delta_\perp$	δ_{iso}	δ_{liq}
C*≡O	−48	305	187	182.2
O=C*=O	−90	245	133	132.2
S=C*=O	−90	275	153	154.0
S=C*=S	−92	332	191	192.8
O=C=C*=C=O	−90	24	−14	−14.6
O=C*=C=C*=O	−90	235	127	127.7
H−C*≡C*−H	−90	150	70	71.9
CH_3−C≡C*−H	−93	166	80	79.8
CH_3−C*≡C−H	−74	140	69	68.4
C*H_3−C≡C−H	−4	7	3.3	3.3
CH_3−C*≡C*−CH_3	−75	152	76	74.8
C*H_3−C≡C−C*H_3	−3	8	4.3	3.3

6.2 Axial Chemical Shift Tensors in Linear and C_3 Symmetry Related Molecules

As the symmetry of a linear molecule quenches the paramagnetic currents about the long axis of the molecule, only diamagnetic shielding currents may affect the ^{13}C chemical shift. The C_∞ symmetry element present in a completely linear molecule also requires an axial chemical shift tensor. The theoretical considerations used to construct Figure 15 indicate that diamagnetic shifts, in the absence of any paramagnetic contributions, leave the ^{13}C resonance at around −90 ppm from TMS. A collection[39] of chemical shifts for selected linear or near-linear molecules is given in Table 2 to illustrate this effect of orbital angular momentum quenching upon paramagnetic currents. Note, the $\delta_\parallel$ components for all linear molecules are close to −90 ppm, except for carbon monoxide, CO, and for those linear alkyne carbons directly attached to the methyl group in methylacetylene and dimethylacetylene.

Carbon monoxide appears to be the exception that clearly breaks the −90 ppm rule. However, theoretical calculations indicate that the paramagnetic contribution to $\delta_\parallel$ is indeed quenched. The diamagnetic currents in carbon monoxide have been altered sufficiently by a charge polarization from the electronegative oxygen to account for the increased $\delta_\parallel$ shift. The C_{3v} symmetry of the methyl group, whilst also guaranteeing an axial tensor for the methyl carbon and for the directly attached carbon, is insufficient to symmetry-quench the paramagnetic currents along the parallel axis of these molecules. The terminal alkyne carbon in methylacetylene is apparently sufficiently removed from the methyl group to allow it also to reflect the same $\delta_\parallel$ shift value as acetylene. The pattern of $\delta_\perp$ values for the compounds listed in Table 2 may be explained by charge effects arising from the electronegativity of adjacent atoms attached to the linear carbon atoms.

The very narrow range in the chemical shift tensors for the methyl carbons in Table 2 are quite typical of methyl tensors in general. All of the electrons in the immediate vicinity of a methyl carbon are contained in σ bonds. Since these C−C and C−H bonds are comparable in energy, the contribution of both diamagnetic and paramagnetic currents along various directions from tetrahedral carbon atoms are quite similar, reducing the anisotropy between components. This equivalence does not imply a quenching of

the paramagnetic currents, merely a lack of anisotropy in the various directional components.

6.3 Asymmetric Chemical Shift Tensors in Molecules with Mirror Symmetry

Planar molecules with mirror symmetry elements require that at least one principal axis of the shift tensor has its orientation perpendicular to the molecular plane. This rule even holds for molecules in single crystals, where intermolecular shielding terms or modest planar deformations seldom distort the δ_{33} principal axis by more than a few degrees from the normal to the molecular plane. Such data support the hypothesis that intermolecular interactions produce only small indirect shifts in molecules when only van der Waals forces are involved. Furthermore, the negligible twist in the δ_{33} orientations also supports the conclusion that remote intermolecular shielding currents are also modest. Planar systems encountered in organic systems invariably involve sp^2 carbon atoms, and the π-electron systems oriented perpendicular to the molecular plane contribute large in-plane paramagnetic shifts. Table 3 contains the chemical shift tensors for a small representative number of planar molecules with sp^2 carbons. Ethylene and benzene are model compounds that provide illustrations of the importance of π electrons in the chemical shift anisotropy arising from the unique three-dimensional characteristics associated with π bonds. Figure 16 schematically illustrates the spatial orientation of electron orbitals that dominate the paramagnetic shifts in these two molecules.

In Figure 16 the δ_{33} tensor shift components, lying along the normal to the molecular plane, arise in both ethylene and benzene from circular shielding currents that lie in the molecular plane and involve only σ-bonding electrons. Such σ bonds are energetically stable and these tightly held electrons are less easily promoted into paramagnetic shielding currents. Thus, δ_{33} sp^2 values (i.e., -10 ppm to $+25$ ppm) are reduced accordingly and fall in the aliphatic hydrocarbon region of the ^{13}C spectrum. Observe also the corresponding δ_{33} values for naphthalene in Table 1.

The two in-plane components in sp^2 molecules (i.e., δ_{11} and δ_{22}) are oriented in a direction perpendicular to the 2p π electrons in both ethylene and benzene, as may be visualized in Figure 16. The δ_{22} in-plane component is parallel to the C–C π bond in ethylene and arises from paramagnetic currents that mix the π electrons with the σ electrons involved in the two C–H bonds. The δ_{22} shift in benzene is the component that arises from a paramagnetic current involving the π electrons and primarily the σ electrons of the C–H bond. This δ_{22} shift in benzene also involves to a lesser extent the σ electrons of the two adjacent C–C bonds.

The δ_{11} in-plane component in benzene lies along the C–H bond and mixes the π electrons with the σ electrons of the two adjacent C–C bonds. Similarly, the δ_{11} component in ethylene lies perpendicular to the C=C bond and involves paramagnetic currents that mix the π electrons primarily with the σ electrons in the C=C bond, while in ethylene the σ electrons in the C–H bonds also participate to a lesser extent in this paramagnetic component. Figure 16 illustrates graphically which electrons participate primarily in the circular currents that affect the various principal shift components.

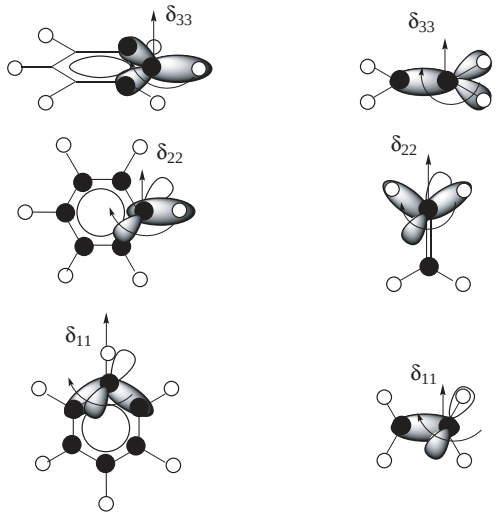

Figure 16 Electron orbitals contributing to shielding currents present in benzene and ethylene. The molecular orientations, the circular electron currents, and their associated principal shift components are represented for δ_{11}, δ_{22}, and δ_{33}

The principal chemical shifts for the α and β positions in naphthalene are listed in Table 1. Whereas the perpendicular mirror planes in benzene provide a symmetry basis for assigning the δ_{11} and δ_{22} chemical shift directions as indicated in Figure 16, no such perpendicular mirror planes exist for the carbons in naphthalene except at the bridgehead positions. Consequently, the δ_{11} directions for C-1 through C-4 in naphthalene deviate slightly from the C–H bond vectors. The orientation of the δ_{11} principal axis has been drawn in Figure 12 and the direction of this principal axis rotates slightly from the C–H bond direction in the molecular plane towards the C–C bond with the highest π-bond order. This is consistent with the concept that the largest paramagnetic currents are associated with a mixture of the π electrons into the carbon σ electrons of the C=C double bond. Thus, the δ_{11} component lies in the molecular plane but attempts to orient perpendicular to π bonds present in the molecule. When two or more π bonds are connected to a carbon atom, the δ_{11} direction will tend to orient perpendicular to the C–C bond of highest π-bond order (see Figure 12).

Table 3 Asymmetric Chemical Shift Tensors in Representative Planar Molecules (ppm from TMS)

Compound	δ_{11}	δ_{22}	δ_{33}	δ_{iso}	δ_{liq}
$CH_2{=}CH_2$	234	120	24	126	123.3
C_6H_6	234	146	9	130	128.7
$C_5H_5^-$	182	114	21	106	103.0
$C_7H_7^+$	280	168	22	157	156.3

6.4 Bond Energy Considerations and Chemical Shift Values

Three types of bonds appear in the sp^2 model compounds used in Figure 16 to illustrate the structural basis of the chemical shift tensor: they are the σ_{C-H}, σ_{C-C}, and π_{C-C}. The relative stability of these three bonds is given by $E(\sigma_{C-H}) > E(\sigma_{C-C}) > E(\pi_{C-C})$. As the admixture of angular momentum

components is inversely proportional to the bond energy of the affected electrons, other factors being equal it follows that the chemical shift tensor components will be related to the energy and the orientation of the bonding electrons. Thus, in benzene, the δ_{11} shift components employ electrons from the π_{C-C} and two σ_{C-C} bonds; the δ_{22} shift involve π_{C-C}, σ_{C-H}, and to a lesser extent the σ_{C-C} electrons; and finally δ_{33} involves the two σ_{C-C} and the σ_{C-H} bonds. The largest δ_{11} shift is therefore associated with the weakest set of bonds and the smallest δ_{33} shift with the strongest bonds. Note, the distinction between $E(\pi_{C-C})$ and $E(\sigma_{C-C})$ made here should not be confused with the total energy of a double bond consisting of the sum of these two energies. Similarly, for ethylene, the tensor component shifts and the contributing bonds are δ_{11} (π_{C-C}, σ_{C-C}, and to a lesser extent σ_{C-H}), δ_{22} (π_{C-C} and σ_{C-H}) and δ_{33} (σ_{C-C} and σ_{C-H}). These somewhat simplistic energy arguments need to be applied with some care as mixing of angular momentum components into the ground-state wavefunctions are dominated also by electron polarization and symmetry considerations which can override the somewhat simpler energy arguments presented here.

6.5 Aromatic Bond Orders in Fused Aromatic Bridgehead Carbons

Table 1 indicates that the chemical shift tensor of the bridgehead carbons for naphthalene are nearly axially symmetric. For example, the value for $\delta_{11} - \delta_{22}$ in bridgehead carbons is only 6.3 ppm, while $\delta_{11} - \delta_{22}$ for benzene is 88 ppm. The nonbridgehead carbon tensors in naphthalene are essentially like those indicated for benzene, with $\delta_{11} - \delta_{22}$ values in the vicinity of 80–90 ppm. Both of the in-plane bridgehead tensor components mix the π_{C-C} bond electrons with only σ_{C-C} bond electrons, and the tensor would be axial if the three π bonds to the three adjacent carbon atoms were to be equivalent. The diversity of π bonds varies greatly in fused aromatic hydrocarbons as may be observed in Figure 17 where the principal shift components of representative bridgehead carbons are plotted for a set of naphthalene-related molecules. The relevant bond orders are also indicated in Figure 17. Note, $\delta_{11} - \delta_{22}$ is smaller when all three bonds have comparable bond orders. When one of the three adjacent carbon atoms in a bridgehead fails to exhibit a significant π-electron population, the carbon shift tensor reverts to a more typical asymmetric pattern. The bond order between C-6a and C-6b moieties in perylene is very small (i.e., 1.07) and reflects only the presence of a σ_{C-C} bond. Hence, the value of $\delta_{11} - \delta_{22}$ = 59 ppm for perylene is similar to the corresponding 70 ppm anisotropy observed for the α-carbons of 1,4,5,8-tetramethylnaphthalene.[40] However, the $\delta_{11} - \delta_{22}$ values for C-3a and C-12c are both ca. 2 ppm and still retain their near-axial character similar to the corresponding bridgehead shifts in naphthalene. This brief discussion of bridgehead shift tensors in naphthalene-related molecules illustrates the potential power of chemical shift tensor data in characterizing the electronic structural details in molecules.

6.6 The Effect of Charge Polarization in Sugar Chemical Shift Tensors

In tetrahedral carbon atoms, the simple energy arguments that are used to account for the large anisotropic shifts in

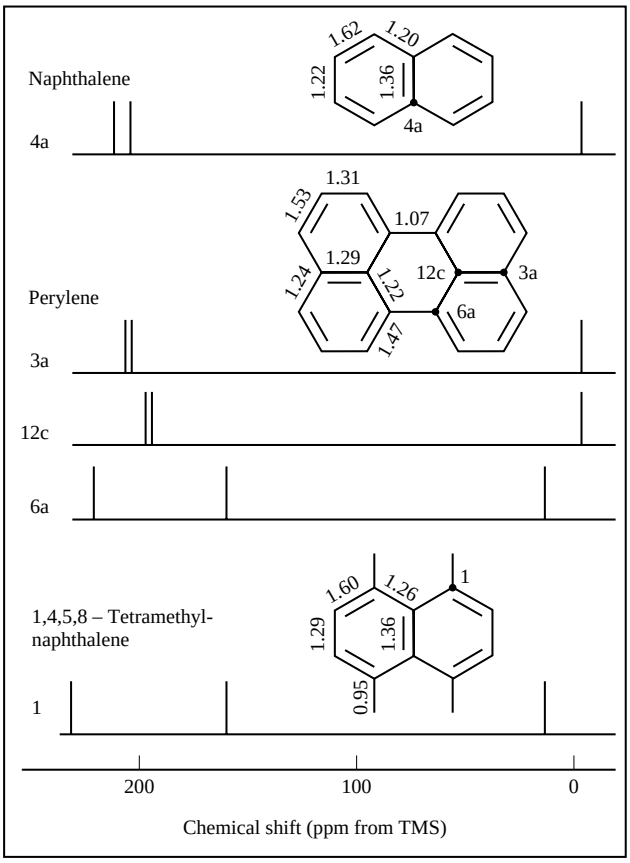

Figure 17 Bridgehead and substituted shift tensor components for naphthalene and related compounds. Small in-plane anisotropy in δ_{11} and δ_{22} is noted whenever all three adjacent carbons have sizable bond orders, indicating comparable π-electron populations. The C-6a bridgehead in perylene has similar bond orders to those at the substituted carbons in 1,4,5,8-tetramethylnaphthalene. Consequently, the large in-plane anisotropy in δ_{11} and δ_{22} results from the C-6a to C-6b bond exhibiting typical single σ-bond character

sp^2 aromatic carbons are less important because only σ-bonds are involved in such molecules, and these bonds tend to be much more similar to each other than corresponding bonds involving sp^2 carbons. Thus, other effects such as charge polarization and distortions in bond angles and internuclear distances are relatively more important in sugars. Bond angle distortions usually arise with steric perturbations of the molecular structure. Further, the absence of dominating symmetry features (e.g., mirror planes) in sugars leaves all of the principal values relatively free to orient in space such that simple recognizable patterns are not available to assist the systematization of the data. Even so, sugar shifts must also continue to reflect the three-dimensional structure of the molecular electrons, and the tensor shifts in the sp^3 sugar carbons are just as sensitive to electronic features as are the sp linear and sp^2 planar molecules discussed above.

Extensive data[41–43] have been accumulated on a number of important sugar systems to delineate the effect of oxygen charge polarization and the rich conformational features found in various sugar molecules. Systematic trends are observed in these data, but when simple rules such as used to discuss aromatic and linear molecules are unavailable to systematize the data only a complete quantum mechanical treatment is

available to sort out the important structural factors in the shift tensors. Quantum simulations of chemical shifts give proper weight to a variety of factors, viz. symmetry, electronic energy, charge polarization and possible steric effects, etc. Fortunately, such theoretical methods are now approaching the point where their reliability provides sufficient independent information to resolve ambiguities in the assignment of very similar tensors not distinguished clearly by either the crystal symmetry or diffraction structural information.

6.7 Quantum Mechanical Calculations of Chemical Shift Tensors

Space in this article is insufficient to discuss every subtle nuance and structural detail found in chemical shift tensors, but a short discussion of the theoretical prediction of these shifts is valuable. The quantum chemical results have been effective in correlating a large body of experimental data and provide a means of comparing NMR tensor data with structural parameters obtained from diffraction studies. Using interatomic distances and bond angles obtained from either X-ray or neutron diffraction results, it is possible to calculate molecular wavefunctions that reflect even minor structural variations. These quantum mechanical wavefunctions are then used to predict chemical shift tensors, and it is found that very modest changes in interatomic bond distances and bond angles can lead to variations in predicted chemical shifts of several ppm. As the experimental NMR accuracy of crystal measurements is about ± 0.3 to ± 0.5 ppm, errors in structural data often cause scatter in the predicted shifts that are nearly an order of magnitude larger than limitations in the NMR data.

Figure 18 contains two plots of the theoretical versus experimental chemical shift tensor components for eight related sugar molecules. In Figure 18(a) the theoretical results depend solely on the diffraction structures in the literature. Where possible the neutron diffraction results have been used as they establish the positions of the protons in molecules much better. In one sugar, methyl β-D-glucopyranoside, a neutron structure was not available and the X-ray data had to be used. The neutron diffraction data provide wavefunctions that predict the chemical shift tensors with less scatter than the X-ray data, primarily because the C–H distances are better determined. A closer study of the neutron data, however, indicates very large Debye–Waller factors for methyl protons in these methylated sugars due to extensive librational motion. Thus, the neutron data provide quality proton positions for ring protons but still experience larger uncertainties in the methyl proton positions.

The plot in Figure 18(b) was obtained first by quantum mechanically optimizing all C–H bond distances in the eight sugar molecules. These refinements in the nuclear positions were then used to obtain wavefunctions for simulating chemical shift tensors. This process considerably improves both the slope and the scatter found in the correlation plot given in Figure 18(a). The improvement in Figure 18(b) presumably may be attributed to better proton positions. The improved wavefunctions predict sugar chemical shifts ranging over 100 ppm with only a scatter of ± 2.4 ppm. These results portend high promise for chemical shift tensors in the area of structural chemistry.

A similar theoretical study[44] of the shift tensors in naphthalene indicates that the errors in the diffraction parameters are

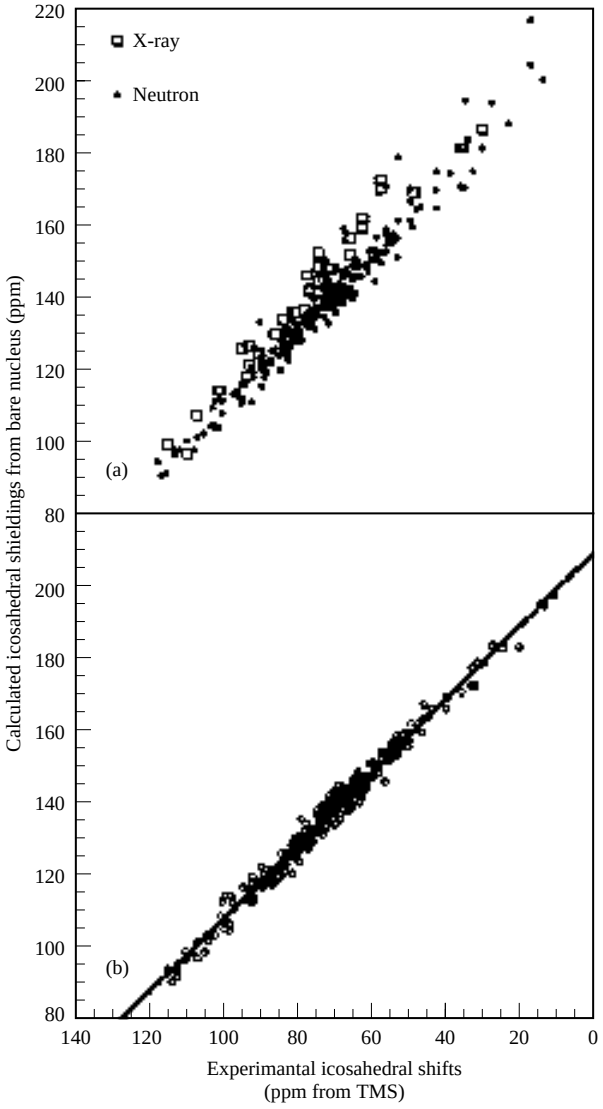

Figure 18 (a) GIAO calculations with X-ray and neutron diffraction structures versus experimental shift tensor components. (b) GIAO calculations with quantum mechanically optimized CH bond lengths versus experimental shift tensor components. (Courtesy of Fang Liu)

sufficient to account for variations of ± 4.9 ppm scatter found between the theoretical predictions and the experimental chemical shifts. This study used the neutron diffraction structure of Pawley and Yates[36] to obtain the naphthalene wavefunctions. Uncertainties of 0.01 Å in bond distances may lead to changes in the wavefunctions that can alter the predicted shifts by up to 2 ppm. Such uncertainties are common in diffraction studies and thus the present scatter in theoretical predictions of shifts can only be reduced by improvements in the structural parameters. A combination of quantum calculations and tensor shift data therefore provides a verifiable means of refining diffraction data. These results portend a bright future for chemical shift studies of single crystals as NMR solid measurements, with errors of less than ± 0.5 ppm, offer a considerable improvement in the relative accuracy of the measured quantity. This is especially important when neutron diffraction structures are not available or if the diffraction structure is on a very large molecule where diffraction uncertainties can be much larger.

7 CONCLUSIONS

From its first discovery in 1950, the chemical shift has made NMR spectroscopy an ubiquitous analytical method in chemistry. The applications are legend and every year literally thousands of research papers make significant chemical conclusions based on chemical shift results. Even though liquid chemical shifts have been extremely important, they reflect only part of the power of the full chemical shift tensor. Chemical shift tensors contain considerably more information on subtle changes in the electronic and chemical structures of all materials. Furthermore, important information on the three-dimensional structure of molecular systems may be obtained from chemical shift tensors. As many of the shift tensor developments have been realized in recent years, one can only conclude that chemical shift studies should be promising for many years to come.

8 RELATED ARTICLES

Carbon and Nitrogen Chemical Shifts of Solid State Enzymes; Shielding Calculations: LORG and SOLO Approaches; Chemical Shift Scales on an Absolute Basis; Chemical Shift Tensor Measurement in Solids; Chemical Shift Tensors in Single Crystals; Chemical Shifts in Biochemical Systems; Dipolar and Indirect Coupling Tensors in Solids; Electric Field Effects on Shielding Constants; Magic Angle Turning and Hopping; Proton Chemical Shift Measurements in Biological Solids; Semiempirical Chemical Shift Calculations; Shielding Calculations: IGLO Method; Shielding Calculations: Perturbation Methods; Shielding: Overview of Theoretical Methods; Shielding in Small Molecules; Shielding Tensor Calculations; Shielding Theory: GIAO Method; Two-Dimensional Powder Correlation Methods; Variable Angle Sample Spinning.

9 REFERENCES

1. W. G. Proctor and F. C. Yu, *Phys. Rev.*, 1950, **77**, 717.
2. W. C. Dickenson, *Phys. Rev.*, 1950, **77**, 736.
3. G. Lindström, *Phys. Rev.*, 1950, **78**, 817.
4. H. A. Thomas, *Phys. Rev.*, 1950, **80**, 901.
5. J. T. Arnold, S. S. Dharmatti, and M. E. Packard, *J. Chem. Phys.*, 1951, **19**, 507.
6. C. P. Slichter, *Principles of Magnetic Resonance*, 3rd edn., Harper & Row, New York, 1989, Chap. 4
7. M. Mehring, High Resolution NMR Spectroscopy in Solids, in *NMR Basic Principles and Progress*, eds. P. Diehl, E. Fluck, and R. Kosfeld, Springer-Verlag, Berlin, 1976, Vol. 11, Chap. 5.
8. U. Haeberlin, High Resolution NMR in Solids—Selective Averaging, in *Advances in Magnetic Resonance*, Academic Press, New York, 1976, Supp. 1, Chap. 3
9. C. A. Fyfe, *Solid State NMR for Chemists*, C.F.C. Press, Guelph, 1983, Chap. 5, pp. 180–209.
10. R. K. Harris, *Nuclear Magnetic Resonance Spectroscopy*, Pitman, London, 1983, Chap. 8
11. B. C. Gerstein and C. R. Dybowski, *Transient Techniques in NMR of Solids*, Academic Press, Orlando, FL, 1985, pp. 103–119.
12. T. M. Duncan, *A Compilation of Chemical Shift Anisotropies*, Farragut Press, Chicago, IL, 1990.
13. M. Bloembergen and J. A. Rowland, *Acta Metall.*, 1953, **1**, 731.
14. J. C. Jackson, *Classical Electrodynamics*, 2nd edn., Wiley, New York, 1975, Appendix 1, p. 811.
15. R. N. Zare, *Angular Momentum*, Wiley-Interscience, New York, 1988, pp. 79–81.
16. M. E. Rose, *Elementary Theory of Angular Momentum*, Wiley, New York, 1967, pp. 62–65.
17. M. Mehring, in *NMR Basic Principles and Progress*, eds. P. Diehl, E. Fluck, and R. Kosfeld, Springer-Verlag, Berlin, 1976, Vol. 11, pp. 215–218.
18. S. A. Smith, W. E. Palke, and J. T. Gerig, *Concepts Magn. Reson.*, 1992, **4**, 107, 181.
19. R. N. Zare, *Angular Momentum*, Wiley-Interscience, New York, 1988, pp. 186–188.
20. R. N. Zare, *Angular Momentum*, Wiley-Interscience, New York, 1988, pp. 85–91.
21. D. W. Alderman, M. H. Sherwood, and D. M. Grant, *J. Magn. Reson., Ser. A*, 1993, **101**, 188.
22. D. W. Alderman, M. H. Sherwood, and D. M. Grant, *J. Magn. Reson.*, 1990, **86**, 60.
23. A. Abragam, *The Principles of Nuclear Magnetism*, Oxford University Press, London, 1961, p. 166.
24. T. M. Duncan, *A Compilation of Chemical Shift Anisotropies*, Farragut Press, Chicago, IL, 1990, p. 3.
25. J. Mason, *Solid State NMR*, 1993, **2**, 285.
26. D. W. Alderman, M. S. Solum, and D. M. Grant, *J. Chem. Phys.*, 1986, **84**, 3717.
27. A. Bax, N. M. Szeverenyi, and G. E. Maciel, *J. Magn. Reson.*, 1983, **51**, 400; 1983, **52**, 147; 1983, **55**, 494; 1985, **61**, 440.
28. Z. Gan, *J. Am. Chem. Soc.*, 1992, **114**, 8307.
29. J. Z. Hu, A. M. Orendt, D. W. Alderman, R. J. Pugmire, C. Ye, and D. M. Grant, *Solid State NMR*, 1994, **3**, 181; J. Z. Hu, W. Wang, F. Liu, M. S. Solum, D. W. Alderman, R. J. Pugmire, and D. M. Grant, *J. Magn. Reson., Ser. A*, 1995, **113**, 210.
30. C. D. Hughes, D. W. Alderman, and D. M. Grant, *J. Magn. Reson., Ser. A*, 1993, **102**, 58.
31. B. F. Chmelka, K. Schmidt-Rohr, and H. Spiess, *Macromolecules*, 1993, **26**, 2282.
32. K. W. Zilm and D. M. Grant, *J. Am. Chem. Soc.*, 1981, **103**, 2913.
33. W. P. Powers and R. E. Wayslishen, *Annual Reports on NMR Spectroscopy*, Ed. G. W. Webb, Academic Press, San Diego, CA, 1991, Vol. 23.
34. M. H. Sherwood, D. W. Alderman, and D. M. Grant, *J. Magn. Reson.* 1989, **84**, 466; C. M. Carter, D. W. Alderman, and D. M. Grant, *J. Magn. Reson.*, 1985, **65**, 183.
35. W. H. Bragg, *Proc. Phys. Soc.*, 1921, **34**, 33.
36. G. S. Pawley and E. A. Yates, *Acta Crystallogr.*, 1969, **B25**, 2009.
37. M. H. Sherwood, J. C. Facelli, D. W. Alderman, and D. M. Grant, *J. Am. Chem. Soc.*, 1991, **113**, 750.
38. C. P. Slichter, *Principles of Magnetic Resonance*, 3rd edn., Harper & Row, New York, 1989, p. 89.
39. A. J. Beeler, A. M. Orendt, D. M. Grant, P. W. Cutts, J. Michl, K. W. Zilm, J. W. Downing, J. C. Facelli, M. S. Schindler, and W. Kutzelnizz, *J. Am. Chem. Soc.*, 1984, **106**, 7672.
40. A. M. Orendt, N. K. Sethi, J. C. Facelli, W. J. Horton, R. J. Pugmire, and D. M. Grant, *J. Am. Chem. Soc.*, 1992, **114**, 2832.
41. D. L. Sastry, K. Takegoshi, and C. A. McDowell, *Carbohydr. Res.*, 1987, **165**, 161.

42. M. H. Sherwood, D. W. Alderman, and D. M. Grant, *J. Magn. Reson., Ser. A* 1993, **104**, 132.
43. F. Liu, C. G. Phung, D. W. Alderman, and D. M. Grant, to be published.
44. J. C. Facelli and D. M. Grant, *Nature (London)*, 1993, **365**, 325.

Biographical Sketch

David M. Grant. *b* 1931. B.S., 1954, Ph.D., 1957, Chemistry, University of Utah, USA. DuPont Instructor, University of Illinois, 1957–58, introduced to NMR by Herb Gutowsky and Martin Karplus. Faculty in Chemistry, University of Utah since 1958, presently Distinguished Professor. Over 300 publications. Awards: 1969 Calif. Section Gold Medal (ACS); 1973 Utah ACS Section Award; 1973–74; Sherman Fairchild Distinguished Scholar, Cal. Inst. Tech.; 1987 Univ. of Utah Rosenbalt Prize; 1991 ACS Award in Petroleum Chem.; 1992 Utah Governor's Medal for Science. Current research specialties: methods and theoretical foundations of carbon-13 NMR, coupled spin relaxation and molecular motions, chemical shifts in liquids and solids with emphasis on carbon-13 shift tensors and their origins in electronic and molecular structure.

Chemical Shifts in Biochemical Systems

Angel C. de Dios and Eric Oldfield

University of Illinois, Urbana-Champaign, IL, USA

1	Introduction	1
2	Empirical Shift–Structure Correlations in Proteins	1
3	The Ab Initio Approach to Protein Shielding	2
4	Nucleic Acids	5
5	Carbohydrates	6
6	Structure from Shielding: Prediction, Refinement, and Validation	6
7	Conclusions	6
8	Related Articles	6
9	References	6

1 INTRODUCTION

The purpose of this article is to outline briefly recent progress in understanding chemical shifts in biochemical systems–proteins, nucleic acids, carbohydrates, and lipids. The chemical shift is probably the most sensitive spectroscopic probe of local structure and environment, but until quite recently it has been quite refractory to detailed analysis, at least in macromolecules. In small molecules, this sensitivity manifests itself in isotope shifts, temperature dependence, gas-to-liquid shifts, and solvent shifts. In macromolecules, sensitivity is manifested as chemical shift nonequivalencies. The NMR chemical shift in biological systems contains a wealth of encoded structural information, and in order to decode this information it is first necessary to be able to predict chemical shifts from known structures.

From a theoretical standpoint, insights gained in studying chemical shifts in biological systems should also greatly help in testing, modifying, and improving present theories of the chemical shift. For example, proteins provide a unique test case for investigating the dependencies of the chemical shift on factors such as torsion angles, hydrogen bonding, and electrostatics. In sharp contrast, gas phase studies of small molecules would not be capable of yielding the torsional dependencies of the chemical shift. This is because variable-temperature measurements, in which the torsional effects would be visible, also include significant contributions from centrifugal distortion, and, in addition, a change in one torsion angle may significantly change the overall shape of a small molecule, and consequently the way it interacts with its environment. Proteins, on the other hand, do not require variable-temperature studies, since sites which differ only in torsion angles are already present. Hence, the ability to interpret and reproduce chemical shift nonequivalencies in biological systems should not only be useful for structure elucidation, but is also of fundamental importance for the evaluation, development, and design of methods for chemical shift computation in general.

Chemical shift nonequivalencies due to folding have been known in proteins for more than two decades. McDonald and Phillips[1] first observed that several residues in hen egg white lysozyme could be resolved in ^{1}H NMR, and this was then followed by Allerhand et al. who observed a ∼6 ppm range for the ^{13}C chemical shift of C-γ of the six tryptophan residues in hen egg white lysozyme.[2] Although such chemical shift inequivalencies have made multidimensional NMR studies of proteins possible,[3,4] understanding of the origins of such chemical shift nonequivalencies remained a very major challenge until recently, when a first-principles reproduction of the NMR spectra of the heavier nuclei (^{13}C, ^{15}N, and ^{19}F) in proteins was demonstrated to be feasible.[5] Here, we trace the development of NMR chemical shift interpretations in biological systems, starting from the discovery of empirical correlations between shift and structure in proteins, up to the present ab initio interpretation of protein, nucleic acid, and carbohydrate chemical shifts, and the derivation of structure from shielding.

2 EMPIRICAL SHIFT–STRUCTURE CORRELATIONS IN PROTEINS

The earliest attempts at unraveling the relationship be-tween secondary structure and chemical shifts were focused on H-α.[6–8] Due to the small chemical shift range and the sensitivity of ^{1}H shielding to not only electrostatic effects but also magnetic factors, such as ring currents and the anisotropy of the diamagnetic susceptibility of peptide groups, only general trends were found between structure and shielding.[9,10] In contrast to ^{1}H NMR, the heavier nuclei exhibit a much wider chemical shift range, rendering such magnetic effects of minor importance. Hence, ^{13}C and ^{15}N nuclei offer more promise, and considerable efforts were made in interpreting these shifts as soon as they became available.

In early work, Kricheldorf et al.[11] and Saito et al.[12] showed that ^{13}C chemical shifts in peptides were mainly influenced by the torsion angles ϕ and ψ. Theoretical attempts involving a semiempirical finite perturbation–incomplete neglect of differential overlap (FPT–INDO) method aimed at reproducing these observations were somewhat successful in demonstrating the nonequivalency between helical and sheet residues,[13] but the calculated differences were much smaller than the range observed experimentally. With an increasing number of assigned C-α and C-β resonances in various proteins—bovine pancreatic trypsin inhibitor (BPTI), calmodulin, interleukin-1β and staphylococcal nuclease—Spera and Bax introduced the first empirical ϕ, ψ chemical shift surface for C-α and C-β using known X-ray data,[14] shown in Figures 1(a) and (b). Figure 1(c) shows histograms of the secondary shift distribution in α-helical and β-sheet residues. From the presently available database of ^{13}C chemical shifts it is clear that C-α resonances of helical sites are deshielded compared with those residues which occur in sheet regions. The opposite trend is evident for C-β, where helical sites are more shielded.[14] Such empirical observations have found use in the chemical shift index,[15] which permits prediction of helical and sheet structure, based on C-α C-β, C^{o}, and H-α shifts.

Considerable attention was also given early on to ^{15}N shifts in proteins.[16,17] However, the problem of whether or

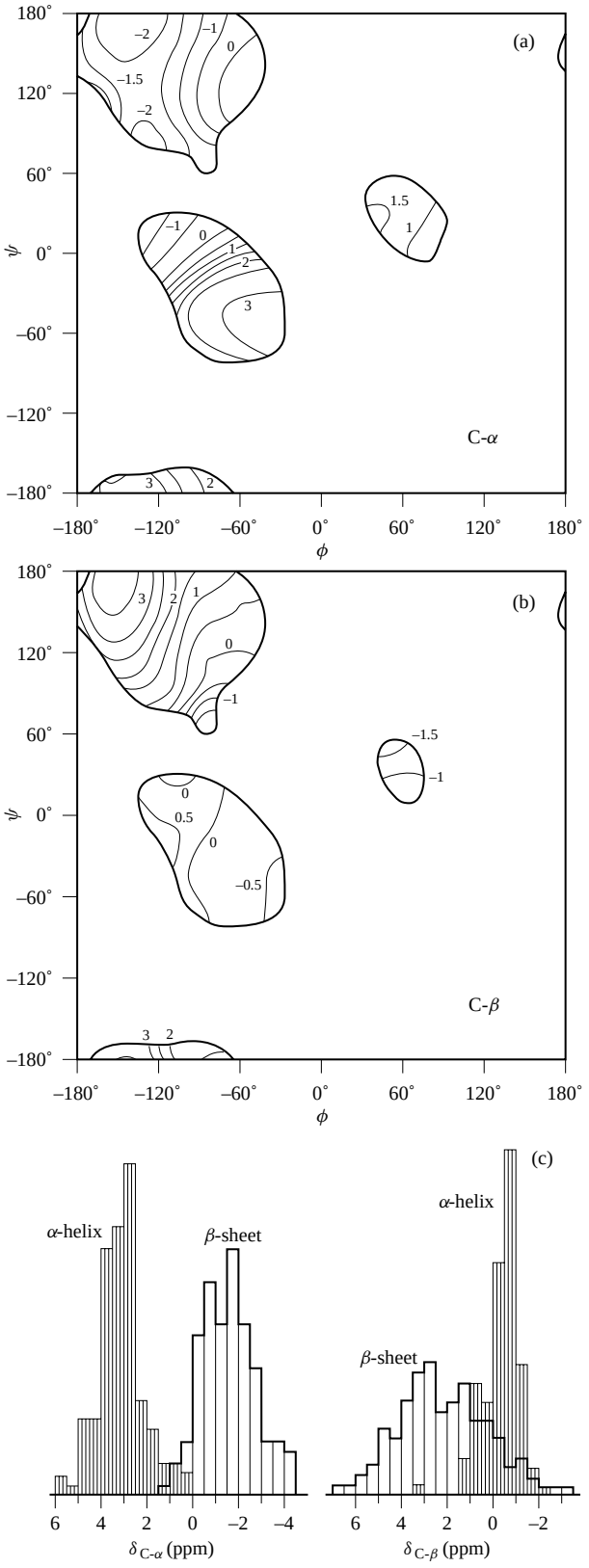

Figure 1 Secondary chemical shift surfaces $\Delta\delta(\phi,\psi)$ and secondary chemical shift histograms for C-α and C-β sites in proteins. (a) Empirical secondary chemical shift surface for C-α nuclei in proteins; (b) as in part (a) but for C-β; (c) histogram showing the distribution of observed secondary shifts for C-α and C-β. (Reproduced by permission of the American Chemical Society from S. Spera and A. Bax, *J. Am. Chem. Soc.*, 1991, **113**, 5490)

not ^{15}N chemical shifts can provide information regarding local structure remained unanswered. Glushka et al. then noticed a correlation between ^{15}N chemical shifts and the torsion angle ψ_{i-1} for residues in sheet regions in BPTI and apamin, but no other structural or 'interaction' features were found.[18] More recently, using a much larger database (consisting of 14 proteins and 1477 ^{15}N chemical shifts), Le and Oldfield[19] found a better empirical correlation between the peptide ^{15}N chemical shift and the torsion angles ϕ_i and ψ_{i-1}, indicating that there is indeed a significant relationship between ^{15}N chemical shifts and secondary structure. The larger number of points permitted study of individual amino acid shift surfaces. Figures 2(a)–(c) show the agreement obtained between experimentally obtained ^{15}N chemical shifts and those derived from the empirically fitted individual shift surfaces, for aspartic acid, lysine, and valine. The presence of an intrinsic relationship between ^{15}N chemical shifts and secondary structure becomes evident from these studies. However, it can also be inferred that there are other factors, such as electrostatic interactions, side-chain conformation, and hydrogen bonding, which all potentially influence ^{15}N shielding. The side chain of valine, for example, introduces an additional angle χ^1, which can modify the ^{15}N chemical shift behavior, since the presence of a substituent at the β-carbon site introduces a γ-*gauche* effect, as noted earlier by Tonelli.[20] In order to take this into account, a much larger database would be needed in order to create separate shift surfaces for each of the three common χ^1 conformers. Empirical database approaches are thus useful in indicating trends, but it would clearly be desirable to be able to predict shifts accurately using first principles or ab initio approaches. For example, the ^{15}N-valine χ^1-torsional problem is one which can easily be solved if the torsional dependencies can be derived from first principles. As demonstrated recently, this is now possible.[15] In addition, sensitivity to side-chain conformation is not exclusive to ^{15}N, since ^{13}C shifts for C-α and C-β sites are also expected to exhibit a χ^1 dependence. This, however, would be difficult to see with only a small database of assigned ^{13}C shifts. Ab initio methods therefore clearly have an advantage over empirical approaches since chemical shift surfaces for individual amino acids, as well as for various χ^1 conformers, can in principle be evaluated.

With the rapidly growing database of ^{1}H chemical shifts,[21] there has been renewed interest in using ^{1}H NMR in protein structure studies.[22–27] These studies have taken advantage of the availability of large numbers of ^{1}H chemical shifts to relate chemical shifts to structure. In addition to the correlation found between secondary structure and the chemical shifts of H-α and H-N, the large amount of spectroscopic information available has also permitted a breakdown of ^{1}H shielding into electrostatic and peptide magnetic anisotropy effects. Thus, the coefficients needed in order to evaluate electrostatic contributions from nearby polar groups, as well as the anisotropy effects arising from peptide bonds, have been derived empirically. The complexity and number of factors that affect ^{1}H chemical shifts, however, make a direct chemical shift to structure route very difficult, although structure refinement using H-α shifts has promise.[30]

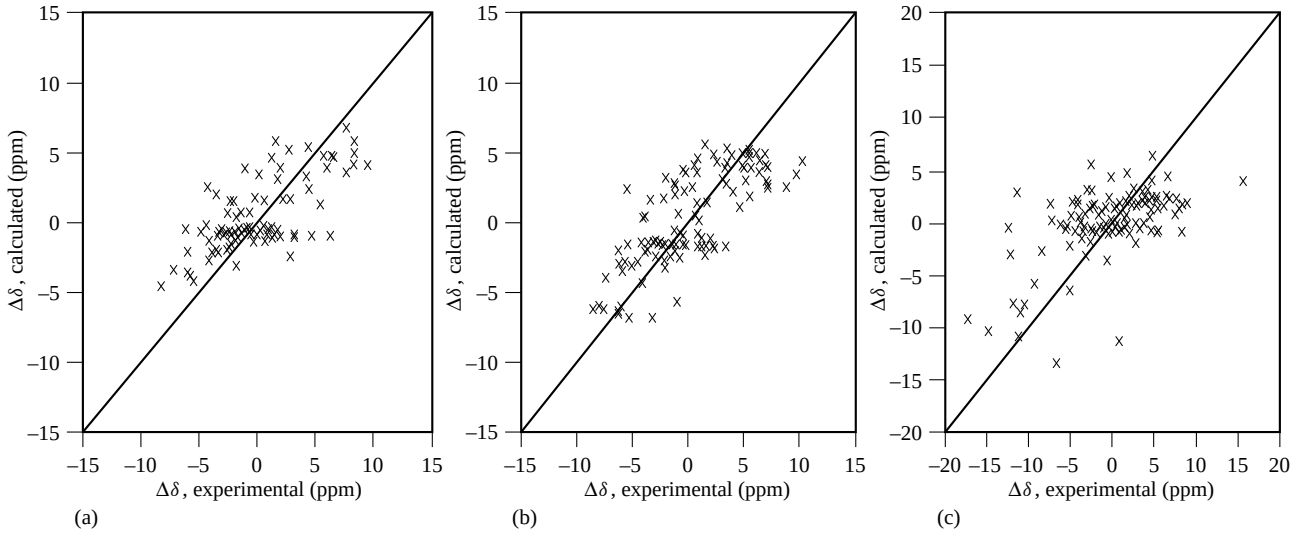

Figure 2 Correlation between experimental secondary ^{15}N chemical shifts and those computed from empirically fitted individual secondary chemical shift surfaces. (a) Aspartic acid; (b) lysine, and (c) valine. (Reproduced by permission of ESCOM Science Publishers BV from H. Le and E. Oldfield, *J. Biomol. NMR*, 1994, **4**, 341)

3 THE AB INITIO APPROACH TO PROTEIN SHIELDING

Although empirical and semiempirical approaches for ^{1}H NMR are useful for analyzing secondary structures, these approaches are more limited for the heavier nuclei. The reason for this is that long range magnetic anisotropy effects will be very small for ^{13}C and ^{15}N, due to the large ^{13}C and ^{15}N shift ranges (~8–30 ppm). Moreover, C-α and C-β, being both sp^3-hybridized carbons, are not expected to have their chemical shift greatly influenced by electrostatic factors. Thus, in order successfully to predict and interpret the chemical shift of heavy nuclei in proteins, it is desirable to apply ab initio methods. These, in general, successfully predict shielding for such heavy elements—at least for ^{13}C, ^{15}N, and ^{19}F. The system, however, consists of so many atoms that a computation which includes the whole protein would be prohibitive, even with supercomputers. Fortunately, however, since the chemical shift is inherently a localized property, it is wrong to suppose that the effects of all atoms in a protein need to be incorporated into the computation. One approach is to separate the total shielding, σ_t, into three parts[31]

$$\sigma_t = \sigma_s + \sigma_l + \sigma_0 \quad (1)$$

where σ_s refers to the short-range contribution, σ_l corresponds to long range electrostatic effects, and σ_0 contains the magnetic effects. Although orthogonality may not be achieved, such a partitioning of the various chemical shift contributions helps develop computational strategies for solving each contribution.

The short range contribution can be further divided into several categories: local structure, repulsive interactions, and strong hydrogen bonding. Local structure includes the dependencies of the chemical shift on bond lengths, bond angles, and torsion angles. For the long range electrostatic contributions, several methods can now be used. One can either incorporate the charge field at the self-consistent field (SCF) level,[32] or use the multipole shielding polarizability (MSP) approach.[33] Lastly, σ_0 can be calculated by a variety of classical methods, basically as discussed above for ^{1}H NMR. This contribution is, however, still within the error limits of present ab initio methods for calculating σ_s and σ_l, although it can still be expected to help somewhat with shift predictions. For further discussions on intra- and intermolecular factors which influence shielding, several recent reviews are available.[34,35]

Hence, for a protein, atoms belonging to the residue which contains the nucleus of interest can be regarded as contributing to σ_s, while the rest of the protein contributes to σ_l. This partitioning greatly reduces the size of the fragment on which full ab initio calculations need to be performed. When combined with recent improvements in hardware (such as powerful workstations) and a method which avoids gauge errors in calculating the shielding property [the gauge-including atomic orbital (GIAO) method],[36] together with the application of new algorithms to improve code efficiency,[37] the ab initio reproduction of chemical shifts in proteins is now at hand.

In recent work,[5] it was shown that a small molecular fragment, *N*-formyl-L-alanine amide, interacting with formamide molecules (used to represent hydrogen bond partners) and point charges (representing the rest of the protein) successfully reproduced the experimentally observed ^{13}C chemical shifts for the 12 alanine C-α and C-β sites in the protein staphylococcal nuclease, as shown in Figure 3. The ability to predict the chemical shift opens up a new avenue for protein structure elucidation, especially if the factors which lead to such nonequivalencies can be identified. The partitioning of the shielding as described above greatly facilitated this quest.[5,38] As expected, C-α and C-β chemical shift nonequivalencies were found to be dominated by the local structure, or short-range factors, σ_s.[36] In addition, based upon an examination of the dependencies of C-α and C-β shielding on bond lengths, bond angles, and torsion angles, it was established that torsion angles clearly dominate the experimentally observed trends. In particular, it was also noted that the chemical shifts at these

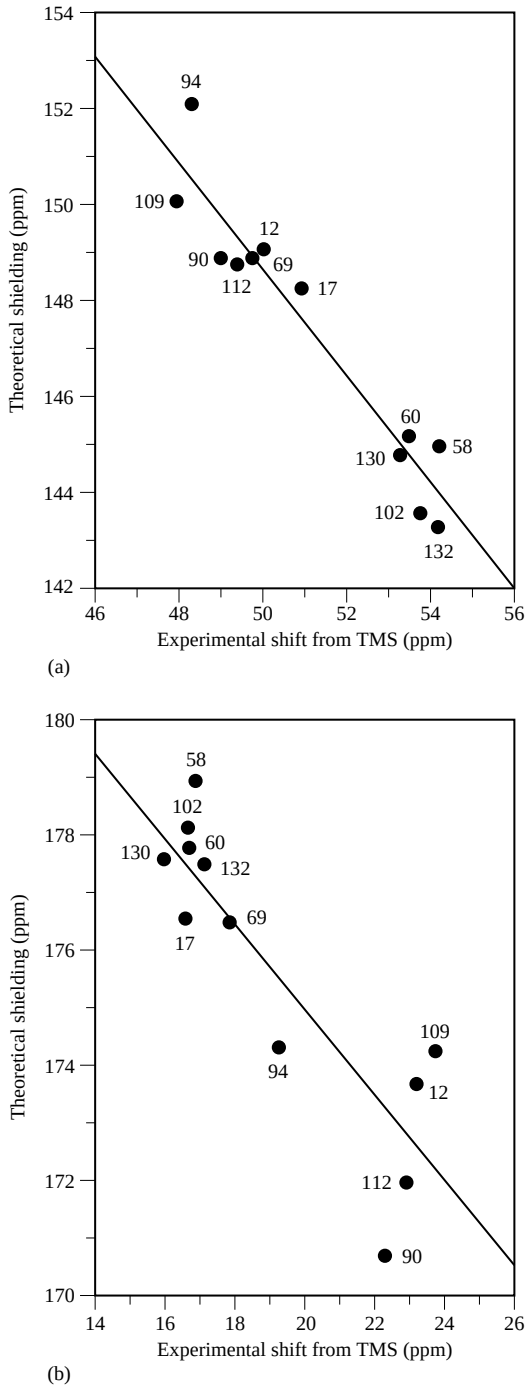

Figure 3 Comparison between calculated ^{13}C NMR shieldings and experimental chemical shifts for alanine residues in staphylococcal nuclease. (a) C-α, (b) C-β. (Reproduced by permission of the American Association for the Advancement of Science from A. C. de Dios, J. G. Pearson, and E. Oldfield, *Science*, 1993, **260**, 1491)

sites were extremely sensitive to bond lengths. In fact, the variations in bond lengths of the same type of residue seen in a single-crystal X-ray structure were shown to lead to a chemical shift range as large as the experimentally measured range, but the predicted shifts were wholly uncorrelated with experiment.[39] Residues of the same type in a protein therefore have bond lengths that are much more similar to each other than X-ray structures would suggest. Nevertheless, from these same studies, ϕ- and ψ-angles were found to be highly correlated with C-α and C-β shifts. Shielding surfaces have therefore been constructed using a model fragment, *N*-formyl-L-alanine amide, in order to map out the effects of ϕ and ψ on C-α and C-β shieldings.[38] With this surface serving as a look-up table, and knowledge of ϕ and ψ, ^{13}C shieldings (or chemical shifts) for any alanine site in a protein can readily be obtained—at least in the absence of large-amplitude motions.

Nitrogen-15 shieldings are expected to be more difficult to predict, since well-defined ϕ and ψ correlations have not been observed, and hydrogen bonding and electrostatic effects could also be important. Recent work,[5] however, has shown that ^{15}N chemical shifts in proteins can now be predicted using the GIAO method, with explicit hydrogen bond partners, and point charges representing the rest of the protein. Figure 4 shows results for valine residues in staphylococcal nuclease.[5] The results in Figure 4(a) were obtained by using a molecular fragment; formyl-L-alanyl-L-valine amide. In Figure 4(b), hydrogen bond partners were explicitly included (as formamide molecules), while Figure 4(c) includes the rest of the protein, represented as point charges. Although the dominance of torsion angles found in ^{13}C chemical shifts is less dramatic with ^{15}N, the generally good accord between calculated and observed values when long range factors are included indicates that ^{15}N NMR is a potentially powerful technique for structure validation. Its sensitivity to long range interactions extends the structural information that can be obtained beyond the local torsion angles, thus complementing ^{13}C NMR.

Although not naturally occurring in most proteins, ^{19}F is a particularly sensitive probe of electrostatic field effects in proteins. Its incorporation, for example, into tryptophan residues of *Escherichia coli* galactose-binding protein (GBP)[40] and hen egg white lysozyme[41] has generated information on how long range factors, such as van der Waals and electrostatic interactions, influence the chemical shift. Using point charges, GIAO has been shown[5] to reproduce satisfactorily the observed ^{19}F NMR spectrum of 5-F-Trp-labeled GBP, except for solvent-exposed sites. With prior knowledge of how shielding is affected by a uniform electric field, field gradient, and field hypergradient (the MSP approach), dynamic averaging becomes tractable,[5] and even shielding at sites that are highly mobile and solvent exposed can be satisfactorily reproduced.[39]

Overall, ^{13}C chemical shifts show great promise in structure elucidation, as noted above for alanine. Successful prediction of ^{13}C chemical shifts has also been shown for glycine and valine residues.[39] Here, the dominance of ϕ and ψ is similarly evident. The correlation between calculated and experimental shieldings for glycine sites is less satisfactory than with alanine and valine, possibly due to glycine mobility. On the other hand, the presence of the side chain in valine introduces an additional angle that can influence both C-α and C-β shieldings. Taking advantage of this additional dependency, crystal-to-solution structural differences became apparent upon close examination of the C-α and C-β shifts of valine residues in calmodulin.[42] Corroborated by coupling constant information, this work demonstrated that five out of the seven valine residues assume a side-chain conformation different from that seen by X-ray crystallography.

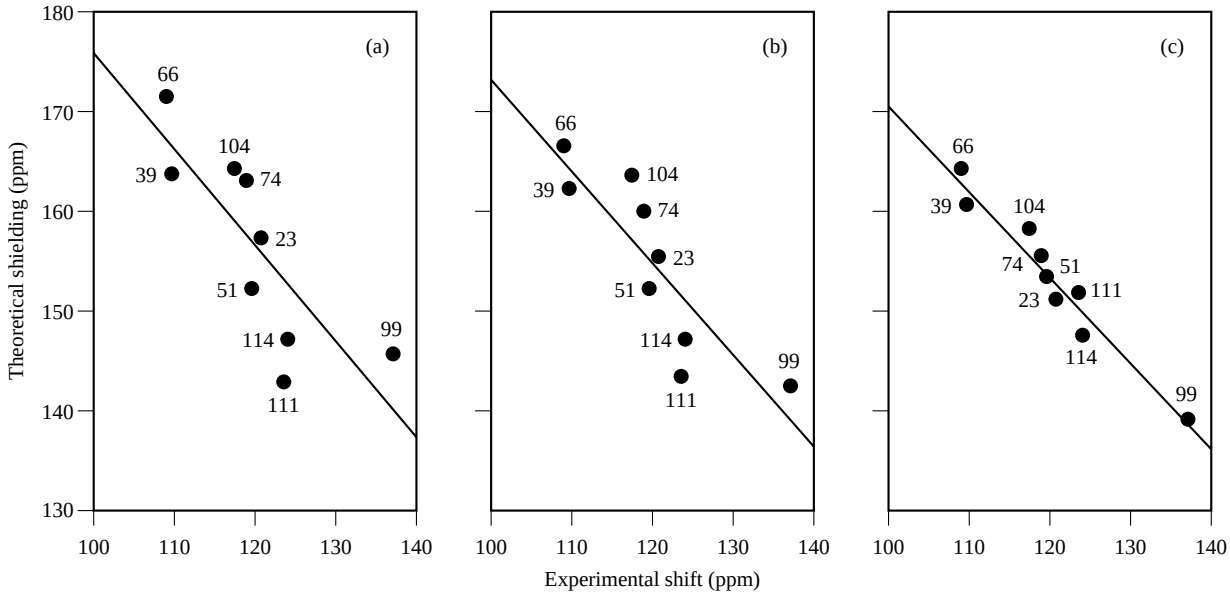

Figure 4 Calculated ^{15}N chemical shieldings versus experimental shifts for the valine sites in staphylococcal nuclease. (a) Using isolated valine fragments; (b) as in part (a) but with inclusion of a hydrogen bond partner; (c) as in part (b) but with incorporation of point charges to represent the rest of the protein. (Reproduced by permission of the American Association for the Advancement of Science from A. C. de Dios, J. G. Pearson, and E. Oldfield, *Science*, 1993, **260**, 1491)

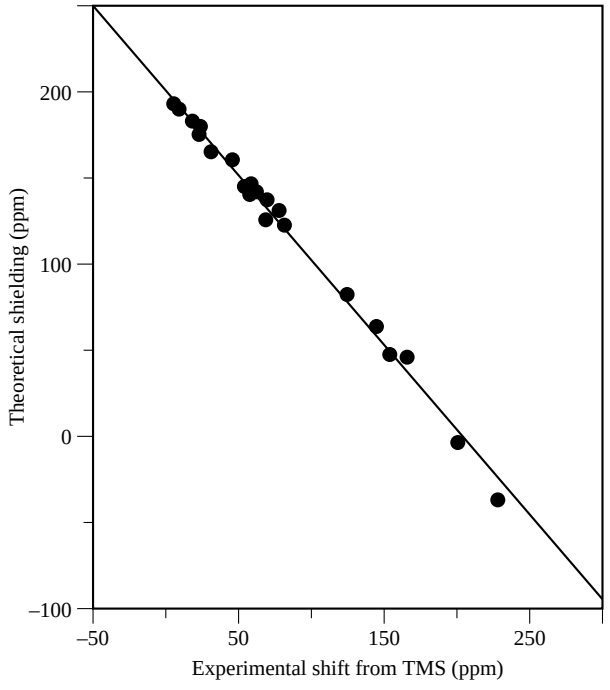

Figure 5 Experimental and theoretical ^{13}C shielding tensor elements for L-threonine in the icosahedral representation. Reprinted with permission from A. C. De Dios et al., *J. Am. Chem. Soc.*, **116**, 5307. Copyright 1994 American Chemical Society

Finally, we briefly consider shielding as a tensor quantity. Here, all elements and their directions need to be evaluated—six parameters versus one isotropic shift, representing a serious challenge for theory. For amino acid crystals, the charge field perturbation gauge including atomic orbital (CFP–GIAO) method gives excellent agreement with experiment.[43] Figure 5 shows a comparison between calculated and experimental shielding components for the ^{13}C nuclei in L-threonine[43] in the icosahedral representation[44] of the shielding tensor. The results shown here clearly illustrate the adequacy of present theoretical methods of predicting chemical shieldings, even in complex (zwitterionic, polar amino acid) systems.

4 NUCLEIC ACIDS

The usefulness of chemical shifts in studying biological systems is naturally not restricted to proteins. Chemical shifts of nucleic acids should similarly encode a wealth of information regarding structure, protonation sites, hydrogen bonding, and electrostatic field effects. The shielding caused by magnetic anisotropy effects on ^{1}H NMR spectra has already been studied using semiempirical methods,[45] and more recently ab initio methods have been used to study the pyrimidine base cytosine.[46] However, these early results were obtained using only a split valence set, insufficiently saturated with basis functions. A more recent study using a larger basis was performed by Schindler[47] using the individual gauge for localized molecular orbitals (IGLO) method.[48] The shielding tensors, as well as the magnetic susceptibilities, were calculated for cytosine, thymine, and uracil, as well as adenine and guanine. The calculated values compared favorably with experiment, but in general the computation of shielding tensors in nucleic acid bases is difficult because definite molecular structures that correspond to the systems on which the NMR measurements were taken are usually not available. In particular, the relative amounts of tautomers depend strongly on the solvent and pH, and the ^{15}N chemical shifts were found to be very sensitive to such environmental effects. Nevertheless, using ab initio optimized structures, it was shown that the calculated ^{15}N shielding trends caused by

protonation could indicate which species dominate in solution. However, the lack of a supportive trend from ^{13}C shieldings did not permit a more precise determination of the dominant tautomer.

5 CARBOHYDRATES

With the importance of carbohydrates in lipid and (glyco)protein structure, as well as in, for example, substrate/inhibitor binding (e.g. in lysozyme), and the occurrence of carbohydrates in metabolism, cell surface antigens, etc., it is surprising that so little work has been reported on ^{13}C and ^{17}O NMR shielding, at the ab initio level. An exception to this is the pioneering work of Grant et al.[49] on ^{13}C shieldings in methyl α-D-glycopyranoside and sucrose. Grant et al. showed that a root mean square deviation (rmsd) of $\sim$3 ppm between theory and experiment (the rmsd from the straight line connecting shift and shielding) with R^2 $\sim$0.97 and a slope of -0.99 (methyl glucoside), could be obtained at the 6-31G level, permitting a convincing reassignment of some earlier chemical shift assignments.

6 STRUCTURE FROM SHIELDING: PREDICTION, REFINEMENT, AND VALIDATION

The ability to predict the NMR spectra of biologically important molecules via ab initio methods heralds a new era in the use of the easiest NMR parameter to measure, the isotropic chemical shift. For proteins, the intimate relationship found between the torsion angles ϕ and ψ and the ^{13}C chemical shifts of C-α and C-β sites strongly suggests that it should be possible to derive structural information from chemical shifts in ways not founded on empirical relationships, size of database, or on X-ray structures. One such method of extracting torsion angles from spectroscopic parameters has recently been proposed.[48] Referred to simply as the 'Z-surface method', it begins with the assumption that a given spectroscopic parameter, P, can be represented as a function of a torsion angle α

$$P = f(\alpha) \tag{2}$$

and the probability that a given value P_i corresponds to a value of α can be cast as in

$$Z_i = \exp[-(P_i - f(\alpha))^2 / W] \tag{3}$$

W is a search width of typically about 1 ppm, and takes into account uncertainties in theoretical and experimental results, e.g. basis deficiencies, referencing errors, etc. Equation (3), of course, assumes a knowledge of $f(\alpha)$, which can be obtained via ab initio methods or from experiment. A plot of Z_i over possible values of α constitutes a probability surface for the angle α. Since the chemical shifts of C-α and C-β are both functions of torsion angles ϕ and ψ, a map of the whole Ramachandran space that shows which pair of ϕ- and ψ-angles closely agree with the observed chemical shifts can be easily constructed. For alanine residues in a variety of proteins, using this approach and the theoretical shielding surfaces for C-α and C-β, plus an experimental surface for H-α, yields values for ϕ and ψ that have only $\sim$10° rmsd values from the X-ray values.[50]

Although ^{15}N chemical shifts are more susceptible to environmental effects, and ^{19}F shift inequivalencies are largely due to electrostatic interactions, this sensitivity of the ^{19}F and ^{15}N shieldings to electrostatic interactions can be utilized in testing present force fields, molecular dynamics programs, and electrostatic field calculations.[51] Moreover, ^{15}N being sensitive to factors other than local structure, it can complement ^{13}C NMR in validating the overall structure of a protein.

7 CONCLUSIONS

Chemical shifts have been reported in biochemical systems for about 30 years. However, only very recently has it been possible to solve the chemical shift problem, and successfully predict chemical shifts in macromolecules, such as proteins.[5] Since chemical shifts can now be intimately related to structure, and vice versa, it seems likely that many new applications to structure prediction, refinement, and validation will stem from these developments. Until recently, it was thought by many to be impossible to predict protein chemical shifts. However, the continuing revolution in computer/disk price/performance ratios now enables study of much larger fragments than heretofore possible. In the future, we believe that many such applications of 'biochemical shifts' and quantum chemistry will contribute greatly to our studies of lipid, protein, nucleic acid, and carbohydrate structure.

8 RELATED ARTICLES

Shielding Calculations: LORG and SOLO Approaches; Chemical Shift Scales on an Absolute Basis; Chemical Shift Tensor Measurement in Solids; Chemical Shift Tensors in Single Crystals; Shielding Calculations: IGLO Method; Shielding Calculations: Perturbation Methods; Shielding: Overview of Theoretical Methods; Shielding in Small Molecules; Shielding Tensor Calculations; Shielding Theory: GIAO Method.

9 REFERENCES

1. C. C. McDonald and W. D. Phillips, *J. Am. Chem. Soc.*, 1969, **91**, 1513.
2. A. Allerhand, R. F. Childers, and E. Oldfield, *Biochemistry*, 1973, **12**, 1335.
3. A. Bax, M. Ikura, L. E. Kay, D. A. Torchia, R. Tschudin, *J. Magn. Reson.*, 1991, **86**, 304.
4. G. M. Clore and A. M. Gronenborn, *Prog. Nucl. Magn. Reson. Spectros.*, 1991, **23**, 43.
5. A. C. de Dios, J. G. Pearson, and E. Oldfield, *Science*, 1993, **260**, 1491.
6. J. L. Markley, D. H. Meadows, and O. Jardetzky, *J. Mol. Biol.*, 1967, **27**, 25.
7. H. Sternlicht and D. Wilson, *Biochemistry*, 1967, **6**, 2881.
8. H. L. Tigelaar and W. H. Flygare, *J. Am. Chem. Soc.*, 1972, **94**, 343.

9. N. J. Clayden and R. J. P. Williams, *J. Magn. Reson.*, 1982, **49**, 383.
10. A. Pardi, G. Wagner, and K. Wuthrich, *Eur. J. Biochem.*, 1983, **137**, 445.
11. H. R. Kricheldorf, W. E. Hull, and D. Muller, *Macromolecules*, 1985, **18**, 2135.
12. H. Saito, R. Tabeta, A. Shoji, T. Ozaki, I. Ando, and T. Asakura, in *Magnetic Resonance in Biology and Medicine*, ed G. Govil, C. L. Khetrapal, A. Saran, Tata McGraw-Hill, New Delhi, 1985, pp. 195–215.
13. I. Ando, H. Saito, R. Tabeta, A. Shoji, and T. Ozaki, *Macromolecules*, 1984, **17**, 457.
14. S. Spera and A. Bax, *J. Am. Chem. Soc.*, 1991, **113**, 5490.
15. D. S. Wishart and B. D. Sykes, *J. Biomol. NMR*, 1994, **4**, 171.
16. G. C. Levy and R. L. Lichter, in *Nitrogen-15 NMR spectroscopy*, Wiley-Interscience, New York, 1979.
17. M. Witanowski, L. Stefaniak, G. A. Webb, *Annu. Rev. NMR Spectrosc.*, 1986, **18**, 65.
18. J. Glushka and D. Cowburn, *J. Am. Chem. Soc.*, 1987, **109**, 7879.
19. H. Le and E. Oldfield, *J. Biomol. NMR*, 1994, **4**, 341.
20. A. E. Tonelli, *J. Am. Chem. Soc.*, 1980, **102**, 7635.
21. B. R. Seavey, E. A. Farr, W. M. Westler, and J. L. Markley, *J. Biomol. NMR*, 1991, 217.
22. M. A. Jiménez, J. L. Nieto, J. Herranz, M. Rico, and J. Santoro, *FEBS Lett.*, 1987, **221**, 320.
23. L. Szilágyi and O. Jardetzky, *J. Magn. Reson.*, 1989, **83**, 441.
24. M. P. Williamson, *Biopolymers*, 1990, **29**, 1423.
25. A. Pastore and V. Saudek, *J. Magn. Reson.*, 1990, **90**, 165.
26. D. S. Wishart, B. D. Sykes, and F. M. Richards, *J. Mol. Biol.*, 1991, **222**, 311.
27. I. D. Kuntz, P. A. Kosen, and E. C. Craig, *J. Am. Chem. Soc.*, 1991, **113**, 1406.
28. K. Ösapay and D. A. Case, *J. Am. Chem. Soc.*, 1991, **113**, 9436.
29. M. P. Williamson and T. Asakura, *FEBS Lett.*, 1992, **302**, 185.
30. K. Ösapay and D. A. Case, *NATO Adv. Study Inst.*, ed. J. A. Tossel, Kluwer, Dordrecht, 1993, 572; D. A. Case and P. E. Wright, in *NMR of Proteins*, ed. G. M. Clore, and A. M. Gronenborn, Macmillan, New York, 1993, pp. 53–91.
31. A. C. de Dios and E. Oldfield, *Chem. Phys. Lett.*, 1993, **205**, 108.
32. A. D. Buckingham and K. P. Lawley, *Mol. Phys.*, 1960, **3**, 219.
33. J. D. Augspurger, C. E. Dykstra, and E. Oldfield, *J. Am. Chem. Soc.*, 1991, **113**, 2447.
34. C. J. Jameson and A. C. de Dios, in *Nuclear Magnetic Shieldings and Molecular Structure*, ed. J. A. Tossell, Kluwer, Dordrecht, 1993, pp. 95–116.
35. A. C. de Dios and C. J. Jameson, *Annu. Rep. NMR Spectrosc.*, 1994, **29**, 1.
36. R. Ditchfield, *J. Chem. Phys.*, 1972, **56**, 5688.
37. K. Wolinski, J. F. Hinton, and P. Pulay, *J. Am. Chem. Soc.*, 1990, **112**, 8251.
38. A. C. de Dios, J. G. Pearson, and E. Oldfield, *J. Am. Chem. Soc.*, 1993, **115**, 9768.
39. D. D. Laws, A. C. de Dios, and E. Oldfield, *J. Biomol. NMR*, 1993, **3**, 607.
40. L. A. Luck and J. J. Falke, *Biochemistry*, 1991, **30**, 4248.
41. C. Lian, H. Le, B. Montez, J. Patterson, S. Harrell, D. D. Laws, I. Matsumura, J. G. Pearson, and E. Oldfield, *Biochemistry*, 1994, **33**, 5238.
42. A. C. de Dios and E. Oldfield, *J. Am. Chem. Soc.*, 1994, **116**, 5307.
43. A. C. de Dios, D. D. Laws, and E. Oldfield, *J. Am. Chem. Soc.*, 1994, **116**, 7784.
44. D. W. Alderman, M. H. Sherwood, and D. M. Grant, *J. Magn. Reson.* 1993, **101**, 188.
45. C. Giessner-Prettre and B. Pullman, *Biochem. Biophys. Res. Commun.*, 1976, **70**, 578.
46. F. R. Prado and C. Giessner-Prettre, *J. Magn. Reson.*, 1982, **47**, 103.
47. M. Schindler, *J. Am. Chem. Soc.*, 1988, **110**, 6623.
48. M. Schindler and W. Kutzelnigg, *J. Chem. Phys.*, 1982, **76**, 1919.
49. D. M. Grant, J. C. Facelli, D. W. Alderman, and M. H. Sherwood, in *Nuclear Magnetic Shieldings and Molecular Structure*, ed. J. A. Tossell, Kluwer, Dordrecht, 1993, pp. 367–384.
50. H. Le, J. G. Pearson, A. C. de Dios, and E. Oldfield, *J. Am. Chem. Soc.*, 1995, **117**, 3800.
51. J. G. Pearson, E. Oldfield, F. S. Lee, and A. Warshel, *J. Am. Chem. Soc.*, 1993, **115**, 6851.

Acknowledgments

Work supported by NIH grant HL-19481.

Biographical Sketches

Angel C. de Dios. *b* 1965. B.S., 1985, Ateneo de Manila University, Philippines, Ph.D., 1992 (supervisor Cynthia Jameson), University of Illinois at Chicago, USA. Postdoctoral work at University of Illinois at Urbana-Champaign, USA (with Eric Oldfield). Postdoctoral research associate, University of Illinois at Urbana-Champaign, 1992–present. Approx. 20 publications. Research specialities: intra- and intermolecular effects on chemical shifts, gas phase NMR spectroscopy.

Eric Oldfield. *b* 1948. B.Sc., 1969, University of Bristol, Ph.D., 1972 (supervisor Dennis Chapman), University of Sheffield, D.Sc., 1982, University of Bristol, UK. Postdoctoral work at Indiana University, Bloomington (with Adam Allerhand) and Massachusetts Institute of Technology, Cambridge (with John S. Waugh). Professor, University of Illinois at Urbana-Champaign, 1975–present. Approx. 170 publications. Research specialties: inorganic and biochemical applications, especially proteins, membranes, and heterogeneous catalysts.

Electric Field Effects on Shielding Constants

W. T. Raynes
University of Sheffield, Sheffield, UK

1	Brief Historical Introduction	1
2	Theoretical Background	1
3	Calculation of Electric Field Coefficients	2
4	Electric Field Gradients	4
5	Applications	4
6	Conclusions	9
7	Related Articles	9
8	References	9

1 BRIEF HISTORICAL INTRODUCTION

The idea that electric fields could alter chemical shifts was first proposed by Schneider, Bernstein and Pople[1] to account for the 'association shifts' in hydrogen-bonded systems observed by proton magnetic resonance. To help confirm this notion a calculation of the electric field dependence of the nuclear shielding in the hydrogen atom was carried out by Marshall and Pople.[2] A more formal treatment of intermolecular interactions on chemical shifts which included the effects of electric fields was presented by Stephen.[3] A general formulation of the effect of a uniform electric field upon nuclear shielding was then given by Buckingham.[4] His treatment takes the shielding to second order in the electric field. Thus for the $\alpha\beta$ component of a nuclear shielding tensor $\boldsymbol{\sigma}$:

$$\sigma_{\alpha\beta} = \sigma^{(0)}_{\alpha\beta} + \sigma^{(1)}_{\alpha\beta\gamma} E_\gamma + \tfrac{1}{2}\sigma^{(2)}_{\alpha\beta\gamma\delta} E_\gamma E_\delta \qquad (1)$$

where $\sigma^{(0)}_{\alpha\beta}$ is a component of $\sigma^{(0)}$, the shielding tensor in the absence of the field $\boldsymbol{E}$, and $\sigma^{(1)}_{\alpha\beta\gamma}$ and $\sigma^{(2)}_{\alpha\beta\gamma\delta}$ are field-independent components of tensors $\boldsymbol{\sigma}^{(1)}$ and $\boldsymbol{\sigma}^{(2)}$. The Einstein summation convention is used in equation (1): the appearance of a suffix twice in a term denotes summation over all axes. Buckingham considered the effect of an electric field produced by a polar group within a molecule acting on a proton in another part of the same molecule and so contributing to the shielding change at that proton brought about by the introduction of the polar group. Upon averaging over all orientations of the molecule in the external magnetic field of the NMR spectrometer, but with the electric field held fixed relative to the molecule, the change in mean shielding was found to be:

$$\Delta\sigma = -AE_z - BE^2 \qquad (2)$$

The parameters A and B were characteristic of the X–H bond involving the proton of interest, and the negative signs were included explicitly in equation (2) to render A and B positive quantities since it was expected that an electric field along the z axis (from X to H) would lead to a reduction in shielding, as would the effect of the field at second order. In equation (2) the X–H bond is treated as cylindrically symmetric at first order and the electron distribution about the proton is treated as spherically symmetric at second order. Equation (2) frequently appears in textbooks and is referred to as 'the Buckingham equation'. Musher[5] offered some early calculations of the value of A for C–H bonds.

Electric fields were soon invoked to account in part for observed solvent effects on chemical shifts in liquids[6] and for the density dependence of nuclear shielding in gases.[7] To help explain the density dependence of the proton shielding in polar gases a statistical mechanical treatment using equation (2) was developed and this was supplemented by formulating the van der Waals contribution to the shielding as a mean electric field squared contribution $\bar{E}^2$ with a coefficient B identical with that in equation (2).[7] This appeared very successful for proton shielding in gases[7–10] and it was soon extended to ^{19}F shielding.[11,12]

Experimental results from NMR studies of both gases and solutions combined with the results of a number of semiempirical calculations meant that by 1972 it was possible to draw up a table of A and B values for protons and other nuclei in various bonding situations.[13] In the 1970s, attention switched to ^{13}C chemical shifts upon which electric field effects are more difficult to describe, partly because of the much greater lack of uniformity of the bonding situation at a carbon atom than at a hydrogen or fluorine atom, and partly because of the greater likelihood of the presence of through-bond effects which are intrinsically more difficult to formulate in mathematical terms. The only major theoretical attempt to study electric field effects on ^{13}C shielding was the semiempirical study by Seidman and Maciel.[14] There were, however, several good ab initio studies of electric field effects on the nuclear shielding in the small molecules H_2[15] and HF[16] during this period, together with some general studies by Aminova and Gubaidullina[17] and Mukhomorov[18] on C–H bonds.

In the 1980s, little was done on the subject apart from the important work of Volodicheva and Rebane,[19] but since 1990 the situation has been transformed. This is largely because good ab initio calculations of the electric field coefficients are now possible on small and medium-sized molecules. In addition, work on the changes in chemical shifts for different conformations of proteins has also stimulated interest. It seems likely that within a few years coefficients for the effects of uniform electric fields on nuclear shielding [i.e. the coefficients defined in equation (1)] will be available which even take account of electron correlation. The effects of electric field gradients may also be well understood.

2 THEORETICAL BACKGROUND

In the presence of a uniform magnetic field $\boldsymbol{B}_0$ there is an interaction between a nuclear magnetic moment $\boldsymbol{\mu}^{\mathrm{N}}$ in a molecule and the magnetic field. The energy of this interaction W is given by:

$$W = -\mu^{\mathrm{N}}_\alpha(\delta_{\alpha\beta} - \sigma_{\alpha\beta})B_{0\beta} \qquad (3)$$

where $\sigma_{\alpha\beta}$ is, as above, an element of the shielding tensor (see ***Chemical Shift Tensors***.). In the most general case

when the environment of the nucleus possesses no symmetry, nine independent coefficients are required to specify the nuclear shielding, since $\sigma_{\alpha\beta}$ is clearly not symmetric in α and β. Thus, for example, for the molecule CHFClBr nine independent coefficients are required to specify the magnetic field experienced by any one of the nuclei when the molecule is placed in an external field $\boldsymbol{B}_0$. For more symmetrical molecules fewer coefficients are required. The symmetry involved here is the so-called 'site symmetry' which may be the same or lower than the point group symmetry of the molecule. Table 1 gives some examples of site symmetry for the nuclei in several simple molecules. Table 2 shows the numbers of nonvanishing and of independent tensor components for all possible nuclear site symmetries.[20]

Table 1 Some Examples of Site Symmetry for Nuclei in Selected Compounds

	C	H	O	F
CH_4	T_d	C_{3v}	–	–
CO_2	$D_{\infty h}$	–	$C_{\infty v}$	–
HCCH	$C_{\infty v}$	$C_{\infty v}$	–	–
CH_3F	C_{3v}	C_s	–	C_{3v}
H_2CO	C_{2v}	C_s	C_{2v}	–
CH_2CCH_2	C-1, C_{2v} C-2, D_{2d}	C_s	–	–

When a uniform electric field is present, $\sigma_{\alpha\beta}$ is given by equation (1). The first requirement is to establish which of the components of the tensors $\boldsymbol{\sigma}^{(1)}$ and $\boldsymbol{\sigma}^{(2)}$ are nonzero for a particular nucleus. This also depends on the site symmetry at that nucleus. The answers can be obtained by using group theoretical techniques.[21]

For $\boldsymbol{\sigma}^{(1)}$ there are 27 nonvanishing, independent coefficients in the case of no site symmetry. Fewer exist when some site symmetry is present. This is made clear in Table 3, which lists all the nonvanishing components for all the main nuclear site symmetries. A more complete list is given elsewhere.[22] The axis systems used in obtaining the nonvanishing coefficients given in Table 3 are as follows: for the site symmetries C_{2v}, C_{3v}, and $C_{\infty v}$ the single axis of symmetry is chosen as the z axis; for the symmetries C_s, D_{2d}, and D_{3h} the plane or principal plane of symmetry is the xz plane. (This last choice differs from that used elsewhere.[22]) For T_d site symmetry any axis system can be chosen.

For $\boldsymbol{\sigma}^{(2)}$ there are 54 not 81, nonvanishing, independent coefficients in the general case since there is an intrinsic symmetry in the last two suffixes, i.e. $\sigma^{(2)}_{\alpha\beta\gamma\delta} = \sigma^{(2)}_{\alpha\beta\delta\gamma}$, even in the absence of any site symmetry. Table 4 lists the nonvanishing components of $\boldsymbol{\sigma}^{(2)}$ for some site symmetries. For components that are equal due to intrinsic symmetry only one is listed in the table. A more complete list is given elsewhere.[22]

In practice, as stated earlier, one needs to calculate the electric field dependence of the mean shielding σ_{E}, i.e. the dependence of the shielding averaged over all directions of the magnetic field but with the electric field kept fixed with respect to the molecule. One then has:

$$\sigma_{\mathrm{E}} = -A_\gamma F_\gamma - B_{\gamma\delta} F_\gamma F_\delta \tag{4}$$

where

$$A_\gamma = -\tfrac{1}{3}\sigma^{(1)}_{\alpha\alpha\gamma} \tag{5}$$

and

$$B_{\gamma\delta} = -\tfrac{1}{6}\sigma^{(2)}_{\alpha\alpha\gamma\delta} \tag{6}$$

The number of independent A and B parameters depends on the site symmetry as shown in Table 5 for some selected site symmetries. A more complete list is given elsewhere.[22] (It is to be noted that Table 4 in Raynes and Ratcliffe[22] omits a third quadratic coefficient B_{zz} for C_s symmetry.) Thus for C_s symmetry:

$$\sigma_{\mathrm{E}} = -A_x E_x - A_z E_z - B_{xx} E_x^2 - B_{yy} E_y^2 - B_{zz} E_z^2 - B_{xz} E_x E_z \tag{7}$$

whilst for C_{3v} and $C_{\infty v}$ symmetry

$$\sigma_{\mathrm{E}} = -A_z E_z - B_{xx} F_x^2 - B_{zz} F_z^2 \tag{8}$$

3 CALCULATION OF ELECTRIC FIELD COEFFICIENTS

The computation of the components of $\boldsymbol{\sigma}^{(1)}$ and $\boldsymbol{\sigma}^{(2)}$ for nuclei in specific molecules by quantum mechanical methods has only been systematically carried out since 1990. Before that, as stated above, only the nuclei in the hydrogen atom[2] and in the H_2 and HF molecules[15,16] had been studied at the ab initio level.

It is usual to recognize two stages in the ab initio calculation of molecular properties (see ***Shielding Calculations: Perturbation Methods***, ***Shielding: Overview of Theoretical Methods*** and ***Shielding in Small Molecules***). At the Hartree–Fock level—in practice the self-consistent field (SCF) level—the motion of each electron in the field of the atomic nuclei and a smoothed out field of all the other electrons is considered. It is at this level that most of the calculations of the electric field coefficients are carried out. The second stage involves taking into account 'electron correlation', the additional contributions arising from the interactions between individual electrons which are not included at the SCF level. A few calculations on small molecules in uniform electric fields in which some electron correlation was included have been performed.[23,24] They show that electron correlation does make a significant contribution to the coefficients, especially those at the quadratic level. At any level of calculation it is essential to use large basis set wavefunctions.

Results at the SCF level for the tensor component of $\boldsymbol{\sigma}^{(1)}$ and $\boldsymbol{\sigma}^{(2)}$ for nuclei in a wide variety of molecules have been calculated with large basis set wavefunctions by Grayson and Raynes.[25–28] Table 6 presents just a few of these results for carbon shielding possessing $C_{\infty v}$ and C_{3v} site symmetries in some simple molecules.[26] In all these cases the z axis is directed from the carbon nucleus of interest along the axis of symmetry towards the proton attached to that carbon (for C_2H_2 and HCN) or towards the plane containing the three protons (for CH_3CN and CH_3F). For C_{3v} symmetry the xz

Table 2 Nonvanishing Components of $\sigma^{(0)}$ for Various Nuclear Site Symmetries

	Total	Independent	Nonvanishing components
C_1, C_i	9	9	All nine
C_2, C_s, C_{2h}	5	5	$\sigma_{xx}^{(0)}; \sigma_{yy}^{(0)}; \sigma_{zz}^{(0)}; \sigma_{xz}^{(0)}; \sigma_{zx}^{(0)}$
C_3, C_{3h}, C_4, C_{4h}, C_6, C_{6h}, S_4, S_6	5	3	$\sigma_{xx}^{(0)} = \sigma_{zz}^{(0)}; \sigma_{xz}^{(0)} = -\sigma_{zx}^{(0)}; \sigma_{yy}^{(0)}$
C_{2v}, D_2, D_{2h}	3	3	$\sigma_{xx}^{(0)}; \sigma_{yy}^{(0)}; \sigma_{zz}^{(0)}$
C_{3v}, C_{4v}, C_{6v}, $C_{\infty v}$, D_{2d}, D_3, D_{3d}, D_{3h}, D_4, D_{4h}, D_6, D_{6h}, $D_{\infty h}$	3	2	$\sigma_{xx}^{(0)} = \sigma_{yy}^{(0)}; \sigma_{zz}^{(0)}$
T, T_h, T_d, O, O_h, K_h	3	1	$\sigma_{xx}^{(0)} = \sigma_{yy}^{(0)} = \sigma_{zz}^{(0)}$

Table 3 Nonvanishing Components of the Tensor $\sigma^{(1)}$ for Some Nuclear Site Symmetries[a]

Site symmetry	No. of nonvanishing components Total	Independent	Nonvanishing components
C_s	14	14	$\sigma_{xxx}^{(1)}; \sigma_{xyy}^{(1)}; \sigma_{yxy}^{(1)}; \sigma_{yyx}^{(1)}; \sigma_{xxz}^{(1)}; \sigma_{xzx}^{(1)}; \sigma_{xzz}^{(1)}; \sigma_{zzz}^{(1)}; \sigma_{zyy}^{(1)}; \sigma_{yzy}^{(1)}; \sigma_{yyz}^{(1)}; \sigma_{zzx}^{(1)}; \sigma_{zxz}^{(1)}; \sigma_{zxx}^{(1)}$
C_{2v}	7	7	$\sigma_{xxz}^{(1)}; \sigma_{yyz}^{(1)}; \sigma_{xzx}^{(1)}; \sigma_{yzy}^{(1)}; \sigma_{zxx}^{(1)}; \sigma_{zyy}^{(1)}; \sigma_{zzz}^{(1)}$
C_{3v}	11	5	$\sigma_{xyy}^{(1)} = \sigma_{yxy}^{(10)} = \sigma_{yyx}^{(1)} = -\sigma_{xxx}^{(1)}; \sigma_{xxz}^{(1)} = \sigma_{yyz}^{(1)}; \sigma_{xzx}^{(1)} = \sigma_{yzy}^{(1)}; \sigma_{zxx}^{(1)} = \sigma_{zyy}^{(1)}; \sigma_{zzz}^{(1)}$
$C_{\infty v}$	7	4	$\sigma_{xxz}^{(1)} = \sigma_{yyz}^{(1)}; \sigma_{xzx}^{(1)} = \sigma_{yzy}^{(1)}; \sigma_{zxx}^{(1)} = \sigma_{zyy}^{(1)}; \sigma_{zzz}^{(1)}$
D_{2d}	6	3	$\sigma_{xxz}^{(1)} = -\sigma_{yyz}^{(1)}; \sigma_{xzx}^{(1)} = -\sigma_{yzy}^{(1)}; \sigma_{zxx}^{(1)} = -\sigma_{zyy}^{(1)}$
T_d	6	1	$\sigma_{xyz}^{(1)} = \sigma_{yzx}^{(1)} = \sigma_{zxy}^{(1)} = \sigma_{zyx}^{(1)} = \sigma_{yxz}^{(1)} = \sigma_{xzy}^{(1)}$
D_{3h}	4	1	$\sigma_{xzz}^{(1)} = \sigma_{zxz}^{(1)} = \sigma_{zzx}^{(1)} = -\sigma_{xxx}^{(1)}$
C_i, D_{2h}, D_{6h}, D_{3d}, T_h, O_h, K_h	0	0	None

[a]The axis systems used for the various site symmetries are given in the text.

Table 4 Nonvanishing Components of the Tensor $\sigma^{(2)}$ for Some Nuclear Site Symmetries

Site symmetry	No. of nonvanishing components Total	Independent	Nonvanishing components
C_s	41	28	$\sigma_{xxxx}^{(2)}; \sigma_{xxxz}^{(2)}; \sigma_{xzxx}^{(2)}; \sigma_{zxxx}^{(2)}; \sigma_{xxzz}^{(2)}; \sigma_{xzxz}^{(2)}; \sigma_{zzzz}^{(1)}; \sigma_{zzzx}^{(2)}; \sigma_{zxzz}^{(2)}; \sigma_{xzzz}^{(2)}; \sigma_{zzxx}^{(2)}; \sigma_{zxzx}^{(2)}; \sigma_{xxyy}^{(2)}; \sigma_{xyxy}^{(2)}; \sigma_{yyxx}^{(2)}; \sigma_{yxyx}^{(2)}; \sigma_{zzyy}^{(2)}; \sigma_{zyzy}^{(2)}; \sigma_{yyzz}^{(1)}; \sigma_{yzyz}^{(2)}; \sigma_{xzyy}^{(1)}; \sigma_{zyyx}^{(2)}; \sigma_{yxzy}^{(2)}; \sigma_{yyxz}^{(2)}; \sigma_{xzyy}^{(2)}; \sigma_{xyyz}^{(2)}; \sigma_{yzxy}^{(2)}; \sigma_{yyyy}^{(2)}$
C_{2v}	21	15	$\sigma_{xxxx}^{(2)}; \sigma_{xxyy}^{(2)}; \sigma_{xyxy}^{(2)}; \sigma_{xzxz}^{(2)}; \sigma_{zxzx}^{(2)}; \sigma_{zzxx}^{(2)}; \sigma_{xxzz}^{(2)} \sigma_{yyyy}^{(2)}; \sigma_{yyxx}^{(2)}; \sigma_{yxyx}^{(2)}; \sigma_{yzyz}^{(2)}; \sigma_{zyzy}^{(2)}; \sigma_{zzyy}^{(2)}; \sigma_{yyzz}^{(2)} \sigma_{zzzz}^{(2)}$
C_{3v}	37	10	$\sigma_{xxxx}^{(2)} = \sigma_{yyyy}^{(2)}; \sigma_{xxyy}^{(2)} = \sigma_{yyxx}^{(2)}; \sigma_{xyxy}^{(2)} = \frac{1}{2}(\sigma_{xxxx}^{(2)} - \sigma_{xxyy}^{(2)}) = \sigma_{yxyx}^{(2)}; \sigma_{zzzz}^{(2)}; \sigma_{yyxz}^{(2)} = \sigma_{yxyz}^{(2)} = \sigma_{xyyz}^{(2)} = -\sigma_{xxxz}^{(2)}; \sigma_{yzyx}^{(2)} = \sigma_{xzyy}^{(2)} = -\sigma_{xzxx}^{(2)}; \sigma_{zyyx}^{(2)} = \sigma_{zxyy}^{(2)} = -\sigma_{zxxx}^{(2)}; \sigma_{xzxz}^{(2)} = \sigma_{yzyz}^{(2)}; \sigma_{xxzz}^{(2)} = \sigma_{yyzz}^{(2)}; \sigma_{zxzx}^{(2)}; \sigma_{zyxy}^{(2)}; \sigma_{zzxx}^{(2)} \sigma_{zzyy}^{(2)}$
D_{3h}, $C_{\infty v}$, $D_{\infty h}$	21	7	$\sigma_{xxxx}^{(2)} = \sigma_{yyyy}^{(2)}; \sigma_{xxyy}^{(2)} = \sigma_{yyxx}^{(2)}; \sigma_{xyxy}^{(2)} = \frac{1}{2}(\sigma_{xxxx}^{(2)} - \sigma_{xxyy}^{(2)}) = \sigma_{yxyx}^{(2)}; \sigma_{xxzz}^{(2)} = \sigma_{yyzz}^{(2)}; \sigma_{xxxz}^{(2)} = \sigma_{yzyz}^{(2)}; \sigma_{zzxx}^{(2)} = \sigma_{zzyy}^{(2)}; \sigma_{zxzx}^{(2)} = \sigma_{zyzy}^{(2)}; \sigma_{zzzz}^{(2)}$
T_d, O_h	21	3	$\sigma_{xxxx}^{(2)} = \sigma_{yyyy}^{(2)} = \sigma_{zzzz}^{(2)}; \sigma_{xxzz}^{(2)} = \sigma_{zzyy}^{(2)} = \sigma_{xxyy}^{(2)} = \sigma_{yyxx}^{(2)} = \sigma_{zzxx}^{(2)} = \sigma_{xzxz}^{(2)} = \sigma_{yzyz}^{(2)} = \sigma_{yxyx}^{(2)} = \sigma_{xyxy}^{(2)} = \sigma_{zyzy}^{(2)} = \sigma_{zxzx}^{(2)}$
K_h	21	2	$\sigma_{xxxx}^{(2)} = \sigma_{yyyy}^{(2)} = \sigma_{zzzz}^{(2)}; \sigma_{yzyz}^{(2)} = \sigma_{xzxz}^{(2)} = \sigma_{xyxy}^{(2)} = \frac{1}{2}(\sigma_{xxxx}^{(2)} - \sigma_{xxyy}^{(2)}) = \sigma_{yxyx}^{(2)} = \sigma_{zxzx}^{(2)} = \sigma_{zyzy}^{(2)}; \sigma_{xxyy}^{(2)} = \sigma_{yyzz}^{(2)} = \sigma_{xxzz}^{(2)} = \sigma_{zzyy}^{(2)} = \sigma_{yyxx}^{(2)}$

[a] The axis systems used for the various site symmetries are given in the text.

Table 5 Nonvanishing Linear and Quadratic Coefficients for the Mean Shielding of a Nucleus for Different Site Symmetries

Site symmetry	Linear	Quadratic
C_s	A_x, A_z	B_{xx}, B_{yy}, B_{zz}, B_{xz}
C_{2v}	A_z	B_{xx}, B_{yy}, B_{zz}
C_{3v}, $C_{\infty v}$	A_z	$B_{xx} = B_{yy}$, B_{zz}
T_d, K_h	None	$B_{xx} = B_{yy} = B_{zz}$

Table 6 Values (ppm a.u.) of Components of the Tensors $\sigma^{(1)}$ and $\sigma^{(2)}$ for the Shielding of Carbon Nuclei Possessing C_{3v} Site Symmetry

	C_2H_2	HCN	$CH_3\underline{C}N$	$\underline{C}H_3CN$	CH_3F
$\sigma^{(1)}_{xxx}$	0	0	18.4	−38.8	86.9
$\sigma^{(1)}_{xxz}$	−1025.8	−620.3	−880.3	−29.2	−343.2
$\sigma^{(1)}_{zzz}$	−56.5	−45.3	−133.1	148.5	20.3
$\sigma^{(2)}_{xxxx}$	−542.0	−998.5	−378.1	−642.8	−1107.8
$\sigma^{(2)}_{xxyy}$	2659.0	3855.5	1922.0	−1584.8	−2949.6
$\sigma^{(2)}_{xxzz}$	−1619.8	2299.3	−622.1	−1397.8	−2489.6
$\sigma^{(2)}_{zzxx}$	−2815.5	−1112.5	−1205.3	−956.1	−1547.8
$\sigma^{(2)}_{zzzz}$	−258.8	−129.8	9.5	2080.7	828.3

plane contains a C–H bond. It can be seen that for both $\boldsymbol{\sigma}^{(1)}$ and $\boldsymbol{\sigma}^{(2)}$ components vary widely between molecules (e.g. $\sigma^{(2)}_{xxyy}$ for the five carbon nuclei in Table 6).

Table 7 gives all results for the A and B coefficients of proton shielding so far obtained by calculation at the SCF level, except for some of the earlier results for H_2, HF, and CH_3F[29] which have now been superseded by those given. For all unreferenced results in Table 7 with $C_{\infty v}$ and C_{3v} site symmetries the proton of interest lies on the z axis and has the most positive z coordinate of all nuclei present; for C_s site symmetries (i.e. when A_x and B_{xz} differ from zero) the z axis is directed along the X–H bond towards the proton and the positive x axis points towards the other proton (or protons) present. Except where indicated, all the results in Table 7 are taken from two papers by Raynes and Grayson.[27,28] Augspurger, Dykstra and co-workers[30,31] chose the z axis (referred to by them as the x axis) always to lie along molecule symmetry axes. In all their calculations the electric field was directed along this axis.

Table 8 gives ab initio SCF results so far obtained for the shielding of carbon and several other nuclei. Earlier results for HF[16] and CH_3F[29] have now been superseded by those given in Table 8. For $C_{\infty v}$ and C_{3v} site symmetries the z axes of the molecules in Table 8 are taken along the principal symmetry axis, with the molecule arranged so that protons lie on the positive z axis or that the nearest protons to the nucleus of interest lie on the positive z axis. For C_{2v} site symmetry the z axis is along the two-fold axis towards the proton with the xz plane being that of the molecule. Except where indicated, all results in Table 8 are taken from two papers by Grayson and Raynes.[25,26]

All the results in Table 6, 7 and 8 are given in units of ppm a.u.; these units are commonly used by workers who calculate the coefficients ab initio. For applications one must convert first to SI units. The appropriate conversion factors are 1 ppm a.u. = 1.94469×10^{-18} m V^{-1} for the linear coefficients and 1 ppm a.u = 3.78182×10^{-30} m^2 V^{-2} for the quadratic coefficients. Two other useful conversion factors are those from c.g.s. units (i.e. e.s.u.) to SI units which involve multiplying A values by 0.33357×10^{-4} and B values by 0.1113×10^{-8}, and those from c.g.s. units (or e.s.u.) to ppm a.u. which require linear coefficients to be multiplied by 17.153×10^{12} and quadratic coefficients by 2.943×10^{20}.

As mentioned earlier, electron correlation, which is not very important for the shielding constants, makes substantial contributions to the electric field coefficients, especially at second order. This has been established by the work of Bishop and Cybulski[24] who used second order Møller–Plesset (MP2) theory to include the effects of correlation. Some of their results are presented in Table 9, where a comparison with SCF results obtained from the same basis set is made. The signs of A are positive for all nuclei in Table 9, indicating that the nucleus of interest lies on the z axis with the other nucleus having a less positive z coordinate.

4 ELECTRIC FIELD GRADIENTS

The electric fields encountered at the molecular level are highly nonuniform, and therefore it is necessary to study the effects of electric field gradients on nuclear shielding. This was first done by Buckingham and Lawley[32] for a hydrogen atom in a uniform field gradient. They found that the contribution due to the field gradient should normally be negligible compared with the quadratic electric field effect.

Later, Batchelor[33,34] invoked the importance of electric field gradients to explain ^{13}C shielding changes brought about by the protonation of amino acids and peptides. Although an improved agreement between theory and experiment was achieved by the introduction of field gradients, an insufficient number of cases was studied to establish with certainty that field gradients cannot be ignored. Augspurger and Dykstra[30] calculated the coefficients of magnetic shielding for a range of nuclei in a number of simple axially symmetric molecules with the field gradient along the axis of symmetry. As with the A and B coefficients, the field gradient coefficients C are very sensitive to the bonding for a particular nuclear species.

5 APPLICATIONS

So far our concern has been with the general theory of the electric field dependence of shielding and with the coefficients which multiply the various components of the electric field. We now turn to the electric fields themselves. This introduces the problems to which the theory can be applied. It is convenient to divide these applications into several areas in which the treatments are of, perhaps, decreasing order of sophistication. These are, first, the area of intermolecular interactions in gases where the interaction between a pair of molecules is involved. The second one is that of solvent effects in liquids where dielectric theories are used to introduce the idea of a 'reaction field'. However, models based upon interactions between individual pairs of molecules—the so-called 'cage-models'—are also used for liquids. A third area is that of intramolecular electric fields due to the introduction of a polar group in a molecule. Difficulties arise here because of the problems of other shielding contributions such as magnetic anisotropy effects or through-bond effects. Another area is that of electric fields in solids. We first consider gases.

Table 7 Values (ppm a.u.) of the *A* and *B* Parameters for the Shielding of Protons in the Hydrogen Atom and in Some Simple Molecules Obtained by ab initio Calculation at the SCF Level[a]

	A_x	A_z	B_{xx}	B_{yy}	B_{zz}	B_{xz}
H atom	0	0	217.0[2]	217.0[2]	217.0[2]	0
H_2	0	41.2,[19] 50.5,[23] 50.3[30]	93.2[23]	93.2[23]	92.9,[23] 93.9[30]	0
CH_4	0	80.2, 45.1[30]	80.5	80.5	−7.7, 57.2[30]	0
NH_3	−8.0	89.8, 27.7[30]	135.1	119.0	−84.1, 139.2[30]	49.7
H_2O	−10.7	91.0, 47.3[30]	114.4	97.2	−152.2, 40.2[30]	−17.5
HF	0	49.5,[19] 79.4,[23] 83.5, 81.5[30]	40.1, 51.9[23]	40.1, 51.9[23]	−157.4, 162.5,[23] −164.3[30]	0
SiH_4	0	61.9, 35.8[30]	118.8	111.8	198.7, 138.2[30]	0
PH_3	−5.6	93.0	100.4	121.0	107.2	28.9
H_2S	−7.7	108.2	135.1	172.9	−83.9	−10.3
HCl	0	101.9,[19] 117.9	89.3	89.3	−172.3	0
HBr	0	110.7[19]				
HI	0	137.6[19]				
C_2H_6	4.0	93.8	102.5	161.9	−10.4	29.4
CH_3F	5.6	62.0	63.9	108.5	−22.7	
CH_3Cl	17.7	67.8	128.7	96.1	15.3	48.3
CH_3CN	3.5	71.6	140.9		19.6	126.0
C_2H_4	36.9	66.7	121.8	76.6	18.3	−11.0
C_6H_6		87.5				
H_2CO	0.9	12.1, 0.1[30]	103.6	44.2	−311.0, 237.3[30]	
HCN	0	54.9, 54.1[30]	26.9	26.9	66.2, 86.6[30]	0
C_2H_2	0	70.1, 67.2[30]	71.3	71.3	−191.0, 6.8[30]	0

[a]Except where explicitly indicated, all results have been taken from the papers of Grayson and Raynes.[27,28] The various axis systems used by authors are defined in the text; the systems differ in some cases (CH_4, NH_3, H_2O, SiH_4, C_2H_4, and H_2CO).

Table 8 Values (ppm a.u.) of the *A* and *B* Parameters for the Shielding of Carbon Nuclei and a Variety of other Nuclei in Some Simple Molecules Obtained by Ab Initio Calculation at the SCF Level[a]

	Nucleus	A_z	B_{xx}	B_{yy}	B_{zz}
CH_4	C	0	134.8, 179.9[30]	134.8, 179.9[30]	134.8, 179.9[30]
C_2H_6	C	−49.2	1722.9	1722.9	639.5
C_2H_4	C	1144.5[31]	671.7	−1017.7	217.1
C_2H_2	C	750.7, 733.9[30]	116.4	116.4	583.1, 553.5[30]
C_6H_6	C	645.0[31]			
HCN	C	428.6, 422.6[30]	−290.8	−290.8	−744.8, −751.5[30]
$CH_3\underline{C}N$	C	631.2	56.4	56.4	205.8
$\underline{C}H_3CN$	C	−30.0	530.6	530.6	119.2
CH_3F	C	222.0	934.2	934.2	691.8
H_2NCHO	C	215.9[31]			
H_2CO	C	697.4,[30] 769.0	59.4	−842.8	−1977.5, 1937.5[30]
CO	C	376.9[23], 374.5[30]	−1373.8[23]	−1373.8[23]	224.1,[23] 267.8[30]
HCN	N	−1927.0, −1910.1[30]	651.2	651.2	5667.0, 5668.1[30]
CH_3CN	N	−2093.7	−84.1	−84.1	6495.9
N_2	N	1051.7[23]	−294.7[23]	−294.7[23]	1380.6[23]
NH_3	N	−87.7, −50.8[30]	762.2	762.2	−529.0, −806.7[30]
H_2NCHO	N	902.8[31]			
H_2O	O	−381.6, −401.1[30]	2946.1	−363.3	2074.0, 2169.7[30]
CO	O	1561.5,[23] 1526.7[30]	1312.9[23]	1312.9[23]	2968.8,[23] 2953.1[30]
H_2CO	O	−6555.3, −7018.9[31]	6076.5	15172.7	23931.0, 35421.5[30]
H_2NCHO	O	3195.7[31]			
CH_3F	F	−505.2, −597.1,[23] −551.4[31]	2366.1	2366.1	5343.3
HF	F	−585.5, −597.1,[23] 636.5[30]	224.0, 240.8[23]	224.0, 240.8[23]	3837.4, 3880.3,[23] 4243.1[30]
SiH_4	Si	0	−3290.5, −3469.8[30]	−3290.5, 3469.8[30]	−3290.5, −3469.8[30]
PH_3	P	181.5	−3365.3	−3365.3	−7828.8
H_2S	S	−534.1	−1578.8	−2206.6	2677.8
HCl	Cl	−1149.8	−1590.8	−1590.8	5682.3

[a]The axis systems used are defined in the text. Except where explicitly indicated all results have been taken from the papers of Grayson and Raynes.[25,26]

Table 9 Electric Field Coefficients (ppm a.u.) of Nuclear Shielding for H_2, N_2, HF, and CO Calculated at the SCF and MP2 Levels of Theory

		H_2	N_2	HF		CO	
				H	F	C	O
A	SCF	50.45	1051.7	79.42	597.1	376.9	1561.5
	MP2	49.4	777.0	79.08	490.2	393.6	1242.4
B_{xx}	SCF	93.2	−294.7	51.9	241.4	−1372.7	1315.0
	MP2	94.5	−1029.6	75.5	263.3	−1522.2	448.3
B_{zz}	SCF	92.9	1378.1	−162.5	3880.0	231.7	2970.0
	MP2	95.6	796.8	−134.6	3061.5	−143.2	540.0

[a] The origin of the vector potential was taken at the nucleus of interest.

5.1 Binary Interactions in Gases

The nuclear shielding in a gas varies with the density (see also ***Gases at High Pressure*** and ***Gas Phase Studies of Chemical Exchange Processes***). In most cases there is a linear dependence, so that one may write formally:[35]

$$\sigma = \sigma_0 + \sigma_1 / V_m \tag{9}$$

where σ_0 is the shielding at very low density and V_m is the molar volume. For a gas mixture of two components labeled 1, which contains the nucleus of interest, and 2, one has:

$$\sigma_1 = x\sigma_1^{(11)} + (1-x)\sigma_1^{(12)} \tag{10}$$

where x is the mole fraction of species 1. The term $\sigma_1^{(11)}$ allows for the interactions of molecule 1 with a like molecule and $\sigma_1^{(12)}$ that with a molecules of species 2. We shall proceed to work with $\sigma_1^{(12)}$, since $\sigma_1^{(11)}$ is just a special case of it. $\sigma_1^{(12)}$ is made up of four contributions:

$$\sigma_1^{(12)} = (\sigma_1)_b + (\sigma_1)_a + (\sigma_1)_E + (\sigma_1)_w \tag{11}$$

where $(\sigma_1)_b$ and $(\sigma_1)_a$ are the bulk susceptibility and magnetic anisotropy contributions which do not involve electric fields; these can be accurately calculated,[6,7] if the magnetic susceptibility and the magnetic susceptibility anisotropy of molecule 2 are known. $(\sigma_1)_E$ is the 'polar effect' due to the electric fields arising from the permanent electric dipole and quadrupole moments in 2. $(\sigma_1)_w$ is the van der Waals contribution and is usually described by an electric field squared, which involves the B parameters previously considered.

We first examine $(\sigma_1)_E$. Let us consider both molecules 1 and 2 to be axially symmetric and to be arranged as shown in Figure 1. For the particular orientation shown, the change in shielding of a nucleus in molecule 1 (assumed to lie on the molecular axis) due to the permanent and induced electric dipole and the permanent quadrupole moments of 2, using equation (2), is

$$(\sigma_{pair})_E = -AE_z - BE^2 \tag{12}$$

where E_z is the electric field along the molecular axis of 1 and E^2 is the square of the electric field at 1. In equation (12) we assume that the electric field due to 2 is uniform at molecule 1 so that the coefficients A and B can be used. We also assume that the distinction between $B_\parallel$ and $B_\perp$ can be ignored. Then[7]

$$\begin{aligned} E_z = {} & -\mu_2 r^{-3}(2\cos\theta_1\cos\theta_2 + \sin\theta_1\sin\theta_2\cos\phi) + \mu_1\alpha_2 r^{-6} \\ & \times(3\cos^2\theta_1 + 1) - \tfrac{3}{2}\Theta_2 r^{-4} \\ & \times[\cos\theta_1(3\cos^2\theta_2 - 1) + 2\sin\theta_1\sin\theta_2\cos\theta_2\cos\phi] \end{aligned} \tag{13}$$

where μ_1 and μ_2 are the permanent dipole moments of 1 and 2, respectively, and α_2 and Θ_2 are the mean polarizability and electric quadrupole moment, respectively, of 2. We assume that the molecular polarizability is isotropic. The square of the total field at molecule 1 is:

$$\begin{aligned} E^2 = {} & \mu_2^2 r^{-6}(3\cos^2\theta_2 + 1) - 2\mu_1\mu_2\alpha_2 r^{-9} \\ & \times(8\cos\theta_1\cos\theta_2 + \sin\theta_1\sin\theta_2\cos\phi) + \tfrac{9}{4}\Theta_2^2 r^{-8} \\ & \times(1 - 2\cos^2\theta_2 + 5\cos^4\theta_2) \end{aligned} \tag{14}$$

$(\sigma_1)_E$ and $(\sigma_{pair})_E$ are related[7,35] through the expression:

$$(\sigma_1)_E = \frac{1}{2}N\int(\sigma_{pair})_E \exp(-u/kT)\,d\tau \tag{15}$$

where u is the intermolecular potential and N is the Avogadro constant; u is usually represented by the Stockmayer potential which is the sum of a Lennard–Jones (6–12) potential and the interaction energy of two dipoles, viz.:

$$\begin{aligned} u = {} & 4\varepsilon_0\left[\left(\frac{r_0}{r}\right)^{12} - \left(\frac{r_0}{r}\right)^{6}\right] + \mu_1\mu_2 r^{-3} \\ & \times(2\cos\theta_1\cos\theta_2 + \sin\theta_1\sin\theta_2\cos\phi) \end{aligned} \tag{16}$$

where

$$\tau = \mu_1\mu_2/\varepsilon_0 r_0^3 \tag{17}$$

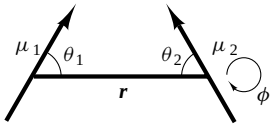

Figure 1 Orientation of axially symmetric molecules 1 and 2

and

$$y = 2(\varepsilon_0/kT)^{\frac{1}{2}} \tag{18}$$

The integration in equation (15) is taken over all mutual orientations and distances of separation. It can be carried out analytically and leads to the functions[36]

$$H_n(y) = y^{\frac{27-n}{6}} \sum_{k=0}^{\infty} \Gamma\left(\frac{6k+n-3}{12}\right) \frac{y^k}{k!} \tag{19}$$

The final result is

$$\begin{aligned}(\sigma_1)_{\mathrm{E}} = & -(\pi NA/6y^2)\{\mu_2[(\tau/3)H_6(y) + (y^4\tau^3/200)H_{12}(y) + \dots] \\ & + (4\mu_1\alpha_2/r_0^3y^2)[H_6(y) + (\tau^2y^4/40)H_{12}(y) + \dots] \\ & + (2\mu_1\Theta_2^2/y^2kTr_0^5)[H_8(y) + \dots]\} \\ & - (\pi NB/3y^4)\{(2\mu_2^2/r_0^3)[H_6(y) + (\tau^2y^4/40)H_{12}(y) + \dots] \\ & + (\mu_1\mu_2\alpha_2/r_0^6)[y^2\tau H_{12}(y) + (y^6\tau^3/60)H_{18}(y) + \dots] \\ & + 3(\Theta_2^2/r_0^5)[H_8(y) + \dots] + \dots\}\end{aligned} \tag{20}$$

Equation (20) is the expression that has been used for the polar effect. As stated above it involves assuming that (a) the polarizability of molecule 2 is isotropic, (b) that $B_{\parallel} = B_{\perp}$, and (c) that u can be described by the Stockmayer potential. At the time of writing these assumptions are being relaxed and the author expects to obtain improved expressions in the near future. Even after this improvement the uniform field approximation [equation (8)] is still required. It has been difficult to establish the validity of equation (20) since, until recently, good values of A and B were not available and it is even more difficult (as discussed below) to formulate the van der Waals contribution which is always present.

$(\sigma_1)_{\mathrm{w}}$ is regarded as being due to the fluctuating electric fields of instantaneous electric dipoles in 2 which average to zero but the mean square of which does not average to zero. Thus[7]

$$(\sigma_{\mathrm{pair}})_{\mathrm{w}} = -B\overline{E^2} \tag{21}$$

where B is identified with B in equation (20). For $\overline{E^2}$ the expression

$$\overline{E^2} = 3\alpha_2 I_2/r^6 \tag{22}$$

has been widely used, where I_2 is the ionization potential of 2. Substitution of equation (22) into equation (21) and replacement of $(\sigma_{\mathrm{pair}})_{\mathrm{E}}$ by $(\sigma_{\mathrm{pair}})_{\mathrm{w}}$ in equation (15) leads to

$$\begin{aligned}(\sigma_1)_{\mathrm{w}} = & -(\pi NB/y^4r_0^3)\alpha_2 I_2\{H_6(y) \\ & + (\tau^2/48)y^4H_{12}(y) + \dots\}\end{aligned} \tag{23}$$

All early values of A and B obtained from experiment were found by fitting equation (11) to the experimental data for which the only unknowns were A and B. Although, as stated above, it is difficult to test equation (20) because of the ubiquitous van der Waals forces, it is possible to test equation (23) since one can study systems for which permanent dipole and quadrupole moments are absent, leaving only $(\sigma_1)_{\mathrm{w}}$, and hence B, to be determined.

This has been done using methane as the test molecule. The density dependences of both the ^{1}H and ^{13}C shielding must involve only $(\sigma_1)_{\mathrm{w}}$ after correction for $(\sigma_1)_{\mathrm{b}}$. Values of $(\sigma_1)_{\mathrm{w}}$ have been measured for both resonances over a very wide temperature range.[37,38] It is found that the temperature dependences of $(\sigma_1)_{\mathrm{w}}$ for both resonances are substantially greater than predicted by the factor $H_6(y)/y^4$ in equation (23) and that the magnitudes of $(\sigma_1)_{\mathrm{w}}$, especially for the ^{13}C shielding, are many times greater than predicted using calculated B values (see Raynes[39] Table 3). It would appear that a mean square field model is unable to account for the observed results.

5.2 Interactions in Liquids

In the liquid phase we again have shielding changes due to the fields of permanent electric moments and those associated with van der Waals forces. In the former case it is usual to separate the situation when the solute molecule, which contains the nucleus of interest, has a permanent electric moment and the surrounding solvent molecules do not, from that in which the solvent molecules themselves also possess permanent electric dipole (or perhaps quadrupole) moments. When the solvent and solute molecules both possess permanent moments one is approaching the area of complex formation, including hydrogen bonding. This is usually treated not in terms of electric fields but in terms of chemical equilibrium theory.

For polar solutes in nonpolar solvents 'reaction field' theory is usually applied. This originates from the Onsager model.[40] The application to chemical shifts was first made by Buckingham et al.[6] They treated the solute molecule as a point dipole at the center of a spherical polarizable cavity surrounded by the solvent which is taken to be a dielectric continuum of dielectric constant ϵ. The point dipole polarizes the neighboring solvent medium and this leads to a uniform 'reaction field' $\boldsymbol{E}_{\mathrm{R}}$ across the cavity parallel to the point dipole $\boldsymbol{\mu}$. This gives

$$\boldsymbol{E}_{\mathrm{R}} = \frac{2(\varepsilon-1)(n^2-1)}{3(2\varepsilon+n^2)}\frac{\boldsymbol{\mu}}{\alpha} \tag{24}$$

where n is the solvent refractive index and α is the polarizability of the solvent molecule.

Diehl and Freeman[41] improved the model by considering the cavity to be nonspherical. They obtained

$$\boldsymbol{E}_R = \frac{\boldsymbol{\mu}}{abc}3\xi_a[1 + (n^2-1)\xi_a]\frac{\varepsilon-1}{\varepsilon + (n^2\xi_a/1-\xi_a)} \tag{25}$$

where

$$\xi_a = \frac{1}{2}abc\int_0^{\infty}\frac{\mathrm{d}\lambda}{(a^2+\lambda)^{\frac{3}{2}}(b^2+\lambda)^{\frac{1}{2}}(c^2+\lambda)^{\frac{1}{2}}} \tag{26}$$

and a, b and c are the axes of the cavity ellipsoid. Diehl and Freeman chose the proton shielding in acetonitrile and paraldehyde to test equation (25). They found that widely

different values of the parameter A for the C–H bonds in these molecules had to be used before equation (24) would agree with the experimental results. However, with equation (25) they found that very similar values of A (viz. A = 3.0 and 3.4 c.g.s. units) gave good agreement. They concluded that equation (25) was to be preferred. What they could not know was that their A values are in good agreement with the modern calculated values of A in 'normal' C–H bonds. Their mean value of A, viz. 3.2 c.g.s. units, is equivalent to 55 ppm a.u., which is only some 10% or so smaller than the A_z values for the C–H proton in CH_3F, CH_3Cl, and C_2H_4 given in Table 7. (It should be noted that reaction fields are sufficiently small that the contribution which is quadratic in the field is negligible.)

Following the work of Diehl and Freeman, another test of the reaction field model was undertaken by Laszlo and Musher.[42] They concluded that no existing reaction field model was adequate to explain the observed results and that the reaction field must have very different values at different points in the solute molecule. No subsequent work appears to have been carried out to develop the theory further. However, with the A parameters now obtained independently from ab initio calculation, it should be possible to do this.

Contributions to the reaction fields of molecules with electric quadrupole moments have been studied by Biemond and co-workers.[43,44] Their conclusion is that the electric quadrupole field contribution is not negligible in comparison with the van der Waals contribution. This is extended to include the octopole moment in the case of methane.[45] Another refinement is to allow for the fact that molecular vibrations produce an oscillating electric dipole moment which modifies the reaction field.[46]

The dielectric theory is meant to be applicable when solvent dielectric constants are small. As stated above, for high dielectric constant solvents (i.e. highly polar solvents) chemical equilibrium theory is generally used. Exceptions to this are the work by Schmidt et al.[47]a and by Akitt[47]b who successfully used electric field models in such cases.

In attempting to deal with the contribution of intermolecular van der Waals interactions to nuclear shielding in liquids most authors start from a simpler form of equation (21):

$$\sigma_w = -B\overline{E^2} \tag{27}$$

where $\overline{E}^2$ is now the mean square electric field experienced by the solute molecule from the surrounding solvent molecules and B is an empirical constant. Two distinct approaches are used to obtain an expression for $\overline{E}^2$. One is to use an expression [usually equation (22)] for the interaction between the solute molecule and one solvent molecule and then to multiply it by the number of solvent molecules in the immediate vicinity of the solute. This is the 'cage model' or 'gas model' and was first used by Rummens et al.[48] The second approach, which uses the reaction field model and hence treats the solvent as a continuous dielectric, was introduced by Howard, Linder and Emerson.[49,50] A detailed treatment of these two approaches is given by Rummens.[51] Homer[52] has also given an early review of the field. In later years much work was done by Homer and co-workers. Their approach was described most fully in 1984.[53] It separates σ_w into two parts—one which can be described in terms of a reaction field model, and one involving a short-range 'buffeting' interaction. Both interactions involve the coefficient B.

Table 10 Comparison of Ab Initio[55] and Empirically Determined Values of B (in 1×10^{-18} e.s.u., 1×10^{-18} cm^2 Statvolt^{-2}) Using Various Models for Noble Gases Dissolved in Liquids[53]

		Empirical[53]			
	Ab initio[55]	Linder	Rummens	RBB	BR
He	0.13	0.25	0.75	1.2	0.7
Ne	1.06	11	27	52	35
Kr	12.03	200	220	350	350
Xe	14.96	580	630	750	820

Further confirmation of the inadequacy of the simple mean square field approach to calculating σ_w values comes from a comparison of theoretical and experimental determinations of B values. Seydoux et al.[54] studied the shifts of He, Ne, Kr, and Xe dissolved in a variety of solvents. Using various models they obtained the B values given in Table 10. The true B values have now been calculated by Bishop and Cybulski.[55] It is clear that the empirical approaches grossly overestimate B, showing that the mean square field model with the uniform field B is inadequate. This point has also been made by de Dios and Jameson.[56]

5.3 Intramolecular Electric Fields

It was realized very early that the small changes in nuclear shielding upon passing along a homologous series or upon substitution of a polar group in a molecule could not be understood by calculations using the Ramsey equation, and so the suggestion that the total shielding of a nucleus could be broken down approximately into a number of contributions was made.[57] It was in this context that Buckingham[4] introduced that idea that, as well as contributing to intermolecular effects, electric fields arising from polar substituents could explain shielding differences between the substituted and the unsubstituted compound. The notion was first applied to proton shielding and then extended to the shielding of ^{19}F, ^{13}C, and other nuclei.

The central idea is to regard the shielding change at a given nucleus upon the substitution of a polar group at some distance away (usually greater than 0.3 nm) in a molecule as being due to the electric field emanating from a point electric dipole situated in the polar group. In carrying out calculations the following features arise: (i) it is assumed, for distances greater than 0.3 nm, that the electric field of the point dipole is sufficiently uniform for the coefficients A and B, as defined previously, to be used; (ii) allowance must be made for any other mechanism which could affect the shielding; and (iii) as the magnetic anisotropy of the polar groups is important here, it is assumed, for distances greater than 0.3 nm, that all inductive and mesomeric effects, which act through bonds rather than through space, can be neglected—the seat of the point dipole in the polar groups is determined so as to give the best overall agreement with experiment.

The first systematic study of intramolecular electric field effects was that by Zürcher.[58] He studied the effects of a number of polar groups upon proton shielding in conformationally rigid steroid molecules. He took magnetic anisotropy and other effects into account. For A he obtained a value of 4.2×10^{-12} e.s.u. (72 ppm a.u.). At the time this was higher than the A value generally accepted ($\sim 3 \times 10^{-12}$ e.s.u.) but, as shown in Table 7, somewhat lower than the true, typical A value

for a C–H bond. He took an optimistic view that in time it would 'be possible eventually to find the refined physical models with which to ascertain quantitatively the chemical shift changes due to some reactions field and specific group interactions'. This has, unfortunately, not proved possible, although the recent availability of reliable values of the *A* and *B* parameters could very well stimulate renewed activity towards this goal.

Following Zürcher, a detailed study of electric field effects was made by Hamer, Peat and Reynolds[59–61] who studied 4-substituted styrenes using both ^{1}H and ^{13}C shielding. Their work confirmed the existence of intramolecular electric fields. For proton shielding they obtained values for *A* of 3.11×10^{-12} e.s.u. (53.3 ppm a.u.) when the field of the dipole was calculated at the C–H bond midpoint, and 4.77×10^{-12} e.s.u. (81.8 ppm a.u.) when the field was calculated at the proton.[59] Later they obtained values of $4.6–6.5 \times 10^{-12}$ e.s.u. (79–111 ppm a.u.) for protons in C–H bonds in aromatic compounds.[61] Green and Martin[62] obtained 56 ppm a.u. for the *A* value of the proton in $CHCl_3$. A value for *A* of -3.0×10^{-11} e.s.u. (−51 ppm a.u.) was later obtained for ^{19}F shielding in C–F bonds.[63] This agreed with other experimental data, but disagrees with the ab initio value of −505.5 ppm a.u. for CH_3F in Table 8.

Considerable attention has been devoted to studying electric field effects on ^{13}C chemical shifts. Some of this work[14,64–68] invokes the idea of an electric field but involves semiempirical calculations, and the effect is formulated in terms of ^{13}C electron densities or total shielding changes rather than in terms of *A* and *B* parameters. Other papers have explicitly involved the electric field coefficients,[69–71] but have also involved highly empirical methods to estimate *A*. Values in the range $2–12 \times 10^{-11}$ e.s.u. (300–1800 ppm a.u.) have been obtained. This range is partly coincident with that of the new ab initio values given in Table 8.

In recent years there has been an upsurge in activity due to greatly increased interest in the chemical shifts brought about by changes in protein conformation[72–77] (see ***Structures of Larger Proteins, Protein-Ligand, and Protein-DNA Complexes by Multi-Dimensional Heteronuclear NMR***). This has led to the calculations already referred to.[30,31] There have also been semiempirical studies of electric field effects of substituents on nuclear shielding.[78]

Intramolecular van der Waals effects on shielding can be treated by a mean square field approach, as was done by Tribble et al.[79] for ^{1}H shielding in hydrocarbons. From this work they obtained $B = 0.27 \times 10^{-18}$ e.s.u. (79 ppm a.u.), which is in fact in fairly good agreement with the *B* values for C–H protons given in Table 7. Earlier, Schaefer et al.[80] had pointed out the significance of intramolecular dispersion effects for ^{1}H on ^{13}C chemical shifts, and Yonemoto[81] studied the van der Waals deshielding caused by halogen atoms.

5.4 Solid State Studies

Measurement of electric fields in solids by the determination of chemical shift changes has also been made. Muha and Yates[82] started this topic with a proton resonance study of ethylene absorbed on a zeolite. A more recent study is that by Clayden[83] who studied ^{13}C shifts on aryl ether compounds. Applications to solid polymers are also possible (see ***Solid Polymers: Shielding and Electronic States***).

6 CONCLUSIONS

The recent availability of ab initio calculated *A* and *B* values together with both new values and improvements to the old values yet to come should act as a spur not only to studies of chemical shifts in proteins but to the whole area of electric fields on chemical shifts. The *A* values obtained by calculation appear to be somewhat larger than those obtained from experiment. This may indicate the importance of electric field gradient effects. However, this can only be determined after there have been developments in the formal theory of field gradient effects combined with more ab initio calculations of the field gradient coefficients.

Other topics which stand to gain from the existence of good *A* and *B* values are associated with pair interactions in gases and reaction fields in liquids. An improved theory for van der Waals effects on shielding is required but it is not clear whether this can be expressed in terms of a mean square field model.

7 RELATED ARTICLES

Anisotropy of Shielding and Coupling in Liquid Crystalline Solutions; Shielding Calculations: LORG and SOLO Approaches; Chemical Shift Tensor Measurement in Solids; Chemical Shift Tensors; Chemical Shift Tensors in Single Crystals; Chemical Shifts in Biochemical Systems; Gas Phase Studies of Chemical Exchange Processes; Gases at High Pressure; Hydrogen Bonding; Noble Gas Elements; Shielding Calculations: Perturbation Methods; Shielding: Overview of Theoretical Methods; Shielding in Small Molecules; Shielding Tensor Calculations; Solid Polymers: Shielding and Electronic States; Structures of Larger Proteins, Protein-Ligand, and Protein-DNA Complexes by Multi-Dimensional Heteronuclear NMR.

8 REFERENCES

1. W. G. Schneider, H. J. Bernstein, and J. A. Pople, *J. Chem. Phys.*, 1958, **28**, 601.
2. T. W. Marshall and J. A. Pople, *Mol. Phys.*, 1957, **1**, 199.
3. M. J. Stephen, *Mol. Phys.*, 1958, **1**, 223.
4. A. D. Buckingham, *Can. J. Chem.*, 1960, **38**, 300.
5. J. I. Musher, *J. Chem. Phys.*, 1962, **37**, 34.
6. A. D. Buckingham, T. Schaefer, and W. G. Schneider, *J. Chem. Phys.*, 1960, **32**, 1227.
7. W. T. Raynes, A. D. Buckingham, and H. J. Bernstein, *J. Chem. Phys.*, 1962, **36**, 3481.
8. L. Petrakis and H. J. Bernstein, *J. Chem. Phys.*, 1962, **37**, 2731.
9. G. Widenlocher and E. Dayan, *Compt. Rend.*, 1965, **260**, 6856.
10. A. D. H. Clague, G. Govil, and H. J. Bernstein, *Can. J. Chem.*, 1969, **47**, 625.
11. L. Petrakis and H. J. Bernstein, *J. Chem. Phys.*, 1963, **38**, 1562.
12. S. Mohanty, *Phys. Rev. A*, 1971, **4**, 136.
13. W. T. Raynes, *Spec. Period. Rep.–NMR*, 1972, **1**, 36.
14. K. Seidman and G. E. Maciel, *J. Am. Chem. Soc.*, 1977, **99**, 659.
15. (a) J. Gruninger and H. F. Hameka, *J. Chem. Phys.*, 1968, **48**, 4878; (b) J. P. Riley and W. T. Raynes, *Mol. Phys.*, 1976, **32**, 569; (c) A. J. Sadlej and W. T. Raynes, *Mol. Phys.*, 1978, **35**, 101.

16. (a) B. Day and A. D. Buckingham, *Mol. Phys.*, 1976, **32**, 343; (b) M. Zaucer and A. Azman, *Z. Naturforsch., A*, 1979, **34**, 1279.
17. R. M. Aminova and R. Z. Gubaidullina, *Zh. Strukt. Khim.*, 1969, **10**, 253.
18. V. K. Mukhomorov, *Zh. Struct. Khim.*, 1971, **12**, 326.
19. M. I. Volodicheva and T. K. Rebane, *Teor. Eksp. Khim.*, 1985, **21**, 373.
20. A. D. Buckingham and S. M. Malm, *Mol. Phys.*, 1971, **22**, 1127.
21. S. Bhagavantam, *Crystal Symmetry and Physical Properties*, Academic, London, 1966.
22. W. T. Raynes and R. Ratcliffe, *Mol. Phys.*, 1979, **37**, 571.
23. D. M. Bishop and S. M. Cybulski, *Mol. Phys.*, 1993, **80**, 199.
24. D. M. Bishop and S. M. Cybulski, *Mol. Phys.*, 1993, **80**, 209.
25. M. Grayson and W. T. Raynes, *Chem. Phys. Lett.*, 1993, **214**, 473.
26. M. Grayson and W. T. Raynes, *Mol. Phys.*, 1994, **81**, 533.
27. M. Grayson and W. T. Raynes, *Chem. Phys. Lett.*, 1994, **218**, 270.
28. M. Grayson and W. T. Raynes, *Magn. Res. in Chem.*, 1995, **33**, 138.
29. M. J. Packer and W. T. Raynes, *Mol. Phys.*, 1990, **69**, 391.
30. J. D. Augspurger and C. E. Dykstra, *J. Phys. Chem.*, 1991, **95**, 9230.
31. J. D. Augspurger, J. G. Pearson, E. Oldfield, C. E. Dykstra, K. D. Park, and D. Schwartz, *J. Magn. Reson.*, 1992, **100**, 342.
32. A. D. Buckingham and K. P. Lawley, *Mol. Phys.*, 1960, **3**, 219.
33. J. G. Batchelor, *J. Am. Chem. Soc.*, 1975, **97**, 3410.
34. J. G. Batchelor, J. Feeney, and G. C. K. Roberts, *J. Magn. Reson.*, 1975, **20**, 19.
35. A. D. Buckingham and J. A. Pople, *Discuss. Faraday Soc.*, 1956, **22**, 17.
36. A. D. Buckingham and J. A. Pople, *Trans. Faraday Soc.*, 1955, **51**, 1173.
37. A. K. Jameson, J. Moyer, and C. J. Jameson, *J. Chem. Phys.*, 1978, **68**, 2873.
38. B. Bennett and W. T. Raynes, *Magn. Reson. Chem.*, 1991, **29**, 946.
39. W. T. Raynes, in *Nuclear Magnetic Shieldings and Molecular Structure*, ed. J. Tossell, Kluwer, Dordrecht, 1993, p. 401.
40. L. Onsager, *J. Am. Chem. Soc.*, 1936, **58**, 1486.
41. P. Diehl and R. Freeman, *Mol. Phys.*, 1961, **4**, 39.
42. P. Laszlo and J. I. Musher, *J. Chem. Phys.*, 1964, **41**, 3906.
43. J. F. M. Van Pell, J. J. Brondijk, V. W. M. Claessen, and J. Biemond, *J. Chem. Soc., Faraday Trans. 2*, 1981, **77**, 1789.
44. H. G. W. Guerds, H. E. Regtoit, M. G. J. A. van der Meerendonk, and J. Biemond, *J. Chem. Soc., Faraday Trans. 2*, 1984, **80**, 1039.
45. M. Huizinga, H. A. W. Ragas, A. H. J. Schrijvers, and J. Biemond, *J. Chem. Soc., Faraday Trans. 2*, 1987, **83**, 2067.
46. D. J. Pennino and E. R. Malinowski, *J. Chem. Soc., Faraday Trans. 2*, 1987, **83**, 933, 939.
47. (a) R. L. Schmidt, R. S. Butler, and J. H. Goldstein, *J. Phys. Chem.*, 1969, **73**, 1117; (b) J. W. Akitt, *J. Chem. Soc., Dalton Trans.*, 1974, 175; *J. Chem. Soc., Faraday Trans. 1*, 1977, **73**, 1622.
48. F. H. A. Rummens, W. T. Raynes, and H. J. Bernstein, *J. Chem. Phys.* 1968, **72**, 2111.
49. B. Linder, *J. Chem. Phys.*, 1960, **33**, 668.
50. B. B. Howard, B. Linder, and M. T. Emerson, *J. Chem. Phys.*, 1962, **36**, 485.
51. F. H. A. Rummens, in *NMR Basic Principles and Progress*, ed. P. Diehl, E. Fluck, and R. Kosfeld, Springer, Berlin, 1975, Vol. 10.
52. J. Homer, *Appl. Spectrosc. Rev.*, 1975, **9**, 1.
53. J. Homer and C. Perceval, *J. Chem. Soc., Faraday Trans. 2*, 1984, **80**, 1.
54. P. Seydoux, P. Diehl, R. K. Mazitov, and J. Jokisaari, *J. Magn. Reson., Ser. A*, 1993, **101**, 78.
55. D. M. Bishop and S. M. Cybulski, *Chem. Phys. Lett.*, 1993, **211**, 255.
56. A. C. de Dios and C. J. Jameson, *Annu. Rep. NMR Spectrosc.*, 1994, **29**, 1.
57. A. Saika and C. P. Slichter, *J. Chem. Phys.*, 1954, **22**, 26.
58. R. F. Zürcher, *Prog. NMR* 1967, **2**, 205.
59. G. K. Hamer and W. F. Reynolds, *Can. J. Chem.*, 1968, **46**, 3813.
60. G. K. Hamer, I. R. Peat, and W. F. Reynolds, *Can. J. Chem.*, 1973, **51**, 897.
61. G. Hamer, I. R. Peat, and W. F. Reynolds, *Can. J. Chem.*, 1973, **51**, 915.
62. R. D. Green and J. S. Martin, *J. Am. Chem. Soc.*, 1968, **90**, 3659.
63. W. F. Reynolds, V. G. Gibb, and N. Plovec, *Can. J. Chem.* 1980, **58**, 839.
64. T. Tokuhiro and G. Fraenkel, *J. Am. Chem. Soc.*, 1969, **91**, 5005.
65. H. J. Schneider and W. Freitag, *J. Am. Chem. Soc.*, 1977, **99**, 8363.
66. L. W. Jacques, J. B. Macaskill, and W. Weltner, *J. Phys. Chem.*, 1979, **83**, 1412.
67. C. Piccinni-Leopardi and J. Reisse, *J. Magn. Reson.*, 1981, **42**, 60.
68. H. J. Schneider and W. Geschwendtner, *J. Org. Chem.*, 1982, **42**, 216.
69. W. J. Horsley and H. Sternlicht, *J. Am. Chem. Soc.*, 1968, **90**, 3738.
70. M. E. van Dommelen, J. W. de Haan, and H. M. Buck, *Org. Magn. Reson.*, 1980, **13**, 447.
71. M. E. van Dommelen, J. W. de Haan, and H. M. Buck, *Org. Magn. Reson.*, 1980, **14**, 497.
72. N. J. Clayden and R. J. P. Williams, *J. Magn. Reson.*, 1982, **49**, 383.
73. A. C. de Dios, J. G. Pearson, and E. Oldfield, *Science*, 1993, **260**, 1491.
74. A. C. de Dios and E. Oldfield, *Chem. Phys. Lett.* 1993, **205**, 108.
75. M. P. Williamson and T. Asakura, *J. Magn. Reson.*, 1991, **94**, 557.
76. T. Asakura, Y. Niizawa, and M. P. Williamson, *J. Magn. Reson.*, 1992, **98**, 646.
77. M. P. Williamson and T. Asakura, *J. Magn. Reson., Ser. B*, 1993, **101**, 63.
78. T. Herr, M. B. Ferraro, and R. H. Contreras, *J. Mol. Struct. (Theochem)*, 1992, **254**, 261.
79. M. T. Tribble, M. A. Miller, and N. L. Allinger, *J. Am. Chem. Soc.*, 1971, **93**, 3894.
80. T. Schaefer, W. F. Reynolds, and T. Yonemoto, *Can. J. Chem.*, 1963, **41**, 2969.
81. T. Yonemoto, *Can. J. Chem.*, 1966, **44**, 223.
82. G. M. Muha and D. J. C. Yates, *J. Chem. Phys.*, 1968, **49**, 5073.
83. N. J. Clayden, *Magn. Reson. Chem.*, 1989, **27**, 692.

Biographical Sketch

W. T. Raynes. *b* 1935. B.Sc., 1956, Ph.D., 1959, D.Sc., 1989, University of London, UK. Postdoctoral research fellow, NRC, Ottawa

Introduced to NMR by H. J. Bernstein. Postdoctoral fellowships at Caltech and Oxford University. lecturer, senior lecturer, and reader in Chemistry, University of Sheffield, UK, 1965–present. Approximately 110 publications. Research interests include the magnetic properties of molecules, especially NMR chemical shifts and coupling constants.

Isotope Effects on Chemical Shifts and Coupling Constants

Cynthia J. Jameson

University of Illinois, Chicago, IL, USA

1	Introduction	1
2	Isotope Shifts: Observations	1
3	Rovibrational Theory of Isotope Shifts	2
4	General Trends in the Electronic Factors	11
5	Isotope Shifts Over Two or More Bonds	11
6	Isotope Effects on Spin–Spin Coupling	13
7	Related Articles	16
8	References	16

1 INTRODUCTION

Where an isotopic label is introduced into a molecule, every neighboring resonant nucleus experiences a slight chemical shift. If the labeling is less than 100%, the resonant nuclei in both the labeled and the unlabeled molecules are observed, with intensities according to statistical distribution. The magnitude of the shift depends on the fractional mass change at the isotope substitution site, on the remoteness of the resonant nucleus from the substitution site, and on the sensitivity of the shielding of the resonant nucleus. Every resonant nucleus in the isotopically labeled molecule experiences this chemical shift due to isotopic substitution, but the shift is only observable under favorable conditions, such as when the shift is larger than the halfwidth of the peaks. Isotope shifts as small as a few ppb have been observed, from zero bonds (the isotopic label itself is the resonant nucleus) to 12 bonds away from the substitution site.[1–3] When the isotopic label itself is the resonant nucleus, the isotope shift is called a primary isotope shift. Such primary isotope shifts can only be observed indirectly, when two in different molecules are compared. There are also attendant effects on the spin–spin coupling constants in the molecule.[4] Here, the primary and secondary effects have to be deduced from the proper combination of observed couplings, and it is more appropriate to do this in the reduced coupling constant from which the gyromagnetic ratios have been removed altogether.

Isotope effects on chemical shifts and coupling constants are very important in two distinct ways. First, they have a multitude of practical applications, such as in the determination of molecular structure and the verification of mechanisms of reactions. This is just one more powerful tool in which a very selective tag carries with it the same wealth of information as the chemical shift itself. Second, isotope shifts provide a more stringent test of ab initio calculations of chemical shifts in specific molecules, being directly related to the slopes on the shielding surface (a mathematical surface), and, in a more general sense, the trends in the thousands of isotope shifts that have been accumulated[1–3] provide insight into the general nature of these shielding surfaces, in terms of the dependence of the details of the surface on the nature of the chemical bond, the net charge of the molecule, bond orders, presence of lone pairs, etc.[5,6] Isotope effects on coupling constants lack practical applications, but are invaluable from the second point of view. For the most part, coupling constants are obtained in rapidly tumbling systems, and only the isotropic average of the tensor is obtained. The full tensor is very difficult to extract from experiments in oriented molecules, since it is always observed as a sum with the larger dipolar tensor. Since coupling mechanisms other than the Fermi contact mechanism are the ones that give rise to the anisotropy of the tensor, the lack of tensor information leaves us with a severe dearth of critical tests of the ab initio calculations. Isotope effects on coupling constants provide additional critical tests, since they depend on the spin–spin coupling surface, not just a single calculated value. The earliest questions asked of theoretical calculations of chemical shifts demanded only that the relative order of chemical shifts be reproduced and that the relative magnitudes agree with experiment. More recently, we have asked how well the calculations reproduce the absolute shielding in specific molecules, not just their relative shifts, and also how well they reproduce the shielding tensor components. These are more stringent tests of theory. In the isotope shift experiments, we ask for even more detailed agreement: how well do the calculations reproduce the shapes of the shielding surfaces as the nuclear coordinates are displaced away from the immediate vicinity of the equilibrium geometry of the molecule? A similar question is posed for the spin–spin coupling surface by the primary and secondary isotope effects on J.

2 ISOTOPE SHIFTS: OBSERVATIONS

We follow the notation introduced by Gombler[7] for the isotope shift observed for nucleus A upon substitution of the neighboring $^{m'}$X isotope:

$$ {}^{n}\Delta\mathrm{A}(^{m'/m}\,\mathrm{X}) = \frac{\nu_{\mathrm{A}}(\mathrm{A}^{\,m'}\mathrm{X}\ldots) - \nu_{\mathrm{A}}(\,\mathrm{A}^{\,m}\mathrm{X}\ldots)}{\nu_{\mathrm{A}}(\mathrm{A}^{\,m}\mathrm{X}\ldots)} \quad (m'\rangle m) \tag{1} $$

where $\nu_{\mathrm{A}}(\mathrm{A}^{\,m'}\mathrm{X}\ \ldots\ )$ is the resonance frequency of the A nucleus in the molecule having the heavier $^{m'}$X isotope, which is n bonds away from the observed nucleus. The molecules (A $^{m'}$X …) and (A ^{m}X …) are isotopomers. The isotope shift can also be written in terms of the nuclear shielding difference:

$$ \begin{aligned} {}^{n}\Delta\ \mathrm{A}(^{m'/m}\,\mathrm{X}) &= \sigma^{\mathrm{A}}(\,\mathrm{A}^{\,m}\,\mathrm{X}\ldots) - \sigma^{\mathrm{A}}(\,\mathrm{A}^{\,m'}\,\mathrm{X}\ldots) \\ &= \sigma - \sigma^{*} \end{aligned} \tag{2} $$

where the asterisk applies to the heavy isotopomer. Just as for spin–spin couplings, this notation becomes ambiguous when A and X are atoms in cyclic compounds in which there are at least two paths connecting the observed nucleus and substituted atom, in which case the observed quantity is an isotope shift corresponding to two or more bond paths.

There are several general observations that have been made about magnitudes and signs of isotope shifts:[1,8]

1. Upon substitution with a heavier isotope, the NMR signal of the nearby nucleus usually shifts towards lower frequencies (higher shielding). Thus, as defined in equations (1) and (2), isotope shifts are generally negative in sign.
2. The magnitude of the isotope shift depends on how remote the isotopic substitution is from the observed nucleus. Although there are exceptions, one-bond isotope shifts are larger than two-bond or three-bond shifts. In the examples shown in Table 1, there is a clear attenuation of the isotope shift with the number of bonds separating the NMR nucleus and the substitution site.[9,10]
3. The magnitude of the isotope shift is a function of the observed nucleus, and reflects its chemical shift range. Comparisons can be made in analogous compounds, as in Table 2.
4. The magnitude of the shift is related to the fractional change in mass upon isotopic substitution. The larger the fractional change in mass, $(m' - m)/m'$, the larger the isotope shift, as is obvious in the examples in Table 3. (The signals can be easily assigned according to the abundance of the masses m' and m.) When two different atoms can be substituted in the molecule, the isotopic shifts are commensurate with the fractional change in masses, as in the example in Table 4.
5. The magnitude of the shift is approximately proportional to the number of equivalent atoms that have been substituted by isotopes. In other words, isotope shifts exhibit additivity. When there are multiple equivalent sites and the labeling is less than 100%, the resonant nuclei in the variously labeled and the unlabeled molecules are observed. For example, for a deuterium fraction d (based on the solvent isotopic composition for the exchange), for N equivalent replaceable hydrogens, the statistical limit for the relative intensity of the $XH_{N-n}D_n$ isotopomer will be

$$I_n = \frac{N!}{n!(N-n)!}(1-d)^{(N-n)}d^n \tag{3}$$

This strictly statistical formula neglects any isotope effects on the equilibrium constant for the exchange. By doing more than one labeling experiment (using different heavy atom fractions), the identification of the signals with the isotopomers can be unequivocal. Fortunately, in many cases, there is also spin–spin coupling information in the NMR spectrum, so that only one labeling experiment is necessary. When there are several equivalent substitution sites, the additivity of the isotope shifts is obvious, as in the examples in Table 5.[15–18] Deviations from strict additivity are small, and their 0:3:4:3:0 ratio in CH_4-like systems has been explained.[19] Additivity is observed in long-range isotope shifts as well. For example, the two-bond deuterium-induced isotope shifts of ^{59}Co in hexaamminecobalt(III) chloride are all −5.2 ppm per D in each of the 18 different isotopomers of $[Co(NH_3)_6]^{3+}$. Less obvious, but also observed, is the additivity of isotope shifts due to substitution at nonequivalent sites.

Table 1

n	$^n\Delta^{31}$P($^{13/12}$C) in Ph_3P (ppm)	$^n\Delta^{13}$C($^{2/1}$H) in butane-1-d_1 (ppm)
1	−0.0227	−0.298
2	−0.0039	−0.088
3	−0.0018	−0.0291
4	—	+0.0051

Table 2

X	$^1\Delta$X($^{13/12}$C) (ppm)	Chemical shift range (ppm)
^{77}Se in Me_2Se	−0.228	2200
^{125}Te in Me_2Te	−0.341	3160
^{29}Si	−0.006	600
^{119}Sn	−0.018	3000
^{207}Pb	−1.089	9000
X	$^1\Delta$X($^{18/16}$O) (ppm)	Chemical shift range (ppm)
^{29}Si	−0.0218	600
^{13}C	−0.019	680
^{31}P	−0.018 to −0.036	950
^{15}N	−0.056, −0.138	1200
^{55}Mn	−0.599	3440
^{99}Tc	−0.22	4500
^{95}Mo	−0.25	7000
^{129}Xe	−0.58	7850
X	$^1\Delta$X($^{2/1}$H) (ppm)	Chemical shift range (ppm)
^{51}V in $[CpVH(CO)_3]^-$	−4.7	6000
^{93}Nb in $[CpNbH(CO)_3]^-$	−6.0	5000
^{183}W in $CpWH(CO)_3$	−10.0	11500

These are the general trends found for all isotope shifts. These general experimental trends provide the testing grounds for the theory of isotope shifts. There are also some tendencies that are less global in nature but that are perceived as correlations in observations of related classes of compounds; for example, one-bond isotope shifts tend to be larger when the bond order between the observed nucleus and the substituted nucleus is higher. These correlations have to be considered separately, since they involve comparisons between different molecules that have many differences other than in the parameters that are being correlated with the isotope shifts.

3 ROVIBRATIONAL THEORY OF ISOTOPE SHIFTS

The effects of intramolecular dynamics (vibration and rotation) on nuclear shielding were theoretically predicted by Ramsey,[20] and have been observed in two ways. First, there is an observable temperature dependence of the resonance frequency, even for the 'isolated' molecule (apart from the temperature dependence due to intermolecular interactions). Second, there is an observable shift upon isotopic substitution of neighboring nuclei. Both are effects of differences in averaging over nuclear configuration as the molecule undergoes vibration and rotation.[21] The temperature dependence of nuclear shielding is observed in the dilute gas phase.[22–25] The nuclear shielding in an 'isolated' molecule, $\sigma_0(T)$, is an average of the nuclear magnetic shielding tensor over all possible orientations of the molecule in the magnetic field, and is actually observed as the nuclear shielding in the limit as the pressure approaches zero. One does not extrapolate the results to a true zero pressure, but to a pressure so low that collisional deformation of the molecule no longer contributes to σ, while there are still enough collisions to provide the required rate of transition between vibrational and rotational states. Thus, $\sigma_0(T)$ is an average over all possible rovibrational states of

Table 3

Molecule	m'	m	Isotope shifts (ppm)	Reference
$(CH_3)_2CO$	3	1	$^2\Delta\ ^{13}C(^{3/1}H) = +0.076$	Arrowsmith et al.[11]
	2	1	$^2\Delta\ ^{13}C(^{2/1}H) = +0.054$	
$(CH_3)_2CO$	3	1	$^1\Delta\ ^{13}C(^{3/1}H) = -0.356$	Arrowsmith et al.[11]
	2	1	$^1\Delta\ ^{13}C(^{2/1}H) = -0.250$	
CO	17	16	$^1\Delta\ ^{13}C(^{17/16}O) = -0.0247$	Wasylishen et al.[12]
	18	16	$^1\Delta\ ^{13}C(^{18/16}O) = -0.0476$	
SeF_6	76	74	$^1\Delta\ ^{19}F(^{76/74}Se) = -0.0154$	Jameson et al.[13]
	77	74	$^1\Delta\ ^{19}F(^{77/74}Se) = -0.021$	
	78	74	$^1\Delta\ ^{19}F(^{78/74}Se) = -0.0301$	
	80	74	$^1\Delta\ ^{19}F(^{80/74}Se) = -0.0442$	
	82	74	$^1\Delta\ ^{19}F(^{82/74}Se) = -0.0576$	

Table 4

Molecule	m'	m	Isotope shift[14] (ppm)
$[CpVH(CO)_3]^-$	2	1	$^1\Delta\ ^{51}V(^{2/1}H) = -4.7$
	13	12	$^1\Delta\ ^{51}V(^{13/12}C) = -0.51$

the molecule, weighted according to the fraction of molecules occupying that state at that temperature.

The average shielding for a given rovibrational state is different for each of several isotopically related species, because the masses enter into the solution of the vibrational–rotational Hamiltonian.[26] Thus, the thermal average shielding $\sigma_0(T)$ is different for the isotopomers. These differences are measured as isotope shifts. It is important to know which aspects of isotope shifts are due to dynamical factors (rovibrational averaging of internuclear separations) and which can be attributed to electronic factors (changes in nuclear shielding with bond extension or bond angle deformation). If the theory can sort out the former, isotope shifts can be used to extract the latter, thus providing chemically interesting information that would establish the isotope shift as an easily measurable index of the chemical bond.

3.1 Vibrational Averaging in Diatomic Molecules

The potential energy surface (PES) of a diatomic molecule can be written in terms of a Dunham potential, or more approximately in terms of a Morse potential. The Dunham potential function expresses the potential energy in terms of a Taylor series expansion in $x = (r - r_e)/r_e$:

$$V = a_0x^2(1 + a_1x + a_2x^2 + a_3x^3 + \dots) \tag{4}$$

The potential parameters a_0, a_1, ... can be obtained from the spectroscopic constants of the molecule. The vibrational levels and functions shown in Figure 1 for the H_2^+ molecule are typical. The first thing to note is that the anharmonic nature of the potential function leads to an unsymmetrical probability distribution function: there is a higher probability of finding the diatomic molecule extended than compressed. Second, this asymmetry becomes more pronounced as we move up in the potential well. Third, the vibrational levels for D_2^+ (shown also as dashed lines) lie lower in the potential well than those for H_2^+, corresponding to its lower vibrational frequency, $\omega_e = 1643.0\,cm^{-1}$ for D_2^+ compared with $2323.5\,cm^{-1}$ for H_2^+. Since we are interested in vibrational averaging and the mass dependence of shielding, we show in Figure 2 the vibrational functions of D_2^+ and H_2^+. It is obvious that the anharmonic potential will give rise to different vibrational averages for the isotopomers, since the more sharply peaked and compact probability density of D_2^+ should lead to a different average than that for H_2^+, in which the probability density is more spread out at the larger separations. This is true for the vibrational ground state, and the differences become even more pronounced at higher vibrational levels. The average values $\langle x^n \rangle$ can be obtained. Complete calculations for some isotopomers of H_2^+ lead to the results for the ground vibrational state shown in Table 6, which also shows the results for the case where the vibration is truly that of a harmonic oscillator (HO).

In order to observe more easily the largest terms that contribute to the above equations and explicitly express their mass dependence, we write only the leading terms, expressed in the measured spectroscopic constants of the molecule.[8]

$$\langle x \rangle_{vJ} = -3(v + \tfrac{1}{2})a_1\frac{B_e}{\omega_e} + 4J(J+1)\frac{B_e}{\omega_e^2} \tag{5}$$

$$\langle x^2 \rangle_{vJ} = 2(v + \tfrac{1}{2})\frac{B_e}{\omega_e} \tag{6}$$

Of these quantities, a_1 is mass-independent, and the others depend on the reduced mass of the diatomic molecule as follows:

$$\omega_e^* = \left(\frac{\mu}{\mu^*}\right)^{1/2}\omega_e, \quad B_e^* = \frac{\mu}{\mu^*}B_e \tag{7}$$

Furthermore, the thermal average $\langle v + \frac{1}{2} \rangle^T$ is also mass-dependent, since the populations of the vibrational energy levels over which this average is taken depend on the vibrational frequency ω_e. Note that $B_e/{\omega_e}^2$ is mass-independent, so the rotational contribution to the thermal average shielding in the diatomic molecule is independent of mass.

Note also that if we include only the leading terms then

$$\langle x \rangle_v = -\tfrac{3}{2}a_1\langle x^2 \rangle_v \tag{8}$$

The difference between two isotopomers is

$$\langle x^2 \rangle_{vJ} - \langle x^2 \rangle_{vJ}^* = 2\frac{B_e}{\omega_e}\left[1 - \left(\frac{\mu}{\mu^*}\right)^{1/2}\right](v + \tfrac{1}{2}) + \dots \tag{9}$$

Table 5

	Isotopomer	δ, observed (ppm)	δ, if exactly additive (ppm)	Deviation (ppm)
^{119}Sn	SnH_3^-	0.0	0.0	0
	SnH_2D^-	−3.093	−3.108	−0.015
	$SnHD_2^-$	−6.202	−6.217	−0.015
	SnD_3^-	−9.325	−9.325	0
^{119}Sn	SnH_4	0.0	0.0	0
	SnH_3D	−0.4266	−0.4026	+0.024
	SnH_2D_2	−0.8369	−0.8052	+0.032
	$SnHD_3$	−1.2306	−1.2077	+0.023
	SnD_4	−1.6103	−1.6103	0
^{31}P	PH_3	0.0	0.0	0
	PH_2D	−0.8045	−0.8458	−0.041
	PHD_2	−1.6491	−1.6916	−0.042
	PD_3	−2.5373	−2.5373	0
^{15}N	NH_3	0.0	0.0	0
	NH_2D	−0.6264	−0.6229	0.0035
	NHD_2	−1.2491	−1.2458	0.0033
	ND_3	−1.8687	−1.8687	0
^{15}N	NH_4^+	0.0	0.0	0
	NH_3D^+	−0.3077	−0.2933	+0.0144
	$NH_2D_2^+$	−0.6048	−0.5865	+0.0183
	NHD_3^+	−0.8937	−0.8798	+0.0139
	ND_4^+	−1.1730	−1.1730	0
^{13}C	CH_4	0.0	0.0	0
	CH_3D	−0.2016	−0.19865	+0.003
	CH_2D_2		−0.3973	
	CHD_3	−0.6006	−0.5960	+0.004
	CD_4	−0.7946	−0.7946	0

$$\langle x\rangle_{vJ} - \langle x\rangle^*_{vJ} = -3a_1\frac{B_e}{\omega_e}\left[1-\left(\frac{\mu}{\mu^*}\right)^{1/2}\right](\,v+\tfrac{1}{2}) + \ldots \qquad (10)$$

The leading term in $\langle x^3\rangle_{vJ}$ has the same mass dependence as the next higher order term in $\langle x\rangle$ and $\langle x^2\rangle$; thus, it is consistent to include only the above two terms. We find the ratios from the full calculations:

$$\frac{\langle x\rangle_{H_2^+} - \langle x\rangle_{HT^+}}{\langle x\rangle_{H_2^+} - \langle x\rangle_{HD^+}} = 1.370 \qquad (11)$$

$$\frac{\langle x^2\rangle_{H_2^+} - \langle x^2\rangle_{HT^+}}{\langle x^2\rangle_{H_2^+} - \langle x^2\rangle_{HD^+}} = 1.369 \qquad (12)$$

whereas using *only* the leading terms leads in both cases to the ratio

$$\frac{1-(\mu_{H_2^+}/\mu_{HT})^{1/2}}{1-(\mu_{H_2^+}/\mu_{HD^+})^{1/2}} = 1.370 \qquad (13)$$

Qualitatively, the mass change accompanying the replacement of ^{m}X by its heavier isotope $^{m'}$X leads to a shorter average bond length. In Figure 2, we show for the lowest vibrational levels the probabilities of finding the diatomic molecule at the various internuclear separations. For the same anharmonic potential, the lighter isotopomer H_2^+ clearly shows greater probabilities of being found in a more extended configuration compared with D_2^+ at each vibrational state. Since the vibrational frequencies are lower for the heavier isotopomer, the populations of its higher vibrational states are somewhat greater. Both effects constitute the mass dependence of the thermal average $\langle x\rangle^T$, with the latter being less important than the former:

$$\{\langle x\rangle^T - \langle x\rangle^{*T}\} \approx -3a_1\frac{B_e}{\omega_e}\left[1-\left(\frac{\mu}{\mu^*}\right)^{1/2}\right]\langle\, v+\tfrac{1}{2}\rangle^T \qquad (14)$$

If we use a harmonic oscillator density of vibrational states, we get a simple form

$$\langle\, v+\tfrac{1}{2}\rangle^T_{HO} = \tfrac{1}{2}\coth(hc\omega_e/2k_BT) \qquad (15)$$

which itself has a mild mass dependence, which is not too important when ω_e is large, in which case coth $(hc\omega_e/2k_\beta T)$

Table 6

$x = (r - r_e)/r_e$	H_2^+	HD^+	HT^+	D_2^+
$\langle x\rangle_{v=0}$	0.033 12	0.028 63	0.026 97	0.023 32
$\langle x^2\rangle_{v=0}$	0.014 47	0.012 35	0.011 58	0.009 90
$\langle x^3\rangle_{v=0}$	0.001 66	0.001 24	0.001 09	0.000 81
HO $\langle x\rangle_v$, $\langle x^3\rangle_v$	0	0	0	0
HO $\langle x^2\rangle_{v=0}$	0.012 98	0.011 24	0.010 598	0.009 178
ω_e (cm^{-1})	2323.5	2012.2	1897.2	1643.0

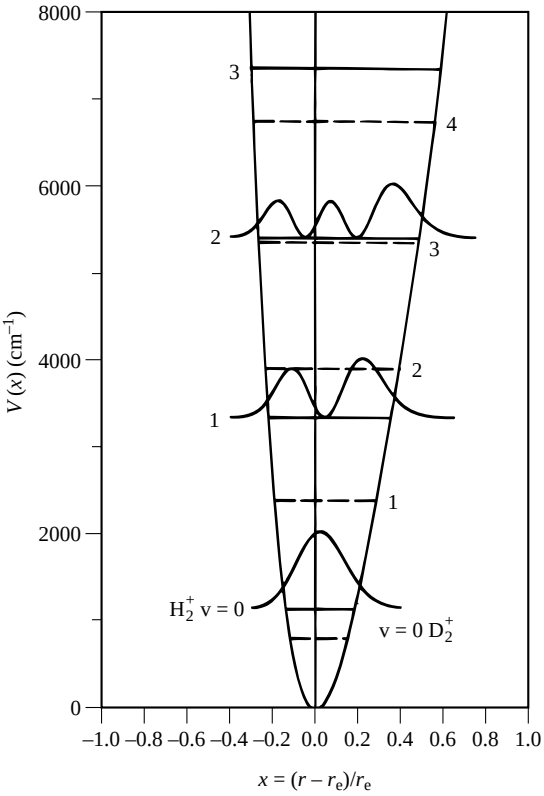

Figure 1 Vibrational levels and wavefunctions (squared) for the $H_2{}^+$ molecule. Also shown, by dashed lines, are the vibrational levels of the $D_2{}^+$ molecule

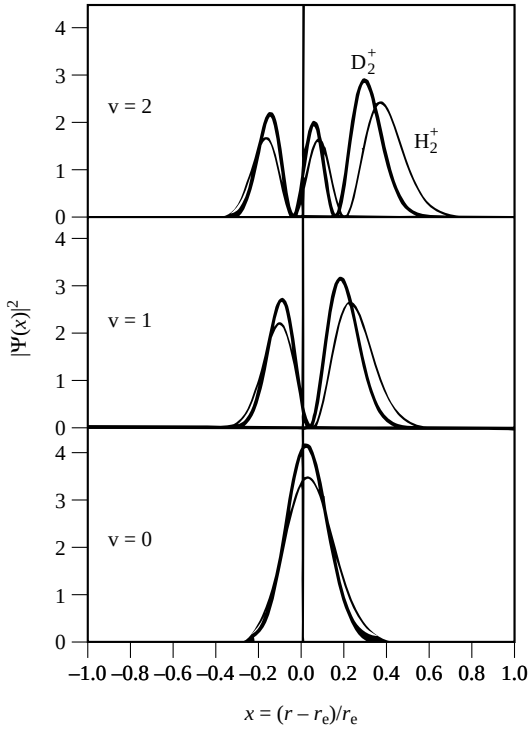

Figure 2 Vibrational wavefunctions (squared) for the $D_2{}^+$ molecule (heavy lines) and the $H_2{}^+$ molecule (light lines)

is very close to 1. A useful form of an approximate potential for the diatomic molecule is the Morse function

$$V = D_e\{1 - \exp[-a(r - r_e)]\}^2 \tag{16}$$

where D_e is the dissociation energy and a is called the Morse parameter, ar_e being a dimensionless quantity related to the ratio

$$\frac{1}{3!}\left(\frac{d^3V}{dx^3}\right)_e \Big/ \frac{1}{2!}\left(\frac{d^2V}{dx^2}\right)_e = -ar_e = a_1 \tag{17}$$

and

$$\langle x\rangle = \tfrac{3}{2}ar_e\langle x^2\rangle \tag{18}$$

At this level of theory, the mass dependence of $\langle x^2\rangle$ is the same as that of $\langle x\rangle$. Thus, we find that for diatomic molecules, neglecting the mass dependence in the coth function,

$$\langle x\rangle^T - \langle x\rangle^{*T} \approx \frac{3ar_e}{2}\frac{B_e}{\omega_e}\left[1 - \left(\frac{\mu}{\mu^*}\right)^{1/2}\right]\coth\left(\frac{hc\omega_e}{2k_BT}\right)$$
$$\approx \langle x\rangle^T\left[1 - \left(\frac{\mu}{\mu^*}\right)^{1/2}\right] \tag{19}$$

or

$$\langle \Delta r\rangle^T - \langle \Delta r\rangle^{*T} \approx \langle \Delta r\rangle^T_{vib}\left[1 - \left(\frac{\mu}{\mu^*}\right)^{1/2}\right] \tag{20}$$

$$\langle \Delta r\rangle^T_{vib} \approx \frac{3ar_e^2}{2}\frac{B_e}{\omega_e}\coth\left(\frac{hc\omega_e}{2k_BT}\right) \tag{21}$$

When μ/μ^* is very close to 1 (which is true for most situations not involving hydrogen), $1 - (\mu/\mu^*)^{1/2}$ can be further approximated by $(\mu^* - \mu)/2\mu^*$ or, in the comparison of the isotopomers A ^{m}X and A $^{m'}$X, by[27]

$$1 - \left(\frac{\mu}{\mu^*}\right)^{1/2} \approx \frac{1}{2}\frac{(m' - m)}{m'}\frac{m_A}{(m_A + m)} \tag{22}$$

$$\langle \Delta r\rangle^T - \langle \Delta r\rangle^{*T} \approx \langle \Delta r\rangle^T_{vib}\frac{1}{2}\frac{(m' - m)}{m'}\frac{m_A}{(m_A + m)} \tag{23}$$

with an analogous expression for $\langle(\Delta r)^2\rangle$. Here we find already the origin of general trend 4 in Section 2. The dynamic factors contain the mass dependence, and in diatomic molecules this mass dependence takes a simple form. It is interesting to point out here that, even for polyatomic molecules, this mass dependence has been found to hold: for $^{m'/m}SeF_6$, a plot of $\langle \Delta r_{SeF}\rangle^T$ and $\langle(\Delta r_{SeF})^2\rangle^T$ versus $(m' - m)/m'$ for m = 74 and m' = 76, 77, 78, 80, 82 leads to straight lines passing through the origin.[28]

A very interesting global description of potential functions for diatomic molecules was given by Herschbach and Laurie.[29] They found that the second and third derivatives of the potential could be described by exponential functions of the equilibrium internuclear distance, each described by a family of curves which are determined by the locations of the bonded atoms in rows of the Periodic Table:

$$(-1)^n F_n = 10^{-(r_e - p_n)/q_n} \tag{24}$$

where

$$F_3 \equiv \frac{1}{3}\left(\frac{\mathrm{d}^3V}{\mathrm{d}r^3}\right)_\mathrm{e}, \quad F_2 \equiv \left(\frac{\mathrm{d}^2V}{\mathrm{d}r^2}\right)_\mathrm{e} \tag{25}$$

and p_n and q_n are parameters that characterize any two rows of the Periodic Table. It was proposed by Jameson and Osten[27] that the averages $\langle x\rangle_\mathrm{v}$ and $\langle x^2\rangle_\mathrm{v}$ can be determined entirely from a knowledge of the r_e and the rows of the Periodic Table to which the atoms belong, using the following relations:

$$\langle \Delta r\rangle_\mathrm{v} = r_\mathrm{e}\langle x\rangle_\mathrm{v} \approx \frac{3h}{8\pi}\mu^{-1/2}10^{-D}(2\ \mathrm{v}+1) \tag{26}$$

$$\langle(\Delta r)^2\rangle_\mathrm{v} = r_\mathrm{e}^2\langle x^2\rangle_\mathrm{v} \approx \frac{h}{4\pi}\mu^{-1/2}10^{-d}(2\ \mathrm{v}+1) \tag{27}$$

where

$$D \equiv \frac{r_\mathrm{e}-p_3}{q_3} - \frac{3(r_\mathrm{e}-p_2)}{2q_2} \tag{28}$$

$$d \equiv \frac{r_\mathrm{e}-p_2}{2q_2} \tag{29}$$

Figure 3 shows a plot of $\langle\Delta r\rangle_\mathrm{vib}$ calculated at 300 K for a large set of diatomic molecules using their individual spectroscopic constants. It appears that the global relation given in equation (26) provides a reasonably good description of the vibrationally averaged bond displacement for diatomic molecules. It has been shown that these equations can be used as well to estimate the dynamic parts for polyatomic molecules, except that the constant factor is closer to $\frac{3}{7}$ than $\frac{3}{8}$.

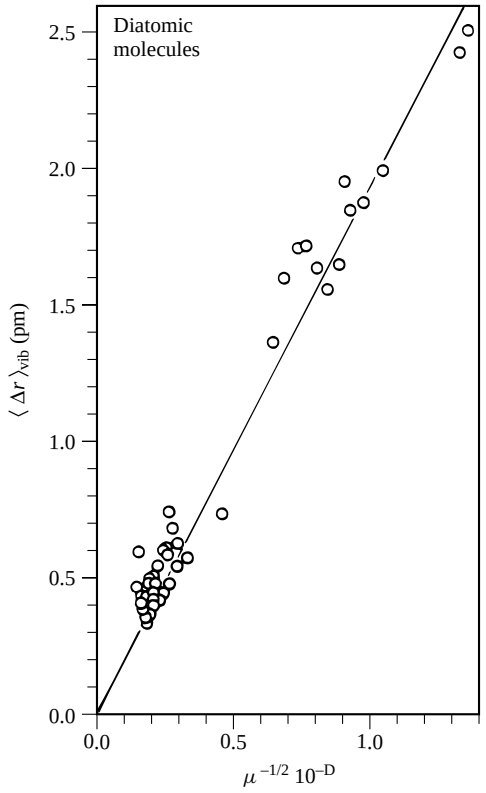

Figure 3 Mean bond displacement in diatomic molecules calculated by vibrational averaging over their individual potential surfaces compared with the global form $\langle\Delta r\rangle_\mathrm{vib} \approx (3\mathrm{h}/8\pi)\mu^{-1/2}10^{-D}$ (the straight line), where D is defined in equation (28). (Reproduced by permission of the American Insitute of Physics from Jameson and Osten[27])

3.2 The Shapes of Shielding Surfaces

In the context of the Born–Oppenheimer approximation, analogous to the potential energy surface, which is a mass-independent electronic property of a molecule in a given electronic state, there is likewise a mass-independent nuclear shielding surface that describes the variation of the shielding as a function of nuclear configuration. For a diatomic molecule, this surface can be described entirely in terms of the internuclear separation. Two examples are shown in Figures 4 and 5. At the united atom limit (r = 0), the diamagnetic shielding of the He^+ ion is (not shown) 35.5009 ppm. At the equilibrium geometry of $H_2{}^+$, the proton shielding is 11.4296 ppm, and at the separated atom limit, the diamagnetic shielding corresponds to half that of the free hydrogen atom ($\frac{1}{2}$)17.75 ppm.[30] The other example is ^{23}Na shielding in NaH, in which the shielding at the equilibrium geometry is lower than for the separated system (either Na^+ or Na atom).[31] Figure 4 is a typical shielding surface for diatomic molecules in that the shielding surface has negative first and second derivatives.[32,33] For example, ^{19}F in the HF molecule and in the F_2 molecule, and ^{35}Cl in the HCl molecule and in the ClF molecule, all have negative first and second derivatives; that is, deshielding accompanies bond extension. It is also typical for the proton shielding in the molecule at its equilibrium geometry to be greater than that for the free H atom in the separated systems. On the other hand, the heavy nuclei are generally deshielded in the molecule at its equilibrium geometry compared with the diamagnetic shielding of the free atom. For example, nearly all ^{19}F nuclei have shielding less than 470.71 ppm. (^{19}F in ClF is a notable exception, and ^{19}F in CH_3F has an isotropic shielding nearly the same as that of the free F atom.) Every ^{19}F shielding first derivative at the equilibrium geometry, including ^{19}F in the ClF molecule, has been found to be negative, and the second derivative is negative as well.[34] On the other hand, the shielding surfaces for ^{23}Na in NaH and ^{7}Li in LiH have positive first derivatives at the equilibrium geometry.[31] The shapes of the shielding surfaces in Figures 4 and 5 are fairly similar; the major difference is which point on the shielding surface corresponds to the pocket in the PES and to which side of the shielding minimum this point corresponds. We have seen that the general behavior in vibrational averaging in the anharmonic PES is that the probabilities are greater on the $r > r_\mathrm{e}$ side. Thus, dynamic averaging always leads to deshielding when the pocket in the PES is to the short-r side of the shielding minimum, whereas dynamic averaging leads to increased shielding relative to the shielding at the equilibrium geometry when the pocket in the PES is to the longer-r side of the shielding minimum. Most nuclei that are observed in NMR are found on the right-hand side of the Periodic Table, where the shielding surface and the PES are related as in Figure 4; there are fewer observations of the alkali and alkaline earth nuclei, whose shielding surfaces and PES are related as in Figure 5. Therefore, the usual case

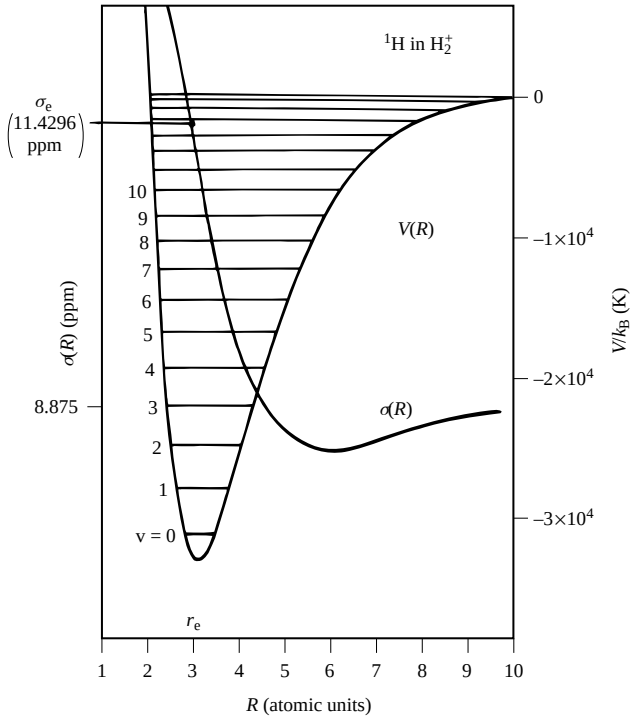

Figure 4 The ^{1}H shielding surface for the H_2^+ molecule is shown with the potential energy surface. The shielding surface is from ab initio calculations by Hegstrom.[30] (Reproduced by permission of the American Institute of Physics from Jameson and de Dios[31])

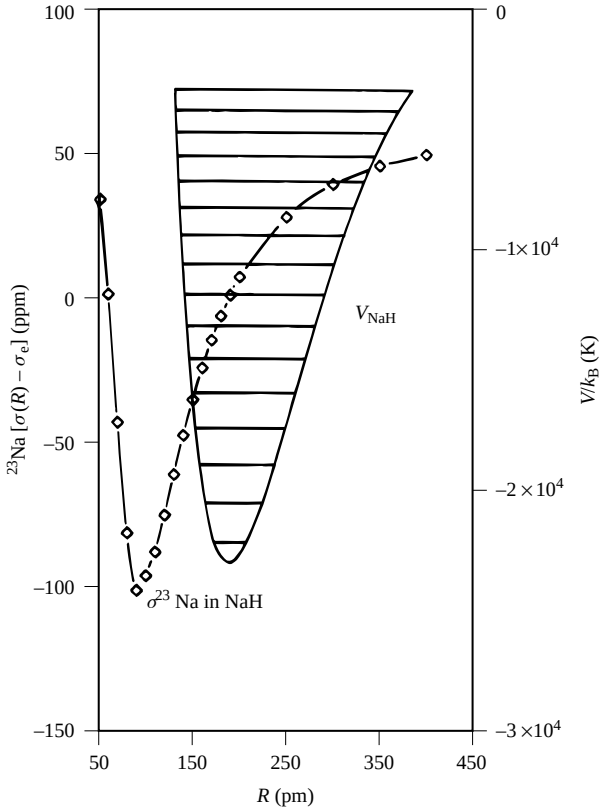

Figure 5 The ^{23}Na shielding surface for the NaH molecule is shown with the potential energy surface. The shielding surface is from ab initio calculations by Jameson and de Dios. (Reproduced by permission of the American Institute of Physics from Jameson and de Dios[31])

is more like Figure 4. Here then is the explanation for general trend 1 in Section 2: superposition of Figure 2 on Figure 4 would lead to a nucleus in the lighter isotopomer being less shielded than the same nucleus in the heavy isotopomer. Preponderance of this situation would lead to a nearly universal sign of one-bond isotope shifts. The exceptions will be Li and Na in the hydrides, for example.

The magnitudes of the isotope shifts would correspond to the ranges of chemical shifts of the observed nucleus if the shielding surfaces themselves scale to these. Let us see. We present the shielding surfaces in the vicinity of the equilibrium geometry in analogous compounds in Figure 6, where ^{19}F in F_2 is compared with ^{35}Cl in ClF (both are bonded to fluorine). ^{19}F in HF is compared with ^{35}Cl in HCl (both are bonded to an H atom). Finally, ^{23}Na in NaH is compared with ^{7}Li in LiH. It is found that if the change in shielding, $\sigma(r) - \sigma(r_e)$, is scaled by the factor $r_e\langle a_0^3/r^3\rangle$, the equilibrium bond distance in the molecule and the purely electronic quantity $\langle a_0^3/r^3\rangle$ characteristic of the atom, for the observed nucleus, the surfaces that describe the change in the shielding of different nuclei in analogous bonding situations superimpose.[31] This then is an explanation for general trend 3 in Section 2: the magnitude of the isotope shift is a function of the observed nucleus and reflects its chemical shift range. A general discussion of shielding surfaces is given by de Dios and Jameson.[35]

3.3 Averaging Over Shielding Surfaces

It is sometimes actually necessary to evaluate the average over a large part of the shielding surface.[36] For example, the PES of the NH_3 molecule has a rather broad double minimum in the inversion coordinate. The trace on the ^{15}N shielding surface along this inversion coordinate is shown in Figure 7. To obtain the contribution to the average ^{15}N shielding from this degree of freedom, it was necessary to find the numerical PES (which are highly anharmonic) and solve for the vibrational wavefunctions. These are shown in Figure 7. The average for each state 0^s, 0^a, 1^s, 1^a, 2^s, 2^a was numerically calculated with these functions, $\langle\Psi_v|\hat{\sigma}|\Psi_v\rangle$, and the thermal average is obtained as

$$\langle\sigma\rangle^T = \frac{\sum_v e^{-E_v/k_BT}\langle\sigma\rangle_v}{\sum_v e^{-E_v/k_BT}} \tag{30}$$

For semirigid molecules that we often observe in NMR (excluding molecules that are fluxional or that undergo low-frequency torsion), the motions involved in the averaging take place in a small pocket of the potential energy surface close to the equilibrium configuration. It is therefore not necessary to calculate the entire shielding surface, as we have shown in Figures 4, 5, and 7. In the same way that averages such as $\langle x\rangle$, $\langle x^2\rangle$, $\langle x^3\rangle$, etc. could be evaluated in terms of the derivatives of the PES such as represented by the quantities a_0, a_1, a_2, a_3, etc. in the Dunham potential function, it is possible to calculate the average shielding from derivatives of the shielding surface at the equilibrium geometry, since we only need to average over very small displacements away from the minimum in the PES.

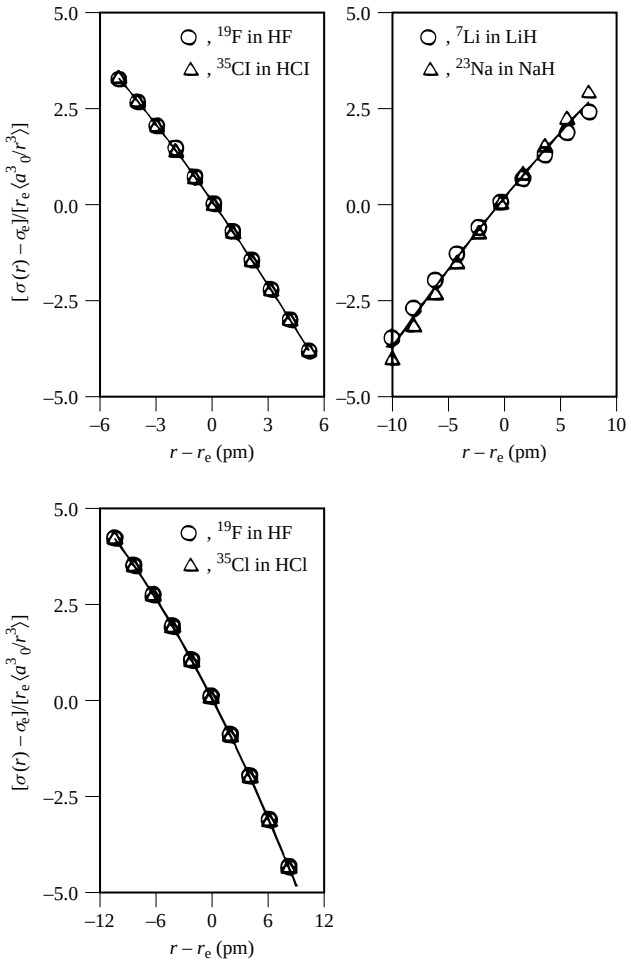

Figure 6 The shielding surfaces of analogous diatomic molecules in the vicinity of the equilibrium geometry, in the range of nuclear displacements spanning the classical turning points of the ground vibrational state. (Reproduced by permission of the American Institute of Physics from Jameson and de Dios[31])

For a diatomic molecule, it is convenient to expand the shielding surface as a power series in $x = (r - r_e)/r_e$. For a particular molecular state characterized by vibrational and rotational quantum numbers v and J,

$$\langle\sigma\rangle_{vJ} = \sigma_e + \left(\frac{d\sigma}{dx}\right)_e \langle x\rangle_{vJ} + \frac{1}{2}\left(\frac{d^2\sigma}{dx^2}\right)_e \langle x^2\rangle_{vJ} + \cdots \qquad (31)$$

Here $\langle x\rangle_{vJ}$, $\langle x^2\rangle_{vJ}$, ... are the averages over the vibrational–rotational wavefunctions corresponding to the (v, J) level, which we have already described in Section 3.1. The isotope shift is therefore given by

$$\langle\sigma\rangle^T - \langle\sigma\rangle^{*T} = \left(\frac{d\sigma}{dx}\right)_e (\langle x\rangle^T - \langle x\rangle^{*T}) + \frac{1}{2}\left(\frac{d^2\sigma}{dx^2}\right)_e (\langle x^2\rangle^T - \langle x^2\rangle^{*T}) + \cdots \qquad (32)$$

With the approximations described in Section 3.1, using the Morse parameter,

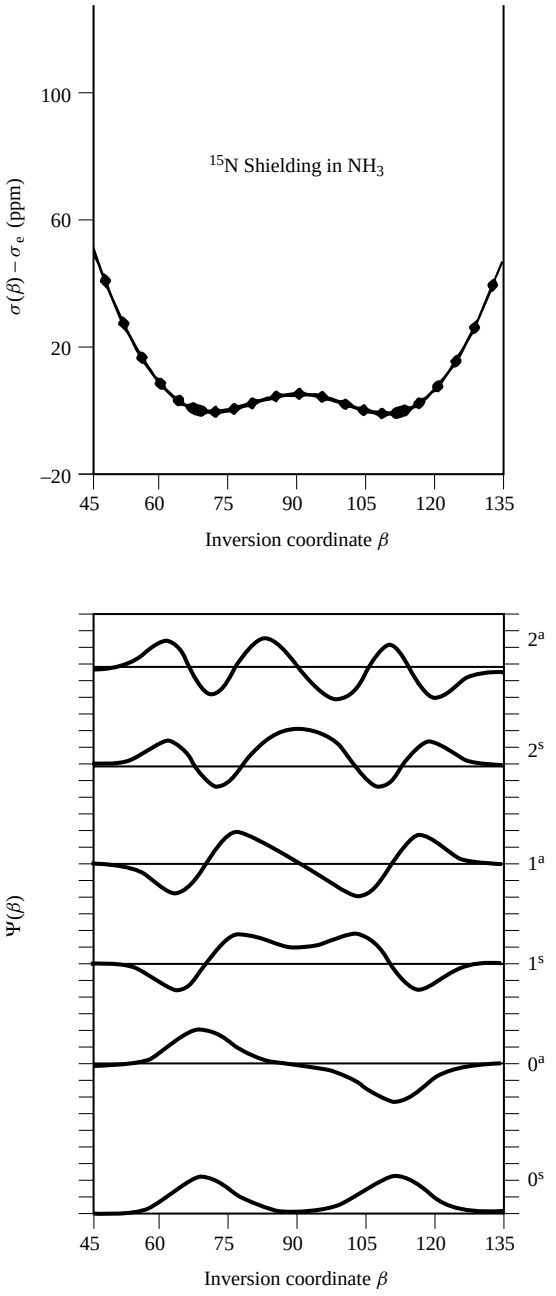

Figure 7 The ^{15}N shielding surface of NH_3 along the inversion coordinate β (the angle between the symmetry axis and a N–H bond) is shown with the vibrational wavefunctions for the lowest inversion levels. The shielding average can be obtained by numerical integration as $\langle\sigma\rangle_v = \int \Psi_v^*(\beta)\sigma(\beta)\Psi_v(\beta)\, d\beta$. (Reproduced by permission of the American Institute of Physics from Jameson et al.[36])

$$\langle x\rangle^T \approx \tfrac{3}{2} a r_e \langle x^2\rangle^T \qquad (33)$$

the isotope shift in diatomic molecules is given by

$$\langle\sigma\rangle^T - \langle\sigma\rangle^{*T} \approx \left[\left(\frac{d\sigma}{dx}\right)_e + \frac{1}{3ar_e}\left(\frac{d^2\sigma}{dx^2}\right)_e\right](\langle x\rangle^T - \langle x\rangle^{*T}) + \cdots \approx \left[\left(\frac{d\sigma}{dr}\right)_e + \frac{1}{3a}\left(\frac{d^2\sigma}{dr^2}\right)_e\right](\langle\Delta r\rangle^T - \langle\Delta r\rangle^{*T}) \qquad (34)$$

and, when coth ($hc\omega_e/2k_BT$) is close to 1,

$$\langle\sigma\rangle^T - \langle\sigma\rangle^{*T} \approx \left[\left(\frac{d\sigma}{dr}\right)_e + \frac{1}{3a}\left(\frac{d^2\sigma}{dr^2}\right)_e\right] \times \langle\Delta r\rangle^T_{vib}\left[1 - \left(\frac{\mu}{\mu^*}\right)^{1/2}\right] \quad (35)$$

In equations (34) and (35), the first quantity (in square brackets) is a mass-independent purely electronic quantity; the second quantity is a mass-dependent dynamic factor. As we have seen, both the first and second derivatives of the shielding surface are most often negative. Right here, we see that the sign of the isotope shift is negative owing to $(d\sigma/dr)_e$ being negative, since the shift is defined such that the dynamic factor is positive; that is, the nucleus in the light isotopomer is less shielded (appears at higher frequency) than the nucleus in the heavy isotopomer. The unusual (positive) sign of the isotope shift will be observed when the shielding derivative is positive, such as for ^{23}Na in NaH or ^{7}Li in LiH. For polyatomic molecules, it makes physical sense to expand the nuclear shielding in terms of the normal coordinates Q_s (a concept of significance only for small displacements):[21,37]

$$\sigma = \sigma_e + \sum_s \left(\frac{\partial\sigma}{\partial Q_s}\right)_e Q_s + \frac{1}{2}\sum_{s,r}\left(\frac{\partial^2\sigma}{\partial Q_r\,\partial Q_s}\right)_e Q_r Q_s + \cdots \quad (36)$$

where the shielding derivatives are taken at the equilibrium configuration. Normal coordinates are a logical choice for this expansion, since methods of evaluating the average values $\langle Q_s\rangle$ and $\langle Q_r Q_s\rangle$ are well known in vibrational spectroscopy. However, the derivatives of the nuclear shielding with respect to the mass-dependent normal coordinates are not invariant under isotopic substitution. For the purpose of discussing the isotope shift, it is more convenient to expand the shielding in terms of mass-independent internal displacement coordinates:[5,21]

$$\sigma = \sigma_e + \sum_i \left(\frac{\partial\sigma}{\partial\mathcal{R}_i}\right)_e \mathcal{R}_i + \frac{1}{2}\sum_{i,j}\left(\frac{\partial^2\sigma}{\partial\mathcal{R}_i\,\partial\mathcal{R}_j}\right)_e \mathcal{R}_i\mathcal{R}_j + \cdots \quad (37)$$

where $\mathcal{R}$ stands for the bond displacements (Δr_i) and the bond angle deformations ($\Delta\alpha_{ij}$).

The theoretical interpretation of isotope shifts in polyatomics therefore involves the mass-independent electronic quantities such as

$$\left(\frac{\partial\sigma}{\partial\mathcal{R}_i}\right)_e = \left(\frac{\partial\sigma}{\partial r_i}\right)_e \quad \left(\frac{\partial\sigma}{\partial\alpha_{ij}}\right)_e \quad (38)$$

which describe the change in nuclear shielding with bond extension or angle deformation, and the mass-dependent thermal averages $\langle\mathcal{R}_i\rangle^T$, which are $\langle\Delta r\rangle^T$, $\langle\Delta\alpha\rangle^T$, ... and $\langle\mathcal{R}_i\mathcal{R}_j\rangle^T$, which are $\langle(\Delta r)^2\rangle^T$, $\langle(\Delta\alpha)^2\rangle^T$, $\langle\Delta r\ \Delta\alpha\rangle^T$, ... The isotope shift is given by

$$\sigma - \sigma = \sum_i \left(\frac{\partial\sigma}{\partial\mathcal{R}_i}\right)_e \langle\mathcal{R}_i\rangle^T + \frac{1}{2}\sum_{i,j}\left(\frac{\partial^2\sigma}{\partial\mathcal{R}_i\,\partial\mathcal{R}_j}\right)_e \langle\mathcal{R}_i\mathcal{R}_j\rangle^T + \cdots \quad (39)$$

In order to be able to evaluate $\langle\mathcal{R}_i\rangle^T$, $\langle\mathcal{R}_i\mathcal{R}_j\rangle^T$ etc., we need a potential surface in which the vibrational motion of the molecule takes place. The known derivatives of this surface are the quadratic, cubic, etc. force constants. Normal coordinate analysis with the quadratic force constants gives the solutions to the harmonic problem, which are the harmonic frequencies ω_s, the normal coordinates Q_s, and the **L** matrix. The internal displacement coordinates $\mathcal{R} = \Delta r_i, \Delta\alpha_{ij}$, etc. can be expressed in terms of these normal coordinates in the general relation[38]

$$\mathcal{R} = \mathbf{L}Q \quad (40)$$

where is a tensor containing the transformation coefficients between the curvilinear internal coordinates and various powers of Q_s. The vibrational part of Δr_i is then

$$\Delta r_i = \sum_i L_i^r Q_r + \frac{1}{2}\sum_{r,s} L_i^{rs} Q_r Q_s + \frac{1}{6}\sum_{r,s,t} L_i^{rst} Q_r Q_s Q_t + \cdots \quad (41)$$

Thus, the vibrational average $(\Delta r)_{vib}$ can be expressed in terms of $\langle Q_r\rangle$, $\langle Q_r Q_s\rangle$, etc. The analytical expressions for elements of the **L** tensor are given by Hoy et al.,[38] in which the linear terms L_i^r are identical to the elements L_{ir} of the **L** matrix. The above equation is exact, but in practice, of course, the series must be truncated; in general, it converges well, each term being smaller than the preceding by a factor of about 10 for typical vibrational amplitudes. The expectation values of only totally symmetric coordinates Q_s are required:[39]

$$\langle Q_s\rangle = \left(\frac{h}{4\pi^2 c}\right)^{1/2}\omega_s^{-3/2}\left[3k_{sss}(\mathrm{v}_s + \tfrac{1}{2}) + \sum_r{}' k_{srr}(\mathrm{v}_r + \tfrac{1}{2}g_r)\right] \quad (42)$$

where ω_s are the normal frequencies and k_{srr} are the cubic force constants, both in wavenumbers. g_r denotes the degeneracy of the rth vibration. $\langle Q_r Q_s\rangle = 0$ if $\omega_r \neq \omega_s$, and

$$\langle Q_s^2\rangle = \frac{h}{4\pi^2 c\omega_s}(\mathrm{v}_s + \tfrac{1}{2}) \quad (43)$$

To obtain the thermal average shielding, we again need $\langle \mathrm{v}_s + \frac{1}{2}\rangle^T$. For larger molecules, it becomes impossible to calculate a sufficient number of rovibrational states in order to use the exact method for the thermal averaging, so the only practical way of calculating expectation values of molecular properties over different rotational and vibrational states for a given temperature is by using the harmonic approximation for the vibrational partition function, that is,

$$\langle \mathrm{v}_s + \tfrac{1}{2}\rangle^T = \tfrac{1}{2}\coth(hc\omega_s/2k_BT) \quad (44)$$

3.4 Relative Magnitudes of Terms That Contribute to the Isotope Shift

Mass substitution at one site in the molecule affects dynamic averages of all electronic properties. If, in particular, we have nuclear spins at various sites, all of these will have different average shifts; some will experience larger changes than others. In general, the entire molecule participates in the dynamic averaging. Depending on the nature of each nuclear shielding surface, the change in chemical shift may be of either sign. Each molecule offers a unique situation, and, especially for the long-range isotope effects, vibrations involving many atoms may play a part. To illustrate the types of terms that contribute to a one-bond isotope shift, we use the

$^1\Delta\ ^{13}C\ (^{2/1}H)$ in CH_4 as an example. During vibration, the displacements away from the equilibrium nuclear configuration can be small enough that a Taylor series expansion can be used:[40]

$$\begin{aligned}\langle\sigma^C\rangle = \sigma_e &+ P_r(\langle\Delta r_1\rangle + \langle\Delta r_2\rangle + \langle\Delta r_3\rangle + \langle\Delta r_4\rangle)\\ &+\tfrac{1}{2}P_{rr}[\langle(\Delta r_1)^2\rangle + \langle(\Delta r_2)^2\rangle + \langle(\Delta r_3)^2\rangle + \langle(\Delta r_4)^2\rangle]\\ &+P_{rs}(\langle\Delta r_1\Delta r_2\rangle + \langle\Delta r_1\Delta r_3\rangle + \langle\Delta r_1\Delta r_4\rangle\\ &+\langle\Delta r_2\Delta r_3\rangle + \langle\Delta r_2\Delta r_4\rangle + \langle\Delta r_3\Delta r_4\rangle)\\ &+\tfrac{1}{2}P_{\alpha\alpha}[\langle(\Delta\alpha_{12})^2\rangle + \cdots] + P_{\alpha\beta}(\langle\Delta\alpha_{12}\Delta\alpha_{13}\rangle + \cdots)\\ &+P_{r\alpha}(\langle r_1\Delta\alpha_{12}\rangle + \cdots) + P_{\alpha\omega}(\langle\Delta\alpha_{12}\Delta\alpha_{34}\rangle + \cdots)\\ &+ \text{higher-order terms}\end{aligned} \tag{45}$$

where $P_r \equiv (\partial\sigma^C/\partial r_1)_e$, while P_{rr} and P_{rs} are the second derivatives of the ^{13}C shielding with respect to the C–H bond distances; $P_{\alpha\alpha}$, $P_{\alpha\beta}$, and $P_{\alpha\omega}$ are the second derivatives of the ^{13}C shielding with respect to the HCH bond angles, and $P_{r\alpha}$ is the mixed second derivative $(\partial^2\sigma^C/\partial r_1\ \partial\alpha_{12})_e$. In some molecules, there are first derivatives with respect to the angle as well, for example, for ^{17}O in H_2O and ^{31}P in PH_3.[41,42] In yet others, the averaging cannot be carried out by considering small displacements, as in the inversion motion of the NH_3 molecule. The complexity of the equation increases with increasing number of atoms. Nevertheless, many general trends may be observed in the huge body of information represented in tables of thousands of isotope shifts.[1–3] These trends have become apparent, despite the uniqueness of the dynamic averaging of each molecule, because some terms in the full theory are more dominant than others. It is the persistence of the dominant contributions in most molecules that allows us to consider isotope shifts in much simpler terms, short of full averaging of full shielding surfaces in every case. In Table 7, we examine the relative magnitudes of terms that contribute to the isotope shift in selected molecules, where the calculations of the many terms (as shown above for CH_4) have been carried out to gain some insight into what might be expected in other molecules.[36,42–46] Clearly, the mixed terms and higher-order terms (listed in Table 7 as 'Other') are negligible compared with the total isotope shift. The P_r term, which is due entirely to the anharmonicity of the vibration, provides the largest contribution, but P_{rr} terms are not negligible. The stretch (P_r and P_{rr} terms together) dominate, even in the case of NH_3, where the inversion mode gives significant angle deformation contributions. If we can extrapolate these results to larger molecules, we can say that the bond stretching contributions dominate one-bond isotope shifts, and the anharmonic part of this, which goes with the first shielding derivative $(\partial\sigma/\partial r)_e$, gives the largest contribution. However, the terms involving the second derivative $(\partial^2\sigma/\partial r^2)_e$ are also important. Bond angle contributions are uniformly less important than the bond stretching contributions to the isotope shift.

Table 8 Comparison of Shielding Derivatives Estimated from Isotope Shifts with Those Obtained from Ab Initio Quantum Mechanical Calculations

	$(\partial\sigma/\partial r)_e$ (ppm Å^{-1})	
	Estimated from isotope shifts	Ab initio theoretical
^{15}N in CN^-	−872[47]	−809.8[34]
^{13}C in CN^-	−473[47]	−494.4[34]
^{15}N in NH_3	−124[17]	−123.2[36]
^{15}N in NH_4^+	−65[27]	−67.9[52]
^{31}P in PH_3	−180[15]	−148.83[42]
^{13}C in CH_4	−38[48]	−52.62[53]
^{17}O in H_2O	−294[17]	−270.9[41]
^{77}Se in H_2Se	−1250[49]	−1056.5[46]
^{13}C in CO	−456[12]	−538.1[34]
^{17}O in CO	−1150[12]	−1061.1[34]
^{15}N in N_2	−912[50]	−1011.4[34]
^{11}B in BH_4^-	−26.7[27]	−27.0[52]
^{13}C in CO_2	−214[51]	−156.4[34]
^{15}N in NO_2^-	−990[51]	−1438.1[34]
^{15}N in NO_3^-	−410[51]	−498.0[34]

If we take the experimental isotope shift and use an estimate for the dynamic factor $\langle\Delta r_{XH}\rangle - \langle\Delta r_{XD}\rangle$, we arrive at a reasonable estimate of the shielding derivative $(\partial\sigma/\partial r)_e$ in the molecule. Indeed, Table 8 shows that the estimated shielding derivatives compare reasonably well with the derivatives obtained from the ab initio shielding surfaces.

3.5 Additivity of Isotope Shifts

We can use the isotopomers of the CH_4 molecule to illustrate the additivity of NMR isotope shifts. The mean bond displacements in the methane family $CX_{4-n}Y_n$ (where X,Y = H,D,T) have been calculated using the anharmonic force field of methane.[19] It has been found that the substitution effects on the vibrational contribution to mean bond displacements are strictly additive. Each substitution of a hydrogen by a deuterium shortens the appropriate bond by nearly the same amount Δ. The mean bond displacements in $^{12}CH_{4-n}T_n$ and $^{12}CD_{4-n}T_n$ exhibit the same strictly linear dependence on n. We can express $\langle\Delta r_{CH}\rangle$ and $\langle\Delta r_{CD}\rangle$ in $^{12}CH_{4-n}D_n$ as follows. If we let

$$d = \langle\Delta r_{CH}\rangle \quad \text{in } CH_4 \text{ at } 300\,K \tag{46}$$

Table 7 Isotope Shifts $\sigma^X(XH_n) - \sigma^X(XD_n)$ (in ppm) Calculated for ^{13}C, ^{15}N, ^{31}P, ^{17}O, and ^{77}Se Nuclei

Term	CH_4[43]	NH_3[36]	PH_3[42]	H_2O[44]	H_2Se[a]
P_r	−1.169	−2.05	−2.44	−2.847	−11.66
P_{rr}	0.453	−0.97	−1.68	−1.316	−5.59
$P_\alpha + P_{\alpha\alpha}$	+0.686	+0.66	+0.67	+0.404	+1.25
Other	−0.042	−0.004	0.002	+0.08	neglect
Total	−0.978	−2.36	−3.45	−3.68	−16.0
Experimental	−0.774	−1.87	−2.53	−3.09	−14.04

[a]Calculated by Jameson,[45] based on the points on the ab initio shielding surface of Tossell and Lazzeretti.[46]

$$d - \Delta = \langle \Delta r_{CD} \rangle \quad \text{in } CD_4 \text{ at } 300\,K \tag{47}$$

where d = 2.0881 pm and Δ = 0.553 45 pm, we find for $CH_{4-n}D_n$ that

$$\langle \Delta r_{CD} \rangle = d - \Delta + (4-n)\delta_D \tag{48}$$

$$\langle \Delta r_{CH} \rangle = d + n\delta_H \tag{49}$$

Similar relations can be found for the other series of isotopomers. That is, for a given bond, substitution of an isotope involved in this bond had an effect Δ on its own mean bond length (a primary effect on the mean bond displacement); each substitution of an isotope at some other bond has a much smaller effect δ (a secondary effect). The $^{2/1}$H-induced ^{13}C NMR isotope shift between any two isotopomers of $CH_{4-n}D_n$ can then be expressed as

$$\begin{aligned} \sigma^C(\,CH_{4-n}\,D_n) - \sigma^C(\,CH_{4-n'}\,D_{n'}) &= \left(\frac{\partial\sigma^C}{\partial r}\right)_e \\ &\quad \times[(n'-n)\Delta + \text{ terms in } \delta] \\ &\approx \left(\frac{\partial\sigma^C}{\partial r}\right)_e (n'-n)\Delta \end{aligned} \tag{50}$$

This is the basis for the near-additivity of isotope shifts due to substitution at equivalent sites. If we leave out the terms in δ (which are about two orders of magnitude smaller than Δ), we have strict additivity: the magnitude of the shift is proportional to the number $n' - n$ of atoms that have been substituted by isotopes. Even when all the terms in P_{rr}, P_{rs}, $P_{r\alpha}$, etc. are included and calculated properly, the nearly strict additivity of isotope shifts is preserved. Although there are many smaller changes that are not quite the same as each ^{m}X is replaced by $^{m'}$X, it has been shown that these smaller changes lead to only slight deviations from additivity, which deviations incidentally have been observed[15–18] just as predicted.[19]

4 GENERAL TRENDS IN THE ELECTRONIC FACTORS

We have already seen that the dynamical factors in one-bond isotope shifts are fairly predictable, and can even be estimated without a good force field because the mass-independent part of the dynamic factor is largely determined by the bond length and the rows of the Periodic Table of the pair of bonded atoms. We have also seen that the mass dependence of the isotope shift and its additivity can be explained entirely by the dynamic factors for one-bond isotope shifts. All other trends must therefore be attributable to trends in the electronic factor and the first and second derivatives of the nuclear shielding. If we estimate the dynamic factors $\langle \Delta r \rangle - \langle \Delta r \rangle^*$ as described in Section 3.1, it is possible to obtain the magnitudes and signs of the electronic factor $[(\partial\sigma/\partial r)_e + (1/3a)(\partial^2\sigma/\partial r^2)_e]$, which we shall denote simply by $(\partial\sigma/\partial r)_e$, with the understanding that the first-derivative terms nearly always dominate, although the ratio of the above two terms may range from 10:1 to 3:1.

Some trends in $(\partial\sigma/\partial r)_e$ have been predicted from the observed trends in isotope shifts.[5,6] Recent ab initio calculations have explored the generality of these trends and the limits and conditions of their applicability.[34]

1. $(\partial\sigma/\partial r)_e$ is usually negative. The general shape of the shielding surface shown in Figure 4 seems to be typical for a diatomic molecule, and, for most nuclei, the minimum in the shielding surface occurs at separations larger than the equilibrium internuclear separation, leading to a negative $(\partial\sigma/\partial r)_e$. The exceptional sign of $(\partial\sigma/\partial r)_e$ arises when the minimum in the shielding surface lies inside the equilibrium internuclear separation, as in Figure 5. In polyatomic molecules, negative $(\partial\sigma/\partial r)_e$ are also much more commonly found than positive ones, leading to the usual (negative) sign of the isotope shift.
2. $(\partial\sigma/\partial r)_e$ generally increases with the chemical shift range of the nucleus. We have seen in Figure 6 that changes in the shielding upon displacement away from the equilibrium geometry do scale in analogous compounds according to $\langle a_0^3/r^3 \rangle$ for the free atom, which is the same factor that varies periodically across the Periodic Table in the same way as the ranges of chemical shifts.[54,55] Because of this correlation, an easy way to obtain an estimate of an isotope shift is to use the scaling factor of $\langle a_0^3/r^3 \rangle$ values to provide a Periodic-Table-wide set of 'reduced isotope shifts', which need only be multiplied by the mass factors $[(m' - m)/m']$ $\times (m_A + m)/2m_A$ to get an estimate of the one-bond isotope shift induced by any isotopic substitution for any nucleus in any molecule.[56]
3. $(\partial\sigma/\partial r)_e$ has been found to correlate with the absolute shielding σ_0 in related molecules: at the equilibrium geometry, the most deshielded environments have more steeply changing shielding surfaces. When the dynamic terms are very similar, this forms the basis for the correlations of $^1\Delta$ with chemical shifts, which have been observed in some cases. Such correlations of isotope shifts are more likely to be noticed in diatomic-like situations such as $^{13/12}$C-induced ^{19}F isotope shifts or $^{18/16}$O-induced ^{13}C isotope shifts in O=C situations.[57] Chesnut and Wright have found that calculated shielding derivatives do roughly correlate with shielding itself for ^{19}F and for ^{13}C, ^{15}N, and ^{17}O involved in multiple bonds.
4. The magnitudes of the derivatives of shielding with respect to extension of a bond increase with increasing bond order. Since bond lengths tend to anticorrelate with bond order (higher bond order, shorter bond length), this trend in the shielding derivative is also the basis for the observed increasing magnitudes of one-bond isotope shifts for shorter bond lengths between the NMR nucleus and the substitution site.
5. The shielding derivative tends to be more negative with increasing negative net charge and with the presence of lone pairs on the observed nucleus. This has been found in the comparisons of ^{15}N in NO_2^- and NO_3^-, ^{15}N in NH_3 and NH_4^+, ^{31}P in PH_4^+, PH_3 and PH_2^-, ^{119}Sn in SnH_3^+, SnH_4 and SnH_3^-, and ^{13}C and also ^{15}N in HCN and CN^-.
6. Since the one-bond coupling constant is a purely electronic quantity, it must be the electronic factors in the one-bond isotope shifts that allow the observation of linear correlations with the one-bond coupling constant, and likewise the incremental effects of substitution of H by Ph or H by CH_3 in the examples in Table 9.[10–61] These above data translate to increasingly negative $(\partial\sigma^X/\partial r_{XH})_e$ upon successive Ph substitution at X.

Table 9

	$^1\Delta$ (ppm per D)		$^1\Delta^{13}C(^{2/1}H)$ (ppm per D)
^{15}N in NH_3	−0.623	^{13}C in CH_3D	−0.187
in $PhNH_2$	−0.715	in $PhCH_2D$	−0.2755
^{31}P in PH_3	−0.846	in $(Ph)_2CHD$	−0.342
in $PhPH_2$	−1.21	in $(Ph)_3CD$	−0.4377
^{13}C in CH_4	−0.192	^{13}C in CH_3D	−0.187
in $PhCH_3$	−0.28	in H_3CCH_2D	−0.284
^{77}Se in SeH_2	−7.02	in $(H_3C)_2CHD$	−0.3759
in PhSeH	−7.96	in $(H_3C)_3CD$	−0.4722

5 ISOTOPE SHIFTS OVER TWO OR MORE BONDS

Isotope shifts due to substitution with a heavier atom at a site remote from the observed nucleus show the same general trends as one-bond isotope shifts.

1. The sign is still generally negative, although some are positive, with some alternation of signs being observed in the same molecule.
2. The magnitude reflects the chemical shift range of the observed nucleus.
3. The magnitude is related to the fractional mass change.
4. The effect is additive.

These are generally smaller than one-bond shifts; nevertheless, a large number of them have been observed, some over a distance of seven or more bonds. The question is, what information is contained in these long-range shifts? What we propose to show here is that these long-range shifts are a property of the electronic transmission path from the site of substitution up to the resonant nucleus.

To illustrate the types of terms that contribute to a long-range isotope shift, let us consider a two-bond isotope shift such as $^2\Delta\ ^1H(^{2/1}H)$ in CH_4.[19] The average proton shielding for proton H_1 can be written as

$$\begin{aligned}\langle\sigma^{H_1}\rangle = {} & \sigma_e + P_r\langle\Delta r_1\rangle + P_s(\langle\Delta r_2\rangle + \langle\Delta r_3\rangle + \langle\Delta r_4\rangle) \\ & + \tfrac{1}{2}P_{rr}\langle(\Delta r_1)^2\rangle + \tfrac{1}{2}P_{ss}[\langle(\Delta r_2)^2\rangle + \langle(\Delta r_3)^2\rangle + \langle(\Delta r_4)^2\rangle] \\ & + P_{rs}(\langle\Delta r_1\Delta r_2\rangle + \langle\Delta r_1\Delta r_3\rangle + \langle\Delta r_1\Delta r_4\rangle) \\ & + P_{st}(\langle\Delta r_2\Delta r_3\rangle + \langle\Delta r_2\Delta r_4\rangle + \langle\Delta r_3\Delta r_4\rangle) + \cdots \end{aligned} \tag{51}$$

where

$$P_r \equiv \left(\frac{\partial\sigma^{H_1}}{\partial r_1}\right)_e, \quad P_s \equiv \left(\frac{\partial\sigma^{H_1}}{\partial r_2}\right)_e \tag{52}$$

and P_{rr}, P_{ss}, P_{rs}, and P_{st} are the appropriate second derivatives of the shielding with respect to the various C–H distances. Therefore, the two-bond deuterium-induced proton isotope shifts between CH_3D and CH_4 is (with D replacing proton number 2)

$$\begin{aligned}{}^2\Delta^1\,H(^{2/1}\,H) = {} & \langle\sigma^{H_1}\rangle_{CH_4} - \langle\sigma^{H_1}\rangle_{CH_3D} \\ = {} & (P_r + 2P_s)(\langle\Delta r_1\rangle_{CH_4} - \langle\Delta r_1\rangle_{CH_3D}) \\ & + P_s(\langle\Delta r_2\rangle_{CH_4} - \langle\Delta r_2\rangle_{CH_3D}) \\ & + (\tfrac{1}{2}P_{rr} + P_{ss})[\langle(\Delta r_1)^2\rangle_{CH_4} - \langle(\Delta r_1)^2\rangle_{CH_3D}] \\ & + \tfrac{1}{2}P_{ss}[\langle(\Delta r_2)^2\rangle_{CH_4} - \langle(\Delta r_2)^2\rangle_{CH_3D}] \\ & + (P_{rs} + 2P_{st})(\langle\Delta r_1\Delta r_2\rangle_{CH_4} - \langle\Delta r_1\Delta r_2\rangle_{CH_3D}) \\ & + (2P_{rs} + P_{st})(\langle\Delta r_1\Delta r_3\rangle_{CH_4} - \langle\Delta r_1\Delta r_3\rangle_{CH_3D}) \\ & + \cdots \end{aligned} \tag{53}$$

With D replacing proton number 2, $\delta = \langle\Delta r_i\rangle_{CH_4} - \langle\Delta r_i\rangle_{CH_3D}$ is (the same for i = 1,3,4) a slight change of about 10^{-3} pm in the other C–H average bond lengths due to deuteration, and $\langle\Delta r_2\rangle_{CH_4} - \langle\Delta r_2\rangle_{CH_3D}$ is the typical $\Delta = \langle r_{CH}\rangle - \langle\Delta r_{CD}\rangle$, which is of order about 0.5 pm:

$$\begin{aligned}{}^2\Delta^1\,H(^{2/1}\,H) \approx {} & (P_r + 2P_s)\delta + P_s\Delta + \left(\tfrac{1}{2}P_{rr} + P_{ss}\right)\delta_{rr} + \tfrac{1}{2}P_{ss}\Delta_{rr} \\ & + (P_{rs} + 2P_{st})\Delta_{rs} + (2P_{rs} + P_{st})\delta_{rs} \end{aligned} \tag{54}$$

If we invoke the relationship $\langle\Delta r\rangle \approx \frac{3}{2}ar_e\ \langle(\Delta r)^2\rangle$ used earlier, we find

$$\begin{aligned}{}^2\Delta^1\,H(^{2/1}\,H) \approx {} & \left(P_s + \frac{1}{3a}P_{ss}\right)\Delta + \left(P_r + \frac{1}{3a}P_{rr} + 2P_s + \frac{2}{3a}P_{ss}\right)\delta \\ & + \text{mixed terms} + \text{higher-order terms} \end{aligned} \tag{55}$$

or, more succinctly,

$$\begin{aligned}2\Delta^1\,H(^{2/1}\,H) \approx {} & \mathcal{S}\Delta + (\mathcal{P} + 2\mathcal{S})\delta \\ & + \text{mixed terms} + \text{higher-order terms} \end{aligned} \tag{56}$$

Here $\mathcal{P}$ stands for the following combination of primary first and second derivatives:

$$\mathcal{P} \equiv \left(\frac{\partial\sigma^{H_1}}{\partial r_1}\right)_e + \frac{1}{3a}\left(\frac{\partial^2\sigma^{H_1}}{\partial r_1^2}\right)_e \tag{57}$$

and is a measure of the sensitivity of the shielding of a nucleus to stretching of a bond to it. $\mathcal{S}$ stands for the following combination of secondary first and second derivatives:

$$\mathcal{S} \equiv \left(\frac{\partial\sigma^{H_1}}{\partial r_2}\right)_e + \frac{1}{3a}\left(\frac{\partial^2\sigma^{H_1}}{\partial r_2^2}\right)_e \tag{58}$$

and is a measure of the sensitivity of the shielding of a nucleus to stretching of a remote bond.[19] When we recall that $\Delta \approx 0.5$ pm whereas $\delta \approx 10^{-3}$ pm, we see that the term $\mathcal{S}\Delta$ would dominate the isotope shift unless $\mathcal{P}$ is two orders of magnitude larger than $\mathcal{S}$. It is therefore valid to consider a long-range isotope shift as largely described by a product of a primary change in the average bond length at the heavy atom substitution site (the dynamic factor) and a secondary shielding derivative(s) that measures the change in shielding upon a change with bond length at the remote site. This is very encouraging, because the secondary dynamic factor δ is so dependent on the entire molecular framework and potential energy surface in which vibrations take place that it is difficult to estimate. On the other hand, we have seen that Δ has a very straightforward dependence on r_e and the masses in the local fragment, and can be easily estimated. This means that if the δ terms are unimportant, the sign and magnitude of the long-range isotope shifts are a direct measure of the sign and

magnitude of $(\partial\sigma/\partial r_{\text{remote}})_e$. This derivative is stereospecific, dependent on electron-withdrawing/donating abilities of substituents, and has the usual electronic-transmission-path dependence of various observables such as long-range spin–spin coupling and substituent effects on chemical shifts. Thus, in $^{13}CH_3(CH_2)_{n-2}NHD$, for example,

$$ {}^{n}\Delta\,{}^{13}\mathrm{C}(^{2/1}\mathrm{H}) \approx \left[\left(\frac{\partial\sigma^{\mathrm{C}}}{\partial r_{\mathrm{NH}}}\right)_e + \frac{1}{3a}\left(\frac{\partial^2\sigma^{\mathrm{C}}}{\partial r_{\mathrm{NH}}^2}\right)_e\right] \times(\langle\Delta r_{\mathrm{NH}}\rangle - \langle\Delta r_{\mathrm{ND}}\rangle) \tag{59} $$

it is easy to see why *n*-bond isotope shifts are in general smaller than one-bond isotope shifts. The farther away the substitution site is from the observed nucleus, the smaller the secondary derivative is expected to be. For example, in the H_2O molecule,[41]

$$ \left(\frac{\partial\sigma^{\mathrm{H}_1}}{\partial r_{\mathrm{OH}_1}}\right)_e = -0.353 \text{ ppm pm}^{-1} $$
$$ \left(\frac{\partial\sigma^{\mathrm{H}_1}}{\partial r_{\mathrm{OH}_2}}\right)_e = -0.046 \text{ ppm pm}^{-1} \tag{60} $$

that is, a trace along the increasing coordinate r_{OH_1} gives a sharply decreasing H_1 shielding surface near the equilibrium geometry, but a trace along the coordinate r_{OH_2} on the same shielding surface is rather flat. Also, the nearly flat portion of the shielding surface could be sloping slightly in either direction; thus, either sign is possible for long-range isotope shifts. The secondary derivatives should still reflect the shielding sensitivity of various nuclei as manifested in the ranges of their chemical shifts.

The experimental evidence for the dominance of the term $\mathcal{S}\Delta$ is convincing.

1. The observed additivity of long-range isotope shifts is completely consistent with this. Isotope shifts from equivalent substitution sites such as a remote CH_3 group involve the secondary derivative multiplied by one Δ term for each C–D replacing a C–H.
2. The mass dependence of the two-bond isotope shift is the same as that of the one-bond shift, that is, $1\text{-}(\mu/\mu^*)^{1/2}$, where μ and μ^* are the local reduced masses *at the substitution site*. Furthermore, the ratio of the effects of substitution of H by T to that of H by D is the same as would be expected if the Δ term dominated the isotope shift. Vibrational calculations show that[48]

$$ \frac{\langle\Delta r_{\mathrm{CH}}\rangle_{\mathrm{CH_4}} - \langle\Delta r_{\mathrm{CT}}\rangle_{\mathrm{CT_4}}}{\langle\Delta r_{\mathrm{CH}}\rangle_{\mathrm{CH_4}} - \langle\Delta r_{\mathrm{CD}}\rangle_{\mathrm{CD_4}}} = 1.426 \tag{61} $$

   In $(CH_3)_2C{=}O$, the observed ratio of isotope shifts for tritium and deuterium substitution is[11]

$$ \frac{{}^{1}\Delta\,{}^{13}\mathrm{C}(^{3/1}\mathrm{H})}{{}^{1}\Delta\,{}^{13}\mathrm{C}(^{2/1}\mathrm{H})} = 1.424 \pm 0.025 \tag{62} $$

   That this ratio is indistinguishable from 1.426 serves to reassure us that the leading term is dominant in one-bond shifts, with $(\partial\sigma/\partial r)_e$ $(\langle\Delta r_{\mathrm{CH}}\rangle - \langle\Delta r_{\mathrm{CD}}\rangle)$ for deuterium substitution and $(\partial\sigma/\partial r)_e$ $(\langle\Delta r_{\mathrm{CH}}\rangle - \langle\Delta r_{\mathrm{CT}}\rangle)$ for tritium substitution. The two-bond isotope shifts have also been observed in $CH_3{}^{13}C(O)CH_3$, and these have the ratio[11]

$$ \frac{{}^{2}\Delta\,{}^{13}\mathrm{C}(^{3/1}\mathrm{H})}{{}^{2}\Delta\,{}^{13}\mathrm{C}(^{2/1}\mathrm{H})} = 1.41 \pm 0.12 \tag{63} $$

   This ratio is also indistinguishable from 1.426, which indicates that the dominant contribution is $(\partial\sigma^{\mathrm{C(O)}}/\partial r_{\mathrm{CH}})_e \times (\langle\Delta r_{\mathrm{CH}}\rangle - \langle\Delta r_{\mathrm{CT}}\rangle)$ for tritium substitution and $(\partial\sigma^{\mathrm{C(O)}}/\partial r_{\mathrm{CH}})_e(\langle\Delta r_{\mathrm{CH}}\rangle - \langle\Delta r_{\mathrm{CD}}\rangle)$ for deuterium substitution.
3. The relative signs of one-bond and *n*-bond isotope shifts for the same nucleus in the same molecule are not always the same. Consider, for example, the carbonyl carbon isotope shifts in $(CH_3)_2$ $^{13}C{=}O$. The $^{1}\Delta$ $^{13}C(^{18/16}O)$ and $^{2}\Delta$ $^{13}C(^{2/1}H)$ are opposite signs. Thus, the important term in $^{2}\Delta$ $^{13}C(^{2/1}H)$ must not involve $(\partial\sigma^{\mathrm{C(O)}}/\partial r_{\mathrm{CO}})_e$ δ.
4. The long-range isotope shifts correlate with indicators of electronic transmission paths such as dihedral angle dependence of three-bond isotope shifts (similar to the Karplus relation for three-bond coupling constants, although not with one set of coefficients), stereospecificity (*cis* versus *trans* versus *gauche*, and *syn* versus *anti*) of isotope shifts parallels that of spin–spin coupling, and the correlation of long-range isotope shifts with electron-withdrawing/donating ability of substituents, even across a path traversing seven bonds. These correlations of long-range isotope shifts with purely electronic quantities can only be observed if the isotope shift is itself dominated by an electronic factor that depends on the transmission of electronic information between the observed nucleus and the mass-modified site: a fortunate occurrence, since the long-range electronic factor is far more interesting and useful than the long-range dynamic factor. Since the primary dynamic factor Δ is easily estimated, long-range isotope shifts can provide direct invaluable information about the changes in shielding of a nucleus upon a minor perturbation at a distant site.

In summary, the electronic factor $(\partial\sigma^{\mathrm{A}}/\partial r_{\mathrm{XY}})_e$ in the long-range isotope shifts is found to have the following attributes.

1. The magnitude decreases (usually) as the Y–X bond becomes more remote from nucleus A. Ab initio calculations have shown that for the first- and second-row hydrides XH_n, the ratio $(\partial\sigma^{\mathrm{H}_1}/\partial r_2)_e/(\partial\sigma^{\mathrm{H}_1}/\partial r_1)_e = 0.06\text{–}0.14$. However, the two-bond secondary derivative is not necessarily much smaller than primary derivatives, especially when multiple bonds are involved.[34]
2. It is stereospecific. For three-bond isotope shifts, it is found that *cis*, *trans* > *gauche*, and in some cases the dihedral angle dependence has been clearly observed and it is not unlike the Karplus relation of three-bond spin–spin coupling with angle ϕ. This stereospecificity is purely electronic in nature.
3. It correlates with other purely electronic quantities that are dependent on the same electronic transmission path, such as substituent effects on chemical shifts by electron-withdrawing or -donating groups. The electronic transmission path is most easily explored by the isotope shift, because substitution of an atom by a heavier one leads to the fewest complications compared with other methods of investigation such as replacement by atoms or groups of different electronegativity or size.

6 ISOTOPE EFFECTS ON SPIN–SPIN COUPLING

The indirect spin–spin coupling constant J is a useful index of the chemical bond, and isotope effects on it provide

information about the sensitivity of J to bond extension. Since the isotope effects on the isotropic average J can be determined more precisely than the individual J tensor components or the anisotropy, the isotope effects can be considered as *the* major source of experimental information for assessing the quality of ab initio theoretical calculations of indirect spin–spin coupling.

The working definitions of the isotope effects on J are as follows.[4] $\Delta_s\, {}^nJ(\mathrm{AB})[{}^{m'/m}\mathrm{X}]$ is the *secondary* isotope effect on the n-bond coupling constant between nuclei A and B due to the substitution of ${}^m\mathrm{X}$ by the heavier isotope ${}^{m'}\mathrm{X}$ somewhere in the molecule:

$$\Delta_s\, {}^nJ(\mathrm{AB})[{}^{m'/m}\mathrm{X}] = |{}^nJ(\mathrm{AB})|^* - |{}^nJ(\mathrm{AB})| \tag{64}$$

$\Delta_p\, {}^nJ(\mathrm{A}^{2/1}\mathrm{H})$ is the *primary* isotope effect on the coupling constant between nuclei A and H due to the substitution of H by D, the coupled nuclei being separated by n bonds:

$$\Delta_p\, {}^nJ(\mathrm{A}^{2/1}\mathrm{H}) = |{}^nJ(\mathrm{AD})|^* \frac{\gamma_\mathrm{H}}{\gamma_\mathrm{D}} - |{}^nJ(\mathrm{AH})| \tag{65}$$

where $\gamma_\mathrm{H}/\gamma_\mathrm{D} = 6.514\,398\,04(120)$. Of course, if we instead use the purely electronic quantities, namely, the reduced coupling constants

$${}^nK(\mathrm{AH}) \equiv 4\pi^2 \frac{{}^nJ(\mathrm{AH})}{h\gamma_\mathrm{A}\gamma_\mathrm{H}} \tag{66}$$

usually expressed in reduced units of $10^{19}\,\mathrm{J^{-1}\,T^2}$, then the primary isotope effect is simply a difference:

$$\Delta_p\, {}^nK(\,{}^{2/1}\mathrm{H}) = |{}^nK(\mathrm{AD})|^* - |{}^nK(\mathrm{AH})| \tag{67}$$

Only the absolute values are compared, for practical reasons, since the absolute signs of spin–spin coupling constants are not always known. As in isotope shifts, the asterisk * denotes the heavier isotopomer. Where both secondary and primary isotope effects are observed, the primary isotope effect should be obtained from, for example, $J(\mathrm{SnD})$ in SnH_2D^- and $J(\mathrm{SnH})$ in SnH_3^-, rather than $J(\mathrm{SnD})$ and $J(\mathrm{SnH})$ in the same isotopomer SnH_2D^-. The latter difference includes both primary and secondary isotope effects.

Isotope effects on nuclear shielding are usually visually obvious in a high-resolution NMR spectrum, since the peaks of the isotopomer are shifted from the parent species. On the other hand, isotope effects on coupling constants are only observed as very slightly different multiplet splittings for each isotopomer (secondary isotope effects) or as a slightly smaller (usually) or larger $J(\mathrm{AD})$ than that expected from $J(\mathrm{AH})/6.514\,398\,04$ (primary isotope effects). Because of this factor of $6.514\ldots$, the isotope effects on J are less precisely determined than the isotope effects on shielding. According to these working definitions, a positive isotope effect on J means that the reduced coupling is larger in the deuterated species.

6.1 Observed General Trends in Isotope Effects on J

The general trends and their theoretical explanation have been presented by Jameson and Osten.[4]

1. The sign of the primary or secondary isotope effect on the coupling constant is not directly related to the absolute sign of the coupling constant. Whether it is related to the absolute sign of the reduced coupling constant is not yet established, since one-bond coupling isotope effects are presently available for positive reduced coupling constants only.
2. Primary isotope effects are negative or positive, the positive signs being found only in molecules involving one or more lone pairs of the coupled nuclei. For example, primary isotope effects are positive in H_2Se, in PH_3, and in other 3-coordinate phosphorus, but negative in PH_4^+ and in 4- and 5-coordinate phosphorus. It is positive in SnH_3^- (one lone pair) and negative in SnH_4 and SnH_3^+ (no lone pairs).
3. Secondary isotope effects can have either sign, but are often negative. Positive signs have been observed where triple bonds are involved (as in HC≡CH and HC≡N), but also in some of the same systems with positive primary isotope effects.
4. Secondary isotope effects are roughly additive upon substitution of several equivalent sites neighboring the coupled nuclei. For example, in the NH_4^+ ion, each D substitution decreases ${}^1J({}^{14}\mathrm{NH})$ by $0.05 \pm 0.02\,\mathrm{Hz}$, and in PH_3, each D substitution decreases ${}^1J(\mathrm{PH})$ by $2.5\,\mathrm{Hz}$. Small deviations from additivity have been observed.
5. The magnitudes of isotope effects are small, the largest primary effect being about 10% of the coupling constant in SnH_3^-, so that only the effects of deuterium (and tritium) substitution, where the largest fractional changes in mass are involved, have been observed. Some of the larger primary isotope effects are $+11.5\,\mathrm{Hz}$ for $\Delta_p\, {}^1J(\mathrm{PH})$ in PH_3 and $+10.5\,\mathrm{Hz}$ in SnH_3^-. Secondary isotope effects as large as $-2.0\,\mathrm{Hz}$ per D [for ${}^1J(\mathrm{SiF})$] and $+3.0\,\mathrm{Hz}$ per D [for ${}^1J(\mathrm{SnH})$] have been observed.
6. The magnitudes of the isotope effects are roughly proportional to the fractional change in mass, in the very few instances where effects of isotopic substitution of ${}^1\mathrm{H}$ by ${}^2\mathrm{H}$ and ${}^3\mathrm{H}$ have been reported.

6.2 Rovibrational Averaging of J, the Leading Terms

Just as in isotope shifts, the isotope effect on J can be written in terms of products of electronic and dynamic factors as follows.[6] For a diatomic molecule,

$$\langle J\rangle^* - \langle J\rangle = \left(\frac{\partial J}{\partial r}\right)_\mathrm{e} (\langle \Delta r\rangle^* - \langle \Delta r\rangle) + \frac{1}{2}\left(\frac{\partial^2 J}{\partial r^2}\right)_\mathrm{e} [\langle (\Delta r)^2\rangle^* - \langle (\Delta r)^2\rangle] + \ldots \tag{68}$$

The dynamic factors are the same as we have already discussed (and, indeed, the same for all rovibrational averaging of any molecular electronic properties). Only the electronic factors need be discussed here. Of course, γ of some nuclei are negative, so we really should compare derivatives of the reduced coupling such as $(\partial K/\partial r)_\mathrm{e}$, etc., where

$$\left(\frac{\partial J}{\partial r}\right)_\mathrm{e} = \frac{h\gamma_\mathrm{N}\gamma_{\mathrm{N}'}}{4\pi^2}\left(\frac{\partial K}{\partial r}\right)_\mathrm{e} \tag{69}$$

One important difference between J and σ is that the latter is a one-center property whereas the former is a two-center

Table 10

	Experimental[15]		Calculated	
	K(SnH) (reduced units)	K(SnD) (reduced units)	K(SnH) (reduced units)	K(SnD) (reduced units)
SnH_3^-	24.09 ± 0.01		24.09	
SnH_2D^-	24.76 ± 0.02	27.09 ± 0.14	24.76	27.08
$SnHD_2^-$	25.40 ± 0.03	27.72 ± 0.22	25.43	27.75
SnD_3^-		28.53 ± 0.43		28.42

property. In polyatomic molecules, there are usually several electronic factors of comparable size that contribute to the isotope effects on J. For polyatomic molecules, if ^1J is most sensitive to the bond length, the one-bond shifts can also be written in the same way as for diatomic molecules, with the terms such as $(\partial J/\partial\alpha)_e(\langle\Delta\alpha\rangle^* - \langle\Delta\alpha\rangle) + \ldots$ being less important. ^2J and ^3J, on the other hand, are very sensitive to bond and torsion angles.[62]

Let us consider SnH_4 as an example rather than CH_4, since fairly large isotope effects on SnH coupling have been observed. The types of terms that contribute to the vibrationally averaged spin–spin coupling are the same as those that contribute to the proton shielding in CH_4 as given in equation (51):

$$\langle K(\mathrm{SnH_1})\rangle = K_e + P_r\langle\Delta r_1\rangle + P_s(\langle\Delta r_2\rangle + \langle\Delta r_3\rangle + \langle\Delta r_4\rangle) + \text{terms in } P_{rr}, P_{ss}, P_{rs}, P_{st}, P_\alpha, \text{ etc.} \quad \ldots \tag{70}$$

where the primary derivative is $P_r \equiv (\partial K(\mathrm{SnH_1})/\partial r_{\mathrm{SnH_1}})_e$ and the secondary derivative is $P_s \equiv (\partial K(\mathrm{SnH_1})/\partial r_{\mathrm{SnH_2}})_e$. If we let $d \equiv \langle\Delta r_{\mathrm{SnH}}\rangle$ in SnH_4 and $d - \Delta \equiv \langle\Delta r_{\mathrm{SnD}}\rangle$ in SnD_4 then $d \approx 1.780$ pm and $\Delta \approx 0.5161$ pm can be obtained for $r_e = 170$ pm using the method described in Section 3.1. K_e is the reduced coupling constant at the equilibrium molecular geometry. The leading terms are[6]

$$\mathrm{SnH_4}: \quad \langle K(\mathrm{SnH})\rangle = K_e + (P_r + 3P_s)d + \ldots \tag{71}$$

$$\mathrm{SnH_3D}: \quad \langle K(\mathrm{SnH})\rangle = K_e + (P_r + 2P_s)d + P_s(d - \Delta) + \ldots \tag{72}$$

$$\langle K(\mathrm{SnD})\rangle = K_e + P_r(d - \Delta) + 3P_s d + \ldots \tag{73}$$

$$\mathrm{SnH_2D_2}: \quad \langle K(\mathrm{SnH})\rangle = K_e + (P_r + P_s)d + 2P_s(d - \Delta) + \ldots \tag{74}$$

$$\langle K(\mathrm{SnD})\rangle = K_e + (P_r + P_s)(d - \Delta) + 2P_s d + \ldots \tag{75}$$

$$\mathrm{SnHD_3}: \quad \langle K(\mathrm{SnH})\rangle = K_e + P_r d + 3P_s(d - \Delta) + \ldots \tag{76}$$

$$\langle K(\mathrm{SnD})\rangle = K_e + (P_r + 2P_s)(d - \Delta) + P_s d + \ldots \tag{77}$$

$$\mathrm{SnD_4}: \quad \langle K(\mathrm{SnH})\rangle = K_e + (P_r + 3P_s)(d - \Delta) + \ldots \tag{78}$$

From the above, we see that the primary isotope effect, the difference[63]

$$\Delta_p{}^1K(\mathrm{Sn}^{2/1}\mathrm{H}) = |^1K(\mathrm{SnD})|^*_{\mathrm{SnH_3D}} - |^1K(\mathrm{SnH})|_{\mathrm{SnH_4}} = (428.21 \pm 0.14) - (429.19 \pm 0.02) \approx -P_r\Delta \tag{79}$$

leads to $P_r \approx 1.90$ reduced units pm^{-1}. The primary isotope effect may also be taken from any of the differences $|^1K(\mathrm{SnD})|_{\mathrm{SnH_2}D_2} - |^1K(\mathrm{SnH})|_{\mathrm{SnH_3D}}$ or $|^1K(\mathrm{SnD})|_{\mathrm{SnHD_3}} - |^1K(\mathrm{SnH})|_{\mathrm{SnH_2D_2}}$ or $|^1K(\mathrm{SnD})|_{\mathrm{SnD_4}} - |^1K(\mathrm{SnH})|_{\mathrm{SnHD_3}}$, leading to an average value $P_r = (\partial K(\mathrm{SnH_1})/\partial r_{\mathrm{SnH_1}})_e \approx 2.00$ reduced units pm^{-1}. Note that at this level of approximation, only the primary derivative P_r is involved in the primary isotope effect.

At the same time, the difference

$$\Delta_s{}^1K(\mathrm{SnH})[^{1/2}\mathrm{H}] = |K(\mathrm{SnH})|^*_{\mathrm{SnH_3D}} - |K(\mathrm{SnH})|_{\mathrm{SnH_4}} = (428.81 \pm 0.02) - (429.19 \pm 0.02) \approx -P_s\Delta \tag{80}$$

leads to $P_s \approx 0.74$ reduced units pm^{-1}. Since this secondary isotope effect may be taken from three other differences such as $|^1K(\mathrm{SnH})|_{\mathrm{SnH_2D_2}} - |^1K(\mathrm{SnH})|_{\mathrm{SnH_3D}}$, etc., we get an average value $P_s = (\partial K(\mathrm{SnH_1})/\partial r_{\mathrm{SnH_2}})_e \approx 0.75$ reduced units pm^{-1} and $K_e = 421.63$ reduced units. The primary isotope effect involves largely the primary derivative of the coupling constant, and the secondary isotope effect on the coupling involves largely the (secondary) derivative of the coupling constant with respect to stretching a remote bond.

We can do the same analysis for the isotopomers of SnH_3^-, and we find that the values $P_r = -5.80$ reduced units pm^{-1}, $P_s = -1.30$ reduced units pm^{-1}, and $K_e = 39.04$ reduced units reproduce the experimental values reasonably well, as seen in Table 10.

The agreement with the six experimental numbers is very good. These quantities can be translated back to Hz pm^{-1} as in Table 11.

It is interesting that, although the magnitude of the SnH coupling constant is about one order of magnitude smaller in SnH_3^- than in SnH_4, the sensitivity of the spin–spin coupling to bond extension is almost three times as great. The lone pair is generally known to be responsible for negative contributions to the reduced coupling, leading to a much smaller magnitude of the spin–spin coupling. Apparently, it is also the lone pair (on Sn in SnH_3^-) that is responsible for the greater sensitivity to bond extension. By similar procedures, the changes in the reduced coupling constant with extension of the bond, $(\partial K/\partial r)_e$, or of an adjacent bond, $(\partial K/\partial r')_e$, can be estimated in other systems such as SnH_3^+, PH_4^+, PH_3, PH_2^-, and SeH_2 from experimental values of J(AH) and

Table 11

	SnH_4	SnH_3^-
$(\partial J(\mathrm{SnH})/\partial r)_e$ (Hz pm^{-1})	−9.00	+26.00
$(\partial J(\mathrm{SnH})/\partial r')_e$ (Hz pm^{-1})	−3.40	+5.80
$\langle J(\mathrm{SnH})\rangle - J_e$ (Hz)	−34.1	+67.3
J_e (Hz)	−1899.3	−175.8

Table 12 Derivatives of the Reduced Spin–Spin Coupling Constant with Respect to Extension of the Bond Between the Coupled Nuclei (r) and With Respect to Extension of the Other Bond (r')[6]

	Empirical		Theoretical	
Molecule	$(\partial K/\partial r)_e$ (reduced units pm^{-1})	$(\partial K/\partial r')_e$ (reduced units pm^{-1})	$(\partial K/\partial r)_e$ (reduced units pm^{-1})	$(\partial K/\partial r')_e$ (reduced units pm^{-1})
Without lone pairs:				
HD			+1.4979	
CH_4			+0.973 24	+0.5884
PH_4^+	+1.04 ± 0.20	+0.075 ± 0.02		
SnH_4	+2.00 ± 0.30	+0.75 ± 0.07		
SnH_3^+	+6.00 ± 4.00	≈0		
With lone pairs:				
$^{13}C^{17}O$			negative	
$^{14}N^{15}N$			negative	
HF			−0.5156	
PH_3	−4.22	+0.465		
PH_2^-	−1.25	−0.26		
SeH_2	−1.90 ± 0.60	−0.71 ± 0.09		
SnH_3^-	−5.80 ± 0.40	−1.30 ± 0.10		

J(AD) combined with values of the dynamic factor calculated by the methods described in Section 3.1. These values are compared with some published theoretical values in Table 12. Since all are expressed as γ-free reduced coupling constants, these are purely electronic quantities, which can be directly compared with each other in sign and magnitude. Theory has shown that the Fermi contact term is most sensitive to bond stretch.[64,65] Thus, it is not surprising that the magnitudes of the empirical derivatives in Table 12 increase with increasing spin density at the nucleus, just as the reduced coupling constants are known to do. The secondary derivative is generally smaller than the primary derivative, and both usually have the same sign. The earlier prediction by Jameson and Osten[4] that $(\partial K(\mathrm{AH})/\partial r)_e$ will generally be negative when A has lone pairs but will be positive otherwise appears to be correct.

In summary, the electronic factor in the one-bond coupling constant $(\partial K(\mathrm{AH})/\partial r_{\mathrm{AH}})_e$ has been found to have the following attributes that explain the observed trends.

1. For A without lone pairs, it is positive; that is, the magnitude of the coupling increases as the bond becomes stretched.
2. It is largely dominated by the Fermi contact term, which is very sensitive to the distance between the two nuclei, much more so than the spin–dipolar and orbital contributions to coupling.
3. Probably because of the dominance of the Fermi contact term, it is larger for nucleus A having larger atomic number.
4. For A with lone pairs, this electronic factor is negative. It is known that lone pairs make negative contributions to the spin–spin coupling. The sign of this electronic factor confirms that the lone pair contributions are very sensitive to bond extension.
5. The secondary electronic factor $(\partial K(\mathrm{AH})/\partial r_{\mathrm{AX}})_e$ is generally 2–5 times smaller than the primary electronic factor, and is a measure of the sensitivity of the coupling across one bond to the lengthening of another bond involving one of the coupled atoms.

In summary, the dynamic factors and electronic factors in isotope effects on NMR parameters have been characterized. The theoretical model is general for any molecular electronic property.[26] The effects can be completely understood within the context of the Born–Oppenheimer approximation. Complete calculations can be carried out for individual molecules within this theoretical framework. Where such calculations have been carried out, the agreement with experiment is good. Under conditions where the leading terms are dominant, the molecule-specific higher order terms can be neglected so as to find explanations for and make predictions of the sweeping generalities that have surfaced empirically in isotope effects on NMR parameters. The dynamic factor that has been derived by assuming dominance of the bond stretching successfully predicted the mass dependence of the isotope effects observed later. The empirical electronic factors deduced from this model are found to be consistent (in sign, in magnitude, and in correlations with various quantities such as net charge, presence or absence of lone pairs, bond order, etc.) with the theoretical electronic factors obtained by ab initio calculations.

7 RELATED ARTICLES

Chemical Shift Scales on an Absolute Basis; Gas Phase Studies of Intermolecular Interactions and Relaxation.

8 REFERENCES

1. H. Batiz-Hernandez and R. A. Bernheim, in *Progress in Nuclear Magnetic Resonance Spectroscopy*, eds. J. W. Emsley, J. Feeney, and L. H. Sutcliffe, Pergamon Press, Oxford, 1967, Vol. 3, p. 63
2. P. E. Hansen, in *Annual Reports on NMR Spectroscopy*, ed. G. A. Webb, Academic Press, London, 1983, Vol. 15, p. 105.
3. P. E. Hansen, in *Progress in Nuclear Magnetic Resonance Spectroscopy*, eds. J. W. Emsley, J. Feeney, and L. H. Sutcliffe, Pergamon Press, Oxford, 1988, Vol. 20, p. 207.
4. C. J. Jameson and H. J. Osten, *J. Am. Chem. Soc.*, 1986, **108**, 2497.
5. C. J. Jameson and H. J. Osten, in *Annual Reports on NMR Spectroscopy*, ed. G. A. Webb, Academic Press, London, 1986, Vol. 17, p. 1.

6. C. J. Jameson, in *Isotopes in the Physical and Biomedical Sciences*, eds. E. Buncel and J. R. Jones, Elsevier, Amsterdam, 1991, Vol. 2, p. 1.
7. W. Gombler, *J. Am. Chem. Soc.*, 1982, **104**, 6616.
8. C. J. Jameson, *J. Chem. Phys.*, 1977, **66**, 4983.
9. R. Maple, J. E. Carson, and A. Allerhand, *J. Am. Chem. Soc.*, 1989, **111**, 7293.
10. J. R. Wesener, D. Moskau, and H. Gunther, *J. Am. Chem. Soc.*, 1985, **107**, 7307.
11. C. H. Arrowsmith, L. Baltzer, A. J. Kresge, M. F. Powell, and Y. S. Tang, *J. Am. Chem. Soc.*, 1986, **108**, 1356.
12. R. E. Wasylishen, J. O. Friedrich, S. Mooibroek, and J. B. Macdonald, *J. Chem. Phys.*, 1985, **83**, 548.
13. C. J. Jameson, A. K. Jameson, and D. Oppusunggu, *J. Chem. Phys.*, 1986, **85**, 5480.
14. M. Hoch and D. Rehder, *Inorg. Chim. Acta*, 1986, **111**, L13.
15. R. E. Wasylishen and N. Burford, *Can. J. Chem.*, 1987, **65**, 2707.
16. A. K. Jameson and C. J. Jameson, *J. Magn. Reson.*, 1978, **32**, 455.
17. R. E. Wasylishen and J. O. Friedrich, *Can. J. Chem.*, 1987, **65**, 2238.
18. B. Bennett and W. T. Raynes, *Spectrochim. Acta A*, 1989, **45**, 1267.
19. C. J. Jameson and H. J. Osten, *J. Chem. Phys.*, 1984, **81**, 4293.
20. N. F. Ramsey, *Phys. Rev.*, 1952, **87**, 1075.
21. C. J. Jameson, *J. Chem. Phys.*, 1977, **66**, 4977.
22. C. J. Jameson, A. K. Jameson, and S. M. Cohen, *J. Chem. Phys.*, 1977, **67**, 2771.
23. A. K. Jameson, K. Schuett, C. J. Jameson, S. M. Cohen, and H. Parker, *J. Chem. Phys.*, 1977, **67**, 2821.
24. C. J. Jameson, *Bull. Magn. Reson.*, 1980, **3**, 3.
25. C. J. Jameson, *Chem. Rev.*, 1991, **91**, 1375.
26. C. J. Jameson, in *Theoretical Models of Chemical Bonding*, ed. Z. B. Maksic, Springer-Verlag, Berlin, 1991, Part 3, p. 457.
27. C. J. Jameson and H. J. Osten, *J. Chem. Phys.*, 1984, **81**, 4300.
28. C. J. Jameson and A. K. Jameson, *J. Chem. Phys.*, 1986, **85**, 5484.
29. D. R. Herschbach and V. W. Laurie, *J. Chem. Phys.*, 1961, **35**, 458.
30. R. A. Hegstrom, *Phys. Rev. A*, 1979, **19**, 17.
31. C. J. Jameson and A. C. de Dios, *J. Chem. Phys.*, 1993, **98**, 2208.
32. R. Ditchfield, *Chem. Phys.*, 1981, **63**, 185.
33. D. B. Chesnut and C. K. Foley, *J. Chem. Phys.*, 1986, **84**, 852.
34. D. B. Chesnut and D. W. Wright, *J. Comput. Chem.*, 1991, **12**, 546.
35. A. C. de Dios and C. J. Jameson, in *Annual Reports on NMR Spectroscopy*, ed. G. A. Webb, Academic Press, London, 1994, vol. 29, p. 1.
36. C. J. Jameson, A. C. de Dios, and A. K. Jameson, *J. Chem. Phys.*, 1991, **95**, 1069.
37. G. Riley, W. T. Raynes, and P. W. Fowler, *Mol. Phys.*, 1979, **38**, 877.
38. A. R. Hoy, I. M. Mills, and G. Strey, *Mol. Phys.*, 1972, **24**, 1265.
39. M. Toyama, T. Oka, and Y. Morino, *J. Mol. Spectrosc.*, 1964, **13**, 193.
40. W. T. Raynes, P. W. Fowler, P. Lazzeretti, R. Zanasi, and M. Grayson, *Mol. Phys.*, 1988, **64**, 143.
41. P. W. Fowler, G. Riley, and W. T. Raynes, *Mol. Phys.*, 1981, **42**, 1463.
42. C. J. Jameson, A. C. de Dios, and A. K. Jameson, *J. Chem. Phys.*, 1991, **95**, 9042.
43. W. T. Raynes, *Mol. Phys.*, 1988, **63**, 719.
44. P. W. Fowler and W. T. Raynes, *Mol. Phys.*, 1981, **43**, 65.
45. C. J. Jameson, in *Specialist Periodical Reports on NMR*, ed. G. A. Webb, Royal Society of Chemistry, London, 1989, Vol. 19, p. 1.
46. J. A. Tossell and P. Lazzeretti, *J. Magn. Reson.*, 1988, **80**, 39.
47. R. E. Wasylishen, *Can. J. Chem.*, 1982, **60**, 2194.
48. H. J. Osten and C. J. Jameson, *J. Chem. Phys.*, 1985, **81**, 4288.
49. H. J. Osten and C. J. Jameson, *J. Chem. Phys.*, 1985, **82**, 4595.
50. J. O. Friedrich and R. E. Wasylishen, *J. Chem. Phys.*, 1985, **83**, 3707.
51. C. J. Jameson and H. J. Osten, *J. Chem. Phys.*, 1984, **81**, 2556.
52. D. B. Chesnut, *Chem. Phys.*, 1986, **110**, 415.
53. P. Lazzeretti, R. Zanasi, A. J. Sadlej, and W. T. Raynes, *Mol. Phys.*, 1987, **62**, 605.
54. C. J. Jameson and H. S. Gutowsky, *J. Chem. Phys.*, 1964, **40**, 1714.
55. C. J. Jameson and J. Mason, in *Multinuclear Nuclear Magnetic Resonance*, ed. J. Mason, Plenum Press, London, 1987, p. 51.
56. C. J. Jameson and H. J. Osten, *J. Am. Chem. Soc.*, 1985, **107**, 4158.
57. C. J. Jameson, *Mol. Phys.*, 1985, **54**, 73.
58. A. A. Borisenko, N. M. Sergeyev, and Y. A. Ustynyuk, *Mol. Phys.*, 1971, **22**, 715.
59. M. Alei and W. E. Wageman, *J. Chem. Phys.*, 1978, **68**, 783.
60. T. Schaefer, J. Peeling, and R. Sebastian, *Can. J. Phys.*, 1987, **65**, 534.
61. H. J. Jakobsen, A. J. Zozulin, P. D. Ellis, and J. D. Odom, *J. Magn. Reson.*, 1980, **38**, 219.
62. W. T. Raynes, J. Geertsen, and J. Oddershede, *Chem. Phys. Lett.*, 1992, **197**, 516.
63. K. L. Leighton and R. E. Wasylishen, *Can. J. Chem.*, 1987, **65**, 1469.
64. J. Oddershede, J. Geertsen, and G. Scuseria, *J. Phys. Chem.*, 1988, **92**, 3056.
65. J. Geertsen, J. Oddershede, and G. E. Scuseria, *J. Chem. Phys.*, 1987, **87**, 2138.

Biographical Sketch

Cynthia J. Jameson. *b* 1937. B.S., University of the Philipines; Ph.D., 1963, University of Illinois at Urbana-Champaign. Introduced to NMR by Herb Gutowsky. Faculty in Chemistry, University of Illinois at Chicago, 1968–present. Approx. 130 publications. Research interests include theoretical and experimental studies of the chemical shift in simple systems in the gas phase and in molecules absorbed in microporous solids, with particular emphasis on intramolecular and intermolecular shielding surfaces and averages therein; also, spin relaxation in gases and their connection with the anisotropy of intermolecular potentials and molecular dynamics.

Magnetic Susceptibility and High Resolution NMR of Liquids and Solids

David L. Vander Hart
National Institute of Standards and Technology, Gaithersburg, MD, USA

1	Introduction	1
2	Physical Origins of Susceptibility, Definitions, and Equations	1
3	Magnetic Susceptibility Effects in the High-Resolution NMR of Liquids	2
4	Magnetic Susceptibility Effects in Solid State NMR	4
5	Miscellaneous Considerations	7
6	Related Articles	8
7	References	8

1 INTRODUCTION

The principal aspects of high-resolution (HR) NMR which are influenced by magnetic susceptibility (MS) effects in nonconducting materials are spectral resolution and the accurate measurement of chemical shift. Also, with the wide application of NMR to imaging, particularly the imaging of heterogeneously structured materials, MS effects can influence the quality and interpretation of the images obtained. It is also possible to obtain MS information about materials using high-resolution NMR techniques. In this presentation, the physical origins of susceptibility in nonconducting materials are sketched, a few basic equations are given, the tensorial nature of susceptibility is pointed out, and a number of practical considerations are offered including the influence of sample spinning, particularly at the magic angle. Only diamagnetic and paramagnetic susceptibility are considered; ferromagnetism and antiferromagnetism are not discussed. Finally, a few comments are included regarding the use of high-resolution NMR to measure MS values, both molecular MS and the MS of condensed phases.

2 PHYSICAL ORIGINS OF SUSCEPTIBILITY, DEFINITIONS, AND EQUATIONS

In classical electromagnetism, the magnetic induction $\boldsymbol{B}$ and the magnetic field strength $\boldsymbol{H}$ inside a medium, are related by the equation

$$\boldsymbol{B} = \mu_0(\boldsymbol{H} + \boldsymbol{M}) \tag{1}$$

where $\boldsymbol{M}$ is the magnetization or magnetic moment per unit volume. Quantities appearing in equation (1) are in rationalized SI units where $\boldsymbol{H}$ and $\boldsymbol{M}$ are expressed in A m^{-1} and $\boldsymbol{B}$ has the units of tesla. Quantities given in bold-face type are either vectors or tensors. The permeability of free space, μ_0, takes the value $4\pi \times 10^{-7}$ T m A^{-1} (Bennett et al. have published a useful reference paper[1] delineating appropriate conversions from cgs to SI units for quantities related to magnetism.) For isotropic nonferromagnetic materials,

$$\boldsymbol{M} = \kappa \boldsymbol{H} = (d/M)\kappa_{\mathrm{M}}\boldsymbol{H} \tag{2}$$

where κ and κ_{M} are respectively called the rationalized volume and molar magnetic susceptibilities, d is the density in kg m^{-3} and M is the molar mass in kg mol^{-1}. (κ is equivalent to the quantity $4\pi\chi_{\mathrm{v}}$ in the cgs system, where χ_{v} is the volume MS; κ and χ_{v} are both dimensionless. The relationship between κ_{mole}, having units of m^3 mol^{-1}, and χ_{M} in the cgs system, having units of cm^3 mol^{-1}, is that numerically $4\pi\chi_{\mathrm{M}} = 10^6\,\kappa_{\mathrm{mole}}$.) MS is a bulk property of materials. Thus, MS is associated with an ensemble of molecules and is not intended to describe the details of the response to an external field over molecular distances. At the same time, individual molecules possess molecular susceptibility tensors.[2,3] Moreover, for nonconducting materials, the uniformity of κ_{M} for solid, liquid, and gaseous forms of the same material implies that bulk MS values probably derive from summed molecular magnetic susceptibilities.[3,4] Indeed, the molecular theory of diamagnetism is described in terms of molecular wavefunctions.

2.1 Diamagnetic and Paramagnetic Susceptibility

The two kinds of MS considered are diamagnetic and paramagnetic. Diamagnetic susceptibility is a generalized response to the magnetic field of the orbiting paired electrons in a sample.[2] This response is most often negative in sign and usually weak,[5] i.e. $\kappa \approx -10^{-5}$. Owing to the fact that the diamagnetic susceptibility arises from the reaction of electrons in their orbitals to the presence of the magnetic field, this quantity is usually quite independent of temperature. There are generally two terms contributing to the diamagnetic susceptibility,[2]

$$\kappa_{\mathrm{mole}} = -\frac{Ne^2\mu_0}{4m}\sum_i \overline{x_i^2 + y_i^2} + \frac{Ne^2\mu_0}{2m^2}\sum_{n(\neq 0)}\frac{|(0|\hat{L}_z|n)|^2}{E_n - E_0} \tag{3}$$

where N is Avogadro's number, e is the charge on the electron in coulombs, m is the mass of the electron in kg, i is an index over all electrons in the molecule, and n is an index over all excited electronic states of corresponding energies E_n (in joules) in the molecule. The first term is an average over all of the electrons in the ground state, where the z direction lies along $\boldsymbol{H}$. The size of this term is usually associated with the ability of the electrons, especially the outer electrons, to circulate freely in planes perpendicular to $\boldsymbol{H}$. The second term involves the mixing of ground and excited electron states by the angular momentum operator $\hat{L}_z$. The first term is negative and the second term is positive but usually smaller than the first; hence the sum is usually negative.

Paramagnetic susceptibility most often arises from unpaired electrons whose net polarizations in the magnetic field yield an MS which is positive in sign and somewhat larger than

the diamagnetic contribution. The latter is still there but is usually masked by the paramagnetic contribution. The electronic polarization which gives rise to the paramagnetic contribution is temperature-dependent and the paramagnetic susceptibility reflects that. For example, suppose a molecule of molar mass M has unpaired electrons, then, according to Langevin,[6]

$$\kappa_{\text{mole}} = N\mu^2\mu_0/3kT \tag{4}$$

where μ is the magnetic moment of the unpaired spins on the molecule; μ, in J T^{-1}, is given by

$$\mu = 2\beta[S(S+1)]^{1/2} \tag{5}$$

where S is the total spin which is equal to half the number of unpaired spins and β is the Bohr magneton in units of J T^{-1}. Substituting equation (5) into equation (3) gives

$$\begin{aligned}\kappa_{\text{mole}} &= 4N\mu_0\beta^2 S(S+1)/3kT \\ &= [6.286 \times 10^{-6} S(S+1)/T]\,\text{m}^3\,\text{mol}^{-1}\end{aligned} \tag{6}$$

Paramagnetic susceptibilities are usually larger than diamagnetic susceptibilities; ratios of 10 to 100 are not uncommon. Molecular oxygen has unpaired electrons and a relatively small molar mass; its presence in dissolved form can be a measurable perturbation on the measurement of diamagnetic susceptibility.[7]

2.2 Tensorial Character of Magnetic Susceptibility

In principle, the molecular MS and the bulk MS in solids is anisotropic,[2,3,8] giving rise to a *tensorial* interaction, i.e. the general definition of $\boldsymbol{M}$ in equation (2) is

$$\boldsymbol{M} = \boldsymbol{\kappa}\cdot\boldsymbol{H} \tag{7}$$

where $\boldsymbol{\kappa}$ is a tensor. Thus, $\boldsymbol{M}$ may, in principle, depart from the direction of $\boldsymbol{H}$. Anisotropic bulk MS (ABMS) is most often associated with the crystalline state of matter in contrast with the glassy or liquid states of matter where isotropic bulk MS (IBMS) is most commonly found. For diamagnetic crystals, ABMS can arise because both the magnetic susceptibility of each molecule is anisotropic and the molecules in the unit cell preserve a net orientation of their different susceptibility axes. A common molecular source of ABMS in organic compounds is the aromatic ring.[3,8,9] Ring currents, which are induced by the magnetic field when there is some projection of the normal to the ring along the magnetic field, offer a significant contribution to the MS tensor. If an aromatic compound has a crystal habit where the ring normals have a net projection along some axis, then there is a high probability that such a crystal will display ABMS. Graphite, as an extreme example, has a very large anisotropy[10] because of its dense planar fused-ring structure.

For paramagnetic materials, the existence of an anisotropic electron $\boldsymbol{g}$ tensor, for example, can give rise to ABMS since net electron polarization then becomes a function of orientation. The $\boldsymbol{g}$ tensor can become very anisotropic, particularly for certain transition metal compounds where crystal field splittings and electron spin–orbit couplings both play a role in determining the anisotropy of $\boldsymbol{g}$.[11] For example, the electrons in high-spin iron in the heme group have $g_{\parallel}$ close to the free-electron value of 2, whereas $g_{\perp}$ is about 6. As will be seen, there is considerable difference in the NMR resolution one obtains with magic angle spinning (MAS) if ABMS, rather than IBMS, is present.

2.3 Relationship Between Sample Shape and Uniform Internal Fields

For many NMR experiments, a uniform internal magnetic field is desired (uniform on a scale significantly larger than the molecular scale) so that interactions on the molecular scale can be exposed. In principle, one can make the external field very homogeneous, but the introduction of a material with finite MS into this homogeneous field generally modifies the field, both outside and inside the material. Thus, one is interested in how sample shape influences the field internal to the material and what shapes will give rise to a uniform internal field when the body is placed in a uniform external field.

For a body described by a single MS tensor, the general ellipsoid is the only finite body shape which, in the presence of a uniform external field, gives rise to a uniform internal field.[12] Cylinders of infinite length and spheres are ellipsoids of rotation; high-resolution NMR samples often approximate these shapes. It is possible, in principle, that if an ellipsoid, probably a single crystal, has an ABMS tensor whose principal axes do not coincide with the axes of the ellipsoid, that the direction of the uniform internal field will not coincide with the direction of the external field. However, for diamagnetic and paramagnetic materials, deviations from the external field direction will be negligible.

At this point we will separately consider MS effects in high-resolution liquid NMR and in solid state NMR. In liquid state NMR the measurement of chemical shifts can often be made very accurately; moreover, resolution is of primary importance. Also, most materials associated with the high-resolution experiment, including the sample, possess IBMS. In contrast, for solid state NMR, the so-called 'high-resolution' techniques generally achieve resolution which is, at best, an order of magnitude worse than in the liquid state and, more typically, two or more orders of magnitude worse. Thus, for solids, one is less concerned with the influence of MS on accurate chemical shift measurements. At the same time, in the solid state, MS effects can influence the measurement of chemical shifts in ways that do not happen for liquids. Of probably greater interest is the role which MS plays in determining resolution in the solid state. The added possibility that samples have ABMS also increases the complexity of dealing with MS, since strategies for reducing IBMS broadening only work partially when ABMS is present.

3 MAGNETIC SUSCEPTIBILITY EFFECTS IN THE HIGH-RESOLUTION NMR OF LIQUIDS

3.1 Resolution

For spectroscopic NMR applications, one generally desires the best resolution possible. MS considerations have dictated

several items in the standard practice of high-resolution NMR. Usually, sample tubes are cylindrical and are ideally filled with liquid which extends both above and below the rf coil so as to approximate an ellipsoid, thereby promoting internal field uniformity in the region of the coil. When sample volume is limited, one often uses a spherical sample tube, again approximating an ellipsoid, although the stem attached to the sphere is a significant perturbation on the uniformity of the field inside the sphere.

Sample spinning is a second way of dealing with MS effects to improve resolution, although a primary motivation for sample spinning is that it averages out inhomogeneities in the static field perpendicular to the spinning axis. Variations in the wall thickness of the NMR tube and/or a lack of concentricity cause the magnetic field to be warped in the sample region since the magnetic susceptibility of the glass is usually different from the liquid. Spinning about the tube axis helps to average these effects to smaller values. This averaging is more effective in the iron magnet geometry, where $\boldsymbol{H} \perp \boldsymbol{s}$ ($\boldsymbol{s}$ is the unit vector in the spinning-axis direction), than it is in the usual superconducting-magnet geometry where $\boldsymbol{H} \parallel \boldsymbol{s}$. This difference comes about because only in the former case does the orientation of $\boldsymbol{H}$, with respect to the vectors connecting the liquid and the tube imperfections, become modulated by spinning.

Discontinuities of MS within the sample also degrade resolution. Air bubbles, precipitates, etc. in a sample are all undesirable. Even a spherical air bubble creates a large perturbation since, in general, an ellipsoid of one susceptibility inside of an ellipsoid of a different susceptibility will result in nonuniform fields inside of both ellipsoids, even though the external field was originally uniform.

Finally, MS effects dictate certain things about probe construction. Aside from electromagnetic interferences, the asymmetric disposition of the probe elements (electronic components, mechanical supports, etc.) perturb the field lines on a distance scale comparable with the size of the object. The strategies for minimizing degradation of resolution include (a) maintaining sufficient distance between the elements and the sample so that the perturbations at the sample change slowly enough, spatially, that shim-coil compensation is possible, (b) distributing perturbing elements symmetrically, and (c) attempting to match the MS of the probe elements to that of air. The method for achieving the latter is usually to combine some paramagnetic character with the diamagnetic character of a material. For example, a substantial improvement in resolution has been demonstrated[13] by replacing a copper rf coil with one having an MS much closer to that of air. A minor drawback to this approach of MS matching is that the paramagnetic contribution will be temperature-dependent.

3.2 Chemical Shift Measurements

The NMR resonance frequency observed in a liquid for a magnetic nucleus at a given chemical site on a molecule is often a very well-defined frequency, especially for a spin-$\frac{1}{2}$ nucleus. In general, one uses measured frequencies to deduce something about the molecule, about a chemical site in the molecule, or about how a site is influenced by its immediate intermolecular interactions (e.g. hydrogen bonding, solvation shells, etc.) Of less interest are those influences on the chemical shift which derive from mean fields averaged over many molecules. The MS effects fall into this latter category. The resonance frequency ω_0 ($= 2\pi\nu_0$) for a given nucleus, ignoring spin couplings, is given by the Larmor relationship,

$$\omega_0 = \gamma \mu_0 H_{\mathrm{n}} \tag{8}$$

where H_{n} is the magnetic field strength seen by the nucleus and γ is the gyromagnetic ratio of the observed nucleus in units of rad T^{-1}. Zimmerman and Foster[12] took the approach that $\boldsymbol{H}_{\mathrm{n}}$ is the vector sum of five parallel vector fields,

$$\boldsymbol{H}_n = \boldsymbol{H}_0 + \boldsymbol{h}_1 + \boldsymbol{h}_2 + \boldsymbol{h}_3 + \boldsymbol{h}_4 \tag{9}$$

where $\boldsymbol{H}_0$ is the applied external field, $\boldsymbol{h}_1$ is the demagnetizing field, proportional to the susceptibility, arising from the shape of the sample, $\boldsymbol{h}_2$ is the contribution due to magnetization external to the Lorentz sphere,[14,15] $\boldsymbol{h}_3$ is the field associated with local intermolecular interactions, e.g. hydrogen bonding, and $\boldsymbol{h}_4$ is the field arising from intramolecular contributions, e.g. the response to the magnetic field of electrons, particularly those surrounding the nucleus observed, plus the influence of molecular conformation, etc. It is the quantity ($\boldsymbol{h}_3$ + $\boldsymbol{h}_4$) which one seeks to measure and interpret via the chemical shift measurements. For liquid samples of IBMS, having overall ellipsoidal shapes and placed into a uniform field $\boldsymbol{H}_0$,

$$\boldsymbol{h}_1 = -\alpha\kappa \boldsymbol{H}_0 \tag{10}$$

where α is the demagnetizing factor tabulated for the general ellipsoid by Osborne.[16] This factor depends on the axis ratios of the ellipsoid and the direction of the magnetic field with respect to these axes. Values of α for certain ellipsoids are as follows: 0 for $\boldsymbol{H}_0$ parallel to the axis of a long cylinder and $\frac{1}{2}$ perpendicular to the same cylinder, $\frac{1}{3}$ for a sphere, and 1 for $\boldsymbol{H}_0$ perpendicular to the plane of a thin disk. The field ($\boldsymbol{H}_0$ + $\boldsymbol{h}_1$) is considered to be the average magnetic field internal to the liquid. It is thus, perhaps, not so obvious why the field $\boldsymbol{h}_2$ must be added to this mean internal field in order to take proper account of the mean internal field seen at the nucleus.[14,15] The quantity $\boldsymbol{h}_2$ arises, in a sense, from the consideration that the mean internal field ($\boldsymbol{H}_0$ + $\boldsymbol{h}_1$) is the mean field *after* the liquid has been magnetized. Since the molecule containing the nucleus in question is also in an induced-magnetism state, it is fair to ask whether the mean effective field which magnetized a given volume is not slightly different from the final mean field. The suggestion then is that the mean field seen by the nucleus is this slightly different field. To address this problem, one considers the fictitious removal of a very small sphere of magnetized liquid surrounding a molecule. Removal is especially fictitious because one 'freezes' in the field lines prior to the removal of the sphere so that the sphere is uniformly magnetized and the magnetic field lines in the liquid near the hole are also unperturbed.[15] When one considers this problem in this so-called Lorentz sphere, one finds that the compensating field $\boldsymbol{h}_2$ is given by

$$\boldsymbol{h}_2 = (1/3)\boldsymbol{M} = (1/3)\kappa \boldsymbol{H}_0 \tag{11}$$

Therefore, the MS-corrected field $\boldsymbol{H}_{\mathrm{c}}$ seen by the molecule in its average local environment is[12]

$$\boldsymbol{H}_c = \boldsymbol{H}_0 + \boldsymbol{h}_1 + \boldsymbol{h}_2 = \boldsymbol{H}_0\{1 + [(1/3) - \alpha]\kappa\} \tag{12}$$

For a spherical liquid sample, $\boldsymbol{H}_c$ is $\boldsymbol{H}_0$; for long cylindrical spinning samples,[12,17]

$$\boldsymbol{H}_c = \boldsymbol{H}_0[1 + (1/6)(3\cos^2\beta - 1)\kappa] \tag{13}$$

where β is the angle between $\boldsymbol{H}_0$ and the spinning axis vector, $\boldsymbol{s}$. equation (13) indicates that the susceptibility corrections are very different for $\boldsymbol{H}_0$ perpendicular or parallel to $\boldsymbol{s}$; moreover, if $\boldsymbol{s}$ assumes the magic angle, β_M = arccos $(3^{-1/2})$, then the susceptibility term vanishes[17] and $\boldsymbol{H}_c = \boldsymbol{H}_0$.

A usual method of making a referenced chemical shift measurement in high-resolution NMR is to mix an internal chemical shift standard with a test liquid. This works quite well in that both kinds of molecules experience the same perturbations from MS, assuming the mixture to be a true solution. On occasion, however, chemicals are not compatible or contamination is an important issue. Then one often uses a concentric tube arrangement with one liquid in the central tube and the other in the annular space. It does not matter, from the point of view of the MS corrections to be applied, which of the spaces is occupied by the reference so long as tubes are spun. (Static concentric tubes with $\boldsymbol{H}_0$ perpendicular to the tube axis, generate a substantial distribution of internal fields over the two sample regions.[12]) Moreover, equation (13) is used to determine $\boldsymbol{H}_c$ in both liquid regions.

Recognize that the convention for chemical shift, δ, is that shifts to higher resonance frequency imply more *positive* δ values. (Note that this sign convention is also consistent with Knight shifts[18] as well as the more conventionally used chemical shift scales for protons, ^{13}C nuclei, etc.) If one measures the apparent chemical shift difference $\Delta\delta_{obs}$ (= $\delta - \delta_{ref}$) between two resonances originating from each of the sample regions, then for the iron-core magnet geometry with $\boldsymbol{H}_0 \perp \boldsymbol{s}$, the susceptibility-corrected shift $\Delta\delta_{corr}$ is given by

$$\Delta\delta_{corr} = \Delta\delta_{obs} - (1/6)(\kappa^{ref} - \kappa) \tag{14}$$

and for the superconducting geometry with $\boldsymbol{H}_0 \parallel \boldsymbol{s}$

$$\Delta\delta_{corr} = \Delta\delta_{obs} + (1/3)(\kappa^{ref} - \kappa) \tag{15}$$

where κ^{ref} is the MS of the reference liquid and κ is the MS of the test-sample liquid.

Application of equations (14) and (15) is not always convenient when one of the MS values is not known. This situation arises often for mixtures as well as neat liquids. It is possible to estimate κ, if one knows the composition and density of a material, using Pascal's constants.[3,8,19,20] This method assumes additivity relationships for the contributions from the various atoms. Corrections which depend on the nature of the bonding are also included. For known mixtures whose individual κ values are known, a molar-volume additivity assumption works quite well[21] for estimating κ for the mixture:

$$\kappa_{mixt} = \phi_1\kappa_1 + \phi_2\kappa_2 \tag{16}$$

where ϕ_1 and ϕ_2 are respectively the volume fractions of components 1 and 2.

4 MAGNETIC SUSCEPTIBILITY EFFECTS IN SOLID STATE NMR

4.1 Influence on Resolution

Solid particles come in all shapes and sizes. Particles can be crystalline, semicrystalline (e.g. polymers), amorphous or glassy materials, or even rubbery liquid-like materials. Generally, solid particles do not naturally occur as ellipsoids with ideal shape factors. This section offers a framework for estimating the spread of internal magnetic fields inside of an arbitrary particle; also an estimate of broadening in a powder sample is given. In addition, the question is raised as to what can be done, if anything, to reduce the susceptibility broadening in an NMR spectrum. The short answer is that magic angle sample spinning (MAS) will fully average to zero broadening from IBMS for particles of any shape, but when ABMS is present, MAS will result in incomplete averaging. In general, one must use single crystals of an ellipsoidal shape to eliminate ABMS broadening.

Given a particle, characterized by a single MS tensor and of a general shape, introduced into a uniform magnetic field, one can calculate the distribution of internal magnetic fields due to particle shape in the following way.[17] About any given point in the particle, where one wishes to calculate the internal field, define a primary sphere which is the largest sphere that remains within the particle. Subdivide the remaining regions of the particle into i spherical volumes, V_i, choosing the spheres of different sizes so as to account for all of the remaining particle volume. According to equation (7), the magnetic field induces a magnetic moment per unit volume in the particle; thus, each of these spheres represents a magnetic moment $\boldsymbol{\mu_i}$ given by

$$\boldsymbol{\mu}_i = V_i\boldsymbol{\kappa}\cdot\boldsymbol{H} \tag{17}$$

and the projection along $\boldsymbol{H}$ of the dipolar field $\boldsymbol{h}_i$ due to $\boldsymbol{\mu}_i$, evaluated at the center of the primary spheres will be

$$h_i = (\mu_i/r_i^3)(3\cos^2\theta_i - 1) \tag{18}$$

where, in polar coordinates centered at the origin of the primary sphere, r_i is the distance to the center of V_i and θ_i is the angle between the field direction and the line connecting the centers of the primary and the ith spheres. The sample-shape-dependent contribution to the field dispersion at the center of the primary sphere is the sum of the h_i values since the contribution from the first sphere does not contribute to the dispersion. A similar calculation can be performed at all points in the particle in order to obtain the distribution of internal fields for an arbitrary particle shape. We begin by discussing broadening for particles possessing IBMS.

4.1.1 Samples with Isotropic Magnetic Susceptibility

Drain[22] estimated the MS broadening of NMR lines in powder samples having IBMS by considering the broadening due to the shape of each particle and due to the packing of the particles. The contribution from shape was calculated by assuming that the particles were isolated prolate or oblate ellipsoids with axial ratios of 2 or 0.5, respectively. A

uniform distribution of ellipsoid orientations in the field [leading to a distribution of α values in equation (10)] gives rise to lineshapes which are asymmetric, resembling powder lineshapes for axially symmetric chemical shift tensors.[23] Drain estimated the interparticle contribution to MS broadening by using the dipole approximation to calculate the distribution within a spherical particle due to spherical cubic-close-packed arrays of neighboring particles. The result was that comparable broadening arose from sample shape and from neighbor distributions. The full width, in Hz, of the resulting resonance was about $\kappa\nu_0/4$, where it is assumed that either air or vacuum surrounds each particle. This corresponds to about 2 ppm for the typical organic material. Obviously, a significant improvement in resolution could be obtained if a liquid with a matching susceptibility were introduced into the sample chamber.[24] Then, MS broadening would be reduced to about $\Delta\kappa\nu_0/4$ where $\Delta\kappa$ is the difference in κ between the particles and the liquid. Note that Drain's estimate of line broadening assumes that the overall shape of the powder sample does not deviate strongly from an ellipsoid; if it does, there is an additional MS broadening due to overall sample shape. Another way to eliminate MS broadening in solid materials with IBMS is to melt-cast or melt-crystallize them into ellipsoidal shapes. In the absence of voids, MS broadening then ought to be very small.

One can also average to zero the broadening from IBMS effects by using MAS.[17] The dipolar form of equation (18) suggests that the angular averages of all $\boldsymbol{h}_i$ will vanish with MAS. Hence, the average dispersion will also vanish. The efficacy of MAS has also been demonstrated for samples containing liquids together with solids, such as glass beads.[17] These authors reported linewidths for the liquid-component nuclei consistent with expectations involving the rotational averages of equation (18), namely, that spinning samples with $\boldsymbol{s} \perp \boldsymbol{H}$ simply reduced the static-sample linewidth by a factor of two, whereas MAS eliminated the MS broadening when the diffusion length of the molecules in the liquid over a rotor period was small in comparison to the bead diameter. The success of eliminating MS broadening from solid state spectra is very vividly seen in the MAS ^{13}C spectrum of a cubic material such as adamantane where, in the presence of MAS, broadening due to other sources is also minimal and observed linewidths approach those expected from the inhomogeneities of the applied field.[25]

4.1.2 Samples with Anisotropic Bulk Magnetic Susceptibility

We turn now to the more complicated case of ABMS where κ is a tensor, rather than a scalar, and this tensor has principal values κ_1, κ_2, and κ_3, given in order of decreasing magnitude. In the sense that the ABMS tensor can formally be separated into an isotropic part, characterized by the mean of the principal values, and an anisotropic part, characterized by deviations from the mean, the behavior of the isotropic part will be the same as discussed above. It is only the anisotropic part which will require further consideration.

As an example of ABMS, let us consider the aromatic ring which is the most common source of diamagnetic ABMS in organic systems. Aromatic molecules typically have anisotropic molecular magnetic susceptibilities;[3] thus, their crystalline counterparts often possess ABMS as well. It is useful to think of the aromatic ring itself as an analog of ABMS in solids since, in liquid state NMR, the aromatic ring gives rise to the familiar ring current shifts.[26] These shifts are illustrated in Figure 1 where an aromatic ring is drawn and atoms A1 and A2 are placed outside of the ring, A1 along the hexad axis and A2 in the plane of the ring. If there is isotropic tumbling in a liquid containing an aromatic ring, and if the atoms A1 and A2 maintain their position with respect to this ring, then the resonance of A1 will shift to higher field and the resonance of A2 will shift to lower field. Even though the influence of the ring current on the atoms A1 and A2, at any fixed orientation, can be described as a dipolar interaction, isotropic reorientation does not average this interaction to zero because the *strength of the dipole moment is a function of orientation*. Only for a dipole moment of *fixed* magnitude, will the average dipolar field at all surrounding points vanish upon isotropic tumbling. The sign of the ring current shift at a given point in space usually takes the sign of the dipolar field when the induced moment on the ring is strongest, i.e. when $\boldsymbol{H}$ is parallel to the hexad axis.

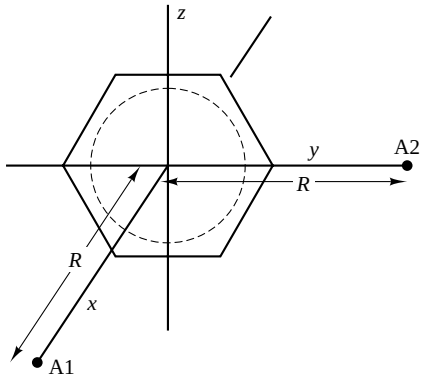

Figure 1 Geometry illustrating, at atoms A1 and A2, ring current shifts arising from the induced circulation of electrons in the π orbitals of the benzene ring. The C_6 axis of the ring, i.e. the direction of the maximum induced dipole, lies along x, and A1 is situated on x. Atom A2 lies along y. If, during isotropic tumbling or MAS, atoms A1 and A2 maintain their orientation with respect to the benzene ring, then A1 will experience an average reduction in its local field. This change in field is opposite in sign and twice the magnitude seen at A2. The interaction between the ring and the atoms is a dipolar interaction, but shifts arise because of the orientation dependence of the induced dipole. In glassy materials, aromatic rings give rise to a spread of frequencies for nearby atoms. In the presence of MAS, crystals possessing ABMS produce analogous shifts. Replace the benzene ring by a crystal with an axially symmetric κ tensor oriented along x. Similar shifts will occur for atoms in surrounding regions over distances comparable to the crystal size

For ABMS in solids, one might think of replacing the aromatic ring in Figure 1 with, say, a spherical single crystal which possesses ABMS. At some distance outside of this sphere, a change in the orientation of $\boldsymbol{H}$ with respect to the ABMS tensor of the sphere will create a change in the strength of the induced magnetic moment of the spherical crystal. This change will alter the strength of the dipolar fields emanating from this sphere. Hence, the isotropic average of the sphere's dipolar field at all external points will not, in general, vanish.

From the foregoing discussion we may draw qualitative conclusions about ABMS line broadening *in the presence of MAS*, given that MAS was effective in eliminating line broadening when only IBMS is present:

1. An isolated ellipsoidal single crystal will have no ABMS broadening since the field inside of the ellipsoid is uniform for all orientations.
2. A spherical hole inside of a sphere with ABMS will cause broadening.
3. A nonellipsoidally shaped single crystal with ABMS will cause ABMS broadening unless κ is axially symmetric and its unique axis lies along the spinning axis.
4. In a powder sample where each particle is a single crystal, ABMS broadening arises from both particle shape and from interparticle perturbations.
5. Densification via, say, melt crystallization, of a polycrystalline sample possessing ABMS increases ABMS broadening.
6. Dilution of ABMS crystallites with a material having IBMS reduces the interparticle contribution to ABMS broadening for resonances associated with these crystallites but creates ABMS broadening for resonances in the material with IBMS. The efficacy of such dilution depends rather strongly on having ABMS particles which are themselves single crystals, i.e. diluting polycrystalline ABMS particles is not very effective.

An empirical estimate of ABMS line broadening is based on MAS linewidth data[27] for hexamethylbenzene, a substance having an axially symmetric MS tensor. In a melt crystallized (densely polycrystalline) sample, ABMS line broadening yielded a full width at a halfheight of 0.93 ppm which, for hexamethylbenzene is a linewidth, in Hz, of $0.18\Delta\kappa\nu_0$ where $\Delta\kappa = \kappa_{\parallel} - \kappa_{\perp}$. In the work just referred to, points 3, 5, and 6 listed above were also demonstrated and a very crude calculation of interparticle broadening was attempted.

In the absence of MAS, ABMS line broadening is, of course, also eliminated for a *static* single crystal in the form of an ellipsoid.

4.2 Influence of Magnetic Susceptibility on Chemical Shift Measurements

4.2.1 Referencing the Anisotropic Chemical Shift

In the discussion which follows, the assumption is made that one wishes to determine the isotropic or anisotropic chemical shift values, relative to some reference material, *to a precision exceeding the magnitude of potential susceptibility corrections*. In many cases, the precision of the determination is such that one cannot justify a preoccupation with MS corrections. For example, MS issues are important in the measurement of chemical shifts for protons in organic materials because of the usually small range (8–10 ppm) of proton chemical shifts. In comparison, MS corrections for ^{13}C shifts are less important; yet MS effects can be seen because of the relatively high resolution achievable on observing dilute spin-$\frac{1}{2}$ nuclei such as ^{13}C. In paramagnetic materials or certain inorganic materials with larger susceptibilities, a consideration of the impact of MS on chemical shift is also in order.

One way to measure a chemical shift tensor is to rotate a single crystal in a magnetic field about orthogonal axes. This allows one to map the chemical shift and, by correlating these shifts with other measurements, e.g. X-ray, one can relate these shifts to directions in the molecules. Since each determination of a resonance position is undertaken using a static sample, shape effects for the crystal come into play. Obviously, the narrowest lines will be for ellipsoids. If one does not wish to make shape-dependent MS corrections at each orientation, then a sphere should be employed. If the spherical crystal has IBMS, then the chemical shift anisotropy measured will be correct. If the crystal has ABMS, then one knows that $\boldsymbol{M}$ in equation (7) has a magnitude that is a function of orientation. Yet, according to the foregoing discussion on susceptibility corrections in liquids, where equation (9) was used, if the contribution from the Lorentz sphere is included, then $(\boldsymbol{h}_1 + \boldsymbol{h}_2) = 0$ for a sphere, i.e. there should be no correction term which depends on κ at any orientation. Yet, Spiess et al.,[28] in a very careful study of ferrocene, observed small deviations from an axially symmetric shielding tensor for the protons of ferrocene in a spherical single crystal. They attributed these deviations to ABMS effects, arguing that motional averaging of the ferrocene rings and crystal symmetry combine to predict an axially symmetric shift tensor. If ABMS effects persist in a single-crystal sphere, then the appropriateness of the Lorentz correction $\boldsymbol{h}_2$ is questioned. Since the observed deviations were small, there may be alternative explanations. Nevertheless, it still seems that when the magnitude of the potential susceptibility corrections is a significant fraction of the apparent chemical shift anisotropy, the most reasonable recipe for determining true chemical shift anisotropies in materials with ABMS is to use a spherical single crystal and make no MS corrections.

4.2.2 Referencing the Isotropic Chemical Shift

The question arises as to effective strategies for referencing *isotropic* chemical shifts in solids. For solids with IBMS, an effective approach is to utilize MAS with a sample geometry such that an unknown material surrounds a central glass capillary containing a primary liquid reference, such as tetramethylsilane (TMS) for ^{13}C or ^{1}H nuclei. It does not matter whether the walls of the glass have uneven thickness or whether the spinning creates bubbles in the liquid. The main precaution, related to $\boldsymbol{B}_0$ homogeneity, is to distribute the liquid over the same axial range of the rotor that the sample occupies. The chemical shift measured between reference and solid needs no correction for MS, although there can be some other solid state contributions to the apparent chemical shift, e.g. from second-order dipolar effects.[29,30] Once the chemical shift of a suitable solid is measured in the way outlined above, that solid can be used as a secondary shift standard. For materials with IBMS, unknown and standard can be mixed in any fashion, utilizing MAS, and the measured shift differences will need no further MS correction.

The geometry for referencing the chemical shift in samples with ABMS is a more complicated problem. An approximate method is to employ MAS on a sample in which a liquid reference in a capillary is surrounded by a powder sample of the ABMS material, where the grain size of the powder is much smaller than the wall thickness of the capillary, and the particles in the powder have no preferred orientation. In this case the signal from the powder will have substantial ABMS broadening; yet, to the liquid in the capillary, the powder will look like a material with IBMS. Therefore, within the approximation that ABMS broadening in the powder is symmetric, one will get a chemical shift difference which is correct. Symmetric broadening is not necessarily

expected since broadening arises from effective dipolar interactions which typically have asymmetric, powder-average field distributions associated with them. Also, in contrast to the IBMS case, for arbitrary powder samples having ABMS, it is not required that the mean resonance position, i.e. that position about which the first moment of the resonance intensity vanishes, is without influence from ABMS. Qualitatively, one expects ABMS-induced powder-average shifts to be closely related to the existence of regular and highly asymmetric shapes for the individual powder particles.

This author is unaware of any geometry for a sample, whereby an unknown material with ABMS, *in the form of a single crystal of some shape*, can be combined with a chemical shift reference material possessing IBMS in such a way that differences in the isotropic values of unknown and reference chemical shifts can be measured reliably without a prior knowledge of the orientation of the ABMS tensor in that material. The complicated nature of chemical shift referencing has been demonstrated for a polymer film possessing ABMS.[25] In the presence of MAS, variations in shifts of about 1.5 ppm were observed between ^{13}C nuclei in TMS, contained in a central capillary tube, and ^{13}C nuclei in the oriented polymer film. These differences arose when the orientation of the unique axis of the ABMS tensor was changed from parallel to the rotor axis to perpendicular to the cylindrical walls of the rotor.

If one presumes that the Lorentz sphere correction applies to all diamagnetic and paramagnetic solids, then for a spherical single crystal possessing ABMS as well as for a spherical liquid sample, the field seen by the nucleus is just the external field $\boldsymbol{H}_0$. Hence, a true chemical shift difference, in the absence of ABMS broadening, could be measured by sequential substitution of such samples. Of course, the use of MAS for the single crystal or the employment of rotation patterns would be required in order to identify the isotropic chemical shift; moreover, for the liquid sample, the influence of the container wall will be present and this is also most easily dispensed with using MAS.

5 MISCELLANEOUS CONSIDERATIONS

5.1 Influence on Multidimensional NMR

The development of 'high-resolution' techniques in solids has enabled spectroscopists to design multidimensional NMR strategies for solids. When the chemical shifts of one nucleus form the basis for one of the NMR dimensions, then it is possible that MS effects can appear. The author has seen such effects using proton multiple pulse techniques combined with MAS. The dipolar fields arising from either IBMS or ABMS in a glassy or semicrystalline solid can be distributed in a way which is not highly correlated with the anisotropic chemical shift tensors on the molecules. The net influence of MS is to create a distribution of effective chemical shift tensors. For a given chemical site, effective tensors throughout the sample have dispersions of principal values but the same isotropic average for IBMS. For ABMS, a dispersion of isotropic shifts also exists. Thus, in a proton 2D experiment, for example, where MS effects can be a modest fraction of the chemical shift range or of chemical shift anisotropies, one tends to create spatially based as well as chemically based correlations of polarization as one increments the time for chemical shift evolution. As usual in NMR, this can be a nuisance as well as a source of information.

5.2 Use of NMR to Measure Unknown Magnetic Susceptibilities

From the foregoing discussions, it is clear that if one has two liquids in the concentric-tube geometry and utilizes MAS, any chemical shift difference associated with the two liquids will need no MS correction. A second measurement with either $\boldsymbol{s} \perp \boldsymbol{H}_0$ or $\boldsymbol{s} \parallel \boldsymbol{H}_0$ will yield the susceptibility difference between two liquids [equations (14) and (15)]. Provided the MS is known for one of the liquids, this measurement will yield the MS of the unknown liquid. One could forego the magic angle measurement above and simply use chemical shift data employing internal standards. However, any contribution to the shift arising, for example, from a change in intermolecular associations would produce an error in the susceptibility determination. Another approach[31] to measuring diamagnetic susceptibilities in liquids involves measuring a chemical shift difference from sequential experiments for some nucleus belonging to a liquid for which κ is desired. First the measurement is made for the neat liquid; then the measurement is repeated for that liquid suspended as a separate phase, in spherical droplets, in another immiscible liquid for which κ is known. This method gave reported κ values to within a few per cent of literature values.

It is also possible to estimate paramagnetic susceptibilities using NMR signals. Feher and Knight[32] in 1955 used two capillaries, filled with water, and oriented them inside of a tube filled with Mn_2O_3 powder. One capillary was parallel and one perpendicular to $\boldsymbol{B}_0$. The tube axis was in the remaining orthogonal direction. The difference in resonance frequency between the two tubes of water allowed them to estimate κ to within 6% of the listed value. Other variants of this experiment using different geometries have also been employed. For example, Li et al. measured the shift of the proton resonance in a sphere of water when that sphere was sequentially placed in a powder of an unknown and then in a powder of a reference material.[33] It is also possible to estimate the MS of a paramagnetic substance by simultaneously measuring, using concentric-tube geometry, the shift difference for a nucleus in a reference material in two solutions. One solution is the reference dissolved in a pure solvent; the other solution is the same but augmented by a known amount of paramagnetic material.[34,35]

5.3 Measurement of Anisotropic Molecular Magnetic Susceptibilities

A molecule possessing anisotropic molecular magnetic susceptibility experiences a weak alignment in a magnetic field. Its order parameter is proportional[36,37] to $\Delta\kappa H^2/kT$, where $\Delta\kappa$ is the anisotropy in the molecular magnetic susceptibility tensor. The first evidence for this alignment[36] was observed at 9.3 T in solutions of multiring aromatic compounds where deuteron resonances were split by less than 1 Hz. Subsequently, several halomethanes were examined[37] at

14.35 T, again revealing deuteron splittings of a few tenths of a Hz. The precision of these measurements is not high, but clearly the precision ought to improve rapidly as one moves to higher fields. Deuterons are ideal nuclei for observing this alignment since their natural linewidths in low viscosity liquids are quite narrow; yet, the quadrupolar interaction responsible for the splitting is conveniently large. A significant increase in the quadrupolar interaction would make the linewidths unacceptably broad for detecting small splittings.

5.4 A Basic Strategy for Suppressing MS Effects in Magnetic Resonance Imaging

One often wishes to image the density of a liquid, like water, in the vicinity of solid (e.g. bones) or rarified (e.g. as occurs for lungs[38]) phases (see ***Lung and Mediastinum: A Discussion of the Relevant NMR Physics***.). Corresponding abrupt changes in MS have the effect of modifying resonance frequencies in a local manner.[39] To the extent that the resonance frequency of a nucleus determines its spatial position in an imaging application, where field gradients are applied, the MS shift will create an undesirable apparent 'spatial shift'. A strategy[40,41] for minimizing such shifts involves creating imaging sequences where chemical shifts and MS-induced shifts are refocused but gradient pulses are applied during the dephasing and rephasing times in such a way that the resonance offsets due to these external gradients do not refocus. The result is that the 'spatial shifts' arising from MS effects get scaled approximately by the ratio of the local gradient field strength to the static field strength; hence the spatial shift becomes negligible in most materials.

6 RELATED ARTICLES

Chemical Shift Tensor Measurement in Solids; Chemical Shift Tensors in Single Crystals; Diffusion in Porous Media; Lung and Mediastinum MRI; Magnetic Field Induced Alignment of Molecules; Oil Reservoir Rocks Examined by MRI; Probe Design and Construction; Probes for High Resolution; Susceptibility and Diffusion Effects in NMR Microscopy; Susceptibility Effects in Whole Body Experiments.

7 REFERENCES

1. L. H. Bennett, C. H. Page, and L. J. Swartzendruber, *J. Res. Nat. Bur. Stand.*, 1978, **83**, 9.
2. J. H. Van Vleck, *Electric and Magnetic Susceptibilities*, Oxford University Press, Oxford, UK, 1932.
3. W. H. Flygare, *Chem. Rev.*, 1974, **74**, 653.
4. R. K. Reber and G. F. Boeker, *J. Chem. Phys.*, 1947, **15**, 508.
5. *Handbook of Chemistry and Physics*, 73rd edn., ed. D. R. Lide, CRC Press, Boca Raton, FL, 1992, Sect. 9.
6. P. Langevin, *Ann. Chim. Phys.*, 1905, **5**, 70; *J. Phys.*, 1905, **4**, 678.
7. B. C. Eggleston, D. F. Evans, and R. E. Richards, *J. Chem. Soc.*, 1954, 941.
8. J. A. Pople, W. G. Schneider, and H. J. Bernstein, *High Resolution Nuclear Magnetic Resonance*, McGraw-Hill, New York, 1959, Chaps. 2 and 4.
9. L. Pauling, *J. Chem. Phys.*, 1936, **4**, 673.
10. K. S. Krishnan, *Nature (London)*, 1934, **133**, 174.
11. J. E. Wertz and J. R. Bolton, *Electron Spin Resonance, Elementary Theory and Applications*, McGraw-Hill, New York, 1972.
12. J. R. Zimmerman and M. R. Foster, *J. Phys. Chem.*, 1957, **61**, 282.
13. L. F. Fuks, F. S. C. Huang, C. M. Carter, W. A. Edelstein, and P. B. Roemer, *J. Magn. Reson.*, 1992, **100**, 229.
14. M. A. Lorentz, *The Theory of Electrons*, Dover, New York, 1952.
15. R. P. Feynman, R. B. Leighton, and M. Sands, *The Feynman Lectures on Physics*, Addison-Wesley, Reading, MA, 1964, Vol. II, Chaps. 10, 11, 34.
16. J. A. Osborne, *Phys. Rev.*, 1945, **67**, 351.
17. D. Doskočilová, D. D. Tao, and B. Schneider, *Czech. J. Phys. B*, 1975, **25**, 202.
18. C. P. Slichter, *Principles of Magnetic Resonance*, Springer-Verlag, Berlin, 1978, Chap. 4
19. P. Pascal, *Chemie generale*, Masson et Cie, Paris, 1949.
20. C. K. Ingold, *Structure and Mechanism in Organic Chemistry*, Cornell University Press, Ithaca, NY, 1953.
21. W. R. Angus and D. V. Tilston, *Trans. Faraday Soc.*, 1947, **43**, 221.
22. L. E. Drain, *Proc. Phys. Soc.*, 1962, **80**, 1380.
23. N. Bloembergen and J. A. Rowland, *Acta Metall.*, 1953, **1**, 731.
24. M. E. Stoll and T. J. Majors, *J. Magn. Reson.*, 1982, **46**, 283.
25. W. L. Earl and D. L. VanderHart, *J. Magn. Reson.*, 1982, **48**, 35.
26. J. S. Waugh and R. W. Fessenden, *J. Am. Chem. Soc.*, 1957, **79**, 846.
27. D. L. VanderHart, W. L. Earl, and A. N. Garroway, *J. Magn. Reson.*, 1981, **44**, 361.
28. H. W. Spiess, H. Zimmermann, and U. Haeberlen, *Chem. Phys.*, 1976, **12**, 123.
29. D. L. VanderHart, *J. Chem. Phys.*, 1986, **84**, 1196.
30. M. P. Augustine, K. W. Zilm, and D. B. Zax, *J. Chem. Phys.*, 1993, **98**, 9432.
31. J. Homer and H. K. Al-Daffaee, *J. Chem. Soc., Faraday Trans. 2*, 1985, **81**, 803.
32. G. Feher and W. D. Knight, *Rev. Sci. Instrum.*, 1955, **26**, 293.
33. J. Li, M. E. Lashier, G. L. Schrader, and B. C. Gerstein, *Appl. Catal.*, 1991, **73**, 83.
34. D. F. Evans, *J. Chem. Soc.*, 1959, 2003.
35. S. K. Sur, *J. Magn. Reson.*, 1989, **82**, 169.
36. J. A. B. Lohman and C. MacLean, *Chem. Phys.*, 1978, **35**, 269.
37. A. A. Bothner-By, J. Dadok, P. K. Mishra, and P. C. M. Van Zijl, *J. Am. Chem. Soc.*, 1987, **109**, 4180.
38. D. C. Ailion, T. A. Case, D. D. Blatter, A. H. Morris, A. G. Cutillo, C. H. Durney, and S. A. Johnson, *Bull. Magn. Reson.*, 1984, **6**, 130.
39. T. A. Case, C. H. Durney, D. C. Ailion, A. G. Cutillo, and A. H. Morris, *J. Magn. Reson.*, 1987, **73**, 304.
40. P. Bendel, *IEEE Trans. Med. Imag.*, 1985, **MI-4**, 114.
41. J. B. Miller and A. N. Garroway, *J. Magn. Reson.*, 1986, **67**, 575.

Acknowledgments

The author wishes to acknowledge the assistance of L. H. Bennett, L. J. Swartzendruber, J. F. Douglas, A. N. Garroway, G. Eaton, J. Carolan, and A. Vega in the preparation of this manuscript.

Biographical Sketch

David L. VanderHart. *b* 1941. B.A., 1963, Ph.D., 1968, Physical Chemistry, University of Illinois, supervisor, H. S. Gutowsky. Postdoctoral work with W. H. Flygare (molecular Zeeman effect), 1968–69. Polymers Division, National Institute of Standards and Technology, Gaithersburg, MD, USA, 1969–present. Approx. 70 publications. Current research specialty: solid state NMR of polymers with an emphasis on obtaining morphological information.

Nitrogen-15 Chemical Shift Tensors and Organic Structure

Ronald J. Pugmire

Department of Chemical and Fuels Engineering, University of Utah, Salt Lake City, UT, USA

1 Introduction 1
2 Chemical Shielding 1
3 Experimental Techniques 3
4 Results 4
5 Conclusions 7
6 References 7

1 INTRODUCTION

During the past two decades solid state NMR spectroscopy and its applications have grown rapidly among the chemistry and biochemistry community. The availability of increasingly sophisticated instrumentation and software has created opportunities for conducting experiments in areas that have not previously been available to the general chemical community. These new opportunities have been especially helpful in the study of solids. While the majority of such solid state applications have utilized ^{13}C nuclei, a much broader range of interesting nuclei (e.g., ^{11}B, ^{14}N, ^{15}N, ^{17}O, ^{19}F, ^{23}Na, ^{27}Al, ^{29}Si, ^{31}P, ^{113}Cd, ^{209}Pb, etc.) has emerged for use by solid state scientists and engineers.

Interest in magnetic resonance studies of nitrogen has increased significantly in the past decade. The distribution of nitrogen containing substances in materials important to the chemical, biological, medical, agricultural, and environmental sciences is well documented. The ^{14}N nucleus (99.6% natural abundance, nuclear spin 1) is quadrupolar giving rise to a broad signal while the ^{15}N nucleus has spin 1/2. The relative sensitivity of both nuclei is approximately 1×10^{-3} compared to ^{1}H. Nitrogen NMR data have been extensively reviewed by Witanowski et al.[1] and by Mason.[2] Most of the literature describes liquid state isotropic shifts and their relationship to structure elucidation, the importance of solvent effects, and tautomeric equilibria. The combination of a large isotropic shift range, approximately 1350 ppm,[1] and sensitivity to electronic interactions involving the lone pair of electrons make ^{15}N shifts a very sensitive probe of both structural changes and intermolecular interaction.[3] These attractive features of the ^{15}N nucleus are off-set by the sensitivity challenges arising from a low natural abundance (0.365%), long relaxation times, small magnetogyric ratio, and a subsequent receptivity factor 2.19×10^{-2} relative to ^{13}C for an equivalent number of nuclei. Hence, much of the data reported has been obtained from ^{15}N labeled materials although modern high field spectrometers have proven their value in studies at the natural abundance level. A significant amount of attention has recently been focused on the role of nitrogen in biological structures[4] because of its sensitivity to both hydrogen bonding and intermolecular and long-range interactions. In this document the discussion will be restricted to the ^{15}N nucleus.

2 CHEMICAL SHIELDING

The well known relationship between magnetic field strength B_o(arbitrary orientation in the z direction), the magnetogyric ratio γ_I of nuclear spin I, and the NMR Larmor frequency ν_o (in frequency units, Hz) is given in equation (1)

$$\nu_o = \frac{\gamma_I B_o}{2\pi} \tag{1}$$

where ν_o is the difference in energy between any two of the allowed states. The magnetic inductive affect at the nucleus is equal to the vector sum of the static magnetic field and an induced magnetization vector arising from electronic currents that exist in the sample. The induced magnetization is proportional to B_o and the proportionality constant is the sum of the chemical shielding and the magnetic susceptibility of the material surrounding the nucleus of interest. In solids, where rapid motional averaging is absent, all intramolecular currents within the molecule of interest are assigned to chemical shielding. Electronic currents arising from neighboring molecules are assigned to magnetic susceptibility. A more detailed and very useful outline of these interactions is provided by Grant.[5]

The electronic circulation set up by the magnetic induction of the applied field perturbs the effects of B_o at the nucleus of interest. These electronic currents induce a shielding field, B_s, which may be either paramagnetic or diamagnetic (deshielding or shielding) and this induced field must be added to B_o in order to obtain the effective field, B_{eff}, experienced by the nucleus of interest (equation (2)).

$$B_{eff} = B_s + B_o \tag{2}$$

This effect is portrayed in vector form in Figure 1.

The shielding of the nuclear spin is a tensor quantity, described below, that depends on the electronic environment as well as the molecular orientation in the magnetic field. In solids the molecular orientation is locked into a powder pattern in which the nuclear resonance frequency is a function of the orientation of the microcrystalline particles. The random orientation of these particles leads to broad resonance patterns for each unique nuclear spin. The rich informational content of these powder patterns provides more information about electronic structure than the isotropic shifts observed in rapidly tumbling liquid molecules. Unfortunately, the diversity of the banding arising from multiple unique chemical environments in these broad powder patterns obscures the information content that is available in the isotropic chemical shift. However, the components of the shift tensor in the solid state reveal even more information regarding the subtle differences in electronic and geometrical structural characteristics and

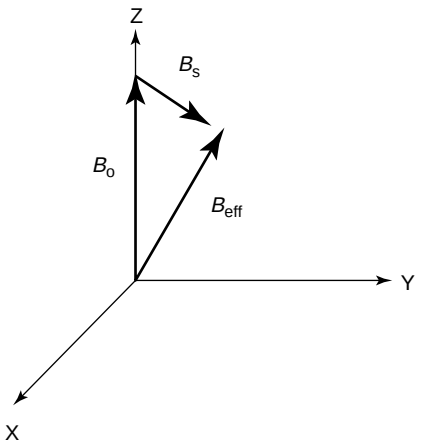

Figure 1 Relationship between the applied field, B_o, and the shielding field and effective fields (not drawn to scale) B_s and B_{eff}

the various experimental techniques employed to extract this information from solid samples is summarized in Section 3.

The shielding interaction with a nucleus is different for each unique chemical environment or symmetry position relative to the remainder of the lattice structure. Furthermore, the orientation dependence of the magnetic field to the screening currents induced around the nucleus presents an anisotropic environment that can be described by the chemical shift tensor. In principal, a different resonance frequency will be observed for each orientation of the nuclear spin with respect to the external magnetic field and the difference in this screening effect from that of a reference material is defined as the chemical shift. The reference that has emerged in the field is

$$\delta = \begin{bmatrix} \delta_{xx} & \delta_{xy} & \delta_{xz} \\ \delta_{yx} & \delta_{yy} & \delta_{yz} \\ \delta_{zx} & \delta_{zx} & \delta_{zz} \end{bmatrix} \tag{3}$$

external nitromethane ($\delta = 0$) with the convention of negative values for more shielded resonance positions. The chemical shift tensor δ in a general reference frame may be represented by a 3×3 Cartesian matrix that is called a second rank tensor (equation (3)) which can be decomposed into three individual tensors of rank zero, one, and two which are defined as the scalar isotropic chemical shift, the symmetric, and antisymmetric chemical shifts denoted (equation (4)) as

$$\delta = \delta_o + \delta_{sym} + \delta_{anti} \tag{4}$$

The isotropic shift, δ_o, of zeroeth rank, is the trace of the Cartesian tensor, e.g., $1/3(\delta_{xx} + \delta_{yy} + \delta_{zz})$, and is invariant to any rotational transformation of the coordinate frame. Hence, δ_o is the only part of the chemical shift tensor that can be measured in solution samples; this the result of rapid tumbling motion of the molecules. The antisymmetric (first rank) and symmetric (second rank,) chemical shifts are given in equations (5) and (6), respectively.

$$\delta_{ij}^{(a)} = \tfrac{1}{2}(\delta_{ij} - \delta_{ji}) \tag{5}$$

$$\delta_{ij}^{(s)} = \tfrac{1}{2}(\delta_{ij} + \delta_{ji}) \tag{6}$$

The absence of diagonal elements in the first rank tensor renders these second order infinitesimal shift frequencies immeasurable. The traceless second-rank symmetric matrix contains diagonal elements that can provide first-order anisotropic shifts that add to or subtract from the Zeeman frequencies and are measurable in the NMR spectrum of solids. In the symmetric matrix any change in orientation of the magnetic field in the molecular frame will still leave anisotropic shifts along the diagonal of the transformed second-rank matrix. Unlike the antisymmetric components, the off-diagonal shifts in the symmetric portion of the chemical shift tensor will affect the principal values under the transformations associated with matrix diagonalization.

There always exists some frame in which the matrix in equation (3) is diagonal, in which case the three diagonal elements of the chemical shift tensor are designated as the principal values, δ_{11}, δ_{22}, and δ_{33}. By convention the order of the principal values are given as $\delta_{11} \geq \delta_{22} \geq \delta_{33}$, with δ_{11} representing the highest frequency (least shielded) component. The axis system in which the symmetric chemical shift matrix is diagonal is designated the principal axis system (PAS). The diagonal components are the principle values in the PAS while the remaining three (off-diagonal) terms are the Euler angles which define the directions of these principal values in the molecular frame. Hence, the complete description of the chemical shift tensor requires six elements of the shift tensor. The breakpoints in a powder pattern provide the principal values of the chemical shift tensor. The off-diagonal terms can only be obtained experimentally by tracking the chemical shift of each unique nucleus as a molecule (e.g., a molecule in a single crystal) is rotated in the magnetic field. These data can then be transformed into any of a number of reference frames that can be used to determine the orientation of the tensor in the molecular frame. The details of these experiments and transformations are described in a general outline by Orendt[6] and in detail by Grant[5] and Sherwood.[7]

The difficulties associated with growing single crystals and then acquiring the necessary orientational data is daunting, time consuming, and complicated by the reality that acquiring a single crystal of sufficient size for NMR experiments is usually not practical. However, sufficient single crystal data, together with theoretical simulations of the shift tensors, have been acquired to demonstrate that quite good approximations can be obtained for the orientation of the shift tensor principal axis system on the molecular frame.[8,9] Hence, the various types of experiments that provide only the principal values of the shift tensor on powder samples[6,10] are sufficient, when combined with appropriate theoretical calculations, to describe the off-diagonal elements which fix the orientation in the molecular frame with reasonable accuracy (see Section 4.3). To date, the majority of chemical shift tensor data appearing in the literature has been restricted to the ^{13}C nucleus and the latest, but somewhat dated, compilation of these data together with available data on ^{15}N shift tensor principal values has been provided by Duncan.[11] The acquisition of shift tensor data on solid materials, however, has expanded considerably in the past 10–15 years as line narrowing methods and techniques have become available. A review has described these experimental advances[6] but additional major advances in multidimensional experiments have recently appeared[12–14] and are described in another article in this encyclopedia,

Magic-angle Turning Spectra of Solids Involving 5π-pulse Sequences.

Despite the challenges faced with obtaining shift tensor data, new experimental techniques now enable investigators to obtain high quality ^{13}C shift tensor data on molecules containing more than sixty unique carbon atoms[10] and ^{15}N shift tensors at the natural abundance level on molecules containing as many as five nitrogens (guanine)[15] and eight non-equivalent nitrogens in potassium penicillin V.[13]

3 EXPERIMENTAL TECHNIQUES

^{15}N chemical shift tensor data have been reported using five different types of experimental techniques: (1) single crystal studies; (2) analysis of static powder patterns and off-magic-angle spinning on simple ^{15}N enriched heterocycles; (3) analysis of powder patterns utilizing the dipolar interaction between ^{1}H–^{5}N or adjacent ^{13}C–^{15}N labeled pairs; (4) powder patterns obtained by means of dynamic nuclear polarization experiments; (5) two-dimensional experiments such as polarization inversion spin exchange at the magic angle (PISEMA), and the five-π pulse experiment five pi replicated magic angle turning (FIREMAT).

3.1 Single Crystals

A single crystal study of L-hystidine·HCl·H_2O[16] reported the full tensor of the two imidazole nitrogens in the amino acid while a single crystal study of [1-^{13}C]glycyl[^{15}N]glycine provided the principal values of the ^{15}N tensor and its orientation in the molecular frame.[17]

3.2 Static Powders and Off-Magic Angle Spinning

The major portion of the ^{15}N shift tensor data has been obtained by static powder pattern analysis. Illustrative examples of static experiments on ^{15}N-enriched materials include: studies of the various phases of NH_4NO_3,[18] protonated and non-protonated species in simple five- and six-member nitrogen heterocycles,[19] porphyrin complexes,[20] cation binding in a membrane-bound polypeptide,[21] substituted benzonitriles,[22] off-angle fast sample spinning of an isolated ^{15}N–^{15}N diazo system,[23] static and off-angle fast sample spinning of substituted pyrazoles,[24] secondary structure of peptides containing L-alanine[25] and poly(β-benzyl L-aspartate),[26] substituted benzonitriles,[27] the amide fragment of acetanilide and *N*-methylacetanilide,[28] and the relationship of the δ_{33} principal value to the hydrogen bond length in the glycine residue of some oligopeptides.[29]

3.3 Dipolar Interactions in Powders

^{15}N shift tensor principal values and their orientation in the molecular frame have been determined through the dipolar interaction between proton and nitrogen dipolar coupling in peptides,[30] tryptophan and histidine side chains,[31] the phenylalanine residue,[32] the dipolar tensors for the peptide bond in [1-^{13}C]glycyl[^{15}N]glycine·HCl·H_2O,[33] peptides of the form *N*-acetyl[1-^{13}C]glycyl[^{15}N]-X-amide where X = glycine, alanine, and tyrosine[34] and L[-^{13}C]alanyl-L-[^{15}N]alanine,[35] an analytical approach for the determination of the principal value σ_{33} of the amide ^{15}N chemical shift tensor element with respect to the molecular frame,[36] studies of the nitroso-groups in nitrobenzene and *p*-nitroso-N,N-dimethyl aniline (in which a very large CSA anisotropy of 1472 ppm was observed),[37] the two-dimensional PISEMA data on [1-^{15}N]-2′-deoxyguanosine,[38] the three-dimensional powder patterns of $^{15}N_{\varepsilon 1}$-tryptophan and $^{15}N_{\pi}$-hystidine side chains,[39] shift tensor values and orientation in the molecular frame in ^{13}C and ^{15}N labeled uracil.[40,41]

3.4 Dynamic Nuclear Polarization Experiments on Powders

Hu et al.[42,43] reported large ^{15}N DNP enhancement factors in benzamide (260, compared to CP data) and greater than 900 in carbazole and were able to compare the principal values of the shift tensors in powdered samples of these two molecules with those obtained by standard cross polarization and single pulse experimental techniques.

3.5 Two-Dimensional Experiments

A variety of two-dimensional experiments designed for separating the isotropic and anisotropic chemical shift information were instrumental in advancing resolution and data analysis of complex molecular systems.[44–50] The magic angle turning experiments, first conceived by Gan,[51] paved the way

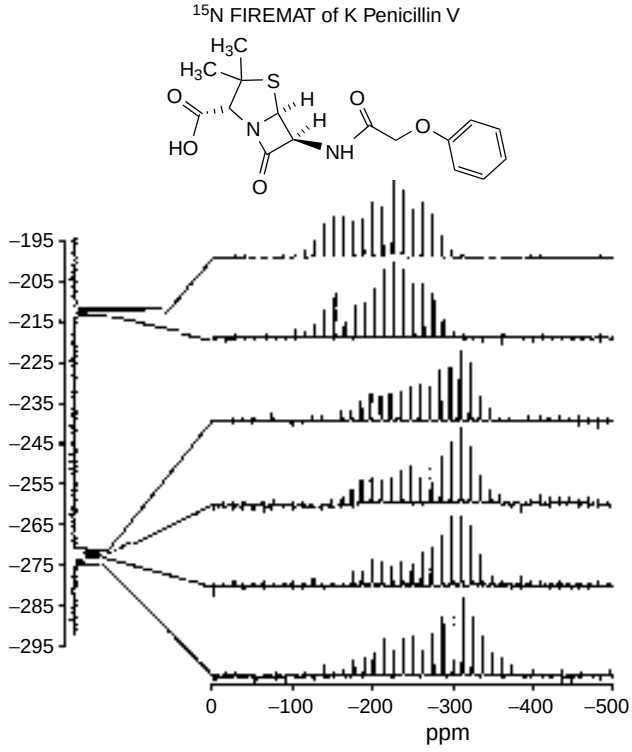

Figure 2 A two-dimensional natural abundance ^{15}N spectrum is shown in which the isotropic shift spectrum with no spinning side bands is plotted vertically on the left while the isolated spinning sideband patterns for the six resolved peaks are plotted on the right, connected to the corresponding isotropic peaks by guide lines

for development of experimental tools[12,13] that can reveal an amazing amount of detail regarding CSA in complex molecular systems. Recent modifications to the 5-π pulse experiments, FIREMAT[13] and 2D-PASS[14] have been particularly exciting in significantly expanding the range and complexity of molecules that can be studied. These two experiments, while related by virtue of a common 5-π pulse sequence for generating the two-D data set, possess important differences that are detailed in Ref.[10] Taking advantage of TIGER data processing in the FIREMAT experiment,[52] one is able to optimize S/N and resolution in the evolution dimension and obtain high quality ^{13}C data on molecules with more than 60 different tensors. The power of the FIREMAT experiment can be seen by examining the ^{15}N spectrum of penicillin V in Figure 2. Potassium penicillin V has two nitrogen atoms and, at ambient temperature, four molecules per asymmetric unit.[13] Conformational differences in these molecules split the NH nitrogen into the four peaks shown between −271.7 ppm and −275.3 ppm. The conformational differences do not affect the ring nitrogen to the same extent and three of the resonances are degenerate at −212.5 while the fourth is at −214.0 ppm. The FIREMAT experiment has also been used to obtain ^{15}N shift tensor data at the natural abundance level on nucleic acid bases,[15] purine,[53] and indolazines.[54]

4 RESULTS

4.1 Characteristics of Principal Values in Nitrogen Heterocycles

For convenience in consideration of ^{15}N shift tensors in organic molecules the discussion will be restricted to nitrogen heterocycles since this general class of compounds is ubiquitous in nature. The relatively simple five-and six-member heterocycles have been shown to provide the framework for understanding the shift tensor data in more complex heterocyclic structures including indolazines, the nucleic acid bases and related compounds. Consideration of ionic species also

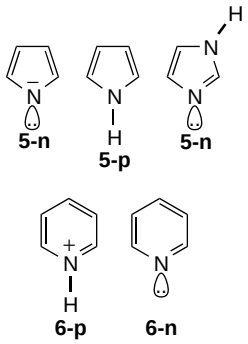

Figure 3 Definition of the different types of nitrogen atoms present in five-and six-member nitrogen heterocycles. The terms "n" and "p" represent non-bonded lone pair and protonated or bonded, lone pair, respectively

reflects the effects of hydrogen bonding interactions on the nitrogen shift tensors. This is especially interesting because of the lone pair of electrons. The structures portrayed in Figure 3 provide a useful framework from which to understand the experimental shift tensor data.

It is found that four different types of nitrogen tensors are present in simple nitrogen heterocycles. For convenience, the nitrogens with non-bonded lone electron pairs in five- and six-member rings shall be referred to as **5-n** and **6-n** types (such as pyrrole anion and the non-protonated nitrogens in imidazole and benzimidazole) and protonated **5-p** and **6-p** types (e.g., pyrrole, the protonated sites in imidazole and benzimidazole, the imidazolium cation, and the pyridinium cation).

Figure 4 presents a correlation diagram of the principal values of 12 simple heterocyclic structures. Quantum mechanical calculations were used to assign the orientation of the principal values to the molecular frame and to provide insight into the effects of electronic structure on the chemical shielding. These orientation assignments can be made with reasonable accuracy (estimated error of ±10 degrees based on work on uracil)[55] if

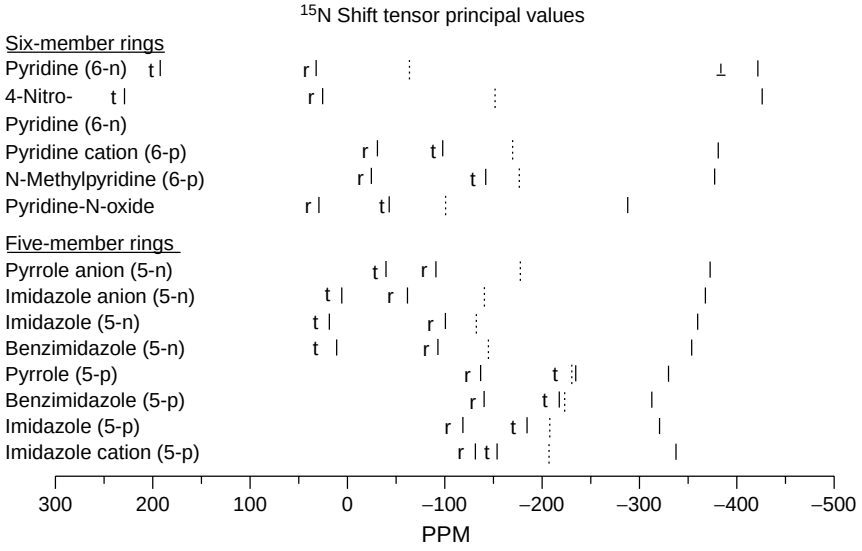

Figure 4 Correlation of the ^{15}N chemical shift principal values in 5-and 6-member heterocycles. The principal values are marked by solid lines, and the symbols indicate their approximate orientation in the molecular frames as described in Figure 5

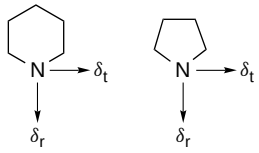

Figure 5 Orientation of the in-plane principal components in nitrogen heterocycles. δ_r and δ_t are depicted in the figure and lie in the plane of the ring approximately in the tangential and radial directions of the ring. $\delta_\perp$ is perpendicular to the ring. (*J. Am. Chem. Soc.*, published with permission)

sufficient structural data (e.g., crystal structure, bond length,) is available.[56,57]

A cursory inspection of Figure 4 illustrates the differences in the spans of the principal values of the nitrogen types. That the span of pyridine (622 ppm) is not unique as demonstrated by the span of 4-nitropyridine (674 ppm). In pyridine one observes that the δ_{11} shift component is oriented tangential to the ring, a direction that is also perpendicular to the lone pair (see Figure 6). When the hybridization of the nitrogen is changed from the **6-n** to the **6-p** type either by protonation, alkylation, or by *N*-oxide formation the tangential component crosses over the radial component, thus reducing the span of the shift tensor components by approximately 1/2 (to a range of 338−351 ppm). A similar affect is noted for the **5-n**/**5-p** case. The span in the pyrrole anion (333 ppm) is reduced to 192 ppm in pyrrole. Comparable effects are noted in each molecular pair studied. The data of Hoelger et al.[24] exhibit the same phenomena in the amine/imine pair of nitrogens in substituted pyrazoles.

The orientation of the shift tensor on the molecular frame of the compounds containing **5-n** type nitrogens corresponds to that found in pyridine (**6-n**). The span of the **5-n** tensor components is 337−374 ppm, a range that is nearly identical to that of the **6-p** nitrogens. In a manner similar to that noted for pyridine, protonation of the **5-n** loan pair inverts the order of the radial and tangential components and also significantly reduces (again, by approximately 1/2) the span of the **5-p** type nitrogens (to a range of 172−206 ppm). This reduction of span for the **5-n** and **5-p** species, compared to the respective **6-n** and **6-p** species, may be attributed to the larger degree of localization of the six π-electrons in five-member heterocycles compared with the six-member rings.[58] The increase of the localization of the π-electrons increases the electronic repulsion energy, thereby increasing the energy gaps corresponding to the $\sigma-\pi^*$ and $\pi-\sigma^*$ orbitals which dominate the paramagnetic contribution to the in-plane components. Thus, the paramagnetic contribution to the in-plane components of the shielding term decreases which reduces the shift tensor span.

The effects of interaction of the lone pair with neighboring atoms, whether bonded or non-bonded, is a matter of extreme interest and will be described in Section 4.3.

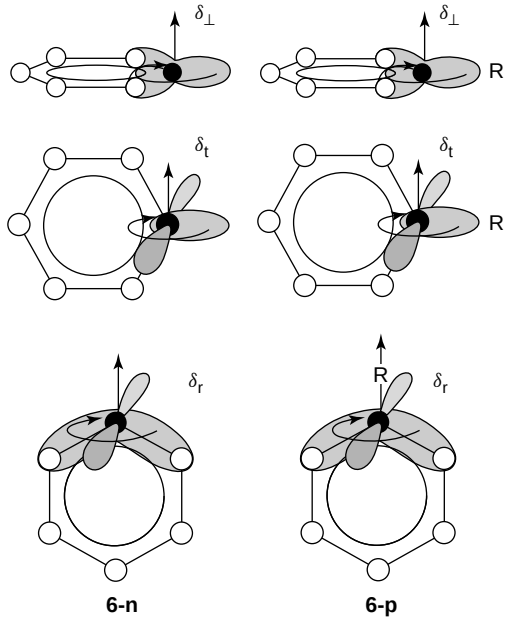

Figure 6 Electron orbitals making the largest contributions to the chemical shift principal components in pyridine. R corresponds to the lone pair in pyridine and R=H, O, or CH_3 in pyridine hydrochloride, pyridine-*N*-oxide, and *N*-methylpyridine. (*J. Am. Chem. Soc.*, published with permission)

4.2 The Nucleic Acid Bases

The simple nitrogen heterocycles can be used as a guide to understanding the electronic structure and intermolecular interactions in the nucleic acid bases. Employing a combination of two-dimensional experimental techniques (PHORMAT, TIGER data processing, and FIRMAT) that were dependent on the complexities of the ^{15}N spectra, the shift tensors were

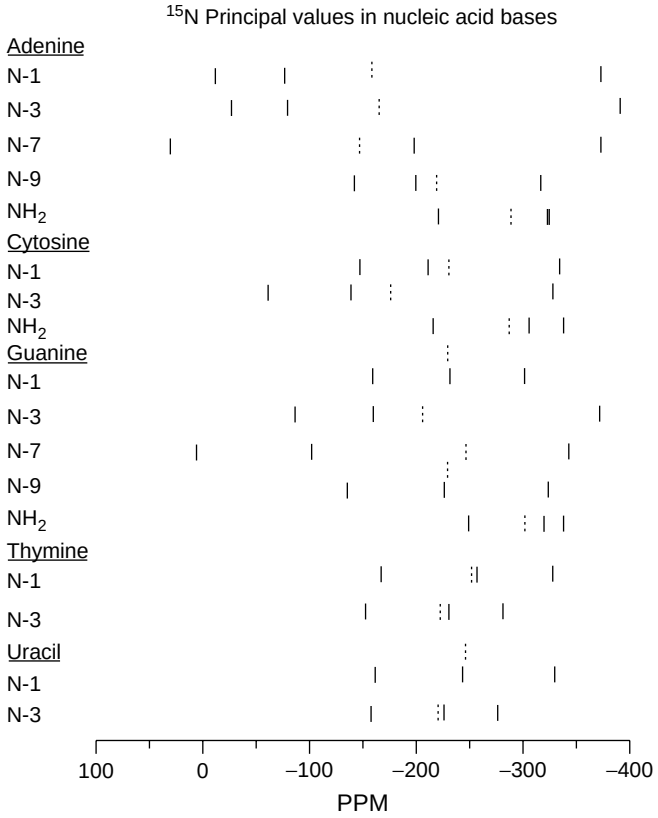

Figure 7 Correlation diagram of the ^{15}N shift tensor principal values in nucleic acid bases. Dashed lines are isotropic shift values

obtained on isotopically enriched adenine, and at natural abundance on thiamine, guanine, and cytosine.[15] The principal values obtained, together with data previously reported on uracil,[40] are presented as a bar graph in Figure 7 in order to visualize the relationship between the various shift tensor patterns.

The ^{13}C and ^{15}N shift tensor data obtained on purine[53] provides a useful model for interpreting the patterns observed in the nucleic acid bases. The purine data were obtained under separate sets of conditions and the position of the tautomeric proton could be definitely identified (by means of the ^{13}C isotropic shift data) as residing at either the N-7 or the N-9 position. The interpretation of the data is further confirmed by comparing the purine ^{15}N data with that of the simple nitrogen heterocycles previously described. In the five- and six-member heterocycles (Figure 4) the span ($\delta_{11}-\delta_{33}$) of the shift tensors of the **5/6-p** nitrogens are of the order of 1/2 that of the **5/6-n** nitrogens (compare, for example, the spans of N-1 and N-3 in benzimidazole in Figure 4). The N-7 and N-9 tautomeric structures in purine mirror this effect and, by comparing the spans of the N-7/9 positions in adenine and guanine (Figure 8), the position of the tautomeric proton is clearly evident in these two compounds. Furthermore, the spans of the N-1 and N-3 tensors in uracil and thiamine clearly indicate that the two labile protons occupy these sites while the cytosine data suggest that N-1 is the preferred site, in accordance with x-ray data. In the case of guanine the shift tensor data is consistent with the proton occupying the N-1 site.

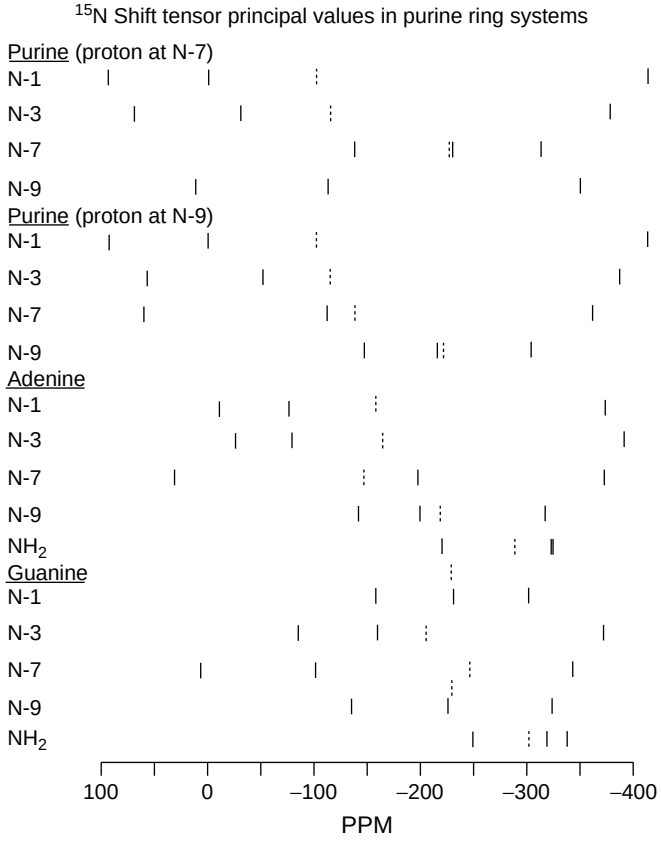

Figure 8 Comparison of shift tensor principal values in purine ring structures. The purine data is taken from Ref.[9] while the adenine and guanine data were taken from Ref.[15]

4.3 Effects of Hydrogen Bonding

The large changes in the shift tensor principal values provide a means for assessing hydrogen bonding in a wide range of heterocyclic ring systems. Using density functional theory (DFT) Facelli[3] simulated the shift tensor data in benzamide and these results, together with simulations of uracil,[40] highlighted the importance of including hydrogen bonding, and in general, intermolecular interactions in the calculation of ^{15}N chemical shift tensors. Further evidence for the importance of these intermolecular interactions in the calculation of ^{15}N chemical shift tensors can be found by analysis of these tensors in the series of heterocycles portrayed in Figure 4.

For these compounds the rms error between experimental and DFT calculated values, which did not include intermolecular effects, was approximately 30–40 ppm. This large scatter is approximately an order of magnitude greater than that found in simulated data on polyaromatic hydrocarbons.[56,57]

Utilizing the imidazole structural information obtained from neutron diffraction data it is possible to improve the chemical shift calculations and to examine the effects of hydrogen bonding on the ^{15}N shift principal values using a dimer model.[19] The correlation between experimental and calculated shift principal values in imidazole, with and without intermolecular interactions, is shown in Figure 9. The rms error of the predicted shift principal values is 40.9 ppm using an optimized geometry and is 13.8 ppm when the structural data includes the position of the hydrogens in the lattice structure along with the effects of hydrogen bonding.[19] Using the neutron diffraction data without including the intermolecular hydrogen bonding

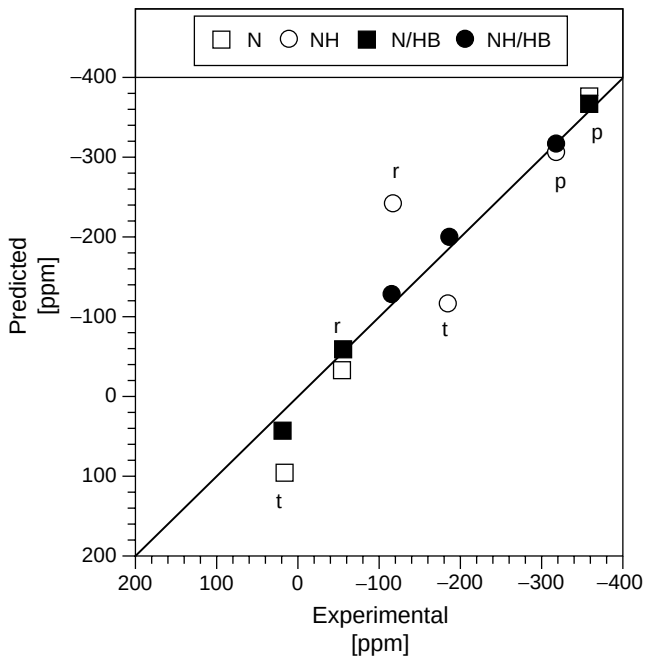

Figure 9 Experimental versus predicted chemical shift values for imidazole. The DFT method was used to calculate the ^{15}N shift tensor values using the neutron diffraction structure and including the effects of intermolecular interactions due to hydrogen bonding. The letters r, t, and p refer to the radial, tangential, and perpendicular components of the shift tensors. The legends N/HB and NH/HB designate predictions based on intermolecular interactions due to hydrogen bonding for the **5-n** and **5-p** nitrogens, respectively. (*J. Am. Chem. Soc.*, with permission)

effects produces only a modest improvement in the calculated values over those obtained with the optimized geometry. Introduction of intermolecular effects in the simulation of the nucleic acid bases plays a significant role in improving the correlation of experimental and theoretical result, reducing the rms error by a factor of two.[15] Given the 3–4 fold greater span of the nitrogen shift tensor, a rms error of 14 ppm in imidazole and 16 ppm for the nucleic acid bases compares favorably with the 3–5 ppm rms errors obtained in simulations of ^{13}C chemical shift tensors in polycyclic aromatic hydrocarbons based on x-ray structure data.[56,57]

5 CONCLUSIONS

^{15}N chemical shift tensors in heterocyclic compounds are very sensitive to the hybridization of the nitrogen atom and changes in the tangential component can vary from 200 ppm to as much as 340 ppm in five-and six-member rings, respectively, when the nitrogen lone-pair hybridization is changed. The changes in the magnitude of the in-plane components are so large that these effects may be useful in probing intermolecular interactions associated with hydrogen bonding in biological systems. It is possible to measure and spacially assign the principal components of the ^{15}N chemical shift tensors obtained from powder samples in heterocyclic compounds. The assignments of the chemical shift tensor components are critical for analyzing the relationship between the electronic structure and shift tensors. In all the compounds studied, the most deshielded component, δ_{11}, is in the plane of the ring and approximately perpendicular to the plane containing the bonding-antibonding or HOMO-LUMO pair of orbitals with the smallest energy gap. The most shielded component, δ_{33}, is always perpendicular to the plane of the ring, as in the ^{13}C tensors of aromatic compounds and is less sensitive to changes in the hybridization of the nitrogen atom than the principal components in the plane of the ring.

Employing modern instrumentation and experimental techniques that have been optimized for obtaining shift tensor data, it is now possible to study nucleic acid materials at the natural abundance level or with isotropic enrichment depending on the relaxation times and spectral complexity. The nucleic acid bases exhibit the same sensitivity to small changes in molecular geometry and environment noted for the five- and six-member heterocycles. Even for nitrogens with similar hybridization, differences as large as 50 ppm are found in corresponding principal shift components. Theoretical techniques now available enable the investigator to simulate the molecular environment with reasonable confidence. The agreement between experiment and theory is highly dependent on the molecular model used in the calculations, and molecular models that include the intermolecular interactions show superior correlation with the experimental values.

6 REFERENCES

1. M. Witanowski, L. Stefaniak, and G. A. Webb, in 'Annual Reports on NMR Spectroscopy', ed G. A. Webb, Academic Press: London, 1993, Vol. 25, p. 2 and reviews of these authors in this series.
2. J. Mason, in 'Encyclopedia of Nuclear Magnetic Resonance', eds D. M. Grant and R. K. Harris, Wiley: London, 1996, p. 3222.
3. J. C. Facelli, R. J. Pugmire, and D. M. Grant, *J. Am. Chem. Soc.*, 1996, **118**, 5488.
4. See for example: (a) Q. Teng, M. Iqbal, and T. A. Cross, *J. Am Chem. Soc.*, 1992, **114**, 5312; (b) A. Shoji, T. Ozaki, T. Fujito, K. Deguchi, I. Ando, and S. Ando, *J. Am. Chem. Soc.*, 1990, **112**, 4693; (c) H. Le and E. J. Oldfield, *J. Biomol. NMR*, 1994, **4**, 341; (d) C. J. Hartzell, T. K. Pratum, and G. Drobny, *J. Phys. Chem.*, 1987, **87**, 4324; (e) G. Harbison, J. Herzfeld, and R. G. Griffin, *J. Am. Chem. Soc.*, 1981, **103**, 4752; (f) G. A. Lorigan, R. McNamara, R. A. Jones, and S. J. Opella, *J. Magn. Reson.*, 1999, **140**, 315; (g) M. Hong, J. D. Gross, W. Hu, and R. G. Griffin, *J. Magn. Reson.*, 1998, **135**, 169; (h) Q. Teng and T. A. Cross, *J. Magn. Reson.*, 1989, **85**, 439; (i) K. T. Dayie and G. Wagner, *J. Am. Chem. Soc.*, 1999, **119**, 7797; (j) M. Ashikawa, A. Shoji, T. Ozaki, and I. Ando, *Macromolecules*, 1999, **32**, 2288; (k) J. R. Bender, D. M. Taylor, and A. Ramamoorthy, *J. Am. Chem. Soc.*, 2001, **123**, 914; (l) A. Ramamoorthy, C. H. Wu, and S. J. Opella, *J. Am. Chem. Soc.*, 1997, **119**, 10 479; (m) D. K. Lee, J. S. Santos, and A. Ramamoorthy, *Chem. Phys. Lett.*, 1999, **309**, 209; (n) K. G. Valentine, A. L. Rockwell, L. M. Gierasch, and S. J. Opella, *J. Magn. Reson.*, 1987, **73**, 519; (o) T. G. Oas, C. J. Hartzell, F. W. Dahlquist, and G. P. Drobny, *J. Am. Chem. Soc.*, 1987, **109**, 5962; (p) R. E. Stark, L. W. Jelinski, D. J. Ruben, D. A. Torchia, and R. G. Griffin, *J. Magn. Reson.*, 1983, **55**, 266; (q) G. S. Harbison, L. W. Jelinski, R. E. Stark, D. A. Torchia, J. Herzfeld, and R. G. Griffin, *J. Magn. Reson.*, 1984, **60**, 79; (r) J. F. Hinton, P. L. Guthrie, P. Pulay, K. Wilinski, and G. Fogarasi, *J. Magn. Reson.*, 1992, **96**, 154; (s) M. D. Lumsden, R. E. Wasylishen, K. Eichele, M. Schindler, G. H. Penner, W. P. Powell, and R. D. Curtis, *J. Am. Chem. Soc.*, 1994, **116**, 1403; (u) S. Kuroki, N. Asakawa, S. Ando, I. Ando, A. Shoji, and T. Ozaki, *J. Mol. Structure*, 1991, **245**, 69.
5. D. M. Grant, in 'Encyclopedia of Nuclear Magnetic Resonance', eds D. M. Grant and R. K. Harris, Wiley: London, 1996, p. 1298.
6. A. M. Orendt, in 'Encyclopedia of Nuclear Magnetic Resonance', eds D. M. Grant and R. K. Harris, Wiley: London, 1996, p. 1282.
7. M. H. Sherwood, in 'Encyclopedia of Nuclear Magnetic Resonance', eds D. M. Grant and R. K. Harris, Wiley: London, 1996, p. 1322.
8. J. C. Facelli, in 'Encyclopedia of Nuclear Magnetic Resonance', eds D. M. Grant and R. H. Harris, Wiley: London, 1996, p. 4327.
9. See, for instance, Modeling NMR Chemical Shift Tensors, Gaining Insights into Structure and Environment, ACS Symposium Series 732, eds J. C. Facelli and A. C. deDios, 1999.
10. D. M. Grant, in 'Encyclopedia of Nuclear Magnetic Resonance', eds D. M. Grant and R. K. Harris, Wiley: Chichester, 2002, Volume 9.
11. T. M. Duncan, 'A Compilation of Chemical Shift Anisotropies', 2nd edn, Farragut Press: Chicago, 1997.
12. J. Z. Hu, D. W. Alderman, C. Ye, R. J. Pugmire, and D. M. Grant, *J. Magn. Reson. A*, 1993, **105**, 82.
13. D. W. Alderman, G. McGeorge, J. Z. Hu, R. J. Pugmire, and D. M. Grant, *Mol. Phys.*, 1998, **95**, 1113.
14. O. N. Antzutkin, S. C. Shekar, and M. H. Levitt, *J. Magn. Reson.*, 1995, **115**, 7.
15. J. Z. Hu, J. C. Facelli, D. W. Alderman, R. J. Pugmire, and D. M. Grant, *J. Am. Chem. Soc.*, 1998, **120**, 9863.
16. G. Harbison, J. Herzfeld, and R. G. Griffin, *J. Am. Chem. Soc.*, 1981, **103**, 4752.
17. G. S. Harbison, L. W. Jelinski, R. E. Stark, D. A. Torchia, J. Herzfeld, and R. G. Griffin, *J. Magn. Reson.*, 1984, **60**, 79; R. E. Stark, L. W. Jelinski, D. J. Ruben, D. A. Trochia, and R. G. Griffin, *J. Magn. Reson.*, 1983, **55**, 266.
18. K. L. Anderson-Altmann and D. M. Grant, *J. Phys. Chem.*, 1993, **97**, 11 096.
19. M. S. Solum, K. L. Anderson, M. Strohmeier, D. A. Berges, Y. Zhang, J. C. Facelli, R. J. Pugmire, and D. M. Grant, *J. Am. Chem. Soc.*, 1997, **119**, 9804.

20. M. Strohmeier, A. M. Orendt, J. C. Facelli, M. S. Solum, R. J. Pugmire, R. W. Parry, and D. M. Grant, *J. Am. Chem. Soc.*, 1997, **119**, 7114.
21. F. Tian and T. A. Cross, *J. Magn. Reson.*, 1998, **135**, 535.
22. M. Sardashti and G. E. Maciel, *J. Phys. Chem.*, 1988, **92**, 4620.
23. R. Challoner, R. K. Harris, and J. A. Tossell, *J. Magn. Reson.*, 1997, **126**, 1.
24. E. G. Hoelger, F. Aguilar-Parrilla, J. Elguero, O. Weintraub, S. Vega, and H. H. Limbach, *J. Magn. Reson. Series A*, 1996, **120**, 46.
25. A. Shoji, T. Ozaki, T. Fujito, K. Deguchi, S. Ando, and I. Ando, *J. Am. Chem. Soc.*, 1990, **112**, 4693–4697.
26. M. Ashikawa, A. Shoji, T. Ozaki, and I. Ando, *Macromolecules*, 1999, **32**, 2288.
27. M. Sardashti and G. E. Maciel, *J. Phys. Chem.*, 1988, **92**, 4620.
28. M. D. Lumsden, R. E. Wasylishen, K. Eichele, M. Schindler, G. H. Penner, W. P. Power, and R. D. Curtis, *J. Am. Chem. Soc.*, 1994, **116**, 1403.
29. S. Kuroki, N. Asakawa, S. Ando, I. Ando, A. Shoji, and T. Ozaki, *J. Mol. Struct.*, 1991, **245**, 69.
30. M. Hong, J. D. Gross, W. Hu, and R. G. Griffin, *J. Magn. Reson.*, 1998, **135**, 169.
31. A. Ramamoorthy, C. H. Wu, and S. J. Opella, *J. Am. Chem. Soc.*, 1997, **119**, 10 479.
32. D. K. Lee, J. S. Santos, and A. Ramamoorthy, *Chem. Phys. Lett.*, 1999, **309**, 209.
33. G. S. Harbison, L. W. Jelinski, R. E. Stark, D. A. Torchia, J. Herzfeld, and R. G. Griffin, *J. Magn. Reson.*, 1984, **60**, 79.
34. T. G. Oas, C. J. Hartzell, F. W. Dahlquist, and G. P. Drobny, *J. Am. Chem. Soc.*, 1987, **109**, 5962.
35. C. J. Hartzell, M. Whitfield, T. B. Oas, and G. P. Drobny, *J. Am. Chem. Soc.*, 1987, **109**, 5966.
36. Q. Teng and T. A. Cross, *J. Magn. Reson.*, 1989, **85**, 439.
37. M. D. Lumsden, G. Wu, R. E. Wasylishen, and R. D. Curtis, *J. Am. Chem. Soc.*, 1993, **115**, 2825.
38. G. A. Lorigan, R. McNamara, R. A. Jones, and S. J. Opella, *J. Magn. Reson.*, 1999, **140**, 315.
39. A. Ramamoorthy, C. H. Wu, and S. J. Opella, *J. Am. Chem. Soc.*, 1997, **119**, 10 479.
40. K. L. Anderson-Altmann, Cu. G. Phung, S. Mavromoustakos, Z. Zheng, J. C. Facelli, C. D. Poulter, and D. M. Grant, *J. Phys. Chem.*, 1995, **99**, 10 454.
41. J. Leppert, B. Heise, and R. Ramachandran, *J. Magn. Reson.*, 2000, **145**, 307.
42. J. Z. Hu, J. Zhou, B. Yang, L. Li, J. Qui, C. Ye, M. S. Solum, R. A. Wind, R. J. Pugmire, and D. M. Grant, *Solid State NMR*, 1997, **8**, 129.
43. J. Z. Hu, M. S. Solum, R. A. Wind, B. L. Nilsson, M. A. Peterson, R. J. Pugmire, and D. M. Grant, *J. Phys. Chem., A*, 2000, **104**, 4413.
44. Y. Yarim-Agaev, P. M. Tutunjian, and J. S. Waugh, *J. Magn. Reson.*, 1982, **47**, 51.
45. A. Bax, N. M. Szeverenyi, and G. E. Maciel, *J. Magn. Reson.*, 1983, **51**, 400.
46. A. Bax, N. M. Szeverenyi, and G. E. Maciel, *J. Magn. Reson.*, 1983, **55**, 494.
47. R. Tycko, G. Dabbagh, and P. Mirau, *J. Magn. Reson.*, 1989, **85**, 265.
48. T. Terao, T. Fujii, T. Onodera, and A. Saiks, *Chem. Phys. Lett.*, 1984, **107**, 145.
49. L. Frydman, G. C. Chingas, Y. K. Lee, P. J. Grandinetti, M. A. Eastman, B. A. Barrall, and A. Pines, *J. Chem. Phys.*, 1992, **97**, 4800.
50. A. C. Kolbert and R. G. Griffin, *Chem. Phys. Lett.*, 1990, **166**, 87.
51. Z. Gan, *J. Am. Chem. Soc.*, 1992, **114**, 8307.
52. See discussion in Reference 10.
53. J. C. Facelli, J. Z. Hu, M. S. Solum, R. J. Pugmire, and D. M. Grant, in 'Modeling NMR Chemical Shift Tensors, Gaining Insights into Structure and Environment', ACS Symposium Series 732. eds J. C. Facelli and A. C. deDios, 1999, p. 162.
54. J. Z. Hu, D. Barich, R. J. Pugmire, and D. M. Grant, '^{15}N chemical Shift Tensors in Indolazines', in preparation.
55. K. L. Anderson-Altmann, C. G. Phung, S. Mavromoustakos, Z. Zheng, J. C. Facelli, C. D. Poulter, and D. M. Grant, *J. Phys. Chem.*, 1995, **99**, 10 454.
56. C. M. Carter, D. W. Alderman, J. C. Facelli, and D. M. Grant, *J. Am. Chem. Soc.*, 1987, **109**, 2639.
57. D. M. Grant, F. Liu, R. J. Iuliuci, C. G. Phung, J. C. Facelli, and D. W. Alderman, *Acta Crystallogr.*, 1995, **B51**, 540.
58. J. C. Facelli, R. H. Contreras, D. G. de Kowalewski, V. J. Kowalewski, and R. N. Piegaia, *J. Mol. Struct., Theochem*, 1983, **94**, 163.

Biographical Sketch

Ronald J. Pugmire, *b* 1937. B.S. 1959, Idaho State College; Ph.D., 1966, Chemistry, University of Utah, USA, where he was introduced to NMR by David M. Grant. Post Doctoral, 1966–68, University of Utah. Faculty in Chemical and Fuels Engineering and Chemistry (adjunct), and Associate Vice President for Research, University of Utah. Approximately 200 publications. Research specialties: carbon-13 and nitrogen-15 NMR, chemical shielding in solids, theoretical correlation of shielding tensors, coal chemistry, and applications of NMR spectroscopy to coal science and combustion science.

Nucleic Acids: Chemical Shifts

David Cowburn

The Rockefeller University, New York, NY, USA

1	Introduction	1
2	DNA Oligomers	1
3	^{13}C and ^{15}N Shifts	1
4	Temperature Dependence of ^{13}C Shifts	2
5	Issues with RNA	3
6	^{15}N Sites as Structural Indicators	3
7	Conclusions	3
8	Related Articles	3
9	References	3

1 INTRODUCTION

This article concentrates on chemical shifts in nucleic acids as indicators of conformation. Shifts of ^{1}H, ^{13}C, and ^{15}N are reviewed. A complete treatment of ^{31}P shifts is given elsewhere by Gorenstein (see ***Nucleic Acids: Phosphorus-31 NMR***), as is the characterization of unusual bases by Agris (see ***RNA Structure and Function: Modified Nucleosides***). The nomenclature used is that of Saenger.[1] In this short article, it is not possible to review the whole subject, so emphasis is placed on areas of major impact, without attempt to be comprehensive or to apply historical credit.

Nucleic acid structures in solution continue to be a major research topic, because of both general chemical interest and the burgeoning industry of understanding the detailed interactions of nucleic acids in biological processes. Two examples of special interest are how proteins and nucleic acids recognize each other and whether there are general rules, and how some ribonucleic acids (RNAs) achieve catalytic activities. The use of chemical shifts continues to be of importance because the structures of many nucleic acids are dynamic and polymorphic. Shift analysis can attempt to achieve the simple objective of defining whether there is predominantly a single structure (or small family) to be analyzed, and can, in favorable cases, achieve the more complex objective of a reasonable level of secondary structural information. To address the more complex biological areas, higher molecular weight complexes require study, since the structures of the nucleic acid components alone rarely provide any clear perspective on the mode of binding and interaction, as vividly illustrated in the dramatic twisting of the deoxyribonucleic acid (DNA) strands in complexes with Transcriptional Binding Protein (TBP)[2] a result entirely unanticipated from solution studies of the DNA oligomers alone. Higher molecular weight complexes, often with proteins or other nonnucleic acid components, have extensively overlapped spectra, so the additional dispersion from the use of heteronuclei and multidimensional NMR becomes imperative.

2 DNA OLIGOMERS

The naming of atom positions in the bases and in deoxyribose are shown in Figure 1, which also illustrates the base pairing expected in the Watson–Crick form. In this form, imino and amino hydrogens have reduced rates of exchange with solvent hydrogen, and so the appearance of these normally exchangeable hydrogens in the spectrum is diagnostic of base pairing. The observation of well-resolved imino resonances of comparable width and intensity to nonexchangeable hydrogen resonances then provides definitive evidence for a single well-defined structure. Successful structural investigations appear to rely heavily on this characteristic to find conditions of temperature, pH, cations, etc., favorable to the determination.

Standard procedures exist for assignment of most exchangeable[3,4] and nonexchangeable hydrogens.[5–8] The shifts of nonexchangeable hydrogens in B type DNA have been thoroughly analyzed in over 600 nucleotides. The shifts of H-2′, H2″, H3′, H4′ and H6/H8 are dominated by the identity of the attached base. Cytidine (C) H-5 and thymine (T) CH_3 are influenced by the adjacent 5′ base, while H-1′ is influenced by the adjacent 3′ base. The averaged values and their distribution profiles are for oligonucleotides observed under fairly wide solution conditions and temperatures, so highly precise reference values are probably best obtained by using those from a closely related sequence under similar solution and temperature conditions.[5]

Shifts outside the normal ranges can be used as preliminary identification of sites of binding or modification. For example, the shifts of base and sugar H-1′ in a modified duplex with benzopyrene diol epoxide have been used as supporting evidence for the stacking of the benzopyrene ring directly over the sugar of one base in the minor groove.[9] In closely analogous sequences, similarities of many shifts of the unchanged residues can then be used to infer similarity of structure. For example, the base and 2′,2″ shift of an A_3 bulge (A = adenosine) from a duplex are virtually identical to those in an AIA bulge (I = inosine), when the I substitution is used to separate otherwise isochronous A H8 signals for the purposes of sequential assignment by COSY and NOESY.[10]

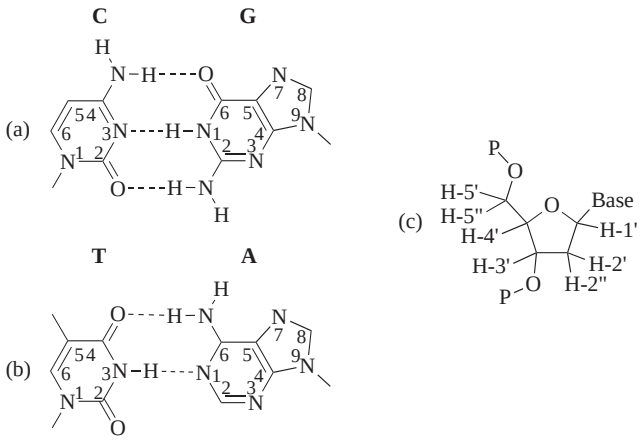

Figure 1 Scheme of Watson–Crick base pairing in deoxynucleotides for (a) cytosine and guanine, and (b) thymine, and adenine. (c) Nomenclature for the deoxyribose ring

3 ^{13}C AND ^{15}N SHIFTS

The extension of these uses of shifts of hydrogens to other nuclei was a natural development, impeded by the difficulties of synthetic incorporation of stable isotope labels, and/or by low NMR sensitivity. Incorporation of labels still remains very expensive, and for DNA the precursor deoxynucleotides present difficulties. Labeling of RNA has become practical and efficient for designed sequences,[11,12] and transfer RNAs have been biosynthetically labeled for assignment purposes for many years. Indirect detection methods, and their elaboration into methods for connectivity determination using multidimensional NMR,[13] have similarly alleviated sensitivity issues. Indirect detection methods have made it practical to observe ^{13}C and ^{15}N shifts without enrichment, and these have provided, complementarily to earlier studies with short oligonucleotides,[14] an adequate base for assignment and interpretation for DNA oligomers.[15–17] For example, for ^{13}C shifts, purine C-2 resonances are sufficiently separated from purine C-8 and pyrimidine C-6 resonances, that the overlap in the hydrogen spectra of the appropriate H2, H8, and H6 resonances can be partially resolved by inspection. Similarly, H1′ and pyrimidine H5 can be type assigned by two-dimensional (2D) separation of the C-1′ and C5 resonances, and H3′, H4′, H5′, and H5″ are separable also. Purine C-8 can be discriminated from pyrimidine C6 by the C8s larger $^{1}J(^{13}\mathrm{C},^{1}\mathrm{H})$ value in coupled spectra. For ^{15}N parameters, in the critical imino area, pyrimidine N3 and purine N1 are separated by about 10 ppm, permitting considerable additional resolution of the imino hydrogens in a $^{15}\mathrm{N}/^{1}\mathrm{H}$ 2D map. These experiments are still relatively little used, despite their clear and rich information content.[18–20]

4 TEMPERATURE DEPENDENCE OF ^{13}C SHIFTS

The profiles of chemical shifts with temperature have received considerable attention, especially those for hydrogen. This approach provides a potential avenue to understanding the contributions of individual components to the melting phenomena, in contrast to the bulk properties observed by ultraviolet absorption or circular dichroism. The interpretation of the changes of shifts observed has not proved to be entirely simple, and increasingly elaborate models have been used.[21] Variable temperature studies using ^{13}C have been more limited. This is in spite of the potential for using relaxation dynamics, or the effects of pseudorotation of the ribose ring on shifts.[22] Detailed temperature profiles of a small number of oligomers are available for base[16] and sugar[22] carbons. These provide a highly detailed grounding from which to consider the origin of shifts in oligonucleotides.

The observations for bases may be summarized as follows. A range of shifts of about 3 ppm for each class of carbon in the low-temperature duplex narrows to <1 ppm range at high temperature. Residues at the termini show smaller transitions than others. The slopes of $\mathrm{d}\delta/\mathrm{d}T$ are mixed (positive, negative, around zero), with most showing the largest change at around the melting temperature, but with clear evidence for one or more 'pretransitions' below that temperature, especially at carbons at guanosine G2, G6, and T4. There is essentially no obvious neighboring dependence for each pair of base types.

Detailed quantum mechanical calculations of the shifts for bases[23,24] and sugars[25] are available. Naturally, the match of experiment and theory will be limited by neglect of conformation averaging, of solvation, and by the limited orbital sets used. For bases, the melting effects have been summarized[16] as arising from changes in hydrogen bonding, both that to a partner base and that to solvent, from base stacking effects, and from steric compression. Hydrogen bond related changes occur on those carbons adjacent to a nitrogen or carbonyl participating in hydrogen bonding. Since those sites may be involved in hydrogen bonding with other bases, or with solvent water, changes are then the summation of multiple effects depending on the relative strengths of the different hydrogen bonds involved. The expectation is then that substantial negative $\mathrm{d}\delta/\mathrm{d}T$ values should be seen for C2 and 6 in G, and 4 in T, with lesser effects at 2, 5, and 6 in A, and 2, 4, 5, and 6 in C. Base stacking effects are similarly complex in effect, and it may be concluded that a geometric effect similar to a ring current shift would be expected to produce a positive $\mathrm{d}\delta/\mathrm{d}T$ going from a stacked to a single-stranded form. It seems unlikely that steric compression effects could play a major role in shifts in such duplexes, where there are considerable degrees of backbone freedom.[1] The most reasonable hypothesis concerning the temperature dependence of base shifts then centers on the cooperative transition of melting changing simultaneously the oppositely signed contributions of geometric stacking and of hydrogen bonding. The individual changes then reflect the different roles of each carbon with respect to the geometry of the stacking, or the adjacency to a hydrogen bonding site. A plausible hypothesis for the premelting changes is that there is apparent weakening of the hydrogen bonding prior to the principal transition.

In the case of deoxyribose sugars,[22] the temperature dependence of carbon shifts might be expected to shed light on the much discussed issue of pseudorotation in the sugar ring. Early work[26] suggested that fitting the observed vicinal coupling constants in deoxyribosides needed at least a two-state model, incorporating the 'N' (North), 3′-*endo*, or 'S' (South), 2′-*endo* conformers of the ring.[1] This is now generally,[27] though not universally,[28,29] accepted for oligonucleotide analysis also, with the caveat that other sugar puckers may be significantly populated, but cannot be easily experimentally analyzed, so Occam's razor reduces us to using the simplest model.[27] This and other issues[30,31] continue to point out possible limitations of high-precision attempts to determine DNA oligomer using single conformer models. Sugar ^{13}C shifts might be a useful additional characteristic of ring pucker, and this has been established for some RNA oligonucleotides,[20,32] in a relatively straightforward way. Detailed studies of DNA oligomers do not support this kind of analysis, and deviations of shifts with respect to temperature show quite different patterns.[22] A general explanation is that indeed multiple ring conformers do exist, and that the deoxyribose and ribose rings naturally have different sets of conformers. The general magnitude of the alteration of shift with melting is, however, quite small (about 1–2 ppm), so it is very difficult to make a complete differentiation of shift effects arising solely through ring conformation, from those arising from ring current (magnetic anisotropy) and other more distant effects. In general, the conclusion that these melting curves require a more complex explanation than an S–N conversion

alone is fully justified, and more detailed studies of the effects of sequence seem appropriate.

5 ISSUES WITH RNA

Spectral assignment in RNA had previously been difficult, because of the overlap of sugar hydrogens in the 4–5 ppm region. Resolution by multidimensional heteronuclear shift correlation with ^{13}C provides a straightforward additional dispersion, with C-5′, C-3′, C-2′, C-4′, and C-1′ being ordered in increasing shift in relatively well-separated groups.[33] It remains to be seen, in the large structural variations of bulges, internal loop, duplexes, and hairpins, whether these simple classifications will suffice. The success of a multidimensional, triple resonance approach using $^{13}C/^{15}N$ dual-labeled duplex dodecamer,[34] bodes well for complete assignment of significantly larger RNAs. This approach similarly depends on the large ^{13}C dispersion to separate out sugar hydrogens.

Using the characteristic imino hydrogen region, several laboratories made remarkable progress in assigning larger RNAs, especially transfer RNAs and 5S RNA. Additional information from ^{15}N shifts has also been widely used, mainly for group-specific assignments.

6 ^{15}N SITES AS STRUCTURAL INDICATORS

It will be readily apparent by inspection of Figure 1, that nitrogens are potentially reporters at the sites of the major interactions of the bases. They participate in the Watson–Crick hydrogen bonding (C,3,4; G,1,2; T,3; and A,1,6), serving as donor in all cases, and recipient at C3 and A1. The major groove of a double helix is also lined with the amino groups of A and C, and the nitrogen at position 7 in purines A and G, while the purine position 3 is exposed in the minor groove. The known perturbations of shifts on hydrogen bonding, for donor or recipient, then provide a specific window into the major recognition elements of the bases. This simple reporting may be invaluable in larger complexes where full determination of structure is presently impractical. Some existing studies include the investigation of Hoogsteen hydrogen bonding in triple helices[19] and guanine tetrads,[35] investigations of the effects of *O*-methylation,[36,37] and studies of netropsin/duplex complexes.[17,38]

DNA triplexes can be readily formed by appropriate sequences in which a purine-rich tract makes Watson–Crick contacts with a pyrimidine-rich strand, and then a subsequent pyrimidine-rich strand make predominantly Hoogsteen pairing to the central purine-rich portion, and the Watson–Crick pairing is readily apparent in the shifts of G1 and T3 nitrogens.[19] In guanine-rich tetrads, the shift variation between duplex, tetrad, and single strand forms for the N-7 of G in two sequences was found to be rather small, and while hydration effects and hydrogen bonding may be usefully investigated in lower molecular weight complexes,[35] the prospects for use in larger complexes are not clear.

Several oligomers containing [1′-^{15}N]- and [2-^{15}N]-O^6-methyl-2′-deoxyguanosine have been studied, confirming expected base pairings in mismatches against C and T. These studies elegantly illustrate the positional specificity available from NMR studies for base–base hydrogen bonding and for the pH and temperature dependence of such bonding. For the O^6MeGT pair, there is direct hydrogen bonding at N-2 but not N-1, with N-1 probably fully solvated.[36] In contrast, the O^6MeGC pair has a very complex, pH-dependent, wobble pairing.[37] The low-frequency melting shift of the [1-^{15}N]O^6MeGC resonance (3 ppm) is similar to that for other hydrogen bond acceptors, whereas the high-frequency shift of [2-^{15}N]O^6MeGC (8 ppm) is not similarly matched. This is in line with expected differences in hydrogen bond strength: the apparent high-frequency shift of an O^6MeG $^{15}N2$ as an sp^3 hydrogen bond donor to an sp^2 nitrogen acceptor is significantly greater than that associated with NH_2–O interaction.

The structures of netropsin/DNA oligomer complexes have been extensively studied by X-ray and NMR methods. Nitrogen-15 studies are fully consistent with the general view that netropsin displaces water of hydration from the minor groove, without significant perturbation of the duplex structure. Shifts from positions 3 in A,[38] 1 in G, and 3 in T[17] are all indicative of modulated hydrogen bonding on complexation at the expected positions. The suggestion[17] that larger perturbations of 3 in T result from the alterations of the adjacent carbonyl's hydrogen bonding indicates a possible sensor of the critical pyrimidine 2-position in the minor groove, but requires further experimental support.

7 CONCLUSIONS

The major motivation for continuing interest in this area is the need for better tools to study macromolecular interactions involving larger pieces of nucleic acids than are currently normally studied. Shifts on formation of DNA–protein complexes have been reported for several cases.[39–41] In general, these shifts are interpretable using the same rationales, interrelation, major or minor groove binding, disruption of pairing and/or stacking, and possible displacement of water, and it may be expected that their extension with ^{13}C and ^{15}N labeled nucleic acid components would be invaluable. Continuing efforts in rationalizing the observed shift effects then also remain a priority.

8 RELATED ARTICLES

Nucleic Acid Flexibility and Dynamics: Deuterium NMR; Nucleic Acid Structures in Solution: Sequence Dependence; Nucleic Acids: Base Stacking and Base Pairing Interactions; Nucleic Acids: Phosphorus-31 NMR; Nucleic Acids: Spectra, Structures, and Dynamics.

9 REFERENCES

1. W. Saenger, *Principles of Nucleic Acid Structure*, Springer, New York, 1983.
2. J. L. Kim, D. B. Nikolov, and S. K. Burley, *Nature (London)*, 1993, **365**, 520.
3. D. J. Patel, L. Shapiro, and D. Hare, *Q. Rev. Biophys.*, 1987, **20**, 35.

4. J. Feigon, V. Sklenár, E. Wang, D. E. Gilbert, R. F. Macaya, and P. Schultze, *Methods Enzymol.*, 1992, **211**, 235.
5. F. J. M. v. d. Ven, and C. W. Hilbers, *Nucleic Acids Res.*, 1988, **16**, 5713.
6. S. H. Chou, D. R. Hare, D. E. Wemmer, and B. R. Reid, *Biochemistry*, 1983, **22**, 3037.
7. A. Kintanar, R. E. Klevit, and B. R. Reid, *Nucleic Acids Res.*, 1987, **15**, 5845.
8. K. Wüthrich, *NMR of Proteins and Nucleic Acids*, Wiley, New York, 1986.
9. C. de los Santos, M. Cosman, B. E. Hingerty, V. Ibanez, L. A. Margulis, N. E. Geacintov, S. Broyde, and D. J. Patel, *Biochemistry*, 1992, **31**, 5245.
10. I. Radhakrishnan, C. de los Santos, and D. J. Patel, *J. Mol. Biol.*, 1993, **234**, 188.
11. E. P. Nikonowicz, A. Sirr, P. Legault, F. M. Jucker, L. M. Baer, and A. Pardi, *Nucleic Acids Res.*, 1992, **20**, 4507.
12. R. T. Batey, M. Inada, E. Kujawinski, J. D. Puglisi, and J. R. Williamson, *Nucleic Acids Res.*, 1992, **20**, 4515.
13. G. M. Clore and A. Gronenborn, *Science*, 1991, **252**, 1390.
14. P. P. Lankhorst, C. A. Haasnoot, C. Erkelens, H. P. Westerink, G. A. van der Marel, J. H. van Boom, and C. Altona, *Nucleic Acids Res.*, 1985, **13**, 927.
15. W. Leupin, G. Wagner, W. A. Denny, and K. Wüthrich, *Nucleic Acids Res.*, 1987, **15**, 267.
16. S. R. La Plante, E. A. Boudreau, N. Zanatta, G. C. Levy, P. N. Borer, J. Ashcroft, and D. Cowburn, *Biochemistry*, 1988, **27**, 7902.
17. J. Ashcroft, D. H. Live, D. J. Patel, and D. Cowburn, *Biopolymers*, 1991, **31**, 45.
18. D. H. Live, I. Radhakrishnan, V. Misra, and D. J. Patel, *J. Am. Chem. Soc.*, 1991, **113**, 4687.
19. I. Radhakrishnan, X. Gao, C. de los Santos, D. Live, and D. J. Patel, *Biochemistry*, 1991, **30**, 9022.
20. G. Varani and I. Tinoco, *J. Am. Chem. Soc.*, 1991, **113**, 9349.
21. J. M. L. Pieters, J. R. Mellema, H. van den Elst, G. A. van der Marel, J. H. van Boom, and C. Altona, *Biopolymers*, 1989, **28**, 717.
22. S. R. LaPlante, N. Zannatta, A. Hakkinen, A. H.-J. Wang, and P. N. Borer, *Biochemistry*, 1994, **33**, 2430.
23. C. Giesner-Prettre, *J. Biomol. Struct. Dyn.*, 1984, **2**, 233.
24. C. Giessner-Prettre, *J. Biomol. Struct. Dyn.*, 1986, **4**, 99.
25. C. Giessner-Prettre, *J. Biomol. Struct. Dyn.*, 1985, **3**, 145.
26. C. Altona and M. Sundaralingam, *J. Am. Chem. Soc.*, 1972, **94**, 8205.
27. K. D. Bishop, F. J. H. Blocker, W. Egan, and T. L. James, *Biochemistry*, 1994, **33**, 427.
28. J. T. Davis, S. Hirani, C. Bartlett, and B. R. Reid, *J. Biol. Chem.*, 1994, **269**, 3331.
29. S. G. Kim and B. R. Reid, *Biochemistry*, 1992, **31**, 12103.
30. W. J. Metzler, C. Wang, D. B. Kitchen, R. M. Levy, and A. Pardi, *J. Mol. Biol.*, 1990, **214**, 711.
31. F. J. M. van de Ven and C. W. Hilbers, *Eur. J. Biochem.*, 1988, **178**, 1.
32. P. P. Lankhorst, C. Erkelens, C. A. G. Haasnoot, and C. Altona, *Nucleic Acids Res.*, 1983, **11**, 7215.
33. G. Varani and I. Tinoco, Jr., *Q. Rev. Biophys.*, 1991, **24**, 479.
34. E. P. Nikonowicz and A. Pardi, *J. Mol. Biol.*, 1993, **232**, 1141.
35. B. L. Gaffney, C. Wang, and R. A. Jones, *J. Am. Chem. Soc.*, 1992, **114**, 4047.
36. B. Goswami, B. L. Gaffney, and R. A. Jones, *J. Am. Chem. Soc.*, 1993, **115**, 3832.
37. B. L. Gaffney, B. Goswami, and R. A. Jones, *J. Am. Chem. Soc.*, 1993, **115**, 12607.
38. Y. S. Rhee, C. Wang, B. L. Gaffney, and R. A. Jones, *J. Am. Chem. Soc.*, 1993, **115**, 8742.
39. G. Otting, Y. Q. Qian, M. Billeter, M. Muller, M. Affolter, W. J. Gehring, and K. Wüthrich, *EMBO J.*, 1990, **9**, 3085.
40. M. Shirakawa, H. Matsuo, Y. Serikawa, N. Suzuki, and Y. Kyogoku, in *Molecular Structure and Life: Molecular Recognition of Nucleic Acids*, eds. Y. Kyogoku and Y. Nishimura, Japan Science Society Press, Tokyo, 1992.
41. R. M. J. N. Lamerichs, R. Boelens, G. A. van der Marel, J. H. van Boom, R. Kaptein, F. Buck, B. Fera, and H. Rüterjans, *Biochemistry*, 1989, **28**, 2985.

Biographical Sketch

David Cowburn. *b* 1945. B.Sc., 1965, University of Manchester Institute of Science and Technology; Ph.D., 1970, London University; D.Sc., 1980, London University. Fascinated during Ph.D. by the potential for NMR as a structural tool in biochemistry. Faculty of Rockefeller University, 1973–present. Approx. 100 publications. Research interests include structure–function relationships in biological chemistry, development of magnetic resonance techniques in biomedical research, determination of molecular conformation by spectroscopic techniques, particularly magnetic resonance and applications of these to understanding molecular mechanism of control of genetic expression, and of intracellular signal transduction.

Relativistic Computation of NMR Shieldings and Spin–Spin Coupling Constants

Jochen Autschbach and Tom Ziegler

University of Calgary, Calgary, Canada

1 Introduction 1
2 Relativistic Theory of NMR Shieldings and Spin–Spin Coupling Constants 1
3 Heavy Atom Nuclear Shieldings 8
4 Heavy Atom Spin–Spin Couplings 13
5 Summary 16
6 Related Articles in this Volume 16
7 Related Articles in Volumes 1–8 16
8 References 16

1 INTRODUCTION

A long time has passed since the formulation of relativistic quantum mechanics. Meanwhile, it has become chemistry textbook knowledge that atoms and molecules containing heavy nuclei exhibit so-called relativistic effects which, e.g., cause mercury to be liquid and are responsible for the color and the chemical inertness of gold. A qualitative explanation based on the Bohr model for one-electron atoms is straightforward. Special relativity has to be considered when velocities are no longer small compared to the speed of light. The Bohr formulae can be interpreted such that, in atomic units (see below), the electron in the ground state has a velocity of Z, with Z being the nuclear charge. The speed of light, c, has a value of approximately 137 in the same units. This illustrates that electrons in heavy atoms can reach a substantial fraction of the speed of light, and it is therefore clear that core orbitals in heavy atoms show sizable relativistic effects. It has been somewhat surprising, however, that valence orbitals exhibit relativistic effects of the same order in c^{-2} as core orbitals, which cause significant changes in the chemical properties of heavy element compounds. Relativistic effects for valence orbitals are nowadays well investigated and understood. For elements of the 6th row of the periodic table (Cs–Rn), the correction terms are so large that nonrelativistic quantum chemical computations often do not yield even a qualitatively correct answer. It is generally accepted that relativistic computations have to be carried out for such atoms and their compounds. c^{-2} appears in the relativistic theory – due to its smallness – as an expansion parameter, by which perturbational orders of relativistic corrections are characterized. The nonrelativistic limit is approached for $c \to \infty$.

Nuclear shieldings and spin–spin couplings are very sensitive experimental probes for the electronic and geometrical structure of a compound. For the same reason, however, they are difficult to compute accurately. In the presence of heavy nuclei, any attempt to achieve a reasonable agreement between theory and experiment has to consider relativistic effects in the computations. Both the current state of relativistic quantum chemical methods and the art of computing NMR parameters have advanced far enough that a large body of computational results for heavy element systems obtained with a variety of methods is available. Remarkable results have been achieved, e.g., the explanation of certain experimental trends such as the 'halogen dependence', or the ability to compute NMR parameters with the heavy nuclei as the probe. Therefore it is appropriate to give a short overview here of the methodologies being used so far as well as results that have been obtained for a number of heavy atom systems.

Concerning the methodology, we focus on methods that are capable of treating both light and heavy nuclei with respect to NMR shieldings and spin–spin couplings on a first-principles basis (meaning ab initio methods and approximate Kohn–Sham density functional theory (DFT)). Variational methods are emphasized, but the possibility of treating relativity as a perturbation is frequently mentioned. In particular for nuclear shieldings, certain chemical trends have successfully been explained upon inclusion of spin-orbit coupling to first order alone, and a number of such results are quoted in Section 3. Concerning the spin–spin couplings, we focus on couplings involving a heavy nucleus. Dimensionless atomic units (unit of charge $e = 1$, electron mass $m = 1$, $4\pi\varepsilon_0 = 1$, $h = 2\pi$, $c \approx 137.036$) are used in the theoretical section. The electronic g-factor is assumed to be exactly 2, as predicted by the Dirac equation, and not written explicitly.

Computed or experimental nuclear shieldings and chemical shifts are quoted in ppm (10^{-6}), spin–spin couplings either as reduced couplings K in SI units of $\mathrm{kg\,m^{-2}\,s^{-2}\,A^{-2}}$, or as coupling constants J in Hertz ($\mathrm{s^{-1}}$). The discussion of theoretical results and interpretations refer to a time-independent treatment of closed-shell molecules with fixed nuclei.

In Section 2, we outline the theoretical approach to heavy atom NMR. Illustrative results and interpretations for chemical shifts and spin–spin couplings presented in Sections 3 and 4, respectively, are chosen in order to cover a range of chemical applications and trends and a number of different methodologies.

2 RELATIVISTIC THEORY OF NMR SHIELDINGS AND SPIN–SPIN COUPLING CONSTANTS

In this section the theoretical methodology that allows for the relativistic computation of NMR parameters of molecules is outlined. Due to the vast amount of literature and the many different techniques in the field of relativistic quantum chemistry, no attempt has been made to give a complete overview. Instead, a hierarchy of currently common approximations from which magnetic properties can be extracted is sketched in a pragmatic way. For details we refer to some of the books and review articles on relativistic quantum chemistry.[1–4]

2.1 Relativity in Quantum Chemistry

'Ordinary' nonrelativistic quantum chemistry deals with the solution of the time-independent many-electron Schrödinger equation

$$\hat{\mathcal{H}}^{\mathrm{nrel}}\Psi = \Psi E \tag{1}$$

where Ψ is the many-electron wavefunction of an atom or molecule with fixed nuclei, and E is the total energy.

$$\hat{\mathcal{H}}^{\mathrm{nrel}} = \sum_{i=1} \frac{\hat{\boldsymbol{p}}_i^2}{2} + \sum_{i=1} V_{Ni} + V_{ee} + V_{\mathrm{nuc}} \tag{2}$$

is the nonrelativistic Hamiltonian consisting of the nonrelativistic kinetic energy operator $\hat{\boldsymbol{p}}_i^2/2$ for each electron i, the electron-nucleus attraction potential V_{Ni} for each electron, the nonrelativistic electron−electron Coulomb repulsion $V_{ee} = \sum_{j>i} 1/r_{ij}$, and the internuclear repulsion potential V_{nuc}. $\hat{\boldsymbol{p}} = -i\boldsymbol{\nabla}$ is the momentum operator in space representation. Since analytic solutions of equation (1) for many electron systems are not known, approximations have to be made. As a starting point, the N-electron equation is usually separated into N effective one-electron equations for one-particle wavefunctions ψ (so called atomic or molecular orbitals) which depend on an effective potential V. For simplicity, we implicitly refer to such effective one-electron equations (or true one-electron systems) in the following, by using the symbol ψ for the one-electron wavefunction or orbital. Particular details of common approximations are not discussed in this section.

In relativistic quantum chemistry, $\hat{\mathcal{H}}^{\mathrm{nrel}}$ in equation (1) is replaced by its relativistic counterpart. All of the problems of the nonrelativistic many-electron theory are present in the relativistic formulation as well. Hence, similar techniques are common in order to find approximate solutions; in particular, use of orbitals is made. However, relativistic quantum chemistry has its own specific problems associated with it, one of them being the lack of a consistent relativistic many-particle Hamiltonian being derived from quantum electrodynamics. Therefore, relativistic many-electron atomic and molecular computations rely on the use of the four-component 'no-pair' Dirac−Coulomb−Breit Hamiltonian or some approximation obtained from it:

$$\hat{\mathcal{H}}^{\mathrm{DCB}} = \hat{P}^+ \left[\sum_{i=1}^{N} (c\boldsymbol{\alpha}_i\hat{\boldsymbol{p}}_i + \beta_i c^2) + V_{Ni} + V_{ee} + \sum_{j>i=1}^{N} \hat{\mathcal{H}}_{ij}^{\mathrm{B}} + V_{\mathrm{nuc}} \right] \hat{P}^+ \tag{3}$$

Here, $\boldsymbol{\alpha}$ and β are 4×4 matrices introduced by Dirac in order to obtain a relativistic wave equation for spin-1/2 particles from the 'classical' relativistic Hamilton function. In its standard representation, $\boldsymbol{\alpha}$ is written in terms of the well-known Pauli spin-matrices $\boldsymbol{\sigma}_s$ (not to be confused with the symbol for the nuclear shielding tensor). The $\hat{\mathcal{H}}_{ij}^{\mathrm{B}}$ (Breit interaction, see, e.g., Ref.[4]) are relativistic corrections to V_{ee} that contain the so-called magnetic interaction and further account for the fact that the electron−electron interaction is not instantaneous but is transmitted with a finite speed. Use of the projection operators $\hat{P}^+$ cures some of the problematic features of the Dirac−Coulomb(−Breit) operator by restricting its solutions to the positive energy spectrum, the eigenfunctions of which are identified with the desired electronic states (no-pair approximation[2,5]). We have to stress here that though $\hat{\mathcal{H}}^{\mathrm{DCB}}$ is in general not truly Lorentz invariant, it "provides an excellent approximation to the full theory".[3]

The main difference between the four-component relativistic and the nonrelativistic Hamiltonian is seen to be in the kinetic energy operator for an electron, which is $c\boldsymbol{\alpha}\hat{\boldsymbol{p}} + \beta c^2$ in equation (3) instead of $\hat{\boldsymbol{p}}^2/2$ in $\hat{\mathcal{H}}^{\mathrm{nrel}}$. It takes into account the relativistic increase of electron mass due to high velocities, it includes the electron's rest mass energy, it incorporates the electron spin, and also causes the spin-orbit coupling. Although electron spin needs to be considered in the nonrelativistic theory in an ad hoc manner in order to account for experimental facts, a coupling between spin and spatial degrees of freedom occurs only in the relativistic theory. For simplicity of notation, we omit the $\hat{P}^+$ in the following, and we do not explicitly consider the Breit interaction since it is actually being neglected in many computations. Its relative importance to, e.g., total atomic energies was found to decrease with increasing nuclear charge from ∼50% in He to ∼2% in Hg relative to the one-electron relativistic corrections.[6]

A conceptually straightforward way of performing a relativistic molecular computation in order to obtain a starting point for a calculation of NMR properties is to use directly the time-independent Dirac equation

$$\hat{\mathcal{H}}^{\mathrm{D}}\psi^{\mathrm{D}} = \psi^{\mathrm{D}}E \tag{4}$$

with

$$\hat{\mathcal{H}}^{\mathrm{D}} = c\boldsymbol{\alpha}\hat{\boldsymbol{p}} + \beta c^2 + V \tag{5}$$

Note that we used here the aforementioned simple notation for (effective) one-electron equations. ψ^{D} is a four-component relativistic orbital. Because $\boldsymbol{\alpha}$ and β are 4×4 matrices, the wavefunction has to be a four-component vector for which each component is a complex function of space. Due to the four components, such molecular computations are unfortunately quite expensive as compared to nonrelativistic ones, and the explicit inclusion of electron correlation is a formidable task.

Many attempts have been made to transform the four-component equation (4) into two-component form, in order to keep interpretations simpler and to reduce the computational effort. However, so-called picture change effects occur, a discussion of which is beyond the scope of this overview (see, e.g., Ref.[7] and references cited therein.) Here we give an account of some of these methods. Writing $\boldsymbol{\alpha}$ explicitly in terms of the 2×2 Pauli spin-matrices $\boldsymbol{\sigma}_s$, the Dirac equation (4) reads

$$(\hat{\mathcal{H}}^{\mathrm{D}} - E)\psi^{\mathrm{D}} = \begin{pmatrix} V - E & c\boldsymbol{\sigma}_s\hat{\boldsymbol{p}} \\ c\boldsymbol{\sigma}_s\hat{\boldsymbol{p}} & V - E - 2c^2 \end{pmatrix} \begin{pmatrix} \varphi \\ \chi \end{pmatrix} = 0 \tag{6}$$

The zero of the energy scale has been shifted in equation (6) to $+mc^2$, $m = 1$, the rest mass energy of the electron, so that bound states have negative energy as usual in nonrelativistic quantum chemistry. Here, φ and χ are the so-called 'upper' and 'lower' components of the four-component orbital ψ^{D}, each of them made up of two components. The functions φ

and χ are also frequently referred to as the 'large' and 'small' components because of the $1/2c$ prefactor in equation (7) below. (Note, however that, depending on the potential and the location, the 'small component' can be much larger than the 'large' one, e.g., for $p_{1/2}$ orbitals close to the nucleus.) From the second row of the matrix one obtains explicitly

$$\chi = X\varphi = \frac{1}{2c} k \boldsymbol{\sigma}_s \hat{\boldsymbol{p}} \varphi \tag{7}$$

with $k = (1 - [(V - E)/2c^2])^{-1}$, which yields the relation between the upper and the lower component. Because φ and χ are not independent of each other, it should be possible to obtain a relativistic two-component equation for φ or χ alone, the solutions of which contain the same information as ψ^{D}. In the elimination of the small component (ESC) scheme, equation (7) is directly substituted in the equation obtained from the first row of the matrix in (6) and yields the two-component Hamiltonian:

$$\hat{\mathcal{H}}^{\mathrm{ESC}} = V + \frac{1}{2}(\boldsymbol{\sigma}_s \hat{\boldsymbol{p}}) k (\boldsymbol{\sigma}_s \hat{\boldsymbol{p}}) \tag{8}$$

In the nonrelativistic limit, $c \to \infty$, $k \to 1$, and then, with $(\boldsymbol{\sigma}_s \hat{\boldsymbol{p}})^2 = \hat{\boldsymbol{p}}^2$, the nonrelativistic Schrödinger Hamiltonian is recovered from the ESC operator (8):

$$\hat{\mathcal{H}}^{\mathrm{nrel}} = V + \frac{1}{2}(\boldsymbol{\sigma}_s \hat{\boldsymbol{p}})^2 \tag{9}$$

Another way in which to obtain the nonrelativistic limit is to multiply (4) with $\hat{\mathcal{H}}^{\mathrm{D}}$ before taking the limit $c \to \infty$. Although the ESC equation appears to be very illustrative, the Hamiltonian depends (through k) on the unknown energy and is not usable in actual linear variational calculations. In order to arrive at an energy-independent two-component equation, the Foldy–Wouthuysen (FW) transformation of $\hat{\mathcal{H}}^{\mathrm{D}}$ to block-diagonal form is achieved by

$$\hat{\mathcal{H}}^{\mathrm{FW}} = U \hat{\mathcal{H}}^{\mathrm{D}} U^{-1} \tag{10}$$

When $\hat{\mathcal{H}}^{\mathrm{FW}}$ is block diagonal, this completely uncouples the upper and lower component and yields the desired two-component equation and $\chi = X\varphi$, an energy-independent relation between upper and lower component [see equation (7)]. U can be written in terms of X, see, e.g., the literature cited in Ref.[7] For many-electron systems, the exact form of X and U and therefore the exact form of $\hat{\mathcal{H}}^{\mathrm{FW}}$ are not known. Different approximations for X yield different approximate two-component Hamiltonians in which the uncoupling of the two components is only achieved to a certain order in c^{-2}. These approximate two-component Hamiltonians are sometimes collectively denoted as 'quasi relativistic'.

A rather simple approach is to expand (7) to zeroth order in c^{-2}. This yields $X \approx c\boldsymbol{\sigma}_s \hat{\boldsymbol{p}}/2c^2$, which results in the famous Pauli Hamiltonian[8] after carrying out the transformation (10) with $U(X)$:

$$\hat{\mathcal{H}}^{\mathrm{Pauli}} = \hat{\mathcal{H}}^{\mathrm{nrel}} - \frac{\hat{\boldsymbol{p}}^4}{8c^2} - \frac{(\hat{\boldsymbol{p}}^2 V)}{8c^2} + \frac{i}{4c^2}\boldsymbol{\sigma}_s[(\hat{\boldsymbol{p}} V) \times \hat{\boldsymbol{p}}] \tag{11}$$

The second, third, and fourth term on the right-hand side of (11) are the mass–velocity (MV), Darwin (DAR), and spin-orbit (SO) terms, respectively, representing corrections of order c^{-2} to the nonrelativistic Hamiltonian. The Pauli operator has certain pathological features due to the fact that close to a nucleus where V is very large (it goes to $-\infty$ for point-like nuclei), $(V - E)/2c^2$ is not small and neglecting this term in equation (7) is not justified. As a result, the Pauli operator affords severe singularities. Moreover, it is not variationally stable and permits only a perturbational treatment to first order. Higher order contributions yield diverging terms. Variational computations based on the Pauli operator have been frequently carried out, by using frozen cores and minimal basis sets in the core regions for valence orbitals, under which circumstances the variational instability can be kept somewhat under control in many cases. We refer to such frozen core methods in Sections 3 and 4 when speaking about variational Pauli computations. A *scalar relativistic* approach is obtained by omitting the SO term. This yields a one-component formalism analogous to the nonrelativistic scheme with pure α- and β-spin orbitals, that contain the – in many cases dominant – scalar relativistic effects. It is also possible to separate off a spin-orbit part in the Dirac equation.

One of the possible alternatives for the Pauli Hamiltonian is offered by the so-called zeroth order regular approximation (ZORA) method.[9] Some authors refer to the ZORA Hamiltonian as the Chang–Pélissier–Durand (CPD) operator. It is obtained from the zeroth order of an expansion of k in powers of $E/(2c^2 - V)$ in equation (7). This expansion parameter remains rather small in particular where the potential V goes to $-\infty$. The two-component ZORA Hamiltonian resulting from the transformation (10) reads

$$\hat{\mathcal{H}}^{\mathrm{ZORA}} = V + \frac{1}{2}(\boldsymbol{\sigma}_s \hat{\boldsymbol{p}}) \mathcal{K} (\boldsymbol{\sigma}_s \hat{\boldsymbol{p}}) \tag{12a}$$

$$= V + \frac{1}{2}\hat{\boldsymbol{p}} \mathcal{K} \hat{\boldsymbol{p}} + \frac{i}{2}\boldsymbol{\sigma}_s[(\hat{\boldsymbol{p}}\mathcal{K}) \times \hat{\boldsymbol{p}}] \tag{12b}$$

with $\mathcal{K} = 2c^2/(2c^2 - V)$. Note the formal similarity to the ESC Hamiltonian in (8), with k replaced by $\mathcal{K}$. The nonrelativistic limit corresponds to $\mathcal{K} \to 1$, $(\hat{\boldsymbol{p}}\mathcal{K}) = 0$. The first and the second term in (12b) yield $\hat{\mathcal{H}}^{\mathrm{nrel}}$ plus scalar relativistic corrections, while the third term is the ZORA SO operator. For small V, $(\hat{\boldsymbol{p}}\mathcal{K}) \approx (\hat{\boldsymbol{p}} V)/2c^2$, and the ZORA SO term is similar to the Pauli SO term. Close to a nucleus, both operators differ substantially. The use of the ZORA method in heavy element computations is becoming increasingly popular, and the results are in most cases superior to those obtained with the Pauli operator. Conceptually, the ZORA operator has the disadvantage of not being invariant with respect to a change of the origin of the energy scale (gauge invariance), as can be seen from the fact that only V but not $(V - E)$ occurs in the operator. The standard choice for the potential is $V(\boldsymbol{r}) \to 0$ for $\boldsymbol{r} \to \infty$. Most of the resulting problems can be circumvented by a "scaling" procedure or by the use of frozen core potentials or model potentials for the construction of $\mathcal{K}$.

A different way of transforming the Dirac Hamiltonian to two-component form is used in the Douglas–Kroll (DK) method. Here, U in equation (10) is obtained via subsequent transformations that uncouple the upper and lower components to some order n in c^{-2} written as

$$U_n = \sqrt{1 + W_n^2} + W_n \tag{13}$$

where W_n is anti-hermitian. For U_0, the FW transformation for the free electron is used. To higher orders, equations for W_n have to be solved in order to achieve further uncoupling. Already with U_1, most of the relativistic effects are recovered. We refer the reader to, e.g., Ref.[3] for details and original references. In particular due to the work of Hess and coworkers, the DK method has been established as a reliable tool in quantum chemistry for the computation of heavy element compounds. To some extent, the ZORA and the DK method to lowest order yield quite comparable results for many molecular properties. As an advantage, the DK method does not suffer from a gauge invariance problem, at the disadvantage of a somewhat more complicated formalism, if spin-orbit coupling and magnetic fields are included.

In order to arrive at a relativistic perturbation theory that avoids the infinities of the Pauli Hamiltonian to higher orders, so-called 'direct' or 'Dirac' four-component perturbation theory (DPT) can be employed. By a simple change of metric between upper and lower components in the Dirac equation (6), an expansion of the resulting four-component equation in powers of c^{-2} is straightforward and leads to nonsingular first and higher order expressions for E and ψ. A treatment of magnetic properties has been described in detail in the literature.[10] However, higher order expressions become computationally rather expensive, while at the same time it is well known that first-order relativistic perturbation theory is not sufficient for such 'relativistic' elements as, e.g., Au, Hg or Pb for the determination of bond energies or molecular geometries. It can be assumed that relativistic corrections up to order c^{-4} at least are also necessary for NMR parameters for such nuclei, in which case a variational procedure (Dirac, ZORA, DK) might be easier to implement and computationally not much more or even less expensive.

As an alternative to the aforementioned methods which incorporate relativity directly into the calculations, the use of relativistic effective core potentials (ECPs) allows for consideration of relativistic effects in molecular computations. Inclusion of spin-orbit coupling is also possible in these methods. Recent benchmark calculations[11] have shown that ECPs can yield very reliable properties of heavy element compounds.

As already mentioned, the potential V in the equations in this section might not simply refer to the external potential (e.g., V_{Ni}) for one-electron systems but to an effective many-electron potential. In this case, V implicitly contains effects that are due to the electron–electron Coulomb repulsion $1/r_{ij}$. The explicit transformation of $1/r_{ij}$ to two-component form yields new relativistic operators of order c^{-2} instead, for example the two-electron spin-orbit operator. Use of the effective electronic potential in V in the one-electron SO operator accounts, to some extent, for these two-electron terms in a mean-field sense. Transformation of the Breit interaction to two-component form yields further two-electron terms, such as the spin-other-orbit operator.

2.2 Nuclear Shieldings and Spin–Spin Couplings

A basic quantity that formally allows access to many properties of atoms and molecules is the total (electronic + nuclear repulsion) energy E of the system. It is readily available, to some degree of accuracy depending on the approximations that have been made, from quantum chemical computations, either from a relativistic or nonrelativistic formalism, based on variational or perturbational approaches. We refer to the wavefunction or the set of orbitals that produced this energy as the 'zeroth order solution'. In practice, it does not initially contain the effects from external magnetic fields or nuclear spins, but it might incorporate relativistic effects. Many observables, among them NMR shielding and spin–spin coupling tensors, can be defined as derivatives of the total energy of the system under investigation. The shielding tensor $\boldsymbol{\sigma}$ for a nucleus A is given by

$$\boldsymbol{\sigma}(A) = \left.\frac{\partial^2 E}{\partial \boldsymbol{B}^{\mathrm{ext}} \partial \boldsymbol{\mu}_A}\right|_{\boldsymbol{B}^{\mathrm{ext}}=0, \boldsymbol{\mu}_A=0} \tag{14a}$$

while the reduced nuclear spin–spin coupling tensor $\mathbf{K}$ involving two nuclei A and B is obtained from

$$\mathbf{K}(A, B) = \left.\frac{\partial^2 E}{\partial \boldsymbol{\mu}_A \partial \boldsymbol{\mu}_B}\right|_{\boldsymbol{\mu}_A=0, \boldsymbol{\mu}_B=0} \tag{14b}$$

Here, $\boldsymbol{B}^{\mathrm{ext}}$ is the applied external magnetic field, and $\boldsymbol{\mu}_A$ is the magnetic moment of nucleus A, related to its intrinsic angular momentum $\boldsymbol{I}_A$ by $\boldsymbol{\mu}_A = \gamma_A \hbar \boldsymbol{I}_A$ with γ_A being the magnetogyric ratio of the nucleus. We refer to some of the many excellent review articles focusing on the nonrelativistic computation of NMR parameters for details.[12–15] Equations (14a,b) conceptually serve as the starting point for a perturbational approach by which the energy derivatives can be evaluated once the zeroth order solution has been obtained. For the spin–spin coupling, the direct (through space) coupling between two nuclei does not yield a contribution to the coupling constants for rapidly rotating molecules (i.e., for measurements in gas phase or in solution) and is not discussed further. We implicitly refer to indirect spin–spin couplings throughout the rest of this article.

For the general case of two perturbations, described by the perturbation parameters $\boldsymbol{\kappa}$ and $\boldsymbol{\lambda}$ with Cartesian components κ_x, κ_y, κ_z etc., the mixed second derivative of the total energy

$$E = \langle \Psi | \hat{\mathcal{H}} | \Psi \rangle \tag{15}$$

with respect to the perturbation parameters is given from standard double perturbation theory by equation (16). There it is assumed that the Hellmann–Feynman theorem holds with respect to the first perturbation $\boldsymbol{\lambda}$ for approximate zeroth-order solutions. In the NMR case, the nuclear magnetic moments or the external magnetic field are directly interpreted as the perturbation parameters due to their relative 'smallness'.

$$\begin{aligned} E^{(1,1)} :&= \left.\frac{\partial^2 E}{\partial \boldsymbol{\kappa} \partial \boldsymbol{\lambda}}\right|_{\boldsymbol{\kappa}=0, \boldsymbol{\lambda}=0} \\ &= \langle \Psi^{(0,0)} | \hat{\mathcal{H}}^{(1,1)} | \Psi^{(0,0)} \rangle + 2\mathrm{Re} \langle \Psi^{(0,1)} | \hat{\mathcal{H}}^{(1,0)} | \Psi^{(0,0)} \rangle \end{aligned} \tag{16}$$

The superscripts denote the order of perturbation with respect to $\boldsymbol{\lambda}$ and $\boldsymbol{\kappa}$, respectively. Because $\boldsymbol{\lambda}$ and $\boldsymbol{\kappa}$ are vectors, $E^{(1,1)}$ is a 2nd rank tensor. $\hat{\mathcal{H}}^{(1,0)} = \partial \hat{\mathcal{H}} / \partial \boldsymbol{\lambda}|_{\boldsymbol{\lambda}=0}$, $\Psi^{(0,1)} = \partial \Psi / \partial \boldsymbol{\kappa}|_{\boldsymbol{\kappa}=0}$, etc. $\Psi^{(0,1)}$ represents the change of the wavefunction due to the presence of the perturbation denoted by $\boldsymbol{\kappa}$, i.e., either the external magnetic field, or the magnetic field arising from one

of the nuclear spins. $\Psi^{(0,1)}$ can be formally obtained from solving the first-order perturbed wave equation

$$(\hat{\mathcal{H}}^{(0,0)} - E^{(0,0)})\Psi^{(0,1)} + (\hat{\mathcal{H}}^{(0,1)} - E^{(0,1)})\Psi^{(0,0)} = 0 \qquad (17)$$

showing that $\hat{\mathcal{H}}^{(0,1)}$ has to be known in order to compute $\Psi^{(0,1)}$. In DFT, formally similar expressions involving a sum over the Kohn–Sham orbitals instead of the many-electron wavefunction Ψ are used to compute $\boldsymbol{\sigma}$ and $\mathbf{K}$.

In the sum-over-states formulation it is assumed that the unperturbed ground state $\Psi_0 = \Psi^{(0,0)}$ with $E_0 = E^{(0,0)}$ and *all* the excited states (energies E_i and wavefunctions Ψ_i) corresponding to the field-free Hamiltonian $\hat{\mathcal{H}}^{(0,0)}$ are known. The Ψ_i form a complete basis set in which $\Psi^{(0,1)}$ can be expressed as

$$\Psi^{(0,1)} = \sum_{a\neq 0} \Psi_a C_a \qquad (18)$$

with yet unknown coefficients C_a. With the first-order equation (17), one obtains for the C_a after some manipulation

$$C_a = \sum_{a\neq 0} \frac{\langle\Psi_a|\hat{\mathcal{H}}^{(0,1)}|\Psi_0\rangle}{E_0 - E_a} \qquad (19)$$

and therefore for the nuclear shielding or spin–spin coupling

$$E^{(1,1)} = \langle\Psi_0|\hat{\mathcal{H}}^{(1,1)}|\Psi_0\rangle + 2\mathrm{Re}\sum_{a\neq 0} \frac{\langle\Psi_0|\hat{\mathcal{H}}^{(0,1)}|\Psi_a\rangle\langle\Psi_a|\hat{\mathcal{H}}^{(1,0)}|\Psi_0\rangle}{E_0 - E_a} \qquad (20)$$

We have to stress here that although equation (20) is *formally* correct, in practice not all (or any) of the excited states of $\hat{\mathcal{H}}^{(0,0)}$ are (or can be) known. However, equation (20) serves as a convenient basis for an interpretation of the final results and approximations to it can be easily identified within orbital models. Employing variational perturbation theory, $E^{(1,1)}$ is in practice usually directly computed from the zeroth order solution based upon the set of occupied and unoccupied (virtual) orbitals that serve as a one-particle basis in most theoretical methods.[16] In simple cases, for each occupied orbital a sum over virtual orbitals similar to (20) can be derived as the contributions to $E^{(1,1)}$, in which $E_0 - E_a$ is replaced by differences between occupied and virtual orbital energies, $\epsilon_i - \epsilon_a$. However, these orbital contributions also take into account possible first-order change in the potential caused by the perturbation, and a possible dependence of the basis set on the perturbation. Neglecting any change in the potential V leads to so-called uncoupled equations that are much easier and computationally cheaper to solve. (In DFT, neglecting the current-density dependence of the density functional leads to the mentioned uncoupled approach when the first-order perturbations of the orbitals due to the external magnetic field are evaluated.) For interpretation purposes, the potential change is often negligible, in which case the orbital contributions can have exactly the form (20), but with Ψ_0 replaced by an occupied orbital ψ_i (with energy ϵ_i) and Ψ_a and E_a replaced by virtual orbitals ψ_a and their energies ϵ_a. In particular the HOMO-LUMO gap plays an important role here, since it leads to the largest individual $1/(\epsilon_i - \epsilon_a)$. Another factor is, of course, the magnitude of the $\langle\psi_i|\hat{\mathcal{H}}^{(0,1)}|\psi_a\rangle$ and $\langle\psi_a|\hat{\mathcal{H}}^{(1,0)}|\psi_i\rangle$ matrix elements. For chemical shifts (not shieldings) and spin–spin couplings, it turns out that $\langle\Psi_0|\hat{\mathcal{H}}^{(1,1)}|\Psi_0\rangle$, the diamagnetic term (see below), is often of only minor importance. It is also possible to write the diamagnetic term in a sum-over-states form.[17] *For simplicity of notation, we refer to equation (20) as the working equation for evaluating* $\boldsymbol{\sigma}$ *and* $\mathbf{K}$ *regardless of the actual method being used.*

Once the zeroth order solution is known, and the perturbation operators with respect to $\boldsymbol{\mu}_A$ and $\boldsymbol{B}^{\mathrm{ext}}$ have been formulated, $\boldsymbol{\sigma}$ and $\mathbf{K}$ can be computed based on equation (20) in some chosen computational approximation. For the relativistic case of heavy element systems, E, Ψ and the perturbation operators refer to a relativistic zeroth-order treatment. In case relativity is treated as a perturbation itself, this leads to at least second- and third-order perturbation expressions for $\boldsymbol{\sigma}$ and $\mathbf{K}$ in which the order of derivatives is arbitrary. In this case, relativity can be conceptually regarded as a perturbation of an initially nonrelativistic expression for (14a,b).

In order to apply equation (20) for the computation of NMR shieldings or spin–spin couplings, the presence of the external magnetic field $\boldsymbol{B}^{\mathrm{ext}}$ and the magnetic field due to the nuclear spins has thus to be considered in the theory. More specifically, within a chosen theoretical level (nonrelativistic, four-component, a variational two-component scheme, relativistic perturbation theory, ...) the Hamiltonian $\hat{\mathcal{H}}(\boldsymbol{B}^{\mathrm{ext}}, \boldsymbol{\mu})$ is to be formulated in order to determine $\hat{\mathcal{H}}^{(1,1)}$, $\hat{\mathcal{H}}^{(1,0)}$ and $\hat{\mathcal{H}}^{(0,1)}$. Magnetic fields $\boldsymbol{B}$ are usually incorporated into quantum chemistry by finding the corresponding magnetic vector potential $\boldsymbol{A}$ which is related to the magnetic field $\boldsymbol{B}$ by $\boldsymbol{B} = \nabla \times \boldsymbol{A}$, and making the so-called minimal substitution for the momentum operator in the field-free Hamiltonian,

$$\hat{\boldsymbol{p}} \longrightarrow \hat{\boldsymbol{\pi}} = \hat{\boldsymbol{p}} - q\boldsymbol{A} \qquad (21)$$

with respect to a particle of charge q. We use $q = -e = -1$ for an electron in the following.

The well-known gauge-invariance problem arises here, viz. a given magnetic field does not uniquely define the vector potential, since adding the gradient $\nabla f(\boldsymbol{r})$ of any scalar function to $\boldsymbol{A}$ does not change $\boldsymbol{B}$, because $\nabla \times \nabla f(\boldsymbol{r}) = 0$. Often, f is chosen such that $\nabla\boldsymbol{A} = 0$ (Coulomb gauge). We use this gauge in the following. A different gauge of $\boldsymbol{A}$ can, e.g., be represented by choosing a different origin for the coordinate representation of $\boldsymbol{A}$. Although for a large class of variationally determined *exact* wavefunctions, expectation values do not depend on the chosen gauge, this is not generally true for approximate wavefunctions in a finite basis.[16]

For a point-like nuclear magnetic dipole, the vector potential is

$$\boldsymbol{A}^{\mu}_A = \frac{1}{c^2}\frac{\boldsymbol{\mu}_A \times \boldsymbol{r}_A}{r_A^3} \qquad (22)$$

$\boldsymbol{r}_A$ being the distance vector with respect to nucleus A, and r_A its length. Due to the strong inhomogeneity of $\boldsymbol{A}^{\mu}_A$, the position of the nucleus A is generally used as the origin for $\boldsymbol{A}^{\mu}_A$. The vector potential of an external, homogeneous magnetic field reads

$$\boldsymbol{A}^{\mathrm{ext}} = \frac{1}{2}\boldsymbol{B}^{\mathrm{ext}} \times \boldsymbol{r} \qquad (23)$$

For a molecule with many atoms there exists no obvious gauge origin since $\boldsymbol{r}$ refers to an arbitrarily chosen coordinate system. Nuclear shieldings obtained with wavefunctions approximated in a finite basis depend more or less strongly on the chosen origin. The $\boldsymbol{A}^{\text{ext}}$ gauge problem is circumvented in, e.g., the gauge-independent or gauge-including atomic orbitals (GIAO) or the individual gauge for localized orbitals (IGLO) methods. In these methods, field dependent basis functions or molecular orbitals are employed to ensure gauge invariance of expectation values. Such distributed gauge origin methods are commonly used in computations of nuclear shieldings. Another, less effective procedure is to supplement the basis sets by functions that are chosen such as to remove the gauge dependence to some extent without being of critical importance for the determination of the energy or the molecular structure. The gauge origin problem has been extensively discussed in the literature (see, e.g., Refs.[12,13,18] and literature cited therein for details).

Equation (22) is the most frequently used expression for the nuclear magnetic vector potential. It is known that for very accurate relativistic results, a finite nucleus model should be adopted both to obtain the zeroth-order solution as well as in the NMR perturbation calculation. However, almost all of the results quoted later in this work have been obtained with the point-nucleus approximation, and the influence of finite-nucleus corrections on the final results does not seem to be of critical importance.

Substituting (21) into the nonrelativistic one-electron Schrödinger Hamiltonian, equation (9), yields the additional 'magnetic' terms

$$\hat{\mathcal{H}}^{\text{mag}}_{\text{nrel}} = \frac{1}{2}(\boldsymbol{A}\hat{\boldsymbol{p}} + \hat{\boldsymbol{p}}\boldsymbol{A} + i\boldsymbol{\sigma}_s[\hat{\boldsymbol{p}} \times \boldsymbol{A} + \boldsymbol{A} \times \hat{\boldsymbol{p}}] + \boldsymbol{A}^2) \tag{24}$$

The operators linear in $\boldsymbol{A}$ are called the paramagnetic terms, while those proportional to $\boldsymbol{A}^2$ are called the diamagnetic terms. The second term on the right-hand side of equation (24) describes the interaction of the electronic spin with a magnetic field and is not present if one starts with the one-component Schrödinger equation where $(\boldsymbol{\sigma}_s\hat{\boldsymbol{p}})^2$ of equation (9) is replaced by $\hat{\boldsymbol{p}}^2$ before the minimal substitution is made (this implies that the substitution $\hat{\boldsymbol{p}} \rightarrow \hat{\boldsymbol{\pi}}$ has to be made before transformation to two-component form and then the limit $c \rightarrow \infty$ is taken). In the ZORA or ESC case, formally very similar magnetic operators are obtained that contain relativistic corrections due to the presence of $\mathcal{K}$ or k. For the ZORA case, see Refs.[19,20] For a derivation of the magnetic terms arising from the second-order DK transformation and from the Pauli Hamiltonian, see Refs.[21,22] The ESC case is illustrated elsewhere.[23]

Substituting $\hat{\boldsymbol{p}}$ with $\hat{\boldsymbol{\pi}}$ in the one-electron Dirac operator (5) yields a single paramagnetic term

$$\hat{\mathcal{H}}^{\text{mag}}_{\text{D}} = c\boldsymbol{\alpha}\boldsymbol{A} \tag{25}$$

Since the nonrelativistic limit (24) as well as relativistic two-component Hamiltonians afford a diamagnetic term, this should be contained in a result for $E^{(1,1)}$ obtained from (25). It has been shown that a diamagnetic contribution to $E^{(1,1)}$ in equation (16) indeed arises in the four-component scheme due to the contributions from negative energy eigenfunctions of $\hat{\mathcal{H}}^{\text{D}}$, that are used as a basis set in a sum-over-states expression for $\Psi^{(0,1)}$ in equation (16),[24] even though there is only a paramagnetic perturbation operator (25).

Upon explicit substitution of $\boldsymbol{A} = \boldsymbol{A}^{\text{ext}} + \sum_A \boldsymbol{A}^{\mu}_A$ from equation (23), and equation (22) or a finite-size magnetic dipole version of it, $\hat{\mathcal{H}}^{\text{mag}}(\boldsymbol{B}^{\text{ext}}, \boldsymbol{\mu})$ is finally obtained. Taking the derivatives with respect to $\boldsymbol{B}^{\text{ext}}$ and $\boldsymbol{\mu}_A$, $\boldsymbol{\mu}_B$ then yields $\hat{\mathcal{H}}^{(1,1)}$, $\hat{\mathcal{H}}^{(0,1)}$ and $\hat{\mathcal{H}}^{(1,0)}$ for a specific nonrelativistic or relativistic theoretical scheme. In the case of nuclear shieldings, it is most economic to take $\hat{\mathcal{H}}^{(1,0)} = \partial\hat{\mathcal{H}}/\partial\boldsymbol{\mu}_A|_{\boldsymbol{\mu}_A=0}$, while $\Psi^{(0,1)} = \partial\Psi/\partial\boldsymbol{B}^{\text{ext}}|_{\boldsymbol{B}^{\text{ext}}=0}$. In the nonrelativistic case, one obtains the one-electron operators

$$\begin{aligned}\hat{\mathcal{H}}^{\text{mag}}_{\text{nrel}}(\boldsymbol{B}^{\text{ext}}, \boldsymbol{\mu}) = \boldsymbol{A}^{\text{ext}^2} + \hat{\mathcal{H}}^{\text{OZ}} + \hat{\mathcal{H}}^{\text{SZ}} + \hat{\mathcal{H}}^{\text{OP}} \\ + \hat{\mathcal{H}}^{\text{DS}} + \hat{\mathcal{H}}^{\text{FC}} + \hat{\mathcal{H}}^{\text{SD}} + \hat{\mathcal{H}}^{\text{OD}}\end{aligned} \tag{26}$$

Here,

$$\hat{\mathcal{H}}^{\text{OZ}} = \frac{1}{2}\boldsymbol{B}^{\text{ext}} \cdot (\boldsymbol{r} \times \hat{\boldsymbol{p}}) = \frac{1}{2}\boldsymbol{B}^{\text{ext}} \cdot \hat{\boldsymbol{L}} \tag{27a}$$

$$\hat{\mathcal{H}}^{\text{SZ}} = \frac{1}{2}\boldsymbol{B}^{\text{ext}} \cdot \boldsymbol{\sigma}_s \tag{27b}$$

$$\hat{\mathcal{H}}^{\text{OP}} = \frac{1}{c^2}\sum_A \boldsymbol{\mu}_A \left(\frac{\boldsymbol{r}_A}{r_A^3} \times \hat{\boldsymbol{p}}\right) \tag{27c}$$

$$\begin{aligned}\hat{\mathcal{H}}^{\text{DS}} = \frac{1}{2c^2}\sum_A \Bigg[(\boldsymbol{\mu}_A \cdot \boldsymbol{B}^{\text{ext}})\left(\frac{\boldsymbol{r}_A}{r_A^3} \cdot \boldsymbol{r}\right) \\ -(\boldsymbol{\mu}_A \cdot \boldsymbol{r})\left(\boldsymbol{B}^{\text{ext}} \cdot \frac{\boldsymbol{r}_A}{r_A^3}\right)\Bigg]\end{aligned} \tag{27d}$$

$$\begin{aligned}\hat{\mathcal{H}}^{\text{FC}} + \hat{\mathcal{H}}^{\text{SD}} = \frac{1}{2c^2}\sum_A \boldsymbol{\sigma}_s \Bigg[\boldsymbol{\mu}_A \left(\nabla \cdot \frac{\boldsymbol{r}_A}{r_A^3}\right) \\ -(\boldsymbol{\mu}_A \cdot \nabla)\frac{\boldsymbol{r}_A}{r_A^3}\Bigg]\end{aligned} \tag{27e}$$

$$\hat{\mathcal{H}}^{\text{OD}} = \frac{1}{2c^4}\sum_{B\neq A} \frac{(\boldsymbol{\mu}_A \cdot \boldsymbol{\mu}_B)(\boldsymbol{r}_A \cdot \boldsymbol{r}_B) - (\boldsymbol{\mu}_A \cdot \boldsymbol{r}_B)(\boldsymbol{\mu}_B \cdot \boldsymbol{r}_A)}{r_A^3 r_B^3} \tag{27f}$$

(27a) is the orbital Zeeman term, (27b) spin Zeeman, (27c) paramagnetic orbital, (27d) diamagnetic shielding, (27e) Fermi-contact + spin-dipole, (27f) diamagnetic orbital term, respectively. The individual FC and SD operators, in particular the well-known δ function for the FC term, are obtained by explicitly carrying out the differentiation of $\boldsymbol{r}_A/r_A^3$ in (27e). Note that the presence of c in the nonrelativistic magnetic operators does *not* denote any relativistic terms, but c emerges from the magnetic units in equation (22) and the fact that the fine structure constant equals $1/c$ in the chosen atomic units. As already mentioned, the operators in the ZORA or ESC case are formally quite similar to the nonrelativistic ones, but include $\mathcal{K}$ or k and their derivatives, yielding different spatial contributions in particular for the FC term, but similar physical interpretations. We therefore use the same names for the operators when referring to these two-component relativistic schemes.

As compared to the nonrelativistic or two-component ones, the Dirac form of the one-electron magnetic operators look rather simple:

$$\hat{\mathcal{H}}^{\text{mag}}_{D}(\boldsymbol{B}^{\text{ext}}, \boldsymbol{\mu}) = -\frac{c}{2}\boldsymbol{B}^{\text{ext}} \cdot (\boldsymbol{\alpha} \times \boldsymbol{r}) - \frac{1}{c}\sum_A \boldsymbol{\mu}_A \cdot \left(\boldsymbol{\alpha} \times \frac{\boldsymbol{r}_A}{r_A^3}\right) \tag{28}$$

Taking the derivatives with respect to $\boldsymbol{B}^{\mathrm{ext}}$ and $\boldsymbol{\mu}_A$ in order to apply equation (20) is conceptually straightforward. Since (26) is connected to (28) as its nonrelativistic limit, the apparent simplicity of the four-component operators results in the many two-component terms through the coupling of the upper and lower components of the wavefunction by the Dirac operators. The 'Gordon-decomposition' of the Dirac shielding tensor provides a route to interpret the four-component results in the more common way of paramagnetic and diamagnetic contributions.[25] See, e.g., Ref.[26] for numerical examples.

Referring to the two-component scheme, equations (27a–f), it can be seen that the OZ, OP and DS operators contribute to the nuclear shielding. Explicitly,

$$\hat{\mathcal{H}}^{(1,1)} = \left.\frac{\partial^2 \hat{\mathcal{H}}^{\mathrm{DS}}}{\partial \boldsymbol{B}^{\mathrm{ext}} \partial \boldsymbol{\mu}_A}\right|_{\boldsymbol{B}^{\mathrm{ext}}=0,\,\boldsymbol{\mu}_A=0}$$

$$\hat{\mathcal{H}}^{(1,0)} = \left.\frac{\partial (\hat{\mathcal{H}}^{\mathrm{OP}} + \hat{\mathcal{H}}^{\mathrm{FC}} + \hat{\mathcal{H}}^{\mathrm{SD}})}{\partial \boldsymbol{\mu}_A}\right|_{\boldsymbol{\mu}_A=0}$$

$$\hat{\mathcal{H}}^{(0,1)} = \left.\frac{\partial \hat{\mathcal{H}}^{\mathrm{OZ}}}{\partial \boldsymbol{B}^{\mathrm{ext}}}\right|_{\boldsymbol{B}^{\mathrm{ext}}=0} \tag{29}$$

are used in equation (20). Here, the external field and the nuclear spin induce electronic paramagnetic orbital currents through $\hat{\mathcal{H}}^{\mathrm{OZ}}$ and $\hat{\mathcal{H}}^{\mathrm{OP}}$, respectively, the magnetic fields of which cause the paramagnetic nuclear shielding. The diamagnetic shielding contribution from $\hat{\mathcal{H}}^{\mathrm{DS}}$ is due to the diamagnetic electronic currents induced in the electronic system. As already mentioned, we restrict the discussion here to the spin-compensated case (closed-shell molecules). Without spin-orbit coupling, the FC and SD terms do not contribute to the nuclear shielding in closed shell systems, i.e., with pure spin-orbitals the contributions from spin-up and spin-down orbitals due to $\hat{\mathcal{H}}^{\mathrm{FC}}$, $\hat{\mathcal{H}}^{\mathrm{SD}}$ exactly cancel because the external magnetic field does not induce spin density.

For nonrelativistic spin–spin couplings, one uses

$$\hat{\mathcal{H}}^{(1,1)} = \left.\frac{\partial^2 \hat{\mathcal{H}}^{\mathrm{OD}}}{\partial \boldsymbol{B}^{\mathrm{ext}} \partial \boldsymbol{\mu}_A}\right|_{\boldsymbol{\mu}_A=0,\,\boldsymbol{\mu}_B=0}$$

$$\hat{\mathcal{H}}^{(1,0)} = \left.\frac{\partial (\hat{\mathcal{H}}^{\mathrm{OP}} + \hat{\mathcal{H}}^{\mathrm{FC}} + \hat{\mathcal{H}}^{\mathrm{SD}})}{\partial \boldsymbol{\mu}_A}\right|_{\boldsymbol{\mu}_A=0}$$

$$\hat{\mathcal{H}}^{(0,1)} = \left.\frac{\partial (\hat{\mathcal{H}}^{\mathrm{OP}} + \hat{\mathcal{H}}^{\mathrm{FC}} + \hat{\mathcal{H}}^{\mathrm{SD}})}{\partial \boldsymbol{\mu}_B}\right|_{\boldsymbol{\mu}_B=0} \tag{30}$$

Similar to NMR shieldings, the OP and OD terms introduce paramagnetic and diamagnetic electronic currents due to a nuclear magnetic moment that can further interact with the perturbations from another nucleus. The SD and in particular the FC term both yield nonzero contributions and cause a different coupling mechanism. These operators introduce a net electronic spin density at or around, say, nucleus A, which is transferred through the electronic system (chemical bonds) to nucleus B and interacts with its spin magnetic moment there. There is also a mixed term between the FC and the SD contribution, that contributes to the anisotropy of the $\mathbf{K}$ tensor. Again, in the nonrelativistic case, where spin and spatial degrees of freedom are completely independent from each other, all 'mixed' contributions to $\mathbf{K}$ between orbital- and spin-dependent operators yield zero (e.g., the contribution due to $\hat{\mathcal{H}}^{\mathrm{FC}}$ in $\hat{\mathcal{H}}^{(1,0)}$ with the one due to $\hat{\mathcal{H}}^{\mathrm{OP}}$ in $\hat{\mathcal{H}}^{(0,1)}$ and vice versa in equation (20)). The same arguments concerning vanishing terms involving both spin- and orbital-dependent operators apply in the scalar relativistic case.

The situation is much different at the presence of SO coupling. Spatial and spin degrees of freedom are then coupled and not longer independent from each other. Not unexpectedly therefore, in, e.g., the Pauli, ESC, DK, or ZORA case including the one-electron spin-orbit (1e-SO) operator, mixed contributions involving both spin- and orbital-dependent operators occur for $\boldsymbol{\sigma}$ and $\mathbf{K}$ in this case. In particular, the spin-dependent FC and SD terms contribute to the chemical shielding because, through SO coupling, an external magnetic field induces net spin-density even in a closed-shell system. Likewise, for spin–spin couplings, mixed terms between spin- and orbital-dependent operators in $\hat{\mathcal{H}}^{(1,0)}$ and $\hat{\mathcal{H}}^{(0,1)}$ are no longer zero. In variational two-component procedures in which the zeroth-order computation and the magnetic operators are based on the same formalism and no terms have been omitted initially, no new operators or new terms in the expressions for $\boldsymbol{\sigma}$ or $\mathbf{K}$ arise due to SO coupling. In case that the (usually Pauli) 1e-SO operator is introduced as a first-order perturbation, the additional terms are formulated and calculated explicitly, which is convenient for interpretations. The same holds for additional scalar relativistic corrections. The operators arising from the minimal substitution $\hat{\boldsymbol{p}} \rightarrow \hat{\boldsymbol{\pi}}$ in the spin-orbit operator itself have thereby been overlooked for a long time.[22] For nuclear shielding, the most important contribution due to spin-orbit coupling has been shown to arise from the FC term in the external magnetic field, while for spin–spin couplings, the FC-OP cross term appears to be dominant in the cases being investigated so far. See Sections 3.1 and 4.2 for further comments and explanations. All the 1e-SO contributions are, of course, contained in the four-component treatment based on equation (28).

As already mentioned, transformation of the electron–electron interaction to two-component form yields various new terms, among them the two-component two-electron spin-orbit and spin-other-orbit operators (collectively being denoted here by '2e-SO'), which give rise to various additional magnetic contributions in the presence of magnetic fields. See, e.g., Refs.[4,16,27] for theoretical details. Unless explicitly mentioned, we refer to the 1e-SO effects in the following. Actual program implementations may make use of an effective potential in the 1e-SO operator and the results may therefore contain two-electron SO effects to some extent.

2.3 Computational Methods

While the importance of Hartree–Fock computations in quantum chemistry is generally decreasing in favor of either correlated ab initio methods or DFT, it is still one of the common methods in the field of computation of heavy atom NMR parameters. A four-component implementation of Hartree–Fock shielding tensors and spin–spin couplings has been reported by Visscher and co-workers[28,29] and an implementation for nuclear shieldings by Nakatsuji and co-workers.[26,30,31] Both implementations use a common gauge origin for the external magnetic field. Pioneering NMR Hartree–Fock calculations including scalar relativistic effects based on the Pauli operator or the DK transformation, and

spin-orbit effects based either upon explicit consideration of the Pauli SO operator or the use of spin-orbit ECPs, have been reported by Nakatsuji et al.[32,33] and by Fukui et al.[21,22,34] Theoretically somewhat less justified 'mixed' methods such as using the scalar part of the DK operator together with Pauli SO for the zeroth-order solution and nonrelativistic + Pauli SO operators for NMR shieldings have also been used with reasonable success.[35] The main disadvantage of the Hartree–Fock based methods is, of course, the neglect of electron correlation, that has been demonstrated to be of high importance for the determination of NMR parameters in general and of heavy atom spin–spin couplings in particular.

To the best of our knowledge, four-component post Hartree–Fock or DFT implementations of NMR parameters have not yet been carried out, but can be expected in the near future at least for the DFT case. Post Hartree–Fock MCSCF computations of heavy atom nuclear shieldings (employing GIAO) and spin–spin couplings have so far considered spin-orbit effects only, based on a perturbational first-order treatment of the Pauli SO operator.[36–40] Scalar relativistic effects from the heavy atom were neglected in this case. This method is often suitable for NMR of light nuclei close to a heavy atom and has been successfully applied to small molecules. Likewise, SO ECPs are able to recover the important spin-orbit effects on neighbor atom shieldings that are being neglected by scalar relativistic ECPs.

The first-order SO approach has already been utilized in the pioneering approaches for the computation of nuclear shieldings in heavy atom compounds, involving simple semiempirical wavefunctions.[41–44] For spin–spin couplings, relativistic effects have been first considered in the form of correction factors applied on top of nonrelativistic Hartree–Fock or semiempirical wavefunctions.[45,46] Four-component extended Hückel theory (REX) has been developed and extensively applied to both heavy atom shieldings and spin–spin couplings by Pyykkö and co-workers.[47]

The restriction of excluding the heavy nuclei in the NMR computations applies technically to a common use of ECPs in heavy element computations. Existing methodology for NMR parameters that has been derived for all-electron calculations cannot be used without modification for NMR parameters of those atoms for which an ECP is used. In this case, either a NMR methodology directly derived from the pseudopotential formalism would have to be used, or at least the pseudo-orbitals need to be orthogonalized on the relativistic heavy atom cores before applying a standard all-electron code.

Density functional theory (DFT)[48] has been very successful in the field of heavy atom NMR computations. Methodological development for relativistic NMR computations has been performed in particular by Kaupp, Malkin, Malkina and co-workers[49–51] (using the IGLO method for shieldings), and by Ziegler and co-workers (GIAO for shieldings).[19,20,52–54] Taking into account that the electron density, the spin density and the current density define the one-electron magnetic contributions to $\boldsymbol{\sigma}$ and $\mathbf{K}$, and that these densities are (of course only in principle) obtained exactly from Kohn–Sham DFT,[55] its application to NMR parameters has a theoretically well founded base. From the experience gained so far it seems that the current-density dependence and also relativistic corrections of the exchange-correlation functional are not very large, and quite reasonable results can be obtained with standard nonrelativistic local-density (LDA) or generalized gradient (GGA) approximations (in which, however, the density can be a relativistic one). The fact that electron correlation is to some extent accounted for in contemporary Kohn–Sham DFT, and due to its computational effectiveness with regard to the number of atoms that can be treated simultaneously, most of the relativistic NMR computations on larger systems such as transition metal complexes are currently based on DFT. For the heavy atom DFT NMR computations carried out so far, various relativistic methods have been utilized, among them perturbational use of the Pauli SO operator, variational computations with the Pauli operator and frozen cores excluding or including SO coupling, the use of the ZORA Hamiltonian, and use of scalar relativistic and spin-orbit ECPs.

We further note that some authors subdivide the relativistic effects of NMR parameters into 'direct' and 'indirect' effects, the latter being related to the change of the NMR parameters with respect to a change of the computed molecular structure due to relativity. It is known that small geometrical changes can result in sizeable changes of shieldings and couplings. The choice of experimentally determined structures, if available, for the computations is unambiguous and leaves only the 'direct' effects to be discussed.

Apart from acronyms already specified in the previous sections, we make use of the following abbreviations from now on: vPSO, vPSC, vPauli for variational Pauli SO only, scalar only, and scalar + SO, respectively; similarly, pPSO, pPSC, pPauli denote first-order perturbational relativistic calculations; HF for Hartree–Fock; DKSC, DK for Douglas–Kroll, first order without and with SO corrections, respectively, and MCSCF for multiconfigurational Hartree–Fock (ab initio).

3 HEAVY ATOM NUCLEAR SHIELDINGS

Suggestions on the importance of relativistic corrections to nuclear shieldings and first numerical estimates for atoms date back to the 1960s. In 1969, Nakagawa argued that spin-orbit coupling would be an important factor for nuclear shieldings of light nuclei in the neighborhood of heavy halides.[56] Subsequently, semiempirical calculations of the respective SO effect in hydrogen and methyl halides were carried out by Morishima et al.,[41] Volodicheva and Rebane[42] and Cheremisin and Schastnev.[43] In the early 1980s, several authors published the formalism of nuclear shieldings within the four-component (Dirac) scheme.[25,57,58] This work and its future importance was subsequently reviewed by Jameson.[59] We also refer the reader to subsequent articles by Jameson and Jameson et al. who review the literature in the computational NMR field on a yearly basis. In particular the more recent articles show a large increase of publications based on relativistic methods. See, e.g., Ref.[60] for a relativistic NMR application in solid-state physics. Already anticipated by Pyykkö[57] in his remark "A rigorous implementation of the present theory will [...] probably take some time", four-component ab initio (Hartree–Fock) calculations of NMR shieldings in molecules have been reported only rather recently.[26,28,31]

Following the historical computational development we discuss SO effects on NMR shieldings prior to scalar relativistic effects.

3.1 Spin-orbit Coupling Effects

The proton chemical shift in the series of hydrogen halides HX (X = F, Cl, Br, I) and the ^{13}C shifts in CH_3X are probably the most thoroughly studied parameters in heavy atom NMR computations. The reason is that these molecules are among the smallest samples in which the strong SO dependence of NMR chemical shifts can be computed and compared to experiment. The HX and CH_3X series therefore serve as benchmarks for heavy atom NMR computations where, due to the smallness of the systems, high quality basis sets can be employed nowadays. The trend being obtained from the computations is always similar, regardless of which method has been used: excluding SO coupling does not recover the experimentally observed trend, but with inclusion of SO effects the calculated values follow the experimental trend. The numerical quality of the results is, of course, much dependent on the chosen method, and also somewhat on whether scalar relativistic effects have been additionally considered or not. Table 1 displays some of the results for the HX series that have been obtained during the last three decades. The data establish that the experimental trend can indeed be explained on the basis of SO effects only, while exclusion of SO effects does not reproduce the right trend even if scalar relativistic effects are considered.

Explanations of the SO contribution to nuclear shielding have been given in almost all of the articles quoted in Table 1 and many other papers. Qualitatively, let us consider the singlet (closed shell) ground state wavefunction without SO coupling first. As in equation (18), we assume that Ψ_0 and all the excited states of the Hamiltonian (without SO coupling) are available as a complete basis set. Expanding the spin-orbit coupled wavefunction on this basis means that, due to the nature of the SO operator, contributions also from excited triplet states will enter the SO wavefunction. Now the perturbed SO wavefunction in an external magnetic field, represented in the same basis, will have different coefficients for the singlet and triplet states and thereby the magnetic field can effectively induce a net spin density in the electronic system. The FC and SD operators also induce spin density and therefore the contribution from these operators to the NMR shielding are no longer zero.

In the case of the shielding of a light nucleus L in the neighborhood of a heavy atom Y, the spin density is induced by the external field around Y, transferred through the chemical bond(s) to the light nucleus L, and is there 'detected' by the FC and SD perturbations (heavy-atom effect on the light-atom shielding (HALA) in contrast to the heavy atom effect on the heavy nucleus shielding itself, HAHA[61]). This suggests a qualitative similarity to the nonrelativistic FC/SD mechanism of nuclear spin–spin coupling, where the spin density is not induced by the external field but by the FC and SD perturbation from another nucleus. This similarity has already been proposed in 1969 by Nakagawa et al.,[56] but no unambiguous numerical evidence could be provided. Recent DFT computations[62] on a number of systems convincingly demonstrate the correlation between K(L,Y) and the spin-orbit contribution to σ(L) induced by Y. In particular, a familiar Karplus-type dihedral angle relation known for three-bond spin–spin couplings has been obtained for the SO contribution to proton shielding in iodoethane that closely follows the behavior of ^3K(H,I). Many numerical results obtained by different authors show that the SD contribution to spin-orbit induced shielding can often be neglected, and the FC part is usually dominant. The same holds for nuclear spin–spin couplings (Section 4). Similar to spin–spin couplings, too, is that the magnitude of the FC contribution to nuclear shielding depends on the σ-character of the L–Y bond(s). This allows for similar chemical interpretations.[51,62]

The case of $\delta(^{13}C)$ in methyl halides is not as spectacular as the hydrogen halides. Still, qualitative agreement with experimental data can only be achieved upon inclusion of SO coupling in the shieldings calculation, while scalar relativistic corrections are of minor importance. Benchmark data for

Table 1 Proton Chemical Shifts in Hydrogen Halidex HX

$-\delta(^1H)$[a] method/year	X = Cl		X = Br		X = I	
	nrel[d]	rel	nrel	rel	nrel	rel
Semiemp. pPSO/1973[41]	8.02	8.24	11.24	13.85	13.08	20.92
Semiemp. pPSO/1978[42]	2.1	2.7	5.75	10.0	3.22	16.8
REX/1987[47]		0.45		3.35		11.01
HF pPSO/1995[32]	2.43	3.17	2.57	7.72	3.07	18.93
HF DK + vPSO/1996[35]	1.92	2.69	2.36	7.87	0.04	19.93
DFT pPSO/1996[49]	1.68	2.31	1.23	5.34	1.61	13.24
DFT vPSC/1997[52]	1.4	1.5	1.7	1.8	2.1	2.3
MCSCF pPSO/1998[36]	1.98	2.57	2.19	6.04	2.74	14.68
DFT vPauli/1998[53]		1.43		5.34		11.79
HF SCDK/1999[34]	2.08	2.17	2.39	3.06	2.62	4.95
HF Dirac/1999[28]	2.39	3.13	2.82	8.21	3.32	20.11
HF Dirac/1999[26]		2.68		4.91		10.71
DFT ZORA/2001[b]	1.57	2.45	1.84	5.31	2.19	13.6
DFT SO-ECP/2001[63]	1.68	2.39	1.21	6.42	1.61	14.87
exp ($\pm$0.02)[c]		2.58		6.43		15.34

[a]In ppm, with respect to HF, all values $\times$ (−1).
[b]This work, DFT ZORA, (BP86 functional).
[c]Experimental values as quoted in Ref.[53] Uncertainty due to the experimental value for HF (measured with respect to CH_4).
[d]Nonrelativistic values listed if reported in reference.

these and other small molecules have been published, e.g., in Refs.[32,36,43,47,49,53,63]

The importance of the influence of two-electron (2e−) SO operators or the Breit correction in the Dirac scheme has been investigated by some authors.[30,36,50] For $\sigma(^1H)$ in HX and $\sigma(^{13}C)$ in MeX, the 2e-SO contributions were found to be small and of opposite sign to the 1e-SO shielding terms. The relative importance of the two-electron terms appears to be generally decreasing for these cases as the heavy atom becomes heavier, contributing about 30% to the (small) SO shift caused by F substituents and about 7% to the (large) SO shift caused by iodine substituents. Similar conclusions for the relative importance of the 2e-SO terms were obtained for the shielding of the heavy atom,[36] for which (see next section) the scalar relativistic effects should not be neglected. For increasingly heavy X, the scalar relativistic corrections may be of higher importance than the two-electron SO terms. See, e.g., the DK results in Table 1. On the other hand, the vPSC DFT values of Ref.[52] do not indicate such large scalar relativistic corrections. At the present level of accuracy that can currently be achieved by either nonrelativistic + pPSO or four component ab initio methods, or relativistic DFT, the two-electron SO contributions appear to be rather negligible for heavy element molecules.

One of the major successes of relativistic NMR shieldings computations has been the explanation of the origin of the 'normal' and 'inverse' halogen dependence (NHD and IHD) in many compounds. Well known to experimentalists and theoreticians, shieldings of light atoms L bound to a halogen X quite often strongly increase as X becomes heavier (NHD) and its electronegativity decreases. Examples are HX, shown above, CH_3X, CH_2X_2, etc., and many other main group compounds in particular in high oxidation states. However, counter examples are known, where the L nucleus becomes less shielded for decreasing electronegativity (and increasing nuclear charge) of X, at least for Cl (sometimes Br) compared to F. Sometimes, in those compounds the NHD is observed again for X = I (and sometimes Br). Examples are SiX_4, AlX_4^-, and many transition metal compounds. As in HX (Table 1), in the investigated cases the NHD is caused by the SO contribution to nuclear shielding, while the nonrelativistic computations predict an IHD behavior. Figure 1 displays the Hartree–Fock data obtained for some silicon halides in 1995. Very similar results for these and other compounds were obtained in the same year by a semiempirical approach.[44]

Extremely large SO corrections to the phosphorus chemical shift in PX_4^+ have been reported in Ref.[64] and were attributed to the pronounced s-character of the L–X bonds due to the high oxidation state of phosphorus. Similar NHD results can be found in many theoretical studies of the SO shielding contribution. The authors of Ref.[65] investigated a number of Ti tetrahalides and Nb hexahalides. Rather typical for early transition metal halides, almost vanishing net SO effects on the metal shielding were observed even for the tetra- and hexa-iodides, caused by a cancellation of positive SO contributions from the FC term and negative changes of the paramagnetic shielding at the presence of SO coupling. In this case, IHD for the series F → I is observed for the chemical shifts in agreement with experiment. This has been interpreted in terms of the different nature of the metal d-orbitals binding to the ligands as compared to (s- and) p-orbitals in the case of main group elements exhibiting NHD.

If one bases the interpretation for the IHD on equation (20), the decreasing HOMO-LUMO gap due to decreasing electronegativity of the halogen in the series X = F → I results in a larger magnitude of the paramagnetic shielding, if the matrix elements in the sum over excited states are assumed to be approximately constant. (In Ref.[66], excellent linear correlation of ^{95}Mo chemical shifts with the lowest magnetically allowed d-d* excitation energy has been observed for a number of Mo complexes.) Since the nonrelativistic paramagnetic shielding contribution is typically negative, this results in increasingly positive chemical shifts (IHD). From the investigations quoted above it becomes clear that the NHD, on the other hand, is due to the more pronounced influence of spin-orbit coupling, which often increases the shielding and therefore causes increasingly negative chemical shifts. The diamagnetic shielding, as a core property, is usually found to be of small influence concerning the chemical shifts. From the relativistic nature of the NHD it becomes clear why previous

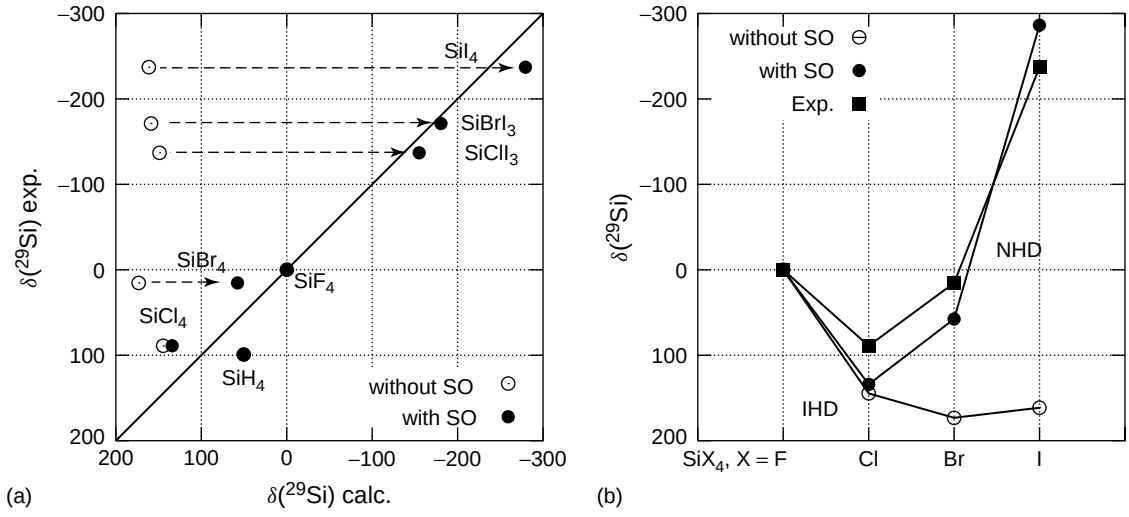

Figure 1 ^{19}Si chemical shifts with respect to SiF_4 in silane and some silicon halides, from Hartree–Fock data.[33] Scalar rel. and SO effects considered here via ECPs on the halide ligands. (a) experimental vs. computed Si shifts. (b) NHD and IHD along the SiX_4 series. See Section 3.1

explanations of the NHD that only take the (nonrelativistic) paramagnetic shielding into account have not generally been convincing.

Density functional theory (DFT) has been particularly successful in the case of transition metal compounds, and generally in cases for which electron correlation has a strong influence on the NMR shielding, and where a correlated ab initio method including relativistic effects has not been available or has not been applicable due to the size of the system (see also the section on spin–spin couplings). An example where electron correlation is believed to be very important is the ^{13}C shift in the series of CX_3^+. Nonrelativistic DFT and MP2 calculations show very similar results exhibiting IHD. This trend is also observed, but strongly overestimated, by nonrelativistic Hartree–Fock calculations, indicating the importance of electron correlation. Further inclusion of SO coupling in the DFT calculations recovers the experimentally observed NHD for $X = Cl \rightarrow Br \rightarrow I$ with good accuracy.[67]

Most of the relativistic DFT studies of transition metal compounds include scalar relativistic effects and are discussed in the next section.

3.2 Including Scalar Relativistic Effects

From a computational point of view, the most simple way of including scalar relativistic effects in a NMR shieldings calculation is to use an available scalar relativistic ECP on the heavy atom. When HALA effects are studied, existing nonrelativistic NMR code can be (and is) used without modifications. Many studies have been carried out using this approach, see, e.g., Refs.[51,68] for overviews of density functional applications in particular to transition metal complexes. In view of the importance of SO corrections to $\boldsymbol{\sigma}$ as seen in the previous section, however, the range of applications of this method seems to be limited. Spin-orbit ECPs have been applied to a number of NMR ligand shieldings including heavy main group and transition metal compounds.[33,63] Restrictions with respect to HALA effects also apply to the purely scalar relativistic approach of Ref.[52], in which HX and a number of transition metal complexes are studied. However, the method is capable of treating the heavy metal shift (and HAHA effects) itself, with reasonable accuracy as shown for the W shifts in Table 2. In Ref.[69], an overview of this variational scalar Pauli method is given. Among other data, a large number of ^{125}Te shifts are presented. In comparison with experiment, the relativistic computations achieved good accuracy, therefore SO effects can be regarded as mostly unimportant for Te chemical shifts. An increase of the scalar relativistic effects of the shielding of the heavy nucleus X with $\sim Z^{3.5}$ has been found from SCDK calculations for the HX series.[21] This underlines the importance of scalar relativistic corrections for heavy nucleus shieldings. Computational methods that include both scalar relativistic and SO effects and have been applied to both light and heavy nucleus shieldings are, of course, the four-component methods,[26,28,30] and, e.g., Douglas–Kroll including SO effects,[70–72] Pauli including SO,[22,53] or the ZORA approach.[19,73] A collection of transition metal tetroxo- and hexacarbonyl complexes appears to represent a benchmark test set for DFT NMR implementations. Oxygen shifts of group 6–8 transition metal tetroxo-complexes were studied, e.g., in Refs.[52,74] with a scalar relativistic approach. The rather good agreement with experimental shifts suggests that SO coupling does not play an important role in this case. Scalar relativistic effects on the ligand shifts appeared to be of high importance only for the 5d metals and are almost negligible for the 3d metals. The metal shifts in the same set of complexes were studied by variational scalar + SO Pauli and ZORA SO DFT.[75] Unfortunately, no oxygen shifts were reported there for comparison. The results for the metal shifts have been satisfactory, with ZORA emerging as the superior method in this case. Table 2 displays some ^{183}W shifts that were obtained by DFT methods and by a Hartree–Fock approach[70] including scalar + SO effects. The results indicate that scalar and SO effects are probably of equal importance for the W shifts. In Ref.[76], a larger number of W shifts than quoted in Table 2 have been computed by both vPauli and by ZORA DFT. ZORA resulted in a mean error of approximately 3% of the total shift range of 7000 ppm for the investigated samples when compared to experiment. The Pauli approach performed worse in this case, with an error of about 6%. ZORA produced a similar accuracy for a number of ^{207}Pb chemical shifts reported in the same study (4% error compared to the covered shift range), whereas the mean error from the Pauli approach was found to be four times larger in this case. The ZORA computations predicted an enormous SO shift of the Pb shielding of PbI_4 of more than −8000 ppm, a number yet to be supported by experimental results.

Carbon chemical shifts for 5d transition metal carbonyl complexes studied with DFT are displayed in Table 3. SO effects play a less significant role for the ^{13}C chemical shift in these complexes as compared to HX, but systematically improve the computed results. The SO shifts do not easily follow intuitive arguments based on the size of the HOMO-LUMO gap (HLG).[53] From equation (20) the individual contributions to the shielding can be expected to decrease with increasing HLG along a row of the periodic table. Despite the fact that the HLG increases from approximately 2 to 6 eV from $[Hf(CO)_6]^{2-}$ to $[Ir(CO)_6]^{3+}$, the spin-orbit contribution to the nuclear shielding and to the chemical shift is nevertheless seen to be increasing from Hf to Ir. As illustrated in Ref.[53], the trend can be rationalized on the basis that, due to the relative energies of the metal d_σ, d_π and the CO σ and π^*

Table 2 Some ^{183}W Chemical Shifts

Compound	δ exp.[a]	DFT vPSC[52]		DFT vPauli[76]	DFT ZORA[76]	HF SCDK + vPSO[70b]	
		nrel	rel	rel	rel	nrel	rel
$W(CO)_6$	−3446	−4075	−3703	−3306	−3876		
WF_6	−1121			−107	−630	−1795	−1135
WCl_6	2181			1773	1932	2266	2686

[a]With respect to WO_4^{2-}, as compiled in Ref.[76]
[b]Reported in [70] with respect to WF_6.

orbitals, the bonding in Hf carbonyl is dominated by $d_\pi - \pi^*_{CO}$ interaction, whereas the bonding in Ir carbonyl is dominated by $d_\sigma - \sigma_{CO}$ interaction. CO is more likely to σ-donate charge to the highly positively charged Ir, whereas metal-ligand π-back-donation dominates in the Hf complex. Only in the former case, however, can spin density be effectively transferred to the carbon nucleus, therefore the magnitude of the SO induced carbon shift is increasing along the 5d transition metal carbonyl series despite the increasing HLG. It has been shown previously that the decreasing $\delta(^{13}C)$ along the series at the scalar relativistic level is due to a complex interplay of different factors in which the amount of π-back-donation is predominant.[77,78]

In a ZORA DFT study of ^{195}Pt chemical shifts,[79] the authors also found that simple arguments based on the magnitude of $1/(\epsilon_i - \epsilon_a)$ are not always able to provide an explanation of the observed trends. The magnitude of the matrix elements in the numerator of the sum in equation (20) has to be considered as well and needs to be explained by intuitive chemical arguments. In the case of Pt shifts, NHD is observed in many cases. An analysis of the computational data shows that both the SO contributions and the paramagnetic shielding approximately equally contribute to the NHD. For the paramagnetic Pt shielding, this was attributed to a preference of the soft acid Pt(II) to bind to the soft base I instead of Cl. The authors in Ref.[79] could numerically and graphically illustrate that this results in a smaller magnitude of the (negative) paramagnetic shielding for iodine ligands due to smaller paramagnetic matrix elements in equation (20) that overcompensate the opposite HLG influence. The overall accuracy of the ZORA DFT method for Pt shieldings resulted in a mean error of approximately 10% of the investigated chemical shift range for 23 samples.[79]

Mercury shieldings have been computed by DFT and Hartree–Fock methods.[19,71,72] Table 4 lists some results that have been obtained. As can be seen from the data for HgMeX and HgX_2, the mercury halide compounds exhibit NHD, largely caused by the SO effects on the nuclear shieldings.[19,71] Large 'coupling' between scalar and SO corrections to mercury shifts were noted in Ref.[71] This means that the inclusion of both relativistic mechanisms is important in order to achieve reasonable results, because the SO correction based on a nonrelativistic zeroth order solution is much different from the one obtained from a scalar relativistic one. It is well known that scalar relativistic effects substantially stabilize and contract the 6s orbital in Hg, while the Hg 5d shell is destabilized and spatially expanded as compared to nonrelativistic computations.

Table 3 ^{13}C Chemical Shifts in 5d Transition Metal Carbonyls, from DFT Calculations

Compound	δ exp.[a]	vPSC [78]	vPauli [53]	SO ECP [63]
$[Hf(CO)_6]^{2-}$	244	228.3	234.5	228.2
$[Ta(CO)_6]^{-}$	211	211.8	214.8	206.0
$W(CO)_6$	192	197.7	196.7	188.6
$[Re(CO)_6]^{+}$	171	183.9	176.2	173.7
$[Os(CO)_6]^{2+}$	147	172.4	149.5	153.9
$[Ir(CO)_6]^{3+}$	121	153.6	125.8	130.9
$[Au(CO)_2]^{+}$	174		165.3	164.0
$[Hg(CO)_2]^{2+}$	169		158.2	154.0

[a]As compiled in Refs.[53,63], with respect to TMS.

Table 4 ^{199}Hg Chemical Shifts

Compound[a]	δ exp.[b]	DFT ZORA[19]	HF DK
$Hg(SiH_3)_2$	+196		+232[72]
$Hg(GeH_3)_2$	−147		−289[72]
HgMe(CN)	−766	−861	
$Hg(CN)_2$	−1386	−1724	
HgMeCl	−861	−943	
HgMeBr	−915	−1068	
HgMeI	−1097	−1025	
$HgCl_2$	−1519	−1556	(−1519)[c]
$HgBr_2$	−2213	−2684	−2134/−3191[c]
HgI_2	−3447	−3506	−2371/−4130[c]
$HgCl_2\ (NH_3)_2$[d]	−1280[e]	−1086	
$HgBr_2\ (NH_3)_2$[d]	−1622[e]	−1858	
$HgI_2\ (NH_3)_2$[d]	−2355[e]	−2836	

[a](Me = CH_3).
[b]With respect to $HgMe_2$, as compiled in Refs.[19,72]. Solvent for HgX_2 has been THF.
[c]SCDK + vPSO, Ref.[71] Data reported with respect to $HgCl_2$, therefore the value for $HgCl_2$ has been set equal to the experimental shift here. Results were obtained with two different basis sets. The shifts obtained with the external field projectors are displayed.
[d]NH_3 to simulate the solvent pyridine in the computations.
[e]Experimental values for HgX_2 in pyridine.

In effect, the scalar relativistic Hg–ligand bonds are much different from the nonrelativistic ones, meaning that the s and d contributions in the occupied and virtual metal-ligand orbitals, that determine to some extent the magnitude of the SO corrections to the chemical shifts, will be very different as well. In Ref.[71], the rather unsatisfactory performance of the computations, in particular the strong overestimation of the SO shift corrections for the HgX_2 series (Table 4, large basis set) was attributed to the missing treatment of 2e-SO terms. The authors proposed that 20–40% of the 1e-SO contribution to the chemical shift may be canceled by the two-electron contributions, which seems to be excessive taking the previously quoted findings about the relative importance of the two-electron SO terms for heavy atom compounds into account. Considering the reasonable overall performance of the DFT calculations for Hg shifts (they do not include 2e-SO operators explicitly), the inaccuracies of the Hartree–Fock results for HgX_2 could also be attributed to the missing treatment of electron correlation. Another problem might be the inconsistent treatment of relativity, viz. the use of the problematic Pauli SO operator in conjunction with the scalar relativistic DK Hamiltonian. This has been criticized by Fukui.[21]

For the series $Hg(LCH_3)_2$, L = C, Si, Ge, which has been computed with a DK transformed Hamiltonian including SO coupling, it was found that the rather small magnitudes of Hg chemical shifts are caused by cancellation of large relativistic and nonrelativistic contributions.[72] Even the usually negligible SD contribution to the chemical shift is here comparable in magnitude to the shift itself. In that respect, the achieved results must be regarded as quite accurate and testify to the accuracy of the relativistic treatment with the DK Hamiltonian. The authors also consider missing solvent effects as a possible source of error, an issue that has already been addressed regarding mercury chemical shifts.[19] Experimentally confirmed, the solvent dependence of, e.g., the Hg shift in HgI_2 can amount to more than 1000 ppm (pyridine vs.

THF). It has been computationally demonstrated in Ref.[19], that direct coordination of the metal by a nucleophilic solvent (pyridine, simulated by NH_3 in the ZORA computations) is largely responsible for the large experimental solvent effects on chemical shifts. The computations were able to qualitatively simulate a strong positive contribution to $\delta(^{199}\mathrm{Hg})$ due to the coordination of the solvent to Hg. The resulting geometry change (bending of X–Hg–X by approximately 30°) upon complexation was found to increase the magnitude of the (negative) chemical shift by ∼600 ppm for $HgCl_2$, while the direct interaction of the solvent with the heavy atom caused a large shift of δ by ∼+1100 ppm. THF was supposed to coordinate much less strongly to Hg and not to cause a significant change of the linear structure of HgX_2. A possible influence on the chemical shift due to THF that might account for the differences between theory and experiment in Table 4 has therefore not been investigated.

It should be noted here that absolute shielding values of, e.g., 8020 ppm from ZORA DFT,[19] and of 15 128 ppm from spin-orbit DK Hartree–Fock[72] for ^{199}Hg in $Hg(CH_3)_2$ have been reported. While the paramagnetic and diamagnetic shieldings are approximately equal in both methods, the reported spin-orbit corrections differ by ∼7000 ppm. The differences obviously largely cancel regarding the chemical shift and demonstrate that due to cancellation of systematic errors, chemical shifts are much easier to compute accurately than absolute shieldings in particular for such heavy nuclei. We therefore do not list reported absolute shielding values in the tables.

Chemical shifts in compounds containing elements as heavy as uranium have been investigated[73,80] with DFT. In Ref.[80], variational Pauli and ZORA calculations have been employed together with standard GGA functionals, as well as a scalar relativistic ECP in conjunction with the B3LYP hybrid functional. ^{19}F chemical shifts in a number of U-halide complexes were obtained with moderate absolute accuracy with both the ZORA and the Pauli approaches, while certain trends between different compounds could not be reproduced by the GGA functionals. SO effects for the F shifts were found to be of low importance (typically ∼30 ppm for Pauli and somewhat less for ZORA, as compared to experimental shifts between 750 and 790 ppm). The scalar relativistic ECP/B3LYP did yield systematically between 80 and 270 ppm too large chemical shifts, but certain trends were better reproduced. From this, the authors concluded that the ECP approach is beyond its limit for actinide NMR and that improved XC functionals are needed for the nonhybrid DFT methods in order to reproduce some trends among a series of compounds more accurately. A clearly better performance of ZORA vs. Pauli could not be observed in this study.

Many of the studies cited so far also provide relativistic effects on the shielding tensor anisotropy, $\Delta\sigma$. See Refs.[28,36,37] for examples. The practical application of these quantities for heavy atom systems is, however, rather limited so far. We therefore refer to the literature for detailed discussions of relativistic effects on $\Delta\sigma$, and only mention here that huge effects have been reported so far.

4 HEAVY ATOM SPIN–SPIN COUPLINGS

Nuclear spin–spin couplings are not very easy to compute accurately, in particular for heavy elements, but can often be measured with high precision. Unlike the case of chemical shifts, where systematic errors in the computation may cancel when the shifts are obtained from the difference of the two computed shielding values of the probe and the reference compounds, there is no such cancellation of errors for spin–spin couplings. Another problem is that the interest is often in couplings involving a heavy nucleus itself, and scalar relativistic effects can be enormously large. Therefore, attempts to calculate spin–spin couplings similarly to the NMR shieldings case just by considering the Pauli SO operator to first order did not yield very satisfactory results for couplings involving a heavy nucleus.[38–40] However, this method seems to be applicable for the study of HALA effects in some cases.[38] Likewise, ECPs can be employed for this type of application (e.g., in Ref.[81]). However, in the following we focus on couplings to a heavy nucleus itself. As compared to chemical shieldings, much less computational data are yet available.

4.1 (Mostly) Scalar Relativistic Effects

Scalar relativistic effects are usually believed to yield the major influence on heavy nuclear spin–spin couplings. The reason for this is related to the fact that the FC term (27e) was found to represent the dominant contribution for an overwhelming number of couplings that have been investigated (of course, counter examples are known). In its usual nonrelativistic form for point-like nuclei, the FC term originates from the value of the induced spin-density *directly at* the nuclei, while its relativistic generalizations probe the space very close to the nuclei.[20,29] There, in particular, the electron density is substantially modified due to the scalar relativistic operators (MV + DAR in the Pauli formalism, equation (11)), and a huge influence on the FC perturbations can be expected. This was noted in 1968[82] regarding the contact term in NMR spin–spin coupling and has been known since 1930[83] from the theory of atomic hyperfine splittings.

The authors of Refs.[45,46] introduced relativistic correction factors (RCFs) for hyperfine integrals of atomic orbitals (AOs), which account for the relativistic increase of the electron density at the respective nucleus. The RCFs can then be used in nonrelativistic molecular computations to scale the AO integrals entering the FC expression for the coupling tensor in equation (20). The authors of Ref.[84] reported a somewhat related procedure that is applicable to couplings involving a heavy nucleus, based on the variational scalar Pauli treatment. The semiempirical approaches described in, e.g., Refs.[85–88] also make use of integrals based on four-component atomic computations in an otherwise nonrelativistic formalism.

To give the reader an idea of the magnitude of the RCFs, we note that, e.g., a value of 2.4386 has been reported[45] for the Hg 6s orbital. This means that, if the coupling Hg–L (L = light nucleus) is dominated, as it is often the case, by the FC contribution and by the 6s orbital on the Hg side, the coupling relativistically increases by almost a factor of 3. Likewise, Hg–Hg and other couplings between 6th row elements can be expected to relativistically increase by almost an order of magnitude. Even for rather light fourth row nuclei, nonnegligible relativistic effects on coupling constants of ∼10% can be expected. This should be compared to the celebrated huge relativistic bond contraction of many Au(I) compounds, which is of the order of 10%.

A problem connected with the RCFs is that they do not account for relativistic changes of the molecular orbitals that determine the spin–spin coupling. Such changes would be obtained from a variational or higher than first-order perturbational relativistic molecular computation. The RCFs are also not able to describe relativistic effects of L–L′ couplings in the neighborhood of a heavy nucleus for the same reason. In many cases, relativistic changes of the zeroth-order solution may either enhance or quench the strong relativistic effects of the AO integrals and lead to much different answers than obtained from the RCFs. In these, and other cases for which the coupling is not dominated by the FC term, a consistent first-principles variational or perturbational scheme for molecules is desirable.

The four-component formalism of nuclear spin–spin couplings has been subsequently published by Pyykkö, who provided a simple LCAO example for K(Hg–C) in dimethylmercury.[89] The results are very typical for heavy-atom spin–spin couplings. They exhibit a huge relativistic increase of K(Hg–C) by a factor of 2.7, with the new mixed contributions due to spin-orbit coupling being almost negligible for the isotropic coupling and yielding a somewhat larger contribution to the anisotropy ΔK of the coupling tensor. ΔK thereby increased even stronger by a factor of 3.3 due to relativity. A formulation for spin–spin couplings within the four-component scheme based on the polarization propagator method has been published by Aucar and Oddershede.[90] An implementation for spin–spin couplings within the relativistic extended Hückel theory (REX) was applied to many systems and often recovered the experimentally observed trends and provided explanations.[91] Recently, an ab initio Hartree–Fock four-component implementation and benchmark results for HX, H_2Y, (Y = O, S, Se, Te), and some plumbanes have been reported.[24,28,29] Also rather recently, the two-component ZORA DFT approach for spin–spin couplings has been formulated and implemented by the present authors.[20,54] Earlier semiempirical approaches based on the MNDO, AM1 and PM3 Hamiltonians, and ab initio methods including the Pauli SO operator, have already been mentioned. See Ref.[23] for a review on hyperfine interaction in metals from the solid-state physics point of view.

The series YH_4, Y = C, Si, Ge, Sn, Pb, has been studied as benchmark systems in many of the references cited so far. The results show a strong scalar relativistic increase in the FC contribution to the Y–H coupling, that amounts to roughly a factor of two in the case of Y = Pb. Table 5 displays spin–spin couplings in plumbanes obtained from different theoretical methods. Nonrelativistically, the FC term to the couplings is dominant and all other contributions are almost negligible. In the relativistic case, the situation is not much different. The new mixed contributions due to SO coupling are not negligible, but rather small.[40,54,91] The scalar relativistic corrections to FC terms of the Pb–L couplings clearly dominate and it can be seen from Table 5 that the total relativistic corrections to the Pb–L couplings are very substantial. The correlated ab initio study of Kirpekar et al.,[40] only including SO effects, was not able to achieve qualitative agreement with experiment, but could provide evidence that SO effects on K(Pb–H) in PbH_4 are indeed not very large (and negative in this case). The largest SO contribution is due here to the OP-FC cross term (which is zero in the nonrelativistic limit).[40,54] Therefore, large SO effects on the coupling constants can be expected only for those systems where SO coupling is of high importance (typically heavy p-block elements such as Tl, Bi, Pb), and both the FC and the paramagnetic coupling contribution are not very small already at the non- or scalar-relativistic limit. This is not the case for the plumbanes, and therefore the scalar relativistic effects on the FC term dominate the picture. This also rationalizes the quite accurate results for PbH_4 and $PbMe_4$ in Refs.[84,86]. Compared to other studies of sixth row element one-bond couplings, the data in Table 5 appear to be rather typical and qualitatively similar results have been, e.g., obtained for couplings involving W, Pt and Hg in a number of heavy metal complexes.[20,84] As for the plumbanes in Table 5, chemical trends for very similar compounds are often already reproduced at the nonrelativistic level while magnitudes of coupling constants typically increase by a factor of two due to scalar relativistic corrections. Already at the scalar relativistic level, good agreement with experiment has been achieved for most of the systems in Refs.[20,84].

From the data in Table 5, the importance of electron correlation for obtaining reasonable estimates of spin–spin coupling constants becomes obvious. The effect of correlation

Table 5 Reduced Pb–L Spin–Spin Coupling Constants in Plumbanes, in $10^{20}\,kg\,m^{-2}\,s^{-2}\,A^{-2}$

Compound coupling[a]	PbH_4 Pb–H	$PbMe_2H_2$ Pb–H	$PbMe_3H$ Pb–H	$PbMe_4$ Pb–C	$PbCl_4$ Pb–Cl
REX[91]	84.4			46.5	
	(37.3)			(16.4)	
AM1[86]	97.2			33.5	−32.0
DFT vPSC[84]	85.1			20.7	
DFT ZORA[20,54]	122.8	98.3	89.1	−26.8[b]	−321.5[b]
	(59.9)	(57.8)	(56.6)	(10.4)	(−211.6)
HF Dirac[29]	181.9		166.8		
	(71.1)				
MCSCF pPSO[40]	48.3				
	(56.2)				
Experiment[95]	112[c]	98.7	92.3	39.6	288.9[d]

[a]Nonrelativistic values in parentheses, Me = CH_3.
[b]$PbMe_4$, this work BP86 functional; $PbCl_4$, scalar ZORA.
[c]Extrapolated from $PbMe_2H_2$ and $PbMe_3H$.
[d]Not directly measured, sign not determined.

at the nonrelativistic ab initio level is seen from a comparison of the nrel. number in parentheses listed for the Dirac approach with the one from the MCSCF computation. Based on a respective nonrelativistic ratio for SiH_4, Enevoldsen et al.[29] estimated a Pb–H coupling constant in PbH_4 of $\sim 138 \times 10^{20}\,\mathrm{kg\,m^{-2}\,s^{-2}\,A^{-2}}$ for a correlated approach. This is very close to the ZORA DFT result and underlines on the one hand the sensitivity of spin–spin coupling constants with respect to the quality of the zeroth-order solution and on the other hand the fact that standard DFT functionals partially account for the influence of correlation. The semiempirical methods try to incorporate these effects via their parametrization. As seen from Table 5, the results for PbH_4 and $PbMe_4$ are in rather good agreement with experiment. However, the Pb–Cl coupling in $PbCl_4$ appears to be strongly underestimated by the AM1 method. The authors list a better coupling constant of $-80.6 \times 10^{20}\,\mathrm{kg\,m^{-2}\,s^{-2}\,A^{-2}}$ obtained with the PM3 semiempirical Hamiltonian in Ref.[86], but on the other hand K(Pb–H) in PbH_4 is overestimated by more that a factor of five with PM3. In a comparison of theory and experiment for the YCl_4 series, Y = C, Si, Sn, Pb, the semiempirical methods systematically underestimate the magnitude of the Y–Cl coupling constant, with the PM3 results being substantially larger than the AM1 (and MNDO) results. REX performs rather well in comparison.[91] The strong overestimation of some coupling constants in the semiempirical methods has been attributed to the 'triplet instability' problem that also plagues the Hartree–Fock approaches.[12] The DFT methods seem to be much more robust in this case. Both scalar and SO ZORA DFT have predicted a negative Pb–C coupling constant for $PbMe_4$ despite the fact that the nonrelativistic limit, other computations, and the quoted experimental coupling (from 1978) agree on a positive value. In all other cases we have investigated so far, ZORA did yield the experimentally predicted sign of K and in most cases the magnitudes were reproduced with good accuracy.

As already mentioned in Section 3, solvent effects can substantially influence NMR parameters for heavy atom compounds. In particular, it was found that complexation of the heavy atom by solvent molecules, if possible, yields huge effects on shieldings of the heavy nucleus. It is therefore not very surprising that this is the case for NMR spin–spin couplings as well. More surprising, however, is the magnitude of the effects even for rather weakly coordinating solvents that do not cause a significant change in the geometry of the compound under investigation. In Ref.[92], a number of linear mercury and square-planar platinum complexes have been investigated. Even for such weakly coordinating solvents such as $CHCl_3$ or CH_2Cl_2, a significant shift of the FC contribution to the spin–spin coupling has been observed. Experimental trends for different solvents ($CHCl_3$ vs. DMSO) have been quantitatively reproduced. The solvent coordination effect has been analyzed in detail for $Hg(CN)_2$. K(Hg–C) increases from 237.9 to 443.4 to $576.2 \times 10^{20}\,\mathrm{kg\,m^{-2}\,s^{-2}\,A^{-2}}$ at the nonrelativistic, scalar ZORA relativistic, scalar rel. + $4CH_3OH$ solvent molecules level, respectively (DFT, VWN functional). SO corrections were small in the samples studied in Ref.[92] It was found that charge donation from the solvent into the metal-ligand σ bonds is responsible for the large positive shift of K(Hg–C). It does not seem very likely that unspecific solvent effects for coordinatively saturated complexes are of such high importance, but they will be not negligible for high-accuracy computations. In Ref.[93], complexation of the complex $[(NC)_5Pt–Tl(CN)]^-$ by water was found to explain a rather unintuitive experimental result for the Tl–C couplings. In aqueous solution, $^2K(\mathrm{Tl–C}) \gg {}^1K(\mathrm{Tl–C})$ has been observed experimentally. In the same complex, the huge Pt–Tl coupling (expt. $\sim$57 kHz in water) has been shown to increase by more than 20 kHz upon coordination by solvent molecules in the ZORA DFT computations.

4.2 Spin-orbit Effects

Not many cases have been investigated so far, where SO coupling is of essential importance for heavy nucleus spin–spin coupling constants. Very often it is possible to achieve a good comparison between theory and experiment at the computationally much cheaper and easier to interpret scalar relativistic level. As a counter example, we would like to emphasize the case of Tl halides, TlX.

Figure 2 shows the coupling constants that have been obtained with the ZORA DFT approach[54] on different levels of approximation. Clearly, SO effects yield the dominant contribution to the coupling constants for TlI and a completely wrong trend for the series is obtained at the scalar relativistic level. The explanation for the SO effects follows that for the chemical shieldings. Mixed terms between the spin-dependent FC and SD operators and the orbital dependent OP operator are no longer zero in the presence of SO coupling. Through SO coupling, the spin-density that is induced by the FC perturbation at a nucleus 'leaks' through into the orbital shapes and causes orbital current densities that yield nonzero coupling contributions with the orbital currents induced by the OP term at the other nucleus. Likewise, the OP operator induces spin-density in the SO coupled system. As for nuclear shieldings, the FC-OP cross term was found to be dominant and the SD-OP term small.[39,40,54] For TlX, the paramagnetic contribution is dominant at the nonrelativistic level and the FC term represents

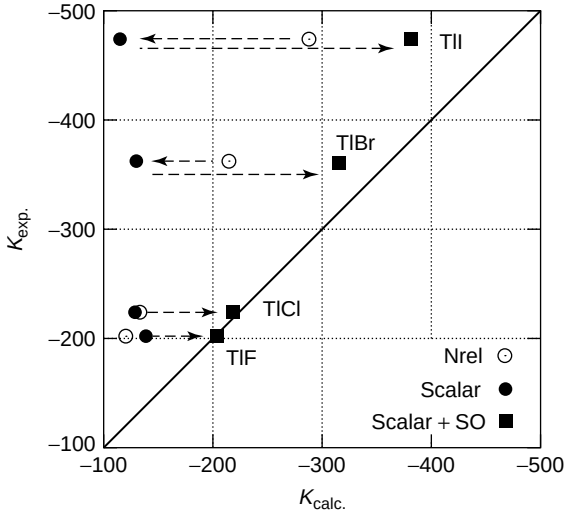

Figure 2 Reduced spin–spin coupling constants in thallium halides TlX from ZORA DFT computations (Ref.[54], BP86 functional), in $10^{20}\,\mathrm{kg\,m^{-2}\,s^{-2}\,A^{-2}}$. Calculated vs. experimental values. Experimental data compiled in Ref.[94]

the second largest contribution. This leads to the large FC-OP cross terms at the SO coupled level. In the case of TlI, this cross term represents the largest individual relativistic correction to the coupling constant and is essential in order to obtain the correct trend for the TlX series.[54] The DFT approach appears to be of somewhat reduced accuracy for the case of TlBr and TlI which has been largely attributed to deficiencies in the GGA functional.[54]

The authors of Ref.[38] concluded from a study of K(H−H) in H_2Y (Y = O, S, Se, Te) that the SO effects may generally yield the dominant contribution for HALA effects as is the case for many nuclear shieldings. A large relativistic change of K(H−H) in PbH_4 has been observed from four-component Hartree−Fock computations[29] where SO effects are naturally present. On the other hand, Ref.[40] reports rather small SO corrections to K(H−H) in PbH_4, based on a nonrelativistic Hartree−Fock wavefunction. Furthermore, huge changes of the FC term due to electron correlation were found. Clearly, more relativistic studies including both scalar and SO effects are needed in this case in order to draw a definite conclusion.

Available studies have shown that even in those cases where the SO effect on the coupling constant is rather small, the anisotropy ΔK can be quite strongly influenced by SO coupling. Relativistic changes of ΔK have been reported in several of the papers cited so far, e.g., in Refs.[24,28,38,54,87,91] However, the applications of ΔK for the heavy atom case are, as in the $\Delta\sigma$ case, very limited so far. It is already established that future investigations of ΔK and interpretations of respective experimental findings will need to include relativistic effects if heavy atom systems are studied, and both scalar and SO effects will be of importance in this case. Experimental data for the TlX series have, along with a number of other light and heavy diatomic systems, been investigated in Ref.[94] and periodic trends of K and ΔK have been analyzed. ΔK can generally be expected to increase with increasing charge of the heavy nuclei involved, with very large anisotropies for couplings with sixth row atoms in particular at the right end of the periodic table.

5 SUMMARY

It is nowadays possible to compute relativistic heavy nucleus NMR parameters by a variety of different approaches at different levels of accuracy and computational expense. A number of available quantum chemical program systems are capable of such computations. From the numerical evidence provided so far by many computational studies of NMR parameters in heavy atom systems, it becomes obvious that relativistic effects can be responsible for the main chemical trends that have been observed experimentally. In particular, spin-orbit coupling must be considered for shieldings of light nuclei in the neighborhood of heavy p-block elements. Both scalar and spin-orbit relativistic corrections are important for shielding tensors of heavy nuclei and ligand shieldings in heavy transition metal complexes. It is imperative to use scalar relativistic corrections in order to compute reliable magnitudes for spin−spin couplings involving heavy nuclei. Spin-orbit corrections to spin−spin couplings can be very substantial if both the paramagnetic and the Fermi-contact contributions to the coupling are large and a heavy p-block element is involved.

6 RELATED ARTICLES IN THIS VOLUME

Shielding Calculations; Indirect Nuclear Spin−Spin Coupling Tensors.

7 RELATED ARTICLES IN VOLUMES 1–8

Chemical Shift Tensors, Volume 2; Dipolar & Indirect Coupling Tensors in Solids, Volume 3; Indirect Coupling: Semiempirical Calculations, Volume 4; Indirect Coupling: Theory & Applications in Organic Chemistry, Volume 4; Shielding Calculations: IGLO Method, Volume 7; Shielding Calculations: LORG & SOLO Approaches, Volume 7; Shielding Calculations: Perturbation Methods, Volume 7; Shielding in Small Molecules, Volume 7; Shielding: Overview of Theoretical Methods, Volume 7; Shielding Tensor Calculations, Volume 7.

8 REFERENCES

1. P. Pyykkö, *Chem. Rev.*, 1988, **88**, 563.
2. J. Almlöf and O. Gropen, in 'Reviews in Computational Chemistry', eds K. B. Lipkowitz and D. B Boyd, VCH Publishers: New York, Vol. 8, pp. 203−244.
3. B. A. Hess, in 'Encyclopedia of Computational Chemistry', ed P. v. R. Schleyer, John Wiley & Sons: Chichester, 1998, pp. 2499−2508.
4. R. E. Moss, 'Advanced Molecular Quantum Mechanics', Chapman and Hall: London, 1973.
5. A. J. Sadlej, in 'Lecture Notes in Chemistry II', ed B. O. Roos, Springer: Berlin, 1994, Vol. 64, pp. 203−230.
6. S. Okada, M. Shinada, and O. Matsuoka, *J. Chem. Phys.*, 1990, **93**, 5013.
7. J. Autschbach and W. H. E. Schwarz, *Theor. Chem. Acc.*, 2000, **104**, 82.
8. W. Pauli, in 'Handbuch der Physik', Springer: Berlin, 1958, Vol. 5.
9. E. van Lenthe, E. J. Baerends, and J. G. Snijders, *J. Chem. Phys.*, 1993, **99**, 4597.
10. W. Kutzelnigg, *J. Comput. Chem.*, 1999, **20**, 1199.
11. P. Schwerdtfeger, J. R. Brown, J. K. Laerdahl, and H. Stoll, *J. Chem. Phys.*, 2000, **113**, 7110.
12. T. Helgaker, M. Jaszuński, and K. Ruud, *Chem. Rev.*, 1999, **99**, 293.
13. U. Fleischer, C. van Wüllen, and W. Kutzelnigg, in 'Encyclopedia of Computational Chemistry', ed P. v. R. Schleyer, John Wiley & Sons: Chichester, 1998, pp. 1827−1835.
14. D. B. Chesnut, in 'Reviews in Computational Chemistry', eds K. B. Lipkowitz and D. B Boyd, VCH Publishers: New York, 1996, Vol. 8, pp. 245−297.
15. J. Kowalewski, *Annu. Rep. NMR Spectrosc.*, 1982, **12**, 81.
16. R. McWeeny, 'Methods of Molecular Quantum Mechanics', 2nd edn., Academic Press: London, 1992.
17. S. P. A. Sauer, *J. Chem. Phys.*, 1993, **98**, 9220.
18. H. Fukui, *Nucl. Magn. Reson.*, 1994, **23**, 124.
19. S. K. Wolff, T. Ziegler, E. van Lenthe, and E. J. Baerends, *J. Chem. Phys.*, 1999, **110**, 7689.
20. J. Autschbach and T. Ziegler, *J. Chem. Phys.*, 2000, **113**, 936.
21. H. Fukui and T. Baba *J. Chem. Phys.*, 1998, **108**, 3854.
22. H. Fukui, T. Baba, and H. Inomata, *J. Chem. Phys.*, 1996, **105**, 3175.

23. H. Akai, M. Akai, S. Blügel, B. Drittler, H. Ebert, K. Terakura, R. Zeller, and P. H. Dederichs, *Prog. Theor. Phys. Suppl.*, 1990, **101**, 11.
24. G. A. Aucar, T. Saue, L. Visscher, and H. J. A. Jensen, *J. Chem. Phys.*, 1999, **110**, 6208.
25. N. C. Pyper, *Chem. Phys. Lett.*, 1983, **96**, 204; **96**, 211.
26. M. Hada, Y. Ishikawa, J. Nakatani, and H. Nakatsuji, *Chem. Phys. Lett.*, 1999, **310**, 342.
27. J. E. Harriman, 'Theoretical Foundations of Electron Spin Resonance', Academic Press: New York, 1978.
28. L. Visscher, T. Enevoldsen, T. Saue, H. J. A. Jensen, and J. Oddershede, *J. Comput. Chem.*, 1999, **20**, 1262.
29. T. Enevoldsen, L. Visscher, T. Saue, H. J. A. Jensen, and J. Oddershede, *J. Chem. Phys.*, 2000, **112**, 3493.
30. Y. Ishikawa, T. Nakajima, M. Hada, and H. Nakatsuji *Chem. Phys. Lett.*, 1998, **283**, 119.
31. M. Hada, R. Fukuda, and H. Nakatsuji, *Chem. Phys. Lett.*, 2000, **321**, 452.
32. H. Nakatsuji, H. Takashima, and M. Hada, *Chem. Phys. Lett.*, 1995, **233**, 95.
33. H. Nakatsuji, T. Nakajima, M. Hada, H. Takashima, and S. Tanaka, *Chem. Phys. Lett.*, 1995, **247**, 418.
34. T. Baba and H. Fukui, *J. Chem. Phys.*, 1999, **110**, 131.
35. C. B. Ballard, M. Hada, H. Kaneko, and H. Nakatsuji, *Chem. Phys. Lett.*, 1996, **254**, 170.
36. J. Vaara, K. Ruud, O. Vahtras, H. Ågren, and J. Jokisaari, *J. Chem. Phys.*, 1998, **109**, 1212.
37. J. Vaara, K. Ruud, and O. Vahtras, *J. Chem. Phys.*, 1999, **111**, 2900.
38. J. Vaara, K. Ruud, and O. Vahtras, *J. Comput. Chem.*, 1999, **20**, 1314.
39. S. Kirpekar, H. J. A. Jensen, and J. Oddershede, *Theor. Chim. Acta.*, 1997, **95**, 35.
40. S. Kirpekar and S. P. A. Sauer, *Theor. Chem. Acc.*, 1999, **103**, 146.
41. I. Morishima, K. Endo, and T. Yonezawa, *J. Chem. Phys.*, 1973, **59**, 3356.
42. M. I. Volodicheva and T. K. Rebane, *Teoreticheskaya i Éksperimental'naya Khimiya (engl. ed Theor. and Exp. Chemistry)* 1978, **14**, 348.
43. A. A. Cheremisin and P. V. Schastnev, *J. Magn. Reson.*, 1980, **40**, 459.
44. K. Endo, K. Yamamoto, and H. Okada, *Bull. Chem. Soc. Jpn.*, 1995, **68**, 3341.
45. P. Pyykkö, E. Pajanne, and M. Inokuti, *Int. J. Quantum Chem.*, 1973, **7**, 785.
46. D. K. Dalling and H. S. Gutowsky, *J. Chem. Phys.*, 1971, **55**, 4959.
47. P. Pyykkö, A. Görling, and N. Rösch, *Mol. Phys.*, 1987, **61**, 195.
48. R. G. Parr and W. Yang, 'Density Functional Theory of Atoms and Molecules', Oxford University Press: New York, 1989.
49. V. G. Malkin, O. L. Malkina, and D. R. Salahub, *Chem. Phys. Lett.*, 1996, **261**, 335.
50. O. L. Malkina, B. Schimmelpfennig, M. Kaupp, B. A. Hess, P. Chandra, U. Wahlgren, and V. G. Malkin, *Chem. Phys. Lett.*, 1998, **296**, 93.
51. M. Kaupp, V. G. Malkin, and O. L. Malkina, in 'Encyclopedia of Computational Chemistry', ed P. v. R. Schleyer, John Wiley & Sons: Chichester, 1998, pp. 1857–1866.
52. G. Schreckenbach and T. Ziegler, *Int. J. Quantum Chem.*, 1997, **61**, 899.
53. S. K. Wolff and T. Ziegler, *J. Chem. Phys.*, 1998, **109**, 895.
54. J.Autschbach and T. Ziegler, *J. Chem. Phys.*, 2000, **113**, 9410.
55. E. K. U. Gross, J. F. Dobson, and M. Petersilka, *Top. Curr. Chem.*, 1996, **81**, 181.
56. Y. Nomura, Y. Takeuchi, and N. Nakagawa, *Tetrahedron Lett.*, 1969, **8**, 639.
57. P. Pyykkö, *Chem. Phys.*, 1983, **74**, 1.
58. Z. C. Zhang and G. A. Webb, *J. Mol. Struct.*, 1983, **104**, 439.
59. C. J. Jameson, *Nucl. Magn. Reson.*, 1984, **13**, 1.
60. R. L. Hota, R. C. Patnaik, G. S. Tripathi, and P. K. Misra, *Phys. Rev. B*, 1995, **51**, 7291.
61. U. Edlund, T. Lejon, P. Pyykkö, T. K. Venkatachalam, and E. Buncel, *J. Am. Chem. Soc.*, 1987, **109**, 5982.
62. M. Kaupp, O. L. Malkina, V. G. Malkin, and P. Pyykkö, *Chem. Eur. J.*, 1998, **4**, 118.
63. J. Vaara, O. L. Malkina, H. Stoll, V. G. Malkin, and M. Kaupp, *J. Chem. Phys.*, 2001, **114**, 61.
64. M. Kaupp, C. Aubauer, G. Engelhardt, T. M. Klapötke, and O. L. Malkina, *J. Chem. Phys.*, 1999, **110**, 3897.
65. H. Nakatsuji, Z.-M. Hu, and N. Nakajima, *Chem. Phys. Lett.*, 1997, **275**, 429.
66. H. Nakatsuji, M. Sugimoto, and S. Saito, *Inorg. Chem.*, 1990, **29**, 3095.
67. M. Kaupp, O. L. Malkina, and V. G. Malkin, *Chem. Phys. Lett.*, 1997, **265**, 55.
68. M. Bühl, M. Kaupp, O. L. Malkina, and V. G. Malkin, *J. Comput. Chem.*, 1998, **20**, 91.
69. G. Schreckenbach and T. Ziegler, *Theor. Chem. Acc.*, 1998, **99**, 71.
70. M. Hada, H. Kaneko, and H. Nakatsuji, *Chem. Phys. Lett.*, 1996, **261**, 7.
71. H. Nakatsuji, M. Hada, H. Kaneko, and C. C. Ballard, *Chem. Phys. Lett.*, 1996, **255**, 195.
72. J. Wan, R. Fukuda, M. Hada, and H. Nakatsuji, *J. Phys. Chem., A* 2001, **105**, 128.
73. G. Schreckenbach, S. K. Wolff, and T. Ziegler, in 'Modeling NMR Chemical Shifts', ACS Symposium Series no. 732, eds J. C. Facelli and A. C. de Dios, American Chemical Society: Boston, MA, 1999, pp. 101–114.
74. M. Kaupp, V. G. Malkin, O. L. Malkina, and D. R. Salahub, *J. Am. Chem. Soc.*, 1995, **117**, 1851; erratum 1995, **117**, 8492.
75. R. Bouten, E. J. Baerends, E. van Lenthe, L. Visscher, G. Schreckenbach, and T. Ziegler, *J. Chem. Phys.*, 2000, **104**, 5600.
76. A. Rodriguez-Fortea, P. Alemany, and T. Ziegler, *J. Phys. Chem. A*, 1999, **103**, 8288.
77. Y. Ruiz-Morales, G. Schreckenbach, and T. Ziegler, *J. Phys. Chem.*, 1996, **100**, 3359.
78. A. W. Ehlers, Y. Ruiz-Morales, E. J. Baerends, and T. Ziegler, *Inorg. Chem.*, 1997, **36**, 5031.
79. T. M. Gilbert and T. Ziegler, *J. Phys. Chem. A*, 1999, **103**, 7535.
80. G. Schreckenbach, S. K. Wolff, and T. Ziegler, *J. Phys. Chem. A*, 2000, **104**, 8244.
81. G. B. Bacskay, I. Bytheway, and N. S. Hush, *J. Am. Chem. Soc.*, 1996, **118**, 3753.
82. J. Feeney, R. Haque, L. W. Reeves, and C. P. Yue, *Can. J. Chem.*, 1968, **46**, 1389.
83. G. Breit, *Phys. Rev.* 1930, **35**, 1447.
84. J. Khandogin and T. Ziegler, *J. Phys. Chem. A*, 2000, **104**, 113.
85. G. A. Aucar and R. H. Contreras, *J. Magn. Reson.*, 1991, **93**, 413.
86. R. M. Lobayan and G. A. Aucar, *J. Mol. Struct.*, 1998, **452**, 1.
87. J. A. Gonzaléz, G. A. Aucar, M. C. Ruiz de Azúa, and R. H. Contreras, *Int. J. Quantum Chem.*, 1997, **61**, 823.
88. G. A. Aucar, E. Botek, S. Gómez, F. Sproviero, and R. H. Contreras, *J. Organomet. Chem.*, 1996, **524**, 1.
89. P. Pyykkö, *Chem. Phys.*, 1977, **22**, 289.
90. G. A. Aucar and J. Oddershede, *Int. J. Quantum Chem.*, 1993, **47**, 425.
91. P. Pyykkö and L. Wiesenfeld, *Mol. Phys.*, 1981, **43**, 557.
92. J. Autschbach and T. Ziegler, *J. Am. Chem. Soc.*, 2001, **123**, 3341.
93. J. Autschbach and T. Ziegler, *J. Am. Chem. Soc.*, 2001, **123**, 5320.
94. D. L. Bryce and R. E. Wasylishen, *J. Am. Chem. Soc.*, 2000, **122**, 3197.
95. B. Wrackmeyer and K. Horchler, *Annu. Rep. NMR Spectrosc.*, 1989, **22**, 249.

Acknowledgements

This work has received financial support from the National Science and Engineering Research Council of Canada (NSERC). J. A. thanks Dr. S. Patchkovskii for stimulating discussions.

Biographical Sketches

Jochen Autschbach, *b* 1968. M.Sc. (Chemistry), 1996, Ph.D., 1999, Siegen, Germany. Ph.D. thesis on relativistic effects in atoms and chemical bonds. Since 1999 member of Tom Ziegler's research group in Calgary, Canada. Current research interests: computation of heavy atom NMR spin–spin coupling constants and chemical shifts, solvent effects in spectroscopy, theory of optical activity, density functional response theory, relativistic quantum chemistry. J. A. has contributed, among other code, a program for the computation of heavy atom spin–spin couplings to the Amsterdam Density Functional program.

Tom Ziegler, *b* 1944. T. Z. was raised in Denmark and graduated from the University of Copenhagen in 1972 with a Cand. Scient. degree in theoretical chemistry. He obtained a Ph.D. from University of Calgary (1978) where he has been a full professor since 1991. He has in the last 25 years worked with the development of density functional theory as a practical tool in transition metal chemistry and homogeneous catalysis. This has led to computational methods of use in spectroscopy, thermochemistry, structure determination and molecular dynamics. He is a fellow of both the Royal Danish and Royal Canadian Societies.

Semiempirical Chemical Shift Calculations

Renate Wolff and Reiner Radeglia
Federal Institute for Materials Research and Testing (BAM), Berlin, Germany

1	Introduction	1
2	Basic Considerations	1
3	Semiempirical Calculations	2
4	Related Articles	8
5	References	9

1 INTRODUCTION

The measurement of chemical shifts of the resonating nuclei ^{1}H, ^{13}C, ^{15}N, ^{17}O, ^{19}F, ^{29}Si, and ^{31}P, and their relation to molecular structure has led to NMR spectroscopy becoming the leading method for structural determination in organic and inorganic chemistry. This relationship was recognized[1–3] only a few years after the discovery of the NMR effect by Purcell[4] and Bloch[5] and their co-workers. (see ***Carbon-13 Spectral Simulation***; ***Inorganic Chemistry Applications***; ***Chemical Shift Tensors***, and ***Organic Chemistry Applications***)

The complicated connection between experimental chemical shifts and molecular structure was first described by Ramsey.[6] The semiempirical interpretation of chemical shifts mainly goes back to the extended work of Pople, who presented a theory of NMR chemical shifts[7–9] applied to ^{1}H and ^{13}C nuclei on the basis of an approximate molecular orbital (MO) theory.[10] Semiempirical chemical shift calculations were an active field of research for about 20 years. The development of the theory accompanied the development of NMR measurement techniques.

Because of the approximate character of semiempirical calculations, two aims may be set:

1. comparing experimental and calculated trends in chemical shifts to obtain information on the electronic structure of molecules and solids in terms of general chemical concepts;
2. obtaining quantitative agreement between experimental and theoretical results by adjusting the empirical parameters.

Since the 1980s high-level ab initio methods have become available for calculating chemical shifts for resonant nuclei up to the second row in medium-sized molecules. Such calculations give good agreement with experimental values without the need for any empirical parameters (see ***Shielding Calculations: LORG and SOLO Approaches***; ***Shielding Calculations: IGLO Method***; ***Shielding Theory: GIAO Method***; ***Shielding: Overview of Theoretical Methods***; ***Shielding in Small Molecules***). These methods have brought and are expected to bring more insight into the real connection between chemical shifts and electronic structure, though the interpretation of the results in terms of general chemical concepts is not always easy. Ab initio results may prove the validity and limits of semiempirical correlations and may be used to calibrate semiempirical results.

Semiempirical interpretation continues to have its place in practical NMR structural analysis. The relations between chemical shifts and structural parameters are easy and quick to apply, and there is much experience in their use in different fields of organic and inorganic chemistry. Semiempirical methods are still necessary for very heavy nuclei and for very large molecular systems including nuclei of the first and second rows.

There are a number of books and review articles concerning semiempirical methods and calculations.[10–22] Since 1972, chemical and physical aspects of nuclear shielding and, inter alia, semiempirical results have been reported annually.[23]

2 BASIC CONSIDERATIONS

2.1 NMR Chemical Shifts

The chemical shift δ is measured as the difference between a given NMR signal and that of a reference compound. It is defined as

$$\delta = \frac{\nu - \nu_{\mathrm{ref}}}{\nu_{\mathrm{ref}}} \tag{1}$$

in terms of the measured frequencies. (The 10^6-fold value is customarily declared, without units or else as ppm.) The resonance condition

$$\nu = \frac{|\gamma|}{2\pi}|\boldsymbol{B}| \tag{2}$$

connects the chemical shift with the electronic structure of the investigated material via the local magnetic field $\boldsymbol{B}$. γ is the gyromagnetic ratio of the resonating nucleus. The local magnetic field is determined by the externally applied uniform magnetic field, $\boldsymbol{B}_0$, and an additional shielding field induced at the nucleus by $\boldsymbol{B}_0$ owing to its influence on electronic motion, mainly in the vicinity of the resonating nucleus. The total field at the nucleus is given by

$$\boldsymbol{B} = (\mathbf{1} - \boldsymbol{\sigma}) \cdot \boldsymbol{B}_0 \tag{3}$$

where σ is the magnetic shielding tensor describing the spatial magnetic shielding of the resonating nucleus by the surrounding electrons. It is an intrinsic property of the investigated substance. **1** is the unit dyadic. (See ***Chemical Shift Tensors*** and ***Shielding Calculations: Perturbation Methods***.)

In isotropic liquids the molecular motion averages the direction dependence of the shielding to its isotropic shielding constant σ

$$\sigma = \tfrac{1}{3}(\sigma_{xx} + \sigma_{yy} + \sigma_{zz}) \tag{4}$$

In high-resolution solid state NMR, the averaging is achieved by experimental techniques, e.g. magic angle spinning (MAS). (see ***Magic Angle Spinning***)

The observed chemical shift δ from equation (1) is described in terms of the shielding constant σ and that of a reference nucleus, σ_{ref}, as

$$\delta = \frac{\sigma_{\mathrm{ref}} - \sigma}{1 - \sigma_{\mathrm{ref}}} \tag{5}$$

In the following semiempirical considerations the following approximation is used:

$$\delta = \sigma_{\mathrm{ref}} - \sigma \tag{6}$$

2.2 Magnetic Shielding Constants

Magnetic shielding of the resonating nucleus in an atom has been described by Lamb[24] as a diamagnetic shielding σ^{d} due to electron circulation around the nucleus produced by an externally applied magnetic field. The greater the electron density around the nucleus, the greater the shielding. In molecules, the electron circulation in the atom in question is perturbed by the other nuclei and electrons. The relation between electronic structure and magnetic shielding becomes much more complex. Ramsay[6,25,26] introduced an additional paramagnetic shielding term σ^{p} to take these perturbations into account:

$$\sigma = \sigma^{d} + \sigma^{p} \tag{7}$$

Knowledge of the electronic groundstate and all excited states, including the continuum states, of the whole molecule is required to calculate the magnetic shielding constant exactly.

Approximate results depend on the gauge origin of the magnetic vector potential. Since the magnetic shielding σ, as a physical quantity, must be independent of the choice of origin of the coordinate system, different methods have been developed to remove the gauge dependence of the results. In semiempirical calculations, the gauge origin is frequently located at the resonating nucleus in question.

Saika and Slichter[27] introduced a very useful partition of the magnetic shielding constant in order to consider the main influences on chemical shifts. They took into account the local diamagnetic and paramagnetic contributions due to the atom in question, together with the nonlocal contributions due to all the other atoms in the molecule:

$$\sigma = \sigma_{A}^{d}(\text{loc}) + \sigma_{A}^{p}(\text{loc}) + \sum_{B \neq A} \sigma_{AB} \tag{8}$$

The local diamagnetic term is similar to the Lamb term for an atom, and depends mainly on the electron density on the atom A. The local paramagnetic term is determined by the electron charge density and its imbalance in the atom in question, as well as on energy excitations. The nonlocal terms may be described as magnetic anisotropy effects, ring current effects, and electric field effects.

There is a distinct difference between the main influences on proton chemical shifts and those on the shifts of nuclei other than protons. For proton chemical shifts, the local paramagnetic term vanishes owing to the symmetry of the electronic s wavefunction in the electronic ground state and the high excitation energies of the hydrogen atom. However, all other terms may be important. For nuclei other than protons, the local paramagnetic term is found to be the most sensitive to structural changes. The nonlocal contributions are of minor importance.

3 SEMIEMPIRICAL CALCULATIONS

3.1 Semiempirical Quantum Chemical Methods

The electronic structure of molecules can be calculated approximately using semiempirical quantum chemical methods. These are based on first principles, but take into account serious approximations in the calculation of matrix elements and contain sets of empirical parameters. The advantages of semiempirical methods are their relatively small demand for computer time and the possibility of describing the results in terms of general chemical concepts, such as orbital occupation and energy, electron density, bond order, and net atomic charge as input quantities for the calculation of magnetic shielding constants.

Some commonly used semiempirical methods include HMO (Hückel molecular orbital) theory[28] and the PPP (Pariser–Parr–Pople) method,[29,30] which take into account only π electrons for the calculation of molecular π systems. Methods that take into account valence electrons include EHT (extended Hückel theory)[31] and schemes considering the ZDO (zero differential overlap) approximation[32] to different extents, such as CNDO[32] (complete neglect of differential overlap), INDO[32] (intermediate neglect of differential overlap), MINDO (modified intermediate neglect of differential overlap),[33] and MNDO (modified neglect of differential overlap).[34]

The empirical parameters in all these methods have been determined using different bond characteristics and ab initio results to give reliable results for molecular structure and energy. Parameterizations of the CNDO/S and INDO/S methods[35] have been introduced to describe spectroscopic parameters. These parameterizations have led to a good quantitative description of chemical shifts. In general, using semiempirical methods, a correct description of chemical shift *trends* rather than of the actual values may be expected.

3.2 Magnetic Shielding Contributions

3.2.1 Diamagnetic Shielding Constants

Flygare and co-workers[36–38] have given a widely used expression for the diamagnetic shielding constant of the atom A:

$$\sigma_{A}^{d} = \sigma_{A}(\text{free atom}) + \frac{\mu_0 e^2}{12\pi m} \sum_{B \neq A} \frac{Z_B}{R_{AB}} \tag{9}$$

The free atom term for the atom A is completed by additional terms coming from the point charges at the sites of the other atoms B in the molecule. μ_0 is the vacuum permeability, and $-e$ and m are the electron charge and mass, respectively. Z_B denotes the nuclear charge and R_{AB} is the distance between atoms A and B. The magnetic shielding for free atoms is available from nonrelativistic[39] and relativistic[40] calculations. For the hydrogen atom, σ_H = 17.8 ppm.[10] The free atom values increase with increasing atomic number: for example, σ_C = 260.7 ppm, σ_{Si} = 874.1 ppm, and σ_{Co} = 2166.4 ppm.[39] In equation (9), the diamagnetic shielding constant is calculated considering all atoms in the molecule. It has been shown[16] that for the local contribution only the nearest neighbor atoms of the resonance nucleus need be taken into account.

The quantum chemical expression for the local diamagnetic shielding contribution is[7,8]

$$\sigma_{A}^{d}(\text{loc}) = \frac{\mu_0 e^2}{12\pi m} \sum_{\mu}^{A} P_{\mu\mu} \langle \phi_\mu | r^{-1} | \phi_\mu \rangle_A \tag{10}$$

In terms of an independent electron model, the ith molecular orbital (MO) ψ_i is given as a linear combination of atomic orbitals ϕ_μ (LCAO) of the valence shells:

$$\psi_i = \sum_{\mu} C_{i\mu} \phi_\mu \tag{11}$$

In equation (10), $P_{\mu\mu}$ are the elements of the charge density–bond order matrix:

$$P_{\mu\nu} = 2\sum_{i}^{\text{occ}} c_{i\mu}c_{i\nu} \tag{12}$$

where the summation runs over all occupied molecular orbitals. With the radial part of the Slater functions, the matrix element is given as

$$\langle\phi_\mu|r^{-1}|\phi_\mu\rangle_{\text{A}} = Z_{\mu\text{A}}/n^2a_0 \tag{13}$$

where $Z_{\mu\text{A}}$ is the effective nuclear charge number for the atom A in a molecule, n is the effective principal quantum number, and a_0 is the Bohr radius. $Z_{\mu\text{A}}$ can be calculated from Slater's rules.[41] For atoms of the first and second rows, $Z_{n\text{sA}}$ and $Z_{n\text{pA}}$ are given as

$$Z_{n\text{sA}} = Z_{n\text{pA}} = Z_{0\text{A}} + 0.35q_{\text{A}} \tag{14}$$

while for H,

$$Z_{1\text{sH}} = 1.00 + 0.30q_{\text{H}} \tag{15}$$

where $Z_{0\text{A}}$ is the effective nuclear charge number of the free atom A. The net atomic charge q_{A} of atom A with N_{A} valence electrons in the free atom is given by

$$q_{\text{A}} = N_{\text{A}} - \sum_{\mu}^{\text{A}} P_{\mu\mu} \tag{16}$$

Alternatively, for the determination of $Z_{\mu\text{A}}$ Burn's rules[42] can be used.

The diamagnetic shielding constant σ^{d} shows a linear dependence on electron density, with a small quadratic correction. Therefore, the respective chemical shift term is proportional to the net charge of the considered atom.

3.2.2 Paramagnetic Shielding Constants

The sum-over-states (SOS) approximation of the local paramagnetic shielding constants in the independent electron model, developed by Pople[7,8] from second-order perturbation theory, has been extensively used to discuss chemical shift properties (see ***Shielding Calculations: Perturbation Methods***). In this model,

$$\begin{aligned}\sigma_{\text{A}}^{\text{p}}(\text{loc}) = &-\frac{\mu_0}{4\pi}\frac{2e^2\hbar^2}{3m^2}\langle r^{-3}\rangle_{n\text{pA}}\sum_{i}^{\text{occ}}\sum_{j}^{\text{unocc}}(E_j - E_i)^{-1}\\ &\times\Big[(c_{iy}^{\text{A}}c_{jz}^{\text{A}} - c_{iz}^{\text{A}}c_{jy}^{\text{A}})\sum_{\text{B}}(c_{iy}^{\text{B}}c_{jz}^{\text{B}} - c_{iz}^{\text{B}}c_{jy}^{\text{B}})\\ &+(c_{iz}^{\text{A}}c_{jx}^{\text{A}} - c_{ix}^{\text{A}}c_{jz}^{\text{A}})\sum_{\text{B}}(c_{iz}^{\text{B}}c_{jx}^{\text{B}} - c_{ix}^{\text{B}}c_{jz}^{\text{B}})\\ &+(c_{ix}^{\text{A}}c_{jy}^{\text{A}} - c_{iy}^{\text{A}}c_{jx}^{\text{A}})\sum_{\text{B}}(c_{ix}^{\text{B}}c_{jy}^{\text{B}} - c_{iy}^{\text{B}}c_{jx}^{\text{B}})\Big]\end{aligned} \tag{17}$$

The constants are the same as in equation (9) with $\hbar = h/2\pi$, where h is Planck's constant. The $c_{i\mu}^{\text{A}}$ ($\mu = x, y, z$) are the coefficients of the atomic orbitals p_x, p_y, and p_z on atom A in an LCAO development of the unperturbed MOs as in equation (11). The summation runs over all occupied (i) and unoccupied (j) states. The singlet excitation energy differences are

$$E_j - E_i = \epsilon_j - \epsilon_i + J_{ij} + 2K_{ij} \tag{18}$$

where ϵ_i and ϵ_j are the eigenvalues of the MOs of the unperturbed system. J_{ij} and K_{ij} are the molecular Coulomb and exchange integrals. The sum over B includes B = A and B ≠ A. $\langle r^{-3}\rangle_{n\text{pA}}$ is the mean inverse cube of the radius of the p valence orbitals on atom A. From the matrix element in equation (13), $\langle r^{-3}\rangle_{n\text{pA}}$ becomes

$$\langle r^{-3}\rangle_{n\text{pA}} = \langle\phi_{n\text{p}}|r^{-3}|\phi_{n\text{p}}\rangle_{\text{A}} = \frac{2}{n(n-1)(2n-1)}\left(\frac{Z_{n\text{pA}}}{na_0}\right)^3 \tag{19}$$

for n = 2 or 3, with $Z_{n\text{pA}}$ from equation (14).

The finite perturbation theory (FPT) approach[43] using gauge-including atomic orbitals (GIAO) avoids the excited states of the SOS approach (which are difficult to estimate) by considering small perturbations of the magnetic field. The results are given as a sum of one-, two-, and three-center terms (***Shielding Theory: GIAO Method***).

3.2.3 Magnetic Anisotropy Effects of Neighboring Bonds

Nonlocal influences on magnetic shielding of the considered resonating nucleus can have their origin in distant bonds in the molecule. This effect has been described in detail by Raynes.[44] The externally applied magnetic field induces currents of the electrons forming the distant bonds, which give rise to a small secondary magnetic field at the resonating nucleus of interest. Since the molecule tumbles, this field is partly averaged, corresponding to the anisotropy of the magnetic susceptibility $\Delta\chi$ of the bond. The simplest quantitative equation for this shielding contribution σ_{m} is the point dipole approximation of McConnell:[45]

$$\sigma_{\text{m}} = \frac{\Delta\chi}{12\pi R^3}(1 - 3\cos^2\theta) \tag{20}$$

where R is the distance from the resonating nucleus to the point dipole at the distant bond, and θ is the angle between the bond and the connection line R between nucleus and dipole. R > 3 nm has been recommended in order to minimize errors in the exact location of the dipole. A list of $\Delta\chi$ values has been given.[46]

The shielding effect of the magnetic anisotropy is most frequently observed for proton chemical shifts, since the chemical shift range of ^{1}H is particularly small. In other elements, the nuclei are much more shielded than in hydrogen, and the magnetic anisotropy effect may be negligible compared with other influences.

The formulation for σ_{m} in equation (20) is strictly valid only for cylindrically symmetric bonds or groups. It can be applied, for example, to C–H, C–Cl, and CH_3, but not to NO_2, C=O, and C=C. In the latter cases, the longitudinal and transverse components of susceptibility with respect to the bond direction and the corresponding geometrical parameters must be taken into account.

3.2.4 Ring Currents

Induced electron motion in neighboring bonds, which is responsible for the magnetic anisotropy effect, can lead to intramolecular currents in molecules with delocalized π-electron systems. The concept of ring currents is widely used in discussing the proton chemical shifts of aromatic hydrocarbons satisfying Hückel's $4n + 2$ rule. Pople[47,48] calculated the secondary magnetic field due to the ring current by a magnetic

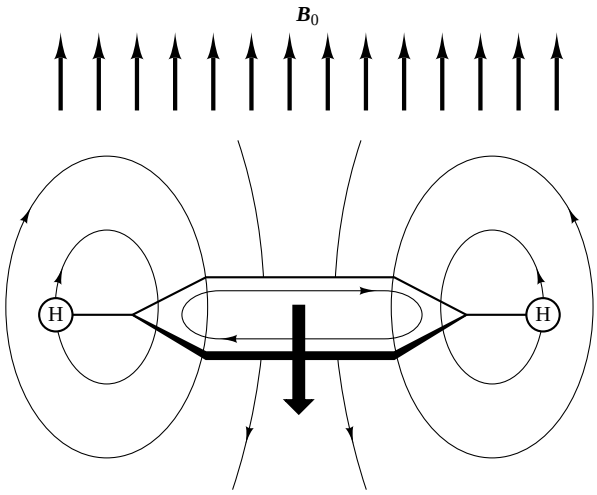

Figure 1 Ring current in the benzene ring caused by an externally applied uniform magnetic field $\boldsymbol{B}_0$ and the induced secondary magnetic field at the ring

point dipole at the center of the ring. Figure 1 shows the secondary magnetic field for a benzene ring where a static magnetic field is applied perpendicular to the ring plane. The application of a magnetic field in the ring plane does not give rise to a secondary field—thus, a high anisotropy of the shielding arises. The contribution of the ring current to the isotropic proton chemical shift is determined by this high anisotropy. Waugh and Fessenden[49,50] and Johnson and Bovey[51] refined this model. They described the ring current as two loops above and below the ring according to the delocalized π-electron density. The tables of Johnson and Bovey include the induced secondary field and the changes in the nuclear shielding for the benzene ring[52] depending on the distance from the ring.

Quantum chemical considerations of ring current effects have been given by Pople[48] and McWeeny[53] using the Hückel theory. The theory of McWeeny gives the secondary field B′ at the considered proton as

$$B' = k\beta \frac{S^2 B_0}{a^3} \sum_i J_i[-K(r_i)] \tag{21}$$

where k is a constant factor, β is the resonance integral of the HMO theory, S is the area of the aromatic ring, a is the length of a C–C bond, B_0 is the externally applied magnetic field, J_i is the intensity of the current in the ith ring, and $K(\mathrm{r}_i)$ is a geometrical factor depending on the position of the proton in question relative to the ring. Haigh and Mallion[54] considered the 'sigma ratio' B'/B_b', where B_b' is the secondary field for benzene. The sigma ratio depends only on the induced current intensity, J_i, and the geometric factor $K(r_i)$:

$$\frac{B'}{B_\mathrm{b}'} = \sum_{i=1}^{N} \frac{J_i}{J_\mathrm{b}} \frac{K_i(r)}{K_\mathrm{b}} \tag{22}$$

where N is the number of rings. Slight nonplanarity of benzenoid hydrocarbons can also be treated using an extension of the McWeeny theory.[55] Tables of numerical values have been given for the calculation of ring currents.[56]

Ring currents (RC) and local magnetic anisotropy of different bonds (LA) can have influences on proton chemical shifts in macrocyclic systems. The quantum chemical considerations of Ege and Vogler[57,58] allow one to calculate and separate these influences:

$$\delta = \delta^{\mathrm{RC}} + \delta^{\mathrm{LA}} + \delta^0 + \delta^{\mathrm{q}} \tag{23}$$

where δ^{q} is the chemical shift contribution proportional to the net electronic π charge of the contiguous carbon atom, and δ^0 fits the correlation to experimental values.

3.2.5 Electric Field Effects

A strong polar group gives rise to an intramolecular electric field $\boldsymbol{E}$, which changes the electron density at the resonating nucleus. Additionally, a direct through-space influence on magnetic shielding may become effective. This effect was first discussed by Buckingham[59] for proton shielding constants, and is described by

$$\sigma_E = -AE_z - BE^2 \tag{24}$$

where E_z is the electric field strength in the X–H direction. A and B are constants depending on the neighboring atom X. (see ***Electric Field Effects on Shielding Constants***)

3.3 Some Applications of Semiempirical Calculations

3.3.1 Proton NMR Chemical Shifts

Proton chemical shifts depend mainly on the local diamagnetic shielding and on shielding contributions from nonlocal influences:

$$\sigma = \sigma^{\mathrm{d}}(\mathrm{loc}) + \sum_{\mathrm{B}\neq\mathrm{A}} \sigma_{\mathrm{AB}} + \sigma_{\mathrm{r}} + \sigma_E \tag{25}$$

One or more contributions may be operative, depending on the chemical structure of the investigated molecule. The dependence on the diamagnetic shielding suggests a relation between chemical shift and hydrogen net charge:

$$\delta(^1H) \propto q_{\mathrm{H}} \tag{26}$$

However, this is only true when large effects can be observed. The relation in equation (26) gives the basis for different shielding rules, such as the Dailey–Shoolery rule for the compounds CH_3CH_2X. In these compounds, the proton chemical shift differences of the CH_2 and CH_3 protons are proportional to the electronegativity of the substituents X.[60]

In organic molecules, the net charge of the adjacent carbon atom can be decisive for ^{1}H chemical shifts. The 'atom-in-a-molecule' approximation of the local diamagnetic term in equation (10) may be extended to the 'atom + ligand' approximation, taking into account the diamagnetic shielding of the nearest neighbor atom:

$$\delta(^1\mathrm{H}) \propto q_{\mathrm{C}} \tag{27}$$

For a C–H bond with bond length of 0.108 nm a slope of 8.70 ppm/a.u. has been given from theoretical considerations[61] (the atomic unit for the net charge, a.u., is the elementary charge). Spiesecke and Schneider[62] found an empirical correlation of this kind with HMO π net charges of carbon atoms in aromatic ions, with a slope of 10.0 ppm/a.u. Another

example is the correlation of proton chemical shifts and PPP π net charges of the adjacent carbon atoms in polymethinium salts $[\,N{-}(CH)_{2n+1}{-}N\,]^+$ with a slope of 7.1 ppm/a.u.[63] In both cases, good correlations exist between ^1H and ^{13}C chemical shifts of the contiguous nuclei although the origins of the shieldings are different from each other (see below).

In most cases, additional contributions from distant parts of the molecule arise. For the proton chemical shift in *n*-pentanes,[64] the sum of diamagnetic contributions and anisotropy effects of neighboring bonds gives the right trend for the shift with the decisive influence of the anisotropy of the susceptibility of the C–C bonds in equation (20). The anisotropy effect is also responsible for the trend in the observed ^1H chemical shifts to higher frequency in the surprising order of C_2H_6, C_2H_2, C_2H_4. The C≡C triple bond has a negative $\Delta\chi$, in contrast to positive $\Delta\chi$ values for C–C and C=C bonds.[21] With a negative geometrical factor in equation (20), a low-frequency shift results for acetylene owing to the magnetic anisotropy, which works against the high-frequency shift from the diamagnetic shielding due to the positive charge on the H atom in C_2H_2.

The calculation of proton chemical shifts in alanine oligopeptides[65] as the sum of the magnetic anisotropy term and the electric field contribution of equation (24) using CNDO/2 calculations illustrates an application to a large system. The proton chemical shifts for all α-CH protons and all NH protons in a series of alanine oligomers were calculated and compared with experimental proton spectra. The agreement with the antiparallel β pleated sheet structure is good. This method may be useful for the study of conformations of oligopeptides and polypeptides.

The high-frequency shift of 1.5 ppm of aryl protons compared with olefinic protons can be understood in terms of the ring current effect using the point-dipole model. Outside the ring in its plane, the secondary field (Figure 1) adds to the field $\boldsymbol{B}_0$, leading to deshielding of the protons outside the ring. For [18]annulene (**1**), the secondary fields in the molecular plane outside and inside the ring determine the observed high-frequency shifts of the outer protons and the low-frequency shift of the inner protons.[19] The ring current contributions for proton chemical shifts in polycyclic systems can be obtained by summation over the different ring contributions, as in equation (22), which depend only on the intensity of the ring currents and a geometrical factor. This concept has been used for large systems.[54] For the description of ^1H chemical shifts in porphyrin molecules, ring currents and magnetic anisotropies are decisive.[66]

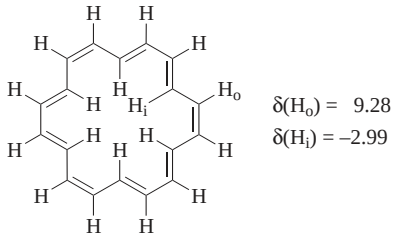
H
H
H

differences in chemical shifts. ^{29}Si chemical shifts of zeolites have also been discussed.[77] The assignment of the ^{13}C chemical shifts of a molecule chemisorbed on zeolites has been investigated using the INDO-CS method.[78] FPT-CNDO/2 calculations of ^{29}Si chemical shifts in the system n-Si_nH_{2n+2} (n = 7–15) have been carried out to assign the conformations of poly(methylphenylsilane).[79]

For a correct description of chemical shifts, reparameterizations of the semiempirical methods is often used. However, the change in the original parameters leads to problems.[80] The validity of the new parameters is restricted to special applications, and the methods are no longer applicable to the calculation of other electronic properties. Another method for the adaptation of theoretical results to experimental data was used by Chesnut and Zhang.[81] They employed MINDO/3 calculations for hydrocarbons, and found that the occupied orbital energies correspond to the ab initio (STO-5G) energies, while the vacant orbital energies are not equal to but have a linear relation with their ab initio counterparts. Therefore, rather than the MINDO/3 parameters, the ^{13}C shielding constant was fitted, in order to avoid the deficiencies in describing the excitation energies and electron distribution arising in the MINDO/3 method.

Another approach that has been adopted is density functional calculation of shielding. Using GIAOs into the LCAO-Xα approach, good results have been achieved for the shielding of the resonating nuclei ^{1}H, ^{7}Li, ^{11}B, ^{13}C, ^{15}N, ^{17}O, and ^{19}F in small molecules[82] compared with IGLO results and available experimental shielding constants in the gas phase (***Chemical Shift Scales on an Absolute Basis*** and ***Shielding Calculations: IGLO Method***).

3.3.2.1 Average Excitation Energy (AEE) Approximation. The average excitation energy (AEE) approximation[83,84] of the paramagnetic shielding constant is probably the approximation most widely used in discussion of the gross chemical shift trends of related compounds in terms of general chemical and quantum chemical characteristics. For the different excitation energies in equation (17), an average value ΔE is introduced. Simultaneously, in the ZDO approximation in the Pople theory, the following closure relation holds:

$$\sum_i {}^{\text{occ}} c_{\mu i} c_{\nu i} \sum_j {}^{\text{unocc}} c_{\mu j} c_{\nu j} = \delta_{\mu\nu} \tag{29}$$

where the Kronecker delta $\delta_{\mu\nu}$ is 1 for $\mu = \nu$ and is 0 for $\mu \neq \nu$. The paramagnetic shielding constant $\sigma_A{}^p$ of the resonating nucleus A in the average excitation energy approximation is given by

$$\sigma_A^p = -\frac{4}{3}\frac{\mu_0}{4\pi}\frac{e^2\hbar^2}{2m^2}\langle r^{-3}\rangle_{npA}(\Delta E)^{-1}\sum_B Q_{AB} \tag{30}$$

The constants have their usual meanings. The paramagnetic term in this Karplus–Pople equation depends only on the ground state of the unperturbed molecular orbitals. It comprises three structure-dependent factors.

The term $\sum_B Q_{AB}$ characterizes the imbalance of the electron distribution around the considered nucleus and the influences of hybridization. Q_{AA} and Q_{AB} (B $\neq$ A) are given by

$$\begin{aligned} Q_{AB} = {} & \delta_{AB}(P_{xAxB} + P_{yAyB} + P_{zAzB}) \\ & -\tfrac{1}{2}(P_{xAxB}P_{yAyB} + P_{xAxB}P_{zAzB} + P_{yAyB}P_{zAzB}) \\ & +\tfrac{1}{2}(P_{xAyB}P_{xByA} + P_{xAzB}P_{xBzA} + P_{yAzB}P_{yBzA}) \end{aligned} \tag{31}$$

The Q_{AB} terms depend on the elements of the charge density–bond order matrix of semiempirical calculations according to equation (12). They arise from the p orbital occupation of the atom of interest and the other first- and higher-row elements in the molecule.

The average excitation energy ΔE in equation (30) is a parameter that may also be structure-dependent. However, there is no explicit instruction for the calculation of ΔE.. It follows from equation (17) that the smallest possible energy transition mostly contributes to $\sigma_A{}^p$. Therefore, sometimes the difference of the eigenvalues of the LUMO (lowest unoccupied MO) and the HOMO (highest occupied MO) of an MO calculation is used as ΔE. However, only the MOs with sufficiently high p character of the atom A contribute to the paramagnetic shielding. Alternatively, ΔE has also been taken from optical and X-ray spectra.

The term $\langle r^{-3}\rangle_{npA}$ from equation (19) depends nearly linearly on the atomic net charge q_A according to equation (19).

Usually, all three structure-dependent factors contribute to the chemical shift. In molecules of similar structure, one of the three structure-dependent quantities may dominate in structural change, or all factors may have the same structural dependence. Sometimes, an explanation can be given for empirical correlations.

3.3.2.2 Empirical Relations. Empirical relations between NMR chemical shifts and characteristics of the geometrical and electronic structure, substituent parameters, and spectroscopic and physical properties have been established to classify the overwhelming number of chemical shift data, to support the assignment of resonance signals to molecular structure, and to obtain insight into the mutual connections between the considered quantities. Care has to be taken in using these correlations, because they are restricted to special applications. Some examples will be given in the following.

δ versus q. Linear correlations between chemical shifts δ and atomic net charges q have been found—for example, for ^{13}C[14,15,85] and ^{19}F[85] chemical shifts. In conjugated carbon chains, hetero atoms have an influence on ^{13}C chemical shifts over many bonds. Simultaneously, changes in π electron net charges q_π on the carbon atoms have a linear effect on chemical shifts:

$$\Delta\delta(^{13}\text{C}) \propto \Delta q_\pi \tag{32}$$

For polymethinium salts, for example, a factor of proportionality of 184 ppm/a.u. was found when q_π was calculated using the PPP method.[86] This value is in the typical region for related correlations[14] for carbon chemical shifts. The local diamagnetic term, equation (10), or the term $\langle r^{-3}\rangle_{2pC}$ from the local paramagnetic term, equation (30), might be responsible for this correlation. Since the regression coefficient with the diamagnetic term is about 8 ppm/a.u.[14] the origin of the observed relation for ^{13}C is mainly due to the factor $\langle r^{-3}\rangle_{2pC}$ in the local paramagnetic term of equation (30). For polymethinium salts, there is a good correlation between the ^{13}C and ^{1}H chemical shifts of the related C and H atoms (see above), showing the carbon chemical shift to be about 20 times more sensitive than the proton chemical shift. It is evident that the same qualitative correlations have different origins: diamagnetic shielding is responsible for ^{1}H chemical shifts, while paramagnetic shielding is mainly responsible for ^{13}C chemical shifts.

The correlations between substituent chemical shifts and substituent parameters of the Hammett type that have been observed for *para*-substituted benzenes and related systems can also be regarded to a certain extent as correlations with net charges of the considered resonating atoms[13,15,85] (see ***Organic Chemistry Applications***).

δ versus r. Correlations between chemical shifts and bond distances r can be understood as correlations of chemical shifts with the bond order terms and hybridization in $\sum Q_{AB}$ from σ^p_A. An example is the correlation between parallel components of the silicon shielding tensor $\sigma_\parallel$ for solid silicates with C_{3v} symmetry and the corresponding Si–O bond lengths.[87] The correlations between the isotropic ^{29}Si chemical shifts and the mean Si–O bond lengths in silicates were given by[88]

$$\overline{\delta(^{29}\text{Si})(\text{ppm})} = -2014 + 1.187 \times 10^4 \overline{d(\text{Si–O})(\text{nm})} \tag{33}$$

showing the very high sensitivity of silicon chemical shifts to bond length differences (see ***Silicon-29 NMR of Solid Silicates***).

δ versus f (φ). In solid silicates, the Si–O bond lengths are closely related to the OSiO angles at the resonating nucleus and to the SiOT (T = Si or Al) angles φ at the neighboring oxygen atoms. Relations of silicon chemical shifts to different functions of the SiOT angles in silicates have been given.[89] These relations have been found to arise from the influence of hybridization of the oxygen bonding orbital in the term $\sum Q_{AB}$ from σ^p_{Si} of equation (30).[90,91] The s character α^2_O of the bonding oxygen orbital, given by

$$\alpha^2_O = \cos\varphi/(\cos\varphi - 1) \tag{34}$$

is a suitable function to correlate with silicon chemical shifts of silicates. Another function χ'' of structural parameters of silicates was deduced by Sherriff and Grundy[92] and gives good correlation with ^{29}Si chemical shifts over a range of 60 ppm:

$$\chi'' = \sum_i s_i \frac{1 - 3\cos^2\theta_i}{3R_i^3} \frac{\cos\varphi_i}{\cos\varphi_i - 1} \tag{35}$$

where s_i is an empirical parameter for bond strength in the solid state, R_i is the distance between the midpoint of the O–T bond and the considered silicon atom, and θ_i is the angle between R_i and the O–T bond, i runs over the second neighbors of the silicon atom in question. The formula for χ'' connects the s character α^2_O in equation (34) with a term similar to the magnetic anisotropy of McConnell in equation (20).

For the same systems, other linear correlations have been established between silicon chemical shifts and electronegativities,[93] ΔE of σ^p_{Si} in equation (30),[94] and negative silicon net charges q_{Si}.[95,96] These correlations can be brought together by the results of semiempirical CNDO/2 calculations,[97] which show that all three factors of the paramagnetic term are linearly correlated with the same quantity, namely, the silicon net charge. The correlation with $\langle r^{-3}\rangle_{3pSi}$ is positive, while the correlations with $\sum Q_{AB}$ and $(\Delta E)^{-1}$ are negative. The latter two factors are responsible for the correct description of the trend of silicon chemical shifts due to SiOT bond angle variations in silicates (see ***Silicon-29 NMR*** and ***Silicon-29 NMR of Solid Silicates***).

δ versus λ. A correlation between ^{59}Co chemical shifts[3,98] and the wavelengths of the first optical absorption maximum for each compound of a series of cobalt complexes has been observed and interpreted as an effect of the average excitation energy in the paramagnetic shielding constant of equation (30).[10]

3.3.2.3 Semiempirical Correlations. In general, more than one term of equation (30) is decisive for the chemical shift. For the interpretation of the ^{19}F chemical shifts of fluorobenzenes, Karplus and Das[99] reduced the imbalance term to Q_{AA} and discussed its influence on the chemical shift. Saika and Slichter[27] calculated the difference in magnetic shielding between the F_2 molecule and the F^- ion. This difference represents the whole chemical shift range of about 800 ppm, because of the extreme values for the imbalance term Q_{AA} in both cases. For the symmetric F^- ion, the electron distribution is fully symmetric, and Q_{AA} vanishes. In contrast, the covalently bonded F_2 molecule has the highest possible imbalance of the electron distribution (i.e. 1). The ^{19}F chemical shifts for other compounds fall into this region (see ***Fluorine-19 NMR***).

The bonding situation in carbon compounds is completely different. The charge distribution around a carbon nucleus is usually more symmetric than that for a fluorine nucleus. The Q_{AA} term is approximately constant, and, therefore, less important than the Q_{AB} terms for B ≠ A in equation (30), especially if multiple bonds are present. The ^{13}C chemical shifts to higher frequency in the order ethane, acetylene, and ethylene were interpreted by Pople.[84] The anisotropy of the Q_{AB} term for acetylene is greater than that for ethylene. However, a smaller value for acetylene results because of the averaging of the isotropic chemical shift values. This smaller value for acetylene is responsible for the relatively low-frequency position of the resonance signal compared with that of ethylene. Good agreement with the experimental values was found with ΔE = 10 eV for ethane and a smaller ΔE = 8 eV for ethylene and acetylene.

Jameson and Gutowsky[100] included d orbital influences in the paramagnetic term to extend the chemical shift calculations beyond the first row:

$$\sigma^p(\text{loc}) = -\frac{4}{3}\frac{\mu_0}{4\pi}\frac{e^2\hbar^2}{2m^2}\frac{1}{\Delta E}[\langle r^{-3}\rangle_{np} P_u + \langle r^{-3}\rangle_{nd} D_u] \tag{36}$$

where $P_u = Q_{AA}$ as in the Karplus–Das equation; the imbalance term D_u for the d electron distribution was given explicitly. This theory was used by Letcher and Van Wazer[12] to develop a semiempirical theory of ^{31}P NMR chemical shifts. In equation (36) the $\langle r^{-3}\rangle_{nd}$ term is found to be smaller than the $\langle r^{-3}\rangle_{np}$ term by a factor of about 100 for P(III) and P(V). For the same coordination number, the quotient $\langle r^{-3}\rangle_{np}/\Delta E$ was considered to be constant. The imbalance term P_u was studied as a function of electronegativity for a number of phosphorus-containing molecules, and as a function of bond angles using valence bond (VB) orbitals constructed from s, p_x, p_y, and p_z atomic orbitals and bond polarity indices h_{AB} of an A–B bond. The latter can be expressed as

$$h_{AB} = 1.0 + (0.16 + 0.035|EN_A - EN_B|)(EN_A - EN_B) \tag{37}$$

where EN_A is the electronegativity of the considered atom A and EN_B is the electronegativity of the nearest neighbor atom B.

It has been shown for a manifold of parameter combinations that, as a function of electronegativity, P_u first increases, reaches a maximum, and then decreases. This pattern of the P_u term yields an explanation of the 'sagging pattern' observed

for ^{31}P chemical shifts in substitution series like $PX_{3-n}Y_n$ (n = 0, ... ,3) in dependence of n or on the phosphorus net charge[12] (see ***Phosphorus-31 NMR***).

The same theory was applied to the interpretation of ^{29}Si chemical shifts in the substitution series $(CH_3)_{4-n}SiX_n$ (n = 0 ... 4).[101,102] The d orbital term in equation (36) was neglected and ΔE was regarded as constant. To consider only the structure-dependent term in the 'electronegativity model', a relative paramagnetic shielding constant σ^{p*} was introduced as

$$\sigma^{p*} = R_p^* P_u^* \tag{38}$$

by relating the first term of equation (36) to the paramagnetic shielding constant of a nucleus in a totally unpolar surrounding. P_u* and R_p* are given by

$$P_u^* = \frac{1}{2}\sum_B h_{AB} - \frac{1}{6}\sum\sum_{B>B'} h_B h_{B'} \tag{39}$$

$$R_p^* = [1 + 0.35(f/Z_{0A})q_A]^3 \tag{40}$$

with

$$q_A = 4 - \sum_B h_{AB} \tag{41}$$

where f is an empirical factor that fits the results to experimental values. Simultaneously, f corrects for the possible structural dependence of ΔE. P_u* has a similar pattern, as described by Letcher and Van Wazer, for the phosphorus paramagnetic shielding constant. The R_p* term increases approximately linearly with increasing net charge. The factor f changes the slope of R_p* and fits σ^{p*} to experimental values by changing the maximum and the form of P_u*. The latter consideration is also applicable to ^{13}C chemical shifts of carbon atoms of coordination number four.[101] In this way, the observed differences in the influence of electronegative substitution on ^{13}C and ^{29}Si chemical shifts can be understood. For ^{13}C chemical shifts, the R_p* or $\langle r^{-3}\rangle_p$ part is decisive, and leads to high-frequency shifts with increasing net charge at the respective carbon atom. For ^{29}Si, the P_u* or P_u term explains the high-frequency ^{29}Si chemical shift with increasing net charge in the region of small charges and the low-frequency shift with increasing net charge in the region of greater charges (a roughly parabolic dependence—'sagging pattern'). For a restricted part of the whole range of silicon chemical shifts as in SiO_2 polymorphs with four surrounding oxygen atoms and large silicon net charge, the correlation

$$\delta(^{29}\text{Si}) \propto -q_{Si} \tag{42}$$

holds for the structural dependence of the imbalance term P_u (see ***Silicon-29 NMR of Solid Silicates***).

The roughly parabolic dependence of ^{31}P and ^{29}Si chemical shifts on substituent electronegativity has also been observed for ^{27}Al chemical shifts. Using equation (36) and the 'electronegativity model' for silicon chemical shifts, Hallas and Sternberg[103] verified this pattern, ranging from $[AlH_4]^-$ to $[Al(OH)_4]^-$ and from $[AlCl_6]^{3-}$ to $[Al(H_2O)_6]^{3-}$. To describe the wide range of ^{27}Al chemical shifts observed in systems having AlO_4 units, they used the bond polarization energy that can be calculated from the charges on the next neighbor atoms and their geometrical arrangement. This model can be applied to explain the influences of substituents of the second coordination sphere if the directly bonded substituents remain unchanged, as for ^{31}P chemical shifts in phosphates, ^{29}Si chemical shifts in SiO_2 polymorphs, ^{13}C chemical shifts in vinyl compounds, and ^{1}H chemical shifts of hydrogen-bonded protons.[104]

The interpretation of magnetic shielding in transition metal complexes can be improved over the $\sigma \propto -1/\Delta E$ relation mentioned above for cobalt complexes, taking into account the nephelauxetic ratio β, which varies with the complex:[80,105,106]

$$\sigma \propto -\beta/\Delta E \tag{43}$$

The slope is the effective r^{-3} value $\langle r^{-3}\rangle_{nd}/\beta$ describing the influences of the ligands on the radial term in equation (36). The ligand shielding can be discussed using the partition

$$\sigma = \sigma(\text{free ligand}) + \sigma_{cov} + \sigma_m \tag{44}$$

The shielding of the covalency of the metal–ligand bond σ_{cov} and the shielding σ_m due to the neighboring atoms (mainly the transition metal) in terms of the McConnell equation, equation (20), complete the shielding in the free ligand to give the ligand shielding in the complex.

Magnetic shielding calculations of nuclei in very heavy elements require relativistic corrections.[22,107] They have a strong influence on σ^d [40] and σ^p.[22] Calculations of σ^p have been carried out—for example, for linear molecules involving ^{13}C, ^{17}O, ^{33}S, ^{77}Se, and ^{125}Te using the REX (relativistic extended Hückel) theory.[108] Since relativistic effects are largest for the 1s core, they may be less important for chemical shifts than for absolute shieldings. Using nonrelativistic wavefunctions, the ^{207}Pb chemical shifts of lead halides correlate with the paramagnetic shielding constant in equation (36) on the basis of pseudopotential calculations of the electronic structure.[109] P_u and D_u are calculated from the orbital populations of p and d valence orbitals. The average excitation energy ΔE is taken as the mean difference between LUMO and occupied valence MOs. Heavy atoms such as bromine and iodine cause abnormally low frequency shifts of their neighbor nuclei, e.g. proton shifts in HX and ^{13}C shifts in CH_3X.[110] This 'heavy atom effect' has been interpreted in terms of a third-order perturbation theory as spin–orbit interaction.[108,110] The interaction gives 51% of the total proton shielding in HI.[110]

4 RELATED ARTICLES

Carbon-13 Spectral Simulation; Shielding Calculations: LORG and SOLO Approaches; Chemical Shift Scales on an Absolute Basis; Chemical Shift Tensors; Electric Field Effects on Shielding Constants; Fluorine-19 NMR; Inorganic Nuclei: Low Sensitivity Transition Metals; Magic Angle Spinning; Nitrogen NMR; Organic Chemistry Applications; Oxygen-17 NMR; Phosphorus-31 NMR; Shielding Calculations: IGLO Method; Shielding Calculations: Perturbation Methods; Shielding: Overview of Theoretical Methods; Shielding in Small Molecules; Shielding Tensor Calculations; Shielding Theory: GIAO Method; Silicon-29 NMR; Silicon-29 NMR of Solid Silicates.

5 REFERENCES

1. W. D. Knight, *Phys. Rev.*, 1949, **76**, 1259.
2. W. C. Dickinson, *Phys. Rev.*, 1950, **78**, 339.
3. W. G. Proctor and F. C. Yu, *Phys. Rev.*, 1951, **81**, 20.
4. E. M. Purcell, H. C. Torrey, and R. V. Pound, *Phys. Rev.*, 1946, **69**, 37.
5. F. Bloch, W. W. Hansen, and M. Packard, *Phys. Rev.*, 1946, **69**, 127.
6. N. F. Ramsey, *Phys. Rev.*, 1950, **78**, 699.
7. J. A. Pople, *J. Chem. Phys.*, 1962, **37**, 53.
8. J. A. Pople, *J. Chem. Phys.*, 1962, **37**, 60.
9. J. A. Pople, *Discuss. Faraday Soc.*, 1962, **34**, 7.
10. J. A. Pople, W. G. Schneider, and H. J. Bernstein, *High-Resolution Nuclear Magnetic Resonance*, McGraw-Hill, New York, 1959.
11. J. W. Emsley, J. Feeney, and L. H. Sutcliffe, *High Resolution Nuclear Magnetic Resonance Spectroscopy*, 2 Vols., Pergamon Press, Oxford, 1965.
12. J. H. Letcher and J. R. Van Wazer, in *Topics in Phosphorus Chemistry*, eds. M. Grayson and E. J. Griffith, Wiley-Interscience, New York, 1967, Chap. 2
13. P. R. Wells, *Linear Free Energy Relationships*, Academic Press, London, 1968.
14. G. J. Martin, M. L. Martin, and S. Odiot, *Org. Magn. Reson.*, 1975, **7**, 2.
15. G. L. Nelson and E. A. Williams, in *Progress in Physical Organic Chemistry*, eds. A. Streitwieser and R. W. Taft, Wiley-Interscience, New York, 1976, Vol. 12, p. 229.
16. K. A. K. Ebraheem and G. A. Webb, in *Progress in NMR Spectroscopy*, eds. J. W. Emsley, J. Feeney, and L. H. Sutcliffe, Pergamon Press, Oxford, 1977, Vol. 11, Chap. 5
17. D. L. Beveridge, in *Modern Theoretical Chemistry*, ed. G. A. Segal, Plenum Press, New York, 1977, Vol. 8, Part B, Chap. 5
18. G. A. Webb, in *NMR and the Periodic Table*, eds. R. K. Harris and B. E. Mann, Academic Press, London, 1978, Chap. 3
19. H. Günther, *NMR Spectroscopy. An Introduction*, 2nd edn., Wiley, Chichester, 1995.
20. I. Ando and G. A. Webb, *Theory of NMR Parameters*, Academic Press, London, 1983.
21. R. K. Harris, *Nuclear Magnetic Resonance Spectroscopy*, Longman, Harlow, UK, 1986.
22. C. J. Jameson and J. Mason, in *Multinuclear NMR*, ed. J. Mason, Plenum Press, New York, 1987, Chap. 3
23. *Specialist Periodical Reports on NMR*, ed. R. K. Harris (Vols. 1–5), R. J. Abraham (Vols. 6–8), and G. A. Webb (Vol. 9 onwards), The Chemical Society (Vols. 1–8)/ The Royal Society of Chemistry (Vol. 9 onwards), London, 1972 onwards.
24. W. E. Lamb, Jr., *Phys. Rev.*, 1941, **60**, 817.
25. N. F. Ramsay, *Phys. Rev.*, 1951, **83**, 540.
26. N. F. Ramsay, *Phys. Rev.*, 1952, **86**, 243.
27. A. Saika and C. P. Slichter, *J. Chem. Phys.*, 1954, **22**, 26.
28. A. Streitwieser, Jr., *Molecular Orbital Theory for Organic Chemists*, J. Wiley, New York, 1961.
29. R. Pariser and R. G. Parr, *J. Chem. Phys.*, 1953, **21**, 466.
30. J. A. Pople, *Trans. Faraday Soc.*, 1954, **50**, 901.
31. R. Hoffmann, *J. Chem. Phys.*, 1963, **39**, 1397.
32. J. A. Pople and D. L. Beveridge, *Approximate Molecular Orbital Theory*, McGraw-Hill, New York, 1970.
33. R. C. Bingham, M. J. S. Dewar, and D. H. Lo, *J. Am. Chem. Soc.*, 1975, **97**, 1285.
34. M. S. J. Dewar and W. Thiel, *J. Am. Chem. Soc.*, 1977, **99**, 4899 and 4907.
35. K. Krogh-Jespersen and M. Ratner, *J. Chem. Phys.*, 1976, **65**, 1305.
36. W. H. Flygare and J. Goodisman, *J. Chem. Phys.*, 1968, **49**, 3122.
37. T. D. Gierke, H. L. Tigelaar, and W. H. Flygare, *J. Am. Chem. Soc.*, 1972, **94**, 330.
38. T. D. Gierke and W. H. Flygare, *J. Am. Chem. Soc.*, 1972, **94**, 7277.
39. G. Malli and C. Froese, *Int. J. Quantum Chem.*, 1967, **1S**, 95.
40. D. Kolb, W. R. Johnson, and P. Shorer, *Phys. Rev. A*, 1982, **26**, 19.
41. J. C. Slater, *Phys. Rev.*, 1930, **36**, 57.
42. G. Burns, *J. Chem. Phys.*, 1964, **41**, 1521.
43. R. Ditchfield, *J. Chem. Phys.*, 1972, **56**, 5688.
44. W. T. Raynes, in *Specialist Periodical Report on NMR*, ed. R. K. Harris, The Chemical Society, London, 1972, Vol. 1, Chap. 1
45. H. M. McConnell, *J. Chem. Phys.*, 1957, **27**, 226.
46. W. T. Raynes, *Mol. Phys.*, 1971, **20**, 321.
47. J. A. Pople, *J. Chem. Phys.*, 1956, **24**, 1111.
48. J. A. Pople, *Mol. Phys.*, 1958, **1**, 175.
49. J. S. Waugh and R. W. Fessenden, *J. Am. Chem. Soc.*, 1957, **79**, 846.
50. J. S. Waugh, *J. Am. Chem. Soc.*, 1958, **80**, 6697.
51. C. E. Johnson, Jr., and F. A. Bovey, *J. Chem. Phys.*, 1958, **29**, 1012.
52. J. W. Emsley, J. Feeney, and L. H. Sutcliffe, *High Resolution Nuclear Magnetic Resonance Spectroscopy*, Pergamon Press, Oxford, 1965, Vol. 1, Appendix B.
53. R. McWeeny, *Mol. Phys.*, 1958, **1**, 311.
54. C. W. Haigh and R. B. Mallion, *Mol. Phys.*, 1970, **18**, 767.
55. C. W. Haigh and R. B. Mallion, *Mol. Phys.*, 1971, **22**, 955.
56. C. W. Haigh and R. B. Mallion, *Org. Magn. Reson.*, 1972, **4**, 203.
57. G. Ege and H. Vogler, *Tetrahedron*, 1975, **31**, 569.
58. H. Vogler, *J. Am. Chem. Soc.*, 1978, **100**, 7464.
59. A. D. Buckingham, *Can. J. Chem.*, 1960, **38**, 300.
60. B. P. Dailey and J. N. Shoolery, *J. Am. Chem. Soc.*, 1955, **77**, 3977.
61. J. Niwa, *Bull. Chem. Soc. Jpn.*, 1975, **48**, 118.
62. H. Spiesecke and W. G. Schneider, *Tetrahedron Lett.*, **1961**, 468.
63. R. Radeglia, E. Gey, K.-D. Nolte and S. Dähne, *J. prakt. Chem.*, 1970, **312**, 877 (CA **74**: 118119b).
64. I. Ando and A. Nishioka, *Bull. Chem. Soc. Jpn.*, 1973, **46**, 1040.
65. T. Asakura, *Makromol. Chem.*, 1981, **182**, 1097.
66. C. Giessner-Prettre and B. Pullman, *Biochem. Biophys. Res. Commun.*, 1981, **101**, 921.
67. R. B. Mallion, in *Specialist Periodical Reports on NMR*, ed. R. K. Harris, The Chemical Society, London, 1975, Vol. 4, Chap. 1
68. M. Jallali-Heravi and G. A. Webb, *Org. Magn. Reson.*, 1978, **11**, 524.
69. M. Jallali-Heravi and G. A. Webb, *J. Magn. Reson.*, 1978, **32**, 429.
70. P. T. Czech, X.-Q. Ye, and R. F. Fenske, *Organometallics*, 1990, **9**, 2016.
71. X.-Z. You, W.-X. Wu, and A.-B. Dai, *Pure Appl. Chem.*, 1990, **62**, 1087.

72. T. P. Fehlner, P. T. Czech, and R. F. Fenske, *Inorg. Chem.*, 1990, **29**, 3103.
73. P. D. Ellis, G. E. Maciel and J. W. McIver, Jr., *J. Am. Chem. Soc.*, 1972, **94**, 4069.
74. G. E. Maciel, J. L. Dallas, R. L. Elliott, and H. C. Dorn, *J. Am. Chem. Soc.*, 1973, **95**, 5857.
75. W.-X. Wu, X.-Z. You, A.-B. Dai, and S.-P. Jing, *Polyhedron*, 1990, **9**, 1849.
76. T. Asakura, H. Yoshimizu, S. Ando, and I. Ando, *J. Mol. Struct. (Theochem)*, 1988, **168**, 135.
77. V. G. Malkin, O. V. Gritsenko, and G. M. Zhidomirov, *Chem. Phys. Lett.*, 1988, **152**, 44.
78. V. G. Malkin, V. V. Chesnokov, E. Paukshtis, and G. M. Zhidomirov, *J. Am. Chem. Soc.*, 1990, **112**, 666.
79. T. Takayama and I. Ando, *J. Mol. Struct.*, 1990, **222**, 275.
80. C. J. Jameson, in *Specialist Periodical Reports on NMR*, ed. G. A. Webb, The Royal Society of Chemistry, 1990, Vol. 19, Chap. 1
81. D. B. Chesnut and C. Zhang, *J. Comput. Chem.*, 1988, **9**, 416.
82. K. Friedrich, G. Seifert, and G. Grossmann, *Z. Phys. D*, 1990, **17**, 45 (*Chem. Abstr.* **113**, 203600v).
83. M. Karplus and J. A. Pople, *J. Chem. Phys.*, 1963, **38**, 2803.
84. J. A. Pople, *Mol. Phys.*, 1964, **7**, 301.
85. W. J. Hehre, R. W. Taft and R. D. Topsom, in *Progress in Physical Organic Chemistry*, eds. A. Streitwieser and R. W. Taft, Wiley-Interscience, New York, 1976, Vol. 12, p. 159.
86. R. Radeglia, *J. Prakt. Chem.*, 1973, **315**, 1121 (CA **80**: 81592w).
87. A.-R. Grimmer, *Chem. Phys. Lett.*, 1985, **119**, 416.
88. A.-R. Grimmer and R. Radeglia, *Chem. Phys. Lett.*, 1984, **106**, 262.
89. G. Engelhardt and D. Michel, *High-Resolution Solid-State NMR of Silicates and Zeolites*, Wiley, Chichester, 1987.
90. G. Engelhardt and R. Radeglia, *Chem. Phys. Lett.*, 1984, **108**, 271.
91. R. Radeglia and G. Engelhardt, *Chem. Phys. Lett.*, 1985, **114**, 28.
92. B. L. Sherriff and H. D. Grundy, *Nature (London)*, 1988, **332**, 819.
93. N. Janes and E. Oldfield, *J. Am. Chem. Soc.*, 1985, **107**, 6769.
94. J. A. Tossell, *Phys. Chem. Minerals*, 1984, **10**, 137.
95. R. Wolff, R. Radeglia, and J. Sauer, *J. Mol. Struct. (Theochem)*, 1986, **139**, 113.
96. R. Wolff, R. Radeglia, C. Vogel, and J. Sauer, *J. Mol. Struct. (Theochem)*, 1989, **183**, 223.
97. R. Wolff, R. Radeglia, and C. Vogel, *J. Phys. Chem. Solids*, 1990, **51**, 123.
98. R. Freeman, G. R. Murray and R. E. Richards, *Proc. R. Soc. Lond. Ser. A*, 1957, **242**, 455.
99. M. Karplus and T. P. Das, *J. Chem. Phys.*, 1961, **34**, 1683.
100. C. J. Jameson and H. S. Gutowsky, *J. Chem. Phys.*, 1964, **40**, 1714.
101. G. Engelhardt, R. Radeglia, H. Jancke, E. Lippmaa, and M. Mägi, *Org. Magn. Reson.*, 1973, **5**, 561.
102. R. Radeglia, *Z. Phys. Chem., Leipzig*, 1975, **256**, 453 (CA **83**: 139526h).
103. E. Hallas and U. Sternberg, *Mol. Phys.*, 1989, **68**, 315.
104. U. Sternberg, in *Nuclear Magnetic Shieldings and Molecular Structure*, ed. J. A. Tossell, Kluwer, Dordrecht, 1993, p. 435.
105. C. J. Jameson, in *Specialist Periodical Reports on NMR*, ed. G. A. Webb, The Royal Society of Chemistry, London, 1986, Vol. 15, Chap. 1
106. C. J. Jameson, in *Specialist Periodical Reports on NMR*, ed. G. A. Webb, The Royal Society of Chemistry, London, 1988, Vol. 17, Chap. 1
107. C. J. Jameson, in *Specialist Periodical Reports on NMR*, ed. G. A. Webb, The Royal Society of Chemistry, London, 1984, Vol. 13, Chap. 1
108. J. Jokisaari, P. Lazzeretti, and P. Pyykkö, *Chem. Phys.*, 1988, **123**, 339.
109. M. Nizam, M. Allavena, Y. Bouteiller, B. H. Suits, and D. White, *J. Magn. Reson.*, 1989, **82**, 441.
110. I. Morishima, K. Endo, and T. Yonezawa, *J. Chem. Phys.*, 1973, **59**, 3356.

Biographical Sketches

Renate Wolff. *b* 1936. Diploma (physics), 1973, Technical University of Dresden, Germany; Dr. rer. nat., 1978, Academy of Sciences, Berlin. Introduced to NMR by R. Radeglia. Central Institute of Physical Chemistry of the Academy of Sciences, Berlin, 1973–91; Federal Institute for Materials Research and Testing, Berlin, 1992–present. 26 publications. Research speciality: theoretical interpretation of NMR parameters.

Reiner Radeglia. *b*. 1937. Diploma (chemistry) 1961, Dr. ret. nat. (supervisor Kurt Schwabe) 1963, Technical University of Dresden. Central Institute of Physical Chemistry of the Academy of Sciences, Berlin (East) 1963–1991. Dr. habil. Humboldt University, Berlin (East) 1969; Professor of Physical Chemistry 1988. Federal Institute for Materials Research and Testing, Berlin 1992–present. Approx. 300 publications. Research specialties: NMR parameters and molecular structure.

Shielding Calculations: IGLO Method

Werner Kutzelnigg, Ulrich Fleischer, and Christoph van Wüllen

Ruhr-Universität Bochum, Bochum, Germany

1	Introduction	1
2	The Hamiltonian in a Magnetic Field and the Gauge Problem	2
3	Chemical Shifts	3
4	Basic Principles of the IGLO Method	3
5	DIGLO and MC-IGLO	5
6	Some Results and Applications	5
7	Correlation and Relativistic Effects	6
8	Related Articles	8
9	References	8

1 INTRODUCTION

Until about 1980, the ab initio calculation of NMR chemical shifts was regarded as possible in principle, but rather demanding as far as computer time was concerned, and only calculations on rather small systems with moderate accuracy had been published. A considerable breakthrough came with the invention of the IGLO (individual gauge for localized orbitals) method,[1,2] which made ab initio calculations on chemically interesting molecules possible. Early applications included the ab initio derivation of an increment system for hydrocarbons,[3] a definite confirmation of the nonclassical structure of the 2-norbornyl cation,[4] the assignment of the shift tensors of cyclopropane, bicyclobutane and [1.1.1]propellane,[5] and the prediction[5] of the ^{19}F shift in SF_2 prior to its measurement.[6] (For other applications, see, e.g., the review by Kutzelnigg et al.[5])

In an investigation of various carbocations,[4] it was observed that the agreement between computed and experimental chemical shifts was usually very good for nonclassical carbonium ions, but less so for classical ones. At this point, P.v.R. Schleyer suggested that the disagreement might be due to the use of generally assumed incorrect—in fact too symmetric—structures for the classical ions. It turned out that, for example, the isopropyl cation $HC(CH_3)_2^+$ has only C_2 rather than C_{2v} symmetry.[5] Subsequently, the combination of NMR measurements, ab initio structure optimizations, and IGLO calculations for competitive structures has become an efficient approach to decide which structure is realized under the conditions of an experiment. This need not be the structure of lowest energy for the isolated molecule. Especially in the chemistry of boron hydrides,[7] this combined method has led to the determination of improved structures, which differ from the X-ray or electron diffraction structures—in some cases significantly. IGLO calculations have often been helpful in ruling out assumed structures. It has been shown[8] that a reaction product of P_4 with alkali metal in an organic solvent, characterized by its NMR spectrum, was not P_4H^- as had been claimed[9]—at least not in the suggested bicyclobutane-type structure.[9] The measured ^{31}P shifts (71, −330, and −355 ppm) did not agree with those computed[8] for either an *endo* (161, 172, and −319 ppm) or an *exo* structure (−51, −176, and −352 ppm). In many other cases (see Section 6), IGLO calculations served to confirm proposed structures; for example, for the adamantanediyl dication,[5] where the IGLO values for δ(C) were 6.6 and 35.6 ppm, and the corresponding experimental shifts were 7 and 33 ppm. For more examples, see Section 6.

A few years after the advent of the IGLO method, the LORG approach was presented.[10] It is similar to IGLO in the basic idea of using individual gauge origins for different localized orbitals, but rather different in technical details and in the way in which errors are controlled. We believe that IGLO is better justified, since it can be derived from a stationarity principle.[11–13] Nevertheless, it is most noteworthy that the results of calculations with the two methods are usually rather close. Which method performs better computationally depends somewhat on which versions one compares. The most recent IGLO implementation[15] is probably hard to beat. Various types of shift calculations are described in Ref. 14.

The GIAO method is, in principle, older than both IGLO and LORG, but really efficient implementations have been possible only quite recently[16], taking advantage of knowledge from gradient evaluations (see ***Shielding Theory: GIAO Method***). The main difference between GIAO and IGLO is that in the former different gauge origins are used for different basis functions, while in IGLO (or LORG) they are used for different localized MOs. Again, the results are close to those of IGLO calculations. Recent comparisons between GIAO and IGLO by authors of GIAO programs have mainly stressed that GIAO calculations converge somewhat faster to basis limit results than IGLO calculations, while for sufficiently large basis sets the agreement is very good[17]. In noting the faster convergence with extension of the basis sets for GIAO versus IGLO or LORG (the three together are often referred to as *distributed-gauge* methods), one must not forget that all three methods converge spectacularly faster to the basis set limit than the traditional coupled Hartree–Fock (CHF) approach with a *common gauge origin*. The somewhat slower convergence of IGLO versus GIAO is due to the evaluation of the so-called exchange coupling terms in IGLO by means of a completeness insertion. However, this very step implies that in IGLO no more two-electron integrals are needed than in an ordinary SCF calculation, while GIAO also needs the derivatives of the integrals with respect to the nuclear coordinates. Therefore, for the same basis size, GIAO is significantly more expensive than IGLO, so that, for the same computational cost, one can afford a larger basis in IGLO than in LORG. For molecules of high symmetry such as C_{60}, a special implementation of GIAO[18] has some advantages. A nice feature of IGLO is that the computed chemical shifts result as sums of contributions of localized orbitals, which helps in interpreting the results. IGLO has also the advantage that it furnishes magnetic susceptibilities in addition to chemical shifts, which for some of the other methods is either not possible (as for LORG) or has not yet (or only very recently) been implemented (as for GIAO[17]).

It has recently been shown[19] that for very small molecules (essentially diatomic or triatomic with one hydrogen), high accuracy can be achieved using a common gauge origin. A

rather powerful implementation of CHF with a common gauge has allowed reliable calculations even of benzene,[20] but this is probably the absolute limit, since extremely large basis sets are needed.

A fourth distributed gauge origin method has recently been proposed.[21] Here the balance between diamagnetic and paramagnetic terms is treated differently from IGLO, LORG, or GIAO. While in the latter methods the diamagnetic terms are obtained exactly, and one tries to get the paramagnetic ones *almost* exactly, here one introduces an error into the diamagnetic terms that should cancel that of the paramagnetic ones. An apparently different method proposed by Bader et al.[22] was later shown by Lazzeretti et al.[23] to be equivalent to that of Geertsen.[21]

All methods mentioned so far, such as IGLO, LORG, GIAO, and CHF, are of coupled Hartree–Fock type, i.e., the many-electron wavefunction is approximated as a single Slater determinant. Effects that go beyond the single Slater determinant approximation are usually referred to as 'electron correlation' and are obviously neglected. One further neglects relativistic effects. These effects are important only in exceptional cases, to which we shall come in Section 7.

Details of the IGLO method and its applications can be found in a recent review[5] and a complementary one.[12] For technical details, especially for prospective users, a description of the most recent release of IGLO is recommended.[15]

2 THE HAMILTONIAN IN A MAGNETIC FIELD AND THE GAUGE PROBLEM

We are only interested in closed-shell states, where the interaction of the electron spin with the external magnetic field can be ignored. We also limit ourselves to the nonrelativistic regime, where spin–orbit interactions can be neglected.

The Hamiltonian for a one-electron system in a magnetic field described by the vector potential $\boldsymbol{A}$ is

$$\hat{\mathcal{H}} = \frac{1}{2m}\left(\hat{\boldsymbol{p}} + \frac{e}{c}\boldsymbol{A}\right)^2 + V = \hat{\mathcal{H}}_0 + \hat{\mathcal{H}}_{10} + \hat{\mathcal{H}}_{20} \tag{1}$$

$$\hat{\mathcal{H}}_{10} = \frac{e}{mc}\boldsymbol{A}\cdot\hat{\boldsymbol{p}}, \quad \hat{\mathcal{H}}_{20} = \frac{e^2}{2mc^2}A^2 \tag{2}$$

Here $\hat{\boldsymbol{p}}$ is the momentum, V is the nuclear potential, $\hat{\mathcal{H}}_0$ is the Hamiltonian in the absence of the magnetic field, e and m are the electron charge and mass, and c is the velocity of light. The magnetic field strength $\boldsymbol{B}$ is related to the vector potential by

$$\boldsymbol{B} = \operatorname{curl}\boldsymbol{A} \tag{3}$$

The inverse of equation (3) is not unique. One can, in fact, add to $\boldsymbol{A}$ the gradient $\nabla\chi$ of an arbitrary scalar function χ without affecting the validity of equation (3). For a homogeneous magnetic field $\boldsymbol{B}$, a possible choice of $\boldsymbol{A}$ compatible with equation (3) is

$$\boldsymbol{A}(\boldsymbol{r}) = \tfrac{1}{2}\boldsymbol{B}\times(\boldsymbol{r}-\boldsymbol{R}) \tag{4}$$

where $\boldsymbol{R}$ is a fixed point in space, called the 'gauge origin'. In choosing $\boldsymbol{A}$ in the form given in equation (4), we have considerably reduced the arbitrariness of $\boldsymbol{A}$. Now only the choice of $\boldsymbol{R}$ is arbitrary. To get the eigenvalue E and eigenfunction ψ of $\hat{\mathcal{H}}$ as functions of $\boldsymbol{B}$, one can apply perturbation theory. There are two perturbations, $\hat{\mathcal{H}}_{10}$ and $\hat{\mathcal{H}}_{20}$, the first of which is linear in the field strength and the second quadratic. One sees easily that for the choice in equation (4), both $\hat{\mathcal{H}}_{10}$ and $\hat{\mathcal{H}}_{20}$ contain $\boldsymbol{R}$, i.e., that $\hat{\mathcal{H}}$ depends on the gauge origin. All measurable quantities must be gauge-independent. This means that if one solves the Schrödinger equation exactly, E as well as its derivatives with respect to the field strength $\boldsymbol{B}$ will be independent of $\boldsymbol{R}$. However, the wavefunction (which is not measurable) will depend on $\boldsymbol{R}$, and so will the contributions to the perturbation expansion to be discussed later.

One can show that a change of the gauge origin in $\hat{\mathcal{H}}$ from $\boldsymbol{R}$ to $\boldsymbol{R}'$ is equivalent to a unitary transformation (gauge transformation)

$$\hat{\mathcal{H}} \to \hat{\mathcal{H}}' = \hat{U}^\dagger\hat{\mathcal{H}}\hat{U} \tag{5a}$$

$$U = \exp(\mathrm{i}\Lambda), \quad \Lambda = \tfrac{e}{2c}\boldsymbol{B}\times(\boldsymbol{R}'-\boldsymbol{R})\cdot\boldsymbol{r} \tag{5b}$$

If ψ is an eigenfunction of $\hat{\mathcal{H}}$ then the eigenfunction ψ' of $\hat{\mathcal{H}}'$ is given as $\psi' = \hat{U}^\dagger\psi$.

In perturbation theory, one expands the energy and the wavefunction in analogy to equation (1) as

$$E = E_0 + E_{10} + E_{20} + \cdots \tag{6a}$$

$$\psi = \psi_0 + \psi_{10} + \psi_{20} + \cdots \tag{6b}$$

which yields

$$E_{10} = \langle\psi_0|\hat{\mathcal{H}}_{10}|\psi_0\rangle \tag{7}$$

$$\begin{aligned} E_{20} &= E_{20}^{\mathrm{d}} + E_{20}^{\mathrm{p}} \\ E_{20}^{\mathrm{d}} &= \langle\psi_0|\hat{\mathcal{H}}_{20}|\psi_0\rangle \\ E_{20}^{\mathrm{p}} &= \mathrm{Re}\langle\psi_0|\hat{\mathcal{H}}_{10}|\psi_{10}\rangle \end{aligned} \tag{8}$$

where ψ_{10} is the solution of

$$(\hat{\mathcal{H}}_0 - E_0)\psi_{10} = (\hat{\mathcal{H}}_{10} - E_{10})\psi_0 \tag{9}$$

If the system has no permanent magnetic moment—which is what we usually assume—then $E_{10} = 0$.

E_{20} can be written as

$$E_{20} = -\frac{1}{2}\sum_{\alpha,\beta} B_\alpha\chi_{\alpha\beta}B_\beta, \quad \alpha,\beta = x,y,z \tag{10}$$

where $\boldsymbol{\chi} = \{\chi_{\alpha\beta}\}$ is the magnetic susceptibility tensor. E_{20}^{d} and E_{20}^{p} are called the *diamagnetic* and *paramagnetic* contributions to E_{20}. Both E_{20}^{d} and E_{20}^{p} are strongly gauge-origin-dependent. In their sum E_{20}, this dependence only cancels if equation (9) is solved exactly, otherwise E_{20}^{d} is obtained rather accurately but $E_{20}{}^{\mathrm{p}}$ has a possibly large error. All this holds for the individual $\chi_{\alpha\beta}$ and for the isotropic susceptibility

$$\chi = \tfrac{1}{3}(\chi_{xx} + \chi_{yy} + \chi_{zz}) \tag{11}$$

There are, in principle, two ways to solve the gauge origin problem (at least to a high degree of accuracy).

1. One tries to solve equation (9) as accurately as possible. In a basis expansion method, this means that one uses nearly saturated basis sets.
2. One tries to find an optimum gauge origin $\boldsymbol{R}$ for which the error with respect to an exact solution is as small as possible—even if the basis is small.

For atoms, the second approach is successful. There is, in fact, a *natural gauge origin* at the position of the nucleus. For this choice, $E_{20}^{\mathrm{p}} = 0$, and E_{20}^{d} is evaluated rather easily. For molecules, there is no natural gauge origin, but one should try to find something similar, as one does in the distributed gauge methods.

While in closed-shell atoms E_{20} is always positive (energy-raising), corresponding to diamagnetism, in molecules E_{20}^{p} may be larger in absolute value than E_{20}^{d}, so that an overall paramagnetism may result. This is often the case if a low-lying excited state has a nonvanishing matrix element of a relevant angular momentum operator with the considered state. This paramagnetism is temperature-independent, and is often called *van Vleck paramagnetism*. It must be clearly distinguished from the ordinary temperature-dependent paramagnetism that arises for atoms or molecules in a degenerate state with the degeneracy split by the magnetic field.

3 CHEMICAL SHIFTS

In the preceding section, we have considered a single (external) magnetic field. To study chemical shifts, we have to add the magnetic field $\boldsymbol{B}_{\mathrm{N}}$ created by the magnetic moment of a nucleus. In equation (1), we must replace $\boldsymbol{A}$ by $\boldsymbol{A} + \boldsymbol{A}_{\mathrm{N}}$. We use the first label to count orders in $\boldsymbol{A}$ and the second for orders in $\boldsymbol{A}_{\mathrm{N}}$:

$$\hat{\mathcal{H}} = \hat{\mathcal{H}}_0 + \hat{\mathcal{H}}_{10} + \hat{\mathcal{H}}_{01} + \hat{\mathcal{H}}_{11} + \hat{\mathcal{H}}_{20} \tag{12}$$

$$\hat{\mathcal{H}}_{01} = \frac{e}{mc}\boldsymbol{A}_{\mathrm{N}} \cdot \hat{\boldsymbol{p}}, \quad \hat{\mathcal{H}}_{11} = \frac{e^2}{2mc^2}\boldsymbol{A} \cdot \boldsymbol{A}_{\mathrm{N}} \tag{13}$$

[The other terms are as in equations (1) and (2)]. A possible expression for $\boldsymbol{A}_{\mathrm{N}}$ is

$$\frac{\boldsymbol{A}_{\mathrm{N}} = \boldsymbol{\mu} \times (\boldsymbol{r} - \boldsymbol{\varrho})}{|\boldsymbol{r} - \boldsymbol{\varrho}|^3} \tag{14}$$

This choice corresponds to taking the gauge origin for $\boldsymbol{A}_{\mathrm{N}}$ at the position $\boldsymbol{\varrho}$ of the respective nucleus (with magnetic moment $\boldsymbol{\mu}$). Other gauges are possible, but there is no point in *not* choosing the 'natural' gauge origin $\boldsymbol{\varrho}$ for $\boldsymbol{A}_{\mathrm{N}}$. Only for the vector potential $\boldsymbol{A}$ of the *external* field does the gauge origin $\boldsymbol{R}$ remain arbitrary.

Expanding the energy in analogy to equations (5) and (10), one obtains E_{11} as the term bilinear in $\boldsymbol{A}$ and $\boldsymbol{A}_{\mathrm{N}}$. Like E_{20}, E_{11} consists of two contributions,

$$\begin{aligned} E_{11} &= E_{11}^{\mathrm{d}} + E_{11}^{\mathrm{p}} \\ E_{11}^{\mathrm{d}} &= \langle\psi_0|\hat{\mathcal{H}}_{11}|\psi_0\rangle \\ E_{11}^{\mathrm{p}} &= 2\,\mathrm{Re}\langle\psi_0|\hat{\mathcal{H}}_{01}|\psi_{10}\rangle \end{aligned} \tag{15}$$

in perfect analogy to equation (8).

The relation of E_{11} to the chemical shift tensor $\boldsymbol{\sigma}$ is

$$E_{11} = \sum_{\alpha,\beta} \mu_\alpha \sigma_{\alpha\beta} B_\beta, \quad \alpha, \beta = x, y, z \tag{16}$$

For a closed-shell atom and with the gauge origin $\boldsymbol{R}$ (for the homogeneous external field) at the position of the nucleus, the paramagnetic contribution E_{11}^{p} vanishes, and the expression for E_{11}^{d} becomes very simple.

If one uses an off-center gauge origin for an atom, one gets a spurious nonvanishing E_{11}^{p}. This cancels with an extra term in E_{11}^{d} only if the basis is large enough that ψ_{10}, which is needed in equation (15) and which is constructed from equation (9), is obtained with sufficient accuracy. The extra term in E_{11}^{d} is usually obtained much more accurately than E_{11}^{p}.

Both E_{20} and E_{11} are formally defined in terms of second derivatives of the energy, i.e., as second-order response properties, but one can also rationalize these quantities by means of a two-step mechanism. We note that the external homogeneous field induces a current density in the atom or molecule. This current density generates an induced magnetic field, which interacts both with the external field (giving rise to diamagnetism) and with the magnetic moments of the nuclei (giving rise to the chemical shift). Current density plots[5,12] may contribute to a better understanding of the origin of chemical shifts.

A characteristic feature of the IGLO method is that E_{11} (as well as E_{20}) is obtained as a sum of MO contributions, but that for different MOs different gauge origins are used, so that the decomposition of E_{11} into E_{11}^{d} and E_{11}^{p} refers to a different gauge origin for each MO. The sum of E_{11}^{d} for all MOs is then a *local diamagnetic contribution*, which must not be confused with a *global* contribution, where the same gauge is used for all MOs.

While the susceptibility tensor $\boldsymbol{\chi}$ is symmetric (i.e. $\chi_{xy} = \chi_{yx}$), the shift tensor $\boldsymbol{\sigma}$ is asymmetric. Eigenvectors and eigenvalues of $\boldsymbol{\sigma}$ are constructed from its symmetric part, i.e., by replacing $\sigma_{\alpha\beta}$ by $\frac{1}{2}(\sigma_{\alpha\beta} + \sigma_{\alpha\beta})$.

The sign convention for shieldings is such that $\sigma > 0$ means shielding and $\sigma < 0$ deshielding. For the relative shift $\delta = \sigma_{\mathrm{ref}} - \sigma$, the sign has the opposite meaning.

4 BASIC PRINCIPLES OF THE IGLO METHOD

We are now prepared to understand the main features of the IGLO method, at least qualitatively. More detailed presentations can be found elsewhere.[5,12,15]

Let us first consider a supersystem of two H_2 molecules with a large distance r between them. If r is large enough, the two H_2 molecules can be regarded as independent. One could calculate σ(H) for each separately, choosing the midpoint of either molecule as respective gauge origin. If, however, we want to treat $(H_2)_2$ as one supermolecule, and choose one gauge origin, the best choice would be the center of mass of this supermolecule. This gauge origin would be largely off-center for either H_2 subunit. Errors of the type illustrated in Section 3 will arise. One would certainly try to avoid this by using independent gauge origins for the two subunits.

However, if r is no longer very large, the two subunits can no longer be regarded as independent. If one now wants to introduce independent gauge origins for either H_2, one gets

rather complicated coupling terms, which are the price to pay for the freedom to take independent gauge origins. Fortunately, this price is not very high as far as computer time is concerned.

The IGLO method is, like most existing methods like LORG or GIAO, of coupled Hartree–Fock (CHF) type. This means that the $2n$-electron wavefunction is approximated as a Slater determinant, Φ, built up from $2n$ spin orbitals. We consider closed-shell states, where spin orbitals with α and β spin have the same orbital factor. The energy expectation value

$$E = \langle\Phi|\hat{\mathcal{H}}|\Phi\rangle \tag{17}$$

is made stationary with respect to variation of the spin orbitals, subject to their orthogonality condition. The $\hat{\mathcal{H}}$ in equation (17) is that given by equation (12), i.e., it is expanded in powers of the field strength $\boldsymbol{B}$ and the magnetic moment $\boldsymbol{\mu}$ of the nucleus. The orbitals φ_i occupied in Φ will also be expanded in powers of $\boldsymbol{B}$ and $\boldsymbol{\mu}$, so that E will be given as an expansion of the same type. If we require stationarity of E for all values of $\boldsymbol{B}$ and $\boldsymbol{\mu}$ (in a neighborhood of $\boldsymbol{B} = 0$ and $\boldsymbol{\mu} = 0$), we end up with coupled Hartree–Fock theory.

To zeroth order, one has to solve the ordinary Hartree–Fock equations

$$\hat{F}^{(0)}\varphi_i^{(0)} = \varepsilon_i^{(0)}\varphi_i^{(0)}, \quad \hat{F}^{(0)} = \hat{h}^{(0)} + \sum_{j=1}^{n}(2\hat{J}_j^{(0)} - \hat{K}_j^{(0)}) \tag{18}$$

where $F^{(0)}$ is the unperturbed Fock operator, ${\varphi_i}^{(0)}$ are the unperturbed orbitals and ${\varepsilon_i}^{(0)}$ their energies, $\hat{h}^{(0)}$ is the one-electron part of the unperturbed Hamiltonian, and ${\hat{J}_j}^{(0)}$ and $\hat{K}_j^{(0)}$ are the contributions of ${\varphi_j}^{(0)}$ to the Coulomb and exchange operators, respectively.

To first order in $\boldsymbol{B}$, one gets an equation for the first-order corrections ${\varphi_i}^{(1)}$ to the orbitals. In terms of the ${\varphi_i}^{(0)}$ and ${\varphi_i}^{(1)}$, the components of the chemical shift tensors can then be calculated as simple expectation values. If one has chosen a common gauge origin (e.g., the position of the nucleus for an atom), one is dealing with conventional CHF theory.

Remembering that a change of the gauge origin can be achieved by a gauge transformation as in equation (5) one may choose to replace the expectation value in equation (17) by $E = \langle\Phi|\hat{U}^{\dagger}\hat{\mathcal{H}}\hat{U}|\Phi\rangle$. By choosing $\hat{U}$ according to equation (5) nothing is gained, since a change of the gauge origin can also be formulated directly, just by replacing $\boldsymbol{R}$ by $\boldsymbol{R}'$. However, one can use a more general unitary transformation, $\hat{U}$, than that given by equation (6), allowing different gauge origins for different orbitals. Details of such nonlocal gauge transformations can be found elsewhere.[12,15]

Performing this transformation, we obtain the working equations of the IGLO method for chemical shifts (for the susceptibilities, see e.g. Kutzelnigg et al.[5])

$$\{(1-\hat{P}_0)\hat{\tilde{F}}_k^{(1)} - \hat{\tilde{P}}_k^{(1)}\hat{F}^{(0)} + (1-\hat{P}_0)\hat{F}^{(0)}\}\psi_k^{(1)} = 0 \tag{19}$$

$$\hat{P}^{(0)} = \sum_{j=1}^{n}|\psi_j^{(0)}\rangle\langle\psi_j^{(0)}| \tag{20}$$

$$\hat{\tilde{P}}_k^{(1)} = \sum_{j=1}^{n}|\psi_j^{(1)}\rangle\langle\psi_j^{(0)}| - |\psi_j^{(0)}\rangle\langle\psi_j^{(1)}| + [|\psi_j^{(0)}\rangle\langle\psi_j^{(0)}|, \Lambda_k - \Lambda_j] \tag{21}$$

$$\hat{\tilde{F}}_k^{(1)} = \hat{\tilde{h}}_k^{(1)} - \sum_{j=1}^{n}\hat{\tilde{K}}_j^{(1)} - \sum_{j=1}^{n}[\hat{K}_j^{(0)}, \Lambda_j - \Lambda_k] \tag{22}$$

$$\Lambda_k(r) = \frac{e}{2c\hbar}(\boldsymbol{R}_k \times \boldsymbol{B})\cdot\boldsymbol{r} \tag{23}$$

All wavefunctions and operators in these working equations are real. The first-order operators, characterized by a tilde, are then antisymmetric.

After having solved equation (18) and before considering equation (19), one transforms from the canonical orbitals ${\varphi_i}^{(0)}$ to the localized orbitals ${\psi_i}^{(0)}$ according to the criterion of Boys. $\hat{P}^{(0)}$ is the projector onto the occupied unperturbed states, $\hat{\tilde{P}}_k^{(1)}$ is a projector involving unperturbed orbitals ${\psi_k}^{(0)}$ and their first-order corrections ${\psi_k}^{(1)}$, as well as the commutator of the unperturbed operator with a difference of gauge functions Λ_k. $\hat{\tilde{F}}_k^{(1)}$ is a first-order coupled Fock operator typical of coupled Hartree–Fock theory, and $\hat{\tilde{K}}_j^{(1)}$ is a first-order exchange operator, defined by its matrix elements

$$\langle a|\hat{\tilde{K}}_j^{(1)}|b\rangle = (a\psi_j^{(1)}|\psi_j^{(0)}b) - (a\psi_j^{(0)}|\psi_j^{(1)}b) \tag{24}$$

with the two-electron integrals on the right-hand side in Mulliken notation. $[\hat{A}, \hat{B}]$ always means the commutator $\hat{A}\hat{B} - \hat{B}\hat{A}$. An essential feature of the IGLO equations is that $\hat{\tilde{F}}_k^{(1)}$ contains the one-electron operator $\hat{\tilde{h}}_k^{(1)}$ with the gauge appropriate for the orbital ψ_k:

$$\hat{\tilde{h}}_k^{(1)} = \frac{e}{2mci}\boldsymbol{B}\times(\boldsymbol{r}-\boldsymbol{R}_k)\cdot\hat{\boldsymbol{p}} \tag{25}$$

The only approximation with respect to the exact IGLO equations is that the commutator in equation (22) is evaluated by means of a completeness insertion. The chemical shifts are evaluated as

$$\sigma = \sigma^{\mathrm{d}} + \sigma^{\mathrm{p0}} + \sigma^{\mathrm{p1}} \tag{26}$$

$$\sigma^{\mathrm{d}} = 2\sum_{k=1}^{n}\langle\psi_k^{(0)}|\hat{h}'_{k2}|\psi_k^{(0)}\rangle \tag{27}$$

$$\sigma^{\mathrm{p0}} = -4\sum_{j,k=1}^{n}\langle\psi_k^{(0)}|\hat{\tilde{h}}_{01}|\psi_j^{(0)}\rangle\langle\psi_j^{(0)}|\Lambda_j - \Lambda_k|\psi_k^{(0)}\rangle \tag{28}$$

$$\sigma^{\mathrm{p1}} = -4\sum_{k=1}^{n}\langle\psi_k^{(0)}|\hat{\tilde{h}}_{01}(1-\hat{P}_0)|\psi_k^{(1)}\rangle \tag{29}$$

$$\hat{\tilde{h}}_{01} = \frac{e}{mci}\frac{\boldsymbol{\mu}\times(\boldsymbol{r}-\boldsymbol{\varrho})\cdot\hat{\boldsymbol{p}}}{|\boldsymbol{r}-\boldsymbol{\varrho}|^3} \tag{30}$$

$$\hat{h}'_{k2} = \frac{e^2}{2mc^2}\frac{\{\boldsymbol{B}\times(\boldsymbol{r}-\boldsymbol{R}_k)\}\cdot\{\boldsymbol{\mu}\times(\boldsymbol{r}-\boldsymbol{\varrho})\}}{|\boldsymbol{r}-\boldsymbol{\varrho}|^3} \tag{31}$$

In fact, equations (26)–(29) refer to each tensor component of $\boldsymbol{\sigma}$. Formally, one repeats the calculation for both $\boldsymbol{B}$ and $\boldsymbol{\mu}$ in the direction of the three Cartesian axes.

Unlike in the case of a theory with a common gauge origin, σ consists of not only a diamagnetic and a paramagnetic term—there are in fact three terms. The first, σ^{d}, is easily identified as a local diamagnetic term, since it involves

the $\psi_k^{(0)}$ and a second-order operator, the third, equation (29), is clearly paramagnetic, since it involves a first-order perturbation $\psi_k^{(1)}$ of an orbital, and a first-order operator $\hat{h}_{01}$. The second term, equation (28), which vanishes for a common gauge origin, i.e., if $\Lambda_j = \Lambda_k$, shares with the genuine paramagnetic term σ^{p1} the fact that it involves only $\hat{h}_{01}$, but with a diamagnetic term that is completely expressible in terms of the unperturbed orbitals $\psi_k^{(0)}$.

We have usually regarded σ^{p0} as a local paramagnetic contribution and have defined

$$\sigma^{p} = \sigma^{p0} + \sigma^{p1} \tag{32}$$

but this is not compulsory. Anyhow, the contributions to σ are not observables—they are only useful for interpretative purposes.

5 DIGLO AND MC-IGLO

Direct IGLO or DIGLO[24] is related to ordinary IGLO in the same sense as 'direct SCF' is to ordinary SCF. While in ordinary IGLO, all two-electron integrals that are needed are evaluated at the beginning and stored on peripheral memory, in direct IGLO (based on the semidirect SCF of the TURBOMOLE package[25]), most integrals are calculated whenever they are needed, and only a small number of (expensive) integrals are stored. In using DIGLO, one achieves independence of the size of available disk space, and the number of basis functions, related to the size of the molecule, is only limited by the available computer time.

MC-IGLO[26,27] differs from IGLO insofar as it takes care of so-called *nondynamic* correlation effects. The variational wavefunction is no longer a single Slater determinant, but a linear combination of Slater determinants with both the orbitals and the expansion coefficients being varied. The standard option for MC-IGLO is the full-valence CAS (CAS = 'complete active space'), but other choices of the active space are possible. MC-IGLO has to be applied whenever the state to be considered is not well described by a single Slater determinant reference function.

6 SOME RESULTS AND APPLICATIONS

Results of IGLO calculations and applications to the elucidation of molecular structures or to the assignment of tensor components have been published in many original papers, and have been documented in reviews,[5,12] which contain a lot of material not published before. Here, we shall not discuss results that have been reviewed before, unless we regard them as particularly illustrative. In giving examples, we go from light to heavy nuclei as in Kutzelnigg et al.[5] We start with proton shifts.

It has often been conjectured that ^{1}H chemical shifts in OH groups correlate with atomic charges or even with local acidities. In a detailed study[28] it was shown that generally such a relation does not hold, but that it can be justified if one considers only a limited class of closely related molecules—in this context, to surface hydroxyls that are bounded to B, Al, Si, or P and are completely coordinated by O atoms as in zeolites.

In the field of boron hydrides, the combination of NMR measurements and IGLO calculations has turned out to be particularly fruitful for the elucidation of structures and to be a serious alternative to classical X-ray methods.[7] The ^{10}B or ^{11}B shifts are very useful in this context, since IGLO calculations for σ(B) are rather accurate even with small basis sets. This is, in part, related to the absence of lone pairs.

Table 1 shows the correlation coefficients and standard deviations of a linear regression between measured and calculated values of σ(B) for a large number of boron hydrides for various choices of structures. Although the correlation is quite good for the experimental structures, it is significantly improved if one uses ab initio optimized structures, and its quality rises with the level of the ab initio method. A final slight improvement is achieved if one does the IGLO calculation with a larger basis. The message is that the theoretical structures are more accurate than those from experiment (X-ray or electron diffraction). In some cases (e.g., B_5H_{11}), too high a degree of symmetry had been assumed in the *experimental structure*. An analogous correlation for some carboranes was poorer unless two *critical* molecules were left out. For one of these (1,5-$C_2B_3H_5$), it was found that electron correlation effects are non-negligible (see Section 7); for the other critical molecule (1,2-$C_2B_3H_7$), the (rather old) NMR spectrum was erroneous.

For ^{13}C shifts of neutral molecules, there has been increased interest in recent years in theoretical studies of the conformational dependence of σ(C). An investigation by Barfield on the *γ-gauche* effect[29] can be mentioned here. In polymers such as poly(isobutene) the chemical shifts depend on whether the polymer is isotactic, syndiotactic, or amorphous. For an amorphous polymer, the distribution of various conformations gives rise to broad, unresolved resonances in the ^{13}C NMR. These can be simulated (and analyzed) by IGLO calculations on conformations of model oligomers.[30]

The existence of ring currents in benzene and similar molecules has been a controversal subject for some time. A few definite statements can now be made.[31] The high-frequency shift of σ(H) in olefins has a different origin to the additional high-frequency shift in benzene and other aromatic compounds. This extra shift is due to the ring current in the π system, which deshields the out-of-plane component σ_{zz} by a few ppm with respect to nonaromatic systems, of which only about 1 ppm remains in the isotropic shift. In neutral idealized Hückel annulenes, one finds a ring current contribution to σ(H) that is roughly proportional to the number of π electrons.[12]

The most spectacular applications of IGLO calculations to ^{13}C shifts are probably those in carbocations. It has been verified[5] that the 2-norbornyl cation is non-classic, that in the norbornadienyl cation there is a three-center rather than a five-center bond, and that the cyclobutadiene dication $C_4H_4^{2+}$ has a nonplanar equilibrium structure.

After ^{1}H, ^{13}C, and ^{19}F, one of the most widely studied nuclei is ^{31}P. A systematic collection of IGLO results for σ(P) has been published,[5,32] and more work is in progress. Recently, the synthesis of PS_3^- has been claimed;[33] however, the reported ^{31}P shift[33] of 52.3 ppm is inconsistent with that computed for PS_3^- (D_{3h}, basis II), namely 436 ppm. It would fit better with $P_2S_6^{2-}$, for which the IGLO value is 77 ppm.

While cubic P_8 does not exist (the equilibrium structure of P_8 is less symmetric[34]), some cubic systems derived formally

Table 1 Statistical Analysis[a] of the Performance of IGLO Calculations[7]

IGLO basis (geometry)	Slope	Correlation coefficient	Deviation (ppm) Largest	Standard
DZ (experiment)	1.08	0.984	18.5	5.3
DZ (3-21G)	1.02	0.990	10.4	5.5
DZ (6-31G*)	1.00	0.994	5.4	2.9
DZ (MP2/6-31G*)	1.01	0.999	3.1	1.2
II′ (MP2/6-31G*)	1.01	0.999	2.2	1.4

[a]Results of a least-squares analysis, IGLO versus experimental ^{11}B chemical shifts.

Table 2 Chemical Shifts of Some Phosphacubanes[a]

	$P_4C_4R_4$		$P_4Si_4R_4$		P_8
	δ_P	δ_C	δ_P	δ_{Si}	δ_P
IGLO[b]	235	−11.7	−182	−15.3	−36
Experiment[c]	257.4	−29.1	−177.0	−28.5	

[a]Chemical shifts in ppm with respect to 85% H_3PO_4 (δ_P) and TMS (δ_C and δ_{Si}).
[b]R = H.
[c]R = t-C_4H_9.

from P_8 have been synthesized, namely, $(RCP)_4$ and $(RSiP)_4$. The measured and computed shifts are compared in Table 2.[35] The poorer agreement for δ(C) and δ(Si) is in part due to the difference of R in experiment and theory.

An important feature of theoretical studies, such as IGLO calculations, is that information about principal values and the orientation of principal axis systems are directly available, since the full shielding tensor is calculated. Thus, interesting comparisons with results from solid state NMR can be made. Quite often, these data, especially those on the orientation of principal axis systems, are not available from experiment. The calculations then give additional and complementary information. The phosphorus shielding tensors in dithiadiphosphetanes[36] and iminophosphanes[37] have been studied.

In a cooperation with M. Jansen et al., the chemical shift tensors of molecules of the type $P_4O_6S_x$, x = 0, ... 4, have been calculated and compared with the experimental counterparts.[38] The results are shown in Table 3. The agreement between theory and experiment for the isotropic shifts is usually satisfactory. It is also not unexpected that the agreement is usually better for the formally five-valent than for the three-valent P, because the former has no lone pairs. While there is fair agreement between experimental and theoretical tensor components for four of the five molecules, in one case, namely, P_4O_6S, a large discrepancy appears for P(III). However, this discrepancy can be completely removed if one assumes that in the crystal there is free rotation around the threefold axis going through the PS bond. Transformation of the shift tensors to the new reference frame reestablishes the consistency between theory and experiment.

Rather little has been published on IGLO calculations involving nuclei of atoms of the fourth and higher rows. Some results for Ge and Se are displayed in Table 4. To give an example of a fifth-row atom, we mention some recent calculations on Xe. It has been observed that Xe adsorbed in an Na^+-containing zeolite shows a downfield shift (+60 ppm with respect to free Xe), while Xe adsorbed in an Ag^+-containing zeolite exhibits an upfield shift (−70 ppm).[39] Model calculations on Na^+Xe and Ag^+Xe at the respective equilibrium distances ($5.5a_0$ and $6.0a_0$, respectively) led to shifts of +61 and −66 ppm.[40]

7 CORRELATION AND RELATIVISTIC EFFECTS

Since IGLO is a method based on a single Slater determinant wavefunction, i.e., one in which effects of electron correlation are ignored, it is surprising that it works so well in many cases, while for many other properties electron correlation cannot generally be ignored. A partial answer lies in the fact that the chemical shift is a one-electron property (as is the magnetic susceptibility). Two-electron properties are usually much more sensitive to electron correlation.

If one distinguishes between dynamic correlation and nondynamic correlation, in the sense that the former is related to the short-range electron interaction, and the latter to near degeneracy or avoided crossing (i.e., the presence of low-lying excited states), then one expects that only nondynamic correlation will have a *strong* effect on one-electron properties. While the treatment of dynamic correlation requires long expansions in Slater determinants (configuration interaction, CI)—or, at a low level of approximation, Møller–Plesset perturbation theory—the method of choice for the treatment of nondynamic correlation is a multiconfiguration SCF (MC-SCF) approach, as implemented in MC-IGLO[26] or, more recently, MC-GIAO.[41]

In those cases where SCF-IGLO (or GIAO) is a good starting approximation, the results can be somewhat improved by means of Møller–Plesset perturbation theory, for example, the GIAO-MP2 method of Gauss.[42] MP2 is not very helpful for those cases where nondynamic correlation matters, like for O_3.

How can one know when strong correlation effects are to be expected? This is usually the case if strong paramagnetic (deshielding) contributions are present. Their existence is also related to the presence of low-lying excited states. While local diamagnetic contributions are well reproduced on an SCF level, paramagnetic ones are usually overestimated (in absolute value). For example, the ^{17}O chemical shieldings in ozone are much too paramagnetic at the SCF level (about −3000 ppm), and an MC-IGLO calculation yields about −1200 ppm for the terminal and about −700 ppm for the central oxygen atom, in accordance with experimental values.[12] In fact, the shieldings in ozone are extremely paramagnetic (strongly deshielded), but this effect is greatly overestimated at the SCF level.

Table 3 Phosphorus Chemical Shift Tensors[a]

Nucleus		P_4O_6		P_4O_6S[b]	$P_4O_6S_2$	$P_4O_6S_3$	$P_4O_6S_4$
				IGLO			
P(V)	δ_{33}		−227	−227	−233	−245	−254
	δ_{22}		141	141	145	151	149
	δ_{11}		141	141	154	159	149
	δ_{iso}			18.2	22.1	21.2	14.9
				Experiment			
	δ_{33}			−205	−200	−226	−240
	δ_{22}			125	136	145	137
	δ_{11}			125	136	145	137
	δ_{iso}			15.3	23.7	20.6	11.1
				IGLO			
P(III)	δ_{33}	−139	−133	59	−131	−138	
	δ_{22}	202	201	59	189	171	
	δ_{11}	202	209	158	209	171	
	δ_{iso}	88.2	92.4	92.4	89.2	68.2	
				Experiment			
	δ_{33}			95	−90	−103	
	δ_{22}			95	218	176	
	δ_{11}			178	218	176	
	δ_{iso}			122.6	115.6	83.6	

[a]In ppm with respect to 85% H_3PO_4.
[b]The data given in the second column are values averaged over a rotation around the threefold axis.

Table 4 Chemical Shifts of Some Germanium and Selenium Compounds[a]

Molecule	Experiment	IGLO	Molecule	Experiment	IGLO
Ge_2H_6	−13.1	−10.0	SeH_2	−226	−251
GeH_3CH_3	89.5	87.1	$SeHCH_3$	−116	−103
$GeH_2(CH_3)_2$	171.1	163	$Se(SiH_3)_2$	−666	−629
$GeH(CH_3)_3$	241.8	229	SeF_4	1083	886
$Ge(CH_3)_4$	298.7	296	SeF_6	610	532
GeH_3SiH_3	−25.9	−19.7	CF_2Se	688	644
$GeCl_4$	329.6	335	C_4H_4Se	605	645, 542[b]
			SeCO	−447	−419
			SeCS	102	123

[a]Chemical shifts in ppm with respect to GeH_4 and $Se(CH_3)_2$; the shieldings $\sigma_{Ge}(GeH_4)$ and $\sigma_{Se}[Se(CH_3)_2]$ are 1738.0 and 1860.6.
[b]Data for two different geometries.

Although this is a general trend, there are notable exceptions: in F_2, which is also strongly deshielded, the SCF result is too diamagnetic by about 30 ppm, while MC-IGLO gives a reasonable value. This tendency to *under*estimate the paramagnetic contribution can be observed with some other ^{19}F shieldings as well. As an aside, the rovibronic corrections in F_2 are exceptionally large (−40 ppm), which has to be taken into account when comparing theory and experiment.

An interesting example concerns the ^{15}N shieldings in the dinitrogen oxides. These molecules have low-lying excited states due to the weak (and long) N–N bond. At the SCF level, σ(N) is predicted to be much too diamagnetic in N_2O_2 and too paramagnetic in N_2O_4. The MC-IGLO values compare much better with experiment (see Table 5). N_2O_3 is somewhere in between. The experimental values of these shieldings were difficult to obtain, and are possibly not very accurate.[43]

For organic molecules, there is a rule of thumb that correlation effects are non-negligible if both π bonds and lone pairs are present, giving rise to low-lying $n \rightarrow \pi^*$ transitions.

Since none of the available methods so far allows the treatment of relativistic effects, one can draw conclusions regarding these only indirectly (or by means of semiempirical methods). A detailed IGLO study of HX and CH_nX_{4-n}, with X = F, Cl, Br, I, revealed that relativistic effects are rather small for X = F, Cl, non-negligible for X = Br, but very large for X = I. The so-called heavy-atom effect, i.e., an increased shielding of H or C if a heavy atom is a neighbor, has largely, but not entirely, a relativistic origin.[12]

Table 5 Absolute Nitrogen Shieldings in Dinitrogen Oxides

Molecule		IGLO	MC - IGLO	Experiment[43]
N_2O_2	σ(N)	−1194	−1735	−1971
N_2O_2	$\sigma(N_1)$	−407	−470	−428
	$\sigma(N_2)$	−340	−224	−199
N_2O_4	σ(N)	−186	−125	−123

8 RELATED ARTICLES

Shielding Calculations: LORG and SOLO Approaches; Chemical Shift Scales on an Absolute Basis; Chemical Shift Tensor Measurement in Solids; Chemical Shift Tensors; Semiempirical Chemical Shift Calculations; Shielding Calculations: Perturbation Methods; Shielding: Overview of Theoretical Methods; Shielding in Small Molecules; Shielding Theory: GIAO Method.

9 REFERENCES

1. W. Kutzelnigg, *Isr. J. Chem.*, 1980, **19**, 193.
2. M. Schindler and W. Kutzelnigg, *J. Chem. Phys.*, 1982, **76**, 1916.
3. M. Schindler and W. Kutzelnigg, *J. Am. Chem. Soc.*, 1983, **105**, 1360.
4. M. Schindler, *J. Am. Chem. Soc.*, 1987, **109**, 1020.
5. W. Kutzelnigg, U. Fleischer, and M. Schindler, in *NMR basic principles and progress*, eds. P. Diehl, E. Fluck, and R. Kosfeld, Springer-Verlag, Berlin, 1990.
6. W. Gombler, J. Schaebs, and H. Willner, *Inorg. Chem.*, 1990, **29**, 2697.
7. M. Bühl and P.v.R. Schleyer, *J. Am. Chem. Soc.*, 1992, **114**, 477.
8. F. Reichel, Thesis, Köln, 1991.
9. M. Baudler, Ch. Adamek, S. Opiela, M. Budzikiewicz, and D. Ouzounis, *Angew. Chem.*, 1988, **100**, 1110.
10. A. E. Hansen and T. D. Bouman, *J. Chem. Phys.*, 1985, **82**, 5035.
11. W. Kutzelnigg, *J. Mol. Struct. (THEOCHEM)*, 1989, **202**, 11.
12. W. Kutzelnigg, U. Fleischer, Ch. van Wüllen, R. Franke, and T. van Mourik, in *Nuclear Magnetic Shieldings and Molecular Structure*, ed. J. A. Tossell, Kluwer, Dordrecht, 1993, p. 141.
13. W. Kutzelnigg, *Theor. Chim. Acta*, 1992, **83**, 263.
14. J. A. Tossell, ed., *Nuclear Magnetic Shieldings and Molecular Structure*, Kluwer, Dordrecht, 1993.
15. Ch. van Wüllen and W. Kutzelnigg, in *METECC-94*, ed. E. Clementi, STEF, Cagliari, 1993, Vol. B, p. 383.
16. P. Pulay, J. F. Hinton, and K. Wolinski, in *Nuclear Magnetic Shieldings and Molecular Structure*, ed. J. A. Tossell, Kluwer, Dordrecht, 1993, p. 243.
17. K. Ruud, T. Helgaker, K. L. Bak, and H. J. Aa. Jensen, *J. Chem. Phys.*, 1993, **99**, 3847.
18. M. Häser, R. Ahlrichs, A. P. Baron, P. Weiss, C. Horn, *Theor. Chim. Acta*, 1992, **83**, 435.
19. S. M. Cybulski and D. M. Bishop, *J. Chem. Phys.*, 1993, **98**, 8057.
20. P. Lazzeretti, M. Malagoli, and R. Zanasi, *J. Mol. Struct. (THEOCHEM)*, 1991, **234**, 127.
21. J. Geertsen, *J. Chem. Phys.*, 1989, **90**, 4892.
22. T. A. Keith and R. W. F. Bader, *Chem. Phys. Lett.*, 1993, **210**, 223.
23. P. Lazzeretti, M. Malagoli, and R. Zanasi, *Chem. Phys. Lett.*, 1994, **220**, 299.
24. U. Meier, Ch. van Wüllen, and M. Schindler, *J. Comp. Chem.*, 1992, **13**, 551.
25. R. Ahlrichs, B. Bär, M. Häser, H. Horn, and C. Kölmel, *Chem. Phys. Lett.*, 1989, **162**, 165.
26. Ch. van Wüllen and W. Kutzelnigg, *Chem. Phys. Lett.*, 1993, **205**, 563.
27. Ch. van Wüllen and W. Kutzelnigg, *J. Chem. Phys.*, in press.
28. U. Fleischer, W. Kutzelnigg, A. Bleiber, and J. Sauer, *J. Am. Chem. Soc.*, 1993, **115**, 7833.
29. M. Barfield, in *Nuclear Magnetic Shieldings and Molecular Structure*, ed. J. A. Tossell, Kluwer, Dordrecht, 1993, p. 523.
30. R. Born, H. W. Spiess, W. Kutzelnigg, U. Fleischer, and M. Schindler, *Macromolecules*, 1994, **27**, 1500.
31. U. Fleischer, and W. Kutzelnigg, Phosphorus, *Sulfur Silicon Relat. Elem.*, 1993, **77**, 105.
32. H. W. Roesky, R. Ahlrichs, and S. Brode, *Angew. Chem.*, 1986, **98**, 91.
33. D. Hohl and R. O. Jones, *J. Chem. Phys.*, 1990, **92**, 6710.
34. U. Fleischer, Ch. van Wüllen and W. Kutzelnigg, *Phosphorus, Sulfur Silicon Relat. Elem.*, 1994, **93**, 365.
35. K. Krüger, G. Grossmann, U. Fleischer, R. Franke, and W. Kutzelnigg, *Magn. Reson. Chem.*, 1994, **32**, 596.
36. D. Gudat, W. Hoffbauer, E. Niecke, W. W. Schoeller, U. Fleischer, and W. Kutzelnigg, *J. Am. Chem. Soc.*, 1994, **116**, 7325.
37. M. Jansen, F. Frick, W. Hoffbauer, A. R. Grimmer, W. Kutzelnigg, and U. Fleischer, *Naturwissenschaften*, 1993, **80**, 465.
38. R. Grosse, R. Burmeister, B. Boddenberg, A. Gedenon, and J. Fraissard, *J. Phys. Chem.*, 1991, **95**, 2443.
39. A. Freitag, Ch. van Wüllen, and V. Staemmler, *Chem. Phys.*, 1995, **192**, 267.
40. K. Ruud, T. Helgaker, R. Kobayashi, P. Jørgensen, K. L. Bak, and H. J. Aa. Jensen, *J. Chem. Phys.*, 1994, **100**, 8178.
41. J. Gauss, *Chem. Phys. Lett.*, 1992, **191**, 614.
42. J. Mason, in *Nuclear Magnetic Shieldings and Molecular Structure*, ed. J. A. Tossell, Kluwer, Dordrecht, 1993, p. 449.

Biographical Sketches

Werner Kutzelnigg. *b* 1933. Diplom, 1958, Dr.rer.nat., 1960, Freiburg i.B. Postdoctoral work, Paris and Uppsala. Dr. habil., Göttingen, 1967. Professor, Karlsruhe, 1970; Professor, Bochum 1973. Approx. 180 publications. Research interests: various aspects of theoretical chemistry, from the development of new methods to a qualitative understanding.

Ulrich Fleischer. *b* 1958. Diplom, 1984, Dr.rer.nat., 1992, Bochum. 25 publications. Research interests: theory of molecular structure and properties.

Christoph van Wüllen. *b* 1963. Diplom, 1988, Münster; Dr.rer.nat., 1992, Bochum. 12 publications. Research interests: theory of electronic and molecular structure.

Shielding Calculations: LORG and SOLO Approaches

Aage E. Hansen and Merete Bilde

University of Copenhagen, Copenhagen, Denmark

1	Introduction	1
2	Theory	1
3	Options	2
4	Applications	4
5	Concluding Remarks	6
6	Related Articles	7
7	References	7

1 INTRODUCTION

The LORG (localized orbital–local origin) approach to the calculation of nuclear magnetic shieldings[1–4] is a variant of coupled Hartree–Fock (CHF) theory[5] where local gauge origins are associated with localized molecular orbitals. In SOLO (second-order LORG),[4,6] the approach is extended to second order in electron correlation.[7] For general surveys of theoretical approaches, see ***Shielding: Overview of Theoretical Methods***.

The LORG and SOLO approaches are formulated and presently implemented[8] as post-Hartree–Fock methods allowing several choices of localization schemes and gauge options, as described in Section 3, and allowing analyses of relationships between shielding properties and geometric as well as electronic molecular structure features, as described in Section 4. Section 4 also surveys representative applications, while relationships to other approaches using local gauge origins are included in Section 5.

2 THEORY

2.1 LORG

The LORG approach was first derived[1] from Ramsey's expression[9] for the shielding tensor by identifying the matrix elements and energy differences in the paramagnetic contributions as the transition moments and energies in a localized molecular orbital version of the random phase approximation (RPA).[7] Local gauge origins were assigned to each occupied localized orbital, and orthogonality and completeness properties of the RPA provided the following expression for a Cartesian component of the shielding tensor:[1]

$$\begin{aligned}\sigma_{ij}(\mathrm{LORG}) &= \sigma_{ij}^{\mathrm{d}}(\mathrm{LORG},1) + \sigma_{ij}^{\mathrm{d}}(\mathrm{LORG},2) + \sigma_{ij}^{\mathrm{p}}(\mathrm{LORG}) \\ &= c^{-2}\sum_{\alpha}\langle\alpha|\{(\boldsymbol{r}-\boldsymbol{R}_\alpha)\cdot\boldsymbol{r}\delta_{ij} - [\boldsymbol{u}_i\cdot(\boldsymbol{r}-\boldsymbol{R}_\alpha)](\boldsymbol{u}_j\cdot\boldsymbol{r})\}/r^3|\alpha\rangle \\ &\quad + \mathrm{i}c^{-2}\sum_{\alpha}\sum_{\beta}(\boldsymbol{u}_i\cdot\langle\alpha|\hat{\ell}/r^3|\beta\rangle)\{\boldsymbol{u}_j\cdot[(\boldsymbol{R}_\alpha-\boldsymbol{R}_\beta)\times\langle\beta|\boldsymbol{r}|\alpha\rangle]\} \\ &\quad - 2c^{-2}\sum_{\alpha m}\sum_{\beta n}(\boldsymbol{u}_i\cdot\langle\alpha|\hat{\ell}/r^3|m\rangle)\Omega_{\alpha m,\beta n}(\boldsymbol{u}_j\cdot\langle n|\hat{\ell}^{(\alpha)}|\beta\rangle) \qquad (1)\end{aligned}$$

in atomic units. The localized orbitals α and β are doubly occupied in the Hartree–Fock ground state $|\Delta_0\rangle$, and m and n are virtual orbitals. The quantities $\boldsymbol{u}_i$ and $\boldsymbol{u}_j$ are Cartesian unit vectors, the angular momentum operator $\hat{\boldsymbol{l}}$ and position vectors $\boldsymbol{r}$ are referred to the magnetic nucleus, and $\boldsymbol{R}_\alpha$ is a local origin assigned to orbital α, so that $\hat{\boldsymbol{l}}^{(\alpha)} \equiv (\boldsymbol{r}-\boldsymbol{R}_\alpha)\times\hat{\boldsymbol{p}}$ is the angular momentum relative to this origin. $\boldsymbol{\Omega}$ is an inverse energy matrix

$$\Omega = (\mathbf{A}-\mathbf{B})^{-1},\ \begin{cases} A_{\alpha m,\beta n} = \langle\alpha\to m|\hat{\mathcal{H}}-E_0|\beta\to n\rangle \\ B_{\alpha m,\beta n} = \langle\alpha\to m,\beta\to n|\hat{\mathcal{H}}|\Delta_0\rangle \end{cases} \qquad (2)$$

where E_0 is the energy of $|\Delta_0\rangle$. Expressions for the matrix elements $A_{\alpha m,\beta n}$ and $B_{\alpha m,\beta n}$ have been given previously.[1,3] In equation (1) all references to a common origin are replaced by internal distance vectors, cf. equations (8)–(12) in ***Shielding: Overview of Theoretical Methods***. However, the conventional distinctions[9] between dia- and paramagnetic terms no longer apply; in particular σ_{ij}^{d} (LORG, 2) mixes erstwhile dia- and paramagnetic terms. Diamagnetic labels, d, now imply that these terms are computed solely from occupied orbitals, and the paramagnetic label, p, implies contributions involving the virtual orbital space.

Explicit evalution of σ_{ij}^{p} (LORG) is time-consuming and impractical, unless analysis into individual excitations $\alpha\to m$ is exploited. Introducing instead the linear equations[2]

$$\sum_{\alpha,m}(\boldsymbol{A}-\boldsymbol{B})_{\beta n,\alpha m}\langle\alpha|\hat{\boldsymbol{\rho}}|m\rangle = \mathrm{i}\langle\beta|\hat{\boldsymbol{p}}|n\rangle \qquad (3)$$

$$\sum_{\alpha,m}(\boldsymbol{A}-\boldsymbol{B})_{\beta n,\alpha m}\langle\alpha|\hat{\boldsymbol{\eta}}|m\rangle = \mathrm{i}\langle\beta|\hat{\boldsymbol{l}}|n\rangle \qquad (4)$$

which can be solved iteratively for the implied matrix elements $\langle\alpha|\hat{\boldsymbol{\eta}}|m\rangle$, the paramagnetic term becomes[2]

$$\begin{aligned}\sigma^{\,p}_{ij}(\mathrm{LORG}) &= \sum_{\alpha}\sigma_{ij}^{\mathrm{p}}(\mathrm{LORG},\alpha) \\ &\equiv -2\mathrm{i}c^{-2}\sum_{\alpha}\sum_{m}(\boldsymbol{u}_i\cdot\langle\alpha|\hat{\ell}/r^3|m\rangle)[\boldsymbol{u}_j\cdot(\langle m|\hat{\boldsymbol{\eta}}|\alpha\rangle - \boldsymbol{R}_\alpha\times\langle m|\hat{\boldsymbol{\rho}}|\alpha\rangle)] \qquad (5)\end{aligned}$$

which is now a sum of bond contributions. The diamagnetic terms can similarly be condensed to bond contributions

$$\sigma_{ij}^{\mathrm{d}}(\mathrm{LORG},1) + \sigma_{ij}^{\mathrm{d}}(\mathrm{LORG},2) \equiv \sum_{\alpha}\sigma_{ij}^{\mathrm{d}}(\mathrm{LORG},\alpha) \qquad (6)$$

For simplicity the term 'bond' includes cores and lone pairs.

The original derivation[1] represented a reduction of RPA to its static limit, identical to coupled Hartree–Fock (CHF) theory.[5] A later derivation[10] established the connection to CHF theory, and showed that equation (1) can be rewritten as:

$$\begin{aligned}&\sigma_{ij}(\mathrm{LORG}) = \sigma_{ij}(\mathrm{CHF},\boldsymbol{R}=0) \\ &-c^{-2}\sum_{\alpha}\langle\alpha|[\boldsymbol{R}_\alpha\cdot\boldsymbol{r}\delta_{ij} - (\boldsymbol{u}_i\cdot\boldsymbol{R}_\alpha)(\boldsymbol{u}_j\cdot\boldsymbol{r})]/r^3|\alpha\rangle \\ &+\mathrm{i}c^{-2}\sum_{\alpha}\sum_{\beta}(\boldsymbol{u}_i\cdot\langle\alpha|\hat{\ell}/r^3|\beta\rangle)[\boldsymbol{u}_j\cdot(\boldsymbol{R}_\alpha-\boldsymbol{R}_\beta)\times\langle\beta|\boldsymbol{r}|\alpha\rangle] \\ &-2\mathrm{i}c^{-2}\sum_{\alpha}\sum_{m}(\boldsymbol{u}_i\cdot\langle\alpha|\hat{\ell}/r^3|m\rangle)[\boldsymbol{u}_j\cdot(\boldsymbol{R}_\alpha\times\langle m|\hat{\boldsymbol{\rho}}|\alpha\rangle)] \qquad (7)\end{aligned}$$

where $\sigma_{ij}(\mathrm{CHF},\ \boldsymbol{R}=0)$ is the CHF result using a common origin at the magnetic nucleus.[5] In the Hartree–Fock limit

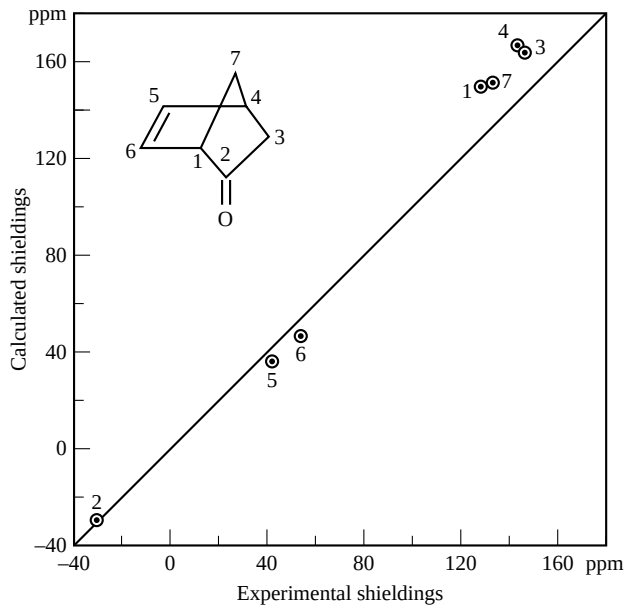

Figure 1 LORG isotropic ^{13}C shieldings in 2-norbornenone[2] versus experimental values. (Reproduced from Jameson[11] by permission of the Royal Society of Chemistry)

$\langle m|\hat{\boldsymbol{\rho}}|\alpha\rangle = \langle m|\boldsymbol{r}|\alpha\rangle$,[1] and orbital completness then makes the correction terms on the right-hand side of equation (7) cancel identically. CHF and LORG hence converge in the Hartree–Fock limit,[1,10] by the same token demonstrating the origin independence of CHF theory in this limit.

It was noted already by Ramsey[9] that severe numerical problems arise in inexact, i.e. finite basis, calculations of chemical shielding because of improper balancing of long range dia- and paramagnetic terms. It follows from equation (7) that the computationally important aspect of local origins in fact lies in the damping of such unbalanced long range terms, as has been shown explicitly in Table I and Appendix C of Hansen and Bouman.[1]

In many practical applications only the isotropic part of the shielding tensor

$$\bar{\sigma}(\mathrm{LORG}) = (1/3)\sum_i \sigma_{ii}(\mathrm{LORG}) \tag{8}$$

is of interest, and the overall performance of LORG for the ^{13}C isotropic shieldings in 2-norbornenone[2] using a small atomic basis set ([3s2p/2s]) is illustrated in Figure 1; experimentally computed agreements are within ± 10 ppm over a total range of about 200 ppm.

2.2 SOLO

Equations (1), (2) and (7) are consistent through first order in the fluctuation potential relative to $|\Delta_0\rangle$.[7] LORG, and CHF in general, can hence be considered consistent through first order in electron correlation. To extend the LORG approach to second order in electron correlation,[6] we utilized the second-order polarization propagator (SOPPA) approach of Oddershede et al.,[7,12] and to establish contact with this approach we rewrite the paramagnetic contribution in equation (1) as follows:

$$\sigma^{\mathrm{p}}_{ij}(\mathrm{LORG}) = -2c^{-2}\sum_{\alpha m}\sum_{\beta n} t[\boldsymbol{u}_i\cdot\hat{\boldsymbol{l}}/r^3]^{(1)}_{\alpha m}\Omega^{(1)}_{\alpha m,\beta n}t[\boldsymbol{u}_j\cdot\hat{\boldsymbol{l}}^{(\alpha)}]^{(1)}_{n\beta} \tag{9}$$

where superscripts indicate evaluation to first order in electron correlation and $[\boldsymbol{\Omega}^{(1)}]^{-1} = [\mathbf{A}^{(1)} - \mathbf{B}^{(1)}]$ can be identified with the principal propagator $\mathbf{P}(E = 0)$ to first order.[7,12] The terms $t[\boldsymbol{u}_i\cdot\hat{\boldsymbol{l}}/r^3]_{\alpha m}$ and $t[\boldsymbol{u}_j\cdot\hat{\boldsymbol{l}}^{(\alpha)}]_{n\beta}$ represent transition moments.

Following this line of approach we defined[4,6] the working second-order LORG (SOLO) expression for an element of the shielding tensor as follows:

$$\begin{aligned}
&\sigma_{ij}(\mathrm{SOLO}) \equiv \sigma^{\mathrm{d}}_{ij}(\mathrm{LORG},1) + \sigma^{\mathrm{d}}_{ij}(\mathrm{LORG},2) + \sigma^{\mathrm{p}}_{ij}(\mathrm{SOLO})\\
&= c^{-2}\sum_{\alpha}\langle\alpha|\{(\boldsymbol{r}-\boldsymbol{R}_\alpha)\cdot\boldsymbol{r}\delta_{ij} - [\boldsymbol{u}_i\cdot(\boldsymbol{r}-\boldsymbol{R}_\alpha)](\boldsymbol{u}_j\cdot\boldsymbol{r})\}/r^3|\alpha\rangle\\
&\quad + \mathrm{i}c^{-2}\sum_{\alpha}\sum_{\beta}(\boldsymbol{u}_i\cdot\langle\alpha|\hat{\ell}/r^3|\beta\rangle)\{\boldsymbol{u}_j\cdot[(\boldsymbol{R}_\alpha-\boldsymbol{R}_\beta)\times\langle\beta|\boldsymbol{r}|\alpha\rangle]\}\\
&\quad - 2c^{-2}\sum_{\alpha m}\sum_{\beta n} t[\boldsymbol{u}_i\cdot\hat{\ell}/r^3]^{(2)}_{\alpha m}\Omega^{(2)}_{\alpha m,\beta n}t[\boldsymbol{u}_j\cdot\hat{\ell}^{(\alpha)}]^{(2)}_{n\beta}
\end{aligned} \tag{10}$$

This differs from equation (1) only in the last term, where the transition moments now include second-order corrections, and where $[\boldsymbol{\Omega}^{(2)}]^{-1}$ is the principal propagator $\mathbf{P}(E = 0)$ to second order. We have followed Paidarova et al.[12] in assuming that diamagnetic terms can be evaluated directly from the Hartree–Fock ground state, and explicit expressions for the required second-order expansions are available elsewhere.[7] An iterative second-order method, mutatis mutandis equations (3) and (4), has been implemented,[8] and the terms in equation (10) can hence be written as sums of bond contributions, mutatis mutandis equations (5) and (6).

To illustrate the performance of SOLO, Figure 2 compares LORG, SOLO, and experimental results for the ^{15}N isotropic shielding in pyridine and the *n*-azines using a [3s3p1 d/2s] atomic basis.[13] Here the isotropic shieldings change by up to about 50 ppm on going from LORG to SOLO, generally improving the agreements with experiments.

3 OPTIONS

LORG and SOLO calculations require a choice of localization scheme and of local origins, as discussed in Sections 3.1 and 3.2 In addition, LORG and SOLO share with other ab initio methods the chore of choosing an atomic orbital basis. In Section 3.3 we comment on computational strategies and discuss the interplay between localization, local origin, and basis set.

3.1 Localization Schemes

As presently implemented,[8] LORG and SOLO assume that the occupied orbitals are localized by the Foster–Boys procedure which maximizes the quantity $\Sigma_{\alpha,\beta}|\boldsymbol{\mathcal{R}}_\alpha - \boldsymbol{\mathcal{R}}_\beta|^2$, where

$$\boldsymbol{\mathcal{R}}_\alpha \equiv \langle\alpha|\mathbf{r}|\alpha\rangle \tag{11}$$

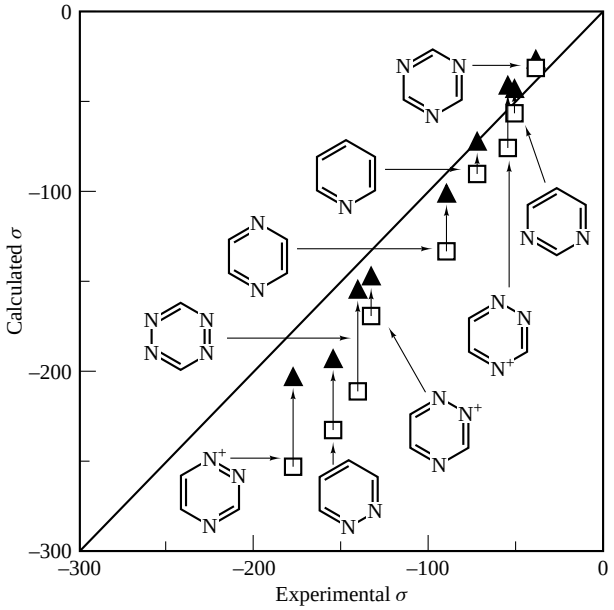

Figure 2 Absolute nitrogen shieldings in azines. Calculated versus experimental isotropic shieldings for the nitrogen atoms at both first-order (LORG) and second-order (SOLO) levels of electron correlation; (□) LORG; (▲) SOLO. (Reproduced from Bouman and Hansen[13] by permission of *Chemical Physics Letters*)

is the centroid of the localized orbital α.[14] The separation of the centroids is hence maximized, and the immediate results of this procedure are localized core orbitals and essentially spheroidal localized σ orbitals in typical single bonds, while multiple bonds will be represented by τ ('banana') orbitals. Hence, conjugated hydrocarbons and simple aromatics will show structures with alternating single bonds and τ bonds, while heteroatomic compounds (in particular those with multiple bonds and lone pairs) can exhibit complicated patterns that do not lend themselves easily to structural interpretations.

For many purposes the actual orbital pattern is of no interest or consequence, and LORG and SOLO calculations can proceed directly from localized orbitals resulting from the above procedures. However, for structural interpretations of the results, e.g. in order to extract σ and π contributions, or to ensure proper representation of symmetry, it may be advantageous to design the localization procedure. In its simplest form this is done by diagonalization of the Fock matrix within a subset of localized orbitals,[15] transforming two-center τ orbitals into σ and π orbitals, or a pair of sp^2-type lone-pair orbitals into conventional nonbonding and σ-type lone-pair orbitals. More generally, groups of orbitals, e.g. core, σ, and π orbitals in planar unsaturated or aromatic systems, can be localized separately with the additional option of leaving a group such as the π orbitals delocalized. The localizations amount to different unitary transformations within the occupied orbital space, and leave the Hartree–Fock ground state and the RPA invariant.[15] However, different localizations lead to different sets of local origins, and in small basis sets the LORG shieldings are somewhat sensitive to the choice of localization.

The local origins refer to occupied orbitals only and localization of the virtual orbitals is normally immaterial, but can be introduced[15] if analysis of the paramagnetic terms into localized orbital excitations is desired.

3.2 Local Origins

Since equations (1) and (7) converge to common as well as local origin independence in the Hartree–Fock limit, the choice of a set of $\boldsymbol{R}_\alpha$ can be viewed as a means of accelerating convergence to the Hartree–Fock limit for a given atomic orbital basis set and localization scheme. Conversely, the choice becomes less critical as the basis set is improved. We have identified[1] two standard origin options,

$$\text{FULL LORG/SOLO:}\boldsymbol{R}_\alpha \equiv \mathcal{R}_\alpha \equiv \langle\alpha|\mathbf{r}|\alpha\rangle \quad \text{for all } \alpha \tag{12}$$

and

$$\text{LORG/SOLO:} \quad \boldsymbol{R}_\alpha \equiv 0 \quad \text{for } \mathcal{R}_\alpha\rangle R_{\min} \tag{13a}$$

$$\boldsymbol{R}_\alpha \equiv \mathcal{R}_\alpha \equiv \langle\alpha|\mathbf{r}|\alpha\rangle \quad \text{for } \mathcal{R}_\alpha\rangle R_{\min} \tag{13b}$$

where equation (13a) colloquially speaking selects the orbitals that are bonded to the magnetic nucleus. LORG is hence a compromise between a local common origin CHF and FULL LORG, and Table 1 of Hansen and Bouman[1] provided the initial rationale for such a compromise for the calculation of ^{13}C shieldings. The quantity $R_{\min}$ will normally be chosen to be smaller than a typical bond distance, and is often quite uncritical. However for molecules with polarized bonds experimentation may be required, as discussed in a recent study of shieldings in the peptide unit.[16] The respective merits of the FULL LORG and LORG options are discussed below.

3.3 Strategies, Choice of Options

Since the LORG and SOLO approaches are formulated and presently implemented[8] as post-Hartree–Fock methods, these calculations presuppose an SCF calculation generating canonical molecular orbitals and two-electron integrals in atomic or molecular orbital bases; in the former case the integrals are subsequently transformed to molecular orbital basis.[15] The advantage of a post-Hartree–Fock strategy is that experimentation with the various options is quite fast and inexpensive once the molecular orbital and two-electron integral files are available for a given molecule and a given atomic orbital basis.

The interplay between options can be illustrated for ^1H and ^{13}C in benzene.[17] Figures 3(a) and (b) show the isotropic shielding in four atomic basis sets for FULL LORG and LORG using two different localization schemes, viz. a Kekulé-type structure with alternating single and σ, π double bonds, and a structure generated by separate localization of core and σ orbitals leaving π orbitals delocalized (canonical). Basis A is double-zeta [3s2p/2s],[18] basis B is [3s2p/2s1p] where the polarization function on H is a 50–50 contraction of Gaussians (α_1 = 0.50, α_2 = 1.50), basis C is [3s3p1d/2s],[3] and basis D is [3s3p1d/2s1p]. Similarly, Figures 4(a) and (b) show the *span*,[19] i.e. $\boldsymbol{\Omega} = \boldsymbol{\sigma}_{33} - \boldsymbol{\sigma}_{11}$, where $\boldsymbol{\sigma}_{33} \geq \boldsymbol{\sigma}_{22} \geq \boldsymbol{\sigma}_{11}$ are principal shieldings. The figures include estimated Hartree–Fock limits[20] and experimental results.[21,22]

For the isotropic shieldings, Figures 1(a) and (b), the FULL LORG–LORG distinction is more critical than localization

Table 1 Bond Decomposition of Isotropic LORG Shieldings[a] for ^{13}C in 2-Norbornenone (in ppm)

Bond/Nucleus	C–1	C–2	C–3	C–4	C–5	C–6	C–7
O-C–2(σ)	−1	**−59**	−1	–	–	–	–
O-C–2(π)	–	**−16**	–	–	–	–	–
C–2-C–1	**−12**	**−76**	−2	−1	–	–	–
C–2-C–3	−3	**−76**	**−9**	–	–	–	−1
C–1-C–6	**−12**	−1	–	−1	−3	**−36**	–
C–1-C–7	**−12**	−2	–	–	–	–	**−14**
C–6-C–5(σ)	−1	–	–	−1	**−50**	**−49**	−1
C–6-C–5(π)	1	−1	–	–	**−34**	**−33**	–
C–5-C–4	−1	–	–	**−9**	**−42**	−1	–
C–4-C–3	–	−1	**−11**	**−9**	–	–	–
C–4-C–7	–	−1	–	**−10**	–	–	**−15**
C–1-H–9	**−7**	−1	–	−1	–	−1	–
C–6-H–10	−1	–	–	−1	−4	**−28**	–
C–5-H–11	−1	–	–	−1	**−29**	−4	–
C–4-H–12	−1	−1	–	**−5**	−1	−1	–
C–3-H–13	–	−2	**−7**	–	–	–	–
C–3-H–14	–	−2	**−7**	–	–	–	–
C–7-H–16	–	–	–	–	−1	−1	**−12**
C–7-H–15	–	−1	–	–	–	–	**−8**
C(1s)	**203**	**203**	**203**	**203**	**203**	**203**	**203**
O(1s)	–	–	–	–	–	–	–
O(nonbonding)	−3	20	−2	–	–	–	–
O(lone pair)	–	−14	–	–	–	–	–
Total	148	−29	161	164	36	46	150

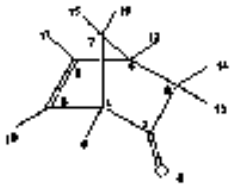

[a]Shieldings are obtained in basis A (see text) and contributions smaller than 1 ppm are neglected. The 1s(C) contributions are for the carbon nucleus given at the top of the particular column.

choice in the smaller basis sets. LORG is quite stable with respect to basis set for ^{13}C in accord with previous findings,[11] while for ^{1}H FULL LORG is the more stable option. A 'locally dense basis set' effect[23] can be detected, since increasing the basis on ^{1}H (basis B) and ^{13}C (basis C) selectively improves FULL LORG–LORG agreements for the respective nuclei. Full use of the 'locally dense basis set' concept[23] within the LORG approach is reported elsewhere.[24] For tensorial shielding properties, Figures 2(a) and (b) suggest, not unexpectedly, that basis sets of less than triple-zeta polarized quality, i.e. [3s3p1d/2s1p], are computationally unsafe.

4 APPLICATIONS

4.1 Bond and Symmetry Analyses

Equations (5) and (6) allow decomposition of the shieldings into bond contributions,[1] and Table 1 shows the contributions to the ^{13}C isotropic shielding in 2-norbornenone[17] for which the overall results are shown in Figure 1. Contributions from orbitals directly bonded to the respective nuclei are shown in bold face, and the orbital labeled O (lone pair) is directed along the C=O bond. The local nature of the shielding is quite apparent, as is the difference in local σ and π double bond contributions.

A different type of analysis obtains by exploitation of symmetry, since the paramagnetic terms can be built up one symmetry block at a time[1,25] utilizing the fact that in canonical bases the (**A** − **B**) matrix, equation (2), and hence equations (3) and (4) are block diagonal with respect to molecular point group symmetry. Equations (3) and (4) can accordingly be solved separately within irreducible representations before being transformed to localized basis. In Table 2 we illustrate this for the Cartesian elements of the shielding tensor of a ^{1}H nucleus in benzene calculated[17] in basis D of Figures 3 and 4, using in-plane x and y axes, along and perpendicular to the C-^{1}H bond, respectively. In the present case only the C_h subgroup symmetry is exploited, and the table shows the individual paramagnetic contributions from $\sigma \rightarrow \sigma^*$ ($^1A'$), $\pi \rightarrow \pi^*$ ($^1A'$), $\sigma \rightarrow \pi^*$ ($^1A''$), and $\pi \rightarrow \sigma^*$ ($^1A''$) excitations. Paramagnetic contributions from excitations out of C(1s) orbitals are neglected, while their minuscule diamagnetic contributions are included in the σ(sigma) terms. As indicated, the orbital excitations transform pairwise as the same irreducible representation; this feature persists in full D_{6h} symmetry. For the sake of the analysis, the tensors in the upper part of Table 2 hence neglect (**A** − **B**) matrix elements coupling excitations within the pairs. The agreement with the results of the complete calculation reported in the lower part of Table 2 indicates that such couplings are indeed small in the present case. Point group selection rules for the tensor elements and the relative importance of the various orbital contributions are clearly demonstrated in the table. We note in particular the small, but unique, *negative* π contribution to $\boldsymbol{\sigma}_{zz}$, ascribed to the 'ring current effect' in common NMR lore.[26] A LORG study of the ring current model is reported elsewhere.[27]

4.2 Representative Applications

LORG and SOLO calculations have been performed almost exclusively ab initio and have been based, again almost

Table 2 Symmetry and Orbital Analysis of LORG Shielding Contributions for ^{1}H in Benzene (in ppm)[a]

Transitions allowed	sigma → sigma*			sigma → π*			π → sigma*			π → π*			Sum		
σ^d	σ^d(sigma) = 34.99						$\sigma^d(\pi)$ = 1.26						36.23		
Diamagnetic tensor	38.92	0.33	0.00				11.34	1.54	0.00				50.78	1.87	0.00
	−0.56	33.41	0.00				−2.02	−3.53	0.00				−2.58	29.59	0.00
	0.00	0.00	32.64				0.00	0.00	−4.04				0.00	0.00	28.34
σ^p	−2.88			−9.63			0.60			0.46			−11.45		
Paramagnetic tensor	0.00	0.00	0.00	−17.29	0.28	0.00	−5.93	−1.62	0.00	0.00	0.00	0.00	−23.22	−1.34	0.00
	0.00	0.00	0.00	−0.20	−11.61	0.00	2.29	7.72	0.00	0.00	0.00	0.00	2.09	−3.89	0.00
	0.00	0.00	−8.65	0.00	0.00	0.00	0.00	0.00	0.00	0.00	0.00	1. 38	0.00	0.00	−7.27
σ	σ^d(sigma) = 22.47						$\sigma^d(\pi)$ = 2.31						24.78		
Sum	21.63	0.61	0.00				5.41	−0.08	0.00				27.04	0.53	0.00
	−0.76	21.80	0.00				0.27	4.19	0.00				−0.49	25.99	0.00
	0.00	0.00	23.99				0.00	0.00	−2.66				0.00	0.00	21.33

Complete	sigma			π			Sum		
Total tensor	21.26	0.65	0.00	4.43	−0.21	0.00	26.21	0.44	0.00
	−0.76	21.41	0.00	0.41	5.27	0.00	−0.35	26.38	0.00
	0.00	0.00	23.70	0.00	0.00	−3.18	0.00	0.00	20.26

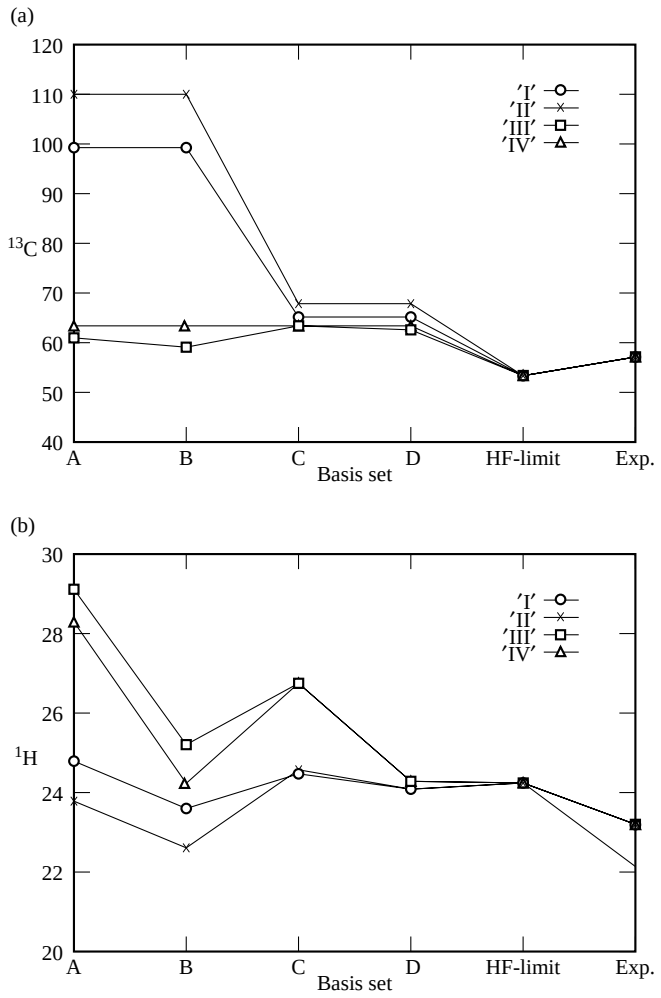

Figure 3 (a) Isotropic shieldings for ^{13}C in benzene (in ppm). (b) Isotropic shieldings for ^{1}H in benzene (in ppm). 'I', FULL LORG, Kekulé-type localization; 'II', FULL LORG, delocalized π orbitals; 'III', LORG, Kekulé-type localization; 'IV', LORG, delocalized π orbitals. See text for basis sets A–D. (HF-limit from Lazzeretti et al.,[20] experimental data from Jameson and Jameson[21,22])

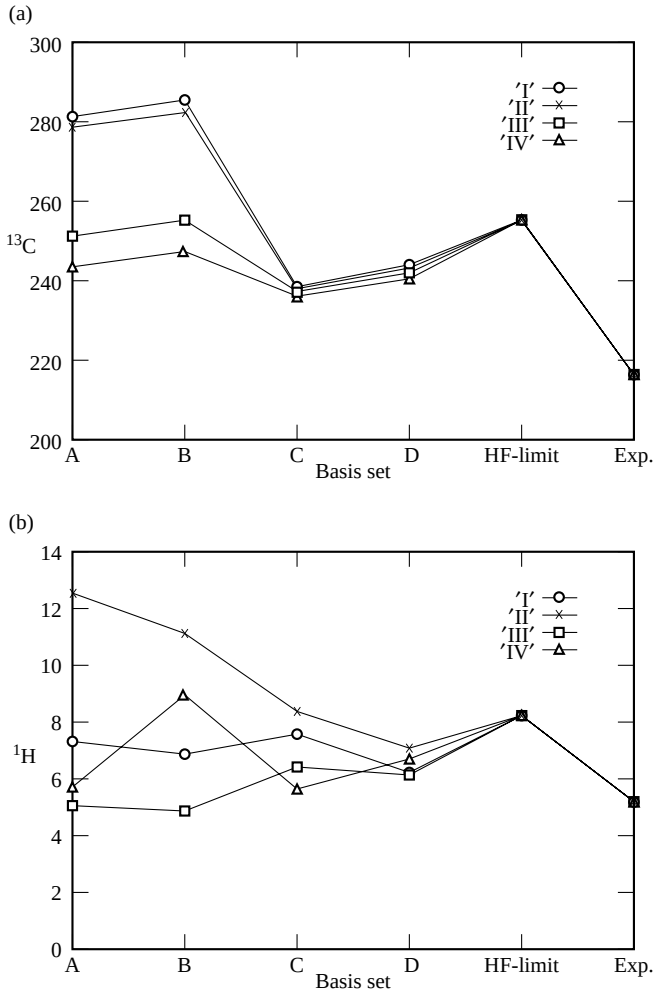

Figure 4 (a) Span, $\Omega=\sigma_{33}-\sigma_{11}$ for ^{13}C in benzene (in ppm). (b) Span, $\Omega=\sigma_{33}-\sigma_{11}$ for ^{1}H in benzene (in ppm). 'I', FULL LORG, Kekulé-type localization; 'II', FULL LORG, delocalized π orbitals; 'III' LORG, Kekulé-type localization; 'IV' LORG, delocalized π orbitals. See text for basis sets A–D. (CHF-limit from Lazzeretti et al.,[20] experimental data from Jameson[22])

exclusively, on the RPAC implementation,[8] although an application based on equation (7) has also been reported.[28] A study[29] employing a semiempirical approach concluded that the parameterization cannot adequately overcome the problems inherent in the use of a minimal basis set for shielding calculations.

Representative applications utilizing features of the LORG approach include molecular symmetry analyses of nonsymmetric shielding tensors,[4,25] a study of the importance of solvation[30] and molecular embedding[31] for deuterium isotope effects, and a study of point charge and dipolar perturbations on the shielding of the heavy atoms in the peptide unit.[16] A study of the ring current model for proton shieldings in aromatic molecules[27] is mentioned above, and a novel approach for the visual display of shielding tensors[3,25,27] has been proposed. The study of solvation effects in isotope effects[30] is based on the calculation of shielding surfaces involving hydrogen bonding; see also Orendt et al.[32] for a LORG study of hydrogen bonding effects for ^{17}O shielding tensors in larger molecules. Other LORG studies of shielding surfaces include applications to intramolecular modes in small hydrides,[33,34] in the PHO_3^{2-} ion,[35] and LORG[36] and SOLO[37] studies of weakly bound systems. LORG calculations of ligand and central atom shifts in transition metal complexes have been reported,[38,39] however as pointed out by Ellis et al.[39] calculations at the CHF level neglecting spin–orbit effects cannot be expected to be quantitatively adequate for the shielding of transition metal nuclei. Of course, an important function of theoretical shielding calculations lies in the analysis and assignment of experimental data; examples are LORG[40] and SOLO[41] assisted studies of ^{15}N shielding tensors. See also ***Shielding Tensor Calculations***.

5 CONCLUDING REMARKS

The LORG and SOLO approaches belong to a family of methods that use local origins to ensure gauge origin independence and to increase convergence towards complete basis results. The latter feature, which results from a damping

of unbalanced long range shielding contributions as discussed in Section 2.1, is essential for the comparison of shieldings between molecules of very different size, i.e. for a faithful representation of chemical shifts.[1]

The use of local origins can be traced to Kirkwood's theory[42,43] of optical rotatory power, where magnetic dipole transition moments are expanded relative to local origins, and to London's theory[44] of diamagnetic susceptibilities, where complex local gauge factors are introduced in the atomic orbital basis. LORG and SOLO took the Kirkwood approach as the point of departure,[1] and grew out of a localized orbital RPA approach to calculating and analyzing electronic spectra and circular dichroism of chiral molecules.[8,43] London's approach formed the basis for the GIAO[45] method (Gauge Invariant/Including Atomic Orbitals), see ***Shielding Theory: GIAO Method***; a perhaps more appropriate acronym is LAO (London Atomic Orbitals).[46] The IGLO[47] method (Individual Gauge for Localized Orbitals) method introduces local gauge factors in a localized molecular orbital basis, see ***Shielding Calculations: IGLO Method***. An IGAIM (Individual Gauges for Atoms in Molecules) has also been proposed,[48] and a gauge approach based on a propagator formulation of the diamagnetic shielding contribution has been explored, see Sauer et al.[49] and discussion therein. At the CHF level all these approaches converge to the same results in the Hartree–Fock limit;[10] in particular the difference between LORG and IGLO can be viewed as a difference in the evaluation of the last term in equation (7).[10]

Extensions of the above methods to electron correlation levels beyond CHF include SOLO (second-order LORG) described in Section 2.2, and a second-order Møller–Plesset (MP2) version of GIAO.[50] Although consistent through second order, these two methods are distinctly different and the relationship between SOPPA/SOLO and MP2-GIAO is being investigated.[51] Multiconfigurational versions of the GIAO/LAO method (MC-LAO[52]) and of IGLO (MC-IGLO[53]) have also been developed. At present, the merits and limitations of these post-CHF approaches cannot be considered fully explored.

6 RELATED ARTICLES

Shielding Calculations: IGLO Method; Shielding Calculations: Perturbation Methods; Shielding: Overview of Theoretical Methods; Shielding in Small Molecules; Shielding Tensor Calculations; Shielding Theory: GIAO Method.

7 REFERENCES

1. Aa. E. Hansen and T. D. Bouman, *J. Chem. Phys.*, 1985, **82**, 5035.
2. T. D. Bouman and Aa. E. Hansen, *Chem. Phys. Lett.*, 1988, **149**, 510.
3. T. D. Bouman and Aa. E. Hansen, *Int. J. Quant. Chem.*, 1989, **Symp. 23**, 381.
4. Aa. E. Hansen and T. D. Bouman, in *Nuclear Magnetic Shieldings and Molecular Structure*, ed. J. A. Tossell, Kluwer, Dordrecht, 1993, pp. 117–140.
5. W. N. Lipscomb, in *Advances in Magnetic Resonance*, ed. J. S. Waugh, Academic Press, New York, 1966, Vol. 2, pp. 138–176.
6. T. D. Bouman and Aa. E. Hansen, *Chem. Phys. Lett.*, 1990, **175**, 292.
7. J. Oddershede, P. Jørgensen, and D. L. Yeager, *Comput. Phys. Rep.*, 1984, **2**, 33.
8. T. D. Bouman and Aa. E. Hansen, *RPAC Molecular Properties Package, Version 9.0*, University of Copenhagen, 1991.
9. N. F. Ramsey, *Phys. Rev.*, 1952, **86**, 243.
10. J. C. Facelli, D. M. Grant, T. D. Bouman, and Aa. E. Hansen, *J. Comput. Chem.*, 1990, **11**, 32.
11. C. J. Jameson, in *Nuclear Magnetic Resonance, A Specialist Periodical Report*, ed. G. A. Webb, Royal Society of Chemistry, Cambridge, 1990, Vol. 19, Chap. 1
12. I. Paidarova, J. Komasa, and J. Oddershede, *Mol. Phys.*, 1991, **72**, 559.
13. T. D. Bouman and Aa. E. Hansen, *Chem. Phys. Lett.*, 1992, **197**, 59.
14. J. M. Foster and S. F. Boys, *Rev. Mod. Phys.*, 1960, **32**, 300.
15. T. D. Bouman, B. Voigt, and Aa. E. Hansen, *J. Am. Chem. Soc.*, 1979, **101**, 550; T. D. Bouman, Aa. E. Hansen, B. Voigt, and S. Rettrup, *Int. J. Quant. Chem.*, 1983, **23**, 595.
16. P. E. Hansen, J. Abildgaard, and Aa. E. Hansen, *Chem. Phys. Lett.*, 1994, **224**, 275.
17. M. Bilde, M.Sc. dissertation, University of Copenhagen, 1994.
18. T. H. Dunning and P. J. Hay, in *Methods of Electronic Structure Theory*, ed. H. F. Schaefer III, Plenum, New York, 1977.
19. J. Mason, *Solid State Nucl. Magn. Reson*, 1993, **2**, 285.
20. P. Lazzeretti, M. Malagoli, and R. Zanasi, *J. Mol. Struct. (Theochem.)*, 1991, **234**, 127.
21. A. K. Jameson and C. J. Jameson, *Chem. Phys. Lett.*, 1987, **134**, 461.
22. C. J. Jameson, in *Nuclear Magnetic Resonance, A Specialist Periodical Report*, ed. G. A. Webb, Royal Society of Chemistry, Cambridge, 1993, Vol. 22, Chap. 1
23. D. B. Chesnut and K. D. Moore, *J. Comp. Chem.*, 1989, **10**, 648; D. B. Chestnut, B. E. Rusiloski, K. D. Moore, and D. A. Egolf, *J. Comp. Chem.*, 1993, **14**, 1364.
24. R. A. Kirby and Aa. E. Hansen, *Int. J. Quant. Chem.*, 1995, in press.
25. Aa. E. Hansen and T. D. Bouman, *J. Chem. Phys.*, 1989, **91**, 3552.
26. C. W. Haig and R. B. Mallion, *Prog. NMR Spectrosc.*, 1980, **13**, 303.
27. M. Bilde and Aa. E. Hansen, to be published.
28. C. M. Smith, R. D. Amos, and N. C. Handy, *Mol. Phys.*, 1992, **77**, 381.
29. J. D. Baker and M. C. Zerner, *Int. J. Quant. Chem.*, 1992, **43**, 327.
30. M. Munch, Aa. E. Hansen, P. E. Hansen, and T. D. Bouman, *Acta. Chem. Scand.*, 1992, **46**, 1065.
31. P. E. Hansen, Aa. E. Hansen, A. Lycka, and A. Buvari-Barcza, *Acta Chem. Scand.*, 1993, **47**, 777.
32. A. M. Orendt, R. R. Biekofsky, A. B. Pomilio, R. H. Contreras, and J. C. Facelli, *J. Phys. Chem.*, 1991, **95**, 6179.
33. C. J. Jameson, A. C. DeDios, and A. K. Jameson, *J. Chem. Phys.*, 1991, **95**, 1069.
34. C. J. Jameson, A. C. DeDios, and A. K. Jameson, *J. Chem. Phys.*, 1991, **95**, 9042.
35. T. C. Farrar and J. D. Trudeau, *J. Phys. Chem.*, 1990, **94**, 6277.
36. C. J. Jameson and A. C. DeDios, *J. Chem. Phys.*, 1993, **98**, 2208.
37. C. J. Jameson and A. C. DeDios, *J. Chem. Phys.*, 1992, **97**, 417.

38. J. E. Combariza, M. Barfield, and J. H. Enemark, *J. Phys Chem.* 1991, **95**, 5463; J. E. Combariza, J. H. Enemark, M. Barfield, and J. C. Facelli, *J. Am. Chem. Soc.*, 1989, **111**, 7619.
39. P. D. Ellis, J. D. Odom, A. S. Lipton, and J. M. Gulick, *J. Am. Chem. Soc.*, 1993, **115**, 755; P. D. Ellis, J. D. Odom, A. S. Lipton, Q. Chen, and J. M. Gulick, in *Nuclear Magnetic Shieldings and Molecular Structure*, ed. J. A. Tossell, Kluwer, Dordrecht, 1993, pp. 539–555.
40. M. D. Lumsden, G. Wu, R. E. Wasylishen, and R. D. Curtis, *J. Am. Chem. Soc.*, 1993, **115**, 2825; R. D. Curtis, J. W. Hilborn, G. Wu, M. D. Lumsden, R. E. Wasylishen, and J. A. Pincock, *J. Phys. Chem.*, 1993, **97**, 1856.
41. P. J. Patrick, C. J. Groombridge, J. Mason, and E. A. Moore, *Chem. Phys. Lett.*, 1994, **219**, 491.
42. J. G. Kirkwood, *J. Chem. Phys.*, 1937, **5**, 479.
43. Aa.E. Hansen and T. D. Bouman, *J. Math. Chem.*, 1992, **10**, 221, and references therein.
44. F. London, *J. Phys. Rad.*, 1937, **8**, 397.
45. R. Ditchfield, in *MTP International Review of Science, Physical Chemistry, Series I. Molecular Structure and Properties*, Butterworths, London, 1972, Vol. II.
46. E. Dalgaard, *Chem. Phys. Lett.*, 1977, **47**, 279; T. Helgaker and P. Jørgensen, *J. Chem. Phys.*, 1991, **95**, 2595.
47. W. Kutzelnigg, *Isr. J. Chem.* 1980, **19**, 193; M. Schindler and W. Kutzelnigg, *J. Chem. Phys.*, **76**, 1919.
48. T. A. Keith and R. F. Bader, *Chem. Phys. Lett.*, 1992, **194**, 1.
49. S. P. A. Sauer, I. Paidarovà, and J. Oddershede, *Mol. Phys.*, 1994, **81**, 87.
50. J. Gauss, *Chem. Phys. Lett.*, 1992, **191**, 614.
51. J. Fagerström and J. Oddershede, *J. Chem. Phys.*, 1994, **101**, 10 775.
52. K. Ruud, T. Helgaker, R. Kobayashi, P. Jørgensen, K. L. Bak, and H. J.Aa. Jensen, *J. Chem. Phys.*, 1994, **100**, 8187; M. Jaszunski, T. Helgaker, K. Ruud, K. L. Bak, and P. Jørgensen, *Chem. Phys. Lett.*, 1994, **220**, 154.
53. C. van Wüllen and W. Kutzelnigg, *Chem. Phys. Lett.*, 1993, **205**, 563.

Biographical Sketches

Aage E. Hansen. *b* 1937. M.Sc., 1962, Ph.D., 1964, Technical University of Denmark, D.Sc., 1977, University of Copenhagen, Denmark. Faculty in Chemistry, University of Copenhagen, 1965–present. Approx. 60 publications. Research interests: quantum theory of molecular electromagnetic properties, including, in particular, chiroptical spectroscopy and nuclear magnetic resonance.

Merete Bilde. *b* 1969. M.Sc., 1994, University of Copenhagen, Denmark. Presently working towards a Ph.D. degree at Risø National Laboratories, Roskilde, Denmark.

Shielding Calculations: Perturbation Methods

Julio C. Facelli

University of Utah, Salt Lake City, UT, USA

1	Introduction	1
2	Symmetry Properties of the Shielding Tensor	1
3	Exact Perturbation Theory	1
4	Gauge Origin Dependence of the Chemical Shielding	2
5	Relativistic Effects and $L \cdot S$ Coupling	3
6	Perturbation Schemes	4
7	London Orbitals and Gauge-Independent Theories of Chemical Shielding	6
8	Origin-Independent Formulation of Chemical Shielding	7
9	Related Articles	7
10	References	7

1 INTRODUCTION

Perhaps the most important discovery after the successful detection of the NMR signal has been the observation that the nuclear resonance frequencies depend on the chemical or electronic environment of the nuclei,[1,2] or, as Norman Ramsey states in his landmark papers of 1950:[3,4] 'In measurements of nuclear magnetic moments, a correction must be made for the magnetic field arising from the motions of the molecular electrons which are induced by the externally applied field.' Ramsey realized that corrections using only Lamb's diamagnetic theory were inadequate for molecules, because in molecules there are additional shielding contributions arising from the second-order paramagnetism. To address this problem, he developed the necessary theoretical framework to explain and eventually to calculate the 'chemical effect' that would become the chemical shift nowadays commonly used for structural elucidation. The calculation of the second-order paramagnetic contribution using perturbation theory has been a challenge to theoreticians for more than 40 years. In this article, we present a detailed discussion of the perturbative schemes that can be used in the calculation of chemical shieldings. In addition, we have included a small amount of material describing the symmetry properties of shielding tensors, some references to more comprehensive derivations of the Hamiltonian describing the magnetic shielding constants, and a detailed discussion of the gauge dependence of the chemical shielding. Practical implementations of the theories described here and their applications to solve chemical problems are presented elsewhere in this Encyclopedia, see Related Articles.

2 SYMMETRY PROPERTIES OF THE SHIELDING TENSOR

The formal definition of the components of the chemical shielding tensor is

$$\sigma_{\alpha\beta} = \frac{\partial^2 E}{\partial \mu_\alpha \, \partial B_\beta} \tag{1}$$

where E is the total electronic energy of the molecule, $\boldsymbol{B}$ is the external magnetic field, and $\boldsymbol{\mu}$ is the magnetic moment of the nucleus of interest. There are two important observations that can be made from equation (1)

1. The chemical shielding tensor is an antisymmetric tensor because

$$\sigma_{\alpha\beta} = \frac{\partial^2 E}{\partial \mu_\alpha \, \partial B_\beta} = \frac{\partial^2 E}{\partial B_\beta \, \partial \mu_\alpha} \neq \frac{\partial^2 E}{\partial \mu_\beta \, \partial B_\alpha} = \sigma_{\beta\alpha} \tag{2}$$

   This property of the tensor should not be confused with the fact that the first-order response function (the NMR spectrum) is sensitive only to the symmetric part of the tensor and that the antisymmetric components contribute only to the second-order response, i.e., the relaxation of the spin magnetization.[5,6]
2. When using perturbation theory, the chemical shielding tensor components can be identified as the coefficients in the expansion of the electronic energy that correspond to bilinear terms in the nuclear magnetic moment and the external magnetic field.

The chemical shielding tensor has nine independent components, the number of which may be reduced by molecular symmetry. The independent components of the chemical shielding tensor for different molecular symmetries are given in Table 1.[7] Note that the diamagnetic contribution to the chemical shielding tensor is a symmetric quantity—this will become apparent when we develop the perturbation expansions for the shielding tensors.

3 EXACT PERTURBATION THEORY

In order to obtain the exact expressions, using the nonrelativistic Born–Oppenheimer approximation, for the calculation of the chemical shieldings, it is necessary to include in the electronic Hamiltonian the vector potential representing the external magnetic field and the dipolar field originated in the magnetic moment of the nucleus.[8–10] In the Coulomb gauge, the vector potential defining these fields at the position of electron k can be written as

$$\boldsymbol{A}_k(\boldsymbol{r}) = \tfrac{1}{2}\boldsymbol{B} \times \boldsymbol{r}_k + \frac{\boldsymbol{\mu}_N \times \boldsymbol{r}_{Nk}}{r_{Nk}^3} \tag{3}$$

where we follow the standard notation used in this Encyclopedia. The origin of the vector potential is at the position O and $\boldsymbol{r}_k$ and $\boldsymbol{r}_{Nk}$ are defined according to Figure 1. Note that, for simplicity, we are assuming that only one nucleus in the molecule has a nonzero magnetic moment. $\boldsymbol{r}_k$ is the position of electron k measured from the origin of the coordinate system, and $\boldsymbol{r}_{Nk}$ is the position of electron k measured from the nucleus N. Following the standard procedures for the inclusion of magnetic interactions in the electronic Hamiltonian, the full electronic Hamiltonian in the presence of the two magnetic fields becomes

$$\hat{\mathcal{H}} = \frac{1}{2}\sum_k \left[\frac{1}{\mathrm{i}}\nabla_k - \frac{1}{c}\boldsymbol{A}_k(\boldsymbol{r})\right]^2 + V(\boldsymbol{r}) \tag{4}$$

Using the properties of the Coulomb gauge, i.e. $\nabla \cdot \boldsymbol{A} = 0$, the expansion of this Hamiltonian leads to six terms, only three of which are relevant to the calculation of chemical shieldings. These are

$$\hat{\mathcal{H}}_\alpha^{(1,0)} = \frac{-\mathrm{i}}{2c}\sum_k (\hat{\boldsymbol{L}}_k)_\alpha = \frac{-\mathrm{i}}{2c}\sum_k (\boldsymbol{r}_k \times \nabla_k)_\alpha \tag{5}$$

Table 1 Nonvanishing Components of the Chemical Shielding Tensor for Different Point Groups (Reproduced by Permission of Taylor and Francis, from A. D. Buckingham and S. M. Malm, *Mol. Phys.*, 1971, **22**, 1127)

Point group appropriate to the shielded nucleus	Number of independent components		Nonvanishing components for the symmetric(s) and antisymmetric(a) components
	$\sigma^{\mathrm{d}}_{\alpha\beta}$	$\sigma^{\mathrm{p}}_{\alpha\beta}$	
C_1, C_i	6	9	σ_{zz}, σ_{xx}, σ_{yy}, σ^{s}_{xy}, σ^{s}_{xz}, σ^{s}_{yz}; σ^{a}_{xy}, σ^{a}_{xz}, σ^{a}_{yz}
C_2, C_s, C_{2h}	4	5	σ_{zz}, σ_{xx}, σ_{yy}, σ^{s}_{xy}; σ^{a}_{xy}
C_{2v}, D_2, D_{2h}	3	3	σ_{zz}, σ_{xx}, σ_{yy}
C_4, S_4, C_{4h}	2	3	σ_{zz}, σ_{xx}, σ_{yy}; σ^{a}_{xy}
C_3, S_6, C_{3h}, C_6, C_{6h}	2	3	σ_{zz}, $\sigma_{xx} = \sigma_{yy}$; σ^{a}_{xy}
C_{4v}, D_{2d}, D_4, D_{4h}, C_{3v}, D_3, D_{3d}, D_{3h}, D_{4h}, D_{3h}, C_{6v}, D_6, D_{6h}	2	2	σ_{zz}, $\sigma_{xx} = \sigma_{yy}$
$C_{\infty v}$, $D_{\infty h}$	2	1	σ_{zz}, $\sigma_{xx} = \sigma_{yy}$ ($\sigma^{\mathrm{p}}_{zz} = 0$)
T, T_h, T_d, O, O_h	1	1	$\sigma_{zz} = \sigma_{xx} = \sigma_{yy}$

$$\hat{\mathcal{H}}^{(0,1)}_{\alpha} = \frac{-\mathrm{i}}{c}\sum_k \frac{(\hat{\boldsymbol{L}}_{Nk})_\alpha}{r^3_{Nk}} = \frac{-\mathrm{i}}{2c}\sum_k \frac{(\boldsymbol{r}_{Nk}\times\nabla_k)_\alpha}{r^3_{Nk}} \tag{6}$$

$$\hat{\mathcal{H}}^{(1,1)}_{\alpha\beta} = \frac{1}{c^2}\sum_k \frac{\boldsymbol{r}_k\cdot\boldsymbol{r}_{Nk}\delta_{\alpha\beta} - (\boldsymbol{r}_k)_\alpha(\boldsymbol{r}_{Nk})_\beta}{r^3_{Nk}} \tag{7}$$

where the superscripts indicate the order in the external magnetic field, $\boldsymbol{B}$, and in the nuclear magnetic moment, $\boldsymbol{\mu}$, respectively. If we restrict our analysis to closed shell molecules, for which the electronic ground state is of the Σ type, $\hat{\mathcal{H}}^{(1,0)}$ and $\hat{\mathcal{H}}^{(0,1)}$ give no contribution to the energy at first-order in Raleigh–Schrödinger (RS) perturbation theory. The third term, $\hat{\mathcal{H}}^{(1,1)}$, gives at first order a nonzero contribution that is proportional to $1/c^2$; the other contribution of order $1/c^2$ can be obtained from the second-order cross term between $\hat{\mathcal{H}}^{(1,0)}$ and $\hat{\mathcal{H}}^{(0,1)}$. Using the definition of chemical shielding given by equation (1), we can define the diamagnetic and paramagnetic contributions to the chemical shielding as the first- and second-order terms in the energy expansion that are bilinear in the external magnetic field and the nuclear magnetic moment, respectively. The final expressions for the diamagnetic and paramagnetic contributions are

$$\sigma^{\mathrm{d}}_{\alpha\beta}(O) = \frac{1}{2c^2}\langle\psi_0|[\boldsymbol{r}_k\cdot\boldsymbol{r}_{Nk}\delta_{\alpha\beta} - (\boldsymbol{r}_k)_\alpha(\boldsymbol{r}_{Nk})_\beta]r^{-3}_{Nk}|\psi_0\rangle \tag{8}$$

$$\sigma^{\mathrm{p}}_{\alpha\beta}(O) = \frac{-1}{2c^2}\sum_n \frac{1}{E_n - E_0}\langle\psi_0|(\hat{\boldsymbol{L}}_k)_\alpha|\psi_n\rangle\langle\psi_n|(\hat{\boldsymbol{L}}_{Nk})_\beta r^{-3}_{Nk}|\psi_0\rangle + \text{c.c.} \tag{9}$$

where we have indicated explicitly that equations (8) and (9) are valid when the origin of the vector potential is at the position O. The sum in equation (9) is over all the excited states of the molecule. Before discussing the methods for practical evaluation of equations (8) and (9), it is important to understand the behavior of the diamagnetic and paramagnetic terms under translations of the origin of the coordinate system.

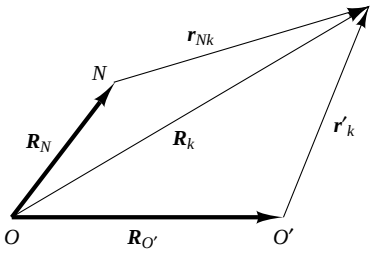

$$\boldsymbol{r}_{Nk} = \boldsymbol{r}'_{Nk}$$
$$\boldsymbol{r}_k = \boldsymbol{r}'_k + \boldsymbol{R}_{O'}$$

Figure 1 Coordinate system used to illustrate the gauge origin dependence of the diamagnetic and paramagnetic contributions of the chemical shielding

4 GAUGE ORIGIN DEPENDENCE OF THE CHEMICAL SHIELDING

Using the notation of Figure 1, we can calculate the effect of a translation of the origin of coordinates on the diamagnetic and paramagnetic contribution by using the replacements

$$\left.\begin{aligned}\boldsymbol{r}_{Nk} &= \boldsymbol{r}'_{Nk}\\ \boldsymbol{r}_k &= \boldsymbol{r}'_k + \boldsymbol{R}_{O'}\end{aligned}\right\} \tag{10}$$

in equations (8) and (9) to obtain the expressions for σ^{d} and σ^{p} in the new coordinate system with origin at O'. For the diamagnetic components, we obtain

$$\sigma^{\mathrm{d}}_{\alpha\beta}(O) = \frac{1}{2c^2}\langle\psi_0|[\boldsymbol{r}'_k\cdot\boldsymbol{r}_{Nk}\delta_{\alpha\beta} + \boldsymbol{R}_{O'}\cdot\boldsymbol{r}_{Nk}\delta_{\alpha\beta} - (\boldsymbol{r}'_k)_\alpha(\boldsymbol{r}_{Nk})_\beta - (\boldsymbol{R}_{O'})_\alpha(\boldsymbol{r}_{Nk})_\beta]r^{-3}_{Nk}|\psi_0\rangle \tag{11}$$

which becomes

$$\sigma^{\mathrm{d}}_{\alpha\beta}(O) = \sigma^{\mathrm{d}}_{\alpha\beta}(O') + \frac{\boldsymbol{R}_{O'}}{2c^2}\cdot\langle\psi_0|\frac{\boldsymbol{r}_{Nk}}{r^3_{Nk}}|\psi_0\rangle\delta_{\alpha\beta} - (\boldsymbol{R}_{O'})_\alpha\langle\psi_0|\frac{(\boldsymbol{r}_{Nk})_\beta}{r^3_{Nk}}|\psi_0\rangle \tag{12}$$

The same replacements can be made for the paramagnetic contribution

$$\sigma^{\mathrm{p}}_{\alpha\beta}(O) = \frac{-1}{2c^2}\sum_n \frac{1}{E_n - E_0}\langle\psi_0|[(\boldsymbol{r}'_k + \boldsymbol{R}_{O'}) \times \nabla]_\alpha|\psi_n\rangle \times \langle\psi_n|(\boldsymbol{L}_{Nk})_\beta r_{Nk}^{-3}|\psi_0\rangle + \text{c.c.} \tag{13}$$

which becomes

$$\sigma^{\mathrm{p}}_{\alpha\beta}(O) = \sigma^{\mathrm{p}}_{\alpha\beta}(O') + \left[\frac{-1}{2c^2}\sum_n \frac{1}{E_n - E_0}\langle\psi_0|(\boldsymbol{R}_{O'} \times \nabla)_\alpha|\psi_n\rangle \times \langle\psi_n|(\boldsymbol{r}_{Nk} \times \nabla_k)_\beta r_{Nk}^{-3}|\psi_0\rangle + \text{c.c.}\right] \tag{14}$$

At this point of the derivation, it is crucial to assume that we are working with the exact solution of the Schrödinger equation; therefore the $|\psi_n\rangle$ form a complete set, for which the virial relationship

$$(E_n - E_0)\langle\psi_0|\boldsymbol{r}|\psi_n\rangle = \langle\psi_0|\nabla|\psi_n\rangle \tag{15}$$

holds exactly. Note that this relationship is also true for any variational solution of the Schrödinger equation in a complete Hilbert space. This, as we shall see later, makes the chemical shielding calculations gauge-invariant for any variational wavefunction in a complete Hilbert space.

Using equation (15), it is possible to eliminate the energy denominator in equation (14):

$$\sigma^{\mathrm{p}}_{\alpha\beta}(O) = \sigma^{\mathrm{p}}_{\alpha\beta}(O') + \left[\frac{-1}{2c^2}\sum_n (\boldsymbol{R}_{O'} \times \langle\psi_0|\boldsymbol{r}_{Nk}|\psi_n\rangle)_\alpha \times \langle\psi_n|(\boldsymbol{r}_{Nk} \times \nabla_k)_\beta r_{Nk}^{-3}|\psi_0\rangle + \text{c.c.}\right] \tag{16}$$

which, making use of the closure relationship $\Sigma_n|\psi_n\rangle\langle\psi_n| = \hat{1}$ and the commutator $[\boldsymbol{r}, \nabla] = -1$, can be written as

$$\sigma^{\mathrm{p}}_{\alpha\beta}(O) = \sigma^{\mathrm{p}}_{\alpha\beta}(O') - \frac{\boldsymbol{R}_{O'}}{2c^2} \cdot \langle\psi_0|\frac{\boldsymbol{r}_{Nk}}{r_{Nk}^3}|\psi_0\rangle\delta_{\alpha\beta} + (\boldsymbol{R}_{O'})_\alpha\langle\psi_0|\frac{(\boldsymbol{r}_{Nk})_\beta}{r_{Nk}^3}|\psi_0\rangle \tag{17}$$

There are several important observations that can be derived from equations (12) and (17).

1. The total chemical shielding, i.e., the sum of the paramagnetic and diamagnetic parts, is invariant under changes of the origin of the coordinate system. Note that all the terms in equations (12) and (17) that depend on $\boldsymbol{R}_{O'}$ cancel each other in the sum of the two expressions. In the language of electromagnetic interactions, this is equivalent to saying that the chemical shielding tensor is invariant under gauge transformations that preserve $\nabla \cdot \boldsymbol{A} = 0$, i.e, the Coulomb gauge. For calculations of the chemical shieldings in other gauges, see the work by Ferarro et al.[11]
2. The diamagnetic and paramagnetic components depend on the origin of the coordinate system, and their values can be changed at will by changing the relative position of the nucleus with respect to the origin. The origin-dependent contributions to the diamagnetic and paramagnetic terms are linear in the distance between the nucleus and the origin.
3. For exact wavefunctions—actually for any variational approximation of the wavefunction in a complete Hilbert space—the selection of the origin of the coordinate system is inconsequential, because the origin-dependent terms in the diamagnetic and paramagnetic contributions are calculated exactly, and they cancel each other.
4. For atomic systems, there is a natural choice for the origin of the vector potential, namely, the position of the nucleus. For this choice, using equations (12) and (17), it is straightforward to prove that the paramagnetic contribution is identically zero, and therefore the shielding is totally diamagnetic (Lamb's diamagnetic theory).
5. For approximate wavefunctions, i.e., any calculation that we can do, the selection of the origin of the gauge is a serious problem, because the origin-dependent terms, which cancel each other in exact theories, are calculated using different approximations with different errors, and they do not cancel each other. Note that the diamagnetic contributions are calculated using the more accurate zeroth-order perturbation theory, while the paramagnetic contributions are calculated using second-order perturbation theory, which is much more sensitive to truncation errors in the sum over the excited states. Numerical examples of the effect of changing the gauge origin in shielding calculations abound in the literature,[12] and later in this article we discuss several strategies that have been proposed to minimize the gauge problem.
6. There is one particular selection of the origin of the gauge that deserves special mention. If one chooses the origin of the vector potential at the center of mass of the molecule, it is possible to prove that the paramagnetic contribution at the center of mass is proportional to the spin–rotation constant, which can be measured by microwave spectroscopy.[13] By measuring the spin–rotation constant and calculating the diamagnetic contribution to the shielding at the center of mass, it is possible to obtain very accurate determinations of the absolute shieldings of the nuclei in small molecules, which can be used to establish absolute chemical shielding scales. These scales are critical for comparing calculated chemical shieldings with their corresponding shift values (see also ***Chemical Shift Scales on an Absolute Basis***).
7. For molecules with C_∞ symmetry, if we choose the origin of the coordinate system on the C_∞ axis, the component of the paramagnetic contribution along the axis is identically zero, and therefore the shielding along the C_∞ axis is totally diamagnetic.[14]
8. Practical experience as well as theoretical derivations have demonstrated that the best results can be obtained when the gauge origin is located at the center of the electronic distribution of the molecule. This choice produces the best overall selection when the chemical shieldings of all the nuclei in the molecule are computed from one single calculation; when only the shielding of one nucleus is required, the best choice for the origin of the vector potential is the nucleus under consideration.

5 RELATIVISTIC EFFECTS AND $l \cdot S$ COUPLING

In the derivations presented in the previous section, we have assumed that there is no coupling between the molecular angular momentum $\boldsymbol{L}$ and the electronic spin $\boldsymbol{S}$, retaining only

terms of order $1/c^2$ in the Hamiltonian. This is equivalent to saying that equations (8) and (9) do not include any relativistic effects. Limitations of space preclude a complete discussion of the problem of relativistic effects on chemical shieldings, but it is worth mentioning that several authors have discussed this problem—at least from a formal point of view. Numerical estimations of the $\boldsymbol{L}\cdot\boldsymbol{S}$ coupling and relativistic effects on chemical shieldings are still poorly documented. The interested reader can find derivations of the relativistic theory of magnetic shielding in the literature.[5,15] A very detailed derivation of the hyperfine Hamiltonians relevant to molecular magnetic interactions has been presented by Michelot.[16]

The effect of the $\boldsymbol{L}\cdot\boldsymbol{S}$ coupling on the chemical shieldings has been studied by adding to the Hamiltonian given by equation (4) the $\boldsymbol{L}\cdot\boldsymbol{S}$ coupling and the interaction between the electronic spin and the external and nuclear moment magnetic fields.[17,18] Within this approximation, the molecular Hamiltonian becomes

$$\hat{\mathcal{H}} = \frac{1}{2}\sum_k \left\{ \left[\frac{1}{\mathrm{i}}\nabla_k - \frac{1}{c}\boldsymbol{A}_k(\boldsymbol{r}) \right]^2 + 2\beta \hat{\boldsymbol{S}}_k \cdot [\nabla_k \times \boldsymbol{A}_k(\boldsymbol{r})] + \lambda \hat{\boldsymbol{L}}_k \cdot \hat{\boldsymbol{S}}_k \right\} + V(\boldsymbol{r}) \tag{18}$$

where λ is the coupling energy between the spin and the angular momentum and β is the Bohr magneton. The perturbational treatment of this Hamiltonian leads to the usual diamagnetic and paramagnetic terms discussed above, plus several terms bilinear in the external magnetic field and the nuclear magnetic moment, which represent the $\boldsymbol{L}\cdot\boldsymbol{S}$ contribution to the magnetic shielding. The additional terms can be evaluated using third-order perturbation theory, but only limited calculations of this effect have been presented.[17,18]

6 PERTURBATION SCHEMES

In this section, we describe different perturbation schemes that can be used in practical calculations of chemical shieldings. To avoid unnecessary complications with the gauge problem discussed above, we shall discuss the perturbation schemes assuming that we are using a complete basis set. Schemes to alleviate the gauge problem are discussed at the end of this article and elsewhere in the Encyclopedia (see 'Related Articles'). To simplify our expressions, we have chosen the position of the nucleus under consideration as the origin of the vector potential. The expressions for the diamagnetic and paramagnetic parts become

$$\sigma^{\mathrm{d}}_{\alpha\beta}(N) = \frac{1}{2c^2}\langle\psi_0|[r^2_{Nk}\delta_{\alpha\beta} - (\boldsymbol{r}_{Nk})_\alpha(\boldsymbol{r}_{Nk})_\beta]r^{-3}_{Nk}|\psi_0\rangle \tag{19}$$

$$\sigma^{\mathrm{p}}_{\alpha\beta}(N) = \frac{-1}{2c^2}\sum_n \frac{1}{E_n - E_0}\langle\psi_0|(\hat{\boldsymbol{L}}_{Nk})_\alpha|\psi_n\rangle\langle\psi_n|(\hat{\boldsymbol{L}}_{Nk})_\beta r^{-3}_{Nk}|\psi_0\rangle + \text{c.c.} \tag{20}$$

The calculation of the diamagnetic part presents no complications, and can be evaluated for any kind of wavefunction, requiring only the evaluation of one-electron integrals of the type $1/r$, $1/r^3$, and xy/r^3, which are readily available in most quantum mechanical codes. The calculation of the diamagnetic term is computationally simple, requiring a negligible amount of effort after the calculation of the zeroth-order approximation to the wavefunction. Moreover, because the ground electronic state is less sensitive to the approximations used in the calculation, it is possible to calculate the diamagnetic contribution accurately, even when using modest approximations to the wavefunction.

The more complicated paramagnetic term requires, in principle, knowledge of all the excited electronic states of the molecule, in which case the direct evaluation of equation (20) would be immediate. Unfortunately, this is not the case, and a great deal of effort is necessary to obtain reliable results for the paramagnetic contribution. It is always important, if possible, to calculate the paramagnetic contribution with the same accuracy as the diamagnetic contribution in order to achieve as high a degree as possible of gauge invariance of the numerical results. Unfortunately, this may increase the computational complexity beyond practical limits, and the evaluation of the paramagnetic contribution has always been the limiting factor in the theoretical calculation of chemical shieldings. Historically, better and better approximations have been feasible owing to advances in computational sciences as well as a better understanding of perturbation theory in many-electron systems. In the following subsections, we review the most common approximations to calculate the paramagnetic contribution to the chemical shieldings.

6.1 Coupled Hartree–Fock Perturbation Theory

While most of the early work in the calculation of chemical shieldings was based on very simple approximations, it is convenient for pedagogical reasons to develop the exact coupled Hartree–Fock (CHF) theory of the chemical shielding and then to simplify the expressions to obtain less complex approximations. In this way, we hope that the reader will be able to understand the physical assumptions made for the different approximations.

Using the Hartree–Fock approximation and standard notation[19] the second-order change in the molecular electronic energy for a singlet perturbation $\hat{\mathcal{H}}_1$ is

$$E^{(2)} = \sum_{\{i,a\}}[c^2_{ia}(\varepsilon_a - \varepsilon_i + \langle ia|ia\rangle) + 2c_{ia}\langle i|\hat{\mathcal{H}}_1|a\rangle] + 2\sum_{i,a\neq j,b}\sum c_{ia}c_{jb}(4\langle ia|jb\rangle - \langle ab|ij\rangle - \langle ja|ib\rangle) \tag{21}$$

where the c_{ia} are the coefficients corresponding to the excited state determinants, in which we have expanded the perturbed wavefunction as

$$|\psi\rangle = |\psi_0\rangle + \sum_{i,a} c_{ia}|\psi_{i\to a}\rangle + \sum_{\substack{i,a\\ j,b}} c_{ia}c_{jb}|\psi_{i\to a, j\to b}\rangle + \ldots \tag{22}$$

The Hartree–Fock solution for the ground state corresponds to the single determinant wavefunction that minimizes the electronic energy of the system. Therefore, to be consistent with this definition, we shall require that the second-order energy $E^{(2)}$ be a minimum with respect to changes in the expansion coefficients c_{ia}. Using this condition, $\delta E^{(2)}/\delta c_{ia} = 0$, in equation (21), we obtain the following system of linear equations to calculate the coefficients c_{ia}:

$$c_{ia}(\varepsilon_a - \varepsilon_i + \langle ia|ia\rangle) + \langle i|\hat{\mathcal{H}}_1|a\rangle + 2\sum_{j,b\neq i,a} c_{jb}(4\langle ia|jb\rangle - \langle ab|ij\rangle - \langle ja|ib\rangle) = 0 \tag{23}$$

The second-order Hartree–Fock energy can be calculated by replacing the coefficients c_{ia} determined from the system of linear equations, given by equation (23) into equation (21).

Several schemes have been developed to solve exactly or approximately the system of linear equations given by equation (23). The simplest approximation is to neglect all of the two-electron integrals in equation (23); this leads to a very simple expression for the second-order energy:

$$E^{(2)} = \sum_{i,a} \frac{\langle i|\hat{\mathcal{H}}_1|a\rangle\langle a|\hat{\mathcal{H}}_1|i\rangle}{\varepsilon_i - \varepsilon_a} \tag{24}$$

Direct use of equation (24) is problematic, because the Hartree–Fock orbital energies for the unoccupied orbitals are always too high; therefore, even when using uncoupled schemes, it is necessary to take into account the repulsion integrals $\langle ia|ia\rangle$ to correct for this deficiency in the orbital energies of the unoccupied orbitals. With this addition, equation (24) becomes

$$E^{(2)} = \sum_{i,a} \frac{\langle i|\hat{\mathcal{H}}_1|a\rangle\langle a|\hat{\mathcal{H}}_1|i\rangle}{\varepsilon_i - \varepsilon_a + \langle ia|ia\rangle} \tag{25}$$

Practical application of equation (24) or equation (25) to the calculation of the paramagnetic contribution of the chemical shielding is immediate, replacing $\hat{\mathcal{H}}_1$ by the appropriate operators given by equations (5) and (6) and by expanding the molecular orbitals $|i\rangle$ in a linear combination of atomic orbitals. In general, the uncoupled approaches have been less than successful, but many semiempirical theories of chemical shieldings have been developed by further simplification of equation (25). In these theories, which assume that only the first term in the sum in equation (25) makes a significant contribution to the chemical shielding, the sum over the exited states is replaced by a quantity solely dependent on the electronic ground state and an average excitation energy, which are usually treated as semiempirical parameters. By eliminating the sum over states, they provide very compact expressions for the semiqualitative analysis of the chemical shieldings.[20] Note that the uncoupled approach is physically equivalent to the assumption that the external perturbation does not change the average Hartree–Fock potential in which the molecular electrons move.

The next step in complexity for the calculation of chemical shieldings is to solve the system of equations given by equation (23), including all the coupling terms. This takes into account the change in the average Hartree–Fock potential induced by the external perturbation and the consequent change in the electronic distribution. This physical interpretation has been used as a reason for solving equation (23) in an iterative fashion, solving first the uncoupled problem, using its solution to calculate the correction terms in equation (23) and iterating thereafter this procedure until convergence. This procedure is commonly called a coupled Hartree–Fock (CHF) calculation, and the working equations are

$$c_{ia}^{(n+1)} = \frac{-\langle i|\hat{\mathcal{H}}_1|a\rangle}{\varepsilon_a - \varepsilon_i} - \frac{1}{\varepsilon_a - \varepsilon_i} \sum_{jb} S_{ia,\,jb} c_{jb}^{(n)} \tag{26}$$

where n indicates the order of the iteration and $S_{ia,\,jb}$ is given by:

$$S_{ia,\,jb} = 4\langle ia|jb\rangle - \langle ab|ij\rangle - \langle ja|ib\rangle \tag{27}$$

Note that $S_{ia,\,jb}$ is independent of the perturbation, and depends only on the properties of the Hartree–Fock electronic ground state. The iterative procedure prescribed by equation (26) converges if all the eigenvalues of $S_{ia,jb}$ are smaller than one in absolute value. In contrast with the serious problems encountered in solving these equations for the calculation of J couplings,[21] the convergence of the CHF equations for chemical shielding calculations is satisfactory.

It is also possible to express the CHF equations in the language of the polarization propagator approach or linear response theory[22] by introducing the inverse of the polarization propagator $\mathbf{P}$:

$$(\mathbf{P}^{-1})_{ia,\,jb} = (\varepsilon_a - \varepsilon_i)\delta_{ij}\delta_{ab} + 4\langle ia|jb\rangle - \langle ab|ij\rangle - \langle ja|ib\rangle \tag{28}$$

Using this definition of $\mathbf{P}^{-1}$, it is possible to express the second-order contribution to the electronic energy as

$$E^{(2)} = \sum_{ia,\,jb} \langle i|\hat{\mathcal{H}}_1|a\rangle P_{ia,\,jb} \langle b|\hat{\mathcal{H}}_1|j\rangle \tag{29}$$

There are several relevant features of equation (29) that are important to discuss:

1. The propagator $\mathbf{P}$ depends only on quantities that are known from the Hartree–Fock calculations [see equation (28)].
2. Once the polarization propagator $\mathbf{P}$ has been calculated by inverting $\mathbf{P}^{-1}$, it is possible to calculate any second-order property depending on it by using equation (29). It should be noted that the calculation of $\mathbf{P}^{-1}$ and its inversion are computationally very expensive, while the evaluation of equation (29) represents a trivial ammount of computational effort.
3. An alternative solution of equation (29), commonly named SOS/2 (for sum over states/2), consists in expressing the second-order energy as an explicit sum over states similar to the exact expression given by RS perturbation theory. Within this approach, $\mathbf{P}^{-1}$ is constructed according to equation (28), but it is diagonalized instead of inverted. In the new basis, in which $\mathbf{P}^{-1}$ is diagonal, it is possible to express the second-order energy as

$$E^{(2)} = \sum \frac{\langle i'|\hat{\mathcal{H}}_1|a'\rangle\langle a'|\hat{\mathcal{H}}_1|i'\rangle}{E'_i - E'_a} \tag{30}$$

where $|i'\rangle$ are the eigenvectors of $\mathbf{P}^{-1}$ and E its eigenvalues. This formulation is totally equivalent to equation (29), but can be used explicitly to analyze the contributions of different orbitals to the chemical shielding.

For simplicity, all the equations discussed above have been expressed in terms of molecular orbitals (MO), but the reader should to keep in mind that the actual calculation of the shielding constants normally requires one to rewrite the equations in the atomic orbital (AO) basis or to transform the necessary two-electron integrals from the AO basis into the MO basis. This transformation is the most demanding part of the chemical shielding calculations in terms of CPU, storage and memory requirements. Direct methods for the solution of equation (29), which avoid the two-electron integral bottleneck, promise great advances in our ability to compute chemical shieldings in the future.[23]

6.2 Finite Perturbation Theory

The perturbation schemes described in the previous section were based on approximations to the exact perturbation theory; the notion of finite perturbation theory (FPT) or finite field perturbation theory (FFPT) is based on the direct use of equation (1) to calculate chemical shieldings. In the FPT approach, the electronic energy of the system is calculated with and without the magnetic fields derived from the vector potential given by equation (3), and the derivatives of the energy with respect to the magnetic fields are estimated numerically by finite differences:

$$\sigma_{\alpha\beta} = \left.\frac{\partial^2 E}{\partial \mu_\alpha \, \partial B_\beta}\right|_{B_\beta=\mu_\alpha=0} \approx \frac{E(\Delta\mu_\alpha, \Delta B_\beta) - E(0,0)}{\Delta\mu_\alpha \Delta B_\beta} \tag{31}$$

In equation (31), the values of ΔB_β and $\Delta\mu_\alpha$ are selected in such way that they produce a large enough change in the electronic energy of the system to calculate the denominator with the desired precision without introducing higher-order terms in the derivatives. Normally, it is necessary to calibrate these increments for each MO method, but this does not represent a significant problem for the application of equation (31) to calculate chemical shieldings. The FPT method can be easily programmed; therefore it can be used to calculate the chemical shielding for any high-order approximation to the electronic wavefunction without major modifications of the necessary computer programs. Its most serious disadvantage is the need for a complete SCF energy calculation for each component of each of the shielding tensors in the molecule. The FPT method is useful for highly correlated methods for which the algebraic expressions for the second-order energy are not readily available.

6.3 Perturbation Theory Including Correlation Effects

When appropriate techniques to mitigate gauge origin problems are used, the Hartree–Fock level calculations of chemical shieldings have been very successful—even when relatively modest basis sets were used. For instance, the chemical shift tensors in sucrose, calculated using the GIAO method, agree with their experimental measurements with standard marginal deviations of 4.6 and 2.7 ppm when using the STO-3G and 3-21G basis sets, respectively (see Figure 2).[24] But many cases have also been documented in the literature in which the Hartree–Fock calculations produce fairly poor results, even in the limit of very large basis sets: examples of this behavior can be found for CO[25] and in the systematic overestimation of the δ_{11} principal components of the ^{13}C chemical shift tensors for olefinic and aromatic carbons.[26]

To correct these deficiencies, several attempts have been made to include dynamic electronic correlation in calculations of chemical shieldings. One important consideration in including electron correlation in the calculation of chemical shieldings is to preserve the gauge invariance of the total shielding. As we discussed above, only the exact wavefunction and its variational approximations preserve the gauge invariance of the chemical shieldings in the limit of complete basis sets. This is a severe restriction, because many methods commonly used to include correlation effects in quantum mechanical calculations do not satisfy this requirement. In these cases, numerical experiments are necessary to evaluate the sensitivity of the results with respect to changes in the origin of the vector potential. It has been established that the correlation effects are very sensitive to the basis set used in the calculations; therefore correlation effects calculated with unsaturated basis sets may be misleading.[25]

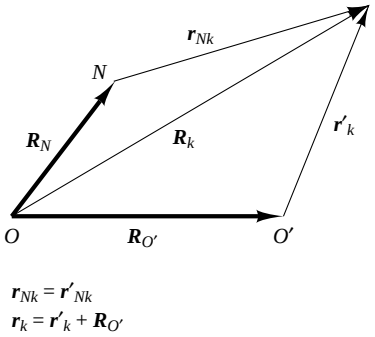

Figure 2 Comparison between the GIAO calculated chemical shift values, in the icosahedral representation, and their experimental values. Reproduced by permision of Kluwer Academic Publishers from D. M. Grant, J. C. Facelli, D. W. Alderman, and M. H. Sherwood, in 'Nuclear Magnetic Shielding and Structure', eds. J. A. Tossell, Kluwer, Dordrecht, 1993, p. 367

In Table 2, we have given a number of numerical examples of electronic correlation effects on calculated chemical shieldings. Note that these are probably the most accurate calculations of chemical shieldings available today; in most cases the results have been obtained using extended basis sets near the Hartree–Fock limit. It is apparent from these results that the importance of correlation effects is strongly dependent on the bonding situation of the nucleus. For a singly bonded nucleus, correlation effects are extremely small—to the degree that it is not possible to assess their impact in improving agreement with the experimental data without taking into account vibrational, medium, and temperature corrections to chemical shieldings. Correlation effects are much more important for nuclei in multiply bonded situations, in which case the agreement between experimental and calculated values shows a significant improvement.

7 LONDON ORBITALS AND GAUGE-INDEPENDENT THEORIES OF CHEMICAL SHIELDING

In practical applications, the gauge origin dependence of chemical shieldings is a significant problem, because in most cases it is not possible to use large basis sets to achieve or even to be near the Hartree–Fock limit. Several methods have been proposed to eliminate this problem by making the results formally gauge-invariant even for incomplete basis sets. The most common methods—GIAO, IGLO, and LORG—are described in detail elsewhere in this Encyclopedia (see 'Related Articles'), but the reader should realize that all of them are based on the use of the same kind of explicit gauge-dependent functions for the atomic (GIAO), or molecular, (IGLO and LORG) orbitals.

The exact wavefunctions transform as

$$\psi(\boldsymbol{A}') = \mathrm{e}^{-\mathrm{i}\Delta}\psi(\boldsymbol{A}) \tag{32}$$

Table 2 Calculated Effects of Electron Correlation on Chemical Shifts Using Different Methods (All Values in ppm in Absolute Shieldings)

	MC/IGLO		MP2/GIAO		SOLO/LORG		
	SCF	MC	SCF	MP2	SCF	SOLO	Exp.
H_2O, ^{17}O	321.39	323.04	323.18	339.79	377.94	379.79	344.0
CO, ^{13}C	−23.40	13.39	−29.2	11.1	−17.42	−1.50	3.0
^{17}O	−83.86	−36.66	−113.47	−54.06	−87.77	−60.37	−36.7
CH_4, ^{13}C	193.82	198.39	195.7	201.5	198.71	200.36	200.36
C_2H_6, ^{13}C	—	—	184.0	188.0	184.78	184.69	180.9
C_2H_4, ^{13}C	—	—	59.9	71.2	64.41	72.07	64.5

under a gauge transformation given by

$$\boldsymbol{A}(\boldsymbol{r}) \rightarrow \boldsymbol{A}(\boldsymbol{r}') = \boldsymbol{A}(\boldsymbol{r}) + \nabla\lambda(\boldsymbol{r}) \tag{33}$$

where

$$\Delta = c^{-1} \sum_i \lambda(\boldsymbol{r}_i) \tag{34}$$

For complete variational sets equation (32) is automatically satisfied, the energy of the system is gauge-invariant, and the electronic current derived from the wavefunctions is conserved, i.e., $\nabla \cdot \boldsymbol{j} = 0$.[27,28] An approximate wavefunction can be forced to satisfy equation (32) by expanding it in the so-called London orbitals or GIAOs given by

$$\chi_p(\boldsymbol{r}, \boldsymbol{A}) = \chi_p(\boldsymbol{r}) \exp\left[-\frac{\mathrm{i}}{c}\boldsymbol{A}(\boldsymbol{R}_p) \cdot \boldsymbol{r}\right] \tag{35}$$

where the $\chi_p(\boldsymbol{r})$ are real atomic orbitals (Slaters, Gaussians, etc.) and $\boldsymbol{R}_p$ is the position of the center of the $\chi_p(\boldsymbol{r})$. When the wavefunction is optimized within the space expanded by orbitals of the type given in equation (35), the explicit field dependence of the AOs constrains the search in such a way that only wavefunctions satisfying equation (32) are taken into account. That is to say, the set of trial functions change from one gauge to another in such a way that the energy is invariant. Unfortunately, the use of GIAOs does not guarantee the conservation of the electronic current.[27] It is also important to realize that, a priori, there is no reason to expect better results when using this enforced gauge invariance of the energy, but, because the GIAOs are the first-order solutions for the one-electron, one-center, uniform magnetic field problem when $\chi_p(\boldsymbol{r})$ is the solution of the problem for $\boldsymbol{B} = 0$, they do provide a more flexible basis for expanding the wavefunction in the presence of a magnetic field. As a consequence, in practical applications, calculations using GIAOs produce better results.

The above discussion was based on using GIAOs for the atomic basis set in the expansion of the wavefunctions. The IGLO and LORG methods avoid the use of GIAOs in the calculation of the zeroth-order wavefunctions, but they expand the first-order perturbation of the wavefunction in a set of localized molecular orbitals with individual gauge origins, producing a similar effect. For a detailed discussion of the differences between the IGLO and LORG methods, the reader can consult the literature.[29] Finally, it is important to cite the work by Helgaker and Jørgensen[30] showing that it is possible to use London orbitals in the calculation of chemical shieldings employing the techniques developed to calculate polarization propagators for MCSF wavefunctions.

8 ORIGIN-INDEPENDENT FORMULATION OF CHEMICAL SHIELDING

The approaches described above to mitigate the gauge origin problem are all based on the idea of shifting the phase of either atomic or molecular orbitals to compensate for the changes in the origin of the coordinate system. All of them can be characterized by an enforced gauge invariance of the electronic energy by restricting the trial functions to those satisfying equation (32). In contrast to this approach Geertsen[31] and Sauer and Oddershede[25] have expressed the diamagnetic contribution as a second-order property using the polarization propagator formalism. In this formalism, both the paramagnetic and diamagnetic contributions are calculated as second-order properties, and the cancelation of errors discussed above is no longer present, because both contributions are calculated with the same degree of accuracy. Unfortunately, this approach does not provide any practical advantages, because it requires large basis sets to calculate the diamagnetic contributions.

9 RELATED ARTICLES

Anisotropy of Shielding and Coupling in Liquid Crystalline Solutions; Shielding Calculations: LORG and SOLO Approaches; Chemical Shift Scales on an Absolute Basis; Chemical Shift Tensor Measurement in Solids; Chemical Shift Tensors; Electric Field Effects on Shielding Constants; Shielding Calculations: IGLO Method; Shielding: Overview of Theoretical Methods; Shielding in Small Molecules; Shielding Tensor Calculations; Shielding Theory: GIAO Method.

10 REFERENCES

1. E. M. Purcell, *Phys. Rev.*, 1949, **76**, 1262.
2. H. L. Anderson, *Phys. Rev.*, 1949, **76**, 1460.
3. N. F. Ramsey, *Phys. Rev.*, 1950, **78**, 699.
4. N. F. Ramsey, *Phys. Rev.*, 1950, **77**, 567.
5. J. B. Robert and L. Wiesenfeld, *Phys. Rep.*, 1982, **86**, 363.
6. F. A. L. Anet and D. J. O'Leary, *Concepts Magn. Reson.*, 1991, **3**, 193.
7. A. D. Buckingham and S. M. Malm, *Mol. Phys.*, 1971, **22**, 1127.
8. W. N. Lipscomb, in *Advances in Nuclear Magnetic Resonance*, ed. J. S. Waugh, Academic Press, New York, 1966, Vol. 2, p. 138.
9. J. I. Musher, in *Advances in Nuclear Magnetic Resonance*, ed. J. S. Waugh, Academic Press, New York, 1966, Vol. 2, p. 177.

10. W. Kutzelnigg, U. Fleischer, and M. Schindler, in *NMR Basic Principles and Progress*, eds. P. Diehl, E. Fluck, H. Günther, R. Kosfeld, and J. Seelig, Springer-Verlag, Berlin, 1990, Vol. 23, p. 167.
11. M. B. Ferraro, T. E. Her, P. Lazzeretti, M. Malagoli, and R. Zanasi, *J. Chem. Phys.*, 1993, **98**, 4030.
12. R. Höller and H. Lischka, *Mol. Phys.*, 1980, **41**, 1017.
13. W. H. Flygare, *J. Chem. Phys.*, 1964, **41**, 793.
14. A. J. Beeler, A. M. Orendt, D. M. Grant, P. Cutts, J. Michl, K. W. Zilm, J. W. Downing, J. C. Facelli, M. S. Schindler, and W. Kutzelnigg, *J. Am. Chem. Soc*., 1984, **106**, 7672.
15. Z. C. Zhang and G. A. Webb, *J. Mol. Struct. (THEOCHEM)*, 1983, **104**, 439.
16. F. Michelot, *Mol. Phys.*, 1982, **45**, 949.
17. A. A. Cheremisin and P. V. Schastnev, *J. Magn. Reson*, 1980, **40**, 459.
18. I. Morishima, K. Endo, and T. Yonezawa, *J. Chem. Phys*. 1973, **59**, 3356.
19. A. Szabo and N. S. Ostlund, *Modern Quantum Chemistry*, McGraw-Hill, New York, 1982.
20. J. A. Pople, *J. Chem. Phys.*, 1962, **37**, 53.
21. R. H. Contreras and J. C. Facelli, in *Annual Reports on NMR Spectroscopy*, ed. G. A. Webb, Academic Press, London, 1993, Vol. 27, p. 255.
22. P. Jørgensen and J. P. Simons, *Quantum Chemistry: Second Quantization-Based Methods*, Academic Press, New York, 1981.
23. M. Feyereisen, J. Nichols, J. Oddershede, and J. Simons, *J. Chem. Phys.*, 1992, **96**, 2978.
24. D. M. Grant, J. C. Facelli, D. W. Alderman, and M. H. Sherwood, in *Nuclear Magnetic Shielding and Structure*, ed. J. A. Tossel, Kluwer, Dordrecht, 1993, p. 367.
25. S. P. A. Sauer and J. Oddershede, in *Nuclear Magnetic Shielding and Structure*, ed. J. A. Tossell, Kluwer, Dordrecht, 1993, p. 351.
26. J. C. Facelli and D. M. Grant, *Nature (London)*, 1993, **365**, 325.
27. S. T. Epstein, *J. Chem. Phys.*, 1973, **58**, 1592.
28. S. T. Epstein, *Isr. J. Chem.*, 1980, **19**, 154.
29. J. C. Facelli, D. M. Grant, T. D. Bouman, and A. E. Hansen, *J. Comp. Chem.*, 1990, **11**, 32.
30. T. Helgaker and P. Jørgensen, *J. Chem. Phys.*, 1991, **95**, 2595.
31. J. Geertsen, in *Nuclear Magnetic Shielding and Structure*, ed. J. A. Tossell, Kluwer, Dordrecht, 1993, p. 335.

Biographical Sketch

Julio C. Facelli. *b* 1953. Licenciado in Physics, 1977 and Doctor in Physics, 1981, University of Buenos Aires, Argentina. Postdoctoral work at the University of Arizona 1983–84. University of Utah 1984–present. Approx. 80 publications. Current research interests quantum chemical calculations of NMR parameters, relationships between NMR parameters and molecular structure and large scale scientific computing.

Shielding Calculations

Julio C. Facelli

University of Utah, Salt Lake City, UT, USA

1 Introduction 1
2 Developments Leading to the Modern Methods to Calculate Shielding Constants 1
3 Software Available and Hardware Needed for Shielding Calculations 4
4 Chemical and Structural Research Using Modern Methods 5
5 Conclusions 9
6 Related Articles in Volumes 1–8 9
7 References 9

1 INTRODUCTION

Since the publication of the Encyclopedia of NMR[1] there has been a significant increase in our ability to calculate shielding tensors. These increased capabilities have originated in new theoretical developments, advances in the algorithms used in quantum mechanical software and great improvements in the performance of computer hardware. This article gives a general overview of these developments and illustrates the use of NMR shielding calculations as a tool for solving common problems in structural chemistry and NMR spectroscopy.

Several methods to calculate shielding constants were described in the original volumes of the *Encyclopedia of Nuclear Magnetic Resonance*.[2–6] The methods described in the encyclopedia plus other methods, such as IGAIM (individual gauges for atoms in molecules)[7] and CSGT (continuous gauge transformation),[8] have become part of the standard toolkit of structural chemists. The implementation of routines to calculate NMR shieldings in popular quantum chemical packages, such the Gaussian series of programs,[9] has provided the greatest impetus for the routine use of NMR shielding calculations in structural chemistry.

In this article we discuss significant advances in the calculation of NMR shielding constants reported since the publication of the Encyclopedia of NMR in 1996. The material included in this article is by no means comprehensive and it is intended for physical or biological science researchers who are not specialists in the field of NMR. Comprehensive reviews in the field can be found in the accounts published annually by Jamenson and more recently by de Dios and Jameson.[10] Additional reviews on shielding calculations that have been published since the publication of the Encyclopedia of NMR, are: Fukui's review,[11] Fleischer et al. article in the Encyclopedia of Computational Chemistry,[12] and Chestnut's review in Reviews in Computational Chemistry.[13] Also the proceedings of two international meetings[14,15] provide a good overview of the state of the art developments in this field.

In Section 2 of this article we discuss the development of distributed gauge methods and the use of modern density functional theory (DFT) to calculate shielding constants. The section ends with a brief discussion of the open problems in the field of shielding calculations. In Section 3 we give a short account of the software available to perform shielding calculations and the hardware necessary for this task. Section 4 presents selected examples of state of the art shielding calculations from the author's work. Finally, the reader is advised that the references presented in Section 8 are by no means comprehensive, representing just a small sample of the work reported in the field in the last five years.

2 DEVELOPMENTS LEADING TO THE MODERN METHODS TO CALCULATE SHIELDING CONSTANTS

The state of the art in the calculation of NMR shielding constants has changed dramatically since the publication of the Encyclopedia of NMR in 1996. At that time the calculation of NMR shieldings was a highly specialized field, with a relative modest number of practitioners. While other computational modeling techniques were already highly developed and popular among non-specialists, the calculation of NMR shielding constants was still in its developmental stages. The principal reasons for this state of affairs were the complications associated with the so-called "gauge" problem and the well-known need to include electronic correlation effects in the calculation of NMR shielding constants.

Both problems were particularly severe for calculations in large molecules of practical interest. In these systems the need for large basis sets required to eliminate gauge invariance problems and the steep scaling with the size of the system, which is characteristic of electron structure methods that include electronic correlation effects, made the calculations unfeasible. In the next two subsections we describe new computational techniques that can be used to alleviate these problems, making calculations of shielding constants in large molecules possible.

2.1 Distributed Gauge Origin Methods

The so called "gauge" problem in shielding calculations or more precisely the lack of gauge invariance of the calculated shielding constants is a consequence of using a finite basis in the expansion of the wave function or electron density. Facelli has reviewed the gauge problem in detail in the *Encyclopedia of NMR*,[2] and another recent treatment of this problem can be found in Fukui's review.[11] It has been known for many years that this problem can be eliminated by using complex functions to expand the wave function. In spite of this theoretical understanding, it has taken a long time to derive practical and efficient formulations from this principle. It can be shown that the use of complex functions in the expansion of the wave function is equivalent to using different gauge origins for different regions of the electron density, therefore these methods to calculate shielding constants using complex expansions of the wave function have been designated as

distributed gauge origin methods. Many of the distributed gauge origin methods, like individual gauge for localized orbitals (IGLO),[5] localized orbitals local origin (LORG),[6] gauge including atomic orbital (GIAO),[4] individual gauges for atoms in molecules (IGAIM)[7] and continuous gauge transformation (CSGT),[8] have been efficiently implemented (see below) in common chemical modeling packages making possible for non-specialists to calculate shieldings routinely.

The distributed gauge methods can be classified into several different classes, those that use individual gauges for localized orbitals (LORG and IGLO); those that use a formulation based on the current of the electron density and the Bader's topological atom in a molecule description (IGAIM) or an empirical function for the continuous transformation of the gauge origin (CSGT) and finally, the GIAO method, which accomplishes the invariance of the results by using individual gauge origins for each atomic function in the basis set. For practical applications the selection of a method to calculate shielding is quite arbitrary, depending on such practical factors as software availability, cost and/or familiarity of the user with a particular method, hardware compatibility, etc. Methods using a localized orbital description, such as LORG and IGLO, can provide a somehow intuitive decomposition of the shielding into contributions arising from different localized orbitals, a feature quite appealing to chemists. The IGAIM method provides a decomposition of the shielding constants into contributions arising from the electronic density of each atomic basin, as defined by Bader's topological atom in a molecule description.[7] These types of decompositions are not available when using the GIAO or the CSGT methods, but the later provides an accurate three-dimensional representation of the distribution of induced electron current. Finally, it is interesting to mention Geertsen's method,[16] which gives a gauge origin independent formulation of the shielding constants by using second order perturbation theory to calculate its diamagnetic part. Unfortunately, while quite elegant, this formulation has not lead to practical applications due to the difficulties associated with the calculation of second order properties.

While all the methods discussed above take different approaches to mitigate the gauge problem, all of them are exact and converge to the same shielding values in the limit of very large basis. Of course, the converged values are identical to those obtained with the common origin method when the same extended basis is used in the calculations. In Figure 1 we present the basis set dependence of the calculated chemical shifts in glycine for different distributed gauge methods compared with the results obtained using the common origin method. The calculations were done using the Gaussian98 system,[9] the basis sets used correspond to the Dunning's correlation consistent basis, which includes polarization functions,[17] and the standard STO-3G from Pople et al.[18] It is apparent from the Figure that for the very small basis set, STO-3G, none of the methods is able to recover a significant fraction of the infinite basis limit; but significant improvements are observed when using the double zeta (DZ) basis set. Finally, the calculated values for all the methods consider here are almost identical when the quadruple zeta (QZ) basis set is used. While in some of the graphs of Figure 1 the IGAIM method appears to converge faster than the GIAO method, to the author's knowledge this is not a general conclusion, for instance the opposite results have been reported by Cheesman.[19]

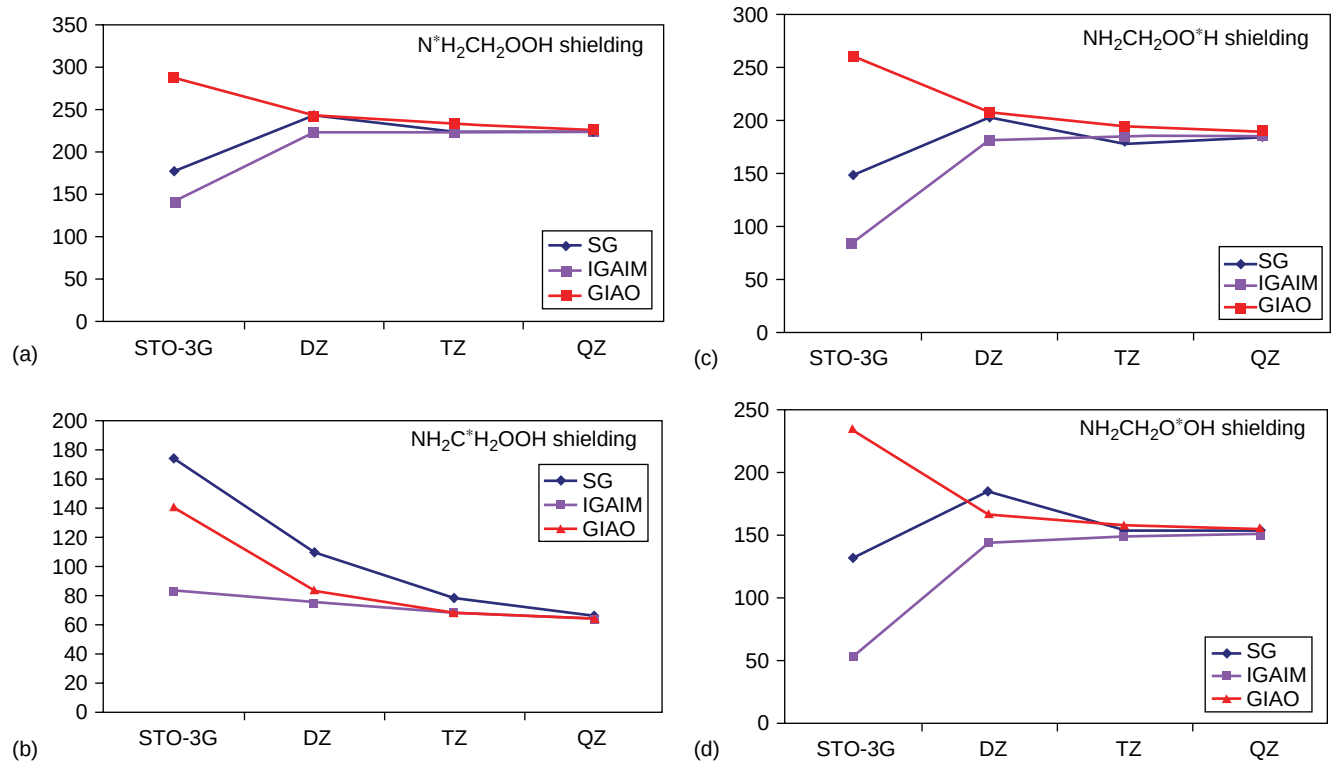

Figure 1 Basis set dependence of the shieldings in Glycine with different distributed gauge methods. All the values are in ppm referenced to the bare nucleus. The asterisk indicates the nucleus for which the shielding was calculated

2.2 Density Functional Theory Methods

The second important improvement in the calculation of shielding tensors, has been the development of generalized gradient approximations (GGAs) for the exchange-correlation functional in the density functional theory (DFT). While this theory, DFT, has been known for many years the development of GGAs and hybrid exchange-correlation functionals has increased the accuracy of the DFT to the point of making it suitable for shielding calculations.[20] Previous DFT theories, based on the local density approximation (LDA), did not have the accuracy necessary to provide the detailed description of the molecular electronic density needed to reproduce shielding constants quantitatively.[19]

The importance of the electron correlation effects in the calculation of shielding constants has been known for long time. Calculations at the Hartree–Fock level, while useful, were not as precise as needed for solving structural or assignment problems. Methods including contributions of the electronic correlation in the calculation of shielding constants also have been known for quite some time, for instance calculations using highly correlated Coupled Cluster methods have been published recently.[21] Unfortunately these methods, even at the MP2 level, do not provide a practical alternative to calculate shielding constants in large molecules because they scale as N^5 to N^7, depending of the approximation, with the size of the system. The development of effective DFT theories, which include electronic correlation effects, has proven a revolutionary tool in the field of shielding calculations. Using the DFT theory, which scales as N^2, it is possible to calculate shielding constants in molecular systems of practical interest including electronic correlation effects. Moreover, new DFT methods with quasi-linear scaling are becoming available and certainly they will be applied to the calculation of shielding constants in the near future.

Modern DFT theories are based on different approximations to calculate the exchange-correlation functional. Two fundamental approaches have been taken to establish this functional, one is based on pure mathematical considerations and the other based on empirical correlations that may include a portion of the Hartree–Fock exchange. Numerous shielding calculations, using a myriad of different functionals, have been reported. Many of these studies claim, depending of the set of molecules studied, to have found the best functional to calculate shielding constants. Careful evaluation of the literature would indicate that, except for the LDA approximation that does not include any gradient correction, all the modern exchange-correlation functionals give shielding constants of similar quality. It has become apparent that the shielding constants are much less sensitive to the selection of the exchange-correlation functional than other molecular properties.[22]

In Table 1 we compare the RMS between experimental and calculated ^{13}C and ^{15}N NMR chemical shifts for different exchange-correlation functionals for the compounds studied by Cheesman.[19] It is apparent that except for the calculations done using the LDA approximation, the DFT calculations are much better than the Hartree–Fock estimates and close to the values obtained for MP2 calculations. Two important observations can be derived from the table: (i) the calculations are not very sensitive to the exchange-correlation functional used, except for the LDA approximation; (ii) DFT methods recover a significant portion of the electronic correlation effect and provide a viable alternative to calculate chemical shifts with accuracies close to those obtained with the much more expensive MP2 method.

2.3 Limitations of the Current Methods

In spite of the great success of shielding calculations, there are several limitations in the current methods that should be taken into account. These limitations can be broadly classified as those inherent to the approximations used in the calculations and those due to the lack of knowledge of the molecular or crystalline structure.

In the first category the greatest deficiency of the current methods is the neglect of relativistic corrections. This is of minor consequence when dealing with molecules including first or second row atoms, but becomes a significant problem when the molecule includes atoms beyond the third row of the periodic table. There is a great deal of literature dealing with relativistic effects on shielding calculations,[14,15] but there are no well-established methods that can be used routinely. Moreover, most of the common approximations to take into account these effects have not been implemented in the most popular software used for shielding calculations. The calculation of shielding constants in molecules containing heavy atoms remains the realm of very specialized research groups.

The second methodological challenge in the calculation of NMR shielding is associated with the uncertainties in the molecular or crystalline geometry and the effects that the lattice may have on the NMR shielding constants. The first problem is a consequence of the great sensitivity of the shielding constants to the molecular geometry, a fact that has been known for some time.[23] While this sensitivity has been instrumental for using NMR chemical shift information to elucidate structural problems,[24] at the same time it can lead to unacceptably large errors in the calculated shielding constants due to the uncertainties in the position of hydrogen atoms observed in common structural methods such as X-ray. It has become common practice to optimize the position of the hydrogens atoms, determined by X-ray structures, before

Table 1 RMS error between calculated and experimental chemical shifts for different exchange correlation functionals[a]

RMS	HF	LSDA	BPW91	BLYP	B3PW91	B3LYP	MP2
^{13}C	11.5	16.1	7.7	9.2	8.7	9.5	2.3
^{15}N	49.3	34.6	20.0	21.7	27.5	29.1	13.4

[a]All values are in ppm from Ref.[19], calculated using the GIAO method with a qz2p basis set and MP2/tz2p geometries.

Table 2 Standard deviation between the experimental and Dunning D95 and D95** calculated ^{13}C chemical shifts in Methyl Bacteriopheophorbide[a]

Geometry	D95		D95**	
	Exp.	Exp. (**NA**)	Exp.	Exp. (**NA**)
X-ray	14.7	8.1	–	–
H-optimized	12.8	4.0	13.0	4.0
Crystal Optimized	12.8	4.0	13.0	4.0
Molecular Optimized	12.9	4.1	13.1	4.0

[a]Values in ppm from Ref.[34].

performing shielding calculations. The dramatic effect of this practice can be observed in the results presented in Table 2, the RMS between the calculated and experimental ^{13}C chemical shifts in methyl bacteriopheophorbide *a* decrease by a factor two, when the H-optimized structure is used in the shielding calculations.

Unfortunately, the practice of using optimized or partially optimized structures to calculate NMR shielding constants leads also to significant questions about possible cancellation of errors between the method used to optimize the geometry and the one used to calculate the NMR shielding constants. When using only the agreement between experimental and calculated NMR shielding constants as criteria for success, it is conceivable that good agreement could be achieved due to the use of a optimized geometry that underestimates the inter atomic bond distances, in conjunction with a method to calculate NMR shielding constants that also underestimates the shieldings or vise versa. Note that almost always $\partial\sigma/\partial r \leq 0$.[25] Comprehensive studies, including intermolecular effects (see below) and vibrational corrections, are needed to fully understand the interplay between geometry optimization and shielding calculations.

The inclusion of intermolecular effects in the calculation of shielding constants has attracted a great deal of attention over the years,[26] but no off the shelf methods are available to take into account these effects in the calculations. Unfortunately, in many cases the intermolecular interactions cannot be neglected without losing the quantitative agreement between experimental and calculated results (see below). In these situations it is necessary to exercise care and complement the standard methods available to calculate shielding constants with appropriate ways to take into account the intermolecular effects. A number of modern methods to address this issue are discussed in Section 4.4.

3 SOFTWARE AVAILABLE AND HARDWARE NEEDED FOR SHIELDING CALCULATIONS

Significant shielding calculations can be done using hardware and software commonly available in most structural chemical labs. With this in mind, it is important to provide a short account of the software available and the hardware necessary for NMR shielding calculations. In the next subsections we describe several of the most common software packages that can be used to calculate shielding constants and the typical hardware requirements for these calculations. The reader should notice that the software list is not comprehensive and that due to the rapidly evolving nature of the field it may become outdated shortly.

3.1 Gaussian98 Software

In terms of making shielding calculations available to a larger community of researchers, the most significant development has been the work by Cheesman et al.[19] Using the framework of the CDFT (Coupled DFT) perturbation theory they implemented the calculation of shielding tensors in the popular Gaussian suite of programs.[9] This implementation makes use of the techniques previously developed by Pulay and co-workers,[4] to efficiently calculate the complex two electron integrals necessary to implement the GIAO formulation. This method has become the most popular tool to calculate shielding constants. A number of additional methods to calculate shielding constants have also been implemented in the Gaussian suite of programs. These include HF, DFT and MP2 electronic approximations as well as single origin, GIAO, IGAIM and CSGT methods to deal with the gauge origin problem.

3.2 Other Commonly Used Programs

In addition to the popular Gaussian suite of programs several well known programs provide capabilities to calculate shielding constants using different approximations. Some of common programs available for shielding calculations are:

ACESII (http://www.qtp.ufl.edu/Aces2/).[27] Analytically evaluated NMR shielding tensors are available at the SCF and MBPT(2) levels using gauge-including atomic orbitals (GIAOs) to ensure exact gauge-invariance.

CADPAC (http://ket.ch.cam.ac.uk/software/cadpac.html).[28] NMR shielding constants can be calculated using the LORG algorithm for the DFT and HF electronic approximations.

deMon (http://www.sims.nrc.ca/sims/deMon/).[29,30] NMR shielding calculations using the DFT approximation within the SOS scheme described by Malkin.[30]

NWChem (http://www.emsl.pnl.gov:2080/docs/nwchem/nwchem.html).[31] Calculation of NMR shielding (GIAO method) for the HF electronic approximation using the coupled Hartree–Fock scheme. The implementation of these calculations using the DFT electronic approximation has been announced for a future release of this program.

It is important to realize that this is only a partial listing of computer programs capable of calculating NMR shielding constants. There are numerous other programs in many research groups with similar capabilities, but these tend to be

less supported and more difficult to use than those listed above. Also the reader should keep in mind that this field is changing rapidly and that the capability to calculate NMR shielding constants is becoming a standard feature of most molecular modeling software packages.

3.3 Hardware Necessary for Shielding Calculations

Modest shielding calculations, up to 10–20 non-hydrogen atoms, with a few hundreds of basis functions can be done in reasonable time using typical desktop computers. While these calculations cannot be done in an interactive fashion, overnight turn around for each shielding calculation is a reasonable expectation. If a geometry optimization of the system is necessary before performing the shielding calculation, this time may increase significantly depending on the quality and magnitude of the geometry optimization needed. Much larger calculations, involving of the order of 100 non-hydrogen atoms and more than one thousand basis functions are more suitable for large SMP (symmetric multi processors), Beowulf clusters or other parallel supercomputer systems. In general the software available for shielding calculations runs in parallel mode, but does not scale well with the number of processors. Very seldom more that 8–10 processors can be used effectively with the existing software. The better scalability performance of NWChem[32] provides hope for improved scalability of shielding calculations when the DFT approach is implemented in this package.

4 CHEMICAL AND STRUCTURAL RESEARCH USING MODERN METHODS

This section gives a few examples of the author's work in which calculations of NMR shielding constants were used to address common problems in NMR spectroscopy and structural chemistry. It is important to realize that this is not a comprehensive review of this topic. There is considerably more work reported in this area than it is possible or even desirable to include in an encyclopedia article. Readers interested in specific applications and/or in gaining a detailed understanding of the field should consult the important reviews published in this field. These references are given in the introductory section of this article.

In Section 4.1 we discuss the issues associated with comparing calculated shielding constants with measured chemical shifts. In Section 4.2 we show an example on how to use shielding calculations to improve the experimental assignment of ^{13}C resonances in methyl bacteriopheophorbide *a*. In Section 4.3 we show how modern techniques to calculate NMR shielding constants can be used to produce relatively large and consistent data sets of chemical shifts and how they can be used to gain insight into their classification. Finally in Section 4.4 we discuss some of the methods than can be used to take into account intermolecular/crystalline interactions.

4.1 Transforming Shieldings into Shifts

A significant complication to assess the quality of calculated shielding constants is the need for a reliable method to compare calculated and experimental values. NMR experiments provide chemical shifts, i.e., the position of a resonance frequency with respect to the resonance frequency of an established standard. The quantum chemical calculations provide absolute shielding constants, i.e., the relative shift of the resonance with respect to the resonance frequency of the bare nucleus. In principle, if the absolute shielding is known for the standard used in the experimental determination of the shift, the calculated shielding constants can be compared with the experimental chemical shifts using the following equation:

$$\delta(\text{shift}) = -\sigma(\text{shielding}) + \sigma_{\text{Ref}}(\text{shielding}) \quad (1)$$

Note that in equation (1) there is an additional minus sign that has been introduced between the shift scale and the shielding scale. This change of sign is introduced to take into account that the chemical shift increases as the nucleus becomes more de-shielded, while the shielding decreases.

Unfortunately, the use of equation (1) is complicated by the lack of precise values for σ_{Ref} (shielding). Absolute values of the shielding of the most common standards have been determined using Flygare's[33] relationship between the spin-rotational constant and the paramagnetic contribution to the shielding calculated at the center of mass. Unfortunately, these values do not take into account the effects that thermal averaging and/or solvent (in liquids) or crystal lattice (in solids) interactions may have on the chemical shifts of the standards. Precise studies of chemical shifts associated with thermal averaging and lattice effects are only known for very few standards.

To address these referencing difficulties it is quite common to correlate the calculated shielding constants with the experimental shift values using a linear regression of the type

$$\delta^{\text{exp}}(\text{shift}) = -A\sigma^{\text{calc.}}(\text{shielding}) + B \quad (2)$$

where *A* and *B* are constants determined by linear regression. The deviations of *A* from unity and *B* from the absolute value of the shielding of the reference standard give an indication of overall systematic errors in the calculations. Typically the deviations in *A* are an indication of the under or over estimation of the electronic correlation effects on the calculated shielding constants, while those in *B* are an indication of the uncertainties in the referencing process associated with thermal averaging and lattice effects.

4.2 Chemical Shifts Assignments

The assignment of NMR resonances has always been problematic and in spite of the great progress in using two-dimensional techniques for assignment purposes, these problems are still serious, particularly in solid state NMR. Calculations of shielding constants can provide additional information that can help in the assignment of experimental spectra.

A good example on how to use shielding calculations in aid to solve assignment problems was recently presented by Facelli in his study of methyl bacteriopheophorbide *a*.[34] The calculated chemical shift values, using the Dunning D95** basis set and the H-optimized geometry, are compared with the experimental values in Table 2 and their linear relationship plotted in Figure 2. A careful comparison between the calculated and experimental results shows that when

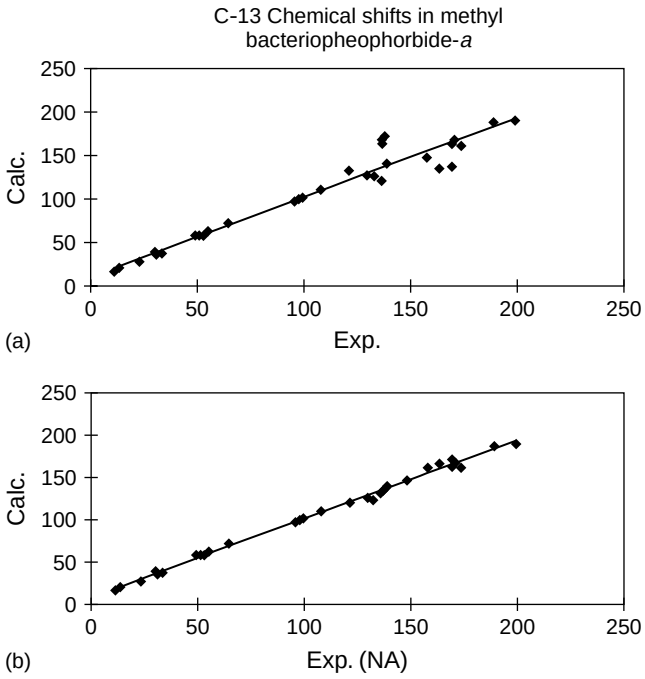

Figure 2 Correlation between the calculated and experimental ^{13}C chemical shifts in Methyl Bacteriopheophorbide *a*. Original assignments (a) and revised ones (b). All values are in ppm. (Reproduced with permission from Ref.[34])

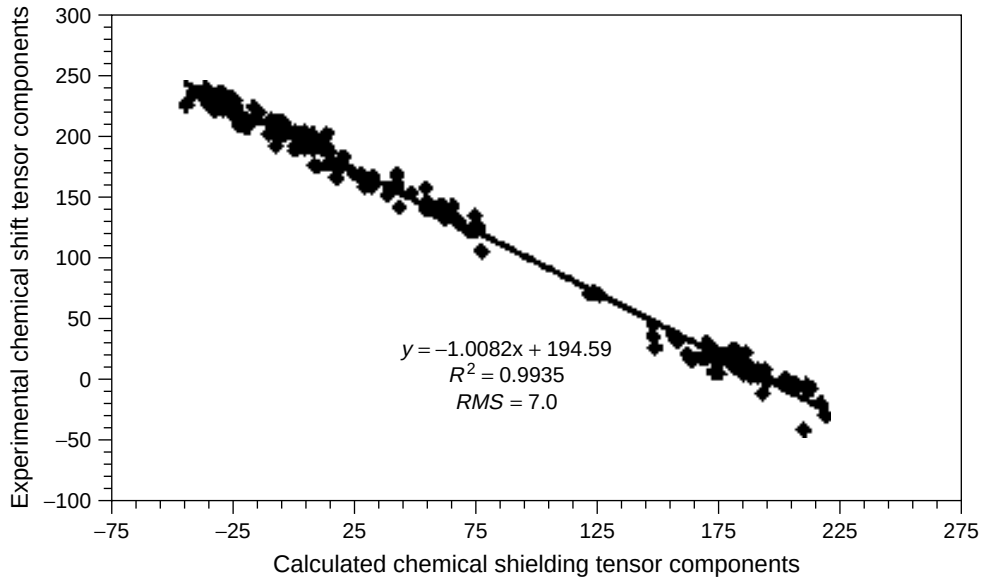

Figure 3 Linear relationship between experimental (shifts) and calculated (shieldings) ^{13}C chemical shifts principal values in PAHs. All values are in ppm. (Reproduced with permission from Ref.[35])

using the literature assignments of the carbon resonances, the residuals for C_{11}, C_{13}, C_{12}, C_{14}, C_1, C_5 C_{17} and C_{16} are at least two times larger than the standard deviation of the linear fit. Moreover, these large residuals appear in pairs (see Figure 2) suggesting that the experimental values may have been incorrectly assigned. If these assignments are exchanged the standard deviation between the calculated and experimental values drops by a factor close to two for the optimized structures. From Table 2 it is also apparent that the improvement in the correlation is independent of the geometry and basis used in the calculations. This dramatic improvement, observed when exchanging the experimental assignments for C_{11}, C_{13}, C_{12}, C_{14}, C_1, C_5 C_{17} and C_{16}, is depicted in the graph at the bottom of Figure 2, where it is shown that all the outliers in the correlation are eliminated when the new assignments are used.

4.3 Large Collections of Shielding Tensors: Hierarchical Cluster Analysis

The developments of the calculation of shielding constants described above allow researchers to tackle problems in novel

ways. For instance, an important problem in using chemical shift information to study complex substances, such as coals and soots, has been the lack of information on the amount of homogeneous broadening expected in the solid state spectra of these materials. It has been known for a long time that a carbon nucleus in a particular chemical environment has a chemical shift tensor with characteristic principal values, but very little quantitative information exists on how much variability exists in these values or how much overlap exists between the characteristic ranges for different chemical environments. Shielding calculations can help to address this problem by providing a practical method to assemble larger collections of data than those available from experiments.

A hierarchical cluster analysis of the principal values of ^{13}C chemical shift tensors encountered in polycyclic aromatic hydrocarbons (PAHs) has been done recently using calculated chemical shifts.[35] The analysis was performed using chemical shift tensors calculated using the DFT (B3PW91) GIAO method, with a D95 basis set on optimized geometries obtained using the CVFF force field and the DISCOVER routine in MSI's InsightII package. The good correlation observed (see Figure 3) between the calculated and experimental values, when available, supports the use of the calculated values in the hierarchical cluster analysis. This analysis was performed for two data sets of increasing size and the classification was found independent of the size of the sample, leading to the conclusion that the results presented here are valid for all PAHs.

The classification of the tensors using the hierarchical cluster analysis produces classes of chemical shift principal values that can be associated with the intuitive classification of chemical types of carbons present in PAHs. Figure 4 presents the results of the hierarchical cluster analysis of all the ^{13}C chemical shift principal values included in the smaller data set (150 different sets of three chemical shift principal values).

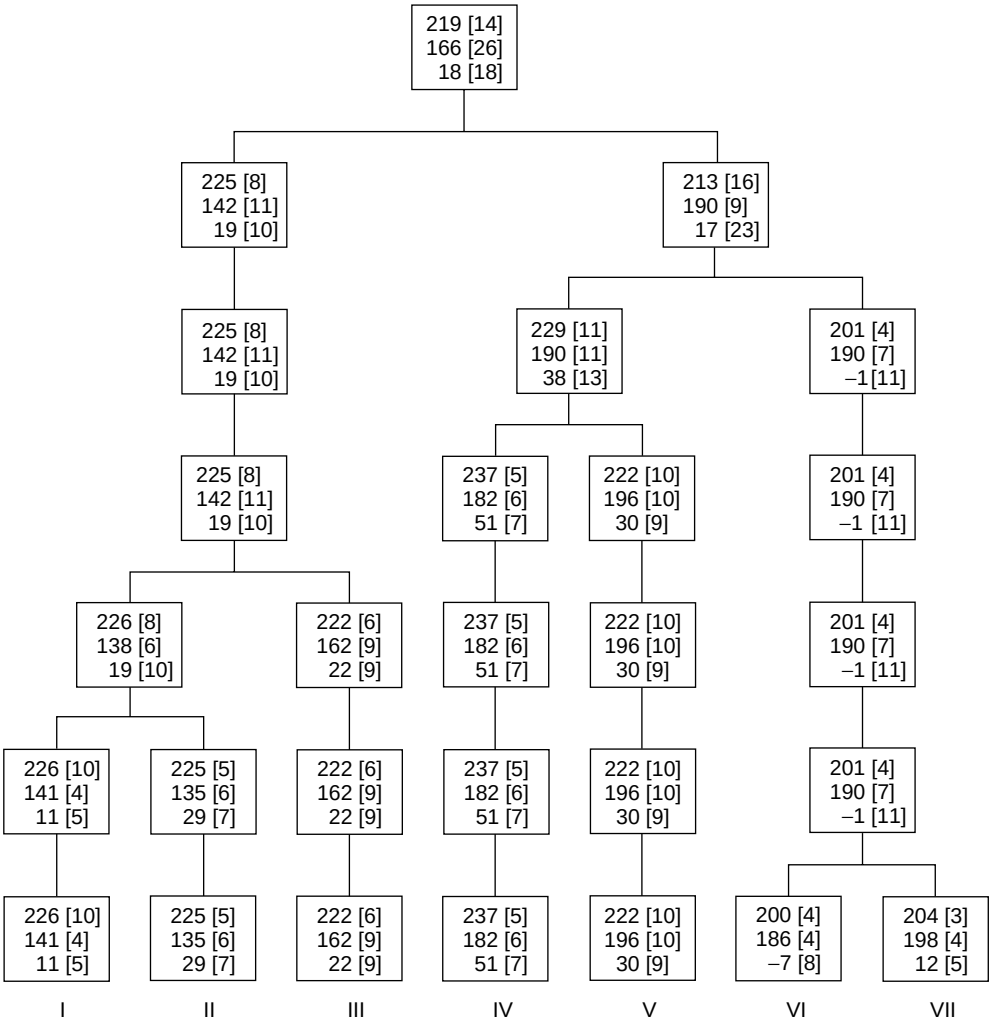

Figure 4 Hierarchical cluster analysis of the ^{13}C chemical shift tensor principal values of PAHs. The hierarchy includes classifications using from one to seven clusters. The number in square brackets after the principal values is the standard deviation. Seven clusters is the number of significant clusters given by the "best cut" procedure. The seven classes can be associated with the following types of carbons: (I) C–H aromatic carbons, (II) C–H aromatic carbons that are subject to steric strain, (III) C–C_a aromatic carbons where C_a is an aliphatic carbon in a planar configuration, (IV) C–C_a aromatic carbons where C_a is an aliphatic carbon in a non-planar configuration, (V) bridgehead aromatic carbons attached to two six member rings and one five member ring (this is always a non-planar configuration), (VI) bridgehead aromatic carbons attached to three six member rings in a planar configuration, (VII) bridgehead aromatic carbons attached to three six member rings in a non-planar configuration. All values are in ppm. (Reproduced with permission from Ref.[35])

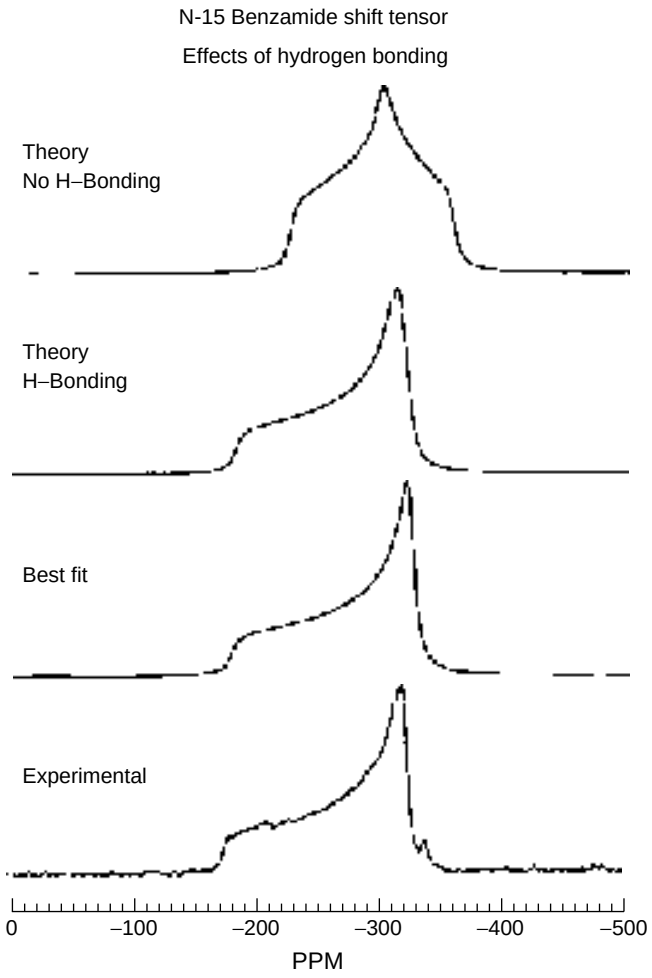

Figure 5 SSNMR ^{15}N Spectra of benzamide. Comparison with the experimental spectra of different simulations performed using ^{15}N chemical shifts calculated with different molecular models. This figure shows the dramatic effects of the HB interactions in the ^{15}N chemical shift tensor principal values

The figure presents the results for classifications including one to seven clusters, which is the maximum allowable number of clusters using the "best cut" method. The classification scheme also provides standard deviations within each class; these can be used as a measure of the inhomogeneous broadening expected for each characteristic NMR signal in complex mixtures of PAHs.

4.4 Intermolecular/Crystalline Effects

An active area of research in the theory of shielding calculations is the development of new methods to take into account intermolecular effects. While there is a long history of including these effects in NMR shielding calculations,[36] with the advent of new powerful computational methods for shielding calculations and new data from solid state NMR there has been an increased interest of reproducing the so called solid state effects. These effects, which originate in intermolecular interactions, are observed as changes in the resonance frequencies in the solid from those observed in liquids, as well as by duplication of spectral lines due to magnetic non-equivalences in the crystallographic cell. These magnetic non-equivalences are averaged, by molecular tumbling in liquid and gas phases, and therefore not observed in the corresponding NMR spectra. Solid state effects have been observed and modeled in both ^{13}C and ^{15}N chemical sifts.[37–40] For instance Figure 5 depicts the effects of including intermolecular effects, using the cluster method, in the calculation of the ^{15}N chemical sifts of benzamide.[40] It is apparent that the spectrum simulated using the ^{15}N chemical shift principal values calculated without including the intermolecular effects does not even resemble the experimental one. This is immediately corrected once these interactions are included in the calculations.

Crystalline effects are implicitly included in the calculation of molecular properties when the calculations are done using a formulation that includes periodic boundary conditions, the most common example of this technique can be found in the CRYSTAL98 program.[41] Recently Mauri et al.[42,43] have introduced a method to calculate NMR shielding constants in periodic systems, which of course includes implicitly all the intermolecular interactions. Unfortunately, this method has been implemented using the LDA approximation,[20] which reproduces chemical shifts with much less accuracy than hybrid functionals.[19] To the author's knowledge there has not been any implementation of a method to calculate shielding constants using periodic boundary conditions in a general

molecular simulation program like CRYSTAL98.[41] Therefore, intermolecular effects must be explicitly modeled when using hybrid exchange correlation functionals in the calculation of chemical shifts.

Many approximate methods have been used to include these effects in ab initio molecular calculations. Currently, there are two general schemes to model intermolecular effects: (i) the cluster models and (ii) the charge point models. A detailed discussion of both schemes is available elsewhere.[36] The cluster model explicitly includes in the calculation of the shielding constants the neighboring molecules or some of their *significant fragments*.[44] The difficulties associated with this method arise from the selection of the *significant fragments*, which is somehow arbitrary, and the considerable increase in the computational resources needed when large fragments are added to the calculations. Charge models, which describe the intermolecular effects by a discrete distribution of point charges, are very attractive because they derive from a very simple idea: the crystalline electrostatic potential can be represented by a finite distribution of point charges. The great advantage of these models is that the cost of shielding calculations does not significantly increase when a distribution of point charges is added to the system. Note also, that most of the existing programs to calculate NMR shielding constants have build-in capabilities to include a distribution of point charges in their calculation. The charges used in the calculations can be derived from simple population analysis methods[45] or from more elaborate methods that may adjust them to electrostatic potentials that mimic either the molecular or crystalline (Madelung) electrostatic potentials. In general the methods that attempt to use charges derived from electrostatic potentials obtained by ab initio calculations produce better results.[46] For instance, Facelli and Ferraro have used Troung's surface charge representation of the electrostatic embedding potential (SCREEP) method,[47] which attempts to reproduce the Madelung potential by a charge distribution on a van der Waals surface surrounding the molecule of interest. Grant and co-workers[48] have used a similar approach to calculate ^{13}C chemical shifts in thiocarbonates using the method proposed by Derenzo et al.[49] to calculate the Madelung potential.

In liquids intermolecular effects have been taken into account by using continuous models,[50] molecular dynamics simulations[51] and thermo dynamical averaging techniques.[52]

5 CONCLUSIONS

This article shows that by using tools, hardware and software, typically available to most researchers in the areas of NMR spectroscopy and/or structural chemistry it is possible to perform meaningful calculations of NMR shielding constants. While there are still unresolved problems with these calculations, like relativistic effects in molecules containing heavy nuclei and systematic treatments of intermolecular effects, there is a large number of systems in which these calculations can be used routinely to solve important structural problems or to elucidate issues of molecular electronic structure.

Several examples of the use of calculated shielding constants in aid to solve common problems encountered in NMR spectroscopy and structural chemistry were used to illustrate how useful these calculations can be.

6 RELATED ARTICLES IN VOLUMES 1–8

Bacteriorhodopsin & Rhodopsin, Volume 2; Chemical Shift Scales on an Absolute Basis, Volume 2; Chemical Shift Tensors, Volume 2; Chemical Shift Tensors in Single Crystals, Volume 2; Coal Structure from Solid State NMR, Volume 2; Fossil Fuels, Volume 3; Semiempirical Chemical Shift Calculations, Volume 7; Shielding Calculations: IGLO Method, Volume 7; Shielding Calculations: LORG & SOLO Approaches, Volume 7; Shielding Calculations: Perturbation Methods, Volume 7; Shielding: Overview of Theoretical Methods, Volume 7; Shielding in Small Molecules, Volume 7; Shielding Theory: GIAO Method, Volume 7; Shielding Tensor Calculations, Volume 7.

7 REFERENCES

1. D. M. Grant and R. K. Harris eds, 'Encyclopedia of Nuclear Magnetic Resonance', Wiley: London, 1996.
2. J. C. Facelli, in 'Encyclopedia of Nuclear Magnetic Resonance', eds D. M. Grant and R. K. Harris, Wiley: London, 1996, p. 4299.
3. G. A. Webb, in 'Encyclopedia of Nuclear Magnetic Resonance', eds D. M. Grant and R. K. Harris, Wiley: London, 1996, p. 4307.
4. P. Pulay and J. F. Hinton, in 'Encyclopedia of Nuclear Magnetic Resonance', eds D. M. Grant and R. K. Harris, Wiley: London, 1996, p. 4334.
5. W. Kutzelnigg, U. Fleischer, and Ch. van Wüllen, in 'Encyclopedia of Nuclear Magnetic Resonance', eds D. M. Grant and R. K. Harris, Wiley: London, 1996, p. 4284.
6. Aa. E. Hansen and M. Bilde, in 'Encyclopedia of Nuclear Magnetic Resonance', eds D. M. Grant and R. K. Harris, Wiley: London, 1996, p. 4292.
7. T. A. Keith and R. F. W. Bader, *Chem. Phys. Lett.*, 1992, **194**, 1.
8. T. A. Keith and R. F. W. Bader, *Chem. Phys. Lett.*, 1993, **210**, 223.
9. Gaussian 98, Revision A.7, M. J. Frisch, G. W. Trucks, H. B. Schlegel, G. E. Scuseria, M. A. Robb, J. R. Cheeseman, V. G. Zakrzewski, J. A. Montgomery, Jr., R. E. Stratmann, J. C. Burant, S. Dapprich, J. M. Millam, A. D. Daniels, K. N. Kudin, M. C. Strain, O. Farkas, J. Tomasi, V. Barone, M. Cossi, R. Cammi, B. Mennucci, C. Pomelli, C. Adamo, S. Clifford, J. Ochterski, G. A. Petersson, P. Y. Ayala, Q. Cui, K. Morokuma, D. K. Malick, A. D. Rabuck, K. Raghavachari, J. B. Foresman, J. Cioslowski, J. V. Ortiz, A. G. Baboul, B. B. Stefanov, G. Liu, A. Liashenko, P. Piskorz, I. Komaromi, R. Gomperts, R. L. Martin, D. J. Fox, T. Keith, M. A. Al-Laham, C. Y. Peng, A. Nanayakkara, C. Gonzalez, M. Challacombe, P. M. W. Gill, B. Johnson, W. Chen, M. W. Wong, J. L. Andres, C. Gonzalez, M. Head-Gordon, E. S. Replogle, and J. A. Pople, Gaussian, Inc.: Pittsburgh, PA, 1998.
10. C. J. Jameson and A. C. de Dios, in 'Special Periodical Reports on NMR', ed G. A. Webb, published annually by the The Royal Chemical Society: London.
11. H. Fukui, *Prog. NMR Spectrosc.*, 1997, **31**, 317.
12. U. Fleischer, Ch. van Wüllen, and W. Kutzelnigg, in 'Encyclopedia of Computational Chemistry', ed P. von Ragué Schleyer, Wiley: London, 1998, p. 1827.
13. D. B. Chestnut, in 'Reviews in Computational Chemistry', eds K. B. Lipkowitz and D. B. Boyd, VCH Publishers: New York, 1996, Vol. 8, p. 245.
14. J. C. Facelli and A. C. de Dios eds, 'Modeling NMR Chemical Shifts: Gaining Insights into Structure and Environment', American Chemical Society Symposium Series, no. 732, Oxford University Press: New York, 1999.

15. M. Kaupp and V. G. Malkin, eds, Special Issue: Quantum Chemical Calculation of NMR and EPR Parameters, *J. Comp. Chem.*, 1999, **20**, 1199.
16. J. Geertsen, *Chem. Phys. Lett.*, 1991, **179**, 479.
17. D. E. Woon and T. H. Dunning, *J. Chem. Phys.*, 1993, **98**, 1358.
18. W. J. Hehre, R. F. Stewart, and J. A. Pople, *J. Chem. Phys.*, 1969, **51**, 2657.
19. J. R. Cheesman, G. W. Trucks, T. A. Keith, and M. J. Frisch, *J. Chem. Phys.*, 1996, **104**, 5497.
20. J. M. Seminario and P. Politzer eds, Modern Density Functional Theory: A Tool for Chemistry. In 'Theoretical and Computational Chemistry' Vol. 2, Elsevier Science: 1995.
21. S. M. Cybulski and D. M. Bishop, *J. Chem. Phys.*, 1997, **106**, 4082.
22. P. J. Wilson, R. G. Amos, and N. C. Handy, *Mol. Phys.*, 1999, **97**, 757.
23. J. C. Facelli and D. M. Grant, *Nature*, 1993, **365**, 325.
24. J. K. Harper and D. M. Grant, *J. Am. Chem. Soc.*, 2000, **122**, 3708; J. Heller, D. D. Laws, M. Tomaselli, D. S. King, D. E. Wemmer, A. Pines, R. H. Havlin, and E. Oldfield, *J. Am. Chem. Soc.*, 1997, **119**, 7831; H. Le, J. G. Pearson, A. G. de Dios, and E. Oldfield, *J. Am. Chem. Soc.*, 1995, **117**, 3800.
25. C. J. Jameson and H. J. Osten, *Annu. Rep. NMR Spectrosc.*, 1986, **17**, 1.
26. A. C. de Dios and E. Oldfield, *Solid State Nucl. Magn. Reson.*, 1996, **6**, 101.
27. ACESII is a program product of the Quantum Theory Project, University of Florida. Authors: J. F. Stanton, J. Gauss, J. D. Watts, M. Nooijen, N. Oliphant, S. A. Perera, P. G. Szalay, W. J. Lauderdale, S. A. Kucharski, S. R. Gwaltney, S. Beck, A. Balková, D. E. Bernholdt, K. K. Baeck, P. Rozyczko, H. Sekino, C. Hober, and R. J. Bartlett. Integral packages included are VMOL (J. Almlöf and P. R. Taylor); VPROPS (P. Taylor); ABACUS (T. Helgaker, H. J. Aa. Jensen, P. Jørgensen, J. Olsen, and P. R. Taylor).
28. CADPAC: The Cambridge Analytic Derivatives Package Issue 6, Cambridge, 1995. A suite of quantum chemistry programs developed by R. D. Amos with contributions from I. L. Alberts, J. S. Andrews, S. M. Colwell, N. C. Handy, D. Jayatilaka, P. J. Knowles, R. Kobayashi, K. E. Laidig, G. Laming, A. M. Lee, P. E. Maslen, C. W. Murray, J. E. Rice, E. D. Simandiras, A. J. Stone, M.-D. Su, and D. J. Tozer.
29. deMon-KS version 3.3, M. E. Casida, C. D. Paul, A. Goursot, A. Koester, L. Petterson, E. Proynov, A. St-Amant, D. R. Salahub, H. Duarte, N. Godbout, J. Guan, C. Amorski, M. Leboeuf, V. Malkin, O. Malkina, F. Sim, A. Vela, deMon Software, Université de Montréal, 1997.
30. V. G. Malkin, O. L. Malkina, L. A. Eriksson, and D. R. Salahub, in 'Modern Density Functional Theory', Vol. 2, eds J. M. Seminario and P. Politzer, Elsevier Science: Amsterdam, 1995.
31. NWChem is a computational chemistry package that is designed to run on high-performance parallel supercomputers as well as on conventional workstation clusters. It aims to be scalable both in its ability to treat large problems efficiently, and in its usage of available parallel computing resources. NWChem has been developed by the High-performance Computational Chemistry group of the Environmental Molecular Sciences Laboratory (EMSL) at the Pacific Northwest National Laboratory (PNNL).
32. A. M. Orendt, private communication, 2001.
33. C. J. Jameson and J. Mason, in 'Multinuclear NMR', ed J. Mason, Plenum: New York, 1987, p. 56.
34. J. C. Facelli, *J. Phys. Chem.*, 1998, **102**, 2111.
35. J. C. Facelli, B. Nakagawa, A. M. Orendt, and R. J. Pugmaire, *J. Phys. Chem.*, 2001, **105**, 7468.
36. M. B. Ferraro, V. Repetto, and J. C. Facelli, *Solid State Nucl. Magn. Reson.*, 1998, **10**, 185.
37. A. C. de Dios, J. G. Pearson, and E. Oldfield, *Science*, 1993, **260**, 1491.
38. A. C. de Dios and E. Oldfield, *Chem. Phys. Lett.*, 1993, **205**, 108.
39. A. C. de Dios and E. Oldfield, *J. Am. Chem. Soc.*, 1994, **116**, 5307.
40. J. C. Facelli, R. J. Pugmaire, and D. M. Grant, *J. Am. Chem. Soc.*, 1996, **118**, 5488.
41. R. Dovesi, V. R. Saunders, C. Roetti, M. Causà, N. M. Harrison, R. Orlando, and E. Aprá, in *CRYSTAL98*, University of Torino, Torino, 1999.
42. F. Mauri, B. Pfrommer, and S. G. Louie, *Phys. Rev. Lett.*, 1996, **77**, 5300.
43. T. Gregor, F. Mauri, and R. Car, *J. Chem. Phys.*, 1999, **111**, 1815.
44. T. A. Kaplan and S. D. Mahanti eds, 'Electronic Properties of Solids Using Cluster Methods', Plenum: New York, 1995.
45. A. Szabo and N. S. Ostlund, 'Modern Quantum Chemistry', McGraw-Hill: New York, 1989.
46. D. E. Williams and J. M. Yan, *Adv. Atom. Mol. Phys.*, 1988, **23**, 87.
47. E. V. Stefanovich and T. N. Truong, *J. Phys. Chem. B*, 1998, **102**, 3018.
48. D. Stueber, F. N. Guenneau, and D. M. Grant, *J. Chem. Phys.*, 2001, **114**, 9236.
49. S. E. Derenzo, M. K. Klintenberg, and M. J. Weber, *J. Chem. Phys.*, 2000, **112**, 2074.
50. I. Ando and G. A. Webb, *Org. Magn. Reson.*, 1981, **15**, 111.
51. D. B. Chestnut and B. E. Rusiloski, *J. Mol. Struct. (THEOCHEM)*, 1994, **314**, 19.
52. R. Ludwig, F. Weinhold, and T. C. Farrar, *Mol. Phys.*, 1999, **97**, 479.

Biographical Sketch

Julio C. Facelli, *b* 1953. Licenciado in Physics (1977) and Doctor in Physics (1981), University of Buenos Aires, Argentina. Postdoctoral work at the University of Arizona. University of Utah 1984–present. Approx. 110 publications. Current research interests: Quantum chemical calculations of NMR parameters; relationship between NMR parameters and molecular structure; structure and properties of soot; and numerical and data intensive scientific computing.

Shielding in Small Molecules

Paolo Lazzeretti, Massimo Malagoli and Riccardo Zanasi

Università degli Studi di Modena, Modena, Italy

1 Introduction 1
2 Electronic Hamiltonians for a Molecule in an Electromagnetic Field 2
3 Linear Response in Magnetic Fields 5
4 Related Articles 9
5 References 9

1 INTRODUCTION

Powerful ad hoc computational approaches are available to predict NMR chemical shifts for medium and large molecules (see ***Shielding Calculations: LORG and SOLO Approaches***; ***Shielding Calculations: IGLO Method***, and Pulay et al.[1]). These methods yield theoretical estimates in reasonably good agreement with experiment, and are useful to rationalize trends, to check the reliability of measured values, etc. The aims of calculations on small molecules, based upon general quantum mechanical procedures, are somewhat different: the main emphasis is placed in understanding physical facts and determining, fully a priori, the exact value of absolute quantities, namely, nuclear magnetic shieldings; the quality of the theoretical predictions is not established by mere comparison with corresponding experimental data, which might be misleading in a number of cases. More exactly, yardsticks of accuracy are sought as by-products of the calculation, by evaluating related properties, namely magnetic susceptibility, quantum mechanical sum rules and constraints, upper and lower bounds, limiting values of the computational scheme based on a given approximation (e.g., the Hartree–Fock method), etc. In this article, after a short overview showing the limits of a classical approach to the shielding mechanism, we shall examine fully theoretical procedures enabling us to assess the accuracy of nuclear magnetic shielding predicted via approximate wavefunctions, independently of comparison with experimental values. The tests of accuracy rely on conditions for origin independence or, more generally, invariance under a gauge transformation of the electromagnetic potentials and associated canonical transformations of the electronic Hamiltonian, conditions for charge conservation, hypervirial theorems, etc. Although the main interest lies in theoretical determination of nuclear shieldings for a molecule in a spatially uniform and time-independent magnetic field, the more general case of a molecule responding linearly to harmonic perturbations is also examined, by introducing the Bloch gauge and the magnetic multipole Hamiltonian.[2,3]

The methods described in this article provide rigorous constraints and severe tests of quality for electronic wavefunctions. Although they are based on very general relationships, valid for any quantum mechanical system, practical applications are presently restricted to small molecules, for which accurate variational wavefunctions are available.

1.1 Magnetic Shielding in Classical Electrodynamics

Let us consider an electrically neutral molecule with N nuclei and an even number n of electrons, with mass m_e, smeared out with charge density $\rho(\boldsymbol{r}) = -e\gamma(\boldsymbol{r})$, a function of position $\boldsymbol{r}$ within the molecular domain. Systems of this type are symmetric under time reversal, and, except a few cases, diamagnetic: an external magnetic field $\boldsymbol{B}$, supposed, for simplicity, static and homogeneous, induces within the electron cloud an average orbital magnetic moment with a component $\langle \boldsymbol{m} \rangle$ antiparallel to $\boldsymbol{B}$. According to the Ampère and Larmor theorems of classical electrodynamics, this orbital moment arises from an induced electronic current density (in agreement with the Lenz law, the electron flow is in a direction such as to oppose the external field)

$$\boldsymbol{J}^B_{\mathrm{L}}(\boldsymbol{r}) = -\frac{e^2}{m_e c}\gamma(\boldsymbol{r})\boldsymbol{A}(\boldsymbol{r}) \tag{1}$$

where $\boldsymbol{A}$ is the vector potential associated with $\boldsymbol{B}$, in the Coulomb gauge,

$$\boldsymbol{B} = \nabla \times \boldsymbol{A}, \quad \nabla \cdot \boldsymbol{A} = 0, \quad \boldsymbol{A} = \tfrac{1}{2}\boldsymbol{B} \times \boldsymbol{r} \tag{2}$$

The stationary field generated at a point $\boldsymbol{r}_0$ by the Larmor precession is given by the Biot–Savart law

$$\boldsymbol{B}_{\mathrm{L}}(\boldsymbol{r}_0) = \frac{1}{c}\int \mathrm{d}^3 r \frac{\boldsymbol{r} - \boldsymbol{r}_0}{|\boldsymbol{r} - \boldsymbol{r}_0|^3} \times \boldsymbol{J}^B_{\mathrm{L}}(\boldsymbol{r}) = -\boldsymbol{\sigma}_{\mathrm{L}}(\boldsymbol{r}_0) \cdot \boldsymbol{B} \tag{3}$$

where $\boldsymbol{r}$ is the distance of the volume element $\mathrm{d}\boldsymbol{r}$ from the origin, so that the local effective field is

$$\boldsymbol{B}(\boldsymbol{r}_0) = \boldsymbol{B} + \boldsymbol{B}_{\mathrm{L}}(\boldsymbol{r}_0) = [\mathbf{1} - \boldsymbol{\sigma}_{\mathrm{L}}(\boldsymbol{r}_0)] \cdot \boldsymbol{B} \tag{4}$$

The magnetic shielding arising at $\boldsymbol{r}_0$, from the electron circulation is described by the tensor

$$\boldsymbol{\sigma}_{\mathrm{L}}(\boldsymbol{r}_0) = \frac{e^2}{2m_e c^2}\int \mathrm{d}^3 r\, \gamma(\boldsymbol{r}) \left(\boldsymbol{r} \cdot \frac{\boldsymbol{r} - \boldsymbol{r}_0}{|\boldsymbol{r} - \boldsymbol{r}_0|^3}\mathbf{1} - \boldsymbol{r}\frac{\boldsymbol{r} - \boldsymbol{r}_0}{|\boldsymbol{r} - \boldsymbol{r}_0|^3} \right) \tag{5}$$

The average shielding of a point at the origin of coordinates is connected with the scalar potential due to the electron cloud,

$$\tfrac{1}{3}\mathrm{Tr}[\boldsymbol{\sigma}_{\mathrm{L}}(\mathbf{0})] = -\frac{e}{3m_e c^2}\phi(\mathbf{0}), \quad \phi(\mathbf{0}) = -e\int \mathrm{d}^3 r\, \gamma(\boldsymbol{r})\frac{1}{r} \tag{6}$$

The first-order magnetic moment arising from the Larmor currents,

$$\langle \boldsymbol{m}_{\mathrm{L}} \rangle = \frac{1}{2c}\int \mathrm{d}^3 r\, \boldsymbol{r} \times \boldsymbol{J}^B_{\mathrm{L}} = \boldsymbol{\chi}_{\mathrm{L}} \cdot \boldsymbol{B} \tag{7}$$

and its second-order interaction energy with the magnetic field,

$$W^{BB}_{\mathrm{L}} = -\tfrac{1}{2}\langle \boldsymbol{m}_{\mathrm{L}} \rangle \cdot \boldsymbol{B} = -\frac{1}{2c}\int \mathrm{d}^3 r \boldsymbol{A} \cdot \boldsymbol{J}^B_{\mathrm{L}} = -\tfrac{1}{2}\boldsymbol{B} \cdot \boldsymbol{\chi}_{\mathrm{L}} \cdot \boldsymbol{B} \tag{8}$$

are expressed via the Langevin magnetic susceptibility

$$\boldsymbol{\chi}_{\mathrm{L}} = -\frac{e^2}{4m_e c^2}\int \mathrm{d}^3 r \gamma(\boldsymbol{r})(r^2\mathbf{1} - \boldsymbol{r}\boldsymbol{r}) \tag{9}$$

Using equation (4), the energy of interaction between an intrinsic magnetic dipole $\boldsymbol{\mu}_I$ on nucleus I, at $\boldsymbol{R}_I$, and the local effective magnetic field is

$$-\boldsymbol{\mu}_I \cdot \boldsymbol{B}(\boldsymbol{R}_I) = -\boldsymbol{\mu}_I \cdot \boldsymbol{B} + \boldsymbol{\mu}_I \cdot \boldsymbol{\sigma}_{\mathrm{L}}^I \cdot \boldsymbol{B}, \quad \boldsymbol{\sigma}_{\mathrm{L}}^I \equiv \boldsymbol{\sigma}_{\mathrm{L}}(\boldsymbol{R}_I) \tag{10}$$

where $\boldsymbol{\sigma}_{\mathrm{L}}^I$ is a tensor describing Larmor shielding of nucleus I. From equation (3) and the expression for the vector potential at $\boldsymbol{r}$ due to the nuclear dipole,

$$\boldsymbol{A}^{\mu_I} = \boldsymbol{\mu}_I \times \frac{\boldsymbol{r} - \boldsymbol{R}_I}{|\boldsymbol{r} - \boldsymbol{R}_I|^3} \tag{11}$$

one obtains the energy of interaction between the nuclear dipole and the local stationary magnetic field arising from the Larmor currents:

$$\boldsymbol{\mu}_I \cdot \boldsymbol{\sigma}_{\mathrm{L}}^I \cdot \boldsymbol{B} \equiv W_{\mathrm{L}}^{\mu_I B} = -\frac{1}{c} \int \mathrm{d}^3 r \boldsymbol{A}^{\mu_I} \cdot \boldsymbol{J}_{\mathrm{L}}^B = -\boldsymbol{\mu}_I \cdot \boldsymbol{B}_{\mathrm{L}}(\boldsymbol{R}_I) \tag{12}$$

An obvious 'interchange theorem' holds, i.e.,

$$W_{\mathrm{L}}^{\mu_I B} = -\frac{1}{c} \int \mathrm{d}^3 r \boldsymbol{A} \cdot \boldsymbol{J}_{\mathrm{L}}^{\mu_I} = -\langle \boldsymbol{m}_{\mathrm{L}}^I \rangle \cdot \boldsymbol{B}, \quad \langle \boldsymbol{m}_{\mathrm{L}}^I \rangle \equiv -\boldsymbol{\mu}_I \cdot \boldsymbol{\sigma}_{\mathrm{L}}^I \tag{13}$$

introducing the Larmor-type current density induced by the nuclear magnetic dipole within the electron distribution:

$$\boldsymbol{J}_{\mathrm{L}}^{\mu_I}(\boldsymbol{r}) = -\frac{e^2}{m_{\mathrm{e}} c} \gamma(\boldsymbol{r}) \boldsymbol{A}^{\mu_I}(\boldsymbol{r}) \tag{14}$$

According to an alternative interpretation to that provided by equation (12), this result accounts for the energy of interaction between the external magnetic field and an average orbital magnetic dipole moment induced within the electron cloud by the nuclear moment.

Classical electrodynamics is unable to describe paramagnetic contributions: quantum mechanical methods given below are necessary to understand these.

2 ELECTRONIC HAMILTONIANS FOR A MOLECULE IN AN ELECTROMAGNETIC FIELD

2.1 Gauge Transformations

Let us consider a charge distribution $\rho(\boldsymbol{r}, t)$, flowing with local velocity $\boldsymbol{v}(\boldsymbol{r}, t)$. The condition for charge conservation is, in component form (with $\alpha = 1, 2, 3$),

$$\nabla_\alpha J_\alpha + \frac{\partial \rho}{\partial t} = 0, \quad J_\alpha = \rho v_\alpha \tag{15}$$

Note that here and in what follows, the Einstein summation convention is adopted, i.e., a summation over pairs of repeated indices is implied: $\nabla_\alpha J_\alpha \equiv \sum_{\alpha=1}^3 \nabla_\alpha J_\alpha$. According to the Maxwell equations, the electromagnetic field can be described by introducing scalar and vector potentials $\phi(\boldsymbol{r}, t)$ and $\mathrm{A}_\alpha(\boldsymbol{r}, t)$:

$$B_\alpha = \epsilon_{\alpha\beta\gamma} \nabla_\beta A_\gamma, \quad E_\alpha = -\nabla_\alpha \phi - \frac{1}{c} \frac{\partial A_\alpha}{\partial t} \tag{16}$$

These potentials are defined to within a gauge transformation, leaving the fields and the Maxwell equations invariant, induced by an arbitrary continuous function $f = f(\boldsymbol{r}, t)$ tending smoothly to 0 at infinity:

$$A_\alpha \to A'_\alpha = A_\alpha + \nabla_\alpha f, \quad \phi \to \phi' = \phi - \frac{1}{c} \frac{\partial f}{\partial t} \tag{17}$$

The classical Lagrangian for one electron in an electromagnetic field is a sum of 'particle' and 'interaction' terms:

$$L = L_{\mathrm{e}} + L_{\mathrm{I}}, \quad L_{\mathrm{e}} = \tfrac{1}{2} m_{\mathrm{e}} \dot{r}^2, \quad L_{\mathrm{I}} = e\phi(\boldsymbol{r}, t) - \frac{e}{c} \dot{r}_\alpha A_\alpha(\boldsymbol{r}, t) \tag{18}$$

A change of gauge yields an equivalent Lagrangian

$$L \to L' = L + \frac{\mathrm{d}g}{\mathrm{d}t}, \quad \frac{\mathrm{d}g}{\mathrm{d}t} = \dot{r}_\alpha \nabla_\alpha g + \frac{\partial g}{\partial t}, \quad g = -\frac{e}{c} f \tag{19}$$

but does not affect the Lagrange equation of motion

$$\frac{\mathrm{d}}{\mathrm{d}t} \frac{\partial L}{\partial \dot{r}_\alpha} - \frac{\partial L}{\partial r_\alpha} = 0 \tag{20}$$

Assuming that the electron is spread out with density ρ, and flows with current density J_α,

$$\rho(\boldsymbol{R}, t) = -e\delta[\boldsymbol{R} - \boldsymbol{r}(t)], \quad J_\alpha(\boldsymbol{R}, t) = -e\dot{r}_\alpha(t)\delta[\boldsymbol{R} - \boldsymbol{r}(t)] \tag{21}$$

satisfying equation (15), an interaction Lagrangian density can be defined by

$$\mathcal{L}_{\mathrm{I}} = -\rho(\boldsymbol{R}, t)\phi(\boldsymbol{R}, t) + \frac{1}{c} J_\alpha(\boldsymbol{R}, t) A_\alpha(\boldsymbol{R}, t), \quad L_{\mathrm{I}} = \int \mathcal{L}_{\mathrm{I}} \, \mathrm{d}^3 R \tag{22}$$

which, under a gauge transformation given by equation (17), where $f = f(\boldsymbol{R}, t)$, transforms as

$$\begin{aligned} \mathcal{L}_{\mathrm{I}} \to \mathcal{L}'_{\mathrm{I}} &= \mathcal{L}_{\mathrm{I}} + \frac{1}{c} \left(\rho \frac{\partial f}{\partial t} + J_\alpha \nabla_\alpha f \right) \\ &= \frac{1}{c} \left[\frac{\partial}{\partial t}(\rho f) + \nabla_\alpha (J_\alpha f) - f \left(\frac{\partial \rho}{\partial t} + \nabla_\alpha J_\alpha \right) \right] \end{aligned} \tag{23}$$

where the last contribution vanishes owing to the continuity constraint, equation (15). Integrating over all space, the second contribution, owing to the Gauss theorem, gives a surface integral vanishing for the boundary conditions on J_α and f, and one is left with a total time derivative, i.e., with an equivalent Lagrangian, equation (19), and the same equation of motion, equation (20): charge-current conservation is a necessary condition for gauge invariance of the equation of motion.

The classical Hamiltonian is defined via the mechanical momentum,

$$h = \dot{r}_\alpha p_\alpha - L = \frac{1}{2m_{\mathrm{e}}} \pi_\alpha \pi_\alpha - e\phi, \quad \pi_\alpha = p_\alpha + \frac{e}{c} A_\alpha \tag{24}$$

Under a change of gauge, the classical dynamical variables in equation (24) transform as

$$\begin{aligned} p_\alpha = \frac{\partial L}{\partial \dot{r}_\alpha} \to p'_\alpha = \frac{\partial L'}{\partial \dot{r}_\alpha} = p_\alpha + \nabla_\alpha g \\ h' = \dot{r}_\alpha p'_\alpha - L' = h - \frac{\partial g}{\partial t} \end{aligned} \tag{25}$$

2.2 Canonical Transformations

Some problems arise when the Hamiltonian is quantized, since the canonical momentum operator $-\mathrm{i}\hbar\nabla_\alpha$ corresponds to different classical variables in unprimed and primed representations: the transformed quantum Hamiltonian is not obtained via equation (25). Therefore let us define 'particle' and 'interaction' operators

$$\hat{h}^{(0)} = \frac{1}{2m_\mathrm{e}}\hat{p}^2$$

$$\hat{h}^{(1)} + \tfrac{1}{2}\hat{h}^{(2)} = \frac{e}{2m_\mathrm{e}c}(A_\alpha\hat{p}_\alpha + \hat{p}_\alpha A_\alpha) + \frac{e^2}{2m_\mathrm{e}c^2}A_\alpha A_\alpha - e\phi \qquad (26)$$

Under a change of gauge, the mechanical momentum undergoes a similarity transformation induced by a unitary operator,

$$\hat{\pi}_\alpha \rightarrow \hat{\pi}'_\alpha = \hat{\pi}_\alpha - \nabla_\alpha\hat{g} \equiv \hat{Q}\hat{\pi}_\alpha\hat{Q}^\dagger, \quad \hat{Q} = \exp\left(\frac{\mathrm{i}}{\hbar}\hat{g}\right) \qquad (27)$$

Owing to the transformations given by equations (17) and (27), different equivalent Hamiltonians can be used for an electron in the electromagnetic field. Allowing for a class of gauge function wider than that retained in equation (19), i.e., $\hat{g} = \hat{g}(\boldsymbol{r}, \boldsymbol{p}, \boldsymbol{A}, \phi)$, a transformed quantum mechanical Hamiltonian will have the general form

$$\hat{h}' = \mathrm{i}\hat{\hbar}\left(\frac{\partial\hat{Q}}{\partial t}\right)\hat{Q}^\dagger + \hat{Q}\hat{h}\hat{Q}^\dagger \qquad (28)$$

As the generating function depends on the canonical momentum, the transformation to the new Hamiltonian is not accompanied by a change, equation (19), of the Lagrangian. In addition, the operators $\hat{g}$ and $\partial\hat{g}/\partial t$ do not generally commute (although we shall limit ourselves to transformations where $[\hat{g}, \partial\hat{g}/\partial t] = \hat{0}$ hereinafter). Under a transformation, equation (17), changing the one-electron wavefunction consistently with equation (28), the Schrödinger equation is invariant:

$$\psi \rightarrow \psi' = \hat{Q}\psi, \quad \hat{h}'\psi' = \mathrm{i}\hbar\frac{\partial}{\partial t}\psi' \qquad (29)$$

Using the quantum mechanical definition of total time derivative,

$$\frac{\mathrm{d}\hat{g}}{\mathrm{d}t} = \frac{\mathrm{i}}{\hbar}[\hat{h}^{(0)}, \hat{g}] + \frac{\partial\hat{g}}{\partial t} \qquad (30)$$

and the Hausdorff formula, to second order in $\hat{g}$, one obtains

$$\hat{h}' = \hat{h} - \frac{\mathrm{d}\hat{g}}{\mathrm{d}t} + \frac{\mathrm{i}}{\hbar}[\hat{g}, \hat{h}^{(1)}] + \tfrac{1}{2}\left(\frac{\mathrm{i}}{\hbar}\right)^2[\hat{g}, [\hat{g}, \hat{h}^{(0)}]] \qquad (31)$$

An alternative first-order Hamiltonian is obtained by choosing $\hat{g}$ so that

$$\hat{h}^{(1)} = \frac{\partial\hat{g}}{\partial t}, \quad \hat{h}'^{(1)} = \hat{h}^{(1)} - \frac{\mathrm{d}\hat{g}}{\mathrm{d}t} = -\frac{\mathrm{i}}{\hbar}[\hat{h}^{(0)}, \hat{g}] \qquad (32)$$

In practice, the gauge transformations that have been studied so far amount merely to a change of origin of the coordinate system for a molecule in the presence of a spatially uniform and time-independent magnetic field:

$$r'_\alpha \rightarrow r''_\alpha = r'_\alpha + d_\alpha, \quad A'_\alpha \rightarrow A''_\alpha = A'_\alpha + d_\beta\nabla_\alpha A'_\beta \qquad (33)$$

$$f = -\tfrac{1}{2}\epsilon_{\alpha\beta\gamma}(r_\alpha - r'_\alpha)B_\beta d_\gamma \equiv A'_\gamma d_\gamma, \quad g \equiv -\frac{e}{c}A'_\alpha d_\alpha \qquad (34)$$

Much more general choices for the gauge function f can, of course, be made. Three changes of gauge of the electromagnetic potentials will be outlined here:

1. the Bloch transformation;
2. the Landau transformation;
3. the canonical transformation leading to the torque formalism.

2.3 The Bloch Potentials

The MacLaurin series for the electric and magnetic fields, e.g.,

$$B(\boldsymbol{r}, t)_\alpha = \sum_{k=0}^{\infty}\frac{1}{k!}r_{\alpha_1}r_{\alpha_2}\cdots r_{\alpha_k}B(\boldsymbol{0}, t)_{\alpha_k\alpha_{k-1}\cdots\alpha_1\alpha} \qquad (35)$$

(where

$$B(\boldsymbol{0}, t)_{\alpha_k\alpha_{k-1}\cdots\alpha_1\alpha} \equiv \left[\frac{\partial^k B(\boldsymbol{r}, t)_\alpha}{\partial r_{\alpha_k}\partial r_{\alpha_{k-1}}\cdots\partial r_{\alpha_1}}\right]_{\boldsymbol{r}=\boldsymbol{0}} \qquad (36)$$

etc. denote the partial derivatives with respect to coordinates, at the origin), are not compatible with the analogous power expansions for vector and scalar potentials, which would not satisfy the equations for the fields, equation (16). Therefore, following Bloch,[2,3] one carries out a transformation, equation (17), where

$$f^\mathrm{B}(\boldsymbol{r}, t) = -\sum_{k=1}^{\infty}\frac{1}{k!}r_{\alpha_1}r_{\alpha_2}\cdots r_{\alpha_k}A(\boldsymbol{0}, t)_{\alpha_k\alpha_{k-1}\cdots\alpha_1} \qquad (37)$$

The new potentials satisfying equation (16) are

$$A^\mathrm{B}(\boldsymbol{r}, t)_\alpha = \sum_{k=0}^{\infty}\frac{k+1}{(k+2)!}\epsilon_{\alpha\beta\gamma}r_\gamma r_{\alpha_1}r_{\alpha_2}\cdots \times r_{\alpha_k}B(\boldsymbol{0}, t)_{\alpha_k\alpha_{k-1}\cdots\alpha_1\beta} \qquad (38)$$

$$\phi^\mathrm{B}(\boldsymbol{r}, t) = -\sum_{k=0}^{\infty}\frac{1}{(k+1)!}r_\alpha r_{\alpha_1}r_{\alpha_2}\cdots r_{\alpha_k}E(\boldsymbol{0}, t)_{\alpha_k\alpha_{k-1}\cdots\alpha_1\alpha} \qquad (39)$$

For a static electric field, one has $A^\mathrm{B}_{\alpha\alpha} = 0$ cf. the condition defining the Coulomb gauge, $A^\mathrm{C}_{\alpha\alpha} = 0 = \phi$, in a static homogeneous magnetic field.

The Bloch gauge is particularly useful, since it leads to a natural definition for the multipolar Hamiltonian adopted hereinafter to describe the properties of a molecule in a nonuniform time-dependent electromagnetic field.[3]

2.4 The Landau Gauge

Let us denote by A^C_α the vector potential in the Coulomb gauge, equation (2). The divergenceless Landau gauge[2] is obtained via the transformation

$$A^\mathrm{L}_\alpha = A^\mathrm{C}_\alpha + \nabla_\alpha f^\mathrm{L} = B_\beta r_\gamma, \quad f^\mathrm{L}(\boldsymbol{r}) = \tfrac{1}{2}(B_x yz + B_y zx + B_z xy) \qquad (40)$$

(α, β, and γ are any cyclic permutations of x, y, and z). The one-electron Hamiltonian in the Landau gauge, $\hat{h}_\mathrm{L}$, is obtained

with a transformation of the Coulomb Hamiltonian based on equation (40). From equation (26),

$$\hat{h}_{\mathrm{C}} \rightarrow \hat{h}_{\mathrm{L}} = \hat{h}^{(0)} + \hat{h}_{\mathrm{L}}^{(1)} + \tfrac{1}{2}\hat{h}_{\mathrm{L}}^{(2)} \tag{41}$$

$$\hat{h}_{\mathrm{L}}^{(1)} = \frac{e}{m_{\mathrm{e}}c} A_{\alpha}^{\mathrm{L}} \hat{p}_{\alpha} = \frac{e}{m_{\mathrm{e}}c}(B_y z \hat{p}_x + B_z x \hat{p}_y + B_x y \hat{p}_z) \tag{42}$$

$$\hat{h}_{\mathrm{L}}^{(2)} = \frac{e^2}{m_{\mathrm{e}}c^2} A_{\alpha}^{\mathrm{L}} A_{\alpha}^{\mathrm{L}} = \frac{e^2}{m_{\mathrm{e}}c^2}(B_x^2 y^2 + B_y^2 z^2 + B_z^2 x^2) \tag{43}$$

A transformation of the origin [cf. equation (33)] can be thought of as a change of gauge of the Landau vector potential:

$$A_{\alpha}^{\prime \mathrm{L}} \rightarrow A_{\alpha}^{\prime\prime \mathrm{L}} = A_{\alpha}^{\prime \mathrm{L}} + \nabla_{\alpha}\mathbb{L}, \quad \mathbb{L} = -(B_y d_z x + B_z d_x y + B_x d_y z) \tag{44}$$

2.5 The One-Electron Torque Hamiltonian

Instead of using the potentials ϕ and A_{α}, one seeks an alternative representation of the electromagnetic field introducing Hertz–Righi polarization potentials.[2] Adopting the Nisbet gauge[2] for the electric Hertz vector $\boldsymbol{Z}$,

$$\phi(\boldsymbol{r}, t) = -\nabla_{\alpha} Z_{\alpha}(\boldsymbol{r}, t) = 0, \quad A_{\alpha}(\boldsymbol{r}, t) = \frac{1}{c}\frac{\partial}{\partial t} Z_{\alpha}(\boldsymbol{r}, t) \tag{45}$$

The one-electron Hamiltonian within the torque formalism[2,4] is obtained according to equation (32). Through first order in the magnetic field,

$$\hat{g}^{(\nabla\times\mathbf{Z})_0} = \frac{e}{2m_e c^2}\epsilon_{\alpha\beta\gamma}\nabla_{\beta} Z_{\gamma}(\mathbf{0}, t)\hat{l}_{\alpha} \tag{46}$$

$$\hat{h}^{(1)} = \tfrac{e}{2m_{\mathrm{e}}c} B_{\alpha}(\mathbf{0}, t)\hat{l}_{\alpha} \equiv \tfrac{\partial}{\partial t}\hat{g}^{(\nabla\times\mathbf{Z})_0}$$

$$\hat{h}'^{(1)} = \epsilon_{\alpha\beta\gamma}\nabla_{\beta} Z_{\gamma}(\mathbf{0}, t)\hat{h}_{\alpha}^{(\nabla\times\mathbf{Z})_0} \tag{47}$$

introducing $\hat{k}_{\alpha}$, the torque about the origin on the unperturbed electron, and a reduced one-electron operator:

$$\hat{h}_{\alpha}^{(\nabla\times\mathbf{Z})_0} = -\frac{e}{2m_{\mathrm{e}}c^2}\hat{k}_{\alpha}, \quad \hat{k}_{\alpha} = \frac{\mathrm{d}\hat{l}_{\alpha}}{\mathrm{d}t} = \frac{\mathrm{i}}{\hbar}[\hat{h}^{(0)}, \hat{l}_{\alpha}] \tag{48}$$

2.6 Electronic Hamiltonians

Let the n electrons in a molecule be assigned coordinate vectors $\boldsymbol{r}_i$, canonical momenta $\hat{\boldsymbol{p}}_i = -\mathrm{i}\hbar\nabla_i$, and angular momenta $\hat{\boldsymbol{l}}_i = \boldsymbol{r}_i \times \hat{\boldsymbol{p}}_i (i = 1, 2, \ldots, n)$. The corresponding quantities for the N nuclei are $Z_{\mathrm{I}}e$, M_I, $\boldsymbol{R}_I$, etc. In the absence of any perturbation, the electronic states of the molecule are the eigenfunctions $|j\rangle$ of the unperturbed Born–Oppenheimer Hamiltonian

$$\hat{H}^{(0)} = \sum_{i=1}^{n}\left[\frac{\hat{p}_i^2}{2m_{\mathrm{e}}} - \sum_{I=1}^{N}\frac{Z_I e^2}{|\boldsymbol{r}_i - \boldsymbol{R}_I|} + \frac{1}{2}\sum_{j\neq i}^{n}\frac{e^2}{|\boldsymbol{r}_i - \boldsymbol{r}_j|}\right] + \frac{1}{2}\sum_{I}^{N}\sum_{J\neq I}^{N}\frac{Z_I Z_J e^2}{|\boldsymbol{R}_I - \boldsymbol{R}_J|} \tag{49}$$

i.e., $\hat{H}^{(0)}|j\rangle = E_j^{(0)}|j\rangle$. In the presence of an electromagnetic field with potentials $\boldsymbol{A}_i \equiv \boldsymbol{A}(\boldsymbol{r}_i, t)$ and $\phi_i \equiv \phi(\boldsymbol{r}_i, t)$, the interaction Hamiltonian is

$$\hat{V} = \sum_{i=1}^{n}\left[\frac{e}{2m_{\mathrm{e}}c}(\boldsymbol{A}_i \cdot \hat{\boldsymbol{p}}_i + \hat{\boldsymbol{p}}_i \cdot \boldsymbol{A}_i) + \frac{e^2}{2m_{\mathrm{e}}c^2}A_i^2 - e\phi_i\right] \tag{50}$$

In the Bloch gauge, to first order in the fields and their derivatives,[3]

$$\hat{H}^{(1)} = -\sum_{k=0}^{\infty}[E(\mathbf{0}, t)_{\alpha_k\alpha_{k-1}\cdots\alpha_1\alpha}\hat{\mu}_{\alpha\alpha_1\alpha_2\cdots\alpha_k} + B(\mathbf{0}, t)_{\alpha_k\alpha_{k-1}\cdots\alpha_1\alpha}\hat{m}_{\alpha\alpha_1\alpha_2\cdots\alpha_k}] \tag{51}$$

where, using Bloch normalization, the unperturbed magnetic multipole operators can be written (omitting contributions from electron spin) as,

$$\hat{m}_{\alpha\alpha_1\cdots\alpha_k} = -\frac{k+1}{(k+2)!}\frac{e}{2m_{\mathrm{e}}c} \times \sum_{i=1}^{n}(\hat{l}_{\alpha} r_{\alpha_1}\cdots r_{\alpha_k} + r_{\alpha_1}\cdots r_{\alpha_k}\hat{l}_{\alpha})_i. \tag{52}$$

If two indices are equal, $\hat{m}_{\alpha\alpha} = 0 = \hat{m}_{\alpha\alpha\beta\ldots}$, etc. The contributions provided by A_i^2 in equation (50) are accounted for by defining 'perturbed' multipoles

$$\hat{m}'_{\alpha} = \hat{m}_{\alpha} + \hat{\chi}^{\mathrm{d}}_{\alpha\beta}B(\mathbf{0}, t)_{\beta} + \hat{\chi}^{\mathrm{d}}_{\alpha\beta;\gamma}B(\mathbf{0}, t)_{\gamma\beta} + \hat{\chi}^{\mathrm{d}}_{\alpha\beta;\gamma\delta}B(\mathbf{0}, t)_{\delta\gamma\beta} + \hat{\chi}^{\mathrm{d}}_{\alpha\beta;\gamma\delta\epsilon}B(\mathbf{0}, t)_{\epsilon\delta\gamma\beta} + \cdots \tag{53a}$$

$$\hat{m}'_{\alpha\beta} = \hat{m}_{\alpha\beta} + \hat{\chi}^{\mathrm{d}}_{\alpha\gamma;\beta}B(\mathbf{0}, t)_{\gamma} + \tfrac{16}{9}\hat{\chi}^{\mathrm{d}}_{\alpha\gamma;\beta\delta}B(\mathbf{0}, t)_{\delta\gamma} + \tfrac{5}{2}\hat{\chi}^{\mathrm{d}}_{\alpha\gamma;\beta\delta\epsilon}B(\mathbf{0}, t)_{\epsilon\delta\gamma} + \cdots \tag{53b}$$

where the following auxiliary tensors have been introduced:

$$\hat{\chi}^{\mathrm{d}}_{\alpha\beta} = -\frac{e^2}{4m_{\mathrm{e}}c^2}\sum_{i=1}^{n}(r_{\nu}^2\delta_{\alpha\beta} - r_{\alpha}r_{\beta})_i \tag{54}$$

$$\hat{\chi}^{\mathrm{d}}_{\alpha\beta;\gamma} = -\frac{e^2}{6m_{\mathrm{e}}c^2}\sum_{i=1}^{n}[(r_{\nu}^2\delta_{\alpha\beta} - r_{\alpha}r_{\beta})r_{\gamma}]_i \tag{55}$$

$$\hat{\chi}^{\mathrm{d}}_{\alpha\beta;\gamma\delta} = -\frac{e^2}{16m_{\mathrm{e}}c^2}\sum_{i=1}^{n}[(r_{\nu}^2\delta_{\alpha\beta} - r_{\alpha}r_{\beta})r_{\gamma}r_{\delta}]_i \tag{56}$$

etc., (symmetric indices separated by a semicolon can be freely permuted).

The torque formalism [cf. equations (47) and (48)], is easily generalized to define an alternative first-order n-electron Hamiltonian. The operator for the torque exerted by the nuclei on the electrons (about the origin $\boldsymbol{r}_0$) is

$$\hat{\boldsymbol{K}}_n^N = \sum_{I=1}^{N}\sum_{i=1}^{n}\hat{\boldsymbol{K}}_i^I, \quad \hat{\boldsymbol{K}}_i^I(\boldsymbol{r}_0) = e^2 Z_I\frac{\boldsymbol{r}_i - \boldsymbol{R}_I}{|\boldsymbol{r}_i - \boldsymbol{R}_I|^3} \times (\boldsymbol{R}_I - \boldsymbol{r}_0) \tag{57}$$

and the n-electron 'reduced Hamiltonian' [cf. equation (48)], is

$$\sum_{i=1}^{n}\hat{h}_{i\alpha}^{(\nabla\times\mathbf{Z})_0} = -\frac{e}{2m_{\mathrm{e}}c^2}\hat{K}_{n\alpha}^N \tag{58}$$

The torque Hamiltonian, equation (47), depends on time: time-dependent perturbation theory must be used to describe the magnetic properties in the torque formalism—even for static fields.

In the presence of a nuclear magnetic dipole $\boldsymbol{\mu}_I$, the terms $-\mu_I\alpha\hat{\boldsymbol{B}}_{I\alpha}^n$ and

$$\hat{H}^{(11)} = \frac{e^2}{m_{\mathrm{e}}c^2}\sum_{i=1}^{n}(A_{\alpha}A_{\alpha}^{\mu_I})_i, \quad A_{i\alpha}^{\mu_I} = \frac{1}{e}\epsilon_{\alpha\beta\gamma}\mu_{I\beta}\hat{E}_{I\gamma}^i \tag{59}$$

must be added to the Hamiltonian of equation (50). In equation (59) the vector potential, equation (11), has been expressed via the operator for the electric field of electron i on nucleus I,

$$\hat{E}^i_{I\alpha} = e\frac{r_{i\alpha} - R_{I\alpha}}{|\boldsymbol{r}_i - \boldsymbol{R}_I|^3} \tag{60}$$

and the operator for the magnetic field of the electrons on nucleus I in the absence of an external perturbation is

$$\hat{B}^n_{I\alpha} = -\frac{e}{cm_e}\hat{M}^n_{I\alpha}, \quad \hat{M}^n_{I\alpha} = \frac{1}{e}\epsilon_{\alpha\beta\gamma}\sum_{i=1}^{n} E^i_{I\beta}\hat{p}_{i\gamma} \tag{61}$$

From equations (38) and (59), in nonuniform fields, the perturbed operator is

$$\begin{aligned}\hat{B}'^n_{I\alpha} = \hat{B}^n_{I\alpha} &- \hat{\sigma}^{\mathrm{d}I}_{\alpha,\beta}B(\mathbf{0},t)_\beta - \hat{\sigma}^{\mathrm{d}I}_{\alpha,\beta\gamma}B(\mathbf{0},t)_{\gamma\beta} \\ &-\hat{\sigma}^{\mathrm{d}I}_{\alpha,\beta\gamma\delta}B(\mathbf{0},t)_{\delta\gamma\beta} + \cdots\end{aligned} \tag{62}$$

where a comma separates the index for a component of the nuclear magnetic moment and a group of indices relative to the magnetic field and its spatial derivatives. The first two operators for the diamagnetic contributions to nuclear shielding are defined by

$$\hat{\sigma}^{\mathrm{d}I}_{\alpha,\beta} = \frac{e}{2m_e c^2}\sum_{i=1}^{n}(r_{i\lambda}\hat{E}^i_{I\lambda}\delta_{\alpha\beta} - r_{i\alpha}\hat{E}^i_{I\beta}) \tag{63}$$

$$\hat{\sigma}^{\mathrm{d}I}_{\alpha,\beta\gamma} = \frac{e}{3m_e c^2}\sum_{i=1}^{n}(r_{i\lambda}\hat{E}^i_{I\lambda}\delta_{\alpha\beta} - r_{i\alpha}\hat{E}^i_{I\beta})r_{i\gamma} \tag{64}$$

3 LINEAR RESPONSE IN MAGNETIC FIELDS

We shall be interested in the average values, formally correct to first order in the perturbing field and its spatial derivatives, of the operators in equations (53) and (62), which themselves involve the perturbation, over the time-dependent perturbed state. Representing the external perturbation as a monochromatic plane wave with frequency ω, and denoting the electronic transition (natural) frequencies by $\omega_{ja} = \hbar^{-1}(E^{(0)}_j - E^{(0)}_a)$, one obtains a formula for the expectation value[2] where the first-order Hamiltonian is expressed in an arbitrary formalism: the response properties obtained corresponding to a different $\hat{H}^{(1)}$ will be the same if the kets $|j\rangle$ are exact eigenvectors of the (model) $\hat{H}^{(0)}$. This equivalence can be checked by means of the off-diagonal Ehrenfest, or hypervirial, relations [a consequence of the definition in equation (30)]

$$\langle a|\hat{R}_\alpha|j\rangle = \frac{\mathrm{i}}{m_e}\omega^{-1}_{ja}\langle a|\hat{P}_\alpha|j\rangle = -\frac{1}{m_e}\omega^{-2}_{ja}\langle a|\hat{F}^N_{n\alpha}|j\rangle \tag{65}$$

$$\langle a|\hat{L}_\alpha|j\rangle = \mathrm{i}\omega^{-1}_{ja}\langle a|\hat{K}^N_{n\alpha}|j\rangle \tag{66}$$

where

$$\begin{aligned}\hat{R}_\alpha = \sum_{i=1}^{n} r_{i\alpha}, \quad \hat{P}_\alpha = \sum_{i=1}^{n}\hat{p}_{i\alpha} \\ \hat{L}_\alpha = \sum_{i=1}^{n}\hat{l}_{i\alpha}, \quad \hat{F}^N_{n\alpha} = -\sum_{I=1}^{N}\sum_{i=1}^{n} Z_I e\hat{E}^i_{I\alpha}\end{aligned} \tag{67}$$

are the operators for electron centroid, total canonical and angular momentum, and force exerted by the nuclei on the electrons.

3.1 Magnetic Dipole Properties

The frequency-dependent, or dynamic, paramagnetic contributions to the susceptibility and nuclear shielding, in the L formalism, are[2]

$$\chi^{\mathrm{p}}_{(LL)\alpha\beta}(\omega) = \frac{e^2}{4m_e^2c^2\hbar}\sum_{j\neq a}\frac{2\omega_{ja}}{\omega^2_{ja} - \omega^2}\,\mathrm{Re}(\langle a|\hat{L}_\alpha|j\rangle\langle j|\hat{L}_\beta|a\rangle) \tag{68}$$

$$\sigma^{\mathrm{p}I}_{(L)\alpha\beta}(\omega) = -\frac{1}{\hbar}\sum_{j\neq a}\frac{2\omega_{ja}}{\omega^2_{ja} - \omega^2}\,\mathrm{Re}(\langle a|\hat{B}^n_{I\alpha}|j\rangle\langle j|\hat{m}_\beta|a\rangle) \tag{69}$$

Using the torque Hamiltonian defined in equations (47), (57), and (58), or the hypervirial relations in equation (66), these properties become, in the KL and K formalisms,

$$\begin{aligned}\chi^{\mathrm{p}}_{(KL)\alpha\beta}(\omega) = -\frac{e^2}{4m_e^2c^2\hbar}&\sum_{j\neq a}\frac{2}{\omega^2_{ja} - \omega^2} \\ &\times\mathrm{Im}(\langle a|\hat{K}^N_{n\alpha}|j\rangle\langle j|\hat{L}_\beta|a\rangle)\end{aligned} \tag{70}$$

$$\begin{aligned}\sigma^{\mathrm{p}I}_{(K)\alpha\beta}(\omega) = -\frac{e^2}{2m_e^2c^2\hbar}&\sum_{j\neq a}\frac{2}{\omega^2_{ja} - \omega^2} \\ &\times\mathrm{Im}(\langle a|\hat{M}^n_{I\alpha}|j\rangle\langle j|\hat{K}^N_{n\beta}|a\rangle)\end{aligned} \tag{71}$$

The paramagnetic susceptibility, in the KK formalism, is

$$\begin{aligned}\chi^{\mathrm{p}}_{(KK)\alpha\beta}(\omega) = \frac{e^2}{4m_e^2c^2\hbar}&\sum_{j\neq a}\frac{2}{\omega_{ja}(\omega^2_{ja} - \omega^2)} \\ &\times\mathrm{Re}(\langle a|\hat{K}^N_{n\alpha}|j\rangle\langle j|\hat{K}^N_{n\beta}|a\rangle)\end{aligned} \tag{72}$$

If $|a\rangle$ and $|j\rangle$ are exact eigenstates of $\hat{H}^{(0)}$ then

$$\boldsymbol{\chi}^{\mathrm{p}}_{(KK)} \equiv \boldsymbol{\chi}^{\mathrm{p}}_{(KL)} \equiv \boldsymbol{\chi}^{\mathrm{p}}_{(LL)} \equiv \boldsymbol{\chi}^{\mathrm{p}}, \quad \boldsymbol{\sigma}^{\mathrm{p}I}_{(K)} = \boldsymbol{\sigma}^{\mathrm{p}I}_{(L)} \equiv \boldsymbol{\sigma}^{\mathrm{p}I} \tag{73}$$

The diamagnetic contributions (independent of ω) are obtained as expectation values of the operators in equations (54) and (63):

$$\chi^{\mathrm{d}}_{\alpha\beta} = \langle a|\hat{\chi}^{\mathrm{d}}_{\alpha\beta}|a\rangle, \quad \sigma^{\mathrm{d}I}_{\alpha\beta} = \langle a|\hat{\sigma}^{\mathrm{d}I}_{\alpha,\beta}|a\rangle \tag{74}$$

and total magnetic dipole response tensors are

$$\chi_{\alpha\beta}(\omega) = \chi^{\mathrm{p}}_{\alpha\beta}(\omega) + \chi^{\mathrm{d}}_{\alpha\beta}, \quad \sigma^{I}_{\alpha\beta}(\omega) = \sigma^{\mathrm{p}I}_{\alpha\beta}(\omega) + \sigma^{\mathrm{d}I}_{\alpha\beta} \tag{75}$$

It is sometimes convenient, for computational purposes, to introduce a perturbation expansion for the electron current density induced by a static external magnetic field and by an intramolecular nuclear magnetic dipole: to first order in B_β and $\mu_{I\beta}$,

$$J(\boldsymbol{r})_\alpha = J^{(0)}_\alpha(\boldsymbol{r}) + \mathcal{J}^{B_\beta}_\alpha(\boldsymbol{r})B_\beta + \mathcal{J}^{\mu_{I\beta}}_\alpha(\boldsymbol{r})\mu_{I\beta} + \cdots \tag{76}$$

defining two second-rank current density tensors, $\mathcal{J}^{B_\beta}_\alpha$ and $\mathcal{J}^{\mu_{I\beta}}_\alpha$. The classical ansatz for the interaction energies, equations (8), (12), and (13), can be retained, using the total quantum current density, equation (76). As energies are gauge-invariant, the condition for charge conservation in a static magnetic field [cf. equation (23)], becomes,[5] using equations (8) and (17) with $f = r_\beta$,

$$\int \mathrm{d}^3r\, J_\alpha = 0 \tag{77}$$

The magnetic susceptibility and the nuclear magnetic shielding of nucleus I, at $\boldsymbol{R}_I$, can be expressed in terms of the current density, equation (76):

$$\chi_{\alpha\delta} = \frac{1}{2c}\epsilon_{\alpha\beta\gamma}\int \mathrm{d}^3r\, r_\beta \mathcal{J}^{B_\delta}_\gamma(\boldsymbol{r}) \tag{78}$$

$$\begin{aligned}\sigma^I_{\alpha\delta} &= -\frac{1}{c}\epsilon_{\alpha\beta\gamma}\int \mathrm{d}^3r \frac{r_\beta - R_{I\beta}}{|\boldsymbol{r}-\boldsymbol{R}_I|^3}\mathcal{J}^{B_\delta}_\gamma(\boldsymbol{r}) \\ &= -\frac{1}{2c}\epsilon_{\beta\gamma\delta}\int \mathrm{d}^3r\, r_\beta \mathcal{J}^{\mu_I\alpha}_\gamma(\boldsymbol{r})\end{aligned}$$

3.2 Magnetic Multipolar Contributions

Paramagnetic contributions to susceptibility and nuclear shielding in the L formalism, arising from higher magnetic moments, are evaluated using the unperturbed operators of equations (52) and (61). Mixed dipolar–multipolar paramagnetic susceptibilities are

$$\begin{aligned}\chi^{\mathrm{p}}_{\alpha,\beta\gamma}(\omega) &= \frac{1}{\hbar}\sum_{j\neq a}\frac{2\omega_{ja}}{\omega^2_{ja}-\omega^2}\,\mathrm{Re}(\langle a|\hat{m}_\alpha|j\rangle\langle j|\hat{m}_{\beta\gamma}|a\rangle) \\ &= \chi^{\mathrm{p}}_{\beta\gamma,\alpha}(\omega)\end{aligned} \tag{80}$$

$$\begin{aligned}\chi^{\mathrm{p}}_{\alpha\beta,\gamma\delta}(\omega) &= \frac{1}{\hbar}\sum_{j\neq a}\frac{2\omega_{ja}}{\omega^2_{ja}-\omega^2}\,\mathrm{Re}(\langle a|\hat{m}_{\alpha\beta}|j\rangle\langle j|\hat{m}_{\gamma\delta}|a\rangle) \\ &= \chi^{\mathrm{p}}_{\gamma\delta,\alpha\beta}(\omega)\end{aligned} \tag{81}$$

etc., where tensor indices are divided in groups (separated by a comma) that can be freely permuted, since they refer to different multipoles, equation (52). The contributions to nuclear magnetic shielding from higher magnetic multipoles are

$$\sigma^{\mathrm{p}I}_{\alpha,\beta\gamma}(\omega) = -\frac{1}{\hbar}\sum_{j\neq a}\frac{2\omega_{ja}}{\omega^2_{ja}-\omega^2}\,\mathrm{Re}(\langle a|\hat{B}^n_{I\alpha}|j\rangle\langle j|\hat{m}_{\beta\gamma}|a\rangle) \tag{82}$$

etc., where a comma separates the index for a component of the nuclear magnetic moment and a group of indices relative to the field gradients. $\chi^{\mathrm{p}}_{\alpha,\beta\beta}(\omega) = 0 = \chi^{\mathrm{p}}_{\alpha\beta,\gamma\gamma}(\omega)$ and $\sigma^{\mathrm{p}I}_{\alpha,\beta\beta}(\omega) = 0 = \sigma^{\mathrm{pI}}_{\alpha\beta,\gamma\gamma}(\omega)$, etc. The diamagnetic contributions, from equations (55) and (64), are

$$\chi^{\mathrm{d}}_{\alpha\beta;\gamma} = \langle a|\hat{\chi}^{\mathrm{d}}_{\alpha\beta;\gamma}|a\rangle, \quad \chi^{\mathrm{d}}_{\alpha\beta;\gamma\delta} = \langle a|\hat{\chi}^{\mathrm{d}}_{\alpha\beta;\gamma\delta}|a\rangle \tag{83}$$

$$\sigma^{\mathrm{d}I}_{\alpha,\beta\gamma} = \langle a|\hat{\sigma}^{\mathrm{d}I}_{\alpha,\beta\gamma}|a\rangle, \quad \sigma^{\mathrm{d}I}_{\alpha,\beta\gamma\delta} = \langle a|\hat{\sigma}^{\mathrm{d}I}_{\alpha,\beta\gamma\delta}|a\rangle \tag{84}$$

etc. Therefore the magnetic moments induced by a nonuniform magnetic field can be written as

$$\begin{aligned}\Delta\langle\hat{m}'_\lambda\rangle = {}& \chi_{\lambda\alpha}B(\mathbf{0},t)_\alpha + \chi_{\lambda,\alpha\beta}B(\mathbf{0},t)_{\beta\alpha} \\ &+\chi_{\lambda,\alpha\beta\gamma}B(\mathbf{0},t)_{\gamma\beta\alpha}+\cdots\end{aligned} \tag{85}$$

$$\begin{aligned}\Delta\langle\hat{m}'_{\lambda\mu}\rangle = {}& \chi_{\lambda\mu,\alpha}B(\mathbf{0},t)_\alpha + \chi_{\lambda\mu,\alpha\beta}B(\mathbf{0},t)_{\beta\alpha} \\ &+\chi_{\lambda\mu,\alpha\beta\gamma}B(\mathbf{0},t)_{\gamma\beta\alpha}+\cdots\end{aligned} \tag{86}$$

etc., where the total dipolar–multipolar susceptibilities are defined, for example, by

$$\chi_{\alpha,\beta\gamma}(\omega) = \chi^{\mathrm{p}}_{\alpha,\beta\gamma}(\omega) + \chi^{\mathrm{d}}_{\alpha\beta;\gamma} \tag{87}$$

$$\chi_{\alpha\beta,\gamma\delta}(\omega) = \chi^{\mathrm{p}}_{\alpha\beta,\gamma\delta}(\omega) + \tfrac{16}{9}\chi^{\mathrm{d}}_{\alpha\gamma;\beta\delta} = \chi_{\gamma\delta,\alpha\beta}(\omega) \tag{88}$$

The magnetic field induced on nucleus I by the electron cloud perturbed by a nonuniform magnetic field is

$$\begin{aligned}\Delta\langle\hat{B}^n_{I\alpha}\rangle = {}& -\sigma^I_{\alpha\beta}B(\mathbf{0},t)_\beta - \sigma^I_{\alpha,\beta\gamma}B(\mathbf{0},t)_{\gamma\beta} \\ &-\sigma^I_{\alpha,\beta\gamma\delta}B(\mathbf{0},t)_{\delta\gamma\beta}+\cdots\end{aligned} \tag{89}$$

where the multipolar contributions to the total dynamic magnetic shieldings are

$$\sigma^I_{\alpha,\beta\gamma}(\omega) = \sigma^{\mathrm{p}I}_{\alpha,\beta\gamma}(\omega) + \sigma^{\mathrm{d}I}_{\alpha,\beta\gamma} \tag{90}$$

etc. Magnetic multipolar effects are invoked to rationalize 'contact shifts'.[3]

3.3 Magnetic Properties in the Landau Gauge

In this gauge [cf. equations (42) and (43)], the total n electron interaction Hamiltonian contains the terms

$$\hat{H}^B_{\mathrm{L}} = \frac{e}{m_{\mathrm{e}}c}\sum_{i=1}^n(A^{\mathrm{L}}_\alpha\hat{p}_\alpha)_i \tag{91}$$

$$\hat{H}^{BB}_{\mathrm{L}} = \frac{e^2}{m_{\mathrm{e}}c^2}\left(B^2_x\sum_{i=1}^n y_i^2 + B^2_y\sum_{i=1}^n z_i^2 + B^2_z\sum_{i=1}^n x_i^2\right) \tag{92}$$

In the reference state $|a\rangle$, the diamagnetic contribution to the susceptibility is[6]

$$\chi^{\mathrm{dL}}_{xx} = -\frac{\partial^2}{\partial B^2_x}\langle a|\tfrac{1}{2}\hat{H}^{BB}_{\mathrm{L}}|a\rangle = -\frac{e^2}{m_{\mathrm{e}}c^2}\langle a|\sum_{i=1}^n y_i^2|a\rangle\,\chi^{\mathrm{dL}}_{xy} = 0,\ldots \tag{93}$$

(other tensor components are obtained by cyclic permutation of the indices x, y, and z). Off-diagonal diamagnetic components vanish for any coordinate system in the Landau gauge. The paramagnetic contribution is

$$\chi^{\mathrm{pL}}_{xx} = \frac{e^2}{m^2_{\mathrm{e}}c^2\hbar}\sum_{j\neq a}\frac{2}{\omega_{ja}}\,\mathrm{Re}\left[\langle a|\sum_{i=1}^n(yp_z)_i|j\rangle\langle j|\sum_{i=1}^n(yp_z)_i|a\rangle\right] \tag{94a}$$

$$\chi^{\mathrm{pL}}_{xy} = \frac{e^2}{m^2_{\mathrm{e}}c^2\hbar}\sum_{j\neq a}\frac{2}{\omega_{ja}}\,\mathrm{Re}\left[\langle a|\sum_{i=1}^n(yp_z)_i|j\rangle\langle j|\sum_{i=1}^n(zp_x)_i|a\rangle\right] \tag{94b}$$

etc. It is a symmetric tensor, as in the Coulomb gauge, diagonal only in its principal axis system: the off-diagonal components of total susceptibility are paramagnetic and, remarkably, origin-independent in the Landau gauge for molecular symmetries equal to or larger than c_{2v}.

In the presence of a nuclear magnetic dipole, the interaction Hamiltonian contains the terms $-\mu_{I\alpha}\hat{B}^n_{I\alpha}$ and $\hat{H}^{\mu_I B}_{\mathrm{L}} = (e^2/m_{\mathrm{e}}c)\sum_{i=1}^{\mathrm{n}}(A^{\mu_I}_\alpha A^{\mathrm{L}}_\alpha)_i$. The diamagnetic contribution to the shielding of nucleus I becomes

$$\sigma^{\mathrm{d}IL}_{xx} = \frac{\partial^2}{\partial\mu_{Ix}\partial B_x}\langle a|\hat{H}^{\mu_I B}_{\mathrm{L}}|a\rangle = \frac{e}{m_{\mathrm{e}}c^2}\langle a|\sum_{i=1}^n y_i\hat{E}^i_{Iy}|a\rangle \tag{95a}$$

$$\sigma^{\mathrm{d}IL}_{yx} = \frac{\partial^2}{\partial\mu_{Iy}\partial B_x}\langle a|\hat{H}^{\mu_I B}_{\mathrm{L}}|a\rangle = -\frac{e}{m_{\mathrm{e}}c^2}\langle a|\sum_{i=1}^n y_i\hat{E}^i_{Ix}|a\rangle \tag{95b}$$

etc. For any coordinate system, $\sigma_{xy}^{dIL} = \sigma_{yz}^{dIL} = \sigma_{zx}^{dIL} = 0$, i.e., the diamagnetic contribution to the shielding of nucleus I is a second-rank asymmetric tensor with a maximum of six independent components. The paramagnetic contribution is

$$\sigma_{xx}^{pIL} = -\frac{e^2}{m_e^2 c^2 \hbar} \sum_{j \neq a} \frac{2}{\omega_{ja}} \mathrm{Re}\left[\langle a|\hat{M}_{Ix}^n|j\rangle\langle j| \sum_{i=1}^{n} (y\hat{p}_z)_i |a\rangle \right] \quad (96a)$$

$$\sigma_{xy}^{pIL} = -\frac{e^2}{m_e^2 c^2 \hbar} \sum_{j \neq a} \frac{2}{\omega_{ja}} \mathrm{Re}\left[\langle a|\hat{M}_{Ix}^n|j\rangle\langle j| \sum_{i=1}^{n} (z\hat{p}_x)_i |a\rangle \right] \quad (96b)$$

etc. It is an asymmetric tensor with nine independent components in the absence of molecular symmetry; σ_{xy}^{IL}, σ_{yz}^{IL}, and σ_{zx}^{IL} are paramagnetic and origin-independent.

Diamagnetic contributions in different gauges are related by

$$\chi_{xx}^{dC} = \tfrac{1}{4}(\chi_{xx}^{dL} + \chi_{yy}^{dL}), \quad \chi_{\alpha\alpha}^{dC} = \tfrac{1}{2}\chi_{\alpha\alpha}^{dL} \quad (97)$$

$$\sigma_{xx}^{dIC} = \tfrac{1}{2}(\sigma_{xx}^{dIL} + \sigma_{yy}^{dIL}), \quad \sigma_{yx}^{dIC} = \tfrac{1}{2}\sigma_{yx}^{dIL}, \quad \sigma_{\alpha\alpha}^{dIC} = \sigma_{\alpha\alpha}^{dIL} \quad (98)$$

From the hypervirial relation

$$\langle a| \sum_{i=1}^{n} (x\hat{p}_y)_i |j\rangle = \tfrac{1}{2}\langle a|\hat{L}_z|j\rangle - \tfrac{1}{2}\mathrm{i}m_e\omega_{ja}\langle a| \sum_{i=1}^{n} (xy)_i |j\rangle \quad (99)$$

the equations connecting the paramagnetic contributions in the Landau and Coulomb gauges are

$$\chi_{xx}^{pL} = \chi_{xx}^{pC} + \tfrac{1}{4}(\chi_{yy}^{dL} - 3\chi_{xx}^{dL}), \quad \chi_{xy}^{pL} = \chi_{xy}^{C} \quad (100)$$

$$\sigma_{xx}^{pIL} = \sigma_{xx}^{pIC} + \tfrac{1}{2}(\sigma_{yy}^{dIL} - \sigma_{xx}^{dIL}), \quad \sigma_{yx}^{pIL} = \sigma_{yx}^{pIC} - \sigma_{yx}^{dIC}$$
$$\sigma_{\alpha\beta}^{IL} = \sigma_{\alpha\beta}^{IC} \quad (101)$$

In calculations based on the algebraic approximation, equations (97) and (98) are satisfied identically for any basis set. On the other hand, equations (100) and (101) are obeyed if and only if equation (99) is satisfied, for example, if $|a\rangle$ and $|j\rangle$ are exact Hartree–Fock states.[2] If a finite basis set is employed according to the self-consistent field scheme, the degree to which equations (100) and (101) are fulfilled gives a measure of the accuracy of the calculation, i.e., information on the quality of the basis set and its degree of completeness with respect to the operators involved: total magnetic properties are invariant in a gauge transformation, equation (40), only if the basis set is complete.

3.4 Diamagnetic Contributions in Propagator Form

For one electron, the diamagnetic contributions to magnetic properties arise from

$$A_\alpha A_\alpha = \frac{1}{4}\epsilon_{\alpha\beta\gamma} B_\beta r_\gamma \epsilon_{\alpha\lambda\mu} B_\lambda r_\mu$$
$$A_\alpha A_\alpha^{\mu_I} = \frac{1}{2e}\epsilon_{\alpha\beta\gamma} B_\beta r_\gamma \epsilon_{\alpha\lambda\mu} \mu_{I\lambda} \hat{E}_{I\mu} \quad (102)$$

Using $[\hat{A}, \hat{B}\hat{C}] = [\hat{A}, \hat{B}]\hat{C} + \hat{B}[\hat{A}, \hat{C}]$ in the commutators

$$\frac{\mathrm{i}}{\hbar}[r_\beta, \hat{l}_\alpha] = \epsilon_{\alpha\beta\gamma} r_\gamma, \quad \frac{\mathrm{i}}{\hbar}[\hat{M}_{I\lambda}, r_\alpha] = \epsilon_{\alpha\lambda\mu}\hat{E}_{I\mu} \quad (103)$$

one obtains the relationships

$$A_\alpha A_\alpha = \frac{\mathrm{i}}{4\hbar} B_\gamma B_\delta \epsilon_{\alpha\beta\gamma}[r_\alpha, r_\beta \hat{l}_\delta]$$
$$= \frac{\mathrm{i}}{8\hbar} B_\gamma B_\delta (\epsilon_{\alpha\beta\gamma}[r_\alpha, r_\beta \hat{l}_\delta] + \epsilon_{\alpha\beta\delta}[\hat{l}_\alpha r_\beta, r_\gamma]) \quad (104)$$

$$A_\alpha A_\alpha^{\mu_I} = -\frac{\mathrm{i}}{2\hbar} B_\gamma \mu_{I\delta} \epsilon_{\alpha\beta\gamma}[r_\beta \hat{M}_{I\delta}, r_\alpha] \quad (105)$$

For n electrons, using these commutators, the first of equation (65), and the resolution of the identity $\sum_j |j\rangle\langle j| = \hat{1}$, the diamagnetic contributions to susceptibility and nuclear shielding are (cf. similar formulae by Geertsen[7])

$$\chi_{\delta\gamma}^{\Delta} = \frac{e^2}{4m_e^2 c^2 \hbar} \epsilon_{\alpha\beta\gamma} \sum_{j \neq a} \omega_{ja}^{-1} \left\{ \langle a| \sum_{i=1}^{n} [(r_\beta - r'_\beta)\hat{l}_\delta]_i |j\rangle\langle j|\hat{P}_\alpha|a\rangle \right.$$
$$\left. + \langle a|\hat{P}_\alpha|j\rangle\langle j| \sum_{i=1}^{n} [(r_\beta - r'_\beta)\hat{l}_\delta]_i |a\rangle \right\} \quad (106)$$

$$\sigma_{\delta\gamma}^{\Delta I} = -\frac{e^2}{2m_e^2 c^2 \hbar} \epsilon_{\alpha\beta\gamma} \sum_{j \neq a} \omega_{ja}^{-1} \left\{ \langle a| \sum_{i=1}^{n} (r_{i\beta} - r'_\beta)\hat{M}_{I\delta}^i |j\rangle\langle j|\hat{P}_\alpha|a\rangle \right.$$
$$\left. + \langle a|\hat{P}_\alpha|j\rangle\langle j| \sum_{i=1}^{n} (r_{i\beta} - r'_\beta)\hat{M}_{I\delta}^i |a\rangle \right\} \quad (107)$$

which reduce to the conventional diamagnetic contributions, equation (74) in the limit of complete basis sets.

3.5 Sum Rules for Origin Independence

The total theoretical magnetic properties of a molecule in a spatially uniform and time-independent magnetic field must be independent of the origin of the coordinate system. In a change of gauge, equation (33), of the Coulomb vector potential, variations of diamagnetic and paramagnetic contributions should cancel each other exactly. The constraints for invariance are expressed via auxiliary tensors

$$(\hat{P}_\alpha, \hat{L}_\beta)_{-1} = \frac{1}{\hbar} \sum_{j \neq a} \frac{2}{\omega_{ja}} \mathrm{Re}(\langle a|\hat{P}_\alpha|j\rangle\langle j|\hat{L}_\beta|a\rangle) \quad (108)$$

$$(\hat{K}_{n\alpha}^N, \hat{P}_\beta)_{-2} = -\frac{1}{\hbar} \sum_{j \neq a} \frac{2}{\omega_{ja}^2} \mathrm{Im}(\langle a|\hat{K}_{n\alpha}^N|j\rangle\langle j|\hat{P}_\beta|a\rangle) \quad (109)$$

$$(\hat{F}_{n\alpha}^N, \hat{L}_\beta)_{-2} = -\frac{1}{\hbar} \sum_{j \neq a} \frac{2}{\omega_{ja}^2} \mathrm{Im}(\langle a|\hat{F}_{n\alpha}^N|j\rangle\langle j|\hat{L}_\beta|a\rangle) \quad (110)$$

$$(\hat{F}_{n\alpha}^N, \hat{K}_{n\beta}^N)_{-3} = \frac{1}{\hbar} \sum_{j \neq a} \frac{2}{\omega_{ja}^3} \mathrm{Re}(\langle a|\hat{F}_{n\alpha}^N|j\rangle\langle j|\hat{K}_{n\beta}^N|a\rangle) \quad (111)$$

$$(\hat{P}_\alpha, \hat{P}_\beta)_{-1} = \frac{1}{\hbar} \sum_{j \neq a} \frac{2}{\omega_{ja}} \mathrm{Re}(\langle a|\hat{P}_\alpha|j\rangle\langle j|\hat{P}_\beta|a\rangle) \quad (112)$$

$$(\hat{F}_{n\alpha}^N, \hat{P}_\beta)_{-2} = -\frac{1}{\hbar} \sum_{j \neq a} \frac{2}{\omega_{ja}^2} \mathrm{Im}(\langle a|\hat{F}_{n\alpha}^N|j\rangle\langle j|\hat{P}_\beta|a\rangle) \quad (113)$$

$$(\hat{F}_{n\alpha}^N, \hat{F}_{n\beta}^N)_{-3} = \frac{1}{\hbar} \sum_{j \neq a} \frac{2}{\omega_{ja}^3} \mathrm{Re}(\langle a|\hat{F}_{n\alpha}^N|j\rangle\langle j|\hat{F}_{n\beta}^N|a\rangle) \quad (114)$$

$$(\hat{P}_\alpha, \hat{M}^n_{I\beta})_{-1} = \frac{1}{\hbar}\sum_{j\neq a}\frac{2}{\omega_{ja}}\,\mathrm{Re}(\langle a|\hat{P}_\alpha|j\rangle\langle j|\hat{M}^n_{I\beta}|a\rangle) \tag{115}$$

$$(\hat{F}^N_{n\alpha}, \hat{M}^n_{I\beta})_{-2} = -\frac{1}{\hbar}\sum_{j\neq a}\frac{2}{\omega^2_{ja}}\,\mathrm{Im}(\langle a|\hat{F}^N_{n\alpha}|j\rangle\langle j|\hat{M}^n_{I\beta}|a\rangle) \tag{116}$$

with the property $(\hat{X}, \hat{Y})_{-q} = (\hat{Y}, \hat{X})_{-q}$. Corresponding to different origins,

$$\begin{aligned}\chi^{\mathrm{p}}_{(LL)\alpha\beta}(\boldsymbol{r}'') = \chi^{\mathrm{p}}_{(LL)\alpha\beta}(\boldsymbol{r}') + \frac{e^2}{4m^2_{\mathrm{e}}c^2}\{&d_\delta[\epsilon_{\alpha\gamma\delta}(\hat{P}_\gamma, \hat{L}_\beta(\boldsymbol{r}'))_{-1}\\ &+\epsilon_{\beta\gamma\delta}(\hat{P}_\gamma, \hat{L}_\alpha(\boldsymbol{r}'))_{-1}]\\ &+\epsilon_{\alpha\gamma\delta}\epsilon_{\beta\lambda\mu}d_\delta d_\mu(\hat{P}_\gamma, \hat{P}_\lambda)_{-1}\}\end{aligned} \tag{117}$$

$$\begin{aligned}\chi^{\mathrm{p}}_{(KL)\alpha\beta}(\boldsymbol{r}'') = \chi^{\mathrm{p}}_{(KL)\alpha\beta}(\boldsymbol{r}') + \frac{e^2}{4m^2_{\mathrm{e}}c^2}\{&d_\delta[\epsilon_{\alpha\gamma\delta}(\hat{F}^N_{n\gamma}, \hat{L}_\beta(\boldsymbol{r}'))_{-2}\\ &+\epsilon_{\beta\gamma\delta}(\hat{P}_\gamma, \hat{K}^N_{n\alpha}(\boldsymbol{r}'))_{-2}]\\ &+\epsilon_{\alpha\gamma\delta}\epsilon_{\beta\lambda\mu}d_\delta d_\mu(\hat{F}^N_{n\gamma}, \hat{P}_\lambda)_{-2}\}\end{aligned} \tag{118}$$

$$\begin{aligned}\chi^{\mathrm{p}}_{(KK)\alpha\beta}(\boldsymbol{r}'') = \chi^{\mathrm{p}}_{(KK)\alpha\beta}(\boldsymbol{r}') + \frac{e^2}{4m^2_{\mathrm{e}}c^2}\{&d_\delta[\epsilon_{\alpha\gamma\delta}(\hat{F}^N_{n\gamma}, \hat{K}^N_{n\beta}(\boldsymbol{r}'))_{-3}\\ &+\epsilon_{\beta\gamma\delta}(\hat{F}^N_{n\gamma}, \hat{K}^N_{n\alpha}(\boldsymbol{r}'))_{-3}]\\ &+\epsilon_{\alpha\gamma\delta}\epsilon_{\beta\lambda\mu}d_\delta d_\mu(\hat{F}^N_{n\gamma}, \hat{F}^N_{n\lambda})_{-3}\}\end{aligned} \tag{119}$$

$$\begin{aligned}\chi^{\mathrm{d}}_{\alpha\beta}(\boldsymbol{r}'') = \chi^{\mathrm{d}}_{\alpha\beta}(\boldsymbol{r}') + \frac{e^2}{4m_{\mathrm{e}}c^2}[&2\langle a|\hat{R}_\gamma(\boldsymbol{r}')|a\rangle d_\gamma\delta_{\alpha\beta} - \langle a|\hat{R}_\alpha(\boldsymbol{r}')|a\rangle d_\beta\\ &-\langle a|\hat{R}_\beta(\boldsymbol{r}')|a\rangle d_\alpha - nd_\gamma d_\gamma\delta_{\alpha\beta} + nd_\alpha d_\beta]\end{aligned} \tag{120}$$

$$\sigma^{\mathrm{p}I}_{(L)\alpha\beta}(\boldsymbol{r}'') = \sigma^{\mathrm{p}I}_{(L)\alpha\beta}(\boldsymbol{r}') - \frac{e^2}{2m^2_{\mathrm{e}}c^2}\epsilon_{\beta\gamma\delta}d_\delta(\hat{M}^n_{I\alpha}, \hat{P}_\gamma)_{-1} \tag{121}$$

$$\sigma^{\mathrm{p}I}_{(K)\alpha\beta}(\boldsymbol{r}'') = \sigma^{\mathrm{p}I}_{(K)\alpha\beta}(\boldsymbol{r}') - \frac{e^2}{2m^2_{\mathrm{e}}c^2}\epsilon_{\beta\gamma\delta}d_\delta(\hat{M}^n_{I\alpha}, \hat{F}^N_{n\gamma})_{-2} \tag{122}$$

$$\sigma^{\mathrm{d}I}_{\alpha\beta}(\boldsymbol{r}'') = \sigma^{\mathrm{d}I}_{\alpha\beta}(\boldsymbol{r}') - \frac{e}{2m_{\mathrm{e}}c^2}(d_\gamma\langle\hat{E}^n_{I\gamma}\rangle\delta_{\alpha\beta} - d_\alpha\langle\hat{E}^n_{I\beta}\rangle) \tag{123}$$

Therefore the sum rules for translational invariance of total susceptibility and nuclear magnetic shielding are

$$\begin{aligned}(\hat{P}_\alpha, \hat{L}_\beta)_{-1} = (\hat{K}^N_{n\alpha}, \hat{P}_\beta)_{-2} = (\hat{F}^N_{n\alpha}, \hat{L}_\beta)_{-2} = (\hat{F}^N_{n\alpha}, \hat{K}^N_{n\beta})_{-3}\\ = m_{\mathrm{e}}\epsilon_{\alpha\beta\gamma}\langle a|\hat{R}_\gamma|a\rangle\end{aligned} \tag{124}$$

$$(\hat{P}_\alpha, \hat{M}^n_{I\beta})_{-1} = (\hat{F}^N_{n\alpha}, \hat{M}^n_{I\beta})_{-2} = \frac{m_{\mathrm{e}}}{e}\epsilon_{\alpha\beta\gamma}\langle a|\hat{E}^n_{I\gamma}|a\rangle \tag{125}$$

$$(\hat{P}_\alpha, \hat{P}_\beta)_{-1} = (\hat{F}^N_{n\alpha}, \hat{P}_\beta)_{-2} = (\hat{F}^N_{n\alpha}, \hat{F}^N_{n\beta})_{-3} = m_e n\delta_{\alpha\beta} \tag{126}$$

These formulas can also be directly established from equations (65) and (66) and from the integral condition for charge conservation, equation (77), i.e., the necessary condition for gauge invariance (cf. equation (23)).

For a transformation, equation (44), in the Landau gauge, one finds for the magnetic susceptibility and shielding of nucleus I,

$$\begin{aligned}\chi^{\mathrm{dL}}_{xx}(\boldsymbol{r}'') = \chi^{\mathrm{dL}}_{xx}(\boldsymbol{r}') + \frac{e^2}{m_{\mathrm{e}}c^2}\\ \times\left[2\langle a|\sum_{i=1}^n(y_i - y')|a\rangle d_y - nd_y^2\right]\end{aligned} \tag{127a}$$

$$\begin{aligned}\chi^{\mathrm{pL}}_{xx}(\boldsymbol{r}'') = \chi^{\mathrm{pL}}_{xx}(\boldsymbol{r}') - \frac{e^2}{m^2_{\mathrm{e}}c^2}\\ \times[2(\hat{T}_x, \hat{P}_z)_{-1}d_y - (\hat{P}_z, \hat{P}_z)_{-1}d_y^2]\end{aligned} \tag{127b}$$

$$\begin{aligned}\chi^{\mathrm{pL}}_{xy}(\boldsymbol{r}'') = \chi^{\mathrm{pL}}_{xx}(\boldsymbol{r}') - \frac{e^2}{m^2_{\mathrm{e}}c^2}[&(\hat{T}_x, \hat{P}_x)_{-1}d_z + (\hat{T}_y, \hat{P}_z)_{-1}d_y\\ &-(\hat{P}_z, \hat{P}_x)_{-1}d_y d_z]\end{aligned} \tag{127c}$$

$$\sigma^{\mathrm{d}IL}_{xx}(\boldsymbol{r}'') = \sigma^{\mathrm{d}IL}_{xx}(\boldsymbol{r}') - \frac{e}{m_{\mathrm{e}}c^2}\langle a|\hat{E}^n_{Iy}|a\rangle d_y \tag{128a}$$

$$\sigma^{\mathrm{p}IL}_{xx}(\boldsymbol{r}'') = \sigma^{\mathrm{p}IL}_{xx}(\boldsymbol{r}') + \frac{e^2}{m^2_{\mathrm{e}}c^2}(\hat{M}^n_{Ix}, \hat{P}_z)_{-1}d_y \tag{128b}$$

$$\sigma^{\mathrm{d}IL}_{yx}(\boldsymbol{r}'') = \sigma^{\mathrm{d}IL}_{yx}(\boldsymbol{r}') + \frac{e}{m_{\mathrm{e}}c^2}\langle a|\hat{E}^n_{Ix}|a\rangle d_y \tag{128c}$$

$$\sigma^{\mathrm{p}IL}_{yx}(\boldsymbol{r}'') = \sigma^{\mathrm{p}IL}_{yx}(\boldsymbol{r}') + \frac{e^2}{m^2_{\mathrm{e}}c^2}(\hat{M}^n_{Iy}, \hat{P}_z)_{-1}d_y \tag{128d}$$

$$\sigma^{\mathrm{p}IL}_{xy}(\boldsymbol{r}'') = \sigma^{\mathrm{p}IL}_{xy}(\boldsymbol{r}') + \frac{e^2}{m^2_{\mathrm{e}}c^2}(\hat{M}^n_{Ix}, \hat{P}_x)_{-1}d_z \tag{128e}$$

Therefore additional conditions for the invariance of theoretical Landau susceptibility under a coordinate transformation are

$$\begin{aligned}(\hat{P}_z, \hat{T}_x)_{-1} = m_{\mathrm{e}}\langle a|\textstyle\sum_{i=1}^n(y_i - y')|a\rangle\\ (\hat{P}_z, \hat{T}_y)_{-1} = (\hat{T}_x, \hat{P}_x)_{-1} = 0\end{aligned} \tag{129}$$

$$(\hat{T}_z, \hat{P}_y)_{-1} = \frac{1}{\hbar}\sum_{j\neq a}\frac{2}{\omega_{ja}}\,\mathrm{Re}\left\{\langle a|\sum_{i=1}^n[(x - x')\hat{p}_y]_i|j\rangle\langle j|\hat{P}_y|a\rangle\right\} \tag{130}$$

The diamagnetic terms in propagator form change according to

$$\begin{aligned}\chi^{\Delta}_{\delta\gamma}(\boldsymbol{r}'') = \chi^{\Delta}_{\delta\gamma}(\boldsymbol{r}') - \frac{e^2}{4m^2_{\mathrm{e}}c^2}\epsilon_{\alpha\beta\gamma}\\ \times\Bigg\{&d_\beta(\hat{P}_\alpha, \hat{L}_\delta)_{-1} - d_\beta d_\lambda\epsilon_{\delta\lambda\mu}(\hat{P}_\alpha, \hat{P}_\mu)_{-1}\\ &+\hbar^{-1}d_\lambda\epsilon_{\delta\lambda\mu}\sum_{j\neq a}\omega^{-1}_{ja}\Bigg[\langle a|\sum_{i=1}^n(r_{i\beta} - r'_\beta)\hat{p}_{i\mu}|j\rangle\langle j|\hat{P}_\alpha|a\rangle\\ &+\langle a|\hat{P}_\alpha|j\rangle\langle j|\sum_{i=1}^n(r_{i\beta} - r'_\beta)\hat{p}_{i\mu}|a\rangle\Bigg]\Bigg\}\end{aligned} \tag{131}$$

$$\sigma^{\Delta I}_{\delta\gamma}(\boldsymbol{r}'') = \sigma^{\Delta I}_{\delta\gamma}(\boldsymbol{r}') + \frac{e^2}{2m^2_{\mathrm{e}}c^2}\epsilon_{\alpha\beta\gamma}d_\beta(\hat{P}_\alpha, \hat{M}^n_{I\delta})_{-1} \tag{132}$$

In the limit of exact variational wavefunctions, equations (131) and (132) are the same as equations (120) and (123) for the conventional diamagnetic contributions. From equations (117) and (131), one can see that the total susceptibility $\chi^{\mathrm{p}}_{(LL)\alpha\beta} + \chi^{\Delta}_{\alpha\beta}$ depends only linearly on $\boldsymbol{d}$ also within the algebraic

approximation, owing to exact cancellation of quadratic terms: the constraint for translational invariance becomes

$$(\hat{P}_\mu, \hat{L}_\gamma)_{-1} = -\frac{1}{\hbar}\epsilon_{\alpha\beta\gamma}\sum_{j\neq a}\omega_{ja}^{-1} \times\left\{\langle a|\sum_{i=1}^{n}[(r_\beta - r'_\beta)\hat{p}_\mu]_i|j\rangle\langle j|\hat{P}_\alpha|a\rangle + \langle a|\hat{P}_\alpha|j\rangle\langle j|\sum_{i=1}^{n}[(r_\beta - r'_\beta)\hat{p}_\mu]_i|a\rangle\right\} \quad (133)$$

which is equivalent to equation (108), as shown by the first hypervirial relation, equation (65). For some molecules, quantities appearing in equation (133) vanish by symmetry (e.g., if there is a center of inversion) and the total susceptibility from equations (117) and (131) is origin-independent also in the algebraic approximation.

It is also worthy of notice, in calculations using finite basis sets and irrespective of symmetry, that all of the total shielding tensor components $\sigma^{pI}_{(L)\alpha\beta} + \sigma^{\Delta I}_{\alpha\beta}$ are independent of the origin, since there is exact cancellation between paramagnetic and Δ contributions (cf. equations (121) and (132)).

4 RELATED ARTICLES

Shielding Calculations: LORG and SOLO Approaches; Shielding Calculations: IGLO Method; Shielding Calculations: Perturbation Methods; Shielding: Overview of Theoretical Methods; Shielding in Small Molecules; Shielding Tensor Calculations; Shielding Theory: GIAO Method.

5 REFERENCES

1. P. Pulay, J. F. Hinton, and K. Wolinski, in *Nuclear Magnetic Shieldings and Molecular Structure*, Kluwer, Amsterdam, 1993, p. 243
2. P. Lazzeretti, *Adv. Chem. Phys.* 1987, **75**, 507.
3. P. Lazzeretti, *Theor. Chim. Acta.*, 1993, **87**, 59.
4. P. Lazzeretti and R. Zanasi, *Phys. Rev. A*, 1985, **32**, 2607.
5. P. Lazzeretti, M. Malagoli, and R. Zanasi, *Chem. Phys.*, 1991, **150**, 173.
6. M. B. Ferraro, T. E. Herr, P. Lazzeretti, M. Malagoli, and R. Zanasi, *Phys. Rev. A*, 1992, **45**, 6272; *J. Chem. Phys.*, 1993, **98**, 4030.
7. J. Geertsen, in *Nuclear Magnetic Shieldings and Molecular Structure*, Kluwer, Amsterdam, 1993, p. 335.

Biographical Sketches

Paolo Lazzeretti. *b* 1943. Doctor in Chemistry, 1967, Bologna University, Italy. Introduced to NMR by L. Lunazzi and to quantum chemistry by P. Palmieri. Chair of Chemical Physics, Modena University, 1990–present. Approx. 150 publications. Current interests: linear and nonlinear responses of molecules to electromagnetic fields.

Riccardo Zanasi. *b* 1951. Doctor in Chemistry, 1975, Modena University, Italy (supervisor Paolo Lazzeretti). Assistant professor, Modena University, 1980–present. Approx. 100 publications. Current interests: linear and nonlinear responses of molecules or electromagnetic fields.

Massimo Malagoli. *b* 1963. Ph.D. in Chemistry, 1994 (supervisors Paolo Lazzeretti and Riccardo Zanasi. Approx. 30 publications. Current interests: linear and nonlinear responses of molecules or electromagnetic fields.

Shielding: Overview of Theoretical Methods

Graham A. Webb

University of Surrey, Guildford, Surrey, UK

1	Introduction	1
2	Basic Theoretical Considerations	1
3	Ab Initio Molecular Orbital Calculations	2
4	Semiempirical Molecular Orbital Calculations	8
5	Related Articles	9
6	References	9

1 INTRODUCTION

In an NMR experiment, the magnetic field $\boldsymbol{B}$ at the nucleus differs from the applied magnetic field $\boldsymbol{B}_0$. In the absence of medium effects, this magnetic field difference is due to the shielding of the nucleus by the electrons in the molecule. In chemically different molecules, the electronic structures vary; consequently, the chemical shielding of a nucleus depends upon the nature of its electronic environment. The relationship between $\boldsymbol{B}$ and $\boldsymbol{B}_0$ is given by

$$\boldsymbol{B} = (\boldsymbol{1} - \boldsymbol{\sigma})\boldsymbol{B}_0 \tag{1}$$

where $\boldsymbol{\sigma}$ is the second-rank chemical shielding tensor.

Experimentally, the term 'chemical shift' is often used in preference to 'chemical shielding'. The chemical shift δ_X of a nucleus X with respect to a given standard is given by

$$\delta_{\mathrm{X}} = \sigma_{\mathrm{std}} - \sigma_{\mathrm{X}} \tag{2}$$

Consequently, an increase is shielding corresponds to a decrease in chemical shift, and vice versa.

In principle, the effects of chemical shielding can take either sign. A positive value of σ results in an increase in chemical shielding, sometimes referred to as a diamagnetic effect. Alternatively, deshielding occurs if σ is negative; this corresponds to a paramagnetic effect.

In general, $\boldsymbol{\sigma}$ is an unsymmetric second-rank tensor, namely $\sigma_{ij} \neq \sigma_{ji}$. In contrast with experiment, theoretical calculations provide values for all of the tensor components. The tensor is usually decomposed into its symmetric, $\boldsymbol{\sigma}^{\mathrm{s}}$, and antisymmetric, $\boldsymbol{\sigma}_{\mathrm{a}}$, components for the purposes of comparison with experimental data:

$$\sigma_{ij}^{\mathrm{s}} = \tfrac{1}{2}(\sigma_{ij} + \sigma_{ji}) \tag{3}$$

$$\sigma_{ij}^{\mathrm{a}} = \tfrac{1}{2}(\sigma_{ij} - \sigma_{ji}) \tag{4}$$

In the expression that describes the interactions between a molecule and an applied magnetic field, σ_{ij}^{a} only appears in terms which are second order in the magnetic field. Thus, the effects of σ_{ij}^{a} are not normally observed in standard NMR experiments, which depend upon interactions that are first order with respect to the applied magnetic field. Consequently, the calculated values of σ_{ij}^{a} are neglected, and the diagonalization of σ_{ij}^{s} results in the determination of the principal axes of the shielding tensor. The isotropic shielding σ_{av}, the shielding anisotropy $\Delta\sigma$, and the asymmetry ξ are then determined from the diagonal elements, σ_{11}, σ_{22}, and σ_{33}, where the usual convention is $\sigma_{11} \leq \sigma_{22} \leq \sigma_{33}$, as follows:

$$\sigma_{\mathrm{av}} = \tfrac{1}{3}(\sigma_{11} + \sigma_{22} + \sigma_{33}) \tag{5}$$

$$\Delta\sigma = \sigma_{33} - \tfrac{1}{2}(\sigma_{11} + \sigma_{22}) \tag{6}$$

$$\xi = \frac{\sigma_{22} - \sigma_{11}}{\sigma_{33} - \sigma_{\mathrm{av}}} \tag{7}$$

From NMR studies on nonviscous liquids, only values of σ_{av} are available for comparison with calculation. However, in the case of aligned molecules such as those in solids or liquid crystals, NMR measurements can provide information on $\Delta\sigma$ and ξ. It should be noted that, in general, the errors in experimental results for $\Delta\sigma$ and ξ are larger than in those for σ_{av}.

2 BASIC THEORETICAL CONSIDERATIONS

In principle, quantum mechanics can produce a full account of all molecular properties. In practice, various approximations are introduced into the calculations to make them tractable. Such approximations produce apodictic limitations on the results obtained. For example, Hartree–Fock (HF) level calculations, involving a single determinant, on rigid isolated molecules ignore the effects of electron correlation, variations of geometry, and media influences on chemical shielding. Normally, such effects are considered separately, as are possible relativistic effects on the shielding of heavier nuclei. Another aspect of theoretical calculations is the requirement of a specified molecular geometry—often, precise experimental geometries are unknown, in which case quantum mechanics can provide a minimum energy or 'optimized' structure. In practice, such calculations tend to be restricted to small and medium sized molecules. Structural information obtained from HF calculations is usually fairly reliable. The agreement with experimental bond lengths is normally within 1–3 pm and the bond angles usually differ by less than 2° or 3°.[1] The results obtained from ab initio molecular orbital calculations often depend upon the choice of basis set used. For reliable results, the calculation should be convergent with respect to the choice of basis set. The preceding comments in this section apply to calculations of all molecular electronic properties. Calculations of magnetic properties, such as chemical shielding, suffer from an additional limitation. This is known as the gauge problem. It arises from the use of perturbation theory to describe the, rather small, contribution to the total electronic energy of the molecule provided by the applied magnetic field. The magnetic perturbation is described by means of the orbital angular momentum operator. Since this operator is not invariant with respect to translations, its influence depends upon the position at which it is evaluated. Consequently, the result obtained for the calculated chemical shielding depends upon the choice of origin for the calculation. This is a theoretical artifact, which needs to be dealt with before comparison between experimental and theoretical shielding data occurs.

The first serious attempt to calculate chemical shielding effects was Ramsey's work in 1950.[2,3] Perturbation theory was used to produce an expression for the elements $\sigma_{\alpha\beta}$ (α, $\beta = x, y, z$) of the shielding tensor in a Cartesian coordinate system (x, y, z):

$$\sigma_{\alpha\beta} = \sigma_{\alpha\beta}^{\mathrm{d}} + \sigma_{\alpha\beta}^{\mathrm{dg}} + \sigma_{\alpha\beta}^{\mathrm{p}} + \alpha_{\alpha\beta}^{\mathrm{pg}} \tag{8}$$

Here d and p indicate the diamagnetic and paramagnetic components and g indicates the gauge-dependent terms. The diamagnetic terms depend only upon the wavefunction of the electronic ground state, while the paramagnetic expressions involve the wavefunctions of all of the molecular excited states, including those of the continuum. The expressions for the four terms appearing in equation (8) are as follows:

$$\sigma_{\alpha\beta}^{\mathrm{d}} = \frac{\mu_0 e^2}{8\pi m}\langle 0|\sum_k \frac{r_k^2\delta_{\alpha\beta} - r_{k\alpha}r_{k\beta}}{r_k^3}|0\rangle \tag{9}$$

$$\sigma_{\alpha\beta}^{\mathrm{dg}} = \frac{\mu_0 e^2}{8\pi m}\langle 0|\sum_k \frac{R_\alpha r_{k\beta} - R_\gamma r_{k\gamma}\delta_{\alpha\beta}}{r_k^3}|0\rangle \tag{10}$$

$$\sigma_{\alpha\beta}^{\mathrm{p}} = \frac{\mu_0 e^2}{8\pi m^2}\sum_r{}' \frac{1}{E_0 - E_n}\Bigg(\langle 0|\sum_k \frac{\hat{l}_{k\alpha}}{r_k^3}|n\rangle\langle n|\sum_k \hat{l}_{k\beta}|0\rangle + \langle 0|\sum_k \hat{l}_{k\beta}|n\rangle\langle n|\sum_k \frac{\hat{l}_{k\alpha}}{r_k^3}|0\rangle\Bigg) \tag{11}$$

$$\sigma_{\alpha\beta}^{\mathrm{pg}} = \frac{\mu_0 e^2}{8\pi m^2}\epsilon_{\beta\gamma\delta}R_\gamma\sum_n{}' \frac{1}{E_0 - E_n}\Bigg(\langle 0|\sum_k \frac{\hat{l}_{k\alpha}}{r_k^3}|n\rangle\langle n|\sum_k \hat{p}_{k\delta}|0\rangle + \langle 0|\sum_k \hat{p}_{k\delta}|n\rangle\langle n|\sum_k \frac{\hat{l}_{k\alpha}}{r_k^3}|0\rangle\Bigg) \tag{12}$$

Here, μ_0 is the permeability of free space, $\boldsymbol{r}_k$ is the position vector of electron k with respect to the origin of the Cartesian coordinates, and $\hat{\boldsymbol{l}}_k = \boldsymbol{r}_k \times \hat{\boldsymbol{p}}_k$ is the orbital angular momentum operator, with $\hat{\boldsymbol{p}}$ the linear momentum operator; the primes on the summations over n indicate that the ground state ($n = 0$) is not included, the Kronecker delta $\delta_{\alpha\beta} = 1$ if $\alpha = \beta$ and 0 if $\alpha \neq \beta$; the alternating tensor $\epsilon_{\beta\gamma\delta} = 1$ if $\beta\gamma\delta$ is an even permutation of xyz, -1 if $\beta\gamma\delta$ is an odd permutation of xyz, and 0 if any two of β, γ or δ are identical. In equations (10) and (12), $\boldsymbol{R}$ is the vector separation between the origin of the Cartesian coordinates and the origin of the vector potential of the applied magnetic field (the gauge origin)

Normally, the shielding is calculated with respect to the origin of the coordinates. Thus, if the nucleus of interest is chosen to be at the gauge origin then $\boldsymbol{R} = 0$ and the right-hand sides of equations (10) and (12) become zero. Evidently, the appropriate choice of nuclear position in the calculation can lead to the removal of gauge dependence in the theoretical shielding value.

The requirement of knowledge of the energies of all of the molecular electronic excited states, together with the continuum, in order to evaluate equation (11) points to a further drawback to Ramsey's shielding formulation. In general, little is known about the discrete high-energy or the continuum states of most molecules. Some detailed calculations for small molecules imply that shielding contributions from the continuum may be at least as important as those from discrete electronic states.[4,5]

To be able to calculate chemical shielding reliably on a fairly routine basis, it is necessary to have molecular orbital equivalents of Ramsey's expressions that do not suffer from the gauge problem or the involvement of the continuum states. The coupled Hartree–Fock (CHF) development by Lipscomb[6] provides the way forward. At present, ab initio molecular orbital (MO) calculations of nuclear shieldings for nuclei from the first and second long rows of the Periodic Table can reproduce experimental data to within about 3 or 4% of an element's shielding range. Consequently, such calculations can be used for predictive purposes as well as providing some information on the molecular electronic factors that determine the extent of nuclear shielding and its variations. Some details of these calculations are considered in the next section.

3 AB INITIO MOLECULAR ORBITAL CALCULATIONS

The electronic shielding of nuclei in molecules is a very small effect when compared with the total electronic energy of a molecule. Thus, very accurate wavefunctions are required to calculate the shielding effect satisfactorily. This, in turn, shows the necessity of using large basis sets in the CHF shielding calculations. Another reason for employing a large basis set is that a complete basis set would provide CHF shielding results that are gauge-independent.[7] In contrast to this, approximate wavefunctions produce gauge-dependent shielding results unless the gauge origin is taken to be at the nucleus of interest.[8]

3.1 Common Origin Calculations

Large-basis-set calculations, using a common gauge origin, can provide nuclear shieldings in very good agreement with experiment. Table 1 shows the results of some calculations of this type for some small hydrocarbons.[9,10] The best gauge origin is found to be at the ^{13}C nucleus. The basis sets used include 3d sets for carbon and 2p sets for hydrogen. This choice of basis sets is in agreement with those employed in similar CHF calculations.[11,12] In general, the choice of an extended basis set is not a practical one for CHF calculations on larger molecules. An example of common origin ^{13}C shielding calculations for a large molecule is provided by C_{60}, buckminsterfullerene. In this molecule, all of the carbons are equivalent, and so symmetry arguments can be used to reduce the number of integrals to be evaluated. ^{13}C shielding results have been obtained using some relatively small basis sets: STO-3G, STO-3G*, 6-31G, and 6-31G*.[13,14] To obtain some idea of the effort involved in these calculations, we consider the case of using the 6-31G* basis set. This calculation involves 900 orbitals and 8.2×10^{10} two-electron integrals. Symmetry requirements show that about 7×10^8 of these integrals are unique. Further arguments reveal that many of these are sufficiently small to be ignored; however, this leaves about 1.29×10^8 integrals to be evaluated. The cpu time required for this calculation is about 233 h i.e., almost 10 days! With such demands on computational facilities, it is unlikely that common origin shielding calculations will become widespread.

Table 1 Comparison of some Common Origin Calculated and Experimental ^{13}C Shieldings (in ppm)[a]

	σ_{xx}	σ_{yy}	σ_{zz}	σ_{au}	Experimental
CH_4	195.8	195.8	195.8	195.8	195.1
C_2H_6	187.7	182.7	193.1	186.2	180.9
C_2H_4	177.9	−81.1	84.3	60.4	64.5
C_2H_2	39.0	39.0	279.4	119.1	117.2

[a]The unique axis is taken to be the z axis; e.g., in C_2H_4, z is along the C−C bond and x is perpendicular to the molecular plane.

Table 2 Comparison of Calculated and Experimental ^{13}C Shieldings (in ppm) for C_{60} Obtained Using Various Basis Sets and Two Choices of Gauge Origin

Basis	(p, p)	σ(cm)	σ(C)
STO-3G	90.1	270.4	656.8
STO-3G*	186.4	211.0	447.0
6-31G	176.3	203.8	461.2
6-31G*	243.9	173.2	306.4
Extrapolation	360.0	97.0	46.2
Experiment		43.0	43.0

In judging the results of the ^{13}C shielding calculations for C_{60}, it is necessary to appreciate that the basis sets employed are inadequate to obtain convergence of the shielding with respect to the basis set. Additionally, it has to be remembered that these common origin calculations, using incomplete basis sets, will produce shieldings that are gauge-dependent. A selection of the results obtained for C_{60} is given in Table 2, where the parameter (p, p) is taken as a measure of the completeness of the basis sets employed. The ^{13}C shielding data are reported both for the gauge origin chosen at the centre of mass (cm) and at one of the carbon atoms in the molecule (c). It is clear that the results are both gauge- and basis-set-dependent. Since (p, p) indicates the number of electrons involved in the calculation, it is possible to perform a linear extrapolation of the calculated shielding results with respect to (p, p). The limit of 360 is chosen, since this is the total number of electrons for C_{60}. In this way, the ^{13}C shielding values are obtained as 97.0 ppm when the gauge origin is taken to be at the centre of mass and 46.2 ppm for the choice of a carbon atom as gauge origin. The latter is clearly in better agreement with the experimental value of 43.0 ppm.[15] The C_{60} shielding results show rather graphically the necessity of using large basis sets to obtain reliable data from common origin calculations and the requirement of an appropriate choice of gauge origin.

3.2 Local Origin Calculations

An alternative to using large basis sets to overcome the gauge problem is to introduce gauge factors into either the atomic orbitals of the basis set or into the MOs of a CHF calculation. This procedure can lead to shielding results that are independent of gauge origin, even though the calculation is an approximate one. London[16] proposed the inclusion of gauge factors in calculations by means of gauge-included atomic orbitals (GIAOs). The resulting complex orbitals ψ_n are used in place of the usual, real, atomic orbitals ϕ_n located at $\boldsymbol{R}_n$:

$$\psi_n = \phi_n \exp\left[-\frac{ie}{h}\boldsymbol{A}(\boldsymbol{R}_n)\cdot\boldsymbol{r}\right] \tag{13}$$

and the complex phase factor contains the vector potential $\boldsymbol{A}(\boldsymbol{R}_n)$ for the magnetic field evaluated at the point $\boldsymbol{R}_n$.

Ditchfield[17–19] and others have used this approach in shielding calculations with some success. A development of the GIAO method, in conjunction with analytical derivative theory, has resulted in the production of some very interesting shielding results with modest basis sets.[20]

In another development, exponential gauge factors have been introduced into the MOs employed in shielding calculations.[21–24] This procedure employs individual gauge origins for different localized molecular orbitals (IGLO). In the IGLO calculations, the MOs used, ψ_k, are related to the usual MOs ϕ_k by

$$\phi_k = \exp(i\hat{\lambda}_k)\,\psi_k \tag{14}$$

where $\hat{\lambda}_k$ is a local multiplicative operator proportional to the applied magnetic field $\boldsymbol{B}$ and the ϕ_k are expanded in powers of $\boldsymbol{B}$. Both the GIAO and IGLO methods may be referred to as local origin variants of the CHF method, since the gauge origins in the calculations are attached to each nucleus in turn. In this way, the gauge problem is overcome. A further advantage of the IGLO procedure is that it furnishes a way of identifying shielding contributions that arise from specific electrons in the molecule. Consequently, shielding contributions can be attributed to electrons on the atom in question, on neighboring atoms, or involved in bonding between atoms. A comparable approach has been proposed in which different gauge origins are chosen for different pairs of orbitals, which may be either atomic or molecular orbitals.[25]

An alternative to CHF calculations of second-order magnetic properties is the equations of motion (EOM) procedure.[26] The random phase approximation (RPA) is a well-known means of obtaining results from the EOM approach. Various methods for calculating nuclear shielding within the RPA have been considered. Some involve a common origin,[27,28] whereas localized MOs with local origins (LORG) have also been employed.[29,30] The LORG approach differs from the GIAO and IGLO methods in that complex orbitals are not explicitly introduced. Rather, angular momentum terms are expanded relative to a local origin for each orbital; by means of the RPA, shielding expressions are produced that are independent of gauge origin. The LORG method results in a localization of the molecular orbitals, which provides a pathway to the decomposition of the nuclear shielding into individual local bond and bond−bond contributions. Thus, the LORG and IGLO methods of calculating nuclear shieldings are analogous to each other.

In comparing the relative merits of the GIAO, IGLO, and LORG methods, it should be mentioned that the GIAO procedure appears to be the more efficient in terms of the convergence of the shielding value with respect to the size of basis set used,[20] whereas the IGLO and LORG calculations furnish shielding contributions that may be attributed to specific molecular regions. Such results are germane to many chemically oriented discussions, and thus have a fairly general appeal. Since the GIAO, IGLO, and LORG calculations can all be performed with different levels of basis set quality, the results are found to be dependent upon the choice of basis sets used. In Table 3, the results of some shielding calculations

Table 3 Comparison of Some ^{13}C Shieldings and Their Anisotropies (in ppm) Produced by IGLO, LORG, and GIAO Calculations, and by Experiment

Molecule	IGLO	LORG	GIAO	Experimental
CH_4	196.7	196.0	193.0	195.1
HCN	72.9	77.3	74.8	82.1
	306	301	304.8	316.3 ± 1.2
C_2H_2	116.4	122.3	118.3	117.2
	243.3	235.0	241.0	240 ± 5
CO	−6.0		−21.3	1.0
	420.0		439.0	405.5 ± 1.4
C_2H_6	183.5	184.7	181.2	180.9
	13.5	8.0	11.3	
CH_3OH	157.2	145.7	134.6	136.6
		60.5	77.3	63.0
H_2CO	−3.8	4.0	2.6	−8.0
	183.8	183.0	196.5	

by these three methods are compared. The results given are obtained by the use of medium sized basis sets; for example, sets of triple zeta quality with a set of d polarization functions for the heavy atoms. In comparison with the experimental results, the calculated data are in reasonable agreement. The success of these local origin methods in nuclear shielding calculations appears to reside in the omission of large terms of opposite sign, which would have canceled exactly in the limit of a complete basis set. This is analogous to the cancelation of the gauge-dependent terms in the Ramsey formulation, equations (8)–(12). Consequently, for an incomplete basis set calculation, the local origins provide a damping of basis set errors in long-range shielding contributions.[31]

An example of the dependence of GIAO-calculated ^{13}C shieldings on the choice of geometry and basis set is provided in Table 4.[32] The use of experimental geometries is indicated by NOOPT; also included are optimized geometries from ab initio calculations using 4-31G and 4-31G** basis sets. The ^{13}C shieldings are calculated with 3-21G, 4-31G, and 4-31G** basis sets. The best agreement with the experimental shieldings is provided by the calculations using experimental geometries and the 4-31G** basis set; in this case, the average least-squares error for the set of molecules studied is 2.7 ppm.

Another method of tackling the gauge problem in nuclear shielding calculations is to use individual gauges for atoms in molecules (IGAIM).[33] The IGAIM method produces the induced current density distribution of a molecule from its constituent atoms; it differs from the GIAO, IGLO, and LORG procedures in that the gauge origins in IGAIM are determined by properties of the charge density in real space rather than by the behavior of the chosen basis functions in the Hilbert space of the molecular wavefunction.

The atom in a molecule model consists of a partitioning of the real space of a molecule into atomic basins.[34] Using this procedure, the shielding tensor is presented as a sum of separate contributions from each atom in a molecule. Consequently, IGAIM shielding calculations result from a sum of atomic contributions that are produced by taking each nucleus in turn as a gauge origin. Each of these atomic calculations employs a small basis set, thus giving a time advantage over the GIAO, IGLO, and LORG methods, which require larger, molecular, basis sets. In contrast to this, the GIAO, IGLO, and LORG methods provide the shieldings of all of the nuclei in a given molecule from one calculation, whereas the IGAIM method requires many calculations if all the shieldings are required. Thus, the time required for IGAIM calculations on larger molecules, with many nuclei of interest, can become prohibitive.

The results of some ^{13}C IGAIM shielding calculations are given in Table 5, where they are compared with the results obtained from conventional CHF calculations using the same basis set. In the latter case, the common gauge origin is placed at the nucleus whose shielding is being computed. As shown in Table 5, the IGAIM results are in much better agreement with experiment than those given by the CHF calculations.

3.3 Calculations on Larger Molecules

In general, satisfactory nuclear shielding results can be obtained from calculations on fairly small molecules containing relatively light atoms. An exception should be mentioned—namely, those cases where electron correlation effects are important. As we shall see later, these can usually be accounted for by calculations extending beyond the CHF limit.

A potential barrier to calculations on larger molecules is the requirement of a relatively large basis set in order to obtain shielding results that are convergent with respect to choice of basis set. One way of dealing with this problem is to use a relatively large, locally dense, set of functions for the atoms containing the nuclei of interest. The other atoms in the molecule are then provided with considerably smaller sets of functions. It has been demonstrated that the calculated nuclear shieldings obtained using locally dense basis sets are in good agreement with those provided by calculations with balanced basis sets, and there is also a significant saving of cpu time.[35]

For atoms from the first long row of the Periodic Table, it is suggested that a suitable locally dense basis set is 6-311G(d, p). This can be successfully coupled with a 3-21G set for the remaining atoms in the molecule. A number of GIAO calculations have used this technique with success, including those for the amide group in glycylglycine,[36] for the –CH=N– group of benzylidineaniline[37] and for the proton shielding anisotropy of $(H_2O)17$ as a model for ice.[38]

In deciding whether a locally dense basis set is an appropriate choice, some consideration has to be given to the bonding situations of the atoms in question. In general, carbon and phosphorus may be taken as singly dense species, whereas hydrogen, oxygen, and nitrogen are best treated as part of a locally dense pair of atoms, the other member being the atom that is directly bonded.

Other approaches to calculating the shieldings of large molecules include 'direct' methods[39] and a method for partitioning the shielding into a number of contributions.[40] 'Direct' techniques reduce the storage requirements for two-electron integrals by calculating the integrals each time they are required, rather than storing them. This approach has been developed in conjunction with IGLO calculations, and is termed DIGLO. It has been applied to molecules with about 1000 basis functions.[41] Since the number of two-electron integrals to be calculated is proportional to the fourth power of the number of electrons included in a molecular calculation, it is clear that 'direct' methods are of great relevance to considerations of shielding calculations on larger molecules. A proposal to partition the shielding contributions into short-range, long-range, and others has been put forward in conjunction with

Table 4 Calculated and Observed Isotropic ^{13}C Chemical Shifts (in ppm from CH_4) of the Resonant Nuclei (*C) Using NOOPT/4-31G, 4-31G/4-31G, NOOPT/3-21G, NOOPT/4-31G**, and 4-31G**/4-31G** Basis Sets[32]

	NOOPT/4-31G	4-31G/4-31G	NOOPT/3-21G	NOOPT/4-31G**	4-31G**/4-31G**	Experimental
CH_4	0.0	0.0	0.0	0.0	0.0	0.0
C_2H_6	4.2	4.8	2.9	5.0	5.5	8.0
C_2H_4	131.2	127.4	119.2	125.4	121.5	125.4
$*CH_3CH_2CH_3$	16.1	15.4	13.5	16.6	16.3	17.7
$CH_3\,*CH_2CH_3$	16.7	13.8	13.7	18.6	16.4	18.2
cis-$*CH_3CH{=}CHCH_3$	12.4	12.9	10.6	12.3	12.6	12.7
cis-$CH_3\,*CH{=}CHCH_3$	130.8	130.1	119.0	126.3	124.9	125.9
trans-$*CH_3CH{=}CHCH_3$	19.9	18.6	17.4	19.5	18.4	19.4
trans-$CH_3\,*CH{=}CHCH_3$	134.2	129.6	121.2	129.3	124.5	127.2
cyclo-C_3H_6	−2.0	−2.6	−2.6	−1.4	−2.2	0.1
cyclo-C_6H_{12}	29.5	25.5	24.9	30.3	26.2	29.9
C_6H_6	133.2	132.1	119.7	129.2	127.3	130.0
$*CH_2{=}CHCH_3$	123.7	128.3	112.8	118.2	115.1	117.5
$CH_2{=}*CHCH_3$	138.7	138.0	124.9	133.7	131.2	137.8
$CH_2{=}CH*CH_3$	17.5	22.9	15.2	17.1	19.3	20.8
$*CH{\equiv}CCH_3$	74.5	74.6	69.2	69.6	69.0	69.0
$CH{\equiv}*CCH_3$	79.2	80.4	71.7	74.1	74.5	82.0
$CH{\equiv}C*CH_3$	5.0	4.0	4.3	4.9	3.9	4.0
Toluene (C-1)	141.3	140.2	126.3	137.7	136.4	140.8
Toluene (C-2)	133.3	132.5	119.9	128.9	128.1	131.4
Toluene (C-3)	134.5	133.6	120.6	130.6	129.6	132.2
Toluene (C-4)	130.2	129.3	117.1	126.1	125.1	128.5
Toluene (CH_3)	21.9	22.1	19.6	21.1	21.5	24.3
$*CH{\equiv}C{-}C{\equiv}CH$	68.4	69.8	63.6	65.1	66.0	69.3
$CH{\equiv}*C{-}C{\equiv}CH$	71.9	73.0	65.4	66.5	66.8	71.0
cyclo-$C_3H_4(CH_2)$		−3.7				3.0
cyclo-$C_3H_4(=C)$		117.1				108.0
Averaged least-squares error (ppm)	3.16	3.24 (without cyclo-C_3H_4)	7.34	2.72	3.20	
Correlation coefficient	0.998	0.995	0.997	0.998	0.999	
Slope	0.96	0.97	1.06	1.00	1.02	

calculations on proteins.[40] It remains to be seen how generally reliable and applicable this approach may be.

Table 5 Comparison of Absolute ^{13}C Shieldings in (ppm) Calculated by the IGAIM Method and the CHF Procedure, Using the Same 6-311G**(2d, 2p) Basis set, with Experimental Values Taken as Thermal Averages at 300 K in the Limit of Zero Gas Density

Molecule	IGAIM	CHF	Experimental
CH_4	197.4	198.5	195.1
HCN	79.9	89.5	82.1
C_2H_2	119.3	127.0	117.2
C_2H_4	66.4	73.4	64.5
C_2H_6	186.3	192.3	180.9
C_3H_4 (C-1)	119.5	130.2	115.2
C_3H_4 (C-2)	−34.8	−22.4	−29.3
C_6H_6	61.5	82.1	57.9
CO	−7.4	−11.9	1.0
CO_2	57.9	78.9	58.8
CS_2	−41.1	51.9	−8.0
CSO	21.9	78.2	30.0
CH_3NH_2	167.0	173.9	158.3
CH_3OH	148.0	155.8	136.6
CH_3F	130.2	140.0	116.8
CF_4	86.0	122.3	64.5
HCOOH	32.2	50.2	23.7

3.4 Effects of Geometry on Nuclear Shielding

Normally, solution state NMR measurements are taken at around 300 K. The molecules in gaseous and liquid samples are usually mobile at such temperatures, and collisions occur, providing the opportunity for molecules to populate excited vibrational and rotational states on the NMR timescale. As noted previously, nuclear shielding calculations are usually performed by assuming a rigid nuclear framework, and usually the equilibrium configuration is taken as the structure on which the calculations are based. Consequently some account of rotational–vibrational effects may be necessary in comparing experimental and calculated nuclear shielding data.[42]

As the accuracy of nuclear shielding calculations increases, the significance of including rotational–vibrational corrections in a comparison of theoretical and experimental results becomes more apparent. It has been reported that the rotational–vibrational effects on ^{19}F shieldings can be as large as −9.5 to −18.0 ppm for some haloethanes at 300 K[43] and from −6.8 to −16.4 ppm for some halomethanes.[44] These data show the difficulty that can arise in choosing a suitable geometry upon which to base shielding calculations when there is a strong geometrical dependence of shielding. In many cases, accurate experimental geometries are unknown, and minimized HF geometries are chosen for shielding calculations.

Some calculated first derivatives of the shielding of some ^{13}C, ^{15}N, ^{17}O, and ^{19}F nuclei in a variety of small molecules

Table 6 Some First Derivatives of IGLO-Calculated Nuclear Shieldings with Respect to Bond Length r_{AX} and Bond Angle α_{XAX} for ^{15}N, ^{29}Si, and ^{31}P

Molecule	$\partial\sigma/\partial r_{AX}$ (ppm Å^{-1})	$\partial\sigma/\partial\alpha_{XAX}$ (ppm deg^{-1})
NH_3	−433	−6
NF_3	−921	−107
HF	−486	
LiF	54	
SiH_4	−66	
SiF_4	80	
P_2	−2055	
PH_3	−464	−332
PF_3	−243	−54

have been reported.[45] The derivatives have negative values, showing that the shielding is expected to decrease as the bond length increases. This is in agreement with the available experimental data.[42] In addition, the observed shielding derivatives become more negative as the magnitude of the nuclear shielding decreases, as is found to be the case experimentally.[42]

Table 6 shows the results of IGLO calculations of some first derivatives of some ^{15}N, ^{29}Si, and ^{31}P shieldings as a function of bond length and bond angle.[46] The dominant contribution to the change of shielding as the bond length varies arises from the paramagnetic shielding term. An increase in bond length produces a decrease in the relevant electronic excitation energies, which furnishes an enhanced paramagnetic contribution to the shielding tensor. Regrettably, a direct comparison between the results given in Table 6 and experiment is not possible, because the appropriate experimental data appear to include assumptions that may not be valid.[46]

In addition to rotational–vibrational effects, there are specific and nonspecific intermolecular interactions that may influence nuclear shielding. These medium effects result from interactions of a given molecule with its environment, thus influencing the electronic structure for a given nuclear configuration, as well as modifying the molecular geometry. Specific interactions, such as hydrogen bonding, may be treated theoretically using the supermolecule approach. Nonspecific interactions can be included by means of Onsager's reaction field treatment of polar molecules.[47] A derivative of this approach is the self-consistent reaction field model (SCRF).[48]

Both solution and solid state experimental NMR shieldings may contain a component due to medium effects. However, these contributions are usually ignored in nuclear shielding calculations at the ab initio level. The SCRF model has been applied to a study of aminoborane.[49] The report deals mainly with the influence of the reaction field on the geometry of aminoborane. IGLO calculations are performed to give the ^{11}B shielding relevant to the geometry produced by the reaction field effects. Unfortunately, the shielding calculations do not appear to have been performed in the presence of the reaction field, and so any influence of this field on the electronic structure of aminoborane has not been included.

Nuclear shielding calculations in the presence of a reaction field are well established in the area of semiempirical calculations. No doubt, they will become part of the ab initio shielding calculation scene in due course.

Table 7 Comparison of Some ^{95}Mo Chemical Shifts (in ppm from $[MoO_4]^{2-}$) as Obtained by Various Calculations and Experiment

Species	SOS	FPT	LORG	Experimental
$[MoO_3S]^{2-}$	161.1	683.0	702.7	497
$[MoO_2S_2]^{2-}$	376.0	1363.0	1507.4	1067
$[MoOS_3]^{2-}$	743.3	1867.0	2367.7	1654
$[MoS_4]^{2-}$	1110.8	2397.0	3185.4	2259
$Mo(CO)_6$			−1898.6	−1856
$[MoNCl_4]^-$			2087.2	−1106

3.5 Calculations of Heavy Metal Shieldings

Ab initio calculations using a common origin and modest basis sets, within finite perturbation theory (FPT), have been performed for the metal shieldings of a number of compounds containing Cu, Zn, Ag, Cd, and Mo.[50–54] In general, the results presented appear to reproduce satisfactorily a number of the experimental trends. However, it seems probable that some of the agreement with experiment may be somewhat fortuitous, since such shieldings are expected to be quite solvent-dependent, the solution geometries of the compounds studied are not well known, and possible electron correlation and relativistic effects are absent from the calculations. To date, there are no ab initio shielding calculations on heavy metals that include electron correlation and relativistic effects. However, it is reasonable to assume that they are not insignificant. A further aspect of heavy metal shielding calculations that requires consideration is the difficulty of comparing them with experimental results. In general, there are no absolute shielding scales available for heavy metals at the present time. Consequently, comparisons of theoretical and experimental data can only be performed for shielding differences, i.e., chemical shifts between two species.

Molybdenum shielding calculations by the LORG[55,56] and the, less accurate, sum over states (SOS) perturbation methods[57] have also been reported. Some of these results are presented as chemical shifts with respect to $[Mo\ O_4]^{2-}$ in Table 7, where they are compared with the results produced by the FPT method[52] and with experiment.[58–60] In the LORG calculations, the best sets used are of triple zeta quality for the metal d orbitals and 4-31G* for the ligand atoms. Thus, the LORG results are expected to be the most accurate and reliable of those given in Table 7. However, they do not appear to be in the best agreement with the available experimental data. Analysis of the LORG shielding results for molybdenum reveals that the ^{95}Mo shielding is not dominated by contributions arising from the metal orbitals. This contrasts with the reports based upon FPT calculations.[49,50] Perhaps this difference is not too surprising, since the FPT method uses a common origin and a modest basis set, which is expected to result in a poor description of ligand electron contributions to the shielding of the metal. FPT common origin calculations have also been reported for the ^{93}Nb shieldings of nineteen niobium hexahalide mixed complexes.[61] The calculations predict a shielding range of 2300 ppm in passing from $NbF^{-:6}$ to $NbBr^{-:6}$, which mirrors the observed chemical shift range.

Other heavy metal ab initio shielding calculations include those on titanium,[62,63] tin, cadmium-53,[64] and zinc.[65,66] In general, these calculations show satisfactory agreement with experimental data. A summary of the current situation

regarding heavy metal nuclear shielding calculations must include reminders that absolute shielding scales for these nuclei are unavailable, that the solution geometries of the species considered are often unknown, and that rather more extensive basis sets appear to be required. Significant advances in these calculations would be made if the basis sets used were optimized such that the shielding calculations were convergent with respect to basis set. In addition, some attempt should be made to estimate the importance of relativistic and electron correlation effects on the results of these nuclear shielding calculations.

3.6 Electron Correlation Effects

In recent years, it has become possible to perform CHF nuclear shielding calculations, using either common or local origins, that are sufficiently close to the HF limit that some imperfections of HF theory are apparent from a comparison of the calculated and experimental shieldings. Predictably, the absence of electron correlation effects in HF calculations shows most noticeably in 'electron-rich' cases, for example, when lone pair electrons are present–especially when multiple bonding occurs simultaneously. Such cases give rise to nearly degenerate and low lying electronic excited states, which are not well described by the single determinant HF MO eigenfunctions. An early attempt to move beyond the HF limit in nuclear shielding calculations was the sum-over-states procedure with configuration interaction (CI).[67] This common origin method was applied to some first and second row hydrides, and the results obtained are in satisfactory agreement with experiment. It should be noted that the molecules studied in this work are ones for which electron correlation effects are not expected to be large. More recently, the local origin methods for calculating nuclear shieldings have been enhanced by the addition of techniques for including electron correlation effects. The GIAO method has been extended by means of many body perturbation theory (MBPT).[68,69] Similarly, a nonperturbative multiconfiguration extension of the IGLO procedure has been reported.[70] This is referred to as MC-IGLO. Finally, the LORG method of calculating nuclear shieldings has been combined with the second-order polarization propagator (SOPPA) technique[71] to produce the second-order LORG or SOLO procedure.[72] Table 8 shows the results of some GIAO-MBPT calculations for ^{17}O shieldings.[68] The effect of including electron correlation is to increase the calculated values of the ^{17}O shieldings, usually bringing them into closer agreement with experiment.

Table 8 Comparison of Some ^{17}O Shieldings (in ppm) Produced by GIAO and GIAO-MBPT Calculations, and Experiment

Molecule	GIAO	GIAO-MBPT	Experimental
H_2O	323.18	339.79	357
H_2O_2	139.01	150.88	134
CO	−113.47	−54.06	−40.1 ± 17.2
H_2CO	−471.40	−345.02	−312.1
CH_3OH	341.55	354.41	344.9
CO_2	200.37	236.37	243.4
OF_2	−471.13	−465.53	−473.1
NNO	107.54	192.12	200.5

Table 9 Comparison of Some ^{1}H, ^{13}C, ^{17}O, and ^{31}P Shieldings (in ppm) Produced by SCF-IGLO and MC-IGLO Calculations, and Experiment

Molecule	Nucleus	SCF-IGLO	MC-IGLO	Experimental
CH_4	C	193.8	198.4	198.7
	H	31.22	31.13	30.61
PH_3	P	583.4	598.2	594.4
	H	29.43	29.65	29.28
F_2	F	−165.3	−204.3	−192.8
CO	C	−23.4	13.4	3.0
	O	−83.9	−36.7	−42.3
O_3	O (central)	2730.1	−657.7	−724.0
	O (terminal)	−2816.7	−1151.8	−1290.0

Table 10 Comparison of Some ^{15}N Shieldings (in ppm) produced by IGLO, LORG, and SOLO Calculations on Some Conjugated Heterocycles, and Experiment

Molecule	IGLO	LORG	SOLO	Experimental
s-Triazine	−41	−33	−28	−39
Pyrimidine	−71	−58	−45	−51
Pyridine	−104	−94	−72	−73
Pyrazine	−121	−136	−102	−90
s-Tetrazine	−221	−213	−159	−141
Pyridazine	−240	−235	−197	−156
1,2,4-Triazine				
N-3		−76	−42	−54
N-2		−171	−151	−134
N-1		−255	−207	−178

A comparable finding is given in Table 9 for some MC-IGLO calculations of ^{1}H, ^{13}C, ^{17}O, and ^{31}P shieldings.[73] Not surprisingly, the electron correlation effects on the nuclear shieldings are small for methane and phosphine, but much more significant for fluorine, carbon monoxide, and ozone, which are 'electron-rich' molecules For the central oxygen of ozone, the effect of including electron correlation in the calculation is to increase the predicted shielding by over 2000 ppm. As in the case of the GIAO-MBPT calculations, the MC-IGLO results show an increase in shielding over that given by the corresponding IGLO calculations. The exception is the fluorine molecule. The results of some LORG and SOLO nitrogen shielding calculations are compared in Table 10.[74] The conjugated heterocycles chosen for the study represent cases where electron correlation effects are expected to be important. As can be seen, the inclusion of electron correlation leads to an increase in the calculated nitrogen shieldings and usually to an improved agreement with experimental results. This is consistent with the view that taking account of electron correlation interactions results in an improved description of the molecular electronic excited states, so that the energies of the lower lying members of the excited states are increased; this results in a smaller paramagnetic contribution to the nuclear shielding, so that the total shielding increases.

A comparison of the LORG and SOLO data given in Table 10 with experiment shows root mean square errors of 49.2 and 19.9 ppm respectively. Thus, the case is strongly made for the necessity of including electron correlation effects in nuclear shielding calculations on 'electron-rich' molecules. As a caveat, it should be mentioned that the amount of influence of electron correlation on the calculated shieldings

Table 11 Comparison of Some ^{15}C, ^{15}N, ^{17}O, ^{19}F and ^{31}P Shieldings (in ppm) Produced by GIAO and CDFT Calculations, and Experiment

Molecule	Nucleus	GIAO	CDFT	Experimental
PN	P	−15.8	42.1	53
	N	−409.4	−347.3	−349
P_2H_2	P	−294.2	−190.9	−166
CO	C	−8.0	−0.3	1
	O	−61.3	−63.4	−42.3
NNO	N (terminal)	89.0	97.0	99.5
	N (central)	−2.0	5.9	11.3
	O	219.4	185.4	200.5
H_2O_2	O	191.5	157.2	133.9
N_2	N	−80.0	−69.3	−61.0
N_2CO	C	14.2	−12.3	−1
	O	−406.2	−362.6	−312.1
F_2	F	−181.4	−197.8	−193.8

depends upon the method chosen, as well as on the basis set and geometry.

Density functional theory (DFT) is an alternative to HF methods for describing molecular electronic structure.[75,76] A particularly appealing aspect of DFT is that electron correlation effects are explicitly included in the calculations. Coupled DFT (CDFT), together with the IGLO method, has been used in some nuclear shielding calculations for molecules where electron correlation effects are anticipated to make a significant contribution to the calculated shieldings.[77] In Table 11 the CDFT shielding results are compared with experiment and with the results of some GIAO calculations in which electron correlation effects are not included.[78,79] It is noteworthy that the CDFT results are in much better agreement with experiment than are the uncorrelated GIAO data. This serves again to stress the importance of electron correlation effects on the observed shieldings of nuclei in 'electron-rich' molecules. However, it should also be noted that the electron correlation methods of calculating nuclear shieldings used to date tend to overemphasize the importance of correlation effects; this shortcoming can be overcome by using more sophisticated electron correlation methods such as multiconfiguration SCF with coupled clusters (MCSCF-CC) and the MP_4 theory, for example.

4 SEMIEMPIRICAL MOLECULAR ORBITAL CALCULATIONS

During the last few years, ab initio calculations of nuclear shieldings have become increasingly popular for smaller molecular systems, mainly because of the widespread availability of enhanced computer power. Prior to that, semiempirical calculations were generally popular and widely accepted. Such calculations have a good record for indicating shielding trends in series of closely related molecules, although they are often unsuitable for predictive purposes—especially for comparison of the nuclear shieldings of molecules whose chemical properties are not closely related. There are still areas where ab initio shielding calculations have not yet been successfully applied, for example, for an extended network of atoms, and for investigating medium effects on nuclear shielding and relativistic effects on the shielding of heavier nuclei.

Pople's GIAO model provides the basis for the more successful semiempirical shielding calculations.[80–83] In cases where only valence s and p electrons need to be considered for an atom A, the expressions for the rotationally averaged values of the local diamagnetic, σ_A^d, and paramagnetic, σ_A^p, terms are

$$\sigma_A^d = \frac{\mu_0 e^2}{12\pi m} \sum_{\mu}^{A} \rho_{\mu\mu} \langle \mu | r_{A_\mu}^{-1} | \mu \rangle \tag{15}$$

$$\begin{aligned}\sigma_A^p = -\frac{\mu_0 e^2 h^2}{6\pi m} \langle r^{-3} \rangle_{r_p} \sum_j^{\text{occ}} \sum_k^{\text{unocc}} \frac{1}{E_k - E_j} \\ \times \Big[(C_{yAj} C_{zAk} - C_{zAj} C_{yAk}) \sum_B (C_{yBj} C_{zBk} - C_{zBj} C_{yBk}) \\ + (C_{zAj} C_{xAk} - C_{xAj} C_{zAk}) \sum_B (C_{xBj} C_{yBk} - C_{yBj} C_{xBk}) \\ + (C_{xAj} C_{yAk} - C_{yAj} C_{xAk}) \sum_B (C_{xBj} C_{zBk} - C_{zBj} C_{xBk}) \Big]\end{aligned} \tag{16}$$

where $\rho_{\mu\mu}$ is the charge density in the atomic orbital μ, which is at an average distance of $r_{A\mu}$ from nucleus A, and C_{xA_j} is the LCAO coefficient of the p_x orbital on atom A in the molecular orbital j, and so on. The summation over the atoms B includes A; consequently, σ_A^p is zero unless both A and B possess valence p electrons. E_k and E_j are the energies of the unoccupied and occupied molecular orbitals k and j, respectively; the excitation energies $E_k - E_j$ are those of the excited singlet states, which are mixed with the ground state by the magnetic field used in the NMR experiment. From these comments, it may be apparent that semiempirical nuclear shielding calculations can provide the basis for an approximate understanding of chemical shifts in terms of molecular electronic structure. In general, the absolute shielding values produced by these calculations are not too reliable, but changes in nuclear shielding as a function of molecular structure can be predicted to a reasonable accuracy by semiempirical methods. More extensive accounts of semiempirical nuclear shielding calculations are to be found in the literature.[84–86] Various semiempirical parameter schemes have been used to calculate nuclear shieldings. Generally, reasonable agreement with experiment has been obtained for ^{13}C, ^{14}N, ^{17}O, and ^{19}F shieldings with CNDO/S and INDO/S parameter schemes (CNDO/S = complete neglect of differential overlap for spectroscopy; INDO/S = intermediate neglect of differential overlap for spectroscopy). In these calculations, almost the full range of observed chemical shifts for a given type of nucleus is attributed to changes in the local paramagnetic term, and this may be discussed in the terminology of charge densities, bond orders and excitation energies as shown by equation (16). For calculations of the shieldings of carbon and nitrogen nuclei, the INDO/S scheme is found to give results that are in closest agreement with experiment.[87,88]

4.1 Nuclear Shielding of Macromolecules

In polymers, electrons are usually not constrained to well-defined regions of a molecule, in contrast to the situation normally found in small molecules. Consequently, molecular orbital calculations on monomeric species are not readily transferable to polymers because of differences in electronic

structure. In calculations on polymers, additional approximations are required; for example, the tight binding (TB) approximation[89] has been successfully used in semiempirical calculations of the nuclear shieldings of nuclei in infinite chains.[90] In general, the best choice of parameter scheme for these calculations is found to be the INDO/S set.[91] An example is provided by the case of *cis*- and *trans*-polyacetylenes, where the ^{13}C shieldings are satisfactorily reproduced by the TB-INDO/S shielding calculations.[91]

4.2 Medium Effects on Nuclear Shielding

Solute and solvent molecules may interact in both specific and nonspecific ways, both of which may influence the nuclear shielding. Specific interactions include hydrogen bonding, protonation, and complex formation, which have been included in many ab initio and semiempirical nuclear shielding calculations.

Nonspecific shielding influences can be produced by bulk susceptibility effects, van der Waals effects, neighbor susceptibility anisotropies, and electric field effects. The modus operandi of these effects is by means of electronic interactions between the dipole moments of the solute and solvent molecules.[92] The solvaton model[93] has been used together with semiempirical molecular orbital calculations to estimate the effects of nonspecific solute–solvent interactions on nuclear shielding in a number of cases. In general, the results obtained from calculations using the solvaton model within the INDO/S–SOS framework are both qualitatively and quantitatively reliable.[94] The presence of the lone electron pair renders nitrogen nuclear shieldings particularly susceptible to solute–solvent interactions. The greatest influence of this kind for neutral species has been reported in a study of some azine heteroaromatics;[95] pyridazine shows a range of about 50 ppm for its solvent-dependent nitrogen shielding. Solvaton-based nuclear shielding calculations show that about half of this range is produced by nonspecific solute–solvent interactions.

4.3 Relativistic Effects for Heavy Nuclei

There are two relativistic effects that should be considered in discussions of the shielding of heavy nuclei.

A relativistic electronic mass increase causes the radii of the innermost orbitals to contract. This contraction may lead to enhanced screening of the nuclear charge as far as the outer electrons are concerned; thus the radii of their orbitals may increase. Equations (15) and (16) show that any change in the separation between a given nucleus and its surrounding electrons is expected to result in marked changes in both the diamagnetic and paramagnetic shielding contributions.

The second relativistic effect to be considered is that arising from the breakdown of Russell–Saunders coupling in favour of j–j coupling of electronic angular momenta. As a consequence of this breakdown, some spin triplet character can be introduced into the singlet ground state of a diamagnetic molecule. Resulting from this, a local magnetic field is produced at the nucleus, which produces a change in nuclear shielding.

The Dirac model has been employed to produce a relativistic analog of Ramsey's theory of nuclear shielding.[96–100] To date, only semiempirical molecular orbital calculations of relativistic contributions to the nuclear shielding of heavy atoms have appeared.[101] The results show that relativistic effects are significant for the proton shieldings of the hydrogen halides, with the major influence arising from the spin–orbit coupling-induced changes in the wavefunctions. In another study, a comparison of CHF and relativistic semiempirically calculated shieldings for the series CX and CX_2, where X = O,S, and Se, shows some expected relativistic contributions to the paramagnetic shielding terms of the heavier nuclei.[102]

It is to be anticipated that the areas outlined here, as still being part of the purview of semiempirical calculations of nuclear shieldings, will become part of the remit of ab initio calculations in the not too distant future. In order to examine more thoroughly the results of more accurate shielding calculations, there are some experimental demands to be met. More careful measurements of solvent effects on nuclear shieldings are required; absolute shielding scales need to be established for more nuclei; and there is a requirement for more gas phase data to permit accurate comparisons of calculated and experimental data. In addition, it should not be forgotten that the effects of rotational–vibrational averaging should be included in experimental results. Such improved measurements are required for most NMR nuclei; they are probably more readily obtained for the lighter nuclei, and it could be several years before a reliable experimental basis is available for a more coruscating investigation of the results of ab initio shielding calculations on heavier nuclei.

5 RELATED ARTICLES

Anisotropy of Shielding and Coupling in Liquid Crystalline Solutions; Average Hamiltonian Theory; Shielding Calculations: LORG and SOLO Approaches; Chemical Shift Scales on an Absolute Basis; Chemical Shift Tensors; Electric Field Effects on Shielding Constants; Shielding Calculations: IGLO Method; Shielding Calculations: Perturbation Methods; Shielding in Small Molecules; Shielding Tensor Calculations; Shielding Theory: GIAO Method.

6 REFERENCES

1. W. J. Hehre, L. Radom, P. von R. Schleyer, and J. A. Pople, *Ab initio Molecular Orbital Theory*, Wiley, New York, 1986.
2. N. F. Ramsey, *Phys. Rev.*, 1950, **77**, 567.
3. N. F. Ramsey, *Phys. Rev.*, 1950, **78**, 699.
4. H. F. Hameka, *J. Chem. Phys.*, 1964, **40**, 3127.
5. L. C. Snyder and R. G. Parr, *J. Chem. Phys.*, 1961, **34**, 827.
6. W. N. Lipscomb, in *Advances in Magnetic Resonance*, ed. J. S. Waugh, Academic Press, New York, 1966, Vol. 2, p. 137.
7. S. T. Epstein, *J. Chem. Phys.*, 1965, **42**, 2897.
8. R. M. Stevens, K. M. Pitzer, and W. N. Lipscomb, *J. Chem. Phys.*, 1963, **38**, 550.
9. R. Hoeller and H. Lischka, *Mol. Phys.*, 1980, **41**, 1017.
10. R. Hoeller and H. Lischka, *Mol. Phys.*, 1980, **41**, 1041.
11. P. Lazzeretti and R. Zanasi, *J. Chem. Phys.*, 1978, **68**, 832.
12. P. Lazzeretti and R. Zanasi, *J. Chem. Phys.*, 1978, **68**, 1523.
13. P. W. Fowler, P. Lazzeretti, and R. Zanasi, *Chem. Phys. Lett.*, 1990, **165**, 79.

14. P. W. Fowler, P. Lazzeretti, M. Malagali, and R. Zanasi, *Chem. Phys. Lett.*, 1991, **179**, 174.
15. R. Taylor, J. G. Hare, A. K. Abdul-Sala, and H. W. Kroto, *J. Chem. Soc., Chem. Commun.*, 1990, 1423.
16. F. London, *J. Phys. Radium*, 1937, **8**, 397.
17. R. Ditchfield, *J. Chem. Phys.*, 1972, **56**, 5688.
18. R. Ditchfield, *Chem. Phys. Lett.*, 1972, **15**, 203.
19. R. Ditchfield, *Mol. Phys.*, 1974, **27**, 789.
20. K. Wolinski, J. F. Hinton, and P. Pulay, *J. Am. Chem. Soc.*, 1990, **112**, 8251.
21. W. Kutzelnigg, *Isr. J. Chem.*, 1980, **19**, 123.
22. M. Schindler and W. Kutzelnigg, *J. Chem. Phys.*, 1982, **76**, 1919.
23. M. Schindler and W. Kutzelnigg, *J. Am. Chem. Soc.*, 1983, **105**, 1360.
24. M. Schindler and W. Kutzelnigg, *Mol. Phys.*, 1983, **48**, 781.
25. B. Levy and J. Ridard, *Mol. Phys.*, 1981, **44**, 1099.
26. D. J. Rowe, *Rev. Mod. Phys.*, 1968, **40**, 153.
27. V. Galasso and G. Fronzoni, *J. Chem. Phys.*, 1986, **34**, 3215.
28. P. Lazzeretti and R. Zanasi, *Phys. Rev. A*, 1985, **32**, 2607.
29. A. E. Hansen and T. D. Bouman, *J. Chem. Phys.*, 1985, **82**, 5035.
30. T. D. Bouman and A. E. Hansen, *Chem. Phys. Lett.*, 1988, **149**, 510.
31. C. J. Jameson, in *Specialist Periodical Reports on NMR*, ed. G. A. Webb, The Royal Society of Chemistry, London, 1980–1993, Vols. 9–22.
32. H. Kurosu, G. A. Webb, and I. Ando, *Magn. Reson. Chem.*, 1992, **30**, 1122.
33. T. A. Keith and R. F. W. Bader, *Chem. Phys. Lett.*, 1992, **194**, 1.
34. R. F. W. Bader, *J. Chem. Phys.*, 1989, **91**, 6989.
35. D. B. Chesnut and K. D. Moore, *J. Comput. Chem.*, 1989, **10**, 648.
36. D. B. Chesnut and C. G. Phung, *Chem. Phys. Lett.*, 1991, **183**, 505.
37. J. F. Hinton, P. L. Guthrie, P. Pulay, K. Wolinski, and G. Fogarasi, *J. Magn. Reson.*, 1992, **96**, 154.
38. J. F. Hinton, P. Guthrie, P. Pulay, and K. Wolinski, *J. Am. Chem. Soc.*, 1992, **114**, 1604.
39. M. Haeser, R. Ahlrichs, H. P. Baron, P. Weis, and H. Horn, *Theor. Chim Acta*, 1992, **83**, 455.
40. A. C. de Dios and E. Oldfield, *Chem. Phys. Lett.*, 1993, **205**, 108.
41. U. Meier, C. van Wuellen, and M. Schindler, *J. Comput. Chem.*, 1992, **13**, 551.
42. C. J. Jameson and H. J. Osten, in *Annual Reports on NMR Spectroscopy*, ed. G. A. Webb, Academic Press, London, 1986, Vol. 17, p. 1.
43. C. J. Jameson and H. J. Osten, *J. Chem. Phys.*, 1985, **83**, 5425.
44. C. J. Jameson and H. J. Osten, *Mol. Phys.*, 1989, **55**, 383.
45. D. B. Chesnut and C. K. Foley, *J. Chem. Phys.*, 1986, **84**, 852.
46. U. Fleischer, M. Schindler, and W. Kutzelnigg, *J. Chem. Phys.*, 1987, **86**, 6337.
47. L. Onsager, *J. Am. Chem. Soc.*, 1936, **58**, 1486.
48. S. C. Tucker and D. G. Truhlar, *Chem. Phys. Lett.*, 1989, **157**, 164.
49. M. Buehl, T. Steinke, P. von R. Schleyer, and R. Boese, *Angew. Chem., Int. Ed. Engl.*, 1991, **30**, 1160.
50. H. Nakatsuji, K. Kanda, K. Endo, and T. Yonezawa, *J. Am. Chem. Soc.*, 1984, **106**, 4653.
51. K. Kanda, H. Nakatsuji, and T. Yonezawa, *J. Am. Chem. Soc.*, 1984, **106**, 5888.
52. H. Nakatsuji and M. Sugimoto, *Inorg. Chem.*, 1990, **29**, 1221.
53. H. Nakatsuji, T. Inoue, and T. Nakao, *Chem. Phys. Lett.*, 1990, **167**, 111.
54. H. Nakatsuji, M. Sugimoto, and S. Saito, *Inorg. Chem.*, 1990, **29**, 3095.
55. J. E. Combariza, M. Barfield, and J. H. Enemark, *J. Phys. Chem.*, 1991, **95**, 5463.
56. J. E. Combariza, J. H. Enemark, M. Barfield, and J. C. Facelli, *J. Amer. Chem. Soc.*, 1989, **111**, 7619.
57. Y. Sun, L. Zhu, X. You, and Y. Jiang, *Theor. Chim. Acta*, 1992, **82**, 213.
58. P. Kroneck, O. Lutz, and A. Nolle, *Z. Naturforsch. A*, 1980, **35**, 226.
59. O. Lutz, A. Nolle, and P. Kroneck, *Z. Naturforsch. A*, 1976, **31**, 454.
60. O. Lutz, A. Nolle, and P. Kroneck, *Z. Naturforsch. A*, 1977, **32**, 505.
61. M. Sugimoto, M. Kanayama, and H. Nakatsuji, *J. Phys. Chem.*, 1992, **96**, 4375.
62. H. Nakatsuji, and T. Nakao, *Chem. Phys. Lett.*, 1990, **167**, 571.
63. J. A. Tossell, *J. Magn. Reson.*, 1991, **94**, 301.
64. H. Nakatsuji, T. Nakao, and K. Kanda, *Chem. Phys.*, 1987, **118**, 25.
65. J. A. Tossell, *J. Phys. Chem.*, 1991, **95**, 366.
66. J. A. Tossell, *Chem. Phys. Lett.*, 1990, **169**, 145.
67. V. Galasso, *Theor. Chim. Acta*, 1983, **63**, 35.
68. J. Gauss, *Chem. Phys. Lett.*, 1992, **191**, 614.
69. H. Fukui, K. Miura, and H. Matsuda, *J. Chem. Phys.*, 1992, **96**, 2039.
70. C. von Wuellen and W. Kutzelnigg, *Chem. Phys. Lett.*, 1993, **205**, 563.
71. J. Geertsen and J. Oddershede, *Chem. Phys.*, 1984, **90**, 301.
72. T. D. Bouman and A. E. Hansen, *Chem. Phys. Lett.*, 1990, **175**, 292.
73. W. Kutzelnigg, C. von Wuellen, U. Fleischer, R. Franke and T. von Mourik, in *Nuclear Magnetic Shieldings and Molecular Structure*, ed. J. A. Tossell, Kluwer, Dordrecht, 1993, p. 141.
74. T. D. Bouman and A. E. Hansen, *Chem. Phys. Lett.*, 1992, **197**, 59.
75. P. Hohenberg and W. Kohn, *Phys. Rev.*, 1964, **136**, B864.
76. W. Kohn and L. J. Sham, *Phys. Rev.*, 1965, **140**, A1133.
77. V. G. Malkin, O. L. Malkina, and D. R. Salahub, *Chem. Phys. Lett.*, 1993, **204**, 87.
78. D. B. Chesnut and C. G. Phung, *J. Chem. Phys.*, 1989, **91**, 6238.
79. D. B. Chesnut and B. E. Rusiloski, *Chem. Phys.*, 1991, **157**, 105.
80. J. A. Pople, *Discuss. Faraday Soc.*, 1962, **34**, 7.
81. J. A. Pople, *J. Chem. Phys.*, 1962, **37**, 53.
82. J. A. Pople, *J. Chem. Phys.*, 1962, **37**, 60.
83. J. A. Pople, *Mol. Phys.*, 1965, **7**, 301.
84. K. A. K. Ebraheem and G. A. Webb, in *Progress in Nuclear Magnetic Resonance Spectroscopy*, eds. J. W. Emsley, J. Feeney, and L. N. Sutcliffe, Pergamon Press, Oxford, 1978, Vol. 11, p. 149.
85. I. Ando and G. A. Webb, *Theory of NMR Parameters*, Academic Press, London, 1983, p. 47.
86. G. A. Webb, in *NMR of Living Systems*, ed. T. Axenrod and G. Ceccarelli, Reidel, Dordrecht, 1986, p. 19.

87. K. A. K. Ebraheem, G. A. Webb, and M. Witanowski, *Org. Magn. Reson.*, 1978, **11**, 27.
88. M. Jallali-Heravi and G. A. Webb, *J. Magn. Reson.*, 1978, **32**, 429.
89. T. Yamanobe, R. Chujo, and I. Ando, *Mol. Phys.*, 1983, **50**, 123.
90. I. Ando, T. Yamanobe, H. Kurosu and G. A. Webb, in *Annual Reports on NMR Spectroscopy*, ed. G. A. Webb, Academic Press, London, 1990, Vol. 22, p. 205.
91. T. Yamanobe, I. Ando, and G. A. Webb, *J. Mol. Struct.*, 1987, **151**, 191.
92. I. Ando and G. A. Webb, *Org. Magn. Reson.*, 1981, **15**, 111.
93. H. A. Germer, *Theor. Chim. Acta*, 1974, **34**, 145.
94. M. Witanowski and G. A. Webb, *Proc. Indian Acad. Sci.*, 1985, **94**, 241.
95. M. Witanowski, W. Sicinska, S. Biernat, and G. A. Webb, *J. Magn. Reson.*, 1991, **91**, 289.
96. P. Pyykko, *Chem. Phys.*, 1983, **74**, 1.
97. N. C. Pyper, *Chem. Phys. Lett.*, 1983, **96**, 204.
98. N. C. Pyper, *Chem. Phys. Lett.*, 1983, **96**, 211.
99. Z. C. Zhang and G. A. Webb, *J. Mol. Struct.*, 1983, **104**, 439.
100. Z. C. Zhang and N. C. Pyper, *Mol. Phys.*, 1988, **64**, 963.
101. P. Pyykko, A. Goerling, and N. Roesch, *Mol. Phys.*, 1987, **61**, 195.
102. J. Jokisaari, P. Lazzeretti, and P. Pyykko, *Chem. Phys.*, 1988, **123**, 339.

Biographical Sketch

Graham A. Webb. *b* 1935. B.Sc., Ph.D., D.Sc., 1974, University of London. Successively lecturer, senior lecturer in chemical physics, reader and Professor in Chemistry at the University of Surrey. Approx. 350 publications and about 50 edited volumes on NMR. Research interests include a study of solute–solvent interactions by nitrogen NMR, solution and solid state NMR studies of molecular structure, theoretical aspects of nuclear shielding and of drug–receptor interactions.

Shielding Tensor Calculations

Julio C. Facelli
University of Utah, Salt Lake City, UT, USA

1	Introduction	1
2	The Use of Calculations of Chemical Shielding Tensors for the Assignment of the Orientations of the Principal Values Obtained from Disordered Samples	1
3	The Use of Chemical Shielding Tensor Calculations for the Assignment of ^{13}C Resonances in the Solid Phase	2
4	Studies of the Additivity of Electronic Substituent Effects in the Tensor Components of Chemical Shift Tensors	3
5	Study of Steric Effects on Chemical Shifts Tensors	3
6	Sensitivity of the Calculated Shieldings to the Molecular Geometry	4
7	Relationship between Calculated ^{13}C Chemical Shift Tensors and Aromaticity	5
8	Calculations of Chemical Shifts in Carbocations	5
9	Angular Dependence of the Principal Components of the ^{13}C Chemical Shift Tensors	6
10	Conclusions	6
11	Related Articles	7
12	References	7

1 INTRODUCTION

In the last 10 years, our ability to calculate chemical shielding tensors has increased greatly. The advances have originated in new theoretical developments to mitigate the gauge origin problem, advances in the algorithms used in the quantum mechanical computer programs, and great improvements in computer hardware performance. In recent years, the improvements of experimental methods to measure the principal values and the full chemical shift tensors (see also ***Chemical Exchange Effects on Spectra***, ***Chemical Shift Tensors***, and ***Chemical Shift Tensors in Single Crystals***) have produced a large collection of experimental values of the principal components of the chemical shift tensors and some information on the full tensors,[1] giving further impetus to the development of better methods for calculating chemical shifts. It is significant to realize that when comparing experimental and calculated values of chemical shifts it is important to compare the full tensors, or at least the principal values, because it is well-documented in the literature[2] that in certain cases the agreement between experimental and calculated isotropic shift may arise from a fortuitous cancellation of errors in the calculated principal components.

Several modern methods for calculating chemical shieldings are described in detail elsewhere in this Encyclopedia (see Related Articles). All these methods can produce fairly accurate results and with the current computational technology calculations involving several hundreds of basis functions in molecules with 20–30 nonhydrogen atoms have become common.

In this article important examples of the use of calculations of chemical shielding tensors as an aid in solving chemical/structural problems are presented. In the examples the importance of calculating the full chemical shielding tensors over the use of the isotropic values is emphasized. The article does not attempt to present a comprehensive description of all the chemical problems that have been or can potentially be addressed using calculations of chemical shieldings; the article is limited to a brief description of some of the most interesting problems which, in the author's opinion, have benefited from this type of calculation. The selection has been somewhat arbitrary and perhaps biased by the author's own research interests. Apologies are made for the omission of many other important pieces of research that have not been included in this article. It is hoped that the material presented here will give the reader a flavor of how to use chemical shift tensor calculations in molecular sciences. For those interested in a comprehensive survey of the applications, reference should be made to the annual accounts on the field published by Jameson.[3] The examples used in this article to illustrate the importance of calculating the chemical shielding tensors are listed in the Table of Contents.

2 THE USE OF CALCULATIONS OF CHEMICAL SHIELDING TENSORS FOR THE ASSIGNMENT OF THE ORIENTATIONS OF THE PRINCIPAL VALUES OBTAINED FROM DISORDERED SAMPLES

The assignment of the principal values of the tensor into the molecular frame is a critical step in obtaining information on the relationship between electronic structure and chemical shielding. Several reasonably simple experimental methods have been developed to measure the principal values of the chemical shielding tensors in disordered solids,[1] but, unfortunately, only the principal values from the tensor are available from these experiments; much more complex ones, involving dipolar coupling, are necessary to obtain the orientation of the principal axes of the tensor. Even in cases of high molecular symmetry, in which the orientations of the principal axes are known by symmetry, it is necessary to use theoretical arguments to decide which principal value corresponds to each principal direction. The only exception to this rule can be found in molecules with a C_3 axis or one of higher symmetry, in which case there are only two principal components of the shielding tensor, one lying along the symmetry axis and the other perpendicular to the axis with a degeneracy factor of two.

A classical example of this problem is the assignment of the principal components of the $^{13}CH_2$ chemical shift tensors in cyclic alkanes.[4] In Table 1 the measured principal values of the tensors in cyclopropane, cyclobutane, and cyclopentane are presented by rank order. From the table we can conclude that the calculations, which have been undertaken using a modest double zeta basis, reproduce the measured principal values quite well, but a simple inspection of this table also indicates that all the principal components are quite sensitive to the size of the alkane ring and to the CCC angle. This

Table 1 ^{13}C Chemical Shift Principal Values in Cyclopropane, Cyclobutane, and Cyclopentane Presented by Rank Order. The Experimental Values are Referenced to External Liquid TMS and the Calculated Values to the Calculated Value of TMS using a Double Zeta Basis[4]

		Cyclopropane	Cyclobutane	Cyclopentane
δ_{11}	experimental value	22	39	49
	IGLO	38	35	49
δ_{22}	experimental value	2	23	21
	IGLO	6	27	31
δ_{33}	experimental value	−36	14	12
	IGLO	−39	9	16

is quite contrary to the actual physical situation depicted in Figure 1, where the experimental principal components have been ordered according to their spatial orientation obtained from the calculations. Figure 1 shows that only the component perpendicular to the CCC plane, δ_{CC}, is highly dependent on the CCC angle. The other two components show only a very modest dependence on the size of the alkane ring. Only theoretical calculation of the chemical shielding tensors can provide the information required to make use of the experimental measurements in a consistent way. Note that the calculations of the chemical shieldings produce the complete tensor in the molecular frame, therefore complete information on the orientation of the principal axis of the shielding is available from the calculations. The agreement between the calculated and the experimental values gives confidence in using spatial assignments based on the orientations of the calculated principal values.

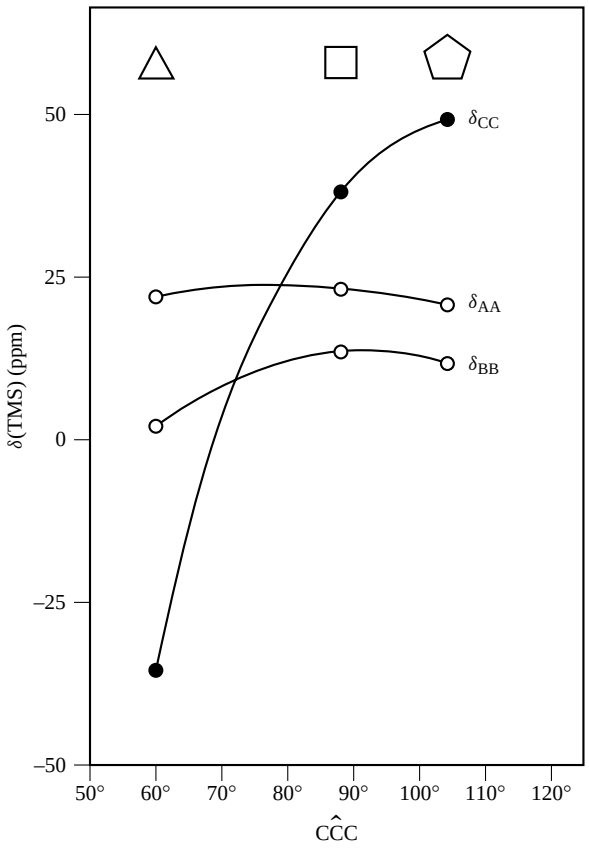

Figure 1 ^{13}C shift principal components are shown as a function of the CCC angle in cyclopropane, cyclobutane, and cyclopentane. The orientation of the principal axes obtained from theoretical calculations of the chemical shielding tensors is as follows: δ_{AA}: lies in the HCH plane bisecting the HCH angle; δ_{CC}: lies perpendicular to the HCH plane; and δ_{CC}: lies perpendicular to the CCC plane. (Reproduced by permission of The American Chemical Society from J. C. Facelli, D. M. Grant, and J. Michl, *Acc. Chem. Res.*, 1987, **20**, 152)

3 THE USE OF CHEMICAL SHIELDING TENSOR CALCULATIONS FOR THE ASSIGNMENT OF ^{13}C RESONANCES IN THE SOLID PHASE

The assignment of resonance frequencies to individual nuclei has always been a significant problem in NMR spectroscopy. Over the years a number of techniques have been developed to make the spectroscopic assignments more reliable in complex molecules. The most common assignment techniques used in modern liquid NMR are based on the additivity effects of the electronic substituent, measurements of coupling constants, backbone connectivities derived from INADEQUATE experiments, and multidimensional experiments correlating chemical shifts and coupling constants of directly bonded nuclei. Unfortunately, these methods are not readily applicable to solid state measurements due to relaxation, sensitivity, and linewidth problems. The most common tool for the assignment of carbon resonances in the solid state is a comparison of the chemical shift values with their liquid shift values. This method is only adequate for assigning resonances separated by several ppm, otherwise the differential shifts observed in going from the liquid to the solid phase are of the same magnitude as the differences between the resonance frequencies of the nuclei and the assignments become unreliable. A classical example of this problem is the assignment of the ^{13}C resonances of crystalline glucose which required the use of selective isotopic enrichment.[5]

In principle, calculations of isotropic chemical shifts can be used for chemical shift assignments, but they also become unreliable when the isotropic shifts differ by less than 2–3 ppm, which is the limit of reliability of our current theoretical methods. The use of the principal tensor components, which magnify the dispersion of the chemical shifts, partially overcomes the problem when at least one of the principal values of the shift tensors in question differs by more than 4–5 ppm, thus making assignments from theoretical calculations reliable. For instance, the ^{13}C chemical shifts of the phenyl carbons directly bonded to the oxygen in solid *p*-tolyl ether, have principal components of δ_{11} = 238.3 ppm, δ_{22} = 147.4 ppm, δ_{33} = 74.4 ppm, and δ_{11} = 238.6 ppm, δ_{22} = 160.7 ppm, δ_{33} = 74.4 ppm, respectively.[6] The isotropic values of 153.3 ppm and 157.9 ppm are too close to make any reliable assignment based on the calculated values, and the liquid values are of no use in this case because the two carbons are equivalent in solution with an isotropic chemical shift of 155.2 ppm. The X-ray structure of this compound shows that the two phenyl moieties form a dihedral angle, α [shown for diphenyl ether (**1**) in Scheme 1], of approximately 90°. Using the X-ray geometry of the compound, the calculated chemical shifts tensors show a large difference of 11.8 ppm between the δ_{22} components of the carbons in question. This

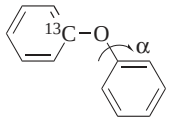

(1)

Scheme 1. Structure of diphenyl ether. The X-ray studies predict a dihedral angle of approximately 10° between the two phenyl moieties.

allows a reliable assignment of these carbons which would not be possible without the calculation and measurement of the principal values. The carbon with the largest δ_{22} component, 160.7 ppm, corresponds to an arylic carbon of the ring for which the C−^{13}C−O−Ph moiety is almost planar. The carbon with the smaller δ_{22} component, 147.4 ppm, corresponds to the aromatic ring for which the dihedral angle C−^{13}C−O−Ph is close to 90°. This larger shift in δ_{22} can be rationalized with the smaller C_{aryl}−O bond order for an out-of-plane configuration compared with the bond order for the planar configuration.

Even when full tensor data are available, calculations of chemical shift tensors can be important in the assignment of the individual carbon resonances and their orientation in the molecular frame when the combined symmetry requirements of the NMR experiments and the crystalline structure lead to ambiguous assignment of the resonances. An example of this problem was described in the analysis of the ^{13}C chemical shift tensors of pyrene.[7]

4 STUDIES OF THE ADDITIVITY OF ELECTRONIC SUBSTITUENT EFFECTS IN THE TENSOR COMPONENTS OF CHEMICAL SHIFT TENSORS

The additivity of the electronic substituent effects has been one of the most powerful tools for the assignment and rationalization of ^{13}C chemical shifts,[8] but most of the work in this area has concentrated on the isotropic shift values. This type of analysis for the full chemical shift tensors and/or their principal values has been very limited, partially due to the absence of precise data on the substituent effects on the tensor values. Note that this type of analysis requires a knowledge of the shift values with an accuracy of <1 ppm in several derivatives of the parent compound. The most comprehensive study of the electronic substituent effects on ^{13}C chemical shift tensors of aromatic carbons has been presented by Carter et al.[9] who analyzed the electronic substituent effect of the methoxy group in polysubstituted methoxybenzenes. The data used in the analysis were derived from single crystal studies.

For conformationally flexible substituents, like the methoxy group, the substituent effects in the liquid or solution phase represent only the thermal average of the substituent effects for different conformations. Frequently in the solid state the substituent is trapped in a fixed conformation and additional substituent parameters are necessary to describe the steric effect. For the methoxy group it is necessary to introduce a steric *ortho* effect to describe the differential substituent effect on the two carbons *ortho* to the substituent.[10,11] Table 2 presents the substituent effect parameters for the methoxy group in substituted benzenes. The steric effect corresponds to the additional shift observed by the *ortho* carbon *cis* to the O−CH_3 bond. The values entered in Table 2 follow the trends commonly known from the rules of substituent effects, but it is noteworthy to observe the large anisotropies present in the substituent effects which in some cases are as large as 40 ppm.

Table 2 Electronic Substituent Effect of the Methoxy Group on the ^{13}C Chemical Shift Principal Values in Polysubstituted Methoxybenzenes[a]

	δ_{11}	δ_{22}	δ_{33}
ipso	11.3	30.0	58.3
ortho	−31.6	−7.7	8.1
steric[b]	−4.5	−1.9	−11.4
meta	−0.2	0.0	−4.4
para	−9.6	−14.3	−4.2

[a]All values in ppm from Carter et al.[9]. The TMS scale has been used in this table, i.e. a positive substituent effect means a deshielding of the carbon nucleus.
[b]The steric effect corresponds to the additional shift observed in the *ortho* carbon *cis* to the O−CH_3 bond.

Using chemical shift data from related compounds, we can use the information available from Table 2 to assign NMR resonances and to obtain conformational information. For example, the principal values of the chemical shift tensors for C-1 and C-3 in 2-methoxynaphthalene (**2**) (see Scheme 2) are δ_{11} = 176.7 ppm, δ_{22} = 120.9 ppm, δ_{33} = 18.1 ppm, and δ_{11} = 198.7 ppm, δ_{22} = 125.2 ppm, δ_{33} = 24.4 ppm, respectively. The conformation of the methoxy group in this compound is not known from diffraction techniques, but certainly the two energetically most favorably conformations, depicted in Scheme 2, are (**2a**) and (**2b**). Using the substituent parameters from Table 2, we can estimate the principal values of the shift tensors of C-1 and C-3 for the two conformations; we obtain for **2a**: (C-1: δ_{11} = 187.6 ppm, δ_{22} = 130.7 ppm, δ_{33} = 19.5 ppm; C-3: δ_{11} = 196.0 ppm, δ_{22} = 130.5 ppm, δ_{33} = 18.5 ppm) and for **2b**: (C-1: δ_{11} = 193.6 ppm, δ_{22} = 132.6 ppm, δ_{33} = 30.9 ppm; C-3: δ_{11} = 192.0 ppm, δ_{22} = 128.6 ppm, δ_{33} = 7.1 ppm). From these data one may immediately conclude that conformation **2a** is the most stable in the solid. Note that this conclusion is also supported by ab initio calculations and by reactivity considerations. While the additivity of the substituent effects in this case does not work perfectly, the amplification of the differences observed in the individual shielding components makes it possible to establish the preferred conformation of 2-methoxynaphthalene in the solid phase using chemical shift tensor information and the additivity of the electronic substituent effects.

(2a) **(2b)**

Scheme 2. Possible conformations of methoxy group in 2-methoxynaphthalene.

5 STUDY OF STERIC EFFECTS ON CHEMICAL SHIFTS TENSORS

A classical example of this application is the study of the principal components of the ^{13}C chemical shift tensor in *cis*- and *trans*-butene. The experimental measurement of these principal components was presented in one of the earliest papers reporting ^{13}C chemical shift principal values at low temperature.[12] However, the assignment of the principal components into the molecular frame and their interpretation had to wait several years until adequate calculations of these chemical shifts became available.[13] The calculated and experimental values of these tensors are displayed in Figure 2, where the calculations were used to assign the principal components into the molecular frame. From Figure 2 it becomes apparent that the γ steric effect is almost exclusively on the component perpendicular to the plane of the molecule, indicating that steric effects are observed in tensor principal components perpendicular to the plane in which the forces that generate the compression lie. The importance of the calculations becomes apparent when it is realized that the assignments in Figure 2 are not possible using only the experimental information. Moreover, the calculations can only provide a detailed analysis of the origin of the steric effect. The analysis of the localized bond contributions to the chemical shielding, in the local bond frame, reveals that the main contribution to the steric shielding effect in *cis*-butene originates in the compression of the C–C bond.[14]

6 SENSITIVITY OF THE CALCULATED SHIELDINGS TO THE MOLECULAR GEOMETRY

Calculations of chemical shieldings have been used to rationalize subtle results on the symmetry of the ^{13}C chemical shift tensors in naphthalene.[15] The crystal of naphthalene belongs to the $P2_{1/a}$ space group which implies that the molecules have C_i symmetry. All the diffraction studies in naphthalene have been unable to resolve, outside of the experimental errors, any departure from the D_{2h} molecular symmetry observed for naphthalene in the gaseous or liquid phase. However, the ^{13}C chemical shift tensors of single crystal naphthalene exhibit C_i symmetry and the departures of the NMR results from D_{2h} symmetry are well above their experimental errors.[16] This apparent contradiction between the experimental results obtained from diffraction and NMR techniques has been resolved by using calculations of the ^{13}C chemical shift tensors and their derivatives with respect to the geometrical parameters used in the calculations. Facelli and Grant in their 1993 paper[15] calculated how sensitive the ^{13}C chemical shift tensors in naphthalene are to the molecular structure by evaluating the derivatives of the chemical shielding tensors with respect to all the independent parameters of the molecular structure of naphthalene. Using this information and standard techniques for the error propagation, they were able to demonstrate that the uncertainties in the diffraction data are large enough to cover the deviations from D_{2h} symmetry observed in the ^{13}C NMR data. That is, the chemical shift tensors present an intrinsic sensitivity to the molecular structure higher than diffraction methods. In Figure 3 a comparison is presented between the experimental and calculated chemical shift tensors in naphthalene and the errors introduced into the calculations by the uncertainties in the molecular structure. When these errors are taken into account, the agreement between the experimental and calculated chemical shift tensors is almost perfect. This high sensitivity of the chemical shift tensors to the molecular structure opens the exciting possibility of using chemical shielding information for quantitative structural

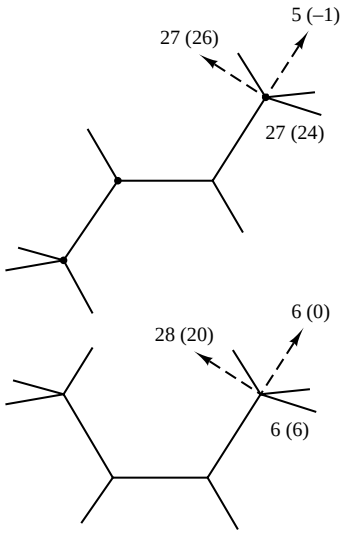

Figure 2 $^{13}CH_3$ shift principal components in the molecular frame according to the LORG calculations in *cis*- and *trans*-butene. There is one component perpendicular to the plane of the paper in each molecule. The calculated values are given in parentheses. (Reproduced by permission of J. Wiley & Sons, Inc. from J. C. Facelli and D. M. Grant, in Topics in Stereochemistry, eds. E. L. Eliel and S. H. Wilen, 1989, Vol. 19, p. 1)

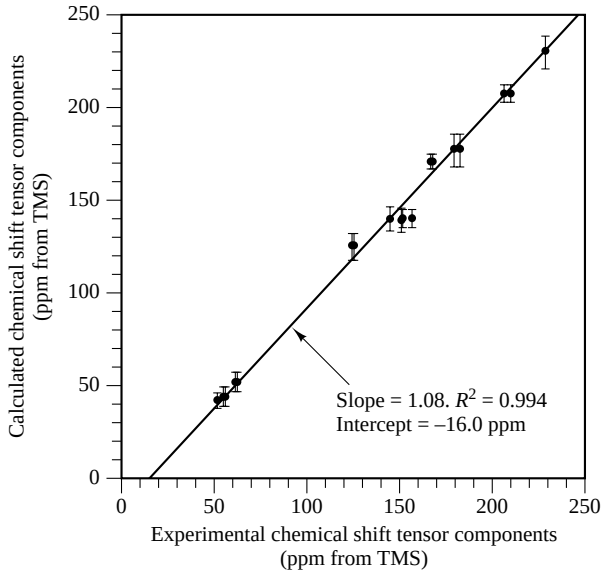

Figure 3 The excellent correlation between experimental and calculated ^{13}C chemical shift tensor components in naphthalene is shown. The error bars represent the uncertainties introduced into the calculations by the limited accuracy of the experimental geometry used in the calculation. (Reproduced by permission of Macmillan Magazines Ltd. from J. C. Facelli and D. M. Grant, *Nature (London)*, 1993, **365**, 325)

determination. It is important to realize that only tensor information of the chemical shieldings has the potential to give quantitative structural determination; the isotropic chemical shifts, which are also very sensitive to the molecular structure, do not provide enough data for solving the refinement problem which requires a minimum of $3N - 6$ independent measurements.

7 RELATIONSHIP BETWEEN CALCULATED ^{13}C CHEMICAL SHIFT TENSORS AND AROMATICITY

The concept of aromaticity has captured the imagination of chemists for more than a century. While the effect of aromaticity on many molecular properties is well understood, many questions remain on how to characterize the aromatic character of individual bonds. Most of the information regarding this question has been based on theoretical concepts derived from Kekulé resonance structures and/or more or less arbitrary definitions of electron populations derived from advanced molecular calculations.

The combined use of experimental measurements and calculations of chemical shift tensors in polycyclic aromatic compounds has provided a very interesting approach to the study of aromaticity. Facelli and Grant[17] have developed a very simple model to calculate the in-plane principal components of the ^{13}C chemical shift tensors in polycyclic aromatic compounds using the Pople[18] model for the chemical shielding and the MNDO[19] approximation for wavefunction. In the limited cases in which experimental information is available, this theoretical method reproduces the in-plane components very well. The in-plane shielding components in these compounds are sensitive to the aromatic characteristics of the molecules, while the lowest-frequency (most upfield) component of the shift tensor, which is oriented perpendicular to the molecular plane, is determined by the σ-electronic structure. Although the experimental determination of ^{13}C chemical shift tensors in polycyclic compounds is extremely difficult due to the very long relaxation times of these compounds, a reliable computational method, which has been calibrated against all the existing experimental data, has allowed the study of a large number of ^{13}C chemical shift tensors in polycyclic compounds.

Our studies reveal that the in-plane anisotropy of the ^{13}C chemical shift tensors is determined by the differences in the aromatic character of the adjacent bonds. The direction of δ_{11} is along or close to the bond with the smaller bond order, i.e. the less aromatic. For protonated carbons this is always the C–H bond, but for quaternary carbons this can be any of the adjacent C–C bonds. Hence the orientation of δ_{11} and the difference between δ_{11} and δ_{22} give information on the aromatic character of the adjacent bonds. In Figure 4 we present the calculated values of δ_{11} and δ_{22} for the quaternary carbons of several polycyclic aromatic compounds.

Several important conclusions emerge from Figure 4. As is expected from arguments using the Kekulé structures of azulene, the large in-plane anisotropy of the quaternary carbon indicates that the central bond does not have any aromatic character. Triphenylene has an aromatic structure that more closely resembles the structure of three benzene rings connected by nonaromatic bonds than a four-membered ring

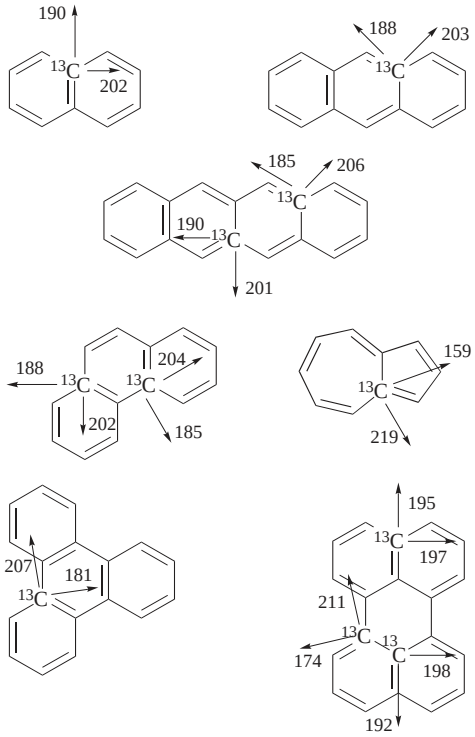

Figure 4 In-plane components of the ^{13}C chemical shift tensors of quaternary carbons in polycyclic aromatic compounds. These components have been calculated using the MNDO/Pople model proposed by Facelli and Grant.[17] The orientation of δ_{11} and the asymmetry between δ_{11} and δ_{22} provide direct information on the aromatic character of the adjacent C–C bonds

system with π electrons delocalized over the whole molecule, and the structure of perylene is closer to the aromatic structure expected for two naphthalene molecules connected by two nonaromatic bonds.

8 CALCULATIONS OF CHEMICAL SHIFTS IN CARBOCATIONS

While the full power of a complete tensor analysis or even the measurement of the ^{13}C chemical shift principal values has not yet been applied to study the structure of carbocations, calculations of ^{13}C isotropic chemical shifts have been used successfully to determine the structure of these compounds. Early calculations of ^{13}C isotropic chemical shifts using the IGLO method[20] were in good agreement with the experimental values for the nonclassical ions, but differences of 20–30 ppm were observed for the classical ones. These results were originally interpreted as a deficiency of the IGLO method in calculating chemical shifts in carbocations, but later analysis[21] indicated that deficiencies in the geometries of the carbocations used in the shielding calculations were responsible for the large discrepancies. In fact, when using carefully optimized ab initio geometries, the agreement between calculated and experimental chemical shifts becomes almost perfect for both classical and nonclassical carbocations, indicating that ^{13}C NMR in combination with quantum mechanical calculations could be used as one of the most effective tools for structural characterization of these compounds.

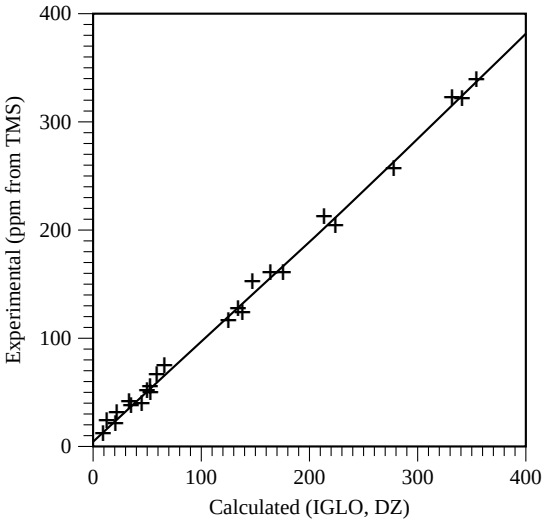

Figure 5 Correlation between the IGLO calculated ^{13}C chemical shifts and their experimental values in carbocations.[21] The experimental values are referenced to TMS and the calculated to the absolute value calculated for TMS using the DZ (double zeta) basis set, 218.1 ppm. The best linear fit has a slope of 0.9544, an intercept of 3.94 ppm, R^2 value of 0.9973, and a standard marginal deviation of 5.24 ppm. This very low marginal standard deviation is characteristic of the results that can be obtained in chemical shift calculations when highly optimized ab intio geometrical structures are used in the ^{13}C chemical shifts calculations

This finding is of great importance because the structural characterization of carbocations has been an almost intractable problem. Note that standard structural techniques such as diffraction, microwave, or NOEs are not readily applicable to carbocations. On comparing the calculated ^{13}C chemical shifts for the possible structures of a carbocation with the experimental values of the chemical shifts it is possible to determine the structure of the carbocations in solution. Several important discoveries have been made in the carbocation field in recent years using this methodology and we expect that even more dramatic discoveries will be possible using the full tensor information. In Figure 5 we present the correlation between the experimental and the IGLO calculated chemical shift for several carbocations.[21]

9 ANGULAR DEPENDENCE OF THE PRINCIPAL COMPONENTS OF THE ^{13}C CHEMICAL SHIFT TENSORS

As discussed previously, our studies with *p*-tolyl ether indicate that the large differences between the δ_{22} components in the shift tensors of the aryl carbons directly bonded to the oxygen ether are of critical importance in making the corresponding chemical assignments of the NMR resonances. In this section we wish to reemphasize the importance of analyzing all the shielding components in any structural analysis. Several examples have been presented in the literature on how different components of the shielding tensors exhibit very different behavior with respect to geometrical parameters.[22]

Carbon-13 chemical shift tensors can be used to extract valuable information on the structure of carbonaceous materials.[23] To accomplish this goal it is necessary to develop a good understanding of the dependence of the chemical shielding on molecular structure. For this work, it is convenient to use model compounds that mimic the most common moieties present in coals. As an example, we have calculated the angular dependence of the principal values of the ^{13}C chemical shift tensors in diphenyl ether. In Figure 6 the angular dependence of the principal components is presented as a function of the ^{13}COCC dihedral angle α, which is indicated in Scheme 1. It is remarkable that while δ_{11} and δ_{33} are almost independent of the dihedral angle, δ_{22} changes by more than 10 ppm over the whole range of α.

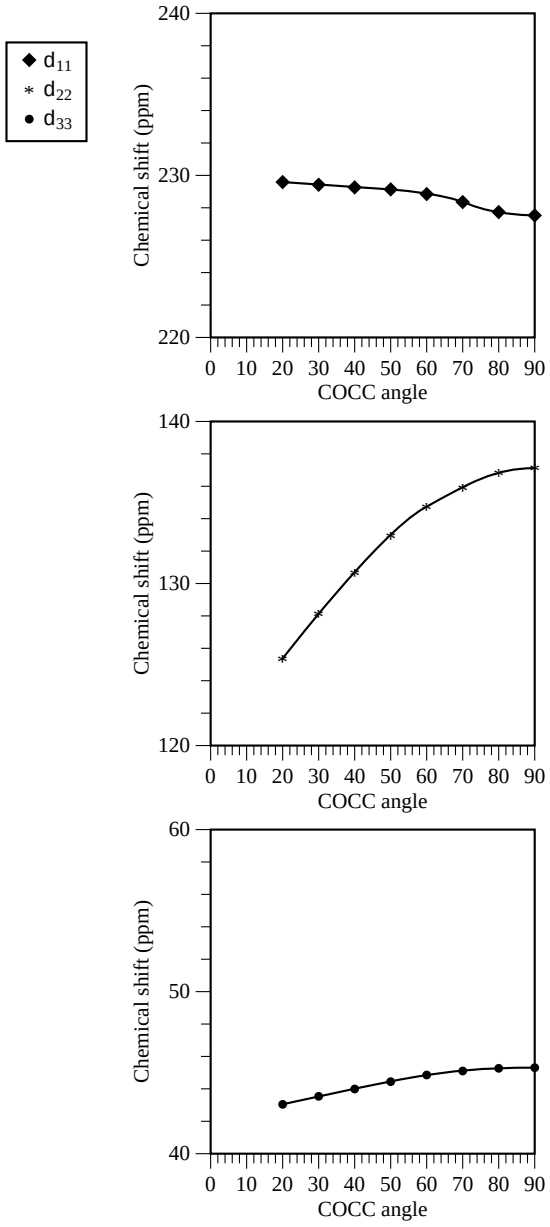

Figure 6 Calculated angular dependence of the ^{13}C chemical shift principal components of the phenyl carbon directly attached to the oxygen ether in diphenyl ether. The angle α is the dihedral angle between ^{13}COCC as indicated in 1. The chemical shifts values are in ppm from TMS and the angle in degrees

10 CONCLUSIONS

The examples presented illustrate how important is the use of the full chemical shielding tensors in structural investigations and how the calculations of the tensors can complement the experimental measurements. In many cases calculations are mandatory to obtain information of any significance, but even in those cases in which the full tensorial data are available from experiments, the calculations provide invaluable information on the physical origins of the shielding and its relationship with the molecular structure.

We have only started using chemical shift tensor information to solve chemical and structural problems. As calculations improve, making possible the study of larger molecular systems, the use of experimental and calculated shielding information may become one of the most powerful tools available for molecular structure determination.

11 RELATED ARTICLES

Anisotropy of Shielding and Coupling in Liquid Crystalline Solutions; Carbon and Nitrogen Chemical Shifts of Solid State Enzymes; Shielding Calculations: LORG and SOLO Approaches; Chemical Shift Scales on an Absolute Basis; Chemical Shift Tensor Measurement in Solids; Chemical Shift Tensors; Chemical Shift Tensors in Single Crystals; Shielding Calculations: IGLO Method; Shielding Calculations: Perturbation Methods; Shielding: Overview of Theoretical Methods; Shielding in Small Molecules; Shielding Theory: GIAO Method.

12 REFERENCES

1. M. T. Duncan, *A Compilation of Chemical Shift Anisotropies*, The Farragut Press, Chicago, IL, 1990.
2. A. M. Orendt, J. C. Facelli, A. J. Beeler, K. Reuter, W. J. Horton, P. Cutts, D. M. Grant, and J. Michl, *J. Am. Chem. Soc*., 1988, **110**, 3385.
3. C. J. Jameson, in *Special Periodical Reports on NMR*, ed. G. A. Webb, published annually by The Royal Chemical Socity, London.
4. J. C. Facelli, A. M. Orendt, A. J. Beeler, M. S. Solum, G. Depke, K. D. Malsch, J. D. Downing, P. S. Murthy, D. M. Grant, and J. Michl, *J. Am. Chem. Soc.*, 1985, **107**, 6749.
5. P. E. Pfeffer, K. B. Hicks, M. H. Frey, S. J. Opella, and W. L. William, *J. Carbohydr. Chem.*, 1984, **3**, 197.
6. J. C. Facelli, J. Z. Hu, A. M. Orendt, A. M. Arif, R. J. Pugmire, and D. M. Grant, *J. Phys. Chem.*, 1994, **98**, 12 186.
7. C. A. Carter, D. W. Alderman, J. C. Facelli, and D. M. Grant, *J. Am. Chem. Soc*., 1987, **109**, 2639.
8. E. G. Paul and D. M. Grant, *J. Am. Chem. Soc*., 1963, **85**, 1701; A. Pross and L. Radon, *Prog. Phys. Org. Chem.*, 1977, **13**, 966.
9. C. M. Carter, J. C. Facelli, D. W. Alderman, D. M. Grant, N. K. Dalley, and B. E. Wilson, *J. Chem. Soc., Faraday Trans. 1* , 1988, **84**, 3673.
10. R. H. Contreras, R. R. Biekofsky, D. G. de Kowalewski, A. M. Orendt, and J. C. Facelli, *J. Phys. Chem.*, 1993, **97**, 91.
11. R. R. Biekofsky, A. B. Pomilio, R. H. Contreras, D. G. de Kowalewski, and J. C. Facelli, *Magn. Reson. Chem.*, 1989, **27**, 158.
12. K. W. Zilm, R. T. Colin, D. M. Grant, and J. Michl, *J. Am. Chem. Soc.*, 1980, **102**, 6672.
13. M. S. Solum, J. C. Facelli, D. M. Grant, and J. Michl, *J. Am. Chem. Soc*., 1986, **108**, 6464.
14. J. C. Facelli, D. M. Grant, and J. Michl, *Int. J. Quantum Chem.*, 1987, **31**, 45.
15. J. C. Facelli and D. M. Grant, *Nature (London)*, 1993, **365**, 325.
16. M. H. Sherwood, J. C. Facelli, D. W. Alderman, and D. M. Grant, *J. Am. Chem. Soc*., 1991, **113**, 570.
17. J. C. Facelli and D. M. Grant, *Theor. Chim. Acta*, 1987, **71**, 277.
18. J. A. Pople, *J. Chem. Phys*., 1962, **37**, **53**, 60.
19. M. J. S. Dewar and W. J. Thiel, *J. Am. Chem. Soc.*, 1977, **99**, 4899.
20. M. Schindler, *J. Am. Chem. Soc*., 1987, **109**, 1020.
21. W. Kutzelnigg, U. Fleischer, and M. Schindler, in *NMR Basic Principles and Progress*, eds. P. Diehl, E. Fluck, H. Günther, R. Kosfeld, and J. Seelig, Spinger-Verlag, Berlin Heidelberg, 1990, Vol. 23, p. 167.
22. J. C. Facelli and D. M. Grant, in *Topics in Stereochemistry*, eds. E. L. Eliel and S. H. Wilen, Wiley, New York, 1989, Vol. 19, p. 1.
23. R. J. Pugmire, A. M. Orendt, J. C. Facelli, and D. M. Grant, *Proc. Int. Conf. Coal Sci., Newcastle-upon-Tyne, UK, 1991* , p. 72.

Biographical Sketch

Julio C. Facelli. *b* 1953. Licenciado in Physics, 1977 and Doctor in Physics, 1981, University of Buenos Aires, Argentina. Postdoctoral work at the University of Arizona 1983–84. University of Utah 1984–present. Approx. 80 publications. Current research interests; quantum chemical calculations of NMR parameters, relationships between NMR parameters and molecular structure and large scale scientific computing.

Shielding Theory: GIAO Method

Peter Pulay and James F. Hinton
University of Arkansas, Fayetteville, AR, USA

1	Introduction	1
2	The Gauge Problem and the Definition of GIAOs	1
3	Molecular Orbital Theory with GIAOs	2
4	Applications of the GIAO Method	4
5	Related Articles	5
6	References	5

1 INTRODUCTION

The gauge-including atomic orbital (GIAO) method is a quantum mechanical technique for the calculation of magnetic properties of chemical systems. It is one of the main methods to solve the so-called gauge problem. In its simplest form, the latter is the unphysical dependence of the calculated results on the arbitrary gauge of the vector potential—in particular, the dependence on the position of the molecule if magnetic fields are present. In the GIAO method, the atomic basis functions depend explicitly on the magnetic field, canceling the gauge dependence of the results. Such basis functions were first used by London[1] to explain magnetic susceptibilities. They were introduced in modern electronic structure theory by Hameka[2] and Pople.[3,4] Hameka[2,5] also performed the first ab initio NMR shielding calculations using GIAOs, and coined the name 'gauge-independent atomic orbital' method. The name 'gauge-including atomic orbital' method is the usual one in the modern literature, since it retains the well-known GIAO acronym but it is more accurate. Some authors use the term 'London atomic orbitals' (LAOs) instead. GIAOs were first used in modern ab initio self-consistent field (SCF) perturbation theory by Ditchfield,[6] who, with Ellis,[7] performed the first applications to polyatomic molecules. Their early review is an excellent overview of the subject.[8]

As explained in more detail in the next section, the origin of the gauge problem is the truncation of the atomic orbital (AO) set used to describe the molecular orbitals (MOs). The perturbation caused by a homogeneous magnetic field B_z in the z direction is proportional to $B_z\hat{l}_z$, where $\hat{l}_z$ is the z component of the angular momentum operator. The latter is not invariant with respect to translations, and its effect on an atomic orbital is essentially an infinitesimal rotation of the orbital around the z axis. If the center of the orbital lies on the z axis, the perturbation leaves it either invariant (for an s orbital) or transforms it to another member of a degenerate set (e.g. p_x to p_y). However, for atomic orbitals centered far from the z axis, the (necessarily limited) AO basis set is usually not flexible enough to provide a satisfactory description of the perturbed wavefunction. This results in a progressively worsening description for atoms situated far from the origin, and is of course particularly serious for large molecules, which can now be treated with ab initio molecular orbital methods.

The most straightforward solution of this problem is to introduce a dependence in the atomic orbitals so that they provide the correct first-order solution to the atomic problem in a homogeneous magnetic field, irrespective of the position of the atom. This leads to the multiplication of the atomic orbitals by a complex exponential factor (*gauge factor*) that depends on the magnetic field, as well as the center coordinates of the AO and the Cartesian coordinates of the electron. Such a field-dependent basis set makes the evaluation of the dependence of the energy and wavefunction on the perturbation more complex, and also more expensive, compared with a fixed AO basis calculation of the same dimension. However, it allows the use of much smaller basis sets, and thus ultimately results in large savings. There are other techniques that restore gauge invariance. The most important of these [IGLO,[9] independent gauge for localized orbitals (***Shielding Calculations: IGLO Method***), and LORG,[10] localized orbital–local origin (***Shielding Calculations: IGLO Method***)] apply gauge factors not to atomic orbitals but to localized molecular orbitals. The success of IGLO, in particular, contributed much to renewed an interest in the ab initio calculation of chemical shieldings.

2 THE GAUGE PROBLEM AND THE DEFINITION OF GIAOs

According to nonrelativistic quantum theory, the momentum operator of an electron in the presence of a static magnetic field is[11,12]

$$\hat{\boldsymbol{p}} = -\mathrm{i}\hbar\nabla + e\boldsymbol{A} \tag{1}$$

where i is the imaginary unit, $\hbar$ is Planck's constant divided by 2π, $-e$ is the electron charge, ∇ is the symbolic vector of differentiation along the three spatial directions, and $\boldsymbol{A}$ is the vector potential of the electromagnetic field. [Note that we use the SI system of units; most older references use the Gaussian system, which differs not only in units but also in the dimensions and formulas, e.g. the second term on the right-hand side of equation (1) is divided by c, the speed of light, in the Gaussian system]. The vector potential $\boldsymbol{A}$ is related to the magnetic flux density $\boldsymbol{B}$ by

$$\boldsymbol{B} = \nabla \times \boldsymbol{A} \tag{2}$$

The gauge problem arises from the fact that $\boldsymbol{A}$ is not uniquely determined by $\boldsymbol{B}$. Addition of the gradient of any scalar function $f(\boldsymbol{r})$ to $\boldsymbol{A}$,

$$\boldsymbol{A}' = \boldsymbol{A} + \nabla f(\boldsymbol{r}) \tag{3}$$

leaves the flux density $\boldsymbol{B}$ and all other observable quantities unchanged, since $\nabla \times \nabla f = 0$. For homogeneous magnetic fields, the simplest choice of the vector potential is

$$\boldsymbol{A} = \tfrac{1}{2}\boldsymbol{B} \times \boldsymbol{r} \tag{4}$$

(Other choices, such as the Landau gauge[11] offer no advantage in the GIAO method). Choosing the scalar function $f = \frac{1}{2}\boldsymbol{B} \times \boldsymbol{r}_0 \cdot \boldsymbol{r}$ in equation (3) changes the vector potential to

$$\boldsymbol{A}' = \boldsymbol{A} + \nabla f = \tfrac{1}{2}\boldsymbol{B} \times (\boldsymbol{r} + \boldsymbol{r}_0) \tag{5}$$

which is equivalent to shifting the origin of the coordinate system to the new gauge origin $-\boldsymbol{r}_0$, or alternatively translating the molecule by $\boldsymbol{r}_0$ in the Cartesian frame.

It is easy to show that the gauge transformation, equation (3), does not change any observable results,[11,12] by showing that simultaneously modifying the wavefunction as

$$\Psi' = \Psi \exp\left[-\frac{\mathrm{i}e}{\hbar}\sum_i f(\boldsymbol{r}_i)\right] \tag{6}$$

transforms the Schrödinger equation, $\hat{\mathcal{H}}\Psi = E\Psi$ to

$$\hat{\mathcal{H}}'\Psi' = E\Psi' \tag{7}$$

In equations (6) and (7), $\boldsymbol{r}_i$ is the position of the ith electron and $\hat{\mathcal{H}}'$ is the Hamiltonian in the new gauge. The transformation in equation (6) does not change any observable quantities; this is trivial for any local operators, since the wavefunction is merely multiplied by a phase factor. For the simple shift in the gauge origin, equation (5), the gauge factor for electron j is

$$\exp[-\tfrac{1}{2}\mathrm{i}\boldsymbol{B}\cdot\boldsymbol{r}_0\times\boldsymbol{r}_j] \tag{8}$$

where we have switched to atomic units ($\hbar = e = 1$).

Unfortunately, the invariance of the exact wavefunction under gauge transformations does not hold for most approximate methods—in particular, for those using finite basis set expansions. To understand the origin of this phenomenon, let us consider a one-electron central field (atomic) problem perturbed by a weak homogeneous magnetic field, described by the vector potential in equation (4). Substituting equation (1) into the Hamiltonian and changing to atomic units shows that the first-order perturbation is $\boldsymbol{B}\cdot\hat{\boldsymbol{l}}$, where $\hat{\boldsymbol{l}} = \boldsymbol{r}\times\hat{p} = -\mathrm{i}\hbar\boldsymbol{r}\times\nabla$ is the angular momentum operator. Only the first-order term, linear in $\boldsymbol{B}$, is needed for chemical shielding calculations. If the center (atom) is placed at the origin, the wavefunction can be chosen as an eigenfunction of the angular momentum operator, and therefore it remains an exact solution (to first order) in the presence of the magnetic field. If the atom is shifted to $\boldsymbol{r}_0$, the correct first-order wavefunction is simply the unperturbed wavefunction multiplied by the gauge factor in equation (8). For a field in the z direction, the first-order wavefunction can be approximately visualized as a rotation around the imaginary z axis. A finite basis set usually lacks the polarization functions needed to describe this rotation, leading to results that deteriorate as the atom moves away from the origin. This is only a cosmetic problem for atoms that have a natural gauge origin, but becomes acute in molecules, particularly large ones, since most atoms are necessarily far from the origin.

The most straightforward way to solve the gauge problem is to modify the atomic basis functions so that they remain the correct first-order eigenfunctions of the central field Hamiltonian for arbitrary positions in the presence of the field.[1] Such basis functions describe correctly a set of noninteracting atoms, and give greatly improved results for molecules, besides restoring translational invariance. The gauge-including atomic orbitals are defined, according to equation (8), as

$$\chi_p(\boldsymbol{B}) = \chi_p(0)\exp[-\tfrac{1}{2}\mathrm{i}\boldsymbol{B}\cdot\boldsymbol{R}_p\times\boldsymbol{r}_i] \tag{9}$$

where $\chi_p(0)$ is an unperturbed atomic basis function and $\boldsymbol{R}_p$ is its center.

Integrals over GIAO basis functions are not origin-independent: a two-center integral (e.g. the overlap $\langle\chi_p|\chi_q\rangle$) is multiplied by the factor $\exp[-\frac{1}{2}\mathrm{i}\ \boldsymbol{B}\times(\boldsymbol{R}_p - \boldsymbol{R}_q)\cdot\boldsymbol{d}]$ if the molecule moved by $\boldsymbol{d}$ in the Cartesian frame. Amos and Roberts,[13] following London,[1] gave a simple proof of the translational invariance of the observables calculated from GIAO-based wavefunctions. The essence of this proof is that a simultaneous transformation of the molecular orbital coefficients C_{pi} to $C_{pi}\exp(\frac{1}{2}\mathrm{i}\ \boldsymbol{B}\cdot\boldsymbol{R}_p\times\boldsymbol{d})$ cancels the translation dependence of the integrals and leaves all observable quantities invariant.

The position of the nucleus is the only natural choice for the gauge origin of the field generated by its magnetic dipole. As the dipole field diminishes rapidly (as r^{-3}) with distance, it is not necessary to consider alternative gauges.

For the widely used Gaussian-type basis functions (and also for Slater-type orbitals), the gauge factor can be formally absorbed into the coordinates of the center of the atomic orbital.[14] The latter become field-dependent complex numbers. The advantage of such a viewpoint is that it emphasizes the analogy with the analytical derivative theory of potential surfaces.[15] In spite of the difference in the physics, the mathematical descriptions are similar, the main difference being that the basis function centers remain real as they follow the nuclei in potential surface calculations, but they become complex in the presence of magnetic fields. Thus many of the highly developed techniques of analytical derivative theory can be used in GIAO calculations of magnetic properties.[16]

3 MOLECULAR ORBITAL THEORY WITH GIAOs

In this section, we shall consider ab initio (nonempirical) results only, since semiempirical methods have only been qualitatively successful.[8] The magnetic shielding of a nucleus can be formally defined as the second derivative of the molecular energy with respect to the external magnetic field and the magnetic dipole moment of the nucleus. This is a dimensionless quantity with nine components, but usually only the six components of its symmetric part are accessible, and in nonoriented samples only the average of the diagonal elements is observed. The formal definition above is equivalent to the intuitive model in which the shielding is interpreted as the fractional change of the external magnetic field at the nuclear position due to induced currents in the molecule.

We begin with the most fundamental and widely used self-consistent field (SCF) approximation with a finite basis set. It is sufficient to consider only closed shell SCF theory, since this applies to the vast majority of molecules of interest in NMR. In the following formulas, we use superscripts for derivative quantities, the first of which corresponds to differentiation with respect to the external field, and the second (if present) to the nuclear magnetic moment.[6,8] The subscript of the magnetic nucleus in question is not shown explicitly. Significant simplification is provided by the fact that only E_1, the one-electron part of the total energy, depends on the nuclear magnetic moment. Thus the chemical shielding becomes, in the finite-basis closed shell SCF case,

$$\sigma^{ab} = \frac{\partial^2 E_1}{\partial B_a \partial \mu_b} = \mathrm{Tr}[\mathbf{D}\mathbf{h}^{ab}] + \mathrm{Tr}[\mathbf{D}^a\mathbf{h}^{0b}] \tag{10}$$

where σ is the chemical shielding, a and b are the x, y, z spatial directions, E_1 is the one-electron part of the total SCF energy, Tr stands for the trace of a matrix, $\mathbf{h}$ is the matrix of the one-electron operator (the sum of the kinetic energy and nuclear attraction) in the AO basis, $\mathbf{D}$ is the first-order reduced density matrix, $D_{pq} = 2\Sigma_i\, C_{pi}C_{qi}$, C_{pi} and C_{qi} are molecular orbital coefficients, p and q are AO indices, and i is an occupied MO. Equation (10) is simpler than the general SCF second-derivative formula (see, e.g. Pulay[15]), because the basis functions are independent of the second perturbation (with respect to the nuclear dipole moment). The evaluation of the derivative one-electron Hamiltonian matrix elements is simple, keeping in mind that the basis functions depend explicitly on the external magnetic field but not on the nuclear magnetic moments:

$$(\mathbf{h}^a)_{pq} = \langle p|\hat{h}^a|q\rangle + \langle p^a|\hat{h}|q\rangle + \langle p|\hat{h}|q^a\rangle \tag{11}$$

$$(\mathbf{h}^{0b})_{pq} = \langle p|\hat{h}^{0b}|q\rangle \tag{12}$$

$$(\mathbf{h}^{ab})_{pq} = \langle p|\hat{h}^{ab}|q\rangle + \langle p^a|\hat{h}^{0b}|q\rangle + \langle p|\hat{h}^{0b}|q^a\rangle \tag{13}$$

Here p and q denote atomic orbitals, and the derivative operators in the above formulas are defined as

$$\hat{h}^a = -\tfrac{1}{2}\mathrm{i}\boldsymbol{r}\times\boldsymbol{\nabla} \tag{14}$$

$$\hat{h}^{0b} = -\mathrm{i}\alpha^2\frac{[(\boldsymbol{r}-\boldsymbol{R})\times\boldsymbol{\nabla}]_b}{|\boldsymbol{r}-\boldsymbol{R}|^3} \tag{15}$$

$$\hat{h}^{ba} = \frac{\alpha^2}{2}\frac{\boldsymbol{r}\cdot(\boldsymbol{r}-\boldsymbol{R})\delta_{\mathrm{ab}} - r_a(\boldsymbol{r}-\boldsymbol{R})_b}{|\boldsymbol{r}-\boldsymbol{R}|^3} \tag{16}$$

with $\boldsymbol{R}$ denoting the position of the magnetic nucleus and α denoting the fine structure constant, i.e. the inverse velocity of light in atomic units ($\alpha \approx 1/137.035\,989$). Equations (15) and (16) follow from the vector potential of the magnetic dipole at the origin (e.g., see, Atkins[17]),

$$\boldsymbol{A} = \frac{\mu_0}{4\pi}\frac{\boldsymbol{m}\times\boldsymbol{r}}{r^3} \tag{17}$$

after converting to atomic units ($\alpha^2 = \mu_0 e^2/4\pi m_e a_0$, where μ_0 is the vacuum permeability).

The first-order perturbed density matrix $\mathbf{D}^a$ needed to evaluate the shielding tensor in equation (10) can be obtained from the solution of the coupled perturbed Hartree–Fock (CPHF) equations. The GIAO case differs from the simpler theory with perturbation-independent basis functions[18] in that all AO integrals have nonvanishing derivatives with respect to the magnetic field. Hartree–Fock perturbation theory for nuclear coordinates[19] is, however, analogous to the GIAO case, and can be used with little change.[6] The most compact and computationally efficient way is to use a density-matrix-based AO formulation.[16] Starting with the derivative of the Hartree–Fock equations, we can express the first-order derivative density matrix as

$$\mathbf{D}^a = -\tfrac{1}{2}\mathbf{D}\mathbf{S}^a\mathbf{D} + \sum_{iv}(\varepsilon_i-\varepsilon_v)^{-1}\mathbf{C}_i^\dagger(\mathbf{F}^a-\varepsilon_i\mathbf{S}^a)\mathbf{C}_v(\mathbf{C}_i\mathbf{C}_v^\dagger - \mathbf{C}_v\mathbf{C}_i^\dagger) \tag{18}$$

where the superscript a denotes differentiation with respect to $\boldsymbol{B}_a$, $\mathbf{S}$ is the AO overlap matrix, $\mathbf{F}$ is the Fock matrix, and $\mathbf{C}_i$ and $\mathbf{C}_v$ are column vectors of occupied and virtual orbital coefficients, respectively. Equation (18) must be solved iteratively, because the first-order Fock matrix $\mathbf{F}^a$ depends on $\mathbf{D}^a$:

$$(\mathbf{F}^a)_{pq} = (\mathbf{h}^a)_{pq} + \sum_{rs}[(\mathbf{D}^a)_{rs}g_{pqrs} + (\mathbf{D})_{rs}g^a_{pqrs}] \tag{19}$$

Here $g_{pqrs} = (pq|rs) - \frac{1}{2}(ps|qr)$ is an unperturbed two-electron integral, and g^a is its derivative (due to the gauge factors) with respect to the field component a. The strategy to solve equations (18) and (19) efficiently has been discussed in detail.[16] The most demanding computational task is the calculation of the two-electron integrals g and g^a and their contraction with the density matrix. (An alternative formulation that interchanges the roles of the two perturbations is not viable in most cases, because there are only three external field directions but $3N$ nuclear magnetic moments.)

Using direct SCF techniques,[20] i.e. by not storing but recalculating the AO integrals, the size of the molecules that can be calculated is limited only by computer time. The most impressive calculation so far is perhaps the evaluation of the chemical shifts in several isomers of C_{84}, using good quality (triple-zeta plus polarization) basis sets[21] containing 1596 atomic basis functions.

It is useful to decompose the total shielding into diamagnetic and paramagnetic contributions, though this is not a unique procedure and different authors propose different decomposition schemes. The most common decomposition designates the first term on the right-hand side of equation (10) as the diamagnetic term and the second as the paramagnetic one. In an alternative decomposition, the contribution from the first term in equation (18) is counted as diamagnetic. Essentially all of the problems in calculating shielding constants arise from the paramagnetic contribution. For an atom at the origin, the diamagnetic contribution, say the zz component, is given, according to equations (10), (13), and (16), as the expectation value of the operator $\frac{1}{2}\alpha^2(r^2 - z^2)/r^3$, and thus the isotropic average is the expectation value of $\frac{1}{3}\alpha^2 r^{-1}$. As this is essentially the electron–nucleus attraction energy, it is very accurate (even with mediocre basis sets) and stable.

The equations above are quite different from the sum over excited states in the Ramsey equation. The latter, although the main conceptual tool for understanding NMR shieldings, is not advantageous for numerical calculations—mainly because it requires that all the excited states of the unperturbed system be known exactly. This is not the case in ab initio theory, and the summary effect of the excited states, hidden in the iterative equations (17) and (18), can be evaluated at much less cost than the sum over excited states.

SCF calculations, although quite successful, particularly for relative shifts, still suffer from the neglect of correlation. In order to achieve higher accuracy, electron correlation must

be included in the wavefunction. The best way of doing this depends on the electronic structure of the system. If correlation effects are not dominant, second-order perturbation Møller–Plesset perturbation theory (MP2) serves as a relatively inexpensive and well-defined technique. NMR chemical shieldings with GIAOs at the MP2 level have been formulated and implemented recently by Gauss.[22] The theory is too complex to include here, but the method is practical and improves significantly upon the SCF results in difficult cases. Applicability of the MP2 method is limited at present by the substantially increased computational and storage requirements compared with the SCF method. It is likely that this method will be extended soon to higher orders of Møller–Plesset perturbation theory, and to coupled cluster wavefunctions, yielding very accurate results, although at considerable computational cost.

For very strongly correlated systems, like F_2 or ozone, the MP2 method fails. These systems require a genuine multiconfigurational description. An alternative method, very successful for other ground state properties, is to use modern density functional theory. No GIAO results were available at the time of writing, but the prospects appear promising.

Although methods that place the gauge factors not on atomic orbitals but on localized molecular orbitals (IGLO[9] and LORG[10]) have been very successful—and, in principle (though not so far in practice), they should be more efficient—the GIAO method has certain advantages over them. First, there is evidence that GIAO calculations require somewhat smaller basis sets than IGLO for the same accuracy.[16] Second, localization of molecular orbitals is not always unique, and some systems are genuinely delocalized. In such cases, localized theories may have somewhat ill-defined results. Third, although localized theories can also deal with electron correlation, it is more straightforward to include correlation in the GIAO approach.

4 APPLICATIONS OF THE GIAO METHOD

In this section, some selected chemical applications of GIAO calculations of NMR shieldings are summarized, mostly at the SCF level. Calculations have been performed with a variety of nuclei (e.g. ^{1}H, ^{13}C, ^{15}N, ^{17}O, ^{19}F, ^{29}Si, ^{31}P, and ^{33}S) using the GIAO approach. We begin with a brief discussion of the comparison between experiment and theory. The definitive test of the accuracy of the chemical shift calculations is the determination of absolute chemical shieldings. Two main factors limit the accuracy of this comparison: environmental effects and nuclear motion. Most calculations are performed on isolated molecules at the equilibrium geometry. Absolute shieldings from gas phase measurements are largely free of environmental effects, but vibrational averaging effects remain, even at absolute zero. In the absence of experimental absolute chemical shieldings, the chemical shift anisotropy of the shielding tensor is the next best parameter to use for a comparison of theory and experiment. This parameter does not require referencing or bulk susceptibility corrections. The principal components of the chemical shielding tensor are generally obtained from solid state NMR measurements, preferably with the solid at very low temperature to minimize contributions from molecular motion. In this case, however, environmental effects, unless included in the calculations, may be significant. Vibrational (temperature) and environmental effects also influence chemical shifts, although some cancellation of these is to be expected for chemically and structurally similar atoms. It is also possible to obtain a fortuitously accurate isotropic shielding value when the errors in the components of the shielding tensor cancel.

NMR chemical shieldings are often sensitive functions of the molecular geometry, and therefore accurate chemical shieldings require good geometries. The main problem with using experimental geometries is that their accuracy is randomly varying, depending on the method used and the molecule itself. Theoretical values, although their absolute accuracy is often not better, provide much more homogeneous data if a single method and basis set is used throughout. The accuracy of relative chemical shifts often improves significantly if accurate computed geometries are substituted for experimental ones.[23]

The chemical shift anisotropy of the hydrogen atom in the water cluster $(H_2O)_{17}$ has been calculated to determine the efficiency and accuracy of the GIAO method applied to relatively large molecular systems.[24] Experimental NMR measurements have been made on ice at very low temperatures, 173–195 K, to determine the chemical shift anisotropy of the hydrogen atom.[25–27] However, significantly different values of the chemical shift anisotropy (28.7 ± 1, 28.5 ± 1, 34 ± 4, and 34.2 ± 1 ppm) were obtained. The chemical shielding anisotropy of the hydrogen atom in the central water molecule of the $(H_2O)_{17}$ cluster was calculated to be 35.17 ppm (a 6-311G + 1p + 1d basis set was used for all atoms) and 34.83 ppm (a 6-311G + 1p + 1d basis set was used for the central water molecule and the 4 molecules in the first hydration sphere, and a 4-31G basis set was used for the remaining 12 water molecules in the second hydration sphere). The results of the calculations support the higher experimental values. This study of ice, modeled with the $(H_2O)_{17}$ cluster, $(H_2O)_5$ cluster, and H_2O, showed the potential importance of considering solvent (i.e. environmental) effects in performing chemical shift calculations.

There is a potential problem that one should be aware of in the use of the GIAO technique to calculate ^{1}H chemical shifts. Although the calculation of ^{1}H chemical shifts is perhaps the easiest to perform, because the number of electrons is the smallest of any atom, the chemical shift range of ^{1}H is concomitantly the smallest. Consequently, variation in the calculated results may not be sufficient to distinguish between protons in similar chemical environments. Another problem is that protons are usually located at the periphery of the molecule, and are sensitive to intermolecular interactions.

The application of the GIAO method to the study of the very important ^{13}C chemical shifts was illustrated in the mid-1970s in the review by Ditchfield and Ellis.[8] A recent GIAO SCF study of the chemical shifts in a number of hydrocarbons yielded good agreement with experiment.[28] Calculations of the dihedral angle-dependent shieldings for *n*-octane reproduced the *γ-gauche* effect to within about 3 ppm.[29] Carbon-13 chemical shielding tensors in sugars have been measured experimentally by solid state NMR studies of single crystals and calculated using the GIAO method.[30] The theoretical results were found to be of sufficient accuracy to aid in making the assignments of resonances arising from very similar carbon atoms. The correlation between theoretical and experimental results suggests that subtle structural features can be addressed with an accuracy comparable to that obtained

with X-ray and neutron diffraction techniques. A similar study of crystalline naphthalene suggests that the use of solid state NMR together with GIAO calculations of ^{13}C chemical shifts can be used to refine structural parameters obtained from diffraction methods.[31] The calculation of ^{13}C chemical shifts was used recently to verify the photolysis product of 7-oxo[2.2.1]hericene.[32]

The principal components of the chemical shielding tensor in the imine moiety of benzylideneaniline and all-*trans*-retinylidenebutylimine have been calculated with the GIAO method.[33] The theoretical results for ^{13}C and ^{15}N were found to be in good agreement with solid state NMR measurements. The GIAO method has been used to calculate the chemical shift tensors of oxygen, carbon, nitrogen, and hydrogen in a study of the hydration of a dipeptide, glycylglycine.[34] It was found that while the orientation of the shift tensors for oxygen, carbon, and nitrogen is affected very little by hydration, the change of the amide proton tensor is significant and appears to follow the orientation of the local hydrogen bonding of water. Perhaps the most elegant and far-reaching application of the GIAO method has been that of Oldfield, in which ^{1}H, ^{13}C, ^{15}N, and ^{19}F chemical shifts were calculated for proteins and used to analyze the secondary and tertiary structure of proteins and to probe protein electrostatics.[35] These results strongly suggest that calculated chemical shifts may provide a new method for structure refinement of proteins.

The chemical shielding parameters for the ^{29}Si nucleus in a variety of compounds have been calculated using the GIAO method.[36] Molecules were chosen for study for which low-temperature solid state NMR spectroscopy had been used to obtain the chemical shielding parameters. Again, good agreement was achieved between the theoretical and experimental values.

The chemical shielding tensor for ^{31}P in phosphine PH_3, has been calculated using the GIAO method[37] at both the SCF and the MP2 levels. Large basis sets and the inclusion of electron correlation were necessary to obtain accurate results, particularly for the absolute shielding. This illustrates the fact that it is much more difficult to calculate accurate results for atoms with lone pairs than, for example, carbon. The NMR shielding depends sensitively on the hybridization of the lone pair, and minor inaccuracies in the hybridization may result in significant errors in the chemical shielding.

Calculated ^{31}P chemical shifts have been used as part of a study of the pH, temperature, and concentration dependences of the chemical shifts in disodium hydrogen phosphite and disodium fluorophosphate solutions.[38] The experimental and theoretical results suggest that changes in pH and temperature cause changes in the average PF, PH, and PO bond distances, which lead to changes in the NMR parameters. Sulfur-33 chemical shifts for carbon disulfide, dimethyl sulfide, dimethyl sulfoxide, dimethyl sulfone, and sulfate and thiosulfate ions have been calculated.[16]

An impressive chemical application of the GIAO method is the confirmation of the existence and structure of stable Al–I compounds.[39]

5 RELATED ARTICLES

Shielding Calculations: LORG and SOLO Approaches; Chemical Shift Scales on an Absolute Basis; Chemical Shift Tensors; Semiempirical Chemical Shift Calculations; Shielding Calculations: IGLO Method; Shielding Calculations: Perturbation Methods; Shielding: Overview of Theoretical Methods; Shielding in Small Molecules; Shielding Tensor Calculations.

6 REFERENCES

1. F. London, *J. Phys. Radium*, 1937, **8**, 397.
2. H. F. Hameka, *Mol. Phys.*, 1958, **1**, 203.
3. J. A. Pople, *Mol. Phys.*, 1958, **1**, 175.
4. J. A. Pople, *Discuss. Faraday Soc.*, 1962, **34**, 7.
5. D. Zeroka and H. F. Hameka, *J. Chem. Phys.*, 1966, **45**, 300.
6. R. Ditchfield, *J. Chem. Phys.*, 1972, **56**, 5688.
7. R. Ditchfield and P. D. Ellis, *Chem. Phys. Lett.*, 1972, **17**, 342.
8. R. Ditchfield and P. D. Ellis, in *Topics in Carbon-13 NMR Spectroscopy*, ed. G. C. Levy, Wiley, New York, 1974, Vol. 1, Chap. 1
9. M. Schindler and W. Kutzelnigg, *J. Chem. Phys.*, 1982, **76**, 1919.
10. A. E. Hansen and T. D. Bouman, *J. Chem. Phys.* 1985, **82**, 5035.
11. L. D. Landau and E. M. Lifshitz, *Quantum Mechanics, (Non-Relativistic Theory)*, Pergamon Press, London, 1958, Chap. 16
12. H. F. Hameka, *Advanced Quantum Chemistry*, Addison-Wesley, Reading, MA, 1965, p. 157.
13. A. T. Amos and H. G. Ff. Roberts, *J. Chem. Phys.*, 1969, **50**, 2375.
14. G. G. Hall, *Int. J. Quantum Chem.*, 1973, **7**, 15.
15. P. Pulay, in *Advances in Chemical Physics*, ed. K. P. Lawley, Wiley, New York, 1987, Vol. 69, p. 241.
16. K. Wolinski, J. F. Hinton, and P. Pulay, *J. Am. Chem. Soc.*, 1990, **112**, 8251.
17. P. W. Atkins, *Molecular Quantum Mechanics*, 2nd edn., Oxford University Press, Oxford, 1983, Chap. 14
18. R. M. Stevens, R. M. Pitzer, and W. N. Lipscomb, *J. Chem. Phys.*, 1963, **38**, 550.
19. S. Bratoz, *Colloq. Int. CNRS*, 1958, **82**, 287; J. Gerratt and I. M. Mills, *J. Chem. Phys.*, 1968, **49**, 1719.
20. J. Almlöf, K. Faegri, Jr., and K. Korsell, *J. Comp. Chem.*, 1982, **3**, 385.
21. U. Schneider, S. Richard, M. M. Kappes, and R. Ahlrichs, *Chem. Phys. Lett.* 1993, **210**, 165.
22. J. Gauss, *Chem. Phys. Lett.*, 1992, **191**, 614.
23. M. Bühl and P. v. R. Schleyer, *J. Am. Chem. Soc.* 1992, **114**, 477.
24. J. F. Hinton, P. Guthrie, P. Pulay, and K. Wolinski, *J. Am. Chem. Soc.*, 1992, **114**, 1604.
25. W. K. Rhim and D. P. Burum, *J. Chem. Phys.*, 1979, **71**, 3139.
26. A. Pines, D. J. Ruben, S. Vegga, and M. Mehring, *Phys. Rev. Lett.*, 1976, **36**, 110.
27. L. M. Ryan, R. C. Wilson, and B. C. Gerstein, *Chem. Phys. Lett.* 1977, **52**, 341.
28. H. Kurosu, G. A. Webb, and I. Ando, *Magn. Reson. Chem.*, 1992, **30**, 1122.
29. H. Kurosu, I. Ando, and G. A. Webb, *Magn. Reson. Chem.*, 1993, **31**, 399.
30. D. M. Grant, J. C. Facelli, D. W. Alderman, and M. H. Sherwood, in *Nuclear Magnetic Shieldings and Molecular Structure*, ed. J. A. Tossell, Kluwer, Dordrecht, 1993, p. 367.
31. J. C. Facelli and D. M. Grant, *Nature (London)*, 1993, **365**, 325.

32. R. Liu, X. Zhou, and J. F. Hinton, *J. Am. Chem. Soc.*, 1992, **114**, 6925.
33. J. F. Hinton, P. L. Guthrie, P. Pulay, K. Wolinski, and G. Fogarasi, *J. Magn. Res.*, 1992, **96**, 154.
34. D. B. Chesnut and C. G. Phung, in *Nuclear Magnetic Shielding and Molecular Structure*, ed. J. A. Tossell, Kluwer, Dordrecht, 1993, p. 221.
35. A. C. de Dios, J. G. Pearson, and E. Oldfield, *Science (Washington, DC)*, 1993, **260**, 1491; J. F. Hinton, P. L. Guthrie, P. Pulay, and K. Wolinski, *J. Magn. Reson.*, 1993, **103**, 188.
36. J. F. Hinton, P. Guthrie, P. Pulay, and K. Wolinski, *J. Magn. Res., Ser. A*, 1993, **103**, 188.
37. K. Wolinski, C.-L. Hsu, J. F. Hinton, and P. Pulay, *J. Chem. Phys.*, 1993, **99**, 7819.
38. T. C. Farrar, J. L. Schwartz, and S. Rodriguez, *J. Phys. Chem.*, 1993, **97**, 7201.
39. J. Gauss, U. Schneider, R. Ahlrichs, C. Dohmeier, and H. Schnöckel, *J. Am. Chem. Soc.*, 1993, **115**, 2402.

Biographical Sketches

Peter Pulay. *b* 1941. Diploma 1963 chemistry, Eötvös University, Budapest; Ph.D., 1970, chemistry, University of Stuttgart (supervisors Heinzwerner Preuss and Josef Goubeau). Research fellow and later associate professor, Eötvös University, Budapest. Department of Chemistry, University of Arkansas, 1982–present. Currently Roger B. Bost Professor of Chemistry. Approx. 150 publications. Research specialties: electronic structure theory, ab initio analytical derivatives, infrared and Raman spectroscopy, magnetic properties of molecules.

James F. Hinton. *b* 1938. B.S. chemistry 1960, University of Alabama; Ph.D., 1964, University of Georgia (supervisor F. J. Johnston). Department of Chemistry, University of Arkansas, 1965–present. Currently University Professor of Chemistry. Approx. 120 publications. Research specialties: application of NMR spectroscopy to the study of biological channels, ^{205}Tl NMR spectroscopy, magnetization inversion transfer applications to cation transport through channels, ab initio calculations of NMR shifts.

Solid Polymers: Shielding and Electronic States

Takeshi Yamanobe
Gunma University, Kiryu, Gunma, Japan
and
Hiromichi Kurosu
Tokyo Institute of Technology, Ookayama, Meguro-ku, Tokyo, Japan

1 Introduction 1
2 Theoretical Aspects of Electronic State and Nuclear Shielding in Solid Polymers 1
3 Interpretation of Nuclear Shielding by the TB Method 2
4 Related Articles 6
5 References 6

1 INTRODUCTION

Nuclear shielding data offer microscopic information about the stereochemical and crystal structures of polymers, which in turn are important factors in understanding physical properties. Details of electronic structure can also be deduced from nuclear shielding data, and this is also important in controlling physical properties.[1] In order to obtain information about the electronic structure of polymers from nuclear shielding data, it is necessary to use a theoretical approach in addition to an experimental one.

In general, there are two possibilities for obtaining such information by theoretical methods. One is to use a fragment of polymer such as a dimer, trimer, etc. for theoretical calculations. Such an approach is useful, because the nuclear shielding is sometimes governed by the local electronic structure. However, there is doubt whether the electronic structure obtained from the model compound appropriately reproduces that of the polymer chain. Another approach is to employ directly an infinite polymer chain with a periodic structure. This leads to the application of the tight-binding (TB) molecular orbital approximation, which was developed in the field of solid state physics.[2] Its advantages are that it treats the polymer directly and that relatively long range intrachain interactions such as hydrogen bonding in the α-helix form of polypeptides can be easily taken into account.

In using the model compound approach, the electronic structure of large chains can be visualized by drawing the orbital energies associated with chains of increasing length. On the other hand, for an infinite polymer chain, the energy levels are built up as a continuous band structure. As the rotation about the bond is strongly restricted in solid polymers, the periodicity of the polymer chain is retained. From the point of view of calculating nuclear shielding, use of the TB model for calculations of the electronic structures of polymers has been successful. Here we describe the basic ideas for deducing the electronic structure and nuclear shielding of solid polymers by the TB approximation.

2 THEORETICAL ASPECTS OF ELECTRONIC STATE AND NUCLEAR SHIELDING IN SOLID POLYMERS

Polymers can be characterized by a possible periodicity in their conformational structure and a large number of electrons. In this system, the potential energy that an electron experiences is periodic. Periodic systems have the advantage of translational symmetry when compared with aperiodic systems. It is possible to exploit this symmetry in order to reduce to reasonable proportions the formidable task of computing the electronic states of an extended system. The TB molecular orbital model is employed to describe the electronic structure of linear periodic polymers within the framework of a 'linear combination of atomic orbitals' approximation for electronic eigenfunctions. By means of Bloch's theory,[3] the eigenfunction $\Phi_n(k)$ for an electron at position r, belonging to the nth crystal orbital is given by

$$\Phi_n(k) = N^{-1/2} \sum_{j=-(N-1)/2}^{(N-1)/2} \sum_{\nu=1}^{s} \mathrm{e}^{\mathrm{i}jkb} C_{\nu n}(k) \phi_\nu(r - jb) \tag{1}$$

where k is the wavenumber, ν is an orbital index for the jth cell, s is the total number of atomic orbitals in a given cell, N is the total number of cells considered, and b is the unit vector of translational symmetry. In equation (1) $\phi_\nu(r - jb)$ represents the νth atomic orbital in the jth cell and $C_{\nu n}(k)$ its expansion coefficient in the linear combination of atomic orbitals. The limits of k, within a given Brillouin zone, are $-\frac{1}{2}\pi$ and $\frac{1}{2}\pi$. Using equation (1), the total energy E of the polymer can be expressed as

$$E(k) = \sum_{n}^{\mathrm{occ}} \langle \Psi_n(k) | \hat{\mathcal{H}} | \Psi_n(k) \rangle \tag{2}$$

where $\Psi_n(k)$ is the Slater determinant composed of the $\Phi_n(k)$. $\hat{\mathcal{H}}$ is the Hamiltonian, consisting of terms representing the kinetic energy, the potential energy of the electronic field of the polymer, and the electron repulsion energy. The advantage of equation (1) is that calculation of the electronic structure of an infinite polymer can be reduced to the calculation for a unit cell (monomer unit) interacting with all other unit cells, using the periodicity of the polymer.

In general, calculations on small molecules using ab initio MO methods can provide very satisfactory estimates of nuclear shielding.[1] For larger monomeric species, semiempirical molecular orbital calculations such as CNDO/2 and INDO/S are still the workhorses. The diagonal and off-diagonal elements of the Fock matrix, $F_{\mu\mu}$ and $F_{\mu\mu'}$, respectively, based on CNDO/2, are expressed as follows:

$$\begin{aligned} F_{\mu\mu}(k) = {} & -\tfrac{1}{2}(I_\mu + A_\mu) + \tfrac{1}{2}(1 - P_{\mu\mu})\gamma_{\mathrm{AA}}^{00} \\ & + \sum_{\mathrm{B}} \sum_{j=-M}^{M} (P_{\mathrm{B}} - Z_{\mathrm{B}})\gamma_{\mathrm{AB}}^{0j} \\ & + 2K_\pi \beta_{\mathrm{A}} \sum_{j=1}^{M} S_{\mu\mu}^{0j} \cos kj - \sum_{j=1}^{M} \gamma_{\mathrm{AA}}^{0j} P_{\mu\mu}^{-jR} \cos kj \end{aligned} \tag{3}$$

$$\begin{aligned} F_{\mu\mu'}(k) = {} & \tfrac{1}{2} K_\pi (\beta_{\mathrm{A}} + \beta_{\mathrm{B}}) \sum_{j=-M}^{M} S_{\mu\mu'}^{0j} \mathrm{e}^{\mathrm{i}kj} \\ & - \tfrac{1}{2} \sum_{j=-M}^{M} P_{\mu'\mu}^{-jR} \gamma_{\mathrm{AB}}^{0j} \mathrm{e}^{\mathrm{i}kj} \end{aligned} \tag{4}$$

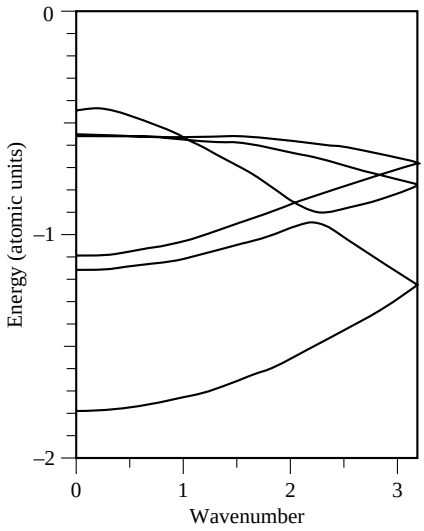

Figure 1 Electronic band structure of polyethylene with *trans* zigzag conformation calculated using CNDO/2 TB MO

where I_μ and A_μ are the ionization potential energy and electron affinity, respectively, γ_{AB} represents the Coulomb repulsion integral between the atomic orbital μ on atom A in the original cell and the atomic orbital μ' on atom B in the jth cell. $S^{0j}_{\mu\mu'}(k)$ is the overlap integral between the μth atomic orbital in the original cell and the μ'th atomic orbital in the jth cell. $P_{\mu\mu'}$ is the bond order matrix, P_B is the electron density on atom B, $P^{-jR}_{\mu'\mu}$ is the bond order matrix between the μth atomic orbital in the original cell and the μ'th atomic orbital in the $\pm j$th cell, and Z_B is the core charge of atom B. K_π is a correction factor for the $\pi-\pi$ electron interaction.[4,5]

By solving the Fock matrix defined by equations (3) and (4), the expansion coefficients in equation (1) can be obtained. These expansion coefficients and energies are dependent on k, which leads to a band structure for the polymer chain. Figure 1 shows the calculated band structure of polyethylene with a *trans* zig–zag conformation. As only six valence electrons in a monomer unit cell are included in the calculation, the corresponding six valence bands can be seen in Figure 1. Calculation with model compounds gives discrete energy levels. In a series of homogeneous molecules, the number of energy levels increases with the molecular size, and correspondingly the separation between these energy levels decreases. For an infinite polymer chain, the energy level is a continuous band structure, as shown in Figure 1. The electronic structure of solid polymers is characterized by this band structure, with a dependence of the energy level on k.

The nuclear shielding for the various nuclei in a given macromolecule can be calculated from the electronic band structure obtained, $C_{\nu n}(k)$, and $E_n(k)$. In general, the nuclear shielding can be written as[1]

$$\sigma = \sigma^{d} + \sigma^{p} + \sigma' \tag{5}$$

where σ^d and σ^p are diamagnetic and paramagnetic contributions, respectively, and σ' is the contribution from neighboring atoms. For a carbon atom, σ' is much less than 1 ppm, and can be considered negligible. Thus, σ can be estimated as the sum of σ^d and σ^p. Based on the TB MO, σ^d and σ^p are obtained by the sum-over-states method as follows:[5–7]

$$\sigma^{d}_{A}(k) = \frac{\mu_0 e^2}{6\pi m_e^2} \sum_{\nu}^{A} \sum_{\nu'}^{A} P_{\nu\nu'}(k) \langle \phi_\nu(r) | r^{-1} | \phi_{\nu'}(r) \rangle \tag{6}$$

$$\begin{aligned}\sigma^{p}_{A,\alpha\beta}(k) = -\frac{\mu_0 h^2 e^2}{4\pi m_e^2} \sum_{m}^{occ} \sum_{n}^{unocc} \sum_{j}^{A} \langle r^{-3} \rangle_{2p} ({}^1E^n_m - {}^1E_0)^{-1} \\ \times \sum_{j}^{B} \sum_{l}^{B} [X(k,j,m,n,\beta,\gamma) X(l,m,n,\gamma,\alpha) \\ - Y(j,m,n,\beta,\gamma) Y(l,n,m,\gamma,\alpha) \\ + X(j,m,n,\gamma,\alpha) X(l,n,m,\beta,\gamma) \\ - Y(j,m,n,\gamma,\alpha) Y(l,n,m,\beta,\gamma)]\end{aligned} \tag{7}$$

Here e is the charge and m_e the mass of the electron, μ_0 is the permeability of free space,

$$P_{\nu\nu'}(k) = \sum_{m}^{occ} C^*_{\nu m}(k) C_{\nu' m}(k) \tag{8}$$

where m refers to the number of occupied crystal orbitals and n to those that are unoccupied, E_0 is the electronic energy of the ground state, and E^n_m is the energy of the state created by promoting an electron from orbital m to orbital n. j and l are atomic orbitals on centers A and B, respectively, and

$$X(j,m,n,\beta,\gamma) = C^{R\beta}_{jm} C^{I\gamma}_{jn} + C^{R\beta}_{jn} C^{I\gamma}_{jm} - C^{R\gamma}_{jn} C^{I\beta}_{jm} - C^{R\gamma}_{jm} C^{I\beta}_{jn} \tag{9}$$

$$Y(j,m,n,\beta,\gamma) = C^{R\beta}_{jm} C^{R\gamma}_{jn} + C^{R\gamma}_{jn} C^{R\beta}_{jm} - C^{I\beta}_{jn} C^{I\gamma}_{jm} - C^{I\gamma}_{jm} C^{I\beta}_{jn} \tag{10}$$

where α, β, and γ refer to the x, y, and z components of the shielding tensor in cyclic order, and R and I indicate the real and imaginary parts of the coefficients $C_{\nu n}(k)$. As shown by equations (6) and (7), the nuclear shielding is calculated as a function of k. In order to be able to compare the calculated and experimental values of the nuclear shielding, it is necessary to average the calculated data over k, within the first Brillouin zone, as given by

$$\sigma = \int_{-\pi/b}^{\pi/b} \sigma(k) D(k)\, dk \tag{11}$$

where $D(k)$ is the density of states, namely, the number of states per unit amount of energy. Thus, the nuclear shielding can be obtained through the electronic band structure of polymers—especially solid polymers.

The quantities calculated using equations (6) and (7) are nuclear shieldings σ, and so the negative sign means deshielding. On the other hand, a negative sign for the observed chemical shift δ means an increase in shielding. Hereinafter, calculated and observed shieldings are expressed as shielding and chemical shift, respectively. The absolute value of the calculated shielding should be compared directly with the observed chemical shift.

3 INTERPRETATION OF NUCLEAR SHIELDING BY THE TB METHOD

The shielding of ^{13}C reflects the magnetic environment of the atom considered, and this depends on the conformation, configuration, and crystal structure of polymers. In order to understand ^{13}C shielding, examples illustrating the applications of TB MO methods to some polymers will be described.

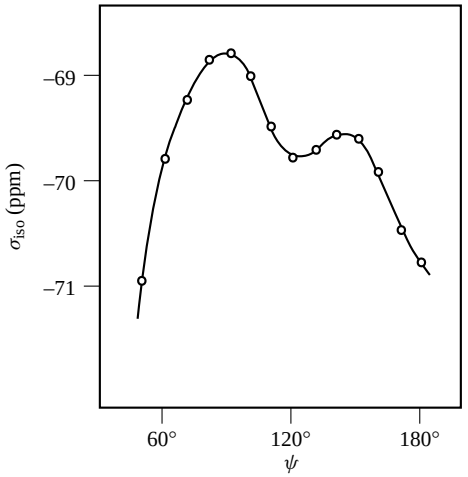

Figure 2 Dependence of the calculated ^{13}C NMR shielding of polyoxymethylene on dihedral angle ψ

3.1 Conformation

It is known from an X-ray diffraction study that a polyoxymethylene chain in the crystalline region takes an all-*gauche* conformation with a 9/5 helix.[8] However, in the noncrystalline region, the structure has not yet been determined exactly, because of the complicated conformation of the chain. It has been reported that the observed ^{13}C chemical shifts of polyoxymethylene in crystalline and noncrystalline regions appear at 88.5 and 89.5 ppm, respectively.[9] Figure 2 shows the dependence of the calculated isotropic ^{13}C shielding on the dihedral angles ψ within the framework of CNDO/2 TB MO.

The isotropic shielding of ^{13}C increases as ψ is increased from 50° to 90°, and the shielding decreases through a minimum value as ψ is increased from 90° to 180°. The values of 60° and 180° for ψ correspond to the all-*gauche* and all-*trans* conformations, respectively. The calculated isotropic ^{13}C shielding of the all-*gauche* conformation appears at lower frequency by about 1 ppm than that of the all-*trans* conformation. Dividing the difference of ^{13}C shielding between all-*gauche* and all-*trans* conformations, for the diamagnetic term, the difference between the all-*gauche* and all-*trans* conformations is 0.1 ppm, and for the paramagnetic term the corresponding difference is 0.9 ppm. The contribution to the relative ^{13}C shielding is due mainly to a change in the paramagnetic term. The diamagnetic term is determined only by the ground state, whereas the paramagnetic term involves interactions between the ground and excited states, as seen from equations (6) and (7). Thus, the observed chemical shift difference between the crystalline and noncrystalline regions comes from a variable interaction due to a conformational change. Therefore, it can be argued that the calculated value confirms well the experimental finding that the ^{13}C shielding for the crystalline region is greater by about 1 ppm than that for the noncrystalline region.

Calculated values of $\Delta\sigma$ ($= \sigma_{yy} - \sigma_{zz}$; spectrum breadth) for the all-*gauche* and all-*trans* conformations are 37.7 and 1.8 ppm, respectively. $\Delta\sigma$ for the all-*gauche* conformation is much larger than that for the all-*trans* conformation. On the other hand, the experimental values of $\Delta\delta$ for the crystalline and noncrystalline regions are about 35 ppm and 7–10 ppm, respectively.[9] The calculated and experimental values agree relatively well with each other. The fact that the calculated value of $\Delta\sigma$ for the all-*trans* conformation is rather small suggests that the electronic environment around the carbon nucleus considered here is relatively symmetric. The small observed value for $\Delta\delta$ may be due mainly to the high symmetry of the electronic environment in addition to the averaging of ^{13}C shielding anisotropy with molecular motion. Further, we are concerned with the behavior of δ_{22}, whose value is obtained from the apex of the tent-like powder pattern. In the experimental data, δ_{22} for the crystalline region appears at about 5 ppm to low frequency when compared with that for the noncrystalline region. However, the calculated value of σ_{xx} for the all-*gauche* conformation appears at lower frequency by about 2.5 ppm when compared with that for the all-*trans* conformation. Thus, the calculation explains the experimental observation reasonably, despite the rough assumption of an all-*trans* conformation for the noncrystalline region.

There has also been some interest in polypeptides. It has been demonstrated that the ^{13}C chemical shifts of C-α, C-β, and the carbonyl carbons are displaced by up to 7 ppm, depending on the particular conformations such as α-helix and β-sheet. Such conformation-dependent chemical shifts of ^{13}C can be understood through changes of the electronic band structure varying with the dihedral angles (ϕ and ψ) of the skeletal bond.

Table 1 shows the calculated and observed ^{13}C shieldings of a polyglycine chain with forms I and II.[7] The observed carbonyl ^{13}C signal for form I is shielded by about 4 ppm compared with that for form II. The calculated ^{13}C shielding for form I is larger by about 11 ppm than that for form II, which matches the experimental finding. There is no significant difference between the methylene ^{13}C chemical shifts for forms I and II within experimental error. At this stage, it cannot be determined whether the methylene shielding for form I or that for II is the larger. The calculated shielding of ^{13}C for form I is smaller by about 3 ppm than that for form II, so the calculation predicts the existence of a shielding difference (about 3 ppm) between forms I and II. It appears that the calculated shieldings are somewhat exaggerated compared

Table 1 Observed and Calculated ^{13}C Chemical Shifts and Shieldings of an Isolated Polyglycine Chain

	δ_{obs} (ppm)[a]		δ_{calc} (ppm)[b]	
	Form I	Form II	Form I	Form II
CH_2	43.5	43.5	−127.2	−124.4
C=O	168.4	172.3	−236.7	−248.1

[a]From TMS. The positive sign means deshielding.
[b]The negative sign means deshielding.

with the observed values. Nevertheless, the observed trend that the ^{13}C chemical shift difference for the methylene carbon is very small when compared with that for carbonyl carbon is reproduced qualitatively by the calculation.

3.2 Configuration

Polyacetylene (PA) is the simplest conjugated polyene, and has two configurations (*cis* and *trans*). It has been reported that shielding of ^{13}C in *cis*-PA appears at lower frequency by about 10 ppm than that of *trans*-PA.[10] Calculations of ^{13}C shielding in PAs have been carried out based on the use of CNDO/2 TB MO and INDO/S TB MO. The differences in the isotropic shielding of ^{13}C between *cis*- and *trans*-PAs, calculated using CNDO/2 and the INDO/S TB MO, are about 2.0 and 3.5 ppm, respectively,[11] i.e., the results differ by a factor of about 2. As the observed difference is about 10 ppm, both types of calculation somewhat underestimate the real values in this case.

Figure 3 shows the observed[12] and calculated components of the ^{13}C shielding tensors of *cis*- and *trans*-PA. As can be seen, the absolute values of σ_{zz} and σ_{xx} calculated using INDO/S TB MO are smaller by about 40 ppm than those obtained using CNDO/2 TB MO. The value of σ_{yy} calculated using INDO/S TB MO is larger by about 10 ppm than that obtained using CNDO/2 TB MO. Consequently, the separation between the values of σ_{xx} and σ_{yy} calculated using INDO/S TB MO is much larger than that obtained using CNDO/2 TB MO. Furthermore, it has been shown that in going from the calculation using CNDO/2 to that using INDO/S, the values of σ_{zz} and σ_{xx} are changed considerably. The most remarkable difference is the estimation of the $\pi-\pi$ overlap integral. Values of σ_{zz} and σ_{xx} are affected by the distribution of π electrons.

The electronic band structure of a PA consists of five valence bands within the framework of the semiempirical method. The highest occupied band has π symmetry. Comparing the electronic band structures calculated using CNDO/2 TB MO with that using INDO/S TB MO, the energies of the three high-energy bands increase, in particular that of the highest occupied band. As can seen from Equation (5), σ^{p} contains a term proportional to the inverse of the excitation energy. The increase in the energies of the three high-energy bands is one of the factors leading to the deshielding of σ_{zz} and σ_{xx}, which implies a lower excitation energy. In fact, the band gaps (the energy difference between the highest occupied and the lowest unoccupied band) for *trans*-PA calculated using CNDO/2 and INDO/S TB MO are about 8.0 and 4.2 eV, respectively. The observed band gap for *trans*-PA is about 1.9 eV. Thus, the contribution of these high-energy bands to σ_{xx} and σ_{zz} is remarkably improved in going from CNDO/2 to INDO/S TB MO.

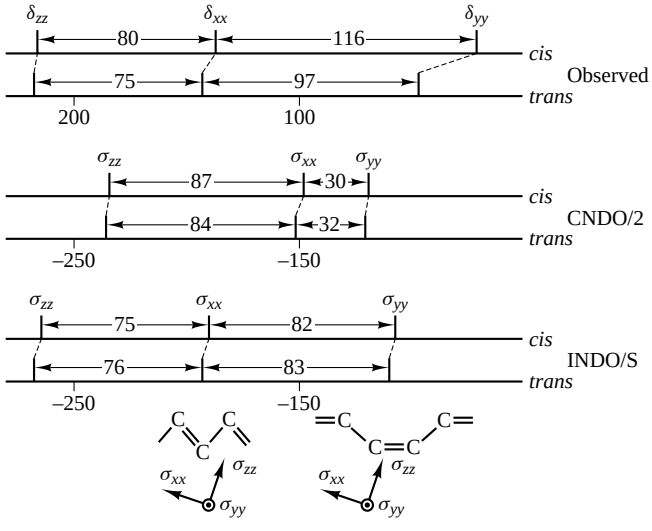

Figure 3 Observed and calculated components of ^{13}C NMR shielding tensors of *cis*- and *trans*-PAs. The directions of the principal axes are indicated at the bottom

It is clear from Figure 3 that the reason why the calculated difference in isotropic shielding of ^{13}C between *cis*- and *trans*-PAs is underestimated is that the difference in σ_{yy} cannot be reasonably reproduced. In order to reproduce more reasonably the observed difference in σ_{yy} between *cis*- and *trans*-PAs, it may be necessary to use MOs that can properly describe band structures that have σ symmetry.

Polypyrrole is one of a series of heterocyclic polymers that has attracted much attention because of its characteristic electric and electronic properties. Fundamental structural formulas have been proposed for undoped and doped polypyrroles, where the aromatic form corresponds to the undoped state and the quinoid form to the doped state. From analysis of high-resolution solid state ^{15}N NMR, it is known that the ^{15}N chemical shift for the quinoid form appears to high frequency from that for the aromatic form. In order to obtain information about ^{15}N chemical shifts and electronic band structures of an infinite polypyrrole chain with aromatic or quinoid forms, calculations were carried out using INDO/S TB MO.[13]

As listed in Table 2, the calculated shielding of ^{15}N for the quinoid form appears to high frequency compared with that for the aromatic form. The calculated results agree with observed ones, suggesting that the electronic band structure has been properly estimated. From the calculated electronic band structure, the band gaps for the aromatic and quinoid forms are 5.1 and 2.9 eV, respectively. This result implies that the electrical conductivity of the quinoid form is larger than that of the aromatic form. Therefore, it can be expected that if the amount of the quinoid form is increased, polypyrrole with a higher electric conductivity can be obtained.

3.3 Crystal Structure

The crystal structure in the solid state, which describes how molecules condense, is an important factor when discussing physical properties. The effect of crystal structure on the nuclear shielding can, in principle, be separated from the effect of conformation and configuration to within the limitations of a quantum chemical model.

Experimentally, it is reported that the ^{13}C chemical shifts of the CH_2 carbon for *n*-paraffins, cyclic paraffins,

Table 2 Calculated ^{15}N Shieldings and Band Gaps for Aromatic and Quinoid Polypyrrole Models Using INDO/S TB MO

Structure	Calculated shielding σ_{iso} (ppm)	Band gap (eV)
Aromatic	−223.50	5.12
Quinoid	−232.51	2.86

and polyethylene with *trans* zigzag conformations in the orthorhombic and triclinic forms are about 33 and 34 ppm, respectively.[14,15] As the conformation is the same in each case, the difference of about 1 ppm may be due to a local change in intermolecular interactions resulting from the change of the orthorhombic to the triclinic form. Paraffins can be considered as models for the crystallographic form of the polyethylene. The results of X-ray diffraction studies suggest that the *trans* zigzag plane of any specified chain in the orthorhombic and triclinic forms is, respectively, perpendicular and parallel to that of the neighboring chains. The chemical shift of ^{13}C in polyethylene with a monoclinic form appears at higher frequency by 1.4 ppm compared with that of polyethylene with a orthorhombic form. The orientation of the *trans* zigzag plane in the monoclinic form is very close to that in the triclinic form.[16] Thus, the solid state ^{13}C NMR chemical shift depends on the orientation of the C–C–C plane in the *trans* zigzag chains.

Since the chains lie periodically in space in the solid state, calculations of chemical shifts should be employed that take account of the three-dimensional structure, including interactions between chains. In order to take into account the interchain interaction, a 'seven-polyethylene-chains model' has been used to compute the ^{13}C shielding.[17] Figure 4 shows models for polyethylenes with an orthorhombic form and a monoclinic form. The setting angle ψ for orthorhombic polyethylene is not clearly determined. Figure 5 shows the ψ dependence of the difference in shielding of ^{13}C between orthorhombic and monoclinic polyethylenes ($\sigma_{orth} - \sigma_{mono}$) calculated using INDO/S TB MO. As can be seen, the calculated difference in shielding of ^{13}C between these forms is positive in the case of $\psi = 25^\circ - 42^\circ$, and negative in the case of $\psi = 20^\circ - 25^\circ$ and $\psi = 42^\circ - 55^\circ$. The largest difference occurs at $\psi = 35^\circ$. From these results, the angle of $\psi = 25^\circ - 42^\circ$ is good for the setting angle of orthorhombic polyethylene, and can reasonably reproduce the observed data. This result shows that the difference in chemical shift between the orthorhombic and monoclinic forms is caused by the difference in interchain interaction through the electronic band structure.

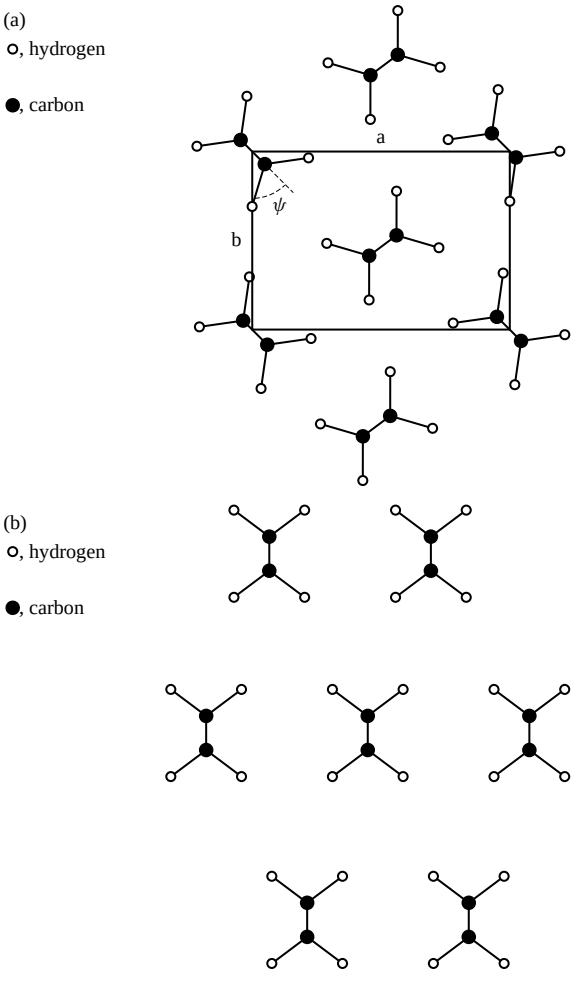

Figure 4 The 'seven-polyethylene-chains' model: (a) orthorhombic form; (b) monoclinic form

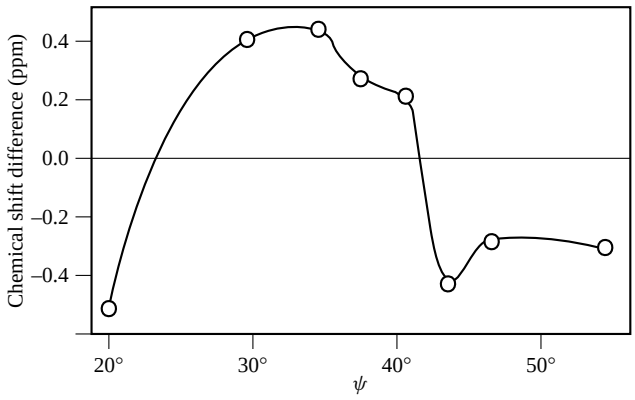

Figure 5 The ^{13}C NMR chemical shift difference between the orthorhombic and monoclinic polyethylene chains calculated using the seven-chains model, as functions of the setting angle ψ

The effect of crystal structure on the nuclear shielding of *cis*- and *trans*-PA is also relevant. A specified polymer chain is surrounded locally by six neighboring chains in the crystal, and these six chains can be separated into three groups. Each chain group consists of two chains, which are equivalent with respect to the central chain. In order to take interchain interaction into account, the 'seven-chains model' has been used to compute the ^{13}C shielding as shown in Figure 6.[18]

The calculated values depend on the chain arrangement. The total energies of *cis*- and *trans*-PAs show minima at $\Delta b = -10$ pm, where Δb is the deviation of b from the value determined by X-ray diffraction. A small decrease from the original crystal lattice values determined by X-ray methods leads to energetically stable results in the calculations for both PAs. This arises from the fact that CNDO/2 slightly underestimates the interaction distances, as is already known.[19] However, an extreme decrease in the interchain distance leads to a large instability. Therefore, when comparing *cis*- and *trans*-PAs, it might be appropriate to consider the arrangement with a somewhat shorter distance. With respect to the band gap, the smaller the value of b, the smaller the band gap becomes. The decreases in the lattice parameters in the calculation correspond to the PA system under high pressure, where a shrinkage of the interchain distance occurs. It is therefore suggested that the electric conductivity of PA samples will increase with an increase in pressure. Comparing the isomers, the band gap value of *trans*-PA is smaller than that of *cis*-PA. This explains the experimental observation that *trans*-PA has a higher conductivity than *cis*-PA. The calculated values

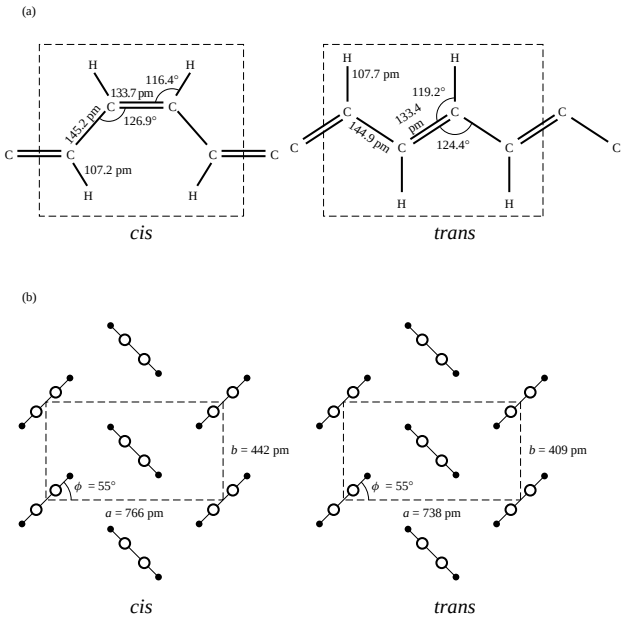

Figure 6 Geometrical parameters of *cis*- and *trans*-PA: (a) valence geometries; (b) lattice parameters

are very large for the arrangement given by the original lattice parameters. The arrangement with a small value of b is near to the real form in the crystal. It has been shown experimentally that the lattice parameters a and b for *cis*-PA are larger than those for *trans*-PA (Figure 6); that is, the interchain distance of *cis*-PA is longer than that of *trans*-PA. This may be due to the different shapes of the PA chains. In the comb-like *cis*-PA chains, some of the hydrogen and carbon atoms tend to be very close in interatomic distance, and so they become repulsive (in fact, the nearest-neighbor C−H distance between the chains in *cis*-PA is shorter than that in *trans*-PA in the case using the original geometries). Therefore, the *cis*-PA crystal becomes more stable at the arrangement with the larger lattice parameters than does the *trans*-PA crystal, and these long interchain distances lead to a large band gap and so to a low conductivity for *cis*-PA.

Figure 7 shows the calculated dependence of the shielding of ^{13}C for *cis*- and *trans*-PA on Δb. In the arrangement with

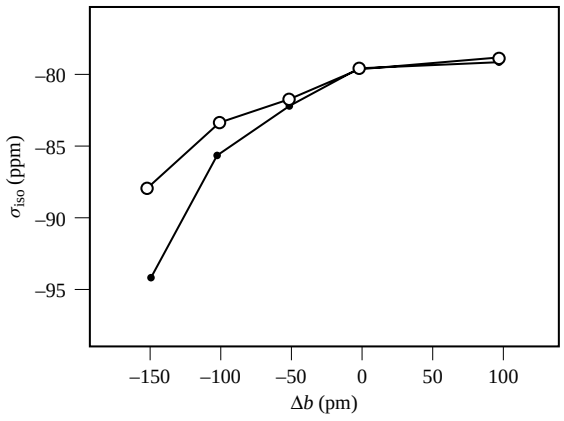

Figure 7 Dependence on b of the calculated isotropic ^{13}C shielding of PA chains in the seven-chains model: ○, *cis*; ●, *trans*

the original lattice parameters, the calculated values of σ_{iso} do not reproduce the observed large difference between the two isomers. However, in the arrangement with short interchain distances, the calculations agree well with the experiments. With regard to the chemical shift tensors, not only σ_{33} but also the components σ_{11} and σ_{22} decrease as the interchain distance is decreased. The most variable component for a change of the interchain distance is σ_{22}, whose direction is along that of the molecular chain. The effect of the interchain interactions might appear strongly in this direction. At $\Delta b = -100$ pm, the difference in σ_{22} between the isomers agrees quantitatively with the experimental data. From these results, the effect of crystal structure on nuclear shielding can be explained via the electronic structure in addition to the effect of the chain configuration.

4 RELATED ARTICLES

Chemical Shift Tensors; Conducting Polymers; Shielding Calculations: IGLO Method; Shielding Calculations: Perturbation Methods; Shielding: Overview of Theoretical Methods; Shielding in Small Molecules; Shielding Tensor Calculations; Shielding Theory: GIAO Method.

5 REFERENCES

1. I. Ando and G. A. Webb, *Theory of NMR Parameters*, Academic Press, London, 1983.
2. A. Imamura, *J. Chem. Phys.*, 1970, **52**, 3168.
3. F. Bloch, *Z. Phys.*, 1928, **52**, 555.
4. M. Kondo, I. Ando, R. Chujo, and A. Nishioka, *J. Magn. Reson.*, 1976, **24**, 315.
5. T. Yamanobe and I. Ando, *J. Chem. Phys.*, 1985, **83**, 3154.
6. T. Yamanobe, R. Chujo, and I. Ando, *Mol. Phys.*, 1983, **50**, 1231.
7. T. Yamanobe, I. Ando, H. Saito, R. Tabeta, A. Shoji, and T. Ozaki, *Bull. Chem. Soc. Jpn.*, 1985, **58**, 23.
8. H. Tadokoro, M. Kobayashi, Y. Kawaguchi, A. Kobayashi, and S. Murashashi, *J. Chem. Phys.*, 1963, **38**, 703.
9. H. Kurosu, T. Yamanobe, T. Komoto, and I. Ando, *Chem. Phys.*, 1987, **116**, 391.
10. M. M. Maricq, J. S. Waugh, A. G. MacDiarmid, H. Shirakawa, and A. T. Heeger, *J. Am. Chem. Soc.*, 1978, **100**, 7729.
11. T. Yamanobe, I. Ando, and G. A. Webb., *J. Mol. Struct.*, 1987, **151**, 191.
12. T. Terao, S. Maeda, T. Yamabe, K. Akagi, and H. Shirakawa, *Chem. Phys. Lett.*, 1984, **103**, 347.
13. M. Kiuchi, H. Kurosu, and I. Ando, *J. Mol. Struct.*, 1992, **29**, 193.
14. T. Yamanobe, T. Sorita, T. Komoto, I. Ando, and H. Sato, *J. Mol. Struct.*, 1985, **131**, 267.
15. D. L. VanderHart, *J. Magn. Reson.*, 1981, **44**, 117.
16. D. L. VanderHart and F. Khoury, *Polymer*, 1984, **25**, 1589.
17. H. Kurosu, I. Ando, and T. Yamanobe, *J. Mol. Struct.*, 1989, **201**, 239.
18. T. Ishii, H. Kurosu, T. Yamanobe, and I. Ando, *J. Chem. Phys.*, 1988, **89**, 7315.
19. K. Morokuma, *Chem. Phys. Lett.*, 1971, **19**, 129.

Biographical Sketches

Takeshi Yamanobe. *b* 1958. B.E., 1981, Ph.D., 1986, Tokyo Institute of Technology. Introduced to NMR by I. Ando. Dept. Industrial Chemistry, Tokyo Institute of Polytechnic, 1987–1993. Currently associate professor of Materials Engineering, Gunma University, Japan, 1993–present. Approx. 30 publications. Research interests include the electronic structure and NMR chemical shift of polymers, and structure and dynamics of polymeric materials by solid state NMR.

Hiromichi Kurosu. *b* 1962. Ph.D., 1990, Tokyo Institute of Technology (supervisor Isao Ando). Postdoctoral work at the University of Surrey (with Graham A. Webb). Assistant professor, Department of Polymer Chemistry, Tokyo Institute of Technology, 1989–present. Approx. 40 publications. Research specialties: solid state NMR and NMR shielding calculations, and structures and electronic states of solid polymers.

Analysis of High-Resolution Solution State Spectra

Paul L. Corio and Stanford L. Smith

Department of Chemistry, University of Kentucky, Lexington, KY, USA

1	Introduction	1
2	Theoretical Basis	1
3	Analysis of Simple Spectra	5
4	Strongly Coupled Systems	7
5	The X Approximation	11
6	Symmetrical Systems	14
7	Other Approaches	17
8	Related Articles	18
9	References	18

1 INTRODUCTION

The analysis of a high-resolution spectrum requires that four questions be addressed. (i) What are the energy eigenvalues and eigenvectors of the system in a strong, stationary magnetic field $\boldsymbol{B}_0$? (ii) What are the selection rules governing transitions in the presence of perturbing magnetic fields? (iii) What are the relative intensities of allowed transitions? (iv) How can the parameters characterizing the system—the chemical shifts and coupling constants—be obtained from an experimental spectrum?

Although these questions are logically ordered from the spectroscopic point of view, experimentalists are principally interested in the structural information that can be derived from chemical shifts and coupling constants, since chemical shift data can be used to identify specific functional groups in many compounds, and coupling constants are often remarkably sensitive to the nature of the bonds between particular nuclei, such as the *cis*, *trans*, and geminal arrangements of protons about a carbon–carbon double bond.

The extraction of chemical shifts and coupling constants from an experimental spectrum is not always a simple matter, though with magnetic field strengths of 10 T or more most high-resolution spectra can be interpreted without much difficulty. In early high-resolution experiments, however, the analysis was almost invariably a difficult problem, since experiments were performed at field strengths of about 0.1 T when spin–spin interactions were comparable with differences in chemical shifts, leading to considerable fine structure. Furthermore, computers were not generally available to solve the algebraic equations of high degree often encountered with systems containing as few as four or five nuclei. Complex spectra occasionally arise even with the magnetic field strengths available today. This is always true for certain symmetrical molecules containing spin-$\frac{1}{2}$ nuclei with different magnetogyric ratios, such as 1,3,5-trifluorobenzene or 1,1-difluoroethylene. A somewhat similar consideration applies to certain symmetrical systems with nuclei having identical magnetogyric ratios, such as *o*-dichlorobenzene; although the specrum is much simpler at 400 MHz than at 60 MHz, the analysis at 400 MHz still requires some knowledge of the subtleties of high-resolution spectra. It is always possible to relegate such problems to the computer, but there are many instances where the analysis is so simple it can be carried out with little or no computation simply through familiarity with certain patterns that occur frequently in practice.

The following development presents a survey of some traditional methods of spectral analysis that eschews certain formal details that may be studied in monographs devoted to the subject.[1–6] The reader is assumed to have some familiarity with quantum mechanics[7] and the quantum theory of angular momentum.[7–9]

2 THEORETICAL BASIS

2.1 Nuclear Angular Momentum

A charged macroscopic body spinning about an axis through it has a magnetic moment by virtue of the circulation of charge, angular momentum by virtue of the circulation of mass, and a straightforward classical calculation shows that the magnetic moment is proportional to the angular momentum. There is an analogous relation for nuclei, but quantum theory requires that the vector operator $\hat{\boldsymbol{\mu}}$ representing the magnetic moment, be proportional to the vector operator $\hbar\hat{\boldsymbol{I}}$, representing the angular momentum:

$$\hat{\boldsymbol{\mu}} = \gamma\hbar\hat{\boldsymbol{I}} \tag{1}$$

where $\hbar$ is Planck's constant divided by 2π, and γ, the magnetogyric ratio, is an empirical constant which may be positive or negative (Table 1). The dimensionless vector operator $\hat{\boldsymbol{I}} = (\hat{I}_x, \hat{I}_y, \hat{I}_z)$ represents the nuclear angular momentum in units of $\hbar$; its components are Hermitian operators satisfying

Table 1 Magnetic Resonance Data for Some Common Nuclei[a,b]

Nucleus	I	μ/μ_N	$\lvert\nu\rvert/2\pi$ (MHz T^{-1})
$^{1}_{1}$H	$\frac{1}{2}$	2.79268	42.5751
$^{2}_{1}$H	1	0.85738	6.53549
$^{10}_{5}$B	3	1.8005	4.57484
$^{11}_{5}$B	$\frac{3}{2}$	2.6880	13.6597
$^{14}_{7}$N	1	0.40358	3.07634
$^{15}_{7}$N	$\frac{1}{2}$	−0.28304	4.31501
$^{19}_{9}$F	$\frac{1}{2}$	2.6273	40.0538
$^{31}_{15}$P	$\frac{1}{2}$	1.1305	17.2347

[a] μ_N is the nuclear Bohr magneton: $e\hbar/2m_p$.

[b] The natural units of ν are rad s^{-1} T^{-1}; $\lvert\nu\rvert/2\pi$ is the (linear) resonance frequency in a field of 1 T.

$$[\hat{I}_x, \hat{I}_y] = i\hat{I}_z \tag{2}$$

$$[\hat{I}_y, \hat{I}_z] = i\hat{I}_x \tag{3}$$

$$[\hat{I}_z, \hat{I}_x] = i\hat{I}_y \tag{4}$$

where $[\hat{A}, \hat{B}] = \hat{A}\hat{B} - \hat{B}\hat{A}$ is the commutator of $\hat{A}$ and $\hat{B}$.

The square of the angular momentum (in units of $\hbar^2$) is

$$\hat{\boldsymbol{I}} \cdot \hat{\boldsymbol{I}} = \hat{\boldsymbol{I}}^2 = \hat{I}_x^2 + \hat{I}_y^2 + \hat{I}_z^2 \tag{5}$$

which commutes with each component of $\hat{\boldsymbol{I}}$:

$$[\hat{\boldsymbol{I}}^2, \hat{I}_x] = [\hat{\boldsymbol{I}}^2, \hat{I}_y] = [\hat{\boldsymbol{I}}^2, \hat{I}_z] = 0 \tag{6}$$

To prove these relations, first observe that $[\hat{\boldsymbol{I}}^2, \hat{I}_x] = [\hat{I}_y{}^2, \hat{I}_x] + [\hat{I}_z{}^2, \hat{I}_x]$, since $[\hat{I}_x{}^2, \hat{I}_x] = 0$. The identity

$$[\hat{A}^2, \hat{B}] = \hat{A}[\hat{A}, \hat{B}] + [\hat{A}, \hat{B}]\hat{A} \tag{7}$$

together with equations (2) and (4) lead to the conclusion that $[\hat{\boldsymbol{I}}^2, \hat{I}_x] = 0$. The others are proved similarly.

Equation (6) states that the scalar product $\hat{\boldsymbol{I}}\cdot\hat{\boldsymbol{I}} = \hat{\boldsymbol{I}}^2$ is rotationally invariant, i.e. if $\hat{\boldsymbol{I}}'$ is the angular momentum referred to an $x'y'z'$ system related to the original xyz system by a rotation about the origin, then $\hat{\boldsymbol{I}}'\cdot\hat{\boldsymbol{I}}' = \hat{\boldsymbol{I}}\cdot\hat{\boldsymbol{I}}$. This is obvious for the scalar product of ordinary vectors which depends only upon the lengths of the vectors and their included angle, quantities independent of the coordinate system to which the vectors are referred. That the corresponding result holds for the scalar product of vector operators is a consequence of the fact that the components of $\hat{\boldsymbol{I}}$ are generators for rotations of the system space that correspond to physical rotations about the coordinate axes. Any rotationally invariant operator $\hat{V}$ associated with the nuclear angular momentum commutes with the components of $\hat{\boldsymbol{I}}$:

$$[\hat{V}, \hat{I}_x] = [\hat{V}, \hat{I}_y] = [\hat{V}, \hat{I}_z] = 0 \tag{8}$$

Rotational invariance has important implications for the theory of high-resolution spectra.

Since $\hat{\boldsymbol{I}}^2$ and $\hat{I}_z$ commute, there exists a set of vectors each of which is an eigenvector of both operators. In fact, there are $2I + 1$ independent eigenvectors $\psi(Im)$:

$$\hat{\boldsymbol{I}}^2\psi(Im) = I(I+1)\psi(Im) \tag{9}$$

$$\hat{I}_z\psi(Im) = m\psi(Im) \tag{10}$$

where I is a non-negative integer, or half an odd positive integer, and $m = I, I - 1, \ldots, -I + 1, -I$. Note that the argument of ψ is not the product of I and m, but a listing of the quantum numbers required to specify a state of angular momentum. For brevity, we omit punctuation between quantum numbers. When $I = \frac{1}{2}$, the two independent states of angular momentum will be denoted as

$$\alpha = \psi(\tfrac{1}{2}, \tfrac{1}{2}), \quad \beta = \psi(\tfrac{1}{2} - \tfrac{1}{2}) \tag{11}$$

The eigenvalues of $\hat{I}_z$ are distinct, so the eigenvectors $\psi(Im)$ are necessarily orthogonal. We shall assume they are also normalized:

$$(\psi(Im'), \psi(Im)) = \delta_{mm'} \tag{12}$$

where (ϕ,ψ) denotes the Hermitian scalar product of ϕ and ψ and $\delta_{m'm} = 1$ if $m = {}_{m'}$, $\delta_{m'm} = 0$, if $m' \neq m$. In particular, when $I = \frac{1}{2}$:

$$(\alpha, \alpha) = (\beta, \beta) = 1 \tag{13}$$

$$(\alpha, \beta) = (\beta, \alpha) = 0 \tag{14}$$

The application of $\hat{I}_x$ or $\hat{I}_y$ to $\psi(Im)$ can be inferred from the useful relations:

$$\hat{I}_\pm\psi(Im) = \{(I \mp m)(I \pm m + 1)\}^{1/2}\psi(Im \pm 1) \tag{15}$$

where the raising and lowering operators $\hat{I}_+$ and $\hat{I}_-$ are defined by:

$$\hat{I}_\pm = \hat{I}_x \mathrm{i}\hat{I}_y \tag{16}$$

The following formulas for $I = \frac{1}{2}$ are used in many computations:

$$\hat{I}_z\alpha = \alpha/2, \quad \hat{I}_z\beta = -\beta/2 \tag{17}$$

$$\hat{I}_+\beta = \alpha, \quad \hat{I}_-\alpha = \beta \tag{18}$$

$$\hat{I}_+\alpha = \hat{I}_-\beta = 0 \tag{19}$$

2.2 Energy Levels and Selection Rules

The Hamiltonian operator for a nucleus in a magnetic field $\boldsymbol{B}$ is:

$$\hat{\mathcal{H}} = -\hat{\boldsymbol{\mu}}\cdot\boldsymbol{B} = -\gamma\hbar(B_x\hat{I}_x + B_y\hat{I}_y + B_z\hat{I}_z) \tag{20}$$

Now the product of the magnetogyric ratio and a magnetic field is an angular velocity whose significance may be deduced from the formula[7]

$$\frac{\mathrm{d}}{\mathrm{d}t}(\Psi, \hat{X}\Psi) = \left(\Psi, \frac{\mathrm{d}\hat{X}}{\mathrm{d}t}\Psi\right) \tag{21}$$

which states that the time derivative of the expectation value is equal to the expectation value of the time derivative. Taking $\hat{X}$ successively as $\hat{\mu}_x, \hat{\mu}_y, \hat{\mu}_z$—which are not explicit functions of the time, so their partial derivatives with respect to t vanish—and making use of the Schrödinger equation

$$\mathrm{i}\hbar\left(\frac{\partial\Psi}{\partial t}\right) = \hat{\mathcal{H}}\Psi \tag{22}$$

the results may be written in the vector form:

$$\frac{\mathrm{d}}{\mathrm{d}t}\langle\hat{\boldsymbol{\mu}}\rangle = -\gamma\boldsymbol{B}\times\langle\hat{\boldsymbol{\mu}}\rangle \tag{23}$$

This classical equation states that the expectation value of $\hat{\mu}$ precesses about the instantaneous direction of $\boldsymbol{B}$ with angular frequency

$$\boldsymbol{\omega} = -\gamma\boldsymbol{B} \tag{24}$$

the sense of the precession being negative or positive according to whether γ is positive or negative. For a constant field, the trace of the vector $\langle\hat{\boldsymbol{\mu}}\rangle$ is a cone (Figure 1). A frequency proportional to the applied field is called a Larmor frequency.

In the special case of a nucleus with spin I in a stationary field $B_0\boldsymbol{k}$, the Hamiltonian is

$$\hat{\mathcal{H}} = -\gamma\hbar B_0\hat{I}_z \tag{25}$$

whose eigenvectors and eigenvalues are $\psi(Im)$ and $E_m = -\gamma\hbar B_0 m$, $m = I, I - 1, I - 2, \ldots, -I$. The levels are uniformly spaced, the spacing of successive levels being $\gamma\hbar B_0$ (Figure 2). Transitions between these levels can be induced by an oscillating radiofrequency field directed along the x axis:

$$B_x\boldsymbol{i} = 2B_1\boldsymbol{i}\cos\omega t \tag{26}$$

where $B_1 \ll B_0$. Classically, the oscillating field exerts an additional torque on $\langle\hat{\boldsymbol{\mu}}\rangle$, which tends to increase the energy of

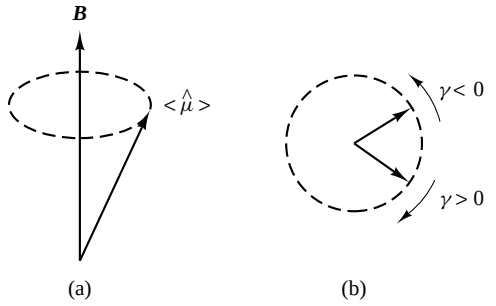

Figure 1 (a) The expectation value of $\hat{\boldsymbol{\mu}}$ precesses about the field $\boldsymbol{B}$ with angular frequency $-\gamma \boldsymbol{B}_0$. (b) The circle of precession drawn looking toward the xy plane from the positive z axis; the sense of precession is negative or positive according to whether γ is negative or positive

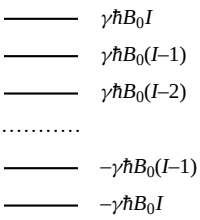

Figure 2 Energy levels of a nucleus with spin I in stationary field $B_0\boldsymbol{k}$

the system by increasing the angle between $\langle\hat{\boldsymbol{\mu}}\rangle$ and $B_0\boldsymbol{k}$. This 'flipping' torque is most effective when the frequency of the oscillating field is equal to the Larmor precession frequency, that is, when $\omega = |\gamma|B_0$.

This result may be obtained quantum mechanically. According to first-order time-dependent perturbation theory, the oscillating field induces transitions between adjacent energy levels, i.e. the selection rule is $m' = m \pm 1$, or, equivalently, $\Delta m = \pm 1$. For $\Delta m = -1$, the system absorbs a single quantum of radiation from the oscillating field and the Bohr frequency rule requires that $E_{m'} - E_m = \hbar\omega$; substituting from $E_m = -\gamma \hbar B_0 m$, we find that $\omega = |\gamma|B_0$.

2.3 Chemical Shifts

The interaction of a nucleus bereft of enveloping electrons with an applied field $\boldsymbol{B}$ is given by equation (20), but this expression must be modified when the nucleus is embedded in a molecule since the field-induced motions of the electrons generate internal fields that also contribute to the field at the nucleus. The net field will, in general, differ from $\boldsymbol{B}$ in magnitude and direction, and will vary with molecular orientation. In fluid systems, where molecules experience random changes in orientation, the averaged induced field is proportional to the applied field: $\boldsymbol{B}_{\text{ind}} = -\sigma\boldsymbol{B}$, where the shielding constant σ is a positive number of the order of 10^{-5} for protons, varying roughly as $Z^{4/3}$ for nuclei with $Z > 1$ (see ***Shielding: Overview of Theoretical Methods***).

The net field at the nucleus is $(1 - \sigma)\boldsymbol{B}$, so that if $\boldsymbol{B}_0$ is the field required for resonance with an unshielded nucleus, the field required for resonance when it is shielded must be increased to a value $\boldsymbol{B}_{\text{R}}$ such that $\boldsymbol{B}_0 = (1 - \sigma)\boldsymbol{B}_{\text{R}}$. This change in the field required for resonance is called the chemical shift; it depends upon the electronic structure of the molecule, is generally different for the same nucleus in different molecules, and may even be different for the same nuclei in the same molecule, the difference in the field or frequency being then called the internal chemical shift. Internal chemical shifts distinguish structurally different nuclei in a molecule, hence their importance in chemical analysis.

In the averaging process mentioned above, it was tacitly assumed that the nucleus maintained its orientation with respect to the applied field, the molecule tumbling about it during the averaging process. A nucleus with $I > \frac{1}{2}$ possesses an electric quadrupole moment which interacts with the electric field gradient set up at the nucleus by the electrons, and this interaction can be strong enough that the orientation with respect to $\boldsymbol{B}$ is not maintained. In such instances, the lifetimes of nuclei in the states $\psi(Im)$ can be so short that the resonance is too broad to detect. This does not, however, preclude consideration of spin quantum numbers $I > \frac{1}{2}$. For instance, deuterium ($I = 1$) has a relatively small quadrupole moment, and does not experience large field gradients. Morever, nuclei with spin $\frac{1}{2}$ can, in certain circumstances, have their spins sum to values greater than $\frac{1}{2}$ but without the complications introduced by quadrupole interactions.

2.4 Spin–Spin Interactions

The analysis of a high-resolution spectrum would be a trivial matter if it was only necessary to take shielding effects into account: there would be one resonance for each distinct chemical environment, with an intensity proportional to the number of nuclei in that environment. Furthermore, the fourth column of Table 1, which gives the resonance frequencies for a field of 1 T, shows that different nuclei undergo resonance in different regions of the radiofrequency spectrum so there would be no interference from isotopes or other nuclei. There are, however, certain spin–spin interactions that survive the averaging processes characteristic of fluid systems, and these interactions, which must be rotationally invariant, generally produce considerable fine structure. The simplest interaction consistent with experiment is a scalar product of magnetic moments: $-K_{ij}\hat{\boldsymbol{\mu}}_i \cdot \hat{\boldsymbol{\mu}}_j$, where the proportionality constant, symmetric in i and j, depends upon the electronic structure of the molecule but is independent of the applied magnetic field. Introducing the spin vectors $\hat{\boldsymbol{I}}_i$, $\hat{\boldsymbol{I}}_j$, and defining the spin–spin coupling constant in Hz by

$$J_{ij} = (2\pi)^{-1}\gamma_i\gamma_j\hbar K_{ij} = J_{ji} \tag{27}$$

the interaction takes the standard form $-J_{ij}h\hat{\boldsymbol{I}}_i \cdot \hat{\boldsymbol{I}}_j$. Representative values of spin–spin coupling constants are given in Table 2.

Table 2 Representative Values of Spin–Spin Coupling Constants

Molecule	Coupled nuclei	$\lvert J\rvert$ (Hz)
H_2	(H,H)	277
HD	(H,D)	43.5
CH_4	(H,H)	12.4
$^{13}CH_4$	(^{13}C,H)	125
PH_3	(P,H)	179
PF_3	(P,F)	1410

Taking into account the various chemical environments and all possible spin–spin interactions, the Hamiltonian operator in the field $\boldsymbol{B}_0$ is given by

$$\hat{\mathcal{H}} = -h\left\{ \sum_i \nu_i \hat{I}_{zi} + \sum_{i<j}\sum J_{ij} \hat{\boldsymbol{I}}_i \cdot \hat{\boldsymbol{I}}_j \right\} \tag{28}$$

where $\nu_i = |\gamma|(1 - \sigma_i)B_0/2\pi$, with σ_i being the averaged shielding constant for nucleus j. As nuclei with different magnetogyric ratios are generally observed in separate experiments, there is no loss of generality in assuming all nuclei in the system have the common magnetogyric ratio γ. The relative intensity of a transition conforming to the selection rule $m' = m - 1$ is proportional to the absolute square of the matrix element of $\hat{I}_-$ connecting the initial and final states:

$$\text{Int}(m \rightarrow m') = |(\phi(m'), \hat{\boldsymbol{I}}_- \phi(m')|^2 \tag{29}$$

2.5 Multispin Systems

Any state of angular momentum for a nucleus of spin-$\frac{1}{2}$ may be written as a linear combination of α and β. The states of N spin-$\frac{1}{2}$ nuclei can be described by 2^N product functions, each factor in a product being α or β, the first factor referring to the first nucleus, the second factor to the second nucleus, and so on. If, for instance, $N = 4$, there are 16 such products: $\alpha\alpha\alpha\alpha$, $\alpha\alpha\alpha\beta$, $\alpha\alpha\beta\alpha$, etc., and any state of angular momentum can be expressed as a linear combination of these 16 product functions. These are not products in the arithmetical sense; the product notation is merely a convenient way of writing out a complete set of states for the system. The product functions for $N = 2$, 3, 4 are given in Table 3.

Each product function has a definite value for the net z component of angular momentum, equal to $m_\text{T} = (r - s)/2$, where r and s, respectively, denote the number of αs and βs. The number of product functions having the same value of m_T, which is equal to the number of ways $N = r + s$ objects can be divided into two groups having r and s objects in each group, is:

$$\eta(m_\text{T}) = \frac{N!}{(N/2 - m_\text{T})!(N/2 + m_\text{T})!} \tag{30}$$

Since α and β are orthonormal the product functions constructed from them are also orthonormal, the scalar product of product functions being equal to the product of individual scalar products. For example, $(\alpha\beta,\beta\alpha) = (\alpha,\beta)(\beta,\alpha) = 0{\cdot}0 = 0$ and $(\alpha\beta,\alpha\beta) = (\alpha,\alpha)(\beta,\beta) = 1{\cdot}1 = 1$.

The spin vector for nucleus j is denoted $\hat{\boldsymbol{I}}_j = (\hat{I}_{jx}, \hat{I}_{jy}, \hat{I}_{jz})$; its components act only on the states of nucleus j and its components commute with the components of $\hat{\boldsymbol{I}}_k$:

$$[\hat{I}_{xj}, \hat{I}_{yk}] = \mathrm{i}\hat{I}_{zj}\delta_{jk} \tag{31}$$

$$[\hat{I}_{yj}, \hat{I}_{zk}] = \mathrm{i}\hat{I}_{xj}\delta_{jk} \tag{32}$$

$$[\hat{I}_{zj}, \hat{I}_{xk}] = \mathrm{i}\hat{I}_{yj}\delta_{jk} \tag{33}$$

It is often essential in the consideration of a multispin system to compound several angular momenta to a resultant. In particular, two angular momenta $\hat{\boldsymbol{I}}_1$, $\hat{\boldsymbol{I}}_2$ may be compounded to a resultant $\hat{\boldsymbol{F}} = \hat{\boldsymbol{I}}_1 + \hat{\boldsymbol{I}}_2$, characterized by the total spin quantum numbers:

$$F = I_1 + I_2, \quad I_1 + I_2 - 1, \quad I_1 + I_2 - 2, \ldots, \quad |I_1 - I_2| \tag{34}$$

For example, if $I_1 = I_2 = \frac{1}{2}$, the values of F are 1 and 0. The number of states corresponding to each value of F is $2F + 1$, so the total number of states in this case is $(2 \times 1 + 1) + (2 \times 0 + 1) = 4 = 2^2$.

To compute the values of F for three spin-$\frac{1}{2}$ nuclei, we add the third spin to the values of the total spin obtained when $N = 2$, obtaining $\frac{3}{2}$, $\frac{1}{2}$, the latter occuring twice, once as $\frac{3}{2} - 1$, and again as $0 + \frac{1}{2}$. The number of times a total spin quantum number appears is called the statistical weight and denoted g_F. The total number of states should be $2^3 = 8$, and on computing $2F + 1$ for $F = \frac{3}{2}$, $\frac{1}{2}$, taking into account that $g_{3/2}$, = 1, $g_{1/2} = 2$, we find that there are indeed eight states.

The values of the total spin quantum numbers and their statistical weights resulting from the additional of several spin-$\frac{1}{2}$ nuclei are given in Table 4. These results are important in the study of systems composed of groups of magnetically equivalent nuclei.

The states corresponding to the various values of F are eigenvectors of the operators:

$$\begin{aligned}\hat{\boldsymbol{F}}^2 &= (\hat{\boldsymbol{I}}_1 + \hat{\boldsymbol{I}}_2 + \ldots)^2 \\ &= \sum_i \hat{\boldsymbol{I}}_i^2 + 2\sum_{i<j}\sum \hat{\boldsymbol{I}}_i \cdot \hat{\boldsymbol{I}}_j\end{aligned} \tag{35}$$

Table 3 Product Functions for Spin $\frac{1}{2}$ Nuclei

Product function	m_T	$\eta(m_\text{T})$
$\alpha\alpha$	1	1
$\alpha\beta$, $\beta\alpha$	0	2
$\beta\beta$	−1	1
$\alpha\alpha\alpha$	$\frac{3}{2}$	1
$\alpha\alpha\beta$, $\alpha\beta\alpha$, $\beta\alpha\alpha$	$\frac{1}{2}$	3
$\beta\beta\alpha$, $\beta\alpha\beta$, $\alpha\beta\beta$	$-\frac{1}{2}$	3
$\beta\beta\beta$	$-\frac{3}{2}$	1
$\alpha\alpha\alpha\alpha$	2	1
$\alpha\alpha\alpha\beta$, $\alpha\alpha\beta\alpha$, $\alpha\beta\alpha\alpha$, $\beta\alpha\alpha\alpha$	1	4
$\alpha\alpha\beta\beta$, $\alpha\beta\alpha\beta$, $\alpha\beta\beta\alpha$, $\beta\beta\alpha\alpha$, $\beta\alpha\beta\alpha$, $\beta\alpha\alpha\beta$	0	6
$\beta\beta\beta\alpha$, $\beta\beta\alpha\beta$, $\beta\alpha\beta\beta$, $\alpha\beta\beta\beta$	−1	4
$\beta\beta\beta\beta$	−2	1

Table 4 Total Spin Quantum Numbers for N Spin $\frac{1}{2}$ Nuclei

N	Total spin F	Statistical weight g_F
2	1	1
	0	1
3	$\frac{3}{2}$	1
	$\frac{1}{2}$	2
4	2	1
	1	3
	0	2
5	$\frac{5}{2}$	1
	$\frac{3}{2}$	4
	$\frac{1}{2}$	5
6	3	1
	2	5
	1	9
	0	5

$$\hat{F}_z = \sum_i \hat{I}_{zi} \tag{36}$$

with the eigenvalues $F(F + 1)$, $m_T = F, F - 1, \ldots, -F$, for each value of F in the sequence shown in equation (34).

3 ANALYSIS OF SIMPLE SPECTRA

3.1 The A_N System

The word *simple* is used here to characterize spectra that are simple in the sense that they exhibit only a single resonance, or simple in the sense that they can be described by the perturbation formulas of quantum mechanics. We shall begin with the first case—the A_N system—all of whose nuclei have the same Larmor frequency ν_0, such as the protons in hydrogen, methane, and benzene. The protons in these molecules are symmetrically equivalent, as any one may be (conceptually) transformed into any other by a symmetry of the molecule, namely, a rotation, reflection, or inversion. Nuclei that are chemically equivalent by virtue of an exchange of positions through rapid internal motions will, in general, also have the same (averaged) Larmor frequency. Neopentane is an A_{12} system because of the relatively uninhibited rotations of the methyl groups about the bonds joining them to the central carbon atom.

The spectrum of an A_N system consists of a single line at the frequency ν_0—even though the nuclei are coupled by spin–spin interactions of the form $J_{jk}\,\hat{\boldsymbol{I}}_j \cdot \hat{\boldsymbol{I}}_k$. The reason is that the equality of Larmor frequencies and the rotational invariance of spin–spin interactions result in the conservation of the square of the total spin angular momentum and the spin–spin interactions. To clarify the physical ideas, consider a magnetic resonance experiment with fluorine atoms, when it is obvious only one resonance would be observed. Yet the fluorine nucleus contains nine protons and 10 neutrons whose spins couple to a resultant spin of $\frac{1}{2}$. The coupling of the nucleons does not lead to fine structure because a magnetic resonance experiment deals with the interactions of resultant magnetic moments with each other and with applied fields. An A_N system behaves similarly, in that the coupling of the nuclei with each other leads to resultant magnetic moments that interact with applied fields and each other, but produce no fine structure.

The theory is straightforward. The stationary Hamiltonian for an A_N system is

$$\hat{\mathcal{H}} = -h(\nu_0 \hat{F}_z + \hat{V}) \tag{37}$$

where $\hat{V}$ denotes the spin–spin interactions:

$$\hat{V} = \sum_{i<j} \sum J_{ij} \hat{\boldsymbol{I}}_i \cdot \hat{\boldsymbol{I}}_J \tag{38}$$

Since $\hat{V}$ is rotationally invariant, it commutes with $\hat{F}_x$, $\hat{F}_y$, $\hat{F}_z$, and, therefore, also with $\hat{\boldsymbol{F}}^2$, so that states of the system are characterized by the eigenvalues E, m_T, v, $F(F + 1)$ of $\hat{H}$, $\hat{F}_z$, $\hat{V}$, and $\hat{\boldsymbol{F}}^2$. Writing F rather than $F(F + 1)$ for brevity, the eigenfunctions take the form $\psi(Evm_TF)$ and the energies are:

$$E = -h(\nu_0 m_T + v) \tag{39}$$

The time-dependent Hamiltonian is

$$\hat{\mathcal{H}}(t) = -h(\nu_0 \hat{F}_z + \hat{V} + 2B_1 \hat{F}_x \cos \omega t) \tag{40}$$

The shielding correction to the amplitude of the oscillating field has not been included in the Hamiltonian since $B_1 \ll B_0$. Evidently $\hat{V}$ and $\hat{\boldsymbol{F}}^2$ commute with $\hat{\mathcal{H}}$, so these operators are conserved even in the presence of the oscillating field. Conservation of $\hat{\boldsymbol{F}}^2$ requires $F'(F' + 1) = F(F + 1)$; hence $F' = F$, since the total spin quantum number must be non-negative. Thus the allowed transitions are $\psi(Evm_TF) \rightarrow \psi(E'vm_T'F)$ and the frequency of the transition is $\nu = (m_T - m_T')\nu_0$, which is independent of the spin–spin interactions. Thus, the energy levels between which transitions are allowed are shifted equally and in the same direction by the spin–spin interactions. The selection rule $\Delta m_T = -1$ now yields $\nu = \nu_0$.

A group of nuclei such that its total angular momentum and the spin–spin interactions within it are conserved is defined as a group of magnetically equivalent nuclei. The A_N system consists of a single group of magnetically equivalent nuclei and the interactions of the nuclei with each other cannot be observed. It is possible to estimate the coupling constants between magnetically equivalent nuclei by isotopic substitution. For example, the coupling constant between hydrogen and deuterium in HD is 43.5 Hz. Making the assumption that the substitution of deuterium for hydrogen does not alter the electronic structure significantly, the coupling in H_2 is obtained by multiplication with $\gamma_H/\gamma_D = 6.51$, which yields 277 Hz.

The concept of a group of magnetically equivalent nuclei can be generalized to systems with several groups G = A, B, C, ... of nuclei with Larmor frequencies ν_A, ν_B, ν_C, ... A group S is a group of magnetically equivalent nuclei if the following conditions are satisfied:

$$\left.\begin{aligned} &\nu_{Si} = \nu_{Sj} = \ldots \equiv \nu_S \\ &J_{SiGr} = J_{SjGr} = J_{SkGr} = \ldots = J_{SGr} \\ &r = 1, 2, \ldots, n_G \\ &G = A,B, \ldots, \neq S \end{aligned}\right\} \tag{41}$$

where J_{SiGr} is the coupling constant for nucleus i in group S and nucleus r in group G. These conditions state that only one coupling constant is required to describe the interactions of group S with group G. If these conditions apply to the interactions of the nuclei in group G with those in group S, so that G is also a group of magnetically equivalent nuclei, the coupling between groups S and G can be described by a single coupling constant J_{SG}. When these conditions are satisfied, the total angular momentum and the spin–spin interactions within each group are conserved. The result is that the energy difference between any two levels for which a transition is allowed will be shifted by the same amount and in the same direction. It is permissible, therefore, to omit the interactions within magnetically equivalent groups from the Hamiltonian.

Groups of magnetically equivalent nuclei may be realized in practice by virtue of molecular symmetry, or an effective symmetry brought about by internal molecular motions. The protons adjacent to the chlorine atoms in 1,2,3-trichlorobenzene form a group of two magnetically equivalent nuclei as only a single coupling constant is required to describe the coupling to the third proton. Similarly, the protons in propane constitute an A_6B_2 system.

The stationary Hamiltonian for a system consisting of groups of magnetically equivalent nuclei is

$$\hat{\mathcal{H}} = -h\left(\sum_{\mathrm{G}} \nu_{\mathrm{G}} \hat{I}_{\mathrm{G}z} + \sum_{G<G'} \sum J_{\mathrm{GG}'} \hat{\boldsymbol{I}}_{\mathrm{G}'} \cdot \hat{\boldsymbol{I}}_{\mathrm{G}'} \right) \tag{42}$$

where the notation G < G′ means that G precedes G′ alphabetically. The intensities of allowed transitions are given by the absolute squares of the matrix elements of[1]

$$\hat{F} = \sum_{\mathrm{G}} \boldsymbol{F}_{\mathrm{G}-} \tag{43}$$

connecting the initial and final states. The implications of magnetically equivalent groups in the analysis of high-resolution spectra will be discussed in Section 4.

3.2 Zero-Order Spectra

Zero-order spectra occur when the interactions of the nuclei are negligible compared with their interactions with the applied magnetic field. If the nuclei under consideration are divided into magnetically equivalent groups A, B, C, ... , containing n_{A}, n_{B}, n_{c}, ... spin-$\frac{1}{2}$ nuclei with the same magnetogyric ratio, the spectrum will consist, in general, of one line for each group with relative intensities in the ratios n_{A}:n_{B}:n_{C}: ... . The proton spectrum of 1,1-dineopentyl-2-*t*-butylethylene (Figure 3) is an example. The *t*-butyl groups occupy structurally nonequivalent positions in the molecule, as exhibited by the three lines of equal intensity in the right side of the spectrum. (Further information would be required to assign a particular one of these resonances to the protons in a particular *t*-butyl group.) Similar remarks apply to the protons in the methylene groups. The remaining resonance is unambiguously identified as the olefinic proton. Four points should be particularly noted. (a) Rapid, internal rotations about carbon–carbon single bonds result in an averaging of local environments, leading to the structural equivalence of the protons in both the methylene and methyl groups. (b) Similar averaging processes lead to the structural equivalence of the methyl groups within each *t*-butyl group. (c) The integrated signal intensities, as measured by the area under each resonance, are in the ratios 1:2:2:9:9:9. (d) Although the spectrum does not distinguish the individual *t*-butyl groups or methylene groups, the olefinic, methylene, and *t*-butyl groups are unambiguously identified.

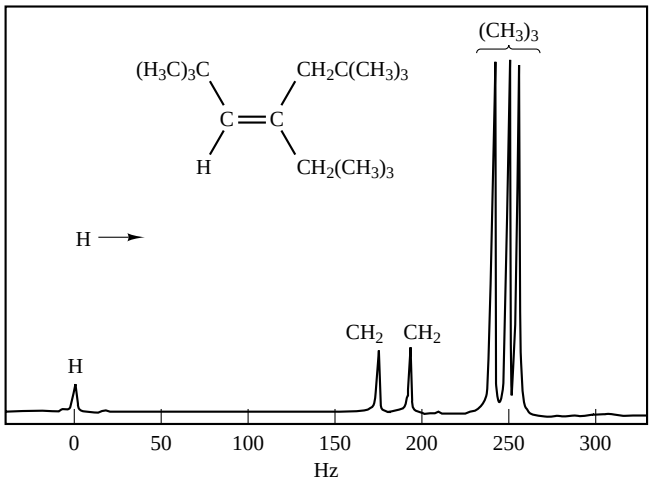

Figure 3 The proton magnetic resonance spectrum of 1,1-dineopentyl-2-*t*-butylethylene at 60 MHz

3.3 First-Order Spectra

First-order spectra occur when spin–spin interactions introduce small corrections to the energy of the system in the applied field $\boldsymbol{B}_0$. Physically, two nuclei with magnetic moments interact by virtue of the electrons occupying intervening bonds, the result being that one nucleus experiences additional magnetic fields that vary with the orientation of the other with respect to field $\boldsymbol{B}_0$. Consider two spin-$\frac{1}{2}$ nuclei, A, X. In the absence of a spin–spin interaction, nucleus A experiences a (shielded) magnetic field along the *z* axis and the oscillating radiofrequency field generates a single resonance at the frequency ν_{A}. When A interacts with X, the *z* field at A will depend upon the orientation of nucleus X. In some molecules the *z* component of angular momentum for X will be parallel to the *z* axis, while in other molecules it will be antiparallel, the populations in these states being nearly equal according to the Boltzmann distribution. Nucleus A will thus exhibit two resonance lines of equal intensity equally shifted $|J_{\mathrm{AX}}|/2$ above and below ν_{A}, so that the frequency separation of the lines is $|J_{\mathrm{AX}}|$. As the interaction is reciprocal, X will also exhibit two resonance lines of equal intensity with frequency separation $|J_{\mathrm{AX}}|$.

When there are n_{A} and n_{X} spin-$\frac{1}{2}$ nuclei in groups A and X, there will be n_{X} + 1 resonances for A with the common frequency separation $|J_{\mathrm{AX}}|$ and with relative intensities

$$\binom{n_{\mathrm{X}}}{n_{\mathrm{X}}/2 + m_{\mathrm{X}}}, \quad m_{\mathrm{X}} = n_{\mathrm{X}}/2,\ n_{\mathrm{X}}/2 - 1,\ \ldots,\ -n_{\mathrm{X}}/2 \tag{44}$$

Similarly, there will be n_{A} + 1 resonances for X with the common frequency separation $|J_{\mathrm{AX}}|$ and with relative intensities

$$\binom{n_{\mathrm{A}}}{n_{\mathrm{A}}/2 + m_{\mathrm{A}}}, \quad m_{\mathrm{A}} = n_{\mathrm{A}}/2,\ n_{\mathrm{A}}/2 - 1,\ \ldots,\ -n_{\mathrm{A}}/2 \tag{45}$$

The case n_{A} = 1, n_{X} = 9 is illustrated in Figure 4, which shows the ^{31}P resonances for trimethyl phosphite. Eight of the predicted 10 resonances are cleanly resolved; the remaining two lines are buried in the noise. The lines are uniformly spaced with $|J_{\mathrm{AX}}|$ = 10.5 Hz. The proton spectrum (not shown) consists of two lines of equal intensity with spacing 10.5 Hz. The first-order spectrum of the protons in diethyl ether at 400 MHz is shown in Figure 5.

3.4 Second-Order Spectra

The description of higher order spectra requires some rather tedious formal computations.[1] The following formulas for frequencies and intensities are obtained from the perturbation theory of quantum mechanics:

$$\nu_{\mathrm{G}} + \sum_{\mathrm{G}' \neq \mathrm{G}} J_{\mathrm{GG}'} m_{\mathrm{G}'} + \frac{1}{2} \sum_{\mathrm{G} \neq \mathrm{G}'} \frac{J_{\mathrm{GG}'}^2}{\nu_{\mathrm{GG}'}} \{ F_{\mathrm{G}'}(F_{\mathrm{G}'} + 1) - m_{\mathrm{G}'}(m_{\mathrm{G}'} + 1) + 2 m_{\mathrm{G}} m_{\mathrm{G}'} \} \tag{46}$$

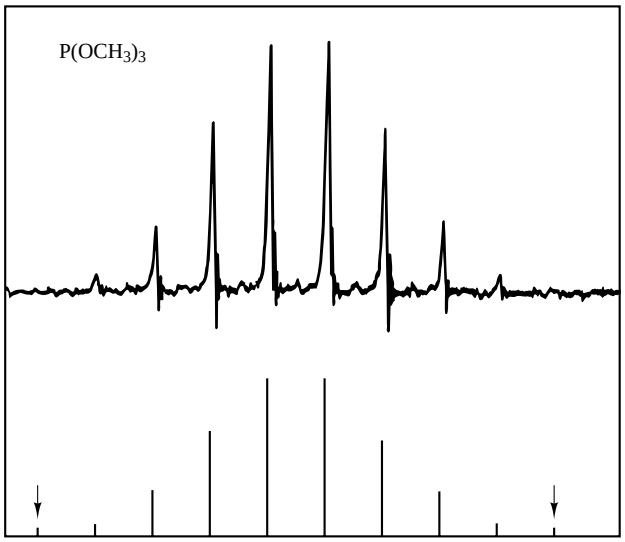

Figure 4 The experimental (top) and theoretical (bottom) phosphorus magnetic resonance spectra of trimethyl phosphite at 23.4 MHz

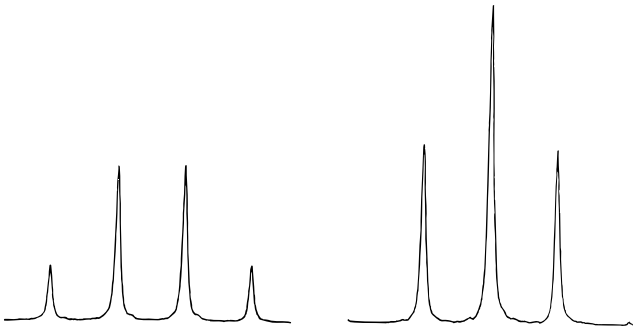

Figure 5 The proton magnetic resonance spectrum of diethyl ether at 400 MHz. The multiplet spacings in the methyl triplet and the methylene quartet yield $J = 7.02$ Hz. The chemical shift is 907.69 Hz, so $J/\delta = 0.008$

$$g_{F_G}(F_G - m_G + 1)(F_G + m_G)\left\{1 - \sum_{G' \neq G} \frac{2J_{GG'}m_G}{\nu_{GG'}}\right\} \prod_{G' \neq G} g_{F_{G'}} \qquad (47)$$

where G = A, B, C, ... and where $\nu_{GG'} = \nu_G - \nu_{G'}$. The total spin quantum numbers F_G and $F_G{}'$ and their statistical weights are computed by the procedure described in Section 2.5 Note that the formulas for first-order spectra are obtained by omitting the second summation in the formula for the frequencies, and omitting the second term within the curled brackets in the formula for the intensities.

For two groups A, B, the preceding formulas reduce to:

$$\nu_A + Jm_B + \frac{1}{2}\left(\frac{J^2}{\delta}\right)\{F_B(F_B + 1) - m_B(m_B + 1) + 2m_Am_B\} \qquad (48)$$

$$g_{F_A}g_{F_B}(F_A + m_A)(F_A - m_A + 1)\left(1 - \frac{2Jm_B}{\delta}\right) \qquad (49)$$

The zero, first, and second-order spectra computed by perturbation theory are illustrated in Figure 6 for the A_3B_2 system.

In the case of the ABC system, i.e., three spin-$\frac{1}{2}$ nuclei, second-order perturbation theory yields the results given in Table 5. Twelve transitions are predicted; the frequencies and intensities of the remaining lines are obtained by cyclically permuting A, B, C. It should be noted that on changing the sign of each coupling constant the spectrum is transformed into itself. The same result holds for two-group systems, on recalling that to each value of m_B there is a corresponding value $-m_B$. Subject to the condition that the populations of the various levels are approximately equal, a high-resolution spectrum is independent of the signs of the coupling constants;[1] only the relative signs can be determined. When there is only one coupling constant we shall arbitrarily assume it to be positive.

The vinyl group protons in vinyl acetate at 60 MHz (Figure 7) provide an example of an ABC system to which second-order theory is applicable.

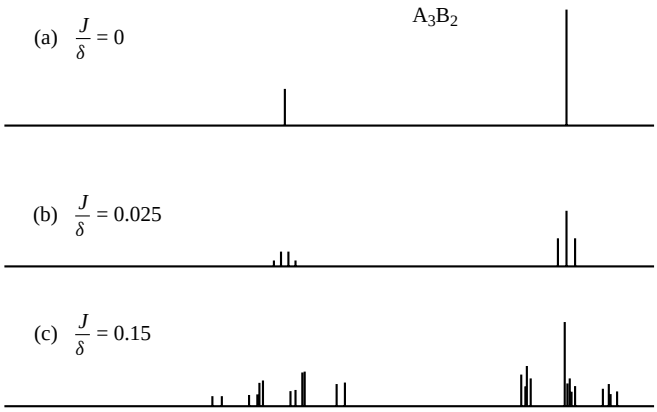

Figure 6 Zero, first, and second-order spectra for an A_3B_2 system

Table 5 Second-Order Perturbation Analysis of the ABC System[a]

Frequency	Relative intensity
$\nu_A + \frac{1}{2}(J_{AB} + J_{AC}) + \frac{1}{4}\left(\frac{J_{AB}^2}{\nu_{AB}} + \frac{J_{AC}^2}{\nu_{AC}}\right)$	$1 - \frac{J_{AB}}{\nu_{AB}} - \frac{J_{AC}}{\nu_{AC}}$
$\nu_A + \frac{1}{2}(J_{AB} - J_{AC}) + \frac{1}{4}\left(\frac{J_{AB}^2}{\nu_{AB}} + \frac{J_{AC}^2}{\nu_{AC}}\right)$	$1 - \frac{J_{AB}}{\nu_{AB}} + \frac{J_{AC}}{\nu_{AC}}$
$\nu_A - \frac{1}{2}(J_{AB} - J_{AC}) + \frac{1}{4}\left(\frac{J_{AB}^2}{\nu_{AB}} + \frac{J_{AC}^2}{\nu_{AC}}\right)$	$1 + \frac{J_{AB}}{\nu_{AB}} - \frac{J_{AC}}{\nu_{AC}}$
$\nu_A - \frac{1}{2}(J_{AB} + J_{AC}) + \frac{1}{4}\left(\frac{J_{AB}^2}{\nu_{AB}} + \frac{J_{AC}^2}{\nu_{AC}}\right)$	$1 + \frac{J_{AB}}{\nu_{AB}} + \frac{J_{AC}}{\nu_{AC}}$

Here, and subsequently, $\nu_{AB} = \nu_A - \nu_B$, $\nu_{AC} = \nu_A - \nu_C$, etc.

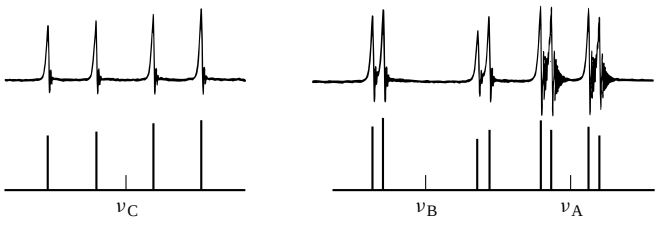

Figure 7 The proton magnetic resonance spectrum of the vinyl group protons in vinyl acetate at 60 MHz. The second-order spectrum was calculated for $\nu_{AB} = 18.71$ Hz, $\nu_{BC} = 146.09$ Hz, $|J_{AB}| = 1.45$ Hz, $|J_{AC}| = 6.37$ Hz, and $|J_{BC}| = 14.01$ Hz

4 STRONGLY COUPLED SYSTEMS

4.1 The AB System

The AB system consists of two spin-$\frac{1}{2}$ nuclei with the same magnetogyric ratio and resonance frequencies ν_A, ν_B in the absence of spin–spin interactions. We shall assume $\nu_A > \nu_B$, and write $\delta = \nu_A - \nu_B$ for the intramolecular (internal) chemical shift.

There are four independent states of angular momentum, so that operators will be represented by 4×4 matrices. As a basis we use the product functions $\alpha\alpha$, $\alpha\beta$, $\beta\alpha$, $\beta\beta$, writing the factors in alphabetical order. Operators referring to nucleus A operate only on the first factor of a product function; operators for nucleus B operate only on the second factor.

The stationary Hamiltonian operator is

$$\hat{\mathcal{H}} = -h(\nu_A \hat{I}_{Az} + \nu_B \hat{I}_{Bz} + J\hat{\boldsymbol{I}}_A \cdot \hat{\boldsymbol{I}}_B) \tag{50}$$

where for brevity we have written J for J_{AB}. The coupling operator $\hat{\boldsymbol{I}}_A \cdot \hat{\boldsymbol{I}}_B$ is rotationally invariant, so it commutes with $\hat{F}_z$. But the latter commutes with $\hat{I}_{Az}$ and $\hat{I}_{Bz}$, which implies $[\hat{\mathcal{H}}, \hat{F}_z] = 0$. Consequently, the matrix of $\hat{\mathcal{H}}$ relative to the product basis will be decomposed into three submatrices of dimensions 1×1, 2×2, 1×1, corresponding to the eigenvalues 1, 0, 0, -1 of $\hat{F}_z$.

To compute the energy eigenvalues it proves convenient to write the interaction operator in terms of raising and lowering operators:

$$\hat{\boldsymbol{I}}_A \cdot \hat{\boldsymbol{I}}_B = \hat{I}_{Az}\hat{I}_{Bz} + \tfrac{1}{2}(\hat{I}_{A+}\hat{I}_{B-} + \hat{I}_{A-}\hat{I}_{B+}) \tag{51}$$

Operating on the product functions with $\hat{\mathcal{H}}$, we obtain:

$$\left.\begin{aligned} \hat{\mathcal{H}}\alpha\alpha &= -\tfrac{1}{2}(\nu_A + \nu_B + \tfrac{1}{2}J)\alpha\alpha \\ \hat{\mathcal{H}}\alpha\beta &= -\tfrac{1}{2}(\delta - \tfrac{1}{2}J)\alpha\beta - \tfrac{1}{2}J\beta\alpha \\ \hat{\mathcal{H}}\beta\alpha &= \tfrac{1}{2}(\delta + \tfrac{1}{2}J)\beta\alpha - \tfrac{1}{2}J\alpha\beta \\ \hat{\mathcal{H}}\beta\beta &= \tfrac{1}{2}(\nu_A + \nu_B - \tfrac{1}{2}J)\beta\beta \end{aligned}\right\} \tag{52}$$

Evidently, $\alpha\alpha$ and $\beta\beta$ are eigenvectors of $\hat{\mathcal{H}}$, but $\alpha\beta$ and $\beta\alpha$ are mixed by the interaction operator so that the remaining two eigenvectors are linear combinations of $\alpha\beta$ and $\beta\alpha$. The eigenvalues of these linear combinations are obtained by diagonalizing the 2×2 submatrix generated by $\alpha\beta$ and $\beta\alpha$:

$$\begin{pmatrix} -\delta + \frac{1}{2}J & -J \\ -J & \delta + \frac{1}{2}J \end{pmatrix}$$

The results of this computation are given in Table 6.

The selection rule $\Delta m_T = \Delta m_A + \Delta m_B = -1$ shows that transitions are allowed from each of the two states with $m_T = 0$ to the state with $m_T = -1$, and from the state with $m_T = 1$ to each of the states with $m_T = 0$. The resonance frequencies and relative intensities are computed using the formulas:

$$E_j - E_i = h\nu_{i\to j} \tag{53}$$

$$\text{Int}(i \to j) = |(\psi_j, (\hat{I}_{A-} + \hat{I}_{B-})\psi_i)|^2 \tag{54}$$

Table 6 [a]Eigenvalues and Eigenvectors for the AB System

Eigenvector	m_T	Energy
1. $\alpha\alpha$	1	$-\frac{1}{2}(\nu_A + \nu_B + \frac{1}{2}J)$
2. $\frac{1}{(1+Q^2)^{1/2}}$ $(Q\alpha\beta - \beta\alpha)$	0	$\frac{1}{2}(\frac{1}{2}J + R)$
3. $\frac{1}{(1+Q^2)^{1/2}}$ $(\alpha\beta + Q\beta\alpha)$	0	$\frac{1}{2}(\frac{1}{2}J - R)$
4. $\beta\beta$	-1	$\frac{1}{2}(\nu_A + \nu_B - \frac{1}{2}J)$

[a]$Q = J/(\delta + R)$, $R = (J_2 + \delta^2)^{\frac{1}{2}}$.

where the ψ_i, $i = 1, 2, 3, 4$, are the eigenvectors of $\hat{\mathcal{H}}$ ordered as in Table 6. As an illustration we compute Int($1 \to 2$) and Int($1 \to 3$):

$$(I_{A-} + I_{B-})\psi_1 = \beta\alpha + \alpha\beta = (1 + Q^2)^{-1/2}\{(Q-1)\psi_2 + (Q+1)\psi_3\} \tag{55}$$

$$\text{Int}(1 \to 2) = \frac{(1+Q)^2}{1+Q^2} = 1 + J/R \tag{56}$$

$$\text{Int}(1 \to 3) = \frac{(1-Q)^2}{1+Q^2} = 1 - J/R \tag{57}$$

where

$$R = (J^2 + \delta^2)^{1/2}, \quad Q = \frac{J}{\delta + R} \tag{58}$$

The resonance frequencies and relative intensities are given in Table 7. Here, and subsequently, transitions denoted A are those for which $\Delta m_A = -1$ and $\Delta m_B = 0$ in the limit $J \to 0$; in this limit, the frequencies of A transitions approach ν_A. Similarly, B transitions for which $\Delta m_B = -1$, $\Delta m_A = 0$ as $J \to 0$, approach ν_B.

The spectrum consists of four lines and is symmetrical with respect to the mean resonance frequency, as indicated in Figure 8. The separations of the mean and extreme resonance frequencies may be used to compute the values of J and δ:

$$J = \tfrac{1}{2}\{(A_1 - B_1) - (A_2 - B_2)\}, \quad \delta = [(A_1 - B_1)(A_2 - B_2)]^{1/2} \tag{59}$$

The proton spectrum of 2-bromo-5-chlorothiophene at 23.4 MHz is shown in Figure 9.

In the limit $\delta \to 0$, the AB system reduces to an A_2 system, the central lines coalesce, and the intensities of the outer lines decrease to zero. When δ is large compared with J, the AB system becomes an AX system with all four lines of equal intensity. The variation of the spectrum as J ranges from 0 to ∞ is shown in Figure 10.

Table 7 Frequencies and Intensities for the AB System

Transition[a]	Relative intensity	Frequency
A_1	$1 - J/R$	$\frac{1}{2}(\nu_A + \nu_B + J + R)$
A_2	$1 + J/R$	$\frac{1}{2}(\nu_A + \nu_B - J + R)$
B_1	$1 + J/R$	$\frac{1}{2}(\nu_A + \nu_B + J - R)$
B_2	$1 - J/R$	$\frac{1}{2}(\nu_A + \nu_B - J - R)$

[a]Here, and subsequently, transitions denoted A, B are those having resonance frequencies at ν_A, ν_B, respectively, in the limit $J \to 0$.

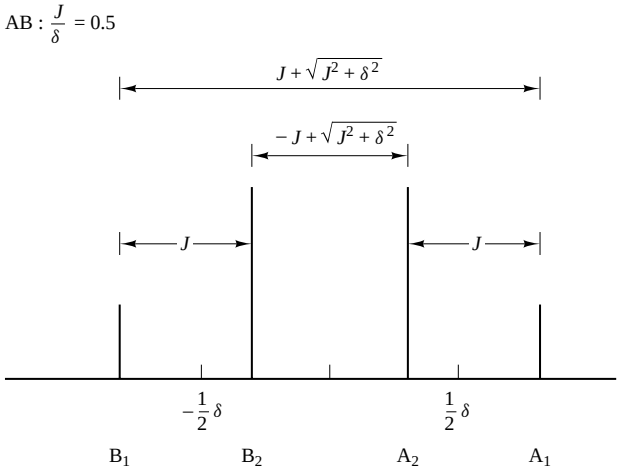

Figure 8 The theoretical AB spectrum for $J/\delta = 0.5$

Figure 9 The proton magnetic resonance spectrum of 2-bromo-5-chlorothiophene at 23.4 MHz

4.2 The A_2B System

The A_2B system is the simplest system containing a nontrivial group of magnetically equivalent nuclei. The coupling within group A does not affect the spectrum, so it is not necessary to include it when making detailed calculations of the spectrum.[1] The results of the calculation are collected in Table 8, where

$$R_\pm = (\delta^2 \pm J\delta + \tfrac{9}{4}J^2)^{1/2} \quad Q_\pm = \frac{J\sqrt{2}}{\delta \pm \frac{1}{2}J + R_\pm} \tag{60}$$

Theoretical spectra are shown in Figures 11 and 12. The values of J and δ are given by the formulas

$$J = \tfrac{1}{3}\{(A_1 - A_4) + (B_1 - B_3)\}, \quad \delta = \tfrac{1}{2}\{(A_2 - B_4) + (A_3 - B_4)\} \tag{61}$$

The experimental spectrum of 1,2,3-trichlorobenzene at 60 MHz is shown in Figure 13. Eight of the nine predicted lines

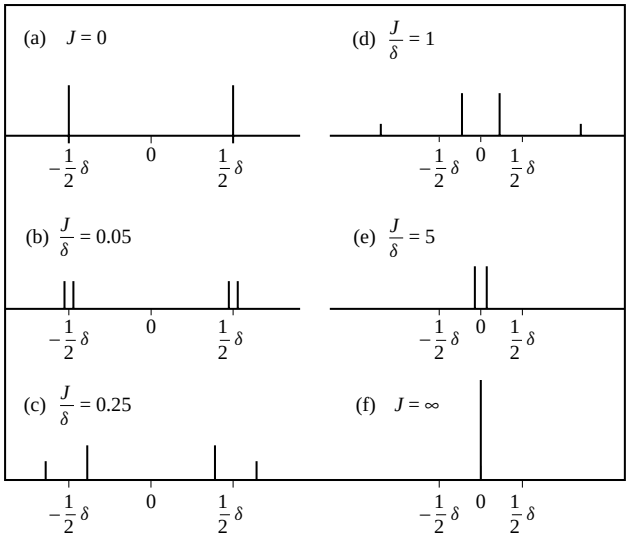

Figure 10 Theoretical AB spectra for various values of J/δ

are cleanly resolved, leading to accurate determinations of J and δ. The ninth line, labeled M in Table 8, is a mixed transition, i.e., in the limit $J \to 0$, the resonance does not approach ν_A nor ν_B but $2\nu_A - \nu_B$, corresponding to the improbable triple spin flip $\alpha\alpha\beta \to \beta\beta\alpha$ for which $\Delta m_A = -2$, $\Delta m_B = +1$. The calculated intensities of mixed transitions are generally negligible in the spectra of two-group systems,[1] but this is not necessarily true for systems of three or more groups.

4.3 Irreducible Components

Analysis of a system containing any number of magnetically equivalent groups with at least one $n_G > 1$ can always be simplified by reduction into irreducible components defined by the total spin quantum numbers. The superposition of appropriately weighted subspectra generated by the irreducible components yields the theoretical spectrum. When the subspectra of previously analyzed irreducible components can be identified in the observed spectrum, the analysis can be materially simplified.

The fundamental idea is to identify the total spin quantum numbers and multiplicities of each magnetically equivalent

Table 8 Frequencies and Intensities for the A_2B System

Resonance	Intensity	Frequency
A_1	$\frac{(\sqrt{2}-Q_-)^2}{1+Q_-^2}$	$\frac{1}{2}(\nu_A + \nu_B + \frac{3}{2}J + R_-)$
A_2	$\frac{Q_-(\sqrt{2}Q_- - 1) + \sqrt{2}^2}{(1+Q_+^2)(1+Q_-^2)}$	$\frac{1}{2}(2\nu_A + R_+ - R_-)$
A_3	$\frac{\{\sqrt{2}+Q_-(1+\sqrt{2}Q_-)\}^2}{(1+Q_+^2)(1+Q_-^2)}$	$\frac{1}{2}(2\nu_A + \nu_B + R_- - R_+)$
A_4	$\frac{(\sqrt{2}+Q_-)^2}{1+Q_-^2}$	$\frac{1}{2}(\nu_A + \nu_B + \frac{3}{2}J + R_+)$
B_1	$\frac{(1+\sqrt{2}Q_-)^2}{1+Q_-^2}$	$\frac{1}{2}(\nu_A + \nu_B + \frac{3}{2}J - R_-)$
B_2	$\frac{\{\sqrt{2}(Q_- - Q_+) - 1\}^2}{(1+Q_+^2)(1+Q_-^2)}$	$\frac{1}{2}(2\nu_A - R_+ - R_-)$
B_3	$\frac{(\sqrt{2}+Q_+-1)^2}{1+Q_-^2}$	$\frac{1}{2}(\nu_A + \nu_B + \frac{3}{2}J - R_+)$
B_4	1	ν_B
M	$\frac{\{(Q_+ - \sqrt{2})Q_- + \sqrt{2}Q_+\}^2}{(1+Q_+^2)(1+Q_-^2)}$	$\frac{1}{2}(2\nu_A + R_+ + R_-)$

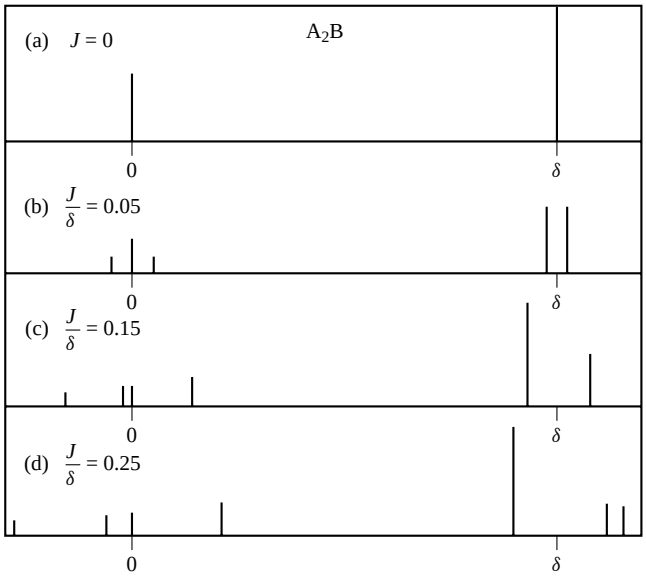

Figure 11 Theoretical A_2B spectra for various values of J/δ

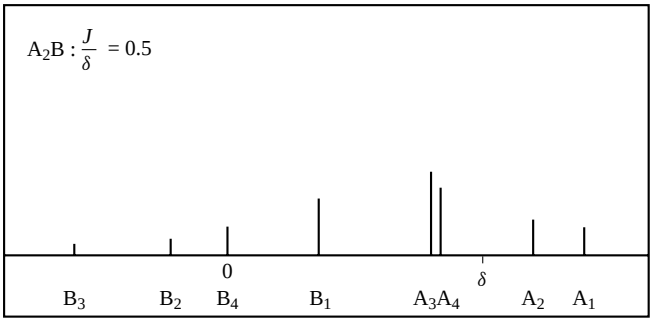

Figure 12 The theoretical A_2B spectrum for $J/\delta = 0.5$

group, assigning total spins in all possible ways to the various groups to form the irreducible component systems. The A_2B system provides the simplest example of a reducible spin system as $F_A = 1, 0$ and $F_B = \frac{1}{2}$ with $g_1 = g_0 = g_{1/2} = 1$. The spectrum of the A_2B system is thus the superposition of two irreducible components: $A_1B_{1/2}$ and $A_0B_{1/2}$, the latter consisting of a single line of unit intensity at ν_B. Thus, the decomposition may be symbolically written:

$$A_2B = A_1B_{1/2} + A_0B_{1/2} \tag{62}$$

In the general case, we can write:

$$A_{n_A}B_{n_B}C_{n_C}\ldots = \sum_{\text{all } F_G} (g_{F_A}g_{F_B}g_{F_C}\ldots)A_{F_A}B_{F_B}C_{F_C}\ldots \tag{63}$$

where the product of the spin multiplicities is the number of times the irreducible component to which it is prefixed occurs in the decomposition. For example, the A_3B system has $F_A = \frac{3}{2}, \frac{1}{2}$ with $g_{3/2} = 1$, $g_{1/2} = 2$, and $F_B = \frac{1}{2}$ with $g_{1/2} = 1$, so that

$$A_3B = A_{3/2}B_{1/2} + 2A_{1/2}B_{1/2} \tag{64}$$

Thus the $A_{1/2}B_{1/2}$, which is just the (irreducible) AB system, occurs twice in the decomposition. If we can detect the AB

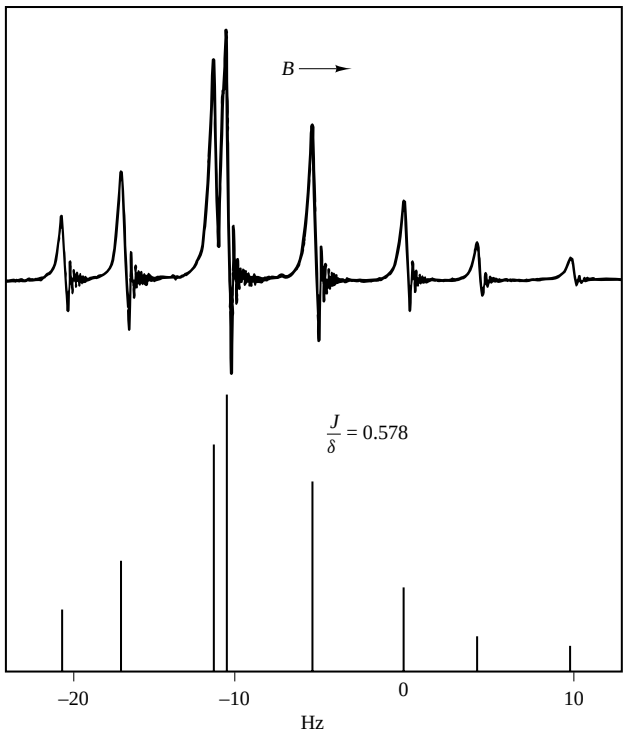

Figure 13 The proton magnetic resonance spectrum of 1,2,3-trichlorobenzene at 60 MHz. The theoretical spectrum was calculated with $J = 8.08$ Hz, $\delta = 13.97$ Hz

subspectrum in the observed spectrum, we can deduce the chemical shift and coupling constant without computing the spectrum of the irreducible $A_{3/2}B_{1/2}$ system.

As an illustration, consider the AB_2C system whose decomposition is

$$AB_2C = A_{1/2}B_1C_{1/2} + A_{1/2}B_0C_{1/2} \tag{65}$$

But $A_{1/2}B_0C_{1/2} \equiv$ to $A_{1/2}C_{1/2}$, since a system with spin zero does not have a magnetic moment and cannot, therefore, interact with internal or external fields. Identification of the $A_{1/2}C_{1/2}$ component in the experimental spectrum will yield $|J_{AC}|$ and ν_{AC}. The spectrum of *m*-dibromobenzene as observed at 60 MHz is shown in Figure 14, in which the irreducible $A_{1/2}C_{1/2}$ is identified by the consideration that for negligible coupling of nucleus C to A and to B the spectrum would be approximately that of an AB_2 system.

Referring to Table 4, we can deduce the following reduction of the A_3B_2 system into its irreducible components:

$$A_3B_2 = A_{3/2}B_1 + A_{3/2}B_0 + 2A_{1/2}B_1 + 2A_{1/2}B_0 \tag{66}$$

Here, the irreducible components with $F_B = 0$ generate a single, undeviated resonance at ν_A. If the $A_{1/2}B_1$ component can be identified, the coupling constant and ν_B can be determined from the known properties of that system. The application of this procedure to tetraethylsilane is illustrated in Figure 15.

When a system contains groups with an even number of spin-$\frac{1}{2}$ nuclei, the irreducible component for which all but one group, say group A, have their total spins equal to zero will generate a single line at ν_A. Similarly, the other

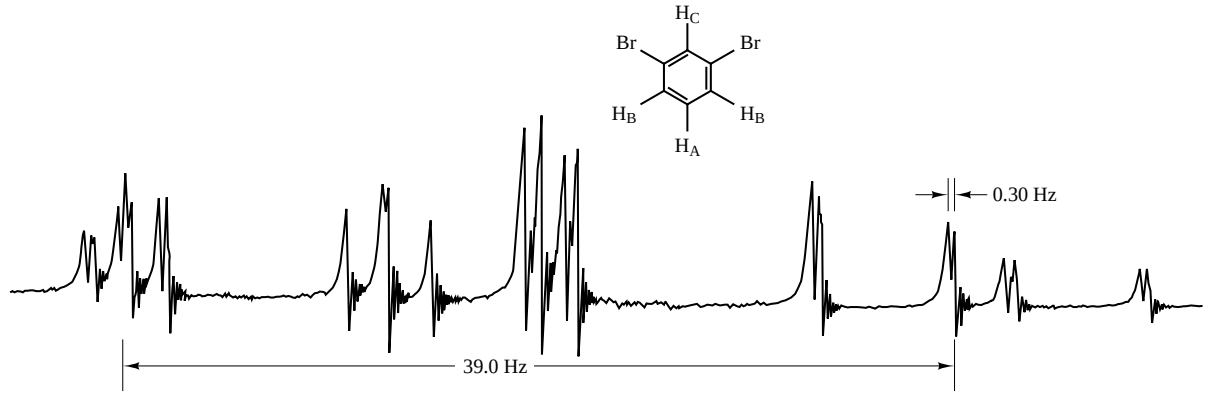

Figure 14 The proton magnetic resonance spectrum of *m*-dibromobenzene at 60 MHz, showing the irreducible $A_{1/2}C_{1/2}$ component with $|J_{AC}| = 0.30$ Hz and $\delta = 39.0$ Hz

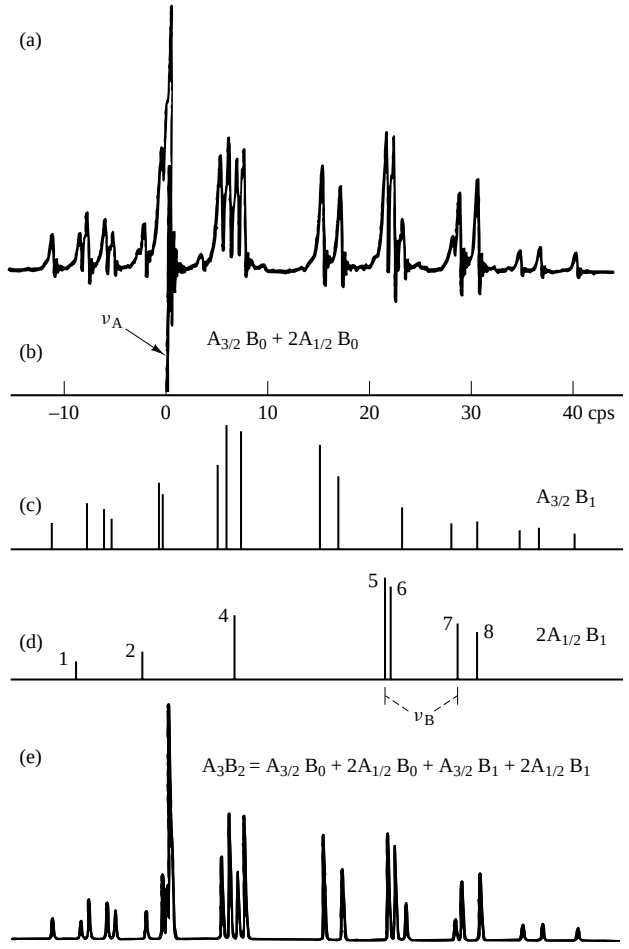

Figure 15 The proton magnetic resonance spectrum of tetraethylsilane at 60 MHz: (a) experimental spectrum; (b)–(d) irreducible components; and (e) calculated composite spectrum. The horizontal axis is in Hz. Analysis of the irreducible components yields $J = 7.98$ Hz, $\delta = 24.91$ Hz

irreducible components will generate lines at each of the uncoupled Larmor frequencies. Identification of these lines in the spectrum will then yield all of the internal chemical shifts. Propane, an A_6B_2 system, is an example. The decomposition of the spectrum is shown in Figure 16. The coupling constant was determined from the properties of the A_2B_2 system.[1]

4.4 Intensity Theorems

The intensity associated with a generic irreducible component is given by the formula

$$\mathrm{Int}A_{F_A}B_{F_B}C_{F_C}\ldots = \frac{2}{3}\left\{\sum_G F_G(F_G+1)\right\}\prod_G(2F_G+1) \qquad (67)$$

in which the sum and product are taken over all groups. Since the component $A_{F_A}B_{F_B}C_{F_C}\ \ldots$ appears $g_{F_A}g_{F_B}g_{F_C}$ times in the reduction of the system, the contribution of all such systems to the total intensity of the system is $(g_{F_A}g_{F_B}g_{F_C}\ldots)\mathrm{Int}A_{F_A}B_{F_B}C_{F_C}\ldots$. Using these formulas, it is possible to compute the contribution of a given irreducible component to the total relative intensity. For N particles with spins $I_1, I_2, \ldots$, the total relative intensity is[1]

$$\frac{2}{3}\prod_{i=1}^{N}(2I_i+1)\left\{\sum_{i=1}^{N}I_i(I_i+1)\right\}$$

which reduces to $2^{N-1}N$ when all $I_i = \frac{1}{2}$. For example, the irreducible $A_{1/2}B_{1/2}$ component occurs 42-times in the A_9B system, such as isobutane, and contributes 3.28% to the total intensity.

5 THE X APPROXIMATION

5.1 The ABX_n System

Systems with several groups of magnetically equivalent nuclei A, B, C, ... , X admit an extremely useful approximation when ν_X is very different from ν_A, ν_B, ν_C, ... The essential idea was implicit in the discussion of first-order spectra, when only the z components of angular momenta and their degeneracies were required for the analysis. In other words, the x and y components of the interaction involving $\hat{\boldsymbol{I}}_X$ can be neglected, so that in the particular case of two groups A and X, the stationary Hamiltonian takes the form

$$\hat{\mathcal{H}} = -h(\nu_A\hat{I}_{Az} + \nu_X\hat{I}_{Xz} + J_{AX}\hat{I}_{Az}\hat{I}_{Xz}) \qquad (68)$$

Since $\hat{I}_{Az}$ and $\hat{I}_{Xz}$ commute with $\hat{\mathcal{H}}$, states of the system can be chosen to be eigenvectors of these operators as well as

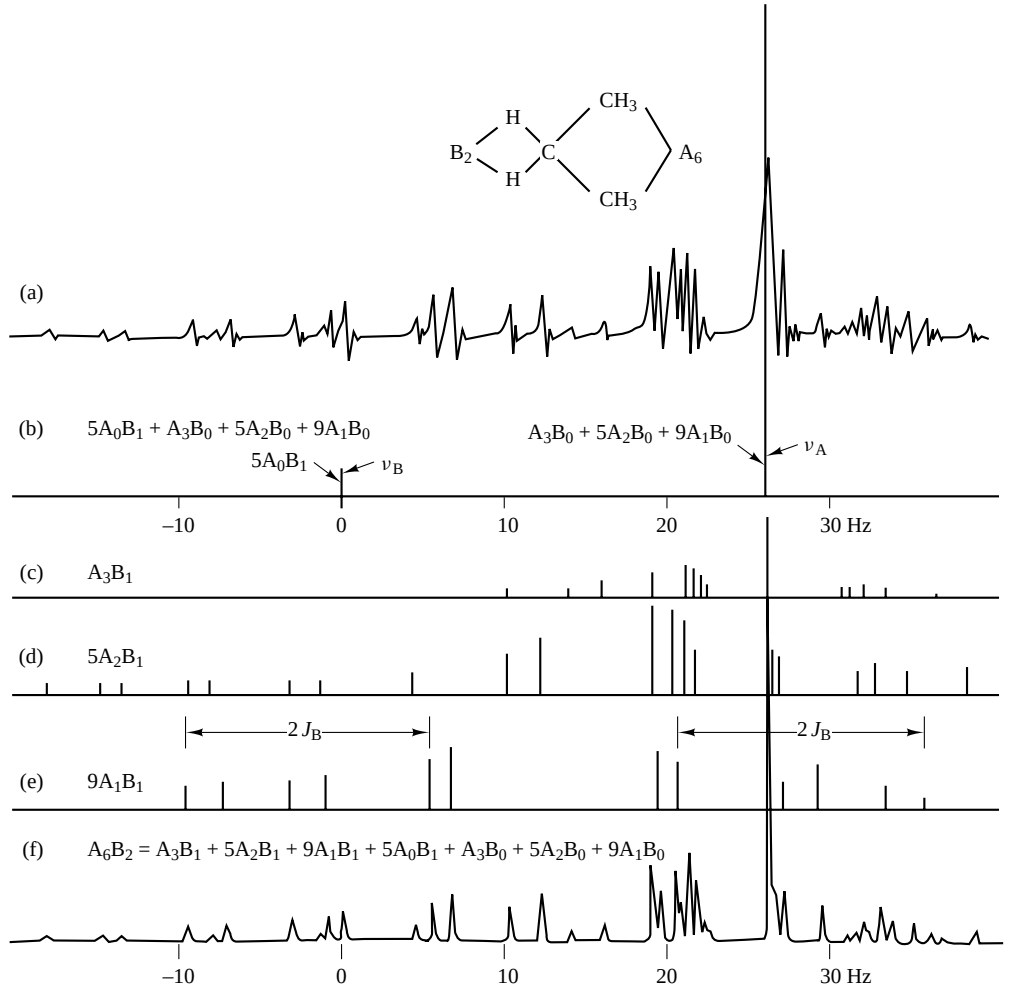

Figure 16 The proton magnetic resonance spectrum of propane at 60 MHz: (a) experimental spectrum; (b)–(e) irreducible components; and (f) calculated composite spectrum. Analysis of the irreducible components yields $J = 7.45$ Hz, $\delta = 26.32$ Hz

the Hamiltonian. For the validity of this approximation it is sufficient that $|\nu_{AX}| \ll |J_{AX}|$. The content of this condition is that states of very different energies can be treated by first-order perturbation theory.

The generalization of the preceding considerations presents no difficulties, but we shall consider only the case of three-group systems when the sufficient conditions for neglect of the x and y components of $J_{AX}\hat{\boldsymbol{I}}_A \cdot \hat{\boldsymbol{I}}_X$ and $J_{BX}\hat{\boldsymbol{I}}_B \cdot \hat{\boldsymbol{I}}_X$ are $|\nu_{AX}|$, $|\nu_{BX}| \gg |\nu_{AB}|$, $|J_{AB}|$, $|J_{AX}|$, $|J_{BX}|$. Excepting experiments at very low magnetic field strengths, these conditions will certainly be satisfied if $\gamma_X \neq \gamma_A = \gamma_B$. In any case, the stationary Hamiltonian is

$$\hat{\mathcal{H}} = -h(\nu_A \hat{I}_{Az} + \nu_B \hat{I}_{Bz} + \nu_X \hat{I}_{Xz} + J_{AB}\hat{\boldsymbol{I}}_A \cdot \hat{\boldsymbol{I}}_B + J_{AX} I_{Az} I_{Xz} + J_{BX} \hat{I}_{Bz} \hat{I}_{Xz}) \tag{69}$$

Since $\hat{I}_{Az} + \hat{I}_{Bz}$ and $\hat{I}_{Xz}$ both commute with $\hat{\mathcal{H}}$ and with each other, the eigenfunctions of the system will be eigenfunctions of $\hat{I}_{Az} + \hat{I}_{Bz}$, $\hat{I}_{Xz}$, and $\hat{\mathcal{H}}$. Taking the ABX_n system as a specific example, the product functions are of the form $\alpha\alpha\phi(F_X m_X)$, $\beta\beta\phi(F_X m_X)$, $\alpha\beta\phi(F_X m_X)$, $\beta\alpha\phi(F_X m_X)$. Only the last two products are coupled by the interaction $J_{AB}\hat{\boldsymbol{I}}_A \cdot \hat{\boldsymbol{I}}_B$, as these products have the same eigenvalue of $\hat{I}_{Az} + \hat{I}_{Bz}$, i.e. $m_A + m_B$.

The values of F_X and their statistical weights for n spin-$\frac{1}{2}$ nuclei may be determined by the procedure explained in Section 2.5, and the same procedure may be used to to determine the corresponding values for nuclei with $I > \frac{1}{2}$, such as n deuterium atoms. The spectrum is worked out along the lines indicated for the AB system and the results are collected in Table 9, where:

$$R(m_X) = \{[\delta + (J_{AX} - J_{BX})m_X]^2 + J_{AB}^2\}^{1/2} \tag{70}$$

$$Q(m_X) = \frac{J_{AB}}{\delta + (J_{AX} - J_{BX})m_X + R(m_X)} \tag{71}$$

The complete spectrum is obtained for any value of n as follows. Starting with a particular value of F_X, we put $m_X = F_X, F_X - 1, \ldots, -F_X$ in each of the tabulated A and B transitions, thus obtaining a total of $4(2F_X + 1)$ A and B transitions. For the X and M transitions, m_X only takes the $2F_X$ values, $F_X, F_X - 1, \ldots, -F_X + 1$, for a total of $12F_X$ X and M transitions. Repeating this procedure for each value of F_X, the entire spectrum is generated.

It is important to recognize that the AB region of the spectrum consists of a superposition of AB systems and the identification of these AB quartets is an important key to the

Table 9 Frequencies and Intensities for the ABX_n System

Transition	Intensity	Frequency
A	$g_{F_X}\left(1 \pm \frac{J_{AB}}{R(m_X)}\right)$	$\frac{1}{2}\{\nu_A + \nu_B \mp J_{AB} + (J_{AX} + J_{BX})m_X + R(m_X)\}$
B	$g_{F_X}\left(1 \pm \frac{J_{AB}}{R(m_X)}\right)$	$\frac{1}{2}\{\nu_A + \nu_B \pm J_{AB} + (J_{AX} + J_{BX})m_X - R(m_X)\}$
X_1	$\frac{g_{F_X}(F_X+m_X)(F_X-m_X+1)Q(m_X)Q(m_X-1)+1^2}{1+Q^2(m_X)1+Q^2(m_X-1)}$	$\frac{1}{2}\{2\nu_X \pm R(m_X - 1) \mp R(m_X)\}$
X_2	$g_{F_X}(F_X + m_X)(F_X - m_X + 1)$	$\frac{1}{2}(2\nu_X \pm J_{AX} \pm J_{BX})$
M	$\frac{g_{F_X}(F_X+m_X)(F_X-m_X+1)Q(m_X)-Q(m_X-1)^2}{1+Q^2(m_X)1+Q^2(m_X-1)}$	$\frac{1}{2}\{2\nu_X \pm R(m_X - 1) \pm R(m_X)\}$

analysis. On comparing the expressions for $R(m_X)$ and $Q(m_X)$ with those of R and Q for the AB system, we see that the apparent internal chemical shift, for a given value of m_X, is:

$$\nu^*_{AB} = |\delta + (J_{AX} - J_{BX})m_X| \tag{72}$$

Since these pseudo AB systems are symmetrical with respect to their mean resonance frequencies, the double quantum transitions for these systems can be used to identify their centers of symmetry[1] (see ***Multiple Quantum Spectroscopy of Liquid Samples***). It should also be noted that the mixed transitions occur only in the X region of the spectrum.

5.2 The ABX System

For the ABX system $F_X = \frac{1}{2}$, so there will be eight AB transitions (two AB quartets), four X transitions, and two mixed transitions. The ABX system is often used to obtain a set of chemical shifts and coupling constants as initial parameters in an exact analysis of an ABC system. The spectrum of 2-fluoro-4,6-dichlorophenol, Figures 17 and 18, provides an excellent example of an ABX spectrum. The theoretical spectrum of the AB region shows the decomposition into (pseudo) AB quartets. The X region, Figure 18, shows the four X transitions and the two mixed transitions. The details of the analysis show that J_{AX} and J_{BX} are of opposite sign.

5.3 The ABX_2 System

For the ABX_2 system F_X = 1, 0, so there will be a total of 28 transitions: 12 AB transitions, 12 X transitions, and four mixed transitions. In particular, the AB region consists of three AB quartets: an actual AB quartet which occurs twice and two pseudo AB quartets each occurring once, with apparent internal chemical shifts

$$\nu^*_{AB} = |\delta + J_{AX} - J_{BX}| \tag{73}$$

$$\nu^{**}_{AB} = |\delta - J_{AX} + J_{BX}|. \tag{74}$$

The fact that the actual AB quartet appears with twice the relative intensity of the pseudo AB quartets may render its identification in an experimental trace easier.

The experimental and theoretical spectra of an approximately equimolar solution of *cis*- and *trans*-1,3-dichloropropene are shown in Figures 19 and 20. Both components conform to the ABX_2 approximation. Although the composite experimental spectrum is somewhat complicated, there is sufficient resolution to disentangle the *cis* and *trans* isomers by

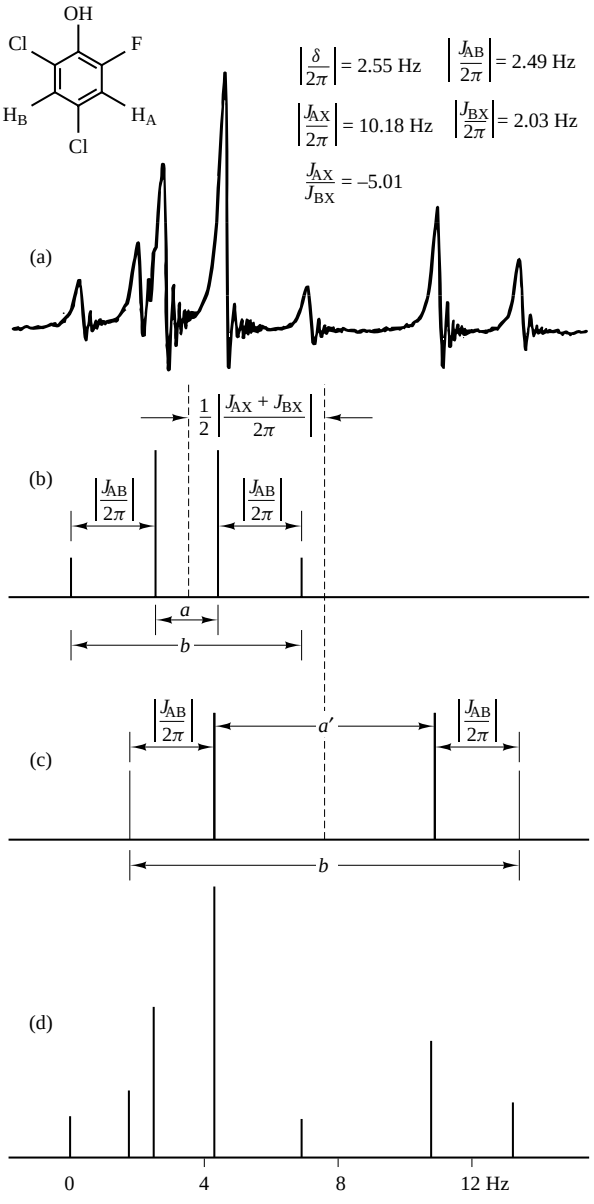

Figure 17 The proton magnetic resonance spectrum of 2-fluoro-4,6-dichlorophenol at 60 MHz. The parameters are in angular frequency units

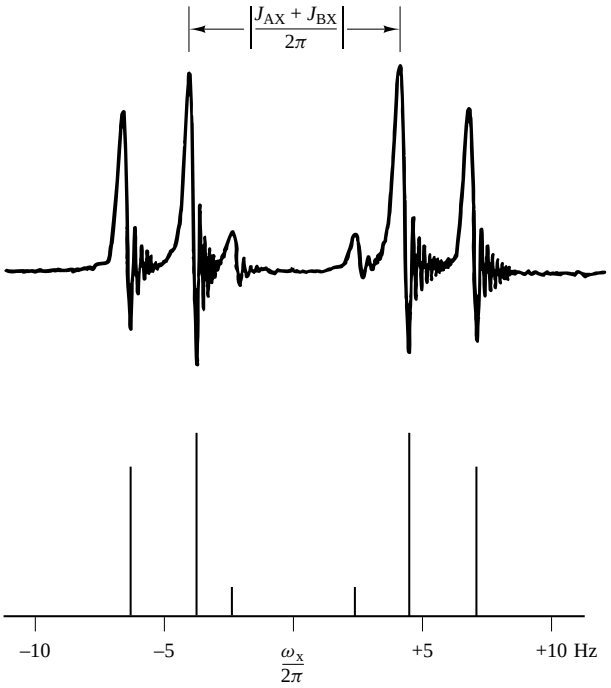

Figure 18 The fluorine magnetic resonance spectrum of 2-fluoro-4,6-dichlorophenol at 56.4 MHz

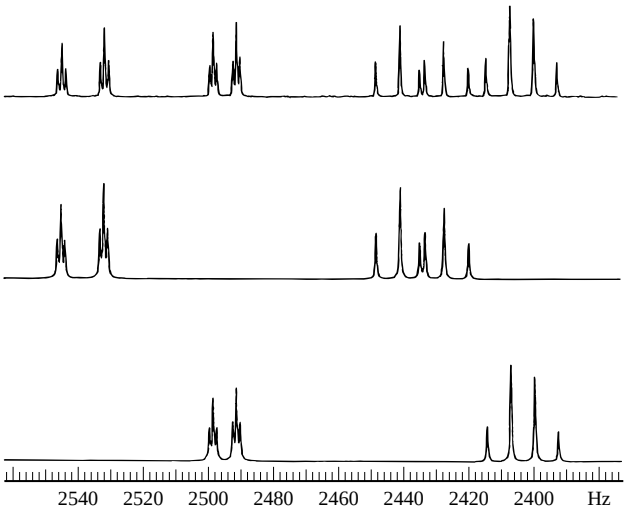

Figure 19 Experimental and theoretical spectra of an approximately equimolar mixture of *cis*- and *trans*-1,3-dichloropropene at 400 MHz: the AB region (top); the calculated *trans* AB region (middle); and the calculated *cis* AB region (bottom)

virtue of the fact that couplings generally decrease in the order *trans* > *cis* > *gem*. This consideration leads to the separation of the isomers indicated in Figures 19 and 20. Taking the AB region of the *trans* isomer first, we recall that it should consist of 12 lines comprising three AB quartets, one of which is a true AB quartet that appears with twice the intensity of the pseudo AB quartets. The four lines of the true AB quartet are easily picked out and they lead at once to $|\nu_{AB}|$ = 103.36 Hz, $|J_{AB}|$ = 13.19 Hz. We can also easily pick out two of the lines belonging to the pseudo AB quartets in the high-frequency region of

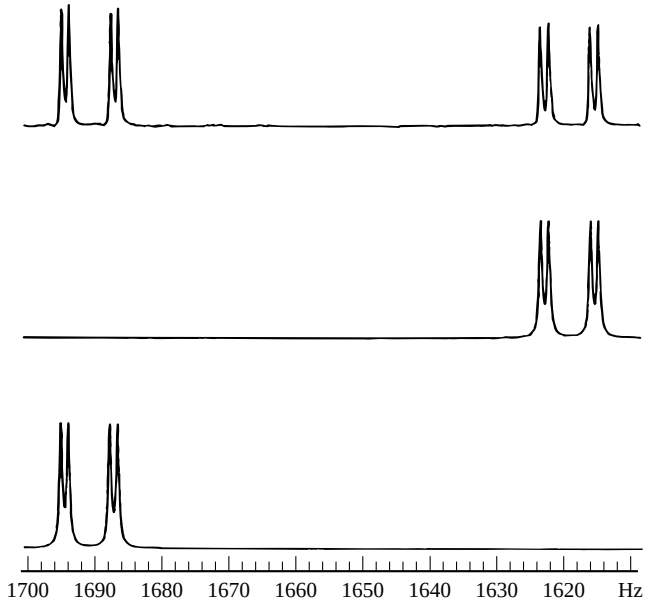

Figure 20 Experimental and theoretical spectra of an approximately equimolar mixture of *cis*- and *trans*- 1,3-dichloropropene at 400 MHz: the X region (top); the calculated *trans* X region (middle); and the calculated *cis* X region (bottom)

the spectrum: the first and third lines of the two triplets at high frequency constitute one pair, the third and sixth the other; but whichever pair of lines we choose, there are two choices for the other pair of lines of the quartet, depending on the relative signs of J_{AX} and J_{BX}. It turns out that the spectrum is independent of the sign of J_{AB} and, in the particular cases under consideration here, the spectra are independent of the relative signs of J_{AX} and J_{BX}. The magnitudes of these coupling constants for the *trans* isomer are $|J_{AX}|$ = 1.22 Hz, $|J_{BX}|$ = 7.44 Hz, and $|\nu_{AX}|$ = 918.8 Hz, $|\nu_{BX}|$ = 815.4 Hz. It should be noted that the coupling of the methylene protons (group X) to *trans* and geminal protons would be expected by first-order perturbation theory to split each of the lines of the AB quartet into triplets, and indeed the four triplets are evident in the AB region. A similar consideration applies to the *cis* isomer, but two lines of the low-frequency triplets overlap so that only 10 of the 12 AB lines are observed. An analysis similar to that for the *trans* isomer yields $|J_{AB}|$ = 7.25 Hz, $|J_{AX}|$ = 1.08 Hz, $|J_{BX}|$ = 7.38 Hz, $|\nu_{AB}|$ = 90.8 Hz, $|\nu_{AX}|$ = 803.61 Hz, $|\nu_{BX}|$ = 712.83 Hz.

6 SYMMETRICAL SYSTEMS

6.1 Symmetry Group of the Spin Hamiltonian

Analysis of symmetrical spin systems can be simplified through the use of group theoretical considerations, since each transformation in the symmetry group of the spin system commutes with the Hamiltonian. More precisely, the symmetry group of the spin system consists of those nonsingular operators $\hat{R}$ that leave the Hamiltonian invariant under a similarity transformation: $\hat{R}\,\hat{\mathcal{H}}\,\hat{R}^{-1} = \hat{\mathcal{H}}$. The symmetry group of the spin system is a subgroup of the symmetry

group of the molecule, where by 'symmetry group of the molecule' we mean the symmetry group of the molecule in its equilibrium configuration. As an illustration, consider the *o*-dichlorobenzene molecule (**1**) whose symmetry group consists of $\hat{E}$, the group identity, a twofold rotation $\hat{C}_2$, a reflection in the plane of the molecule σ_v, and $\sigma_{v'}$, a reflection in a plane through the rotation axis perpendicular to the plane of the molecule.

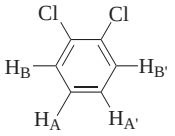

(1)

The symmetry of the molecule requires that $\nu_A = \nu_{A'}$, $\nu_B = \nu_{B'}$, $J_{AB} = J_{A'B'}$, $J_{AB'} = J_{A'B}$. On the other hand, the symmetry group of the spin system contains only two transformations, i.e. $\hat{E}$ and $\hat{C}_2$, as σ_v and $\sigma_{v'}$ are equivalent to $\hat{E}$ and $\hat{C}_2$ insofar as the protons are concerned. The symmetry group of the molecule takes into account the electron distribution which contributes to the values of the shielding and coupling constants. Once the implications of the molecular symmetry group have been incorporated in the symmetry conditions imposed on the shielding and coupling constants, it is only necessary to consider the symmetry group of the nuclear spins, in this case the subgroup $\{\hat{E}, \hat{C}_2\}$.

Similar considerations apply to other molecules. Thus the molecular symmetry group of benzene is D_{6h} but the symmetry group of the protons is D_6. In this case, however, no group theoretical calculations are required since the molecule consists of a single group of magnetically equivalent nuclei and only one resonance would be observed. With the identification of magnetic equivalence—a consequence of the conservation of angular momentum—the essential group theoretical considerations have been taken into account. Thus, the symmetry group of the protons in *m*-dibromobenzene (**2**), i.e.

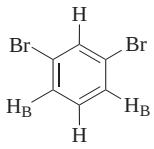

(2)

is $\{\hat{E}, \hat{C}_2\}$, but as the protons denoted by the letter B are magnetically equivalent, it would be superfluous to carry out a group theoretical analysis of the system—the symmetry is taken into account by the conservation of angular momentum of group B. For these reasons, it is not necessary to appeal to group theoretical considerations in many instances where they might seem appropriate. There are, of course, instances where group theoretical considerations are quite useful, the case of *o*-dichlorobenzene being an example we shall consider in detail.

The basic idea in the application of group theory is that each operator in the symmetry group of the spin system commutes with the Hamiltonian operator, so that in the case of an Abelian group all operators in the group commute. Except for the identity operator, there will be additional nontrivial constants of the motion (conserved quantities), and these will lead to further simplification of the Hamiltonian matrix. Moreover the operators of the group will also commute with the time dependent Hamiltonian, so there are additional symmetry restrictions on allowed transitions. Similar remarks apply to the case where the symmetry group of the spin system is non-Abelian, though in this case there will be fewer constants of the motion since not all of the group operators commute.

6.2 The AA′BB′ System

The case of a molecule with spin symmetry $\{\hat{E}, \hat{C}_2\}$ is easily worked out. We have $[\hat{\mathcal{H}}, \hat{F}_z] = [\hat{\mathcal{H}}, \hat{C}_2] = 0$, so that it is possible to find a set of eigenvectors that are eigenvectors of $\hat{\mathcal{H}}$, $\hat{F}_z$, and $\hat{C}_2$.

Since $\hat{C}_2^2 = \hat{E}$, the eigenvalues of $\hat{C}_2$ satisfy $\lambda^2 = 1$, so that $\lambda = \pm 1$. If, therefore, we chose the initial basis vectors to be eigenvectors of $\hat{C}_2$, the Hamiltonian matrix will consist of two submatrices, one corresponding to the states with $\lambda = +1$ and the other to the states with $\lambda = -1$.

A symmetrized set of basis vectors may be constructed from the product basis by the application of projection operators, using the group character table which, in this case, is

	$\hat{E}$	$\hat{C}_2$
$\mathcal{A}$	1	1
$\mathcal{B}$	1	−1

The symmetrized basis vectors belonging to the irreducible representation, $\mathcal{A}$, the symmetric representation, will be eigenvectors of $\hat{C}_2$ with $\lambda = +1$, whereas those belonging to $\mathcal{B}$, the antisymmetric representation, will be eigenvectors of $\hat{C}$ with $\lambda = -1$. The projection operators are $\hat{E} + \hat{C}_2$ for the symmetric representation and $\hat{E} - \hat{C}_2$ for the antisymmetric representation, the coefficients for $\hat{E}$ and $\hat{C}_2$ having been taken from the character table. A symmetrized basis is obtained by applying these operators to each element in the product basis, retaining only the linearly independent vectors thus derived. The normalized vectors are given in Table 10, from which it is evident that the Hamiltonian matrix will consist of two submatrices, one a 10×10 matrix corresponding to $\lambda = +1$, the other a 6×6 matrix corresponding to $\lambda = -1$. To prove that these vectors are eigenvectors of $\hat{C}_2$, observe that if ψ is any product vector for which $(\hat{E} \pm \hat{C}_2)\psi \neq 0$, then

$$\hat{C}_2(\hat{E} \pm \hat{C}_2)\psi = (\hat{C}_2 \pm \hat{E})\psi = \pm(\hat{E} \pm \hat{C}_2)\psi \tag{75}$$

An alternative procedure for deriving a symmetrized basis for the AA′BB′ system is to construct symmetrized vectors for the AA′ nuclei and BB′ nuclei separately, and then form their products. Applying the projection operators $\hat{E} \pm \hat{C}_2$ to the products $\alpha\alpha$, $\alpha\beta$, $\beta\alpha$, $\beta\beta$, we obtain the normalized basis vectors of Table 11. Using these vectors for the AA′ and BB′ nuclei, we obtain the basis vectors given in Table 12 A product belongs to the symmetric or antisymmetric representation according to whether the product of the $\hat{C}_2$ eigenvalues of the factors is +1 or −1. The advantage of this method is that each factor has definite eigenvalues of $\hat{I}_{Az} + \hat{I}_{A'z}$ and $\hat{I}_{Bz} + \hat{I}_{B'z}$ which will be useful in the discussion of the AA′XX′ system.

Table 10 Symmetrized Basis Vectors for the AA′BB′ System

Basis vector	$(\mathcal{S})_{m_T}$
$\alpha\alpha\alpha\alpha$	$(\mathcal{A})_2$
$\frac{1}{\sqrt{2}}(\alpha\alpha\alpha\beta + \alpha\alpha\beta\alpha)$	$1(\mathcal{A})_1$
$\frac{1}{\sqrt{2}}(\alpha\beta\alpha\alpha + \beta\alpha\alpha\alpha)$	$2(\mathcal{A})_1$
$\alpha\alpha\beta\beta$	$1(\mathcal{A})_0$
$\beta\beta\alpha\alpha$	$2(\mathcal{A})_0$
$\frac{1}{\sqrt{2}}(\alpha\beta\alpha\beta + \beta\alpha\beta\alpha)$	$3(\mathcal{A})_0$
$\frac{1}{\sqrt{2}}(\alpha\beta\beta\alpha + \beta\alpha\alpha\beta)$	$4(\mathcal{A})_0$
$\frac{1}{\sqrt{2}}(\alpha\beta\beta\beta + \beta\alpha\beta\beta)$	$1(\mathcal{A})_{-1}$
$\frac{1}{\sqrt{2}}(\beta\beta\alpha\beta + \beta\beta\beta\alpha)$	$2(\mathcal{A})_{-1}$
$\beta\beta\beta\beta$	$(\mathcal{A})_{-2}$
$\frac{1}{\sqrt{2}}(\alpha\alpha\alpha\beta - \alpha\alpha\beta\alpha)$	$1(\mathcal{B})_1$
$\frac{1}{\sqrt{2}}(\alpha\beta\alpha\alpha - \beta\alpha\alpha\alpha)$	$2(\mathcal{B})_1$
$\frac{1}{\sqrt{2}}(\alpha\beta\alpha\beta - \beta\alpha\beta\alpha)$	$1(\mathcal{B})_0$
$\frac{1}{\sqrt{2}}(\alpha\beta\beta\alpha - \beta\alpha\alpha\beta)$	$2(\mathcal{B})_0$
$\frac{1}{\sqrt{2}}(\alpha\beta\beta\beta - \beta\alpha\beta\beta)$	$1(\mathcal{B})_{-1}$
$\frac{1}{\sqrt{2}}(\beta\beta\alpha\beta - \beta\beta\beta\alpha)$	$2(\mathcal{B})_{-1}$

The analysis of an AA′BB′ system requires the solution of an algebraic equation of the fourth degree in five parameters, and is best handled numerically (see ***Analysis of Spectra: Automatic Methods***). Explicit expressions can be derived for 12 of the predicted 28 lines and these can be used to obtain a partial analysis. The spectrum of *o*-dichlorobenzene at 60 MHz is shown in Figure 21 in which the chemical shift and coupling constants are in angular units, hence the factors of 2π. The four lines shown separated by $L_+/2\pi = (J_{AB} + J_{AB'})/2\pi$ form a pseudo AB quartet which yields the values of $|\delta|$ and $|L_+|$. The spectrum of an AA′BB′ system is symmetrical about the mean resonance frequency.

6.3 The AA′XX′ System

When $|\delta| \to \infty$, all coupling constants remaining finite, the AA′BB′ system becomes an AA′XX′ system, and the X approximation yields considerable simplification of the problem. Of the four $(\mathcal{A})_0$ states, only $3(\mathcal{A})_0$ and $4(\mathcal{A})_0$ are mixed by spin–spin coupling, as these states have the same values of $m_{AA'}$ and $m_{XX'}$. The spectrum consists of 20 lines and Table 13 gives the 10 lines in the AA′ region where

$$K_\pm = J_{AA'} \pm J_{XX'}, \quad R_5 = (K_+^2 + L_-^2)^{1/2}$$

$$L_\pm = J_{AX} \pm J_{AX'} \quad Q_5 = -\frac{L_-}{K_+ + R_5}$$

$$R_2 = (K_-^2 + L_-^3)^{1/2} \quad Q_2 = -\frac{L_-}{K_- + R_2}$$

Table 11 Symmetrized Basis Vectors for Two Spin-$\frac{1}{2}$ Nuclei: C_2 Symmetry

Basis vector	m_T	$(\mathcal{S})_{m_T}$
$\alpha\alpha$	1	$(\mathcal{A})_1$
$\frac{1}{\sqrt{2}}(\alpha\beta + \beta\alpha)$	0	$(\mathcal{A})_0$
$\beta\beta$	−1	$(\mathcal{A})_{-1}$
$\frac{1}{\sqrt{2}}(\alpha\beta - \beta\alpha)$	0	$(\mathcal{B})_0$

Table 12 Symmetrized Basis Vectors for the AA′BB′ and AA′XX′ Systems

Basis vector	$m_{AA'}$	$m_{XX'}$	$(\mathcal{S})_{m_T}$
$\alpha\alpha\alpha\alpha$	1	1	$(\mathcal{A})_2$
$\frac{1}{\sqrt{2}}(\alpha\alpha\alpha\beta + \alpha\alpha\beta\alpha)$	1	0	$1(\mathcal{A})_1$
$\frac{1}{\sqrt{2}}(\alpha\beta\alpha\alpha + \beta\alpha\alpha\alpha)$	0	1	$2(\mathcal{A})_1$
$\alpha\ \alpha\ \beta\ \beta$	1	−1	$1(\mathcal{A})_0$
$\beta\ \beta\ \alpha\ \alpha$	−1	1	$2(\mathcal{A})_0$
$\frac{1}{2}(\alpha\beta\alpha\beta + \alpha\beta\beta\alpha + \beta\alpha\beta\alpha + \beta\alpha\alpha\beta)$	0	0	$3(\mathcal{A})_0$
$\frac{1}{2}(\alpha\beta\alpha\beta - \alpha\beta\beta\alpha - \beta\alpha\beta\alpha - \beta\alpha\alpha\beta)$	0	0	$4(\mathcal{A})_0$
$\frac{1}{\sqrt{2}}(\alpha\beta\beta\beta + \beta\alpha\beta\beta)$	0	−1	$1(\mathcal{A})_{-1}$
$\frac{1}{\sqrt{2}}(\beta\beta\alpha\beta + \beta\beta\beta\alpha)$	−1	0	$2(\mathcal{A})_{-1}$
$\beta\beta\beta\beta$	−1	−1	$(\mathcal{A})_{-2}$
$\frac{1}{\sqrt{2}}(\alpha\alpha\alpha\beta - \alpha\alpha\beta\alpha)$	1	0	$1(\mathcal{B})_1$
$\frac{1}{\sqrt{2}}(\alpha\beta\alpha\alpha - \beta\alpha\alpha\alpha)$	0	1	$2(\mathcal{B})_1$
$\frac{1}{2}(\alpha\beta\alpha\beta - \alpha\beta\beta\alpha - \beta\alpha\beta\alpha + \beta\alpha\alpha\beta)$	0	0	$1(\mathcal{B})_0$
$\frac{1}{2}(\alpha\beta\alpha\beta + \alpha\beta\beta\alpha - \beta\alpha\beta\alpha - \beta\alpha\alpha\beta)$	0	0	$2(\mathcal{B})_0$
$\frac{1}{\sqrt{2}}(\alpha\beta\beta\beta - \beta\alpha\beta\beta)$	0	−1	$1(\mathcal{B})_{-1}$
$\frac{1}{\sqrt{2}}(\beta\beta\alpha\beta - \beta\beta\beta\alpha)$	−1	0	$2(\mathcal{B})_{-1}$

Evidently, the resonances are symmetrically disposed about ν_A and the separation of the two most intense lines in the spectrum yields $|L_+|$. There is some ambiguity in the assignment of the remaining eight lines as they are grouped into pairs of lines whose intensities sum to 2. Furthermore, the spectrum is transformed into itself if the sign of $J_{XX'}$ is reversed, or if the sign of $J_{AA'}$ is reversed, so that at best one can only determine $|J_{AA'}|$, $|J_{XX'}|$, and $|L_-| = |J_{AX} - J_{AX'}|$.

The proton magnetic resonance spectrum of *o*-dichlorobenzene at 400 MHz is shown in Figure 22.

6.4 The $A_2A_2'BB'$ System

Symmetrical systems containing magnetically equivalent groups can be decomposed into irreducible components. As an illustration, consider *trans*-1,4-dichloro-2-butene, an $A_2A_2'BB'$ system. The components $A_1A_0'B_{1/2}B_{1/2}'$ and

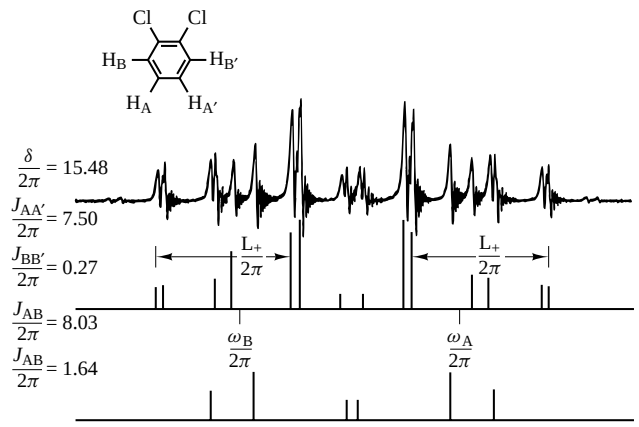

Figure 21 The proton magnetic resonance spectrum of pure *o*-dichlorobenzene at 60 MHz. The upper part of the theoretical spectrum shows the transitions between symmetric states, the lower part the transitions between antisymmetric symmetric states. The chemical shift and coupling constants are in Hz

Table 13 Frequencies and Intensities for the AA′XX′ System

Transition	Intensity	Frequency
A Transitions		
$\mathcal{A}_1$	4	$\nu_A - \frac{1}{2}L_+$
$\mathcal{A}_2$	4	$\nu_A + \frac{1}{2}L_+$
$\mathcal{A}_3$	$\frac{2}{1+Q_5^2}$	$\frac{1}{2}(2\nu_A + K_+ - R_5\}$
$\mathcal{A}_4$	$\frac{2Q_5^2}{1+Q_5^2}$	$\frac{1}{2}(2\nu_A + K_+ + R_5\}$
$\mathcal{A}_5$	$\frac{2}{1+Q_5^2}$	$\frac{1}{2}(2\nu_A - K_+ + R_5\}$
$\mathcal{A}_6$	$\frac{2Q_5^2}{1+Q_5^2}$	$\frac{1}{2}(2\nu_A - K_+ - R_5\}$
B Transitions		
$\mathcal{B}_1$	$\frac{2}{1+Q_2^2}$	$\frac{1}{2}(2\nu_A + K_- - R_2\}$
$\mathcal{B}_2$	$\frac{2Q_2^2}{1+Q_2^2}$	$\frac{1}{2}(2\nu_A + K_- + R_2\}$
$\mathcal{B}_3$	$\frac{2}{1+Q_2^2}$	$\frac{1}{2}(2\nu_A - K_- + R_2\}$
$\mathcal{B}_4$	$\frac{2Q_2^2}{1+Q_2^2}$	$\frac{1}{2}(2\nu_A - K_- - R_2\}$

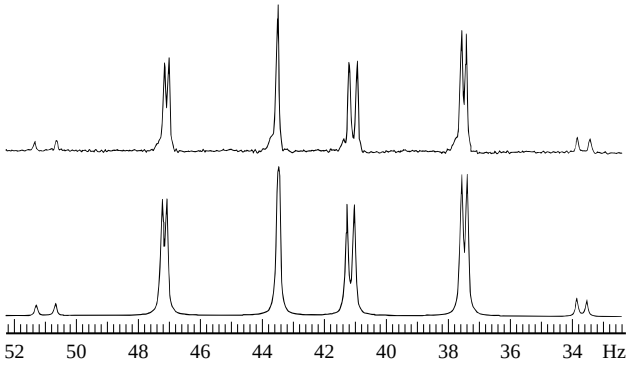

Figure 22 The high-frequency region of the proton magnetic resonance spectrum of 10% solution of *o*-dichlorobenzene in deuterated chloroform at 400 MHz (top), showing the high-frequency half of the symmetrical spectrum. The intense, single line at 98.65 Hz is a superposition of two virtually coincident lines. The theoretical spectrum (bottom) was reproduced with the coupling parameters derived from the 60 MHz spectrum (Figure 21) and an internal shift of 84.57 Hz. The frequency origin is at the symmetry center

$A_0A_1'B_{1/2}B_{1/2}'$ are clearly identical, so that the decomposition is $A_1A_1'B_{1/2}B_{1/2}' + 2A_1A_0'B_{1/2}B_{1/2}{}' + A_0A_0'B_{1/2}B_{1/2}'$.

In the $A_0A_0'B_{1/2}B_{1/2}'$ component, groups A and A′ have zero total spin and are effectively decoupled from the other nuclei. Hence, this component yields a single line of four intensity units at ν_B. The spectrum of the component $A_1A_0'B_{1/2}B_{1/2}'$ is independent of $J_{AA'}$, depending only on ν_A, $J_{BB'}$, $J_{AB} \equiv J$, and $J_{AB'} \equiv J'$. Finally, the component $A_1A_1'B_{1/2}\ B_{1/2}'$ has C_2 symmetry, so that the states of the system may be classified as symmetric and antisymmetric. The experimental and theoretical spectra are shown in Figures 23 and 24.

7 OTHER APPROACHES

Modern, pulsed FT spectroscopy (see ***Fourier Transform and Linear Prediction Methods***) provides additional opportunities for the simplification or analysis of complex high

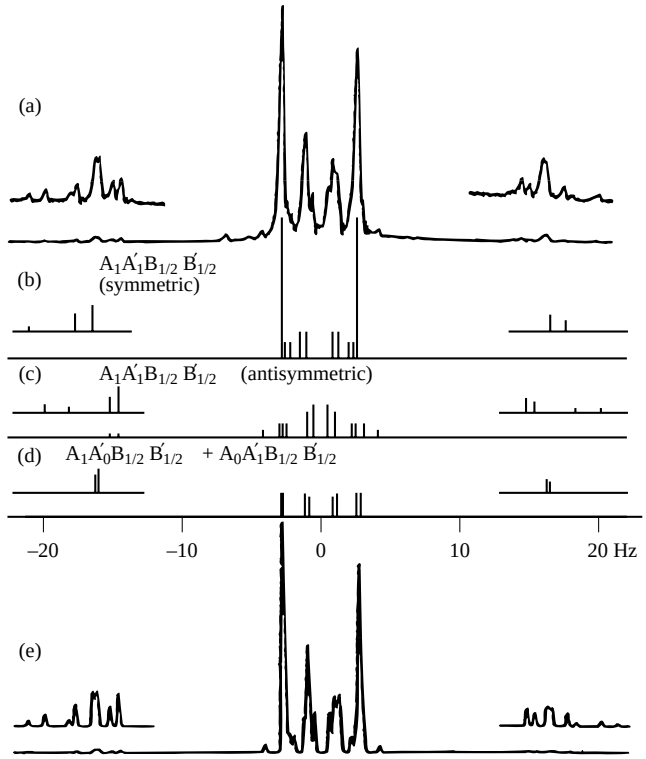

Figure 23 Experimental and theoretical proton magnetic resonance spectra of the A_2A_2' region of *trans*-1,4-dichloro-2-butene at 60 MHz: (a) experimental spectrum; (b) symmetric transitions of the $A_1A_1'B_{1/2}B_{1/2}'$ component; (c) antisymmetric transitions of the $A_1A_1'B_{1/2}B_{1/2}'$ component; (d) $A_1A_0'B_{1/2}B_{1/2}'$ transitions; and (e) calculated composite spectrum

resolution spectra. The most elementary contribution is the availability of spectral information in digital form. Suitable resolution enhancement routinely available on modern spectrometers can resolve lines and eliminate ambiguities in assignments. Add/subtract software permits the removal of spectral lines from one component leaving the 'pure' second-order spectrum of another for analysis. All computers on modern FT systems contain programs to perform the calculations described above, initially as simulations and subsequently to obtain an iterative fit between simulated and experimental spectra. (Effective use of these programs requires some understanding of the material discussed here.)

More advanced techniques provide additional opportunities to simplify spectral analysis. For example, simple population transfer experiments such as INEPT (see ***INEPT***) can be used to provide information about complex systems, particularly heteronuclear systems. Multiple quantum pulse techniques routinely used for filtering, solvent suppression, or coherence transfer may be applied to the multiple quantum analysis procedures described above. Homonuclear *J*-resolved 2D spectra (see ***Two-Dimensional J-Resolved Spectroscopy***) as a minimum remove ambiguities arising from overlap of first or second order systems. Projection of these spectra provides what are effectively 'proton decoupled proton spectra', in which each chemically shifted species appears as a single line uncoupled to other protons. Thus, chemical shifts are immediately available for input to more complex analysis of the coupled systems. Second-order

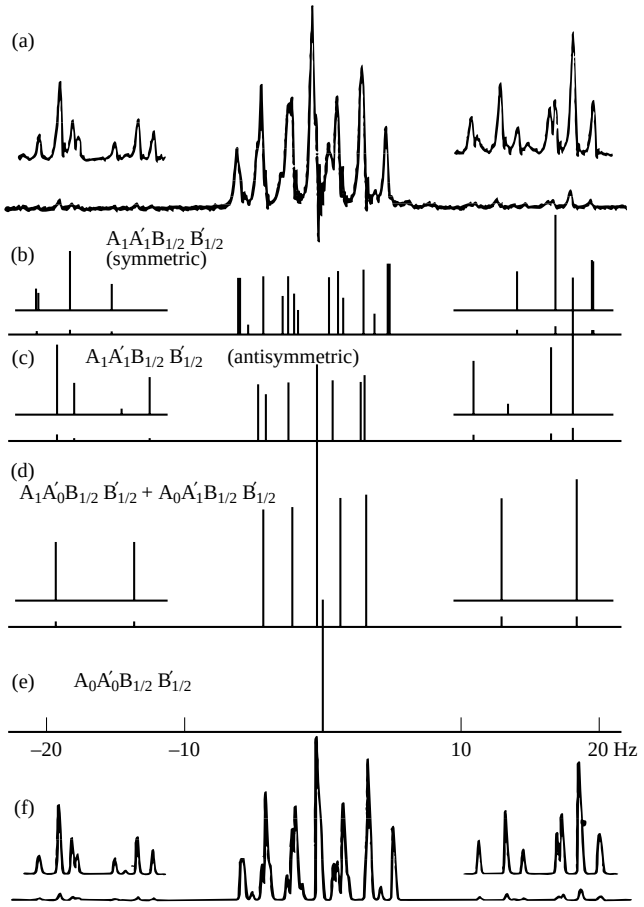

Figure 24 Experimental and theoretical proton magnetic resonance spectra of the BB′ region of *trans*-1,4-dichloro-2-butene at 60 MHz: (a) experimental spectrum; (b) symmetric transitions of the $A_1A_1'B_{1/2}B_{1/2}'$ components; (c) antisymmetric transitions of the $A_1A_1'B_{1/2}B_{1/2}'$ component; (d) $A_1A_0'B_{1/2}B_{1/2}'$ component; (e) $A_0A_0B_{1/2}B_{1/2}'$ component, a single transition of four intensity units at ν_A; and (f) composite calculated spectrum

systems also benefit from *J*-resolved 2D spectra where combination lines appear at appropriate offsets in both dimensions.

As magnetic field strengths have increased, providing greater sensitivity and simpler spectra, the size of molecules being studied has also increased. It is now common to obtain spectra which consist of a large number of relatively simple spectral elements (AB, ABX, AMX_2, etc.) which are mixed together and/or overlapping. In some cases homonuclear COSY experiments (see ***COSY Two-Dimensional Experiments***; ***COSY Spectra: Quantitative Analysis***) provide critical information about which nuclei are coupled to each other, permitting applications of the principles discussed above to the identified subspectra without the need for more sophisticated analysis. They may also assist in determining which nuclei will or will not be included in more sophisticated analyses. Three-dimensional COSY experiments also permit the separation of otherwise complex overlapping systems into tractable subsets. For example, overlapping simple AB or ABX systems in peptides and proteins can be sorted on the basis of ^{15}N chemical shifts.

8 RELATED ARTICLES

Analysis of Spectra: Automatic Methods; Carbon-13 Spectral Simulation; Chemical Shift Tensors; COSY Spectra: Quantitative Analysis; COSY Two-Dimensional Experiments; Coupling Constants Determined by ECOSY; Decoupling Methods; Double Resonance; Fourier Transform and Linear Prediction Methods; Fourier Transform Spectroscopy; Homonuclear Three-Dimensional NMR of Biomolecules; Magnetic Equivalence; Multidimensional Spectroscopy: Concepts; Multiple Quantum Spectroscopy of Liquid Samples; Polarization Transfer Experiments via Scalar Coupling in Liquids; Shielding: Overview of Theoretical Methods; Spin Echo Spectroscopy of Liquid Samples; Three-Dimensional HMQC-NOESY, NOESY-HMQC, and NOESY-HSQC; Three- and Four-Dimensional Heteronuclear Magnetic Resonance; Two-Dimensional J-Resolved Spectroscopy.

9 REFERENCES

1. P. L. Corio, *Structure of High-Resolution NMR Spectra*, Academic Press, New York, 1966.
2. P. L. Corio, *Chem. Rev.*, 1960, **60**, 363.
3. J. W. Emsley, J. Feeney, and L. H. Sutcliffe, *High Resolution Nuclear Magnetic Resonance Spectroscopy*, Pergamon, New York, 1965, Vol. 1.
4. J. D. Roberts, *An Introduction to Spin–Spin Splitting in High Resolution Nuclear Magnetic Resonance Spectra*, Benjamin, New York, 1961.
5. J. A. Pople, W. G. Schneider, and H. J. Bernstein, *High-Resolution Nuclear Magnetic Resonance*, McGraw-Hill, New York, 1959.
6. R. J. Abraham, *Analysis of High Resolution NMR Spectra*, Elsevier, New York, 1971.
7. L. Landau and E. M. Lifshitz, *Quantum Mechanics, Non-Relativistic Theory*, 3rd edn., Pergamon, New York, 1977.
8. E. Feenberg and G. Pake, *Notes on the Quantum Theory of Angular Momentum*, Addison-Wesley, Cambridge, MA, 1953.
9. M. E. Rose, *Elementary Theory of Angular Momentum*, Wiley, New York, 1957.
10. P. L. Corio and R. C. Hirst, *J. Chem. Educ.*, 1969, **46**, 345.

Acknowledgments

The authors wish to express their appreciation to Mr John Layton for obtaining the experimental 400 MHz spectra of *o*-dichlorobenzene, diethyl ether, and the *cis* and *trans* isomers of 1,3-dichloropropene, and to Mrs June Smith for invaluable technical assistance in the preparation of the manuscript. We are also indebted to the *Journal of Chemical Education* for permission to reproduce Figures 4, 6, 8, 11, and 12 from P. L. Corio and R. C. Hirst, *J. Chem. Educ.*, 1969, **46**, 345. Figures 3, 4, 6–14, 17, and 18 are reproduced from P. L. Corio, 'Structure of High-Resolution NMR Spectra', Academic Press, New York, 1966.

Biographical Sketches

Paul L. Corio. *b* 1928. US Navy, 1946–47; A.B., 1953 Columbia College, A.M., 1954, Ph.D., 1957, Columbia University, preceptor, B. P. Dailey. Research associate, Mobil Oil Corporation, 1957–70; Professor

of Chemistry, University of Kentucky, 1970–present. Research specialties: nuclear and electron spin resonance, theory of reaction mechanisms, theoretical chemistry.

Stanford L. Smith. *b* 1935. A.B., 1957, Albion College; Ph.D., 1961, Iowa State University, preceptor Orville Chapman. Professor of Chemistry and Radiology, University of Kentucky, 1962–present. Acting Director of the Magnetic Resonance Imaging and Spectroscopy Center, 1987–1990. University Director of NMR Technology, 1987–present. Research specialties: solvent effects, analysis of biomolecules and complex organic compounds, magnetic resonance imaging.

Analysis of Spectra: Automatic Methods

David S. Stephenson
University of Munich, Munich, Germany

1	Introduction	1
2	Spectral Synthesis	1
3	Nonautomatic Analysis	1
4	Semiautomatic Analysis	1
5	Automatic Analysis	2
6	Improvements to DAVINS	4
7	Applications	5
8	Related Articles	6
9	References	6

1 INTRODUCTION

The NMR spectrum itself is of little intrinsic interest: it is merely a stepping-stone to the parameters of analytical value—usually the chemical shifts and coupling constants, sometimes rate constants and relaxation times. For this reason the extraction of these parameters—the analysis of an NMR spectrum—plays a crucial role in the exploitation of the NMR method.

The synthesis of an NMR spectrum, i.e. its construction from given parameters using the well-known rules of quantum mechanics, may be tedious if the spin system is complex, but it is doomed to failure only if the problem is of a scale such that the rounding errors become significant or the calculation takes an inordinately long time. In contrast, the analysis of an NMR spectrum presents us with a task of such intricacy that only the simplest of spectra may be reduced to their parameters in a straightforward manner.

The reason for this dichotomy lies in the way in which the parameters are encoded into a spectrum, and to appreciate the problems involved in the decoding it is helpful to consider first how an NMR spectrum may be synthesized.

2 SPECTRAL SYNTHESIS

Using the spin system as a framework, we can construct a Hamiltonian operator as a function of the chemical shifts, coupling constants and so on:

$$\hat{\mathcal{H}} = f(\mathbf{p}) \tag{1}$$

where the parameters have been collected into a vector $\mathbf{p}$. Together with an appropriate set of basis functions $|\ \phi_i >$, this operator may be employed to yield the Hamiltonian matrix $\mathbf{H}$ whose elements are

$$H_{ij} = \langle \phi_i | \hat{\mathcal{H}} | \phi_j \rangle \tag{2}$$

Diagonalization of the Hamiltonian matrix using standard numerical procedures yields the static energy levels of the spin system as eigenvalues, as well as the corresponding eigenvectors which represent transformations of the original basis to the stationary states of the Hamiltonian. It is now an easy matter to synthesize the NMR spectrum, for the transition frequencies are merely the differences of suitable eigenvalues and the intensities are simply related to the products of the corresponding eigenvectors.

3 NONAUTOMATIC ANALYSIS

One might expect that the wealth of information contained in an NMR spectrum and quantified into the frequencies and intensities of the transitions might both overdefine the parameters and pave an easy way to their determination. Whilst the former is certainly true (the spectrum of an ABC spin system for instance is characterized by three shifts and three couplings but provides 15 frequencies and 15 intensities), the latter is a delusion!

During the construction of the spectrum, the Hamiltonian matrix $\mathbf{H}$ is subjected to a similarity transformation to bring it into diagonal form

$$\tilde{\mathbf{U}}\mathbf{H}\mathbf{U} = \mathbf{D} \tag{3}$$

and whilst we can formally write

$$\mathbf{H} = \mathbf{U}\mathbf{D}\tilde{\mathbf{U}} \tag{4}$$

this equation is of little practical value since neither $\mathbf{D}$ nor $\mathbf{U}$ is known explicitly from the spectrum: all we can determine are the differences between certain elements of $\mathbf{D}$ and products of certain columns of $\mathbf{U}$. However, if the parameters are known reasonably well, a trial matrix $\mathbf{H}^{(0)}$ may be constructed and a trial spectrum calculated. From this, the true Hamiltonian matrix $\mathbf{H}$ may be obtained using perturbation theory,

$$\mathbf{H} = \mathbf{H}^{(0)} + \mathbf{H}^{(1)} \tag{5}$$

and provided $\mathbf{H}^{(1)}$ is small, its elements may be estimated from the differences in the frequencies of corresponding transitions in the experimental and synthetic spectra. This is the essence of the traditional method of iterative analysis exemplified by the programs NMREN/NMRIT of Swalen and Reilly[1] and the program LAOCOON of Castellano and Bothner-By.[2]

For these methods to work, however, it is necessary both that $\mathbf{H}^{(1)}$ be small enough for a linear approximation to hold, and that sufficient transitions in the synthetic spectrum be assigned to their experimental counterparts. This is the sticking point beyond which such methods fail.

4 SEMIAUTOMATIC ANALYSIS

Apart from some work on specific spin systems, the first serious attempt to automate the analysis generally is the contribution by Keller, Lusebrink, and Sederholm.[3] They saw that two problems faced the user of the Swalen–Reilly method,

viz. the assignment of a sufficient number of experimental transitions and also the determination of the energy levels from these transitions.

The first problem was solved by the development of a program called DECOMP to identify overlapping lines, and the second problem by a program named ASSIGN which built up an energy level diagram in a systematic manner.

5 AUTOMATIC ANALYSIS

The real move into automatic analysis came, however, in the 1970s from two teams who sought a more general approach, and whose endeavors led to the computer programs STREAK and DAVINS.

5.1 STREAK

A decisive breakthrough was achieved by Diehl, Sýkora, and Vogt[4] who realized that the information contained in a spectrum could be concentrated into a small number of data by means of an integral transform.

Anyone who has contemplated the spectrum of a molecule dissolved in a liquid crystal will appreciate the huge amount of information contained therein. An oriented eight spin-$\frac{1}{2}$ system gives rise to 11 440 transitions. Even with overlap a large number of these will be visible, and since the number of parameters which determine the spectrum (eight shifts, 28 isotropic couplings, and 28 anisotropic couplings) is only 64, the problem is obviously overdetermined. A parallel can well be drawn with the information content of a picture, and indeed for the storage and transmission of pictures several data compression techniques are available based on transformations.[5]

Specifically, Diehl et al. considered transforming both the experimental and synthetic spectra into small sets of real numbers which would then be compared with each other. Subsequently the parameters **p** could be varied so that the two sets converged. This approach has the advantage of avoiding the assignment step altogether and furthermore opening the prospect of allowing a solution starting from initial parameters far from their correct values—these are the two major stumbling-blocks in nonautomatic analysis.

This transformation of a spectrum is a very general concept but Diehl et al. restricted it somewhat by concentrating on linear integral transforms using orthogonal bases. This has certain technical advantages.

If the basis set is represented by the functions $w_k(\omega)$, then for each value of k the coefficient $f_{\hat{k}}$, defined as the integral

$$f_{\hat{k}} = \int_{-\infty}^{+\infty} w_k(\omega) I(\omega)\, \mathrm{d}\omega \tag{6}$$

may be obtained from the spectrum $I(\omega)$, which can be either a stick spectrum (defined in terms of a sum of delta functions and thus fulfilling the integrability requirements) or as a regular array of intensities. The coefficients so obtained from the synthetic and experimental spectra may be used to form the functional

$$\Delta^2 = \sum_{k=1}^{n} (f_k^{\mathrm{exp}} - f_k^{\mathrm{syn}})^2 \tag{7}$$

and Δ^2 should then be reduced by varying the parameters using a standard optimization routine.

Diehl et al. originally considered several types of basis sets, but later[6] restricted their choice to a Fourier basis together with a limited number of polynomials.

5.2 DAVINS

Stephenson and Binsch[7] approached the problem from a different standpoint. Setting out from the lineshape analysis of NMR spectra broadened by chemical exchange,[8] a project culminating in the iterative program DNMR5, they treated the high-resolution spectrum not as a set of sharp lines but as a vector of the spectral intensities measured at regular frequency intervals. This, of course, is ideally suited to the output of a modern NMR spectrometer and, indeed, in taking this step the problem of line assignment has been solved, for lines as such no longer exist!

There is certainly nothing new in fitting the lineshape of a high-resolution NMR spectrum. Glidewell, Rankin, and Sheldrick[9] had shown that this was possible, and they also pointed out that although no assignment is necessary good trial values of the parameters are required. In their choice of examples these authors were lucky in taking compounds which had fairly well-known parameters and which in a field of 2.35 T yielded ^{1}H spectra showing relatively little fine structure. This made the analysis similar to that of an exchange-broadened spectrum.

In 1976, Heinzer[10] also published work describing the application of lineshape fitting, and demonstrated the difficulties associated with local minima if the trial parameters are far from their true values.

The innovative idea of Stephenson and Binsch, however, is the recognition that local minima could be avoided by a modification of the error function. In this formulation a measured experimental spectrum is represented as a vector **s** whose elements are the intensities s_i at selected frequency values ω_i. Equally, the synthetic spectrum is a vector $\hat{\mathbf{s}}$ whose elements are functions of the parameters and the frequency:

$$\hat{s}_i = f(\mathbf{p}, \omega_i) \tag{8}$$

In the least-squares approach, the best estimate of **p** is that which minimizes the real functional

$$\phi = (\mathbf{s} - \hat{\mathbf{s}})^{\mathrm{T}} (\mathbf{s} - \hat{\mathbf{s}}) \tag{9}$$

but whilst this is easy to state in principle, it is in practice no trivial task to obtain the unique vector **p**. To see why this should be, consider the experimental doublet shown at the top of Figure 1, and the synthetic doublet shown below it. If the sole element of the parameter vector **p** consists of the chemical shift of the synthetic doublet, the error functional ϕ will have the form shown in the bottom curve of Figure 1—a global minimum where both lines overlap and a local minimum where one line overlaps. A standard minimization program starting from a shift out on the right will find the local minimum and then stop.

What we have to do is somehow tell the synthetic spectrum not to look straight up at the experimental but to take a glance

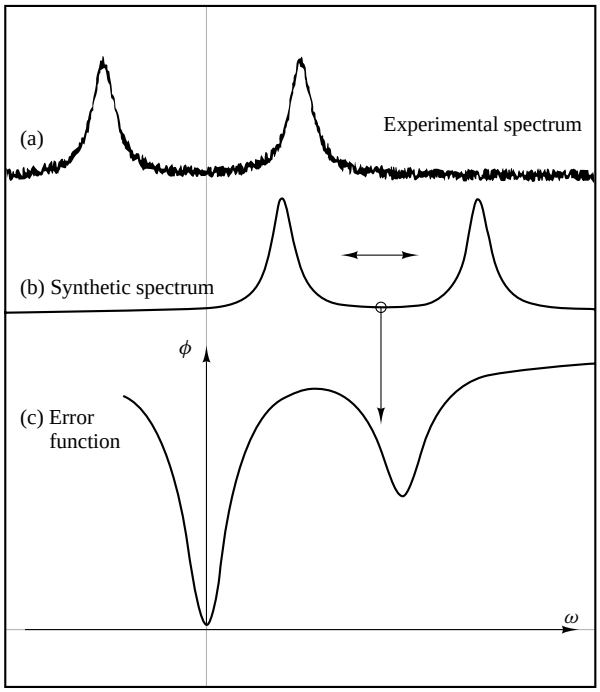

Figure 1 (a) Top: an experimental spectrum **s** consisting of a doublet. (b) Middle: a synthetic spectrum $\hat{\mathbf{s}}$ consisting of a doublet, the center frequency of which (ω) can move left or right. (c) Bottom: the error $\phi = (\mathbf{s} - \hat{\mathbf{s}})^{\mathrm{T}}(\mathbf{s} - \hat{\mathbf{s}})$ as a function of the center frequency ω, showing a global and a local minimum

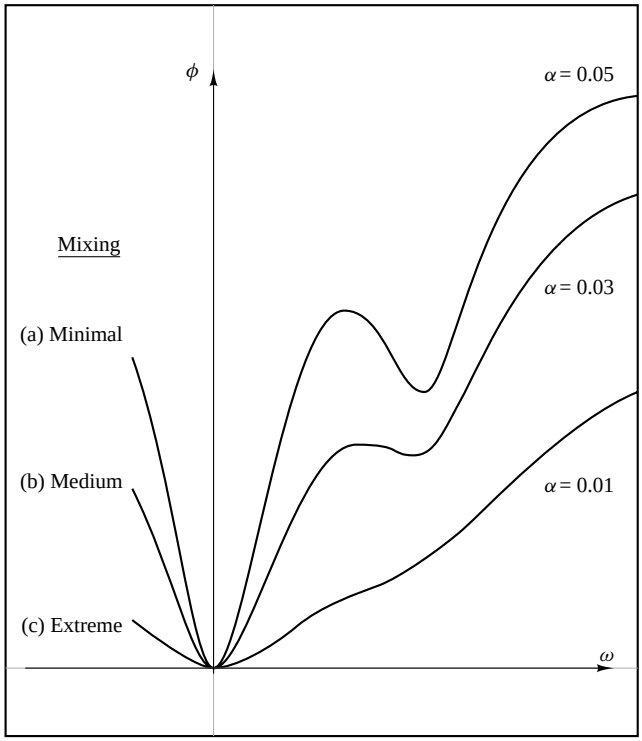

Figure 2 (a) Top: the error functional $\phi' = (\mathbf{s} - \hat{\mathbf{s}})^{\mathrm{T}}\mathbf{W}(\mathbf{s} - \hat{\mathbf{s}})$ with $W_{\mathrm{ij}} = \exp(-\alpha|i - j|)$ for a minimal amount of mixing ($\alpha = 0.05$) as a function of the center frequency ω, still showing a global and a local minimum, compare with Figure 1(c). (b) Middle: similar to (a) but with $\alpha = 0.03$, the mixing is stronger and the local minimum weaker. (c) Bottom: similar to (a) but with $\alpha = 0.01$, the mixing is now strong enough to smooth out the local minimum

sideways, for only then will the true correlation between the synthetic and experimental spectra become obvious.

Now suppose we modify equation (9) to include a general square matrix **W**:

$$\phi' = (\mathbf{s} - \hat{\mathbf{s}})^{\mathrm{T}}\mathbf{W}(\mathbf{s} - \hat{\mathbf{s}}) \tag{10}$$

Then depending on the form of **W** and on the values of its individual elements, the functional ϕ' can be manipulated so as to smooth out the local minima. If this is achieved, the mixing of the residuals $(\mathbf{s} - \hat{\mathbf{s}})$ can be considered equivalent to introducing a pulling mechanism into the system, such that the lines in the experimental spectrum attract their counterparts in the synthetic. This attraction, at a distance, should be strong enough to overcome the direct local attraction which gives rise to local minima.

As an example, let us consider **W** to be a Toeplitz matrix whose elements are given by

$$W_{ij} = \exp(-\alpha|i - j|) \tag{11}$$

The effect on the two-line system is shown in Figure 2 for three values of α. Indeed, for a value of $\alpha < 0.02$, only one minimum exists and any simple optimization routine will be able to find it.

This two-line case does not fully represent the typical NMR spectrum, which can be better appreciated when we consider the ethyl group spectrum of ethylbenzene shown in Figure 3(a). The error surface defined by equation (9) is shown below the spectrum; in this case, both the linewidth and the coupling constant have been held fixed at their true values and the sole variable parameters are the shifts of the methyl and methylene groups, so that we see a two-dimensional surface in three-space. This eggbox-like error surface can, however, give only a rough idea of the myriad of local minima to be expected in the general case of a multidimensional error space. When we introduce the mixing matrix **W**, the shape of the surface is changed as shown in Figure 3(c). Just as for the two-line case, the surface is smoothed and there is a critical value of α for which the surface exhibits one minimum only [Figure 3(d)].

One must, though, not fall into the trap of thinking that this one minimum corresponds directly to the true global minimum of the unmodified surface. That would be too easy! We could then take a strong mixing matrix **W**, locate the unique minimum, replace **W** with the unit matrix **I** and find ourselves in the global minimum. Unfortunately this does not work. But what we can conceive is a gradual reduction in the mixing during which the minimum which we at first locate on ϕ' mutates into the global minimum of ϕ, and if the process is adiabatic then we can follow the change.[11]

This is roughly the policy of DAVINS (Direct Analysis of Very Intricate NMR Spectra), but in the actual computer program a gradual change in **W** was not realized, rather the concept was followed of first locating the minimum on one surface ϕ'_0, then reducing the degree of mixing in order to change to another surface ϕ'_1, locating the minimum on this, then changing to ϕ'_2, and so on. The requirement for such a scheme to be successful is that the minimum on ϕ'_n must lie within the convergence radius of the correct minimum on

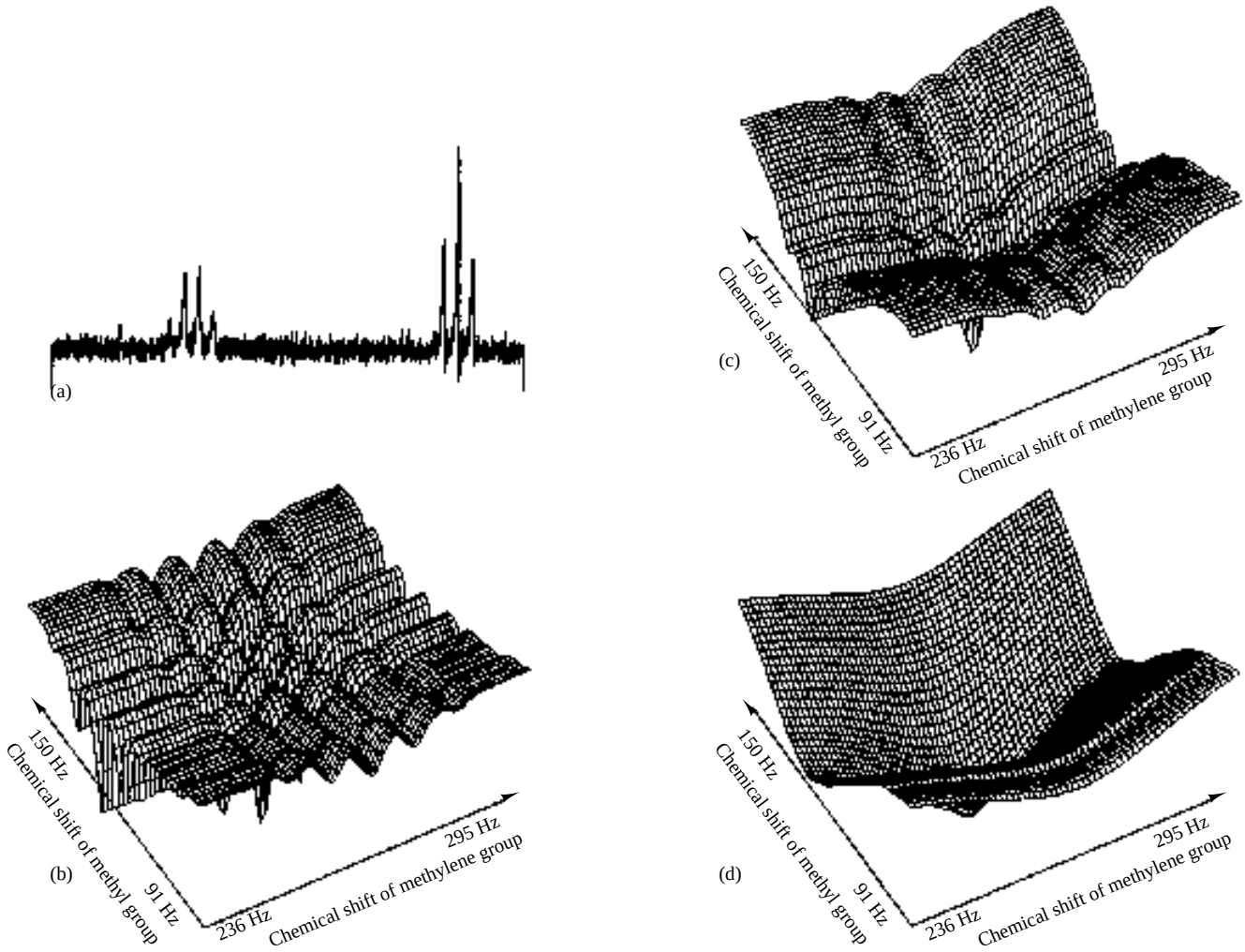

Figure 3 (a) Top left: 100 MHz ^{1}H spectrum of the ethyl group of ethylbenzene. (b) Bottom left: a section of the corresponding error surface ϕ in three-space. (c) Top right: modified error surface ϕ' with exponential mixing $\alpha = 0.1$. (d) Bottom right: similar to (c) but with $\alpha = 0.01$. (Reproduced by permission of Academic Press from D. S. Stephenson and G. Binsch, *J. Magn. Reson.*, 1980, **37**, 395)

ϕ'_{n+1}. With this procedure, we should eventually arrive at the global minimum of the unmodified surface ϕ.

Although specific details of the matrices **W** cannot rigorously be obtained, a few general features are apparent. Firstly, in order to treat all parts of the spectrum equally, the elements should have the property that $W_{ij} = W_{i+k,j+k}$; thus **W** is a Toeplitz matrix. Secondly, the mechanism which we envisage as being responsible for the smoothing-out of local minima is equivalent to that which 'pulls' synthetic lines toward their experimental counterparts. But this is effective only if the contributions to the error arising from the off-diagonal elements of **W** are made dependent on the absolute distance between corresponding lines in such a way that ϕ' increases monotonically as a function of their separation. Thus, the elements W_{ij} should decrease monotonically as a function of their distance from the main diagonal of **W**, i.e. $W_{i,i+k} > W_{i,i+k+1}$. Other restrictions on the form of **W**, such as setting all the diagonal elements equal to unity, may be chosen to fulfill technical requirements, but are not essential. Within this framework the choice of suitable function is completely free, but Stephenson and Binsch found that the exponential $W_{ij} = \exp(-\alpha|i - j|)$ and Lorentzian $W_{ij} = 1/(1 + \beta|i - j|^2)$ forms proved satisfactory.

6 IMPROVEMENTS TO DAVINS

The first modification to which DAVINS was subjected was the substitution of the original synthesis routines by routines allowing the inclusion of anisotropic couplings. The resulting program DANSOM[12] has been shown to be capable of analyzing spectra with thousands of transitions.[13]

The second, and more significant, modification was again the replacement of the original synthesis routines; this time by routines which took into account the full symmetry of the spin system. Whereas the original routines of Quirt and Martin[14] provided for only twofold symmetry and magnetic equivalence, the routines SYMTRY and CYMTRY[15] allow for symmetry in a most general form. The incorporation of these into DAVINS led to the programs DAVSYM and DAVCYM[16] which are now commercially available under the name DAISY.

The most recent modification concerns a general overhaul of DAVINS undertaken by the original authors to eliminate many of its defects and to bring it up-to-date. Specifically, the areas tackled are acceleration of the calculation of the spectrum $\hat{\mathbf{s}}$, acceleration of the calculation of the mixed error function ϕ', and the inclusion of the ability to treat a multitude of Hamiltonians. Furthermore, the program is now furnished with an X-Windows graphical user interface, and the various modules can run on separate networked computers. The first phase of this project, leading to DAVINX, was completed in 1995.

7 APPLICATIONS

Details of the analysis of common NMR spectra using DAVINS together with recipes for successful application have already been published.[17] The guidelines recorded then remain valid even today, although modified by the experience gained using the program interactively. The characterization of spectra on the basis of 'peak clustering' is still an important criterion in deciding how to approach a full automatic analysis. Consequentially, the choice of type and degree of the initial mixing is strongly dependent on the structure of the spectrum.

For clustered spectra, i.e. those in which groups of lines huddle round their respective chemical shifts, the calculation should iterate on all the parameters using initially a moderate exponential mixing. The program should be allowed to move through its repertoire of modified error surfaces until it reaches the global minimum of the unmodified surface ϕ (we christened the ensemble of these operations a 'grand cycle'[7]). It should have reached the correct solution within one grand cycle.

Spectra of this type may well be analyzed by other means, but an automatic analysis is to be preferred not only because of its ease but because the full information content of the spectrum is employed in determining the parameters. An example of such an analysis is provided by the 400 MHz ^{1}H spectrum of 1,2-dimethyl-3-cyanocyclopropane shown in Figure 4. The shifts are readily extracted by inspection and the few couplings are reasonably well known, but line assignments would have been difficult. An automatic analysis is a matter of a few mouse-clicks!

A significant part of our effort concerned the reduction of spectrum artifacts such as baseline anomalies, but these problems can now regularly be taken care of by standard NMR software and no longer need be part of the analysis program itself. However, since the program calculates a synthetic spectrum using a Lorentzian lineshape, it is worthwhile ensuring that the experimental lineshape also has this form—in cases of extreme deviation it is profitable to reconvolute the spectrum.[18] Furthermore, a zero- and first-order correction should always be made to the baseline because the total spectral integral is one of the constraints on the iteration. Both of these forms of preprocessing were applied to the spectrum in Figure 4(a) before the analysis was started.

For spectra in which the clustering is not visible, it is advisable to start with a strong exponential mixing and iterate just on the dominant parameters in the first grand cycle; these are usually the chemical shifts, but for liquid crystal spectra comprise the major dipolar couplings. Subsequent grand cycles should employ moderate Lorentzian mixing iterating on the dominant parameters initially and then on all parameters. This, however, is no panacea, especially if the initial values are taken from the telephone book.[17] In cases where only poor estimates of the parameters exist, it may be necessary to initiate several trial runs starting from combinations of values which broadly cover the expected ranges of the parameters to be varied. This grid search approach is time-consuming but will, provided the grid is chosen finely enough, lead to success.

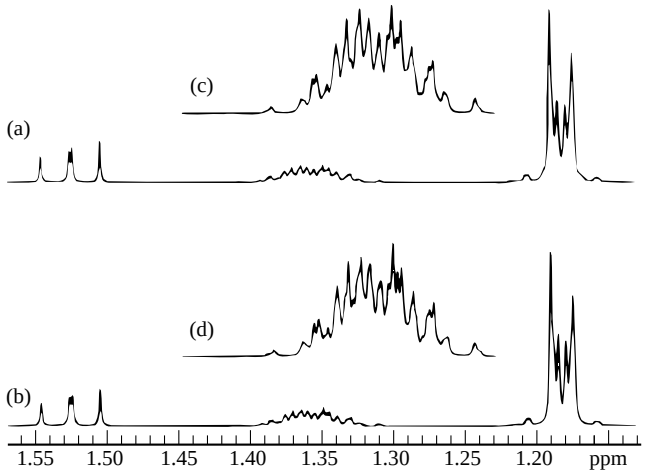

Figure 4 (a) Top: 400 MHz ^{1}H spectrum of 1,2-dimethyl-3-cyanocyclopropane after preprocessing as described in the text. (b) Bottom: synthetic spectrum. (c) Expansion of the region 1.30–1.45 ppm of the experimental spectrum. (d) Expansion of the region 1.30–1.45 ppm of the synthetic spectrum

Just such a method was adopted for the analysis of the spectrum of allyl chloride oriented in the nematogen Phase V and shown in Figure 5(a). Since the dipolar couplings could not be predicted with any accuracy, the coupling between the allylic methylene protons was estimated from the width of the spectrum and eight trial runs made with the other couplings set at ±200 Hz with random sign combinations. Several of these runs completed their first grand cycle with significant reduction of the error function ϕ and could be

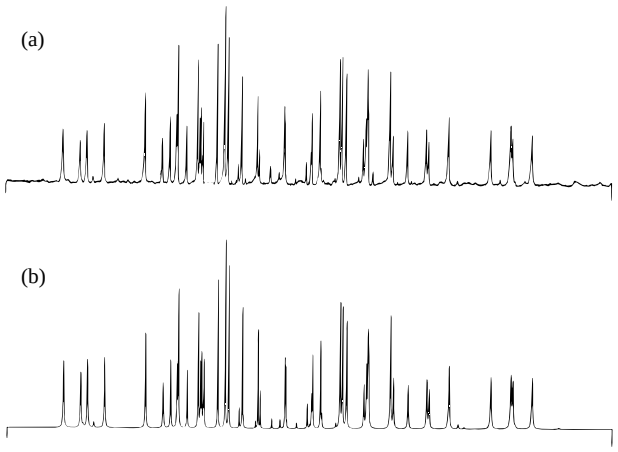

Figure 5 (a) Top: ^{1}H spectrum of allyl chloride oriented in Phase V after baseline correction. (b) Bottom: synthetic spectrum. (Reproduced by permission of Heyden & Son from D. S. Stephenson and G. Binsch, *Org. Magn. Reson.*, 1980, **14**, 226)

used as the basis for subsequent grand cycles iterating on all couplings and shifts. These secondary grand cycles with moderate Lorentzian mixing all yielded essentially the same parameter values, which were further refined under inclusion of the linewidth to produce the spectrum shown in Figure 5(b).

In conclusion, it may be said that with the advent of UNIX workstations as both host and satellite computers linked to NMR spectrometers, the automatic analysis of NMR spectra has come of age. Indeed, the major application might well be in the routine analysis of 'simple' NMR spectra rather than in the unraveling of spectra containing many thousands of lines.

8 RELATED ARTICLES

Analysis of High-Resolution Solution State Spectra; Chemical Exchange Effects on Spectra; Data Processing; Liquid Crystalline Samples: Spectral Analysis; Magnetic Equivalence.

9 REFERENCES

1. J. D. Swalen and C. A. Reilly, *J. Chem. Phys.*, 1962, **37**, 21.
2. S. Castellano and A. A. Bothner-By, *J. Chem. Phys.*, 1964, **41**, 3863.
3. W. D. Keller, T. R. Lusebrink, and C. H. Sederholm, *J. Chem. Phys.*, 1966, **44**, 782.
4. P. Diehl, S. Sýkora, and J. Vogt, *J. Magn. Reson.*, 1975, **19**, 67.
5. A. Rosenfeld and A. C. Kak, *Digital Picture Processing*, 2nd edn., Academic Press, New York, 1982.
6. P. Diehl and J. Vogt, *Org. Magn. Reson.*, 1976, **8**, 638.
7. D. S. Stephenson and G. Binsch, *J. Magn. Reson.*, 1980, **37**, 395.
8. D. S. Stephenson and G. Binsch, *J. Magn. Reson.*, 1978, **32**, 145.
9. C. Glidewell, D. W. H. Rankin, and G. M. Sheldrick, *Trans. Faraday Soc.*, 1969, **65**, 2801.
10. J. Heinzer, *J. Magn. Reson.*, 1977, **26**, 301.
11. W. I. Zangwill and C. B. Garcia, *Pathways to Solutions, Fixed Points, and Equilibria*, Prentice-Hall, Englewood Cliffs, NJ, 1981.
12. D. S. Stephenson and G. Binsch, *Org. Magn. Reson.*, 1980, **14**, 226.
13. D. S. Stephenson and G. Binsch, *Mol. Phys.*, 1981, **43**, 697.
14. A. R. Quirt and J. S. Martin, *Org. Magn. Reson.*, 1971, **5**, 318.
15. V. Lueg and G. Hägele, *J. Magn. Reson.*, 1977, **26**, 505.
16. G. Hägele, M. Engelhardt, and W. Boenigk, *Simulation und Automatisierte Analyse von Kernresonanzspektren*, VCH, Weinheim, 1987.
17. D. S. Stephenson and G. Binsch, *J. Magn. Reson.*, 1980, **37**, 409.
18. A. Gibbs and G. A. Morris, *J. Magn. Reson.*, 1991, **91**, 77.

Biographical Sketches

David S. Stephenson. *b.* 1950. B.A. (Nat. Sci.), 1971, University of Cambridge, UK, Ph.D., 1975 (supervisor Jim Emsley), University of Southampton, UK. Postdoctoral work at University of Munich (with Gerhard Binsch). Currently Akademischer Oberrat at University of Munich. Approx. 30 publications. Current interests: computer games.

Carbon-13 Spectral Simulation

Peter C. Jurs

The Pennsylvania State University, University Park, PA, USA

1	Introduction	1
2	Methodology for the Development of Individual Models	1
3	Regression Model Library	4
4	Model Selection	5
5	Neural Network Prediction of ^{13}C NMR Spectra	7
6	^{13}C NMR Simulation of Pyrans	7
7	Summary	10
8	Related Articles	10
9	References	10

1 INTRODUCTION

Carbon-13 nuclear magnetic resonance, ^{13}C NMR, spectrum simulation involves converting structural information into a simulated spectrum via calculation. Spectral simulation can be very useful in aiding chemists in the solution of complex structure elucidation problems and in the verification of chemical shift assignments.

This article will discuss the simulation of ^{13}C NMR spectra by empirical modeling techniques. The four most common methods of ^{13}C NMR spectral simulation involve linear additivity relationships, database retrieval techniques, quantum mechanical methods, and empirical modeling. The utility of linear additivity relationships has been studied by many researchers including Zupan et al.[1] and Fürst and Pretsch.[2] This technique utilizes a large database of carbon atoms and their associated chemical shifts to derive empirical parameters for a variety of structures and functionalities. The chemical shift of a new atom in a particular environment can then be calculated using the empirical parameters derived from similar atomic environments in the form of simple linear equations. Although this approach can be applied to a wide range of compounds, standard errors in excess of 5 ppm are common.

Database retrieval techniques[3,4] also rely on access to a large database containing carbon atoms and their corresponding known chemical shifts. To simulate the ^{13}C NMR spectrum for a query compound, the most similar atomic match is found from the database for each unique atom in the query. The chemical shift associated with each matched database atom is retrieved as the predicted chemical shift for each atom in the query. This method is applicable to a wide variety of compounds, but its accuracy is highly dependent on the size and breadth of the database and the nature of the similarity metric used for carbon atom retrieval.

Quantum mechanical methods for ^{13}C NMR spectral simulation involve the use of molecular orbital theory calculations such as INDO and MINDO/2.[5,6] Chemical shielding is calculated in two parts: diamagnetic shielding (created by the induced current around the nucleus of interest) and paramagnetic shielding (the degree to which the specific chemical environment quenches the induced current around the nucleus). Recent work by Baker and Zerner[6] reports the calculation of ^{13}C NMR shifts using an intermediate neglect of the differential overlap model for several relatively small hydrocarbons and other simple molecules. Quantum mechanical methods typically require extensive computational time and are applied only to relatively simple molecules.

Empirical modeling techniques involve the development of mathematical models from a dataset of known chemical shifts. These models relate the chemical shift of an atom to various atom-based structural parameters (descriptors). When such a model is derived using multiple linear regression, it may have the following form:

$$S = b_0 + b_1X_1 + b_2X_2 + \ldots + b_nX_n \qquad (1)$$

where S is the chemical shift of an individual carbon atom, the X_i quantities are the descriptor values, and the b_i quantities are coefficients determined by multiple linear regression analysis. Computational neural networks can also be used to develop models which relate descriptors to chemical shifts. Once the model is developed, it can be utilized to predict the chemical shifts for carbons not contained in the original dataset. A limitation of this technique arises because the model equations can only be used to predict the shifts for atoms that are structurally similar to those used to develop the models. Unlike database retrieval techniques however, these models have the ability to interpolate chemical shifts. In addition, this technique typically yields simulated spectra with standard errors on the order of 1.0 ppm. This article will focus on the methodology involved in developing empirical models for ^{13}C NMR spectral simulation and present an extended example of application of the method to tetrahydropyran compounds.

2 METHODOLOGY FOR THE DEVELOPMENT OF INDIVIDUAL MODELS

The methodology used to develop mathematical models for ^{13}C NMR simulation is illustrated in Figure 1, and each step will be described in the following discussion.

2.1 Selecting a Dataset

The first step involved in a ^{13}C NMR spectral simulation study is determining the class of compounds to be studied. Once a set of compounds is selected, their corresponding ^{13}C NMR spectra are obtained from the primary literature or data compilations. One such compilation of ^{13}C NMR data is that of Chemical Concepts GmbH, which currently contains 68 207 compounds (C_1–C_{86}) with 83 591 associated spectra. After chemical shifts are assembled into spectra, they should be checked against the primary literature to minimize the probability of errors. Typically, 90% of the carbon atoms and their associated shifts are used as the training set (a set used to generate the model equations), and the remaining 10% are set aside as a prediction set (a set used to test the external predictive ability of the model equations after model development is complete).

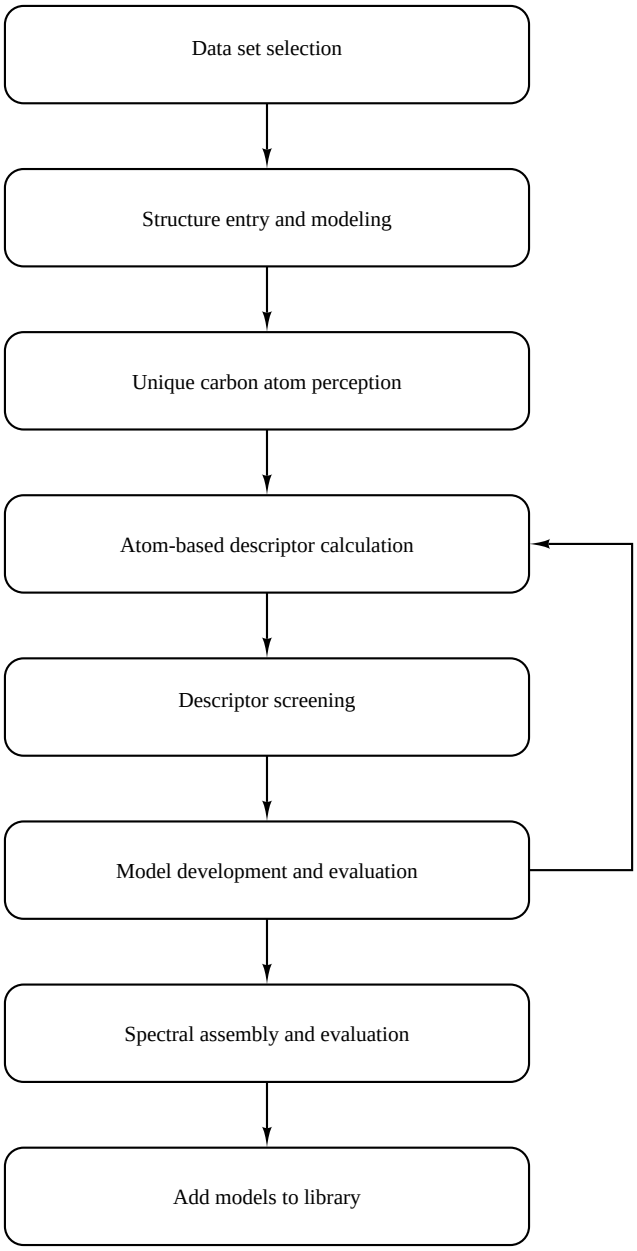

Figure 1 Flow chart of ^{13}C NMR simulation study

2.2 Structure Entry and Modeling

The molecular structures are entered as two-dimensional sketches and stored as connection tables in a database. In addition to the molecular structures, the ^{13}C NMR spectrum for each compound is stored. The two-dimensional representations of the compounds are then submitted to molecular modeling to generate three-dimensional molecular models. A simple, interactive classical molecular mechanics routine is used as a starting point.[7] The models are then refined using the molecular mechanics approach of MM2.[8] Some bond types and atomic arrangements cannot be modeled by MM2, in which case it is necessary to use molecular orbital methods such as MOPAC.[9] Three-dimensional representations of the structures are necessary for subsequent computation of geometrical descriptors. Such geometric descriptors are essential to ^{13}C NMR simulation because shift values are highly dependent on geometric relationships in the structures.

2.3 Unique Atom Perception

It is important to include only the unique atoms (those in structurally unique surroundings) in the dataset when generating models. Unique atoms give rise to unique chemical shifts. If an atom and its corresponding chemical shift are represented more than once in the dataset, then the models can become unduly skewed or biased to account for that particular atom type.

2.4 Atom Subsetting

The carbon atoms in a set of compounds are usually structurally diverse, so it may be difficult to generate one model capable of simulating accurate ^{13}C NMR shifts for all the atoms together. In such cases, the dataset can be divided into smaller, more homogenous sets of atoms. In many studies, subsetting has been primarily based on carbon atom connectivity (1°, 2°, 3°, 4°), or position relative to a functional group (e.g., the number of bonds distant from a carbonyl group). Model equations are then developed independently for each atom subset. Whenever possible, subsetting is not employed and one overall model is generated for all carbon atoms in the set of compounds. The flow chart of Figure 1 does not include subsetting of the data because it is only done when necessary.

2.5 Descriptor Generation

Once the unique carbon atoms have been identified and stored, the structural environment surrounding each carbon atom must be encoded. The chemical environments are represented by numerically encoding the topological, electronic, and geometrical features that surround each carbon atom, as illustrated in Figure 2.

These calculated numerical representations of the chemical environments are called descriptors. Since the chemical shift of a carbon atom is not significantly affected by the chemical environment more than five bonds away, descriptors are only computed based on structural features located one to five bonds distant from the carbon center of interest. More than 700 atom-based descriptors have been implemented in ^{13}C NMR spectral simulation studies. A few examples of the topological, electronic, and geometrical descriptors that have been found to be important in numerous studies are described here. A complete list of the atom-based descriptors that can be calculated has been presented elsewhere.[10]

Topological Descriptors: The simplest descriptors are topological and are calculated directly from the connection table representations of the structures. These descriptors include atom counts, valency counts, and molecular connectivity indices. Molecular connectivity indices are graph theoretical descriptors derived from the topological representation of molecular structures, and they encode size, shape, and branching information.[11] The most commonly used atom count descriptor is the number of carbon atoms located three bonds

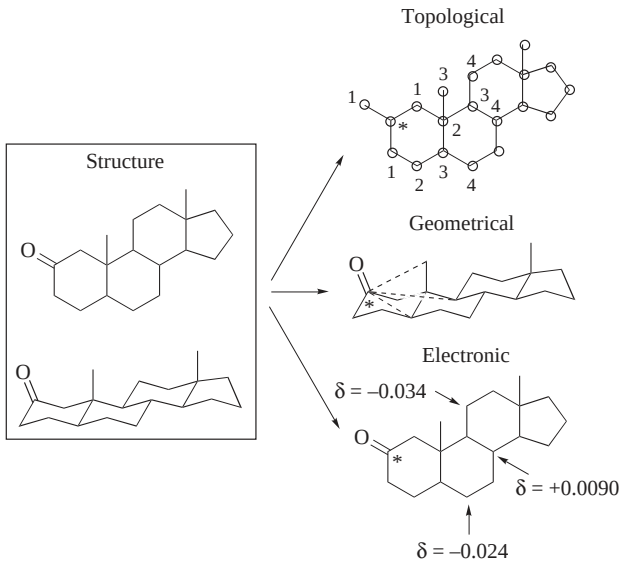

Figure 2 Schematic diagram of atom-based descriptor generation

from the carbon center of interest. This descriptor appeared in five of the first 66 regression models in the library of models for ^{13}C NMR simulation. The most widely used valency count descriptor encodes the number of tertiary carbons that are located one bond from the carbon center of interest. This descriptor has appeared in 10 of the first 66 regression models in the library. Connectivity indices encode the degree of branching that surrounds a given carbon atom. The average connectivity index over the carbon atoms one bond from the carbon center has been the most useful descriptor in this category, appearing in four of the first 66 regression models.

Electronic Descriptors: The electronic properties of the portion of the structure near a given carbon atom are computed by first calculating the partial atomic charges for each heavy atom (nonhydrogen) in the compound. These partial atomic charges are computed using extended Hückel,[12] Del Re,[13] or an empirical method recently reported[14] based on an extension of work by Abraham and Smith.[15] Once these partial charges have been computed, the total atomic charge, the average atomic charge, the most negative atomic charge, and the most positive atom charge are calculated from one to five bonds from the carbon center being described. All three of the partial atomic charge calculation methods have been quite useful, but the most widely used electronic descriptor is based on Del Re methods and computes the sum of the σ charges on all heavy atoms located three bonds from the carbon center of interest. This descriptor has been used in six of the first 66 regression models in the library.

Geometrical Descriptors: The most sophisticated descriptors are geometrical in nature and are dependent on the three-dimensional coordinates obtained from molecular mechanics. Because these descriptors are dependent on calculated geometries, they possess an added degree of experimental uncertainty. Examples of geometrical descriptors include through-space distance calculations and shell counts, illustrated in Figure 3.

As shown, one through-space descriptor encodes the sum of inverse cubed through-space distances from the carbon center (here a carbonyl carbon) to all primary carbons located two bonds away. An example of a shell count descriptor

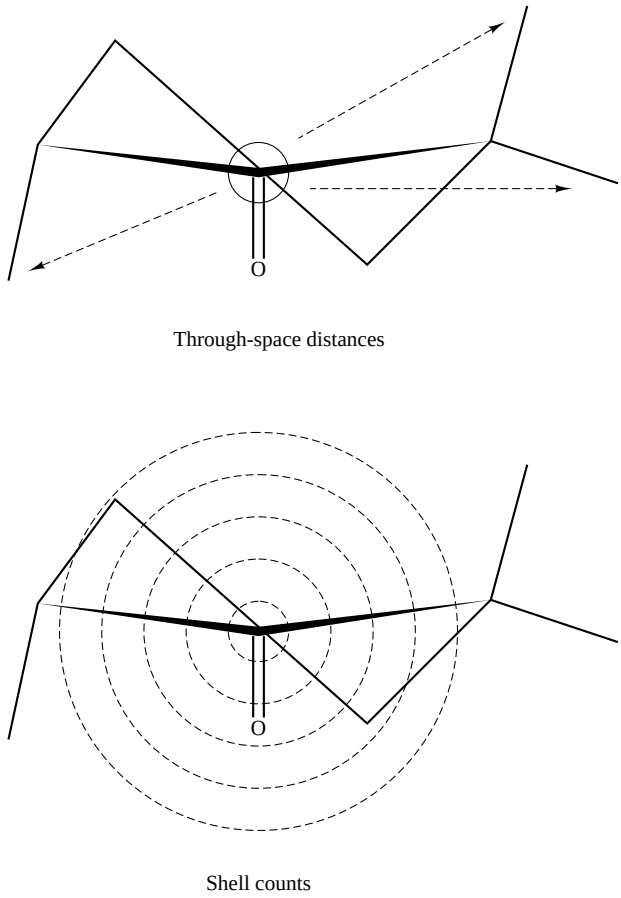

Figure 3 Diagram showing through-space distances and shell counts used for descriptor generation

would be to count the number of hydrogens that are located in the spherical shell from 3.6 Å to 5.0 Å from the carbon center. The radii of the shells used were found by systematic investigation of simple compounds for distances that were most representative of structural classes. The most commonly used geometrical descriptor (present in 20 of the first 66 regression models), however, is a van der Waals energy descriptor.[16] This descriptor calculates the van der Waals energy of the carbon center interacting with all hydrogen atoms in the molecule.

2.6 Descriptor Screening

In order to assure their statistical significance, the descriptors are screened before being submitted to multiple linear regression analysis. Only information-rich descriptors pass the screening step for further analysis. This step is performed independently for each atom subset since a particular descriptor may contain useful information for one subset but not for another. Descriptors are generally removed from consideration if they contain mostly identical or zero values for the entire atom subset, or if they are highly correlated with other descriptors. The overall goal of descriptor screening is to reduce the size of the data matrix (minimize the number of descriptors used) while retaining the maximum amount of information.

2.7 Model Development by Regression

The descriptors that survive screening are submitted to multiple linear regression analysis. Forward selection,[17] backward deletion,[17] and leaps-and-bounds regression[18] are among the methods used to select descriptors and develop final models. Leaps-and-bounds regression is an automated technique that simulates performing all possible regressions by considering optimal subsets of descriptors. The objective is to find the best mathematical model that relates the chemical shifts of the carbon atoms comprising the training set to their experimental ^{13}C NMR shifts using the smallest number of descriptors of those available. Typically, there should be at least five chemical shifts for each descriptor present in a model. If the problem under investigation involves several subsets, a separate model is developed for each atom subset. After the models are developed, the simulated spectra can be assembled from the individual chemical shift predictions.

2.8 Model Evaluation

Various methods are utilized to validate each model. Models with high multiple correlation coefficients, R, and low standard errors of regression, s, are desirable. The goal is to find models with s values less than 1.0 ppm. Plots of calculated versus observed chemical shifts and residual error versus calculated shifts can be used to test visually for outliers, nonconstant variance, and other statistical problems.[19] Each model is also internally validated using jackknifing. This involves regenerating the model coefficients for the training set with one chemical shift removed, and then predicting the value for the removed carbon atom. This is done once for each chemical shift in the training set, and the averaged results obtained are indicative of the quality of the model. Another important model evaluation step is external prediction. Using an external prediction set, the models are used to predict the shifts for atoms which were not included in the original training set.

2.9 Spectral Assembly and Evaluation

Once the individual chemical shifts have been calculated for all of the carbon atoms in the training and prediction sets, they are combined to form simulated ^{13}C NMR spectra for entire compounds. Once assembled, the root mean square (rms) errors between simulated and observed spectra are calculated. Generation of simulated spectra that have rms spectral errors of 1.0 ppm or less is the goal. If the rms spectral errors produced by a model are unacceptable, then new models are generated or subsetting of the data may be tried.

Another technique used to evaluate the quality of the simulated spectra is library searching. Library searching involves comparing a simulated spectrum for a compound against a library of over 1000 stored spectra which contains the observed spectrum for the same compound. If a simulated spectrum is of high quality, then the most similar spectrum (the spectrum retrieved as the top match) should be the observed spectrum of the same compound or a very similar one. The goal is to generate simulated spectra which are accurate enough to retrieve their observed spectra as number one matches in all cases. It has been observed that this is possible when rms spectral errors of 1.0 ppm or below are obtained.

2.10 Adding Models to the Library

Once suitable regression models have been developed and have passed the spectral assembly and evaluation steps, they are stored in the regression model library for future use in automated ^{13}C NMR spectral predictions. Within the regression model library, there are four databases which contain information about all the molecular structures, carbon atoms, regression models, and atom-based descriptors that were used to build the library. The information in these databases is essential for performing automated spectral predictions and must be updated as new models are checked in.

The *structure database* identifies every compound that was used in the development of a regression model. In addition, the energy-minimized three-dimensional coordinates are stored for each of these compounds. The *atom database* contains information about each unique carbon atom that was previously used to develop a regression model. Each carbon atom in this database possesses a unique index number and its observed chemical shift is also stored. The *model database* contains information about each regression model including the statistics associated with each model, the intercept, the regression coefficients, and the descriptor index associated with each coefficient. The *descriptor database* contains the unique indices associated with the 718 descriptors that can be calculated. In addition, this database indicates which ADAPT programs must be executed to compute each descriptor and the necessary settings that must be utilized. This information is necessary during predictions of spectra for unknown compounds.

3 REGRESSION MODEL LIBRARY

The long-term goal of such a system is to develop the capability to simulate accurate ^{13}C NMR spectra for a wide variety of organic compounds directly from their structures in an automated fashion. In order to pursue this goal, a library containing previously developed regression models (predictive equations) was constructed.

In the past, the primary focus was the development of empirical models for limited sets of structurally homogeneous compounds. However, more recently, the utility of combining database retrieval and empirical modeling techniques has been investigated in an attempt to benefit from the advantages offered by both techniques. In this combined approach, predictive equations are retrieved from a library of stored regression models to calculate the chemical shifts for each atom in a query compound. For this approach to be successful, two tasks must be accomplished. First, the library of predictive regression equations must be broadly applicable, i.e. models capable of simulating accurate shifts for many different atomic environments must be developed and stored. Second, an effective algorithm capable of selecting the most appropriate model to use for predicting the shift of a query atom needs to be developed.

A total of 87 regression models capable of simulating ^{13}C NMR spectra for a variety of structural classes has been developed and stored in a library of regression

equations. The structural classes represented are as follows: linear and branched alkanes,[20] cycloalkanes,[21] cyclohexanols and decalols,[22] hydroxysteroids,[23] cyclopentanes and cyclopentanols,[24] norbornanols,[25] cyclohexanones and decalones,[26] piperidines,[27] polychlorinated biphenyls,[28] alkyl-substituted benzenes and polyaromatics,[29] keto-steroids,[30] quinolines and isoquinolines,[31] cyclopentanones and cyclo heptanones,[32] side-chain atoms on ring systems,[33] indoles,[34] hydroaromatics,[33] polysaccharides,[35] and tetrahydropyrans.[36] These models are listed in Table 1.

As shown in Table 1, three to eight models have been developed for each compound class except for polysaccharides and tetrahydropyrans where only one model was necessary. Each model was developed for a subset of the carbon atoms found in the compounds being studied and the number of atoms used in the development of each model are shown in parentheses after the identity of each model. More than 6000 carbons were used to develop the set of 87 models. Models 8, 12, and 63 were each developed with fewer than eight observations. Because fewer than eight observations were not sufficient to generate statistically valid regression models, the average chemical shift of each atom subset was used in place of traditional regression equations. Each compound class was studied independently and the standard set of procedures described above were followed in order to develop the regression models.

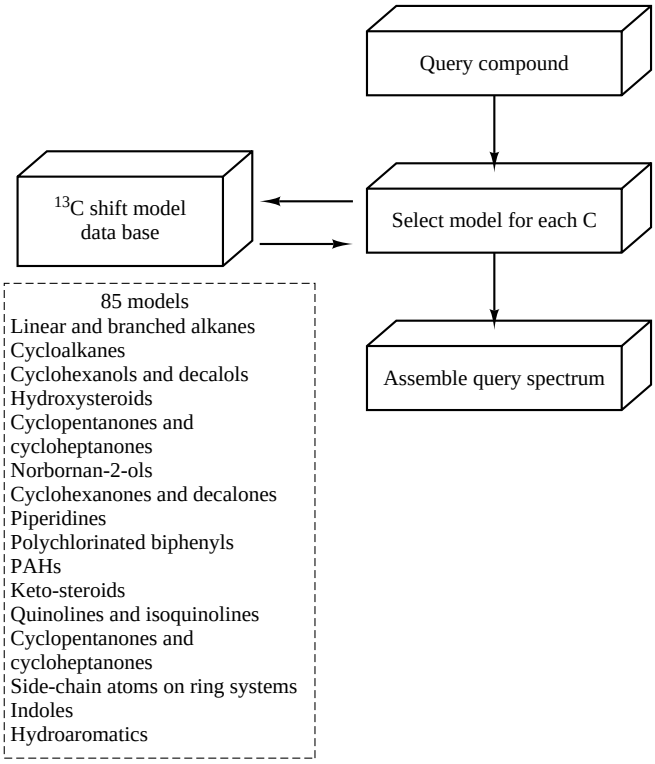

Figure 4 Flow chart of ^{13}C NMR shift prediction using model library

4 MODEL SELECTION

To use the models for predicting the shifts of unknowns, an effective procedure for choosing the best model from the library must be available. A flow chart of this selection process is shown in Figure 4.

Currently, a nearest neighbor approach to model selection is being utilized. The development of this approach has been described.[17] The current model library contains the 87 predictive equations shown in Table 1. The atomic environment surrounding each of these atoms is encoded using a set of seven topological descriptors. These seven descriptors include the six EVEC descriptors[37] used in the original model selection procedure[38] and Randićs atomic ID descriptor.[39] As a set, these seven variables provide sufficient information about the surroundings of each carbon atom to make selection from the library possible.

To select a model for the prediction of a query atom in an unknown, the following procedure is followed. The seven descriptors are calculated for the query atom. In order to find the most similar atomic match, the Euclidean distance, d, between the query atom and each of the 5155 atoms in the database is calculated using equation (2):

$$d = [(D_1 - Q_1)^2 + (D_2 - Q_2)^2 + \ldots + (D_7 - Q_7)^2]^{1/2} \quad (2)$$

where the D_i terms are the descriptor values for an individual database atom and the Q_i terms are the descriptor values for the query atom. The database atom associated with the smallest Euclidean distance is defined as the nearest neighbor atom. In a database retrieval scheme, the shift associated with this nearest neighbor atom would be assigned to the query atom. In our scheme, the model developed from the nearest neighbor atom is used to calculate the chemical shift for the query atom. To do this, the descriptors that were used in the selected model are computed for the query atom. Then, these descriptor values are multiplied by the appropriate coefficients and the chemical shift is predicted. This entire procedure is repeated for each atom in the query compound until the complete ^{13}C NMR spectrum is simulated.

An illustration of this method was developed when the model library contained the first 71 models. The spectrum for 2,2,5-trimethylcyclopentanone was simulated. This compound was not used to develop any models in the database but is similar to the compounds used in the cyclopentanone and cycloheptanone study. The molecular structure, observed ^{13}C NMR spectrum, and simulated ^{13}C NMR spectrum are shown in Figure 5.

For each of the seven carbon atoms in the query compound, an appropriate model was selected from the model library. The figure visually illustrates the high degree of similarity between the simulated and observed spectra. The standard error of estimate for this simulated spectrum was 0.81 ppm. It should be emphasized that this entire procedure is fully automated, and it took less than 4 min to generate a complete simulated spectrum starting from the energy-minimized three-dimensional molecular structure.

This automated model selection procedure can be used to probe the regression model library systematically to determine if any weaknesses are present. A weakness in the library means that the ^{13}C NMR spectra for a class of compounds cannot be simulated with the desired accuracy. When such deficiencies are identified, models which address them can be developed. Two independent studies were recently performed which probed the model library and identified two such weaknesses. The first study involved a set of cyclic compounds

Table 1 List of Regression Models Forming the Library and Numbers of Carbons used to Develop Each Model

Model No.	Model description
	Linear/branched alkanes
1	Primary carbons (128)
2	Secondary carbons (119)
3	Tertiary carbons (53)
4	Quaternary carbons (24)
	Cycloalkanes
5	Primary carbons (50)
6	Secondary carbons (157)
7	Tertiary carbons (79)
8	Quaternary carbons (7)
	Cyclohexanols/decalols
9	Primary carbons (39)
10	Secondary carbons (138)
11	Tertiary carbons (78)
12	Quaternary carbons (8)
	Hydroxysteroids
13	Primary carbons (48)
14	Secondary carbons (224)
15	Tertiary carbons (120)
16	Tertiary carbons with −OH attached (25)
17	Quaternary carbons (53)
	Cyclopentanes/cyclopentanols
18	Primary carbons (35)
19	Secondary carbons (82)
20	Tertiary carbons (36)
21	Tertiary carbons with −OH attached (11)
22	Quaternary carbons (13)
23	All carbons with −OH attached (20)
24	Tertiary and quaternary ring carbons (28)
25	Tertiary and quaternary side chain carbons (13)
26	Secondary carbons (21)
27	Tertiary carbons with −OH attached (32)
	Norbornan-2-ols
28	Primary carbons (50)
29	Secondary carbons (95)
30	Tertiary carbons without −OH attached (82)
31	Tertiary carbons with −OH attached (30)
32	Quaternary carbons (17)
33	Quaternary carbons without −OH attached (15)
	Cyclohexanones/decalones
34	Primary carbons (46)
35	Secondary carbons (170)
36	Tertiary carbons (49)
37	Quaternary carbons (22)
38	Carbonyl carbons (model A) (38)
39	Carbonyl carbons (model B) (38)
40	Carbons one bond from the carbonyl (67)
41	Carbons two bonds from the carbonyl (85)
42	Carbons > two bonds from the carbonyl (135)
	Piperidines
43	Primary carbons (60)
44	Secondary carbons (78)
45	Tertiary carbons (44)
46	Primary carbons attached to a carbon (44)
47	Primary carbons attached to a nitrogen (16)
48	Carbons one bond from a nitrogen (62)
49	Carbons two bonds from a nitrogen (65)
50	Carbons > two bonds from a nitrogen (55)
	Polychlorinated biphenyls
51	Carbons with chlorines attached (84)
52	Bridging carbons (49)
53	Carbons with hydrogens attached (131)
	Alkyl-substituted benzenes/PAHs
54	Aromatic ring carbons (231)
55	Primary carbons (36)
56	Non-ring-bridging aromatic ring carbons (178)
57	Ring-bridging aromatic carbons (53)
	Keto-steroids
58	Carbonyl carbons (26)
59	Carbons one bond from the carbonyl (52)
60	Carbons two bonds from the carbonyl (74)
61	Carbons three bonds from the carbonyl (97)
62	Carbons > three bonds from the carbonyl (208)
	Quinolines/isoquinolines
63	Primary carbons (5)
64	Carbons two bonds from bridge carbons and two bonds from a nitro group (105)
65	Carbons one bond from bridge carbons or two bonds from a bridge carbon and a nitro group (114)
66	Bridge carbons and carbons attached to a nitro group (69)
	Cyclopentanones and cycloheptanones
67	Carbonyl centers (36)
68	Carbons one bond from the carbonyl (64)
69	1° carbons >1 bond from the carbonyl (46)
70	2° carbons >1 bond from the carbonyl (64)
71	3° and 4° carbons >1 bond from the carbonyl (43)
	Side-chain atoms on ring systems
72	Primary carbons (75)
73	Secondary carbons (24)
74	Tertiary carbons (19)
75	Quaternary carbons (35)
	Indoles
76	Carbons 2 and 3 (112)
77	Carbons 1 and 4 (112)
78	Carbons 5 (54)
79	Carbons 6 (56)
80	Carbons 7 (56)
81	Carbons 8 (56)
	Hydroaromatics
82	Carbons 1 bond from bridgehead (113)
83	Bridgehead carbons (122)
84	2°, 3°, 4° carbons >1 bond from bridgehead (94)
85	1° carbons >1 bond from bridgehead (88)
	Polysaccharides
86	All carbons (92)
	Tetrahydropyrans
87	All carbons (201)

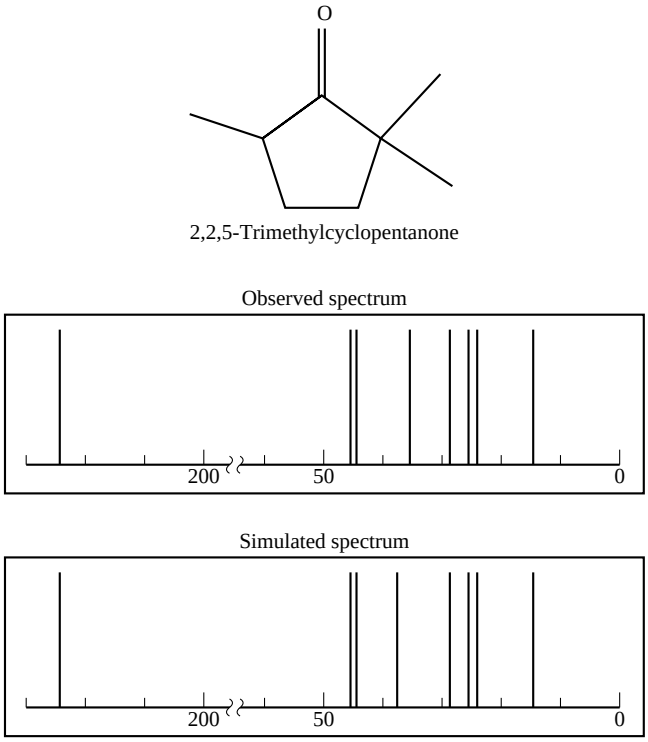

Figure 5 Simulated and observed spectra for 2,2,5-trimethylcyclopentanone

containing various side chains, and the second involved a set of hydroaromatic compounds. Models were developed for these classes of compounds and they were added to the library, forming models 72–75 for side chains[33] and 82–85 for hydroaromatic compounds.[33] Other recent additions to the library include models developed with sets of indoles,[34] polysaccharides,[35] and tetrahydropyrans.[36]

5 NEURAL NETWORK PREDICTION OF ^{13}C NMR SPECTRA

The models discussed up to this point were developed via multiple linear regression analysis and they had the form of equation (1). Such models assume a linear relationship between the individual carbon atom descriptors and the chemical shifts. It is possible to use transformations of individual descriptors to introduce nonlinearities, but this must be done in an ad hoc manner. As seen, the approach with linear models has been successfully used to develop models for many classes of compounds. However, nonlinear relationships between the descriptors and chemical shifts are undoubtedly present, and methods to take advantage of this information should lead to superior simulation ability. The use of computational neural networks provides such an opportunity to utilize nonlinear relationships.

A computational neural network is an assembly of simple units, called neurons, organized in a highly-connected array.[40,41] Three types of neurons comprise a network: *input* neurons which accept the input data characterizing each observation; *output* neurons which provide the predicted value or pattern; and *hidden* neurons connected to the input or output neurons to provide intermediate processing. A fully-connected, feed-forward neural network consists of these three types of neurons arranged in layers with connections linking each neuron in a given layer and all of the neurons in the succeeding layer (Figure 6).

For simplicity, the network shown has just one output neuron which would provide a quantitative value for the predicted chemical shift. The network functions by receiving a set of input values, processing them, and then producing an output value calculated from these input values. A network is trained through repeated presentations of input and target pairs. The adjustable weights associated with the links within the network are systematically altered during training to reduce the error, and their values constitute the memory of the network.

The most widely used training algorithm is called back-propagation because the errors in the outputs are propagated backward through the network to systematically alter the weights. Back-propagation is a gradient descent method. The objective of training a network is to create a system that can properly reproduce all of the target values given the set of input values. Neural networks often have a large number of adjustable parameters (the weights) and they can be prone to overtraining. This occurs when training continues through too many iterations and the network focuses on learning the individual idiosyncrasies of the training set patterns which diminishes its ability to predict for unknowns. Overtraining is avoided by using a cross-validation set of patterns to test the network periodically during training, and terminating training when the cross-validation set error is minimized. After training is complete, the network can then be used to predict the outputs for a new set of inputs.

Recently, there has been a great deal of interest in neural networks in many areas of science and technology including engineering, biology, and the cognitive sciences.[42] Neural networks have been applied to several areas of chemistry,[43] including ^{1}H NMR spectroscopy[44,45] and ^{13}C NMR spectroscopy.[46] A review article covering many applications of neural networks in analytical chemistry has appeared,[47] and a tutorial was recently published.[48]

Several studies have been undertaken in which back-propagation neural networks were used as a supplement to regression analysis to link the atomic structural environment descriptors to the ^{13}C NMR shifts.[35,36,49] Neural networks have also been used for the task of choosing models from the regression model library for use in predicting the ^{13}C NMR spectrum of a query compound.[50] Excellent results have been achieved, which lead us to believe that expanded use of neural networks for the prediction of ^{13}C NMR spectral shifts will follow.

Recently an advanced quasi-Newton neural network training algorithm called BFGS (Broyden–Fletcher–Goldfarb–Shanno)[51] was reported. This method computes the step size for the correction for each weight during the computation, yielding quicker convergence. It provides a superior performance to the standard back-propagation method, both in terms of speed of training and final results, and it was applied to ^{13}C NMR simulation.[35,36]

6 ^{13}C NMR SIMULATION OF PYRANS

As an example of the capabilities of this ^{13}C NMR simulation approach, a recent study of tetrahydropyrans[36] is

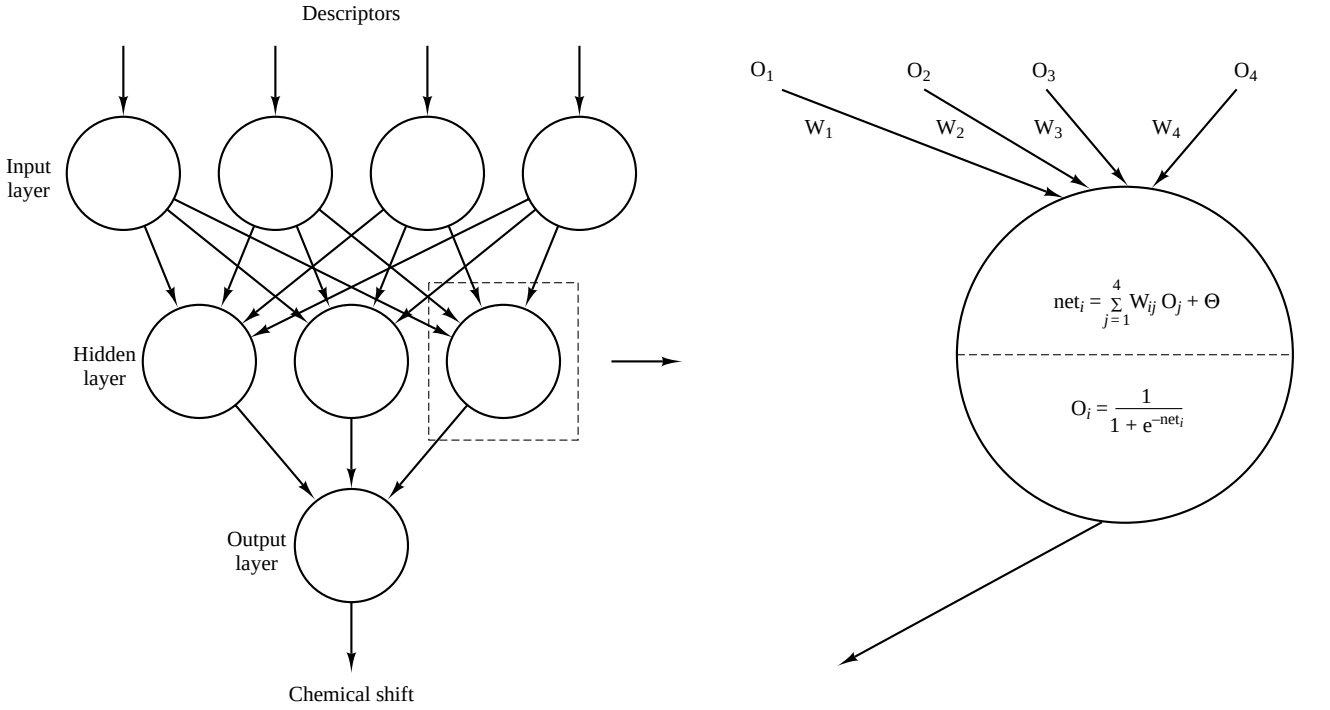

Figure 6 Architecture and function of a fully-connected, feed-forward computational neural network

described. The ^{13}C NMR spectra of the tetrahydropyrans were simulated directly from their molecular structures using the methodology described above. A set of 29 tetrahydropyrans was used as a training set to generate regression equations and to train neural networks, and three additional compounds were used as a cross-validation set. The results of simulations undertaken by regression analysis were found to be extremely sensitive to molecular geometries. To account for this, two different methods of descriptor manipulation, an averaging method and a Boltzmann-weighted averaging method, were developed, and the models generated from the descriptor sets were compared. The results for the Boltzmann-weighted averaging method were found to be superior to those based on descriptors derived from only the lowest energy molecular conformations.

The 32 tetrahydropyran compounds and ^{13}C NMR spectra used for this study were obtained from the Chemical Concepts database (Weinheim, Germany) and are listed in Table 2. Compounds 1–29 were used as a training set, and 30–32 were used as a cross-validation set to test the external predictive ability of the equations generated by regression analysis. The three compounds in the cross-validation set were chosen randomly. The experimentally observed shifts fall into two groups: the atoms not bonded directly to an oxygen (shifts ranging from 5.07 ppm to 46.06 ppm), and the atoms bonded directly to an oxygen (shifts ranging from 63.43 ppm to 80.21 ppm). All the carbons were treated as one dataset, and it was not necessary to divide them into subsets in this study.

Each compound was modeled with molecular mechanics using MM2 to find the lowest strain energy conformation. Then the unique carbon atoms from each compound were identified. The training set is comprised of the 182 unique carbon atoms of compounds 1–29 and the cross-validation set is comprised of the 19 unique carbon atoms of compounds

Table 2 The 32 Tetrahydropyrans used for Simulation Study

Number	Compound
1	2-Methyltetrahydropyran
2	4-Methyltetrahydropyran
3	Tetrahydropyran
4	*cis*-3,5-Dimethyltetrahydropyran
5	3,3-Dimethyltetrahydropyran
6	*trans*-2,4-Dimethyltetrahydropyran
7	*cis*-2,4-Dimethyltetrahydropyran
8	3-Methyltetrahydropyran
9	*cis*-2,3-Dimethyltetrahydropyran
10	*cis*-2,5-Dimethyltetrahydropyran
11	*cis*-3,4-Dimethyltetrahydropyran
12	*trans*-2-Ethyl-6-methyltetrahydropyran
13	*trans*-2,3-Dimethyltetrahydropyran
14	*trans*-2,5-Dimethyltetrahydropyran
15	*trans*-3,4-Dimethyltetrahydropyran
16	*cis*-2,6-Dimethyltetrahydropyran
17	*trans*-2,6-Dimethyltetrahydropyran
18	2,2-Dimethyltetrahydropyran
19	4,4-Dimethyltetrahydropyran
20	3,3,5-Trimethyltetrahydropyran
21	*R*-2, *cis*-3, *trans*-5-Trimethyltetrahydropyran
22	*R*-2, *cis*-3, *trans*-5-Trimethyltetrahydropyran
23	*R*-2, *trans*-3, *cis*-5-Trimethyltetrahydropyran
24	*R*-3, *cis*-4, *cis*-5-Trimethyltetrahydropyran
25	*R*-3, *trans*-4, *cis*-5-Trimethyltetrahydropyran
26	*R*-3, *cis*-4, *trans*-5-Trimethyltetrahydropyran
27	*trans*-***S***-Ethyl-4-methyltetrahydropyran
28	*cis*-2-Ethyl-5-methyltetrahydropyran
29	*cis*-2-Ethyl-6-methyltetrahydropyran
30	*trans*-3,5-Dimethyltetrahydropyran
31	2,2,6-Trimethyltetrahydropyran
32	2-Ethyltetrahydropyran

Table 3 Regression Equation, Descriptors used, and Statistics for Equation Developed using Boltzmann-Weighted Average Descriptors

Descriptor[a]	Mean	SD[b]	Coefficient	Mean effect[c] (ppm)
MNAC 3	−0.133	0.118	6.22 ± 1.8	−0.83 ± 0.23
MPCG 1	−0.00347	0.0478	−23.4 ± 7.0	0.0812 ± 0.024
HHI3 2	0.131	0.0804	66.5 ± 2.8	8.71 ± 1.14
CHVD 1	0.171	0.196	9.23 ± 1.5	1.58 ± 0.25
CXVD 1	0.280	0.228	5.92 ± 0.97	1.66 ± 0.27
STAS 1	0.487	0.353	−1.32 ± 0.41	−0.642 ± 0.20
STBS 1	0.286	0.384	1.45 ± 0.35	0.358 ± 0.10
TOTB 1	0.630	0.618	−1.13 ± 0.37	−0.712 ± 0.23
CHCG 1	0.108	0.232	87.1 ± 1.1	9.41 ± 0.12
COET 1	0.873	0.232	4.79 ± 0.38	4.18 ± 0.33
Intercept			14.7	
	n = 182		s = 1.53 ppm	R = 0.998
	n = 19		s = 3.53 ppm	R = 0.994

[a]Descriptor definition ('heavy atom' denotes all nonhydrogen atoms). MPCG 1, the most positive σ-charge among heavy atoms one bond away from the carbon center, HH13 2, the sum of the inverse cubed through-space distance from the hydrogens attached to the carbon center to other hydrogens four bonds away; CHVD 1, the van der Waals energy due to interactions between the carbon center and hydrogens in the molecule; CHCG 1, the extended Hückel charge on the carbon center; COET 1, the van der Waals energy between the carbon center and all oxygens two or more bonds away; TOTB 1, the sum of the strain associated with torsional angles involving oxygen atoms and the carbon center in torsional bonds; MNAC 3, the most negative charge due to all heavy atoms three bonds from the carbon center; CXVD 1, the van der Waals energy due to the interactions between the carbon center and other heavy atoms; STAS 1, the smallest strain associated with a torsional angle involving the carbon center; STBS 1, the smallest strain associated with a torsional bond involving the carbon center.
[b]SD = standard deviation.
[c]Mean effect = average shielding and deshielding contribution of each descriptor on the predicted chemical shift.

30–32. Descriptors were then generated for the 201 unique carbon atoms and screened to eliminate those with little information content, leaving 65 descriptors.

The remaining descriptors were analyzed using leaps-and-bounds regression and a nine-descriptor equation was found to yield the best results. The standard error for this model was 1.37 ppm, somewhat higher than the 1.00 ppm that is typically desired in order to generate quality spectra. The 19 carbon atoms of the cross-validation set were predicted with a standard error of 2.49 ppm. This value is larger than desirable and it has been adversely influenced by several substantial outliers.

One measure of the quality of the simulated spectra is to use the spectra as queries for library searching. When this was done against a large library, the spectra generated by this model were accurate enough that number one matches were found for all compounds. That is, the authentic spectra were retrieved as best matches to the query spectra. However, the scores, which are a measure of the quality of the spectra, were poor. The presence of several geometrical descriptors in the model indicates that the geometry of the molecule is an important determinant of the chemical shift for these tetrahydropyrans. This led to testing of the sensitivity of this model to the different conformations that tetrahydropyrans can assume.

To perform the test for the tetrahydropyrans, the lowest strain energy conformations of the molecules were regenerated in their ring-flipped, or high strain energy, conformations. Once these conformations were available, the descriptors that appeared in the best regression equation were recalculated for these conformations. These new descriptor values were then used with the regression equation and the previous coefficients. If the descriptor values were similar for both conformations, the results of the predictions would be similar. In fact, there was a large difference in the results obtained when using the descriptors derived from the two conformations. The low strain energy compounds had an rms spectral error of 1.30 ppm, while the high strain energy compounds had an rms spectral error of 3.77 ppm. This shows that the descriptor values and the regression models derived from them produce shift predictions that are very sensitive to conformational changes. Several methods were developed in an attempt to encode other conformations in order to improve results, and a Boltzmann-weighted averaging method was found to perform the best.

To create descriptors that were averaged for the two conformations, geometric and electronic descriptors were calculated for both energy conformations, and these values were averaged using a Boltzmann weighting scheme. Using leaps-and-bounds regression, a successful 10-descriptor model was found. This model is shown in Table 3 along with its statistics. Of these 10 variables, HHI3, CHVD, CXVD, STAS, STBS, TOTB, and COET are geometrical descriptors, showing the importance of conformational information. This regression model has a standard error of 1.53 ppm.

Once regression analysis had been performed and the best descriptors for the dataset had been determined, neural networks were trained using the same data. The quasi-Newton training method was utilized to develop the networks. For the Boltzmann-weighted average conformation dataset, a neural network with the architecture 10–5–1 (five hidden layer neurons) was found to be optimum. The descriptors were presented to the networks in two groups; a training set (182 carbons) and a cross-validation set (19 carbons). Instead of determining the external predictive ability of the model, the cross-validation set was used to help eliminate the problem of overfitting the data. When the rms error for the cross-validation set fails to improve, the network is no longer giving results that are applicable to atoms not found in the dataset, and the training is stopped.

The results obtained with the Boltzmann-weighted averaging method improved dramatically compared with the regression analysis results. The error decreased from 1.53 ppm for

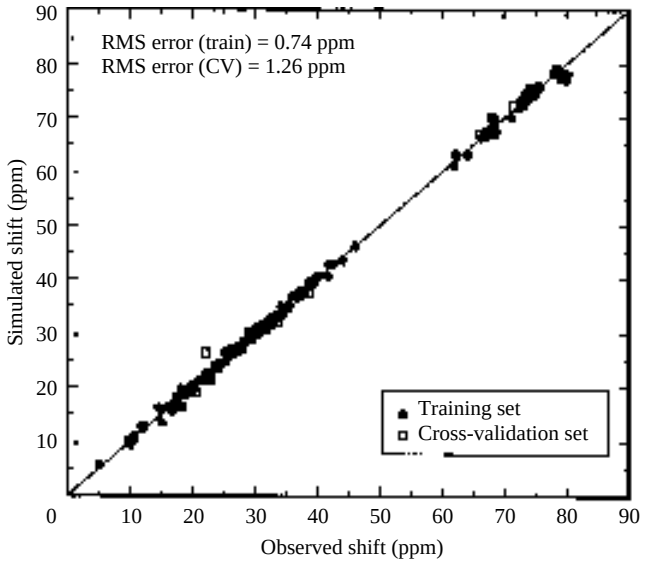

Figure 7 Plot of simulated versus ^{13}C NMR shifts for tetrahydropyrans

regression to an rms error of 0.74 ppm with the neural network. The neural network was able to utilize the information provided by the Boltzmann-weighted averaging method. In addition, nonlinear relationships linking the descriptors to the ^{13}C NMR shifts are accounted for by the neural network. A plot of the predicted versus observed shifts is shown in Figure 7. All of the shifts of the cross-validation set are predicted well, with a lone exception.

An example of the accuracy of the neural network model is shown by the comparison of an entire predicted spectrum to an observed spectrum in Figure 8.

This is compound 32 listed in Table 2, i.e. 2-ethyltetrahydropyran, one of the cross-validation set members. The Boltzmann-weighted averaged descriptors along with a neural network model gives a predicted spectrum that is almost identical to the observed spectrum with an rms error of only 0.68 ppm. The visual similarity between the simulated and observed spectra is striking. Furthermore, just one model has been used for all the carbons in the compound.

Thus, multiple linear regression analysis and quasi-Newton neural networks were used to predict accurately the chemical shifts of tetrahydropyrans. Descriptors based on several conformations of each molecule were shown to be more effective in these simulation studies than descriptors calculated only from low strain energy conformations.

7 SUMMARY

The methodology exists to develop models that directly link calculated structural descriptors for individual carbon atoms with their ^{13}C NMR chemical shifts. Models are developed from sets of compounds with known chemical shifts and then these models have the ability to predict the chemical shifts for new compounds. The descriptors for the carbon atoms are topological, geometrical, or electronic in nature, and they encode the surroundings of the carbons sufficiently for model development. The models can be developed using

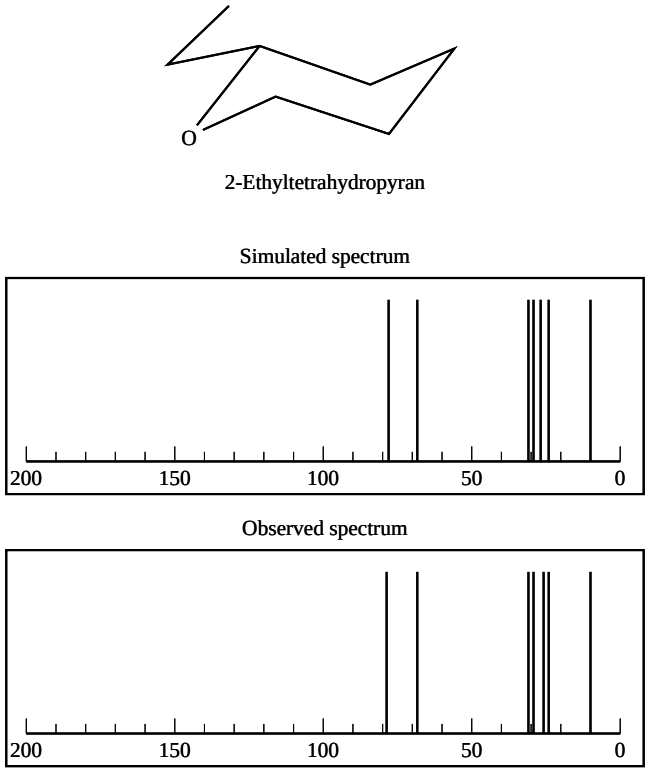

Figure 8 Simulated and observed spectra for 2-ethyltetrahydropyran

multiple linear regression analysis or using computational neural networks. Models with rms spectral errors in the neighborhood of 1.0 ppm have been developed for a wide variety of compound classes and the models have been incorporated into a library. Current work is focusing on the simulation of the ^{13}C NMR spectra of carbohydrates directly from their structures.

8 RELATED ARTICLES

Shielding Calculations: LORG and SOLO Approaches; Organic Chemistry Applications; Computer Assisted Structure Elucidation; Semiempirical Chemical Shift Calculations; Data Processing

9 REFERENCES

1. J. Zupan, M. Novič, S. Bohanec, M. Razinger, L. Lah, M. Tušar, and I. Košir, *Anal. Chim. Acta*, 1987, **200**, 333.
2. A. Fürst and E. Pretsch, *Anal. Chim. Acta*, 1990, **229**, 17.
3. W. Bremser, *Anal. Chim. Acta*, 1978, **103**, 355.
4. S. G. Yuan, Y. W. Wang, D. Chen, and C. Z. Zheng, *Anal. Chim. Acta*, 1989, **221**, 345.
5. H. Fukui, *Magn. Reson. Rev.*, 1987, **11**, 205.
6. J. D. Baker and M. C. Zerner, *Int. J. Quant. Chem.*, 1993, **43**, 327.
7. A. J. Stuper, W. E. Brugger, and P. C. Jurs, *Computer-Assisted Studies of Chemical Structure and Biological Function*, Wiley-Interscience, New York, 1979, pp. 83–90.

8. U. Burkert and N. L. Allinger, *Molecular Mechanics, ACS Monogr. No. 177*, Am. Chem. Soc., Washington, DC, 1982.
9. T. Clark, *A Handbook of Computational Chemistry: A Practical Guide to Chemical Structure and Energy Calculation*, Wiley-Interscience, New York, 1985.
10. G. P. Sutton, *Ph.D. Dissertation*, The Pennsylvania State University, 1990.
11. L. B. Kier and L. H. Hall, *Molecular Connectivity in Structure–Activity Analysis*, Wiley, New York, 1986.
12. J. P. Lowe, *Quantum Chemistry*, Academic Press, New York, 1978.
13. G. Del Re, *J. Chem. Soc.*, **1958**, 4031.
14. S. L. Dixon and P. C. Jurs, *J. Comput. Chem.*, 1992, **13**, 492.
15. R. J. Abraham and P. E. Smith *J. Comput. Chem.*, 1988, **9**, 288.
16. N. L. Allinger, M. T. Tribble, M. A. Miller, and D. H. Wertz, *J. Am. Chem. Soc.*, 1971, **93**, 1637.
17. N. R. Draper and H. Smith, *Applied Regression Analysis*, 2nd. edn., Wiley, New York, 1981.
18. G. M. Furnival and R. W. Wilson, Jr., *Technometics*, 1974, **16**, 499.
19. D. A. Belsley, E. Kuh, and R. E. Welsch, *Regression Diagnostics: Identifying Influential Data and Sources of Collinearity*, Wiley, New York, 1980.
20. L. P. Lindeman and J. Q. Adams, *Anal. Chem.*, 1971, **43**, 1245.
21. D. H. Smith and P. C. Jurs, *J. Am. Chem. Soc.*, 1978, **100**, 3316.
22. G. W. Small and P. C. Jurs, *Anal. Chem.*, 1983, **55**, 1128.
23. G. W. Small and P. C. Jurs, *Anal. Chem.*, 1984, **56**, 2307.
24. D. S. Egolf and P. C. Jurs, *Anal. Chem.*, 1987, **59**, 1586.
25. D. S. Egolf, E. B. Brockett, and P. C. Jurs, *Anal. Chem.*, 1988, **60**, 2700.
26. G. P. Sutton and P. C. Jurs, *Anal. Chem.*, 1989, **61**, 863.
27. M. L. Ranc and P. C. Jurs, *Anal. Chem.*, 1989, **61**, 2489.
28. D. S. Egolf and P. C. Jurs, *Anal. Chem.*, 1990, **62**, 1746.
29. G. P. Sutton and P. C. Jurs, *Anal. Chem.*, 1990, **62**, 1884.
30. G. P. Sutton, L. S. Anker, and P. C. Jurs, *Anal. Chem.*, 1991, **63**, 443.
31. M. L. Ranc and P. C. Jurs, *Anal. Chim. Acta*, 1991, **248**, 183.
32. J. W. Ball, L. S. Anker, and P. C. Jurs, *Anal. Chem.*, 1991, **63**, 2435.
33. P. C. Jurs, J. W. Ball, L. S. Anker, and T. L. Friedman, *J. Chem. Inf. Comput. Sci.*, 1992, **32**, 272.
34. M. L. Ranc and P. C. Jurs, *Anal. Chim. Acta*, 1993, **280**, 145.
35. J. W. Ball and P. C. Jurs, *Anal. Chem.*, 1993, **65**, 3615.
36. D. L. Clouser and P. C. Jurs, *Anal. Chem., Anal. Chim. Acta*, 1994, **295**, 221.
37. G. W. Small and P. C. Jurs, *Anal. Chem.*, 1984, **56**, 1314.
38. G. W. Small, T. R. Stouch, and P. C. Jurs, *Anal. Chem.*, 1984, **56**, 2314.
39. M. Randić, *J. Chem. Inf. Comput. Sci.*, 1984, **24**, 164.
40. J. L. McClelland and D. E. Rumelhart, *Explorations in Parallel Distributed Processing: A Handbook of Models, Programs, and Exercises*, MIT Press, Cambridge, MA, 1988.
41. J. Hertz, A. Krough, and R. Palmer, *Introduction to the Theory of Neural Computation*, Addison-Wesley, Reading, PA, 1991.
42. M. Caudill and C. Butler, *Naturally Intelligent Systems*, MIT Press, Cambridge, MA, 1990.
43. S. Borman, *Chem. Eng. News.* 1989, **67**, 24.
44. J. U. Thomsen and B. Meyer, *J. Magn. Reson.*, 1989, **84**, 212.
45. B. Meyer et al., *Science*, 1991, **251**, 542.
46. V. Kvasnička et al. *J. Chem. Inf. Comput. Sci.*, 1992, **32**, 742.
47. J. Zupan and J. Gasteiger, *Anal. Chim. Acta*, 1991, **248**, 1.
48. B. J. Wythoff, *Chem. Intell. Lab. Syst.*, 1993, **18**, 115.
49. L. S. Anker and P. C. Jurs, *Anal. Chem.*, 1992, **64**, 1157.
50. J. W. Ball and P. C. Jurs, *Anal. Chem.*, 1993, **65**, 505.
51. R. Fletcher, *Practical Methods of Optimization*, John Wiley & Sons, New York, 1980.

Biographical Sketches

Peter C. Jurs. *b* 1943. B.S., 1965, Stanford University, Ph.D., 1969, University of Washington. Department of Chemistry, Penn State University, 1969–present. Approximately 190 publications. Research interests include computer applications in chemistry, studies of correlations between molecular structure and physicochemical properties (^{13}C NMR chemical shifts, chromatographic retention indices, boiling point, surface tension), or biological activity (pharmaceutical effects, chemical toxicity, carcinogenic, or mutagenic potential).

Chemical Shift Scales on an Absolute Basis

Cynthia J. Jameson
University of Illinois, Chicago, IL, USA

1	Introduction	1
2	Absolute Shielding Scales Based on the Proton in Liquid Water	1
3	Absolute Shielding Information from Spin-Rotation Constants	1
4	The Connection Between Absolute Shielding Scales of Two Nuclei	5
5	Magnitudes of the Corrections Linking the Shielding in the Condensed Phase to the Isolated Molecule at its Equilibrium Geometry	6
6	Related Articles	9
7	References	9

1 INTRODUCTION

Nuclear magnetic shielding is a second-order molecular electronic property which provides a severe test of the accuracy of molecular quantum mechanical calculations. While electric dipole polarizability and hyperpolarizabilities provide tests of the wavefunction at the outer regions, nuclear shielding is very sensitive, especially to contributions from high angular momentum functions, in the regions close to a particular nucleus. Precise measurements of differences in shielding are easy to carry out. In most NMR studies the resonance frequencies are measured and a chemical shift is defined as $\delta = (\nu_i - \nu_{\text{ref}})/\nu_{\text{ref}}$. From the relationship between the resonance frequency ν_i, the external magnetic field $\boldsymbol{B}_0$, the magnetogyric ratio γ, and the nuclear shielding σ_i, i.e. $\nu_i = (\gamma/2\pi)(1 - \sigma_i) B_0$, we can write the chemical shifts in terms of the nuclear shielding as $\delta = (\sigma_{\text{ref}} - \sigma_i)/(1 - \sigma_{\text{ref}})$.

Reasonably accurate calculations are now available for nuclei in the first row of the Periodic Table in molecules with a small number of first row atoms and for hydrides of the second row, as may be seen in the articles on IGLO, LORG and SOLO and GIAO shielding calculations described by Kutzelnigg, Hansen and Pulay in this Encyclopedia (***Shielding Calculations: LORG and SOLO Approaches***, ***Shielding Calculations: IGLO Method***, ***Shielding Theory: GIAO Method***). In making a comparison of theoretical ab initio values at the equilibrium molecular geometries with experimental chemical shifts, it is necessary to have absolute quantities (absolute shielding values) to compare with rather than shielding differences or chemical shift values. Accurate chemical shift measurements can be carried out by simultaneous measurement of two frequencies in the same physical sample in the field. If we know the absolute shielding value corresponding to the first frequency, then the accurate chemical shift between the two provides the absolute shielding of the second, or indeed of any number of systems whose chemical shifts can be related to the absolute shielding of any one system. But how do we establish the absolute shielding value of the very first one?

2 ABSOLUTE SHIELDING SCALES BASED ON THE PROTON IN LIQUID WATER

The absolute proton shielding in a spherical sample of pure liquid H_2O at 34.7 °C, σ = 25.790 ± 0.014 ppm, has been established by two experiments. The first was a simultaneous measurement of the frequencies of an electronic transition and a nuclear magnetic transition in atomic hydrogen. The second was a simultaneous measurement of NMR frequencies of protons in a spherical sample of liquid water at 34.7 °C and in a spherical bulb filled with atomic hydrogen in the same magnetic field. The first experiment established the g-factor of the bare proton; the second experiment allows the determination of the absolute nuclear magnetic shielding of protons in liquid water.[1,2]

One standard technique for establishing an absolute shielding scale for a nucleus M is by combining the results of two experiments. The first is an atomic beam magnetic resonance experiment or an optical pumping experiment which measures the ratio of γ for the M nucleus to γ for the electron in the free M atom. Since the (electron) γ can be calculated from the known electron magnetic moment and electronic g-value of the atomic state, the value of γ(M, free atom) may be obtained precisely. The second is an NMR experiment which measures the ratio of the Larmor frequencies of M and ^{1}H in an infinitely dilute $M_{(aq)}{}^{n+}$ ion in aqueous solution. This provides the ratio $\gamma(^1\text{H}, H_2O, \text{liq.})/\gamma(\text{M}, M_{(aq)}{}^{n+})$. The key here is that $\gamma(^1\text{H}, H_2O, \text{liq.})$ is known precisely for pure liquid water from experiments and is assumed to be the same in the infinitely dilute aqueous solution of $M_{(aq)}{}^{n+}$ ion, so γ(M, $M_{(aq)}{}^{n+}$) can be obtained. Then, from the definition of the nuclear magnetic shielding σ relative to the bare nucleus, $\gamma = (1 - \sigma)\gamma_0$, where γ_0 is the magnetogyric ratio of the bare nucleus,

$$\frac{\sigma(\text{M, free atom}) - \sigma(\text{M}, M_{aq}{}^{n+})}{1 - \sigma(\text{M}, M_{q}{}^{n+})} = 1 - \frac{\gamma(\text{M, free atom})}{\gamma(\text{M}, M_{aq}{}^{n+})} \quad (1)$$

Since σ(M, free atom) is theoretically known[3] the absolute shielding of M in the aqueous solution of $M_{(aq)}{}^{n+}$ is thereby established.

This method is applicable when the aqueous solution of the metal ion is a convenient reference and extrapolation to infinite dilution is possible. The ratio γ(M, free atom)/γ(M, liq. ref.) has to be known to 1 part in 10^5 if the σ(M, liq. ref.) − σ(M, free atom) is to be determined to ±10 ppm. The absolute shielding scales for Li, Na, K, Rb, Cs, Zn, Cd, Ga, Hg, and Pb were determined in this way and are summarized in Table 1 in 'Multinuclear NMR' edited by Mason.[4]

3 ABSOLUTE SHIELDING INFORMATION FROM SPIN-ROTATION CONSTANTS

With the gauge origin at the nucleus in question, σ^{p} in Ramsey's expression is related to another molecular property,

Table 1 Absolute σ_0 ^{15}N Shieldings

Molecule	σ_0(^{15}N in the molecule, 300 K) (ppm)
N_2	−61.6
NNO	99.5
N**N**O	11.3
HCN	−20.4

the nuclear spin-rotation tensor. The nuclear spin-rotation tensor arises from the coupling of the magnetic moment of a nucleus with the magnetic field generated by the molecular rotation at that nucleus. Ramsey[5] and Flygare[6] have shown that

$$\sigma_{gg}^{p} = (m_p/2mg_N)C_{gg}/B_{gg}^{(e)} - (\mu_0/4\pi)(e^2/2m) \times \sum_N Z_{N'}[R_{NN'}^2 - (R_{NN'}^2)_{gg}]/R_{NN'}^3 \quad (2)$$

in which m_p and m are the masses of the proton and the electron, g_N is the g-factor for the nucleus of interest, C_{gg} and σ_{gg}^{p} are the diagonal components of the spin-rotation tensor and the paramagnetic shielding tensor in the principal axis system of the molecular moment of inertia, while $B_{gg}^{(e)}$ is the rotational constant at the equilibrium configuration.

The σ_{gg}^{p} values can be related to the components along the principal axes of the shielding tensor by a rotational transformation using the known molecular goemetry. The second term in the equation is the nuclear contribution which depends only on the coordinates and atomic number of all the other nuclei N' in the molecule. The total absolute shielding can then be determined by adding the diamagnetic contribution σ^d, which is obtained from theory, calculated at the nucleus of interest N as the gauge origin:

$$\sigma^d = (\mu_0/4\pi)(e^2/3m)\left\langle \psi^0 \left| \sum 1/r_i \right| \psi^0 \right\rangle \quad (3)$$

It is very important to calculate the nuclear terms using the same structure as that used for calculating diamagnetic terms.

Experimental values of spin-rotation constants are available from molecular beam magnetic and electric resonance experiments and also from high-resolution microwave spectroscopy. In the first two types of experiments the radiofrequency spectrum corresponding to the reorientation of the ^{15}N nuclear moment in a magnetic field, or the interaction of the electric dipole moment of the molecule with a strong external electric field, is composed of transitions from many J and M_J states which may be individually resolved. In the third type of experiment, a specific purely rotational transition is observed. Vibrationally averaged constants are obtained, usually for the ground vibrational state, occasionally for a vibrationally excited state as well. The exact relation between σ^p and C holds for a vibrationless molecule at the equilibrium nuclear configuration. Experimentally one usually obtains $\langle C \rangle_{v=0}$ components of the vibrationally averaged spin-rotation constant.

The first absolute shielding scale which was compiled in an internally consistent way is the one for ^{19}F in a small set of molecules whose chemical shifts have been measured in the limit of zero pressure at room temperature.[6] To establish the first absolute shielding for ^{19}F in a molecule,[7] Hindermann and Cornwell corrected the observed spin-rotation constant in HF to the equilibrium configuration, from which they obtained σ_e^{p}. The latter combined with the theoretical value of σ_e^{d} gave σ_e, which was then converted to σ_0 at room temperature by making the rovibrational correction. Once the absolute σ_0 for HF was known, they could then find the absolute σ_0 for their secondary reference molecule (SiF_4) by measuring the chemical shift between HF and SiF_4 at the zero-pressure limit. The absolute σ_0 for the other molecules on their scale were then determined from measured chemical shifts from SiF_4. Since all the measured chemical shifts correspond to the zero-pressure limit, Hindermann and Cornwell's scale is a list of absolute σ_0 (i.e., for the isolated molecule) at room temperature. In addition, they found the absolute shielding σ(liq., T) of $CFCl_3$. With this connection, other measurements of shifts relative to liquid $CFCl_3$ can be converted to absolute σ(liq. or soln., T) by other workers.

In general, once the absolute shielding of a primary reference molecule (in this case the HF molecule) has been established, the absolute ^{19}F shielding of a series of other molecules can be systematically determined. What is required are simultaneous accurate chemical shift measurements between the primary reference molecule and all the other molecules in the isolated molecule limit. Frequently, the primary reference molecule is not a convenient internal reference and a secondary reference molecule is used instead. In this case, the SiF_4 molecule is ideal, it is relatively inert, and has a long ^{19}F relaxation time in the gas phase so that the signal is sharp. To extend the ^{19}F absolute shielding scale, observed resonance frequencies in gas samples were reduced to the zero-density limit at 300 K using previously measured density and temperature-dependent chemical shifts for each gas. The results corresponding to a rovibrationally-averaged isolated molecule at 300 K are expressed relative to SiF_4 as a standard. The values of $[\sigma_0(300\,K) - \sigma_0^{SiF_4}(300\,K)]/[1 - \sigma_0^{SiF_4}(300\,K)]$ were obtained by dividing the frequency differences by the resonance frequency of SiF_4. The shielding differences $[\sigma_0^{A}(300\,K) - \sigma_0^{SiF_4}(300\,K)]$ were obtained for a large number of molecules[8,9] and were found to be identical to Hinderman and Cornwell's values for all of their molecules (six) which were included in the new set. Based on σ_0(HF, 300 K) = 410.0 ppm, absolute $\sigma_0(SiF_4, 300\,K)$ = 363.2 ppm. The absolute σ_0 for a large number of F-containing molecules have been determined from the ^{19}F chemical shift limit at 300 K, $[\sigma_0(A, 300\,K) - \sigma_0(SiF_4, 300\,K)]$.[8,9] Neat liquid $CFCl_3$ and C_6F_6 provide the connection for converting chemical shifts measured in other laboratories using these references into absolute shielding values; σ(^{19}F neat liq. $CFCl_3$, spherical, 300 K) = 188.7 ppm; σ(^{19}F neat liq. C_6F_6, spherical, 300 K) = 355.5 ppm.

How large can the errors be if the corrections shown in Figure 1 are not carried out, i.e. if $\langle C_{gg}\rangle_{v=0}/\langle B_{gg}\rangle_{v=0}$ are used to calculate $\langle \sigma_{gg}^{p}\rangle_{v=0}$ directly? The difference between the vibrational average of the ratios $\langle C_{gg}/B_{gg}\rangle_{v=0}$ and the ratio of the vibrational averages $\langle C_{gg}\rangle_{v=0}/\langle B_{gg}\rangle_{v=0}$ can be as much as 10% in molecules containing hydrogen. Incomplete knowledge of the first and second derivatives of C with nuclear configuration presently makes it impossible to correct for this error, as Hindermann and Cornwell had done for HF. The thermal average of σ^p can be approximated by using the spin-rotation tensor for the ground vibrational state. However, when a low-frequency vibration exists and the spin-rotation constants

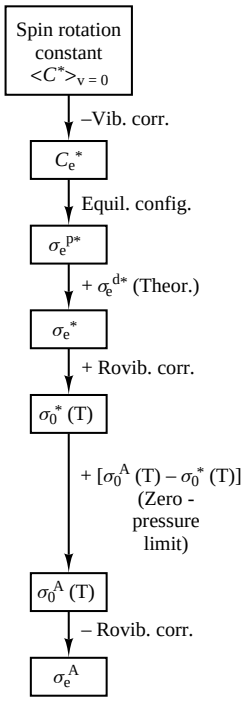

Figure 1 Building up an absolute shielding scale from the absolute shielding of one primary reference whose spin-rotation constant is accurately known. The following notations are used: * denotes the primary reference molecule, A any other compound, subscript 0 the isolated molecule, and subscript e the equilibrium configuration

for the first excited vibrational state are substantially different from those of the ground vibrational state (such as in NNO), a proper thermal average has to be carried out. There are also rotational (centrifugal distortion) corrections which have to be made.

Given the possible sources of error which we have mentioned above, some discrepancies may be observed in comparing shielding values derived from spin-rotation constants with differences in thermal averages of shielding observed in nuclear magnetic resonance spectroscopy in the zero-pressure limit. However, the precision of most available spin-rotation constants is still such that the sources of errors discussed above are not limiting.

Ab initio calculations of the diamagnetic part of the shielding are generally reliable since these depend only on the ground-state wavefunctions. The changes resulting from configuration interaction are very minor, no more than a few tenths of a ppm in σ^{d}, over the Hartree–Fock value. Where ab initio calculations are not available, it is possible to estimate σ^{d} to within 1–2 ppm even without wavefunctions. Flygare has proposed an easy method for evaluating σ^{d} which has been shown to be sufficiently reliable for evaluating the average and the components of σ from the spin-rotation tensor.[10,11] The success of this method is due to the fact that most of σ^{d} is given by the diamagnetic shielding of the free atom and the rest can then be approximately calculated by the method of atomic dipoles. It has been found that the method of Flygare and co-workers is accurate to within 1–2 ppm. Let us consider this method briefly.

By formally partitioning the sum of $1/r_j$ over all j electrons into two sums, one over electrons 'on' nucleus N and the other over all electrons 'on' all the other nuclei, N', Flygare has been able to write the average diamagnetic shielding in terms of a free atom term, a contribution of the electronic point charges centered at the other nuclei, and a third term which arises if the point charges are not centered on the N' nucleus but are displaced by a distance $\langle\rho\rangle_{N'}$:

$$\sigma_{\mathrm{av}}^{\mathrm{d}} = \sigma^{\mathrm{d}}(\text{free atom}) + (\mu_0/4\pi)(e^2/3m)\sum_{N'} Z_{N'}/R_{N'} - (\mu_0/4\pi)(e^2/3m)\sum_{N'} R_{N'}\cdot\langle\rho\rangle_{N'}/R_{N'}^3 \tag{4}$$

The second term in the above equation is identical in form and opposite in sign to the nuclear terms in equation (1) and the last term is a small correction. Thus, the absolute shielding σ can be written in the Flygare method, as

$$\sigma_{\mathrm{av}} = \sigma^{\mathrm{d}}(\text{free atom}) - (\mu_0/4\pi)(e^2/3m) \times \sum_{N'} R_{N'}\cdot\langle\rho\rangle_{N'}/R_{N'}^3 + \frac{m_{\mathrm{p}}}{2mg_N}\cdot\frac{1}{3}\sum\frac{C_{\mathrm{gg}}}{B_{\mathrm{gg}}^{(\mathrm{e})}} \tag{5}$$

This applies to the equilibrium configuration, with extension to thermal averages requiring some corrections which may be a few ppm.

Using the Flygare approximation for the diamagnetic shielding then leads to

$$\sigma_{\mathrm{av}} \simeq \frac{m_{\mathrm{p}}}{2m_{\mathrm{e}}g_N}\cdot\frac{1}{3}\sum\frac{C_{\mathrm{gg}}}{B_{\mathrm{gg}}^{(\mathrm{e})}} + \sigma^{\mathrm{d}}(\text{free atom}) \tag{6}$$

The diamagnetic shieldings of the free atoms are well known from the tabulations of Malli and Froese.[3] For a spherical top molecule,

$$\left.\begin{aligned}\sigma_{\mathrm{av}} &\simeq \frac{m_{\mathrm{p}}}{2m_{\mathrm{e}}g_N}\cdot\frac{C_{\mathrm{av}}}{B} + \sigma^{\mathrm{d}}(\text{free atom})\\ \sigma_{\parallel} - \sigma_{\perp} &\simeq \frac{m_{\mathrm{p}}}{2m_{\mathrm{e}}g_N}\cdot\frac{C_{\parallel} - C_{\perp}}{B}\end{aligned}\right\} \tag{7}$$

and for a linear molecule

$$\left.\begin{aligned}\sigma_{\perp} &\simeq \frac{m_{\mathrm{p}}}{2m_{\mathrm{e}}g_N}\cdot\frac{C_{\perp}}{B} + \sigma^{\mathrm{d}}(\text{free atom})\\ \sigma_{\parallel} &= \sigma_{\parallel}^{\mathrm{d}}\end{aligned}\right\} \tag{8}$$

since $\sigma_{\parallel}^{\mathrm{p}}$ is identically zero for a linear molecule.

The spin-rotation tensor has been used to determine the ^{15}N absolute shielding in NH_3, ^{19}F in HF, ^{13}C and ^{17}O in CO, and ^{31}P in PH_3, and these absolute shieldings have been used to establish all other absolute shieldings in various molecules containing these nuclei. Gas-phase studies provide the relative differences at the zero-density limit and these can be converted to σ_0(300 K) values absolutely. If the commonly used liquid reference is also measured relative to this one molecule, then all past and future measurements of chemical shifts relative to this liquid reference can be converted to absolute shieldings. As we have seen above, rovibrational corrections should be calculated and added to theoretical σ_{e}

before comparing with the experimental values σ_0(300 K). For some molecules this latter value is not very different from the zero-point vibrational average shielding σ_0(0 K). Similarly, the observed spin-rotation constants should be corrected for rovibrational effects before using the identity to obtain σ_e. Nevertheless, the agreement between absolute shielding values derived from spin-rotation constants and those from gas-phase measurements in the zero-pressure limit is remarkably good as shown in Figure 2, which indicates the reliability of the spin-rotation constants.

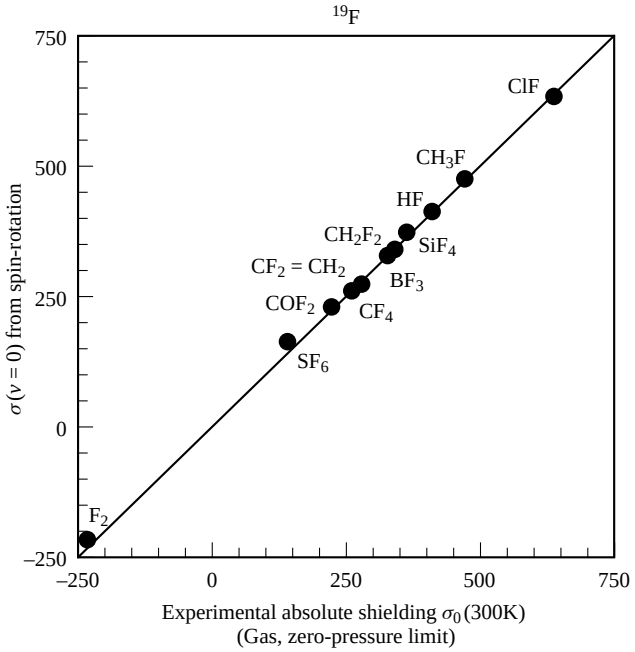

Figure 2 Experimental absolute shielding values of ^{19}F from gas-phase measurements in the zero-density limit. The gas-phase measurements are converted to absolute shielding by using HF as the primary reference molecule. These are compared with the individual absolute shielding values derived from independent measurements of the ^{19}F spin-rotation constants in various molecules

The ^{15}N absolute shielding scale is based on the spin-rotation tensor in the primary reference molecule, NH_3. The spin-rotation-derived shielding for NH_3 is 264.54 ppm.[12] Nitrogen-15 chemical shifts in the gas phase taken to the zero-pressure limit lead to absolute $\sigma_0(^{15}N)$ shieldings in the N_2, NNO, and HCN molecules,[13] see Table 1. At the same time, the absolute shielding of the liquid references were obtained: $\sigma(^{15}N, NH_3, liq., 300\,K) = 380.4$ ppm; $\sigma(^{15}N, CH_3NO_2, liq., 300\,K) = -135.8$ ppm.

The ^{17}O absolute shielding scale is based on the spin-rotation tensor in $C^{17}O$, $C_\perp = 30.4 \pm 1.2$ kHz which leads to $\sigma(^{17}O, CO) = -42.3 \pm 17.2$ ppm.[14] The gas-phase measurements of ^{17}O chemical shifts in H_2O, CO_2, NNO, OCS, OF_2, and CO lead to the absolute $\sigma_0(^{17}O)$ shielding values[14] shown in Table 2.

The ^{13}C shielding scale is based on the primary reference ^{13}C in the $^{13}C^{16}O$ molecule in which $C_\perp = 32.70 \pm 0.12$ kHz in the v = 0, J = 1 state [15] is in good agreement with the previous value of 32.59 ± 0.15 kHz. Rovibrational corrections on the spin-rotation constant to obtain $\sigma_e(^{13}C$ in $^{13}C^{16}O) = 3.0 \pm 0.9$ and then rovibrational corrections on the latter lead to $\sigma_0(^{13}C$ in $^{13}C^{16}O$, 300 K) = 1.0 ± 1.2 ppm.[16] With measurements of ^{13}C chemical shifts in the low-density gas phase under conditions such that intermolecular effects and bulk susceptibility effects are less than 0.05 ppm, the $[\sigma_0 - \sigma_0(CO)]$ have been obtained for a large number of molecules ranging from CH_4 where $\sigma_0(^{13}C, CH_4, 300\,K) = 195.1$ ppm to $CH_2{=}C{=}CH_2$ where $\sigma_0(^{13}CH_2, 300\,K) = 115.2$ ppm, $\sigma_0(={}^{13}C{=}, 300\,K) = -29.3$ ppm. The independent spin-rotation-derived absolute shieldings in $^{13}CH_4$, $D^{13}CN$, and $O^{13}CS$ are completely consistent with the values of σ_0 obtained for these molecules based on $\sigma_0(^{13}CO) = 1.0 \pm 1.2$ ppm.

The $\sigma_0(^{13}C$ in the molecule, 300 K) values for a large number of molecules have been published by Jameson[16] and Jameson (Table 16).[17] A missing value from the latter is isopentane $\cdots$ (CH)**C**H_3, for which $\sigma_0(^{13}C$ in the molecule, 300 K) = 165.0 ppm. These measurements also provide $\sigma(^{13}C$, TMS liquid, spherical, 300 K) = 184.1 ppm and $\sigma(^{13}C, C_6H_6$ liquid, spherical, 300 K) = 55.7 ppm, which are convenient references for converting chemical shift measurements to absolute shieldings.

The ^{31}P absolute shielding scale is based on the primary reference molecule PH_3, in which the spin rotation tensor $C_\perp = -114.90 \pm 0.13$ kHz and $C_\parallel = -116.38 \pm 0.32$ kHz (where the quoted errors are for 99% confidence limits),[18] leading to $\sigma_0(^{31}P, PH_3, 300\,K) = 594.45 \pm 0.63$ ppm. If the spin-rotation tensor is rovibrationally corrected, one gets[19] $\sigma_e(^{31}P$ in the PH_3 molecule) = 599.93 ppm and $(\sigma_\parallel - \sigma_\perp)_e = -64.5$ ppm.

The PF_3 molecule serves as a suitable secondary reference since its chemical shift has a smaller dependence on density. Extrapolation of gas-phase mixtures in argon to the zero-density limit provides the absolute shieldings[20] listed in Table 3. At the same time the absolute shielding of ^{31}P in convenient reference liquids has been obtained: $\sigma(^{31}P$, 85% H_3PO_4 aq., spherical, 300 K) = 328.35 ppm and $\sigma(^{31}P$, $P(OMe)_3$ liquid, spherical, 300 K) = 187.54 ppm. A ^{33}S absolute shielding scale has been derived from the spin-rotation constant $C_\perp = 870 \pm 50$ Hz in the OCS molecule, which leads to $\sigma_0(^{33}S$, OCS molecule) = 843 ± 12 ppm.[21] The ^{33}S chemical shift measurements in the gas phase lead (without full corrections for intermolecular effects) to the values shown in Table 4. A convenient liquid reference is CS_2 for which $\sigma(^{33}S, CS_2$, liquid, spherical, 300 K) = 581 ppm.

Although the proton absolute shielding for water was the first to be established, proton shifts have not been systematically measured in the gas-phase zero-pressure limit and connected to either liquid water or liquid TMS. This situation should be remedied soon as improving proton shielding calculations need some good experimental tests. There are, however, absolute shieldings that can be individually derived

Table 2 Absolute σ_0 ^{17}O Shieldings

Molecule	$\sigma_0(^{17}O$ in the molecule, 300 K) (ppm)
H_2O	344.0
CO_2	243.4
NNO	200.5
OCS	107.9
OF_2	−473.1
CO	(−42.3 ± 17.2)

Table 3 Absolute σ_0 ^{31}P Shieldings

Molecule	σ_0(^{31}P in the molecule, 300 K) (ppm)
PMe_3	391.71
OPF_3	363.43
PF_3	222.69
PCl_2Me	138.65
PCl_3	111.29
P_4	−551.5
PH_3	(594.45 ± 0.63)

Table 4 Absolute σ_0 ^{33}S Shielding Values

Molecule	σ_0(^{33}S in the molecule, 300 K) (ppm)
H_2S	752
CH_3SH	707.3
SF_6	425.6
SO_2	−125.9
OCS	(843 ± 12)

from measured spin-rotation constants by the methods already described, and these are shown in Table 5.

Table 5 Absolute σ_0 Proton Shieldings

Molecule	σ_0 (^{1}H in the molecule, 300 K) (ppm)	Other values (ppm)
CH_3F	28.27 ± 0.5	
PH_3	27.89 ± 0.15	
NH_3	32.10 ± 0.02	
H_2	26.363 ± 0.004	
CH_4	30.80 ± 0.23	30.611 ± 0.024
HCl	31.16 ± 0.09	
HF	28.64 ± 0.01	28.51 ± 0.20
H_2S	31.26 ± 0.40	
SiH_4	27.52 ± 0.44	27.63 ± 0.03

The errors quoted include only those arising from the uncertainty in the spin-rotation tensor itself. Other values reported in the last column are based on a variety of chemical shift measurements which are indirectly connected to liquid water whose absolute shielding is σ(^{1}H, H_2O, liq., spherical, 34.7 °C) = 25.790 ± 0.014 ppm.

4 THE CONNECTION BETWEEN ABSOLUTE SHIELDING SCALES OF TWO NUCLEI

Spin-rotation constants of any two nuclei in the same molecule can be related to one another provided that both nuclei relax entirely by the spin-rotation mechanism. In the gas phase, in the exchange-narrowing limit, there is a single characteristic correlation time τ which is identical for both nuclei.

The nuclear spin relaxation time characteristic of this mechanism is given by

$$(1/T_1)_{SR} = \frac{2}{3}\langle J(J+1)\rangle 4\pi^2 C_{eff}^2 \tau \qquad (9)$$

with C in units of rad s^{-1}, so that for two nuclei k and k' in the same molecule, in the same gas sample,

$$T_1(k)/T_1(k') = C_{eff}^2(k')/C_{eff}^2(k) \qquad (10)$$

For linear molecules $C_{eff}{}^2 = C_\perp{}^2$. For spherical tops

$$\begin{aligned} C_{eff}^2 &= C_{av}^2 + \frac{4}{45}(\Delta C)^2 \\ &= \left[\frac{1}{3}(2C_\perp + C_\parallel)\right]^2 + \frac{4}{45}(C_\parallel - C_\perp)^2 \end{aligned} \qquad (11)$$

A nucleus in the center of a spherical top is a favorable choice since all $C_{gg}{}^{(k)}$ are equal by symmetry and only $C_{av}{}^2$ enters into the relaxation expression. If both nuclei k and k' relax entirely by spin rotation, and if $C_{eff}{}^2$ is known for one nucleus, e.g. ^{19}F in SeF_6 or TeF_6, then C_{av} for the central nucleus (and thus the shielding) can be obtained from the measured ratio of relaxation times in the gas phase. This is supported by empirical observations for CH_4 in various buffer gases, in which the ratio of measured ^{13}C and ^{1}H relaxation times in the gas phase was found to be independent of buffer gas, temperature, or density, and was within experimental error of the inverse ratio of the $C_{eff}{}^2$ values from molecular beam data. These molecular beam data, in turn, were consistent with the ^{13}C shielding scale (based on $C_\perp$ in CO) and the ^{1}H shielding scale (based on γ of the H atom).

It is also possible to determine $C_{eff}{}^2$ from the density dependence of T_1 in the region of the minimum. However, for most systems, the minimum T_1 occurs at such low densities that appropriate measurements are feasible only for ^{1}H and ^{19}F nuclei which have the highest NMR sensitivity, and which also have well-established shielding scales based on spin-rotation constants from molecular beam and high-resolution microwave measurements.

This method was used to establish the ^{77}Se and ^{125}Te shielding scales by concurrent measurement of the ^{19}F and ^{77}Se (or ^{125}Te) spin-relaxation times in SeF_6 (or TeF_6) molecules in the dilute gas phase,[22] and also the ^{29}Si shielding scale based on both SiH_4 and SiF_4 molecules.[23] The sample was gaseous (e.g. SeF_6 or TeF_6, or an equimolar mixture of SiH_4 and SiF_4) contained in a sealed glass tube at a well-regulated temperature. Inversion–recovery experiments were set up in both the observe channel and the decoupling channel, the decoupling channel having been modified so that it could be tuned to ^{19}F as well as ^{1}H.

In one cycle, one-eighth of the total number of transients were taken and stored for each delay time for one nucleus and then the other. The next cycle went through the delay list for one nucleus and the other, acquiring the next eighth and so on. Thus the T_1 experiments were undertaken in the same molecule in the same sample essentially simultaneously. Only the magnitude of C could be obtained from the experiments. The signs were assigned on the basis of the σ values obtained. Defined with the gauge origin at the nucleus in question, σ^p is usually negative for most heavy nuclei. For SeF_6 the two possible values of σ^p which can be calculated from C are 1559.7 or −2160.7 ppm, from which we choose the latter, i.e. C(^{77}Se) is negative. For TeF_6 the two possible values of σ^p are 2570 or −3070 ppm and we choose the latter, which with a negative g(^{125}Te) implies that C(^{125}Te) is positive.

Although the relationship between σ^p and C is exact only for the rigid isolated molecule at its equilibrium configuration, we have used rovibrationally averaged values at room temperature for all quantities. The errors in σ associated with this are smaller than the rovibrational corrections to shielding (-8 and -9 ppm, respectively, for ^{77}Se and ^{125}Te in SeF_6 and TeF_6) since the vibrational corrections to C and σ^p tend to increase slightly the magnitudes of both. Hence, σ_0 (^{77}Se in SeF_6 molecule, 300 K) = 1437.8 ± 64 ppm, σ_0 (^{77}Se in H_2Se molecule, 300 K) = 2401 ± 64 ppm, and σ_0 (^{125}Te in TeF_6 molecule, 300 K) = 3790 ± 130 ppm.

These values are based on 3298 ppm and 6580 ppm for σ^d of the free Se and Te atoms, respectively, including relativistic corrections. Using the absolute shielding values for ^{77}Se in SeF_6(g) and for ^{125}Te in TeF_6(g), and the known gas-to-liquid shifts for SeF_6 and TeF_6, the absolute shielding for the reference liquids σ(^{77}Se, Me_2Se, liq.) = 2069 ppm and σ(^{125}Te, Me_2Te, liq.) = 4333 ppm are obtained. Concurrent measurement of ^{29}Si and ^{1}H spin-relaxation times in a sample of SiF_4 gas provides the ratio $C^2_{av}(^{29}Si)/C^2_{eff}$ (^{1}H), and concurrent measurement of ^{29}Si and ^{19}F spin-relaxation times in SiF_4 gas provides the ratio $C^2_{av}(^{29}Si)/C^2_{eff}(^{19}F)$. The spin-rotation tensors are independently known for ^{1}H and ^{19}F in these molecules. Using $g_{Si} = -1.1106$ and the theoretical value for the diamagnetic shielding σ^d free Si atom = 874.1 ppm, and choosing positive signs for C(^{29}Si) in both molecules, leads to$^{23}\sigma_0$(^{29}Si in SiH_4 molecule, 300 K) = 475.3 ± 10 ppm and σ_0(^{29}Si in SiF_4 molecule, 300 K) = 482.0 ± 10 ppm.

The T_1 experiments in SiH_4 and SiF_4 provide two completely independent determinations of very nearly the same point (separated by only 6.7 ppm) on the ^{29}Si shielding scale. The coincidence of these two truly independent results is remarkable. Since a large part of C^2_{eff} (^{1}H or ^{19}F) is the isotropic average C^2_{av} (^{1}H or ^{19}F) which is directly related to σ_{av} (^{1}H or ^{19}F), the values are constrained to be consistent with the absolute shielding scales of both ^{1}H and ^{19}F and also the 6.7 ppm ^{29}Si shielding difference between SiH_4 and SiF_4. All these conditions are well satisfied within realistic error estimates of ±10 ppm. The ^{19}F shielding scale is well established, with several independent determinations based on the spin-rotation constants in a number of small molecules agreeing with the chemical shifts in the zero-pressure limit. The ^{1}H shielding scale is also well established on the basis of hydrogen atomic beam data. It is satisfying to find that the Si shielding scale is consistent with these. Finally, the measured ^{29}Si chemical shifts in SiH_4 and SiF_4 gas relative to neat liquid Me_4Si lead to σ(^{29}Si, Me_4Si, liquid, spherical) = 368.5 ± 10 ppm.

In favorable systems, simultaneous measurements of T for two spin-$\frac{1}{2}$ nuclei in the same molecule in the gas phase provide a means of determining the absolute nuclear shielding scale of the second nucleus from that of the first. This method can be applied when the spin-rotation tensor of the first nucleus is independently known or can be calculated from its known shielding tensor. The latter can be obtained by measurement of the chemical shift anisotropy and the isotropic absolute shielding based on some primary reference (such as ^{1}H in the H atom, ^{13}C in CO, ^{15}N in NH_3, ^{17}O in CO, ^{19}F in HF, ^{31}P in PH_3, or ^{33}S in OCS). In a linear molecule only the isotropic shielding is necessary since $\sigma_\parallel$ is entirely diamagnetic. For spherical tops the $(\Delta C)^2$ term is 4/45-times as small as the $C^2{}_{av}$ term, so that even when $(\Delta C)^2$ and $\Delta\sigma$ are unknown an estimate may be adequate. An appropriate molecule in which two nuclei relax nearly exclusively by spin-rotation in the gas phase effectively provides a bridge between the absolute shielding scales of these nuclei.

Finally, a method of obtaining the absolute shielding directly from the measured anisotropy $\Delta\sigma \equiv (\sigma_\parallel - \sigma_\perp)$ in a linear molecule takes advantage of the symmetry requirement that the paramagnetic shielding contribution along the axis parallel to the molecular axis vanishes: $\sigma^p_{||} = 0$. A theoretically calculated diamagnetic term $\sigma^d_{||}$ provides the rest of the required information:

$$\sigma_\perp = \sigma^d_\parallel - \Delta\sigma, \qquad \sigma_\parallel = \sigma^d_\parallel \tag{12}$$

so that the absolute average shielding is

$$\sigma = \sigma^d_\parallel - \left(\frac{2}{3}\right)\Delta\sigma \tag{13}$$

albeit containing some unwanted intermolecular effects in $\Delta\sigma$ which is usually obtained from a condensed-phase measurement. One can therefore establish a shielding scale for a nucleus by choosing an appropriate linear molecule. Some examples are shown in Table 6. The absolute shieldings obtained from the anisotropy differ slightly from those obtained in the gas in the zero-pressure limit, from which we see that intermolecular effects are 1 to -8 ppm in the solid. It should be noted that the above relationships hold only for a linear molecule, not for a quasilinear or pseudolinear molecule. Any off-axis atoms break the symmetry and lead to $\sigma^p_{||} \neq 0$. For example, $CH_2{=}{}^{13}C{=}CH_2$ has $\sigma^p_{||} = -250$ ppm for the central ^{13}C. Furthermore, $\sigma^p_{||} = 0$ holds for a linear molecule only at the level of the nonrelativistic theory of shielding.

5 MAGNITUDES OF THE CORRECTIONS LINKING THE SHIELDING IN THE CONDENSED PHASE TO THE ISOLATED MOLECULE AT ITS EQUILIBRIUM GEOMETRY

The exquisite sensitivity of the shielding to the electronic environment is what makes the NMR chemical shift a very

Table 6 Absolute Shielding (ppm) Derived from the Shielding Anisotropy

Molecule/ion	$\Delta\sigma$, solid	$\sigma_\parallel = \sigma_\parallel{}^d$	$\sigma_\perp$	σ_{av}	σ_0(^{13}C in the molecule, 300 K)
OCO	335	274.1	−60.9	50.8	58.8
OCS	365	274.1	−90.9	30.8	30.0
SCS	424	276.1	−147.9	−6.6	−8.0
NCS^-	321	264.7	−56.3	50.7	
SeCSe	506	294	−212	−43.3	

powerful tool in studying structure, intermolecular effects, and dynamic averaging. For the purpose of comparing with theoretical ab initio calculations of the shielding, however, this exquisite sensitivity to the environment appears at first to be a distinct disadvantage. Nevertheless, if one knows the precise relationship between the quantities being calculated (the shielding at some specific set of nuclear coordinates) and the quantities being measured, then the appropriate comparisons against theory can still be made. In fact, a more complete comparison becomes possible when the true connection between the experimental milieu and the theoretical constructs is understood. Since it is never possible to observe a molecule as a fixed arrangement of nuclei (even in the molecular beam where no neighbor effects need to be considered, there is always at least the zero-point vibrational motion), let us consider the nature of the connection between what is measured and what can be calculated. In this respect, the NMR chemical shift is in by far a more advanced stage compared with other molecular electronic properties such as electric dipole polarizability, electric field gradient tensors, etc. It is partly a theoretical advantage, but more important an experimental advantage, that NMR spectroscopy provides. The very high resolution that is possible under the conditions of isotropic averaging in gases and solutions makes it possible to measure chemical shifts of the order of parts per billion. The more advanced temperature control of experiments in NMR spectroscopy, compared with other forms of spectroscopies, combined with the high resolution, has made it possible to measure the temperature dependence of the shielding in a nearly isolated molecule over a 200 K range almost routinely. The small chemical shifts that are the differences in shielding between two molecules differing only in the isotopic masses of some of the nuclei can be measured to a few ppb as well.

Both of these phenomena are related to the dynamic averaging of the vibrating molecule through its various nuclear configurations, each configuration having its appropriate shielding value for a particular nucleus. There are also intermolecular effects, again associated with shielding values that change with nuclear configurations, this time the configurations of supermolecules including not only the molecule bearing the NMR nucleus but all the neighboring interacting molecules. Solvent shifts are a manifestation of this, as are adsorption shifts, as well as a portion of the discrimination between different locations of the same amino acid residues in a protein. The dynamic averaging is discussed further in ***Isotope Effects on Chemical Shifts and Coupling Constants*** and some aspects of the intermolecular shifts are discussed further in the article on ***Gas Phase Studies of Intermolecular Interactions and Relaxation***. In this article, we merely take note of the mechanisms that give rise to the phase-dependent and temperature-dependent differences and how large the corrections are.

Let us first consider an isolated or nearly isolated molecule, i.e. one in which the frequency of collisions with other molecules is still enough to allow the molecule to sample its many rotational and vibrational states while being observed in the NMR spectrometer but not frequent enough to lead to a measureable intermolecular contribution. As the molecule undergoes vibrations, the distances between nuclei change in a periodic fashion, bonds being alternately compressed and expanded, bond angles being alternately enlarged and made smaller, with torsions or frustrated internal rotations possibly occuring as well. For each frozen configuration the shielding of an NMR nucleus in the molecule is different. In the context of the Born–Oppenheimer approximation, the nuclei are moving slowly enough relative to the electronic motion that it is possible to talk about a shielding surface, a highly multidimensional mathematical surface akin to the intramolecular potential energy surface, which describes the shielding at each configuration of the collection of nuclei that make up the framework of the molecule. Of course, the parts of this shielding surface that are sampled during the vibrations are those regions that correspond to the deep pockets in the intramolecular potential energy surface (PES), located at what we call the 'equilibrium' molecular geometry. Thus, it would seem that for the most part, the only interesting regions that we should concern ourselves with are those in the immediate vicinity of the single deep pocket in the PES. This may indeed be the case for the dynamic averaging in small molecules such as diatomics and methane. However, as soon as torsion angles come into the picture, the nature of the averaging changes. Wider excursions are possible, perhaps passing though *cis*-eclipsed, *gauche*, *gauche′*, *trans*-staggered, etc. Even in a simple molecule like NH_3, the umbrella inversion has to be considered in its entirety—no minor small amplitude excursions here! Thus, it becomes necessary to think in terms of not a single shielding tensor associated with a particular nucleus in a molecule, but a continuum, of such tensors changing smoothly with nuclear displacements away from the lowest energy point in the deep pocket. Some shielding surfaces are shown in the article on ***Isotope Effects on Chemical Shifts and Coupling Constants***, and the consequences of the dynamic averaging are discussed there as well.

How large are the shielding changes in going from the equilibrium geometry to the dynamically-averaged shielding? This depends on the molecule. For the ^{19}F shielding in the F_2 molecule, the difference is of the order of 40 ppm; for the ^{15}N in the N_2 molecule it is smaller, about 3 ppm, and for ^{1}H in the HF molecule it is around 0.3 ppm. Most of the dynamic averaging effects lead to a decreased shielding, but instances of increased shielding can also be found. At the time when the theoretical calculations were only good to within 50 ppm for ^{13}C in various molecules, for example, the direct comparison of the shielding calculated in a molecule rigidly fixed at its equilibrium geometry with the chemical shift measurements in solution could be excused. With the present theoretical capability discussed in the articles by Hansen and Kutzelnigg in this Encyclopedia, the real test of the quality of a calculation is really in the shape of the surface in the immediate vicinity of the equilibrium geometry, not just the value at a single one point on the surface. The rationale for determining absolute shielding scales is to be able to compare shieldings rather than differences of shieldings between two different molecules, thereby disallowing any fortuitous agreements in chemical shifts while the shieldings themselves could be far off. We go further at this point and make note not only of the absolute shielding of a nucleus in the particular molecule, but the dynamic average over a portion of the shielding surface for this nucleus; the shape of the surface itself is being tested. Typical magnitudes of the vibrational corrections that arise from this dynamic averaging are shown in Table 7.

Most of the time, we observe molecules in some medium rather than in the zero-pressure limit in the gas phase. Most of the full shielding tensor information is obtained in the solid

Table 7 Vibrational Corrections from Dynamic Averaging

	$[\sigma_0(T) - \sigma_e]$, theor. (ppm)
^{1}H in HF	−0.4
^{13}C in CH_4	−3.6
^{15}N in NH_3	−8.8
^{17}O in H_2O	−13.6
^{19}F in HF	−9.7
^{31}P in PH_3	−12.8
^{77}Se in H_2Se	−58.9

state or in liquid crystal solutions. It is therefore important to understand the ways in which that which we are measuring is affected by the surrounding molecules. We know that medium effects can be large because the gas-to-liquid shifts have been measured in pure substances. The magnitudes of some of these are shown in Table 8, where the chemical shift between the liquid and the vapor in equilibrium with it have been measured at the same temperature. We also know that intermolecular effects in physisorption can be large. Now, this is strictly an intermolecular effect, not involving a change in chemical structure. For ^{129}Xe nuclei of xenon atoms physisorbed in zeolites, the adsorption shifts are of the order of several hundred ppm! In other words, a xenon atom adsorbed in a zeolite cavity or channel has a shielding that differs from that in the gas phase by several hundred ppm. (See ***Adsorbed Species: Spectroscopy and Dynamics***.) This is strictly an intermolecular effect, not much different from the solvent effect in solution, with the only difference being that the solvent is stationary while the solute is relatively free to move. This too is a result of dynamic averaging, just as in solutions. This is clearly a many-body type of situation and the interpretation involves making some approximations.

Table 8 Gas-to-Liquid Shifts

		T(K)	$[\sigma(\text{liquid}, T) - \sigma\ (\text{vapor}, T)]$ (ppm)
^{1}H in	H_2O	298	−4.4
	NH_3	300	−1.75
	HCN	346.6	−2.0
^{13}C in	CO_2	220	−1.28
	HCN	336.6	−7.68
	C_6H_6	300	−1.5
^{15}N in	NH_3	300	−19.47
	HCN	346.7	+10.4
	CH_3CN	227.5	+11.3
^{17}O in	H_2O	488	−36.0
^{19}F in	CF_3H	280	−2.26
	CH_2F_2	280	−3.17
	CF_3Cl	280	−3.65
	CF_2Cl_2	300	−5.15
	CF_3CH_3	300	−4.65
	$CFCl_3$	340	−6.00
	CH_3F	260	−7.7
	SeF_6	300	−4.8
	TeF_6	300	−5.4
	WF_6	300	−7.4
^{31}P in	P_4	526	−77
^{77}Se in	SeF_6	300	−1.38
	H_2Se	300	−120
^{125}Te in	TeF_6	300	−2.0
^{129}Xe in	Xe	244	−200

A simpler situation is found in the gas phase. Intermolecular effects can be treated in the gas phase by the method of Buckingham and Pople by considering a virial expansion of the molecular electronic property, in this case the NMR shielding, in powers of density, i.e. $\sigma(T,\ \rho) = \sigma_0(T) + \sigma_1(T)\rho + \sigma_2(T)\rho^2 + \sigma_3(T)\rho^3 + \ldots$, where $\sigma_0(T)$ is the temperature-dependent shielding in the nearly isolated molecule. By making measurements of the shielding in gas samples of various densities at various temperatures, it is possible to obtain directly the second virial coefficient of nuclear shielding, $\sigma_1(T)$. This is a dynamic average which has a precise interpretation, as shown below.

$$\sigma_1(T) = \int_0^\infty 4\pi R^2\, \mathrm{d}R[\sigma(R) - \sigma(\infty)] \exp^{-V(R)/kT} \qquad (14)$$

In other words, the dynamic averaging occurs over an intermolecular shielding surface, $[\sigma(R) - \sigma(\infty)]$, with various weighting factors, as determined by the intermolecular potential energy, $V(R)$, surface. In a sense, this is entirely analogous to the averaging which occurs in vibration, except that the pockets are very deep in the intramolecular potential surface, whereas they are relatively shallow for intermolecular surfaces. Thus a very wide range of distances are included, and the temperature dependence is explicitly seen in the integration. The intermolecular shielding surface looks rather similar to the shielding surface of a nucleus in a diatomic molecule, except that all parts of the intermolecular surface are important other than at very very close range where the repulsive interactions dominate so strongly that such configurations are not effectively sampled.

This shielding surface is also amenable to theoretical calculations. In effect, the system under consideration is a supermolecule made up of the interacting molecules at all possible orientations and separations. A direct comparison of an intermolecular surface to an intramolecular one is not possible. However, the known differences in shielding sensitivities of nuclei across the Periodic Table allow us to scale the chemical shifts of one type of nucleus relative to another. For example, proton shifts are about 20 ppm to the fluorine shifts of about six hundred ppm. If we do this, then we can put an intramolecular shielding surface on the same plot as an intermolecular shielding surface, keeping their magnitudes in the same proportion as the well-known relative magnitudes of the ranges of their chemical shifts. One such example is shown in Figure 3, where the intramolecular shielding surface for the ^{23}Na nucleus in the NaH molecule is superimposed on the intermolecular shielding surface for the isoelectronic system, the ^{21}Ne nucleus in a Ne atom interacting with a He atom. On an absolute scale the shielding surface for ^{21}Ne in Ne–He has a much steeper change than the ^{23}Na shielding surface, but only because the nuclei on the right-hand side of the Periodic Table have much larger expectation values for the $1/r^3$ value of the electrons. When this is taken into account, it is seen that intramolecular shielding surfaces involve a much greater response of the nucleus to the changing electronic environment (bond extension or compression) than the response of the nucleus to the approach of a neighboring solvent molecule described by the intermolecular shielding surface.

If the shielding of a nucleus in a molecule surrounded by six neighbors, say, can be considered as a sum of six pairwise contributions between itself and each neighbor molecule,

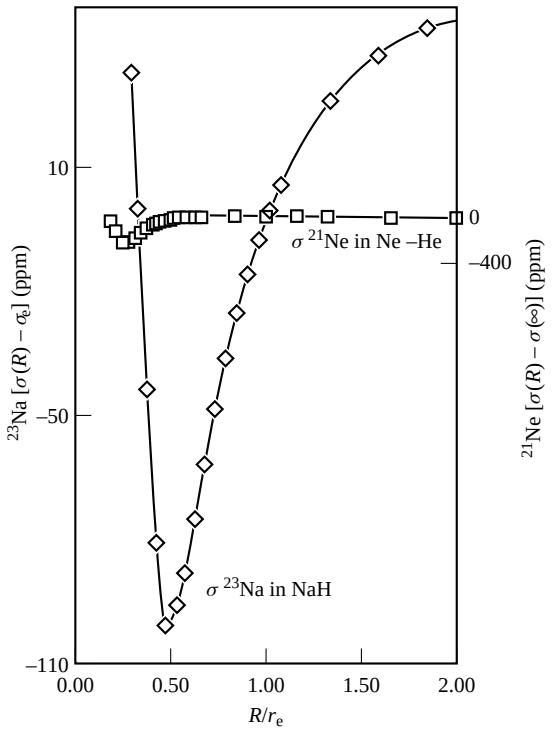

Figure 3 The intramolecular shielding surface for ^{23}Na in NaH and the intermolecular shielding surface for ^{21}Ne in NeHe

and if each pairwise intermolecular shielding function is known (similar to the ^{21}Ne shielding function for NeHe in Figure 3), then dynamic averaging amounts to sampling all such configurations of molecule and neighbors and calculating the intermolecular shielding for each configuration. This has been done for ^{129}Xe shielding in zeolite NaA. The same intermolecular shielding function that reproduces the $\sigma_1(T)$ for xenon in the gas phase reproduces the chemical shifts between the Xe, Xe_2, Xe_3, . . . , Xe_8 clusters trapped inside the cages of zeolite NaA.[24,25] In principle, chemical shifts in condensed phases can be obtained by a similar dynamic averaging.

6 RELATED ARTICLES

Shielding Calculations: LORG and SOLO Approaches; Gas Phase Studies of Intermolecular Interactions and Relaxation; Isotope Effects on Chemical Shifts and Coupling Constants; Shielding Calculations: IGLO Method; Shielding: Overview of Theoretical Methods; Shielding Theory: GIAO Method.

7 REFERENCES

1. P. F. Winkler, D. Kleppner, T. Myint, and F. G. Walther, *Phys. Rev. A.*, 1972, **5**, 83.
2. W. D. Phillips, W. E. Cooke, and D. Kleppner, *Phys. Rev. Lett.*, 1975, **35**, 1619.
3. G. Malli and C. Froese, *Int. J. Quantum Chem.*, 1967, **1S**, 95.
4. C. J. Jameson and J. Mason, in *Multinuclear NMR*, ed J. Mason, Plenum Press, London, 1987, Chap. 3
5. N. F. Ramsey, *Phys. Rev.*, 1950, **78**, 699.
6. W. H. Flygare, *J. Chem. Phys.*, 1964, **41**, 793.
7. D. K. Hindermann and C. D. Cornwell, *J. Chem. Phys.*, 1968, **48**, 4148.
8. C. J. Jameson, A. K. Jameson, and P. M. Burrell, *J. Chem. Phys.*, 1980, **73**, 6013.
9. C. J. Jameson, A. K. Jameson, and J. Honarbaksh, *J. Chem. Phys.*, 1984, **81**, 5266.
10. W. H. Flygare and J. Goodisman, *J. Chem. Phys.*, 1968, **49**, 3122.
11. T. D. Gierke and W. H. Flygare, *J. Am. Chem. Soc.*, 1972, **94**, 7277.
12. S. G. Kukolich, *J. Am. Chem. Soc.*, 1975, **97**, 5704.
13. C. J. Jameson, A. C. Jameson, D. Oppusunggu, S. Wille, P. M. Burrell, and J. Mason, *J. Chem. Phys.*, 1981, **74**, 81.
14. R. E. Wasylishen, S. Mooibroek, and J. B. Macdonald, *J. Chem. Phys.*, 1984, **81**, 1057.
15. W. L. Meerts, F. H. de Leeuw, and A. Dymanus., *Chem. Phys.*, 1977, **22**, 319.
16. A. K. Jameson and C. J. Jameson, *Chem. Phys. Lett.*, 1987, **134**, 461.
17. C. J. Jameson, in *Nuclear Magnetic Resonance*, ed. G. A. Webb, Royal Society of Chemistry, London, 1991, Vol. 20, Chap. 2
18. P. B. Davies, R. M. Neumann, S. C. Wofsy, and W. Klemperer, *J. Chem. Phys.*, 1971, **55**, 3564.
19. C. J. Jameson, A. C. de Dios, and A. K. Jameson, *J. Chem. Phys.*, 1991, **95**, 9042.
20. C. J. Jameson, A. C. de Dios, and A. K. Jameson, *Chem. Phys. Lett.*, 1990, **167**, 575.
21. R. E. Wasylishen, C. Connor, and J. O. Friedrich, *Can. J. Chem.*, 1984, **62**, 981.
22. C. J. Jameson and A. K. Jameson, *Chem. Phys. Lett.*, 1987, **135**, 254.
23. C. J. Jameson and A. K. Jameson, *Chem. Phys. Lett.*, 1988, **149**, 300.
24. C. J. Jameson and A. C. de Dios, *J. Chem. Phys.*, 1992, **97**, 417.
25. C. J. Jameson, A. K. Jameson, B. I. Baello, and H. M. Lim, *J. Chem. Phys.*, 1994, **100**, 5965.

Biographical Sketch

Cynthia J. Jameson. *b* 1937. B.S., University of the Philippines, Ph.D., 1963, University of Illinois at Urbana-Champaign. Introduced to NMR by Herb Gutowsky. Faculty in Chemistry, University of Illinois at Chicago, 1968–present. Approx. 130 publications. Research interests include theoretical and experimental studies of the chemical shift in simple systems in the gas phase and in molecules absorbed in microporous solids, with particular emphasis on intramolecular and inter-molecular shielding surfaces and averages therein; also, spin relaxation in gases and their connection with the anisotropy of intermolecular potentials and molecular dynamics.

Computer Assisted Structure Elucidation

Reinhard Dunkel
Salt Lake City, UT, USA

1 Introduction 1
2 Computerized Analysis of One-Dimensional Spectra 1
3 Automated Analysis of Two-Dimensional INADEQUATE Spectra 2
4 Structure Generation 4
5 Related Articles 5
6 References 5

1 INTRODUCTION

The determination of the structure of an unknown chemical compound is one of the prominent application areas of NMR. The overwhelming number of elucidations are performed by experienced spectroscopists without the help of automated or computer-assisted tools for such data analysis. The goal of computerization of NMR-based structure elucidation is to reduce the need for human intervention over computer assistance to automated systems to obtain an ease-of-use comparable with structure determination using X-ray crystallography. This article presents the basic computerization approaches for the individual structure elucidation phases.

The structure elucidation process can be subdivided into the data acquisition, the data interpretation, and the structure generation and evaluation. The data acquisition is well understood and reasonably well automated. The challenge for the analysis of one-dimensional (1D) NMR spectra arises from the inherent ambiguity between spectral features and the molecular structures. Three basic computerized 1D analysis techniques are discussed: the database search, the knowledge-based approach, and the pattern-recognition approach. The advantage of multidimensional NMR techniques is a significant reduction in the ambiguity of the spectral–structural relationship. However, the size of the resulting datasets and the frequently minimal signal-to-noise (S/N) ratio of the data pose problems for both manual and automated analyses alike. The automated analysis of multidimensional data is described using two-dimensional (2D) INADEQUATE spectra which allow the direct detection of the molecular carbon skeleton.

The results of the spectral data interpretation are identified molecular fragments and/or constraints on the possible structure of an unknown compound. Computers are ideally suited to piece together the structural information from various sources and to generate exhaustively all possible candidate structures of the unknown which are compatible with the available constraints. The list of all candidate structures provides a powerful means of identifying the scope of the remaining structural ambiguities. Due to the lack of available software, the structure evaluation and the identification of additional experiments to discriminate among remaining candidates still requires an experienced spectroscopist. A proper structure elucidation would iterate through the data acquisition, interpretation, structure generation, and evaluation until all but one candidate structure have been ruled out.

2 COMPUTERIZED ANALYSIS OF ONE-DIMENSIONAL SPECTRA

^{13}C spectra offer the most prominent applications for 1D NMR structure elucidations and are used here to introduce the database search, the knowledge-based and the pattern-matching approaches for 1D computerized spectral analysis.

The simplest application of ^{13}C spectra is as a molecular fingerprinting tool. For example, many molecules encountered in natural products are known compounds, and a computerized search in a spectral database may be used to locate the matching reference spectrum and to identify the given compound. Unfortunately, maintaining quality spectral databases is extremely expensive and only a limited number of known compounds can be found in publicly available spectral databases.[1] Nevertheless, even if the spectrum of the unknown is not among available reference data, closely matching spectra might provide clues about the structure of an unknown compound. Besides complete spectrum matching, it is possible to match selected features. A prominent example is the identification of monomer units in a polymer sample by matching the polymer's spectrum against a database of monomer spectra. Despite the obvious limitations, spectral database searches remain the method of choice for most compound identifications.

Closely related to the human analysis of 1D spectra are the knowledge-based approaches ('artificial intelligence methods') for computerized spectral analysis. A correlation table of molecular substructures and related chemical shift ranges (possibly including resonance multiplicities) can be assembled to describe the substructure–subspectral relationship. Normally some 200 substructures will be used, each describing molecular fragments such as >CH–O– with one central ^{13}C resonance and the immediate neighboring atoms. Enlarging the size of the substructures would allow one to specify better the environment of a nucleus of interest and, thereby, to narrow the corresponding resonance range. Enlarging the size of substructures to two resonance fragments, unfortunately, would require tens of thousands of table entries.

By analogy with human use of such correlation tables, a rule-interpreter program can use these table entries ('rules') in a hypothesis-driven or data-driven manner to find all possible constituent substructures consistent—when considered individually—with the experimental spectrum. In its simplest form a data-driven rule interpreter would examine each observed spectral resonance signal and list all matching substructures found in the correlation table. Due to the ambiguities in the substructure–subspectral relationship, many more substructures will be identified in this first analysis step, which are consistent with a given 1D spectrum than are actually present in the unknown. A substructure not only specifies the central atom with a given resonance range but also imposes constraints on the possible environment of neighboring atoms. In the second analysis step elaborate consistency checks can identify mutually consistent sets of possible substructures.

Such knowledge-based interpretation schemes for 1D data are generally fast and provide a valuable insight into the possible structure of an unknown. However, it is unrealistic to expect such simple rule-based schemes to compete successfully with the careful spectral analysis carried out by an experienced spectroscopist. A spectroscopist often uses—consciously or subconsciously—background information, such as general chemical knowledge, the source and assumed class of the unknown, previous experience with similar structures, etc., in addition to the spectral data to add to the spectral analysis and to resolve ambiguities encountered during the data interpretation. This additional information is normally not stored in the rule base and hence is unavailable to the automated interpretation process.

The major limitation of database searches is the unavailability of critical reference spectra, and the major limitation of knowledge-based approaches is a lack of sufficient models to understand and describe the substructure–subspectral relationship. A set of methods, designed to overcome these limitations, involves the derivation of model-free classification rules from database reference spectra. These are known as 'pattern-recognition approaches' and differ radically from any human interpretation scheme in that they do not assign a physical meaning either to individual spectral resonances or to any relationship between individual measurements. An NMR spectrum is regarded as a vector representing a single point in an abstract *n*-dimensional pattern space. For example, a ^{13}C spectrum might be represented by a 200-dimensional vector with each dimension corresponding to a 1 ppm range in the spectrum. Each dimension corresponding to a spectral range with one or more signals is set to 1 and otherwise to 0. In this description each spectrum representing a single point in the assumed 200-dimensional vector space can be compared with a reference spectrum by some abstract distance measure or can be compared with predetermined threshold values.

With this formalism, empirical classifications can be determined from a database of reference spectra (the 'training set') which allow one to make a single binary decision, such as distinguishing between the presence and absence of a molecular feature from a given spectrum. Once determined, such classification criteria can be readily applied to spectra of unknown compounds. For example, the possible presence or absence of the >CH–O–substructure would be decided using knowledge-based approaches by searching for a carbon resonance (a signal doublet if no proton decoupling is used) around 75 ppm in the ^{13}C spectrum. In contrast, a pattern-recognition procedure would subject the complete spectrum to some mathematical transform and the resulting number would be compared with a cut-off value determined from reference data to establish the presence or absence of the >CH–O–substructure. The applications of pattern-recognition methods to NMR data generally have not proven to be of great utility for automated structure elucidation. The major problem is that a classification may indeed be right or wrong but pattern recognition has failed to provide a real justification or confidence estimate for the proposed classification.

Details of the above discussed approaches as well as a description of existing programs can be found in a book by Gray.[2] The goal of the computerized structure elucidation process is the exhaustive generation of possible molecular structures satisfying all constraints. For the structure generation phase only those substructures and structure constraints determined beyond reasonable doubt should be used in the generation process. The highly ambiguous nature of 1D spectral interpretation results gives the ultimate justification for the use of less ambiguous multidimensional NMR data in the structure elucidation process.

3 AUTOMATED ANALYSIS OF TWO-DIMENSIONAL INADEQUATE SPECTRA

The most useful multidimensional NMR spectra for structure elucidation are the homonuclear and heteronuclear short-range and long-range correlation spectra.[3] Multidimensional datasets are often acquired with a minimal S/N ratio and are often of the maximum size which the available computer storage allows one to acquire. The manual interpretation of such data is extremely tedious and is normally the time-determining step in the structure elucidation of an unknown compound. No computer assisted structure elucidation system can be considered complete without automation of this crucial step.

Computer assisted or automated techniques for interpreting 2D NMR spectra have consisted mainly of the application of direct techniques[4] (e.g. cluster analysis and peak picking), linear prediction or maximum entropy methods,[5] or least-squares parameter optimization[6] in the case of severe overlap and/or strong coupling. If signals are strongly overlapping, a model can help to resolve ambiguities and also significantly improves the detection limit of the spectral analysis.

The greatest challenge in the structure elucidation of complex molecules is the determination of the molecular carbon skeleton. A method which allows the direct detection of carbon–carbon bonds is the two-dimensional version of the INADEQUATE experiment.[7] A single spectrum frequently allows one to trace the complete carbon skeleton of a molecule. Unfortunately, difficulties with the insensitivity of the method at natural abundance of ^{13}C (1.1%), the resulting long acquisition times of these spectra, the size of the acquired two-dimensional data sets, and the time-consuming and error prone manual interpretation of often hundreds of megabytes of data have severely limited the routine use of this technique. Two-dimensional INADEQUATE spectra are used here to illustrate automated spectral analysis allowing one to improve the sensitivity, reliability, and speed of the spectral interpretation.

Figure 1 shows a graphical illustration of the 2D INADEQUATE spectrum for a $>CH-CH_2-CH_3$ molecular fragment with the corresponding proton decoupled ^{13}C spectrum. The first bond pattern is found around the chemical shifts ν_A and ν_B as two pairs of antiphase doublets at the double quantum frequency (DQF) $\nu_A + \nu_B$. The second bond pattern belongs to the methylene (ν_B) and methyl (ν_C) carbons, but no bond signal can be found between the methine (ν_A) and methyl carbons (ν_C) in agreement with the bonding in $>CH-CH_2-CH_3$.

The major challenge for every computerized analysis of multidimensional data is rapid and reliable data reduction. Through the automated analysis of the 1D spectrum all carbon resonance frequencies as well as linewidths and intensities can be easily determined. For the interpretation of 2D INADEQUATE data for each pair of resonances identified in the 1D spectrum, two small regions of the spectrum can be defined as shown by the small rectangles in Fig. 1. If a bond exists between the two carbon atoms under consideration,

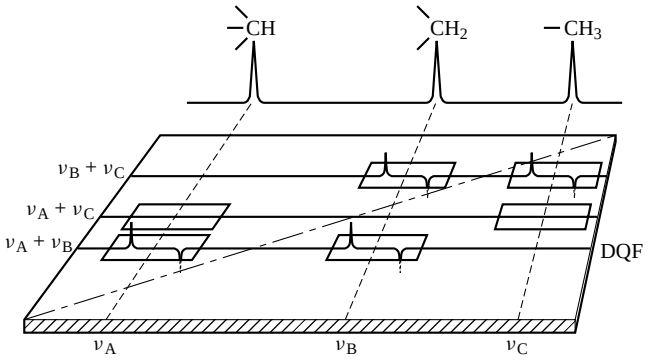

Figure 1 Schematic representation of a 2D INADEQUATE spectrum of a $-CH-CH_2-CH_3$ fragment. (Reproduced by permission of the American Chemical Society from R. Dunkel, C. L. Mayne, R. Pugmire, and D. M. Grant, *Anal. Chem.*, 1992, **64**, 3134)

the characteristic pattern must exist within this 'bond area' which typically comprises less than one-thousandth of the whole spectrum. For n carbon atoms there are $n(n-1)/2$ possible bond regions to be examined. To maximize the sensitivity of this computerized spectral analysis a model equation is used describing the functional form of a possible bond signal.

Two bonded ^{13}C atoms form an AB (or AX) spin system producing four transitions in the shift direction of the 2D INADEQUATE spectrum. From the quantum mechanical description of an AB system all four resonance frequencies and the relative transition intensities can be calculated from the resonance frequencies, ν_A and ν_B, and the one-bond $^{13}C-^{13}C$ coupling constant J. The INADEQUATE pulse sequence uses a double quantum filter to suppress the unwanted and isolated ^{13}C resonances and this filter leaves the four transitions in antiphase. When the difference between the resonance frequencies ν_A and ν_B is large compared with the coupling constant J, the spin system simplifies from AB to AX. For the AX spin system all four transitions have the same absolute intensity, each antiphase doublet is centered at the chemical shift of the corresponding carbon atom, and the doublets are each split by the one-bond $^{13}C-^{13}C$ coupling constant, as shown in Figure 1.

The 2D INADEQUATE lineshape may be calculated as the product of the 1D shift and double quantum lineshapes. These lineshapes themselves are modeled as a convolution of a Lorentzian function caused by exponential spin relaxation and a sinc function caused by truncated data acquisition.

To obtain the best possible spectral resolution multidimensional spectra are normally acquired with phase sensitive detection and hence have to be phase corrected before undertaking any manual data analysis. By introducing phase parameters in the analysis model, phase sensitive experimental data can be analyzed without prior phase correction. For each 1D lineshape function a phase parameter is introduced in the model equation specifying the linear combination of absorption and dispersion modes needed to explain the observed spectral phase. Phase sensitive 2D spectra consist of hypercomplex data with four phase quadrants (real/real, real/imaginary, imaginary/real, imaginary/imaginary). Visual interpretation of 2D spectra is limited to the analysis of one quadrant. The only difference between the signals in the different phase quadrants is a phase shift of 90° between the real and imaginary part in each spectral dimension. Hence, the model equation describes all four quadrants and, since the phase relationship between the phase quadrants is known, all quadrants can be analyzed simultaneously without introduction of additional model parameters. Even though the signals across all four quadrants are correlated, the noise between the quadrants should be uncorrelated, at least partially. Hence, the simultaneous computer analysis of all four quadrants achieves an effective S/N improvement over the analysis of only one quadrant.

The derived model equation describes the shape of all possible bond signals as a function of a few physically defined quantities. Most of the model parameters are known from acquisition parameters and values obtainable from the prior analysis of the 1D carbon spectrum. Using nonlinear regression analysis, the few not-exactly-known model parameters can be determined for each possible bond pattern by fitting the model equation to the corresponding small bond regions of experimental data.

The top spectrum in Figure 2 shows the imaginary/imaginary phase quadrant of the unphased bond signal of carbon atoms 2,3 in 1,1-dimethyltetralin (1,2,3,4-tetrahydro-1,1-dimethylnaphthalene) in a high S/N 2D INADEQUATE spectrum. Regressing the complete hypercomplex data (not just the phase quadrant shown) of this bond signal with the model equation yields the best-fit parameter values. The parameter values can then be used to simulate the signal in the imaginary/imaginary phase quadrant (as shown in the spectrum in the middle of the figure); the bottom spectrum shows the difference between the experimental and the simulated spectra. The residuals between both signal doublets are caused by incomplete suppression of isolated ^{13}C resonances by the INADEQUATE pulse sequence and are unrelated to the analyzed bond signal.

Regressing all potential bond areas in a 2D INADEQUATE spectrum using the described model equation reduces the 2D INADEQUATE information from potentially hundreds of megabytes of spectral data to $n(n-1)/2$ sets of determined best-fit model parameters. The remaining step is to identify those parameter sets describing genuine bond signals. An excellent scale invariant bond criterion is the determined overall intensity value of a spin system scaled by its error value. The related parameter precision defined as the inverse relative error of the measurement[8] of the overall intensity value is used as the sole bond criterion for the following discussion.

To determine the detection probability for the bond pattern shown in Figure 2 at a root-mean-square (rms) S/N ratio of 2.5, 1000 bond regions with pure pseudorandom noise and 1000 bond regions with noise, and the hypercomplex simulated signal from Figure 2 at the appropriate S/N level are generated. The top spectrum in Figure 3 shows one of the generated bond signals in the imaginary/real phase quadrant which shows the highest S/N ratio of the four quadrants. The simulated spectra may be analyzed like experimental data to obtain the intensity parameter precision of each simulated bond region. The bottom spectrum in Figure 3 shows the best-fit determined bond signal for the bond region shown above. The distribution of determined intensity parameter precisions determined from this Monte Carlo simulation of bond signals is shown as the white distribution in Figure 4. The bimodal noise-only distribution is shown in black. One thousand simulations

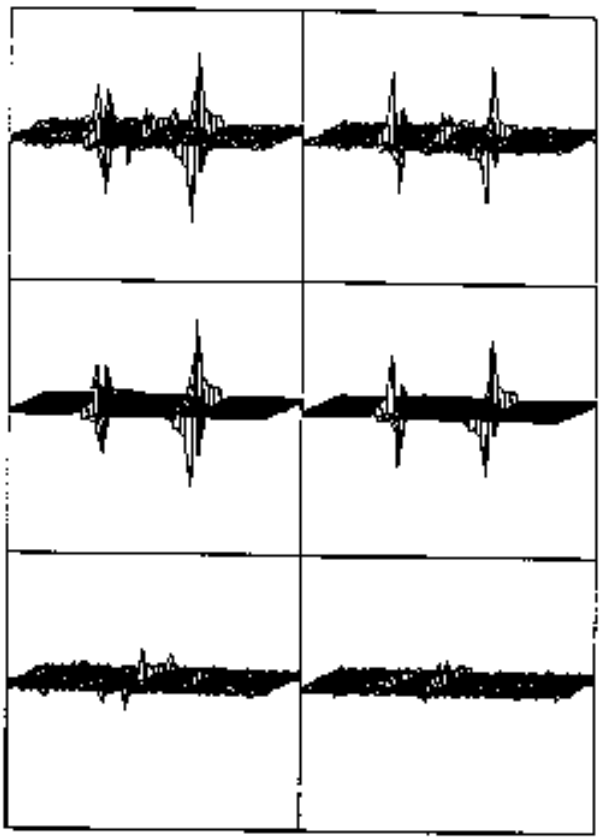

Figure 2 Unphased 2D INADEQUATE bond signal of carbon atoms 2,3 in 1,1-dimethyltetralin in the imaginary/imaginary phase quadrant of: (top) the experimental spectrum; (middle) the simulated spectrum; (bottom) the residual spectrum. (Reproduced by permission of the American Chemical Society from R. Dunkel, C. L. Mayne, R. J. Pugmire, and D. M. Grant, *Anal. Chem.*, 1992, **64**, 3137)

were used to approximate a 99.9% detection probability. Since the distributions do not overlap each other, bond signals can be distinguished from noise patterns with a probability greater than 99.9% at the r.m.s. S/N level of 2.5, which is inconceivable for the visual interpretation of the data. This illustrates the dramatic sensitivity increase obtainable through computerized spectral analysis. Using Monte-Carlo simulations the detection limit of the method at a requested certainty level can be determined for all conceivable model equations, parameter values of experimental patterns, spectral resolutions, and analysis strategies.

Slight extensions of the described computerized analysis have to be made to account for signal aliasing, to guarantee convergence to the correct bond signal in high resolution spectra, to detect rare but possible ambiguities in the 2D INADEQUATE signal assignments, and to list all possible interpretations of identified ambiguous signal assignments. The described automated analysis of 2D INADEQUATE spectra with these extensions is implemented in program XCCBond[9] and has been applied mainly to the structure elucidation of natural products.[10] On typical spectrometer workstations a 2D INADEQUATE spectrum can be analyzed in a few minutes for a 30-carbon-atom compound, using a few thousand spectral points resolution in each dimension.

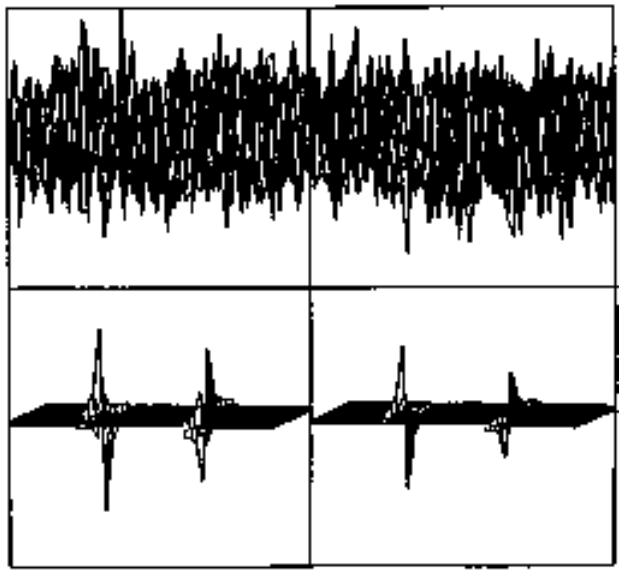

Figure 3 (Top) The Monte Carlo simulated bond signal of Figure 2 in the imaginary/real phase quadrant at an r.m.s. S/N ratio of 2.5. (Bottom) The best-fit bond pattern identified in this hypercomplex data. (Reproduced by permission of the American Chemical Society from R. Dunkel, C. L. Mayne, R. J. Pugmire, and D. M. Grant, *Anal. Chem.*, 1992, **64**, 3144)

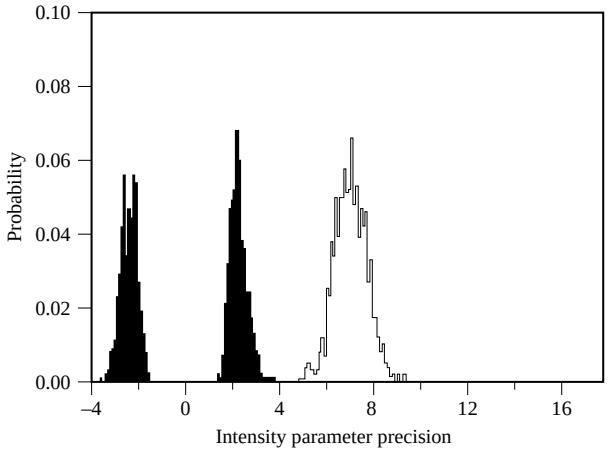

Figure 4 Distribution of intensity parameter precisions determined from 1000 Monte-Carlo simulated bond areas, as shown in Figure 3. The bimodal black distribution shows the 99.9% probability distribution determined from noise-only bond areas, and the distribution for bond signals at an r.m.s. S/N level of 2.5 is shown by the white distribution. (Reproduced by permission of the American Chemical Society from R. Dunkel, C. L. Mayne, R. J. Pugmire, and D. M. Grant, *Anal. Chem.*, 1992, **64**, 3138)

4 STRUCTURE GENERATION

The interpretation results of the analysis of NMR spectra are identified substructures and/or structural constraints for the unknown. For example, in the case of the described automated 2D INADEQUATE spectral analysis the interpretation results are identified carbon–carbon connectivities. Due to heteroatoms in the molecular backbone or due to limitations of the 2D INADEQUATE experiment, only separated carbon

skeleton fragments might be detected rather than the complete molecular backbone. The remaining problem, therefore, is to find in an automated and uniform approach the molecular structures that are consistent with the identified fragments.

No intuitive procedure exists which would allow a spectroscopist to produce manually all possible molecular isomers consistent with given constraints. The success of the structure elucidation, however, depends on carefully ruling out all possible candidate structures of the unknown until only one possible structure remains. An overlooked or not properly ruled-out isomeric structure renders the final result of the structure elucidation meaningless. A computer is ideally suited for the exhaustive generation of possible isomeric structures subject to given bonding constraints, because it is a purely combinational problem. Lederberg[11] has proven that the topology of any chemical compound can be defined in terms of 'tree' and 'vertex' graphs. The resulting vertex graph programs were the first provably correct exhaustive structure generators. The remaining challenge is to obtain a reasonable efficiency of exhaustive structure generators for typical structure elucidation applications.

In principle, a simple recursive algorithm could be used to list all possible isomeric structures consistent with the molecular formula of the unknown (usually obtainable through mass spectrometry) by an exhaustive exploration of all possible bonds among the atoms. In a second step those isomers consistent with all constraints could be filtered out and duplicate isomers eliminated. Unfortunately, the combinational explosion of the number of possible isomers swamps such brute-force approaches. A practical strategy is to generate only those structures consistent with the known constraints and also to avoid duplicate structures rather than to generate isomers which have to be discarded later.

Section 3 describes the computerized analysis of 2D INADEQUATE spectra. The output of the analysis program XCCBond is a carbon–carbon connectivity table. Given the molecular formula of the unknown, this connectivity table can be expanded to contain the noncarbon atoms. A simple recursive algorithm can then be used to complete this partially completed connectivity table by determining all permutations of bonds between the free valences of the specified 'fragments'. This approach guarantees that all resulting isomers (represented by alternate connectivity tables) will satisfy all determined carbon–carbon connectivities and all additional constraints (e.g. the number of protons for each carbon atom) enforced during the completion of the connectivity table.

Each possibility of forming a bond during the completion of the connectivity table starts a new search tree which a simple recursive algorithm would explore exhaustively. However, before assuming the presence of a bond a simple analysis would often reveal that the resulting search tree cannot lead to useful isomers. For example, the analysis could show that the whole search tree can only lead to disconnected molecular substructures. A structure generator should detect and prune such fruitless search tree branches as soon as possible.

Another source of inefficiency in the structure generation is multiple generated copies of an isomer most commonly caused by molecular symmetry. The described algorithm would, for example, list a phenol molecule six times with the hydroxy group located at each of the six carbon atoms of the benzene ring. A possible solution to multiple isomer copies is subsequently to transform all generated isomers to a canonical form and to remove duplicates. More efficient is to transform the connectivity table itself into a canonical form to be able to detect and exploit symmetries during intermediate generation steps.

The structure generators described in the literature differ greatly in their algorithms, capabilities to prune fruitless search trees, and approaches to avoid redundancy in the generated isomers. An example program for the described structure generator for the completion of a partially specified connectivity table, allowing one to specify simple additional constraints and pruning search trees leading to disconnected molecular fragments as well as a comparison of published structure generators, can be found in the book by Gray.[12]

5 RELATED ARTICLES

Analysis of High-Resolution Solution State Spectra; Analysis of Spectra: Automatic Methods; Biological Macromolecules: NMR Parameters; Chemical Shifts in Biochemical Systems; Data Processing; Fourier Transform and Linear Prediction Methods; INADEQUATE Experiment; Multidimensional Spectroscopy: Concepts; Carbon-13 Spectral Simulation; COSY Two-Dimensional Experiments; Heteronuclear Shift Correlation Spectroscopy; NOESY; ROESY.

6 REFERENCES

1. D. L. Dalrymple, C. L. Wilkins, G. W.A. Milne, and S. R. Heller, *Org. Magn. Reson.*, 1978, **11**, 535; Y. Katagiri, K. Kanohta, K. Nagasawa, T. Okusa, T. Sakai, O. Tsumura, and Y. Yotsui, *Anal. Chim. Acta*, 1981, **133**, 535.
2. N. A. B. Gray, *Computer-Assisted Structure Elucidation*, Wiley, New York, 1986, Chaps 4–6.
3. G. E. Martin and A. S. Zektzer, *Two-Dimensional NMR Methods for Establishing Molecular Connectivity. A Chemist's Guide to Experimental Selection, Performance, and Interpretation*, VCH, Weinheim, 1988.
4. S. Glaser and H. R. Kalbitzer, *J. Magn. Reson.*, 1987, **74**, 450; B. U. Meier, Z. L. Mádi, and R. R. Ernst, *J. Magn. Reson.*, 1987, **74**, 565.
5. H. Gesmar and J. J. Led, *J. Magn. Reson.*, 1989, **83**, 53.
6. Z. L. Mádi and R. R. Ernst, *J. Magn. Reson.*, 1988, **79**, 513.
7. A. Bax, R. Freeman, and S. P. Kempsell, *J. Am. Chem. Soc.*, 1980, **102**, 4849; A. Bax, R. Freemen, and T. A. Frenkiel, *J. Am. Chem. Soc.*, 1981, **103**, 2102; A. Bax, *Two-Dimensional Nuclear Magnetic Resonance in Liquids*, Delft University Press, Delft, 1982, pp. 155–174; J. Buddrus and H. Bauer, *Angew. Chem., Int. Ed. Engl.*, 1987, **26**, 625.
8. D. W. Posener, *J. Magn. Reson.*, 1974, **14**, 121.
9. R. Dunkel, C. L. Mayne, J. Curtis, R. J. Pugmire, and D. M. Grant, *J. Magn. Reson.*, 1990, **90**, 290; R. Dunkel, Ph.D. Thesis, University of Utah, December 1990; R. Dunkel, C. L. Mayne, R. J. Pugmire, and D. M. Grant, *Anal. Chem.*, 1992, **64**, 3133.
10. M. P. Foster, C. L. Mayne, R. Dunkel, R. J. Pugmire, D. M. Grant, J.-M. Kornprobst, J.-F. Verbist, J.-F. Biard, and C. M. Ireland, *J. Am. Chem. Soc.*, 1992, **114**, 1110; R. Dunkel, C. L. Mayne, M. P. Foster, C. M. Ireland, D. Li, N. L. Owen, R. J. Pugmire, and D. M. Grant, *Anal. Chem.*, 1992, **64**, 3150; P. Perera, R. Andersson, L. Bohlin, C. Andersson, D. Li, N. L. Owen, R. Dunkel, C. L. Mayne, R. J. Pugmire, D. M. Grant, and P. A. Cox, *Magn. Reson. Chem.*, 1993, **31**, 472.

11. J. Lederberg, *Proc. Natl. Acad. Sci. USA*, 1965, **53**, 134.
12. N. A. B. Gray, *Computer-Assisted Structure Elucidation*, Wiley, New York, 1986, Chap. 10

Biographical Sketch

Reinhard. Dunkel. *b* 1963. Vordiplom Universität Bielefeld, 1985 (chemistry); Diplom Technische Universität Braunschweig, 1987; Vordiplom Fernuniversität Hagen, 1989 (computer science); Ph.D., University of Utah (supervisor David M. Grant), 1990. Research interests include computer applications in chemistry and the automated correction and analysis of experimental data.

Data Processing

George C. Levy, Deborah J. Kerwood and Muppirala Ravikumar

Infomatrix Inc, Ann Arbor, MI, USA

1	Introduction	1
2	History of Computers in NMR	1
3	Data Processing in NMR	2
4	Molecular Modeling	6
5	References	9

1 INTRODUCTION

Much of the progress in NMR spectroscopy over the past 50 years has rested on significant advances in instrumentation and computer hardware and software technologies. There has been an extraordinary transition from the early NMR instruments to today's modern systems. In the mid-1990s, NMR spectrometers are based on multiple computers, mostly tightly coupled, and associated peripherals and smart devices. Software available for control of modern day NMR experiments, and for processing and analysis of the results of those experiments, has reached sophistication that could not be anticipated a decade ago. It is anticipated that, near the turn of the century, NMR instrumentation itself may become truly intelligent, assisting scientists in performing complicated analysis of molecular structures and other applications. Parallel to the developments in NMR spectroscopy have been extraordinary opportunities demonstrated in magnetic resonance imaging (MRI) methods, used in both clinical modalities and the material sciences.

This chapter describes the historical development of computing hardware and software technologies in NMR, with emphasis on current state-of-the-art data processing and data analysis for NMR spectroscopy, and its applications in chemistry, biology, and related sciences. Today, NMR data processing methods greatly extend the utilization of NMR data across a broad range of applications, from industrial process control, to organic and biological molecular structure determination, to understanding basic dynamic properties of molecules.

2 HISTORY OF COMPUTERS IN NMR

The earliest use of digital computers in NMR was for time-averaging of multiple scans, using hard-wired transient recorders in the mid-1960s (the Varian CAT) and then yielding to hybrid systems performing the first Fourier transforms as early as 1969 in commercial NMR instrumentation.[1] In the early 1970s, all research grade NMR instruments were interfaced to dedicated minicomputers which controlled simple pulse NMR data acquisition, as well as performed Fourier transform (FT) and standard post-FT processing. These systems incorporated analog oscilloscopes and plotters for output. By the mid-1970s, NMR instrumentation was designed around minicomputers with 16–20 bit word length, and low-resolution color raster graphics and digital plotters began to appear.[2] In the early 1980s, dedicated NMR instrument computers began to be replaced by modern general design microcomputer and minicomputer systems, augmented by array processors.

The earliest reports of NMR laboratory computer networks predated general purpose workstation computers.[3,4] Those networks were generally connected by several links, and were limited in functionality and speed. They had to contend with nonstandardized data formats, word lengths, and many other inconsistencies among the NMR instrumentation vendors. A few early implementations utilized higher speed parallel connections.[3,4] The main purpose of the initial NMR laboratory networks was to move FT processing, display and plotting offline, away from the NMR instrument. A second important goal was centralized data archiving.

By 1990, virtually all NMR instruments were based on integrated graphics workstation computers. These NMR instruments also incorporated multiple microcomputers in various roles, ranging from control of sample temperature, to highly complex pulse and gradient sequence generation, to data acquisition and control of the user interface. Modern NMR data systems utilize intelligent digital plotters and intelligent subsystems for high-speed, high-resolution color graphics, in some cases also including three-dimensional graphics.

In modern NMR instrumentation, the computer is no longer isolated, but is instead generally networked to other computers and instrumentation in the laboratory and beyond. Laboratory computer networks belong to wide-area networks, including regional networks and the Internet. This was a natural outgrowth of the use in the late 1980s of graphics workstation computers, which from the beginning were network oriented.[5]

In NMR there are three largely separate arenas for computing:

1. Data acquisition and experiment control;
2. Data reduction; and
3. Data analysis and application.

In all modern NMR instrumentation, the tasks of acquiring data and controlling the spectrometer are fully covered by computers embedded in the instrumentation itself, usually through proprietary software which is not fully accessible to the user. Event timing in pulsed FT NMR is on a rapid and sustained timescale (events separated by 10^{-9} or more and sustained for minutes, hours, or days).

On the other hand, the NMR data reduction task has relatively light real-time constraints, although multidimensional NMR experiments can require very extended data reduction periods for larger datasets. Software provided by instrumentation vendors reduces the NMR spectral data to finished output and provides a broad range of standard and some specialized capabilities.

Today, many laboratories add local software routines or software systems provided from other laboratories or commercial sources, to augment the capabilities of software provided by the NMR instrumentation manufacturers. As a result of the almost ubiquitous use of UNIX computers and networking and UNIX-based networking in larger laboratories, the processing and analysis of NMR data has extensively migrated from the instrumentation computers themselves to auxiliary graphics workstations and networked computer servers. Even in smaller laboratories, PC-based data processing software can

Table 1 Evolution of Scientific Computers: 1970s to 1990s

Category of Computer	Mid-1970s	Mid-1980s	Mid-1990s
Smallest	8 bit microcomputer, e.g. Z80 32 kbyte RAM, 250 kbyte disk, Perf. $\ll 0.1$[a]	16 bit PC, 640 kbyte RAM, 40 Mbyte disk, Perf. ca. 0.1–1	32/64 bit PC, 16 Mbyte RAM, 400 Mbyte disk, Perf. 100–250
High-end	16 bit minicomputer, (e.g. PDP-11), 64 kbyte RAM, 5 Mbyte disk, Perf. ca. 0.1	32-bit graphics workstation 8 Mbyte RAM, 300 Mbyte disk, Perf. 10	64 bit multi-processor graphics workstation, 128 RAM, 10 Gbyte, disk Perf. 10^3
Remote site supercomputer	Control data, Cray Perf. ca 10^2	Cray, Parallel, Perf. 10^3–10^4	Various, Perf. 10^4–10^7

[a]Perf., approximate performance relative to the first Digital Equipment Corp. VAX, model 1 1/780. Older machines had disproportionately slower floating point computation, except for supercomputer-class machines.

add additional capabilities beyond that provided by the instrumentation manufacturers. The NMR manufacturers themselves also now offer data processing and analysis software for off-line application, utilizing workstations or PCs.

The trend to off-line NMR data reduction and processing began in the late 1970s, at that time for two reasons. First, NMR instrumentation computers of the period were not true multitasking computers and thus they were not capable of reliably collecting data and performing processing tasks simultaneously. Second, NMR spectrometer-based computers of the time were mostly manufactured specifically for the tasks of NMR data acquisition and these machines did not incorporate effective software development environments, including versatile program development tools (standard language compilers, symbolic debuggers, etc.), nor did many of these systems incorporate high-speed floating point capabilities necessary for many advanced algorithms.[6]

It is difficult to comprehend in the mid-1990s that NMR instrument computers of even 15 years ago might have program address space limitations and total memory storage that would today be greatly exceeded in a toy selling for less than US$10. In fact, it is instructive to view the history of computers (Table 1) available to scientists over the past 30 years in order to gain perspective of the extraordinary changes that have taken place.

It is also instructive to look back at several figures that were prepared for a paper published in early 1988 on the changes in computer technology and their effect on the practice of chemistry.[7] Figure 1 shows that the exponential relationships which were apparent from 1960s to the 1980s have indeed continued (at least thus far) and that the computer revolution in the laboratory remains on-track.

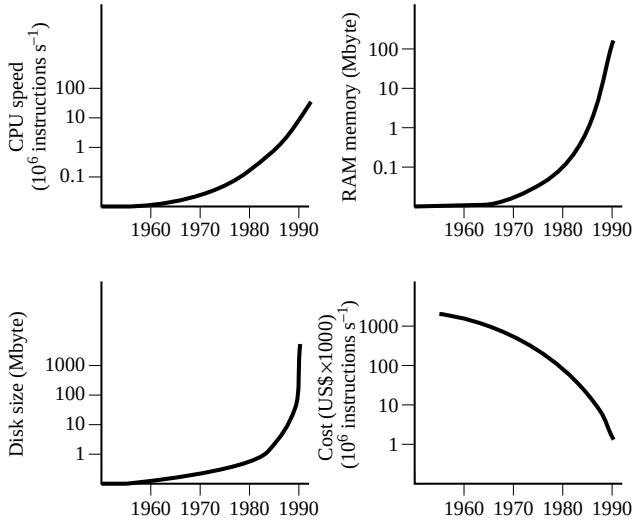

Figure 1 Trends in laboratory computer technology: a surprising logarithmic trend

3 DATA PROCESSING IN NMR

3.1 Averaging and Early Implementations

Data processing gains more importance whenever there is noise. Since noise is generally uncorrelated, n successive additions of noise is only going to add as $\sqrt{n}$. However, the signal adds up linearly as n. Hence successive additions give rise to a signal-to-noise (S/N) ratio improvement of $\sqrt{n}$.

In the very early days of CW NMR, this averaging was performed through box-car integrators which were hardware.[8] In this method there is very little room for further data processing, and what you got was what you had in the box-car integrators. With the introduction of microprocessors a new method was possible, whereby one could store the data and use it for a variety of purposes. This mode of data storage is essential for any useful data processing and has evolved a plethora of data-processing practices that are mostly borrowed or adopted from signal-processing techniques in electrical engineering. Although CW NMR had been routinely practicing signal averaging to enhance the S/N ratio of NMR signals, it was still limited by the time required to collect one scan of an NMR spectrum. This limitation is due to the constraints by the physical theory that dictates the rate at which the 'CW excitation' can be effected to obtain a reliable spectrum. This limitation was circumvented by the development of pulsed FT NMR. This began a new era of NMR which not only

opened a whole range of new experimental techniques, but also extensive data-processing techniques and practices.

3.2 FT Processing

The idea of FT NMR was brought to the attention of the NMR community by Lowe and Norberg.[9] However, the development of the FFT algorithm by Cooley and Tukey[10] enabled Ernst and Anderson[11] to extract the full potential of the method in acquiring NMR spectra with a higher S/N ratio per unit time.

In FT NMR, one acquires the NMR FID in the time domain that corresponds to one scan, and then those data are stored in a computer. The acquired analog signal is converted into a digital signal by using a high precision analog-to-digital converter (ADC), for the purposes of storing and further data processing. S/N ratio averaging is done in the time domain by repeatedly collecting FIDs and coadding the scans in the computer as they are stored. After a requisite amount of averaging is done, a fast FT (FFT) is performed to obtain the spectrum in the frequency domain.

FT NMR has brought with it a large number of data-processing techniques that enhance the appearance and quality of NMR spectra; it also has a few problems. Signal averaging in Fourier transform NMR spectrometers is necessarily preceded by converting the analog signal to digital form. This step involves various hardware and software considerations, which have been described in detail in the literature.[12,13] We will touch on only some of the salient features. The FID is first 'sampled and held', before it is digitized. The number of bits in the digitizer crucially determines the 'dynamic range' and maximum allowable spectral width. The speed of digitization, coupled with Nyquist criteria puts a limit on the number of bits in the ADC. The number of bits in the ADC limits the ratio of maximum observable signal to minimum observable signal, i.e. the dynamic range. The difference between the word size of the computer and the size of the ADC limits the number of transients that can be averaged without altering or reducing the maximum dynamic range achievable by the ADC.

3.2.1 Quadrature Detection or Sign Discrimination

Among many aspects of NMR data processing which are intimately tied with the hardware and experimental practices, quadrature detection is one of the important considerations. In pulsed FT NMR spectroscopy, the frequency of the reading pulse (carrier frequency) determines the relative sign of frequencies in the NMR spectrum.[14,15] If both real and imaginary components of the FID are simultaneously collected for each Nyquist time increment, then FT has to be performed on the complex FID in order to retain the sign information of the frequencies. This method requires that the spectrometer be equipped with two separate receiver channels whose gain and other characteristics are identical. One way to circumvent this difficult task is to use only one receiver channel, while collecting the real and imaginary components of the FID at successive instances of time incrementation, where the time incrementations are half of the value determined by the Nyquist criterion. This latter method involves two separate FIDs of the real and imaginary components, and coadding them. Thus, it involves careful and consistent data representation and FT processing.

3.2.2 Window Functions

The signal-averaged time domain data can be Fourier transformed into frequency domain spectra. It has been found that multiplying the time averaged data with an appropriate function before the FT yields several advantages with respect to the 'apparent' resolution and sensitivity. An excellent account of this has been presented in the book by Ernst et al.[14]

The basic idea of these window functions is as follows.

1. Since, the true NMR signal is decaying in time, while the noise keeps a 'kind of constant amplitude', any decaying window function enhances sensitivity. If the decay of the applied function matches the decay of the true signal, it is called a 'matched filter'. Usually this is a simply decaying exponential, on the presumption that the FID is exponentially damped.
2. Any function that gives more weight to the later part of the FID is generally believed to enhance the resolution. The selection of the resolution enhancement function is, in general, intimately tied with assumptions about the lineshape. If one presumes a Lorentzian shape, with known widths, then a function which is exponentially increasing removes this shape and application of a decreasing Gaussian will result in a more resolved spectrum.
3. An unavoidable consequence of terminating the time domain acquisition after a certain time before the signal has completely decayed (truncation) is the appearance of ripples that are due to the well known 'Gibbs phenomenon'. An exhaustive analysis of several classes of function and their effect on Gibbs phenomenon has been carried out. In general, every function that reduces ripple broadens the spectrum, with the degree of broadening being roughly proportional to their efficacy in reducing the ripples.

A choice of a window function is made such that it would optimally increase sensitivity and resolution, while decreasing the ripple.

It is generally believed that one cannot simultaneously enhance both the resolution and sensitivity using window functions. A choice is made depending on the need and the nature of acquisition. If it is not possible to obtain a sufficient S/N ratio during the time domain acquisition, a matched filter can be used. If the data acquired have a sufficiently high S/N ratio, and if it is desired to improve the resolution, then a combination of resolution enhancement with ripple suppression is used. In this case, Ernst suggests a combination of Lorentz–Gauss apodization with a Hamming window.

It may be remembered that the window functions alter only the apparent resolution or sensitivity, but cannot replace the Utopian goal of achieving unlimited resolution and sensitivity at the acquisition stage. Another important aspect is that the application of window functions does alter the quantification of spectral parameters, such as intensities and linewidths, unless the window function chosen evaluates to unity at the origin.

3.2.3 Zero Filling

It has become common practice to extend artificially the acquired time domain data with zeros prior to the Fourier

transformation. The rationale behind this practice is that, since longer acquisitions improve resolution but nevertheless bring in data with a lower S/N ratio, it would be agreeable to achieve similar resolution without either wasting precious instrumental time in acquisition, or adding noise. Zero filling prior to FT is equivalent to interpolation of the spectrum (decimation of the time domain data) and thus gives better definition or representation of the lineshape. Zero filling once (adding as many zeros as the time domain data points) has been found to incorporate information from the dispersive component into the absorptive component, and hence it is useful to zero fill at least once. Adding more zeros than this extent serves merely to enhance the interpolative effects.

3.2.4 Phasing

The frequency domain spectrum is a mixture of absorptive and dispersive components which can be separated into their component parts. The absorptive and dispersive components correspond to the real and imaginary parts of the spectrum. It is possible to separate these two components in most of the one-dimensional NMR experiments. Many multidimensional NMR experiments are designed ('phase cycled') in such a way that this separation of absorptive and dispersive components is possible. Usually, the absorptive component has the advantage that the spectral lines appear narrower and that they are proportional to the number of spins and that they are symmetric, in contrast to the magnitude or power representations which would obviate the need for phase correction.

Phasing involves two levels of correction. The first level is called 'zeroth-order correction', where the task is to find a phase angle, θ for the whole spectrum such that it satisfies the following equations:

$$\text{New_Real_Part} = \text{Old_Real_Part}^* \cos(\vartheta) - \text{Old_Imaginary_Part}^* \sin(\vartheta) \quad (1)$$

$$\text{New_Imaginary_Part} = \text{Old_Real_Part}^* \sin(\vartheta) + \text{Old_Imaginary_Part}^* \cos(\vartheta) \quad (2)$$

and such that the area under the New_Real_Part is maximum, assuming an ideal baseline. In the first-order correction a similar phase angle θ is found, except that this phase angle varies linearly with the frequency.[16]

Several algorithms have been proposed for automating this phasing process. One such early attempt is that by Ernst,[17] who tries to maximize the total area under the real part of the spectrum while minimizing the total area under the dispersive component. Another widely used algorithm is the DISPA algorithm, where the general principle is that (at least for a resolved line) the two-dimensional plot of well-phased real and imaginary parts is a circle for a Lorentzian line.[18]

3.2.5 Baseline Conditioning

Often, there are even or uneven distortions in the baseline of NMR spectra. A large portion of the uniform baseline distortions arise from dc offsets in the ADC and other hardware sources. This distortion is usually corrected in the time domain by subtracting the complex average of the last 10% of the FID which has been acquired for a reasonable length of time. A number of factors (e.g. temporal effects and instabilities from instrumentation, and extremely broad peaks from known or unknown components of the sample) contribute to the uneven distortions, ridges, etc. Some of the uneven distortions can also be suppressed by deemphasizing the first few data points of the FID with an appropriate window function[19] such as convolution difference.

3.2.6 Peak Analysis

To extract useful information from an NMR spectrum, it is necessary to perform peak analysis. This includes peak-picking, integration, analysis of linewidths and lineshapes, and assignment of spectral lines and their multiplet patterns. Integration can be carried out by using the simple trapezoidal rule, provided that there are no baseline distortions and when all peaks are well separated. In the more typical case, more elaborate methods are required to obtain accurate integrals for spectral peaks.

Analysis of spectral lines (frequencies and intensities) and their multiplet patterns has received considerable attention, especially for one-dimensional NMR spectra. Many programs have been written and tested to simulate one-dimensional NMR of simple spin systems. Two such programs that have become successful and widely used are LACOON5[20] and DAVINS.[21] These programs can be valuable tools in aiding and verifying assignments of simple one-dimensional spectra.

Analysis of spectral lineshapes and linewidths of one-dimensional NMR spectra is another area that has received considerable attention. These programs help in extracting a host of significant information regarding chemical exchange and other dynamic processes.[22,23] Similarly, a large number of programs are available to extract relaxation parameters such as T_1 and T_2.

It may be pointed out that most programs for spectral peak or multiplet simulation and extraction of dynamic or relaxation parameters suffer from various inadequacies of theoretical treatment, unless a complete treatment of strong coupling and relaxation effects is taken into account, as has been described in a recent paper.[24]

3.2.7 Advanced Signal Analysis

As an alternative to the FT, a number of other techniques have become popular for transforming the time domain data into frequency domain spectra. Among these the linear prediction (LP), the maximum entropy method (MEM), the maximum likelihood method (MLM), and the least-squares (LS) or Bayesian methods are significant (see the review by Hoffman and Levy[25]).

The LP methods presume that the future (past) time domain data can be represented as a linear combination of the past (future) time domain data. Whenever the FID is the sum of exponentially damped sinusoids and the S/N ratio is high, this assumption is valid. The advantage of the LP method is that it gives the spectral parameters (frequencies, linewidths, integrals, etc.) directly. Also, LP works well even when some of the early (immediately after the read pulse) time domain data points are missing, a case which results in baseline

distortions using FT processing. For this reason, the LP methods are also popular for predicting missing time domain points in multidimensional NMR spectra.

One significant disadvantage of LP methods is the computational inefficiency of the method. Most LP methods are based on singular value decomposition of the LP matrix created from, say, n time domain points. The method requires of the order of n^3 floating point operations, as compared with FFT which only requires $n \ln(n)$ floating point operations. But, whenever the total number of peaks is relatively small, the size of the LP matrices tends to be small. For this reason and because of operational constraints on acquisition times, LP methods are perceived to be useful in in vivo NMR spectroscopy. However, these spectra generally consist of nonexponential decays due to inhomogeneous samples and consequent broadening.

MEM methods derive their conceptual foundations from Shannon's information theoretic approaches. The basic idea in this approach is that, given some data and a set of possible models, the model is chosen so as to maximize the missing information content. In the NMR adopted version, the procedure is as follows:

1. A trial time domain pseudo-FID is generated.
2. A χ^2 statistic is calculated with an estimated variance, σ^2, for the noise; then, for the correct model of the time domain data χ^2 should equal the number of data points.
3. An appropriate choice of entropy S is defined.
4. The trial time domain data are modified until S is maximized, while simultaneously satisfying the constraints on χ^2 [as described in (2)].

A recent account of MEM and its merits are described in the paper by Jones and Hore.[26]

LS based methods presume a model for the number and characteristics of the NMR signals and minimize the square error between the model and the observed FID. Since very little is generally known about the number of signals, these methods are currently neither successful nor popular.

MLM,[27] as applied to NMR spectra, is quite similar to MEM. MLM purports to find the most likely model that would simultaneously improve resolution and sensitivity. The algorithm attempts to cast the FT in an iterative linear equation form and solves for the most likely model, while simultaneously subjecting it to either some weighting functions or some kind of χ^2 statistic constraints, in addition to performing miscellaneous corrections to the model at each iteration. The method has been shown to improve the contrast not only in one-dimensional NMR spectra but also in multidimensional NMR spectra.[28]

An attractive feature of all the above methods is that, unlike FT, they do not suffer from Gibbs phenomenon (since they essentially attempt to 'fit' a model to the time domain data).[29] Most of the methods can be used such that they yield spectral parameters in a more direct form. However, unlike FT, they are computationally expensive, and almost computationally prohibitive for use on the largest data arrays in multidimensional NMR processing.

3.3 Data Processing in Multidimensional NMR

Multidimensional NMR data processing shares most of the conceptual features of one-dimensional processing, especially with respect to the basic ideas of zero filling, windowing, FT and other techniques of converting the data into spectra. However, several additional features become important because of the large datasets and because of the idiosyncrasies of the experimental implementations used to determine the sign of frequencies in the remote dimensions. We will give an extremely brief overview of some of these features.

FT is the most common choice for initial conversion of multidimensional FIDs into spectra, for the most compelling reason of computational efficiency. However, in three-dimensional and higher multidimensional processing the time domain data cannot be collected with the required resolution in the remote dimensions due to an inordinate increase in the acquisition time. In such cases, it has been found that use of LP methods to predict more time domain data points in these remote dimensions prior to multidimensional FT is advantageous.

A consequence of the extremely large sizes of multidimensional time domain datasets is that FT cannot be carried out along all dimensions while holding the complete dataset in the random access memory (RAM) or its equivalent. It becomes necessary to store the data in mass storage media and then read or write the required portion repetitively. This also necessitates either transposition of the data for processing along remote dimensions, or evolving suitable modifications of the FFT algorithm to achieve the same goal. While the first choice increases the input/output time, the latter choice increases the complexity of programming.

Determining the sign of frequencies in the remote dimensions is another complexity of multidimensional NMR processing, which is intimately tied up with experimental procedures that are designed for the same purpose. Two conceptually important experimental methods have been evolved for this purpose. The first is called the States–Haberkorn (SHR)[30] method in which both the real and imaginary parts of the remote dimensional time domain data are acquired for the same length of the remote time evolution, similar to the two-receiver-channel detection in one-dimensional NMR. The second method, time proportional phase incrementation (TPPI),[31] achieves the same purpose by modifying the phase cycling of the pulse sequence used, similar to the one-receiver-channel detection in one-dimensional NMR. There are many variations of these two basic procedures. Thus it becomes necessary to keep track of the data ordering, representation, and storage method of the real and imaginary components of every dimension in the multidimensional FID, along with the basic scheme used to discriminate the sign of frequencies in the remote dimension. Furthermore, FT processing has to be consistent with the data representation.

Most concepts regarding one-dimensional data processing are also applicable in multidimensional processing. In the case of applying window functions, some new functions have become popular. One of these is the shifted or unshifted sine-bell window[32] and has been found to be useful for phase sensitive spectra, particularly those with antiphased cross peaks. For spectra with inphase cross peaks other resolution enhancing windows are more useful. Caution has to be exercised for quantification purposes, since integrals are unchanged only for window functions that evaluate to unity at the origin. Thus, use of an unshifted sine-bell for quantifying a NOESY spectrum is inappropriate. Some effort has been directed towards automation of peak picking, which would be

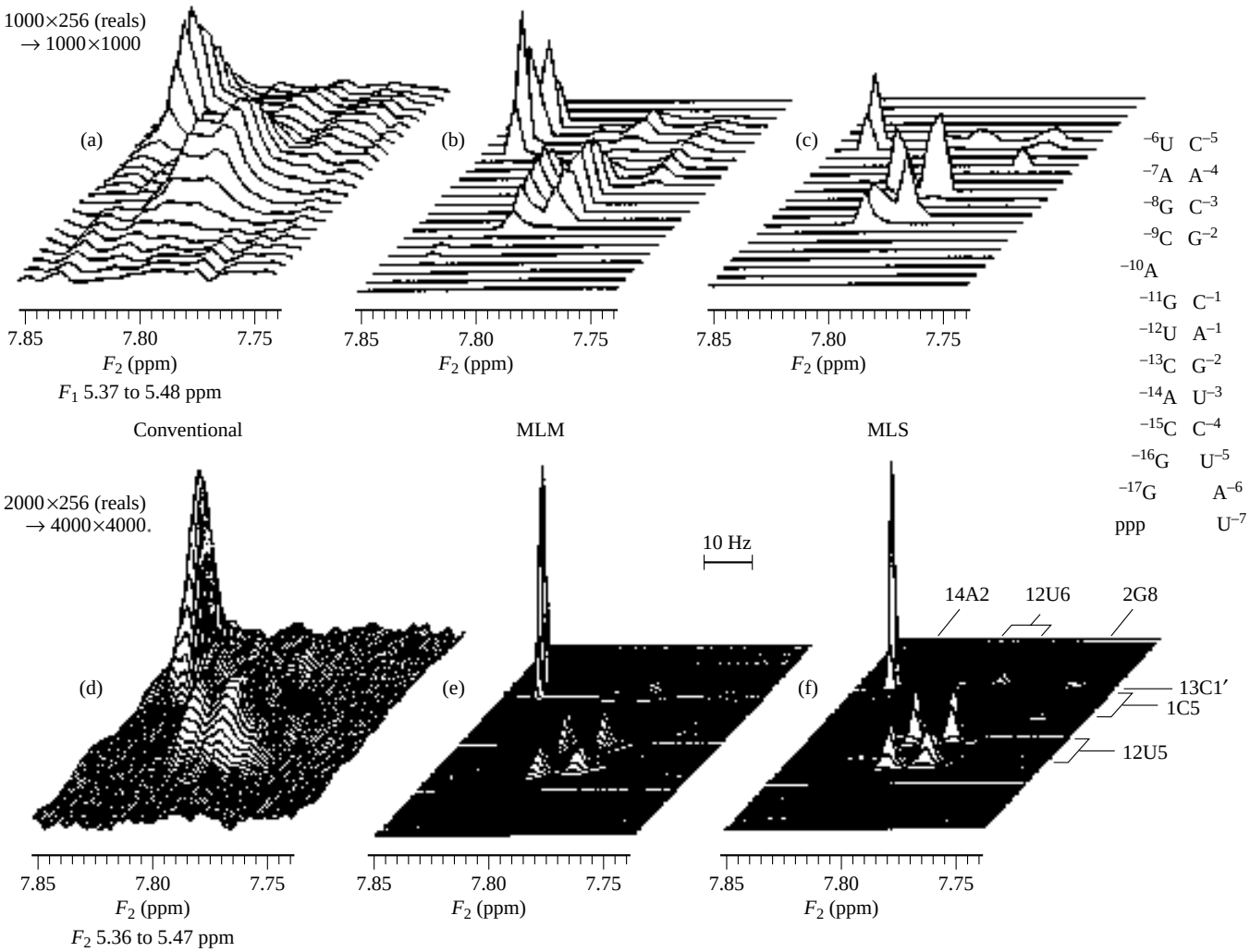

Figure 2 Stacked views of the small subregion (base-1′) of a 500-MHz 24-mer RNA hairpin-loop spectrum. (a–c) Based on 1000 × 1000 data; (d–f) zero filled to 4000 × 4000 total real data. (a and d) Processed conventionally; (b and e) processed using maximum-likelihood method (MLM); (c and f) processed using MLM and symmetrization

an important advantage for multidimensional spectra that may contain thousands of cross peaks.

Baseline distortions and ridges contribute to difficulties in peak identification and quantification. Considerable effort has been expended to obviate this problem. An example of automated removal of these artifacts is shown in Figure 2.[33] Use of MLM to obtain contrast enhancement of peaks from artifacts has also proved useful for peak identification, and the quantification of integrals in such spectra seems to be reliable (Figure 3).[34]

3.4 Automated Analysis of NMR Spectra

As a result of the dramatic growth of new multidimensional NMR techniques, and through concomitant growth of data processing tools (both software and hardware), there is increased interest, need, and demand to automate the study of more and more complex molecules. A critical step in the study of complex molecules, after obtaining the NMR spectral data, is to make resonance assignments. Notable developments in artificial intelligence (AI) methods have added impetus to the need for automation of this process. One area in which there is some hope is in the analysis of ^{13}C NMR spectra of reasonably large organic molecules.[35] Considerable effort has also been directed to easing the process of assignment by using computers. Some effort, with moderate success, has been expended in the following components of the assignment process. Programs have been written either merely to perform book-keeping tasks or to aid the manual assignment process graphically.[36–38] Use has been made of symmetry based algorithms to identify weakly coupled well resolved multiplet patterns.[39] Feed-forward three-layer neural networks with back-propagation training have also been used to identify AX type antiphase cross peaks.[40,41] Similar network architecture has been used to sieve out, with modest success, authentic peaks from spectral artifacts in a NOESY spectrum.[42]

Some methods have been suggested that demonstrate progress towards the automation of the biomolecular NMR spectral assignment methods.[43] Use of neural networks seems to be especially promising in this direction.[44,45]

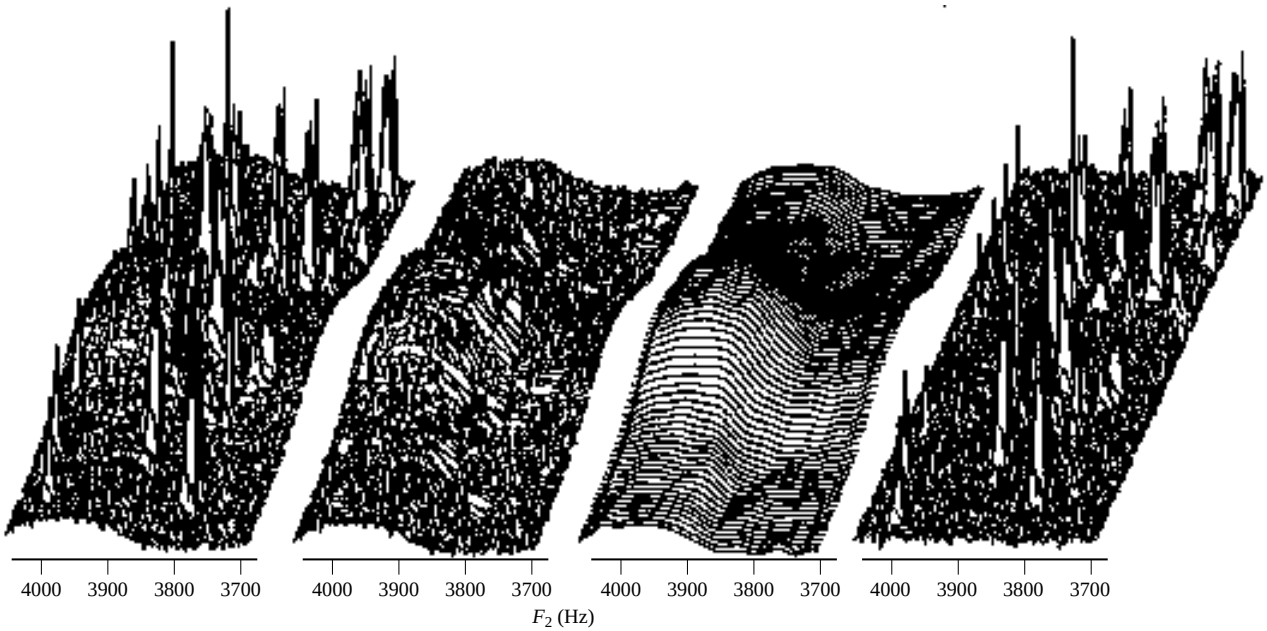

Figure 3 (a) Original spectrum prior to baseplane correction, where a small section (512 × 512 data size) of a two-dimensional experimental NOE spectrum was combined with a synthetic dataset having resonance peaks and baseplane distortion. (b) Stacked plot of baseplane information filled with two-dimensional nonlinear weighted interpolation (the filling lines in the F_2 direction only are shown). (c) Refined baseplane obtained by multiplication in the time domain by a two-dimensional shifted Guassian window function that was generated automatically by a program. (d) Corrected spectrum that was obtained by subtracting the refined baseplane (c) from the original spectrum (a)

4 MOLECULAR MODELING

NMR has become an important, if not essential, tool for the determination of the solution structure of macromolecules. The procedure for structure determination usually proceeds in three steps: (1) several NMR experiments, (2) conversion of information obtained from the NMR experiment into structural information, and (3) structure determination based on the NMR and holonomic information. Steps (2) and (3) can also be combined. There are recent approaches which use NMR parameters directly in the refinement procedure.

Initial molecular structure determinations relied on one-dimensional NOE experiments in which the change in intensity of NMR signals was monitored when neighboring spins were irradiated. The resultant intensity change is proportional to the inverse sixth power of the distance between the two protons under study, since the dominant relaxation mechanism is due to magnetic dipole coupling.[46,47] With the advent of two-dimensional NMR experiments, information can be obtained about the structure of much larger and more complex molecules.[48]

Typically, two types of structural information can be obtained from NMR experiments: (1) distance information from proton–proton NOESY and/or ROESY spectra; and (2) angular information based on COSY-type (or scalar coupling based NMR) experiments. Angular information is usually supplementary to NMR-derived distances due to the lack of accuracy with which J values can be obtained, and sometimes limitations in its conversion to dihedral angles. A more detailed discussion of two-dimensional NMR experiments is presented by R. R. Ernst (see ***Multidimensional Spectroscopy: Concepts***.).

The NOESY experiment has proven to be a challenge in the conversion of NOE intensities to distances. The problem lies in the fact that the cross peak intensities are not only dependent on the distance between protons, but also on the motions of the molecule. In addition, in the case of large molecules, 'spin diffusion' (the indirect transfer of magnetization between protons), contributes to the intensity of the cross peaks.[49] The procedures for determining distances from NOE intensities can be divided into qualitative and quantitative solutions. The latter follow two different approaches: (1) (hybrid) relaxation matrix analysis,[50,51] and (2) gradient-based analysis.[52,53] The gradient-based method involves the analysis of cross peak intensities in a refinement procedure and will therefore be described after the discussion of refinement methods.

The qualitative approach for determining NOE-derived distances is based on the isolated spin pair approximation (ISPA) in which the internuclear distance is estimated by referencing the intensity and the distance to two protons of known distance. This technique can be used for short mixing times and short correlation times, but under conditions where spin diffusion is a factor this method will underestimate the distance if the distance being measured is larger than the reference distance (the usual case) and overestimate the distance if the distance is smaller than the reference distance.[54] Similarly, when a distance range is needed for structure determination techniques, such as in distance geometry (DG) or molecular dynamics (MD) calculations, the range is estimated from the strength of the intensity of the cross peak at different mixing times.

Relaxation matrix approaches give a more quantitative measurement of the distance between protons by taking into account the whole network of spin systems. This technique solves the relaxation matrix to interpret distances, and this is thus referred to as a DIRECT method.[50,55] The problem with this approach is that, in order to solve the relaxation matrix, most of the cross peaks and diagonal peaks have to be resolved

or else the relaxation pathway is not well established.[56] This method is efficient with small molecules, where the S/N ratio is high and where there is minimal overlap of peaks in the NOESY spectrum.

A solution to the incomplete relaxation matrix involves techniques that combine experimental intensities with those calculated based on a starting structure. Iterative relaxation matrix analysis (IRMA) is an iterative program that combines relaxation matrix calculation with restrained molecular dynamics (r-MD). The program starts with available experimental NMR intensities plus a starting structure, from which it then calculates the missing intensities. With this hybrid of both experimental and calculated intensities it solves the relaxation matrix to produce distances.[51,57] These distances are then used in r-MD or distance geometry calculations to produce a new starting structure for IRMA that is more defined by the experimental intensities than the initial starting structure. This cycle is repeated until a final structure is produced which optimally fits the experimental spectra.

MARDIGRAS (matrix analysis of rates for dIscerning geometry in solution) is a similar technique, developed by James et al.[58,59] which generates an augmented intensity matrix. This intensity matrix, which contains all the scaled experimental intensities and the calculated intensities of the starting structure, is then solved for the distances. This technique differs from IRMA in that it does not require a restrained molecular dynamics or restrained distance geometry step, but instead requires internal consistency in the relaxation matrix. This makes MARDIGRAS less time-consuming.

CAMELSPIN/ROESY experiments, like NOESY data, provide information about the distance between protons, but there are different problems associated with ROESY, such as off-resonance and TOCSY/HOHAHA effects. The program CROSREL, developed by Leeflang and Kroon-Batenburg,[60] is able to accept either ROESY or NOESY cross peak intensities as input to solve a full relaxation matrix. This program takes into account spin diffusion, internal motions and anisotropic effects; for the ROESY experiments it accounts for nonrelaxation factors, such as HOHAHA effects. A three-dimensional version of the recently developed LOUSY can unambiguously yield 'ROE-only' effects, by separating HOHAHA/TOCSY effects.

The process of determining the structure of a molecule depends on computational programs that globally search conformational space to find a set of molecular structures consistent with both experimental and holonomic constraints of bond lengths, bond angles, and steric limitations. Distance geometry, a branch of mathematics,[61] is routinely used to determine initial structures of proteins which can then be refined further by means of restrained molecular dynamics calculations. An advantage of distance geometry is that it is able to explore conformational space in a relatively short period of time.[62] The structures produced will fit well with the distance constraints applied, but will have high potential energy due to close nonbonded contacts, which are alleviated in the molecular mechanics step. There are two general methods of distance geometry: (1) the matrix method,[63–66] and (2) the variable target function in dihedral angle space technique.[67,68] In the former, distances between points are converted into coordinates by a procedure called embedding. The coordinates are then optimized against an 'error function' which increases rapidly when the distance constraints are violated. The first solution structure of a protein, proteinase inhibitor IIA from bull seminal plasma (BUSI IIA), was determined in this manner with the program DISGEO in 1985 by Williamson et al.[69] The variable target function approach first randomizes the dihedral angles around single bonds and then proceeds to adjust the conformation to fit a set of experimental constraints, by varying the dihedral angle. The first program to implement this technique was DISMAN, developed by Braun and Go.[67] The current program that is based on this technology is DIANA, which was developed by Wüthrich's group. This new version includes vectorization to reduce the amount of central processing unit (CPU) time.

Another approach used for structure determination, often used in conjunction with distance geometry, is restrained molecular dynamics,[70,71] where the energy of the system is minimized as the structure is allowed to explore conformational space, along with experimental NOE constraints. The molecular dynamics programs most widely used are GROMOS (Groninger molecular simulation),[72] AMBER 4.0,[73] X-PLOR,[74] and CHARMM.[75] Each molecular dynamics simulation program has a force field which consists of a Lennard–Jones potential, a Coulombic interaction, a dihedral potential, and harmonic potential terms that constrain bond lengths, bond angles, and torsion angles; for restrained molecular dynamics an energy potential is included for the NMR constraints. The form of the last potential depends on the user, but usually takes the form of a flat-well potential, where the estimated experimental error can be incorporated as the width of the flat well.[76,77] Restrained molecular dynamics has also found success in the structure determination of nucleic acids, where the choice of initial structure is not usually a problem.

Simulated annealing is widely used for biomacromolecular structure. The goal of molecular dynamics calculations is to find the global minimum in a potential energy surface, containing multiple local minima. In the simulated annealing protocol, the temperature of the system is elevated so that the simulated molecule can overcome energy barriers, and this is followed by slow cooling which will enable the lowest energy form to be achieved.[78]

A relatively new implementation of an old concern is the use of time-averaged distance constraints in molecular dynamics calculations. In the calculations mentioned above it has been assumed that the NOE reflects a static distance, but in reality it reflects a time-averaged distance. A more realistic approach would be to replace the instantaneous distance r in the NOE-pseudo-potential energy term with the time-averaged distance $\langle r \rangle$, where:

$$\langle r \rangle \cong \langle r(t)^{-6} \rangle^{-1/6} \tag{3}$$

Usually since the NOE is assumed to be predominantly due to dipolar interactions the intensity of the NOE cross peaks are proportional to r^{-6}. But the timescale of the molecular dynamics simulation is short compared with the correlation time for the molecular tumbling of the molecule, so the influence of angular fluctuation can be ignored. The additional term involving t is a memory function so that $\langle r \rangle$ is a running average, with the recent history having more weight than past history.[79,80] Theoretical comparison studies of standard and time-averaged refinement methods have been done on the DNA hexamer $d(GAATTC)_2$[81] and on the macrocyclic immunosuppressive agent FK506.[82] For both studies, the

two methods gave similar gross structures, but the time-averaged method gave a superior picture of the fine structure and the inherent flexibility of the molecule. This technique has also been used in the refinement of the DNA octamer [d(GTATAATG)]·[d(CATATTAC)][83] and tendamistat[84] using experimental NOE-derived distances. The results of these studies confirm the theoretical results, in that the time-averaged protocol gave a more realistic picture of the flexibility of the molecules. In addition, the time-averaged structure compared with the standard refinement structure gave better agreement with the experimental data. Torda et al.[85] have recently applied this technique using J coupling constant information. A penalty function was added to the force field which allowed the J coupling information to be enforced as a time-averaged quantity. The results were similar to those for the distance time-averaged constraints, i.e. a greater ability to enforce experimental restraints while exploring a larger region of conformational space.

Yip and Case[52] and Baleja et al.[53] pioneered the gradient-based analysis of NOE intensities in a refinement protocol. This involves incorporation into the force field of a penalty function based on the NOE intensities in which the experimental intensities are compared with NOE intensities calculated using a full relaxation matrix analysis based on the starting model. This method not only takes into account spin diffusion, but also differential motion within the molecule. A gradient of the NOE intensities with respect to structural parameters, such as the Cartesian coordinates, is calculated. This can be done in three ways: (1) by manipulation of the matrix exponential expression, e.g.[86]

$$\frac{\delta}{\delta R_{k,l}} A(\tau)_{i,j} = \sum_{r,u} L_{r_i} L_{r_k} L_{u_l} L_{u_j} \times \left[\frac{\exp(-\lambda_r \tau) - \exp(-\lambda_u \tau)}{\lambda_r - \lambda_u} \right] \qquad (4)$$

where L and λ are eigenvectors and eigenvalue matrices of R, respectively, and $A(\tau)$ represents the NOEs between protons i and j; (2) by numerical integration of $\mathrm{d}(a)/\mathrm{d}t = -(R)(a)$ by Gear's algorithm; and (3) approximation of (a) based on the Taylor expansion series.[87] Determining the gradient of the intensities can be computationally exhausting in terms of time and memory, especially for method (1). It is possible to shorten the time of computation while still maintaining the accuracy of the calculation by evaluating the force of the NOE potential in the first steps and subsequently in every X steps during the molecular mechanics run, or when the proton moves more than x nanometers away. Also, instead of calculating the relaxation matrix for the whole molecule, sets of overlapping submolecules can be created so that cross peaks influence only nearby spins, and not the whole molecule. The advantage that this technique has over others is that the correlation times, in addition to the nuclear coordinates, can be altered to minimize the penalty function.

Heuristic refinement,[88] another refinement technique for proteins, is based on a systematic search of conformational space, but it uses prior knowledge of the system under study, thereby making it less computationally demanding. PROTEAN[89–91] is a program based on this theory for the structure determination of proteins. The protocol used is: (1) to define the secondary structure from NMR data plus a knowledge of the protein sequence; (2) to determine the coarse topology of the folded structure by coarse systematic sampling of conformational space; and (3) to define the spatial distribution of atomic positions.

5 REFERENCES

1. Bruker spectrometers, which initially utilized a Digital Equipment PDP-8 minicomputer and Nicolet hard-wired signal averager.
2. Varian 620L, Texas Instruments 990, Nicolet 1080 and 1180, Bruker BNC-12 computers.
3. G. C. Levy and D. Terpstra, *Computer Networks in the Chemical Laboratory*, Wiley Interscience, New York, 1981.
4. G. C. Levy, D. Terpstra, and C. L. Dumoulin, in chapter 5, ref. 2.2.
5. G. C. Levy, *Comput. Enhanced Spectrosc.*, 1986, **3**, 79.
6. G. C. Levy and J. H. Begemanm, *J. Chem. Inf. Comput. Sci.*, 1985, **25**, 350.
7. G. C. Levy, *J. Chem. Inf. Comput. Sci.*, 1988, **26**, 167.
8. J. A. Pople, W. G. Schneider, and H. J. Bernstein, *High Resolution Nuclear Magnetic Resonance*, McGraw Hill, New York, 1957.
9. I. J. Lowe and R. E. Norberg, *Phys. Rev.*, 1957, **107**, 46.
10. J. W. Cooley and J. W. Tukey, *Math. Comput.*, 1965, **19**, 297.
11. R. R. Ernst and W. A. Anderson, *Rev. Sci. Instrum.*, 1966, **37**, 93.
12. J. C. Lindon and A. G. Ferrige, *Prog. NMR Spectrosc.*, 1980, **14**, 27.
13. Shaw, *Fourier Transform NMR Spectroscopy*, Elsevier, Amsterdam, 1984.
14. R. R. Ernst, G. Bodenhausen, and A. Wokaun, *Principles of Nuclear Magnetic Resonance in One and Two Dimensions*, Oxford Publications, Oxford, 1987.
15. (a) T. C. Farrar and E. D. Becker, *Pulse and Fourier Transform NMR*, Academic Press, London, 1971; (b) E. D. Becker, *High Resolution NMR*, Academic Press, London, 1980.
16. M. L. Martin, J.-J. Delpuech, and G. J. Martin, *Practical NMR Spectroscopy*, Heyden, London, 1980.
17. R. R. Ernst, *J. Magn. Reson.*, 1969, **1**, 7.
18. R. E. Hoffman, F. Delaglio, and G. C. Levy, *J. Magn. Reson.*, 1992, **98**, 231.
19. R. Freeman, *A Handbook of Nuclear Magnetic Resonance*, Wiley, New York, 1987.
20. S. Castellano and A. A. Bothner-By, *J. Chem. Phys.*, 1964, **41**, 3863.
21. D. S. Stephenson and G. Binsch, *QCPE Bull.*, 1978, **11**, 378.
22. J. Sandstrom, *Dynamic NMR Spectroscopy*, Academic Press, New York, 1982.
23. J. I. Kaplan and G. Fraenkel, *NMR of Chemically Exchanging Systems*, Academic Press, New York, 1980.
24. M. Ravikumar, R. Shukla, and A. A. Bothner-By, *J. Chem. Phys.*, 1991, **95**, 3092.
25. R. E. Hoffman and G. C. Levy, *Prog. NMR Spectrosc.*, 1991, **23**, 211.
26. J. A. Jones and P. J. Hore, *J. Magn. Reson.*, 1991, **92**, 363.
27. (a) F. Ni and H. A. Scheraga, *J. Magn. Reson.*, 1989, **82**, 413; (b) R. E. Hoffman, A. Kumar, K. D. Bishop, P. N. Borer, and G. C. Levy, *J. Magn. Reson.*, 1989, **83**, 586.
28. (a) G. W. Jeong, Ph.D. Thesis, Syracuse University, New York, 1992; (b) G. W. Jeong, S. Wang, P. N. Borer, and G. C. Levy, *J. Magn. Reson., Ser. A*, 1993, **102**, 123.

29. E. O. Brigham, *The Fast Fourier Transform*, Prentice Hall, Englewood Cliffs, NJ, 1974.
30. D. J. States, R. A. Haberkorn, and D. J. Ruben, *J. Magn. Reson.*, 1982, **48**, 286.
31. D. Marion and K. Wüthrich, *Biochem. Biophys. Res. Commun.*, 1983, **113**, 967.
32. A. DeMarco and K. Wüthrich, *J. Magn. Reson.*, 1976, **24**, 201.
33. G. C. Levy, G. W. Jeong, J. Yu, and K. Wang, *J. Magn. Reson.*, in press.
34. P. N. Borer and G. C. Levy, *Methods Enzymol.*, 1994, **239**, 257.
35. (a) W. Bremser, *Magn. Reson. Chem.*, 1985, **23**, 271; (b) J. P. Doucet, A. Panaye, E. Feuilleaubois, and P. Ladd, *J. Chem. Inf. Comput. Sci.*, 1993, **33**, 320.
36. H. Grahn, U. Edlund, Y. T. van den Hoogen, F. Delaglio, C. Altona, M. W. Roggenbuck, and P. N. Borer, *J. Biomol. Struct. Dyn.*, 1989, **6**, 1135.
37. T. S. Harvey, S. Bagby, and M. Ikura, in *Frontiers of NMR in Molecular Biology III*, ed. T. L. James, S. W. Fesik, and P. E. Wright, 1993, p. 253.
38. D. G. Kneller and I. D. Kuntz, in *Frontiers of NMR in Molecular Biology III*, ed. T. L. James, S. W. Fesik, and P. E. Wright, 1993, p. 254.
39. B. U. Meier and R. R. Ernst, *J. Magn. Reson.*, 1988, **79**, 540.
40. M. Kjaer and F. M. Poulsen, *J. Magn. Reson.*, 1991, **94**, 659.
41. H. Shen, S. Ludvigsen, and F. M. Poulsen, *J. Magn. Reson.*, 1990, **90**, 346.
42. S. A. Corne, A. P. Johnson, and J. Fisher, *J. Magn. Reson.*, 1992, **100**, 256.
43. R. P. Meadows, E. T. Olejniczak, and S. W. Fesik, *J. Biomol. NMR*, 1994, **4**, 79.
44. R. Anand, K. G. Mehrotra, C. K. Mohan, and S. Ranka, *J. Pattern Recognition*, 1993.
45. B. J. Hare and J. H. Prestagard, *J. Biomol. NMR*, 1994, **4**, 35.
46. J. A. Ferreti and G. H. Weiss, *Methods Enzymol.*, 1989, **176**.
47. J. H. Noggle and R. G. Schirmer, *The Nuclear Overhauser Effect*, Academic Press, New York, 1971.
48. K. Wüthrich, *NMR of Proteins and Nucleic Acids*, Wiley, New York, 1986.
49. A. Kalk and J. C. Berendsen, *J. Magn. Reson.*, 1976, **24**, 343.
50. E. T. Olejniczak, R. T. Gampe, Jr, and S. W. Fesik, *J. Magn. Reson.*, 1986, **67**, 28.
51. R. Boelens, T. M. G. Koning, and R. Kaptein, *J. Mol. Struct.*, 1988, **173**, 299.
52. P. Yip and D. Case *J. Magn. Reson.*, 1989, **83**, 643.
53. J. D. Baleja, J. Moult, and B. D. Sykes, *J. Magn. Reson.*, 1990, **87**, 375.
54. B. A. Borgias and T. L. James, *J. Magn. Reson.*, 1988, **79**, 493.
55. P. A. Mirau, *J. Magn. Reson.*, 1980, **80**, 439.
56. B. A. Borgias and T. L. James, *J. Magn. Reson.*, 1988, **79**, 493.
57. R. Boelens, T. M. G. Koning, G. A. Van der Marel, J. H. van Boom, and R. Kaptein, *J. Magn. Reson.*, 1989, **82**, 290.
58. B. A. Borgias and T. L. James, *J. Magn. Reson.*, 1991,
59. B. A. Borgias, M. Gochin, D. J. Kerwood, and T. L. James *Prog. Nucl. Magn. Reson. Spectrosc.*, 1990, **22**, 83.
60. B. R. Leeflang and L. M. J. Kroon-Batenburg, *J. Biomol. NMR*, 1992, **2**, 495.
61. L. M. Blumenthal, *Theory and Application of Distance Geometry*, Chelsea, Bronx, NY, 1970.
62. I. D. Kuntz, J. F. Thomason, and C. M. Oshiro, *Methods Enzymol.*, 1989, **177**,
63. G. M. Crippen, *J. Comput. Phys.*, 1977, **24**, 96.
64. T. F. Havel, I. D. Kuntz, and G. M. Crippen, *Bull. Math. Biol.*, 1983, **45**, 665.
65. W. Braun, C. Bosch, L. R. Brown, N. Go, and K. Wüthrich, *Biochim. Biophys. Acta*, 1981, **667**, 377.
66. T. F. Havel and K. Wüthrich, *J. Mol. Biol.*, 1985, **182**, 281.
67. W. Braun and N. Go, *J. Mol. Biol.*, 1985, **186**, 611.
68. W. Braun, in *Computational Aspects of the Study of Biological Macromolecules by Nuclear Magnetic Resonance Spectroscopy*, ed. J. C. Hoch, F. M. Poulsen and C. Redfield, Plenum, New York, 1991, *Ser. A, Vol. 225*, p. 225.
69. M. P. Williamson, T. F. Havel, and K. Wüthrich, *J. Mol. Biol.*, 1985, **182**, 295.
70. W. F. van Gunsteren, R. Kaptein, and E. R. P. Zuiderweg, in *Proceedings of a NATO/CECAM Workshop on Nucleic Acid Conformation and Dynamics*, ed. W. K. Olsen, Orsay, 1984, p. 79–82.
71. R. Kaptein, E. R. P. Zuiderweg, R. M. Scheek, R. Boelens, and W. F. van Gunsteren, *J. Mol. Biol.*, 1985, **182**, 179.
72. The GROMOS (Groninger Molecular Simulation) software package (by W. F. van Gunsteren and H. J. C. Berendsen) is available from BIOMOS b.v., Nijenborogh 16, 9747 AG Groningen, The Netherlands.
73. D. A. Pearlman, D. A. Case, J. C. Caldwell, G. L. Seibel, U. C. Singh, P. Weiner, and P. A. Kollman, AMBER 4.0, University of California, San Francisco, 1991.
74. A. T. Brunger, *X-PLOR, A System for X-ray Crystallography and NMR*., Yale University, New Haven, CT, 1987.
75. Molecular Simulations, Inc., MA., 1986 Burlington.
76. J. D. Baleja, R. T. Pon, and B. D. Sykes, *Biochemistry*, 1990, **29**, 4828.
77. D. J. Kerwood, G. Zon, and T. L. James, *Eur. J. Biochem.*, 1991, **197**, 583.
78. M. Nilges, G. M. Clore, and A. M. Gronenborn, *FEBS Lett.*, 1988, **229**, 317.
79. H. Kessler, C. Griesinger, J. Lautz, A. Muller, W. F. van Gunsteren, and H. J. C. Berendsen, *J. Am. Chem. Soc.*, 1988, **110**, 3393.
80. A. E. Torda, R. M. Scheek, and W. F. van Gunsteren, *J. Mol. Biol.*, 1990, **214**, 223.
81. D. A. Pearlman and P. A. Kollman, *J. Mol. Biol.*, 1991, **220**, 457.
82. D. A. Pearlman, *J. Biomol. NMR*, 1994, **4**, 1.
83. U. Schmitz, A. Kumar, and T. L. James, *J. Am. Chem Soc.*, 1992, **114**, 10 654.
84. A. E. Torda, R. M. Scheek, and W. F. van Gunsteren, *J. Mol. Biol.*, 1990, **214**, 223.
85. A. E. Torda, R. M. Brunne, T. Huber, H. Kessler, and W. F. Gunsteren, *J. Biomol. NMR.*, 1993, **3**, 55.
86. R. Bruschweiller and D. A. Case, *Prog. NMR Spectrosc.*, 1994, **26**, 27.
87. B. Stawarz, M. Genest, and D. Genest, *Bipolymers*, 1992, **32**, 633.
88. R. B. Altman and O. Jardetzky, *Methods Enzymol.*, 1989, **177**, Chap. 11
89. R. B. Altman and O. Jardetzky, *J. Biochem.*, 1986, **100**, 1403.
90. J. F. Brinkley, R. B. Altman, B. S. Duncan, B. G. Buchanan, and O. Jardetzky, *J. Chem. Inf. Comput. Sci.*, 1988, **28**, 194.
91. O. Lichtarge, C. W. Cornelius, B. G. Buchanan, and O. Jardetzky, *Protein. Struct. Funct. Genet.*, 1986, **2**, 340.

Biographical Sketches

George C. Levy. *b*. 1944. A.B., 1965. Ph.D. 1968, Chemistry, UCLA, USA. Research staff, General Electric Corporate R&D, 1968–73, associate professor and professor, Florida State University, 1973–81; professor, Syracuse University, 1981–94; founder and chairman, board of directors, New Methods Research, Inc. 1983–92; president, Infomatrix, Inc., Ann Arbor, MI, 1994. Approx. 240 publications including seven books co-authored and edited. Alfred P. Sloan Fellow (1975–7) and Camille and Henry Dreyfus Teacher Scholar, 1976–81. In 1990 received Thomas L. Saaty Prize for Applied Advances in the Mathematical and Management Sciences, from the *American Journal of Mathematical and Management Sciences.*

Deborah J. Kerwood. *b* 1959. B.S., 1981, Ph.D., 1986, Chemistry, Wesleyan University, USA. Postdoctural research scientist, University of California at San Francisco, research scientist, Veterans Administration Hospital, San Francisco, NMR Laboratory Operational Manager, Syracuse University, 1992–present. Approx. 15 publications. Research specialties: structure determination via NMR techniques, ^{13}Crelaxation NMR.

Muppirala Ravikumar. *b* 1958. B.E.(Hons.) Chemical Engineering, M.Sc.(Hons) Chemistry Birla Institute of Technology and Science, Pilani, 1982; Ph.D., chemistry, Tata Institute of Fundamental Research, Bombay, India, 1988. Research associate, Carnegie Mellon University, Pittsburgh, PA, USA, 1988–93; research associate, Syracuse University, NY, USA, 1993–present. Research interests: investigatng physical principles of NMR and their application to problems in biology and chemistry, new multidimensional NMR techniques, structure-dynamics of proteins and nucleic acids.

Diffusion-Ordered Spectroscopy (DOSY)

Gareth A. Morris

University of Manchester, Manchester, UK

1 Introduction 1
2 Historical Background 2
3 Data Analysis 3
4 Experimental Methods 4
5 Examples 8
6 Related Articles in this Volume 9
7 Related Articles in Volumes 1–8 9
8 References 9

1 INTRODUCTION

High resolution NMR spectroscopy is one of the most powerful tools available for chemical structure elucidation. The great majority of high resolution NMR experiments are carried out on more or less pure materials, in which the signals of a single species dominate. NMR has until recently been much less widely used in the study of mixtures, but two techniques are changing this. The first is HPLC-NMR, in which NMR experiments are performed directly on the eluent stream from a chromatography column, in either continuous- or stopped-flow mode. HPLC-NMR is capable of handling complex mixtures, and offers great flexibility through the use of different stationary and mobile phases, but requires special hardware and is expensive both in instrument time and in solvent consumption. In the second, diffusion-ordered spectroscopy (DOSY), the results of pulsed field gradient spin echo experiments are analyzed to determine diffusion coefficients for the individual signals in a spectrum, and hence to distinguish between the signals of different components in a mixture. In most applications, two- or three-dimensional spectra are synthesized in which signals are dispersed in one dimension according to their diffusion coefficients. DOSY uses standard spectrometer hardware and sample handling, requiring only the additional software for data analysis and spectrum synthesis; the field has been authoritatively reviewed by Johnson.[1]

DOSY and HPLC-NMR may be viewed as analogues, DOSY effecting a virtual separation as opposed to the true physical separation used by HPLC. The versatility that changes in stationary and mobile phase afford when separating substances by HPLC is to some extent paralleled by the possibility of manipulating the relative diffusion coefficients of different species by changing solvent, or by adding agents to bind species preferentially. The two techniques are largely complementary, HPLC-NMR generally being the more powerful but slower and more expensive technique. In principle it would be possible to achieve higher resolution by combining stopped-flow HPLC-NMR with DOSY than either technique can provide in isolation.

Figures 1 and 2 illustrate some of the basic principles of DOSY. A series of measurements is made of pulsed field gradient stimulated echo spectra (Figure 1), in which diffusion causes signals to be attenuated. Fitting the signal peak heights as a function of gradient pulse area to the theoretical Gaussian form allows a diffusion coefficient and a standard error to be calculated for each peak in the spectrum. A two-dimensional diffusion-ordered spectrum can then be synthesized (Figure 2) in which the normal spectrum (top) is used to determine the horizontal (chemical shift) domain lineshape for each peak, and the diffusion coefficient and standard error are used to define the position and width of a Gaussian lineshape in the vertical (diffusion) domain. All signals for a given molecule should then appear in a horizontal line, at the same diffusion coefficient D; cross-sections through the 2D spectrum at different values of D then separated subspectra for the different species in a mixture. This simple and effective approach is however restricted to the high resolution case where peaks are well-resolved in the chemical shift domain: where signals overlap in the normal spectrum, analysis can be much more problematic.

The name DOSY deliberately invites comparison with 2D NMR methods such as COSY (correlation spectroscopy) and NOESY (nuclear Overhauser effect spectroscopy). There is however an important distinction to be drawn between the true 2D techniques, in which the positions of signals in the indirectly detected frequency domain (F_1) are encoded as frequencies of amplitude or phase oscillation as a function of the evolution time t_1, and DOSY, in which the positions of signals in the diffusion domain must be determined from the rate with which signal amplitude decreases as the strength of the applied magnetic field gradients is increased. F_1 frequencies in COSY etc. may be straightforwardly and unambiguously obtained by Fourier transformation of the signal oscillations as a function of t_1 (as well as by more sophisticated techniques such as linear prediction, maximum entropy or the filter diagonalization method), but there is no such general way to invert the corresponding experimental data in DOSY experiments. The Fourier transform is highly effective at unraveling superimposed oscillations, which may be treated as complex exponentials, but unfortunately the corresponding method for superimposed real exponential decays, the inverse Laplace transform, is numerically intractable.

DOSY therefore is forced to rely on simplifying approximations when attempting to interpret signal decay in terms of diffusion. By far the most common approximation is to assume, as in Figure 2 above, that each signal originates from a single species; this can allow very accurate estimation of diffusion coefficient, but risks misleading the experimenter if a given signal actually contains contributions from more than one species. Where two signals with different diffusion coefficients overlap, fitting the data to the form expected for a single decay will yield a compromise diffusion coefficient intermediate between the two true values. It seems unlikely that a practical, general solution will be found to the problem of unambiguously inverting an experimental decay of signal amplitude with gradient pulse area into an accurate distribution of signal strength as a function of diffusion coefficient, but a number of useful approximations are available.

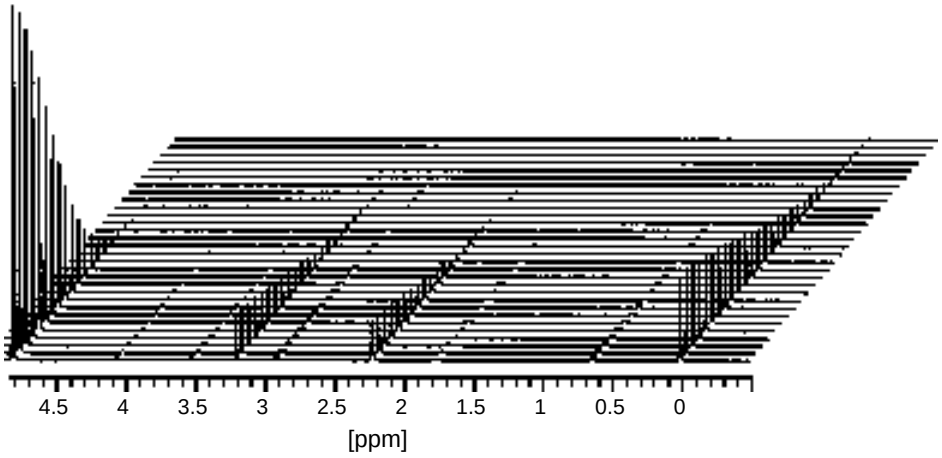

Figure 1 500 MHz ^{1}H pulsed field gradient spin echo spectra for a mixture of acetone (A), choline (C) and DSS (2,2-dimethyl-2-silapentane-5-sulfonate sodium salt, D) in D_2O; a signal is also seen for residual HDO (W). 30 spectra were acquired using the PFGLED sequence of Figure 3(b) using gradient strengths incremented linearly from 0.5 to 15 G cm^{-1}

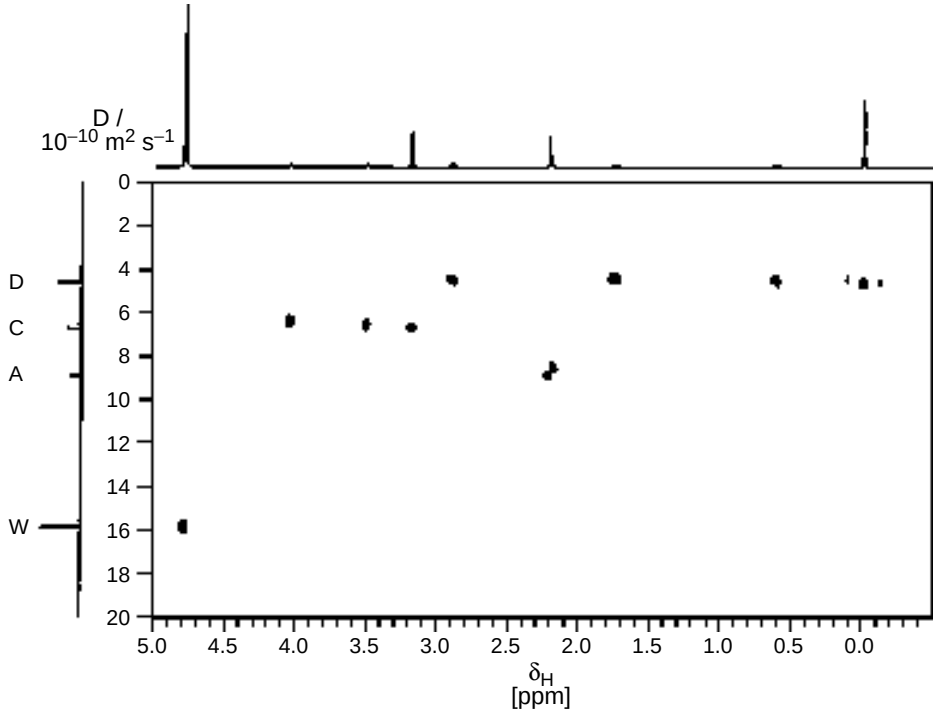

Figure 2 DOSY spectrum calculated from the data of Figure 1

DOSY is, in essence, nothing more than a new form of data presentation applied to a much older family of techniques, that of pulsed field gradient measurements of diffusion coefficient. However, by highlighting the use of such methods for the analysis of mixtures and focusing attention on some of their limitations, DOSY has led both to significant improvements in techniques for diffusion measurement and to a much wider range of applications.

2 HISTORICAL BACKGROUND

It was recognized very early in the development of NMR that diffusion contributes to the attenuation of spin echo signals when experiments are performed in an inhomogeneous magnetic field. Spins that move through a spatially-varying magnetic field during a spin echo experiment will suffer changes in Larmor frequency, leading to changes in signal phase that depend on the motion undergone. Diffusive motion will lead to a distribution of different signal phases, and hence to a diminution in net signal. This principle has been extensively exploited, and NMR remains one of the most widely-used of techniques for measuring diffusion.[2,3]

Experiments carried out using a static field which remains inhomogeneous throughout are limited in application, as the line broadening caused by the field inhomogeneity leads to signal overlap and reduces signal-to-noise ratio. The introduction

of pulsed magnetic field gradients allowed spin echo signals to be measured under high resolution conditions, retaining high sensitivity and allowing signals with different Larmor frequencies to be distinguished. Pulsed field gradient spin echo experiments come in a variety of forms, but all share the same basic features. After initial excitation, the evolution of the spins falls into three distinct phases: a defocusing period, in which field gradient pulses are used to give each spin a position-dependent phase; a delay, during which diffusion takes place; and a refocusing period, in which gradient pulses are applied to reverse the original phase encoding. For a single rectangular field gradient pulse of width δ and amplitude G, the extent of defocusing or refocusing produced is described by the gradient pulse area $q = \gamma\delta G$; an effective gradient pulse area may be defined for more complex sequences of gradient pulses. Spins that experience no net movement during the diffusion period refocus exactly, but where diffusion takes place, a distribution of signal phases results and the net magnetization is therefore attenuated. The net signal attenuation as a result of unrestricted diffusion shows a Gaussian dependence on q (an exponential dependence on q^2):

$$\mathrm{S}(q) = \mathrm{S}(0)\exp[-D\Delta' q^2] \tag{1}$$

where D is the diffusion coefficient, and the effective diffusion time Δ' is the time Δ between the midpoints of the defocusing and refocusing periods less a small correction for diffusion during the gradient pulses. It is important to choose values for q^2 that give an accurate record of diffusional attenuation for all species of interest, without wasting time acquiring spectra which are uninformative.[1]

The idea that pulsed field gradient echo spectra could be used for the analysis of mixtures dates back at least to the 1981 work of Stilbs,[4] but the concept of a diffusion-ordered spectrum was only introduced by Johnson in 1992.[5] Two distinct strands may be distinguished in the development of DOSY: high resolution DOSY, in which relatively complex mixtures can be analyzed with good diffusion accuracy using well-resolved spectra where the majority of peaks arise from a single species, and low resolution DOSY, in which the overlap or complete superimposition of signals limits the reconstruction of the diffusion dimension of the DOSY spectrum to a relatively low resolution. Between these two poles a variety of approaches may be used to constrain the analysis in order to maximize the amount of chemically useful information to be obtained from the experimental data.

3 DATA ANALYSIS

3.1 High Resolution DOSY

The simplest approach to analyzing the results of DOSY experiments is to assume that each individual peak in the NMR spectrum arises from a single species, and hence has an amplitude which varies with gradient pulse area according to equation (1). In simple mixtures with well-resolved signals this is straightforward, and gives the maximum interpretable information for a minimum of effort. The basic data processing follows the pattern described briefly in the Introduction. After measurement, experimental free induction decays are weighted and Fourier transformed as normal; where most signals have the same common linewidth, mild resolution enhancement may be useful. Careful baseline correction is then carried out, to minimize distortions of the diffusion spectrum caused by instrumental shortcomings and crosstalk between signals. Peak heights are tabulated as a function of gradient pulse area for each peak identified in the spectrum, and two-parameter exponential least squares fitting as a function of q^2 is carried out. This yields an apparent diffusion coefficient and a standard error for each peak, which may then be used in synthesizing a DOSY spectrum. For each peak j in the normal spectrum (for convenience, the spectrum with lowest q is generally used) a two-dimensional peak is constructed which has the same shape in the NMR dimension as that $\mathrm{S}_j(F)$ in the normal spectrum, a volume proportional to the peak height in the normal spectrum, and a Gaussian shape in the diffusion dimension which is centered on the fitted diffusion coefficient D_j and has a width determined by the standard error σ_j. The final 2D DOSY spectrum is then the sum of N such 2D peaks:

$$\mathrm{S}(D, F) = \sum_{j=1}^{N} \frac{\mathrm{S}_j(F)}{\sqrt{2\pi\sigma_j^2}} \exp\left[\frac{-(D - D_j)^2}{2\sigma_j^2}\right] \tag{2}$$

Several refinements of this basic approach are possible. Even the best available spectrometer hardware is unable to switch as rapidly as required between a field gradient pulse and high resolution conditions, with the result that spectra show small distortions because of the slow recovery of the main magnetic field B_0 to maximum homogeneity. These distortions may be corrected by reference deconvolution[6] (qv) if there is a suitable reference signal available in the spectrum. To the normal requirement that the reference signal should be a strong, well-resolved singlet, must be added the stipulation that the reference material should preferably diffuse no more rapidly than the slowest of the species under study, so that the reference signal remains strong in all the experimental spectra. One candidate for such a material in non-polar solvents is polydimethylsiloxane. In practice, 2–3 fold improvements in diffusion resolution may readily be obtained using reference deconvolution.

Another common instrumental shortcoming that reduces resolution in the diffusion domain of a DOSY spectrum is non-uniformity of the pulsed linear field gradient, i.e., the presence of gradients of higher orders than one. Variations of 10% across the active volume of the probe are common, with larger discrepancies outside the observe coil. The effect of such variation is make the signal attenuation dependence on q deviate from a Gaussian: effectively the decay becomes the sum of different Gaussians from different regions of the sample. For signals that are only mildly attenuated this is of little consequence: relatively clean Gaussian behavior is seen, corresponding to a gradient strength averaged over the sample. Where, however, signals undergo severe attenuation, the weaker gradient in some parts of the sample leads to significantly stronger signals than expected at high nominal gradient strengths. These deviations from Gaussian behavior lead to an increased error in the fitting process, and are one of the causes of the common observation that DOSY signals are broader in the diffusion domain at high diffusion coefficient. The loss of resolution can be reduced by empirically adjusting the apparent values of q^2 to force the experimental signal decay to adopt the expected Gaussian shape: this improves

the accuracy of fit, and hence the accuracy with which relative diffusion coefficients are determined, at the expense of a small loss in absolute accuracy. A much more effective solution, however, is to determine the form of the distribution of signal strength as a function of gradient strength, and then use this information to calculate the predicted form of the signal attenuation curve as a function of q^2. This may conveniently be done by mapping the experimental distributions of signal strength and gradient strength as functions of position within the sample, and then integrating over the sample to find the overall signal attenuation curve. Fitting to this function, which may conveniently be represented as the exponential of a power series, rather than to a Gaussian, then gives much better statistics for signals that experience strong attenuation. The benefits are particularly apparent when studying mixtures with a wide range of diffusion coefficients, since at high q the signal intensities of rapidly diffusing species will be dominated by contributions from the regions of the samples experiencing the lowest gradients.

Data processing strategies in DOSY depend on the nature of the sample, the characteristics of the spectrum, and the signal-to-noise ratio of the NMR data. Where resolution is good but signal-to-noise ratio poor, as for example with ^{13}C or ^{29}Si, there is little need for baseline correction and little advantage in using reference deconvolution. Conversely, for ^{1}H systems with very high signal-to-noise ratios, baseline correction is important and the improvement in diffusion resolution obtainable by combining reference deconvolution and gradient mapping can approach an order of magnitude.

3.2 Low Resolution DOSY

The problem of identifying an arbitrary distribution of signal intensity as a function of diffusion coefficient (a "diffusion spectrum") from measurements of signal attenuation as a function of gradient pulse area is one that has already been intensively studied in a different context, that of dynamic light scattering. Given the absence of a method for computing accurate inverse Laplace transforms from experimental data, the challenge is to use suitable approximations, constraints and prior knowledge to enable realistic diffusion spectra to be constructed. For polydisperse systems, where there is a continuous distribution of diffusion coefficients, only very general constraints can be applied, typically that the diffusion spectrum remain positive and that it be as simple and featureless as is compatible with the experimental data. This conservative approach minimizes the risk of misinterpretation, but yields large uncertainties in the diffusion coefficients of any monodisperse components in a mixture. The two approaches that have proved most successful in DOSY analysis of polydisperse systems are CONTIN[7] and maximum entropy.[8]

3.3 Intermediate Approximations

Many mixture analysis problems lie between the two extremes of a fully-resolved and an unresolved NMR spectrum. Some spectral lines are well-resolved, others are the sum of two or more components, which may be partially resolved. Under such circumstances low resolution DOSY has little to offer unless the system exhibits only a few diffusion coefficients which are of very different magnitudes. The straightforward monoexponential analysis as a function of q^2 described above is more successful in providing useful chemical information, since where two signals with different diffusion coefficients contribute to a given peak the apparent diffusion coefficient will be intermediate between the two values. Since the effects of overlap are simple where only two signals are involved, DOSY spectra with a minority of signals overlapping are relatively straightforward to interpret, but the ability to extract a complete subspectrum for a given diffusion coefficient is lost.

Between the Procrustes bed of a single exponential fit and the open-ended analyses of CONTIN and maximum entropy lie a range of methods designed to fit the experimental data to more or less constrained models, using prior knowledge of the likely form of the diffusion spectrum to allow the maximum of useful information to be extracted from the experimental data. In moderately crowded spectra the majority of cases of overlap will only involve two signals, so a logical first step is to replace monoexponential fitting with biexponential. Simple four parameter biexponential fitting can be quite satisfactory provided that the two diffusion coefficients differ by a factor of two or more, but the generation of initial guesses for the iterative fitting risks introducing bias. A safer solution is the general package for multiexponential fitting SPLMOD (SPLine Model), which has been used successfully[9] for DOSY by incorporating pragmatic rules for the rejection of spurious fits. A variety of more sophisticated approaches to analyzing multiple overlapping exponentially decaying spectra have been proposed, including the DECRA (direct exponential curve resolution algorithm),[10] MCR (multivariate curve resolution)[11] and CORE (component resolved NMR)[12] methods, but have yet to be widely applied.

4 EXPERIMENTAL METHODS

4.1 Homonuclear 2D DOSY

The earliest experiments used the basic Carr-Purcell pulse sequence in the presence of a continuous field gradient. The introduction of pulsed field gradients has already been mentioned; the next improvement was the shift to using a stimulated $(90 - \tau - 90 - \Delta - 90 - \tau)$ rather than a Carr-Purcell $(90 - \tau - 180 - \tau)$ echo sequence. This carries a factor of two penalty in sensitivity, since on average only half of the initial transverse magnetization is refocused in a stimulated echo, but minimizes the time for which the magnetization remains transverse. This is of value for systems where T_2 is significantly shorter than T_1, but is particularly useful for systems with homonuclear scalar coupling. Restricting the time that magnetization spends in the transverse plane minimizes the impact of J modulation, and hence avoids the introduction of multiplet phase errors. Since high resolution DOSY generally relies on peak heights as a guide to signal intensity, any dispersion mode character to the experimental lineshape greatly increases the risk of signal overlap, and hence of crosstalk between adjacent peak heights and distortion of the diffusion spectrum.

The parent pulse sequence for most DOSY experiments is the pulsed field gradient stimulated echo (PFGSTE) sequence of Figure 3(a), in which the delays τ are just long enough to encompass the transmitter pulse fall time, the width δ of the gradient pulse, and the recovery time for the gradient pulse.

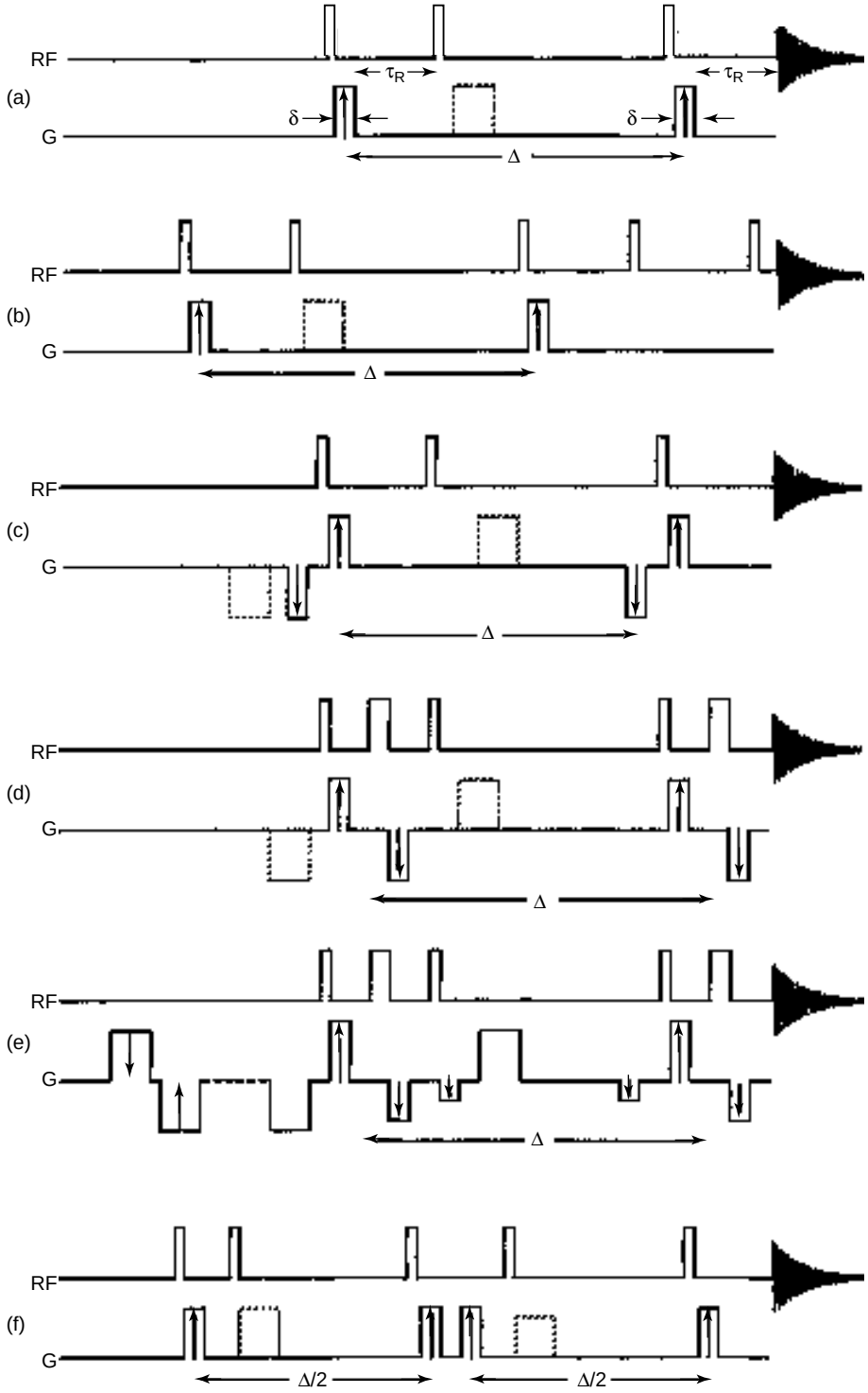

Figure 3 Radiofrequency (RF) and gradient (G) pulse sequences for DOSY: (a) pulsed field gradient stimulated echo (PFGSTE); (b) pulsed field gradient longitudinal echo delay (PFGLED); (c) gradient compensated stimulated echo sequence (GCSTE); (d) bipolar pulse pair stimulated echo (BPPSTE); (e) one-shot BPPSTE; (f) convection compensated double stimulated echo. 90° pulses are indicated by narrow rectangles in the RF traces and 180° by broad. Purge/homospoil pulses as an alternative or adjunct to phase cycling are indicated with dotted lines; up/down arrows indicate gradient pulse amplitudes that are increased/decreased to obtain increased diffusional weighting of signals. In the defocusing and refocusing periods, the spacing between RF pulses is given by the sum of the gradient pulse width δ and the gradient recovery delay τ_R, as shown for sequence (a)

If the diffusion delay Δ is defined as the time between the midpoints of the two gradient pulses, the correction to the diffusion time for diffusion during the gradient pulses is $-\delta/3$, giving $\Delta' = \Delta - \delta/3$ and the familiar attenuation expression

$$S(q) = S(0)\exp[-Dq^2(\Delta - \delta/3)] \quad (3)$$

This basic sequence is perfectly serviceable for many purposes, but is capable of considerable improvement. Two problems which are of particular importance under high resolution NMR conditions are those of slow main field recovery from the gradient pulses, causing distortion of the early part of the free induction decay, and interference with the deuterium field frequency lock. In general the former effect is brief, giving a broad distorted base to lines, and the latter relatively long-lived, giving sharp but "unphaseable" lineshapes.

The problem of main field disturbance, usually due to eddy currents induced in the probe and magnet metalwork, is much less severe in modern instruments, which have self-shielded ("actively shielded") gradient coils. These minimize magnetic flux leakage outside the gradient coil, and hence give rise to much weaker eddy currents. For probes with unshielded gradient coils, a very effective way to circumvent problems from eddy currents is to add a z-filter to the stimulated echo sequence, storing the refocused magnetization for some tens of ms until the field is stable. Such a LED (longitudinal echo delay)[13] step may be included in a variety of DOSY pulse sequences; the simplest is the PFGLED sequence of Figure 3(b).

A more general solution to the problem of eddy currents in modern high resolution spectrometers, which also deals with the problem of gradient pulses suppressing the deuterium lock signal and hence introducing slow B_0 shifts, is to use bipolar pairs of field gradient pulses. Using closely-spaced matched pairs of gradient pulses of opposite polarity cancels eddy current effects to first order, and refocuses the deuterium lock signal in a gradient echo. Such opposed pulse pairs may have one partner outside the defocusing/refocusing periods, or have both pulses within the defocusing/refocusing period but bracketing a 180° radiofrequency pulse. Sequences using the latter construct are generally referred to as bipolar sequences, since the diffusion encoding is carried out by the bipolar pulse pair; such sequences have a number of advantages. In second-order scalar coupled systems, relaxation effects can lead to zero quantum coherence causing phase errors in simple stimulated echo pulse sequences; by refocusing chemical shifts, bipolar sequences avoid exciting such coherences and hence do not suffer from phase errors in strongly coupled multiplets. Bipolar sequences also reduce contributions to diffusion-encoding from static background field gradients; these are not a problem under high resolution conditions, but in heterogeneous systems with strong internal field gradients caused by magnetic susceptibility differences they can complicate matters significantly. Adding balancing gradient pulses to the PFGSTE sequence gives the gradient compensated stimulated echo (GCSTE) sequence of Figure 3(c), which is a good general purpose sequence for systems lacking strong coupling; in the latter case the bipolar pulse pair stimulated echo (BPPSTE) sequence of Figure 3(d) is preferable.

With all pulse sequences for high resolution DOSY it is important to ensure that the desired coherence transfer pathway is followed. At first sight this might seem unimportant for a sequence such as PFGSTE, since the gradient pulses might be expected to suppress the coherence transfer antiecho. However, even with strong gradient pulses the attenuation envelope for rejected signals only decays as the inverse of the pulse area. Small amounts of unwanted signal can therefore survive the pulse sequence, causing small intensity and phase anomalies and distorting the resultant diffusion spectrum. For the best results with PFGSTE-based sequences it is therefore important to use phase cycling. With BPPSTE, the issue is more critical, since without phase cycling any magnetization that does not experience perfect 180° pulses during the defocusing and refocusing periods will form a gradient echo over the relevant period and will not experience significant diffusional attenuation.

Where speed of measurement is important – and useful DOSY data can be obtained in as little as 30 s – a purge/homospoil pulse may be used in the diffusion delay to enforce zero coherence order in this period, and in bipolar sequences the positive and negative gradient pulses may be unbalanced in order to dephase magnetization not refocused by the 180° pulses. A final refinement is to add dummy pulses, where gradient amplifier duty cycle permits, before the start of a pulse sequence. These may be ramped down in amplitude as the diffusion-encoding pulses are ramped up, in order to keep the net energy dissipated the same for each transient; the pulses precondition the gradient amplifier and coil, and reduce gradient pulse area mismatch problems. A bipolar sequence which incorporates all three of these modifications and is suitable for "one-shot" (single transient per gradient value) use is shown in Figure 3(e).

The limitations imposed by non-uniformity of the pulsed field gradient are most effectively dealt with as described in Data Analysis, since this retains full sensitivity and resolution in the NMR data. A much simpler method of reducing the impact of gradient non-uniformity is to restrict the active volume of the sample to the most homogeneous region of the gradient (i.e., the region where the applied gradient is closest to linear). This may be achieved either by using selective excitation in the presence of a field gradient to select just a slice of the sample, or by physically restricting the length of the sample. In the former case care must be taken to avoid spurious echo phenomena, while in the latter case even the best susceptibility matching still results in a substantial degradation of the NMR lineshape.

A more serious limitation on DOSY measurements is the requirement that the motion of the spins in the sample be dominated by diffusion. Typical high resolution DOSY experiments use diffusion times Δ of a few tenths of a second, so for small molecules the mean square displacement over the timescale of the experiment is about 20 μm. Coherent motion of the spins with a velocity of the order of 1 $\mu m\,s^{-1}$ is thus sufficient to interfere with diffusion measurements even for small molecules; studies on macromolecules, and on nuclei with low magnetogyric ratio, can be vitiated by much slower motion (of the same order as continental drift). There is thus a severe potential problem of convection when attempting to use DOSY at temperatures above or below room temperature.

Where mobile solvents such as methanol or acetone are used, the onset of convection in a normal NMR tube with commercial probes is typically only a few degrees away from the quiescent sample temperature. The first sign of convection is usually the appearance of small phase errors

at higher gradient strengths; for low velocities, the phase error is proportional to the product of the gradient pulse width, diffusion time and gradient amplitude. Unfortunately, apparent phase errors are a common symptom of other instrumental problems, including lock disturbance, slow B_0 recovery, and gradient pulse area mismatch. The onset of convection can be delayed by using a capillary tube, particularly if the capillary is surrounded by a mobile (but NMR-silent) solvent, since the convection of the outer liquid helps reduce the temperature gradient along the capillary sample. A more general solution to the problem of coherent motion of the spins during DOSY experiments is to build velocity compensation into the pulse sequence. The sequence of Figure 3(f) uses a double stimulated echo[14] to refocus the phase gradient caused by coherent motion. Such sequences, which can be extended by analogy with sequence 3(e) to avoid lock disturbance and hence give improved lineshapes, allow DOSY measurements to be performed over a much wider temperature range.

4.2 Heteronuclear 2D DOSY

The principal factor limiting the application of DOSY to the analysis of complex mixtures is the requirement that spectra be well-resolved if good diffusion resolution, and hence good discrimination between mixture components, is to be obtained. One way to improve resolution is to select for observation a nucleus such as carbon-13 that has a relatively high ratio of chemical shift dispersion to linewidth. Unfortunately there is a double price to pay on moving from protons to carbon-13, in the form of greatly reduced signal-to-noise ratio and a four-fold decrease in sensitivity to field gradients. The latter problem can be eliminated, and the former somewhat reduced, if the carbon-13 signals measured are the result of polarization transfer from protons. Combining a proton pulsed field gradient stimulated echo sequence with INEPT (insensitive nuclei enhanced by polarization transfer) or DEPT (distortionless enhancement by polarization transfer) transfer to carbon-13 allows carbon signals to be measured which enjoy the usual signal enhancement and recycle time advantages of polarization transfer techniques, and show the same sensitivity to diffusion as proton signals. DOSY-DEPT and DOSY-INEPT[15] can, where sensitivity permits, be very effective mixture analysis tools. One complication is the need to keep power deposition in the sample from decoupling to a minimum, since quite modest decoupling powers are sufficient to generate convection in mobile solvents.

4.3 3D DOSY

A more general approach to improving spectral resolution in DOSY is to extend experiments into a further spectral dimension. 3D DOSY experiments involve the measurement of a series of conventional two-dimensional spectra with increasing diffusion weighting, typically by prepending a pulsed field gradient stimulated echo sequence to the preparation period of a normal 2D experiment. Cross- and diagonal-peak volumes are then fitted to extract diffusion coefficients and standard errors and a 3D DOSY spectrum synthesized in a manner exactly analogous to 2D DOSY. DOSY-COSY,[16] DOSY-NOESY[17] and DOSY-TOCSY (total correlation spectroscopy)[18] experiments have all been described, although most applications have been restricted to labeling 2D peaks with diffusion coefficients rather than carrying out the synthesis of a full 3D spectrum. The highest

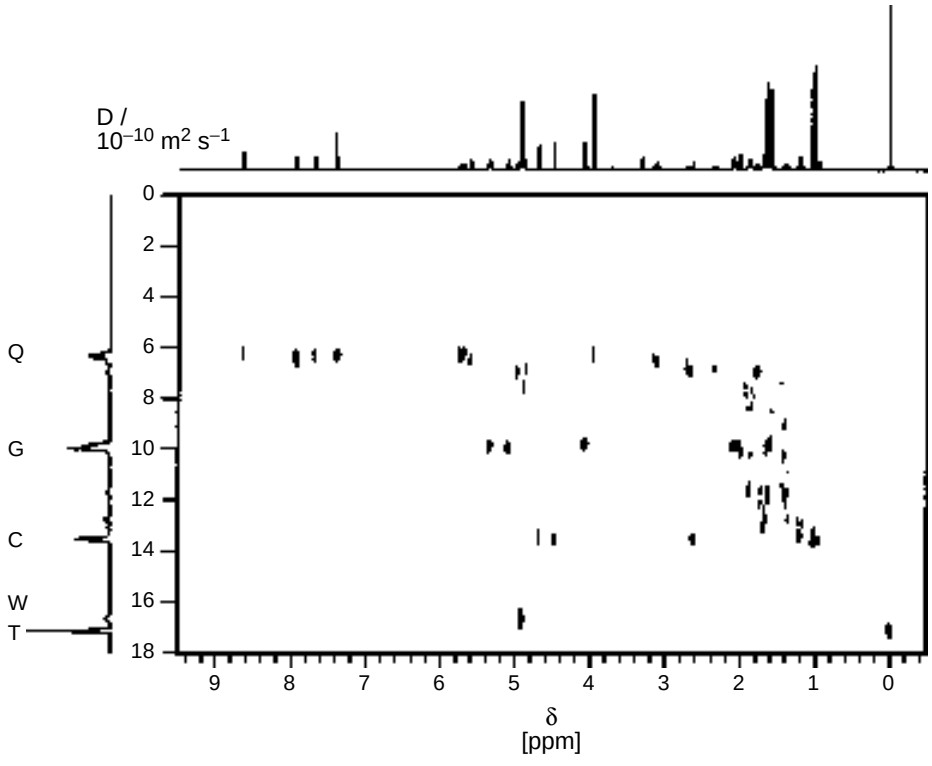

Figure 4 400 MHz proton DOSY spectrum of a mixture of quinine (Q), geraniol (G) and camphene (C) in deuteriomethanol; signals are also seen for HDO (W) and TMS (T)

net resolution technique reported to date is DOSY-HMQC (heteronuclear multiple quantum coherence),[19] which disperse signals according to proton shift, carbon-13 shift and diffusion coefficient.

5 EXAMPLES

Figure 4 shows a typical high resolution proton 2D DOSY spectrum for a simple mixture, illustrating some of the strengths and weaknesses of DOSY as a tool for the analysis of simple mixtures. The sample, a mixture of quinine, geraniol and camphene in deuteriomethanol, also contained TMS (tetramethylsilane) as reference, and residual water and monoprotiomethanol. Spectral data were acquired at 400 MHz using the GCSTE sequence of Figure 3(c); 10 spectra of 16 transients covering the range 0.6–10 G cm^{-1} in equal steps of gradient squared were measured with a diffusion time Δ of 0.5 s and gradient pulse widths δ of 2 ms, in a total time of 45 min. These parameters were chosen to give only modest (ca. 50%) attenuation for the signals of the slowly-diffusing quinine, in order to ensure that there was sufficient TMS signal for reference deconvolution at the higher gradient strengths. Spectra were processed with reference deconvolution based on the TMS line to give a Lorentzian lineshape of 1 Hz at half height, baseline corrected using cubic spline interpolation, and fitted with a modified exponential derived from gradient mapping experiments as described in Section 3.1.

Overall, the distribution of signals in the diffusion domain of spectrum of Figure 4 is dominated as expected by the

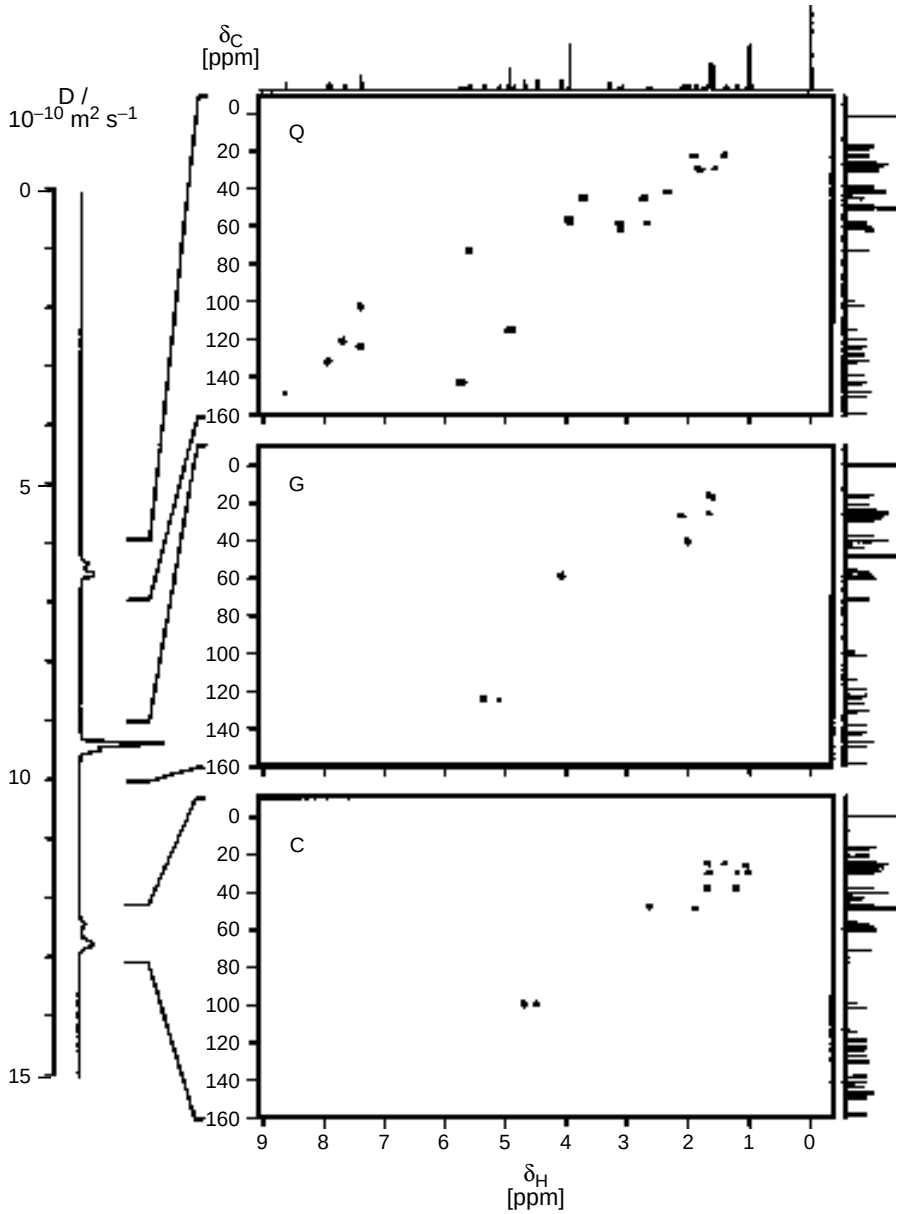

Figure 5 400 MHz ^{1}H-^{13}C DOSY-HMQC data for the same mixture as Figure 4, with (left) the integral projection of the 3D spectrum onto the diffusion axis, and (right, from top) integral projections onto the ^{1}H-^{13}C plane for the diffusion regions 5.9–6.9 × 10^{-10} (quinine, Q), 9.0–10.0 × 10^{-10} (geraniol, G), and 12.1–13.1 × 10^{-10} m^2 s^{-1} (camphene, C)

diffusion coefficients of the four main species present, quinine, geraniol, camphene and TMS. These appear as four strong distinct peaks in the integral projection of the spectrum onto the diffusion axis, shown at the left. Above 2 ppm, all of the signals appear at the expected positions in the diffusion domain, with one exception. At 4.9 ppm the quinine multiplet lies on top of the broader residual water signal, with the result that the apparent diffusion coefficients of the quinine signals are increased and that of the water slightly decreased. This effect can be reduced but not eliminated by the use of resolution enhancement to reduce the overlap between the signals; however, the shifts in the signals are simple, predictable and easily accounted for, and do little to damage the interpretability of the spectrum. Below 2 ppm the large number of aliphatic proton signals from the three main species gives rise to more severe overlap, with the result that a significant number of signals are displaced to lie at averaged apparent diffusion coefficients. As the diffusion projection shows, 95% of the overall signal intensity remains at the correct diffusion coefficient; in this sample only low intensity signals show significant deviations from their expected positions, although the difficulty of reproducing contour plots for spectra with such high chemical shift resolution exaggerates their apparent importance.

Where sensitivity considerations permit, 3D DOSY methods offer a large improvement in resolution. Figure 5 shows data from a 3D DOSY-HMQC (heteronuclear multiple quantum coherence) experiment[19] on a similar sample of quinine, geraniol and camphene. Five diffusion-weighted HMQC datasets of 512×1024 complex data points were acquired in a total time of 17 h, with a diffusion time of 45 ms and pulse gradient strengths from 1 to 30 G cm^{-1}. Peak volumes were determined for all cross peaks and fitted to a simple exponential as a function of q^2. The extra resolution afforded by separating signals according to both ^{1}H and ^{13}C chemical shifts now ensures that all signals, including those for the aliphatic protons, are well-resolved. Thus while the relative accuracy with which diffusion coefficients are determined is reduced compared to Figure 4 because of the small number of different gradient strengths used, the 3D experiment nevertheless successfully resolves all the signals in the mixture.

6 RELATED ARTICLES IN THIS VOLUME

Diffusion-Based Studies of Aggregation, Binding and Conformation of Biomolecules: Theory and Practice; Reference Deconvolution.

7 RELATED ARTICLES IN VOLUMES 1–8

Diffusion & Flow in Fluids, Volume 3; Diffusion Measurements by Magnetic Field Gradient Methods, Volume 3; Electrophoretic NMR, Volume 3; Field Gradients & Their Application, Volume 3.

8 REFERENCES

1. C. S. Johnson Jr., *Prog. NMR Spectrosc.*, 1999, **34**, 203.
2. W. S. Price, *Concepts Magn. Reson.*, 1997, **9**, 299.
3. W. S. Price, *Concepts Magn. Reson.*, 1998, **10**, 197.
4. P. Stilbs, *Anal. Chem.*, 1981, **53**, 2135.
5. K. F. Morris and C. S. Johnson Jr., *J. Am. Chem. Soc.*, 1992, **114**, 3139.
6. G. A. Morris, H. Barjat, and T. J. Horne, *Prog. Nucl. Magn. Reson. Spectrosc.*, 1997, **31**, 197.
7. K. F. Morris and C. S. Johnson Jr., *J. Am. Chem. Soc.*, 1993, **115**, 4291.
8. M. A. Delsuc and T. E. Malliavin, *Anal. Chem.*, 1998, **70**, 2146.
9. K. F. Morris and C. S. Johnson Jr., *J. Am. Chem. Soc.*, 1993, **115**, 4291.
10. B. Antalek and W. Windig, *J. Am. Chem. Soc.*, 1996, **118**, 10 331.
11. L. C. VanGorkom and T. M. Hancewiecz, *J. Magn. Reson.*, 1998, **130**, 125.
12. P. Stilbs, K. Paulsen, and P. C. Griffiths, *J. Phys. Chem.*, 1996, **100**, 8180.
13. S. J. Gibbs and C. S. Johnson Jr., *J. Magn. Reson.*, 1991, **93**, 395.
14. A. Jerschow and N. Müller, *J. Magn. Reson.*, 1997, **125**, 372.
15. D. Wu, A. Chen, and C. S. Johnson Jr., *J. Magn. Reson., A* 1996, **123**, 215.
16. D. Wu, A. Chen, and C. S. Johnson Jr., *J. Magn. Reson., A* 1996, **121**, 88.
17. E. K. Gozansky and D. G. Gorenstein, *J. Magn. Reson., B* 1996, **111**, 94.
18. A. Jerschow and N. Müller, *J. Magn. Reson., A* 1996, **123**, 222.
19. H. Barjat, G. A. Morris, and A. G. Swanson, *J. Magn. Reson.*, 1998, **131**, 131.

Biographical Sketch

Gareth A. Morris, *b* 1954. M.A. (Nat. Sci.), Ph.D. (supervisor Ray Freeman) 1978, Oxford University, UK. Fellow by Examination, Magdalen College, Oxford, 1978–1981; Izaak Walton Killam Postdoctoral Fellow, University of British Columbia (with Laurie Hall) 1978–79. Lecturer (1982–1989) and Reader (1989–1997) in Chemistry, Professor of Physical Chemistry (1998 to date), University of Manchester, UK. Approx. 130 publications. Current research interests: development of novel NMR techniques and their application to problems in chemistry, biochemistry and medicine.

Fourier Transform and Linear Prediction Methods

Jens J. Led and Henrik Gesmar
University of Copenhagen, Copenhagen, Denmark

1	Introduction	1
2	The Fourier Transform of the Free Induction Decay	1
3	The Linear Prediction Method	2
4	Least-Squares Fourier Transform Techniques	6
5	Conclusion	8
6	Related Articles	8
7	References	8

1 INTRODUCTION

In the CW NMR technique, as used in the early days of NMR (see Volume 1 of this Encyclopedia), the frequency spectrum was obtained directly as a function of the input rf or the strength of the magnetic field, B_0. For the modern high resolution pulse NMR experiment a FID is recorded as a function of time, and the frequency spectrum is calculated as the FT (see ***Fourier Transform Spectroscopy***) of this time domain signal. Despite the qualities of the FT, such as computational efficiency and numerical stability, in recent years improved spectral methods have been introduced into the analysis of NMR data. Among these methods the linear prediction method, described in this article, has been one of the most succesful.

There are two main reasons for the application of the linear prediction method to NMR data. One is to produce better spectra, i.e. to avoid the drawbacks that characterize the FT, particularly for multidimensional NMR data (see ***Multidimensional Spectroscopy: Concepts***). The other reason for the use of the linear prediction method is to estimate spectral parameters (frequencies, signal intensities, signal widths, and phases) directly from the FIDs.

The drawbacks of the FT mentioned above are aliasing, $(\sin x)/x$ modulation of the resonance signals, phase distortions, and pseudobaselines. Although we often refer to these effects as artifacts, they are caused by one of the advantages of the FT, i.e. the conservation of information. Thus, the fact that the time domain FID can be sampled only for a finite period of time and only as a limited number of discrete data points, must also be expressed in the frequency spectrum. Unfortunately, this information is kept in the form of the rather annoying effects mentioned above. These characteristics of the FT are quite general. In Section 2 of this article they are described in some detail for the special case of the NMR FID.

From the above it follows that in order to reduce the 'artifacts' in the spectrum we must apply an alternative spectral method that does not preserve all the information of the FID. In particular, we wish to suppress the information about the truncation, and preserve the information about the NMR resonance signals. As described in Section 3, this can be done by using the linear prediction method. Finally, in Section 4 it is described how a detailed knowledge of the artifacts in the FT spectrum together with the principle of least squares can be applied to gain valuable information from NMR spectra.

2 THE FOURIER TRANSFORM OF THE FREE INDUCTION DECAY

On the assumption of multiexponential decay the sampled FID F_k can be expressed as

$$F_k = F(k\Delta t) = \sum_{j=1}^{p} I_j \exp[(\mathrm{i}2\pi\nu_j - R_{2j}^*) \times (k \cdot \Delta t + T_{\mathrm{in}}) + \mathrm{i}\phi_j] \quad (1)$$

where k is an integer in the interval $[0, N-1]$, Δt is the sampling interval, I_j is the amplitude of the jth exponential, and ν_j, R_{2j}*, and ϕ_j are the frequency, the decay rate, and the phase, respectively. For severe overlap, strong coupling, or cross correlation it may not be possible to assign I_j to a specific nucleus, but this has no consequence for the following. Further, the symbol T_{in} is the initial time during which the signal has developed before the sampling is started, and i is the imaginary unit. Equation (1) represents the case of quadrature detection, where the signal is sampled as a series of complex numbers. To describe the real-valued case, which is not covered in this article, equation (1) should be added to its own complex conjugate.

Because of the discrete nature of F_k, the FT must be applied in its discrete form, i.e.

$$S_m = S\left(\frac{m}{n \cdot \Delta t}\right) = S\left(\frac{m}{T_{\mathrm{aq}}}\right) = \sum_{k=0}^{N-1} F_k \exp(\mathrm{i}2\pi km/n) \quad (2)$$

When F_k from equation (1) is introduced into equation (2), the expression can be evaluated as the finite sum of a geometrical progression. Thus, the analytical expression for the FT NMR spectrum is

$$S_m = S\left(\frac{m}{N\ \Delta t}\right) = S(\nu) = \sum_{j=1}^{p} A_j \frac{1 - \exp\{[\mathrm{i}2\pi(\nu_j - \nu) - R_{2j}^*]T_{\mathrm{aq}}\}}{1 - \exp\{[\mathrm{i}2\pi(\nu_j - \nu) - R_{2j}^*]/F\}} \quad (3)$$

Here, ν_j is the independent frequency variable in the spectrum, $T_j = N \cdot \Delta t$ is the acquisition time, $F = (1/\Delta t)$ is the spectral width, and A_j is given by

$$A_j = I_j \exp[(\mathrm{i}2\pi\nu_j - R_{2j}^*)T_{\mathrm{in}} + \mathrm{i}\phi_j] \quad (4)$$

Contrary to k, the number m is not necessarily an integer. This reflects the fact that the spectrum can be evaluated for any value of the frequency ν. However, when the fast FT procedure is applied to the N values of F_k, the spectrum is calculated only for integer values of m in the interval $[0, N-1]$. If zeros are added at the end of the FID before the FT, the right-hand side of equation (3) still holds, because only

zeros are added to equation (2), but the variable m may now be a noninteger. If for example N zeros are added after the N points of the FID, the spectrum is calculated for $m = 0, \frac{1}{2}, 1, \frac{3}{2}, \ldots, N - 1$.

Equation (3) consists of two periodic terms: one in the numerator with the period $1/T_{aq}$, and one in the denominator with the period $F = (1/\Delta t) = (N/T_{aq})$. Thus the entire expression has a period of F, i.e. the Nyquist frequency.[1] In order to avoid the implied aliasing of signals, a sufficiently short dwell time, Δt, must be chosen in order to assure that F is larger than all resonance frequencies in the spectrum. However, as shown in equation (3), the discrete spectrum still differs significantly from the theoretical spectrum, which is given as a sum of nonperiodic complex Lorentzians:

$$s(\nu) = \sum_{j=1}^{p} \exp(i\phi_j)\, I_j / R_{2j}^* \frac{1}{1 - i2\pi(\nu_j - \nu)/R_{2j}^*} \qquad (5)$$

For the discrete spectrum to approximate the theoretical spectrum, F must be large compared with the involved decay rates R_{2j}^*, and to all relevant values of $\nu_j - \nu$. The latter condition corresponds to what is often referred to as 'oversampling', and is rarely fulfilled, particularly in multidimensional spectroscopy. Nonetheless, when these conditions hold, equation (3) is reduced to

$$S(\nu) = \left(F \sum_{j=1}^{p} \frac{A_j}{R_{2j}^*} \frac{1}{1 - i2\pi(\nu_j - \nu)/R_{2j}^*} + \sum_{j=1}^{p} A_j/2 \right) \times \{1 - \exp\{[i2\pi(\nu_j - \nu) - R_{2j}^*]T_{aq}\}\} \qquad (6)$$

as shown by Gesmar et al.[2] If the FID is allowed to decay completely during the sampling, i.e. $T_{aq} \gg (1/R_{2j}^*)$, the term in the second parentheses in equation (6) is very close to unity. This is the ideal discrete FT spectrum in that it is the best approximation to a sum of complex Lorentzians as expressed in equation (5). Even in this case, however, the FT spectrum differs from the theoretical spectrum. Firstly, because a frequency-independent term $\Sigma_{j=1}^{p} A_j/2$ is present, and secondly, because each intensity I_j has been multiplied by the factor $\exp[(i2\pi\nu_j - R_{2j}^*)T_{in}]$, as can be seen from equation (4).

The first deviation results in a pseudobaseline in the FT spectrum. However, this pseudobaseline is removed in the ideal case when the first point of the FID is multiplied by $\frac{1}{2}$ before the Fourier transformation. This is particularly important for multidimensional spectroscopy, where the presence of baselines in the individual FIDs leads to ridges in the various dimensions.

The second deviation, namely the presence of the factor $\exp[(i2\pi\nu_j - R_{2j}^*)T_{in}]$, results in a frequency- and relaxation-dependent phase distortion of the FT spectrum. This phase distortion depends linearly upon the center frequencies ν_j of the individual signals, and not upon the independent spectral frequency variable ν. Therefore, the commonly used linear phase correction procedure, based on a linear relationship between the phase and the spectral frequency ν, is not always appropriate, although it suffices in most cases with modest phase distortions and narrow and well-separated signals. For extreme phase distortions, however, or for signals that are broad and poorly separated, or when small signals are situated on the tail of a larger signal, the spectrum can be correctly phased only at the center of each signal, and undulations of the signal tails will occur. In order to reduce such effects, the value of T_{in} is normally kept as small as possible, despite the fact that the first few points of the FID are often of poor quality due to the electronic filtering and, eventually, overflow in the analog-to-digital converter. Thus, not even the ideal discrete Fourier transform spectrum is the 'true' spectrum as given by equation (5).

In many cases, and particularly in multidimensional spectroscopy, the FID is not sampled until the point where it has decayed completely, i.e. $T_{aq} \approx 1/R_{2j}^*$. In such cases, $1 - \exp\{[i2\pi(\nu_j - \nu) - R_{2j}^*]T_{aq}\}$ in equation (6) cannot be neglected, which results in an apparently misphased signal. Because the phase error depends on the position of the resonance frequency ν_j relative to the specific frequencies $\nu = (m/T_{aq})$ calculated by means of the FT procedure (see above), it appears to be random and cannot be corrected in the general case. Note that for signals with $\nu_j = (m/T_{aq})$ (m is an integer), misphasing due to the truncation will not occur. Furthermore, because the pseudobaseline level $\Sigma_{j=1}^{p} A_j/2$ is also altered by $1 - \exp\{[i2\pi(\nu_j - \nu) - R_{2j}^*]T_{aq}\}$, the above-mentioned multiplication of the first data point by a factor of $\frac{1}{2}$ will not work, and the area between the signal curve and the baseline is no longer a measure of the relative signal intensity. The amount of intensity that has leaked into the pseudobaseline depends on ν_j and R_{2j}^* for individual resonances. As can be seen from equation (6), the pseudobaseline problems are reduced considerably when the spectral width F is significantly larger than the frequency range covered by the resonances, i.e. when the FID is oversampled (see above).

When m is an integer, $1 - \exp\{[i2\pi(\nu_j - \nu) - R_{2j}^*]T_{aq}\} = 1 - \exp[(i2\pi\nu_j - R_{2j}^*)T_{aq}]$ and no oscillations are observed in the spectrum. However, as already mentioned, by zero filling the FID, the frequencies $\nu = (m/T_{aq})$ in the FT spectrum can be calculated for fractional values of m also, in order to increase spectral resolution. In this case the periodicity of the factor $1 - \exp\{[i2\pi(\nu_j - \nu) - R_{2j}^*]T_{aq}\}$ is seen in the spectrum as signal side lobes ('wriggles') with a period of T_{aq}^{-1} in connection with the resonances whose components in the free induction decay have been truncated.

In the following sections it is described how the deviations between the theoretical spectrum [equation (5)] and the discrete FT spectrum can be reduced or even eliminated.

3 THE LINEAR PREDICTION METHOD

Since linear prediction was introduced into the field of NMR spectroscopy by Barkhuijsen et al., it has been used as an effective tool in the analysis of time domain NMR data.[3,4] It is applied in a number of ways, both qualitatively and quantitatively. Qualitatively it is used as a preprocessor to the FT in order to improve the resulting spectra. Quantitatively it can be used as an estimator of the spectral parameters, i.e. the frequencies, linewidths, intensities, and phases. In all cases, it eliminates or reduces considerably the deficiencies of the FT such as aliasing, truncation errors, phase distortions, and ridges in one- and multi-dimensional NMR spectra. In this section the principles of the linear prediction method are reviewed briefly. In Section 3.1 the qualitative application of

the method is illustrated, and the quantitative application of the linear prediction method is demonstrated in Section 3.2.

The FID signal F_k, given as a sum of p exponentially damped sinusoids sampled at regular time intervals [equation (1)], has the following property:

$$F_k = \sum_{m=1}^{p} f_m F_{k-m} \tag{7}$$

disregarding the effect of the noise.[5] Here f_m is the mth forward prediction coefficient. Since f_m is independent of k it can be determined from the experimental data points, and subsequently used to extrapolate the FIDs. An interesting alternative to direct extrapolation of the FID, the linear prediction z-transformation (LPZ) method, has been suggested by Tang and Norris.[6]

The prediction coefficients are related to the frequencies ν_j and the decay rates R_{2j}*, through the characteristic polynomial:

$$z^p - \sum_{m=1}^{p} f_m z^{p-m} = P(z) \tag{8}$$

since the roots C_j of this polynomial are given by[5]

$$C_j = \exp[(\mathrm{i}2\pi\nu_j - R_{2j}^*)\Delta t] \tag{9}$$

For an experimental FID, the precise number of signals contained in the FID is, in general, unknown a priori. Therefore, the applied number of prediction coefficients must be sufficiently large ($>p$) to ensure the determination of all the involved complex exponentials. This results in an excess of roots of the characteristic polynomial in equation (8). However, as shown by Kumaresan,[7] the roots are divided into two classes: one that contains the p signal roots conforming to equation (9), and another that contains the extraneous roots. Furthermore, in the case of backward prediction, i.e.

$$F_k = \sum_{m=1}^{p} b_m F_{k+m} \tag{10}$$

the two classes can be separated, since the extraneous roots still fall inside the unit circle, whereas the signal roots C_j are situated outside the unit circle. In the case of forward prediction [equation (7)], both classes fall inside the unit circle. This is, in principle, of no consequence if the coefficients are used for an extrapolation of the FID, since this requires both classes of coefficient. In practice, however, the presence of noise may occasionally result in roots that fall outside the unit circle, corresponding to noise components with negative decay rates (see below).

3.1 Qualitative Application

Qualitatively, linear prediction is used as a preprocessor to the FT in order to improve the resulting spectra.[4] An example of this application is the reconstruction of the first few data points of an experimental FID where these points have been corrupted by pulse breakthrough or by electronic filtering.[8] The presence of such corrupted data points may result in a severe baseline distortion, as illustrated in Figures 1(a) and (b). Although a deletion of the points would, in principle, remedy this problem, such a deletion would create a new problem, namely a dramatic first-order phase distortion of the FT spectrum. However, as shown in Figures 1(c) and (d), a reconstruction of the first six data points from the succeeding ones using equation (10) results in a straight baseline of the FT spectrum. Obviously, backward linear prediction extrapolation of the FID also provides a method of correcting dramatic first-order phase distortions, as occurs in cases where the experimental conditions introduce significant initial delays, e.g. semiselective soft pulses.

For truncated FIDs, forward extrapolation can be applied in order to reduce the truncation errors, and thus increase the resolution.[9] This is particularly the case in three- or higher-dimensional spectra.[10,11] Because of a limited accumulation time, the time domain data for the slowest incrementing time dimension are normally truncated, which results in a limited resolution. Also, for natural abundance two-dimensional heteronuclear correlation spectra, forward extrapolation has proved useful. Because of the low sensitivity that characterizes these spectra, the data acquisition in the t_1 domain should be confined to only the first and most intense part of the FID. This, however, is meaningful only if the associated truncation errors can be alleviated by forward linear prediction of the FID.

In both cases of forward extrapolation the reliability of the extrapolation depends on the number and the quality of the experimental data used for the extrapolation. This can be realized by considering a noiseless FID containing N sinusoids. Here only $4N$ data points would be necessary to determine the $4N$ parameters that are involved (i.e. the frequencies, the linewidths, the intensities, and the phases of the N signals) and, thereby, to reproduce the entire FID. When noise is present, as in experimental data, the number of data points and linear prediction coefficients used for the extrapolation must be increased considerably. Normally, the number of data points should exceed the number of linear prediction coefficients by at least a factor of 3.

As mentioned above, the noise may also give rise to roots outside the unit circle. Since these roots correspond to noise components with negative decay rates, an extrapolation that includes the corresponding linear prediction coefficients would result in an extrapolated FID which increases with increasing time. Preferably, this problem should be solved by including more experimental information in order to obtain a more stable solution, and thus remove the extracircular roots and ensure the decay of the extrapolated FID. If this is not possible, the roots may simply be reflected to fall inside the unit circle.[8] In any case, it is mandatory to apply equation (10) in order to check for roots outside the unit circle and, if necessary, to construct a modified set of roots from which a new set of linear prediction coefficients can be calculated. Omission of this procedure may result in artifactual peaks in the resulting spectra.

The effect of forward extrapolation is illustrated in Figure 2 which shows an experimental FID along the t_1 dimension in the methyl region of the C–H correlation spectrum of insulin, together with the FT. The original time domain data were Fourier transformed in t_2, so that the FID in Figure 2 is a

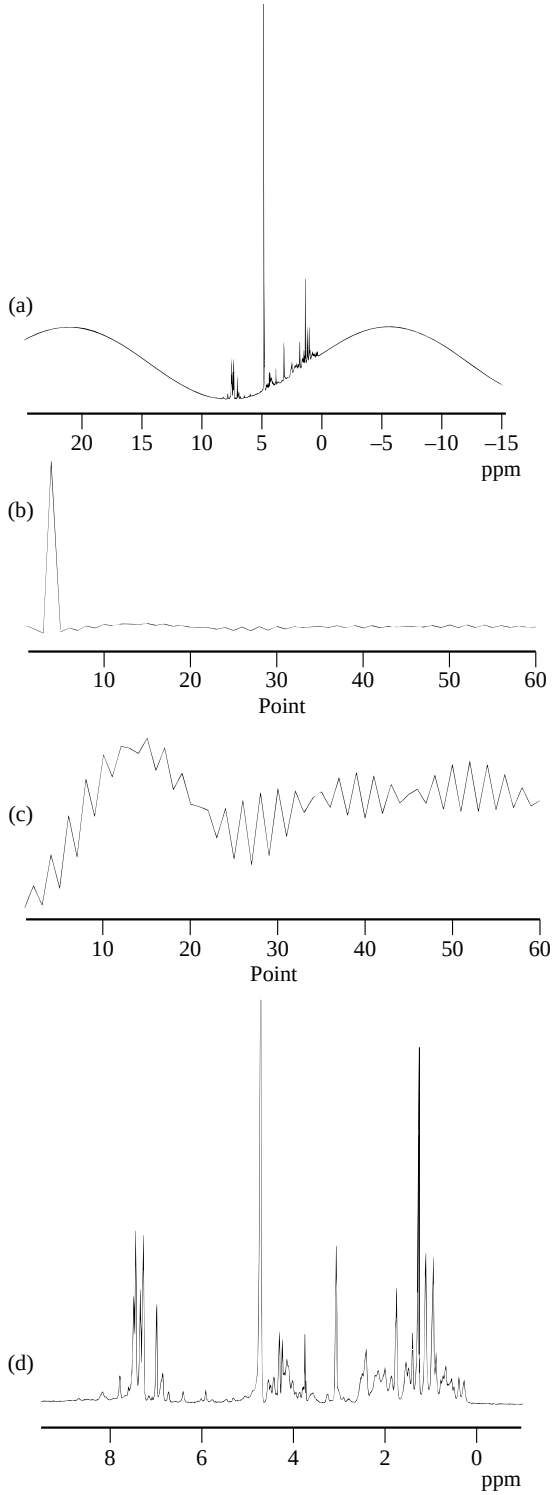

Figure 1 The first slice along the F_2 dimension in a two-dimensional HOHAHA spectrum of dimeric insulin. (a) The FT spectrum. (b) The first 50 data points of the FID. Note that the fourth data point in the FID is severely damaged, which gives rise to the undulating baseline in (a). (c) The first six data points of the FID were deleted and recalculated from 18 linear prediction coefficients using equation (10). The linear prediction coefficients were determined from 36 equations of the type of equation (10), k ranging from 7 to 42. Note that the vertical scale is changed. (d) The FT spectrum of the repaired FID. Note that both scales are changed. (Reproduced by permission of The American Chemical Society from J. J. Led and H. Gesmar, *Chem. Rev.*, 1991, **91**, 1413)

sum of several proton signals modulated by the frequencies of the attached ^{13}C nuclei. Here Fourier transformation of the original 512 experimental data points alone would result in an unacceptably low digital resolution, while zero filling would give rise to truncation errors in the form of a sinc function ('wiggles') superimposed on the signals. Although this artifact can be removed by digital filtering [Figures 2(a) and (c)], it can be done only by sacrifice of resolution. Only if the FID is extrapolated by linear prediction to an almost complete decay [Figure 2(b)] is the information, inherent in the experimental FID, retained [see Figure 2(d)].

It should be emphasized that, whereas the backward reconstruction of the first few corrupted data points of the FID is normally a 'safe' modification, the forward extrapolation of a FID should be applied with care. This holds because the number of reconstructed data points in the backward reconstruction is small compared with the number of linear prediction coefficients that can be calculated, and because the fine structure of the spectrum is not influenced by the initial points in the FID. Similar favorable conditions do not apply in the case of forward prediction, since here a more extensive extrapolation is often desirable in order to ensure a complete decay. In general, the number of complex linear prediction coefficients must be at least equal to the number of resonances in the FID, and preferably exceed it by several factors, the surplus necessary depending on the signal-to-noise ratio. Should this condition not be fulfilled, the accuracy by which the frequencies are reproduced by the extrapolation may be too low, making the extrapolation less valuable, or even meaningless, if carried too far. In such cases a shorter extrapolation in combination with a window function may be appropriate.[10]

3.2 Quantitative Applications

3.2.1 One-Dimensional Data

The aim of the quantitative linear prediction approach is to obtain the spectral information from the FID directly as the parameters I_j, ν_j, R_{2j}*, and ϕ_j, i.e. to estimate the involved intensities, frequencies, decay rates, and phases. In addition, the corresponding standard deviations should be evaluated. The quantitative linear prediction method is based on the classical work by Baron de Prony, further developed by Kumaresan and Tufts, and introduced into the field of NMR spectroscopy by Barkhuijsen et al. as the linear prediction singular value decomposition method (LPSVD).[3,12,13] The basic principle of the method is described below.

In order to find n linear prediction coefficients from N data points, equation (10) is set up for $N - n$ values of the index k, where n should be chosen to be considerably larger than the expected number of resonances. The linear prediction coefficients are found by singular value decomposition of equation (10), and subsequently the roots of the characteristic polynomial in equation (8) are found. As explained in the previous section, the extraneous roots, caused by the excess of linear prediction coefficients, can be separated from the signal roots C_j because the former fall inside the unit circle, while the latter fall outside because of the decay of the complex

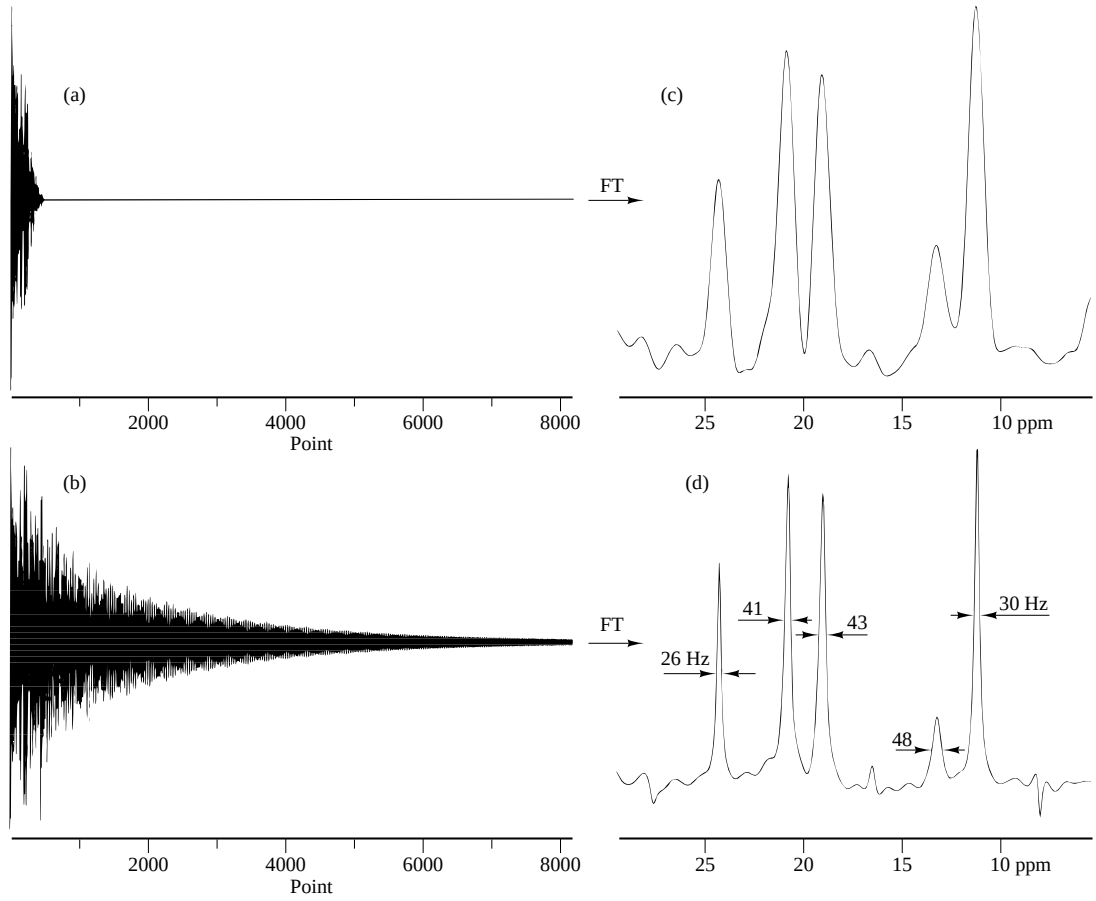

Figure 2 An experimental FID along t_1 (512 data points, t_1 acquisition time 10.2 ms) in a heteronuclear multiple quantum coherence C–H correlated two-dimensional spectrum of insulin. (a) Zero filled to 8192 data points and digital-filtered using a $\cos^2$ window function. (b) Linear prediction extrapolated to 8192 data points using equation (7). (c) FT of the digital-filtered FID in (a). (d) FT of the linear prediction extrapolated FID in (c). (Reproduced by permission of ESCOM Science Publishers B.V. from J. J. Led and H. Gesmar, *J. Biomol. NMR*, 1991, **1**, 237)

exponentials. For backward prediction $C_j = \exp[(-i2\pi\nu_j + R_{2j}^*)\,\Delta t]$ and F_k can be expressed as

$$F_k = F(k\,\Delta t) = \sum_{j=1}^{p} I_j \exp(i\phi) C_j^{-(k+T_{in}/\Delta t)} \qquad (11)$$

where F_k is seen to depend linearly on $I_j \exp(i\phi)$. For N data points, equation (11) can be expressed for N values of k, and because $C_j^{-(k+T_{in}/\Delta t)}$ is known, the complex values of $I_j \exp(i\phi)$ can be determined by a linear least-squares calculation. From the complex values of C_j and $I_j \exp(i\phi)$, the spectral parameters ν_j, R_{2j}^*, I_j, and ϕ_j are easily determined. Thus, the spectral parameters needed to describe the resonances in the FID can be determined without any a priori assumptions about their values. As only the parameters I_j and ϕ_j are included in the final least-squares calculation, true least-squares estimates of the standard deviations cannot be evaluated from the corresponding normal equation matrix. However, as established by Barkhuijsen et al.[14] in a later paper, the Cramèr Rao lower bounds can be used as reasonable substitutes.

Although the spectral parameters contain all the relevant information about the FID, a noiseless FID is often simulated and subsequently Fourier transformed to make a direct comparison with the FT spectrum possible. An example from the original paper by Barkhuijsen et al.[3] is shown in Figure 3.

The fact that no initial assumption about the spectral parameters is needed increases the value of the linear prediction method for complicated spectra with many narrowly spaced and overlapping resonances. In order to ensure sufficient resolution in such cases a very large number of linear prediction coefficients is needed in equation (10). This often results in computations that are unfeasible with the classical procedures for solving linear equations such as singular value decomposition, QR, and Cholesky decomposition, all of which have been applied to the linear prediction method in order to solve equation (10).[15,16] Therefore, dedicated fast algorithms have been developed for both the singular value decomposition method and the QR method.[17,18] Consequently, for one-dimensional linear prediction calculations the computational bottleneck is no longer associated with solving equation (10), but rather with the rooting of the characteristic polynomial. As shown in Figure 4, it is possible, at present, to apply more than 10 000 linear prediction coefficients to ensure sufficient resolution.

3.2.2 Two-Dimensional Data

The complete quantitative linear prediction analysis of two-dimensional NMR data was developed by Gesmar and Led, as

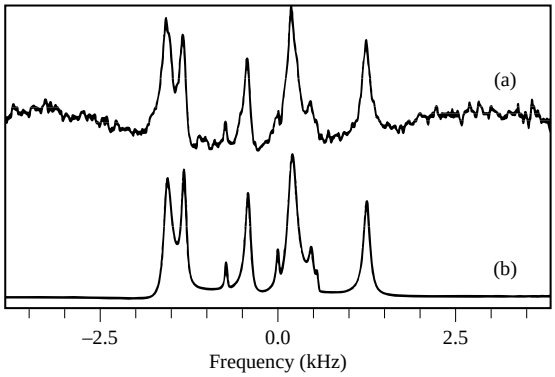

Figure 3 (a) In vivo ^{31}P NMR spectrum, computed by cosine fast Fourier transformation of 768 data points, using the optimal signal-to-noise ratio filter with a time constant of 0.015 s, and putting the three initial data points equal to zero. (b) Graphical display of the linear prediction singular value decomposition results, extracted from data points 4 to 128. This was obtained by cosine fast Fourier transformation of 768 data points computed from the estimated parameters. (Reproduced by permission of Academic Press, Inc. from H. Barkhuijsen, R. de Beer, W. M. M. J. Bovée, and D. van Ormondt, *J. Magn. Reson.*, 1985, **61**, 465)

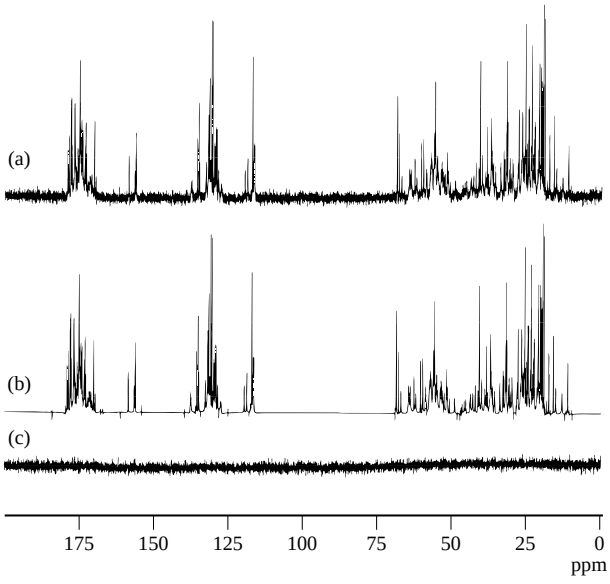

Figure 4 (a) FT ^{13}C spectrum of the dimeric insulin. The corresponding FID was recorded at 305 K and 125.76 MHz in 32 K data points with a sweep width of 50 000 Hz. (b) The FT of the FID recalculated from the spectral parameters produced by a 13 000 order fast linear prediction calculation on the experimental FID. (c) The difference between the FT spectrum in (a) and the fast linear prediction spectrum in (b). (Reproduced by permission of Academic Press, Inc. from H. Gesmar and P. C. Hansen, *J. Magn. Reson.*, 1994, **106**, 236)

reviewed briefly here.[19] A two-dimensional FID, $F_{l,k} = F\ (l\ \Delta t', k\ \Delta t)$, sampled at regularly spaced time intervals Δt and $\Delta t'$ in the two dimensions, conforms with equation (1) only if $I_j \exp(\mathrm{i}\phi_j)$ is substituted by

$$D_{l,j} = \sum_{h=1}^{p_j} I_{h,j} \exp(\mathrm{i}\phi_{h,j}) \exp[(\mathrm{i}2\pi \nu'_h - R^{*\prime}_{2h}) l\ \Delta t'] \qquad (12)$$

where the label prime indicates the second dimension. The parameter $I_{h,j}$ is the intensity of the two-dimensional signal and p_j is the number of correlations of the j th resonance. Equation (10) is still valid for any value of l, and because $\exp[(\mathrm{i}2\pi \nu_j - R_{2j}^*)\ \Delta t]$ does not depend on l, neither do the backward coefficients b_m. Thus, an equation similar to equation (10)

$$F_{l,k} = \sum_{m=1}^{p} b_m F_{l,k+m} \qquad (13)$$

applies in the two-dimensional case for any value of k and l, i.e. the p linear prediction coefficients apply in the t dimension for all values of l. Therefore, equation (13) can be set up and solved for all values of l simultaneously. After the determination of the b_m values, the corresponding characteristic polynomial equation is solved, and the frequencies ν_j and the decay rates R_{2j}* are found from the C_j values for the t dimension exactly as in the one-dimensional case. Since the C_j values are known at this point, the values of the $D_{l,j}$ terms that have replaced the I_j terms can be found for each value of l in the same way as the I_j values were found for the one-dimensional case. Thus, for each resonance ν_j a series of values of $D_{l,j}$ as a function of l can be evaluated. Now, because $D_{l,j}$ itself is a sum of complex exponentials, as can be seen from equation (12), the linear prediction principle applies once again. Therefore,

$$D_{l,j} = \sum_{m=1}^{p_j} b'_{j,m} D_{l+m,j} \qquad (14)$$

where $b'_{j,m}$ represents the t' backward coefficients that belong to the jth resonance. For each resonance ν_j a complete one-dimensional linear prediction calculation, which also includes the rooting of the characteristic polynomial and subsequent linear least-squares determination of the intensities and phases, is carried out. Thus, in addition to ν_j and R_{2j}*, estimates of ν_h' and R'_{2h}* are produced together with the value of $I_{h,j}$ and $\phi_{h,j}$, i.e. a complete determination of the spectral parameters of the two-dimensional FID has been achieved.

The applicability of the two-dimensional quantitative linear prediction procedure was demonstrated in the original paper by the determination of the spectral parameters from the ^{1}H phase modulated COSY FID of threonine in D_2O.[19] The parameters are listed in the original paper, and the quality of the estimation is illustrated in Figure 5 by a two-dimensional Lorentzian-shaped reconstruction of a (β-CH, CH_3) cross peak.

4 LEAST-SQUARES FOURIER TRANSFORM TECHNIQUES

In this section it is described how the spectral parameters I_j, ν_j, R_{2j}*, and ϕ_j can be estimated from the FT spectrum, unbiased by the deviations from the theoretical spectrum described in Section 2.[20] As mentioned previously, no information is lost by the Fourier transformation and, therefore, the spectral parameters can be evaluated from the FT spectrum as well as from the FID. Furthermore, the noise in the FT spectrum is uncorrelated with the zero mean and constant

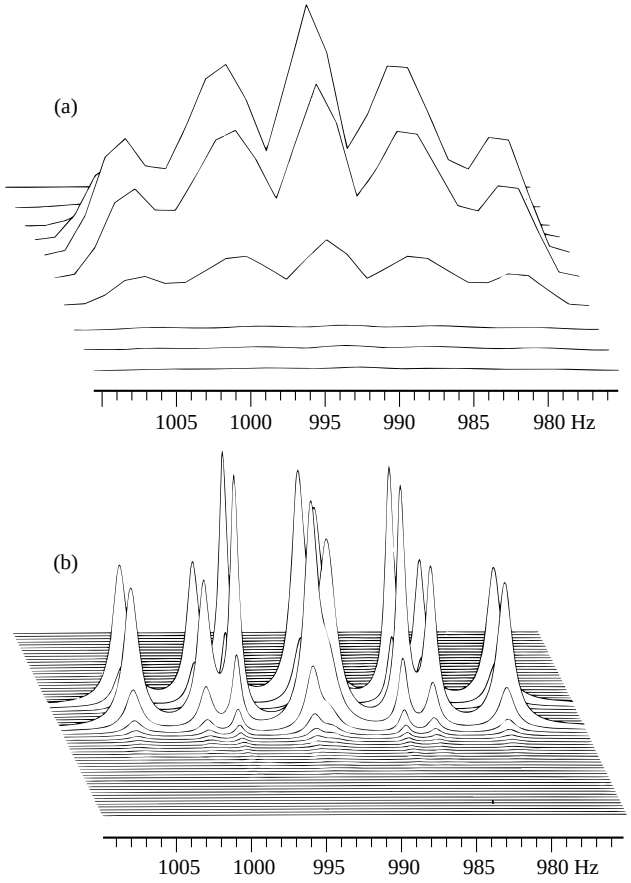

Figure 5 (a) Expansion of the (β-CH,CH_3) multiplet in the sine bell filtered two-dimensional absolute mode Fourier transform spectrum. (b) Spectrum of the same region, calculated from the parameters estimated by the two-dimensional linear prediction procedure. The signals are pairwise in counterphase, but the phases have been set to zero in the displayed spectrum. (Reproduced by permission of Academic Press, Inc. from H. Gesmar and J. J. Led, *J. Magn. Reson.*, 1989, **83**, 53)

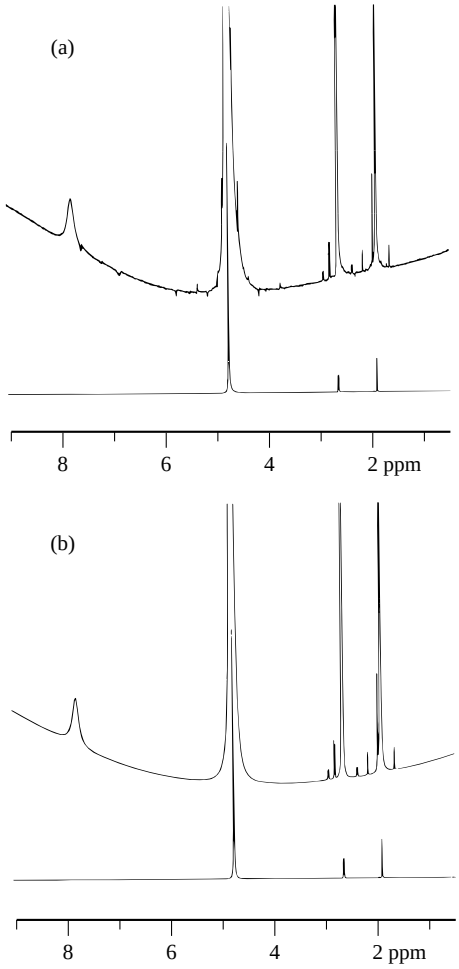

Figure 6 (a) The ^{1}H NMR absorption mode FT spectrum of a 2.5 M solution of *N*-methylacetamide in water at pH 5.2. In the upper spectrum the vertical scale is increased by a factor of 100. (b) Simulated spectrum based on the parameters derived from the experimental spectrum corresponding to (a). The same linear phase correction was used in both spectra. (Reproduced by permission of Academic Press, Inc. from F. Abildgaard, H. Gesmar, and J. J. Led, *J. Magn. Reson.*, 1988, **79**, 78)

variance if the same holds for the FID, a condition that is generally assumed to be true.[2] Thus the spectral parameters I_j, ν_j, R_{2j}*, and ϕ_j can be estimated by a nonlinear least-squares fit of equation (3) to the FT spectrum. It should be emphasized, however, that unbiased estimates of the spectral parameters are obtained only by application of this exact expression for the discrete FT of a multiexponential decaying FID. Any attempt to fit Lorentzian signals to the FT spectrum will lead to biased values of the spectral parameters, as discussed in Section 2. In order to ensure that the spectral noise is uncorrelated, it is also important that the FID is neither zero filled nor manipulated in any other way.

An example that demonstrates the result of a least-squares fit of equation (3) to an FT spectrum is shown in Figure 6. Here the ^{1}H FT NMR spectrum of *N*-methylacetamide in water is presented together with a simulated spectrum, recalculated from the parameters estimated in the least-squares fit. The small signals are ^{13}C satellites from the abundant *trans* isomer and the methyl resonances from the *cis* isomer. Because of the 6000 : 1 intensity ratio between the large water signal and the smallest signals of the solute, the latter are severely affected by aliasing. However, because equation (3) is used in the least-squares analysis, unbiased spectral parameters are obtained for all signals, even the small ones. Thus, the intensity ratio between the methyl signals of the *trans* isomer and their ^{13}C satellites was estimated as 1.11% $\pm$ 0.10%, which is in agreement with the expected concentration ratio of 1.12%. Likewise, the concentration of the *cis* isomer at 300 K was estimated to 1.60% $\pm$ 0.10% of the total amount of *N*-methylacetamide. This also compares favorably with the previously estimated value of 3%. A table, that contains all the estimated spectral parameters and their standard deviations can be found in the original paper.[20]

Because the spectrum $S(\nu)$ represented by equation (3) depends on the resonance frequency ν_j and the decay rate R_{2j}* in a nonlinear fashion, the least-squares analysis must be performed iteratively and requires an estimate of reasonable initial values of these nonlinear parameters. This represents a difficult and time-consuming task and may even be impossible for complicated spectra. One way to solve this problem is to perform a linear prediction analysis of the corresponding FID and use the linear prediction estimate of the frequencies and

decay rates as initial values for the least-squares iterations. Alternatively, one can proceed as proposed by Kumaresan et al.,[21] who have designed a sequence of iterations that requires only very crude initial values. The advantage of this approach is that no polynomial rooting is needed, as in the linear prediction procedure. However, unlike the linear prediction procedure, no 'fast' algorithm exists for the solution of the involved equations, and thus the choise of procedure must depend on the complexity of the NMR spectrum, and on the available computational possibilities. Still, unbiased estimates of the spectral parameters I_j, ν_j, R_{2j}*, and ϕ_j can be obtained with both methods, because both include a least-squares calculation based on equation (3).

5 CONCLUSION

The spectral methods described in this article (extrapolation of the FID by linear prediction, quantitative linear prediction, and least-squares FT) have all proved to be very useful in NMR spectroscopy. The major drawbacks of these methods have been the extensive computing time required and the need for very large amounts of computer memory. However, the new 'fast' algorithms together with the substantial improvements in minicomputers have reduced these drawbacks considerably, and made the use of linear prediction and least-squares analyses feasible on standard computational equipment that is normally available in NMR laboratories today.

6 RELATED ARTICLES

Fourier Transform Spectroscopy; Multidimensional Spectroscopy: Concepts.

7 REFERENCES

1. E. O. Brigham, *The Fast Fourier Transform*, Prentice-Hall, Englewood Cliffs, NJ, 1974, p. 85.
2. H. Gesmar, J. J. Led, and F. Abildgaard, *Prog. NMR Spectrosc.*, 1990, **22**, 255.
3. H. Barkhuijsen, R. de Beer, W. M. M. J. Bovée, and D. van Ormondt, *J. Magn. Reson.*, 1985, **61**, 465.
4. J. J. Led and H. Gesmar, *Chem. Rev*., 1991, **91**, 1413.
5. S. M. Kay and S. L. Marple, Jr., *Proc. IEEE*, 1981, **69**, 1380.
6. J. Tang and R. Norris, *J. Magn. Reson.*, 1986, **69**, 180.
7. R. Kumaresan *IEEE Trans. ASSP*, 1983, **31**, 217.
8. D. Marion and A. Bax, *J. Magn. Reson.*, 1989, **83**, 205.
9. C. F. Tirendi and J. F. Martin, *J. Magn. Reson.*, 1989, **81**, 577.
10. E. T. Olejniczak and H. L. Eaton, *J. Magn. Reson.*, 1990, **87**, 628.
11. G. Zhu and A. Bax, *J. Magn. Reson.*, 1990, **90**, 405.
12. G. R. B. Prony, *J. L'Ecol Polytech. Paris*, 1795, **1**, 24.
13. R. Kumaresan and D. W. Tufts *IEEE Trans. ASSP*, 1982, **30**, 833.
14. H. Barkhuijsen, R. van de Beer, and D. van Ormondt, *J. Magn. Reson.*, 1986, **67**, 371.
15. H. Gesmar and J. J. Led, *J. Magn. Reson.*, 1988, **76**, 183.
16. J. Tang, C. P. Lin, M. K. Bowman, and J. R. Norris, *J. Magn. Reson.*, 1985, **62**, 167.
17. W. W. F. Pijnappel, A. van den Boogaart, R. de Beer, and D. van Ormondt, *J. Magn. Reson.*, 1992, **97**, 122.
18. H. Gesmar and P. C. Hansen, *J. Magn. Reson.*, 1994, **106**, 236.
19. H. Gesmar and J. J. Led, *J. Magn. Reson.*, 1989, **83**, 53.
20. F. Abildgaard, H. Gesmar, and J. J. Led, *J. Magn. Reson.*, 1988, **79**, 78.
21. R. Kumaresan, C. S. Ramalingam, and D. van Ormondt, *J. Magn. Reson.*, 1990, **89**, 562.

Biographical Sketches

Jens J. Led. *b* 1938. M.S. (chemistry), The Technical University of Denmark, 1963. Ph.D., 1968, Sc.D., 1988, University of Copenhagen. Faculty in Chemistry, University of Copenhagen, 1969–present. Visiting research associate, University of Utah, 1971–73. Approx. 60 publications. Current research specialties: NMR studies of protein structure and function, NMR signal analysis.

Henrik Gesmar. *b* 1948. M.S. (chemistry), B.A. (Spanish), 1983, Ph.D. (chemistry), 1988, University of Copenhagen. Faculty in Chemistry, University of Copenhagen, 1988–present. Approx. 25 publications. Primary research interest: NMR studies of proteins, with focus on spectral analysis and computational methods.

Fourier Transform Spectroscopy

Weston A. Anderson
Varian Associates, Palo Alto, CA, USA

1 Introduction 1
2 Historical Background 1
3 The Mathematics of the Fourier Transform 4
4 The Bloch Equations 6
5 The Fourier Transform Spectrometer Electronics 8
6 Related Articles 9
7 References 10

1 INTRODUCTION

Fourier transform (FT) spectroscopy employs wideband excitation to simulate simultaneously all the transition lines of a nuclear magnetic resonance (NMR) spectrum to produce a time-dependent response signal. An FT is applied to the response signal and produces an NMR spectrum. The FT is a mathematical process for converting a signal that is a function of time to one that is a function of frequency.

The wideband excitation may be produced by several different methods, the most common in use today being pulsing of the applied radiofrequency (rf) field. Another method is modulating an rf by a random or pseudorandom noise source. Wideband sources with almost any spectral distribution may be generated using modern pulse programmers and frequency synthesizers controlled by digital logic. A method related to FT spectroscopy uses a very rapid scan of the rf source through the NMR spectral region.

In the pulsed NMR method, the time-dependent NMR response, called the free induction decay (FID), is sampled at uniform time intervals after the termination of the rf pulse. Each time sample is digitized and stored in a digital memory. To improve the sensitivity, the experiment may be repeated, the responses of subsequent pulses sampled at the same uniform time intervals, and the digitized values of each sample added to the value previously stored for the corresponding time interval. When a sufficient number of samples have been stored, the FT is applied, yielding an output spectrum that is a function of frequency. The advantage of FT NMR spectroscopy is the gain in sensitivity that can be obtained. For ^{1}H or ^{13}C NMR in liquid samples the gain can exceed a factor of 100.

2 HISTORICAL BACKGROUND

The FT is named after the French mathematician Jean Baptiste Joseph Fourier (1768–1830). Fourier taught at the École Normale in Paris when it opened in 1795, and later at the École Polytechnique. In 1801 he became Prefect of Isère, based at Grenoble. Here he investigated heat conduction, and in 1807 announced his use of a series of sines and cosines of integral multiples of a variable to represent almost any function. This idea originated in the works of Leonhard Euler (1707–83) and Daniel Bernoulli (1700–82). In 1816, Fourier moved to Paris, and in 1817 was made a Member of the French Academy of Science. In 1822 he published *Théorie Analytique de la Chaleur* in which he fully developed the theory and mathematics of the series now known by his name.

Spectroscopy started with optical spectroscopy, the dispersing of light into its spectral components or colors. In 1607, Isaac Newton illustrated that a beam of light, after passing through a glass prism, forms an elongated multicolored image called a spectrum. In 1802, Thomas Young developed the wave theory of light and related color to wavelength. In 1859, G. R. Kirchoff set out the general law connecting absorption and emission of light and showed that each species of atom has a uniquely characteristic spectrum. In 1881, A. A. Michelson invented the interferometer and used it to measure accurately the wavelengths of a number of atomic emission lines relative to the standard meter. In his monograph of 1907, Michelson explained the connection between the spectral pattern of a light beam and the corresponding time domain signals, i.e. that one can be derived from the other through an FT.[1] The Michelson optical interferometer made possible multiplex spectrometry, i.e. recording of all the spectral intervals simultaneously. The full power of this technique for increasing the sensitivity of infrared spectrometry was pointed out by Fellgett in 1951[2] and is known as the 'Fellgett advantage' or 'multiplex advantage'. The technique is unsuitable for NMR, however, because of the much longer wavelengths of NMR spectral frequencies.

NMR spectroscopy began with the discovery of the technique by Purcell and co-workers at Harvard[3] and Bloch and coworkers at Stanford,[4] reported early in 1946. The method used to obtain a spectrum was either to scan slowly the driving rf or the polarizing magnetic field strength. The resulting resonance could be displayed on an oscilloscope or on a strip chart recorder. This slow passage or continuous wave (CW) method was used for the first 20 years of NMR spectroscopy.

Some of the concepts of pulsed NMR were contained in the introductory section of Bloch's first detailed paper about NMR:[5]

> Not only a weak rf field, acting at resonance over very many Larmor periods, can produce an appreciable nuclear change of orientation, but also a strong field pulse, acting over only a few periods. Once the nuclear moments have been turned into an angle with the constant field, they will continue to precess around it and likewise cause a nuclear induction to occur at an instant when the driving pulse has already disappeared. It seems perfectly feasible to receive thus an induced nuclear signal of radiofrequency well above the thermal noise of a narrow band receiver.

The transient signal described here became known as the FID. Bloch did not specifically treat this case in the remainder of his paper. The concept appears to be covered by some of the broad claims of the Bloch–Hansen patent;[6] however, no specific application is shown that makes use of this technique.

Transient effects, commonly called 'wiggles', were observed in many of the early experiments. They occur when one sweeps so rapidly through resonance that either thermal equilibrium is not achieved or the adiabatic condition is not satisfied. The wiggles were treated theoretically by Jacobsohn and Wangsness.[7] For the conditions mentioned above, the nuclear

moment fails to precess in step with the applied rf, and a beat due to the interference of these two separate frequencies is seen. Later, Torrey[8] analyzed a similar transient case that occurs when one establishes a nonequilibrium situation and then fixes the experimental parameters, including the strength and frequency of the rf field and the value of the polarizing field. Thus some transient effects were observed quite early, but they were not observed in the absence of an rf field as described by Bloch for the FID.

In October 1948, Russell Varian filed a patent application entitled 'Method and Means for Correlating Nuclear Properties of Atoms and Magnetic Fields'.[9] The patent describes a specific method for changing the orientation of the nuclear moments so that they form an angle with the magnetic field, usually the Earth's field. A polarizing field is established at an angle with respect to the field to be measured (which is usually the Earth's magnetic field). After a nuclear polarization is established, the polarizing field is quickly shut off, leaving the nuclear moments at an angle with the Earth's field. They then precess about the direction of the Earth's field and, in so doing, induce a voltage in a coil surrounding the sample. This coil is coupled to a sensitive amplifier, the output of which is connected to a means of measuring the precessional frequency, which is proportional to the Earth's magnetic field strength. In the original systems, a frequency counter was used to determine the frequency. A reed frequency meter, which is a crude Fourier analyzer, was used in a later portable magnetometer.

In the year 1949–50, Hahn performed a number of experiments that made use of the pulsed rf field methods suggested by Bloch. He used a combination of an inversion pulse and a rapid scan through the resonance region to measure the thermal relaxation time of water.[10a] Later he described the FID signals that follow a short pulse and developed the theory and experimental techniques of spin echo NMR. With the spin echo technique he measured the NMR relaxation times T_1 and T_2.[10b,c] Hahn and Maxwell analyzed the complex echo patterns found in molecules that contained spin-coupled chemical groups.[11]

In August 1956, Russell Varian filed a patent[12] which contained the major concepts of FT NMR as a method of increasing the sensitivity of NMR spectrometers. Here a wideband frequency source is used to excite simultaneously all the resonance lines in an NMR spectrum. After storing the responses, an FT analyzer is used to convert the response into a frequency spectrum. The system described in his patent is illustrated in Figure 1. It is stated in the patent that 'the wide band frequency source may comprise, for example, a pulse generator wherein the pulses are regulated to give Fourier components over the desired frequency range or a white noise source having the required bandwidth'. In this system he also provided a field/frequency control using a NMR reference sample. Signals from the analytical and reference samples are mixed together to obtain a signal at the difference frequency, thereby eliminating the effects of frequency or field drift. Two different Fourier analyzer systems are described: in one the signal is recorded on photographic film, and in the other it is recorded on magnetic tape. In the first system, the FT is performed by using the film as a diffraction grating in an optical spectrometer arrangement. The spectrum, i.e. the FT, is recorded on a second film by a beam of light that is diffracted by the image on the first film. After it has been developed, the second film is read with a photoelectric densitometer and recorded on a strip chart recorder. In the magnetic tape system the Fourier analysis is performed by playing the recorded signal to a mixer and sending the output through a low-pass filter and detector to the strip chart recorder. The mixer receives a reference signal from a variable-frequency oscillator. The frequency of this oscillator determines the frequency component of the output spectrum.

Because of their complexity, neither of these systems was built. However, the claims of the patent were sufficiently broad to cover practical systems that were developed later. From a reading of the patent it is obvious that Russell Varian had a clear understanding that the NMR response to a wideband

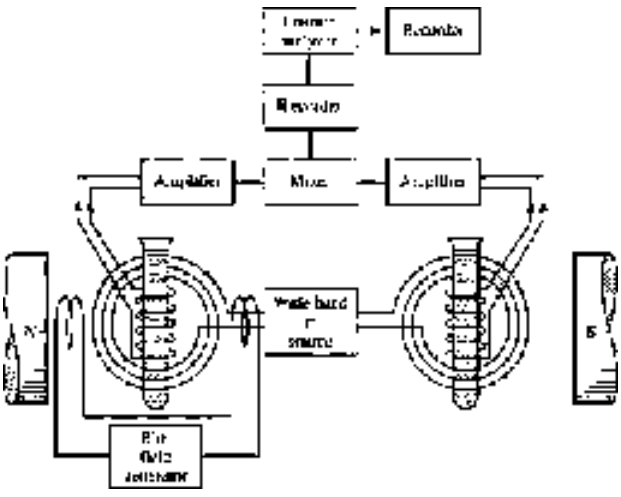

Figure 1 The FT NMR system described in the Russell Varian US Patent[12]

source and the spectrum formed an FT pair. Before the patent issued in 1966, Lowe and Norberg[13] had also pointed out that the FID and spectrum formed an FT pair.

In the early 1960s, the need for greater sensitivity was growing. The increase in strength of the polarizing magnetic field was a help, as was the repetitive averaging of spectra by adding together many spectra in a computer of average transients (CAT) that became available about this time. The multiplex advantage, as suggested by the Varian patent, seemed to offer increased sensitivity without taking additional time to perform time averaging. In 1962, Anderson proposed a multichannel NMR spectrometer to make use of the multiplex advantage. He proposed using a chopper wheel to generate a band of frequencies which, after mixing with an offset frequency, could be applied to produce simultaneous resonance of the sample nuclei. The responses, after mixing with the same offset frequency, could be demodulated by the same chopper wheel and provide simultaneous multiple output signals in real time[14] (see also ***Anderson, Weston A.: Early NMR Experiences and Experiments***). These output signals could be integrated to achieve the desired signal-to-noise ratio. Before the chopper wheel was put into operation, Anderson realized that a series of pulses would be a better way to achieve a band of discrete rf fields. After mixing, the response signals could be stored using a CAT and then Fourier transformed by a computer. This approach was even closer to the Varian patent. The necessary equipment was assembled and the idea successfully tested by Richard Ernst. In the early experiments Ernst and Anderson found a sensitivity enhancement of more than 10 in experiments using the same data acquisition time (Figure 2) (see ***Anderson, Weston A.: Early NMR Experiences and Experiments***).[15]

The improvement in sensitivity provided by the FT technique, compared with the previous field or frequency scanned experiments, is determined primarily by the ratio of the spectrum width F and the linewidth of a single transition $\Delta = 1/\pi T_2$. The time taken to obtain a spectrum by an FT experiment yielding essentially the same signal-to-noise ratio is reduced by a factor of F/Δ. By signal averaging, the signal-to-noise ratio increase is proportional to the square root of the number of averaged spectra. Thus, to first order, the FT technique provides an increase in the signal-to-noise ratio by a factor of approximately $\sqrt{(F/\Delta)}$ for the same total data collection time. With the larger spectral widths arising from the greater magnetic field strengths of modern systems, the gain in the signal-to-noise ratio can be a factor of 100 or more for ^{13}C or ^{1}H experiments in liquid samples.

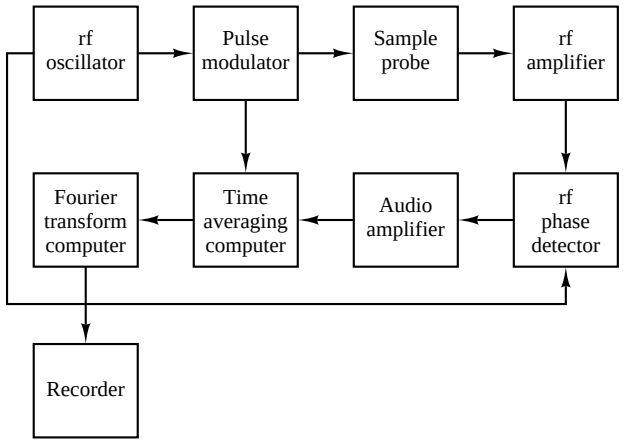

Figure 2 The FT NMR system described by Anderson and Ernst[15]

The use of a broadband noise source was demonstrated independently by Ernst[16] and Kaiser.[17] In these experiments a pseudorandom sequence was used to modulate the rf phase of the excitation to produce a wideband noise source. The advantage of the pseudorandom sequence is its predictable spectral properties and constant rf power. The rf power level is far lower than that required for pulsed FT; however, the simultaneous radiation and detection can lead to line broadening that is absent in pulsed FT spectroscopy.

In the rapid scan approach,[18] the rf field is quickly scanned through the NMR spectral region causing wiggles, as described above. The spectrum is corrected by a convolution with a scan of a single line made under identical conditions, or by one that is simulated on a computer. The signal from a single line resembles its FID, except that the frequency of the wiggles increases as the rf frequency is swept away from the resonance condition.

With flexible pulse programmers and frequency synthesizers that can be digitally controlled, an excitation function can be generated with virtually any spectral distribution by controlling the width, amplitude, phase, and perhaps frequency, of each pulse or pulse segment. This concept was originally applied to spin decoupling by Tomlinson and Hill,[19] and later used to produce composite pulses for the suppression of solvent lines and for other applications.[20]

In 1971, J. Jeener proposed that the Fourier transformation technique be extended into a second dimension, from which information could be extracted using additional pulses.[21] In 1974, Ernst and his group demonstrated the technique and showed how it could be particularly useful in analyzing large molecules.[22] A first pulse or group of pulses was used to establish a coherent nonequilibrium state in the spin system. The state of the spin system then evolves during a period called the 'evolution period'. A second pulse or pulse group then causes mixing of the evolved states. The detection period follows the mixing period. An FT is applied to the signals recorded during the detection period. Repeating the experiment for different evolution times yields a two-dimensional array of data. A second FT is applied with respect to this second time dimension, the evolution time, to produce a two-dimensional frequency spectrum.

Variations of the two-dimensional experiment can yield a wealth of information. Some of the more important applications involve tracing out the molecular structures by resolving spin couplings between protons, protons and ^{13}C, and between ^{13}C atoms. Overhauser types of experiment yield information on the conformation of polypeptides and small proteins. Overlapping lines are often resolved by spreading the spectrum out in a second or a third dimension.[23,24]

Magnetic resonance imaging (MRI) is a field in which FT techniques are essential. MRI began when Paul Lauterbur proposed the use of NMR for imaging in a manner analogous to the use of computerized tomography (CT) in X-ray imaging. Lauterbur's critical idea was to use magnetic field gradients, making the frequencies of the NMR resonance signals dependent upon the spatial position of the resonant nuclei.[25] A number of techniques developed by Hinshaw made use of the multiplex advantage of FT NMR. Generally, the techniques involved simultaneously detecting all the resonances in a

line or plane with the spatial positions coded by magnetic field gradients, and later reconstructing by the back-projection used in CT.[26] In 1975, Ernst proposed a way of acquiring and reconstructing MRI data that was similar to the two-dimensional spectroscopic method.[27] A magnetic field gradient is applied during the evolution period between pulses, and an orthogonal gradient is applied during the detection period. By repeating the experiment a number of times, each time incrementing the duration of the evolution time, a series of responses is collected. Applying a double FT with respect to the different times yields a cross-sectional image. The method was readily extended to three dimensions. This Fourier imaging technique, and a modified form known as spin warp imaging,[28] is the most frequently used method of MRI.

Resonances from nuclei in solid samples are split and shifted by the static dipole–dipole coupling between nuclei and by quadrupole coupling of nuclei that have electric quadrupole moments. Because the splittings and shifts depend upon the orientation of the interaction with respect to the polarizing field, resonances in a polycrystalline sample are further broadened. As a result, the FID from nuclei in a solid can be very short, and instrumental limitations of finite rf pulse lengths and receiver recovery times limit its direct observation.

Spin echo techniques[10] can be used to overcome partially the problem of short FID transients that decay during the receiver dead time following the excitation pulse. The techniques are suitable for a polycrystalline material with strong dipole or quadrupole couplings. The basic spin echo technique uses two excitation pulses separated by a short time interval. The magnetization then rephases to form a dipolar echo[29] or quadrupolar echo.[30] At the echo peak the magnetization is rephased as at the start of the FID. Now, however, the signal is separated from any interfering rf pulses so that it may be recorded accurately. Fourier transformation of the second half of the echo produces the spectral response.

A number of techniques reduce line broadening, allowing the extraction of spectral information by FT methods. Magic angle spinning (MAS), introduced by Andrew et al.[31] and Lowe,[32] can reduce the dipole–dipole contribution to the linewidths in solids.[33] Combining MAS with heteronuclear decoupling and cross polarization[34] (CP MAS) provides high resolution capabilities for dilute nuclear spins such as those of ^{13}C.[35]

Repetitive pulse sequences have also been developed. These effectively average interactions that normally cause broadening of lines in solids. The spin system is subjected to a repetitive sequence of closely spaced pulses. The spin response is digitized once per cycle of the sequence, thus building up the equivalent of a single FID which is then transformed in the usual way to produce a spectrum.[36]

FT techniques have also been used in electron spin resonance (ESR), sometimes called electron paramagnetic resonance (EPR) spectroscopy. Generally, the electron FID signals are much shorter than the nuclear FID response found in liquids and solids; however, as the electronic equipment has improved, many of the multiple pulse and two-dimensional experiments commonly used in NMR have been applied to ESR.[37,38]

FT techniques have been applied to many other forms of spectroscopy, such as ion cyclotron resonance (ICR) mass spectroscopy, nuclear quadrupole resonance (NQR), EPR, dielectric spectroscopy, and microwave spectroscopy. Marshall has reviewed many of these techniques. The way in which FT methods have increased the sensitivity of these techniques is described below.[39]

3 THE MATHEMATICS OF THE FOURIER TRANSFORM

There are a number of different mathematical formulations of the FT and the inverse transform.[40] One pair is given by the equations:

$$F(\nu) = \int_{-\infty}^{\infty} f(t) \exp(-\,\mathrm{i}2\pi\nu t)\ \mathrm{d}t \tag{1}$$

$$f(t) = \int_{-\infty}^{\infty} F(\nu) \exp(\,\mathrm{i}2\pi\nu t)\ \mathrm{d}\nu \tag{2}$$

where $\mathrm{i} = \sqrt{-1}$, $f(t)$ is a function of time t, and $F(\nu)$ is a function of the frequency ν. The inverse transformation converts a frequency spectrum $F(\nu)$ back into the time domain $f(t)$.

The angular frequency $\omega = 2\pi\nu$ is often used for formal expressions yielding the transformation pair:

$$F(\omega) = \int_{-\infty}^{\infty} f(t) \exp(-\,\mathrm{i}\omega t)\ \mathrm{d}t \tag{3}$$

and

$$f(t) = \frac{1}{2\pi} \int_{-\infty}^{\infty} F(\omega) \exp(\,\mathrm{i}\omega t)\ \mathrm{d}\omega \tag{4}$$

Note that the expressions for $F(\omega)$ and $F(\nu)$ differ by 2π.

There are a number of properties or theorems that play a basic role in the application of FT pairs.[40] Some of the more useful ones are summarized below. By interchanging $F(\nu)$ and $f(t)$ and changing i to $-$i, the theorems also apply to the inverse transformations.

3.1 Similarity Theorem

If $f(t)$ has the FT $F(\nu)$, then $f(at)$ has the FT $|1/a|F(\nu/a)$.

This theorem illustrates that if the timescale is compressed by a factor of a ($a < 1$), the frequency scale expands by $1/a$, and, as it expands, the area of the spectrum remains constant.

3.2 Addition Theorem

If $f(t)$ and $g(t)$ have the FTs $F(\nu)$ and $G(\nu)$, respectively, then $f(t) + g(t)$ has the transform $F(\nu) + G(\nu)$.

This theorem illustrates that the FT transform is a linear transform and is suitable for dealing with linear problems. Although the NMR magnetization $\boldsymbol{M}$ does not respond linearly to the rf pulse, the subsequent FID motions are linear and the addition theorem applies.

3.3 Shift Theorem

If $f\ (t)$ has the FT $F(\nu)$, then $f\ (t - t_0)$ has the FT $\exp(-\mathrm{i}2\pi\ \nu\ t_0)\ F(\nu)$.

This theorem illustrates that a change in the time origin of the FID causes a frequency-dependent phase change in the resulting spectrum. Modern NMR spectrometers can correct for frequency-dependent phase errors in the spectrum.

3.4 Convolution Theorem

If $H(\nu)$ represents the convolution of the two functions $F(\nu)$ and $G(\nu)$, then its FT $h(t)$ can be expressed as the product of the two functions $f(t)$ and $g(t)$ where they are the FTs of $F(\nu)$ and $G(\nu)$, respectively.

The convolution operator is expressed as:

$$\hat{H}(\nu) = F(\nu)*G(\nu) = \int_{-\infty}^{\infty} F(\mu)G(\nu - \mu)\ \mathrm{d}\mu \qquad (5)$$

and the corresponding relationship for the FT of these quantities is $h(t) = f(t)g(t)$. This theorem is extremely useful in any filtering process that makes use of convolution. To achieve the maximum possible signal-to-noise ratio, it is necessary to use a matched filter, which is determined by the lineshape. The FID of a Lorentzian spectral line with a relaxation time T_2 corresponds to a decay envelope given by $\exp(-t/T_2)$. Thus to obtain a spectrum with the best possible signal-to-noise ratio, the FID is multiplied by $\exp(-t/T_2)$ before the FT is taken.

Other filter applications that can make use of the convolution theorem include: resolution enhancement, to narrow artificially the resonance lines; lineshape transformations (for example, to transform the Lorentzian lines to Gaussian lines which cut off faster with frequency); apodization of the FID to suppress or eliminate oscillating signal tails in the spectrum; and correction of instrumental distortions, perhaps caused by the limited receiver bandwidth. These processes are trivial when done in the time domain, as compared to performing a convolution in the frequency domain.[23]

3.5 Definite Integral

The definite integral of a function $F(\nu)$ from $-\infty$ to ∞ is equal to the value of its FT at the origin, $f(0)$.

$$f(0) = \int_{-\infty}^{\infty} F(\nu)\ \mathrm{d}\nu \qquad (6a)$$

$$F(0) = \int_{-\infty}^{\infty} f(t)\ \mathrm{d}t \qquad (6b)$$

This states that the initial value of a FID is equal to the area of its FT. With proper attention to the NMR phase adjustments, one can relate the initial value of the FID to the total area in the NMR spectrum.

3.6 Rayleigh's Theorem

The integral of the squared modulus of a function is equal to the integral of the squared modulus of its spectrum.

$$\int_{-\infty}^{\infty} |f(t)|^2\ \mathrm{d}t = \int_{-\infty}^{\infty} f(t)f^*(t)\ \mathrm{d}t = \int_{-\infty}^{\infty} F(\nu)F^*(\nu)\ \mathrm{d}\nu = \int_{-\infty}^{\infty} |F(\nu)|^2\ \mathrm{d}\nu \qquad (7)$$

Here each integral represents the energy of the system. The term $|f(t)|^2$ has some interesting properties in that its value does not depend upon the origin or frequency offset of the transmitter.

3.7 The Sine and Cosine Transforms

The cosine transform $C(\nu)$ and sine transform $S(\nu)$ are obvious extensions of the standard FT:

$$C(\nu) = \int_{-\infty}^{\infty} f(t)\cos(2\pi\nu t)\ \mathrm{d}t \qquad (8a)$$

$$S(\nu) = \int_{-\infty}^{\infty} f(t)\sin(2\pi\nu t)\ \mathrm{d}t \qquad (8b)$$

It is useful to note that the cosine transform is symmetric about $\nu = 0$ and the sine transform is antisymmetric about $\nu = 0$. If $f(t)$ is real, then the real part of $F(\nu)$ is symmetric and the imaginary part antisymmetric about $\nu = 0$.

3.8 The Discrete Fourier Transform

For most NMR applications, the data have a finite time duration and are sampled and recorded at discrete time intervals. The discrete FT (DFT) is based on the use of periodic functions with period N so that $x(n) = x(n + kN)$, where n, N, and k are integers.[40,41] The DFT is defined within the limited region of what would be one period of the periodic function. In contrast to Fourier series, which may have an infinite number of terms, there are only N distinct complex exponentials used in the DFT. The DFT and inverse transform can be written as:

$$F(\nu_k) = \sum_{n=0}^{N-1} f(t_n)\exp(-\ \mathrm{i}2\pi kn/N) \qquad (9)$$

$$f(t_n) = \frac{1}{N}\sum_{k=0}^{N-1} F(\nu_k)\exp(\ \mathrm{i}2\pi kn/N) \qquad (10)$$

The normalizing factor $1/N$ arises from the equality:

$$\sum_{n=0}^{N-1} \exp(\ \mathrm{i}2\pi nk/N) = \begin{cases} \mathrm{N}, & \text{for } k = mN,\ m \text{ an integer} \\ 0, & \text{otherwise} \end{cases} \qquad (11)$$

In NMR, the FID signals are digitized at times $t_n = n\Delta\tau$, where $\Delta\tau$ is the time interval between successive analog-to-digital converter (ADC) samples, and n takes the N integer values from 0 to $N - 1$. The spectral frequencies ν_k measured in the rotating coordinate system extend from $-1/(2\Delta\tau)$ to $1/(2\Delta\tau)$, and have the values $\nu_k = k/(N\ \Delta\tau)$, where N is the total number of FID samples. In a single-channel system, k ranges from 0 to $N/2$, and in a quadrature system (discussed below) k ranges from $-N/2$ to $+N/2$. Modern computers and the fast FT (FFT) algorithms permit rapid computation of the DFT.[43,44]

4 THE BLOCH EQUATIONS

The FT NMR experiments that use rf pulses for excitation are treated in greater detail here, since they are the ones in greatest use today. A FID signal is stimulated by applying a short rf magnetic field pulse at right angles to the constant polarizing magnetic field. Following the conventional notation, the polarizing magnetic field is along the z axis and the rf magnetic field along the x axis. By increasing the phase of the rf drive frequency by 90°, the effective axis of the rf field is changed to lie along the y axis. Thus roles of the x- and y-axes are easily interchanged, thereby permitting experiments where the effective rf field can be applied in any direction in the xy plane.

The phenomenological equations of Bloch[5] and his development of the rotating coordinate system provide an easy way to describe the FT experiment and to resolve many questions regarding the optimization of experimental parameters. The equations in the laboratory system are:

$$\dot{M}_x = \gamma(M_y B_z - M_z B_y) - M_x/T_2 \tag{12a}$$

$$\dot{M}_y = \gamma(M_z B_x - M_x B_z) - M_y/T_2 \tag{12b}$$

$$\dot{M}_z = \gamma(M_x B_y - M_y B_x) - (M_z - M_0)/T_1 \tag{12c}$$

where M is the magnetization vector, $\dot{M}$ is the time derivative of M, and B is the applied magnetic field vector, with the subscripts indicating the particular components. With only a polarizing field B_z and no other magnetic field components, a solution of these equations is:

$$M_x = M_\mathrm{T}\cos(\omega_0 t + \phi)\ \exp(-t/T_2) \tag{13}$$

$$M_y = M_\mathrm{T}\sin(\omega_0 t + \phi)\exp(-t/T_2) \tag{14a}$$

$$M_z = M_0 + M_\mathrm{L}\exp(-t/T_1) \tag{14b}$$

where $\omega_0 = -\gamma B_z$, and M_T is the total transverse magnetization. In a right-handed coordinate system, a positive value of γ yields a negative value of ω_0. These equations describe a magnetization vector precessing about the magnetic field axis at an angular frequency of ω_0, as shown in Figure 3. With the positive z axis taken in the direction of the magnetic field B_z, the sign of ω_0 is the same as the sign of $-\gamma$. The xy component of the magnetization decays toward zero with a time constant T_2, and the z component of magnetization approaches $\boldsymbol{M}_0$ with a time constant T_1.

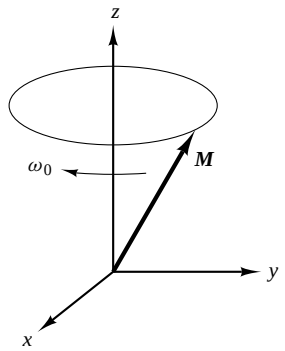

Figure 3 Precessing magnetization in the presence of a constant field B_z along the z axis

Using complex notation $f(t) = M^+ = M_x + \mathrm{i}M_y = M_\mathrm{T}\exp(\mathrm{i}\omega_0 t + \mathrm{i}\phi - t/T_2)$ and inserting it into equation (3) yields

$$F(\omega) = M_\mathrm{T}\exp(\mathrm{i}\phi)\int_0^\infty \exp[\mathrm{i}(\omega_0 - \omega)t - t/T_2]\ \mathrm{d}t$$

$$= M_\mathrm{T}\exp(\mathrm{i}\phi)\frac{1/T_2 + \mathrm{i}(\omega_0 - \omega)}{(\omega_0 - \omega)^2 + (1/T_2)^2} \tag{15}$$

Choosing the transverse magnetization M_T to be aligned along the x axis at time $t = 0$ corresponds to the phase $\phi = 0$. In this case the real part of $F(\omega)$ corresponds to the absorption signal $a(\Delta\omega)$, and the imaginary part corresponds to the dispersion signal $d(\Delta\omega)$ where

$$a(\Delta\omega) = M_\mathrm{T}\frac{1/T_2}{(\Delta\omega)^2 + (1/T_2)^2} \tag{16a}$$

$$d(\Delta\omega) = M_\mathrm{T}\frac{\Delta\omega}{(\Delta\omega)^2 + (1/T_2)^2} \tag{16b}$$

with the frequency offset $\Delta\omega = \omega_0 - \omega$.

4.1 The Rotating Coordinate Frame

The concept of the rotating coordinate frame can be helpful when visualizing the magnetization during the time for which an rf pulse is applied. In most FT experiments the pulse length τ is short compared with T_1 and T_2 so that, while the pulse is being applied, the terms in equations (12a)–(12c) containing T_1 and T_2 can be safely omitted. After the termination of the pulse, the solutions for the magnetization $\boldsymbol{M}$ are again given by equations (13), (14a) and (14b) with new values for M_T, M_L, and ϕ. It may be more useful to express the magnetization $\boldsymbol{M}$ in the rotating coordinate frame even after the termination of the pulse. In most spectrometer systems the signals are mixed with the transmitter frequency, so that the frequencies of the signals at the output of the mixer correspond to those of the rotating frame.

The rf pulse is normally described as a linearly oscillating field $2B_1\cos(\omega_\mathrm{rf}t + \psi)$. This field is equivalent to two counter-rotating fields, each with strength B_1. Only the component that rotates in the same sense as the magnetization is effective in perturbing the nuclear spins. With $|B_1/B_z| \ll 1$ the counter-rotating component is safely ignored. Thus in the

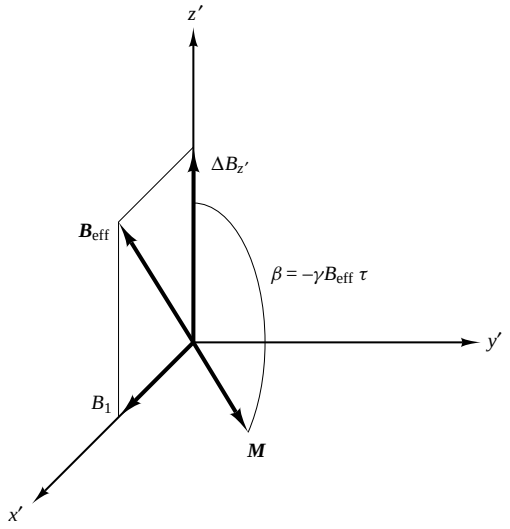

Figure 4 Magnetization precessing about the effective field $\boldsymbol{B}_{\text{eff}}$ in the coordinate frame with axes x', y' and z' rotating with the rf field. The field $\boldsymbol{B}_{\text{eff}}$ is the vector sum of the rf field B_1 along the x' axis and the offset field ΔB_z along the $z' = z$ axis

coordinate frame that rotates with the angular frequency ω_{rf}, the perturbing rf field has static components $B_{x'} = B_1 \cos\psi$ and $B_{y'} = B_1 \sin\phi$. By selecting the field $\Delta B_{z'} = B_z + \omega_{\text{rf}}/\gamma = -(\omega_0 - \omega_{\text{rf}})/\gamma$, the Bloch equations in the rotating system are identical to those of the static system. The solution to the equations is obvious. The magnetization in the rotating frame just precesses about the effective field of magnitude $B_{\text{eff}} = \sqrt{(\Delta B_{z'}^2 + {B_1}^2)}$ at the frequency $\omega' = -\gamma B_{\text{eff}}$, so that at the end of a pulse of length τ the magnetization $\boldsymbol{M}$ has been rotated through an angle $\beta = \gamma B_{\text{eff}}\,\tau$. The fields in the rotating coordinate system with $\phi = 0$ are illustrated in Figure 4.

If the rf frequency corresponds to the resonant frequency of the NMR line, then $\Delta B_{z'} = 0$ and the angle of rotation during an rf pulse $\beta = \gamma B_1 \tau$. If initially the magnetization is at equilibrium, that is directed along the z axis with $M_z = \boldsymbol{M}_0$, then an rf pulse with $\beta = \pi/2$ (90° pulse) will rotate the magnetization from along the z axis to the xy plane ($z = 0$), resulting in the maximum FID signal. The FT of this signal produces a real and an imaginary output. By selecting a combination of these two outputs, one can display either the absorption or dispersion mode NMR lines.

To calculate the rotation of off-resonant lines, the magnetization is assumed initially to be aligned along the $z' = z$ axis. The rf field B_1 is along the x' axis, and the offset field $\Delta B_{z'}$ along the z' axis of the coordinate frame rotating at the angular frequency ω_{rf}. The total field in this rotating coordinate system is the vector addition of ΔB_z and B_1 to yield $\boldsymbol{B}_{\text{eff}}$ along the z'' axis, which makes an angle θ with respect to the z' axis (Figure 4). During the rf pulse, the magnetization, initially along z', rotates about z'' through an angle $\beta = -\gamma B_{\text{eff}}\tau$. At the end of the rf pulse the magnetization in this tilted rotating coordinate system has the following values, as can be deduced with the aid of Figure 4:

$$M_{x''} = -M_0 \sin\theta \cos\beta \tag{17a}$$

$$M_{y''} = M_0 \sin\theta \sin\beta \tag{17b}$$

$$M_{z''} = M_0 \cos\theta \tag{17c}$$

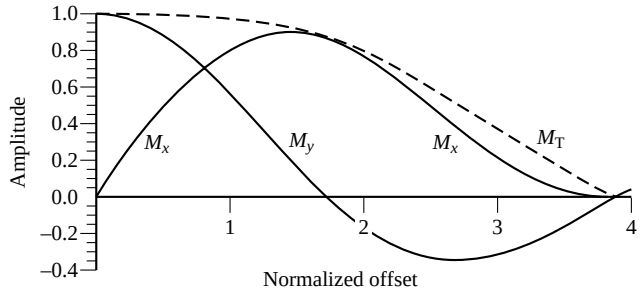

Figure 5 Plot of M_x, M_y, and M_{T} versus the normalized offset $[(\omega_{\text{o}} - \omega_{\text{rf}})/(-\gamma B_1)] = \Delta B_{z'}/B_1$. At an offset $\Delta B_{z'} = B_1$, the magnetization M_x is decreased by over 40% while the total magnetization $M_{\text{T}} = \surd[(M_{x'})^2 + (M_{y'})^2]$ is decreased by about 2%

and expressing these values in the rotating coordinate frame yields:

$$\begin{aligned} M_{x'} &= M_{x''}\cos\theta + M_{z''}\sin\theta \\ &= M_0 \sin\theta \cos\theta(1 - \cos\beta) \end{aligned} \tag{18a}$$

$$M_{y'} = M_{y''} = M_0 \sin\theta \sin\beta \tag{18b}$$

$$\begin{aligned} M_{z'} &= M_{z''}\cos\theta - M_{x''}\sin\theta \\ &= M_0(\cos^2\theta + \sin^2\theta \cos\beta) \end{aligned} \tag{18c}$$

The dependence of the signal amplitude as a function of the field offset $\Delta B_z/B_1$ is shown in Figure 5. The field strength B_1 has been selected by letting $\gamma B_1 \tau = \pi/2$, so the NMR lines near the rf ω_{rf} produce the maximum amplitude. The in-phase signals M_y and the quadrature phase signals M_x are plotted. By tracking the phase adjustment over the spectrum, one can expect to obtain an absorption or dispersion signal equal to the total transverse amplitude of the magnetization M_{T}. The phase shift $\phi = \arctan(M_{x'}/M_{y'})$ and the total pulse rotation angle β are shown in Figure 6. It can be seen that a linear correction of the phase shift will compensate fairly closely for the frequency dependent phase shift over the frequency range comparable with the rf field strength $\gamma B_1/2\pi$.

As can be seen in Figure 5, the transverse magnetization vanishes when the normalized offset equals 3.87. Redfield and Gupta[45] proposed that strong solvent lines could be suppressed by adjusting their resonance to correspond to this offset. There are a number of composite pulse patterns that can be used for

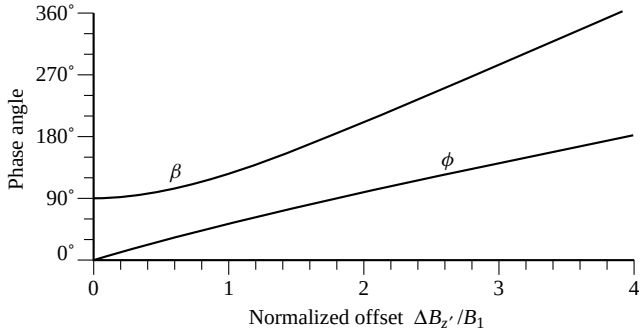

Figure 6 The phase angle ϕ and nutation angle β versus the normalized offset $\Delta B_{z'}/B_1$

solvent suppression and to extend further the useful frequency range for a given pulse power.[20,46]

5 THE FOURIER TRANSFORM SPECTROMETER ELECTRONICS

A block diagram of an early FT NMR spectrometer is shown in Figure 2. In this system the transmitter frequency is normally adjusted to be just beyond one edge of the NMR spectral region. After mixing, the received signal and transmitter frequency are sent through a bandpass filter and then digitized and stored in the digital memory of a computer. A complex DFT is performed to obtain the output spectrum. A phase adjustment that provides a means of selecting the proper ratio of real and imaginary outputs of the DFT enables one to obtain a pure absorption or dispersion mode spectrum.[15]

5.1 Required Pulse Power

For proton resonance the typical value of the rf pulse amplitude is 25 kHz (5.9×10^{-4} T) for 10 μs to produce a 90° pulse. This takes a peak power of about 25 W at 600 MHz. This is sufficient to cover a spectrum width of about 25 kHz, which is quite adequate for proton spectra which have a spectral range of about 10 ppm. Carbon-13 is more of a problem with a spectral range of about 200 ppm and a smaller magnetic moment. At 14.1 T the width of the carbon spectral range is about 30 kHz, requiring a peak rf field strength of 28×10^{-4} T at 150 MHz. This takes a power of about 250 W at the 150 MHz operating frequency.

5.2 Quadrature System

The single-channel system suffers from several drawbacks that are overcome in dual channel or quadrature systems. One problem is that noise from both sides of the transmitter frequency is mixed with the signal frequency and contributes to the output noise. The quadrature system provides a $\sqrt{2}$ increase in sensitivity by eliminating the unwanted sideband noise. Another advantage is the more efficient use of rf pulse power gained by placing the rf at the center of the spectrum.[47] A block diagram of a quadrature system is shown in Figure 7.

The single sideband operation is obtained by splitting the receiver signals into two channels, and mixing one with a reference frequency that is in phase with the transmitter frequency, and mixing the other with a reference frequency in quadrature with the transmitter frequency.[47] After low-pass filtering, each of these two channels is digitized and stored in digital memory. The FT is applied separately to the signals in each of the two channels leading to four frequency domain signals. These can then be combined to select signals from either side of the transmitter frequency and, in addition, to display the desired absorption or dispersion mode spectrum (see Figure 7).

The low-pass filters are designed to cut out all frequencies greater than $1/(2\Delta\tau)$. The bandwidth of the system extends from $f_{\mathrm{rf}} - 1/(2\Delta\tau)$ to $f_{\mathrm{rf}} + 1/(2\Delta\tau)$. Any NMR signals, or noise that is generated outside of this frequency range, to the extent they are not filtered out by the low-pass filter, are present in the output. This process is called 'aliasing'. Aliased signals can usually be detected by their different appearance since their higher frequency experiences a greater phase shift in the low-pass filter.

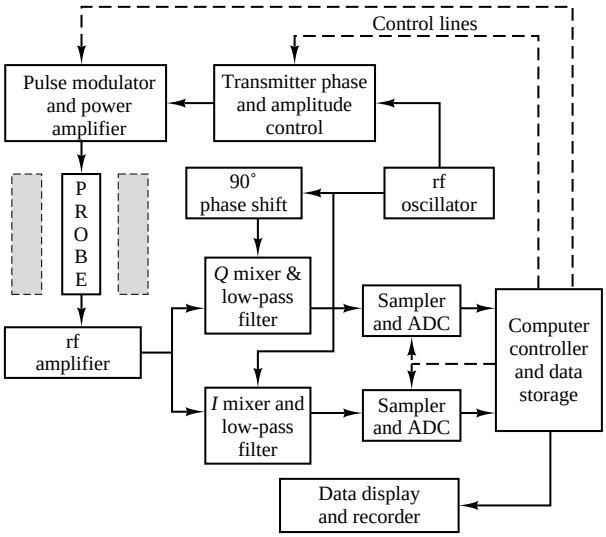

Figure 7 Block diagram of the electronics of an FT NMR spectrometer

5.3 Phase Cycling

One problem that can occur in quadrature detection systems is the incomplete separation between the NMR signals on the two sides of the transmitter frequency. This can happen if the in-phase and quadrature phase channels are not adequately matched. The gains of the two channels must be nearly identical and the two mixers must receive reference signals that have a precise 90° phase difference. In the case of a mismatch, when the signals from the two channels are combined the cancellation of the unwanted sideband is not complete. Phase cycling of the transmitter frequency is a way to get around this problem. Phase cycling is done by shifting the transmitter phase by 90° on each successive readout pulse and routing the data with the correct sign to each of the four memory channels. After a first pulse the real and imaginary data of the I mixer go to memory locations 1 and 2, and the data of the Q mixer go to memory channels 3 and 4. The phase of the next transmitter pulse is increased by 90° and the roles of the I and Q mixers are interchanged. After this pulse, the data from mixer I go to memory channels 3 and 4, taking into account the correct sign, and similarly the data of mixer Q go to memory locations 1 and 2. During the third pulse, the transmitter phase is shifted by 180° compared with the first pulse, and the outputs of the I and Q mixers go to the same locations as in the first pulse, except for a sign change. After the fourth pulse, the routing configuration is identical to that of the first pulse.[48] This process has been called CYCLOPS by Hoult and Richards.[49] With suitable spectrometer programming the task can be performed automatically. After a sufficient number of phase cycles have been completed, the data are Fourier transformed and combined in the usual way to give the complete spectrum.

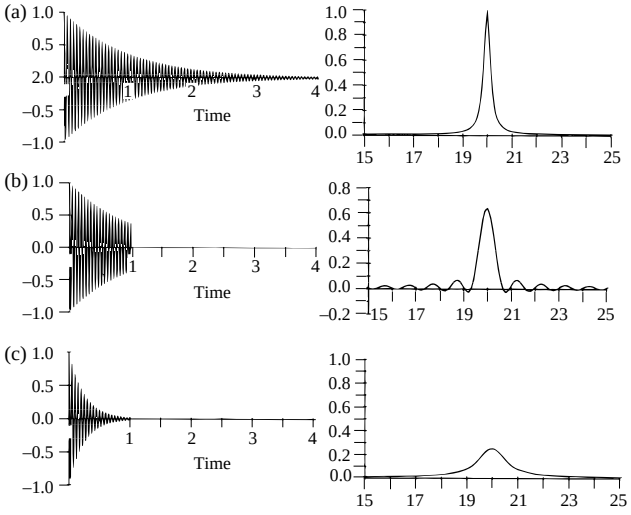

Figure 8 Simulated FID with T_2 = 1 s on the left and the corresponding FT on the right. (a) The full FID and its FT. (b) The FID truncated after 1 s and its FT. (c) The truncated FID, apodized with the function $\exp(-t/T)$ with T = 0.33 s, and its FT. In order to plot smoothed spectra, all FIDs were zero-filled before taking the FT

5.4 Digitization Rates and Number of Data Points

When taking the data, a choice must be made on the digitization rate $1/\Delta\tau$, and the total number of data points taken N. The Nyquist criterion relates the highest frequency at which nonredundant data occur in the spectrum. In a single-channel system the transmitter frequency is normally placed to one side of the NMR spectral region that is to be investigated, and so the output of the mixer contains signal frequencies from 0 to $0.5/\Delta\tau$. In a quadrature system, twice as many data points are obtained and the frequencies on the two sides of the transmitter frequency can be separated, giving spectral data from $-0.5/\Delta\tau$ to $+0.5/\Delta\tau$. The total time spent in obtaining the FID data $T = N\,\Delta\tau$ determines the density of data points in the spectrum. Stopping the data-taking process before the FID has decayed sufficiently produces 'truncation wiggles' in the spectrum (Figure 8). The truncation process is equivalent to multiplying a complete FID by a square wave of duration T. In the frequency domain this is equivalent to a convolution of the NMR spectrum with the spectrum of a square wave of width T. This problem can be avoided by taking more FID data points, N, by increasing $\Delta\tau$, or by applying a windowing function, as discussed in the next section.

5.5 Apodization Windows

To prevent a sharp discontinuity at the end of the FID, it can be multiplied by a window function that goes smoothly toward zero at the end of the FID. One such function is $\exp(-t_n/T^*)$. As mentioned above, a matched filter with the value $T^* = T_2$, goes at least part way and provides a reduction in truncation wiggles. Making T^* even smaller will further reduce the truncation wiggles; however, there is a penalty of some loss in resolution. The smoothing and loss of resolution is apparent in the illustration at the bottom of Figure 8. Another common window function is the Hanning apodization which has the form $h(t_n) = 0.5[1 + \cos(\pi t_n/T)]$. Apodization may be combined with resolution enhancement by using a function such as $0.5[1 + \cos(\pi t_n/T)]\exp(2\pi t_n/T_2)$. A number of other window functions have been used.[23]

5.6 Zero Filling

As was mentioned above, by extending the time used to record the FID, the resolution can be improved at the expense the signal-to-noise ratio. Extending the data collection of the FID after it has decayed nearly to zero will increase the noise contribution more than the signal contribution. Zero filling is the process of inserting zeros in the data field at the end of the FID in order to extend artificially the duration T. With N real FID data points one obtains $N/2$ independent complex Fourier coefficients. In general, the real and imaginary data points in the spectrum are independent. Because of causality and a Hilbert transform relationship (sometimes called the 'Kramers–Krönig relationship') between the absorption and dispersion mode signals, one can obtain N absorption data points and N dispersion data points where now each contains the full information available from the FID. Bartholdi and Ernst[50] have shown that this can be achieved by appending N zeros to the FID data field before making the FT. Appending $(2n - 1)N$ zeros to the FID, with $n > 1$, will provide an additional interpolation of points in the spectrum, thus giving a spectrum which looks smoother but contains no further information.

5.7 Linear Prediction

It may be necessary or desirable to truncate the FID before it has substantially decayed, leading to truncation wiggles. Another problem is that it may not be possible to obtain the first few data points of an FID due to the dead time of the receiver or some other reason. Linear prediction is a process that extrapolates the data already contained in the FID in order to obtain a best guess of points beyond the range of the data, either before the first data point or after the last data point. The FID can be modeled using an arbitrary number of exponentially decaying sinusoidal waves to represent the contributions from the various NMR lines. Each line can be represented by an initial amplitude, decay time constant, frequency, and phase. After determining the best fit to the model, the model can be used to calculate additional points that may be missing before the start of the FID data or beyond the end of the truncated FID. The technique has been particularly useful in straightening out the baseline of a spectrum that was made from a delayed acquisition of the FID. It can also be used for resolution enhancement and smoothing of the data.[51]

The maximum entropy method is sometimes used to obtain the best fit of data to amplitude and frequency parameters. This method of fitting the data to a model has shown encouraging results; however, the lengthy computation required has prevented its wide acceptance.[52]

6 RELATED ARTICLES

Anderson, Weston A.: Early NMR Experiences and Experiments; COSY Two-Dimensional Experiments; Double Resonance; Multidimensional Spectroscopy: Concepts; Probes for High Resolution; Selective Hartmann–Hahn Transfer in Liquids.

7 REFERENCES

1. A. A. Michelson, *Am. J. Sci.*, 1881, **22**, 120; *Phil. Mag. Ser. 5*, 1891, **31**, 256, 338; 1892, **34**, 280; *Light Waves and Their Uses*, University of Chicago Press, Chicago, IL, 1907.
2. P. Fellgett, *J. Phys. Radium*, 1958, **19**, 187; *J. Phys. (Paris)*, 1967, **28**, C2-165.
3. E. M. Purcell, H. C. Torrey, and R. V. Pound, *Phys. Rev.*, 1946, **69**, 37.
4. F. Bloch, W. W. Hansen, and M. Packard, *Phys. Rev.*, 1946, **69**, 127.
5. F. Bloch, *Phys. Rev.*, 1946, **70**, 460.
6. F. Bloch and W. W. Hansen, US Patent 2 561 489, filed 23 December 1946, issued 24 July 1951; reissued as US Patent 23 950, issued 22 February 1955.
7. B. A. Jacobsohn and R. K. Wangsness, *Phys. Rev.*, 1948, **73**, 942.
8. H. C. Torrey, *Phys. Rev.*, 1949, **76**, 1059.
9. R. H. Varian, US Patent 2 561 490, filed 28 October 1948, issued 24 July 1951; reissued as US Patent Re 23 769, issued 12 January 1954.
10. (a) E. L. Hahn, *Phys. Rev.*, 1949, **76**, 145; (b) 1950, **77**, 297; (c) 1950, **80**, 580.
11. E. L. Hahn and D. E. Maxwell, *Phys. Rev.*, 1952, **88**, 1070.
12. R. H. Varian, US Patent 3 287 629, filed 29 August 1956, issued 22 November 1966.
13. I. J. Lowe and R. E. Norberg, *Phys. Rev.*, 1957, **107**, 46.
14. W. A. Anderson, *Radiol. Today*, 1992, **9**, 1.
15. R. R. Ernst and W. A. Anderson, *Rev. Sci. Instrum.*, 1966, **37**, 93; W. A. Anderson and R. R. Ernst, US Patent 3 475 680, filed 26 May 1965, issued 28 October 1969.
16. R. R. Ernst, *J. Magn. Reson.*, 1970, **3**, 10.
17. R. Kaiser, *J. Magn. Reson.*, 1970, **3**, 28.
18. J. Dadok and R. F. Sprechen, *J. Magn. Reson.*, 1974, **13**, 243; R. K. Gupta, J. A. Ferretti, and E. D. Becker, *J. Magn. Reson.*, 1974, **13**, 275; J. A. Ferretti and R. R. Ernst, *J. Chem. Phys.*, 1976, **65**, 4283.
19. B. L. Tomlinson and H. D. W. Hill, *J. Chem. Phys.*, 1973, **59**, 1775.
20. M. H. Levitt and R. Freeman, *J. Magn. Reson.*, 1979, **33**, 473; M. H. Levitt, *Prog. NMR Spectrosc.*, 1986, **18**, 61.
21. J. Jeneer, Ampere Summer School, Basko Polje, Yugoslavia, 1971.
22. W. P. Aue, E. Bartholdi, and R. R. Ernst, *J. Chem Phys.*, 1976, **64**, 2229; R. R. Ernst, US Patent 4 134 058, filed 28 November 1977, issued 9 January 1979; US Patent 4 168 462, filed 5 June 1978, issued 18 September 1979.
23. R. R. Ernst, G. Bodenhausen, and A. Wokaun, *Principles of Nuclear Magnetic Resonance in One and Two Dimensions*, Clarenon, Oxford, 1987, Chaps. 4 and 6–9.
24. A. E. Derome, *Modern NMR Techniques for Chemistry Research*, Pergamon, Oxford, 1987, Chaps. 8–10; D. Shaw, *Fourier Transform NMR Spectroscopy*, 2nd edn, Elsevier, Amsterdam, 1984, Chap. 10
25. P. C. Lauterbur, *Bull. Am. Phys Soc.*, 1972, **18**, 86; *Nature*, 1973, **242**, 190.
26. W. S. Hinshaw, *J. Appl. Phys.*, 1976, **47**, 3709; H. R. Brooker and W. S. Hinshaw, *J. Magn. Reson.*, 1978, **30**, 129.
27. A. Kumar, D. Welti, and R. R. Ernst, *Naturwissenschaffe*, 1975, **62**, 34; A. Kumar, D. Welti, and R. R. Ernst, *J. Magn. Reson.*, 1975, **18**, 69; R. Ernst, US Patent 4 070 611, filed 13 April 1977, issued 24 January 1978.
28. W. A. Edelstein, J. M. S. Hutchinson, G. Johnson, and T. W. Redpath, *Phys. Med. Biol.*, 1980, **25**, 751; G. Johnson, J. M. S. Hutchinson, T. W. Redpath, and L. M. Eastwood, *J. Magn. Reson.*, 1983, **54**, 374.
29. P. Mansfield and D. Ware, *Phys. Lett.*, 1966, **22**, 133.
30. M. Bloom, J. H. Davis, and M. I. Valic, *Can. J. Phys.*, 1980, **58**, 1510.
31. E. R. Andrew, A. Bradbury, and R. G. Eades, *Arch. Sci.*, 1958, **11**, 223.
32. I. J. Lowe, *Phys. Rev. Lett.*, 1959, **2**, 258.
33. M. M. Maricq and J. S. Waugh, *J. Chem Phys.*, 1979, **70**, 3300; D. Muller, W. Gessner, H. J. Behrens, and G. Scheler, *Chem. Phys. Lett.*, 1981, **79**, 59.
34. S. R. Hartmann and E. L. Hahn, *Phys. Rev.*, 1962, **128**, 2042; A. Pines, M. G. Gibby, and J. S. Waugh, *Chem. Phys.*, 1973, **59**, 569.
35. J. Schaefer and E. O. Stejskal, *J. Am. Chem. Soc.*, 1976, **98**, 1031.
36. J. S. Waugh, L. M. Huber, and U. Haeberlen, *Phys. Rev. Lett.*, 1968, **20**, 180; U. Haeberlen, *Adv. Magn. Reson.*, 1976, (Suppl 1), Chaps. 4–6; B. C. Gerstein and C. R. Dybowski, *Transient Techniques in NMR of Solids, An Introduction to Theory and Practice*, Academic, Orlando, FL, 1985, Chaps. 5 and 6; E. O. Stejskal and J. D. Memory, *High Resolution NMR in the Solid State*, Oxford University Press, New York, chap. IID.
37. L. Kevan and M. Bowman, *Modern Pulsed and Continuous-Wave Electron Spin Resonance*, Wiley, New York, 1990; G. L. Mullhauser and J. H. Freed, *J. Chem. Phys.*, 1984, **81**, 37; T. Prisner, O. Dobbert, K. P. Dinse, and H. van Willigen, *J. Am. Chem. Soc.*, 1988, **110**, 1622.
38. S. Lee, B. R. Patyal, and J. H. Freed, *J. Chem. Phys.*, 1993, **98**, 3665.
39. A. G. Marshall, (ed.), *Fourier, Hadamard, and Hilbert Transforms in Chemistry*, Plenum, New York, 1982.
40. R. Bracewell, *The Fourier Transform and Its Applications*, McGraw Hill, New York, 1965, Chaps 6–8.
41. A. V. Oppenheim and R. W. Schafer, *Digital Signal Processing*, Prentice-Hall, Englewood Cliffs, NJ, 1975.
42. W. T. Cochran, J. W. Cooley, D. L. Favin, H. D. Helms, R. A. Kaenel, W. W. Lang, G. C. Maling, D. E. Nelson, C. M. Rader, and P. D. Welch, *Proc. IEEE*, 1967, **55**, 1664.
43. J. W. Cooley and J. W. Tukey, *Math. Comput.*, 1965, **19**, 297; B. Gold and C. Rader, *Digital Processing of Signals*, McGraw-Hill, New York, 1969; R. C. Singleton, *IEEE Trans. Audio Electroacoustics*, 1967, AU-15, 91.
44. For a short history of FFT algorithms see: J. W. Cooley and P. A. Welch, *Proc. IEEE*, 1967, **55**, 1675.
45. A. G. Redfield and R. K. Gupta, *J. Chem. Phys.*, 1971, **54**, 1418.
46. R. Freeman, S. P. Kempsell, and M. H. Levitt, *J. Magn. Reson.*, 1980, **38**, 453; M. H. Levitt, *J. Magn. Reson.*, 1982, **48**, 234; M. H. Levitt and R. R. Ernst, *J. Magn. Reson.*, 1983, **55**, 247.
47. R. R. Ernst, US Patent 3 501 691, filed 8 May 1968, issued 17 March 1970.
48. E. O. Stejkal and J. Schaefer, *J. Magn. Reson.*, 1974, **14**, 160.
49. D. Hoult and R. E. Richards, *Proc. R. Soc. (London), Ser. A*, 1975, **344**, 311.
50. E. Bartholdi and R. R. Ernst, *J. Mag. Reson.*, 1973, **11**, 9.
51. H. Barkhuijsen, R. de Beer, W. M. M. J. Bovée, and S. van Ormondt, *J. Magn. Reson.*, 1985, **61**, 465; C. F. Tirendi and J. F. Martin, *J. Magn. Reson.*, 1989, **81**, 557; J. F. Martin and C. F. Toremdo, *J. Magn. Reson.*, 1989, **82**, 392; D. Marion and A. D. Bax, *J. Magn. Reson.*, 1989, **83**, 205.
52. S. Sibisi, *Nature (London)*, 1983, **301**, 134; S. Sibisi, J. Skilling, R. G. Brerenton, E. D. Laue and J. Staunton, *Nature (London)*, 1984, **311**, 446; P. J. Hore, *J. Magn. Reson.*, 1985, **62**, 561; D. S. Stephenson, *Prog. NMR Spectrosc.*, 1988, **20**, 515.

Biographical Sketch

W. A. Anderson. *b* 1928. B.S., 1950, Ph.D., 1955, Stanford, CA, USA Ph.D. work under Prof. Felix Bloch on NMR. Special Assistant to the Director General of CERN, Geneva, Switzerland, 1955–56. Varian Associates, Palo Alto, CA, USA, 1955–present: Instrument Division Research Group, 1955–63; Director of Research, Instrument Division, 1963–72; Director of Systems & Techniques Laboratory, Varian Corporate Research, 1972–87; Principal Scientist, 1987–present; Varian Fellow, 1988–present. Approx. 40 publications and 40 issued US Patents.

Heteronuclear Assignment Techniques

Christopher J. Turner

Massachusetts Institute of Technology, Cambridge, MA, USA

1	Introduction	1
2	Multiplicity Determination	1
3	Heteronuclear Chemical Shift Correlation	3
4	Related Articles	8
5	References	8

1 INTRODUCTION

These days the acquisition of a proton decoupled carbon-13 spectrum is relatively straightforward; however, the interpretation of the spectrum is often much more challenging. Fortunately, there are a variety of heteronuclear assignment techniques which are available to help with this task. Aside from deductions based upon chemical shifts and relaxation properties, the most common assignment technique involves the transfer of magnetization between nuclei via spin coupling, a process often referred to as coherence transfer.

There are basically two methods of transferring magnetization between nuclei, either free precession or forced precession. In both these processes, a time (τ) is chosen which is related to the reciprocal of a coupling constant. In the former method, pulses are applied separated by a delay τ during which the transmitter is turned off. In the latter method, pulses are applied for a total time τ. Thus, the difference between the two techniques is whether the transmitter is left on, or turned off for the time τ. In the past, heteronuclear assignment techniques relied almost exclusively on the former method, i.e. combinations of pulses and delays. However, the latter method, coherence transfer in the rotating frame via multiple pulse based heteronuclear J cross polarization, also known as hetero-TOCSY, has become increasingly popular.

2 MULTIPLICITY DETERMINATION

Most heteronuclear spectra are acquired with broadband proton decoupling. Despite this, it is often desirable to determine the multiplicity, or number of directly attached protons. In theory, this information could be obtained from a proton coupled spectrum; however, in practice, this is often inconvenient because of spectral overlap and low sensitivity. Therefore, experiments have been developed which encode multiplicity information into broadband decoupled spectra. This process is often referred to as spectral editing.

2.1 APT

The attached proton test (APT) interrupts the decoupling for a time (τ) between excitation and detection. The delay τ is related to the reciprocal of an appropriate heteronuclear coupling constant, usually ^1J(C,H). During the period τ the different components of the proton coupled multiplets precess at their individual frequencies, which are governed by their heteronuclear J coupling. The recombination of these components, when the decoupler is turned back on, produces a constructive or destructive interference. The signals from methine and methyl carbons appear inverted with respect to those from quaternary and methylene carbons. However, the use of this simple sequence leads to a severe frequency dependent phase shift across the spectrum, which is normally unacceptable. This phase shift can be removed by the use of a spin echo. The echoes can be modulated by either gating the decoupler,[1–3] or by use of a 180° proton pulse synchronized with the 180° carbon pulse.[4] The two methods, shown in Figure 1, are referred to as the gated decoupler and proton flip techniques by analogy to heteronuclear two-dimensional J spectroscopy.[5] The gated decoupler method is normally used; however, the proton flip method is more interesting because it can be seen, conceptually, as a step toward the SEMUT (subspectral editing using a multiple quantum trap) experiment.

Semiclassical vector models are often used to explain echo sequences.[6] However, it is necessary to use the product operator formalism here, because of the importance of techniques based upon the generation of multiple quantum coherence. The product operator approach uses a form of shorthand algebra to follow the spin gymnastics.[7,8] Let us start with a step-by-step analysis of the product operator transformations associated with the proton flip version of the attached proton test shown in Figure 1(b), for a ^{13}C,^{1}H spin system. For simplicity only terms that contribute to the final spectrum are shown. The first step is a 90° excitation pulse acting on the z magnetization of the carbons; thus equation (1) contains an operator representing the state of the magnetization (in this case, the carbon magnetization at thermal equilibrium; $\hat{C}_z$) which is acted upon by a rotation operator (in this case, a

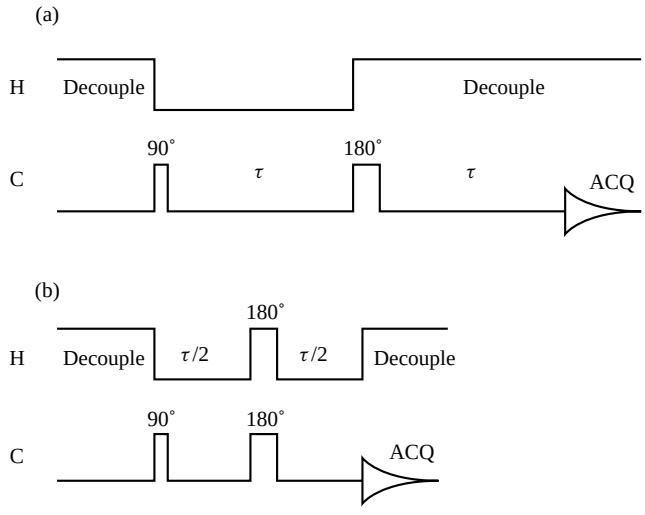

Figure 1 Basic echo sequences for heteronuclear multiplicity selection (APT). (a) Gated decoupler method; (b) spin flip method. τ is set to $1/J$ for an even/odd subspectrum. In this, and subsequent, diagrams the phase of all 180° pulses is of no practical importance, apart from the necessity of inverting the receiver reference phase if the phase of a 180° pulse is changed by 90°

rotation of the carbon magnetization about the x axis; $\hat{C}_x$):

$$\hat{C}_z \xrightarrow{(\pi/2)\hat{C}_x} -\hat{C}_y \quad (1)$$

Heteronuclear spin coupling evolves during the subsequent delay τ. The operator for spin–spin coupling is represented by $2\hat{C}_z\hat{H}_z$, that is, a rotation about the z axis for both nuclei, leading to the following:

$$-\hat{C}_y \xrightarrow{(\pi J_{CH}\tau)2\hat{C}_z\hat{H}_z} -\hat{C}_y \cos(\pi J_{CH}\tau) + 2\hat{C}_x\hat{H}_z \sin(\pi J_{CH}\tau) \quad (2)$$

If the interval τ is chosen such that $\tau = 1/(2J_{CH})$ then the cosine term becomes zero and we are left with:

$$-\hat{C}_y \xrightarrow{(\pi/2)2\hat{C}_z\hat{H}_z} +2\hat{C}_x\hat{H}_z \quad (3)$$

that is to say, two carbon magnetization vectors aligned in opposition along the $\pm x$ axes. We can ignore the simultaneous 180° pulses on both spins because they have the same effect as a single 180° pulse in a homonuclear spin system, i.e. they refocus the chemical shift while having no effect upon either homo- or heteronuclear coupling. After a further delay $\tau = 1/(2J_{CH})$ we find the two vectors are realigned again, but along the $+y$ rather than the $-y$ axis:

$$+2\hat{C}_x\hat{H}_z \xrightarrow{(\pi/2)2\hat{C}_z\hat{H}_z} \hat{C}_y \quad (4)$$

For an odd multiplicity (e.g. CH and CH_3) we can summarize this whole process as

$$\hat{C}_z \xrightarrow{(\pi/2)\hat{C}_x} -\hat{C}_y \xrightarrow{(\pi/2)2\hat{C}_z\hat{H}_z} 2\hat{C}_x\hat{H}_z \xrightarrow{(\pi/2)2\hat{C}_z\hat{H}_z} \hat{C}_y \quad (5)$$

Whereas for an even multiplicity (e.g. CH_2) these transformations become

$$\hat{C}_z \xrightarrow{(\pi/2)\hat{C}_x} -\hat{C}_y \xrightarrow{(\pi/2)2\hat{C}_z\hat{H}_z} 2\hat{C}_y\hat{H}_z \xrightarrow{(\pi/2)2\hat{C}_z\hat{H}_z} -\hat{C}_y \quad (6)$$

Notice that in the second case the magnetization passes through a magnetization state represented by the operator $2\hat{C}_y\hat{H}_z$ rather than $2\hat{C}_x\hat{H}_z$. This leads to a pairwise separation of multiplicities. Improved J compensated APT experiments have been proposed, which reduce the problems of cross-talk between the spectra due to the inevitable spread in the values of the coupling constants.[9]

2.2 SEMUT

The major disadvantage with APT is that the spectra are sorted only on the basis of even or odd multiplicity; thus, methine and methyl carbons are indistinguishable. In practice, it is more convenient to produce subspectra containing each multiplicity separately. The SEMUT pulse sequence, which is set out in Figure 2, is superior to APT in these regards.[10]

Let us follow the product operator transformations which take place during SEMUT. They take the following form when

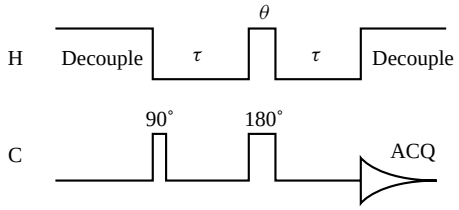

Figure 2 SEMUT pulse sequence; τ is set to $1/(2J)$

the multiplicity (n) is odd (e.g. CH_3 and CH), $\tau = 1/(2J_{CH})$ and the flip angle of the proton pulse is θ:

$$\hat{C}_z \xrightarrow{(\pi/2)\hat{C}_x} -\hat{C}_y \xrightarrow{(\pi/2)2\hat{C}_z\hat{H}_z} 2\hat{C}_x\hat{H}_z \xrightarrow{(\theta/2\pi)\hat{H}_x,(\pi)\hat{C}_x} 2\hat{C}_x\hat{H}_z \cos^n\theta \xrightarrow{(\pi/2)2\hat{C}_z\hat{H}_z} \hat{C}_y \cos^n\theta \quad (7)$$

When n is even, the product operator takes the same form at the end of the sequence, despite the fact that the magnetization passes through a state of $2\hat{C}_y\hat{H}_z$. In both cases, the spectra are edited as a function of $\cos^n\theta$. That is, the flip angle dependence for the individual CH_n intensities, $I(CH_n)$, may be written as

$$I(C) = 1 \quad (8)$$

$$I(CH) = \cos\theta \quad (9)$$

$$I(CH_2) = \cos^2\theta \quad (10)$$

$$I(CH_3) = \cos^3\theta \quad (11)$$

In practice, four different spectra are acquired with different flip angles θ, e.g. $\theta = 0°$, $\theta = 60°$, $\theta = 120°$, and $\theta = 180°$. These are combined in various proportions to produce the final C, CH, CH_2, and CH_3 subspectra. The precision of the editing procedure has been improved in the SEMUT GL sequence[11] by the introduction of a purging sandwich ($90°-\tau/2-180°-\tau/2-90°$). A further modification is that the various delays need not be equal.

2.3 INEPT

The INEPT (see ***INEPT***) was originally designed to improve the sensitivity of proton coupled heteronuclear spectra.[12] However, a modification of INEPT was later shown to be capable of multiplicity selection.[13] The pulse sequence for INEPT is set out in Figure 3. The first pulse, a 90° proton pulse about the $+x$ axis, generates transverse proton magnetization. During the following period $1/4J-180°(H,C)-1/4J$, the heteronuclear coupling (J_{CH}) evolves, while the chemical shifts of both nuclei are refocused. This produces two proton magnetization vectors aligned in opposition along the $\pm x$ axes. If a 90° pulse is applied to the protons about the $+y$ axis, longitudinal two-spin order is created, often represented by proton spin vectors aligned along the $\pm z$ axes. These population disturbances affect the carbon magnetization because

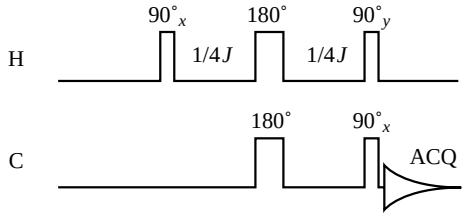

Figure 3 INEPT pulse sequence. To eliminate undesired contributions from the native ^{13}C spin magnetization, the second ^{1}H 90° should be alternately applied along the $+y$ and $-y$ axes, combined with inversion of the receiver reference phase

of their common energy levels and can be studied by a 90° pulse applied to the carbons. This process can be summarized as

$$\hat{H}_z \xrightarrow{(\pi/2)\hat{H}_x} -\hat{H}_y \xrightarrow{(\pi/2)2\hat{H}_z\hat{C}_z} 2\hat{H}_x\hat{C}_z \xrightarrow{(\pi/2)\hat{H}_y} -2\hat{H}_z\hat{C}_z \xrightarrow{(\pi/2)\hat{C}_x} 2\hat{H}_z\hat{C}_y \tag{12}$$

Proton-coupled spectra are obtained, but multiplets do not display the normal intensity distribution, because the magnetization is detected in the form $2\hat{H}_z\hat{C}_y$; thus doublets appear as +1, −1, triplets +1, 0, −1, and quartets +1, +1, −1, −1.

In order to decouple such multiplets, a delay must be added in order to allow the various components of the multiplet to interfere constructively. The length of this delay is related to both J and the multiplicity. At the center of the delay, 180° pulses are applied to both nuclei, to minimize off-resonant effects.[13] This sequence, shown in Figure 4, has been called refocused INEPT. If only a single proton is attached to each carbon then the condition for optimum signal strength is $\tau_2 = 1/4J$. However, when signals with varying multiplicities are present, a compromise value of $\tau_2 = 1/6J$ can be used which treats all multiplicities approximately equally. Alternatively, three separate spectra can be acquired with different values of τ_2, such as $\tau_2 = 1/8J$, $\tau_2 = 1/4J$, and $\tau_2 = 3/8J$, which can be used to disentangle the various multiplicities.

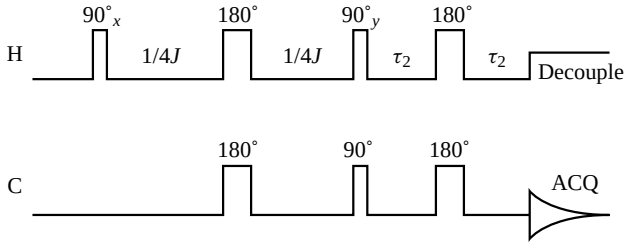

Figure 4 Refocused INEPT pulse sequence; τ_2 varies with the multiplicity of the signal to be decoupled. See text for details

Refocused INEPT has been modified to yield INEPT$^+$.[14] This improvement concerns the addition of a $90°_x$ purging pulse immediately before data acquisition so that multiplets with the normal binomial distribution pattern are obtained if the spectra are not decoupled. The INEPT$^+$ sequence is shown in Figure 5.

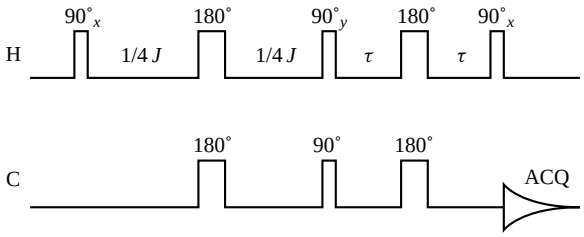

Figure 5 INEPT$^+$ pulse sequence; τ_2 is set as in refocused INEPT

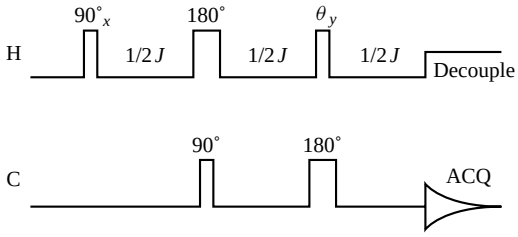

Figure 6 DEPT pulse sequence

2.4 DEPT

The DEPT experiment[15] resembles an early heteronuclear multiple quantum coherence experiment.[16] It has been widely adopted as a method of multiplicity selection because it is much less sensitive to J cross-talk than refocused INEPT. However, as a method of sensitivity enhancement it has the disadvantage that it takes three times longer than the basic INEPT sequence. The pulse sequence is set out in Figure 6.

Let us analyze the DEPT sequence for a CH group. Since the two 180° pulses serve only to refocus the chemical shift, we can ignore them in the following discussion, as well as the evolution of the chemical shift:

$$\hat{H}_z \xrightarrow{(\pi/2)\hat{H}_x} -\hat{H}_y \xrightarrow{(\pi/2)2\hat{H}_z\hat{C}_z} 2\hat{H}_x\hat{C}_z \xrightarrow{(\pi/2)\hat{C}_x} -2\hat{H}_x\hat{C}_y \xrightarrow{(\pi/2)2\hat{H}_z\hat{C}_z} -2\hat{H}_x\hat{C}_y \xrightarrow{(\theta/2\pi)\hat{H}_y} 2\hat{H}_z\hat{C}_y \sin\theta \xrightarrow{(\pi/2)2\hat{H}_z\hat{C}_z} -\hat{C}_x \sin\theta \tag{13}$$

The editing function is, to a first approximation, dependent only upon the flip angle θ, i.e. it does not depend upon J, which accounts for the superiority of DEPT over refocused INEPT as a method of multiplicity determination. Further improvements in spectral editing can be obtained with the DEPT-GL sequence.[11]

In general, multiplicity selection, or spectral editing, can be thought of as a kind of building block, which can be added to other techniques. For example, multiplicity selection has been applied to HMQC,[17] HSQC,[18] and hetero-TOCSY[19] experiments.

3 HETERONUCLEAR CHEMICAL SHIFT CORRELATION

Heteronuclear chemical shift correlation can involve either direct or indirect detection of the heteronucleus. Indirect

detection offers a sensitivity advantage of $\gamma^{3/2}$ compared with direct heteronuclear correlation. This means a sensitivity advantage of a factor of eight per transient in a ^{1}H detected ^{13}C correlation experiment, or 30 for ^{1}H detected ^{15}N correlation. For historical reasons, we start by discussing direct detection.

3.1 2D INEPT and 2D DEPT

It is useful to think of INEPT and DEPT as precursors of 2D heteronuclear chemical shift correlation experiments, despite the fact that this reverses the true chronology. The corresponding 2D experiments are formed by the introduction of an evolution period after the initial 90° pulse. Removing the heteronuclear coupling in F_1 is accomplished by the addition of a 180° pulse on the heteronucleus at the middle of the evolution time. The expansion of INEPT into a 2D experiment is shown in Figure 7.[20,21]

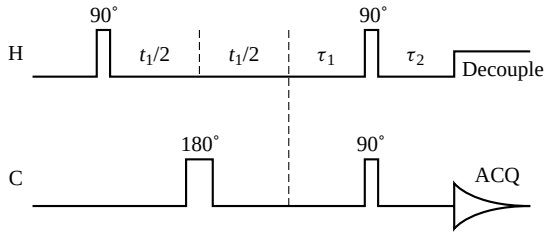

Figure 7 2D INEPT pulse sequence for heteronuclear chemical shift correlation; τ_1 is set to $1/(2J)$ while τ_2 is often set to a compromise value of $1/(3J)$. The spectra are normally displayed in the magnitude mode to avoid the problems of phase correction

Figure 8 shows the corresponding 2D DEPT experiment.[22] The 2D DEPT experiment is fully refocused, and therefore requires less frequency dependent phase correction. It also allows multiplicity determination because the correlations from CH and CH_3 moieties appear with the opposite phase to those from CH_2 moieties. Both these factors mean that 2D DEPT is probably preferable to 2D INEPT for phase sensitive work with small molecules, despite the fact that 2D DEPT is 50% longer.[23]

3.2 COLOC

2D INEPT or 2D DEPT was designed to utilize the large direct (one bond) coupling constant for the heteronuclear coherence transfer. While it is possible to use these sequences

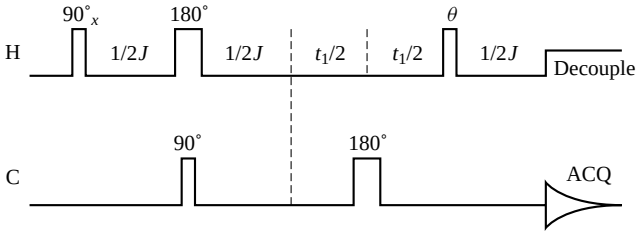

Figure 8 2D DEPT pulse sequence. Phase sensitive displays are often used which enable even/odd multiplicity determination

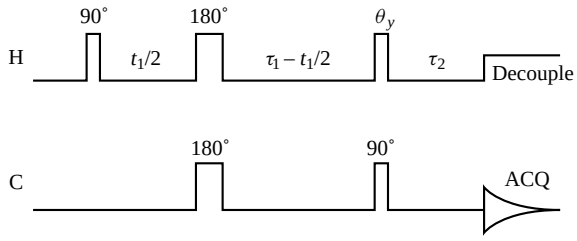

Figure 9 COLOC pulse sequence for heteronuclear chemical shift correlation through multiple bonds

for the study of long-range (multiple bond) heteronuclear correlation, it is preferable to use a sequence designed to incorporate a constant value of the evolution time,[24] because there is considerable loss of magnetization due to proton relaxation during t_1 and the delay τ_1, as well as carbon relaxation during the delay τ_2. In so-called 'constant time' experiments the evolution time is placed inside the τ_1 delay, as shown in Figure 9. This reduces the total time during which proton transverse relaxation takes place. The most popular technique is called COLOC,[25] although a variety of other sequences have been proposed.[26,27]

3.3 Relay

If a homonuclear correlation step is inserted into a heteronuclear correlation experiment we arrive at the sequence shown in Figure 10 which can be described as a proton relayed heteronuclear correlation experiment.[28] Additional signals, so-called 'relayed' peaks, appear in the spectrum which provide indirect information on connectivity of the heteronuclei. The 2D spectrum has the heteronuclear chemical shift on one axis, with signals from the directly bonded protons and protons to which they are coupled, for example their ^{3}J(HCCH) neighbors, along the other axis. Thus, the relay experiment provides complementary data to a long-range heteronuclear correlation experiment.

After proton evolution with heterodecoupling, a homonuclear transfer takes place from one proton to other protons which are spin coupled to it. The evolution of the proton chemical shift is refocused during this transfer by the first proton 180° pulse. It is also desirable to refocus the proton chemical shift during the subsequent heteronuclear transfer. This leads to a sequence with two adjacent 180° proton pulses, as shown in Figure 10. However, this can be simplified because it is

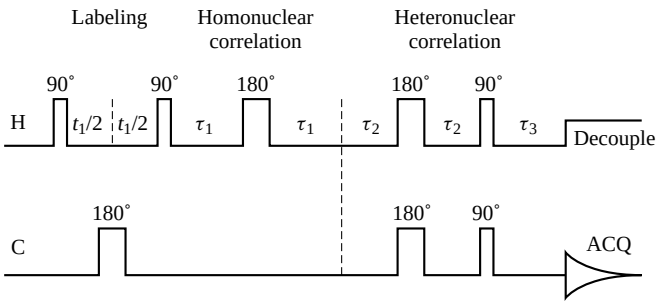

Figure 10 Proton relayed heteronuclear chemical shift correlation sequence

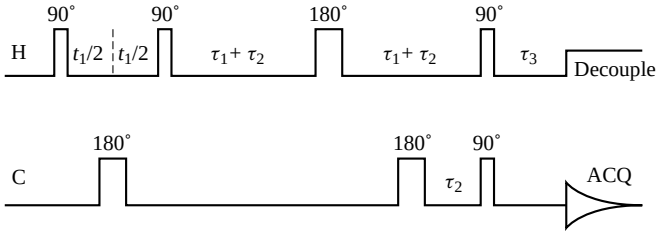

Figure 11 Optimized proton relayed heteronuclear chemical shift correlation sequence

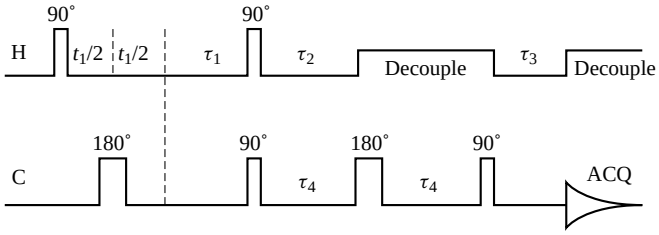

Figure 12 Carbon relayed heteronuclear chemical shift correlation sequence

often possible to concatenate 180° pulses; thus the two adjacent proton 180° pulses can be replaced by a single one in the middle of the delays $2\tau_1$ and $2\tau_2$ without changing the net effect,[29–31] as shown in Figure 11. The reverse experiment is also possible, that is, to relay the magnetization via the heteronucleus, as shown in Figure 12.[32]

3.4 Indirect Detection

Indirect detection has become the standard method of performing heteronuclear correlation. Both single or multiple quantum correlation techniques are in use. The heteronuclear multiple quantum experiments are derivatives of experiments originally proposed by Müller.[16] Most of the heteronuclear single quantum experiments are variations of a double INEPT experiment first proposed by Bodenhausen and Ruben.[33] It can be shown, both theoretically and practically, that experiments involving single quantum correlation have several advantages.[34,35]

3.5 HMQC

Heteronuclear multiple quantum correlation (HMQC) was initially very popular as a method of performing indirect detection experiments.[36] The HMQC pulse sequence is shown in Figure 13. For a heteronuclear H–C system, the experiment can be described as

$$\hat{H}_z \xrightarrow{(\pi/2)\hat{H}_x} -\hat{H}_y \xrightarrow{(\pi/2)2\hat{H}_z\hat{C}_z} -2\hat{H}_x\hat{C}_z \xrightarrow{(\pi/2)\hat{C}_x} -2\hat{H}_x\hat{C}_y$$
$$\xrightarrow{t_1} -2\hat{H}_x\hat{C}_y\cos\Omega_c t_1 \xrightarrow{(\pi/2)\hat{C}_x} -2\hat{H}_x\hat{C}_z\cos\Omega_c t_1 \qquad (14)$$

where Ω_c denotes the angular offset frequency of the carbon spin. The above expression predicts that the detected in-phase ^{1}H signal (H_y) is modulated in amplitude by Ω_c, giving

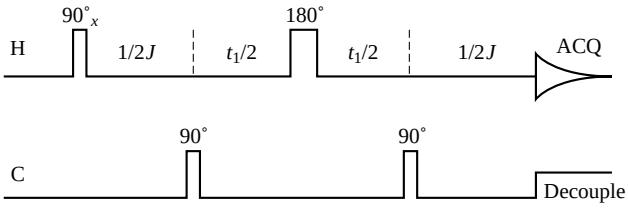

Figure 13 HMQC pulse sequence for ^{1}H detected heteronuclear chemical shift correlation utilizing heteronuclear multiple quantum coherence during the evolution period

rise to a single absorptive correlation in the 2D spectrum. Unfortunately this is not the whole story. Additional protons have an important effect. Consider an I–K–S spin system (where both I, K = ^{1}H, S = ^{13}C or ^{15}N), that is, the effect of a second proton K. The relatively small homonuclear coupling J_{IK} can safely be neglected during the delay τ. However, it cannot be neglected during the evolution time. Consequently the magnetization at the beginning of the detection period can be summarized as

$$-\hat{I}_y\cos\pi J_{IK}t_1\cos\Omega_s t_1 + 2\hat{I}_x\hat{K}_z\sin\pi J_{IK}t_1\cos\Omega_s t_1 \qquad (15)$$

The multiplet pattern resembles that of a 2D J spectrum, in that it is phase modulated in t_1. Thus, it is impossible to obtain pure phases. Another disadvantage of HMQC is that the spectrum will display homonuclear J coupling in the F_1 dimension. There is yet another problem with the resolving power of HMQC, in that the linewidth in the F_1 dimension is determined by the relaxation rate of the multiple quantum coherence $\hat{H}_x\hat{C}_y$. This often leads to broadening, since multiple quanta usually relax faster than single quanta.[34,35]

Quite a few modifications to the basic HMQC sequence have been proposed.[37–40] For example, it is often desirable to perform heteronuclear correlation without presaturation of the water signal. One method of achieving this is to replace the 90° and 180° ^{1}H pulses with jump-and-return pulses as shown in Figure 14.[41]

The suppression of spurious signals which originate from protons not bonded to the heteronucleus can be improved in a variety of ways. The most common of these is to precede HMQC by a so-called BIRD (bilinear rotational decoupling) sequence as shown in Figure 15.[42] The BIRD sequence inverts the z magnetization of protons attached to ^{12}C while leaving the magnetization of the protons attached to ^{13}C unaffected. A relaxation delay is added between the BIRD and the start of the HMQC sequence, in a manner reminiscent of WEFT.[43] The idea is to use differential relaxation as a method of improving the suppression of the unwanted signals from ^{12}C. Since ^{13}C has a spin, protons attached to ^{13}C will relax faster than those attached to ^{12}C. Thus, it may be possible to choose a delay

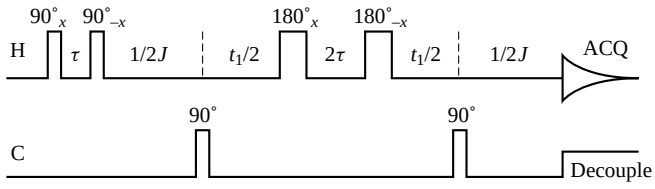

Figure 14 HMQC correlation in H_2O without presaturation

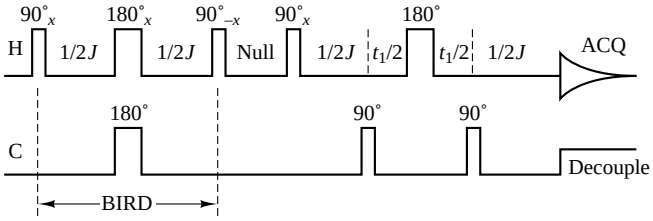

Figure 15 HMQC pulse sequence with BIRD presaturation of protons coupled to ^{12}C

such that the signal from all the protons attached to ^{12}C are approximately nulled, while all the protons attached to ^{13}C have relaxed. However, this method is unattractive for large molecules because they often exhibit a negative NOE, in which case, cross relaxation between the inverted protons attached to ^{12}C and the noninverted protons attached to ^{13}C will decrease the signal intensity.

3.6 Flip-back

An alternative approach, which avoids the problem of sensitivity loss by cross relaxation, is to refocus the magnetization of the protons attached to ^{12}C prior to the evolution period.[16] The in-phase magnetization from the protons attached to ^{12}C can then be flipped back to the $+z$ axis while the heteronuclear antiphase magnetization is unaffected. The sequence is shown in Figure 16. The sequence starts with $90^\circ_x(^1\text{H})-1/(4J)-180^\circ(^1\text{H},^{13}\text{C})-1/(4J)-$, where the simultaneous 180° pulses refocus chemical shift evolution. At the end of this period, all protons coupled to the heteronucleus are antiphase ($\hat{I}_x\hat{S}_z$) with respect to the heteronuclear coupling. Since the proton homonuclear coupling constants J(H, H) are usually much smaller than ^1J(C,H), all protons attached to ^{12}C still have essentially only in-phase magnetization (I_y). This allows a separation of protons attached to ^{12}C and ^{13}C by the action of a $90^\circ_x(^1\text{H})$ pulse at the end of the preparation period. The $90^\circ_x(^1\text{H})$ pulse flips the in-phase ^{1}H magnetization I_y of the protons attached to ^{12}C to the $-z$ axis while the antiphase I_xS_z remains unaffected. However, at the same time the $90^\circ_x(^{13}\text{C})$ converts the antiphase magnetization, I_xS_z, into heteronuclear two-spin coherence I_xS_y, which evolves during t_1. The 180° pulse at the midpoint of the evolution time interchanges the zero and double quantum frequencies. Not only does this eliminate the ^{1}H chemical shift component from the multiple quantum frequency, as in HMQC, but it also it flips the protons attached to ^{12}C back to the $+z$ axis. Cross relaxation then causes the rapid recovery of the longitudinal magnetization of the protons attached to ^{13}C.

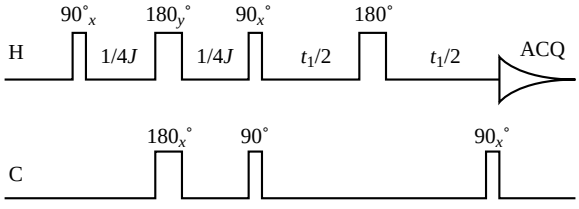

Figure 16 Flip-back chemical shift correlation

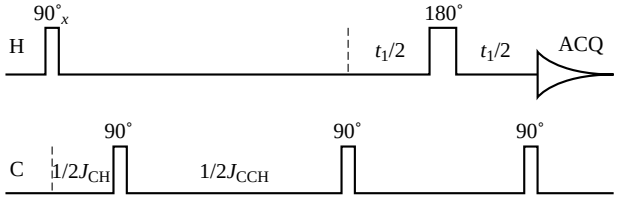

Figure 17 HMBC pulse sequence for ^{1}H detected heteronuclear multiple bond correlation utilizing heteronuclear multiple quantum coherence during the evolution period. The first ^{13}C 90° serves as a low-pass J filter. The spectra are normally displayed in the magnitude mode to avoid the problems of phase correction

Unfortunately, this modification is unsuitable if ^{13}C decoupling is desired during data acquisition, because the ^{1}H chemical shifts are in-phase at the end of the evolution period, whereas the decoupling should be started at a time $1/(2J_{\text{CH}})$ later.

3.7 HMBC

A simple extension of the HMQC experiment can be used to determine long range (two and three bond) correlations. It is convenient to add a low-pass J filter, to suppress the direct one bond correlations.[44] The resulting HMBC sequence is shown in Figure 17.[45]

Many applications of indirect detection focus on nuclei such as ^{13}C and ^{15}N; however, other interesting applications of long-range heteronuclear correlation techniques concern the indirect detection of phosphorus. In these cases, where the T_1 of the heteronucleus is shorter than the T_1 of the protons but its T_2 is longer than that of the protons, a different approach may be preferable.[46]

3.8 HSQC

The heteronuclear single quantum correlation experiment has become increasingly popular in recent years.[33] The pulse sequence is set out in Figure 18. This experiment employs an INEPT sequence[12] to transfer proton z magnetization into antiphase nitrogen magnetization. Proton decoupling during the evolution time is accomplished with a 180° proton pulse at the midpoint of the evolution time. A subsequent reverse INEPT transfer reconverts the transverse ^{13}C magnetization into observable ^{1}H magnetization. This can be summarized as

$$\hat{H}_z \xrightarrow{\text{INEPT}} -2\hat{H}_z\hat{C}_y \xrightarrow{t_1} -2\hat{H}_z\hat{C}_y\cos\Omega_c t_1 \xrightarrow{\text{reverseINEPT}} -\hat{H}_x\cos\Omega_c t_1 \qquad (16)$$

The 2D spectrum displays neither ^{1}H–^{1}H nor ^{1}H–^{13}C spin coupling in the F_1 dimension. However, ^{13}C–^{13}C spin coupling is active in the F_1 dimension, but this will normally only be visible in isotopically enriched samples. The transverse relaxation rate of $\hat{H}_z\hat{C}_y$ corresponds to the sum of the relaxation rate of $\hat{C}_y$, i.e. the reciprocal of the ^{13}C T_2, and the longitudinal relaxation rate of $\hat{H}_z$. This latter contribution is often described as scalar relaxation of the

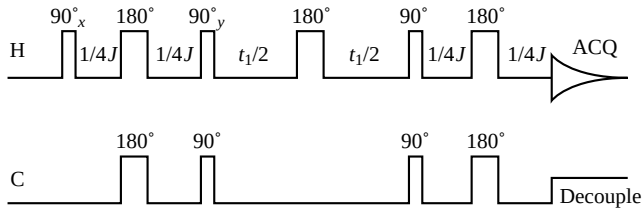

Figure 18 HSQC pulse sequence (sometimes known as the Overbodenhausen correlation experiment) utilizing heteronuclear single quantum coherence during the evolution time, and a 180° ^{1}H pulse to remove the net effect of heteronuclear coupling

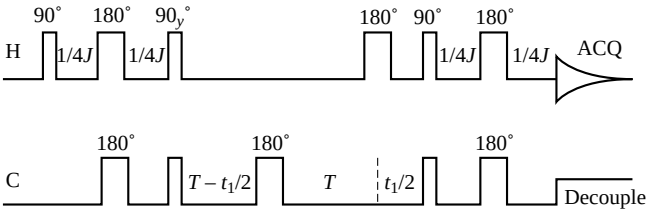

Figure 19 Constant time HSQC pulse sequence for heteronuclear correlation of isotopically enriched species

second kind.[47] Whenever H_z changes its spin state, the ^{13}C doublet component changes its frequency by J(C, H), therefore the F_1 linewidth corresponds to the ^{13}C linewidth in a ^{1}H coupled ^{13}C spectrum.

There are two major modifications to the HSQC experiment. They both pertain to resolution enhancement. Firstly, the constant time HSQC experiment shown in Figure 19 removes the effects of ^{13}C–^{13}C coupling in the F_1 dimension.[48–50] Secondly, much narrower lines can be obtained by decoupling during the evolution time as shown in Figure 20.[35]

3.9 Inverse Relay

Since relay experiments involve a combination of a heteronuclear and a homonuclear correlation step, i.e. a combination of two separate 2D experiments, they are particularly suitable for the application of 3D spectroscopy. In the past, the relay step was performed by pulsed methods; however, it is now more common to use TOCSY for this purpose. We examine two examples here, that of 2D HMQC–TOCSY[51] and 3D TOCSY–HMQC.[52] The 2D HMQC–TOCSY sequence is shown in Figure 21. The sequence combines HMQC and TOCSY in a straightforward manner. At the beginning of the TOCSY mixing step, the ^{1}H magnetization is aligned along the y axis and modulated in

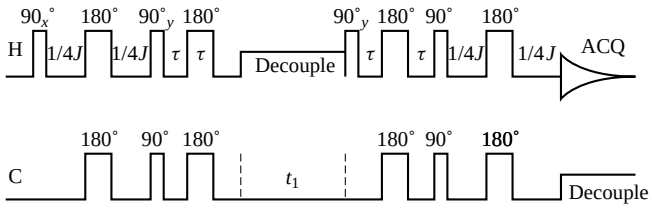

Figure 20 Decoupled HSQC pulse sequence utilizing a composite pulse decoupling scheme preceded by a refocusing interval

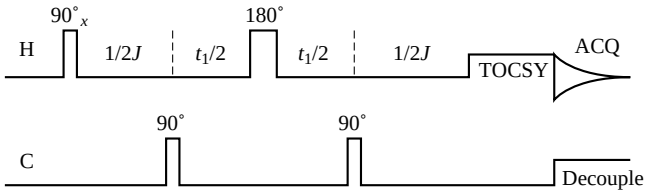

Figure 21 2D HMQC–TOCSY pulse sequence

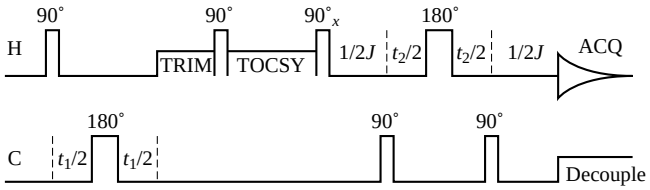

Figure 22 3D TOCSY–HMQC pulse sequence

amplitude by the heteronuclear chemical shift. The TOCSY mixing scheme then redistributes the magnetization of the heteronuclear coupled proton over all its coupling partners. So, in the final 2D spectrum, all coupled protons will be modulated by the frequency of the heteronucleus. A 3D version of the opposite combination is shown in Figure 22.

3D ^{1}H–^{15}N TOCSY–HMQC spectra can be used to identify spin systems in macromolecules, such as proteins.[53] The idea is to correlate the NH ^{1}H and ^{15}N chemical shifts of each amino acid residue with the corresponding C-αH ^{1}H chemical shifts. The first step of this process is to allow the aliphatic ^{1}H chemical shifts to evolve during the period t_1. The magnetization of the aliphatic protons is transferred by TOCSY to the corresponding intraresidue NH protons. Subsequently the NH ^{1}H magnetization is transferred to the directly bonded ^{15}N spins by HMQC. A 3D ^{1}H–^{15}N TOCSY–HMQC spectrum has the appearance of a regular 2D TOCSY spectrum apart from the fact that the signals are spread out over a series of slices edited by the ^{15}N chemical shifts.

3.10 Hetero-TOCSY

Since its first description by Hartmann and Hahn,[54] coherence transfer in the rotating frame has found wide application as a method of improving the repetition rate in solid state experiments. Although the possibility of using heteronuclear cross polarization as a method of chemical shift correlation in liquids was recognized and demonstrated long ago,[55,56] technical problems have prevented its widespread use. The solution to many of these problems has appeared as a byproduct of the interest generated by homonuclear cross polarization, otherwise known as TOCSY.[57]

Cross polarization experiments are normally carried out by applying a 90° pulse to one of the spins, followed by simultaneously spin locking both nuclei. When these spin lock fields are larger than the chemical shift, the Hamiltonian reduces to the spin–spin interaction terms, which are dipolar in origin for solids and scalar for isotropic liquids. Cross polarization occurs when the effective secondary nutation frequency of both rotating frames is the same. This is referred to as the Hartmann–Hahn condition, and has to be matched

better than the interaction frequency between the spins.[58] This is easy in solids where the large dipolar fields constitute the interaction between the spins. However, in isotropic liquids, the interaction is spin–spin coupling, giving rise to the name *J* cross polarization. The one bond coupling between ^{13}C and ^{1}H is about 140 Hz, while rf fields of the order of 10 kHz are necessary to excite the nuclei evenly. Thus, in liquids the rf amplitudes need to be matched to better than 1%, which renders the experiment technically very demanding. However, the simultaneous use of multiple pulse mixing schemes on both channels has alleviated this problem.[59–62]

The advantages of hetero-TOCSY become most apparent when long range correlation experiments are considered; for example, hetero-TOCSY has been shown to be extremely useful for ^{1}H detected ^{31}P correlation spectroscopy of nucleic acids.[63,64]

4 RELATED ARTICLES

Composite Pulses; COSY Two-Dimensional Experiments; Half-Filter Experiments: Proton–Carbon-13; Heteronuclear Shift Correlation Spectroscopy; INADEQUATE Experiment; INEPT; Multidimensional Spectroscopy: Concepts; Multiple Quantum Spectroscopy of Liquid Samples; NOESY; Phase Cycling; Relayed Coherence Transfer Experiments; ROESY; Two-Dimensional J-Resolved Spectroscopy; Water Signal Suppression in NMR of Biomolecules.

5 REFERENCES

1. C. Le Cocq and J.-Y. Lallemand, *J. Chem. Soc., Chem. Commun.*, 1981, 150.
2. D. W. Brown, T. T. Nakashima, and D. L. Rabenstein, *J. Magn. Reson.*, 1981, **45**, 302.
3. S. L. Patt and J. N. Shoolery, *J. Magn. Reson.*, 1982, **46**, 535.
4. F.-K. Pei and R. Freeman, *J. Magn. Reson.*, 1982, **48**, 318.
5. G. Bodenhausen, R. Freeman, and D. L. Turner, *J. Chem. Phys.*, 1976, **65**, 839; G. Bodenhausen, R. Freeman, R. Niedermeyer, and D. L. Turner, *J. Magn. Reson.*, 1977, **26**, 133.
6. C. J. Turner, *Progr. Nucl. Magn. Reson. Spectrosc.*, 1984, **16**, 311.
7. O. W. Sørensen, G. W. Eich, M. H. Levitt, G. Bodenhausen, and R. R. Ernst, *Progr. Nucl. Magn. Reson. Spectrosc.*, 1983, **16**, 163.
8. H. Kessler, M. Gehrke, and C. Griesinger, *Angew. Chem., Int. Ed. Engl.*, 1988, **27**, 490.
9. A. M. Torres, T. T. Nakashima, and R. E. D. McClung, *J. Magn. Reson., Ser. A*, 1993, **101**, 285.
10. H. Bildsoe, S. Donstrup, H. J. Jakobsen, and O. W. Sørensen, *J. Magn. Reson.*, 1983, **53**, 154.
11. O. W. Sørensen, S. Donstrup, H. Bildsoe, and H. J. Jakobsen, *J. Magn. Reson.*, 1983, **55**, 347.
12. G. A. Morris and R. Freeman, *J. Am. Chem. Soc.*, 1979, **101**, 760.
13. D. P. Burum and R. R. Ernst, *J. Magn. Reson.*, 1980, **39**, 163.
14. O. W. Sørensen and R. R. Ernst, *J. Magn. Reson.*, 1983, **51**, 477.
15. D. M. Doddrell, D. T. Pegg, and M. R. Bendall, *J. Magn. Reson.*, 1982, **48**, 323.
16. L. Müller, *J. Am. Chem. Soc.*, 1979, **101**, 4481.
17. L. E. Kay and A. Bax, *J. Magn. Reson.*, 1989, **84**, 598.
18. D. G. Davis, *J. Magn. Reson.*, 1991, **91**, 665.
19. T. Domke and L. McIntyre, *J. Magn. Reson.*, 1992, **96**, 143.
20. R. Freeman and G. A. Morris, *J. Chem. Soc., Chem. Commun.*, 1978, 684.
21. M. W. Edwards and A. Bax, *J. Am. Chem. Soc.*, 1986, **108**, 918.
22. M. R. Bendall and D. T. Pegg, *J. Magn. Reson.*, 1983, **53**, 144.
23. H. Kessler, C. Griesinger, and G. Zimmermann, *Magn. Reson. Chem.*, 1987, **25**, 579.
24. A. Bax and R. Freeman, *J. Magn. Reson.*, 1981, **44**, 542.
25. H. Kessler, C. Griesinger, J. Zarbock, and H. R. Loosli, *J. Magn. Reson.*, 1984, **57**, 331.
26. G. E. Martin and A. S. Zektzer, *Magn. Reson. Chem.*, 1988, **26**, 631.
27. W. F. Reynolds, S. McLean, M. Perpick-Dumont, and R. G. Enriquez, *Magn. Reson. Chem.*, 1989, **27**, 162.
28. P. H. Bolton and G. Bodenhausen, *Chem. Phys. Lett.*, 1982, **89**, 139.
29. A. Bax, *J. Magn. Reson.*, 1983, **53**, 149.
30. P. H. Bolton, *J. Magn. Reson.*, 1983, **54**, 333.
31. H. Kessler, M. Bernd, H. Kogler, J. Zarbock, O. W. Sørensen, G. Bodenhausen, and R. R. Ernst, *J. Am. Chem. Soc.*, 1983, **105**, 6944.
32. H. Kessler, W. Bermel, and C. Griesinger, *J. Magn. Reson.*, 1985, **62**, 573.
33. G. Bodenhausen and D. J. Ruben, *Chem. Phys. Lett.*, 1980, **69**, 185.
34. T. J. Norwood, J. Boyd, J. E. Heritage, N. Soffe, and I. D. Campbell, *J. Magn. Reson.*, 1990, **87**, 488.
35. A. Bax, M. Ikura, L. E. Kay, D. A. Torchia, and R. Tschudin, *J. Magn. Reson.*, 1990, **86**, 304.
36. A. Bax, R. H. Griffey, and B. L. Hawkins, *J. Am. Chem. Soc.*, 1983, **105**, 7188.
37. A. G. Redfield, *Chem. Phys. Lett.*, 1983, **96**, 537.
38. D. Brühwiler and G. Wagner, *J. Magn. Reson.*, 1986, **69**, 546.
39. G. Otting and K. Wüthrich, *J. Magn. Reson.*, 1988, **76**, 569.
40. E. R. P. Zuiderweg, *J. Magn. Reson.*, 1990, **86**, 346.
41. S. Roy, M. Z. Papastavros, V. Sanchez, and A. G. Redfield, *Biochemistry*, 1984, **23**, 4395.
42. A. Bax and S. Subramanian, *J. Magn. Reson.*, 1986, **67**, 565.
43. S. L. Patt and B. D. Sykes, *J. Chem. Phys.*, 1972, **56**, 3182.
44. H. Kogler, O. W. Sørensen, G. Bodenhausen, and R. R. Ernst, *J. Magn. Reson.*, 1983, **55**, 157.
45. A. Bax and M. F. Summers, *J. Am. Chem. Soc.*, 1986, **108**, 2093.
46. V. Sklenar, H. Miyashiro, G. Zon, H. T. Miles, and A. Bax, *FEBS Lett.*, 1986, **208**, 94.
47. A. Abragam, *The Principles of Nuclear Magnetism*, Clarendon Press, Oxford, 1961.
48. J. Santoro and G. C. King, *J. Magn. Reson.*, 1992, **97**, 202.
49. F. J. M. Van de Ven and M. E. P. Philippens, *J. Magn. Reson.*, 1992, **97**, 637.
50. G. W. Vuister and A. Bax, *J. Magn. Reson*, 1992, **98**, 428.
51. L. Lerner and A. Bax, *J. Magn. Reson.*, 1986, **69**, 375.
52. D. Marion, P. C. Driscoll, L. E. Kay, P. T. Wingfield, A. Bax, A. M. Gronenborn, and G. M. Clore, *Biochemistry*, 1989, **28**, 6150.
53. G. M. Clore, A. Bax, P. C. Driscoll, P. T. Wingfield, and A. M. Gronenborn, *Biochemistry*, 1990, **29**, 8172.
54. S. R. Hartmann and E. L. Hahn, *Phys. Rev.*, 1962, **128**, 2042.
55. A. A. Maudsley, L. Müller, and R. R. Ernst, *J. Magn. Reson.*, 1977, **28**, 463.
56. L. Müller and R. R. Ernst, *Mol. Phys.*, 1979, **38**, 963.

57. L. Braunschweiler and R. R. Ernst, *J. Magn. Reson.*, 1983, **53**, 521.
58. G. C. Chingas, A. N. Garroway, R. D. Bertrand, and W. B. Moniz, *J. Chem. Phys.*, 1981, **74**, 127.
59. D. W. Bearden and L. R. Brown, *Chem. Phys. Lett.*, 1989, **163**, 432.
60. E. R. P. Zuiderweg, *J. Magn. Reson.*, 1990, **89**, 533.
61. D. Y. Artemov, *J. Magn. Reson.*, 1991, **91**, 405.
62. G. A. Morris, *Magn. Reson. Chem.*, 1991, **29**, 83.
63. G. W. Kellogg, A. A. Szewczak, and P. B. Moore, *J. Am. Chem. Soc.*, 1992, **114**, 2727.
64. K. Y. Wang, I. Goljer, and P. H. Bolton, *J. Magn. Reson., Ser. B*, 1994, **103**, 192.

Biographical Sketch

Christopher J. Turner. *b* 1945. B.Sc., 1967, Ph.D., 1972, Chemistry, University of London, UK. Postdoctoral work, City of London Polytechnic, 1972–75, Queen Elizabeth College, 1975–77. NMR applications chemist, Varian, 1977–82. Manager of the NMR Facility, Department of Chemistry, Columbia University, New York, 1982–92. NMR spectroscopist, Francis Bitter National Magnet Laboratory, Massachusetts Institute of Technology, 1992–present. Approx. 50 publications. Research specialties: steady state effects in multidimensional data acquisition.

Liouville Equation of Motion

Charles L. Mayne
University of Utah, Salt Lake City, UT, USA

1	Introduction	1
2	Operators and Operator Bases	1
3	Some Commonly Used Bases	7
4	The Density Operator	10
5	Superoperators	13
6	Related Article	14
7	References	14

1 INTRODUCTION

Nuclear magnetic resonance is uniquely capable of revealing structure and dynamics on a molecular level. An understanding of nuclear spin relaxation is fundamental to an understanding of nuclear magnetic resonance in general. The theoretical framework needed to promote this understanding is conveniently constructed in terms of the time evolution of the density operator under the influence of some Hamiltonian as expressed by the Liouville–von Neuman equation. The emphasis here will be on molecules in liquids, though many of the principles presented are applicable to solids and gases. The experimental observables of NMR are oscillatory magnetizations induced in a sample as a consequence of subjecting it to various static and time-varying magnetic fields. The quantum mechanical operators corresponding to these observables act only on the nuclear spin degrees of freedom of the system. Furthermore, these operators are proportional to the spin angular momentum operators or products thereof, and, hence, can be dealt with using finite basis sets of states or operators. Relaxation, however, is a consequence of interactions between the nuclear spins and the rest of the system, referred to as the 'lattice'. In most cases, the lattice cannot be treated exactly using quantum mechanics, because the density operator and the Hamiltonian cannot be defined exactly. The strategy generally employed, then, is to treat the effects of the lattice classically as a random time-dependent modulation of the nuclear spin operators while retaining a quantum mechanical description of the nuclear spins themselves. All externally applied magnetic fields are likewise treated classically. Our goal is to derive equations that correctly describe the observed temporal behavior of the experimental observables. This is done by proposing a Hamiltonian for the system under study, solving the Liouville–von Neuman equation for the time evolution of the density operator, computing the expected time evolution of the experimental observables, and comparing the result with measured values of these observables. Secondly, one wants to extract from this temporal behavior of the observables information about the fundamental nature of the system under investigation. For example, internuclear distances and rates of molecular reorientation due to Brownian motion can dramatically affect the results of an NMR experiment. How can this kind of information be extracted from the behavior of the magnetization in a sample as a function of time? This article will lay out the theoretical framework of NMR experiments, with emphasis on an understanding of nuclear spin relaxation in liquids.

This article presumes a basic knowledge of the nuclear magnetic resonance phenomenon, including nuclear spin polarization in an external static magnetic field and interaction of nuclear spins with applied radiofrequency fields. For those not acquainted with these concepts, several basic texts may be consulted.[1–3] The reader is assumed to have some grasp of basic quantum mechanics and angular momentum theory at the level generally taught in undergraduate physical chemistry courses. Some command of linear algebra and integral and differential calculus is also assumed. All abbreviations and symbols are either defined in the endpapers or are defined in context. Vectors and matrices will be distinguished by bold italic and bold roman type, respectively, and the same symbol in normal weight type will denote the magnitude of a vector or, with appropriate subscripts, components of a vector or elements of a matrix. Quantum mechanical operators will have a hat, for example, $\hat{\mathcal{H}}$. Liouville space operators will have a double hat, for example $\hat{\hat{\mathcal{L}}}$.

It is a familiar concept that the wavefunction embodies all that can be known about a quantum mechanical system and that any wavefunction can be expressed as a linear combination of the members of a complete set of eigenfunctions of the Hamiltonian of the system. However, in NMR, the density operator has proven to be a more convenient vehicle for this information, and the density operator, the Hamiltonian, and all other operators associated with the system can be cast as linear combinations of a complete set of orthonormal operators. These two descriptions are completely equivalent, and each can be formulated from the general concepts embodied in the bracket notation introduced by Dirac[4] to describe abstract vector spaces. For nuclear spin systems in liquids, it is often possible to focus on a small number of spins (all the spins in one molecule, for example) and to consider the macroscopic sample as an ensemble of such systems, identical in their dependence on quantum mechanical operators but sampling the distribution of random classical variables. Since each nuclear spin has only a small number of eigenstates and the number of eigenstates for the whole system is the product of the numbers for each of the component spins, the necessary mathematics reduces, by means of an ensemble average, to a problem in linear algebra of reasonable dimension. In the following sections, the mathematics needed to discuss most of the experiments done on liquid samples will be formulated. Space limitations make it impossible to give a completely detailed exposition; for this, the reader may consult several excellent texts.[5–9]

2 OPERATORS AND OPERATOR BASES

When a quantum mechanical system has a finite number of discrete energy levels (suppose there are n of them), the operators and states of the system can be represented as matrices and vectors in an n-dimensional vector space. Thus, the algebra of abstract n-dimensional vector spaces is essential to the theory we wish to develop. Dirac developed a convenient notation for describing these concepts.

2.1 Dirac Bracket Notation

For now, let us develop the bracket notation in a very abstract sense. It is important to realize that the bracket notation is just a formalism and can be applied to represent any desired vector space. Later, we shall apply it to both Hilbert and Liouville representations of the density operator. In the following equation is defined something called a *bra* and something called a *ket*:

$$\langle bra|(c)|ket\rangle \tag{1}$$

Bras and kets may have any kind of label inside to distinguish one from another. A ket may be converted into the corresponding bra by taking the Hermitian conjugate or adjoint, i.e., the complex conjugate transpose, and, of course, a bra can be converted into a ket in the same manner:

$$\langle bra| = [(|ket\rangle)^*]^{\mathrm{T}} = (|ket\rangle)^\dagger \tag{2}$$

Multiplication of a bra and a ket in that order yields a number that can be real, imaginary, or complex:

$$\langle bra|ket\rangle = \mathrm{c} \tag{3}$$

Note that this *scalar product* is not commutative, as we shall see in equation (9). Equation (3) is a key concept. In what follows, one must be able to recognize the $\langle\ |\ \rangle$ construct as a number that commutes with operators, bras, and kets. The scalar product is linear:

$$\left.\begin{aligned}\langle \mathrm{bra}|(|\mathrm{ket}_1\rangle + |\mathrm{ket}_2\rangle) &= \langle \mathrm{bra}|\mathrm{ket}_1\rangle + \langle \mathrm{bra}|\mathrm{ket}_2\rangle \\ (\langle \mathrm{bra}_1| + \langle \mathrm{bra}_2|)|\mathrm{ket}\rangle &= \langle \mathrm{bra}_1|\mathrm{ket}\rangle + \langle \mathrm{bra}_2|\mathrm{ket}\rangle\end{aligned}\right\} \tag{4}$$

Next we define something called an *operator* that converts a ket into some other ket:

$$\widehat{Op}|\mathrm{ket}\rangle = |\mathrm{new\ ket}\rangle \tag{5}$$

Operators will be distinguished by a hat (circumflex). Operators do not, in general, commute. The identity operator $\hat{E}$ just leaves a ket unaltered:

$$\hat{E}|\mathrm{ket}\rangle = |\mathrm{ket}\rangle \tag{6}$$

The identity operator does commute with all other operators.

Taking the adjoint of both sides of equation (5) yields the following relationship, which shows how an operator can act to the left on a bra:

$$(\widehat{Op}|\mathrm{ket}\rangle)^\dagger = \langle \mathrm{bra}|\widehat{Op}^\dagger = \langle \mathrm{new\ bra}| \tag{7}$$

If $\widehat{Op}^\dagger = \widehat{Op}$, the operator is said to be *Hermitian* or *self-adjoint*.

If an operator acting on a ket yields the same ket multiplied by a number c (perhaps complex), the ket is said to be an *eigenket* of the operator, and c is the *eigenvalue*:

$$\widehat{Op}|\mathrm{ket}\rangle = c|\mathrm{ket}\rangle \tag{8}$$

As mentioned above, multiplication of bras and kets is not commutative, so the question arises of the meaning of the following product of a ket with a bra:

$$|\mathrm{ket}\rangle\langle \mathrm{bra}| = \mathrm{operator} \tag{9}$$

This is called the *outer product* or *tensor product* of the bra and ket. Equation (9) asserts that this combination is an operator. This assertion can be easily proven by operating on some ket:

$$|a\rangle\langle b\|c\rangle = |a\rangle\langle b|c\rangle = |a\rangle n_{bc} = n_{bc}|a\rangle \tag{10}$$

Remember that $\langle b|c\rangle$ is just a number, by equation (3), and a number will commute with a ket. Thus, $|a\rangle\langle b|$ satisfies the definition of an operator as in equation (5), because it produces a new ket $|a\rangle$ from $|c\rangle$. The numerical coefficient involved is not a problem, because a number times a ket is still a ket. The fact that one can reinterpret or regroup bras and kets in this way is a key concept of the formalism. In Section 2.2 it will become more obvious why these alternative interpretations are possible. We shall not put a hat over these operators, since there is no possibility of confusion; expressions of the type $|\ \rangle\langle\ |$ will always be interpretable as operators.

If we have a set of kets $\{|i\rangle,\ i = 1, 2, 3, \ldots, n\}$ such that

$$\langle i|\ j\rangle = \delta_{ij} \quad \text{for all} \quad i, j = 1, 2, 3, \ldots, n \tag{11}$$

then the set is said to be an *orthonormal* (orthogonal and normalized) basis. The Kronecker delta function is defined by

$$\delta_{ij} = \begin{cases} 1 & (i = j) \\ 0 & (i \neq j) \end{cases} \tag{12}$$

If for some member of the set $\langle i|i\rangle \neq 1$ then we simply define a new ket $|i'\rangle = |i\rangle/\langle i|i\rangle^{\frac{1}{2}}$ to replace $|i\rangle$ until all members of the set are normalized.

With just these simple rules for manipulating operators, bras, and kets as postulates, one can develop the mathematics necessary to treat nuclear spin dynamics.

2.2 Representations

Suppose we have some system in a state that corresponds to an abstract vector or ket designated as $|\psi(t)\rangle$. The indicated time dependence shows that the system may be evolving in time. We attempt to expand this state in the stationary orthonormal set of equation (11) as follows, and we want to know the form of the coefficients $c_i(t)$:

$$|\psi(t)\rangle = \sum_{i=1}^{n} c_i(t)|i\rangle \tag{13}$$

Multiplying from the left by $\langle i|$, a bra corresponding to one of the members of the basis set, and using equation (11) yields

$$\begin{aligned}\langle i|\psi(t)\rangle &= \langle i|\sum_{j=1}^{n} c_j(t)|\ j\rangle \\ &= \sum_{j=1}^{n} c_j(t)\langle i|\ j\rangle \\ &= \sum_{j=1}^{n} c_j(t)\delta_{ij} = c_i(t)\end{aligned} \tag{14}$$

The last step follows because, by equation (12), only the ith term survives in the sum. This is a formal prescription for computing the expansion coefficients; later, we shall see how it is implemented in real cases. The question of whether the set $\{|i\rangle\}$ is complete, i.e., contains all the basis vectors necessary to represent $|\psi(t)\rangle$, will not be addressed here. It will simply be asserted that such a set can be found. Taking the adjoint of both sides of equation (14) yields the analogous equation for bras:

$$\langle\psi(t)|i\rangle = c_i^*(t) \tag{15}$$

Having chosen a basis set, we can compute all the coefficients needed for equation (14) or equation (15). If these coefficients are arranged in a column or a row vector then we have the Hilbert space representation of the state (bra or ket) in the basis:

$$|\psi\rangle \xrightarrow{|i\rangle} \begin{bmatrix} \langle 1|\psi\rangle \\ \langle 2|\psi\rangle \\ \langle 3|\psi\rangle \\ \vdots \\ \langle n|\psi\rangle \end{bmatrix} = \begin{bmatrix} c_1 \\ c_2 \\ c_3 \\ \vdots \\ c_n \end{bmatrix} \tag{16a}$$

$$\begin{aligned} \langle\psi| \xrightarrow{|i\rangle} & [\langle\psi|1\rangle \quad \langle\psi|2\rangle \quad \langle\psi|3\rangle \quad \dots \quad \langle\psi|n\rangle] \\ & = [c_1^* \quad c_2^* \quad c_3^* \quad \dots \quad c_n^*] \end{aligned} \tag{16b}$$

A mapping of this sort is sometimes written with an equals sign in the literature. This is not consistent with the notation we have developed, because the state $|\psi\rangle$ is an abstraction implying no particular basis, whereas the vector representing $|\psi\rangle$ requires that a particular basis be chosen. It is also inconsistent to equate a wavefunction to a ket, because a wavefunction is a representation of the ket in a continuous rather than a discrete basis. The result is a function rather than a vector with discrete elements; that is why it is called a wave*function*. In this article, mappings of this sort will be indicated by an arrow as in equation (16). The basis used will be indicated as shown or will be obvious from the context.

Of course, the members of the basis set can themselves be represented in the basis. If the jth member of the basis is represented then all the elements of the vector will be zero except the jth, which is one:

$$|\,j\rangle \xrightarrow{|i\rangle} \begin{bmatrix} \langle 1|\,j\rangle \\ \langle 2|\,j\rangle \\ \vdots \\ \langle\,j|\,j\rangle \\ \vdots \\ \langle n|\,j\rangle \end{bmatrix} = \begin{bmatrix} 0 \\ 0 \\ \vdots \\ 1 \\ \vdots \\ 0 \end{bmatrix} \tag{17a}$$

$$\begin{aligned} \langle\,j| \xrightarrow{|i\rangle} & [\langle\,j|1\rangle \quad \langle\,j|2\rangle \quad \dots \quad \langle\,j|\,j\rangle \quad \dots \quad \langle\,j|n\rangle] \\ & = [0 \quad 0 \quad \dots \quad 1 \quad \dots \quad 0] \end{aligned} \tag{17b}$$

If we rewrite equation (13) using the result in equation (14) and commute the number with the ket on the right, we have

$$\begin{aligned} |\psi(t)\rangle &= \sum_{i=1}^{n} \langle i|\psi(t)\rangle|i\rangle \\ &= \sum_{i=1}^{n} |i\rangle\langle i|\psi(t)\rangle \\ &= \left(\sum_{i=1}^{n} |i\rangle\langle i|\right)|\psi(t)\rangle \end{aligned} \tag{18}$$

Written this way, the implication is

$$\sum_{i=1}^{n} |i\rangle\langle i| = \hat{E} \tag{19}$$

Rearranging and reinterpreting the brackets in this way may seem quite strange at first, but the examples given below should clarify the formalism. The operators $|i\rangle\langle i|$ are called *projection operators* because they project from any state the part that projects on the ith basis state. Summing over all the projection operators then just gives the unit operator.

Suppose we have two alternative sets of basis states, $\{|a,i\rangle\}$ and $\{|b,i\rangle\}$, spanning the same vector space; then we can effect a transformation between the bases using projection operators as in equation (19). Projecting the b basis onto the a basis, we have

$$\begin{aligned} |b,i\rangle &= \left(\sum_{j=1}^{n} |a,j\rangle\langle a,j|\right)|b,i\rangle \\ &= \sum_{j=1}^{n} |a,j\rangle\langle a,j|b,i\rangle \\ &= \sum_{j=1}^{n} \langle a,j|b,i\rangle|a,j\rangle \end{aligned} \tag{20}$$

If we have an arbitrary state represented in the b basis, it can be transformed to the a basis as follows:

$$\begin{aligned} \psi\rangle &= \sum_{i=1}^{n} \langle b,i|\psi\rangle|b,i\rangle \\ &= \sum_{i=1}^{n} \langle b,i|\psi\rangle \sum_{j=1}^{n} \langle a,j|b,i\rangle|a,j\rangle \\ &= \sum_{i,j=1}^{n} \langle a,j|b,i\rangle\langle b,i|\psi\rangle|a,j\rangle \end{aligned} \tag{21a}$$

$$\begin{aligned} \langle\psi| &= \sum_{i=1}^{n} \langle\psi|b,i\rangle\langle b,i| \\ &= \sum_{i=1}^{n} \langle\psi|b,i\rangle \sum_{j=1}^{n} \langle b,i|a,j\rangle\langle a,j| \\ &= \sum_{i,j=1}^{n} \langle\psi|b,i\rangle\langle b,i|a,j\rangle\langle a,j| \end{aligned} \tag{21b}$$

Comparing these results with equations (16a) and (16b), it is apparent that equations (21a) and (21b) can be represented as follows:

$$\begin{bmatrix} \langle a,1|\psi\rangle \\ \langle a,2|\psi\rangle \\ \langle a,3|\psi\rangle \\ \vdots \\ \langle a,n|\psi\rangle \end{bmatrix}$$

$$= \begin{bmatrix} \langle a,1|b,1\rangle & \langle a,1|b,2\rangle & \langle a,1|b,3\rangle & \dots & \langle a,1|b,n\rangle \\ \langle a,2|b,1\rangle & \langle a,2|b,2\rangle & \langle a,2|b,3\rangle & \dots & \langle a,2|b,n\rangle \\ \langle a,3|b,1\rangle & \langle a,3|b,2\rangle & \langle a,3|b,3\rangle & \dots & \langle a,3|b,n\rangle \\ \vdots & \vdots & \vdots & \ddots & \vdots \\ \langle a,n|b,1\rangle & \langle a,n|b,2\rangle & \langle a,n|b,3\rangle & \dots & \langle a,n|b,n\rangle \end{bmatrix}$$

$$\times \begin{bmatrix} \langle b,1|\psi\rangle \\ \langle b,2|\psi\rangle \\ \langle b,3|\psi\rangle \\ \vdots \\ \langle b,n|\psi\rangle \end{bmatrix} \tag{22a}$$

$$[\langle\psi|a,1\rangle \quad \langle\psi|a,2\rangle \quad \langle\psi|a,3\rangle \quad \dots \quad \langle\psi|a,n\rangle]$$

$$= [\langle\psi|b,1\rangle \quad \langle\psi|b,2\rangle \quad \langle\psi|b,3\rangle \quad \dots \quad \langle\psi|b,n\rangle]$$

$$\times \begin{bmatrix} \langle b,1|a,1\rangle & \langle b,1|a,2\rangle & \langle b,1|a,3\rangle & \dots & \langle b,1|a,n\rangle \\ \langle b,2|a,1\rangle & \langle b,2|a,2\rangle & \langle b,2|a,3\rangle & \dots & \langle b,2|a,n\rangle \\ \langle b,3|a,1\rangle & \langle b,3|a,2\rangle & \langle b,3|a,3\rangle & \dots & \langle b,3|a,n\rangle \\ \vdots & \vdots & \vdots & \ddots & \vdots \\ \langle b,n|a,1\rangle & \langle b,n|a,2\rangle & \langle b,n|a,3\rangle & \dots & \langle b,n|a,n\rangle \end{bmatrix} \tag{22b}$$

Note that the columns of the first transformation matrix are merely the representation of the b basis kets in the a basis, while the rows are the representation of the a bras in the b basis. The second transformation matrix is the adjoint (complex conjugate transpose) of the first. If the two matrices are multiplied in either order, the result is a unit matrix, because the basis states are normalized. But this is just the definition of a unitary matrix. In compact matrix notation, we have

$$\boldsymbol{\psi}_a = \mathbf{T}\boldsymbol{\psi}_b, \quad \boldsymbol{\psi}_a^\dagger = \boldsymbol{\psi}_b^\dagger \mathbf{T}^\dagger \tag{23}$$

The unitary nature of the transformation is expressed as

$$\mathbf{T}\mathbf{T}^\dagger = \mathbf{T}^\dagger\mathbf{T} = \mathbf{E} = \mathbf{T}\mathbf{T}^{-1} = \mathbf{T}^{-1}\mathbf{T} \tag{24}$$

From these two equations, it is evident that the normalization of the state is preserved, regardless of the representation used:

$$\boldsymbol{\psi}_a^\dagger\boldsymbol{\psi}_a = \boldsymbol{\psi}_b^\dagger\mathbf{T}^\dagger\mathbf{T}\boldsymbol{\psi}_b = \boldsymbol{\psi}_b^\dagger\boldsymbol{\psi}_b \tag{25}$$

The inverse transformation can easily be derived. If $\boldsymbol{\psi}_\mathrm{a} = \mathbf{T}\boldsymbol{\psi}_\mathrm{b}$ then we have

$$\mathbf{T}^{-1}\mathbf{T}\boldsymbol{\psi}_b = \mathbf{T}^{-1}\boldsymbol{\psi}_a, \quad \boldsymbol{\psi}_b = \mathbf{T}^{-1}\boldsymbol{\psi}_a \tag{26}$$

But the inverse transformation is

$$\begin{aligned} |\psi\rangle &= \sum_{i=1}^{n} \langle a,i|\psi\rangle |a,i\rangle \\ &= \sum_{i=1}^{n} \langle a,i|\psi\rangle \sum_{j=1}^{n} \langle b,j|a,i\rangle |b,j\rangle \\ &= \sum_{i,j=1}^{n} \langle b,j|a,i\rangle\langle a,i|\psi\rangle |b,j\rangle \end{aligned} \tag{27}$$

Comparing equations (21a) and (27), the relationship between the a to b and b to a transforms is found to be

$$T_{ji}^* = \langle b,i|a,j\rangle^* = \langle a,j|b,i\rangle = T_{ij}^\dagger \tag{28}$$

which shows that the inverse transformation matrix $\mathbf{T}^{-1}$ is just the adjoint of the original matrix—but this is again just the definition of a unitary matrix. Examining equations (22a) and (22b), it is clear that the complex conjugate transpose of the transformation matrix is, indeed, the desired inverse transformation. This may be shown more easily by noting from equation (24) that $\mathbf{T}^\dagger = \mathbf{T}^{-1}$. Then, from equation (23), we have

$$\left.\begin{aligned} \mathbf{T}^\dagger\boldsymbol{\psi}_a = \mathbf{T}^\dagger\mathbf{T}\boldsymbol{\psi}_b = \boldsymbol{\psi}_b \\ \boldsymbol{\psi}_a^\dagger\mathbf{T} = \boldsymbol{\psi}_b^\dagger\mathbf{T}^\dagger\mathbf{T} = \boldsymbol{\psi}_b^\dagger \end{aligned}\right\} \tag{29}$$

We now turn to some relationships involving operators. Suppose one has some arbitrary operator $\hat{\mathrm{O}}$. Using equation (19), we can write

$$\begin{aligned} \hat{O} &= \left(\sum_{i=1}^{n} |i\rangle\langle i|\right)\hat{O}\left(\sum_{j=1}^{n} |\,j\rangle\langle\,j|\right) \\ &= \sum_{i,j=1}^{n} |i\rangle\langle i|\hat{O}|\,j\rangle\langle\,j| \\ &= \sum_{i,j=1}^{n} \langle i|\hat{O}|\,j\rangle |i\rangle\langle\,j| \\ &= \sum_{i,j=1}^{n} c_{ij}|i\rangle\langle\,j| \end{aligned} \tag{30}$$

A unit operator can be inserted anywhere without affecting the equality. This equation is a prescription for writing any operator as a sum of operators $|i\rangle\langle\,j|$. Clearly, if there are n basis states $|i\rangle$ then there are n^2 basis operators $|i\rangle\langle\,j|$. If we multiply this equation from the left and right by a basis state, the result is a prescription for the coefficients c_{ij}:

$$\begin{aligned} \langle k|\hat{O}|l\rangle &= \langle k|\left(\sum_{i,j=1}^{n} c_{ij}|i\rangle\langle\,j|\right)|l\rangle \\ &= \sum_{i,j=1}^{n} c_{ij}\langle k|i\rangle\langle\,j|l\rangle \\ &= \sum_{i,j=1}^{n} c_{ij}\delta_{ki}\delta_{jl} = c_{kl} \end{aligned} \tag{31}$$

These coefficients are commonly called the *matrix elements* of the operator, and can be arranged in a matrix to form a Hilbert space representation of the operator:

$$\hat{O} \xrightarrow{|i\rangle} \mathbf{O} = \begin{bmatrix} \langle 1|\hat{O}|1\rangle & \langle 1|\hat{O}|2\rangle & \langle 1|\hat{O}|3\rangle & \dots & \langle 1|\hat{O}|n\rangle \\ \langle 2|\hat{O}|1\rangle & \langle 2|\hat{O}|2\rangle & \langle 2|\hat{O}|3\rangle & \dots & \langle 2|\hat{O}|n\rangle \\ \langle 3|\hat{O}|1\rangle & \langle 3|\hat{O}|2\rangle & \langle 3|\hat{O}|3\rangle & \dots & \langle 3|\hat{O}|n\rangle \\ \vdots & \vdots & \vdots & \ddots & \vdots \\ \langle n|\hat{O}|1\rangle & \langle n|\hat{O}|2\rangle & \langle n|\hat{O}|3\rangle & \dots & \langle n|\hat{O}|n\rangle \end{bmatrix} \tag{32}$$

Proceeding as in equation (25), we can write

$$\boldsymbol{\psi}_a^\dagger \mathbf{O}_a \boldsymbol{\psi}_a = \boldsymbol{\psi}_b^\dagger \mathbf{T}^\dagger \mathbf{T} \mathbf{O}_a \mathbf{T}^\dagger \mathbf{T} \boldsymbol{\psi}_b = \boldsymbol{\psi}_b^\dagger \mathbf{O}_b \boldsymbol{\psi}_b \tag{33}$$

where we have defined the operator in the b basis as

$$\mathbf{O}_b = \mathbf{T} \mathbf{O}_a \mathbf{T}^\dagger \tag{34}$$

Analogously, the basis operators themselves can be represented as follows to yield a matrix of all zero elements except the ijth:

$$|i\rangle\langle j| \xrightarrow{|i\rangle} \begin{bmatrix} \langle 1|i\rangle\langle j|1\rangle & \langle 1|i\rangle\langle j|2\rangle & \dots & \langle 1|i\rangle\langle j|j\rangle & \dots & \langle 1|i\rangle\langle j|n\rangle \\ \langle 2|i\rangle\langle j|1\rangle & \langle 2|i\rangle\langle j|2\rangle & \dots & \langle 2|i\rangle\langle j|j\rangle & \dots & \langle 2|i\rangle\langle j|n\rangle \\ \vdots & \vdots & \ddots & \vdots & & \vdots \\ \langle i|i\rangle\langle j|1\rangle & \langle i|i\rangle\langle j|2\rangle & \dots & \langle i|i\rangle\langle j|j\rangle & \dots & \langle i|i\rangle\langle j|n\rangle \\ \vdots & \vdots & & \vdots & \ddots & \vdots \\ \langle n|i\rangle\langle j|1\rangle & \langle n|i\rangle\langle j|2\rangle & \dots & \langle n|i\rangle\langle j|j\rangle & \dots & \langle n|i\rangle\langle j|n\rangle \end{bmatrix}$$

$$= \begin{bmatrix} 0 & 0 & \dots & 0 & \dots & 0 \\ 0 & 0 & \dots & 0 & \dots & 0 \\ \vdots & \vdots & \ddots & \vdots & & \vdots \\ 0 & 0 & \dots & 1 & \dots & 0 \\ \vdots & \vdots & & \vdots & \ddots & \vdots \\ 0 & 0 & \dots & 0 & \dots & 0 \end{bmatrix} \tag{35}$$

This result can also be obtained from equations (17a) and (17b) by writing

$$\begin{bmatrix} \langle 1|i\rangle \\ \langle 2|i\rangle \\ \vdots \\ \langle j|i\rangle \\ \vdots \\ \langle n|i\rangle \end{bmatrix} \begin{bmatrix} \langle j|1\rangle & \langle j|2\rangle & \dots & \langle j|j\rangle & \dots & \langle j|n\rangle \end{bmatrix}$$

$$= \begin{bmatrix} \langle 1|i\rangle\langle j|1\rangle & \langle 1|i\rangle\langle j|2\rangle & \dots & \langle 1|i\rangle\langle j|j\rangle & \dots & \langle 1|i\rangle\langle j|n\rangle \\ \langle 2|i\rangle\langle j|1\rangle & \langle 2|i\rangle\langle j|2\rangle & \dots & \langle 2|i\rangle\langle j|j\rangle & \dots & \langle 2|i\rangle\langle j|n\rangle \\ \vdots & \vdots & \ddots & \vdots & & \vdots \\ \langle i|i\rangle\langle j|1\rangle & \langle i|i\rangle\langle j|2\rangle & \dots & \langle i|i\rangle\langle j|j\rangle & \dots & \langle i|i\rangle\langle j|n\rangle \\ \vdots & \vdots & & \vdots & \ddots & \vdots \\ \langle n|i\rangle\langle j|1\rangle & \langle n|i\rangle\langle j|2\rangle & \dots & \langle n|i\rangle\langle j|j\rangle & \dots & \langle n|i\rangle\langle j|n\rangle \end{bmatrix} \tag{36}$$

The basis operators are orthogonal, just as the basis states are; however, the inner product exemplified by equation (11) must be replaced by the trace operation:

$$\begin{aligned} \mathrm{Tr}(|\,j\rangle\langle k|l\rangle\langle m|) &= \sum_{i=1}^{n} \langle i|\,j\rangle\langle k|l\rangle\langle m|i\rangle \\ &= \langle k|l\rangle\langle m|\,j\rangle \\ &= \delta_{kl}\delta_{mj} \end{aligned} \tag{37}$$

In equation (37), the right-hand side will be nonzero if and only if $j = m$ and $k = l$; then

$$|\,j\rangle\langle k|k\rangle\langle\,j| = |\,j\rangle\langle k|(|\,j\rangle\langle k|)^\dagger \tag{38}$$

In order to simplify notation, we now make a mapping of the indices j and k of $|j\rangle\langle k|$ onto a single index i of $\hat{U}_i$. This is simply a relabeling of the basis operators. The exact nature of the mapping is arbitrary, except that there must be a one-to-one correspondence between the pair of indices j, k and the index i. The expression corresponding to equation (37) is then

$$\mathrm{Tr}(\hat{U}_i \hat{U}_j^\dagger) = \delta_{ij} \tag{39}$$

This equation is the normalization condition for basis operators analogous to equation (11). Note that if the basis states used in equation (37) are normalized then these basis operators will also be normalized.

If we expand the generic operator $\hat{O}$ in terms of this basis set, the result is

$$\hat{O} = \sum_{i=1}^{n^2} c_i \hat{U}_i \tag{40}$$

Now, if this equation is multiplied by ${\hat{U}_j}^\dagger$ and the trace taken, a prescription is obtained for the expansion coefficients c_i:

$$\begin{aligned} \mathrm{Tr}(\hat{O}\hat{U}_j^\dagger) &= \mathrm{Tr}\left(\sum_{i=1}^{n^2} c_i \hat{U}_i \hat{U}_j^\dagger \right) \\ &= \sum_{i=1}^{n^2} c_i \mathrm{Tr}(\hat{U}_i \hat{U}_j^\dagger) = \sum_{i=1}^{n^2} c_i \delta_{ij} = c_j \end{aligned} \tag{41}$$

Equation (40) may then be rewritten as

$$\hat{O} = \sum_{i=1}^{n^2} \mathrm{Tr}(\hat{O}\hat{U}_i^\dagger)\hat{U}_i \tag{42}$$

The coefficients in this equation can be arranged in a vector to form the Liouville space representation of the operator:

$$\hat{O} \xrightarrow{\hat{U}_i} \begin{bmatrix} \mathrm{Tr}(\hat{O}\hat{U}_1^\dagger) \\ \mathrm{Tr}(\hat{O}\hat{U}_2^\dagger) \\ \mathrm{Tr}(\hat{O}\hat{U}_3^\dagger) \\ \vdots \\ \mathrm{Tr}(\hat{O}\hat{U}_{n^2}^\dagger) \end{bmatrix} \tag{43}$$

Note that this space is n^2-dimensional.

As was done with basis states, it is possible to transform among alternative sets of basis operators. Consider a new operator basis $\{\hat{V}_i, i = 1, 2, 3, \ldots, n^2\}$. These operators can be expressed in the original basis as

$$\hat{V}_i = \sum_{j=1}^{n^2} \mathrm{Tr}(\hat{V}_i \hat{U}_j^\dagger)\hat{U}_j \tag{44}$$

Equation (42) can be written in terms of the $\hat{V}_i$; then equation (44) can be substituted:

$$\begin{aligned}\hat{O} &= \sum_{j=1}^{n^2} \mathrm{Tr}(\hat{O}\hat{V}_j^\dagger)\hat{V}_j \\ &= \sum_{j=1}^{n^2} \mathrm{Tr}(\hat{O}\hat{V}_j^\dagger) \sum_{i=1}^{n^2} \mathrm{Tr}(\hat{V}_j \hat{U}_i^\dagger)\hat{U}_i \\ &= \sum_{i,j=1}^{n^2} \mathrm{Tr}(\hat{V}_j \hat{U}_i^\dagger)\mathrm{Tr}(\hat{O}\hat{V}_j^\dagger)\hat{U}_i \end{aligned} \tag{45}$$

Comparing equations (42) and (45), it is evident that the conversion of operator bases is accomplished as follows:

$$\mathrm{Tr}(\hat{O}\hat{U}_i^\dagger) = \sum_{j=1}^{n^2} \mathrm{Tr}(\hat{V}_j \hat{U}_i^\dagger)\mathrm{Tr}(\hat{O}\hat{V}_j^\dagger) \tag{46}$$

In terms of the Liouville space representation, this can be written as

$$\begin{bmatrix} \mathrm{Tr}(\hat{O}\hat{U}_1^\dagger) \\ \mathrm{Tr}(\hat{O}\hat{U}_2^\dagger) \\ \mathrm{Tr}(\hat{O}\hat{U}_3^\dagger) \\ \vdots \\ \mathrm{Tr}(\hat{O}\hat{U}_{n^2}^\dagger) \end{bmatrix} = \begin{bmatrix} \mathrm{Tr}(\hat{V}_1\hat{U}_1^\dagger) & \mathrm{Tr}(\hat{V}_2\hat{U}_1^\dagger) & \mathrm{Tr}(\hat{V}_3\hat{U}_1^\dagger) & \ldots & \mathrm{Tr}(\hat{V}_{n^2}\hat{U}_1^\dagger) \\ \mathrm{Tr}(\hat{V}_1\hat{U}_2^\dagger) & \mathrm{Tr}(\hat{V}_2\hat{U}_2^\dagger) & \mathrm{Tr}(\hat{V}_3\hat{U}_2^\dagger) & \ldots & \mathrm{Tr}(\hat{V}_{n^2}\hat{U}_2^\dagger) \\ \mathrm{Tr}(\hat{V}_1\hat{U}_3^\dagger) & \mathrm{Tr}(\hat{V}_2\hat{U}_3^\dagger) & \mathrm{Tr}(\hat{V}_3\hat{U}_3^\dagger) & \ldots & \mathrm{Tr}(\hat{V}_{n^2}\hat{U}_3^\dagger) \\ \vdots & \vdots & \vdots & \ddots & \vdots \\ \mathrm{Tr}(\hat{V}_1\hat{U}_{n^2}^\dagger) & \mathrm{Tr}(\hat{V}_2\hat{U}_{n^2}^\dagger) & \mathrm{Tr}(\hat{V}_3\hat{U}_{n^2}^\dagger) & \ldots & \mathrm{Tr}(\hat{V}_{n^2}\hat{U}_{n^2}^\dagger) \end{bmatrix} \times \begin{bmatrix} \mathrm{Tr}(\hat{O}\hat{V}_1^\dagger) \\ \mathrm{Tr}(\hat{O}\hat{V}_2^\dagger) \\ \mathrm{Tr}(\hat{O}\hat{V}_3^\dagger) \\ \vdots \\ \mathrm{Tr}(\hat{O}\hat{V}_{n^2}^\dagger) \end{bmatrix} \tag{47}$$

2.3 Direct Product Bases

It is quite common that one is able to derive a basis for two or more parts of a system using the techniques described in the previous section, but it is then desired to represent the whole system so that interactions among the parts can be considered. For example, a molecule might contain two spins, say a ^{13}C nucleus and a ^{1}H nucleus. For this purpose, we introduce the *direct* or *outer product* of the subspaces to form the space appropriate for the whole system. One can form the direct products in either Hilbert space or Liouville space. The only new definitions needed are as follows. For vectors (states),

$$|\psi_1\rangle|\psi_2\rangle = |\psi\rangle \tag{48a}$$

$$\begin{bmatrix} \langle 1,1|\psi_1\rangle \\ \langle 1,2|\psi_1\rangle \\ \langle 1,3|\psi_1\rangle \\ \vdots \\ \langle 1,n|\psi_1\rangle \end{bmatrix} \otimes \begin{bmatrix} \langle 2,1|\psi_2\rangle \\ \langle 2,2|\psi_2\rangle \\ \langle 2,3|\psi_2\rangle \\ \vdots \\ \langle 2,m|\psi_2\rangle \end{bmatrix} = \begin{bmatrix} \langle 1,1|\psi_1\rangle \begin{bmatrix} \langle 2,1|\psi_2\rangle \\ \langle 2,2|\psi_2\rangle \\ \langle 2,3|\psi_2\rangle \\ \vdots \\ \langle 2,m|\psi_2\rangle \end{bmatrix} \\ \langle 1,2|\psi_1\rangle \begin{bmatrix} \langle 2,1|\psi_2\rangle \\ \langle 2,2|\psi_2\rangle \\ \langle 2,3|\psi_2\rangle \\ \vdots \\ \langle 2,m|\psi_2\rangle \end{bmatrix} \\ \langle 1,3|\psi_1\rangle \begin{bmatrix} \langle 2,1|\psi_2\rangle \\ \langle 2,2|\psi_2\rangle \\ \langle 2,3|\psi_2\rangle \\ \vdots \\ \langle 2,m|\psi_2\rangle \end{bmatrix} \\ \vdots \\ \langle 1,n|\psi_1\rangle \begin{bmatrix} \langle 2,1|\psi_2\rangle \\ \langle 2,2|\psi_2\rangle \\ \langle 2,3|\psi_2\rangle \\ \vdots \\ \langle 2,m|\psi_2\rangle \end{bmatrix} \end{bmatrix} \tag{48b}$$

A slightly more condensed notation is required to make the corresponding definition for matrices (operators) manageable:

$$\hat{O} = \hat{O}^{(1)} \otimes \hat{O}^{(2)} \tag{49a}$$

$$\mathbf{O} = \begin{bmatrix} O_{1,1}^{(1)}\mathbf{O}^{(2)} & O_{1,2}^{(1)}\mathbf{O}^{(2)} & O_{1,3}^{(1)}\mathbf{O}^{(2)} & \ldots & O_{1,n}^{(1)}\mathbf{O}^{(2)} \\ O_{2,1}^{(1)}\mathbf{O}^{(2)} & O_{2,2}^{(1)}\mathbf{O}^{(2)} & O_{2,3}^{(1)}\mathbf{O}^{(2)} & \ldots & O_{2,n}^{(1)}\mathbf{O}^{(2)} \\ O_{3,1}^{(1)}\mathbf{O}^{(2)} & O_{3,2}^{(1)}\mathbf{O}^{(2)} & O_{3,3}^{(1)}\mathbf{O}^{(2)} & \ldots & O_{3,n}^{(1)}\mathbf{O}^{(2)} \\ \vdots & \vdots & \vdots & \ddots & \vdots \\ O_{n,1}^{(1)}\mathbf{O}^{(2)} & O_{n,2}^{(1)}\mathbf{O}^{(2)} & O_{n,3}^{(1)}\mathbf{O}^{(2)} & \ldots & O_{n,n}^{(1)}\mathbf{O}^{(2)} \end{bmatrix} \tag{49b}$$

$$\mathbf{O}^{(2)} = \begin{bmatrix} O_{1,1}^{(2)} & O_{1,2}^{(2)} & O_{1,3}^{(2)} & \ldots & O_{1,m}^{(2)} \\ O_{2,1}^{(2)} & O_{2,2}^{(2)} & O_{2,3}^{(2)} & \ldots & O_{2,m}^{(2)} \\ O_{3,1}^{(2)} & O_{3,2}^{(2)} & O_{3,3}^{(2)} & \ldots & O_{3,m}^{(2)} \\ \vdots & \vdots & \vdots & \ddots & \vdots \\ O_{m,1}^{(2)} & O_{m,2}^{(2)} & O_{m,3}^{(2)} & \ldots & O_{m,m}^{(2)} \end{bmatrix} \tag{49c}$$

Note that the dimension of the product space is always the product of the dimensions of the subspaces.

In equation (43) the Liouville space was introduced. With the introduction of the concept of direct products, it is possible to give a more satisfying explanation of the mapping from Hilbert space to Liouville space. The Hilbert space operators $|i\rangle\langle j|$ can be mapped onto a Liouville space with the following basis states:

$$|i\rangle|\ j\rangle = |ij\rangle \tag{50}$$

Clearly, a one-to-one mapping is possible. In Section 5, the use of Liouville space representations will be explored further with the introduction of superoperators.

It is common in the NMR literature to have implied direct products. For example, one might write $\hat{I}_z{}^{(1)} + \hat{I}_z{}^{(2)}$, where (1) and (2) refer to different spins. This is meant to imply $\hat{I}_z{}^{(1)} \otimes \hat{E}^{(2)} + \hat{E}^{(1)} \otimes \hat{I}_z{}^{(2)}$. Alternatively, one might encounter $\hat{I}_z\hat{I}_+$, where no direct product is implied, or $\hat{I}_+{}^{(1)}\hat{I}_-{}^{(2)}$, where we are to understand that this means $\hat{I}_+{}^{(1)} \otimes \hat{I}_-{}^{(2)}$. It is necessary to understand from the context and notation what is really meant.

3 SOME COMMONLY USED BASES

Next let us consider some examples of bases commonly used in NMR, using simple spin systems to illustrate how this formalism can be applied to nuclear spins.

3.1 The Single Spin Eigenstate Basis

A single isolated spin-$\frac{1}{2}$ nucleus has two energy eigenstates. They are commonly represented as $|\alpha\rangle$ and $|\beta\rangle$; however, since this notation is applicable only for spin-$\frac{1}{2}$, we shall also use the notation $|\frac{1}{2}\rangle$ and $|-\frac{1}{2}\rangle$, respectively, where each state is labelled by its $\hat{I}_z$ eigenvalue (this will be discussed in more detail below). It is assumed that these states are orthonormal. Using equation (17a), we can write the Hilbert space representation of the basis states as

$$\left.\begin{aligned} |\alpha\rangle = |\tfrac{1}{2}\rangle \rightarrow \begin{bmatrix}\langle\alpha|\alpha\rangle\\ \langle\beta|\alpha\rangle\end{bmatrix} = \begin{bmatrix}1\\0\end{bmatrix} \\ |\beta\rangle = |-\tfrac{1}{2}\rangle \rightarrow \begin{bmatrix}\langle\alpha|\beta\rangle\\ \langle\beta|\beta\rangle\end{bmatrix} = \begin{bmatrix}0\\1\end{bmatrix} \end{aligned}\right\} \tag{51}$$

The corresponding Hilbert space representation of the basis operators can be obtained most easily using equation (36) to write

$$\left.\begin{aligned} \hat{U}_1 = |\alpha\rangle\langle\alpha| \rightarrow \begin{bmatrix}1\\0\end{bmatrix}[1\quad 0] = \begin{bmatrix}1&0\\0&0\end{bmatrix} \\ \hat{U}_2 = |\alpha\rangle\langle\beta| \rightarrow \begin{bmatrix}1\\0\end{bmatrix}[0\quad 1] = \begin{bmatrix}0&1\\0&0\end{bmatrix} \\ \hat{U}_3 = |\beta\rangle\langle\alpha| \rightarrow \begin{bmatrix}0\\1\end{bmatrix}[1\quad 0] = \begin{bmatrix}0&0\\1&0\end{bmatrix} \\ \hat{U}_4 = |\beta\rangle\langle\beta| \rightarrow \begin{bmatrix}0\\1\end{bmatrix}[0\quad 1] = \begin{bmatrix}0&0\\0&1\end{bmatrix} \end{aligned}\right\} \tag{52}$$

It is easily verified that these matrices satisfy the orthonormality conditions by comparing with equation (39) for all pairs.

For spins with a higher angular momentum quantum number, the bases are similar but with higher dimension. For example, a spin-1 nucleus, like ^{2}H, has three eigenstates and nine basis operators. Representations of basis states and operators for any nucleus can be obtained just as above knowing only the number of eigenstates and assuming that they are orthonormal.

3.2 The Basis Derived from Direct Products of Single Spin Bases

When the system of interest includes more than one spin, a direct product of single spin bases described in the previous section (one set corresponding to the correct spin for each nucleus) yields a basis for the combined system. The first state and the first operator for two spin-$\frac{1}{2}$ nuclei, for example, would be

$$\left.\begin{aligned} |\alpha\rangle \otimes |\alpha\rangle = |\alpha\alpha\rangle \rightarrow \begin{bmatrix}1\\0\end{bmatrix} \otimes \begin{bmatrix}1\\0\end{bmatrix} \\ = \begin{bmatrix}1\begin{bmatrix}1\\0\end{bmatrix}\\ 0\begin{bmatrix}1\\0\end{bmatrix}\end{bmatrix} = \begin{bmatrix}1\\0\\0\\0\end{bmatrix} \\ \hat{U}_1 \otimes \hat{V}_1 \rightarrow \begin{bmatrix}1&0\\0&0\end{bmatrix} \otimes \begin{bmatrix}1&0\\0&0\end{bmatrix} = \begin{bmatrix}1\begin{bmatrix}1&0\\0&0\end{bmatrix} & 0\begin{bmatrix}1&0\\0&0\end{bmatrix}\\ 0\begin{bmatrix}1&0\\0&0\end{bmatrix} & 0\begin{bmatrix}1&0\\0&0\end{bmatrix}\end{bmatrix} \\ = \begin{bmatrix}1&0&0&0\\0&0&0&0\\0&0&0&0\\0&0&0&0\end{bmatrix} \end{aligned}\right\} \tag{53}$$

The other 3 basis states and 15 operators are composed in the same fashion using all the pairs of single spin matrices.

3.3 The Basis Derived from the Eigenstates of the Hamiltonian

The states given in equation (51) for a single spin $\frac{1}{2}$ are the eigenstates of the Hamiltonian, but for two identical spin-$\frac{1}{2}$ nuclei (an A_2 spin system), the eigenstates are

$$\left.\begin{aligned} |\mathrm{A}_2, 1\rangle = |\alpha\alpha\rangle \rightarrow \begin{bmatrix}1\\0\\0\\0\end{bmatrix} \\ |\mathrm{A}_2, 2\rangle = \sqrt{\tfrac{1}{2}}(|\alpha\beta\rangle + |\beta\alpha\rangle) \rightarrow \begin{bmatrix}0\\\sqrt{\frac{1}{2}}\\\sqrt{\frac{1}{2}}\\0\end{bmatrix} \\ |\mathrm{A}_2, 3\rangle = \sqrt{\tfrac{1}{2}}(|\alpha\beta\rangle - |\beta\alpha\rangle) \rightarrow \begin{bmatrix}0\\\sqrt{\frac{1}{2}}\\-\sqrt{\frac{1}{2}}\\0\end{bmatrix} \\ |\mathrm{A}_2, 4\rangle = |\beta\beta\rangle \rightarrow \begin{bmatrix}0\\0\\0\\1\end{bmatrix} \end{aligned}\right\} \tag{54}$$

These equations show a representation of the eigenstates in the basis of the spin product states. Assembling these vectors into a unitary matrix according to equation (22a) gives the following transformation matrix from the spin product basis to the eigenbasis:

$$\mathbf{U} = \begin{bmatrix} 1 & 0 & 0 & 0 \\ 0 & \sqrt{\frac{1}{2}} & \sqrt{\frac{1}{2}} & 0 \\ 0 & \sqrt{\frac{1}{2}} & -\sqrt{\frac{1}{2}} & 0 \\ 0 & 0 & 0 & 1 \end{bmatrix} \tag{55}$$

It is easily verified that $\mathbf{U}\mathbf{U}^{\dagger} = \mathbf{U}\mathbf{U}^{-1} = \mathbf{E}$. Applying this transformation to the spin product states or operators yields the desired eigenstate basis for the Hilbert space representation or the Liouville space representation, respectively.

3.4 The Angular Momentum Operator Basis

For a single spin-$\frac{1}{2}$ nucleus, the components of the angular momentum vector operator $\hat{\boldsymbol{I}} = \{\hat{I}_x, \hat{I}_y, \hat{I}_z\}$ augmented by the identity operator $\hat{E}$ are a complete basis. For a development of the angular momentum operators from first principles, the reader is referred to the standard texts.[6,7,10] We shall be content to define them according to their effect on the basis states as in equation (5). For any spin-I nucleus there are $2I + 1$ quantum states $|m\rangle$ such that

$$\left.\begin{aligned} \hat{I}_x|m\rangle &= \tfrac{1}{2}\{[I(I+1) - m(m+1)]^{1/2}|m+1\rangle \\ &\quad + [I(I+1) - m(m-1)]^{1/2}|m-1\rangle\} \\ \hat{I}_y|m\rangle &= \tfrac{1}{2\mathrm{i}}\{[I(I+1) - m(m+1)]^{1/2}|m+1\rangle \\ &\quad - [I(I+1) - m(m-1)]^{1/2}|m-1\rangle\} \\ \hat{I}_z|m\rangle &= m|m\rangle \end{aligned}\right\} \tag{56}$$

The eigenvalue m ranges in integer steps such that $-I \leq m \leq I$. For spin-$\frac{1}{2}$, using the $\{|\frac{1}{2}\rangle, |-\frac{1}{2}\rangle\}$ basis, the angular momentum operators and their representations are

$$\begin{aligned} \hat{I}_x &\rightarrow \tfrac{1}{2}\begin{bmatrix} 0 & 1 \\ 1 & 0 \end{bmatrix}, \quad \hat{I}_y \rightarrow \tfrac{1}{2\mathrm{i}}\begin{bmatrix} 0 & 1 \\ -1 & 0 \end{bmatrix} \\ \hat{I}_z &\rightarrow \tfrac{1}{2}\begin{bmatrix} 1 & 0 \\ 0 & -1 \end{bmatrix}, \quad \hat{E} \rightarrow \begin{bmatrix} 1 & 0 \\ 0 & 1 \end{bmatrix} \end{aligned} \tag{57}$$

It is easily verified that these operators are orthogonal but not normalized using equation (39). Normalization can easily be achieved by multiplying by the appropriate constants to satisfy equation (39); this yields the desired basis for spin-$\frac{1}{2}$:

$$\left.\begin{aligned} \hat{U}_1 &= \frac{1}{\sqrt{2}}\hat{E} \rightarrow \frac{1}{\sqrt{2}}\begin{bmatrix} 1 & 0 \\ 0 & 1 \end{bmatrix} \\ \hat{U}_2 &= \sqrt{2}\hat{I}_z \rightarrow \frac{\sqrt{2}}{2}\begin{bmatrix} 1 & 0 \\ 0 & -1 \end{bmatrix} \\ \hat{U}_3 &= \sqrt{2}\hat{I}_x \rightarrow \frac{\sqrt{2}}{2}\begin{bmatrix} 0 & 1 \\ 1 & 0 \end{bmatrix} \\ \hat{U}_4 &= \sqrt{2}\hat{I}_y \rightarrow \frac{\sqrt{2}}{2\mathrm{i}}\begin{bmatrix} 0 & 1 \\ -1 & 0 \end{bmatrix} \end{aligned}\right\} \tag{58}$$

For a spin-1 nucleus, using equation (56), the angular momentum operators are

$$\left.\begin{aligned} \hat{I}_x &\rightarrow \tfrac{1}{\sqrt{2}}\begin{bmatrix} 0 & 1 & 0 \\ 1 & 0 & 1 \\ 0 & 1 & 0 \end{bmatrix}, \quad \hat{I}_y \rightarrow \tfrac{1}{\mathrm{i}\sqrt{2}}\begin{bmatrix} 0 & 1 & 0 \\ -1 & 0 & 1 \\ 0 & -1 & 0 \end{bmatrix} \\ \hat{I}_z &\rightarrow \begin{bmatrix} 1 & 0 & 0 \\ 0 & 0 & 0 \\ 0 & 0 & -1 \end{bmatrix} \end{aligned}\right\} \tag{59}$$

However, since nine basis operators are required for spin 1, augmenting this set with $\hat{E}$ would clearly not be sufficient to produce a complete basis. However, we shall defer enumerating the other members of this basis until the next section, because the task becomes much easier once the spherical tensor operators have been introduced.

3.5 The Spherical Tensor Operator Basis

Examination of equation (56) rapidly leads one to conclude that a simpler basis might be composed including the following operators:

$$\left.\begin{aligned} \hat{I}_+|m\rangle &= [I(I+1) - m(m+1)]^{1/2}|m+1\rangle \\ \hat{I}_-|m\rangle &= [I(I+1) - m(m-1)]^{1/2}|m-1\rangle \end{aligned}\right\} \tag{60}$$

These operators are commonly called the *raising* or *step-up* and *lowering* or *step-down* operators, because they convert a given eigenket of $\hat{I}_z$ into one with the eigenvalue increased or decreased, respectively, by one. In terms of these operators, we have

$$\hat{I}_x = \tfrac{1}{2}(\hat{I}_+ + \hat{I}_-), \quad \hat{I}_y = \tfrac{1}{2\mathrm{i}}(\hat{I}_+ - \hat{I}_-) \tag{61}$$

The inverse relationship is

$$\hat{I}_+ = \hat{I}_x + \mathrm{i}\hat{I}_y, \quad \hat{I}_- = \hat{I}_x - \mathrm{i}\hat{I}_y \tag{62}$$

Applying these relations to equation (57) leads to a new basis:

$$\left.\begin{aligned} \hat{I}_+ &\rightarrow \begin{bmatrix} 0 & 1 \\ 0 & 0 \end{bmatrix}, \quad \hat{I}_- \rightarrow \begin{bmatrix} 0 & 0 \\ 1 & 0 \end{bmatrix} \\ \hat{I}_z &\rightarrow \tfrac{1}{2}\begin{bmatrix} 1 & 0 \\ 0 & -1 \end{bmatrix}, \quad \hat{E} \rightarrow \begin{bmatrix} 1 & 0 \\ 0 & 1 \end{bmatrix} \end{aligned}\right\} \tag{63}$$

The orthonormal basis corresponding to equation (58) is given by

$$\left.\begin{aligned} \hat{U}_1 &= \hat{T}^{(0)}_{0,0} = \frac{1}{\sqrt{2}}\hat{E} \rightarrow \frac{1}{\sqrt{2}}\begin{bmatrix} 1 & 0 \\ 0 & 1 \end{bmatrix} \\ \hat{U}_2 &= \hat{T}^{(1)}_{0,0} = \sqrt{2}\hat{I}_z \rightarrow \frac{\sqrt{2}}{2}\begin{bmatrix} 1 & 0 \\ 0 & -1 \end{bmatrix} \\ \hat{U}_3 &= \hat{T}^{(1)}_{1,0} = -\hat{I}_+ \rightarrow \begin{bmatrix} 0 & -1 \\ 0 & 0 \end{bmatrix} \\ \hat{U}_4 &= \hat{T}^{(1)}_{-1,0} = \hat{I}_- \rightarrow \begin{bmatrix} 0 & 0 \\ 1 & 0 \end{bmatrix} \end{aligned}\right\} \tag{64}$$

The $\hat{T}^{(k)}_{q,j}$ designation for these operators is that characterizing the *irreducible spherical tensor operators*. There will be

$2k + 1$ members in a set of operators of rank k with projection q ranging from $-k$ to k in integer steps. Note that the index j is not needed here, but will come into play when more complicated spin systems are considered with more than one set of operators of a given k. In what follows, the index j will be suppressed when it is not needed. It is easily verified that this basis is orthonormal. The minus sign associated with $\hat{U}_3$ does not affect the orthonormality of the set. It is common practice to choose this 'phase factor' to correspond to that of the spherical harmonic functions, i.e., such that

$$\hat{T}_q^{(k)\dagger} = (-1)^q \hat{T}_{-q}^{(k)} \tag{65}$$

The operators then satisfy equation (39) in the form

$$\mathrm{Tr}(\hat{T}_q^{(k)} \hat{T}_{q'}^{(k)\dagger}) = (-1)^q \mathrm{Tr}(\hat{T}_q^{(k)} \hat{T}_{-q'}^{(k')}) = \delta_{kk'}\delta_{q-q'} \tag{66}$$

The defining characteristic of the irreducible spherical tensor operators is that when they are subjected to a rotation of the coordinate system, they behave like the spherical harmonic functions, i.e., they transform to linear combinations of the set such that operators of differing k or j never mix:

$$\hat{R}(\phi, \theta, \chi)\hat{T}_{q,j}^{(k)}\hat{R}^{-1}(\phi, \theta, \chi) = \sum_{q'=-k}^{k} D_{q'q}^{(k)}(\phi, \theta, \chi)\hat{T}_{q',j}^{(k)} \tag{67}$$

The rotation operator $\hat{R}(\phi, \theta, \chi)$ and its inverse (defined by equation (68)) transform any operator from the original coordinate system $\{x,y,z\}$ into a new one $\{x',y',z'\}$:

$$\left.\begin{aligned} \hat{R}(\phi, \theta, \chi) &= \exp(-\mathrm{i}\phi\hat{I}_z)\exp(-\mathrm{i}\theta\hat{I}_y)\exp(-\mathrm{i}\chi\hat{I}_z) \\ \hat{R}^{-1}(\phi, \theta, \chi) &= \exp(\mathrm{i}\phi\hat{I}_z)\exp(\mathrm{i}\theta\hat{I}_y)\exp(\mathrm{i}\chi\hat{I}_z) \end{aligned}\right\} \tag{68}$$

The Euler angles $\{\phi,\theta,\chi\}$ define rotations about the z, then y, then z again axes of the original coordinate system, which rotations carry the original coordinate system to coincide with the new one. The $D_{q'q}^{(k)}(\phi, \theta, \chi)$ are called the *Wigner rotation matrix elements*. The definition of these coefficients is rather involved, and will not be given here. They are defined and tabulated in numerous texts, such as the excellent one by Zare.[10] Exponential operators like those in equation (68) as generators of rotations play a central role in the theoretical development of NMR. They, too, are discussed in great detail in Zare's text.

It was noted in Section 2.1 that operators do not necessarily commute. A special shorthand notation is commonly used for *commutators* of operators, defined as follows:

$$\hat{A}\hat{B} - \hat{B}\hat{A} \equiv [\hat{A}, \hat{B}] \tag{69}$$

Using this notation, an equivalent, though perhaps less intuitive, definition of irreducible spherical tensor operators is provided by the following commutation relations:

$$\left.\begin{aligned} [\hat{I}_\pm, \hat{T}_{q,j}^{(k)}] &= \{(k \mp q)(k \pm q + 1)\}^{1/2}\hat{T}_{q\pm1,j}^{(k)} \\ [\hat{I}_z, \hat{T}_{q,j}^{(k)}] &= q\hat{T}_{q,j}^{(k)} \end{aligned}\right\} \tag{70}$$

Note that one is free to choose either the positive or the negative square root in the coefficient in equation (70), and the result will still satisfy both commutation relations. Thus, we choose the one that satisfies equation (65). The following commutators are easily verified for spin-$\frac{1}{2}$ from equation (63):

$$[\hat{I}_z, \hat{I}_\pm] = \pm\hat{I}_\pm, \quad [\hat{I}_\pm, \hat{I}_\mp] = \pm 2\hat{I}_z \tag{71}$$

From equation (59), using equation (62), one can generate the following operators and verify that equation (71) holds for spin 1 also:

$$\left.\begin{aligned} \hat{I}_+ \to \sqrt{2}\begin{bmatrix} 0 & 1 & 0 \\ 0 & 0 & 1 \\ 0 & 0 & 0 \end{bmatrix}, \quad \hat{I}_- \to \sqrt{2}\begin{bmatrix} 0 & 0 & 0 \\ 1 & 0 & 0 \\ 0 & 1 & 0 \end{bmatrix} \\ \hat{I}_z \to \begin{bmatrix} 1 & 0 & 0 \\ 0 & 0 & 0 \\ 0 & 0 & -1 \end{bmatrix} \end{aligned}\right\} \tag{72}$$

It can be shown[6] that these commutation relations are true in general. These three matrices represent an irreducible spherical tensor operator of rank one just as was the case for spin-$\frac{1}{2}$ in equation (64), and the zeroth-order operator can be written as well. Note, however, that the required normalization factors are different:

$$\left.\begin{aligned} \hat{T}_0^{(0)} &= \frac{1}{\sqrt{3}}\hat{E} \to \frac{1}{\sqrt{3}}\begin{bmatrix} 1 & 0 & 0 \\ 0 & 1 & 0 \\ 0 & 0 & 1 \end{bmatrix} \\ \hat{T}_1^{(1)} &= -\tfrac{1}{2}\hat{I}_+ \to -\frac{1}{\sqrt{2}}\begin{bmatrix} 0 & 1 & 0 \\ 0 & 0 & 1 \\ 0 & 0 & 0 \end{bmatrix} \\ \hat{T}_{-1}^{(1)} &= \tfrac{1}{2}\hat{I}_- \to \frac{1}{\sqrt{2}}\begin{bmatrix} 0 & 0 & 0 \\ 1 & 0 & 0 \\ 0 & 1 & 0 \end{bmatrix} \\ \hat{T}_0^{(1)} &= \frac{1}{\sqrt{2}}\hat{I}_z \to \frac{1}{\sqrt{2}}\begin{bmatrix} 1 & 0 & 0 \\ 0 & 0 & 0 \\ 0 & 0 & -1 \end{bmatrix} \end{aligned}\right\} \tag{73}$$

It is easily verified that these operators are orthonormal and satisfy equation (70).

Using these four operators as a starting point, the problem of finding the other five basis operators for spin 1 can now be addressed. The required operators must be mutually orthogonal and orthogonal to the four already proposed. A logical extension of what has been done so far would be the five elements of an irreducible spherical tensor operator of rank two. For spin 1, the step-up operator can be applied twice to the eigenstate $|-1\rangle$ to produce first the $|0\rangle$ then the $|1\rangle$ eigenstate. The corresponding second-rank operator is $\hat{I}_+\hat{I}_+$. The representation of this operator can be obtained in several ways according to what we have learned so far. Perhaps the easiest way is to square the matrix given in equation (72) and normalize the result to give

$$\hat{T}_2^{(2)} = \tfrac{1}{2}\hat{I}_+\hat{I}_+ \to \begin{bmatrix} 0 & 0 & 1 \\ 0 & 0 & 0 \\ 0 & 0 & 0 \end{bmatrix} \tag{74}$$

which is easily shown to satisfy equation (70). Equation (70) can now be used to successively generate the other members of the set as follows:

$$[\hat{I}_-, \hat{T}_2^{(2)}] = \{(2 + 2)(2 - 2 + 1)\}^{1/2}\hat{T}_1^{(2)} = -2\hat{T}_1^{(2)} \tag{75}$$

The negative square root is chosen so as to satisfy equation (65). Hence, we have

$$\begin{aligned}\hat{T}_1^{(2)} &= -\tfrac{1}{2}[\hat{I}_-, \tfrac{1}{2}\hat{I}_+\hat{I}_+] = -\tfrac{1}{4}[\hat{I}_-, \hat{I}_+\hat{I}_+] \\ &= -\tfrac{1}{4}(\hat{I}_-\hat{I}_+\hat{I}_+ - \hat{I}_+\hat{I}_+\hat{I}_-)\end{aligned} \tag{76}$$

Then substituting from equation (71) yields

$$\begin{aligned}\hat{T}_1^{(2)} &= -\tfrac{1}{4}\{\hat{I}_-\hat{I}_+\hat{I}_+ - \hat{I}_+(2\hat{I}_z + \hat{I}_-\hat{I}_+)\} \\ &= -\tfrac{1}{4}\{(\hat{I}_-\hat{I}_+ - \hat{I}_+\hat{I}_-)\hat{I}_+ - 2\hat{I}_+\hat{I}_z\} \\ &= -\tfrac{1}{4}(-[\hat{I}_+, \hat{I}_-]\hat{I}_+ - 2\hat{I}_+\hat{I}_z)\end{aligned} \tag{77}$$

Using equation (71) again gives the desired operator, and substitution from equation (72), gives the representation:

$$\hat{T}_1^{(2)} = \tfrac{1}{2}(\hat{I}_z\hat{I}_+ + \hat{I}_+\hat{I}_z) \rightarrow \frac{1}{\sqrt{2}}\begin{bmatrix}0 & 1 & 0\\ 0 & 0 & -1\\ 0 & 0 & 0\end{bmatrix} \tag{78}$$

Applying the same procedure successively generates the other three operators. The $q = 0$ component is

$$\begin{aligned}\hat{T}_0^{(2)} &= -\sqrt{\tfrac{1}{6}}[\hat{I}_-, \hat{T}_1^{(2)}] \\ &= -\tfrac{1}{2}\sqrt{\tfrac{1}{6}}[\hat{I}_-, (\hat{I}_z\hat{I}_+ + \hat{I}_+\hat{I}_z)] \\ &= -\tfrac{1}{2}\sqrt{\tfrac{1}{6}}(\hat{I}_-\hat{I}_z\hat{I}_+ - \hat{I}_z\hat{I}_+\hat{I}_- + \hat{I}_-\hat{I}_+\hat{I}_z - \hat{I}_+\hat{I}_z\hat{I}_-) \\ &= -\tfrac{1}{2}\sqrt{\tfrac{1}{6}}\{(\hat{I}_- + \hat{I}_z\hat{I}_-)\hat{I}_+ - \hat{I}_z\hat{I}_+\hat{I}_- + \hat{I}_-\hat{I}_+\hat{I}_z \\ &\quad -\hat{I}_+(-\hat{I}_- + \hat{I}_-\hat{I}_z)\} \\ &= -\tfrac{1}{2}\sqrt{\tfrac{1}{6}}(\hat{I}_+\hat{I}_- + \hat{I}_-\hat{I}_+ + \hat{I}_z[\hat{I}_-, \hat{I}_+] + [\hat{I}_-, \hat{I}_+]\hat{I}_z) \\ &= \sqrt{\tfrac{1}{6}}\{2\hat{I}_z^2 - \tfrac{1}{2}(\hat{I}_+\hat{I}_- + \hat{I}_-\hat{I}_+)\} \rightarrow \frac{1}{\sqrt{6}}\begin{bmatrix}1 & 0 & 0\\ 0 & -2 & 0\\ 0 & 0 & 1\end{bmatrix}\end{aligned} \tag{79}$$

In this case, the negative phase is chosen arbitrarily, because equation (65) places no constraint on the phase of this operator. The $q = -1$ component is

$$\begin{aligned}\hat{T}_{-1}^{(2)} &= \sqrt{\tfrac{1}{6}}[\hat{I}_-, \hat{T}_0^{(2)}] \\ &= \tfrac{1}{6}[\hat{I}_-, \{2\hat{I}_z^2 - \tfrac{1}{2}(\hat{I}_+\hat{I}_- + \hat{I}_-\hat{I}_+)\}] \\ &= \tfrac{1}{6}(2\hat{I}_-\hat{I}_z^2 - 2\hat{I}_z^2\hat{I}_- + \tfrac{1}{2}\hat{I}_+\hat{I}_-\hat{I}_- - \tfrac{1}{2}\hat{I}_-\hat{I}_-\hat{I}_+) \\ &= \tfrac{1}{6}\{2(\hat{I}_- + \hat{I}_z\hat{I}_-)\hat{I}_z - 2\hat{I}_z(-\hat{I}_- + \hat{I}_-\hat{I}_z) \\ &\quad +\tfrac{1}{2}(2\hat{I}_z + \hat{I}_-\hat{I}_+)\hat{I}_- - \tfrac{1}{2}\hat{I}_-(-2\hat{I}_z + \hat{I}_+\hat{I}_-)\} \\ &= \tfrac{1}{2}(\hat{I}_z\hat{I}_- + \hat{I}_-\hat{I}_z) \rightarrow \frac{1}{\sqrt{2}}\begin{bmatrix}0 & 0 & 0\\ 1 & 0 & 0\\ 0 & -1 & 0\end{bmatrix}\end{aligned} \tag{80}$$

Here the positive phase has been chosen to satisfy equation (65). The $q = -2$ component is

$$\begin{aligned}\hat{T}_{-2}^{(2)} &= \tfrac{1}{2}[\hat{I}_-, \hat{T}_{-1}^{(2)}] \\ &= \tfrac{1}{4}[\hat{I}_-, (\hat{I}_z\hat{I}_- + \hat{I}_-\hat{I}_z)] \\ &= \tfrac{1}{4}(-\hat{I}_z\hat{I}_-\hat{I}_- + \hat{I}_-\hat{I}_-\hat{I}_z) \\ &= \tfrac{1}{4}\{-(-\hat{I}_- + \hat{I}_-\hat{I}_z)\hat{I}_- + \hat{I}_-(\hat{I}_- + \hat{I}_z\hat{I}_-)\} \\ &= \tfrac{1}{2}\hat{I}_-\hat{I}_- \rightarrow \begin{bmatrix}0 & 0 & 0\\ 0 & 0 & 0\\ 1 & 0 & 0\end{bmatrix}\end{aligned} \tag{81}$$

The positive phase has been chosen here, again arbitrarily. The same result could also be obtained by starting from $T_{-2}{}^{(2)}$ and stepping it up with I_+. These nine operators given by equations (73), (74), and (78)–(81) form a complete basis set for spin 1. Of course, higher spin bases can be constructed in the same way; spin I will require irreducible spherical tensors of rank $k = 0, 1, 2, \ldots, 2I$.

4 THE DENSITY OPERATOR

It is a familiar concept[7] that an experimental measurement will yield a value corresponding to the bracket of the state of the system under study with the operator corresponding to the observable:

$$\langle\hat{O}(t)\rangle = \langle\psi(t)|\hat{O}|\psi(t)\rangle \tag{82}$$

The notation on the left-hand side carries some connotation that the operator is time-dependent, which need not be the case; the time dependence in this case is carried entirely in the state. Some authors use the notation $\langle\hat{O}\rangle(t)$ or some other variant to avoid possible ambiguity. We shall retain the notation of equation (82), trusting the reader to realize the subtle difference implied. This leads to a discussion of Schrödinger versus Heisenberg versus interaction pictures of quantum mechanics, which will be addressed in Section 4.1. Of course, this result is independent of the 'picture' employed or the basis chosen. Inserting twice the sum on projection operators for some basis as in equation (19) and rearranging yields

$$\begin{aligned}\langle\hat{O}(t)\rangle &= \langle\psi(t)|\sum_{i=1}^{n}|i\rangle\langle i|\hat{O}\sum_{j=1}^{n}|\,j\rangle\langle\,j|\psi(t)\rangle \\ &= \sum_{i,j=1}^{n}\langle\psi(t)|i\rangle\langle i|\hat{O}|\,j\rangle\langle\,j|\psi(t)\rangle \\ &= \sum_{i,j=1}^{n}\langle\,j|\psi(t)\rangle\langle\psi(t)|i\rangle\langle i|\hat{O}|\,j\rangle\end{aligned} \tag{83}$$

As in equation (9), the quantity $|\psi(t)\rangle\langle\psi(t)|$ can be regarded as an operator, which is known as the density operator $\hat{\rho}(t)$:

$$\hat{\rho}(t) = |\psi(t)\rangle\langle\psi(t)| \tag{84}$$

Continuing from equation (83), we can write

$$\begin{aligned}\langle \hat{O}(t)\rangle &= \sum_{i,j=1}^{n} \langle\, j|\hat{\rho}(t)|i\rangle\langle i|\hat{O}|\, j\rangle \\ &= \sum_{j=1}^{n} \langle\, j|\hat{\rho}(t)\hat{O}|\, j\rangle \\ &= \mathrm{Tr}(\hat{\rho}(t)\hat{O}) \end{aligned} \tag{85}$$

This is an important relationship showing that the expected value of any operator can be computed by taking the trace of its product with the density operator. This form is completely equivalent to equation (82), and is the form commonly used for discussion of magnetic resonance phenomena. Just as the state $|\psi(t)\rangle$ contains all that can be known about the state of a system, so does the density operator.

According to equation (42), using an appropriate operator basis, we can write

$$\begin{aligned}\hat{\rho}(t) &= \sum_{i=1}^{n^2} \mathrm{Tr}\{\hat{\rho}(t)\hat{U}_i^{\dagger}\}\hat{U}_i \\ &= \sum_{i=1}^{n^2} \langle \hat{U}_i^{\dagger}(t)\rangle \hat{U}_i \end{aligned} \tag{86}$$

Thus, the expected values of all the basis operators provide the coefficients needed to represent the density operator in any basis, and these values provide a Liouville space representation of the density operator according to equation (43). Extensive use of this concept will be made later in developing the equations needed to explain spin relaxation.

The development so far has implied that the system of interest can be characterized by a state $|\psi(t)\rangle$. Liquid samples can never be so characterized, but can often be viewed as an ensemble of such isolated systems. Thus, it is desirable to take an ensemble average of equation (84). Since all the variation among the members of the ensemble resides in the operator $|\psi(t)\rangle\langle\psi(t)|$, the averaging process commutes with the sums over basis states, and we can write

$$\begin{aligned}\overline{\langle \hat{O}(t)\rangle} &= \sum_{i,j=1}^{n} \overline{\langle\, j|\psi(t)\rangle\langle\psi(t)|i\rangle}\langle i|\hat{O}|\, j\rangle \\ &= \sum_{i,j=1}^{n} \overline{\langle\, j|\hat{\rho}(t)|i\rangle}\langle i|\hat{O}|\, j\rangle \\ &= \sum_{j=1}^{n} \langle\, j|\bar{\hat{\rho}}(t)\hat{O}|\, j\rangle \\ &= \mathrm{Tr}\{\bar{\hat{\rho}}(t)\hat{O}\} \end{aligned} \tag{87}$$

Clearly, $\hat{\rho}(t)$ can be replaced by $\bar{\hat{\rho}}(t)$ in the above equations, leaving the form of the equations the same. In what follows, we shall not retain the overbar notation, but the density operator should be assumed to be averaged over an ensemble.

4.1 Time Evolution of the Density Operator

The time-dependent Schrödinger equation

$$\mathrm{i}\hbar\frac{\mathrm{d}}{\mathrm{d}t}|\psi(t)\rangle = \hat{\mathcal{H}}(t)|\psi(t)\rangle \tag{88}$$

can easily be converted to our density operator formalism. Beginning from equation (84) and using equation (88) and its complex conjugate obtained using equations (2) and (7), we can write

$$\begin{aligned}\frac{\mathrm{d}\hat{\rho}(t)}{\mathrm{d}t} &= \frac{\mathrm{d}}{\mathrm{d}t}\{|\psi(t)\rangle\langle\psi(t)|\} \\ &= \frac{\mathrm{d}}{\mathrm{d}t}\{|\psi(t)\rangle\}\langle\psi(t)| + |\psi(t)\rangle\frac{\mathrm{d}}{\mathrm{d}t}\{\langle\psi(t)|\} \\ &= -\frac{\mathrm{i}}{\hbar}\hat{\mathcal{H}}(t)|\psi(t)\rangle\langle\psi(t)| + \frac{\mathrm{i}}{\hbar}|\psi(t)\rangle\langle\psi(t)|\hat{\mathcal{H}}(t) \\ &= -\frac{\mathrm{i}}{\hbar}\{\hat{\mathcal{H}}(t)\hat{\rho}(t) - \hat{\rho}(t)\hat{\mathcal{H}}(t)\} \\ &= -\frac{\mathrm{i}}{\hbar}[\hat{\mathcal{H}}(t), \hat{\rho}(t)] \end{aligned} \tag{89}$$

Note that the Hamiltonian is Hermitian. The commutator of the Hamiltonian with the density operator determines the time development of the density operator. This relation is referred to as the *Liouville–von Neuman equation*, and will play a central role in what follows. Our goal, generally stated, will be to find solutions of this equation using a Hamiltonian corresponding to various experimental situations. The density operator at some particular time will generally be known—at least parametrically—and equation (89) must then be integrated to obtain the time development of the density operator.

The solution of this equation of motion is fairly simple if the Hamiltonian is not time-dependent. If we suppose that the density operator has the value $\hat{\rho}(0)$ at $t = 0$ then

$$\hat{\rho}(t) = \exp\left(-\frac{\mathrm{i}}{\hbar}\hat{\mathcal{H}}t\right)\hat{\rho}(0)\exp\left(\frac{\mathrm{i}}{\hbar}\hat{\mathcal{H}}t\right) \tag{90}$$

is a solution, as can be verified by differentiation:

$$\begin{aligned}\frac{\mathrm{d}\hat{\rho}(t)}{\mathrm{d}t} &= \left(-\frac{\mathrm{i}}{\hbar}\hat{\mathcal{H}}\right)\exp\left(-\frac{\mathrm{i}}{\hbar}\hat{\mathcal{H}}t\right)\hat{\rho}(0)\exp\left(\frac{\mathrm{i}}{\hbar}\hat{\mathcal{H}}t\right) \\ &\quad + \exp\left(-\frac{\mathrm{i}}{\hbar}\hat{\mathcal{H}}t\right)\hat{\rho}(0)\left(\frac{\mathrm{i}}{\hbar}\hat{\mathcal{H}}\right)\exp\left(\frac{\mathrm{i}}{\hbar}\hat{\mathcal{H}}t\right) \\ &= -\frac{\mathrm{i}}{\hbar}\left\{\hat{\mathcal{H}}\exp\left(-\frac{\mathrm{i}}{\hbar}\hat{\mathcal{H}}t\right)\hat{\rho}(0)\exp\left(\frac{\mathrm{i}}{\hbar}\hat{\mathcal{H}}t\right)\right. \\ &\quad \left. - \exp\left(-\frac{\mathrm{i}}{\hbar}\hat{\mathcal{H}}t\right)\hat{\rho}(0)\exp\left(\frac{\mathrm{i}}{\hbar}\hat{\mathcal{H}}t\right)\hat{\mathcal{H}}\right\} \\ &= -\frac{\mathrm{i}}{\hbar}\{\hat{\mathcal{H}}\hat{\rho}(t) - \hat{\rho}(t)\hat{\mathcal{H}}\} = -\frac{\mathrm{i}}{\hbar}[\hat{\mathcal{H}}, \hat{\rho}(t)] \end{aligned} \tag{91}$$

We have used the fact that an operator commutes with a function of itself.

Now let us examine the expected value of a generic operator with this solution. Substituting equation (90) into equation (87) yields

$$\begin{aligned}\langle \hat{O}(t)\rangle &= \mathrm{Tr}\{\hat{\rho}(t)\hat{O}\} = \mathrm{Tr}\left\{\exp\left(-\frac{\mathrm{i}}{\hbar}\hat{\mathcal{H}}t\right)\hat{\rho}(0)\exp\left(\frac{\mathrm{i}}{\hbar}\hat{\mathcal{H}}t\right)\hat{O}\right\} \\ &= \mathrm{Tr}\left\{\hat{\rho}(0)\exp\left(\frac{\mathrm{i}}{\hbar}\hat{\mathcal{H}}t\right)\hat{O}\exp\left(-\frac{\mathrm{i}}{\hbar}\hat{\mathcal{H}}t\right)\right\} \\ &= \mathrm{Tr}\{\hat{\rho}(0)\hat{O}(t)\} \end{aligned} \tag{92}$$

The fact that the trace operation is invariant under cyclic permutation of the factors has been used, and the time-dependent operator $\hat{O}(t)$ has been introduced according to

$$\hat{O}(t) = \exp\left(\frac{\mathrm{i}}{\hbar}\hat{\mathcal{H}}t\right)\hat{O}\exp\left(-\frac{\mathrm{i}}{\hbar}\hat{\mathcal{H}}t\right) \tag{93}$$

Equation (87) expresses the Schrödinger picture of quantum mechanics, whereas equation (92) transforms into the Heisenberg picture. Clearly, the two forms are equivalent.

Differentiating equation (93) yields the equation of motion for the time-dependent operators of the Heisenberg picture, corresponding to equation (89) for the Schrödinger picture:

$$\frac{\mathrm{d}\hat{O}(t)}{\mathrm{d}t} = \frac{\mathrm{i}}{\hbar}[\hat{\mathcal{H}}, \hat{O}(t)] \tag{94}$$

The derivation proceeds like that of equation (91). The equations for the Schrödinger and the Heisenberg pictures are similar in form, but the sign differences in the various terms should be noted.

When the Hamiltonian is time-dependent, the situation is considerably more complex, and no attempt will be made here to discuss this case in general terms. However, suppose the Hamiltonian can be separated into a term that is time-dependent and another that is not:

$$\hat{\mathcal{H}}(t) = \hat{\mathcal{H}}_0 + \hat{\mathcal{H}}_1(t) \tag{95}$$

Equation (89) may then be rewritten as

$$\begin{aligned}\frac{\mathrm{d}\hat{\rho}(t)}{\mathrm{d}t} &= -\frac{\mathrm{i}}{\hbar}[\hat{\mathcal{H}}_0 + \hat{\mathcal{H}}_1(t), \hat{\rho}(t)] \\ &= -\frac{\mathrm{i}}{\hbar}\{[\hat{\mathcal{H}}_0, \hat{\rho}(t)] + [\hat{\mathcal{H}}_1(t), \hat{\rho}(t)]\}\end{aligned} \tag{96}$$

If $\hat{\mathcal{H}}_1(t) = 0$ then the solution is as in equation (90). By analogy with equation (90), let us define the transformed operators

$$\hat{\rho}'(t) = \exp\left(\frac{\mathrm{i}}{\hbar}\hat{\mathcal{H}}_0 t\right)\hat{\rho}(t)\exp\left(-\frac{\mathrm{i}}{\hbar}\hat{\mathcal{H}}_0 t\right) \tag{97}$$

$$\hat{\mathcal{H}}_1'(t) = \exp\left(\frac{\mathrm{i}}{\hbar}\hat{\mathcal{H}}_0 t\right)\hat{\mathcal{H}}_1(t)\exp\left(-\frac{\mathrm{i}}{\hbar}\hat{\mathcal{H}}_0 t\right) \tag{98}$$

Differentiating equation (97) and substituting from equations (96) and (98) then gives

$$\begin{aligned}\frac{\mathrm{d}\hat{\rho}'(t)}{\mathrm{d}t} &= \frac{\mathrm{i}}{\hbar}\hat{\mathcal{H}}_0\exp\left(\frac{\mathrm{i}}{\hbar}\hat{\mathcal{H}}_0 t\right)\hat{\rho}(t)\exp\left(-\frac{\mathrm{i}}{\hbar}\hat{\mathcal{H}}_0 t\right) \\ &\quad + \exp\left(\frac{\mathrm{i}}{\hbar}\hat{\mathcal{H}}_0 t\right)\frac{\mathrm{d}\hat{\rho}(t)}{\mathrm{d}t}\exp\left(-\frac{\mathrm{i}}{\hbar}\hat{\mathcal{H}}_0 t\right) \\ &\quad + \exp\left(\frac{\mathrm{i}}{\hbar}\hat{\mathcal{H}}_0 t\right)\hat{\rho}(t)\exp\left(-\frac{\mathrm{i}}{\hbar}\hat{\mathcal{H}}_0 t\right)\left(-\frac{\mathrm{i}}{\hbar}\hat{\mathcal{H}}_0\right) \\ &= \frac{\mathrm{i}}{\hbar}[\hat{\mathcal{H}}_0, \hat{\rho}'(t)] + \exp\left(\frac{\mathrm{i}}{\hbar}\hat{\mathcal{H}}_0 t\right)\left(-\frac{\mathrm{i}}{\hbar}\{[\hat{\mathcal{H}}_0, \hat{\rho}(t)]\right. \\ &\quad \left. + [\hat{\mathcal{H}}_1(t), \hat{\rho}(t)]\}\right)\exp\left(-\frac{\mathrm{i}}{\hbar}\hat{\mathcal{H}}_0 t\right) \\ &= -\frac{\mathrm{i}}{\hbar}[\hat{\mathcal{H}}_1'(t), \hat{\rho}'(t)]\end{aligned} \tag{99}$$

Thus, in this 'interaction picture', part of the time dependence is placed in the operators and part remains in the density operator. The effect of $\hat{\mathcal{H}}_0$ appears only implicitly in the exponential transformation operator. Of course, this is not a solution of the equation of motion, but it will prove to be a useful technique to be applied later on.

4.2 The Reduced Density Operator

In NMR experiments, it is usually the case that the nuclear spins interact weakly with the other degrees of freedom of the sample of interest. For the moment, let us assume that they do not interact at all. The state of the system can be written as a direct product, as in equation (48a), of a ket corresponding to the spin degrees of freedom with one corresponding to the rest of the system, the lattice:

$$|S\rangle|L\rangle = |SL\rangle \tag{100}$$

The number of degrees of freedom, i.e., the number of basis states, necessary to span the spins is modest, while that necessary to span the lattice is very large—effectively infinite.

Consider the expected value of an operator that acts only on the spin degrees of freedom. If $\{|sl\rangle\}$ is a basis set spanning both the spins and the lattice, we can write

$$\begin{aligned}\langle\hat{O}\rangle &= \mathrm{Tr}(\hat{\rho}\hat{O}) = \mathrm{Tr}(|SL\rangle\langle SL|\hat{O}) \\ &= \sum_{sl}\langle sl|SL\rangle\langle SL|\hat{O}|sl\rangle\end{aligned} \tag{101}$$

Since $\hat{O}$ commutes with the lattice operators, this can be rearranged to yield

$$\begin{aligned}\langle\hat{O}\rangle &= \sum_s\langle s|S\rangle\langle S|\hat{O}|s\rangle\sum_l\langle l|L\rangle\langle L|l\rangle \\ &= \sum_s\langle s|S\rangle\left(\sum_l\langle l|L\rangle\langle L|l\rangle\right)\langle S|\hat{O}|s\rangle\end{aligned} \tag{102}$$

We can now define the reduced density operator by

$$\hat{\sigma} = |S\rangle\left(\sum_l\langle l|L\rangle\langle L|l\rangle\right)\langle S| = \mathrm{Tr}_l(\hat{\rho}) \tag{103}$$

The expected value of $\hat{O}$ can then be written as

$$\langle\hat{O}\rangle = \mathrm{Tr}_s(\hat{\sigma}\hat{O}) \tag{104}$$

Thus, observing experimental quantities corresponding to spin operators requires only a knowledge of this reduced density operator, and the problem has, at least in principle, only the small dimensionality of the spin degrees of freedom and not the very large dimensionality of the spins and the lattice. In particular, the Liouville equation, equation (99), can be cast in this form. However, if there were, indeed, no interaction of the spins with the lattice, as was assumed above, there would be no relaxation. Of course, this is observed not to be the case, but the interaction is sufficiently weak that it can be treated by perturbation methods, and the very large number of

degrees of freedom in the lattice permits treating the lattice classically to achieve excellent correspondence of theory to experiment. In what follows, then, solutions will be sought of the Liouville–von Neuman equation for the reduced density operator:

$$\frac{\mathrm{d}\hat{\sigma}(t)}{\mathrm{d}t} = -\frac{\mathrm{i}}{\hbar}[\hat{\mathcal{H}}(t), \hat{\sigma}(t)] \tag{105}$$

5 SUPEROPERATORS

The representation of operators in Liouville space has been discussed in Section 2.2. In this section, we shall introduce superoperators that act on operators in Liouville space in much the same way as operators act on states in Hilbert space, i.e., superoperators transform one operator into another.

Consider the operator product

$$\hat{C} = \hat{B}_1 \hat{A} \hat{B}_2 \tag{106}$$

Let us attempt to cast $\hat{A}$ in a Liouville space representation and then find a superoperator $\hat{\hat{B}}$ such that $|\hat{C}\rangle = \hat{\hat{B}}|\hat{A}\rangle$. The operator product can be written as follows and rearranged as shown by applying equations (7) and (15):

$$\begin{aligned}\langle i|\hat{C}|\ j\rangle &= \sum_{k,l=1}^{n} \langle i|\hat{B}_1|k\rangle\langle k|\hat{A}|l\rangle\langle l|\hat{B}_2|\ j\rangle \\ &= \sum_{k,l=1}^{n} \langle i|\hat{B}_1|k\rangle\langle\ j|\hat{B}_2^{\dagger}|l\rangle\langle k|\hat{A}|l\rangle \end{aligned} \tag{107}$$

The superoperator matrix elements can now be defined by

$$\langle ij|\hat{\hat{B}}|kl\rangle = \langle i|\hat{B}_1|k\rangle\langle\ j|\hat{B}_2^{\dagger}|l\rangle \tag{108}$$

This expression can be viewed as the matrix elements of a direct product in a space with basis $|i\rangle|j\rangle = |ij\rangle$, the direct product of two identical Hilbert space bases as in equation (50):

$$\hat{\hat{B}} = \hat{B}_1 \otimes \hat{B}_2^{\dagger} \tag{109}$$

The matrix elements of $\hat{A}$ may be mapped into a vector in this same space just as in equation (43). In fact, the operator basis $\{\hat{U}_i\}$ introduced in equation (43) is equivalent to the basis $\{|ij\rangle\}$. The matrix elements of $\hat{A}$ may be written as

$$\langle ij|\hat{A}\rangle = \langle i|\hat{A}|\ j\rangle \tag{110}$$

Then equation (107) can be written as

$$|\hat{C}\rangle = \hat{\hat{B}}|\hat{A}\rangle \tag{111}$$

The utility of this formalism is evident from several examples.

5.1 Unitary Transformations

Unitary transformations like $\hat{U}\hat{A}\hat{U}^{\dagger}$ in Hilbert space can easily be translated to Liouville space using equation (109) to define the relevant superoperator

$$\hat{\hat{U}} = \hat{U} \otimes \hat{U} \tag{112}$$

Note that $(\hat{U}^{\dagger})^{\dagger} = \hat{U}$. Then the unitary transformation becomes

$$\hat{\hat{U}}|\hat{A}\rangle \tag{113}$$

The superoperator $\hat{\hat{U}}$ is unitary. To show this, we can write

$$\hat{A} = \hat{U}^{\dagger}\hat{U}\hat{A}\hat{U}^{\dagger}\hat{U} \tag{114}$$

But this implies

$$|\hat{A}\rangle = (\hat{U}^{\dagger} \otimes \hat{U}^{\dagger})(\hat{U} \otimes \hat{U})|\hat{A}\rangle = \hat{\hat{U}}^{\dagger}\hat{\hat{U}}|\hat{A}\rangle \tag{115}$$

where the second equality in equation (115) follows immediately by considering the adjoint of equation (108). Thus, it must be that

$$\hat{\hat{U}}^{\dagger}\hat{\hat{U}} = \hat{\hat{E}} \tag{116}$$

5.2 Commutators

Consider the commutator $[\hat{A}, \hat{B}]$ as the action of something denoted by $[\hat{A}, \ ]$ on the operator $\hat{B}$ to produce a new operator $\hat{C}$. This relationship can be written as

$$[\hat{A}, \hat{B}] = \hat{A}\hat{B} - \hat{B}\hat{A} = \hat{A}\hat{B}\hat{E} - \hat{E}\hat{B}\hat{A} \tag{117}$$

Applying equation (109) then yields

$$\hat{\hat{A}} = \hat{A} \otimes \hat{E} - \hat{E} \otimes \hat{A}^{\dagger} \tag{118}$$

5.3 The Liouvillian

Using equation (118), the equation of motion for the density operator equation (89) can be re-written as

$$\frac{\mathrm{d}|\hat{\rho}(t)\rangle}{\mathrm{d}t} = -\frac{\mathrm{i}}{\hbar}\hat{\hat{\mathcal{L}}}(t)|\hat{\rho}(t)\rangle \tag{119}$$

The Liouvillian superoperator corresponding to the commutator with the Hamiltonian is defined as

$$\hat{\hat{\mathcal{L}}}(t) = \hat{\mathcal{H}}(t) \otimes \hat{E} - \hat{E} \otimes \hat{\mathcal{H}}(t) \tag{120}$$

Note that the Hamiltonian is Hermitian, so that $\hat{\mathcal{H}}(t) = \hat{\mathcal{H}}(t)^{\dagger}$.

6 RELATED ARTICLES

Rudimentary NMR: The Classical Picture.

7 REFERENCES

1. T. C. Farrar, and E. D. Becker, *Pulse and Fourier Transform NMR: Introduction to Theory and Methods*, Academic Press, New York, 1971.
2. H. Friebolin, *Basic One- and Two-Dimensional NMR Spectroscopy*, VCH, New York, 1991.
3. A. E. Derome, *Modern NMR Techniques for Chemistry Research*, Pergamon Press, Oxford, 1987.
4. P. A. M. Dirac, *The Principles of Quantum Mechanics*, 4th edn., Oxford University Press, Oxford, 1958.
5. T. C. Farrar and J. E. Harriman, *Density Matrix Theory and its Applications in NMR Spectroscopy*, 2nd edn., The Farragut Press, Madison, WI, 1992.
6. M. Goldman, *Quantum Description of High-Resolution NMR in Liquids*, Oxford University Press, Oxford, 1988.
7. C. P. Slichter, *Principles of Magnetic Resonance*, 3rd edn., Springer-Verlag, Berlin, 1990.
8. R. R. Ernst, G. Bodenhausen, and A. Wokaum, *Principles of Nuclear Magnetic Resonance in One and Two Dimensions*, Oxford University Press, Oxford, 1987.
9. A. Abragam, *The Principles of Nuclear Magnetism*, Oxford University Press, Oxford, 1961.
10. R. N. Zare, *Angular Momentum*, Wiley, New York, 1988.

Biographical Sketch

Charles L. Mayne. *b* 1942. B.S., 1970, New Mexico State University, U.S.A., Ph.D., 1976, University of Utah. Introduced to NMR by George A. Gray and subsequently tutored by David M. Grant. Manager of NMR Laboratories, University of Utah, Department of Chemistry, 1973–present. Academic appointment as Adjunct Associate Professor of Chemistry, University of Utah. Approx. 40 publications in NMR. Research interests include nuclear-spin relaxation, NMR at high pressure, structure elucidation of natural products, various aspects of multidimensional NMR, and computerized analysis of NMR data.

Liquid Crystalline Samples: Spectral Analysis

M. Longeri and G. Celebre
Università della Calabria, Cosenza, Italy

1	Introduction	1
2	Computer Programs for Spectral Analysis	2
3	Obtaining Starting Parameters for Iterations	3
4	Strategies in Spectral Analysis	4
5	Related Articles	7
6	References	7

1 INTRODUCTION

Proton (or other spin-$\frac{1}{2}$ nuclei) NMR spectra of molecules dissolved in liquid crystalline solvents differ from their isotropic analogues in a significant way. Thus, the well-known proton isotropic spectrum of ethylbenzene (composed of a triplet, a quadruplet and a broad singlet) changes into the ugly looking spectrum shown in Figure 1. Only by displaying the spectrum with a much smaller Hz/cm ratio is it possible to recognize the few thousand closely spaced, well-resolved, single transitions dispersed over a range of a few kilohertz which compose the spectrum. For molecules with a higher number of interacting spins the situation is even worse; the total intensity is dispersed over so many closely spaced, single transitions that their anisotropic spectra, except for a few highly symmetric spin systems, appear as a single unresolved band a few kilohertz in width. For this reason it is not necessary to use deuterated compounds as anisotropic solvents because the liquid crystalline phases used contain more than 20 interacting protons and contribute to the total spectrum only as the lumps and bumps which form the baseline. The lines due to the solute, which are much more intense because their total intensity is dispersed over relatively fewer transitions, can be distinguished from the baseline.[1]

These differences arise because two extra terms have to be considered in the anisotropic Hamiltonian.[1] Within the usual high field approximation the Hamiltonian is given by

$$\begin{aligned}\hat{\mathcal{H}} = {} & \frac{1}{2\pi}\sum_i \gamma_i \hat{I}_{iz}(1-\sigma_i^{\mathrm{iso}}-\bar{\sigma}_{zzi})B_z \\ & + \sum_{i<j}\{J_{ij}^{\mathrm{iso}}[\hat{I}_{iz}\hat{I}_{jz}+\tfrac{1}{2}(\hat{I}_i^+\hat{I}_j^- + \hat{I}_i^-\hat{I}_j^+)]\} \\ & + \sum_{i<j}[\bar{J}_{zzij}+2\bar{D}_{zzij}][\hat{I}_{iz}\hat{I}_{jz}-\tfrac{1}{2}(\hat{I}_i^+\hat{I}_j^- + \hat{I}_i^-\hat{I}_j^+)] \\ & + \sum_i \frac{\bar{q}_{zzi}}{4I_i(2I_i-1)}[3\hat{I}_{iz}\hat{I}_{iz}-I_i(I_i+1)] \qquad (1)\end{aligned}$$

where γ_i is the magnetogyric ratio of the ith nucleus. The fourth term is included only if $I_i \geq 1$, while the σ_i^{iso} and J_{ij}^{iso} scalars, the trace of the $\boldsymbol{\sigma}$ shielding and $\boldsymbol{J}$ indirect spin–spin coupling tensors, are the well-known spectral parameters which determine isotropic spectra; $\bar{\sigma}_{zzi}$, $\bar{J}_{zzij}$, $\bar{D}_{zzij}$ and $\bar{q}_{zzi}$ are the averaged components of the shielding, indirect coupling, direct dipolar coupling, and quadrupolar coupling tensors, respectively. The last two tensors have a null trace and so do not influence the frequencies or intensities of the peaks in isotropic spectra.

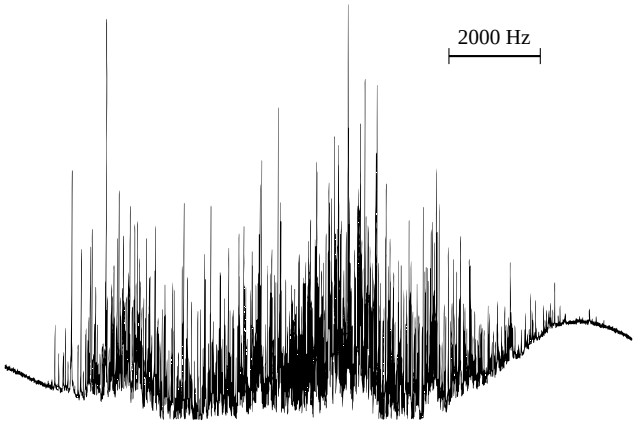

Figure 1 300 MHz (7.06 T) proton spectrum of ethylbenzene dissolved in ZLI 1132, a nematic solvent obtained from Merck

The direct dipolar couplings are related to the molecular geometries by

$$\bar{D}_{zzij} = K_{ij}\sum_{\alpha\beta} G_{ij\alpha\beta}S_{\alpha\beta}, \quad \alpha,\beta = x,y,z \qquad (2)$$

for rigid molecules, or

$$\bar{D}_{zzij} = K_{ij}\sum_n p^n \sum_{\alpha\beta} G^n_{ij\alpha\beta}S^m_{\alpha\beta} \qquad (3)$$

if internal rotational motions are present. K_{ij} depends on the magnetogyric ratio of the ith and jth nuclei, p^n is the population of conformer n, $S^m_{\alpha\beta}$ are the elements of $\mathbf{S}^n$, the Saupe orientational matrix for conformer n, $G^n_{ij\alpha\beta}$ are related to the internuclear distance r_{ij} and to its orientation with respect to a Cartesian system x, y, z fixed on the molecule.

It should be noted that the observed differences are not just due to the extra parameters present, but also, and more importantly, to the wider range of values that they can assume (from 2.5 to −5 kHz for direct couplings, and up to several kilohertz for quadrupolar couplings). If spin systems composed of only spin-$\frac{1}{2}$ nuclei are considered (for a description of how quadrupolar couplings influence anisotropic, spectra, see ***Liquid Crystalline Samples: Deuterium NMR***), the fourth term in equation (1) is zero and the spectrum shape depends mainly on the values of the dipolar couplings. Two important consequences ensue from this fact: (a) all the nuclei in the molecule have dipolar couplings larger than the experimental linewidth (4–5 Hz); and (b) no first-order features are present in the spectra of homonuclear spin systems.

Two points follow from equation (1). First, the direct spin–spin coupling $\bar{D}_{zzij}$ cannot be measured separately from $\bar{J}_{zzij}$ because only the quantity

$$\bar{T}_{zzij} = \bar{D}_{zzij} + \tfrac{1}{2}\bar{J}_{zzij} \qquad (4)$$

can be determined experimentally,[1c] and so liquid crystal NMR can be used to determine the geometry only if the pseudodipolar couplings $\bar{J}_{zzij}$ are known independently. Experimental and theoretical studies have shown that the pseudodipolar term is usually much smaller than the dipolar coupling and so, with the exception of F–F couplings, $\bar{D}_{zzij}$ can be safely equated to $\bar{T}_{zzij}$ (see ***Anisotropy of Shielding and Coupling in Liquid Crystalline Solutions***).

The second point involves magnetically equivalent nuclei (see ***Magnetic Equivalence***). The frequencies and intensities in isotropic spectra do not depend on the values of the indirect couplings between nuclei belonging to the same magnetically equivalent group, but this is not the case for anisotropic spectra. In many spectra this just means that there is one more direct coupling for each magnetically equivalent group to be taken into account in anisotropic spectral analysis, but the effects are quite dramatic for A_n (where n is the number of interacting spins) spin systems. Benzene is a very good example; all six protons have the same chemical shift and so, even though there are three different indirect couplings (J_{ortho}, J_{meta}, and J_{para}), the isotropic spectrum shows only a single transition. The spin system is correctly defined as A_6. The spectrum of benzene dissolved in an orienting medium will instead contain a maximum of 72 lines and is analyzable in terms of a chemical shift and three indirect and three direct couplings. The correct notation for the spin system is $AA'A''A'''A''''A'''''$.[1b]

2 COMPUTER PROGRAMS FOR SPECTRAL ANALYSIS

For anisotropic spectra, analytical solutions are possible only for a very limited number of simple spin systems,[1a,1b] but simulation/iteration programs are available for spectral analysis. These programs will: (a) calculate the spectrum from a trial starting set of spectral parameters using the spin Hamiltonian in equation (1); and (b) refine the parameters to fit some spectral quantities.[2]

A few methods have been proposed which use different spectral quantities in the fit, but only three of them have found application in anisotropic spectral analysis.

1. *Fully automated analysis*[3] According to this approach the full spectrum (defined by a vector containing intensity values at a fixed frequency interval) is used in the iteration procedure. No operator intervention is needed during the iteration cycles; at the end of the procedure the operator checks if the experimental spectrum has been reproduced correctly and no false minimum found (for a more detailed description of the method and computer programs, see ***Analysis of Spectra: Automatic Methods***).
2. *Swalen–Reilly method*[4] The 'experimentally' determined energy level diagram (ELD) is used in the refinement program NMRIT.[2,4b] The final parameter set, refined assuming a given assignment of calculated to experimental levels, is used to calculate the spectrum which is then compared with the experimental one. The procedure is repeated for a different assignment and the parameters giving the best fit between the calculated and experimental spectrum are assumed to be correct. The procedure can be easily automated, its main advantage deriving from the relatively low number of distinct assignments.[5] The algorithm which computes the ELD [part (a) of the program] must take into account the correct symmetry of the spin system.
3. *Castellano–Bothner-By method*[6] By far the most widely used approach,[2] this method makes use of the experimental frequencies in the parameters' refinement procedure. The method is particularly attractive because the derivatives

$$\frac{\partial F_{mn}}{\partial p_j} = \frac{\partial \Lambda_m}{\partial p_j} - \frac{\partial \Lambda_n}{\partial p_j} \tag{5}$$

where p_j is the jth spectral parameter, Λ_m is the mth eigenvalue, and F_{mn} is the calculated frequency of the transition between the mth and nth levels, can be calculated analytically. In fact,

$$\frac{\partial \Lambda_m}{\partial p_j} = \left(\mathbf{U} \frac{\partial \mathbf{H}}{\partial p_j} \mathbf{U} \right)_{mm} \tag{6}$$

where $\mathbf{U}$ is the matrix which diagonalizes the Hamiltonian matrix representation $\mathbf{H}$ in a given basis set. Care must be taken when choosing the basis set, in order to make as simple as possible the algorithm which computes the matrix $(\partial\ \mathbf{H}/\partial p_j)$.

Line identification numbers from a spectrum calculated with a trial, starting set of spectral parameters are assigned by the operator to experimental frequencies; the program will modify a selected subset of parameters to minimize the root mean square (rms) of the differences between the assigned calculated and experimental frequencies and will output the spectrum calculated with the new parameter set. The operator will compare the two spectra, recognize more lines to assign, modify or delete old assignments and choose a new subset of parameters to iterate. The cycles will be repeated until nearly all the experimental lines are assigned and a low rms obtained, having iterated the whole set of spectral parameters. The procedure is cumbersome, requiring a great deal of time and effort by the operator in the assignment step, and cannot be easily automated because only the operator can discriminate between the $N!$ different assignments (N being the number of observed transitions) on the basis of their intensities and relative positions. The probability of achieving success in the spectral analysis is low, decreases quickly as the complexity of the spin system increases, and is strictly related to the quality of the starting set, i.e. how near the starting parameter values are to the final ones.

To reduce the computational requirements [central processing unit (CPU) time and storage requirements] of part (a) of the program, much effort has been devoted to making full use of the possibilities of simplifying the Hamiltonian by using suitable basis function sets, but keeping operational the Castellano–Bothner-By iterative method. The first programs (LAOCOON[6b] and its anisotropic counterpart LAOCONOOR) took into account the so-called F_Z and X approximation factorization; magnetic equivalence factorization based on the Ferguson–Marquardt formalism[7] (composite particle formalism) was introduced in the LEQUOR program[8] in the early 1970s.

Molecular symmetry can also be used to factorize the Hamiltonian matrix if the basis function sets which are used belong to the irreducible representation of the permutation

group of the spin system.[2] This leads to an increase in the complexity of the algorithm which computes: (i) the elements of the Hamiltonian and transition probability matrices, and (ii) the analytical derivatives ($\partial \mathbf{H}/\partial_{p_i}$) in the basis set used. However, computational efficiency is greatly increased. Simulation programs which make full use of molecular symmetry exist,[9] but the iterative part has been implemented only for the C_2 permutation group (program LACX[2,10]).

The two formalisms (composite particle and symmetry factorization) have been combined in the ARCANA program,[11] which has been used to analyze such complex spin systems as those arising from the 11 protons in 4-methoxy-4′-cyanobiphenyl[12] (an AA′BB′CC′DD′E_3 spin system).

CPU times can be further reduced if more efficient ordering routines are used. The gain is quite impressive for complex spin systems, resulting in the astonishingly short time of 2 min when a Shell–Metzner ordering[13] routine was used. This compares with 102 min for the commonly used Bubble–Sort[13] for the AA′BB′CC′XX′Y_3 $\{I_A = I_B = I_C = \frac{1}{2}, I_X = I_Y = 1\}$ spin system which gives more than 10 000 transitions, and was simulated on a VAX 11/780[14] using the ARCANA program. More efficient diagonalization routines give better total performance in the simulation step, but some problems arise when they are used in the iterative step. In fact, depending on the diagonalization algorithm used, pairs of eigenvalues can change their positions arbitrarily; the line numbers change in an unpredictable way and the iteration fails. Rough prediagonalization, according to Castellano et al.,[6a] can eliminate this inconvenience if Jacobi based diagonalization routines are used.

Computer hardware is now improving at such a fast rate that the latest generation of workstations have performances in terms of mips (million instructions per second), main memory and mass storage, which are similar to, if not greater, than the largest mainframes of 10 years ago. In fact, the most important differences between programs is not now in their efficiency in simulating the spectra, or even in the iteration procedure, but rather in their ability to produce a visual representation of the spectrum on the terminal, and in the ease of assigning transitions to observed frequencies.

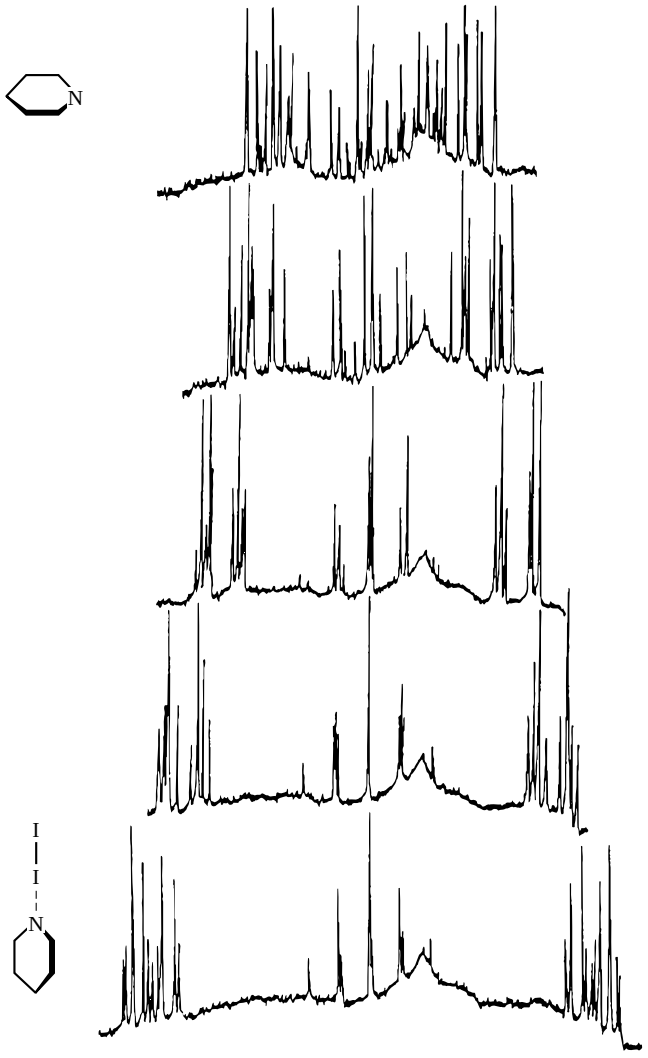

Figure 2 100 MHz (2.34 T) proton spectra of [^{14}N]pyridine in phase IV (Merck); the quantity of added I_2 increases from the top (0 mol% with respect to pyridine) to the bottom (60 mol%). The axis of highest order is perpendicular to the ring for free pyridine, parallel to the N–I–I direction for the complex. (Reproduced by permission of Royal Chemical Society from D. Catalano, C. A. Veracini, P. L. Barili, and M. Longeri, *J. Chem. Soc., Perkin Trans. II*, 1983, 171)

3 OBTAINING STARTING PARAMETERS FOR ITERATIONS

Remembering the wide range of allowed values of D_{ij}, it is easy to understand the enormous difficulties faced in analyzing anisotropic spectra. When the line density in the spectrum is low (few nuclei, strongly oriented spin systems), very approximate estimates of the D_{ij} values can quite easily give frequency/intensity patterns in the calculated spectra that can be recognized in the experimental spectra. When the spectra become crowded (the one shown in Figure 1 is a good example), a completely random trial-and-error approach is hopeless; more systematic and efficient methods have to be devised to ensure at least some probability of success in the analysis. Sometimes the spectral parameters can be guessed either from a comparison with data for similar molecules (or the same molecule in a different solvent) or from the shape of the spectrum.

The spectra of the pyridine–I_2 complex[15] shown in Figure 2 illustrate this point very well. At high concentrations of the complex, the spectrum looks fairly simple, displaying even some first-order features such as the pentuplet-like multiplet in the center of the spectrum. The two outer groups can then be thought to be due to the *ortho* and *meta* protons, the distance between the groups being related to the D_{om} coupling, while the spacing between two consecutive lines in the central multiplet is equal to $D_{op} + D_{mp}$. In addition, the chemical shifts can be guessed approximately. This behavior is due to the fact that the molecule is strongly oriented with its molecular long axis tending to lie parallel to the mesophase director. When this happens, D_{om} has a large negative value (below −1000 Hz), while both D_{op} and D_{mp} are, in absolute value, much smaller. (Note that the *ortho–meta* and *meta–para* distances are nearly the same but the direction of the interproton vector with respect to the director is very different.) For pyridine, where the N–*para*-proton axis is, on average, perpendicular to the mesophase

director, the spectrum is featureless, and no estimates of spectral parameters can be made.

A more general strategy is to prepare a solution of the fully protonated and perdeuterated isotopomers. The $S_{\alpha\beta}$ obtained from the analysis of the ^{2}H spectra (see ***Liquid Crystalline Samples: Deuterium NMR***) can be used to calculate approximate dipolar couplings from trial structures. The method works fairly well for rigid molecules, but it is not so efficient when internal rotation motions are present in the molecule (see ***Liquid Crystalline Samples: Structure of Nonrigid Molecules***). Examples of this approach are the analysis of the ^{1}H spectra of biphenyl[16] and 4-cyanobiphenyl.[17]

Alternatively, keeping an approximate molecular structure constant, it is possible to iterate over the $S_{\alpha\beta}$ values. Because the number of the variables is small (usually two or three), the approximate solution is quickly found.[18] The final parameter set is then obtained by iterating over the dipolar couplings independently.

As soon as the number of interacting spins increases, such simple considerations can no longer be applied. Monosubstituted benzenes display a behavior similar to the one already described. When the substituent does not contain protons, its spectrum looks like the one at the bottom of Figure 2, but if some interacting nucleus is present the complexity of the spectrum increases in two ways: (i) the number of the transitions increases because of the extra couplings; and (ii) groups of transitions due to these nuclei can overlap with some of the features due to the aromatic protons. This is precisely what happens for the spectrum of anisole, where the OCH_3 transitions fall in the same spectral region as the *para* proton.[19]

If these extra nuclei have different magnetogyric ratios only point (i) has to be taken into account, and first-order features due to the couplings between nuclei with different magnetogyric ratios appear in the spectrum. Such is the case for trideuteromethoxybenzene[20] (anisole-d_3) for example, where each transition of the aromatic protons is split into a septet: the septets in the outer wings are spaced by a distance approximately equal to the sum of the *ortho*-CD_3 and *meta*-CD_3 couplings, whilst the central septets are spaced by the *para*-CD_3 coupling. Being able to recognize all these structures in the spectrum, makes it possible to obtain very good values for the extra couplings and, in addition, to obtain the 'decoupled' spectrum due to the aromatic protons by selecting the central lines of each multiplet. What is left to be analyzed is just a five-spin AA′BB′C system, the spectrum of which would look like the one shown at the bottom of Figure 2. Such a spectrum can be analyzed easily. This is the case for anisole dissolved in ZLI 1115; the spectrum in I35 showed very few septet structures, and so it was not possible to determine the 'decoupled' AA′BB′C spin system.[20]

A similar approach proved to be possible for the four-proton, six-deuterium $AA'A''A'''X_3X'_3$ spin system of 1,4-bis(trideuteromethoxy)benzene.[11] The proton spectrum is composed of two complex, well-spaced groups of lines, the spacing of which is related to the coupling between the two *ortho* aromatic protons. The AA′A″A‴ spin subsystem would give the very simple spectrum shown in Figure 3, according to that obtained for symmetrically *para*-disubstituted halobenzenes. Each line would then be split into 13 subspectra corresponding to the values of m_T, the total deuteron spin quantum number, by coupling with the six deuterons: for $m_T = \pm6$, ±5, ±4, ±3, ±2, ±1, and 0, the intensities would be 1, 6, 21, 50, 90, 126, and 141, respectively. Trying to recognize all the 13 subspectra by eye is hopeless; in this case the task was easily accomplished by doing a two-dimensional homonuclear correlation experiment.

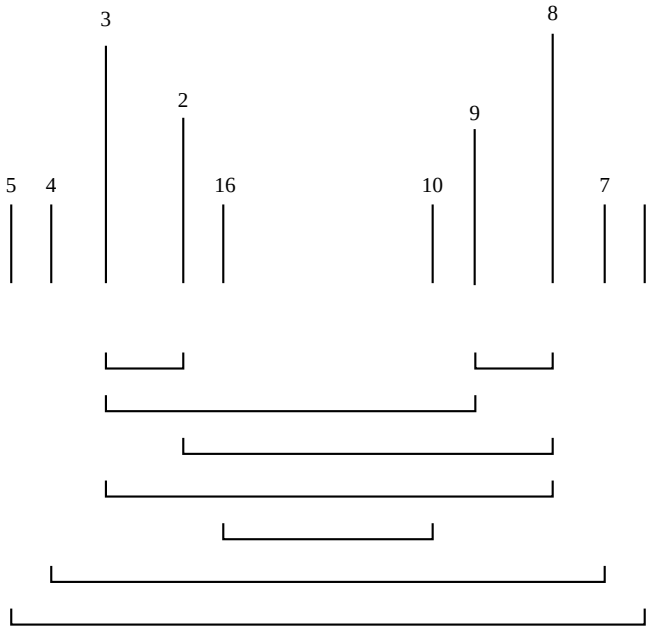

Figure 3 Sketch of the spectrum of an AA′A″A‴ system of spin-1/2 nuclei with dipolar coupling constants typical for a *para*-homodisubstituted benzene, showing how transitions are connected. (Reproduced by permission of Royal Chemical Society from J. W. Emsley, D. L. Turner, A. Giroud, and M. Longeri, *J. Chem. Soc., Faraday Trans. 2*, 1985, **81**, 603)

For an AA′A″A‴ spin system spectrum, such as the one shown in Figure 3, only two lines (the most intense ones) within the two groups share the same energy level, all the other connections being between symmetric lines belonging to the different groups. As a consequence, the off-diagonal peaks near the diagonal reveal the position of the two connected lines in each subspectrum. As shown in Figure 4, only 8 of the 13 off-diagonal peaks expected on each side of the main diagonal are visible. The lines belonging to the $m_T = 0$ subspectrum were easily spotted and then, with little effort, nearly all the subspectra (the less intense lines of the $m_T = \pm6$ subspectra are lost in the noise) were recognized.

Such elegant ways of analyzing anisotropic spectra are quite uncommon. Very often spectral analysis is an unglamorous, boring, and long task, with many unrewarding days spent in front of a terminal with little or no hope of disentangling patterns that can be recognized from the maze of lines in the experimental spectrum and few exciting moments occur when the lines begin to assume the right frequency and intensity pattern and the main features appear in the calculated spectrum.

4 STRATEGIES IN SPECTRAL ANALYSIS

Two main strategies have been developed to try to simplify the analysis of spectra: one is aimed mainly at reducing human

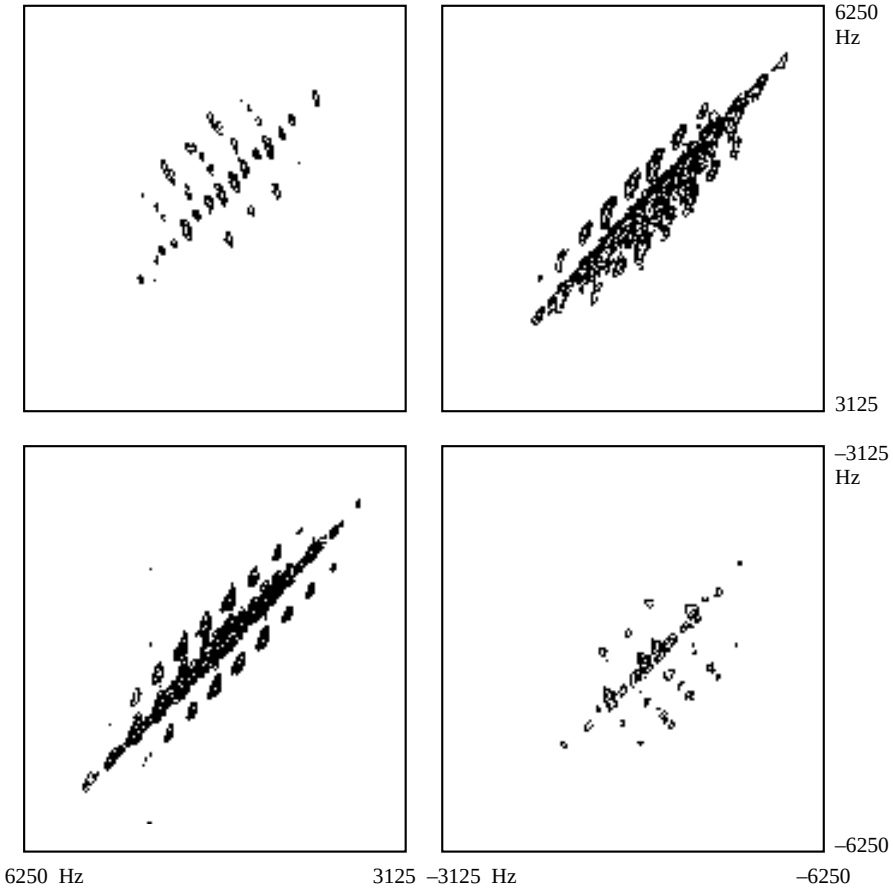

Figure 4 200 MHz (4.69 T) proton autocorrelation spectrum of 4-bis(trideuteromethoxy)benzene dissolved in the liquid crystal PCH 1132 (Merck). (Reproduced by permission of Royal Chemical Society from J. W. Emsley, D. L. Turner, A. Giroud, and M. Longeri, *J. Chem. Soc., Faraday Trans. 2*, 1985, **81**, 603)

intervention by using automated methods, and the other is aimed at simplifying spectral analysis by obtaining simpler experimental spectra.

4.1 Fully Automated Approaches

Two different approaches use the first strategy. The first approach (mentioned previously) has been used to analyze the anisotropic spectra of three allyl halides[21] and of cyclopentene,[22] an eight-spin system. The second approach makes use of the Swalen–Reilly iterative method. The use of the latter method is limited, mainly because an 'experimental' ELD is needed. Programs and/or experimental methods devoted to this task have been proposed,[2] but the complexity and peculiar characteristics of anisotropic spectra make them unsuitable candidates for analysis in this way. Pfändler and Bodenhausen[5] have proposed a two-dimensional *z* correlation spectroscopy (*z* COSY) experiment for constructing experimentally the ELD for a given spin system. Using different values of the β flip angle of the pulse sequence

$$\frac{\pi}{2} - t_1 - \beta - \tau_m - \beta - t_2 \qquad (7)$$

the authors showed that it is possible to determine the topology of two connected frequencies by observing how the intensity of the cross peak varies with β. Knowing the topology of the connections for nearly all the observed lines in the spectrum, the energy level subdiagram for an A_3B and an A_2BC spin system were constructed, even when some connections were determined incorrectly. For each different possible assignment (864 for the A_2BC, and 8 for the A_3B spin system), the spectral parameter set was refined according the Swalen–Reilly iterative method. The spectrum was calculated and the best assignment was chosen by comparing the calculated and experimental spectra.

A generalization of the method would require a library containing topologies of ELDs for spin systems of different symmetries. Improvements are needed to take into account the extensive degeneracy that can occur for larger spin systems. Such degeneracies can be due either to accidental overlaps of lines in crowded spectral regions or to the poor digital resolution of the two-dimensional spectra of liquid crystalline phases.

4.2 Spectral Simplification Based Approaches

As an alternative approach to the automated methods, experiments aimed at reducing the complexity of spectra can be planned. In this way spectral analysis will be simplified and the rate of success increased.

4.2.1 Spectral Simplification via Deuterium Decoupling

Selectively deuterated molecules give quite complex ^{1}H spectra (the anisole-d_3 spectrum in ZLI 1115 being a lucky exception), even if, at first glance, they look fairly simple. There are, in fact, a larger number of lines in such spectra, as deuterium has $I = 1$ while the larger linewidth, due to the ^{2}H quadrupolar relaxation, combined with the lower values of the D_{HD} couplings ($\gamma_H/\gamma_D \simeq 6$), causes widespread overlapping of transitions.

Spectral simplification can be obtained by performing $\{^2H\}-^1H$ decoupling experiments, and good results have been obtained with solenoid probes. Using short acquisition times (<0.2 s) when the decoupler is on, and a delay of typically 3 s to allow cooling to occur and to reduce thermal inhomogeneities, decoupled spectra from complex spin systems such the eight protons in 4-trideuteromethoxy-4′-cyanobiphenyl[12] have been recorded and successfully analyzed.

The procedure just described is the one usually followed when complex spectra are analyzed using this approach: ^{1}H spectra (with and without deuterium decoupling) of different selectively perdeuterated isotopomers are recorded under similar experimental conditions (solvent, temperature and concentration) and analyzed from the simpler to the more complex spin systems in order to obtain a good starting parameter set for the analysis of the spectrum of the fully protonated molecule. The full procedure requires much synthetic and spectral analysis work, but it is applicable whenever selective deuteration is possible and gives a very high success rate—its upper limits being an analyzable ^{1}H spectrum of the fully protonated species.

As an alternative to the high power decoupling technique, the sequence which refocuses heteronuclear coupling,

$$\left(\frac{\pi}{2}\right) - \tau_1 - (\pi) - \tau_1 - \text{Sample} \tag{8}$$

can be used:[23] τ_1 is increased at fixed intervals and the first point of each FID taken at the top of the echo is stored in a vector. The vector is Fourier transformed to give the decoupled, $\Delta\nu_i = 0$ spectrum. In fact the selective pulse sequence is such that at the top of the echo the magnetization does not depend on the heteronuclear couplings. The experiment takes a long time and has lower sensitivity than decoupling. In addition, artifacts due to pulse and phase imperfections have to be considered, but these can be significantly reduced in modern instrumentation. The spin echo experiment has the great advantage that all the heteronuclear couplings due to nuclei with different γ values are decoupled at once. If the antiecho is recorded, homonuclear couplings are refocused and the spectrum depends only on heteronuclear couplings (see ***Spin Echo Spectroscopy of Liquid Samples***).

4.2.2 Spectral Simplification via Multiple Quantum Spectroscopy

This approach is discussed elsewhere (see ***Multiple Quantum Spectroscopy in Liquid Crystalline Solvents***). Here it is sufficient to remember that for a given spin system composed of N nonequivalent spins $\frac{1}{2}$, the maximum possible number of transitions of order p is

$$Z_p = \binom{2N}{N-p} \tag{9}$$

for $1 \leq p \leq N$.[24] It is clear that even a very complex spin system will give simple spectra when p is $N - 1$ or $N - 2$ and these spectra will contain the same information that can be obtained from the single quantum ordinary spectrum with

$$Z_p = \binom{2N}{N-1} \tag{10}$$

4.2.3 Double Quantum Two-Dimensional Correlated Experiments

In a series of very elegant papers, Pines et al. applied multiple quantum (MQ) spectroscopy to a class of compounds, the n-alkanes, whose proton spectra are too complex to analyze. The molecules chosen, from n-hexane[25] to n-decane,[26] were randomly perdeuterated in such a way to have a negligible population of isotopomers with more than three protons left, but with all the possible two- and three-protonated isotopomers having a nearly uniform population distribution. This is easily done via a catalytic exchange reaction for n-alkanes, but the required population distribution may not be reached in such a direct way for other molecules having functional groups. This limits the generalization of the method to other organic compounds. A two quantum filtered experiment reduces the complexity of the spectrum leaving only AB and A_2 (16 for n-hexane) spin systems. A four-step phase cycling keeps the total number of averaged FIDs for each t_1 (96 for 24 increments in τ[25]) acceptably low, to ensure a digital resolution of nearly 30 Hz per point. The phase cycling selects even quantum coherences: the sweep width is then kept small by the isotopomer population distribution because no four or higher coherences are possible. On the other hand, it is crucial that the double quantum coherence of all the AB spin systems is present. As the D_{ij} values cover a wide range, this can be achieved only by coadding FIDs obtained with different τ values; the data acquisition time will thus be lengthened significantly. To distinguish signals belonging to different spin systems, a two-dimensional correlation experiment can be performed. The two last steps are possible using the pulse sequence

$$\left(\frac{\pi}{2}\right)_\phi - \tau - \left(\frac{\pi}{2}\right)_\phi - \frac{t_1}{2} - (\pi) - \frac{t_1}{2} - \left(\frac{\pi}{2}\right)_x - \frac{\tau_2}{2} - (\pi) - \frac{\tau_2}{2} - t_2 \tag{11}$$

All the spectra were recorded with continuous deuterium decoupling,[27] which causes considerable heating and thermal inhomogeneities, despite air-flow temperature control. All the couplings (up to 20 for n-decane) were determined with an experimental error of about 25 Hz, the low accuracy being a consequence of the low digital resolution and thermal gradients.

4.2.4 Spectral Simplification via Scaling of Dipolar Couplings

As previously stated, one of the reasons for the complexity of anisotropic spectra is the non-first-order character of the

spectra. Another way to simplify the analysis of such spectra is to scale the direct couplings by some factor, thus leaving only a few couplings (the biggest) that are greater than the spectral linewidth. In this way first-order features will appear in the spectrum if the chemical shift differences are large enough, and the number of lines in the spectrum will be reduced. In principle, all these improvements could be achieved simply by changing the experimental conditions that decrease the solute order (temperature and/or solute concentration), but this is in practice unachievable because the **S** matrix changes discontinuously at the nematic–isotropic transition temperature T_{NI}.

Courtieu et al.[28] applied the variable angle technique (using a spinning angle of 51°), developed for NMR in solids, to scale dipolar couplings, thus reducing the ABC pattern in CF_2CFBr to a first-order, easily analyzable AMX spectrum. At lower angles, non-first-order features began to appear but, because the authors were able to register the spectra at lower spinning angles, the line patterns can be easily followed and the dipolar couplings calculated at a spinning angle of 0° (***Spinning Liquid Crystalline Samples***).

Scaling of dipolar couplings can be achieved by using a suitable pulse sequence (PARDES) derived from the well-known WAHUHA and MREV sequences,[29] as described by Frydman et al.[30] The reduction in the splitting of the doublet due to CH_2Cl_2 dissolved in a nematic mesophase was followed by varying the parameters in the sequence.

5 RELATED ARTICLES

Liquid Crystals: General Considerations; Structure of Rigid Molecules Dissolved in Liquid Crystalline Solvents; Two-Dimensional NMR of Molecules Oriented in Liquid Crystalline Phases.

6 REFERENCES

1. (a) J. W. Emsley and J. C. Lindon, *NMR Spectroscopy Using Liquid Crystal Solvents*, Pergamon, Oxford, 1975; (b) P. Diehl and C. L. Khetrapal, in *NMR Basic Principles and Progress*, eds. P. Diehl, E. Fluck, and R. Kosfeld, Springer, Berlin, 1969, Vol. 1; (c) C. A. Veracini, in *NMR of Liquid Crystals*, ed. J. W. Emsley, Reidel, Dordrecht, 1985.
2. P. Diehl, H. Kellerhals, and E. Lustig, in *NMR Basic Principles and Progress*, eds. P. Diehl, E. Fluck, and R. Kosfeld, Springer, Berlin, 1972, Vol. 6.
3. (a) D. S. Stephenson and G. Binsch, *J. Magn. Reson.*, 1980, **37**, 395; (b) D. S. Stephenson and G. Binsch, *J. Magn. Reson.*, 1980, **37**, 409.
4. (a) J. D. Swalen and C. A. Reilly, *J. Chem. Phys.*, 1962, **37**, 21; (b) J. D. Swalen, in *Computer Programs for Chemistry*, ed. D. F. DeTar, Benjamin, New York, 1968, Vol. 1.
5. P. Pfändler and G. Bodenhausen, *J. Magn. Reson.*, 1991, **91**, 65.
6. (a) S. Castellano and A. A. Bothner-By, *J. Chem. Phys.*, 1964, **41**, 3863, (b) S. Castellano, in *Computer Programs for Chemistry*, ed. D. F. DeTar, Benjamin, New York, 1968, Vol. 1.
7. R. C. Ferguson and D. W. Marquardt, *J. Chem. Phys.*, 1964, **41**, 2087.
8. P. Diehl, H. P. Kellerhals, and W. Niederberger, *J. Magn. Reson.*, 1971 **4**, 352.
9. G. Hagële, M. Engelhardt, and W. Boenigk, *Simulation and automatisierte Analyse von Kernresonanzspektren*, VCH, Weinheim, 1987.
10. C. W. Haigh, *Ann. Rep. NMR Spectrosc.* 1971, **4**, 311.
11. J. W. Emsley, D. L. Turner, A. Giroud, and M. Longeri, *J. Chem. Soc. Faraday Trans. 2*, 1985, **81**, 603.
12. J. W. Emsley, G. Celebre, G. De Luca, M. Longeri, and F. Lucchesini, *Liquid Cryst.*, 1994, **16**, 1037.
13. N. Wirth, *Algorithms + Data Structures = Programs*, Prentice Hall, Englewood Cliffs, NJ, 1980.
14. E. Sicilia, Tesi di Laurea, Università della Calabria, 1988.
15. D. Catalano, C. A. Veracini, P. L. Barili, and M. Longeri, *J. Chem. Soc., Perkin Trans. II*, 1983, 171.
16. G. Celebre, G. De Luca, M. Longeri, D. Catalano, C. A. Veracini, and J. W. Emsley, *J. Chem. Soc., Faraday Trans.*, 1991, **87**, 2623.
17. J. W. Emsley, T. J. Horne, G. Celebre, G. De Luca, and M. Longeri, *J. Chem. Soc., Faraday Trans.*, 1992, **88**, 1679.
18. P. Diehl, in *NMR of Liquid Crystals*, ed. J. W. Emsley, Reidel, Dordrecht, 1985.
19. P. Diehl, H. Huber, A. C. Kunwar, and M. Reinhold, *Org. Magn. Reson.*, 1977, **9**, 374.
20. G. Celebre, G. De Luca, M. Longeri, and J. W. Emsley, *J. Phys. Chem.*, 1992, **96**, 2466.
21. D. S. Stephenson and G. Binsch, *Org. Magn. Reson.*, 1980, **14**, 226.
22. D. S. Stephenson and G. Binsch, *Mol. Phys.*, 1981, **43**, 697.
23. J. W. Emsley and D. L. Turner, *J. Chem. Soc., Faraday Trans. 2*, 1981, **77**, 1493.
24. G. Bodenhausen, *Prog. NMR Spectrosc.*, 1981, **14**, 137.
25. M. Gochin, A. Pines, M. E. Rosen, S. P. Rucker, and C. Schmidt, *Mol. Phys.*, 1990, **69**, 671.
26. M. E. Rosen, S. P. Rucker, C. Schmidt, and A. Pines, *J. Phys. Chem.*, 1993, **97**, 3858.
27. A. Pines, S. Vega, and M. Mehring, *Phys. Rev. B*, 1978, **18**, 112.
28. (a) J. Courtieu, D. W. Alderman, D. M. Grant, and J. P. Bayles, *J. Chem. Phys.*, 1982, **77**, 723; (b) J. Courtieu, D. W. Alderman, and D. M. Grant, *J. Am. Chem. Soc.*, 1983, **103**, 6783.
29. J. D. Ellett, M. G. Gibby, U. Haeberlen, L. M. Huber, M. Mehring, A. Pines, and J. S. Waugh, in *Advances in Magnetic Resonance*, ed. J. S. Waugh, Academic, San Diego, 1971, Vol. 5, p. 117.
30. L. Frydman, P. C. Rossomando, and B. Frydman, *J. Magn. Reson.*, 1991, **95**, 484.

Biographical Sketches

M. Longeri. *b* 1947. Laurea (with Professor C. A. Veracini). Pisa, 1972. Dipartimento di Chimica, Università della Calabria, 1973–present. Approx. 60 publications. Research interests: spectral and conformational analysis of molecules dissolved in liquid crystalline mesophases.

G. Celebre. *b* 1958. Laurea (with Professor M. Longeri), Calabria, 1984. Dipartimento di Chimica, Università della Calabria, 1986–present. Approx. 20 publications. Research interests: conformational analysis of molecules dissolved in liquid crystalline mesophases.

Magic Angle Spinning Carbon-13 Lineshapes: Effect of Nitrogen-14

Charles A. McDowell

University of British Columbia, Vancouver, Canada

1	Introduction	1
2	Magic Angle Spinning	1
3	Effects of an Axially Symmetric Electric Field Gradient	2
4	^{14}N Effects of an Asymmetric Electric Field Gradient	3
5	Influence of J Coupling	6
6	Other Spin-$\frac{1}{2}$ Nuclei Bonded to ^{14}N: ^{1}H CRAMPS	6
7	Related Articles	8
8	References	8

1 INTRODUCTION

The introduction of the Hartmann–Hahn[1] technique of cross polarization into solid state nuclear magnetic resonance spectroscopy, particularly when combined with multiple pulse methods[2] to remove homo- and heteronuclear, dipolar broadening, was a significant addition to the methods available for the study of solid compounds by NMR. When cross polarization and proton decoupling were incorporated into the magic angle spinning technique,[3] there was produced a significant enlargement of the repertoire of sensitive NMR spectrometric procedures available for obtaining high-resolution spectra of solid state compounds and materials.[4] This important new spectroscopic method became known as cross polarization magic angle spinning (CP MAS) NMR. When the ^{13}C spectra of compounds containing nitrogen were studied by CP MAS some lines appeared as broadened asymmetric doublets. It was soon realized that this characteristic lineshape resulted from the ^{14}N nuclear quadrupole moment interfering with the ability of the magic angle spinning to average out the ^{13}C–^{14}N dipolar interactions. This interpretation was based on earlier observations of the ^{13}C lineshapes of carbon nuclei bonded to nitrogen in the NMR of single crystals. We shall now briefly describe the main features of such high-resolution NMR spectra of single crystals to provide a suitable background for understanding the theoretical interpretation of the asymmetrical ^{13}C–^{14}N lineshapes in CP MAS spectra.

1.1 Single Crystal NMR Spectra

Within a short time after their introduction, the new NMR spectroscopic techniques were applied to obtain ^{13}C chemical shielding data on a wide range of organic compounds. It was soon found in compounds containing a nitrogen nucleus adjacent to the carbon nucleus being studied that splittings from ^{13}C–^{14}N dipolar couplings were observed. Griffin et al.[5] found that the NMR spectrum of a single crystal of glycine at a certain orientation with respect to the magnetic field exhibited three lines from the methylene carbons split by adjacent ^{14}N nuclei. In measurements of the ^{13}C chemical shielding tensor in the metal complex $K_2Pt(CN)_4Br_{0.3}\cdot 3H_2O$, Stoll et al.[6] observed large effects clearly shown to be caused by ^{14}N quadrupolar interactions. In that compound, the electric quadrupolar interactions are of comparable size to the ^{13}C–^{14}N dipolar interaction; consequently, mixing with the pure Zeeman eigenfunctions occurs. These required eigenfunctions were obtained by the application of first-order perturbation theory and subsequent diagonalization of the combined Zeeman-quadrupole Hamiltonian. Stoll et al. assumed an axially symmetric electric field gradient tensor with its symmetry axis along the C–N bond. Good quantitative agreement was found between the theoretical and experimental spectral lineshapes for all the angular variations studied.

Because amino acids are of great biological importance, the observations of ^{13}C–^{14}N dipolar–quadrupolar interactions clearly meant that single crystal NMR spectra of amino acids would soon be investigated. Thus simultaneously there were reported such detailed studies of alanine[7] and glycine.[8] Though these two detailed single crystal studies cover similar ground, we shall give details about the more complete studies of alanine and use some of the theoretical ideas later in our discussion of the effects of ^{14}N quadrupolar interactions causing asymmetry in certain magic angle spectral lineshapes of compounds with C–N bonds.

The proton-enhanced proton-decoupled ^{13}C NMR spectra of a single crystal of L-alanine were studied by Naito et al.[7] The C-α line showed a triplet pattern arising from dipolar coupling with the ^{14}N ($S = 1$) nuclei (Figure 1). These splittings were asymmetric, especially in the a-axis orientation. The dipolar interactions in the presence of the ^{14}N quadrupolar interaction were calculated by applying ideas first employed by VanderHart et al.[9] to provide a theoretical analysis of the static proton resonance spectra of polycrystalline $HMn(CO)_5$ and $HCo(CO)_4$. The appropriate Hamiltonian for the case where the quadrupole asymmetry parameter η is zero is written in the following form for later convenience:

$$\mathcal{H} = -\gamma_N \hbar B_0 S_z + \frac{\chi h}{4S(2S-1)}[3S_z^2\cos^2\theta + 3S_x^2\sin^2\theta + 3(S_zS_x + S_xS_z)\sin\theta\cos\theta - S^2] \quad (1)$$

where the quadrupolar coupling constant is $\chi = e^2qQ/h$ This Hamiltonian was used to determine the required eigenfunctions of the ^{14}N nucleus, and these in turn employed to calculate the eigenfunctions of the ^{13}C–^{14}N dipolar interaction as a function of θ, the angle between the direction of the external magnetic field and the symmetry axis of the electric field gradient tensor, i.e., the C_θ–N bond direction. It was thus possible to calculate the three ^{13}C resonances predicted (and observed experimentally for the C-α nucleus) which correspond to the nitrogen Zeeman states $|+1\rangle$, $|0\rangle$, and $|-1\rangle$, respectively. When the sign of the quadrupole coupling constant was assumed to be positive, good agreement was found between the calculated and experimental data for all the angles studied. The experimental results thus give the sign of the quadrupole coupling constant.

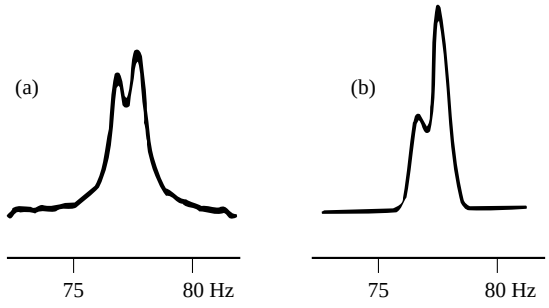

Figure 1 Lineshape of the C-α nucleus in the ^{13}C CP MAS spectrum of polycrystalline L-alanine taken at a field of 4.6 T. (a) Experimental spectrum; (b) computer-simulated spectrum assuming an axially symmetric quadrupolar parameter. (Reproduced by permission of the American Institute of Physics from Naito et al.[14])

2 MAGIC ANGLE SPINNING

As is well known, MAS tends to average out anisotropic interactions to their corresponding isotropic values when they are very weak as compared with their Zeeman interactions. Theoretical consideration of the effect of the ^{14}N quadrupolar interaction on the ^{13}C MAS spectra based on the above ideas, show that for ^{13}C nuclei bonded to ^{14}N an asymmetric doublet pattern is expected. Lippmaa et al.[10] reported that a high-resolution rotational-synchronized proton-enhanced magic angle spinning ^{13}C NMR spectrum of the polycrystalline solid of the one-dimensional compound tetrathiofulvalene–tetracyanoquinodimethane (TTF–TCQN) exhibited a three-line spectrum, one line of which consisted of an asymmetric doublet which they attributed to the C–N group. The splitting was found to be field-dependent and identified as arising from dipole–dipole interaction with the ^{14}N nuclei having a quadrupole interaction of comparable magnitude to their Zeeman interaction. This was the first observation of an asymmetric lineshape in a ^{13}C magic angle spinning NMR spectrum of a compound containing a ^{13}C–^{14}N bond.

3 EFFECTS OF AN AXIALLY SYMMETRIC ELECTRIC FIELD GRADIENT

The influence of spinning on the solid state NMR spectrum of a molecular system consisting of spin pairs in which one of the two spins has a quadrupole moment was first treated theoretically by Kundla and Alla.[11] The quadrupolar interaction fixes the spin moment at a definite orientation in the principal axis system (PAS) of the molecule. Rotation of the sample causes a rotational synchronized movement of the spin moment which does not permit the complete averaging of the dipole–dipole interaction between the spin-$\frac{1}{2}$ nucleus I and the quadrupole nucleus $S = 1$. The degree of the averaging depends on the ratio of the quadrupolar and Zeeman energies of the S nucleus.

The Hamiltonian may be written as

$$\mathcal{H} = \mathcal{H}_{\mathrm{Z}}^{I} + \mathcal{H}^{S} + \mathcal{H}_{\mathrm{D}}^{IS} \tag{2}$$

Here $\hat{\mathcal{H}}_{\mathrm{Z}}^{I}$ is the Zeeman term of the I nucleus, $\mathcal{H}^{S}$ is the quadrupolar Hamiltonian, and $\mathcal{H}_{\mathrm{D}}^{IS}$ the dipolar interaction Hamiltonian between the I and S spins. It is assumed that $\mathcal{H}_{\mathrm{D}}^{IS}$ is small so that first-order perturbation theory may be applied to calculate the resonance frequencies of the I-spin spectral lines. Because of the rotation of the sample at frequency ω_{r}, the eigenfunctions and eigenvalues of the unperturbed system become time-dependent. These were calculated for the case where the quadrupole coupling is symmetric. The energy levels were expressed in terms of parameters such as $k = \omega_{\mathrm{Q}}/\omega_{\mathrm{Z}}^{S}$; θ, the angle between the rotation axis and the magnetic field; the Euler angles α, β, and γ of the sample-fixed coordinate system, in which the α axis coincided with the rotational axis; and the PAS. When $\theta = 0$, the eigenvalue equations became the same as those giving the dependences of the spectral lines on the orientation of the nonrotating single crystal as described by Stoll et al.[6] To obtain the lineshapes and resonances of the polycrystalline sample at high spinning speeds, the average positions, $\overline{\Delta_n^{\mathrm{D}}}$, were obtained by averaging over all orientations represented by the angle β. Numerical calculations for the magic angle case showed that the line splittings and total widths depend strongly on the relative strengths of the Zeeman and quadrupolar interactions. Moreover, it was shown that in a strong magnetic field, the I-spin spectrum is an asymmetric doublet, one of the lines being the sum of two components, the full width of the single line being twice as large as that of the composite line. The splitting increased with increasing k leading to a regular triplet. The isotropic spin–spin interaction between the I and S nuclei was predicted to shift the I-spin spectral lines, the effect decreasing with increasing values of k.

Apparently unaware of the above work of the Estonian scientists, several groups reported CP MAS spectra of polycrystalline organic compounds containing C–N bonds such as amino acids, peptides, and proteins in which significant differences were observed between the solid state spectra and those in solution.[12,13] Most of the resonances from carbons bonded to nitrogens were split into broadened doublets, and some of the resonances from more distant carbons were also affected.

A classical and much studied example is the CP MAS spectrum of polycrystalline alanine.[14] The observed splittings of the asymmetric doublet of the C-α resonance was 45 Hz with a 200 MHz magnet and $\sim$ 100 Hz when measured at 90 MHz. The spectra can be fully interpreted and quantitatively explained by the following theoretical treatment.[14] First, the ^{14}N quadrupolar interaction is of comparable magnitude to the Zeeman interaction, so the ^{14}N spin eigenfunctions must be determined by diagonalizing the nitrogen Zeeman quadrupole Hamiltonian, and those eigenfunctions used in the calculation of the ^{13}C–^{14}N dipolar interactions. At the outset it should be understood that in this problem it is important to be mindful of the timescale of the magic angle spinning. In the experiments described by Naito et al.[14] the spinning frequency was 4.5 kHz, which is small compared with the ^{14}N quadrupolar interaction in L-alanine for which $\chi = 1.205$ MHz; the adiabatic approximation can therefore be employed to determine the nitrogen spin functions at time t from the following equation

$$\mathcal{H}_{\mathrm{ZQ}}\psi_{\mathrm{N}}(t) = E(t)\psi_{\mathrm{N}}(t) \tag{3}$$

Here, $\mathcal{H}_{\mathrm{ZQ}}(t)$ is the Zeeman quadrupole Hamiltonian of the nitrogen nuclei at time t. For the amino nitrogen in amino

acids and the cyano nitrogen in nitriles, one may assume with a high degree of accuracy that the electric field gradient tensor is axially symmetric, i.e., $\eta = 0$. Thus for the MAS spectrum of L-alanine we can write the Zeeman quadrupole Hamiltonian as

$$\mathcal{H}_{ZQ}(t) = -\gamma_N \hbar S_z B_0 + \frac{\chi h}{4S(2S-1)}[3S_z^2 \cos^2\theta(t) + 3S_x^2 \sin^2\theta(t) + 3(S_z S_x + S_x S_z)\sin\theta(t) \times \cos\theta(t) - S^2] \quad (4)$$

Here, $\theta(t)$ is the periodic value of the angle between the field direction $\boldsymbol{B}_0$ and the internuclear vector $\boldsymbol{r}_{CN}$. Under MAS, when a rigid array of nuclei is rotated with an angular velocity ω_r about an axis inclined at an angle β to the direction of the external magnetic field $\boldsymbol{B}_0$, and at an angle β' to $\boldsymbol{r}_{CN}$, we may write that $\theta(t)$ can vary as follows:

$$\cos\theta(t) = \cos\beta\cos\beta' + \sin\beta\sin\beta'\cos(\omega t + \psi) \quad (5)$$

where ψ is the azimuthal angle of $\boldsymbol{r}_{CN}$ at time $t = 0$.

In this case the $^{13}C-^{14}N$ dipolar interaction is very small compared with the Zeeman interaction, so first-order perturbation theory can be used to calculate the $^{13}C-^{14}N$ dipolar interaction at time t. The dipolar splitting of the ^{13}C resonance resulting from that calculation using the Hamiltonian $\mathcal{H}_{ZQ}$ represented by equation (3) yields

$$\Delta E_i(t) = -\gamma_C \gamma_N \hbar^2 / r_{CN}^3 \{[a_i(t)^2 - c_i(t)^3 2][1 - 3\cos^2\theta(t)] - (9/2)^{1/2}[a_i(t) + c_i(t)]b_i(t)\sin 2\theta(t)\} \quad (6)$$

Here, $a_i(t)$, $b_i(t)$, and $c_i(t)$ (i = 1, 2, and 3) are the coefficients at time t of the Zeeman quantized spin functions of the nitrogen nuclei, namely, $|1\rangle$, $|0\rangle$, and $|-1\rangle$, respectively. In L-alanine the $^{13}C-^{14}N$ dipolar interaction, 0.6636 kHz, is small compared with the spinning frequency 4.5 kHz, so in such cases the $\Delta E_i(t)$ have to be averaged from $t = 0$ to $t = \infty$ to obtain the $^{13}C-^{14}N$ dipolar energy of the spinning sample. The values of $\Delta E_i(t)$ were calculated for each 5° of $\omega t + \psi$ in the range 0° to 360° with constant β', and these values were then averaged to yield $\overline{\Delta E_{i\beta'}(t)}$. The theoretical lineshapes for polycrystalline samples rotating at the magic angle $\beta = 54.7°$ are obtained by calculating the numerical values of $\overline{\Delta E_{i\beta'}(t)}$ when β' is varied in steps of 2° in the interval 0° to 90°, each $\overline{\Delta E_{i\beta'}(t)}$ being weighted by its probability $\sin\beta'$. Finally, convoluting the theoretical lineshapes with a Gaussian function gave the actual lineshape. The linewidth of the Gaussian function is an adjustable parameter which takes into account any instrumental line broadening, such as effects arising from improper decoupling setting, any slight misalignment of the magic angle, and any magnetic field inhomogeneities, etc.

As shown in Figure 1, the calculated and experimental spectra agreed well. Clearly the calculated lineshape is an asymmetric doublet with a splitting of 48 Hz for a ^{13}C resonance frequency of 50.3 MHz and 108 Hz for a resonance frequency of 22.6 MHz, both values in good agreement with experimental observations.[12,14] This field-dependence of the asymmetric doublet splitting arises because a weak field causes a relative increase in the contributions from the off-diagonal elements of the matrix representation of the Hamiltonian $\hat{\mathcal{H}}_{ZQ}(t)$. Noteworthy also was the finding that when the sign of the term χh in the lineshape calculation was chosen as negative, the shape was reversed, i.e., the intensity of the high-frequency (low-field) peak was now stronger than the other one. This observation thus presents a means of determining the sign of the quadrupole coupling constant of ^{14}N bonded to ^{13}C by lineshape analysis of the CP MAS ^{13}C NMR spectra.

When the spectrum of cyanoacetamide was studied the same theoretical treatment was applicable because here also the $^{13}C-^{14}N$ dipolar interaction, 1.46 kHz, was smaller than the rotor spinning frequency. The lineshape exhibited a reversal of the intensities of the doublet components. When the value of χh was taken to be negative, the simulated lineshape was in good agreement with that observed experimentally. The splitting of the asymmetric doublet for the nitrile was 338 Hz in the simulated spectrum, in good agreement with the experimentally measured splittings of 305 Hz to 356 Hz for different cyano compounds.

The above theoretical treatment and the simulated MAS lineshapes were based on the important assumption that the rotor spinning speed was very small in comparison with the size of the quadrupole interaction of the ^{14}N nucleus in the molecule. It was, however, shown that if the spinning speeds were as large as the ^{14}N quadrupolar interaction (i.e., in the MHz range), which seems highly unlikely, the lineshape predicted is quite different from those obtained at low spinning frequencies. For the extremely high spinning frequency case, a truncated Zeeman quadrupole Hamiltonian $\overline{\mathcal{H}_{ZQ}(t)}$ (the time-dependent part is truncated) can be used for the MAS lineshape calculation. Using the same parameters as employed in the simulation of the spectra of nitrile compounds with a value of χ = 3.87 MHz and 24 Hz for the halfwidth of the Gaussian broadening function, it was found that the predicted splitting is less than one-third of the slow-spinning case, giving a broad powder pattern as the expected lineshape.

Contemporaneously with the above work, Zumbulyadis et al.[15] presented an extensive analysis of the influence of quadrupole nuclei on the magic angle spinning spectra of spin-$\frac{1}{2}$ nuclei. Here also, as above, the treatment was restricted to the case with an axially symmetric quadrupolar tensor. The formal theory described was similar to that described above; it also made use of the adiabatic approximation, in which a time-dependent wavefunction is approximated by an eigenfunction of the instantaneous Hamiltonian multiplied by a time-dependent phase factor. Theoretical powder patterns were calculated for a range of values of parameters typical of ^{13}C coupled to ^{14}N, the results being given as a function of ratio of the spin-1 Zeeman frequency Z to the quadrupole coupling constant χ. Each spectrum consisted of double-peaked bands with an intensity ratio of 1:2; the ratio of the S-spin Zeeman to the quadrupolar interaction (Z/χ) determined the widths of the bands and the splittings between them. This was also implicit in the theories of Naito et al.[14,16] as was the finding that both the widths and splittings of the bands decrease at higher magnetic fields where the quadrupolar interaction induces less mixing of the S-spin Zeeman eigenstates. It was also shown that the appearance of the bands depended critically on the mutual orientations of the unique principal axes of the dipolar and quadrupolar interaction tensors, the doublet splitting going through a minimum when the two principal axes were oriented at the magic angle *with respect to each other*.

4 ^{14}N EFFECTS OF AN ASYMMETRIC ELECTRIC FIELD GRADIENT

Though the above theoretical treatments[14,15] were successful in providing an interpretation of the CP MAS ^{13}C spectra of a number of nitrogen-containing compounds and, in particular, explaining the asymmetric lineshapes associated with C–N bonds, the restriction to cases with symmetric ^{14}N quadrupolar tensors was limiting. When the quadrupole coupling parameter $\eta \neq 0$, the C–N bond direction may not be parallel to the principal axis of the quadrupolar tensor. In this situation the off-diagonal elements in the matrix representation of the Hamiltonian $\mathcal{H}_{ZQ}$ will contain η, and hence a large value of the quadrupolar asymmetry parameter will be quite effective in determining the resulting MAS lineshape.

To extend the theory to include the ^{13}C CP MAS spectra of important organic molecules such as nitroanilines, and biomolecules like imidazoles, polypeptides, and proteins in which the influence of asymmetry of the ^{14}N quadrupole coupling tensor may play an important role in determining the lineshapes of the spectra, it was necessary to extend the theoretical formulation though the basic ideas were still sufficient to permit the required extension to encompass a wider range of molecular environments.[16]

The adiabatic approximation represented by equation (2) is still used but the Zeeman quadrupole Hamiltonian for ^{14}N must be modified to reflect the asymmetry of η, the nitrogen asymmetry parameter. The Hamiltonian is now written as

$$\mathcal{H}_{ZQ}(t) = -\gamma_N \hbar B_0 S_{z'} + \frac{eQq_{zz}}{4S(2S-1)} \times\{(3S_z^2(t) - S^2) + \eta[S_x^2(t) - S_y^2(t)]\} \qquad (7)$$

where $\eta = (q_{xx} - q_{yy})/q_{zz}$; eq_{ii} are the principal values of the electric field gradient tensor at the ^{14}N nucleus in the compound. They obey the convention that $|q_{zz}| \geq |q_{yy}| \geq |q_{xx}|$. The quantity e^2Qq_{ii} ($i = x, y, z$) is one of the principal values of the quadrupole coupling tensor and e^2Qq_{zz} is the quadrupole coupling constant. In this case there are two different coordinate systems to be considered. The Zeeman coordinate system is specified by (x', y', z'), and the principal axis system coordinates of the ^{14}N electric field gradient tensor of the compound by (x, y, z). The Euler angles of the spinner rotation axes (x^R, y^R, z^R) are written as β', θ, and ψ. The magic angle spinning axis, z^R, is inclined at an angle β' with the z axis, and at the magic angle β to the static magnetic field (Z'). The angle ψ is time-dependent and given by $\psi = \omega_r t + \psi_0$, where ψ_0 is the initial angle when $t = 0$ and ω_r is the angular velocity of spinning. Transformations of the coordinate systems (see Figure 2) give the ^{14}N Zeeman quadrupole Hamiltonian in the Zeeman coordinate system, and the resulting eigenstates are used to calculate the ^{13}C–^{14}N dipolar energy. Since, in general, the internuclear vector $\boldsymbol{r}_{CN}$ is not collinear with the z axis of the electric field gradient tensor, its direction is defined by the polar angles (θ, ψ) in the principal axis system of the electric field gradient tensor. First order perturbation theory can again be used to calculate the ^{13}C–^{14}N dipolar energy of the ^{13}C resonance of a certain

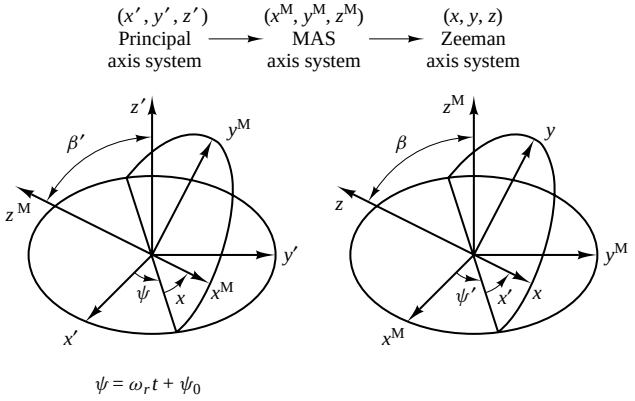

Figure 2 Diagrammatic representation of the coordinate transformations required to calculate the ^{13}C lineshapes when the quadrupolar parameter η is asymmetric. They can be summarized as follows:

x, y, z	x^R, y^R, z^R	x', y', z'
Principal $\xrightarrow{(\beta',\phi,\psi)}$	Rotating $\xrightarrow{(\beta,0,0)}$	Zeeman
axis system	axis system	axis system

molecular orientation at time t and is given by

$$\Delta E_{i\beta'\Phi}(t) = \langle\beta\psi_N(t)|\mathcal{H}_D(t)|\beta\psi_N(t)\rangle - \langle\alpha\psi_N(t)|\mathcal{H}_D(t)|\alpha\psi_N(t)\rangle \qquad (8)$$

Here, $|\alpha\rangle$ and $|\beta\rangle$ are the ^{13}C Zeeman spin functions. As before, the ^{13}C–^{14}N dipolar interaction is smaller than the spinning frequency, so $\Delta E_{i\beta'\Phi}(t)$ must be averaged over one rotor cycle, i.e., from $t = 0$ to $t = \infty$, to give the ^{13}C–^{14}N dipolar energy in the spinning sample, namely

$$\overline{\Delta E_{i\beta'\Phi}(t)} = (1/2\pi)\int_0^{2\pi} \Delta E_{i\beta'\Phi}(\psi)\,d\psi \qquad (9)$$

The values of $\overline{\Delta E_{i\beta'\Phi}(t)}$ were calculated numerically for small increments of the appropriate angles and the resulting values averaged. The resulting theoretical averaged line positions for the spinning sample were weighted by their probability, sin β', and then convoluted with a suitable lineshape function to yield the actual lineshape.

One of the first compounds chosen to test the above theory for calculating the MAS lineshapes of molecules containing ^{14}N nuclei with nonasymmetric quadrupolar tensors, i.e., with $\eta \neq 0$, was polycrystalline 2,6-dimethyl-3-nitroaniline. This molecule has two different types of ^{14}N nuclei. The ^{13}C MAS NMR spectrum showed that the resonances for both the nitro and amino carbon nuclei exhibited asymmetric doublet patterns (Figure 3). The high-frequency line in the nitro doublet was more intense than the other component, whereas the reverse was the case for the amino peak. Clearly the differences in the lineshapes arose from the different signs, orientations, and magnitudes of the respective electric field gradient tensors for the two ^{14}N nuclei. Calculations of the theoretical lineshapes by the method outlined above using the appropriate molecular parameters and a reasonable assignment for the orientation of the ^{14}N electric field gradient tensor based on that of *p*-nitrotoluene yielded lineshapes similar to those observed

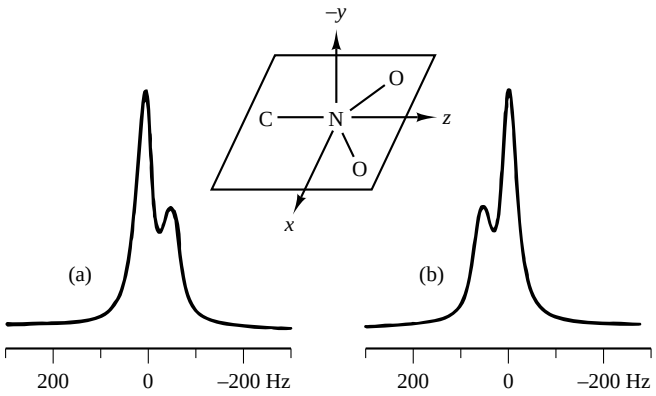

Figure 3 Lineshape of the resonance of the carbon nucleus adjacent to the NO_2 group in the ^{13}C CP MAS spectrum of 2,6-dimethyl-3-nitroaniline. Computer-simulated spectrum calculated with a quadrupolar asymmetry parameter $\eta = 0.408$ and (a) the ^{14}N quadrupolar coupling constant $e^2Qq_{zz}/h = -1.340$ MHz; (b) the quadrupolar coupling assumed to be positive. (Reproduced by permission of Academic Press from Naito et al.[16])

experimentally. With the value of χ being 1.340 MHz and η = 0.408 for ^{14}N of the $-NO_2$ group, good agreement was found with the experimental lineshape only when the sign of the quadrupole coupling constant was taken as negative. The simulation of the lineshape of the amino peak required more insight. Values for χ, η, and $\gamma_C\gamma_N\hbar/(2\pi r_{CN}^3)$, based on literature information, were chosen to be 3.977 MHz, 0.263, and 0.8466 kHz, respectively. In the case where the z axis of the quadrupole coupling constant was chosen to lie normal to the plane of the NH_2 group and the y axis assumed to be tilted 40° from the C–N bond direction, with the sign of the quadrupole coupling constant negative the resulting simulated lineshape was in excellent agreement with that observed experimentally. Also, the calculated value for the doublet splitting was 110 Hz, in good agreement with the observed value of 102 Hz.

It proved more difficult to provide an unambiguous interpretation of the lineshapes of the ^{13}C CP MAS NMR spectrum of polycrystalline glycylglycine and glycyl-L-alanine. Here again the orientation of the principal axes of the ^{14}N quadrupole coupling tensor was unknown. Proceeding as before, the calculated lineshapes for the case where the z axis was assumed to lie along the direction of the N–H bond led to a narrow singlet pattern not in agreement with the experimental spectrum. When the z axis was chosen to be normal to the C–N–C plane and the y axis along the N–H bond, the simulated lineshapes again did not agree with the observed lineshape. Several possible orientations of the axes were tried, but only when the z axis of the quadrupole tensor of the amino nitrogen was assumed to lie along the C–N bond direction and the sign of the quadrupole coupling constant taken as positive, together with acceptable values of the other constants, was a satisfactory lineshape simulation obtained. Moreover, the calculated doublet splitting for the C-α carbon in glycylglycine was 49 Hz, which was in good agreement with the experimental value of 41 Hz.

Given the satisfactory simulations of the observed lineshapes from the theory for amino acids and polypeptides, attention was then turned to a more sophisticated molecule of biological interest, namely, trimethylimidazole. This molecule has two different types of nitrogen nuclei. The quadrupole coupling constants and asymmetry constants of the two nitrogen nuclei are for N-1, χ = 1.424 MHz and η = 0.980, and for N-2 χ = 3.267 MHz and η = 0.129. The large difference in the two quadrupolar tensors for the two nitrogen nuclei is obviously mainly the cause of the notable difference between the lineshapes observed for the C-4 and C-5 carbon atoms in the CP MAS spectrum of ^{13}C in this compound. Nevertheless, it was only possibly to simulate the experimental lineshapes successfully after a judicious choice of the orientations with respect to the molecular axes of the respective quadrupolar tensor axes.

Furthermore, this work clearly showed that in nitrogen-containing organic compounds, if the correct quadrupole coupling tensor and the relative orientations of the principal axes with respect to the molecular axes are known for a particular nitrogen nucleus, it is possible to calculate the theoretical lineshape for the carbon nucleus bonded to the nitrogen. That the sign of the quadrupole coupling constant for the nitro and amino nitrogen atom in organic compounds differed was new. Since each group containing a nitrogen atom has a characteristic quadrupole coupling tensor, it follows that the ^{13}C resonances in the CP MAS NMR spectra of the carbon atoms in such groups, e.g., $-NO_2, -NH_2, \equiv N, -NH_3^+$, and −CN, all exhibit characteristic lineshapes. This information is obviously of considerable practical importance for the assignment of the solid state ^{13}C CP NMR spectra of organic compounds, particularly those of biological importance and heterocyclic compounds, pharmaceuticals, dyestuffs, etc.

Another approach to calculating the lineshapes of the ^{13}C MAS spectra of nitrogen-containing organic compounds was put forward by Hexem et al.[17] This was based on writing the Hamiltonian of the spin system in terms of irreducible spherical tensor operators, namely

$$\mathcal{H} = \sum_{\lambda} \sum_{l} \sum_{m=-l}^{l} (-1)^m R_{l-m}^{\lambda} T_{lm}^{\lambda} \qquad (10)$$

In this equation, λ represents the type of interaction, including the Zeeman interactions for the carbon, Z_C, and nitrogen spins, Z_N; the quadrupole interaction of the nitrogen spin, Q; D, the $^{13}C-^{14}N$ dipolar interaction; and CS, the chemical shielding of the carbon spins. The quantity J, the indirect spin–spin interaction, is ignored because it was assumed to be negligible. The rotational properties of the irreducible spherical tensors were used to obtain the Hamiltonian in a more convenient form. The time-dependence of the resulting Hamiltonian was removed by applying average Hamiltonian theory. The part of the average Hamiltonian representing the dominant interactions of the carbon atoms and which commutes with the appropriate Zeeman Hamiltonian can be written as

$$\mathcal{H}^C(\phi) = C^Z \rho_{00}^Z T_{00}^Z + C^{CS} \rho_{00}^{CS} T_{00}^{CS} + \sum_{m=-2}^{2} C^D (-1)^m R_2^D - (\phi) T^D 3_{2m} \qquad (11)$$

where $C^Z = \gamma_C\hbar$, $C^{CS} = \gamma_C$, $\rho_{00}^{CS} = \sigma_{iso}$, $T_{00}^Z = B_{00}I_z$, $C^D = -2\gamma_C\gamma_N\hbar^2$, and σ_{iso} is the isotropic chemical shift. Making use of Wigner rotation matrices, one set of Euler angles transforms the principal axis system of the dipolar interaction

to the principal axis system of the electric field tensor, while the angles (0, θ_M, ψ) transforms further the spatial components to the axis system of the spinning rotor. In this last transformation, θ_M is the magic angle (54.7°) and ψ is the azimuthal angle of rotation about the rotor axis.

The shifts in the energy levels of ^{13}C were calculated using zero-order average Hamiltonian theory, which is equivalent to first-order perturbation theory, this procedure being possible because the small size of the dipolar coupling means that it can be treated as a perturbation. Because of the relative orders of magnitude of the ^{14}N quadrupole coupling constant and the lower achievable spinning rates, one cannot use zero-order average Hamiltonian theory to average $\hat{\mathcal{H}}^D_{CN}$, the heteronuclear Hamiltonian over one rotational period. The ^{14}N matrix was diagonalized and the induced carbon shifts calculated. The carbon shifts were calculated for a sufficient number of points as described in the earlier theoretical treatments. These dipolar shifts were averaged over one rotation period $\overline{\omega_n^C}$ by numerical integration over the azimuthal angle of rotation, ϕ. This is equivalent to assuming the adiabatic approximation for calculating the change of the nitrogen states over the rotational period described in detail earlier by Naito et al.[14,16] and by Zumbulyadis et al.[15]

As a preliminary test of theory, and to compare the results from diagonalizing the nitrogen Hamiltonian matrix with those obtained by using first-order perturbation theory to obtain the coefficients in the eigenfunction $\Phi_n^N(\phi)$ representing a linear combination of the Zeeman spin states, Hexem et al.[17] calculated the expected powder ^{13}C spectrum for a C–N bond. Typical values of the parameters were used and the quadrupole coupling tensor was assumed to be axially symmetric with η = 0. When these theoretical predictions for the lineshapes were compared with the experimental observations for polycrystalline alanine, it was clear that the spectra lacked the resolution to show the fine structure predicted by the powder pattern. The calculated spectrum obtained using a value of 0.26 for the quadrupole asymmetry parameter, η, and taking its sign as positive was in good agreement with the experimental spectrum, in general accord with the findings of Naito et al.[16]

Explaining the ^{13}C lineshape of the α-carbon in *N*-acetylvaline was more challenging. In this case η = 0.31 and in the case of the polypeptide bond study of Naito et al.[16] it was necessary to consider carefully the relative orientations of the principal axes of the electric field gradient tensor with respect to the molecular axes. Consideration of several orientations soon yielded a set of parameters which produced good agreement between the computer simulated lineshape and that observed experimentally.

The extensive studies of Hexem et al.[17] and Naito et al.[16] showed clearly that comparing the experimental and computer-calculated spectra provides a ready method for obtaining information concerning the relative orientations of the dipolar and electric field gradient tensors from the manifestations of the influences of those parameters on the ^{13}C NMR lineshapes. Moreover, such studies also enable the sign of the asymmetry parameter of the ^{14}N nucleus bonded to the carbon to be established. Also, as is clearly apparent from the theoretical treatments outlined earlier in this article, the extent of the splitting between the doublet peaks characteristic of the ^{13}C resonance of a C–N bond depends on the magnitude and the asymmetry parameter of the ^{14}N quadrupole tensor, the internuclear distance, the strength of the applied magnetic field, and the orientation of the internuclear vector $\boldsymbol{r}_{CN}$ in the principal axis system of the electric field gradient tensor.[18]

Kundla and Alla[11] had earlier shown that the line splittings and total widths depended on the relative strengths of the Zeeman and quadrupolar interactions. The magnitude of the splitting is directly dependent on the dipolar interaction and the asymmetry parameter, which is different for differing values of the Euler angles defining its spatial orientation, with the Zeeman frequency of the ^{14}N nucleus being Z_N, the dipolar coupling $D = \gamma_C\gamma_N\hbar/4\pi^2 r_{CN}^3$, and the polar and azimuthal angles as β^D and α^D, the doublet splitting S is given by:

$$S = \tfrac{9}{20}(D\chi/Z_N)(3\cos^2\beta^D - 1 + \eta\sin^2\beta^D\cos 2\alpha^D) \quad (12)$$

which is in terms of all the geometric ($\boldsymbol{r}$, α^D, β^D) and energy variables (χ, Z_N, η) up to first order in (χ/Z_N). As a test of equation (13) the values of the splitting S predicted by that equation were plotted against the experimentally observed splittings for more than 20 compounds containing different types of C–N bonds.[19] An excellent linear relationship was found which may, at first sight, seem surprising because of the wide range of different molecular species involved.

5 INFLUENCE OF *J* COUPLING

In the Hamiltonians used in all the theoretical treatments described, the term $\mathcal{H}_J$ representing the indirect J coupling was ignored. This was because the value of J_{iso} was expected to be so small that it would have little, or no effect, on the CP MAS lineshapes of ^{13}C–^{14}N-containing compounds. The excellent agreements found between the experimental and theoretical lineshapes shows that this was usually an easily justifiable assumption. The inclusion of J coupling leads to the introduction of the term:[20]

$$[-(\Delta J/3)(3\cos^2\beta^J - 1 + \eta\sin^2\beta^J\cos 2\alpha^J)] \quad (13)$$

where β^J and α^J give the orientation of the unique z axis of the $\boldsymbol{J}$ tensor in the PAS of the quadrupole tensor. To illustrate the effect of the J coupling, Figure 4 shows how the normal two-peak powder spectrum becomes a three-peak spectrum for the case of ^{14}N. The theoretical spectra were calculated from the computer program of Naito et al.,[14,16] modified to include the term $\mathcal{H}_J$ in the Hamiltonian. The introduction of the indirect spin–spin coupling results in a splitting of the $m_{^{14}N} = -1$ and +1 levels, while the $m_{^{14}N} = 0$ peak is unaffected. In the calculations, the ^{14}N electric field gradient tensor was assumed to be axially symmetric with the largest principal component parallel to the ^{13}C–^{14}N dipolar vector. A similar procedure was employed by Eichele and Wasylishen,[21] though they used a different computer program based on the perturbation method to interpret and simulate the spectrum demonstrating the first observation of the indirect spin–spin coupling $^1J(^{14}N,^{13}C)$ effect which they discovered in the ^{13}C CP MAS NMR spectrum of [(*n*-$C_3H_7)_4N$][$Cd(SCN)_3$]. Because of the excellent agreement found between the simulated and the experimental spectra they estimated the value of $^1J(^{14}N,^{13}C)$ = 11 ± 3 Hz.

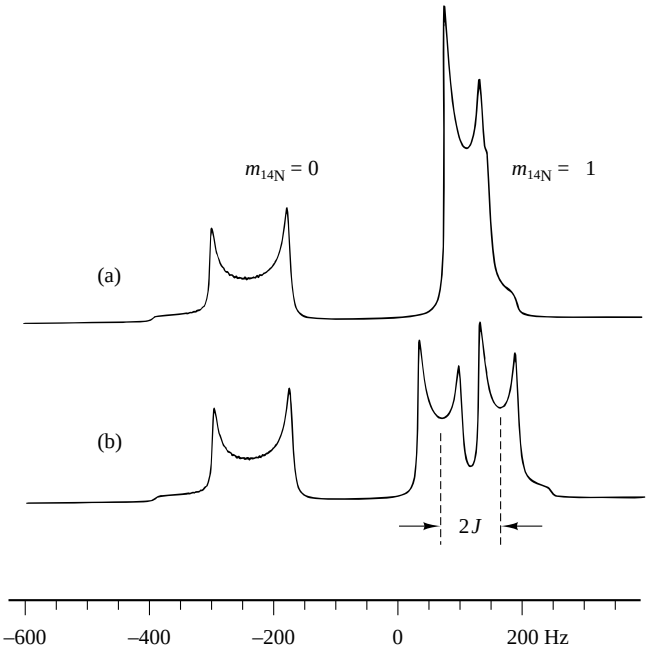

Figure 4 Diagrammatic representation of the effect of including the term $\mathcal{H}_J$ in the Hamiltonian before calculating the lineshape

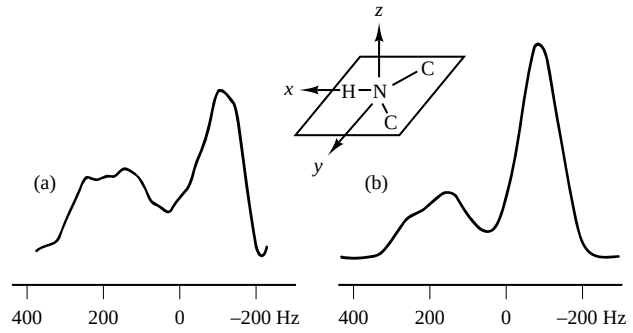

Figure 5 Lineshape of the CP MAS spectrum of a proton bonded to the peptide nitrogen nucleus in *N*-acetylglycine. (a) Experimental spectrum obtained by using CRAMPS with the MREV-8 pulse sequence. (b) Computer-simulated spectrum obtained using a quadrupolar asymmetry parameter $\eta = 0.32$ and $e^2Qq_{zz}/h = -3.21$ MHz. (Reproduced by permission of the American Chemical Society from Naito et al.[23])

6 OTHER SPIN-$\frac{1}{2}$ NUCLEI BONDED TO ^{14}N: ^{1}H CRAMPS

Protons are ubiquitous in nature and bond to many different types of nuclei. Of these the bonding to ^{14}N is important because N–H bonds are fundamental in the molecular composition of amino acids, polypeptides, and proteins. Unfortunately, the ^{1}H CP MAS spectra of such compounds were generally found to be lacking in structure because of the dipolar broadening caused by homonuclear interactions and magnetic shielding anisotropies. The introduction of the technique of combining sample rotation and multiple pulse NMR spectroscopy, the so-called CRAMPS procedure pioneered by Gerstein et al.,[22] was a major innovative addition to the CP MAS methodology which considerably enlarged its range of applications, making it possible to obtain high-resolution proton spectra of hydrogen-containing solids many of which are of great industrial importance. When applied to solid amino acids the CRAMPS technique yielded proton CP MAS spectra in which there were identified[23] asymmetric peaks clearly arising from the ^{1}H–^{14}N dipolar interaction and the ^{14}N quadrupole interaction not being averaged out, as earlier described for the analogous ^{13}C–^{14}N case. The resolution of the characteristic asymmetric lineshapes varied with the type of multiple pulse sequence used. This was presumably because a faster spinning frequency was required to reduce the N–H dipolar interactions. In all cases, characteristic asymmetric doublets were observed for the ^{1}H–^{14}N bonds, with the exception of the N-2 and N-3 nuclei in the imidazole ring of L-histidine hydrochloride monohydrate. Those two bonds exhibited broad asymmetric peaks, possibly being the result of strong hydrogen bonding.

The asymmetric peaks in the CRAMPS MAS spectra of amino acids were simulated by Naito et al.[23] using the computer programs based on the theoretical treatments described earlier.[14,16] In addition, it was necessary to multiply the quadrupole and Zeeman terms in the Hamiltonian by the scaling factors $S_m S_r$. The term S_m is the scaling factor for the multiple pulse scheme used, and $S_r = \frac{1}{2}(3\cos^2\theta - 1)$ is the scaling factor caused by a group rotation where θ is the angle between the rotation axis and the N–H direction. The lineshapes were simulated successfully. That of the peptide proton was well simulated (see Figure 5) using the ^{14}N coupling constant of -3.2 MHz and $\eta = 0.31$, the parameters having been determined in a single crystal ^{14}N NMR study on *N*-acetylvaline though the sign of the quadrupole coupling constant had been established previously from a comparison of the experimental and computer-simulated peptide carbon nuclei.[16] In addition, it was necessary to interchange the assigned axes of the electric field gradient tensor so that the *x* axis was parallel to the N–H bond direction. The spectral peaks for the proton bonded to the imidazole nitrogen N nuclei were simulated using the ^{14}N coupling constants earlier determined from ^{14}N NMR single crystal studies. The simulated spectra showed that broad lines were to be expected and that a clear asymmetric doublet was not to be anticipated in this case. It was also to be expected that the proton bonded to the N-2 nucleus should have a broader lineshape than that for the N-3 nucleus. These predicted lineshapes were in good agreement with those observed experimentally.

The interesting ^{14}N-containing spin-pairs ^{14}N≡^{15}N^{+}–and ^{15}N≡^{14}N^{+}–yield unusual lineshapes.[24] It should also be mentioned that the ^{13}C MAS lineshapes of the parent compounds 5-methyl-2-[α-^{15}N]diazobenzenesulfonic acid and its isotopomer with [β-^{15}N] exhibit characteristic novel lineshapes. It was, however, possible to obtain approximate lineshape simulations for the ^{13}C–^{14}N residual dipolar couplings even though the resulting ragged appearances of the simulations were clearly caused by the use of insufficient increments of the orientations of the angles β^Q and γ^Q in the calculations. Convolution of the two simulated spectra yielded a lineshape which was a good reproduction of the spectrum resulting from convoluting the observed ^{13}C MAS spectra of the two isotopomers. An apparent triplet lineshape was observed for the carbon nucleus bonded to the α- and β-^{14}N nuclei of the diazo group, which arises from two different residual ^{13}C–^{14}N dipolar couplings acting on the same carbon nucleus. It proved possible to simulate that feature.

Mention should be made of related studies of the lineshapes found for off-magic angle, or variable-angle, ^{13}C NMR spectra of compounds which exhibit $^{13}C-^{14}N$ dipolar–quadrupolar interaction effects.[25] Though to some extent peripheral to the main thrust of this article, the phenomena described in those studies are of considerable interest.

7 RELATED ARTICLES

Average Hamiltonian Theory; CRAMPS; Cross Polarization in Solids; Magic Angle Spinning; Quadrupolar Interactions; Quadrupolar Nuclei in Solids; Rotating Solids.

8 REFERENCES

1. S. R. Hartmann and E. L. Hahn, *Phys. Rev.*, 1962, **128**, 2042.
2. A. Pines, M. G. Gibby, and J. S. Waugh, *J. Chem. Phys.*, 1973, **59**, 569.
3. E. R. Andrew, A. Bradbury, and R. G. Eades, *Nature*, **182**, 1639; I. J. Lowe, *Phys. Rev. Lett.*, 1959, **2**, 285.
4. J. Schaefer, E. O. Stejskal, and R. Buchdahl, *Macromolecules*, 1975, **8**, 291.
5. R. G. Griffin, A. Pines, and J. S. Waugh, *J. Chem. Phys.*, 1975, **63**, 3676.
6. M. E. Stoll, R. W. Vaughan, R. B. Saillant, and T. Cole, *J. Chem. Phys.*, 1974, **61**, 2896.
7. A. Naito, S. Ganapathy, K. Akasaka, and C. A. McDowell, *J. Chem. Phys.*, 1981, **74**, 3190.
8. R. A. Haberkorn, R. E. Stark, H. van Willigen, and R. G. Griffin, *J. Am. Chem. Soc.*, 1981, **103**, 2534.
9. D. L. VanderHart, H. S. Gutowsky, and T. C. Farrar, *J. Am. Chem. Soc.*, 1967, **89**, 5056.
10. E. Lippmaa, M. Alla, H. Raude, R. Teeäär, I. Heinmaa, and E. Kundla, *Proc. 20th Congr. AMPERE, Tallin*, eds. E. Kundle, E. Lipmaa, and T. Saluvere, Springer-Verlag, Berlin, 1987, p. 87.
11. E. Kundla and M. Alla, *Proc. 20th Congr. AMPERE, Tallin*, eds. E. Kundle, E. Lipmaa, and T. Saluvere, Springer-Verlag, Berlin, 1987, p. 92.
12. C. J. Groombridge, R. K. Harris, K. J. Packer, B. J. Say, and S. F. Tanner, *J. Chem. Soc., Chem. Commun.*, 1980, 174.
13. M. H. Frey and S. J. Opella, *J. Chem. Soc., Chem. Commun.*, 1980, 474.
14. A. Naito, S. Ganapathy, and C. A. McDowell, *J. Chem. Phys.*, 1981, **74**, 5393.
15. N. Zumbulyadis, P. M. Hendricks, and R. L. Young, *J. Chem. Phys.*, 1981, **75**, 1603.
16. A. Naito, S. Ganapathy, and C. A. McDowell, *J. Magn. Reson.*, 1982, **48**, 367.
17. J. G. Hexem, M. H. Frey, and S. J. Opella, *J. Chem. Phys.*, 1982, **77**, 3847.
18. Z. Gan and D. M. Grant, *J. Magn. Reson.*, 1990, **90**, 522.
19. A. C. Olivieri, L. Frydman, and L. E. Diaz, *J. Magn. Reson.*, 1987, **75**, 50.
20. A. C. Olivieri, *J. Magn. Reson.*, 1988, **81**, 201.
21. K. Eichele and R. E. Wasylishen, *Solid State NMR*, 1992, **1**, 159.
22. B. C. Gerstein, R. G. Pembleton, R. C. Wilson, and L. M. Ryan, *J. Chem. Phys.*, 1977, **66**, 361.
23. A. Naito, A. Root, and C. A. McDowell, *J. Phys. Chem.*, 1991, **95**, 3578.
24. R. K. Harris, P. Jonsen, and K. J. Packer, *Magn. Reson. Chem.*, 1985, **23**, 565.
25. N. K. Sethi, D. W. Alderman, and D. M. Grant, *Mol. Phys.*, 1990, **71**, 217.

Biographical Sketch

Charles A. McDowell. *b* 1918. B.Sc., 1941, M.Sc., 1942, D.Sc., 1955, Queen's University of Belfast, UK; D.Sc., 1984, honoris causa, University of British Columbia, Canada. National service, UK, 1941–45; lecturer, University of Liverpool, UK, 1945–55; Professor and Head, Department of Chemistry, University of Liverpool, 1955–81; University Professor, 1981–84. Currently University Professor Emeritus, Department of Chemistry, University of British Columbia, Canada. Approx. 360 publications. Current research specialties; mainly in solid state NMR.

Magic Angle Spinning: Effects of Quadrupolar Nuclei on Spin-1/2 Spectra

Robin K. Harris
University of Durham, UK

1	Introduction	1
2	Theoretical Background	1
3	Consequences of Perturbation Theory	2
4	Results and Discussion	3
5	Departure from Perturbation Theory	4
6	Quadrupolar Coupling Dominant	5
7	Related Articles	6
8	References	6

1 INTRODUCTION

As explained in detail in ***Magic Angle Spinning Carbon-13 Lineshapes: Effect of Nitrogen-14***, magic angle spinning does not always eliminate from spin-$\frac{1}{2}$ spectra the influence of dipolar coupling to quadrupolar nuclei. In particular, when quadrupolar energies are not negligible compared with Zeeman energies, spin-$\frac{1}{2}$ spectra may show splittings and/or lineshapes which arise from residual dipolar coupling to quadrupolar nuclei. This phenomenon was first discovered and thoroughly investigated for the (^{13}C, ^{14}N) nuclear pair, but it soon became apparent that the effect was more widespread, indeed ubiquitous. The present article will discuss a wide range of examples and will place particular emphasis on the perturbation approach, which is adequate to explain many cases. The discussion will be limited to the centers of gravity of what are, strictly speaking, powder bandshapes. The reader is referred to ***Magic Angle Spinning Carbon-13 Lineshapes: Effect of Nitrogen-14*** for details of more exact theory, for questions of powder bandshapes, and for all examples involving ^{14}N. The whole subject has received attention in a review article[1] which summarizes the theoretical approaches and also lists cases for many different nuclear spin pairs.

2 THEORETICAL BACKGROUND

Consider a pair of nuclei I and S, where the former has the spin quantum number $\frac{1}{2}$ and the latter is quadrupolar. For simplicity in this discussion, it will be assumed that the electric field gradient at S is axially symmetric, but the reader must be careful not to infer that the results below apply to the general case of $\mu \neq 0$. The phenomenon mentioned above can be traced to the influence of terms in the quadrupolar Hamiltonian involving nuclear spin operators other than $\hat{S}_z$. When Zeeman terms dominate, the energy levels of quadrupolar nuclei are properly characterised by the spin component quantum number m_S, associated with $\hat{S}_z$. Since the relevant Hamiltonian terms have angular dependences $\frac{1}{2}(3\cos^2\theta_Q - 1)$, where θ_Q is the angle between the major principal axis of the quadrupolar tensor and the applied magnetic field ($\boldsymbol{B}_0$), their effects are averaged to zero by magic angle spinning at a fast enough rate. Moreover, in such circumstances, the only terms in the dipolar Hamiltonian connecting the quadrupolar nucleus with the spin-$\frac{1}{2}$ nucleus which are secular involve similar angular dependence $\frac{1}{2}(3\cos^2\theta_D - 1)$ where θ_D is the angle between $\boldsymbol{B}_0$ and the internuclear distance between the spin $\frac{1}{2}$ and the quadrupolar nuclei. Thus, magic angle spinning at a sufficiently high rate is enough to eliminate these dipolar interactions. Therefore, resonance frequencies in spin-$\frac{1}{2}$ MAS spectra are unaffected by dipolar interactions to quadrupolar nuclei in such circumstances. Similar considerations apply to anisotropy and asymmetry in the indirect ('scalar') coupling between a spin-$\frac{1}{2}$ nucleus and a quadrupolar nucleus: MAS suffices to remove the influence of such coupling components on the frequencies in the spin-$\frac{1}{2}$ spectrum, though the isotropic part of the coupling is retained.

However, when quadrupolar and Zeeman terms in the Hamiltonian become comparable, the situation is drastically changed. The detailed theoretical treatment using the full Hamiltonian is discussed in ***Magic Angle Spinning Carbon-13 Lineshapes: Effect of Nitrogen-14***. Here, the perturbation treatment, which is frequently applicable, will be presented. The use of perturbation theory was pioneered by Olivieri and co-workers[2] for the (^{13}C, ^{14}N) case (though it was implicit in earlier treatments), and rapidly extended[3] to situations involving higher-spin quadrupolar nuclei.

The spin-$\frac{3}{2}$ case is chosen here for illustration purposes. Consider the so-called 'alphabet expansion' of the dipolar and axially-symmetric quadrupolar interactions (Table 1). In the high-field approximation the Zeeman levels may be designated as $|m_S\rangle$, where $m_S = \frac{3}{2}, \frac{1}{2}, -\frac{1}{2}$ or $-\frac{3}{2}$. Under the influence of terms C, D, E, and F of the 'quadrupolar alphabet', these wavefunctions are mixed to become

$$|(-\tfrac{3}{2})'\rangle = \quad |-\tfrac{3}{2}\rangle + a_1^*|-\tfrac{1}{2}\rangle - a_2^*|\tfrac{1}{2}\rangle \tag{1a}$$

$$|(-\tfrac{1}{2})'\rangle = -a_1|-\tfrac{3}{2}\rangle + \quad |-\tfrac{1}{2}\rangle + a_3^*|\tfrac{1}{2}\rangle - a_2^*|\tfrac{3}{2}\rangle \tag{1b}$$

$$|(\tfrac{1}{2})'\rangle \quad = \quad a_2|-\tfrac{3}{2}\rangle - a_3|-\tfrac{1}{2}\rangle + \quad |\tfrac{1}{2}\rangle - a_1^*|\tfrac{3}{2}\rangle \tag{1c}$$

$$|(\tfrac{3}{2})'\rangle \quad = \quad +a_2|-\tfrac{1}{2}\rangle + a_1|\tfrac{1}{2}\rangle + \quad |\tfrac{3}{2}\rangle \tag{1d}$$

where, in the perturbation approach, $a_1 = \langle\frac{1}{2}|\hat{\mathcal{H}}_Q|\frac{3}{2}\rangle/\gamma_s\hbar B_0$, $a_2 = \langle-\frac{1}{2}|\hat{\mathcal{H}}_Q|-\frac{3}{2}\rangle/2\gamma_s\hbar B_0$ and $a_3 = \langle-\frac{1}{2}|\hat{\mathcal{H}}_Q|\frac{1}{2}\rangle/\gamma_s\hbar B_0$, etc.

The alphabet terms C and D are relevant for a_1 and a_3 whereas terms E and F are effective for a_2. However, it can be shown that $a_3 = 0$ and that a_2 cannot affect the I spectrum. Now, because of the mixed nature of the Zeeman levels, terms C and D of the (I, S) 'dipolar alphabet' become secular, the additional energy contributions being

$$\langle(-\tfrac{3}{2})'m_I|\hat{\mathcal{H}}_D|(-\tfrac{3}{2})'m_I\rangle = \langle(\tfrac{3}{2})'m_I|\hat{\mathcal{H}}_D|(\tfrac{3}{2})'m_I\rangle \propto -a_1 D m_I \tag{2a}$$

$$\langle(-\tfrac{1}{2})'m_I|\hat{\mathcal{H}}_D|(-\tfrac{1}{2})'m_I\rangle = \langle(\tfrac{1}{2})'m_I|\hat{\mathcal{H}}_D|(\tfrac{1}{2})'m_I\rangle \propto +a_1 D m_I \tag{2b}$$

Table 1 The NMR Internal Hamiltonian: The Alphabet Expansion

Term	Geometric factor[c]	Spin factors[a] Dipolar	Quadrupolar[b]	Connectivity
A	$1 - 3\cos^2\theta$	$I_z S_z$	$(I_z)^2$	Secular
B	$-\frac{1}{4}(1 - 3\cos^2\theta)$	$I_+S_- + I_-S_+$	$I_+I_- + I_-I_+$	Flip-flop[a]
C	$-\frac{1}{2}\sin\theta\cos\theta\exp(-i\phi)$	$I_zS_+ + I_+S_z$	$I_zI_+ + I_+I_z$	Single quantum
D	$-\frac{1}{2}\sin\theta\cos\theta\exp(i\phi)$	$I_zS_- + I_-S_z$	$I_zI_- + I_-I_z$	Single quantum
E	$-\frac{1}{4}\sin^2\theta\exp(-2i\phi)$	I_+S_+	$(I_+)^2$	Double quantum
F	$-\frac{1}{4}\sin^2\theta\exp(2i\phi)$	I_-S_-	$(I_-)^2$	Double quantum

[a] Secular for the quadrupolar and homonuclear dipolar interactions, but nonsecular for heteronuclear dipolar interactions.
[b] For the axially symmetric case ($\eta = 0$).
[c] There are also constant numerical factors (hD for the dipolar case and $h\chi/2S(2S-1)$ for the quadrupolar case).

where D is the dipolar coupling constant, $\gamma_I\gamma_S(\mu_0/4\pi)(\hbar/2\pi)r_{IS}^{-3}$ (to be distinguished from the alphabet term D!). Therefore the energy levels are modified as shown in Figure 1, and the outer lines of the I multiplet will be shifted in one direction, while the inner lines will shift to the same extent but in the opposite direction. Of course the terms in the Hamiltonian also involve geometric factors which depend on the Euler angles connecting the dipolar and quadrupolar tensors with the magnetic field $\boldsymbol{B}_0$. Since these are *not* of the form $(3\cos^2\theta - 1)$, they are not eliminated by MAS although they are reduced. Thus each of the multiplet components in the I spectrum will be powder patterns under MAS. However, the structure of these powder patterns is not usually observed, and consequently the useful information normally comes from consideration of the centers of gravity of the bands. Of course the indirect coupling tensor $\boldsymbol{J}$ has some common features with $\boldsymbol{D}$, and therefore it will in principle also need to be considered.

Full evaluation for the general case results[1] in the following perturbation expression for the shift induced in the center of gravity of the spin-$\frac{1}{2}$ transition frequency associated with quadrupolar basis state m_S

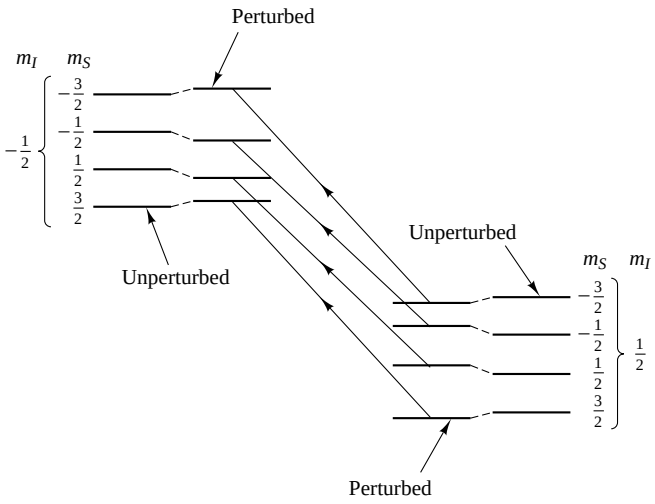

Figure 1 Energy-level diagram for an IS nuclear spin pair with $I = \frac{1}{2}$, $S = \frac{3}{2}$ to show the perturbations induced by quadrupolar and dipolar interactions. The extent of the perturbations is greatly exaggerated. It is assumed that γ_I, γ_S, and J_{iso} are all positive

$$^2\Delta\nu(m_S) = \frac{3\chi}{20\nu_S}\left[\frac{S(S+1) - 3m_S^2}{S(2S-1)}\right] \times \left[Df(\alpha^D, \beta^D, \eta) - \frac{\Delta J}{3}f(\alpha^J, \beta^J, \eta)\right] \quad (3)$$

where $f(\alpha, \beta, \eta) = 3\cos^2\beta - 1 + \eta\sin^2\beta\cos 2\alpha$, α and β are the relevant Euler angles (see Harris and Olivieri[1]), η is the asymmetry in the electric field gradient, χ is the quadrupole coupling constant, ν_S is the Larmor frequency of the quadrupolar nucleus and ΔJ is the anisotropy in $\boldsymbol{J}$. The above equation assumes that $\boldsymbol{J}$ is an axially symmetric tensor. Simplifications result if there are further assumptions. In particular, if $\boldsymbol{J}$ and $\boldsymbol{D}$ are co-axial, and if η is ignored, the complete equation for the spin-$\frac{1}{2}$ transition frequency is

$$\nu(m_S) = \nu_I - m_S J_{\text{iso}} + \frac{3D'\chi}{20\nu_S}\left[\frac{S(S+1) - 3m_S^2}{S(2S-1)}\right] \quad (4)$$

where ν_I is the Larmor frequency of the spin-$\frac{1}{2}$ nucleus, J_{iso} is the isotropic part of $\boldsymbol{J}$, and D' is an effective dipolar coupling constant, incorporating the anisotropy in J

$$D' = D - \frac{\Delta J}{3} \quad (5)$$

The second-order shift itself, $\nu(m_S) - \nu_I + m_S J_{\text{iso}}$, depends only on the square of m_S, and for $m_S = \pm S$ it is independent of S. It is therefore convenient to normalize effects to the shift of the 'outermost' lines, defined as

$$\Delta = -\frac{3}{10}\frac{\chi D'}{\nu_S} \quad (6)$$

This enables the second-order shifts of all lines to be written as

$$^2\Delta\nu(m_S) = -\left[\frac{S(S+1) - 3m_S^2}{S(2S-1)}\right]\Delta \quad (7)$$

Table 2 lists the shifts of all lines, for various half-integral values of S, in terms of Δ.

Table 2 Second-Order Shifts in the Spectra of Spin-$\frac{1}{2}$ Nuclei Arising from Coupling to a Half-Integral Quadrupolar Nucleus S[a]

	m_S				
S	$\pm\frac{1}{2}$	$\pm\frac{3}{2}$	$\pm\frac{5}{2}$	$\pm\frac{7}{2}$	$\pm\frac{9}{2}$
$\frac{3}{2}$	-1	1			
$\frac{5}{2}$	$-\frac{4}{5}$	$-\frac{1}{5}$	1		
$\frac{7}{2}$	$-\frac{5}{7}$	$-\frac{3}{7}$	$\frac{1}{7}$	1	
$\frac{9}{2}$	$-\frac{2}{3}$	$-\frac{1}{2}$	$-\frac{1}{6}$	$\frac{1}{3}$	1

[a]Note: The values are normalized to the shift of the outermost lines as expressed in equation (6).

3 CONSEQUENCES OF PERTURBATION THEORY

A number of significant features can be understood from equations (3)–(7).

1. While perturbation theory holds, second-order shifts are inversely proportional to $\boldsymbol{B}_0$, so that no new information is obtained by using several spectrometers. However, such experiments can be used to check that the origin of splittings in the spectra does indeed involve second-order effects, since the behavior with $\boldsymbol{B}_0$ differs from that of splittings caused by either J_{iso} or differences in chemical shifts.
2. Since second-order shifts depend on m_S^2, their values occur in pairs, with the outermost multiplet lines moving most. Figure 2 illustrates the situation as a function of $\chi D/\nu_S$ when $\Delta J = 0$.
3. The average second-order shift is zero, so the isotropic chemical shift is simply obtained by averaging the frequencies of all the lines.
4. The isotropic coupling constant, $|J_{\text{iso}}|$, is also readily obtained as the average spacing between lines, though care must be taken if there is any crossover of frequencies. The value of $|J_{\text{iso}}|$ is also available from the central spacing $|\nu(m_S = \frac{1}{2}) - \nu(m_S = -\frac{1}{2})|$.
5. Since the innermost lines shift in the opposite direction to the effect on the outermost lines, there is a 'bunching' of lines at one end of the spectrum. The extent of coalescence is more apparent for lower values of S for a given $\chi D/\nu_S$. The sense depends on the sign of Δ, and in favorable cases it gives important information on relative signs.
6. In particular, if $\boldsymbol{J}$ and $\boldsymbol{D}$ are co-axial the following general rule results: 'bunching' occurs to low frequency (i.e. Δ is positive) if *either* χ is negative (with D and D' of the same sign) *or* χ is positive (with D and D' of opposite signs). An analogous statement can be made if Δ is negative. This rule takes into account the effects of signs of magnetogyric ratios. Thus, if the magnitude and sign of χ is known, together with r_{IS}, and if η is ignored, then ΔJ can be derived unambiguously. However, if only r_{IS} and $|\chi|$ are available, two possible values of ΔJ can be calculated but they cannot be distinguished.
7. When perturbation theory holds, neither the magnitude nor the sign of J_{iso} influences Δ.
8. If the value of $|J_{\text{iso}}|$ is negligible compared to linewidths, then there will be $S + \frac{1}{2}$ lines. The relative frequencies at which 'bunching' takes place will give the sign of χ. The magnitude of Δ will enable r_{IS} to be determined if $|\chi|$ is known, and vice versa. However, $S = \frac{3}{2}$ is a special case, since a 1:1 doublet will be seen [Figure 3(a)], of spacing $\frac{3}{10}(\chi D/\nu_S)(3\cos^2\beta^D - 1 + \eta\sin^2\beta^D\cos 2\alpha^D)$ in the general case, and information on the sign of χ is lost.
9. Since the denominator in equation (7) reflects the fact that the validity of the perturbation approach depends on $\chi/2S(2S-1)\nu_S$, higher spins are more accurately treated than lower spins for equivalent values of χ.

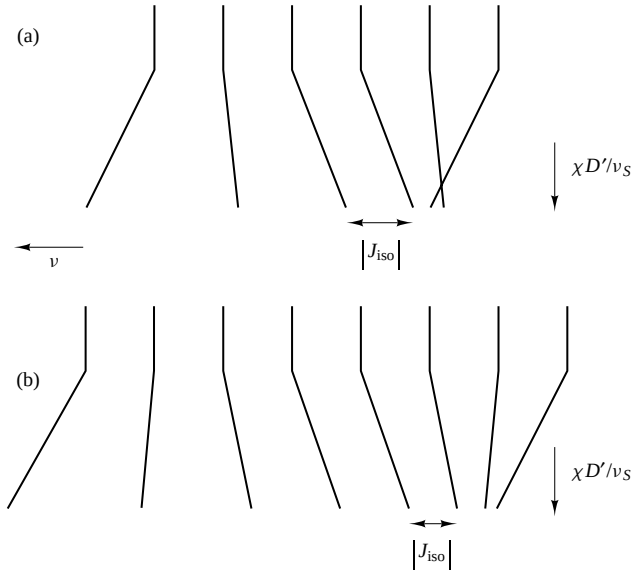

Figure 2 Second-order shifts in spin-$\frac{1}{2}$ MAS spectra arising from coupling to a quadrupolar nucleus S, as a function of the parameter $\chi D'/\nu_S$ under a perturbation approach according to equation (7): (a) $S = \frac{5}{2}$; (b) $S = \frac{7}{2}$. A positive value of Δ is assumed

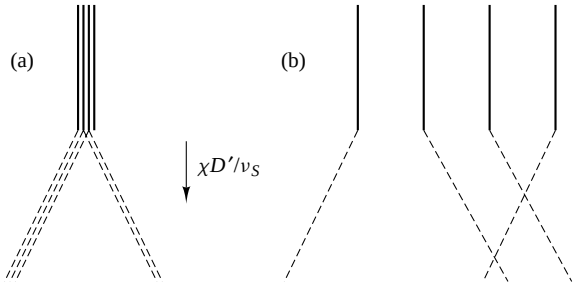

Figure 3 Second-order shifts in spin-$\frac{1}{2}$ MAS spectra arising from coupling to a quadrupolar nucleus $S = \frac{3}{2}$ as a function of the parameter $\chi D'/\nu_S$ under a perturbation approach according to equation (7): (a) $J_{\text{iso}} = 0$; (b) $-J_{\text{iso}}- > 0$. A positive value of Δ is assumed

4 RESULTS AND DISCUSSION

Many examples are now known where perturbation theory is reasonably applicable. In particular, the (^{119}Sn, $^{35/37}$Cl) situation is appropriate[3,4] since in such cases $|\chi|$ is generally modest (~35 MHz). Thus even for a 4.7 T spectrometer, the perturbation parameter $\chi/2S(2S-1)\nu_S$ is only in the region of 0.30. The splitting arising from $|J_{\text{iso}}|$ cannot be ignored. However, since chlorine is monovalent, coaxiality of $\boldsymbol{J}$ and $\boldsymbol{D}$ is a reasonable approximation for directly-bonded Sn–Cl groups except when chlorine is in a bridging situation. In fact,

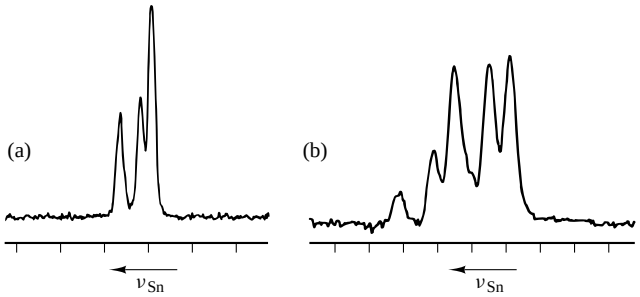

Figure 4 Tin-119 CP MAS NMR spectra at 74.63 MHz for (a) $(PhCH_2)_3SnCl$ and (b) Et_2SnCl_2, showing the second-order effects of coupling to the chlorine nuclei.[4] The markers are at 1 kHz and 0.5 kHz intervals for (a) and (b), respectively

a typical spectral pattern is a 1:1:2 triplet with relative spacings 2:1 [Figure 4(a)], which is strictly the case only when $|J_{iso}| = 2\Delta$. Values of $|J(\text{Sn,Cl})|$ have therefore been derived, as have approximate data for ΔJ. When more than one chlorine is coupled to the same Sn, simple convolution suffices to predict the spectral appearance. If the chlorines are equivalent, then $|J_{iso}| = 2\Delta$ leads to a 1:2:4:1:4:4 multiplet (with the first spacing twice the others), such as has been observed [Figure 4(b)] for Et_2SnCl_2.[4]

Cases involving ^{31}P coupled to metal nuclei are also common, and have been shown[5,6] to occur for a range of S-spin metals, e.g. $^{63/65}$Cu ($S = \frac{3}{2}$), ^{55}Mn ($S = \frac{5}{2}$), ^{59}Co ($S = \frac{7}{2}$), and ^{93}Nb ($S = \frac{9}{2}$). Figure 5 shows an example where the second-order effects are relatively small. In a number of such cases perturbation theory is not appropriate, and in others questions of nonaxiality reduce the usefulness of the observed second-order effects. However, the case of $Mn_2(CO)_9PPh_3$ proved[6] to be appropriate, since the molecular symmetry has axiality and spinning sideband analysis indicates that this is retained in the solid state. Such an analysis also gives a value for $|D'|$, so that $|\chi|$ can be derived (42 MHz). The value of $\chi/2S(2S-1)\nu_S$ for a spectrometer operating at 7.1 T is thus 0.028, which confirms that perturbation theory is applicable. Several (^{31}P, $^{63/65}$Cu) examples have been analyzed[7] using perturbation theory to yield data for $\Delta J \sim 0.6$ kHz.

Numerous other examples of residual dipolar coupling have been reported, some of which come into the category of a perturbation treatment. In particular, examples of (^{13}C, ^{2}H) have been given.[1,8,9] Although ^{2}H has a low value of χ, the residual effects of dipolar coupling are appreciable because r_{CH} is small and hence D is relatively large. With rigid molecules,[1,8] there is a nice contrast to the (^{13}C, ^{14}N) case since, although 2:1 doublets are observed in both instances, the origins differ. For the (^{13}C, ^{14}N) pair J_{iso} can usually be ignored, so there is overlap for the lines connected to states $|+1\rangle$ and $|-1\rangle$ for ^{14}N, whereas for (^{13}C, ^{2}H), the overlap is of transitions involving $|0\rangle$ and $|-1\rangle$ for ^{2}H. The latter situation arises coincidentally because $|J_{iso}(^{13}\text{C}, ^{2}\text{H})|$ is approximately equal to $\frac{9}{10}D\chi/\nu_S$. The spectra have a different appearance[9] for inclusion compounds of urea and thiourea with deuterated guest molecules, such as straight-chain alkanes and corresponding carboxylic acids. The guest molecules are relatively mobile, so that values of $\chi(^{2}\text{H})$ are substantially reduced (to ca. 50–70 kHz for CD_2 groups) by averaging. Second-order effects on the ^{13}C spectra are therefore relatively modest, simply resulting in a small asymmetry in the splittings

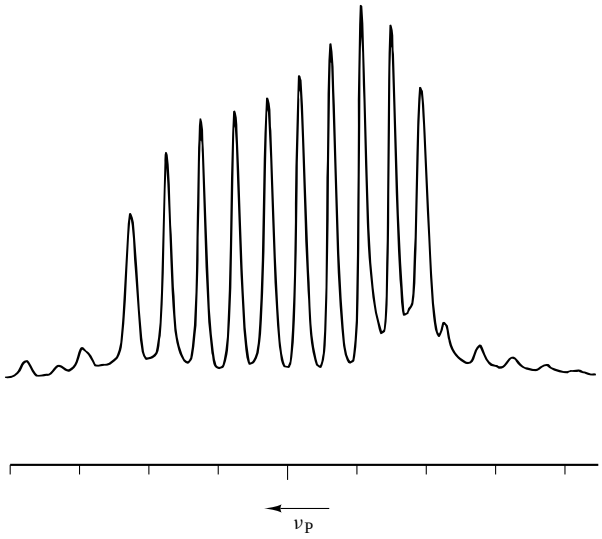

Figure 5 Phosphorus-31 CP MAS NMR spectra at 81.0 MHz for $(C_5H_5)(Me_3P)Cl_2Nb{=}N(o\text{-}tBuC_6H_4)$, showing the second-order effects of coupling to the niobium nucleus: the multiplet spacing decreases slightly from high to low frequency. The lines outside the main decet are spinning sidebands. The markers are at 1 kHz intervals

of the 1:2:3:2:1 quintet patterns. The spectra can be used to determine, at least qualitatively, the relative values of χ at different positions in a chain, which in turn depend on variations in local molecular mobility.

Of course, the appearance of splittings arising from either dipolar coupling, whether residual or full, or indirect coupling is contingent upon the lifetimes of the quadrupolar spin states being long compared with the frequency separations in the spin-$\frac{1}{2}$ spectra. If spin–lattice relaxation times of the quadrupolar nuclei become sufficiently short, the result is 'self-decoupling' (such as is frequently observed in solution state situations). In such cases a single line will be seen in the spin-$\frac{1}{2}$ spectrum. This is the situation[10] for the ^{31}P spectrum of PCl_5 where sharp singlets are observed for the PCl_4^+ and PCl_6^- ions at room temperature but multiplets at low temperature. Of course, molecular motion (e.g. rotation of ions, as for PCl_5) may affect residual dipolar splittings both directly (by averaging $\boldsymbol{D}$) and indirectly (by relaxing the S nucleus). 'Self-decoupling' can in principle also occur because of chemical exchange involving I–S bond breaking.

5 DEPARTURE FROM PERTURBATION THEORY

The first clear case of effects of dipolar coupling residual which did not involve the (^{13}C, ^{14}N) nuclear pair concerned the (^{31}P, ^{63}Cu) nuclei in bis(triphenylphosphine)copper(I) and related complexes, presented by Menger and Veeman.[5] These authors published detailed theory, but the situation was beyond the validity of perturbation theory. Many examples involving the (^{31}P, ^{63}Cu) pair have since come to light, though some are susceptible to the perturbation approach.

The (^{13}C, $^{35/37}$Cl) case is interesting.[11,12] Although there are simplifying features, since chlorine is univalent (and hence coaxiality of $\boldsymbol{J}$ and $\boldsymbol{D}$ can be assumed) and J(C, Cl) is negligibly small, the value of $|\chi|$ is sufficiently large (ca.

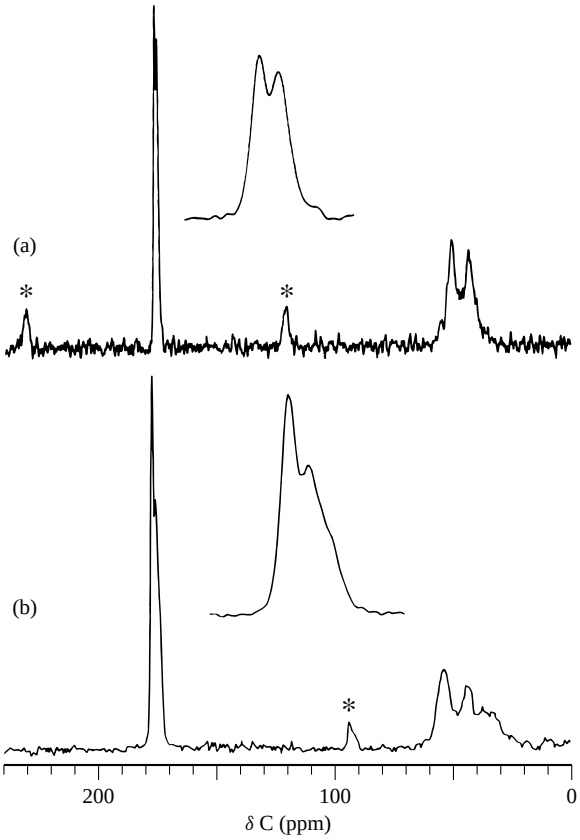

Figure 6 Carbon-13 CP MAS NMR spectra of sodium monochloroacetate: (a) 75.4 MHz; (b) 50.3 MHz, showing the second-order effects of coupling to chlorine.[12] The insets show expansions of the carboxyl region. The asterisks denote spinning sidebands

−70 MHz) that departures from perturbation theory can be observed. At modest magnetic fields (7.1 T and above), the 1:1 doublet predicted by perturbation theory is indeed observed [Figure 6(a)], but the splitting is smaller than predicted and is not inversely proportional to $\boldsymbol{B}_0$. However, it has been shown[13] by simulation using exact theory that for the case $S = \frac{3}{2}$ the doublet splitting, s, can be adequately represented in the range $0.8 < R = |\chi/\nu_S| < 3.0$ by the cubic polynomial

$$s = D(0.581R + 0.033R^2 - 0.021R^3) \tag{8}$$

A cubic equation for s has also been derived for the $S = \frac{3}{2}$ case in which J_{iso} cannot be ignored.

For the (^{13}C, $^{35/37}$Cl) case, even equation (8) is inadequate at 4.7 T, since a broad 2:1:1 triplet is both predicted and observed[11,12] [Figure 6(b)]. Figure 7 shows the theoretical line positions (centers of gravity) as a function of R for the case $I = \frac{1}{2}$, $S = \frac{3}{2}$ for positive χ and in the absence of $\boldsymbol{J}$. At high values of R, four lines are expected, and this links up with the expectation from inverse perturbation theory discussed below.

Molecular-level motion has a drastic effect on the ^{13}C spectra of sodium chloroacetates.[12] For the monochloro compound a clear doublet is seen for both the CH_2Cl and carbonyl carbons at 7.1 T and above, with the expected 2:1:1 triplet at 4.7 T. However sodium trichloroacetate shows a sharp line for each carbon at 7.1 T, not only at room temperature but also down to 163 K. The reason for this behavior undoubtedly lies in the facile internal rotation of the $C-CCl_3$ group.

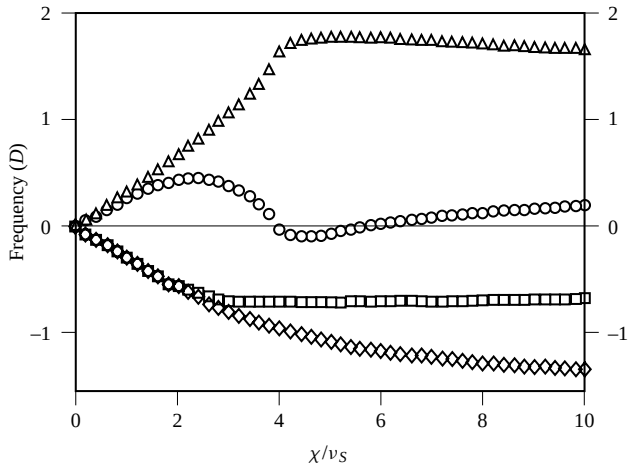

Figure 7 Line positions (centers of gravity, units of D) for a spin-1/2 nucleus coupled to a spin-3/2 nucleus as a function of $R = \chi/\nu_S$ as obtained[13] by the full theory for positive χ and assuming $J_{\text{iso}} = \Delta J = \eta = \beta^D = 0$

When J_{iso} needs to be taken into consideration and perturbation theory is inadequate, it has been shown[13] that the sign of J_{iso} can be obtained from the spectrum (if the sign of χ is known). Thence $J(^{63}\text{Cu}, ^{31}\text{P})$ has been found[13] to be negative.

6 QUADRUPOLAR COUPLING DOMINANT

Olivieri has considered[14,15] the case where the quadrupole coupling constant is very large. The dipolar and indirect couplings will still transfer the quadrupole information to the spin-$\frac{1}{2}$ nucleus under MAS conditions, giving rise to splittings in the spectra. For the case where $\boldsymbol{J}$ is axially symmetric and the three tensors $\boldsymbol{D}$, $\boldsymbol{q}$, and $\boldsymbol{J}$ are all co-axial, Olivieri showed[14] that a quartet results when $S = \frac{3}{2}$. Each component is a powder pattern, with the centers of gravity forming two doublets with splittings, independent of the applied magnetic field, given by

$$s(\pm\tfrac{1}{2}) = |1.709J_{\text{iso}} + D'| \tag{9a}$$

$$s(\pm\tfrac{3}{2}) = \tfrac{3}{2}|2D' - J_{\text{iso}}| \tag{9b}$$

When the Zeeman S term begins to be significant with respect to the quadrupolar interaction, an inverse perturbation approach ('inverse' when compared to the considerations of Section [2] above) may be used.[14] In this case equations (9a) and (9b) need to be modified, and the four centers of gravity are

$$\langle \Delta\nu(\pm\tfrac{1}{2})\rangle = \mp(0.8546J_{\text{iso}} + 0.5D') - 2(J_{\text{iso}} + D')\frac{\nu_S}{\chi} \tag{10a}$$

$$\langle \Delta\nu(\pm\tfrac{3}{2})\rangle = \pm\tfrac{3}{4}(2D' - J_{\text{iso}}) + 2(J_{\text{iso}} + D')\frac{\nu_S}{\chi} \tag{10b}$$

The spectrum is no longer symmetric, and the sense of the asymmetry depends on the relative signs of $J_{\text{iso}} + D'$, ν_S, and χ. Olivieri has also extended calculations[15] of this type to

situations where $\boldsymbol{q}$ is not axially symmetric and for arbitrary relative orientations of $\boldsymbol{q}$ and $\boldsymbol{D}$.

Frequently, large χ implies the likelihood of rapid spin–lattice relaxation and therefore self-decoupling of S from the spin-$\frac{1}{2}$ nucleus in question. However, (^{13}C, $^{79/81}$Br) systems have been shown[16] to approach the inverse perturbation case, and an example of a (^{31}P, ^{201}Hg) spin pair (with $D \ll J_{\mathrm{iso}}$ in magnitude) even nearer the low-field limit has been reported.[15,17]

7 RELATED ARTICLES

Magic Angle Spinning Carbon-13 Lineshapes: Effect of Nitrogen-14; Quadrupolar Interactions; Quadrupolar Nuclei in Solids.

8 REFERENCES

1. R. K. Harris and A. C. Olivieri, *Prog. NMR Spectrosc.*, 1992, **24**, 435.
2. A. C. Olivieri, L. Frydman, and L. E. Diaz, *J. Magn. Reson.*, 1987, **75**, 50; A. C. Olivieri, *J. Magn. Reson.*, 1989, **81**, 201.
3. R. K. Harris, *J. Magn. Reson.*, 1988, **78**, 389; D. C. Apperley, H. Bai, and R. K. Harris, *Mol. Phys.*, 1989, **68**, 1277.
4. R. K. Harris, A. Sebald, D. Furlani, and G. Tagliavini, *Organometallics* 1988, **7**, 388.
5. E. M. Menger and W. S. Veeman, *J. Magn. Reson.*, 1982, **46**, 257.
6. R. Gobetto, R. K. Harris, and D. C. Apperley, *J. Magn. Reson.*, 1992, **96**, 119.
7. A. C. Olivieri, *J. Am. Chem. Soc.*, 1992, **114**, 5758.
8. P. Jonsen, S. F. Tanner, and A. H. Haines, *Chem. Phys. Lett.*, 1989, **164**, 325; S. D. Swanson, S. Ganapathy, and R. G. Bryant, *J. Magn. Reson.*, 1987, **73**, 239.
9. A. E. Aliev, K. D. M. Harris, D. C. Apperley, R. K. Harris, and M. M. Sünnetçioglu, *J., Chem. Soc., Faraday Trans. 1*, 1993, **89**, 3791.
10. R. K. Harris and A. Root, *Mol. Phys.*, 1989, **66**, 993.
11. R. M. Cravero, M. González-Sierra, C. Fernández, and A. C. Olivieri, *J. Chem. Soc., Chem. Commun.*, 1993, 1253; R. K. Harris, M. M. Sünnetçioglu, K. S. Cameron, and F. G. Riddell, *Magn. Reson. Chem.*, 1993, **31**, 963.
12. S. H. Alarcón, A. C. Olivieri, S. A. Carss, and R. K. Harris, *J. Magn. Reson.*, 1995, in press..
13. S. H. Alarcón, A. C. Olivieri, and R. K. Harris, *Solid State NMR*, 1993, **2**, 325.
14. A. C. Olivieri, *J. Magn. Reson. Ser. A*, 1993, **101**, 313.
15. A. C. Olivieri, *Solid State NMR*, 1992, **1**, 345.
16. S. H. Alarcón, A. C. Olivieri, S. A. Carss, and R. K. Harris, *Magn. Reson. Chem.*, 1995, **33**, 603.
17. L.-J. Baker, G. A. Bowmaker, P. C. Healy, B. W. Skelton, and A. H. White, *J. Chem. Soc., Dalton Trans.*, 1992, 989.

Acknowledgments

The author is grateful to Professor A. C. Olivieri for fruitful collaborative research on the topic in question, and for valuable comments on the text of this article.

Biographical Sketch

Robin K. Harris. *b* 1936. B.A. (Nat.Sci.), Ph.D., (supervisor Norman Sheppard), Sc.D., University of Cambridge, UK. Postdoctoral work at Mellon Institute, Pittsburgh, PA (with Aksel Bothner-By). Successively lecturer, senior lecturer, and professor, University of East Anglia, UK. Currently Professor of Chemistry, University of Durham, UK. Secretary-General of ISMAR, 1986–92. Approx. 350 publications. Current research specialty: solid state NMR and its applications in materials chemistry.

Magnetic Equivalence

Thomas H. Siddall III

University of New Orleans, New Orleans, LA, USA

1	Introduction	1
2	A Hypothetical Molecule	1
3	Dimethylformamide: Internal Rotation	2
4	Biphenyl-Like Rotation in certain Anilides	2
5	Rotation of Methyl Groups as a Dynamic Symmetry Operation	3
6	Geared Isopropyl Groups	3
7	An Amine/Amine Hydrochloride Equilibrium with Amine Inversion	4
8	Exchange in an Iron Hydride	5
9	Change of Shape: Polyhedral Exchange	5
10	Interchange of Hydride Hydrogen with Molecular Hydrogen as Ligands	5
11	Inversion and Isomerization in Metal Tris(diketonates)	6
12	Slow Rotation and Possible Ring Inversion in a Lanthanum Compound	7
13	Ring Whizzing	8
14	Bridge/Terminal Exchange and Isomerism in a Bridged Iron Compound	9
15	Conclusions	9
16	General References	10
17	Related Articles	10
18	References	10

1 INTRODUCTION

Magnetic equivalence arises from symmetry. It is convenient to divide symmetry into two parts. The first is the point group symmetry of the molecule (or ion). The second is the symmetry that involves rapid intramolecular motions such as internal rotation of parts of the molecule against other parts, molecular inversion, or shifting of bonds between atoms in the molecule. As the temperature is lowered, these motions or rearrangements may slow down so much that nuclei (or sets of nuclei) that were equivalent at higher temperature become magnetically nonequivalent. (Magnetic equivalence that is achieved by interaction between molecules and/or intermolecular events is excluded from discussion in this article.)

Rapid processes are those by definition that occur with a frequency greater than the chemical shift difference between the NMR signals from the nuclei if they were nonequivalent. The spectrum that occurs at higher temperature when processes are rapid and the nuclei are equivalent is known as the *fast exchange spectrum*. The spectrum at lower temperature and when processes are slow is known as the *slow exchange spectrum*. The spectra at intermediate temperatures are said to be *intermediate exchange spectra*. Typically signals are broadened to become perhaps almost featureless humps for nuclei in the temperature region of intermediate exchange. Signal shape analysis of broadened signals can yield rate data and kinetic parameters. The kinetic window for signal shape analysis can vary substantially for different situations. However, typically rates of $10-1000\,s^{-1}$ can be determined by signal shape analysis. (The free energy of activation, $\Delta G^{\ddagger}$, as reported in the literature for various processes is quoted in this article. The temperature is always 298 K, unless otherwise noted.)

For convenience in discussion, point group symmetry will be referred to as *static symmetry*. The effect of internal motions will be referred to as *dynamic symmetry*. In fact, manifestation of dynamic symmetry is commonly called DNMR (dynamic NMR).

The operations of static symmetry and dynamic symmetry can be brought together to form a *permutation group* for the nuclei or groups of nuclei under discussion. This may seem strange since static symmetry depends only on geometry and does not actually move nuclei, while dynamic symmetry depends on actually moving nuclei. However, mathematically there is no qualitative distinction between the outcome of the two kinds of symmetry. In any event the nuclei are permuted (or in more common language they are exchanged). Permutation group theory is not discussed as such in this article, but it will be useful to use some of the ideas of permutation groups.

It is important to note that NMR of itself does not necessarily specify uniquely the dynamic physical process that permutes nuclei in any given case. It may, however, reveal which nuclei are exchanging with which nuclei. The detection of mutual exchange will be discussed in the main body of this article. But any analysis as to detailed mechanism requires additional information or theory outside the NMR experiment. However, a knowledge of mutual exchange may rule out certain mechanisms from a list of otherwise plausible mechanisms.

In spite of this caveat as to the limits of mechanistic information from NMR alone, the main article is organized to some extent around demonstrations of rotation around bonds, molecular inversion, and other specific internal motions, shifting of bonds, or combinations of such as these. The choice of interpretation of the nuclear exchange has always been assisted by outside considerations, even though these considerations may not be explicitly stated in the discussion that follows.

Individual studies have been selected for discussion in this article to represent principles. There is no attempt to give a review-like coverage of the very large literature that is continuing to emerge on the subject. Selection has not been made on the basis of clear superiority of one report over similar reports. The literature is too large and choice too subjective to guarantee that the selection has been made entirely on the basis of merit or of scientific importance.

Finally, a large share of the literature covered in this article was published in the approximate period from 1960 to 1975. The principles that were established in that period are now almost a matter of routine, but of course with newly interesting manifestations. Section 16, General References, refers to a variety of reviews and literature collections and should be consulted for a much wider coverage of magnetic equivalence and dynamic NMR than was possible to give in composing the present article. Also the bulk of the NMR studies have been undertaken by proton NMR methods. Unless otherwise specified or obvious, NMR stands for proton NMR in this article.

2 A HYPOTHETICAL MOLECULE

Some of the discussion in the Introduction can be illustrated with simple examples. The first example deals with a hypothetical molecule (**1**). So long as the R^1, R^2, and R^3 groups are all different, the carbon atom, C*, is asymmetric and the molecule has no symmetry plane. As a consequence, the hydrogen atoms, H_A and H_B, are nonequivalent since there is no static symmetry between them. Inversion of the asymmetric carbon atom would be a dynamic symmetry operation, but inversion of such a carbon atom is much too slow by many orders of magnitude to be an effective dynamic symmetry operation.

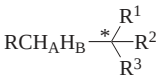

(1)

It might be supposed that rotation around the bond between the carbon atoms could constitute a dynamic symmetry operation, but this is not correct. Rapid rotation around that bond might tend to average out the environments of the hydrogen atoms, but the averaging could never be complete. It is suggested here that this last point is best demonstrated by experimenting with molecular models. On the other hand, if any two of the R^1, R^2, or R^3 groups were the same, there could be a symmetry plane between the hydrogen atoms. This static symmetry element would make the hydrogen atoms magnetically equivalent.

The usual twisting and turnings, rotations and vibrations of the rest of the molecule would ordinarily be much too rapid on the NMR timescale to destroy this equivalence. Variable temperature NMR studies are at the heart of much of the discussion of magnetic equivalence or the lack of it. If an internal rearrangement is so rapid that it cannot be 'frozen out' at the lowest experimentally attainable temperature, then it is just part of the background. It does not stand out as a dynamic symmetry operation, the effect of which is amenable to study by variable temperature NMR.

Given the asymmetric carbon atom, the hydrogen atoms are *diastereotopic*. This term will be used frequently in later discussions. In principle any geminal species can be diastereotopic. Isopropyl radicals are often included in molecules chosen for study. The methyl groups within an isopropyl group can be diastereotopic. Molecular inversion is the only dynamic operation that can render the methyl groups equivalent. If the methyl groups remain nonequivalent, then rapid inversion is not occurring. Of course other geminal pairs can serve the same purpose but their utility is usually lessened by the complex spectra that can occur, while methyl nonequivalence can lead to signal patterns that are easy to analyze, often at a glance.

3 DIMETHYLFORMAMIDE: INTERNAL ROTATION

The observation by Phillips[1] of the effect of temperature on the proton magnetic resonance spectrum of *N*,*N*-dimethylformamide and its explanation as internal rotation is one of the earliest records of intramolecular exchange in NMR. The core framework of amides is planar. There is partial double bond character in the carbonyl-to-nitrogen bond (the amide bond). Pauling[2] calculated the resonance energy to be 88 kJ mol^{-1}. For present purposes, resonance energy and the partial double bond character are manifest as the barrier to rotation around the amide bond.

Phillips observed that there is only one methyl signal at the fast exchange limit, but that this signal splits into two methyl signals at the slow exchange limit. He explained this behavior as being due to rapid rotation around the amide bond at higher temperature with the rotation slowing down as the slow exchange limit is reached at lower temperature.

Gutowsky and Holm[3] utilized the techniques of Gutowsky's earlier signal shape studies to determine the rate of rotation in dimethylformamide. They obtained a $\Delta G^{\ddagger}$ value of 92 kJ mol^{-1}. Since this pioneering work, there has been and continues to be a veritable torrent of applications to a large variety of intermolecular as well as intramolecular rate problems.

The symmetry considerations that are involved are straightforward. In the planar ground state, both methyl groups lie in the amide plane. Since there is no static symmetry element between the methyl groups, they are nonequivalent in the ground state. One methyl group is *cis* to the carbonyl oxygen and the other is *trans*. Rapid rotation around the amide bond is the dynamic symmetry operation that makes the methyl groups equivalent.

This set of symmetry considerations applies for amides in general and even more generally to rotation around the bond between trigonally bonded atoms in a variety of molecules that have a planar ground state. On the other hand, biphenyls, as examples, have the rotating parts in an out-of-plane ground state, and the barrier to rotation is substantially steric rather than electronic as it is in rotation around the amide bond.

4 BIPHENYL-LIKE ROTATION IN CERTAIN ANILIDES

Dynamic NMR of anilides with unsymmetrical substitution in the benzene ring demonstrates how a missing static symmetry operation can be replaced by a dynamic symmetry operation and magnetic equivalence is then achieved.

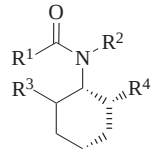

(2)

In ground state anilides of the general type (**2**) the benzene ring is perpendicular to the amide plane. If the ring is symmetrically substituted, the perpendicular plane through the ring is a symmetry plane (a static symmetry element). If both *ortho* substituents are not the same, this symmetry plane is lost, a chiral center is established, and the molecule becomes chiral. This situation was first reported by Adams and his students[4] well before the advent of NMR in chemistry.

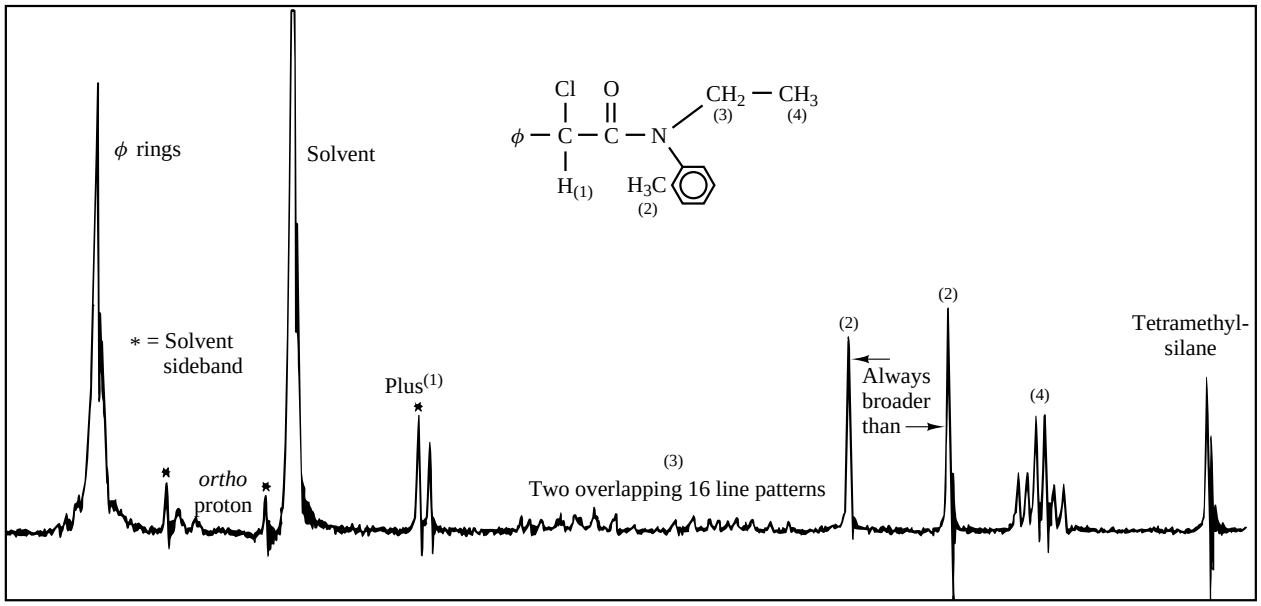

Figure 1 Double proton signals at 40 °C of an anilide dissolved in $CHCl_2CHCl_2$. [Reprinted with permission from Siddall and Stewart, *J. Phys. Chem.*, **73**, 40. Copyright (1969) American Chemical Society]

Rotation around the benzene-to-nitrogen bond is generally slow on the NMR timescale at room temperature, but becomes rapid at elevated temperature. Rapid rotation then becomes a dynamic symmetry operation and substitutes for the lost symmetry plane. (Generally, the *cis*/*trans* isomerism due to slow rotation around the carbonyl-to-nitrogen bond is not observed in anilides of this type except in formanilides. Probably this is due to the predominance of one geometric isomer over the other to the point of excluding the lesser isomer from observation.)

This situation is demonstrated in a striking manner if a second chiral center is introduced into the anilide molecule.[5] With two chiral centers the molecule exists as two diastereoisomers. In the slow exchange limit each of the two isomers exhibits its own set of NMR signals. This in effect doubles the signals in the NMR spectrum as can be seen in Figure 1.

However, raising the temperature increases the rate of rotation around the benzene-to-nitrogen bond and the doubled signal sets coalesce into a single set of signals. The single set is the average over the rapid equilibrium between the two isomers. Rapid rotation has substituted for the lost symmetry plane and leads to magnetic equivalence.

5 ROTATION OF METHYL GROUPS AS A DYNAMIC SYMMETRY OPERATION

The barrier to rotation of methyl groups is typically quite small, 12–13 kJ mol^{-1}. As a consequence, rotation of the methyl group is very rapid on the NMR timescale and is usually not explicitly considered as a dynamic symmetry operation in evaluating symmetry for NMR purposes. However, extreme crowding in 1-*t*-butyl-5,6,7,8-tetrachloro-1,4-dihydronaphthalene 1,4-endoxide (**3**) slows methyl group rotation down sufficiently to be detectable.[6]

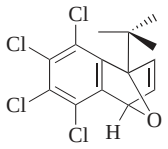

(3)

At room temperature, the *t*-butyl group gave a sharp singlet. At −60 °C, the methyl groups within the *t*-butyl group are nonequivalent and the orginal singlet becomes three sharp singlets. Rotation around the bond to the *t*-butyl group evidently has slowed down. As the temperature was lowered still further to − 121 °C and finally to − 133 °C, two of the three methyl signals broadened almost to the point of decoalescence, while the singlet from the third methyl group remained little changed. Apparently the temperature could not be lowered sufficiently to give the slow exchange spectrum. The authors examined possibilities other than slow methyl rotation as explanations for the broadening, but were able to dismiss these other possible explanations.

6 GEARED ISOPROPYL GROUPS

Rapid rotation of isopropyl groups is usually automatically taken for granted as part of a big background of rapid internal molecular motions that are not singled out as dynamic symmetry operations, since they are rapid on the NMR timescale at accessible temperatures. However, there is considerable evidence that isopropyl rotation can be slow, especially if isopropyl groups are in close enough proximity to each other to interact sterically. This steric interaction apparently can take the form of synchronous rotation. Such isopropyl rotations have been quite aptly labeled as geared rotation[7] or cogwheeling. Furthermore, the rotation of other groups that are adjacent to the geared isopropyl groups can

be slowed because of steric interactions with the isopropyl groups.

In the molecule described below, benzyl group rotation is slowed because of interaction with the isopropyl groups. (The NMR studies were made both with proton NMR and with carbon-13 NMR. The two spectroscopies substantiated each other in detail. This being the case and in the interest of economy in discussion, only the proton behavior is described below.)

The room temperature spectrum[7] of 1,3-dibenzyl-4,5-diisopropyl-2-thione (**4***a*, **4***b*) is just as would be expected. At highest frequency, the benzene ring protons give a multiplet; moving to low frequency, the methylene protons give a singlet, then there is the methine septet, and finally at lowest frequency there is the expected methyl doublet. The static symmetry is C_{2v}. The molecule lies in one plane. The plane perpendicular to the molecular plane makes the isopropyl groups equivalent as whole groups and also the benzyl groups equivalent as whole groups. The molecular symmetry plane makes the protons within a methylene group equivalent and the methyl groups within an isopropyl group equivalent.

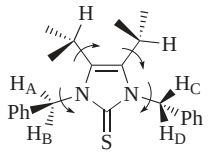

anti
(4*a*)

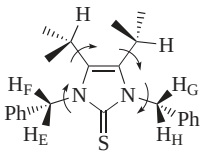

syn
(4*b*)

The spectrum at $-112\,^{\circ}$C is anything but routine. The C_{2v} symmetry is destroyed. There are no longer any symmetry planes nor a C_2 axis. Methylene protons give four separate AB patterns and are clearly diastereotopic. The methine signals have disappeared into baseline noise, but there are four methyl doublets. The increase to four AB patterns definitely shows that there are four different low temperature environments for the methylene groups and eight environments for the methylene protons.

The existence of only four methyl doublets from the isopropyl groups might be unexpected. If there are eight environments for the methylene protons, eight environments would be expected for the methyl groups. This could lead to eight doublets rather than just four. Precise signal overlap to give just four pairs of doublets could be an explanation, but does require an uncomfortable degree of coincidence. However, since no alternative explanation is readily forthcoming, the discussion will be continued, while ignoring this difficulty, which is what the authors of the paper did.

The spectra taken between $-20\,^{\circ}$C and $-90\,^{\circ}$C indicate that more than one rate process is taking place. The process that is observed below $-20\,^{\circ}$C is assigned to the synchronous rotation of the isopropyl groups. At lower temperature, the process of rotation around the bond of one of the benzyl groups is being slowed down. At still lower temperature, the rotation of the other benzyl group is slowing. The $\Delta G^{\ddagger}$ value was calculated to be 48 kJ mol^{-1} at 223.6 K for the isopropyl process, and 45 and 36 kJ mol^{-1} for the two different benzyl rotations.

The process shown below is central to rationalizing the spectral observations. The isopropyl groups, acting as gears, tend to lock into one or the other of two positions. The positions are mirror images of each other. The gears rotate rapidly on the NMR timescale at room temperature. The gears lock and unlock so quickly that the locked positions average out. At about $-20\,^{\circ}$C the lock–unlock rotation slows down to the slow exchange limit as far as the isopropyl rotations are concerned. Meanwhile, the rotamer lifetime of the benzyl groups is still very short, still at rapid exchange. Many benzyl rotations occur during the lifetime of one lock of the isopropyl gears.

As the temperature is lowered still further, first one of the benzyl rotations slows to the slow exchange limit. Finally, at still lower temperature, the other benzyl rotation slows to the slow exchange limit. Once all three of these rotations have slowed enough, the slow exchange NMR spectrum obtains.

In ground states a benzyl rotamer can have two positions. In one position the benzene ring is above the molecular ring plane. In the other position the benzene ring is below that plane. This leads to *syn*/*anti* isomerism, both benzene rings on one side of the ring plane or one benzene ring on one side of the plane and the other on the other side of the plane. In each of the *syn*/*anti* isomers the benzyl groups are in different environments and within each methylene group the protons are in a different environment. Since $2 \times 2 \times 2 = 8$, there are eight proton environments and four AB quartets.

As the temperature is raised from the overall slow exchange limit, each of these dynamic symmetry operations are involved to give finally the fast exchange spectrum, to result in C_{2v} molecular static symmetry, and to give magnetic equivalences consistent with that symmetry.

7 AN AMINE/AMINE HYDROCHLORIDE EQUILIBRIUM WITH AMINE INVERSION

This example[8] is interesting enough that it is included even though it may be a violation of the restriction to intramolecular events as stated in the Introduction. The discussion involves the static symmetry and also molecular inversion as a dynamic symmetry operation.

Nitrogen inversion in simple acyclic amines and with hydrocarbon substituents is usually too rapid to be observed directly by NMR. On the other hand, inversion of the hydrochloride of amines is very slow and magnetic equivalence is dictated by static symmetry alone. However, with an amine/amine hydrochloride equilibrium, nonequivalent protons in the hydrochloride can become equivalent in the amine. The amine in this example is dibenzylmethylamine.

The symmetry plane between the benzyl groups in the amine hydrochloride makes the benzyl radicals equivalent as entire radicals, but there is no static symmetry element that makes the protons of the methylene group magnetically equivalent within a benzyl radical. As a consequence the methylene protons with the methylene groups give an AB quartet. Inversion is much too slow within the hydrochloride to act as a dynamic symmetry operation.

On the other hand, inversion of the amine is rapid and acts as a dynamic symmetry operation to make the methylene protons equivalent. As the pH of the hydrochloride solution is raised, enough amine exists in the equilibrium mixture that the methylene AB quartet coalesces as the methylene protons become equivalent.

Since inversion occurs only during the amine lifetime, and the amine/amine salt equilibrium is fast, the exchange of methylene proton identities is given by k(exchange) = k(inversion) × (amine)/[(salt) + (amine)]. With a pH of 2.5, using the pK_a value of the amine as 7.5 and obtaining k(exchange) from signal shape analysis, the authors were able to calculate the inversion rate of the amine as 2×10^5 s^{-1}. In effect the salt sequestered enough of the amine to make the inversion rate measurable.

8 EXCHANGE IN AN IRON HYDRIDE

Inorganic compounds can be a very rich source for all sorts of NMR studies. The examination of the temperature-dependent proton spectra and ^{31}P spectra of $H_2Fe[P(OC_2H_5)_3]_4$ illustrates this richness.[9] (Of the proton spectra only the hydride part is relevant to the discussion. The spectra of ethyl protons are omitted.)

The compound exists as the *cis* isomer, (**5**), where the Ps represent ligand triethyl phosphite molecules and the Hs the ligand hydrogen atoms. The subscripted numbers will be used in the continued discussion. Because of space limitations, the discussion is drastically curtailed. Readers may wish to consult the original paper.

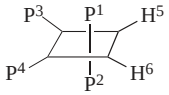

(5)

At 68 °C, the spectrum of the hydride hydrogens is a binomial quintet which indicates that the protons are magnetically equivalent as are the phosphorus atoms. The proton-decoupled phosphorus spectrum is just one singlet which also indicates that the phosphorus atoms are equivalent. It must be that some exchange processes are rapid enough at this temperature to be dynamic symmetry operations that lead to the patterns of magnetic equivalence.

At −50 °C, the magnetic equivalence of the phosphorus atoms has disappeared. The proton-decoupled phosphorus spectrum gives an A_2B_2 pattern which is just what would be expected from C_{2v} symmetry for the *cis* isomer.

The low temperature proton spectrum for the hydride hydrogens is a deceptively simple triplet of doublets which represents an $AA'XX'Y_2$ pattern (A for protons, X and Y for phosphorus). The authors found six different coupling constants which is consistent with such a pattern.

As the temperature is lowered from 68 °C, the three central peaks of the proton quintet broaden, as would be expected if the relevant exchanges were occurring. However, the wing peaks of the quintet remain sharp and unaffected by exchange. This shows that two of the phosphorus atoms remain equivalent as the temperature is lowered. The axial phosphorus atoms are magnetically equivalent and are the Y_2 part of the $AA'XX'Y_2$ spectrum. On the other hand, the equatorial phosphorus atoms are the XX' part of the spectrum and are not magnetically equivalent.

The phosphorus spectra at intermediate temperatures were compared with calculated spectra assuming various phosphorus atom exchange schemes. The only exchange scheme that fits the experimental spectra was to have P^1 exchange with P^3 or P^4 and to have P^2 exchange with P^3 or P^4. Or, in other words, there was axial–equatorial exchange, but no axial–axial or equatorial–equatorial exchange of phosphorus atoms. The observed exchanges are the fundamental dynamic symmetry operations, but without revealing the mechanistic detail as to how they occur.

The authors felt that the complexity of this molecule is appropriate to demonstrate this kind of permutational analysis. Less complex molecules would not exhibit interesting exchange patterns, while more complex molecules might present too much of a computational problem. It should be noted that the development of two-dimensional NMR techniques after this paper was published provides direct instrumental access to revealing which nuclei are exchanging with which nuclei.

9 CHANGE OF SHAPE: POLYHEDRAL EXCHANGE

Four-coordinate nickel compounds often exist in solution as an equilibrium of 'square planar' and 'tetrahedral' isomers. (Generally the square planar complexes are not strictly D_{4h} and the tetrahedral complexes are not strictly T_d, but this distinction in the isomers is common in the literature and is useful. The quotation marks will be dropped in the discussion below.) The square planar isomers are diamagnetic while the tetrahedral isomers are paramagnetic. The paramagnetism in the tetrahedral isomers leads to very large shifts of NMR signals from their normal positions in diamagnetic isomers (or molecules in general). These very large shifts facilitate signal assignment in the slow exchange limit where the signal sets of the two isomers can be seen as two separate sets. It may stretch the definition somewhat, but the conversion between isomers could be called a dynamic symmetry operation. There have been detailed mechanistic proposals as to how the conversion occurs but they will not be discussed here. The components of these mechanisms could be more properly labeled as dynamic symmetry operations rather than the overall conversion.

Unfortunately in most instances the slow exchange limit is evidently below attainable temperatures and the only spectra obtained are the spectra averaged between isomers. The molecule, $[MeP(Ph)_2]_2NiBr_2$, and related molecules, provide fortunate exceptions.[10] At −65 °C, the slow exchange spectrum demonstrates the very large chemical shifts that are induced by paramagnetism. For example, the signal from the *meta* protons in the tetrahedral isomer occurs at almost δ − 30 ppm, while the corresponding signal for the square planar isomer occurs at the normal position for aromatic proton signals.

As the temperature is raised the separate signals begin to coalesce. Finally at 40 °C, the averaged spectrum is obtained and with it, magnetic equivalence. The authors obtained 57 kJ mol^{-1} for $\Delta G^{\ddagger}$.

10 INTERCHANGE OF HYDRIDE HYDROGEN WITH MOLECULAR HYDROGEN AS LIGANDS

The dynamic symmetry operation here is the exchange back and forth, on the one hand, of two hydrogen atoms

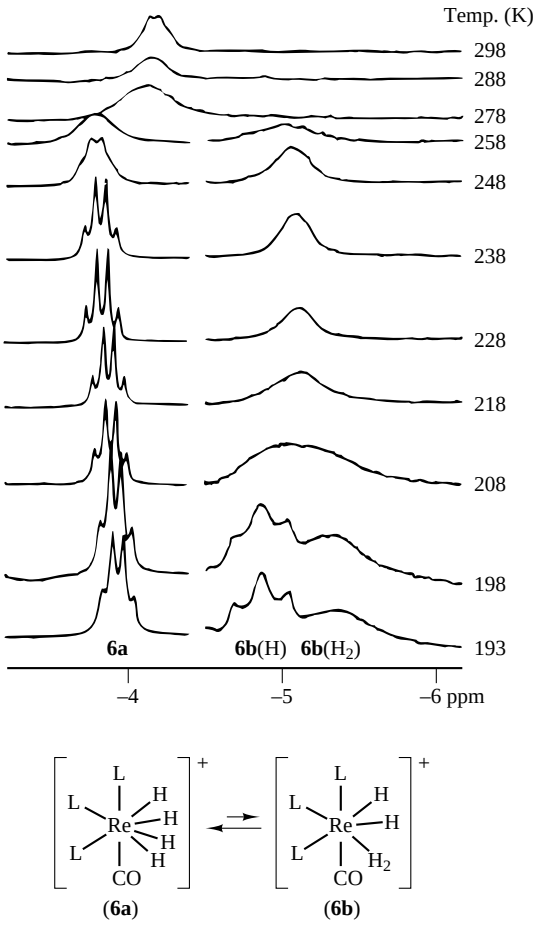

Figure 2 The hydrogen/hydride equilibrium and the hydride region of the 250 MHz spectrum of the ion $[ReH_4(CO)(PMe_2Ph)_3]^+$. (Reproduced with permission from Crabtree, *Acc. Chem. Res.*, 1990, **23**, 95)

as a hydrogen molecule bound as one ligand, with the two hydrogen atoms bound separately as two separate hydride ligands, on the other hand.

This change between molecule and hydride manifests itself in several features of the variable temperature NMR spectra[11] of the ion $[ReH_4(CO)(PMe_2Ph)_3]^+$. The hydride region of the spectra is shown in Figure 2.

At 298 K, the entire hydride spectrum is just one broadened quartet with coupling to the three phosphorus atoms. The fast exchange limit and magnetic equivalence are being approached. As the temperature is lowered, this signal decoalesces quickly to give an AB quartet at high frequency (low field) and to produce an unresolved hump at lower frequency. At the lowest temperature, the low-frequency hump has decoalesced into a somewhat broadened AB quartet and a smaller hump. There must be two rate processes at work.

The higher temperature coalescence depends on the slowing down of the isomer equilibrium. The value of $\Delta G^{\ddagger}$ for the isomerization was found to be 49 kJ mol^{-1} at 213 K. The sharp, high frequency quartet is assigned to isomer (**6a**). In (**6a**) all the hydrogen atoms are bound to the metal as hydride hydrogens and, as a consequence, there is no further change in the spectrum of that isomer as the temperature is lowered. The spectrum of isomer (**6b**) continues to change as the temperature is lowered, which indicates that some dynamic operation is coming into play. The final partial decoalescence of the spectrum of (**6b**) reflects the slowing down of the hydride/molecule interconversion within that isomer. The value of $\Delta G^{\ddagger}$ was found to be 41 kJ mol^{-1}. The interconversion has then played a role twice. This is one interesting example of the role of a dynamic process as occurring more than once in the same molecule. A number of examples have been published of multiple rotations, inversions, and combinations of these and other processes.

An interesting sidelight arises from the above experiment. Generally, 7- and 8-coordinate structures are *fluxional*. Interconversions between competing polyhedra are so rapid that the slow exchange spectrum is not attainable at the lowest temperatures that are available to NMR experiments. In the case discussed above, not only is the slow exchange spectrum of one such structure achieved, but also that of the other, competing polyhedron with a different coordination number. The 7-coordinate structure involves a molecule of hydrogen occupying only one coordination site. The 8-coordinate structure involves two hydrogen atoms, each occupying a coordination site.

11 INVERSION AND ISOMERIZATION IN METAL TRIS(DIKETONATES)

The octahedral complexes in which a metal is bonded to three β-diketone ligands provide instructive examples of the role of symmetry in NMR. ('Octahedral' is at best only approximately octahedral, but the term is used widely when discussing these complexes.) There is a very large amount of literature on this subject, but discussion here is focused on the complexes of (a) symmetrical diketones, $RC(O)CH_2C(O)R$, and (b) unsymmetrical diketones, $RC(O)CH_2^-C(O)R'$, and where a given complex has all three diketones as either (a) or (b).

The static symmetry of the symmetrical complexes (a) is D_3 (and not O_h). The three diketone chelate rings with the metal are all magnetically equivalent as entire rings. The complex is chiral and chirality will be apparent if diastereotopic nuclei or groups of nuclei are included. In practice it has been very useful for both R groups to be isopropyl. With this choice of ligand all the isopropyl groups are magnetically equivalent as entire groups, but the methyl groups within an isopropyl group are nonequivalent. In the slow exchange limit there will be two methyl doublets and the two will become one methyl doublet at the fast exchange limit. The dynamic symmetry operation is inversion of the complex.

The simplest visualization of the actual inversion mechanism is to assume a trigonal prism as the transition state. The transition state molecule could then either fall back into its original ground state geometry or into its enantiomer. While this mechanism has the virtue of simplicity, it is not generally accepted. Instead a dissociative mechanism is preferred. One end of one of the ligands breaks its bond to the metal such that the metal then becomes five-coordinate. The transition state geometry around the metal is supposed to be either a trigonal bipyramid or a square pyramid. The ligand that became unidentate in the transition state reattaches itself either to reform the original ground state or to form its enantiomer. These complexities admittedly stretch the concept of a single dynamic symmetry operation.

Complexes of type (b) can exist as *cis* or *trans* isomers. For the *cis* isomer there is one triangular face defined by three R groups. The vertices of the triangle opposite to this triangle are occupied by R′ groups. The *cis* isomer has C_3 symmetry with the C_3 axis through the centers of the triangles above. As a consequence the three chelate rings are equivalent as entire rings. With R being isopropyl, the methyl groups are diastereotopic. The fast exchange spectrum of the methyl groups in an isopropyl group would consist of one doublet. The slow exchange spectrum would consist of two methyl doublets. Qualitatively the isopropyl spectrum of the *cis* isomer of a type (b) complex would be the same as for a type (a) complex.

On the other hand, the *trans* isomer of a type (b) complex has no static symmetry. The chelate rings are magnetically nonequivalent. With R being isopropyl, there would be six methyl doublets, two from each ring, at the slow exchange limit. However, the fast exchange limit would exhibit only one methyl doublet.

The dynamic symmetry operation for both *cis* and *trans* isomers is inversion. However, *cis* and *trans* isomers do not stand alone, each by itself. A *cis*/*trans* interconversion can also occur at the same time and can be considered as a dynamic symmetry operation. The discrete separation into racemization and isomerization events is considered to be difficult-to-impossible to achieve experimentally. The dissociation mechanism followed by arrangement into a five-coordinate geometry and a return to six-coordinate geometry could accomplish one or the other or both at once.

This complex situation with the tris(chelates) reflects the caveat stated in the Introduction. Straightforward dynamic NMR may reveal permutation patterns but cannot of itself supply mechanistic details.

Two studies of temperature-dependent NMR spectra particularly exemplify the discussion above. In both cases the metal was aluminum. The first[12] involved Al(Isopr(CO)CH(CO)Isopr)$_3$ as type (a). The second[13] study was with Al(PhCH$_2$(CO)CH(CO)Isopr)$_3$ as a type (b) complex. (The formula for the isopropyl group is abbreviated as Isopr and that for the benzene ring as Ph.)

At 37 °C the symmetrical complex, type (a), gives a slow exchange methyl spectrum that consists of two equal intensity doublets. At 120 °C the two doublets coalesce and at 145 °C the fast exchange spectrum as just one doublet is reached. At the lowest temperature isopropyl groups are equivalent as entire groups, but the diastereotopic methyl groups exhibit their nonequivalence as two doublets.

At 93 °C the spectrum of the unsymmetrical complex shows 13 of the expected 16 methyl signals. At 139 °C these doublets coalesce into one broad doublet. Finally, at 156 °C, the one doublet sharpens. The fast exchange limit and magnetic equivalence obtain. There is no clear indication at intermediate temperatures that isomerization and inversion may be occurring as separate events in two well-defined temperature regions. The two dynamic symmetry operations must be very much entangled.

12 SLOW ROTATION AND POSSIBLE RING INVERSION IN A LANTHANUM COMPOUND

As a rule, complexes, molecules, and ions with central metal atoms with coordination number greater than six rearrange so rapidly that the slow exchange limit and spectrum are not attainable. (They are said to be fluxional or *stereochemically nonrigid*.) Analysis indicates that with higher coordination numbers there are a number of competing polyhedra with nearly the same free energy. As a consequence there are one or more low-lying excited states that are readily accessible even at very low temperatures. As a result, magnetic equivalence persists in the variable temperature spectra of such compounds. However, macrocyclic ligands can confer enough rigidity to the structure of the complex species that slow exchange spectra become accessible. An example[14a] is available with the lanthanum(III) complex ion (**7**) with 1,4,7,10-tetrakis(2-carbamoylethyl)-1,4,7,10-tetraazacyclododecane (**8**).

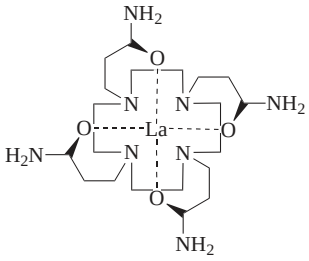

(7)

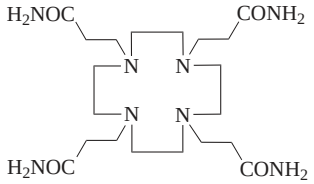

(8)

Ring inversion and rotation around the amide bonds are both dynamic symmetry operations for this complex ion. (The authors do not specifically label the first process as ring inversion, but this seems to be one likely explanation of what is observed. This label is used throughout the rest of the discussion below.) The lanthanum atom is eight-coordinate. It is bound to the octadentate ligand through the four ring nitrogens and the oxygen atoms of the four amide groups. The lanthanum ion lies above the approximate plane of the macrocycle ring. There is a C_4 axis through the lanthanum atom and the center of the ring. Rotation around this axis is the static symmetry operation and it renders the four chelate rings equivalent as entire rings and the four amide groups equivalent as entire groups. The C_4 axis is the only static symmetry element. There is no symmetry plane. Much of the detail of the slow exchange structure of the complex in solution is suggested by the solid state structure of the complex.

The slow exchange disposition of the ring ethylene moieties is very important in rationalizing the slow exchange spectrum. Carbon-13 NMR shows that the carbon atoms within an ethylene moiety are nonequivalent. One carbon atom is closer to the lanthanum atom than is the other. For convenience in discussion, the carbon atoms within each ring ethylene group are described below as head- and tail-ends of the group. Also, the attached hydrogen atoms can be either axial or equatorial. Therefore, there are four environments for the ring ethylene hydrogen atoms. Also the head-and-tail arrangement of the carbon atoms alternates in going around the macrocycle ring. Hence, each of the ring nitrogens is chiral. These nitrogens are bound to four different atoms: (1) the lanthanum atom; (2) a carbamoylethyl carbon atom; (3) a head carbon atom; and (4) a tail carbon atom. The hydrogen atoms are diastereotopic in both the methylene groups of the carbamoyl moieties. Also at the slow exchange limit, rotation around the amide bond in each amide group is slow.

The net result of all this is that the slow exchange spectrum for the protons should consist of two ABCD patterns, one

pattern for the ring hydrogens and one for the methylene hydrogens of the carbamoyl moiety, and finally an AB pattern for the amide nitrogen protons. Five different ^{13}C signals would be expected.

The experimental spectra in the slow exchange limit (0 °C) confirmed these expectations, except that the protons attached to the amide nitrogen atom have a very small or even zero coupling constant to each other. As a consequence, two separate singlets were obtained for these protons rather than the expected AB quartet. Also the spectra for the ring hydrogens and for the hydrogens of the methylene groups of the carbamoyl moiety are so complicated, and with considerable overlap, that it is not easily possible to discern clearly two ABCD patterns. However, the authors did assign parts of these signals to specific protons or groups of protons.

A complete proton spectrum in the fast exchange limit was not given. However, the two amide proton singlets collapsed into one singlet as these protons became magnetically equivalent at 92 °C. Signal shape analysis showed that the activation energy for rotation around the amide bond is 69 kJ mol^{-1}.

The ring carbon atoms coalesced in the ^{13}C spectrum at 29 °C and a barrier of 60 kJ mol^{-1} was obtained. The ring carbons become magnetically equivalent, the head-to-tail difference is lost, and with it the chirality of the ring nitrogens. It would be expected that the loss of the head-to-tail difference and the axial/equatorial distinction between ring protons would lead to a collapse into a singlet for those protons at the fast exchange limit. If on the other hand some dynamic operation other than ring inversion is occurring, and the axial/equatorial difference is preserved, a doublet or possibly an AB quartet would be observed. The loss of chirality should alter the low temperature ABCD pattern of the methylene protons of the carbamoyl moiety to an AA′ BB′ pattern since these protons would no longer be diastereotopic in the chemical shift sense.

NMR studies of the complexes with paramagnetic lanthanides would be interesting, since chemical shift differences would be enhanced and first-order NMR patterns could result with easy analysis of these patterns. The variable temperature spectra of the paramagnetic complexes of the related tetraacetate macrocycle have been reported.[14b] With this macrocycle the situation is further complicated by the coexistence of two isomers of the complexes. However, the expanded chemical shift scales that are obtained tend to compensate for this complication.

13 RING WHIZZING

Cyclopentadiene rings can be bonded to metals in either of two modes. In one mode, the bonding (pentahapto bonding symbolized as η^5 bonding) is to the ring as a whole. In this mode the metal is bonded to the ring as a whole rather than being bonded to one specific carbon atom in the ring (monohapto bonding or η^1). For the pentahapto situation, the protons of the ring are all magnetically equivalent as are the carbon atoms. The monohapto mode gives three sets of nuclei that are not equivalent between the sets. The proton attached to the bonded carbon atom is by itself one set (H_a, shown as A in Figure 3). The two protons in the once removed positions (H_b, shown as B) are the second set and are magnetically equivalent

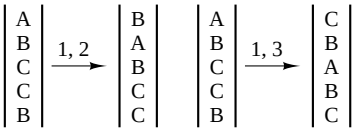

Figure 3 Exchange patterns in a cyclopentadiene ring

to each other. The remaining two protons (H_c, shown as C) form the third set and are equivalent to each other.

In effect, the static symmetry of the monohapto-bonded ring is a symmetry plane perpendicular to the ring, including the bonding site and passing between the carbon atoms of each of the pairs of carbon atoms. The dynamic symmetry operation is the changing of site of the bonded-to-metal carbon atom. This operation is commonly called *ring whizzing*.

From the pentahapto-bonded ring, the proton resonance should just be a sharp singlet at all temperatures. In the fast exchange limit for the protons of the monohapto-bonded ring, rapid change in the bonding site should also lead to a singlet. While in the slow exchange limit (slow change in the bonding site), the magnetically equivalent sets should give signals from each set. In practice the lone proton gives a singlet and the remaining four protons give an AA′BB′ pattern.

The ring complex (η^5-C_5H_5)(η^1-C_5H_5)$Fe(CO)_2$ has a ring of each kind in the molecule and demonstrates this behavior.[15] The results of a variable temperature study are shown in Figure 4.

At 30 °C the fast exchange limit is achieved. The whole proton spectrum consists of just two singlets. The signal at lower frequency is from the pentahapto-bonded ring and the one at higher frequency the signal averaged over all the protons of the monohapto-bonded ring.

The signals at the slow exchange limit are assigned as follows, going from high frequency to low frequency. The multiplet at highest frequency is assigned to the two H_b and the two H_c protons as the expected AA′BB′ pattern. The lower half of this pattern is assigned to the H_b protons and the other half to the H_c protons. This particular part of the overall assignment of proton signals is absolutely crucial to the rationalization of the variable temperature spectra as given below. The singlet at

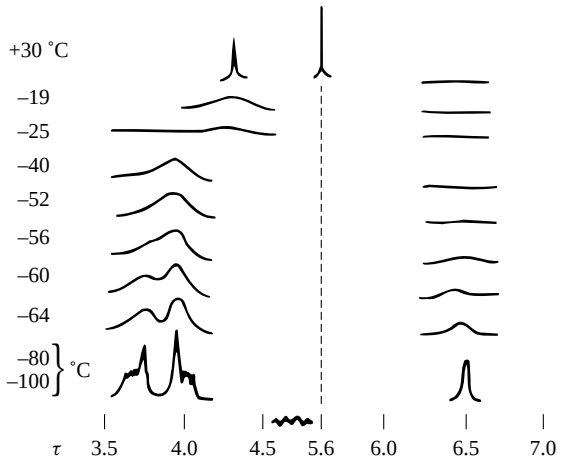

Figure 4 Ring whizzing and its effect on the proton spectrum of (η^5-C_5H_5)(η^1-C_5H_5)$Fe(CO)_2$. (Reproduced with permission from Cotton, *Acc. Chem. Res.*, 1968, **1**, 257)

about 5.6 ppm is from the pentahapto ring protons and remains unaltered throughout the temperature changes. The singlet at about 6.5 ppm is from the lone hydrogen that is attached to the bonding carbon atom.

As the temperature is raised all the signals from the bonded ring broaden, but the high frequency half of the AA′BB′ set broadens more rapidly than the lower frequency half. This shows that exchange of the H_b protons is occurring more rapidly than of the H_c protons. This, in turn, provides the decisive evidence as to how the bonding site shifts around the ring as ring whizzing (or, more elegantly, metal migration around the ring) takes place. The two plausible mechanisms are (1) a 1,2-shift or (2) a 1,3-shift. The exchange (or permutation) patterns that result are shown in Figure 3.

With the 1,2-shift, both H_bs are exchanged in each migration of the iron atom, but only one H_c. For one metal migration, the H_b exchange is twice as fast and the higher-frequency wing of the AA′ BB′ pattern would be expected to broaden twice as fast as the lower-frequency wing when the temperature is increased. On the other hand, with a 1,3-shift, the situation is reversed and the lower-frequency wing should broaden first.

This analysis, overall, is impressive and seems to demonstrate that not only in a general way is ring whizzing the dynamic symmetry operation, but in more detail that the 1,2-shift is the dynamic symmetry operation. A ^{13}C temperature study could make the analysis even more impressive.

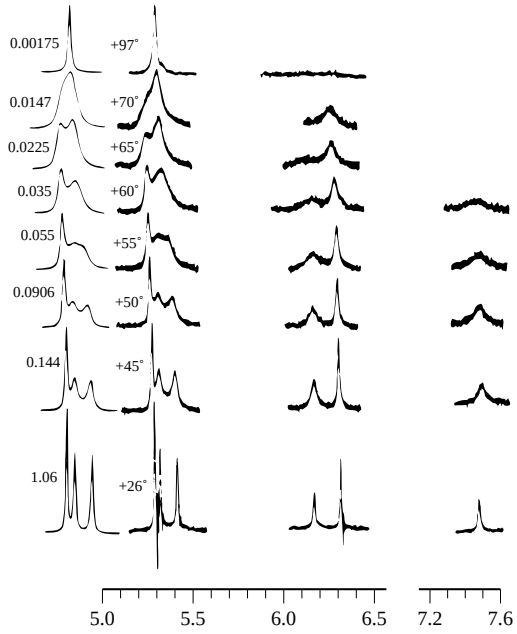

Figure 5 Variable temperature proton spectra of the compound (η^5-$C_5H_5)_2Fe_2(CO)_2(CNCH_3)_2$. [Reprinted with permission from Adams and Cotton, *J. Am. Chem. Soc.*, **95**, 6589. Copyright (1973) American Chemical Society]

14 BRIDGE/TERMINAL EXCHANGE AND ISOMERISM IN A BRIDGED IRON COMPOUND

The compound under discussion could exist as any one or several of the isomers shown below.

cis *trans*

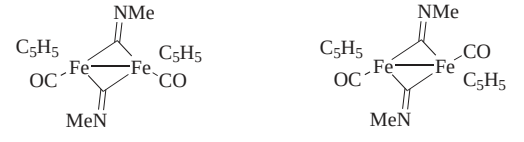

(9) **(10)**

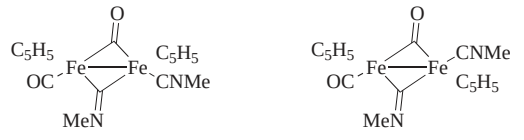

(11) **(12)**

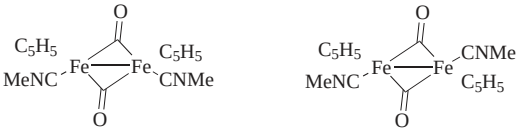

(13) **(14)**

By a combination of infrared and NMR spectroscopy and elegant reasoning, the authors[16] were able to eliminate all possibilities except isomers (**9**) and (**14**). Isomer (**9**) has C_{2v} static symmetry with one $CNCH_3$ group above the plane of the paper and the other below that plane. (The above-the-plane, below-the-plane detail is omitted from the structural formulas.) There is a C_2 axis through the nitrogen atoms. (The dispositions of the CH_3 groups is represented in an arbitrary fashion and does not affect the symmetry.) On the other hand, isomer (**12**) has no static symmetry.

The slow exchange proton spectrum at 26 °C (Figure 5) reflects these symmetry considerations. The static symmetry of isomer (**9**) renders the cyclopentadienyl groups magnetically equivalent within the pair of these groups and does the same for the methyl groups. The signals at 5.33 and 6.37 ppm and with relative intensity 5:3 are assigned to the cyclopentadienyl and methyl groups of isomer (**9**). The set of signals at 5.38, 5.47, 6.23, and 7.48 ppm with relative intensity within the set of 5:5:3:3 are assigned to one cyclopentadienyl group, to the other cyclopentadienyl group, to the bridging $CNCH_3$ group, and to the terminal $CNCH_3$ group, respectively, all for isomer (**12**).

The signals for isomer (**9**) remain relatively sharp as the temperature is raised at first. Meanwhile the signals from isomer (**12**) are noticeably broadened even at 45 °C. At about 60 °C and higher the isomer (**9**) signals also broaden. At 97 °C all the cyclopentadienyl signals coalesce into one sharp singlet and fast exchange is approached. The methyl signals have coalesced, but due to large chemical shift differences have not yet emerged from the baseline.

Two dynamic processes (or symmetry operations) must be taking place. The first, at lower temperature, is the exchange of bridge and terminal cyclopentadienyl and $CNCH_3$ groups within isomer (**12**). The second process, at higher temperature, must be that the isomerization process itself becomes rapid.

15 CONCLUSIONS

Two closely related aspects of NMR, magnetic equivalence and dynamic NMR, have been foci of investigations at least

since the Phillips paper[1] on dimethylformamide. Magnetic equivalence in the slow exchange limit can often be analyzed to reveal the static symmetry of a chemical species or at least to limit the choices of static symmetry. Structural details of species in solution (or even the gas phase) are deducible from static symmetry. Structural determination in whatever phase is always an important goal in chemistry. Structural determination by NMR is now in an advanced state of development.

1. Dynamic NMR can provide two sorts of information. Signal shape analysis can yield rate data in a range of rates that are much too fast to be accessible by classical rate experiments. Signal shape analysis is also now in an advanced state of development.
2. Dynamic NMR can provide information that bears on the mechanisms for various intramolecular motions and rearrangements. Mechanisms are always dear to the hearts of chemists. Mechanism elucidation, aided by dynamic NMR, has been successful in many cases. Nevertheless, this is a *relatively* undeveloped approach to the study of mechanisms.

It seems likely that continued development will depend heavily on an expanding combination of two endeavors. The first of these is the use of two-dimensional NMR (and perhaps, other NMR instrumental techniques) to identify mutually exchanging nuclei. The second is the application of the theory of permutation groups.

16 GENERAL REFERENCES

1. L. M. Jackson and F. A. Cotton (eds.), *Dynamic Nuclear Magnetic Resonance Spectroscopy*, Academic Press, New York, 1975. A major part of this volume bears directly on dynamic symmetry operations that contribute to achieving magnetic equivalence.
2. R. G. Jones, The Use of Symmetry in Nuclear Magnetic Resonance, in *NMR Principles and Progress*, Springer-Verlag, New York, 1969, Vol. 1.
3. J. D. Atwood, *Inorganic and Organometallic Reaction Mechanisms*, Brooks/Cole, Monterey, CA, 1985.
4. F. A. Cotton, *Chemical Applications of Group Theory*, 2nd edn., Wiley, New York, 1971. Generations of American chemists have been introduced to group theory via the editions of this work. The book is directed toward static symmetry (as defined in this article).
5. M. Hammermesh, *Group Theory and its Application to Physical Problems*, Addison-Wesley, Reading, MA, 1962. Chapter 7 provides an introduction to permutation groups. Other chapters introduce continuous groups such as the group of the sphere and also higher groups.
6. I. G. Kaplan, *Symmetry of Many Electron Systems*, English edition published by Academic Press, New York, 1975. Although this book is primarily devoted to electronic problems, Chap. II is an especially useful introduction to permutation groups. There are useful tables in the appendices.
7. K. Vrieze and P. W. N. M. Van Leeuwen, Studies of Dynamic Organometallic Compounds of The Transition Metals by means of Nuclear Magnetic Resonance, in *Prog. Inorg. Chem.*, 1971, **14**, 1.
8. J. W. Emsley, J. Feeney, and L. H. Sutcliffe, *The Effects of Chemical Equilibria and Molecular Conformational Motion on NMR Spectra*, Chap. 9 of 'High Resolution Nuclear Magnetic Resonance Spectroscopy', Pergamon Press, New York, 1965. This chapter provides an excellent review through 1964 of a variety of exchange processes. It is a good starting point for reading on dynamic processes and symmetry.
9. G. N. Lamar, W. DeW. Horrocks, Jr., and R. H. Holm (eds.), *NMR of Paramagnetic Molecules. Principles and Application*, (especially Chaps. 7 and 8), Academic Press, New York, 1973.
10. B. E. Mann, Dynamic NMR Spectroscopy in Inorganic and Organometallic Chemistry in *Annu. Rep. NMR Spectrosc.*, 1982, **12**, 12.
11. S. Szymanski and G. Binsch, Permutation Symmetry in NMR Relaxation and Exchange, in *Annu. Rep. NMR Spectrosc.*, 1991, **23**, 210.
12. Michinori Öki, *Applications of Dynamic NMR Spectroscopy to Organic Chemistry*, published as *Volume 4 of Methods in Stereochemical Analysis*, VCH Publishers, Inc., Deerfield Beach, FL, 1985. This valuable volume is an exhaustive review of the title material over the entire period, 1955–83. It contains over 1000 references. Chapter 1, entitled'General Considerations', is an excellent introduction to dynamic NMR. However, symmetry and group theoretical considerations are not emphasized.

17 RELATED ARTICLES

Aluminum-27 NMR of Solutions; Boron NMR; Chemical Exchange Effects on Spectra; COSY Spectra: Quantitative Analysis; COSY Two-Dimensional Experiments; Coupling Constants Determined by ECOSY; Fluxional Motion; Hydrogen–Metal Systems; Hydrogen Molecules; Inorganic Chemistry Applications; Organic Chemistry Applications; Organometallic Compounds; Phosphorus-31 NMR; Quantitative Measurements; Stereochemistry and Long Range Coupling Constants; Two-Dimensional J-Resolved Spectroscopy; Two-Dimensional Methods of Monitoring Exchange.

18 REFERENCES

1. W. D. Phillips, *J. Chem. Phys.*, 1955, **23**, 1363.
2. L. Pauling, *The Nature of the Chemical Bond*, Cornell University Press, Ithaca, NY, 1944.
3. H. S. Gutowsky and C. H. Holm, *J. Chem. Phys.*, 1956, **25**, 1228.
4. R. Adams, *Record Chem. Prog.*, 1949, **10**, 91.
5. T. H. Siddall, III and W. E. Stewart, *J. Phys. Chem.*, 1969, **73**, 40.
6. H. Nakanishi and O. Yamamoto, *Tetrahedron Lett.*, **1973**, 727.

7. U. Berg and C. Roussel, *J. Am. Chem. Soc.*, 1980, **102**, 7848.
8. M. Saunders and F. Yamada, *J. Am. Chem. Soc*., 1963, **85**, 1882.
9. P. Meakin et al., *J. Am. Chem. Soc.*, 1973, **95**, 75.
10. G. N. La Mar and E. O. Sherman, *J. Am. Chem. Soc.*, 1970, **92**, 2691.
11. R. H. Crabtree, *Acc. Chem. Res*., 1990, **23**, 95.
12. B. Jurado and C. S. Springer, *Chem. Commun.*, **1971**, 85.
13. J. R. Hutchison et al., *Inorg. Chem.*, 1971, **10**, 1004.
14. (a) J. R. Morrow et al., *Inorg. Chem.*, 1993, **32**, 4566; (b) S. Aime et al., *Inorg. Chem.*, 1992, **31**, 4291.
15. F. A. Cotton, *Acc. Chem. Res.*, 1968, **1**, 257.
16. R. D. Adams and F. A. Cotton, *J. Am. Chem. Soc.*, 1973, **95**, 6589.

Biographical Sketch

T. H. Siddall, III. *b* 1922. B.A., 1942, University of North Carolina, M.S., 1948, University of Chicago, Ph.D., 1951, Duke University. G. W. Wheland stimulated interest in molecular rearrangements and intramolecular motions. Atomic Energy Division of DuPont, 1950–69; Professor of Chemistry, University of New Orleans, 1969–89; Professor Emeritus, 1989–present. Approx. 95 publications. Research interests have included a variety of problems in NMR, chemistry, chemical engineering, and physics. Present research interest: application of group theory, especially higher groups, to NMR of higher spin nuclei.

Maximum Entropy Reconstruction

Jeffrey C. Hoch and Alan S. Stern
Rowland Institute for Science, Cambridge, MA, USA

1	Introduction	1
2	Limitations of the DFT	1
3	Spectrum Analysis as an Inverse Problem	2
4	Solving the Inverse Problem Using Maximum Entropy Reconstruction	2
5	Numerical Algorithm	2
6	Analytic Solution	4
7	Example Applications	5
8	Quantification	7
9	Computational Cost	8
10	Concluding Remarks	8
11	Related Articles	8
12	References	8

1 INTRODUCTION

Efficient algorithms for computing the discrete Fourier transform (DFT) served as one of the enabling technologies behind the development of modern NMR spectroscopy.[1] While use of the fast Fourier transform (FFT) was widespread in science and engineering in the 1960s, it was nevertheless a fairly audacious proposal in 1965 to use the FFT to analyze time domain data as an alternative to conventional field or frequency swept experiments, since the marriage of a computer capable of performing the FFT to an NMR spectrometer had yet to be consumated. The implications turned out to be profound, of course, opening the way to the development of multidimensional NMR and magnetic resonance imaging. Yet while providing a crucial capability, the DFT is not without inherent limitations, some of which can be avoided by the use of alternative methods that would have been impractical in 1965, or even as recently as 1990.

2 LIMITATIONS OF THE DFT

The reasons for using the DFT are compelling, beyond even the efficiency of FFT algorithms. Among them are the linearity of the DFT (which simplifies quantification and error analysis and also permits applications such as difference spectroscopy) and the full weight of the theory behind the continuous Fourier transform.[2] A time series can be characterized as a finite sum of periodic functions, given by the inverse DFT

$$d_k = \frac{1}{\sqrt{N}} \sum_{n=0}^{N-1} f_n \mathrm{e}^{2\pi \mathrm{i} kn/N} \qquad (1)$$

where d_k is the value of the time series at time $k\Delta T$, ΔT is the interval between samples, f_n is the coefficient of the Fourier component with frequency $n/N\Delta T$, and N is the number of Fourier components (which is equal to the number of samples in the time series). The Fourier coefficients are computed by the forward DFT

$$f_n = \frac{1}{\sqrt{N}} \sum_{k=0}^{N-1} d_k \mathrm{e}^{-2\pi \mathrm{i} kn/N} \qquad (2)$$

Differences between the DFT and the continuous Fourier transform result from sampling and truncation, in both time and frequency. Sampling in the time domain can introduce artifacts in the spectrum, in which components with frequencies greater than $1/\Delta T$ appear at lower frequencies (aliasing). Truncation in the time domain introduces spurious spread of the components in the spectrum (leakage). Characterization of a time series beyond the sampled interval by means of Fourier coefficients computed from the interval (which is equivalent to estimating the spectrum with a digital resolution higher than $1/N\Delta T$) is correct only for periodic time series, since each Fourier component in equation (1) satisfies $\mathrm{e}^{2\pi \mathrm{i} kn/N} = \mathrm{e}^{2\pi \mathrm{i}(k+N)n/N}$.

Another difficulty associated with the DFT stems from the relationship between the number of data samples and the digital frequency resolution. The term digital frequency resolution is used to refer to the frequency difference between adjacent points in a discrete spectral estimate, and it should be distinguished from the resolution of the spectral estimate, which is a measure of the ability of a spectral estimate to distinguish between closely spaced frequency components. The digital resolution places a lower bound on the resolution of a spectral estimate. The spacing between points in the frequency domain is given by $1/N\Delta T$; therefore, to achieve high digital frequency resolution it is desirable to collect as long a data record as possible. In pulsed NMR experiments, however, the signal of interest usually diminishes with time. Thus collecting long data records to improve resolution rapidly leads to diminishing returns by degrading the signal-to-noise ratio (S/N) of the resulting spectrum. A technique for overcoming this degradation is to collect data for a short period of time and then append zeroes to the end (zero filling). This process also introduces discontinuities into the time series, resulting in leakage. The leakage can be severe if the signal of interest has not decayed sufficiently before the end of the sampled interval. Weighting functions (also referred to as apodization, window, or taper functions) can be applied to the time data, to minimize the extent of leakage by reducing the intensity of the signal near the end of the sampled interval, although this generally incurs an accompanying loss of resolution due to broadening of the spectral components. A virtual zoo of weighting functions exists, each function fulfilling a different goal (leakage reduction, resolution enhancement, sensitivity enhancement) or striking a compromise between various goals.[3] In particular the matched filter (which mimics the decay of the FID envelope), because of its theoretical properties, has long been employed to enhance sensitivity.[4]

One way to extend a time series in a more intelligent fashion than appending zeroes, is to extrapolate using linear prediction. Linear prediction is based on a model in which each value of a time series is assumed to be a linear combination of the preceding values. However, linear prediction is not

always appropriate. It is strictly correct only for exponentially decaying sinusoids, it requires a relatively high S/N, and it is only applicable to time series that have been sampled at uniform intervals. (See ***Fourier Transform and Linear Prediction Methods***.)

3 SPECTRUM ANALYSIS AS AN INVERSE PROBLEM

A more general approach, that avoids the limitations of the DFT and linear prediction, treats spectrum analysis of a time series as an inverse problem. Inverse problems are those in which the properties of interest can only be viewed indirectly. A famous example is Plato's allegory of the cave,[5] in which the problem is to infer the characteristics of an object from the shadows in the firelight it casts on the walls of a cave. In NMR spectrum analysis, the inverse problem can be stated as that of recovering the spectrum f_n of an ensemble of spins, when the only observations we have are the FID at various times (d_k), contaminated by noise (ϵ_k):

$$\hat{d}_k = d_k + \epsilon_k \tag{3}$$

We can approach this inverse problem by placing restrictions on the possible solutions f_n. The first restriction comes from the obvious requirement that f_n must be consistent with the experimental observations. The agreement can be quantified through the use of a constraint statistic that measures how well the reconstructed spectrum agrees with the available data. The statistic is determined by comparing a 'mock' FID, given by the inverse DFT of the reconstructed spectrum, with the actual data. When the noise and experimental error in the measured data are normally distributed, an appropriate statistic is the (unweighted) χ^2 statistic,

$$\chi^2 = \sum_{k=0}^{M-1} |m_k - \hat{d}_k|^2 \tag{4}$$

where M is the number of data samples collected, and m_k is the mock FID. Other forms of the constraint statistic, C, are possible, but χ^2 is the one generally used, because of its simplicity and the difficulty in justifying any other distribution of errors in the data. (A weighted χ^2 statistic can also be used, for example, if there is good reason to believe that some of the data points are more subject to error than others.) Whatever the form of C, the constraint that the reconstructed spectrum must be consistent with the measured data takes the form

$$C \leq C_0 \tag{5}$$

where C_0 is an upper bound on the allowed error. Given a prior estimate of the amount of noise in the data, C_0 should be comparable to the root-mean-square (RMS) noise level.

4 SOLVING THE INVERSE PROBLEM USING MAXIMUM ENTROPY RECONSTRUCTION

The constraint statistic alone does not provide enough of a restriction on the possible reconstructions to be of much use. In fact, any mock FID that matches the experimental FID to within C_0 for the first M points will satisfy the constraint. If we are to improve over the DFT, we need some additional criteria for regularizing the reconstructed spectrum, that will effectively constrain the values of the mock FID beyond M. One such criterion is the maximum entropy principle, which says that a reasonable reconstruction should add no new information beyond that contained in the experimental data. The principle originated in the work of Claude Shannon on the information-carrying capacity of circuits,[6] where he showed that the entropy of a probability distribution p, defined by

$$S(p) = -\sum_n p_n \log p_n \tag{6}$$

is a measure of the lack of information. There is a formal link between Shannon's entropy and the statistical entropy of an ensemble, and this link can be used to provide a constraint on possible spectrum reconstructions. On a more pragmatic level, the maximum entropy principle can be viewed simply as a means of obtaining a smooth, bounded reconstruction. The use of the maximum entropy principle to regularize the possible solutions to the spectrum analysis inverse problem is called maximum entropy (MaxEnt) reconstruction. [Maximum entropy reconstruction should be distinguished from the maximum entropy method (MEM) introduced by Burg,[7] which is more closely related to linear prediction.] Entropy is not unique as a regularizer, however, and there are other functionals that have similar properties.[8]

An important distinction between MaxEnt reconstruction and methods of spectrum analysis (such as those based on linear prediction) that implicitly assume Lorentzian lineshapes, is that MaxEnt reconstruction per se makes no assumptions about the signal to be recovered. Yet it is flexible enough to allow prior information to be incorporated into the reconstruction. A particularly simple means for incorporating prior knowledge is through a convolution kernel. Typical kernels might include exponential decay at some known rate, or J modulation at a known frequency. The reconstruction then yields the *deconvolved* spectrum having the highest entropy.

5 NUMERICAL ALGORITHM

The maximum entropy principle provides a formal basis for reconstructing the spectrum f_n, but some additional details must be addressed in order to apply MaxEnt reconstruction to NMR data. For modern NMR experiments, we need to be able to reconstruct complex spectra containing both positive and negative components. The Shannon formula [equation (6)] clearly does not apply to complex-valued spectra. A more suitable approach is to find the spectrum corresponding to a maximum entropy ensemble of spin-$\frac{1}{2}$ particles.[9] The resulting formula is

$$S(f) = -\sum_{n=0}^{N-1} \frac{|f_n|}{def} \log\left(\frac{|f_n|/def + \sqrt{4 + |f_n|^2/def^2}}{2}\right) - \sqrt{4 + |f_n|^2/def^2} \tag{7}$$

where *def* is a scale factor. The maximum entropy distribution prescribes the value of *def* (it depends on the spectrometer

response and the total number of spins in the sample). However, it is more convenient to treat *def* as an adjustable parameter.

The next detail that we are faced with is how to solve the constrained optimization problem, that is, the problem of maximizing $S(f)$ subject to the constraint that $C \leq C_0$. An equivalent unconstrained optimization problem is to maximize the objective function

$$Q = S - \lambda C \tag{8}$$

where λ is a Lagrange multiplier. The solution we seek corresponds to a critical point of Q, i.e., a point where $\nabla Q = 0$. In the general case there is no analytic solution to this problem, and we are forced to seek numerical solutions. For many problems of this type, a numerical search using the gradient of the objective function (steepest ascent or conjugate gradients) is a reasonably efficient method for finding the critical point. Unfortunately, an objective function constructed from two such dissimilar functionals as the χ^2 statistic and the entropy is quite difficult to maximize. Practical solution of the general MaxEnt reconstruction problem requires a fairly complex optimizer, and the most efficient algorithms require of the order of 100 (or more) times the computational effort of the FFT.

Since the entropy [given by equation (7)] and the constraint statistic [equation (4)] are both everywhere convex, there is a unique, global solution to the constrained optimization problem. Furthermore, this maximum satisfies $C = C_0$ provided that the trivial solution $f_n = 0$ does not also satisfy the constraint.

There have been several algorithms published for computing MaxEnt reconstructions. A particularly robust and efficient algorithm was described by Skilling and Bryan.[10] This method uses multiple search directions and a variable metric to determine the size of the step at each iteration. We describe here a variant we have found useful in our laboratory.

The algorithm begins with a flat trial spectrum equal to zero everywhere. At each iteration, a mock FID is computed from the current value of the trial spectrum. In the general case this involves inverse Fourier transformation and multiplication by a decay kernel, which is specified by the user as an input parameter. A decay does not need to be applied, but when it is, the reconstructed spectrum is an approximation of what would have been observed had the decay not been present. The first M points of the N point mock FID are used to compute the value of C, according to equation (4). The algorithm constructs a small set of direction vectors, and computes a quadratic approximation to the entropy in the subspace spanned by these vectors. Since the constraint is itself quadratic, it is possible to maximize analytically the entropy approximation subject to the constraint in this subspace. This results in the trial spectrum for the next iteration.

The quadratic approximation to the entropy is accurate only for small step sizes, so when the value of C for the mock FID is far from the desired value C_0, it is better to solve the analytic maximization using a constraint value C', intermediate between C_0 and the current value of C, rather than attempt one large step. Consequently the algorithm proceeds in two phases. In the first phase, C is larger than C_0 and the algorithm attempts to lower C. In the second phase, C_0 has been attained and the algorithm seeks to maximize the entropy.

This approach could be based on direction vectors that include ∇S, the gradient of the entropy (with respect to f). The problem is that the gradient can be dominated by small values of f, and the algorithm would spend more time adjusting values that are close to zero than adjusting signal peaks. The key insight of Skilling and Bryan was that the introduction of an 'entropy metric' produces an algorithm that more evenly weights the contributions of large and small values of the spectrum. Using the entropy metric amounts to replacing ∇S and ∇C (the gradient of the constraint with respect to the trial spectrum) with $\mathbf{H}^{-1}\nabla S$ and $\mathbf{H}^{-1}\nabla C$, where $\mathbf{H}$ is $-\nabla^2 S$, the negative of the Hessian (the matrix of second derivatives) of S. The matrix $\mathbf{H}$ is nearly diagonal, so its inverse is easy to compute. The search directions used during the first phase of the algorithm are:

$$\begin{aligned} &\nabla C \\ &\mathbf{H}^{-1}\nabla C \\ &\mathbf{H}^{-1}\nabla Q \\ &\mathbf{H}^{-1}(\nabla^2 C)\mathbf{H}^{-1}\nabla Q \\ &Q = S - \lambda C \end{aligned} \tag{9}$$

and λ is set to $|\nabla S|/|\nabla C|$. During the second phase, the second search direction is replaced by ∇Q. In the original algorithm of Skilling and Bryan, neither ∇C nor ∇Q are used as search directions. We found that including them speeds convergence. The major effort in computing these vectors stems from four discrete Fourier transformations (two each to compute ∇C and to apply $\nabla^2 C$) and multiplication by $\mathbf{H}^{-1}$.

With these direction vectors, a quadratic model for the entropy and the constraint can be constructed using a second-order Taylor expansion about the trial spectrum. A spectrum f' in the subspace spanned by the direction vectors can be represented by a vector of length four, $\bar{a}$; the correspondence is given by

$$f' = a_1 v_1 + a_2 v_2 + a_3 v_3 + a_4 v_4 + f_0 \tag{10}$$

where v_1 through v_4 are the direction vectors and f_0 is the current trial spectrum. The quadratic approximations then become

$$S(\bar{a}) \approx S(\ f_0) + \bar{B} \cdot \bar{a} + \tfrac{1}{2}\bar{a} \cdot \mathbf{M} \cdot \bar{a} \tag{11a}$$

and

$$C(\bar{a}) \approx C(\ f_0) + \bar{G} \cdot \bar{a} + \tfrac{1}{2}\bar{a} \cdot \mathbf{N} \cdot \bar{a} \tag{11b}$$

where vectors $\overline{B}$ and $\overline{G}$ are inner products of ∇C and ∇S with the direction vectors

$$\bar{B}_i = \nabla S \cdot v_i \tag{12a}$$

$$\bar{G}_i = \nabla C \cdot v_i \tag{12b}$$

Similarly, the 4×4 matrices $\mathbf{M}$ and $\mathbf{N}$ are the inner products of $\nabla^2 S$ and $\nabla^2 C$ with the direction vectors:

$$M_{ij} = v_i \cdot \nabla^2 S \cdot v_j \tag{13a}$$

$$N_{ij} = v_i \cdot \nabla^2 C \cdot v_j \tag{13b}$$

Computing these values requires several more Fourier transformations and large matrix products. The Lagrange condition $\nabla S - \lambda \nabla C = 0$ for the maximum of the objective function in the subspace becomes

$$(\bar{B} + \mathbf{M} \cdot \bar{a}) - \lambda(\bar{G} + \mathbf{N} \cdot \bar{a}) = \bar{0} \tag{14}$$

By a suitable change of coordinates in the subspace it is possible to simplify this equation by simultaneously diagonalizing **M** and **N**. The solution then is given by

$$a_i = \frac{B_i - \lambda G_i}{\lambda N_{ii} - M_{ii}} \tag{15}$$

λ can be found by using a binary search to determine the value for which $C(\bar{a})$ equals the target value C'.

Convergence criteria for determining when the trial spectrum is sufficiently close to the MaxEnt reconstruction derive from the Lagrange condition and the requirement that $C \approx C_0$. The Lagrange condition implies that ∇C and ∇S are parallel, so convergence can be monitored by computing the value

$$Test = \left| \frac{\nabla S}{|\nabla S|} - \frac{\nabla C}{|\nabla C|} \right| \tag{16}$$

The algorithm terminates when $C \approx C_0$ and $Test \ll 1$. In practice, we stop the algorithm when $Test < 10^{-3}$, or when a preset maximum number of iterations has been executed.

The value of C_0 can be estimated from the data by examining a portion of an FID that is essentially free of signal, or alternatively, by examining a signal-free region of the DFT spectrum. For MaxEnt reconstructions, C_0 should generally be somewhat larger than the estimate of the RMS noise level. Very large values of C_0 result in overly smooth reconstructions in which weaker components are washed out.

The other adjustable parameter, *def*, is rather more difficult to prescribe. *def* represents the scale at which the nonlinear effects of MaxEnt reconstruction become significant. A large value of *def* results in nearly linear reconstructions. When *def* is large and C_0 is zero, the resulting reconstruction is essentially the same as the DFT of the zero-filled FID. However, very low values of *def* can give rise to spurious artifacts. As a rule of thumb, we use values of *def* somewhat lower than the noise level. Fortunately, the results are not overly sensitive to the choice of *def*. We know of no algorithmic procedure for determining the best value.

6 ANALYTIC SOLUTION

While numerical solution is required in the general case, there is a special case of MaxEnt reconstruction that has an analytical solution. Though unrealistic in several respects, examination of this special case can give some insights into how MaxEnt reconstruction works. When N (the number of points in the reconstructed spectrum) is equal to M (the number of experimental data points), and when the relationship between the trial spectrum and the mock FID is given simply by the inverse Fourier transform (i.e. we are not trying to deconvolve a decay), the solution can be found analytically. Parseval's theorem, which states that the sum of the squared magnitudes of a vector is equal to the sum of the squared magnitudes of its Fourier coefficients, permits the constraint statistic to be computed in the frequency domain. Under these circumstances the Lagrange condition becomes

$$0 = \nabla Q = \nabla S - 2\lambda(f - F) \tag{17}$$

where F is the DFT of the data $\hat{d}$. The solution is given by

$$|f_n| = \delta_\lambda^{-1}(|F_n|) \tag{18a}$$

$$\text{phase}(f_n) = \text{phase}(F_n) \tag{18b}$$

where δ_λ is the function

$$\delta_\lambda(x) = x - s'(x)/2\lambda \tag{19}$$

and $s(x)$ is the contribution of a spectral component with magnitude x to the overall entropy S [see equation (7)]. This result corresponds to a nonlinear transformation, applied point by point to the DFT of the time domain data. The transformation depends on the value of λ, and has the effect of scaling every point in the spectrum down, but points closer to the baseline are scaled down more than points far above the baseline. Figure 1 illustrates $\delta_\lambda^{-1}(x)$ for various values of λ. As λ increases, the relative weight given to the constraint term in the objective function increases, and the transformation becomes more nearly linear.

This helps to explain the characteristic of MaxEnt reconstructions that noise near the baseline is suppressed more than noise away from the baseline (for example, superimposed on a broad peak). A further point to note is that there is a very important distinction between S/N and sensitivity. Sensitivity is the ability to distinguish signal from noise. Applying the same transformation to both the signal and the noise cannot improve this ability, since peaks that are comparable in height to the noise level will be reduced by the same amount as the noise. The ratio between the highest signal peaks and the noise

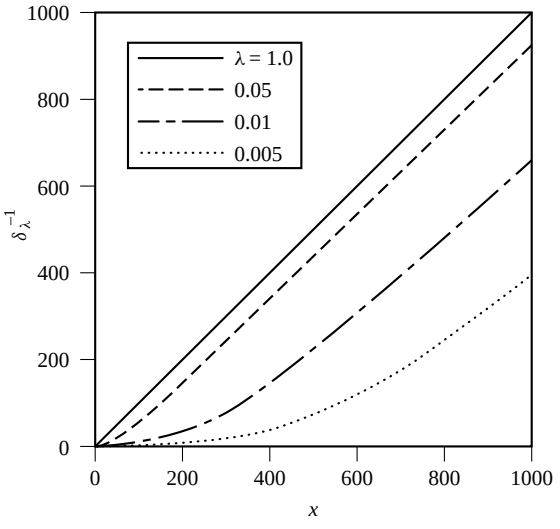

Figure 1 The nonlinear transformation $\delta_\lambda{}^{-1}(x)$ applied to the DFT spectrum that results in the MaxEnt reconstruction when $N = M$, for various values of the Lagrange multiplier λ

may increase, but small peaks will be just as difficult to distinguish as before. For linear operations (such as apodization), an improvement in S/N necessarily implies an improvement in sensitivity; for nonlinear operations (such as MaxEnt reconstruction) this is not so. In this special case, gains in S/N in the MaxEnt reconstruction are purely cosmetic. In the more general case, for example when an approximately known decay is deconvolved from the reconstructed spectrum, there may be real sensitivity gains. However, a prudent investigator will always question whether gains in S/N really correspond to gains in sensitivity.[11]

7 EXAMPLE APPLICATIONS

Armed with an efficient optimizer, the Cambridge Maximum Entropy group and their collaborators performed the earliest applications of MaxEnt reconstruction to NMR.[12] Properties of MaxEnt reconstruction depend on both the data and the parameters of the reconstruction, such as the decay kernel, and so are best illustrated by examples using typical NMR data. In addition to providing a concrete means of exploring the use of MaxEnt reconstruction for improving resolution or enhancing sensitivity, they provide a means of comparing the performance of alternate methods.

7.1 One-Dimensional

7.1.1 Resolution

Figure 2 illustrates the methyl and aliphatic region of spectra obtained for a sample of 20 mM L-Ala-L-Pro in D_2O at pD 6.0 and 25°C. Data consisting of 1024 complex points were collected at 400 MHz on a JEOL GX-400 spectrometer. Shown are the zero-filled (to 8192 points) DFT spectrum without (a) and with (b) windowing (60°-shifted sine-bell). Figure 2(c) is the DFT spectrum obtained by extrapolating from 1024 points to 8192 with linear prediction, using a filter order of 60 and reflecting roots of the characteristic polynomial that fall outside the unit circle to the inside. Figure 2(d) illustrates the MaxEnt reconstruction, computed using 1.0 for C_0 and 0.1 for *def*. All parts of Figure 2 are plotted using the same scale. The region near the methyl peaks (around 1.55 ppm, arising from both the *cis* and *trans* forms of the peptide bond) shows the artifacts due to truncation. Windowing the FID ameliorates the artifacts, at the expense of lower resolution due to broadening. More aggressive resolution enhancement (for example a 30°-shifted sine-bell) improves the resolution at the expense of more pronounced negative 'wings' surrounding the methyl peaks. Extrapolation by linear prediction [Figure 2(c)] dampens the artifacts somewhat; further reduction could be obtained by windowing the extrapolated FID. The MaxEnt reconstruction [Figure 2(d)] is virtually free of artifacts and has narrow lines; further line narrowing could be achieved by deconvolving the natural linewidth.

7.1.2 Signal-To-Noise Ratio

Figure 3 illustrates gains in S/N that can be achieved using MaxEnt reconstruction. Figure 3(a) contains the aliphatic

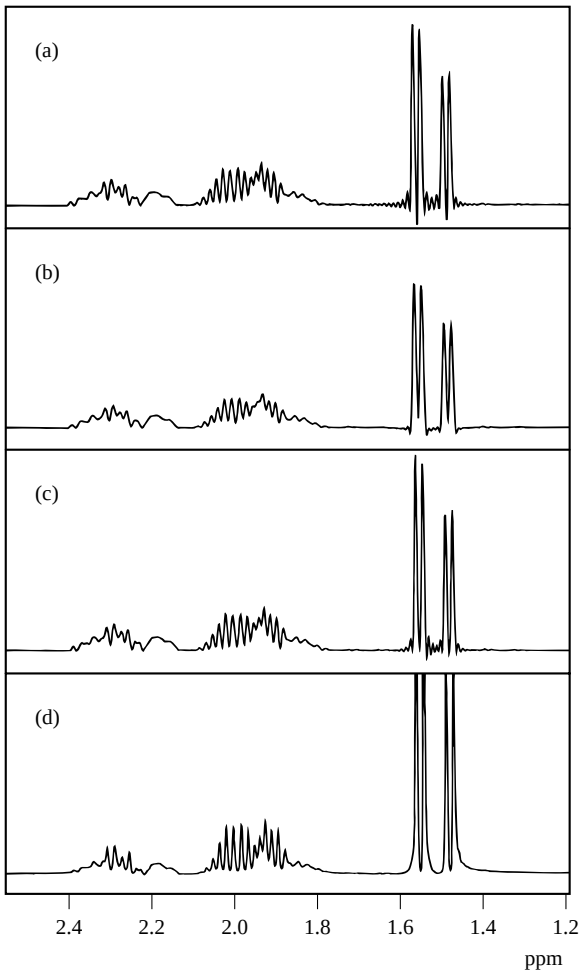

Figure 2 Aliphatic region of the ^1H spectrum of L-Ala-L-Pro, from 1024-point data: (a) zero filled to 8192 and Fourier transformed; (b) zero filled, apodized using a 60°-shifted sine-bell and Fourier transformed; (c) extrapolated to 8192 points using linear prediction and Fourier transformed; (d) MaxEnt reconstruction

region of the DFT spectrum for a sample of 0.1% ethylbenzene in deuterochloroform, using a single 90° observe pulse; 1024 complex points were zero-filled to 4096 and windowed using a 60°-shifted sine-bell prior to Fourier transformation. Figure 3(b) shows the DFT spectrum of data collected using a 7° observe pulse, and processed as in Figure 3(a). Figure 3(c) shows the MaxEnt reconstruction obtained using 2.8 for C_0 and 0.01 for *def*; no decay was deconvolved. Although striking, the improvement in S/N does not necessarily correspond to a real gain in sensitivity, as discussed earlier. Note that the multiplet structure of the peak near 3.25 ppm is not much more evident in (c) than in (b).

7.1.3 Robustness

A characteristic of MaxEnt reconstruction that distinguishes it from parametric methods, such as linear prediction, is that it makes no implicit assumptions about the nature of the data (although using MaxEnt reconstruction to perform deconvolution does presume the convolution kernel to be correct). Linear prediction, however, is strictly correct only for exponentially decaying sinusoids. MaxEnt is thus less

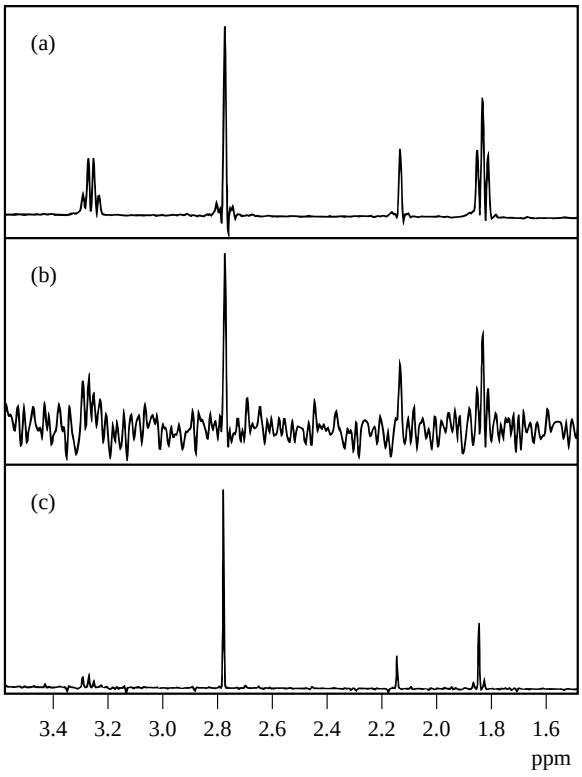

Figure 3 Aliphatic region of the ^{1}H spectrum of ethylbenzene: (a) obtained using a 90° observe pulse; (b) obtained using a 7° observe pulse followed by 60°-shifted sine-bell apodization, zero filling, and Fourier transformation; (c) obtained using a 7° observe pulse followed by MaxEnt reconstruction

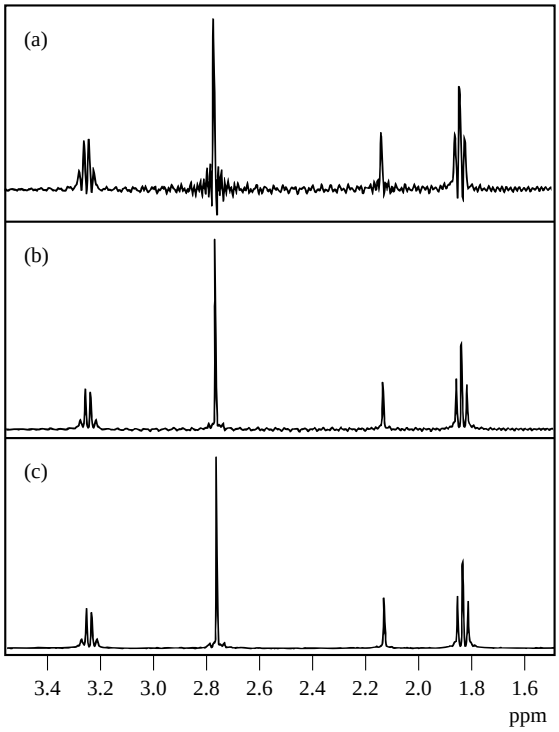

Figure 4 Spectra computed from data corrupted at two interior stretches of the FID using: (a) Fourier transformation, (b) MaxEnt reconstruction utilizing the entire data set, and (c) MaxEnt reconstruction excluding the corrupted data points

susceptible to bias when the signal has unusual characteristics such as markedly nonexponential decay, when the S/N is low, or when the data have been corrupted. It is quite common for points at the begining of a FID to be corrupted, which can result in distorted baselines. In these circumstances, backwards linear prediction can be used to correct the corrupted points. However, if the corrupted data points are in the middle of a FID, or distributed in some unusual fashion throughout the FID, linear prediction is less useful. MaxEnt reconstruction, however, does not require the data to be sampled at uniformly spaced intervals, and so can be applied quite easily to data that are corrupted in an irregular fashion. It is our own sad experience that points in the indirect dimensions of long multidimensional experiments are occasionally contaminated by intermittent instrument failure or environmental influences. Maximum entropy reconstruction provides a means of recovering useful spectra from such data.

To demonstrate the possibilities, we consider a contrived example, constructed by manually corrupting the one-dimensional FID used to generate Figure 3(a). The complex 1024-point FID was corrupted by setting to zero the real and imaginary parts of the points from 350 to 359 and 750 to 759. Figure 4(a) shows the DFT spectrum of the corrupted FID, zero-filled to 4096 points. Figure 4(b) and (c) are 4096-point MaxEnt reconstructions, using 1.0 for C_0 and 0.1 for *def*, and without deconvolving a decay. In Figure 4(b) all 1024 points of the FID were included in the computation of χ^2, while in Figure 4(c) the corrupted points were left out. Figure 4(b) illustrates that MaxEnt reconstruction is much more robust to data contamination than the DFT. Figure 4(c) shows the flexibility of MaxEnt reconstruction for treating data corrupted at arbitrary locations when the points of corruption are known.

7.2 Multidimensional

Maximum entropy reconstruction can also be applied to multidimensional data, and it is here that the ability to obtain high-resolution spectra from short data records offers the most significant benefits. Since the data collection time increases linearly with the amount of data collected in indirect dimensions of a multidimensional data set, resolution in these dimensions is often limited by practical considerations of the amount of experiment time available. An advantage of MaxEnt reconstruction over linear prediction for ameliorating those constraints is that the data samples need not be collected at uniform intervals, allowing data collection to be tailored to the type of experiment, sampling more frequently when the S/N is high and hence making more efficient use of available measuring time.

There are a number of ways MaxEnt reconstruction can be extended to multiple dimensions. The most general is simply to compute the entropy of the entire spectrum. As a practical matter, however, this can present a formidable computational challenge for large data sets, since each iteration of the reconstruction algorithm requires several transformations from the time to the frequency domain (and back). An alternative that is far less demanding is to apply MaxEnt reconstruction to each FID in one dimension independently. With this approach, MaxEnt reconstructions of large multidimensional data sets

can be performed efficiently on typical workstations. With a small modification to the algorithm, this approach using a series of one-dimensional reconstructions yields results that are nearly equivalent to the more general multidimensional reconstruction.

In one-dimensional MaxEnt reconstruction, one seeks the local maximum of the objective function for which $C = C_0$. This occurs for a specific value of λ. When computing MaxEnt reconstruction for the rows of a multidimensional data set, normal variations in the noise and the signal can result in different values of λ for each row. The consequences of this variation are often insignificant, but they can be important if they are large enough to perturb the lineshapes, or if quantification of the reconstructed spectrum is performed. Since the nonlinearity of MaxEnt reconstruction depends on the relative weights applied to the entropy and the constraint statistic, it is important to ensure that the same weight (value of λ) applies to each row. This is relatively easy to accomplish by choosing a typical row, estimating the noise, and computing a normal one-dimensional MaxEnt reconstruction. For the multidimensional data set, each row is then reconstructed using the value of λ obtained from the reconstruction of the trial row, instead of iterating to achieve $C = C_0$.

While the resolution of a spectrum determined by MaxEnt reconstruction is mainly determined by the time of the last data sample (as for the DFT), higher sensitivity for the same number of measurements can be achieved by tailoring the sampling schedule to the expected signal.[13–15] The optimal schedule depends on whether the signal is an exponentially damped sinusoid, is cosine modulated, or is stationary (such as that in a constant time experiment).

Figure 5 shows the methyl region of the two-dimensional ^{1}H–^{13}C HMQC spectra for a 10 mM sample of the 16-residue peptide α_1B in D_2O at pH 5.0 and 25°C, obtained with natural abundance of ^{13}C at 9.4 T. The data used to compute the spectra in (a) and (b) consisted of 1024 complex points in the ^{1}H dimension (t_2) and 128 complex points in the ^{13}C dimension (t_1). The spectrum in Figure 5(a) was computed by windowing with a 30°-shifted sine-bell, and zero filling to 2048 complex points prior to Fourier transformation in t_2, followed by linear prediction using a filter order of 10 to extrapolate the data to 512 points in t_1, windowing using a 45°-shifted sine-bell, zero filling to 1024 points and Fourier transformation. The data used to compute the spectrum in Figure 5(b) were obtained similarly to the data for (a) in t_2, but exponential sampling using an effective decay time of 30 ms was used to collect 128 complex points, selected from a linear schedule of 512 points. Processing in t_2 was performed as before, but MaxEnt reconstruction was performed in t_1, with values of 10 for *def* and 0.0554 for λ, and deconvolving a 20 Hz linewidth kernel. The data for Figure 5(c) consisted of 64 points exponentially sampled from a linear schedule of 256 points; the spectrum was computed as in (b). Comparison of (a) and (b) shows that nonlinear sampling in conjunction with MaxEnt reconstruction yields higher resolution than is achieved using conventional data acquisition and processing. In particular, the couplings between the leucine methyl protons and the γ proton are more clearly evident in (b). Comparison of (a) and (c) shows that exponential sampling can also be used to obtain resolution comparable to or better than conventional methods using less data. For long multidimensional experiments, even a reduction by a factor of 2 in experiment time can be significant.

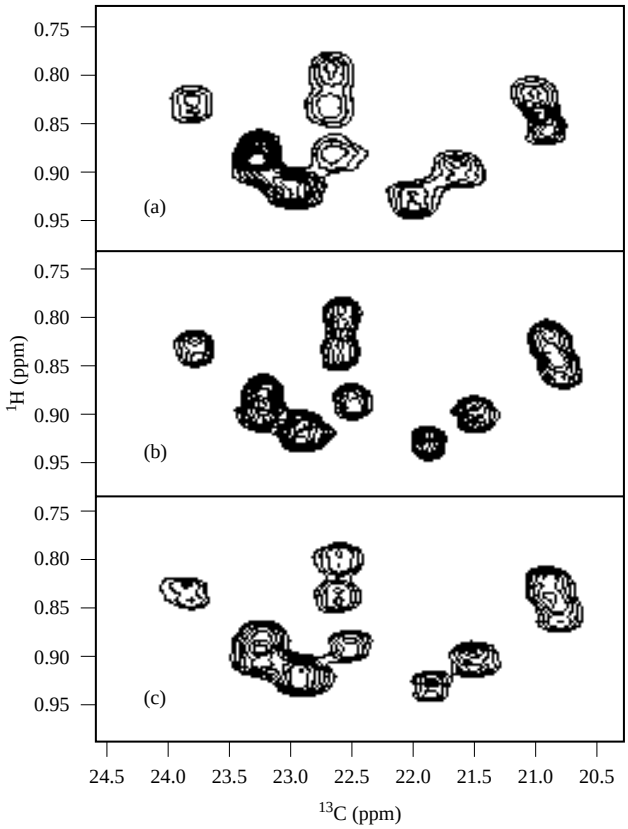

Figure 5 Methyl region of the ^{1}H–^{13}C HMQC spectra of α_1B: (a) computed from 128-point (in t_1) conventionally acquired data using linear prediction, extrapolation, windowing, and Fourier transformation, (b) using MaxEnt reconstruction of 128-point exponentially sampled t_1 data, and (c) using MaxEnt reconstruction of 64-point exponentially sampled t_1 data

7.3 Deconvolution

MaxEnt reconstruction can also be used to deconvolve an arbitrary modulation. One application is to deconvolve J modulation. Figure 6 shows the same region of the HMQC spectrum of α_1B as Figure 5, but MaxEnt reconstruction has been used in the ^{1}H dimension to deconvolve the 7 Hz coupling. This method is equally applicable to spectra exhibiting antiphase modulation; however, it is only capable of deconvolving a single, fixed modulation frequency.

8 QUANTIFICATION

The nonlinearity of MaxEnt reconstruction is an inherent characteristic, and is responsible for the method's ability to achieve noise suppression without sacrificing resolution to the extent associated with linear filtering (such as the windowed DFT). This nonlinearity has important implications in situations where quantification of peak intensities or volumes is required, such as nuclear Overhauser effect measurements or difference spectroscopy. For difference spectroscopy, it may be sufficient to compute the difference using the time domain data and compute the MaxEnt reconstruction of the difference. This assures that the same

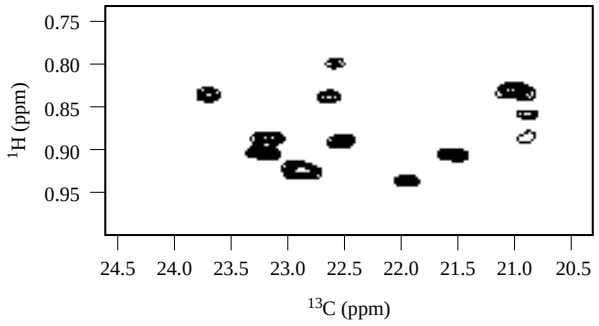

Figure 6 Methyl region of the ^{1}H–^{13}C HMQC spectrum of α_1B, with 7 Hz J modulation deconvolved in the ^{1}H dimension using MaxEnt reconstruction

nonlinearity applies to both experiments. When measuring nuclear Overhauser effects, or otherwise quantifying peak intensities, there are two possible approaches. One is to constrain tightly the reconstruction to match the data, which forces the reconstruction to be more nearly linear (although at the expense of noise suppression). Another is to inject synthetic signals of known relative intensity into the time domain data prior to reconstruction. A calibration curve can then be constructed by quantifying the intensities of the known signals.

The nonlinear nature of MaxEnt reconstruction also renders the S/N a poor estimate of sensitivity. Sensitivity estimates are perhaps best obtained by adding signals of known intensity to the data prior to reconstruction.

9 COMPUTATIONAL COST

The computational cost of MaxEnt reconstruction for one-dimensional spectra is typically 2 orders of magnitude greater than the cost of computing an FFT. For large, multidimensional reconstructions, the elapsed time is dominated by memory requirements, rather than the number of computations: the algorithm described above requires of the order of 16 times the size of the reconstructed spectrum for intermediate storage. While row-wise reconstruction can be used to ameliorate this requirement, fully multidimensional MaxEnt reconstructions remain the province of supercomputer-class machines with large amounts of high-speed random-access memory.

10 CONCLUDING REMARKS

Maximum entropy reconstruction is a powerful method for computing spectral estimates from time domain NMR data that avoids some of the limitations inherent in the discrete Fourier transform. It is more general than parametric methods, such as those based on linear prediction, that are restricted to Lorentzian signals, yet is capable of incorporating prior knowledge about the signal when it is available. The computational cost, while significantly greater than the FFT, is in a range that is practical on modern workstations, even for large data sets. Some of the power of the method stems from its nonlinearity, which dictates that the method must be used cautiously. Its ability to use nonlinearly sampled data provides a powerful tool for improving the resolution and sensitivity of multidimensional experiments. Used prudently, MaxEnt reconstruction can extend the limits of sensitivity and resolution in NMR, simplify analysis, and enable the study of larger molecules and molecules at lower concentrations than is feasible using the DFT.

11 RELATED ARTICLES

Data Processing; Fourier Transform and Linear Prediction Methods; Fourier Transform Spectroscopy.

12 REFERENCES

1. R. R. Ernst, in *Computational Aspects of the Study of Biological Macromolecules by Nuclear Magnetic Resonance Spectroscopy*, eds. J. C. Hoch et al., Plenum, New York, 1991.
2. E. O. Brigham, *The Fast Fourier Transform*, Prentice-Hall, Englewood Cliffs, NJ, 1974.
3. R. R. Ernst, G. Bodenhausen, and A. Wokaun, *Principles of Nuclear Magnetic Resonance in One and Two Dimensions*, Clarendon, Oxford, 1987.
4. R. R. Ernst, *Adv. Magn. Reson.*, 1966, **2**, 1.
5. Plato, *Republic*, Hacket, Indianapolis.
6. C. E. Shannon, *Bell Syst. Tech. J.*, 1948, **27**, 379.
7. J. P. Burg, in *Modern Spectrum Analysis*, ed. D. G. Childers, IEEE Press, New York, 1978.
8. D. L. Donoho, I. A. Johnstone, J. C. Hoch, and A. S. Stern, *Proc. R. Stat. Soc. B*, 1992, **54**, 41.
9. J. A. Jones and P. J. Hore, *J. Magn. Reson.*, 1991, **92**, 276.
10. J. Skilling and R. Bryan, *Mon. Not. R. Astron. Soc.*, 1984, **211**, 111.
11. D. L. Donoho, I. A. Johnstone, and A. S. Stern, *Proc. Natl. Acad. Sci. USA*, 1990, **87**, 5066.
12. S. Sibisi, J. Skilling, R. Brereton, E. Laue, and J. Staunton, *Nature (London)*, 1984, **311**, 446.
13. J. C. J. Barna, E. D. Laue, M. R. Mayger, J. Skilling, and S. J. P. Worrall, *J. Magn. Reson.*, 1987, **73**, 69.
14. M. Robin, M.-A. Delsuc, E. Guittet, and J.-Y. Lallemand, *J. Magn. Reson.*, 1991, **92**, 645.
15. P. Schmieder, A. S. Stern, G. Wagner, and J. C. Hoch, *J. Biol. NMR*, 1993, **3**, 569.

Acknowledgments

We are grateful to David Donoho, Ian Johnstone, Peter Schmieder, Gerhard Wagner, and Peter Connolly for many stimulating discussions and continuing fruitful collaborations on aspects of maximum entropy reconstruction in NMR. We also thank John Osterhout and Marcela Oslin for providing the sample of α_1B, and George Maalouf and Peter Connolly for collecting NMR data.

Biographical Sketches

Jeffrey C. Hoch. *b* 1954. A.B. Boston University, 1976; A.M. Harvard, 1978; Ph.D. Harvard, 1983. Introduced to NMR by M. Karplus and C. M. Dobson. Member of Rowland since founding in 1981. Approx. 30 publications. Director of NATO Workshop ‘Computational Aspects of

the Study of Biological Macromolecules by NMR Spectroscopy', and editor with C. Redfield and F. M. Poulsen of the published proceedings. Research interests include NMR data processing, analysis, and protein structure determination.

Alan S. Stern. *b* 1958. A. B. Harvard, 1979; Ph.D. U.C. Berkeley, 1984. Member of Rowland since 1988. Approx. 15 publications. Research interests include signal processing and mathematical logic.

Microprobes and Methodologies for Spectral Assignments: Applications

Gary E. Martin

Global Pharmaceutical Sciences, Pharmacia Corporation, Kalamazoo, MI, USA

1	Introduction	1
2	High Sensitivity, Small Volume Probe Performance Comparisons	6
3	Applications of Small Volume NMR Probes in the Solution of Chemical Structure Problems	9
4	Conclusions	12
5	References	12

1 INTRODUCTION

Nuclear magnetic resonance or NMR has become the cornerstone of modern chemical structure elucidation. The technique is unparalleled in its ability to determine chemical structures by tracking atom-to-atom connectivity. Experiments are now available that allow one to determine homonuclear (^{1}H–^{1}H and ^{13}C–^{13}C) and heteronuclear (^{1}H–X where X = ^{13}C, ^{15}N, ^{19}F and ^{31}P among other heteronuclear pairs) connectivity information that is invaluable in assembling unknown chemical structures. Despite the considerable power of NMR methods, the technique unfortunately suffers from inherently low sensitivity when compared to other analytical spectroscopic methods such as mass spectrometry. This rather stringent limitation has prompted very considerable effort in the development of small volume, high sensitivity NMR probe designs. In part, these efforts have been necessary as it is not always possible to isolate additional sample for analysis.

The earliest detailed description of NMR spectroscopy using small rf coils that the author is aware of is found in the work of Odelblad in 1966.[1] In this study, solenoidal microcoils were used in conjunction with continuous wave (CW) NMR methods to study human cervical mucous secretions. The study examined ^{1}H chemical shifts and spin-lattice (T_1) relaxation behavior of the secretions. From that study, there was a gap of more than a decade before the pioneering work of Shoolery in 1979.[2] Shoolery's work focused on the use of 1.7 mm capillary NMR probes for direct observe ^{13}C NMR measurements. Shoolery demonstrated that it was possible to substantially reduce data acquisition times, acquiring decoupled ^{13}C NMR spectra for samples as small as 1 mg of cholesterol in 16 h. Corresponding gains were reported for ^{1}H spectra, with data acquired for a 1 μg sample of cortisone acetate.

These early studies set the stage for the development of 3 mm micro NMR probes that started in 1991 in a collaboration between the author, colleagues and staff at Nalorac Corporation. The first report utilizing 3 mm micro NMR probe technology appeared in 1992.[3] Using the simple indoloquinoline alkaloid cryptolepine **(1)** as a model compound for the study, the authors reported the acquisition of inverse-detected direct heteronuclear shift correlation HMQC data[4] using a 12 μg (0.05 μMole) sample of the alkaloid dissolved in 145 μl of d_6-DMSO in 16 h. These data are shown in Figure 1. Long-range heteronuclear correlations were measured using the substantially less sensitive HMBC experiment[5] on a 35 μg sample (0.15 μmole) of the alkaloid in 145 μl of d_6-DMSO in 21 h. These studies ushered in new capabilities for the characterization of small samples by NMR spectroscopy. It would have been necessary to isolate substantially larger samples than those reported for characterization using conventional 5 mm NMR probeheads.

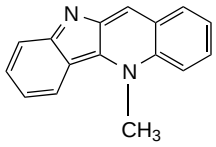

(1)

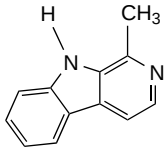

(2)

Later in 1992, a direct comparison of the performance of 3 mm and 5 mm inverse-detection NMR probes for the acquisition of heteronuclear shift correlation data was reported.[6] Using 1 μMole samples of the alkaloid harmane **(2)** prepared in appropriate volumes for the two probe formats, HMQC spectra were acquired with identical s/n (signal-to-noise) ratios. It took four times as long to acquire comparable s/n data in a 5 mm probe with an identical quantity of sample as for the same data in a 3 mm micro inverse NMR probe design (Figure 2). Clearly, for structural characterization problems when limited quantities of sample are available, there is a significant time advantage to acquiring the data using a 3 mm rather than 5 mm probehead.

Several years after the introduction of the 3 mm micro NMR probes, another innovation appeared in the form of the Varian Nano-probe™.[7–9] Shoolery, the driving force behind this probe technology, had the vision of having 100% of the sample within the confines of the rf coils of the probe. Obviously, however, this would result in considerable inhomogeneity over the sample due to the discontinuity of the magnetic susceptibility at the cell boundary. To circumvent this problem, the sample cell was oriented at the magic angle, 54.7°, and spun at high speed (>1 kHz) to average all of the magnetic dipoles to zero. The small volume of the nano-cell, 40 μl, makes it well suited to small samples. Nano-probe technology has made it possible to acquire ^{1}H spectra on samples of an aromatic alkaloid, **1**, as small as 75 ng (32 picomoles)

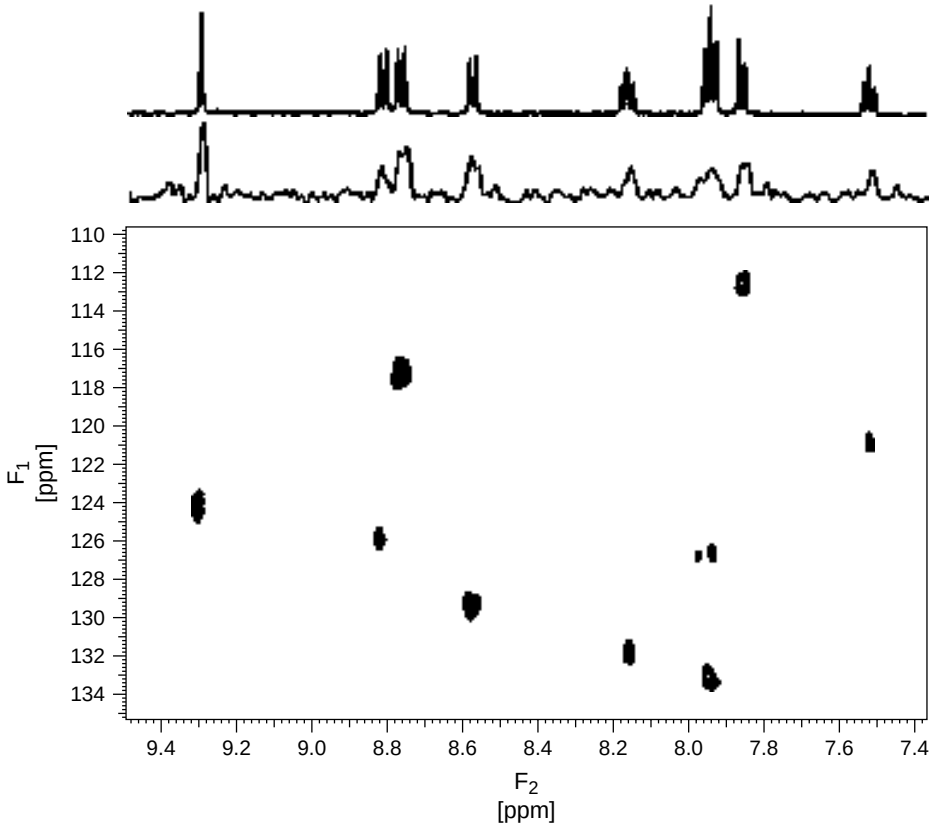

Figure 1 HMQC spectrum of a 12 μg (0.05 μmole) sample of the alkaloid cryptolepine **(1)** acquired overnight using a 3 mm micro inverse-detection NMR probe. The projection of the 2D data matrix through the proton frequency domain (F_2) is shown immediately above the contour plot; the ^{1}H reference spectrum is shown at the top

and COSY spectra overnight on an 85 picomole (200 ng) sample of the same model alkaloid.[10] The ^{1}H spectrum of an 32 picomole sample of cryptolepine **(1)** in shown in Figure 3; the corresponding COSY spectrum is shown in Figure 4. Using a heteronuclear version of the probe in conjunction with specialized processing software, Shoolery demonstrated that an INADEQUATE spectrum of a 3.8 mg sample of sucrose could be acquired in 62 h.[8] Since the initial development of the Nano-probe, a gradient inverse-detection version of the probe has also been developed yielding impressive results.[11] Applications of the Nano-probe for the characterization of small samples are discussed below.

The next step in the development of high-sensitivity, small volume NMR probes was the initial report of the μ-coil NMR probe by Sweedler and co-workers in 1995, which essentially overlapped the development of the nano-probe.[12] Unlike conventional NMR probes or the nano-probe described above, the μ-coil probe was instead a flow probe design, with the rf coil wrapped around a polyimide-coated fused-silica capillary. To obtain usable lineshape, it was necessary to immerse the coil in Fluorinert FC-43 when in use. While a linewidth of 0.6 Hz was initially reported, lineshape, based on visual inspection of figures in the initial report, was evidently not well optimized. Nevertheless, the authors reported a detection limit, defined as a s/n = 3 : 1, for a 19 ng sample of sucrose (56 picomoles) using a 1 min acquisition. It is also worth noting that since the μ-coil probe was a flow probe design that a smaller percentage of the actual sample, <20%, was calculated to be contained within the rf coil of the probe.

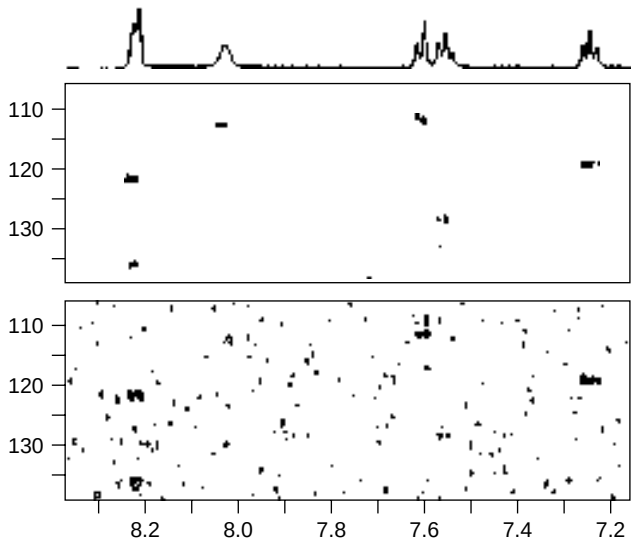

Figure 2 Comparison HMQC spectra of 1 μmole samples of the simple alkaloid harmane **(2)**. The spectrum shown in the bottom panel was acquired with a sample dissolved in 600 of d_6-DMSO using a 5 mm inverse detection probe. The data were acquired in 23 min. The same quantity of material was dissolved in 160 μl of d_6-DMSO and the data were acquired using a 3 mm micro inverse probe in 12 min to afford the spectrum shown in the top panel. To achieve comparable signal-to-noise using the 5 mm probe required ∼70 of data acquisition

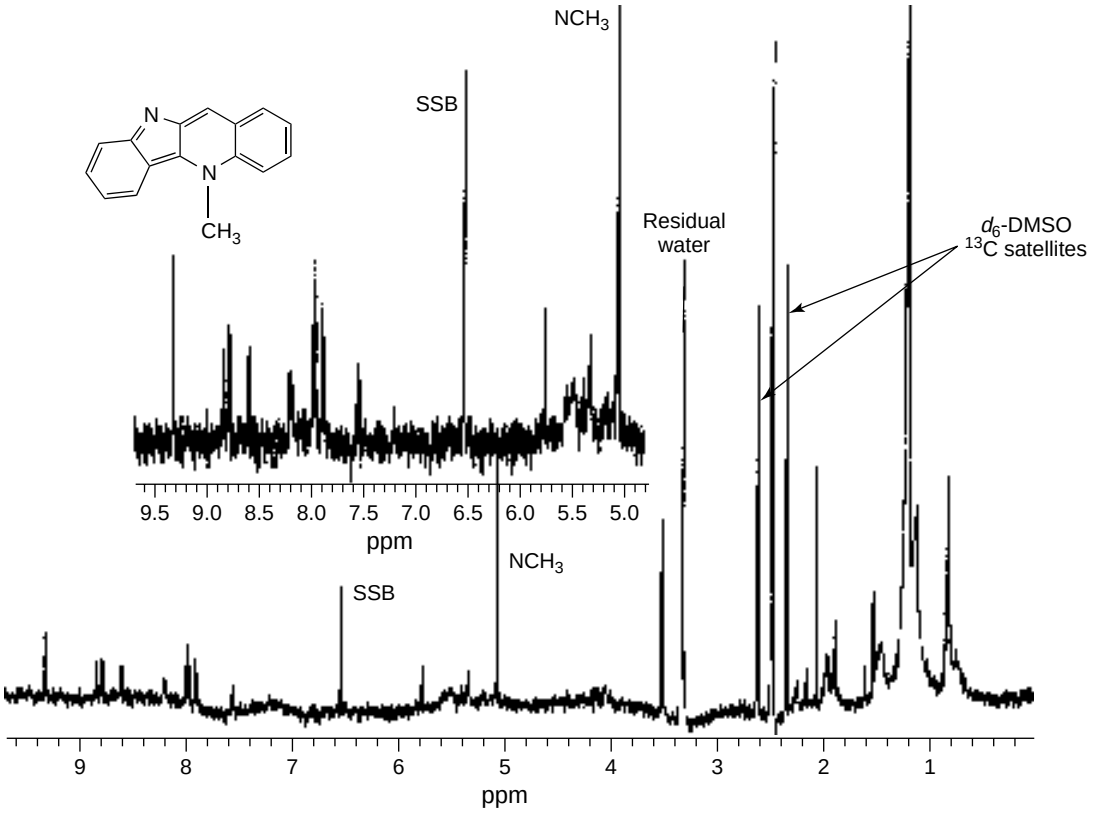

Figure 3 Proton NMR spectrum of a 75 ng (32 picomoles) sample of the indoloquinoline alkaloid cryptolepine (**1**, inset structure) acquired overnight using a Varian Nano-probe™. Both the residual water and the protio DMSO signals were suppressed in the experiment. Note the intensity of the ^{13}C satellite lines of the solvent relative to the intensity of the N-methyl group (~5.05 ppm) of cryptolepine

In contrast, conventional NMR probe designs can load up to ~80% of the sample within the confines of the rf coils in conventional NMR tubes and >95% of the sample when Shigemi micro cells are employed, or 100% with a nano-cell.

Following the initial report, refinements of the μ-coil NMR probe design have been reported. Designs have included probes for ^{13}C detection, although only labeled samples have thus far been studied.[13] Multiple solenoidal microcoil probes for possible applications to high-throughput screening have been developed.[14] Susceptibility matching plugs used in conjunction with microcoils have also been described for limited sample applications.[15] Using this approach it was possible to position ~43% of the sample within the coil volume, a substantial improvement over initial flow designs. Perhaps the most interesting report has been a probe design for inverse-detection experiments.[16] In the latter study, the authors reported the acquisition of a ^{13}C decoupled HMQC spectrum of a 13 μg sample of chloroquine diphosphate dissolved in 745 nl of D_2O. These data were acquired by accumulating 32 transients for each of 2048 × 128 increments of the 2D NMR data matrix. The few applications of the μ-coil probe that have appeared thus far have all be contained in papers reporting the development of these probes and are discussed below.

Following in 1998, the development of 1.7 mm gradient submicro inverse-detection or SMIDG NMR probes was reported.[17,18] This probe design returned to the 1.7 mm format pioneered in the 1970's by Shoolery.[2] The SMIDG probe design employs a conventional 1.7 mm NMR tube format that can be inserted pneumatically as with 5 mm or 3 mm micro NMR probes. Sample volumes range from 22–30 μl depending on the coil dimensions and allow ~78% of the sample to be located within the coil volume when careful sample positioning and shimming are done. In one of the original reports, an 8% cryptolepinone impurity contained in a 0.55 μmole sample of cryptolepine was fully characterized by a combination of GHMQC and GHMBC experiments despite the dynamic range problems inherent to the sample.[18] The SMIDG probe has also been used for a number of low-level, long-range $^{1}H-^{15}N$ 2D NMR studies at natural abundance, dramatically lowering sample requirements for this very insensitive experiment.[19,20] A number of applications of 1.7 mm SMIDG NMR probe technology for natural product and pharmaceutical impurity characterization have been reported and are discussed below.

In 2001, the development of a 1 mm gradient inverse NMR probe was reported.[21] Using this probe technology, it was possible to record the HMQC spectrum of a 1 μg sample of ibuprofen **(3)** overnight. To date, there have not been any reported applications of this probe technology to the best of the author's knowledge.

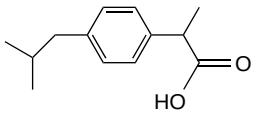

(3)

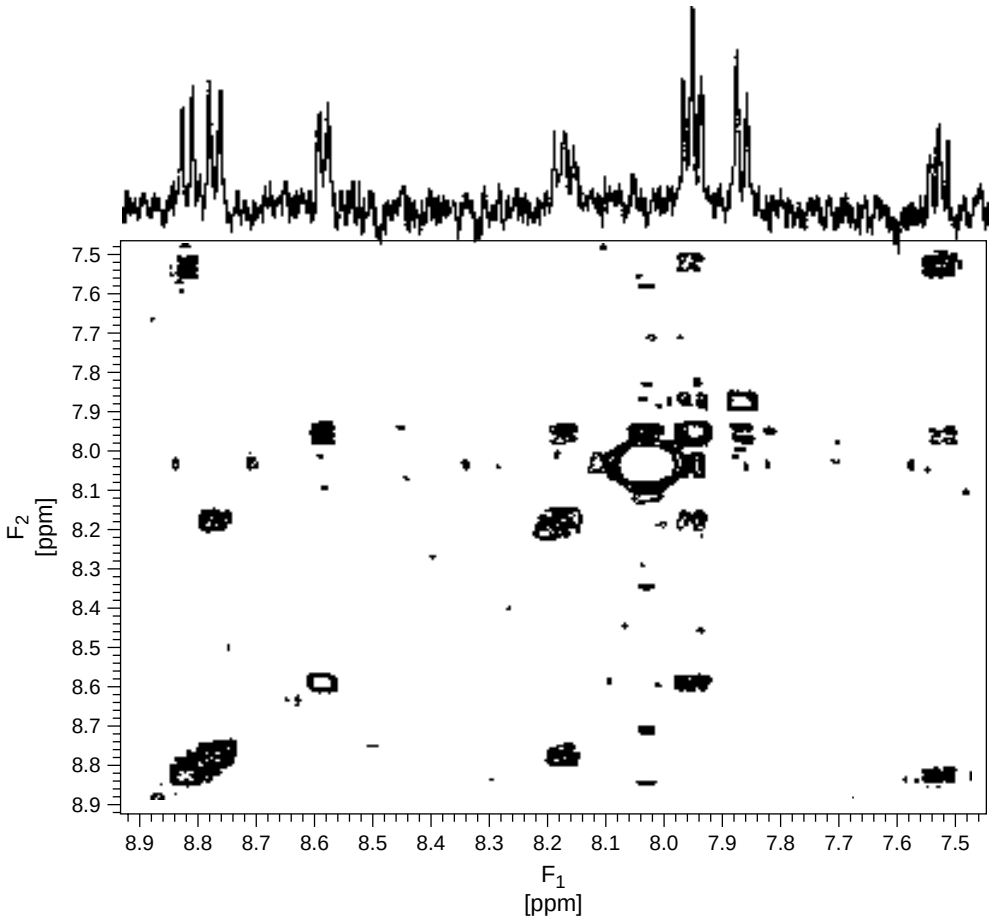

Figure 4 Overnight COSY spectrum obtained using a 200 ng sample of the simple alkaloid cryptolepine **(1)** dissolved in 40 μl d_6-DMSO and acquired using a Varian Nano-probe™

More recently, intensive effort has been directed toward the development of cryogenic NMR probes. Thus far, 5 and 3 mm designs have been reported by various manufacturers. Several studies using prototype cryogenic 3 mm probes have been presented as posters[22–24] and several reports have appeared in the published literature.[25,26] Cryogenic NMR probes operate by cooling the rf coils to temperatures in the range of 10–25 K to reduce noise; preamplifiers used in conjunction with these probes are also frequently cooled to temperatures in the range of from 40–60 K. Considerable sensitivity gains are obtained by using this complex and technologically demanding design strategy. Early versions of the 3 mm cryogenic NMR probe tested in the author's laboratory gave s/n ratios for the anomeric proton of a 2 mM sucrose sample in the range of ~180 : 1. More recent designs have given s/n ratios as high as 242 : 1. In comparison, a conventional 3 mm probe can be expected to give s/n ratios in the range of 62–67 : 1 for the same sample tube. The extremely high sensitivity of the cryogenic NMR probes translates to very considerable time savings to achieve identical s/n ratios when compared to conventional NMR probeheads. In the initial report from the author's laboratory using a prototype Nalorac 3 mm CryoSPEC™ (CryoM{H}C500-3) probe[25] a 40 μg sample of strychnine **(4)** was employed as a model compound and HSQC data were acquired. All of the responses were observable in 45 min albeit with noise still present in the spectrum; an essentially noise-free spectrum was recorded in 90 min. In comparison, to achieve a comparable s/n ratio using a conventional 3 mm micro NMR probe, the sample had to be run for 17.5 h, which is a factor of 12.5 in time. These comparative spectra are shown in Figure 5. Although not performed in a small volume probe, still more impressive results have been obtained for long-range $^{1}H-^{15}N$ experiments run on a 2 mg sample of the antibiotic eperezolid **(5)** in 160 μl of solvent in a 3 mm NMR tube run coaxially in

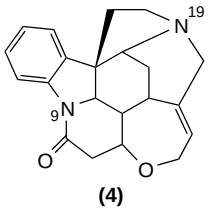

(4)

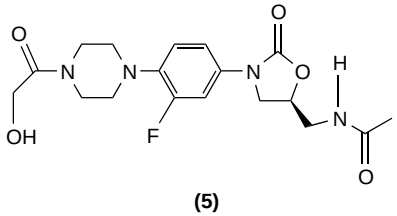

(5)

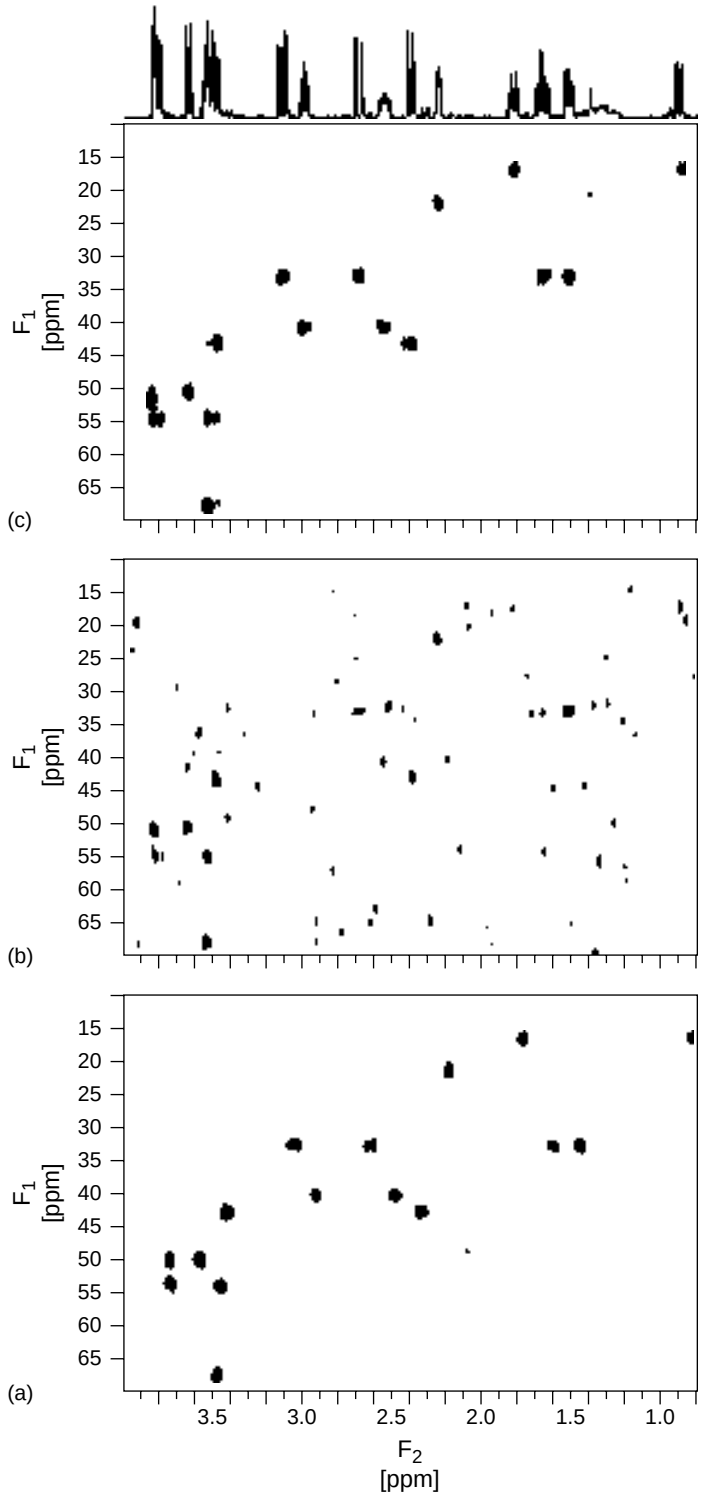

Figure 5 Comparison of 3 mm gradient inverse triple resonance and 3 mm cryoprobe performance comparison using a 40 μg (120 nanomole) sample of strychnine **(4)**. The same sample, prepared by serial dilution, was used for the acquisition of the HSQC spectra (non-gradient) shown in all three panels. The data shown in (a) were acquired by accumulating 32 transients/t_1 increment as 2048 × 48 (hypercomplex files × 2) data points, which were linear predicted to 192 points in the second frequency domain and zero-filled to 256 points during Fourier transformation using a Nalorac CryoSPEC 3 mm cryogenic micro inverse NMR probe. The data acquisition time was 90 min. Data shown in (b) were acquired identically except that a conventional Nalorac MIDTG-500-3 gradient inverse 3 mm triple resonance NMR probe was employed. Processing and scaling were identical to the data presented in (a), obviously lower in quality since these data were acquired using a conventional NMR probe. Data shown in (c) were again acquired using the Nalorac MIDTG-500-3 gradient inverse triple resonance probe except that 352 transients were accumulated/t_1 increment giving an acquisition time of 17.5 h. Processing and scaling were identical to that used to prepare panel (a). S/n ratios in panels (a) (90 min) and (c) (17.5 h) are comparable

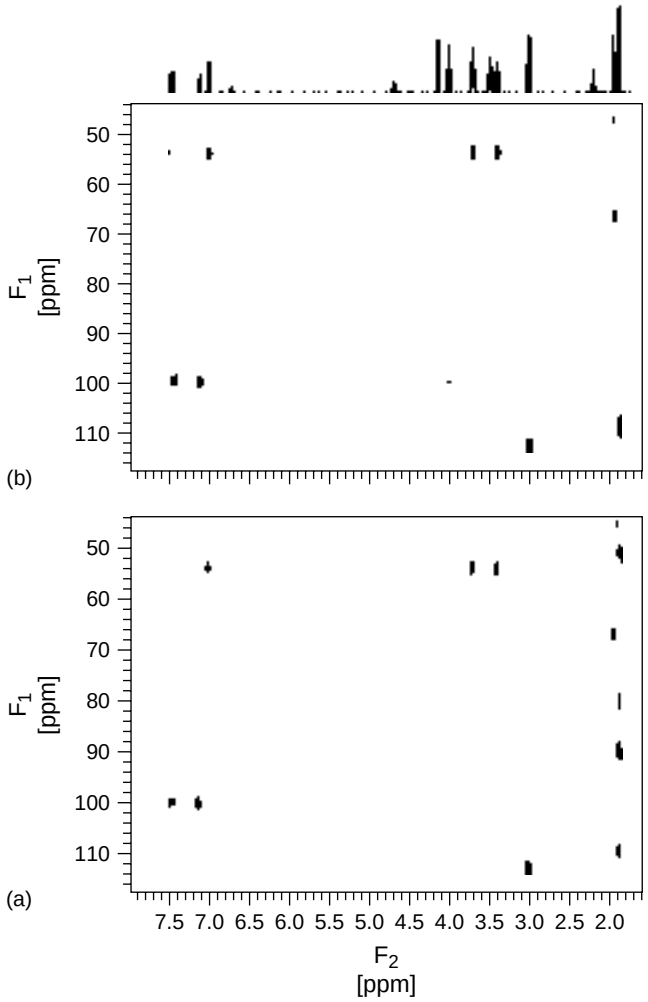

Figure 6 Comparison $^{1}H-^{15}N$ CIGAR-HMBC[27] 5–10 Hz optimized long-range heteronuclear shift correlation data for the oxazolidinone antibiotic eperezolid **(5)** at natural abundance ^{15}N. The data shown in (a) were acquired using a Varian Cryo-Q 500 MHz HN gradient cryogenic NMR probe in 26 min with a s/n ratio of 101 : 1. To acquire comparable s/n data using a conventional Nalorac MIDTG-500-3 gradient inverse triple resonance probe using the same sample required 17 h 40 min (b)

a 5 mm Varian Cryo-Q 500 MHz HN probe.[26] A CIGAR-HMBC[27] spectrum in which all of the anticipated long-range $^{1}H-^{15}N$ 2D NMR responses were observed was recorded in 26 min. To achieve comparable s/n ratio in a conventional 3 mm gradient inverse triple resonance probe required 17 h 40 min, corresponding to a factor of 38 in time. These results are shown in Figure 6.

2 HIGH SENSITIVITY, SMALL VOLUME PROBE PERFORMANCE COMPARISONS

One question that immediately comes to the mind of an investigator when faced with the problem of acquiring NMR data for a small sample is what probe should be used? This question has prompted a number of comparisons of various probe formats since the introduction of the 3 mm micro NMR probes in 1992. A complete set of all possible comparisons is unfortunately not available. Indeed, there are no direct comparisons at all between any of the formats discussed in the contribution vs. any of the μ-coil NMR probes. Nevertheless, those comparisons that have been reported are summarized below.

2.1 3 mm Micro Inverse vs. 5 mm Inverse NMR Probe Performance Comparison

The first comparison of a small volume NMR probe to the standard 5 mm probe was reported in late 1992 following the introduction of the 3 mm micro NMR probes.[6] Using a 1 μmole sample of the simple alkaloid harmane **(2)** dissolved in appropriate volumes of d_6-DMSO for 3 and 5 mm NMR probes, comparison HMQC spectra were recorded. When data were acquired for identical times, the pair of spectra shown in Figure 2 were obtained. The advantage of the 3 mm micro probe over the conventional 5 mm probe when dealing with the 167 μg (1 μmole) sample of harmane **(2)** is obvious. When data were acquired in 12 min (4 transients/t_1 increment, 2048 × (2 × 32) hypercomplex files) using the 3 mm micro inverse probe, it was necessary to acquire data for 69 min (32 transients/t_1 increment 2048 × (2 × 32) hypercomplex files) to achieve comparable performance with a conventional 5 mm inverse-detection probe. These data heralded the beginning of renewed interest in the utilization of high-sensitivity, small volume NMR probes.

2.2 3 mm Micro Dual vs. Heteronuclear Nano-probe Performance Comparison

A rigorous comparison of these probe formats has not been reported. There are, however, several examples in the literature where both probe formats were used to acquire ^{13}C reference spectra. One example is contained in a paper describing the elucidation of the structure of the alkaloid cryptolepicarboline **(6)** from the Ghanaian plant *Cryptolepus sanguinolenta*.[28] The total available sample of the alkaloid was ∼100 μg (∼0.25 μmole). The acquisition of a ^{13}C reference spectrum of the alkaloid sample in 40 μl of d_6-DMSO using a heteronuclear nano-probe was accomplished overnight giving a spectrum with a s/n ratio of 9 : 1. In comparison, the same sample of alkaloid, after transfer to a 3 mm micro NMR probe in the process of which the sample was diluted to 140 μl gave a spectrum with 9 : 1 s/n over a weekend. A similar non-rigorous comparison of the performance of the 3 mm micro dual and heteronuclear nano-probes is found in a report of the characterization of an N-acetyl keto derivative of fumonisin-B_1 **(7)**.[29] An overnight acquisition of a ^{13}C reference spectrum of an ∼200 μg sample of the material gave a carbon spectrum with a s/n ratio of 5.5 : 1 when a 3 mm micro dual probe was employed. Curiously, a ketone carbonyl resonance expected on the basis of mass spectrometric fragmentation data was not observed in the spectrum. The acquisition of the ^{13}C reference spectrum was repeated with the same sample after concentration to 40 μl to allow the use of a heteronuclear nano-probe. The overnight nano-probe acquisition gave a spectrum with a s/n ratio of 11 : 1 and the carbonyl resonance at 219.5 ppm was observed in the spectrum. These data are presented in Figure 7. There is no obvious reason why carbonyl resonance wasn't observed in the spectrum recorded using the 3 mm micro dual probe;

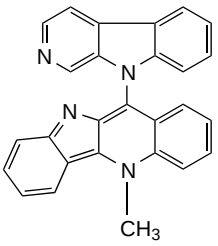

(6)

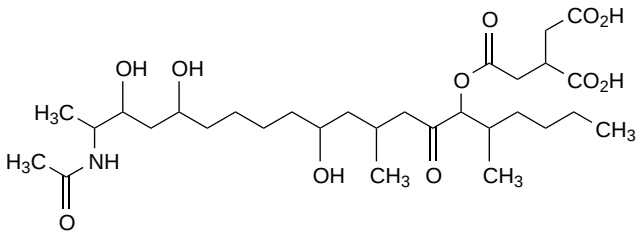

(7)

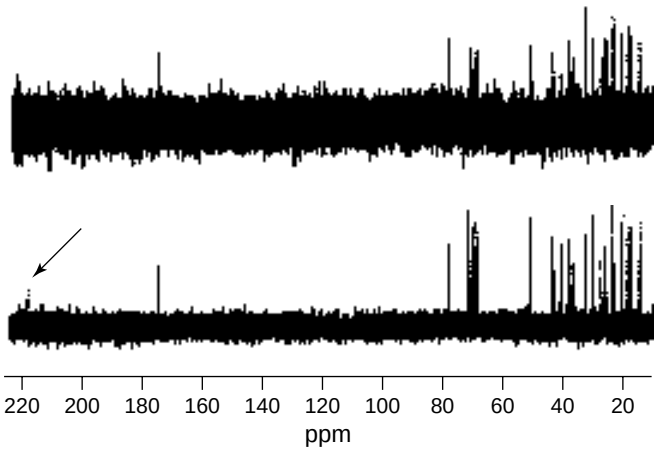

Figure 7 Overnight ^{13}C reference spectra of an ~200 μg sample of a secondary fungal metabolite, fumonisin-B_1 **(7)**, in D_2O. The data shown in the top panel were acquired using a 3 mm micro dual NMR probe in 145 μl of solvent and gave a signal-to-noise ratio of 5.5 : 1. A ketone carbonyl resonance expected on the basis of mass spectrometric fragmentation data was not observed in the spectrum. Following the concentration of the sample to 40 μl to allow the use of a heteronuclear Nano-probe™, the data shown in the bottom panel were acquired. The overnight Nano-probe™ acquisition gave a spectrum with a s/n ratio of 11 : 1 and the carbonyl resonance at 219.5 ppm was observed in the spectrum

the relaxation delay between transients was identical. From these data, however, it can be concluded that the per transient efficiency of the conventional micro dual probe is somewhat better than that of the nano-probe. This conclusion derives from the nearly four-fold concentration of the sample for acquisition of the nano-probe data. If probe efficiencies were identical, a s/n ratio for the nano-probe approaching 22 : 1 should have been obtained on the basis of the concentration factors.

2.3 1.7 mm SMIDG vs. 3 mm Micro Inverse Probe Performance Comparison

A rigorous comparison of the 1.7 mm submicro gradient inverse or SMIDG and a 3 mm micro inverse detection NMR probes has been reported for both $^{1}H-^{13}C$ direct and long-range and $^{1}H-^{15}N$ long-range heteronuclear shift correlation experiments.[30] In addition, the results obtainable by running a 1.7 mm sample coaxially in a 3 mm micro probe were also reported in this study. Using an 0.5 μmole sample of the non-steroidal anti-inflammatory agent ibuprofen **(3)** in either 30 or 150 μl of d_6-DMSO, gradient $^{1}H-^{13}C$ HSQC spectra were acquired using both probes. Data accumulation for the three experiments performed was 48 min for each spectrum. Using the 1.7 mm SMIDG probe, a s/n ratio of 148 : 1 was obtained. All of the expected responses were observed in the spectrum, including that of the relatively weak *sec*-butyl methine resonance. When the 1.7 mm sample was run in the 3 mm micro inverse probe, again all of the responses were observed; the s/n ratio was 75 : 1. When the GHSQC data were acquired using the 3 mm micro inverse probe, the *sec*-butyl methine resonance was absent from the spectrum; the s/n ratio was 62 : 1. Similar results were obtained for the same series of $^{1}H-^{13}C$ GHSQC experiments using a 1 μmole sample of strychnine **(4)**. These comparison GHSQC spectra are presented and described in Figure 8.

Using a 1 mg sample of strychnine **(4)**, long-range $^{1}H-^{15}N$ GHMBC experiments were also performed using both the 1.7 mm SMIDG and the 3 mm micro inverse probes; these data are presented in Figure 9. The 1.7 mm SMIDG data gave all of the expected long-range $^{1}H-^{15}N$ responses;[30–33] all responses were well above the noise floor of the spectrum. When the 1 mg sample in the 1.7 mm tube was run coaxially in the 3 mm micro inverse probe, again, all of the expected long-range responses to the two strychnine nitrogen resonances were observed although there were some noise spikes contained in the spectrum with comparable intensity to the desired, long-range responses. For the 3 mm sample, all but one of the expected long-range responses was observed. However, there were substantial numbers of spurious peaks with greater intensity than the desired long-range responses. It was concluded that a sample containing ~3 μmoles (~1 mg in the case of strychnine) was borderline for an overnight long-range $^{1}H-^{15}N$ 2D NMR experiment at natural abundance in a 3 mm probe.

2.4 Conventional vs. Cryogenic NMR Probe Performance Comparison

To date there are two studies in the literature that report comparisons of conventional and cryogenic NMR probe performance. The first is a direct comparison of 3 mm cryogenic inverse and conventional 3 mm inverse-detection probes.[25] Using a 40 μg (120 nanomoles) sample of strychnine dissolved in 150 μl d_6-benzene, identical HSQC spectra were recorded using a Nalorac 3 mm CryoSPEC inverse probe and a conventional Nalorac Z•SPEC™ MIDTG-500-3 gradient inverse-detection probe. With the cryogenic probe, all of the aliphatic direct correlation responses were observable within 45 min and a noise-free spectrum was obtained in 90 min. To achieve a comparable s/n ratio using the conventional probe required 17 h of data acquisition. With the initial prototype

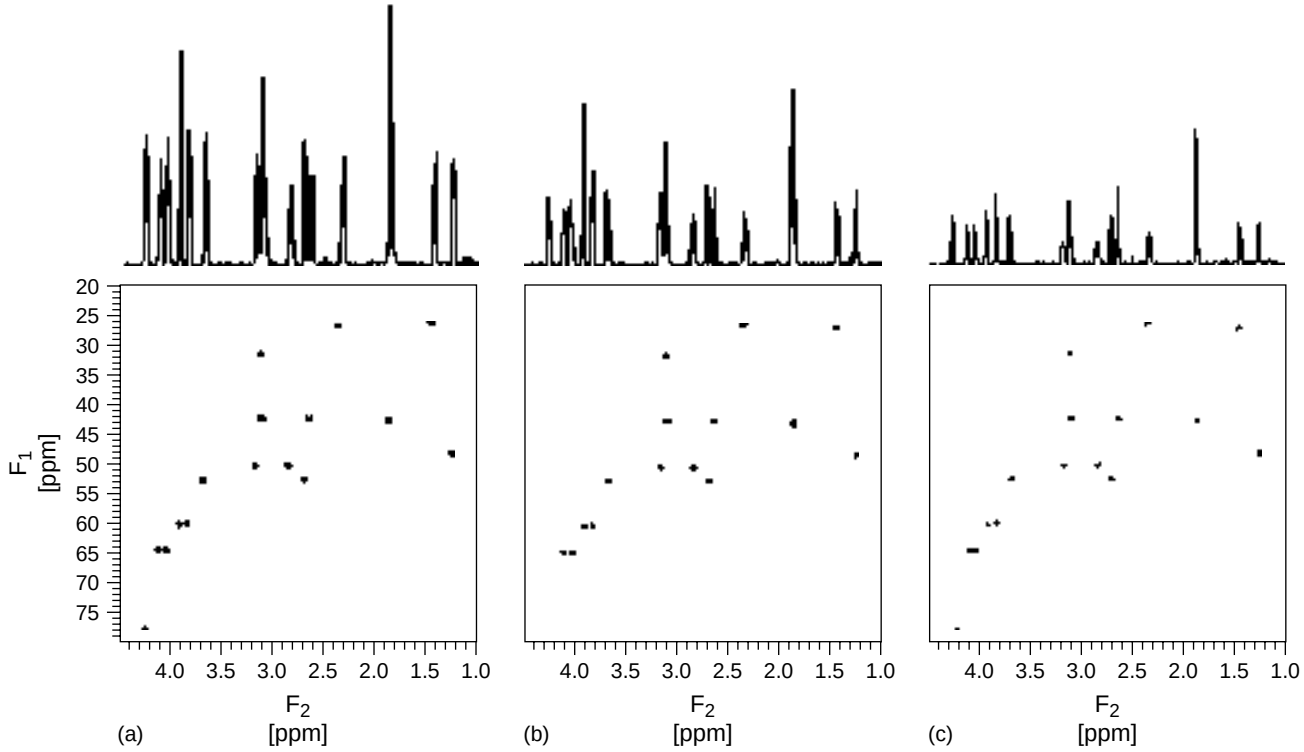

Figure 8 Comparison 600 MHz $^{1}H-^{13}C$ GHSQC spectra acquired for a 1 μmol sample of strychnine **(4)** in $CDCl_3$ in either a 1.7 or 3 mm NMR tube in a volume appropriate to the tube format. All data were acquired by accumulating four transients at each of 64 increments of the evolution time, t_1, giving identical data acquisition times. All data were processed and scaled identically to prepare the three panels shown. Data shown in (a) were acquired using a 1.7 mm sample in a Nalorac SMIDG-600-1.7 submicro gradient inverse detection NMR probe; using the region from 5.5 to 4.5 ppm as representative noise, the s/n ratio for this spectrum was 112 : 1. The data shown in (b) were acquired by running the 1.7 mm sample coaxially in a conventional Nalorac MIDTG-600-3 gradient triple resonance micro inverse NMR probe. The s/n ratio for these data was 75 : 1. Finally, the data shown in (c) were acquired using a 1 μmol sample in a 3 mm tube, the data again acquired using the conventional Nalorac MIDTG-600-3 probe. The s/n ratio for this experiment was 62 : 1. Projections through the F_2 frequency domain are plotted above each of the contour plots to provide a more effective portrayal of the relative s/n ratio in the three experiments

cryoprobe used for this comparison, a 3.5 × improvement in signal-to-noise was afforded by the cryoprobe, which corresponds to a 12.5-fold time advantage to equivalent signal-to-noise. The comparison 90 min HSQC spectra are shown in Figure 5.

More recently, a comparison was drawn for the acquisition of long-range $^{1}H-^{15}N$ 2D experiments at natural abundance.[26] Using a 2 mg sample of the oxazolidinone antibiotic eperezolid **(5)** dissolved in 160 μl d_3-acetonitrile in a 3 mm NMR, $^{1}H-^{15}N$ CIGAR-HMBC 2D NMR spectra optimized for a long-range coupling range of from 5 to 10 Hz[34–36] were acquired using a Varian 5 mm Cryo-Q HN probe (because of the considerable variability of long-range $^{1}H-^{15}N$ couplings, it is advisable to use an accordion-optimized long-range 2D NMR experiment such as IMPEACH-MBC or CIGAR-HMBC to record long-range $^{1}H-^{15}N$ 2D NMR spectra at natural abundance. See Ref.[34]). In less than 10 min, most of the anticipated long-range $^{1}H-^{15}N$ responses were observed. A second experiment run in 26 min afforded a spectrum with 101 : 1 (projecting through the F_1 or ^{15}N frequency domain) s/n in which even the weakest response had ∼40 : 1 s/n. Acquisition of a 26 min data set using a conventional Nalorac Z•SPEC MIDTG-500-3 gradient inverse probe gave only the N7-9CH_3 response. A longer 4 h experiment gave all of the expected long-range responses albeit with <50 : 1 s/n. To attain a s/n ratio comparable to that of the 26 min cryoprobe experiment, it was necessary to acquire data with the conventional 3 mm probe for 17 h 40 min (112 : 1 s/n). A comparison of the 26 min 5 mm cryoprobe data with the 17 h 40 min 3 mm $^{1}H-^{15}N$ CIGAR-HMBC spectra optimized over the range of 5–10 Hz is shown in Figure 6. Thus, for long-range $^{1}H-^{15}N$ experiments, the cryogenic NMR probe afforded a >38× time advantage relative to a conventional 3 mm micro probe despite potential losses of signal due to filling factor associated with running a 3 mm tube coaxially in the 5 mm probe. Unfortunately, at present, it is not possible to make a direct comparison of 3 mm NMR probes for long-range $^{1}H-^{15}N$ 2D NMR experiments at natural abundance as a 3 mm cryogenic NMR probe with an X-coil tunable to ^{15}N or doubly tuned to ^{13}C and ^{15}N has yet to be developed.

While 5 mm cryogenic NMR probes are not in the category of small volume NMR probes by any means, the extremely high sensitivity which they offer makes them competitive when dealing with small samples, particularly when 3 mm tubes are run coaxially or specialized micro cells are employed to restrict sample volume. To date, there have not been any reports of tubes smaller than 3 mm in diameter being run coaxially in a cryogenic probe; it is likely that filling factor losses would substantially offset the gains in sensitivity offered by the probe if a small tube such as 1.7 mm were run coaxially in a 5 mm cryogenic probe. Thus, it is likely that as cryogenic probes

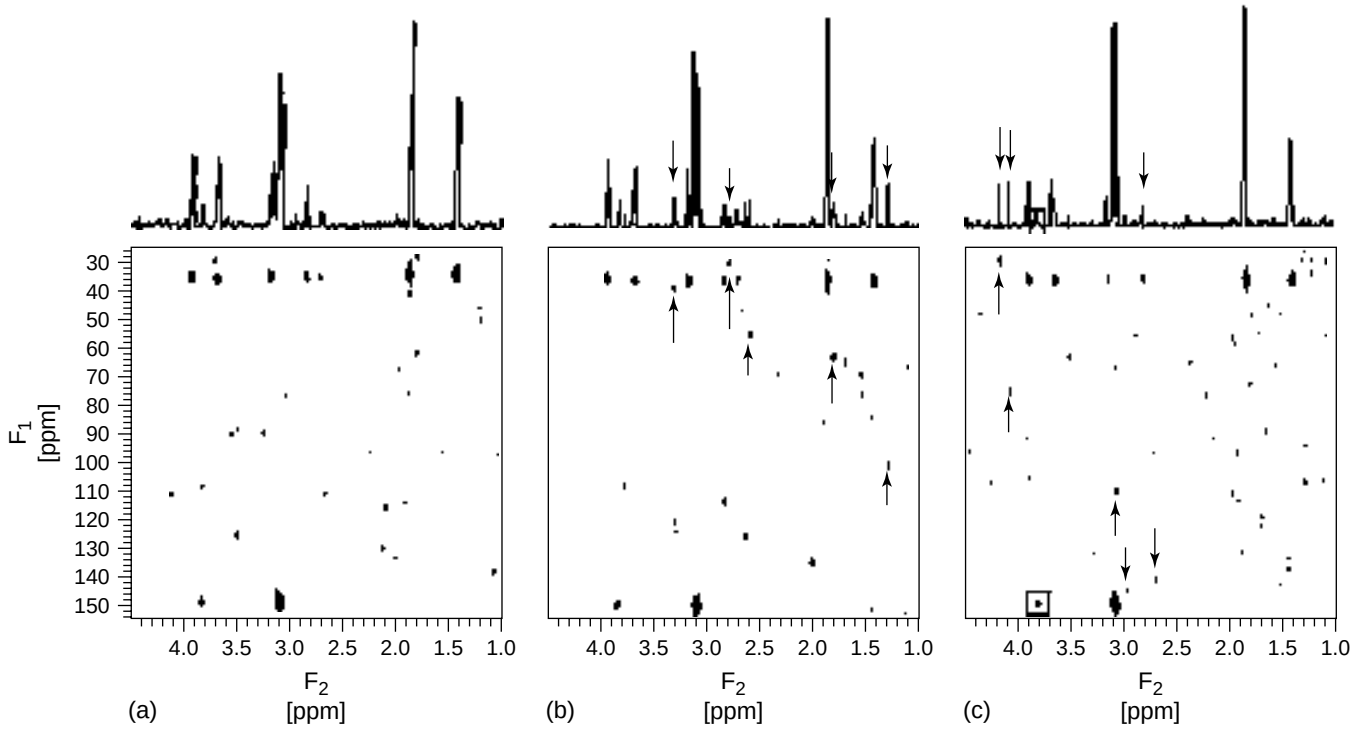

Figure 9 Comparison $^{1}H-^{15}N$ 8 Hz optimized GHMBC spectra of 3 μmole samples of strychnine **(4)** at natural abundance prepared in either a 1.7 or 3 mm NMR tube in a volume appropriate to the tube format. All spectra were recorded at 600 MHz, accumulating 4096 transients for each of 40 increments of the evolution time, t_1, giving identical 18 h data acquisitions. The data shown in (a) were acquired using a 1.7 mm sample in a Nalorac SMIDG-600-3 gradient inverse submicro NMR probe. Again using the region of the proton spectrum from 5.5 to 4.5 ppm for representative noise, the SMIDG data gave a s/n ratio of 60 : 1. All anticipated responses were observed either directly in the contour plot or readily in the traces from the N9 amide or N19 aliphatic nitrogen resonances. When the 1.7 mm sample was run coaxially in a Nalorac MIDTG-600-3 gradient inverse triple resonance probe, the data shown in (b) were obtained, giving a s/n ratio of 41 : 1. Some spurious responses are observed in the projection through F_2 as well as in the contour plot. Finally, when a 3 mm sample was used in a 3 mm probe, the result shown in (c) was obtained. In this case, spurious responses in the projection are of greater intensity than some legitimate responses, suggesting that either a longer data acquisition or larger sample would be desirable with this probe technology to obtain reliable data. The s/n ratio of the spectrum shown in (c) was 26 : 1

become more widely available that 5 mm versions of this probe technology will be used to deal with small NMR samples in those labs not equipped with more specialized probeheads.

2.5 Conventional NMR Tubes vs. Specialized Sample Cells

One alternative available to researchers without access to any of the specialized NMR probeheads described in this contribution is to use a specialized sample cell to restrict overall sample volume, thereby keeping a greater percentage of a scarce sample within the confines of the rf coils of the probe being used. Various tactics have been employed to achieve this goal. Approaches have included the development of plastic NMR tube inserts, the properties of which are matched as closely as possible to those of the solvent being employed. Shigemi, using a more novel approach, has employed specialized glass that matches the magnetic susceptibility of several NMR solvents, to make both the NMR tube and a precision bore 'plunger'. Tubes have been manufactured thus far for use with $CDCl_3$, CD_3OD, D_2O and d_6-DMSO. With a conventional 5 mm NMR tube, sample volumes can be reduced from ~500 μl to roughly 225–250 μl. The resulting two-fold increase in sample concentration will correspondingly quarter acquisition time to a given s/n ratio.

To date, two studies have appeared in the literature that compare the results obtainable with normal NMR tubes vs. specialized NMR cells. The earliest report was a study of Caribbean ciguatoxin.[37] A substantial improvement in the HMQC data that could be recorded for an ~0.95 μmole sample of Caribbean ciguatoxin was noted when the data were acquired in 67 μl d_5-pyridine when the sample was run in a 3 mm Shigemi D_2O-matched micro NMR cell (despite the mismatch of the solvent to the optimization of the micro cell) vs. data acquired in 120 μl in a conventional 3 mm NMR tube. No quantitative comparison was drawn. A similar improvement was noted by Reynolds, Yu and Enriquez[38] for ^{13}C-detected 2D heteronuclear NMR experiments when run in Shigemi micro NMR cells vs. data acquired in normal 3 mm NMR tubes. Although 1.7 mm Shigemi cells have been developed, there have not been any reported applications of this type of tube in the literature.

3 APPLICATIONS OF SMALL VOLUME NMR PROBES IN THE SOLUTION OF CHEMICAL STRUCTURE PROBLEMS

There is a wide range of potential applicability of specialized NMR probe technology in the solution of structural

problems, not all of which have yet been reported. Some research areas where specialized NMR probe heads can be highly advantageous include: characterization of scarce natural product samples; identification of metabolites of pharmaceuticals; characterization of forensic samples; protein characterization; and the identification of chemically unstable species. Given that the first of the new generation of small volume specialized probes to be described were the 3 mm micro inverse and dual probes, applications utilizing these probeheads will be surveyed first, followed by applications utilizing Nano-probe technology. To date, there have not been any applications of μ-coil probes in the solution of structural problems of which the author is aware. The examples that have been reported in conjunction with the development of this probe technology will be summarized next. Examples of potential applications and structural problems solved using 1.7 mm SMIDG probes, and then cryogenic probe applications will complete this section.

3.1 Existing Reviews

Several reviews have been published that deal with either probe-specific or the general topic of small sample NMR spectroscopy.[39–44] Various aspects of dealing with small samples by NMR have also been discussed in reviews of specific classes of molecules, which include alkaloids,[45] carbohydrates,[46] and a recent review of long-range $^{1}H-^{15}N$ 2D NMR applications.[47]

3.2 Applications of 3 mm Micro Probes

Following the initial reports on the development of 3 mm micro NMR probe technology in the authors laboratories, then at Burroughs Wellcome, Co., the first reported 'real world' application of this technology was in the characterization of a 30 μg (0.07 μmoles) metabolite sample through the use of a combination of 3 mm micro and heteronuclear nano-nmr probe technology.[48] A heteronuclear nano-nmr probe was used to record a ^{13}C reference spectrum and a homonuclear nano-nmr probe was used to record a COSY spectrum. Following transfer of the sample and dilution to 120 μl, heteronuclear shift correlation spectra were recorded using a 3 mm micro inverse NMR probe. In 1995, the structure of an N-acetyl keto derivative of fumonisin-B_1 **(7)** was determined, again using a combination of probeheads. Two-dimensional NMR spectra were recorded using a 3 mm micro probe while a ^{13}C reference spectrum was recorded using both a 3 mm micro dual and heteronuclear nano-nmr probe. Interestingly, the keto resonance at 219 ppm was not observed in the data from the 3 mm micro dual probe while it was readily observed in the data recorded with the nano-nmr probe.[28] Later in 1995, the structure of the complex indoloquinoline alkaloid cryptolepicarboline was reported.[27] The homo- and heteronuclear 2D NMR data were recorded using a 3 mm micro inverse nmr probe. A comparison of the ^{13}C spectra recorded using a 3 mm micro dual and heteronuclear nano-nmr probe were also contained in the report.[27] Later in 1995, in a report by the author and co-workers[37] the benefits of using reduced volume Shigemi micro nmr cells was reported in the context of a study of Caribbean ciguatoxin. In a related study, the proton and carbon NMR spectra of the marine toxin brevetoxin-2 were fully assigned on less than 1 μmole of material through the use of 3 mm micro nmr probe technology.[49]

Late in 1995, the structure of the indolobenzazepine alkaloid homocryptolepinone, which serves as a structural component of the complex spiro nonacyclic alkaloid cryptospirolepine, was reported.[50] Continuing in the indoloquinoline series of alkaloids in 1996, two new members of this series with novel ring fusion between the indole and quinoline portions of the molecule were reported.[51] Cryptosanguinolentine was based on an indolo[3,2*c*]quinoline ring fusion rather than the more common [3,2-*b*] ring fusion. Cryptotakiine was based on a indolo[2,3-*b*]quinoline ring system which placed both annular nitrogens on the same side of the molecule. Later in 1996 the structure of the novel, dimeric alkaloid cryptomisrine was reported.[52]

In 1997, Reynolds and co-workers,[38] as noted above, examined the limits of ^{13}C detected heteronuclear shift correlation experiments through the combined usage of 3 mm micro probes and Shigemi micro nmr cells. Although the sensitivity of ^{13}C-detected heteronuclear 2D nmr methods is inarguably lower than that of newer, proton-detected methods, there are still occasions when high digitization requirements in the ^{13}C frequency domain are better addressed by direct ^{13}C detection, provided that sufficient sample is available.[53]

3.3 Applications of Nano-nmr Probes

Magic angle spinning (MAS) liquid NMR probes, or nano-nmr probes as they are frequently referred to *in lieu* of Varian's trademarked Nano-probe™ nomenclature, have been applied in the study of a diverse range of chemical structure problems. A very useful subdivision of these applications is suggested in the review by Keifer.[39] For discussion, it is convenient to separate applications into heterogeneous and homogeneous sample types. The former encompasses samples as diverse as whole cells, tissue samples and solid phase synthesis (SPS) supports used for combinatorial chemistry and related applications. Homogeneous samples, as the name implies, refers to solutions in the usual NMR sense.

3.3.1 Heterogeneous Samples

Nano-nmr probes, which spin at the magic angle (54.7°) at speeds of up to several KHz, are quite useful for the study of heterogeneous samples. The earliest such application, of which the author is aware, is a 1994 report dealing with SPS beads on which the synthetic chemistry was being carried out. The first report, which employed ^{1}H NMR, used a Varian homonuclear Nano-probe.[54] Results that can be obtained with various SPS resins using various types of probes were reported in 1996 by Keifer and co-workers.[55] The effect of tether length between the resin and the synthetic site has been examined[56] as has the use of MAS liquids probes to monitor the extent of reaction completion on SPS supports.[57,58] More recently, Seffler and Gerritz[59] have used 1D and 2D NMR methods to characterize reaction products bound to Chiron SynPhase crowns used in the elaboration of combinatorial chemical libraries. Finally, although not chemically bound, Mohri and co-workers[60] have studied the mobility of surface-adsorbed molecules on insoluble pigment particles using ^{1}H T_1 relaxation measurements in a nano-nmr probe. Reviews on the analysis of materials on solid supports include those of Keifer[39] and Gallop and Fitch.[61]

Another interesting heterogeneous nano-nmr probe application has been used in an attempt to biochemically classify kidney carcinoma biopsy samples.[62] While by no means a rapid analytical or screening tool, this study does provide a glimpse of where the probe technology may be applied in the future.

3.3.2 Homogeneous Samples

Numerous reports of applications of nano-nmr probes to homogeneous solution samples have been reported. Broadly, these applications can be further subgrouped into natural products or small molecules and biomacromolecule studies. One of the first reported small molecule applications was a combined 3 mm micro NMR probe/nano-nmr probe study of a metabolite structure.[48] The 3 mm micro probe was used to record the heteronuclear 2D nmr data on a 30 μg sample of a low molecular weight metabolite while a heteronuclear nano-nmr probe was used to record the ^{13}C reference spectrum. Combined 3 mm micro probe/nano-nmr probe applications have also been reported in the elucidation of a complex indoloquinoline alkaloid structure[27] and a fumonisin-B_1 fungal metabolite structure.[28] In both of these studies, comparative ^{13}C NMR spectra acquired in a 3 mm micro dual probe and a heteronuclear nano-nmr probe are presented. Another combined 3 mm micro probe/nano-nmr probe application is found in the structural characterization of laingolide, a novel 15-membered macrolide from a blue green alga.[63] In this study, the direct and long-range heteronuclear chemical shift correlation experiments were performed in a 3 mm micro probe while the ^{13}C reference spectrum was recorded using a heteronuclear nano-nmr probe.

The sensitivity of heteronuclear nano-nmr probes, combined with the small volume of a nano cell (40 μl) has led to the application of this probe technology for the characterization of a novel steroid skeleton[64] through the use of the INADEQUATE[65,66] experiment.

More recently, several additional applications of nano-nmr probe technology have been reported in the characterization of natural product samples. Bierer and co-workers[67] reported using a nano-nmr probe in the characterization of the indoloquinoline alkaloid cryptolepinone, which was independently characterized by Martin and co-workers[68] using 3 mm micro probe hardware. A modified tetrapeptide, lyngbyapeptin A, has been characterized, in part, using nano-nmr to acquire a ^{13}C reference spectrum.[69] Lyngbapeptin A was described as being produced by a cyanobacterium in 'trace' amounts and thus it is likely that the heteronuclear shift correlation data were recorded using a 3 mm micro NMR probe although this was not specified in the report. Most recently, the structure of a new macrocyclic trichotehcene produced by a marine-derived fungus has been reported.[70] In this case, a Varian Nano-probe was used for the acquisition of all of the NMR data reported, including the heteronuclear shift correlation spectra.

The first reported application of nano-nmr probes in the study of biomacro-molecules is found in the report of Manzi et al.[71] on the identification of a novel glycosaminoglycan core-like molecule. Delepierre and co-workers[72] next reported studies of the structure of a potassium channel blocking toxin (peptide) from the scorpion *Pandinua imperator* using a homonuclear nano-nmr probe. That report was followed by another from the same laboratory that examined the kinetics of secondary structure recovery during the refolding of reduced hen egg white lysozyme.[73] Further work on potassium channel blocking peptide toxins was also reported later in 1997 by Delepierre and co-workers.[74] Delepierre and colleagues[75] next reported the results of a study of renatured lysozyme using nano-nmr techniques. In 1999, Delepierre, et al.,[76] reported the analysis of the structure of Pi7, an orphan peptide from the scorpion *Pandinus imperator* using ^1H nano-nmr methods. Van Halbeek and co-workers[77] initiated studies of glycan classes and their analysis by nano-nmr methods that were first reported in 2000. Finally, the biosynthesis of ganglioside mimics of *Campylobacter jejuni* has been studied at the nanomole level through the use of nano-nmr methods.[78]

Most recently, Kupce et al.[79] have examined the issue of adiabatic TOCSY MAS in liquids, demonstrating that adiabatic mixing sequences are less susceptible to modulation effects due to both rf and magnetic field homogeneities than are conventional mixing sequences.

3.4 Applications of Small Volume Cryoprobes

To date, only a scant few reports on the use of small volume cryogenic NMR probes have been reported. Withers and co-workers[22–24] have presented several posters describing the utilization of a 2.5 or 3 mm cryogenic probes for the acquisition of heteronuclear shift correlation data needed for metabolite characterization. The author and colleagues[25] have reported a comparison of conventional and cryogenic 3 mm NMR probes using a 40 μg (120 nanomoles) sample of strychnine **(4)** shown in Figure 5. Finally, although not using a small volume cryogenic probe, the author and co-workers[26] have reported a comparison of long-range $^1H-^{15}N$ heteronuclear shift correlation data (shown in Figure 6) acquired using a 3 mm sample in both a 5 mm cryogenic and conventional 3 mm NMR probes. Undoubtedly more applications of small volume cryogenic probes will appear given the substantial sensitivity advantage which these probes afford.

3.5 Phase Cycled vs. Gradient NMR Experiments When Dealing with Very Small Samples

Work in the author's laboratories at Pharmacia, directed to the characterization of very small samples of isolated and impurities of potential drug candidates, has shown that at very low concentrations the use of gradient NMR experiments is disadvantageous. Reynolds and Enriquez[80] after a discussion of this observation have gone on to report a rigorous experimental verification of this observation. They demonstrated that at high concentrations, the t_1 ridges due to incomplete suppression of $^1H-^{12}C$ components of magnetization (or that from protons bound to heteroatoms) constitutes the main source of noise in phase-cycled 2D NMR spectra. Gradient NMR pulse sequences strongly suppress this noise, as would be expected. This observation is consistent with the generally accepted advantage of gradient-based NMR experiments when only a few transients/t_1 increment will be accumulated. However, as also reported by Reynolds and Enriquez, the intensity of the t_1 ridges appears to be directly proportional to the signal strength and consequently, for very dilute samples, t_1 ridges contribute to the total noise in an HMBC experiment to only a minor extent. When sufficient numbers of transients are accumulated

per t_1 increment, the intrinsically higher sensitivity of phase-cycled experiments vs. gradient-based experiments makes the former preferable.

To illustrate this observation rather dramatically, Russell[81] has recorded gradient and phase-cycled HMBC data for a 20 μg sample of retrorscine **(8)**. These data are shown in Figure 10 compared to data from a 700 μg sample of the same molecule. The 700 μg data were acquired overnight at 500 MHz using a conventional Nalorac MIDTG-500-3 gradient micro inverse 3 mm NMR probe and provide a references for the responses expected to be observed in the spectrum.

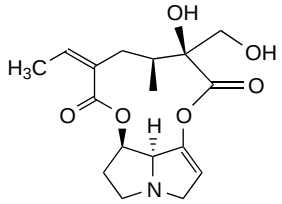

(8)

The reference gradient HMBC spectrum acquired overnight using the 700 μg sample of the alkaloid is shown in Figure 10 Panel a and contains all of the responses expected for the molecule. The phase-cycled, non-gradient HMBC spectrum acquired using a 20 μg sample of the alkaloid in 160 h is shown in Panel b. A significant percentage of the possible responses are observed in the spectrum, particularly when traces for the individual carbons are extracted from the data matrix. In contrast, the gradient HMBC spectrum on the same 20 μg sample after an identical data acquisition, shown in Panel c, shows only the most intense responses in the spectrum. This result is consistent with the work of Reynolds and Enriquez[80] which was done with substantially larger samples.

4 CONCLUSIONS

Small volume, high sensitivity NMR probes have had a significant impact on the conduct of research in many areas of chemistry and biochemistry that depends on NMR methods since the first reports on the contemporary versions of these probes appeared about a decade ago. Probes have been developed in a number of formats for conventional tube configurations including 3, 2.5, 1.7 and 1 mm. New probe technologies such as Varian's Nano-probe and the μ-Coil probes have also been reported. The development of small volume, cryogenic NMR probes is now on-going. With the continuing developments and refinements in this rapidly advancing field of NMR research, sample requirements have concomitantly decreased. COSY spectra on samples as small as 200 ng of cryptolepine **(1)**, HMQC spectra on 1 μg of ibuprofen **(3)**, and HMBC spectra on 6 μg of cryptolepinone, an oxidative degradation product contained in a sample of cryptolepine **(1)** have been discussed in this report. While it is difficult to foresee how much further sample requirements will diminish in the coming years, it is assured that with the advent of small volume, cryogenic NMR probes that the frequency of studies with very small samples will increase in the near future.

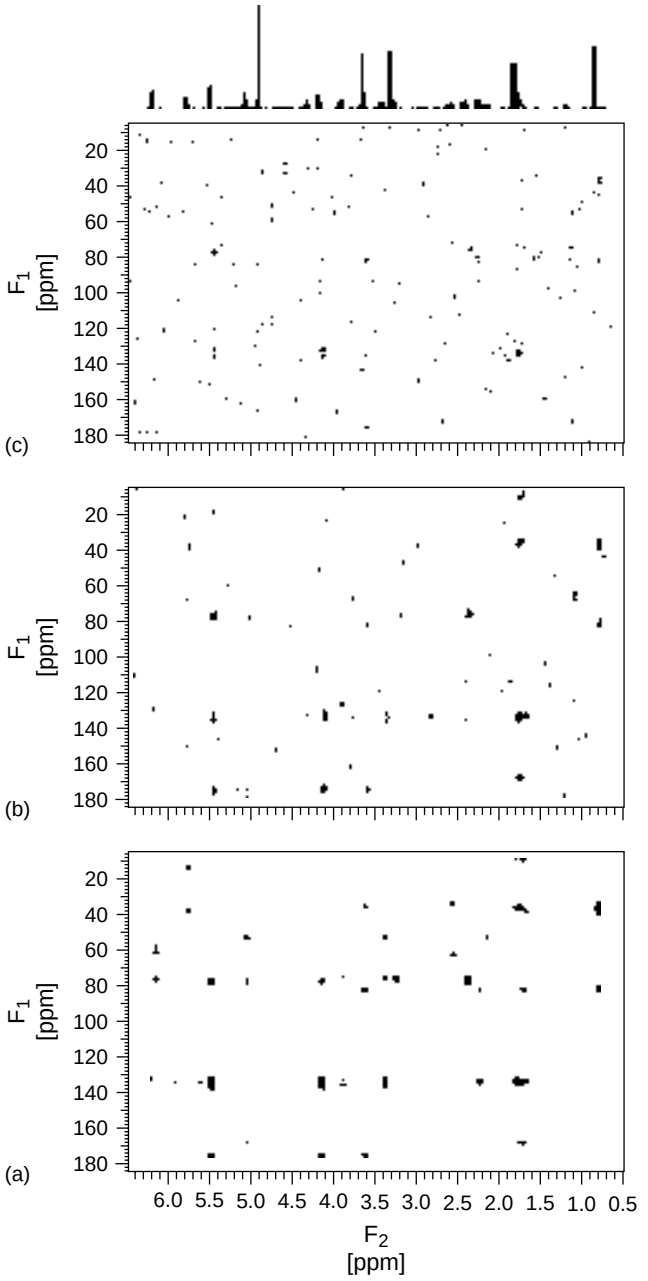

Figure 10 Comparison HMBC spectra of retrorscine **(8)**.[81] The 8 Hz optimized gradient HMBC reference spectrum shown in panel (a) was acquired overnight using a 700 μg sample of the alkaloid dissolved in 150 μl of d_4-methanol. The data shown in panels (b) and (c) were accumulated using a 20 μg sample of the alkaloid dissolved in 150 μl of d_4-methanol. The data shown in panel (b) were acquired using a conventional phase-cycled, non-gradient HMBC pulse sequence. In comparison, the data shown in panel (c) were obtained using the more contemporary gradient HMBC experiment. The superior performance at these low levels of the phase-cycled non-gradient HMBC experiment is consistent with the recent report of Reynolds and Enriquez[80]

5 REFERENCES

1. E. Odelblad, 'Nordisk Forening for Obsterik och Gyynekologi', Karolinska Institute: Stockholm, 1966.
2. J. N. Shoolery, 'Topics in Carbon-13 NMR Spectroscopy', ed G. C. Levy, Wiley: New York, 1979, Vol. 3, p 28.

3. R. C. Crouch and G. E. Martin, *J. Nat. Prod.*, 1992, **55**, 1343.
4. A. Bax and S. Subramanian, *J. Magn. Reson.*, 1986, **67**, 565.
5. A. Bax and M. F. Summers, *J. Magn. Reson.*, 1986, **108**, 2093.
6. R. C. Crouch and G. E. Martin, *Magn. Reson. Chem.*, 1992, **30**, S66.
7. T. Barbara, *J. Magn. Reson.*, 1994, **109A**, 265.
8. J. N. Shoolery, *Prog. NMR Spectrosc.*, 1995, **28**, 37.
9. P. A. Kifer, L. Baltusis, D. M. Rice, A. A. Tymiak, and J. N. Shoolery, *J. Magn. Reson.*, 1996, **119A**, 65.
10. G. E. Martin, unpublished results, 1995.
11. V. V. Krishnamurthy, unpublished results, 1998.
12. D. L. Olson, T. L. Peck, A. G. Webb, R. L. Magin, and J. V. Sweedler, *Science*, 1995, **270**, 1967.
13. R. Subramanian and A. G. Webb, *Anal. Chem.*, 1998, **70**, 2454.
14. Y. Li, A. M. Wolters, P. V. Malawey, J. V. Sweedler, and A. G. Webb, *Anal. Chem.*, 1999, **71**, 4815.
15. B. Behnia and A. G. Webb, *Anal. Chem.*, 1998, **70**, 5326.
16. R. Subramanian, J. V. Sweedler, and A. G. Webb, *J. Am. Chem. Soc.*, 1999, **121**, 2333.
17. G. E. Martin, R. C. Crouch, and A. P. Zens, *Magn. Reson. Chem.*, 1998, **36**, 551.
18. G. E. Martin, J. E. Guido, R. H. Robins, M. H. M. Sharaf, A. N. Tackie, and P. L. Schiff, Jr., *J. Nat. Prod.*, 1998, **61**, 555.
19. C. E. Hadden and G. E. Martin, *J. Nat. Prod.*, 1998, **61**, 969.
20. C. E. Hadden and G. E. Martin, *Magn. Reson. Chem.*, 1999, **37**, 385.
21. G. Schlotterbeck, A. Ross, H. Senn, R. Hochstrasser, H. Tschirky, R. Seydoux, D. Marek, T. Kühn, O. Schett, and M. Warden, *42nd Experimental Nuclear Magnetic Resonance Conference*, Orlando, FL, March 11–16, 2001, Abst. W&Th, p 143.
22. J. Pease, R. Withers, R. Nast, A. Deese, P. Calderon, M. Saumil, T. Kelly, and F. Laukein, *40th Experimental Nuclear Magnetic Resonance Conference*, Orlando, FL, February 28–March 5, 1999, Abst. W&Th, p 202.
23. Y. Liu, J. Pease, B. Potts, A. Deese, Y. D. Liu, M. O'Neil-Johnson, R. Withers, and R. Nast, *SMASH 2000 – Small Molecule NMR Conference*, Argonne, IL, July 16–19, Abstr. 21.
24. M. A. O'Neil-Johnson, J. Pease, Y. Liu, B. Potts, A. Deese, R. Withers, and R. Nast, *42nd Experimental Nuclear Magnetic Resonance Conference*, Orlando, FL, March 11–16, 2001, Abst. W&Th, p 162.
25. D. J. Russell, C. E. Hadden, G. E. Martin, A. A. Gibson, A. P. Zens, and J. L. Carolan, *J. Nat. Prod.*, 2000, **63**, 1047.
26. R. C. Crouch, W. Llanos, K. G. Mehr, Chad E. Hadden, D. J. Russell, and G. E. Martin, *Magn. Reson. Chem.*, 2001, **39**, 555.
27. For a review of accordion-optimized long-range heteronuclear 2D NMR experiments, see G. E. Martin, in *Annu. Rep. NMR Spectrosc.*, ed G. A. Webb, Academic Press: New York, 2000, Vol. H6, pp. 37–100.
28. M. H. M. Sharaf, P. L. Schiff, Jr., A. N. Tackie, C. H. Phoebe, Jr., L. Howard, C. Meyers, C. E. Hadden, S. K. Wrenn, A. O. Davis, C. W. Andrews, D. Minick, R. L. Johnson, J. P. Shockcor, R. C. Crouch, and G. E. Martin, *Magn. Reson. Chem.*, 1995, **33**, 767.
29. S. M. Musser, R. M. Eppley, E. P. Mazzola, C. E. Hadden, J. P. Shockcor, R. C. Crouch, and G. E. Martin, *J. Nat. Prod.*, 1995, **58**, 1392.
30. G. E. Martin and C. E. Hadden, *Magn. Reson. Chem.*, 1999, **37**, 721.
31. G. E. Martin, R. C. Crouch, and C. W. Andrews, *J. Heterocyclic Chem.*, 1995, **32**, 1759.
32. H. Koshino and J. Uzawa, *Kagaku to Seibutsu*, 1995, **33**, 252.
33. C. E. Hadden and G. E. Martin, *J. Nat. Prod.*, 1998, **61**, 969.
34. G. E. Martin and C. E. Hadden, *Magn. Reson. Chem.*, 2000, **38**, 251.
35. C. E. Hadden, G. E. Martin, and V. V. Krishnamurthy, *J. Magn. Reson.*, 1999, **140**, 274.
36. C. E. Hadden, G. E. Martin, and V. V. Krishnamurthy, *Magn. Reson. Chem.*, 2000, **38**, 143.
37. R. C. Crouch, G. E. Martin, S. M. Musser, H. R. Grenade, and R. W. Dickey, *Tetrahedron Lett.*, 1995, **38**, 6827.
38. W. F. Reynolds, M. Yu, and R. G. Enriquez, *Magn. Reson. Chem.*, 1997, **35**, 614.
39. P. A. Keifer, *Drug Discovery Today*, 1997, **2**, 468.
40. P. A. Keifer, *Curr. Opin. Biotech.*, 1997, **10**, 34.
41. N. Wu, T. L. Peck, A. G. Webb, R. L. Magin, and J. V. Sweedler, *Anal. Chem.*, 1994, **66**, 3849.
42. D. L. Olson, M. E. Lacey, and J. V. Sweedler, *Anal. Chem.*, 1998, **70**, A257.
43. M. E. Lacey, R. Subramanian, D. L. Olson, A. G. Webb, and J. V. Sweedler, *Chem. Rev.*, 1999, **99**, 3133.
44. M. Delepierre, *J. Chim. Phys.*, 1998, **95**, 235.
45. G. E. Martin and R. C. Crouch, in 'Modern Methods of Plant Analysis', eds H. F. Linskens and J. F. Jackson, Springer-Verlag: Berlin, 1994, Vol. 15, pp. 25–89.
46. J. Ø. Duus, C. H. Gotfredsen, and K. Bock, *Chem. Rev.*, 2000, **100**, 4589.
47. G. E. Martin and C. E. Hadden, *J. Nat. Prod.*, 2000, **63**, 543.
48. J. P. Shockcor, R. M. Wurm, I. S. Silver, R. C. Crouch, and G. E. Martin, *Tetrahedron Lett.*, 1994, **35**, 4919.
49. R. C. Crouch, G. E. Martin, R. W. Dickey, D. G. Baden, R. E. Gawley, K. S. Rein, and E. P. Mazzola, *Tetrahedron*, 1995, **51**, 8409.
50. M. H. M. Sharaf, P. L. Schiff, Jr., A. N. Tackie, C. H. Phoebe, Jr., A. O. Davis, C. W. Andrews, R. C. Crouch, and G. E. Martin, *J. Heterocyclic Chem.*, 1995, **32**, 1631.
51. M. H. M. Sharaf, P. L. Schiff, Jr., A. N. Tackie, C. H. Phoebe, Jr., and G. E. Martin, *J. Heterocyclic Chem.*, 1996, **33**, 239.
52. M. H. M. Sharaf, P. L. Schiff, Jr., A. N. Tackie, C. H. Phoebe, Jr., R. L. Johnson, D. Minick, C. W. Andres, R. C. Crouch, and G. E. Martin, *J. Heterocyclic Chem.*, 1996, **33**, 789.
53. W. F. Reynolds, S. McLean, H. Jacobs, and W. W. Harding, *Can. J. Chem.*, 1999, **77**, 1922.
54. W. L. Fitch, G. Detre, C. P. Homes, J. N. Shoolery, and P. A. Keifer, *J. Org. Chem.*, 1994, **59**, 7955.
55. P. A. Keifer, L. Baltusis, D. M. Rice, A. A. Tymiak, and J. N. Shoolery, *J. Magn. Reson.*, 1996, **199A**, 65.
56. P. A. Keifer, *J. Org. Chem.*, 1996, **61**, 1558.
57. T. Wehler and J. Westman, *Tetrahedron Lett.*, 1996, **37**, 4771.
58. M. Pursch, G. Schlotterbeck. L.-H. Tseng, K. Albert, and W. Rapp, *Angew. Chem., Intl. Ed., Engl.*, 1996, **35**, 2867.
59. A. M. Seffler and S. W. Gerritz, *J. Comb. Chem.*, 2000, **2**, 127.
60. T. Mohri, Y. Nakahara, W. Zhang, Y. Nakatsuji, T. Murreishi, Y. Miyoji, and I. Ikeda, *Chem. Lett.*, 2000, 998.
61. M. A. Gallop and W. L. Fitch, *Curr. Opin. Chem. Biol.*, 1997, **1**, 94.
62. D. Moka, R. Vorreuther, H. Schicha, M. Spraul, E. Humpfer, M. Lipinski, P. J. D. Foxall, J. K. Nicolson, and J. C. Lindon, *J. Pharm. Biomed. Anal.*, 1998, **17**, 125.
63. D. Klein, J.-C. Braekman, D. Daloze, L. Hoffmann, and V. Demoulin, *Tetrahedron Lett.*, 1996, **37**, 7519.
64. D. C. Chauret, T. Durst, J. T. Amason, P. Sanchez-Vindas, L. San Roman, L. Poveda, and P. A. Keifer, *Tetrahedron Lett.*, 1996, **44**, 7575.
65. A. Bax, R. Freeman, and T. A. Frenkiel, *J. Am. Chem. Soc.*, 1981, **103**, 2102.
66. A. Bax, R. Freeman, and T. A. Frenkiel, *J. Magn. Reson.*, 1981, **43**, 478.
67. D. M. Fort, J. Vlitvak, J. L. Chm. Q. Lu, P.-W. Phuan, R. Cooper, and D. E. Bierer, *J. Nat. Prod.*, 1998, **61**, 1528.
68. M. H. M. Sharaf, P. L. Schiff, Jr., A. N. Tackie, and G. E. Martin, *J. Heterocyclic Chem.*, 1998, **35**, 1365.
69. D. Klein, J.-C. Brakeman, D. Daloze, L. Hoffmann, G. Castillo, and V. Demoulin, *Tetrahedron Lett.*, 1999, **40**, 695.
70. M. Namikoshi, K. Akano, S. Meguro, I. Kasuga, Y. Mine, T. Takahashi, and H. Bobayashi, *J. Nat. Prod.*, 2001, **64**, 396.
71. A. Manzi, P. V. Salimath, R. C. Spiro, P. A. Keifer, and H. H. Freeze, *J. Biol. Chem.*, 1995, **270**, 9154.

72. M. Delpierre, A. Prochnicka-Chalufour, and L. D. Possani, *Biochemistry*, 1997, **36**, 2649.
73. P. Roux, M. Delepierre, M. E. Goldberg, and A.-F. Chaffotte, *J. Biol. Chem.*, 1997, **272**, 24 843.
74. M. Delepierre, A. Prochnicka-Chalufour, and L. D. Possani, *Toxicon*, 1997, **36**, 1599.
75. M. Delepierre, P. Roux, A.-F. Chaffotte, and M. E. Goldberg, *Magn. Reson. Chem.*, 1998, **36**, 645.
76. M. Delepierre, A. Prochnicka Chalufour, J. Boisbouvier, and L. D. Possani, *Biochemistry*, 1999, **38**, 16 756.
77. A. E. Manzi, K. Norgard-Sumnicht, S. Argade, J. D. Marth, H. van Halbeek, and A. Varki, *Glycobiology*, 2000, **10**, 669.
78. M. Bilgert, J.-R. Brisson, M.-F. Karwaski, J. Michniewicz, A.-M. Cunningham, Y. Wu, N. M. Young, and W. W. Wakarchuk, *J. Biol. Chem.*, 2000, **I275**, 3896.
79. E. Kupce, P. A. Keifer, and M. DelPiere, *J. Magn. Reson.*, 2001, **148**, 115.
80. W. F. Reynolds and R. G. Enriquez, *Magn. Reson. Chem.*, 2001, **39**, 531.
81. D. J. Russell, unpublished data.

Acknowledgements

The author would like to acknowledge the assistance of his colleagues, C.E. Hadden and D.J. Russell at Pharmacia Corp., K. Krishnamurthy at Eli Lily and R.C. Crouch at Varian, Inc. for discussions pertaining to the Nano-probe. Thanks also go to Professor W.F. Reynolds of the University of Toronto for many stimulating discussions on the topic of small sample NMR probes and to Professor P.L. Schiff, Jr. of the University of Pittsburgh for providing many of the natural product samples that have been studied and used as model compounds during the development of small volume NMR probe technology over the past decade.

Biographical Sketch

Gary Edwin Martin, *b* 1949. Ph.D. 1975 Pharmaceutical Sciences, University of Kentucky. Professor, University of Houston, 1975–89. Principal Scientist Burroughs Wellcome Co., Research Triangle Park, NC 1989–1995. Senior Fellow, Pharmacia Corp. 1996–present. Approx. 250 publications. Current research interests: high sensitivity, small volume and cryogenic NMR probe development and applications; development of new long-range heteronuclear shift correlation experiments; application of long-range $^{1}H-^{15}N$ heteronuclear shift correlation at natural abundance.

Multiple Quantum Spectroscopy in Liquid Crystalline Solvents

Leslie D. Field
Sydney University, NSW, Australia

1	Introduction	1
2	Multiple Quantum NMR of Samples Dissolved in Liquid Crystalline Solvents	1
3	Excitation of Multiple Quantum Coherences	2
4	Detection of Multiple Quantum Coherences	3
5	Methods of Spectral Analysis and Spectral Simulation	5
6	Applications of MQ NMR to Samples Dissolved in Liquid Crystalline Solvents	5
7	Related Articles	8
8	References	8

1 INTRODUCTION

Liquid crystals can be loosely defined as materials with properties intermediate between those of solids and liquids (mesophases). Liquid crystals typically flow like viscous liquids but the phase exhibits some degree of molecular packing or structure whereby individual molecules tend to align, making the mesophase anisotropic.

1.1 NMR in Liquid Crystalline Solvents

Most molecules that form a nematic mesophase are able to dissolve a small amount of solute compound without destroying the mesophase. Since the first reports of using liquid crystals as solvents for NMR spectroscopy, high resolution NMR in liquid crystalline solution has developed into an important area.[1] The amount of solute that can be dissolved in a nematic mesophase depends on the mesophase and the solute, but solute concentrations of 5 wt % are common and concentrations of 10–15 wt % are sometimes achievable without disrupting the liquid crystalline properties of the solvent.

The motion of solute molecules dissolved in a nematic mesophase is restricted by the arrangement of the mesophase molecules. The anisotropy of the arrangement of the solvent molecules induces anisotropy in the movement of the solute molecules via dispersion forces. A solute dissolved in an oriented mesophase is forced to undergo nonrandom (anisotropic) motion because of its interactions with the aligned solvent. If the nematic mesophase is aligned in a magnetic field then alignment of the mesophase is reflected in the anisotropy of the motion of the solute molecules.

The rapid motion of molecules in an oriented mesophase results in the averaging of the intermolecular dipolar interactions to zero. However, the intramolecular dipolar interactions have a nonzero average.

Qualitatively the NMR spectra of solutes oriented in mesophases are more complex than the spectra obtained in isotropic solvents, for two reasons (see ***Liquid Crystalline Samples: Spectral Analysis***):

1. The nonzero averaging of dipolar couplings results in many more coupling constants (splittings) being expressed in the spectrum. A dipolar coupling constant appears for every pair of interacting nuclei.
2. The magnitude of the dipolar coupling constants (D_{ij}), between a pair of interacting nuclei is generally large (up to a few kilohertz) compared with the indirect coupling constants (typically a few hertz). This results in virtually all spectra of solutes dissolved in an oriented mesophase being highly second order and adds to the spectral complexity.

2 MULTIPLE QUANTUM NMR OF SAMPLES DISSOLVED IN LIQUID CRYSTALLINE SOLVENTS

The signals observed in a conventional NMR spectrum (single rf pulse followed by signal acquisition and FT of the resulting FID) are governed by selection rules which dictate that transitions can only be induced between energy levels differing in total spin quantum number by $\Delta M = \pm 1$ (single quantum transitions). Multiple quantum NMR (MQ NMR)[2] is concerned with the observation of nuclear transitions where $\Delta M \neq \pm 1$.

The number of transitions in the single quantum NMR spectrum of a solute dissolved in an anisotropic solvent increases rapidly with the number of coupled spins. A molecule with a single proton would have a ^{1}H spectrum with only one transition. A system containing two protons would have four possible transitions, and a spin system composed of three nonequivalent protons has 15 transitions.

The number of transitions for an unsymmetrical spin system (disregarding symmetry considerations) can be calculated as[3]

$$\text{No. single quantum transitions} = (2N)!/[(N-1)!(N+1)!] \quad (1)$$

This is an exponential function where the number of transitions increases dramatically as the number of interacting spins increases (Figure 1). In an 8-spin system there would be 1.14×10^3 transitions in the single quantum spectrum; in a 10-spin system there would be 1.67×10^5 transitions.

If there is symmetry present in the spin system (i.e. chemically or magnetically equivalent nuclei) the number of transitions is reduced. For the symmetrical six proton spin system of benzene there are 72 transitions, compared with 792 transitions in a six proton system with no symmetry.

Given a reasonable linewidth for each transition, substantial overlap occurs in the single quantum spectrum of a large spin system, and the spectrum rapidly degenerates to an unresolved broad lump. In higher spin systems, it becomes impossible to resolve or assign individual transitions for an iterative computer analysis. MQ NMR can considerably reduce the complexity of the spectrum of a solute dissolved in a liquid crystalline solvent, and the main benefit of MQ NMR lies in the fact that there are fewer transitions in the very high MQ spectra.

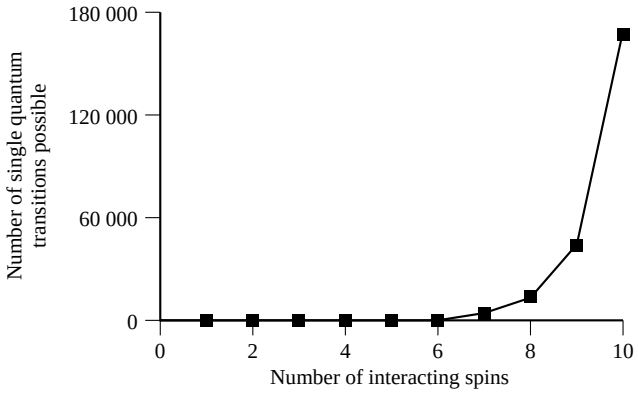

Figure 1 The number of single quantum transitions as a function of the number of interacting nuclei ($I = \frac{1}{2}$)

The number of M quantum transitions in a system of N nuclei ($I = 1/2$), neglecting symmetry, is given by

$$\text{No. of } M \text{ quantum transitions} = (2N)!/[(N - M)!(N + M)!] \quad (2)$$

Representative values are summarized in Table 1.

In the N quantum spectrum of an N-spin system, there will always be only one transition. The $(N - 1)$ quantum spectrum of an N-spin system will contain only $2N$ transitions. For large N, the $N - 1$ and $N - 2$ quantum spectra will contain only a few transitions and will be much less complex and more easily analyzed than the single quantum spectrum.

3 EXCITATION OF MULTIPLE QUANTUM COHERENCES

Coherence between states separated by $\Delta M \neq 1$ cannot be observed directly, but is usually detected indirectly by its modulation of single quantum coherence in a two-dimensional NMR experiment. A two-dimensional NMR experiment[4] for exciting and detecting MQ spectra can be divided schematically into five time frames, as shown in Table 2.

Providing that MQ coherences (MQCs) can be produced by a suitable preparation sequence, and mixed to observable single quantum coherence with an appropriate 'mixing' sequence, the MQ frequencies of a spin system can be obtained by systematically varying the duration of the 'evolution' period (t_1) followed by Fourier transformation over t_1. Compared with samples in isotropic solution, MQCs can be excited relatively easily in samples dissolved in liquid crystalline solution. The large dipolar coupling constants expressed ensure that coherences evolve rapidly and MQC can be excited efficiently before the effects of relaxation complicate coherence development in the spin system.

3.1 Nonselective Excitation

The most common (and simplest) method for preparing MQC is by use of two $\pi/2$ pulses separated by a fixed delay. The simplest mixing sequence is a single $\pi/2$ pulse and this means that a three-pulse sequence (Figure 2) can be used to record multiple quantum spectra.

The sequence of two hard pulses in the preparation part in Figure 2 nonselectively generates coherence of all orders possible in the spin system. Coherences are not excited uniformly and the efficiency with which MQC is excited depends specifically on the couplings and chemical shifts of the nuclei in the spin system and the choice of the interval d_1. Broad band excitation techniques have been proposed[5] where the value of d_1 in the preparation sequence is varied either in a pseudorandom or systematic fashion to achieve a more uniform excitation in the multiple quantum domain. Weitekamp et al.[6] have devised an experimental search procedure for optimizing the delays in the preparation period of the MQ excitation sequence.

Table 1 The Number of Transitions in the M Quantum Spectra as a Function of the Number of Interacting Nuclei ($I = \frac{1}{2}$)

	Number of spins ($I = \frac{1}{2}$)						
ΔM	2	4	6	8	10	15	20
1	4	56	792	11440	1.68×10^5	1.45×10^8	1.31×10^{11}
2	1	28	495	8008	1.26×10^5	1.19×10^8	1.13×10^{11}
4		1	220	1820	38760	5.46×10^7	6.28×10^{10}
6			1	120	4845	1.43×10^7	2.32×10^{10}
8				1	190	2.04×10^6	5.58×10^9
10					1	1.42×10^5	8.48×10^8
15						1	6.58×10^5
20							1

Table 2 The Five Time Frames in the Two-dimensional MQ NMR Experiment[a]

Relaxation	Preparation	Evolution	Mixing	Detection
Spin system relaxes between experiments	Generate MQC in the coupled spin system	MQC evolves with time (t_1)	Mixes MQC to observable SQC	Detect SQC as a FID (t_2)

[a]MQC, multiple quantum coherence; SQC, single quantum coherence.

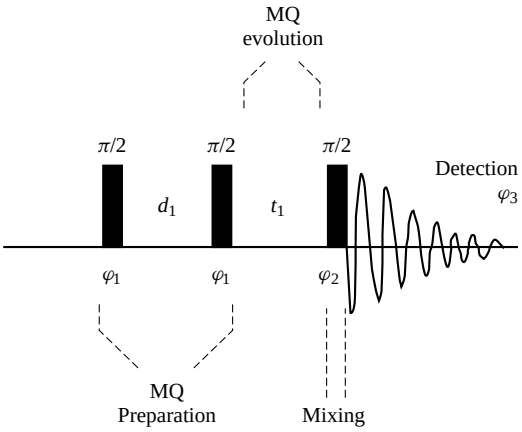

Figure 2 Three-pulse sequence for the observation of MQ spectra

3.2 Selective Excitation

Nonselective excitation of MQC excites all possible coherences, but leaves most of the spectral intensity in the single quantum and low multiple quantum spectra because these spectra have the most transitions.[3b] As a result, the simpler high-order coherences are comparatively weak. An alternative approach to the excitation of MQC is selectively to excite only a few orders of coherence and more effectively channel or focus the available signal into one order (or a few selected orders).

Order selective excitation has been achieved by the use of phase-cycled sequences of rf pulses[7] and composite pulse trains.[8] Pines et al.[7,9] have established that an nk quantum selective excitation sequence ($k = 0, \pm1, \pm2, \cdots$) can be constructed by repeating an appropriate sequence with a phase increment $2\pi/n$ between repetitions:

$$\varphi = 0 \quad \varphi = 2\pi/n \; \varphi = 4\pi/n \quad \varphi = 2(n-1)\pi/n$$
$$[p_1 \ldots p_q]\,[p_1 \ldots p_q]\,[p_1 \ldots p_q] \ldots [p_1 \ldots p_q]$$

The pulse sequences $[p_1 \cdots p_q]$ employed in each section of the sequence can be nonselective; however, only certain sequences are effective in efficiently generating the desired orders of MQC. Sequences involving several thousand cycled pulses have been explored.[7,9] An upper limit on the length of the excitation sequence is set by relaxation processes in the spin system. Effective phase-cycled excitation sequences must generate MQC efficiently and compensate for the effects of imperfect rf hardware and pulses.

4 DETECTION OF MULTIPLE QUANTUM COHERENCES

The frequencies of MQCs are obtained indirectly using two-dimensional NMR sequences whereby the multiple quantum frequencies modulate the observable single quantum spectrum. The two-dimensional spectrum contains multiple quantum frequencies in F_1 and single quantum frequencies in F_2. The frequencies of the multiple quantum spectrum are most conveniently obtained as F_1 projections from the two-dimensional spectrum.

It is not necessary to acquire an entire two-dimensional data set to obtain the multiple quantum frequencies. MQ spectra can be obtained by acquiring a single point in t_2 (at $t_2 = 0$ or some other value) and then transforming the resulting one-dimensional sequence of points as a function of t_1. In theory, the FT of the $t_2 = 0$ row of a two-dimensional data set is identical to the F_1 projection of the entire two-dimensional data set.[10]

If the MQ preparation sequence does not perfectly select coherences from an individual MQ order, then the MQ spectrum detected will be a complex superposition of subspectra from the various MQCs excited. There are several methods available to filter or separate the MQ spectra of various orders.

4.1 Order Selective Detection

4.1.1 Dependence on Resonance Offset

n Quantum coherence evolves n-fold more rapidly during the t_1 evolution period of the MQ experiment than does single quantum coherence. If the single quantum spectrum is centered at a frequency approximately $\Delta\omega$ from the rf transmitter, transitions in the n quantum spectrum are centered at a frequency $n\Delta\omega$. With nonselective excitation, multiple quantum spectra are separated by $\Delta\omega$ and by judicious selection of the transmitter offset, the spectra of various multiple quantum orders can be cleanly separated (Figure 3) in the frequency domain.

The main disadvantages of using transmitter offsets to separate various orders of MQC are: (i) offset frequencies of 10–30 kHz are often required to obtain clean separation of the coherence orders and the large offset results in nonuniform rf distribution and homogeneity across the spectrum: and (ii) for a nonselective experiment where all orders of coherence (up to $\pm N$ orders in an N-spin system) are detected, the total sweep width required in F_1 is prohibitively large. The F_1 sweep width is approximately $N*SW$, where SW is the approximate spectral width of any of the orders of coherence in the spin system; SW may be 100–300 kHz and necessarily gives rise to poor digital resolution.

4.1.2 Time Proportional Phase Incrementation

Time proportional phase incrementation (TPPI) enables the separation of spectra of various coherence orders. If the phase of the excitation radiation is incremented by $\Delta\phi = \Delta\omega{\cdot}\Delta t_1$ each time that t_1 is incremented by Δt_1, the n quantum spectrum is centered at a frequency $n\Delta\omega$ from the transmitter in the two-dimensional MQ NMR spectrum. MQ orders are separated in frequency by $\Delta\omega$ in the same fashion as if an offset had been employed.

4.1.3 Order Selective MQ Filtration Using Phase Cycling

Order selective detection of the spectrum of a desired order n is achieved by coadding $4n$ FIDs at each value of τ_1 with the phase of the preparation rf radiation (φ_1 in Figure 2) incremented from $2\pi/4n$ to 2π in steps of $2\pi/4n$ with the receiver phase (φ_3 in Figure 2) incremented by $\pi/2$ at each step.[11] Two-dimensional Fourier transformation over τ_1 and τ_2 affords a two-dimensional spectrum which has the MQ

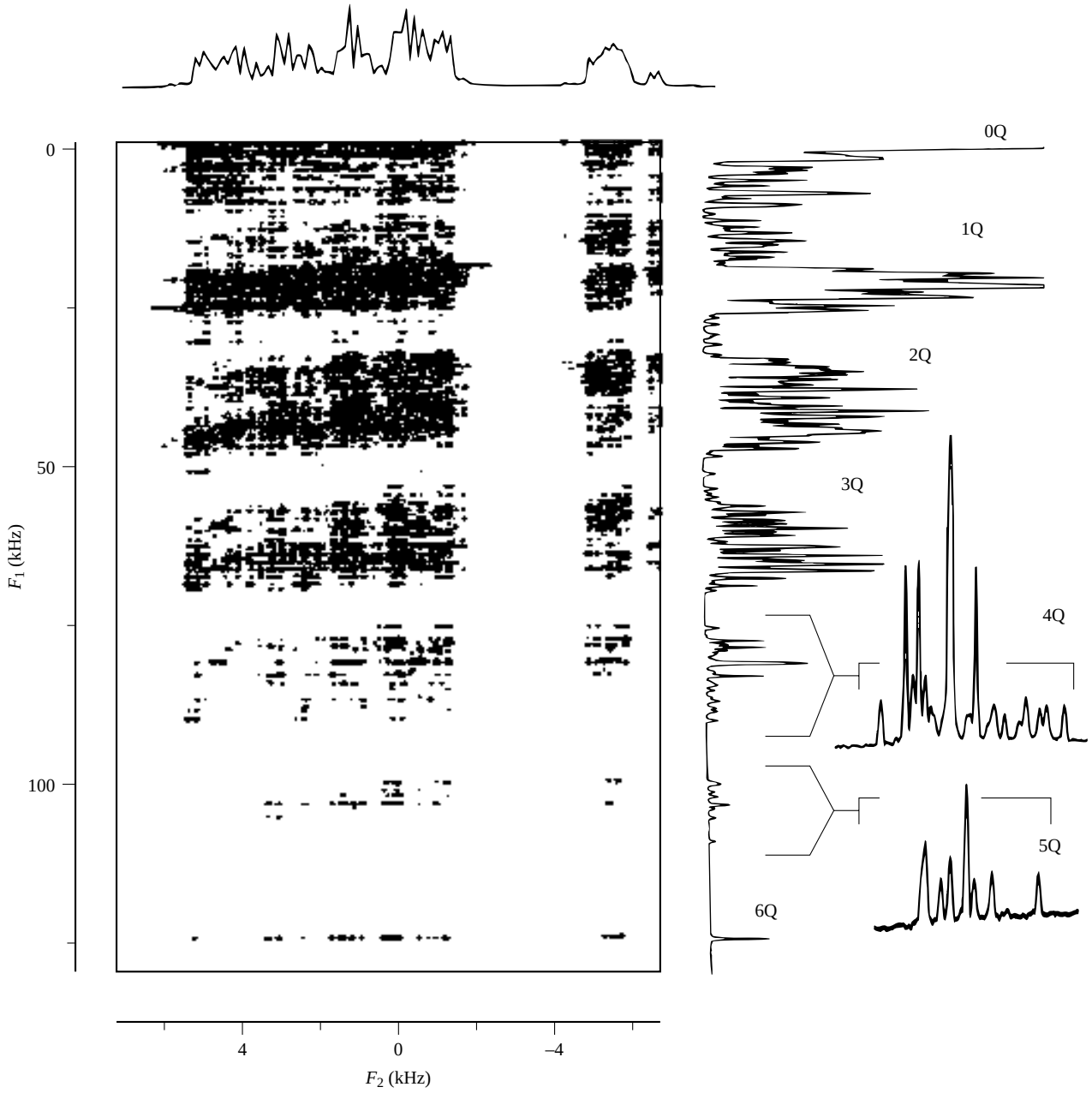

Figure 3 The separation of MQ spectra by employing a transmitter offset: ^{1}H spectrum of 2-methylthiophene aligned in a liquid crystalline solvent. The spectrum was acquired with the pulse sequence shown in Figure 2 with the transmitter offset approximately 20.7 kHz from the center of spectrum. The full spectrum is symmetrical about $F_1 = 0$ and only half of the spectrum is shown. Frequencies in the MQ spectrum are obtained from an F_1 projection of the two-dimensional data set

frequencies of the desired order of MQC in F_1 and the MQ filtered single quantum spectrum in F_2.

4.1.4 Coherence Echo Filtration

Order selective detection of the spectrum of a desired order n has been achieved by exploiting the phase properties of MQC transfer echoes. An additional (fixed) period d_e is inserted in the MQ pulse sequence, prior to the mixing pulse of the MQ pulse sequence (Figure 4). The delay d_e results in the MQCs evolving beyond the normal τ_1 period and coherence transfer echoes of the n quantum coherences maximize in the detection period at nd_e.[12] Different coherence orders give rise to echoes which maximize at different times in the detection period. The spectra derived from individual orders of coherence can be obtained by selecting a detection window to coincide with the maximum signal of the desired order of coherence.

4.1.5 Use of Magnetic Field Gradients

Order selective detection of the spectrum of a desired order n has been achieved by using field gradients.[13] A field gradient pulse of amplitude g is applied at the end of the MQ evolution

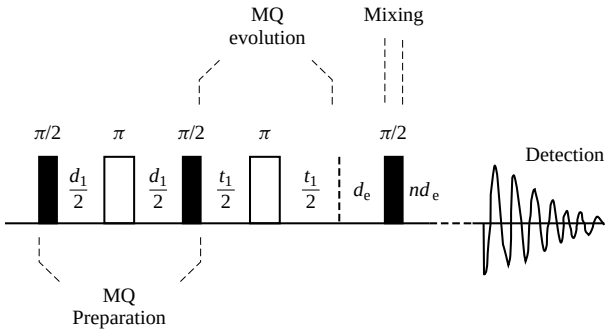

Figure 4 Pulse sequence for selectively observing MQC transfer echoes

period, prior to the mixing section of the MQ pulse sequence (Figure 5). A refocusing gradient of amplitude *ng* immediately after the mixing sequence selects only signals from the *n*-quantum spectrum.[12a,14]

4.1.6 Phase Sensitive MQ Spectra

A disadvantage of most simple mixing sequences which convert MQCs to detectable single quantum coherence is that the detectable single quantum spectrum has both absorption and dispersion components. As spin systems become larger, the single quantum spectrum degenerates to a mass of overlapping resonances, and any mixing sequence which results in signals of differing phase causes signal cancellation. In larger, more complex spin systems, the single quantum spectrum becomes weaker and inherently more difficult (or impossible) to detect. Pines et al.[15] have developed a general class of MQ experiments where the MQ preparation sequence is matched with a mixing sequence (a time reversal sequence) to give a single quantum spectrum which is in-phase. There are a number of matched preparation/mixing sequences and these have been used to observe high-order MQ spectra, including those in solids.

Another consequence of simple MQ sequences is that the MQ spectra obtained are obtained as spectra that cannot be phased. Most MQ spectra which have been recorded from samples dissolved in liquid crystalline solution have been transformed as magnitude spectra. Using appropriately matched preparation and mixing sequences, pure absorption spectra

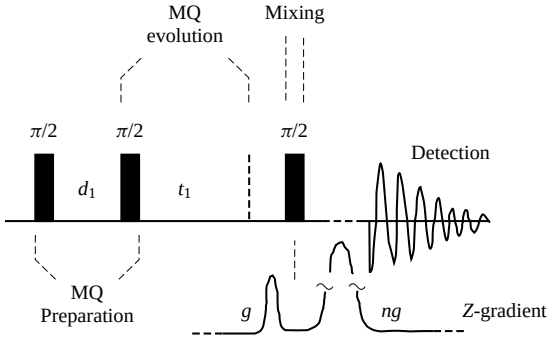

Figure 5 Pulse sequence for selectively observing MQC using field gradient filtration

have been recorded,[2b,16] and these show improved sensitivity and resolution compared with corresponding magnitude spectra.

5 METHODS OF SPECTRAL ANALYSIS AND SPECTRAL SIMULATION

The energy levels of an *n*-spin system can be calculated if the dipolar coupling constants D_{ij}, scalar coupling constants J_{ij}, chemical shifts ν_i, and quadrupolar coupling constants q_{ij} are known. The energy levels are grouped into manifolds according to their Zeeman quantum number (M) and irreducible symmetry representations. m Quantum transitions occur between energy levels of the same symmetry where $\triangle M = m$. The frequencies of MQ transitions are not difficult to calculate and the frequencies in experimental MQ spectra have been fitted iteratively to calculated frequencies using modifications of LAOCOON type[17] computer algorithms. The calculation of the correct intensities of MQ transitions is more demanding since the transition intensities are a complex function of the specific pulse sequence used to generate the spectrum. Transition intensities in MQ spectra derived from a simple three-pulse sequence (Figure 2) have been estimated using a statistical approach whereby all symmetry-allowed transitions are assumed to be equally excited. Averaging over a range of d_1 values, the integrated intensity per order decreases as $\triangle M$ increases, but the average intensity per transition increases as $\triangle M$ increases.[3b] The estimation of transition intensities in MQ spectra has been extended to excitation sequences involving order selective composite pulse excitation, and the calculations provide a reliable means for theoretically optimizing the efficiency of the excitation sequence.[18]

6 APPLICATIONS OF MQ NMR TO SAMPLES DISSOLVED IN LIQUID CRYSTALLINE SOLVENTS

6.1 Structural Studies

In the spectra of compounds dissolved in liquid crystalline solution, dipolar interactions between nuclei are not averaged to zero and the spectra can, in principle, be analyzed to obtain values for the dipolar coupling constant D_{ij} between each pair of nuclei (i and j) in the solute spin system. Since the D_{ij} are inversely proportional to the cube of the internuclear distances r_{ij} [equation (3)], the relative positions of the nuclei in the spin system can be determined and the shape of the molecule as well as its average orientation in the magnetic field can be deduced, providing enough independent D_{ij} values can be measured. For a system of coupled $I = 1/2$ nuclei, the transition frequencies in the MQ spectra are determined by the dipolar coupling constants, the scalar coupling constants, and the chemical shifts of the nuclei. In theory, the spectra of order $n - 1$ and $n - 2$ contain sufficient transitions to measure all the dipolar coupling constants and chemical shifts in an *n*-spin system:

$$D_{ij} = -(h\gamma_H^2/4\pi^2)S_{ij}/r_{ij}^3 \qquad (3)$$

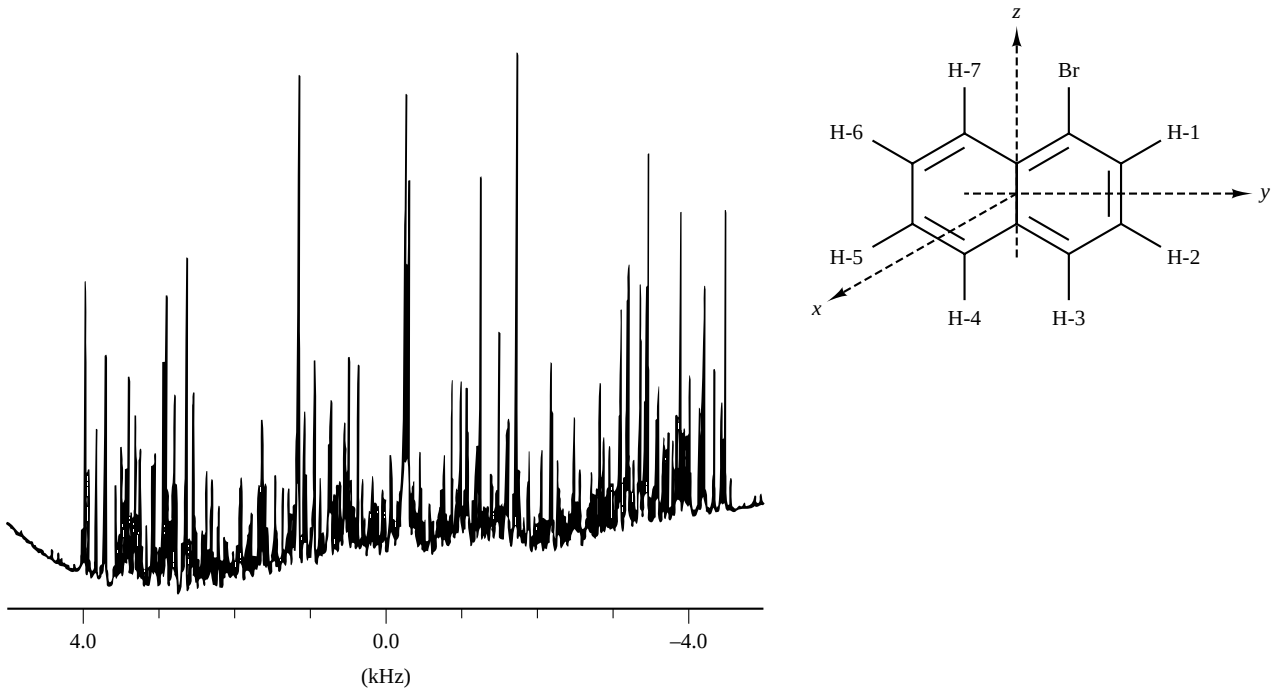

Figure 6 Single quantum proton spectra of 1-bromonaphthalene aligned in liquid crystalline solution. Reproduced by permission of Academic Press from Reference [20a]

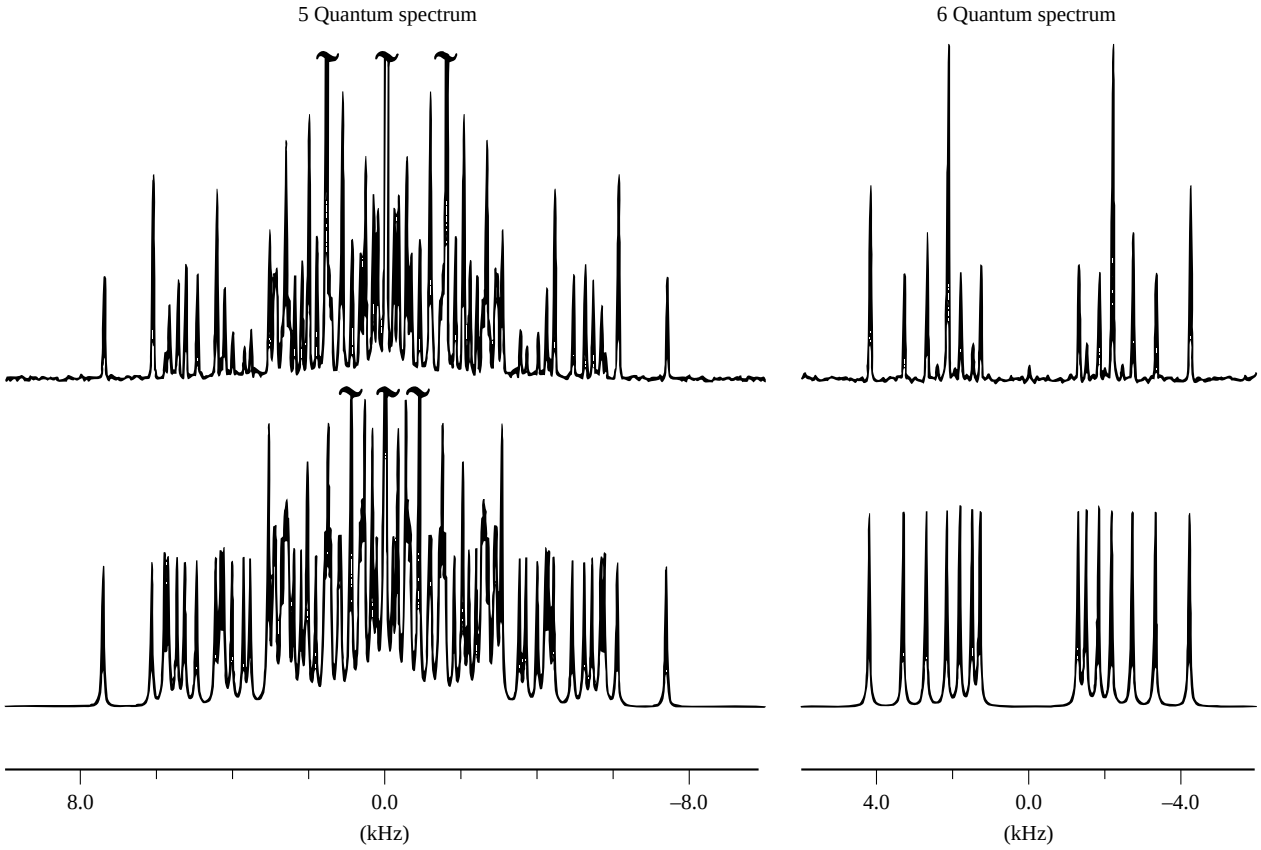

Figure 7 Experimental (upper) and simulated (lower) multiple quantum spectra of 1-bromonaphthalene aligned in liquid crystalline solution. Experimental spectra were acquired with chemical shift refocusing in F_1 and spectra were symmetrized about $F_1 = 0$. Simulations assume all transitions have the same intensity. Reproduced by permission of Academic Press from Reference [20a]

where γ_H is the proton magnetogyric ratio, r_{ij} is the internuclear distance between protons i and j, and S_{ij} is the order of the internuclear vector between i and j.[19] There have been only a few studies in which the geometry of a spin system has been established using MQ NMR.

6.1.1 Structure of Rigid Molecules: Structure of 1-Bromonaphthalene

1-Bromonaphthalene has a proton spin system containing seven nonequivalent spins. In liquid crystalline solution the ^{1}H NMR spectrum contains more than 3000 transitions (Figure 6).[20] The five and six quantum spectra have been recorded and solved simultaneously (Figure 7) to give values for the 21 independent dipolar coupling constants, and from the D_{ij} values the geometry of the planar seven spin system was determined.[20]

6.1.2 Chain Mobility in n-Hexane-d_6

MQ NMR has been employed to study chain mobility in alkanes dissolved in liquid crystalline solution. Drobny[2b] has reported the MQ spectra of *n*-hexane-d_6 (deuterated in the terminal methyl groups) dissolved in a nematic solvent. MQ spectra were recorded and the high quantum spectra (six and seven quantum) analyzed to give dipolar couplings. The six quantum proton spectrum contains 36 transitions and the seven quantum spectrum contains four transitions, as expected for an eight proton spin system with C_{2h} symmetry. The best fit of theoretically generated MQ NMR spectra to the experimental spectra was obtained with a model where only the minimum energy conformations of the alkane chain were appreciably populated.

6.1.3 Structure of 4-Cyano-4′-n-pentylbiphenyl

4-Cyano-4′-*n*-pentylbiphenyl is a nematic liquid crystal at room temperature. The five, six, and seven quantum MQ NMR spectra of the eight proton spin system of a partially deuterated compound (with the pentyl side chain completely deuterated) have been analyzed to give the interproton dipolar couplings in the biphenyl core of the molecule.[21] The best match between the experimental and simulated MQ NMR spectra were obtained when the biphenyl system was not planar, but when there was an angle of about 32° between the linked phenyl groups.

6.2 Counting Spins in Clusters

In MQ NMR, individual spins become correlated with each other over time through their dipolar couplings. The rate at which MQCs develop is a complex function of the coupling constants present in the spin system. In solids, where the distribution of dipole coupled spins is effectively infinite, the correlations between spins develop in a monotonic fashion. As time progresses, more spins can absorb more quanta and high order MQC can be generated.[22] In systems where there are effectively isolated clusters of spins (e.g. liquid crystals, molecules dissolved in liquid crystalline phases, and polycrystalline solids) the time development of MQC is interrupted and the system can only support MQC up to the size of coupled spin clusters. In the 21-spin system of the liquid crystal 4-cyano-4′-heptylbiphenyl, the effective spin system size increases to a maximum of 21 spins as the preparation time for MQC increases (Figure 8).

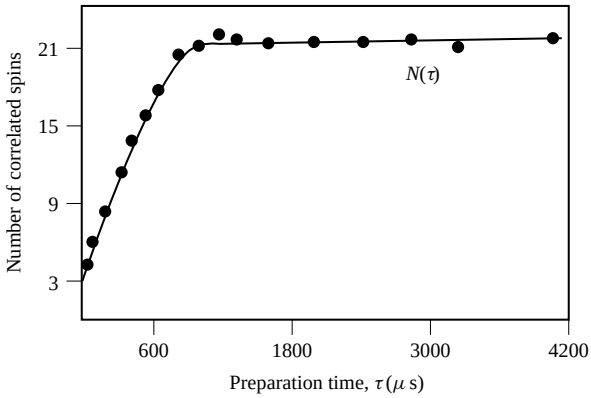

Figure 8 The effective system size $N(\tau)$ as a function of the preparation time τ for the liquid crystal 4-cyano-4′-heptylbiphenyl. After an induction period of approximately 1000 μs, $N(\tau)$ levels off to a value of 21, reflecting the number of spins in the isolated molecular cluster. Reprinted by permission of the American Chemical Society from Baum and Pines[22]

The rate of MQC development in a mixture of liquid crystalline materials has also been used to identify and observe distinct subsections of molecules comprising the liquid crystals. Separate MQ signals were observed for effectively isolated spin pairs (phenyl rings) and weakly coupled multispin clusters (alkyl tails)[23] in a mixture of 4-cyanophenyl 4′-butylbenzoate and 4-cyanophenyl 4′-heptylbenzoate.

6.3 Measurements of Diffusion

MQC has been used to extend the normal NMR spin echo measurement of diffusion. In typical spin echo experiments, molecules are labeled by their position in a magnetic field gradient after an initial rf pulse and diffusion is measured by monitoring the amplitude of the spin echo following a second pulse. MQ NMR spectroscopy exploits the fact that *n* quantum coherence dephases *n*-times more quickly than does single quantum coherence, so higher quantum coherences are significantly more sensitive to diffusion.

Martin et al.[24] measured the diffusion of dichloromethane (CH_2Cl_2) in various liquid crystal solvents by following the decay of the double quantum coherence. In measurements of the diffusion of benzene in a nematic liquid crystal, Zax and Pines[25] used a pulse sequence [Figure 9(a)] to excite MQC nonselectively and then selectively monitored the decay of the coherence echo of the $n = 1$ to $n = 6$ orders of coherence following field gradient pulses. The amplitude of echo decay for all orders of coherence was fitted to a modified Stejskal–Tanner equation[26] (Figure 9), thus verifying that the rate of echo decay is proportional to n^2.

6.4 Molecular Motion and Relaxation

The spectral densities of molecule motion $J_q(\omega)$ are usually estimated by simultaneously analyzing a combination of

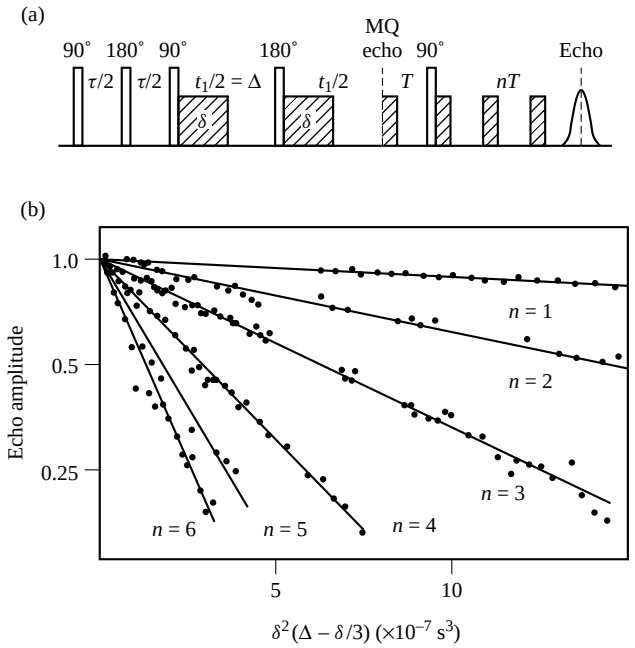

Figure 9 (a) Pulse sequence for an NMR pulsed field gradient experiment. (b) Normalized echo amplitudes plotted against the gradient pulse timing parameter $[\delta^2(\Delta - \delta/3)]$ of the Stejskal–Tanner equation.[26] (Reproduced by permission from D. Zax and A. Pines, *J. Chem. Phys.*, 1983, **78**, 6333)

relaxation measurements. Spectral densities may be measured from the decay of MQC and, particularly in $I = 1$ systems where the relaxation mechanism is dominated by the nuclear quadrupole, the relaxation of zero, double, triple and higher order coherences have been used to determine the spectral densities of motion for small deuterated organic molecules ($CDCl_3$,[27] $D{-}C{\equiv}C{-}C{\equiv}N$,[27b] CD_2Cl_2,[28] and $CD_3{-}C{\equiv}N$,[29]) dissolved in liquid crystalline solution. The relaxation of the two and three quantum resonances of ^{23}Na ($I = \frac{3}{2}$) and the four and five quantum resonances of ^{17}O ($I = \frac{5}{2}$) have been measured in lyotropic liquid crystals.[30]

6.5 Heteronuclear MQC

Heteronuclear MQC (HMQC) (coherence involving spins of different type, e.g. $^1H/^2H$ or $^1H/^{15}N$) have been used to study molecules in liquid crystal solution. Minoretti et al.[31] have demonstrated that there is a significant sensitivity advantage when the MQCs of a relatively insensitive nucleus (e.g. ^2H) can be detected indirectly by observing ^1H nuclei coupled to the heteronuclear spin system.

7 RELATED ARTICLES

Amphiphilic Liquid Crystalline Samples: Nuclear Spin Relaxation; Liquid Crystalline Samples: Deuterium NMR; Liquid Crystalline Samples: Diffusion; Liquid Crystalline Samples: Relaxation Mechanisms; Liquid Crystalline Samples: Spectral Analysis; Liquid Crystalline Samples: Structure of Nonrigid Molecules; Liquid Crystals: General Considerations; Lyotropic Liquid Crystalline Samples; Multidimensional Spectroscopy: Concepts; Multiple Quantum NMR in Solids; Multiple Quantum Spectroscopy of Liquid Samples; Structure of Rigid Molecules Dissolved in Liquid Crystalline Solvents; Two-Dimensional NMR of Molecules Oriented in Liquid Crystalline Phases.

8 REFERENCES

1. For leading references on NMR in liquid crystalline solvents see: (a) J. W. Emsley and J. C. Lindon, *NMR Spectroscopy Using Liquid Crystal Solvents*, Pergamon, Oxford, 1975; (b) J. W. Emsley (ed.), *Nuclear Magnetic Resonance of Liquid Crystals*, Riedel, Dordrecht, 1985.
2. For leading references on multiple quantum NMR spectroscopy, including studies of molecules in ordered phases see: (a) M. Munowitz and A. Pines, *Adv. Chem. Phys.*, 1987, **66**, 1; (b) G. P. Drobny, *Ann. Rev. Phys. Chem.*, 1985, **36**, 451; (c) D. Weitekamp, *Adv. Magn. Reson.*, 1983, **11**, 111; (d) G. Bodenhausen, *Progr. NMR Spectrosc.*, 1981, **14**, 137.
3. (a) S. Sinton, *Ph.D. Thesis*, University of California, Berkeley, 1982; (b) J. B. Murdoch, W. S. Warren, D. Weitekamp, and A. Pines. *J. Magn. Reson.*, 1984, **60**, 205; (c) A. Wokaun and R. R. Ernst, *Mol. Phys.*, 1978, **36**, 317; (d) R. A. Hoffman, *Adv. Magn. Reson.*, 1970, **4**, 87.
4. For general references to two-dimensional NMR spectroscopy see, for example: (a) A. E. Derome, *Modern NMR Techniques for Chemistry Research*, Pergamon, Oxford, 1989; (b) R. R. Ernst, G. Bodenhausen, and A. Wokaun, *Principles of Nuclear Magnetic Resonance in One and Two Dimensions*, Clarendon, Oxford, 1987.
5. (a) G. Drobny, A. Pines, S. Sinton, D. P. Weitekamp, and D. Wemmer, *Faraday Div. Chem. Symp.*, 1979, **13**, 49; (b) L. Braunschweiler, G. Bodenhausen, and R. R. Ernst, *Mol. Phys.*, 1983, **48**, 535; (c) O. W. Sorenson, M. Levitt, and R. R. Ernst, *J. Magn. Reson.*, 1983, **55**, 104.
6. D. P. Weitekamp, J. R. Garbow, and A. Pines, *J. Magn. Reson.*, 1982, **46**, 529.
7. (a) W. S. Warren and A. Pines, *J. Chem. Phys.*, 1981, **74**, 2808; (b) W. S. Warren, S. Sinton, D. P. Weitekamp, and A. Pines, *Phys. Rev. Lett.*, 1979, **43**, 1791; (c) W. S. Warren, D. P. Weitekamp, and A. Pines, *J. Magn. Reson.*, 1980, **40**, 581; (d) W. S. Warren, D. P. Weitekamp, and A. Pines, *J. Chem. Phys.*, 1980, **73**, 2084; (e) W. S. Warren and A. Pines, *Chem. Phys. Lett.*, 1982, **88**, 441.
8. T. M. Barbara, R. Tycho, and D. P. Weitekamp, *J. Magn. Reson.*, 1985, **62**, 54.
9. G. Drobny, A. Pines, S. Sinton, W. S. Warren, and D. P. Weitekamp, *Phil. Trans. R. Soc. London, Ser. A*, 1981, **299**, 585.
10. K. Nagayama, P. Bachmann, K. Wurthrich, and R. R. Ernst, *J. Magn. Reson.*, 1978, **31**, 133.
11. Order Selective detection: (a) A. Wokaun and R. R. Ernst, *Chem. Phys. Lett.*, 1977, **52**, 407; (b) G. Drobny, *Chem. Phys. Lett.*, 1984, **109**, 132.
12. Coherence transfer echoes: (a) A. Bax, P. G. DeJong, A. F. Mehlkopf, and J. Schmidt, *Chem. Phys. Lett.*, 1980, **69**, 567; (b) Y. S. Yen and D. P. Weitekamp, *J. Magn. Reson.*, 1982, **47**, 476; (c) D. P. Weitekamp, J. R. Garbow, and A. Pines, *J. Chem. Phys.*, 1982, **77**, 2870.
13. G. K. Pierens, T. A. Carpenter, L. D. Colebrook, L. D. Field, and L. D. Hall, *J. Magn. Reson.*, 1992, **99**, 398.
14. (a) R. L. Vold, J. S. Waugh, M. P. Klein, and D. E. Phelps, *J. Chem. Phys.*, 1968, **48**, 3831; (b) J. F. Martin, L. S. Selwyn, R. R. Vold, and R. L. Vold, *J. Chem. Phys.*, 1982, **76**, 2632; (c)

D. Zax and A. Pines, *J. Chem. Phys.*, 1983, **78**, 6333; (d) A. A. Maudsley, A. Wokaun, and R. R. Ernst, *Chem. Phys. Lett.*, 1978, **55**, 9.

15. Time reversal sequences: (a) W. S. Warren, S. Sinton, D. P. Weitekamp, and A. Pines, *Phys. Rev. Lett.*, 1979, **43**, 1791; (b) W. S. Warren, D. P. Weitekamp, and A. Pines, *J. Magn. Reson.*, 1980, **40**, 581; (c) W. S. Warren, D. P. Weitekamp, and A. Pines, *J. Chem. Phys.*, 1980, **73**, 2084.
16. G. Drobny and J. Listerud, *Mol. Phys.*, 1986, **58**, 1021.
17. (a) S. Castellano and A. A. Bothner-By, *J. Chem. Phys.*, 1964, **41**, 3863; (b) J. A. Ferretti, R. K. Harris, and R. B. Johannesen, *J. Magn. Reson.*, 1970, **84**, 3.
18. W. S. Warren, J. B. Murdoch, and A. Pines, *J. Magn. Reson.*, 1984, **60**, 236.
19. P. Diehl and C. L. Khetrapal, in *NMR, Basic Principles and Progress*, ed. P. Diehl, E. Fluck, and R. Kosfeld, Springer, Berlin, 1969, Vol. 1.
20. (a) L. D. Field, G. K. Pierens, K. J. Cross, and M. L. Terry, *J. Magn. Reson.*, 1992, **97**, 451; (b) L. D. Field and M. L. Terry, *J. Magn. Reson.*, 1986, **69**, 176.
21. (a) S. W. Sinton, D. Zax, J. B. Murdoch, and A. Pines, *Mol. Phys.*, 1984, **53**, 333; (b) S. W. Sinton and A. Pines, *Chem. Phys. Lett.*, 1980, **76**, 263.
22. J. Baum and A. Pines, *J. Am. Chem. Soc.*, 1986, **108**, 7447.
23. W. V. Gerasimowicz, A. N. Garroway, and J. B. Miller, *J. Am. Chem. Soc.*, 1990, **112**, 3726.
24. J. F. Martin, L. S. Selwyn, R. R. Vold, and R. L. Vold, *J. Chem. Phys.*, 1982, **76**, 2632.
25. D. Zax and A. Pines, *J. Chem. Phys.*, 1983, **78**, 6333.
26. E. O. Stejskal and J. E. Tanner, *J. Chem. Phys.*, 1965, **42**, 288.
27. (a) R. R. Vold and R. L. Vold, *J. Chem. Phys.*, 1977, **66**, 4018; (b) R. R. Vold, R. L. Vold, and N. Szerverenyi, *J. Phys. Chem*, 1981, **85**, 1934.
28. (a) R. Poupko, R. R. Vold, and R. L. Vold, *J. Magn. Reson.*, 1979, **34**, 67; (b) G. Bodenhausen, R. R. Vold, and R. L. Vold, *J. Magn. Reson.*, 1980, **37**, 93; (c) R. R. Vold, R. L. Vold, R. Poupko, and G. Bodenhausen, *J. Magn. Reson.*, 1980, **38**, 141.
29. (a) D. Jaffe, R. R. Vold, and R. L. Vold, *J. Magn. Reson.*, 1982, **46**, 475; (b) D. Jaffe, R. R. Vold, and R. L. Vold, *J. Magn. Reson.*, 1982, **46**, 496; (c) D. Jaffe, R. R. Vold, and R. L. Vold, *J. Chem. Phys.*, 1983, **78**, 4852.
30. I. Furo and B. Halle, *Mol. Phys.*, 1992, **76**, 1169.
31. A. Minoretti, W. P. Aue, M. Reinhold, and R. R. Ernst, *J. Magn. Reson.*, 1980, **40**, 175.

Biographical Sketch

Leslie D. Field. *b* 1953. B.Sc., 1975, Ph.D., 1979, Sydney. Faculty in Chemistry, Sydney University, 1982–present. Approx. 100 publications. Research interests: organometallic chemistry (C–H bond activation, catalytic activation of hydrocarbons, organometallic polymers, the mechanism of organometallic reactions); organic, organometallic, and inorganic synthesis; chemical applications of multinuclear MR spectroscopy, multiple quantum NMR spectroscopy, and NMR spectroscopy of molecules aligned in ordered solvents.

Proton Chemical Shift Measurements in Biological Solids

Ann McDermott
Columbia University, New York, NY, USA

and

Cynthia F. Ridenour
Otsuka Electronics, Inc., Fort Collins, CO, USA

1 Introduction 1
2 Approaches to Narrowing Proton Resonances 1
3 Information From the Lineshape 2
4 Hydrogen Bonding: Chemical Shift and Hydrogen Exchange 2
5 2D Correlation with Carbon 3
6 Conclusions 4
7 Related Articles 4
8 References 4

1 INTRODUCTION

There are strong motivations for pursuing solid state NMR of protons, namely the inherently good sensitivity and the possibilities for study of hydrogen bonding via chemical shifts. Despite its enormous potential, solid state NMR of protons in biomolecules has had surprisingly few applications in comparison with other high-resolution NMR methods for studying biological macromolecules. In this article we discuss experimental solutions to the problem of spectral resolution and the analysis of spectra for chemical information. Although essentially all of the successful measurements of chemical shift and shift anisotropy were obtained on simple crystalline solids we also discuss possible future applications in structural biology.

2 APPROACHES TO NARROWING PROTON RESONANCES

Producing narrow proton linewidths is the most significant challenge to solid state proton NMR. For the case of a typical rigid organic solid, ^{1}H NMR spectra obtained without sample spinning or with moderate speed sample spinning show very broad lines, on the order of a few tens of kilohertz. Narrowing of these lines by the technique of combined rotation and multiple pulse spectroscopy, CRAMPS,[1–4] or by dilution of the protons[5–7] has been demonstrated in crystalline small molecules. These methods have provided the means to study hydrogen bonding and proton exchange in solids, but practically no high-resolution solid state ^{1}H NMR applications to macromolecules have been reported. In contrast to rigid organic solids, solids with high molecular mobility such as lipids and membrane structures often provide well-resolved ^{1}H NMR simply by Bloch decay acquisition with slow magic angle spinning.[8–11]

The CRAMPS method is the most common experimental approach to achieving high-resolution ^{1}H spectra of materials in the solid state. It has been used in interesting applications of chemical analysis,[12–15] and probably has the most potential for general studies of amorphous biological solids. Proton NMR linewidths obtained by CRAMPS or magnetic dilution can be as low as 0.2 ppm, which could be sufficient to separate the typical functional groups found in a protein but of course would never be adequate for site-specific assignments of even a small peptide. Highly crystalline compounds typically produce the narrowest lines, while compounds with some amorphous character produce somewhat broader lines.[14] Macroscopic susceptibility due to the shape of the microcrystal presumably contributes to the linewidth, and specific anisotropic bulk susceptibility effects in aromatic systems have been discussed.[14]

An alternative method that has been little pursued to date is the detection of deuterons during magic angle spinning (MAS). With this approach resolution comparable to that of CRAMPS or dilution can often be obtained without special effort,[16,17] and spectral overlap can be avoided by utilizing selective labeling. Considerable spectral intensity is squandered into spinning sidebands, so application of methods to fold the sidebands together is important. On the other hand, the quadrupolar constants and dynamic information normally obtained from static ^{2}H NMR can be derived from the sideband patterns in these spectra. Several reports of cross polarization between deuterium and protons have appeared.[16,18]

In the following discussion we will focus more on CRAMPS than the other two approaches because of the much larger existing literature and the far fewer complications with sample preparation. We illustrate the typical appearance of CRAMPS spectra of simple organic biological solids with a series of CRAMPS spectra of amino acids and dipeptides in Figure 1; some of these samples have also been characterized by measurement of dilute protons[6] or by spinning ^{2}H spectra.[17] It is apparent from Figure 1 that the linewidths are significantly below 1 ppm in every case and the spectra allow resolution

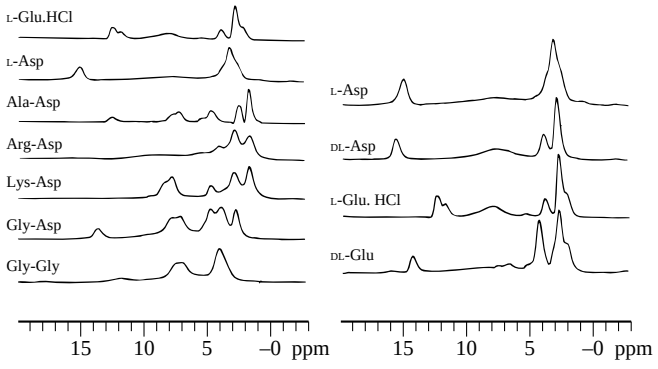

Figure 1 The 200 MHz BR-24 spectra of crystalline amino acids (as indicated). Pulse length was 1.3 μs with a τ value of 2.3–3.0 μs and spinning speeds of 1.0–1.5 kHz. Sixteen transients were accumulated. Glu = glutamic acid, Asp = aspartic acid, Ala = alanine, Arg = arginine, Lys = lysine, Gly = glycine

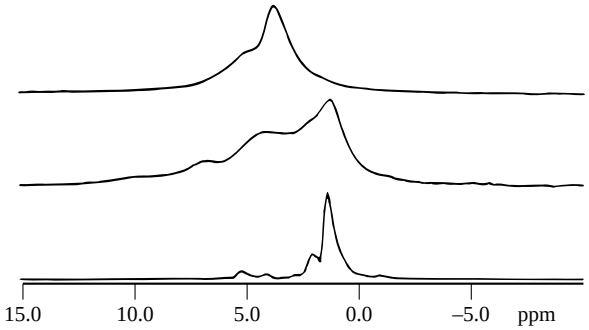

Figure 2 Typical CRAMPS spectra of biological molecules, measured at 187 MHz with the BR-24 pulse sequence.[19] Top: amylopectin; middle: γ-globulin; bottom: coconut oil. Spectra were acquired with MAS spinning speed of 1–2 kHz, pulse width = 1.0–1.2 μs, τ = 3.0 μs, repetition time 1.7 s

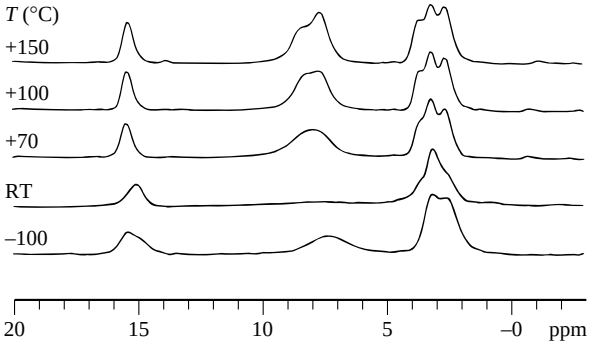

Figure 3 The 200 MHz BR-24 spectrum of l-aspartic acid at various temperatures. Note that the amine resonance at 7.7 ppm disappears near room temperature (RT) due to the microsecond correlation time for the amine's threefold hopping rate. This behavior is quite common for amine groups although the critical temperature is variable

of one chemical classification from another. For aliphatic or aromatic protons the chemical shifts are comparable to those known from solution state experiments, that is −1 to 2 ppm for methyl groups, 1–3 ppm for methylene, 3–5 ppm for methine, and 6–8 ppm for aromatic protons. Unlike solution spectroscopy, in solid state experiments observing acid and other exchangeable protons is possible, and in particular for the case of carboxylic acids the range in typical shifts is quite a lot broader than the linewidths. The amine and many of the other N–H functionalities are often around 7–8 ppm, while imidazole protons and structural water protons and carboxylic acids can be found at a broad range of shift values depending on hydrogen bonding, with strongly hydrogen-bonded groups being significantly deshielded (10–20 ppm). The chemical shifts and lineshapes for resonances in hydrogen bonding groups are discussed in detail in the following sections.

Typical ^{1}H CRAMPS spectra of other biological materials are also exhibited in Figure 2.[19] The carbohydrate spectrum (top) is dominated by methine and hydroxyl protons. The protein spectrum (middle) shows contributions from methyl, methylene, methine, amine, and other groups but is largely unresolved. A methylene resonance at 1.3 ppm dominates the lipid spectrum (bottom). As noted above, MAS-only spectra of lipids provide good ^{1}H resolution. Proton linewidths of lipids and highly mobile materials are often narrower in MAS-only spectra than in CRAMPS spectra[19] due to pulse imperfections in the multiple pulse sequence.

3 INFORMATION FROM THE LINESHAPE

All three detection methods show certain potentially confusing effects that deserve special comment. As has been reported previously[1,20] dynamic processes can interfere with the CRAMPS detection of groups undergoing motion if the correlation times are comparable to the pulse width, the multiple pulse cycle time, or to the sample spinning speed. This effect is often seen at room temperature in the form of missing amine resonances. Amine groups enact a three-site hopping motion on the microsecond timescale near room temperature since they have activated barriers in the range of 30 kJ mol^{-1}. This motion has been previously characterized by wideline ^{1}H T_1 measurements[21] but not by lineshape methods. Such amine lines that are broad or undetected near room temperature are readily detected at temperatures above 70 °C or below −100 °C in typical cases. Figure 3 shows variable temperature ^{1}H CRAMPS spectra of L-aspartic acid in which the amine line at 7.7 ppm illustrates this effect. Other effects on the lineshapes as a function of temperature are often observed, and analysis of these lineshapes by explicit simulation would be informative but has not yet been accomplished. Other than the amine rotation, common local motions in proteins rarely result in loss of signal because the rates are not on the microsecond timescale near room temperature. The ^{2}H MAS spectra exhibit lineshape and intensity effects for amines in a comparable temperature range: here the sampling rate of data collection is usually in the submegahertz range so again motions in the microsecond range interfere with detection. Proton spectra of magnetically diluted (deuterated) samples detected using Bloch decay during MAS would presumably show lineshape effects due to much slower motions, approximately on the millisecond timescale. Hence detection of sharp spectra due to the amine peaks is usually straightforward by ^{1}H MAS spectra. In all three methods interpretation of line intensities is quite unreliable because of all of these lineshape effects and/or the uncertainties involved in the extent of chemical incorporation of deuterium.

Protons that are directly bound to nitrogens often exhibit a lineshape that is obviously affected by the incomplete averaging of dipolar coupling to the ^{14}N resulting from the fact that the strongly quadrupolar ^{14}N is not in the high-field limit. These effects are most clear in lower field spectra[22] and can be seen in the 200 MHz high-temperature CRAMPS spectrum of aspartic acid (Figure 3) but also have been seen in well-resolved high field spectra.[5] They offer the possibility of characterization of the bonding geometry and the quadrupole parameters for the nitrogen from the ^{1}H lineshapes[22] as has been done for ^{13}C lineshapes for ^{13}C^{14}N pairs.[23–26]

4 HYDROGEN BONDING: CHEMICAL SHIFT AND HYDROGEN EXCHANGE

For protons that participate in hydrogen bonding, there are well-known correlations between the shielding of the ^{1}H isotropic chemical shift, the ^{1}H shielding anisotropy, the ^{2}H coupling constant, and hydrogen bonding distances[1,27–29] for

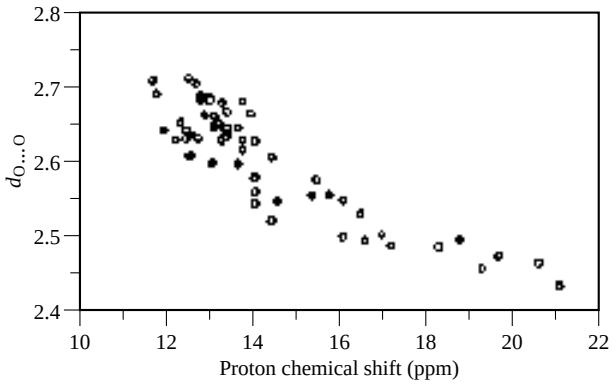

Figure 4 The ^{1}H chemical shifts of the amino acids in Figure 1 plotted against their O ... O distances as indicated by crystallography. Filled circles show proton chemical shifts derived from our data, as shown in Figure 1; crystal structures for these compounds can be found in Rao,[40] Eggleston and Hodgson,[41–43] Derissen et al.,[44] Bhat and Vijayan,[45] Sequeira et al.,[46] and Hamilton and Parthasarathy.[47] The open circles are from previous measurements in Harris et al.[1]

small crystalline compounds. Quantification of hydrogen bonding is of great interest for studies in structural biology because of the role in recognition and conformational preferences. Solid state NMR could potentially be far more sensitive to details of hydrogen bonding and ionization states than crystallography. The chemical shifts for the acid protons for carboxyl groups in amino acids (shown in Figure 1) correlate with hydrogen-bonding length and this plot is shown in Figure 4 in filled circles. In comparison with previous measurements[1] which are entered here as open circles, our data encompass a rather restricted range because of the limited scope of compounds that are both relevant as model systems for proteins and sufficiently characterized. Clearly there is some scatter in the data but there is also a general trend that reproduces previous correlations.

Anisotropy of the proton shielding has been reported in a variety of solids with very simple structures; a thorough compilation and reviews are available.[30–32] Many of these values were obtained from static multiple pulse measurements on either single crystals or powders or from rotation plots of the deuterium signal of a single crystal. The shielding anisotropy, $|\Delta\sigma| = |(\sigma_\perp - \sigma_\parallel)|$, is quite narrow (about 4–7 ppm) for alkyl or aromatic protons (except for methyl groups which are 1–2 ppm), but for some ionizable protons the anisotropy is more pronounced, with values of approximately 17 ppm for amides and 16–30 ppm for acids, alcohols, and water, but only about 5 ppm for amines. A detailed analysis of tensor values and orientations would presumably be useful in studying nonbonded interactions but is probably not possible in biological solids in the near future. Many complications affect the CSA measurements by CRAMPS, such as residual homonuclear and heteronuclear dipolar interactions, molecular motion, and chemical shift scaling. Magnetically dilute protons in organic solids give rise to spinning sidebands during low-speed MAS, and when the percentage of hydrogens that are replaced with deuterons is approximately 99% or larger these sidebands appear to be dominated by CSA effects (A. McDermott, unpublished).

A point of specific interest in solid state studies of hydrogen bonding is the fact that hydrogen bonds can have profound effects upon reactivity in biological catalysis. For example, acid–base chemistry or proton mobility in the solid state is presumably strongly affected by local nonbonded interactions, a point which is relevant in many enzyme mechanisms. The geometric preferences of hydrogen bonds and the specific control of reactivity can be probed in the solid state studies since particular networks are arrested on an experimentally accessible timescale. Protons that participate in typical thermally driven and near-reversible exchange processes in proteins are found on the 'ionizable' hydrogen bonded groups such as carboxyl, imidazole, water, amine, alcohol, and guanidinium. The typical exchange timescales of microseconds to hours are presumably sensitive to the specific hydrogen-bonding geometry in a way that might be predicted by ab initio[33] or semiempirical methods. A systematic study of chemical exchange processes as a function of geometry in structurally characterized solids by NMR would help to clarify the theory of proton exchange.

Recent advances in ^{1}H NMR of deuterated simple model compounds for proteins show that such measurements of exchange processes are possible. Variable temperature two-dimensional (2D) methods applied to one example of a low symmetry hydrogen-bonded network of carboxylic acids and crystallographic water molecules demonstrated unambiguously that a proton is transferred between water and a carboxyl group[6] in an activated process with a barrier of 37 kJ mol^{-1}. Additional measurements will be necessary for the purpose of creating a database that correlates rates of exchange with structural features.

5 2D CORRELATION WITH CARBON

The more ambitious goal of utilizing ^{1}H NMR for detailed structural analyses of amorphous solid materials or complex solid state macromolecules is not practical without addressing the problem of resolution of one ^{1}H resonance from the others of the same chemical functional group. The approach taken by solution NMR spectroscopy to correlate the ^{1}H resonance with nearby or attached heteronuclei is applicable in solids as well. The ^{15}N or ^{13}C NMR spectra in the solid state are considerably broader than solution spectra but nonetheless often allow distinction of a handful of selectively labeled residues. Two important classes of 2D H–X experiments for solid state NMR of H–X pairs are dipolar chemical shift correlation methods or 'DIPSHIFT'[34] for determination of the bond distance to a great accuracy in a spin pair and heteronuclear correlation methods or 'HETCOR',[35–37] which maps the chemical shifts of the X nucleus to nearby protons via the dipolar coupling. The latter is clearly the experiment of choice when more than one proton connected with the heteronucleus of interest should be resolved and rather approximate distance information will suffice. Our recent work with HETCOR and modified versions of the pulse sequence demonstrate the observation of longer H–X distances including C–O ... H hydrogen bonds which appear as weak cross peaks. Rotor-synchronized transfer sequences have been used to increase the range of H–X distances probed by this method.[38] As an example, the HETCOR spectrum of alanyl aspartic acid is shown in Figure 5. In particular the ^{1}H–^{13}C correlation peaks between the carboxyl groups around 170 ppm in the ^{13}C dimension and the acid proton near 12.5 ppm in the

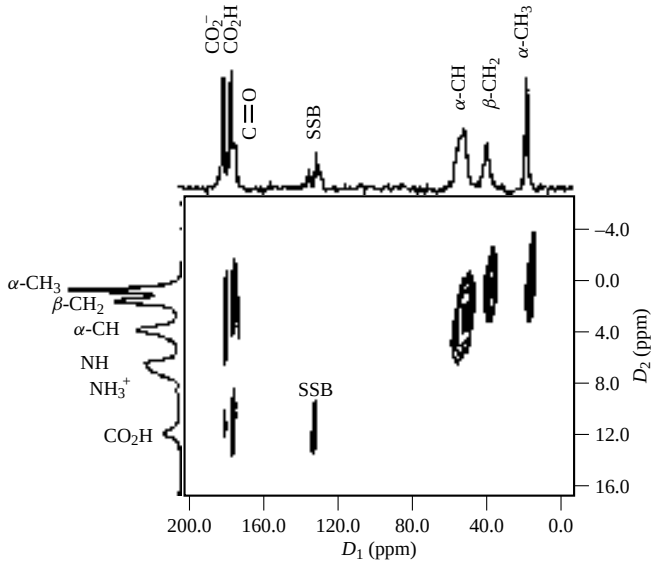

Figure 5 Rotor-synchronized HETCOR spectrum of alanyl aspartic acid at 200 MHz and room temperature. Magnetization transfer was accomplished by 2.5 WIM-24 cycles per rotor period during four sequential rotor periods. The 90° pulse lengths were 3.2 μs for both channels. Experimental repetition time was 1.7 s. Data matrix was 80 × 512 points zero-filled to 512 × 512 with 20 Hz linebroadening in D_2 and a Kaiser window applied to D_1. SSB = spinning sidebands

^{1}H dimension are indirectly connected pairs; several of the ^{13}C resonances show more than one ^{1}H cross peak.

Since essentially all of the resolution in the HETCOR experiment comes from the heteronuclear dimension, it is probably worthwhile to reiterate the virtues of such a 2D experiment in comparison with a one-dimensional (1D) heteronuclear measurement. Although detailed information about hydrogen bonding is available from heteronuclear NMR, the information from the ^{1}H shifts is often independent of that obtained from the heteronuclear shift. A case in point is the carboxylate group: the ^{1}H shift depends on the interaction of the detected acid proton with the nearest hydrogen bond acceptor, while σ_{22} of the ^{13}C shift depends on the distance between the carboxyl oxygen, which acts as a hydrogen bond acceptor, and the nearest proton.[39] The 2D HETCOR experiment provides the possibility of identifying the chemical nature of the hydrogen bonding partners to a carbon-containing functional group, even if the partners are water molecules. In a more practical light, we have found the HETCOR experiment to be quite useful in determining or confirming ^{13}C assignments for larger peptides and pharmaceuticals. As for disadvantages, obviously the time investment in such an experiment is enormously greater than that necessary for a 1D heteronuclear experiment. In the 2D spectra interpretation of the proton dimension is subject to similar complications as the CRAMPS experiment. In particular the intensities of the lines depend strongly on the presence or absence of mid-kHz motions.

Some of these issues are well illustrated with the spectrum of natural abundance alanyl aspartic acid. The three carbonyl-type carbons are readily identified by the HETCOR spectrum with one being a protonated carboxyl, one being deprotonated but hydrogen bonded to the protonated carbonyl, and the third being an amide carbonyl with no cross peak to the acid proton. A strong hydrogen bond between the two carboxyl groups is indicated by both the deshielded acid proton (14 ppm) that was detected in the HETCOR spectrum and the σ_{22} value for the deprotonated carboxyl group (184 ppm) that was determined in 1D low-spinning CP MAS sideband analysis. Moreover the assignment of both the ^{13}C and ^{1}H dimensions can be verified by comparison of the ^{1}H shifts in the cross peaks of the carbonyl resonances with those in the methylene/methine region. From such a comparison one could have identified, for example, that the protonated carboxyl is alpha to a methylene while the deprotonated carboxyl is alpha to a methine. The fact that good sensitivity was obtained for a naturally abundant dipeptide implies that moderate-sized proteins can be studied by this approach if they are selectively labeled.

6 CONCLUSIONS

The long-established relationships between proton shift and hydrogen-bonding distances were confirmed in the more restricted data base of amino acids and peptides. Utilization of these 1D CRAMPS methods for proteins is unlikely because of the 0.3–1 ppm linewidths. These measurements might be of use in more complex solids if the spectrum is separated into two dimensions using correlations to attached heteronuclei in the HETCOR experiment. Demonstrations of HETCOR spectra on small peptides with naturally abundant ^{13}C demonstrate the requisite sensitivity for biological work and indicate the potential for measuring hydrogen bonding parameters and confirming assignments.

7 RELATED ARTICLES

HETCOR in Organic Solids; Hydrogen Bonding; Line Narrowing Methods in Solids; Magic Angle Spinning Carbon-13 Lineshapes: Effect of Nitrogen-14.

8 REFERENCES

1. R. K. Harris, P. Jackson, L. H. Merwin, B. J. Say, and G. Hagele, *J. Chem. Soc., Faraday Trans. 1*, 1988, **84**, 3649.
2. B. C. Gerstein, R. G. Pembleton, R. C. Wilson, and L. M. Ryan, *J. Chem. Phys.*, 1977, **66**, 361.
3. D. P. Burum and W. K. Rhim, *J. Chem. Phys.*, 1979, **71**, 944.
4. B. C. Gerstein, *Philos. Trans. R. Soc. London, Ser. A*, 1981, **299**, 521.
5. A. E. McDermott, F. J. Creuzet, A. C. Kolbert, and R. G. Griffin, *J. Magn. Reson.*, 1992, **98**, 408.
6. L. Zheng, K. Fishbein, R. Griffin, and J. Herzfeld, *J. Am. Chem. Soc.*, 1993, **115**, 6254.
7. J. Yesinowski, H. Eckart, and G. Rossman, *J. Am. Chem. Soc.*, 1988, **110**, 1367.
8. S. Un, Ph.D. Dissertation, University of California, Berkeley, 1987.
9. C. Lee and R. G. Griffin, *Biophys. J.*, 1989, **55**, 355.
10. J. Forbes, C. Husted, and E. Oldfield *J. Am. Chem. Soc.*, 1988, **110**, 1059.
11. V. Rutar, *J. Agric. Food Chem.*, 1989, **37**, 67.

12. G. Maciel, C. Bronniman, and B. Hawkins, *Adv. Magn. Reson.*, 1990, **14**, 125.
13. C. E. Bronnimann, R. C. Zeigler, and G. E. Maciel, *J. Am. Chem. Soc.*, 1988, **110**, 2023.
14. C. E. Bronnimann, B. L. Hawkins, M. Zhang, and G. E. Maciel, *Anal. Chem.*, 1988, **60**, 1743.
15. P.-J. Chu, M. J. Potrzebowski, Y. Gao, and A. I. Scott, *J. Am. Chem. Soc.*, 1990, **112**, 881.
16. L. Muller, *Chem. Phys.*, 1981, **61**, 235.
17. L. Zheng, Ph.D. Dissertation, Brandeis University, Waltham, MA, 1993.
18. A. J. Kim and L. G. Butler, *J. Magn. Reson.*, 1992, **99**, 292.
19. C. F. Ridenour, Ph.D. Dissertation, Colorado State University, Fort Collins, CO, 1992.
20. U. Haeberlin and J. Waugh, *Phys. Rev.*, 1969, **185**, 420.
21. E. R. Andrew, *Mol. Phys.*, 1976, **31**, 1479.
22. A. Naito, A. Root, and C. A. McDowell, *J. Phys. Chem.*, 1991, **95**, 3578.
23. A. C. Olivieri, L. Frydman, and L. E. Diaz, *J. Magn. Reson.*, 1987, **75**, 50.
24. J. W. Diesveld, E. M. Menger, H. T. Edjes, and W. S. Veeman, *J. Am. Chem. Soc.*, 1980, **102**, 7935.
25. J. G. Hexem, M. Frey, and S. J. Opella, *J. Chem. Phys.*, 1982, **77**, 3847.
26. N. Zumbulyadis, P. M. Henrichs, and R. H. Young, *J. Chem. Phys.*, 1981, **75**, 1603.
27. B. Berglund and R. W. Vaughan, *J. Chem. Phys.*, 1980, **73**, 2037.
28. G. A. Jeffrey and Y. Yeon, *Acta Crystallogr., Sect. B*, 1986, **42**, 410.
29. M. C. Etter and G. M. Vojta, *J. Magn. Reson.*, 1991, **93**, 609.
30. T. M. Duncan, *A Compilation of Chemical Shift Anisotropies*, Farragut Press, Chicago, 1990, pp. H-1–H-12.
31. U. Haeberlin, *High Resolution NMR in Solids; Selective Averaging*, Academic Press, New York, 1976.
32. M. Mehring, *Principles of High Resolution NMR in Solids*, 2nd edn., Springer, New York, 1983.
33. K. Luth and S. Scheiner, *Int. J. Quantum Chem., Quantum Chem. Symp.*, 1992, **26**, 817.
34. M. G. Munowitz and R. G. Griffin, *J. Chem. Phys.*, 1982, **76**, 2848.
35. P. Caravatti, G. Bodenhausen, and R. R. Ernst, *Chem. Phys. Lett.*, 1982, **89**, 363.
36. J. E. Roberts, S. Vega, and R. G. Griffin, *J. Am. Chem. Soc.*, 1984, **106**, 2506.
37. D. P. Burum and A. Bieleski *J. Magn. Reson.*, 1991, **94**, 645.
38. C. E. Bronnimann, R. A. Santos, and R. A. Wind, *J. Magn. Reson.*, 1994, **105**, 183.
39. Z. Gu and A. McDermott, *J. Am. Chem. Soc.*, 1993, **115**, 4282.
40. S. T. Rao, *Acta Crystallogr., Sect. B*, 1973, **29**, 1718.
41. D. S. Eggleston and D. J. Hodgson, *Int. J. Peptide Protein Res.*, 1985, **25**, 242.
42. D. S. Eggleston and D. J. Hodgson, *Int. J. Peptide Protein Res.*, 1983, **21**, 288.
43. D. S. Eggleston and D. J. Hodgson, *Int. J. Peptide Protein Res.*, 1982, **19**, 206.
44. J. L. Derissen, H. J. Endeman, and A. F. Peerdman, *Acta Crystallogr., Sect. B*, 1968, **24**, 1349.
45. T. N. Bhat and M. Vijayan, *Acta Crystallogr., Sect. B*, 1976, **32**, 891.
46. A. Sequeira, H. Rajagopal, and R. Chidambaram, *Acta Crystallogr., Sect. B*, 1972, **28**, 2514.
47. T. F. W. C. Hamilton and R. Parthasarathy, *Acta Crystallogr., Sect. B*, 1972, **28**, 2083.

Biographical Sketches

Ann McDermott. *b* 1960. B.S., 1981, Harvey Mudd College; Ph.D., 1987, University of California, Berkeley, with Professor Ken Sauer and Dr. Melvin Klein; postdoctoral research, 1988–1990, MIT and Francis Bitter National Magnet Laboratory with Professor Robert Griffin, postdoctoral research 1990–1991, Université Catholique de Louvain, Institute for Clinical Pathology, Tropical Diseases Unit; Assistant Professor of Chemistry, Columbia University, 1991–present.

Cynthia F. Ridenour. *b* 1962. B.A., 1984, University of Colorado, Boulder; Ph.D., 1992, Colorado State University, with Professor Gary E. Maciel, applications scientist, Otsuka Electronics (USA), Inc., 1992–present.

Reference Deconvolution

Gareth A. Morris

University of Manchester, Manchester, UK

1 Introduction 1
2 Historical Background 2
3 Theory 2
4 Applications 4
5 Related Article in this Volume 6
6 Related Articles in Volumes 1–8 6
7 References 6

1 INTRODUCTION

All experiments are imperfect. Advances in the engineering and design of NMR spectrometers mean that NMR experiments have steadily improved in quality over the last 50 years, and are certainly closer to perfection than many other types of spectroscopic measurement, but nevertheless all NMR measurements carry internal evidence of the shortcomings of the experimental equipment and techniques used. Some sources of imperfection are inevitable: any electronic measurement that takes place above absolute zero contains random noise originating in the thermal motion of charge carriers. Many other sources could be avoided in an ideal NMR instrument: line broadening or spinning sidebands caused by static magnetic field inhomogeneity, difference artifacts caused by instabilities in field-frequency ratio, and phase errors caused by impure radiofrequency sources. One feature shared by all the members in this list is that they affect all the signals in a spectrum in the same way: each can be described as a multiplication of the expected free induction decay by some sort of error function. It is therefore possible in principle to correct for the effects of these sources of imperfection by using prior knowledge of the form expected for a given line in the spectrum. This is the basis of reference deconvolution,[1] in which the experimental spectrum is deconvoluted with the experimental form of a reference signal and reconvoluted with the theoretical ideal form, to yield a spectrum in which instrumental distortions are suppressed for all signals. In keeping with its original use for the correction of lineshapes, the method is often referred to by the acronym FIDDLE (Free Induction Decay Deconvolution for Lineshape Enhancement), although strictly it is the experimental spectrum, rather than the free induction decay, that is deconvoluted.

The basic principles of reference deconvolution are illustrated in Figure 1, which uses data from a 300 MHz proton experiment in which the homogeneity of the static field was deliberately perturbed. The spectrum contains a signal from acetone which should be a simple singlet, but which in common with all the other signals in the spectrum shows severe lineshape errors and spinning sidebands because of the combination of poor B_0 homogeneity and sample spinning. If the Fourier transform of the raw experimental free induction decay, Figure 1(b), is treated by zeroing all the spectrum apart from the region containing the acetone signal, inverse Fourier transformation of this windowed spectrum will yield a time-domain signal which is that component of the original free induction decay attributable to the acetone reference signal. This time-domain acetone signal is the product of the signal that would have been recorded by a perfect instrument, multiplied by a complex time-dependent envelope function which describes the modulation of the signal by the spatially and temporally varying magnetic field experienced by different parts of the sample, and supplemented by a background of random noise.

The ideal form of the signal expected from theory is straightforward: in the frequency domain, a Lorentzian line centered on the acetone chemical shift, and in the time domain, a complex exponential that rotates at the acetone chemical shift and decays exponentially. It is thus possible both to deduce the form of the error modulation experienced by the experimental signal, and to produce a spectrum corrected for its effects, by taking the complex ratio of the theoretical and experimental forms of the reference signal. Multiplying the original experimental free induction decay by this time-dependent complex ratio yields a corrected signal, shorn of the unwanted modulation, which can be Fourier transformed to yield a corrected spectrum with ideal lineshapes (Figure 1b). The price paid is a small increase in the complexity of data processing, and an increased (and non-white) noise background.

Reference deconvolution is not limited to the correction of lineshape errors: many different instrumental errors are multiplicative in the time domain and hence susceptible to

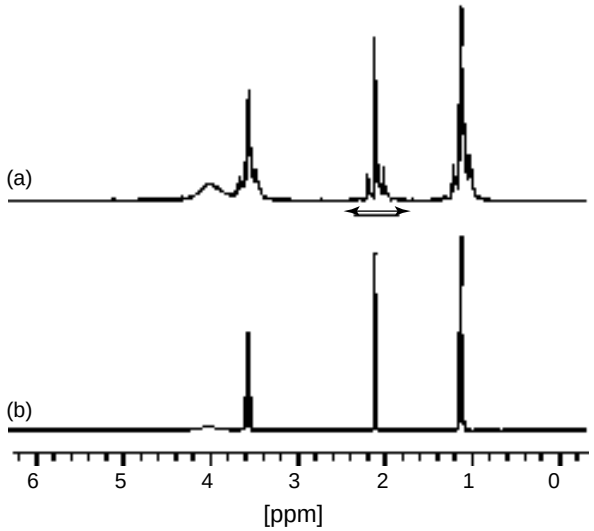

Figure 1 Schematic illustration of simple reference deconvolution. Deconvoluting the raw experimental spectrum (a) with the acetone lineshape contained in the arrowed frequency range and reconvoluting with a 1 Hz wide Lorentzian gives the corrected spectrum (b), in which signals have essentially perfect lineshapes. (Adapted from 'Progress in Nuclear Magnetic Resonance Spectroscopy', Vol. 31, G. A. Morris, H. Barjat and T. J. Horne, Reference Deconvolution Methods, pp 197–257, Copyright (1997), with permission from Elsevier Science)

correction in this way. Examples include changes in receiver gain, field-frequency ratio, receiver phase, and many of the sources of t_1-noise in 2D NMR spectroscopy. Unlike other post-processing methods for improving the interpretability of NMR data, such as maximum entropy reconstruction or linear prediction, reference deconvolution is essentially a linear process. Prior knowledge of the theoretical form of the reference signal is used to allow the experimental signal(s) to be factorized into a corrected spectrum and an experimental lineshape, with no change in the overall information content. This linearity represents both a strength and a weakness. The risk of over-interpretation of the experimental evidence, ever present with nonlinear methods, is small. However, reference deconvolution cannot produce corrected data where there is no experimental evidence. The range of experimental imperfections that may be corrected is thus finite: if the time-domain envelope of an experimental signal touches zero, division of the ideal time-domain signal by its experimental form will produce a singularity. In such circumstances there is a choice between restricting the correction of the signal to times before the experimental signal disappears, and invoking nonlinear methods.

2 HISTORICAL BACKGROUND

Experimental spectroscopists frequently use the principle of reference deconvolution implicitly: if a small shoulder appears on one side of an NMR line, the immediate reaction is to check for the same feature elsewhere in the spectrum. If absent, the shoulder represents a real signal; if present throughout, it probably indicates a shimming error and can safely be ignored. Giving this principle quantitative form, numerical fitting of complex multiplets with an experimental lineshape dates back at least to 1966.[2,3] Reference deconvolution proper has been independently proposed at least four times in different guises, for correcting pulse Fourier Transform FT NMR,[4,5] correlation NMR[6] (Reference Lineshape Adjustment, RLSA) and in vivo NMR[7] (Quantification Improvement by Converting Lineshapes to the Lorentzian Type, QUALITY) data. Although the algorithms proposed differ somewhat in detail, all share the same basic features. In addition to these methods, which seek to use all the experimental information available in the correction process, a variety of less general methods have been proposed which seek to correct just one or two classes of error. Examples include time-dependent phase correction in in vivo experiments using pulsed field gradients,[8] and phase[9] or phase and amplitude[10] tracking for t_1-noise reduction in 2D NMR experiments.

3 THEORY

The basic algorithm described in the Introduction can be quite effective, but in all but the simplest spectra it suffers from a significant disadvantage. In order to obtain the experimental free induction decay for the reference signal alone it is necessary to filter out contributions from all other signals. At first sight this is straightforward; zeroing all but the arrowed reference signal region of Figure 1(a) should have the desired effect. However, in order to obtain the complete time-domain reference signal it is necessary to use both real (absorption mode) and imaginary (dispersion) mode parts of the raw experimental spectrum. Because the dispersion mode signal falls off only hyperbolically with frequency offset, it is much more difficult to choose a reference region which neither truncates the dispersion mode reference signal nor includes signal from other resonances. The solution is to perform the filtering of the experimental spectrum on the absorption mode signal alone, and reconstruct the missing contribution from the dispersion signal using the Hilbert transform relationship between the two. Provided that the raw experimental free induction decay is zero-filled at least once before Fourier transformation, no net loss of information results.

A practical algorithm for reference deconvolution proceeds as follows. The raw experimental free induction decay $s_e(t)$ is zero-filled once, Fourier transformed and phase corrected to yield an experimental spectrum $S_e(\omega)$. The experimental free induction decay for the reference signal $s_r(t)$ alone may be obtained by taking the first half of the inverse Fourier transform of the windowed spectrum:

$$s_r(t) = \mathrm{FT}^{+}[\mathrm{Re}\{S_e(\omega)\} \prod(\omega_R, \omega_L)] \prod(0, t_{max}) \qquad (1)$$

Here FT^{+} and FT^{-} indicate inverse Fourier transformation and Fourier transformation respectively:

$$\mathrm{FT} \pm [A(\omega)\} = \frac{1}{2\pi} \int_{-\infty}^{+\infty} A(\omega) e^{\pm i\omega t} d\omega \qquad (2)$$

the window function $\Pi(a,b)$ is unity between a and b and zero elsewhere, the reference signal (and nothing else) is entirely contained within the frequency range ω_R to ω_L, and t_{max} is the time for which the experimental free induction decay is recorded. The windowing $\Pi(0,t_{max})$ is necessary because transforming only the real part of $S_e(\omega)$ generates a time-symmetric function consisting of the required signal followed by its reflection. The use of zero-filling before the initial Fourier transformation ensures that no information is lost when this reflection is discarded.

The next step is to calculate the ideal form $s_i(t)$ of the ideal reference signal. This may be done either by direct calculation in the time domain, or by inverse Fourier transformation of the theoretical spectrum; in both cases it is necessary to include explicitly any known satellite signals, isotope shifts etc. The choice of lineshape for the ideal reference signal is critical. The obvious choice, the natural lineshape, is almost always far too ambitious: because most experimental spectra are significantly broadened by field inhomogeneity, setting a target lineshape which is much narrower than the experimental lineshape generally yields unacceptably low signal-to-noise ratio. As with other forms of resolution enhancement, the uninformative limit is an infinitely sharp spectrum with zero signal-to-noise ratio. The solution is to select a target lineshape, typically Lorentzian, Gaussian, or some mixture of the two, which gives a suitable compromise between resolution and signal-to-noise ratio in the corrected spectrum. In general the ideal reference signal can be described as a sum of rotating complex exponentials multiplied by an envelope function $W(t)$:

$$s_i(t) = \sum_{j=1}^{n} a_j \exp(i\omega_j t) \times W(t) \qquad (3)$$

where the summation is over the known components of the reference signal, and $W(t)$ typically has the form

$$W(t) = \exp\left[-\frac{t}{t_e}\right]\exp\left[-\frac{t^2}{t_g^2}\right] \quad (4)$$

with exponential and Gaussian components defined by the time constants t_e and t_g receptively.

The correction function required is then the complex ratio $c(t)$ between the theoretical and experimental reference free induction decays:

$$c(t) = \frac{s_i(t)}{s_r(t)} \quad (5)$$

Since the experimental reference free induction decay is derived from a phase-corrected spectrum (in order to avoid dispersion mode contributions), any frequency-dependent component of the phase correction will have had the effect of giving a small time shift to the time-domain signal. Therefore to ensure exact time correspondence between the full and the reference experimental free induction decays, a time-shifted version $s'_e(t)$ of the former should be produced:

$$s'_e(t) = \mathrm{FT}^+[\mathrm{Re}\{S_e(\omega)\}]\prod(0, t_{max}) \quad (6)$$

The corrected spectrum is finally obtained by Fourier transforming the product of the time-shifted full experimental free induction decay and the correction function $c(t)$:

$$S_c(\omega) = \mathrm{FT}^-[s'_e(t)c(t)] \quad (7)$$

The complete process is summarized in Figure 2. The raw experimental free induction decay (a) is zero-filled, Fourier transformed and phase corrected (b), and then inverse Fourier transformed with (d) and without windowing to yield the reference free induction decay (c) $s_r(t)$ and the time-shifted (phase-corrected) full free induction decay (i) $s'_e(t)$. The ideal reference signal (e) $s_i(t)$ is calculated either directly or by inverse Fourier transformation of the ideal spectrum (f). Finally the time-shifted signal (i) is divided by the experimental reference signal (c) and multiplied by the ideal reference signal (e) to give the corrected free induction decay (g), which may be transformed to give a corrected spectrum (h) $S_c(\omega)$.

Not all experimental spectra contain a suitable singlet reference signal. There is a fundamental difficulty in using reference signals which are simple multiplets, in that such signals contain zeroes in the time domain. It is however still possible to use such signals in spectra with good signal-to-noise ratio, by interpolating the correction function $c(t)$ over the gaps in the experimental data. Although this compromises slightly the linearity of the process, in practice the extra information generated is a very small proportion of the whole, and the interpolation works well. The principal problem is the need for the ideal reference signal to be very accurately characterized, as visible artifacts can result from errors of just a few MHz in coupling constant or a fraction of a percent amplitude asymmetry. Fortunately the effects of such errors are simple and predictable (spurious sidebands at harmonics of the multiplet splitting), and iterative minimization of such sidebands can be used to refine the form of the ideal signal. Provided care is taken, very good results can be obtained with doublet reference signals.[11]

Reference deconvolution is not restricted to one-dimensional spectra, but different multidimensional experiments may

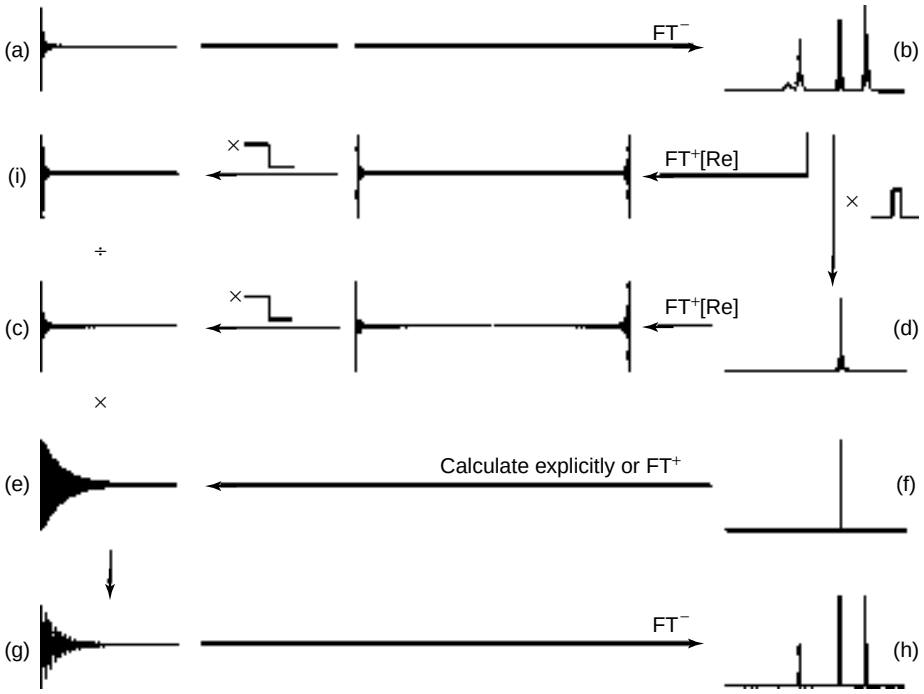

Figure 2 Schematic summary of a practical algorithm for reference deconvolution. (Reprinted from 'Progress in Nuclear Magnetic Resonance Spectroscopy', Vol. 31, G. A. Morris, H. Barjat and T. J. Horne, Reference Deconvolution Methods, pp 197–257, Copyright (1997), with permission from Elsevier Science)

require different implementations. The discussion which follows concerns the application to 2D NMR, but similar considerations apply to all multidimensional NMR experiments. Reference deconvolution for the simple correction of lineshape errors can be applied to any 2D experiment by using a correction function derived from a conventional 1D experiment. The same correction function is applied to every experimental free induction decay, correcting the lineshape in F_2; where appropriate, the same correction can be used in F_1. A much more powerful use of reference deconvolution in 2D NMR is for the correction of t_1-noise, but here two complications intrude. The first is that reference deconvolution only corrects for instrumental errors which affect all signals equally; in 2D NMR, this can effectively limit reference deconvolution to correcting a single coherence transfer pathway. The second problem is that reference deconvolution cannot be used where there is no reference signal, preventing (or at least greatly complicating) its application to experiments in which the reference signal is amplitude modulated as a function of t_1.

Reference deconvolution has been applied very successfully to two different classes of 2D experiment: those in which t_1-noise is dominated by a single unwanted pathway (e.g., HMBC (heteronuclear multiple bond coherence)), and those in which pulsed field gradients are used to ensure that only a single coherence transfer pathway survives (e.g., gradient enhanced COSY (correlation spectroscopy), gradient NOESY (nuclear Overhauser effect spectroscopy)). In the former case, the normal phase cycle is split into two halves in which the unwanted signals are of opposite phase, and reference deconvolution is used to ensure that the reference signal is nulled when data for the two halves are combined.[12] In the latter case, reference deconvolution is used as normal except that the ideal reference signal is phase-modulated as a function of t_1, and the extraction of the experimental reference signal requires automatic phase and baseline adjustment of the reference region of the (t_1,F_2) spectra.[13]

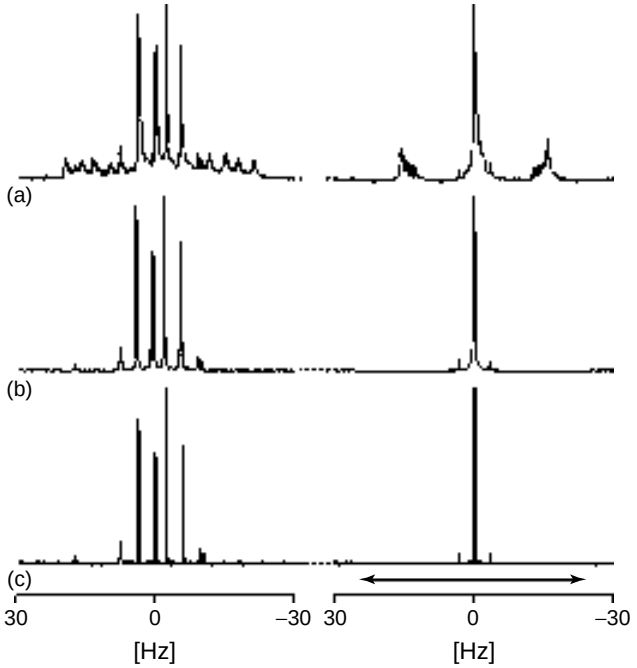

Figure 3 Reference deconvolution of a 300 MHz proton spectrum of a solution of orthodichlorobenzene and TMS in deuterioacetone. (a) Raw spectrum; (b) after reference deconvolution with a target lineshape of a 0.2 Hz wide Lorentzian; and (c) after reference deconvolution with a target lineshape of a 0.2 Hz wide Gaussian. The horizontal arrow indicates the reference region used. (Adapted from Progress in Nuclear Magnetic Resonance Spectroscopy, Vol. 31, G. A. Morris, H. Barjat and T. J. Horne, Reference Deconvolution Methods, pp 197–257, Copyright (1997), with permission from Elsevier Science)

4 APPLICATIONS

4.1 Lineshape Correction

One of the earliest applications of reference deconvolution, and still the most widespread, is for the correction of instrumental errors in lineshape. Figure 3 offers an extreme example, in which a 300 MHz proton spectrum of a sample of orthodichlorobenzene and tetramethylsilane (TMS) was acquired under conditions of sample spinning and poor shimming. The raw spectrum of Figure 3(a) shows severe lineshape asymmetry and spinning sidebands. Reference deconvolution with a target lineshape of a 0.2 Hz wide Lorentzian ($t_e = 5/\pi$ s, $t_g = \infty$ in equation 4) using a 50 Hz wide region of the spectrum containing the TMS signal yielded the corrected spectrum of Figure 3(b), while setting a target lineshape of a 0.2 Hz Gaussian ($t_e = \infty$, $t_g = 2.65$ s in equation 4) gave the spectrum of Figure 3(c). Note the ^{29}Si and ^{13}C satellites visible in the TMS region of Figures 3(b) and 3(c); if these are omitted from the ideal reference signal, spurious negative sidebands appear in the corrected spectrum.

Figure 3 is illustrative of the sort of improvement obtainable, at relatively modest cost in signal-to-noise ratio, even where there are severe lineshape distortions. In spectra where the natural widths of the lines of interest are significantly greater than that of the reference signal, as is generally the case, resolution enhancement is easily obtained by using a negative time constant t_e and a positive t_g in equation (4). This leads to over-enhancement of the reference line, generating negative side-lobes, but enhanced resolution for the remainder of the spectrum. The application of reference deconvolution is not restricted to spectra, such as that of Figure 3, which have relatively high signal-to-noise ratio. The basic requirement is that the signal-to-noise ratio of the reference signal be at least as good as that of the signals of interest, as otherwise the noise in the reference region would lead to visible noise being convoluted onto the remainder of the spectrum. Reference deconvolution is not uniformly successful; in the small minority of situations where there is significant multiplet character to the experimental lineshape, so that nodes appear in the time-domain signal, the width of target lineshape for which clean results are obtained is limited by the time at which the first zero appears in the experimental signal envelope.

Lineshape correction by reference deconvolution finds a wide variety of uses in NMR. It is particularly helpful in dynamic NMR, where instrumental contributions to the experimental lineshape interfere with attempts to extract dynamic information by bandshape fitting;[14] in diffusion-ordered spectroscopy, where small magnetic field perturbations following the application of field gradient pulses can distort lineshapes and lead to overestimation of diffusion coefficients;[15] and in

in vivo NMR,[7] where accurate shimming is frequently impossible. It has also been used in single crystal solid state NMR, and for the suppression of unwanted sidebands from a variety of sources. Although not strictly an application of lineshape correction, examination of the correction function $c(t)$ for 1D spectra can be a valuable diagnostic tool in tracking down instrumental problems.

4.2 Difference Spectroscopy

One of the families of NMR techniques most susceptible to instrumental irreproducibility is that of difference spectroscopy. The most common example is the NOE (nuclear Overhauser effect) difference technique, in which a difference is typically taken between an unperturbed spectrum and one acquired following selective saturation of a particular proton signal. Because Overhauser effects are typically small for small molecules in mobile solution, this technique is normally carried out only on samples with strong signals. This has the result that almost all such spectra show substantial difference artifacts, typically in the form of spurious signals which appear to be in dispersion mode. In fact such artifacts usually arise from small frequency differences between the saturated and unperturbed spectra, and hence cannot be adjusted to pure absorption mode. Although frequency errors frequently dominate, small changes in lineshape (especially if there is some probe heating as a result of the saturating irradiation), pulse phase errors etc., also contribute. All of these ills can be treated by using reference deconvolution to ensure that the reference signal has the same frequency, amplitude, phase and shape in both spectra. Provided that precautions are taken to avoid frequency-dependent perturbations of the spectra, the resultant difference spectra can be extremely clean.[16]

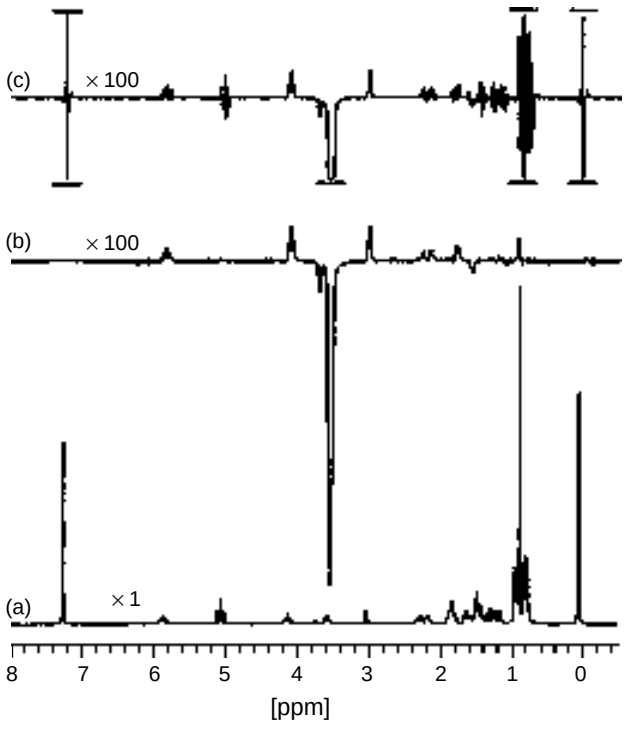

Figure 4 300 MHz proton spectra of compound **1**. (a) Normal spectrum; (b) NOE difference spectrum corrected by reference deconvolution using a 140 Hz wide reference region centered on the chloroform signal at 7.24 ppm, and expanded vertically ×100; and (c) uncorrected difference spectrum, with the same expansion but truncated as indicated by the horizontal bars

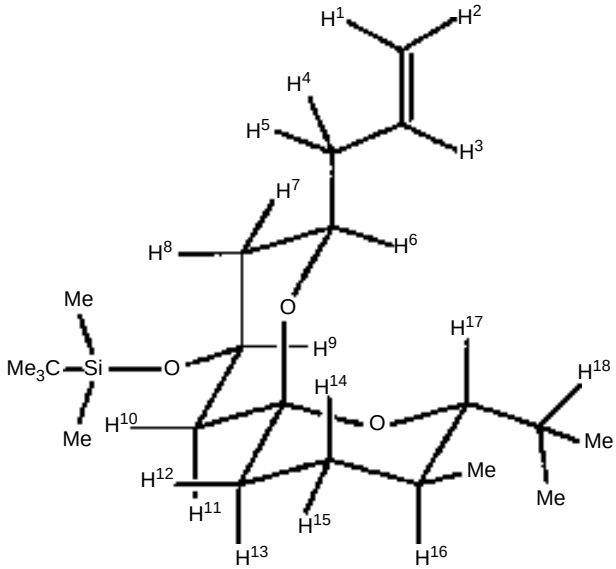

(1)

Figure 4(a) shows the normal spectrum of the species **1**, Figure 4(b) a hundred-fold vertical expansion of the corrected NOE difference spectrum following irradiation of proton 6, and Figure 4(c) the uncorrected difference spectrum. At such an expansion the uncorrected spectrum shows severe difference artifacts, but these are almost completely absent in the corrected spectrum. In the uncorrected spectrum only Overhauser effects greater than about 1% can be identified unequivocally, whereas the corrected spectrum shows a clean 0.5% NOE to the methyl signal at 0.9 ppm. The complete nulling of the signal of the trimethylsilyl blocking group, which is not expected to show any NOE, is particularly gratifying. This shows that the reference deconvolution process matches the signal amplitudes in the two parent spectra to better than 1 part in 10^4, or in other words would allow the detection of NOE's as small as 0.01% for such a signal.

4.3 2D NMR

Considerable improvements in spectral quality can be obtained by the use of reference deconvolution to correct the t_1-noise that results when instrument instability causes – as it inevitably does – different increments of a 2D NMR experiment to be acquired under slightly different conditions. If reference deconvolution is to correct in 2D NMR all of the errors that it can correct in 1D, it is necessary that all the signals of interest follow the same coherence transfer pathway, as otherwise any errors in pulse phase will have different effects on signals following different pathways. Of course, in experiments where other sources of t_1-noise that do not affect the relative phases of pulses and signals are dominant, the requirement of a single pathway may be relaxed.

The simplest example of a single pathway 2D experiment is gradient-enhanced COSY,[17] in which field gradient pulses

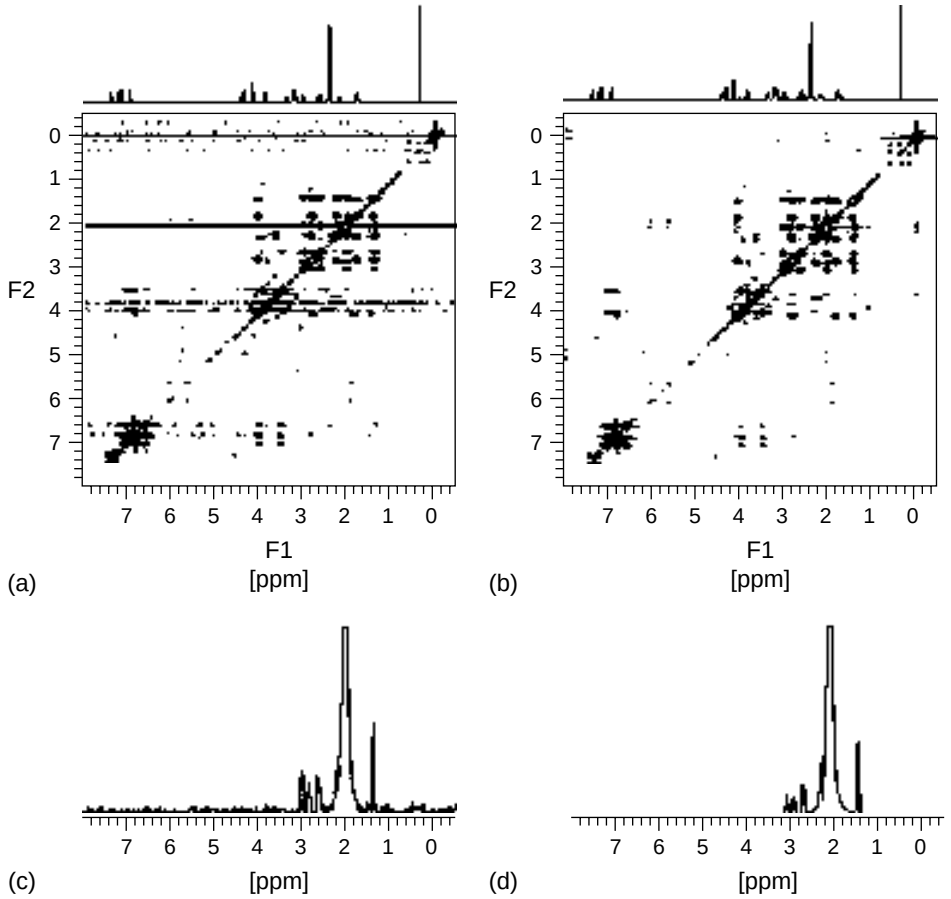

Figure 5 500 MHz gradient COSY spectra of compound 2. (a) Raw and (b) corrected COSY spectra, with (c) and (d) vertical expansions of the corresponding F_1 cross-sections through the residual proton signal from the solvent. (Adapted from T. J. Horne and G. A. Morris, *J. Magn. Reson. Ser A*, 1996, **123**, 246, by permission of Academic Press)

either side of the mixing pulse are used to enforce either the coherence transfer echo or the antiecho pathway.

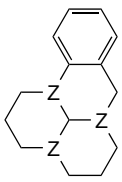

(2)

Figure 5 shows the results of a simple gradient COSY experiment on a solution of the tetracyclic orthoamide **2** in deuterioacetone with TMS as reference. To correct the experimental data, the raw free induction decays were treated with a mild Gaussian weighting to prevent truncation artifacts, zero-filled, and Fourier transformed with respect to t_2. Each of the resultant spectra was then subjected to reference deconvolution using an 88 Hz wide region around the TMS signal, and the corrected free induction decay stored. Automatic zero-order phase and linear baseline correction were applied to the reference region, and a target lineshape of a 3 Hz wide Lorentzian, phase modulated as a function of t_1 at the TMS offset from resonance, was used. The 2D spectra of Figure 5(a) and (b) show the raw and corrected data respectively, following sinebell multiplication, zero-filling and double Fourier transformation. The corresponding F_1 cross-sections Figure 5(c) and (d) through the residual solvent peak at 2.04 ppm show the reduction in t_1-noise achieved by reference deconvolution. The signal-to-t_1-noise ratio increases from 2600 : 1 to 110 000 : 1, a 40-fold improvement. Interestingly, the reduction in the noise level reveals some small signals attributable to dipolar demagnetization field effects, which are not normally seen in spectra of relatively dilute samples.

5 RELATED ARTICLE IN THIS VOLUME

Diffusion-Ordered Spectroscopy (DOSY).

6 RELATED ARTICLES IN VOLUMES 1–8

COSY Two-Dimensional Experiments, Volume 3, Data Processing, Volume 3, Maximum Entropy Reconstruction, Volume 5, Nuclear Overhauser Effect, Volume 5.

7 REFERENCES

1. H. Barjat, T. J. Horne, and G. A. Morris, *Prog. Nucl. Magn. Reson. Spectrosc.*, 1997, **31**, 197.

2. W. D. Keller, T. R. Lusebrink, and C. H. Sederholm, *J. Chem. Phys.*, 1966, **44**, 782.
3. R. R. Ernst, R. Freeman, B. Gestblom, and T. R. Lusebrink, *Mol. Phys.*, 1967, **13**, 283.
4. J. Taquin, *C.R. Acad. Sci. Paris*, 1975, **280B**, 485; *C.R. Acad. Sci. Paris*, 1976, **283B**, 257; *Rev. Phys. Appl.*, 1979, **14**, 669.
5. G. A. Morris, *J. Magn. Reson.*, 1988, **80**, 547.
6. J. M. Wouters and G. A. Petersson, *J. Magn. Reson.*, 1977, **28**, 81; J. M. Wouters, G. A. Petersson, W. C. Agosta, F. H. Field, W. A. Gibbons, H. Wyssbrod, and D. Cowburn, *J. Magn. Reson.*, 1977, **28**, 93.
7. A. A. DeGraaf, J. E. van Dijk, and W. M. M. J. Bovée, *Magn. Reson. Med.*, 1990, **13**, 343.
8. R. J. Ordidge and I. D. Cresshull, *J. Magn. Reson.*, 1986, **69**, 151.
9. G. A. Zhu, A. Renwick, and A. Bax, *J. Magn. Reson. Ser. A*, 1994, **110**, 257.
10. A. Ziegler, M. Izquierdo, C. Rémy, and M. Décorps, *J. Magn. Reson. Ser. B*, 1995, **107**, 10.
11. H. Barjat, G. A. Morris, A. G. Swanson, S. Smart, and S. C. R. Williams, *J. Magn. Reson. Ser. A*, 1995, **116**, 206.
12. A. Gibbs, G. A. Morris, A. G. Swanson, and D. Cowburn, *J. Magn. Reson. Ser. A*, 1993, **101**, 351.
13. T. J. Horne and G. A. Morris, *J. Magn. Reson. Ser. A*, 1996, **123**, 246.
14. D. V. S. Green, I. H. Hillier, G. A. Morris, and L. Whalley, *Magn. Reson. Chem.*, 1990, **28**, 820.
15. H. Barjat, G. A. Morris, S. Smart, A. G. Swanson, and S. C. R. Williams, *J. Magn. Reson. Ser. B*, 1995, **108**, 170.
16. G. A. Morris and D. Cowburn, *Magn. Reson. Chem.*, 1989, **27**, 1085.
17. R. E. Hurd, *J. Magn. Reson.*, 1990, **87**, 422.

Biographical Sketch

Gareth A. Morris, *b* 1954. M.A. (Nat. Sci.), Ph.D. (supervisor Ray Freeman) 1978, Oxford University, UK. Fellow by Examination, Magdalen College, Oxford, 1978–1981; Izaak Walton Killam Postdoctoral Fellow, University of British Columbia (with Laurie Hall) 1978–1979. Lecturer (1982–1989) and Reader (1989–1997) in Chemistry, Professor of Physical Chemistry (1998 to date), University of Manchester, UK. Approx. 130 publications. Current research interests: development of novel NMR techniques and their application to problems in chemistry, biochemistry and medicine.

Sideband Analysis in Magic Angle Spinning NMR of Solids

Judith Herzfeld and Xiaobing Chen
Brandeis University, Waltham, MA, USA

1	Introduction	1
2	Moments	2
3	Sideband Ratios	5
4	Simulations	6
5	Complications	7
6	Related Articles	7
7	References	7

1 INTRODUCTION

In general, the effective magnetic field at a nucleus depends on the orientation of the molecule in the applied field. In the simplest case of a dilute spin-$\frac{1}{2}$ system, the orientation dependence is due to the anisotropy of the chemical shielding. Typically, the electron density in a molecule is highly anisotropic, with accumulations along the bond axes between neighboring nuclei. This leads to complicated electron currents which depend on the direction of the applied magnetic field relative to the bond axes. At experimentally accessible applied field strengths, where only the first-order effects on the electrons are observed, the chemical shielding is most generally expressed in linear algebraic terms as a second-rank tensor with elements ${}^{A}\sigma_{ij}$ which specify the magnitude of the ith element of the induced magnetic field vector at nucleus A when the applied magnetic field is along direction j. In most cases, the asymmetry of the tensor is not measurable[1–3] and the effective chemical shielding tensor is the symmetric tensor equal to half of the sum of the exact tensor and its transpose. This symmetric tensor has a principal axis system in which it is diagonal and three principal values (conventionally $\sigma_{11} \leq \sigma_{22} \leq \sigma_{33}$) corresponding to the chemical shielding along the three principal axes. Detailed information about the electron distribution around the nucleus is thus summarized in six chemical shielding parameters (the six elements of the symmetric tensor, or the three principal values and the three Euler angles for the principal axis system). For this reason chemical shielding tensors have attracted considerable experimental and theoretical interest.[4,5]

All six chemical shielding parameters can be measured if a single crystal of sufficient size is available which allows the molecules to be studied in at least six appropriately chosen orientations relative to the applied field.[6] In powder samples, all molecular orientations are represented at the same time, with corresponding chemical shifts. The result is a broad signal with a characteristic shape known as a powder pattern [see, for example, Figure 1]. Although all orientational information has been lost, the three principal values of the shielding tensor, which specify the maximum, minimum, and most common

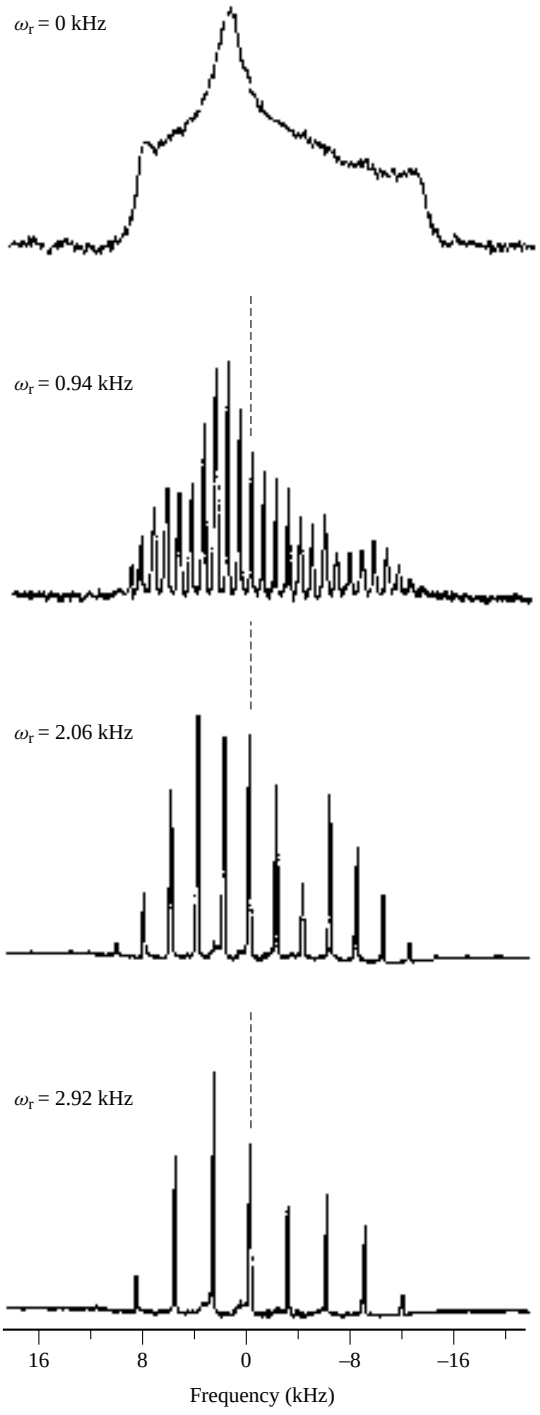

Figure 1 Proton decoupled ^{31}P spectra, at 119.05 MHz, of barium diethyl phosphate spinning at the magic angle[20]

chemical shifts, are apparent in the discontinuities of the powder pattern.[7] This is the most straightforward way to measure the three principal values of the shielding tensor. However, in many samples (notably biological ones) the discontinuities of the powder pattern may be obscured by overlap of multiple powder patterns and by poor signal-to-noise ratio due to the dispersal of the signal intensity over the breadth of the powder pattern. Two-dimensional (2D) correlation spectroscopy on reoriented samples can be used to sort overlapped powder patterns,[8] but the signal-to-noise

ratio is further deteriorated by the dispersal of signal intensity over 2D powder patterns.

Motional averaging reduces the effective range of chemical shielding, thereby improving both resolution and signal-to-noise ratio. In the limit of rapid isotropic tumbling, all of the signal is found at the average of the principal values of the chemical shielding (i.e. one-third of the trace of the tensor which is invariant to rotation). This isotropically averaged signal is observed for molecules in solution unless they are so large that the rotational diffusion is too slow. When the natural motion is not sufficiently fast or isotropic, the isotropic average of the chemical shift (or any second-rank tensor, such as the dipolar interaction) can be produced mechanically by spinning sufficiently rapidly about an axis tilted at the 'magic angle', $\cos^{-1}(\frac{1}{3}) = 54^\circ 44'$, relative to the direction of the applied field.[9,10]

While rapid magic angle spinning (MAS) provides high-resolution spectra of solid, dilute spin-$\frac{1}{2}$ systems, all information about the chemical shielding anisotropy (and hence the underlying anisotropy of the electron density) is lost. Use of rotor-synchronized rf pulses to prevent averaging in a second evolution period yields 2D spectra with powder patterns in the second dimension positioned at the isotropic chemical shift in the first dimension.[11] Similar results can be obtained by purely mechanical means, using 'magic angle hopping'[12] or 'stop-and-go spinning'.[13] This use of a second dimension to separate powder patterns that overlap in one dimension allows direct determination of the principal values of the chemical shift. However, the experiments are relatively demanding and do not address the signal-to-noise problem of powder patterns.

Anisotropic information can also be recovered by MAS at rates that are too small to average the chemical shielding anisotropy completely.[14] Spinning a crystallite at a frequency ω_r in the laboratory frame of reference, results in an applied field that swings around a cone with a frequency ω_r in the crystallite frame of reference [see equation (1) in Herzfeld and Berger[15]]. The chemical shielding of spins in the crystallite therefore oscillates around the isotropic value during the rotor period. The corresponding modulation of the Larmor precession produces a free induction decay for each crystallite with frequency components at integral multiples of ω_r above and below the isotropic value [see equation (21) in Herzfeld and Berger[15]]. The magnitudes and phases of these components will depend on the differences between the three principal values of the chemical shielding and on the initial orientation of the crystallite (given by three Euler angles). However, for a 'carousel'[16] of crystallites with orientations related by a uniform distribution of rotations around the rotor axis (corresponding to integration over the Euler angle γ in Herzfeld and Berger[15]), out-of-phase contributions cancel to produce a pure absorption NMR spectrum, consisting of a band at the isotropic frequency (the centerband) flanked by sidebands spaced at the spinning frequency with magnitudes depending on the values of the other two Euler angles and the differences between the principal values of the chemical shielding [see equation (24) in Herzfeld and Berger[15]]. It follows that the spectrum of a powder sample, representing contributions from the full range of the other two Euler angles, is also purely absorptive (see also Levitt,[16] Maricq and Waugh,[17] and Gullion and Conradi[18]) and that the magnitudes of the sidebands in the MAS powder spectrum will depend on the differences between the three principal values of the chemical shielding. The span, $\Omega = \sigma_{33} - \sigma_{11}$, and the skew, $\kappa = (\sigma_{11} + \sigma_{33} - 2\sigma_{22})/(\sigma_{33} - \sigma_{11})$,[19] can therefore be derived from the sideband intensities, while the isotropic average, $\sigma_{iso} = (\sigma_{11} + \sigma_{22} + \sigma_{33})/3$, is given by the position of the centerband. Analysis of slow MAS spectra thus presents an opportunity to determine experimentally all three principal values of the chemical shift without sacrificing resolution or signal-to-noise ratio.

Fortunately, the assignment of band order in slow MAS spectra is straightforward because the position of the centerband is independent of spinning speed and the associated sidebands are all spaced at the spinning frequency. Unfortunately, however, the dependence of the sideband intensities on the principal values of the chemical shielding is complicated, as illustrated by the example in Figure 1. Two approaches have been taken to extract the span and skew from the sideband intensities. Maricq and Waugh[21] have made use of the relatively simple dependence of the second and third moments of the sideband pattern on the span and skew. On the other hand, Herzfeld and Berger[15] have focused on the practical benefits of working with the ratios of the sideband intensities. We review both of these methods.

2 MOMENTS

Using I_N to represent the intensity of the Nth sideband (the signal at the frequency $N\omega_r$ above the isotropic frequency), the kth moment of a slow MAS spectrum is given by

$$M_k = \omega_r^k \sum_N N^k I_N \Big/ \sum_N I_N \tag{1}$$

Maricq and Waugh[21] found that the span and skew can be derived from the second and third moments according to the equations

$$\Omega = (1/2)\delta(3 - \eta) \tag{2}$$

and

$$\kappa = (3/2)\delta(1 + \eta)/\Omega \tag{3}$$

where δ is given by

$$8\delta^3 - 30M_2\delta - 35M_3 = 0 \tag{4}$$

and η is given by

$$\eta^2 = [15(M_2/\delta^2) - 3] = [1 - (35/2)(M_3/\delta^3)] \tag{5}$$

Equations (4) and (5) have three solutions for δ, each with two solutions for η. These six solutions correspond to the six permutations of the three principal values of the chemical shielding.

The accuracy of this method of sideband analysis clearly depends critically on the accuracy of the determination of the two moments. In practice, this requires that all the sidebands be resolved from other contributions to the spectrum. In addition, the sensitivity of the moments to the intensities of the higher order sidebands necessitates accurate measurement

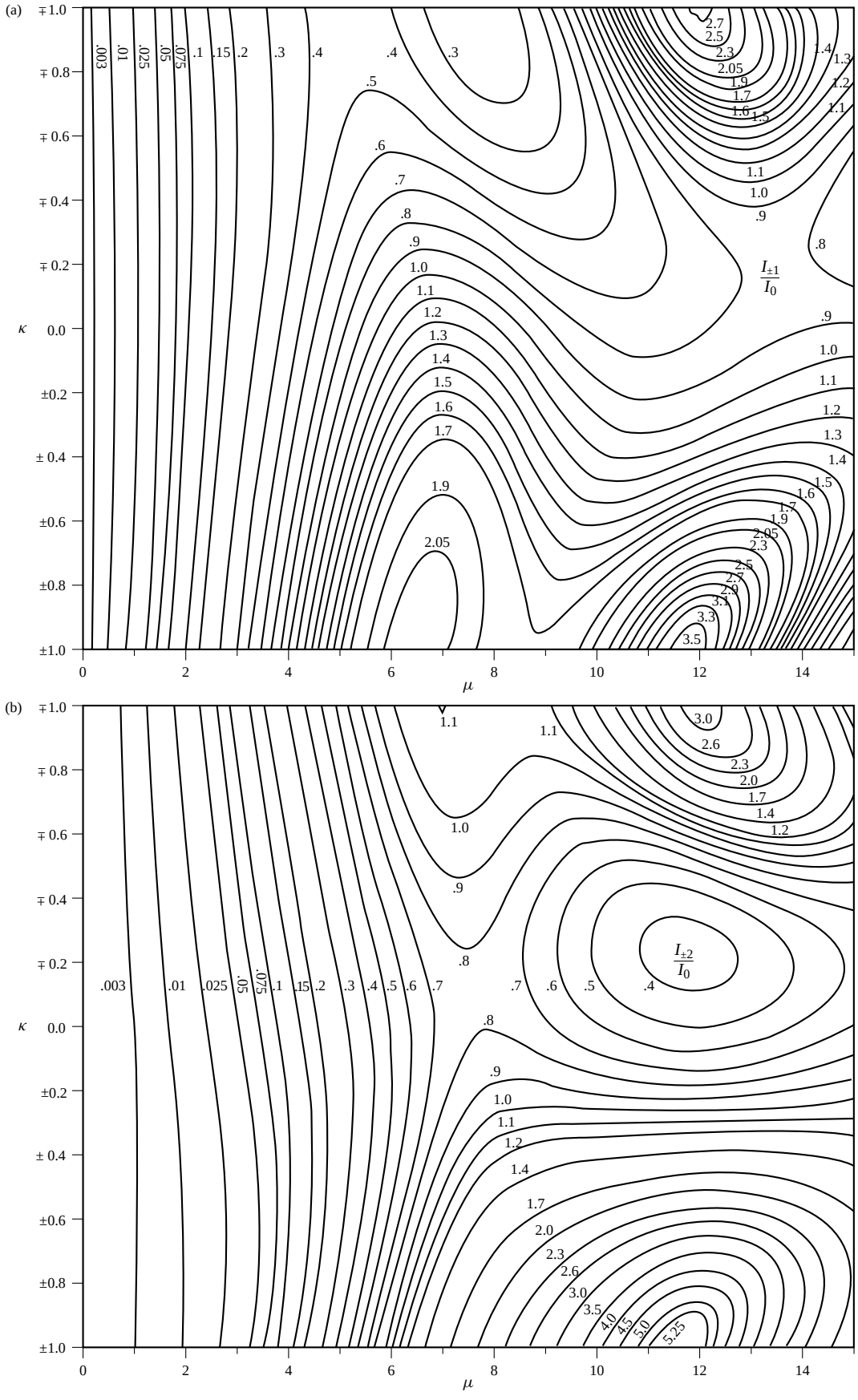
(a)
(b)
$\frac{I_{\pm 1}}{I_0}$
$\frac{I_{\pm 2}}{I_0}$
κ
μ
∓1.0
∓ 0.8
∓ 0.6
∓ 0.4
∓ 0.2
0.0
±0.2
± 0.4
±0.6
±0.8
±1.0
0
2
4
6
8
10
12
14
.003
.01
.025
.05
.075
.1
.15
.2
.3
.4
.5
.6
.7
.8
.9
1.0
1.1
1.2
1.3
1.4
1.5
1.6
1.7
1.9
2.05
2.3
2.5
2.7
2.9
3.1
3.3
3.5
1.1
1.0
.9
.8
.7
.6
.5
.4
3.0
2.6
2.3
2.0
1.7
1.4
1.2
1.1
1.0
.9
.8
.7
.6
.5
.4
.3
.2
.15
.1
.075
.05
.025
.01
.003
.8
.9
1.0
1.1
1.2
1.4
1.7
2.0
2.3
2.6
3.0
3.5
4.0
4.5
5.0
5.25

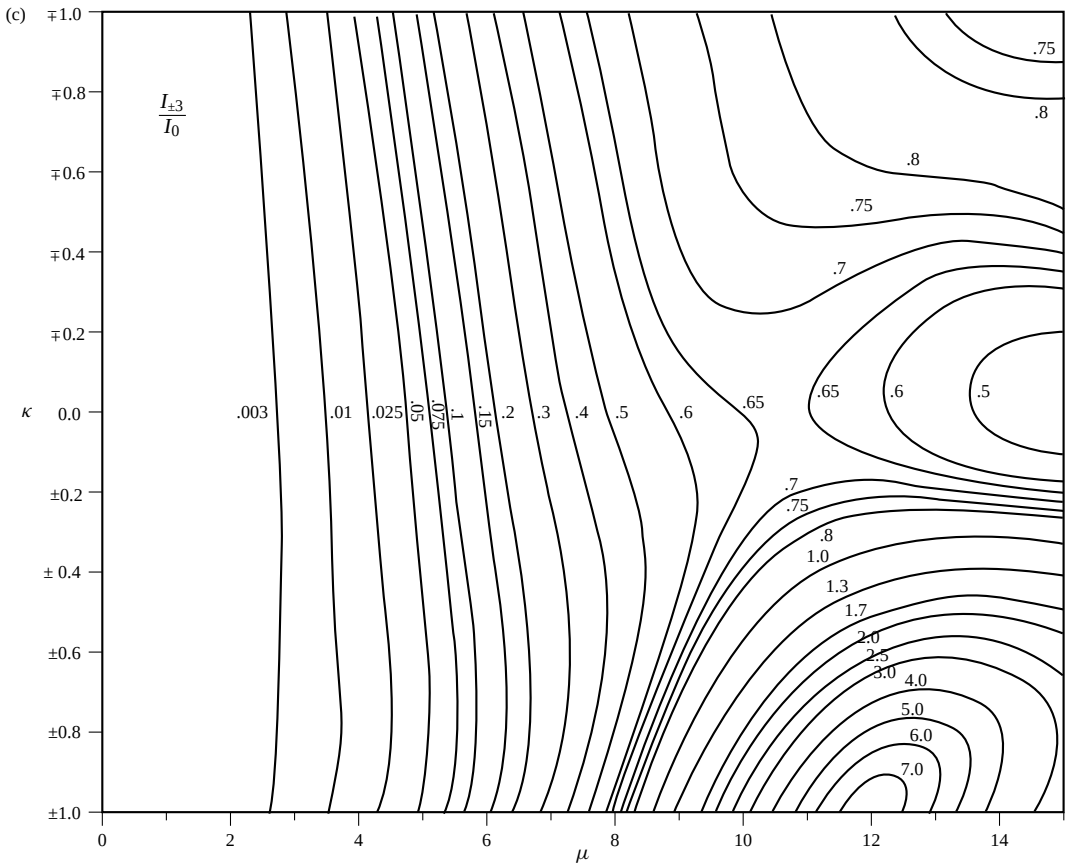
(c)
$\frac{I_{\pm 3}}{I_0}$
κ
μ
∓1.0
∓0.8
∓0.6
∓0.4
∓0.2
0.0
±0.2
± 0.4
±0.6
±0.8
±1.0
0
2
4
6
8
10
12
14
.003
.01
.025
.05
.075
.1
.15
.2
.3
.4
.5
.6
.65
.7
.75
.8
1.0
1.3
1.7
2.0
2.5
3.0
4.0
5.0
6.0
7.0

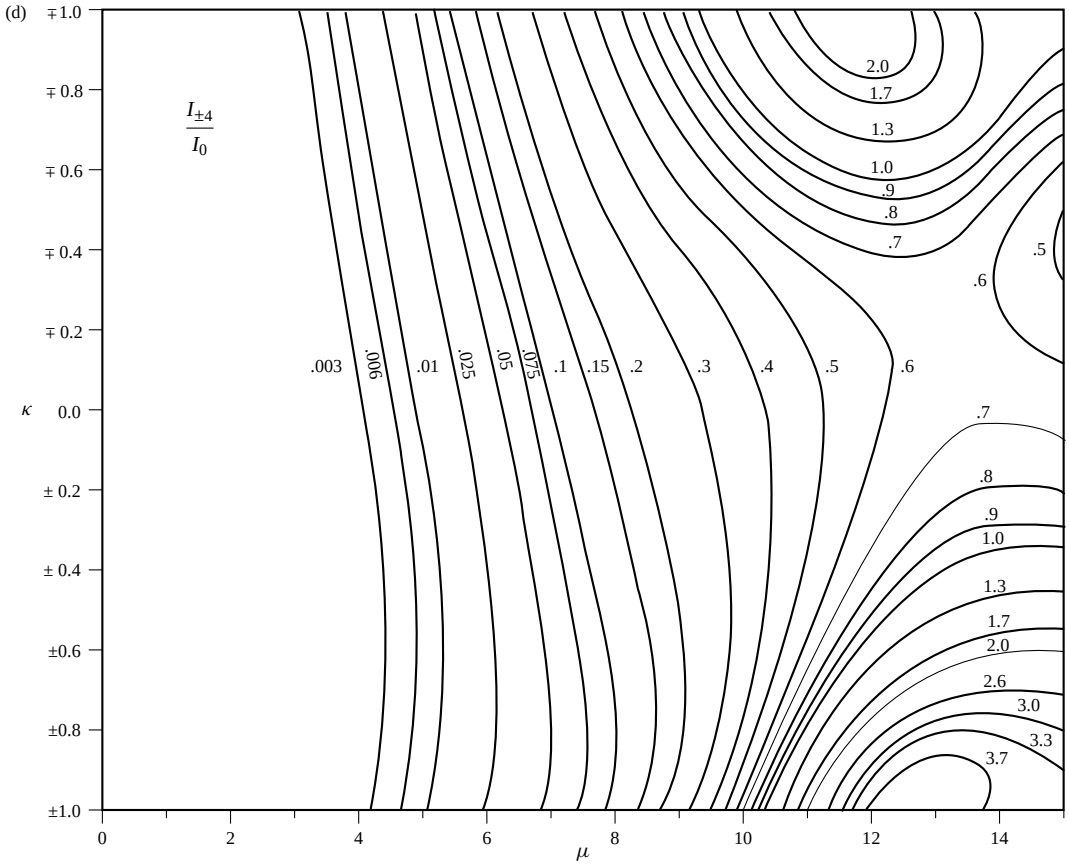
(d)
$\frac{I_{\pm 4}}{I_0}$
κ
μ
∓1.0
∓ 0.8
∓ 0.6
∓ 0.4
∓ 0.2
0.0
± 0.2
± 0.4
±0.6
±0.8
±1.0
0
2
4
6
8
10
12
14
.003
.006
.01
.025
.05
.075
.1
.15
.2
.3
.4
.5
.6
.7
.8
.9
1.0
1.3
1.7
2.0
2.6
3.0
3.3
3.7

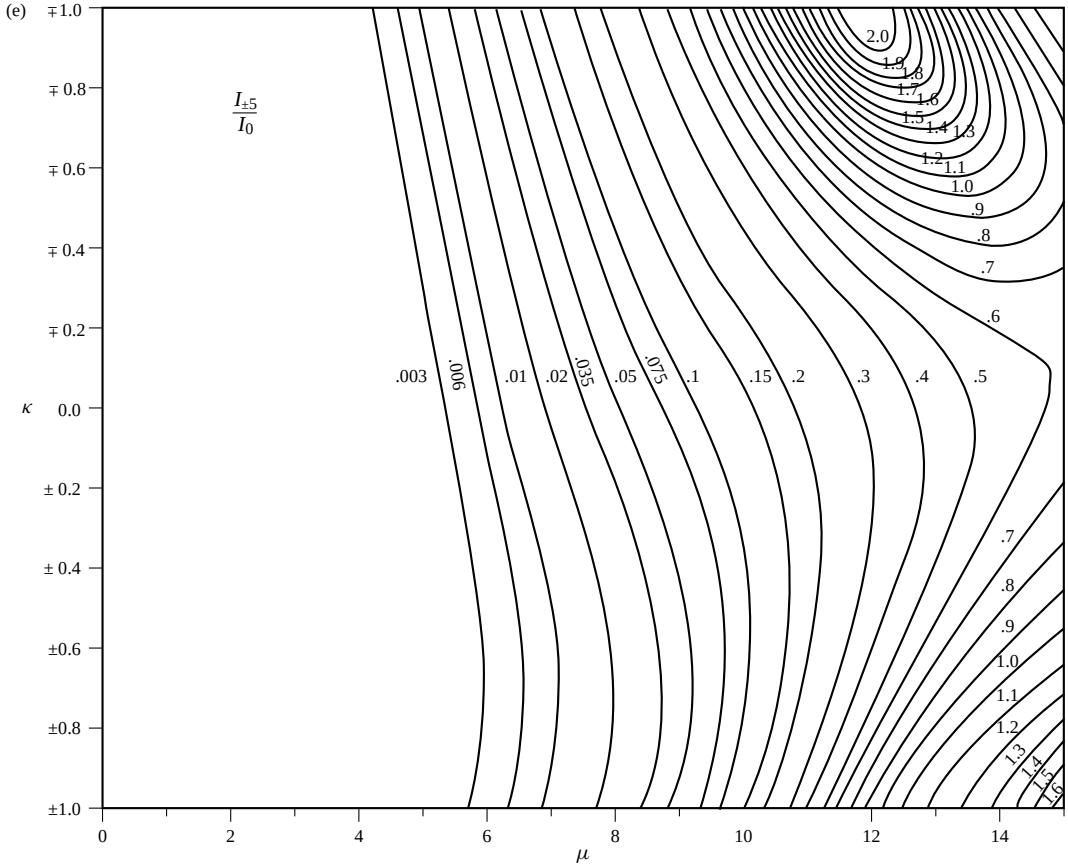

Figure 2 Contour plots of I_N/I_0 for values of N as indicated in (a)–(e).[15] This half strip corresponds to the convention $\sigma_{11} \leq \sigma_{22} \leq \sigma_{33}$. The five other permutations of the principal values correspond to the half strip for $\mu < 0$ and the four quadrants above and below the half strips

of weak signals that may be obscured by noise. The effects of inaccuracies in the measurement of higher order sidebands have been considered by Clayden et al.[22] in applications to slow MAS ^{31}P spectra of sodium dihydrogen orthophosphate, with a nonaxial shielding tensor, and triphenylphosphine oxide, with an axial shielding tensor. It was found that omitting sidebands of only 1% of the intensity of the most intense sideband was enough to produce significant variability in the derived principal values of the shielding. M_3 is the more vulnerable to inaccuracy than M_2 and examination of equations (4) and (5) shows that if $|M_3| > (\frac{2}{35})(5M_2)^{\frac{3}{2}}$ there is only one real solution for δ and no real values for η. This is a particular problem in the case of near axial tensors, for which $|M_3|$ is especially large compared with M_2 and η^2 tends toward zero. Inaccuracies in this regime easily lead to imaginary values of η. (See for example the case of triphenylphosphine oxide in Herzfeld et al.[20]) In general, moment analysis demands superb signal-to-noise ratio, especially for near axial tensors.

3 SIDEBAND RATIOS

Reliance on high-order sidebands, or any particularly inconvenient sidebands, can be avoided by using a search procedure to find those values of the span and skew that provide the best match to the intensities of the relatively accessible sidebands alone. In this process it is necessary to use ratios of sideband intensities for normalization.[15] Usually the centerband is one of the relatively strong sidebands and so it is convenient to use that for normalization. This places a special burden on accurate measurement of the intensity of the centerband and if this is not convenient other ratios can be used instead (see, for example, Fenzke et al.[23]). In the search for the best fit of the available intensity ratios, it is computationally demanding to calculate sideband intensities directly for every change in span and skew [e.g., using equations (24) and (33) Herzfeld and Berger,[15] for example]. Excellent accuracy can be obtained with much improved speed by bicubic spline interpolation between values calculated on a grid of points in the parameter space.[15] Such a grid of values is available for the intensities of the N = 0, ±1, ±2, ±3, ±4, ±5 bands, for values of the scaled span $\mu = (\gamma B/\omega_r)\ \Omega$ (where γ is the gyromagnetic ratio of the nucleus and B is the strength of the applied field) from 0 to 15,[15] and can be extended to larger spans[24] and higher orders,[23] as necessary.

In order to make good use of sideband intensity ratios, it is helpful to examine their dependence on the span and the skew graphically. Figure 2 shows contour plots for the intensity ratios $I_{\pm N}/I_0$, for N = 1 to 5. These graphs have several uses. First, they can be used to estimate graphically the span and skew for a particular set of experimental intensity ratios by locating the intersections of the corresponding contours. An example is shown in Figure 3 for barium diethyl phosphate. The graphical estimate of span and skew may suffice for some

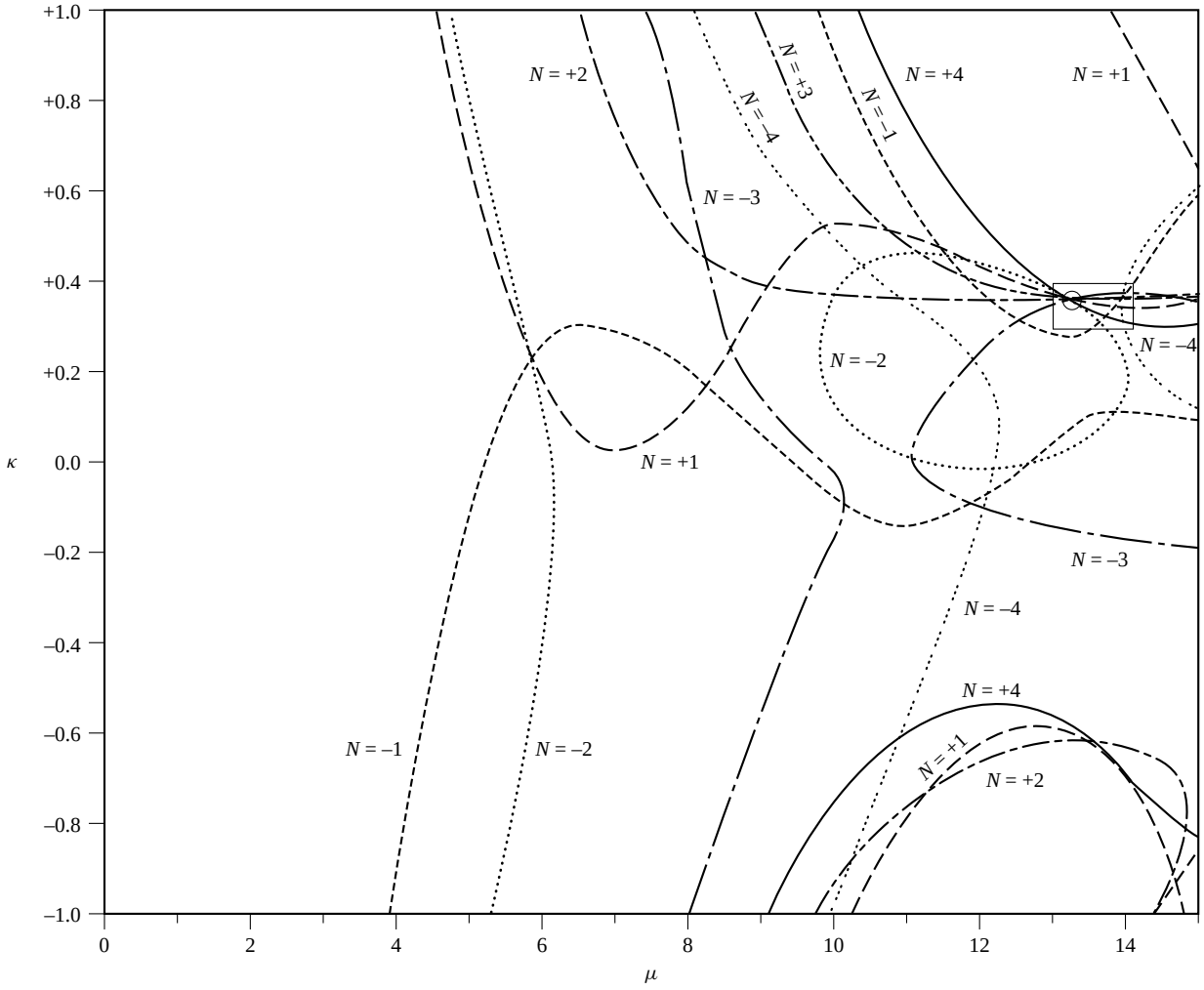

Figure 3 Graphical analysis of sideband intensity ratios I_N/I_0 from a ^{31}P spectrum, at 119.05 MHz, of barium diethyl phosphate spinning at 1.705 kHz.[15] Notice that the contours for $N > 0$ appear as they do in Figure 2, while the contours for $N < 0$ appear flipped over. This is necessary to superimpose corresponding values of κ. The estimated values of the scaled span, μ, and the skew, κ, are indicated with two different estimates of uncertainty by the circle and rectangle at $\mu \approx 13$ and $\kappa \approx 0.4$

purposes (see, for example, graphical ^{31}P results for sodium dihydrogen orthophosphate and triphenylphosphine oxide in Tables 1 and 3 of Clayden et al.[22]) or may be used as the starting point of a numerical fitting procedure for greater refinement.

The graphs in Figure 2 can also be used to design experiments. For example, it is clear that the intensity ratios are insensitive to the skew (as indicated by nearly vertical contours) for small values of μ. Thus a sufficiently low spinning speed must be chosen for μ to be large enough to obtain information about the skew. For near axial tensors (κ tending toward ± 1), the graphs show that μ must be even larger to obtain spectra sensitive to the skew. This difficulty has been noted by Clayden et al. for the nearly axially symmetric ^{31}P tensor of triphenylphosphine oxide, as compared with the nonaxial ^{31}P tensor of sodium dihydrogen orthophosphate (see Figures 3 and 8 of Clayden et al.[22]). Nevertheless, in both cases, graphical analysis of sideband ratios gives reasonably good estimates for the principal values of the chemical shielding, in contrast to the results of moment analysis (see Tables 1 and 3 of Clayden et al.[22]). For small spans, the spinning speed may need to be impractically low to obtain informative values of μ. However, for such narrow tensors, the skew is not of great practical interest because the three principal values are so similar.

4 SIMULATIONS

The reliability of the above methods depends on the extraction of accurate intensities for individual bands in slow MAS spectra. If the centerbands are well resolved, then overlap of sidebands with centerbands can be avoided by careful choices of spinning speeds or, for busier spectra, by a 2D experiment that sorts sidebands according to their isotropic chemical shifts.[25,26] However for spectra with overlapping centerbands or poor signal-to-noise ratio, extraction of accurate band intensities is not possible. In these cases, a more suitable approach is a direct least-squares fit of the full spectrum.[22] A relatively rapid scheme for such a fit was developed by deGroot et al.[27] Spectra are simulated for trial parameters by convolving a simple lineshape with sideband

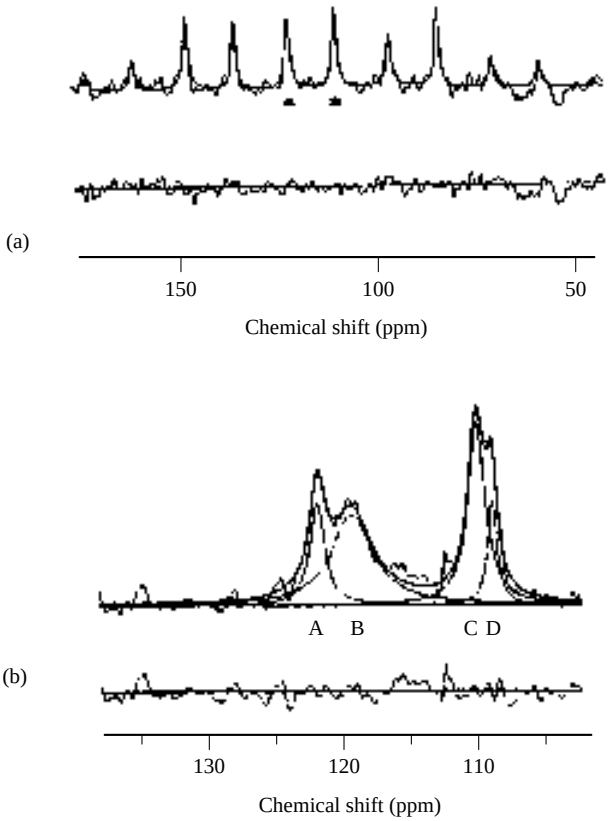

Figure 4 Carbon-13 MAS difference spectra and simulations for 14-^{13}C-retinal-labeled bacteriorhodopsin at (a) neutral pH with spinning speed 2.0 kHz[27] and (b) at low pH with spinning speed 3.0 kHz.[28] Chemical shifts are relative to TMS. The centerband is marked for each species by an asterisk or a letter. The least-squares simulations are represented by smooth lines. For the overlapped signals at low pH, the components that constitute the fit are also shown. Below each spectrum the residues are shown

intensities calculated by interpolation between stored values on a grid of points in span–skew space (from Herzfeld and Berger[15]). These calculated bands are positioned on a polynomial background according to the isotropic shifts and spinning speed. Least-squares iteration of the parameter search is pursued until the residuals reach the noise level. Figure 4 shows the results of such fits for a sample of 14-^{13}C-retinal-labeled bacteriorhodopsin at neutral pH and at low pH. At neutral pH, there are two species and their signals are fully resolved. In this case, the virtue of the fit is in the objective treatment of the noise. At low pH, four species are present, with some overlap of centerbands. In this case, the fit is essential for treating overlap, as well as noise.

5 COMPLICATIONS

Errors in sideband analysis may arise from noise in the spectrum or from mistaken theoretical assumptions. For analyses using moments or sideband ratios, the most straightforward means of assessing noise-limited accuracy is to repeat the analysis for variations of the measured sideband intensities over the range of values consistent with the noise.[29] This is preferable to arbitrary cut-offs in the acceptable overall deviations between theory and experiment.[23,29] For simulations, more rigorous sensitivity analysis is possible. In this case, it is convenient to choose a nonlinear least-squares fitting package that includes built-in statistical error estimation.[27]

The fundamental theoretical assumption made in the usual sideband analysis is that the chemical shielding is the only source of anisotropy. This is appropriate for a dilute spin-$\frac{1}{2}$ system with proton decoupling. However, cross polarization is an important tool in solid state NMR. In MAS experiments with cross polarization, Jeschke and Grossmann[30] reported systematic deviations between simulated and the experimental sidebands. They point out that the normal assumption that the magnetization of spins is independent of molecular orientation may be invalid for cross-polarized spins due to: (i) Hartmann–Hahn mismatch anisotropy, (ii) for short contact times, anisotropic orientation of the heteronuclear pair axis, and (iii) for long contact times, anisotropic relaxation in the rotating frame.

Other sources of anisotropy are also of interest. Spin-$\frac{1}{2}$ systems with heteronuclear dipolar interactions still behave inhomogeneously and various strategies of sideband analysis can be used to determine the strength of the dipolar interaction and the orientation of the heteronuclear axis relative to the principal axes of the chemical shielding.[21,31,32] Sideband analysis is also useful for systems with weak quadrupolar interactions.[21,33] However, systems with homonuclear dipolar interactions or strong quadrupolar interactions do not behave inhomogeneously and do not lend themselves to sideband analysis.[21,34,35]

6 RELATED ARTICLES

Anisotropy of Shielding and Coupling in Liquid Crystalline Solutions; Carbon and Nitrogen Chemical Shifts of Solid State Enzymes; Carbon-13 Spectral Simulation; Chemical Shift Tensor Measurement in Solids; Chemical Shift Tensors; Chemical Shift Tensors in Single Crystals; Dipolar and Indirect Coupling Tensors in Solids; Line Narrowing Methods in Solids; Magic Angle Spinning; Magic Angle Turning and Hopping; Proton Chemical Shift Measurements in Biological Solids; Rotating Solids; Variable Angle Sample Spinning.

7 REFERENCES

1. R. G. Griffin, J. D. Ellett, M. Mehring, J. G. Bulitt, and J. S. Waugh, *J. Chem. Phys.*, 1972, **57**, 2147.
2. F. K. Kneubühl, *Phys. Kondens. Mater.*, 1963, **1**, 410.
3. U. Haeberlen, *High Resolution NMR in Solids: Selective Averaging, Advances in Magnetic Resonance*, Suppl. 1, ed. J. S. Waugh, Academic Press, New York, 1976, p. 31.
4. M. Mehring, *High Resolution NMR in Solids*, 2nd edn., Springer, New York, 1983.
5. J. A. Tossell (ed.), *Nuclear Magnetic Shieldings and Molecular Structure*, Kluwer Academic, Dordrecht, 1993.
6. W. S. Veeman, *Prog. NMR Spectrosc.*, 1984, **16**, 193.
7. N. Bloembergen and J. A. Rowland, *Acta Metall.*, 1953, **1**, 731.
8. C. D. Hughes, M. H. Sherwood, D. W. Alderman, and D. M. Grant, *J. Magn. Reson. A*, 1993, **102**, 58.

9. E. R. Andrew and R. G. Eades, *Proc. R. Soc. London, Ser. A*, 1953, **216**, 398.
10. I. L. Lowe, *Phys. Rev. Lett.*, 1959, **2**, 285.
11. R. Tycko, G. Dabbagh, and P. A. Mirau, *J. Magn. Reson.*, 1989, **85**, 265.
12. A. Bax, N. M. Szeverenyi, and G. E. Maciel, *J. Magn. Reson.*, 1983, **52**, 147.
13. R. G. Ziegler, R. A. Wind, and G. E. Maciel, *J. Magn. Reson.*, 1988, **79**, 299.
14. E. O. Stejskal, J. Schaefer, and R. A. McKay, *J. Magn. Reson.*, 1977, **25**, 569.
15. J. Herzfeld and A. E. Berger, *J. Chem. Phys.*, 1980, **73**, 6021.
16. M. H. Levitt, *J. Magn. Reson.*, 1989, **82**, 427.
17. M. Maricq and J. S. Waugh, *Chem. Phys. Lett.*, 1977, **47**, 327.
18. T. Gullion and M. S. Conradi, *J. Magn. Reson.*, 1990, **86**, 39.
19. J. Mason, *Solid State Nucl. Magn. Reson.*, 1993, **2**, 285.
20. J. Herzfeld, A. Roufosse, R. A. Haberkorn, R. G. Griffin, and M. J. Glimcher, *Philos. Trans. R. Soc. London, Ser. B*, 1980, **289**, 459.
21. M. Maricq and J. S. Waugh, *J. Chem. Phys.*, 1979, **70**, 3300.
22. N. J. Clayden, C. M. Dobson, L. Y. Lian, and D. J. Smith, *J. Magn. Reson.*, 1986, **69**, 476.
23. D. Fenzke, B. Macb, and H. Pfeifer, *J. Magn. Reson.*, 1990, **88**, 172.
24. C. J. Groombridge, *Magn. Reson. Chem.*, 1993, **31**, 380.
25. A. C. Kolbert and R. G. Griffin, *Chem. Phys. Lett.*, 1990, **166**, 87.
26. D. P. Raleigh, E. T. Olejniczak, and R. G. Griffin, *J. Magn. Reson.*, 1991, **93**, 472.
27. H. J. M. deGroot, S. O. Smith, A. C. Kolbert, J. M. L. Courtin, C. Winkel, J. Lugtenburg, J. Herzfeld, and R. G. Griffin, *J. Magn. Reson.*, 1991, **91**, 30.
28. H. J. M. deGroot, S. O. Smith, J. Courtin, E. van den Berg, C. Winkel, J. Lugtenburg, R. G. Griffin, and J. Herzfeld, *Biochemistry*, 1990, **29**, 6873.
29. G. E. Hawkes, K. D. Sales, L. Y. Lian, and R. Gobetto, *Proc. R. Soc. London, Ser. A*, 1980, **424**, 93.
30. G. Jeschke and G. Grossmann, *J. Magn. Reson. A*, 1993, **103**, 323.
31. J. Herzfeld, J. E. Roberts, and R. G. Griffin, *J. Chem. Phys.*, 1987, **86**, 2.
32. P. J. Chu, R. R. Carvajal, and J. H. Lunsford, *Chem. Phys. Lett.*, 1990, **175**, 407.
33. T. H. Walter, L. Reven, and E. Oldfield, *J. Phys. Chem.*, 1989, **93**, 1320.
34. S. Hayashi, and K. Hayamizu, *Chem. Phys. Lett.*, 1991, **157**, 381.
35. A. Kubo and C. A. McDowell, *J. Chem. Phys.*, 1990, **92**, 7156.

Biographical Sketches

Xiaobing Chen. *b* 1967. B.E., 1990, Tsinghua University, China; M.A., 1992, Brandeis University. Currently Ph.D. candidate at Harvard University.

Judith Herzfeld. *b* 1948. A. B. 1967, Barnard College, Columbia University, Ph.D., 1972, Massachusetts Institute of Technology, USA, M. P. P., 1973, John F. Kennedy School of Government, Harvard University. Faculty in Chemistry, Amherst College, USA, 1973–74, Faculty in Physiology and Biophysics, Harvard Medical School, 1975–85, Faculty in Chemistry, Brandeis University, 1985–present. Currently Professor of Biophysical Chemistry. Approx. 115 publications. Research specialties: solid state NMR studies of the structure and function of membrane proteins, statistical mechanical studies of entropically driven long-range order in crowded solutions of self-assembling amphiphiles.

Spectral Editing Techniques: Hydrocarbon Solids

Kurt W. Zilm

Yale University, New Haven, CT, USA

1	Introduction	1
2	Background on Spectral Editing of Liquids	1
3	Challenges Posed by Solids	1
4	Experimental Considerations and Caveats	5
5	Summary	6
6	Related Articles	6
7	References	6

1 INTRODUCTION

Spectral editing techniques in NMR in general are methods that aid the spectroscopist in assigning or simplifying complex high-resolution spectra. Most approaches to spectral editing have been developed in the context of NMR of ^{13}C where the emphasis has been on separating ^{13}C resonances on the basis of their multiplicity, i.e. the number of directly attached ^{1}Hs. This type of information, when combined with the analysis of ^{13}C chemical shifts, is very often sufficient for determining the chemical structure of rather complex organic molecules. As such, spectral editing of solution NMR finds wide application in industry for the structural characterization of polymers, drugs, and petroleum based products. Development of similar methods which are applicable to solid samples has been motivated by a large number of important applications to geochemical and material science.

This article deals with spectral editing approaches developed specifically for high-resolution solid state NMR of ^{13}C. Many different strategies have been applied to this problem, and the space provided here unfortunately does not permit covering every aspect of this subfield. Most of the relevant literature is cited in two recent papers,[1,2] and the interested reader may find more extensive citations contained therein.

2 BACKGROUND ON SPECTRAL EDITING OF LIQUIDS

The high information content of ^{13}C NMR spectra of liquids is well known. It follows directly from the large dispersion of the ^{13}C chemical shift and the remarkably tight correlation of ^{13}C chemical shifts with structure. The beautiful stick-spectrum simplicity of ^{13}C spectra is made possible by ^{1}H decoupling and the low natural abundance of ^{13}C which eliminates complications from ^{13}C–^{13}C J couplings. Their information content is greatly increased if the multiplicity of the ^{13}C resonances can be determined.

Editing techniques for ^{13}C NMR of liquids rely on the fairly narrow range of values for $^{1}J(^{13}\mathrm{C},^{1}\mathrm{H})$. This permits one to devise pulse sequences in which the evolution of the ^{13}C magnetization can be made to depend principally upon the number n of directly attached ^{1}Hs in CH_n groups. The attached proton test (APT) is the simplest example. In its most basic form, a $\pi/2$, τ, π, τ, acquire echo sequence is applied to the ^{13}C with ^{1}H decoupling during acquisition. A π pulse is also applied to the ^{1}Hs after the first τ, resulting in J modulation of the ^{13}C spin echo. During the 2τ evolution period the dephasings of the ^{13}C chemical shifts are refocused, while those due to $^{1}J(^{13}\mathrm{C},^{1}\mathrm{H})$ accumulate. Setting τ to $\frac{1}{2}J$ produces a spectrum in which the CH_3 and CH_1 resonances are inverted, while the CH_2 and CH_0 resonances are absorptive.

For complex ^{13}C spectra, more powerful methods are required, but all rely upon J couplings in some manner. In editing protocols based on INEPT, J modulation is used to label the ^{1}H magnetization which is then transferred to the ^{13}C (see ***INEPT***). The various CH_n groups can be amplitude modulated in distinct ways depending upon the length of the time evolution due to J coupling. On this basis schemes can be devised in which linear combinations of a few different experiments produce CH_3-only, CH_2-only, CH_1-only, and CH_0-only spectra. Techniques utilizing DEPT provide some improvement in selectivity, as the differentiation of CH_n groups depends upon a pulse flip angle rather than a period τ of free evolution under $^{1}J(^{13}\mathrm{C},^{1}\mathrm{H})$. Especially clean separation of CH_n subspectra has been achieved using multiple quantum coherence among the J-coupled spins. This *s*ubspectral *e*diting using a *mu*ltiple-quantum *t*rap (SEMUT) has the advantage of being relatively insensitive to the value of $^{1}J(^{13}\mathrm{C},^{1}\mathrm{H})$.

3 CHALLENGES POSED BY SOLIDS

As discussed elsewhere in the Encyclopedia, obtaining high-resolution ^{13}C spectra of organic solids requires both magic angle spinning (MAS) and high-power decoupling of the protons. These techniques are usually combined with cross polarization (CP) in a CP MAS experiment. The need to remove broadening associated with chemical shift anisotropy and ^{13}C–^{1}H dipolar couplings presents a new set of problems in the design of methods for spectral editing. Over the last 20 years of development in high-resolution NMR of solids three basic strategies have been applied to this problem. The first has been to design pulse sequences which produce J-modulated signals in solids, and thereby directly adapt the techniques just discussed to solids. The others use ^{13}C–^{1}H dipolar couplings as the basis for selection of CH_n. Some of these methods use the relative strengths of dipolar couplings or rates of CP to differentiate ^{13}C signals of different multiplicities. Others rely upon the establishment of quasi-equilibrium states in the CP process and thus differentiate the ^{13}C multiplicities on the basis of the ratio of the inverse rotating frame spin temperature of the ^{13}C to that for its directly bonded protons.

3.1 *J* Modulation in Solids

Observing resolved $^{1}J(^{13}\mathrm{C},^{1}\mathrm{H})$-coupled multiplets in CP MAS ^{13}C spectra of solids is made difficult by the strong

$^1H-^1H$ and $^1H-^{13}C$ dipolar couplings. In the absence of strong on-resonance ^1H decoupling, CP MAS spectra of typical rigid samples are broad and relatively featureless. The $^1H-^{13}C$ dipolar broadening is by itself inhomogeneous, and should therefore be suppressed by MAS. However the spin-exchange mediated by the $^1H-^1H$ dipolar couplings is faster than typical rates of MAS. Therefore the spin states of ^1H can change several times during a MAS cycle, and the average of the $^1H-^{13}C$ dipolar interaction is then no longer zero. In a simplified picture one can consider this to be a lifetime broadening of the ^{13}C resonances due to the short lifetime of the spin states of the directly attached protons. Terao and co-workers[3] first demonstrated that suppression of the $^1H-^1H$ dipolar couplings could make it possible to observe $^1J(^{13}C,^1H)$-coupled multiplets in solids. In their work, ^1H decoupling at the magic angle in the rotating frame was first used. Subsequently a number of homonuclear sequences such as MREV-8 have been applied as homonuclear multiple pulse decoupling (MPD) for this purpose. For systems such as plastic crystals where molecular motion has already appreciably averaged the dipolar couplings, MPD produces CP MAS spectra with well-resolved $^1J(^{13}C,^1H)$ coupled multiplets. The couplings observed are reduced by the scaling factor appropriate to the particular MPD sequence used.

This approach has been extended to editing schemes that most resemble those used in liquids. The basic approach is to insert MPD sequences in the periods of free evolution under $^1J(^{13}C,^1H)$. APT-type spectra of motionally narrowed solids have been acquired in this fashion, but in the general case the MPD does not produce sufficient narrowing of the proton NMR spectra to permit sustained J modulation. Terao and co-workers[4] have investigated the limitations of this approach most extensively for rigid solids. One sequence they have successfully used in producing J modulation for rigid solids consists of CP followed by a J-modulated rotor synchronized echo. During the first half of the echo, magnetization of the ^{13}C nuclei evolves under proton homonuclear decoupling. This period, t_1, is adjusted to be equal to one rotor cycle. Over the course of the rotor period J modulation accumulates, but any modulation by the $^{13}C-^1H$ dipolar coupling and the ^{13}C CSA is refocused. After the π pulse, high-power dipolar decoupling is applied for another period t_1. This second interval refocuses the isotropic chemical shift and effects of any bulk susceptibility broadening that accumulated during the first t_1 period. FIDs taken as a function of t_1 then are largely only modulated by $^1J(^{13}C,^1H)$. In this manner a 2D heteronuclear J-resolved spectrum can be obtained with multiplets in the ω_1 dimension. However this approach still does not yield clean multiplets. For instance, the outer lines in quartets for CH_3 groups are very much broader than the central pair, and they are barely resolved.

At the moment, J modulation based editing techniques for solids will remain useful only for systems with significant motional narrowing. Advances in the efficiency of homonuclear decoupling, especially under conditions of MAS, are needed before such techniques can become widely applicable. Problems also remain in combining these homonuclear decoupling requirements with the typical hardware used for CP MAS NMR. While the approach has been proven in principle, development of generally applicable methods for solids along these lines remains a challenge for the future.

3.2 Dipolar Dephasing and Related Schemes

The most generally applicable editing techniques for solids take advantage of the strong dipolar couplings inherent in solids, rather than treating them as a nuisance to be eliminated. The simplest approach to spectral editing in CP MAS NMR of organic solids is the venerable technique[5] of dipolar dephasing (DD) or interrupted decoupling. After CP, the ^1H decoupler is turned off for $\sim 50\,\mu s$. This is a sufficient time for the $^{13}C-^1H$ dipolar coupling to dephase the transverse magnetization for any ^{13}C with a directly bonded ^1H, as long as the dipolar coupling is not motionally averaged. Therefore the lines for rigid CH_1 and CH_2 groups are effectively suppressed. Rapid rotation of CH_3 groups at room temperature leads to different behavior for these protonated carbons. This rotation renders the three $^{13}C-^1H$ dipolar couplings equal, and reduces them to one-third of their static value. Depending upon the spin state of the protons, the ^{13}C in a CH_3 group can experience one of two possible dipolar fields. Whenever the three protons are in the same state ($\alpha\alpha\alpha$ or $\beta\beta\beta$), the three couplings reinforce one another, and the ^{13}C experiences the field of a single full $^{13}C-^1H$ dipolar coupling. However, three-quarters of the time the ^1Hs are in a state such as $\alpha\alpha\beta$ or $\beta\beta\alpha$. In this instance the fields due to two of the couplings will exactly cancel. The net dipolar field then is usually only one-third of a single $^{13}C-^1H$ dipolar coupling, and this is similar to that often experienced through nonbonded contacts by a CH_0. Thus, in most instances, methyl groups at room temperature behave like nonprotonated carbons under dipolar dephasing. The DD spectrum then consists of slightly attenuated resonances for just the CH_0 and CH_3 groups. Comparison with a fully polarized CP MAS spectrum provides a simple qualitative method for categorizing resonances as either CH_3 + CH_0 or CH_2 + CH_1. In many instances, a simple CP MAS spectrum can be fully assigned using this approach in combination with information from linewidth or chemical shifts.

Several approaches have been taken to improve on the basic DD technique. In some instances the dephasing interval leads to an unacceptable linear phase correction due to the delayed acquisition. A π pulse may be inserted in the interrupted decoupling interval to alleviate this to some degree. However, as first pointed out by Munowitz and Griffin,[6] the π pulse should be applied only after a full rotor period to ensure that both the isotropic and anisotropic portions of the ^{13}C chemical shift are refocused. Other groups have investigated the spin dynamics of the DD experiment with the desire to separate CH_n resonances more completely or quantitatively.[7] The approach has been to fit the dephasing of the ^{13}C resonances as a function of the dephasing time, τ_D, to some type of model dephasing function. Since it can be argued the different CH_n groups may have characteristic dephasing characteristics, this approach would seem to have some validity. In this manner one can then extrapolate back in dephasing time to recover the initial intensities of the CH_3 and CH_0 resonances.

The best way to view the DD experiment is actually as a low-resolution 1D version of separated local field (SLF) spectroscopy under MAS conditions. During τ_D the ^{13}C FID is dominated by the $^{13}C-^1H$ dipolar couplings, and is damped by the $^1H-^1H$ dipolar interactions. An isolated CH_1 group then has a decay profile that is essentially a damped Pake doublet FID, that for a CH_2, i.e. a Pake 'triplet'. Since the local structure of isolated CH_n groups of a given n does not

vary appreciably in organic solids, these decays would be quite characteristic were it not for the $^1H-^1H$ dipolar couplings. This complication can be removed by applying MPD during the dephasing interval. In this manner the number of dipolar couplings is determined from a spectral pattern, i.e. sideband intensities, rather than from a less structure-specific average dephasing rate.

The first proposal for this type of MAS SLF spectroscopy was by Munowitz and Griffin[6] as a means of measuring C–H distances. Webb and the author[8] later investigated using the spinning sideband patterns characteristic of the different CH_n groups for spectral editing. The proposed 2D experiment consists of CP followed by MPD (usually MREV-8) for t_1 to produce dipolar evolution in the first frequency dimension. This is followed by a $\pi/2(\phi_i)$, τ, $\pi/2(x)$ sequence to selectively project the ^{13}C magnetization onto one axis of the rotating frame. The period, τ, is a few hundred μs and is used to dephase magnetization not placed along z by the $\pi/2(\phi_i)$ pulse. Following the $\pi/2(x)$ pulse, the normal dipolar decoupled ^{13}C FID is acquired during time period t_2. Cycling the phase ϕ_i in a time proportional phase incrementation scheme avoids the need to acquire a quadrature data set in t_1. The sideband patterns generated this way in the ω_1 dimension retain both dipolar and CSA effects. However, at low-to-moderate field strengths the patterns are so dominated by the $^{13}C-^1H$ dipolar couplings that they can still be easily deconvolved into their CH_n components. Since CH_2 groups have two dipolar couplings, they have nearly twice as many sidebands, and are readily distinguished from CH_1 groups by this technique. Decomposition of complex CP MAS spectra with many overlapping lines has been demonstrated using this approach. At higher fields the same deconvolution methods can be applied using Munowitz and Griffin's rotor-synchronized sequence to eliminate the complications due to CSA. The requirement for delaying acquisition to several rotor periods after the initial CP interval, however, can result in substantial losses in sensitivity. A further simplification has been proposed by Sethi.[9] Since the temporal evolution during t_1 in the MAS SLF experiments is well understood, only a few special times t_1 need be acquired. Using this approach Sethi has introduced 1D editing schemes that also can be used to separate CH_1 and CH_2 resonances.

3.3 Schemes Using CP Dynamics

The previous methods rely upon the relative strengths of $^{13}C-^1H$ dipolar couplings or the different numbers of dipolar couplings to discriminate between different CH_n groups. The dipolar couplings are used essentially to dephase or modulate the ^{13}C resonances in a predictable manner. Another strategy is to use the ways in which these differences in the dipolar coupling network result in differences in the CP dynamics between the CH_n groups.

The simplest description of the CP process considers the transfer as a first-order kinetic process with a time constant T_{CH}. However, it is well known that this description is only qualitatively correct, and only phenomenologically describes the long-time behavior ($t \gg T_2$). At short CP times the Hartmann–Hahn transfer is dominated by the details of the dipolar coupling network between a ^{13}C and its directly bonded ^1Hs. In single crystals, one even observes transient oscillations in the polarization transfer. For powdered samples under moderate MAS, the transient effect manifests itself as a rapid initial period of CP transfer in which the ^{13}C and its attached ^1Hs come into a quasi-equilibrium. Spin diffusion to the more distant protons transports polarization more slowly to these ^1Hs coupled to the ^{13}C. This slower process determines the rate at which the ^{13}C reaches its final fully polarized state. In the quasi-equilibrium state, the initially unpolarized ^{13}C nuclei share the polarization equally with their directly attached protons. CH_1 and CH_2 groups then polarize to one-half and two-thirds of their full intensity, respectively, on the short timescale. Because of their motionally averaged dipolar field, CH_3 groups behave similarly to nonprotonated carbons. Both the CH_0 and CH_3 groups then polarize more slowly, with the polarization bottleneck to full enhancement usually being the rate of $^1H-^1H$ spin diffusion. As long as the transfer of transient polarization among the closely coupled spins is faster than the $^1H-^1H$ spin diffusion and direct transfer from more distant protons, it can be put to good use in spectral editing schemes.

One particularly useful approach for distinguishing the signals of $CH_1 + CH_2$ from those of $CH_0 + CH_3$ based on the previous ideas is the depolarization (DEP) technique.[10] After a several ms CP interval, the spin locked ^1H magnetization is allowed to dephase by turning off the ^1H rf for several hundred μs, while keeping the ^{13}C spin locked. Turning the ^1H rf back on reestablishes the CP contact, and the ^{13}C magnetization can be used to repolarize the depolarized ^1Hs. If the phase of the ^1H rf is switched 90° every 25–50 μs over a total period of a few hundred μs, there will be no net buildup in the ^1H magnetization, only a net drain from the ^{13}C. Since only the $CH_1 + CH_2$ carbons polarize on this timescale, their signals are fully depleted after the depolarization, while the $CH_0 + CH_3$ signals are attenuated only slightly. The resulting DEP spectrum is much like a DD spectrum. However since the ^{13}C are spin locked until the depolarization is finished, there are no problems with linear phase errors as in DD.

Polarization inversion (PI) can also be used in a similar fashion.[11] In this technique the ^{13}C are first fully polarized by CP, and the phase of the rf in the ^1H channel suddenly inverted. Since the ^1H spin temperature has now been inverted, the ^{13}C will try to follow. Those ^{13}C with strong $^{13}C-^1H$ dipolar couplings first quickly depolarize, and then repolarize in the opposite direction. Since the zero crossings for CH_1 and CH_2 groups are different, they can be used in some instances to distinguish resonances. Nulling of resonances in this manner has also been referred to as cross depolarization[12] (CPD). A further variant adds a final short polarization period onto the CPD sequence.[13] The depolarization and repolarization periods in this cross-depolarization–repolarization technique (CPDR) can be adjusted so as simultaneously to null the CH_1 and CH_2 groups. This is not in general possible with the cross-depolarization interval alone.

Sangill et al.[2] have presented a thorough study of the use of CPD and CPDR in spectral editing. Their analysis focused on using optimized combinations of CPD and CPDR spectra to produce CH_n-only spectra, $n = 0–3$, while maintaining good sensitivity. By paying careful attention to the CP dynamics, they were able successfully to separate complex CP MAS spectra into their CH_n subspectral components.

Burum and Bielecki[14] have introduced a particularly clever method based on CP dynamics for selectively detecting CH_2

groups in CP MAS NMR. Their method, WIMSE (*w*indowless *i*sotropic *m*ixing for *s*pectral *e*diting), starts with a CP interval under a multiple pulse cycle which eliminates the $^1H-^1H$ dipolar couplings during the CP step while maintaining the $^{13}C-^1H$ couplings. Over a MAS rotor period under these conditions, no net polarization is transferred to ^{13}C nuclei in CH groups. Instead, whatever magnetization is transferred at the start of the rotor cycle 'echoes' back from the ^{13}C to the ^1H at the end. However, the presence of two dipolar couplings in a CH_2 group defeats this 'rotational polarization echo' effect. The resulting spectrum then consists solely of the CH_2 component in a complex CP MAS spectrum. CH_3 and CH_0 lines do not appear as their CP rates are too slow.

3.4 Techniques Using Quasi-Equilibrium States

Another successful method based on differences in CP dynamics between the different CH_n groups is the solid state attached proton test, or SSAPT method. Initially the ^{13}C are fully polarized using a 2–3 ms CP interval. Immediately following this, a short PI period is applied, typically on the order of 50 μs. At the beginning of the PI time the ^{13}C and their directly attached ^1Hs are equally polarized. Upon reversal of the phase in the ^1H spin locking rf, this equilibrium is broken, and the spins try to reequilibrate. Since the CH_3 and CH_0 groups polarize slowly, they are relatively unaffected by this short PI interval. The CH_2 and CH_1 groups, on the other hand, have sufficient time to reach a quasi-equilibrium state through a rapid transient CP transfer. In the case of the CH_1 group, the ^{13}C and the ^1H have equal but opposite polarizations at the start of the PI. During the short PI time these magnetizations cancel, and the signal for the CH_1 carbons is very effectively nulled. The ^{13}C nuclei in the CH_2 groups carry 1 unit of polarization as opposed to the -2 units in the ^1Hs at the beginning of the PI interval. This results in -1 unit of total polarization to be shared among the three spins in the quasi-equilibrium state. At the end of the PI period, the CH_2 signal is then inverted with an intensity of $-\frac{1}{3}$ of its fully polarized signal. The SSAPT spectrum then has CH_3 + CH_0 signals nearly fully polarized and positive, CH signals nulled, and CH_2 signals inverted at one-third intensity. In many instances this provides a very straightforward means of separating the contributions from the different CH_n groups to a ^{13}C CP MAS spectrum.[15,16]

This approach has been extended to a complete spectral editing protocol by Wu, Burns, and the author.[1] Since the establishment of the quasi-equilibrium state depends upon the ratio of the inverse rotating frame spin temperatures of the ^{13}C and its directly bonded ^1Hs, this technique is less sensitive to the CP rates. In this sense it is a relatively robust editing procedure.

The complete spectral editing procedure due to Wu et al. uses four basic experiments (see Figure 1). One begins by acquiring a CH_2-only spectrum. The sequence used starts with a short CP contact which polarizes the CH and CH_2 groups to their quasi-equilibrium intensities of $\frac{1}{2}$ and $\frac{2}{3}$ respectively. This is followed by a short PI interval of roughly the same length. During PI the CH signals null, as does any small CH_3 or CH_0 polarization built up during the CP step. The CH_2 ^{13}C magnetization goes to $-\frac{1}{3}$ of its initial value, resulting in a spectrum with $-\frac{2}{9}$ the intensity for these carbons. This

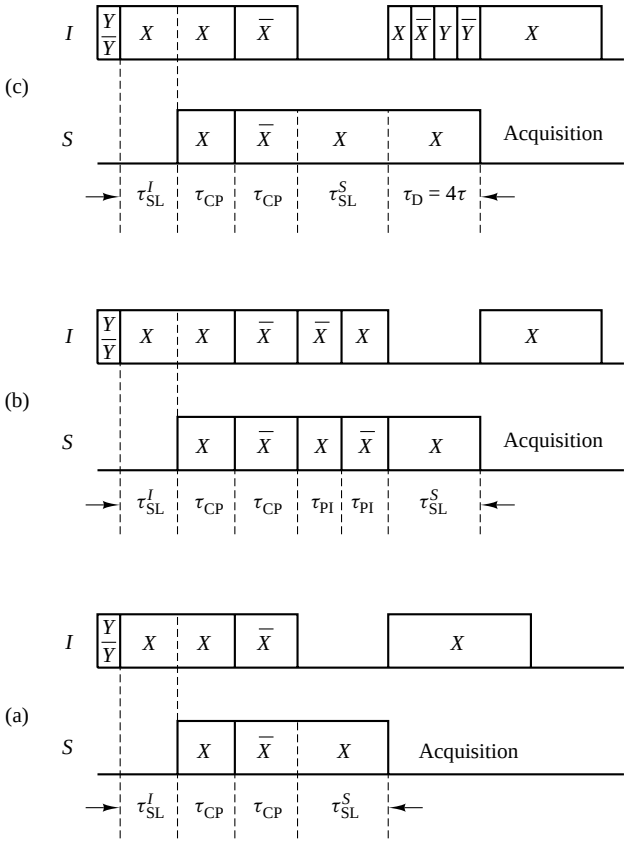

Figure 1 Sequences used in the editing protocol of Wu et al. All employ simultaneous phase inversion to alleviate problems with Hartmann–Hahn mismatches. (a) CP sequence. The additional spin locking delay τ_{SL}^S is used to make the total ^{13}C spin locking time the same in all of the sequences. (b) SCPPI sequence used to acquire CH_2-only spectra. (c) Depolarization sequence. The time τ_{SL}^I is added in these sequences mainly to minimize distortions from ^1H rotating frame relaxation

short CP polarization inversion (SCPPI) spectrum then has contributions from only the CH_2 groups.

The second experiment is a short contact CP (SCP). This will have intensity principally from the CH and CH_2 carbons. Another short CP spectrum with a depolarization interval is also acquired (SCPD). The SCPD spectrum can be used to subtract out the contamination of the SCP data from CH_3 and CH_0 groups. Unfortunately the CH_3 and CH_0 carbons have sufficiently different CP dynamics that they are differentially attenuated, and this subtraction alone is insufficient. In most instances, however, the shift ranges for CH_3 and CH_0 groups are adequately separated so that a dividing line on the ^{13}C chemical shift scale can be chosen to separate these groups. Different weighting factors can then be applied to the upfield (CH_3) and downfield (CH_0) regions for this purpose. The result of this procedure is a relatively clean CH-only spectrum.

To acquire semiquantitatively correct CH_0 and CH_3 spectra, a long CP depolarization spectrum is acquired (LCPD). This spectrum is again split into CH_0 and CH_3 regions, and each part corrected for the differential signal loss of the two types of groups in the depolarization step.

The cleanest and most quantitative results are obtained with this method if the intensity factors for spectral decomposition are determined experimentally on a known model system.

Table 1 Typical Intensities for CH_n Resonances in Pulse Sequences Used for Spectral Editing

	CH_n			
Experiment	CH_0	CH_1	CH_2	CH_3
LCP	100	100	100	100
SCP	10.5	57.5	68	22.6
SCPPI	0	0	−22	0
SCPD	7.2	0	0	10.4
LCPD	82.5	0	0	57.5

Using the set of sequences shown in Figure 1, the intensity matrix in Table 1 is found to be typical. LCP is used to denote a standard (long) CP experiment which is used as the 100% intensity reference.

As the entries demonstrate, the CH and CH_2 group intensities in the SCPPI and SCP experiments are quite close to those expected from the quasi-equilibrium description of the CP dynamics.

Figure 2 compares the four spectra acquired in the editing protocol for cholesteryl acetate to the normal CP MAS spectrum. In the solid state there are two molecules in the unit cell producing a doubling of the lines. Furthermore, changes in conformation lead to significant shifts in many resonances. Using the intensity matrix in Table 1, the CH_n, $n = 0-3$, only spectra can be reconstructed from these data. The results of this data manipulation are shown in Figure 3, clearly demonstrating the simplifications made possible by this spectral editing approach. As a check on this editing protocol, one may sum the CH_n subspectra to produce a synthetic CP MAS spectrum. This is compared with the normal CP MAS spectrum in Figure 4, along with the difference of the two. The small differences observed indicate the reliability of the approach used.

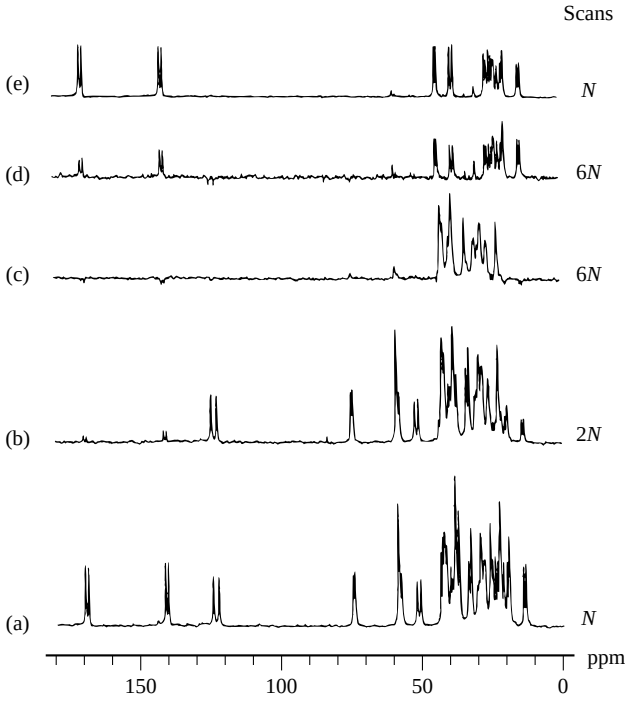

Figure 2 Data from a spectral editing experiment on cholesteryl acetate. (a) Normal CP spectrum for comparison. (b) SCP spectrum. (c) SCPPI spectrum. (d) SCPD spectrum. (e) LCPD spectrum. In practice larger numbers of scans are acquired for the lower signal-to-noise experiments as indicated in the figure

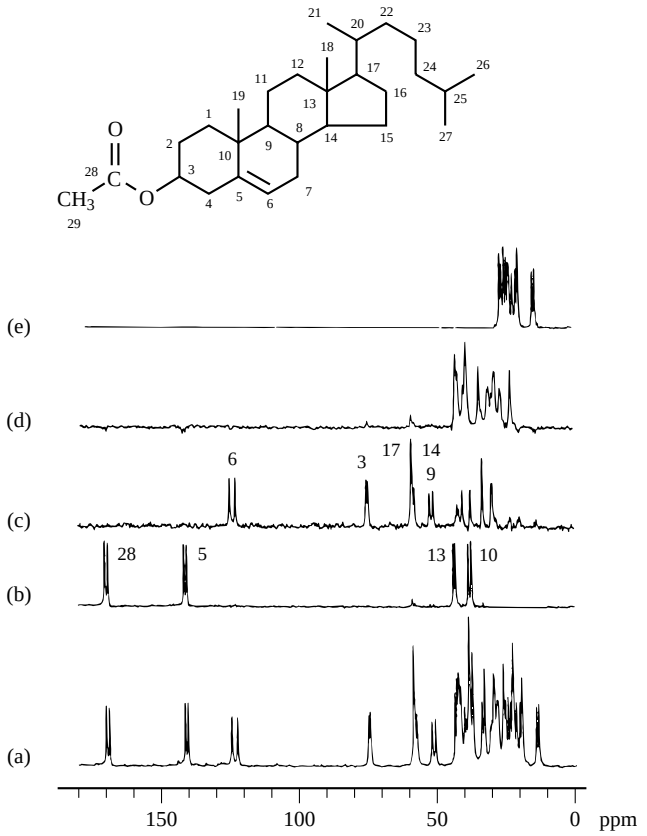

Figure 3 Subspectra constructed from the data in Figure 2. (a) Normal CP MAS spectrum again for comparison. (b) CH_0-only. (c) CH_1-only. (d) CH_2-only. (e) CH_3-only. Some of the assignments made possible by the editing technique are given in the inset

4 EXPERIMENTAL CONSIDERATIONS AND CAVEATS

Except for the simplest approaches to spectral editing in solids, one must pay some extra attention to the experimental setup. In particular, very high MAS spin rates and rf inhomogeneity can adversely affect the CP dynamics relied upon in most methods. The sharpening of the Hartmann–Hahn condition, and the need to match typically on a sideband condition, $\omega_1 = \omega_2 + \omega_r$, makes a homogeneous rf field more important than in a standard CP MAS experiment. Good experimental practice requires stable rf levels, restricting the sample to well within the rf coil, and a stable spin rate. For experiments utilizing short CP, PI, or depolarization periods, additional modifications that make the matching condition less sensitive are needed. Our group has found the simultaneous phase inversion method[1,14,15] easy to incorporate in editing schemes. The pulse sequences in Figure 1 utilize this approach to make the results much less sensitive to how well the matching condition is set and maintained throughout the experiment.

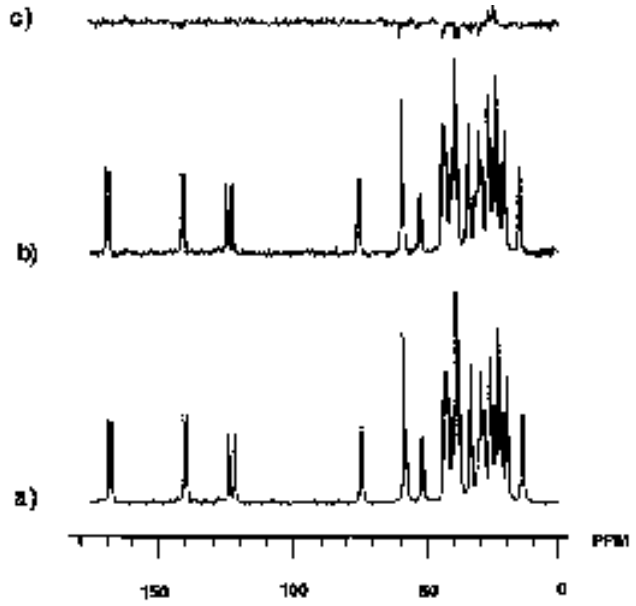

Figure 4 Comparison of the (a) normal CP MAS spectrum and (b) the synthetic one produced by direct summation of the subspectra in Figure 3(b)–(e). (c) The difference between the normal and synthetic CP MAS spectra

When spectra are to be combined in an editing procedure, it is also important to consider rf heating, droop in the rf levels, and $T_{1\rho}$ relaxation. Whenever possible, it is a good practice then to keep the rf fields on for comparable periods of time in the different experiments to be combined. The sequences in Figure 1 have been constructed to take these additional complications into account. Table 2 gives the set of delays in reference to Figure 1 that have been found to give optimal performance in editing applications on rigid solids at moderate fields and MAS rates. These parameters have been used and tested in applications to many coals and polymers as well as on model systems.

Methods which employ homonuclear decoupling sequences require additional care in spectrometer alignment. For these methods one must more carefully adjust all rf levels, and pay especial attention to rf homogeneity. In practice one must follow the same procedures as used to prepare for a ^{1}H CRAMPS experiment. Similar complications from the interaction of the MAS and the MPD also occur as found in CRAMPS.

The majority of the methods that have been discussed here rely on differences in the dipolar coupling networks found between the various CH_n groups. These are washed out when there is significant motional averaging, and as such all of these methods have limitations. On the other hand, such motional narrowing has many signatures which are easy to recognize, and provides another means of discriminating between resonances in a complex spectrum. When very fast MAS rates are employed, the spin dynamics also change.[17] Most methods presented here work best at low to moderate MAS rates (5 kHz or below). Additional complications can arise at high fields because of the CSA spinning sidebands. Since different molecular orientations with respect to the rotor contribute more intensity to some sidebands than others, the inhomogeneous nature of the CP dynamics can be accentuated. Under many editing schemes the center and sidebands can then behave differently, complicating analysis. In the light of these difficulties, most applications to complex systems have employed low field operation ($B_0 < 4$ T). Additional work is needed to delineate how high-field and high-speed MAS operation can be accommodated with the majority of these methods.

Table 2 Delay Parameters for Spectral Editing

	Delay (μs)				
Experiment	$\tau_{SL}{}^I$	$2\tau_{CP}$	$2\tau_{PI}$	$\tau_{SL}{}^S$	τ_D
LCP	140	1500	0	400	0
SCP	1600	40	0	400	0
SCPPI	1600	40	35	365	0
SCPD	1600	40	0	300	100
LCPD	140	1500	0	300	100

5 SUMMARY

At present there are many methods available for distinguishing CH_3 + CH_0 groups from CH and CH_2 centers in CP MAS spectra. A number of reliable approaches for separating CH and CH_2 groups have also appeared, and some of these have been combined in complete spectral editing protocols which separate resonances by multiplicity. These methods have many applications in organic geochemistry and polymer science. Further advances are required before most of these techniques can be combined with operation at the highest available field strengths and spin rates.

6 RELATED ARTICLES

CRAMPS; Cross Polarization in Rotating Solids: Spin-1/2 Nuclei; Cross Polarization in Solids; Fossil Fuels; Heteronuclear Assignment Techniques; INEPT; Magic Angle Spinning; Quantitative Measurements; Rotating Solids; Solid State Probe Design; Spin Echo Spectroscopy of Liquid Samples.

7 REFERENCES

1. X. Wu, S. T. Burns, and K. W. Zilm, *J. Magn. Reson. Ser. A*, 1994, **107**, in press.
2. R. Sangill, N. Rastrup-Andersen, H. Bildsøe, H. J. Jakobsen, and N. C. Neilsen, *J. Magn. Reson. Ser. A*, 1994, **107**, 67.
3. T. Terao, H. Miura, and A. Saika, *J. Chem. Phys.*, 1981, **75**, 1573.
4. H. Miura, T. Terao, and A. Saika, *J. Chem. Phys.*, 1986, **85**, 2458.
5. M. Alla and E. Lippmaa, *Chem. Phys. Lett.*, 1976, **37**, 260.
6. M. G. Munowitz and R. G. Griffin, *J. Chem. Phys.*, 1982, **76**, 2848.
7. L. B. Alemany, D. M. Grant, R. J. Pugmire, T. D. Alger, and K. W. Zilm, *J. Am. Chem. Soc.*, 1983, **105**, 2133.
8. G. W. Webb and K. W. Zilm, *J. Am. Chem. Soc.*, 1989, **111**, 2455.
9. N. K. Sethi, *J. Magn. Reson.*, 1991, **93**, 265.

10. X. Wu, S. Zhang, and X. Wu, *Chem Phys. Lett.*, 1989, **162**, 321.
11. X. Wu, S. Zhang, and X. Wu, *J. Magn. Reson.*, 1988, **77**, 343.
12. M. T. Melchior, *22nd Exp. NMR Conf., Asilomar, CA, March 1991*, poster B-29.
13. J. S. Hartman and J. A. Ripmeester, *Chem. Phys. Lett.*, 1990, **168**, 219.
14. D. P. Burum and A. Bielecki, *J. Magn. Reson.*, 1991, **95**, 184.
15. X. Wu and K. W. Zilm, *J. Magn. Reson., Ser. A*, 1993, **104**, 119.
16. X. Wu and K. W. Zilm, *J. Magn. Reson., Ser. A*, 1993, **102**, 205.
17. X. Wu and K. W. Zilm, *J. Magn. Reson., Ser. A*, 1993, **104**, 154.

Acknowledgments

I wish to acknowledge the especially important contributions of two of my colleagues in this field. The first is Dr Gretchen Webb, my first graduate student, who was instrumental in working out 2D MAS SLF methods for editing, as well as developing much of the hardware that still makes these experiments work so well in our laboratory. The second is Dr Xiaoling Wu, my long-time associate, collaborator, and friend. It is because of Xiaoling's experimental acumen and theoretical insight that our laboratory has been able to contribute so successfully to the development of spectral editing methods for solids.

Biographical Sketch

Kurt W. Zilm. *b* 1955. B.S., 1976, Ph.D., 1981, University of Utah. Introduced to NMR by D. M. Grant. Faculty in Chemistry Yale University, 1983–present. Approx. 80 publications. Research interests: theory and development of NMR techniques for solving problems of chemical interest, studies of transition metal polyhydrides, supported metal catalysts, matrix-isolated organic intermediates and metal clusters, applications of optical pumping in gas phase NMR, tunneling in NMR, dipolar demagnetizing field effects in NMR and development of new solids NMR techniques for structural studies in polymers and organic geochemistry.

Spinning Sideband Analysis for Spin-1/2 Nuclei

Robin K. Harris

Department of Chemistry, University of Durham, South Road, Durham, UK

&

Alejandro C. Olivieri

Universidad Nacional de Rosario, Rosario, Argentina

1	Introduction	1
2	Theory	1
3	Retrieval of Tensor Parameters	3
4	Error Analysis	4
5	Interplay of Tensors	5
6	Related Articles in this Volume	9
7	Related Articles in Volumes 1–8	9
8	References	9

1 INTRODUCTION

In the ideal situation for applying NMR spectroscopy, a homogeneous solution is placed inside a homogeneous external magnetic field, leading to single and narrow resonances for each non-equivalent NMR-active nucleus contained in the sample. However, this paradise is almost never reached. Whenever the sample is a liquid crystal, a solid or a slowly reorienting macromolecule, and/or when the magnetic field is not perfectly homogenous within the sample, usually unwanted spinning sidebands appear, flanking the relevant peaks at integral multiples of the sample spinning frequency. The presence of sidebands causes two main problems: (1) a decrease in the height of the central peak, since the overall signal intensity is distributed among the components of the sideband manifold, and (2) a possibility of sidebands overlapping with other interesting peaks, thereby complicating the spectral analysis.

However, sidebands usually contain useful information. The intensity distribution varies according to the sample spinning speed and to the changes of the chemical shift and/or relevant dipolar interactions and/or quadrupolar interactions across the sample. Particularly interesting are the effects observed in high-resolution magic-angle spinning (MAS) NMR spectroscopy, which is the standard technique to analyze powdered solid samples. Suitable analysis of the intensities may allow the characterization of the shielding and/or dipolar and/or quadrupolar tensor(s) affecting the studied nucleus. This explains why a considerable effort has been devoted to the theoretical calculation of sideband intensities, to the development of methods capable of extracting such information, and to their use for many different nuclei and for a variety of chemical systems.

In the present review, methods for retrieval of the principal components of the relevant tensors from MAS NMR spectroscopic data are revisited, along with suitable analysis of the experimental errors affecting them. Also, a range of applications for structural and dynamic problems is briefly covered. The article builds on the paper by Herzfeld[1] (see **Sideband Analysis in Magic Angle Spinning NMR of Solids,** Volume 7, which was relatively short, though it contained the plots for the graphical method). We will not, herein, describe spinning-sideband analysis for quadrupolar nuclei or for two-dimensional experiments or for situations of rotational resonance. The article will also be restricted to sample-spinning about the magic angle (i.e., VAS or variable angle spinning situations will not be treated). However, cases where dipolar interactions with quadrupolar nuclei affect spinning sidebands for spin-1/2 nuclei will be discussed.

2 THEORY

2.1 The Approach of Maricq and Waugh[2]

We commence with a discussion of the simplest situation, where only shielding is under consideration. The shielding tensor $\boldsymbol{\sigma}$ is of second-rank, with principal components defined in the principal axis system (PAS) as σ_{11}, σ_{22} and σ_{33}. These components are labeled in such a way that

$$|\sigma_{33} - \sigma_{\text{iso}}| \geq |\sigma_{11} - \sigma_{\text{iso}}| \geq |\sigma_{22} - \sigma_{\text{iso}}| \tag{1}$$

where $\sigma_{\text{iso}} = (\sigma_{11} + \sigma_{22} + \sigma_{33})/3$ is the isotropic chemical shift. In the σ scale, more positive values correspond to lower resonance frequencies, i.e., increased shielding (notice that $\sigma - \sigma_{\text{ref}} = -\delta$).

It is customary to define the parameters $\Delta\sigma$ (shielding anisotropy) and η (asymmetry parameter) in order to characterize the $\boldsymbol{\sigma}$ tensor as

$$\Delta\sigma = \sigma_{33} - (\sigma_{11} + \sigma_{22})/2 \tag{2}$$

$$\eta = (\sigma_{22} - \sigma_{11})/(\sigma_{33} - \sigma_{\text{iso}}) \tag{3}$$

Sideband intensities in MAS NMR have been calculated by a number of methods. A general review of numerical simulation of solid-state NMR experiments, including those for rotating samples, has appeared.[3] We present here a brief derivation of Maricq and Waugh's equations,[2] and show how intensities can be conveniently calculated from the latter, in order to introduce computer programs for retrieving the tensor components.

For a single nucleus within a static microcrystalline sample, the shielding Hamiltonian is given in the high-field case by

$$\hbar^{-1}\widehat{\mathcal{H}} = -\omega_0\sigma_{zz}\widehat{I}_z \tag{4}$$

where ω_0 is the resonance frequency in angular units and σ_{zz} is the appropriate component of the $\boldsymbol{\sigma}$ tensor relating the spin component I_z and the magnetic field $\boldsymbol{B}_0$ (assumed to point

along the z axis). The required σ_{zz} component is obtained from the diagonal $\boldsymbol{\sigma}$ tensor (as defined in its PAS)

$$\boldsymbol{\sigma} = \begin{pmatrix} \sigma_{11} & 0 & 0 \\ 0 & \sigma_{22} & 0 \\ 0 & 0 & \sigma_{33} \end{pmatrix} \tag{5}$$

In order to obtain σ_{zz} in a MAS experiment, the tensor $\boldsymbol{\sigma}$ is subjected to the following transformations: (1) from its PAS to the MAS frame (where the z axis coincides with the spinning axis), and (2) from the latter frame to the laboratory (LAB) frame (where the z axis is coincident with $\boldsymbol{B}_0$). The latter rotations are accomplished by using the following sets of Euler angles: (α, β, γ) for the first rotation, and $(\psi, \xi, 0)$ for the second. Now $\psi = \alpha_o + \omega_r t$, where ω_r is the sample spinning frequency, and ξ is the angle between $\boldsymbol{B}_0$ and the spinning axis, i.e., $\xi = 54.7°$ for the magic-angle situation (Figure 1)*. Therefore

$$\begin{aligned} \boldsymbol{\sigma}(\text{MAS}) &= \boldsymbol{R}_z(\gamma)\boldsymbol{R}_x(\beta)\boldsymbol{R}_z(\alpha)\boldsymbol{\sigma}(\text{PAS})\boldsymbol{R}_z^{-1}(\alpha)\boldsymbol{R}_x^{-1}(\beta)\boldsymbol{R}_z^{-1}(\gamma) \\ \boldsymbol{\sigma}(\text{LAB}) &= \boldsymbol{R}_x(\xi)\boldsymbol{R}_z(\psi)\boldsymbol{\sigma}(\text{MAS})\boldsymbol{R}_z^{-1}(\psi)\boldsymbol{R}_x^{-1}(\xi) \end{aligned} \tag{6}$$

where $\boldsymbol{R}$ are generalized rotation matrixes, the rotation axes are denoted as subscripts, and the rotation angles are in parentheses.

The result is

$$\begin{aligned} \sigma_{zz} = \sigma_{\text{iso}} + \frac{2}{3}\left[\frac{\cos 2\psi'}{2}(\sigma'_{22} - \sigma'_{11}) + \sin 2\psi'\ \sigma'_{12}\right] \\ + \frac{2\sqrt{2}}{3}(\sigma'_{13}\sin\psi' + \sigma'_{23}\cos\psi') \end{aligned} \tag{7}$$

where

$$\psi' = \psi + \gamma$$

$$\sigma'_{22} = (\sigma_{11}\sin^2\alpha + \sigma_{22}\cos^2\alpha)\cos^2\beta + \sigma_{33}\sin^2\beta \tag{8}$$

$$\sigma'_{11} = \sigma_{11}\cos^2\alpha + \sigma_{22}\sin^2\alpha \tag{9}$$

$$\sigma'_{12} = (\sigma_{11} - \sigma_{22})\sin\alpha\cos\alpha\cos\beta \tag{10}$$

$$\sigma'_{13} = (\sigma_{11} - \sigma_{22})\sin\alpha\cos\alpha\sin\beta \tag{11}$$

$$\sigma'_{23} = (\sigma_{11}\sin^2\alpha + \sigma_{22}\cos^2\alpha)\sin\beta\cos\beta - \sigma_{33}\sin\beta\cos\beta \tag{12}$$

Notice from equation (7) that σ_{zz} is time dependent, and oscillates with frequencies 0, $\omega_r t$ and $2\omega_r t$ ($\psi = \omega_r t$). Hence the shielding becomes time-dependent. Since the relevant Hamiltonian $\widehat{\mathcal{H}}$ commutes with itself at all times, the propagator $U(t)$ of the spin system is given by $U(t) = \exp[i\hbar^{-1}\int_0^t \widehat{\mathcal{H}}(t)\,dt$. Therefore, the time-dependent FID can be written as[1,2]

$$f(t) = f_0 \exp[i\theta(t)] \tag{13}$$

where

$$\theta(t) = \int_0^t \omega_0\sigma_{zz}(t)\,dt \tag{14}$$

* An alternative but equivalent approach is the use of Wigner rotation formulae. For a discussion, see B.C. Gerstein and C.R. Dybowski, 'Transient Techniques in NMR of Solids', Academic Press, 1985.

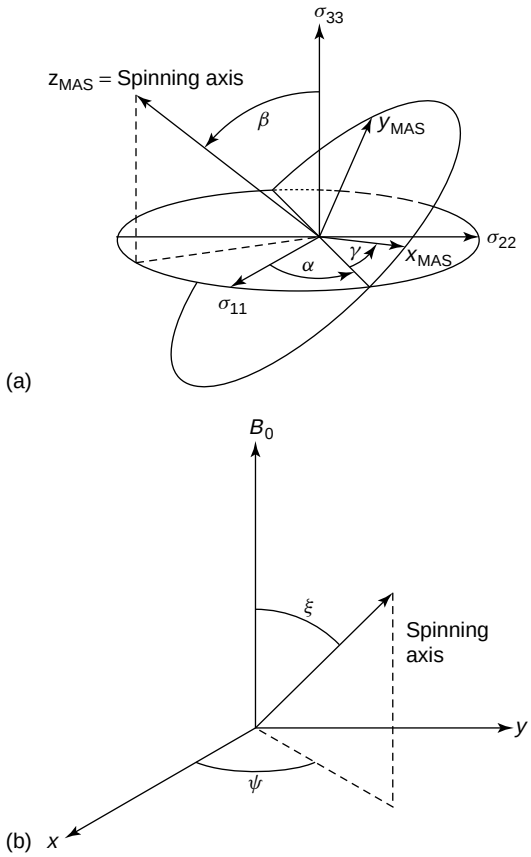

Figure 1 (a) mutual relationship between the magic-angle spinning frame (MAS) and the frame defined by the principal components of the shielding tensor. (b) orientation of the spinning axis with respect to the external magnetic field

Integrating equation (14) for a MAS cycle yields[1]

$$\begin{aligned} \theta(t) = \omega_0 \Bigg\{ \sigma_{\text{iso}} t + \frac{1}{3\omega_r}\left[\frac{\sin 2\psi'}{2}(\sigma'_{22} - \sigma'_{11}) - \cos 2\psi'\ \sigma'_{12}\right] \\ + \frac{2\sqrt{2}}{3\omega_r}(\sigma'_{23}\sin\psi' - \sigma'_{13}\cos\psi') - \\ - \frac{1}{3\omega_r}\left[\frac{\sin 2\gamma}{2}(\sigma'_{22} - \sigma'_{11}) - \cos 2\gamma\ \sigma'_{12}\right] \\ + \frac{2\sqrt{2}}{3\omega_r}(\sigma'_{23}\sin\gamma - \sigma'_{13}\cos\gamma)\Bigg\} \end{aligned} \tag{15}$$

Frequency information can be gathered from equations (13–15) by applying a Fourier transformation. Since $\theta(t)$ is periodic (with period $2\pi/\omega_r$), the observed spectrum will consist of peaks centred at $(\omega_0\sigma_{\text{iso}} + k\omega_r)$, where k is an integer (positive or negative). The corresponding Fourier coefficients provide the amplitudes F_k of the frequency components, and are given by:

$$\begin{aligned} F_k = \frac{1}{2\pi}\int_0^{2\pi} \exp\left[i\,(k\psi + A_2\sin 2\psi + B_2\cos 2\psi\right. \\ \left. + A_1\sin\psi + B_1\cos\psi)\right]\,d\psi \end{aligned} \tag{16}$$

$$A_1 = 2\sqrt{2}\omega_0\sigma'_{23}/(3\omega_r) \tag{17}$$

$$A_2 = \omega_0(\sigma'_{22} - \sigma'_{11})/(6\omega_r) \tag{18}$$

$$B_1 = -2\sqrt{2}\omega_0\sigma'_{13}/(3\omega_r) \quad (19)$$

$$B_2 = -\omega_0\sigma'_{12}/(3\omega_r) \quad (20)$$

The peak intensities are obtained from the squared modulus $|F_k|$.[1] However, it should be noticed that the above discussion corresponds to a single nucleus whose σ tensor is oriented in the LAB frame according to the angles (α, β, γ). For a microcrystalline sample, therefore, the peak intensities are given by the following powder average[1]

$$I_k = \frac{1}{4\pi}\int_0^{\pi}\int_0^{2\pi} |F_k|^2 d\alpha \ \sin\beta \ d\beta \quad (21)$$

An approximate method of calculation based on the above equations has been discussed, which uses a series expansion, and does not require the computation of integrals such as those in equation (21).[4] This method is accurate for values of $\omega_0\Delta\sigma/\omega_r$ up to ca. 3. However, better accuracy is obtained by employing computer-based approaches to calculate each sideband at a time, using equation (21), while an alternative method consists of calculating the FID [equation (13)] and then performing a computer Fourier transformation. In the latter approach, the Fourier transform contains the intensities of all sidebands at the same time. Spinning sideband manifolds arising from paramagnetic shift anisotropy can be similarly calculated.[5] When overlapping peaks occur, it may be useful to apply maximum entropy deconvolution before spinning sideband intensities are calculated, in order to isolate different sideband manifolds which would otherwise be unresolvable,[6] though in principle direct fitting of the complete sidebands, including their shapes, may be better.

The range of applicability of the above equations should be mentioned. As explained above, equation (21) applies to cases where the spin Hamiltonian commutes with itself at all times. These include, besides the case of a single non-interacting nucleus, other situations such as: (1) nuclei subjected to heteronuclear dipolar or indirect coupling interactions and (2) nuclei under homonuclear AX-type dipolar or indirect interactions (see below). Conversely, the above approach is no longer applicable when strongly coupled homonuclear interactions occur.

2.2 Other Approaches

When homonuclear interactions occur, and provided the coupled pairs of nuclei are isolated, one can apply Floquet theory, average Hamiltonian theory or a numerical evaluation of the spin density matrix in order to calculate the sideband intensities.[7–13] An interesting example is provided by the ^{31}P,^{31}P coupling in a phosphole tetramer and in an *ortho* diphosphino benzene derivative, where information concerning the orientations of the phosphorus chemical shift tensors and the sign of $J(^{31}\text{P},^{31}\text{P})$ have been deduced.[9]

Another area where the above theory cannot be applied is when chemical exchange takes place in the intermediate regime (i.e., when the exchange rates are comparable to the difference in frequency between the exchanging $\boldsymbol{\sigma}$ tensors). Here again a Liouville treatment of the exchange, together with Floquet theory, can successfully account for the sideband intensities.[14–16] However, it should be noticed that, for rapidly exchanging systems, the equations of Maricq and Waugh[2] can be confidently applied by considering the nuclei under the influence of an effective tensor $\boldsymbol{\sigma}_{\text{eff}}$ given by a population-weighted average of the contributing $\boldsymbol{\sigma}$ tensors. Pertinent examples of this latter situation are illustrated by the fast solid-state proton transfer taking place between individual phosphate units in the dihydrogen phosphates,[17] in the phosphoric acid:urea adduct[18] and in the complexes formed by phenols and a phosphine oxide.[19]

For homonuclear coupling interactions which are extended to the whole sample, none of the above methods can be applied. Two such cases are worth of mention: (1) the effect of ^{1}H,^{1}H dipolar coupling on ^{1}H spinning sideband intensities of hexamethylbenzene, which has been related to M_n dipolar moments ($n = 2, 4, 6$ and 8),[20] and (2) dipolar ^{31}P,^{31}P coupling in MH_2PO_4 phosphates ($M = K^+$, Rb^+ and NH_4^+), accounted for by assuming that the ^{31}P nuclei are acting as if they were non-equivalent, and that the coupling extends to only a nearest neighbor sphere.[21,22]

3 RETRIEVAL OF TENSOR PARAMETERS

In this Section we review the methods which are usually employed for retrieving tensor parameters from sideband intensities when the equations of Maricq and Waugh[1] apply, again using the notation for a simple shielding case. This is also relevant to cases where intensities are not solely determined by the shielding tensor $\boldsymbol{\sigma}$, but also by effective tensors resulting from the interplay of the latter with other relevant interactions (see below).

Several approaches have been described in the literature in order to retrieve shielding tensor parameters from sideband intensities. One of them is Maricq and Waugh's method of moments,[2] in which the computation of the second and third moments M_2 and M_3 respectively allows the parameters $\Delta\sigma$ and η to be obtained by solving the following system of equations

$$8(\Delta\sigma)^3 - 30M_2(\Delta\sigma) - 35M_3 = 0 \quad (23)$$

$$\eta^2 = 1 - 35M_3/2(\Delta\sigma)^3 \quad (24)$$

where $M_n = \omega_r^n \sum k^n I_k / \sum I_k$. Equations (23) and (24) have three solutions for $\Delta\sigma$, and each of them, in turn, provides two solutions for η. The six pairs of values of $\Delta\sigma$, η correspond to the six possible permutations of the three principal components of the $\boldsymbol{\sigma}$ tensor. Due to the presence of the factor k^n in the definition of the nth moment, the accuracy of applying the above method depends critically on the intensities of outer sidebands, which are usually small and therefore are the most affected by experimental noise.

To avoid the latter problems, Herzfeld and Berger devised a graphical method based on a relatively small set of accessible sideband intensities.[1] Specifically, they generated plots of the intensity ratios I_k/I_0 ($k \neq 0$) as a function of two parameters, μ and ρ, which conveniently replace $\Delta\sigma$ and η

$$\mu = \omega_0\Delta\sigma(1 + \eta/3)/\omega_r \quad (25)$$

$$\rho = \pm(1 - \eta)/(1 + \eta/3) \quad (26)$$

Since the plots are based on ratios of intensities rather than on absolute values of I_k, the latter need not be normalized.

Only ratios involving experimentally accessible values of I_k are considered. The method is based on localizing the values of μ and ρ for which the experimental intensity ratios closely match the theoretical ones.[1] Additionally, a qualitative view of the errors in estimating the retrieved parameters can be obtained by comparing the shielding tensors calculated from different values of k. Neither the moments method nor the graphical method of Herzfeld and Berger are now greatly used.

The generalized use of computers in the chemical laboratory has led to convenient computer-based methods for obtaining shielding parameters (or 'paramagnetic shift anisotropies'[5]), mainly based on iterative methods.[23–26] Figure 2 shows an example.[27,28] In such cases one starts from a given set of initial parameter guesses (these can be the Herzfeld-Berger parameters μ and ρ, or directly $\Delta\sigma$ and η), and refines them iteratively, using standard routines for non-linear parameter estimation. Simplex or Newton-Gauss methods are used to minimize the standard deviation s_{fit} (or, alternatively, χ^2)

$$s_{\text{fit}} = \left\{ \frac{[I_k(\text{calc}) - I_k(\text{exp})]^2}{(n-2)} \right\}^{\frac{1}{2}} \tag{28}$$

where n is the number of experimentally accessible sidebands.

Computer-based methods which use the full sideband manifold are considered to be the most reliable ones. However, the choice of the optimum number of sidebands to obtain for fitting (i.e., the decision as to the best value of ω_r) is a matter for discussion.[29] The software packages from the Varian and Bruker manufacturers now contain programs for spinning sideband analysis. A ^{119}Sn example[30] of ssb fitting using the STARS program[31] is shown in Figure 3.

The use of Floquet theory for calculating spinning sideband manifolds has been reviewed.[32] A further method, described by Fenzke et al.,[33] generates a series of computer files from equation (22) for values of μ, ρ in the ranges (0,20) and (−1,1) respectively, containing the theoretical sideband intensities, with k ranging from −10 to 10 (this may constitute a drawback of the method, although one may produce files for a larger ranges of μ, ρ and k). From a measured set of experimental intensities, a statistical error indicator $\varepsilon = 1 - [\Sigma I_k(\text{calc}) I_k(\text{exp})]^2 / \Sigma I_k^2(\text{calc}) \Sigma I_k^2(\text{exp})$ is computed, and a computer search is made for the values of μ and ρ which lead to its minimum value. A plot of this error indicator as a function of μ, ρ in the vicinity of the minimum provides an estimation of the experimental errors. Figure 4 gives such a three-dimensional plot of ε as a function of μ and ρ for the case of the [^{2}H$_7$]-urea/phosphoric acid adduct.[18] The projection of the plot onto the μ, ρ plane (Figure 4b) gives a qualitative view of the fitting errors.

4 ERROR ANALYSIS

Two sources of errors should be considered in retrieving shielding parameters from MAS sideband intensities: (1) experimental errors leading to observed sideband intensities which deviate from those theoretically expected, and (2) computer-fitting errors, which depend on the characteristics of the minimization procedure, and also on the shielding parameters themselves.

A number of publications have considered several experimental factors affecting the accuracy in the derived parameters.[24,25,30,33,34] When using cross-polarization methods, for example, variations of the polarization efficiency with the orientation within the sample may be a source of error. This error stems from the anisotropy of the Hartmann-Hahn mismatch.[25] To overcome this problem, use of a modified pulse

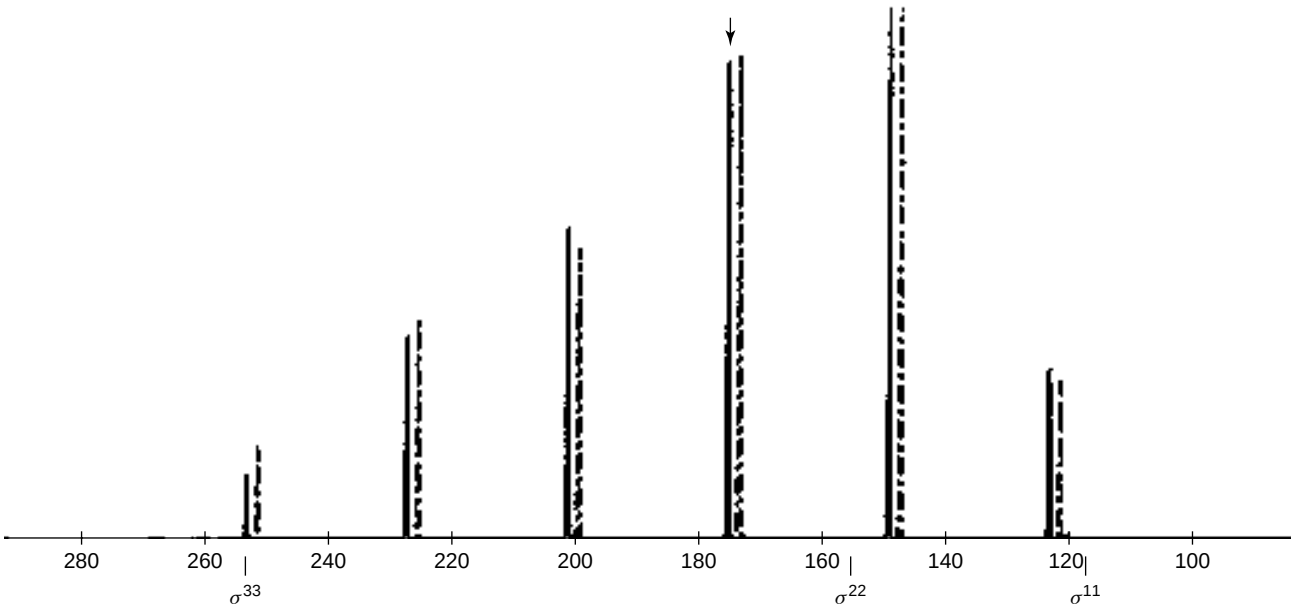

Figure 2 Example of the iterative fitting of a ^{13}C spinning sideband manifold, obtained at a spin rate of 1.3 kHz using an in-house computer program.[28] The C22 band of Form II of cortisone acetate is illustrated.[27] The vertical arrow indicates the centerband. The solid line (to which the shift scale refers) represents the experimental spectrum, while the dashed line (arbitrarily offset) is as computer-fitted with the parameters $\zeta = -78$ ppm, $\eta = 0.49$. (Note: (a) these values differ slightly from those in Table 2 of Ref.[27] and (b) Figure 2 of Ref.[27] incorrectly refers to C5 rather than C22.) (Reproduced by permission from E. A. Christopher, R. K. Harris and R. A. Fletton, *Solid State NMR*, 1992, **1**, 93)

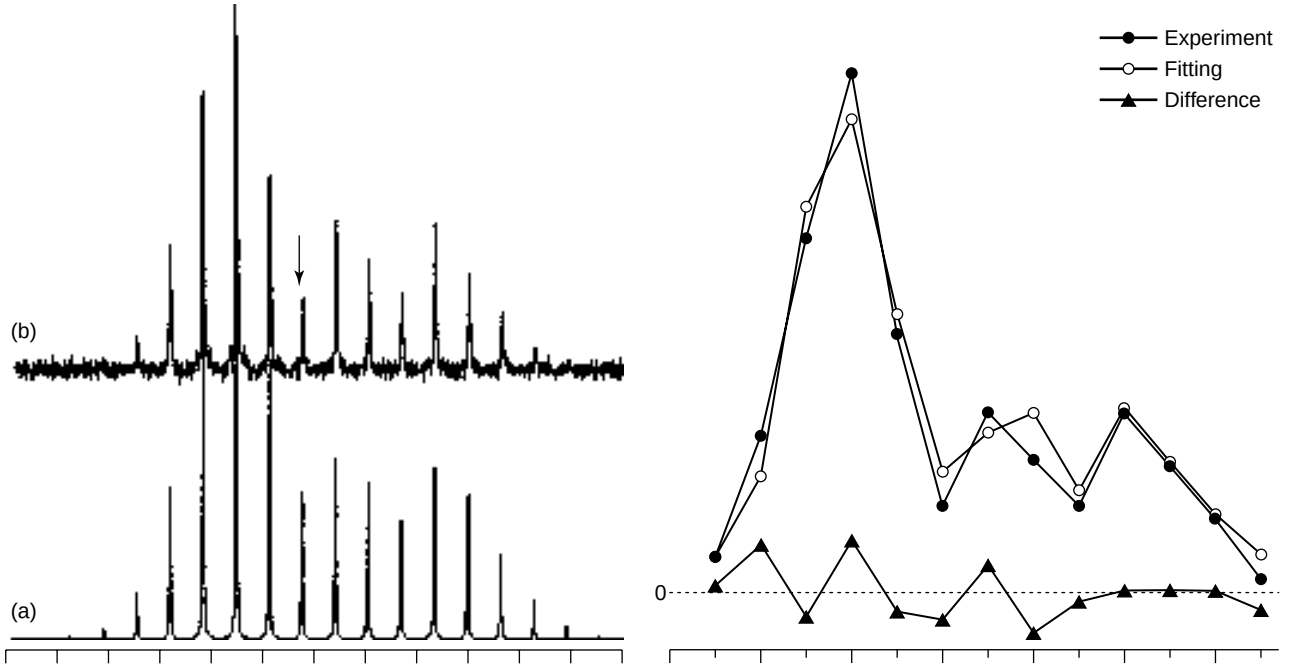

Figure 3 (a) Computed-fitted and (b) experimental (111.9 MHz) ^{119}Sn-{^{1}H} spinning sideband patterns for tin sulfate. The parameters obtained by the use of the Varian STARS program are $\zeta = 553$ ppm, $\eta = 0.14$. The rotation rate was 9.0 kHz. The fitting is carried out with a constant linewidth, so the peak-heights of (a) and (b) do not necessarily match well. The integrals and the differences between experimental and simulated values are plotted to the right, the horizontal dashed line being at zero level

sequence called multiple-contact isotropic cross-polarization (MCICP) has been proposed, together with an empirical intensity correction function.[25] On the other hand, for single-pulse excitation (direct polarization), an important factor is the variation in the degree of polarization of the nuclei over the full frequency range of the spectrum, as a result of the finite duration of the pulse used in the excitation process.[31,34] This latter problem becomes serious for heavy nuclei such as ^{199}Hg, for which shielding anisotropies of thousands of ppm may occur. Attempts have been made to correct for these deviations by utilizing the theoretical RF field amplitude as a function of frequency.

The estimation of fitting errors has been discussed several times,[24–26,35,36] and in special detail in a recent publication.[37] Once the best-fit parameters and the standard deviation s_{fit} (equation (28)) are obtained by the program, one may estimate the errors in $\Delta\sigma$ and η by computing the so-called marginal standard deviations

$$s_{\text{marg}}(i) = s_{\text{fit}}[(B^{-1})_{\text{ii}}]^{1/2} \tag{29}$$

where B is a covariance matrix defined as $B_{\text{ij}} = \sum \left[dI_k(\text{calc})/di\right]\left[dI_k(\text{calc})/dj\right]$, and i,j are refined parameters. Additionally, the following ratio of variances is useful in assessing whether the parameters are properly defined by the experimental intensities

$$R_{\text{i}} = \frac{(B^{-1})_{\text{ii}}}{(B_{\text{ii}})^{-1}} \tag{30}$$

Another recent article[29] has considered the accuracy of tensor parameters measured using solid-state NMR and has used a similar approach. Comparison to the static limit shows that the determination of the anisotropy is more reliable in spinning experiments than in static ones, and an optimum number of sidebands has been found for which the estimation of the anisotropy is the most accurate. However, an analogous analysis for the asymmetry parameter shows it to be consistently more reliably determined from a static spectrum.

In fact, it has been pointed out several times[28,36–38] that the uncertainty in asymmetry values derived from ssb analysis is very high when the magnitude is low. Indeed, it becomes difficult to distinguish axial symmetry from non-axial cases when $\eta < 0.2$. The comparison of R_{i} with critical values of F from standard statistical tables allows one to determine if the parameters have been adequately modelled.[37] However, though the parameters may appear to be well defined, the standard errors in η may be too high to draw definite conclusions regarding axiality. This problem is highlighted when the value of the ratio $\omega_0\Delta\sigma/\omega_{\text{r}}$ is sufficiently small.[37]

Questions of errors and correlations between parameters have also been discussed by Skibsted et al.[39] They have illustrated contour plots of rms deviations between experimental and simulated intensities for the spinning sidebands in the ^{133}Cs MAS spectrum of $CsVO_3$, but the emphasis in their work is on the interplay of shielding and quadrupolar tensors.

5 INTERPLAY OF TENSORS

In many cases, more than one type of tensor will affect static NMR bandshapes and hence spinning sideband manifolds. The matter is relatively simple when only inhomogeneous interactions are involved since these can be considered to contribute independently to the Hamiltonian. It is instructive to consider the simplest situation involving three such tensors,

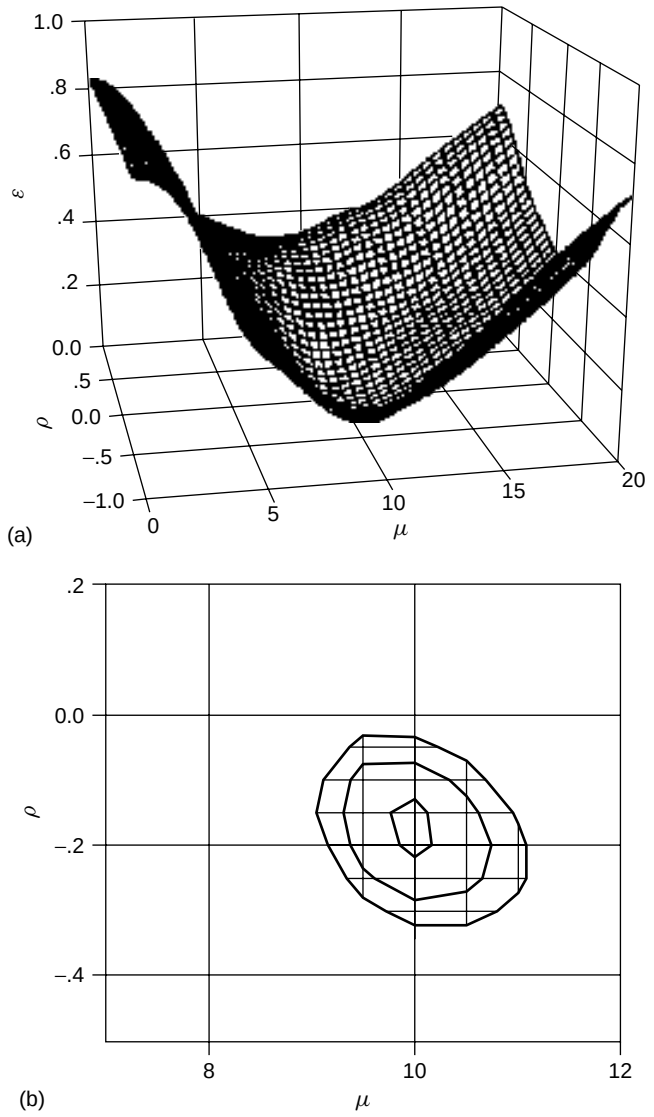

Figure 4 Minimization graphs relevant to ^{31}P spinning sideband analysis for the ($^2H_7$)-urea phosphoric acid adduct[18]: (a) Plot of ε as a function of μ, ρ. (b) Projection of the plot onto the μ, ρ plane for a closer inspection of the minimum

namely shielding, dipolar coupling and indirect ('scalar') coupling. The influence of a sufficiently large isotropic indirect coupling constant is necessary in order to give resolvable subspectra of spinning sideband manifolds (see below), which allows spectral analysis to proceed. In this section a common alternative definition of anisotropy to that given in equation (2) will be used, namely

$$\zeta = \sigma_{33} - \sigma_{\text{iso}} \tag{31}$$

It is clear that the two definitions are equivalent, with $\Delta\sigma = 3\zeta/2$.

5.1 Interplay of σ, D and J[40–43]

The simplest case, which illustrates the essential features, occurs for isolated heteronuclear two-spin (AX) systems with $I_A = I_X = 1/2$, in which axial symmetry prevails, so that asymmetry in $\boldsymbol{\sigma}$ and $\boldsymbol{J}$ can be ignored. All three tensors for, say, the A spins, are co-axial (with the major principal axis along the internuclear A, X distance, r_{AX}), and the anisotropy in $\boldsymbol{J}$ has exactly the same form as the dipolar coupling, $\boldsymbol{D}$, so that an effective parameter D' may be defined as

$$D' = D - \frac{\Delta J}{3} \tag{32}$$

where D is the dipolar coupling constant in frequency units, $(\mu_o/4\pi)\gamma_A\gamma_X\hbar/2\pi r_{AX}^3$, and ΔJ is the anisotropy in $\boldsymbol{J}$ (see **Dipolar & Indirect Coupling Tensors in Solids,** Volume 3; **Indirect Nuclear Spin–Spin Coupling Tensors**) expressed as $J_\parallel - J_\perp$. Note that this implies that there is no NMR experimental method which is able to separate D and ΔJ. The discussion will proceed under the assumption that γ_A and γ_X are both positive, but the results can be readily adjusted if this is not the case. The NMR Hamiltonian may be written as

$$\begin{aligned} h^{-1}\widehat{\mathcal{H}} = &-\nu_A^o\left[1 - \left\{\sigma_A^{iso} + \frac{1}{2}\zeta_A\ (3\cos^2\theta - 1)\right\}\right]\widehat{I}_{zA} \\ &- \nu_X^o\left[1 - \left\{\sigma_X^{iso} + \frac{1}{2}\zeta_X\ (3\cos^2\theta - 1)\right\}\right]\widehat{I}_{zX} \\ &+ J_{AX}^{iso}\widehat{I}_{zA}\widehat{I}_{zX} - D'(3\cos^2\theta - 1)\widehat{I}_{zA}\widehat{I}_{zX} \end{aligned} \tag{33}$$

where $\nu_o^A = \gamma_A B_o/2\pi$ and $\nu_o^X = \gamma_X B_o/2\pi$ are the A and X Larmor frequencies in the absence of shielding, σ_A^{iso} and σ_X^{iso} are the isotropic A and X shielding constants, ζ_A and ζ_X are the shielding anisotropies expressed as $\sigma_A^\parallel - \sigma_A^{iso}$ and $\sigma_X^\parallel - \sigma_X^{iso}$, respectively, J_{AX} is the isotropic (A, X) coupling constant and θ is the angle between $\boldsymbol{r}_{AX}$ and $\boldsymbol{B}_o$. The transitions of the A nucleus are therefore described by

$$\begin{aligned} \nu_A = &\nu_A^o\left[1 - \left\{\sigma_A^{iso} + \frac{1}{2}\zeta_A\ (3\cos^2\theta - 1\right\}\right] \\ &- J_{AX}m_X + D'(3\cos^2\theta - 1)m_X \end{aligned} \tag{34}$$

where m_X is the appropriate spin component quantum number for the X spin. This equation reduces to

$$\nu_A = \nu_A^{iso} - \frac{1}{2}\nu_A^o\zeta_A^{eff}(3\cos^2\theta - 1) - J_{AX}m_X \tag{35}$$

where ζ_A^{eff} is an effective tensor anisotropy given by

$$\zeta_A^{eff} = \zeta_A - \frac{2D'm_X}{\nu_A^o} \tag{36}$$

The A transitions therefore form two sub-spectra ($m_X = \pm\frac{1}{2}$), in one of which the shielding and dipolar tensors reinforce one another whereas in the other they partially cancel

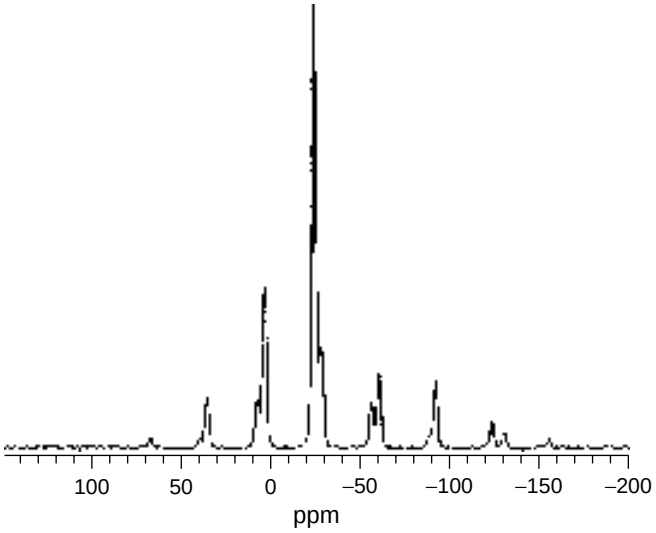

Figure 5 Proton-decoupled ^{19}F CPMAS NMR spectrum of $(Ph_2FPNMe)_2$ at 188 MHz, and spin rate 6 kHz showing the difference in centerband intensities of the two doublet components, arising from the 'squeezing' and 'stretching' of the relevant subspectra. (Figure adapted from that in R. K. Harris and L. A. Crowe, *J.C.S. Dalton*, 1999, 4315, with permission)

each other. Thus one static powder subspectrum is 'stretched' whereas in the other is 'squeezed'.

Under slow MAS conditions, the influence of the angle-dependent term $3\cos^2\theta - 1$ is translated into a distribution of intensities among the relevant spinning sidebands, which extend over a larger frequency range for the 'stretched' subspectrum than for the 'squeezed' subspectrum. The isotropic coupling serves to resolve the subspectra, enabling the spinning sideband manifolds to be analysed separately, thus yielding the two values of ζ_A^{eff}. One consequence is that the centerbands of the two components, split by J_{AX}, have different intensities (see Figure 5).[44] The magnitudes of ζ_A, D' and J_{AX} are readily obtained by the analysis. Since the sign of ζ_A will normally be obvious (and can be obtained separately by spinning sideband analysis of an A spectrum obtained with X-decoupling) sign information on J_{AX} and D' are obtained, albeit with some ambiguity. Only the relative signs of D' and J_{AX} are determined, the rule being as follows: If the high-frequency spinning sideband manifold has the larger magnitude of ζ_A^{eff}, then (i) for positive ζ_A, D' and J_{AX} have the same sign, whereas (ii) for negative ζ_A, D' and J_{AX} have opposite signs. The inverse is true if the larger magnitude of ζ_A^{eff} belongs to the low-frequency subspectrum. If r_{AX} is known (e.g., from diffraction studies), D can be calculated, so ΔJ can be derived, though with an ambiguity unless the sign of J_{AX} is known. On the other hand, if the relative magnitudes of D and $\Delta J/3$ can be assumed, the absolute sign of J_{AX} can be determined.[40,42]

The extension to a linear AX_2 case is straightforward. There will now be three spinning sideband manifolds in the A spectrum, with effective tensor anisotropies given by

$$\zeta_A^{eff} = \zeta_A - \left(\frac{2D'}{\nu_o^A}\right)\sum m_X \qquad (37)$$

where $\sum m_X = 1, 0$ or -1, associated with centerbands at $\nu_A^{iso} - J_{AX}\sum m_X$. The central sideband manifold gives ζ_A directly, because it is independent of D'. Clearly this is an advantage, particularly if A-{X} spectra cannot be obtained because of spectrometer limitations.

Zilm and Grant[45] derived expressions for heteronuclear two-spin (AX) solid-state spectra of static samples, and these have been adapted for MAS cases and further discussed by Harris et al.[40] and Haubenreisser et al.[41] The theory involved can form the basis of a computer program involving the Euler angles between the tensor axes. This has been done by Cherryman and Harris[43] for the AX and AX_2 cases, though still under the assumptions that $\boldsymbol{J}$ is axially symmetric and co-axial with $\boldsymbol{D}$. These authors analysed the spectra to triple-fit the coupled and A-{X} decoupled spectra of the AX case (see Figure 6) simultaneously (and correspondingly for the three subspectra of the AX_2 case). Triple fitting can also be carried out for spectra with satellite peaks arising from isotopic mixtures, e.g., for ^{19}F spectra influenced by coupling to ^{119}Sn[42,45] or for ^{31}P spectra of compounds exhibiting ^{31}P, ^{195}Pt coupling.[46] Recently, errors in the simultaneous fit of shielding tensor components and in the Euler angles which fix the orientation of the tensor in the molecular frame have been discussed, and clues have been given concerning the experimental variables to be set in order to obtain the desired accuracy in the orientation angles.[47]

Cases involving homonuclear coupling (dipolar and indirect) together with shielding are more complex and have been mentioned briefly above, references 9 and 10 supplying ideal cases.

Practical application of the above theory has been made for the two-spin (^{13}C, ^{31}P) case,[40,41] for the two-spin (^{119}Sn,

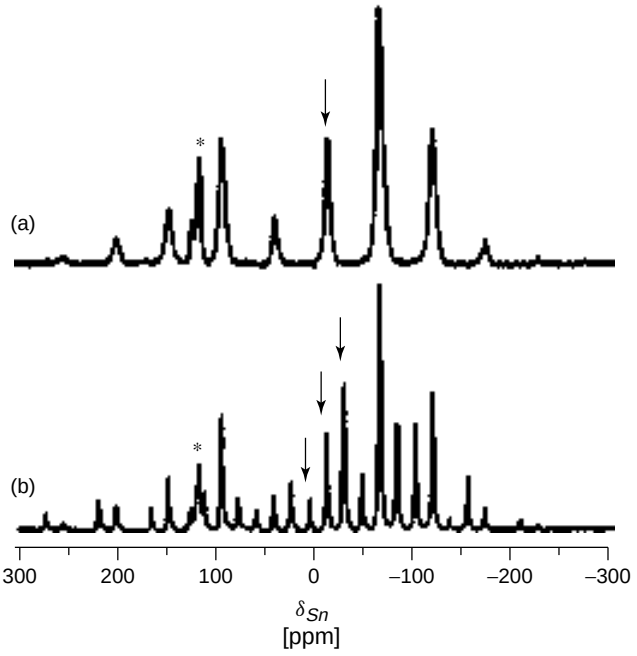

Figure 6 Proton-decoupled ^{119}Sn CPMAS NMR spectra of $^{n}Bu_3SnF$ at 74.6 MHz and spin rate 4 kHz. (a) Triple-resonance case (i.e., ^{19}F-decoupled). (b) Spectra with fluorine coupling effects to show the three subspectra. Triple-fit procedures for the spinning sideband patterns shown in (b) give tensor information which, for the shielding interaction, are consistent with those derived from (a). (Reproduced by permission from J. C. Cherryman and R. K. Harris, *J. Magn. Reson.*, 1997, **128**, 21)

^{19}F) situation,[43] and for (^{119}Sn, ^{19}F) AX_2 spectra.[42,43] The lack of observable differences in intensity distribution between spinning sideband manifolds of subspectra arising from (^{195}Pt, ^{31}P) indirect coupling has been taken[48] as evidence that ^{195}Pt shielding anisotropy dominates over dipolar coupling in *cis*-$PtMe_2(PPh_3)_2$.

5.2 Interplay of σ, D and q[49–51]

For spin-1/2 nuclei coupled to quadrupolar spins, second-order effects occur because the influence of the quadrupolar interaction is transferred to the spin-1/2 by the coupling (see **Magic Angle Spinning Carbon-13 Lineshapes: Effect of Nitrogen-14,** Volume 5; **Magic Angle Spinning: Effects of Quadrupolar Nuclei on Spin-1/2 Spectra,** Volume 5). This has two effects: (i) it alters the multiplet splittings which would otherwise be equal to $|J_{AX}|$, and (ii) it causes each multiplet peak to be a powder pattern (see Ref.[52] for a review). Such complications do not affect the spinning sideband analysis described above as long as the multiplet components are clearly resolved (and provided integrals rather than peak heights are used as intensities since the powder patterns vary in shape). Thus, similar principles to those of the above Section can be invoked for AX cases in which dipolar coupling is between the observed spin-1/2 and a single quadrupolar nucleus. Equation (35) can still be used, but now m_X takes $2I + 1$ possible values ($m_X = I, I-1, I-2 \ldots . -I$), resulting in $2I+1$ subspectra. Clearly spinning sideband analysis becomes more accurate since the number of parameters involved is the same as for two spin-1/2 nuclei. Such spectra have been examined[49] for (^{31}P, ^{55}Mn), (^{31}P, ^{59}Co) and (^{31}P, ^{93}Nb) spin systems (Figure 7).

However, this simple situation is seldom true for ^{13}C spectra involving (^{13}C, ^{14}N) spin pairs, since in this case the relevant isotropic indirect coupling constants are generally small, even negligible. The powder patterns for the subspectra involving $m_N = \pm 1$ overlap, giving a 2 : 1 or 1 : 2 appearance to the spectrum in the limit of fast spinning. However, the powder bandshapes will vary over the spinning sideband manifold,[50] so that in the simplest situation,

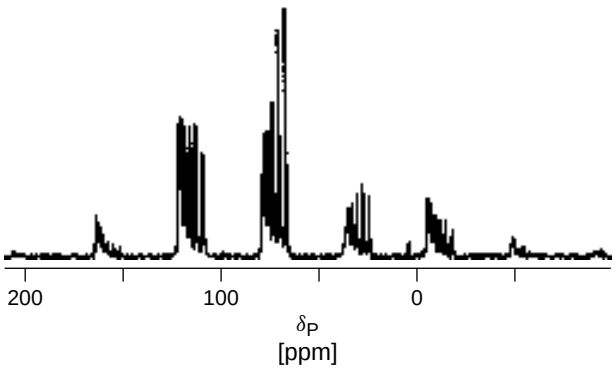

Figure 7 Phosphorus-31 direct polarization spectrum of $Mn_2(CO)_9PPh_3$ at 121.4 MHz showing the differences in spinning sideband intensities for the subspectra from the multiplet components (arising from ^{55}Mn, ^{31}P coupling) because of the interplay between the shielding, quadrupolar and indirect coupling tensors. (Reproduced by permission from R. Gobetto, R. K. Harris and D. C. Apperley, *J. Magn. Reson.*, 1992, **96**, 119)

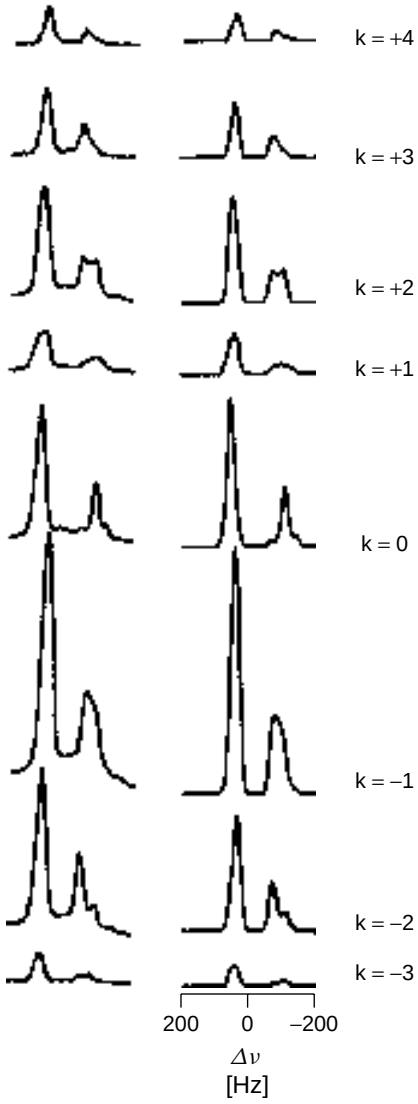

Figure 8 Centerband and sidebands for the high-frequency cyanide ^{13}C CPMAS signals of ($\{(CH_3)_3Pb\}_4Ru(CN)_6$) at 75.4 MHz. Left: experimental bandshapes (rotation rate 4.3 kHz). Right: computer simulation. (Reproduced by permission from N. A. Davies, R. K. Harris and A. C. Olivieri, *Mol. Phys.*, 1996, **87**, 669)

i.e., when $\boldsymbol{\sigma}$, $\boldsymbol{D}$ and $\boldsymbol{q}$ are axially symmetric and co-axial, the angle β between their unique axes and the spinning axis becomes an important variable. The theory has been discussed by Davies et al.[50] and applied (using a perturbation approach) to the cyanide carbon signals of a coordination polymer, $[\{(CH_3)_3Pb\}_4Ru(CN)_4]_\infty$ (see Figure 8). The shape of the centerband at infinite spinning speed is dominated by the intensities of the major singularities at $\beta = 54.7°$ and 90°. As the rotation rate is lowered, the former loses intensity in comparison to the latter. The splitting of the centerband therefore apparently increases as the rotation speed decreases (see Figure 9). There are concomitant changes in the shapes of the spinning sidebands. Their patterns and their intensities can be simulated using standard theory,[53] and therefore information on ζ_C, D_{CN} (in principle, D') and q obtained. Off-MAS ^{13}C spinning sideband manifolds for the cyanide signal of CH_3CN have also been simulated,[51] and used together

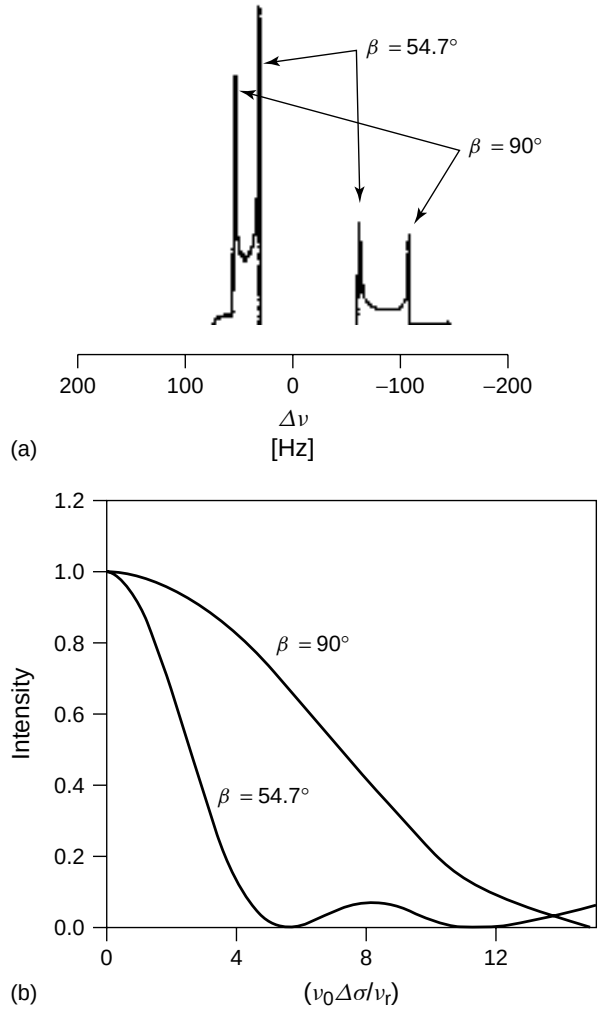

Figure 9 (a) calculated bandshape for an asymmetric 2 : 1 splitting produced by residual second-order ^{13}C, ^{14}N dipolar coupling. The peaks associated with the orientations $\beta = 90°$ and 54.7° (where β is the angle made by the unique axes of the co-axial tensors $\boldsymbol{\sigma}$, D and q with the spinning axis) are indicated by arrows. (b) calculated (normalized) centerband intensities for crystallites with $\beta = 90°$ and 54.7° as a function of the ratio between the shielding anisotropy (expressed in Hz) and the spinning frequency. (Reproduced by permission from N. A. Davies, R. K. Harris and A. C. Olivieri, *Mol. Phys*., 1996, **87**, 669)

with other NMR spectra to yield detailed data on $\boldsymbol{\sigma}$, $\boldsymbol{D}$ and $\boldsymbol{q}$.

Ding and McDowell[54] have pointed out the limitations of most calculations of spectra involving coupling between spin-1/2 and quadrupolar nuclei. They give a general and exact description of the problem within the framework of the density matrix, including the spinning sidebands in a natural manner. They apply the theory to ^{13}C spectra of $KPt(CN)_4.3H_2O$, including the ^{195}Pt satellites, and show that the complex spectra are fitted extremely well at different spinning rates, yielding the relevant parameters. A density matrix approach has also been used by Amoureux et al.[55] to produce a general computer program, PULSAR, to simulate a wide range of NMR situations involving interplay of different tensors, including the Euler angles between their axes.

6 RELATED ARTICLES IN THIS VOLUME

Magic-angle Spinning Extensions; Satellite Transition NMR Spectroscopy of Half-Integer Quadrupolar Nuclei under Magic-Angle Spinning.

7 RELATED ARTICLES IN VOLUMES 1–8

Chemical Shift Tensor Measurement in Solids, Volume 2; Dynamic Angle Spinning, Volume 3; High Speed MAS of Half-Integer Quadrupolar Nuclei in Solids, Volume 4; Magic Angle Spinning, Volume 5; Sideband Analysis in Magic Angle Spinning NMR of Solids, Volume 7; Variable Angle Sample Spinning, Volume 8.

8 REFERENCES

1. J. Herzfeld and A. E. Berger, *J. Chem. Phys.*, 1980, **73**, 6021.
2. M. M. Maricq and J. S. Waugh, *J. Chem. Phys.*, 1979, **70**, 3300.
3. P. Hodgkinson and L. Emsley, *Prog. NMR Spectrosc.*, 2000, **36**, 201.
4. B. Q. Sun and E. A. Pines, *Appl. Magn. Reson.*, 1993, **5**, 43.
5. A. R. Brough, C. P. Grey, and C. M. Dobson, *J. Am. Chem. Soc.*, 1993, **115**, 7318.
6. J. Hjorth, J. Skibsted, and H. J. Jakobsen, in 'Methodology and Applications of Inversion within Geophysics, Astronomy, Geodesy and Physics', Proceedings of the Interdisciplinary Inversion Workshop II, ed K. Mosegaard, Copenhagen, 1993.
7. N. K. Sethi, D. W. Alderman, and D. M. Grant, *Mol. Phys.*, 1990, **71**, 217.
8. A. Schmidt and S. Vega, *Isr. J. Chem.*, 1992, **32**, 215.
9. G. Wu, B. Sun, R. E. Wasylishen, and R. G. Griffin, *J. Magn. Reson.*, 1997, **124**, 366.
10. R. Challoner, T. Nakai, and C. A. McDowell, *J. Chem. Phys.*, 1991, **94**, 7038.
11. R. Challoner, C. A. McDowell, M. Yoshifuji, K. Toyota, and J. A. Tossell, *J. Magn. Reson. Ser. A*, 1993, **104**, 258.
12. G. Wu, R. E. Wasylishen, and R. D. Curtis, *Can. J. Chem.*, 1992, **70**, 863; G. Wu and R. E. Wasylishen, *Inorg. Chem.*, 1992, **31**, 145; *J. Chem. Phys.*, 1993, **99**, 6321.
13. A. Kubo and C. A. McDowell, *J. Chem. Phys.*, 1990, **92**, 7156.
14. A. Schmidt, S. O. Smith, D. P. Rayleigh, J. E. Roberts, R. G. Griffin, and S. Vega, *J. Chem. Phys.*, 1986, **85**, 4248.
15. A. Schmidt and S. Vega, *J. Chem. Phys.*, 1987, **87**, 6895.
16. M. J. Duer and M. H. Levitt, *Solid State NMR*, 1992, **1**, 211.
17. A. C. Olivieri, C. M. Lagier, D. C. Apperley, and R. K. Harris, *Solid State NMR.*, 1992, **1**, 205.
18. C. M. Lagier, D. C. Apperley, U. Scheler, A. C. Olivieri, and R. K. Harris, *J. Chem. Soc. Faraday Trans.*, 1996, **92**, 5047.
19. C. M. Lagier, A. C. Olivieri, and R. K. Harris, *J. Chem. Soc. Perkin Trans.*, 1998, **2**, 1791.
20. Y. Shen, T. Wu, and Y. Yang, *Chem. Phys. Lett.*, 1995, **242**, 83.
21. K. Eichele and R. E. Wasylishen, *J. Phys. Chem.*, 1994, **98**, 3108.
22. C. M. Lagier and A. C. Olivieri, *J. Magn. Reson.*, 1997, **126**, 138.
23. J. R. Ascenso and R. K. Harris, unpublished (1985) (first referred to in the open literature in R. K. Harris and A. Sebald, *J. Organomet. Chem.*, 1987, **331**, C9); L. H. Merwin, Ph.D. Thesis, University of Durham, 1987 (reported in the open literature in R. K. Harris, L. H. Merwin, and G. Hägele, *J. Chem. Soc. Faraday Trans. I*, 1989, **85**, 1409).
24. H. J. M. de Groot, S. O. Smith, A. C. Kolbert, J. M. L. Courtin, C. Winkel, J. Lugtenburg, J. Herzfeld, and R. G. Griffin, *J. Magn. Reson.*, 1991, **91**, 30.

25. G. Jeschke and G. Grossmann, *J. Magn. Reson. Ser. A*, 1993, **103**, 323.
26. N. J. Clayden, C. M. Dobson, L.-Y. Lian, and D. J. Smith, *J. Magn. Reson.*, 1986, **69**, 476.
27. E. A. Christopher, R. K. Harris, and R. A. Fletton, *Solid State NMR*, 1992, **1**, 93.
28. L. H. Merwin, Ph.D. Thesis, University of Durham, 1987; H.-P. Bai, Ph.D. Thesis, University of Durham, 1991.
29. P. Hodgkinson and L. Emsley, *J. Chem. Phys.*, 1997, **107**, 4808.
30. R. K. Harris, D. C. Apperley, P. Avalle, and P. Amornsakchai, unpublished work.
31. Varian Incorporated, NMR Systems STARS software.
32. A. D. Bain and R. S. Dumont, *Concepts Magn. Reson.*, 2001, **13**, 159.
33. D. Fenzke, B. Maess, and H. Pfeiffer, *J. Magn. Reson.*, 1990, **88**, 172.
34. G. A. Bowmaker, R. K. Harris, and S.-W. Oh, *Coord. Chem. Rev.*, 1998, **167**, 49.
35. G. E. Hawkes, K. D. Sales, L. Y. Lian, and E. R. Gobetto, *Proc. R. Soc. Lond. A*, 1989, **424**, 93.
36. P. D. Ellis and H. Bildsøe, referred to in H. Jakobsen, P. D. Ellis, R. R. Inners, and C. F. Jensen, *J. Am. Chem. Soc.*, 1982, **104**, 7442.
37. A. C. Olivieri, *J. Magn. Reson. Ser. A*, 1996, **123**, 207.
38. R. K. Harris, P. Jackson, L. H. Merwin, B. J. Say, and G. Hägele, *J. Chem. Soc. Faraday Trans. 1*, 1988, **84**, 3649.
39. J. Skibsted, T. Vosegaard, H. Bildsøe, and H. J. Jakobsen, *J. Phys. Chem.*, 1996, **100**, 14 872.
40. R. K. Harris, K. J. Packer, and A. M. Thayer, *J. Magn. Reson.*, 1985, **62**, 284.
41. U. Haubenreisser, U. Sternberg, and A.-R. Grimmer, *Mol. Phys.*, 1987, **60**, 151.
42. H. Bai and R. K. Harris, *J. Magn. Reson.*, 1992, **96**, 24.
43. J. C. Cherryman and R. K. Harris, *J. Magn. Reson.*, 1997, **128**, 21.
44. R. K. Harris and L. A. Crowe, *J.C.S. Dalton*, 1999, 4315.
45. K. W. Zilm and D. M. Grant, *J. Am. Chem. Soc.*, 1981, **103**, 2913.
46. L. A. Crowe, Ph.D. Thesis, University of Durham, 1999; L. A. Crowe, K. B. Dillon, R. K. Harris, J. A. K. Howard, and M. D. Roden, to be published.
47. A. C. Olivieri, *Solid State NMR*, **11**, 1998, 181.
48. R. K. Harris, P. Reams, and K. J. Packer, *J. Mol. Struct.*, 1986, **141**, 13.
49. R. Gobetto, R. K. Harris, and D. C. Apperley, *J. Magn. Reson.*, 1992, **96**, 119.
50. N. A. Davies, R. K. Harris, and A. C. Olivieri, *Mol. Phys.*, 1996, **87**, 669.
51. J. Sepa, R. J. Gorte, B. H. Suits, and D. White, *Chem. Phys. Lett.*, 1996, **252**, 281.
52. R. K. Harris and A. C. Olivieri, *Prog. NMR Spectrosc.*, 1992, **24**, 435.
53. A. C. Olivieri, *Solid State NMR*, 1997, **10**, 19.
54. S. Ding and C. A. McDowell, *J. Chem. Phys.*, 1997, **107**, 7762.
55. J. P. Amoureux, C. Fernandez, and Y. Dumazy, *J. Chem. Phys.*, 1995, **92**, 1939.

Biographical Sketches

Robin K. Harris, *b* 1936. B.A. (Nat. Sci.), Ph.D. (supervisor Norman Sheppard), Sc.D., University of Cambridge, UK. Postdoctoral work at Mellon Institute, Pittsburgh, PA (with Aksel Bothner-By). Successively lecturer, senior lecturer, and professor, University of East Anglia, UK. Currently Professor of Chemistry, University of Durham, UK. Secretary-General of ISMAR, 1986-92. Approx. 460 publications. Current research specialty: solid-state NMR and its applications in materials chemistry.

Alejandro C. Olivieri, *b* 1958. B.Sc. (Catholic University, Argentina), Ph.D. (supervisor Manuel G. Sierra), National University of Rosario, Argentina. Postdoctoral work at the University of Illinois at Urbana-Champaign, USA (with Iain Paul and David Curtin). Successively Associate Professor and currently Full Professor, Department of Analytical Chemistry, National University of Rosario, Argentina. Approx. 100 publications. Current research interests: NMR and its applications to organic and analytical chemistry.

Average Hamiltonian Theory

John S. Waugh

Massachusetts Institute of Technology, Cambridge, MA, USA

1	Introduction	1
2	Magnus Expansion	1
3	Representations and Frames of Reference: Truncation	2
4	Applications	3
5	Additional Topics	6
6	References	7

1 INTRODUCTION

When a system is subject to a time-dependent Hamiltonian $\hat{\mathcal{H}}(t)$, it may sometimes happen that its development over some interval (t_1,t_2) could have been caused by a hypothetical time-independent average Hamiltonian. The requirements for this replacement and the circumstances under which it is useful are the subjects of this article. We also exhibit the forms that $\bar{\hat{\mathcal{H}}}$ takes in several cases of practical importance in NMR.

Consider the following simple example: a spin or group of spins has a frequency shift δ which varies cosinusoidally with time: $\delta(t) = \delta_0 + \alpha \cos \omega t$. The magnetization $\boldsymbol{m}_0$ is initially placed along the x axis of a rotating frame, after which the FID $g(t)$ depends on the precessional phase accumulation φ:

$$g(t) = \frac{m_x(t)}{m_0} = \cos\varphi(t),$$
$$\varphi(t) = \int_0^t \delta(t')\,\mathrm{d}t' = \delta_0 t + \frac{\alpha}{\omega}\sin\omega t \qquad (1)$$

By trigonometric identities and the Jacobi–Anger formula, this gives

$$g(t) = \cos\delta_0 t\left\{J_0(k) + 2\sum_{n=0}^{\infty} J_{2n}(k)\cos 2n\omega t\right\}$$
$$-\sin\delta_0 t\sum_{n=1}^{\infty} J_{2n-1}(k)\sin(2n-1)\omega t \qquad (2)$$

with $k = \alpha/\omega$. The Fourier transform of equation (2) is the familiar spectrum consisting of a central resonance and an array of sidebands spaced by ω with intensities proportional to the corresponding Bessel functions. The sideband structure is a consequence of the periodicity of $\hat{\mathcal{H}}(t)$.

In practice FIDs are usually sampled at some convenient but otherwise arbitrary interval t_s, anticipating discrete Fourier transformation. The sideband pattern just described is seen if $t_s \ll 2\pi/\omega$. Suppose instead that the data sampling is synchronized with ω and occurs only once in each N periods, $N = 1, 2, \ldots$. Substituting $t_s = 2\pi N/\omega$, we see that the trigonometric functions disappear and $g(t) = g(mt)_s = \cos\delta_0 t$. As a consequence of synchronous sampling, all sidebands have disappeared from the spectrum, having been folded into the center band. The same result is obtained if the oscillating parts of equation (2) are replaced by their averages, namely 0. In quantum mechanical language, the time-dependent spin Hamiltonian has been replaced by a time-independent average Hamiltonian:

$$\hat{\mathcal{H}}(t) = (\delta_0 + \alpha\cos\omega t)\hat{I}_z \rightarrow \bar{\hat{\mathcal{H}}} = \delta_0\hat{I}_z \qquad (3)$$

The requirements of (i) the periodic time dependence of the Hamiltonian and (ii) synchronous sampling are characteristic of average Hamiltonians. It is also typical that in the course of averaging, some part of the original Hamiltonian (here the part containing information about α) is lost and the spectrum is correspondingly simplified.

The example discussed is incomplete in that $\hat{\mathcal{H}}(t)$ was chosen as a single spin operator with a time-dependent scalar coefficient, so that $[\hat{\mathcal{H}}(t), \hat{\mathcal{H}}(t')] = 0$. When this is not so, the meaning of $\bar{\hat{\mathcal{H}}}$ must be modified. In the next section we review the formal theory that deals with these matters.[1]

2 MAGNUS EXPANSION

We consider the time development of a quantum state between times 0 and T:

$$|a(T)\rangle = \hat{U}(T,0)|a(0)\rangle \qquad (4)$$

If $\hat{\mathcal{H}}$ were independent of time, we would have simply $\hat{u} = \exp(-i\hat{\mathcal{H}}t)$, but more generally

$$\hat{U}(T,0) = \mathcal{T}\exp\left\{-\mathrm{i}\int_0^T \hat{\mathcal{H}}(t)\,\mathrm{d}t\right\} \qquad (5)$$

where the symbol is a reminder that the infinitesimal propagators

$$\hat{u}(t'+\mathrm{d}t, t') = \exp\{-\mathrm{i}\hat{\mathcal{H}}(t')\,\mathrm{d}t\} \qquad (6)$$

of which $\hat{U}$ is composed must be multiplied together with t' increasing from right to left.

There is no general way of accomplishing this unless $\hat{\mathcal{H}}$ is weak enough or t short enough that not much happens to the system: $\hat{U} \approx 1$, or, informally put, $\hat{\mathcal{H}}t \ll 1$. Normal time-dependent perturbation theory gives a recipe based on repeated iteration of the following pair of relations:

$$|a(T)\rangle = |a(0)\rangle + \int_0^T \frac{\partial|a(t)\rangle}{\partial t}, \quad \frac{\partial|a(t)\rangle}{\partial t} = -\mathrm{i}\hat{\mathcal{H}}(t)|a(t)\rangle \qquad (7)$$

$$\hat{U}(T,0) = 1 - \mathrm{i}\int_0^T \hat{\mathcal{H}}(t)\,\mathrm{d}t - \int_0^T \mathrm{d}t\int_0^t \mathrm{d}t'\,\hat{\mathcal{H}}(t)\hat{\mathcal{H}}(t') + \ldots \qquad (8)$$

If the Hamiltonian is periodic, there is an advantage in evaluating $\hat{U}$ over a full period. Then the same $\hat{U}$ can be used to describe the long time development of the system as long as one is content with observing the system stroboscopically in synchrony with $\hat{\mathcal{H}}(t)$. We would like to express $\hat{U}$ in terms of an average Hamiltonian

$$\begin{aligned}\hat{U}(t_c, 0) &= \exp(-i\hat{\bar{\mathcal{H}}}t_c)\\ \hat{U}(Nt_c, 0) &= \{\hat{U}(t_c, 0)\}^N = \exp\{-i\hat{\bar{\mathcal{H}}}(Nt_c)\}\end{aligned} \tag{9}$$

However, while the operator $\hat{A} = -\hat{\bar{\mathcal{H}}}t_c$ must be Hermitian, and the function exp $(i\hat{A})$ of any Hermitian operator $\hat{A}$ is unitary, the truncated propagator of equation (8) is not unitary.

The Magnus expansion provides an escape from this problem: one tries from the beginning to find a unitary propagator in terms of a power series in $\lambda = -i$ as follows:

$$\hat{U}(T, 0) = \exp\{\lambda(\hat{a} + \lambda\hat{b} + \lambda^2\hat{c} + \dots)\} \tag{10}$$

One equates the coefficients of equal powers of λ in equations (8) and (10) [noting that equation (8) is such a series] to find the operators $\hat{a}$, $\hat{b}$, $\hat{c}$, ... The result, after putting the result in the form of equation (10), replacing λ by $-i$, and choosing $T = t_c$, is

$$\hat{\bar{\mathcal{H}}} = \sum_n \hat{\bar{\mathcal{H}}}^{(n)} \tag{11}$$

$$\hat{\bar{\mathcal{H}}}^{(0)} = \frac{1}{t_c}\int_0^{t_c} \hat{\mathcal{H}}(t')\,dt' \tag{12}$$

$$\hat{\bar{\mathcal{H}}}^{(1)} = \frac{-i}{2t_c}\int_0^{t_c} dt \int_0^t dt'[\hat{\mathcal{H}}(t), \hat{\mathcal{H}}(t')] \tag{13}$$

$$\begin{aligned}\hat{\bar{\mathcal{H}}}^{(2)} = \frac{-1}{6t_c}\int_0^{t_c} dt \int_0^t dt' \int_0^{t'} dt''\{&[\hat{\mathcal{H}}(t), [\hat{\mathcal{H}}(t'), \hat{\mathcal{H}}(t'')]]\\ &+[\hat{\mathcal{H}}(t''), [\hat{\mathcal{H}}(t'), \hat{\mathcal{H}}(t)]]\}\end{aligned} \tag{14}$$

This series converges of course at a rate similar to equation (8), and is not useful unless the first few terms (in practice, usually the first and second) suffice.

3 REPRESENTATIONS AND FRAMES OF REFERENCE: TRUNCATION

The convergence of the Magnus series can be greatly influenced by one's choice of representation or frame of reference. As an example, begin with a laboratory frame Hamiltonian which includes static and radiofrequency fields as well as an internal Hamiltonian which might include chemical shifts, dipolar interactions, etc.:

$$\hat{\mathcal{H}}(t) = \omega_0\hat{I}_z + 2\omega_1\cos\omega t\ \hat{I}_x + \hat{\mathcal{H}}_{\text{int}} \tag{15}$$

$\hat{\mathcal{H}}(t)$ is periodic modulo $t_c = 2\pi/\omega$, and one might imagine applying equations (11)–(14) directly. But, if the rf frequency is near the Larmor frequency, $\hat{\mathcal{H}}t_c \approx \omega_0/\omega \approx 1$ and the perturbation theory will not converge. We take advantage of the elementary principle of quantum mechanics that no physical consequences are altered if all states $|a\rangle$ and all operators $\hat{Q}$ in a problem are transformed to a new representation by an arbitrary unitary operator $\hat{R}$:

$$|\tilde{a}\rangle = \hat{R}|a\rangle, \quad \tilde{\hat{Q}} = \hat{R}\hat{Q}\hat{R}^{-1} \tag{16}$$

In the new representation the time evolution is governed by an effective Hamiltonian:

$$\frac{\partial|a\rangle}{\partial t} = -i\,\hat{\mathcal{H}}_{\text{eff}}|a\rangle, \quad \hat{\mathcal{H}}_{\text{eff}} = \hat{R}\hat{\mathcal{H}}\hat{R}^{-1} - iU\frac{\partial\hat{U}^{-1}}{\partial t} \tag{17}$$

In the case of equation (15) the choice $\hat{R} = \exp(i\omega t\hat{I}_z)$ leads to

$$\begin{aligned}\hat{\mathcal{H}}_{\text{eff}} = (\omega_0 - \omega)\hat{I}_z + \omega_1\{(1 + \cos 2\omega t)\hat{I}_x - \sin 2\omega t\ \hat{I}_y\}\\ +\tilde{\hat{\mathcal{H}}}_{\text{int}}(t)\end{aligned} \tag{18}$$

with $\tilde{\hat{\mathcal{H}}}_{\text{int}} \equiv \hat{R}\hat{\mathcal{H}}_{\text{int}}\hat{R}^{-1}$. In this interaction representation the size of the Hamiltonian is greatly reduced but t_c is the same as before, so the series in equation (11) converges very rapidly. (Because an operator of the form $\hat{R} = \exp(i\theta\hat{I}_z)$ generates a rotation in spin space through the angle θ, here about the z axis, the interaction representation can be associated with a *rotating frame of reference*. The fortunate circumstance that most of the transformations that are useful in magnetic resonance are of this form gives us this useful geometrical picture. A dominant quadrupolar coupling, for example, is not so kind.) The rotating frame also coincides with the laboratory frame at intervals of t_c, so that calculations made with reference to the rotating frame have relevance to experimental measurements. Indeed the requisite synchronization is often realized in practice by means of an rf phase detector referenced to ω.

To lowest order equation (18) gives just

$$\hat{\bar{\mathcal{H}}}^{(0)} = (\omega_0 - \omega)\hat{I}_z + \omega_1\hat{I}_x + \hat{\bar{\mathcal{H}}}^{(0)}_{\text{int}} \tag{19}$$

whose first two terms describe the familiar effective field $\boldsymbol{B}_{\text{eff}}$ of magnitude $[(\omega_0 - \omega)^2 + {\omega_1}^2]^{1/2}$, inclined at the angle $\xi = \tan^{-1}[\omega_1/(\omega_0 - \omega)]$ to the main Zeeman field $\boldsymbol{B}_0$. To evaluate the third term, one must first write out the internal Hamiltonian explicitly. We take the example of the chemical shift:

$$\hat{\mathcal{H}}_{\text{int}} = \gamma\boldsymbol{B}\cdot\boldsymbol{\sigma}\cdot\hat{\boldsymbol{I}} \tag{20}$$

Since $\boldsymbol{B}_0$ is dominant and in the z direction, this simplifies to

$$\hat{\mathcal{H}}_{\text{int}} = -\omega_0(\sigma_{zx}\hat{I}_x + \sigma_{zy}\hat{I}_y + \sigma_{zz}\hat{I}_z) \tag{21}$$

Transforming to the rotating frame and averaging over one period t_c, we are left with the familiar result

$$\begin{aligned}\tilde{\hat{\mathcal{H}}}_{\text{int}} = \ &-\omega_0\{\sigma_{zz}\hat{I}_z + \sigma_{zx}(\hat{I}_x\cos\omega t - \hat{I}_y\sin\omega t)\\ &+\sigma_{zy}(\hat{I}_y\cos\omega t + \hat{I}_x\sin\omega t)\}\end{aligned} \tag{22}$$

$$\bar{\hat{\mathcal{H}}}^{(0)}_{\text{int}} = -\omega_0 \sigma_{zz} \hat{I}_z \tag{23}$$

At this point we remind the reader that σ_{zz} refers to a coordinate system fixed in the laboratory, not in the molecule containing the spin $\hat{\boldsymbol{I}}$. If $\boldsymbol{B}_0$ is in the direction (θ, φ) with respect to the principal axes (X,Y,Z) of the shielding tensor then

$$\sigma_{zz} = \sigma_{ZZ} \cos^2\theta + \sigma_{XX} \sin^2\theta \cos^2\varphi + \sigma_{YY} \sin^2\theta \sin^2\varphi \tag{24}$$

If the molecule is tumbling rapidly and isotropically in a liquid, we must supplement the average already taken in spin space by an independent average over angles:

$$\bar{\sigma}_{zz} = \left(\frac{1}{3}\right)(\sigma_{XX} + \sigma_{YY} + \sigma_{ZZ}) = \frac{1}{3}\,\text{Tr}\,\boldsymbol{\sigma} \tag{25}$$

Even though the motion of the molecule is not periodic, the average over angles is complete in a time much shorter than the sampling interval of the FID (see below).

So far we have looked only at the lowest order term in the Magnus expansion. The oscillations in the first and second terms of equation (19) give a correction

$$\bar{\hat{\mathcal{H}}}^{(1)}_{\text{rf}} = \left(\frac{\omega_1}{2\omega}\right)^2 \hat{I}_z + \frac{\omega_1(\omega_0 - \omega)}{2\omega}\hat{I}_x \tag{26}$$

If the resonance frequency ω_{res} is defined as the frequency for which the coefficient of $\hat{I}_z$ vanishes then the first term of equation (26) represents the small Bloch–Siegert shift of the resonance condition away from its nominal frequency $\omega_{\text{res}} = \omega_0$ when the rf field is not of vanishing intensity.

Other internal Hamiltonians can be treated similarly. Consider the dipole–dipole interaction of a single pair of spins $\hat{\boldsymbol{I}}$ and $\hat{\boldsymbol{S}}$ having Larmor frequencies ω_{0I} and ω_{0S} which may or may not be different:

$$\hat{\mathcal{H}}_{\text{D}} = \frac{\gamma_I \gamma_S \hbar}{r^3}\left\{\hat{\boldsymbol{I}}\cdot\hat{\boldsymbol{S}} - 3\left(\hat{\boldsymbol{I}}\cdot\frac{\boldsymbol{r}}{r}\right)\left(\hat{\boldsymbol{S}}\cdot\frac{\boldsymbol{r}}{r}\right)\right\} \tag{27}$$

where $\boldsymbol{r}$ is a vector pointing from one spin to the other in space. By expanding the spin operators in Cartesian coordinates and $\boldsymbol{r}/r$ in spherical polar coordinates referred to $\boldsymbol{B}_0$, one finds, as Van Vleck[2] showed,

$$\hat{\mathcal{H}}_{\text{D}} = \gamma_I \gamma_S \hbar r^{-3}(\hat{A} + \hat{B} + \hat{C} + \hat{D} + \hat{E} + \hat{F}) \tag{28}$$

where

$$\left.\begin{aligned}
&\hat{A} = -(3\cos^2\theta - 1)\hat{I}_z\hat{S}_z \\
&\hat{B} = \tfrac{1}{2}(3\cos^2\theta - 1)(\hat{I}_x\hat{S}_x + \hat{I}_y\hat{S}_y) \\
&\hat{C} + \hat{D} = -3\sin\theta\cos\theta\,\{(\hat{I}_z\hat{S}_x + \hat{I}_x\hat{S}_z)\cos\varphi + (\hat{I}_z\hat{S}_y + \hat{I}_y\hat{S}_z)\sin\varphi\} \\
&\hat{E} + \hat{F} = -\tfrac{3}{2}\sin^2\theta\,\{(\hat{I}_x\hat{S}_x - \hat{I}_y\hat{S}_y)\cos 2\varphi + (\hat{I}_x\hat{S}_y + \hat{I}_y\hat{S}_x)\sin 2\varphi\}
\end{aligned}\right\} \tag{28a}$$

We can imagine a rotating frame transformation $\hat{S}$ = exp ($i\omega_{0I}t\hat{I}_z$ + $i\omega_{0S}t\hat{S}_z$) which makes various terms of $\hat{C}$ and $\hat{D}$ oscillatory at frequencies ω_{0I} and ω_{0S}, terms $\hat{E}$ and $\hat{F}$ oscillatory at $\omega_{0I} + \omega_{0S}$, $\hat{B}$ oscillatory at $\omega_{0I} - \omega_{0S}$, and leaves $\hat{A}$ independent of time. Removing oscillatory terms gives a truncated Hamiltonian which depends on whether the spins are alike or different. In the latter case only term $\hat{A}$ survives. In the former, containing terms $\hat{A}$ and $\hat{B}$, the result is frequently written as

$$\bar{\hat{\mathcal{H}}}^{(0)}_{\text{D},kl} = \hat{\mathcal{H}}_{\text{D},kl} = \gamma_I \gamma_S \hbar r_{kl}^{-3}\left(\frac{3\cos^2\theta_{kl} - 1}{2}\right) \times(\hat{\boldsymbol{I}}_k\cdot\hat{\boldsymbol{I}}_l - 3\hat{I}_{zk}\hat{I}_{zl}) \tag{29}$$

Here the same symbol I is used for both spins to emphasize that they are of the same species, at the expense of the necessity of labels k and l.

Higher order corrections to the chemical shift and spin–spin Hamiltonians can be calculated in a manner similar to those that led to the Bloch–Siegert shift, but these are not of much practical importance.

4 APPLICATIONS

We have seen that the average Hamiltonian offers a convenient conceptual framework for approaching the truncation of Hamiltonians, and also a systematic way of evaluating corrections to the lowest order truncations. However, it also provides a guide for the synthesis of new and useful experiments. For example, one could have regarded the application of an intense external field as a deliberate measure for transforming the system Hamiltonian from one form, for example $\hat{\mathcal{H}}_{\text{D}}$, to another, $\hat{\mathcal{H}}'_{\text{D}}$. The requirement for this to be successful is that the external influence be *strong* compared with $\hat{\mathcal{H}}_{\text{int}}$ and that it generate an $\hat{\tilde{\mathcal{H}}}_{\text{int}}(t)$ which is *periodic* in a manner that can be synchronized with experimental observations. There are enough variables at the experimenter's disposal that average Hamiltonians can, to a surprising degree, be tailored to measure. In this section we illustrate this with several important examples.

4.1 Experiments with Steady rf Fields: Second Rotating Frame

4.1.1 Decoupling of Unlike Spins

Consider the situation in equation (20) when $\omega_{\text{eff}} = \gamma B_{\text{eff}}$ is large. We apply a second transformation $\hat{R}_2$ which removes $\boldsymbol{B}_1$ in the same way that $\hat{R}$ removed $\boldsymbol{B}_0$ (or most of it). It is convenient to do this in two stages: $\hat{R}_2 = \hat{S}\hat{T}$, with $\hat{T} = \exp(i\xi\hat{I}_y)$. This creates a new z axis parallel to $\boldsymbol{B}_{\text{eff}}$. The second transformation $\hat{S}$ = exp ($i\omega_{\text{eff}}t\hat{I}_z$) then induces the *second tilted rotating (STR) frame*, in which

$$\hat{\tilde{\mathcal{H}}}^{(\text{STR})}_{\text{eff}}(t) = \hat{S}\hat{T}\bar{\hat{\mathcal{H}}}^{(0)}_{\text{int}}\hat{T}^{-1}\hat{S}^{-1} \tag{30}$$

Take as an example $\bar{\hat{\mathcal{H}}}^{(0)}_{\text{int}} = K\hat{I}_z\hat{S}_z$, the coupling between two unlike spins truncated as described above. (In the case of

dipolar coupling $K = -\gamma_I\,\gamma_S\hbar r^{-3}(3\cos^2\theta - 1)$. For scalar coupling in liquids, expressible as $J\hat{\mathbf{I}}\cdot\hat{\mathbf{S}}$ in the laboratory, one gets the same form with $K = J$.) We imagine that the rf field of equation (16) and equation (20) is applied near the I-spin resonance, so that the transformations T and S involve only I-spin variables as indicated. (It is easily verified that the final results are unchanged if we apply an arbitrary transformation to the S-spin operators.) The result of the two transformations is

$$\hat{\tilde{\mathcal{H}}}^{(\mathrm{STR})}_{\mathrm{eff}}(t) = K\hat{S}_z\{\hat{I}_z\cos\xi - (\hat{I}_x\cos\omega_{\mathrm{eff}}t - \hat{I}_y\sin\omega_{\mathrm{eff}}t)\sin\xi\} \tag{31}$$

and the average Hamiltonian is

$$\hat{\bar{\mathcal{H}}}^{(0,\mathrm{STR})} = K_{\mathrm{eff}}\hat{I}_z\hat{S}_z, \quad K_{\mathrm{eff}} = K\cos\xi = K\left(\frac{\omega_0-\omega}{\omega_{\mathrm{e}}}\right) \tag{32}$$

The coupling constant has been effectively reduced: for irradiation exactly at resonance it vanishes altogether.

Note that $\hat{\tilde{\mathcal{H}}}_{\mathrm{eff}}(t)$ is periodic modulo $t_{\mathrm{c}} = 2\pi/\omega_{\mathrm{e}}$, which depends on the irradiation conditions and is not conveniently synchronized with data acquisition. The average Hamiltonian concept is therefore not well suited to this experiment: in fact equation (32) is correct for certain values of ω_{e}, but for all other values K_{eff} is smaller than predicted.

4.1.2 Recoupling of Unlike Spins: The Hartmann–Hahn Effect

We have just shown that applying a strong rf field at the Larmor frequency of one of two species of unlike coupled spins removes their coupling. We now show that simultaneous irradiation at both Larmor frequencies not only restores the coupling, but makes the spins appear to be of the same species, in the sense that they can undergo mutual spin flips. For the first time we allow explicitly for the presence of many spins of both types:

$$\hat{\mathcal{H}}'_{\mathrm{D}} = \hat{\mathcal{H}}_{II} + \hat{\mathcal{H}}_{SS} + \hat{\mathcal{H}}_{IS} \tag{33a}$$

where

$$\hat{\mathcal{H}}_{IS} = -\gamma_I\gamma_S\hbar\sum_k\sum_p r_{kp}^{-3}(3\cos^2\theta_{kp} - 1)\hat{I}_{zk}\hat{S}_{zp} \tag{33b}$$

is a sum over all pairs of unlike spins, and $\hat{\mathcal{H}}_{II}$ and $\hat{\mathcal{H}}_{SS}$ are sums of terms of the form of equation (26). The transformation to be applied is now

$$\hat{S}\hat{T} = \exp\{\mathrm{i}(\omega_{\mathrm{eff},I}\hat{I}_z + \omega_{\mathrm{eff},S}\hat{S}_z)t\}\exp\{\mathrm{i}(\xi_I\hat{I}_y + \xi_S\hat{S}_y)\} \tag{34}$$

where $\hat{I}_z = \Sigma\hat{I}_{zk}$, etc. As before, all Zeeman terms are removed but attach their respective oscillations to the I and S spin operators in equation (33), etc., resulting in oscillatory time-dependences at $\omega_{\mathrm{eff},I}$, $\omega_{\mathrm{eff},S}$ and their sum and difference, as well as a time-independent part. We average first over all oscillating terms except the one at the lowest frequency $\Delta = \omega_{\mathrm{eff},I} - \omega_{\mathrm{eff},S}$:

$$\hat{\bar{\mathcal{H}}}^{(0,\mathrm{STR})} = \hat{\mathcal{H}}_{II}P_2(\cos\xi_I) + \hat{\mathcal{H}}_{SS}P_2(\cos\xi_S) + \hat{\mathcal{H}}_{IS}\cos\xi_I\cos\xi_S + \hat{\mathcal{H}}_{\mathrm{ff}}(t) \tag{35}$$

$$\hat{\mathcal{H}}_{\mathrm{eff}}(t) = \tfrac{1}{2}\exp\{-\tfrac{1}{2}\mathrm{i}\,\Delta t\,(\hat{I}_z - \hat{S}_z)\} \times\sum_k\sum_{l\rangle k} K'_{kl}(\hat{I}_{+k}\hat{I}_{-l} + \hat{I}_{-k}\hat{I}_{+l})\exp\{\tfrac{1}{2}\mathrm{i}\,\Delta t\,(\hat{I}_z - \hat{S}_z)\} \tag{36}$$

$$K'_{kl} = K_{kl}\sin\xi_I\sin\xi_S \tag{37}$$

The best known application of this result is the irradiation of both species at resonance and adjustment of Δ to zero (Hartmann–Hahn condition.[3] The now static term $\hat{\mathcal{H}}_{\mathrm{ff}}$ leads to mutual flips of interacting I and S spins, which could not occur under the normal truncated spin–spin Hamiltonian [equation (33)].

The actual behavior in many-spin systems is complicated by the terms in $\hat{\mathcal{H}}_{II}$ and $\hat{\mathcal{H}}_{SS}$ (although most applications are to systems in which the S spins are very dilute and $\hat{\mathcal{H}}_{SS}$ can be neglected). The Hartmann–Hahn effect in concert with *IS* decoupling [cf. equation (33)] forms the basis of a widely used technique for resolved dilute spin spectroscopy in solids.[4]

4.2 Pulsed RF Fields: The Toggling Frame

Consider a solid having only a single spin species, I. Everything drops out of equation (35) except the first term, which vanishes as well if the irradiation is performed at the magic angle in the rotating frame, $\xi_{\mathrm{m}} = \tan^{-1}\sqrt{2}$. Such an experiment evidently accomplishes decoupling of like spins. Early experimenters who recognized this fact[5] did not notice the contrast of this behavior with the effect on chemical shifts [equation (23)] for which

$$\hat{\bar{\mathcal{H}}}^{(0,\mathrm{STR})} = -\omega_0\sum_k \text{œ}_{zzk}(\hat{I}_{zk}\cos\xi_I + \hat{I}_{yk}\sin\xi_I) \tag{38}$$

does not vanish. Returning equation (38) to the z axis by reversing the transformation $\hat{T}$, we recover just equation (23) with a scale factor of $1/\sqrt{3}$. That is, chemical shifts are in principle extractable from a background of static dipole–dipole broadening in solids.

At this point we need to remember the higher order corrections to the Magnus series, which we have been ignoring for the most part. In experiments on rf irradiation of solids, practical rf fields are not sufficient to dominate the internal Hamiltonian to the extent that $\boldsymbol{B}_0$ does in the laboratory frame, and $\hat{\bar{\mathcal{H}}}^{(1)}_{II}$ can often be comparable in size to equation (35). To remove $\hat{\bar{\mathcal{H}}}^{(1)}_{II}$, we need further degrees of freedom in the design

of rf irradiation, in particular modulation of the amplitude and phase of the rf carrier. The analysis is especially simple if we idealize the rf envelope as a train of Δ-functions. Each such pulse contains a particular carrier phase, which we choose for simplicity from the set 0°, 90°, 180°, and 270°, which lead to instantaneous rotations about the x, y, $-x$, and $-y$ axes of the rotating frame. We imagine repetition of a short sequence which has cyclic behavior, so that stroboscopic observations made once per cycle have relevance to the laboratory frame of reference.

The propagator $\hat{U}$ for a sequence of n pulses in the rotating frame can be abbreviated as

$$\hat{U} = [\hat{\mathcal{H}}, \tau_n]\hat{P}_n[\hat{\mathcal{H}}, \tau_{n-1}]\cdots[\hat{\mathcal{H}}, \tau_1]\hat{P}_1 \tag{39}$$

where $[\hat{\mathcal{H}}, \tau_k]$ represents a free development of the spin system under its internal Hamiltonian $\hat{\mathcal{H}}$ during the interval τ_k and $\hat{P}_k$ represents the rotation produced by the pulse about some axis $\mu = x, y, \ldots$, during which the internal Hamiltonian is neglected:

$$[\hat{\mathcal{H}}, \tau_k] = \exp(-\mathrm{i}\hat{\mathcal{H}}\tau_k), \quad \hat{P}_k = \exp(-\mathrm{i}\theta_k \hat{I}_\mu) \tag{40}$$

By convention, the observations of the system are made at the end (left) of the sequence as written. We wish to find a transformation which removes the rf pulses, by analogy to the second rotating frame transformation which removed a steady rf field. This can be done by judicious insertion of identity transformations $\hat{P}_m\hat{P}_m^{-1}$ in such a way as to accumulate all the $\hat{P}$ terms in $\hat{U}$ at the end (left) and to replace the free interpulse developments under the normal Hamiltonian $\hat{\mathcal{H}}$ by a sequence of developments under transformed Hamiltonians $\tilde{\hat{\mathcal{H}}}_k$:

$$\hat{U} = \hat{\mathcal{P}}_n[\tilde{\hat{\mathcal{H}}}_n, \tau_n][\tilde{\hat{\mathcal{H}}}_{n-1}, \tau_{n-1}]\cdots[\tilde{\hat{\mathcal{H}}}_1, \tau_1] \tag{41}$$

where

$$\tilde{\hat{\mathcal{H}}}_k = \hat{\mathcal{P}}_k^{-1}\hat{\mathcal{H}}\hat{\mathcal{P}}_k, \quad \hat{\mathcal{P}}_k = \hat{P}_k\hat{P}_{k-1}\cdots\hat{P}_1 \tag{42}$$

The cyclic property makes $\hat{\mathcal{P}}_n = 1$.

4.2.1 Removal of Inhomogeneous Shifts: Spin Echoes

As an example consider the case of inhomogeneous shifts $\hat{\mathcal{H}}_\delta$, arising from chemical shift as in equation (23), from an inhomogeneous Zeeman field or from coupling to unlike spins. We apply a sequence of equally spaced 180° pulses alternately along the y and $-y$ axes of the rotating frame: since these pulses are inverses of one another,

$$\hat{U} = 1\cdot[\tilde{\hat{\mathcal{H}}}_2, \tau][\tilde{\hat{\mathcal{H}}}_1, \tau], \quad \tilde{\hat{\mathcal{H}}}_2 = \hat{\mathcal{H}}_\delta,$$
$$\tilde{\hat{\mathcal{H}}}_1 = \hat{P}_1\hat{\mathcal{H}}_\delta\hat{P}_1^{-1} = -\hat{\mathcal{H}}_\delta \tag{43}$$

and $\tilde{\hat{\mathcal{H}}}$ switches sign. Note the following.

1. $\tilde{\hat{\mathcal{H}}}^{(0)} = 0$: the system returns to its original quantum state at intervals $t_c = 2\tau$. If a nonzero magnetization was present at $t = 0$, it returns at the end of each cycle in the form of a spin echo.
2. The reversed sign of the $\tilde{\hat{\mathcal{H}}}_1$ in the toggling frame is equivalent to a reversal in the direction of time.
3. While in this example the system was observed just before a pulse, the results are easily seen to be independent of the observing phase.
4. Since $[\tilde{\hat{\mathcal{H}}}_1, \tilde{\hat{\mathcal{H}}}_2] = 0$, all higher orders $\tilde{\hat{\mathcal{H}}}^{(n)0)}$ vanish: the result is correct even if $\delta\tau \gg 1$.

4.2.2 Decoupling of Like Spins: Multiple Pulse Sequences

The last two of these results are special to the inhomogeneous Hamiltonian. A contrary example is provided by the WAHUHA sequence—the one for which the average Hamiltonian theory was developed in the first place.[6] The cycle consists of four unequally spaced 90° pulses along the x, y, $-x$, and $-y$ directions in the rotating frame:

$$\hat{U} = [\hat{\mathcal{H}}, \tau]\hat{P}_{-y}[\hat{\mathcal{H}}, 2\tau]\hat{P}_y[\hat{\mathcal{H}}, \tau]\hat{P}_{-x}[\hat{\mathcal{H}}, 2\tau]\hat{P}_x \tag{44}$$

Equation (42) can be written as

$$\hat{U} = 1\cdot[\hat{\mathcal{H}}_Z, \tau][\hat{\mathcal{H}}_X, 2\tau][\hat{\mathcal{H}}_Z, \tau], [\hat{\mathcal{H}}_Y, 2\tau] \tag{45}$$

where $\hat{\mathcal{H}}_Z$ is the normal rotating frame Hamiltonian, e.g. equation (23) or equation (29), the subscript being a reminder that z component operators $\hat{I}_{zk}$ appear explicitly. The terms $\hat{\mathcal{H}}_x$ and $\hat{\mathcal{H}}_Y$ are the same except that these operators are replaced by $\hat{I}_{xk}$ or $\hat{I}_{yk}$, respectively. Now it is easy to see that the average Hamiltonian for inhomogeneous shifts is

$$\bar{\hat{\mathcal{H}}}^{(0)}_{\delta,k} = \frac{1}{3}\delta_k(\hat{I}_{xk} + \hat{I}_{yk} + \hat{I}_{zk}) \tag{46}$$

and that for like-spin dipolar interactions is

$$\bar{\hat{\mathcal{H}}}^{(0)}_{\mathrm{D},kl} = \frac{\gamma^2\hbar}{r_{kl}^3}\left(\frac{3\cos^2\theta_{kl} - 1}{2}\right)$$
$$\times\{\hat{\mathbf{I}}_k\cdot\hat{\mathbf{I}}_l - (\hat{I}_{xk}\hat{I}_{xl} + \hat{I}_{yk}\hat{I}_{yl} + \hat{I}_{zk}\hat{I}_{zl})\} = 0 \tag{47}$$

These results are the same (modulo a rotation through 45° about the z axis) as for steady rf irradiation at the magic angle mentioned at the beginning of this section. The difference is that in the pulsed case it is possible to make the next order in the dipolar average Hamiltonian vanish. However, to do so, the observation point in the cycle must be properly chosen. If the cycle is phased as:

$$\hat{U} = [\hat{\mathcal{H}}, \tau]\hat{P}_x[\hat{\mathcal{H}}, \tau]\hat{P}_{-y}[\hat{\mathcal{H}}, 2\tau]\hat{P}_y[\hat{\mathcal{H}}, \tau]\hat{P}_{-x}[\hat{\mathcal{H}}, \tau] \tag{48}$$

the development in the toggling frame is

$$\hat{U} = 1\cdot[\hat{\mathcal{H}}_Z, \tau][\hat{\mathcal{H}}_Y, \tau][\hat{\mathcal{H}}_X, 2\tau][\hat{\mathcal{H}}_Y, \tau][\hat{\mathcal{H}}_Z, \tau] \tag{49}$$

The symmetry about the midpoint of the cycle causes the integral in equation (13) to vanish. [In fact, experimental constraints dictate the phasing in equation (50) in any case.]

4.3 Mechanical Rotation

Most of the averaging discussed so far has been over precessional motions in spin space. However, spin Hamiltonians such as that in equation (29) can also be made time-dependent by physical motions in coordinate space. These can be random motions of individual molecules or coherent motions of the entire sample. In the latter category, we consider the bodily rotation of a sample with truncated dipolar interactions, either like or unlike, at frequency ω_r about an axis making an angle χ with $\boldsymbol{B}_0$. By expressing θ in terms of χ and $\omega_r t$, it is easily found that the average of $\hat{\mathcal{H}}'_D$ over the time $t_{cr} = 2\pi/\omega_r$ is

$$\langle \hat{\mathcal{H}}'_D \rangle_{Av} = \frac{1}{2}(3\cos^2\chi - 1)\hat{\mathcal{H}}'_D \qquad (50)$$

which vanishes for 'magic angle' rotation, $\chi = \tan^{-1}\sqrt{2}$. The same is true for other interactions, such as chemical shielding, which transform as second-rank tensors under spatial rotations. Tensors of higher rank possess more than one 'magic angle' (i.e. nodal cone) and cannot be averaged by uniaxial rotation. Second- and fourth-rank tensors can both be averaged by sequential or simultaneous rotations about two axes:[7] this has special relevance to quadrupolar interactions, which to first order in e^2qQ/ω_0 transform as second-rank tensors but in second order have a fourth-rank part.

Magic angle rotation is more effective than one might expect for inhomogeneous interactions[8] such as chemical shielding and quadrupolar coupling, for which the Hamiltonian is a sum of single-spin terms. There the question of commutation of $\hat{\tilde{\mathcal{H}}}(t)$ at different times does not arise, since each spin develops independently and its part of the Hamiltonian is a fixed spin operator multiplied by a time-dependent scalar coefficient. Then the lowest order average Hamiltonian $\hat{\bar{\mathcal{H}}}^{(0)}$ is exact. Important advantage of this is taken in the CP MAS technique[9] for extracting sharp chemical shift spectra from dilute species in solids. (Homogeneous interactions, dipolar in particular, do not have this property: the interaction between spins j and k does not commute with the interaction between k and l at different orientations of the triplet unless the three spins are collinear.)

5 ADDITIONAL TOPICS

5.1 Asynchronism

We have emphasized the importance of the periodicity of effective Hamiltonians $\hat{\tilde{\mathcal{H}}}(t)$ and synchronism of such periods with experimental measurement. These requirements can be relaxed to a degree if the timescale over which $\hat{\tilde{\mathcal{H}}}(t)$ varies is much shorter than the interval t_s between measurements. First consider the use of a truncated (rotating frame) average Hamiltonian to describe a typical FID. In principle, the truncated Hamiltonian describes the system only over full Larmor periods. If t_s is not an integer multiple of t_c, the last fractional Larmor period should be associated with a different average Hamiltonian. Clearly, since several thousand Larmor periods $t_c = 2\pi/\omega_0$ occur between samples, the time-weighted average of these two Hamiltonians is essentially the same as the usual truncated Hamiltonian and the correction can be ignored.

The same considerations apply in evaluating the average Hamiltonian in a second rotating frame or toggling frame, where the cycle time associated with the second average is long compared to laboratory Zeeman periods. Here, however, it is essential that data acquisition be synchronized with the slower cycle time.

A similar argument allows us to deal with averaging due to random molecular motion, at least in the limit of extreme narrowing. The average of the Hamiltonian over a time T converges to a constant value as T becomes long compared with the correlation time τ_c. If t_s is long compared with τ_c, this average can be used. However, the theory provides no guidance to behavior in the transition from slow to fast motion.

5.2 Multiple Time Dependences: Interference

Some two- (and higher) dimensional NMR experiments depend on applying different external perturbations, thereby generating different average Hamiltonians during different epochs of the same experiment. An example is separated local field (SLF) NMR,[10] in which chemical shifts and dipolar couplings are separated into two dimensions.

A different situation arises when two or more different time dependences are present simultaneously. Sometimes these can be turned to practical advantage, as in the recovery of chemical shift anisotropies from MAS experiments by applying pulses synchronous with the sample rotation.[11] Perhaps more commonly they are a nuisance: the addition of MAS to multiple pulse experiments (CRAMPS)[12] in order to remove chemical shift anisotropies inevitably compromises the effectiveness of the multiple pulse train in reducing dipolar broadening. Random molecular motions which are too slow to affect conventional NMR spectra may show themselves when sample spinning with $\omega_r \approx \tau_c{}^{-1}$ or decoupling with $\gamma B_1 \approx \tau_c{}^{-1}$ are present.

5.3 Thermodynamics

A conservative system of many interacting particles, such as an assembly of spins with dipolar interactions as in equation (30), is expected to approach thermodynamic equilibrium with a density matrix

$$\sigma_{eq} = \frac{\exp(-\hat{\mathcal{H}}/k_B T)}{\mathrm{Tr}\{\exp(-\hat{\mathcal{H}}/k_B T)\}} \qquad (51)$$

The essence of the average Hamiltonian concept is the treatment of an explicitly time-dependent system as if it were conservative with Hamiltonian $\hat{\bar{\mathcal{H}}}$. The application of thermodynamics to such systems has been questioned[13] and extensively discussed.[14] Thermodynamics is a practical

science: it does not require that the system remain in the equilibrium expressed in equation (51) forever, but only that it reaches that condition and remains long enough to permit measurements. Therefore one is free to speak of spin temperatures in the laboratory frame despite the existence of (slow) spin–lattice relaxation. Redfield's extension of the spin-temperature concept to the rotating frame,[15] even in the presence of rf irradiation as in equation (18) and equation (19), explained many previously mystifying observations. One can understand these successes by observing that the frequencies contained in the time-dependent parts of $\hat{\tilde{\mathcal{H}}}(t)$, for example phonons or the terms dropped in going from equation (18) to equation (19) or from equation (28) to equation (29), are far from resonant, with eigenvalue differences belonging to the static part of $\hat{\tilde{\mathcal{H}}}(t)$. Of course, a second averaging done with respect to the STR frame or toggling frame is more questionable, but in many cases satisfies the requirements of equation (51) adequately. In any case, the principal applications of the average Hamiltonian are to spectroscopy.

6 REFERENCES

1. U. Haeberlen and J. S. Waugh, *Phys. Rev.*, 1968, **175**, 453; U. Haeberlen, *High Resolution NMR in Solids: Selective Averaging*, Academic Press, New York, 1976; M. Mehring, *High Resolution NMR in Solids*, 2nd edn., Springer, Berlin Heidelberg New York, 1983.
2. J. H. Van Vleck, *Phys. Rev.*, 1948, **74**, 1168.
3. S. Hartmann and E. L. Hahn, *Phys. Rev.*, 1962, **128**, 2042.
4. A. Pines, M. G. Gibby, and J. S. Waugh, *J. Chem. Phys.*, 1973, **59**, 569.
5. M. Lee and W. I. Goldburg, *Phys. Rev.*, 1965, **140**, A1261.
6. J. S. Waugh, L. M. Huber, and U. Haeberlen, *Phys. Rev. Lett.*, 1968, **175**, 453.
7. A. Samoson, E. Lippmaa, and A. Pines, *Mol. Phys.*, 1988, **65**, 1013.
8. A. M. Portis, *Phys. Rev.*, 1953, **91**, 1971.
9. E. O. Stejskal, J. Schaefer, and R. A. McKay, *J. Magn. Reson.*, 1977, **25**, 569.
10. R. K. Hester, J. L. Ackerman, B. L. Neff, and J. S. Waugh, *Phys. Rev. Lett.*, 1976, **36**, 1081.
11. E. Lippmaa, M. Alla, and T. Tuherm, *Proc. XIX Congr. AMPERE*, Heidelberg, 1976, p. 113.
12. L. M. Ryan, R. E. Taylor, A. J. Paff, and B. C. Gerstein, *J. Chem. Phys.*, 1980, **72**, 508.
13. Y. N. Ivanov, B, N. Provotorov, and E. B. Fel'dman, *Zh. Eksp. Teor. Fiz Pis'ma Red.*, 1978, **27**, 164 (*JETP Lett.*, 1978, **3**, 153); E. B. Fel'dman, *Phys. Lett.*, 1984, **104A**, 479.
14. M. M. Maricq, *Adv. Magn. Reson.*, 1990, **14**, 151.
15. A. G. Redfield, *Phys. Rev.*, 1955, **98**, 1787.

Biographical Sketches

John S. Waugh. *b* 1929. A.B., 1949, Dartmouth College, Ph.D., 1953, California Institute of Technology. Faculty of Chemistry, MIT, Instructor, A. A. Noyes Professor, 1953–89; Institute Professor at MIT, 1989–present. Research specialty: NMR, mostly in solids.

Cross Polarization in Rotating Solids: Spin-$\frac{1}{2}$ Nuclei

Frank Engelke

Ames Laboratory, IA, USA

1	Introduction	1
2	Magnetization Transfer in the Radiofrequency Rotating Frame	1
3	Cross Polarization and Dipolar Coupling	2
4	Dipolar Couplings in Rotating Solids	3
5	Cross Polarization in Rotating Solids[28]	4
6	Modified CP Experiments and MAS	5
7	Related Articles	6
8	References	6

1 INTRODUCTION

The development of cross polarization (CP) techniques, allowing the transfer of magnetization from a system of spins I with high abundance (e.g. ^{1}H, ^{19}F, and ^{31}P) to a system of spins S with low natural abundance (e.g. ^{13}C and ^{15}N) was a major step to *enhance the sensitivity* of these rare nuclei in solid state NMR.[1–3] As the sensitivity thresholds for rare nuclear spins have been lowered, NMR has become available for extensive studies of solid materials.

A second problem peculiar to solid state NMR originates from the fact that, in solids, molecules or molecular groups are generally not subject to fast isotropic motions as they are in liquids. Consequently, NMR applied to solid samples, e.g. polycrystalline or amorphous materials, is characterized by spatially anisotropic spin interactions. The dominating interactions for spin-$\frac{1}{2}$ nuclei in solids are the direct dipole–dipole coupling between spins, and the magnetic shielding due to the electronic environment of a given nucleus, causing the chemical shift of resonance lines. The resulting spectra of polycrystalline or amorphous samples typically reveal broad lineshapes reflecting these anisotropic interactions. It was a major technical goal in NMR to invent techniques which play, at least in part, a role analogous to that of thermal motion in liquids, i.e. to average out or reduce the anisotropic contribution of the spin interactions. This averaging can take place either in spin space or in ordinary coordinate space,[4,5] depending on the interaction. To remove homonuclear dipolar couplings, averaging in spin space requires the application of multiple pulse sequences (see ***CRAMPS***). In order to eliminate broadening of resonance lines of rare S spins due to heteronuclear dipolar interactions with abundant I spins, rf irradiation near the Larmor frequency of I spins can be applied (heteronuclear high power decoupling[3]). The removal of line broadening originating from the chemical shift anisotropy (CSA) can be accomplished by averaging performed in coordinate space, i.e. by rotating the sample around a spatially fixed axis inclined by a specific angle θ_m, called the 'magic angle', relative to the direction of the external field $\boldsymbol{B}_0$. Magic angle spinning (MAS) and some descendent techniques are nowadays well established and routinely included in high-resolution solid state NMR studies, allowing the identification of chemical environments by the isotropic chemical shift.

Fast sample rotation also affects homo- and heteronuclear dipole–dipole couplings.[6,7] Because these interactions provide the physical basis on which polarization transfer between different spin systems occurs, they are here considered first in some detail (see Sections 2 and 3). Following these considerations, the influence of sample spinning on the CP process will be discussed (Sections 4 and 5). Because sample spinning may impose dramatic effects on the CP process, effects which are undesirable from an experimental point of view, the possibilities of circumventing some of these difficulties are reviewed in Section 6. Since the majority of applications are based on the spin lock, cross polarization technique, proposed by Hartmann and Hahn,[1] and Pines, Gibby, and Waugh,[2] the present article is concerned with this method.[28] For details of other techniques, such as adiabatic demagnetization in the rotating frame[1,3] and the nuclear solid effect,[8,12] the reader is referred to the literature (see also ***Cross Polarization in Solids***).

2 MAGNETIZATION TRANSFER IN THE RADIOFREQUENCY ROTATING FRAME

Figure 1 shows the basic pulse sequence used in CP experiments.[2,3] Initially, a 90° ($\pi/2$) pulse is applied at the resonance frequency ω_{0I} of the abundant I spins with magnetogyric ratio γ_I, creating transverse magnetization. In the subsequent time interval, denoted by τ_{CP}, the rf field (strength in angular frequency units $\Omega_{1I} = \gamma_I B_{1I}$) is applied parallel to the transverse I-spin magnetization, thus locking the magnetization in the direction of the $\boldsymbol{B}_{1I}$ rf field. Simultaneously, rf irradiation (strength $\Omega_{1S} = \gamma_S B_{1S}$) occurs at the resonance frequency ω_{0S} for the rare S spins with magnetogyric ratio γ_S, the initial transverse magnetization of which is zero. If the Hartmann–Hahn condition[1]

$$\gamma_I B_{1I} = \gamma_S B_{1S} \tag{1}$$

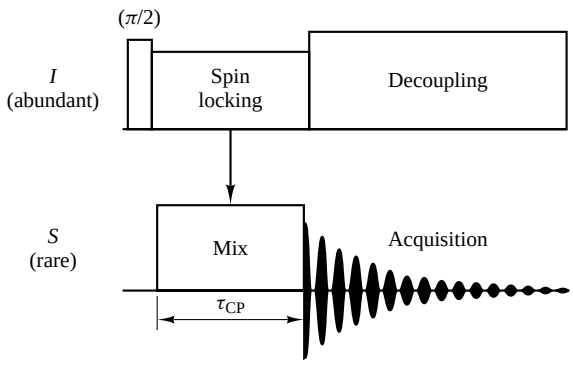

Figure 1 Pulse sequence for standard cross polarization. Radiofrequency irradiation occurs at the Larmor frequencies ω_{0I} and ω_{0S} for I and S spins simultaneously

for the rf field strengths is satisfied, transfer of magnetization from the I-spin system to the S-spin system can take place during the cross polarization mixing time τ_{CP}, resulting in a build-up of transverse S-spin magnetization, which can be observed after switching off the rf field in the S-spin channel. During this acquisition period, the rf irradiation in the I-spin channel may continue to provide decoupling of the $I-S$ dipolar interaction.[3]

The elementary process for cross polarization involves transitions of dipolar-coupled I and S spins, frequently called flip-flop transitions or mutual spin flips, because one spin is changing its state from a higher to a lower energy, while simultaneously a neighboring spin moves from a state with lower to a state with higher energy. If a solid, containing systems of spins I and S with different magnetogyric ratios γ_I and γ_S, is subjected only to the external magnetic field $\boldsymbol{B}_0$, then the energy levels for both systems are given by the Zeeman interaction in the laboratory frame. The splitting of energy levels (in angular frequency units) is different for I and S spins, and is equal to their respective Larmor frequencies ω_{0I} and ω_{0S} [Figure 2(a)]. Under these circumstances flip-flop transitions involving $I-S$ spin pairs possess a vanishingly small probability rate, because the (virtual) photon which would be emitted during an I-spin transition could not be absorbed by an S-spin transition between Zeeman energy levels. This situation changes if rf fields are present for both spin systems [Figure 2(b)]. The total Hamiltonian of the two spin systems in the laboratory frame of reference becomes oscillatory time dependent due to the presence of rf fields. It is convenient to choose a frame of reference which is rotating with the applied rf fields (doubly rotating frame), generally known in quantum mechanics as the transformation from the Heisenberg operator representation to the interaction representation.[9] In this frame the time dependence originating from the rf fields (frequencies ω_k, $k = I$ or S) vanishes[10] for $\omega_k = \omega_{0k}$ (on-resonance). Identifying the new z axis with the direction of the rf field vectors $\boldsymbol{B}_{1I}$ and $\boldsymbol{B}_{1S}$, the total spin Hamiltonian in this tilted rotating frame (TRF)[3,13] with spin components $\hat{I}_{zk}$, $\hat{I}_{xk}$ for the spins I_k, $\hat{I}_z = \Sigma_k \hat{I}_{zk}$ and the spin components $\hat{S}_z$, $\hat{S}_x$ for a single S spin is:

$$\hat{\mathcal{H}} = \hat{\mathcal{H}}_I + \hat{\mathcal{H}}_S + \hat{\mathcal{H}}_{IS}$$

$$\hat{\mathcal{H}}_I = -\Omega_{1I}\hat{I}_z + \hat{\mathcal{H}}_{II} \quad \hat{\mathcal{H}}_S = -\Omega_{1S}\hat{S}_z$$
$$\hat{\mathcal{H}}_{IS} = 2\sum_k D_k \hat{I}_{xk}\hat{S}_x \qquad (2)$$

where it has been assumed that both rf fields are in resonance with the I and S spins, respectively. $\hat{\mathcal{H}}_I$ denotes the Hamiltonian for the I-spin system, whereas $\hat{\mathcal{H}}_{II}$ and $\hat{\mathcal{H}}_{IS}$ are the $I-I$ homonuclear and $I-S$ heteronuclear dipolar Hamiltonians. The homonuclear dipolar couplings among S spins can be neglected, due to the low abundance of S spins. D_k denotes the dipolar coupling strength between spin S and spin I_k. The above Hamiltonian includes the two terms $\Omega_{1I}\hat{I}_z$ and $\Omega_{1S}\hat{S}_z$, which represent the Zeeman interaction in the TRF for I and S spins, respectively. The corresponding splitting of Zeeman energy levels in the TRF, therefore, is given by Ω_{1I} and Ω_{1S}, which are experimental parameters. Satisfying the Hartmann–Hahn matching condition $\Omega_{1I} = \Omega_{1S}$ [equation (1)] provides equal TRF–Zeeman splittings for both spin systems, such that an energy transfer can take place between I and S spins [Figure 2(b)].

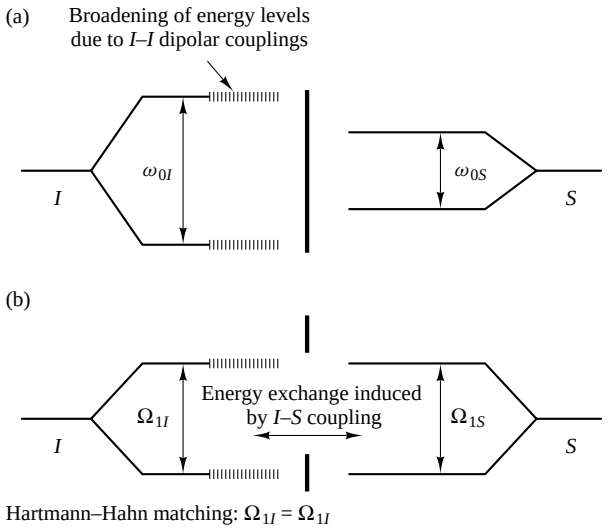

Figure 2 Energy levels of I and S spins (a) in the laboratory frame and (b) in the rf rotating frame

3 CROSS POLARIZATION AND DIPOLAR COUPLING

It is instructive to consider first a simple system, consisting of an isolated dipolar-coupled $I-S$ spin pair, providing some basic concepts necessary to show the impact which MAS has on cross polarization. The energy levels of the spin system, i.e. the possible total energies of both spins, are shown in Figure 3(a). $|++\rangle$, $|+-\rangle$, etc., denote product TRF–Zeeman spin-state vectors $|m_I,m_S\rangle$ (with magnetic quantum numbers $m_{I,S} = +\frac{1}{2}$ for the z-spin component parallel, and $m_{I,S} = -\frac{1}{2}$ for the z-spin component antiparallel to the rotating rf field). If dipolar couplings are not present and $\Delta\Omega = \Omega_{1I} - \Omega_{1S} = 0$, then Zeeman state vectors are eigenvectors of the TRF Hamiltonian. The two states with antiparallel spin orientations are degenerate (i.e. having the same energy). $\Delta\Omega \neq 0$ removes this degeneracy, the eigenstates are now $|2\rangle$ and $|3\rangle$. For small $\Delta\Omega$ the magnetic quantum numbers m_I and m_S are still 'good' quantum numbers. The presence of $\hat{\mathcal{H}}_{IS}$ leads to transitions between Zeeman states or, in general, between $|2\rangle$ and $|3\rangle$, and $|1\rangle$ and $|4\rangle$. In Figure 3(a) the probabilities of these transitions are labeled W_0 and W_2. The same holds for $\Delta\Omega = 0$ for the Zeeman states $|++\rangle$,$|+-\rangle$, $|-+\rangle$, and $|--\rangle$. The energy levels in the TRF, including the dipolar Hamiltonian $\hat{\mathcal{H}}_{IS}$ and $\Delta\Omega$ being non-zero, can be obtained from the Hamiltonian $\hat{\mathcal{H}}$ in equation (2) (with $\hat{\mathcal{H}}_{II} = 0$) by using a matrix representation with the Zeeman state vectors, and solving the eigenvalue problem for $\hat{\mathcal{H}}$. The transition probabilities W_0 and W_2 are then given as the square modulus of the corresponding matrix elements of the time evolution operator[9] $\hat{U}(t) = \exp(-i\hat{\mathcal{H}}t)$. If the sum of the two rf fields, $\Sigma = \Omega_{1I} + \Omega_{1S}$, is large compared to their difference $\Delta\Omega = \Omega_{1I} - \Omega_{1S}$, and to the dipolar coupling strength D between I and

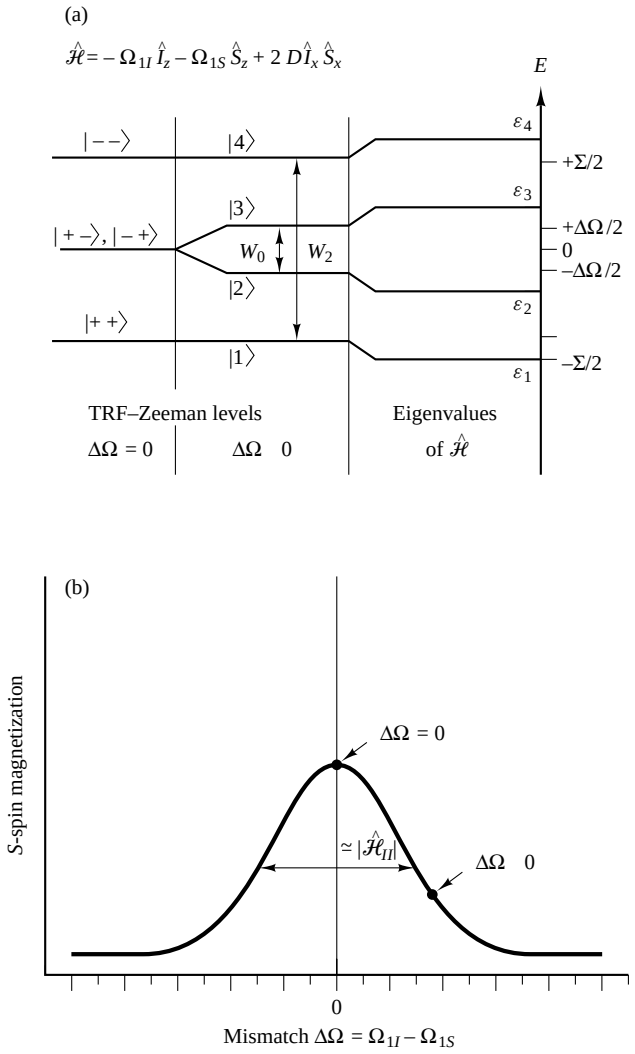

Figure 3 (a) Energy levels of an $I-S$ two-spin system in the tilted rotating frame for matching ($\delta\Omega = 0$) and mismatching ($\delta\Omega \neq 0$) the Hartmann–Hahn condition; (b) Hartmann–Hahn matching curve for a nonrotating solid

S spins, and if, in addition, the quantity $\Delta\Omega$ (referred to in the following as Hartmann–Hahn mismatch) is small compared to D, then the flip-flop transition probability W_0 dominates. W_0 depends on the coupling strength D, and is much larger than W_2:

$$W_0 \propto \frac{D^2}{D^2 + \Delta\Omega^2} \approx 1, \quad W_2 \propto \frac{D^2}{D^2 + \Sigma^2} \ll 1 \qquad (3)$$

for D, $\Delta\Omega \ll \Sigma$, and $\Delta\Omega \ll D$. In general, $I-I$ dipolar couplings are present in the solid, giving rise to a broadening of the I-spin levels.[11,12] With increasing mismatch $\Delta\Omega$, the two energy levels for the states $|\,2\rangle$ and $|\,3\rangle$ of the $I-S$ spin system shift relative to each other [Figure 3(a)], and for $\Delta\Omega > D$ [equation (3)] and $\delta\Omega$ larger than the $I-I$ dipole couplings, the transition probability W_0 decreases significantly.

An entirely isolated $I-S$ spin system would periodically exchange magnetization between I and S spin. The presence of many spins interacting with each other introduces the statistical, or thermodynamic, aspect[3,13,14] into cross polarization. Under standard CP conditions (Figure 1) the initial I-spin magnetization is transferred irreversibly to the S-spin system. However, the behavior of the elementary flip-flop transition allows one to understand, at least qualitatively, the efficiency of CP under mismatch conditions ($|\,\Delta\Omega\,| \neq 0$), as illustrated in Figure 3(b). The polarization transfer is most efficient for $\Delta\Omega = 0$. Increasing mismatch leads to a gradual decrease of S-spin magnetization as long as the levels of the spin states $|\,2\rangle$ and $|\,3\rangle$ still overlap, originating from their finite width due to $I-I$ dipolar couplings. CP becomes completely inefficient if the mismatch becomes larger than the $I-I$ dipolar coupling strengths. The plot of S-spin magnetization obtained by CP versus mismatch $\Delta\Omega$ is called the Hartmann–Hahn or CP-matching curve, and is drawn schematically in Figure 3(b). As will be shown below, the CP-matching curve, as an indicator of efficiency for $I-S$ magnetization transfer, is of utmost importance when combining CP and MAS.

The result that magnetization transfer conserving the total spin energy occurs predominantly for small mismatch $\Delta\Omega$ can be expressed by the selection rules

$$\Delta m_I + \Delta m_S = 0, \quad |\Delta\Omega| \leq D_{IS}, D_{II} \qquad (4)$$

i.e. CP takes place via flip-flop transitions (total change of the magnetic quantum numbers m_I and m_S is zero). The second condition in equation (4) includes the broadening of TRF–Zeeman levels, leading to a CP-matching curve of finite width.

4 DIPOLAR COUPLINGS IN ROTATING SOLIDS

The dipolar coupling strengths D_{jk} between two spins j and k depend on their mutual distance r_{jk} and on the orientational angle ϑ_{jk} of the internuclear vector $\boldsymbol{r}_{jk}$ relative to the static field $\boldsymbol{B}_0$ (see also ***Internal Spin Interactions and Rotations in Solids***):

$$D_{jk} = \frac{\mu_0 \gamma_j \gamma_k \hbar^2}{4\pi r_{jk}^3} \frac{1}{2}(3\cos^2\vartheta_{jk} - 1) \qquad (5)$$

Spinning of the sample around an axis tilted by the angle θ_m relative to $\boldsymbol{B}_0$ leads to a periodic time dependence of the angle ϑ_{jk} with the frequency ω_r of rotation as shown in Figure 4. The time-dependent term $\cos\vartheta_{jk}(t)$ can be expressed as a function of the angles θ_m, θ_{jk} and $\omega_r t$, and the angle-dependent part of D_{jk} then reads

$$\begin{aligned}(3\cos^2\vartheta_{jk}(t) - 1) = {} & \tfrac{1}{2}(3\cos^2\theta_m - 1)(3\cos^2\theta_{jk} - 1) \\ & + \tfrac{3}{2}\sin 2\theta_m \sin 2\theta_{jk} \cos(\omega_r t) \\ & + \tfrac{3}{2}\sin^2\theta_m \sin^2\theta_{jk} \cos(2\omega_r t) \end{aligned} \qquad (6)$$

Decomposing the time-dependent cosine terms into complex exponentials, the Fourier expansion (with Fourier coefficients $d_{jk}^{(n)}$) is obtained:

$$D_{jk}(t) = \sum_{n=-2}^{+2} d_{jk}^{(n)}[\exp(in\omega_r t)] \qquad (7)$$

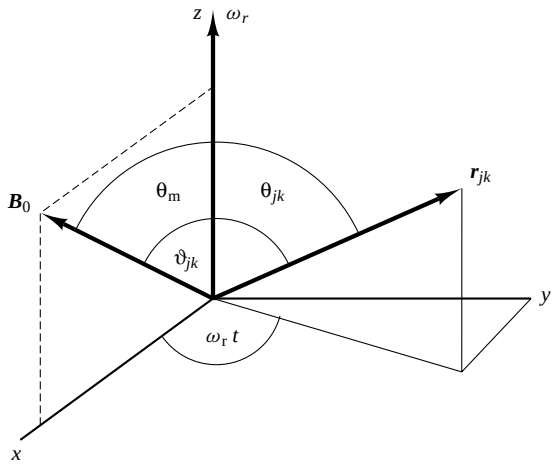

Figure 4 Coordinate frame of reference for a sample spinning around the axis ω_r, and the vector $\boldsymbol{r}_{jk}$ rotating with a polar angle $\omega_r t$

The first term on the right-hand side of equation (6) is time independent [Fourier coefficient $d_{jk}^{(0)}$ in equation (7)], and becomes equal to zero for $\theta_m = 54.7°$—this is called the 'magic angle'. The other two terms in equation (6) show that sample rotation results in a modulation of the dipolar coupling strengths D_{jk} with spinning frequencies ω_r and $2\omega_r$ and an average value equal to zero. Therefore, under sample rotation the dipolar Hamiltonians $\hat{\mathcal{H}}_{II}$ and $\hat{\mathcal{H}}_{IS}$ become periodically time-dependent with the period $2\pi/\omega_r$ of sample rotation.

5 CROSS POLARIZATION IN ROTATING SOLIDS[28]

As illustrated in Section 3, the CP rate, as a function of the transition probabilities of $I-S$ flip-flop transitions, and the form of the CP-matching curve depend on the $I-S$ and $I-I$ dipolar coupling strengths. In order to proceed with the quantum mechanical model discussed above, the resulting time periodicity of dipolar Hamiltonians originating from MAS has to be included. For an isolated $I-S$ spin system in the presence of sample spinning the problem can be solved, for example, using the Floquet formalism (see ***Floquet Theory***).[15,16] Within this theory, originally proposed as a general method for solving linear differential equations with periodic coefficients, an average Hamiltonian, called the Floquet Hamiltonian, can be derived by using the Fourier decomposition of the periodic time-dependent dipolar coupling strengths [equation (7)]. For very fast sample spinning (i.e. when the MAS frequency ω_r is comparable to or larger than the dipolar coupling coefficients $d_{jk}^{(n)}$, $n = \pm1$ or ±2), the flip-flop transitions responsible for $I-S$ magnetization transfer are subject to conditions which are more rigorous than the selection rules given in equation (4), because they now include the MAS frequency ω_r:[16]

$$\Delta m_I + \Delta m_S = 0, \quad |\Delta\Omega + n\omega_r| \leq \tfrac{1}{2} d_{jk}^{(n)}, \quad n = \pm1, \pm2 \quad (8)$$

which means, that CP is possible for mismatch values $\Delta\Omega = \pm\omega_r$ and $\pm2\omega_r$, and becomes small for $n = 0$ because of the disappearance of the zero-order Fourier coefficient $d_{jk}^{(0)}$ at the magic angle [see equations (5)–(7)]. From the conditions given in equation (8), it follows that the CP-matching curve, being rather broad and featureless for a nonrotating solid [Figure 3(b)], splits into sidebands separated by the MAS frequency ω_r, as shown in Figure 5. For very fast spinning, maximum CP does not occur at $\Delta\Omega = 0$, as in the static case, but takes place at $\Delta\Omega$ close to the first and second-order sidebands. The widths of these sidebands depend on the dipolar coupling parameters $d_{jk}^{(n)}$ ($n \neq 0$), and on ω_r as increasing spinning rates provide a more complete averaging of dipolar couplings. The CP-matching curves shown in Figure 5 are calculated by means of a statistical theory,[17] taking into account that: (1) in a solid, usually many I spins interact with each other; and (2) each S spin may be coupled to more than one I spin. The dipolar couplings are introduced as parameters, which represent average values for the I and S spin systems (so-called 'second moments'[12]), while the spin dynamics are described by statistical spin-correlation functions.

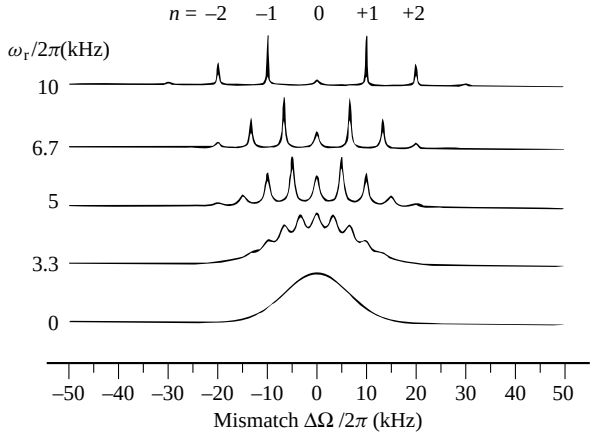

Figure 5 CP-matching curves for various spinning rates for a solid with relatively weak dipolar couplings, e.g. hexamethylbenzene

Experimental evidence for the break-up of the CP-matching curve into a sideband pattern was first provided by Stejskal et al.[18] for adamantane. Many other examples of CP-matching behavior under MAS have been found experimentally.[19–22] Figure 6 shows the $^1H-^{13}C$ CP matching curve for aromatic carbon in polycrystalline hexamethylbenzene (HMB) obtained at a spinning rate of $\omega_r/2\pi = 5$ kHz. In this experiment the

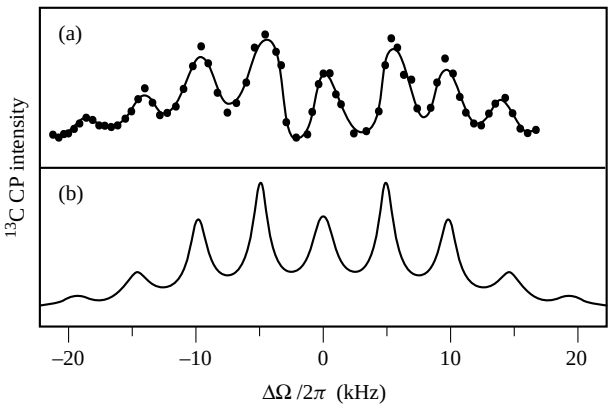

Figure 6 CP-matching curves for aromatic ^{13}C nuclei in hexamethylbenzene: (a) experimental curve obtained at $\omega_r/2\pi = 5$ kHz; (b) theoretical curve

proton rf field was fixed at $\Omega_{1I}/2\pi$ = 40 kHz and the ^{13}C rf field was varied in the range $\Omega_{1S}/2\pi$ = 18 to 57 kHz. Each experimental data point in Figure 6 represents an intensity value of the ^{13}C NMR line resonating at ca. 130 ppm (isotropic chemical shift relative to tetramethylsilane), attributed to aromatic carbon nuclei in HMB. The theoretical curve was obtained[17] using values for the $I-I$ and $I-S$ dipolar coupling parameters determined from the internuclear distances and the crystal structure of HMB.

The appearance of sharp CP-matching sidebands at high spinning rates causes various experimental difficulties. First, the maximum of S-spin magnetization is not obtained at $\Delta\Omega$ = 0, as for the static case. The mismatch has to be adjusted to one of the sidebands, the location of which depends on ω_r. Second, the sidebands become narrow at high MAS rates, requiring highly stable rf amplitudes Ω_{1I} and Ω_{1S}, and accurate spinning rates which have to remain constant over extended periods of time. Otherwise, slight deviations lead to dramatic losses of the CP enhancement for S-spin magnetization. Furthermore, the spectrum of the S spins may possess a variety of resonance lines with different resonance frequencies; for example, ^{13}C NMR spectra of organic solids very often reveal resonance frequencies over a range of 200 ppm, which leads to resonance offsets resulting in different mismatch values $\Delta\Omega$ for each resonance line. This means that some S spins are properly cross polarized, while other S spins with different $\Delta\Omega$ values due to resonance offsets are only weakly polarized. Any of the latter cases results in distortions of the relative intensities in CP MAS spectra.

6 MODIFIED CP EXPERIMENTS AND MAS

Because of the usefulness of the CP MAS technique, much effort has been made in recent years to develop methods which circumvent the experimental disadvantage originating from the Hartmann–Hahn condition under MAS. These methods can be grouped as follows:

1. Mechanical techniques, for example, off-magic angle spinning[20] and stop-and-go magic angle spinning.[21]
2. Techniques based on modifications of the standard CP rf-pulse scheme (Figure 1), including rf phase or amplitude modulation,[16,23,24] or rf amplitude variation.[25]
3. Alternative ways of magnetization transfer, for example, via the nuclear solid effect.[8,12] or dynamic nuclear polarization.[12,26]

The following brief discussion will focus on methods (1) and (2).

Off-magic angle spinning exploits the fact that the zero-order coefficients $d_{jk}^{(0)}$ of the Fourier expansion [equation (7)] become unequal to zero for spinning angles θ different from the magic angle θ_m, which should lead to an increase in the CP-matching centerband (at high spinning rates) and to a broadening of the center- and sidebands. Sardashti and Maciel[20] employed a CP technique, using the angle $\theta = 90^\circ$ during the CP period, and switching to the magic angle before starting acquisition of the NMR signal. According to equation (6), only centerbands and second-order sidebands appear in the CP-matching curve. A broadening of the center- and sidebands originating from the less severe averaging of $I-I$ dipolar couplings for $\theta \neq \theta_m$ is also observed in this experiment.

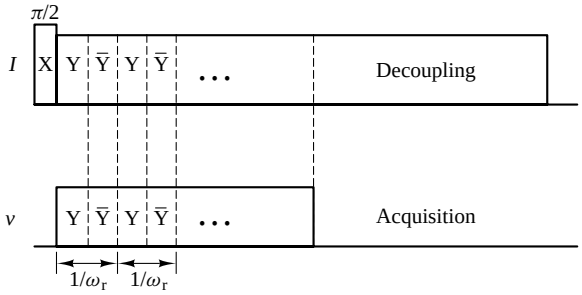

Figure 7 CP pulse sequence with simultaneous phase inversion

Stop-and-go sample spinning, proposed by Zeigler et al.,[21] is even more straightforward in its attempt to avoid CP-matching sidebands. During the CP period the sample is not spinning, or it is slowed down, while during detection MAS is turned on. Both techniques require advanced mechanical capabilities for the spinner system, either being able quickly to switch the spinner axis or to turn the spinning on and off during the CP experiment.

A general way to improve the magnetization transfer under MAS conditions is based on modifications of the CP rf-irradiation scheme.[16,23–25] One possibility[25] consists of applying stepwise rf-amplitude variations of the spin lock field [variable amplitude CP (VACP)], thus creating a whole series of slightly different Hartmann–Hahn matching conditions during one CP period. In this way an averaging over rf-amplitude mismatches is achieved, resulting in a remarkable smoothing of CP-matching curves. Another strategy, which may give an idea of the general philosophy involved, introduces an additional time dependence into the CP Hamiltonian [equation (2)] by periodically inverting the phases of the rf fields in the I and S spin channels simultaneously,[16,23,24] synchronized with sample spinning (Figure 7). The time dependence of the TRF Hamiltonian then originates from: (1) the MAS modulation of the dipolar interactions, and (2) the modulation of the rf fields. One effect of this pulse sequence, which is important from a practical point of view, consists of averaging or compensating for $\Delta\Omega$ deviations due to rf inhomogeneities.[24,27] The pulse sequence of Figure 7 has been shown to provide a significant broadening of the CP-matching curve.[16,24] Improvements have been proposed[16] leading to a whole new class of general amplitude-modulation CP (AMCP) schemes based on the study of detailed time dependences of the TRF Hamiltonian, and allowing the design of pulse sequences to restore CP-matching conditions under MAS, which are similar to those in nonrotating solids.

7 RELATED ARTICLES

CRAMPS; Cross Polarization in Solids; Dynamic Angle Spinning; Internal Spin Interactions and Rotations in Solids; Floquet Theory; Line Narrowing Methods in Solids; Magic Angle Spinning; Rotating Solids; Spectral Editing Techniques: Hydrocarbon Solids; Spin Diffusion in Solids; Variable Angle Sample Spinning

8 REFERENCES

1. S. R. Hartmann and E. L. Hahn, *Phys. Rev.*, 1962, **128**, 2042.
2. A. Pines, M. G. Gibby, and J. S. Waugh, *J. Chem. Phys.*, 1972, **56**, 1176; 1973, **59**, 569.
3. M. Mehring, *Principles of High Resolution NMR in Solids*, 2nd edn., Springer, Berlin, 1983, Chaps 2 and 4.
4. U. Haeberlen, *High Resolution NMR in Solids—Selective Averaging*, *Advances in Magnetic Resonance*, Suppl. 1, Academic, New York, 1976, Chap. IV.
5. B. C. Gerstein and C. R. Dybowski, *Transient Techniques in NMR of Solids—An Introduction to Theory and Practice*, Academic, Orlando, FL, 1985, Chaps 5 and 6.
6. E. R. Andrew, A. Bradbury, and R. G. Eades, *Nature*, 1958, **182**, 223; 1959, **183**, 1802.
7. I. J. Lowe, *Phys. Rev. Lett.*, 1959, **2**, 285.
8. R. A. Wind and C. S. Yannoni, *J. Magn. Reson.*, 1986, **68**, 373; 1987, **72**, 108.
9. M. Weissbluth, *Atoms and Molecules*, Academic, New York, 1978, Chap 9.3; S. Gasiorowicz, *Quantum Physics*, Wiley, Chichester, 1974, Chap. 14
10. This transformation can be achieved for circularly polarized rf fields only. However, a linearly polarized rf field (frequency ω_k, $k = I, S$) can be decomposed into two circular polarized fields, rotating with angular frequencies $\omega_{0k} - \omega_k$ and $\omega_{0k} + \omega_k$ in the rotating frame. If the resonance offset $\omega_{0k} - \omega_k$ is small compared with $\omega_{0k} + \omega_k$, and if the rf field amplitudes Ω_{1k} are small compared with ω_{0k}, only the circular polarized component rotating with ω_{0k}—ω_k needs to be considered; the other one has negligible influence (Bloch–Siegert effect, see Shirley,[15] Section III).
11. A. Das and A. C. Melissinos, *Quantum Mechanics*, Gordon & Breach, New York, 1986, Chap. 5
12. A. Abragam, *The Principles of Nuclear Magnetism*, Clarendon, Oxford, 1961, Chaps IV and IX.
13. D. E. Demco, J. Tegenfeldt, and J. S. Waugh, *Phys. Rev. B*, 1975, **11**, 4133.
14. D. Suter and R. R. Ernst, *Phys. Rev. B*, 1985, **32**, 5608; M. H. Levitt, D. Suter, and R. R. Ernst, *J. Chem. Phys.*, 1986, **84**, 4243.
15. J. H. Shirley, *Phys. Rev. B*, 1965, **138**, 979.
16. S. Hediger, B. H. Meier, and R. R. Ernst, *Chem. Phys. Lett.*, 1993, **213**, 627.
17. F. Engelke, T. Kind, D. Michel, M. Pruski, and B. C. Gerstein, *J. Magn. Reson.*, 1991, **95**, 286.
18. E. O. Stejskal, J. Schaefer, and J. S. Waugh, *J. Magn. Reson.*, 1977, **28**, 105.
19. E. O. Stejskal, J. Schaefer, and R. A. McKay, *J. Magn. Reson.*, 1984, **57**, 471; J. Schaefer, E. O. Stejskal, J. R. Garbow, and R. A. McKay, *J. Magn. Reson.*, 1984, **59**, 150.
20. M. Sardashti and G. E. Maciel, *J. Magn. Reson.*, 1987, **72**, 467; R. A. Wind, S. F. Dec, H. Lock, and G. E. Maciel, *J. Magn. Reson.*, 1988, **79**, 136.
21. R. C. Zeigler, R. A. Wind, and G. E. Maciel, *J. Magn. Reson.*, 1988, **79**, 299.
22. M. Pruski, L. DelaRosa, and B. C. Gerstein, *Energy Fuels*, 1990, **4**, 160.
23. T. M. Barbara and E. H. Williams, *J. Magn. Reson.*, 1992, **99**, 439.
24. X. Wu and K. W. Zilm, *J. Magn. Reson., Ser. A*, 1993, **104**, 154.
25. O. B. Peersen, X. Wu, I. Kustanovich, and S. O. Smith, *J. Magn. Reson., Ser. A*, 1993, **104**, 334.
26. R. A. Wind, F. E. Anthonio, M. J. Duijvestijn, J. Schmidt, J. Trommel, and G. M. C. DeVette, *J. Magn. Reson.*, 1983, **52**, 424.
27. X. Wu and K. W. Zilm, *J. Magn. Reson.*, 1991, **93**, 265.
28. D. Michel and F. Engelke, in *NMR Basic Principles and Progress*, Springer, Berlin, 1994, vol. 32, pp. 69–125.

Biographical Sketches

Frank Engelke. *b* 1955. M.Sc. (physics), Ph.D. (supervisor Dieter Michel), habilitation, University of Leipzig, Germany. Postdoctoral work at Saarbruecken University, Germany (with Jorn Petersson), and since 1992 at Ames Laboratory, USA (with Bernie Gerstein, Marek Pruski and Terry King). Approx. 20 publications. Current research specialties: solid state NMR in rotating solids and solid state NMR applications on metal surfaces.

Cross Polarization in Solids

Douglas P. Burum

Bruker Instruments, Inc., Billerica, MA, USA

1	Introduction	1
2	Strategies for Achieving High-Resolution NMR in Solids	1
3	Theory of Cross Polarization in Solids	2
4	Cross Polarization at High Spinning Speeds	4
5	Spectral Editing and Other Tricks Using Cross Polarization	7
6	Conclusions	7
7	Related Articles	8
8	References	8

1 INTRODUCTION

A number of techniques exist for producing well resolved NMR spectra of solid samples. Some, including very rapid rotation about the 'magic' angle[1] of 54.7° and CRAMPS (see ***CRAMPS***) multiple pulse irradiation, attempt to produce well resolved spectra of abundant nuclei such as ^{1}H or ^{19}F. However, much greater success has been achieved in obtaining high-resolution solid state spectra of 'rare' NMR isotopes such as ^{13}C and ^{15}N. Typically, three techniques are combined: cross polarization[2] to increase signal strength and measurement repetition rate, heteronuclear decoupling[3] to remove line broadening due to surrounding abundant spins, and magic angle spinning[4] to eliminate chemical shift anisotropy (CSA) effects.

This article deals primarily with cross polarization in solids. Heteronuclear decoupling and magic angle spinning are briefly mentioned, but more detailed discussions of these techniques are presented in other articles (see ***Magic Angle Spinning*** and ***Rotating Solids***).

2 STRATEGIES FOR ACHIEVING HIGH-RESOLUTION NMR IN SOLIDS

It is helpful to begin by considering the various interactions that occur in the solid state.[5] In order of their relative magnitudes, the interactions may be summarized as follows:

1. *Quadrupolar* This is an interaction involving electric field gradients that occurs only for nuclei of spin quantum number greater than $\frac{1}{2}$. Since most important NMR nuclei, including ^{1}H, have spin-$\frac{1}{2}$, they are not subject to quadrupolar effects.
2. *Dipolar* This is the effect that the nuclear dipole field generated by each nuclear spin has on its neighboring spins, and it is the dominant interaction for abundant nuclei such as ^{1}H spins in solids. Dipolar interactions are often referred to as either 'homonuclear', for interaction between nuclei of the same species (e.g. ^{1}H–^{1}H), or heteronuclear, for interaction between nuclei of different species (e.g. ^{1}H–^{13}C). Due to rapid, isotropic molecular motion, dipolar interactions are averaged to zero in liquids, but do contribute to the longitudinal relaxation parameter T_1.
3. *Chemical Shift Anisotropy (CSA)* The magnitude of the diamagnetic effect that surrounding electrons have on the nucleus usually depends on molecular orientation. The average, or isotropic, shift is observable in both liquids and solids. In addition, resonance lines for most solids exhibit an additional shift based on molecular orientation. For single crystals this is manifested as a dependence of the resonance frequency on orientation. For a powder sample, all orientations are represented simultaneously and the result is a broad CSA 'powder pattern'. These powder patterns often overlap and cause loss of resolution.
4. *Isotropic Chemical Shift* In a liquid, rapid molecular reorientation allows only the average, or isotropic chemical shift to be observed. In solids, the same result is often achieved by rapid rotation of the sample about an axis tilted away from the magnetic field by 54.7°, often referred to as the 'magic' angle. Magic angle spinning is discussed in more detail in other articles (see ***Magic Angle Spinning*** and ***Rotating Solids***).
5. *J Coupling* This is an indirect coupling of nuclei to each other, mediated by shared electrons. As such, it is a 'through-bond' coupling, and is of great importance in liquids. However, it is too weak to be observable in most spectra of solids.

Elimination of the direct dipolar interaction between nuclei is clearly the first step in achieving high-resolution NMR in solids. The dipolar interaction between a given pair of spin-$\frac{1}{2}$ nuclei, as expressed by the dipolar Hamiltonian[6] $\hat{\mathcal{H}}_{\mathrm{D}}$, can be written as

$$\hat{\mathcal{H}}_D \propto \left(\frac{1}{r^3}\right)(1 - 3\ \cos^2\theta)\ \text{spin part} \qquad (1)$$

where r is the internuclear distance, and θ is the angle that the internuclear vector makes with the magnetic field. The 'spin part' varies, depending on whether the two nuclei are of the same species (homonuclear) or different species (heteronuclear). For example, the spin part for two coupled ^{1}H spins is given by:

$$\text{Homonuclear spin part} = \{\hat{I}_1 \cdot \hat{I}_{2-3}\hat{I}_{z1}\hat{I}_{z2}\} \qquad (2)$$

where the labels 1 and 2 refer to the two ^{1}H spins. On the other hand, the spin part for dipolar coupling between a ^{1}H and a ^{13}C nucleus is given by:

$$\text{Heteronuclear spin part} = \{\hat{I}_z\hat{S}_z\} \qquad (3)$$

where I and S refer to the ^{1}H and ^{13}C nuclei, respectively.

Clearly, the dipolar interaction may be eliminated by causing any of the three terms in equation (1) to vanish. In some cases, rapid rotation of the sample about the magic angle can be used to eliminate the second term.[7] However, for most rigid solids it is usually not possible to spin fast enough for this approach to be effective in eliminating dipolar couplings. For heteronuclear coupling, the spin part can usually be eliminated by strong rf irradiation of one of the nuclear

species,[3] whereas for homonuclear coupling the spin part can sometimes be sufficiently reduced by the CRAMPS multiple rf pulse technique (see ***CRAMPS***).

The most commonly used approach is to observe a nuclear spin for which the NMR active isotope has a low abundance. For these 'rare' spins, such as ^{13}C, the homonuclear coupling is automatically eliminated since the large distances between NMR active nuclei cause the first term of equation (1) to be vanishingly small. At the same time, the heteronuclear interaction with surrounding abundant spins, usually ^{1}H nuclei, is eliminated by strong continuous rf irradiation[3] of the abundant nuclei to cause the spin part given in equation (3) to average to zero. For powder samples, magic angle spinning is also applied to eliminate CSA broadening.

There are two important disadvantages associated with NMR of rare nuclei in solids, namely low sensitivity and, in most cases, long relaxation times. The low sensitivity is an obvious result of low natural abundance.

The long relaxation times,[8] or T_1 values, are essentially due to an accident of nature. For spin-$\frac{1}{2}$ nuclei, the nuclear spin energy is coupled to the surrounding environment, or 'lattice', via locally generated time varying magnetic fields. The strength of the coupling, and therefore the rate at which the nuclear spins return to equilibrium, is governed by the magnetogyric ratio. Unfortunately, all of the spin-$\frac{1}{2}$ NMR nuclei with rare isotopic abundance have relatively low gyromagnetic ratios, and therefore long relaxation times, compared with the most commonly observed abundant NMR spins, namely ^{1}H, ^{19}F, and ^{31}P.

Low sensitivity can be improved by using a very high magnetic field, but the expense is often prohibitive and, for some nuclei, especially ^{13}C, a very high field can make it difficult or impossible to eliminate CSA effects. Another approach is to enrich isotopically the rare nucleus to a higher abundance. This approach can be very successful for improving sensitivity and for spectral editing, but it can also be very time consuming and expensive. In addition, enrichment beyond approximately 10% can cause broadening due to dipolar interactions between the 'rare' nuclei.

T_1 can sometimes be reduced by introducing paramagnetic impurities[9] into the sample, or in some cases by varying the sample temperature. However, these are inconvenient and specialized techniques.

The most commonly used method for increasing the sensitivity and experiment repetition rate when observing rare spins in solids is to transfer polarization from surrounding abundant spins, usually ^{1}H nuclei, to the rare spins. This is referred to as 'cross polarization'. Cross polarization not only enhances the signal strength of the rare spins, but also allows the experiment to be repeated at a rate governed by the T_1 of the abundant spins.

3 THEORY OF CROSS POLARIZATION IN SOLIDS

At equilibrium, the degree of nuclear polarization P_0 depends on the strength of the applied magnetic field $\boldsymbol{B}_0$, the magnetogyric ratio γ, and the 'lattice' temperature T_{L}:[2]

$$P_0 \propto \frac{\gamma B_0}{kT_L} \tag{4}$$

where k is Boltzmann's constant. The polarizations of different nuclear species will therefore be proportional to their magnetogyric ratios:

$$\frac{P_{0I}}{P_{0S}} = \frac{\gamma_I}{\gamma_S} \tag{5}$$

The key to understanding cross polarization in solids is the concept of mutual spin flips. This is a process whereby two coupled spins undergo simultaneous, opposite transitions in their spin states. Essentially, one spin makes a transition from 'spin up' to 'spin down', while the other goes from 'spin down' to 'spin up'. This process occurs spontaneously among abundant nuclei in solids. Since the total polarization is unchanged, the process conserves energy, and the spin part of the homonuclear dipolar coupling contains appropriate mutual spin flip terms. In order to show this better, equation (2) can be rewritten in terms of raising and lowering operators:

$$\text{Homonuclear spin part} = \left\{ \frac{1}{2}[\hat{I}_+\hat{S}_- + \hat{I}_-\hat{S}_+ - 2\hat{I}_z\hat{S}_z] \right\} \tag{6}$$

Because of this process of mutual spin flips, which is often referred to as nuclear 'spin diffusion', abundant spins tend to maintain a uniform degree of polarization despite localized perturbations such as paramagnetic impurities. For this reason, they are often described as a 'thermodynamic bath' of spins with an effective spin 'temperature'.

Of course, mutual spin flips do not occur between rare spins since they are not coupled to each other. Also, they do not occur spontaneously between nuclei of different species, since a mutual spin flip of this sort does not conserve energy, and the spin part given in equation (3) does not contain the necessary raising and lowering operators.

Cross polarization in solids is normally achieved by using rf irradiation to induce heteronuclear mutual spin flips. Since the abundant spins far outnumber the rare spins, this process causes the polarization of the rare spins to be made equal to that of the abundant spins. According to equation (5) this means that the polarization of the rare spins is increased by a factor equal to the ratio of their magnetogyric ratios. For coupled ^{1}H and ^{13}C spins, the ratio is approximately 4. Due to relaxation phenomena and other imperfections, a polarization enhancement factor of 3 is more typically achieved.

The basic method for inducing mutual spin flips between different nuclear species was introduced by Hartmann and Hahn, and is commonly called 'Hartmann–Hahn' cross polarization.[10] The pulse sequence is shown in Figure 1. An initial I-spin pulse places the I magnetization along the y axis in the I-spin rotating frame. This is followed by continuous irradiation along y in the I frame, together with simultaneous irradiation of the S spins. The rf power levels for the two nuclear species are adjusted such that the 'Hartmann–Hahn' condition is met:

$$\omega_{1I} \equiv \gamma_I B_{1I} = \gamma_S B_{1S} \equiv \omega_{1S} \tag{7}$$

In practical terms, this means that the length of a $\pi/2$ pulse is the same for both spin systems. During a few milliseconds of simultaneous irradiation, a substantial magnetization develops along the irradiation axis in the S-spin rotating frame. In

order to acquire a FID, it is then only necessary to turn off the rf on the S channel and observe the signal while the I-spin irradiation is continued for the purpose of heteronuclear decoupling.

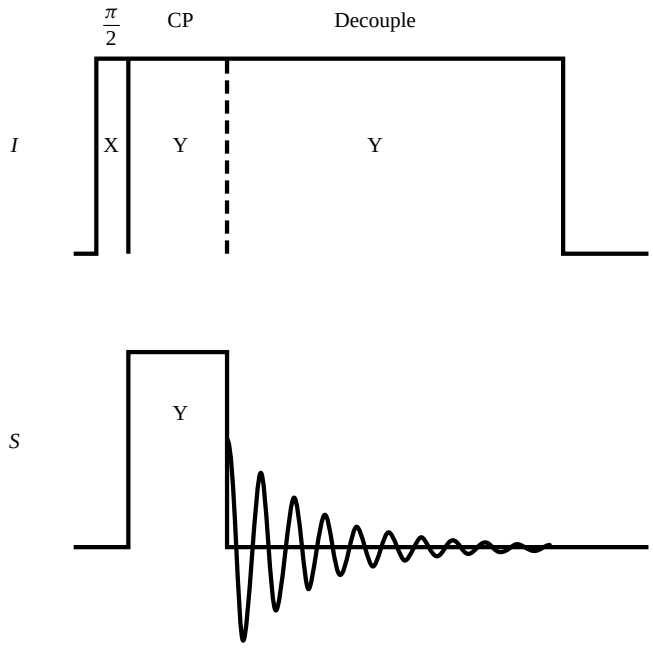

Figure 1 Basic pulse sequence for Hartmann–Hahn cross polarization

Hartmann–Hahn cross polarization can best be understood by carrying out a few simple quantum mechanical manipulations. In the doubly rotating reference frame of the Zeeman interactions for spins I and S, the Hamiltonian for the system may be written as:

$$\hat{\mathcal{H}}_{\mathrm{R}} = \omega_{1I}\hat{I}_Y + \omega_{1S}\hat{S}_Y + \beta_{IS}\hat{I}_z\hat{S}_z \tag{8}$$

where ω_1 is the rf nutation frequency, β_{IS} is a constant, and all other Hamiltonian terms such as chemical shift have been omitted for the sake of clarity. When the Hartmann–Hahn condition is matched, $\omega_{1I} = \omega_{1S}$, and equation (8) may be written as:

$$\hat{\mathcal{H}}_{\mathrm{R}} = \omega_1(\hat{I}_Y + \hat{S}_Y) + \beta_{IS}\hat{I}_z\hat{S}_z \tag{9}$$

The two terms in equation (9) do not commute, but if $\omega_1 \gg \beta_{IS}$ the situation can be further simplified by transforming to the frame of the interaction $(I_y + S_y)\omega_1$. The Hamiltonian in this frame is:

$$\hat{\mathcal{H}}^I_{\mathrm{R}} = \beta_{IS}[\hat{I}_z\cos(\omega_1 t) + \hat{I}_x\sin(\omega_1 t)] \times[\hat{S}_z\cos(\omega_1 t) + \hat{S}_x\sin(\omega_1 t)] \tag{10}$$

Keeping only the time independent, 'secular' part gives:

$$\hat{\mathcal{H}}^I_{\mathrm{R}} = \tfrac{1}{2}\beta_{IS}[\hat{I}_z\hat{S}_z + \hat{I}_x\hat{S}_x] \tag{11}$$

which is the first order average Hamiltonian, and commutes with the major interaction $\omega_1(I_y + S_y)$.

The significance of $\hat{\mathcal{H}}^I_{\mathrm{R}}$ can be better seen if both the I and S coordinate axes are tilted by 90°, such that I_z' and S_z' are parallel with the applied rf fields, i.e. they point along I_y and S_y, which is to say the axis of quantization has been changed to the direction along I_y,S_y. In this doubly tilted frame, the Hamiltonian becomes

$$\hat{\mathcal{H}}^{I'}_{\mathrm{R}} = \tfrac{1}{2}\beta_{IS}(\hat{I}_x\hat{S}_x + \hat{I}_y\hat{S}_y) \tag{12}$$

which can be rewritten in terms of raising and lowering operators as:

$$\hat{\mathcal{H}}^{I'}_{\mathrm{R}} = \tfrac{1}{4}\beta_{IS}(\hat{I}_+\hat{S}_- + \hat{I}_-\hat{S}_+) \tag{13}$$

Clearly, mutual spin flips will occur under these circumstances, but they will occur between magnetization aligned along the y axes in the I and S spin reference frames. Note that if the Hartmann–Hahn condition is not met, there is no secular part in equation (11), and the effect of simultaneous irradiation will simply be to eliminate the heteronuclear coupling.

This simple quantum mechanical treatment applies strictly to an isolated pair of spins. In such a case, the result of Hartmann–Hahn irradiation is an oscillation of magnetization between the two spins. However, in most cases the I spin is coupled to a large number of other I spins via homonuclear dipolar coupling. This coupling to a 'bath' of I spins quickly damps out any oscillation and results in a smooth buildup of S spin magnetization along the y axis.

Note that a similar quantum mechanical treatment may be used to show that application of CW irradiation to two spins coupled by homonuclear dipolar coupling yields an effective Hamiltonian that remains dipolar in form but is rotated in spin space and reduced in magnitude by a factor of 2. The result is that CW rf irradiation slows, but does not quench, spin diffusion between the I spins.

The rate of polarization buildup in the S spins will be governed by the strength of the heteronuclear coupling and by the rate of I spin diffusion. The characteristic time for this process[11] is often called T_{CH}, emphasizing the fact that the method is most commonly applied to cross polarization of ^{13}C spins coupled to ^{1}H spins. At the same time that the S spin polarization is growing, the I spin polarization will tend to decay according to the characteristic 'spin locked' or 'rotating frame' relaxation time[12] $T_{1\rho}$. The competition between these two rates will determine what level of polarization enhancement is actually achieved, how critical the cross polarization time is, and how quantitative the resulting spectrum will be.

Figure 2 presents two ^{13}C spectra of glycine, both obtained with magic angle spinning and heteronuclear decoupling and equal numbers of scans. The first spectrum shows the sensitivity obtained without cross polarization, while the second shows the spectrum obtained using Hartmann–Hahn cross polarization. It can be seen from Figure 2 that a substantial increase in signal strength is realized, although not quite the theoretical increase of 4. Also, a slight perturbation in the relative intensities of the resonance lines is evident. This is due to different values of T_{CH} and $T_{1\rho}$ for the two

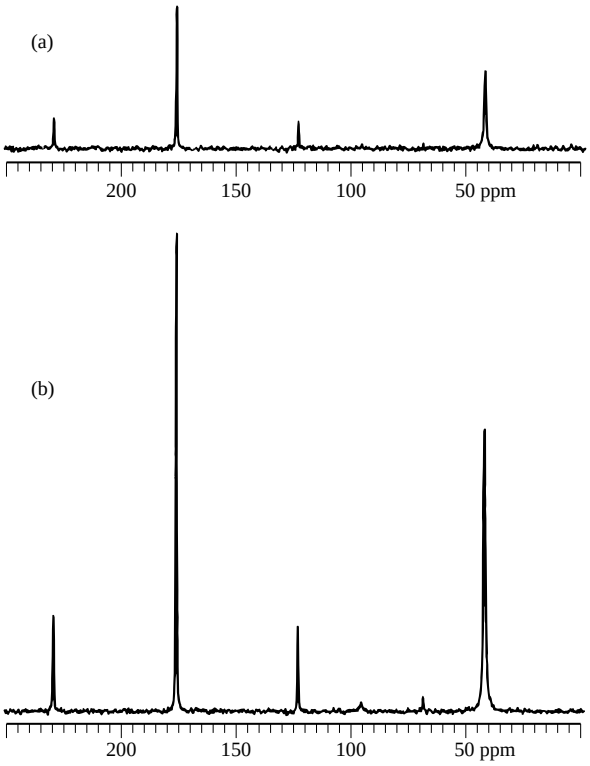

Figure 2 Comparison of ^{13}C MAS spectra for glycine obtained by (a) block decay (single pulse) with heteronuclear decoupling, and (b) Hartmann–Hahn cross polarization followed by heteronuclear decoupling

lines. When multiple scans are to be accumulated, an additional gain in sensitivity is realized due to the shorter relaxation time, or T_1, of the ^1H spins in glycine as compared with the ^{13}C spins (approximately 3 s as compared to 30 s). Figure 3 presents the 'T_{CH}' polarization curve for Hartmann–Hahn cross polarization of glycine. The effects of the competing T_{CH} and $T_{1\rho}$ time constants can easily be seen from the figure.

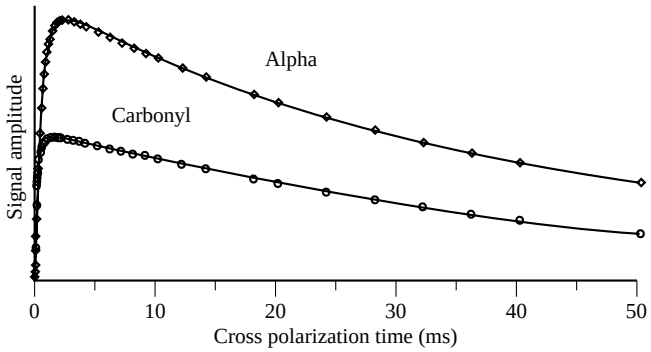

Figure 3 T_{CH} cross polarization curves for glycine

It should be pointed out that Hartmann–Hahn cross polarization can also be described in thermodynamic terms.[13] The abundant I spins are treated as a 'bath', with a 'spin' temperature determined by the degree of polarization and the energy associated with a nuclear spin state transition, i.e. spin 'flip'. Although the S spins are not in direct contact with each other, they are also treated as if they were a thermodynamic bath, and their low abundance is incorporated by assigning them a very low heat capacity. During the Hartmann–Hahn cross polarization period, the I and S spins are quantized along y, and are said to have spin temperatures determined by their polarizations and the strengths of the applied rf fields. The Hartmann–Hahn irradiation has the effect of thermally connecting the two spin baths and, since the S spins have very low heat capacity, they tend to approach the I spin temperature. As the rf fields are equal (in units of 1/second), equal temperatures imply equal degrees of polarization.

It should also be pointed out that there are other methods of cross polarization in solids. One approach uses rf irradiation with adiabatically varied amplitude to transfer magnetization via a 'dipolar' polarization state.[14,15] Another uses the 'Jener–Brockhard' pulse sequence to transfer polarization via multiple quantum states.[16] Still others transfer magnetization using nonthermodynamic techniques similar to those commonly used for liquids.[17] However, all of these alternative techniques have significant disadvantages in comparison with Hartmann–Hahn cross polarization, and none of them is widely used.

4 CROSS POLARIZATION AT HIGH SPINNING SPEEDS

As was mentioned in the introduction, cross polarization in solids is usually combined with magic angle spinning in order to eliminate chemical shift anisotropies, or CSAs. This combined experiment is often called CP MAS, and it is without doubt the most commonly used experimental method in solid state NMR.

In order completely to eliminate CSA effects, the MAS spinning rate must be faster than the width (in hertz) of the broadest CSA pattern in the spectrum. CSA magnitudes depend heavily on the nuclear species and chemical environment. For example, CSAs for ^{15}N and ^{29}Si are typically less than 20 ppm, while CSAs for ^{31}P can be as large as 300 ppm or more. For ^{13}C,

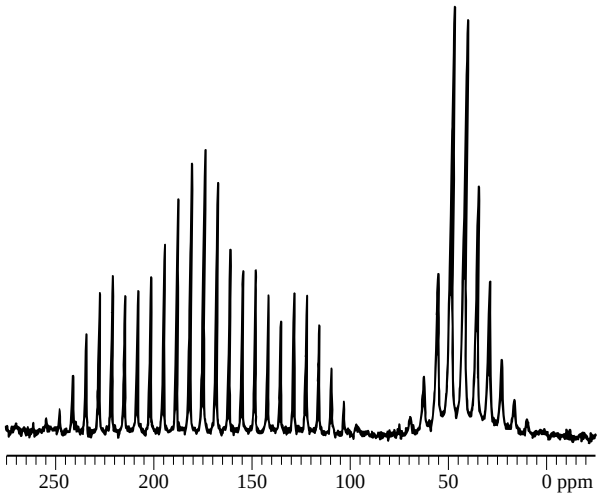

Figure 4 Glycine ^{13}C spectrum with slow spinning MAS. The spinning sidebands approximately trace out the CSA pattern

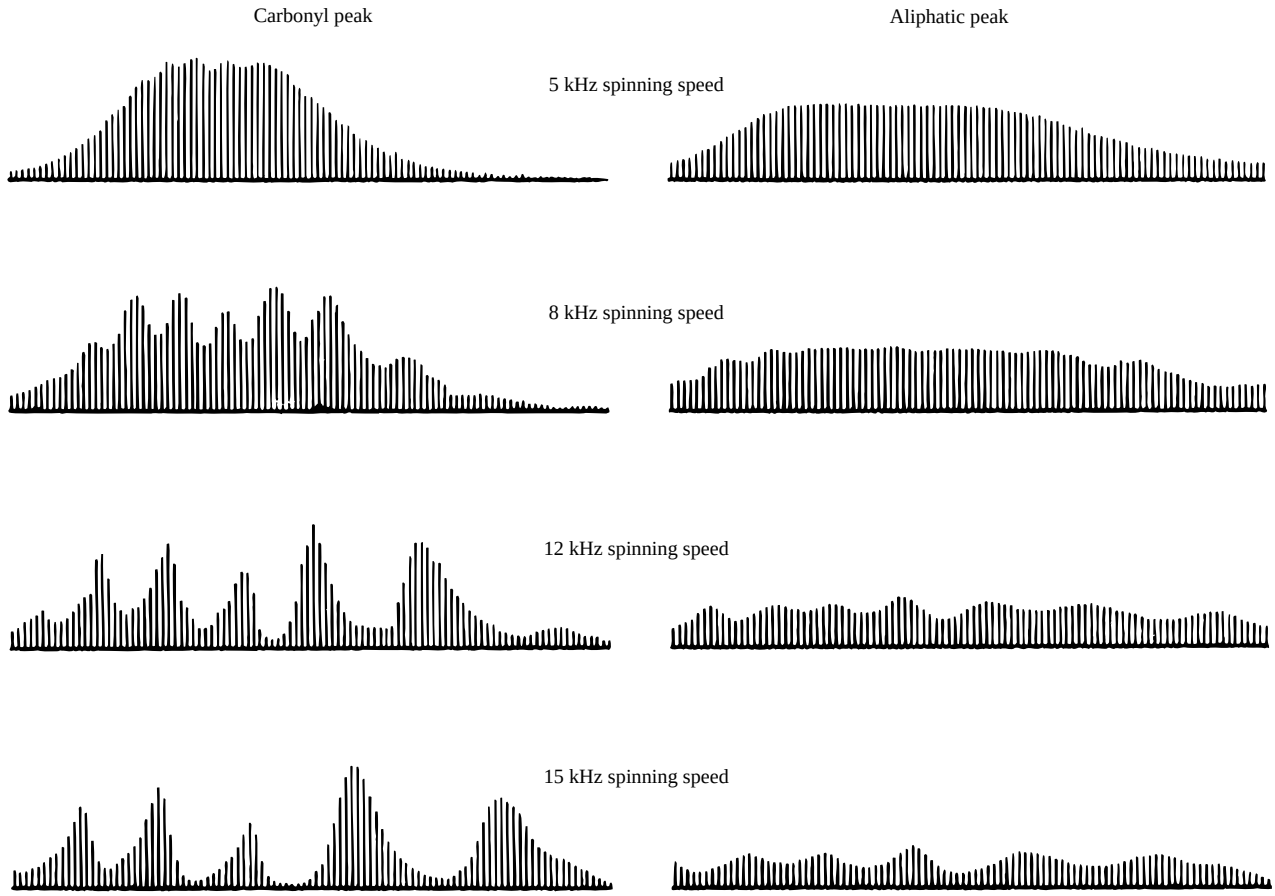

Figure 5 Glycine CP MAS signal strength as a function of Hartmann–Hahn mismatch and spinning speed. The match condition breaks into mismatch sidebands as the spinning speed is increased

CSA widths range from a few parts per million for methyl carbons atoms to 150 ppm or more for rigid aromatic carbon atoms.

If the MAS spinning rate is smaller than the CSA width, the CSA pattern breaks into 'sidebands' that are spaced at the MAS rate and approximately trace out the CSA pattern.[18] An example of this is presented in Figure 4 for glycine. A small number of sidebands can generally be tolerated, especially in highly crystalline samples like glycine that yield spectra with sharp lines. In fact, well resolved sidebands can be analyzed to extract the principal values of the CSA tensor.[18] Nevertheless, it is usually desirable to minimize the occurrence of CSA spinning sidebands by spinning rapidly. Since the CSA width is proportional to the magnetic field strength, the need for fast magic angle spinning increases at higher fields.

MAS spinning above approximately 20 kHz is a difficult mechanical and materials problem, and it also interferes with cross polarization because it tends to suppress heteronuclear dipolar coupling. Although the spinning rate is rarely fast enough completely to eliminate dipolar coupling, it is often sufficient to cause the Hartmann–Hahn match condition to become very critical and inefficient. As the spinning rate increases, additional 'match' conditions appear,[19] making it possible to cross polarize when the rf strength of one channel is mismatched from the other by either one or two times the spinning rate. At very high spinning speeds, cross polarization under these special mismatched conditions remains relatively efficient, even when almost no cross polarization is possible under normal matched conditions. An example of this high speed spinning effect for ^{13}C in glycine is shown in Figure 5.

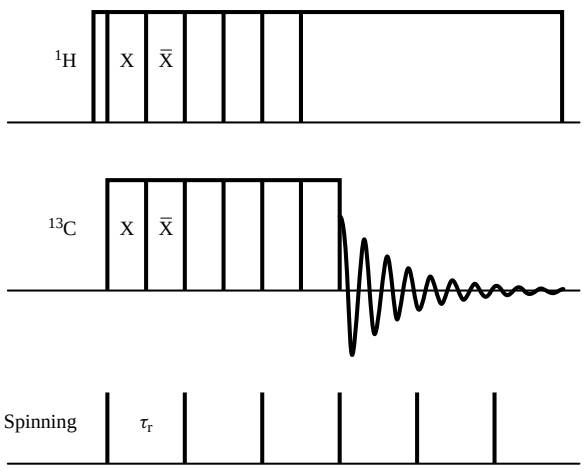

Figure 6 Pulse sequence using alternating π pulses to improve cross polarization during high speed MAS

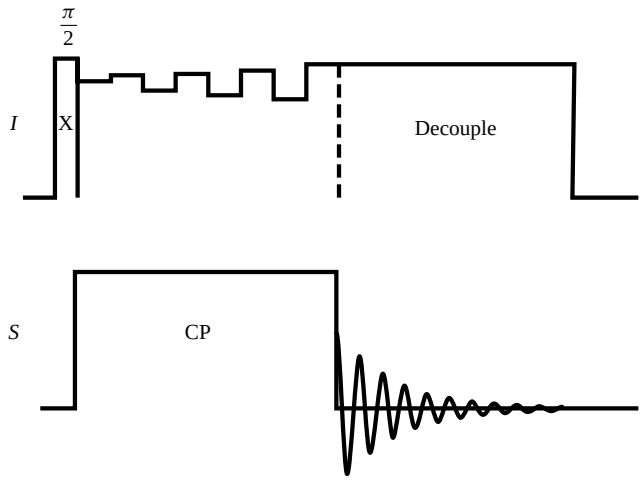

Figure 7 Variable amplitude cross polarization pulse sequence as it was originally proposed. The 'stair step' rf amplitude variation may be replaced by other functions such as a ramp or 'sawtooth'

that will provide sufficient signal intensity and yet will not overly complicate the data analysis by introducing too many spinning sidebands. Typically, CP MAS spectra of ^{13}C are measured in NMR spectrometers with ^{1}H resonance frequencies of 200–300 MHz, and are rarely attempted above 400 MHz. MAS rates are usually kept in the range 4–8 kHz, although spinning up to 15 kHz and beyond is not mechanically difficult. Even under these optimum conditions, ^{13}C CP MAS spectra of rigid solids are rarely free of CSA sidebands.

Several methods have been proposed to improve cross polarization during high speed spinning. In some, the spinning rate[20] or even the spinning angle[21] is changed between the cross polarization and signal detection phases of the experiment. Other approaches use 180° rf pulses to 'spoil' MAS dipolar suppression during the cross polarization[22] A typical pulse sequence for this method is shown in Figure 6.

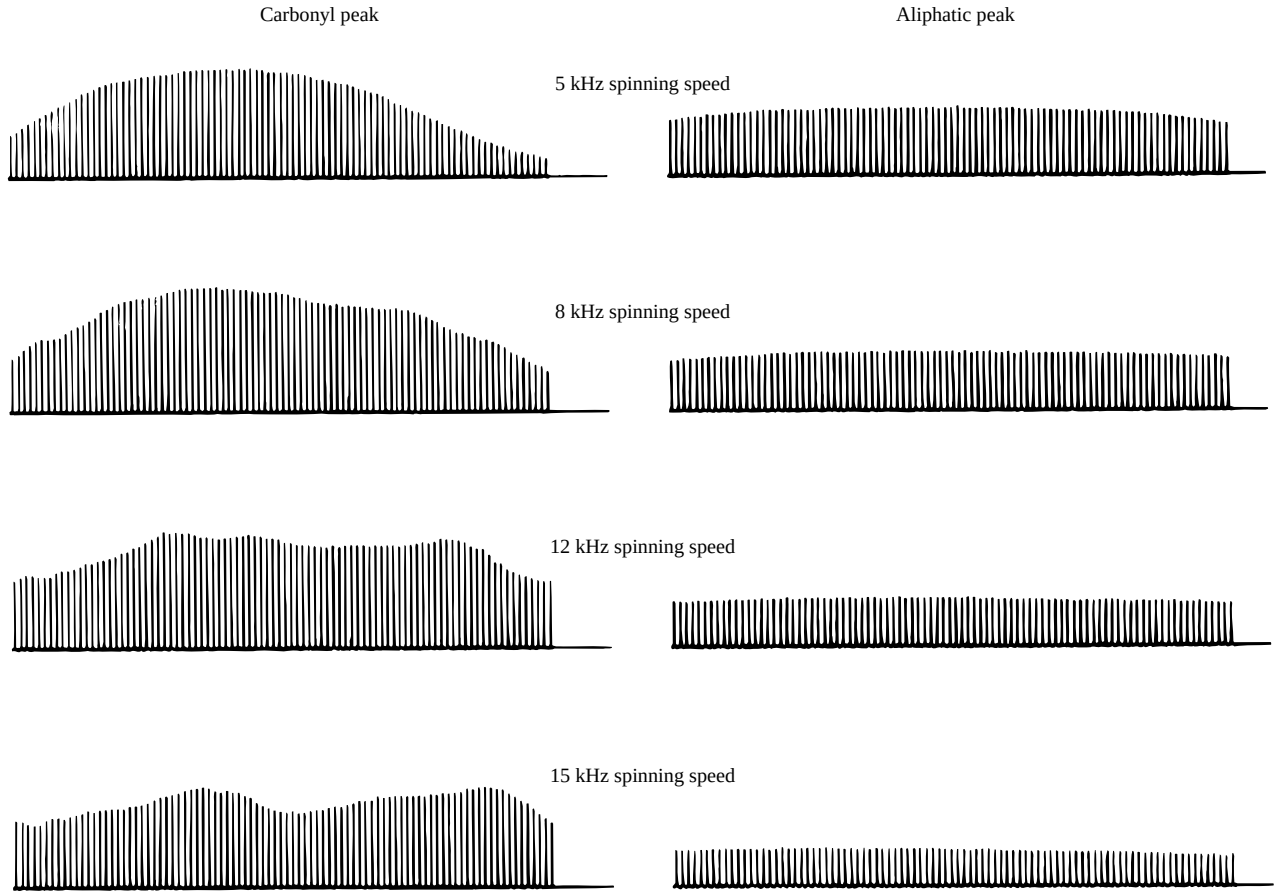

Figure 8 Glycine VACP signal strength as a function of Hartmann–Hahn mismatch and spinning speed.

Unfortunately, it is difficult to achieve stable and reproducible results using mismatched Hartmann–Hahn cross polarization, because the mismatched conditions are very critical and strongly dependent on the spinning rate.

Because of the problems associated with high speed spinning, it is often necessary to select a magnetic field strength

The technique that currently appears to offer the greatest promise for cross polarization at high spinning speeds is called 'variable amplitude cross polarization' (VACP).[23] A diagram of the experiment as it was originally introduced is shown in Figure 7. Essentially, the method depends on the fact that, in many cases, especially for ^{13}C in most

samples, the cross polarization rate T_{CH} is much faster than $T_{1\rho}$. Therefore, there is time to vary the rf levels over a range of values, essentially searching for one or more of the special mismatched Hartmann–Hahn conditions. At most rf settings, no match will occur and the I and S spins will simply remain 'spin locked'. Hopefully, however, at least one of the rf level settings will be near enough to a mismatched Hartmann–Hahn condition to result in significant cross polarization.

For many samples, VACP works very well. An example is given in Figure 8 for glycine spinning at 15 kHz. For experimental convenience, the 'stair step' approach illustrated in Figure 7 is often replaced by a simple amplitude ramp, and the range of rf levels is made large enough to extend from the exact Hartmann–Hahn match to an offset of twice the MAS frequency. Typical VACP cross polarization times are 10–20 ms, as compared to 1–5 ms for traditional Hartmann–Hahn cross polarization.

5 SPECTRAL EDITING AND OTHER TRICKS USING CROSS POLARIZATION

Experiments that serve to identify what functional group a given resonance belongs to are commonly referred to as 'spectral editing' techniques (see ***Spectral Editing Techniques: Hydrocarbon Solids***). This is because they normally cause certain lines in the spectrum to be suppressed or inverted. There are several variations of the Hartmann–Hahn cross polarization method that are useful for spectral editing. Two examples that identify CH_2 carbon resonances are reverse polarization,[24] which depends on differences in T_{CH}, and WIMSE,[25] which uses a sophisticated heteronuclear multiple pulse cross polarization technique known as 'windowless isotropic mixing' or 'WIM'.[26] Whereas most spectral editing methods depend on differences in coupling strength or polarization time, WIMSE makes use of basic differences in spin dynamics. During WIM cross polarization the I spins are isolated from each other, and a dynamic rather than thermodynamic behavior results. A diagram of the WIMSE experiment is presented in Figure 9, and WIMSE spectra of solid gelatin are presented in Figure 10.

WIM cross polarization is also very useful for heteronuclear two-dimensional spectroscopy in solids.[27] A diagram of the WIM based two-dimensional HETCOR experiment is presented in Figure 11. During the first part of this experiment, the BLEW-24 and BB-24 multiple pulse sequences are used to suppress both the homonuclear and heteronuclear dipolar couplings. As a result, the I spins evolve only under

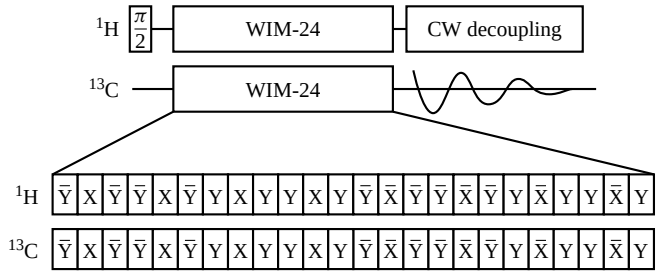

Figure 9 WIMSE spectral editing pulse sequence

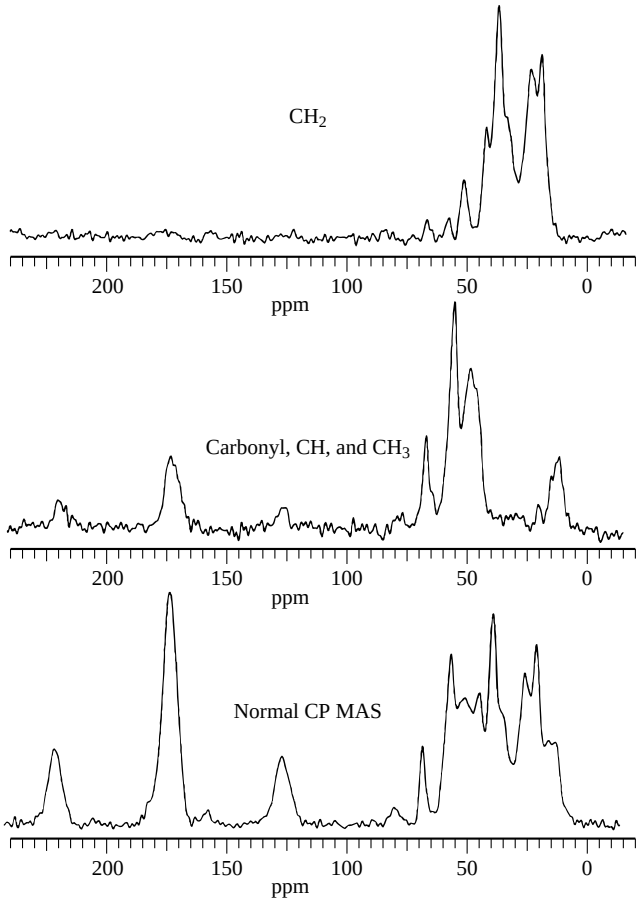

Figure 10 WISME spectra for solid gelatin showing only CH_2 resonances (top), carbonyl, CH and CH_3 resonances (middle) and all resonances (bottom)

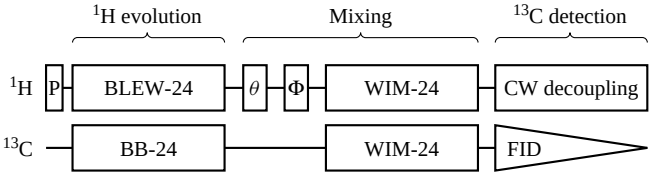

Figure 11 Two-dimensional HETCOR pulse sequence

the influence of resonance offset and chemical shift. The magnetization is then cross polarized to the S spins using WIM, and the S signal is detected. An example of two-dimensional HETCOR applied to ibuprofen is presented in Figure 12. Because WIM is used for cross polarization, peaks occur in the spectrum only at positions that correlate directly coupled ^1H–^{13}C spins. If the usual Hartmann–Hahn method were used, rapid ^1H spin diffusion would occur during the cross polarization time, and 'cross peaks' would appear for all possible combinations of ^1H and ^{13}C.

A number of other methods have been used to isolate spin groups during cross polarization, including simultaneously applied CRAMPS pulse sequences,[28] frequency switched Lee–Goldburg irradiation,[29] and very rapid Hartmann–Hahn irradiation.[30] So far, WIM appears to be the most successful of these methods.

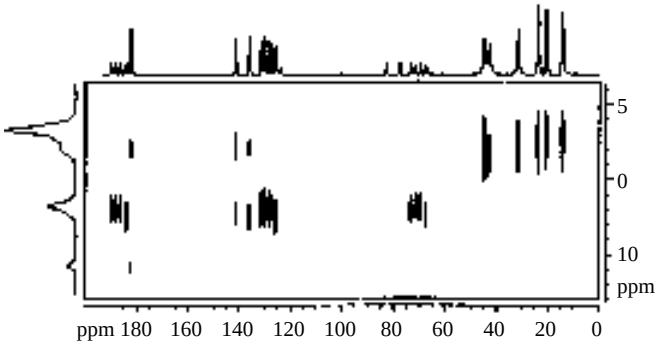

Figure 12 Two-dimensional HETCOR spectrum of ibuprofen. The one-dimensional spectra shown along the axes are a BR-24 CRAMPS spectrum (vertical) and a conventional CP MAS spectrum (horizontal) which were obtained in separate measurements

6 CONCLUSIONS

Hartmann–Hahn cross polarization is widely used to improve sensitivity and experiment repetition rate for rare spins in solids. Although some loss of quantitative information often occurs, the benefits usually far outweigh the disadvantages. At high MAS spinning speeds, cross polarization becomes problematic, but the recently introduced variable amplitude method appears to reduce greatly these difficulties in many cases. A variety of specialized techniques based on Hartmann–Hahn cross polarization have been developed, including spectral editing methods and pulse sequences that suppress spin diffusion during cross polarization.

7 RELATED ARTICLES

CRAMPS; Dipolar and Indirect Coupling Tensors in Solids; Internal Spin Interactions and Rotations in Solids; Magic Angle Spinning; Rotating Solids; Spectral Editing Techniques: Hydrocarbon Solids

8 REFERENCES

1. See for example: E. R. Andrew, W. S. Hinshaw, and R. S. Riffen, *Phys. Lett., Ser. A.*, 1973, **46**, 57.
2. M. Mehring, *Principles of High Resolution NMR in Solids*, 2nd edn, Springer, Berlin, 1983, Sections 4.2 and 4.3.
3. M. Mehring, *Principles of High Resolution NMR in Solids*, 2nd edn, Springer, Berlin, 1983, Section 4.4.
4. M. Mehring, *Principles of High Resolution NMR in Solids*, 2nd edn, Springer, Berlin, 1993, Section 2.6.
5. M. Mehring, *Principles of High Resolution NMR in Solids*, 2nd edn, Springer, Berlin, 1983, Sections 2.1 and 2.2.
6. M. Mehring, *Principles of High Resolution NMR in Solids*, 2nd edn, Springer, Berlin, 1983, p. 16.
7. (a) E. R. Andrew, and R. G. Eades, *Proc. R. Soc. London, Ser. A*, 1953, **216**, 398; (b) references given in M. Mehring, *Principles of High Resolution NMR in Solids*, 2nd edn, Springer, Berlin, 1983, Section 2.6.
8. A. Abragam, *Principles of Nuclear Magnetism*, Clarendon, Oxford, 1961, Section IX.IV.A–C.
9. A. Abragam, *Principles of Nuclear Magnetism*, Clarendon, Oxford, 1961, Section IX.II.A–B.
10. S. R. Hartmann and E. L. Hahn, *Phys. Rev.*, 1962, **128**, 2042 and A. Pines, M. G. Gibby, and J. S. Waugh, *J. Chem. Phys.*, 1973, **59**, 569.
11. M. Mehring, *Principles of High Resolution NMR in Solids*, 2nd edn, Springer, Berlin, 1983 p. 153.
12. M. Mehring, *Principles of High Resolution NMR in Solids*, 2nd edn, Springer, Berlin, 1983, p. 132.
13. M. Mehring, *Principles of High Resolution NMR in Solids*, 2nd edn, Springer, Berlin, 1983 Section 4.1.
14. R. R. Ernst, G. Bodenhausen, and A. Wokaun, *Principles of Nuclear Magnetic Resonance in One and Two Dimensions*, Clarendon, Oxford, 1987, Section 4.145.
15. R. R. Ernst, G. Bodenhausen, and A. Wokaun, *Principles of Nuclear Magnetic Resonance in One and Two Dimensions*, Clarendon, Oxford, 1987, Section 4.146.
16. R. R. Ernst, G. Bodenhausen, and A. Wokaun, *Principles of Nuclear Magnetic Resonance in One and Two Dimensions*, Clarendon, Oxford, 1987, Section 4.298.
17. A. Bax, N. M. Szeverenyi, and G. E. Maciel, *J. Magn. Reson.*, 1982, **50**, 227.
18. J. Herzfeld and A. Berger, *J. Chem. Phys.*, 1980, **73**, 6021.
19. E. O. Stejskal, J. Schaefer, and J. S. Waugh, *J. Magn. Reson.*, 1977, **28**, 105.
20. R. C. Ziegler, R. A. Wind, and G. E. Maciel, *J. Magn. Reson.*, 1988, **79**, 299.
21. M. Sardashti, and G. E. Maciel, *J. Magn. Reson.*, 1987, **72**, 467.
22. T. M. Barbara and E. H. Williams, *J. Magn. Reson.*, 1992, **99**, 439.
23. O. B. Peersen, X. Wu, I. Kustanovich, and S. O. Smith, *J. Magn. Reson., Ser. A*, 1993, **104**, 334.
24. X. Wu, and K. W. Zilm, *J. Magn. Reson., Ser. A*, 1993, **102**, 205.
25. D. P. Burum and A. Bielecki, *J. Magn. Reson.*, 1991, **95**, 184.
26. P. Caravatti, L. Braunschweiler, and R. R. Ernst, *Chem. Phys. Lett.*, 1983, **100**, 305.
27. D. P. Burum and A. Bielecki, *J. Magn. Reson.*, 1991, **94**, 645.
28. J. E. Roberts, S. Vega, and R. G. Griffin, *J. Am. Chem. Soc.*, 1984, **106**, 2506.
29. A. Bielecki, A. C. Kolbert, H. J. M. De Groot, R. G. Griffin, and M. H. Levitt, *Adv. Magn. Reson.*, 1990, **14**, 111.
30. P. Caravatti, G. Bodenhausen, and R. R. Ernst, *Chem. Phys. Lett.*, 1982, **89**, 363.

Biographical Sketch

Douglas P. Burum. *b* 1952. B.S., Harvey Mudd College, 1974; Ph.D., California Institute of Technology (advisor R. W. Vaughan), 1979. Postdoctoral Assistant under R. R. Ernst 1979–80. Joined Bruker Instruments as an applications specialist in solid state NMR in 1982. Currently Bruker USA national product manager for analytical NMR. Approx. 25 publications. Research interests center around development of coherent averaging pulse techniques, including CRAMPS, two-dimensional HETCOR, spectral editing, etc.

Dipolar Spectroscopy: Transient Nutations and Other Techniques

Mario Engelsberg

Universidade Federal de Pernambuco, Recife, Pernambuco, Brazil

1	Introduction	1
2	Dipolar Spectroscopy of Isolated Pairs	1
3	Suppression of other Broadening Interactions	2
4	Dipolar Spectra	4
5	Related Articles	5
6	References	5

1 INTRODUCTION

The application of dipolar spectroscopy as a structural tool in solids can be realized with the help of transient nutations and other similar techniques. The main objective is to take advantage of the unambiguous geometric and dynamical interpretation of purely homonuclear dipolar spectra involving a small number of interacting spins. Thus, the requirements to be met not only involve the removal of broadening caused, for example, by shielding interactions and static field inhomogeneities, but also that homonuclear dipolar couplings remain either unchanged or are affected in a easily accountable way.

Dipolar spectroscopy in solids using transient nutations was pioneered by Yannoni and Kendrick[1] as a method for obtaining structural information in systems where the lack of some degree of long-range order excludes the use of diffraction techniques. The method, which involves enrichment of an isotopically rare spin-$\frac{1}{2}$ nucleus at two selected molecular positions, followed by dilution of the pairs either in the unenriched material or in a matrix, is ideally suited for structural studies in amorphous solids, reaction intermediates, catalysts, etc.

Transient nutation is just one of the available strategies for dipolar spectroscopy in solids. The suppression of inhomogeneous broadening can also be achieved by employing a train of properly chosen rf pulses. Of the possible pulse sequences, the venerable Carr–Purcell sequence[2] and its variations, with some additions and corrections, has also been shown[3] to be quite effective as a structural tool in disordered solids, giving some advantage in overall spectral resolution.

2 DIPOLAR SPECTROSCOPY OF ISOLATED PAIRS

In order to extract useful geometrical and dynamical information in disordered solids from the homonuclear magnetic dipole–dipole interaction, it is required that the spectra contain sharp and well-defined features, even when the dipoles are randomly oriented. This can be achieved, for example, by creating small clusters of mutually interacting dipoles through isotopic enrichment and matrix isolation or dilution. The simplest strategy is to attempt to approximate a regime of isolated pairs.

For a pair of identical nuclear spins $\boldsymbol{I}_1$ and $\boldsymbol{I}_2$ and magnetogyric constant γ in a strong magnetic field $B_0 = \omega_0/\gamma$ along the z axis, the secular[4] Hamiltonian $\hat{\mathcal{H}}_{12}$ involving Zeeman and dipolar interactions can be written as

$$\hat{\mathcal{H}}_{12} = -\hbar\omega_0(\hat{I}_{z1} + \hat{I}_{z2}) + A_{12}(\hat{\boldsymbol{I}}_1 \cdot \hat{\boldsymbol{I}}_2 - 3\hat{I}_{z1}\hat{I}_{z2}) \qquad (1)$$

where

$$A_{12} = \hbar^2\gamma^2(3\cos^2\theta_{12} - 1)/2r_{12}^3 = \hbar^2\gamma^2 P_2(\cos\theta_{12})/r_{12}^3 \quad (2)$$

$P_2(\cos\theta_{12})$ in equation (2) denotes a second-order Legendre polynomial, $\boldsymbol{r}_{12}$ represents the internuclear vector, and θ_{12} is the angle between $\boldsymbol{r}_{12}$ and $\boldsymbol{B}_0$.

The eigenfunctions and eigenvalues of $\hat{\mathcal{H}}_{12}$ for spin-$\frac{1}{2}$ nuclei can be verified from equation (1) to be the triplet states $|t_+\rangle = |+\ +\rangle$, $|t_-\rangle = |-\ \ -\ \rangle$ and $|t_0\rangle = (|+-\rangle + |-+\rangle)/\sqrt{2}$, with energies $E_{t+} = \hbar\omega_0 + A_{12}/2$, $E_{t-} = -\hbar\omega_0 + A_{12}/2$, and $E_{t0} = -A_{12}$, respectively, and the singlet state $|t_0\rangle = (|+-\rangle - |-+\rangle)/\sqrt{2}$ with energy $E_{s0} = 0$. Since the latter is not connected to the triplet states by a rf magnetic field, the spectrum consists of only two lines, the famous Pake[5] doublet, with a frequency separation given by:

$$\begin{aligned}\delta\nu_{\mathrm{p}} &= 3\hbar\gamma^2(3\cos^2\theta_{12} - 1)/4\pi r_{12}^3 \\ &= 3\hbar\gamma^2 P_2(\cos\theta_{12})/2\pi r_{12}^3 \end{aligned} \qquad (3)$$

Most important as a structural tool in systems lacking long-range order is the spectrum of randomly oriented isolated pairs of spin-$\frac{1}{2}$ nuclei. It can be obtained from equation (3) under the assumption of vectors $\boldsymbol{r}/r$ uniformly distributed on a unit sphere. The spectral weight in the frequency interval $\mathrm{d}\nu$ is then proportional to the solid angle $2\pi\ \sin\theta\ \mathrm{d}\theta$ and to $1/(\mathrm{d}\nu/\mathrm{d}\theta)$, where $\nu - \nu_0 = \pm\delta\nu_p/2$ [equation (3)] are the positions of the two members of the Pake doublet relative to the Larmor frequency $\nu_0 = (\gamma/2\pi)B_0$. Thus, the frequency spectrum for randomly oriented[5] isolated pairs can be seen to be proportional to $1/|\cos\theta|$ and, consequently, to display singularities for $\theta = \pi/2$ corresponding to $\nu - \nu_0 = \pm 3\hbar\gamma^2/8\pi r_{12}{}^3 = \pm\Delta_{\mathrm{p}}/2$.

Not only can useful geometrical information be obtained from a spectrum of isolated pairs (Figure 1), but also a description of the dynamics. If the internuclear vector $\boldsymbol{r}_{12}$ is assumed to execute a hindered rotational motion reorienting about a fixed direction in space by random jumps between several positions, the changes in the spectrum shown in Figure 1 can be accurately predicted from the postulated dynamical model for the motion.[6] Moreover, if the reorientation rate is fast compared with $\delta\nu_{\mathrm{p}}$ [equation (3)], a simple average of $P_2(\cos\theta_{12})$ can be performed in order to determine the changes in the spectrum corresponding to this fast motional regime. If the fixed polar angle of $\boldsymbol{B}_0$ relative to the reorientation axis is denoted by Γ, and the constant angle between $\boldsymbol{r}_{12}$ and the reorientation axis is denoted by ψ_{12}, the addition theorem for spherical harmonics

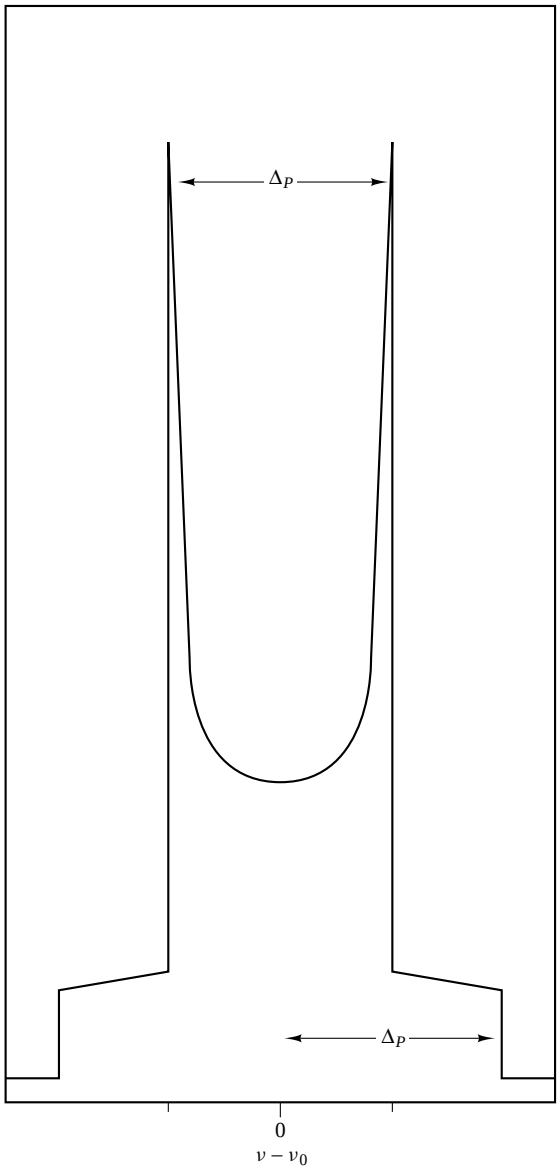

Figure 1 Spectrum of randomly oriented isolated pairs of dipolar-coupled spin-$\frac{1}{2}$ nuclei. The frequency separation between the singularities in the distribution of Pake doublets has the value $\Delta_p = 3\gamma^2\hbar/4\pi r_{12}^3$

can be used to perform the average $\langle P_2(\cos\ \theta_{12})\rangle$ over the time-dependent azimuthal angle associated with $\boldsymbol{r}_{12}$, yielding[7]

$$\langle P_2(\cos\theta_{12})\rangle = P_2(\cos\Gamma)(3\cos^2\psi_{12} - 1)/2 \qquad (4)$$

Equation (4) is valid in the fast motion limit, for hindered rotation between positions of three-fold or higher symmetry, regardless of the details of the motion.

One concludes from equations (3) and (4) that the spectrum corresponding to random directions of the reorientation axis remains identical to the rigid case (Figure 1), but its width can be seen from equation (4) to be reduced by the factor $(3\cos^2\psi_{12} - 1)/2$.

3 SUPPRESSION OF OTHER BROADENING INTERACTIONS

In order to use dipolar spectra of isolated pairs as a structural tool, one needs to suppress other couplings. For spin-$\frac{1}{2}$ nuclei, heteronuclear dipole–dipole interactions, broadening by anisotropic chemical shifts or Knight shifts, and susceptibility broadening in small metallic particles, are among the most frequently found interactions that can mask the spectrum of dipole–dipole coupled isolated pairs.

3.1 Coherent Averaging

As a first step, the choice of an appropriate sequence of pulses for suppressing these couplings without affecting the homonuclear dipolar interactions is worth examining within the framework of average Hamiltonian theory.[8] For δ function excitation pulses, the evolution of the density operator in the rotating frame in the limit of closely spaced pulses has been shown to be governed, after many cycles, by an average Hamiltonian:

$$\bar{\hat{\mathcal{H}}} = (1/T)\sum_{k=1}^{n}\hat{\mathcal{H}}_{nk}\tau_k \qquad (5)$$

where τ_k represents the time interval between the kth and the $(k + 1)$th pulse in a cycle consisting of n pulses with period $T = \sum_{k=1}^{n}\tau_k$. The $\hat{\mathcal{H}}_{nk}$ values in equation (5) can be controlled by the experimenter by a suitable choice of pulses, adequate to the particular internal interactions present.

For the Carr–Purcell sequence, one has $n = 2$ and $\tau_1 = \tau_2 = 2\tau$. Representing the π pulses by the spin rotation operators $\hat{P}_1 = \hat{P}_2 = \exp(-i\pi\hat{I}_y)$ it can be shown[8] that the average Hamiltonian reduces to:

$$\bar{\hat{\mathcal{H}}} = \tfrac{1}{2}(\hat{\mathcal{H}} + \hat{P}_2\hat{\mathcal{H}}\hat{P}_2^{-1}) \qquad (6)$$

which satisfies the requirements for dipolar spectroscopy. Terms in $\hat{\mathcal{H}}$ corresponding to various types of shifts have the general form:

$$\hat{\mathcal{H}}_S = \sum_i \Delta\sigma_i\hat{I}_{zi} \qquad (7)$$

where, for the case of secular chemical shifts, the shielding anisotropy $\Delta\sigma_i$ terms depend upon the orientation of the principal axes of the shielding tensor[8] at the ith site relative to $\boldsymbol{B}_0$. From equation (7) it is clear that $\bar{\hat{\mathcal{H}}}_S = 0$, since the π pulses represented by $\hat{P}_2$ in the second term of the equation simply change the sign of $\hat{\mathcal{H}}_S$. On the other hand, the homonuclear dipolar interaction [equation (1)], being bilinear in the individual spin operators, remains unaffected.

Although the secular heteronuclear interaction is also linear in the individual $\hat{I}_{zi}$ operators and can also be suppressed by the Carr–Purcell sequence and its variations, it is generally more convenient in practice to use strong rf irradiation at the Larmor frequency of these spins for an effective decoupling from the resonant nuclei.

Other pulse sequences also satisfy the requirements for dipolar spectroscopy. For example, several variations of the Carr–Purcell sequence have been proposed in order to compensate for the cumulative error caused by imperfect π pulses. In the Carr–Purcell–Meiboom–Gill (CPMG) sequence[9] this is achieved by a 90° shift between the phase of the π pulses and the phase of the preparation pulse. Other compensated sequences, which have been proposed[10] with a similar aim, involve cycles for 4, 8, or 16 π pulses.

3.2 Transient Nutations

A different approach is needed in order to examine the applicability of transient nutation as a tool for dipolar spectroscopy. This approach permits, at the same time, an evaluation of the effect of π pulses of finite width on dipolar spectra obtained using the CPMG sequence. In the laboratory frame, the total Hamiltonian $\hat{\mathcal{H}}$ includes, in addition to the Zeeman interaction $\hat{\mathcal{H}}_Z$, an interaction with a time-dependent rf field at resonance which may be amplitude modulated by pulses. It also includes a distribution of shifts [equation (7)] and the secular homonuclear dipole–dipole couplings $\hat{\mathcal{H}}_d$:

$$\hat{\mathcal{H}} = -\hbar\omega_0\hat{I}_z - 2\hbar\omega_1(t)\hat{I}_x\cos\omega_0 t - 2t\omega_1(t)I_x\cos\omega_0 t + \sum_i \Delta\sigma_i\hat{I}_{zi} + \hat{\mathcal{H}}_d \tag{8}$$

where, from equations (1) and (2),

$$\hat{\mathcal{H}}_d = \sum_{i\rangle j} A_{ij}(\hat{\boldsymbol{I}}_i\cdot\hat{\boldsymbol{I}}_j - 3\hat{I}_{zi}\hat{I}_{zj}) \tag{9}$$

In the transient nutation experiment, an oscillating rf field of constant amplitude $2\omega_1/\gamma$ is applied suddenly along the x axis of the laboratory frame starting from equilibrium. The ensuing transient precession about the effective field in the rotating frame is then recorded, either point by point after an rf field of variable duration or by sampling through appropriately chosen receiver windows, and Fourier transformed. For simplicity, the conditions for decoupling of the nonresonant spins are assumed to hold, and consequently heteronuclear dipolar interactions have not been included in $\hat{\mathcal{H}}$.

One is interested in the evolution of the density operator $\hat{\rho}'$, in a rotating tilted frame,[11] where one of the two rotating components of the oscillating magnetic field is stationary along the z axis. The transformed density operator $\hat{\rho}'$ can be obtained from the laboratory frame operator $\hat{\rho}$ through the transformation $\hat{\rho}' = \hat{P}\hat{R}\hat{\rho}\hat{R}^{-1}\hat{P}^{-1}$ where

$$\hat{P} = \exp(i\pi\hat{I}_y/2); \quad \hat{R} = \exp(i\omega_0 t\hat{I}_z) \tag{10}$$

Starting from the time evolution of the density operator in the laboratory frame, the evolution of $\hat{\rho}'$ can be shown[11] to be governed by an effective Hamiltonian

$$\hat{\mathcal{H}}'_e = \hat{P}\hat{R}\hat{\mathcal{H}}_e\hat{R}^{-1}\hat{P}^{-1} \tag{11}$$

where $\hat{\mathcal{H}}_e = \hat{\mathcal{H}} - \hat{\mathcal{H}}_Z$, and $\hat{\mathcal{H}}_Z = -\hbar\omega_0\hat{I}_z$ denotes the Zeeman interaction.

Since the secular interactions in $\hat{\mathcal{H}}$ [equations (8) and (9)] commute with $\hat{R}$, the calculation of $\hat{\mathcal{H}}'_e$ from equations (10) and (11) is simplified. Neglecting terms oscillating at frequency $2\omega_0$, the effective Hamiltonian in the rotating tilted frame reduces to

$$\hat{\mathcal{H}}'_e = -\hbar\omega_1\hat{I}_z + \sum_{i\rangle j} A_{ij}(\hat{\boldsymbol{I}}_i\cdot\hat{\boldsymbol{I}}_j - 3\hat{I}_{xi}\hat{I}_{xj}) - \sum_i \Delta\sigma_i\hat{I}_{xi} \tag{12}$$

Furthermore, if the amplitude of the rotating magnetic field ω_1/γ is large compared to the strength of the internal fields, and the system is initially in a state described by an equilibrium density operator $\hat{\rho}(0) = \text{const} \times \hat{I}_z$ in the laboratory frame [and hence by $\hat{\rho}'(0) = -\text{const} \times \hat{I}_x$ in the rotating tilted frame], the *decay* of the transient nutation signal is governed by the terms in equation (13) which commute with $\hat{I}_z$. It is therefore convenient to write, with the help of raising and lowering operators, the last two terms in equation (12) as a purely secular part, obeying the selection rule[4] $\Delta(m_i + m_j) = 0$, plus nonsecular terms satisfying $\Delta(m_i + m_j) \neq 0$. This leads to:

$$\hat{\mathcal{H}}'_e = -\hbar\omega_1\hat{I}_z - \frac{1}{2}\hat{\mathcal{H}}_d - \frac{3}{4}\sum_{i\rangle j} A_{ij}(\hat{I}_{i+}\hat{I}_{j+} + \hat{I}_{i-}\hat{I}_{j-}) - \frac{1}{2}\sum_i \Delta\sigma_i(\hat{I}_{i+} + \hat{I}_{i-}) \tag{13}$$

Equation (13) shows that the transient nutation signal satisfies the requirements for dipolar spectroscopy. Since the last two terms have become nonsecular and do not contribute to the decay, inhomogeneous broadening caused by resonance shifts is suppressed, although an inhomogeneous rf field may still cause broadening.[12] In addition, the strength of the secular dipolar term in equation (14) is one-half the value of the dipolar interaction in the laboratory frame[13] [equation (9)]. Hence the width of the spectrum of isolated pairs shown in Figure 1 is expected to be half the value calculated from equation (3).

3.3 CPMG Sequence with Finite Pulse Widths

The system is prepared by an initial $\pi/2$ pulse and evolves during a time interval τ. A train of π pulses of width t_w, separated by intervals 2τ, and phase shifted by 90° with respect to the initial $\pi/2$ pulse is then applied. The signal amplitudes at the echo maxima are further recorded as a function of time, and Fourier transformed to obtain the frequency spectrum.

Since for the CPMG case, $\omega_1(t)$ in equation (8) represents a periodic function of period $T = 2\tau + t_w$ consisting of rectangular pulses with amplitudes $\omega_{1a} = \pi/t_w$, the steps leading from equation (8) to equation (13) yield an effective Hamiltonian identical to $\hat{\mathcal{H}}'_e$ [equation (13)], but with a time-dependent term $\hbar\omega_1(t)\hat{I}_z$. Moreover, since one is observing the evolution stroboscopically, it is convenient to transform $\hat{\mathcal{H}}'_e$ to a 'toggling frame' where the precession about externally

applied fields, either static or time-dependent, is removed. This is achieved by the transformation[11]

$$\hat{\rho}'_{\rm et}(t) = \exp[-{\rm i}\phi(t)\hat{I}_z/2]\,\hat{\rho}'_{\rm e}(t)\exp[{\rm i}\phi(t)\hat{I}_z/2)] \qquad (14)$$

where:

$$\phi(t) = 2\int_0^t \omega_1(t')\,{\rm d}t' \qquad (15)$$

The evolution of $\hat{\rho}'_{\rm et}(t)$, given by equations (14) and (15), is governed by the effective Hamiltonian

$$\hat{\mathcal{H}}'_{\rm et} = -\frac{1}{2}\hat{\mathcal{H}}_{\rm d} - \frac{3}{4}\sum_{i\rangle j} A_{ij}\{\hat{I}_{i+}\hat{I}_{j+}\exp[{\rm i}\phi(t)] + {\rm c.c.}\}$$
$$-\frac{1}{2}\sum_i \Delta\sigma_i\{\hat{I}_{i+}\exp[-{\rm i}\phi(t)/2] + {\rm c.c.}\} \qquad (16)$$

where c.c. denotes the Hermitian conjugate of the operators within the braces.

As pointed out by Waugh and Wang,[11] only the zero-frequency components of the time-dependent terms in equation (16) can contribute to the observed decay, because the time-dependent parts correspond to frequencies much higher than A_{ij} and $\Delta\sigma_i$ if $1/(t_{\rm w} + 2\tau)$ is sufficiently large. For the periodic functions in equation (16), which involve sine and cosine functions of $\phi(t)$ and $\phi(t)/2$, the zero-frequency components can be obtained graphically in a relatively simple manner by calculating the corresponding averages over one period. Assuming the first π pulse at time from τ from the origin and a sequence of perfect rectangular π pulses of width $t_{\rm w}$, the zero-frequency component of exp $[\pm{\rm i}\phi(t)/2]$ can be seen to vanish leading to a suppression of shifts in equation (16). On the other hand, the dc component of exp $[{\rm i}\phi(t)]$, denoted by $\mathcal{L}$, is given by[3]

$$\mathcal{L} = \frac{1}{T}\int_0^T \cos\phi(t')\,{\rm d}t' = 1 - D \qquad (17)$$

where $T = 2\tau + t_{\rm w}$ is the period, and $D = 2\tau/T$ denotes the duty factor of the sequence of π pulses.

In order to evaluate the effect of π pulses of finite width upon the spectrum of isolated pairs (Figure 1), one can diagonalize the static part of $\hat{\mathcal{H}}'_{\rm et}$ [equation (16)] given by

$$\hat{\mathcal{H}}'_{\rm et} = -\tfrac{1}{2}A_{12}(\hat{\boldsymbol{I}}_1\cdot\hat{\boldsymbol{I}}_2 - 3\hat{I}_{z1}\hat{I}_{z2}) - \tfrac{3}{4}A_{12}(\hat{I}_{1+}\hat{I}_{2+}\mathcal{L}$$
$$+\hat{I}_{1-}\hat{I}_{2-}\mathcal{L}^*) \qquad (18)$$

For spin-$\frac{1}{2}$ nuclei, an adequate basis is composed of the singlet and triplet states introduced earlier in connection with equations (1) and (2). The states $|t_0\rangle$ and $|s_0\rangle$ are still eigenfunctions of $\hat{\mathcal{H}}'_{\rm et}$, whereas two appropriate linear combinations of $|t_+\rangle$ and $|t_-\rangle$ constitute the other two eigenstates.

The quantity of interest in the CPMG experiment is proportional to ${\rm Tr}\,(\hat{\rho}'_{\rm et}(t)\hat{I}_{\rm z})$ and can be explicitly computed[3] from the known eigenvalues and eigenvectors yielding a spectrum of two lines for a given orientation of $\boldsymbol{B}_0$. The frequency separation Δ between the lines for $\theta_{12} = \pi/2$, corresponding to the singularities in the spectrum of randomly oriented pairs (Figure 1) is governed by the second term in equation (18), since the first term commutes with $\hat{\rho}'_{\rm et}(0) = {\rm const}\times\hat{I}_z$ and does not cause any decay. It can be shown[3] that Δ is given by

$$\Delta = 3\gamma^2\hbar(1-D)/4\pi\boldsymbol{r}_{12}^3 \qquad (19)$$

4 DIPOLAR SPECTRA

Figure 2 shows a ^{13}C spectrum of polycrystalline acetic acid at T = 80 K; there is a very close correspondence with the theoretical spectrum shown in Figure 1. The sample contains 4% doubly ^{13}C-labeled acetic acid dissolved in ^{13}C-depleted acetic acid. A modified CPMG sequence with 2τ = 86.4 μs and $t_{\rm w}$ = 9.6 μs, including proton decoupling and cross polarization,[14] was employed. A central peak partially caused by spin locking[7] in the average rf field is omitted for clarity.

Dipolar spectra obtained by employing transient nutations generally display poorer resolution than do those obtained with CPMG sequences, because of the reduction in spectral range by a factor of 2 [equation (13)]. Good resolution is especially important when pairs with more than one interatomic distance are involved.[15] On the other hand, for the CPMG sequence, the splitting Δ(Figure 2) depends on the duty factor, but

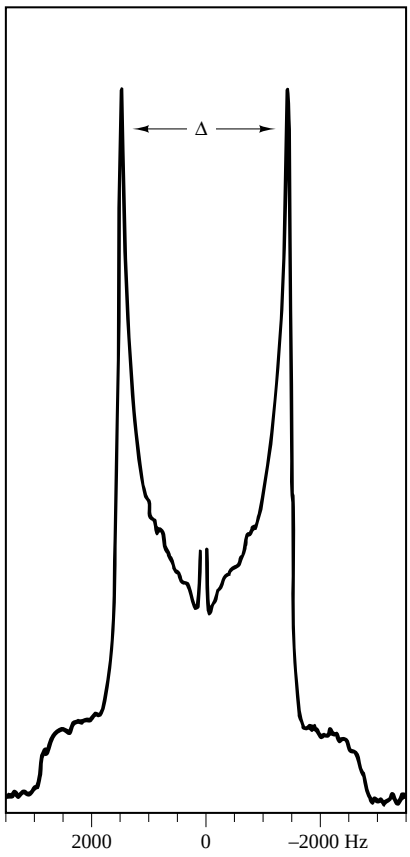

Figure 2 ^{13}C spectrum of polycrystalline acetic acid at T = 80 K. The sample contains 4% doubly ^{13}C-labeled acetic acid dissolved in ^{13}C-depleted acetic acid. A modified CPMG sequence with pulse separation 2τ = 86.4 μs and pulse width t_ω = 9.6 μs was employed (Reproduced by permission from M. Engelsberg and C. S. Yannoni, *J. Magn. Reson.*, 1990, **88**, 393)

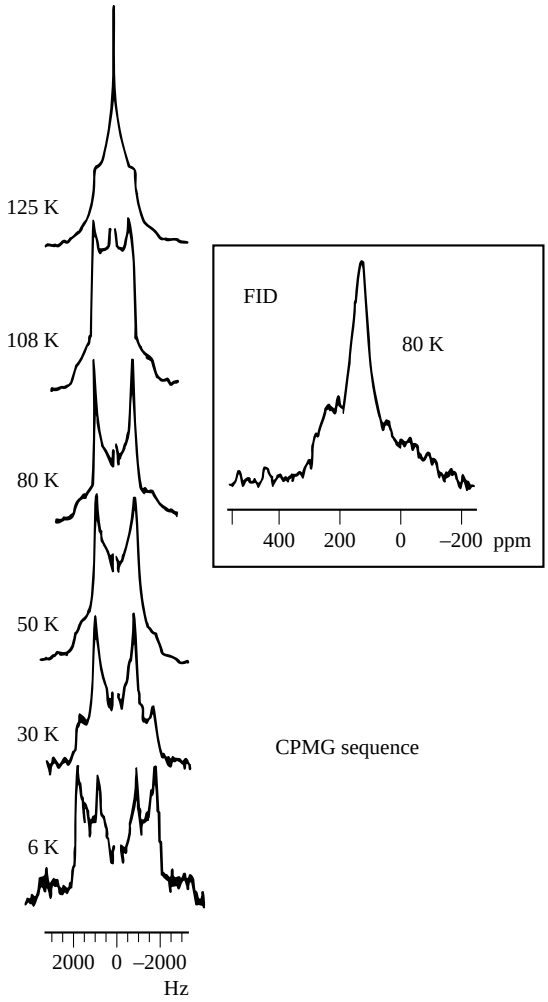

Figure 3 ^{13}C dipolar spectra of benzene (1,2-$^{13}C_2$) chemisorbed on Pt/η-Al_2O_3 obtained by a modified CPMG sequence at various temperatures. The narrow central peak, partially due to spin locking, has been omitted for clarity in all spectra, except the one at 125 K. (Inset) Conventional (FT of FID) proton-decoupled spectrum in the same system at T = 80 K, with shifts measured with respect to a TMS reference (Reproduced by permission from M. Engelsberg, C. S. Yannoni, M. A. Jacintha, C. Dybowski, and R. E. de Souza, *J. Phys. Chem.*, 1994, **98**, 2397. © 1994 American Chemical Society)

the variation has been shown experimentally[3] to agree with the linear dependence predicted by equation (19). Thus a simple correction permits accurate measurement of interatomic distances.[3]

One example of dipolar spectroscopy which helps to illustrate its applicability is provided by the study of benzene chemisorbed on an η-alumina-supported platinum catalyst.[6] The inset in Figure 3 shows a conventional proton-decoupled ^{13}C spectrum of benzene (ν_0 = 15 MHz), doubly labeled in *ortho* positions, chemisorbed on Pt/η–Al_2O_3 at T = 80 K, obtained by FT of the FID. Also shown in Figure 3 are spectra of the same system at various temperatures obtained from a modified CPMG sequence, where the suppression of inhomogeneous broadening uncovers a rich variety of geometrical and dynamical information. The four peaks at the lowest temperature correspond to benzene molecules at different sites, not to different bond lengths.[6,16] For some sites the molecules are rapidly reorienting about the hexad axis,[17] corresponding to $\psi_{12} = \pi/2$ in equation (4), while for others this reorientation rate is small. This explains the difference of a factor of 2 in the splittings of the two inner peaks compared with the outer peaks. At temperatures above 80 K, the spectra can be simulated[6] assuming that the axis of hindered rotation no longer remains perpendicular to the plane of the molecule.

Other examples[15,18,19] of dipolar spectra in a variety of systems further illustrate the usefulness of the techniques described in Section 3 for probing the structure and dynamics of solids.

5 RELATED ARTICLES

Average Hamiltonian Theory; Echoes in Solids; Homonuclear Recoupling Schemes in MAS NMR; Internal Spin Interactions and Rotations in Solids; Nutation Spectroscopy of Quadrupolar Nuclei.

6 REFERENCES

1. C. S. Yannoni and R. D. Kendrick, *J. Chem. Phys.*, 1981, **74**, 747.
2. H. Y. Carr and E. M. Purcell, *Phys. Rev.*, 1954, **94**, 630.
3. M. Engelsberg and C. S. Yannoni, *J. Magn. Reson.*, 1990, **88**, 393.
4. A. Abragam, *The Principles of Nuclear Magnetism*, Oxford University Press, London, 1961, Chap. 4
5. G. E. Pake, *J. Chem. Phys.*, 1948, **16**, 327.
6. M. Engelsberg, C. S. Yannoni, M. A. Jacintha, C. Dybowski, and R. E. de Souza, *J. Phys. Chem.*, 1994, **98**, 2397.
7. C. P. Slichter, *Principles of Magnetic Resonance*, 2nd edn., Springer, Berlin, 1980, Chaps. 3 and 6.
8. J. S. Waugh, C. H. Wang, L. M. Huber, and R. L. Vold, *Phys. Rev.*, 1968, **48**, 662.
9. S. Meiboom and D. Gill, *Rev. Sci. Instrum.*, 1958, **29**, 688.
10. T. Gullion, D. B. Baker, and M. S. Conradi, *J. Magn. Reson.*, 1990, **89**, 479.
11. J. S. Waugh and C. H. Wang, *Phys. Rev.*, 1967, **162**, 209.
12. D. Horne, R. D. Kendrick, and C. S. Yannoni, *J. Magn. Reson.*, 1980, **38**, 493.
13. D. Barnaal and I. J. Lowe, *Phys. Rev. Lett.*, 1963, **11**, 258.
14. A. Pines, M. G. Gibby, and J. S. Waugh, *J. Chem. Phys.*, 1973, **59**, 569.
15. C. S. Yannoni and T. C. Clarke, *Phys. Rev. Lett.*, 1983, **51**, 1191.
16. M. Engelsberg, C. S. Yannoni, M. A. Jacintha, and C. Dybowski, *J. Am. Chem. Soc.*, 1992, **114**, 8319.
17. E. R. Andrews and R. G. Eades, *Proc. R. Soc. Lond., Ser A*, 1953, **218**, 537.
18. J. F. M. Post, B. W. Cook, S. R. Dowd, I. J. Lowe, and C. Ho, *Biochemistry*, 1984, **23**, 6138.
19. C. S. Yannoni, P. P. Bernier, D. S. Bethune, G. Meijer, and J. R. Salem, *J. Am. Chem. Soc.*, 1991, **113**, 3190.

Biographical Sketch

Mario Engelsberg. *b* 1939. Lic. Física 1966, Universidad de Buenos Aires, Argentina. Ph.D. (Physics), Washington University (St. Louis)

(supervisor R. E. Norberg), 1971. Postdoctoral work, University of Pittsburgh (with I. J. Lowe). Professor of Physics, Universidade Federal de Pernambuco, Recife, Brazil, 1974–present. Approx. 55 publications in applications of solid state NMR to physics and chemistry of materials and in NMR imaging at very low magnetic fields.

Double Quantum Coherence

Michael Munowitz
Naperville, IL, USA

1	Introduction	1
2	Vector Precession Model and Coherence	2
3	Properties of Double Quantum Coherence	3
4	Double Quantum Effects in Quadrupolar Systems	5
5	Double Quantum Effects in Spin-$\frac{1}{2}$ Systems	7
6	Related Articles	9
7	References	9

1 INTRODUCTION

Double quantum coherence, a dipole-forbidden degree of freedom in a multilevel spin system, is an important feature of many time domain techniques. Connecting a pair of states where the Zeeman quantum numbers differ by ± 2, a coherent two quantum superposition is the simplest manifestation of the general phenomenon of multiple quantum coherence. Already, however, it exhibits the same phase properties and time development characteristic of more complicated modes, and it serves as an indispensable building block for both theoretical and experimental purposes. Double quantum and related nondipole coherences often provide the mechanism by which modern multidimensional pulse sequences operate.[1–9]

Magnetic resonance is about oscillations, particularly those of a time-dependent magnetization as picked up by a receiving coil. The most basic picture, exemplified best by a collection of uncoupled spin-$\frac{1}{2}$ nuclei, is of a magnetization vector precessing about an applied field with a given amplitude, frequency, and phase. The amplitude of the vector is, of course, its length, from which the strength of the signal is derived. Frequency indicates the number of revolutions completed each second, while the phase denotes the degree of advancement within a cycle. It is phase—where the magnetization is at any point, and not its length or angular velocity—that is the key to coherence, and it is coherence that makes time domain NMR possible.

Consider first the physical meaning of single quantum coherence, which underpins the usual model of transverse magnetization. For an ensemble of identical, noninteracting spin-$\frac{1}{2}$ nuclei, we picture a set of independent oscillators each precessing with the same frequency and amplitude (Figure 1). The net magnetization, which arises as the sum of these separate contributions, is determined entirely by the phase relationships among the different vectors. In an array where the phases are randomly distributed between 0 and 2π, as in Figure 1(a), the transverse components vanish owing to destructive interference. There remains only a time-independent longitudinal component along the field. This *absence* of phase coherence is the normal condition for a spin system in thermal equilibrium. *Coherent* oscillations, by contrast, develop following a $\pi/2$ pulse, which acts to synchronize the phases of all the vectors [Figure 1(b)].

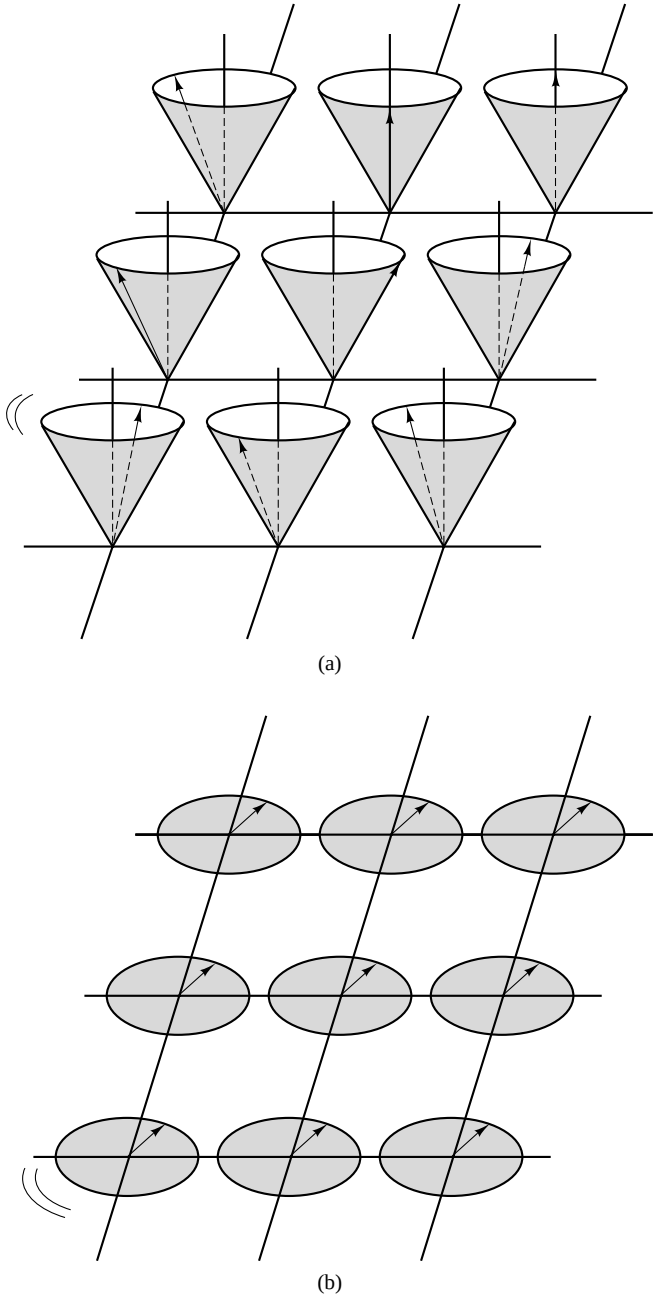

Figure 1 (a) Incoherent and (b) coherent phase relationships in an ensemble of two-level systems

Everything moves together, and a net magnetization is detected in the plane perpendicular to the field.

Viewed as a collection of oscillators, the spin-$\frac{1}{2}$ system thus exhibits coherence when all its component vectors precess with the same phase. Quantum mechanically, one describes the state as a *coherent superposition* (or linear combination) of the spin-up and spin-down states—$|\alpha\rangle$ and $|\beta\rangle$—for which the difference in Zeeman quantum numbers ($\frac{1}{2}$, $-\frac{1}{2}$) is one unit. The phase of precession appears as a phase in the wavefunction, and in this way the physical picture of magnetization is translated into a more abstract, yet more general concept of single quantum coherence. The same quantum mechanical interpretation of phase coherence can

then be extended, by analogy, to double quantum coherence and beyond, for which the simpler model of magnetization does not apply.

2 VECTOR PRECESSION MODEL AND COHERENCE

Any quantitative understanding of quantum mechanical coherence begins with an ensemble of two-level systems evolving under some Hamiltonian $\hat{\mathcal{H}}$. Let the two possible states, denoted as $|1\rangle$ and $|2\rangle$, be left unspecified for now, although presently we will associate them with spins. By taking a general approach to coherence at least initially, we are reminded that the concept is not restricted to NMR. Many of the same ideas find application in microwave and electron paramagnetic resonance (EPR) spectroscopy, as well as certain optical phenomena.

Thus understood, each individual wavefunction

$$|\psi\rangle = c_1|1\rangle + c_2|2\rangle \tag{1}$$

may be reorganized into a density operator $\hat{\boldsymbol{\rho}}$ whose three linearly independent and orthogonal components form a vector in a three-dimensional Liouville space:

$$\rho_x = c_1c_2^* + c_1^*c_2 \tag{2a}$$

$$\rho_y = -\mathrm{i}(c_1c_2^* - c_1^*c_2) \tag{2b}$$

$$\rho_z = c_1^*c_1 - c_2^*c_2 \tag{2c}$$

These quantities are just numerical representations of the basis operators

$$\hat{\rho}_x = |1\rangle\langle 2| + |2\rangle\langle 1| \tag{3a}$$

$$\hat{\rho}_y = -\mathrm{i}(|1\rangle\langle 2| - |2\rangle\langle 1|) \tag{3b}$$

$$\hat{\rho}_z = |1\rangle\langle 1| - |2\rangle\langle 2| \tag{3c}$$

used by Pauli to describe electron spin. A fourth component ($c_1c^*{}_1 + c_2c^*{}_2 = 1$) merely restates the normalization condition, and is of no further interest.

If the Hamiltonian matrix elements $H_{rs} = \langle r|\hat{\mathcal{H}}|s\rangle$ are similarly combined into the vector

$$\Omega_x = H_{12} + H_{21} \tag{4a}$$

$$\Omega_y = -\mathrm{i}(H_{12} - H_{21}) \tag{4b}$$

$$\Omega_z = H_{11} - H_{22} \tag{4c}$$

then the time-dependent Schrödinger equation can be recast into a precession equation,

$$\frac{\mathrm{d}\boldsymbol{\rho}}{\mathrm{d}t} = \boldsymbol{\rho} \times \boldsymbol{\Omega} \tag{5}$$

The density vector $\boldsymbol{\rho}$ thus precesses about $\boldsymbol{\Omega}$ in analogy to the precession of a spin-$\frac{1}{2}$ magnetization about an applied field.[10] This motion is made explicit when ρ_x and ρ_y are combined into a single transverse component, $\rho_{xy} = \rho_x + \mathrm{i}\rho_y$, to give

$$\frac{\mathrm{d}\rho_{xy}}{\mathrm{d}t} = -\mathrm{i}\Omega_z\rho_{xy} \tag{6}$$

and thence

$$\rho_{xy}(t) = \rho_{xy}(0)\exp(-\mathrm{i}\Omega_z t) \tag{7}$$

The longitudinal population, ρ_z, remains constant.

Nothing has happened so far, for we have only *rearranged* the Schrödinger equation for one spin. The vector cross-product form in equation (5) is recognized instantly as the Bloch equations in the absence of relaxation, and no new features have yet appeared.

The notion of coherence enters now through the *phase* of precession, which is related to the coefficients in the original two-state superpositions. Writing each complex coefficient c_j as

$$c_j = |c_j|\exp(\mathrm{i}\phi_j) \tag{8}$$

we have [using equations (2a) and (2b)]

$$\rho_{xy}(t) = 2|c_1|\,|c_2|\exp[-\mathrm{i}(\Omega_z t + \Delta\phi)] \tag{9}$$

for which the phase is established by $\Delta\phi = \phi_2 - \phi_1$. Since each wavefunction may exhibit a different value of $\Delta\phi$, phase coherence is determined by the extent to which the individual precessional motions are correlated throughout the ensemble. The proper relationships appear when the $\boldsymbol{\rho}$ vectors are averaged over the ensemble to yield a statistical description of the mixed state.[1,11,12]

The two extreme cases discussed above now appear in more quantitative form:

1. *No coherence*, or random phases as in Figure 1(a). Here the mixed states is an incoherent superposition of the two basis states, with the population difference given by the time-dependent z component $|c_1|^2 - |c_2|^2$. For spins $\frac{1}{2}$, the situation corresponds to thermal equilibrium.
2. *Full transverse coherence*. The populations $|c_1|^2$ and $|c_2|^2$ become equal, and the phases $\Delta\phi$ are uniform across the ensemble. All vectors precess synchronously in the xy plane, as already illustrated in Figure 1(b).

For the prototype example of a spin-$\frac{1}{2}$ nucleus, the ensemble-averaged vector $\boldsymbol{\rho}$ is isomorphic to the physical magnetization. Its z component is proportional to the population difference, whereas the x and y components correspond to the transverse magnetization in the rotating frame. We need simply take $\hat{\boldsymbol{I}} = \frac{1}{2}\hat{\boldsymbol{\rho}}$ to recover the usual angular momentum operators,

$$\hat{I}_x = \tfrac{1}{2}(|\alpha\rangle\langle\beta| + |\beta\rangle\langle\alpha|) \tag{10a}$$

$$\hat{I}_y = -\tfrac{\mathrm{i}}{2}(|\alpha\rangle\langle\beta| - |\beta\rangle\langle\alpha|) \tag{10b}$$

$$\hat{I}_z = \tfrac{1}{2}(|\alpha\rangle\langle\alpha| - |\beta\rangle\langle\beta|) \tag{10c}$$

and thus appreciate the one-to-one correspondence. The real power of the vector precession model, however, only becomes apparent in *multilevel* spin systems, where the underlying physical picture is less readily apprehended. Here the wavefunctions are generalized to

$$|\psi\rangle = c_1|1\rangle + c_2|2\rangle + \ldots + c_N|N\rangle \tag{11}$$

so the density operator $|\psi\rangle\langle\psi|$ now contains N^2 elements of the form $|r\rangle\langle s|$, instead of the four elements found in the two-level case. Nevertheless, for any pair of levels r and s we can form pseudospin operators analogous to those in equation (10),

$$\hat{I}_x^{r-s} = \tfrac{1}{2}(|r\rangle\langle s| + |s\rangle\langle r|) \quad (12a)$$

$$\hat{I}_y^{r-s} = -\tfrac{\mathrm{i}}{2}(|r\rangle\langle s| - |s\rangle\langle r|) \quad (12b)$$

$$\hat{I}_z^{r-s} = \tfrac{1}{2}(|r\rangle\langle r| - |s\rangle\langle s|) \quad (12c)$$

and thereby re-establish contact with the vector precession model. These fictitious spin-$\frac{1}{2}$ operators form a basis for the density operator of an arbitrary N-level spin system.[13–15] They permit one to treat a transition between *any* two states $|r\rangle$ and $|s\rangle$ using the same physical picture as for spin $\frac{1}{2}$. The x and y components describe the phase coherence, and the z component again supplies the population difference between the two states. And with each state $|r\rangle$ understood to be a Zeeman eigenstate having z component equal to m_r,

$$\hat{I}_z|r\rangle = m_r|r\rangle \quad (13)$$

there is no restriction on the order of coherence, $k = m_r - m_s$. The multiple quantum coherence is just the physical manifestation of a uniform phase relationship between states $|r\rangle$ and $|s\rangle$, deriving from the particular linear combinations specified by c_r and c_s.

Two spin-$\frac{1}{2}$ nuclei, for instance, may be described by four direct-product states—$|1\rangle = |\alpha\alpha\rangle$, $|2\rangle = |\beta\alpha\rangle$, $|3\rangle = |\alpha\beta\rangle$, $|4\rangle = |\beta\beta\rangle$—out of which a set of fictitious spin-$\frac{1}{2}$ operators can be constructed according to equation (12). Double quantum coherence, corresponding to coherent superposition of $|\alpha\alpha\rangle$ and $|\beta\beta\rangle$, is then represented by the operators $\hat{I}_x^{1-4}$ and $\hat{I}_y^{1-4}$, while the population difference between the $\alpha\alpha(m = 1)$ and $\beta\beta(m = -1)$ states is given by $\hat{I}_z^{1-4}$. The three fictitious spin-$\frac{1}{2}$ operators commute as angular momenta within the 1–4 double quantum subspace, and consequently the well-understood properties of three-dimensional rotations fully apply.

The fictitious spin-$\frac{1}{2}$ operators, along with equivalent representations such as the product operator basis, thus bring out a fundamental characteristic of all complex spin systems: there exist *orthogonal modes of coherence*,[16] analogous to the normal modes of other spectroscopic methods, which can be excited individually and monitored dynamically. These independent degrees of freedom are the irreducible units from which complex assemblies of spins are formed. Each mode is a coherent superposition of a certain order, rendered graphically as an independent vector precessing in an abstract three-dimensional space. With frequency-selective excitation, for example, a spectroscopist can address a particular pair of levels within the large system and interact with it as a spin $\frac{1}{2}$. The usual resonant phenomena associated with spin-$\frac{1}{2}$ nuclei—$\pi/2$ pulses, formation of coherence, evolution under chemical shifts and spin–spin couplings, relaxation, and so forth—have transparent analogies within the two-level subspace, as suggested in Figure 2.

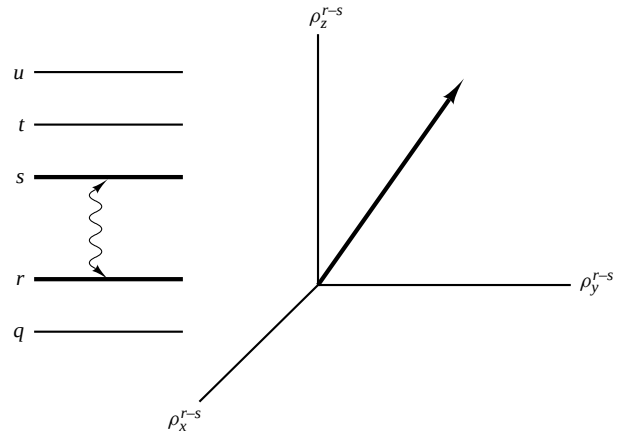

Figure 2 Isolation of two states in a multilevel system

3 PROPERTIES OF DOUBLE QUANTUM COHERENCE

The minimum configuration needed to sustain double quantum coherence is provided by the three levels of a spin-1 nucleus (Figure 3). Here the Zeeman states typically are perturbed by an electric quadrupole coupling, whereby the nonspherical charge distribution of the nucleus interacts with the electric field gradient of the surrounding electrons. This interaction, characterized by a quadrupolar coupling constant ω_Q, shifts the $m = 1$ level by $-\frac{1}{3}\omega_Q$, the $m = 0$ level by

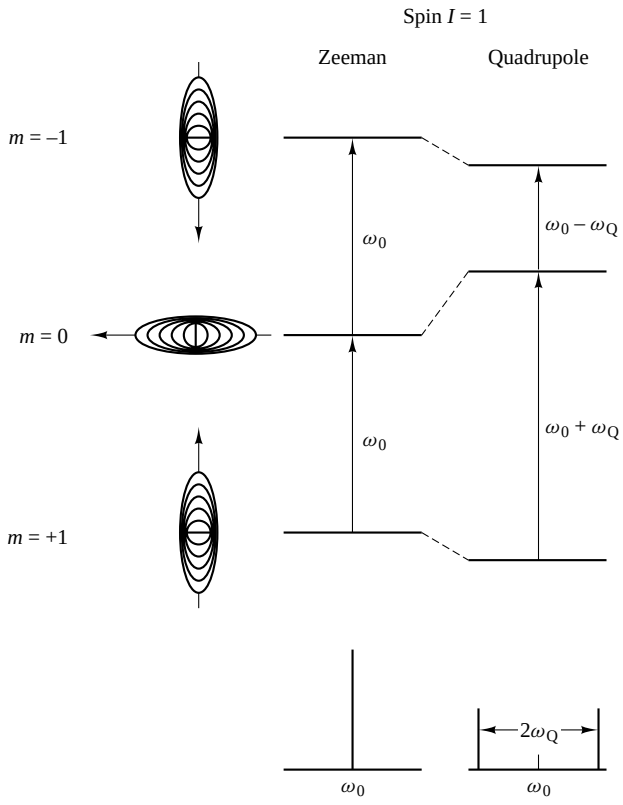

Figure 3 Spin-1 energy levels in the presence and absence of an electric quadrupole coupling. Only the single quantum transitions (and not the double quantum) are split by the quadrupolar interaction

$\frac{2}{3}\omega_Q$, and the $m = -1$ level by $-\frac{1}{3}\omega_Q$ relative to the Larmor frequency ω_0. Single quantum transitions corresponding to (1, 0) and (0, −1) consequently appear at $\omega_0 \pm \omega_Q$, often resulting in a broad spectrum difficult to measure when ω_Q is large.

The double quantum transition (1, −1), however, remains unaffected by the quadrupolar coupling, and resonates at $2\omega_0$. When prepared as a coherent superposition, it evolves independently of the quadupolar Hamiltonian, and develops instead only under the influence of smaller internal interactions such as chemical shifts and spin–spin couplings. Further, the double quantum coherence displays two essential spectral properties: (1) it precesses in the rotating frame at exactly twice the resonant offset of a single quantum transition; (2) its phase (understood to be the instantaneous position of the transverse vector ρ_{xy} in an abstract double quantum space) is shifted by 2ϕ in response to a shift in radiofrequency phase by ϕ.

These key aspects of the double quantum response, when generalized to k quantum coherence ($2\ \Delta\omega \rightarrow k\ \Delta\omega$, $2\phi \rightarrow k\phi$), are exploited in numerous spectroscopic techniques. Among the most important are those designed to separate signals with different orders of coherence, and to excite or detect signals from different orders selectively. The method of time proportional phase incrementation, for example, is rooted in the $n\phi$ phase behavior of double quantum coherence, which was originally observed for double quantum coherence in a three-level system.

A third property, of critical importance experimentally, is 'invisibility'. Single quantum coherence is detectable as ordinary magnetization precisely because it exhibits a nonvanishing magnetic dipole moment. The dipole receiver records the oscillations of $\langle \hat{I}_x \rangle$ and $\langle \hat{I}_y \rangle$ which are nonzero only between states where $\Delta m = \pm 1$. But double quantum coherence, which connects Zeeman states with $\Delta m = \pm 2$, generates no such observable magnetization and therefore must be detected indirectly.

Cast in general spectroscopic terms, the idea is to monitor a forbidden transition through its effect on an allowed transition. Indirect schemes are by no means limited to NMR, and indeed one of the earliest demonstrations involved the detection, by optical techniques, of coherent microwave effects exhibited by molecules in excited triplet states.[17] Coherence between the electron spin levels, although not directly observable owing to symmetry restrictions, nevertheless was measured through changes in phosphorescence. The optical transitions are coupled to the magnetic sublevels of the triplet, and a striking modulation develops when resonant microwave pulses are applied to the electron spins. Electron free precession and electron spin echoes, normally 'hidden' from view, were observed in this way, and the indirect detection of double quantum coherence soon followed.[18]

NMR pulse sequences for indirect detection are generally designed with four distinct periods:

1. *Excitation* of the double quantum coherence, by which a suitable nonequilibrium state is prepared.
2. *Evolution* of the coherence in the presence of natural or externally manipulated couplings and local fields. During this period, the double quantum coherence responds to its environment and oscillates at its characteristic spectral frequencies.
3. *Conversion* of the coherence from an unobservable double quantum form to ordinary single quantum magnetization.
4. *Detection* of the newly created single quantum coherence using ordinary means.

In the usual procedure, one halts the evolution of the double quantum coherence after a specified interval, converts it to an observable single quantum mode, and then records a free induction decay. The first point of the free induction signal, however, depends on the prior history of the double quantum coherence, and thus the progress of the hidden mode is reflected in the observable spectrum. An entire double quantum 'interferogram' can be mapped out in this way, point by point, through systematic incrementation of the evolutionary period. Fourier transformation of the interferogram reveals the spectral response of the double quantum mode to the surrounding local fields. The procedure clearly is the same as for two-dimensional spectroscopy,[19] and in some ways the indirect detection of double quantum spectra in the mid-1970s was a precursor of two-dimensional NMR.

All these properties and considerations pertain to systems of coupled spins as well, the simplest being two spin-$\frac{1}{2}$ nuclei linked by a dipolar or J interaction (Figure 4). The double quantum transition is again between states with $m = \pm 1$, existing now as the direct products $|\alpha\alpha\rangle$ and $|\beta\beta\rangle$. The coherence, as before, evolves independently of the coupling between the two outermost levels. In this system, though, it is the spin–spin interaction that is removed from the dynamics, rather than the analogous quadrupolar coupling. The phase shifts too are enhanced by the expected factor of 2.

Double quantum coherence is the maximum that can be supported between two spin-$\frac{1}{2}$ nuclei. As the *total spin coherence*, it is exemplary of the more complex collective modes from which large coupling networks are built. Consider, in this context, the two spins to constitute a closed system, and picture first a *single quantum* coherence as arising from just one of the spins alone, say 'A'. The transverse magnetization of A then precesses coherently in the local field produced by spin B, which we assume to have magnitude J. Now spin B, roughly speaking, may be up or down, and therefore the A coherence responds to two possible local field configurations: J and $-J$. The single quantum spectrum shows, accordingly, resonances at the two frequencies. But the double quantum coherence, which demands the active participation of *both* spins, is left with no local field to which it can respond. Both spins are tied up in the formation of the coherent superposition, and so the double quantum mode can only evolve as if no spin–spin coupling exists.

In general, collective modes of coherence involve n active spins (which 'flip') and q passive spins (which 'watch'). The order of coherence is established by the Zeeman quantum numbers of the active participants, while the local field is determined by the remaining passive spins. The spectrum of

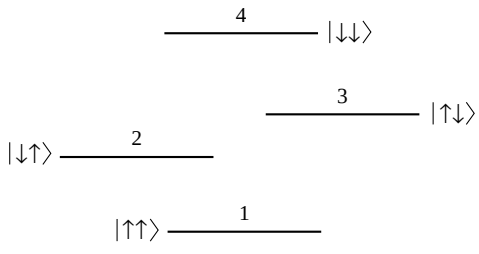

Figure 4 Energy levels for a pair of weakly coupled spin-$\frac{1}{2}$ nuclei

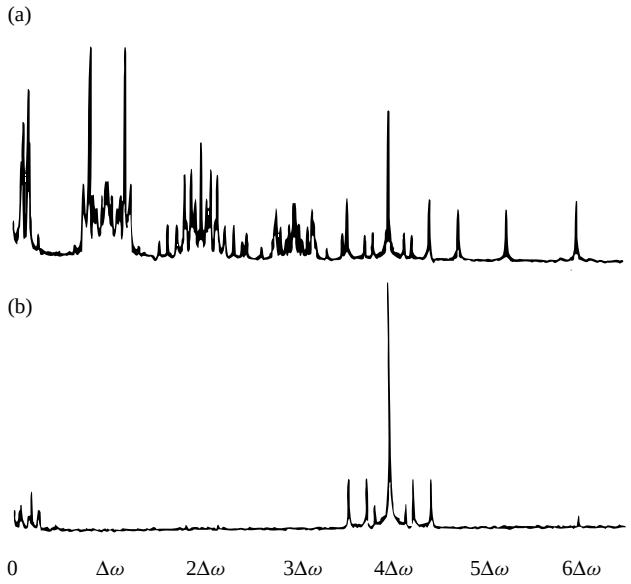

Figure 5 Proton multiple quantum spectra ($|k| = 1, 2, \ldots, 6$) for benzene in an anisotropic solvent. Preparation sequences are built around a two quantum propagator. (a) Nonselective excitation. There are 76 lines in the normal one quantum spectrum, but only two in the five quantum spectrum, and one in the six quantum spectrum. (b) Selective excitation of coherences for which $|k| = 0$ and $|k| = 4$. (Reproduced by permission of the American Institute of Physics from Warren et al.[20])

a multiple quantum coherence, which reflects all the algebraic combinations of the q passive spins, becomes progressively simpler as more spins are allowed to participate actively. The limit is reached with N-quantum coherence in an N-spin system, where the local field vanishes (except for combined chemical shifts and resonance offsets).

One of the early goals of multiple quantum NMR, in fact, was to simplify spectra obtained from oriented systems without sacrificing information about the coupling. A complete picture of the local fields frequently can be extracted from the few resonances available to a high-order coherence, whereas the equivalent single quantum spectrum remains an inpenetrable tangle of lines.

Figure 5(a) illustrates how such simplification is brought about for the case of benzene partially oriented in a liquid crystal solvent. The hydrogen nuclei of each molecule constitute an isolated six-spin system from which multiple quantum signals of orders 1 through 6 can be elicited. The number of lines decreases dramatically with increasing order k, to the point where the six quantum spectrum shows only the one resonance characteristic of the total spin coherence.

Figure 5(b) demonstrates further that multiple quantum coherences can be excited selectively, the example here being primarily four quantum excitation. Selectivity is achieved by exploiting the phase properties of the coherences. Iterative excitation sequences, assembled by concatenating appropriately phase-shifted pulse cycles, are used to channel the coherence into the desired degrees of freedom.[20]

Collective spin modes also form the basis for a number of spin *filtering* techniques. Often designed to exploit the total spin coherence, these methods can be used to select signals from clusters of various sizes—beginning with pairs. Double quantum coherence is the basis for one of the first successful filtering schemes, the detection of $^{13}C-^{13}C$ pairs at natural abundance (see Section 5).

4 DOUBLE QUANTUM EFFECTS IN QUADRUPOLAR SYSTEMS

Experiments carried out in the early to mid-1970s demonstrated many of the properties of double quantum coherence in quadrupolar nuclei such as ^{2}H, ^{23}Na, and ^{27}Al. Frequency-selective excitation by narrowband, 'soft' pulses typically was used to interact with designated pairs of levels, creating circumstances well suited for treatment within the fictitious spin-$\frac{1}{2}$ formalism.

Some of the initial applications demonstrated how double quantum techniques could be used effectively to eliminate dominant quadrupolar or dipole–dipole interactions, while leaving intact smaller couplings of spectroscopic interest. As an alternative to multiple pulse coherent averaging sequences, for example, one might want to study the residual protons in a heavily deuterated material. If hydrogen–hydrogen dipolar interactions are sufficiently attenuated in the dilute system, then the underlying chemical shifts will become visible once the deuterium–hydrogen couplings are eliminated. Unfortunately a technical difficulty arises with conventional decoupling, since the radiofrequency amplitude ω_1 must greatly exceed a quadrupole coupling constant ω_Q of over 100 kHz. If, however, the abundant deuterium nuclei (I) are irradiated continuously with a *weak* radiofrequency field, then *double quantum* decoupling[21–23] can proceed within the fictitious double quantum subspace spanned by the states $|m = 1\rangle$ and $|m = -1\rangle$. For soft irradiation at the deuterium Larmor frequency there is induced a continuous double quantum nutation at an effective angular velocity

$$\omega_e = \sqrt{(2D_{IS})^2 + (\omega_1^2/\omega_Q)^2} \tag{14}$$

where D_{IS} denotes the heteronuclear coupling constant. This latter term, off-resonance by D_{IS}, is accelerated to $2D_{IS}$ as described in Section 3. Rotated about the x axis in double quantum space (recall Figure 2), the dipolar interaction now averages to zero when ω_e exceeds D_{IS}, a condition much less stringent than the requirement that ω_1 cover the full width of the deuterium spectrum. Hence a radiofrequency amplitude of

$$\omega_1 \gg \sqrt{\omega_Q D_{IS}} \tag{15}$$

rather than $\omega_1 \gg \omega_Q$ suffices. With the $(1, -1)$ transition stirred continuously by the narrowband decoupling field, only the $|m = 0\rangle$ state (which exerts no z field on the S spin) is left.

A deuterium-decoupled chemical shift anisotropy powder pattern of the residual ^{1}H nuclei in deuterated ice, shown in Figure 6, illustrates the ability of the technique to improve the resolution of dilute proton systems in the solid state.[22,23] Effects of motion show up in the temperature-dependent powder patterns as well, with the lineshapes undergoing motional averaging characteristic of tetrahedral jumps. The behavior is consistent with the protons hopping around the four hydrogen bonds in the ice lattice.

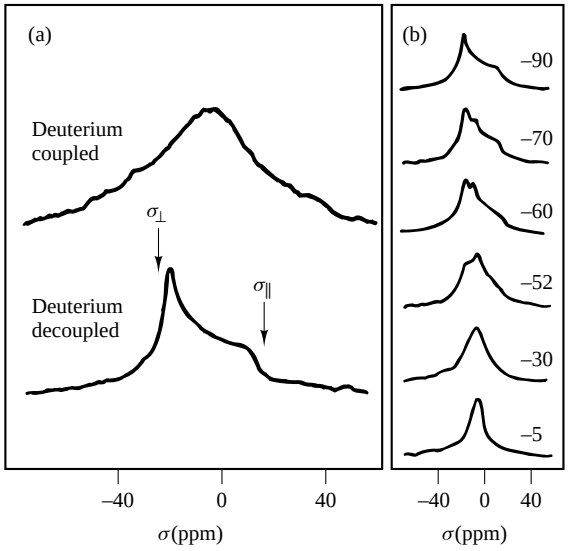

Figure 6 (a) NMR spectra of residual protons in heavy ice (99% deuterium) at $-90\,^{\circ}$C with and without deuterium decoupling. The chemical shift anisotropy of the hydrogen-bonded protons is approximately 34 ppm. (Reproduced by permission of the American Physical Society from Pines et al.[22a]) (b) The spectra are motionally narrowed at higher temperatures, developing lineshapes consistent with tetrahedral jumps. (By courtesy of D. E. Wemmer)

Another use of double quantum excitation is to *bypass* the quadrupolar coupling itself, by looking directly at the unbroadened $(1, -1)$ transition. Narrowband excitation again is used to address only the double quantum subspace, within which the resonant nutation frequency is ω_1^2/ω_Q. The condition for a $\pi/2$ pulse is therefore

$$\frac{\omega_1^2 \tau_p}{\omega_Q} = \frac{\pi}{2} \tag{16}$$

for a burst of duration τ_p. Hence an effective $\pi/2$ pulse can be applied to convert a double quantum population difference into a double quantum transverse coherence. If the m = 1, 0, and -1 Zeeman states are designated as $|1\rangle$, $|2\rangle$, and $|3\rangle$, respectively, then the effect is to rotate $\hat{I}_z^{1-3}$ into $\hat{I}_x^{1-3}$. Once created, the 1–3 transverse coherence vector precesses in a local field due only to the chemical shift and is unaffected by the quadrupolar coupling. The response is mapped out point by point to obtain a double quantum interferogram in the manner discussed in Section 3.

An example of a quadrupole-free double quantum spectrum is provided in Figure 7, with both the time domain and Fourier transform shown.[23] The spectrum is of the chemical shift anisotropy of deuterium in benzene (a powder pattern only 6 ppm wide), obtained in the presence of a 100 kHz quadrupolar coupling constant. What the double quantum approach thus demonstrates is an ability to *avoid* rather than eliminate a large and obstructive coupling. Neither spatial nor spin averaging is employed in a frontal attack on the unwanted interaction, which is left untouched. A mode of coherence indifferent to the offending Hamiltonian is used instead.

Another application involves *spin locking*, by which the lifetime of a double quantum coherence is prolonged in the rotating frame. Analogous to conventional spin locking, the idea is to align the coherence along an applied radiofrequency field. Thus a single quantum coherence parallel to, say, the x axis might be prepared by a $\pi/2$ pulse applied about the y axis of the rotating frame, whereupon the radiofrequency phase would be shifted by $\pi/2$ to realign the effective field along x. With ω_1 now on the x axis, the x magnetization is held fixed along the effective field and is relaxed primarily by lower-frequency motions comparable to ω_1. The same treatment can be imposed on a *double quantum* coherence as well, provided that its nutation and phase characteristics are respected. First, the two quantum mode is aligned along the x axis by a soft pulse resonant only with the $(1, -1)$ transition. Second, the spin locking burst must be shifted by $\pi/4$ (rather than $\pi/2$) in keeping with the two-fold sensitivity to radiofrequency phase. The applied shift of $\pi/4$ is perceived by the double quantum coherence as $\pi/2$, and the spin lock is established.[18]

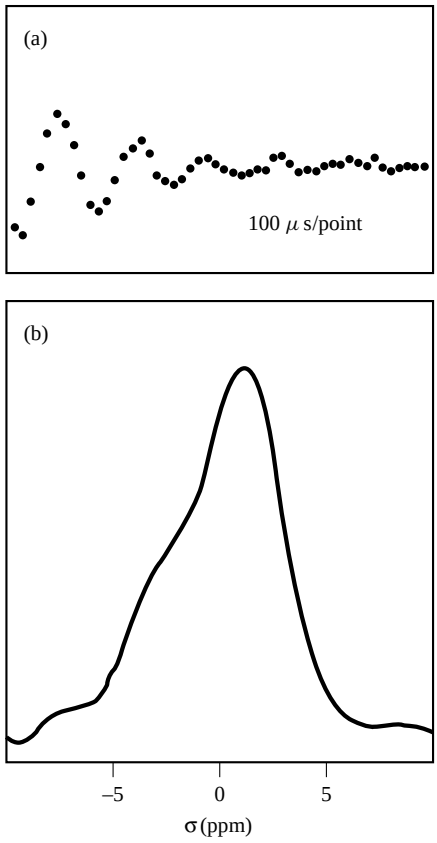

Figure 7 (a) Double quantum free induction decay of deuterium in solid benzene-d_1 doped (10%) into benzene, detected indirectly. Signals were recorded at $-40\,^{\circ}$C, with proton decoupling. (b) Fourier transform, revealing the chemical shift anisotropy. The left edge of the pattern corresponds to the field oriented along the benzene plane normal; the peak at the right corresponds to the perpendicular direction. (By courtesy of S. Vega)

Figure 8 demonstrates the slow decay of a spin locked two quantum signal in deuterated benzene, where ordinarily the transverse relaxation time is only a few hundred microseconds. Held by the phase-shifted locking field, the coherence now endures for some milliseconds.

Spinor behavior and interferometric effects, too, have been observed in multilevel systems where selective excitation creates fictitious spin-$\frac{1}{2}$ characteristics. Simultaneous irradiation of all transition frequencies in a spin 1, for example, allows the

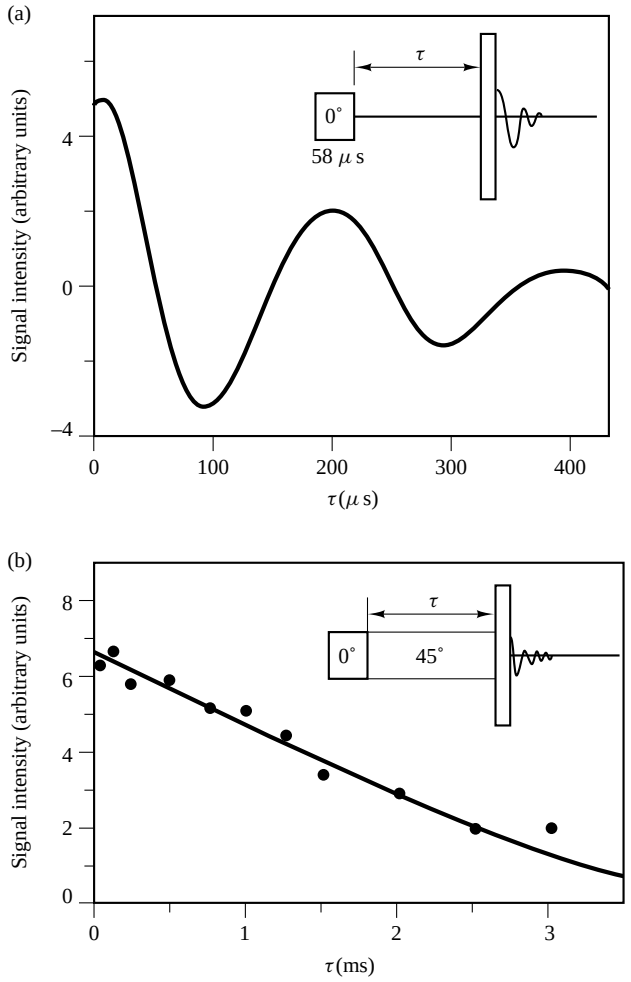

Figure 8 Double quantum phenomena observed for the carboxyl deuterons of crystalline oxalic acid dihydrate. The solid lines represent fits to theoretical models. (a) Free induction decay. A weak $\pi/2$ pulse (τ_p = 58 μs) establishes double quantum coherence across the (1, −1) transition. The coherence evolves undetected for a time τ before being converted to observable magnetization by the strong pulse at the end. (b) Under a spin locking pulse, shifted in phase by $\pi/4$, the double quantum coherence persists for a few milliseconds in the rotating frame. The requisite phase shift of $\pi/4$ (compared with $\pi/2$ in single quantum spin locking sequences) was an early indication that k-quantum coherences display k-fold sensitivity to phase shifts. (By courtesy of S. Vega)

particle to behave as a boson, with its state vector invariant to a rotation by 2π. Selection of just *one* pair of levels within a fictitious spin-$\frac{1}{2}$ subspace, however, creates a pseudofermion. Here the state vector changes sign under a rotation of 2π, going from $|\psi\rangle$ to $-|\psi\rangle$, and returning back to $|\psi\rangle$ only upon rotation by 4π. Detection of this antisymmetry requires interference with a reference state, since the negative sign is lost when the wavefunction is squared. A striking demonstration of spinor periodicity is offered in Figure 9.[24]

Numerous other double quantum effects have been reported, including analogs of familiar NMR phenomena such as spin echoes, rotary echoes, rotary saturation, cross polarization, and population inversion.[18,25,26] Many of these experiments also involve nonintegral spins, in which systems of more than three levels are manipulated. Both single pulse excitation and multistep transfers of coherence between different pairs of

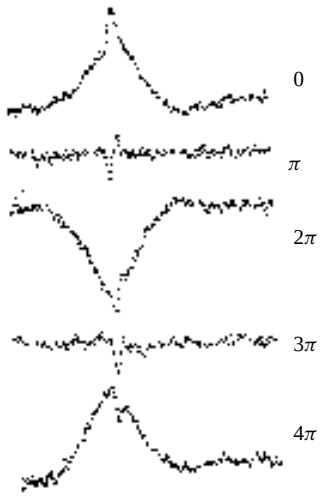

Figure 9 Fermionic behavior in a spin 1, observed within a fictitious spin-$\frac{1}{2}$ subspace. A narrowband $\pi/2$ pulse with frequency ω_{rs} first creates coherence between two of the three levels r, s, t. When irradiated at ω_{st}, the coherence then nutates at the rate $\omega_1/2$, displaying the period of 4π characteristic of spin-$\frac{1}{2}$ particles. The sample is a single crystal of perdeuterated hexamethylbenzene. (Reproduced by permission of the American Physical Society from Stoll et al.[24])

levels are described, and extensive references to the original literature are compiled in a number of books and review articles.[1,6–8]

5 DOUBLE QUANTUM EFFECTS IN SPIN-$\frac{1}{2}$ SYSTEMS

Spin-$\frac{1}{2}$ nuclei can be linked into extended coupling networks through mutual interactions, usually isotropic J couplings in liquids and dipole–dipole couplings in solids and liquid crystals. Double quantum coherence and other nonmagnetization modes, together, have played prominent roles in the rapid development of pulse methods applicable to all phases.

Coupling networks in liquids typically are small, restricted by the limited reach of the through-bond J coupling. The finite size of the clusters is advantageous for spin-selective methods, which are designed to tailor either the excitation or detection to match particular coupling patterns. Of particular interest is the application of spin filtering to ^{13}C spectroscopy where, under ^{1}H decoupling, bonded pairs of ^{13}C nuclei provide two-spin subsystems amenable to double quantum filtering.[27] With ^{13}C naturally abundant at only 1%, though, over 98% of the carbon–carbon pairs are formed by the nonmagnetic isotope ^{12}C. Of the others, most contain just one ^{13}C and therefore can support only single quantum coherence. But there is a 1 in 10 000 chance that adjacent carbons are both ^{13}C—the pair well removed from any other nuclei—and signals derived from these groups can be isolated despite the unfavorable statistics. Since double quantum coherence represents the total spin coherence in the ^{13}C–^{13}C subsystems, there is only one frequency of response: the sum of the chemical shifts from each of the connected carbons. Hence in a filtered two-dimensional spectrum (Figure 10), a double quantum → single

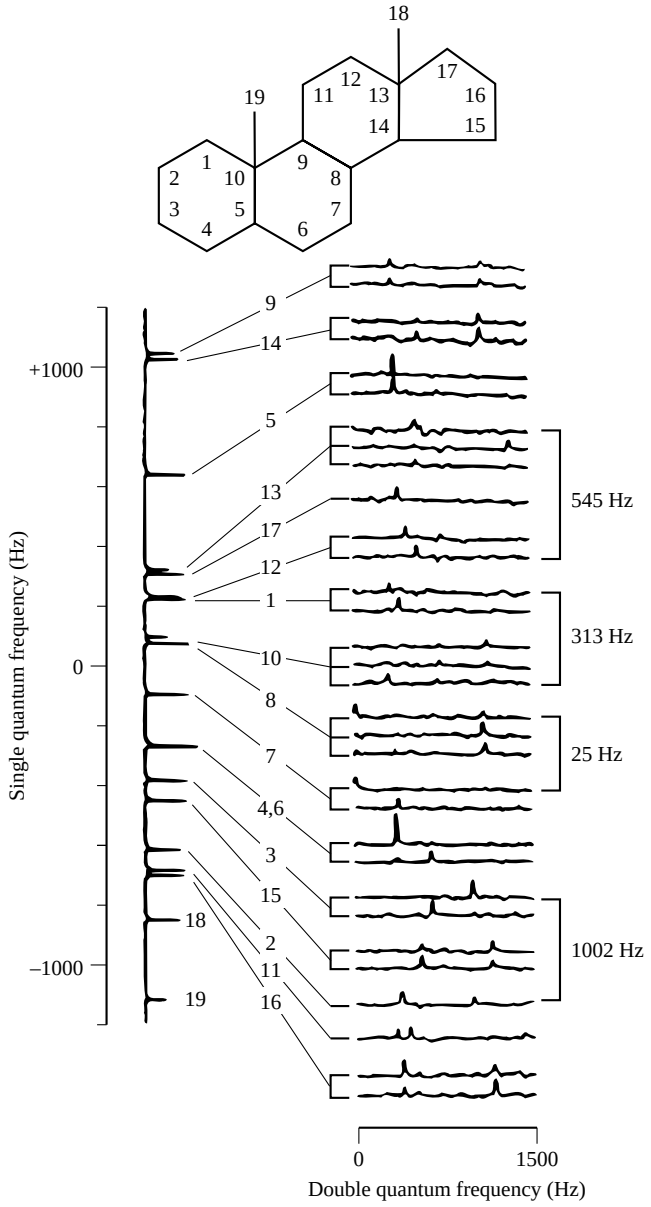

Figure 10 Correlations between double quantum and single quantum frequencies in a two-dimensional ^{13}C spectrum of 5α-androstane. Connections between C-2 and C-3, C-7 and C-8, C-10 and C-1, and C-12 and C-13 are indicated on the spectrum. (Reproduced with permission of the American Chemical Society from Bax et al.[27])

quantum pathway is marked by a common frequency along one axis. Any pair of *single quantum* signals sharing this frequency on the other axis is immediately recognized as originating from the same pair of coupled carbons. Analysis of all the spectral connections permits the reconstruction of the carbon skeleton of the molecule, atom by atom, and provides a first step toward a complete understanding of the structure.

Double quantum coherence, homonuclear and heteronuclear, plays at least some part in vast numbers of pulse sequences, too many to describe adequately in a limited space. Just a few of its manifestations might include BIRD, DEPT, and various spectral editing schemes. But perhaps the most common mode of all is not two quantum but *two spin*. The *antiphase magnetization*, arising from the coherent superpositions $\alpha\alpha \leftrightarrow \beta\alpha$ and $\alpha\beta \leftrightarrow \beta\beta$ in a spin pair, is ubiquitous in its role as a coherence transfer pathway. It is intrinsic to two-dimensional correlated spectroscopy and to the vast majority of sophisticated pulse sequences applied to liquids.

For two nuclei A and B, the antiphase magnetization is proportional to $\hat{I}_{x\mathrm{A}}\hat{I}_{z\mathrm{B}}$ in the product operator representation of the density operator. Fully equivalent to the fictitious spin-$\frac{1}{2}$ description, product operators decompose a system of coupled spins $\frac{1}{2}$ into constituent particles each with two levels.[28] The coherence is imagined as built up spin by spin, rather than by isolation of pairs of states. An antiphase coherence, specifically, is described as a one-quantum two-spin degree of freedom, namely a collective mode with one active spin and one passive. Qualitatively it is pictured as the transverse, single quantum coherence of spin A ($\hat{I}_{x\mathrm{A}}$) responding simultaneously to the two possible orientations of the local field of spin B ($\hat{I}_{z\mathrm{B}}$). Unlike normal in-phase coherence$\hat{I}_x$, however, the antiphase mode appears as the *difference* of two operators: $\hat{I}_x^{1-2} - \hat{I}_x^{3-4}$. One component corresponds to B in the α state; the other component, diametrically opposed in the rotating frame, corresponds to B in the β state (Figure 11). An antiphase coherence, although lacking any net magnetization itself, is readily converted to other modes, including both observable one-quantum one-spin terms such as $\hat{I}_{y\mathrm{B}}$ as well as double quantum terms such as $\hat{I}_{x\mathrm{A}}\hat{I}_{x\mathrm{B}}$.

Solids and other oriented systems, in contrast to liquids, often develop extremely large coupling networks via the through-space dipole interactions. Except perhaps in small, relatively isolated molecules, subsystems containing only two spins (and therefore limited to double quantum coherence) are rare. Nevertheless, double quantum *excitation* sequences are used for selective excitation of k-quantum signals and also to 'pump' coherences of very high order, up to 100 or more in dipolar solids. Specially designed pulse trains successively add two quanta to existing superpositions, thereby creating k-quantum modes where $|k| = 2, 4, 6, \ldots$. These sequences, moreover, are easily manipulated by phase shifts, and can be configured to yield both a two quantum Hamiltonian $\hat{\mathcal{H}}_{yx}$ and its negative, $-\hat{\mathcal{H}}_{yx}$. Negating the Hamiltonian in any unitary propagator

$$\hat{U}(t) = \exp(-\mathrm{i}\hat{\mathcal{H}}t) \tag{17}$$

cannot be distinguished from negating the time, and so the effect is tantamount to reversing the sense of time as the system evolves.[20] Time reversal of this sort is crucial for obtaining high-order multiple quantum spectra in solids.

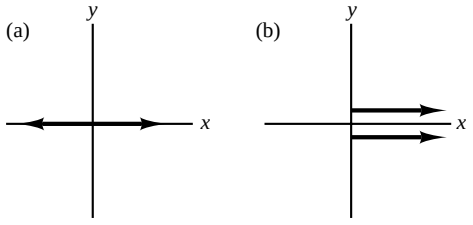

Figure 11 Single-quantum two-spin coherences. (a) Antiphase magnetization, represented as antiparallel vectors. (b) In-phase magnetization

6 RELATED ARTICLES

Average Hamiltonian Theory; Internal Spin Interactions and Rotations in Solids; Multidimensional Spectroscopy: Concepts; Multiple Quantum Coherence in Spin-1/2 Dipolar Coupled Solids; Multiple Quantum Coherences in Extended Dipolar Coupled Spin Networks; Multiple Quantum NMR in Solids; Multiple Quantum Spectroscopy in Liquid Crystalline Solvents; Three- and Four-Dimensional Heteronuclear Magnetic Resonance.

7 REFERENCES

1. M. Munowitz, *Coherence and NMR*, Wiley, New York, 1988.
2. M. Goldman, *Quantum Description of High-Resolution NMR in Liquids*, Oxford University Press, Oxford, 1988.
3. R. R. Ernst, G. Bodenhausen, and A. Wokaun, *Principles of Nuclear Magnetic Resonance in One and Two Dimensions*, Oxford University Press, Oxford, 1987.
4. N. Chandrakumar and S. Subramanian, *Modern Techniques in High-Resolution FT-NMR*, Springer-Verlag, New York, 1987.
5. A. Pines, in *Proc. S.I.F., Course C*, North-Holland, Amsterdam, 1988.
6. M. Munowitz and A. Pines, *Adv. Chem. Phys.*, 1987, **66**, 1.
7. D. P. Weitekamp, *Adv. Magn. Reson.*, 1983, **11**, 111.
8. G. Bodenhausen, *Prog. NMR Spectrosc.*, 1981, **14**, 137.
9. H. Kessler, M. Gehrke, and C. Griesinger, *Angew, Chem., Int. Ed. Engl.*, 1988, **27**, 490.
10. R. P. Feynman, F. L. Vernon, Jr., and R. W. Hellwarth, *J. Appl. Phys.*, 1957, **28**, 49.
11. C. P. Slichter, *Principles of Magnetic Resonance*, 3rd edn., Springer-Verlag, Berlin, 1990.
12. A. Abragam, *Principles of Nuclear Magnetism*, Oxford University Press, Oxford, 1961.
13. S. Vega, *J. Chem. Phys.*, 1978, **68**, 5518.
14. S. Vega and A. Pines, *J. Chem. Phys.*, 1977, **66**, 5624.
15. A. Wokaun and R. R. Ernst, *J. Chem. Phys.*, 1977, **67**, 1752.
16. U. Fano, *Rev. Mod. Phys.*, 1957, **29**, 74.
17. W. G. Breiland, C. B. Harris, and A. Pines, *Phys. Rev. Lett.*, 1973, **30**, 158.
18. (a) S. Vega and A. Pines, *Proceedings of the 19th Ampere Congress, Heidelberg, Germany, September 1976*, ed. K. Hausser, Beltz-Offsetdruck, Hernsback, 1977, p. 183. (b) A. Pines, S. Vega, D. J. Ruben, T. W. Shattuck, and D. E. Wemmer, *Proceedings of the IVth Ampere International Summer School, Pula, Yugoslavia, September 13–23. 1976—Magnetic Resonance in Condensed Matter: Recent Developments*, ed. R. Blinc and G. Lahajnar.
19. W. P. Aue, E. Bartholdi, and R. R. Ernst, *J. Chem. Phys.*, 1976, **64**, 2229.
20. W. S. Warren, D. P. Weitekamp, and A. Pines, *J. Chem. Phys.*, 1980, **73**, 2084.
21. (a) R. C. Hewitt, S. Meiboom, and L. C. Snyder, *J. Chem. Phys.*, 1973, **58**, 5089. (b) L. C. Snyder and S. Meiboom, *J. Chem. Phys.*, 1973, **58**, 5096.
22. (a) A. Pines, D. J. Ruben, S. Vega, and M. Mehring, *Phys. Rev. Lett.*, 1976, **36**, 110. (b) A. Pines, S. Vega, and M. Mehring, *Phys. Rev. B*, 1978, **18**, 112.
23. D. Wemmer, Ph.D. Thesis, University of California, Berkeley, 1978 (Lawrence Berkeley Laboratory Report LBL-8042).
24. M. E. Stoll, E. K. Wolff, and M. Mehring, *Phys. Rev. A*, 1978, **17**, 1561.
25. (a) H. Hatanaka, T. Terao, and T. Hashi, *J. Phys. Soc. Jpn.*, 1975, **39**, 835. (b) H. Hatanaka and T. Hashi, *J. Phys. Soc. Jpn.*, 1975, **39**, 1139. (c) H. Hatanaka, T. Ozawa, and T. Hashi, *J. Phys. Soc. Jpn.*, 1977, **42**, 2069. (d) H. Hatanaka and T. Hashi, *Phys. Lett.*, 1978, **67A**, 183.
26. (a) S. Vega, T. W. Shattuck, and A. Pines, *Phys. Rev. Lett.*, 1976, **37**, 43. (b) S. Vega. T. W. Shattuck, and A. Pines, *Phys. Rev. A*, 1980, **22**, 638.
27. A. Bax, R. Freeman, and T. A. Frenkiel, *J. Am. Chem. Soc.*, 1981, **103**, 2102.
28. O. W. Sørensen, G. W. Eich, M. H. Levitt, G. Bodenhausen, and R. R. Ernst, *Prog. NMR Spectrosc.*, 1983, **16**, 163.

Biographical Sketch

Michael Munowitz. *b* 1955. B.S., Yale University, 1977; Ph.D., Harvard University, 1982 (R. G. Griffin and C. M. Dobson). Postdoctoral work at University of Leiden (J. Schmidt), University of California, Berkeley (A. Pines). Amoco Corporation, 1986–94. Approx. 50 publications. Research specialties: solid state NMR, multiple quantum and local field spectroscopy, design of optical waveguides, modeling of nonlinear optical phenomena.

Double-Quantum NMR Spectroscopy of Dipolar Coupled Spins Under Fast Magic-Angle Spinning

Hans Wolfgang Spiess

Max-Planck-Institut für Polymerforschung, Mainz, Germany

1 Introduction 1
2 High Resolution Solid State NMR 1
3 Applications 5
4 Conclusions and Outlook 12
5 Related Articles in this Volume 14
6 Related Articles in Volumes 1–8 14
7 References 14

1 INTRODUCTION

Double-quantum (DQ) NMR spectroscopy of dipolar coupled spins in solids under fast magic angle spinning (MAS) is new a tool, by use of which topics of general interest in materials science and bioscience can be addressed. For instance, in advanced synthetic as well as in biological systems self assembly of carefully chosen building blocks is of central importance.[1–4] Hydrogen bonding and aromatic π-π interactions are key features of supramolecular chemistry.[5] Despite being highly ordered on a local scale, such systems often do not crystallize. Therefore, their structures cannot be determined by conventional X-ray crystallography or neutron scattering. Alternatives are needed which should provide structural and dynamic information, preferably requiring only small amounts of as-synthesized samples, without the need for isotopic labeling. High resolution solid state ^{1}H-NMR can meet these requirements,[6–8] provided that sufficiently selective information can be extracted from the corresponding spectra.

Since 1994 we have systematically pursued the development of solid state ^{1}H NMR for that purpose by combining fast MAS[9] and DQ NMR spectroscopy,[10] which makes use of the homonuclear dipole–dipole coupling between protons.[11,12] The spectral resolution can be increased by use of similar methods exploiting heteronuclear ^{1}H–^{13}C dipole–dipole couplings.[13] These techniques take advantage of the significant simplification of the multispin dipolar coupled network under fast MAS, where two-spin correlations predominate,[14] and have provided new insight in

- hydrogen bonded structures in the solid state[15]
- columnar stacking and molecular dynamics of discotics[16]
- chain order and translational motion in polymer melts[17]
- chain organization on surfaces.[18]

This review briefly outlines these new approaches for studying supramolecular organization and demonstrate their advantages with specific examples.

2 HIGH RESOLUTION SOLID STATE NMR

Various aspects of solid state NMR are subjects of other articles in this Encyclopedia. For a full treatment of earlier work including multidimensional techniques, we refer to our extended monograph.[19]

2.1 Magic Angle Spinning

A particularly important recent advance in solid state NMR is fast MAS with rotor frequencies $\omega_R > 2\pi \cdot 25\,\text{kHz}$[9] up to $2\pi \cdot 50\,\text{kHz}$ as described by Samoson (see **Magic-angle Spinning Extensions**).[20] For most organic solids, the strongest ^{1}H–^{1}H dipole–dipole coupling, e.g., in CH_2 groups with a proton–proton distance of 0.18 nm are of the order of $\omega_D \approx 2\pi \cdot 20.6\,\text{kHz}$. Thus, the condition $\omega_R \geq \omega_D$ can be met even for the strongest dipole–dipole couplings. Since in most cases the remaining spins are further away, the corresponding remote couplings can effectively be 'spun out'

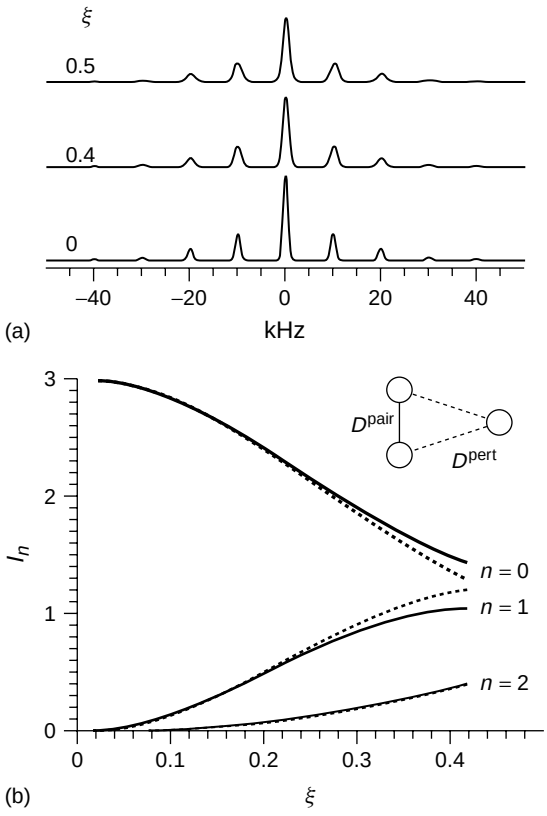

Figure 1 (a) Simulated MAS NMR spectra f or a spin-pair subject to a perturbing spin in an isosceles triangle arrangement for various ratios ξ of the perturbing dipole–dipole coupling ω_D^{pert} to the rotor frequency ω_R. (b) Centreband ($n = 0$) and sideband ($n = 1$, 2) intensities in MAS spectra for the three-spin system in (a) as function of ξ. Solid lines, two- and three-spin correlations; dotted lines, only two-spin correlations.[21] (Reproduced by permission of Academic Press)

and only the strongest couplings, originating from the shortest distances, are retained. This simple picture is indeed borne out in an elaborate theoretical treatment of multi-spin systems under fast MAS, combining Floquet theory and perturbation theory.[14] The higher-spin contributions are found to scale with increasing powers of the inverse rotor frequency and become less and less important at higher and higher ω_R.

As an example, Figure 1(a) shows MAS NMR spectra for a spin-pair subject to a perturbing spin in an isosceles triangle arrangement for various ratios ξ of the perturbing dipole–dipole coupling ω_D^{pert} to the rotor frequency ω_R.[21] Sideband patterns are observed, from which the dominant dipole–dipole coupling D^{pair} can be determined straightforwardly as indicated in Figure 1(b). The simulated center and sideband intensities, calculated from simply adding the contributions of pair correlations are very good approximations for the full treatment including three-spin correlations. The linewidths, however, significantly increase with ξ as the dominant term there involves three-spin correlations. Thus, the strongest dipole–dipole couplings can simply be determined from one-dimensional (1D) MAS sideband patterns.

2.2 Homonuclear Double-Quantum Coherences

In order to obtain a structure, the weaker remote dipole–dipole couplings, relating protons of different chemical entities are particularly informative. They can now be determined by DQ MAS NMR spectroscopy.[11,12] The basic experimental scheme, a specific pulse sequence and a coherence pathway diagram,[22] are shown in Figure 2(a): firstly, a double-quantum coherence (DQC) is excited, which subsequently evolves during an incremented time period t_1. Afterwards, the DQC is converted into observable single-quantum coherence (SQC), which is detected in the acquisition period. Pure absorption mode 2D spectra are ensured by generating amplitude modulated signals in t_1 through proper selection of symmetric pathways.[19,22] During excitation and reconversion the *homonuclear* dipole–dipole interaction is recoupled. Numerous ways for achieving this have been developed, as described by Levitt (see **Symmetry-Based Pulse Sequences in Magic-Angle Spinning Solid-State NMR**)[23] (see also Ref.[24])

The nature of the corresponding 2D spectra is illustrated in Figure 2(b,c). Here we consider two kinds of pairs of spins, labeled 1 and 2, with different chemical shifts. The excitation of DQ coherence is based on the dipole–dipole coupling between the two spins involved. Thus, if the two kinds of groups are separated (Figure 2(b)), DQ signals can only occur at $2\omega_1$ and $2\omega_2$ along the DQ dimension, i.e., on the diagonal of a 2D plot with proper frequency scaling. These signals reflect the dipolar couplings within the respective groups. Note that distinct from the INADEQUATE experiment in isotropic liquids based on the isotropic scalar

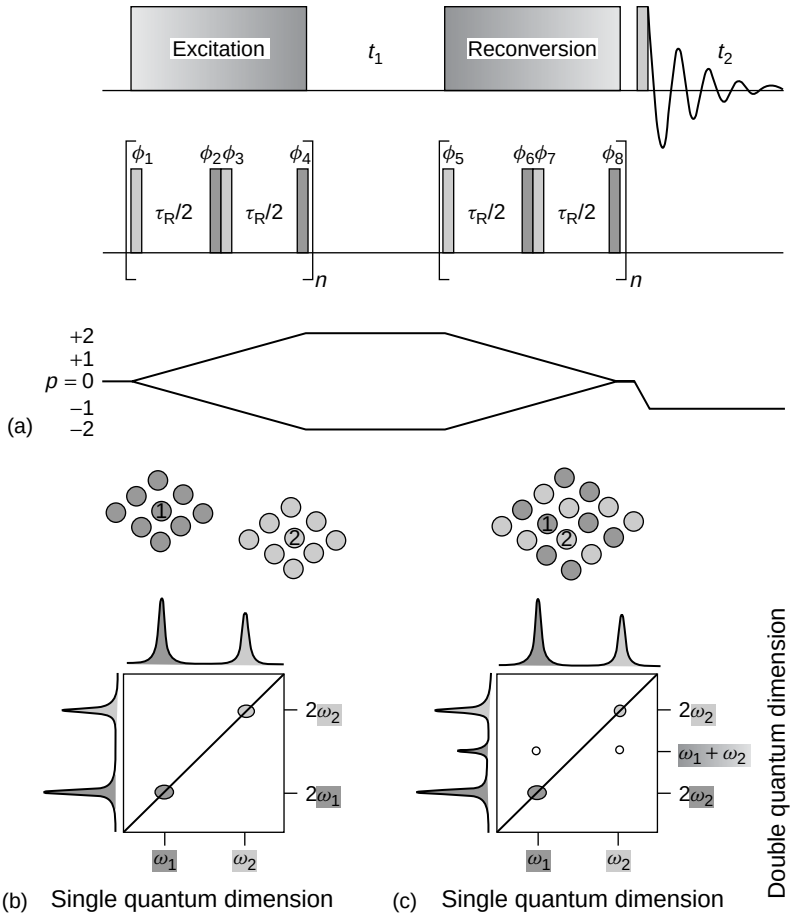

Figure 2 (a) Pulse sequence and coherence transfer pathway of a homonuclear DQ MAS experiment, all pulses have 90° flip angles. (b) Scheme of DQ MAS NMR spectrum for separated spin pairs, (c) for spin pairs in spatial proximity

couplings,[22] the intragroup coherences occur despite the fact that the isotropic chemical shifts of the two spins are equal. This reflects the fact that in solids the DQ coherence is generated by the anisotropic dipole–dipole coupling. If the groups are intermixed (Figure 2(c)), DQ coherences between spins of different groups can also be excited. They occur at the sum-frequency $\omega_1 + \omega_2$ in the DQ dimension and can be detected at both frequencies ω_1 and ω_2 in the single quantum dimension. Thus, such a pair of lines in the 2D-NMR spectrum directly maps the spatial proximity between group 1 and group 2. For short excitation times the intensities of the DQ signals are proportional to D_{ij}^2 where D_{ij} describes the dipole–dipole coupling between the two spins involved.

Spectra as discussed in the previous section are obtained in a *rotor-synchronized fashion*, i.e., the t_1 increment is set equal to the rotor period τ_R and yield distance constraints for the dipolar coupled nuclei. More accurate values for dipole–dipole couplings may be obtained from build-up curves of DQC, which for isolated spin pairs, such as doubly labeled ^{13}C–^{13}C, exhibit an oscillatory behavior.[25] Strongly coupled ^1H–^1H systems, however, quickly develop multi-spin character and the oscillations are damped out. Nevertheless, even there the initial build-up is dominated by DQCs and can quantitatively be analyzed.[26,27]

The dipole–dipole coupling constants as well as the geometry of dipolar coupled clusters as, e.g., in triple- or quadruple hydrogen bonds, can much better be elucidated if DQ *spinning sidebands* are generated by choosing a t_1 time increment well below τ_R.[11,12] Examples calculated for an isolated spin pair are plotted in Figure 3 as a function of $D_{ij}\tau_{exc}$. Note that these sidebands occur despite the fact that the DQC for an isolated spin-pair does not evolve during the evolution time t_1. Instead, the *reconversion* is *rotor encoded* because the dipole–dipole Hamiltonian modulated by MAS differs at the beginning of excitation and reconversion. This mechanism is termed *reconversion rotor encoding* (RRE) and occurs whenever the Hamiltonians involved have an amplitude modulation on the rotor phase, which is also the case in MQ MAS experiments on quadrupolar nuclei.[28,29] The two cases have been compared in detail.[30] In actual applications, the rotor frequency ω_R and the excitation time τ_{exc} will be chosen to generate up to third

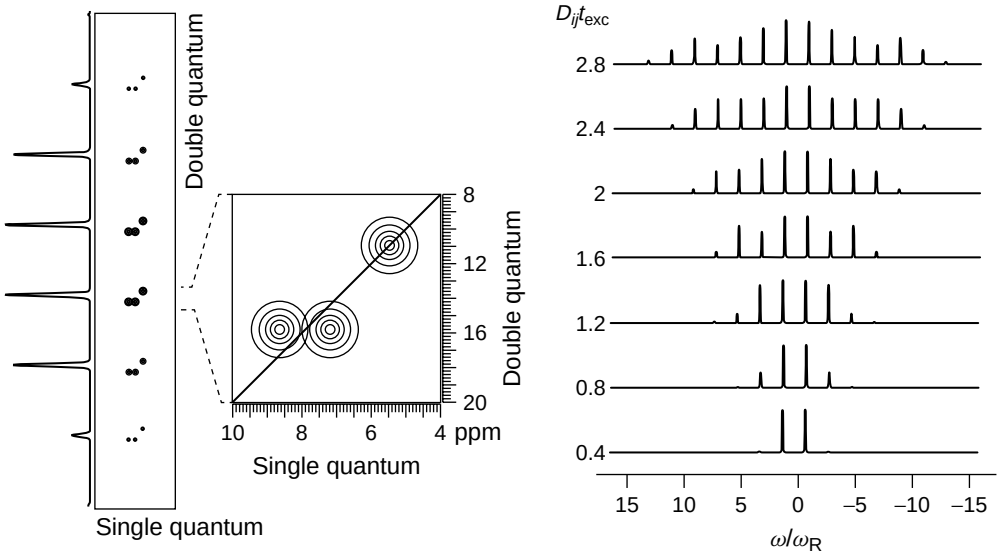

Figure 3 DQ spinning sideband patterns calculated for increasing values of the product of the dipolar coupling and the excitation time

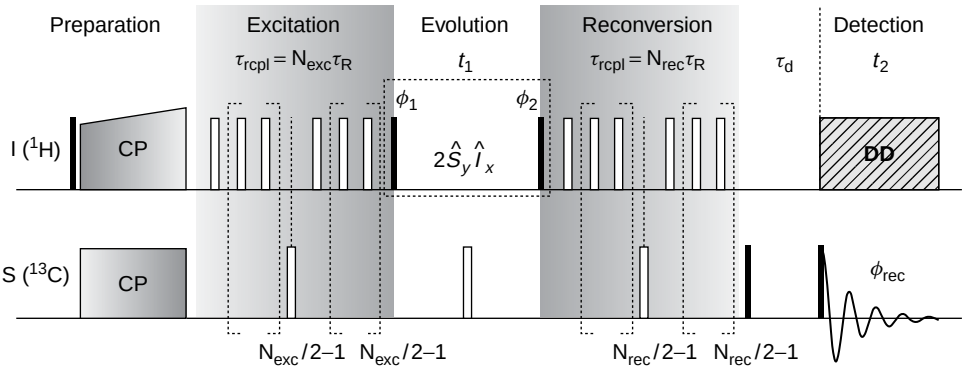

Figure 4 Pulse sequence for heteronuclear ^1H–^{13}C correlation experiments based on combining the concepts of REDOR and HMQC. For details see Ref.[38] Solid and open bars indicate 90° and 180° pulses, respectively. (Reproduced by permission of American Institute of Physics)

order sidebands in order to achieve sufficient signal-to-noise ratios, yet avoid multi-spin effects, which lead to *evolution rotor modulation* (ERM).[30] Notably, multi-spin effects give rise to additional (even-order) sidebands and can, therefore, be easily identified.

2.3 Heteronuclear Multiple-Quantum Coherences

Two-dimensional ^{1}H DQ MAS experiments as described in Section 2.2 still suffer from the limited spectral resolution in solid state ^{1}H NMR. Therefore, heteronuclear methods involving ^{13}C or ^{15}N offer significant advantages for obtaining more specific distance constraints. Indeed, if combined with homonuclear ^{1}H–^{1}H decoupling by rotor synchronized multiple pulse sequences[31] or frequency switched Lee-Goldburg experiments,[32] remarkable resolution has been achieved in model compounds[33] as well as biologically relevant systems.[34] Once specific ^{1}H–^{13}C spin pairs are identified, precise measurement of their dipole–dipole couplings via spinning sidebands also offers a new and efficient way to study molecular dynamics in analogy to ^{2}H-NMR experiments,[19] yet without the need for elaborate isotope labeling. Rotational-echo double-resonance (REDOR)[35,36] currently is most popular for determining heteronuclear dipole–dipole couplings in solids. It is based on a particularly simple approach of *recoupling*, i.e., the application of equally spaced π-pulses twice per rotor period on one of the isotopes. When applied under fast MAS in order to efficiently reduce the homonuclear dipole–dipole coupling, REDOR can be combined with multiple-quantum spectroscopy in a whole class of dipolar heteronuclear multiple spin correlation (DIP-HMSC) experiments[37,38] which are more selective than determining distance constraints via cross polarization and spin diffusion experiments.[39,40] The basic pulse sequence for a ^{1}H–^{13}C heteronuclear multiple-quantum correlation (HMQC) experiment is depicted in Figure 4. As in homonuclear DQ-NMR, the first half of the REDOR recoupling is identified as the excitation period, and the second as the reconversion period. In between, HMQC evolution occurs during t_1. The ^{13}C chemical shift is fully refocused by π-pulses during excitation, evolution and reconversion.

Similar to the homonuclear case, Section 2.2, precise values for heteronuclear dipole–dipole couplings can be determined via sideband patterns, which are generated through rotor encoding (RRE) as well as evolution (ERM). Consequently, the sideband patterns for an isolated heteronuclear spin pair, plotted as a function of the excitation time in Figure 5(a), exhibit the same features as in the homonuclear case (Figure 3). Again, in actual experiments the excitation times are chosen short enough such that a limited number of sidebands is created and multi-spin effects are minimized for C–H groups. The unavoidable three-spin coherences in rigid CH_2 groups, in fact, lead to efficient dephasing.[37,38] This can be used for spectral simplification, but also offers an easy way to distinguish mobile methylene groups from rigid ones.

DQ sideband patterns also offer new ways to study the rate and the geometry of rotational motions,[16,38] where the site selectivity is particularly high for heteronuclear DQ coherences. In Figure 5(b) simulated sideband patterns are plotted for the C–H group which is a sensitive probe of phenylene rotation, often met in practice.[19] At low temperatures one would expect small-angle librations. With increasing temperatures the angular excursions will increase until full rotation might be reached. The resulting motionally averaged dipolar couplings are readily calculated via the internet by use of our NMR-WEBLAB.[41] As shown in Figure 5(b), the sideband patterns show a marked dependence of the flip angle α. A recent experimental example is provided by the restricted phenylene motion in polyphenylene dendrimers,[42] a new type of nanomaterials.[1]

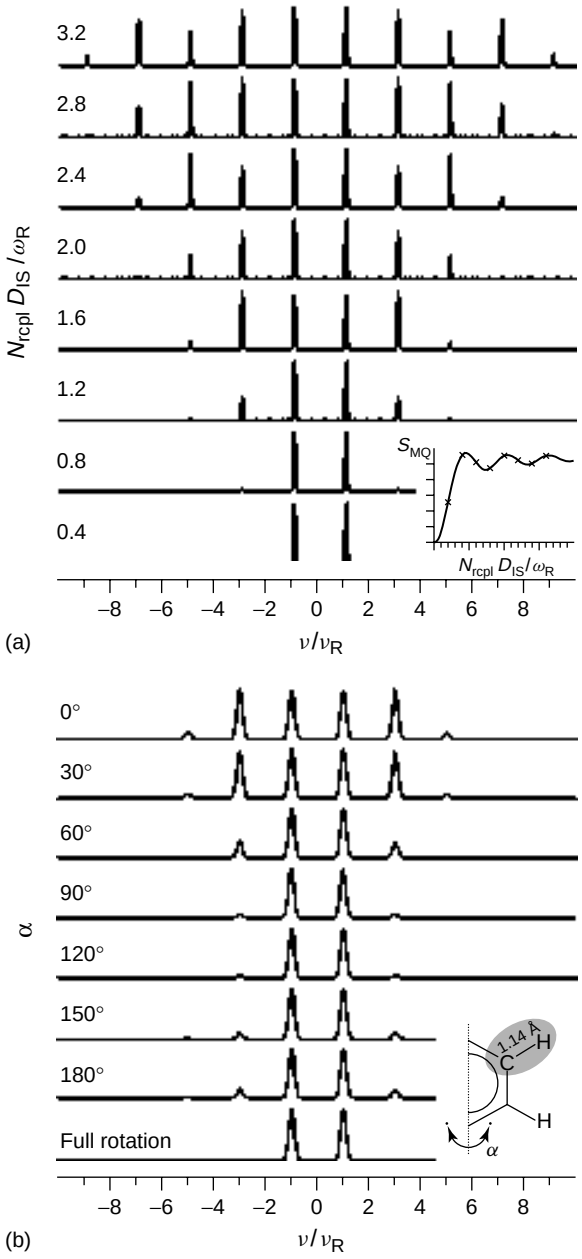

Figure 5 (a) Calculated HMQ spinning sideband patterns for a single IS spin pair for increasing values of the ratio of the product of the dipolar coupling strength D_{IS} multiplied by the number of pump cycles N_{rcpl} and the rotor frequency ω_R. For details see.[38] (b) Calculated heteronuclear DQ MAS NMR spinning sideband patterns for rotating phenylene groups and different flip angles α as indicated ($N_{rcpl}D_{IS}/\omega_R = 1.67$). (Reproduced by permission of American Institute of Physics)

3 APPLICATIONS

3.1 Spin Counting

The classic application of MQ NMR in solids as pioneered by A. Pines in the early 1980s is spin counting.[43] He showed that it is possible to excite homonuclear MQCs comprising more than 100 spins, by exploiting the through-space dipole–dipole coupling. With this technique it was possible, for instance, to prove the existence of small clusters of proton spins on the surface of silica catalyst supports.[44] In fact, the growth of MQCs in a spin cluster as depicted in Figure 6(a) can be described by a statistical model. The intensities of the coherence orders follow a Gaussian distribution, the width of which increases with excitation time. Such behavior indicates that the build-up of homonuclear MQCs amongst strongly coupled spins occurs via a random walk. The different pathways indicated in Figure 6(a) result from the non-localized and, therefore, non-selective growth of the spin-cluster. As demonstrated in Figure 6(c), this behavior is also found under MAS conditions, provided efficient recoupling is achieved.[27]

Distinct from that, MQCs in the I-spin subspace of a heteronuclear IS NMR experiment are excited via the dipole–dipole coupling of all these spins to a single S spin. For this selected site the multitude of surrounding I spins creates

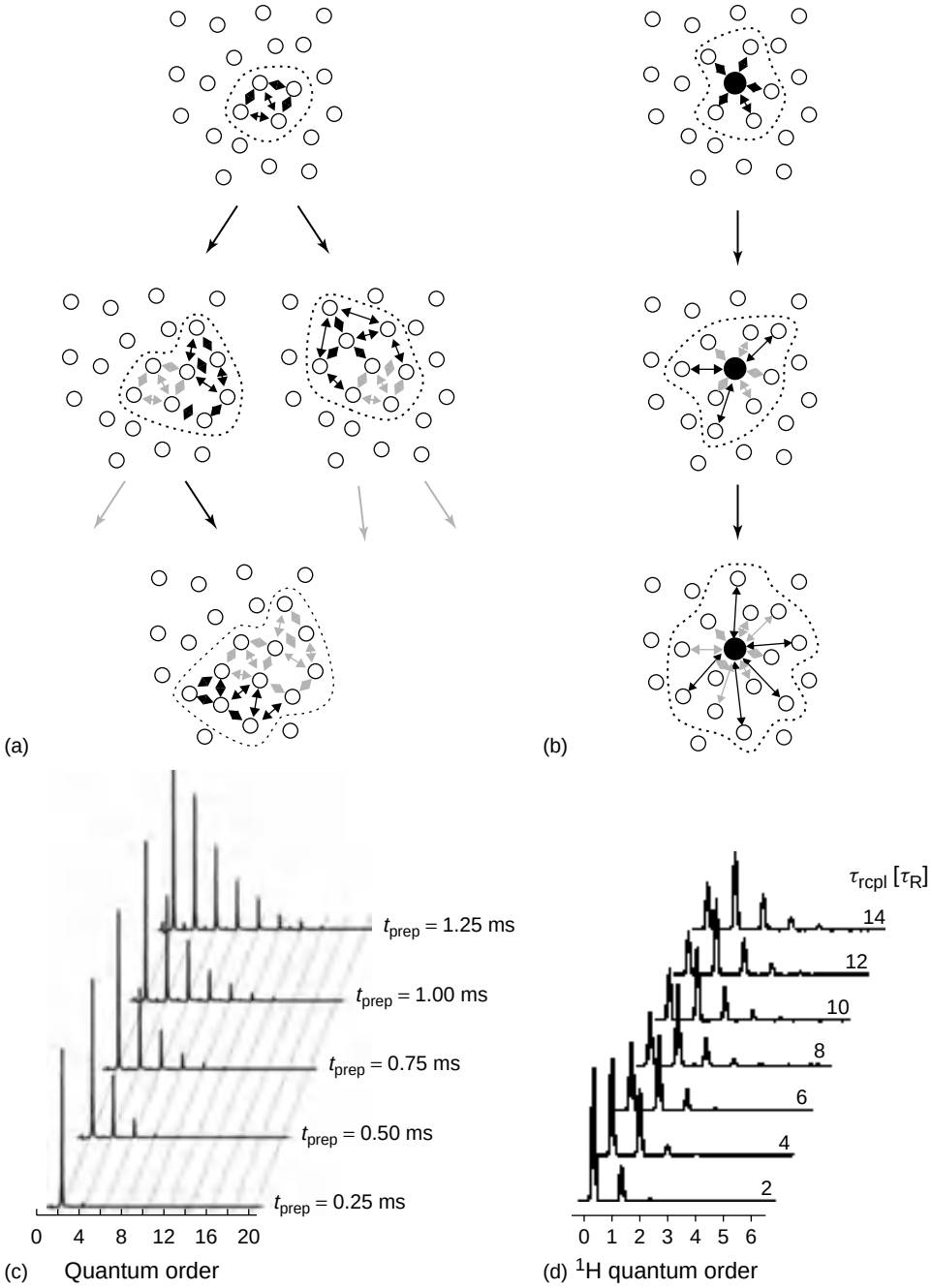

Figure 6 Growth of spin clusters as probed in homonuclear (a) and heteronuclear (b) MQ NMR experiments. Experimental examples for adamantane (^{1}H···^{1}H homonuclear, (c)), for details see Ref.[27] and L-alanine (^{1}H···^{13}C heteronuclear, (d)), for details see Ref.[38] (Reproduced by permission of American Institute of Physics, (a), (b), (d) and Academic Press, (c))

a local field. The number of proton (I) spins incorporated in the HMQ can only grow by including remote spins with sufficient couplings to the S spin [Figure 6(b)]. Thus, build-up of higher spin coherences will converge with time. As shown in Figure 6(d), higher order MQCs are indeed observed for the carboxyl carbon in uniformly ^{13}C labeled L-alanine,[38] but the intensity distribution obviously is not Gaussian. Thus, heteronuclear spin counting indeed probes a selected local environment and therefore is anticipated as a new tool for structural investigations.

3.2 Structure

3.2.1 Hydrogen Bonding

Protons in hydrogen bonded structures exhibit ^1H chemical shifts well away from the aliphatic peaks. Therefore, high resolution ^1H solid state NMR is ideally suited for investigating such systems as noted early on.[45] Moreover, correlations between the ^1H isotropic chemical shifts and the hydrogen-bond strength specified by O···H or O···O distances from single-crystal analyses have been established.[46] The first example of the new kind of information about proton–proton distance constraints available from solid state DQ MAS NMR was the investigation of the unusual hydrogen bonded structures in benzoxazine dimers.[15] These dimers are of interest as model compounds for a new class of phenolic materials, the polybenzoxazines prepared by Ishida and coworkers.[47] These systems combine several favorable properties, such as near-zero shrinkage on polymerization as well as low water absorption, which are attributed to their favorable hydrogen-bonding.

Figure 7(a) shows the superimposed ^1H MAS NMR spectra of both the methyl (solid line) and ethyl (dashed line)

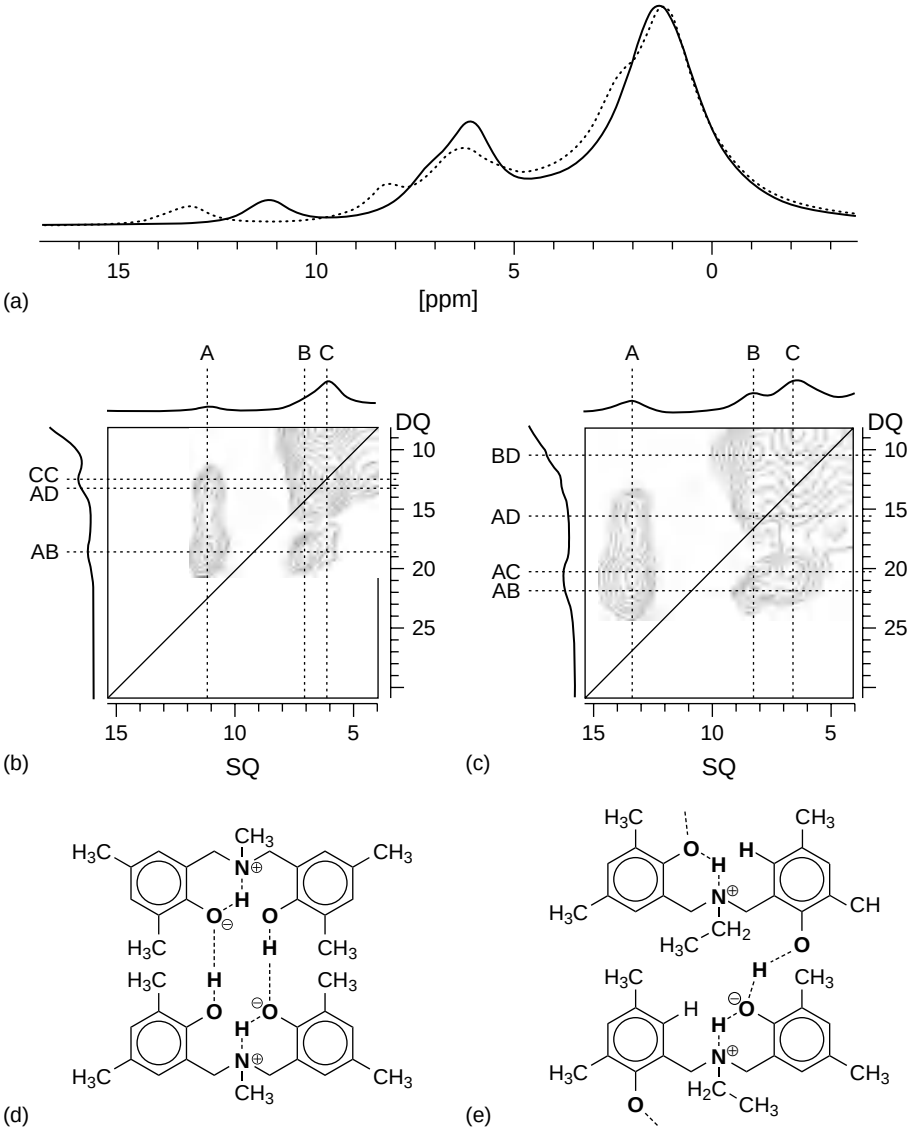

Figure 7 (a) ^1H MAS NMR spectra of benzoxazine dimers at 500 MHz. Solid line, methyl derivative; dotted line, ethyl derivative. (b), (c) Low field region of the ^1H DQ MAS NMR spectrum of the methyl and ethyl derivative, respectively. (d), (e) Schematic arrangement of the methyl dimers into pairs (d) and the ethyl dimers into extended chains (e). For details see Ref.[15] (Reproduced by permission of American Chemical Society)

derivative. The spectra differ markedly in the low-field region, which gives a first hint towards different hydrogen bond arrangements in the two cases. The differences are even more marked in the ^{1}H DQ MAS NMR spectra, whose low-field regions are displayed in Figures 7(b) and 7(c). The labels (A, B, C, and D) refer to the SQ resonances of the hydrogen bonded, aromatic, and aliphatic protons, respectively. The peaks in the DQ spectrum indicate proximities of protons within about 0.35 nm[15] and are labeled accordingly as AB, AC, etc. The most striking differences between the methyl- and ethyl-dimer spectra are the strong aromatic auto peak (CC) and only weak intensity (AC) indicating a DQC between a O···H···N and an aromatic proton for the methyl-dimer, while the situation is reversed for the ethyl-derivative. As discussed in detail elsewhere,[15] this indicates pair formation from two dimers, Figure 7(d) in the methyl-derivative, and extended hydrogen bonded chains, Figure 7(e) for the ethyl-dimers. These structural differences have meanwhile been confirmed by X-ray diffraction.

Another example of elucidating complex hydrogen bonded structures is provided by our study of supramolecular polymers[48] coupled via quadrupole bonds in 2-ureido-4-pyrimidone units, where keto- and enol tautomers in the solid state could clearly be distinguished by DQ MAS NMR.[49] DQ spinning sideband patterns have also been used to locate the protons in bilirubin, a compound of considerable medical importance. It is a product of the metabolism of hemoglobin from red blood cells. Due to an unusually strong intramolecular hydrogen bonding arrangement, bilirubin itself is insoluble in water and can only be removed from the body after being conjugated enzymatically with glucuronic acid.[50] Inefficient removal of bilirubin from the body manifests itself as jaundice. Solid state NMR now has provided proton−proton distances with an accuracy of ±0.002 nm in this important system.[51]

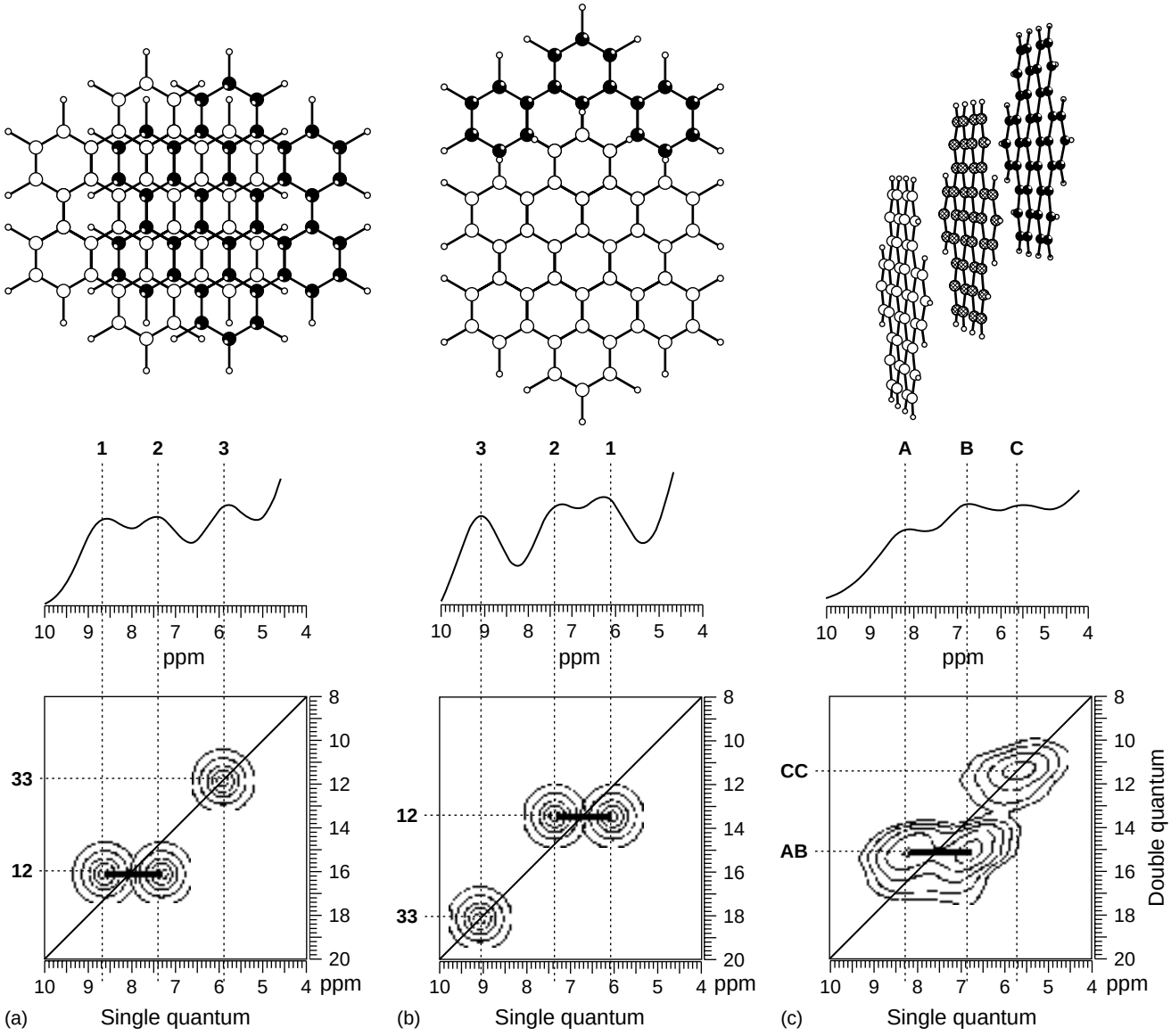

Figure 8 Calculated ^{1}H MAS NMR spectra and schematic ^{1}H DQ MAS NMR spectra for different arrangements of HBC discs, staggered in different directions (a, b). Experimental ^{1}H spectra of HBC–C_{12} together with staggered arrangement (c). For details see Ref.[54] (Reproduced by permission of American Chemical Society)

3.2.2 Aromatic π-π Interactions in Columnar Structures and Guest-Host Complexes

In addition to hydrogen-bonding, the ^{1}H chemical shifts are very sensitive to ring currents associated with π-electrons in aromatic moieties.[52] While in solution, the isotropic molecular tumbling removes most of the π-shifts, in the solid state the protons are exposed to the π-electrons of nearby aromatic moieties, be they intra- or intermolecular. The latter information is particularly valuable for elucidating supramolecular structures.[2,5] A clear-cut example is provided by the columnar stacking of substituted hexa-*peri*-hexabenzocoronene (henceforth referred to as HBC). Opposed to solution or the liquid crystalline phase, where the discs tumble isotropically or rotate rapidly around the column axis, in the solid three distinct aromatic lines are observed in the aromatic region of the ^{1}H-NMR spectrum[16] (Figure 8). The DQ-spectrum exhibits a strong CC auto and two AB cross peaks, which implies the presence of only two types of pairs of aromatic protons, H_A-H_B, H_C-H_C. For quantitative analysis, advanced quantum chemical calculations of NMR chemical shifts are needed.[53] They show that staggered arrangements of the HBC moieties indeed give rise to π-shifts of several ppm.[54] The assignment, which of the chemically shifted protons form pairs is achieved by DQ-NMR and is essential to determine the type of staggering. In a herringbone-structure which corresponds to that of unsubstituted HBC (Figure 8(a)) none of the carbons are aligned, whereas in structure (b) half of the carbons are located directly above or below a carbon of the adjacent layer resembling the packing in graphite. The latter (Figure 8(b)) could clearly be excluded, because it does not match the experimental 2D NMR pattern (Figure 8(c)). The pattern in Figure 8(a), however, agrees well with the experimental one. This proves the specific packing arrangement hypothesized earlier,[16] that this alkylsubstituted system adopts the structure of unsubstituted HBC itself. Through-space π-shifts are remarkably long-range, with an aromatic ring at a distance of 0.7 nm still exerting a measurable influence. Thus, in the final simulation, three HBC moieties had to be taken into account (Figure 8(c)).

The combination of ^{1}H DQ MAS-NMR with advanced ab initio quantum chemical calculations also proved essential for elucidating the structure of a supramolecular guest-host complex. The receptor shown in Figure 9(a) belongs to the family of molecules termed molecular tweezers due to their concave–convex topology and ability to selectively form complexes with electron-deficient compounds.[55] An X-ray crystal structure is available for this system, offering an opportunity to check the reliability of the spectroscopic approach.[56] Figure 9(b) presents a rotor-synchronized ^{1}H DQ MAS spectrum of the complex (Figure 9(a)). Despite the high field (700 MHz) used, the spectral resolution for the many aromatic protons is unsatisfactory. The different sites can much better be distinguished in a heteronuclear correlation spectrum (Figure 9(c)) which was recorded with the REPT-HSQC experiment.[37] The two overlapping ^{13}C lines at 128.7 and 129.6 ppm are assigned to the guest CH groups (5a and 5b), which are well separated by 3.6 ppm in the ^{1}H-dimension. This demonstrates that the π-shifts are much more significant for the protons than they are for the carbons.[54,56] In the present case, the binding of the electron-deficient 1,4-dicyanobenzene guest in the complex is such that the symmetry of the molecular tweezer is broken (Figure 9(a)) and the two adjacent guest protons experience the π-shifts due to the host to largely different degrees. Moreover, the end pair of aromatic protons are directed into the ring current of the naphthalene unit of the next host, which explains the π-shifted 4 ar^{II} resonance.[56] Thus both, the guest–host complexation, as well as the packing of the "loaded" tweezers within the supramolecular solid can be probed by solid state NMR and quantified by ab initio calculation.

3.2.3 Surface Studies

The high sensitivity of ^{1}H NMR makes it possible to study defect sites and molecules adsorbed at surfaces in a straightforward way.[44] Two examples are discussed. The first concerns a ^{1}H-MQ MAS NMR study of defect sites in a zeolite.[57] As in supramolecular systems, the structures of defects are difficult to study in these industrially important microporous solids,[58] because the defects are usually not ordered in the crystallographic sense and, therefore, are not easily amenable to analysis by diffraction methods. Figure 10(a) shows the 2D ^{1}H DQ MAS NMR spectrum of an as-made all silica ZSM-12 zeolite.[57] The signal at 10 ppm in the SQ dimension is due to a DQC generated by the cluster of silanol protons of the defect site. The observation of a strong centreband in the ^{1}H DQ MAS spinning sideband pattern (Figure 10(b)) proves that at least three silanol groups are engaged in hydrogen bonding within the defect site. These results have important implications concerning the nucleation mechanism of high-quality zeolites, as they provide new information on the structure of charge-compensating units in the zeolite colloidal precursors.

In another example ^{1}H DQ MAS NMR recently has also provided new insight in the packing of polyelectrolyte multilayers (PEMs) on silica colloids.[18] These systems, generated by alternate adsorption of anionic and cationic polymers are being explored for numerous applications ranging from photonics to enzyme encapsulation.[59,60] Fast MAS NMR at high fields (700 MHz) of such systems is able to distinguish, e.g., water adsorbed at the surface from that in the PEM and the silanol groups. Two-dimensional ^{1}H DQ MAS NMR, however, is needed to probe the organization of the polyelectrolytes within the multilayers. The DQ spectra (Figure 10) exhibit cross-peaks between the aromatic protons of the poly(styrene sulfonate) (PSS) polyanion and the poly(diallyldimethyl-ammonium) (PDADMAC) polycation in both, the bulk complex and the multilayers. These findings[18] are consistent with conclusions based on less direct experimental probes that these polyelectrolyte multilayers are structurally very similar to the corresponding bulk complexes.[61]

3.3 Dynamics

3.3.1 Axial Motion of Discs in Columnar Liquid Crystals

A unique strength of solid state NMR is its ability to probe molecular dynamics over many orders of magnitude with site selectivity and specific geometric sensitivity.[19,62] High resolution DQ MAS of dipolar coupled spins has further broadened our tools in this area. This is illustrated by a few examples. Consider as a particularly simple case the rotation of the discs around the column axis in discotic liquid crystals.[63]

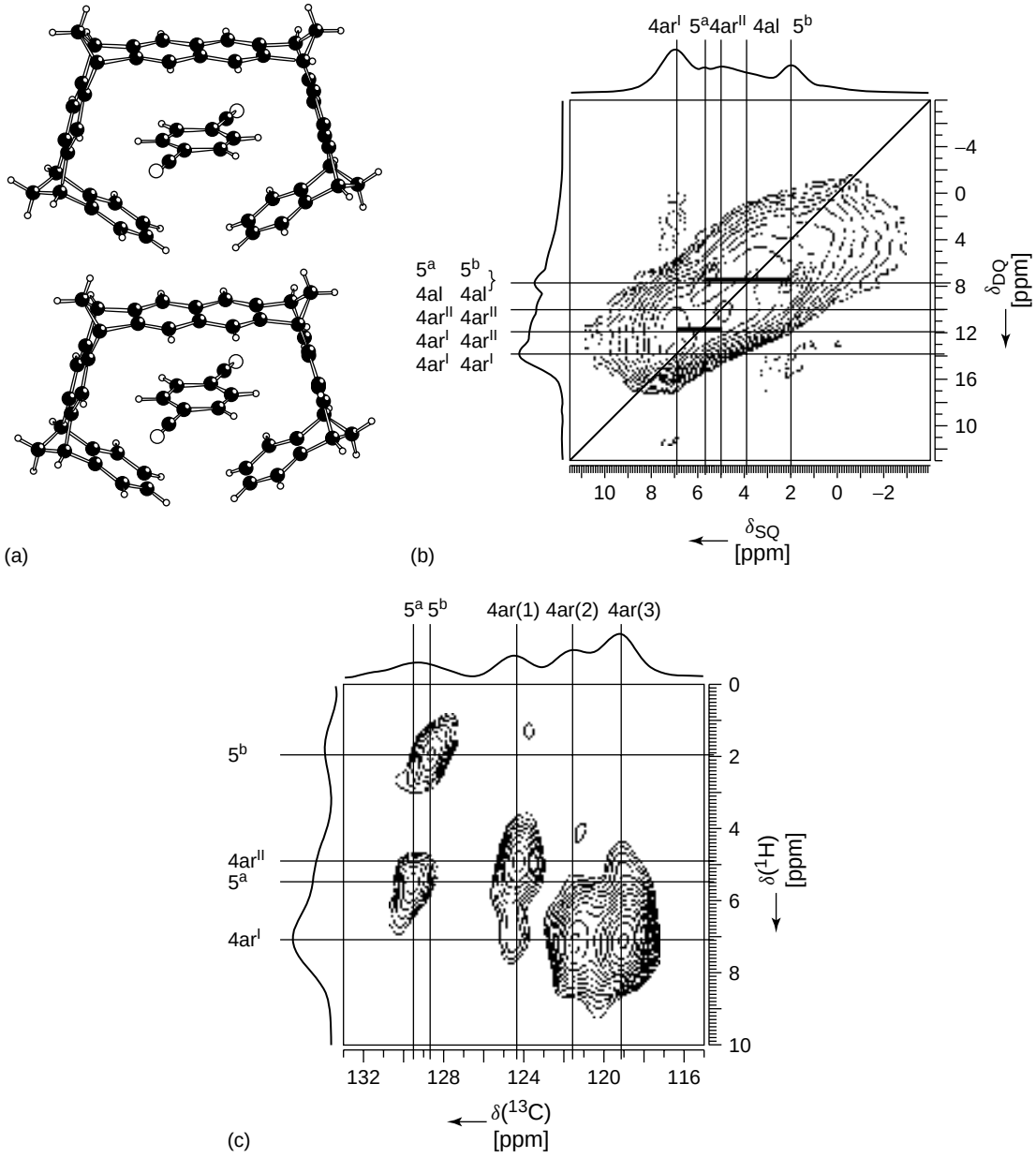

Figure 9 (a) Solid state packing of a molecular tweezer. (b) ^{1}H DQ MAS NMR spectrum at 700 MHz, and (c) ^{1}H–^{13}C HSQS MAS NMR correlation spectrum, for details see Ref.[56]

In the past, studying this motional process required ^{2}H NMR of selectively labeled systems, which was indeed done for HBC.[64] The effort seemed justified in view of the favorable properties of these systems, i.e., extremely stable mesophase and record charge carrier mobility along the column axis.[65] This tedious approach can now be circumvented. Figure 12 presents ^{1}H DQ MAS spinning sidebands of HBC-C_{12}, containing C_{12} alkyl chains, in (a) the crystalline and (b) the LC phases.[16] The aromatic protons are grouped as well separated pairs and, thus, an analysis within the spin-pair approximation is appropriate. As is evident from the insets on the right of Figure 12 the DQ-spinning sideband patterns are very sensitive to the strength of the dipolar coupling, which can be determined with high accuracy to yield values of (15 ± 0.9) kHz and (6 ± 0.5) kHz in the solid and the LC phase, respectively. The reduction factor due the axial motion of the discs is thus 0.4 corresponding to an order parameter of 0.8, remembering that for a completely regular column the H–H vectors would be at right angles to the column axis and the reduction factor would be 0.5.[19] The reduced order parameter indicates additional out-of-plane motion in addition to the axial rotation.

The limited order of these systems also shows up in the X-ray diffraction pattern displayed in Figure 13(a). The order can be increased by inserting phenylene units between the core and the alkyl chains (HBC-PhC_{12}),[66] as is evident from the sharper X-ray reflections in Figure 13(b). In ^{1}H NMR, however, we cannot resolve the core and the exophenyl moieties. This can be achieved by heteronuclear ^{1}H–^{13}C DQ NMR applying REPT-HMQC techniques.[37] Indeed, analysis of the sideband patterns for the C–H groups (Figure 13, lower part) yields core

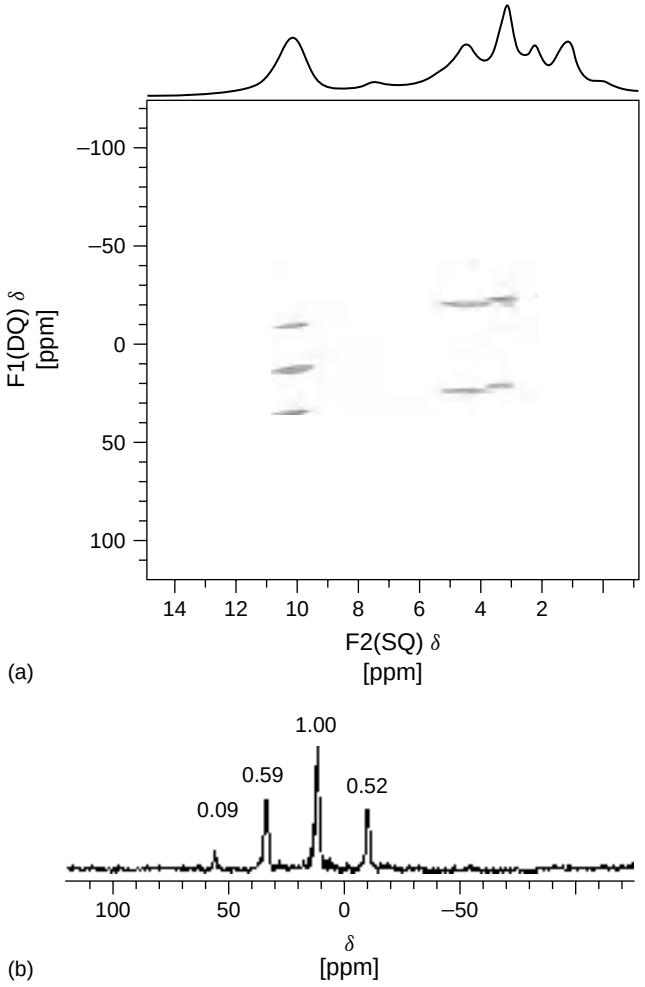

Figure 10 (a) ^{1}H DQ MAS NMR spectrum (500 MHz) of an all silica ZSM zeolite. (b) Sideband pattern for the hydrogen bonded protons, for details see Ref.[57] (Reproduced by permission of American Chemical Society)

order parameters of 0.78 ± 0.09 and 0.93 ± 0.09 for HBC-C_{12} and HBC-PhC_{12}, respectively, indicating less out-of-plane mesogen mobility in the latter. The ease with which this information is obtained with 10 mg of as-synthesized samples made it possible to report such findings together with the synthesis of these new materials.[66]

3.3.2 Slow Motions from Double-Quantum Exchange NMR

Multidimensional exchange NMR spectroscopy provides unique information about the time scale as well as the geometry of slow molecular motions,[19] latest developments are described by Schmidt-Rohr (see **Centerband-Only Detection of Exchange (CODEX): Efficient NMR Analysis of Slow Motions in Solids**).[67] Extending DQ NMR spectroscopy into that area, therefore, represented a special challenge. Recently, such a homonuclear DQ-DQ exchange experiment has been designed[68] by combining two DQ experiments as depicted in Figure 14(a). The dipole−dipole coupling between two distinct spins is used to generate a DQ coherence, and the orientation dependent coupling is measured by means of the DQ-MAS sideband pattern before and after a mixing time. In a reduced three-dimensional experiment, the two DQ-sideband patterns are correlated, resulting in a DQ-DQ sideband pattern which is sensitive to the reorientation angle. By referencing the DQ-DQ time signal, the information content of the pattern is divided into the sidebands and the centreband, with the former reflecting only the moieties which have undergone a reorientation changing the dipole−dipole coupling, and the latter predominantly containing contributions from moieties which retained their dipole−dipole coupling because they remained in, or returned to, their initial position. Hence a single sideband pattern provides access to the reorientation angle and the relative number of sites characteristic of the motional process. As a first example, Figure 14(b) displays calculated (black) and experimental (gray) ^{13}C–^{13}C DQ MAS sideband patterns for the crystalline phase of doubly labeled poly(ethylene). The exchange spectra reflect the 180° flip motion due to the slow α-process of this material, yielding a C–C reorientation angle of $70 \pm 5°$ in accord with 2D dipolar exchange NMR experiments on the same sample under static conditions.[69] One of the advantages of the MAS technique is its ability to probe the chain motion also in the non-crystalline regions, which is particularly important in view of the reviewed interest in the crystallization process of semicrystalline polymers[70] and the relation of the α-process to ultradrawability of such polymers.[71]

3.3.3 Chain Order and Translational Motion in Polymer Melts

High resolution DQ MAS NMR also offers new possibilities to probe dynamic processes involving considerably longer length scales. Figure 15 displays the ^{1}H DQ MAS NMR spectrum of 1.4 poly(butadiene) (PB) in the melt. The rapid segmental motion largely averages intra- and intermolecular dipole−dipole couplings, such that narrow lines result. Despite of that, strong auto- and cross-DQ peaks are observed, from which residual dipole−dipole couplings between the different protons can be determined.[17] They result from the fact that the chain motion in an entangled melt is not completely isotropic on intermediate length- and timescales. Numerous ways have been designed to probe the resulting dynamic order parameters by NMR.[72] ^{1}H DQ MAS NMR is the only way which can clearly distinguish *intra-* and *intergroup* couplings, and therefore determine order parameters for vectors directed *along* the chain, which were found to be considerably higher than anticipated.[17]

In order to quantify our findings, the measured order parameters are analyzed in terms of the celebrated reptation model of chain motion, formulated by De Gennes[73] and Doi and Edwards.[74] As depicted in Figure 16(a) the reptation model considers single chains subject to spatial restrictions due to entanglements, which are considered to act effectively like a tube through which the selected chain reptates. Four separate length- and timescales are distinguished (Figure 16(a)). In the different regimes different scaling laws for the mean-square displacement of chain segment due to *translational* motion are predicted, which also show up in the correlation function $C_R(t)$ probed by the residual dipole−dipole couplings, Figure 16(b). Here, the crossover from regime II ($t^{-1/4}$) to regime III ($t^{-1/2}$) is most indicative of reptation.[17,75,76] This crossover is indeed observed in polymer melts as shown for

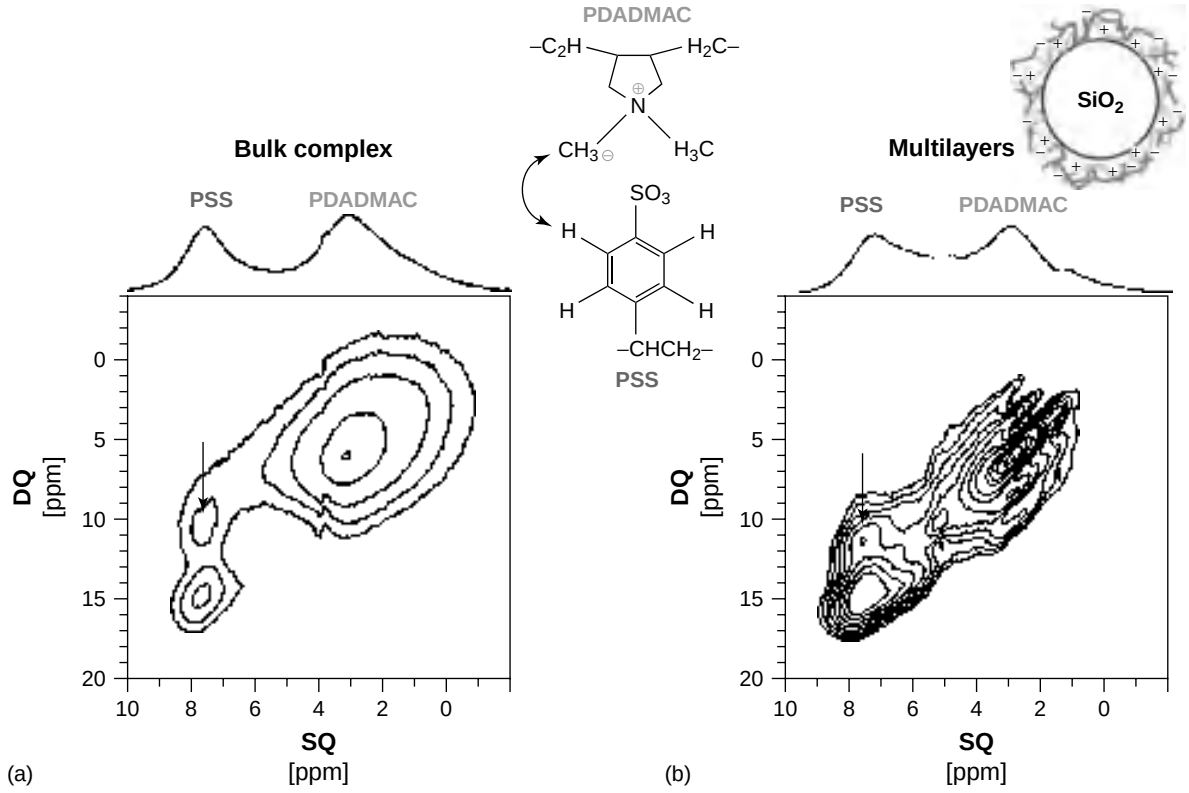

Figure 11 ^{1}H DQ MAS NMR spectra (700 MHz) for a PSS/PDADMAC polyelectrolyte complex (a) and polyelectrolyte multilayer on a silica surface (b). For details see Ref.[18]

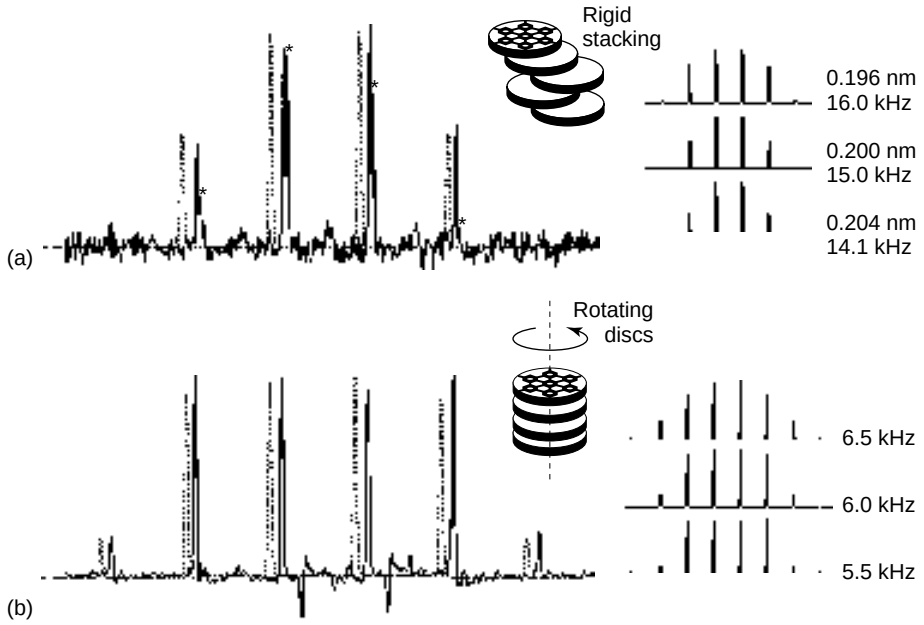

Figure 12 ^{1}H–^{1}H DQ spinning sideband patterns of HBC–C_{12} in the solid state (a) and in the columnar liquid crystalline phase (b), where the discs rotate around the column axis as indicated. For details see Ref.[16] (Reproduced by permission of American Chemical Society)

PB in Figure 16(c),[17,76] which forces us to conclude that the characteristic length scale for the residual dipole–dipole couplings is indeed the entanglement length, i.e., nanometers.[73,74] Thus, DQ NMR emerges as a simple alternative to neutron scattering for probing the chain organization of polymers.[77] Further insight was provided through a recent study,[76] where the effect of restricting the chain motion by anchoring one or both chain ends in polystyrene (PS)-PB blockcopolymers

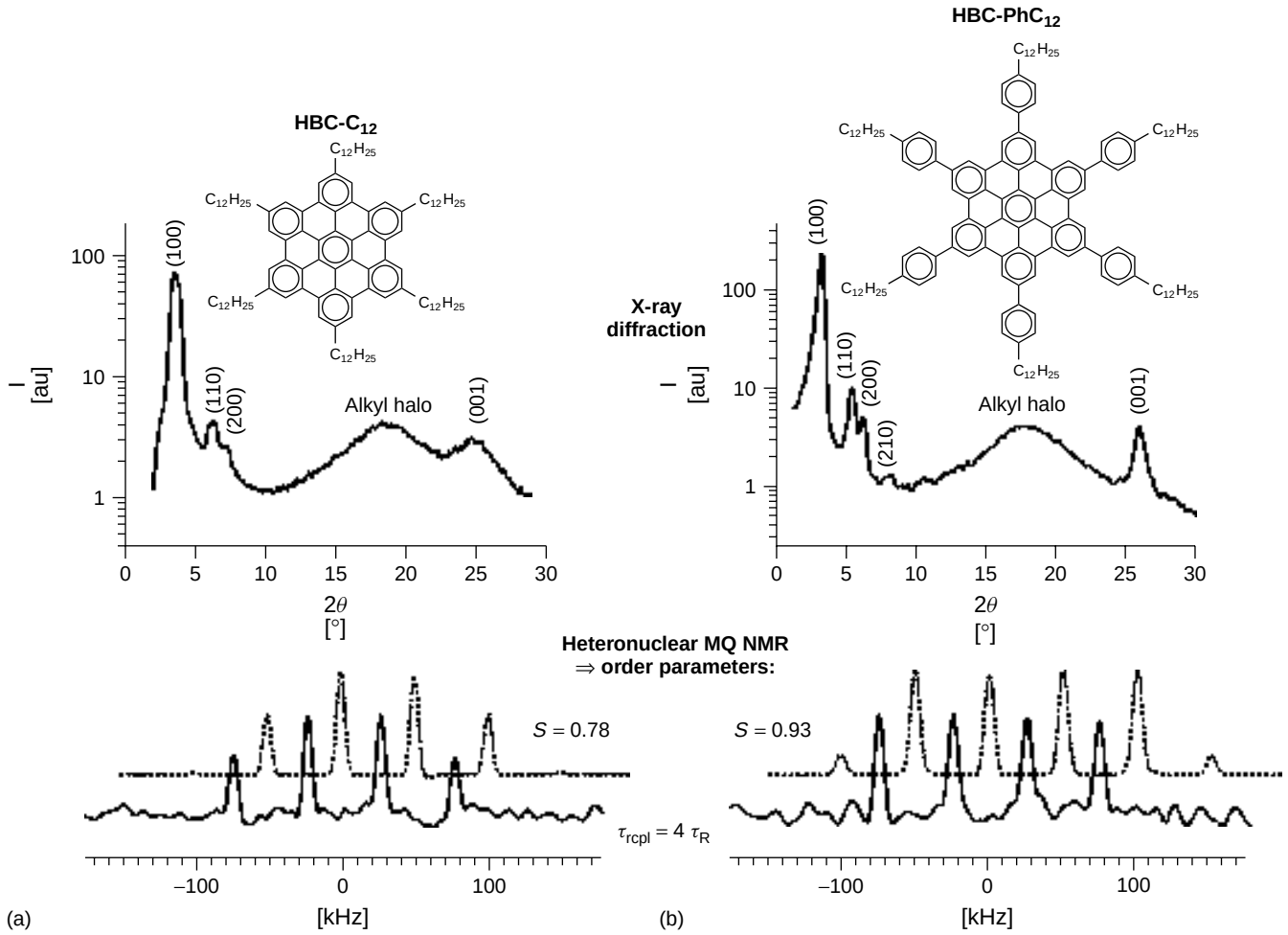

Figure 13 Comparison of powder wide angle X-ray patterns (a) and heteronuclear ^{1}H–^{13}C DQ spinning sideband patterns (b) of HBC–C_{12} (a) and HBC-PhC_{12} (b). For details see Ref.[66]

was investigated (Figure 16(c)). Not only did the chain motion slow down, the order parameters were found to increase drastically in these systems, where the polymer melt is confined to lamellae of a few tens of nm. These observations lead us to conclude that amorphous polymers are, in fact, structured in terms of nanodomains,[76] which is also consistent with new views of polymer crystallization from the melt.[70]

4 CONCLUSIONS AND OUTLOOK

Only a few years after the first DQ MAS spectra of strongly dipolar coupled solids have been recorded[11] this type of spectroscopy has emerged as a powerful tool for structural and dynamical elucidation of complex systems. This overview has focused on applications in soft matter research, i.e., on supramolecular organic systems, where spectra are recorded on small amounts (10–15 mg) of as-synthesized samples and the results are obtained overnight; but the methodology can be applied in general. For instance, high resolution DQ MAS NMR spectroscopy of isotopically labeled systems of biological interest yields torsional angles in peptides[78,79] and thus important information about the chain conformation. The sensitivity of ^{1}H chemical shifts to ring current in aromatic systems has been exploited in determining the packing of porphyrines.[34] The full information about distances and the relative orientation of specific moieties is available from DQ-NMR spectroscopy on static samples of specifically labeled materials[80] and has provided important information about the chain conformation and packing of synthetic macromolecules.[81] Last, but not least, DQ MAS NMR spectroscopy has provided hitherto inaccessible information about the connectivity of building blocks and medium range order of inorganic glasses.[82,83]

The development of the technique is far from complete. Major advances are expected in the years to come. For instance, selection of coherence pathways by pulsed field gradients, well-established in high-resolution NMR in liquids, has recently been demonstrated in rotating solids.[84,85] Likewise, inverse detection and heteronuclear editing has been realized in MAS NMR in both, synthetic polymers and biopolymers.[86,87] Indeed, an increase of the signal to noise ratio by a factor of 10 has been achieved for ^{15}N by such an approach.[49] Thus solid state NMR is envisaged to become as valuable a tool for the supramolecular chemist as solution state NMR is for the synthetic chemist today.

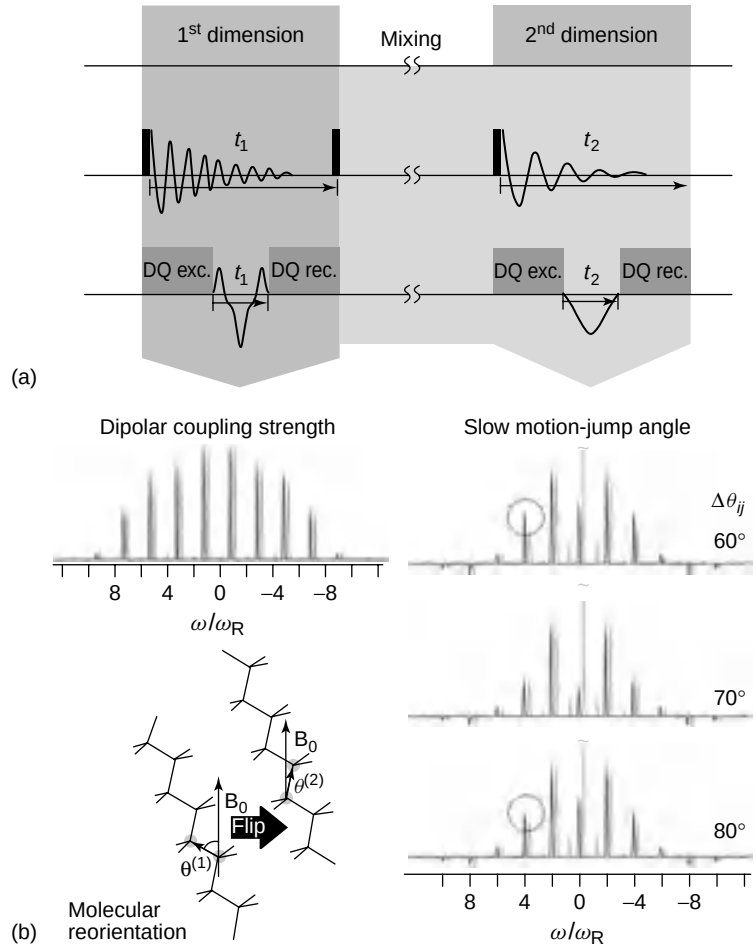

Figure 14 (a) Schematic representation of DQ exchange experiments for elucidation of slow molecular dynamics, lower trace compared to a conventional exchange experiment, middle trace.[19] (b) Calculated (black) and observed (gray) ^{13}C–^{13}C DQ MAS NMR sideband pattern of crystalline poly(ethylene) yielding the dipolar coupling strength and DQ-DQ exchange sideband patterns for different jump angles. For details see Ref.[68] (Reproduced by permission of Academic Press)

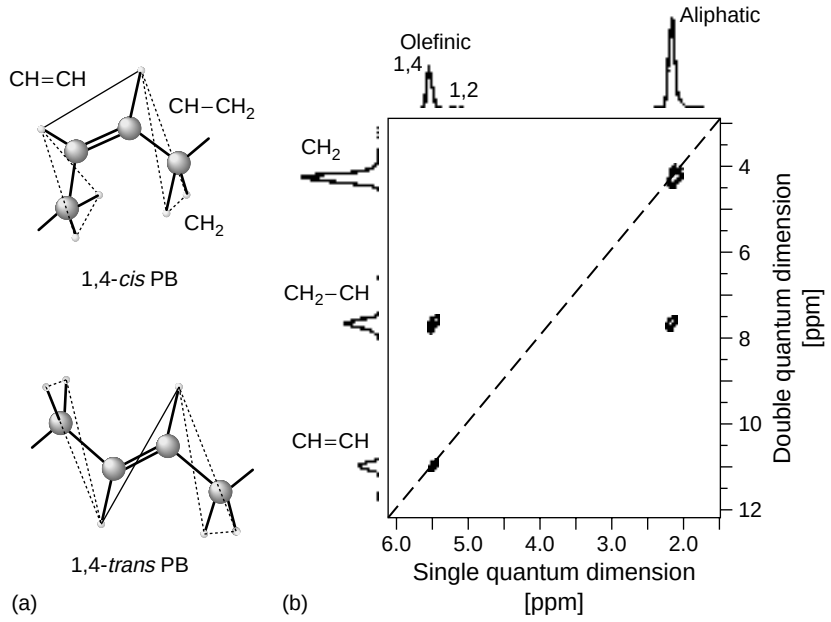

Figure 15 (a) Spin pair dipolar couplings in *cis* and *trans* polybutadiene (PB) units. (b) ^1H DQ MAS NMR spectrum (500 MHz) of a PB melt well above T_g. For details see Ref.[17] (Reproduced by permission of American Physical Society)

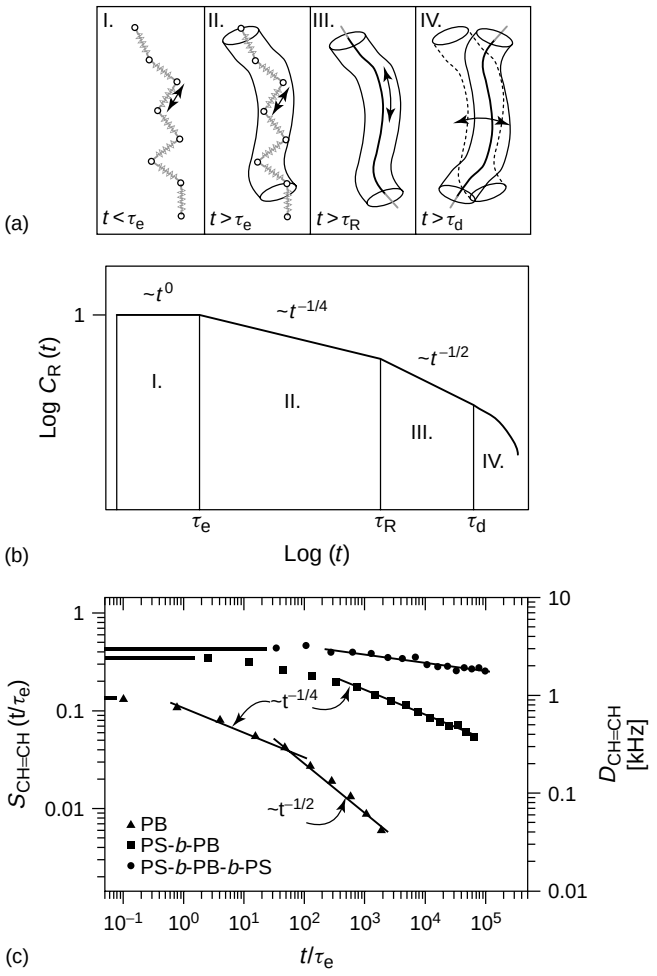

Figure 16 (a) Illustration of the different dynamic regimes considered in the reptation model. (b) Scaling behavior of the correlation function $C_R(t)$ available through ^{1}H DQ MAS NMR in the different dynamic regimes shown in (a). (c) Experimental dipolar couplings for PB and polystyrene-PB diblock (PS-PB) and triblock (PS-PB-PS) copolymers. For details see Ref.[76] (Reproduced by permission of American Chemical Society)

5 RELATED ARTICLES IN THIS VOLUME

Adiabatic Polarization-Transfer Methods in MAS Spectroscopy; Centerband-Only Detection of Exchange (CODEX): Efficient NMR Analysis of Slow Motions in Solids; Dynamics of Hydrogen Transfer in Liquids and Solids; Magic-angle Spinning Extensions; Symmetry-Based Pulse Sequences in Magic-Angle Spinning Solid-State NMR; Spinning Sideband Analysis for Spin-1/2 Nuclei; Structural and Dynamic Characterization of Soft Polymers by Solid State NMR and Field Gradient NMR; Supramolecular Chemistry; Through-Bond Experiments in Solids.

6 RELATED ARTICLES IN VOLUMES 1–8

CRAMPS, Volume 3; Cross Polarization in Rotating Solids: Spin-1/2 Nuclei, Volume 3; Double Quantum Coherence, Volume 3; Floquet Theory, Volume 3; HETCOR in Organic Solids, Volume 4; High Speed MAS of Half-Integer Quadrupolar Nuclei in Solids, Volume 4; Homonuclear Recoupling Schemes in MAS NMR, Volume 4; Hydrogen Bonding, Volume 4; Magic Angle Spinning, Volume 5; Multidimensional Spectroscopy: Concepts, Volume 5; Multiple Quantum Coherence in Spin-1/2 Dipolar Coupled Solids, Volume 5; Multiple Quantum Coherences in Extended Dipolar Coupled Spin Networks, Volume 5; Multiple Quantum NMR in Solids, Volume 5; Polymer Dynamics & Order from Multidimensional Solid State NMR, Volume 6; Polymer Physics, Volume 6; REDOR & TEDOR, Volume 6; Rotating Solids, Volume 7; Shielding: Overview of Theoretical Methods, Volume 7; Sideband Analysis in Magic Angle Spinning NMR of Solids, Volume 7.

7 REFERENCES

1. 'Encyclopedia of Materials: Science and Technology', Pergamon: Amsterdam, 2001.
2. J. M. Lehn, 'Supramolecular Chemistry', Wiley-VCH: Weinheim, 1995.
3. K. Müllen and G. Wegner, eds 'The Oligomer Approach', Wiley-VCH: Weinheim, 1998.
4. G. A. Jeffrey and W. Saenger, 'Hydrogen Bonding in Biological Structures', Springer-Verlag: New York, 1991.
5. J. L. Atwood, J. E. D. Davies, D. D. MacNiol, and F. Vögtle eds, 'Comprehensive Supramolecular Chemistry', Elsevier: Oxford, 1996.
6. M. Mehring, 'Principles of High Resolution NMR in Solids', Springer: Berlin, 1983.
7. R. E. Taylor, R. G. Pmbleton, L. M. Ryan, and B. C. Gerstein, *J. Chem. Phys.*, 1979, **71**, 4541.
8. G. Scheler, U. Haubenreisser, and H. Rosenberger, *J. Magn. Reson.*, 1981, **44**, 134.
9. H. J. Jakobsen, in 'Encyclopedia of Nuclear Magnetic Resonance', eds D. M. Grant and R. K. Harris, Wiley: Chichester, 1996, Vol. 1, p. 398.
10. M. Munowitz and A. Pines, *Adv. Chem. Phys.*, 1987, **66**, 1.
11. H. Geen, J. J. Titman, J. Gottwald, and H. W. Spiess, *Chem. Phys. Lett.*, 1994, **227**, 79.
12. J. Gottwald, D. E. Demco, R. Graf R, and H. W. Spiess, *Chem. Phys. Lett.*, 1995, **243**, 314.
13. W. Sommer, J. Gottwald, D. E. Demco, and H. W. Spiess, *J. Magn. Reson.*, 1995, **A 113**, 131.
14. C. Filip, S. Hafner, I. Schnell, D. E. Demco, and H. W. Spiess, *J. Chem. Phys.*, 1999, **110**, 423.
15. I. Schnell, S. P. Brown, H. Y. Low, H. Ishida, and H. W. Spiess, *J. Am. Chem. Soc.*, 1998, **120**, 11 784.
16. S. P. Brown, I. Schnell, J. D. Brand, K. Müllen, and H. W. Spiess, *J. Am. Chem. Soc.*, 1999, **121**, 6712.
17. R. Graf, A. Heuer, and H. W. Spiess, *Phys. Rev. Lett.*, 1998, **80**, 5738.
18. L. N. J. Rodriguez, S. De Paul, C. J. Barrett, L. Reven, and H. W. Spiess, *Adv. Mater.*, 2000, **12**, 1934.
19. K. Schmidt-Rohr K. and H. W. Spiess, 'Multidimensional Solid State NMR and Polymers', Academic Press: New York, 1994.
20. A. Samoson, 'Encyclopedia of Nuclear Magnetic Resonance', eds D. M. Grant and R. K. Harris, Wiley: Chichester, 2002, Vol. 9.
21. I. Schnell, I. and H. W. Spiess, *J. Magn. Reson.*, 2001, **151**, 153.
22. R. R. Ernst, G. Bodenhausen, and A. Wokaun, 'Principles of Nuclear Magnetic Resonance in One and Two Dimensions', Clarendon Press: Oxford, 1987.
23. M. H. Levitt, 'Encyclopedia of Nuclear Magnetic Resonance', eds D. M. Grant and R. K. Harris, Wiley: Chichester, 2002, Vol. 9.

24. A. Brinkmann, M. Edén, and M. H. Levitt, *J. Chem. Phys.*, 2000, **112**, 8539.
25. R. Graf, D. E. Demco, J. Gottwald, S. Hafner, and H. W. Spiess, *J. Chem. Phys.*, 1997, **138**, 167.
26. R. Graf, D. E. Demco, S. Hafner, and H. W. Spiess, *Solid State NMR*, 1998, **12**, 139.
27. H. Geen, R. Graf, A. S. Heindrichs, B. S. Hickman, I. Schnell, H. W. Spiess, and J. J. Titman, *J. Magn. Reson.*, 1999, **125**, 224.
28. L. Frydman and J. S. Harwood, *J. Am. Chem. Soc.*, 1995, **20**, 11 784.
29. C. Fernandez and J. P. Amoureux, *Chem. Phys. Lett.*, 1995, **242**, 449.
30. U. Friedrich, I. Schnell, S. P. Brown, A. Lupulescu, D. E. Demco, and H. W. Spiess, *Mol. Phys.*, 1998, **95**, 1209.
31. S. Hafner and H. W. Spiess, *Concepts Magn. Reson.*, 1998, **10**, 99.
32. A. Bielecki, A. C. Kolbert, H. J. M. de Groot, R. G. Griffin, and M. H. Levitt, *Adv. Magn. Reson.*, 1990, **14**, 111.
33. A. Lesage, L. Duma, D. Sakellariou, and L. Emsley, *J. Am. Chem. Soc.*, 2001, **123**, 5747.
34. B.-J. van Rossum, D. B. Steensgaard, F. M. Mulder, G. J. Boender, K. Schaffner, A. R. Holzwarth, and H. J. M. de Groot, *Biochemistry*, 2001, **40**, 1587.
35. T. Gullion and J. Schaefer, *Adv. Magn. Reson.*, 1989, **13**, 57.
36. T. Gullion, *Magn. Reson. Rev.*, 1997, **17**, 83.
37. K. Saalwächter, R. Graf, and H. W. Spiess, *J. Magn. Reson.*, 1999, **140**, 471.
38. K. Saalwächter and H. W. Spiess, *J. Chem. Phys.*, 2001, **114**, 5707.
39. B. van Rossum, H. Förster, and H. J. M. de Groot *J. Magn. Reson.*, 1996, **124**, 516.
40. M. Baldus and B. H. Meier, *J. Magn. Reson.*, 1997, **128**, 172.
41. V. Macho, L. Brombacher, and H. W. Spiess, *Appl. Magn. Reson.*, 2001, **20**, 405.
42. M. Wind, U.-M. Wiesler, K. Saalwächter, K. Müllen, and H. W. Spiess, *Adv. Mater.*, 2001, **13**, 752.
43. J. Baum, M. Munowitz, A. N. Garroway, and A. Pines, *J. Chem. Phys.*, 1985, **83**, 2105.
44. S. J. Hwang, D. O. Uner, T. S. King, M. Pruski, and B. C. Gerstein, *J. Phys. Chem.*, 1995, **99**, 3697.
45. U. Haeberlen, 'Advances in Magnetic Resonance Suppl.1', Academic Press: San Diego, CA, 1976.
46. R. K. Harris, in 'Encyclopedia of Nuclear Magnetic Resonance', eds D. M. Grant and R. K. Harris, Wiley: Chichester, 1996, Vol. 5, p. 3314.
47. H. Ishida and H. Y. Low, *Macromolecules*, 1997, **30**, 1099.
48. R. P. Sijbesma, F. H. Beijer, L. Brunsveld, B. J. B. Folmer, J. H. K. K. Hirschberg, R. F. M. Lange, J. K. L. Lowe, and E. W. Meijer, *Science*, 1997, **278**, 1601.
49. I. Schnell, B. Langer, S. H. M. Söntjens, M. H. P. van Genderen, and H. W. Spiess, *J. Magn. Reson.*, 2001, **150**, 57.
50. J. R. Chowdhury, A. S. Wolkoff, N. R. Chowdhury, I. M. Arias in 'The Metabolic and Molecular Bases of Inherited Diseases', eds C. R. Scriver, A. L. Beaudet, W. S. Sly, and D. Valle, McGraw-Hill: New York, 1995, Vol. II, pp. 2161–2208.
51. S. P. Brown, X. X. Zhu, K. Saalwächter, and H. W. Spiess, *J. Am. Chem. Soc.*, 2001, **123**, 4275.
52. P. Lazzeretti, *Prog. NMR Spectrosc.*, 2000, **36**, 1.
53. A. C. de Dios, *Prog. NMR Spectrosc.*, 1996, **29**, 229.
54. C. Ochsenfeld, S. P. Brown, I. Schnell, J. Gauss, and H. W. Spiess, *J. Am. Chem. Soc.*, 2001, **123**, 2597.
55. F.-G. Klärner, U. Burkert, M. Kamieth, R. Boese, and J. Benet-Buchholz, *Chem. Eur. J.*, 1999, **5**, 1700.
56. S. P. Brown, T. Schaller, U. P. Seelbach, F. Koziol, C. Ochsenfeld, F.-G. Klärner, and H. W. Spiess, *Angew. Chem. Int. Ed. Engl.*, 2001, **40**, 717.
57. D. F. Shantz, J. Schmedt auf der Günne, H. Koller, and R. F. Lobo, *J. Am. Chem. Soc.*, 2000, **122**, 6659.
58. H. van Beckum, E. M. Flanigen, and J. C. Jansen, 'Introduction to Zeolite Science and Practice', Elsevier: Amsterdam, 1991.
59. G. Decher, *Science*, 1997, **277**, 1232.
60. F. Caruso and H. Möhwald, *J. Am. Chem. Soc.*, 1999, **121**, 6039.
61. S. T. Dubas and J. B. Schlenoff, *Macromolecules*, 1999, **32**, 8153.
62. H. W. Spiess, *Ber. Bunsenges. Phys. Chem.*, 1997, **101**, 153.
63. D. Demus, J. W. Goodby, G. W. Gray, H. W. Spiess, and V. Vill, eds 'Handbook of Liquid Crystals', Wiley-VCH: Weinheim, 1998.
64. P. Herwig, C. W. Kayser, K. Müllen, and H. W. Spiess, *Adv. Mater.*, 1996, **8**, 510.
65. A. M. van de Craats, J. M. Warman, A. Fechtenkötter, J. D. Brand, M. A. Harbison, and K. Müllen, *Adv. Mater.*, 1999, **11**, 1469.
66. A. Fechtenkötter, K. Saalwächter, M. A. Harbison, K. Müllen, and H. W. Spiess, *Angew. Chem. Int. Ed. Engl.*, 1999, **38**, 3039.
67. K. Schmidt-Rohr, 'Encyclopedia of Nuclear Magnetic Resonance', eds D. M. Grant and R. K. Harris, Wiley: Chichester, 2002, Vol. 9.
68. I. Schnell, A. Watts, and H. W. Spiess, *J. Magn. Reson.*, 2001, **149**, 90.
69. W.-G. Hu, C. Boeffel, and K. Schmidt-Rohr, *Macromolecules*, 1999, **32**, 1619.
70. G. Hauser, J. Schmidtke, and G. Strobl, *Macromolecules*, 1998, **31**, 6250.
71. W.-G. Hu and K. Schmidt-Rohr, *Acta Polym.*, 1999, **50**, 271.
72. J. P. Cohen-Addad, *Prog. NMR Spectrosc.*, 1993, **25**,1.
73. P. G. de Gennes, *J. Chem. Phys.*, 1971, **55**, 572.
74. M. Doi and S. F. Edwards, 'The Theory of Polymer Dynamics', Clarendon Press: Oxford, 1986.
75. R. C. Ball, P. T. Callaghan, E. T. Samulski, *J. Chem. Phys.*, 1997, **106**, 7352.
76. T. Dollase, R. Graf, A. Heuer, and H. W. Spiess *Macromolecules*, 2001, **33**, 298.
77. D. Richter, *Physica B*, 2000, **276–278**, 22.
78. M. Hong, J. D. Gross, and R. G. Griffin, *J. Phys. Chem.*, 1997, **B101**, 5869.
79. X. Feng, P. J. E. Verdegem, Y. K. Lee, D. Sandstrom, M. Eden, P. Bovee Gueurts, W. J. de Grip, J. Lugtenburg, H. J. M. de Groot, and M. H. Levitt, *J. Am. Chem. Soc.*, 1997, **119**, 6853.
80. K. Schmidt-Rohr, *Macromolecules*, 1996, **29**, 3375.
81. K. Schmidt-Rohr, W. Hu, and N. Zumbulyadis, *Science*, 1998, **280**, 714.
82. M. Feike, C. Jäger, and H. W. Spiess, *J. Non-Cryst. Solids*, 1998, **223**, 200.
83. K. Glock, O. Hirsch, P. Rehak, B. Thomas, and C. Jäger, *J. Non-Cryst. Solids*, 1998, **234**, 113.
84. T. Fritzhanns, S. Hafner, D. E. Demco, H. W. Spiess, and F. Laukien, *J. Magn. Reson.*, 1998, **134**, 355.
85. T. Fritzhanns, D. E. Demco, S. Hafner, and H. W. Spiess, *Mol. Phys.*, 1999, **97**, 931.
86. Y. Ishii and R. Tycko, *J. Magn. Reson.*, 2000, **142**, 199.
87. Y. Ishii, J. P. Yesinowski, and R. Tycko, *J. Am. Chem. Soc.*, 2001, **123**, 2921.

Biographical Sketch

Hans Wolfgang Spiess, *b* 1942. Ph.D., 1968, Physical Chemistry, University of Frankfurt, Germany. Research associate, Florida State University, 1968–1970; Max-Planck Institute, Heidelberg with K. H. Hausser, 1970–1975; University of Mainz, 1975–1978. Professor at University of Mainz, 1978–1980, University of Munster, 1981–1982, University of Bayreuth, 1983–1984. Director, Max-Planck-Institut for Polymer Research, Mainz since 1984. Approx. 350 publications and a monograph on multidimensional solid-state NMR and polymers. Current research interests: solid state NMR and its applications in polymer science and supramolecular systems.

Dynamic Frequency Shift

Lawrence G. Werbelow

Universite d'Aix-Marseille I, Marseille, France

1	Introduction	1
2	Semiclassical Theory of Spin Relaxation	1
3	The Dynamic Frequency Shift	2
4	Dynamic Frequency Shifts for Some Simple Spin Systems	2
5	Dynamic Frequency Shifts for Quadrupolar Nuclei	4
6	Summary	7
7	Related Articles	7
8	References	7

1 INTRODUCTION

The proper treatment of a spin subject to two or more noncommuting interactions is a familar problem in nuclear magnetic resonance. In practice, various interactions usually differ markedly in magnitude, which enables one to choose the eigenfunctions of the dominant term as a zeroth-order approximation. (Throughout this discussion, the Zeeman interaction is considered dominant. Hence, the high-field approximation obtains). The effect of lesser interactions can be treated in the context of standard perturbation theory. A classic example is the case of a spin under the influence of a laboratory-fixed Zeeman interaction and a static, molecule-fixed quadrupole interaction. However, in certain situations, the first-order correction vanishes identically and it may be necessary to consider effects derived from higher-order perturbation theory. A well-known example is the treatment of the $\frac{1}{2} \leftrightarrow -\frac{1}{2}$ central transition of a half-integer spin subject to both Zeeman and quadrupolar interactions.

In contrast, when motions effectively average molecule-fixed interactions, first-order effects associated with quadrupole, dipole–dipole, or anisotropic electronic shieldings disappear completely in spherically symmetric or isotropic media. Nevertheless, if the averaging motions are slow on the timescale associated with reciprocal Larmor frequencies, a second-order shift of the Zeeman energy occurs even though first-order corrections are quenched.

Relaxation phenomena in the motionally narrowed regime are described using second-order perturbation theory and it is anticipated that second-order dynamic frequency shifts of Zeeman energies are embodied in relaxation theory. In principle, the dynamic frequency shift yields both structural and dynamic information similar to conventional relaxation parameters such as $(1/T_1)$, $(1/T_2)$ or $(1/T_{1\rho})$, over a nominal range of molecular motions.

In Redfield's seminal exposé on the subject of second-order perturbation theory applied to relaxation phenomena, the dynamic frequency shift was explicitly ignored. However, in the more widely accessible version[1] of this theory, the dynamic frequency shift was acknowledged. Abragam, in his classic monograph,[2] also considered this term. More detailed discussions of the dynamic frequency shift, both in context of the ESR[3,4] or NMR[5,6] experiment, exist in the published literature.

2 SEMICLASSICAL THEORY OF SPIN RELAXATION

In the absence of applied rf fields, the interaction between a nuclear spin and the extranuclear environment can be written as $\hat{\mathcal{H}}(t) = \hat{\mathcal{E}} + \hat{\mathcal{F}}(t)$, where $\hat{\mathcal{E}} = \langle \mathcal{H}(t) \rangle$ and $\hat{\mathcal{F}}(t) = \hat{\mathcal{H}}(t) - \hat{\mathcal{E}}$. The influence of $\hat{\mathcal{E}}$ is revealed through chemical shift and multiplet structure. The term responsible for nuclear spin relaxation, $\hat{\mathcal{F}}(t)$, can be cast is in the form:

$$\hat{\mathcal{F}}(t) = \sum_{\eta} \hat{\mathcal{F}}^{\eta} = \sum_{\eta} \xi_{\eta} \sum_{k} (-1)^k \hat{T}_{\eta}^{k} V_{\eta}^{-k}(t) \qquad (1)$$

In general, the total interaction Hamiltonian, $\hat{\mathcal{F}}(t)$, is composed of a number of distinct couplings or relaxation pathways (η). Each interaction has been partitioned into a symmetrized product of classical lattice functions (V), characteristic interaction coupling constants (ξ), and spin operators ($\hat{T}$) which occur in Hermitian adjoint pairs, $(\hat{T}_{\eta}^{k})^{\dagger} = (-1)^n \hat{T}_{\eta}^{-k}$. The simple decomposition implicit in equation (1) obtains for interactions with axial symmetry.

In the limit where it is possible to define a time τ such that $\langle \hat{\mathcal{F}}(\tau)\hat{\mathcal{F}}(0) \rangle \ll |\hat{\mathcal{F}}|^2$ and $\tau|\hat{\mathcal{F}}| \ll 1$, the time evolution of individual matrix elements of a thermally normalized, reduced spin density operator, $\chi(t)$, are described by a simple set of linearly coupled first-order equations,[1]

$$(\mathrm{d}/\mathrm{d}t)\chi_{\alpha\alpha'}(t) = -\mathrm{i}\omega_{\alpha\alpha'}\chi_{\alpha\alpha'}(t) + \sum_{\alpha''}\sum_{\alpha'''} \mathcal{R}_{\alpha\alpha'\alpha''\alpha'''}\chi_{\alpha''\alpha'''}(t) \qquad (2)$$

where

$$\begin{aligned}\mathcal{R}_{\alpha\alpha'\alpha''\alpha'''} = &\sum_{k}\sum_{\eta}\sum_{\eta'}[G_k^{\eta\eta'}(\omega_{\alpha\alpha''}) + G_k^{\eta\eta'}(\omega_{\alpha'''\alpha'})] \\ &\times (T_{\eta}^{k})_{\alpha\alpha''}(T_{\eta'}^{-k})_{\alpha'''\alpha'} \\ &-\delta_{\alpha\alpha''}\sum_{\beta} G_k^{\eta\eta'}(\omega_{\alpha'''\beta})(T_{\eta}^{k})_{\alpha'''\beta}(T_{\eta'}^{-k})_{\beta\alpha'} \\ &-\delta_{\alpha'''\alpha'}\sum_{\beta} G_k^{\eta\eta'}(\omega_{\beta\alpha''})(T_{\eta}^{k})_{\alpha\beta}(T_{\eta'}^{-k})_{\beta\alpha''} \qquad (3)\end{aligned}$$

The complex spectral density is defined as

$$\begin{aligned}G_k^{\eta\eta'}(\omega) &= \xi_{\eta}\xi_{\eta'}\int_0^{\infty}\langle V_{\eta}^{-k}(t-\tau)V_{\eta'}^{k}(t)\rangle \exp(-\mathrm{i}\omega\tau)\,\mathrm{d}\tau \\ &= J_k^{\eta\eta'}(\omega) - \mathrm{i}L_k^{\eta\eta'}(\omega) \qquad (4)\end{aligned}$$

The abbreviated matrix elements introduced in equations (3) and (4) are defined by the expressions, $\chi_{\alpha\beta} = \langle\alpha|\hat{\chi}|\beta\rangle$, $(T_{\eta}^{k})_{\alpha\beta} = \langle\alpha|\hat{T}_{\eta}^{k}|\beta\rangle$, and $\omega_{\alpha\beta} = -\omega_{\beta\alpha} = \langle\alpha|\hat{\mathcal{E}}|\alpha\rangle - \langle\beta|\hat{\mathcal{E}}|\beta\rangle$. Equation (3) includes both autocorrelation ($\eta = \eta'$) and cross-correlation ($\eta \neq \eta'$) spectral densities.

Detailed derivations, implicit limitations and subsequent simplifications of equations (2)–(4) can be found in articles by Redfield[1] or Hubbard.[7]

The imaginary contribution, $L_k^{\eta\eta'}(\omega)$, is defined as the Hilbert transform of $J_k^{\eta\eta'}(\omega)$ and identifies with a frequency shift. Equation (4) is an affirmation of the Kramers–Kronig relationship which relates the real and imaginary components of the Fourier transform of a causal function.

3 THE DYNAMIC FREQUENCY SHIFT

In the absence of overlapping transitions, equation (2) can be written in a simpler form. For populations $\alpha = \alpha'$ and $\alpha'' = \alpha'''$,

$$-(\mathrm{d}/\mathrm{d}t)\chi_{\alpha\alpha}(t) = \sum_{\alpha''\neq\alpha} W_{\alpha\alpha''}[\chi_{\alpha\alpha}(t) - \chi_{\alpha''\alpha''}(t)] \qquad (5)$$

where

$$W_{\alpha\alpha''} = 2\sum_k \sum_\eta \sum_{\eta'} (T_\eta^k)_{\alpha\alpha''}(T_{\eta'}^{-k})_{\alpha''\alpha} J_{k'}^{\eta\eta'}(\omega_{\alpha\alpha''}).$$

Because

$$L_k^{\eta\eta'}(\omega) + L_k^{\eta\eta'}(-\omega) = 0 \qquad (6)$$

populations are unaffected by the imaginary contribution.

Similarly, the free evolution of the coherence between states $|\alpha\rangle$ and $|\alpha'\rangle$ is described as:

$$-(\mathrm{d}/\mathrm{d}t)\chi_{\alpha\alpha'}(t) = [\mathrm{i}(\omega_{\alpha\alpha'} + \Omega_{\alpha\alpha'}) + (1/T_2)_{\alpha\alpha'}]\chi_{\alpha\alpha'}(t) \qquad (7)$$

where

$$\begin{aligned}(1/T_2)_{\alpha\alpha'} = -\sum_\eta \sum_{\eta'} J_0^{\eta\eta'}(0)\Bigg\{ & 2(T_\eta^0)_{\alpha\alpha}(T_{\eta'}^0)_{\alpha'\alpha'} \\ & + \sum_\eta \{[(T_\eta^0)_{\alpha\alpha}]^2 + [(T_\eta^0)_{\alpha'\alpha'}]^2\} \\ & + (1/2)\Bigg\{\sum_{\beta\neq\alpha} W_{\alpha\beta} + \sum_{\beta\neq\alpha'} W_{\alpha'\beta}\Bigg\}\end{aligned} \qquad (8)$$

The dynamic frequency shift is defined as

$$\begin{aligned}\Omega_{\alpha\alpha'} = \sum_{\beta\neq\alpha}\sum_k\sum_\eta\sum_{\eta'}[& (T_\eta^k)_{\alpha'\beta}(T_{\eta'}^{-k})_{\beta\alpha'} L_k^{\eta\eta'}(\omega_{\beta\alpha'}) \\ & + (T_\eta^k)_{\beta\alpha}(T_{\eta'}^{-k})_{\alpha\beta} L_k^{\eta\eta'}(\omega_{\alpha\beta})]\end{aligned} \qquad (9)$$

For dipole–dipole (D_{IS}), axially symmetric anisotropic shielding (SA_I), and axially symmetric quadrupolar (Q_I) interactions modulated by symmetric-top, diffusional reorientation characterized by the two diffusion constants, $D_\parallel = D_{zz}$ and $D_\perp = D_{xx} = D_{yy}$, $L_k^{\eta\eta'}(\omega)$ is defined as

$$\begin{aligned}L^{\eta\eta'}(\omega) = (16\omega\pi)^{-1}\xi_\eta\xi_{\eta'}\Bigg[& \frac{(3\cos^2\theta_\eta - 1)(3\cos^2\theta_{\eta'} - 1)}{1 + (\omega\tau_{20})^{-2}} \\ & + \frac{12\cos\theta_\eta\cos\theta_{\eta'}\sin\theta_\eta\sin\theta_{\eta'}\cos(\phi_\eta - \phi_{\eta'})}{1 + (\omega\tau_{21})^{-2}} \\ & + \frac{3\sin^2\theta_\eta\sin^2\theta_{\eta'}\cos(2\phi_\eta - 2\phi_{\eta'})}{1 + (\omega\tau_{22})^{-2}}\Bigg]\end{aligned} \qquad (10)$$

Equation (10) applies to isotropic media where the suppressed k index is superfluous. The angle θ defines the angle between the principal axes of the diffusion and interaction tensors. The three correlation times are defined as $1/\tau_{2n} = 6D_\perp + n^2(D_\parallel - D_\perp)$. For isotropic motions, $\tau_{2n} \sum \tau_2$, equation (10) simplifies accordingly, $L^{\eta\eta'}(\omega) = (8\omega\pi)^{-1}(\xi_\eta\xi_{\eta'})(3\cos^2\Theta_{\eta\eta'} - 1)(1 + (\omega\tau_2)^{-2})^{-1}$. The angle $\Theta_{\eta\eta'}$ is defined as the angle between the principal axes of interactions η and η'. If $\omega\tau_{20}$, $\omega\tau_{21}$, $\omega\tau_{22} \gg 1$, $L^{\eta\eta'}(\omega) = (8\omega\pi)^{-1}(\xi_\eta\xi_{\eta'})(3\cos^2\Theta_{\eta\eta'} - 1)$. In this slow motion limit, the maximum shift associated with an autocorrelated term is simply $(4\omega\pi)^{-1}(\xi_\eta)^2$. Appropriate interaction constants for a spin I subject to (I,S) dipole–dipole, anisotropic shielding or quadrupolar interactions are $\xi_{D_{IS}} = (6\pi/5)^{1/2}\gamma_I\gamma_S\hbar(r_{IS})^{-3}$, $\xi_{SA_I} = (2\pi/15)^{1/2}\Delta\sigma_I\omega_I$ (with $\omega_I = \gamma_I B_0$) and $\xi_{Q_I} = (3\pi/40)^{1/2}e^2q_IQ_I/h$.

Only in the limit where motions are relatively isotropic—*and* $\omega\tau_2$ is close to one—will the dynamic shift be comparable to the adiabatic linewidth parameter.[8] In general, this argument is used to justify the neglect of second order dynamic frequency shifts in magnetic resonance. However, for relaxation studies in the vicinity of the T_1 minimum, or for the investigation of systems where linewidths have no adiabatic contribution, the dynamic frequency shift may play an important role.

In Figure 1, the adiabatic term, $G^{\eta\eta}(0) \sum G^\eta(0) = J^\eta(0)$, and the real and imaginary components of the spectral density, $G^\eta(\omega_I)$, are plotted as functions of an isotropic reorientational correlation time (τ_2) measured in units of the reciprocal Larmor frequency, ${\omega_I}^{-1}$. Because the interaction is unspecified, the ordinate is not scaled. The ratio of plateau values for $J^\eta(0)$ and $L^\eta(\omega_I)$ is on the order of ω_I/ξ_η.

4 DYNAMIC FREQUENCY SHIFTS FOR SOME SIMPLE SPIN SYSTEMS

4.1 The Two Unlike Spin-$\frac{1}{2}$ System

Consider the scalar coupled, $I = \frac{1}{2}$, $S = \frac{1}{2}$ spin system with both spins being relaxed by anisotropic shieldings and a mutual dipole–dipole interaction. In the absence of second-order shifts, the four single quantum transitions occur at frequencies $\omega_S \pm J/2$ and $\omega_I \pm J/2$, where J is the scalar

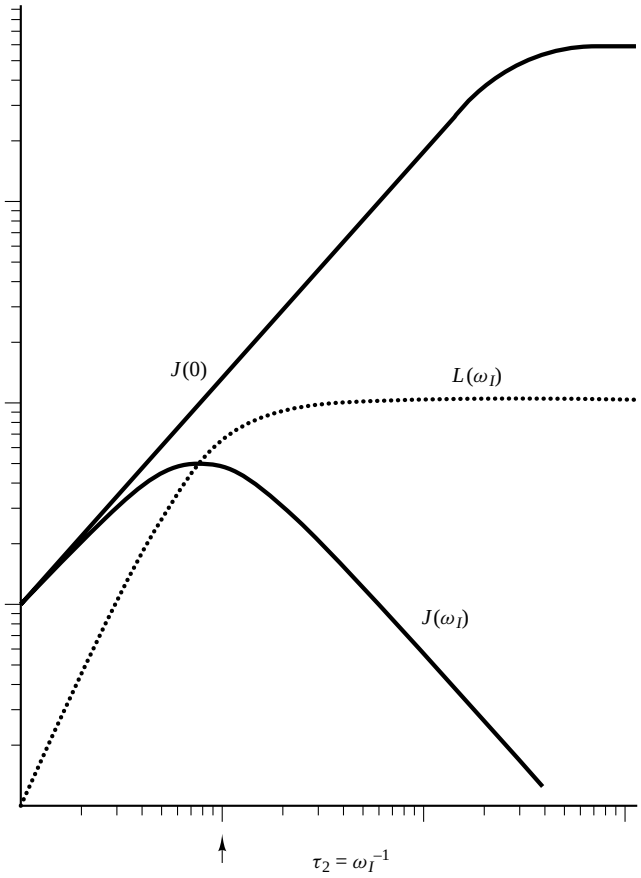

Figure 1 Schematic plots of various relaxation parameters versus the isotropic, reorientational correlation time, τ_2. The real $[J(\omega_I)]$ and imaginary $[L(\omega_I)]$ components of the complex spectral density, $G(\omega_I)$, as well as the zero-frequency or adiabatic term $[J(0)]$, are shown. The plateau values of $J(0)$ and $L(\omega_I)$ are $|\mathcal{F}|$ and $|\mathcal{F}|^2/\omega_I$, respectively

coupling constant. If dynamic frequency shifts are considered, these transitions occur at the modified frequencies

$$\begin{aligned}\omega_S &+ (1/6)L_0^{D_{IS}}(\omega_S - \omega_I) + (1/2)L_1^{D_{IS}}(\omega_S)\\ &+ L_2^{D_{IS}}(\omega_S + \omega_I) + 2L_1^{SA_S}(\omega_S)\\ &\pm (1/2)[J + 4L_1^{D_{IS},SA_S}(\omega_S) + 4L_1^{D_{IS},SA_I}(\omega_I)] \quad (11)\end{aligned}$$

$$\begin{aligned}\omega_I &+ (1/6)L_0^{D_{IS}}(\omega_I - \omega_S) + (1/2)L_1^{D_{IS}}(\omega_I)\\ &+ L_2^{D_{IS}}(\omega_S + \omega_I) + 2L_1^{SA_I}(\omega_I)\\ &\pm (1/2)[J + 4L_1^{D_{IS},SA_S}(\omega_S) + 4L_1^{D_{IS},SA_I}(\omega_I)] \quad (12)\end{aligned}$$

Notice that the splitting between the two components of each doublet, $[J + 4L_1^{D_{IS},SA_S}(\omega_S) + 4L_1^{D_{IS},SA_I}(\omega_I)]$, is modified by cross-correlation terms. The shifts identified with the autocorrelation spectral densities affect both doublet components equally.

Similarly, the double and zero quantum transition frequencies are

$$\begin{aligned}(\omega_I + \omega_S) &+ (1/2)[(L_1^{D_{IS}}(\omega_S) + L_1^{D_{IS}}(\omega_I)] + 2L_2^{D_{IS}}(\omega_I + \omega_S)\\ &+ 2[L_1^{SA_S}(\omega_S) + L_1^{SA_I}(\omega_I)] \quad (13)\end{aligned}$$

and

$$\begin{aligned}(\omega_I - \omega_S) &+ (1/2)[(L_1^{D_{IS}}(\omega_I) - L_1^{D_{IS}}(\omega_S)]\\ &+ (1/3)L_0^{D_{IS}}(\omega_I - \omega_S)\\ &+ 2[L_1^{SA_I}(\omega_I) - L_1^{SA_S}(\omega_S)] \quad (14)\end{aligned}$$

Neither the zero nor double quantum coherences are dephased by adiabatic dipolar contributions. Hence, if extreme narrowing fails, the dynamic frequency shift may be *larger* than the homogeneous linewidth of either of these coherences. However, this is somewhat academic. For example, in a homonuclear spin system ($\omega_I \simeq \omega_S$), the zero quantum dynamic frequency shift is vanishingly small whereas the maximum dipole–dipole induced dynamic frequency shift of the double quantum coherence, $(\frac{3}{5})[\gamma_I\gamma_S\hbar(r_{IS})^{-3}]^2/\omega_I$, is typically less than 1 Hz.

4.2 The Three Identical Spin-$\frac{1}{2}$ System

Although differential dynamic frequency shifts between the various transitions in this important spin grouping have been noticed by many workers, few researchers have attempted to exploit this fact.[9]

For three identical spin-$\frac{1}{2}$ nuclei (I, I', I'') relaxed by mutual dipole–dipole and shielding anisotropy interactions, the dynamic frequency shifts of the three single quantum coherences within the quartet manifold are

$$\begin{aligned}\Omega_{3/2,1/2} = -[&L_1^{D_{II'}}(\omega_I) + 5L_1^{D_{II'},D_{II''}}(\omega_I) + 2L_2^{D_{II'}}(2\omega_I)\\ &-2L_2^{D_{II'},D_{II''}}(2\omega_I) + 2L_1^{SA_I}(\omega_I)\\ &-12L_1^{D_{II'},SA_I}(\omega_I)] \quad (15)\end{aligned}$$

$$\begin{aligned}\Omega_{-1/2,-3/2} = -[&L_1^{D_{II'}}(\omega_I) + 5L_1^{D_{II'},D_{II''}}(\omega_I)\\ &+ 2L_2^{D_{II'}}(2\omega_I) - 2L_2^{D_{II'},D_{II''}}(2\omega_I)\\ &+ 2L_1^{SA_I}(\omega_I) + 12L_1^{D_{II'},SA_I}(\omega_I)] \quad (16)\end{aligned}$$

$$\begin{aligned}\Omega_{(1/2,-1/2)_{3/2}} = -[&L_1^{D_{II'}}(\omega_I) - 7L_1^{D_{II'},D_{II''}}(\omega_I) + 2L_2^{D_{II'}}(2\omega_I)\\ &+ 4L_2^{D_{II'},D_{II''}}(2\omega_I) + 2L_1^{SA_I}(\omega_I)\\ &+ 4L_1^{D_{II'},SA_I}(\omega_I) - 4L_1^{D_{II'},SA_{I''}}(\omega_I)]\end{aligned} \quad (17)$$

The dynamic frequency shift of the doublet's doubly degenerate single quantum coherence is

$$\begin{aligned}\Omega_{(1/2,-1/2)_{1/2}} = -[&L_1^{D_{II'}}(\omega_I) - L_1^{D_{II'},D_{II''}}(\omega_I) + 2L_2^{D_{II'}}(2\omega_I)\\ &-2L_2^{D_{II'},D_{II''}}(2\omega_I) + 2L_1^{SA_I}(\omega_I)\\ &+2L_1^{D_{II'},SA_I}(\omega_I) - 2L_1^{D_{II'},SA_{I''}}(\omega_I)] \quad (18)\end{aligned}$$

where $L_k^{D_{II'},SA_I}(\omega)$ designates the interference or cross correlation between a dipole–dipole interaction and the shielding anisotropy of one of the participating spins. Likewise, $L_k^{D_{II'},SA_{I''}}(\omega)$ arises from the interference between a

dipole–dipole interaction and the shielding anisotropy of the spin not participating in the dipole–dipole coupling.

In the absence of cross correlation, all four of these coherences share identical dynamic frequency shifts, $-[L_1^{D_{II'}}(\omega_I) + 2L_2^{D_{II'}}(2\omega_I) + 2L_1^{SA_I}(\omega_I)$, and the spectral degeneracy of these transitions is not removed. Conversely, in the limit of complete correlation ($L_k^{D_{II'}} = L_k^{D_{II'},D_{II''}}$ and $L_1^{D_{II'},SA_I} = L_1^{D_{II'},SA_I''}$),

$$\Omega_{3/2,1/2} = -6L_1^{D_{II'}}(\omega_I) - 2L_1^{SA_I}(\omega_I) + 12L_1^{D_{II'},SA_I}(\omega_I) \quad (19)$$

$$\Omega_{-1/2,-3/2} = -6L_1^{D_{II'}}(\omega_I) - 2L_1^{SA_I}(\omega_I) - 12L_1^{D_{II'},SA_I}(\omega_I) \quad (20)$$

$$\Omega_{(1/2,-1/2)_{3/2}} = 6L_1^{D_{II'}}(\omega_I) - 6L_2^{D_{II'}}(2\omega_I) - 2L_1^{SA_I}(\omega_I) \quad (21)$$

$$\Omega_{(1/2,-1/2)_{1/2}} = -2L_1^{SA}(\omega_I) \quad (22)$$

For commonly available magnetic field strengths, the maximum dipole–dipole induced frequency shift, $(\frac{27}{10})(\gamma_I^2\hbar(r_{II'})^{-3})^2/\omega_I$, between the various single quantum transition frequencies of a proton triad characterized by the geometry of a methyl group, are on the order of 2 Hz.

4.3 The $I = 1$ Spin System

For a collection of isolated $I = 1$ spins relaxed by intramolecular anisotropic shieldings and quadrupolar interactions, the dynamic frequency shifts of the two single quantum coherences are defined as

$$\Omega_{1,0} = -[2L_1^{Q_I}(\omega_I) + 4L_2^{Q_I}(2\omega_I) + 2L_1^{SA_I}(\omega_I) + 12L_1^{Q_I,SA_I}(\omega_I)] \quad (23)$$

$$\Omega_{0,-1} = -[2L_1^{Q_I}(\omega_I) + 4L_2^{Q_I}(2\omega_I) + 2L_1^{SA_I}(\omega_I) - 12L_1^{Q_I,SA_I}(\omega_I)] \quad (24)$$

Once again, it is seen that the differential dynamic frequency shift between these two coherences, given by $\Omega_{1,0} - \Omega_{0,-1} = -[24L_1^{Q_I,SA_I}(\omega_I)]$, depends only on the cross correlation between competitive relaxation pathways.

The dynamic frequency shift of the double quantum coherence is

$$\Omega_{1,-1} = -[4L_1^{Q_I}(\omega_I) + 8L_2^{Q_I}(2\omega_I) + 4L_1^{SA_I}(\omega_I)] \quad (25)$$

Interestingly, the relaxation rate of the double quantum coherence has no adiabatic quadrupolar contribution and is defined by the expression

$$(1/T_2)_{1,-1} = 4J_1^{Q_I}(\omega_I) + 8J_2^{Q_I}(2\omega_I) + (32/3)J_0^{SA_I}(\omega_I) + 4J_1^{SA_I}(\omega_I) \quad (26)$$

Once again, if extreme narrowing fails then the dynamic frequency shift will be larger than the homogeneous linewidth. The maximum dynamic frequency shift of this double quantum coherence is $(3/20)(e^2q_IQ_I/h)^2/\omega_I$ and can easily exceed 1 kHz—even for a deuteron.

For quadrupolar nuclei, significant—and easily measured—dynamic frequency shifts can be anticipated.

5 DYNAMIC FREQUENCY SHIFTS FOR QUADRUPOLAR NUCLEI

The constant $e^2q_IQ_I/h$ for commonly studied quadrupolar nuclei in representative electronic environments typically ranges from 0.2 to 5 MHz. Thus, dynamic frequency shifts of quadrupolar nuclei generally fall within the range of one to several hundred kHz. These are significant shifts and obviously the greatest interest in the dynamic frequency shift has arisen in the study of quadrupolar nuclei.[10–18] However, one should be reminded that, except near the T_1 minimum, this shift is small compared with the adiabatic linewidth.

The dynamic frequency shift for the specific component $\chi_{m,m-n}$ of the n-quantum coherence for arbitrary spin (either integer or half-integer) relaxed via quadrupolar couplings is given by the expression[19]

$$\begin{aligned}\Omega_{m,m-n} = &\frac{2n}{I^2(2I-1)^2}\{[4I(I+1) - 24m(m-n) - 8n^2 - 1]L_1^{Q_I} \\ &\times(\omega_I) + [-4I(I+1) + 12m(m-n) + 4n^2 + 2]L_2^{Q_I} \\ &\times(2\omega_I)\} = \frac{2n}{I^2(2I-1)^2}\{[4I(I+1)(L_1^{Q_I}(\omega_I) - L_2^{Q_I} \\ &\times(2\omega_I)] - [L_1^{Q_I}(\omega_I) - 2L_2^{Q_I}(2\omega_I)] \\ &- 4[3m(m-n) + n^2][2L_1^{Q_I}(\omega_I) - L_2^{Q_I}(2\omega_I)]\}\end{aligned} \quad (27)$$

These expressions are valid whether or not the various transitions are well-resolved or degenerate. The dynamic frequency shifts of all transitions for half-integral spin ($1 \le n \le 9$; $\frac{3}{2} \le I \le \frac{9}{2}$) are summarized in Table 1.

In Figure 2, the dynamic frequency shifts [measured in units of $2(e^2q_IQ_I/h)^2/25\omega_I$] of the various transitions of an $I = \frac{5}{2}$ spin are plotted as a function of an isotropic reorientational correlation time, τ_2 (measured in units of the reciprocal Larmor frequency, ω_I). For a coupling strength $e^2q_IQ_I/h$ = 1 MHz and a Larmor frequency $\omega_I/2\pi$ = 80 MHz, the ordinate has been scaled such that the dynamic frequency shift is read in kHz.

In Figure 2, the three dynamic frequency shifts, $\Omega_{3/2,-3/2}$, $\Omega_{5/2,-5/2}$ and $\Omega_{1/2,-1/2}$ have been set apart from the other shifts. For each of these transitions, the corresponding linewidth has no adiabatic contribution. Thus, in the limit where $\omega_I\tau_2 > 1$, these linewidths narrow as $\omega_I\tau_2$ increases. In this situation, the dynamic frequency shift will exceed the linewidth and the general assertion that the dynamic frequency shift is small compared with the homogeneous linewidth fails.

Table 1 Dynamic Frequency Shifts for Various Transitions of Half-Integral Spin

n = 1	$I = \frac{3}{2}$	$I = \frac{5}{2}$	$I = \frac{7}{2}$	$I = \frac{9}{2}$
$\frac{1}{2} \leftrightarrow -\frac{1}{2}$	$\frac{8}{3}(L_1^Q - L_2^Q)$	$\frac{2}{25}(8L_1^Q - 8L_2^Q)$	$\frac{8}{147}(5L_1^Q - 5L_2^Q)$	$\frac{1}{54}(8L_1^Q - 8L_2^Q)$
$\frac{3}{2} \leftrightarrow \frac{1}{2}$	$\frac{8}{3}(-L_1^Q)$	$\frac{2}{25}(2L_1^Q - 5L_2^Q)$	$\frac{8}{147}(3L_1^Q - 4L_2^Q)$	$\frac{1}{54}(6L_1^Q - 7L_2^Q)$
$\frac{5}{2} \leftrightarrow \frac{3}{2}$		$\frac{2}{25}(-16L_1^Q + 4L_2^Q)$	$\frac{8}{147}(-3L_1^Q - L_2^Q)$	$\frac{1}{54}(-4L_2^Q)$
$\frac{7}{2} \leftrightarrow \frac{5}{2}$			$\frac{8}{147}(-13L_1^Q + 4L_2^Q)$	$\frac{1}{54}(-10L_1^Q + L_2^Q)$
$\frac{9}{2} \leftrightarrow \frac{7}{2}$				$\frac{1}{54}(-24L_1^Q + 8L_2^Q)$
n = 2	$I = \frac{3}{2}$	$I = \frac{5}{2}$	$I = \frac{7}{2}$	$I = \frac{9}{2}$
$\frac{3}{2} \leftrightarrow -\frac{1}{2}$	$\frac{8}{3}(-L_2^Q)$	$\frac{2}{25}(10L_1^Q - 13L_2^Q)$	$\frac{8}{147}(8L_1^Q - 9L_2^Q)$	$\frac{1}{54}(14L_1^Q - 15L_2^Q)$
$\frac{5}{2} \leftrightarrow \frac{1}{2}$		$\frac{2}{25}(-14L_1^Q - L_2^Q)$	$\frac{8}{147}(-4L_2^Q)$	$\frac{1}{54}(6L_1^Q - 11L_2^Q)$
$\frac{7}{2} \leftrightarrow \frac{3}{2}$			$\frac{8}{147}(-16L_1^Q + 3L_2^Q)$	$\frac{1}{54}(-10L_1^Q - 3L_2^Q)$
$\frac{9}{2} \leftrightarrow \frac{5}{2}$				$\frac{1}{54}(-34L_1^Q + 9L_2^Q)$
n = 3	$I = \frac{3}{2}$	$I = \frac{5}{2}$	$I = \frac{7}{2}$	$I = \frac{9}{2}$
$\frac{3}{2} \leftrightarrow -\frac{3}{2}$	$\frac{8}{3}(-L_1^Q - L_2^Q)$	$\frac{2}{25}(12L_1^Q - 18L_2^Q)$	$\frac{8}{147}(11L_1^Q - 13L_2^Q)$	$\frac{1}{54}(20L_1^Q - 22L_2^Q)$
$\frac{5}{2} \leftrightarrow -\frac{1}{2}$		$\frac{2}{25}(-6L_1^Q - 9L_2^Q)$	$\frac{8}{147}(5L_1^Q - 10L_2^Q)$	$\frac{1}{54}(14L_1^Q - 19L_2^Q)$
$\frac{7}{2} \leftrightarrow \frac{1}{2}$			$\frac{8}{147}(-13L_1^Q - L_2^Q)$	$\frac{1}{54}(-4L_1^Q - 10L_2^Q)$
$\frac{9}{2} \leftrightarrow \frac{3}{2}$				$\frac{1}{54}(-34L_1^Q + 5L_2^Q)$
n = 4		$I = \frac{5}{2}$	$I = \frac{7}{2}$	$I = \frac{9}{2}$
$\frac{5}{2} \leftrightarrow -\frac{3}{2}$		$\frac{2}{25}(-4L_1^Q - 14L_2^Q)$	$\frac{8}{147}(8L_1^Q - 14L_2^Q)$	$\frac{1}{54}(20L_1^Q - 26L_2^Q)$
$\frac{7}{2} \leftrightarrow -\frac{1}{2}$			$\frac{8}{147}(-8L_1^Q - 6L_2^Q)$	$\frac{1}{54}(4L_1^Q - 18L_2^Q)$
$\frac{9}{2} \leftrightarrow \frac{1}{2}$				$\frac{1}{54}(-28L_1^Q + 2L_2^Q)$
n = 5		$I = \frac{5}{2}$	$I = \frac{7}{2}$	$I = \frac{9}{2}$
$\frac{5}{2} \leftrightarrow -\frac{5}{2}$		$\frac{2}{25}(-20L_1^Q - 10L_2^Q)$	$\frac{8}{147}(5L_1^Q - 15L_2^Q)$	$\frac{1}{54}(20L_1^Q - 30L_2^Q)$
$\frac{7}{2} \leftrightarrow -\frac{3}{2}$			$\frac{8}{147}(-5L_1^Q - 10L_2^Q)$	$\frac{1}{54}(10L_1^Q - 25L_2^Q)$
$\frac{9}{2} \leftrightarrow -\frac{1}{2}$				$\frac{1}{54}(-20L_1^Q - 10L_2^Q)$
n = 6			$I = \frac{7}{2}$	$I = \frac{9}{2}$
$\frac{7}{2} \leftrightarrow -\frac{5}{2}$			$\frac{8}{147}(-8L_1^Q - 11L_2^Q)$	$\frac{1}{54}(10L_1^Q - 29L_2^Q)$
$\frac{9}{2} \leftrightarrow -\frac{3}{2}$				$\frac{1}{54}(-14L_1^Q - 17L_2^Q)$
n = 7			$I = \frac{7}{2}$	$I = \frac{9}{2}$
$\frac{7}{2} \leftrightarrow -\frac{7}{2}$			$\frac{8}{147}(-21L_1^Q - 7L_2^Q)$	$\frac{1}{54}(-28L_2^Q)$
$\frac{9}{2} \leftrightarrow -\frac{5}{2}$				$\frac{1}{54}(-14L_1^Q - 21L_2^Q)$
n = 8,9				$I = \frac{9}{2}$
$\frac{9}{2} \leftrightarrow -\frac{7}{2}$				$\frac{1}{54}(-24L_1^Q - 20L_2^Q)$
$\frac{9}{2} \leftrightarrow -\frac{9}{2}$				$\frac{1}{54}(-48L_1^Q - 12L_2^Q)$

In Figure 3, the (dynamic-frequency-shift/linewidth) ratio of various adiabatic-free transitions for $I = \frac{3}{2}$ or $I = \frac{5}{2}$ are plotted as a function of $\omega_I\tau_2$. Once again, quadrupolar relaxation is assumed. The parameter $(\Omega/{T_2}^{-1})_{m,-m}$ is the ratio of the dynamic frequency shift compared with the halfwidth at half-height of the coherence, $\chi_{m,-m}$. In Figure 3, only the absolute value of the dynamic frequency shift is considered. [Note that although the validity of equation (27) is independent of the secular approximation, one must be more cautious in defining a T_2 value when overlapping transitions are involved. However, since secular couplings also contain no adiabatic contribution, a well-defined linewidth parameter can be identified with the coherence $\chi_{m,-m}$ in the interesting limit when $J(0) \gg J(\omega_I)$]

As mentioned earlier, the second-order dynamic and static frequency shifts are different manifestations of the same phenomenon. This is illustrated by comparing expressions for the static, second-order quadrupolar shift of a single quantum coherence $\chi_{m,m-1}$[20]

$$(3/16)\frac{(e^2q_IQ_I/\hbar)^2}{I^2(2I-1)^2}(\omega_I)^{-1}\{[4I(I+1)-24m(m-1)-9] \times\langle\tfrac{3}{2}\sin^2\theta\cos^2\theta\rangle + [-2I(I+1)+6m(m-1)+3]\langle\tfrac{3}{8}\sin^4\theta\rangle\} \quad (28)$$

with equation (27).

In the motionally narrowed limit, the isotropically averaged angular terms appearing in equation (28) each reduce to $\frac{1}{5}$ which reproduces equation (27) in the limit where $L_1^{Q_I}(\omega_I) = 2L_2^{Q_I}(2\omega_I) = (\frac{3}{160})(e^2q_IQ_I/\hbar)^2/\omega_I$.

Although uncommon, couplings other than the electric quadrupolar coupling may play a role in relaxing high-spin nuclei. Dynamic frequency shifts associated with these competitive relaxation pathways should not be forgotten. For example, the dynamic frequency shift for the specific

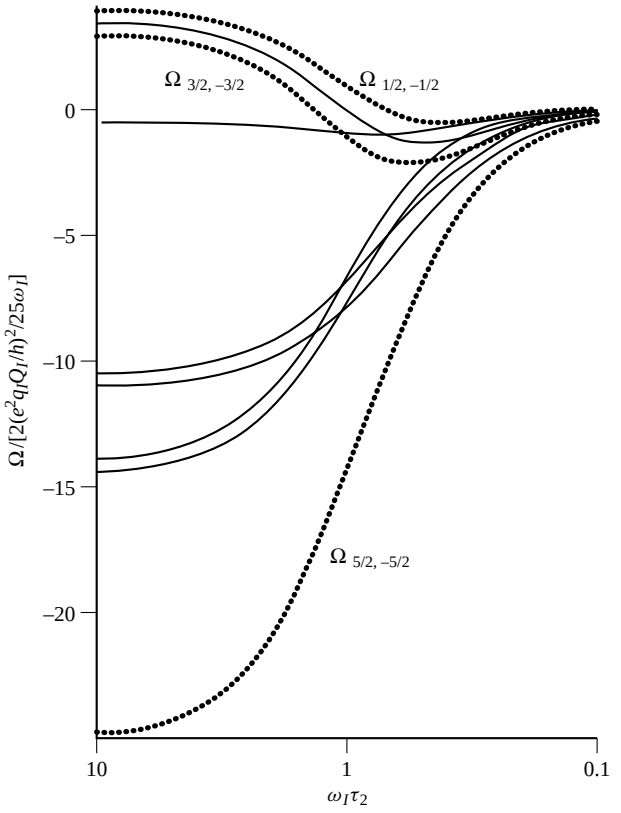

Figure 2 Plot of the quadrupole-induced dynamic frequency shifts of an $I = 5/2$ spin versus the isotropic, reorientational correlation time, τ_2. The three coherences lacking adiabatic linewidth contributions are shown by dotted curves. The ordering of the curves in the limit $\omega_I\tau_2 \gg 1$ is as follows: $\Omega_{1/2,-1/2} > \Omega_{3/2,-1/2} > \Omega_{3/2,-3/2} > \Omega_{3/2,1/2} > \Omega_{5/2,-1/2} > \Omega_{5/2,-3/2} > \Omega_{5/2,3/2} > \Omega_{5/2,1/2} > \Omega_{5/2,-5/2} >$. For a quadrupolar coupling ($e^2q_IQ_I/\hbar$) equal to 1 MHz and a Larmor frequency $\omega_I/2\pi = 80$ MHz, the dynamic frequency shift can be read directly in kHz

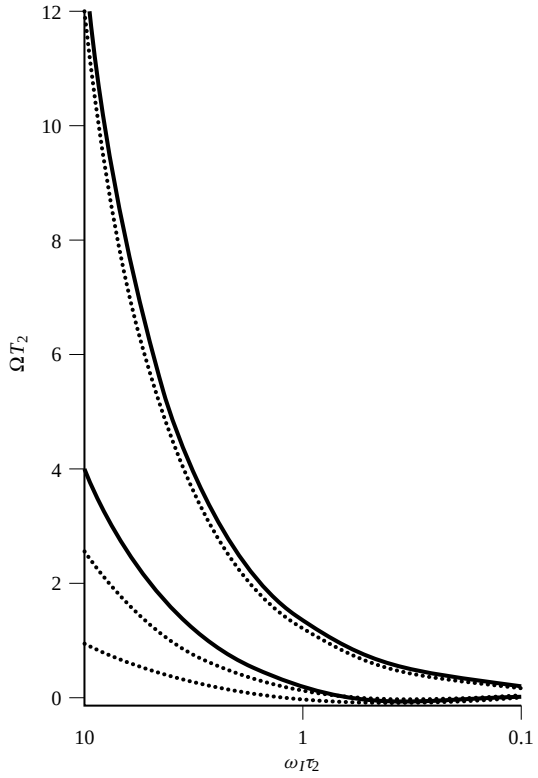

Figure 3 Plot of the quadrupole-induced dynamic frequency shift $\Omega_{m,m'}$, measured in units of $(1/T_2)_{m,m'}$ for various coherences having no adiabatic linewidth contribution. The parameter ΩT_2 equals the dynamic-frequency-shift/halfwidth-at-halfheight ratio. Only the magnitude and not the sign of the shift is considered. The ordering of the curves in the limit $\omega_i\tau_2 > 1$ is as follows: $\Omega;_{3/2,-3/2}\,(I = \frac{3}{2})\rangle\Omega;_{5/2,-5/2}\,(I = \frac{5}{2})\rangle\Omega_{1/2,-1/2}(I = \frac{3}{2})\rangle\Omega_{1/2,-1/2}(I = \frac{5}{2})\rangle\Omega_{3/2,-3/2}(I = \frac{5}{2})\rangle$. The two solid curves distinguish the dynamic frequency shifts of an $I = 3/2$ spin

component $\chi_{m,m-n}$ of the n-quantum coherence, relaxed via shielding anisotropy, is given by the expression

$$\Omega_{m,m-n} = -2nL_1^{SA_I}(\omega_I) \tag{29}$$

More importantly, the dynamic frequency shift associated with the cross correlation between quadrupolar and other interactions can be significant even when quadrupolar interactions dominate. For the case of interference between quadrupolar and shielding anisotropy, the dynamic frequency shifts are given by the expression

$$\Omega_{m,m-n} = \left[\frac{-12n(2m-n)}{I(2I-1)}L_1^{Q_I,SA_I}(\omega_I)\right] \tag{30}$$

Whereas both quadrupolar and shielding anisotropy interactions shift the pair of spin inverted coherences $\chi_{m,m-n}$ and $\chi_{-m+n,-m}$ by like amounts, interference terms shift these two coherences apart. Equation (30) demonstrates that $Q_I - SA_I$ interferences cannot effect any coherence between two spin-inverted states. Thus, unlike dynamic frequency shifts induced by quadrupole interactions alone, $Q_I - SA_I$ cross correlation does not shift any coherence lacking an adiabatic linewidth contribution.

Efficiently relaxed quadrupolar nuclei can effectively dissipate the single quantum coherences of coupled spin-$\frac{1}{2}$ nuclei (scalar relaxation of the second kind), and through interferences with direct or indirect dipole–dipole interactions[21] can induce dramatic dynamic frequency shifts of these same single quantum coherences.

To appreciate the basis of this phenomenon, consider the scalar coupled two-spin system where spin $S = \frac{1}{2}$ and spin $I > \frac{1}{2}$. Assume that the relaxation of spin I is effected by an axially symmetric quadrupolar interaction ($\hat{\mathcal{F}}^{Q_I}$). Spin S is relaxed directly by an I–S dipolar interaction ($\hat{\mathcal{F}}^{D_{IS}}$). It is assumed that $|\hat{\mathcal{F}}^{Q_I}| \gg |\hat{\mathcal{F}}^{D_{IS}}|$. (Spin I) quadrupole–(spin I or S) anisotropic shielding interferences result in no second-order dynamic frequency shifts of spin-S single quantum coherence.

In the limit where all multiplet components are well-resolved, the S multiplet, $\Im(\omega)$, is described as a simple sum of $2I + 1$ Lorentzians,

$$\Im(\omega) = \sum_{m=-I}^{I} (1/T_2)_{(I,m)}/[(\omega_S - \omega - mJ + \Omega_{(I,m)})^2 + (1/T_2)^2_{(I,m)}] \tag{31}$$

where J is the $I-S$ scalar coupling constant and ω_S is the Larmor frequency of spin S. The relaxation rate, $(1/T_2)_{(I,m)}$, and dynamic frequency shift, $\Omega_{(I,m)}$, are defined as

$$(1/T_2)_{(I,m)} = \left[\frac{2}{I(2I-1)}\right]^2 \{[I(I+1)(4m^2+1) - m^2(4m^2+5)] \times J^{Q_I}(\omega_I) + [(I(I+1) - (m^2+1))^2 + 3m^2 - 1]J^{Q_I}(2\omega_I)\} + (8m^2\sqrt{3})J^{D_{IS}}(0) \quad (32)$$

$$\Omega_{(I,m)} = \left[\frac{4}{I(2I-1)}\right][I(I+1) - 3m^2]L^{Q_I, D_{IS}}(\omega_I) \quad (33)$$

Only adiabatic, dipole–dipole contributions have been included in equation (32). Although the quadrupolar interaction generally determines the linewidths of the $2I + 1$ members of the S multiplet, there is no adiabatic quadrupolar contribution. Thus, in the regime where $\omega_I\tau_2 \gg 1$, the S multiplet may be characterized by anomalously narrow components exhibiting relatively large, easily measured, second-order dynamic frequency shifts. In Figure 4, simulated ^{13}C spectra of the ^{13}C–^{2}H spin system, using standard interaction constants illustrate the relative magnitude of these second order shifts.[21]

6 SUMMARY

The dynamic frequency shift is a second-order effect that arises from the basic noncommutivity of the Zeeman interaction with other spin interactions such as dipole–dipole, quadrupolar, or anisotropic shieldings. In the high-field limit, dynamic frequency shifts become less important with increasing field strength.

Usually, dynamic frequency shifts are detectable only in the vicinity of the T_1 minimum. In this region, the shift is on the order of the homogeneous linewidth. In general, motional anisotropy will diminish the relative importance of the dynamic frequency shift.

Since maximal dynamic frequency shifts are on the order of $|\mathcal{F}|^2/\mathcal{E}$ in high-field NMR, only quadrupolar interactions will induce shifts larger than a few Hz. More importantly, the linewidths associated with the coherence between spin-inverted pairs of states have no adiabatic contribution (assuming quadrupole relaxation). For these coherences, the dynamic frequency shift, no longer hidden within the linewidth, surfaces as the dominant relaxation parameter. Furthermore, interference (cross correlation) of dipole–dipole and quadrupole interactions can result in visually dramatic second-order NMR frequency shifts for spin-$\frac{1}{2}$ nuclei which are scalar coupled to quadrupolar nuclei.

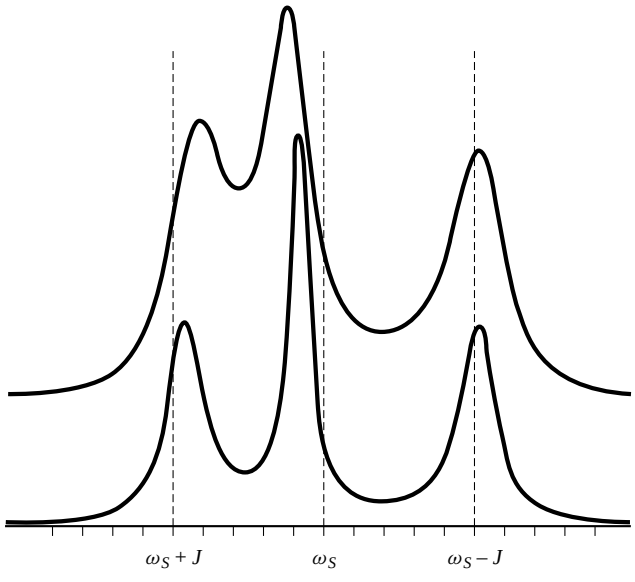

Figure 4 Spectral simulations of the ^{13}C spectra for the ^{13}C–^{2}H spin grouping. Typical values for the ^{13}C–^{2}H dipole–dipole coupling constant ($\gamma_C\gamma_D r_{CD}^{-3}h/2\pi$ = +3.6 kHz), $^1J_{(C,D)}$ scalar coupling constant (+20 Hz), and quadrupole coupling constant, (e^2qQ_S/h = + 170 kHz), are used in these simulations. Additional assumed parameters include isotropic reorientational correlation time $\tau_2 \approx 30$ ns and correlation factor $\Theta_{Q_I,D_{IS}} = 0$. Upper and lower traces correspond to B_0 = 11.75 T and 17.6 T, respectively. Vertical scaling factors are arbitrary. For reference, a first-order, stick spectrum is overlaid

7 RELATED ARTICLES

Quadrupolar Interactions; Quadrupolar Nuclei in Liquid Samples; Relaxation: An Introduction; Relaxation Processes: Cross Correlation and Interference Terms; Relaxation Theory: Density Matrix Formulation; Relaxation Theory for Quadrupolar Nuclei.

8 REFERENCES

1. A. G. Redfield, *Adv. Magn. Reson.*, 1965, **1**, 1.
2. A. Abragam, *Principles of Nuclear Magnetic Resonance*, Oxford University Press, Oxford, 1970.
3. G. K. Fraenkel, *J. Chem. Phys.*, 1965, **42**, 4275.
4. R. Poupko, A. Baram, and Z. Luz, *Mol. Phys.*, 1974, **27**, 1345.
5. L. G. Werbelow, *J. Chem. Phys.*, 1979, **70**, 5381.
6. J. L. Bjorkstam, *J. Mol. Struct.*, 1983, **111**, 135.
7. P. S. Hubbard, *Rev. Mod. Phys.*, 1961, **33**, 249.
8. C. E. M. Fouques and L. G. Werbelow, *Can. J. Chem.*, 1979, **57**, 2329.
9. L. G. Werbelow, A. Thevand, and G. Pouzard, *J. Chem. Soc., Faraday Trans. 2*, 1979, **75**, 971; L. G. Werbelow, *J. Magn. Reson.*, 1979, **34**, 439.
10. D. Brinkmann, M. Mali, J. Roos, R. Messner, and H. Birli, *Phys. Rev. B*, 1982, **26**, 4810.
11. L. G. Werbelow and A. G. Marshall, *J. Magn. Reson.*, 1981, **43**, 443.
12. J. M. Aramini, D. D. McIntyre, and H. J. Vogel, *J. Am. Chem. Soc.*, 1994, **116**, 11506.
13. A. Butler and H. Eckert, *J. Am. Chem. Soc.*, 1989, **111**, 2805.
14. R. H. Tromp, J. de Bleijser, and J. C. Leyte, *Chem. Phys. Lett.*, 1990, **175**, 568.
15. S. Zhong, F. Jordan, C. Ketter, and L. Polgan, *J. Am. Chem. Soc.*, 1991, **113**, 9429.

16. U. Eliav and G. Navon, *J. Chem. Phys.*, 1991, **95**, 7114; U. Eliav, H. Shinar, and G. Navon, *J. Magn. Reson.*, 1991, **94**, 439.
17. W. Price, N.-H. Ge, and L.-P. Hwang, *J. Magn. Reson.*, 1992, **98**, 134.
18. P. H. Kenéz, G. Carlström, I. Furó, and B. Halle, *J. Phys. Chem.*, 1992, **96**, 9524.
19. L. G. Werbelow and G. Pouzard, *J. Phys. Chem.*, 1981, **85**, 3887.
20. M. H. Cohen and F. Reif, *Solid State Phys.*, 1957, **5**, 321.
21. R. E. London, D. M. LeMaster, and L. G. Werbelow, *J. Am. Chem. Soc.*, 1994, **116**, 8400; S. Grzesiek and A. Bax, *J. Am. Chem. Soc.*, 1994, **116**, 10 196; L. G. Werbelow and R. E. London, *J. Chem. Phys.*, 1995, **102**, 5181.

Biographical Sketch

Lawrence G. Werbelow. *b* 1947. B.S., 1970, Humboldt State University, Ph.D., 1974, University of British Columbia (A. G. Marshall, Thesis advisor), D.Sc., 1979, Université de Provence. Research associate (with D. M. Grant) and Instructor, University of Utah, 1974–78. Professor, New Mexico Tech, 1980–present. Approximately 70 publications in the field of magnetic resonance. Current research interests include the study of relaxation-induced polarization/coherence transfer and the development of methods for isolation/identification of ultrafine interactions involving nuclear spin.

Dynamic Spin Ordering of Matrix Isolated Methyl Rotors

David White
University of Pennsylvania, Philadelphia, PA, USA
and
Michael D. Murphy
St. Frances College, Loretta, PA, USA

1	Introduction	1
2	Methyl Group Rotational and Spin Levels	2
3	Homonuclear Dipolar and Spin–Rotation Polarizations	4
4	Heteronuclear Dipolar Polarization	8
5	The Solid Rare Gas Matrix	11
6	Related Articles	12
7	References	12

1 INTRODUCTION

The application of NMR relaxation as a probe of molecule and molecular group motion in solids has provided a wealth of dynamical information and some important insights as to the nature of intra- and intermolecular barriers to rotation. Of special interest have been solids where the internal rotations of symmetrical molecular groups such as $-NH_4^+$, $-CH_3$, etc., lead to macroscopic quantum effects at low temperatures.[1] Whereas at high temperatures the reorientation dynamics can be described by incoherent thermally activated processes (classical diffusion or jumps), at sufficiently low temperatures the motion becomes a coherent quantum tunneling. Since the motion has the effect of interchanging spatial coordinates of identical particles, the requirements of the Exclusion Principle must be taken into account. Thus for molecules containing methyl groups, indistinguishability of the protons leads to observable quantum effects such as the thermally-induced dynamic spin polarization process described below. This is a consequence of a coupled spin and rotational relaxation processes, dynamically linking the observable spin magnetization to the angular momentum of the methyl group.

There are only two known cases where thermally-induced spin polarization has been observed in pure solids.[2,3] This was first reported by Haupt in 1971 for 4-methylpyridine.[2] Haupt discovered that at low temperatures, a large polarization or ordering of the methyl protons with respect to the proton–proton dipolar local field occurs after a change in temperature of the solid. The polarization persists up to several hours depending on the temperature and is associated with a slow relaxation coupled to the interconversion of the proton spin species $I = \frac{3}{2}$ and $I = \frac{1}{2}$. The magnitude and duration of the Haupt effect is critically dependent on the magnitude and symmetry of the potential function describing the barrier to one-dimensional rotation. In general, free or nearly free rotation of the methyl group about its symmetry axis is required, a situation rarely found in molecular solids. Typically, the barrier height is found to greatly exceed the methyl group rotational constant $B/k = 7.56\,\mathrm{K}$ and the motion is more characteristic of tunneling between equivalent potential wells. Nevertheless it is possible to prepare solids artificially in which an impurity molecule containing a methyl group is subject to a relatively low hindering barrier using the technique of matrix isolation.

Since the technique of trapping atoms and molecules in solid rare gas matrices was first introduced,[4] it has been applied to a wide range of questions regarding the chemistry and physics of molecules.[5] Most of the studies have focused on molecular and electronic structure determinations of trapped atoms, stable molecules, aggregates, reactive species, and other reaction products, as well as the exploration of the nature of the matrix environment including the interactions of the impurity molecule with the rare gas lattice. The structural probes have included optical absorption, Raman, electron spin resonance (ESR)[5] and, more recently, nuclear magnetic resonance (NMR)[6,7] and inelastic neutron scattering (INS).[8] The NMR of matrix isolated molecules has been especially useful in probing reorientational dynamics,[9] in particular of methyl groups in matrices.[10] From the proton NMR line shapes of molecules having the structure CH_3X where X is a linear substituent such as $-C{\equiv}N$, $-C{\equiv}CH$, or a halide, it is evident that the symmetry axis is essentially fixed in the rare gas lattice, while rotation about this axis is only weakly hindered. This is illustrated by the comparison of proton spectra of matrix isolated CH_3CCl_3, CH_3CN, and CH_4 in Figure 1. The bottom trace shows a single narrow line for CH_4 due to isotropic reorientation in the matrix.[11] For CH_3CN, the molecule is sufficiently large that the molecular axis is fixed in a cavity or lattice site of the matrix, but the barrier to rotation about this axis is small.[10] This is not the case for CH_3CCl_3 which has a large intramolecular barrier to rotation of the methyl group. The observed spectrum[12] is identical to the theoretical spectrum of a stationary triangle of spin $I = \frac{1}{2}$ nuclei.[13] The intermediate case proves to be the most interesting as the molecule exhibits all the features of a fixed-axis rotator in well-defined rotational states at low temperatures.[14] This is substantiated by an intense Haupt effect observed for CH_3X molecules in matrices.[15]

The spatial and magnetic isolation of methyl molecules achieved with matrix isolation provides a unique opportunity for a detailed exploration of the mechanism leading to spin polarization that is not possible in pure solids. Isolation suppresses intermolecular dipolar couplings so that spin ordering takes place with respect to the *intramolecular* dipolar local field. Experimentally this leads to well-resolved spectral features (see Figure 1) normally obscured due to the intermolecular dipolar broadening. This permits the observation of anisotropy in the polarization process and, more importantly, has led to the discovery of spin ordering with respect to two additional local fields. One of these is associated with heteronuclear dipolar coupling between the methyl protons and another spin in the molecule.[16] The other corresponds to the molecular magnetic field arising from the rotation of nuclear and electronic charges.[17] The lineshape associated with the latter spin order has revealed for the first

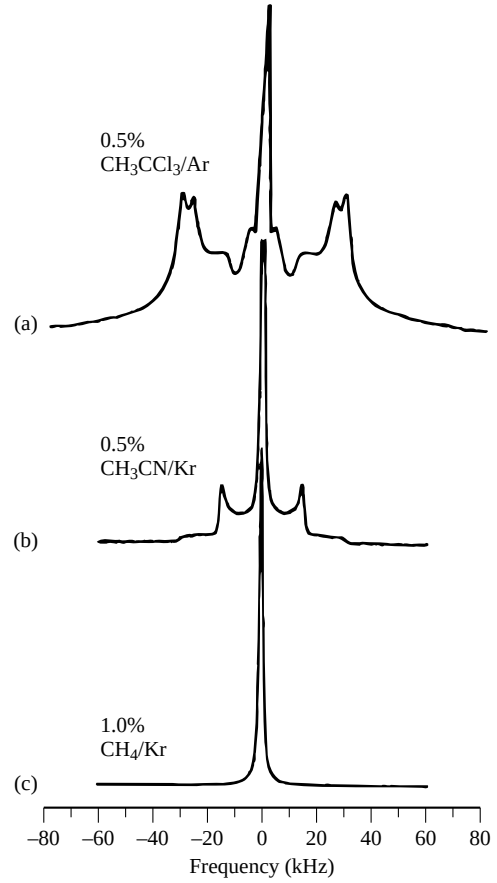

Figure 1 Proton NMR lineshapes of matrix isolated molecules at 5 K. (a) CH_3CCl_3, no rotation. (b) CH_3CN, anisotropic rotation about symmetry axis. (c) CH_4, isotropic rotation

time spin–rotation fine structure in the NMR spectrum of a solid.[17] Essentially the fine structure is due to the fact that the angular momentum of the methyl group is sufficiently large in magnitude and fixed in direction so the full tensorial character of the spin–rotation interaction is preserved.

Matrix isolation also introduces a considerable simplification in the interpretation of the experimental results. The spin Hamiltonian, treated as a quantum mechanical operator in both spin and spatial coordinates, need only include *intramolecular* couplings, and it is possible to treat the rotation of each methyl group independently. To a good approximation, the methyl groups couple independently to a phonon bath provided by the rare gas lattice, with the nuclear spins interacting only indirectly with the phonon bath via the spatial part of the methyl group state function. Using this framework and the assumption of free rotation in the matrix, a theoretical basis for spin polarization with respect to local fields within the methyl group is presented below. These fields are identified as the proton–proton dipolar (II), heteronuclear dipolar (IS), and spin–rotation (IJ), each of which corresponds to a spin energy reservoir dynamically coupled to the rotational relaxation of the methyl group. The theory is shown to be consistent with NMR lineshapes recorded during the evolution of the polarization.

The assumption of free methyl rotation in the solid rare gas matrix, while useful in the discussion of rotational relaxation, is clearly an oversimplification. Indeed optical and INS studies have shown that the unannealed matrix is a highly disordered structure which is characterized by a distribution of trapping sites. Remarkably however, the spin polarizations process is site-selective.[15,17] Thermal annealing, which more or less tends to produce spatial site uniformity by matrix reconstruction, tends to destroy the polarization. In the last section, we explore this issue in more detail.

2 METHYL GROUP ROTATIONAL AND SPIN LEVELS

Our model for a matrix isolated symmetric top molecule CH_3X, where X is a linear substituent, is one where the symmetry axis is fixed while the molecule is free to rotate about this axis, a motion equivalent to the free rotation of a methyl group. This motion can be described by the one-dimensional Hamiltonian

$$\hat{\mathcal{H}}_{\mathrm{R}} = -B\frac{\partial^2}{\partial\phi^2} \tag{1}$$

where B is the rotational constant and ϕ is the rotational coordinate describing the motion of the protons in the plane perpendicular to the fixed axis. The rotational states and energies are $\psi_{\mathrm{R}} = (2\pi)^{-1/2}\exp(\mathrm{i}r\phi)$; $E_{\mathrm{R}} = r^2B$, where $r = 0, \pm1, \pm2, \ldots$ These states can be classified according to the three one-dimensional irreducible representations of the C_3 symmetry group $\lambda = A, E^{\mathrm{a}}, E^{\mathrm{b}}$. States with $r = 0, \pm3, \pm6, \ldots$ belong to the A representation, $r = -1, 2, -4, 5, \ldots$ to E^{a}, and $r = 1, -2, 4, -5, \ldots$ to E^{b}.

Neglecting the small chemical shift interaction of methyl protons, we write the spin Hamiltonian for a methyl group as the sum of Zeeman ($I\mathrm{Z}$), dipolar (II), and spin–rotation (IJ) interactions:

$$\hat{\mathcal{H}}_{\mathrm{s}} = \hat{\mathcal{H}}_{I\mathrm{Z}} + \hat{\mathcal{H}}_{II} + \hat{\mathcal{H}}_{II}(t) + \hat{\mathcal{H}}_{IJ} \tag{2}$$

where

$$\hat{\mathcal{H}}_{I\mathrm{Z}} = -\omega_{0I}\sum_{i}^{3}\hat{I}_Z^i = -\omega_{0I}\hat{I}_Z \tag{2a}$$

and

$$\hat{\mathcal{H}}_{II} = \tfrac{4}{3}\omega_{\mathrm{D}}\sum_{i<j}\left[\hat{I}_Z^i\hat{I}_Z^j - \tfrac{1}{4}(\hat{I}_+^i\hat{I}_-^j + \hat{I}_-^i\hat{I}_+^j)\right] \tag{2b}$$

where $\omega_{\mathrm{D}} = (\kappa/2)(1 - 3\cos^2\psi)$, $\kappa = \frac{3}{4}\gamma_I^2\hbar/R_1^3 = 15.1\,\mathrm{kHz}$, ω_{0I} is the proton Larmor frequency, γ_I the proton magnetogyric ratio, and R_1 the proton–proton distance. The angle ψ defines the orientation of the methyl group axis with respect to the external magnetic field as depicted in Figure 2. Terms of the dipolar interaction depending explicitly on time are grouped into $\hat{\mathcal{H}}_{II}(t)$. These terms are responsible for the relaxation of spin and rotational level populations. The secular terms (those that commute with $\hat{\mathcal{H}}_{\mathrm{Z}}$) represented by $\hat{\mathcal{H}}_{II}$ have been written in the motionally narrowed limit corresponding to anisotropic free rotation about the methyl axis.

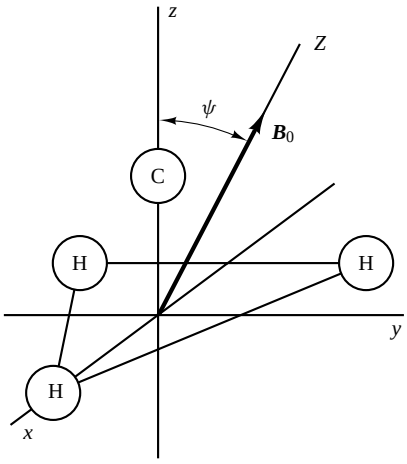

Figure 2 Molecular reference frame (x, y, z) of a methyl group relative to laboratory frame (X, Y, Z)

Setting aside for the moment $\hat{\mathcal{H}}_{IJ}$, the spin basis functions may be chosen as eigenfunctions of $\hat{\mathcal{H}}_{IZ} + \hat{\mathcal{H}}_{II}$. These functions are well known and have been listed in Table 1.[18] The eight spin functions are labeled with the corresponding irreducible representation of symmetry group C_3 and eigenvalue with respect to I_z ($m = \pm\frac{1}{2}, \pm\frac{3}{2}$).

Table 1 Spin Eigenfunctions

$A_{3/2} = \alpha\alpha\alpha$
$A_{1/2} = 3^{-1/2}(\alpha\alpha\beta + \alpha\beta\alpha + \beta\alpha\alpha)$
$A_{1/2} = 3^{-1/2}(\alpha\beta\beta + \beta\alpha\beta + \beta\beta\alpha)$
$A_{3/2} = \beta\beta\beta$
$E^{\mathrm{a}}_{1/2} = 3^{-1/2}(\alpha\alpha\beta + \epsilon\alpha\beta\alpha + \epsilon^*\beta\alpha\alpha)$
$E^{\mathrm{a}}_{1/2} = 3^{-1/2}(\beta\beta\alpha + \epsilon\beta\alpha\beta + \epsilon^*\alpha\beta\beta)$
$E^{\mathrm{a}}_{1/2} = 3^{-1/2}(\alpha\alpha\beta + \epsilon^*\alpha\beta\alpha + \epsilon\beta\alpha\alpha)$
$E^{\mathrm{a}}_{1/2} = 3^{-1/2}(\beta\beta\alpha + \epsilon^*\beta\alpha\beta + \epsilon\alpha\beta\beta)$
$\epsilon = \exp(\mathrm{i}2\pi/3)$

The Exclusion Principle requires that the state function be antisymmetric with respect to permutation of any two identical protons. The feasible symmetry operation for a methyl group however is a rotation by 120°, an operation equivalent to a double permutation of the spins. Thus the total state for the methyl group need only be symmetrized with respect to C_3 rotation which is equivalent to two permutations of identical particles. The allowed spin and rotation combinations are then given by

$$A_r \times A_m, \qquad E^{\mathrm{a}}_r \times E^{\mathrm{b}}_m, \qquad E^{\mathrm{b}}_r \times E^{\mathrm{a}}_m \tag{2c}$$

Taking these restrictions into account, the energy levels are shown in Figure 3. Only the five lowest rotational levels are included as higher levels are not significantly populated below 50 K. The eigenstates are labeled by symmetry A, E^{a}, or E^{b}. The doubly degenerate E rotational levels are shown as double lines. The Zeeman interaction $\hat{\mathcal{H}}_{IZ}$ splits the A_0 rotational level into a quartet of spin levels and the E levels into doublets. The

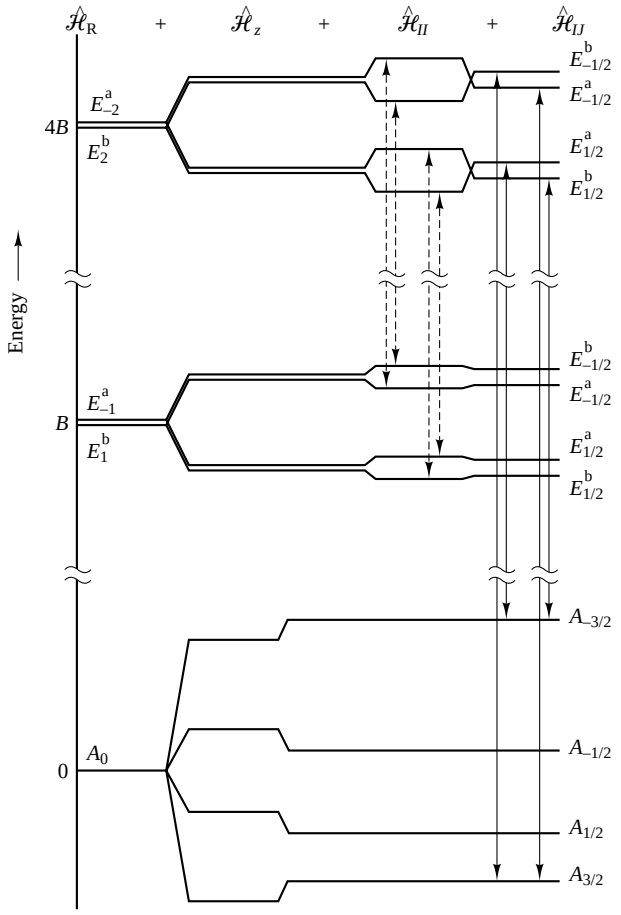

Figure 3 Methyl group rotational and spin energies. The columns from left to right indicate rotational levels, Zeeman, proton–proton dipolar, and spin–rotation splittings. Thermal averaging of the spin–rotation coupling due to the dashed transitions results in the cumulative splittings in the last column. The solid transitions represent relaxation through $\hat{\mathcal{H}}_{II}(t)$

dipolar interaction $\hat{\mathcal{H}}_{II}$ shifts the A spin levels by $+\omega_{\mathrm{D}}\hbar$ but does not affect the E spin levels.

Having identified a basis set of spin and rotational functions, the spin–rotation interaction can now be considered. The general form of this coupling, given in the molecular reference frame, is

$$\hat{\mathcal{H}}_{IJ} = \sum_i \boldsymbol{I}^{\mathrm{i}} \cdot \boldsymbol{C}^{\mathrm{i}} \cdot \boldsymbol{J} \tag{3}$$

where $\boldsymbol{C}^i$ is a Cartesian tensor and $\boldsymbol{J}$ is the angular momentum of the methyl group. Transforming to the laboratory frame and retaining only terms that commute with $\hat{\mathcal{H}}_{IZ}$, equation (3) becomes for the case of anisotropic motion restricted to free rotation about the methyl axis,[19]

$$\hat{\mathcal{H}}_{IJ} = C_{ZZ} \cos\psi\, J_z I_Z \tag{4}$$

where C_{zz} is the principal value of $\boldsymbol{C}$ along the C_3 axis. The term J_z refers to the angular momentum in the molecular frame and is thus identical to the operator $-\mathrm{i}\hbar\,\partial/\partial\phi$. We note that the spin–rotation interaction contains no time-dependent

components in the laboratory frame and so does not contribute to spin or rotational relaxation.

Because the spin–rotation operator in equation (4) is diagonal in the chosen basis of rotational and spin functions, its effect on the spin states is readily evaluated and shown in Figure 3. The resulting spin level shifts depend on the expectation value of the angular momentum $\langle \hat{J}_z \rangle_r = r\hbar$. The angular momentum in the A rotational state is zero so no spin–rotation shifts occur. For the excited rotational state E_1^{b} (total wavefunction $E_1^{\mathrm{b}} E_{\pm 1/2}^{\mathrm{a}}$), the $E_{1/2}^{\mathrm{a}}$ spin level is shifted by $+(C_{zz} \cos \psi)/2$ and the $E_{-1/2}^{\mathrm{a}}$ by $-(C_{zz} \cos \psi)/2$. For the rotational state E_{-1}^{a}, the $E_{\pm 1/2}^{\mathrm{b}}$ spin levels are shifted the same amounts but in opposite directions. The angular momentum for rotational states with $r = \pm 2$ is twice as large as that for $r = \pm 1$ so that the spin–rotation shifts are twice as large, as shown in Figure 3 under $\hat{\mathcal{H}}_{IJ}$. Experimentally, however, one does observe shifts corresponding to specific rotational states, but only dynamically averaged shifts that depend on the temperature.[17] The averaging results from rapid transitions between rotational states due to coupling with lattice phonons. Since this coupling contains no spin operators, the transitions can only occur among rotational levels having the same symmetry representation as indicated by the dashed lines of Figure 3. These transitions maintain a Boltzmann distribution of populations of rotational levels with a common symmetry.[20] The observed spin–rotation frequency shifts

$$\omega_J = \Theta \cos \psi \tag{5}$$

then represent an average over all populated levels with the same symmetry weighted by their Boltzmann factors. For the E^{b} rotational states, the spin–rotation constant Θ is given by the expression

$$\Theta = C_{zz} \frac{\left[\sum_r^{E^{\mathrm{b}}} \langle \hat{J}_z \rangle_r \, \mathrm{e}^{-(E_r - E_1)/kT} \right]}{\left[\sum_r^{E^{\mathrm{b}}} \mathrm{e}^{-(E_r - E_1)/kT} \right]} \tag{6}$$

For the E^{a} rotational levels, the spin–rotation shifts are in the opposite directions so that we may write an interaction that depends only on spin operators as

$$\hat{\mathcal{H}}_{IJ} = \begin{cases} \omega_J \hat{I}_z & E^{\mathrm{b}} \text{ levels} \\ -\omega_J \hat{I}_z & E^{\mathrm{a}} \text{ levels} \\ 0 & A \text{ levels} \end{cases} \tag{7}$$

The thermally averaged spin–rotation shifts are shown at the far right of Figure 3. The NMR spectrum for methyl groups in A spin states will consist of three lines—one at zero frequency and a pair of lines at $\pm 2\omega_{\mathrm{D}}$. For methyl groups in E states, only a pair of lines at $\pm \omega_J$ will be observed. The line spectrum corresponding to a temperature of approximately 10 K for an orientation $\psi = 70^\circ$ is shown in Figure 4. At this temperature the population of A to E rotational levels is approximately 1.9 : 1. In the matrix, the random distribution of the methyl group orientations results in a powder averaged spectrum. The theoretical unbroadened spectrum is the sum of the A and E contributions, a characteristic Pake shape over the frequency range $\pm 2\kappa$ (± 30.2 kHz), and a rectangular spin–rotation powder pattern over the range $\pm \Theta$. Since the spin–rotation contribution is relatively small, temperature-dependent ($0 \leq \Theta \leq 10$ kHz, see Figure 6), and overlaps the intense zero frequency line, it is easily masked in the measured NMR spectrum of Figure 4. At 5 K and below, Θ is large and the broad rectangular powder pattern is easily lost in the dipolar powder pattern. At high temperatures, Θ becomes small and the spin–rotation contribution merges into the zero-frequency feature. It is possible using spin–echo sequences to measure the spin–rotation splitting,[17] but the measurement can be carried out far more easily during a dynamic polarization experiment as described in the next section.

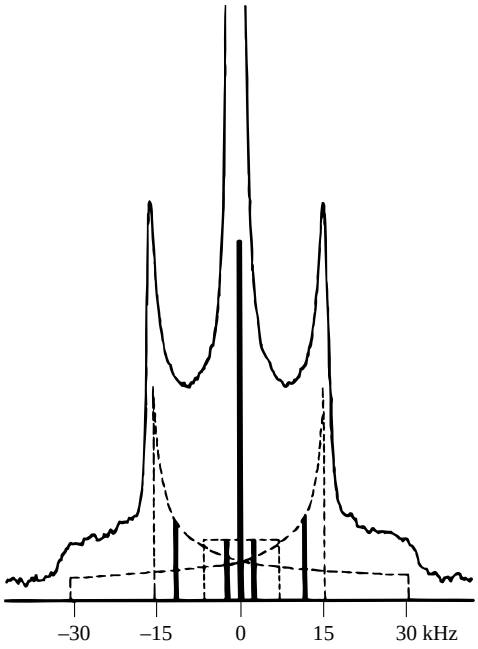

Figure 4 Lower trace: methyl proton transition frequencies and powder average. Upper trace: proton NMR spectrum of 0.5% CH_3/Kr matrix at 10 K

3 HOMONUCLEAR DIPOLAR AND SPIN–ROTATION POLARIZATIONS

The terms $\hat{\mathcal{H}}_{IZ}, \hat{\mathcal{H}}_{II}$, and $\hat{\mathcal{H}}_{IJ}$ of the spin Hamiltonian commute with each other and therefore may be thought of as reservoirs of spin energy each with a characteristic spin temperature. For spins in thermal equilibrium at the lattice temperature, dipolar and spin–rotation magnetizations, corresponding to net alignment of the spins with respect to dipolar and spin–rotation local fields, are extremely small. There are various methods for creating dipolar order such as the application of the Jeener–Broekaert pulse sequence[21] or performing an adiabatic demagnetization in the rotating frame (ADRF). These methods basically involve establishing contact between dipolar and Zeeman spin reservoirs. The enhancement of methyl group dipolar and spin–rotation magnetizations through the Haupt effect also involves coupling of these magnetizations, but to a much larger reservoir namely a nonequilibrium population of rotational levels created by a sudden change in the matrix temperature.

The dynamics of this process has been described in detail by Beckmann et al.[20] and is summarized and extended below.

The evolution of the magnetizations is conveniently evaluated using the density operator formalism. We write the density operator as a product of rotational and spin operators[22,23]

$$\hat{\rho} = \hat{\sigma}_s \frac{e^{-\hat{\mathcal{H}}_R/kT}}{Z} \tag{8}$$

where $\hat{\sigma}_s$ represents the spin operator and $Z = \mathrm{Tr}_r\{\exp(-\hat{\mathcal{H}}_R/kT)\}$. The rotational density operator written in this form (at thermal equilibrium) is only appropriate at times which are long compared with the rotational relaxation time. After a temperature jump, however, equilibration requiring spin-independent transitions (dashed lines in Figure 3) are fast but equilibration requiring symmetry conversion (solid lines in Figure 3) is very slow. It is nevertheless possible to represent the density operator after the lattice temperature is suddenly changed as before, but with the modification

$$\hat{\rho} = \hat{\sigma}_s \frac{e^{-\hat{\mathcal{H}}_R/kT_f}}{Z} e^{\beta_r \hat{\mathcal{H}}_r} = \hat{\sigma} \frac{e^{-\hat{\mathcal{H}}_R/kT_f}}{Z} \tag{9}$$

where T_f is the final temperature after the temperature jump and the operator $\hat{\mathcal{H}}_r$ is defined by its eigenvalues $\langle A_r|\hat{\mathcal{H}}_r|A_r\rangle = 1$, $\langle E_r^a|\hat{\mathcal{H}}_r|E_r^a\rangle = \langle E_r^b|\hat{\mathcal{H}}_r|E_r^b\rangle = -1$. The parameter β_r can be treated as a constant of the motion representing the inverse temperature of the energy reservoir associated with the operator $\hat{\mathcal{H}}_r$. Following the temperature jump, β_r has an initial value $\beta_r(0)$ that depends on the initial and final temperatures of the jump. Its explicit form is given by Beckmann et al. Although E^a and E^b levels are independent, they have the same energies and populations. Thus β_r represents the departure of the populations E and A from equilibrium. Its value decreases to zero through the relaxing transitions as the equilibrium is established.

Because A and E spin states are restricted to A and E rotational states, $\hat{\mathcal{H}}_r$ may be considered as a spin operator and included in the spin density operator $\hat{\sigma}$ as has been done in equation (9). In the high-temperature limit, $\hat{\sigma}$ can be written as

$$\hat{\sigma} = 1 + \beta_r\hat{\mathcal{H}}_r - \beta_{IZ}H_{IZ} - \beta_{II}\hat{\mathcal{H}}_{II} - \beta_{IJ}\hat{\mathcal{H}}_{IJ} \tag{10}$$

The time dependence of the β quantities can be calculated from the master equation[23]

$$\frac{d\rho_{rm}}{dt} = \sum_{r'm'} W_{r'm',rm}(\rho_{r'm'} - \rho_{r'm'}^{eq}) \tag{11}$$

Summing over r, this becomes

$$\frac{d\sigma_m}{dt} = \sum_{r,r',m'} W_{r'm',rm} \frac{e^{-\langle\hat{\mathcal{H}}_R\rangle_{r'}/kT_p}}{Z}(\sigma_{m'} - \sigma_{m'}^{eq}) \tag{12}$$

with

$$W_{r'm',rm} = \int_{-\infty}^{\infty} \overline{\langle r'm'|\hat{\mathcal{H}}_{II}(t)|rm\rangle \langle rm|\hat{\mathcal{H}}_{II}(t+\tau)|r'm'\rangle} \times e^{-\omega_{rr'}\tau}\, d\tau \tag{12a}$$

and

$$\hat{\mathcal{H}}_{II}(t) = \frac{1}{3}\sum_{\lambda}\sum_{i=-2}^{2}(-1)^i A_{2,i}(\lambda)\hat{T}_{2,-i}(\lambda^*) \tag{12b}$$

where the time-dependent dipolar interaction has been written in a symmetry-adapted form convenient for calculating the spin matrix elements. The terms of $\hat{\mathcal{H}}_{II}(t)$ have been written explicitly by Haupt.[1] Separating the spin matrix elements $K_{mm'} = \langle m|\hat{T}_{2,-i}|m'\rangle$ and making the usual assumption that the autocorrelation function is random in time and decays exponentially with a characteristic decay time τ_c, we see that

$$\frac{d\sigma_m}{dt} = \sum_{m'} K_{m,m'}^2 F_2(\sigma_{m'} - \sigma_{m'}^{eq}) \tag{13}$$

where

$$F_n = \sum_{r,r'} |\langle r|2\cos(n\phi)|r'\rangle|^2 \frac{\tau_c}{1+\omega_{r,r'}^2\tau_c^2} \frac{e^{-\langle\hat{\mathcal{H}}_R\rangle_{r'}/kT_f}}{Z} \tag{13a}$$

includes the spectral density function. We note that F_2, the transition probability, depends on cos (2ϕ) which in the limit of free rotation imposes a rotational selection rule of $\Delta r = \pm 2$. The spin transition probabilities, $K_{mm'}$, are nonzero only for $A \leftrightarrow E^a$ and $A \leftrightarrow E^b$ transitions, so that the allowed spin and rotational transitions are restricted to $\Delta r = \pm 2$, $\Delta m = 0$, ± 1, ± 2. Of the 12 allowed transitions, only four are shown as the vertical solid lines in Figure 3. In the case of hindered rotation, both $\Delta r = \pm 2$ and $\Delta r = \pm 1$ transitions are allowed and the relaxation is much faster due to a larger spectral density function.

The evolution of the kth spin temperature with time can be calculated using

$$\frac{d\beta_k}{dt} = \mathrm{Tr}\left[\hat{\mathcal{H}}_k \frac{d\sigma}{dt}\right] \Big/ \mathrm{Tr}[\hat{\mathcal{H}}_k^2] = \sum_m \langle\hat{\mathcal{H}}_k\rangle_m \frac{d\sigma_m}{dt} \Big/ \sum_m \langle\hat{\mathcal{H}}_k\rangle_m^2 \tag{14}$$

which follows from equation (10) and the orthogonality of the operators. Expressed in matrix form, the coupled evolution of the inverse spin temperatures is

$$\frac{d}{dt}\begin{bmatrix}\beta_{IZ}\\ \beta_r\\ \beta_{II}\\ \beta_{IJ}\end{bmatrix} = -\begin{bmatrix} S_{IZ} & 0 & 0 & 0\\ 0 & S_r & S_{r,II} & S_{r,IJ}\\ 0 & S_{II,r} & S_{II} & S_{II,IJ}\\ 0 & S_{IJ,r} & S_{IJ,II} & S_{IJ}\end{bmatrix} \times \begin{bmatrix}\beta_{IZ} - \beta_{IZ}^{eq}\\ \beta_r\\ \beta_{II}\\ \beta_{IJ}\end{bmatrix} \tag{15}$$

where the the equilibrium values of β_{II} and β_{IJ} are assumed to be negligibly small. Expressions for the matrix elements of equation (15) are written explicitly in Table 2 (see below) when $\hat{\mathcal{H}}_1$ and $\hat{\mathcal{H}}_2$ are set equal to zero. A significant feature of equation (15) is that the Zeeman magnetization, proportional to β_{IZ}, is not coupled to β_I or the other inverse spin temperatures.

Table 2 Matrix Elements for Coupled Relaxation in the Heterospin Systems

$S_{IZ} = 2\mathrm{G}(1 + 3\cos^2\psi) + 2H_1(3 - \cos^2\psi) + 2H_2(1 + \cos^2\psi)$
$S_{SZ} = 6H_1(3 - \cos^2\psi) + 6H_2(1 + \cos^2\psi)$
$zS_{IZ,SZ} = z^{-1}S_{SZ,IZ} = 4\sqrt{3}(H_1\sin^2\psi + H_2\cos^2\psi)$
$\frac{1}{2}S_r = S_{II} = S_{IJ} = 3\mathrm{G} + 12H_1 + 6H_2$
$S_{IS} = 8H_1(2 - \cos^4\psi) + H_2(5 + 6\cos^2\psi + \cos^4\psi)$
$d^{-1}S_{r,II} = dS_{II,r} = \frac{3}{2}\sqrt{2}(1 - 3\cos^2\psi)(\mathrm{G} - H_1 + H_2)$
$s^{-1}S_{r,IS} = sS_{IS,r} = -6\sqrt{3}(H_1\sin^2\psi + H_2\cos^2\psi)$
$j^{-1}S_{r,II} = jS_{II,r} = -3\sqrt{2}\cos\psi(\mathrm{G} + H_1 + H_2)$
$ds^{-1}S_{II,IS} = d^{-1}sS_{IS,II} = 3\sqrt{6}(H_1\sin^2\psi + H_2\cos^2\psi)$
$dj^{-1}S_{II,IJ} = d^{-1}jS_{IJ,II} = -\frac{3}{2}\mathrm{G}\cos\psi(1 - 3\cos^2\psi)$
$+6\cos\psi(H_1 - H_2)$
$sj^{-1}S_{IS,IJ} = s^{-1}jS_{IJ,IS} = 6\sqrt{2}\cos\psi\{4H_1(2 - \cos^2\psi)$
$+H_2(5 + \cos^2\psi)\}$
$s = \sqrt{3}\omega_\mathrm{s}, \quad d = \omega_\mathrm{D}/\sqrt{2}; \quad j = \omega_\mathrm{j}/2\sqrt{2}; \quad z = \sqrt{3}\omega_{0I}/\omega_{0S}$
$\mathrm{G} = \frac{9}{16}(\gamma_I^2\hbar/R_1^3)^2F_2$
$H_1 = \frac{3}{8}\sin^2\chi\cos^2\chi(\gamma_I\gamma_S\hbar/R_2^3)^2F_1$
$H_2 = \frac{3}{16}\sin^4\chi(\gamma_I\gamma_S\hbar/R_2^3)^2F_2$

This means that the Zeeman system is unaffected by the absence of rotational equilibrium after a temperature jump. The Zeeman magnetization does equilibrate with the lattice temperature with relaxation time T_1, which is equal to $1/S_{IZ}$. The relaxation time for dipolar magnetization can similarly be identified with $1/S_{II}$ and the spin–rotation relaxation time with $1/S_{IJ}$.

Following a temperature jump, a nonzero value of β_r results from the deviation from equilibrium of the rotational level populations. The sign of β_r depends on whether the temperature is increased or decreased and its magnitude decays from its initial value to zero due to the $A \leftrightarrow E$ transitions. These transitions result in a net change in the dipolar and spin–rotation energies to produce a polarization of these systems. The time dependence is given by equation (15) for the coupled evolution of β_r, β_{II}, and β_{IJ}. In general, the spin magnetizations increase to a maximum after the abrupt change in temperature and then slowly decrease to their equilibrium values as illustrated in Figure 5. These curves represent the amplitude of the proton NMR signal measured at intervals following the temperature jump and are typical of the degree of polarization in matrix isolated CH_3CN.

In order to describe the time dependence of the spin magnetizations after a temperature jump, it is necessary to examine the contribution of each reservoir to the observed NMR spectrum. This consists of Zeeman, dipolar, and spin–rotation components, each having a characteristic lineshape. It is possible to separate these components using the methods described in the following. We consider the effect of a single rf pulse applied at time t after the temperature jump. If the pulse is applied along the X axis of the rotating reference frame exactly at frequency $\omega_{0\mathrm{I}}$, the spin–density matrix evolves under the influence of the internal Hamiltonian and it can be shown[15] that the components of the FID along the X and Y axes at a time τ later are given by

$$\left.\begin{aligned} S_Y(t,\tau) &= \sin\theta\beta_{IZ}(t)\omega_{0I}\Gamma(\tau)[2 + \Lambda\cos(\omega_J\tau) + 3\cos(2\omega_\mathrm{D}\tau)] \\ S_X(t,\tau) &= 6\sin\theta\cos\theta\,\Gamma(\tau)[\beta_{II}(t)\omega_\mathrm{D}\sin(2\omega_\mathrm{D}\tau)] \\ &\quad + \sin\theta\Gamma(\tau)[\beta_{IJ}(t)\omega_J\sin(\omega_J\tau)] \end{aligned}\right\} \quad (16)$$

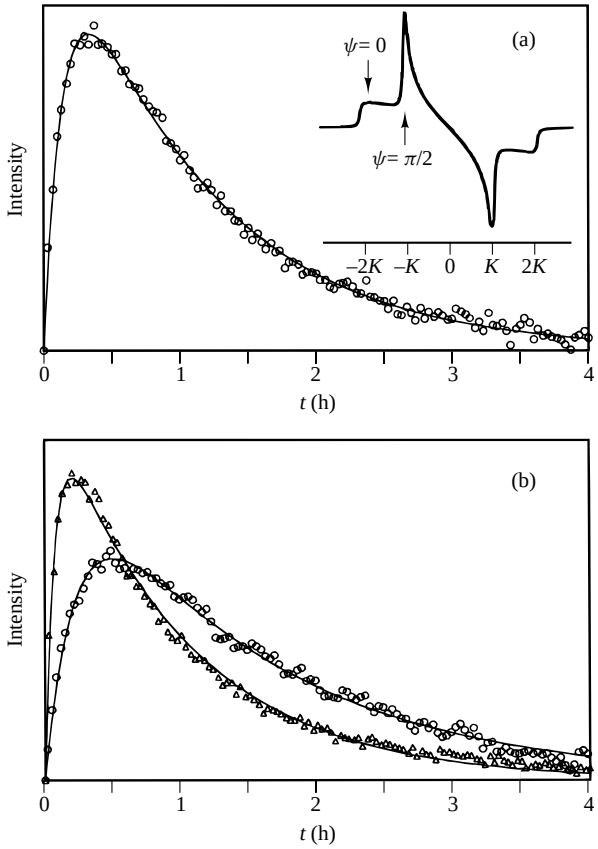

Figure 5 Time dependence of dipolar and spin–rotation magnetizations for a 0.2% CH_3CN/Kr matrix after a 20 → 5 K temperature jump. (a) Dipolar intensity at $\psi = \pi/2$. The solid line is a fitted to equation (18) with $a^{-1} = 3855$ s and $b^{-1} = 510$ s. (b) Dipolar intensity at $\psi = 0$ (circles) with $a^{-1} = 5404$ s and $b^{-1} = 252$ s and spin–rotation intensity at $\psi = 0$ (triangles)

In these equations, $\Gamma(\tau)$ represents inhomogeneous damping and θ is the angle through which the magnetization is rotated by the rf field. The square brackets indicate quantities that must be powder-averaged to describe the signal in polycrystalline matrices. The quantity Λ is defined as the instantaneous ratio of E to A spinstate populations and is thus related to β_r.[17] We assume Λ does not depart greatly from its thermal equilibrium value.

Equation (16) suggests that Zeeman, dipolar, and spin–rotation contributions to the signal can be separated by a suitable choice of the phase and tip angle of the rf pulse. If the reference phase of a quadrature receiver is adjusted so that the Zeeman component of the FID is obtained in the Y channel (pure absorption mode), the dipolar and spin–rotation components appear on the X channel. The Fourier transforms then give the Zeeman (cosine) or combined dipolar and spin–rotation (sine) lineshapes. The latter are shown in Figure 6 for a 0.5% CH_3CN/Kr matrix for several temperature jumps with different final temperatures. These were recorded with a single 45° pulse near the maximum in the polarization. In order to obtain a selective detection of the spin–rotation lineshape, a 90° pulse need be applied. These lineshapes are also shown in Figure 6 for the same temperature jumps. Note that the width of the line varies with the temperature, the maxima and minima of the powder pattern locating the frequencies

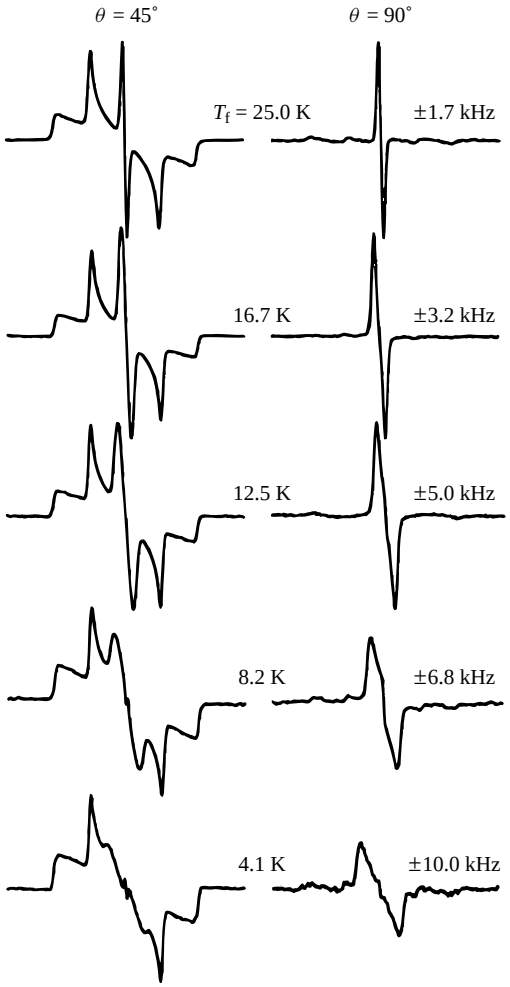

Figure 6 Dipolar and spin−rotation spectra for 0.5% CH_3CN/Kr matrix after a temperature jump to the indicated final temperature. Left column: Overlapping dipolar and spin−rotation powder patterns following 45° pulse. Right column: Spin−rotation lines following a 90° pulse and measured values of Θ

$\pm\Theta(\psi = 0)$. A more accurate procedure for measuring Θ is to fit the spin−rotation component of the FID to the analytical function representing the powder average:

$$S_x(t, \tau, \theta = 90^\circ) = \beta_{IJ}\Gamma(\tau)(\sin\Theta\tau - \Theta\tau\cos\Theta\tau)/\Theta\tau^2 \quad (17)$$

In this procedure, the inhomogeneous linewidth is treated as a simple damping rather than convoluted with the powder pattern in the frequency domain.

The temperature dependence of the spin−rotation coupling constant, Θ, for 0.5% CH_3CN in Ar, Kr, and Xe is shown in Figure 7. The solid lines through the data were calculated using equation (9) with C_{zz} = 9.0 kHz and assuming free rotation in Kr and Xe but hindered rotation in Ar. The reduced angular momentum in the Ar matrix is presumably a consequence of the smaller lattice constant. From the molecular structure of the gas phase and chemical shift data, one would estimate $C_{zz} \sim 17$ kHz.[17] The smaller value in the matrix is a possible indication of some motional averaging of this interaction due to wobbling of the figure axis in the rare gas lattice. This is

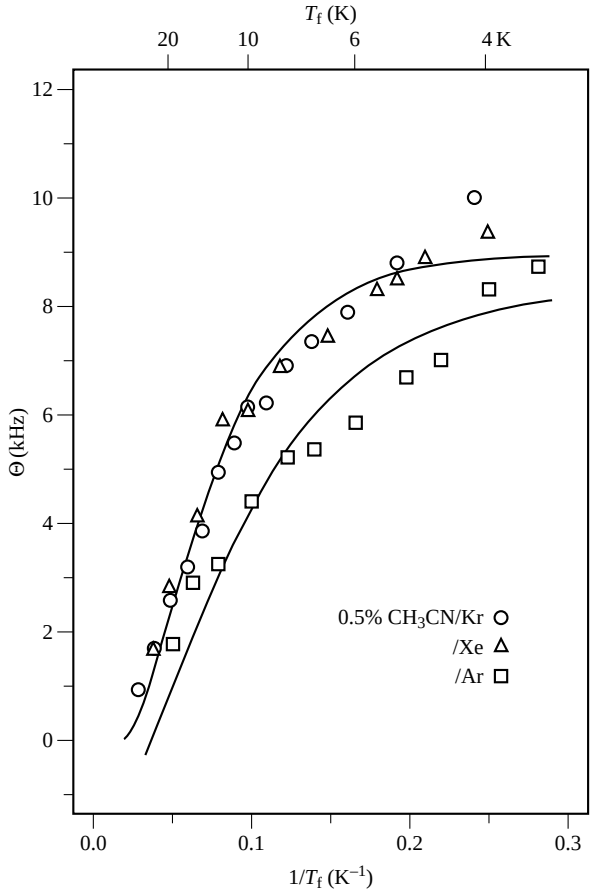

Figure 7 Spin−rotation coupling constant as a function of temperature for 0.5% CH_3CN in Ar, Kr, and Xe matrices. Solid lines were calculated using equation (6)

consistent with the fact that only weak spin−rotation lines are observed in matrix isolated CH_3Cl,[15] a molecule with a shorter figure axis than CH_3CN or CH_3CCH. On the other hand, the failure of equation (6) to describe the spin−rotation splittings at low temperature implies that a large value of C_{zz} can only be consistent with a temperature-dependent quenching of the methyl group angular momentum. It has been suggested by Clough[24] that the angular momentum of the methyl group is modified by fluctuations of the surrounding lattice that are coherent with the methyl group rotation, but this, as yet, has not led to a more accurate description of spin−rotation splitting.[17]

It is worthwhile at this point to comment on the antisymmetric shape of the resonance lines arising from dipolar and spin−rotation magnetization. This comes about as a consequence of using the sine Fourier transform of the FID, but is ultimately due to inversion of the spin level populations during relaxation after the temperature jump. For example, the four transitions pictured at the right of Figure 3 increase the population of the $A_{\pm 3/2}$ levels relative to the $A_{\pm 1/2}$ levels, a situation corresponding to dipolar order. In the presence of the rf field, the $A_{3/2} \leftrightarrow A_{1/2}$ transition causes absorption while the $A_{-3/2} \leftrightarrow A_{-1/2}$ transition causes stimulated emission and an antisymmetric line shape overall. Similarly, spin−rotation order corresponds to a population difference of $E^a_{\pm 1/2}$ levels that is reversed for $E^b_{\pm 1/2}$ levels.

With a knowledge of the NMR lineshapes, it is now possible to consider the time evolution of dipolar and spin–rotation magnetizations after a temperature jump. From. equation (15) it follows that the expressions for $\beta_{II}(t)$ and $\beta_{IJ}(t)$ contain three exponential terms with coefficients and rate constants found by solving cubic equations. We will not be interested in the general form, but will focus instead on two special cases representing methyl group orientations of $\psi = 0$ and $\pi/2$ with respect to the external magnetic field. Because of the isolation of the molecules in the matrix, the relaxation of methyl groups having a common orientation can be followed from the intensity of the corresponding frequency component of the powder spectrum. Considering first the case $\psi = \pi/2$, the spin–rotation splitting ω_J is equal to zero and only the dipolar magnetization is coupled to β_r. The solution of equation (15) leads to the expression

$$M_{II}(t) \propto \beta_{II} = C(\mathrm{e}^{-at} - \mathrm{e}^{-bt}) \tag{18}$$

with $C = \beta_r(0)S_{II,r}/(b - a)$; $a,b = \frac{1}{2}\{S_r + S_{II} \pm [(S_r - S_{II})^2 + 4S_{II,r}S_{r,II}]^{1/2}\}$.

The dipolar polarization for a 0.2% CH_3CN/Kr matrix suddenly cooled from 20 to 5 K is shown in Figure 5(a). The dipolar lineshape has been inserted to indicate the $\psi = \pi/2$ frequency component monitored during the evolution. The solid line through the points is the fit to equation (18) with rate constants given in the figure caption. These rate constants are related to the final temperature of the jump through the expressions for the $S_{k,l}$ and equation (13). The magnitude of the polarization can be estimated by comparing the sizes of Zeeman and dipolar components of the FID. For the temperature jump shown in Figure 5(a), the dipolar component at maximum polarization is on the order of 10^2-times greater than the Zeeman component. For jumps to higher final temperatures, the dipolar magnetization may be 10^3-times greater than the Zeeman magnetization, corresponding to $1/\beta_{II}$ in the microdegree Kelvin range. Also with increasing final temperature, the time of the decay decreases significantly from the period of hours measured for a jump to 5 K.

For orientation angle $\psi = 0$, the methyl group axis is parallel to the external magnetic field. In this case the dipolar and spin–rotation magnetizations are coupled, but the time evolutions of β_{II} and β_{IJ} reduce to the double exponential form of equation (18). The measured polarization curves for the 0.2% CH_3CH/Kr matrix after a 10 → 5 K temperature jump are shown in Figure 5(b). For these curves, the intensity of the $\psi = 0$ frequency components of dipolar (circles) and spin–rotation (triangles) parts of the lineshape were monitored. The solid lines were calculated using equation (18) with the indicated rate constants. Comparison of the dipolar evolution for the two methyl orientations $\psi = 0$ and $\pi/2$ in Figure 5(a) and (b) indicates that the polarization is clearly anisotropic (compare the intensities at 2 h relative to the maxima). At long times after the temperature jump, the intensities of the $\psi = 0$ and $\pi/2$ frequency components are even reversed, as shown graphically in Figure 8.

The qualitative dependence of the rate constants on orientation is that predicted theoretically. The rate constant a in equation (18), for example, is found by using Table 2 to be $a = 0$ for $\psi = 0$ and $a = 5.07$ G for $\psi = \pi/2$. These values predict that the dipolar magnetization for methyl groups at $\psi = 0$ should persist indefinitely. The observed decay is due to weak interactions such as direct and indirect dipolar couplings to nitrogen and krypton nuclei which were not included in the spin Hamiltonian of equation (2). However, the large difference in rate constants as a function of orientation demonstrates the lack of a uniform dipolar spin temperature throughout the matrix. For nonisolated molecules as is usually encountered in solids, the process of spin diffusion establishes a common spin temperature and relaxation is uniform for all molecules.[23] For nominally isolated molecules as in a matrix however, a uniform spin temperature can only be assumed among methyl groups with a common dipolar splitting.

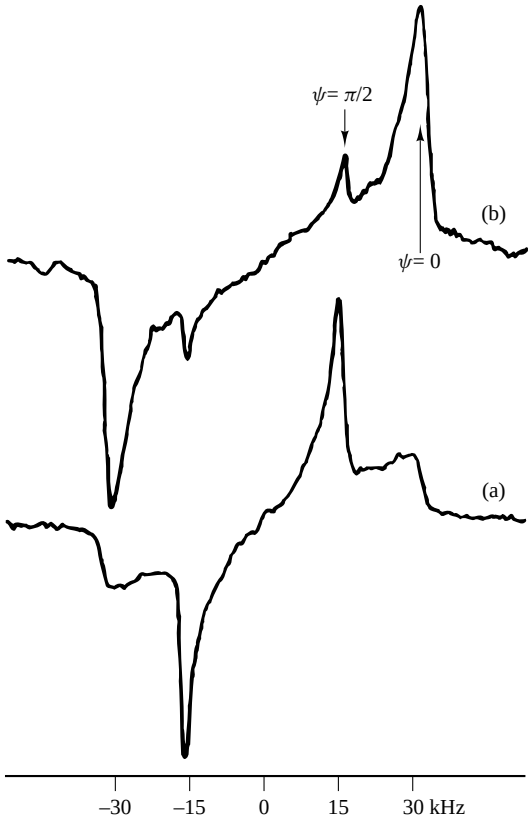

Figure 8 Anisotropy of dipolar polarization. (a) Dipolar spectrum of 0.2% CH_3CN/Kr 30 min after a 20 → 5 K temperature jump. (b) Dipolar spectrum approximately 2 h later

4 HETERONUCLEAR DIPOLAR POLARIZATION

In the spin Hamiltonian of equation (2), dipolar couplings between the methyl protons and other spins in the molecule were neglected. This is a good approximation for CH_3CN and CH_3CCD due to the small coupling between the protons and ^{14}N and ^{2}H nuclei. A relatively large coupling can be introduced, however, by labeling the molecule with an isotope with spin S in close proximity to the methyl protons. An example is $^{13}CH_3CN$ in which the ^{13}C nucleus has a spin $S = \frac{1}{2}$ and causes a resolvable splitting of the proton resonance line through the heteronuclear dipolar interaction.[19] This interaction has an associated magnetization corresponding to a net alignment of the proton spins with respect to the ^{1}H–^{13}C dipolar local field. In matrix isolated molecules undergoing

free rotation about the methyl axis at low temperatures, it is found that this heteronuclear (IS) dipolar magnetization is polarized at the same time as the homonuclear (II) dipolar and spin–rotation (IJ) magnetizations following a temperature jump.[16] The effect, however, is not a simple extension of the analysis of the previous section because the IS dipolar coupling includes time-dependent terms that provide an additional mechanism for relaxation. Although the new mechanism has the same overall qualities as the II dipolar mechanism described in the previous section, it has unique features that provide an interesting contrast with spin polarization in unlabeled molecules and an insight into the spin polarization process in general.

The simplest form of heteronuclear dipolar coupling is obtained for a heterospin with spin $S = \frac{1}{2}$ located on the methyl group axis a short distance from the plane of the protons. The molecular frame parameters describing this spin system are shown in Figure 9. Little generality is lost as a result of this restricted geometry because only symmetric top molecules exhibit low enough barriers to methyl group rotation for the polarization process to take place. The rotational Hamiltonian for such a molecule is identical to that considered earlier, equation (1), and the spin Hamiltonian is that of equation (2) with the addition of terms representing the S-spin Zeeman interaction, $\hat{\mathcal{H}}_{SZ} = -\omega_{0S} S_Z$, the secular heteronuclear dipolar interaction $\hat{\mathcal{H}}_{IS}$,

$$\hat{\mathcal{H}}_{IS} = 4\omega_s \sum_i^3 I_Z^i S_Z = 4\omega_s I_Z S_Z \qquad (19)$$

and the time-dependent heteronuclear dipolar coupling, $\hat{\mathcal{H}}_{IS}(t)$. In equation (19), $\omega_S = (\eta/2)\,(1 - 3\cos^2\psi)$, $\eta = \frac{1}{4}\gamma_I\gamma_S\hbar(1 - 3\cos^2\chi)/R_2^3$, and γ_S is the S-spin magnetogyric ratio. As before, ψ is the orientation of the methyl group axis with respect to the external magnetic field direction. The Hamiltonian has been written in the motional narrowing limit as in the case of the larger II dipolar coupling. In order to evaluate the effect of $\hat{\mathcal{H}}_{IS}$ on the proton spin levels, a suitable choice of basis states is a simple product of I and S spin states. The I spin states are the set λ_{m_I} of Table 1 and the S spin states are the eigenfunctions of S_Z, α ($m_S = \frac{1}{2}$) and

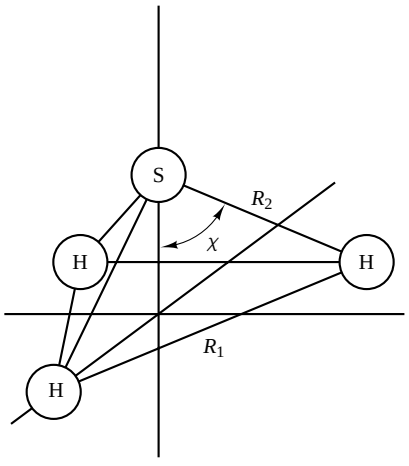

Figure 9 Molecular frame for a methyl group and a spin $S = \frac{1}{2}$ located along the methyl axis

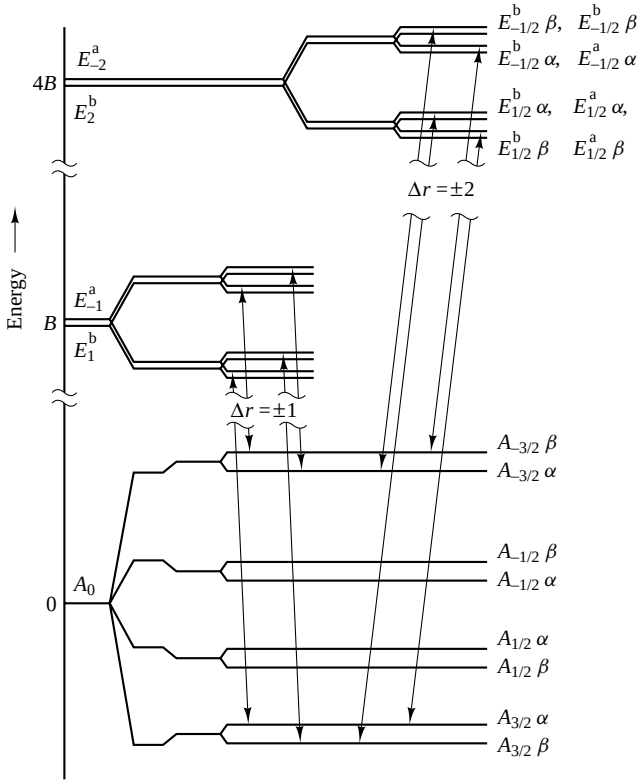

Figure 10 Rotational and spin levels for a methyl group coupled to a heterospin S excluding spin–rotation shifts. The solid lines represent transitions that produce a net IS dipolar polarization after a temperature jump

β ($m_S = -\frac{1}{2}$). The operator $\hat{\mathcal{H}}_{IS}$ is diagonal in this product basis and the result of the coupling is a splitting of the proton levels as depicted in Figure 10. For simplicity, spin–rotation shifts of the E levels are not shown.

From the selection rules $\Delta m_I = \pm 1$, $\Delta m_S = 0$, the proton NMR frequencies are located at $\pm 2\omega_S$, $2\omega_D \pm 2\omega_S$, and $-2\omega_D \pm 2\omega_S$ and are shown in the line spectrum of Figure 11(a). The powder lineshape was calculated for $^{13}CH_3CN$ using the gas phase structure,[24] $R_2 = 1.104$ Å and $\chi = 70.5^\circ$, to give $\eta = 3.73$ kHz. Also shown is the experimental spectrum for a 0.50% $^{13}CH_3CN$/Kr matrix in thermal equilibrium at 5.0 K. The extra lines are due to unlabeled CH_3CN molecules in the matrix, the frequencies corresponding to the powder pattern of Figure 4.

As in the previous discussion of unlabeled carbon atoms, a nonequilibrium difference in A and E populations following a temperature jump provides the driving force for polarizing the methyl group II and IJ spin systems With the S spin present, polarizing transitions are induced through the time-dependent IS dipolar interaction, which by analogy to equation (12) can be written as

$$\hat{\mathcal{H}}_{IS}(t) = \frac{1}{3}\sum_\lambda \sum_{i=-2}^{2} (-1)^i \hat{B}_{2,i}(\lambda)\hat{U}_{2,-i}(\lambda^*) \qquad (20)$$

where the $B_{2,i}$ and $U_{2,-i}$ operate on spatial and spin coordinates respectively. Like $\hat{\mathcal{H}}_{II}(t)$, this coupling has rotational and spin matrix elements that couple only A and

E states, but with two important differences. First, $\hat{\mathcal{H}}_{IS}(t)$ contains S-spin operators that provide for a polarization of the IS dipolar magnetization. The transitions that effect a net change in this magnetization are shown as the vertical lines in Figure 10. Second, the rotational selection rule is $\Delta r = \pm 1, \pm 2$, leading to two sets of transitions. Only those transitions that result in a net change in the IS magnetization are shown. At low temperatures, the spectral density function $\tau_c/(1+\omega_{rr'}^2\tau_c^2)$ in equation (13a) is far larger for ω_{01} than ω_{02}, and thus the IS mechanism is the dominant relaxation mechanism for the whole system. In the case of hindered rotation about the methyl axis, $\Delta r = \pm 1$ transitions are also allowed through $\hat{\mathcal{H}}_{II}(t)$ and the two mechanisms are competitive in the relaxation.

In order to determine the coupled evolution of the rotational system and the spin magnetizations, we use the same approach as in the previous section. Included in the master equation, equation (11), is a spin-density operator that contains the additional terms corresponding to the SZ and IS spin systems. Performing the summations, we find for the time-dependence of the inverse spin temperatures

$$\frac{\mathrm{d}}{\mathrm{d}t}\begin{bmatrix}\beta_{IZ}\\ \beta_{SZ}\\ \beta_r\\ \beta_{II}\\ \beta_{IS}\\ \beta_{IJ}\end{bmatrix} = -\begin{bmatrix} S_{IZ} & S_{IZ,SZ} & 0 & 0 & 0 & 0\\ S_{SZ,IZ} & S_{SZ} & 0 & 0 & 0 & 0\\ 0 & 0 & S_r & S_{r,II} & S_{r,IS} & S_{r,IJ}\\ 0 & 0 & S_{II,r} & S_{II} & S_{II,IS} & S_{II,IJ}\\ 0 & 0 & S_{IS,r} & S_{IS,II} & S_{IS} & S_{IS,IJ}\\ 0 & 0 & S_{IJ,r} & S_{IJ,II} & S_{IJ,IS} & S_{IJ}\end{bmatrix}\begin{bmatrix}\beta_{IZ}-\beta_{IZ}^{\mathrm{eq}}\\ \beta_{SZ}-\beta_{SZ}^{\mathrm{eq}}\\ \beta_r\\ \beta_{II}\\ \beta_{IS}\\ \beta_{IJ}\end{bmatrix} \tag{21}$$

where the coupling matrix elements are written explicitly as in Table 2. From equation (21) we can see that the I- and S-spin Zeeman systems are coupled with each other but uncoupled from the rotational system, and thus are not polarized as the result of a temperature jump.

The coupled evolution of the rotational system and the II, IS, and IJ magnetizations lead to a complex time-dependence after a temperature jump. Qualitatively, however, the observed time-dependence of each magnetization is similar to the double exponential form seen in Figure 5. The relative contributions of each of these spin systems to the overall spin polarization can be determined by examining the proton lineshape as it evolves with time after a temperature jump. If an rf pulse applied on resonance at time t after the temperature jump rotates the magnetization through an angle θ, and if the phase of the pulse is chosen as to correspond to the X direction of the rotating frame, then the expressions for the FID detected along X and Y directions are

$$\left.\begin{aligned} S_Y(t,\tau) &= \sin\theta\ \beta_{IZ}(t)\omega_{0I}\Gamma(\tau)[\cos(2\omega_S\tau)\,(2+\Lambda\cos(\omega_J\tau)\\ &\quad +3\cos(2\omega_D\tau))]\\ S_X(t,\tau) &= 6\sin\theta\cos\theta\ \Gamma(\tau)[\beta_{II}(t)\omega_D\cos(2\omega_S\tau)\sin(2\omega_D\tau)]\\ &\quad +\sin\theta\ \Gamma(\tau)[\beta_{IJ}(t)\omega_J\cos(2\omega_S\tau)\sin(\omega_J\tau)]\\ &\quad +2\sin\theta\ \Gamma(\tau)[\beta_{IS}(t)\omega_S\{2+\Lambda\cos(\omega_J\tau)\\ &\quad +3\cos(\omega_D\tau)\}\sin(2\omega_S\tau)] \end{aligned}\right\} \tag{22}$$

where τ is the time following the pulse. These expressions are identical to equation (16) when $\omega_s = 0$. If the reference phase of the receiver is carefully adjusted, the Zeeman component of the FID [proportional to $\beta_{IZ}(t)$] appears on the Y channel and the II, IS, and IJ components [proportional to $\beta_{II}(t)$, $\beta_{IS}(t)$, and $\beta_{IJ}(t)$, respectively] appear on the X channel. It is possible to separate the IS and IJ components of the FID from the II component by setting $\theta = 90°$. The result is shown in the bottom trace of Figure 11(c) for a 0.50% $^{13}CH_3CN$/Kr matrix 240 s after a 12.5 → 5 K temperature jump. This lineshape can be described exactly with only the IS component of the FID. Although equation (21) shows that the spin–rotation system is also polarized by the temperature jump, the IJ component of the FID appears to have a very low intensity and is obscured by the IS component. These spin–rotation splittings should have the same values as in Figure 7 for unlabeled CH_3CN, but are not resolved due to a further splitting by the IS coupling. The IS dipolar and spin–rotation powder lineshapes have, however, been resolved for matrix isolated $CH_3{}^{13}CN$ which has a smaller IS coupling constant of $\eta = 1.1$ kHz.[11]

The characteristic lineshape for II magnetization in matrix isolated $^{13}CH_3CN$ is shown in Figure 11(b). This spectrum was recorded 30 s after a 5 → 21 K temperature jump by applying a $90°_x\ \tau'\ 45°_x$ pulse sequence with $\tau = 2$ ms. The first pulse

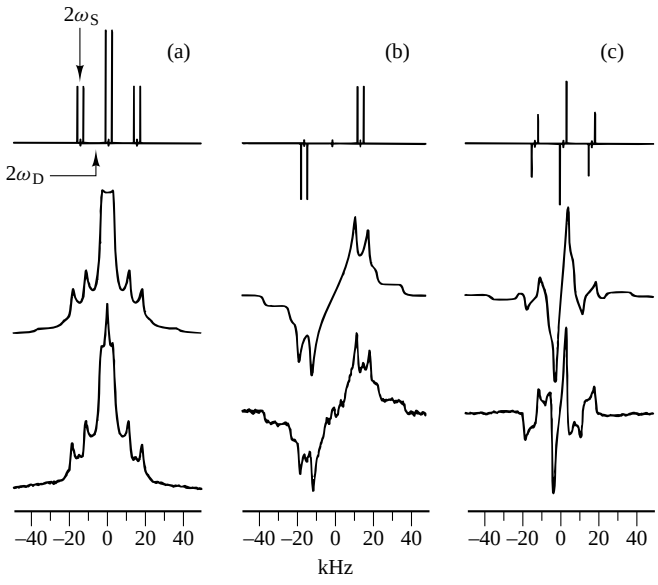

Figure 11 Calculated line and powder spectra for (a) Zeeman, (b) II dipolar, and (c) IS dipolar magnetizations. Bottom traces: Experimental spectra measured for a 0.5% $^{13}CH_3CN$/Kr matrix

converts *IS* and *IJ* magnetizations to transverse magnetization while scaling the *II* magnetization by $-\frac{1}{2}$. After a time τ', during which the *IS* and *IJ* magnetizations decay, the 45° pulse produces *II* transverse magnetization which appears on the *X* channel of the receiver. It is also possible to extend the acquisition so that the echo of the original *IS* magnetization is recorded at time τ' after the 45° pulse. In this way one can measure both β_{II} and β_{IS} simultaneously.

In Figure 11 the calculated and experimental powder lineshapes are compared. The agreement is excellent for the Zeeman and *II* dipolar lineshapes, but not so for the *IS* dipolar lineshape of (c). This difference points to an important characteristic of the $\hat{\mathcal{H}}_{IS}(t)$ polarization mechanism. Not only is there an orientation dependence in the polarization rate constants similar to that seen for the $\hat{\mathcal{H}}_{II}(t)$ mechanism in Figure 8, but also an orientation dependence in the coupling to the rotational system that has a more profound effect. This can be seen by neglecting the coupling among the *II*, *IS*, and *IJ* systems and focusing on the coupling of these systems with the rotational system. Using the matrix elements of Table 2, these are

$$\left.\begin{aligned} \beta_{II} &\propto S_{II,r} = (6/\kappa)(G - H_1 + H_2) \\ \beta_{IJ} &\propto S_{IJ,r} = (12/\Theta)(-G - H_1 + H_2) \\ \beta_{IS} &\propto S_{IS,r} = -(12/\eta)(H_1 \sin^2\psi + H_2 \cos^2\psi) \\ &\quad \times (1 - 3\cos^2\psi)^{-1} \end{aligned}\right\} \quad (23)$$

We see that for the *II* and *IJ* polarizations the inverse spin temperatures do not depend on the orientation of the methyl group. It is thus possible, at least in the early stages of the polarization, to factor β_{II} and β_{IJ} out of the brackets in equation (22) to calculate the lineshapes shown in Figure 11(a) and (b). But this is not true for the *IS* magnetization. If one treats β_{IS} as a constant in the expression for the FID, the resulting calculated lineshape of Figure 11(c) is clearly incorrect. If, however, the orientation dependence in β_{IS} shown above is included, the experimental lineshape is reproduced when $H_1/H_2 = 4.0$.[15,16] This is again a consequence of the spatial isolation of molecules in the matrix. In interacting molecular solids after a temperature jump, rapid spin diffusion would act to establish inverse spin temperatures $\langle\beta_{II}\rangle$, $\langle\beta_{IJ}\rangle$, and $\langle\beta_{IS}\rangle$ that are uniform throughout the sample. In the matrix, the anisotropy in the polarization process is preserved and reflected in the powder lineshape. This must be taken into consideration when accounting for the time-dependence of the experimentally observed *IS* polarizations.[15]

5 THE SOLID RARE GAS MATRIX

While a great deal has been written in the scientific literature about the matrix environment in the vicinity of a trapped molecular species as obtained from optical and INS spectroscopic studies, it is worthwhile to mention some insights concerning the matrix isolation technique from spin polarization studies. The main advantage of this technique is the spatial isolation of molecules. With rare gases this is achieved by the rapid deposition of a room temperature gaseous mixture on a cold target contained in an environment free from background impurities such as atmospheric gases. With low target temperatures, ∼4 K, and reasonably high vacuums, 10^{-6} to 10^{-7} torr, molecular aggregation can be avoided but at the expense of a highly disordered microcrystalline matrix. An adaptation of this technique for proton NMR studies[26] is shown in Figure 12. The hollow cylindrical (4 × 6 mm) sapphire sample cell is supported by a copper adapter at the tip of an Air Products Helitran and maintained at a temperature below 10 K during the matrix deposition. Unlike the thin films used in optical and IR studies, but like INS studies, the volume of the porous matrix is large, occupying one-third of the sample cell and containing approximately 10^{18} spins of interest.

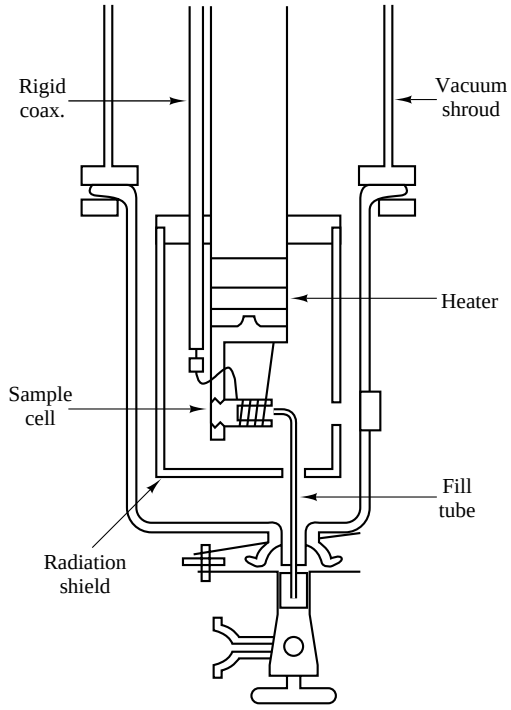

Figure 12 Schematic of experimental apparatus employed for matrix isolation NMR. The externally tuned circuit consists of a grounded single coil surrounding the sapphire sample cell and a cryogenic transmission line

Except in the case of molecules with large rotational constants, e.g., hydrogen halides, CH_4, etc., there have been few infrared or Raman studies of hindered rotation in rare gas matrices that permit an estimation of barrier heights.[6,27,28] Hindered rotation results in frequency shifts and the site multiplicity to inhomogeneous broadening of rotation–vibration spectra.[29] Employing very dilute matrices, the inhomogeneities of the initially formed matrix can be small, 1–2 cm^{-1}, and often reduced by matrix reconstruction on annealing (usually 50–60 K for Kr). As a result, the only characterization of the matrix from such studies is with respect to some average barrier to molecular rotation rather than details concerning site distribution.[30,31] Only in the case of matrix isolated CH_4, where the tendency for molecular aggregation on thermal annealing is small, do the INS studies, which require large and relatively high concentration matrices, provide direct information on site nonuniformity potential barriers to rotation.[32,33]

After initial deposition, the matrix can best be described as a distribution of potential barriers to the rotation of methyl groups which can range from zero to several times the rotational constant B. The presence of a potential barrier to guest molecule rotation affects the proton NMR directly through the spin–rotation splitting, which depends on the methyl group angular momentum, and the degree of spin polarization after a temperature jump, which depends on the separation of the rotational levels. This introduces a *selectivity* for molecules based on their matrix environment that is uncommon among other spectroscopic methods. Following a temperature jump, only molecules in sites where the potential barrier is very low contribute to the polarization. Thus, the dipolar and spin–rotation spectra are characteristic of free rotor molecules while the Zeeman spectrum reflects the entire distribution of environments. Unfortunately, it is difficult to relate quantitatively the intensities of Zeeman and dipolar components of the FID to site occupations. It is possible, however, to compare the population of E spin states in low and high barrier sites based on the spin–rotation splitting in spin echo spectra. In an unannealed 0.5% CH_3CN/Kr matrix, it is found that about one-half of the molecules occupy sites with a negligible potential barrier.[17]

Thermal annealing provides further insight to the matrix environment. Remarkably, the quenching of the spin polarization associated with annealing occurs at temperatures as low as 25 K in Kr and 20 K in Ar, i.e. far below the usual annealing temperatures for rare gas matrices.[30,34] It appears that this effect is due to diffusion, which brings the guest molecules into closer proximity, because annealing also causes a concomitant increase in the thermal equilibrium linewidths and a decrease in the spin–lattice relaxation times both indicative of increased intermolecular dipolar interactions. The effect is most drastic for annealing at higher temperatures ($>$40 K for Kr) after which a jump to a low temperature yields a severely broadened Zeeman lineshape from the Y component of the FID and a very small but still sharp dipolar lineshape from the X component of the FID. Finally, heating matrices formed using the arrangement of Figure 12 to bulk rare gas annealing temperatures leads to such severe molecular aggregation as to eliminate any advantages of the spatial isolation that permits observation of the interesting macroscopic quantum effects described earlier.

Despite the above comments, the site distribution cannot be attributed solely to the interaction of pairs or larger clusters of guest molecules. That there is also a site dependence for isolated molecules is obvious from the spin–rotation splittings seen in Figure 7. Using the same measuring procedures, the splittings in the Ar matrix are smaller than in Kr and Xe matrices. If, as we have maintained, the splittings are characteristic of isolated molecules at sites with low barrier to rotation, the reduced splitting in Ar must be due to an increase in the potential barrier. We expect that such differences in matrix barriers to methyl rotation will prove to be a useful test for molecular dynamics calculations in solid lattices.

6 RELATED ARTICLES

Dynamic Nuclear Polarization and High-Resolution NMR of Solids; Quantum Tunneling Spectroscopy; Thermodynamics of Nuclear Magnetic Ordering.

7 REFERENCES

1. Some examples are: J. Haupt, *Z. Naturforsch.*, 1971, **26a**, 1578; S. Emid, R. J. Baarda, J. Smidt, and R. A. Wind, *Physica*, 1978, **93B**, 327; W. Müller-Warmuth, R. Schuler, M. Prager, and A. Kollmar, *J. Chem. Phys.*, 1978, **69**, 2382; W. Press, *Single Particle Rotations in Molecular Crystals*, Springer-Verlag, New York, 1981; S. Clough, A. Heidemann, A. J. Horsewill, J. D. Lewis, and M. N. J. Paley, *J. Phys. C*, 1982, **15**, 2495; Bih-Yau Jin and R. Silbey, *J. Chem. Phys.*, 1991, **94**, 2077.
2. J. Haupt, *Phys. Lett.*, 1972, **38A**, 389; J. Haupt, *Z. Naturforsch.*, 1973, **28a**, 98.
3. P. S. Allen and P. Branson, *J. Phys. C*, 1978, **11**, L121; P. S. Allen, *Faraday Symp. Chem. Soc.*, 1979, **13**, 133.
4. B. Meyer, *Low Temperature Spectroscopy*, American Elsevier Publishing, New York, 1971.
5. H. E. Hallam (ed.), *Vibrational Spectroscopy of Trapped Species*, J. Wiley & Sons Ltd., London, 1983; D. W. Ball, Z. H. Kafafi, L. Fredin, R. H. Hauge, and J. L. Margrave (eds.), *A Bibliography of Matrix Isolation, 1954–1985*, Rice University Press, Houston, TX, 1989.
6. J. E. Kohl, M. G. Semack, and D. White, *J. Chem. Phys.*, 1978, **69**, 5378.
7. K. W. Zilm, D. M. Grant, R. T. Conlin, and J. Michl, *J. Am. Chem. Soc.*, 1978, **100**, 8038.
8. W. Langel, H. Kollhoff, E. Knözinger, and M. Prager, *Ber. Bunsenges. Phys. Chem.*, 1985, **89**, 927; *ibid*., 1987, **91**, 1257.
9. J. E. Kohl, M.G. Semack, and D. White, *Phys. Rev. Lett.*, 1979, **42**, 1072.
10. M. Murphy, M. G. Semack, and D. White, *J. Magn. Reson.*, 1987, **72**, 143.
11. M. Murphy and D. White, unpublished results.
12. M. Semack and D. White, unpublished results.
13. E. R. Andrew and R. Bersohn, *J. Chem. Phys.*, 1950, **18**, 159.
14. F. Apaydin and S. Clough, *J. Phys. C*, 1968, **1**, 932.
15. M. Murphy, Ph.D. Dissertation, University of Pennsylvania, 1987.
16. M. Murphy and D. White, *J. Chem. Phys.*, 1987, **86**, 1640.
17. M. Murphy and D. White, *J. Chem. Phys.*, 1989, **91**, 4504.
18. J. H. Freed, *J. Chem. Phys.*, 1965, **43**, 1710.
19. M. Mehring, *Principles of High Resolution NMR in Solids*, 2nd edn., Springer-Verlag, New York, 1983.
20. P. Beckmann, S. Clough, J. W. Hennel, and J. R. Hill, *J. Phys. C*, 1977, **10**, 729.
21. J. Jeener and P. Broekaert, *Phys. Rev.*, 1967, **157**, 232.
22. M. Goldman, *Spin Temperatures and Nuclear Magnetic Resonance in Solids*, Oxford University Press, Oxford/New York, 1970; J. Jeener, *Adv. Magn. Reson.*, 1968, **3**, 205.
23. A. Abragam, *The Principles of Magnetic Resonance*, Oxford University Press, London, 1961, Chap. 7
24. S. Clough, *J. Phys. C*, 1985, **18**, L32; S. Clough, *J. Phys. Condens. Matter*, 1989, **1**, 501.
25. C. C. Costain, *J. Chem. Phys.*, 1958, **29**, 864.
26. K. Carduner, M. Villa, and D. White, *Rev. Sci. Instrum.*, 1984, **55**, 68.
27. L. J. Schoen, D. E. Mann, C. Knobler, and D. White, *J. Chem. Phys.*, 1962, **37**, 1147; D. E. Mann, N. Acquista, and D. White, *J. Chem. Phys.*, 1966, **44**, 3453.
28. A. Cabana, G. B. Savitsky, and D. F. Honig, *J. Chem. Phys.*, 1963, **39**, 2942.
29. M. Allavena, H. Chakroun, and D. White, *J. Chem. Phys.*, 1982, **77**, 1757.
30. V. I. Lang and J. S. Winn, *J. Chem. Phys.*, 1991, **94**, 5270.

31. W. H. Flygare, *J. Chem Phys.*, 1963, **39**, 2263; H. Friedmann and S. Kimel, *J. Chem. Phys.*, 1967, **47**, 3589; C. Giradet and D. Robert, *J. Chem. Phys.*, 1973, **58**, 4110.
32. M. Prager and W. Langel, *J. Chem. Phys.*, 1988, **88**, 7995; 1989, **90**, 5889.
33. B. Asmussen, M. Prager, W. Press., H. Blank, and C. J. Carlile, *J. Chem Phys.*, 1992, **97**, 1332; W. L. Langel, M. Prager, H. W. Fleger, E. Knözinger, H. Lauter, H. Blank, and C. J. Carlile, *J. Chem. Phys.*, 1993, **98**, 4838.
34. M. Klein (ed.), *Rare Gas Solids*, Academic Press, London, 1976.

Biographical Sketches

David White. *b* 1925. B.Sc., 1943, McGill University, Ph.D., 1946, University of Toronto. Director of Cryogenic Laboratory and Professor of Chemistry, Ohio State University, 1947–66; Chairman, Department of Chemistry, University of Pennsylvania, 1966–79; Director, Laboratory for Research on the Structure of Matter, 1981–88; Professor of Chemistry University of Pennsylvania, 1988–present. Approx. 160 publications. Research specialties: molecular dynamics in quantum solids; solid rare gas matrices; molecular seives at low temperatures.

Michael D. Murphy. *b* 1957. B.S., 1979, Ph.D., 1988, University of North Carolina, Charlotte. Postdoctoral Fellow, University of Pennsylvania, 1989; Assistant Professor, St. Frances College, Loretta, PA, 1989–present. 10 publications. Research specialty: spin relaxation of matrix isolated molecules.

Echoes in Solids

Bernard C. Gerstein

Ames Laboratory of Iowa State University, Ames, Iowa, USA

1	Introduction	1
2	Basic Ideas	1
3	Time-Dependent Quantum Mechanics of the Spin Echo	1
4	Rotations in Spin Space: Selective Averaging	2
5	The Average Hamiltonian and Echoes	3
6	The Modulated Spin Echo	4
7	The Dipolar Echo and the First-Order Quadrupolar Echo	5
8	Transient Nutations: A Variant	5
9	Multiple Quantum Coherence	5
10	Related Articles	6
11	References	6

1 INTRODUCTION

When a person stands at the edge of a deep canyon and sharply shouts their own name, it may happen that this name, somewhat distorted, and not as loud, will come back to them after a second or so. This return of the initial signal we call an echo. We think of the opposite wall of the canyon reflecting the signal back toward us. In the jargon of NMR, we could say that a sharp signal was broadcast, something is there to 'reflect' this signal, and a somewhat attenuated and distorted response, an 'echo' of the original, is detected at a later time. There is a sense in which we might say that time has been reversed in this experience—except that, for exact time reversal, we might expect that the name would return to us spoken backwards.

One use of echoes in materials science is that in nondestructive testing on metals by sharp sonic signals. Here, a transducer is used to broadcast a pulse of sound into the solid, and the echo, received back by a detector, is used to infer voids, cracks, or general faults in the material. In this case, the echo received from the initial pulse of sound is modulated by the information from macroscopic defects in the solid, and this modulation is unwound to infer the nature of the defect. This case is almost an exact analog of the 'modulated spin echo' first reported by Hahn and Maxwell.[1] In this article, we provide an introduction to the subject of echoes in the study of solids by NMR, with specific attention to those echoes produced by the rotations of internal interactions by the radiofrequency field, $\boldsymbol{B}_1$. We can call these 'spin echoes'. As is discussed in ***Rotating Solids*** there are also echoes produced by physical rotations of the sample, e.g., by 'magic angle spinning'. We call these 'spun echoes'. In this article, we pay specific attention to the case of 'spin echoes' in solids, and their production and detection under radiofrequency excitations.

2 BASIC IDEAS

A spin echo[2] in NMR is quite analogous to that produced when calling one's name in a canyon. A transient transverse magnetization is created, something is done to cause this magnetization to be 'reflected' backwards, and, at a later time, this magnetization transient, somewhat attenuated, flashes back into our detector. We can then repeat the event that refocused the magnetization, and again we shall see an echo. If we are able to watch the signal on the detector, let us say an oscilloscope screen that is exhibiting the memory of a digitizer, from the moment of the broadcast of the initial signal to the return of the echo, and we repeat the refocusing event five times, we might see a signal such as that shown in Figure 1.

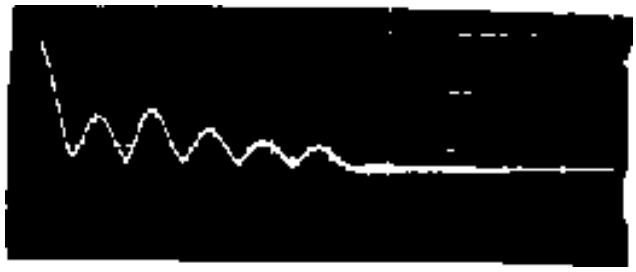

Figure 1 Magnetization amplitude $I(t)$ versus time t. Left, initial decay after a 90° pulse. Five echoes follow five 180° refocusing pulses

This signal is in fact a series of spin echoes when the nucleus in question is ^{1}H in water; the sequence used to produce this effect is the Carr–Purcell[3] version of the Hahn spin echo sequence. The system is prepared with the magnetization along the y direction in the rotating frame by a $90°_x$ pulse, and then a series of 180° pulses, switched in phase by 90° from the preparation pulse (which is to say, along the y axis in the rotating frame), are used to produce the echoes: we designate the sequence by the shorthand notation $90°_x$, τ, $(180°_y, 2\tau) \times 5$.

The signal shown in Figure 1 is observed with the reference phase adjusted for detection along the y axis in the rotating frame. It has a number of interesting features. First, we see a hint of the transient 90° pulse at the beginning, on the left of the figure, as the few points from the baseline up. Second, we see the free induction decay after this pulse. Then, we see a hint of the 180° pulse, and subsequently a signal 'refocusing' back up, reaching an echo maximum, and then decaying back down. This situation is repeated four more times. If we look just at the echo envelope, i.e., the maximum at the beginning of the FID, and the succeeding maxima of the echoes, we see that this envelope roughly describes something looking like an exponential decay. However, in the case shown, there is clearly an oscillation in the envelope—a modulation of the echoes. The spin echo experiment and the modulation of the echo envelope are the subjects here. Finally, we see that the envelope of the echo lasts longer than the FID itself; i.e., if we denote the decay constant for the FID by T_2*, and the decay constant for the echo envelope by T_2 then we see that the effective decay time of the FID, T_2, has been lengthened compared with T_2* by the sequence of 180° refocusing pulses. A classical picture of the initial excitation and the 180° refocusing is shown in Figure 2 for a single refocusing pulse.

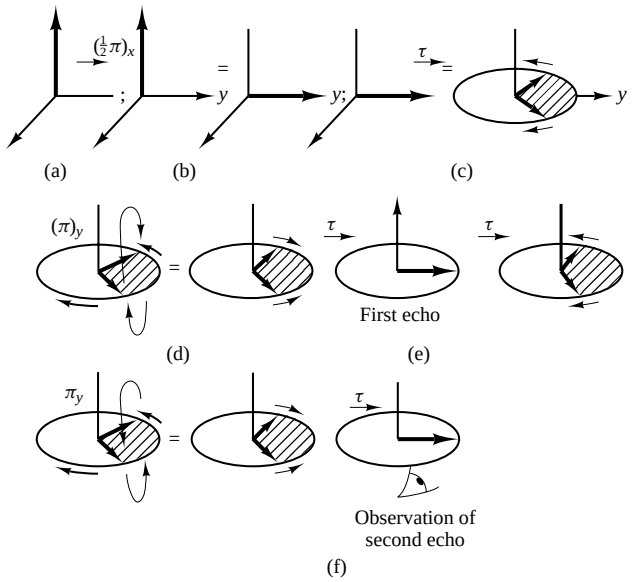

Figure 2 Classical picture of the spin echo: top, polarization, and 90° pulse, followed by dephasing on resonance. Bottom, 180° refocusing pulses, followed by rephasing

3 TIME-DEPENDENT QUANTUM MECHANICS OF THE SPIN ECHO

To place our discussion in perspective, it is necessary to recognize explicitly what has been implicit in the above introduction, namely, that there are two fundamental facts about NMR.

1. A nucleus with a magnetic moment proportional to a constant γ, will resonate at an angular frequency ω in a static magnetic field $\boldsymbol{B}$ given by $\omega = \gamma B$. The sensitivity to detection is proportional to γ, and to the natural abundance of the nucleus in question.
2. Hidden in fundamental fact 1 is the time-dependent mechanics tersely summarized in the following equations:

$$\mathrm{i}\frac{\mathrm{d}\hat{\rho}}{\mathrm{d}t} = [\hat{\mathcal{H}}, \hat{\rho}] \quad \text{(energies in units of radial frequency)} \tag{1}$$

$$\langle \hat{I}_y(t) \rangle = \mathrm{Tr}\, \hat{\rho}(t)\hat{I}_y \tag{2}$$

$$\hat{\rho}(t) = \hat{U}(t, 0)\hat{\rho}(0)\hat{U}^{-1}(t, 0) \tag{3}$$

Equation (1) is the time-dependent Schrödinger equation, expressed in density matrix formalism.[4] equation (2) shows how the solution of equation (1) is used to obtain the time dependence of observables, e.g., the time decay of the magnetization of a nuclear spin system under a resonant excitation. In equation (2) detection is made along the y axis of the rotating frame. The Fourier transform of the time decay is the NMR spectrum. Implicit in equation (2) is the fact that we are using matrix representations to describe our system. Tr $\hat{A}$ denotes the trace, or sum of the diagonal elements, of the matrix representing the operator $\hat{A}$. Equation (3) indicates the formal solution of equation (1). The absolutely critical term here is the propagator $\hat{U}(t,0)$, which drives the ensemble of magnetically resonant nuclei under study from time zero to time t (quite a lovely introduction to the subject of propagators in quantum mechanics is given by Mattuck[5]). It is exactly an understanding of how the experimenter controls $\hat{U}(t,0)$ that makes NMR such a powerful technique for probing the properties of inert and living matter.

4 ROTATIONS IN SPIN SPACE: SELECTIVE AVERAGING

All spectroscopy experiments implicitly or explicitly involve solutions of the time-dependent Schrödinger equation. An understanding of NMR involves at least a rudimentary knowledge of the solutions of this equation in the density operator formulation. Fortunately, there are texts for students at both the entry level[6,7] and advanced levels[8–10] presenting both of these pictures. Abragam's monumental 1961 monograph 'Principles of Nuclear Magnetism'[11] is still a standard reference in the field, with gems yet to be mined so long after its publication.

As a basis for understanding the spin echo experiment, we tersely summarize the results of selective averaging theory on first the result of the spin echo sequence upon an ensemble of spins $\frac{1}{2}$ in a solid, e.g., protons in solid gypsum, $CaSO_4.2H_2O$. Here, the principal internal interactions are, in decreasing order of magnitude,

1. anisotropic shielding;
2. the homonuclear dipolar interaction.

We start in the rotating frame of the Zeeman interaction, the frame in the laboratory in which NMR signals are detected after demodulation removes the carrier frequency from the information content of the signal. In the rotating frame, the principal effective magnetic fields that cause a spin-$\frac{1}{2}$ nucleus such as a proton to resonate for detection by NMR are

1. The externally applied radiofrequency field $\boldsymbol{B}_1$, which is constant in the rotating frame on resonance, with, e.g., an interaction Hamiltonian for a pulse along the phase x being

$$\hat{\mathcal{H}}_1 = -\gamma B_1 \hat{I}_x = -\omega_1 \hat{I}_x \tag{4}$$

2. The sample-supplied, or internal, average of the fields associated with all other internal interactions. For non-spin-$\frac{1}{2}$ nuclei, the major interaction is the electric field gradient, which perturbs the energy levels of quadrupolar nuclei. For concentrated spin-$\frac{1}{2}$ nuclei such as ^{1}H and ^{19}F, the major fields are the dipolar fields of all other protons or fluorine nuclei, $\boldsymbol{B}_\mathrm{D}$, in which a proton or fluorine will precess with a frequency

$$\omega_\mathrm{D} = \gamma B_\mathrm{D} \tag{5}$$

A smaller perturbation is the anisotropic shielding field associated with the reaction of electrons in the environment of the nucleus under observation to the externally imposed static field. With each field is associated an energy and a quantum mechanical energy operator $\hat{\mathcal{H}}$. Thus the energy operator in the rotating frame is given by

$$\hat{\mathcal{H}} = \hat{\mathcal{H}}_\mathrm{rf} + \hat{\mathcal{H}}_\mathrm{int} \tag{6}$$

where the magnitude of $\hat{\mathcal{H}}_{\rm rf}$ for purposes of solid state experiments is about 5 mT. The magnitude of $\hat{\mathcal{H}}_{\rm int}$ is never greater than a few tenths of a millitesla in the case discussed here. The equation of motion of the system is then given by the solution to equation (1) with $\hat{\mathcal{H}}$ being the sum of the rf and internal interactions, as specified in equation (6). The average values of observables, e.g., $\langle \hat{I}_y(t) \rangle$, the free induction decay detected along the y phase in the rotating frame, are given by equation (2).

With the interactions separated in magnitude in this manner, it makes sense to treat $\hat{\mathcal{H}}_{\rm int}$ as a perturbation of $\hat{\mathcal{H}}_{\rm rf}$. Recall that the transformation to the frame of the Zeeman interaction (the rotating frame) simplifies the description of a nuclear spin in the presence of other interactions: for example, the oscillating on-resonance rf field becomes static in the rotating frame. Similarly, transformation to the frame of the now largest interaction $\hat{\mathcal{H}}$ further simplifies the description of the system. The transformation to the frame of the rf is accomplished by the following relations:

$$\hat{\rho} = \hat{U}_{\rm rf} \tilde{\hat{\rho}} \hat{U}_{\rm rf}^{-1} \tag{7}$$

$$\mathrm{i} \frac{\mathrm{d}\hat{U}_{\rm rf}}{\mathrm{d}t} = \hat{\mathcal{H}}_{\rm rf} \hat{U}_{\rm rf} \tag{8}$$

$$\hat{U}_{\rm rf}(0,0) \equiv \hat{U}_{\rm rf}(t=0) = \hat{1} \tag{9}$$

$$\tilde{\hat{\mathcal{H}}}(t) = \hat{U}_{\rm rf}^{-1}(t,0) \hat{\mathcal{H}} \hat{U}_{\rm rf}(t,0) \tag{10}$$

As mentioned above, the notation $\hat{U}(t,0)$ is a formal way of saying that the propagator, $\hat{U}$, drives the system from time 0 to time t. An explicit operational form of $\hat{U}$ will be given below; for now, accept it as that quantity causing the system to proceed in time, with physical origin in the time-dependent sequence of rf pulses and the internal interactions as affected by these pulses. The result,

$$\frac{\mathrm{i}\mathrm{d}\tilde{\hat{\rho}}}{\mathrm{d}t} = [\tilde{\hat{\mathcal{H}}}_{\rm int}, \tilde{\hat{\rho}}\,] \tag{11}$$

where $\tilde{\hat{\mathcal{H}}}_{\rm int}$ is given by equation (10), is that the motion of the system in the new frame, the frame of the rf field, now no longer explicitly contains the rf interaction (recall that transforming to the frame of the Zeeman field removed that interaction from the description of the system).

We next make a second transformation to the frame of $\hat{\mathcal{H}}_{\rm int}$, simply reproducing equations (7)–(10) with the appropriate change in symbols:

$$\tilde{\hat{\rho}} = \hat{U}_{\rm int}(t,0) \tilde{\tilde{\hat{\rho}}} \hat{U}_{\rm int}^{-1}(t,0) \tag{12}$$

$$\frac{\mathrm{i}\mathrm{d}\hat{U}_{\rm int}}{\mathrm{d}t} = \tilde{\hat{\mathcal{H}}}_{\rm int} \hat{U}_{\rm int} \tag{13}$$

$$\hat{U}_{\rm int}(0,0) = \hat{1} \tag{14}$$

Thus $\hat{\rho}$ is replaced by $\tilde{\hat{\rho}}$, $\tilde{\hat{\rho}}$ is replaced by $\tilde{\tilde{\hat{\rho}}}$, $\hat{U}_{\rm rf}$ is replaced by $\hat{U}_{\rm int}$, etc. The system in this frame is static:

$$\mathrm{i} \frac{\mathrm{d}\tilde{\tilde{\hat{\rho}}}}{\mathrm{d}t} = [0, \tilde{\tilde{\hat{\rho}}}\,] = 0 \tag{15}$$

We formally identify this static system with the system at time zero; $\hat{\rho}$ then becomes identical to $\hat{\rho}(0)$. In this perturbation picture, with $\hat{\mathcal{H}}_{\rm int}$ being a perturbation of $\hat{\mathcal{H}}_{\rm rf}$, the motion of the system is described by

$$\hat{\rho}(t) = \hat{U}_{\rm rf}(t,0) \hat{U}_{\rm int}(t,0) \hat{\rho}(0) \hat{U}_{\rm int}^{-1}(t,0) \hat{U}_{\rm rf}^{-1}(t,0) \tag{16}$$

5 THE AVERAGE HAMILTONIAN AND ECHOES

Before becoming explicit about the operational forms of the propagators $\hat{U}$, let us examine equation (16) more closely. It is clear that if both $\hat{U}_{\rm rf}(t_{\rm c},0)$ and $\hat{U}_{\rm int}(t_{\rm c},0)$ are unity at some particular time $t_{\rm c}$ then, at this special time, it appears that the system has simply not changed, i.e., equations (2) and (16) at time $t_{\rm c}$, tell us that the value of any observable at this time is the value of that operator at time zero; at time $t_{\rm c}$, $\hat{\rho}(t_{\rm c}) = \hat{\rho}(0)$. There is therefore an enormous simplicity in the behavior of the system, which the experimenter may accomplish with proper arrangements of sufficiently powerful rf pulses, since both $\hat{U}_{\rm rf}$ and $\hat{U}_{\rm int}$ depend upon $\hat{\mathcal{H}}_{z\rm rf}$, the rf pulses that we supply! The fields (5 mT) generated by the rf pulses are much larger than the 'internal fields' due to dipolar interactions and shielding (<0.3 mT) (but not, in general, electric field gradients on quadrupolar nuclei). That is to say, the initial broadcast of our excitation is 'sharp', as in the name-calling event described at the beginning of this article. In that case, if we had called our name slowly and softly compared with the background noise of the wind sighing through the trees, and the calls of the eagle circling below, we would not have received back an echo response to our call. In more mathematically explicit terms, as long as $\hat{U}_{\rm rf}$ operates for times short compared with times in which $\hat{U}_{\rm int}$ affects the system, its motion is predominantly controlled by $\hat{U}_{\rm rf}$. Then, if the sequence of rf pulses generating $\hat{U}_{\rm rf}(t_{\rm c},0)$ returns the system to its initial state, $\hat{U}_{\rm rf}(t_{\rm c},0)$ is formally equal to unity—a result inferred from physics rather than mathematics. Examples of such pulse sequences are easily imagined if the physics is kept clearly in mind. One example is the sequence $(t,\ 180^\circ_y,\ \tau,\ 180^\circ_y,\ \tau)$ which results in a rotation by 2π about the y axis, leaving the system invariant at a cycle time $t_{\rm c} = 3\tau$. The sequence $(\tau,\ 90^\circ_x,\ \tau,\ 90^\circ_y,\ 2\tau,\ 90^\circ_{-y},\ \tau,\ 90^\circ_{-x},\ \tau)$ has pairs of pulses that cancel each other (the y pulse cancels the $-y$ pulse, and similarly for x) and leave the system invariant at a cycle time $t_{\rm c} = 6\tau$. Such sequences are said to be *cyclic*. If these groups of pulses are repeated periodically, they are both cyclic and *periodic*. As long as $\hat{U}_{\rm rf}(nt_{\rm c},0)$ is the dominant propagator, in the 'windows' between these groups of pulses, the system will behave as if it is not moving in time. The behavior of the system becomes refocused at these 'echo times' $nt_{\rm c}$.

We have here a situation analogous to that which we might imagine if we had been able to use a strobe light to watch the glitter and dynamic flowing that was a performance by the late Janice Joplin. To see her perform at her most intense,

belting out a song like 'Try (Just a Little Bit Harder)', was to experience a visual sensation of watching mercury boiling. Under a strobe, however, we might have been able to recognize that her motions, which were rhythmatic with the beat of the music, viewed in the windows of time periodic with these motions, would make her appear to us to be almost not moving. However, since she was not just an automaton repeating a periodic motion in sync with the strobe, we should see that nuances that were lost without the strobe now become visible. She would appear to move very slowly, in analogy to a modulated spin echo (see below). We might say that her motion appears to vary quite slowly relative to her motion when seen in the absence of a strobe. The rapid motion that we should see without a strobe has been selectively averaged to zero. In this circumstance, we are able to see details of much slower motion that we might have missed had we viewed her doing her full routine—which could be quite rapid and stunning.

6 THE MODULATED SPIN ECHO

With the performance of Janice Joplin viewed in a strobe light kept in mind, let us take a close look at equation (16). We see here that as time progresses, $\hat{U}_{\rm int}(nt_{\rm c},0)$ begins to affect the motion of the system. If the propagator $\hat{U}_{\rm rf}(t,0)$ dominates the situation at short times, meaning that the magnitude of $\hat{\mathcal{H}}_{\rm rf}$ is much larger than the magnitude of $\hat{\mathcal{H}}_{\rm int}$, then, as time progresses, observation in the windows $nt_{\rm c}$ will reveal some motion due to $\hat{U}_{\rm int}(nt_{\rm c},0)$. Now this propagator, $\hat{U}_{\rm int}(nt_{\rm c},0)$, is determined by $\hat{\mathcal{H}}_{\rm int}$. The interaction $\hat{\mathcal{H}}_{\rm int}$ in the case considered is the sum of $\hat{\mathcal{H}}_{\rm D}$ and $\hat{\mathcal{H}}_{\rm CS}$, the dipolar and shielding interactions as manipulated by the rf pulses. If somehow the dipolar interaction (but not the shielding interaction) can be selectively set in motion so that its time average at times $nt_{\rm c}$ is zero, the remaining information in the windows of the stroboscopic observation will be the shielding. The nuances of a Joplin performance become visible if the rapid periodic motion in time with the rhythm is selectively averaged out of our vision by using a strobe. This is exactly what multiple pulse homonuclear decoupling attempts to accomplish. To see how this works, one needs an explicit operational form for the internal propagator $\hat{U}_{\rm int}(nt_{\rm c},0)$. The form is illustrated with the spin echo sequence, (τ, 180°_y, τ, 180°_y, τ). In the sequence, we take the internal Hamiltonian to represent any interaction proportional to the operator $\hat{I}_z$, e.g., shielding, resonance offset, static field inhomogeneities, and scalar couplings to unlike nuclei. Homonuclear dipolar coupling, as shown below, is not simply proportional to $\hat{I}_z$.

When we manipulate $\hat{\mathcal{H}}_{\rm int}$ by cyclic and periodic sequences of rf pulses [$\hat{U}_{\rm rf}(nt_{\rm c},\ 0) = 1$] the form of the propagator $\hat{U}_{\rm int}$ becomes an exponential (see Chapter 4 of Gerstein and Dybowski[6]), with the leading term in the result, observed at cycle times $nt_{\rm c}$, given by

$$\begin{aligned}\hat{\rho}(nt_{\rm c}) &= \hat{U}_{\rm int}(nt_{\rm c})\hat{\rho}(0)\hat{U}_{\rm int}^{-1}(nt_{\rm c},0)\\ &= \exp(-{\rm i}\hat{\bar{\mathcal{H}}}_{\rm int}^{(0)})\,\hat{\rho}(0)\,\exp({\rm i}\hat{\bar{\mathcal{H}}}_{\rm int}^{(0)})\end{aligned} \tag{17}$$

Here, $\hat{\bar{\mathcal{H}}}_{\rm int}^{(0)}$ is equal to the integral over a cycle of the internal Hamiltonian as manipulated in time by the rf pulses:

$$\hat{\bar{\mathcal{H}}}_{\rm int}^{(0)} = \frac{1}{t_{\rm c}}\int_0^{t_{\rm c}} \hat{\tilde{\mathcal{H}}}_{\rm int}(t)\,{\rm d}t \tag{18}$$

This time average of the internal Hamiltonian, as manipulated by the rf pulses, may be interpreted as an average internal Hamiltonian. If this time average is zero, then, for a cyclic, periodic sequence, both $\hat{U}_{\rm rf}(nt_{\rm c})$ and $\hat{U}_{\rm int}(nt_{\rm c})$ will be unity, and at times $nt_{\rm c}$ the system will behave as if there is nothing driving it; it will 'echo' its initial state in time.

The manner of manipulation of $\hat{\tilde{\mathcal{H}}}_{\rm int}$ is as follows:

$$\hat{\tilde{\mathcal{H}}}(t) = \hat{U}_{\rm rf}^{-1}(t,0)\hat{x}_{\rm int}\hat{U}_{\rm rf}(t,0) \tag{19}$$

$\hat{\tilde{\mathcal{H}}}_{\rm int}(t)$ is the *instantaneous* value of the internal Hamiltonian as determined by the rf pulses. $\hat{U}_{\rm rf}(t,0)$ is the propagator due to the rf pulses from time zero to time t. For n time intervals δ_1, followed by δ_2, ... , followed by δ_n, $\hat{U}_{\rm rf}$ is clearly the propagator during interval δ_1, followed by the propagator during δ_2, ... :

$$\hat{U}_{\rm rf}(t,0) = \hat{U}_{\rm rf}(\delta_n)\cdots\hat{U}_{\rm rf}(\delta_1) \tag{20}$$

The inverse of this product of matrix operators is given by

$$\hat{U}_{\rm rf}^{-1}(t,0) = \hat{U}_{\rm rf}^{-1}(\delta_1)\hat{U}_{\rm rf}^{-1}(\delta_2)\cdots\hat{U}_{\rm rf}^{-1}(\delta_n) \tag{21}$$

The physical meaning of the exponentials in equation (17) can be seen from the fact that they can always be expressed as a product of rotations in spin space acting on components of angular momentum operators. For example, consider the rf pulse sequence with perfect delta-function pulses (τ, 180°_y, 2τ, 180°_y, τ), shown in Figure 3.

This sequence is used to produce $\hat{\mathcal{H}}_{\rm rf}$, and thus $\hat{U}_{\rm rf}$, equal to $\exp(-i\int_0^t \hat{\tilde{\mathcal{H}}}{\rm d}t)$, as indicated in Figure 3. At times $0 < t < \tau$ when the rf Hamiltonian is zero, $\hat{U}_{\rm rf}(t,0)$ takes the form $e^0 = 1$, and in this time interval the value of $\hat{I}_z$ as manipulated by the rf pulse sequence in Figure 3 is given by equation (19). We may physically identify $\hat{U}_{\rm int}(0 < t < \tau)$ as given in equation (19) with a rotation $\hat{R}$ of unity, performed on $\hat{I}_z$, symbolized by $\hat{R}\hat{I}_z = 1\cdot\hat{I}_z$. At time $t = \tau$, the rf Hamiltonian corresponds to an infinitely fast rotation about the y axis of 180°. $\hat{U}_{\rm rf}(t = \tau) = \exp(i\pi\hat{I}_y)$, and the physical result is a 180°_y rotation, $\hat{R}_{180y}$, which sends the operator $\hat{I}_z$ into the operator $-\hat{I}_z$. For $\tau < t < 2\tau$ the rf again is zero, and $\hat{U}_{\rm rf}$ is unity. At $t = 3\tau$, another 180°_y takes place. Under this sequence, therefore, with the spin portion of $\hat{\mathcal{H}}_{\rm int}$ being proportional to $\hat{I}_z$, and keeping in mind the time ordering dictated by equations (20) and (21), we find the sequence of values of $\hat{I}_z$ in the frame of the rf pulses (see Figure 3)

$$0 < t < \tau:\quad \hat{I}_z \to {\rm e}^{-0}\hat{I}_z{\rm e}^0 = 1\cdot\hat{I}_z\cdot 1 = 1\cdot\hat{I}_z = \hat{I}_z \tag{22a}$$

$$t = \tau:\quad \hat{I}_z \to 1\cdot\hat{R}_{180y}\hat{I}_z = -\hat{I}_z \tag{22b}$$

$$\tau < t < 3\tau:\quad \hat{I}_z \to 1\cdot\hat{R}_{180y}\cdot 1\cdot\hat{I}_z = -\hat{I}_z \tag{22c}$$

$$3\tau < t \le 4\tau:\quad \hat{I}_z \to -\hat{I}_z \tag{22d}$$

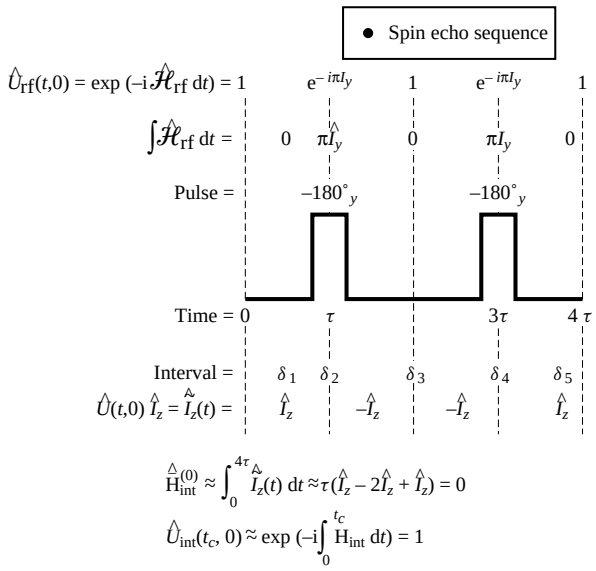

Figure 3 Spin echo sequence, illustrating the pulses (square waves), the propagator associated with the pulses, $\hat{U}_{rf}(t,0)$, and the average Hamiltonian associated with an internal interaction proportional to $\hat{I}_z$

The familiar result is that at periodic cycle times $4n\tau$, under the spin echo sequence $(\tau,\ 180^\circ_y,\ 2\tau,\ 180^\circ_y) \times n$, chemical shifts and field inhomogeneities, with spin operators $\hat{I}_{zk}$, vanish, but other interactions, such as homonuclear dipolar coupling, do not. That is to say, at cycle times $4n\tau$, with the internal Hamiltonian being proportional to $\hat{I}_z$, $\hat{\tilde{\mathcal{H}}}^{(0)}_{int}$ is zero:

$$\begin{aligned}\hat{\tilde{\mathcal{H}}}^{0}_{int} &\propto \int_0^{4\tau} dt\ \hat{U}_{rf}^{-1}(t)\hat{\mathcal{H}}_{cs}\hat{U}_{rf}(t) \\ &= 2\omega_{cs}[\hat{I}_z\tau + (-\hat{I}_z)\tau] = 0 \end{aligned} \tag{23}$$

Here ω_{CS} is a product of a constant (ΔB_{eff}) and the part of the chemical shift Hamiltonian that is a function of the real space angular variables θ and ϕ. We may think of observation at periodic cycle times $t = 4n\tau = nt_c$ as observation in the frame of $\hat{\rho}$.

7 THE DIPOLAR ECHO AND THE FIRST-ORDER QUADRUPOLAR ECHO

The above are the basic ideas behind the use of rf pulses to produce echoes in solids. With these ideas, it is possible to see how rf sequences may be tailored to average to zero a specific interaction, and leave other interactions for observation. Two other interactions that immediately come to mind are the homonuclear dipolar interaction and the first-order quadrupolar interaction. Both of these have interactions that are bilinear in spin operators (***Internal Spin Interactions and Rotations in Solids***). For example, the first-order quadrupolar interaction scales as

$$\hat{\mathcal{H}}_Q \propto \hat{I}^2 - 3\hat{I}_z^2 \tag{24}$$

and the two-body homonuclear dipolar interaction scales as

$$\hat{\mathcal{H}}_{DII} \propto \hat{\boldsymbol{I}}_1 \cdot \hat{\boldsymbol{I}}_2 - 3\hat{I}_{z1}\hat{I}_{z2} \tag{25}$$

A sequence that averages both of these interactions to zero at cycle time 3τ is $(\tau,\ 90^\circ_x, \tau, 90^\circ_y,\ \tau)$. The mechanics may be worked out by the reader, or one can refer to ***CRAMPS*** for an example of how this works. We must remind ourselves here that the condition for the production of an echo is that the initial signal be 'sharp' enough, and the reflecting wall 'hard' enough. This translates to the physical fact already alluded to that the magnitude of $\hat{\mathcal{H}}_{rf}$ must be larger than the magnitudes of the internal Hamiltonians being attacked by the rf. While this can be made generally true for dipolar interactions, it is not generally so for quadrupolar interactions, where in general the magnitude of $\hat{\mathcal{H}}_{rf}$ will be of the order of or smaller than $\hat{\mathcal{H}}_Q$. A case where the rf field is sufficiently larger than the quadrupolar interaction is that of aluminum metal, and Mehring has used this sequence to average the first-order quadrupolar interaction in this system to zero (see page 80 of Mehring[8]). These sequences are further discussed in ***CRAMPS***.

8 TRANSIENT NUTATIONS: A VARIANT

An interesting variant of an echo in a solid, meaning an internal Hamiltonian has been averaged to zero at the echo time, is that of the transient nutation[12] experiment, in which the spins of an ensemble of dipolar coupled spin-$\frac{1}{2}$ nuclei are 'nutated' (spun around) the x axis in the rotating frame by a strong rf field in the x phase. The field is turned off at intervals, and the magnetization along the y axis sampled, in a closely analogous way to a multiple pulse experiment, where the magnetization is sampled in the windows of the experiment where some internal Hamiltonian is averaged to zero. In this case, the dipolar Hamiltonian may be written as

$$\begin{aligned}\hat{\mathcal{H}}_D/\omega \equiv \hat{\mathcal{H}}_{zz} &= \hat{\boldsymbol{I}}_1 \cdot \hat{\boldsymbol{I}}_2 - 3\hat{I}_{z1}\hat{I}_{z2} \\ &\equiv -\tfrac{1}{2}(\hat{\boldsymbol{I}}_1 \cdot \hat{\boldsymbol{I}}_2 - 3\hat{I}_{x1}\hat{I}_{x2}) \\ &\quad +\tfrac{3}{2}(\hat{I}_{y1}\hat{I}_{y2} + 3\hat{I}_{z1}\hat{I}_{z2}) \\ &\equiv -\tfrac{1}{2}\hat{\mathcal{H}}_{xx} + \tfrac{3}{2}(\hat{I}_{y1}\hat{I}_{y2} + 3\hat{I}_{z1}\hat{I}_{z2}) \end{aligned} \tag{26}$$

The terms in $\hat{\mathcal{H}}_{xx}$, commuting with $\hat{I}_x$, the dominant interaction from the rf in the rotating frame, are secular. The other terms are nonsecular, do not commute with the major Hamiltonian, and therefore oscillate themselves out of sight. Under this sequence, therefore, the dipolar Hamiltonian is scaled by a factor of $\frac{1}{2}$, the chemical shift is averaged to zero, and for systems in which the shielding anisotropy is of order of magnitude of the dipolar interaction, e.g., $^{13}C-^{13}C$ pairs in which both shielding anisotropy and homonuclear dipolar coupling are about 3 kHz at fields of roughly 2.3 T, the dipolar coupling can be clearly dug out from under the combined dipolar shielding signal.

9 MULTIPLE QUANTUM COHERENCE

Further, with a bit of imagination, one can see that it might not be desirable to average a given interaction to zero, but to manipulate it in order to obtain information hitherto not available, e.g., counting of the number of spins in a small cluster. This subject is discussed in ***Multiple Quantum Coherence Imaging***, ***Multiple Quantum Coherence in Spin-1/2 Dipolar Coupled Solids*** and ***Multiple Quantum Coherences in Extended Dipolar Coupled Spin Networks***

10 RELATED ARTICLES

Average Hamiltonian Theory; CRAMPS; Dipolar Spectroscopy: Transient Nutations and Other Techniques; Echo-Planar Imaging; Internal Spin Interactions and Rotations in Solids; Line Narrowing Methods in Solids; Multiple Quantum Coherence Imaging; Multiple Quantum Coherence in Spin-1/2 Dipolar Coupled Solids; Multiple Quantum NMR in Solids; Rotating Solids; Quadrupolar Nuclei in Solids; Rotating Solids; Ultrasonic Irradiation and NMR.

11 REFERENCES

1. E. L. Hahn and D. E. Maxwell, *Phys. Rev.*, 1951, **82**, 748.
2. E. L. Hahn, *Phys. Rev.*, 1950, **80**, 580.
3. H. Y. Carr and E. M. Purcell, *Phys. Rev.*, 1954, **94**, 630.
4. T. C. Farrar and J. E. Harriman, *Density Matrix Formalism and its Applications in NMR Theory*, Farragut Press, Madison, WI, 1992.
5. R. D. Mattuck, *A Guide to Feynman Diagrams and the Many Body Problem*, 2nd edn., McGraw-Hill, New York, 1976, (reprinted by Dover, New York, 1992).
6. B. C. Gerstein and C. R. Dybowski, *Transient Techniques in NMR of Solids; An Introduction to the Theory and Practice*, Academic Press, Orlando, 1985.
7. M. Goldman, *Quantum Description of High-Resolution NMR in Liquids*, Oxford University Press, Oxford, 1988.
8. M. Mehring, *Principles of High Resolution NMR in Solids*, 2nd edn., Springer-Verlag, Berlin, 1983.
9. U. Haeberlen, *High Resolution NMR in Solids: Selective Averaging*, Academic Press, New York, 1976.
10. R. R. Ernst, G. Bodenhausen, and A. Wokaun, *Principles of Nuclear Magnetic Resonance in One and Two Dimensions*, Clarendon Press, Oxford, 1987.
11. A. Abragam, *Principles of Nuclear Magnetism*, Oxford University Press, Oxford, 1961.
12. C. S. Yannoni and R. D. Kendrick, *J. Chem. Phys.*, 1981, **74**, 747.

Biographical Sketch

Bernard C. Gerstein. *b* 1932. B.S. Purdue, 1953, Ph.D., 1960, Iowa State University, USA. Introduced to NMR by R. W. Vaughan. Faculty in Chemistry Iowa State University, 1962–present. Approximately 150 publications, with H. F. Franzen the text 'Rudimentary Thermodynamics', and with C. R. Dybowski, the book 'Transient Techniques in NMR of Solids; An Introduction to the Theory and Practice'. Research interests include the applications of solid state NMR to problems in the physics and chemistry of materials, fossil fuels, and heterogeneous catalysis.

Electron–Nuclear Hyperfine Interactions

Karl H. Hausser and Hermann Brunner
Max-Planck-Institut, Heidelberg, Germany

1	Introduction	1
2	Principle	1
3	^{1}H NMR	2
4	NMR with Other Nuclei	3
5	NMR of Radical Ions	4
6	Related Articles	5
7	References	5

1 INTRODUCTION

The literature on electron–nuclear hyperfine coupling as measured by NMR is so large that a comprehensive survey would by far exceed the scope of this article. Hence we concentrate on the principles which determine the applicability and the limitations of this method. The selection of the few examples given is necessarily subjective; for reasons discussed below, we have restricted ourselves to free radicals in solution.

The electron–nuclear hyperfine interaction between a nuclear spin and an unpaired electronic spin causes a splitting of the resonance absorption lines of electron paramagnetic resonance (EPR) which is termed 'hyperfine splitting' (HFS). The splitting is usually described in terms of a coupling constant a_i for the ith nucleus given either in tesla or in hertz; it was measured in the first 20 years of NMR by analyzing the splitting in the EPR spectrum. While the obtainable resolution of NMR depends mainly on the homogeneity of the external magnetic field $\boldsymbol{B}_0$, the resolution of EPR depends on the relaxation phenomena of the unpaired electrons which contribute to the transverse relaxation time T_2 of the electronic spin and hence to the linewidth. It would be outside the scope of this paper to discuss the various mechanisms which contribute to the linewidth—in particular the spin–orbit interaction can broaden the line in metal complexes beyond the resolvability of HFS. It turns out that free radicals in solution are the most suitable systems for studying hyperfine interactions.

The HFS can frequently not be resolved, even in solutions of free radicals consisting of first row elements in low viscosity liquids where the spin–orbit interaction and dipolar broadening are negligible. This is often due to the interaction of the unpaired spins of the electrons with the paramagnetic oxygen O_2 present in most solvents in contact with air. Therefore, the linewidth can be drastically decreased and the resolution correspondingly increased by carefully removing O_2 from the solvent.[1] This is illustrated by the example given in Figure 1, the EPR spectrum of 2,4,6-triphenylphenoxyl in benzene.[2]

However, even without oxygen the HFS in EPR spectra cannot be resolved in many cases. This is due to the large number of lines in an EPR spectrum because the total number of HFS components equals the product of the number of lines

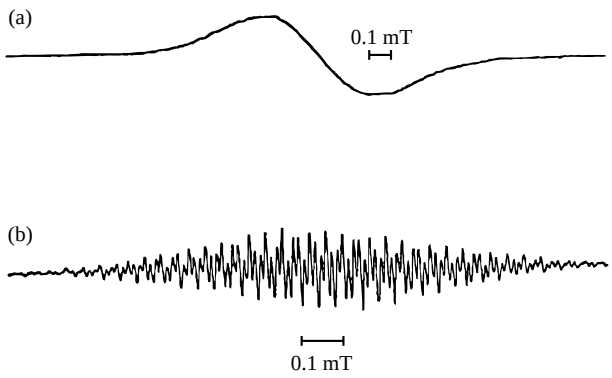

Figure 1 EPR spectra of 2,4,6-triphenylphenoxyl in benzene (concentration 5×10^{-4} mol l^{-1}): (a) saturated with air, (b) after the exclusion of oxygen

originating from nonequivalent nuclei (nuclei with identical HFS coupling constants are termed 'equivalent'). If a free radical contains three types of equivalent protons, namely l_i protons with coupling constant a_i, m_j with coupling constant a_j, and n_k with coupling constant a_k, the total number of HFS lines is $(l + 1)(m + 1)(n + 1)$, which easily leads to several hundreds and even thousands of HFS components. If this large number of HFS lines cannot be resolved, the coupling constants can be measured in many cases by means of electron–nuclear double resonance (ENDOR) or electron–nuclear triple resonance.[3–5] For the example given above, one expects six ENDOR absorption lines, two for each type of equivalent protons. One drawback of ENDOR is that the number of equivalent nuclei that cause an ENDOR transition can usually not be deduced from an ENDOR spectrum, since the intensity of the lines is not proportional to the number of equivalent nuclei, but depends in a complicated manner on the relaxation processes within the sample; we shall not discuss this further here since it is not the topic of this paper, but it is dealt with in another article in this Encyclopedia (see ***Electron–Nuclear Multiple Resonance Spectroscopy***).

Although ENDOR may help by very drastically reducing the number of absorption lines in cases where the coupling constants cannot be measured by high-resolution ESR because the number of HFS components is too high, both methods fail in the case of small coupling constants.

2 PRINCIPLE

The interaction of a nucleus with spin $I = \frac{1}{2}$ and a magnetogyric ratio γ_I and an unpaired electron with spin $S = \frac{1}{2}$ and a magnetogyric ratio γ_S in an external magnetic field $\boldsymbol{B}_0$ can be described by the Hamiltonian

$$\hat{\mathcal{H}} = \gamma_S \hbar(\hat{\boldsymbol{S}} \cdot \boldsymbol{B}_0) + \gamma_I \hbar(\hat{\boldsymbol{I}} \cdot \boldsymbol{B}_0) + \gamma_S \gamma_I \hbar^2 \times \left[\tfrac{8}{3}\pi |\Psi_{(0)}|^2 (\hat{\boldsymbol{I}} \cdot \hat{\boldsymbol{S}}) + \frac{3(\hat{\boldsymbol{I}} \cdot \boldsymbol{r})(\hat{\boldsymbol{S}} \cdot \boldsymbol{r})}{\boldsymbol{r}^5} - \frac{(\hat{\boldsymbol{I}} \cdot \hat{\boldsymbol{S}})}{\boldsymbol{r}^3} \right] \quad (1)$$

The first two terms are the electronic and nuclear Zeeman term; the third term is the scalar Fermi contact term which causes the hyperfine splitting.

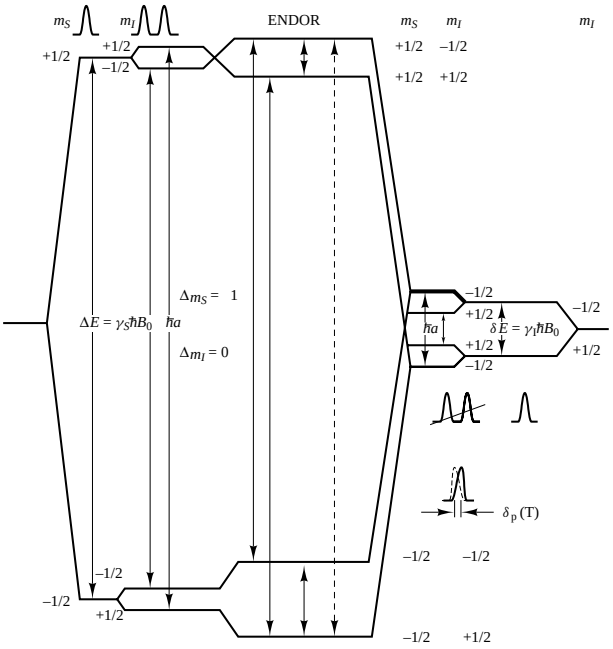

Figure 2 Energy levels and transitions in a coupled two-spin system of one electronic spin $S = \frac{1}{2}$ and one nuclear spin $I = \frac{1}{2}$

The fourth term, (the dipolar term) depends explicitly on the angle Θ between the vector $\boldsymbol{r}$ connecting $\boldsymbol{S}$ and $\boldsymbol{I}$ and the magnetic field $\boldsymbol{B}_0$. The term is averaged out to zero by the molecular motion in low viscosity liquids and hence does not contribute to the time-independent interaction, i.e. the energy levels, but it must be taken into account for the time-dependent interactions, such as relaxation and dynamic nuclear polarization (DNP).

It is instructive to consider the energy levels and possible transitions given by the first three time-independent terms of this two-spin system (Figure 2) the method is easily extended to more nuclei as are present in most practical cases, but the simple example shown in Figure 2 is suitable for understanding the principle. On the left, we recognize the four energy levels originating from the secular parts (the z components) of the first and third terms in the Hamiltonian [equation (1)] and the corresponding EPR transitions. When considering ENDOR, the second term in equation (1), the nuclear Zeeman term, must be taken into account. This leads to the energy levels and the corresponding ENDOR transitions shown in the center of Figure 2.

In principle, the energy levels of the NMR shown on the right in Figure 2 should also be split into two lines with the same splitting constant a. However, this splitting cannot be observed because the NMR lines are broadened by at least two types of time-dependent phenomena associated with the unpaired electrons; first, electronic spin–lattice relaxation with the time constant $T_{1,S}$ and second, electronic exchange with the time constant τ_{ex}. In general, these time constants are sufficiently short to satisfy the following condition

$$T_{1,S} \ll \frac{1}{2\pi a} \quad \text{and/or} \quad \tau_{ex} \ll \frac{1}{2\pi a} \tag{2}$$

Hence one obtains in this case, instead of a splitting, a paramagnetic shift $\Delta B = B_d - B_p$ or $\Delta\nu = \nu_p - \nu_d$.[6,7] In this paper we use frequency units rather than magnetic field units since they give a direct measure of the energy differences and since the coupling constant a is identical whether it is measured by EPR or by NMR, while in magnetic field units the ratio of the magnetogyric ratios of the electron and the nucleus must be taken into account.

A paramagnetic shift δ_p termed the isotropic hyperfine contact interaction shift was defined[6] in analogy to the diamagnetic chemical shift but with the opposite sign, i.e. with a positive sign for a downfield shift and a negative sign for an upfield shift. Since the magnitude of δ_p depends on the Boltzmann factor of the electronic Zeeman energy levels, it is temperature dependent. Its magnitude measured in ppm is given by

$$\delta_p(T) = \frac{B_d - B_p}{B_d} = \frac{a'\hbar\gamma_S^2}{4kT\gamma_I} \tag{3a}$$

$$\delta_p(T) = \frac{\nu_p - \nu_d}{\nu_d} = \frac{ah\gamma_S}{4kT\gamma_I} \tag{3b}$$

where the coupling constant a' is measured in tesla and a is in hertz. For protons at room temperature the result is

$$\delta_p(295\,\text{K}) = a \cdot 26.8\,\text{ppm MHz}^{-1} \tag{3c}$$

Note that with this definition the paramagnetic shift is not measured with respect to any standard, but is measured with respect to the same nucleus in a diamagnetic molecule as similar as possible to the radical.

As $\delta_p(T)$ is proportional to the coupling constant a, the latter can be determined by measuring $\delta_p(T)$ using NMR as well as from the HFS of EPR. At room temperature the coupling constant a_i of the ith nucleus is given by

$$a_i = \frac{4kT\gamma_I}{h\gamma_S}\delta_p(295\,\text{K})\,\text{MHz} \tag{4a}$$

Inserting the constants, one obtains for protons

$$a_i = 3.73 \times 10^{-2}\delta_p(295\,\text{K})\,\text{MHz} \tag{4b}$$

Measuring the coupling constant a by NMR has one additional advantage: while EPR renders only the absolute value of a, $\delta_p(T)$ gives the sign as well. This is particularly valuable for small coupling constants. While in the case of medium or large coupling constants the sign can usually be calculated theoretically with high certainty, this is not so for small coupling constants, the measurement of which is the main domain of NMR.

3 ^{1}H NMR

The first NMR spectrum of a free radical, namely di-*t*-butyl nitroxide (DBNO), which is a liquid at room temperature, is shown (with TMS as an internal standard) in Figure 3.[6] The linewidth is found to be $\Delta\nu = 230$ Hz and the shift δ_p (295 K) $= -8.0$ ppm which, following equation (4), give a coupling constant $a_i = -0.298$ MHz. Note that in this case $\delta_p(T)$ was

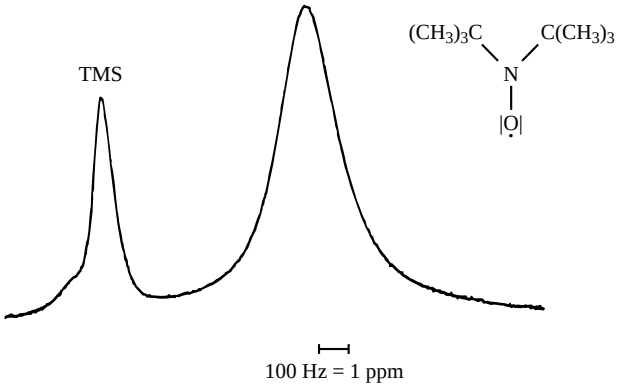

Figure 3 ^{1}H NMR spectrum of the liquid free radical di-*t*-butyl nitroxide with TMS as internal standard

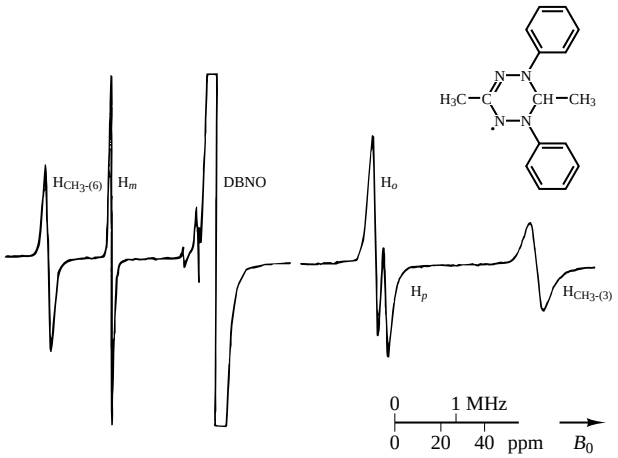

Figure 4 ^{1}H NMR spectrum of 3,6-dimethyl-1,5-diphenylverdazyl in DBNO

measured with respect to the internal standard TMS because no diamagnetic molecule of similar structure was available; since the ^{1}H nuclei in TMS are also in methyl groups, the deviation can be assumed to be rather small. It has been pointed out[8] that to obtain the correct paramagnetic shift $\delta_p(T)$ for neutral radicals its dependence on the concentration of the paramagnetic species must be measured and extrapolated to zero, because otherwise the varying magnetic susceptibility falsifies the result. This is certainly true when using an external standard. However, when using an internal standard, either a general standard like TMS for ^{1}H nuclei or an atom in a molecule that is as similar as possible, this effect is compensated for by the fact that the standard is in a medium with the same bulk susceptibility as the radical. In this case, the error when measuring the different concentrations up to a neat liquid radical stays usually below 10%, i.e. it does not exceed the typical solvent effect.

It is obvious that the critical quantity in NMR measurements of paramagnetic species is the linewidth, since this determines both the possible resolution and the sensitivity. For nuclei with spin $I = \frac{1}{2}$ in paramagnetic compounds the linewidth $\Delta\nu$ is proportional to the square of the interaction between the nucleus and the unpaired electron. The two main types of interaction are the scalar contact interaction discussed above and the dipolar interaction. For larger coupling constants a_i, the scalar interaction dominates, but for small a_i values the two can become comparable.

Since the linewidth $\Delta\nu \propto a_i^2$, medium and large values of a_i lead in general to very broad, unobservable NMR absorption lines. However, this broadening effect can be averaged out by sufficiently short time constants. The condition for obtaining narrow lines is much more limiting than equation (2), namely

$$T_{1,S} \ll \frac{1}{2\pi\nu_S} \tag{5}$$

$$\tau_{ex} \ll \frac{1}{2\pi\nu_S} \tag{6}$$

where ν_S is the Larmor frequency of the electron. Equation (5) and/or equation (6) may be satisfied in favorable cases of certain metal chelate compounds for which very narrow lines have been obtained.

Several attempts can be made to reduce the linewidth to come closer to the condition given in equation (6). One possibility is to use the liquid free radical DBNO as solvent.[9] Figure 4 shows as an example the NMR spectrum of 3,6-dimethyl-1,5-diphenylverdazyl in DBNO at a resonance frequency of 90 MHz.[7] The linewidth varies from about 0.09 MHz to 0.3 MHz, and the different NMR absorption lines are well resolved. The paramagnetic shifts δ_p(295 K) with respect to the corresponding ^{1}H resonances of the diamagnetic leucoverdazyl vary between −148 and +63.5 ppm. As expected, the linewidth increases with the coupling constant, but even the absorption line of the ^{1}H atoms in the methyl group in the R^3 position in the central ring, with a linewidth of about 250 kHz, is easily seen although it has a coupling constant as large as $a_i = -5.52$ MHz. One problem with DBNO is that some absorption lines may be hidden below the broad absorption line of DBNO, in this example the line due to the H atom at the C atom in the central ring. In general, the gain in resolution when using DBNO as a solvent is one order of magnitude for larger coupling constants, but much lower for absorption lines of nuclei with small coupling constants.

4 NMR WITH OTHER NUCLEI

Another approach to increasing the resolution is to use ^{2}H NMR instead of ^{1}H NMR. The paramagnetic shift of the deuterons (in ppm) is, of course, identical to the shift of the protons. Because of the much smaller magnetogyric ratio of the deuterons one expects a reduction of the shift measured in hertz by a factor of γ_P/γ_D, but a reduction of the linewidth by the square of this quantity $(\gamma_P/\gamma_D)^2$. Hence the net increase in resolution when using deuterons instead of protons should be proportional to $\gamma_P/\gamma_D \approx 6.5$.

The ^{2}H NMR spectrum of 3-*t*-butyl-1,5-bis(pentadeuterophenyl)verdazyl in DBNO is reproduced as an example in Figure 5.[7] The gain in resolution when using ^{2}H NMR instead of ^{1}H NMR is found to be about a factor of 2 to 3, but not 6 as expected from theory, considering the Fermi contact interaction only. It follows that the best possible resolution can be obtained using ^{2}H NMR in DBNO; the maximum gain in resolution $\Delta\nu/\nu$ which is obtained in practice is a factor of about 20.

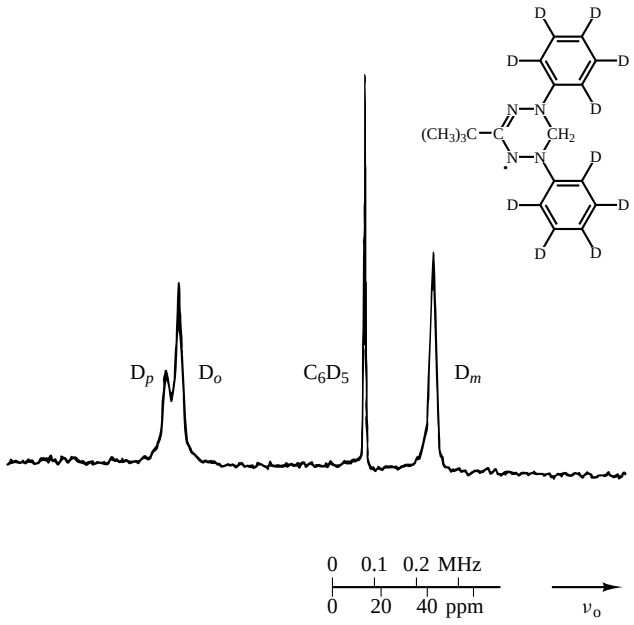

Figure 5 ^{2}H NMR spectrum of 3-*t*-butyl-1,5-bis(pentadeuterophenyl)verdazyl in DBNO

The measurement of the coupling constant a_i was extended to ^{13}C NMR.[10] In cases where a_i could be measured by ESR as well, good agreement was found in general. Differences are of the same order (about 10%) as found with ESR in different solvents; the concentration dependence mentioned above also plays a role, since the NMR is usually measured at high concentration (>2 M), while the concentration with the ESR measurements was mostly about 10^{-3}–10^{-4} M.[11] While the coupling constant a_i of the ^{1}H nucleus is generally mainly determined by the spin density at the atom to which the ^{1}H is bound (with some geometrical effects), ^{13}C NMR measurements of a series of nitroxide radicals showed that the coupling constants a_i depend in a more complex manner on the polarization of the electrons in the nitrogen–carbon bond and on the carbon–carbon bonds, as well as on geometrical effects.[11] The situation is even more complicated with aromatic fluoro compounds where the spin polarization between the 2p orbital of the fluorine and the spin in the 2p orbital of the adjacent carbon atom has to be considered. In favorable cases the sign and magnitude of the fluorine coupling could be obtained.[12]

5 NMR OF RADICAL IONS

A somewhat different situation is encountered when measuring the NMR of radical ions in solution. In general, in the solution both neutral molecules M and the corresponding negative radical ions M^- will be present. In this case there is an electron transfer reaction between these two species, which may be symbolized by[13]

$$M + M^- \rightleftharpoons M^- + M \tag{7}$$

Here the paramagnetic shift $\delta_p(T)$ of a nucleus in the molecule is not given directly by equation (3), but the fraction f_p of paramagnetic radicals in the solution must be taken into account; this is given by

$$f_p = M^-/(M + M^-) \tag{8}$$

Hence the paramagnetic shift $\delta'_p(T)$ becomes

$$\delta'_p(T) = f_p \delta_p(T) \tag{9}$$

Since the measured quantity in this case is $\delta'_p(T)$, in equation (4), $\delta_p(T)$ must be replaced by $\delta_p(T)/f_p$ in order to obtain the coupling constant a_i. The fraction f_p can be determined from the solvent shift due to the change in the susceptibility of the solution as a function of the reduction of the molecule M.[13]

It was stated above that measurement of the coupling constant a_i of a nucleus within a neutral free radical by NMR is usually restricted to small coupling constants. However, in the case of radical ions the chemical exchange with the time constant τ_{ex}^{ch} can be so fast that it approaches the much stricter conditions of equations (5) and (6); it was estimated to be of the order of $\tau_{ex}^{ch} \simeq 10^{-11}$.[14] This is illustrated by the example of biphenyl in diglyme.

Figure 6 shows the ^{1}H NMR spectrum of biphenyl in diglyme. The ^{1}H NMR line of the *meta* protons is much sharper and shifted downfield, as would be expected from the negative spin density at the *meta* carbon atom in biphenyl, as opposed to the much broader lines of the *ortho*- and *para*-^{1}H atoms. The paramagnetic shift $\delta_p(T)$ of the *ortho*- and *meta*-^{1}H atoms is plotted in Figure 7[14] as a function of the solvent shift $\delta_S(T)$ in diglyme when the biphenyl is gradually reduced with sodium.

Over the past 20 years the coupling constants between ^{1}H and ^{2}H nuclei and the unpaired electron spins have been measured in many such chemical exchange systems. In the case of ion radicals, even the coupling between the negative ion radicals and the alkali metal counterions (^{6}Li, ^{23}Na, ^{39}K, etc.) could be measured from the NMR of the alkali metals and the solvent, temperature and concentration dependence could be studied.[15] For more information on hyperfine interaction in NMR, the reader is referred to a series of review articles on the subject which cover the period from 1972 until 1990.[16]

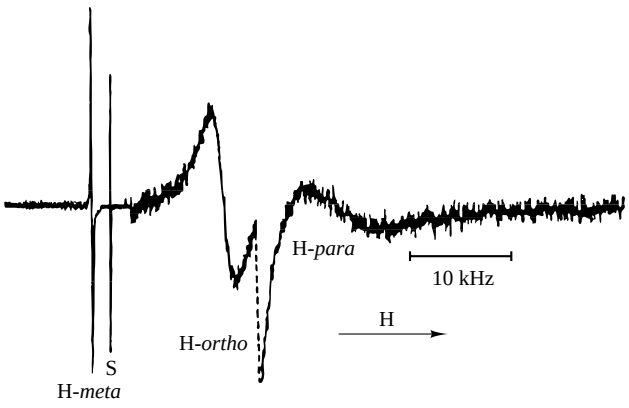

Figure 6 ^{1}H NMR spectrum at room temperature of a completely reduced 1 M solution of biphenyl in diglyme, with sodium as the reducing agent. S, solvent peak. All the peaks were measured with different rf power, gain, and modulation

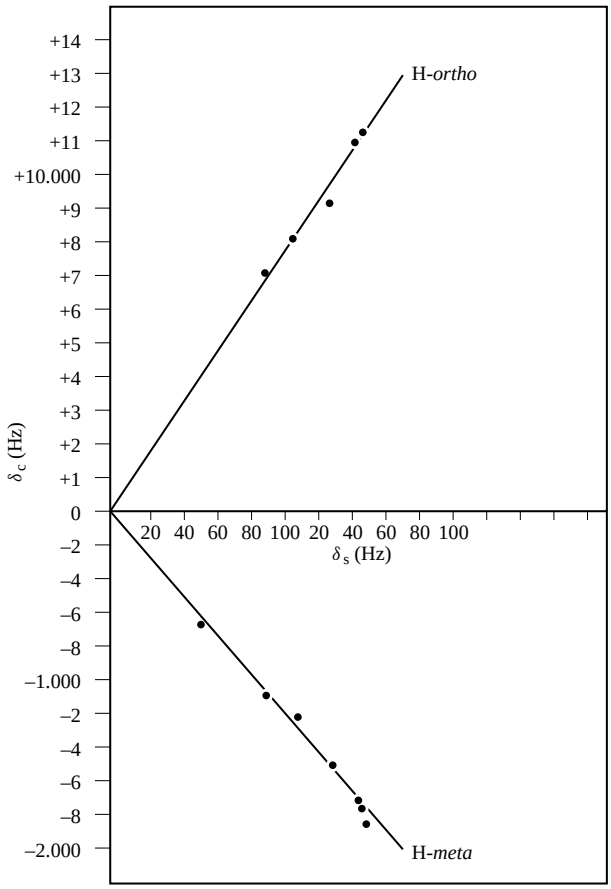

Figure 7 Contact shift δ_c at room temperature of *ortho*-^{1}H and *meta*-^{1}H of biphenyl as a function of the solvent shift δ_s for a solution of diglyme (concentration 1 M) gradually reduced with sodium

6 RELATED ARTICLES

Chemical Exchange Effects on Spectra; Electron–Nuclear Multiple Resonance Spectroscopy.

7 REFERENCES

1. K. H. Hausser, *Naturwissenschaften*, 1960, **47**, 251.
2. K. H. Hausser, C. R. 9^e Coll. Ampère, Pisa, 1960.
3. G. Feher, *Phys. Rev.*, 1956, **103**, 834.
4. J. S. Hyde and A. H. Maki, *J. Chem. Phys.*, 1964, **40**, 3117.
5. K. P. Dinse, R. Biehl, and K. Möbius, *J. Chem. Phys.*, 1974, **61**, 4335.
6. K. H. Hausser, H. Brunner, and J. C. Jochims, *Mol. Phys.*, 1966, **10**, 253.
7. H. Brunner, K. H. Hausser, and F. A. Neugebauer, *Tetrahedron*, 1971, **27**, 3611.
8. P. A. Petillo, J. De Felippis, and S. F. Nelsen, *J. Org. Chem.*, 1991, **56**, 6496.
9. R. W. Kreilick, *Mol. Phys.*, 1968, **14**, 495.
10. G. F. Hatch and R. Kreilick, *Chem. Phys. Lett.*, 1971, **10**, 490.
11. G. F. Hatch and R. W. Kreilick, *J. Chem. Phys.*, 1972, **57**, 3696.
12. W. G. Espersen and R. W. Kreilick, *Mol. Phys.*, 1969, **16**, 577.
13. E. de Boer and C. MacLean, *Mol. Phys.*, 1965, **9**, 191; *J. Chem. Phys.*, 1966, **44**, 1334.
14. G. W. Canters and E. de Boer, *Mol. Phys.*, 1967, **13**, 395.
15. G. N. La Mar, W. DeW. Horrocks, Jr, and R. H. Holm, *NMR of Paramagnetic Molecules. Principles and Applications*, Academic, New York, 1973.
16. G. A. Webb, *Nuclear Magnetic Resonance*, Royal Society of Chemistry, London, 1972–90, Vols 1–19.

Biographical Sketches

Karl H. Hausser. *b* 1919. Ph.D., Tübingen University, 1950. Visiting scientist, Physics Department, University of Chicago (Prof. Mulliken), 1956–57. Scientific member of the Max-Planck-Gesellschaft and Director of Department of Molecular Physics at Max-Planck-Institut für Medizinische Forschung, Heidelberg, 1966–87. Emeritus since 1987. More than one hundred publications. Research specialties: electron paramagnetic resonance, nuclear magnetic resonance and relaxation, dynamic nuclear polarization.

Hermann Brunner. *b* 1931. Diploma, 1959; Ph.D. 1964, Physics, Heidelberg University/Max-Planck-Institut für Medizinische Forschung, Heidelberg–present. Approx. 25 publications. Research fields: EPR in free radicals and organic conductors, optical nuclear polarization, and organic superconductors.

Electron–Nuclear Interactions

Timothy E. Machonkin and John L. Markley

Department of Biochemistry and National Magnetic Resonance Facility at Madison, University of Wisconsin, Madison, WI, USA

1 Introduction 1
2 Electron–Nuclear Interactions in Mononuclear Systems 1
3 Exchange Coupling and its Influence on Electron–Nuclear Interactions 5
4 Concluding Remarks 14
5 References 15

1 INTRODUCTION

NMR has proven to be of great utility in the study of paramagnetic proteins. Although the presence of the paramagnetic center creates inherent difficulties in obtaining structural information from nearby residues, numerous solution structures now exist for certain classes of paramagnetic proteins.[1–3] In addition, the interactions between the unpaired electron and surrounding nuclei create new effects that provide sensitive probes of the electronic and geometric structure of the paramagnetic center. Traditionally, it has been very difficult to obtain quantitative information from these electron–nuclear interactions, but with the advent of reliable, high-level computational techniques and the development of new NMR methodologies, this has begun to change. In coupled systems, a vector coupling model has been of great utility in providing a qualitative picture. In this review, we focus exclusively on FeS proteins, which have been extensively studied by NMR, and although they pose some of the greatest challenges, they have yielded some of the most satisfying agreement between theory and experiment.

2 ELECTRON–NUCLEAR INTERACTIONS IN MONONUCLEAR SYSTEMS

Paramagnetic proteins containing a single transition metal site represent the simplest case for the study of electron–nuclear interactions. Even in these systems, however, the analysis of the resulting effects can be quite complex.

2.1 Theory

We discuss here three types of electron–nuclear interactions: hyperfine shifts,[4,5] paramagnetic relaxation,[4–6] and residual dipolar couplings.[7,8] Electron–nuclear interactions provide an additional contribution to the chemical shift, called the hyperfine shift. This frequently results in peaks appearing far outside the region typical for diamagnetic shifts. Electron–nuclear interactions also give rise to additional NMR relaxation mechanisms that can broaden peaks and make them inaccessible to detection by traditional multidimensional NMR approaches. Residual dipolar couplings appear when a molecule becomes partially ordered with respect to the external magnetic field of the NMR experiment. A protein with an anisotropic magnetic susceptibility tensor will become ordered in a strong magnetic field; and this ordering will show up as changes in couplings between the nuclei of nearby magnetically active atoms. All three effects, hyperfine shifts, paramagnetic relaxation, and residual dipolar couplings, can be rich sources of information about protein structure and the properties of the metal site.

Hyperfine shifts arise from the sum of two distinct interactions: the Fermi contact shift, δ_{con}, and the electron–nuclear dipolar or pseudocontact shift, δ_{pc}. The observed chemical shift, δ_{tot}, is the sum of these two plus the diamagnetic chemical shift, δ_{dia}:

$$\delta_{\text{tot}} = \delta_{\text{con}} + \delta_{\text{pc}} + \delta_{\text{dia}} \tag{1}$$

The Fermi contact shift arises from delocalization of unpaired electron density onto ligand orbitals. Only unpaired spin density at the nucleus contributes to the Fermi contact coupling. The equation for the Fermi contact shift in ppm is:

$$\delta_{\text{con}} = 10^6 \left(\frac{\Delta\nu}{\nu_0}\right)^{\text{con}} = -10^6 \frac{A}{\hbar\gamma_N B_0}\langle S_z\rangle \tag{2}$$

where A is the isotropic hyperfine constant in Joules and $\langle S_z\rangle$ is the expectation value of S_z. (Note that hyperfine coupling is usually reported as $A/\hbar$, which has units of hertz.) In the absence of first-order orbital angular momentum or zero-field splitting (ZFS), this simplifies to:

$$\delta_{\text{con}} = 10^6 \left(\frac{\Delta\nu}{\nu_0}\right)^{\text{con}} = 10^6 \left(\frac{A}{\hbar}\right) \frac{g\mu_B S(S+1)}{3\gamma_N kT} \tag{3}$$

where g is the average molecular electron g-value (frequently assumed to be $\sim g_e$, the free electron g-value). This isotropic hyperfine coupling constant can in turn be related to the unpaired spin density at the nucleus:

$$A = \frac{\mu_0}{3S}\hbar\gamma_N g\mu_B \sum_i [|\psi_i^-(0)|^2 - |\psi_i^+(0)|^2] \tag{4}$$

where $|\psi_i^-(0)|^2$ and $|\psi_i^+(0)|^2$ are the negative and positive spin density at the nucleus of the ith molecular orbital.

The pseudocontact shift is the other contribution to the hyperfine shift. The electron magnetic moment is anisotropic as a result of coupling with the orbital angular momentum, and thus it does not average to zero with molecular tumbling. This yields an isotropic shift that is dependent upon the electron–nuclear distance. The 'point-dipole' approximation is usually invoked, in which all of the unpaired electron density is localized at the metal center. This yields:

$$\delta_{\text{pc}} = 10^6 \left(\frac{\Delta\nu}{\nu_0}\right)^{\text{pc}} = 10^6 \frac{1}{8\pi r^3} \Bigg[(3\cos^2\theta - 1) \times \left(\frac{2}{3}\chi_{zz} - \frac{1}{3}\chi_{xx} - \frac{1}{3}\chi_{yy}\right) + \sin^2\theta \cos 2\phi (\chi_{xx} - \chi_{yy}) \Bigg] \tag{5}$$

where r is the electron–nuclear distance, χ_{zz}, χ_{xx}, and χ_{yy} are the principle components of the magnetic susceptibility tensor, and θ and ϕ are the angles formed by r and the molecular z axis and the projection of r in the xy plane with the molecular x axis. Again, assuming no ZFS, this simplifies to:

$$\delta_{\text{pc}} = 10^6 \left(\frac{\Delta\nu}{\nu_0}\right)^{\text{pc}} = 10^6 \frac{\mu_0}{4\pi} \frac{\mu_B^2 S(S+1)}{18kTr^3} \times \{[2g_{zz}^2 - (g_{xx}^2 + g_{yy}^2)](3\cos^2\theta - 1) + 3(g_{xx}^2 - g_{yy}^2)\sin^2\theta\cos 2\phi\} \quad (6)$$

In analyzing hyperfine shifts, a first step is the separation of the Fermi contact and pseudocontact contributions. As seen in equation (5), the pseudocontact shift is related to the magnetic susceptibility anisotropy. In FeS systems at room temperature, this is small, and for nuclei that are only a few bonds away from the Fe, the Fermi contact term will overwhelmingly dominate. For nuclei close in space but many bonds away from the Fe, the pseudocontact shift will dominate, and can in principle provide useful distance information.

As in the case of hyperfine shifts, the paramagnetic contribution to the nuclear T_1 and T_2 relaxation rates arise from several different contributions: electron–nuclear dipolar, contact, and Curie spin. The equations for these are

$$T_{1_{\text{dip}}}^{-1} = \frac{2}{15}\left(\frac{\mu_0}{4\pi}\right)^2 \frac{\gamma_N^2 g^2 \mu_B^2 S(S+1)}{r^6} \times \left[\frac{\tau_c}{1+(\omega_I-\omega_S)^2\tau_c^2} + \frac{3\tau_c}{1+\omega_I^2\tau_c^2} + \frac{6\tau_c}{1+(\omega_I+\omega_S)^2\tau_c^2}\right] \quad (7)$$

$$T_{1_{\text{con}}}^{-1} = \frac{2}{3}\left(\frac{A}{\hbar}\right)^2 S(S+1)\frac{\tau_e}{1+(\omega_I-\omega_S)^2\tau_e^2} \quad (8)$$

$$T_{2_{\text{dip}}}^{-1} = \frac{1}{15}\left(\frac{\mu_0}{4\pi}\right)^2 \frac{\gamma_N^2 g^2 \mu_B^2 S(S+1)}{r^6} \times \left[4\tau_c + \frac{\tau_c}{1+(\omega_I-\omega_S)^2\tau_c^2} + \frac{3\tau_c}{1+\omega_I^2\tau_c^2} + \frac{6\tau_c}{1+(\omega_I+\omega_S)^2\tau_c^2} + \frac{6\tau_c}{1+\omega_S^2\tau_c^2}\right] \quad (9)$$

$$T_{2_{\text{con}}}^{-1} = \frac{1}{3}\left(\frac{A}{\hbar}\right)^2 S(S+1)\left[\tau_e + \frac{\tau_e}{1+(\omega_I-\omega_S)^2\tau_e^2}\right] \quad (10)$$

$$T_{2_{\text{Curie}}}^{-1} = \frac{1}{5}\left(\frac{\mu_0}{4\pi}\right)^2 \frac{\omega_I^2 g^4 \mu_B^4 S^2(S+1)^2}{(3kT)^2 r^6}\left[4\tau_r + \frac{3\tau_r}{1+\omega_I\tau_r^2}\right] \quad (11)$$

where ω_I and ω_S are the nuclear and electron Larmor precession frequencies, τ_r is the rotational correlation time, τ_e is the electronic relaxation rate, and τ_c is the total correlation time, given as:

$$\tau_c^{-1} = \tau_r^{-1} + \tau_e^{-1} \quad (12)$$

In these equations, several simplifying assumptions have again been made: the point-dipole approximation holds, g is isotropic, and ZFS is negligible. More complex equations have been derived that include g anisotropy and ZFS.[6] Of these simplifications, the point-dipole approximation generally is the one that fails in a quantitative analysis of relaxation rates. This is especially the case in Fe–S proteins, where the Fe is highly covalent and the electron density is delocalized significantly out onto the ligands. This is sometimes referred to as the 'ligand-centered' dipolar contribution to the relaxation rate, and attempts have been made to account for it.[9] In the high-temperature limit, the electronic transverse and longitudinal relaxation rates (T_{1e}, T_{2e}) are essentially equal, and this can be taken as the value of τ_e. The contributions to τ_e are numerous, and in general, prevent its independent determination. Nonetheless, τ_e is assumed to be $\sim 10^{-10}$–10^{-11} s for mononuclear high-spin (h.s.) Fe^{3+} and $\sim 10^{-11}$–10^{-12} s for mononuclear h.s. Fe^{2+}.[6] Curie spin relaxation, which arises from the interaction of the nuclear magnetic moment with the large static magnetic moment provided by the unpaired electrons of the metal center, can be by far the dominant contribution to T_2, especially at high fields, for proteins with a high-spin metal site (e.g., h.s. Fe^{3+}) and/or high molecular weight. The Curie spin contribution to T_1 is very small and can be ignored. Because of the strong dependence of the relaxation rate on the nuclear magnetogyric ratio, γ, hyperfine signals from nuclei with a low γ (e.g., ^{15}N and ^{2}H) are more readily observed than signals from nuclei with high γ (^{1}H). Thus, one strategy for the study of paramagnetic systems is to collect 1D ^{15}N and ^{2}H NMR data on isotopically labeled samples. Note that the chemical shifts of ^{1}H and ^{2}H are essentially equivalent.

The third type of electron–nuclear interaction is residual dipolar coupling. In solution-state NMR, rapid molecular tumbling normally averages out dipolar couplings. However, in a system with a sufficiently anisotropic magnetic susceptibility tensor, a high magnetic field can lead to partial ordering of the molecules. Because the effect is proportional to the square of the magnetic field, the dipolar couplings can be extracted from analysis of one-bond ^{1}H–X couplings at two different fields. The magnitude of $^{1}D_{\text{HX}}$ is related to the magnetic susceptibility anisotropy:

$${}^{1}D_{\text{HX}} = \frac{-\gamma_{\text{X}}\gamma_{\text{H}}B_o^2}{40kT\pi^2 r^3}\left[(3\cos^2\theta - 1)\left(\chi_{zz} - \frac{1}{2}\chi_{xx} - \frac{1}{2}\chi_{yy}\right) + \frac{3}{2}\sin^2\theta\cos 2\phi(\chi_{xx} - \chi_{yy})\right] \quad (13)$$

Note that the form of this equation is very similar to that for the pseudocontact shift (equation 5); however, residual dipolar couplings can be measured directly, whereas pseudocontact shifts must be deconvoluted from the Fermi contact and diamagnetic components of the observed chemical shift.

2.2 Applications to Fe(Cys)$_4$ Proteins

The most extensive study of hyperfine shifts in Fe(Cys)$_4$ proteins is for *Clostridium pasteruianum* rubredoxin (CpRd). Extensive and definitive assignments were obtained for the H and N atoms of the ligating Cys residues and eight nearby amide N atoms in both oxidation states through the use of selective ^{2}H and ^{15}N labeling, including chirally deuterated Cys and single-site labeling (Figure 1(a)–(f), Table 1).[10–13] Also, the Cys C^{β} resonances from reduced CpRd were identified by selective labeling (Figure 1(g), Table 1).[12]

For CpRd, Fermi contact shifts were calculated with hybrid density functional theory (HDFT) using 104-atom models[14] derived from three published crystal structures of oxidized CpRd at 1.1–1.2 Å resolution.[15–17] Extremely good agreement was obtained between the calculated Fermi contact shifts and all of the observed ^{2}H and ^{15}N hyperfine shifts for all three models (in one model, a correction to the placement of the amide H atoms was required). The pseudocontact shift was small enough that it could safely be ignored. The agreement between calculated and experimental hyperfine shifts was excellent. All assignments achieved by selective labeling were confirmed in the calculations, and the calculations allowed definitive sequence-specific assignments for nearly all the remaining hyperfine-shifted ^{2}H and ^{15}N signals. These results validate the approach and indicate that HDFT calculations are a powerful tool for obtaining a quantitative understanding of hyperfine shifts and electronic structure of metalloproteins.

In the case of CpRd, this approach demonstrated the importance of hydrogen bonding to the ligating Cys S^{γ} atoms. In CpRd, six backbone amides donate H-bonds to the Cys S^{γ} atoms: residues Val8, Cys9, Tyr11, Leu41, Cys42, and Val44. In particular, the N atoms of Tyr11 and Val44 exhibit large hyperfine shifts but are eight covalent bonds from the Fe. The conclusion, corroborated by the HDFT calculations, is that H-bonds are capable of delocalizing spin density, a feature that may be important in the electron transfer function of these systems. The calculations further showed an inverse correlation between the magnitude of the hyperfine shift and $H\cdots S^{\gamma}$ distance. (Signals from the ^{15}N atoms of the ligating Cys residues have a separate intercept because they also derive appreciable unpaired spin density through covalent bonds.) Another effect of spin delocalization through H-bonds is the large ($\geq$8 ppm) negative one-bond $^{1}H/^{2}H$ isotope effects on the chemical shifts of the Val8, Tyr11, Leu41, and Val44 N atoms (Table 1).[13] Again, HDFT calculations were able to quantitatively account for this isotope effect.[13] Recent ^{15}N NMR data[18] on a mutant of CpRd with a very different N–S^{γ} length for one of the H-bonds as determined by X-ray crystallography[19] are consistent with the correlation between H-bond length, spin density, and in turn, hyperfine shift. The calculations also helped interpret the ^{2}H, ^{15}N, and ^{13}C chemical shifts for reduced CpRb.[14] Since only coordinates for oxidized CpRd were available, the correlation between the experimental and calculated chemical shifts were not as good, and therefore the residue-specific assignments are only preliminary. Subsequent calculations based on the recently

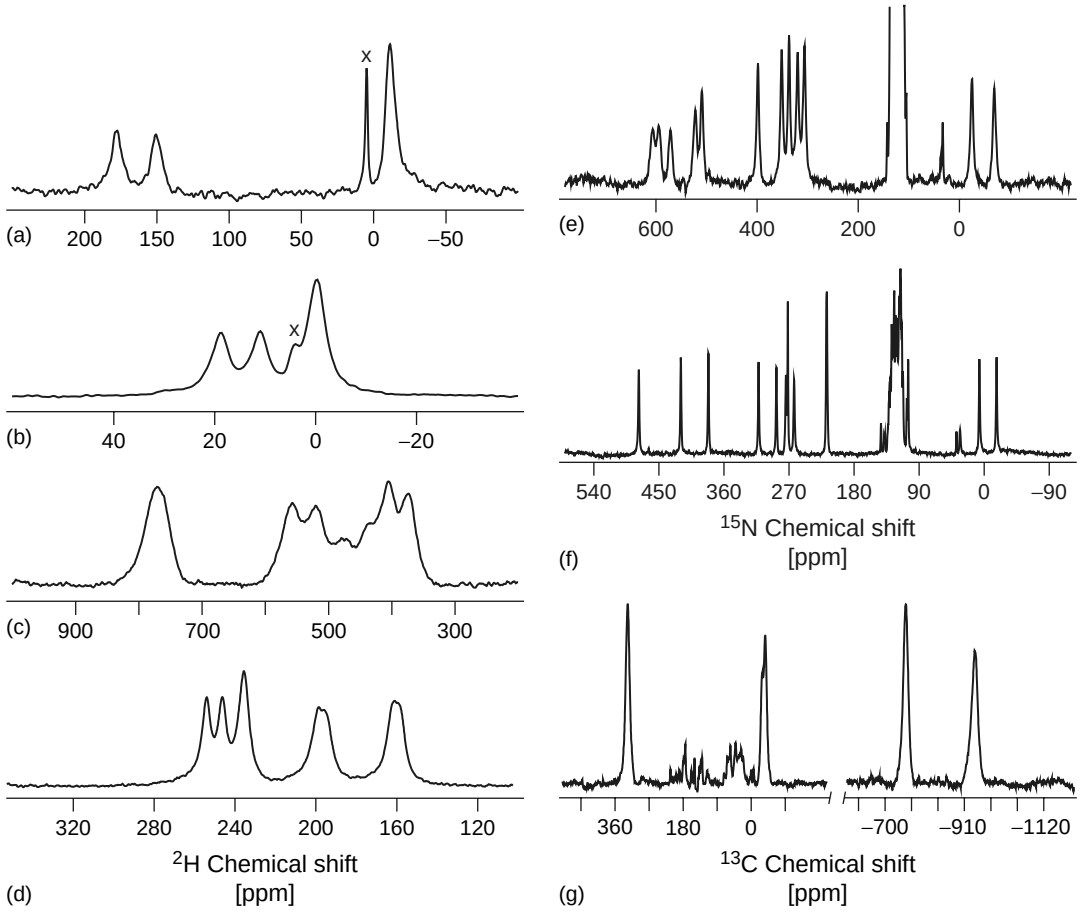

Figure 1 NMR spectra of ^{2}H-, ^{15}N-, and ^{13}C-labeled CpRd at 35 °C. (a) ^{2}H NMR spectrum of oxidized [$^{2}H^{\alpha}$]Cys-labeled CpRd. The peak labeled 'x' arises from $^{1}H^{2}HO$. (b) ^{2}H NMR spectrum of reduced [$^{2}H^{\alpha}$]Cys-labeled CpRd. The peak labeled 'x' arises from $^{1}H^{2}HO$. (c) ^{2}H NMR spectrum of oxidized [$^{2}H^{\beta}$]Cys-labeled CpRd. (d) ^{2}H NMR spectrum of reduced [$^{2}H^{\beta}$]Cys-labeled CpRd. (e) ^{15}N NMR spectrum of oxidized [U–^{15}N]-labeled CpRd. (f) ^{15}N NMR spectrum of reduced [U–^{15}N]-labeled CpRd. (g) ^{13}C NMR spectrum of reduced [$^{13}C^{\beta}$]Cys-labeled CpRd. Parts (a–d) reproduced with permission from Ref.[10] Copyright 1995 American Chemical Society. Parts (e) and (f) adapted from Ref.[13]

Table 1 Experimental chemical shifts of hyperfine resonances in the rubredoxin from *Clostridium pasteruianum* (CpRd)

Assignment	Chemical shifts (ppm)	
	Oxidized	Reduced
Cys6 $H^{\beta 3}$	478.5	196.0
Cys6 $H^{\beta 2}$	406.7	157.0/158.6
Cys9 $H^{\beta 3}$	520.6	233.0
Cys9 $H^{\beta 2}$	771.7	243.7
Cys39 $H^{\beta 3}$	437.0	193.4
Cys39 $H^{\beta 2}$	376.9	158.6/157.0
Cys42 $H^{\beta 3}$	557.4	233.0
Cys42 $H^{\beta 2}$	771.7	251.3
Cys6 H^{α}	−11.5	10.9/18.6
Cys9 H^{α}	150.4/177.3	−0.4
Cys39 H^{α}	−11.5	18.6/10.9
Cys42 H^{α}	177.3/150.4	−0.4
Cys6 C^{β}	nd	327
Cys9 C^{β}	nd	−939
Cys39 C^{β}	nd	−36
Cys42 C^{β}	nd	−755
Cys6 N	571.1	287.4/311.9
Cys9 N	−25.1/−68.8	−17.3/6.5
Cys39 N	594.4	311.9/287.4
Cys42 N	−68.8/−25.1	6.5/−17.3
Thr7 N	351.0	274.1
Val8 N	508.9 (494.5)[a]	477.7 (465.2)
Gly10 N	319.5/305.9	217.5
Tyr11 N	606.0 (588.3)	381.6 (372.8)
Pro40 N	398.2	271.4
Leu41 N	521.3 (507.5)	419.6 (408.6)
Gly43 N	305.9/319.5	217.5
Val44 N	336.6 (328.4)	262.8 (256.4)

[a]Chemical shifts in parentheses are for CpRd in D_2O; four resonances shift to higher frequency owing to a one-bond $^1H/^2H$ isotope effect (see text for details).

published X-ray structure for reduced CpRd[20] are yielding improved agreement with experiment and hence more insight into the electronic structure.[21]

HDFT calculations were extended to a obtain a quantitative understanding of the ^{15}N T_1 relaxation rates in oxidized CpRd.[22] In this system, the contact contribution is small even for the most strongly hyperfine-shifted resonances and the T_1 rates are dominated by electron–nuclear dipolar relaxation. However, given that the unpaired spin density in this system is known to be highly delocalized, the point-dipole approximation is a poor model. This was accounted for by replacing the r^{-6} distance dependence in equation (7) with an effective reciprocal distance, r_{eff}^{-6}:

$$r_{\text{eff}}^{-6} = \frac{1}{4}\left[\frac{1}{3}(\langle q_{xx}\rangle_{\text{spin}} - \langle q_{yy}\rangle_{\text{spin}})^2 + \langle q_{xx}\rangle_{\text{spin}}^2 + \frac{4}{3}(\langle q_{xy}\rangle_{\text{spin}}^2 + \langle q_{xz}\rangle_{\text{spin}}^2 + \langle q_{yz}\rangle_{\text{spin}}^2)\right] \quad (14)$$

In equation (14), the $\langle q_{\alpha\beta}\rangle_{\text{spin}}$ terms are the matrix elements of the spin-differential field gradient tensor:

$$\langle q_{\alpha\beta}\rangle_{\text{spin}} = \sum_{st} D_{st}\langle s|\hat{q}|t\rangle \quad (15)$$

where D_{st} is the normalized, spin-only density matrix and $q_{\alpha\beta}$ is the electric field gradient operator:

$$\hat{q}_{\alpha\beta} = \frac{3r_\alpha r_\beta - \delta_{\alpha\beta}r^2}{r^5} \quad (16)$$

This approach provided excellent agreement between experimental and calculated ^{15}N T_1 rates, whereas the point-dipole model failed for nuclei closer than 7 Å. A comparison of r_{eff} with the crystallographic distance demonstrates this (Figure 2). These calculations yielded a τ_c of $\sim 4 \times 10^{-10}$ s. In this system, $\tau_c \approx \tau_e$, and this value for τ_e is typical for Fe^{3+}.

The magnetic field-dependence of one-bond ^1H–^{15}N and $^1H^{\alpha}$–$^{13}C^{\alpha}$ couplings were measured in order to determine the residual dipolar couplings in oxidized and reduced CpRd.[8] These, in combination with the crystallographic data, were used to obtain the magnitude and orientation of the magnetic susceptibility anisotropy, $\Delta\chi_{\text{ax}}$ and $\Delta\chi_{\text{rh}}$ (Figure 3). By subtracting the calculated diamagnetic contribution from the protein, $\Delta\chi_{\text{ax}}$ and $\Delta\chi_{\text{rh}}$ for the metal center can be determined: 7.93×10^{-28} and 3.24×10^{-28} cm^3 molecule^{-1} for oxidized and 22.3×10^{-28} and 10.5×10^{-28} cm^3 molecule^{-1} for reduced CpRd, respectively (Table 2).

These values, in turn, can be compared with ZFS parameters and g-values previously obtained by other methods for rubredoxins and $Fe(SR)_4$ model complexes. Since the magnetic susceptibility anisotropies were measured at 10 °C, the values are very sensitive to small differences in both the **D**-

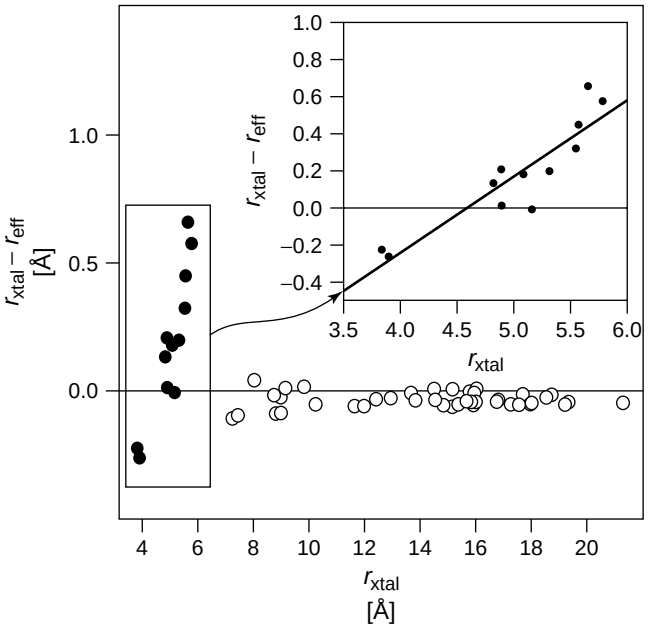

Figure 2 Plot of $r_{\text{xtal}} - r_{\text{eff}}$ versus r_{xtal}, where r_{xtal} is the measured distance between individual ^{15}N nuclei and the Fe atom in the 4RXN crystal structure and where r_{eff} is the effective distance calculated from the wave function using the spin-differential field gradient tensor method. Black circles represent ^{15}N nuclei that give rise to hyperfine-shifted resonances and open circles represent the 'diamagnetic' ^{15}N nuclei. The horizontal line is drawn at the zero of the abscissa. The inset plot shows an expansion of the ordinate for nuclei that are close to the metal center. Reproduced with permission from Ref.[22] Copyright 1998 American Chemical Society

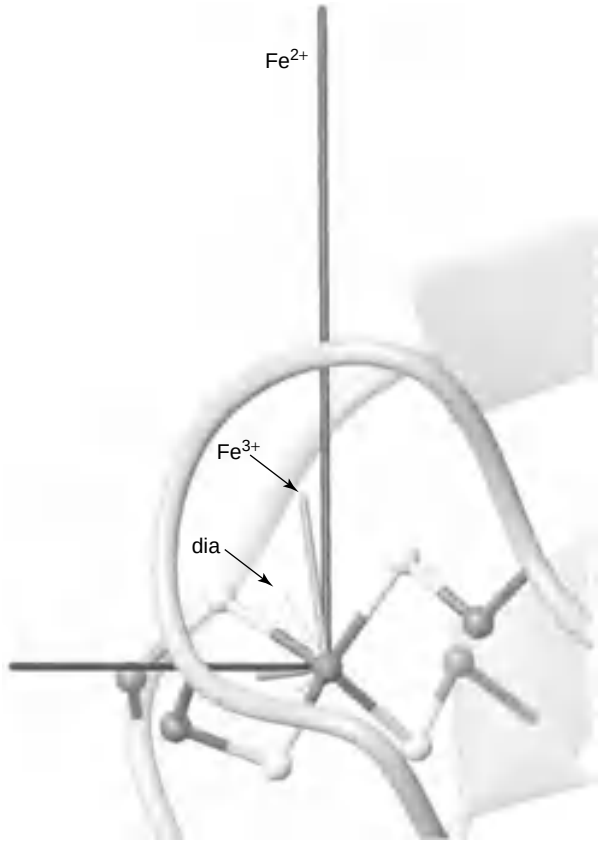

Figure 3 Structural representation of magnetic susceptibility anisotropies. A ribbon diagram of the structure of CpRd is shown, including the atoms of the $Fe(Cys)_4$ center. Vectors originating at the Fe indicate the magnitudes and show the orientations of the $\Delta\chi_{ax}$ and $\Delta\chi_{rh}$ terms obtained from fits to the 5RXN structure of dipolar splittings from oxidized and reduced CpRd. The diamagnetic $\Delta\chi_{ax}$ and $\Delta\chi_{rh}$ values calculated for 5RXN are also shown. Reproduced with permission from Ref.[8] Copyright 1998 American Chemical Society

and **g**-tensors and their relative orientation; thus, they can only be compared to the previous data in general terms.

ZFS parameters have been obtained for oxidized CpRd from Mössbauer spectroscopy[23,24] and for oxidized *Pseudomonas oleovorans* rubredoxin from variable-temperature X-band EPR spectroscopy[25] (Table 2). Both approaches yielded a D that is small and positive, consistent with an approximately D_{2d} geometry; in these calculations, g was assumed to be isotropic and ∼2.0. The values of D, E, and g obtained from EPR can be used to calculate $\Delta\chi_{ax}$ and $\Delta\chi_{rh}$, which yields the qualitatively consistent values of 7.27×10^{-28} and $4.15 \times 10^{-28}\,cm^3\,molecule^{-1}$, respectively. Agreement with the NMR-derived values can be improved substantially by assuming a g-anisotropy of 0.004; this small value is reasonable on the basis of data for a $Fe^{3+}(SR)_4$ model complex.[26]

ZFS parameters have been obtained for reduced CpRd from Mössbauer spectroscopy (Table 2)[23] and for a model complex, $[Fe(SPh)_4]^{2-}$, from Mössbauer,[27] high-frequency EPR (HFEPR),[28] and far-infrared (FIR) absorption spectroscopies.[29] In the latter system, the ZFS parameters obtained from HFEPR and FIR were in agreement and significantly smaller than from those obtained from Mössbauer. Results from the model system were used to derive ZFS parameters for CpRd (Table 2).[28] In all cases, g-values were inferred from expressions derived from second-order perturbation theory (Table 2).[30] $\Delta\chi_{ax}$ and $\Delta\chi_{rh}$ values calculated from Mössbauer-derived values of D, E, and g are approximately twice the experimental values determined by NMR, whereas those derived from HFEPR (22.5×10^{-28} and $13.4 \times 10^{-28}\,cm^3\,molecule^{-1}$, respectively) are in good agreement. Again, small changes in the g-anisotropy would account for the remaining difference.

Once the magnitude and orientation of the magnetic susceptibility anisotropy were determined for oxidized and reduced CpRd, these data could be used to estimate the pseudocontact shifts for nuclei >11 Å from the Fe center. From this it was found that pseudocontact shifts entirely accounted for the observed chemical shift differences between the oxidized and reduced states for the diamagnetic resonances. This, in turn, indicated that the structure of the protein 7 Å or more from the Fe remains the same in the two redox states.

3 EXCHANGE COUPLING AND ITS INFLUENCE ON ELECTRON–NUCLEAR INTERACTIONS

Electron–nuclear interactions in exchange coupled multinuclear systems are considerably more complicated than those in simple single-metal site systems. As with simpler systems, NMR data can be used to evaluate theoretical models describing the paramagnetic center. In particular, the nature of exchange coupling in the mixed-valence states of these clusters has been a topic of great interest. The types of exchange-coupled FeS clusters that have been studied by NMR spectroscopy and their different formal redox states are listed in Table 3. An extensive list of NMR results on different FeS proteins is provided in Table 4.

In this section, we present the theory of how exchange coupling impacts hyperfine shifts and paramagnetic relaxation. We then show how the vector coupling model of hyperfine shifts has been applied to representative FeS clusters and the insight this has provided.

3.1 Theory

In a coupled system, the exchange coupling can be described by the phenomenological spin Hamiltonian:

$$\mathcal{H} = \sum_{i<j} -2J_{ij}\mathbf{S}_i \cdot \mathbf{S}_j \qquad (17)$$

where J is the isotropic or Heisenberg exchange coupling constant and $\mathbf{S}_i$ and $\mathbf{S}_j$ are the local spin operators for each metal site. For a system with two metal centers, such $[2Fe–2S]^{2+}$, this yields a set of levels or "spin ladder" for the total spin S, in which S ranges from $|S_1 + S_2|$ to $|S_1 - S_2|$, the relative energies of which are given by:

$$E(S) = -JS(S+1) \qquad (18)$$

J can be positive (ferromagnetic coupling) or negative (antiferromagnetic coupling). In FeS clusters J is always negative. In mixed-valence systems, such as $[2Fe–2S]^{+}$, the extra electron can be on either Fe; this doubles the number of total spin states. Consideration of this effect, called double

Table 2 Comparison of the magnetic susceptibility anisotropy of oxidized and reduced rubredoxin obtained from NMR with the ZFS parameters and g-values obtained from Mössbauer and EPR and the magnetic susceptibility anisotropy calculated from these

		Oxidized rubredoxin	Reduced rubredoxin
Magnetic susceptibility anisotropy from NMR:	$\Delta\chi_{ax}$ (10^{-28} cm^3 molecule^{-1})	7.93	22.3
	$\Delta\chi_{rh}$	3.24	10.5
ZFS parameters and g-values from Mössbauer:	D (cm^{-1})	1.74[a]	7.58[b]
	E	0.30	2.1
	g_z	2.0	2.00
	g_x	2.0	2.11
	g_y	2.0	2.19
ZFS parameters and g-values from EPR:	D (cm^{-1})	1.76[c]	5.3[d]
	E	0.495	1.5
	g_z	2.0	2.01
	g_x	2.0	2.06
	g_y	2.0	2.10
Calculated magnetic susceptibility anisotropy:	$\Delta\chi_{ax}$ (10^{-28} cm^3 molecule^{-1})	7.27[e]	22.5[e]
	$\Delta\chi_{rh}$	4.15	13.4

[a]Fit included a fourth-order fine structure term, which is not listed here and was not included in the calculation of the magnetic susceptibility anisotropy.[24]
[b]g-values were inferred based upon second-order perturbation theory expressions.
[c]*Pseudomonas oleovorans* rubredoxin.[25]
[d]ZFS parameters were estimated from HFEPR results for the model complex $[Fe(SPh)_4]^{2-}$; g-values were inferred from analysis based on second-order perturbation theory.[28]
[e]Calculated based upon the ZFS parameters and g-values obtained from EPR.

Table 3 Formal redox states in Fe–S clusters

Cluster and protein type	Oxidized state		Reduced state	
[2Fe-2S] clusters	$[2Fe\text{-}2S]^{2+}$	$2Fe^{3+}$	$[2Fe\text{-}2S]^{+}$	Fe^{3+}, Fe^{2+}
[3Fe-4S] clusters	$[3Fe\text{-}4S]^{+}$	$3Fe^{3+}$	$[3Fe\text{-}4S]^{0}$	2 Fe^{3+}, 1 Fe^{2+}
[4Fe-4S] HiPIPs	$[4Fe\text{-}4S]^{3+}$	$3Fe^{3+}$, 1 Fe^{2+}	$[4Fe\text{-}4S]^{2+}$	2 Fe^{3+}, 2 Fe^{2+}
[4Fe-4S] clusters in Fds and other systems	$[4Fe\text{-}4S]^{2+}$	2 Fe^{3+}, 2 Fe^{2+}	$[4Fe\text{-}4S]^{+}$	1 Fe^{3+}, 3 Fe^{2+}

exchange or spin-dependent delocalization, yields the following equation for the energies of the total spin states are now defined by:

$$E(S) = -JS(S+1) \pm B\left(S + \frac{1}{2}\right) \tag{19}$$

where B is the double exchange term. The interplay between J and B determines the ground state (g.s.) of the system. Two additional effects must be considered: static and dynamic asymmetry. Static asymmetry arises from differences in the coordination geometry, H-bonding, and protein electrostatics at the two Fe sites that cause the extra electron to be preferentially localized on one side. Dynamic asymmetry, or vibronic coupling, arises from the change in geometry upon transferring the extra electron from one side to the other. The magnitude of this nuclear distortion defines the height of the barrier to electron transfer between the two sides. Thus, in the limit of large B and small vibronic coupling, there is no barrier to intersite electron transfer and the system is said to be completely valence-delocalized. For example, a valence-delocalized $[2Fe–2S]^{+}$ cluster would be described as $2Fe^{2.5+}$. Together, static asymmetry and vibronic coupling counteract the effect of double exchange. In the limit where these effects are large relative to B, the system is valence-localized and can be described by equations (17) and (18), where J is replaced by a J_{eff}, which is the Heisenberg J plus a correction factor to account for B, static asymmetry, and vibronic coupling. For systems of higher nuclearity, the exchange coupling can be described by decomposing the system into subunits and first considering the coupling within the subunits, and then the coupling between the subunits. For a more detailed account of exchange coupling, see Ref.[31] and references therein.

In an exchange coupled system, the Fermi contact shift can still be described by equation (2), but now one must calculate the Fermi contact shift for each total spin state, each of which will have a different isotropic hyperfine coupling constant, A_i, and sum over the Boltzmann population of the total spin states. The difficulty lies in determining each A_i; however, this can be accomplished readily because the hyperfine coupling constant for each total spin state S, in turn, can be related to the intrinsic hyperfine coupling constant for each metal site, A_j. Thus, equation (2) may be rewritten as:[32]

$$\delta_{con} = 10^6\left(\frac{\Delta\nu}{\nu_0}\right)^{con} = -10^6\frac{1}{\hbar\gamma_N B_0}\sum_i\sum_j A_j C_{ji}\langle S_z\rangle_i \tag{20}$$

where C_{ji} are spin projection coefficients for each metal site j for each total spin state i. These are derived from the

Wigner–Eckart theorem and vector coupling.[33] For a binuclear system, C_1 is given by[31–34]

$$C_1 = \frac{S(S+1) + S_1(S_1+1) - S_2(S_2+1)}{2S(S+1)} \tag{21}$$

where S is the total spin and S_1 and S_2 are the spin states of each metal site. C_2 is given by simply reversing the indices in equation (21). This can be easily extended to systems of higher nuclearity by use of a chain rule.[34] Consider a tetranuclear system that can be divided into two subunits of spin S_p and S_q. From equation (21), spin projection coefficients C_1^p and C_2^p can be calculated by replacing S with S_p and C_p by replacing S_1 and S_2 with S_p and S_q. Coefficients projecting out the spin onto the total spin state are then:

$$C_1 = C_1^p C_p \tag{22}$$

Note also that the spin projection coefficients for each total spin state always sum to one. Considering an explicit expression for the spin expectation value in equation (20) yields:

$$\delta_{\text{con}} = 10^6 \left(\frac{\Delta\nu}{\nu_0}\right)^{\text{con}} = -10^6 \frac{g\beta}{\hbar\gamma_N 3kT} \times \sum_j \frac{A_j \sum_i C_{ji} S(S+1)(2S+1)\exp(-E_S/kT)}{\sum_i (2S+1)\exp(-E_S/kT)} \tag{23}$$

Application of equation (23) is still difficult, and as shown below, has only been attempted qualitatively.

Paramagnetic relaxation can be analyzed by a treatment similar to equations (20) and (23). For example, the point-dipole approximation of the electron–nuclear dipolar contribution to T_1 may be written as:[32]

$$T_{1j}^{-1} = \frac{2}{15}\left(\frac{\mu_0}{4\pi}\right)^2 \frac{\gamma_N^2 g^2 \beta^2}{r_j^2} \frac{\sum_i C_{ji}^2 S(S+1)(2S+1)\exp(-E_S/kT)}{\sum_i (2S+1)\exp(-E_S/kT)} \times \left[\frac{\tau_c}{1+(\omega_I-\omega_S)^2\tau_c^2} + \frac{3\tau_c}{1+\omega_I^2\tau_c^2} + \frac{6\tau_c}{1+(\omega_I+\omega_S)^2\tau_c^2}\right] \tag{24}$$

where T_{1j} is the dipolar relaxation from metal site j, r_j is the distance to that metal site, and τ_c is given as in equation (12). This is then summed over all metal sites. Similar equations may be derived for the other types of paramagnetic relaxation. The issue arises as to what value to use for the electronic relaxation rate. In the limit of strong exchange coupling, where the coupling frequency is large relative to the electronic relaxation rates for the uncoupled spins (τ_{ej}) but small relative to the electronic correlation time (τ_{vj}) the electronic relaxation rate is the same for all metal sites.[35]

$$\frac{|J|}{\hbar} \gg \tau_{ej}^{-1} \tag{25}$$

Table 4 NMR data available on different FeS proteins

Protein type	Oxidized	Reduced
2Fe ferredoxins		
Anabaena PCC7120 vegetative	**43, 44**	**43, 44, 51**
Spinach	**32**	**32**
Porphyra umbicalis,	**32, 52**	**32, 52**
Spirulina platensis	**52, 121**	**52, 121**
Azotobacter vinelandii	**122**	**122**
Phytolacca americana	**121**	**121**
Halobacterium halobium	**121**	**121**
Human	**42, 44**	**42, 44**
Pseudomonas putida	**123–127**	**123–126**
Rieske proteins		
Alkene monooxygenase of *Xanthobacter* strain Py2	**128**	**128**
bc_1 complex of *Paracoccus denitrificans*	**129**	**129**
Toluene-4 monooxygenase of *Pseudomonas mendocina*	**60**	**60**
3Fe ferredoxins		
Bacillus stearothermophilus	**121**	**121**
Bacillus thermoproteolyticus	**121**	**121**
Desulfovibrio gigas	**61, 67**	
Thermococcus litoralis	**66, 71**	
Pyrococcus furiosus	**66, 79**	
4Fe ferredoxins		
Bacillus polymyxa	**121, 130**	**121, 130**
Bacillus stearothermophilus	**121**	**121**
Bacillus thermoproteolyticus	**121**	**121**
Desulfovibrio gigas	**61, 121**	**61, 121**
Desulfovibrio africanus	**131, 132**	
Thermococcus litoralis	**71, 133**	**71**
Thermotoga maritima	**134**	
Pyrococcus furiosus	**115–117**	**115–117**
Desulfovibrio desulfuricans	**135**	

Table 4 (*continued*)

Protein type	Oxidized	Reduced
7Fe ferredoxins		
Thermus thermophilus	**74**	**74**
Mycobacterium smagmatis	**74**	**74**
Pseudomonas ovalis	**74**	**74**
Azotobacter vinelandii	**121**	**121**
Pseudomonas putida	**75, 76**	
Rhodopseudomonas palustris	**70, 77**	**70, 77**
Desulfurolobus ambivalens	**68**	**68**
Bacillus schlegleii	**69, 80**	**69, 80**
Pseudomonas nautica	**78**	
Sulfolobus sp. Strain 7	**72**	
Sulfolobus acidocaldarius	**73**	**73**
Desulfovibrio africanus	**73, 136**	**73**
8Fe ferredoxins		
Clostridium pasteurianum	**102, 107, 108, 137–142**	**102, 107, 108**
Clostridium acidi-urici	**102, 137**	**102**
Clostridium perfringens	**137**	
Peptococcus aerogenes	**137**	
Chromatium vinosum	**105, 143**	**105, 143**
High-potential iron proteins		
Chromatium vinosum	**96, 144–147**	**96, 144, 145, 147–149**
Rhodocyclus gelatinosus	**144, 150, 151**	**144, 150, 151**
Ectothiorhodospira halophila iso I	**38, 83–85**	**38, 85, 152**
Ectothiorhodospira halophila iso II	**85–87**	**85**
Ectothiorhodospira vacuolata iso I	**85, 153**	**85, 153**
Ectothiorhodospira vacuolata iso II	**85, 99**	**85**
Chromatium gracile	**154**	**154**
Rhodospirillum tenue	**155**	**155**
Rhodopseudomonas globiformis	**100**	**100**
Rhodoferax fermentans	**101**	**101**
Nitrogenase Fe protein		
Clostridium pasteurianum		**156**
Azotobacter vinelandii		**120**
PsaC subunit of photosystem I		
Synechococcus elongatus	**157**	**157**
Synechococcus PCC7002	**158**	**158**

$$\frac{|J|}{\hbar} \ll \tau_{vj}^{-1} \tag{26}$$

This case holds for FeS clusters. See[6] and[35] for more details. Although detailed analyses of nuclear and electronic relaxation in coupled systems are few, equation (24) has been of great utility in providing distance constraints for solution structure determination.[36–39]

3.2 Applications to Fe–S Cluster Proteins

3.2.1 [2Fe–2S] Clusters

[2Fe–2S] proteins can be divided into two classes: 2Fe ferredoxins (Fds), in which each Fe is ligated by two Cys residues, and Rieske proteins, in which one Fe is ligated by two Cys and the other by two His.[40,41] The 2Fe Fds can be subdivided further into several types, two of which have been studied by NMR: plant-type and hydroxylase-type. In the oxidized state of both types, the ^{1}H hyperfine-shifted resonances are extremely broad and unresolved. The Cys H^{β} and H^{α} protons have been assigned by selective labeling, as have the Cys C^{β} and N resonances (Table 5).[42–44] All the hyperfine resonances move to higher frequency with increasing temperature or exhibit little temperature-dependence.

The electronic structure of the reduced state is very highly conserved among plant-type 2Fe Fds, based upon EPR, Mössbauer, and other studies.[45–48] Similar studies on reduced hydroxylase-type 2Fe Fds indicate that they, too, have a very highly conserved spectral signature that differs considerably from that of plant-type Fds,[45–48] despite their very similar geometries in the oxidized state (cf., e.g.,[49] and[50]). In the plant-type Fds, the hyperfine resonances are far narrower in the reduced state than in the oxidized state, thus facilitating their assignment. In reduced *Anabaena* PCC7120 vegetative Fd, extensive assignments were obtained for the Cys H^{β}, H^{α}, C^{β}, and N resonances through selective labeling, 2D NOESY (tailored for fast-relaxing resonances), 2D ^{1}H{^{13}C} HSQC, and 1D heteronuclear decoupling experiments (Table 5).[43,44,51] The ^{1}H NMR spectrum is shown in Figure 4(a).

One very important conclusion from these studies is that the $[2Fe–2S]^+$ cluster is valence trapped even at room temperature on the NMR timescale and that the electron resides entirely on the Fe ligated to Cys 41 and 46.[52] This is consistent with, although not necessarily predicted by, the large negative

value of J_{eff} that has been measured by magnetic susceptibility and temperature-dependent EPR. Less work has been done on reduced hydroxylase-type Fds. Partial assignments derived from selective ^{2}H labeling are available for human Fd: H^{β} resonances occur at 103, 80, −10, and −15 ppm, and H^{α} resonances at 37 and 13 ppm.[44] As in the case of plant-type Fds, these data indicate valence-trapping.

A theoretical model was developed by Dunham[53] and later extended by Banci and Bertini[32,54] by use of equation (23) to explain the sign, magnitude, and temperature dependence of the chemical shifts of the ^{1}H hyperfine resonances in reduced Fds. In this model, the intrinsic hyperfine coupling constants for Cys H^{β} and H^{α} protons were assumed to be 1.0 and 0.1 MHz, respectively, and to be only coupled to the closer of the two Fe sites; thus, J_{eff} becomes the only scalable parameter. From magnetic susceptibility and temperature-dependent EPR, J_{eff} is approximately $-100\,\text{cm}^{-1}$ in plant-type Fds[46,55–59] and $-250\,\text{cm}^{-1}$ in hydroxylase Fds.[45,46,59] Remarkably good agreement with this model is obtained for the ^{1}H hyperfine data on plant-type Fds, but only if J_{eff} is assumed to be half the experimental value (Figure 5(b)).

In this case, at room temperature, the H^{β} and H^{α} protons on the Fe^{3+} side are predicted to be at 123 and 17 ppm, respectively, and to shift to lower frequency with increasing

Table 5 Chemical shifts and temperature dependencies of the hyperfine resonances in representative oxidized and reduced [2Fe-2S] and [3Fe-4S] clusters

Oxidized				Reduced			
Peak label	Assignment	Chemical shift (ppm)	Temperature increases, peak moves…	Peak label	Assignment	Chemical shift (ppm)	Temperature increases, peak moves…
			Anabaena PCC7120 2Fe Ferredoxin (at 298 K)				
	Cys H^{β}	25–50	←	A	Cys49/79 $H^{\beta 2}$	134.6	→
			←	B	Cys49/79 $H^{\beta 3}$	125	→
			←	C	Cys79/49 $H^{\beta 2}$	104.2	→
				D	Cys79/49 $H^{\beta 3}$	98	→
				F	Cys41 $H^{\beta 2}$	24.4	←
				G	Cys41 $H^{\beta 3}$	24.4	←
				H	Cys46 $H^{\beta 2}$	19.7	←
				I	Cys46 $H^{\beta 3}$	16.7	←
	Cys H^{α}	15	←	E	Cys49 H^{α}	43.5	→
	Cys H^{α}	9	←	J	Cys79 H^{α}	16.7	→
					Cys46 H^{α}	5.05	nd
					Cys41 H^{α}	3.2	nd
	Cys C^{β}	89.3	←		Cys79 C^{β}	150.2	→
	Cys C^{β}	89.3	←		Cys49 C^{β}	123.4	←
	Cys C^{β}	62.7	←		Cys46 C^{β}	63.1	→
	Cys C^{β}	56.9	←		Cys41 C^{β}	−32.7	→
	Cys49/79 N	155.0	←		Cys49/79 N	362.1	→
	Cys79/49 N	152.9	←		Cys79/49 N	324.5	→
	Cys46 N	131.3	∼0		Cys46 N	155.6	→
	Cys41 N	113.7	∼0		Cys41 N	61.9	→
			Toluene 4-monooxygenase Rieske protein from *P. mendocina* (at 293 K)				
	Cys H^{β}	20–30	←	A	Cys H^{β}	82.7	→
				B	Cys H^{β}	76.7	→
				C	Cys H^{β}	61.1	→
				D	Cys H^{β}	52.6	→
				E	His $H^{\varepsilon 1}$	25.2	→
	Cys45/64 N	143.5	←		Cys45/64 N	201.8	→
	Cys64/45 N	142.1	←		Cys64/45 N	200.6	→
	His47/67 $N^{\varepsilon 2}$	233.8	←		His47/67 $N^{\varepsilon 2}$	119.7	nd
	His67/47 $N^{\varepsilon 2}$	231.5	←		His67/47 $N^{\varepsilon 2}$	116.3	nd
	His47/67 N	158.7	←		His47/67 N	304.2	→
	His67/47 N	122.6	←		His67/47 N	270.3	→
		D. gigas 3 Fe Fd (303 K)				*P. Schlegii* 7 Fe Fd (297 K)	
A	Cys50 H^{β}	29.1	→		Cys H^{β}	190	→
B	Cys50 H^{β}	24.4	→		Cys H^{β}	190	→
C	Cys8 H^{β}	18.1	←		Cys H^{β}	−192	←
D	Cys14 H^{β}	15.3	←		Cys H^{β}	−290	←
Y	Cys14 H^{β}	8.5	nd				
	Cys8 H^{β}	3.5	nd				
E	Cys14 H^{α}	9.9	←				
	Cys8 H^{α}	1.5	nd				

temperature, and the H^{β} and H^{α} protons on the Fe^{2+} side are predicted to be at 26 and 7 ppm, respectively, and to shift to higher frequency with increasing temperature. Qualitative agreement is found for the hydroxylase-type Fds using the experimental value for J_{eff}: the H^{β} and H^{α} protons on the Fe^{3+} side are predicted to be at 67 and 11 ppm, respectively, and to shift to lower frequency with increasing temperature, and the H^{β} and H^{α} protons on the Fe^{2+} side are predicted to be at -29 and 1.5 ppm, respectively, and to shift to higher frequency with increasing temperature (Figure 5(b)). The model breaks down when comparing temperature dependence of the ^{15}N and ^{13}C hyperfine shifts, where there is not a clear pattern of two resonances shifting to higher frequency and two to lower frequency. A similar approach can be used for understanding the hyperfine shifts in $[2Fe–2S]^{2+}$ clusters. Since in this case the g.s. is $S = 0$, only thermal population of paramagnetic excited states yields hyperfine shifts. Here J is large ($-175\,cm^{-1}$),[46] so all of the resonances shift to higher frequency with increasing temperature as the population of paramagnetic excited states increases (Figure 5(a), solid lines).[54] Overall, the success of the vector coupling model in qualitatively explaining hyperfine shifts in [2Fe–2S] clusters justifies its use in more complex systems.

Among the Rieske proteins, the one from the toluene-4 monooxygenase system of *P. mendocina* (TMOC) is the best characterized by NMR. In the reduced state, the ^{1}H spectrum exhibits five resonances at high frequency (Figure 4(b), Table 5) that have been assigned as Cys H^{β} and His $H^{\varepsilon 1}$ protons based upon selective ^{2}H labeling.[60] This study also provided a thorough examination of the ^{15}N hyperfine shifts of H-bonded N nuclei.[60] In both the redox states, six amide and two His $H^{\varepsilon 2}$ N nuclei were found to exhibit paramagnetic shifts and were assigned by selective ^{15}N-labeling. Four of these are H-bonded to the [2Fe–2S] cluster in the crystal structure of a homologous Rieske protein. The crystal structure also showed a fifth amide that was H-bonded to the cluster, but the homologous residue in this system did not exhibit any

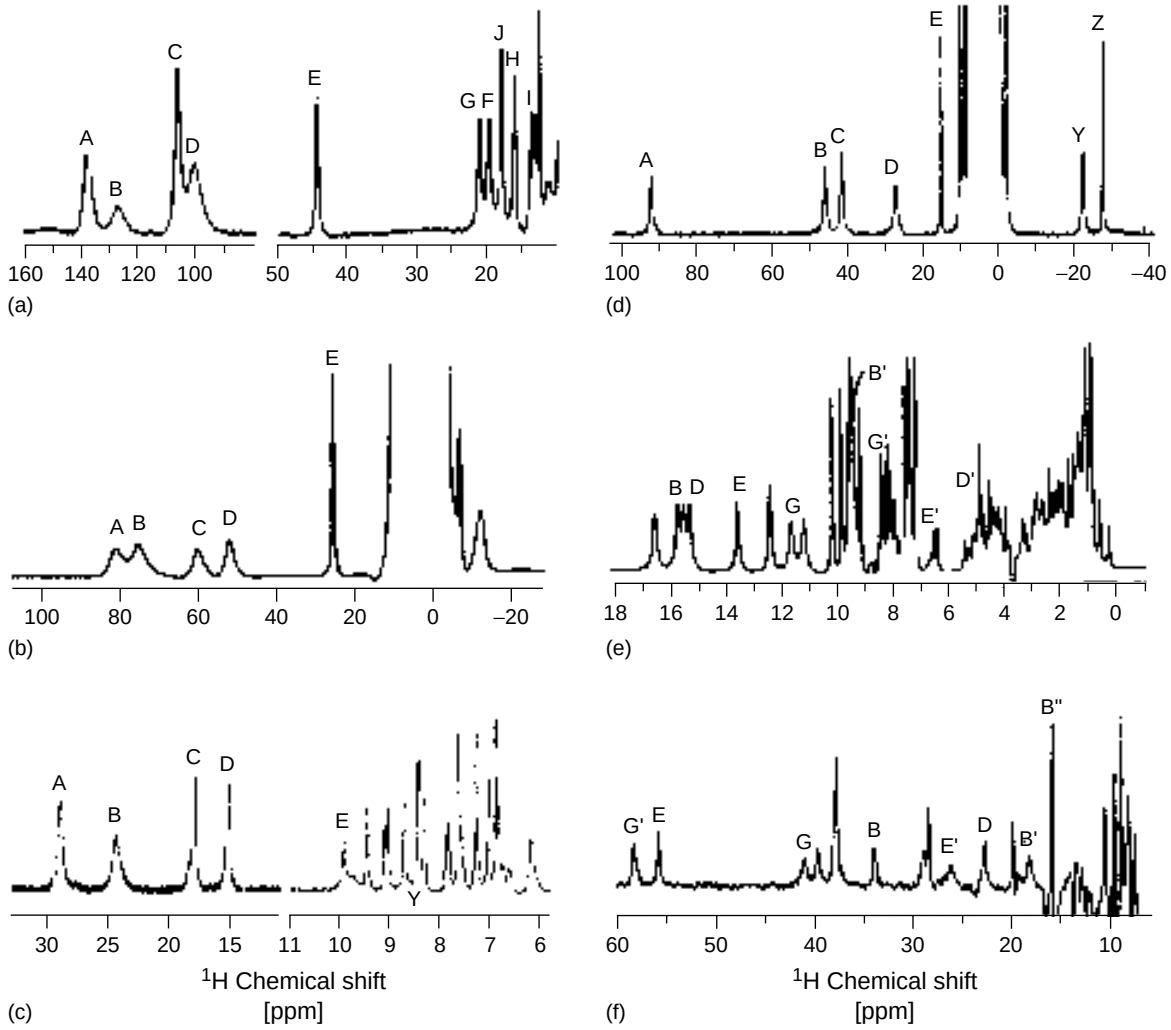

Figure 4 ^{1}H NMR spectra of various FeS Clusters. Peak labels correspond to those listed in Tables 5 and 6. (a) Reduced *Anabaena* PCC7120 2Fe Fd at 283 K. Left-hand panel is scaled up arbitrarily. Adapted from Ref.[43] (b) Reduced toluene 4-monooxygenase Rieske protein from *P. mendocina* at 303 K. Adapted from Ref.[60] (c) Oxidized *D. gigas* 3Fe Fd at 303 K. Left-hand panel is scaled up arbitrarily. Adapted from Ref.[61] (d) Oxidized *E. halophila* HiPIP I at 288 K. Adapted from Ref.[83] (e) Oxidized *C. acidi-urici* at 298 K. Left-hand panel is scaled up arbitrarily. Adapted from Ref.[102] (f) Reduced *C. acidi-urici* at 298 K. Adapted from Ref.[102]

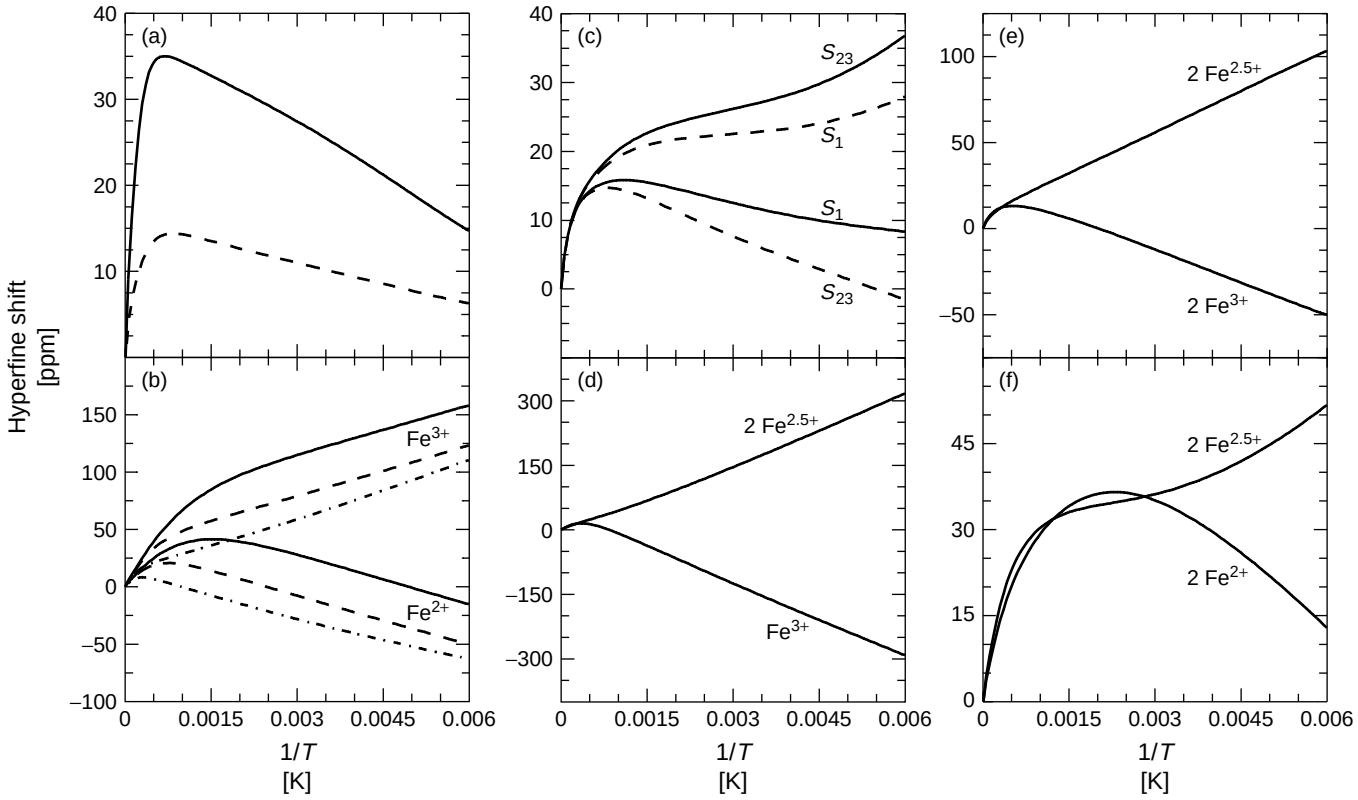

Figure 5 Plots of the temperature dependence of the hyperfine shift of Cys H^{β} resonances versus $1/T$ for different FeS clusters. $A/h = 1$ MHz except where noted. (a) $[2Fe\text{-}2S]^{2+}$, $J = -175\,cm^{-1}$, $A/h = 1.8$ MHz (solid line). $[4Fe\text{-}4S]^{2+}$, $J = -150\,cm^{-1}$, $B = 400\,cm^{-1}$ (dashed line). (b) $[2Fe\text{-}2S]^{+}$, $J = -50\,cm^{-1}$ (solid line), $J = -100\,cm^{-1}$ (dashed line), $J = -250\,cm^{-1}$ (dot-dash line). (c) $[3Fe\text{-}4S]^{+}$, $J_{12} = J_{13} = -185\,cm^{-1}$, $J_{23} = -192\,cm^{-1}$ (solid line). $J_{12} = J_{13} = -185\,cm^{-1}$, $J_{23} = -178\,cm^{-1}$ (dashed line) (d) $[3Fe\text{-}4S]^{0}$, $J = -125\,cm^{-1}$, B= $650\,cm^{-1}$. (e) $[4Fe\text{-}4S]^{3+}$, $J = -130\,cm^{-1}$, $\Delta J_{12} - 32\,cm^{-1}$, $B_{34} = 250\,cm^{-1}$. (f) $[4Fe\text{-}4S]^{+}$, J= $-62\,cm^{-1}$, $\Delta J_{12} = 28\,cm^{-1}$, $B_{34} = 75\,cm^{-1}$

hyperfine shift. The origin of the hyperfine shifts in Rieske proteins has not yet been analyzed in detail.

3.2.2 [3Fe–4S] Clusters

The [3Fe–4S] clusters that have been studied by NMR are found in two types of proteins: 3Fe Fds and 7Fe Fds. The 3Fe Fds are formed from Fds that contain one [4Fe–4S] cluster in which one Fe is labile and is readily removed to yield a stable [3Fe–4S] cluster. The 7Fe Fds contain one $[3Fe–4S]^{+}$ cluster and one $[4Fe–4S]^{2+}$ cluster, in which only the former can be readily reduced. The hyperfine-shifted ^{1}H resonances in $[3Fe–4S]^{+}$ clusters have substantially narrower linewidths than in $[2Fe–2S]^{2+/+}$ clusters. Hyperfine-shifted signals from $[3Fe–4S]^{+}$ clusters have been extensively assigned by 1D NOEs, 2D NOESY, 2D magnitude COSY, and 2D TOCSY. In all cases, the Cys H^{β} resonances are found in the 35 to -1 ppm range; some shift to higher frequency with increasing temperature and some to lower frequency. A representative example is *D. gigas* 3Fe Fd (Figure 4(c), Table 5).[61]

The chemical shifts and temperature dependencies of the hyperfine-shifted resonances are readily understood using the vector coupling model outlined above. The pattern of hyperfine-shifted resonances depends upon the relative values of the three exchange coupling parameters, J_{12}, J_{13}, and J_{23}. From Mössbauer[62] and temperature-dependent EPR,[63,64] all J-values are close in magnitude but not equal. From magnetic susceptibility, J is large and negative ($|J| > 100\,cm^{-1}$).[65] S_2 and S_3 are coupled to yield spin S_{23}, which ranges from 0 to 10, and S_{23} is coupled with S_1 to yield states of the form $|S_{23}, S\rangle$.[62] One can consider three cases.[66–70] (1) If $|J_{12}| = |J_{13}| < |J_{23}|$, then $|2, 1/2\rangle$ is the g.s., and one expects one pair of Cys H^{β} protons to exhibit large high-frequency shifts that decrease in frequency with increasing temperature since they are coupled to the larger spin ($S_1 = 5/2$), and the other two pairs of Cys H^{β} protons exhibit smaller high-frequency shifts that increase in frequency with increasing temperature (Figure 5(c), solid lines). (2) If $|J_{12}| = |J_{13}| > |J_{23}|$, then $|3, 1/2\rangle$ is the g.s., and two pairs of Cys H^{β} protons are expected to exhibit large high-frequency shifts that decrease in frequency with increasing temperature, since they area coupled to the larger spin ($S_{23} = 3$), and the third pair of Cys H^{β} protons to exhibit low-frequency shifts that increase in frequency with increasing temperature (Figure 5(c), dashed lines). (3) In the intermediate case, $|J_{12}| > |J_{13}| > |J_{23}|$, the g.s. is a mixture of $|2, 1/2\rangle$ and $|3, 1/2\rangle$, and one pair of Cys H^{β} protons will have high-frequency shifts that decrease with temperature, one will have minor hyperfine shifts that increase in frequency with temperature, and the third will be slightly shifted to higher frequency and weakly temperature-dependent, with the direction dependent on the exact strength of the coupling.[66–70] Indeed, this range of behavior has been observed. The 3Fe Fds of

D. gigas[61,67] and *T. litoralis*[66,71] and the 7Fe Fds from *D. ambivalens*,[68] *Sulfolobus* sp. Strain 7,[72] and *S. acidocaldarius*[73] are examples of the first case. Most of the other 7Fe Fds exhibit behavior of the third type[69,70,74–78] *Pyrococcus furiosus* 3Fe Fd is somewhat different in that the two Cys H^{β} protons that shift to lower frequency with temperature are at slightly lower frequency than in other [3Fe–4S] clusters and have a much larger chemical shift difference between them (23.6 and 11.8 ppm).[66,79] This was originally ascribed to magnetic coupling of the first type, but with the $S_1 = 5/2$ Fe ligated to Cys11 (equivalent to Cys8 in *D. gigas*) rather than Cys56 (equivalent to Cys50) as is found in other 3Fe Fds;[79] however, this interpretation has recently been challenged.[70,73] In *Desulfovibrio africanus* 7Fe Fd, four resonances were found at high frequency that moved to lower frequency with increasing temperature. This would appear to be an example of the case where $|J_{12}| \approx |J_{13}| > |J_{23}|$; however, detailed assignments were not reported, and no signals were found at frequencies below the diamagnetic region as expected from the above model. Thus, in the $[3Fe–4S]^{+}$ clusters, the vector coupling model has provided a firm basis for beginning to understand how differences among proteins modulate electronic structure.

For many years, there were essentially no reports on the hyperfine-shifted resonances in $[3Fe–4S]^{0}$ clusters, despite an attempt to selectively ^{2}H-label the Cys residues[80] and exploit the slower relaxation rate expected for ^{2}H, as had been done for CpRd.[10] $[3Fe–4S]^{0}$ clusters are a case where double exchange must be considered, and it was revealed by Mössbauer that the coupling could be viewed as mixed-valent iron pair in which double exchange exceeds the effects of isotropic exchange, vibronic coupling, and static asymmetry to yield a valence-delocalized (i.e., $2Fe^{2.5+}$)$S_{23} = 9/2$ state that is in turn coupled to the remaining Fe^{3+}.[81] In the simplest model (all J-values are equal), the Hamiltonian describing this is:

$$\mathcal{H} = -2J \sum_{i<j=1-3} \mathbf{S}_i \cdot \mathbf{S}_j \pm B\left(S_{23} + \frac{1}{2}\right) \tag{27}$$

yielding energies for the total spin states of

$$E(S) = -JS(S+1) \pm B\left(S_{23} + \frac{1}{2}\right) \tag{28}$$

From Mössbauer, the g.s. is $|9/2, 2\rangle$ which indicates that $B > 4|J|$.[81] It is likely that the location of the valence-delocalized $Fe^{2.5+}$ pair can exchange among the three irons, and such an exchange, with a rate constant of $\sim 10^{5}–10^{6}\,s^{-1}$, was invoked as the reason the hyperfine-shift Cys resonances were not observed.[82] Indeed, a new signal appears in the Mössbauer spectrum at higher temperatures (150 K) that indicates that all Fe sites are equivalent as a result of complete delocalization of the extra electron.[81] Reduction of the $[3Fe–4S]^{+}$ cluster at neutral pH is believed to involve protonation of the μ-sulfido bridges. Thus, chemical exchange resulting from dynamic protonation/deprotonation of the sulfides could provide the mechanism for signal broadening. Consistent with this view is the observation of very broad hyperfine-shifted NMR signals at high pH, where the protonation/deprotonation mechanism should be minimal. These signals, shifted both to higher and lower frequencies by 100–300 ppm have been preliminarily assigned to Cys H^{β} protons (Table 5).[82]

3.2.3 [4Fe–4S] Clusters

[4Fe–4S] clusters have been extensively studied by NMR, much more so than all of the other classes of FeS proteins, in part because their relatively narrow hyperfine-shifted signals greatly aid in sequence-specific assignment. As listed in Table 3, they can exist in three different redox states. The $[4Fe–4S]^{3+}$ state is found in the oxidized HiPIPs. In most of these, the protons of the ligating Cys residues have been extensively assigned by 1D NOEs, 2D NOESY, 2D magnitude COSY, 2D TOCSY, 1D saturation-transfer, and 2D EXSY. Representative ^{1}H NMR data from *E. halophila* HiPIP I is given in Figure 4(d) and Table 6; the latter also lists ^{13}C and ^{15}N data obtained from 2D experiments.[38,83,84]

In the oxidized HiPIPs, the Cys H^{β} resonances are found throughout the 150 to −70 ppm range and vary significantly among different HiPIPs, despite their close structural homology. In all cases, however, four Cys H^{β} resonances shift to lower frequency with increasing temperature, and four to higher frequency. To understand this behavior it is necessary to first consider the case of *E. halophila* HiPIP II. This is the only HiPIP that exhibits four Cys H^{β} resonances at high field (95–45 ppm) that shift to lower frequency with increasing temperature and four at low field (−10 to −25 ppm) with the opposite temperature-dependence.[85–87] From Mössbauer, the oxidized HiPIPs consist of a Fe^{3+} pair and a valance-delocalized $Fe^{2.5+}$ pair that are coupled to yield a net $S = 1/2$ g.s.,[88–90] as also shown by EPR.[54,90,91] Noodleman explained this behavior based upon the following Hamiltonian:

$$\mathcal{H} = \sum_{i<j=1-4} -2J_{ij}\mathbf{S}_i \cdot \mathbf{S}_j \pm B_{34}\left(S_{34} + \frac{1}{2}\right) \tag{29}$$

where S_1 and S_2 are the spins of the Fe^{3+} pair and S_3 and S_4 are the spins of the $Fe^{2.5+}$ pair ($S_1 = S_2 = 5/2$ and $S_3, S_4 = 5/2, 2$).[34,92,93] Since J_{12} is the Heisenberg exchange coupling parameter for the Fe^{3+} pair, it is assumed to be the largest. B_{34} is the double exchange term for the valance-delocalized $Fe^{2.5+}$ pair. This then yields the following for the energies of the total spin states:

$$E(S) = -JS(S+1) - \Delta J_{12}S_{12}(S_{12}+1) \pm B_{34}\left(S_{34} + \frac{1}{2}\right) \tag{30}$$

where $J = J_{13} = J_{14} = J_{23} = J_{24} = J_{34}$ and $\Delta J_{12} = J_{12} - J$. There are multiple states with total spin $S = 1/2$. Based upon single-crystal X-band ENDOR data on a $[4Fe–4S]^{3+}$ model complex with very similar Mössbauer and EPR spectral properties, the correct g.s. is $|7/2, 3, 1/2\rangle$ (nomenclature is $|S_{34}, S_{12}, S\rangle$).[94] With $J_{12} > J$, this requires $6 < B_{34}/\Delta J_{12} < 8$.[95] With the same vector coupling model (see below), $J = -130\,cm^{-1}$, $J_{12} = -162\,cm^{-1}$, and $B_{34} = 250\,cm^{-1}$ yields qualitatively correct agreement with the behavior of the Cys H^{β} resonances of *E. halophila* HiPIP II (Figure 5(d)).[32,86,96,97] In a slightly more sophisticated model in which $J_{34} \neq J$, B_{34} and J_{34} are covariant, and hence it currently is not possible to determine any of the parameters independently. This has led to considerable debate as to the exact values to use for the Heisenberg and double exchange parameters.[95,98] Regardless, the picture remains the same: signals of the Cys ligated to the $Fe^{2.5+}$ pair will be shifted to higher frequency and those ligated

Table 6 Chemical shifts and temperature dependencies of the hyperfine resonances in representative [4Fe-4S] clusters

Oxidized				Reduced			
Peak label	Assignment	Chemical shift (ppm)	Temperature increases, peak moves	Peak label	Assignment	Chemical shift (ppm)	Temperature increases, peak moves
			E. halophila HiPIP I (at 288 K)				
A	Cys50 $H^{\beta 3}$	92.0	→		Cys33 $H^{\beta 3}$	16.5	←
B	Cys36 $H^{\beta 2}$	47.0	→		Cys50 $H^{\beta 3}$	14.3	←
C	Cys36 $H^{\beta 3}$	42.4	→		Cys66 $H^{\beta 2}$	10.8	←
D	Cys50 $H^{\beta 2}$	27.8	→		Cys36 $H^{\beta 2}$	9.06	nd
	Cys66 $H^{\beta 2}$	6.26	←		Cys36 $H^{\beta 3}$	7.5	nd
	Cys66 $H^{\beta 3}$	2.59	←		Cys33 $H^{\beta 3}$	7.5	←
Y	Cys33 $H^{\beta 2}$	−21.58	←		Cys66 $H^{\beta 3}$	5.81	←
Z	Cys33 $H^{\beta 3}$	−26.7	←		Cys50 $H^{\beta 2}$	4.7	nd
	Cys66 H^{α}	16.2	←		Cys66 H^{α}	7.74	←
	Cys50 H^{α}	6.48	nd		Cys50 H^{α}	4.16	←
	Cys36 H^{α}	0.62	nd		Cys36 H^{α}	3.81	nd
	Cys33 H	9.75[a,b]	nd		Cys33 H	9.28[a]	nd
	Cys36 H	7.60[a,b]	nd		Cys50 H	8.88[a]	nd
	Cys50 C^{β}	440	→		Cys50 C^{β}	112.4	nd
	Cys36 C^{β}	390	→		Cys36 C^{β}	103.7	nd
	Cys66 C^{β}	59.3	nd		Cys33 C^{β}	102.3	nd
	Cys33 C^{β}	41.1	←		Cys66 C^{β}	88.7	nd
	Cys50 C^{α}	152.2	nd		Cys50 C^{α}	89.0	nd
	Cys66 C^{α}	129.0	←		Cys33 C^{α}	86.7	nd
	Cys33 C^{α}	54.7	nd		Cys66 C^{α}	85.8	nd
	Cys36 C^{α}	28.6	nd		Cys36 C^{α}	78.2	nd
	Cys36 N	150[a,b]	nd		Cys50N	137.27[a]	nd
	Cys33 N	127.5[a,b]	nd		Cys33 N	128.93[a]	nd
			Cluster I of *C. acidi-urici* (at 293 K)				
B	Cys11 $H^{\beta 3}$	15.4	←	G'	Cys8 $H^{\beta 3}$	56.5	→
D	Cys14 $H^{\beta 2}$	15.0	←	E	Cys47 $H^{\beta 3}$	55.9	←
E	Cys47 $H^{\beta 3}$	13.4	←	G	Cys8 $H^{\beta 2}$	41.5	→
G	Cys8 $H^{\beta 2}$	11.4	←	B	Cys11 $H^{\beta 3}$	32.7	←
B'	Cys11 $H^{\beta 2}$	9.2	←	E'	Cys47 $H^{\beta 2}$	26.0	←
G'	Cys8 $H^{\beta 3}$	8.2	←	D	Cys14 $H^{\beta 3}$	23.9	→
E'	Cys47 $H^{\beta 2}$	6.5	←	B'	Cys11 $H^{\beta 2}$	18.5	←
D'	Cys14 $H^{\beta 3}$	4.8	←				
	Cys11 H^{α}	10.0	←		Cys40 H^{α}	15.7	nd
	Cys14 H^{α}	7.4	←	B"	Cys11 H^{α}	15.5	nd
	Cys47 H^{α}	4.7	←				
	Cys8 H^{α}	3.5	←				
	Cys14 C^{β}	121	nd				
	Cys47 C^{β}	109	nd				
	Cys11 C^{β}	97	nd				
	Cys8 C^{β}	91	nd				
	Cys14 C^{α}	92	nd				
	Cys11 C^{α}	81	nd				

[a]298 K.
[b]These values were not reported in tabulated form, but were read off the published spectrum[84] and are therefore approximate.

to the Fe^{3+} pair will be shifted to lower frequency. ^1H hyperfine data of the other HiPIPs, in which only two resonances are at lower frequency than the diamagnetic region, have been explained by invoking a spin equilibrium mechanism, in which the location of the delocalized $Fe^{2.5+}$ pair alternates between two different sets of Fe atoms with the exchange rapid on the NMR timescale.[99] Based upon the *E. halophila* HiPIP I sequence, Cys 33, 36, 50 and 66 are designated I, II, III, and IV, respectively. In *E. halophila* HiPIP II, Cys I and IV ligated to the Fe^{3+} pair and Cys II and III are ligated to the delocalized $Fe^{2.5+}$ pair. All other HiPIPs exist in equilibrium between this arrangement and a second one, in which Cys I and II are ligated to the Fe^{3+} pair and Cys III and IV are ligated to the delocalized $Fe^{2.5+}$ pair. Thus, in *E. halophila* HiPIP I, Cys II experiences ∼20% Fe^{3+} character, and Cys IV ∼20% $Fe^{2.5+}$ character. The degree in which the delocalized $Fe^{2.5+}$ pair is found ligated to Cys III and IV increases in the order *E. halophila* iso I, *R. globiformis*, *E. vacuolata* iso I, *E. vacuolata* iso II, *C. vinosum*, *R. gelatinosus*, and *R. fermentans*. In the last two HiPIPs, Cys II experiences ∼70% Fe^{3+} character, and Cys IV ∼70% $Fe^{2.5+}$ character.[100,101] This spin equilibrium model also explains the noticeable deviation in linearity in the temperature dependencies of the Cys H^{β} protons in *E. vacuolata* HiPIP II, behavior that is not readily accounted for

by other models.[99] In addition, the EPR spectra of oxidized HiPIPs exhibit a mixture of $S = 1/2$ species in all cases except *E. halophila* iso II. These results have been described in terms of the same model as given above, where now the two species are either frozen out or are exchanging on a timescale slower than the EPR experiment.[99] The vector coupling picture and the spin equilibrium model provide a remarkably reliable basis for understanding a range of features seen among the oxidized HiPIPs. The exception again is the failure of the simple vector coupling picture to explain the hyperfine shifts of ^{13}C nuclei, in particular the Cys C^{α} resonances.[38]

The $[4Fe{-}4S]^{2+}$ state is found among all [4Fe–4S] proteins: HiPIPs, the 4Fe, 7Fe, and 8Fe ferredoxins (which in the oxidized state contain 2 $[4Fe{-}4S]^{2+}$ clusters), and two other systems that have been examined by NMR, the nitrogenase Fe-protein and the PsaC subunit of photosystem I. The Cys protons are found in the 22–0 ppm range and always increase in frequency with increasing temperature. In a number of systems, they have been sequence-specifically assigned by the usual assortment of 1D and 2D NMR experiments. Representative data from cluster I of the *C. acidi-urici* 8Fe Fd is given in Figure 5(e) and Table 6.[102] The $[4Fe{-}4S]^{2+}$ cluster consists of two nearly identical $Fe^{2.5+}$ pairs that are antiferromagnetically coupled to yield a net $S = 0$ g.s., as shown by Mössbauer spectroscopy on reduced HiPIPs,[88,89] oxidized 8Fe and 4Fe Fds,[103–105] and oxidized nitrogenase Fe-protein.[106] Thus, as in the case of the $[2Fe{-}2S]^{2+}$ clusters, the hyperfine shifts arise solely from thermal population of paramagnetic excited states. This behavior can be readily fit by using a Hamiltonian of the sort in equation (29) and adding another $B_{12}(S_{12} + 1/2)$ term to account for double exchange in the second valence-delocalized $Fe^{2.5+}$ pair.[34,93,96,97,107] In the simplest possible model all J-values are equal, yielding the following for the energy of the total spin states:

$$E(S) = -JS(S+1) \pm B_{12}\left(S_{12} + \frac{1}{2}\right) \pm B_{34}\left(S_{34} + \frac{1}{2}\right) \qquad (31)$$

This readily accounts for the observed hyperfine shifts of the Cys H^{β} resonances (Figure 5(a), dashed lines).[96,97,107]

The $[4Fe{-}4S]^{+}$ state occurs in the reduced 4Fe and 8Fe ferredoxins, nitrogenase Fe-protein, and PsaC subunit of photosystem I. The Cys protons are found in the 65 to −5 ppm range and exhibit a mixture of temperature-dependent behavior: some shift to higher frequency and some to lower frequency with increasing temperature. Representative data from cluster I of the *C. acidi-urici* 8Fe Fd is given in Figure 5(f) and Table 6.[102] In this system and a number of others, the Cys protons have been sequence-specifically assigned by 1D and 2D NMR experiments and in particular, with the use of 2D EXSY and existing assignments of the oxidized form.[102,108] In reduced *C. acidi-urici* 8Fe Fds and in most other cases, the H^{β} resonances of two Cys residues shift to higher frequency with increasing temperature, and the other two to lower frequency, and all occur in roughly the same chemical shift range.[102,108] Mössbauer spectroscopy indicates that the $[4Fe{-}4S]^{+}$ cluster consists of a Fe^{2+} pair and a valance-delocalized $Fe^{2.5+}$ pair.[103–106,109] In general, the g.s. is $S = 1/2$, although there are notable exceptions, discussed below.[47] The exchange coupling in the $[4Fe{-}4S]^{+}$ cluster is significantly more complex than in other FeS clusters. The decrease in the average valence of the four Fe atoms leads to a decrease in the magnitude of J, which in turns means that B has a proportionally greater influence and that the total spin states are closer in energy.[34,93,110–113] Nonetheless, some insight may be gained by the same simple model as used in equations (29) and (30), where now S_1 and S_2 are the spins of the Fe^{2+} pair and S_3 and S_4 are the spins of the $Fe^{2.5+}$ pair ($S_1 = S_2 = 2$ and $S_3, S_4 = 5/2, 2$). With reasonable estimates for J and B_{34} one obtains the qualitatively correct behavior of the Cys H^{β} resonances: those ligated to the $Fe^{2.5+}$ pair shift to lower frequency with increasing temperature and those ligated to the Fe^{2+} pair shift to higher frequency, and all of them will be higher frequency than the diamagnetic region (Figure 5(f)).

P. furiosus 4Fe Fd is an unusual case. First, one of the ligands to the cluster is an Asp instead of a Cys. Second, the g.s. is a physical mixture of $S = 3/2$ and $S = 1/2$ species based upon EPR.[114] The temperature dependencies of the hyperfine-shifted resonances in the reduced state are complex and very unusual; for example, the H^{β} protons of Cys17 exhibit *opposite* temperature dependence.[115–117] In contrast, the D14C mutant exhibits hyperfine behavior extremely similar to those of other 4Fe and 8Fe Fds; specifically, the H^{β} protons of Cys11 and 17 shift to lower frequency with increasing temperature and are assigned to the $Fe^{2.5+}$ pair, and Cys14 and 56 shift to higher frequency and are assigned to the Fe^{2+} pair.[116] Similarly, from EPR, the g.s. is purely $S = 1/2$.[118] The unusual hyperfine temperature-dependent behavior observed in the wild-type was explained by invoking a spin-equilibrium model similar to that for the oxidized HiPIPs. In one arrangement, Cys 14 and 56 ligate the $Fe^{2.5+}$ pair and Cys 11 and 17 the Fe^{2+} pair, and in the other, Cys 14 and 17 ligate the $Fe^{2.5+}$ pair and Cys 11 and 56 the Fe^{2+} pair, indicating that Asp stabilizes the mixed-valence $Fe^{2.5+}$ pair.[116] Notably, the hyperfine shifts and relaxation rates of the ligand protons in the wild-type protein are not significantly different from other $[4Fe\text{-}4S]^{+}$ clusters, leading to the conclusion that the presence of $S = 3/2$ species in the EPR spectrum is an artifact of freezing and that in solution the g.s. is purely $S = 1/2$.[115] A similar picture exists for the nitrogenase Fe-protein, which also exists as a mixture of $S = 3/2$ and $S = 1/2$ species based upon EPR and Mössbauer.[106,109] Addition of urea increases the fraction of the $S = 3/2$, and addition of ethylene glycol decreases it.[106] Again, the NMR spectra are not significantly different from those of other $[4Fe{-}4S]^{+}$ clusters.[119,120] Indeed, the addition of urea or ethylene glycol had little effect, leading to the conclusion that in solution the g.s. is purely $S = 1/2$.

4 CONCLUDING REMARKS

The last decade has seen a dramatic increase in our understanding of electron–nuclear interactions. We have progressed from merely noting the different sorts of the hyperfine-shifted resonances in paramagnetic proteins to being able to accurately calculate them. Relaxation rates are now often used as distance constraints in solution structure determination. The use of residual dipolar couplings holds similar promise. The vector coupling model has been enormously successful in explaining the ^{1}H hyperfine data in FeS clusters and has contributed greatly to our understanding of the exchange coupling in these complex systems. Further refinement of this model to help better explain ^{13}C and ^{15}N hyperfine data is needed and may lead

to further insights. With these tools in hand, NMR will be capable of answering detailed questions regarding how H-bonds and other aspects of the protein matrix tune the properties of metal active sites and thus their function. Thus, while paramagnetic NMR already is acknowledged as one of the most powerful spectroscopic methods available for investigating the biophysics of metalloproteins, it is now poised to assume similar importance for studies of metalloprotein biochemistry.

5 REFERENCES

1. I. Bertini, C. Luchinat, and A. Rosato, *Prog. Biophys. Mol. Biol.*, 1996, **66**, 43–80.
2. B. J. Goodfellow and A. L. Macedo, *Annu. Rep. NMR Spectrosc.*, 1999, **37**, 119–177.
3. I. Bertini, C. Luchinat, and A. Rosato, *Adv. Inorg. Chem.*, 1999, **47**, 251–282.
4. I. Bertini and C. Luchinat, 'NMR of Paramagnetic Molecules in Biological System', Benjamin/Cummings: Menlo Park, CA, 1986.
5. I. Bertini and A. J. Vila, *Chem. Rev.*, 1993, **93**, 2833–2932.
6. L. Banci, I. Bertini, and C. Luchinat, 'Nuclear and Electron Relaxation', VCH: Weinheim: Germany, 1991.
7. A. A. Bothner-By, P. J. Domaille, and C. Gayathri, *J. Am. Chem. Soc.*, 1981, **103**, 5602–5603.
8. B. F. Volkman, S. J. Wilkens, A. L. Lee, B. Xia, W. W. Westler, R. Beger, and J. L. Markley, *J. Am. Chem. Soc.*, 1999, **120**, 4677–4683.
9. L. Banci, I. Bertini, C. Luchinat, and A. Scozzafava, *J. Am. Chem. Soc.*, 1987, **109**, 2328–2334.
10. B. Xia, W. M. Westler, H. Cheng, J. Meyer, J.-M. Moulis, and J. L. Markley, *J. Am. Chem. Soc.*, 1995, **117**, 5347–5350.
11. B. Xia, Thesis, University of Wisconsin, 1996.
12. B. Xia, B. F. Volkman, D. S. King, D. Jenk, D. M. LeMaster, W. M. Westler, S. J. Wilkens, and J. L. Markley, unpublished data.
13. B. Xia, S. J. Wilkens, W. W. Westler, and J. L. Markley, *J. Am. Chem. Soc.*, 1998, **120**, 4893–4894.
14. S. J. Wilkens, B. Xia, F. Weinhold, J. L. Markley, and W. M. Westler, *J. Am. Chem. Soc.*, 1998, **120**, 4806–4814.
15. K. D. Watenpaugh, L. C. Sieker, and L. H. Jensen, *J. Mol. Biol.*, 1979, **131**, 509–522.
16. K. D. Watenpaugh, L. C. Sieker, and L. H. Jensen, *J. Mol. Biol.*, 1980, **138**, 615–633.
17. Z. Dauter, K. S. Wilson, L. C. Sieker, J. M. Moulis, and J. Meyer, *Proc. Natl. Acad. Sci. USA*, 1996, **93**, 8836–8840.
18. J. Lin, E. Gebel, W. M. Westler, and J. L. Markley, unpublished data.
19. Z. Xiao, M. J. Maher, M. Cross, C. S. Bond, J. M. Guss, and A. G. Wedd, *J. Biol. Inorg. Chem.*, 200, **5**, 75–84.
20. T. Min, C. E. Ergenekan, M. K. Eidsness, T. Ichiye, and C. Kang, *Protein Sci.*, 2001, **10**, 613–621.
21. W. M. Westler and J. L. Markley, unpublished results.
22. S. J. Wilkens, B. Xia, B. F. Volkman, F. Weinhold, J. L. Markley, and W. M. Westler, *J. Phys. Chem. B*, 1998, **102**, 8500–8505.
23. C. Schulz and P. G. Debrunner, *J. Physique*, 1976, **37**, C6-153–C6-158.
24. P. G. Debrunner, E. Münck, L. Que, and C. E. Schulz, in 'Iron-Sulfur Proteins', Vol. III, ed W. Lovenberg, Academic Press: New York, 1977, pp. 381–417.
25. J. Peisach, W. E. Blumberg, E. T. Lode, and M. J. Coon, *J. Biol. Chem.*, 1971, **256**, 5877–5881.
26. M. S. Gebhard, J. C. Deaton, S. A. Koch, M. Millar, and E. I. Solomon, *J. Am. Chem. Soc.*, 1990, **112**, 2217–2231.
27. V. Petrouleas, A. Simopoulos, A. Kostikas, and D. Coucouvanis, *J. Physique*, 1976, **37**, C6-159–C6-164.
28. M. J. Knapp, J. Krzystek, L.-C. Brunel, and D. N. Hendrickson, *Inorg. Chem.*, 2000, **39**, 281–288.
29. P. M. Champion and A. J. Sievers, *J. Chem. Phys.*, 1977, **66**, 1819–1825.
30. A. Abragam and B. Bleaney, 'Electron Paramagnetic Resonance of Transition Ions', Dover: New York, 1970.
31. O. Kahn, 'Molecular Magnetism', Wiley-VCH: New York, 1993.
32. L. Banci, I. Bertini, and C. Luchinat, *Struct. Bonding*, 1990, **72**, 113–136.
33. R. P. Scaringe, D. J. Hodgson, and W. E. Hatfield, *Mol. Phys.*, 1978, **35**, 701–713.
34. L. Noodleman, C. Y. Peng, D. A. Case, and J.-M. Mouesca, *Coord. Chem. Rev.*, 1995, **144**, 199–244.
35. I. Bertini, O. Galas, C. Luchinat, G. Parigi, and G. Spina, *J. Magn. Reson.*, 1998, **130**, 33–44.
36. I. Bertini, M. M. J. Couture, A. Donaire, L. D. Eltis, I. C. Felli, C. Luchinat, M. Piccioli, and A. Rosato, *Eur. J. Biochem.*, 1996, **241**, 440–452.
37. J. G. Huber, J.-M. Moulis, and J. Gaillard, *Biochemistry*, 1996, **35**, 12 705–12 711.
38. I. Bertini, A. Donaire, I. C. Felli, C. Luchinat, and A. Rosato, *Inorg. Chem.*, 1997, **36**, 4798–4803.
39. I. Bertini, A. Donaire, C. Luchinat, and A. Rosato, *Proteins: Struct. Funct. Genet.*, 1997, **29**, 348–358.
40. R. Cammack, *Adv. Inorg. Chem.*, 1992, **38**, 281–322.
41. H. Matsubara and K. Saeki, *Adv. Inorg. Chem.*, 1992, **38**, 223–280.
42. L. Skjeldal, J. L. Markley, V. M. Coghlan, and L. E. Vickery, *Biochemistry*, 1991, **30**, 9078–9083.
43. H. Cheng, W. M. Westler, B. Xia, B.-H. Oh, and J. L. Markley, *Arch. Biochem. Biophys.*, 1995, **316**, 619–634.
44. B. Xia, D. Jenk, D. M. LeMaster, W. M. Westler, and J. L. Markley, *Arch. Biochem. Biophys.*, 2000, **373**, 328–334.
45. P. Bertrand and J.-P. Gayda, *Biochim. Biophys. Acta*, 1979, **579**, 107–121.
46. R. H. Sands and W. R. Dunham, *Q. Rev. Biophys.*, 1975, **7**, 443–504.
47. B. Guigliarelli and P. Bertrand, *Adv. Inorg. Chem.*, 1999, **47**, 421–497.
48. W. Fu, P. M. Drozdzewski, M. D. Davies, S. G. Sligar, and M. K. Johnson, *J. Biol. Chem.*, 1992, **267**, 15 502–15 510.
49. R. Morales, M.-H. Chron, G. Hudry-Clergeon, Y. Pétillot, S. Norager, M. Medina, and M. Frey, *Biochemistry*, 1999, **38**, 15 764–15 773.
50. A. Müller, J. J. Müller, Y. A. Muller, H. Uhlmann, R. Bernhardt, and U. Heinemann, *Structure*, 1998, **6**, 269–280.
51. L. Skjeldal, W. M. Westler, B.-H. Oh, A. M. Krezel, H. M. Holden, B. L. Jacobson, I. Rayment, and J. L. Markley, *Biochemistry*, 1991, **30**, 7363–7368.
52. L. B. Dugad, G. N. La Mar, L. Banci, and I. Bertini, *Biochemistry*, 1990, **29**, 2263–2271.
53. W. R. Dunham, G. Palmer, R. H. Sands, and A. J. Bearden, *Biochim. Biophys. Acta*, 1971, **253**, 373–384.
54. I. Bertini, S. Ciurli, and C. Luchinat, *Struct. Bonding*, 1995, **83**, 1–53.
55. G. Palmer, W. R. Dunham, J. A. Fee, R. H. Sands, T. Ikuza, and T. Yonetani, *Biochim. Biophys. Acta*, 1971, **245**, 201–207.
56. J.-P. Gayda, J. F. Gibson, R. Cammack, D. O. Hall, and R. Mullinger, *Biochim. Biophys. Acta*, 1976, **434**, 154–163.
57. R. E. Anderson, W. R. Dunham, R. H. Sands, A. J. Bearden, and H. L. Crespi, *Biochim. Biophys. Acta*, 1975, **408**, 306–318.
58. S. G. Lloyd, R. Franco, J. J. G. Moura, I. Moura, G. C. Ferreira, and B. H. Huynh, *J. Am. Chem. Soc.*, 1996, **118**, 9892–9900.
59. J. C. Salerno, T. Ohnishi, H. Blum, and J. S. Leigh, *Biochim. Biophys. Acta*, 1977, **494**, 191–197.

60. B. Xia, J. D. Pikus, W. Xia, K. McClay, R. J. Steffan, Y. K. Chae, W. M. Westler, J. L. Markley, and B. G. Fox, *Biochemistry*, 1999, **38**, 727–739.
61. A. L. Macedo, P. N. Palma, I. Moura, J. LeGall, V. Wray, and J. J. G. Moura, *Magn. Reson. Chem.*, 1993, **31**, S59–S67.
62. T. A. Kent, B. H. Huynh, and E. Münck, *Proc. Natl. Acad. Sci. USA*, 1980, **77**, 6574–6576.
63. J.-P. Gayda, P. Bertrand, and F.-X. Theodule, *J. Chem. Phys.*, 1982, **77**, 3387–3391.
64. J. Telser, H.-I. Lee, and B. M. Hoffman, *J. Biol. Inorg. Chem.*, 2000, **5**, 369–380.
65. E. P. Day, J. Peterson, J. J. Bonvoisin, I. Moura, and J. J. G. Moura, *J. Biol. Chem.*, 1988, **263**.
66. S. C. Busse, G. La Mar, L. P. Yu, J. B. Howard, E. T. Smith, Z. H. Zhou, and M. W. W. Adams, *Biochemistry*, 1992, **31**, 11 952–11 962.
67. A. L. Macedo, I. Moura, J. J. G. Moura, J. LeGall, and B. H. Huynh, *Inorg. Chem.*, 1993, **32**, 1101–1105.
68. D. Bentrop, I. Bertini, C. Luchinat, J. Mendes, M. Piccioli, and M. Teixeira, *Eur. J. Biochem.*, 1996, **236**, 92–99.
69. S. Aono, I. Bertini, J. A. Cowan, C. Luchinat, A. Rosato, and M. S. Viezzoli, *J. Biol. Inorg. Chem.*, 1996, **1**, 523–528.
70. I. Bertini, A. Dikiy, C. Luchinat, R. Macinai, M. S. Viezzoli, and M. Vincenzini, *Biochemistry*, 1997, **36**, 3570–3579.
71. A. Donaire, C. M. Gorst, Z. H. Zhou, M. W. W. Adams, and G. La Mar, *J. Am. Chem. Soc.*, 1994, **116**, 6841–6849.
72. T. Iwasaki, E. Watanabe, D. Ohmori, T. Imai, A. Urushiyama, M. Akiyama, Y. Hayashi-Iwasaki, N. J. Cosper, and R. A. Scott, *J. Biol. Inorg. Chem.*, 2000, **276**, 25 391–25 401.
73. J. P. Hannan, J. L. H. Busch, J. Breton, R. James, A. J. Thompson, G. R. Moore, and S. L. Davy, *J. Biol. Inorg. Chem.*, 2000, **5**, 432–447.
74. K. Nagayama, D. Ohmori, T. Imai, and T. Oshima, *FEBS Lett.*, 1983, **158**, 208–212.
75. H. Cheng, K. Grohmann, and W. Sweeney, *J. Biol. Chem.*, 1990, **265**, 12 388–12 392.
76. H. Cheng, K. Grohmann, and W. Sweeney, *J. Biol. Chem.*, 1992, **267**, 8073–8080.
77. G. Battistuzzi, M. Borsari, S. Ferretti, C. Luchinat, and M. Sola, *Arch. Biochem. Biophys.*, 1995, **320**, 149–154.
78. A. L. Macedo, S. Besson, C. Moreno, G. Fauque, J. J. Moura, and I. Mouara, *Biochem. Biophys. Res. Commun.*, 1996, **229**, 524–530.
79. C. M. Gorst, Y.-H. Yeh, Q. Teng, L. Calzolai, Z.-H. Zhou, M. W. W. Adams, and G. La Mar, *Biochemistry*, 1995, **34**, 600–610.
80. I. Bertini, C. Luchinat, G. Mincione, and A. Soriano, *Inorg. Chem.*, 1998, **37**, 969–972.
81. V. Papaefthymiou, J.-J. Girerd, I. Moura, J. J. G. Moura, and E. Münck, *J. Am. Chem. Soc.*, 1987, **109**, 4703–4710.
82. D. Bentrop, I. Bertini, M. Borsari, G. Cosenza, C. Luchinat, and Y. Niikura, *Angew. Chem. Int. Ed.*, 2000, **29**, 3620–3622.
83. I. Bertini, F. Capozzi, L. D. Eltis, I. C. Felli, C. Luchinat, and M. Piccioli, *Inorg. Chem.*, 1995, **34**, 2516–2523.
84. I. Bertini, L. D. Eltis, I. C. Felli, D. H. W. Kasrau, C. Luchinat, and M. Piccioli, *Chem. Eur. J.*, 1995, **1**, 698–607.
85. R. Krishnamoorthi, J. L. Markley, M. A. Cusanovich, C. T. Przysiecki, and T. E. Meyer, *Biochemistry*, 1986, **25**, 60–67.
86. L. Banci, I. Bertini, F. Briganti, A. Scozzafava, M. Vincens-Oliver, and C. Luchinat, *Inorg. Chim. Acta*, 1991, **180**, 171–175.
87. L. Banci, I. Bertini, F. Capozzi, P. Carloni, S. Ciurli, C. Luchinat, and M. Piccioli, *J. Am. Chem. Soc.*, 1993, **115**, 3431–3440.
88. D. P. E. Dickson, C. E. Johnson, R. Cammack, M. C. W. Evans, D. O. Hall, and K. K. Rao, *Biochem. J.*, 1974, **139**, 105–108.
89. P. Middleton, D. P. E. Dickson, C. E. Johnson, and J. D. Rush, *Eur. J. Biochem.*, 1980, **104**, 289–296.
90. I. Bertini, A. P. Campos, C. Luchinat, and M. Teixeira, *J. Inorg. Biochem.*, 1993, **52**, 227–234.
91. B. C. Antanaitis and T. H. Moss, *Biochim. Biophys. Acta*, 1975, **405**, 262–279.
92. L. Noodleman, *Inorg. Chem.*, 1988, **27**, 3677–3679.
93. L. Noodleman and D. A. Case, *Adv. Inorg. Chem.*, 1992, **38**, 423–470.
94. J.-M. Mouesca, G. Ruis, and B. Lamotte, *J. Am. Chem. Soc.*, 1993, **115**, 4714–4731.
95. L. Noodleman, D. A. Case, J.-M. Mouesca, and B. Lamotte, *J. Biol. Inorg. Chem.*, 1996, **1**, 177–182.
96. I. Bertini, F. Briganti, C. Luchinat, A. Scozzafava, and M. Sola, *J. Am. Chem. Soc.*, 1991, **113**, 1237–1245.
97. I. Bertini, F. Briganti, C. Luchinat, A. Scozzafava, and M. Sola, *J. Am. Chem. Soc.*, 1991, **113**, 7084.
98. M. Belinskiy, I. Bertini, O. Galas, and C. Luchinat, *Inorg. Chim. Acta*, 1996, **243**, 91–99.
99. L. Banci, I. Bertini, S. Ciurli, S. Ferretti, C. Luchinat, and M. Piccioli, *Biochemistry*, 1993, **32**, 9387–9397.
100. I. Bertini, F. Capozzi, C. Luchinat, and M. Piccioli, *Eur. J. Biochem.*, 1993, **212**, 69–78.
101. S. Ciurli, M. A. Cremonini, P. Kofod, and C. Luchinat, *Eur. J. Biochem.*, 1996, **236**, 405–411.
102. I. Bertini, F. Capozzi, C. Luchinat, M. Piccioli, and A. Vila, *J. Am. Chem. Soc.*, 1994, **116**, 651–660.
103. C. L. Thompson, C. E. Johnson, D. P. E. Dickson, R. Cammack, D. O. Hall, U. Weser, and K. K. Rao, *Biochem. J.*, 1974, **139**, 97–103.
104. P. Middleton, D. P. E. Dickson, C. E. Johnson, and J. D. Rush, *Eur. J. Biochem.*, 1978, **88**, 135–141.
105. P. Kyritsis, R. Kümmerle, J. G. Huber, J. Gaillard, B. Guigliarelli, C. Popescu, E. Münck, and J.-M. Moulis, *Biochemistry*, 1999, **38**, 6335–6345.
106. P. A. Lindahl, E. P. Day, K. Thomas A., W. H. Orme-Johnson, and E. Münck, *J. Biol. Chem.*, 1985, **260**, 11 160–11 173.
107. I. Bertini, F. Briganti, C. Luchinat, and A. Scozzafava, *Inorg. Chem.*, 1990, **29**, 1874–1880.
108. I. Bertini, F. Briganti, C. Luchinat, L. Messori, R. Monnanni, and A. Scozzafava, *Eur. J. Biochem.*, 1992, **204**, 831–839.
109. P. A. Lindahl, N. J. Gorelick, E. Münck, and W. H. Orme-Johnson, *J. Biol. Chem.*, 1987, **262**, 14 945–14 953.
110. L. Noodleman, *Inorg. Chem.*, 1991, **30**, 246–256.
111. L. Noodleman, *Inorg. Chem.*, 1991, **30**, 256–264.
112. J.-M. Mouesca, L. Noodleman, D. A. Case, and B. Lamotte, *Inorg. Chem.*, 1995, **34**, 4347–4359.
113. F. Moriaud, S. Gambarelli, B. Lamotte, and J.-M. Mouesca, *J. Phys. Chem. B*, 2001, **105**, 9631–9642.
114. R. C. Conover, A. T. Kowal, W. Fu, J.-B. Park, S. Aono, M. W. W. Adams, and M. K. Johnson, *J. Biol. Chem.*, 1990, **265**, 8533–8541.
115. L. Calzolai, C. M. Gorst, Z.-H. Zhao, Q. Teng, M. W. W. Adams, and G. La Mar, *Biochemistry*, 1995, **34**, 11 373–11 384.
116. L. Calzolai, C. M. Gorst, K. L. Bren, Z.-H. Zhou, M. W. W. Adams, and G. N. La Mar, *J. Am. Chem. Soc.*, 1997, **119**, 9341–9350.
117. C. M. Gorst, Z. H. Zhou, K. Ma, Q. Teng, J. B. Howard, M. W. W. Adams, and G. La Mar, *Biochemistry*, 1995, **34**, 8788–8795.
118. Z. H. Zhou and M. W. W. Adams, *Biochemistry*, 1997, **36**, 10 892–10 900.
119. J. Meyer, J. Gaillard, and J.-M. Moulis, *Biochemistry*, 1988, **27**, 6150–6156.
120. W. N. Lanzilotta, R. C. Holz, and L. C. Seefeldt, *Biochemistry*, 1995, **34**, 15 646–15 653.
121. K. Nagayama, Y. Ozaki, Y. Kyogoku, T. Hase, and H. Matsubara, *J. Biochem. (Tokyo)*, 1983, **94**, 893–902.
122. J. Lou, F. Moshiri, M. K. Johnson, M. E. Lafferty, D. L. Sorkin, A.-F. Miller, and R. J. Maier, *Biochemistry*, 1999, **38**, 5563–5571.

123. G. Ratnaswamy and T. C. Pochapsky, *Magn. Reson. Chem.*, 1993, **31**, S73–S77.
124. B. Coxon, N. Sari, M. J. Hoden, and V. L. Vilker, *Magn. Reson. Chem.*, 1997, **35**, 743–751.
125. N. Sari, M. J. Holden, M. P. Mayhew, V. L. Vilker, and B. Coxon, *Biochem. Biophys. Res. Commun.*, 1998, **249**, 773–780.
126. N. U. Jain and T. C. Pochapsky, *J. Am. Chem. Soc.*, 1998, **120**, 12 984–12 985.
127. N. U. Jain and T. C. Pochapsky, *Biochem. Biophys. Res. Commun.*, 1999, **258**, 54–59.
128. R. C. Holz, F. J. Small, and S. A. Ensign, *Biochemistry*, 1997, **36**, 14 690–14 696.
129. S. DeVries, A. Cherepanov, A. Berg, and G. W. Canters, *Inorg. Chim. Acta*, 1998, **275/276**, 493–499.
130. W. D. Phillips, C. C. McDonald, N. A. Stombaugh, and W. H. Orme-Johnson, *Proc. Natl. Acad. Sci. USA*, 1974, **71**, 140–143.
131. S. L. Davy, J. Breton, M. J. Osborne, A. J. Thomson, A. P. Thurgood, L.-Y. Lian, Y. Pétillot, C. Hatchikian, and G. R. Moore, *Biochim. Biophys. Acta*, 1994, **1209**, 33–39.
132. S. L. Davy, M. J. Osborne, J. Breton, G. R. Moore, A. J. Thompson, I. Bertini, and C. Luchinat, *FEBS Lett.*, 1995, **363**, 199–204.
133. A. Donaire, Z.-H. Zhou, M. W. W. Adams, and G. La Mar, *J. Biomol. NMR*, 1996, **7**, 35–47.
134. G. Wildegger, D. Bentrop, A. Ejchart, M. Alber, A. Hage, R. Sterner, and P. Rösch, *Eur. J. Biochem.*, 1995, **229**, 658–668.
135. E. Lebrun, C. Simenel, F. Guerlesquin, and M. Delepierre, *Magn. Reson. Chem.*, 1996, **34**, 873–880.
136. J. L. H. Busch, J. L. Breton, S. L. Davy, R. James, G. R. Moore, F. A. Armstrong, and A. J. Thomson, *Biochem. J.*, 2000, **346**, 375–384.
137. E. L. Packer, W. V. Sweeney, J. C. Rabinowitz, H. Sterlicht, and E. N. Shaw, *J. Biol. Chem.*, 1977, **252**, 2245–2253.
138. I. Bertini, F. Briganti, C. Luchinat, L. Messori, R. Monnanni, A. Scozzafava, and G. Vallini, *FEBS Lett.*, 1991, **289**, 253–256.
139. S. C. Busse, G. La Mar, and J. B. Howard, *J. Biol. Chem.*, 1991, **266**, 23 714–23 723.
140. S. D. B. Scrofani, P. S. Brereton, A. M. Hamer, M. J. Lavery, S. G. McDowall, G. A. Vincent, R. T. C. Brownlee, N. J. Hoogenraad, M. Sadek, and A. G. Wedd, *Biochemistry*, 1994, **33**, 14 486–14 495.
141. S. D. B. Scrofani, R. T. C. Brownlee, M. Sadek, and A. G. Wedd, *Inorg. Chem.*, 1995, **34**, 3942–3952.
142. I. Bertini, A. Donaire, B. A. Feinberg, C. Luchinat, M. Piccioli, and H. Yuan, *Eur. J. Biochem.*, 1995, **232**, 192–205.
143. J. G. Huber, J. Gaillard, and J.-M. Moulis, *Biochemistry*, 1995, **34**, 194–205.
144. D. G. Nettesheim, T. E. Meyer, B. A. Feinberg, and J. D. Otvos, *J. Biol. Chem.*, 1983, **258**, 8235–8239.
145. J. A. Cowan and M. Sola, *Biochemistry*, 1990, **29**, 5633–5637.
146. D. G. Nettesheim, S. R. Harder, B. A. Feinberg, and J. D. Otvos, *Biochemistry*, 1992, **31**, 1234–1244.
147. I. Bertini, F. Capozzi, S. Ciurli, C. Luchinat, L. Messori, and M. Piccioli, *J. Am. Chem. Soc.*, 1992, **114**, 3332–3340.
148. J. Gaillard, J.-P. Albrand, J.-M. Moulis, and D. E. Wemmer, *Biochemistry*, 1992, **31**, 5632–5639.
149. L. Banci, I. Bertini, A. Dikiy, D. H. W. Kastrau, C. Luchinat, and P. Sompornpisut, *Biochemistry*, 1995, **34**, 206–219.
150. L. Banci, I. Bertini, F. Briganti, C. Luchinat, A. Scozzafava, and M. Vincens-Oliver, *Inorg. Chem.*, 1991, **30**, 4517–4524.
151. I. Bertini, F. Capozzi, C. Luchinat, M. Piccioli, and M. Vincens-Oliver, *Inorg. Chim. Acta*, 1992, **198–200**, 483–491.
152. I. Bertini, I. C. Felli, D. H. W. Kastrau, C. Luchinat, M. Piccioli, and M. S. Viezzoli, *Eur. J. Biochem.*, 1994, **225**, 703–714.
153. I. Bertini, A. Gaudemer, C. Luchinat, and M. Piccioli, *Biochemistry*, 1993, **32**, 12 887–12 893.
154. M. Sola, J. A. Cowan, and H. B. Gray, *Biochemistry*, 1989, **28**, 5261–5268.
155. R. Krishnamoorthi, M. A. Cusanovich, T. E. Meyer, and C. T. Przysiecki, *Eur. J. Biochem.*, 1989, **181**, 81–85.
156. J. Meyer, J. Fujinaga, J. Gaillard, and M. Lutz, *Biochemistry*, 1994, **33**, 13 642–13 650.
157. D. Bentrop, I. Bertini, C. Luchinat, W. Nitschke, and U. Mühlenhoff, *Biochemistry*, 1997, **36**, 13 629–13 637.
158. M. L. Antonkine, D. Bentrop, I. Bertini, C. Luchinat, G. Shen, D. A. Bryant, D. Stehlik, and J. H. Golbeck, *J. Biol. Inorg. Chem.*, 2000, **5**, 381–392.

Biographical Sketches

Timothy E. Machonkin, *b* 1971, B.S. Chemistry, 1993, Ph.D., 2000, Stanford University. Dr. Machonkin has been working in the area of bioinorganic chemistry since an undergraduate. In the laboratory of Prof. Edward Solomon at Stanford, he was involved in spectroscopic studies of metalloproteins and model systems, and in particular, EPR and magnetic susceptibility of Cu-containing systems. Since joining the laboratory of Prof. Markley, he has worked on NMR of FeS systems and the development of new methods to study paramagnetic systems with slow electronic relaxation rates by NMR.

John L. Markley, *b* 1941, B.A. Chemistry, 1963, Ph.D., 1969, Harvard University. Dr. Markley is Steenbock Professor of Biomolecular Structure in the Department of Biochemistry at the University of Wisconsin-Madison. He is Head of the National Magnetic Resonance Facility at Madison and the BioMagResBank, the international repository for biomolecular NMR data. Recently, he became Director of the Center for Eukaryotic Structural Genomics at the University of Wisconsin-Madison.

Electron–Nuclear Multiple Resonance Spectroscopy

Hans Thomann and Marcelino Bernardo

Exxon Research and Engineering Company, Annandale, NJ, USA

1	Introduction	1
2	Basic Principles	2
3	Experimental Techniques with Selected Applications	6
4	Concluding Remarks	15
5	Related Articles	15
6	References	16

1 INTRODUCTION

The term 'pulsed electron–nuclear multiple resonance' (PE NMR) spectroscopy refers to a broad range of experimental methods in which pulsed NMR techniques are combined with pulsed electron paramagnetic resonance (EPR) techniques. This combination provides the capability to measure the spectra and spin dynamics of nuclei which are magnetically coupled to unpaired electrons by the hyperfine interaction. Related experimental techniques for measuring the interactions of nuclei coupled to unpaired electrons are paramagnetically shifted NMR, dynamic nuclear polarization (DNP), electron spin resonance (ESR), the pulsed ESR technique of electron spin echo envelope modulation (ESEEM), and continuous wave (CW) electron–nuclear double resonance (ENDOR). These techniques are complementary rather than competing methods for measuring different aspects of the magnetic interactions of the coupled electron–nucleus spin system. Each technique offers certain advantages as well as certain limitations. The most appropriate experimental approach for a given problem also depends on the type of information desired.

The PE NMR techniques discussed in this article are best suited for measuring the magnetic interactions of nuclei in the local coordination structure of a paramagnetic electron. A distinguishing characteristic of nuclei which are detected in PE NMR experiments is that the NMR transition frequencies are shifted by very large values when compared with NMR spectra of diamagnetic samples. These large shifts arise from the large local magnetic fields originating from the unpaired electron spins. Consequently, the resonance frequency is described by the hyperfine coupling and is measured in units of kilohertz or megahertz as opposed to a resonance frequency shift of parts per million referenced to the nuclear Larmor frequency of a standard.

Nuclei which experience large local magnetic fields originating from unpaired electrons are encountered in a wide spectrum of research areas, including chemistry, materials science, polymer science, environmental science, and the biological sciences. Specific examples include: organic and inorganic radical molecules;[1–3] fossil fuels;[4,5] organic conductors, semiconductors and electroactive polymers; organometallic transition metal complexes;[6,7] dopants and other localized states in semiconductors;[8] surfaces such as on oxides and semiconductors; at the internal interfaces of semiconductors, superlattice structures, polymers, and composite materials; catalysis; transition metal ions in zeolites; and at the active sites for electron transfer or substrate binding in metalloproteins and metalloenzymes.[9]

If the unpaired electron spins can be treated as independent (or only weakly coupled) dipoles, their magnetic susceptibility is described by paramagnetism. Nuclei which sustain a hyperfine coupling with such electrons are therefore also referred to as paramagnetically coupled nuclei. Under certain conditions the NMR spectrum of paramagnetically coupled nuclei can be observed directly in the NMR spectrum as a paramagnetic shift. This is usually identified by the magnitude of the frequency shift and its temperature dependence. The local magnetic field originating from the unpaired electron spin shifts the NMR frequency and broadens the linewidth for those nuclei which sustain a hyperfine interaction. Both the magnitude of the frequency shift and the linewidth depend on the magnitude of the hyperfine coupling and on the details of the spin dynamics, specifically on the spin relaxation rates of the electron and nuclei. Well-resolved NMR lines can be observed if the electron spin–lattice relaxation time T_{1e}, or electron spin correlation time τ_e, which describes the time dependence of the local magnetic field, is short enough to assure that the orientation dependence of the local field is time averaged to its isotropic value. The paramagnetic shift is then determined by the isotropic hyperfine coupling arising from the unpaired spin density on the nucleus. Several texts have been written which describe the theory and applications of NMR to paramagnetic molecules including proteins and enzymes with paramagnetic transition metal ions.[10–12]

The short electron spin relaxation time required to observe paramagnetically shifted nuclei directly in NMR spectra also typically result in very broad ESR linewidths. In fact, as a rough guide, paramagnetically shifted NMR transitions are usually only observed in cases where the ESR spectrum is too broad to be observed. However, very broad ESR linewidths can also originate from inhomogeneous line broadening, even if the electron spin relaxation times are very long. In either case, if an ESR spectrum is observed, several experimental approaches are potentially applicable for the measurement of the magnetic interactions of the hyperfine coupled nuclei in these cases. These include DNP, ESR, ESEEM, ENDOR, and the extension of the latter to PE NMR.

In DNP spectroscopy the hyperfine coupling is used as a mechanism to enhance the nuclear polarization. The details of the mechanism for this enhancement and the magnitude of the enhancement depend on the details of the hyperfine interaction, particularly on the time dependence of the hyperfine coupling, and on the details of the ESR spectrum, such as the ESR linewidth and relaxation time. The theory and applications of DNP spectroscopy have been discussed in several texts and review articles.[13–18] (See ***Dynamic Nuclear Polarization and High-Resolution NMR of Solids***.) Here we discuss only those aspects of DNP spectroscopy that are relevant for comparison and contrast with the related techniques mentioned above.

In DNP spectroscopy the NMR signal is detected directly. The ESR transition is used only as a source for achieving enhanced nuclear polarization. Theoretically a maximum enhancement of the NMR signal of the order of ω_e/ω_n can be achieved, but in practice significantly lower values are

usually observed. Direct detection of the NMR signal has the advantage that the high resolution of NMR spectroscopy is maintained. At the same time, this excludes from detection those nuclei which have large hyperfine couplings. This is a result of the combination of low sensitivity and the large shift in transition frequencies. DNP spectroscopy has been applied most successfully in cases where the ESR spectrum consists of a narrow line which is easily saturated. Examples include studies of fossil fuels[19] and polymer interfaces.[20–22]

Paramagnetically coupled nuclei may be observed directly as hyperfine splittings in the ESR spectrum. Such splittings are often observed in ESR spectra of organic radical molecules in liquids (see ***Electron–Nuclear Hyperfine Interactions***). However, if the spin dynamics are not in the fast motion limit, hyperfine splittings are generally not resolved because of inhomogeneous line broadening.

Two different general approaches are available for measuring the magnetic couplings of nuclei which are not resolved in the ESR spectra. One approach is ESEEM.[23–26] In this technique both the allowed and the semiforbidden ESR transitions are coherently excited using two or more short, intense microwave pulses. The nuclear hyperfine and quadrupole interactions (in the case of nuclei with spin multiplicity $I \geq 1$) are observed as a periodic modulation of the envelope of the primary spin echo or stimulated echo intensity. Fourier transformation of this modulation pattern yields a spectrum of frequencies corresponding to the hyperfine (and quadrupolar for $I \geq 1$) frequencies.

One of the advantages of the ESEEM experiment is its high sensitivity, which is roughly comparable with that obtained in an ESR experiment. Furthermore, by selecting the appropriate microwave excitation frequency and applied magnetic field conditions, it is possible to measure the pure nuclear quadrupolar resonance frequencies for nuclei with $I \geq 1$.[27,28] This is possible despite the fact that the experiment is performed at finite magnetic field and the only spin transitions that are excited are the ESR transitions. One limitation of this type of experiment is that nuclear modulation can only be observed if the hyperfine interaction has finite anisotropic coupling components. The second criteron for modulation to be observed is that the microwave pulses must be able to excite both allowed and semiforbidden ESR transitions. This places constraints on the nature of the hyperfine interaction which will yield observable modulation. The theory, techniques, and applications of ESEEM spectroscopy have been reviewed in several texts and review articles.[23–27,29]

The second approach for measuring the magnetic couplings of nuclei which are not resolved in the ESR spectra is directly to excite both the NMR and ESR transitions with rf and microwave excitation. The first double resonance experiment of this type, known as an 'electron–nuclear double resonance', or simply ENDOR, experiment was reported by Feher in 1956.[30] The continuous wave (CW) ENDOR experiment is performed by applying a strong microwave field which is selected to irradiate continuously an EPR transition while simultaneously applying a strong rf field. The rf field is swept through the range of frequencies that encompass the NMR spectrum while continuously observing the intensity of the EPR transition. The intensity of the latter changes whenever the rf frequency matches an NMR transition frequency. The intensity of the EPR transition plotted as a function of the rf frequency generates the ENDOR spectrum. Thus, the ENDOR spectrum is a spectrum of the NMR transitions detected indirectly via the EPR transition. This is in contrast to the ESEEM experiment where the nuclear spin flip is a consequence of exciting a semiforbidden ESR transition. As a result, anisotropic hyperfine interactions are not necessary to observe hyperfine frequencies in the ENDOR experiment.

The ENDOR technique and applications have been documented in several texts and review articles.[1,8,9,31–36] In the case of one electron coupled to a spin-$\frac{1}{2}$ nucleus, and considering for simplicity that the hyperfine interaction is isotropic, the ENDOR spectrum comprises two transitions corresponding to one NMR transition for each of the two electron spin states. There exists a one-to-one correspondence between the number of coupled inequivalent nuclei and the number of ENDOR transitions observed. This can be contrasted to the number of transitions observed in the EPR spectrum where the number of transitions observed is a multiplicative function of the number of inequivalent nuclei coupled to the unpaired electron spin. The reduced number of transitions results in spectral simplification and, consequently, in enhanced spectral resolution.

While the success of the CW ENDOR experiment has been well documented, certain inherent problems in the technique have also limited its applicability. One well-documented limitation of the CW ENDOR experiment is the constraints on the relationship between NMR and ESR relaxation rates that must be satisfied in order to observe an ENDOR signal.[31,32,37–41] These constraints are changed (although not removed) with pulsed excitation techniques. This was recognized by W. B. Mims who reported the first pulsed ENDOR experiment in 1965, roughly a decade after Feher's initial report of the CW ENDOR experiment. Since then the advantages and applications of employing pulsed excitation techniques for both the ESR and NMR transitions have been demonstrated in publications from several laboratories.[37,38,41–46]

A second significant advantage of employing pulsed excitation techniques for both the ESR and NMR transitions is the potential for extending the type of experiments which can be performed. This is in many respects analogous to the extension of the experimental capabilities which become possible using pulsed excitation techniques in NMR spectroscopy. There are, however, distinct differences that must be kept in mind when using the analogy to pulsed NMR. These will be discussed in more detail in the next section. Furthermore, since multiple irradiation frequencies may be used to excite both the NMR and EPR transitions, the modern combined pulsed NMR and pulsed EPR experiments will be referred to as 'pulsed electron NMR' (PE NMR) spectroscopy. In this article, we describe the basic principles of these techniques, their implementation, including the pulse schemes and specific examples of experimental techniques, and illustrate the type of information that can be derived with examples in selected applications.

2 BASIC PRINCIPLES

In this section the magnetic interactions that determine the frequencies and amplitudes in pulsed ENDOR spectra are briefly reviewed. More comprehensive treatments can be found in several texts.[2,6,31,32,47,48] The analysis of the pulsed ENDOR spectrum provides the starting point for understanding the extensions of the basic pulsed ENDOR technique. After

the properties of the pulsed ENDOR spectrum have been presented, the general approach for the PE NMR techniques will be introduced. This is followed by specific experimental techniques with examples of applications.

2.1 Nuclear Spin Interactions and the Spectrum

2.1.1 Transition Frequencies

For spin-$\frac{1}{2}$ nuclei, the NMR spectrum of the paramagnetically coupled nuclei is dominated by the local magnetic field generated by the unpaired electron spin and by the applied magnetic field. The magnitude and orientation of this local field depends on whether the electron spin is aligned along or opposed to the direction of the external magnetic field. The effect of the combined local field and applied field on the nuclear spin is described by the nuclear spin Hamiltonian (expressed in units of frequency)

$$\hat{\mathcal{H}}_n = \sum_{i=1}^{3} (\hat{\boldsymbol{S}}' \cdot \boldsymbol{A} - g_n \beta_n B_0 b_i) \hat{I}_i \tag{1}$$

where the subscript i = 1, 2, 3 on $\hat{I}_i$ refers to the x, y, z components of the nuclear spin operator $\hat{\boldsymbol{I}}$. The prime on the electron spin operator $\hat{\boldsymbol{S}}'$ indicates that a coordinate system is selected in which the $\boldsymbol{g}$ tensor is diagonal. The b_i are the unit vectors of the applied magnetic field expressed in spherical polar coordinates:

$$(b_1, b_2, b_3) = (\cos\phi \sin\theta, \sin\phi \sin\theta, \cos\phi) \tag{2}$$

In most pulsed EPR experiments, particularly on transition metal ions, the microwave pulses excite only a small region of the spectrum centered about the magnetic field for resonance. This magnetic field position selects a subset of molecular orientations defined by the resonance condition, $h\nu = g\beta B_0$, where the orientation dependence of the electronic g factor is expressed by

$$g(\theta, \phi) = \left[\sum_{i=1}^{3} (g_i b_i)^2 \right]^{1/2} \tag{3}$$

The number of molecular orientations which contribute to the ENDOR spectrum is minimum for values of (θ,ϕ) that correspond to the principal axes of the $\boldsymbol{g}$ tensor. This phenomenon is referred to as g-factor orientation selectivity.[49] Since a lower number of molecular orientations contribute, higher spectral resolution can be observed in ENDOR spectra recorded at magnetic field values corresponding to those values of (θ,ϕ) which correspond to these principal axes.

The local field is described by the term $\hat{\boldsymbol{S}}' \cdot \boldsymbol{A}$, where $\boldsymbol{A}$ is the hyperfine interaction tensor. The magnitude of the local field depends on the distance between the electron and the nucleus and on the nature of the chemical bonding that pertains to the electron and nucleus, i.e. on the electronic state in which the electron resides. The distance separating the electron and nucleus determines a classical dipolar interaction. Since the gyromagnetic ratio of the electron is very large, this local magnetic field can be very large. The classical dipolar field will only provide a valid description of the distance between the electron and nucleus if the electron can be treated as a point dipole. Contributions to the hyperfine anisotropy also depend on the nature of the electronic wavefunction. The latter also determines whether the nucleus has a finite unpaired electron spin density at the nucleus. A finite unpaired spin density at the nucleus can only occur if the molecular orbital that describes the unpaired electron has some atomic s-orbital contribution in the wavefunction. The nonclassical contribution to the hyperfine anisotropy is sometimes referred to as 'pseudodipolar coupling'.

The orientation dependence of the local field can be expressed by an orientation-dependent hyperfine coupling $A(\theta, \phi)$. The NMR transition frequencies are then given by

$$\nu_{\pm} = \nu_n \pm \tfrac{1}{2}|A(\theta, \phi)| \tag{4a}$$

$$\nu_{\pm} = \tfrac{1}{2}|A(\theta, \phi)| \pm \nu_n \tag{4b}$$

where the first expression applies if $2\nu_n > |A|$ and the second expression applies if $2\nu_n < |A|$, while in both cases it is assumed that $I = \frac{1}{2}$.

The two limiting expressions [equations (4a) and (4b)] for the NMR frequencies are a recognition of the fact that the local magnetic field described by the hyperfine interaction can be comparable to or larger than the applied magnetic field. This is especially the case at the low applied field strengths, typically 0.35 T, at which many ENDOR and PE NMR experiments are performed. If the local field is greater than the applied field, then the local field is the dominant term that defines the nuclear quantization axis and the applied field is a perturbation. In either case, equations (4a) and (4b) indicate that for a nucleus with $I = \frac{1}{2}$, two NMR transitions will be observed in the ENDOR spectrum, with one transition originating from each of the two electron spin manifolds defined by the eigenvalue, $m_{S'}$, of $\hat{\boldsymbol{S}}'$. These NMR transitions will either be centered on the nuclear Larmor frequency if $2\nu_n > |A|$ or on one-half of the hyperfine coupling if $2\nu_n < |A|$.

In the case of organic radicals, the anisotropy of the g factor can be ignored in the first order analysis of the paramagnetically shifted NMR transitions. The NMR transition frequencies $\nu_{\pm}$ are then given by[50]

$$\begin{aligned} \nu_{\pm} = [&(S_z A_{xx} - \nu_n)^2 \sin^2\theta \cos^2\phi \\ &+ (S_z A_{yy} - \nu_n)^2 \sin^2\theta \sin^2\phi \\ &+ (S_z A_{zz} - \nu_n)^2 \cos^2\theta]^{1/2} \end{aligned} \tag{5}$$

where θ and ϕ are the spherical polar angles relating the applied static field $\boldsymbol{H}_0$ to the principal axis of the hyperfine tensor (A_{xx}, A_{yy}, A_{zz}). Equation (5) assumes that the high-field approximation is valid where the electron and nuclear spin operators $\hat{\boldsymbol{S}}$ and $\hat{\boldsymbol{I}}$ are completely decoupled from the molecular framework and quantized along the applied magnetic field direction. An energy level structure corresponding to an arbitrary selected set of (θ, ϕ) values is shown in Figure 1.

In general, the g factor for the electron will not be isotropic as assumed in the expressions described by equations (4a), (4b) and (5). Anisotropy of the electron g factor is usually

significant in ESR spectra of transition metal ions.[6,7] If the g factor is anisotropic, the NMR frequencies and lineshape will depend on the magnetic field position and microwave frequency selected.[6,48,51,52] In a noncrystalline solid, a single pair of NMR transitions will only be observed if the principal axes of the $\boldsymbol{g}$ and $\boldsymbol{A}$ matrices are collinear. Otherwise a powder pattern lineshape will be observed because of the angular dependence of the $\boldsymbol{g}$ and $\boldsymbol{A}$ matrices.

The NMR frequencies described in equation (5) do not account for the second-order frequency shifts of the ENDOR lines observed for large hyperfine couplings. Since these second-order frequency shifts are proportional to $A^2/4\nu_e$, they can usually be ignored under most experimental conditions. However, even for relatively small hyperfine coupling values, these second-order effects, arising from the spin Hamiltonian terms $\hat{S}_x\hat{I}_x$ and $\hat{S}_y\hat{I}_y$ must be included to calculate correct wave functions that reproduce the rf frequency dependence of the ENDOR amplitudes. These spin coupling terms lead to an enhancement, known as the 'hyperfine enhancement', of the rf field seen by the nucleus. Note that the enhancement can also be negative, i.e. a decrease in the rf field at the nucleus, depending on the eigenvalue m'_S of $\hat{\boldsymbol{S}}'$.

The simple four-level system with isotropic hyperfine coupling described by the spin Hamiltonian:

$$h^{-1}\hat{\mathcal{H}}_0 = \nu_e\hat{S}_z - \nu_n\hat{I}_z + aS_z\hat{I}_z \tag{6}$$

is usually adequate for describing the basic concepts for the sublevel polarization transfer experiments as well as several other PE NMR experiments described later in this article. In the high temperature limit, i.e. $g_e\beta_eB_0/kT \ll 1$, the spin eigenvalues, $h^{-1}E_0(M_S,M_I)$, are given by:

$$h^{-1}E_0(M_S, M_I) = \nu_eM_S - \nu_nM_I + aM_SM_S \tag{7}$$

The energy levels in Figure 1 also describe these eigenstates which arise from the coupling of an $S = I = \frac{1}{2}$ system with isotropic hyperfine coupling. With this level of simplification it is possible to gain considerable insight into the spin dynamics of PE NMR experiments using the spin operator formalism[42] frequently used in NMR spectroscopy.[53]

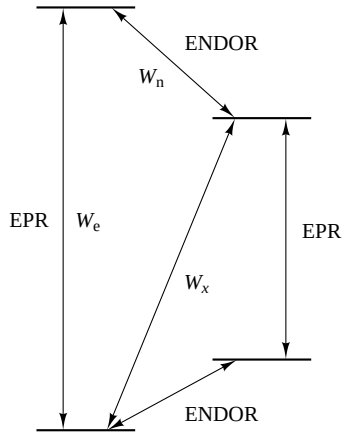

Figure 1 Energy level structure corresponding to the spin Hamiltonian of a four-level system. EPR, ENDOR, and relaxation transitions are identified

In the literature on pulsed ENDOR and PE NMR spectroscopy, the hyperfine splitting of the electron spin eigenstates are referred to as 'hyperfine sublevels' or simply as 'sublevels'. The EPR, NMR, and spin relaxation transitions relevant in the discussion of the ENDOR experiment are identified in Figure 1. The ENDOR transitions indicated in the figure are NMR transitions detected indirectly by the ESR transition. The electron and nuclear relaxation transition probabilities W_e and W_n correspond to effective T_{1e}^{-1} and T_n^{-1} rates; these are also identified in Figure 1. In the analysis of signal amplitudes in the CW ENDOR experiment, the effective rates are the intrinsic rates enhanced by the application of the microwave or rf excitation fields.

If the nuclear spin multiplicity $I \geq 1$, the quadrupolar interaction will result in additional splittings of the hyperfine sublevels. The quadrupolar interaction is described by adding the nuclear self-coupling term, $\hat{\boldsymbol{I}} \cdot \boldsymbol{P} \cdot \hat{\boldsymbol{I}}$ to the spin Hamiltonians of either equation (1) or equation (6). If the principal axes of the $\boldsymbol{g} \cdot \boldsymbol{A} \cdot \boldsymbol{P}$ are collinear and the magnetic field $\boldsymbol{B}_0$ is oriented parallel to one of these principal axes, the first-order ENDOR frequencies are given by[2,6,48]

$$\nu_{ENDOR} = \left| \frac{A_i}{2} \pm \nu_n \pm \frac{3}{2}|P_i|(2m_i + 1) \right| \tag{8}$$

where A_i and P_i denote the principal values of the $\boldsymbol{A}$ and $\boldsymbol{P}$ tensors along the i axis. The nuclear transitions in equation (8) are assumed to increase in the nuclear spin quantum number, i.e. $m_I \rightarrow m_I + 1$. It has also been assumed that ($|A| > 2\nu_n > 3|P_i|$). The principal values of the quadrupolar tensor $\boldsymbol{P}$ are defined as $|P_{zz}| > |P_{yy}| > |P_{xx}|$. These principal values are related to the magnitude of the quadrupolar coupling constant χ and asymmetry parameter η by

$$\chi = 2I(2I - 1)P_zz \tag{9a}$$

$$\eta = \frac{P_xx - P_yy}{P_zz} \tag{9b}$$

According to equation (8), four ENDOR transitions are expected for a nucleus with $I = 1$. However, not all ENDOR transitions may be observed when exciting an ESR transition at a given magnetic field value, since it is possible that each m_I state may be selectively excited. For example, a two-line ENDOR spectrum will be observed if the ESR transition connects the $m_I = 1$ to $m_I = 1$ sublevels of the $m_S = +\frac{1}{2}$ and $m_S = -\frac{1}{2}$ electron spin manifolds.

2.1.2 ENDOR Amplitudes

ENDOR signal amplitudes are proportional to the change in the EPR signal intensity, ΔE, induced by an NMR transition. Since the EPR signal intensity E is proportional to the electron spin susceptibility χ_e, a relative ENDOR susceptibility can be defined by

$$\frac{\Delta\chi_e}{\chi_e} = \frac{\Delta E}{E} \tag{10}$$

The transition frequencies and amplitudes that are described by the time-independent terms in the spin Hamiltonian are independent of the method of exciting and detecting the transitions. However, the dynamic terms of the total spin Hamiltonian that describe the spin system have different effects on the amplitudes in the CW and pulsed experiment. In the CW experiment, the ENDOR signal amplitude depends on the rate at which the ESR and NMR transitions are excited by the applied microwave and rf magnetic fields compared with the rate of intrinsic relaxation pathways that will compete to restore the spin system to thermal equilibrium. Once the spin eigenstates and relaxation rates that connect the eigenstates have been defined, coupled rate equations can be used to model the ENDOR signal amplitude. In contrast, the pulsed ENDOR or ENMR experiment is performed on a timescale which is short compared with the intrinsic spin relaxation rates. The amplitudes can therefore be analyzed without resorting to coupled rate equations.

In the CW experiment, the interplay between the transition intensity induced by the applied magnetic fields and the intrinsic spin relaxation rates is further complicated by the effect of the hyperfine enhancement on the ENDOR amplitudes.[31,32,50,54] For intense rf fields, the ENDOR amplitudes can be independent of the rf frequency. For very weak rf fields, the ENDOR amplitudes increase with the square of the rf frequency. For intermediate values, the ENDOR amplitudes can be a complex function of the transition moments and relaxation parameters, especially since both the transition moments and the relaxation rates can be orientation dependent.

In pulsed ENDOR experiments, the analysis of the hyperfine enhancement and the effects of the spin relaxation on the ENDOR amplitudes is less complex. The pulsed ENDOR experiment is usually performed on a timescale which is short compared with the electron, nuclear, and the electron–nucleus cross-relaxation rates. In this case the relaxation rates do not influence the relative ENDOR amplitudes. The loss of electron spin polarization by T_{1e} processes during the mixing period (described in Section 2.2) results in a uniform decrease in the signal amplitudes, $\Delta\chi_e/\chi_e$, across the ENDOR spectrum. The hyperfine enhancement of the NMR transition moment is then simply observed as a change in the sublevel nutation angle as a function of rf frequency. The sublevel nutation angle θ_R is given by $\theta_R = \gamma_n \epsilon B_2 t_{rf}$, where ϵ is the hyperfine enhancement factor. If the hyperfine interaction is isotropic, the hyperfine enhancement factor is given by $\epsilon = |1 + m_s a/\nu_n|$. The hyperfine enhancement can be observed directly in EPR detected sublevel transient nutation experiments.[43,55]

As described in the next section, the pulsed ENDOR experiment can be divided into pulse periods. The ENDOR amplitude is a function of the microwave pulses in the preparation period and detection period as well as of the nutation angle of the sublevel polarization in the mixing period. The latter can be expressed by

$$EA(\nu_{rf}) = \tfrac{1}{2}(1 - \cos(\theta_{R\pm})) \qquad (11)$$

In the limit of small nutation angles, the cosine term can be expanded in a power series:

$$EA(\nu_{rf}) \approx \frac{(\theta_{R\pm})^2}{4} = \frac{(m_s A)^2}{(2\nu_n)^2} = \frac{(m_s)^2}{(2\nu_n)^2}(\nu_\pm - \nu_n)^2 \qquad (12)$$

Equation (12) explicitly indicates that the Fermi golden rule result for the rf frequency dependence of the transition probability is obtained in the limit of small nutation angle. If the nutation angle is adjusted to correspond to a π pulse at each ENDOR frequency, the ENDOR amplitudes should be independent of the hyperfine enhancement factor. It is straightforward, although time consuming, to measure the sublevel nutation frequency at each ENDOR frequency in the ENDOR spectrum for a quantitative analysis of the ENDOR amplitudes. Additional contributions to the ENDOR amplitudes arise from the effect of hyperfine contrast selectivity in the preparation period and from possible electron–nucleus coherence effects in the detection period.[37,38] These effects are discussed in more detail in Section 3. Contributions originating from the hyperfine anisotropy[6,48] and g-factor orientation selectivity[6,48] will also affect the amplitudes in both the CW and pulsed ENDOR experiments.

2.2 Pulse Schemes

Many of the PE NMR experimental techniques can be understood by analogy to heteronuclear NMR experiments. However, in making this comparison between PE NMR and heteronuclear NMR experiments, some important differences must be recognized. These originate from the fundamental properties of the unpaired electron compared with a nucleus. The two most significant differences are the γ values of the electron and nucleus and the differences between the nature of the wave functions that describe the electron and the nucleus.

The larger γ for the electron compared with any nucleus has two important consequences. The first is the practical consequence for the type of instrumentation required for PE NMR experiments compared with heteronuclear NMR experiments. The heteronuclear NMR experiment requires a transmitter, probe, and receiver capable of handling two (or more) different rf frequencies. In contrast, for the double resonance experiment between the electron and nucleus, the hardware must be capable of handling both rf and microwave frequency components.

A second consequence of the larger γ of the electron is that the local magnetic field generated by the electron is much larger than is generated by any nucleus. This has several consequences on the properties of the spectra observed for nuclei that are coupled to this local field and also has implications on the types of experiments which can be performed. In most cases, PE NMR experiments must be analyzed within the so-called ‘soft pulse limit’, i.e. the bandwidth of the excitation pulses for both the ESR and NMR transitions are much smaller than the spectral bandwidth. In other words, both the ESR and NMR pulses are generally selective excitation pulses. The broad linewidths also exclude certain techniques such as cross polarization in the rotating frame and magic angle spinning which have had such an important impact on NMR of solids from being directly adapted to PE NMR experiments.

The second important difference to bear in mind when comparing PE NMR spectroscopy with pulsed heteronuclear NMR is the difference in the nature of the total wavefunction associated with the electron compared with the nucleus. The electron is generally in an eigenstate, such as an atomic or

molecular orbital, which has a much greater spatial extent than the localized eigenstate which describes the nucleus. This has the consequence that the electron spin is delocalized so that the electron is generally coupled to many more nuclei than would be the case if the electron were represented by a point dipole. The delocalization of the electron spin density in molecular orbitals that have well defined spatial extents can also contribute large anisotropic components to the local (i.e. hyperfine) field. The anisotropy of the hyperfine interaction also assures that the quantization axis for the nucleus does not point in the same direction in the two electron spin eigenstates. This anisotropy in the hyperfine interaction is therefore responsible for the broad spectral widths observed for the NMR transitions and also affects the transitions which are observed, since formally forbidden transitions become 'semiforbidden' transitions.

Another consequence of the nature of the electronic states that host the unpaired electron is that spin coupling mechanisms such as the spin–orbit coupling are effective in broadening the ESR linewidth and in enhancing the spin relaxation rate. Both the broad lines and the shorter relaxation times have implications on the types of PE NMR experiments that can be performed.

The pulse sequences employed in PE NMR experiments can be conveniently divided into pulse periods in direct analogy to NMR spectroscopy. With the above-mentioned caveats in mind, the pulse periods can be analyzed by analogy to a pulsed heteronuclear NMR solids experiment within the soft pulse limit, wherein selective excitation is considered in the analysis. The most basic experiment consists of a preparation, mixing, and detection period. The purpose of the preparation period is to create an initial state perturbed from the equilibrium spin polarization established by the conditions of the temperature and external field (as well as by the level structure of the electron–nuclear coupled spin system). In all PE NMR experiments reported to date, one or two microwave pulses are applied to excite ESR transitions in the preparation period.

Two basically different types of PE NMR experiments will be performed depending on whether the microwave preparation pulses have created sublevel nuclear spin polarization or electron spin coherence at the end of the preparation period. The former are the starting points for ESR detected sublevel polarization transfer experiments and for ESR detected nuclear coherence experiments. The latter is the starting point for coherence transfer ENDOR experiments. In this experiment, a single microwave pulse, ideally a $\pi/2$ pulse, creates electron spin coherence in the preparation period.

In the mixing period, one or more rf pulses are applied to manipulate the sublevel polarization or sublevel coherence. The nature of the perturbation determines the type of experiment performed. The mixing period may include an evolution period, again depending on the type of experiment performed. If sublevel nuclear coherence has been created and is to be indirectly observed via the ESR transition intensity, the mixing period must end with a $\pi/2$ rf pulse that converts the sublevel coherence to sublevel polarization.

In the detection period one or more microwave pulses are applied to create electron spin coherence which is detected in the PE NMR experiment. The electron spin transverse magnetization provides a readout of the electron–nucleus longitudinal order. The transverse magnetization can be detected by a primary spin echo,[56] a stimulated echo,[57] or as a free induction signal.[58] It is also possible to use CW irradiation to detect the transverse electron magnetization[42] or to detect the longitudinal electron magnetization directly.[29]

3 EXPERIMENTAL TECHNIQUES WITH SELECTED APPLICATIONS

3.1 ESR Detected Sublevel Polarization Transfer

It is possible to envisage many pulse sequences which create sublevel nuclear spin polarization. The most common methods, shown in Figure 2, are a single microwave pulse which selectively excites one ESR transition or two microwave pulses. The former was first proposed by Davies[56] and is the starting point for what has become known as the Davies ENDOR experiment. The latter was first proposed by Mims[57] and is the preparation pulse sequence for the experiment now known as Mims ENDOR.

Referring to Figure 3, the selective excitation of one of the two allowed ESR transitions converts the electron spin polarization, represented by the boxes, into electron–nucleus two-spin longitudinal order. The spin polarization from the nuclear Zeeman and hyperfine interactions is negligible compared with the electron spin polarization and can be ignored. The two spin order refers to the fact that the nuclear spins in both NMR transitions are polarized.

Two spin electron–nucleus longitudinal order can also be created using two selective microwave pulses or two nonselective microwave excitation pulses if an evolution time separates the two pulses.[42] Sublevel polarization is created from the transverse components of the magnetization that evolves following the first pulse in the local field of the hyperfine interaction. The second pulse converts the transverse magnetization to two-spin longitudinal order. This suggests that the two pulses should be $\pi/2$ pulses for maximum efficiency in creating sublevel polarization. After the second

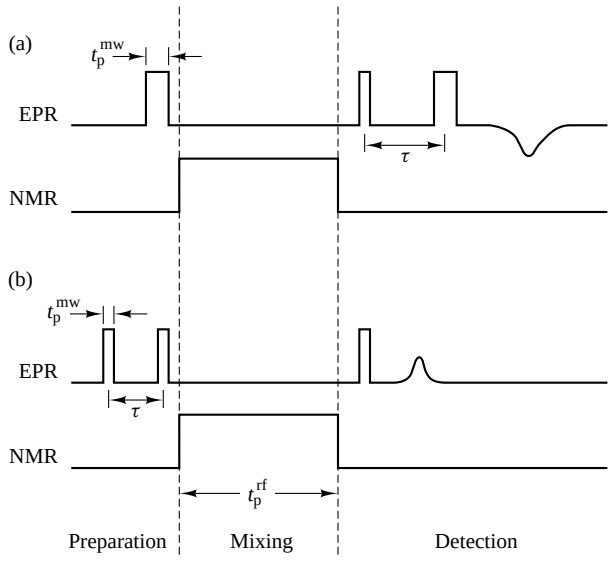

Figure 2 Davies ENDOR (a) and Mims ENDOR (b) pulse sequences

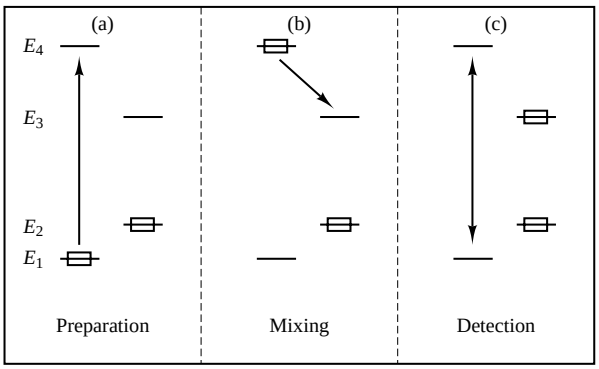

Figure 3 The transfer of spin polarization during the preparation (a), mixing (b) and detection (c) periods of the Davies ENDOR sequence for the four level system shown in Figure 1

pulse, the net sublevel polarization is approximately $\sin(a\tau/2)$ $\sin(\Omega_S\tau)$, where a is the hyperfine coupling in equation (6) and Ω_S is a resonance offset. Note that no sublevel polarization exists for values $a\tau/2 = n\pi$, where n is an integer. These are known as blind spots in the Mims ENDOR experiment.

For an ESR lineshape which is inhomogeneously broadened, the sublevel polarization created by the microwave pulses in the preparation period burn a hole into the envelope of the ESR absorption lineshape as shown in Figure 4(a). The width of the hole is determined by the excitation bandwidth of the preparation pulse. In the case of two pulse excitation, a serrated pattern of magnetization is superimposed on the hole, as shown in Figure 4(b).

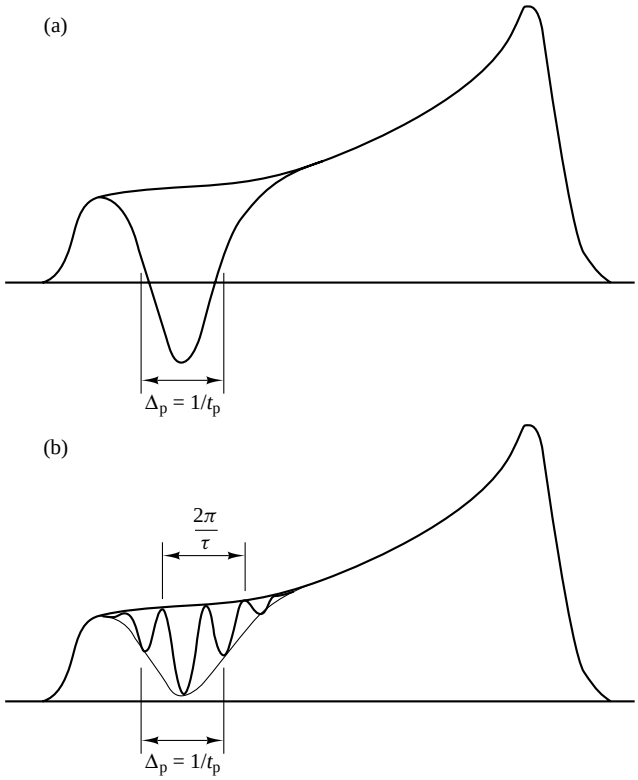

Figure 4 EPR spectra of an inhomogeneously broadened line after the preparation period in the Davies ENDOR (a) and Mims ENDOR (b) pulse sequences. (Reproduced by permission of Academic Press from H. Thomann and M. Bernardo, in 'Methods in Enzymology', eds. J. F. Riordan and B. L. Vallee, 1993, Vol. 227, Chap. 6)

3.1.1 Davies and Mims ENDOR

The pulse sequences for the two most commonly used experiments for the ESR detection of sublevel polarization transfer are shown in Figure 2. The hole-burning effect created by the preparation pulses on an inhomogeneously broadened ESR absorption envelope is shown in Figure 4. The effect of a selective ESR excitation on the electron spin polarization in a four level system described by equation (7) is shown in Figure 3(a). The electron spin polarization associated with these two energy levels will be inverted if the selective microwave pulse is a π pulse. Note that the sublevel longitudinal polarization of both the upper and lower NMR sublevels are not at equilibrium at the end of the preparation period.

In the next step of the pulse sequence, an rf pulse transfers and thereby 'mixes' the electron spin polarization between the sublevels. This is shown in Figure 3(b) for an rf pulse on resonance with the upper sublevel. In the hole-burning picture shown in Figure 4, the sublevel polarization transfer corresponds to the transfer of polarization from within the hole to a frequency offset by the value of the hyperfine coupling. This sublevel polarization transfer occurs at frequencies corresponding to the NMR frequency shifted by the hyperfine interaction (see Section 2.1.1).

The sublevel polarization transfer could, in principle, be detected directly as an NMR signal. Indeed, this would correspond to a pulsed DNP experiment. Note, however, that the sublevel polarization transfer has also changed the electron longitudinal polarization of the two ESR transitions. The sublevel polarization transfer can therefore be detected by measuring the change in the ESR transition intensity. This can be accomplished using a variety of techniques, as discussed in Section 2.2. In the Davies and Mims ENDOR pulse sequences the change in electron longitudinal polarization is detected by observing the change in intensity of a primary or stimulated spin echo. This electron spin coherence is indicated by the double arrow in Figure 3(c).

The spectrum of NMR transition frequencies shifted by the hyperfine coupling, i.e. the ENDOR spectrum, usually far exceeds the excitation bandwidth of the rf pulses. The complete spectrum must therefore be recorded by incrementing stepwise the rf frequency on successive iterations of the pulse sequences shown in Figure 2. The limit of resolution in the spectrum is determined by the excitation bandwidth of the rf pulse.

The Davies ENDOR spectrum of a single crystal of malonic acid which has been irradiated by X-rays to generate carbon π radicals[59] is shown in Figure 5. The transitions at approximately 5 and 30 MHz are the two sublevel transitions associated with the α proton of the CH fragment of the $\dot{C}H(COOH)_2$ radical molecule. The other proton lines originate from the carboxylic protons, from coupling to protons on neighboring malonic molecules, and from overlapping ESR signals from different malonic acid radical molecules.[59] The increase in spectral resolution obtained by decreasing the excitation bandwidth of the rf mixing pulse is shown in the inset of the figure.

The relative amplitudes of the ENDOR transitions are determined by the spin Hamiltonian (as discussed in

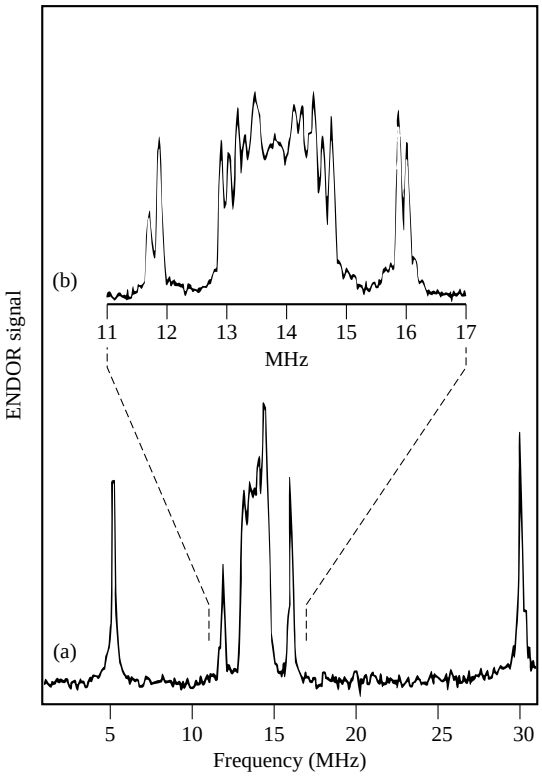

Figure 5 Davies ENDOR spectrum of an X-ray irradiated crystal of malonic acid with rf pulse widths of 5 μs (a) and 10 μs (b). (Reproduced by permission of the American Chemical Society from H. Thomann and M. Bernardo, in 'Advances in Chemistry Series 229: Magnetic Resonance of Carbonaceous Solids', eds. R. E. Botto and Y. Sanada, Washington, DC, 1993, Chap. 4)

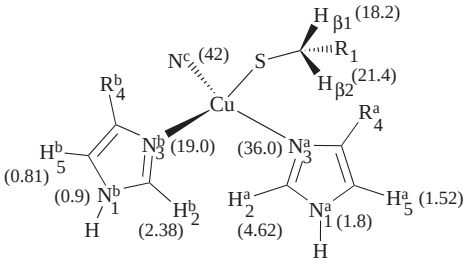

Figure 6 Spectroscopic model for the copper coordination structure in the high pH form of stellacyanin showing the hyperfine couplings (in MHz). (Reproduced by permission of Academic Press from H. Thomann and M. Bernardo, in 'Methods in Enzymology', eds. J. F. Riordan and B. L. Vallee, London, 1993, Vol. 227, Chap. 6)

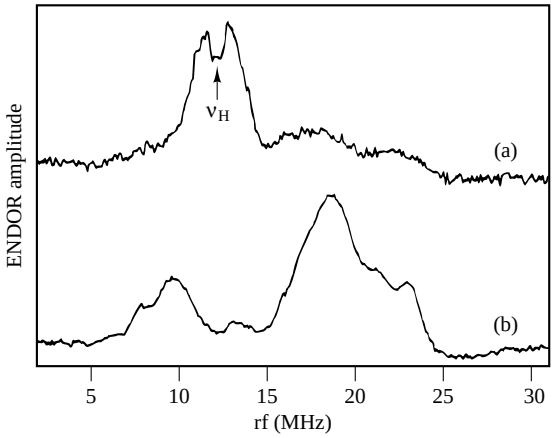

Figure 7 Davies ENDOR spectra of stellacyanin using microwave inversion and detection pulse widths t_{mw} of 0.40, 0.20, 0.40 μs (a) and 0.04, 0.02, 0.04 μs (b). (Reproduced by permission of Academic Press from H. Thomann and M. Bernardo, in 'Methods in Enzymology', eds. J. F. Riordan and B. L. Vallee, 1993, London, Vol. 227, Chap. 6)

Section 2.1.2) but also by the excitation bandwidth, Δ_p of the preparation pulse. In order for a sublevel polarization transfer signal to be detected indirectly using the Davies ENDOR pulse sequence [Figure 2(a)], the condition that $\Delta_p > a$, where a is the hyperfine coupling, must be satisfied.[56] If $\Delta_p > a$, the transfer of polarization remains within the hole burned into the absorption envelope. In this case the change in electron polarization is reduced, resulting in a weaker ENDOR signal. This relationship between Δ_p and a has been referred to as 'hyperfine contrast selectivity',[37–39] as a 'spin alignment hole',[41] and as a 'self-ELDOR effect'.[42] The relationship between Δ_p and a can be used to eliminate or reduce the overlap of ENDOR signals originating from nuclei with different hyperfine couplings.[37–39,60]

Davies ENDOR spectra on a blue copper protein, stellacyanin,[61] will serve to illustrate the application of pulsed ENDOR (and PE NMR) spectroscopy. Transition metal ions and ion clusters are found at the active site for electron transfer in metalloproteins and at the active site for substrate conversion in metalloenzymes. The electron spin echo detected ESR (ED ESR) absorption envelope recorded by plotting the intensity of the primary electron spin echo as a function of magnetic field is shown in the inset of Figure 9. A spectroscopic model for the ligand coordination structure of the Cu^{2+} ion for the high-pH form of the protein is shown in Figure 6. The hyperfine coupling frequencies for each nucleus on the copper ligands are indicated in Figure 6. The NMR transitions for nuclei in the primary ligand coordination structure of the Cu^{2+} ion would be difficult to measure by any other spectroscopic technique.

The hyperfine contrast selectivity mechanism for eliminating the overlap of ENDOR lines is illustrated in Figure 7, where two Davies ENDOR spectra of stellacyanin[61] are shown. When a preparation pulse with narrow excitation bandwidth is used [Figure 7(a)], the proton ENDOR lines which have small hyperfine coupling values that originate from protons on the two imidazole ligands overlap the nitrogen ENDOR lines, particularly the nitrogen line centered at roughly 8 MHz. When a larger excitation bandwidth is used [Figure 7(b)] the amplitudes for these proton ENDOR lines are significantly attenuated. The 1 : 2 relative intensities of the two ^{14}N ENDOR lines centered at 8 and 18 MHz in Figure 7(b) are in agreement with the expected intensity difference due to the hyperfine enhancement factor.[37,38]

The proton ENDOR signals from protons with small hyperfine couplings can also be observed using preparation pulses with large excitation bandwidths with the Mims ENDOR pulse sequence. A comparison of the Davies and Mims ENDOR spectra for the stellacyanin protein is shown in Figure 8. The arrows in the Mims ENDOR spectrum indicate the positions of the 'blind spots' where no ENDOR signal is observed. The position of these blind spots in the spectrum

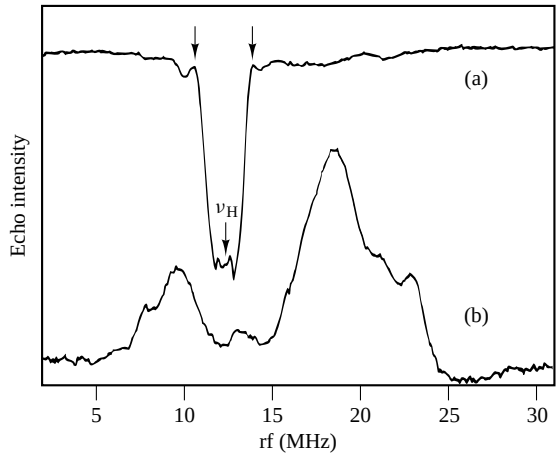

Figure 8 Comparison of the Davies and Mims ENDOR spectra for the stellacyanin protein. (Reproduced by permission of Academic Press from H. Thomann and M. Bernardo, in 'Methods in Enzymology', eds. J. F. Riordan and B. L. Vallee, London, 1993, Vol. 227, Chap. 6)

can be selected by the value of τ chosen in the Mims ENDOR pulse sequence. Note that the ENDOR signal for the protons with small hyperfine couplings is significantly enhanced in the Mims ENDOR spectrum. This is a consequence of the fact that a larger fraction of the electron magnetization can be sampled without suppressing the ENDOR signals from the nuclei with small hyperfine couplings.

An example of the advantage of the increased sensitivity achieved by the indirect detection scheme of the pulsed ENDOR experiment is shown in Figure 9, where the ENDOR signals from the central metal Cu^{2+} ion as well as those from all the (NMR active) ligand nuclei on the metal ligands are observed. The position in the ED ESR spectrum at which this Davies ENDOR spectrum was recorded is shown in the inset of the figure. Although the hyperfine splitting of the Cu^{2+} ion can be observed at the high-field end of the ESR spectrum, the hyperfine splittings are not resolved in the low-field region of the ESR spectrum. Note also that the pulsed ENDOR spectrum reveals the quadrupolar splitting of the Cu^{2+} nucleus. It is not possible to measure these quadrupolar interactions in the ESR spectrum.

3.1.2 Transient Nuclear Nutations

The sublevel nuclear transient nutations can be detected indirectly with the pulse sequences in Figure 2 by incrementing stepwise the rf pulse length on successive pulse sequence iterations. An example is shown for the malonic acid radical in Figure 10. The effect of the time dependence of the signal from the electron spin–lattice relaxation during the mixing time can be eliminated by choosing a fixed, long mixing time before detection or by subtracting the signal recorded without the rf pulse applied (or with the rf frequency set to an off-resonance position in the ENDOR spectrum). The electron spin echo amplitude in the detection period oscillates with a periodicity proportional to $\cos \theta_2$ where θ_2 is the sublevel nutation angle (see Section 2.1.2). These oscillations are sometimes referred to as Rabi oscillations. The influence of the hyperfine enhancement factor on the nutation angle is evident in Figure 10.

The sublevel nutation experiment provides a method for setting the rf mixing pulse conditions to the selected nutation angle. For ESR detected sublevel polarization transfer experiments, the optimum pulse is a π pulse. For the ESR detection of sublevel coherence, the rf mixing pulse would be set for a $\pi/2$ pulse. For samples which are not single crystals and that exhibit hyperfine anisotropy, the Rabi oscillations are rapidly damped after the first period.[37,38] Consequently, the effect on the ENDOR amplitudes due to the hyperfine enhancement can be reduced by selecting a long rf pulse length. However, this produces power broadened lines, and therefore a lower resolution in the spectrum. When two or more magnetically equivalent nuclei are coupled to the electron, harmonics may be observed in the sublevel nutation pattern.[42] An example is shown in Figure 11. Analysis of these

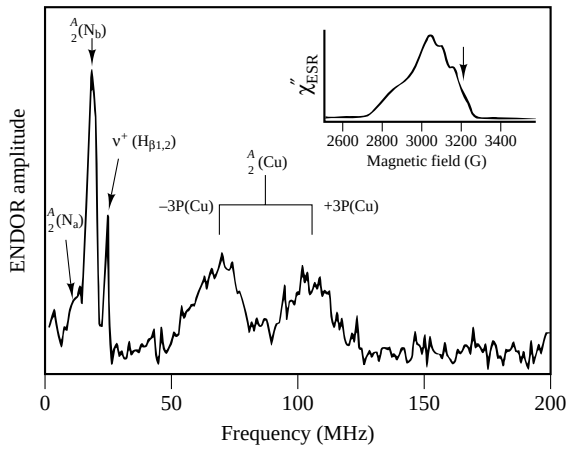

Figure 9 Davies ENDOR spectra of stellacyanin showing the Cu, N, and H resonances. Inset shows the position in the ED ESR spectra where the ENDOR spectra was recorded. (Reproduced by permission of Plenum Press from H. Thomann and M. Bernardo, in 'Biological Magnetic Resonance', eds. L. J. Berliner and J. Reuben, New York, 1993, Vol. 13, Chap. 7)

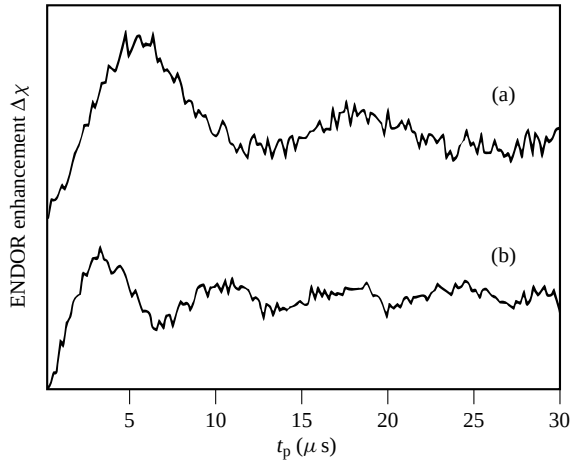

Figure 10 Sublevel nuclear transient nutations detected for the irradiated malonic acid radical at an rf of (a) 7.32 and (b) 21.29 MHz. (Reproduced by permission of the American Chemical Society from H. Thomann and M. Bernardo, in 'Advances in Chemistry Series 229: Magnetic Resonance of Carbonaceous Solids', eds. R. E. Botto and Y. Sanada, Washington, DC, 1993, Chap. 4)

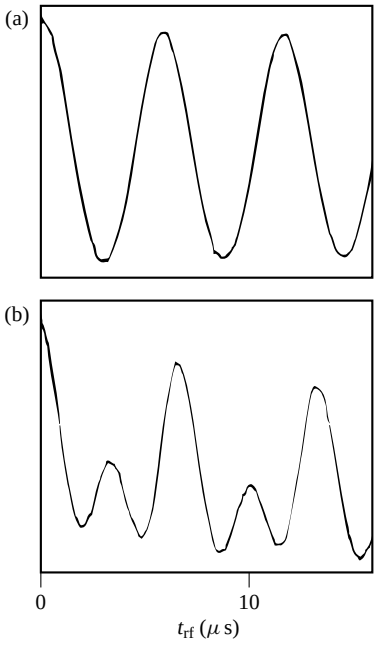

Figure 11 Sublevel nuclear transient nutation patterns of protons in VO(IV)- and Cu(II)-doped $Mg(NH_4)_2(SO_4)_2{\cdot}6H_2O$ single crystals: (a) one proton in $VO(H_2O)_5^{2+}$ and (b) two magnetically equivalent protons in $Cu(H_2O)_6^{2+}$. (Reproduced by permission of the American Chemical Society from C. Gemperle and A. Schweiger, *Chem. Rev.*, 1991, **91**, 1481)

harmonics provides a method for determining the number of equivalent nuclei coupled to the electron.

3.1.3 Optimized Davies and Mims ENDOR

The Davies or Mims ENDOR pulse sequences produce a maximum ENDOR enhancement of $\Delta\chi_e/\chi_e = 1$. A pulse scheme for theoretically increasing this efficiency to $\Delta\chi_e/\chi_e = 2$ has been proposed and demonstrated.[42] This is accomplished by inserting a microwave π pulse and a second rf π pulse following the first rf π pulse in the mixing period. This pulse sequence is the pulsed analog of the Special TRIPLE resonance technique which was also introduced to improve the efficiency in the CW ENDOR experiment.[34,62,63] In practice, the improvement in efficiency of the Davies or Mims ENDOR signal intensity is much smaller than theoretically possible, primarily because of pulse imperfections. Nevertheless, a gain in ENDOR enhancement is observed, as shown in the example given in Figure 12. Nonideal nutation angles due to pulse imperfections are particularly problematic for noncrystalline samples where the ENDOR lines are significantly overlapped.

3.1.4 Electron–Nucleus Coherence Effects

Electron–nucleus coherence effects can be observed in the Davies ENDOR experiment if the microwave pulses in the detection period excite both allowed and semiforbidden ESR transitions.[38,37] These coherence effects generate a nuclear modulation on the envelope of the primary electron spin echo in the detection period analogous to the ESEEM experiment. An example of this phenomenon is shown in Figure 13 where two Davies ENDOR spectra for the blue copper protein,

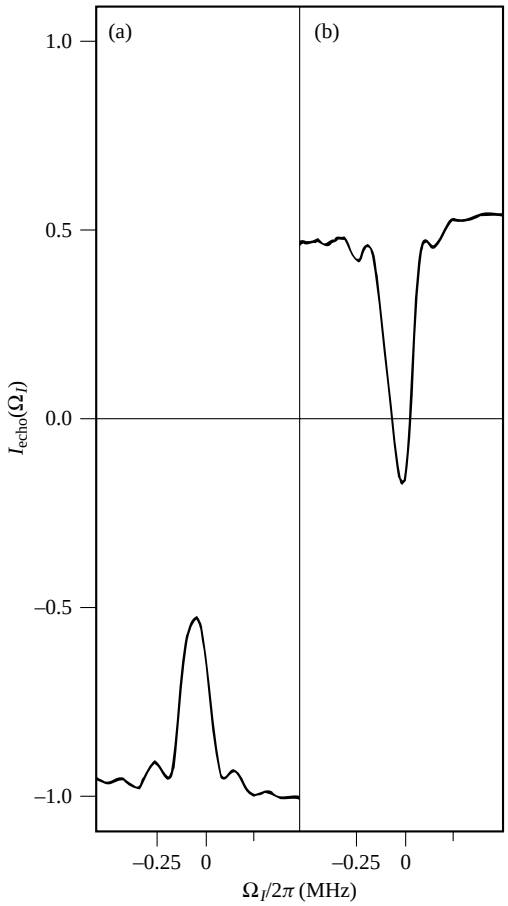

Figure 12 Mims-ENDOR spectra (a) of Cu(II)-doped TGS single crystal around the proton transition at $\omega_p/2\pi = 10.15$ MHz and the optimized spectra obtained using the pulse sequence described in the text. (Reproduced by permission of Academic Press from C. Gemperle et al., *J. Magn. Reson.*, 1990, **87**, 502)

stellacyanin, are shown recorded for two different values of the spin echo delay time τ in the detection period. The values of τ used in the detection period are indicated on the echo envelope waveform shown in the inset. These coherence effects can have important consequences for the analysis of the ENDOR spectrum. Note that the relative amplitudes of the ENDOR intensities depend on the value of τ in the detection period. This effect can be used as a spectral editing technique.[38,37]

3.1.5 Electron–Nucleus–Nucleus Triple Resonance

The Double ENDOR was originally introduced as a CW ENDOR technique to establish the connectivity of hyperfine sublevels and to determine the relative signs of the hyperfine interaction for nonequivalent nuclei.[63,64] The pulsed implementation of the Double ENDOR experiment is shown in Figure 14.[41] The experiment is analogous to the Davies ENDOR experiment, except that a second rf π pulse is inserted in the mixing period to irradiate a preselected ENDOR transition. The Double ENDOR difference spectrum, obtained from the difference between the ENDOR and Double ENDOR spectrum, identifies any changes in intensities of the ENDOR transitions induced by pumping at the second rf frequency. A peak in the Double ENDOR difference spectrum will only be

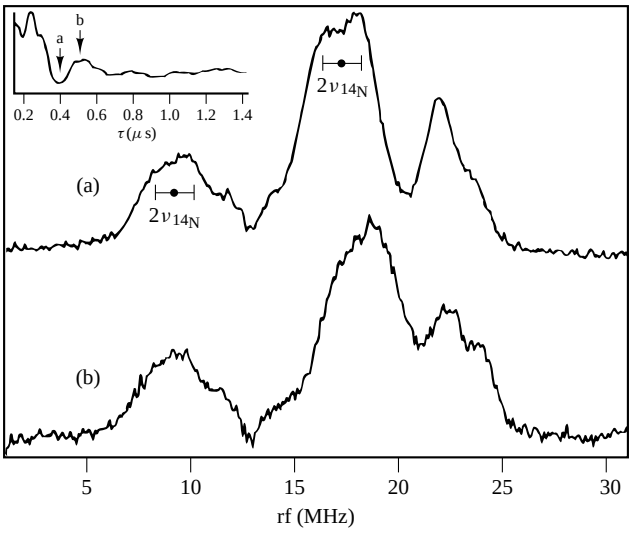

Figure 13 Davies ENDOR spectra of stellacyanin at the two pulse modulation minimum at τ = 0.40 μs (a) and at the maximum at τ = 0.51 μs (b). (Reproduced by permission of Academic Press from H. Thomann and M. Bernardo, in *Methods in Enzymology*, eds. J. F. Riordan and B. L. Vallee, London 1993, Vol. **227**, Chap. 6)

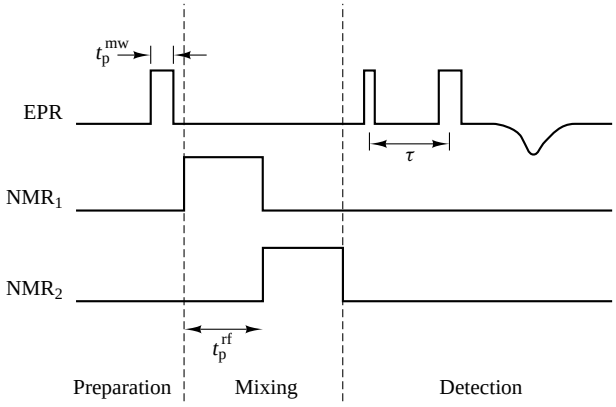

Figure 14 Pulsed implementation of double ENDOR. (Reproduced by permission of Academic Press from H. Thomann and M. Bernardo, in 'Methods in Enzymology', eds. J. F. Riordan and B. L. Vallee, London 1993, Vol. 227, Chap. 6)

observed if the two sublevels each have a level in common with the ESR transition.

An example of the pulsed Double ENDOR and Double ENDOR difference spectrum recorded for the radical in the conjugated conducting polymer, polyacetylene, is shown in Figure 15.[41] The Double ENDOR difference spectra indicate that the unpaired electron is coupled to protons with both positive and negative hyperfine interactions. In this case, similar conclusions were obtained using the CW Double ENDOR experiment and the results were used to determine an electron–electron correlation energy using a Hartree–Fock molecular orbital calculation.[65] However, the CW Double ENDOR experiment was only successful over a restricted temperature range, which is not the case for the pulsed version of the experiment. The pulsed Double ENDOR experiment has also been applied to studies of the irradiated malonic acid radical molecule[45,43] and to studies of the coordination

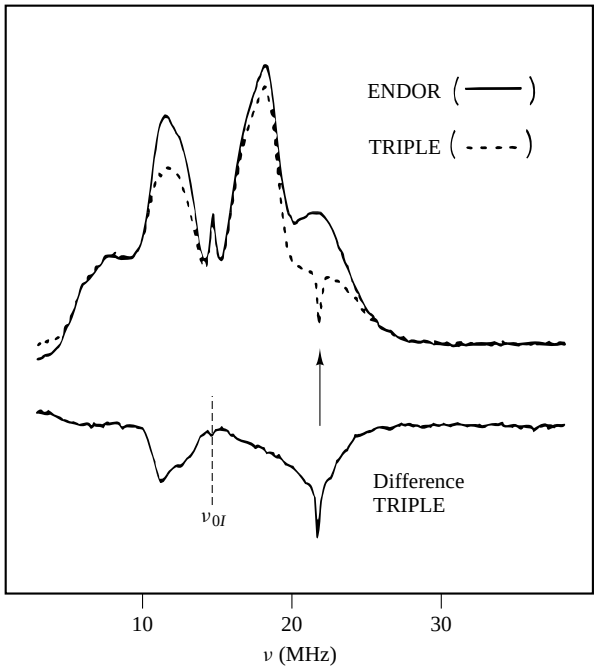

Figure 15 Pulsed Double and Double ENDOR difference spectrum of the polyacetylene radical. (Reproduced by permission of John Wiley & Sons from A. Grupp and M. Mehring in 'Modern Pulsed and Continuous Wave Electron Spin Resonance', eds. L. Kevan and M. K. Bowman, Chichester, 1979, Chap. 4)

structure of transition metal ions and metal clusters in metalloenzymes.[38]

3.1.6 Electron–Nucleus–Electron Triple Resonance

Another variation of a pulsed triple resonance experiment is shown in Figure 16.[38,37] This experiment is related to the Davies ENDOR experiment, except that the frequency of the detection pulses are offset by a frequency Δ from the frequency of the preparation pulse. This is shown schematically in Figure 17 by the magnetic positions at which the preparation, indicated by B_p, and detection, indicated by B_d, irradiation pulses are applied within the ESR absorption envelope. Sublevel polarization transfer that connects the positions B_p and B_d must originate from rf driven sublevel NMR transitions. Polarization transfer by mechanisms other than rf driven nuclear spin flips, such as by spin diffusion, are ineffective because of the short time interval between the preparation and detection period. The value of Δ therefore preselects nuclei with the hyperfine coupling $A = \Delta$. For this reason, the ENDOR spectrum generated for $\Delta = A$ is referred to as a hyperfine selective (HS) ENDOR spectrum. An HS ENDOR spectrum can also be generated by jumping the applied magnetic field.[42]

The HS ENDOR technique is illustrated in Figure 18. The Davies ENDOR spectra for the blue copper protein, stellacyanin, recorded for the native pH 7 form of the protein and for the high-pH (pH 11) perturbed blue form of the protein are shown in Figures 18(a) and 18(b), respectively. The spectra are identical except for the intensity of a transition at 21 MHz observed in the spectrum of the high-pH form. The assignment of this peak is facilitated using the HS ENDOR experiment, as

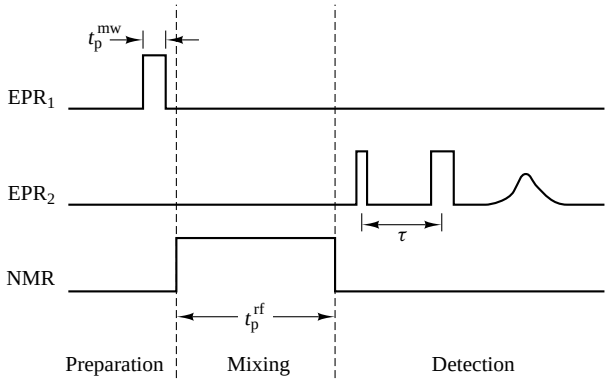

Figure 16 Pulsed electron–nucleus–electron triple resonance pulse sequence. (Reproduced by permission of Academic Press from H. Thomann and M. Bernardo, in 'Methods in Enzymology', eds. J. F. Riordan and B. L. Vallee, London 1993, Vol. 227, Chap. 6)

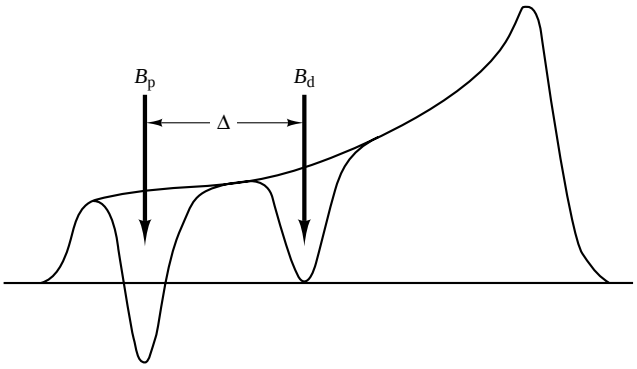

Figure 17 EPR spectra of an inhomogeneously broadened line showing the inversion 'hole' at B_p after the preparation period and the position B_d of the detection pulses. (Reproduced by permission of Academic Press from H. Thomann and M. Bernardo, in 'Methods in Enzymology', eds. J. F. Riordan and B. L. Vallee, London, 1993, Vol. 227, Chap. 6)

illustrated by the three HS ENDOR spectra recorded for values of Δ = 19, 42, and 36 MHz, which are shown in Figures 18(c), 18(d) and 18(e) respectively.

3.2 EPR Detected Sublevel Nuclear Coherence

Sublevel coherence can be created by a $\pi/2$ rf pulse applied at the end of the preparation period. Once created, this sublevel coherence can be manipulated in analogy to many other solid state NMR experiments. Specific examples of these type of experiments are described in this section.

3.2.1 Nuclear Free Induction

The evolution of the sublevel coherence under free precession in the local field can be detected indirectly using the pulse sequence shown in Figure 19.[41,43] The frequency of the rf pulses are set to excite a transition in the ENDOR spectrum. The sublevel coherence evolving during the evolution time t_1 is converted back to electron spin longitudinal polarization by a second rf $\pi/2$ pulse. The sublevel coherence signal at evolution time t_1 is then detected indirectly from the intensity

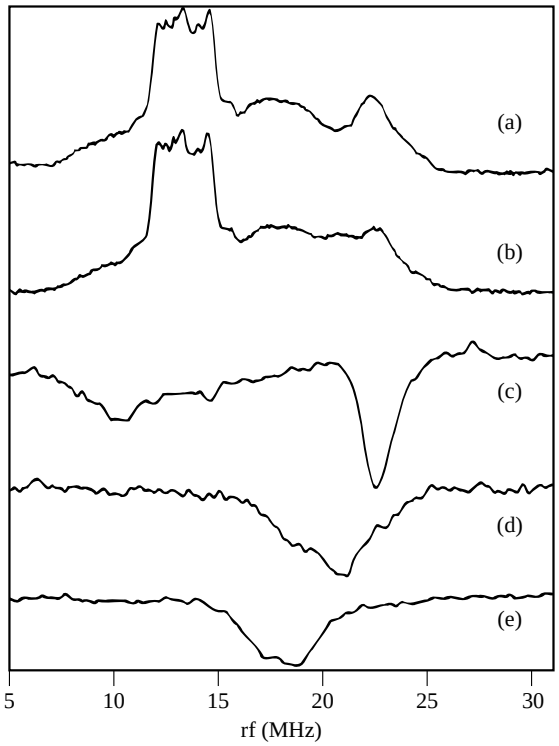

Figure 18 Davies ENDOR spectra of the native (pH 7) form (a) and the high-pH (pH 11) form (b) of stellacyanin. HS ENDOR spectra of the high pH form with Δ = 19.0 (c), 42.0 (d), and 36 (e) MHz were used to assign the feature at 21 MHz to nitrogen. (Reproduced by permission of Academic Press from H. Thomann and M. Bernardo, in 'Methods in Enzymology', eds. J. F. Riordan and B. L. Vallee, London, 1993, Vol. 227, Chap. 6)

modulation of the primary electron spin echo in the detection period. The sublevel free induction signal is then detected point by point by incrementing t_1 on successive pulse sequence iterations. Both the in-phase and phase-quadrature sublevel free precession signals can be detected by phase shifting the relative phase of the two rf pulses by $\pi/2$. Additional phase cycling by π can be used to cancel the effects of electron spin–lattice magnetization recovery during the t_1 evolution period. The rf pulse excitation bandwidth is usually much smaller than the spectral spread of the ENDOR spectrum. In order to record the entire ENDOR spectrum, the pulse sequence shown in Figure 19 must be repeated with the rf frequency incremented on successive experiments. A spectral slice of the overall ENDOR spectrum, determined by the bandwidth of the rf excitation pulse, is recorded for each selected rf. The whole ENDOR spectrum is reconstructed by adding the slices of the limited spectral regions recorded in each experiment.

The ESR detected sublevel free precession experiment is illustrated in Figure 20. These data are collected for a crystal of irradiated malonic acid. In the Davies ENDOR spectrum, a transition that shows no evidence of fine structure is observed at 14.42 MHz. The in-phase and phase-quadrature sublevel free precession signals recorded using the pulse sequence in Figure 19 and the procedure described above are shown in Figure 20(a). The complex Fourier transform of these waveforms is shown in Figure 20(b). This spectrum indicates that the ENDOR line is composed of three overlapping

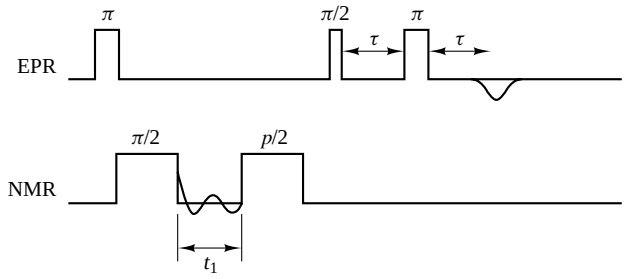

Figure 19 Pulse sequence for EPR detection of sublevel FID. (Reproduced by permission of the American Chemical Society from H. Thomann and M. Bernardo, in 'Advances in Chemistry Series 229: Magnetic Resonance of Carbonaceous Solids', eds. R. E. Botto and Y. Sanada, Washington, DC, 1993, Chap. 4)

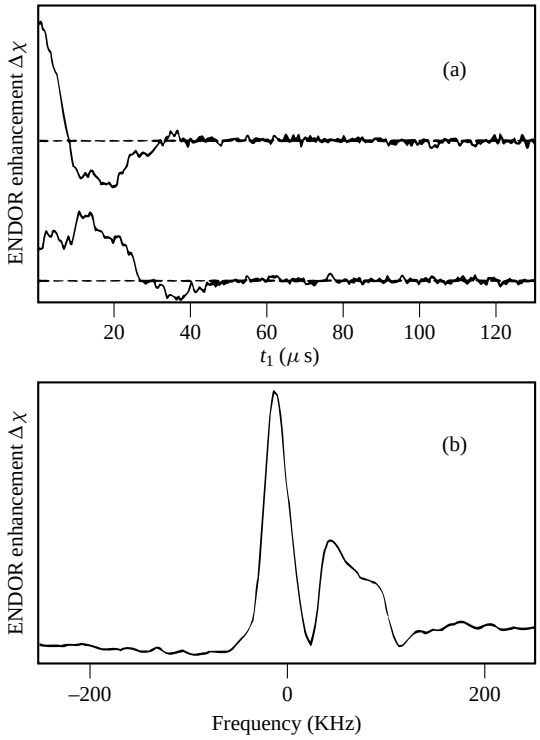

Figure 20 Quadrature sublevel FID signals of malonic acid with ν_{rf} = 14.42 MHz (a) and corresponding complex FT spectrum (b). (Reproduced by permission of the American Chemical Society from H. Thomann and M. Bernardo, in 'Advances in Chemistry Series 229: Magnetic Resonance of Carbonaceous Solids', eds. R. E. Botto and Y. Sanada, Washington, DC, 1993, Chap. 4)

transitions which are not resolved in the Davies ENDOR spectrum.

3.2.2 Multiple Quantum Electron–Nucleus Coherence

The coupling of two or more nuclei with equivalent hyperfine couplings can be detected indirectly using the pulse sequences shown in Figure 21.[41,66] The sublevel polarization can be created using either the inversion–recovery technique with primary spin echo detection (i.e. as in the Davies ENDOR pulse sequence) or by the two pulse excitation in the preparation period with a single pulse in the detection

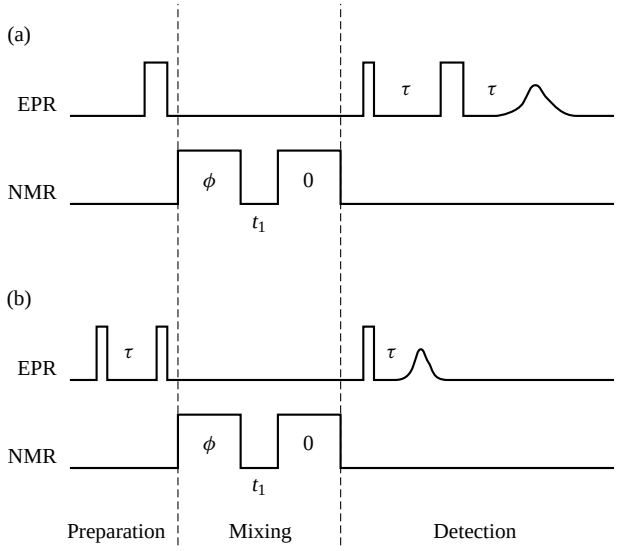

Figure 21 Multiple quantum (MQ) ENDOR pulse sequences: Davies MQ ENDOR (a) and Mims MQ ENDOR (b). (Reproduced by permission of Laser Pages Publishing from H. Thomann and M. Bernardo, *Isr. J. Chem.*, 1992, **32**, 323)

period to create a stimulated echo (i.e. as in the Mims ENDOR pulse sequence). An n-quantum sublevel coherence is detected using the phase incrementation technique in analogy to the NMR experiment.[53,67] An n-quantum coherence accumulates a phase $\theta_n = n\omega_{ENDOR}t_{evol}$ where t_{evol} is an evolution time and ω_{ENDOR} is the sublevel transition frequency.

In the present experiments the phase accumulation occurs during the nutation of the sublevel polarization so that $t_{evol} = t_p^{rf}$. This phase accumulation can be detected by incrementing the phase of the rf mixing pulse in the middle of the mixing period. Theoretically, the optimum ENDOR signal is obtained by applying two $\pi/2$ rf pulses. Each point on the plot of the phase interferogram is collected by incrementing the phase of the second rf pulse on successive pulse sequence iterations.

An example of a multiple quantum spectrum recorded using the pulse sequence in Figure 21(a) for the malonic acid radical molecule is shown in Figure 22.[66] Multiple quantum coherences up to n = 3 are observed for an ENDOR transition at 14.42 MHz recorded for the malonic acid radical molecule in a crystal at an arbitrary orientation. This is consistent with the three lines observed in the ESR detected sublevel FID spectra recorded under identical conditions [Figure 20(b)]. Multiple quantum spectra recorded for several evolution times for free precession are also shown in Figure 22. The oscillation for each order of coherence originates from the free precession of transverse sublevel magnetization in the presence of the local field.

3.2.3 Nuclear Spin Echoes

Hyperfine sublevel spin echoes can be created and detected indirectly by inserting a refocusing rf pulse in the evolution period of the mixing period for the pulse sequence shown in Figure 20. The pulse sequence for this indirect detection of sublevel spin echoes is shown in Figure 23.[40,41] The first rf pulse in the mixing period creates sublevel coherence. This coherence evolves under free precession for time τ_n and is

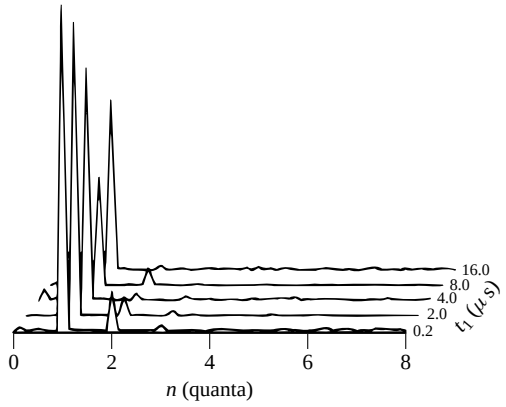

Figure 22 Davies multiple quantum ENDOR spectra of the malonic acid radical for various evolution times. (Reproduced by permission of Laser Pages Publishing from H. Thomann and M. Bernardo, *Isr. J. Chem.*, 1992, **32**, 323)

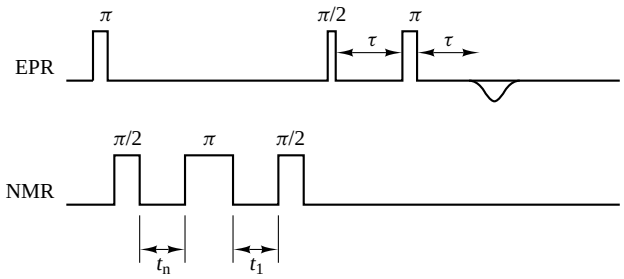

Figure 23 Pulse sequence for EPR detection of sublevel spin echo. (Reproduced by permission of the American Chemical Society from H. Thomann and M. Bernardo, in 'Advances in Chemistry Series 229: Magnetic Resonance of Carbonaceous Solids', eds. R. E. Botto and Y. Sanada, Washington, DC, 1993, Chap. 4)

then refocused by the rf π pulse. The sublevel spin echo formed at time τ_n after the refocusing pulse can be detected by incrementing the time t_1 of the third rf mixing pulse. The third rf pulse transforms the sublevel coherence into two spin electron–nucleus longitudinal order. This is transformed to electron spin coherence for detection of the electron spin polarization by the microwave pulses in the detection period.

The sublevel echo can be detected point by point by incrementing the value of t_1 from $t_1 < \tau_n$ to $t_1 > \tau_n$ on successive pulse sequence iterations. In each pulse sequence iteration the sublevel coherence is detected by the change in intensity of the electron spin echo in the detection period. An example of sublevel spin echoes detected by this procedure for an X-ray irradiated malonic acid crystal are shown in the inset of Figure 24. The two sublevel spin echoes shown were recorded for τ_n values of 5 and 20 μs.

The circles shown in the inset of Figure 24 indicate the echo envelope intensities recorded for several values of $t_1 = \tau_n$. The full sublevel spin echo decay envelope along with a fit to a single exponential and the residuals for the fit are also shown in Figure 24. These sublevel echoes and envelope decay were recorded for the ν_+ = 30.19 MHz ENDOR transition. This corresponds to the proton NMR transition for the α proton of the $\cdot CH(COOH)_2$ radical molecule which is shifted to the high-frequency side of the proton Larmor frequency. The sublevel T_{2n} decay time obtained from the single exponential fit shown

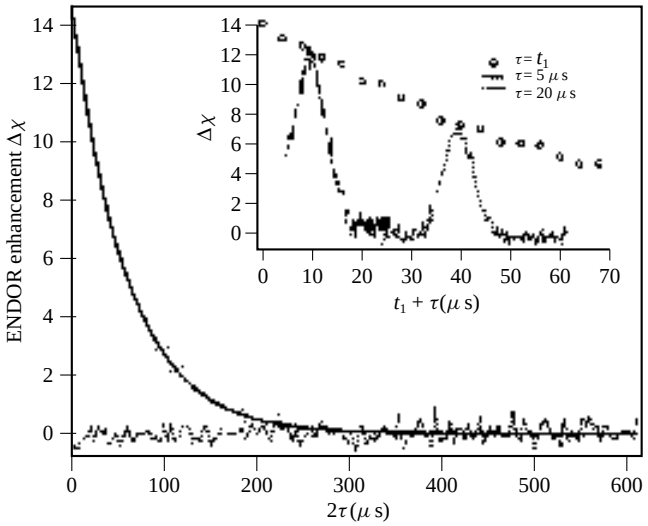

Figure 24 The sublevel spin echo decay recorded with $t_1 = \tau_n$ along with the fit to a single exponential and the residuals of the fit. (Reproduced by permission of the American Chemical Society from H. Thomann and M. Bernardo, in 'Advances in Chemistry Series 229: Magnetic Resonance of Carbonaceous Solids', eds. R. E. Botto and Y. Sanada, Washington, DC, 1993, Chap. 4)

in Figure 24 is 60 μs. The proton T_{2n} values measured for $\nu_{rf} = \nu_n$ are shorter than the values measured at frequencies shifted away from the proton Larmor frequency.

Similar results have been obtained in sublevel nuclear T_{2n} studies of protons in coal samples.[46] In these coal studies, the ESR detected sublevel T_{2n} values measured at $\nu_{rf} = \nu_n$ were similar to the value measured directly by NMR.[68] The ESR detected sublevel T_{2n} values increased for NMR transitions shifted further away from the proton Larmor frequency. Apparently the time-dependent local magnetic field from the hyperfine interaction is not an effective sublevel T_{2n} relaxation mechanism. The T_{2n} value measured directly by NMR is determined by the proton homonuclear dipolar coupling. The equivalence of the value measured in the ESR detected sublevel T_{2n} experiment for $\nu_{rf} = \nu_n$ suggests that the T_{2n} value is also determined by the proton dipolar interaction with the hyperfine coupling serving only as a mechanism for detecting the sublevel coherence signal. Quite different results can be expected if the time dependence of the local field is an effective T_{2n} mechanism. In this case the T_{2n} values would be expected to decrease as the NMR transition frequency is shifted away from the proton Larmor frequency.

3.3 Coherence Transfer ENDOR

In analogy to the coherence transfer experiments known in NMR spectroscopy, it is also possible to detect the hyperfine sublevel transitions by an electron–nuclear double resonance coherence transfer experiment.[41,43,69] Three different pulse sequences for coherence transfer ENDOR experiments are shown in Figure 25. The basic principle in all three types of experiment is similar. The rf pulses applied during the period of free precession of the electron spin coherence created by a $\pi/2$ microwave pulse interfere with the refocusing of this electron coherence following the microwave π pulse.

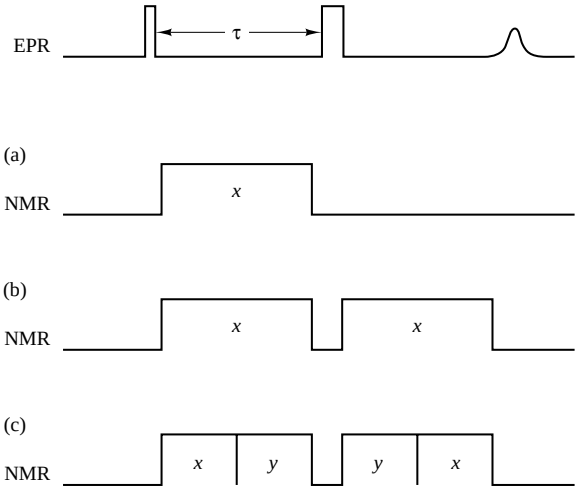

Figure 25 Pulse sequences for coherence transfer ENDOR

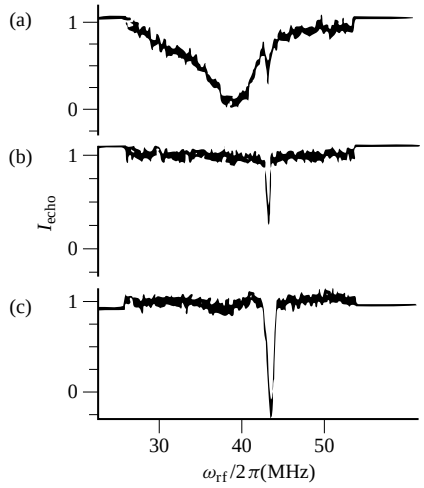

Figure 26 Coherence transfer single crystal ENDOR spectra of the malonic acid radical recorded with corresponding pulse sequences shown in Figure 25. (Reproduced by permission of the American Chemical Society from C. Gemperle and A. Schweiger, *Chem. Rev.*, 1991, **91**, 1481)

This occurs if the rf pulse is on resonance with an NMR transition that has a sublevel in common with the electron spin eigenlevel that belongs to the states from which the electron spin coherence was created. In this case, the sublevel NMR transition shifts the phase of the electron spin coherence which is detected as an attenuation of the electron spin echo. If the rf pulse is a π pulse the electron spin echo intensity is reduced to zero resulting in $\Delta\chi_e/\chi_e = 1$. If the rf pulse is a 2π pulse, the echo intensity changes sign resulting in $\Delta\chi_e/\chi_e = 2$. If a 4π pulse is applied, the electron spin echo intensity returns to its original intensity. This response of the electron spin echo intensity to the rotational symmetry of the sublevel nutation angle is called the 'spinor property' and is a property of wavefunctions for spin-$\frac{1}{2}$ particles.

The ENDOR spectrum recorded using the pulse sequence shown in Figure 25(a) is sufficient to observe the coherence transfer ENDOR effect. However, the application of a single rf pulse also produces a large Bloch–Siegert (BS) frequency shift $\omega_{BS} = -\gamma_e(B_2^2/B_0)$, which results in a phase shift of $\omega_{BS}t_p^{rf}$. Since the rf magnetic field strength is not constant as a function of frequency across the ENDOR spectrum, the Bloch–Siegert phase shift is observed as a broad feature, as shown in Figure 26(a), which can mask the ENDOR transitions. The Bloch–Siegert phase shift can be refocused by applying a second rf pulse, as shown in Figure 25(b), which is symmetrically displaced about the microwave refocusing pulse. This eliminates the broad feature in the ENDOR spectrum as shown in Figure 26(b). The maximum ENDOR effect of $\Delta\chi_e/\chi_e = 1$ is observed when the two rf pulses are π pulses. The efficiency of the ENDOR effect can theoretically be increased to $\Delta\chi_e/\chi_e = 2$ if the two rf pulses are 2π pulses but with a 90° shift introduced, as shown in Figure 25(c).[41,43] The enhancement in the ENDOR signal intensity is shown in Figure 26(c). In practice, the ENDOR efficiency is improved for this phase shifted spinor ENDOR pulse sequence, but because of technical limitations (primarily pulse imperfections) the increase in efficiency is much smaller than theoretically expected. Another limitation of coherence transfer ENDOR experiments is that the ENDOR lines are usually power broadened because of the short electron phase memory time encountered for most samples. It is rare that phase memory times are longer than a few microseconds, even at liquid helium temperatures. Nevertheless, the coherence transfer ENDOR experiment has revealed fundamentally interesting properties of the spin dynamics of the electron–nucleus spin system.

4 CONCLUDING REMARKS

ENDOR and the extension to PE NMR spectroscopy are presently tools of the specialist. They are very powerful techniques in specific cases where the spectra and/or spin dynamics for the nuclei of interest are strongly influenced by the large local magnetic fields originating from the hyperfine coupling with unpaired electron spins. In such cases the NMR transition frequencies are shifted by very large values when compared with NMR spectra of diamagnetic samples. When these circumstances do apply, ENDOR and PE NMR spectroscopy are often the only techniques which can provide the desired information. In this review we have included examples of applications in organic solids, metallobiochemistry, and organometallic chemistry. With the introduction of pulsed excitation techniques, extension to multiple irradiation frequencies, and the introduction of commercially available pulsed instrumentation, continued development of the methodology and an increasing range of applications can be expected for these techniques in the near future. Recent developments in high-frequency ESR,[70] including the extension to high-frequency ENDOR,[71] will also likely expand the range of research applications. The combination of pulsed ESR and pulsed NMR should continue to be a vibrant area of research as new technology becomes available and as new methodologies and applications are developed.

5 RELATED ARTICLES

Chemically Induced Dynamic Nuclear Polarization; Cobalt(II)- and Nickel(II)-Substituted Proteins; Contrast

Agents in MRI: Superparamagnetic Iron Oxide; Contrast Agents in Whole Body Magnetic Resonance: An Overview; Contrast Agents in Magnetic Resonance: Operating Mechanisms; Copper Proteins; Dynamic Nuclear Polarization and High-Resolution NMR of Solids; Electron–Nuclear Hyperfine Interactions; EPR and In Vivo EPR: Roles for Experimental and Clinical NMR Studies; Heme Peroxidases; Iron—Sulfur Proteins; EPR and In Vivo EPR: Roles for Experimental and Clinical NMR Studies.

6 REFERENCES

1. H. Kurreck, B. Kirste, and W. Lubtiz, *ENDOR Spectroscopy of Radicals in Solution*, VCH, New York, 1988.
2. J. E. Wertz and J. R. Bolton, *Electron Spin Resonance: Elementary Theory and Practical Applications*, Chapman & Hall, London, 1986.
3. J. A. Weil (ed.), *Electronic Magnetic Resonance of the Solid State*, Canadian Society for Chemistry, Ottawa, 1987.
4. L. Petrakis and J. R. Fraissard (eds), *Magnetic Resonance. Introduction to Advanced Topics and Applications to Fossil Energy* (*NATO ASI Series C, Vol. 124*), Reidel, Dordrecht, 1984.
5. R. E. Botto and Y. Sanada (eds), *Advances in Chemistry Series: Magnetic Resonance of Carbonaceous Solids*, American Chemical Society, Washington, DC, 1993.
6. A. Abragam and B. Bleaney, *Electron Paramagnetic Resonance of Transition Ions*, (*International Series of Monographs on Physics*), Oxford University Press, Oxford, 1970.
7. J. R. Pilbrow, *EPR of Transition Metal Ions* (*International Series of Monographs on Physics*), Clarendon, Oxford, 1991.
8. J.-M. Spaeth, J. R. Niklas, and R. H. Bartram, *Structural Analysis of Point Defects in Solids*, Springer, New York, 1992.
9. L. J. Berliner and J. Reuben (eds), *EMR of Paramagnetic Molecules* (*Biological Magnetic Resonance, Vol. 13*), Plenum, New York, 1993.
10. L. J. Berliner and J. Reuben (eds), *NMR of Paramagnetic Molecules* (*Biological Magnetic Resonance, Vol. 12*), Plenum, New York, 1993.
11. I. Bertini and C. Luchinat, *NMR of Paramagnetic Molecules in Biological Systems*, Benjamin Cummings, Menlo Park, CA, 1986.
12. G. N. LaMar (ed.), *NMR of Paramagnetic Molecules*, Academic, New York, 1973.
13. A. Abragam, *The Principles of Nuclear Magnetism* (*International Series of Monographs on Physics*), Oxford University Press, Oxford, 1961.
14. C. D. Jeffries, *Dynamic Nuclear Orientation*, Wiley, New York, 1963.
15. M. Goldman, *Spin Temperature and Nuclear Magnetism in Solids* (*International Series of Monographs on Physics*), Oxford University Press, Oxford, 1970.
16. A. Abragam and M. Goldman, *Nuclear Magnetism: Order and Disorder* (*International Series of Monographs on Physics*), Oxford University Press, Oxford, 1982.
17. R. A. Wind, M. J. Duijvestijn, C. van der Lugt, A. Manenschijn, and J. Vriend, *Prog. NMR Spectrosc.*, 1985, **17**, 33.
18. R. D. Bates, Jr, *Magn. Reson. Rev.*, 1993, **16**, 237.
19. R. A. Wind, R. Lewis, H. Lock, and G. E. Maciel, in *Advances in Chemistry Series: Magnetic Resonance of Carbonaceous Solids*, ed. R. E. Botto and Y. Sanada, American Chemical Society, Washington, DC, 1993, Vol. 229, Chap. 3, p. 45.
20. M. Afeworki, R. McKay, and J. Schaefer, *Macromolecules*, 1992, **25**, 4084.
21. G. G. Maresch, R. D. Kendrick, C. S. Yannoni, and M. E. Galvin, *J. Magn. Reson.*, 1989, **82**, 41.
22. R. A. Wind, in *Modern NMR Techniques and their Applications in Chemistry*, eds. A. I. Popov and A. I. Hallenga, Marcel Dekker, New York, 1991.
23. W. B. Mims, in *Electron Paramagnetic Resonance*, ed. S. Geschwind, Plenum, New York, 1973.
24. S. A. Dikanov and Yu. D. Tsvetkov, *Electron Spin Echo Envelope Modulation (ESEEM) Spectroscopy*, CRC, Boca Raton, FL, 1992.
25. L. Kevan and R. N. Schwartz (eds.), *Time Domain Electron Spin Resonance*, Wiley, New York, 1979.
26. L. Kevan and M. K. Bowman (eds.), *Modern Pulsed and Continuous Wave Electron Spin Resonance*, Wiley, New York, 1990.
27. W. B. Mims and J. Peisach, in *Biological Magnetic Resonance*, Plenum, New York, 1981, Vol. 3, p. 213.
28. D. J. Singel, in *Advanced EPR: Applications in Biology and Biochemistry*, ed. A. J. Hoff, Elsevier, Amsterdam, 1989.
29. A. Schweiger, *Angew. Chem., Int. Ed. Engl.*, 1991, **30**, 265.
30. G. Feher, *Phys. Rev.*, 1956, **103**, 834.
31. L. Kevan and L. D. Kispert, *Electron Spin Double Resonance Spectroscopy*, Wiley, New York, 1976.
32. M. M. Dorio and J. Freed (eds.), *Multiple Electron Resonance Spectroscopy*, Plenum, New York, 1979.
33. B. M. Hoffman, *Acc. Chem. Res.*, 1992, **24**, 164.
34. K. Moebius, M. Plato, and W. Lubitz, *Phys. Rep.*, 1982, **87**, 171.
35. A. J. Hoff (ed.), *Advanced EPR: Applications in Biology and Biochemistry*, Elsevier, Amsterdam, 1989.
36. A. Schweiger, in *Structure & Bonding*, Springer, Berlin, 1982, Vol. 51, p. 1.
37. H. Thomann and Marcelino Bernardo, in *Biological Magnetic Resonance*, eds. L. J. Berliner and J. Reuben, Plenum, New York, 1993, Vol. 13, Chap. 7, p. 275.
38. H. Thomann and M. Bernardo, in *Methods in Enzymology*, eds. J. F. Riordan and B. L. Vallee, Academic, San Diego, 1993, Vol. 227, Chap. 6, p. 118.
39. H. Thomann and W. B. Mims, in *Pulsed Magnetic Resonance: NMR, ESR, and Optics*, ed. D. M. S. Bagguley, Clarendon, Oxford, 1992, p. 362.
40. P. Hoefer, A. Grupp, and M. Mehring, in *Electronic Magnetic Resonance of the Solid State*, ed. J. A. Weil, Canadian Society for Chemistry, Ottawa, 1987.
41. A. Grupp and M. Mehring, in *Modern Pulsed and Continuous Wave Electron Spin Resonance*, eds. L. Kevan and M. K. Bowman, Wiley, New York, 1979, Chap. 4, p. 195.
42. C. Gemperle and A. Schweiger, *Chem. Rev.*, 1991, **91**, 1481.
43. M. Mehring, P. Hoefer, and A. Grupp, *Ber. Bunsenges. Phys. Chem.*, 1987, **91**, 1132.
44. W. A. J. A. van der Poel, D. J. Singel, J. Schmidt, and J. H. van der Waals, *Mol. Phys.*, 1983, **49**, 1017.
45. H. Thomann and M. Bernardo, in *Magnetic Resonance of Carbonaceous Solids* (*Advances in Chemistry Series, Vol. 229*), ed. R. E. Botto and Y. Sanada, American Chemical Society, Washington, DC, 1993, Chap. 4, p. 65.
46. H. Thomann, M. Bernardo, and B. G. Silbernagel, in *Magnetic Resonance of Carbonaceous Solids*, (*Advances in Chemistry Series, Vol. 229*), eds. R. E. Botto and Y. Sanada, American Chemical Society, Washington, DC, 1993, Chap. 30, p. 561.
47. C. P. Slichter, *Principles of Magnetic Resonance* (*Springer Series in Solid State Sciences*), 3rd edn., Springer, New York, 1990.

48. N. M. Atherton, *Principles of Electron Spin Resonance*, Ellis Horwood, Chichester, 1993.
49. G. H. Rist and J. H. Hyde, *J. Chem. Phys.*, 1970, **52**, 4633.
50. L. R. Dalton and A. L. Kwiram, *J. Chem. Phys.*, 1972, **57**, 1132.
51. G. C. Hurst, T. A. Henderson, and R. W. Kreilick, *J. Am. Chem. Soc.*, 1985, **107**, 7294.
52. B. M. Hoffman, J. Martinsen, and R. A. Venters, *J. Magn. Reson.*, 1984, **59**, 110.
53. R. R. Ernst, G. Bodenhausen, and A. Wokaun, *Principles of Nuclear Magnetic Resonance in One and Two Dimensions*, Clarendon, Oxford, 1987.
54. V. L. Hochmann, V. Ya. Zevin, and B. D. Shanina, *Sov. Phys. Solid State*, 1968, **10**, 269.
55. C. Gemperle, A. Schweiger, and R. R. Ernst, *Chem. Phys. Lett.*, 1988, **1**, 145.
56. E. R. Davies, *Phys. Lett. Ser. A*, 1974, **47**, 1.
57. W. B. Mims, *Proc. R. Soc. London*, 1965, **283**, 452.
58. T. Wacker, G. A. Sierra, and A. Schweiger, *Isr. J. Chem.*, 1992, **32**, 305.
59. R. C. McCalley and A. L. Kwiram, *J. Phys. Chem.*, 1993, **97**, 2888.
60. P. E. Doan, C. Fan, C. E. Davoust, and B. M. Hoffman, *J. Magn. Reson.*, 1991, **95**, 169.
61. J. Peisach, W. G. Levine, and W. E. Blumberg, *J. Biol. Chem.*, 1967, **242**, 2847.
62. K. Moebius, W. Lubitz, and M. Plato, in *Advanced EPR: Applications in Biology and Biochemistry*, ed. A. J. Hoff, Elsevier, Amsterdam, 1989, p. 441.
63. K. Moebius, in *Multiple Electron Resonance Spectroscopy*, eds. M. M. Dorio and J. Freed, Plenum, New York, 1979.
64. R. J. Cook and D. H. Whiffen, *Proc. R. Soc. London*, 1964, **84**, 845.
65. H. Thomann and L. R. Dalton, in *Handbook of Conducting Polymers*, ed. T. A. Skotheim, Marcel Dekker, New York, 1986, p. 1157.
66. H. Thomann and M. Bernardo, *Isr. J. Chem.*, 1992, **32**, 323.
67. J. Baum, M. Munowitz, A. N. Garroway, and A. Pines, *J. Chem. Phys.*, 1985, **83**, 2015.
68. B. C. Gerstein, C. Chow, R. G. Pembleton, and R. C. Wilson, *J. Phys. Chem.*, 1977, **81**, 565.
69. I. M. Brown, D. J. Sloop, and D. P. Ames, *Phys. Rev. Lett.*, 1969, **22**, 324.
70. S. S. Eaton and G. R. Eaton, *Magn. Reson. Rev.*, 1993, **16**, 157.
71. O. Burghaus, A. Kischkat-Toth, R. Klette, and K. Mobius, *J. Magn. Reson.*, 1988, **80**, 383.

Biographical Sketches

Hans Thomann. *b* 1954. B.S., 1976, Ph.D., 1982, Chemistry, State University of New York at Stony Brook, USA. Research interests: development of pulsed electron NMR techniques and their application to problems in catalysis, metallobiochemistry, and molecular solids; spin relaxation and molecular motion of fluids in porous media.

Marcelino Bernardo. *b* 1957. B.S., 1979, Rochester Institute of Technology, NY, USA. Research interests: development of pulsed electron NMR techniques and their application to problems in catalysis, metallobiochemistry, and molecular solids; MRI.

Floquet Theory

Shimon Vega
Weizmann Institute of Science, Rehovot, Israel

1	Introduction	1
2	The Floquet Formalism	1
3	Stroboscopic Detection	9
4	Examples	11
5	References	15

1 INTRODUCTION

This article is devoted to Floquet theory and its applications to NMR spectroscopy. The formalism presented here is based on that introduced by Shirley[1] in 1965 for describing the interaction between an oscillating field and a quantum system. This theory provides a solution of the Liouville–von Neumann equation for the spin density operator $\hat{\rho}(t)$ of a system that experiences a periodically time-dependent spin Hamiltonian $\hat{\mathcal{H}}(t)$. In NMR this Hamiltonian can be the spin Hamiltonian of a spin system rotating in the magnetic field, or a Hamiltonian that describes a time-dependent rf spin excitation scheme. The need to obtain accurate solutions for the density operator is essential in NMR spectroscopy, because during NMR experiments, one monitors the time evolution of a set of spin coherences (i.e., superposition states) of a system either sequentially or simultaneously. The calculations necessary to solve the Liouville–von Neumann equation for the density operator,[2,3]

$$\frac{\mathrm{d}}{\mathrm{d}t}\hat{\rho}(t) = \mathrm{i}[\hat{\rho}(t), \hat{\mathcal{H}}(t)] \tag{1}$$

can become very complicated. A variety of theoretical approaches can be exploited[2–10] for dealing with this equation for the description of NMR experiments.

One of the widely used approaches for the evaluation of $\hat{\rho}(t)$, at constant time intervals, is the average Hamiltonian theory (AHT).[5,11] This theory provides the methodology to evaluate a time-independent average Hamiltonian that governs the effective time dependence of $\hat{\rho}(t)$ at the end of these intervals. The actual evaluation of this average Hamiltonian is performed by calculating successive terms of a Magnus expansion.[12] The AHT has been used especially for the construction of average Hamiltonians that describe multiple pulse experiments,[3–8,13] and for the design of selective excitation and decoupling schemes.[14,15] For a detailed discussion of AHT, see ***Average Hamiltonian Theory***.

An additional approach that offers a way to solve the equation of motion of the density operator, with a periodically time-dependent Hamiltonian, can be found in the form of Floquet theory.[1,4,16] Maricq[17] has discussed the utilization of this theory and has made a comparative study of AHT and the Floquet approach. This approach provides the tools to evaluate effective Hamiltonians following an expansion procedure. An additional comparison between the two theories has been presented by Llor,[18] showing that the two theories are equivalent when the Floquet Hamiltonians are expanded with the help of the Van Vleck transformation.[19] Goldman et al.[10] have shown how Floquet theory can be exploited in terms of a perturbation expansion, based on operator commutators, for evaluating effective Hamiltonians.

The Floquet formalism, as discussed in this article, does not make use of these expansion methods for the calculation of effective Hamiltonians. However, it does provide a basic methodology for solving the Liouville–von Neumann equation at all times. Wherever necessary, approximation or numerical methods are applied to estimate the solutions. Our Floquet approach follows the dressed states[17,18,20,21] viewpoint, and is a straightforward extension of Shirley's theory.[1] It can be considered as a semiclassical analog of the dressed state quantum description of a system in an electromagnetic field.[1,20,21]

A variety of applications of the Floquet theory for magnetic resonance problems can be found in the literature. Freed et al.[22] used it for calculating saturation effects in ESR spectra. N-photon pulses[23] as well as broadband and narrowband excitation schemes[24] have been designed using this theory. Goelman et al.[25] explained in terms of this formalism the appearance of nonlinear irradiation fields in multiband adiabatic inversion pulses. In MAS NMR spectroscopy, the Floquet approach has been exploited to explain a variety of spectroscopic effects.[26–29] Using perturbation theory, McDowell et al.[28] applied the Floquet formalism to describe experiments on homonuclear spin pairs, and Augustine et al.[29] used it for calculating field-dependent second-order dipolar shifts in MAS NMR. Rotational resonance has been explained in terms of degeneracies of the Floquet state,[30] and effective Hamiltonians have been derived for dipolar recoupling experiments.[31,32] An extension of the theory was also utilized by Schmidt et al.[33] and by Luz et al.[34] in calculations of dynamic MAS spectra.

The rest of this article is divided into three sections. First, the basic Floquet theory is introduced in a general way, without giving examples; secondly, stroboscopic detection of spin parameters is discussed; finally, some examples of the use of this theory are given. The last example deals with the extension of the theory for describing dynamic MAS spectra. The discussions in this article do not deal with large multispin systems. Thus, multiple spin diffusion and spin temperature concepts will not be discussed here. An effort has been made to introduce basic concepts, derive the essential equations, and to present the methodologies of the Floquet theory for application in NMR. The derivations of a large part of the equations are self-contained.

In the modern era of computers, the equation of motion of the density matrix can be solved numerically for a wide variety of problems. Thus, to simulate spectra or to predict and explain spin responses, it no longer always seems necessary to use a 'theory'. However, these theories provide physical insights and ways of thinking about problems. With this in mind, it is appropriate to discuss Floquet theory in this Encyclopedia. Although the representation of the theory might sometimes look cumbersome and the mathematical derivations rather lengthy, the Floquet formalism has enabled a better understanding of a variety of NMR results, created different and stimulating insights into spectroscopic phenomena, and helped to generate new experimental approaches.

2 THE FLOQUET FORMALISM

2.1 The Schrödinger Equation

In this section, the Floquet Hamiltonian of a spin system, experiencing a periodically time-dependent spin Hamiltonian $\hat{\mathcal{H}}(t)$, is introduced, and the expression for the matrix elements of its spin evolution operator is derived. The solution of the Liouville–von Neumann equation for the spin density operator $\hat{\rho}(t)$ of such a system can be obtained by evaluating the unitary spin evolution operator[3–8]

$$\hat{U}(t) = \mathcal{T}\exp\left[-\mathrm{i}\int_0^t \hat{\mathcal{H}}(t')\mathrm{d}t'\right] \tag{2}$$

and by inserting the initial state of the density operator $\hat{\rho}(0)$ at $t = 0$ in the solution of equation (1):

$$\hat{\rho}(t) = \hat{U}(t)\hat{\rho}(0)\hat{U}^{-1}(t) \tag{3}$$

$\mathcal{T}$ is the Dyson time-ordering operator.

Any evolution operator can be expressed in terms of a unitary operator $\hat{F}(t)$, ensuring that $\hat{U}(0) = 1$ and satisfying the Schrödinger equation:[35,36]

$$\frac{\mathrm{d}}{\mathrm{d}t}\hat{F}(t) = -\mathrm{i}\hat{\mathcal{H}}(t)\hat{F}(t) \tag{4}$$

with

$$\hat{U}(t) = \hat{F}(t)\hat{F}^{-1}(0) \tag{5}$$

When the Hamiltonian and the evolution operator are represented in a manifold of spin states $\{|p\rangle, |q\rangle, |r\rangle \ldots\}$, equation (4) will take the form of a set of coupled homogeneous differential equations for the elements $\langle p|\hat{F}(t)|q\rangle$ and with coefficients $\langle p|\hat{\mathcal{H}}(t)|q\rangle$. The generalized form of the solution of such a set of coupled equations, with periodically time-dependent coefficients, was derived by Floquet.[37]

When the time period of the Hamiltonian is T, and its fundamental frequency $\omega = 2\pi/T$, its matrix elements can be expanded as

$$\langle p|\hat{\mathcal{H}}(t)|q\rangle = \sum_{n=-\infty}^{\infty}\langle p|\hat{\mathsf{h}}^n|q\rangle\exp(\mathrm{i}n\omega t) \tag{6}$$

and the solutions for the matrix elements of $\hat{F}(t)$ are, according to Floquet[1,16] of the form

$$\langle p|\hat{F}(t)|q\rangle = \sum_{n=-\infty}^{\infty}\langle p|\hat{f}_n|q\rangle\ \exp(-\mathrm{i}\lambda_0^q t)\ \exp(\mathrm{i}n\omega t) \tag{7}$$

Thus, these matrix elements can be expressed as products of the elements of a periodically time-dependent matrix, $\langle p|\sum_n \hat{f}_n\exp(\mathrm{i}n\omega t)|q\rangle$, and an exponent, $\exp(-\mathrm{i}\lambda_0^q t)$. The dimension of the periodically time-dependent matrix is equal to the dimension of the matrix representation of $\hat{F}(t)$, and the number of λ_0^q parameters is equal to this dimension as well. Insertion of equations (6) and (7) into equation (4) yields a set of equations for the Fourier coefficients of the matrix elements of $\hat{F}(t)$:

$$\sum_r\sum_{m=-\infty}^{\infty}(\langle p|\hat{\mathsf{h}}^{n-m}|r\rangle + n\omega\delta_{nm}\delta_{pr})\langle r|\hat{f}_m|q\rangle = \lambda_0^q\langle p|\hat{f}_n|q\rangle \tag{8}$$

2.2 The Floquet Hamiltonian

The set of coupled equations in equation (8) has the form of an eigenvalue–eigenvector equation. Shirley[1] suggested rewriting this set by defining a Hermitian Floquet Hamiltonian $\hat{\mathcal{H}}_\mathrm{F}$ of infinite dimension, represented in the manifold of dressed spin states $\{|pn\rangle\}$, with the Fourier mode indices $n = -\infty, \ldots, \infty$:

$$\langle pn|\hat{\mathcal{H}}_\mathrm{F}|qm\rangle = \langle p|\hat{\mathsf{h}}^{n-m}|q\rangle + n\omega\delta_{nm}\delta_{pq} \tag{9}$$

The general form of the matrix representation of the Floquet Hamiltonian is shown in Figure 1. The elements of $\hat{\mathcal{H}}_\mathrm{F}$ are time-independent and satisfy an eigenvalue–eigenvector equation of the form

$$\sum_r\sum_{m=-\infty}^{\infty}\langle pn|\hat{\mathcal{H}}_\mathrm{F}|rm\rangle\langle rm|\lambda_k^q\rangle = \lambda_k^q\langle pn|\lambda_k^q\rangle \tag{10}$$

Comparing this equation with equation (8) reveals that the eigenvalues of $\hat{\mathcal{H}}_\mathrm{F}$ are equal to

$$\lambda_k^q = \lambda_0^q + k\omega \tag{11}$$

and that the elements of the eigenvectors of $\hat{\mathcal{H}}_\mathrm{F}$ are equal to

$$\langle pn|\lambda_k^q\rangle = \langle pn-k|\lambda_0^q\rangle = \langle p|\,\hat{f}_{n-k}|q\rangle \tag{12}$$

Because $\hat{\mathcal{H}}_\mathrm{F}$ is of infinite dimension and its eigenvalues satisfy equation (11), the values of the principal eigenvalues λ_0^q are not uniquely determined.[1,16–18] It is always possible, however, to choose $-0.5\omega < \lambda_0^q \leq 0.5\omega$ and to adjust the n indices in the eigenvector elements accordingly.

In Figure 2 the comparison between equations (8) and (9) is demonstrated schematically. Using the definitions for the parameters λ_0^q and the elements of $\hat{f}_n$ in the expression for matrix elements of $\hat{F}(t)$ in equation (7), the evolution operator becomes

$$\begin{aligned}\langle p|\hat{U}(t)|q\rangle &= \sum_r\langle p|\hat{F}(t)\hat{F}^{-1}(0)|q\rangle \\ &= \sum_r\sum_{n,m=-\infty}^{\infty}\langle pn|\lambda_0^r\rangle\exp(-\mathrm{i}\lambda_0^r t)\langle\lambda_0^r|qm\rangle\exp(\mathrm{i}n\omega t) \\ &= \sum_r\sum_{n,m=-\infty}^{\infty}\langle pn-m|\lambda_{-m}^r\rangle \\ &\quad\times\exp(-\mathrm{i}\lambda_{-m}^r t - \mathrm{i}m\omega t)\langle\lambda_{-m}^r|q0\rangle\exp(\mathrm{i}n\omega t)\end{aligned} \tag{13a}$$

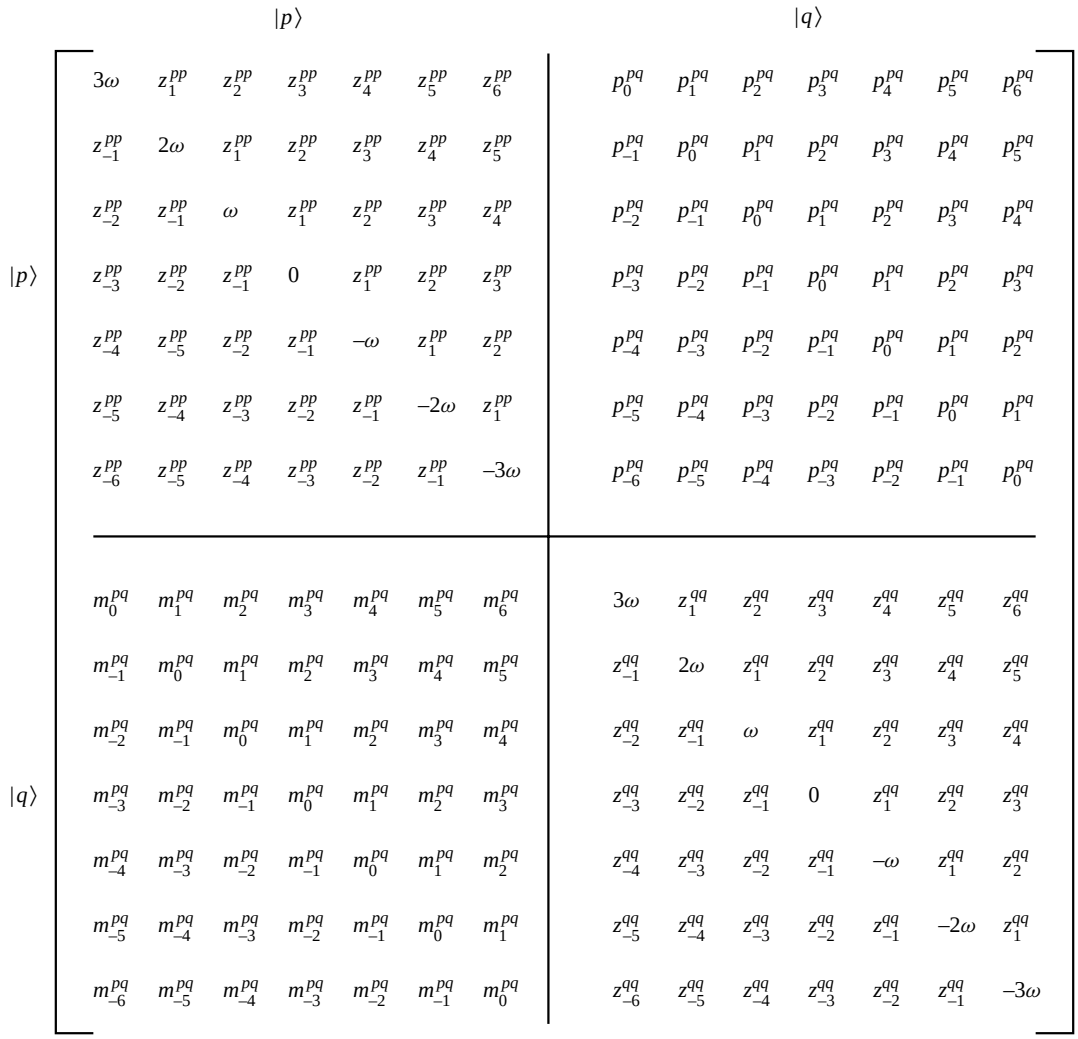

Figure 1 A schematic representation of the infinite $p-q$ blocks of a Floquet matrix

$$\hat{\mathcal{H}}^F = \sum_{p<q} \sum_{n=-\infty, n\neq 0}^{\infty} \omega \hat{N}^{pp} + 2z_n^{pp}\hat{Z}_n^{pp} + 2x_n^{pq}\hat{X}_n^{pq} + 2y_n^{pq}\hat{Y}_n^{pq}$$

with elements $\langle pn|\hat{\mathcal{H}}_F|pm\rangle = z_{n-m}^{pp} + \omega\delta_{nm}$, $\langle pn|\hat{\mathcal{H}}_F|qm\rangle = x_{n-m}^{pq} - iy_{n-m}^{pq} = P_{n-m}^{pq}$ and $\langle qn|\hat{\mathcal{H}}_F|pm\rangle = x_{n-m}^{pq} + \mathrm{i}y_{n-m}^{pq} = m_{n-m}^{pq}$ and $p_n^{pq} = m_{-n}^{pq*}$

which results in

$$\langle p|\hat{U}(t)|q\rangle = \sum_{n=-\infty}^{\infty} \langle pn|\exp(-\mathrm{i}\hat{\mathcal{H}}_F t)|q0\rangle \exp(\mathrm{i}n\omega t) \quad (13b)$$

In this derivation, we have used $\sum_{r,m}\langle \mathrm{pn}|\lambda_{-m}^r\rangle\lambda_{-m}^r\langle\lambda_{-m}^r|q0\rangle = \langle pn|\hat{\mathcal{H}}_F|q0\rangle$ and replaced $n-m$ by n.

The dependence of the matrix elements of the spin evolution operator on the Floquet Hamiltonian in equation (13b) forms the basic equation of Shirley's Floquet formalism.[1] It demonstrates that the Floquet Hamiltonian governs the evolution of the spin system and suggests that this time-independent Hamiltonian can be utilized to derive the exact time dependences of coherences and polarizations of this system.

The time-independent Floquet Hamiltonian $\hat{\mathcal{H}}_F$ replaces the periodically time-dependent Hamiltonian $\hat{\mathcal{H}}(t)$ (see Figure 1). For each $N \times N$ matrix representation of $\hat{\mathcal{H}}(t)$, a Floquet Hamiltonian matrix can be derived by a Fourier transformation of all matrix elements of $\hat{\mathcal{H}}(t)$ and by an insertion of the Fourier coefficients in equation (9). Thus, $\hat{\mathcal{H}}_F$ consists of $N \times N$ infinite matrix blocks and has a special diagonal band structure as shown in Figure 1.

The Floquet matrices can in principle be diagonalized as

$$\hat{\mathcal{H}}_F = \hat{D}_F\hat{\Lambda}_F\hat{D}_F^{-1} \quad (14)$$

and have eigenvalues equal to $\langle qn|\hat{\Lambda}_F|qn\rangle = \lambda_n^q$ and eigenvector elements equal to $\langle pn|\hat{D}_F|qm\rangle = \langle pn|\lambda_m^q\rangle$. The number of independent parameters λ_0^q that define the eigenvalues is equal to N, and the eigenvectors satisfy equation (12). The unitary diagonalization matrix $\hat{D}_F$ is composed of these eigenvectors, and has a similar diagonal band structure to $\hat{\mathcal{H}}_F$, as shown in Figure 3.

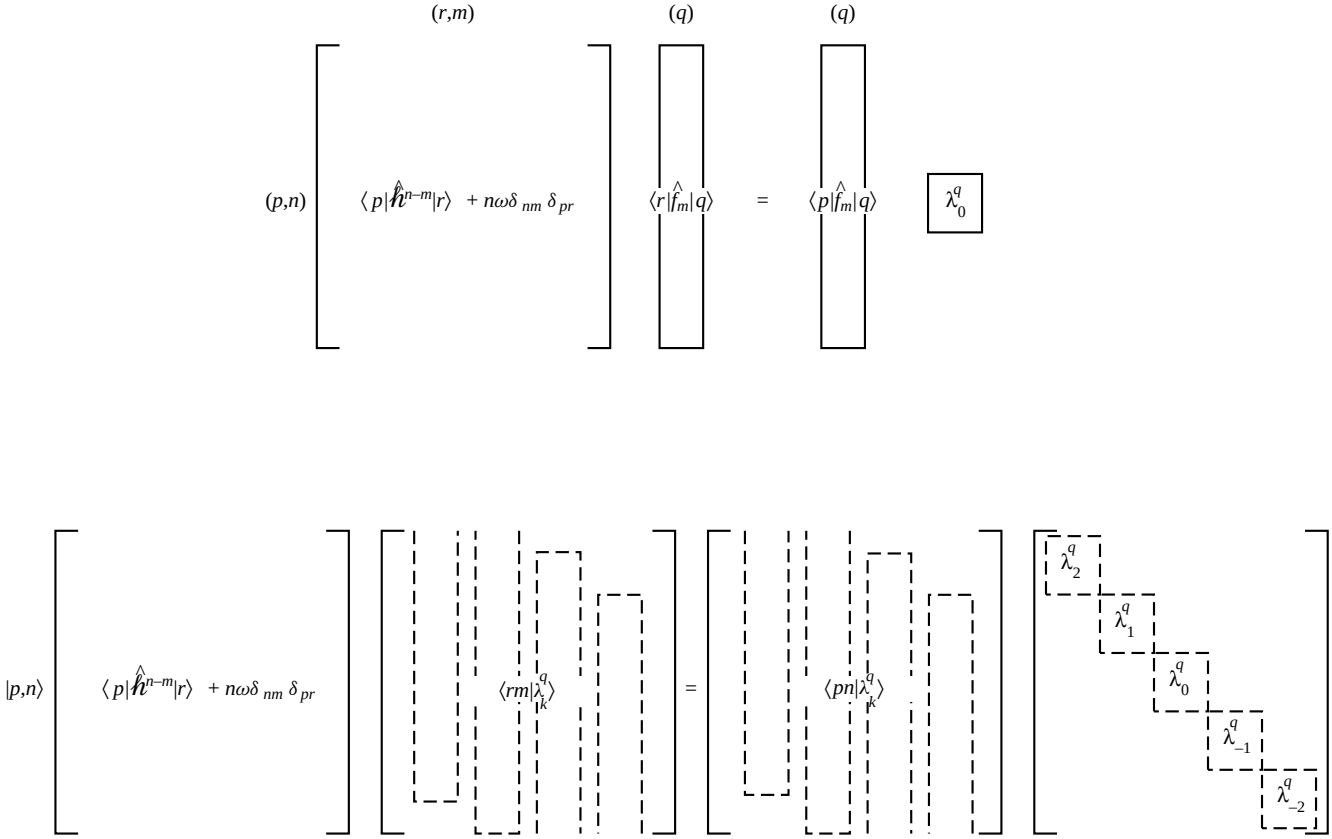

Figure 2 A schematic representation of equation (8) and (10). The eigenvalue equation at the top corresponds to equation (8). In this matrix representation, defined by elements according to the indices (p, n) and (r, m), the qth eigenvector has an eigenvalue $\lambda q/0$. The set of eigenvalue equations at the bottom corresponds to equation (10), and shows that in the dressed state matrix representation defined by elements between $\langle pn|$ and $|rm\rangle$, a set of eigenvectors can be created that are obtained from each other by shifting their elements up or down, and also a corresponding set of eigenvalues that are obtained by adding or substracting $n\omega$ from $\lambda^q{}_0$

The computational stages for the utilization of the Floquet formalism consist of the composition of the Floquet Hamiltonian $\hat{\mathcal{H}}_{\mathrm{F}}$ and the insertion of the exponent $\exp(-\mathrm{i}\hat{\mathcal{H}}_{\mathrm{F}}t)$ in the expression for the matrix elements of the spin evolution operator in equation (13b). In order to evaluate the matrix elements of this exponent it is necessary to diagonalize $\hat{\mathcal{H}}_{\mathrm{F}}$.

2.3 The Floquet Evolution Operator

In order to obtain a better understanding of the utilization of the Floquet Hamiltonian and to emphasize its physical significance we can introduce a Floquet propagator and a Floquet density operator.[38] Thus, the analogy between these operators, the spin evolution and the spin density operators, can then help us to visualize the utilization of this theory.

Let us define a Floquet evolution operator as follows:

$$\hat{U}_{\mathrm{F}}(t) \equiv \exp(-\mathrm{i}\hat{\mathcal{H}}_{\mathrm{F}}t) \tag{15}$$

This operator can be considered as the solution of an equation of motion for a Floquet density matrix $\hat{R}(t)$,

$$\frac{\mathrm{d}}{\mathrm{d}t}\hat{R}(t) = \mathrm{i}[\hat{R}(t), \hat{\mathcal{H}}_{\mathrm{F}}] \tag{16}$$

namely,

$$\hat{R}(t) = \hat{U}_{\mathrm{F}}(t)\hat{R}(0)\hat{U}_{\mathrm{F}}^{-1}(t) \tag{17}$$

The similarity between these equations and the Liouville–von Neumann equation with its solution for a spin system with a time-independent Hamiltonian is apparent. A straightforward inspection, using equation (13), reveals[38]

$$\left.\begin{aligned}\langle p|\hat{U}(t)|q\rangle &= \sum_{n=-\infty}^{\infty}\langle pn|\hat{U}_{\mathrm{F}}(t)|q0\rangle\exp(\mathrm{i}n\omega t)\\ \langle p|\hat{\rho}(t)|q\rangle &= \sum_{n=-\infty}^{\infty}\langle pn|\hat{R}(t)|q0\rangle\exp(\mathrm{i}n\omega t)\end{aligned}\right\} \tag{18}$$

with

$$\langle pn|\hat{R}(0)|qm\rangle \equiv \langle p|\hat{\rho}(0)|q\rangle\delta_{nm} \tag{19}$$

The first equation is the same as equation (13b). With these definitions and relations, we can describe the evolution of spin systems with periodically time-dependent Hamiltonians, in terms of time-independent Floquet Hamiltonians that govern density matrices and create evolution operators (Figure 4). The energy levels of these Hamiltonians are defined in Floquet space and are equal to their eigenstates. The elements

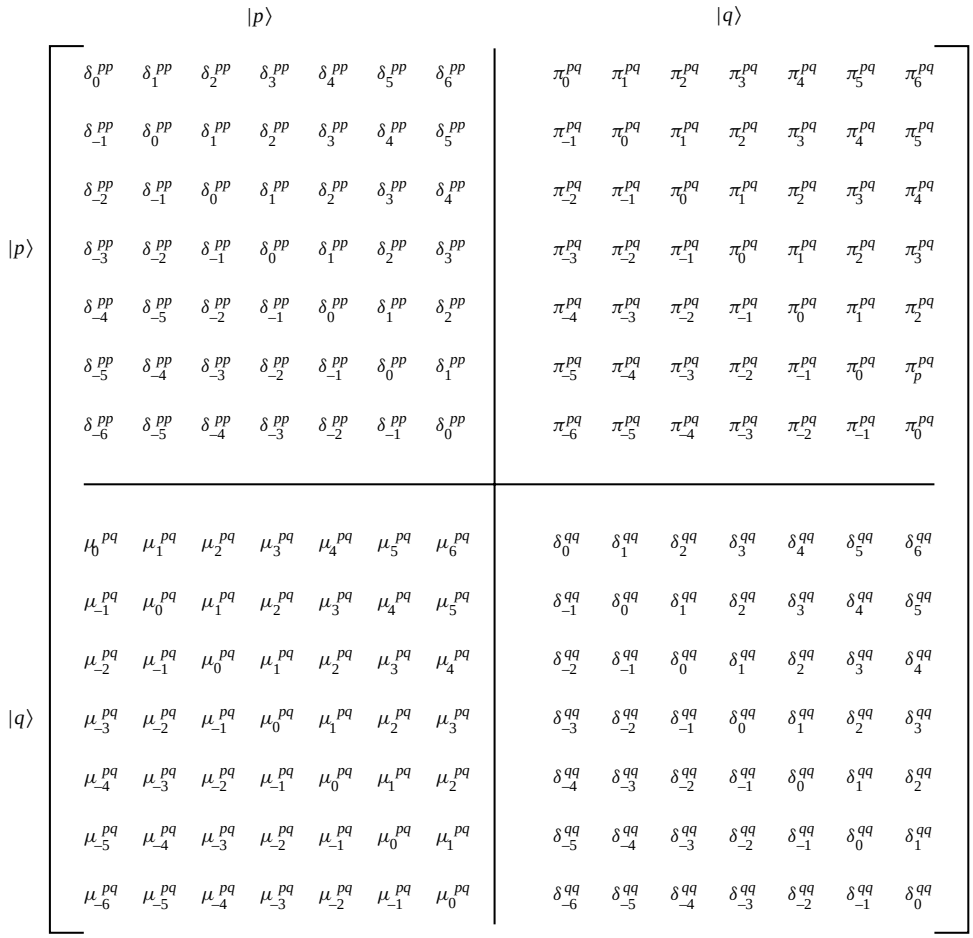

Figure 3 A schematic representation of the (pq) blocks of the diagonalization matrix $\hat{D}_{\mathrm{F}} = \sum_{p<q} \sum_{n=-\infty}^{\infty} 2\, d_n^{pp} \hat{Z}_n^{pp} + \pi_n^{pq} \hat{P}_n^{pq} + \mu_n^{pq} \hat{M}_n^{pq}$

of $\hat{R}(t)$ contain oscillating terms with frequencies that are equal to Floquet energy differences and coefficients that are functions of the eigenvectors of $\hat{\mathcal{H}}_{\mathrm{F}}$. The evaluation of the time dependence of coherences and polarizations of spin systems requires, of course, the transformation of $\hat{R}(t)$ to $\hat{\rho}(t)$, as shown in equation (18).

At this stage of the discussion, it has become evident that the Floquet description of a spin system, with a spin Hamiltonian satisfying $\hat{\mathcal{H}}(t + nT) = \hat{\mathcal{H}}(t)$, is the same as for a system that has a time-independent Hamiltonian. The price we pay for the transformation of the time-dependent Hamiltonian $\hat{\mathcal{H}}(t)$ to the time-independent Hamiltonian $\hat{\mathcal{H}}_{\mathrm{F}}$ is the fact that we must deal with a multiple infinite matrix $\hat{\mathcal{H}}_{\mathrm{F}}$.

2.4 Expectation Values of Observables

The expectation value of an observable $\hat{O}$ of the spin system is evaluated by[36]

$$\langle \hat{O} \rangle = \mathrm{tr}[\rho(t) O] = \sum_{p,r} \langle p|\hat{\rho}(t)|r\rangle \langle r|\hat{O}|p\rangle \qquad (20)$$

An expression for $\langle \hat{O} \rangle$ can also be obtained, when we use the dependence of $\hat{R}(t)$ on $\hat{\rho}(t)$, as given in equation (18):

$$\langle \hat{O} \rangle = \sum_{n=-\infty}^{\infty} \sum_{p} \langle pn|\hat{R}(t)\hat{O}_{\mathrm{F}}|p0\rangle \exp(\mathrm{i}n\omega t) \qquad (21)$$

where the matrix elements of $\hat{O}_{\mathrm{F}}$ are given by elements of a block-diagonal matrix,

$$\langle pn|\hat{O}_{\mathrm{F}}|qm\rangle = \langle p|\hat{O}|q\rangle \delta_{nm} \qquad (22)$$

To show that the expectation values are indeed functions of terms that oscillate with frequencies equal to the differences between Floquet eigenstates, we insert in equation (21) the solution for $\hat{R}(t)$ [equation (16)] and the expression for $\hat{\mathcal{H}}_{\mathrm{F}}$, in terms of its eigenvalues and eigenvectors [below equation (13b)]. The result after a straightforward calculation yields[38]

$$\langle \hat{O} \rangle = \sum_{n=-\infty}^{\infty} \sum_{p<q} A^{pq} \langle \lambda_n^q|\hat{O}_{\mathrm{F}}|\lambda_0^p\rangle \exp[\mathrm{i}(\lambda_n^q - \lambda_0^p)t] \qquad (23)$$

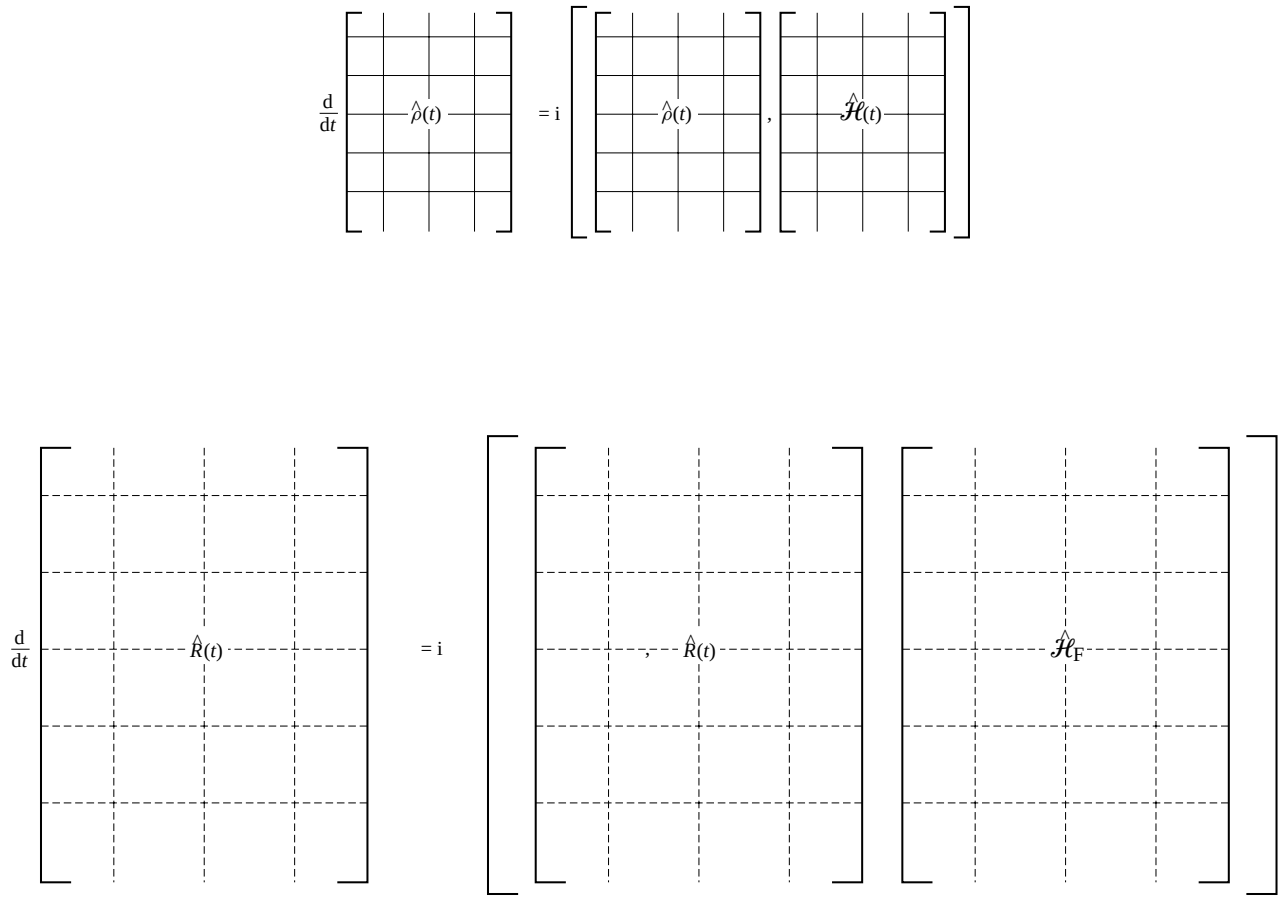

Figure 4 A schematic representation of the comparison between the equation of motions of $\hat{\rho}(t)$ and $\hat{R}(t)$. The matrix elements of the spin Hamiltonian $\hat{\mathcal{H}}(t)$ are time-dependent, and the dimension of the matrix is defined by the number of independent basis functions $\{|p\rangle\}$ of the spin system. The matrix elements of the Floquet Hamiltonian $\hat{\mathcal{H}}_{\mathrm{F}}$ are time-independent, but the dimension of the matrix is infinite, i.e., an infinite block matrix exists for each pair of basis functions $\{|p\rangle,|q\rangle\}$

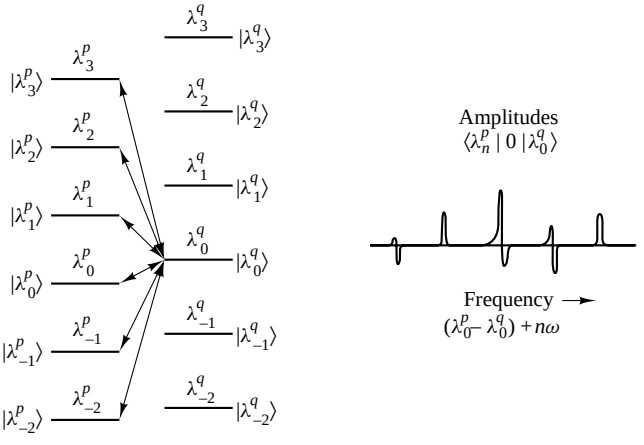

Figure 5 Part of the Floquet energy level scheme of the eigenvectors $\{|\lambda_n^p\rangle\}$ of a Floquet matrix. Allowed transitions between eigenstates $|\lambda_n^p\rangle$ and $|\lambda_0^q\rangle$ result in oscillating terms $\exp[\mathrm{i}(\lambda_n^p - \lambda_0^q)]$ in the expectation values of observables O, and create frequency spectra after Fourier transformations of these time-dependent expectation values $\langle O\rangle$. When these values are multiplied by a decaying function, the Fourier transform spectrum has bands at the frequencies $\lambda_n^p - \lambda_0^q$ and amplitudes proportional to $\langle\lambda_n^p|\hat{O}_{\mathrm{F}}|\lambda_0^q\rangle$

where the normalization coefficients for each group of terms with frequencies $(\lambda_n^q - \lambda_0^p) = (\lambda_0^q - \lambda_0^p) + n\omega$ are equal to

$$A^{pq} = \sum_{m=-\infty}^{\infty} \langle\lambda_0^p|\hat{R}(0)|\lambda_m^q\rangle \tag{24}$$

Thus, the expectation values monitor the differences between the eigenvalues of $\hat{\mathcal{H}}_{\mathrm{F}}$ of allowed Floquet transitions. A schematic representation of this discussion is given in Figure 5.

At this stage of the discussion, a general strategy for the use of Floquet theory can be presented. After the definition of the spin system and its periodically time-dependent Hamiltonian, the following steps must be made in order to take full advantage of this approach.

1. The Floquet Hamiltonian must be constructed from the Fourier components of the periodically time-dependent spin Hamiltonian [equation (9)].
2. Then the eigenstates and eigenvalues of the Floquet Hamiltonian must be evaluated via the diagonalization of $\hat{\mathcal{H}}_{\mathrm{F}}$ [equation (14)].
3. The initial value of the spin density matrix of the spin system must be transformed to $\hat{R}(0)$ and the desired observable $\hat{O}$ to $\hat{O}_{\mathrm{F}}$ [equations (19) and (22)].

4. Finally, the matrix elements of $\hat{O}_{\mathrm{F}}$ and $\hat{R}(0)$ between the eigenstates of the Floquet Hamiltonian must be calculated and inserted into the expression for $\langle \hat{O} \rangle$ [equations (23) and (24)].

The above procedure is only practical when we know how to diagonalize $\hat{\mathcal{H}}_{\mathrm{F}}$. Thus, it is necessary to discuss the diagonalization procedures for the Floquet matrices. In many cases, perturbation theory or other approximation methods will be necessary to estimate the eigenvalues and eigenvectors of this matrix.[1,16–19]

2.5 The Fictitious Spin-1/2 Floquet Matrices

To simplify the presentation of the infinite Floquet matrices, a set of basis matrices, in the manifold of dressed spin states $\{|pn\rangle, |qm\rangle, \ldots\}$, can be introduced.[32,38] These matrices resemble the fictitious spin-$\frac{1}{2}$ operators,[39,40] and can be defined as follows:

$$\left.\begin{aligned}
&\langle pm|\hat{N}^{pp}|pm\rangle = m, \quad \langle pm|\hat{I}^{pp}|pm\rangle = 1 \\
&\langle pm+n|\hat{Z}_n^{pp}|pm\rangle = \langle p|I_z^{pp}|p\rangle = \tfrac{1}{2} \\
&\langle pm+n|\hat{P}_n^{pq}|qm\rangle = \langle p|I_+^{pq}|q\rangle = 1 \\
&\langle qm+n|\hat{M}_n^{pq}|pm\rangle = \langle q|I_-^{pq}|p\rangle = 1 \\
&\langle pm+n|\hat{Z}_n^{pq}|pm\rangle = -\langle qm+n|\hat{Z}_n^{pq}|qm\rangle \\
&\qquad = \langle p|\hat{I}_z^{pq}|q\rangle = \tfrac{1}{2} \\
&\langle pm+n|\hat{X}_n^{pq}|qm\rangle = \langle qm+n|\hat{X}_n^{pq}|pm\rangle \\
&\qquad = \langle p|\hat{I}_x^{pq}|q\rangle = \tfrac{1}{2} \\
&\langle pm+n|\hat{Y}_n^{pq}|qm\rangle = \langle qm+n|\hat{Y}_n^{pq}|pm\rangle^* \\
&\qquad = \langle p|\hat{I}_y^{pq}|q\rangle = -\tfrac{1}{2}\mathrm{i}
\end{aligned}\right\} \tag{25}$$

A schematic representation of these operators is shown in Figure 6

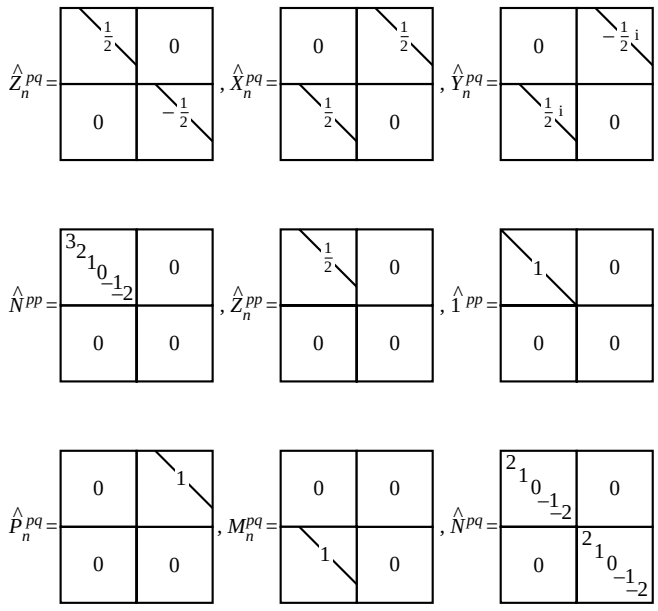

Figure 6 Representations of the Floquet matrices defined in equation (25)

As a result, the spin Hamiltonian

$$\hat{\mathcal{H}}(t) = \sum_{p<q} \sum_{n=-\infty}^{\infty} 2(\omega_{zn}^{pq} \hat{I}_z^{pq} + \omega_{xn}^{pq} \hat{I}_x^{pq} + \omega_{yn}^{pq} \hat{I}_y^{pq}) \exp(\mathrm{i}n\omega t) \tag{26}$$

generates a Floquet Hamiltonian of the form

$$\begin{aligned}
\hat{\mathcal{H}}_{\mathrm{F}} &= \sum_{p<q} \sum_{n=-\infty}^{\infty} (\omega \hat{N}^{pp} + 2\omega_{zn}^{pq} \hat{Z}_n^{pq} + 2\omega_{xn}^{pq} \hat{X}_n^{pq} + 2\omega_{yn}^{pq} \hat{Y}_n^{pq}) \\
&= \sum_{p<q} \sum_{n=-\infty}^{\infty} [\omega \hat{N}^{pp} + 2\omega_{zn}^{pq} (\hat{Z}_n^{pp} - \hat{Z}_n^{qq}) \\
&\quad + (\omega_{xn}^{pq} - \mathrm{i}\omega_{yn}^{pq}) \hat{P}_n^{pq} + (\omega_{xn}^{pq} + \mathrm{i}\omega_{yn}^{pq}) \hat{M}_n^{pq}]
\end{aligned} \tag{27}$$

A similar relationship holds between $\hat{\rho}(t)$ and $\hat{R}(t)$:

$$\begin{aligned}
\hat{\rho}(t) = \sum_{p<q} \sum_{n=-\infty}^{\infty} &[2r_{zn}^{pq}(t) \hat{I}_z^{pq} + 2r_{xn}^{pq}(t) \hat{I}_x^{pq} + 2r_{yn}^{pq}(t) \hat{I}_y^{pq}] \\
&\times \exp(\mathrm{i}n\omega t)
\end{aligned} \tag{28}$$

$$\begin{aligned}
\hat{R}(t) = \sum_{p \le q} \sum_{n=-\infty}^{\infty} &[2r_{zn}^{pq}(t) \hat{Z}_n^{pq} \\
&+ 2r_{xn}^{pq}(t) \hat{X}_n^{pq} + 2r_{yn}^{pq}(t) \hat{Y}_n^{pq}]
\end{aligned} \tag{29}$$

The Floquet operators, as defined in equation (25), satisfy the following commutation relations:

$$\left.\begin{aligned}
&[\hat{N}^{pp} + \hat{N}^{qq}, \hat{X}_n^{pq}] = n\hat{X}_n^{pq}, \quad [\hat{X}_n^{pq}, \hat{X}_m^{pq}] = 0 \\
&[\hat{N}^{pp} + \hat{N}^{qq}, \hat{Y}_n^{pq}] = n\hat{Y}_n^{pq}, \quad [\hat{Y}_n^{pq}, \hat{Y}_m^{pq}] = 0 \\
&[\hat{N}^{pp} + \hat{N}^{qq}, \hat{Z}_n^{pq}] = n\hat{Z}_n^{pq}, \quad [\hat{Z}_n^{pq}, \hat{Z}_m^{pq}] = 0 \\
&[\hat{N}^{pp}, \hat{Z}_n^{pp}] = n\hat{Z}_n^{pp}, \quad [\hat{Y}_n^{pq}, \hat{Z}_m^{pq}] = \mathrm{i}\hat{X}_{n+m}^{pq} \\
&[\hat{X}_n^{pq}, \hat{Y}_m^{pq}] = \mathrm{i}\hat{Z}_{n+m}^{pq}, \quad [\hat{Z}_n^{pq}, \hat{X}_m^{pq}] = \mathrm{i}\hat{Y}_{n+m}^{pq}
\end{aligned}\right\} \tag{30}$$

These relationships can be helpful for the diagonalization of $\hat{\mathcal{H}}_{\mathrm{F}}$ and the evaluation of $\hat{R}(t)$.

Up to this point we have only defined the Floquet Hamiltonian and discussed the possibility of evaluating expectation values. However, as mentioned before, the success of the application of Floquet theory depends on the success of the diagonalization of $\mathcal{H}_{\mathrm{F}}$. This is nontrivial in most cases. Only some simple forms of the Floquet Hamiltonians can be diagonalized analytically. For example, the following terms can be diagonalized, because they consist of an infinite set of 2×2 matrices:

$$\left.\begin{aligned}
\hat{\mathcal{H}}_{\mathrm{F}} &= \omega \hat{N}^{pp} + \omega \hat{N}^{qq} + 2\omega_{zo}^{pp} \hat{Z}_0^{pp} + 2\omega_{z0}^{qq} \hat{Z}_0^{qq} \\
&\quad + 2\omega_{xn} \hat{X}_n^{pq} + 2\omega_{yn} \hat{Y}_n^{pq} \\
\hat{\Lambda}_{\mathrm{F}} &= \omega \hat{N}^{pp} + \omega \hat{N}^{qq} + 2[(\omega_{xn}^{pq})^2 + (\omega_{yn}^{qq})^2 \\
&\quad + \tfrac{1}{4}(\omega_{z0}^{pp} - \omega_{zo}^{qq} + n\omega)^2]^{1/2} \hat{Z}_0^{pq} \\
&\quad + (\omega_{zo}^{pp} - n\omega) \hat{Z}_0^{pp} + (\omega_{zo}^{qq} + n\omega) \hat{Z}_0^{qq}
\end{aligned}\right\} \tag{31}$$

2.6 *z* Diagonalization of the Floquet Hamiltonian

The diagonal blocks of the Floquet Hamiltonian can be diagonalized analytically. The purpose of this section is to show that the diagonalization of the block-diagonal Floquet Hamiltonian

$$\hat{\mathcal{H}}_{\mathrm{F}} = \sum_{p} \left(\omega \hat{N}^{pp} + \sum_{n=-\infty}^{\infty} 2\omega_{zn}^{pp} \hat{Z}_{n}^{pp} \right) \tag{32}$$

results in a diagonalized Hamiltonian of the form

$$\hat{D}_{\mathrm{F}}^{-1} \left[\sum_{p} \left(\omega \hat{N}^{pp} + \sum_{n=-\infty}^{\infty} 2\omega_{zn}^{pp} \hat{Z}_{n}^{pp} \right) \right] \hat{D}_{\mathrm{F}} = \sum_{p} (\omega \hat{N}^{pp} + 2\omega_{z0}^{pp} \hat{Z}_{0}^{pp}) \tag{33}$$

and that the elements of the diagonalization matrix $d_n^{pp} = \langle pm + n | \hat{D}_{\mathrm{F}} | pm \rangle$ for all m satisfy

$$\sum_{n=-\infty}^{\infty} d_n^{pp} \exp(\mathrm{i}n\omega t) = \exp \left\{ \sum_{n=-\infty, n\neq 0}^{\infty} -\frac{\omega_{zn}^{pp}}{n\omega} [\exp(\mathrm{i}n\omega t) - 1] \right\} \tag{34}$$

Thus, the eigenvalues of the block-diagonal Floquet Hamiltonian are equal to its own diagonal elements, and the elements of $\hat{D}_{\mathrm{F}}$ can be obtained by a Fourier expansion, according to equation (34). In the rest of this section these results will be proven.

The Floquet Hamiltonian in equation (32) corresponds to a self-commuting diagonal spin Hamiltonian of the form

$$\hat{\mathcal{H}}(t) = \sum_{p} \sum_{n-\infty}^{\infty} 2\omega_{zn}^{pp} \hat{I}_{z}^{pp} \exp(\mathrm{i}n\omega t) \tag{35}$$

The matrix elements of the evolution operator corresponding to this Hamiltonian can thus be evaluated simply by integration, $\hat{U}(t) = \exp[-\mathrm{i} \int_0^t H(t')\, \mathrm{d}t']$:

$$\langle p | \hat{U}(t) | p \rangle = \exp(-\mathrm{i}\omega_{z0}^{pp} t) \times \exp \left\{ - \sum_{n=-\infty, n\neq 0}^{\infty} \frac{\omega_{zn}^{pp}}{n\omega} [\exp(\mathrm{i}n\omega t) - 1] \right\} \tag{36}$$

An expression for these elements can also be obtained by using the Floquet approach. Equation (33) can actually be derived first by writing the unitary $\hat{D}_{\mathrm{F}}$ matrix in its most general form,

$$\hat{D}_{\mathrm{F}} = \sum_{p} \sum_{n=-\infty}^{\infty} d_n^{pp} \hat{Z}_{n}^{pp}, \quad \hat{D}_{\mathrm{F}}^{-1} = \sum_{p} \sum_{n=-\infty}^{\infty} d_{-n}^{pp*} \hat{Z}_{n}^{pp} \tag{37}$$

and secondly by expressing it in terms of a Hermitian diagonal block-matrix $\Sigma_p \Sigma_n \delta_n^{pp} \hat{Z}_n^{pp}$:

$$\hat{D}_{\mathrm{F}} = \exp \left(\mathrm{i} \sum_{p} \sum_{n=-\infty}^{\infty} \delta_n^{pp} \hat{Z}_n^{pp} \right)$$

$$\hat{D}_{\mathrm{F}}^{-1} = \exp \left(-\mathrm{i} \sum_{p} \sum_{n=-\infty}^{\infty} \delta_n^{pp} \hat{Z}_n^{pp} \right) \tag{38}$$

The diagonalization of $\hat{\mathcal{H}}_{\mathrm{F}}$ results in the following, when we expand the transformation in its Taylor series and use the commutation relations of equations (25) and (33):

$$\hat{D}_{\mathrm{F}}^{-1} \{ \hat{\mathcal{H}}_{\mathrm{F}} \} \hat{D}_{\mathrm{F}} = \hat{\mathcal{H}}_{\mathrm{F}} - \mathrm{i}[D_{\mathrm{F}}, \hat{\mathcal{H}}] = \sum_{p} \left(\omega \hat{N}^{pp} + \sum_{n=-\infty}^{\infty} (2\omega^{pp}_{zn} + \mathrm{i}n\omega \delta^{pp}_{n}) \hat{Z}_{n}^{pp} \right) \tag{39}$$

The only diagonal elements of this transformed Hamiltonian are $\sum_p 2\omega_{z0} \hat{Z}_0^{pp}$ and $\omega \hat{N}^{pp}$, which correspond to equation (33).

Thus, matrix elements of the Floquet evolution operator and the spin evolution operator can be written in terms of the elements of the diagonalization matrix $\hat{D}_{\mathrm{F}}$ and the eigenvalues of $\hat{\mathcal{H}}_{\mathrm{F}}$:

$$\langle pn | \hat{U}_{\mathrm{F}}(t) | p0 \rangle = \sum_{n,m=-\infty}^{\infty} \langle pn | \hat{D}_{\mathrm{F}} | pm \rangle \times \exp(-\mathrm{i}\omega_{z0}^{pp} t - \mathrm{i}m\omega t) \langle pm | \hat{D}_{\mathrm{F}}^{-1} | p0 \rangle \tag{40}$$

and with equations (13a) and (13b)

$$\langle p | \hat{U}(t) | p \rangle = \sum_{n,m=-\infty}^{\infty} d_{n-m}^{pp} \exp(-\mathrm{i}\omega_{z0}^{pp} t - \mathrm{i}m\omega t)\, d_{-m}^{pp*} \exp(\mathrm{i}n\omega t) = \exp(-\mathrm{i}\omega_{z0}^{pp} t) \left[\sum_{m=-\infty}^{\infty} d_{-m}^{pp*} \right] \sum_{n=-\infty}^{\infty} d_n^{pp} \exp(\mathrm{i}n\omega t) \tag{41}$$

A comparison between this result and the result in equation (36) yields the expression in equation (34).[41] For each value of p the sum of all d_n^{pp} coefficients can be made equal to one. This can be derived from the fact that $\hat{U}(0) = 1$ and equation (41)

$$\sum_{n=-\infty}^{\infty} d_n^{pp} = 1 \tag{42}$$

This normalization condition for the $\{d_n^{pp}\}$ elements of the columns of the unitary matrix $\hat{D}_{\mathrm{F}}$ keeps the values of the magnitudes of these elements smaller than one. When $\{\omega_{zn}^{pp}\} \ll \omega$, we get $d_0^{pp} \approx 1$ and $d_n^{pp} \approx 0$ for $n \neq 0$ and, by a Taylor expansion of equation (34), when $\{\omega_{zn}^{pp}\} < \omega$, we get $d_0^{pp} \approx 1 - \sum_n \omega_{zn}^{pp} (n\omega)^{-1}$ and $d_n^{pp} \approx \omega_{zn}^{pp} (n\omega)^{-1}$.

The Fourier expansion in equation (34) for the elements $d_n^{pp}(+)$ of the diagonalization matrix $\hat{D}_{\mathrm{F}}(+)$ of a Floquet Hamiltonian with elements $\{\omega_{zn}^{pp}\}$ is the complex conjugate of the expansion for the elements $d_n^{pp}(-)$ of the diagonalization matrix $\hat{D}_{\mathrm{F}}(-)$ of a Floquet Hamiltonian with elements $\{-\omega_{zn}^{pp}\}$. This follows from the facts that $d_{-n}^{pp*}(-) = d_n^{pp}(+)$ and $\langle pn + m | \hat{D}_{\mathrm{F}}(+) | pm \rangle = \langle pn + m | \hat{D}_{\mathrm{F}}^{-1}(-) | pm \rangle$.

The elements of the diagonalization matrix of the Floquet matrix in equation (35) can also be expressed in terms of Bessel functions:[30]

$$d_n^{pp} = \sum_{\substack{k_1,k_2,\ldots,=-\infty \\ k_{k1}+k_2+\ldots=n}}^{\infty} J_{k_1}\left(-\frac{|\omega_{z1}^{pp}|}{2\omega}\right) J_{k_2}\left(-\frac{|\omega_{z2}^{pp}|}{4\omega}\right) J_{k_3}\left(-\frac{|\omega_{z3}^{pp}|}{6\omega}\right)\cdots \times \exp[\mathrm{i}(k_1\phi_1 + k_2\phi_2 + k_3\phi_3\ldots)] \tag{43}$$

with $\omega_{zn}^{pp} = |\omega_{zn}^{pp}|\exp(\mathrm{i}\phi_n)$.

2.7 Numerical Diagonalization and Perturbation Theory

The diagonalization of the Floquet Hamiltonian is in many instances only possible via numerical calculations. These calculations require a truncation of the infinite matrix. The block size N of the truncated Hamiltonian can be chosen according to the magnitude of the off-diagonal elements and the convergence of the eigenvalues for increasing matrix dimension. For large off-diagonal elements or for elements that are far off-diagonal, it is sometimes recommended to define the truncated matrix in the manifold of Floquet states in the order $\{|pN\rangle|qN\rangle|rN\rangle\}\{|pN-1\rangle|qN-1\rangle|rN-1\rangle\}\cdots\{|p0\rangle|q0\rangle|r0\rangle\}\cdots\{|p-N+1\rangle|q-N+1\rangle|r-N+1\rangle\}\{|p-N\rangle|q-N\rangle|r-N\rangle\}$ rather than in the order $\{|pN\rangle|pN-1\rangle\cdots|p0\rangle\cdots|p-N+1\rangle|p-N\rangle\}\{|qN\rangle|qN-1\rangle\cdots|q0\rangle\cdots|q-N+1\rangle|q-N\rangle\}\{|rN\rangle|rN-1\rangle\cdots|r0\rangle\cdots|r-N+1\rangle|r-N\rangle\}$, when standard diagonalization subroutines are used in computer calculation.

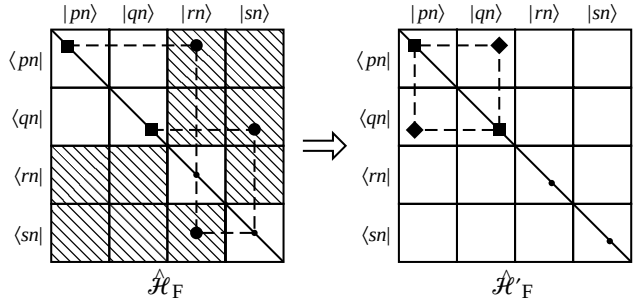

Figure 7 A schematic representation of the degenerate perturbation theory treatment of part of a Floquet matrix $\hat{\mathcal{H}}_F$ that has degenerate diagonal elements, with values $\langle pn+m|\hat{\mathcal{H}}_F|pn+m\rangle \approx \langle qm|\hat{\mathcal{H}}_F|qm\rangle$ = ■ for all m, that are not directly connected via an off-resonance element •. The procedure creates an approximate Floquet matrix $\hat{\mathcal{H}}'_F$ with off-diagonal elements between the degenerate states, and eliminates off-diagonal elements in $\hat{\mathcal{H}}_F$ that are small with respect to the difference between the diagonal elements they connect. The correction element can be calculated according to

$$\langle pn+m|\hat{\mathcal{H}}'_F|qm\rangle = \sum_{r,s}\sum_{k,l=-\infty}^{\infty} \frac{\langle pn+m|\hat{\mathcal{H}}_F|rk\rangle\langle rk|\hat{\mathcal{H}}_F|sl\rangle\langle sl|\hat{\mathcal{H}}_F|qm\rangle}{(E_n^{pq} - \langle rk|\hat{\mathcal{H}}_F|rk\rangle)(E_n^{pq} - \langle sl|\hat{\mathcal{H}}_F|sl\rangle)} + \ldots = \blacklozenge$$

This shows that degenerate Floquet states will be shifted away from each other, even when the interaction Hamiltonian does not exactly exhibit matrix elements between these states

If all off-diagonal elements of $\hat{\mathcal{H}}_F$ are much smaller than the differences between the diagonal elements they connect, standard perturbation theory[16–18,36] can be exploited to estimate eigenvalues and eigenvectors. For example, Nakai et al.[28] used nondegenerate perturbation theory to very high orders for calculating the eigenvalues of the Floquet Hamiltonian of rotating homonuclear two-spin systems. Augustine et al.[29] used perturbation theory to evaluate second-order effects in heteronuclear spin systems.

If some off-diagonal elements connect degenerate diagonal elements of $\hat{\mathcal{H}}_F$, zeroth-order 2 × 2 diagonalization must be performed before a higher-order perturbation expansion can be used. This is commonly necessary for evaluating the energy shifts of the levels at anticrossings (see Section 3.3). However, if the degenerate diagonal elements are not directly connected via nonzero off-diagonal elements, the off-diagonal perturbation approach[3] can be used to estimate an effective off-diagonal element between these degenerate elements (see also the example in Section 4.1). An example of this approach can be found in the paper of Krauss et al.,[23] in which multiphoton effects in NMR on spins with $I = \frac{1}{2}$ are discussed. While the standard perturbation theory approach modifies the diagonal elements and eliminates off-diagonal elements of the Hamiltonian, the off-diagonal perturbation approach replaces existing off-diagonal elements by new small off-diagonal elements between almost-degenerate states (see Figure 7).

3 STROBOSCOPIC DETECTION

3.1 Evolution Operators and Expectation Values

The time dependence of the expectation values of observables is governed, according to equation (23), by the differences between the eigenvalues of the Floquet Hamiltonian. If the observation of these expectation values is restricted to times that are integer multiples of the time constant T of the period of the Hamiltonian ($\exp(\mathrm{i}\omega n_T T) = 1$), the detection is performed stroboscopically. In this case, the matrix elements of the spin evolution operator in equations (13a) and (13b) become

$$\begin{aligned}\langle p|\hat{U}(n_T T)|q\rangle &= \sum_{n=-\infty}^{\infty}\langle pn|\hat{U}_F(n_T T)|q0\rangle \\ &= \sum_r \sum_{n,m=-\infty}^{\infty}\langle pn|\hat{D}_F|rm\rangle \\ &\quad\times \exp(-\mathrm{i}\lambda_m^r n_T T)\langle rm|\hat{D}_F^{-1}|q0\rangle \\ &= \left(\sum_{n=-\infty}^{\infty}\langle pn|\hat{D}_F|r0\rangle\right)\exp(-\mathrm{i}\lambda_0^r n_T T) \\ &\quad\times\left(\sum_{m=-\infty}^{\infty}\langle rm|\hat{D}_F^{-1}|q0\rangle\right)\end{aligned} \tag{44}$$

where we have used the definition of the Floquet evolution operator $\hat{U}_F(t)$ and the diagonalization $\hat{\mathcal{H}}_F = \hat{D}_F\hat{\Lambda}_F\hat{D}_F^{-1}$.

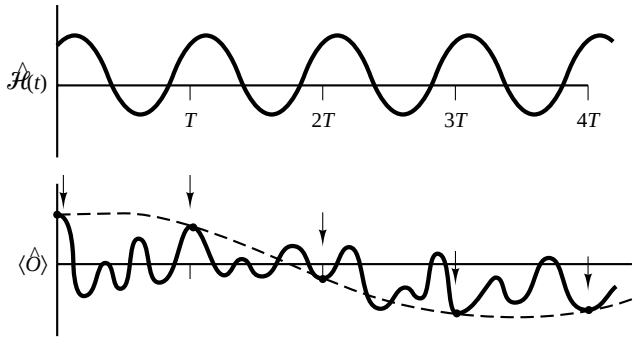

Figure 8 In an experiment that allows only stroboscopic detection of the coherences of a spin system, the data are collected once per each time period T of the spin Hamiltonian with $\hat{\mathcal{H}}(t + n_T T) = \hat{\mathcal{H}}(t)$

The expression for the expectation values of observables in equation (23) can also be simplified during stroboscopic detection (Figure 8):

$$\langle\hat{O}\rangle = \sum_{n=-\infty}^{\infty}\sum_{p}\langle pn|\hat{R}(t)\hat{O}_{\mathrm{F}}|p0\rangle = \sum_{p<q} A^{pq}O^{pq}\exp[-\mathrm{i}(\lambda_0^q - \lambda_0^p)n_T T] \quad (45)$$

with

$$A^{pq} = \sum_{n=-\infty}^{\infty}\langle\lambda_0^p|\hat{R}(0)|\lambda_n^q\rangle, \quad O^{pq} = \sum_{n=-\infty}^{\infty}\langle\lambda_n^q|\hat{O}_{\mathrm{F}}|\lambda_0^p\rangle \quad (46)$$

3.2 Effective Hamiltonians

The spin evolution operator in equation (44) can be written as function of an effective spin Hamiltonian $\hat{\mathcal{H}}_{\mathrm{eff}}$:[10,17,18,38]

$$\hat{U}(n_T T) = \exp(-\mathrm{i}\hat{\mathcal{H}}_{\mathrm{eff}} n_T T) \quad (47)$$

This time-independent Hamiltonian governs the spin system in an exact manner as long as the detection of any observable is restricted to $n_T T$. Comparing equations (47) and (44), the matrix elements of the effective Hamiltonian can be defined by

$$\langle p|\hat{\mathcal{H}}_{\mathrm{eff}}|q\rangle = \langle p|\hat{\tilde{D}}\hat{\Lambda}\hat{\tilde{D}}^{-1}|q\rangle \quad (48)$$

with

$$\left.\begin{aligned}\langle r|\hat{\Lambda}|r\rangle &= \langle r0|\hat{\Lambda}_{\mathrm{F}}|r0\rangle = \lambda_0^r \\ \langle p|\hat{\tilde{D}}|r\rangle &= \sum_{n=-\infty}^{\infty}\langle pn|\hat{D}_{\mathrm{F}}|r0\rangle = \sum_{n=-\infty}^{\infty} d_n^{pr}\end{aligned}\right\} \quad (49)$$

The energies of the effective Hamiltonian are thus equal to the principal eigenvalues of $\hat{\mathcal{H}}_{\mathrm{F}}$, and the elements of its diagonalization matrix are equal to the sums of the elements of $\hat{D}_{\mathrm{F}}$. The principal eigenvalues of $\hat{\mathcal{H}}_{\mathrm{F}}$ can always be chosen between $\frac{1}{2}\omega$ and $-\frac{1}{2}\omega$,[16–18] as expected for a sampling time of $T = 2\pi/\omega$. The actual evaluation of the effective Hamiltonian is again dependent on the diagonalization of the $\hat{\mathcal{H}}_{\mathrm{F}}$. If this can be achieved then the effective Hamiltonian describes the stroboscopic evolution spin of the system in an exact manner. If not, then again approximation methods, such as perturbation theory, must be utilized. A Floquet Hamiltonian that is block-diagonal has a z-diagonalization matrix that satisfies equation (42) and thus $\langle p|\hat{D}|r\rangle = \delta_{pr}$, and generates a diagonal effective Hamiltonian with elements $\langle p|\hat{\mathcal{H}}_{\mathrm{eff}}|p\rangle = \langle p0|\hat{\mathcal{H}}_{\mathrm{F}}|p0\rangle$.

It is desirable to present the effective Hamiltonian in terms of angular momentum operators. Examples are provided by Weintraub and Vega.[38] If the diagonalization is performed numerically, the above equations provide the way to represent the effective Hamiltonian in matrix form. This form can always be transformed to an expression in terms of fictitious spin-$\frac{1}{2}$ operators.[39,40]

3.3 Degenerate Floquet States

Various spectroscopic effects in MAS NMR could be explained by the removal of degeneracies between Floquet states (i.e., the eigenvalues of the Floquet Hamiltonian) of a spin system, due to an interaction Hamiltonian. Rotor frequency lines,[26] the rotary resonance,[42] and the rotational resonance[30,43] phenomena could all be explained in terms of the removal of such a degeneracy. Even the homonuclear recoupling experiments[31,32,40] could be described by the anticrossing of Floquet states in the toggling frame.

In order to explain the anticrossing of Floquet states, let us consider a diagonal Floquet Hamiltonian

$$\hat{\mathcal{H}}_{\mathrm{F}} = \sum_{p}\omega\hat{N}^{pp} + \sum_{p} 2\omega_{z0}^{pp}\hat{Z}_0^{pp} \quad (50)$$

and an additional interaction term of the form

$$\sum_{n=-\infty}^{\infty}(2\omega_{xn}^{st}\hat{X}_n^{st} + 2\omega_{yn}^{st}\hat{Y}_n^{st}) \quad (51)$$

The matrix elements of this addition are only significant when ω_{xn}^{st} and ω_{yn}^{st} are not much smaller than the difference $\omega_{z0}^{ss} - \omega_{z0}^{tt} + n\omega$ between the Floquet energies of the states they connect. However, if this is the case, the interaction term can shift the energies significantly, and an anticrossing of the Floquet states can occur (Figure 9).

A degeneracy $\omega_{z0}^{ss} + n\omega + m\omega \approx \omega_{z0}^{tt} + m\omega$, for all m, between the eigenstates $|s(m+n)\rangle$ and $|tm\rangle$ of $\hat{\mathcal{H}}_{\mathrm{F}}$ will be lifted by an interaction term that connects these states, and will give new eigenvalues

$$\tfrac{1}{2}(\omega_{z0}^{ss} + \omega_{z0}^{tt} + n\omega) + m\omega \pm\{-\tfrac{1}{2}n\omega + [\tfrac{1}{4}(\omega_{z0}^{ss} - \omega_{z0}^{tt} + n\omega)^2 + \omega_{xn}^{st2} + \omega_{yn}^{st2}]^{1/2}\} \quad (52)$$

The part of the effective Hamiltonian that corresponds to the $s-t$ transition will then take the form[38]

$$\hat{\mathcal{H}}_{\mathrm{eff}}^{st} = (\omega_{z0}^{ss} - \omega_{z0}^{tt} + n\omega)\hat{I}_z^{st} + 2\omega_{xn}^{st}\hat{I}_x^{st} + 2\omega_{yn}^{st}\hat{I}_y^{st} - n\omega\hat{I}_z^{st} \quad (53)$$

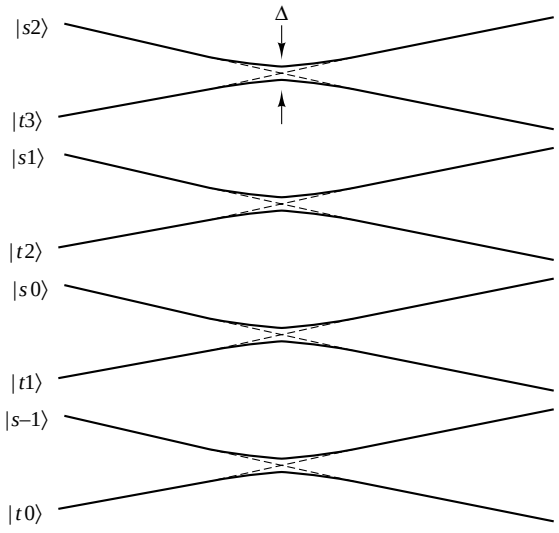

Figure 9 A schematic representation of the anticrossing of almost-degenerate eigenfunctions of a Floquet matrix with $\langle sn+m|\hat{\mathcal{H}}_{\mathrm{F}}|sn+m\rangle = \langle tm|\hat{\mathcal{H}}_{\mathrm{F}}|tm\rangle$ that is caused by an interaction matrix element $\Delta\langle sn+m|\hat{\mathcal{H}}_{\mathrm{F}}^{\mathrm{int}}|tm\rangle$

The anticrossing of the Floquet eigenstates will cause frequency shifts in the expectation values of coherences and polarizations of spin systems. This will occur not only in the case of stroboscopic detection but also in the $(\lambda_0^q - \lambda_0^p) + n\omega$ frequencies of nonsynchronously detected observables.

Thus, the effective Hamiltonian for a stroboscopic observation of a spin system is obtained by the construction of the Floquet Hamiltonian and by its diagonalization. The Floquet principal eigenvalues λ_0^q have become equal to the energies of the effective Hamiltonian, and its operational form can be evaluated by summations over matrix elements d_n^{pq} of the Floquet diagonalization matrix. Where necessary, perturbation theory can be exploited to estimate the parameters λ_0^q and d_n^{pq}, and, where accurate results are required, numerical methods can be used. As mentioned before, expansion methods for the evaluation of effective Hamiltonians, as discussed by Maricq[17] and Llor,[18] are not presented in this article.

4 EXAMPLES

In the rest of this article, some examples of the use of the Floquet approach will be discussed. Only the computational steps relevant to Floquet theory are presented in these examples.

4.1 Modulated rf Excitation

4.1.1 Multifrequency Pulse Excitation

An amplitude- and phase-modulated rf excitation pulse of finite length T that is applied to a spin system with $I = \frac{1}{2}$ has a spin Hamiltonian that can be written in the form

$$\hat{\mathcal{H}}(t) = -\Delta\omega I_z + 2\omega_x(t)\hat{I}_x + 2\omega_y(t)\hat{I}_y = -\Delta\omega\hat{I}_z + \sum_{n=-\infty}^{\infty}[2\omega_{xn}\hat{I}_x + 2\omega_{yn}\hat{I}_y]\exp(\mathrm{i}n\omega t) \quad (54)$$

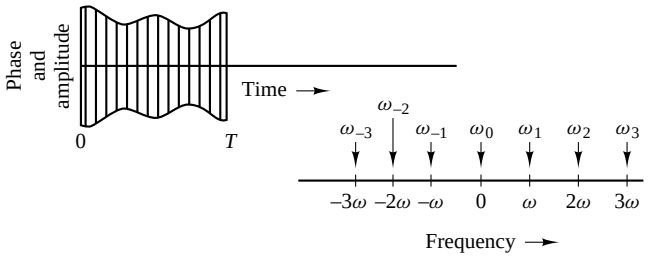

Figure 10 An rf irradiation pulse of finite length can be considered as if it is composed of a set of simultaneously applied rf fields at constant frequency intervals ω

with $\omega = 2\pi/T$. The Fourier transformation describes the time-dependent rf field in terms of multifrequency irradiation (Figure 10). The Floquet Hamiltonian corresponding to this Hamiltonian has the following form, when we consider the length of the pulse as its single time period ($|1\rangle = |\alpha\rangle, |2\rangle = |\beta\rangle$):

$$\hat{\mathcal{H}}_{\mathrm{F}} = \omega(\hat{N}^{11} + \hat{N}^{22}) - \Delta\omega\hat{Z}_0^{12} + \sum_{n=-\infty}^{\infty}(2\omega_{xn}\hat{X}_n^{12} + 2\omega_{yn}\hat{Y}_n^{12}) \quad (55)$$

If we are only interested in the state of the spin immediately after the pulse, it is most convenient to evaluate the effective Hamiltonian of the pulse (see Section 3.2).

For small-amplitude coefficients, $\omega_{nx}, \omega_{ny} \ll \omega$, perturbation theory can be used to evaluate this Hamiltonian. For a special case, with $\Delta\omega \ll \omega$ and $\omega_{x0} = \omega_{y0} = 0$ and thus $\langle 1n|\hat{\mathcal{H}}_{\mathrm{F}}|1n\rangle \approx \langle 2n|\hat{\mathcal{H}}_{\mathrm{F}}|2n\rangle$, the degenerate perturbation approach can be used in order to obtain an approximate Floquet Hamiltonian of the form[23] (see Section 2.7)

$$\hat{\mathcal{H}}'_{\mathrm{F}} = \omega(\hat{N}^{11} + \hat{N}^{22}) - (\Delta\omega + \delta\omega)\hat{Z}_0^{12} + \omega_{\mathrm{eff}}\hat{P}_0^{12} + \omega_{\mathrm{eff}}^*\hat{M}_0^{12} \quad (56)$$

with

$$\omega_{\mathrm{eff}} = \sum_{k,l=-\infty}^{\infty}\frac{\langle 10|\hat{\mathcal{H}}_{\mathrm{F}}|2k\rangle\langle 2k|\hat{\mathcal{H}}_{\mathrm{F}}|1l\rangle\langle 1l|\hat{\mathcal{H}}_{\mathrm{F}}|20\rangle}{(E_0^{12} - \langle 2k|\hat{\mathcal{H}}_{\mathrm{F}}|2k\rangle)(E_0^{12} - \langle 1l|\hat{\mathcal{H}}_{\mathrm{F}}|1l\rangle)} + \cdots \quad (57)$$

$$\delta\omega = -\sum_{k,l=-\infty}^{\infty}\frac{\langle 10|\hat{\mathcal{H}}_{\mathrm{F}}|2k\rangle\langle 2k|\hat{\mathcal{H}}_{\mathrm{F}}|10\rangle}{(E_0^{12} - \langle 2k|\hat{\mathcal{H}}_{\mathrm{F}}|2k\rangle)} - \frac{\langle 20|\hat{\mathcal{H}}_{\mathrm{F}}|1k\rangle\langle 1k|\hat{\mathcal{H}}_{\mathrm{F}}|20\rangle}{(E_0^{12} - \langle 1k|\hat{\mathcal{H}}_{\mathrm{F}}|1k\rangle)} + \cdots \quad (58)$$

and $E_n^{12} = \frac{1}{2}[\langle 1n|\hat{\mathcal{H}}_{\mathrm{F}}|1n\rangle + \langle 2n|\hat{\mathcal{H}}_{\mathrm{F}}|2n\rangle]$. This approximate Hamiltonian contains only corrected diagonal elements and small off-diagonal elements, connecting the almost-degenerate diagonal elements. All other off-diagonal elements are discarded from the Hamiltonian.

The Floquet Hamiltonian in equation (56) generates an effective Hamiltonian of the form

$$\hat{\mathcal{H}}_{\mathrm{eff}} = -(\Delta\omega + \delta\omega)\hat{I}_z + \omega_{\mathrm{eff}}\hat{I}_+ + \omega_{\mathrm{eff}}^*\hat{I}_- \quad (59)$$

When the pulse exhibits only four frequency components, $\omega_{x\pm n} \neq 0$ for $n = n_1, \pm n_2$, equation (59) represents the effective Hamiltonian of an $(n_1 + n_2)$-photon pulse.[23]

4.1.2 Pulse Shaping

For arbitrary frequency amplitudes in the spin Hamiltonian of the excitation pulse in equation (54), numerical diagonalizations of its Floquet Hamiltonian can be performed in order to obtain the eigenvalues $\pm\lambda_0^1$ and the matrix elements d_n^{pq} of the diagonalization matrix of $\hat{\mathcal{H}}_F$. Insertion of these results in equations (48) and (49) in Section 3.2 will yield the effective Hamiltonian.

For designing frequency-selective pulses, the form of the required effective Hamiltonian can be defined, and conditions for $\pm\lambda_0^1$ and the sums of the d_n^{pq} elements, as a function of the off-resonance, can be determined. Numerical search procedures can then be utilized to obtain optimal ω_{xn} and ω_{yn} values that will satisfy these conditions.[24] For example, a broadband pulse that requires an effective Hamiltonian $\hat{\mathcal{H}}_{\text{eff}} = \omega_1 \hat{I}_x$ for a large range of off-resonance values $\Delta\omega$, must satisfy the condition $\lambda_0^1 = 0.5\omega_1$, and $\sum_n d_n^{11} = -\sum_n d_n^{12} = \sqrt{\frac{1}{2}}$ for its Floquet Hamiltonian.

If the Floquet approach is used to design TOCSY sequences,[6] the calculation of the effective Hamiltonian is not sufficient, and all the individual elements of $\hat{D}_F$ become relevant.[44]

4.2 Magic Angle Spinning NMR

4.2.1 MAS Sideband Spectra

The Hamiltonian of a spin system with $I = \frac{1}{2}$ in a single crystallite of a polycrystalline solid that is rotating at the magic angle with a spinning speed ω_R can be written in the form[45]

$$\begin{aligned}\hat{\mathcal{H}}_{CS}(t) &= -\Delta\omega \hat{I}_z + \omega_{CS}[g_1 \cos(\omega_R t + \psi_1) \\ &\quad + g_2 \cos(2\omega_R t + \psi_2)] I_z \\ &= -\Delta\omega \hat{I}_z + \sum_{n=-2, n\neq 0}^{2} 2\omega_n^{CS} \exp(in\omega_R t) \hat{I}_z \end{aligned} \quad (60)$$

The chemical shift parameter ω_{CS} and the explicit forms of the orientational dependent parameters g_n, ψ_n, and $\omega_n^{CS} = \frac{1}{4}\omega_{CS} g_{|n|} \exp(in\psi_n)$, can be derived from the MAS Hamiltonians given in ***Magic Angle Spinning***. The Floquet Hamiltonian corresponding to this Hamiltonian is block-diagonal,

$$\hat{\mathcal{H}}_F^{CS} = \omega_R(\hat{N}^{11} + \hat{N}^{22}) - \Delta\omega \hat{Z}_0^{12} + \sum_{n=-2, n\neq 0}^{2} 2\omega_n^{CS} \hat{Z}_n^{12} \quad (61)$$

and can be z-diagonalized. Its principal eigenvalues are $\lambda_0^1 = \frac{1}{2}\Delta\omega$, and the elements of its diagonalization matrix satisfies $d_n^{11} = d_{-n}^{22*}$, according to the discussion at the end of Section 2.6. The FID signal (ignoring relaxation) after a simple excitation of the rotating spin system, with $\hat{\rho}(0) = 2\hat{I}_x$ and $\hat{R}(0) = 2\hat{X}_0^{12}$, is equal to

$$\begin{aligned}\langle \hat{I}_- \rangle &= \sum_{n=-\infty}^{\infty} A^{12} \langle \lambda_n^2 | \hat{M}_0^{12} | \lambda_0^1 \rangle \exp[\mathrm{i}(\lambda_n^2 - \lambda_0^1)t] \\ &= \exp(\mathrm{i}\Delta\omega t) \sum_{n,m=-\infty}^{\infty} d_{-n-m}^{11} d_m^{11} \exp(in\omega_R t) \end{aligned} \quad (62)$$

with

$$|\lambda_n^1\rangle = \sum_{n=-\infty}^{\infty} d_n^{11} |1n\rangle \quad (63)$$

and, according to equation (42) in Section 2.6,

$$A^{pq} = \sum_{n=-\infty}^{\infty} \langle \lambda_0^1 | \hat{X}_0^{12} | \lambda_n^2 \rangle = \sum_{n,m=-\infty}^{\infty} d_m^{11*} d_{n+m}^{22} = 1 \quad (64)$$

The Fourier transform of the total signal of all crystallites in the sample results in a sideband spectrum. The amplitudes of these frequency bands are equal to the powder integrals of the amplitudes of the individual allowed transitions between Floquet states (see Figure 3). An elegant methodology, similar to the Floquet approach, for the calculation of MAS spectra was introduced by Sethi et al.[46]

4.2.2 Rotor Frequency Lines

If the rotating spin system experiences a weak rf field during signal detection (e.g., a nonzero effective rf field during a multiple pulse experiment[26]), a term $\omega_1 \hat{I}_x$ must be added to $\hat{\mathcal{H}}_{CS}(t)$ and a term $\omega_1 \hat{X}_0^{12}$ to $\hat{\mathcal{H}}_F^{CS}$ with $\omega_1 \ll \omega_R$. The matrix elements of $\hat{X}_0^{12}$ connect the $|1n\rangle$ and $|2n\rangle$ states with Floquet energies $-\frac{1}{2}\Delta\omega + n\omega_R$ and $\frac{1}{2}\Delta\omega + n\omega_R$. These elements can change the eigenvalues and eigenvectors of $\hat{\mathcal{H}}_F$ significantly, even if degeneracies occur between diagonal elements with different n values. For example, when $\Delta\omega \approx n\omega_R$, the Floquet states $|1(n + m)\rangle$ and $|2m\rangle$ for all m are degenerate, and an energy anticrossing can occur. For estimating the dependence on the irradiation term of this energy shift, a z diagonalization of $\mathcal{H}_F$, by a diagonal block matrix $\hat{D}_F$, can be performed (see Section 2.6), and the matrix elements $\delta\omega_1(n) = \frac{1}{2}\omega_1 \langle 1\ \mathrm{n} + m | \hat{D}_F \hat{X}_0^{12} \hat{D}_F^{-1} | 2m \rangle$ between the degenerate states can be evaluated. When this element is different from zero, an effective Hamiltonian of the form (see Sections 3.2 and 3.3)

$$\begin{aligned}\hat{\mathcal{H}}_{\text{eff}}(\Delta\omega \approx n\omega_R) &= -(\Delta\omega - n\omega_R)\hat{I}_z + \delta\omega_1(n)\hat{I}_+ \\ &\quad + \delta\omega_1^*(n)\hat{I}_- \end{aligned} \quad (65)$$

will be obtained. Thus, for stroboscopic measurements, the main resonances are expected at frequencies $[(\Delta\omega - n\omega_R)^2 + 4\delta\omega_1^2(n)]^{1/2}$ and 0, and for nonstroboscopic experiments at

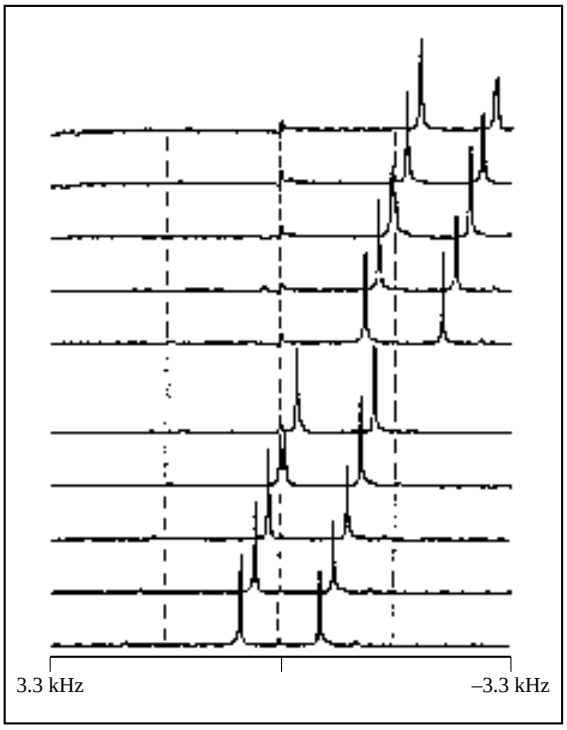

Figure 11 Nitrogen-15 NMR MAS spectrum of doubly ^{15}N-labeled glycylglycine that demonstrates the rotor frequency lines. This spectrum was obtained by a MAS scaling experiment with $q = 0.50$ and $\nu_R = \omega_R/2\pi = 1.67$ kHz. The additional lines in the spectrum are clearly observed at the $(k + n)\omega_R$ positions, when the offset frequency of one of the lines satisfies $\Delta\omega \approx k\omega_R$. (Adapted by permission from Ave et al.[2])

$[(\Delta\omega - n\omega_R)^2 + 4\delta\omega_1^2(n)]^{1/2} + m\omega_R$ and $nm\omega_R$. An example of rotor frequency lines is shown in Figure 11.

4.2.3 Rotational Resonance

The Floquet approach can also be applied to explain the rotational resonance phenomena[43,47] that occur when the interaction between two dipolar-coupled homonuclear spins is monitored during an MAS experiment. If the strength of the interaction is smaller than the spinning speed, the sample rotation will largely eliminate its influence on the MAS spectra of the spins. However, if the difference between the isotropic shifts of the two spins $\Delta\omega = \Delta\omega^{(1)} - \Delta\omega^{(2)}$ is approximately equal to an integer multiple of the spinning frequency ω_R, the interaction will influence the spin evolution significantly. To demonstrate this effect, we can consider the Floquet space defined by the states $\{|pn\rangle\}$, with $p = 1, \ldots, 4$, $|1\rangle = |\alpha\alpha\rangle$, $|2\rangle = |\alpha\beta\rangle$, $|3\rangle = |\beta\alpha\rangle$, and $|4\rangle = |\beta\beta\rangle$. The chemical shift parts of the two spins of the Floquet Hamiltonian as well as the main parts of the dipolar interaction, corresponding to the $\hat{I}_{z1}\hat{I}_{z2}$ terms in the spin Hamiltonian, are block diagonal [see equation (61)]. Only the flip–flop terms, corresponding to $\frac{1}{4}(\hat{I}_{+1}\hat{I}_{-2} + \hat{I}_{-1}\hat{I}_{+2})$, contribute to the off-diagonal blocks 2–3. The terms in the Floquet Hamiltonian corresponding to these blocks have the form $\omega_d \sum_n G_n \hat{X}_n^{23}$, $n = -2, -1, 1, 2$. They connect the states $|2n + m\rangle$ and $|3m\rangle$, for $n = \pm 1$, ± 2 and all m, with Floquet energies $-\frac{1}{2}\Delta\omega + (n + m)\omega_R$ and $\frac{1}{2}\Delta\omega + m\omega_R$, respectively.[30,32,41] These elements will influence the eigenvalues of the whole Floquet Hamiltonian most significantly when they connect degenerate Floquet states, i.e., $\Delta\omega = n\omega_R$. Energy shifts are also expected for n values different from ± 1, ± 2. The changes in the eigenvalues influence the time dependences of the expectation values of the spin angular momentum operators, and thus modify the time dependence of the coherences and populations of the spin system and its MAS spectra.[42]

4.2.4 Effective Hamiltonians of Multipulse Experiments

When rf pulses are applied to rotating spin systems synchronously with the spinning speed, effective Hamiltonians can be evaluated by transforming the spin Hamiltonian to the toggling frame.[5] In that case, the rf terms in the spin Hamiltonian become periodically time-dependent, and a Fourier transformation of these terms is possible. Using the Fourier coefficients of this transformation, a Floquet Hamiltonian that corresponds to the toggling-frame spin Hamiltonian can be constructed. This Hamiltonian governs the spin system again, as long as the toggling-frame transformation is cyclic.[5,11] Examples of this approach can be found in the literature.[31,38,47]

4.2.5 CP MAS Experiments

One of the most important developments in high-resolution solid state NMR spectroscopy was the introduction of cross polarization MAS (CP MAS) experiments on low-abundance $I = \frac{1}{2}$ spins by Schaefer and Stejskal.[48] Floquet theory can provide an elegant way to derive the Hartmann–Hahn conditions of these experiments.[49,50]

The simplest spin system to be considered in order to derive the Hartmann–Hahn condition of CP MAS experiments consists of a high-abundance dipolar-coupled homonuclear spin system (almost always protons) and a single (low-abundance) heteronuclear spin (e.g., X = ^{13}C or ^{15}N).[51] When the high- and low-abundance spins are irradiated simultaneously with CW rf fields of intensities ω_{1H} and ω_{1X}, respectively, an energy level manifold $\{|M\alpha\rangle, |M\beta\rangle\}$ in the doubly rotating frame can be chosen.[4] M are the eigenvalues of the component of the total angular momentum of the abundant spins in the direction of their rf field. α and β are the spin-up and spin-down states of the low-abundance spin in the direction of its rf field. Each state $|M\alpha\rangle$ represents an ensemble of homonuclear coupled spin states. In a rotating sample the dipolar interactions between the spins in the system are periodically time dependent, and the spin Hamiltonian can be replaced by a Floquet Hamiltonian, defined in a manifold of dressed states $\{|M\alpha n\rangle, |M\beta n\rangle\}$.

The heteronuclear dipolar interaction is also periodically time-dependent, and connects the Floquet states $|M\alpha m\rangle$ with $|M + 1\beta m + n\rangle$, owing to its terms in the spin Hamiltonian of the form $\sum_i \omega_{in}^{dip} \hat{I}_{zi}\hat{S}_z \exp(in\omega_R t)$. Thus, in the manifold of Floquet states $\{|M\alpha n\rangle, |M\beta n\rangle\}$, the heteronuclear interaction generates off-diagonal elements. These elements can only have a real influence on the spin system when the above-mentioned Floquet states are almost degenerate. Their Floquet energies are equal to $M\omega_{1H} + \frac{1}{2}\omega_{1X} + \langle\omega(M, m)\rangle + m\omega_R$ and $(M + 1)\omega_{1H} - \frac{1}{2}\omega_{1X} + \langle\omega(M + 1, n + n)\rangle + (m + n)\omega_R$, respectively, where the $\langle\omega(M, m)\rangle$ terms represent the level

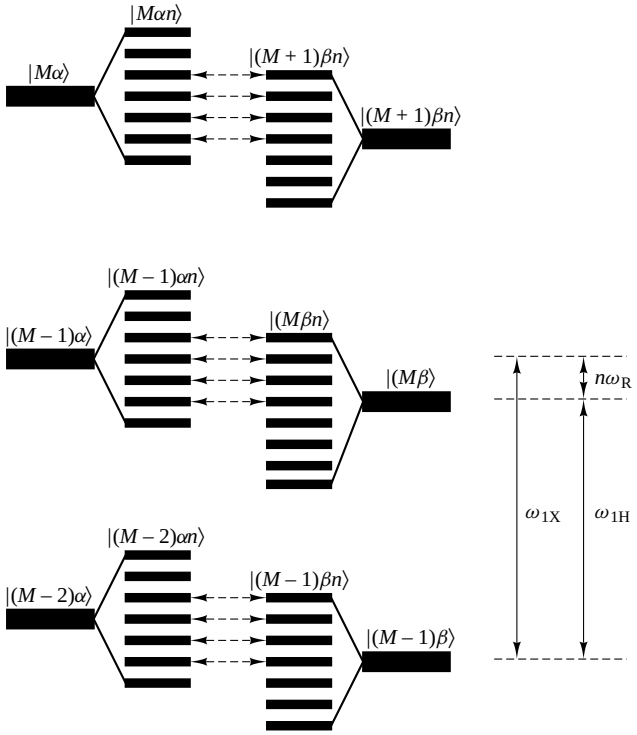

Figure 12 A demonstration of the cross-polarization MAS experiment. The Floquet energy level diagram of an abundant homonuclear spin system, interacting with a single heteronuclear spin, is shown. The states $\{|M\alpha n\rangle, |M\beta n\rangle\}$ of this system, while irradiated by two rf fields, are defined in the text. A degeneracy between the states $|M + 1\beta m + n\rangle$ and $|M\alpha m\rangle$ enables the heteronuclear dipolar interaction to equilibrate their initial spin populations. If at the start of the cross-polarization process the populations of these states are proportional to $(M + 1)\omega_{0H}$ and $M\omega_{0H}$, and at the end of the process these populations are equilibrated, i.e., $(M + \frac{1}{2})\omega_{0H}$, the signal of the low abundance spin becomes proportional to the population difference of the states $|M\alpha n\rangle$ and $|M\beta 0\rangle$, i.e., $[(M + \frac{1}{2}) - (M - \frac{1}{2})]\omega_{0H} = \omega_{0H}$

distribution inside the mth Floquet M manifold (Figure 12). Equilibration of these energies maximizes the influence of the heteronuclear dipolar interaction, defines the Hartmann–Hahn conditions, and enables the cross polarization process for the signal enhancement of the X spin system:

$$\omega_{1H} \approx \omega_{1X} + n\omega_R \tag{66}$$

The spin dynamics of the cross-polarization process can also be described in terms of the Floquet approach. Extensions of this description to low-abundance spins with $I = 1$ can also be made.

4.2.6 Dynamic MAS NMR

Chemical exchange processes in rotating spin systems will influence their MAS sideband spectra. To evaluate these dynamic MAS spectra, various efficient methodologies have been introduced.[52] One of the alternatives for these calculations is the Floquet theory approach.[33,34] With this, an infinite Floquet exchange matrix can be constructed, composed of the coefficients of an infinite set of Bloch–McConnell equations, for the signal components of the exchanging spin systems. The solution of this equation enables the evaluation of the dynamic MAS spectra.

Let us consider a set of spin systems with $I = \frac{1}{2}$ at different sites in a rotating solid with chemical shift Hamiltonians $\hat{\mathcal{H}}^M(t)$ and Floquet matrices $\hat{\mathcal{H}}_F^M$. The signal of the spins at a site M is proportional to $\langle \hat{I}_-^M \rangle$. In Floquet space, this expectation value $S^M(t) = \langle \hat{I}_-^M \rangle(t)$ can be expressed according to equation (21) in Section 2.4, in terms of the Floquet density matrix $\hat{R}^M(t)$ and the lowering operator $\hat{M}_0^{12,M}$:

$$S^M(t) = \sum_{n=-\infty}^{\infty} \langle 1_M n|\hat{R}(t)|2_M 0\rangle\langle 2_M 0|\hat{M}_0^{12,M}|1_M 0\rangle \exp(in\omega_R t) \tag{67}$$

where $|\alpha_M\rangle = |1_M\rangle$, $|\beta_M\rangle = |2_M\rangle$. With $\langle 2_{M0}|\hat{M}_0^{12,M}|1_M 0\rangle = 1$, signal coefficients can be defined as

$$s_n^M(t) = \langle 1_M n|\hat{R}^M(t)|2_M 0\rangle \tag{68}$$

in order to express the signal of site M as

$$S^M(t) = \sum_{n=-\infty}^{\infty} s_n^M(t) \exp(in\omega_R t) \tag{69}$$

A rate equation for the coefficients $s_n^M(t)$ can easily be derived from the equation of motion of $\hat{R}^M(t)$ [equation (16) in Section 2.3]:

$$\frac{d}{dt}s_n^M(t) = -i \sum_{m=-\infty}^{\infty} \{\langle 1_M n|\hat{\mathcal{H}}_F^M|1_M m\rangle - \langle 2_M n|\hat{\mathcal{H}}_F^M|2_M m\rangle + (n - m)\omega_R\} s_m^M(t) \tag{70}$$

This set of equations can be rewritten in a vector–matrix form as

$$\frac{d}{dt}\mathbf{s}^M(t) = -i\boldsymbol{\Omega}^M\mathbf{s}^M(t) \tag{71}$$

where the vector $\mathbf{s}^M(t)$ and the matrix $\boldsymbol{\Omega}^M$ are defined in some infinite manifold of states $\{|n_M\rangle\rangle\}$:

$$\left.\begin{aligned} \mathbf{s}(t) &= \sum_{n=-\infty}^{\infty} \mathbf{s}_n^M(t)|n_M\rangle\rangle \\ \langle\langle n_M|\boldsymbol{\Omega}^M|m_M\rangle\rangle &= \langle 1n|\hat{\mathcal{H}}_F^M|1m\rangle - \langle 2n|\hat{\mathcal{H}}_F^M|2m\rangle + n\delta_{nm} \end{aligned}\right\} \tag{72}$$

The solution of equation (71), together with equation (69), provides the FID MAS signal of site M.

For a dynamic process that exchanges spins between sites M = I,II, ... ,N with rate constants k_{KL}, the Bloch–McConnell equations can be written in the form[53]

$$\frac{d}{dt}\mathbf{s}^M(t) = -i\boldsymbol{\Omega}^M\mathbf{s}^M(t) - \sum_{K=I}^{N} k_{MK}[\mathbf{s}^M(t) - \mathbf{s}^K(t)] \tag{73}$$

The solution of these coupled equations allows the evaluation of the dynamic MAS spectra. These equations can also be

represented in matrix form, when we define a manifold of states $\{|Mn_{\mathrm{M}}\rangle\rangle\}$:

$$\frac{\mathrm{d}}{\mathrm{d}t}\mathbf{S}(t) = -\mathrm{i}\bar{\bar{\mathbf{\Omega}}}\mathbf{S}(t) \tag{74}$$

with the Floquet signal vector

$$\mathbf{S}(t) = \sum_{M=I}^{N}\sum_{n=-\infty}^{\infty} s_n^{\mathrm{M}}(t)|Mn_{\mathrm{M}}\rangle\rangle \tag{75}$$

and the Floquet exchange matrix elements

$$\left.\begin{aligned}\langle\langle Mn_{\mathrm{M}}|\bar{\bar{\mathbf{\Omega}}}|Mm_{\mathrm{M}}\rangle\rangle &= \langle\langle n_{\mathrm{M}}|\mathbf{\Omega}^{\mathrm{M}}|m_{\mathrm{M}}\rangle\rangle - \mathrm{i}\sum_{\mathrm{K=I}}^{N} k_{\mathrm{MK}}\delta_{n_{\mathrm{M}}m_{\mathrm{M}}}\\ \langle\langle Mn_{\mathrm{M}}|\bar{\bar{\mathbf{\Omega}}}|Km_{\mathrm{K}}\rangle\rangle &= \mathrm{i}k_{\mathrm{MK}}\delta_{n_{\mathrm{M}}m_{\mathrm{K}}}\end{aligned}\right\} \tag{76}$$

The construction of this exchange matrix is straightforward, as long as the Hamiltonians of the different sites are known. The Fourier components of these Hamiltonians compose the matrices $\mathbf{\Omega}^{\mathrm{M}}$. Their insertion in $\bar{\bar{\mathbf{\Omega}}}$ generates this exchange matrix. A numerical diagonalization of a truncated form of this matrix provides the solution of equation (74) and allows the evaluation of the time dependence of the elements of the vector $\mathbf{S}$:

$$\mathbf{S}(t) = \exp(-\mathrm{i}\bar{\bar{\mathbf{\Omega}}}t)\mathbf{S}(0) \tag{77}$$

The sum of all elements of the vector $\mathbf{S}(t)$, according to equation (69),

$$\mathbf{S}(t) = \sum_{\mathrm{M=I}}^{N}\sum_{n=-\infty}^{\infty} s_n^{\mathrm{M}}(t)\exp(\mathrm{i}n\omega_{\mathrm{R}}t) \tag{78}$$

then provides the FID signal of the exchanging spin system.[34]

5 REFERENCES

1. J. H. Shirley, Ph.D. Thesis, California Institute of Technology, 1963 (unpublished); J. H. Shirley, *Phys. Rev. B*, 1965, **138**, 979.
2. A. Abragam, *The Principles of Nuclear Magnetism*, Oxford University Press, Oxford, 1961.
3. C. P. Slichter, *Principles of Magnetic Resonance*, 3rd edn., Springer-Verlag, Berlin, 1990.
4. M. Mehring, *Principles of High Resolution NMR Spectroscopy in Solids*, 2nd edn., Springer-Verlag, Berlin, 1983.
5. U. Haeberlen, *High Resolution NMR in Solids: Selective Averaging*, Academic Press, New York, 1976.
6. R. R. Ernst, G. Bodenhausen, and A. Wokaun, *Principles of Nuclear Magnetic Resonance in One and Two Dimensions*, Clarendon Press, Oxford, 1987.
7. B. C. Gerstein and C. Dybowski, *Transient Techniques in NMR of Solids*, Academic Press, New York, 1985.
8. M. Munowitz, *Coherence and NMR*, Wiley-Interscience, New York, 1988.
9. B. C. Sanctuary and T. K. Halstead, in *Advances in Magnetic and Optical Resonance*, ed. W. S. Warren, 1990, Vol. 15, p. 80.
10. M. Goldman, P. J. Grandinetti, A. Llor, Z. Olejniczak, J. R. Schleben, and J. W. Zwanziger, *J. Chem. Phys.*, 1992, **97**, 8947.
11. J. S. Waugh, L. M. Huber, and U. Haeberlen, *Phys. Rev. Lett.*, 1968, **20**, 180; U. Haeberlen and J. S. Waugh, *Phys. Rev.*, 1968, **175**, 453.
12. W. Magnus, *Pure Appl. Math.*, 1954, **7**, 649; P. Pechukas and F. C. Light, *J. Chem. Phys.*, 1966, **44**, 3897.
13. D. P. Burum, *Phys. Rev. B*, 1981, **24**, 3684.
14. M. H. Levitt, R. Freeman, and T. Frenkiel, in *Advances in Magnetic Resonance*, ed. J. S. Waugh, Academic Press, New York, 1983, Vol. 11, p. 47.
15. W. S. Warren and M. S. Silver, in *Advances in Magnetic Resonance*, ed. J. S. Waugh, Academic Press, New York, 1985, Vol. 12, p. 248.
16. D. R. Dior and J. O. Hirschfelder, in *Advances in Chemical Physics*, ed. I. Prigogine and S. Rice, Wiley, New York, 1976, Vol. 35, p. 265; M. M. Maricq, *Phys. Rev. B*, 1982, **25**, 6622; S. I. Chu, in *Advances in Atomic and Molecular Physics*, 1985, Vol. 21, p. 197.
17. M. M. Maricq, *J. Chem. Phys.*, 1986, **85**, 5167; M. M. Maricq, *J. Chem. Phys.*, 1987, **86**, 5647; M. M. Maricq, in *Advances in Magnetic Resonance*, ed. W. S. Warren, Academic Press, New York, 1990, Vol. 14, p. 153.
18. A. Llor, *Chem. Phys. Lett.*, 1992, **199**, 383; A. Llor, *Chem. Phys. Lett.*, 1993, **204**, 217.
19. J. H. Van Vleck, *Phys. Rev.*, 1929, **33**, 467.
20. C. Cohen-Tannoudji and S. Haroche, *J. Phys.*, 1969, **30**, 153.
21. C. Cohen-Tannoudji, B. Diu, and F. Laloe, *Quantum Mechanics*, Wiley, New York, 1977, Vols. 1 and 2.
22. J. H. Freed, G. V. Bruno, and C. F. Polnaszek, *J. Chem. Phys.*, 1971, **75**, 3385; D. J. Schneider and J. H. Freed, in *Advances in Chemical Physics*, eds. J. O. Hirshrfelder, R. E. Wyat, and R. D. Coalson, Wiley, New York, 1986, Vol. 57.
23. Y. Zur, M. H. Levitt, and S. Vega, *J. Chem. Phys.*, 1983, **78**, 5293; E. M. Kraus and S. Vega, *Phys. Rev. A*, 1986, **34**, 333; G. Goelman, D. B. Zax, and S. Vega, *J. Chem. Phys.*, 1987, **87**, 31.
24. G. Goelman, S. Vega, and D. B. Zax, *Phys. Rev. A*, 1988, **39**, 5725; D. B. Zax, G. Goelman, D. Abramovich, and S. Vega, in *Advances in Magnetic Resonance*, ed. W. S. Warren, Academic Press, New York, 1990, Vol. 14, p. 219; D. Abramovich and S. Vega, *J. Magn. Res. A*, 1993, **105**, 30.
25. G. Goelman and J. S. Leigh, *J. Magn. Reson.*, 1993, **101**, 136.
26. W. P. Aue, D. J. Ruben, and R. G. Griffin, *J. Chem. Phys.*, 1984, **80**, 1729; S. Vega, E. T. Ozjejniczak, and R. G. Griffin, *J. Chem. Phys.*, 1984, **80**, 4832.
27. A. Schmidt and S. Vega, *Isr. J. Chem.*, 1992, **32**, 215.
28. A. Kubo and C. A. McDowell, *J. Chem. Phys.*, 1990, **93**, 7156; T. Nakai and C. A. McDowell, *J. Chem. Phys.*, 1992, **96**, 3452.
29. M. P. Augustine, K. Zilm, and D. B. Zax, *J. Chem. Phys.*, 1993, **98**, 9432.
30. A. Schmidt and S. Vega, *J. Chem. Phys.*, 1992, **96**, 2655.
31. T. Gullion and S. Vega, *Chem. Phys. Lett.*, 1992, **194**, 423.
32. A. E. Bennett, R. G. Griffin, and S. Vega, in *NMR Basic Principles and Progress*, ed. B. Blumich, Springer-Verlag, Berlin, 1994, Vol. 33, p. 1.
33. A. Schmidt, S. O. Smith, D. R. Ralaigh, J. E. Roberts, R. G. Griffin, and S. Vega, *J. Chem. Phys.*, 1986, **85**, 4248; A. Schmidt and S. Vega, *J. Chem. Phys.*, 1987, **87**, 6895.
34. Z. Luz, R. Poupko, and S. Alexander, *J. Chem. Phys.*, 1993, **99**, 7544.
35. F. R. Moulton, *Differential Equations*, Macmillan, New York, 1958.

36. A. Messiah, *Quantum Mechanic*, North-Holland, Amsterdam, 1961, Vol. 1.
37. G. Floquet, *Ann. Ecole Norm. Sup.*, 1883, **47**, 12.
38. O. Weintraub and S. Vega, *J. Magn. Res. A*, 1993, **105**, 245.
39. A. Wokaun and R. R. Ernst, *J. Chem. Phys.*, 1977, **67**, 1752.
40. S. Vega, *J. Chem. Phys.*, 1978, **68**, 5518.
41. O. Weintraub and S. Vega, *J. Magn. Res.*, 1994, **109**, 14.
42. T. G. Oas, R. G. Griffin, and M. H. Levitt, *J. Chem. Phys.*, 1988, **89**, 692; M. H. Levitt, T. G. Oas, and R. G. Griffin, *Isr. J. Chem.*, 1988, **28**, 271.
43. E. R. Andrew, S. Clough, L. F. Farnell, T. D. Glendhill, and I. Roberts, *Phys. Lett.*, 1966, **21**, 505; B. M. Meier and W. Earl, *J. Am. Chem. Soc.*, 1987, **109**, 7937; D. P. Raleigh, G. S. Harbison, T. G. Neiss, J. E. Roberts, and R. G. Griffin, *Chem. Phys. Lett.*, 1987, **138**, 285; M. G. Columbo, B. H. Meier, and R. R. Ernst, *Chem. Phys. Lett.*, 1988, **146**, 189; Z. H. Gan and D. M. Grant, *Mol. Phys.*, 1989, **67**, 1419; M. H. Levitt, D. R. Raleigh, F. Creuzet, and R. G. Griffin, *J. Chem. Phys.*, 1990, **92**, 6347.
44. D. Abramovich, Thesis, Weizmann Institute of Science, 1994.
45. M. Maricq and J. S. Waugh, *J. Chem. Phys.*, 1979, **70**, 191.
46. N. K. Sethi, D. W. Alderman, and D. M. Grant, *Mol. Phys.*, 1990, **71**, 217.
47. W. P. Aue, D. J. Ruben, and R. G. Griffin, *J. Chem. Phys.*, 1984, **80**, 1729.
48. J. Schaefer and E. O. Stejskal, *J. Am. Chem. Soc.*, 1976, **98**, 1030.
49. E. O. Stejskal, J. Schaefer, and J. S. Waugh, *J. Magn. Reson.*, 1977, **28**, 105.
50. A. Pines, M. G. Gibby, and J. S. Waugh, *J. Chem. Phys.*, 1973, **59**, 569.
51. X. Wu and K. W. Zilm, *J. Magn. Reson.*, 1991, **93**, 265.
52. L. Frydman and B. Frydman, *Magn. Reson. Chem.*, 1990, **28**, 355; J. H. Kristensen, H. Bildsoe, H. J. Jakobsen, and H. C. Nielsen, *J. Magn. Reson.*, 1992, **100**, 437; M. J. Duer and M. H. Levitt, *Solid State NMR*, 1992, **1**, 211.
53. S. Vega, in *NMR Probes of Molecular Dynamics*, ed. R. Tycko, Kluwer, Dordrecht, 1994, p. 155.

Biographical Sketch

Shimon Vega. *b* 1943. B.S. (kandidaat), 1965, M.S. (doctorandus), 1969, University of Amsterdam. Ph.D. (supervisor Zeev Luz), 1973, Weizmann Institute of Science, Israel. Postdoctoral work at University of California, Berkeley (with Alex Pines), 1974–76. Senior scientist at Weizmann Institute, 1976–80. Tenure position at Weizmann Institute, 1980–present. Sabbatical at MIT, Boston (with Bob Griffin), 1982–83. Sabbatical at Washington University, St. Louis (with Jacob Schaefer), 1990–91. Approx. 75 publications. Research interest: solid state NMR.

Internal Spin Interactions and Rotations in Solids

Michael Mehring

Universität Stuttgart, Stuttgart, Germany

1	Introduction	1
2	Nuclear Spin Hamiltonian Operators	1
3	NMR Spectra	5
4	Rotations	9
5	Origin of Internal Interactions	13
6	Related Articles	17
7	References	17

1 INTRODUCTION

NMR spectroscopy in the solid state has evolved from CW spectroscopy[1,2] via the pulsed and spin echo experiments[3] of the early days to a highly sophisticated spectroscopic technique which allows one to distinguish and determine very subtle nuclear spin interactions either with other nuclear spins or with electrons in any type of solid material.[4–6] Because of the local property of these interactions, information not only on crystalline solids but also on disordered materials (amorphous solids, glasses, polymers, etc.) can be obtained. This makes NMR spectroscopy in the solid state complementary to many other spectroscopic techniques, such as optical spectroscopy. With the advent of special high-resolution techniques for solids,[7–10] different nuclear spin interactions could be resolved, and detailed information on the spatial and electronic structure of solids has become available. The sevenfold ways[10] that nuclear spins can interact with their environment in solid materials are summarized schematically in Figure 1.

External magnetic fields $\boldsymbol{B}_0$ and $\boldsymbol{B}_1$ are usually applied to the sample and also to the nuclear spins (path 1). These fields basically serve the purpose of creating and manipulating the quantum states of the nuclear spins. The most elementary spin–spin interaction is the direct dipole–dipole interaction between nuclear spins (path 2). The dominant contribution to internal interactions of nuclear spins in solids is, however, due to the electron–nucleus interaction (path 3). It is responsible for such interactions as the chemical shift,[11] the Knight shift,[12] quadrupolar interactions,[13] and indirect spin–spin interactions.[14–16] The coupling to phonons (path 4) occurs only in an indirect way and is rather weak, and in general leads only to relaxation phenomena.

Relaxation will not be discussed in this article. I shall restrict myself to the discussion of spectral features and give an introduction to how internal spin interactions influence NMR spectra. In addition, I shall give a brief account of how these quantities might be calculated. Spatial and spin space rotations play an important role in solid state NMR. I shall address the question of how rotations affect the spectra and what kind of mathematical techniques are required to deal with these. The discussion will be restricted to 'basic NMR spectra' that are typically obtained by Fourier transformation of the FID after pulsed excitation. In many cases, however, special multiple pulse techniques are a prerequisite in order to obtain basic NMR spectra of the kind discussed here, because 'unwanted interactions' have to be eliminated first. Nevertheless, no multiple pulse techniques will be discussed in this article. The interested reader is referred to the appropriate articles in the Encyclopedia as well as to special reviews.[9,10,17,18]

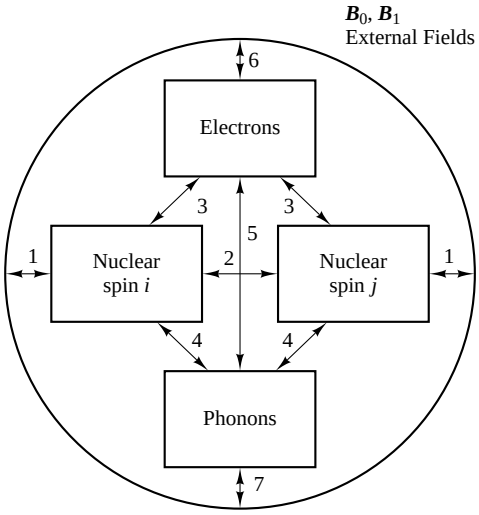

Figure 1 The sevenfold ways a nuclear spin can interact with its environment. The different pathways (1–7) are discussed in the text. (Reproduced by permission of Springer-Verlag from M. Mehring, Principles of High Resolution NMR in Solids, Springer-Verlag, Berlin, 1983, p. 8)

2 NUCLEAR SPIN HAMILTONIAN OPERATORS

NMR spectra are determined by the initial density matrix[19] $\hat{\rho}_0$ and the spin Hamiltonian operators $\hat{\mathcal{H}}$, which we will refer to in the following simply as the 'Hamiltonian'. As in usual spectroscopic theory the eigenvalues E_j and eigenstates $|j\rangle$ of the Hamiltonian can be calculated, leading to dipole-allowed transitions at frequency $\omega_{ij} = (E_i - E_j)/\hbar$ with strength $|\langle i|\hat{I}_+|j\rangle|^2$, which results in the NMR line intensity

$$I_{ij} = |\langle i|\hat{I}_+|j\rangle|^2(p_i - p_j) \tag{1}$$

where p_i and p_j are the populations of the eigenstates or, equivalently, the diagonal elements of the initial density matrix $\hat{\rho}_0$. Because of the flexibility of NMR in manipulating the initial density matrix and the effective Hamiltonian by well-defined pulse sequences the calculation of NMR spectra proceeds, however, in a more advanced way via the calculation of the response function in the time domain (FID) followed by a Fourier transformation. The FID is, of course, governed by the effective Hamiltonian of the internal interaction. The most common Hamiltonian, that for internal interactions in solids, will thus be described in this section.

Guided by Figure 1 we distinguish spin interactions caused by external and internal fields,

$$\hat{\mathcal{H}} = \hat{\mathcal{H}}_{\text{ext}} + \hat{\mathcal{H}}_{\text{int}} \tag{2}$$

where the external fields are the static magnetic field $\boldsymbol{B}_0$, which is usually applied parallel to the z axis of the laboratory

frame, and $\boldsymbol{B}_{\rm rf}$, which is a time-dependent radiofrequency field applied in the (x,y) plane of the laboratory frame, leading to the 'external' Hamiltonian:

$$\hat{\mathcal{H}}_{\rm ext} = \hat{\mathcal{H}}_0 + \hat{\mathcal{H}}_{\rm rf} \tag{3}$$

which can be summarized as

$$\hat{\mathcal{H}}_{\rm ext} = \hbar\omega_0 \hat{I}_z + \hbar\omega_{\rm rf}(\mathrm{e}^{\mathrm{i}\omega t} + \mathrm{e}^{-\mathrm{i}\omega t})\hat{I}_{x,y} \tag{4}$$

where $\omega_0 = -\gamma B_0$ and $\omega_{\rm rf} = -\gamma B_{\rm rf}$. The internal interactions can be represented as a sum of different contributions:

$$\hat{\mathcal{H}}_{\rm int} = \hat{\mathcal{H}}_{\rm S} + \hat{\mathcal{H}}_{\rm Q} + \hat{\mathcal{H}}_{II} + \hat{\mathcal{H}}_{IS} + \hat{\mathcal{H}}_{SS} \tag{5}$$

where the first term is due to shielding contributions, the second term represents the quadrupolar interaction caused by electric field gradients, and the last three terms summarize direct and indirect spin–spin interactions, where two different types of nuclear spins, namely I and S spins, are considered. In order to compare different Hamiltonians, we define

$$\|\hat{\mathcal{H}}\| = [\mathrm{Tr}(\hat{\mathcal{H}}^2)]^{1/2} \tag{6}$$

as the 'magnitude' of a Hamiltonian, where Tr refers to the 'trace operation'. In solids, most of the interactions can be represented by second-rank tensors, leading to the following general formulation of internal interactions in Cartesian coordinates of the laboratory frame (xyz):

$$\hat{\mathcal{H}}_{\rm int} = \hbar\hat{\boldsymbol{I}}\cdot\boldsymbol{A}\cdot\hat{\boldsymbol{X}} = \hbar(\hat{I}_x \quad \hat{I}_y \quad \hat{I}_z)\begin{pmatrix} A_{xx} & A_{xy} & A_{xz} \\ A_{yx} & A_{yy} & A_{yz} \\ A_{zx} & A_{zy} & A_{zz} \end{pmatrix}\begin{pmatrix} \hat{X}_x \\ \hat{X}_y \\ \hat{X}_z \end{pmatrix} \tag{7}$$

where $\hat{\boldsymbol{I}}$ is a nuclear spin operator, $\boldsymbol{A}$ is the interaction tensor, and $\hat{\boldsymbol{X}}$ may be a magnetic field or another nuclear spin or angular momentum operator. In general, nine different components of the interaction Hamiltonian exist, depending on the local symmetry of the nucleus and the type of interaction. Since rotations either in real space or in spin space play an important role, it is convenient to express the interaction Hamiltonian in addition in the form of spherical tensors $A^{(l,m)}$ and spherical tensor operators $\hat{T}^{(l,m)}$ (for details see the literature[9,10,20,21]),

$$\hat{\mathcal{H}}_{\rm int} = \hbar\sum_{l=0}^{l_{\rm max}}\sum_{m=-l}^{+l}(-1)^m A^{(l,m)}\hat{T}^{(l,-m)} \tag{8}$$

which, when expanded explicitly, is represented by nine different terms (for $l_{\rm max} = 2$):

$$\begin{aligned}\hat{\mathcal{H}}_{\rm int} = \hbar\{&A^{(0,0)}\hat{T}^{(0,0)} + A^{(1,0)}\hat{T}^{(1,0)} \\ &-(A^{(1,1)}\hat{T}^{(1,-1)} + A^{(1,-1)}\hat{T}^{(1,1)}) \\ &+A^{(2,0)}\hat{T}^{(2,0)} - (A^{(2,1)}\hat{T}^{(2,-1)} \\ &+A^{(2,-1)}\hat{T}^{(2,1)}) + A^{(2,2)}\hat{T}^{(2,-2)} + A^{(2,-2)}\hat{T}^{(2,2)}\}\end{aligned} \tag{9}$$

where the $A^{(0,0)}$ component represents the isotropic and the $A^{(1,m)}$ components the antisymmetric parts of the interaction, respectively. Although the antisymmetric part may not be zero (as in chemical shift and indirect spin–spin interactions) it does not contribute to the NMR spectrum. In spin–lattice relaxation, however, these parts do contribute. Since we are concentrating on NMR spectra here, the $A^{(1,q)}$ terms will be neglected in the following. In Section 5.4 the spherical tensor representation of the internal interactions discussed in this article is summarized. The basic advantage of spherical tensor notation over Cartesian tensors is their transformation properties under rotations. These will be utilized in Section 2.5.

2.1 Chemical Shift and Knight Shift

Soon after the discovery of NMR, it was realized that the resonance frequency of the nuclear spins deviates from the bare nuclear Larmor frequency.[11,22,23] The chemical shift[11] and the Knight shift[12] belong to the class of spin interactions characterized by spin Hamiltonians that are linear in spin operators and can be expressed in Cartesian form by the generalized shift Hamiltonian responsible for line shifts of the spectra,

$$\hat{\mathcal{H}}_{\rm S} = \hbar\hat{\boldsymbol{I}}\cdot\boldsymbol{S}\cdot\boldsymbol{B} \tag{10a}$$

with

$$S = -\gamma_I\begin{pmatrix} K_{xx}-\sigma_{xx} & K_{xy}-\sigma_{xy} & K_{xz}-\sigma_{xz} \\ K_{yx}-\sigma_{yx} & K_{yy}-\sigma_{yy} & K_{yz}-\sigma_{yz} \\ K_{zx}-\sigma_{zx} & K_{zy}-\sigma_{zy} & K_{zz}-\sigma_{zz} \end{pmatrix} \tag{10b}$$

which contains both the chemical shift and the Knight shift. This is justified because of their similar spin structure in the Hamiltonian. After all, both result from magnetic electron–nuclear coupling; the chemical shift from closed shell electrons, and the paramagnetic or Knight shift from open shell or conduction electron spin interactions with the nuclear spin. This type of paramagnetic shift should not be confused with the paramagnetic contribution to the chemical shift, which is a closed shell property (see Section 5.1). The different sign convention is historical, and stems from the early observation of mostly diamagnetic chemical shifts, which are negative (shielding), in contrast to paramagnetic and Knight shifts, which are, in most cases, positive (depending, however, on the sign of the hyperfine interaction). Both the chemical and Knight shifts can be expressed phenomenologically as ratios of field or frequency shifts with respect to the static magnetic field or Larmor frequency:

$$\sigma_{\alpha\beta} = -\frac{\Delta B_{\alpha\beta}}{B_0} = -\frac{\Delta\omega_{\alpha\beta}}{\omega_0}, \quad K_{\alpha\beta} = \frac{\Delta B_{\alpha\beta}}{B_0} = \frac{\Delta\omega_{\alpha\beta}}{\omega_0} \tag{11}$$

With the conventional orientation of the magnetic field $\boldsymbol{B}_0 = (0,0,B_0)$, we obtain

$$\hat{\mathcal{H}}_{\rm S} = -\hbar\gamma_I[(K_{xz}-\sigma_{xz})\hat{I}_x + (K_{yz}-\sigma_{yz})\hat{I}_y + (K_{zz}-\sigma_{zz})\hat{I}_z]B_0 \tag{12}$$

Note that this notation for the shift Hamiltonian is exact in the sense that no high field approximation has been invoked. The influence of the shift Hamiltonian on NMR spectra and their analysis is briefly discussed in Section 3.1. The physical origin of the different parts of the shift Hamiltonian will be outlined briefly in Sections 5.1 and 5.2.

2.2 Quadrupolar Interactions

The quadrupolar interaction arises from the coupling of an electric field gradient $\boldsymbol{V} = \{\mathrm{V}_{\alpha\beta}\}$ (where $\alpha,\beta = x,y,z$) with the nuclear quadrupole moment Q. The corresponding spin Hamiltonian is bilinear in the spin operator, and can be formally expressed in Cartesian form as

$$\hat{\mathcal{H}}_{\rm Q} = \hbar\hat{\boldsymbol{I}}\cdot\boldsymbol{Q}\cdot\hat{\boldsymbol{I}} \tag{13}$$

where

$$\boldsymbol{Q} = K_{\mathrm{Q}}\boldsymbol{V} \tag{14}$$

with $K_{\mathrm{Q}} = eQ/[2I(2I-1)\hbar]$ and $\boldsymbol{V} = \{\mathrm{V}_{\alpha\beta}\}$, is the quadrupolar interaction tensor. In the principal axis system (X,Y,Z) of the traceless electric field gradient tensor, the quadrupolar Hamiltonian can be written as[13,24,25]

$$\hat{\mathcal{H}}_{\mathrm{Q}} = \tfrac{1}{6}\hbar\omega_{\mathrm{Q}}[3\hat{I}_Z^2 - I(I+1) + \eta(\hat{I}_X^2 - \hat{I}_Y^2)] \tag{15}$$

with $\eta = (V_{XX} - V_{YY})/V_{ZZ}$, where the quadrupolar frequency ω_{Q} is defined as

$$\omega_{\mathrm{Q}} = \frac{3eQ}{2I(2I-1)\hbar}V_{ZZ} \tag{16}$$

The definition of the quadrupolar frequency used here is consistent with the one employed by Cohen and Reif,[24] Abragam,[4] and others.[26] There exist other definitions in the literature, however, where ω_{Q} differs by a factor of two compared with the definition used here.

The formulation in terms of spherical tensor operators is given in Section 5.4. The high field approximation will be discussed in Section 2.4. NMR spectra resulting from quadrupolar interactions are shown in Section 3.2. The physical origin of electric field gradients is outlined briefly in Section 5.3.

2.3 Spin–Spin Couplings

Direct as well as indirect spin–spin interactions[14–16] both lead to a bilinear spin Hamiltonian. In a solid, a large number of nuclei are usually coupled to each other. The spin–spin coupling Hamiltonian can therefore be expressed in Cartesian form as

$$\hat{\mathcal{H}}_{II} = \hbar\sum_{j<k}\hat{\boldsymbol{I}}_j\cdot\boldsymbol{D}_{I_jI_k}\cdot\hat{\boldsymbol{I}}_k, \quad \hat{\mathcal{H}}_{IS} = \hbar\sum_{j,k}\hat{\boldsymbol{I}}_j\cdot\boldsymbol{D}_{I_jS_k}\cdot\hat{\boldsymbol{S}}_k \tag{17}$$

where the coupling occurs pairwise either between two homonuclear (I_j, I_k) or heteronuclear spins (I_j, S_k). The distinction between heteronuclear ($|\omega_{0I} - \omega_{0S}| \gg \omega_{IS}$) and homonuclear ($|\omega_{0I} - \omega_{0S}| \ll \omega_{IS}$) spins is based on their difference in resonance frequencies, where we define the spin–spin interaction frequency as $\omega_{IS} = \|\hat{\mathcal{H}}_{IS}\|\hbar$. This distinction becomes important only when a magnetic field is applied, a case which is discussed in Sections 2.4 and 3.3. We shall use in the following sections the form $\hat{\mathcal{H}}_{II}$ for homonuclear spins exclusively and the form $\hat{\mathcal{H}}_{IS}$ for heteronuclear spins as well as for homonuclear spins if the corresponding expression applies to both. It should be kept in mind also that even between spins of the same type (e.g., two ^{13}C spins) the interaction can be of heteronuclear type if the difference frequency between the two ^{13}C spins is larger than their interaction frequency.

Let us first discuss the (direct) dipole–dipole interaction tensor between two nuclear spins I_j and S_k which can be expressed as

$$D_{\alpha\beta}^{(j,k)} = d_{jk}(\delta_{\alpha\beta} - 3e_\alpha e_\beta) \tag{18}$$

with $d_{jk} = (\mu_0/4\pi)\gamma_I\gamma_S\hbar/r_{jk}^3$ and $\mathrm{Tr}\,\{D_{\alpha\beta}^{(j,k)}\} = 0$. This interaction depends only on the internuclear distance r_{jk} and the product of direction cosines $e_\alpha e_\beta(\alpha,\beta = x,y,z)$ of the distance vector with the (x,y,z) axes. The complete Hamiltonian can be represented in the form of the 'dipolar alphabet'[4] as

$$\hat{\mathcal{H}}_{IS} = \hbar d_{jk}(\hat{A} + \hat{B} + \hat{C} + \hat{D} + \hat{E} + \hat{F}) \tag{19}$$

with

$$\hat{A} = (1 - 3\cos^2\vartheta)\hat{I}_z\hat{S}_z \tag{19a}$$

$$\hat{B} = \tfrac{1}{2}(1 - 3\cos^2\vartheta)(\hat{I}_z\hat{S}_z - \hat{\boldsymbol{I}}\cdot\hat{\boldsymbol{S}}) \tag{19b}$$

$$\hat{C} = -\tfrac{3}{2}\sin\vartheta\cos\vartheta\,\mathrm{e}^{-\mathrm{i}\varphi}(\hat{I}_z\hat{S}_+ + \hat{I}_+\hat{S}_z) \tag{19c}$$

$$\hat{D} = \hat{C}^* = -\tfrac{3}{2}\sin\vartheta\cos\vartheta\,\mathrm{e}^{+\mathrm{i}\varphi}(\hat{I}_z\hat{S}_- + \hat{I}_-\hat{S}_z) \tag{19d}$$

$$\hat{E} = -\tfrac{3}{4}\sin^2\vartheta\;\mathrm{e}^{-\mathrm{i}2\varphi}\hat{I}_+\hat{S}_+ \tag{19e}$$

$$\hat{F} = \hat{E}^* = -\tfrac{3}{4}\sin^2\vartheta\,\mathrm{e}^{+\mathrm{i}2\varphi}\hat{I}_-\hat{S}_- \tag{19f}$$

which, for a large number of homonuclear spins, can be summarized as

$$\hat{\mathcal{H}}_{II} = \hbar\sum_{j<k}d_{jk}\left[\hat{\boldsymbol{I}}_j\cdot\hat{\boldsymbol{I}}_k - 3\frac{1}{r_{jk}^2}(\hat{\boldsymbol{I}}_j\cdot\boldsymbol{r}_{jk})(\hat{\boldsymbol{I}}_k\cdot\boldsymbol{r}_{jk})\right] \tag{20}$$

The same expression applies to heteronuclear spins I_j and S_k where the sum is over j, k. Note that the dipole–dipole interaction tensor is both traceless and axially symmetric, i.e. it can be represented by a single quantity, namely the dipolar interaction strength d_{jk}.

If the spin–spin coupling is mediated by the surrounding electrons (indirect interaction) the representation in equation (18) applies, but with an interaction tensor $\{D_{\alpha\beta}\}$ that is neither traceless nor symmetric in the general case. All nine components of the interaction tensor must be considered. Although NMR spectra are only affected by the symmetric part of the interaction tensor, relaxation processes also involve the antisymmetric part. Relaxation will not be discussed here, however. In those cases where the trace of the indirect spin–spin interaction tensor is dominant (isotropic spin–spin coupling), we can express the corresponding Hamiltonian as

$$\hat{\mathcal{H}}_{II} = \hbar\sum_{j<k}J_{jk}\hat{\boldsymbol{I}}_j\cdot\hat{\boldsymbol{I}}_k \tag{21}$$

where $J_{jk} = \frac{1}{3}\,\mathrm{Tr}\,\{D_{\alpha\beta}\}$. Often local orbital symmetry allows the indirect interaction to be axially symmetric. In those cases the anisotropic spin Hamiltonian has the same spin structure as the dipole–dipole Hamiltonian [equation (20)], with the only difference that the coupling constant d_{jk} is no longer purely geometric, but is a molecular orbital (MO) property. In the general case, the complete symmetric part of the indiret spin interaction tensor must be diagonalized, resulting in three principal values (D_{11}, D_{22}, D_{33}) and three principal axes. The spherical tensor form of spin–spin interactions is summarized in Section 5.4.

2.4 Spin Interactions in Large Magnetic Fields

NMR in solids is usually performed for two extreme cases, namely zero or large magnetic fields. In a zero magnetic field, those spin Hamiltonians that are independent of the magnetic field, such as the quadrupolar and spin–spin interaction

Hamiltonians, lead directly to resolved spectral lines at the difference frequency of their principal elements even in a powder sample. This is what makes zero field NMR/NQR so attractive.[27] However, information on the orientation of the principal elements is lost. In this section, we preferentially cover NMR in large magnetic fields where $\|\hat{\mathcal{H}}_0\| \gg \|\hat{\mathcal{H}}_{\rm int}\|$, leading to a separation of the interaction Hamiltonian into secular ($\hat{\mathcal{H}}'_{\rm int}$) and nonsecular terms ($\hat{\mathcal{H}}''_{\rm int}$):

$$\hat{\mathcal{H}}_{\rm int} = \hat{\mathcal{H}}'_{\rm int} + \hat{\mathcal{H}}''_{\rm int} \tag{22}$$

where $[\hat{\mathcal{H}}_0, \hat{\mathcal{H}}'_{\rm int}] = 0$ and $[\hat{\mathcal{H}}_0, \hat{\mathcal{H}}''_{\rm int}] \neq 0$. The physical reason for this separation is the rapid rotation of the spins by the introduction of the large magnetic field. Those terms of the interaction Hamiltonian that are time-independent under this rotation are 'secular', whereas all time dependent terms are called 'nonsecular'. This suggests transforming the density matrix $\hat{\rho}_l$ from the laboratory frame into the 'rotating frame', leading to the following equation of motion for the density matrix $\hat{\rho}$:

$$\frac{\rm d}{{\rm d}t}\hat{\rho} = -\frac{\rm i}{\hbar}[\,\tilde{\hat{\mathcal{H}}}_{\rm int}, \hat{\rho}] \tag{23}$$

where $\hat{\rho} = \exp[({\rm i}/\hbar)\hat{\mathcal{H}}_0(t)]\hat{\rho}_l(t)\exp[-({\rm i}/\hbar)\hat{\mathcal{H}}_0(t)]$ and $\tilde{\hat{\mathcal{H}}}_{\rm int}(t) = \exp[({\rm i}/\hbar)\hat{\mathcal{H}}_0(t)]\hat{\mathcal{H}}_{\rm int}\exp[-({\rm i}/\hbar)\hat{\mathcal{H}}_0(t)]$. The secular part of the interaction Hamiltonian can now be extracted by the procedure

$$\hat{\mathcal{H}}'_{\rm int} = \frac{1}{t_{\rm c}}\int_0^{t_{\rm c}} {\rm d}\,t\tilde{\hat{\mathcal{H}}}_{\rm int}(t) \tag{24}$$

where $\omega_0 t_{\rm c} = 2\pi$. In spherical tensor operator notation, terms of the type $T^{(l,m)} = \exp(\pm {\rm i}m\omega_0 t)$ appear in the time dependent Hamiltonian. When performing the time averaging [equation (26)], all terms vanish except those with $m = 0$, resulting in the general secular interaction Hamiltonian:

$$\hat{\mathcal{H}}'_{\rm int} = \hbar(A^{(0,0)}\hat{T}^{(0,0)} + A^{(1,0)}\hat{T}^{(1,0)} + A^{(2,0)}\hat{T}^{(2,0)}) \tag{25}$$

where, however, the antisymmetric term $A^{(1,0)}\hat{T}^{(1,0)}$ is irrelevant for the spectrum, as mentioned earlier, and will be dropped. In order to be more specific, we shall now discuss secular parts of different interaction Hamiltonians in turn.

2.4.1 Heteronuclear

We begin with heteronuclear spin–spin interactions, where $\omega_{0I} \neq \omega_{0S}$, which leads to

$$\hat{\mathcal{H}}'_{IS} = \hbar D_{zz}\hat{I}_z\hat{S}_z \tag{26}$$

In the case of dipole–dipole interaction, the z component D_{zz} can be expressed as

$$D_{zz} = -\frac{\mu_0}{4\pi}\gamma_I\gamma_S\hbar r_{IS}^{-3}(3\cos^2\vartheta_{IS} - 1) \tag{27}$$

2.4.2 Homonuclear

The corresponding expression for homonuclear ($\omega_{0I} = \omega_{0S}$) spin–spin interaction is slightly more complicated and can be expressed in general by separating the isotropic part from the anisotropic part:

$$\hat{\mathcal{H}}'_{IS} = \hbar J\hat{\boldsymbol{I}}\cdot\hat{\boldsymbol{S}} + \hbar\tfrac{1}{2}(D_{zz} - J)(3\hat{I}_z\hat{S}_z - \hat{\boldsymbol{I}}\cdot\hat{\boldsymbol{S}}) \tag{28}$$

with $J = \frac{1}{3}\,{\rm Tr}\,\{D_{\alpha\beta}\}$. In the case of dipole–dipole interaction, the secular spin–spin interaction Hamiltonian reduces to

$$\hat{\mathcal{H}}'_{II} = \frac{\hbar}{2}\sum_{j<k} D_{zz}^{(j,k)}(3\hat{I}_{jz}\hat{I}_{kz} - \hat{\boldsymbol{I}}_j\cdot\hat{\boldsymbol{I}}_k) \tag{29}$$

with $D_{zz}^{(j,k)} = -d_{jk}(3\cos^2\vartheta_{jk} - 1)$. The secular quadrupolar Hamiltonian assumes a similar form:

$$\hat{\mathcal{H}}'_{\rm Q} = \tfrac{1}{6}\hbar\omega_{\rm Qz}[3\hat{I}_z^2 - I(I+1)] \tag{30}$$

with $\omega_{\rm Qz} = [3eQ/2I(2I-1)\hbar]V_{zz}$ and $V_{zz} = V_{ZZ}[\frac{1}{2}(3\cos^2\beta - 1) + \frac{1}{2}\eta\sin^2\beta\cos 2\alpha]$. Note that $\omega_{\rm Qz}$ as defined here still contains the asymmetry parameter η and the full orientational dependence.

In the case of the shift Hamiltonian, the situation is rather simple, because only the z component survives the rotating-frame transformation

$$\hat{\mathcal{H}}'_S = -\hbar\gamma_I(K_{zz} - \sigma_{zz})B_0\hat{I}_z \tag{31}$$

leading to a relative shift in resonance frequency of $\delta_{zz} = K_{zz} - \sigma_{zz}$. In order to keep the treatment general, both shift contributions, namely the Knight shift and the chemical shift, are included here. For closed shell materials, only the chemical shift has to be considered. Note that the tensor character (anisotropy) of the shift interactions is still contained in the z component of the tensor. We shall see in the next section how this leads to an orientational dependence of the resonance line.

2.5 Transformation Properties of Spin Interactions

Transformations in NMR are usually rotations either in real space or spin space. The corresponding transformations are represented by unitary matrices. Rotations can be visualized either as rotations of an object like a vector or a tensor (matrix) or alternatively as a counter-rotation of the coordinate system. Both views lead to the same physical result. Here we express the rotation of a vector by $\boldsymbol{r}' = \mathbf{R}\boldsymbol{r}$, whereas a tensor (matrix) rotation is expressed as

$$\boldsymbol{A}' = \mathbf{R}\boldsymbol{A}\mathbf{R}^{-1} \tag{32}$$

where the rotation matrix $\mathbf{R}$ may be represented (in Cartesian notation) in terms of the direction cosines between the vectors $\boldsymbol{r}'$ and $\boldsymbol{r}$ as

$$\mathbf{R} = \{r_{ij}\} = \{\cos(\boldsymbol{r}', \boldsymbol{r})\} \tag{33}$$

with $\{r_{ij}\} = \{r_{ji}\}^{-1}$. The matrix multiplication

$$A'_{ij} = \sum_{ml} A_{ml}r_{im}r_{jl} \tag{34}$$

results, where i,j represent the coordinates of the 'new' (i,j) frame, whereas (m, l) labels the coordinates of the 'old' frame. In the high-field approximation, the z component of the tensor governs the NMR spectrum. If the tensor $\boldsymbol{A}$ is given in the principal axis frame (X,Y,Z) by the principal elements (A_{XX}, A_{YY}, A_{ZZ}) the z component of the corresponding tensor in the laboratory (rotating) frame (x,y,z) is given by

$$A'_{zz} = \sum_m A_{mm}r_{zm}^2 = A_{XX}r_{zX}^2 + A_{YY}r_{zY}^2 + A_{ZZ}r_{zZ}^2 \tag{35}$$

which is readily expressed in terms of Euler angles (α,β) by

$$A'_{zz} = A_{XX}\cos^2\alpha\sin^2\beta + A_{YY}\sin^2\alpha\sin^2\beta + A_{ZZ}\cos^2\beta \tag{36}$$

This is the typical form all anisotropic secular spin interactions assume, where the tensor elements $A_{\alpha\alpha}$ ($\alpha = X, Y, Z$) in equation (38) may be replaced by those of the shift, quadrupolar, or spin−spin interaction tensor. The orientational dependence of the spin interaction as represented in equation (38) determines the orientational dependence of the lineshift, as well as the quadrupolar and dipolar broadening and splitting.

When discussing rotations, we use the sign convention and the Euler angle definition of Rose,[28] where a counterclockwise rotation is defined as positive. Such a rotation by Euler angles ($\alpha\beta\gamma$) can be expressed as a rotation about the z axis by the angle α followed by a rotation about the new y' axis by the angle β, and the final rotation about the new z'' axis by the angle γ, which can be summarized as

$$R(\alpha\beta\gamma) = R_{z''}(\gamma)R_{y'}(\beta)R_z(\alpha) \tag{37}$$

In terms of the original axes, the same rotation can be written as

$$R(\alpha\beta\gamma) = R_z(\alpha)R_y(\beta)R_z(\gamma) \tag{38}$$

In order to provide an example in spin space, we consider the rotation operator about the x axis by an angle α:

$$\begin{aligned}\exp(-\mathrm{i}\alpha\hat{I}_x) &= \exp(\mathrm{i}\tfrac{1}{2}\pi\hat{I}_z)\exp(-\mathrm{i}\alpha\hat{I}_y)\exp(-\mathrm{i}\tfrac{1}{2}\pi\hat{I}_z)\\ &= R(-\tfrac{1}{2}\pi\alpha\tfrac{1}{2}\pi)\end{aligned} \tag{39}$$

The application of these rotation operators to spin operators follows simple transformation rules. The example given here can readily be extended to the operator set ($\hat{I}_x$,$\hat{I}_y$,$\hat{I}_z$). The following example follows directly from the vector picture of spin operators:

$$\exp(-\mathrm{i}\alpha\hat{I}_z)\hat{I}_x\exp(\mathrm{i}\alpha\hat{I}_z) = \hat{I}_x\cos\alpha + \hat{I}_y\sin\alpha \tag{40}$$

It can readily be extended to other rotations by applying classical vector rotation rules. Note, however, that these transformations are quantum mechanically exact and not a classical analogue. Moreover, they apply to any spin operator independent of the spin quantum number.

Since irreducible spherical tensor operators are specially designed to have convenient rotational properties, we can express rotations of these in the compact form[9,10,20,21,28,29]

$$\hat{\tilde{T}}^{(l,m)} = R(\alpha\beta\gamma)\hat{T}^{(l,m)}R(\alpha\beta\gamma)^{-1} = \sum_{n=-l}^{+l}\hat{T}^{(l,n)}D^l_{nm}(\alpha\beta\gamma) \tag{41}$$

by using the Wigner rotation matrix

$$D^l_{nm}(\alpha\beta\gamma) = \mathrm{e}^{-\mathrm{i}n\alpha}d^l_{nm}(\beta)\mathrm{e}^{-\mathrm{i}m\gamma} \tag{42}$$

The reduced rotation matrices $d^l_{nm}(\beta)$ are real and are listed for different values of l in Section 5.5. These transformation properties will be applied in Section 4 in order to discuss rotational properties of NMR spectra in solids.

3 NMR SPECTRA

NMR spectra can be recorded in a number of different ways. Several articles in the Encyclopedia deal with special techniques, and there are textbooks which discuss, for example, special high-resolution techniques in solid state NMR spectroscopy. In this article I restrict myself to 'basic spectra' which are obtained by, for example, Fourier transformation of the free induction decay after $\frac{1}{2}\pi$ pulse excitation. The time evolution of this FID is governed by the internal spin interactions discussed in Section 2, and can be expressed as

$$G(t) = \frac{\mathrm{Tr}\{\hat{I}_+\mathrm{e}^{-(\mathrm{i}/\quad)\hat{\mathcal{H}}t}\rho(0)\mathrm{e}^{(\mathrm{i}/\quad)\hat{\mathcal{H}}t}\}}{\mathrm{Tr}\{\hat{I}_z^2\}} \tag{43}$$

where $\rho(0)$ represents the density matrix at $t = 0$ directly after the $\frac{1}{2}\pi$ pulse and $\hat{\mathcal{H}}$ is the time-independent effective Hamiltonian governing the spin evolution, and $\hat{I}_+ = \hat{I}_x + \mathrm{i}\hat{I}_y$ is the 'detection operator', which includes the two orthogonal (x,y) detection channels. The Hamiltonian used in equation (45) must be considered an effective Hamiltonian depending on the type of pulse (or multiple pulse) experiment performed. In the simple case where the Hamiltonian is diagonal in the Zeeman representation, the trace operation is conveniently expressed by

$$\begin{aligned}G(t) = \frac{1}{\mathrm{Tr}\{\hat{I}_z^2\}}&\sum_{m=-I}^{I-1}\sqrt{I(I+1)-m(m+1)}\rho_{m,m+1}\\ &\times\exp[-\mathrm{i}(H_m - H_{m+1})t]\end{aligned} \tag{44}$$

where $H_m = \langle m|\hat{\mathcal{H}}/\hbar|m\rangle$ and $\rho_{m,m+1} = \langle m|\hat{\rho}(0)|m+1\rangle$. This case is realized in the high-field approximation for all interactions discussed here besides the homonuclear spin−spin interaction. After Fourier transformation, the spectrum

$$\begin{aligned}F(\omega) = \frac{1}{\mathrm{Tr}\{\hat{I}_z^2\}}&\sum_{m=-I}^{I-1}\sqrt{I(I+1)-m(m+1)}\rho_{m,m+1}\\ &\times\delta[\omega - (H_{m+1} - H_m)]\end{aligned} \tag{45}$$

results. This corresponds to line spectra consisting of delta functions at the frequencies

$$\omega_{m,m+1} = H_m - H_{m+1} \tag{46a}$$

with intensities

$$I_{m,m+1} = \frac{\sqrt{I(I+1)-m(m+1)}\rho_{m,m+1}}{\frac{1}{3}I(I+1)(2I+1)} \tag{46b}$$

In the general case the Hamiltonian must be diagonalized and the eigenstates must be used in the evaluation of the trace. In solids, the eigenvalues H_m and the matrix elements $\rho_{m,m+1}$ usually depend on the orientation of the magnetic field with respect to the principal axes of the interaction tensor (see Section 4).

3.1 Lineshift Spectra

Shift spectra are usually recorded in large magnetic fields, i.e., the high-field approximation applies (see Section 2.4). In a single crystal, the NMR spectrum consists of a single line for every nuclear site. Owing to symmetry, several nuclear

sites in a molecule or in the unit cell can be magnetically equivalent, i.e., they give rise to a single line. The line is shifted with respect to the nuclear Larmor frequency and appears at frequency $\omega = \omega_0 + \delta$. In practice, a reference sample is used, to which the observed shift is related by $\delta_{obs} = \delta - \delta_{ref}$. In a solid with low nuclear site symmetry, this shift depends on the orientation of the magnetic field with respect to the principal axis system of the shift tensor. By using a goniometer as discussed in detail in Section 4.1, so-called rotation plots of the orientation-dependent shifts are obtained, from which the shift tensor can be determined. An example of a shift tensor determination from single crystal rotation plots, in which multiple pulse line-narrowing techniques were used in order to obtain resolved spectral lines, was presented by Griffin et al.[30]

In Figure 2 different NMR line spectra of ^{13}C, obtained from a single crystal of the organic conductor (fluoranthenyl)$_2PF_6$, are plotted for different orientations of the magnetic field.[31] Note the variation of the lineshifts with the orientation. The functional form of these 'rotation plots' will be discussed in Section 4.1. Besides the pronounced orientational dependence shown in Figure 2, it is of importance that the lineshifts are caused by both the chemical shift and the Knight shift tensors, which are additive.

In a powder sample the orientation of the principal axis system with respect to the magnetic field occurs with

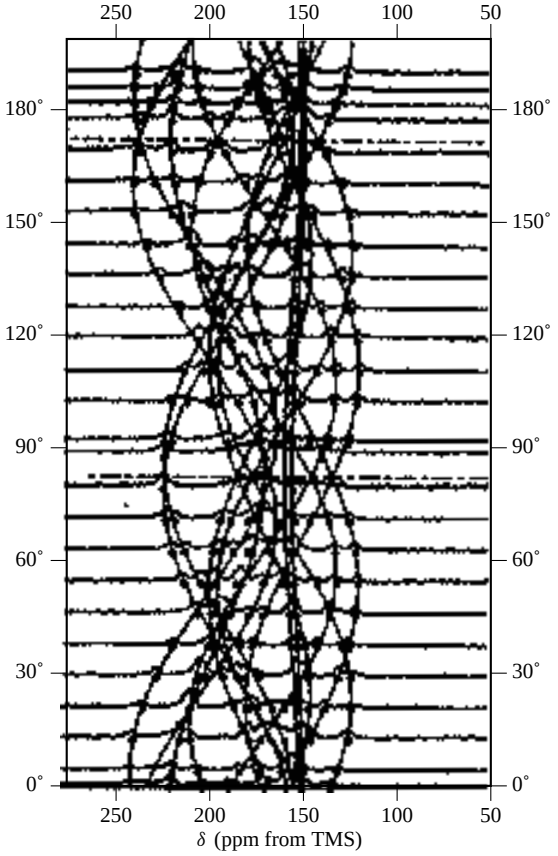

Figure 2 Carbon-13 NMR single crystal spectra of the 1D organic conductor (fluoranthenyl)$_2PF_6$ for different orientations of the magnetic field perpendicular to the stacking axis. (Reproduced by permission of The American Physical Society from D. Köngeter and M. Mehring, *Phys. Rev. B*, 1989, **39**, 6361)

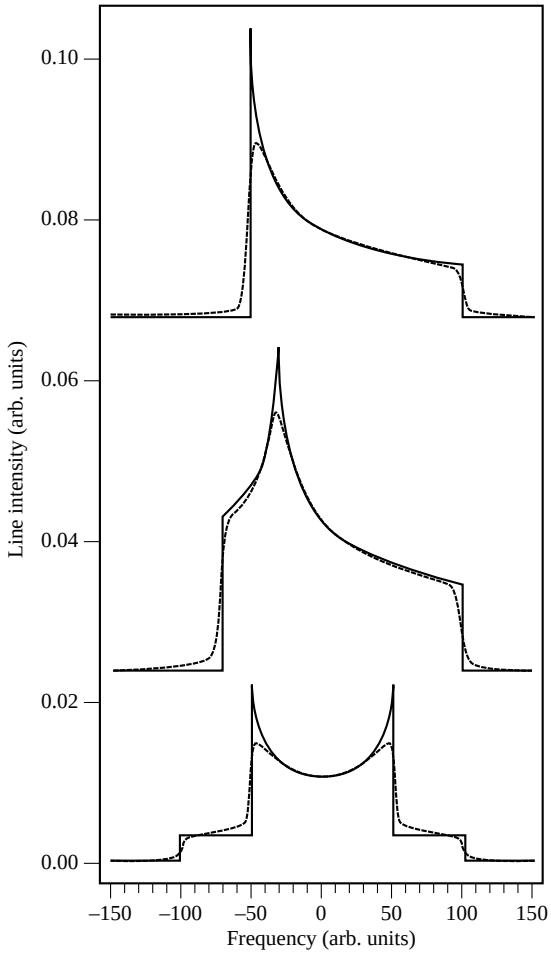

Figure 3 Calculated powder spectra of anisotropic spin interactions, where the dotted lines correspond to unbroadened (ideal) spectra, and the spectra indicated by thick lines are additionally broadened in order to mimic experimental spectra. Top: axially symmetric shift tensor with $\nu_{11} = \nu_{22} = -50$ a.u. and $\nu_{33} = 100$ a.u. Middle: nonaxially symmetric shift tensor with $\nu_{11} = -70$ a.u., $\nu_{22} = -30$ a.u. and $\nu_{33} = 100$ a.u. Bottom: Pake pattern spectra[37] either due to a spin $I = 1$ axially symmetric quadrupole interaction or dipole–dipole coupling of two spin-1/2 nuclei. The maximum coupling strength (ν_{33}, $\boldsymbol{B}_0\|$ unique axis) is 100 a.u

probability $P(\Omega)$, where Ω is the solid angle $(\alpha\beta)$. The 'powder lineshape'

$$I(\omega) = \int \mathrm{d}\Omega P(\Omega) I(\omega, \Omega) \tag{47}$$

results where $\mathrm{d}\Omega = \sin\beta\ \mathrm{d}\beta\ \mathrm{d}\alpha$ and $I(\omega,\Omega)$ is the NMR spectrum for orientation Ω. For an isotropic powder $P(\Omega) = \frac{1}{4\pi}$. Typical examples of powder spectra of axially and nonaxially symmetric shift tensors are shown in Figure 3 (top and middle). Note the edges and the center singularities, which are characteristic features of these spectra and from which the principal elements of the shift tensor can be determined.

In practice it is, however, more appropriate to make a computer fit of the experimental spectra to the calculated lineshape, which can be expressed as

$$I(\omega) = \frac{K(m)}{\pi\sqrt{(\omega - \omega_{11})(\omega_{33} - \omega_{22})}} \quad \text{for} \quad \omega_{33} \geq \omega \rangle \omega_{22} \tag{48}$$

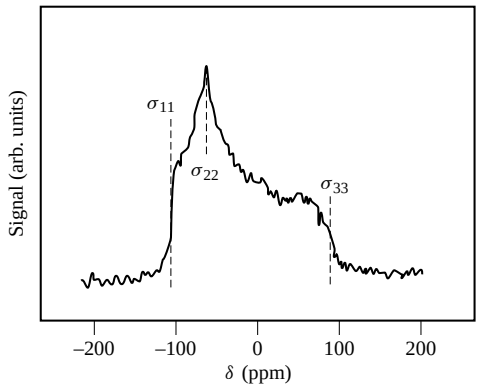

Figure 4 Experimental ^{19}F powder spectrum of fluoranil ($C_6F_4O_2$ at 300 K). The nonaxially symmetric shift tensor elements σ_{11}, σ_{22}, and σ_{33} are indicated. The powder spectrum corresponds to the theoretical spectrum shown in Figure 3 (middle). (Reproduced by permission of The American Physical Society from M. Mehring, R. G. Griffin, and J. S. Waugh, *J. Chem. Phys.* 1971, **59**, 746)

with $m = (\omega_{22} - \omega_{11})(\omega_{33} - \omega)/(\omega_{33} - \omega_{22})(\omega - \omega_{11})$,

$$I(\omega) = \frac{K(m)}{\pi\sqrt{(\omega_{33} - \omega)(\omega_{22} - \omega_{11})}} \quad \text{for} \quad \omega_{22} \rangle \omega \geq \omega_{11} \tag{49}$$

with $m = (\omega - \omega_{11})(\omega_{33} - \omega_{22})/(\omega_{33} - \omega)(\omega_{22} - \omega_{11})$, and $I(\omega) = 0$ for $\omega > \omega_{33}$ and $\omega < \omega_{11}$. $K(m)$ is the complete elliptic integral of the first kind:

$$K(m) = \int_0^{\pi/2} \mathrm{d}\varphi (1 - m \sin^2 \varphi)^{-1/2} \tag{50}$$

In order to compare this lineshape with the experimentally observed lineshape, it must be convoluted with a line-broadening function. In practice, Lorentzian or Gaussian functions are used as line-broadening functions. In Figure 3, a Lorentzian broadening function was applied, leading to a rounding off of the edges and singularities (thick lines). In order to speed up the numerical calculation of powder spectra, Aldermann et al.[32] have proposed a fast algorithm.

The type of powder pattern discussed here was first observed by Bloembergen and Rowland[33] in metallic thallium, where the shift anisotropy is larger than any other interaction. In ordinary solids, this is usually not the case because of dominant dipolar broadenings. With the advent of high-resolution NMR techniques, chemical shift powder patterns became observable in many materials where without these methods only structureless broad lines appeared in the NMR spectra.[8] An early example of such a resolution enhanced powder spectrum is shown in Figure 4.

Resolution was enhanced in Figure 4 by applying a multiple pulse experiment of the WAHUHA type, which eliminates the dipole–dipole interaction among the ^{19}F spins on the average.[34] A summary of experimentally determined chemical shift tensors of different nuclei can be found in the literature,[10] in particular in a review on ^{13}C chemical shift tensors by Duncan.[35]

3.2 Quadrupole Spectra

In cubic solids, the electric field gradient vanishes because of symmetry. The quadrupolar interaction has nevertheless been observed in cubic solids, caused by point defects and dislocations.[36] Surprisingly, it was found that for point defects a Lorentzian lineshape (exponential FID) results, which is usually taken as evidence for homogeneous broadening.[36] Here we restrict ourselves to solids where the local symmetry is low enough to observe quadrupolar splittings directly. In zero magnetic field, the transition frequencies between the different eigenstates of the quadrupole Hamiltonian do not depend on the orientation of the electric field gradient tensor. Therefore, narrow lines are observed even in powder samples. This has been developed into a special kind of 'zero field spectroscopy', covered separately in this Encyclopedia.

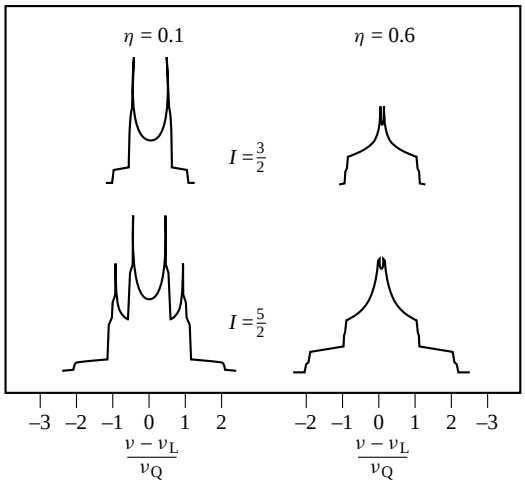

Figure 5 Powder spectra caused by first-order quadrupole interaction (central transition omitted) for nuclear spin I = 3/2 (top) and I = 5/2 (bottom) for two different values of the asymmetry parameter η = 0.1 and 0.6. (Reproduced by permission of Springer-Verlag from D. Freude and J. Haase, in NMR Basic Principles and Progress, eds. P. Diehl, E. Fluch, and R. Kosfeld, Springer-Verlag, Berlin, 1993, Vol. 29, p. 25)

In large magnetic fields only the secular part of the Hamiltonian contributes to the spectrum (see Section 2.4). In the case of the quadrupolar interaction, this results in first-order quadrupolar spectra with transition frequencies

$$\omega_{m,m+1} = \omega_0 + \omega_Q[\tfrac{1}{2}(3\cos^2\beta - 1) + \tfrac{1}{2}\eta \sin^2\beta \cos 2\alpha](m + \tfrac{1}{2}) \tag{51}$$

Because of the spin symmetry, the spectra correspond to pairs of lines symmetrical about ω_0 where the additional line in the center (at ω_0) appears for half-integer spins. The corresponding intensities follow from equation (49). The simplest situation is encountered for a nuclear spin I = 1 (e.g., ^2D), which results in a doublet of lines separated by the quadrupolar frequency. The corresponding powder spectrum depends on the symmetry of the electric field gradient. If the electric field gradient is axially symmetric, the typical 'Pake pattern'[37] [Figure 3 (bottom)] results, which consists of the sum of the axially symmetric shift pattern [Figure 3 (top)] and its mirror image symmetric to zero frequency. For a nonaxially symmetric field gradient, the original and the mirror image of the nonaxially symmetric shift pattern [Figure 3 (middle)] must be added. For half-integer nuclear spins, the procedure is similar, but more complicated spectra result. Some examples are shown in Figure 5.

If the first-order approximation is no longer valid because of an increased quadrupole interaction, it is best to perform a

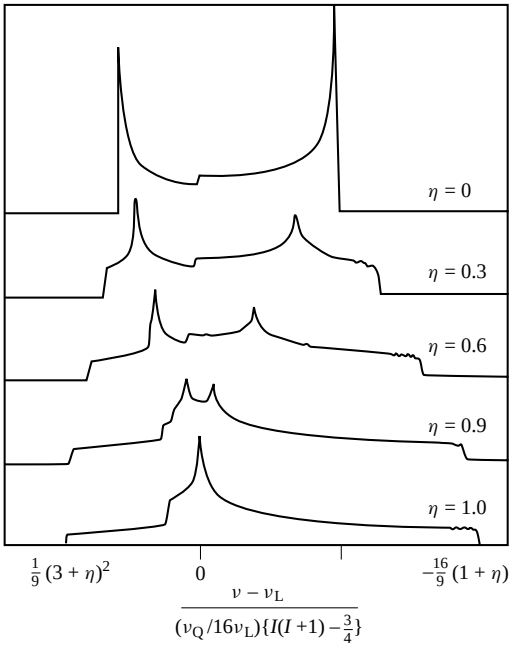

Figure 6 Powder spectra of the central transition ($-1/2 \rightarrow 1/2$) caused by the second-order quadrupole interaction of arbitrary half-integer spin nuclei for different values of the asymmetry parameter η. (Reproduced by permission of Springer-Verlag from D. Freude and J. Haase in NMR Basic Principles and Progress, eds. P. Diehl, E. Fluch, and R. Kosfeld, Springer-Verlag, Berlin, 1993, Vol. 29, p. 27)

numerical diagonalization of the Hamiltonian and to calculate the corresponding spectrum. Although this procedure is numerically rather trivial, second-order quadrupolar transition frequencies have been calculated in the past in order to cope with this situation. For completeness, we include here the transition frequency for the central transition ($-\frac{1}{2} \rightarrow \frac{1}{2}$) of half-integer spins

$$\omega_{-1/2,1/2} = -\frac{\omega_Q^2}{6\omega_0}[I(I+1) - \tfrac{3}{4}] \times [A(\alpha,\eta)\cos^4\beta + B(\alpha,\eta)\cos^2\beta + C(\alpha,\eta)] \quad (52)$$

where

$$A = -\tfrac{27}{8} - \tfrac{9}{4}\eta\cos 2\alpha - \tfrac{3}{8}\eta^2\cos^2 2\alpha \quad (52a)$$

$$B = \tfrac{15}{4} - \tfrac{1}{2}\eta^2 + 2\eta\cos 2\alpha + \tfrac{3}{4}\eta^2\cos^2 2\alpha \quad (52b)$$

$$C = -\tfrac{3}{8} + \tfrac{1}{3}\eta^2 + \tfrac{1}{4}\eta\cos 2\alpha - \tfrac{3}{8}\eta^2\cos^2 2\alpha \quad (52c)$$

Equations (52)–(52c) were first derived by Narita et al.[38] and applied to the calculation of the second-order powder pattern of the central transition for arbitrary half-integer spin-$\frac{1}{2}$ nuclei. Powder spectra of the central transition in half-integer spin systems are shown in Figure 6 for different values of η. Further details about quadrupolar spectra can be found in the recent review by Freude and Haase.[26]

3.3 Spin–Spin Splittings

Spin–spin couplings in the high-field approximation produce line splittings, as is evident from the corresponding Hamiltonian (see Section 2.4). We must distinguish two different cases, namely

1. heteronuclear interactions: $|\omega_{0I} - \omega_{0S}| \gg |\omega_{IS}|$;
2. homonuclear interactions: $|\omega_{0I} - \omega_{0S}| \ll |\omega_{IS}|$.

noindent ω_{IS} is the corresponding interaction frequency between spin I and spin S. These conditions do not require, however, that I and S be different types of nuclear spins, merely that their resonance frequency difference with respect to the interaction frequency determines whether they must be considered as homo- or heteronuclear.

3.3.1 Heteronuclear Interaction

The symmetric part of the secular interaction Hamiltonian can be expressed in this case as

$$\hat{\mathcal{H}}'_{IS} = \hbar \sum_{j,k} D_{zz}^{(j,k)} \hat{I}_{zj} \hat{S}_{zk} \quad (53)$$

as was shown in Section 2.4 Let us assume that we are interested in the spectrum of the I spins. Under the assumption that the $S-S$ spin coupling is much weaker than the $I-S$ coupling, an exact expression can be obtained for the FID of the I_j spin coupled to N_s S spins,[10]

$$G_{IS}(t) = \prod_k \frac{\mathrm{Tr}\{\cos(D_{zz}^{(j,k)} t \hat{S}_{zk})\}}{(2S+1)^{N_s}} \quad (54)$$

which takes the following special forms for some representative values of S:

$$S = \tfrac{1}{2}: \quad G_{IS}(t) = \prod_k \cos(\tfrac{1}{2} D_{zz}^{(j,k)} t) \quad (54a)$$

$$S = 1: \quad G_{IS}(t) = \prod_k \tfrac{1}{3}[1 + 2\cos(D_{zz}^{(j,k)} t)] \quad (54b)$$

$$S = \tfrac{3}{2}: \quad G_{IS}(t) = \prod_k \tfrac{1}{2}[\cos(\tfrac{1}{2} D_{zz}^{(j,k)} t) + \cos(\tfrac{3}{2} D_{zz}^{(j,k)} t)] \quad (54c)$$

The corresponding spectra are readily obtained after Fourier transformation. Note that $D_{zz}^{(j,k)}$ does include the isotropic interaction J. In the case of a single spin $S = \frac{1}{2}$ coupled to a spin I, a pair of lines at frequencies

$$\omega = \omega_0 \pm d_{IS}\tfrac{1}{2}(1 - 3\cos^2\vartheta_{IS}) \quad (55)$$

with $d_{IS} = (\mu_0/4\pi)\gamma_I\gamma_S\hbar/r_{IS}^3$ results. In the case of a powder sample, an average over all angles ϑ_{IS} must be performed, leading to a 'Pake pattern' as displayed in Figure 3 (bottom), where the outermost edges appear at $\omega_0 \pm d_{IS}$.

3.3.2 Homonuclear Interaction

In this case, it is convenient to separate the isotropic from the anisotropic part, leading to

$$\hat{\mathcal{H}}'_{II} = \tfrac{1}{2}\hbar J_{jk} \hat{\mathbf{I}}_j \cdot \hat{\mathbf{I}}_k + \hbar(D_{zz}^{(j,k)} - J_{jk})(3\hat{I}_{jz}\hat{I}_{kz} - \hat{\mathbf{I}}_j \cdot \hat{\mathbf{I}}_k) \quad (56)$$

with $J_{jk} = \frac{1}{3}\ \mathrm{Tr}\ \{D_{\alpha\beta}^{(j,k)}\}$ for the spin–spin coupling between two nuclear spins I_j and I_k. Unfortunately, this Hamiltonian is no longer diagonal, and thus a diagonalization procedure has to be applied for the calculation of the FID and the corresponding spectrum. In the case of the dipole–dipole interaction the

isotropic part vanishes, and for two coupled spin-$\frac{1}{2}$ nuclei a pair of lines results at frequencies

$$\omega = \omega_0 \pm \tfrac{3}{2} d_{II} \tfrac{1}{2}(1 - 3\cos^2 \vartheta_{II}) \tag{57}$$

with $d_{II} = (\mu_0/4\pi)\gamma_I^2 \hbar / r_{II}^3$. For a powder sample, the typical 'Pake pattern' again results [see Figure 3 (bottom)]. In contrast to the heteronuclear case, here the outermost edges appear at $\omega_0 \pm 0.75 d_{II}$.

3.4 The Multispin Lineshape Problem

The multispin lineshape problem for heteronuclear interactions has been discussed in the previous section. Here we consider N homonuclear spins of type I. The truncated (high field) interaction Hamiltonian can be expressed as

$$\hat{\mathcal{H}}'_{II} = \hbar \sum_{j<k} [J_{j,k} \hat{\boldsymbol{I}}_j \cdot \hat{\boldsymbol{I}}_k + \tfrac{1}{2}(D_{zz}^{(j,k)} - J_{j,k})(3\hat{I}_{jz}\hat{I}_{kz} - \hat{\boldsymbol{I}}_j \cdot \hat{\boldsymbol{I}}_k)] \tag{58}$$

For a limited number of spins, a numerical diagonalization is feasible. However, already for 10 spin-$\frac{1}{2}$ nuclei, a 1024×1024 Hamiltonian matrix must be diagonalized. For much larger spin clusters, supercomputer power is needed, and reaches the current computational limit very quickly. In practical cases, one therefore has to resort to approximation schemes. The most obvious procedure is Van Vleck's moment expansion,[39] which is in fact exact in the case where an infinite number of moments is taken into account. It follows from the symmetry of the interaction Hamiltonian that only even order moments must be considered. The FID can in this case be expressed as

$$G(t) = 1 - \frac{1}{2!} M_2 t^2 + \frac{1}{4!} M_4 t^4 - \ldots + \ldots \tag{59}$$

where higher order terms become exceedingly difficult to calculate.[40] In more or less evenly distributed nuclear spins in a solid, the observed lineshape is often Gaussian, as is the FID. In this case, a very good approximation is

$$G(t) = \exp(-\tfrac{1}{2} M_2 t^2) \tag{60}$$

with the corresponding lineshape

$$F(\omega) = \frac{1}{\sqrt{2\pi M_2}} \exp\left(-\frac{\omega^2}{2M_2}\right) \tag{61}$$

The full width at half-height (FWHH) of this lineshape is given by $\Delta\nu = \sqrt{2 \ln 2 M_2}/\pi$. The calculation of the second and fourth moments can be performed rigorously, and results in[4]

$$M_2 = \tfrac{3}{4} I(I+1) p \sum_{j<k} (D_{zz}^{(j,k)})^2 \tag{62}$$

$$\begin{aligned} M_4 = [\tfrac{3}{4} I(I+1)]^2 \Bigg\{ & 3\left[p \sum_k (D_{zz}^{(j,k)})^2 \right]^2 \\ & - \frac{1}{3N} p^2 \sum_{j,k,m\neq} (D_{zz}^{(j,k)})^2 (D_{zz}^{(j,m)} - D_{zz}^{(k,m)})^2 \\ & - \tfrac{1}{5} p \sum_k (D_{zz}^{(j,k)})^4 \left[8 + \frac{3}{2I(I+1)} \right] \Bigg\} \end{aligned} \tag{63}$$

where $\sum_{j,k,m\neq}$ means that all indices must be unequal. Note that a population factor p was introduced in equations (67) and (68), which takes the isotopic abundance p of nuclear spins I into account, where $p = 1$ for 100% abundance. The summation is performed over all possible sites of spin I. Instead of calculating higher order terms a practical approach is to assume special functional forms of the FID, whose second and fourth moments are set to the values calculated according to equations (67) and (68). Prompted by the idea of Abragam, who used a truncated Lorentzian in order to obtain a linewidth expression based only on the second and fourth moments, an attempt was made to derive a simple linewidth expression by applying a memory function approach, which resulted in the expression[10]

$$\Delta\nu = \sqrt{\frac{M_2}{2\pi(\mu - 1.87)}} \tag{64}$$

where $\mu = M_4/M_2^2$ is a dimensionless parameter, which equals 3 in the case of a Gaussian function, and which assumes large values for $\mu \gg 3$ if the character of the lineshape is more Lorentzian. Equation (69) is valid to a good approximation also in the intermediate regime. Note that in a diluted spin system ($p \ll 1$), the moment ratio μ becomes large according to equations (67) and (68), resulting in a narrow line of more Lorentzian character as for $p = 1$.

4 ROTATIONS

Rotation operations are performed by unitary transformations applied to real space tensors or to spin space tensor operators as introduced in Section 2.5. We shall apply the rules quoted there in order to work out the corresponding frequency shifts or splittings observed in NMR spectra in solids. The most general scheme of transformations necessary for obtaining the spatial tensor (operator) $\boldsymbol{A}_1$ in the laboratory frame ($x\ y\ z$) is

$$\begin{array}{ccc} \boldsymbol{A}_{\mathrm{p}} & \xrightarrow{\hat{R}_{\mathrm{p}}(\alpha'\beta'\gamma')} & \boldsymbol{A}_{\mathrm{c}} \\ (XYZ) & & (x_{\mathrm{c}} y_{\mathrm{c}} z_{\mathrm{c}}) \\ \text{principal axis system} & & \text{crystal frame} \\ & \xrightarrow{\hat{R}_{\mathrm{c}}(\alpha\beta\gamma)} & \boldsymbol{A}_{\mathrm{g}} \\ & & (x_{\mathrm{g}} y_{\mathrm{g}} z_{\mathrm{g}}) \\ & & \text{goniometer frame} \\ & \xrightarrow{\hat{R}_{\mathrm{g}}(\varphi\vartheta\psi)} & \boldsymbol{A}_{\mathrm{l}} \\ & & (xyz) \\ & & \text{laboratory frame} \end{array} \tag{65}$$

We start from the principal axis system, i.e., the frame in which the symmetric part of the tensor is diagonal, and distinguish different reference frames such as the *crystal frame*, the *goniometer frame*, and the *laboratory frame*. The goniometer frame is a synonym for any frame with a unique axis about which rotations (flippings) can occur. This includes a real goniometer as well as a spinner and a molecular rotation frame. Each type of rotation will be discussed in turn in the following sections.

There may not always be a crystal frame (as in glasses and polymers). In this case, the two transformations $\hat{R}_{\mathrm{p}}$ and $\hat{R}_{\mathrm{c}}$ can be combined into a single one. The total transformation required when transforming from the principal axis system to the laboratory frame can be written as the product of single step transformations:

Table 1 Relation Between the Parameters A, C, S in Equation [78] and the Cartesian Chemical Shift Tensor Elements for Three Different Orthogonal Settings of the Goniometer Axis with Respect to the Crystal Axes

	x axis: $\alpha = \gamma = 0$, $\beta = \frac{1}{2}\pi$	y axis: $\alpha = \frac{1}{2}\pi$, $\beta = \frac{1}{2}\pi$, $\gamma = \frac{1}{2}\pi$	z axis: $\alpha = \beta = \gamma = 0$
A	$\frac{1}{2}(\sigma_{zz} + \sigma_{yy})$	$\frac{1}{2}(\sigma_{xx} + \sigma_{zz})$	$\frac{1}{2}(\sigma_{xx} + \sigma_{yy})$
S	$-\sigma_{yz}$	σ_{xz}	σ_{xy}
C	$\frac{1}{2}(\sigma_{zz} - \sigma_{yy})$	$\frac{1}{2}(\sigma_{zz} - \sigma_{xx})$	$\frac{1}{2}(\sigma_{xx} - \sigma_{yy})$

$$\hat{R}_{\text{total}} = \hat{R}_{\text{g}}(\varphi\vartheta\psi)\hat{R}_{\text{c}}(\alpha\beta\gamma)\hat{R}_{\text{p}}(\alpha'\beta'\gamma') \tag{66}$$

In terms of Wigner rotation matrices, the total transformation leads to

$$A_1^{(k,q)} = \sum_{m,n,r=-l}^{+k} A_p^{(k,m)} D_{mn}^k(\alpha'\beta'\gamma') D_{nr}^k(\alpha\beta\gamma) D_{rq}^k(\varphi\vartheta\psi) \tag{67}$$

Very often, rotation operations can be contracted into a single operation, and only a subset of the total transformation is required. This will be applied partially in the next sections.

4.1 Sample Rotation

Single crystal investigations were performed in the early days of NMR.[41] They can reveal the complete symmetric part of the shift tensor if performed properly. Consider a sample that is rotated about a specific axis which might be tilted by an angle ϑ with respect to the static magnetic field. A set of Euler angles (φ ϑ ψ) is appropriate to describe these rotations. Spectra taken in the laboratory frame are proportional to $A_1^{(0,0)}$ and $A_1^{(2,0)}$, where $A_1^{(0,0)}$ represents the isotropic part and is therefore invariant under rotation, whereas the anisotropic part $A_1^{(2,0)}$ is transformed according to

$$\underset{\substack{(x_{\text{g}}y_{\text{g}}z_{\text{g}})\\ \text{goniometer frame}}}{\boldsymbol{A}_{\text{g}}} \xrightarrow{R(\varphi\vartheta\psi)} \underset{\substack{(xyz)\\ \text{laboratory frame}}}{\boldsymbol{A}_{\text{l}}} \tag{68}$$

which leads to

$$A_1^{(2,0)} = \sum_{m=-2}^{+2} A_{\text{g}}^{(2,m)} D_{m0}^2(\varphi\vartheta\psi) \tag{69}$$

where $\boldsymbol{A}_{\text{g}}$ represents the tensor in the goniometer frame. Note that the angle ψ becomes irrelevant in this case, and for a fixed tilt angle ϑ only the 'rotation angle' φ is varied from one goniometer setting to the next. In the most general case, $A_1^{(2,0)}$ can be expressed as

$$A_1^{(2,0)} = a_0 + a_1 e^{-i\varphi} + a_{-1} e^{i\varphi} + a_2 e^{-i2\varphi} + a_{-2} e^{i2\varphi} \tag{70}$$

with $a_m = A_g^{(2,m)} d_{m0}^2(\vartheta)$, which leads to the following φ dependence of the z component of the chemical shift tensor:

$$\sigma_{zz}(\varphi) = A + S_1 \sin\varphi + C_1 \cos\varphi + S_2 \sin 2\varphi + C_2 \cos 2\varphi \tag{71}$$

where $A = \sigma_{\text{iso}} + \sqrt{\frac{2}{3}}\, a_0$ and

$$S_1 = i\sqrt{\tfrac{2}{3}}(a_{-1} - a_1), \quad C_1 = \sqrt{\tfrac{2}{3}}(a_{-1} + a_1) \tag{71a}$$

$$S_2 = i\sqrt{\tfrac{2}{3}}(a_{-2} - a_2), \quad C_2 = \sqrt{\tfrac{2}{3}}(a_{-2} + a_2) \tag{71b}$$

Related expressions can be obtained for the dipolar and quadrupolar splittings. Since the a_m contain a combination of the six tensor elements of the symmetric part of the shift tensor all symmetric tensor elements can be determined in a single rotation plot if σ_{iso} is known. This requires, however, that the tilt angle ϑ is chosen appropriately in order to avoid degeneracies. It is more common to chose $\vartheta = \frac{1}{2}\pi$, in which case equation (76) reduces to

$$\sigma_{zz}(\varphi) = A + S \sin 2\varphi + C \cos 2\varphi \tag{72}$$

with $A = \sigma_{\text{iso}} - \sqrt{\frac{1}{6}} A_{\text{g}}^{(2,0)}$, $S = \frac{1}{2} i (A_{\text{g}}^{(2,-2)} - A_{\text{g}}^{(2,2)})$, and $C = (A_{\text{g}}^{(2,-2)} + A_{\text{g}}^{(2,2)})$, where the relation between spherical tensor components $A_{\text{g}}^{(2,m)}$ and the Cartesian tensor elements of the shift tensor in the goniometer frame are given in Table 1. In order to determine the complete shift tensor in the crystal frame, usually three different orthogonal settings of the crystal with respect to the goniometer are required. Let us label the corresponding Euler angles ($\alpha\beta\gamma$) as outlined in the transformation scheme, equation (70), at the beginning of this section. Table 1 summarizes the parameters A, S, and C in terms of the Cartesian chemical shift tensor elements, where only the symmetric part of the shift tensor ($\sigma_{jk} = \sigma_{kj}$) is considered. In the case of quadrupolar interactions the corresponding field gradient tensor elements, and in the case of spin–spin interactions the corresponding spin–spin coupling tensor elements, must be inserted.

An experimental example of rotation plots according to equation (78) has been shown in Figure 2. Fitting the φ dependence of the observed line shifts to equation (78) allows one to determine the parameter set (A, S, C). If this procedure is followed for the three orthogonal axes (x, y, z) of the crystal setting with respect to the goniometer z axis, the column vector $\boldsymbol{A} = (A_x, S_x, C_x, A_y, S_y, C_y, A_z, S_z, C_z)$ results, which can be related according to Table 1 to the column vector $\boldsymbol{s} = (\sigma_{xx}, \sigma_{xy}, \sigma_{xz}\, \sigma_{yy}\, \sigma_{yz}\, \sigma_{zz})$ or to the corresponding tensor elements of other types of interactions. Although the chemical shift tensor elements can be directly determined from the different A_k, S_k, C_k with $k = x,y,z$ according to Table 1, it is more practical to determine the elements of the vector $\boldsymbol{s}$ from the following set of linear equations:

$$\boldsymbol{s} = \mathbf{M}\boldsymbol{A} \tag{73}$$

where the matrix

$$\mathbf{M} = \begin{pmatrix} 0 & 0 & 0 & 0.5 & 0 & -0.5 & 0.5 & 0 & 0.5 \\ 0 & 0 & 0 & 0 & 0 & 0 & 0 & 1 & 0 \\ 0 & 0 & 0 & 0 & 1 & 0 & 0 & 0 & 0 \\ 0.5 & 0 & -0.5 & 0 & 0 & 0 & 0.5 & 0 & -0.5 \\ 0 & -1 & 0 & 0 & 0 & 0 & 0 & 0 & 0 \\ 0.5 & 0 & 0.5 & 0.5 & 0 & 0.5 & 0 & 0 & 0 \end{pmatrix} \tag{74}$$

follows directly from Table 1. If other crystal settings are used, the matrix $\mathbf{M}$ is changed. The overdetermination of the linear equations can be utilized in order to correct for misalignment

of the crystal and other experimental errors. As a result of the whole procedure, the symmetric part of the chemical shift tensor is obtained in the crystal axis frame. As a final step, a diagonalization of the symmetric part of the chemical shift tensor is performed, which leads to the principal elements and the principal axes of the chemical shift tensor in the crystal axis frame.

4.2 Sample Spinning

Whereas sample rotation as discussed in the preceding section is performed by rotating the goniometer axis in steps while taking spectra after each step, sample spinning is performed continuously where the spinner axis, which may be tilted by an arbitrary angle ϑ with respect to the magnetic field, is rotated with angular frequency ω_R. Andrew et al.[42] and Lowe[43] proposed that considerable narrowing of NMR lines could be achieved by sufficiently fast rotation of a sample, where the spinner axis is tilted with respect to the magnetic field axis. Schaefer et al.[44] later applied this technique to polymers. At this point, the reader is referred to ***Magic Angle Spinning***. Here we restrict ourselves to the tensor character of spin interactions under rotation. In order to analyze the spectra, we assume that the angle φ in equations (76) and (78) is replaced by $\varphi = \omega_R t$, which results in a time-dependent frequency

$$\begin{aligned}\omega(t) &= \sigma_{zz}(t)\omega_0 \\ &= \omega_0\Big[\sigma_{iso} + \sqrt{\tfrac{2}{3}}(a_0 + a_1 e^{-i\omega_R t} + a_{-1}e^{i\omega_R t} \\ &\quad + a_2 e^{-i2\omega_R t} + a_{-2}e^{i2\omega_R t})\Big] \end{aligned} \tag{75}$$

which generates oscillatory behavior of the FID and leads to sidebands in the spectrum. Let us first consider the average frequency $\bar{\omega}$, which corresponds to neglecting the sidebands:

$$\bar{\omega} = \omega_0[\sigma_{iso} + \tfrac{1}{2}(3\cos^2\vartheta - 1)(\sigma_{zz} - \sigma_{iso})] \tag{76}$$

We note that this average frequency corresponds to the sum of the isotropic shift and a scaled anisotropy, where the scaling factor is determined by the tilt angle. At the magic angle, i.e. when $\cos^2\vartheta = \frac{1}{3}$ ($\theta = 54^\circ\ 44'$), only the isotropic term survives.

The chemical shift anisotropy is contained in σ_{zz}, where the z axis refers to the spinner axis. If we label the principal values of the chemical shift tensor ($\sigma_{11}\ \sigma_{22}\ \sigma_{33}$) and perform the transformation from the principal axis system to the spinner frame by the Euler angles ($\alpha\ \beta\ 0$), we can express σ_{zz} by

$$\sigma_{zz} = \sigma_{11}\cos^2\alpha\sin^2\beta + \sigma_{22}\sin^2\alpha\sin^2\beta + \sigma_{33}\cos^2\beta \tag{77}$$

In other words, a scaled anisotropic powder pattern is obtained where the shape and width depends on the angle θ. This procedure has led to the method of 'variable angle spinning' (VAS), which is discussed in a separate article (see ***Variable Angle Sample Spinning***). A typical example for the type of sideband spectrum which is observed under magic angle spinning is shown in Figure 7.

If the full time dependence is considered, the FID can be expressed by the product of three phase factors,[10,45,46]

$$g(t) = e^{i\varphi_0}e^{i\Phi_0(t)}e^{i\Phi_a(t)} \tag{78}$$

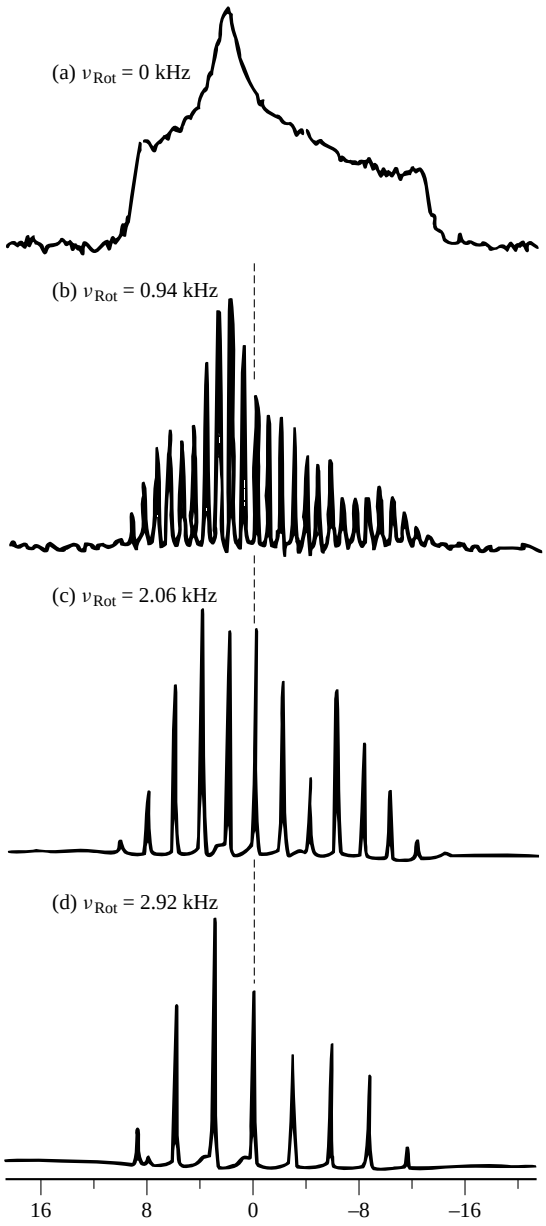

Figure 7 Phosphorus-31 powder spectra of solid dipalmitoylphosphatidylcholine under magic angle spinning conditions for different spinning frequencies ν_{Rot} including $\nu_{Rot} = 0$ (top). (Reproduced by permission of The American Physical Society from J. Herzfeld and A. Berger, *J. Chem. Phys.*, 1980, **73**, 6021. Courtesy of R. G. Griffin)

where

$$\varphi_0 = \frac{\omega_0}{\omega_R}(S_1 + 0.5S_2), \quad \Phi_0(t) = \bar{\omega}t \tag{78a}$$

$$\begin{aligned}\Phi_a(t) &= S_1\sin\omega_R t + C_1\cos\omega_R t + S_2\sin 2\omega_R t \\ &\quad + C_2\cos 2\omega_R t \end{aligned} \tag{78b}$$

with the parameters S_1, S_2, C_1, and C_2 as defined in the previous section [see equation (76)].

The first term in equation (84) sets the initial phase, the second one represents the isotropic part of the shift tensor, and the third one the anisotropic part. All these parameters depend on the tilt angle ϑ of the spinner and the Euler angles ($\alpha\ \beta\ \gamma$). In the case of a powder sample, the FID must be averaged over

the angles ($\alpha\ \beta\ \gamma$), which are conveniently expressed with respect to the principal axis system. The anisotropic part $\Phi_a(t) = \Phi_a(t - n2\pi/\omega_R)$ with $n = 0, 1, 2, \ldots$ shows cyclic behavior, which leads to the creation of sidebands in the spectrum,[45,46]

$$e^{i\Phi_a(t)} = \sum_{n=-\infty}^{\infty} F_n^* F_n\, e^{in\omega_R t} \tag{79}$$

where the sideband intensity $I_n = F^*_n F$ can be calculated from[10]

$$F_n = \sum_{k,l,m=-\infty}^{\infty} J_{n-k-2l-2m}\left(\frac{C_1}{\omega_R}\right) J_k\left(\frac{S_1}{\omega_R}\right) J_l\left(\frac{C_2}{2\omega_R}\right) \times J_m\left(\frac{S_2}{2\omega_R}\right) e^{-i\pi(k+m)/2} \tag{80}$$

Herzfeld and Berger[46] have calculated graphs from which the shift tensor elements can be determined from sideband intensities.

4.3 Rapid Molecular Rotation

The spectra corresponding to rapid molecular rotation follow directly from the treatment presented in Section 4.2. Instead of the spinner axis, a molecular rotation axis must be chosen. Because the rotation is considered to be rapid, i.e., $\omega_R \gg \Delta\omega$, where $\Delta\omega$ represents the frequency spread or anisotropy of the interaction, only the average frequency according to equation (82) contributes to the spectrum. In the case of a powder sample, the appropriate powder average must be calculated.

However, there is no free rotation in solids. Molecular reorientation always proceeds through jumps between potential wells that correspond to different orientations of the molecule. The corresponding line shift or splitting for a particular orientation of the molecule can be readily calculated by using the transformation properties of tensor interactions, as outlined in Section 4.1. Under rapid hopping conditions, an average tensor is observed that results from the average over all possible orientations. In the special case where a unique axis can be defined for the reorientation of the molecule and where the symmetry of this axis is at least threefold, this unique axis plays the role of a 'rotation axis', and the same equations as in Section 4.2 can be applied. As an example of 'rapid flipping', one can consider the limiting spectra in Figure 8.

The procedure for the general case of molecular reorientation is discussed in the following section.

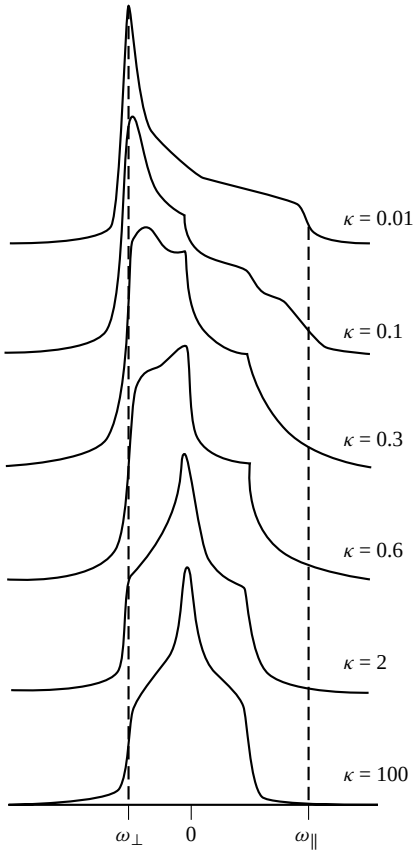

Figure 8 Calculated powder spectra of an axially symmetric shift tensor under 180° jumps about an axis which is tilted by 54° 44′ (magic angle) with respect to the symmetry axis. The relative jump rate κ with respect to the total anisotropy ($\omega_\parallel - \omega_\perp$) is indicated. Note that in the fast motion limit ($\kappa = 100$) a nonaxially symmetric average tensor results. (Reproduced by permission of Springer-Verlag from M. Mehring, Principles of High Resolution NMR in Solids, Springer-Verlag, Berlin, 1983, p. 58)

4.4 Molecular Rotational Exchange

Molecular jumps between different orientations numbered j result in different eigenfrequencies ω_j. For simplicity, we discuss only single lines as observed in chemical shift spectra. However, the extension to line splitting as observed in quadrupolar or spin–spin coupling spectra is straightforward if only single quantum transitions are considered. In this case, the corresponding spectra can be treated as single lines. In fact, soon after the discovery of NMR, line narrowing due to molecular rotation in the solid state was observed by Andrew and Eades[47] in solid benzene. Since then, it was realized that characteristic changes in the NMR/ESR spectra occur under molecular reorientation, and lineshape calculations became mandatory in order to extract the molecular dynamics from the spectra.[48–53] Surprisingly, in inorganic solids, 'molecular' rotations were also observed in temperature-dependent NMR shift spectra.[54]

As an example of a simple molecular two-site jump, we consider an axially symmetric shift or electric field gradient tensor. The corresponding powder spectrum for the shift tensor is shown in Figure 3 (top), while the spectrum for the electric field gradient tensor (spin $I = 1$) would resemble the Pake pattern shown in Figure 3 (bottom). Under rapid 180° molecular jumps about an axis tilted at the magic angle (54° 44′) with respect to the unique axis of the tensor, a complete nonaxially symmetric ($\eta = 1$) tensor results. This could be observed for the shift tensor of ^1H in H_2O and for the electric field gradient tensor of ^2D in D_2O, for example. The variation of the lineshape for different jump rates κ between the extreme situations ($\kappa = 0$ and $\kappa = \infty$) is shown in Figure 8.

In order to calculate spectra like those displayed in Figure 8, we need to write down and solve the corresponding equation of motion. For every orientational site j, a site-specific FID $M_j(t)$ contributes to the total FID, with a probability p_j corresponding to the a priori probability that site j is occupied. Microscopic reversibility requires that $\kappa_{jk}p_k = \kappa_{kj}p_j$ where $\kappa_{jk} = \tau_{jk}^{-1}$ is the

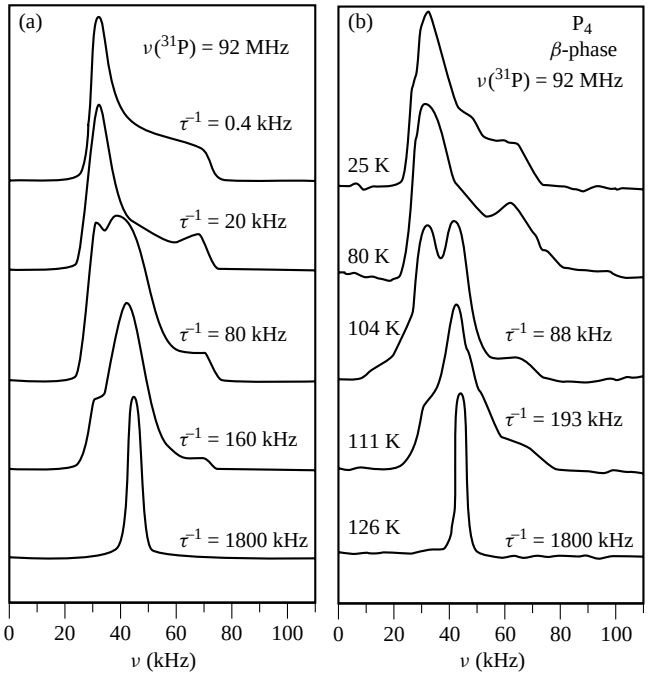

Figure 9 (a) Calculated and (b) measured powder spectra for a random jumping tetrahedron with jump rates τ^{-1}. The measured spectra (b) obtained from ^{31}P in solid white phosphorus in the β phase compare very well with the calculated spectra (a). The values for the jump rates τ^{-1} of the experimental spectra were obtained from T_1 data. (Reproduced by permission of Elsevier Publishing Co. from H. W. Spiess, R. Grosescu, and U. Haeberlen, *Chem. Phys.*, 1974, **6**, 226)

jump rate from site k to site j. The equation of motion for $M_j(t)$ can now be written as

$$\frac{\mathrm{d}}{\mathrm{d}t}M_j(t) = \mathrm{i}\omega_j M_j(t) - \frac{1}{T_{2j}}M_j(t) + \sum_k \kappa_{jk} M_k(t) \tag{81}$$

where additional transversal spin relaxation processes are collected in T_{2j}. By defining the column vector $\boldsymbol{M}(t)$ consisting of N elements $M_j(t)$ with $j = 1, 2, \ldots, N$, equation (88) can be expressed in matrix form as

$$\frac{\mathrm{d}}{\mathrm{d}t}\boldsymbol{M}(t) = (\mathrm{i}\boldsymbol{\Omega} + \boldsymbol{\Gamma})\boldsymbol{M}(t) \tag{82}$$

where $\boldsymbol{\Omega}$ represents a diagonal matrix with diagonal elements ω_j and $\boldsymbol{\Gamma}$ corresponds to the jump matrix with elements $\kappa_{jk} = \tau_{jk}^{-1}$, where the diagonal elements are replaced by $\kappa_{jj} - 1/T_{2j}$. Since the total FID consists of the sum of $M_j(t)$ over all j, the solution of equation (89) can be formally expressed as

$$g(t) = \boldsymbol{1}\exp[(\mathrm{i}\boldsymbol{\Omega} + \boldsymbol{\Gamma})t]\boldsymbol{p} \tag{83}$$

where $\boldsymbol{1} = (1, 1, \ldots 1)$ is an N-dimensional row 'one-vector' and $\boldsymbol{p} = (p_1, p_2, \ldots p_N)$ represents the a priori probability vector. The NMR spectrum is obtained after Fourier transformation of equation (90), which leads to the lineshape expression

$$I(\omega) = \mathrm{Re}[\boldsymbol{1}\boldsymbol{A}(\omega)^{-1}\boldsymbol{p}] \tag{84}$$

where $\mathbf{A}(\omega) = \mathrm{i}(\omega\,\mathbf{E} - \Omega) + \Gamma$ and $\mathbf{E}$ is the $N \times N$ unit matrix.

Although the matrix $\mathbf{A}(\omega)$ is a non-Hermitian complex matrix, there are numerical procedures to diagonalize it. Let us assume a transformation matrix $\mathbf{S}$ exists:

$$\mathbf{S}^{-1}(\boldsymbol{\Omega} + \boldsymbol{\Gamma})\mathbf{S} = \lambda \tag{85}$$

where $\lambda_{ij} = \lambda_j\delta_{ij}$, with eigenvalues λ_j. FID $g(t)$ and lineshape $I(\omega)$ can be expressed as a single sum over N elements as[55]

$$g(t) = \sum_{j=1}^{N}(\mathbf{1S})_j\ \mathrm{e}^{\lambda_j t}(\mathbf{S}^{-1}\boldsymbol{p})_j \tag{86a}$$

$$I(\omega) = \mathrm{Re}\sum_{j=1}^{N}\frac{(\mathbf{1S})_j(\mathbf{S}^{-1}\boldsymbol{p})_j}{\mathrm{i}\omega - \lambda_j} \tag{86b}$$

In the case of powder samples, the appropriate powder average has to be performed. An example of such a calculation is shown in Figure 9. Subtle details of the molecular motion, including the jump angles, can be determined from such an analysis. This type of molecular exchange spectroscopy turned out to be very useful in the investigation of molecular motions in polymers.[56]

5 ORIGIN OF INTERNAL INTERACTIONS

There are articles in this Encyclopedia on the theoretical calculation of spin interactions. Therefore, I shall only outline some essential features of these interactions here.

5.1 Chemical Shift

Shielding of the nuclear spins in condensed matter was noticed and treated theoretically soon after the discovery of NMR.[11,57,58] The local magnetic field $\boldsymbol{B}_{\mathrm{local}}$ at the nuclear site deviates from the externally applied field $\boldsymbol{B}_0$ due to the induced magnetic field $\boldsymbol{B}_{\mathrm{ind}}$

$$\boldsymbol{B}_{\mathrm{local}} = (\mathbf{1} - \boldsymbol{\sigma})\boldsymbol{B}_0 = \boldsymbol{B}_0 - \boldsymbol{B}_{\mathrm{ind}} \tag{87}$$

(with $\mathbf{1}$ the unit tensor), where

$$\boldsymbol{B}_{\mathrm{ind}} = (sigma_{\mathrm{d}} + sigma_{\mathrm{p}})\boldsymbol{B}_0 \tag{88}$$

which can be viewed as being caused by induced orbital currents:

$$\boldsymbol{B}_{\mathrm{ind}} = \frac{\mu_0}{4\pi}\int\frac{(\boldsymbol{r} - \boldsymbol{R}) \times \boldsymbol{j}(\boldsymbol{r})}{|\boldsymbol{r} - \boldsymbol{R}|^3}\mathrm{d}^3r \tag{89}$$

It is convenient to separate the chemical shift tensor and the corresponding currents into 'diamagnetic' ($\boldsymbol{\sigma}_{\mathrm{d}}$, $\boldsymbol{j}_{\mathrm{d}}$) or 'shielding' and 'paramagnetic' ($\boldsymbol{\sigma}_{\mathrm{p}}$, $\boldsymbol{j}_{\mathrm{p}}$) or 'deshielding' contributions. The diamagnetic part is caused by diamagnetic orbital currents resulting from Lenz's rule (shielding), which leads to positive values (by definition) of $\boldsymbol{\sigma}_{\mathrm{d}}$, whereas the paramagnetic part is caused by paramagnetic orbital currents due to partial dequenching of the orbital angular momentum (second-order effect), which leads to an enhanced local field and therefore negative values of $\boldsymbol{\sigma}_{\mathrm{p}}$. From the definition of these orbital currents,

$$\boldsymbol{j} = \boldsymbol{j}_{\mathrm{d}} + \boldsymbol{j}_{\mathrm{p}} \tag{90}$$

$$\boldsymbol{j}_{\mathrm{d}} = -\frac{e}{mc}\boldsymbol{A}\psi^*\psi \tag{91}$$

with vector potential $\boldsymbol{A}$, and

$$\boldsymbol{j}_{\mathrm{p}} = \frac{\mathrm{i}e\hbar}{2m}[\psi^* \text{ grad } \psi - \psi \text{ grad } \psi^*] \tag{92}$$

it follows that knowledge of the electronic wave function in the presence of the static magnetic field is required in order to calculate the chemical shift tensor. Under the condition div $\boldsymbol{j}$ = 0 and $\boldsymbol{A} = \frac{1}{2}\,\boldsymbol{B} \times (\boldsymbol{r} - \boldsymbol{R})$, the induced field vector can be calculated from the expression[11,59–63]

$$\begin{aligned}\boldsymbol{B}_{\mathrm{ind}} = \Bigg\{ &-\frac{\mu_0}{4\pi}\frac{e^2}{2m}\langle 0|\sum_j \frac{1}{r_j^3}(-x_j z_j \boldsymbol{I} - y_j z_j \boldsymbol{j} + (x_j^2 + y_j^2)\boldsymbol{k})|0\rangle \\ &+\frac{\mu_0}{4\pi}\frac{e^2\hbar^2}{2m^2}\sum_n \frac{1}{E_n - E_0}\Bigg[\langle 0|\sum_j \frac{\hat{\boldsymbol{L}}_j}{r_j^3}|n\rangle\langle n|\sum_k \hat{L}_{zk}|0\rangle \\ &+\langle 0|\sum_k \hat{L}_{zk}|n\rangle\langle n|\sum_j \frac{\hat{\boldsymbol{L}}_j}{r_j^3}|0\rangle\Bigg]\Bigg\} B_0\end{aligned} \tag{93}$$

where a summation over the electronic ground state $|0\rangle$ as well as excited states $|n\rangle$ is required. In deriving equation (100), it is assumed that the magnetic field is applied parallel to the z axis and only terms linear in B_0 are retained. $\hat{\boldsymbol{L}}_j$ is the angular momentum operator of electron j. Equation (100) was derived by Ramsey.[11] It consists of the (negative) diamagnetic part, which contains only a summation over electrons in the ground state, as well as the (positive) paramagnetic part, which involves summation over excited states.

The calculation of chemical shift tensors is by no means a trivial task. For reliable calculations on molecules and other delocalized electronic systems 'gauge independent atomic orbitals' (GIAO) must be applied in the LCAO–MO scheme. One of the very successful and more recent methods applies an 'individual gauge for localized orbitals' (IGLO). For a review of this technique consult Kutzelnigg et al.[64,65] From their work, a plot of the diamagnetic, the paramagnetic, and the total orbital current in the benzene molecule is displayed in Figure 10. Note that a simple ring current picture, as is sometimes invoked, is not applicable.

5.2 Knight Shift

The Knight shift is caused by the hyperfine interaction of nuclear spins with electron spins as discussed in Section 2.1. The complete electron–nucleus interaction is summarized in the Hamiltonian

$$\begin{aligned}\hat{\mathcal{H}}_{\mathrm{en}} = \frac{\mu_0}{4\pi}\gamma_{\mathrm{e}}\gamma_{\mathrm{n}}\hbar^2 \sum_{i,j}\Bigg[&\tfrac{8}{3}\pi\hat{\boldsymbol{I}}_i \cdot \hat{\boldsymbol{S}}_j \delta(\boldsymbol{r}_{ij}) \\ &+3\frac{(\hat{\boldsymbol{I}}_i \cdot \boldsymbol{r}_{ij})(\hat{\boldsymbol{S}}_j \cdot \boldsymbol{r}_{ij})}{r_{ij}^5} - \frac{\hat{\boldsymbol{I}}_i \cdot \hat{\boldsymbol{S}}_j}{r_{ij}^3}\Bigg]\end{aligned} \tag{94}$$

where the electron spins S_j couple to the nuclear spins I_i via the Fermi contact term (first part) and the dipolar term (second and third parts). An NMR line shift results only if the electronic spin motion is much faster than the hyperfine interaction. This is the situation in metals, but also in some rapidly exchanging or diffusing electron spin systems.

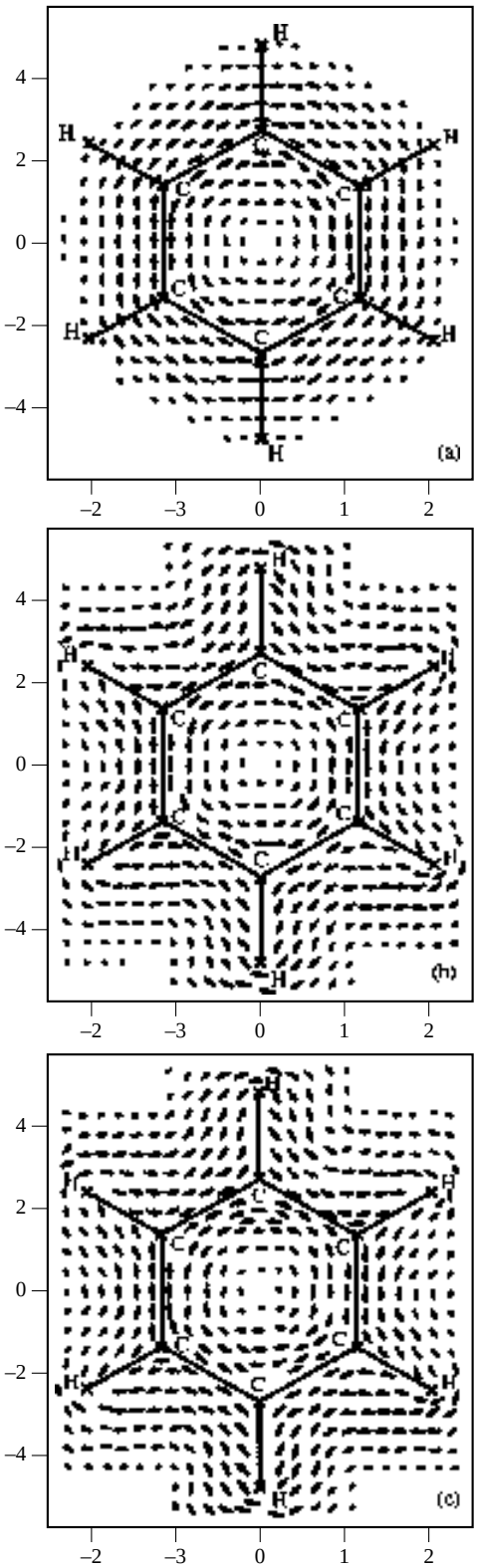

Figure 10 (a) Diamagnetic, (b) paramagnetic, and (c) total orbital currents in benzene, derived by the IGLO method, in an external magnetic field $\boldsymbol{B}_0$ perpendicular to the benzene ring. Chemical shift tensors for protons and ^{13}C can be calculated according to the Biot–Savart law [equation (96)]. (Reproduced by permission of Kluwer from W. Kutzelnigg, C.v. Wüllen, U. Fleischer, R. Franke, and T-v. Mourik, in Nuclear Magnetic Shielding and Molecular Structure, ed. J. Tossell, Kluwer, Dordrecht, 1993, p. 141)

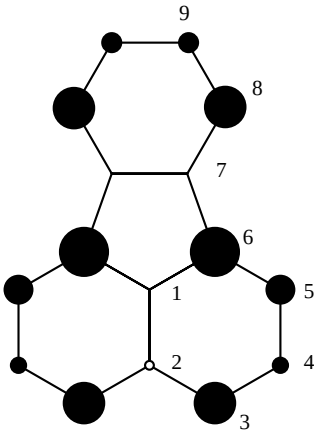

Figure 11 Spin density distribution of the conduction electrons at different carbon sites (numbered 1–9) of the fluoranthene molecule in the one-dimensional organic conductor (fluoranthenyl)$_2$PF$_6$. (Reproduced by permission of The American Physical Society from D. Köngeter and M. Mehring, *Phys. Rev. B*, 1989, **39**, 6361)

Although the corresponding NMR line shift was first reported in metals by W. Knight, it also applies to magnetic systems if the requirement of rapid spin diffusion is met. The classical Knight shift refers to the isotropic Knight shift, which is caused by the Fermi contact term,

$$K_{\mathrm{iso}} = \tfrac{8}{3}\pi \langle |u_k(0)|^2 \rangle_{E_\mathrm{F}} \frac{\chi_\mathrm{s}}{4\pi n_\mathrm{e}} \tag{95}$$

where the electronic wavefunction $\psi_k = u_k(\boldsymbol{r})e^{i\boldsymbol{k}\cdot\boldsymbol{t}}$ for wavevector $\boldsymbol{k}$ is a Bloch function consisting of a lattice periodic function $u_k(\boldsymbol{r})$ and a planewave function $\mathrm{e}^{\mathrm{i}kr}$. Since an average over the Fermi surface is performed, the Knight shift in its classical form is a measure of the s-wave character of the conduction electrons at the nuclear site and the conduction electron susceptibility χ_s. n_e is the number density of the conduction electrons, which must be replaced by Avogadro's number when the molar susceptibility is used. However, in general conductors, including organic conductors, a number of non-s orbitals contribute to the hyperfine interaction, and the Fermi contact term makes only a minor contribution to the Knight shift. For the isotropic Knight shift, 'core polarization' effects usually give larger contributions than the Fermi contact term. Often the dipolar part is significant, and leads to Knight shift anisotropy. Nevertheless, one can rigorously summarize all these contributions in the simple relation

$$K_{zz}^{(j)} = \hbar A_{zz}^{(j)} \left(\frac{\gamma_\mathrm{e}}{\gamma_\mathrm{n}}\right) \chi(q=0) \tag{96}$$

where, besides known parameters, the product of the z component of the local hyperfine tensor $A^{(j)}{}_{zz}$ (in rad s^{-1}) at nuclear site j and the reduced electron spin susceptibility $\chi(q = 0)$ (in J^{-1}) results in the z component of the Knight shift tensor. Note that the full symmetric part of the Knight shift tensor is contained in the orientational dependence of K_{zz}. The reduced electron spin susceptibility $\chi(q = 0)$ depends on the density of states at the Fermi level $D(E_\mathrm{F})$, and is in case of uncorrelated conduction electrons given by $\chi(q = 0) = \frac{1}{4} D(E_\mathrm{F})$. It is related to the ordinary electron spin susceptibility χ_s by $\chi_\mathrm{s} = \mu_0 n_\mathrm{e} \gamma_\mathrm{e}^2 \hbar^2 \chi(q=0)$, where n_e is the electron number density. Once the local hyperfine interaction is known, the Knight shift allows a determination of the electronic spin susceptibility, even in the superconducting state, where the bulk susceptibility is dominated by diamagnetic shielding. Note that all quantities used here are given in SI units and χ_s is a dimensionless parameter.

Since the susceptibility is a global parameter, the site selective Knight shift reflects the hyperfine interaction and therefore the electron spin density at the particular nuclear site. This has been utilized in the determination of the site selective electron spin density, i.e. the amplitude of the conduction electron wave function, as in the organic conductor (fluranthenyl)$_2$PF$_6$ displayed in Figure 11. For more details, the reader is referred to the specialized literature.[4,5,66,67]

5.3 Electric Field Gradients

Quadrupolar interaction parameters such as ω_Q and η determined from NMR/NQR spectra directly lead to the electric field gradient at the nuclear site.[68] In order to calculate this electric field gradient, the charge distribution $\rho(\boldsymbol{r})$ must be known. The calculation of the electric field gradient V_{zz} is conveniently separated into an ionic contribution where summation takes place over all ions with charge q_j at position j and an electronic contribution where integration over the electronic charge density is considered:[69–71]

$$\begin{aligned} V_{zz} = {} & \frac{1}{4\pi\epsilon_0} \sum_j (1-\gamma_\infty) q_j \left(\frac{3\cos^2\vartheta_j - 1}{r_j^3}\right) \\ & - \int [1-\gamma(r)]\rho(\boldsymbol{r}) \left(\frac{3\cos^2\vartheta - 1}{r^3}\right) \mathrm{d}^3 r \end{aligned} \tag{97}$$

The parameters γ_∞ and $\gamma(r)$ are so-called Sternheimer factors which take the enhancement of the electric field gradient at the nuclear site due to 'core polarization' into account. The electronic charge density $\rho(\boldsymbol{r}) = e\psi^*\psi$ is derived from an MO-type calculation which must provide accurate wave functions ψ. Valuable information has been obtained from quadrupole

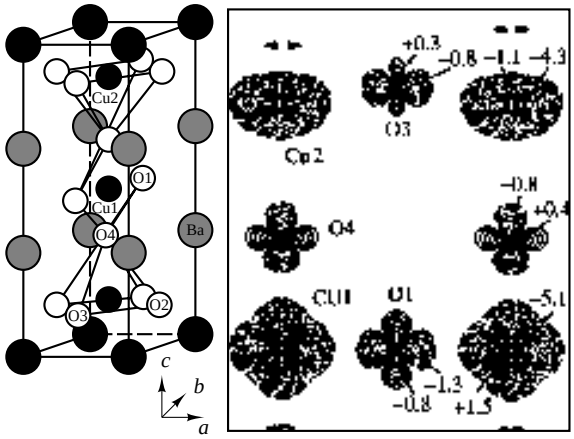

Figure 12 Difference electron density between the crystalline (calculated by the LAPW method) and the superposed ionic charge density in $YBa_2Cu_3O_7$, together with a drawing of the unit cell. The charge density contour plot corresponds to a plane parallel to the b and c axes through the Cu(1)–O(1) chains. Maxima and minima are labelled in units of e Å^{-3}. Dashed lines correspond to negative charge density, and solid lines to positive charge density. (Reproduced by permission of the American Physical Society from K. Schwarz, C. Ambrosch-Draxl, and P. Blaha, *Phys. Rev. B*, 1990, **42**, 2052. Courtesy of K. Schwarz)

Table 2 General Relation Between Spherical Tensors $A^{(l,m)}$ and Cartesian Tensors $A_{\alpha\beta}(\alpha\beta = x,y,z)$ of Internal Spin Interactions

$A^{(0,0)} : -\sqrt{\frac{1}{3}}\ \mathrm{Tr}\ \{A_{\alpha\beta}\}$	$A^{(1,0)} : -\mathrm{i}\sqrt{\frac{1}{2}}(A_{xy} - A_{yx})$	$A^{(1,\pm1)}: -\frac{1}{2}[A_{zx} - A_{xz} \pm \mathrm{i}(A_{zy} - A_{yz})]$
$A^{(2,0)} : \sqrt{\frac{1}{6}}(3A_{zz} - \ \mathrm{Tr}\ \{A_{\alpha\beta}\})$	$A^{(2,\pm1)}: \mp\frac{1}{2}[A_{xz} + A_{zx} \pm \mathrm{i}(A_{yz} + A_{zy})]$	$A^{(2,\pm2)}: \frac{1}{2}[A_{xx} - A_{yy} \pm \mathrm{i}(A_{xy} - A_{yx})]$

Table 3 Relation Between Spherical Tensor Operators $\hat{T}^{(l,m)}$ and the Cartesian Operators $\hat{I}_\alpha$ and $\hat{X}_\beta(\alpha, \beta = x, y, z)$, where $\hat{X}_\beta$ is Any Other Operator Including $\hat{I}_\alpha$

$\hat{T}^{(0,0)} : -\sqrt{\frac{1}{3}}\hat{\boldsymbol{I}} \cdot \hat{\boldsymbol{X}}$	$\hat{T}^{(1,0)} : -\sqrt{\frac{1}{2}}\ \mathrm{i}\ (\hat{I}_x\hat{X}_y - \hat{I}_y\hat{X}_x)$	$\hat{T}^{(1,\pm1)} : -\frac{1}{2}[\hat{I}_z\hat{X}_x - \hat{I}_x\hat{X}_z \pm \mathrm{i}(\hat{I}_z\hat{X}_y - \hat{I}_y\hat{X}_z)]$
$\hat{T}^{(2,0)} : \sqrt{\frac{1}{6}}(3\hat{I}_z\hat{X}_z - \hat{\boldsymbol{I}} \cdot \hat{\boldsymbol{X}})$	$\hat{T}^{(2,\pm1)} : \mp\frac{1}{2}[\hat{I}_x\hat{X}_z + \hat{I}_z\hat{X}_x \pm \mathrm{i}(\hat{I}_y\hat{X}_z + \hat{I}_z\hat{X}_y)]$	$\hat{T}^{(2,\pm2)} : \frac{1}{2}[\hat{I}_x\hat{X}_x - \hat{I}_y\hat{X}_y \pm \mathrm{i}(\hat{I}_x\hat{X}_y - \hat{I}_y\hat{X}_x)]$

Table 4 Relation Between the Spherical Tensor Components $A^{(l,m)}$ and the Cartesian Components of the Chemical Shift Tensor

$A^{(0,0)} : -\sqrt{\frac{1}{3}}\gamma_I\ \mathrm{Tr}\{\sigma_{\alpha\beta}\}$	$A^{(1,0)} : -\sqrt{\frac{1}{2}}\mathrm{i}\gamma_I[\sigma_{xy} - \sigma_{yx}]$	$A^{(1,\pm1)} : \frac{1}{2}\gamma_I[\sigma_{xz} - \sigma_{zx} \pm \ \mathrm{i}(\sigma_{yz} - \sigma_{zy})]$
$A^{(2,0)} : \sqrt{\frac{1}{6}}\gamma_I(3\sigma_{zz} - \ \mathrm{Tr}\ \{\sigma\})$	$A^{(2,\pm1)} : \mp\frac{1}{2}\gamma_I[\sigma_{xz} + \sigma_{zx} \pm \ \mathrm{i}(\sigma_{yz} + \sigma_{zy})]$	$A^{(2,\pm2)} : \frac{1}{2}\gamma_I[\sigma_{xx} - \sigma_{yy} \pm \ \mathrm{i}(\sigma_{xy} + \sigma_{yx})]$

Table 5 Relation Between the Spherical Tensor Operators $\hat{T}^{(l,m)}$ and the Spin Operators $\hat{I}_\alpha(\alpha = +, -, z)$ in Case of Shielding Interactions with Magnetic Field B_0 Parallel to the z Axis

$\hat{T}^{(0,0)} : -\sqrt{\frac{1}{3}}\hat{I}_z B_0$	$\hat{T}^{(1,0)} : 0$	$\hat{T}^{(1,\pm1)} : -\frac{1}{2}\hat{I}_\pm B_0$	$\hat{T}^{(2,0)} : 2\sqrt{\frac{1}{6}}\ \hat{I}_z B_0$	$\hat{T}^{(2,\pm1)} : \mp\frac{1}{2}\hat{I}_\pm B_0$	$\hat{T}^{(2,\pm2)} : 0$

Table 6 Relation Between the Spherical Tensors $A^{(l,m)}$ and the Cartesian Tensors $D_{\alpha\beta}$ of General Spin−Spin Interactions

$A^{(0,0)} : -\sqrt{\frac{1}{3}}\ \mathrm{Tr}\ \{D_{\alpha\beta}\}$	$A^{(1,0)} : -\sqrt{\frac{1}{2}}\ \mathrm{i}\ (D_{xy} - D_{yx})$	$A^{(1,\pm1)}: \frac{1}{2}[D_{xz} - D_{zx} \pm \mathrm{i}(D_{yz} - D_{zy})]$
$A^{(2,0)} : \sqrt{\frac{1}{6}}(3D_{zz} - \ \mathrm{Tr}\{D_{\alpha\beta}\})$	$A^{(2,\pm1)}: \mp\frac{1}{2}[D_{xz} + D_{zx} \pm \mathrm{i}(D_{yz} + D_{zy})]$	$A^{(2,\pm2)}: \frac{1}{2}[D_{xx} - D_{yy} \pm \mathrm{i}(D_{xy} + D_{yx})]$

Table 7 Relation Between the Spherical Tensor Operators $\hat{T}^{(l,m)}$ and the Spin Operators $\hat{I}_\alpha$ and $\hat{S}_\alpha$ ($\alpha = +, -, z$) in Case of Spin−Spin Interactions

$\hat{T}^{(0,0)} : -\sqrt{\frac{1}{3}}\boldsymbol{I} \cdot \hat{\boldsymbol{S}}$	$\hat{T}^{(1,0)} : -\frac{1}{2}\sqrt{\frac{1}{2}}(\hat{I}_+\hat{S}_- - \hat{I}_-\hat{S}_+)$	$\hat{T}^{(1,\pm1)} : \frac{1}{2}(\hat{I}_z\hat{S}_\pm - \hat{I}_\pm\hat{S}_z)$
$\hat{T}^{(2,0)} : \sqrt{\frac{1}{6}}(3\hat{I}_z\hat{S}_z - \hat{\boldsymbol{I}} \cdot \hat{\boldsymbol{S}}$	$\hat{T}^{(2,\pm1)} : \mp\frac{1}{2}(\hat{I}_z\hat{S}_\pm + \hat{I}_\pm\hat{S}_z)$	$\hat{T}^{(2,\pm2)} : \frac{1}{2}\hat{I}_\pm\hat{S}_\pm$

Table 8 Expressions of $d^j_{mm'}(\beta)$ for $j = \frac{1}{2}, 1, \frac{3}{2}, 2$ According to Brink and Satchler[28]

$d^{1/2}_{1/21/2} = d^{1/2}_{-1/2-1/2} = cos\frac{1}{2}\beta d^{1/2}_{-1/21/2} = -d^{1/2}_{1/2-1/2} = sin\frac{1}{2}\beta$	$d^1_{11} = d^1_{-1-1} = cos^2\frac{1}{2}\beta d^1_{1-1} = d^1_{-11} = sin^2\frac{1}{2}\beta$ $d^1_{01} = d^1_{-10} = -d^1_{0-1} = -d^1_{10} = \sqrt{\frac{1}{2}}sin\beta d^1_{00} = cos\beta$
$d^{3/2}_{3/23/2} = d^{3/2}_{-3/2-3/2} = \cos^3\frac{1}{2}\beta$ $d^{3/2}_{3/21/2} = d^{3/2}_{-1/2-3/2} = -d^{3/2}_{1/23/2} = -d^{3/2}_{-3/2-1/2} = -\sqrt{3}\cos^2\frac{1}{2}\beta\sin\frac{1}{2}\beta$ $d^{3/2}_{3/2-1/2} = d^{3/2}_{-1/23/2} = d^{3/2}_{1/2-3/2} = d^{3/2}_{-3/21/2} = \sqrt{3}\cos\frac{1}{2}\beta\sin^2\frac{1}{2}\beta$ $d^{3/2}_{3/2-3/2} = -d^{3/2}_{-3/23/2} = -\sin^3\frac{1}{2}\beta$ $d^{3/2}_{1/21/2} = d^{3/2}_{-1/2-1/2} = cos\frac{1}{2}\beta(3cos^2\frac{1}{2}\beta - 2)$ $d^{3/2}_{1/2-1/2} = -d^{3/2}_{-1/21/2} = \sin\frac{1}{2}\beta(3\sin^2\frac{1}{2}\beta - 2)$	$d^2_{22} = d^2_{-2-2} = cos^4\frac{1}{2}\beta$ $d^2_{2-2} = d^2_{-22} = sin^4\frac{1}{2}\beta$ $d^2_{21} = -d^2_{12} = -d^2_{-2-1} = d^2_{-1-2} = -\frac{1}{2}\sin\beta(1 + \cos\beta)$ $d^2_{2-1} = d^2_{1-2} = -d^2_{-21} = -d^2_{-12} = \frac{1}{2}\sin\beta(\cos\beta - 1)$ $d^2_{20} = d^2_{02} = d^2_{-20} = d^2_{0-2} = \sqrt{\frac{3}{8}}\sin^2\beta$ $d^2_{11} = d^2_{-1-1} = \frac{1}{2}(2\cos\beta - 1)(1 + \cos\beta)$ $d^2_{1-1} = d^2_{-11} = \frac{1}{2}(2cos\beta + 1)(1 - \cos\beta)$ $d^2_{10} = d^2_{0-1} = -d^2_{01} = -d^2_{-10} = -\sqrt{\frac{3}{2}}\sin\beta\cos\beta$ $d^2_{00} = \frac{1}{2}(3\cos^2\beta - 1)$

interactions in different types of solids[25] and, in particular, in metals.[66,67,72]

In recent years, 'local density functional'-type calculations have provided accurate quadrupole coupling parameters in molecules as well as in solids. As an example, Figure 12 shows the charge density difference at different nuclear sites in the unit cell of the high temperature superconductor $YBa_2Cu_3O_7$, which was calculated within the 'local density approximation' (LDA) without any adjustable parameter and which resulted in quadrupolar coupling constants in agreement with experimentally determined values from NMR/NQR experiments.[73,74]

5.4 Spherical Tensors

$$\hat{\mathcal{H}}_{\text{int}} = \hbar \sum_{l=0}^{l_{\max}} \sum_{m=-l}^{+l} (-1)^m A^{(l,m)} \hat{T}^{(l,-m)} \tag{98}$$

$$\begin{aligned}\hat{\mathcal{H}}_{\text{int}} = \hbar\{&A^{(0,0)}\hat{T}^{(0,0)} + A^{(1,0)}\hat{T}^{(1,0)} - (A^{(1,1)}\hat{T}^{(1,-1)} + A^{(1,-1)}\hat{T}^{(1,1)}) \\ &+A^{(2,0)}\hat{T}^{(2,0)} - (A^{(2,1)}\hat{T}^{(2,-1)} + A^{(2,-1)}\hat{T}^{(2,1)}) \\ &+A^{(2,2)}\hat{T}^{(2,-2)} + A^{(2,-2)}\hat{T}^{(2,2)}\}\end{aligned} \tag{99}$$

$$\hat{\tilde{T}}^{(l,m)} = R(\alpha\beta\gamma)\hat{T}^{(l,m)}R^{-1}(\alpha\beta\gamma) = \sum_{p=-l}^{+l} \hat{T}^{(l,p)} D^l_{pm}(\alpha\beta\gamma) \tag{100}$$

Since the electric field gradient tensor $\{V_{\alpha\beta}\}$ is traceless, only the $l = 2$ components of the spherical tensors are relevant in the case of the quadrupolar interaction. The following relations result:

$$\left.\begin{aligned} A^{(2,0)} &= 3\sqrt{\tfrac{1}{6}}K_{\text{Q}}V_{zz} \\ A^{(2,\pm1)} &= \mp K_{\text{Q}}(V_{xz} \pm \text{i}V_{yz}) \\ A^{(2,\pm2)} &= K_{\text{Q}}[\tfrac{1}{2}(V_{xx} - V_{yy}) \pm \text{i}V_{xy}] \\ T^{(2,0)} &= \frac{1}{\sqrt{6}}[3\hat{I}_z^2 - I(I+1)] \\ T^{(2,\pm1)} &= \mp\tfrac{1}{2}(\hat{I}_z\hat{I}_\pm + \hat{I}_\pm\hat{I}_z) \\ T^{(2,\pm2)} &= \tfrac{1}{2}\hat{I}_\pm\hat{I}_\pm \end{aligned}\right\} \tag{101}$$

Spin–spin interactions require in general all nine tensor elements. The relation between the spherical and Cartesian tensors is summarized in Tables 2–7.

Only in the special case of the dipole–dipole interaction does the isotropic part, as well as the antisymmetric part, vanish, and only the $l = 2$ terms survive.

5.5 Wigner Rotation Matrices

Some of the most frequently used Wigner rotation matrices $d^j_{mm'}(\beta)$ are listed in Table 8.

6 RELATED ARTICLES

Average Hamiltonian Theory; Chemical Exchange on Solid Metal Surfaces; Chemical Shift Tensors; Chemical Shift Tensors in Single Crystals; CRAMPS; Dipolar and Indirect Coupling Tensors in Solids; Electron–Nuclear Hyperfine Interactions; Homonuclear Recoupling Schemes in MAS NMR; Knight Shift; Knight Shift; Magic Angle Turning and Hopping; Quadrupolar Nuclei in Solids; Rotating Solids; Sideband Analysis in Magic Angle Spinning NMR of Solids; Variable Angle Sample Spinning; Zero Field NMR.

7 REFERENCES

1. E. M. Purcell, H. C. Torrey, and R. V. Pound, *Phys. Rev.*, 1946, **69**, 37.
2. F. Bloch, W. W. Hansen, and M. Packard, *Phys. Rev.*, 1946, **70**, 474.
3. E. L. Hahn, *Phys. Rev.*, 1950, **80**, 580.
4. A. Abragam, *Principles of Nuclear Magnetism*, Oxford University Press, Oxford, 1961.
5. C. P. Slichter, *Principles of Magnetic Resonance*, 3rd edn., Springer-Verlag, New York, 1990.
6. A. Abragam and M. Goldman, *Nuclear Magnetism: Order and Disorder*, Clarendon Press, Oxford, 1982.
7. J. S. Waugh, L. M. Huber, and U. Haeberlen, *Phys. Rev. Lett.*, 1968, **20**, 180; U. Haeberlen and J. S. Waugh, *Phys. Rev.*, 1968, **175**, 453; U. Haeberlen and J. S. Waugh, *Phys. Rev.*, 1969, **185**, 420.
8. A. Pines, M. G. Gibby, and J. S. Waugh, *J. Chem. Phys.*, 1972, **56**, 1776.
9. U. Haeberlen, *High Resolution NMR in Solids, Selective Averaging*, Academic Press, New York, 1976.
10. M. Mehring, *Principles of High Resolution NMR in Solids*, Springer-Verlag, Berlin, 1983.
11. N. F. Ramsey, *Phys. Rev.*, 1950, **78**, 699; N. F. Ramsey, *Phys. Rev.*, 1952, **86**, 243.
12. W. D. Knight, in *Solid State Physics*, eds. F. Seitz and D. Turnbull, Academic Press, New York, 1956, Vol. 2, p. 93.
13. R. V. Pound, *Phys. Rev.*, 1950, **79**, 685.
14. E. L. Hahn and D. E. Maxwell, *Phys. Rev.*, 1952, **88**, 1070.
15. H. S. Gutowsky, D. W. McCall, and C. P. Slichter, *J. Chem. Phys.*, 1953, **21**, 279.
16. N. F. Ramsey, *Phys. Rev.*, 1953, **91**, 303.
17. R. R. Ernst, G. Bodenhausen, and A. Wokaum, *Principles of Nuclear Magnetic Resonance in One and Two Dimensions*, Oxford University Press, Oxford, 1987.
18. B. C. Gerstein and C. R. Dybowski, *Transient Techniques in NMR of Solids*, Academic Press, San Diego, 1985.
19. K. Blum, *Density Matrix Theory and Applications*, Plenum Press, New York, 1981.
20. H. W. Spiess, in *NMR Basic Principles and Progress*, eds. P. Diehl, E. Fluck, and R. Kosfeld, Springer-Verlag, Berlin, 1978, Vol. 15, p. 55.
21. B. C. Sanctuary and T. K. Halstead, in *Advances in Magnetic and Optical Resonance*, ed. W. S. Warren, Academic Press, San Diego, 1990, Vol. 15, p. 79.
22. W. G. Proctor and F. C. Yu, *Phys. Rev.*, 1950, **77**, 717.
23. A. Saika and C. P. Slichter, *J. Chem. Phys.*, 1954, **22**, 26.
24. M. H. Cohen and F. Reif, *Solid State Phys.*, 1957, **5**, 321.
25. T. P. Das and E. L. Hahn, *Solid State Phys.*, 1958, Suppl. 1.
26. D. Freude and J. Haase, in *NMR Basic Principles and Progress*, eds. P. Diehl, E. Fluck, and R. Kosfeld, Springer-Verlag, Berlin, 1993, Vol. 29, p. 25.
27. D. B. Zax, A. Bielecki, K. W. Zilm, A. Pines, and D. P. Weitekamp, *J. Chem. Phys.*, 1985, **83**, 4877.

28. D. M. Brink and G. R. Satchler, *Angular Momentum*, 3rd edn., Clarendon Press, Oxford, 1993.
29. M. E. Rose, *Elementary Theory of Angular Momentum*, Wiley, New York, 1967.
30. R. G. Griffin, J. D. Ellett, M. Mehring, J. G. Bullitt, and J. S. Waugh, *J. Chem. Phys.*, 1972, **57**, 2147.
31. D. Köngeter and M. Mehring, *Phys. Rev. B*, 1989, **39**, 6361.
32. D. W. Aldermann, M. S. Solum, and D. M. Grant, *J. Chem. Phys.*, 1986, **84**, 3717.
33. N. Bloembergen and J. A. Rowland, *Acta Met.*, 1953, **1**, 731.
34. (a) M. Mehring, R. G. Griffin, and J. S. Waugh, *J. Am. Chem. Soc.*, 1970, **92**, 7222; (b) M. Mehring, R. G. Griffin, and J. S. Waugh, *J. Chem. Phys.*, 1971, **55**, 746.
35. T. M. Duncan, *J. Phys. Chem. Ref. Data*, 1987, **16**, 125.
36. O. Kanert and M. Mehring, *NMR Basic Principles and Progress*, eds. P. Diehl, E. Fluck, and R. Kosfeld, Springer-Verlag, Berlin, 1971, Vol. 3, p. 1.
37. G. E. Pake, *J. Chem. Phys.*, 1948, **16**, 327.
38. K. Narita, J.-I. Umeda, and H. Kusumoto, *J. Chem. Phys.*, 1966, **44**, 2719.
39. J. H. Van Vleck, *Phys. Rev.*, 1948, **74**, 1168.
40. F. Lado, J. D. Memory, and G. W. Parker, *Phys. Rev. B*, 1971, **4**, 1406.
41. G. M. Volkoff, H. E. Petch, and D. Smellie, *Can. J. Phys.*, 1952, **30**, 270.
42. E. R. Andrew, A. Bradbury, and R. G. Eades, *Nature (London)*, 1958, **182**, 1659; E. R. Andrew, A. Bradbury, and R. G. Eades, *Nature (London)*, 1959, **183**, 1802.
43. I. J. Lowe, *Phys. Rev. Lett.*, 1959, **2**, 285.
44. J. Schaefer, E. O. Stejskal, and R. Buchdahl, *Macromolecules*, 1977, **10**, 384.
45. M. M. Maricq and J. S. Waugh, *J. Chem. Phys.*, 1979, **70**, 3300.
46. J. Herzfeld and A. E. Berger, *J. Chem. Phys.*, 1980, **73**, 6021.
47. E. R. Andrew and R. G. Eades, *Proc. R. Soc. London, Ser. A*, 1953, **216**, 398.
48. H. Sillescu and D. Kivelson, *J. Chem. Phys.*, 1968, **48**, 3493.
49. J. H. Freed, G. V. Bruno, and C. Polnaszek, *J. Phys. Chem.*, 1971, **75**, 3385.
50. P. Rigny, *Physica*, 1972, **59**, 707.
51. (a) H. W. Spiess, R. Grosescu, and U. Haeberlen, *Chem. Phys.*, 1974, **6**, 226; (b) H. W. Spiess, *Chem. Phys.*, 1974, **6**, 217.
52. S. Alexander, A. Baram, and Z. Luz, *Mol. Phys.*, 1974, **27**, 441; A. Baram, Z. Luz, and S. Alexander, *J. Chem. Phys.*, 1976, **64**, 4321; S. Alexander, Z. Luz, Y. Naor, and R. Poupko, *Mol. Phys.*, 1977, **33**, 1119.
53. D. E. Wemmer, D. J. Ruben, and A. Pines, *J. Am. Chem. Soc.*, 1981, **103**, 28; D. E. Wemmer and A. Pines, *J. Am. Chem. Soc.*, 1981, **103**, 34.
54. B. Günther, O. Kanert, M. Mehring, and D. Wolf, *Phys. Rev. B*, 1981, **24**, 6747.
55. R. G. Gordon and R. P. McGinnis, *J. Chem. Phys.*, 1968, **49**, 2455.
56. H. W. Spiess, *Adv. Polym. Sci.*, 1985, **66**, 23.
57. J. A. Pople, *Proc. R. Soc. London, Ser. A*, 1957, **239**, 541, 550.
58. H. M. McConnell, *J. Chem. Phys.*, 1957, **27**, 226.
59. W. N. Lipscomb, in *Advances in Magnetic Resonance*, ed. J. S. Waugh, Academic Press, New York, 1966, Vol. 2, p. 137.
60. J. I. Musher, in *Advances in Magnetic Resonance*, ed. J. S. Waugh, Academic Press, New York, 1966, Vol. 2, p. 177.
61. J. D. Memory, *Quantum Theory of Magnetic Resonance Parameters*, Hill, New York, 1968.
62. W. Kutzelnigg, *Isr. J. Chem.*, 1980, **19**, 193; W. Kutzelnigg, *Theochem*, 1989, **202**, 11.
63. W. J. Hehre, L. Radom, P. v. R. Schleyer, and J. A. Pople, *Ab initio Molecular Orbital Theory*, Wiley, New York, 1986.
64. W. Kutzelnigg, U. Fleischer, and M. Schindler, in *NMR Basic Principles Progress*, eds. P. Diehl, E. Fluck, and R. Kosfeld, Springer-Verlag, Berlin 1990, Vol. 23, p. 165.
65. W. Kutzelnigg, C. v. Wüllen, U. Fleischer, R. Franke, and T.-v. Mourik, in *Nuclear Magnetic Shielding and Molecular Structure*, ed. J. Tossell, Kluwer, Dordrecht, 1993, p. 141.
66. T. J. Rowland, *Progr. Mater. Sci.*, 1961, **9**, 1; *Phys. Rev.*, 1960, **119**, 900.
67. W. Kohn and S. H. Vosko, *Phys. Rev.*, 1960, **119**, 912.
68. B. R. Appleman and B. P. Dailey, in *Advances in Magnetic Resonance*, ed. J. S. Waugh, Academic Press, New York, 1974, Vol. 7, p. 231.
69. R. M. Sternheimer, *Phys. Rev.*, 1950, **80**, 102; R. M. Sternheimer, *Z. Naturforsch. A*, 1986, **41**, 24.
70. P. C. Schmidt, K. D. Sen, T. P. Das, and A. Weiss, *Phys. Rev. B*, 1980, **22**, 4167; K. D. Sen, P. C. Schmidt, and A. Weiss, *Z. Naturforsch. A*, 1986, **41**, 37.
71. T. P. Das and P. C. Schmidt, *Z. Naturforsch. A*, 1986, **41**, 47.
72. T. P. Das and M. Pomerantz, *Phys. Rev.*, 1961, **123**, 2070.
73. P. Blaha, K. Schwarz, and P. H. Dederichs, *Phys. Rev. B*, 1988, **37**, 2792.
74. K. Schwarz, C. Ambrosch-Draxl, and P. Blaha, *Phys. Rev. B*, 1990, **42**, 2051.

Acknowledgments

I am indebted to S. Appelt and R. Butscher for careful reading of the manuscript.

Biographical Sketch

Michael Mehring. *b* 1937. Diploma, 1964, Univ. Münster, Dr.rer.nat., 1968, Univ. Münster, Dr. habil., 1971, University Münster. Research Associate, MIT (Waugh), 1969–71; Professor, Univ. Dortmund, 1972–82; Professor, Univ. Stuttgart, 1982–present. Approx. 160 publications. Research interests include theory and applications of high-resolution NMR techniques, in particular multiple pulse, double resonance, and multiquantum NMR to solid state physics problems. Of particular interest are organic conductors and superconductors, conducting polymers, electron-transfer processes, and molecular electronics.

Liouville Equation of Motion

Charles L. Mayne
University of Utah, Salt Lake City, UT, USA

1	Introduction	1
2	Operators and Operator Bases	1
3	Some Commonly Used Bases	7
4	The Density Operator	10
5	Superoperators	13
6	Related Article	14
7	References	14

1 INTRODUCTION

Nuclear magnetic resonance is uniquely capable of revealing structure and dynamics on a molecular level. An understanding of nuclear spin relaxation is fundamental to an understanding of nuclear magnetic resonance in general. The theoretical framework needed to promote this understanding is conveniently constructed in terms of the time evolution of the density operator under the influence of some Hamiltonian as expressed by the Liouville–von Neuman equation. The emphasis here will be on molecules in liquids, though many of the principles presented are applicable to solids and gases. The experimental observables of NMR are oscillatory magnetizations induced in a sample as a consequence of subjecting it to various static and time-varying magnetic fields. The quantum mechanical operators corresponding to these observables act only on the nuclear spin degrees of freedom of the system. Furthermore, these operators are proportional to the spin angular momentum operators or products thereof, and, hence, can be dealt with using finite basis sets of states or operators. Relaxation, however, is a consequence of interactions between the nuclear spins and the rest of the system, referred to as the 'lattice'. In most cases, the lattice cannot be treated exactly using quantum mechanics, because the density operator and the Hamiltonian cannot be defined exactly. The strategy generally employed, then, is to treat the effects of the lattice classically as a random time-dependent modulation of the nuclear spin operators while retaining a quantum mechanical description of the nuclear spins themselves. All externally applied magnetic fields are likewise treated classically. Our goal is to derive equations that correctly describe the observed temporal behavior of the experimental observables. This is done by proposing a Hamiltonian for the system under study, solving the Liouville–von Neuman equation for the time evolution of the density operator, computing the expected time evolution of the experimental observables, and comparing the result with measured values of these observables. Secondly, one wants to extract from this temporal behavior of the observables information about the fundamental nature of the system under investigation. For example, internuclear distances and rates of molecular reorientation due to Brownian motion can dramatically affect the results of an NMR experiment. How can this kind of information be extracted from the behavior of the magnetization in a sample as a function of time? This article will lay out the theoretical framework of NMR experiments, with emphasis on an understanding of nuclear spin relaxation in liquids.

This article presumes a basic knowledge of the nuclear magnetic resonance phenomenon, including nuclear spin polarization in an external static magnetic field and interaction of nuclear spins with applied radiofrequency fields. For those not acquainted with these concepts, several basic texts may be consulted.[1–3] The reader is assumed to have some grasp of basic quantum mechanics and angular momentum theory at the level generally taught in undergraduate physical chemistry courses. Some command of linear algebra and integral and differential calculus is also assumed. All abbreviations and symbols are either defined in the endpapers or are defined in context. Vectors and matrices will be distinguished by bold italic and bold roman type, respectively, and the same symbol in normal weight type will denote the magnitude of a vector or, with appropriate subscripts, components of a vector or elements of a matrix. Quantum mechanical operators will have a hat, for example, $\hat{\mathcal{H}}$. Liouville space operators will have a double hat, for example $\hat{\hat{\mathcal{L}}}$.

It is a familiar concept that the wavefunction embodies all that can be known about a quantum mechanical system and that any wavefunction can be expressed as a linear combination of the members of a complete set of eigenfunctions of the Hamiltonian of the system. However, in NMR, the density operator has proven to be a more convenient vehicle for this information, and the density operator, the Hamiltonian, and all other operators associated with the system can be cast as linear combinations of a complete set of orthonormal operators. These two descriptions are completely equivalent, and each can be formulated from the general concepts embodied in the bracket notation introduced by Dirac[4] to describe abstract vector spaces. For nuclear spin systems in liquids, it is often possible to focus on a small number of spins (all the spins in one molecule, for example) and to consider the macroscopic sample as an ensemble of such systems, identical in their dependence on quantum mechanical operators but sampling the distribution of random classical variables. Since each nuclear spin has only a small number of eigenstates and the number of eigenstates for the whole system is the product of the numbers for each of the component spins, the necessary mathematics reduces, by means of an ensemble average, to a problem in linear algebra of reasonable dimension. In the following sections, the mathematics needed to discuss most of the experiments done on liquid samples will be formulated. Space limitations make it impossible to give a completely detailed exposition; for this, the reader may consult several excellent texts.[5–9]

2 OPERATORS AND OPERATOR BASES

When a quantum mechanical system has a finite number of discrete energy levels (suppose there are n of them), the operators and states of the system can be represented as matrices and vectors in an n-dimensional vector space. Thus, the algebra of abstract n-dimensional vector spaces is essential to the theory we wish to develop. Dirac developed a convenient notation for describing these concepts.

2.1 Dirac Bracket Notation

For now, let us develop the bracket notation in a very abstract sense. It is important to realize that the bracket notation is just a formalism and can be applied to represent any desired vector space. Later, we shall apply it to both Hilbert and Liouville representations of the density operator. In the following equation is defined something called a *bra* and something called a *ket*:

$$\langle bra|(c)|ket\rangle \tag{1}$$

Bras and kets may have any kind of label inside to distinguish one from another. A ket may be converted into the corresponding bra by taking the Hermitian conjugate or adjoint, i.e., the complex conjugate transpose, and, of course, a bra can be converted into a ket in the same manner:

$$\langle bra| = [(|ket\rangle)^*]^{\mathrm{T}} = (|ket\rangle)^\dagger \tag{2}$$

Multiplication of a bra and a ket in that order yields a number that can be real, imaginary, or complex:

$$\langle bra|ket\rangle = \mathrm{c} \tag{3}$$

Note that this *scalar product* is not commutative, as we shall see in equation (9). Equation (3) is a key concept. In what follows, one must be able to recognize the $\langle\ |\ \rangle$ construct as a number that commutes with operators, bras, and kets. The scalar product is linear:

$$\left.\begin{aligned}\langle \mathrm{bra}|(|\mathrm{ket}_1\rangle + |\mathrm{ket}_2\rangle) &= \langle \mathrm{bra}|\mathrm{ket}_1\rangle + \langle \mathrm{bra}|\mathrm{ket}_2\rangle \\ (\langle \mathrm{bra}_1| + \langle \mathrm{bra}_2|)|\mathrm{ket}\rangle &= \langle \mathrm{bra}_1|\mathrm{ket}\rangle + \langle \mathrm{bra}_2|\mathrm{ket}\rangle\end{aligned}\right\} \tag{4}$$

Next we define something called an *operator* that converts a ket into some other ket:

$$\widehat{Op}|\mathrm{ket}\rangle = |\mathrm{new\ ket}\rangle \tag{5}$$

Operators will be distinguished by a hat (circumflex). Operators do not, in general, commute. The identity operator $\hat{E}$ just leaves a ket unaltered:

$$\hat{E}|\mathrm{ket}\rangle = |\mathrm{ket}\rangle \tag{6}$$

The identity operator does commute with all other operators.

Taking the adjoint of both sides of equation (5) yields the following relationship, which shows how an operator can act to the left on a bra:

$$(\widehat{Op}|\mathrm{ket}\rangle)^\dagger = \langle \mathrm{bra}|\widehat{Op}^\dagger = \langle \mathrm{new\ bra}| \tag{7}$$

If $\widehat{Op}^\dagger = \widehat{Op}$, the operator is said to be *Hermitian* or *self-adjoint*.

If an operator acting on a ket yields the same ket multiplied by a number c (perhaps complex), the ket is said to be an *eigenket* of the operator, and c is the *eigenvalue*:

$$\widehat{Op}|\mathrm{ket}\rangle = c|\mathrm{ket}\rangle \tag{8}$$

As mentioned above, multiplication of bras and kets is not commutative, so the question arises of the meaning of the following product of a ket with a bra:

$$|\mathrm{ket}\rangle\langle \mathrm{bra}| = \mathrm{operator} \tag{9}$$

This is called the *outer product* or *tensor product* of the bra and ket. Equation (9) asserts that this combination is an operator. This assertion can be easily proven by operating on some ket:

$$|a\rangle\langle b\|c\rangle = |a\rangle\langle b|c\rangle = |a\rangle n_{bc} = n_{bc}|a\rangle \tag{10}$$

Remember that $\langle b|c\rangle$ is just a number, by equation (3), and a number will commute with a ket. Thus, $|a\rangle\langle b|$ satisfies the definition of an operator as in equation (5), because it produces a new ket $|a\rangle$ from $|c\rangle$. The numerical coefficient involved is not a problem, because a number times a ket is still a ket. The fact that one can reinterpret or regroup bras and kets in this way is a key concept of the formalism. In Section 2.2 it will become more obvious why these alternative interpretations are possible. We shall not put a hat over these operators, since there is no possibility of confusion; expressions of the type $|\ \rangle\langle\ |$ will always be interpretable as operators.

If we have a set of kets $\{|i\rangle,\ i = 1, 2, 3, \ldots, n\}$ such that

$$\langle i|\ j\rangle = \delta_{ij} \quad \text{for all} \quad i, j = 1, 2, 3, \ldots, n \tag{11}$$

then the set is said to be an *orthonormal* (orthogonal and normalized) basis. The Kronecker delta function is defined by

$$\delta_{ij} = \begin{cases} 1 & (i = j) \\ 0 & (i \neq j) \end{cases} \tag{12}$$

If for some member of the set $\langle i|i\rangle \neq 1$ then we simply define a new ket $|i'\rangle = |i\rangle/\langle i|i\rangle^{\frac{1}{2}}$ to replace $|i\rangle$ until all members of the set are normalized.

With just these simple rules for manipulating operators, bras, and kets as postulates, one can develop the mathematics necessary to treat nuclear spin dynamics.

2.2 Representations

Suppose we have some system in a state that corresponds to an abstract vector or ket designated as $|\psi(t)\rangle$. The indicated time dependence shows that the system may be evolving in time. We attempt to expand this state in the stationary orthonormal set of equation (11) as follows, and we want to know the form of the coefficients $c_i(t)$:

$$|\psi(t)\rangle = \sum_{i=1}^{n} c_i(t)|i\rangle \tag{13}$$

Multiplying from the left by $\langle i|$, a bra corresponding to one of the members of the basis set, and using equation (11) yields

$$\begin{aligned}\langle i|\psi(t)\rangle &= \langle i|\sum_{j=1}^{n} c_j(t)|\ j\rangle \\ &= \sum_{j=1}^{n} c_j(t)\langle i|\ j\rangle \\ &= \sum_{j=1}^{n} c_j(t)\delta_{ij} = c_i(t)\end{aligned} \tag{14}$$

The last step follows because, by equation (12), only the ith term survives in the sum. This is a formal prescription for computing the expansion coefficients; later, we shall see how it is implemented in real cases. The question of whether the set $\{|i\rangle\}$ is complete, i.e., contains all the basis vectors necessary to represent $|\psi(t)\rangle$, will not be addressed here. It will simply be asserted that such a set can be found. Taking the adjoint of both sides of equation (14) yields the analogous equation for bras:

$$\langle\psi(t)|i\rangle = c_i^*(t) \tag{15}$$

Having chosen a basis set, we can compute all the coefficients needed for equation (14) or equation (15). If these coefficients are arranged in a column or a row vector then we have the Hilbert space representation of the state (bra or ket) in the basis:

$$|\psi\rangle \xrightarrow{|i\rangle} \begin{bmatrix} \langle 1|\psi\rangle \\ \langle 2|\psi\rangle \\ \langle 3|\psi\rangle \\ \vdots \\ \langle n|\psi\rangle \end{bmatrix} = \begin{bmatrix} c_1 \\ c_2 \\ c_3 \\ \vdots \\ c_n \end{bmatrix} \tag{16a}$$

$$\begin{aligned} \langle\psi| \xrightarrow{|i\rangle} & [\langle\psi|1\rangle \quad \langle\psi|2\rangle \quad \langle\psi|3\rangle \quad \dots \quad \langle\psi|n\rangle] \\ & = [c_1^* \quad c_2^* \quad c_3^* \quad \dots \quad c_n^*] \end{aligned} \tag{16b}$$

A mapping of this sort is sometimes written with an equals sign in the literature. This is not consistent with the notation we have developed, because the state $|\psi\rangle$ is an abstraction implying no particular basis, whereas the vector representing $|\psi\rangle$ requires that a particular basis be chosen. It is also inconsistent to equate a wavefunction to a ket, because a wavefunction is a representation of the ket in a continuous rather than a discrete basis. The result is a function rather than a vector with discrete elements; that is why it is called a wave*function*. In this article, mappings of this sort will be indicated by an arrow as in equation (16). The basis used will be indicated as shown or will be obvious from the context.

Of course, the members of the basis set can themselves be represented in the basis. If the jth member of the basis is represented then all the elements of the vector will be zero except the jth, which is one:

$$|\,j\rangle \xrightarrow{|i\rangle} \begin{bmatrix} \langle 1|\,j\rangle \\ \langle 2|\,j\rangle \\ \vdots \\ \langle\,j|\,j\rangle \\ \vdots \\ \langle n|\,j\rangle \end{bmatrix} = \begin{bmatrix} 0 \\ 0 \\ \vdots \\ 1 \\ \vdots \\ 0 \end{bmatrix} \tag{17a}$$

$$\begin{aligned} \langle\,j| \xrightarrow{|i\rangle} & [\langle\,j|1\rangle \quad \langle\,j|2\rangle \quad \dots \quad \langle\,j|\,j\rangle \quad \dots \quad \langle\,j|n\rangle] \\ & = [0 \quad 0 \quad \dots \quad 1 \quad \dots \quad 0] \end{aligned} \tag{17b}$$

If we rewrite equation (13) using the result in equation (14) and commute the number with the ket on the right, we have

$$\begin{aligned} |\psi(t)\rangle &= \sum_{i=1}^{n} \langle i|\psi(t)\rangle|i\rangle \\ &= \sum_{i=1}^{n} |i\rangle\langle i|\psi(t)\rangle \\ &= \left(\sum_{i=1}^{n} |i\rangle\langle i|\right)|\psi(t)\rangle \end{aligned} \tag{18}$$

Written this way, the implication is

$$\sum_{i=1}^{n} |i\rangle\langle i| = \hat{E} \tag{19}$$

Rearranging and reinterpreting the brackets in this way may seem quite strange at first, but the examples given below should clarify the formalism. The operators $|i\rangle\langle i|$ are called *projection operators* because they project from any state the part that projects on the ith basis state. Summing over all the projection operators then just gives the unit operator.

Suppose we have two alternative sets of basis states, $\{|a,i\rangle\}$ and $\{|b,i\rangle\}$, spanning the same vector space; then we can effect a transformation between the bases using projection operators as in equation (19). Projecting the b basis onto the a basis, we have

$$\begin{aligned} |b,i\rangle &= \left(\sum_{j=1}^{n} |a,j\rangle\langle a,j|\right)|b,i\rangle \\ &= \sum_{j=1}^{n} |a,j\rangle\langle a,j|b,i\rangle \\ &= \sum_{j=1}^{n} \langle a,j|b,i\rangle|a,j\rangle \end{aligned} \tag{20}$$

If we have an arbitrary state represented in the b basis, it can be transformed to the a basis as follows:

$$\begin{aligned} \psi\rangle &= \sum_{i=1}^{n} \langle b,i|\psi\rangle|b,i\rangle \\ &= \sum_{i=1}^{n} \langle b,i|\psi\rangle \sum_{j=1}^{n} \langle a,j|b,i\rangle|a,j\rangle \\ &= \sum_{i,j=1}^{n} \langle a,j|b,i\rangle\langle b,i|\psi\rangle|a,j\rangle \end{aligned} \tag{21a}$$

$$\begin{aligned} \langle\psi| &= \sum_{i=1}^{n} \langle\psi|b,i\rangle\langle b,i| \\ &= \sum_{i=1}^{n} \langle\psi|b,i\rangle \sum_{j=1}^{n} \langle b,i|a,j\rangle\langle a,j| \\ &= \sum_{i,j=1}^{n} \langle\psi|b,i\rangle\langle b,i|a,j\rangle\langle a,j| \end{aligned} \tag{21b}$$

Comparing these results with equations (16a) and (16b), it is apparent that equations (21a) and (21b) can be represented as follows:

$$\begin{bmatrix} \langle a,1|\psi\rangle \\ \langle a,2|\psi\rangle \\ \langle a,3|\psi\rangle \\ \vdots \\ \langle a,n|\psi\rangle \end{bmatrix}$$

$$= \begin{bmatrix} \langle a,1|b,1\rangle & \langle a,1|b,2\rangle & \langle a,1|b,3\rangle & \dots & \langle a,1|b,n\rangle \\ \langle a,2|b,1\rangle & \langle a,2|b,2\rangle & \langle a,2|b,3\rangle & \dots & \langle a,2|b,n\rangle \\ \langle a,3|b,1\rangle & \langle a,3|b,2\rangle & \langle a,3|b,3\rangle & \dots & \langle a,3|b,n\rangle \\ \vdots & \vdots & \vdots & \ddots & \vdots \\ \langle a,n|b,1\rangle & \langle a,n|b,2\rangle & \langle a,n|b,3\rangle & \dots & \langle a,n|b,n\rangle \end{bmatrix}$$

$$\times \begin{bmatrix} \langle b,1|\psi\rangle \\ \langle b,2|\psi\rangle \\ \langle b,3|\psi\rangle \\ \vdots \\ \langle b,n|\psi\rangle \end{bmatrix} \tag{22a}$$

$$[\langle\psi|a,1\rangle \quad \langle\psi|a,2\rangle \quad \langle\psi|a,3\rangle \quad \dots \quad \langle\psi|a,n\rangle]$$

$$= [\langle\psi|b,1\rangle \quad \langle\psi|b,2\rangle \quad \langle\psi|b,3\rangle \quad \dots \quad \langle\psi|b,n\rangle]$$

$$\times \begin{bmatrix} \langle b,1|a,1\rangle & \langle b,1|a,2\rangle & \langle b,1|a,3\rangle & \dots & \langle b,1|a,n\rangle \\ \langle b,2|a,1\rangle & \langle b,2|a,2\rangle & \langle b,2|a,3\rangle & \dots & \langle b,2|a,n\rangle \\ \langle b,3|a,1\rangle & \langle b,3|a,2\rangle & \langle b,3|a,3\rangle & \dots & \langle b,3|a,n\rangle \\ \vdots & \vdots & \vdots & \ddots & \vdots \\ \langle b,n|a,1\rangle & \langle b,n|a,2\rangle & \langle b,n|a,3\rangle & \dots & \langle b,n|a,n\rangle \end{bmatrix} \tag{22b}$$

Note that the columns of the first transformation matrix are merely the representation of the b basis kets in the a basis, while the rows are the representation of the a bras in the b basis. The second transformation matrix is the adjoint (complex conjugate transpose) of the first. If the two matrices are multiplied in either order, the result is a unit matrix, because the basis states are normalized. But this is just the definition of a unitary matrix. In compact matrix notation, we have

$$\boldsymbol{\psi}_a = \mathbf{T}\boldsymbol{\psi}_b, \quad \boldsymbol{\psi}_a^\dagger = \boldsymbol{\psi}_b^\dagger \mathbf{T}^\dagger \tag{23}$$

The unitary nature of the transformation is expressed as

$$\mathbf{T}\mathbf{T}^\dagger = \mathbf{T}^\dagger\mathbf{T} = \mathbf{E} = \mathbf{T}\mathbf{T}^{-1} = \mathbf{T}^{-1}\mathbf{T} \tag{24}$$

From these two equations, it is evident that the normalization of the state is preserved, regardless of the representation used:

$$\boldsymbol{\psi}_a^\dagger\boldsymbol{\psi}_a = \boldsymbol{\psi}_b^\dagger\mathbf{T}^\dagger\mathbf{T}\boldsymbol{\psi}_b = \boldsymbol{\psi}_b^\dagger\boldsymbol{\psi}_b \tag{25}$$

The inverse transformation can easily be derived. If $\boldsymbol{\psi}_\mathrm{a} = \mathbf{T}\boldsymbol{\psi}_\mathrm{b}$ then we have

$$\mathbf{T}^{-1}\mathbf{T}\boldsymbol{\psi}_b = \mathbf{T}^{-1}\boldsymbol{\psi}_a, \quad \boldsymbol{\psi}_b = \mathbf{T}^{-1}\boldsymbol{\psi}_a \tag{26}$$

But the inverse transformation is

$$\begin{aligned} |\psi\rangle &= \sum_{i=1}^{n} \langle a,i|\psi\rangle |a,i\rangle \\ &= \sum_{i=1}^{n} \langle a,i|\psi\rangle \sum_{j=1}^{n} \langle b,j|a,i\rangle |b,j\rangle \\ &= \sum_{i,j=1}^{n} \langle b,j|a,i\rangle\langle a,i|\psi\rangle |b,j\rangle \end{aligned} \tag{27}$$

Comparing equations (21a) and (27), the relationship between the a to b and b to a transforms is found to be

$$T_{ji}^* = \langle b,i|a,j\rangle^* = \langle a,j|b,i\rangle = T_{ij}^\dagger \tag{28}$$

which shows that the inverse transformation matrix $\mathbf{T}^{-1}$ is just the adjoint of the original matrix—but this is again just the definition of a unitary matrix. Examining equations (22a) and (22b), it is clear that the complex conjugate transpose of the transformation matrix is, indeed, the desired inverse transformation. This may be shown more easily by noting from equation (24) that $\mathbf{T}^\dagger = \mathbf{T}^{-1}$. Then, from equation (23), we have

$$\left.\begin{aligned} \mathbf{T}^\dagger\boldsymbol{\psi}_a = \mathbf{T}^\dagger\mathbf{T}\boldsymbol{\psi}_b = \boldsymbol{\psi}_b \\ \boldsymbol{\psi}_a^\dagger\mathbf{T} = \boldsymbol{\psi}_b^\dagger\mathbf{T}^\dagger\mathbf{T} = \boldsymbol{\psi}_b^\dagger \end{aligned}\right\} \tag{29}$$

We now turn to some relationships involving operators. Suppose one has some arbitrary operator $\hat{\mathrm{O}}$. Using equation (19), we can write

$$\begin{aligned} \hat{O} &= \left(\sum_{i=1}^{n} |i\rangle\langle i|\right)\hat{O}\left(\sum_{j=1}^{n} |\,j\rangle\langle\,j|\right) \\ &= \sum_{i,j=1}^{n} |i\rangle\langle i|\hat{O}|\,j\rangle\langle\,j| \\ &= \sum_{i,j=1}^{n} \langle i|\hat{O}|\,j\rangle |i\rangle\langle\,j| \\ &= \sum_{i,j=1}^{n} c_{ij}|i\rangle\langle\,j| \end{aligned} \tag{30}$$

A unit operator can be inserted anywhere without affecting the equality. This equation is a prescription for writing any operator as a sum of operators $|i\rangle\langle\,j|$. Clearly, if there are n basis states $|i\rangle$ then there are n^2 basis operators $|i\rangle\langle\,j|$. If we multiply this equation from the left and right by a basis state, the result is a prescription for the coefficients c_{ij}:

$$\begin{aligned} \langle k|\hat{O}|l\rangle &= \langle k|\left(\sum_{i,j=1}^{n} c_{ij}|i\rangle\langle\,j|\right)|l\rangle \\ &= \sum_{i,j=1}^{n} c_{ij}\langle k|i\rangle\langle\,j|l\rangle \\ &= \sum_{i,j=1}^{n} c_{ij}\delta_{ki}\delta_{jl} = c_{kl} \end{aligned} \tag{31}$$

These coefficients are commonly called the *matrix elements* of the operator, and can be arranged in a matrix to form a Hilbert space representation of the operator:

$$\hat{O} \xrightarrow{|i\rangle} \mathbf{O} = \begin{bmatrix} \langle 1|\hat{O}|1\rangle & \langle 1|\hat{O}|2\rangle & \langle 1|\hat{O}|3\rangle & \dots & \langle 1|\hat{O}|n\rangle \\ \langle 2|\hat{O}|1\rangle & \langle 2|\hat{O}|2\rangle & \langle 2|\hat{O}|3\rangle & \dots & \langle 2|\hat{O}|n\rangle \\ \langle 3|\hat{O}|1\rangle & \langle 3|\hat{O}|2\rangle & \langle 3|\hat{O}|3\rangle & \dots & \langle 3|\hat{O}|n\rangle \\ \vdots & \vdots & \vdots & \ddots & \vdots \\ \langle n|\hat{O}|1\rangle & \langle n|\hat{O}|2\rangle & \langle n|\hat{O}|3\rangle & \dots & \langle n|\hat{O}|n\rangle \end{bmatrix} \tag{32}$$

Proceeding as in equation (25), we can write

$$\boldsymbol{\psi}_a^\dagger \mathbf{O}_a \boldsymbol{\psi}_a = \boldsymbol{\psi}_b^\dagger \mathbf{T}^\dagger \mathbf{T} \mathbf{O}_a \mathbf{T}^\dagger \mathbf{T} \boldsymbol{\psi}_b = \boldsymbol{\psi}_b^\dagger \mathbf{O}_b \boldsymbol{\psi}_b \tag{33}$$

where we have defined the operator in the b basis as

$$\mathbf{O}_b = \mathbf{T} \mathbf{O}_a \mathbf{T}^\dagger \tag{34}$$

Analogously, the basis operators themselves can be represented as follows to yield a matrix of all zero elements except the ijth:

$$|i\rangle\langle j| \xrightarrow{|i\rangle} \begin{bmatrix} \langle 1|i\rangle\langle j|1\rangle & \langle 1|i\rangle\langle j|2\rangle & \dots & \langle 1|i\rangle\langle j|j\rangle & \dots & \langle 1|i\rangle\langle j|n\rangle \\ \langle 2|i\rangle\langle j|1\rangle & \langle 2|i\rangle\langle j|2\rangle & \dots & \langle 2|i\rangle\langle j|j\rangle & \dots & \langle 2|i\rangle\langle j|n\rangle \\ \vdots & \vdots & \ddots & \vdots & & \vdots \\ \langle i|i\rangle\langle j|1\rangle & \langle i|i\rangle\langle j|2\rangle & \dots & \langle i|i\rangle\langle j|j\rangle & \dots & \langle i|i\rangle\langle j|n\rangle \\ \vdots & \vdots & & \vdots & \ddots & \vdots \\ \langle n|i\rangle\langle j|1\rangle & \langle n|i\rangle\langle j|2\rangle & \dots & \langle n|i\rangle\langle j|j\rangle & \dots & \langle n|i\rangle\langle j|n\rangle \end{bmatrix}$$

$$= \begin{bmatrix} 0 & 0 & \dots & 0 & \dots & 0 \\ 0 & 0 & \dots & 0 & \dots & 0 \\ \vdots & \vdots & \ddots & \vdots & & \vdots \\ 0 & 0 & \dots & 1 & \dots & 0 \\ \vdots & \vdots & & \vdots & \ddots & \vdots \\ 0 & 0 & \dots & 0 & \dots & 0 \end{bmatrix} \tag{35}$$

This result can also be obtained from equations (17a) and (17b) by writing

$$\begin{bmatrix} \langle 1|i\rangle \\ \langle 2|i\rangle \\ \vdots \\ \langle j|i\rangle \\ \vdots \\ \langle n|i\rangle \end{bmatrix} \begin{bmatrix} \langle j|1\rangle & \langle j|2\rangle & \dots & \langle j|j\rangle & \dots & \langle j|n\rangle \end{bmatrix}$$

$$= \begin{bmatrix} \langle 1|i\rangle\langle j|1\rangle & \langle 1|i\rangle\langle j|2\rangle & \dots & \langle 1|i\rangle\langle j|j\rangle & \dots & \langle 1|i\rangle\langle j|n\rangle \\ \langle 2|i\rangle\langle j|1\rangle & \langle 2|i\rangle\langle j|2\rangle & \dots & \langle 2|i\rangle\langle j|j\rangle & \dots & \langle 2|i\rangle\langle j|n\rangle \\ \vdots & \vdots & \ddots & \vdots & & \vdots \\ \langle i|i\rangle\langle j|1\rangle & \langle i|i\rangle\langle j|2\rangle & \dots & \langle i|i\rangle\langle j|j\rangle & \dots & \langle i|i\rangle\langle j|n\rangle \\ \vdots & \vdots & & \vdots & \ddots & \vdots \\ \langle n|i\rangle\langle j|1\rangle & \langle n|i\rangle\langle j|2\rangle & \dots & \langle n|i\rangle\langle j|j\rangle & \dots & \langle n|i\rangle\langle j|n\rangle \end{bmatrix} \tag{36}$$

The basis operators are orthogonal, just as the basis states are; however, the inner product exemplified by equation (11) must be replaced by the trace operation:

$$\begin{aligned} \mathrm{Tr}(|\,j\rangle\langle k|l\rangle\langle m|) &= \sum_{i=1}^{n} \langle i|\,j\rangle\langle k|l\rangle\langle m|i\rangle \\ &= \langle k|l\rangle\langle m|\,j\rangle \\ &= \delta_{kl}\delta_{mj} \end{aligned} \tag{37}$$

In equation (37), the right-hand side will be nonzero if and only if $j = m$ and $k = l$; then

$$|\,j\rangle\langle k|k\rangle\langle\,j| = |\,j\rangle\langle k|(|\,j\rangle\langle k|)^\dagger \tag{38}$$

In order to simplify notation, we now make a mapping of the indices j and k of $|j\rangle\langle k|$ onto a single index i of $\hat{U}_i$. This is simply a relabeling of the basis operators. The exact nature of the mapping is arbitrary, except that there must be a one-to-one correspondence between the pair of indices j, k and the index i. The expression corresponding to equation (37) is then

$$\mathrm{Tr}(\hat{U}_i \hat{U}_j^\dagger) = \delta_{ij} \tag{39}$$

This equation is the normalization condition for basis operators analogous to equation (11). Note that if the basis states used in equation (37) are normalized then these basis operators will also be normalized.

If we expand the generic operator $\hat{O}$ in terms of this basis set, the result is

$$\hat{O} = \sum_{i=1}^{n^2} c_i \hat{U}_i \tag{40}$$

Now, if this equation is multiplied by ${\hat{U}_j}^\dagger$ and the trace taken, a prescription is obtained for the expansion coefficients c_i:

$$\begin{aligned} \mathrm{Tr}(\hat{O}\hat{U}_j^\dagger) &= \mathrm{Tr}\left(\sum_{i=1}^{n^2} c_i \hat{U}_i \hat{U}_j^\dagger \right) \\ &= \sum_{i=1}^{n^2} c_i \mathrm{Tr}(\hat{U}_i \hat{U}_j^\dagger) = \sum_{i=1}^{n^2} c_i \delta_{ij} = c_j \end{aligned} \tag{41}$$

Equation (40) may then be rewritten as

$$\hat{O} = \sum_{i=1}^{n^2} \mathrm{Tr}(\hat{O}\hat{U}_i^\dagger)\hat{U}_i \tag{42}$$

The coefficients in this equation can be arranged in a vector to form the Liouville space representation of the operator:

$$\hat{O} \xrightarrow{\hat{U}_i} \begin{bmatrix} \mathrm{Tr}(\hat{O}\hat{U}_1^\dagger) \\ \mathrm{Tr}(\hat{O}\hat{U}_2^\dagger) \\ \mathrm{Tr}(\hat{O}\hat{U}_3^\dagger) \\ \vdots \\ \mathrm{Tr}(\hat{O}\hat{U}_{n^2}^\dagger) \end{bmatrix} \tag{43}$$

Note that this space is n^2-dimensional.

As was done with basis states, it is possible to transform among alternative sets of basis operators. Consider a new operator basis $\{\hat{V}_i, i = 1, 2, 3, \ldots, n^2\}$. These operators can be expressed in the original basis as

$$\hat{V}_i = \sum_{j=1}^{n^2} \mathrm{Tr}(\hat{V}_i \hat{U}_j^\dagger)\hat{U}_j \tag{44}$$

Equation (42) can be written in terms of the $\hat{V}_i$; then equation (44) can be substituted:

$$\begin{aligned}\hat{O} &= \sum_{j=1}^{n^2} \mathrm{Tr}(\hat{O}\hat{V}_j^\dagger)\hat{V}_j \\ &= \sum_{j=1}^{n^2} \mathrm{Tr}(\hat{O}\hat{V}_j^\dagger) \sum_{i=1}^{n^2} \mathrm{Tr}(\hat{V}_j \hat{U}_i^\dagger)\hat{U}_i \\ &= \sum_{i,j=1}^{n^2} \mathrm{Tr}(\hat{V}_j \hat{U}_i^\dagger)\mathrm{Tr}(\hat{O}\hat{V}_j^\dagger)\hat{U}_i \end{aligned} \tag{45}$$

Comparing equations (42) and (45), it is evident that the conversion of operator bases is accomplished as follows:

$$\mathrm{Tr}(\hat{O}\hat{U}_i^\dagger) = \sum_{j=1}^{n^2} \mathrm{Tr}(\hat{V}_j \hat{U}_i^\dagger)\mathrm{Tr}(\hat{O}\hat{V}_j^\dagger) \tag{46}$$

In terms of the Liouville space representation, this can be written as

$$\begin{bmatrix} \mathrm{Tr}(\hat{O}\hat{U}_1^\dagger) \\ \mathrm{Tr}(\hat{O}\hat{U}_2^\dagger) \\ \mathrm{Tr}(\hat{O}\hat{U}_3^\dagger) \\ \vdots \\ \mathrm{Tr}(\hat{O}\hat{U}_{n^2}^\dagger) \end{bmatrix} = \begin{bmatrix} \mathrm{Tr}(\hat{V}_1\hat{U}_1^\dagger) & \mathrm{Tr}(\hat{V}_2\hat{U}_1^\dagger) & \mathrm{Tr}(\hat{V}_3\hat{U}_1^\dagger) & \ldots & \mathrm{Tr}(\hat{V}_{n^2}\hat{U}_1^\dagger) \\ \mathrm{Tr}(\hat{V}_1\hat{U}_2^\dagger) & \mathrm{Tr}(\hat{V}_2\hat{U}_2^\dagger) & \mathrm{Tr}(\hat{V}_3\hat{U}_2^\dagger) & \ldots & \mathrm{Tr}(\hat{V}_{n^2}\hat{U}_2^\dagger) \\ \mathrm{Tr}(\hat{V}_1\hat{U}_3^\dagger) & \mathrm{Tr}(\hat{V}_2\hat{U}_3^\dagger) & \mathrm{Tr}(\hat{V}_3\hat{U}_3^\dagger) & \ldots & \mathrm{Tr}(\hat{V}_{n^2}\hat{U}_3^\dagger) \\ \vdots & \vdots & \vdots & \ddots & \vdots \\ \mathrm{Tr}(\hat{V}_1\hat{U}_{n^2}^\dagger) & \mathrm{Tr}(\hat{V}_2\hat{U}_{n^2}^\dagger) & \mathrm{Tr}(\hat{V}_3\hat{U}_{n^2}^\dagger) & \ldots & \mathrm{Tr}(\hat{V}_{n^2}\hat{U}_{n^2}^\dagger) \end{bmatrix} \times \begin{bmatrix} \mathrm{Tr}(\hat{O}\hat{V}_1^\dagger) \\ \mathrm{Tr}(\hat{O}\hat{V}_2^\dagger) \\ \mathrm{Tr}(\hat{O}\hat{V}_3^\dagger) \\ \vdots \\ \mathrm{Tr}(\hat{O}\hat{V}_{n^2}^\dagger) \end{bmatrix} \tag{47}$$

2.3 Direct Product Bases

It is quite common that one is able to derive a basis for two or more parts of a system using the techniques described in the previous section, but it is then desired to represent the whole system so that interactions among the parts can be considered. For example, a molecule might contain two spins, say a ^{13}C nucleus and a ^{1}H nucleus. For this purpose, we introduce the *direct* or *outer product* of the subspaces to form the space appropriate for the whole system. One can form the direct products in either Hilbert space or Liouville space. The only new definitions needed are as follows. For vectors (states),

$$|\psi_1\rangle|\psi_2\rangle = |\psi\rangle \tag{48a}$$

$$\begin{bmatrix} \langle 1,1|\psi_1\rangle \\ \langle 1,2|\psi_1\rangle \\ \langle 1,3|\psi_1\rangle \\ \vdots \\ \langle 1,n|\psi_1\rangle \end{bmatrix} \otimes \begin{bmatrix} \langle 2,1|\psi_2\rangle \\ \langle 2,2|\psi_2\rangle \\ \langle 2,3|\psi_2\rangle \\ \vdots \\ \langle 2,m|\psi_2\rangle \end{bmatrix} = \begin{bmatrix} \langle 1,1|\psi_1\rangle \begin{bmatrix} \langle 2,1|\psi_2\rangle \\ \langle 2,2|\psi_2\rangle \\ \langle 2,3|\psi_2\rangle \\ \vdots \\ \langle 2,m|\psi_2\rangle \end{bmatrix} \\ \langle 1,2|\psi_1\rangle \begin{bmatrix} \langle 2,1|\psi_2\rangle \\ \langle 2,2|\psi_2\rangle \\ \langle 2,3|\psi_2\rangle \\ \vdots \\ \langle 2,m|\psi_2\rangle \end{bmatrix} \\ \langle 1,3|\psi_1\rangle \begin{bmatrix} \langle 2,1|\psi_2\rangle \\ \langle 2,2|\psi_2\rangle \\ \langle 2,3|\psi_2\rangle \\ \vdots \\ \langle 2,m|\psi_2\rangle \end{bmatrix} \\ \vdots \\ \langle 1,n|\psi_1\rangle \begin{bmatrix} \langle 2,1|\psi_2\rangle \\ \langle 2,2|\psi_2\rangle \\ \langle 2,3|\psi_2\rangle \\ \vdots \\ \langle 2,m|\psi_2\rangle \end{bmatrix} \end{bmatrix} \tag{48b}$$

A slightly more condensed notation is required to make the corresponding definition for matrices (operators) manageable:

$$\hat{O} = \hat{O}^{(1)} \otimes \hat{O}^{(2)} \tag{49a}$$

$$\mathbf{O} = \begin{bmatrix} O_{1,1}^{(1)}\mathbf{O}^{(2)} & O_{1,2}^{(1)}\mathbf{O}^{(2)} & O_{1,3}^{(1)}\mathbf{O}^{(2)} & \ldots & O_{1,n}^{(1)}\mathbf{O}^{(2)} \\ O_{2,1}^{(1)}\mathbf{O}^{(2)} & O_{2,2}^{(1)}\mathbf{O}^{(2)} & O_{2,3}^{(1)}\mathbf{O}^{(2)} & \ldots & O_{2,n}^{(1)}\mathbf{O}^{(2)} \\ O_{3,1}^{(1)}\mathbf{O}^{(2)} & O_{3,2}^{(1)}\mathbf{O}^{(2)} & O_{3,3}^{(1)}\mathbf{O}^{(2)} & \ldots & O_{3,n}^{(1)}\mathbf{O}^{(2)} \\ \vdots & \vdots & \vdots & \ddots & \vdots \\ O_{n,1}^{(1)}\mathbf{O}^{(2)} & O_{n,2}^{(1)}\mathbf{O}^{(2)} & O_{n,3}^{(1)}\mathbf{O}^{(2)} & \ldots & O_{n,n}^{(1)}\mathbf{O}^{(2)} \end{bmatrix} \tag{49b}$$

$$\mathbf{O}^{(2)} = \begin{bmatrix} O_{1,1}^{(2)} & O_{1,2}^{(2)} & O_{1,3}^{(2)} & \ldots & O_{1,m}^{(2)} \\ O_{2,1}^{(2)} & O_{2,2}^{(2)} & O_{2,3}^{(2)} & \ldots & O_{2,m}^{(2)} \\ O_{3,1}^{(2)} & O_{3,2}^{(2)} & O_{3,3}^{(2)} & \ldots & O_{3,m}^{(2)} \\ \vdots & \vdots & \vdots & \ddots & \vdots \\ O_{m,1}^{(2)} & O_{m,2}^{(2)} & O_{m,3}^{(2)} & \ldots & O_{m,m}^{(2)} \end{bmatrix} \tag{49c}$$

Note that the dimension of the product space is always the product of the dimensions of the subspaces.

In equation (43) the Liouville space was introduced. With the introduction of the concept of direct products, it is possible to give a more satisfying explanation of the mapping from Hilbert space to Liouville space. The Hilbert space operators $|i\rangle\langle j|$ can be mapped onto a Liouville space with the following basis states:

$$|i\rangle|\ j\rangle = |ij\rangle \tag{50}$$

Clearly, a one-to-one mapping is possible. In Section 5, the use of Liouville space representations will be explored further with the introduction of superoperators.

It is common in the NMR literature to have implied direct products. For example, one might write $\hat{I}_z{}^{(1)} + \hat{I}_z{}^{(2)}$, where (1) and (2) refer to different spins. This is meant to imply $\hat{I}_z{}^{(1)} \otimes \hat{E}^{(2)} + \hat{E}^{(1)} \otimes \hat{I}_z{}^{(2)}$. Alternatively, one might encounter $\hat{I}_z\hat{I}_+$, where no direct product is implied, or $\hat{I}_+{}^{(1)}\hat{I}_-{}^{(2)}$, where we are to understand that this means $\hat{I}_+{}^{(1)} \otimes \hat{I}_-{}^{(2)}$. It is necessary to understand from the context and notation what is really meant.

3 SOME COMMONLY USED BASES

Next let us consider some examples of bases commonly used in NMR, using simple spin systems to illustrate how this formalism can be applied to nuclear spins.

3.1 The Single Spin Eigenstate Basis

A single isolated spin-$\frac{1}{2}$ nucleus has two energy eigenstates. They are commonly represented as $|\alpha\rangle$ and $|\beta\rangle$; however, since this notation is applicable only for spin-$\frac{1}{2}$, we shall also use the notation $|\frac{1}{2}\rangle$ and $|-\frac{1}{2}\rangle$, respectively, where each state is labelled by its $\hat{I}_z$ eigenvalue (this will be discussed in more detail below). It is assumed that these states are orthonormal. Using equation (17a), we can write the Hilbert space representation of the basis states as

$$\left.\begin{aligned} |\alpha\rangle = |\tfrac{1}{2}\rangle \rightarrow \begin{bmatrix}\langle\alpha|\alpha\rangle\\ \langle\beta|\alpha\rangle\end{bmatrix} = \begin{bmatrix}1\\0\end{bmatrix} \\ |\beta\rangle = |-\tfrac{1}{2}\rangle \rightarrow \begin{bmatrix}\langle\alpha|\beta\rangle\\ \langle\beta|\beta\rangle\end{bmatrix} = \begin{bmatrix}0\\1\end{bmatrix} \end{aligned}\right\} \tag{51}$$

The corresponding Hilbert space representation of the basis operators can be obtained most easily using equation (36) to write

$$\left.\begin{aligned} \hat{U}_1 = |\alpha\rangle\langle\alpha| \rightarrow \begin{bmatrix}1\\0\end{bmatrix}[1\quad 0] = \begin{bmatrix}1&0\\0&0\end{bmatrix} \\ \hat{U}_2 = |\alpha\rangle\langle\beta| \rightarrow \begin{bmatrix}1\\0\end{bmatrix}[0\quad 1] = \begin{bmatrix}0&1\\0&0\end{bmatrix} \\ \hat{U}_3 = |\beta\rangle\langle\alpha| \rightarrow \begin{bmatrix}0\\1\end{bmatrix}[1\quad 0] = \begin{bmatrix}0&0\\1&0\end{bmatrix} \\ \hat{U}_4 = |\beta\rangle\langle\beta| \rightarrow \begin{bmatrix}0\\1\end{bmatrix}[0\quad 1] = \begin{bmatrix}0&0\\0&1\end{bmatrix} \end{aligned}\right\} \tag{52}$$

It is easily verified that these matrices satisfy the orthonormality conditions by comparing with equation (39) for all pairs.

For spins with a higher angular momentum quantum number, the bases are similar but with higher dimension. For example, a spin-1 nucleus, like ^{2}H, has three eigenstates and nine basis operators. Representations of basis states and operators for any nucleus can be obtained just as above knowing only the number of eigenstates and assuming that they are orthonormal.

3.2 The Basis Derived from Direct Products of Single Spin Bases

When the system of interest includes more than one spin, a direct product of single spin bases described in the previous section (one set corresponding to the correct spin for each nucleus) yields a basis for the combined system. The first state and the first operator for two spin-$\frac{1}{2}$ nuclei, for example, would be

$$\left.\begin{aligned} |\alpha\rangle \otimes |\alpha\rangle = |\alpha\alpha\rangle \rightarrow \begin{bmatrix}1\\0\end{bmatrix} \otimes \begin{bmatrix}1\\0\end{bmatrix} \\ = \begin{bmatrix}1\begin{bmatrix}1\\0\end{bmatrix}\\ 0\begin{bmatrix}1\\0\end{bmatrix}\end{bmatrix} = \begin{bmatrix}1\\0\\0\\0\end{bmatrix} \\ \hat{U}_1 \otimes \hat{V}_1 \rightarrow \begin{bmatrix}1&0\\0&0\end{bmatrix} \otimes \begin{bmatrix}1&0\\0&0\end{bmatrix} = \begin{bmatrix}1\begin{bmatrix}1&0\\0&0\end{bmatrix} & 0\begin{bmatrix}1&0\\0&0\end{bmatrix}\\ 0\begin{bmatrix}1&0\\0&0\end{bmatrix} & 0\begin{bmatrix}1&0\\0&0\end{bmatrix}\end{bmatrix} \\ = \begin{bmatrix}1&0&0&0\\0&0&0&0\\0&0&0&0\\0&0&0&0\end{bmatrix} \end{aligned}\right\} \tag{53}$$

The other 3 basis states and 15 operators are composed in the same fashion using all the pairs of single spin matrices.

3.3 The Basis Derived from the Eigenstates of the Hamiltonian

The states given in equation (51) for a single spin $\frac{1}{2}$ are the eigenstates of the Hamiltonian, but for two identical spin-$\frac{1}{2}$ nuclei (an A_2 spin system), the eigenstates are

$$\left.\begin{aligned} |\mathrm{A}_2, 1\rangle = |\alpha\alpha\rangle \rightarrow \begin{bmatrix}1\\0\\0\\0\end{bmatrix} \\ |\mathrm{A}_2, 2\rangle = \sqrt{\tfrac{1}{2}}(|\alpha\beta\rangle + |\beta\alpha\rangle) \rightarrow \begin{bmatrix}0\\\sqrt{\frac{1}{2}}\\\sqrt{\frac{1}{2}}\\0\end{bmatrix} \\ |\mathrm{A}_2, 3\rangle = \sqrt{\tfrac{1}{2}}(|\alpha\beta\rangle - |\beta\alpha\rangle) \rightarrow \begin{bmatrix}0\\\sqrt{\frac{1}{2}}\\-\sqrt{\frac{1}{2}}\\0\end{bmatrix} \\ |\mathrm{A}_2, 4\rangle = |\beta\beta\rangle \rightarrow \begin{bmatrix}0\\0\\0\\1\end{bmatrix} \end{aligned}\right\} \tag{54}$$

These equations show a representation of the eigenstates in the basis of the spin product states. Assembling these vectors into a unitary matrix according to equation (22a) gives the following transformation matrix from the spin product basis to the eigenbasis:

$$\mathbf{U} = \begin{bmatrix} 1 & 0 & 0 & 0 \\ 0 & \sqrt{\frac{1}{2}} & \sqrt{\frac{1}{2}} & 0 \\ 0 & \sqrt{\frac{1}{2}} & -\sqrt{\frac{1}{2}} & 0 \\ 0 & 0 & 0 & 1 \end{bmatrix} \tag{55}$$

It is easily verified that $\mathbf{U}\mathbf{U}^{\dagger} = \mathbf{U}\mathbf{U}^{-1} = \mathbf{E}$. Applying this transformation to the spin product states or operators yields the desired eigenstate basis for the Hilbert space representation or the Liouville space representation, respectively.

3.4 The Angular Momentum Operator Basis

For a single spin-$\frac{1}{2}$ nucleus, the components of the angular momentum vector operator $\hat{\boldsymbol{I}} = \{\hat{I}_x, \hat{I}_y, \hat{I}_z\}$ augmented by the identity operator $\hat{E}$ are a complete basis. For a development of the angular momentum operators from first principles, the reader is referred to the standard texts.[6,7,10] We shall be content to define them according to their effect on the basis states as in equation (5). For any spin-I nucleus there are $2I + 1$ quantum states $|m\rangle$ such that

$$\left.\begin{aligned} \hat{I}_x|m\rangle &= \tfrac{1}{2}\{[I(I+1) - m(m+1)]^{1/2}|m+1\rangle \\ &\quad + [I(I+1) - m(m-1)]^{1/2}|m-1\rangle\} \\ \hat{I}_y|m\rangle &= \tfrac{1}{2\mathrm{i}}\{[I(I+1) - m(m+1)]^{1/2}|m+1\rangle \\ &\quad - [I(I+1) - m(m-1)]^{1/2}|m-1\rangle\} \\ \hat{I}_z|m\rangle &= m|m\rangle \end{aligned}\right\} \tag{56}$$

The eigenvalue m ranges in integer steps such that $-I \leq m \leq I$. For spin-$\frac{1}{2}$, using the $\{|\frac{1}{2}\rangle, |-\frac{1}{2}\rangle\}$ basis, the angular momentum operators and their representations are

$$\begin{aligned} \hat{I}_x &\rightarrow \tfrac{1}{2}\begin{bmatrix} 0 & 1 \\ 1 & 0 \end{bmatrix}, \quad \hat{I}_y \rightarrow \tfrac{1}{2\mathrm{i}}\begin{bmatrix} 0 & 1 \\ -1 & 0 \end{bmatrix} \\ \hat{I}_z &\rightarrow \tfrac{1}{2}\begin{bmatrix} 1 & 0 \\ 0 & -1 \end{bmatrix}, \quad \hat{E} \rightarrow \begin{bmatrix} 1 & 0 \\ 0 & 1 \end{bmatrix} \end{aligned} \tag{57}$$

It is easily verified that these operators are orthogonal but not normalized using equation (39). Normalization can easily be achieved by multiplying by the appropriate constants to satisfy equation (39); this yields the desired basis for spin-$\frac{1}{2}$:

$$\left.\begin{aligned} \hat{U}_1 &= \frac{1}{\sqrt{2}}\hat{E} \rightarrow \frac{1}{\sqrt{2}}\begin{bmatrix} 1 & 0 \\ 0 & 1 \end{bmatrix} \\ \hat{U}_2 &= \sqrt{2}\hat{I}_z \rightarrow \frac{\sqrt{2}}{2}\begin{bmatrix} 1 & 0 \\ 0 & -1 \end{bmatrix} \\ \hat{U}_3 &= \sqrt{2}\hat{I}_x \rightarrow \frac{\sqrt{2}}{2}\begin{bmatrix} 0 & 1 \\ 1 & 0 \end{bmatrix} \\ \hat{U}_4 &= \sqrt{2}\hat{I}_y \rightarrow \frac{\sqrt{2}}{2\mathrm{i}}\begin{bmatrix} 0 & 1 \\ -1 & 0 \end{bmatrix} \end{aligned}\right\} \tag{58}$$

For a spin-1 nucleus, using equation (56), the angular momentum operators are

$$\left.\begin{aligned} \hat{I}_x &\rightarrow \tfrac{1}{\sqrt{2}}\begin{bmatrix} 0 & 1 & 0 \\ 1 & 0 & 1 \\ 0 & 1 & 0 \end{bmatrix}, \quad \hat{I}_y \rightarrow \tfrac{1}{\mathrm{i}\sqrt{2}}\begin{bmatrix} 0 & 1 & 0 \\ -1 & 0 & 1 \\ 0 & -1 & 0 \end{bmatrix} \\ \hat{I}_z &\rightarrow \begin{bmatrix} 1 & 0 & 0 \\ 0 & 0 & 0 \\ 0 & 0 & -1 \end{bmatrix} \end{aligned}\right\} \tag{59}$$

However, since nine basis operators are required for spin 1, augmenting this set with $\hat{E}$ would clearly not be sufficient to produce a complete basis. However, we shall defer enumerating the other members of this basis until the next section, because the task becomes much easier once the spherical tensor operators have been introduced.

3.5 The Spherical Tensor Operator Basis

Examination of equation (56) rapidly leads one to conclude that a simpler basis might be composed including the following operators:

$$\left.\begin{aligned} \hat{I}_+|m\rangle &= [I(I+1) - m(m+1)]^{1/2}|m+1\rangle \\ \hat{I}_-|m\rangle &= [I(I+1) - m(m-1)]^{1/2}|m-1\rangle \end{aligned}\right\} \tag{60}$$

These operators are commonly called the *raising* or *step-up* and *lowering* or *step-down* operators, because they convert a given eigenket of $\hat{I}_z$ into one with the eigenvalue increased or decreased, respectively, by one. In terms of these operators, we have

$$\hat{I}_x = \tfrac{1}{2}(\hat{I}_+ + \hat{I}_-), \quad \hat{I}_y = \tfrac{1}{2\mathrm{i}}(\hat{I}_+ - \hat{I}_-) \tag{61}$$

The inverse relationship is

$$\hat{I}_+ = \hat{I}_x + \mathrm{i}\hat{I}_y, \quad \hat{I}_- = \hat{I}_x - \mathrm{i}\hat{I}_y \tag{62}$$

Applying these relations to equation (57) leads to a new basis:

$$\left.\begin{aligned} \hat{I}_+ &\rightarrow \begin{bmatrix} 0 & 1 \\ 0 & 0 \end{bmatrix}, \quad \hat{I}_- \rightarrow \begin{bmatrix} 0 & 0 \\ 1 & 0 \end{bmatrix} \\ \hat{I}_z &\rightarrow \tfrac{1}{2}\begin{bmatrix} 1 & 0 \\ 0 & -1 \end{bmatrix}, \quad \hat{E} \rightarrow \begin{bmatrix} 1 & 0 \\ 0 & 1 \end{bmatrix} \end{aligned}\right\} \tag{63}$$

The orthonormal basis corresponding to equation (58) is given by

$$\left.\begin{aligned} \hat{U}_1 &= \hat{T}^{(0)}_{0,0} = \frac{1}{\sqrt{2}}\hat{E} \rightarrow \frac{1}{\sqrt{2}}\begin{bmatrix} 1 & 0 \\ 0 & 1 \end{bmatrix} \\ \hat{U}_2 &= \hat{T}^{(1)}_{0,0} = \sqrt{2}\hat{I}_z \rightarrow \frac{\sqrt{2}}{2}\begin{bmatrix} 1 & 0 \\ 0 & -1 \end{bmatrix} \\ \hat{U}_3 &= \hat{T}^{(1)}_{1,0} = -\hat{I}_+ \rightarrow \begin{bmatrix} 0 & -1 \\ 0 & 0 \end{bmatrix} \\ \hat{U}_4 &= \hat{T}^{(1)}_{-1,0} = \hat{I}_- \rightarrow \begin{bmatrix} 0 & 0 \\ 1 & 0 \end{bmatrix} \end{aligned}\right\} \tag{64}$$

The $\hat{T}^{(k)}_{q,j}$ designation for these operators is that characterizing the *irreducible spherical tensor operators*. There will be

$2k + 1$ members in a set of operators of rank k with projection q ranging from $-k$ to k in integer steps. Note that the index j is not needed here, but will come into play when more complicated spin systems are considered with more than one set of operators of a given k. In what follows, the index j will be suppressed when it is not needed. It is easily verified that this basis is orthonormal. The minus sign associated with $\hat{U}_3$ does not affect the orthonormality of the set. It is common practice to choose this 'phase factor' to correspond to that of the spherical harmonic functions, i.e., such that

$$\hat{T}_q^{(k)\dagger} = (-1)^q \hat{T}_{-q}^{(k)} \tag{65}$$

The operators then satisfy equation (39) in the form

$$\mathrm{Tr}(\hat{T}_q^{(k)} \hat{T}_{q'}^{(k)\dagger}) = (-1)^q \mathrm{Tr}(\hat{T}_q^{(k)} \hat{T}_{-q'}^{(k')}) = \delta_{kk'}\delta_{q-q'} \tag{66}$$

The defining characteristic of the irreducible spherical tensor operators is that when they are subjected to a rotation of the coordinate system, they behave like the spherical harmonic functions, i.e., they transform to linear combinations of the set such that operators of differing k or j never mix:

$$\hat{R}(\phi, \theta, \chi)\hat{T}_{q,j}^{(k)}\hat{R}^{-1}(\phi, \theta, \chi) = \sum_{q'=-k}^{k} D_{q'q}^{(k)}(\phi, \theta, \chi)\hat{T}_{q',j}^{(k)} \tag{67}$$

The rotation operator $\hat{R}(\phi, \theta, \chi)$ and its inverse (defined by equation (68)) transform any operator from the original coordinate system $\{x,y,z\}$ into a new one $\{x',y',z'\}$:

$$\left.\begin{aligned} \hat{R}(\phi, \theta, \chi) &= \exp(-\mathrm{i}\phi\hat{I}_z)\exp(-\mathrm{i}\theta\hat{I}_y)\exp(-\mathrm{i}\chi\hat{I}_z) \\ \hat{R}^{-1}(\phi, \theta, \chi) &= \exp(\mathrm{i}\phi\hat{I}_z)\exp(\mathrm{i}\theta\hat{I}_y)\exp(\mathrm{i}\chi\hat{I}_z) \end{aligned}\right\} \tag{68}$$

The Euler angles $\{\phi,\theta,\chi\}$ define rotations about the z, then y, then z again axes of the original coordinate system, which rotations carry the original coordinate system to coincide with the new one. The $D_{q'q}^{(k)}(\phi, \theta, \chi)$ are called the *Wigner rotation matrix elements*. The definition of these coefficients is rather involved, and will not be given here. They are defined and tabulated in numerous texts, such as the excellent one by Zare.[10] Exponential operators like those in equation (68) as generators of rotations play a central role in the theoretical development of NMR. They, too, are discussed in great detail in Zare's text.

It was noted in Section 2.1 that operators do not necessarily commute. A special shorthand notation is commonly used for *commutators* of operators, defined as follows:

$$\hat{A}\hat{B} - \hat{B}\hat{A} \equiv [\hat{A}, \hat{B}] \tag{69}$$

Using this notation, an equivalent, though perhaps less intuitive, definition of irreducible spherical tensor operators is provided by the following commutation relations:

$$\left.\begin{aligned} [\hat{I}_\pm, \hat{T}_{q,j}^{(k)}] &= \{(k \mp q)(k \pm q + 1)\}^{1/2}\hat{T}_{q\pm1,j}^{(k)} \\ [\hat{I}_z, \hat{T}_{q,j}^{(k)}] &= q\hat{T}_{q,j}^{(k)} \end{aligned}\right\} \tag{70}$$

Note that one is free to choose either the positive or the negative square root in the coefficient in equation (70), and the result will still satisfy both commutation relations. Thus, we choose the one that satisfies equation (65). The following commutators are easily verified for spin-$\frac{1}{2}$ from equation (63):

$$[\hat{I}_z, \hat{I}_\pm] = \pm\hat{I}_\pm, \quad [\hat{I}_\pm, \hat{I}_\mp] = \pm 2\hat{I}_z \tag{71}$$

From equation (59), using equation (62), one can generate the following operators and verify that equation (71) holds for spin 1 also:

$$\left.\begin{aligned} \hat{I}_+ \to \sqrt{2}\begin{bmatrix} 0 & 1 & 0 \\ 0 & 0 & 1 \\ 0 & 0 & 0 \end{bmatrix}, \quad \hat{I}_- \to \sqrt{2}\begin{bmatrix} 0 & 0 & 0 \\ 1 & 0 & 0 \\ 0 & 1 & 0 \end{bmatrix} \\ \hat{I}_z \to \begin{bmatrix} 1 & 0 & 0 \\ 0 & 0 & 0 \\ 0 & 0 & -1 \end{bmatrix} \end{aligned}\right\} \tag{72}$$

It can be shown[6] that these commutation relations are true in general. These three matrices represent an irreducible spherical tensor operator of rank one just as was the case for spin-$\frac{1}{2}$ in equation (64), and the zeroth-order operator can be written as well. Note, however, that the required normalization factors are different:

$$\left.\begin{aligned} \hat{T}_0^{(0)} &= \frac{1}{\sqrt{3}}\hat{E} \to \frac{1}{\sqrt{3}}\begin{bmatrix} 1 & 0 & 0 \\ 0 & 1 & 0 \\ 0 & 0 & 1 \end{bmatrix} \\ \hat{T}_1^{(1)} &= -\tfrac{1}{2}\hat{I}_+ \to -\frac{1}{\sqrt{2}}\begin{bmatrix} 0 & 1 & 0 \\ 0 & 0 & 1 \\ 0 & 0 & 0 \end{bmatrix} \\ \hat{T}_{-1}^{(1)} &= \tfrac{1}{2}\hat{I}_- \to \frac{1}{\sqrt{2}}\begin{bmatrix} 0 & 0 & 0 \\ 1 & 0 & 0 \\ 0 & 1 & 0 \end{bmatrix} \\ \hat{T}_0^{(1)} &= \frac{1}{\sqrt{2}}\hat{I}_z \to \frac{1}{\sqrt{2}}\begin{bmatrix} 1 & 0 & 0 \\ 0 & 0 & 0 \\ 0 & 0 & -1 \end{bmatrix} \end{aligned}\right\} \tag{73}$$

It is easily verified that these operators are orthonormal and satisfy equation (70).

Using these four operators as a starting point, the problem of finding the other five basis operators for spin 1 can now be addressed. The required operators must be mutually orthogonal and orthogonal to the four already proposed. A logical extension of what has been done so far would be the five elements of an irreducible spherical tensor operator of rank two. For spin 1, the step-up operator can be applied twice to the eigenstate $|-1\rangle$ to produce first the $|0\rangle$ then the $|1\rangle$ eigenstate. The corresponding second-rank operator is $\hat{I}_+\hat{I}_+$. The representation of this operator can be obtained in several ways according to what we have learned so far. Perhaps the easiest way is to square the matrix given in equation (72) and normalize the result to give

$$\hat{T}_2^{(2)} = \tfrac{1}{2}\hat{I}_+\hat{I}_+ \to \begin{bmatrix} 0 & 0 & 1 \\ 0 & 0 & 0 \\ 0 & 0 & 0 \end{bmatrix} \tag{74}$$

which is easily shown to satisfy equation (70). Equation (70) can now be used to successively generate the other members of the set as follows:

$$[\hat{I}_-, \hat{T}_2^{(2)}] = \{(2 + 2)(2 - 2 + 1)\}^{1/2}\hat{T}_1^{(2)} = -2\hat{T}_1^{(2)} \tag{75}$$

The negative square root is chosen so as to satisfy equation (65). Hence, we have

$$\begin{aligned}\hat{T}_1^{(2)} &= -\tfrac{1}{2}[\hat{I}_-, \tfrac{1}{2}\hat{I}_+\hat{I}_+] = -\tfrac{1}{4}[\hat{I}_-, \hat{I}_+\hat{I}_+] \\ &= -\tfrac{1}{4}(\hat{I}_-\hat{I}_+\hat{I}_+ - \hat{I}_+\hat{I}_+\hat{I}_-)\end{aligned} \tag{76}$$

Then substituting from equation (71) yields

$$\begin{aligned}\hat{T}_1^{(2)} &= -\tfrac{1}{4}\{\hat{I}_-\hat{I}_+\hat{I}_+ - \hat{I}_+(2\hat{I}_z + \hat{I}_-\hat{I}_+)\} \\ &= -\tfrac{1}{4}\{(\hat{I}_-\hat{I}_+ - \hat{I}_+\hat{I}_-)\hat{I}_+ - 2\hat{I}_+\hat{I}_z\} \\ &= -\tfrac{1}{4}(-[\hat{I}_+, \hat{I}_-]\hat{I}_+ - 2\hat{I}_+\hat{I}_z)\end{aligned} \tag{77}$$

Using equation (71) again gives the desired operator, and substitution from equation (72), gives the representation:

$$\hat{T}_1^{(2)} = \tfrac{1}{2}(\hat{I}_z\hat{I}_+ + \hat{I}_+\hat{I}_z) \rightarrow \frac{1}{\sqrt{2}}\begin{bmatrix}0 & 1 & 0\\ 0 & 0 & -1\\ 0 & 0 & 0\end{bmatrix} \tag{78}$$

Applying the same procedure successively generates the other three operators. The $q = 0$ component is

$$\begin{aligned}\hat{T}_0^{(2)} &= -\sqrt{\tfrac{1}{6}}[\hat{I}_-, \hat{T}_1^{(2)}] \\ &= -\tfrac{1}{2}\sqrt{\tfrac{1}{6}}[\hat{I}_-, (\hat{I}_z\hat{I}_+ + \hat{I}_+\hat{I}_z)] \\ &= -\tfrac{1}{2}\sqrt{\tfrac{1}{6}}(\hat{I}_-\hat{I}_z\hat{I}_+ - \hat{I}_z\hat{I}_+\hat{I}_- + \hat{I}_-\hat{I}_+\hat{I}_z - \hat{I}_+\hat{I}_z\hat{I}_-) \\ &= -\tfrac{1}{2}\sqrt{\tfrac{1}{6}}\{(\hat{I}_- + \hat{I}_z\hat{I}_-)\hat{I}_+ - \hat{I}_z\hat{I}_+\hat{I}_- + \hat{I}_-\hat{I}_+\hat{I}_z \\ &\quad -\hat{I}_+(-\hat{I}_- + \hat{I}_-\hat{I}_z)\} \\ &= -\tfrac{1}{2}\sqrt{\tfrac{1}{6}}(\hat{I}_+\hat{I}_- + \hat{I}_-\hat{I}_+ + \hat{I}_z[\hat{I}_-, \hat{I}_+] + [\hat{I}_-, \hat{I}_+]\hat{I}_z) \\ &= \sqrt{\tfrac{1}{6}}\{2\hat{I}_z^2 - \tfrac{1}{2}(\hat{I}_+\hat{I}_- + \hat{I}_-\hat{I}_+)\} \rightarrow \frac{1}{\sqrt{6}}\begin{bmatrix}1 & 0 & 0\\ 0 & -2 & 0\\ 0 & 0 & 1\end{bmatrix}\end{aligned} \tag{79}$$

In this case, the negative phase is chosen arbitrarily, because equation (65) places no constraint on the phase of this operator. The $q = -1$ component is

$$\begin{aligned}\hat{T}_{-1}^{(2)} &= \sqrt{\tfrac{1}{6}}[\hat{I}_-, \hat{T}_0^{(2)}] \\ &= \tfrac{1}{6}[\hat{I}_-, \{2\hat{I}_z^2 - \tfrac{1}{2}(\hat{I}_+\hat{I}_- + \hat{I}_-\hat{I}_+)\}] \\ &= \tfrac{1}{6}(2\hat{I}_-\hat{I}_z^2 - 2\hat{I}_z^2\hat{I}_- + \tfrac{1}{2}\hat{I}_+\hat{I}_-\hat{I}_- - \tfrac{1}{2}\hat{I}_-\hat{I}_-\hat{I}_+) \\ &= \tfrac{1}{6}\{2(\hat{I}_- + \hat{I}_z\hat{I}_-)\hat{I}_z - 2\hat{I}_z(-\hat{I}_- + \hat{I}_-\hat{I}_z) \\ &\quad +\tfrac{1}{2}(2\hat{I}_z + \hat{I}_-\hat{I}_+)\hat{I}_- - \tfrac{1}{2}\hat{I}_-(-2\hat{I}_z + \hat{I}_+\hat{I}_-)\} \\ &= \tfrac{1}{2}(\hat{I}_z\hat{I}_- + \hat{I}_-\hat{I}_z) \rightarrow \frac{1}{\sqrt{2}}\begin{bmatrix}0 & 0 & 0\\ 1 & 0 & 0\\ 0 & -1 & 0\end{bmatrix}\end{aligned} \tag{80}$$

Here the positive phase has been chosen to satisfy equation (65). The $q = -2$ component is

$$\begin{aligned}\hat{T}_{-2}^{(2)} &= \tfrac{1}{2}[\hat{I}_-, \hat{T}_{-1}^{(2)}] \\ &= \tfrac{1}{4}[\hat{I}_-, (\hat{I}_z\hat{I}_- + \hat{I}_-\hat{I}_z)] \\ &= \tfrac{1}{4}(-\hat{I}_z\hat{I}_-\hat{I}_- + \hat{I}_-\hat{I}_-\hat{I}_z) \\ &= \tfrac{1}{4}\{-(-\hat{I}_- + \hat{I}_-\hat{I}_z)\hat{I}_- + \hat{I}_-(\hat{I}_- + \hat{I}_z\hat{I}_-)\} \\ &= \tfrac{1}{2}\hat{I}_-\hat{I}_- \rightarrow \begin{bmatrix}0 & 0 & 0\\ 0 & 0 & 0\\ 1 & 0 & 0\end{bmatrix}\end{aligned} \tag{81}$$

The positive phase has been chosen here, again arbitrarily. The same result could also be obtained by starting from $T_{-2}{}^{(2)}$ and stepping it up with I_+. These nine operators given by equations (73), (74), and (78)–(81) form a complete basis set for spin 1. Of course, higher spin bases can be constructed in the same way; spin I will require irreducible spherical tensors of rank $k = 0, 1, 2, \ldots, 2I$.

4 THE DENSITY OPERATOR

It is a familiar concept[7] that an experimental measurement will yield a value corresponding to the bracket of the state of the system under study with the operator corresponding to the observable:

$$\langle\hat{O}(t)\rangle = \langle\psi(t)|\hat{O}|\psi(t)\rangle \tag{82}$$

The notation on the left-hand side carries some connotation that the operator is time-dependent, which need not be the case; the time dependence in this case is carried entirely in the state. Some authors use the notation $\langle\hat{O}\rangle(t)$ or some other variant to avoid possible ambiguity. We shall retain the notation of equation (82), trusting the reader to realize the subtle difference implied. This leads to a discussion of Schrödinger versus Heisenberg versus interaction pictures of quantum mechanics, which will be addressed in Section 4.1. Of course, this result is independent of the 'picture' employed or the basis chosen. Inserting twice the sum on projection operators for some basis as in equation (19) and rearranging yields

$$\begin{aligned}\langle\hat{O}(t)\rangle &= \langle\psi(t)|\sum_{i=1}^{n}|i\rangle\langle i|\hat{O}\sum_{j=1}^{n}|\,j\rangle\langle\,j|\psi(t)\rangle \\ &= \sum_{i,j=1}^{n}\langle\psi(t)|i\rangle\langle i|\hat{O}|\,j\rangle\langle\,j|\psi(t)\rangle \\ &= \sum_{i,j=1}^{n}\langle\,j|\psi(t)\rangle\langle\psi(t)|i\rangle\langle i|\hat{O}|\,j\rangle\end{aligned} \tag{83}$$

As in equation (9), the quantity $|\psi(t)\rangle\langle\psi(t)|$ can be regarded as an operator, which is known as the density operator $\hat{\rho}(t)$:

$$\hat{\rho}(t) = |\psi(t)\rangle\langle\psi(t)| \tag{84}$$

Continuing from equation (83), we can write

$$\begin{aligned}\langle \hat{O}(t)\rangle &= \sum_{i,j=1}^{n} \langle\, j|\hat{\rho}(t)|i\rangle\langle i|\hat{O}|\, j\rangle \\ &= \sum_{j=1}^{n} \langle\, j|\hat{\rho}(t)\hat{O}|\, j\rangle \\ &= \mathrm{Tr}(\hat{\rho}(t)\hat{O}) \end{aligned} \tag{85}$$

This is an important relationship showing that the expected value of any operator can be computed by taking the trace of its product with the density operator. This form is completely equivalent to equation (82), and is the form commonly used for discussion of magnetic resonance phenomena. Just as the state $|\psi(t)\rangle$ contains all that can be known about the state of a system, so does the density operator.

According to equation (42), using an appropriate operator basis, we can write

$$\begin{aligned}\hat{\rho}(t) &= \sum_{i=1}^{n^2} \mathrm{Tr}\{\hat{\rho}(t)\hat{U}_i^{\dagger}\}\hat{U}_i \\ &= \sum_{i=1}^{n^2} \langle \hat{U}_i^{\dagger}(t)\rangle \hat{U}_i \end{aligned} \tag{86}$$

Thus, the expected values of all the basis operators provide the coefficients needed to represent the density operator in any basis, and these values provide a Liouville space representation of the density operator according to equation (43). Extensive use of this concept will be made later in developing the equations needed to explain spin relaxation.

The development so far has implied that the system of interest can be characterized by a state $|\psi(t)\rangle$. Liquid samples can never be so characterized, but can often be viewed as an ensemble of such isolated systems. Thus, it is desirable to take an ensemble average of equation (84). Since all the variation among the members of the ensemble resides in the operator $|\psi(t)\rangle\langle\psi(t)|$, the averaging process commutes with the sums over basis states, and we can write

$$\begin{aligned}\overline{\langle \hat{O}(t)\rangle} &= \sum_{i,j=1}^{n} \overline{\langle\, j|\psi(t)\rangle\langle\psi(t)|i\rangle}\langle i|\hat{O}|\, j\rangle \\ &= \sum_{i,j=1}^{n} \overline{\langle\, j|\hat{\rho}(t)|i\rangle}\langle i|\hat{O}|\, j\rangle \\ &= \sum_{j=1}^{n} \langle\, j|\bar{\hat{\rho}}(t)\hat{O}|\, j\rangle \\ &= \mathrm{Tr}\{\bar{\hat{\rho}}(t)\hat{O}\} \end{aligned} \tag{87}$$

Clearly, $\hat{\rho}(t)$ can be replaced by $\bar{\hat{\rho}}(t)$ in the above equations, leaving the form of the equations the same. In what follows, we shall not retain the overbar notation, but the density operator should be assumed to be averaged over an ensemble.

4.1 Time Evolution of the Density Operator

The time-dependent Schrödinger equation

$$\mathrm{i}\hbar\frac{\mathrm{d}}{\mathrm{d}t}|\psi(t)\rangle = \hat{\mathcal{H}}(t)|\psi(t)\rangle \tag{88}$$

can easily be converted to our density operator formalism. Beginning from equation (84) and using equation (88) and its complex conjugate obtained using equations (2) and (7), we can write

$$\begin{aligned}\frac{\mathrm{d}\hat{\rho}(t)}{\mathrm{d}t} &= \frac{\mathrm{d}}{\mathrm{d}t}\{|\psi(t)\rangle\langle\psi(t)|\} \\ &= \frac{\mathrm{d}}{\mathrm{d}t}\{|\psi(t)\rangle\}\langle\psi(t)| + |\psi(t)\rangle\frac{\mathrm{d}}{\mathrm{d}t}\{\langle\psi(t)|\} \\ &= -\frac{\mathrm{i}}{\hbar}\hat{\mathcal{H}}(t)|\psi(t)\rangle\langle\psi(t)| + \frac{\mathrm{i}}{\hbar}|\psi(t)\rangle\langle\psi(t)|\hat{\mathcal{H}}(t) \\ &= -\frac{\mathrm{i}}{\hbar}\{\hat{\mathcal{H}}(t)\hat{\rho}(t) - \hat{\rho}(t)\hat{\mathcal{H}}(t)\} \\ &= -\frac{\mathrm{i}}{\hbar}[\hat{\mathcal{H}}(t), \hat{\rho}(t)] \end{aligned} \tag{89}$$

Note that the Hamiltonian is Hermitian. The commutator of the Hamiltonian with the density operator determines the time development of the density operator. This relation is referred to as the *Liouville–von Neuman equation*, and will play a central role in what follows. Our goal, generally stated, will be to find solutions of this equation using a Hamiltonian corresponding to various experimental situations. The density operator at some particular time will generally be known—at least parametrically—and equation (89) must then be integrated to obtain the time development of the density operator.

The solution of this equation of motion is fairly simple if the Hamiltonian is not time-dependent. If we suppose that the density operator has the value $\hat{\rho}(0)$ at $t = 0$ then

$$\hat{\rho}(t) = \exp\left(-\frac{\mathrm{i}}{\hbar}\hat{\mathcal{H}}t\right)\hat{\rho}(0)\exp\left(\frac{\mathrm{i}}{\hbar}\hat{\mathcal{H}}t\right) \tag{90}$$

is a solution, as can be verified by differentiation:

$$\begin{aligned}\frac{\mathrm{d}\hat{\rho}(t)}{\mathrm{d}t} &= \left(-\frac{\mathrm{i}}{\hbar}\hat{\mathcal{H}}\right)\exp\left(-\frac{\mathrm{i}}{\hbar}\hat{\mathcal{H}}t\right)\hat{\rho}(0)\exp\left(\frac{\mathrm{i}}{\hbar}\hat{\mathcal{H}}t\right) \\ &\quad + \exp\left(-\frac{\mathrm{i}}{\hbar}\hat{\mathcal{H}}t\right)\hat{\rho}(0)\left(\frac{\mathrm{i}}{\hbar}\hat{\mathcal{H}}\right)\exp\left(\frac{\mathrm{i}}{\hbar}\hat{\mathcal{H}}t\right) \\ &= -\frac{\mathrm{i}}{\hbar}\left\{\hat{\mathcal{H}}\exp\left(-\frac{\mathrm{i}}{\hbar}\hat{\mathcal{H}}t\right)\hat{\rho}(0)\exp\left(\frac{\mathrm{i}}{\hbar}\hat{\mathcal{H}}t\right)\right. \\ &\quad \left. - \exp\left(-\frac{\mathrm{i}}{\hbar}\hat{\mathcal{H}}t\right)\hat{\rho}(0)\exp\left(\frac{\mathrm{i}}{\hbar}\hat{\mathcal{H}}t\right)\hat{\mathcal{H}}\right\} \\ &= -\frac{\mathrm{i}}{\hbar}\{\hat{\mathcal{H}}\hat{\rho}(t) - \hat{\rho}(t)\hat{\mathcal{H}}\} = -\frac{\mathrm{i}}{\hbar}[\hat{\mathcal{H}}, \hat{\rho}(t)] \end{aligned} \tag{91}$$

We have used the fact that an operator commutes with a function of itself.

Now let us examine the expected value of a generic operator with this solution. Substituting equation (90) into equation (87) yields

$$\begin{aligned}\langle \hat{O}(t)\rangle &= \mathrm{Tr}\{\hat{\rho}(t)\hat{O}\} = \mathrm{Tr}\left\{\exp\left(-\frac{\mathrm{i}}{\hbar}\hat{\mathcal{H}}t\right)\hat{\rho}(0)\exp\left(\frac{\mathrm{i}}{\hbar}\hat{\mathcal{H}}t\right)\hat{O}\right\} \\ &= \mathrm{Tr}\left\{\hat{\rho}(0)\exp\left(\frac{\mathrm{i}}{\hbar}\hat{\mathcal{H}}t\right)\hat{O}\exp\left(-\frac{\mathrm{i}}{\hbar}\hat{\mathcal{H}}t\right)\right\} \\ &= \mathrm{Tr}\{\hat{\rho}(0)\hat{O}(t)\} \end{aligned} \tag{92}$$

The fact that the trace operation is invariant under cyclic permutation of the factors has been used, and the time-dependent operator $\hat{O}(t)$ has been introduced according to

$$\hat{O}(t) = \exp\left(\frac{\mathrm{i}}{\hbar}\hat{\mathcal{H}}t\right)\hat{O}\exp\left(-\frac{\mathrm{i}}{\hbar}\hat{\mathcal{H}}t\right) \tag{93}$$

Equation (87) expresses the Schrödinger picture of quantum mechanics, whereas equation (92) transforms into the Heisenberg picture. Clearly, the two forms are equivalent.

Differentiating equation (93) yields the equation of motion for the time-dependent operators of the Heisenberg picture, corresponding to equation (89) for the Schrödinger picture:

$$\frac{\mathrm{d}\hat{O}(t)}{\mathrm{d}t} = \frac{\mathrm{i}}{\hbar}[\hat{\mathcal{H}}, \hat{O}(t)] \tag{94}$$

The derivation proceeds like that of equation (91). The equations for the Schrödinger and the Heisenberg pictures are similar in form, but the sign differences in the various terms should be noted.

When the Hamiltonian is time-dependent, the situation is considerably more complex, and no attempt will be made here to discuss this case in general terms. However, suppose the Hamiltonian can be separated into a term that is time-dependent and another that is not:

$$\hat{\mathcal{H}}(t) = \hat{\mathcal{H}}_0 + \hat{\mathcal{H}}_1(t) \tag{95}$$

Equation (89) may then be rewritten as

$$\begin{aligned}\frac{\mathrm{d}\hat{\rho}(t)}{\mathrm{d}t} &= -\frac{\mathrm{i}}{\hbar}[\hat{\mathcal{H}}_0 + \hat{\mathcal{H}}_1(t), \hat{\rho}(t)] \\ &= -\frac{\mathrm{i}}{\hbar}\{[\hat{\mathcal{H}}_0, \hat{\rho}(t)] + [\hat{\mathcal{H}}_1(t), \hat{\rho}(t)]\}\end{aligned} \tag{96}$$

If $\hat{\mathcal{H}}_1(t) = 0$ then the solution is as in equation (90). By analogy with equation (90), let us define the transformed operators

$$\hat{\rho}'(t) = \exp\left(\frac{\mathrm{i}}{\hbar}\hat{\mathcal{H}}_0 t\right)\hat{\rho}(t)\exp\left(-\frac{\mathrm{i}}{\hbar}\hat{\mathcal{H}}_0 t\right) \tag{97}$$

$$\hat{\mathcal{H}}_1'(t) = \exp\left(\frac{\mathrm{i}}{\hbar}\hat{\mathcal{H}}_0 t\right)\hat{\mathcal{H}}_1(t)\exp\left(-\frac{\mathrm{i}}{\hbar}\hat{\mathcal{H}}_0 t\right) \tag{98}$$

Differentiating equation (97) and substituting from equations (96) and (98) then gives

$$\begin{aligned}\frac{\mathrm{d}\hat{\rho}'(t)}{\mathrm{d}t} &= \frac{\mathrm{i}}{\hbar}\hat{\mathcal{H}}_0\exp\left(\frac{\mathrm{i}}{\hbar}\hat{\mathcal{H}}_0 t\right)\hat{\rho}(t)\exp\left(-\frac{\mathrm{i}}{\hbar}\hat{\mathcal{H}}_0 t\right) \\ &\quad + \exp\left(\frac{\mathrm{i}}{\hbar}\hat{\mathcal{H}}_0 t\right)\frac{\mathrm{d}\hat{\rho}(t)}{\mathrm{d}t}\exp\left(-\frac{\mathrm{i}}{\hbar}\hat{\mathcal{H}}_0 t\right) \\ &\quad + \exp\left(\frac{\mathrm{i}}{\hbar}\hat{\mathcal{H}}_0 t\right)\hat{\rho}(t)\exp\left(-\frac{\mathrm{i}}{\hbar}\hat{\mathcal{H}}_0 t\right)\left(-\frac{\mathrm{i}}{\hbar}\hat{\mathcal{H}}_0\right) \\ &= \frac{\mathrm{i}}{\hbar}[\hat{\mathcal{H}}_0, \hat{\rho}'(t)] + \exp\left(\frac{\mathrm{i}}{\hbar}\hat{\mathcal{H}}_0 t\right)\left(-\frac{\mathrm{i}}{\hbar}\{[\hat{\mathcal{H}}_0, \hat{\rho}(t)]\right. \\ &\quad \left. + [\hat{\mathcal{H}}_1(t), \hat{\rho}(t)]\}\right)\exp\left(-\frac{\mathrm{i}}{\hbar}\hat{\mathcal{H}}_0 t\right) \\ &= -\frac{\mathrm{i}}{\hbar}[\hat{\mathcal{H}}_1'(t), \hat{\rho}'(t)]\end{aligned} \tag{99}$$

Thus, in this 'interaction picture', part of the time dependence is placed in the operators and part remains in the density operator. The effect of $\hat{\mathcal{H}}_0$ appears only implicitly in the exponential transformation operator. Of course, this is not a solution of the equation of motion, but it will prove to be a useful technique to be applied later on.

4.2 The Reduced Density Operator

In NMR experiments, it is usually the case that the nuclear spins interact weakly with the other degrees of freedom of the sample of interest. For the moment, let us assume that they do not interact at all. The state of the system can be written as a direct product, as in equation (48a), of a ket corresponding to the spin degrees of freedom with one corresponding to the rest of the system, the lattice:

$$|S\rangle|L\rangle = |SL\rangle \tag{100}$$

The number of degrees of freedom, i.e., the number of basis states, necessary to span the spins is modest, while that necessary to span the lattice is very large—effectively infinite.

Consider the expected value of an operator that acts only on the spin degrees of freedom. If $\{|sl\rangle\}$ is a basis set spanning both the spins and the lattice, we can write

$$\begin{aligned}\langle\hat{O}\rangle &= \mathrm{Tr}(\hat{\rho}\hat{O}) = \mathrm{Tr}(|SL\rangle\langle SL|\hat{O}) \\ &= \sum_{sl}\langle sl|SL\rangle\langle SL|\hat{O}|sl\rangle\end{aligned} \tag{101}$$

Since $\hat{O}$ commutes with the lattice operators, this can be rearranged to yield

$$\begin{aligned}\langle\hat{O}\rangle &= \sum_s\langle s|S\rangle\langle S|\hat{O}|s\rangle\sum_l\langle l|L\rangle\langle L|l\rangle \\ &= \sum_s\langle s|S\rangle\left(\sum_l\langle l|L\rangle\langle L|l\rangle\right)\langle S|\hat{O}|s\rangle\end{aligned} \tag{102}$$

We can now define the reduced density operator by

$$\hat{\sigma} = |S\rangle\left(\sum_l\langle l|L\rangle\langle L|l\rangle\right)\langle S| = \mathrm{Tr}_l(\hat{\rho}) \tag{103}$$

The expected value of $\hat{O}$ can then be written as

$$\langle\hat{O}\rangle = \mathrm{Tr}_s(\hat{\sigma}\hat{O}) \tag{104}$$

Thus, observing experimental quantities corresponding to spin operators requires only a knowledge of this reduced density operator, and the problem has, at least in principle, only the small dimensionality of the spin degrees of freedom and not the very large dimensionality of the spins and the lattice. In particular, the Liouville equation, equation (99), can be cast in this form. However, if there were, indeed, no interaction of the spins with the lattice, as was assumed above, there would be no relaxation. Of course, this is observed not to be the case, but the interaction is sufficiently weak that it can be treated by perturbation methods, and the very large number of

degrees of freedom in the lattice permits treating the lattice classically to achieve excellent correspondence of theory to experiment. In what follows, then, solutions will be sought of the Liouville–von Neuman equation for the reduced density operator:

$$\frac{\mathrm{d}\hat{\sigma}(t)}{\mathrm{d}t} = -\frac{\mathrm{i}}{\hbar}[\hat{\mathcal{H}}(t), \hat{\sigma}(t)] \tag{105}$$

5 SUPEROPERATORS

The representation of operators in Liouville space has been discussed in Section 2.2. In this section, we shall introduce superoperators that act on operators in Liouville space in much the same way as operators act on states in Hilbert space, i.e., superoperators transform one operator into another.

Consider the operator product

$$\hat{C} = \hat{B}_1 \hat{A} \hat{B}_2 \tag{106}$$

Let us attempt to cast $\hat{A}$ in a Liouville space representation and then find a superoperator $\hat{\hat{B}}$ such that $|\hat{C}\rangle = \hat{\hat{B}}|\hat{A}\rangle$. The operator product can be written as follows and rearranged as shown by applying equations (7) and (15):

$$\begin{aligned}\langle i|\hat{C}|\ j\rangle &= \sum_{k,l=1}^{n} \langle i|\hat{B}_1|k\rangle\langle k|\hat{A}|l\rangle\langle l|\hat{B}_2|\ j\rangle \\ &= \sum_{k,l=1}^{n} \langle i|\hat{B}_1|k\rangle\langle\ j|\hat{B}_2^{\dagger}|l\rangle\langle k|\hat{A}|l\rangle \end{aligned} \tag{107}$$

The superoperator matrix elements can now be defined by

$$\langle ij|\hat{\hat{B}}|kl\rangle = \langle i|\hat{B}_1|k\rangle\langle\ j|\hat{B}_2^{\dagger}|l\rangle \tag{108}$$

This expression can be viewed as the matrix elements of a direct product in a space with basis $|i\rangle|j\rangle = |ij\rangle$, the direct product of two identical Hilbert space bases as in equation (50):

$$\hat{\hat{B}} = \hat{B}_1 \otimes \hat{B}_2^{\dagger} \tag{109}$$

The matrix elements of $\hat{A}$ may be mapped into a vector in this same space just as in equation (43). In fact, the operator basis $\{\hat{U}_i\}$ introduced in equation (43) is equivalent to the basis $\{|ij\rangle\}$. The matrix elements of $\hat{A}$ may be written as

$$\langle ij|\hat{A}\rangle = \langle i|\hat{A}|\ j\rangle \tag{110}$$

Then equation (107) can be written as

$$|\hat{C}\rangle = \hat{\hat{B}}|\hat{A}\rangle \tag{111}$$

The utility of this formalism is evident from several examples.

5.1 Unitary Transformations

Unitary transformations like $\hat{U}\hat{A}\hat{U}^{\dagger}$ in Hilbert space can easily be translated to Liouville space using equation (109) to define the relevant superoperator

$$\hat{\hat{U}} = \hat{U} \otimes \hat{U} \tag{112}$$

Note that $(\hat{U}^{\dagger})^{\dagger} = \hat{U}$. Then the unitary transformation becomes

$$\hat{\hat{U}}|\hat{A}\rangle \tag{113}$$

The superoperator $\hat{\hat{U}}$ is unitary. To show this, we can write

$$\hat{A} = \hat{U}^{\dagger}\hat{U}\hat{A}\hat{U}^{\dagger}\hat{U} \tag{114}$$

But this implies

$$|\hat{A}\rangle = (\hat{U}^{\dagger} \otimes \hat{U}^{\dagger})(\hat{U} \otimes \hat{U})|\hat{A}\rangle = \hat{\hat{U}}^{\dagger}\hat{\hat{U}}|\hat{A}\rangle \tag{115}$$

where the second equality in equation (115) follows immediately by considering the adjoint of equation (108). Thus, it must be that

$$\hat{\hat{U}}^{\dagger}\hat{\hat{U}} = \hat{\hat{E}} \tag{116}$$

5.2 Commutators

Consider the commutator $[\hat{A}, \hat{B}]$ as the action of something denoted by $[\hat{A}, \ ]$ on the operator $\hat{B}$ to produce a new operator $\hat{C}$. This relationship can be written as

$$[\hat{A}, \hat{B}] = \hat{A}\hat{B} - \hat{B}\hat{A} = \hat{A}\hat{B}\hat{E} - \hat{E}\hat{B}\hat{A} \tag{117}$$

Applying equation (109) then yields

$$\hat{\hat{A}} = \hat{A} \otimes \hat{E} - \hat{E} \otimes \hat{A}^{\dagger} \tag{118}$$

5.3 The Liouvillian

Using equation (118), the equation of motion for the density operator equation (89) can be re-written as

$$\frac{\mathrm{d}|\hat{\rho}(t)\rangle}{\mathrm{d}t} = -\frac{\mathrm{i}}{\hbar}\hat{\hat{\mathcal{L}}}(t)|\hat{\rho}(t)\rangle \tag{119}$$

The Liouvillian superoperator corresponding to the commutator with the Hamiltonian is defined as

$$\hat{\hat{\mathcal{L}}}(t) = \hat{\mathcal{H}}(t) \otimes \hat{E} - \hat{E} \otimes \hat{\mathcal{H}}(t) \tag{120}$$

Note that the Hamiltonian is Hermitian, so that $\hat{\mathcal{H}}(t) = \hat{\mathcal{H}}(t)^{\dagger}$.

6 RELATED ARTICLES

Rudimentary NMR: The Classical Picture.

7 REFERENCES

1. T. C. Farrar, and E. D. Becker, *Pulse and Fourier Transform NMR: Introduction to Theory and Methods*, Academic Press, New York, 1971.
2. H. Friebolin, *Basic One- and Two-Dimensional NMR Spectroscopy*, VCH, New York, 1991.
3. A. E. Derome, *Modern NMR Techniques for Chemistry Research*, Pergamon Press, Oxford, 1987.
4. P. A. M. Dirac, *The Principles of Quantum Mechanics*, 4th edn., Oxford University Press, Oxford, 1958.
5. T. C. Farrar and J. E. Harriman, *Density Matrix Theory and its Applications in NMR Spectroscopy*, 2nd edn., The Farragut Press, Madison, WI, 1992.
6. M. Goldman, *Quantum Description of High-Resolution NMR in Liquids*, Oxford University Press, Oxford, 1988.
7. C. P. Slichter, *Principles of Magnetic Resonance*, 3rd edn., Springer-Verlag, Berlin, 1990.
8. R. R. Ernst, G. Bodenhausen, and A. Wokaum, *Principles of Nuclear Magnetic Resonance in One and Two Dimensions*, Oxford University Press, Oxford, 1987.
9. A. Abragam, *The Principles of Nuclear Magnetism*, Oxford University Press, Oxford, 1961.
10. R. N. Zare, *Angular Momentum*, Wiley, New York, 1988.

Biographical Sketch

Charles L. Mayne. *b* 1942. B.S., 1970, New Mexico State University, U.S.A., Ph.D., 1976, University of Utah. Introduced to NMR by George A. Gray and subsequently tutored by David M. Grant. Manager of NMR Laboratories, University of Utah, Department of Chemistry, 1973–present. Academic appointment as Adjunct Associate Professor of Chemistry, University of Utah. Approx. 40 publications in NMR. Research interests include nuclear-spin relaxation, NMR at high pressure, structure elucidation of natural products, various aspects of multidimensional NMR, and computerized analysis of NMR data.

Low Spin Temperature NMR

Maurice Goldman
Service de Physique de l'Etat Condensé, CEA Saclay, Gif-sur-Yvette, France

1	Introduction	1
2	Methods of Production of Low Nuclear Temperatures	1
3	The Resonance Signal	2
4	Rigorous NMR Results	5
5	Nonlinear Effects in Spin Temperature	8
6	Related Articles	10
7	References	10

1 INTRODUCTION

The manipulation of nuclear spin systems by rf fields and/or the observation of the signal they induce in a pick-up coil nearly always starts from an initial state characterized by one or several temperatures for the nuclear spins. The simplest example, that of a spin system of Hamiltonian $\mathcal{H}$ and single spin temperature T, corresponds to a density matrix for the spins of the form

$$\sigma = \exp(-\mathcal{H}/kT)/\mathrm{Tr}[\exp(-\mathcal{H}/kT)] \tag{1}$$

The description of more complex cases can be found in textbooks.[1–3]

In the vast majority of the uses of NMR, the characteristic frequencies ω associated with the Hamiltonian (for instance, in the Zeeman case, the Larmor frequency) are such that we have

$$\hbar\omega \ll kT \tag{2}$$

In such a case it is permissible, for most practical purposes, to replace the exact density matrix [equation (1)] by the expansion

$$\sigma \simeq (1 - \beta\mathcal{H})/\mathrm{Tr}(1) \tag{3}$$

where $\beta = 1/kT$ is called the 'inverse temperature'. This is known as the 'high-temperature approximation', and it brings about an enormous simplification in the theoretical handling of NMR—most quantities of interest are linear in the inverse temperature β (with the exception of entropy, which is quadratic in β), so that their relative values are independent of spin temperature.

Low spin temperature NMR deals with the case when equation (2) is not valid and one has to use the full expression [equation (1)] for the density matrix. This leads to so-called 'nonlinear effects' in spin temperature, and eventually to nuclear magnetic ordering. There is an exception to the above statement; this is the case when equation (2) is valid as regards the nuclear frequencies, but when the nuclear spins are used to probe the properties of systems at low temperature, which depend strongly on temperature. Examples are electronic ferro-, antiferro-, or ferri-magnets, or superfluid helium-3. These cases are explicitly omitted from the present article.

Low nuclear spin temperatures do not occur spontaneously in nature. Indeed, their production turns out to be extremely laborious, and it can only be justified by the pursuit of a valuable end. This means that, by contrast with the quasigeneral usage in the high-temperature domain, in low spin temperature NMR the nuclear spins are not used as probes of other systems [e.g. proteins or high T_c superconductors (see ***High Temperature Superconductors***)], but they are the system whose properties are studied for their own sake: actors rather than spectators. The 'valuable' aim is essentially nuclear magnetic ordering.

After a brief description of the methods of production of low nuclear spin temperatures, we analyze some of the properties of such systems. In general, the discussion is limited to the domain of paramagnetism. Nuclear ordering, which is described elsewhere in this Encyclopedia (see ***Nuclear Ferromagnetism and Antiferromagnetism*** and ***Thermodynamics of Nuclear Magnetic Ordering***), will only occasionally be touched upon.

This article is to a large extent inspired by Chapter 5 in the book by Abragam and Goldman,[4] although here greater emphasis is put on the ideas behind and the principles of the formal calculations rather than on their detailed description.

2 METHODS OF PRODUCTION OF LOW NUCLEAR TEMPERATURES

The most obvious method is known under the delicate name of the 'brute force' method. It consists of waiting for thermal equilibrium with the lattice at a very low temperature of nuclear spins in a very high magnetic field. Let us give figures. Since both $\hbar\omega = h\nu$ and kT are energies, it is possible to express temperature in terms of frequency, and vice versa. It is useful to remember that $1\,\mathrm{K} \simeq 20.8$ GHz, or

$$1\ \mathrm{mK} \simeq 20.8\ \mathrm{MHz} \tag{4}$$

so that a 'low' Zeeman temperature would correspond to several millikelvin in a field of several tesla. The only problem involves the time required for the nuclear Zeeman interaction to reach equilibrium with the lattice, i.e. the length of the longitudinal relaxation time T_1. In insulators, where nuclear relaxation is due to paramagnetic centers, T_1 becomes extremely long at low lattice temperature and in high field may reach a few hundred hours. Even though much shorter than predicted theoretically, for reasons not yet understood, such values of T_1 deprive the 'brute force' method of its attraction. The situation is different with metals, because their relaxation by the Korringa mechanism is much faster, and the 'brute force' method has been used with success for various metals. It should be noted that at high field, when the Zeeman interaction dominates all other interactions, a low spin temperature corresponds to a high nuclear polarization, through the relationship

$$P = B_I(\hbar\omega/kT) \tag{5}$$

where B_I is the Brillouin function for a nucleus of spin I. For the simplest case, i.e spin $\frac{1}{2}$, this function is

$$B_I(x) = \tanh(x/2) \tag{6}$$

It is apparent from equation (5) that the polarization depends only on the ratio ω/T, i.e. the same physical state would be obtained with a different temperature, by varying the Larmor frequency in proportion. Therefore, the concept of temperature itself is of limited interest and for NMR in high field, 'high-polarization NMR' would be a more appropriate description than 'low spin temperature NMR'. The necessity for a low lattice temperature is a mere consequence of the practical limitations on the value of the external field.

For insulators, a successful alternative to the inefficient 'brute force' method is dynamic nuclear polarization (DNP) which results from the EPR off-resonance irradiation of paramagnetic centers introduced purposely at low concentration in the solid. The basic phenomenon is the following: if electronic spins of Larmor frequency ω_e are irradiated at a frequency $\omega \neq \omega_e$, each time a photon is absorbed the energy of the system increases by $\hbar\omega$, and an upwards electronic spin-flip is produced, resulting in an increase in the electronic Zeeman energy of $\hbar\omega_e$. The energy imbalance $\hbar(\omega_e - \omega)$ serves eventually to modify the Zeeman energy of the nuclear spins.

In its first version, corresponding to the so-called 'solid effect',[5] the irradiation frequency is the difference between or the sum of the electronic and nuclear Larmor frequencies $\omega_e \pm \omega_n$. The transitions are 'forbidden' flip-flop transitions or flip-flip transitions of an electron and a nuclear spin, which can only take place due to the dipolar interaction between these spins. Flip-flop transitions at $\omega_e - \omega_n$ yield a nuclear polarization parallel to the equilibrium value, and flip-flip transitions at $\omega_e + \omega_n$ yield a nuclear polarization of opposite sign. Under strong irradiation and in the absence of parasitic nuclear relaxation, the nuclear polarization modulus eventually becomes equal to that of the thermal equilibrium electronic polarization.

In many cases, when the EPR linewidth exceeds the nuclear Larmor frequency ω_n, the mechanism of DNP is different: off-resonance microwave irradiation produces allowed electronic transitions which lead to a cooling of the electron spin–spin reservoir. As this reservoir is in thermal contact with the nuclear Zeeman reservoir, the latter also becomes cooled, resulting in an increase in its polarization modulus. The sign is the same as for the solid effect: for $\omega < \omega_e$ it corresponds to a positive spin temperature and for $\omega > \omega_e$ to a negative spin temperature. Detailed descriptions of DNP are given by Abragam and Goldman.[4,6]

Physicists are interested not only in nuclear spins with low Zeeman temperatures, but also in spins whose low temperature affects their spin–spin interactions: dipolar, indirect (in heavy nuclei), or RKKY[1,3] (in metals). One can start from nuclei with large polarizations (low Zeeman temperatures) and perform an adiabatic demagnetization. This has been done for 'brute force' polarized nuclei[7,8] and DNP-polarized nuclei in insulators (see e.g. Abragam and Goldman,[4] Chapters 5 and 8). The adiabatic demagnetization can be done by actually reducing the field to zero, in which case the final interactions are the full spin–spin interactions. It can also be done at high field, by slowly sweeping an rf field from a frequency far off-resonance down to on-resonance. As a result of this adiabatic demagnetization in the rotating frame (ADRF),[9] it is the effective field in the rotating frame that is reduced to zero, and the remaining interactions are the so-called 'secular spin–spin interactions', consisting of that part of the spin–spin interactions which commutes with the Zeeman coupling.[1,2]

In zero field, either actual or effective, the nuclear polarization vanishes, and 'high-polarization NMR' is no longer an adequate description. One quantity that is conserved in adiabatic demagnetization is the entropy of the system. The large initial nuclear polarization corresponds to a low entropy, and the only adequate title for this article should therefore be 'low-entropy NMR'.

3 THE RESONANCE SIGNAL

It is well known from general principles (i.e. linear response theory[10]) that the CW nuclear absorption signal is the Fourier transform of the FID signal observed after an infinitely small pulse θ (see e.g. Goldman,[11] Chapter 1). It is then sufficient to analyze the signal observed after such a pulse.

We consider, for simplicity, a system with Zeeman and dipolar interactions having a density matrix of the form

$$\sigma_0 = \exp\left(-\sum_\mu \beta_\mu Z_\mu - \beta_D \mathcal{H}'_D\right) \Big/ \mathrm{Tr}\{\exp(\ldots)\} \tag{7}$$

where Z_μ is the Zeeman interaction $\omega_\mu I_z^\mu$ of the nuclear species μ, β_μ is the corresponding inverse spin temperature, $\mathcal{H}'_D$ is the secular dipolar interaction, and β_D its inverse temperature. This is transformed by a pulse θ at the Larmor frequency of species 0 into

$$\sigma(0) = \exp(-i\theta I_x^0)\,\sigma_0 \exp(i\theta I_x^0) \tag{8}$$

Its subsequent evolution is

$$\sigma(t) = \exp(-i\mathcal{H}t)\,\sigma(0)\exp(i\mathcal{H}t) \tag{9}$$

where $\mathcal{H}$ is the (supposedly static) Hamiltonian. In an appropriate rotating frame, $\mathcal{H}$ reduces to $\mathcal{H}'_D$. The expectation value of a quantity Q is

$$\langle Q\rangle(t) = \mathrm{Tr}\{Q\sigma(t)\} \tag{10}$$

When the angle θ is infinitely small, equation (8) yields, to first order (linear response)

$$\sigma(0) \simeq \sigma_0 - i\theta[I_x, \sigma_0] \tag{11}$$

and the FID signal $\langle I_+\rangle(t)$ (a transverse vector expressed in the form of a complex number) becomes

$$\langle I_+\rangle(t) = -i\theta\ \mathrm{Tr}\{I_+ \exp(-i\mathcal{H}'_D t)[I_x, \sigma_0]\exp(i\mathcal{H}'_D t)\} \tag{12}$$

or, after a few manipulations,

$$\langle I_+\rangle(t) = -i\theta\langle[I_+(t), I_x]\rangle_0 \tag{13}$$

with the notation

$$Q(t) = \exp(+i\mathcal{H}'_D t)\,Q\exp(-i\mathcal{H}'_D t) \tag{14}$$

$$\langle Q\rangle_0 = \mathrm{Tr}\{Q\sigma_0\} \tag{15}$$

3.1 Difference of the High-Temperature Case

We consider, for simplicity, a density matrix corresponding to pure Zeeman order for a system of identical spins $\frac{1}{2}$, I_i:

$$\sigma_0 = \exp\left(-\beta \sum I_z^i\right) \Big/ \mathrm{Tr}\left\{\exp\left(-\beta \sum I_z^i\right)\right\} = \prod_i (1 - t_\beta I_z^i) \tag{16}$$

where

$$t_\beta = \tanh(\tfrac{1}{2}\beta\omega_0) \tag{17}$$

This is transformed by the θ pulse [equation (8)] into

$$\sigma(0) = \prod_i [1 - t_\beta(\cos\theta\, I_z^i + \sin\theta\, I_y^i)] \tag{18}$$

The FID of spin I_i, which is representative of the total FID, is then

$$\langle I_+^i \rangle = -t_\beta \sin\theta\ \mathrm{Tr}\left\{ I_+^i(t) I_y^i \prod_{j\neq i} [1 - t_\beta(\cos\theta\, I_z^j + \sin\theta\, I_y^j)] \right\} \tag{19}$$

In the low θ limit, pertaining to the analysis of the absorption signal, this yields

$$\langle I_+^i \rangle = -t_\beta\theta\ \mathrm{Tr}\left\{ I_+^i(t) I_y^i \prod_{j\neq i} (1 - t_\beta I_z^j) \right\} \tag{20}$$

It is easily shown that this is identical to equation (13). At high temperature, $t_\beta \simeq \frac{1}{2}\beta\omega_0 \ll 1$, so that $\Pi_j(\ \ldots\ ) \simeq 1$, and one obtains

$$\langle I_+^i \rangle = -\tfrac{1}{2}\beta\omega_0\theta\ \mathrm{Tr}\{I_+^i(t) I_y^i\} \tag{21}$$

It is the fact that t is no longer negligible at low temperature which distinguishes the low-temperature case from the high-temperature one. We end this subsection by emphasizing two of the conspicuous consequences of this difference:

1. It is apparent from equation (19) that, even with one nuclear species and purely Zeeman initial order, the FID shape does depend on the pulse angle θ. This observation has had two main consequences.
   (i) A great surprise, after its experimental discovery, for a Ph.D. student of J. S. Waugh (private communication).
   (ii) A disproval, or rather a correction, of the so-called 'Lowe–Norberg theorem'[12] that the CW signal is the Fourier transform of the FID signal. This theorem stems from the fact that under the two conditions of high temperature and purely Zeeman order the FID signal following a rf pulse is proportional to sin θ, but its shape is independent of θ, as can be seen from equation (21). This fact, which was known earlier [E. M. Purcell, NMR Lectures Notes, Harvard (1953); A. Abragam, NMR Lectures Notes, Saclay (1955)], is really an extension of the validity of a general theorem that the CW signal is the Fourier transform of the FID signal following a pulse of infinitely small angle θ, a consequence of linear response theory[10] (see also Abragam and Goldman,[6] Chapter 1, and Goldman,[11] Chapter 1).
2. In the case when there are several different polarized nuclear species, and/or secular dipolar order (nonnegligible β_D) in addition to Zeeman order, the FID signal shape of *one* nuclear species depends on *all* spin temperatures. It should be noted that, in the case of Zeeman plus dipolar order, the FID signal of spins I_μ depends on both β_μ and β_D, and on the angle θ, even at high temperature.[2]

3.2 Qualitative Features of the Zeeman Signal

We refer again to the FID signal following a pulse of infinitely small angle θ, but starting from a state of pure Zeeman order [β_D = 0 in equation (7)]. By contrast with the high-temperature case, the absorption signal shape is, in general, not symmetrical, and not centered on the Larmor frequency. This manifests itself by the fact that this CW signal has no vanishing odd moments. This can be shown by simple qualitative arguments that are not be given here. Furthermore, all moments, whether odd or even, depend on the polarization, i.e. the shapes of the FID signal or absorption signal depend on the polarization. There is, however, a property of the high-temperature case that remains true for low temperature: the area of the absorption signal of a given nuclear species is proportional to its polarization. (This is also the initial FID signal following a small θ pulse). This property, which is associated with the polarization dependence of the first few moments of the absorption signal (i.e. the first few derivatives of the FID at t = 0), makes it possible to perform an absolute calibration of the nuclear polarizations. This has still another advantage, resulting from the following properties:

1. By manipulation of equation (13) one can derive a simple relationship between the integral of the absorption signal $-\int_{-\infty}^{+\infty} \langle I_y \rangle(\omega - \omega_0) d\omega$ and the nuclear polarization. The absorption signal thus defined corresponds to a nonsaturating rf field ω_1/γ along Ox in the rotating frame.
2. The 'absorption' voltage detected is

$$V(\omega) = \xi\omega_1 \langle I_y \rangle(\omega) \tag{22}$$

where ξ is a factor depending on the coil and on the receiver amplification.

Once one has a calibration of the nuclear polarization, the experimental integral

$$\int V(\omega)\, \mathrm{d}\omega \tag{23}$$

yields a calibration of the product $\xi\omega_1$. Since, as will be seen later, ω_1 can be independently calibrated, we obtain the value of the so-called spectrometer 'gain factor' ξ, which can be used to calibrate other physical quantities of interest. This is essential in a domain where everything is highly nonlinear.

Of course, it is equivalent to use the formal expression of the initial FID $\langle I_y \rangle$ following a small-angle pulse and the initial experimentally detected voltage.

3.3 The Moments of the Zeeman Absorption Signal

This section deals only with results, and qualitative comments are made. Detailed calculations can be found in, for example, Abragam et al.[13] and Roinel and Bouffard.[14]

3.3.1 The First Moment

The first moment of the absorption signal (with respect to the Larmor frequency) characterizes the overall shift in the resonance frequency, irrespective of any change in signal shape. The Larmor frequency is determined as the low-polarization limit of the frequency with respect to which the first moment vanishes. One must distinguish between cases when there are one or several spin species.

3.3.1.1 One spin species: the $\frac{3}{2}$ effect. By this we mean nuclear spins with the same chemical shift and the same nuclear environment, e.g. ^{19}F in CaF_2. Conversely, $KMgF_3$ contains three imbricated simple cubic arrays of ^{19}F nuclei which, for a given field orientation, differ both in their secular dipolar couplings and in their chemical shifts.[15]

For a simple spin species, the first moment is not equal to the average (Weiss) field experienced by the spins of other nuclei, rather it is $\frac{3}{2}$ times larger. This can be illustrated as follows. The secular dipolar interaction experienced by a spin I_i is

$$\mathcal{H}'^{(i)}_{\mathrm{D}} = \frac{\gamma^2\hbar}{2}\sum_j \frac{1-3\cos^2\theta_{ij}}{r_{ij}^3}\{2I_z^iI_z^j - I_x^iI_x^j - I_y^iI_y^j\} \quad (24)$$

The term inside the braces can be written

$$\{\ldots\} = \{2I_z^i\langle I_z^j\rangle + 2I_z^i(I_z^j - \langle I_z^j\rangle) - I_x^iI_x^j - I_y^iI_y^j\} \quad (25)$$

It might seem that the first term on the right-hand side will contribute to the shift of the signal, whereas the remaining terms, corresponding to short-range correlations, affect only the lineshape. This argument is wrong. Indeed, we may write the term in braces in equation (24) in the form

$$\{\ldots\} = \{3I_z^iI_z^j - \boldsymbol{I}^i\cdot\boldsymbol{I}^j\} \quad (26)$$

The scalar product commutes with

$$I_+ = I_+^i + I_+^j + \sum_{k\neq i,j} I_+^k \quad (27)$$

and it does not contribute to the FID derivative at $t = 0$ (proportional to $\langle[I_+, \mathcal{H}_{\mathrm{D}}]\rangle$). The remaining term is

$$3I_z^iI_z^j = 3I_z^i\langle I_z^j\rangle + 3I_z^i(I_z^j - \langle I_z^i\rangle) \quad (28)$$

The first term on the right-hand side contributes to the first moment, and the second one to the lineshape; thus the '$\frac{3}{2}$ effect' is recovered. What was wrong with the first reasoning? This was pinpointed by Kittel.[16] We have tacitly assumed in equation (25) that only the longitudinal spin components have nonvanishing average values. In the presence of rf irradiation, the transverse components no longer vanish, and one should use

$$I_x^iI_x^j = I_x^i\langle I_x^j\rangle + I_x^i(I_x^j - \langle I_x^j\rangle) \quad (29)$$

and similarly for the I_y terms. The Weiss fields originating from these transverse components, however small, are sufficient to account for the $\frac{3}{2}$ effect.

Owing to the long range of the dipolar couplings [equation (24)], the NMR first moment depends on the sample shape. The only case for which the Weiss field is the same for all spins is when the sample is ellipsoid in shape. Otherwise, there is a distribution of Weiss fields, and hence an extra broadening of the line. The case when the first moment vanishes is that of a spherical sample of nuclear spins in cubic symmetry, such as ^{19}F in CaF_2. It is only when the first moment does not vanish that it can be used for polarization calibration.

3.3.1.2 Several spin species. We consider the case where there are only two species from different nuclear elements, e.g. LiF or LiH. We call the spins I and S. There is no '$\frac{3}{2}$ effect' between unlike spins, because they precess at different frequencies. The first moments of the two NMR signals are of the form

$$m_{1I} = \tfrac{3}{2}B_{I\to I}Ip_I + B_{S\to I}Sp_S \quad (30a)$$

$$m_{1S} = B_{I\to S}Ip_I + \tfrac{3}{2}B_{S\to S}Sp_S \quad (30b)$$

where p_I and p_S are the polarizations.

The various Weiss fields (or their average values in nonellipsoidal samples) can be calculated theoretically. The variation in the moments with the absorption signal areas then yields an absolute calibration of the polarizations. Figure 1 illustrates the use of this method for LiF. The method is easily extended to more than two species.

3.3.2 The Second Moment

Consider the case when the first moment vanishes, for instance that of ^{19}F in a sphere of CaF_2. The theoretical expression of the second moment is[13]

$$M_2 = \langle[\mathcal{H}'_{\mathrm{D}}, I_+][I_-, \mathcal{H}'_{\mathrm{D}}]\rangle_0/\langle I_+I_-\rangle_0 \quad (31)$$

For spins $\frac{1}{2}$, equation (31) yields the following dependence on the nuclear polarization p:

$$M_2(p) = M_2(0)(1-p^2) \quad (32)$$

One should then observe a linear variation of the experimental M_2 as a function of the square of the signal area.

Figure 2 shows that this is actually the case, for two spherical samples of CaF_2. The only problem is that the value of M_2 extrapolated to zero polarization is larger than its theoretical value, and different in the two samples. The origin is in the presence of paramagnetic centers at low concentration (Tm^{2+} in the present case), which produce a Lorentzian distribution of fields at the ^{19}F sites.[13] The two samples have different Tm^{2+} concentrations, and thus different

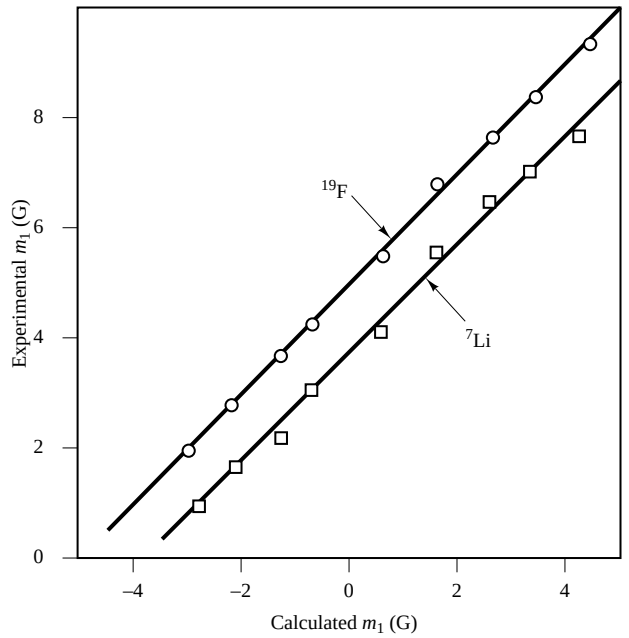

Figure 1 Experimental first moments (to within an arbitrary constant) of ^{7}Li and ^{19}F against their best-fit value in a parallelepiped of LiF. (Reproduced by permission of Oxford University Press from Abragam and Goldman[4])

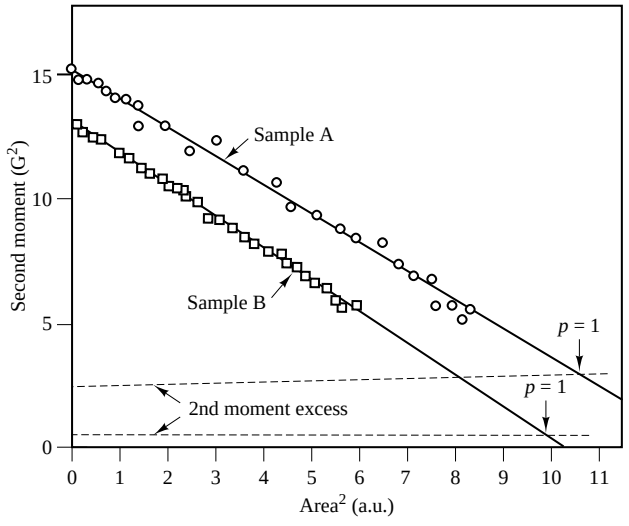

Figure 2 Second moment of the ^{19}F absorption signal against its area squared (in arbitrary units), for two spherical samples of CaF_2, with $\boldsymbol{B}_0 \| [100]$. (Reproduced with permission from Abragam et al.[13])

values of the second-moment excess. This excess depends slightly on nuclear polarization, as derived in Abragam et al.[13]

3.3.3 Higher Moments

These moments also depend on polarization, and could potentially be used for polarization calibration. In particular, for a simple cubic system of spins $\frac{1}{2}$ in a sphere, one predicts for the third moment

$$M_3 \propto p(1 - p^2) \tag{33}$$

which goes through a maximum for $p = 1/\sqrt{3}$. Experimentally, it is extremely difficult to avoid 'contamination' of the absorption signal by a small dispersion contribution, whose antisymmetric shape in the wings is sufficient to deprive experimental third moments of any significance.

4 RIGOROUS NMR RESULTS

We list below several results derived theoretically from equation (13). These results are rigorous for systems in the paramagnetic state, that is with an initial density matrix of the form given by equation (1) in an appropriate reference frame. From plausibility arguments, one is inclined to think that many remain valid even in nuclear magnetic ordered states, that is under conditions of symmetry breaking when equation (1) cannot be rigorous.

Each of these results has been implemented experimentally and used as a practical tool for the investigation of spin systems at low temperature. We cite and comment on these investigations, but no detailed calculations are given. We have already described the first investigation, which is concerned with the area of the absorption signal which, after calibration, yields both the polarization and the 'gain coefficient–rf field' product $\xi\omega_1$.

4.1 Rate of Change of the Polarization

Consider for simplicity a single-species system subjected to a small rf irradiation at a distance Δ from resonance. Its Hamiltonian in the rotating frame is

$$\mathcal{H} = \Delta I_z + \omega_1 I_x + \mathcal{H}'_{\mathrm{D}} \tag{34}$$

According to the Liouville–von Neumann evolution equation for the density matrix, the rate of change in the longitudinal spin expectation is

$$\begin{aligned} \frac{\mathrm{d}}{\mathrm{d}t}\langle I_z\rangle &= \mathrm{Tr}\left\{ I_z \frac{\mathrm{d}\sigma}{\mathrm{d}t} \right\} \\ &= \mathrm{Tr}\{-\mathrm{i} I_z[\mathcal{H}, \sigma]\} \\ &= \mathrm{Tr}\{-\mathrm{i}[I_z, \mathcal{H}]\sigma\} \\ &= \langle -\mathrm{i}[I_z, \mathcal{H}]\rangle_0 \end{aligned} \tag{35}$$

and thus, according to equation (34)

$$\frac{\mathrm{d}}{\mathrm{d}t}\langle I_z\rangle = \omega_1 \langle I_y\rangle \tag{36}$$

If one monitors the absorption signal during an irradiation process, the total change is given by

$$\delta\langle I_z\rangle = \int \omega_1 \langle I_y\rangle \, \mathrm{d}t \tag{37}$$

Use has been made of this method to measure the longitudinal susceptibility in demagnetized spin systems.[17]

The basis of the method is as follows. Starting from equilibrium after ADRF, i.e. an initial density matrix

$$\sigma_i = \exp(-\beta_i \hat{\mathcal{H}}'_{\mathrm{D}})/\mathrm{Tr}\{\dots\} \tag{38}$$

a saturating rf field is suddenly applied at a (small) distance Δ from resonance and one monitors the absorption signal over the course of the evolution of the system towards a new equilibrium of density matrix

$$\sigma_f = \exp[-\beta_f(\mathcal{H}'_{\mathrm{D}} + \Delta I_z + \omega_1 I_x)]/\mathrm{Tr}\{\dots\} \tag{39}$$

If Δ and ω_1 are much smaller than the local field, one has $\beta_f \simeq \beta_i$, and

$$\delta\langle I_z\rangle = \langle I_z\rangle_f = \omega_1 \chi_{\parallel}(\beta) \tag{40}$$

This is measured from the absorption signal using equation (37) and the calibrated value of $\xi\omega_1$.

4.2 Slightly Saturating Linear Passages

We consider a linear sweep of the field (or irradiation frequency) through resonance, with the time of sweep of the linewidth being much longer than T_2. The irradiation produces a saturation of both the polarization and the dipolar energy, which we presume to be small.

4.2.1 Saturation of the Polarization

Let $\mathrm{d}\Delta/\mathrm{d}t = \dot{\Delta}$. Equation (37) then yields

$$\delta\langle I_z\rangle = \frac{\omega_1}{\dot{\Delta}} \int_{-\infty}^{+\infty} \langle I_y\rangle(\Delta)\,\mathrm{d}\Delta \tag{41}$$

The limits can be taken equal to $-\infty$ and $+\infty$ if the sweep starts well below resonance and ends well above it. The integral of the absorption signal is precisely related to the value of $\langle I_z\rangle$, which yields

$$\frac{\delta\langle I_z\rangle}{\langle I_z\rangle} = -\epsilon = -\pi\frac{\omega_1^2}{\dot{\Delta}} \tag{42}$$

an expression which is valid for $\epsilon \ll 1$. By performing n passages, one obtains

$$\frac{\langle I_z\rangle(n)}{\langle I_z\rangle(0)} = (1-\epsilon)^n \simeq \exp(-n\epsilon) \tag{43}$$

through which one measures ϵ. If the sweep rate $\dot{\Delta}$ is known, this provides [from equation (42)] a calibration of ω_1, that is of the rf field amplitude. An experimental result for CaF_2 is shown in Figure 3. From the calibration of ω_1, one obtains a calibration of ξ.

4.2.2 Saturation of Dipolar Energy

A Hamiltonian of the form given by equation (34), at constant Δ, is time independent and the energy associated with it is conserved. If ω_1 is strong enough to ensure a single spin temperature in the rotating frame but is so small that the energy term $\omega_1\langle I_x\rangle$ is negligible, one obtains

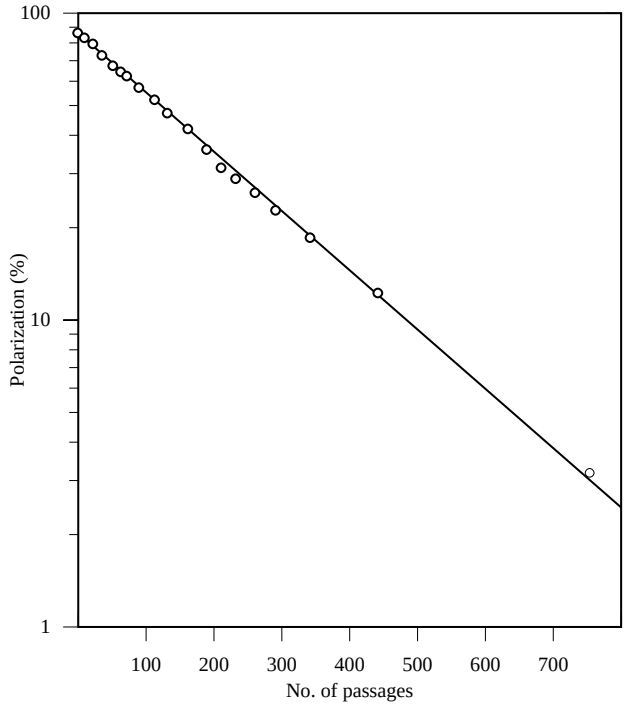

Figure 3 ^{19}F nuclear polarization in CaF_2 as a function of the number of slightly saturating passages. (Reproduced with permission from Abragam et al.[13])

$$\Delta\langle I_z\rangle + \langle\mathcal{H}'_{\mathrm{D}}\rangle = \text{constant} \tag{44}$$

or

$$\Delta\frac{\mathrm{d}}{\mathrm{d}t}\langle I_z\rangle + \frac{\mathrm{d}}{\mathrm{d}t}\langle\mathcal{H}'_{\mathrm{D}}\rangle = 0 \tag{45}$$

which, according to equation (36), gives

$$\frac{\mathrm{d}}{\mathrm{d}t}\langle\mathcal{H}'_{\mathrm{D}}\rangle = -\omega_1\Delta\langle I_y\rangle(\Delta) \tag{46}$$

Under a linear passage through resonance, with a frequency sweep rate $\dot{\Delta}$ so slow that equation (46) remains valid at all times, one obtains

$$\delta\langle\mathcal{H}'_{\mathrm{D}}\rangle = -\frac{\omega_1}{\dot{\Delta}}\int_{-\infty}^{+\infty}\Delta\langle I_y\rangle(\Delta)\,\mathrm{d}\Delta \tag{47}$$

a result which is valid only if $\langle\delta\mathcal{H}'_{\mathrm{D}}\rangle$ is small. What can be measured is the dipolar energy variation corresponding to n passages. Provided the product $\xi\omega_1$ is calibrated as explained above, the experimental results can be connected to the high-temperature linear value

$$\langle\mathcal{H}'_{\mathrm{D}}\rangle = -\beta\ \mathrm{Tr}\ \mathcal{H}'^2_{\mathrm{D}} \tag{48}$$

and thus one obtains a calibrated value of the energy. It makes use of the (nonnormalized) first moment

$$\mathcal{M}_1 = \int_{-\infty}^{+\infty} \Delta\langle I_y\rangle(\Delta)\,\mathrm{d}\Delta \tag{49}$$

and equation (47) becomes

$$\delta\langle\mathcal{H}'_{\mathrm{D}}\rangle = -\frac{\omega_1}{\dot{\Delta}}\mathcal{M}_1 \tag{50}$$

This result is independent of whether there are several spin species or not. This method has been used to calibrate the dipolar energy in LiH.[18]

4.3 First Moment of the Absorption Signal

We return to the first moment as defined by equation (49). This must not be confused with the normalized first moment described in Section 3.2.1. As the absorption signal $I_y(\Delta)$ is the Fourier transform of the (normalized) FID signal [equation (13)], then

$$\begin{aligned}\Delta\langle I_y\rangle(\Delta) &= \frac{\omega_1}{4}\int_{-\infty}^{+\infty}\langle[I_-, I_+(t)]\rangle_0\,\Delta\exp(\mathrm{i}\Delta t)\,\mathrm{d}t \\ &= -\mathrm{i}\frac{\omega_1}{4}\int_{-\infty}^{+\infty}\langle[I_-, I_+(t)]\rangle_0\frac{\mathrm{d}}{\mathrm{d}t}[\exp(\mathrm{i}\Delta t)]\,\mathrm{d}t\end{aligned} \tag{51}$$

Upon integration by parts over t, and then integration over Δ, one obtains finally[19]

$$\mathcal{M}_1 = \frac{\pi}{2}\omega_1\langle[I_-, [I_+, \mathcal{H}'_{\mathrm{D}}]]\rangle_0 \tag{52}$$

The simplest case is when the system contains only one spin species. Through the commutation relations of spin operators, and the form [equation (24)] of the homonuclear secular dipolar interactions, one obtains

$$\mathcal{M}_1 = 3\pi\omega_1\langle\mathcal{H}'_{\mathrm{D}}\rangle_0 \tag{53}$$

What is actually measured is

$$\mathcal{M}'_1 = \xi\mathcal{M}_1 = 3\pi\xi\omega_1\langle\mathcal{H}'_{\mathrm{D}}\rangle_0 \tag{54}$$

The calibration of $\xi\omega_1$ then gives access to a calibrated value of $\langle\mathcal{H}'_{\mathrm{D}}\rangle$.

Consider now the case when there are, say, two spin species I and S. Secular dipolar interactions between unlike spins do not contain flip-flop terms, and it is elementary to show that in such a case

$$\mathcal{M}_1(I) = \pi\omega_1^I\{3\langle\mathcal{H}'_{\mathrm{D}II}\rangle_0 + \langle\mathcal{H}'_{\mathrm{D}IS}\rangle_0\} \tag{55}$$

and for the spins S signal

$$\mathcal{M}_1(S) = \pi\omega_1^S\{\langle\mathcal{H}'_{\mathrm{D}IS}\rangle_0 + 3\langle\mathcal{H}'_{\mathrm{D}SS}\rangle_0\} \tag{56}$$

Together with the measurement of the total dipolar energy

$$\langle\mathcal{H}'_{\mathrm{D}II}\rangle_0 + \langle\mathcal{H}'_{\mathrm{D}IS}\rangle_0 + \langle\mathcal{H}'_{\mathrm{D}SS}\rangle_0 \tag{57}$$

by using the saturation method described in the preceding section, it is possible in principle to derive calibrated values for the three partial energies

$$\langle\mathcal{H}'_{\mathrm{D}II}\rangle_0, \quad \langle\mathcal{H}'_{\mathrm{D}IS}\rangle_0, \quad \langle\mathcal{H}'_{\mathrm{D}SS}\rangle_0 \tag{58}$$

4.4 Qualitative Shape of the Absorption Signal

When a spin system, with a single spin species I (for simplicity), is subjected to an ADRF stopped at the distance Δ_0 from resonance, its density matrix is of the form

$$\sigma = \exp[-\beta(\Delta_0 I_z + \mathcal{H}'_{\mathrm{D}})]/\mathrm{Tr}\{\exp(\dots)\}$$

We assume that $\beta > 0$. If one then looks at the absorption signal $I_y(\Delta)$ with a small, nonsaturating rf field, it can be shown (see Abragam and Goldman,[6] Chapter 5), that this absorption signal is positive for $\Delta \leq \Delta_0$, vanishes at $\Delta = \Delta_0$, and is negative for $\Delta \geq \Delta_0$. This makes it possible to determine the value of Δ_0 in equation (58), that is the effective field. In the particular case when $\Delta_0 = 0$, it can be shown that the absorption signal is antisymmetric at all spin temperatures

$$\langle I_y\rangle(-\Delta) = -\langle I_y\rangle(\Delta) \tag{59}$$

4.5 Linear Response and Transverse Susceptibility

The transverse susceptibility can be defined through two seemingly different approaches:

1. We wait for the thermal equilibrium when a small (but saturating) rf field is applied at a distance Δ_0 from resonance. This corresponds to a density matrix

$$\sigma_{\mathrm{eq}} = \exp[-\beta(\Delta_0 I_z + \omega_1 I_x + \mathcal{H}'_{\mathrm{D}})]/\mathrm{Tr}\{\dots\} \tag{60}$$

which yields a transverse spin expectation value

$$\langle I_x\rangle_{\mathrm{eq}} = \chi_\perp\omega_1 \tag{61}$$

2. Starting from a density matrix

$$\sigma_{\mathrm{eq}} = \exp[-\beta(\Delta_0 I_z + \mathcal{H}'_{\mathrm{D}})]/\mathrm{Tr}\{\dots\} \tag{62}$$

we apply a small rf field of amplitude ω_1/γ and look for the dispersion signal at frequency Δ_0

$$\langle I_x\rangle(\Delta_0) = \chi'_\perp\omega_1 \tag{63}$$

It can be shown, on the basis of linear response theory, that the two transverse susceptibilities are equal

$$\chi_\perp = \chi'_\perp \tag{64}$$

The former definition corresponds to the observation of dispersion during a fast passage (slow enough for the system to be at all times infinitely close to equilibrium, but fast enough for spin–lattice relaxation to be negligible). For the second definition, it is not necessary to look at the dispersion signal.

Instead, one can observe the absorption signal $\langle I_y\rangle(\Delta)$ and compute the dispersion $\langle I_x\rangle(\Delta_0)$ from the Kramers–Kronig relation[1]

$$\langle I_x\rangle(\Delta_0) = -\frac{1}{\pi}\mathcal{P}\int_{-\infty}^{+\infty}\frac{\langle I_y\rangle(\Delta)\,\mathrm{d}\Delta}{\Delta-\Delta_0} \tag{65}$$

Since the absorption signal is calibrated, as shown above, this method yields a calibrated value for the transverse susceptibility.

4.6 Cotanh Transform of the Absorption Signal: Measurement of the Dipolar Temperature

The cotanh transform is one form of the fluctuation–dissipation theorem,[20] as applied to the absorption signal.[18] For a system demagnetized to the distance Δ_0 from the spins I resonance, i.e. for a single spin system, when its density matrix is of the form given by equation (62), the cotanh transform (a neologism) is formally defined by

$$\mathcal{C}(\beta) = \int_{-\infty}^{+\infty}\langle I_y\rangle(\Delta)\,\coth\left[\frac{\beta}{2}(\Delta-\Delta_0)\right]\mathrm{d}\Delta \tag{66}$$

where $\langle I_y\rangle(\Delta)$ is the absorption signal.

It can be shown that

$$\mathcal{C}(\beta) = -\pi\omega_1\langle I_x^2 + I_y^2\rangle_0 \tag{67}$$

This property is valid even when there are several spin species. It can be used when, besides the abundant spins, the system also contains a spin species in low abundance (for instance ^{43}Ca in CaF_2). It is these spins that we call I. Since, for example,

$$I_x = \sum_i I_x^i \tag{68}$$

is the sum of all individual spin components, we have

$$\langle I_x^2\rangle_0 = \sum_i\langle I_x^{i2}\rangle_0 + \sum_{i\neq j}\langle I_x^i I_x^j\rangle_0 \tag{69}$$

For low-abundance spins, their relative distance is large, on average, so that

$$\langle I_x^i I_x^j\rangle_0 \simeq \langle I_x^i\rangle_0\langle I_x^j\rangle_0 \quad (i\neq j) \tag{70}$$

which vanishes when the spins I are not purposely given a transverse polarization. One is then left with

$$\langle I_x^2\rangle_0 + \langle I_y^2\rangle_0 \simeq \sum_i\langle I_x^{i2} + I_y^{i2}\rangle_0 = \sum_i[I(I+1) - \langle I_z^{i2}\rangle_0] \tag{71}$$

In the presence of N_I equivalent spins I, one then has

$$\mathcal{C}(\beta) = -N_I\pi\omega_1[I(I+1) - \langle I_z^{i2}\rangle_0] \tag{72}$$

In the case when nuclear alignment is negligible

$$\langle I_z^{i2}\rangle_0 = \tfrac{1}{3}I(I+1) \tag{73}$$

and one finally obtains

$$\mathcal{C}(\beta) \simeq -\tfrac{2}{3}N_I\pi\omega_1 I(I+1) \tag{74}$$

Using calibrated absorption signals, one adjusts by trial-and-error the value of β in equation (66) so as to satisfy equation (74). This yields a calibrated value of the spin temperature β^{-1}.

5 NONLINEAR EFFECTS IN SPIN TEMPERATURE

Consider, for simplicity, a system with only one spin species, subjected to Zeeman and dipolar interactions. At high field, there are two constants of the motion: the Zeeman energy $\omega_0 I_z$ and the secular dipolar energy $\langle\mathcal{H}'_\mathrm{D}\rangle$. Internal equilibrium corresponds to the most probable state, i.e. that which maximizes the entropy

$$S = -k_\mathrm{B}\ \mathrm{Tr}\{\sigma\ \ln\sigma\} \tag{75}$$

where σ is the spin density matrix, and is consistent with the conservation of the above-mentioned quantities. This corresponds to a density matrix of the form

$$\sigma = \exp(-\beta_\mathrm{Z}\omega_0 I_z - \beta\mathcal{H}'_\mathrm{D})/\mathrm{Tr}\{\exp(\dots)\} \tag{76}$$

where β_Z and β are the Zeeman and dipolar inverse temperatures, respectively. If we introduce the partition function

$$\mathcal{Z}(\beta_\mathrm{Z},\beta) = \mathrm{Tr}\{\exp(-\beta_\mathrm{Z}\omega_0 I_z - \beta\mathcal{H}'_\mathrm{D})\} \tag{77}$$

we have

$$\omega_0\langle I_z\rangle = \omega_0\ \mathrm{Tr}\{\sigma I_z\} = -\frac{\partial}{\partial\beta_\mathrm{Z}}\ln\mathcal{Z} \tag{78}$$

$$\langle\mathcal{H}'_\mathrm{D}\rangle = \mathrm{Tr}\{\sigma\hat{\mathcal{H}}'_\mathrm{D}\} = -\frac{\partial}{\partial\beta}\ln\mathcal{Z} \tag{79}$$

At high temperature, that is to first order with respect to the inverse spin temperature, one obtains the well-known result

$$\omega_0\langle I_z\rangle = -\beta_\mathrm{Z}\omega_0^2\ \mathrm{Tr}\{I_z^2\} \tag{80a}$$

$$\langle\mathcal{H}'_\mathrm{D}\rangle = -\beta\ \mathrm{Tr}\{\mathcal{H}'^2_\mathrm{D}\} \tag{80b}$$

At lower temperature, both $\omega_0\langle I_z\rangle$ and $\langle\mathcal{H}'_\mathrm{D}\rangle$ depend, in a complicated way, on both inverse temperatures, β_Z and β. All the problems arise from the term in $\mathcal{H}'_\mathrm{D}$. If β is zero, that is there is purely Zeeman order, it is elementary to calculate all steady-state expectation values of interest (as seen above, calculating a dynamic quantity such as the FID remains a formidable task). We describe a perturbative approach in which one calculates the physical quantities to all orders with respect

to the inverse Zeeman temperature β_Z, but in the form of a power expansion in dipolar inverse temperature β (it will be shown that, in fact, we can achieve slightly more than that). For secular dipolar interactions, and especially for spins $\frac{1}{2}$, the most convenient approach is through the diagrammatic method devised by Stinchcombe et al.[21,22] The method is not described in detail here. Suffice it to say that the diagram contains bonds, associated with dipolar interaction coefficients, and vertices, the values of which depend on the inverse Zeeman temperature. More precisely, for spins $\frac{1}{2}$, the values depend on

$$t = \tanh(-\tfrac{1}{2}\beta_Z\omega_0) \tag{81}$$

By differentiating equations (78) and (79) with respect to β and with respect to β_Z, respectively, we obtain

$$\frac{\partial}{\partial\beta}\omega_0\langle I_z\rangle = \frac{\partial}{\partial\beta_Z}\langle\mathcal{H}'_D\rangle \tag{82}$$

whence

$$\omega_0\langle I_z\rangle(\beta_Z,\beta) = \omega_0\langle I_z\rangle(\beta_Z,0 + \int_0^\beta \frac{\partial}{\partial\beta_Z}\langle\mathcal{H}'_D\rangle(\beta_Z,\lambda)\,d\lambda \tag{83}$$

This enables one to calculate $\langle I_z\rangle$ as a power expansion in β from the corresponding expansion for $\langle\mathcal{H}'_D\rangle$. One can also obtain β-expansion formulas for the entropy, free energy, etc.

There is an advantage in using this approach for systems where the spins experience a longitudinal average field, that is when, in equation (24)

$$\frac{\gamma^2\hbar}{2}\sum_j \frac{1-3\cos^2\theta_{ij}}{r_{ij}^3} = q \neq 0 \tag{84}$$

a value which is equal for all spins i.

It can be proved that, in such a case, all vertices can be 'renormalized' in such a way that:

1. one considers only diagrams with no free ends; and
2. in each vertex, the term t in equation (81) is replaced by

$$t' = \tanh(-\tfrac{1}{2}\beta_Z\omega_0 - \tfrac{1}{2}\beta q t) \tag{85}$$

For a given physical quantity, the term of zero order corresponds to the mean-field approximation, and the terms in increasing powers of β correspond to the contributions of short-range correlations of increasing order.

We present below several experimental illustrations of nonlinear effects in spin temperature, for ^{19}F spins in spherical samples of CaF_2 (q = 0), together with the theoretical predictions from expansions up to β^3.

5.1 Dipolar Energy versus Polarization in High Effective Field

The experiment consists of measuring $\langle\mathcal{H}'_D\rangle$ as a function of polarization p in a system having a density matrix

$$\sigma = \exp[-\beta(\Delta_0 I_z + \mathcal{H}'_D)]/\mathrm{Tr}\{\ldots\} \tag{86}$$

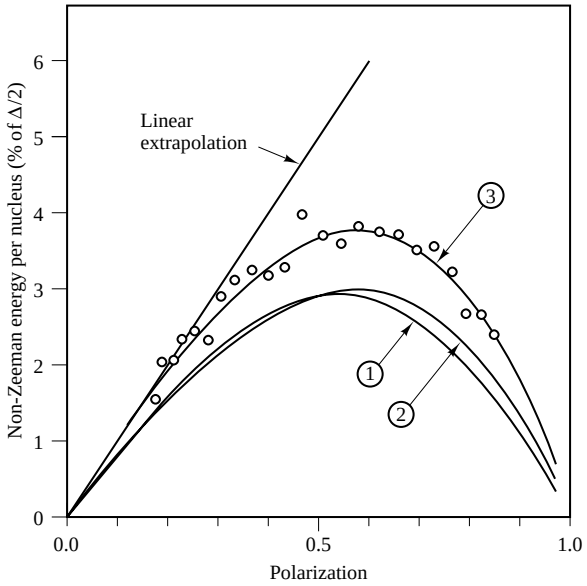

Figure 4 Non-Zeeman energy per fluorine spin as a function of nuclear polarization, in a spherical sample of CaF_2 at thermal equilibrium in the rotating frame in an effective field of 7.12 G·$\boldsymbol{B}_0$‖[100] and $T > 0$. Curves 1 and 2: first- and third-order approximations with dipolar interactions only. Curve 3: after addition of an adjusted contribution from impurities. (Reproduced with permission from Goldman et al.[23])

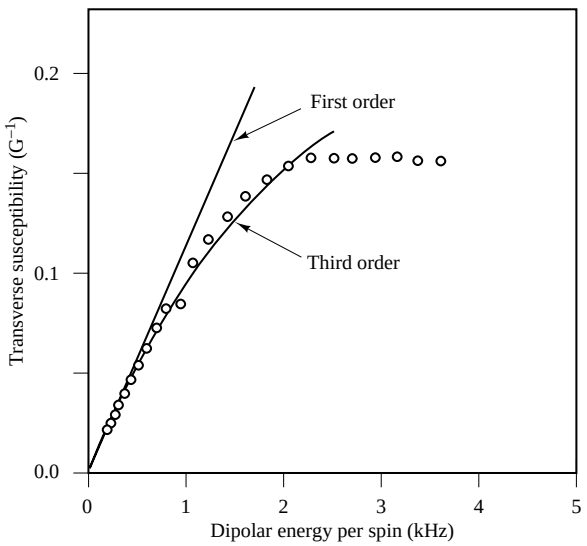

Figure 5 Transverse susceptibility of ^{19}F in a spherical sample of CaF_2 in zero effective field, against dipolar energy, together with first- and third-order approximations. Conditions: $\boldsymbol{B}_0$‖[100], $T < 0$. (Reproduced with permission from Goldman et al.[23])

in the case when Δ_0 is much larger than the local frequency D. When limited to the first order in β, the theoretical expression is

$$\langle\mathcal{H}'_D\rangle = \frac{N}{4}\frac{D^2}{\Delta_0}\ln\left(\frac{1+p}{1-p}\right) \times (1-p^2)(1-\tfrac{2}{3}p^2) \tag{87}$$

where β is expressed as a function of p.

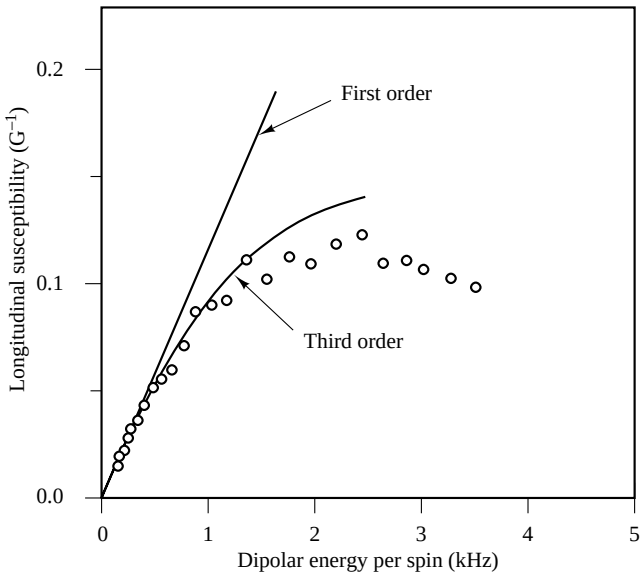

Figure 6 Longitudinal susceptibility of ^{19}F in the same sample and under the same conditions as in Figure 5. (Reproduced with permission from Goldman et al.[23])

Experimentally, one measures the loss of polarization resulting from a sudden rf irradiation at Δ_0 from resonance, starting from a state of pure Zeeman order. Figure 4 shows that agreement with theory requires the addition of an extra term to the secular dipolar reservoir.[23] The extra term has been identified as originating in the random field distribution due to the presence of paramagnetic impurities.

5.2 Transverse and Longitudinal Susceptibilities

Figures 5 and 6 show the transverse and longitudinal susceptibilities in zero effective field as a function of the dipolar energy,[23] together with the theoretical expectation from expansions up to β^3. The experimental method[23] used to obtain these two figures is rather complicated and is not described here. As can be seen in Figures 5 and 6, the results depart markedly from theory at dipolar energies per spin above about 2 kHz. This is no accident: these experiments were part of a general study of nuclear magnetic ordering and, as confirmed by other observations, the departures coincide with the onset of nuclear antiferromagnetism—but that is another story.

6 RELATED ARTICLES

Nuclear Ferromagnetism and Antiferromagnetism; Thermodynamics of Nuclear Magnetic Ordering.

7 REFERENCES

1. A. Abragam, *The Principles of Nuclear Magnetism*, Clarendon, Oxford, 1961.
2. M. Goldman, *Spin Temperature and Nuclear Magnetic Resonance in Solids*, Clarendon, Oxford, 1970.
3. C. P. Slichter, *Principles of Magnetic Resonance*, 3rd edn, Springer, Berlin, 1990.
4. A. Abragam and M. Goldman, *Nuclear Magnetism: Order and Disorder*, Clarendon, Oxford, 1982.
5. A. Abragam and W. G. Proctor, *C. R. Acad. Sci., Paris*, 1958, **246**, 2253.
6. A. Abragam and M. Goldman, *Rep. Prog. Phys.*, 1978, **41**, 395.
7. N. Kurti, F. N. H. Robinson, F. Simon, and D. A. Spohr, *Nature*, 1956, **178**, 450.
8. P. J. Hakonen and S. Yiu, *J. Low Temp. Phys.*, 1991, **85**, 25, and references therein.
9. A. G. Anderson and S. R. Hartmann, *Phys. Rev.*, 1962, **128**, 2023.
10. R. Kubo, *J. Phys. Soc. Jpn*, 1957, **12**, 570.
11. M. Goldman, *Quantum Description of High-Resolution NMR in Liquids*, Clarendon, Oxford, 1988.
12. I. J. Lowe and R. E. Norberg, *Phys. Rev.*, 1957, **107**, 46.
13. A. Abragam, M. Chapellier, J. F. Jacquinot, and M. Goldman, *J. Magn. Reson.*, 1973, **10**, 322.
14. Y. Roinel and V. Bouffard, *J. Magn. Reson.*, 1975, **18**, 304.
15. P. Bonamour, V. Bouffard, C. Fermon, M. Goldman, J. F. Jacquinot, and G. Saux, *Phys. Rev. Lett.*, 1991, **66**, 2810.
16. C. Kittel, *Phys. Rev.*, 1948, **73**, 155.
17. J. F. Jacquinot, M. Chapellier, and M. Goldman, *Phys. Lett. A*, 1974, **48**, 303.
18. M. Goldman, Y. Roinel, and V. Bouffard, *J. Magn. Reson.*, 1982, **46**, 110.
19. M. Goldman, *J. Magn. Reson.*, 1975, **17**, 393.
20. R. Brout, *Phase Transitions*, Benjamin, New York, 1965.
21. R. Stinchcombe, G. Horwitz, F. Englert, and R. Brout, *Phys. Rev.*, 1963, **130**, 155.
22. R. Brout, in *Magnetism*, eds. G. T. Rado and H. Suhl, Academic, New York, 1965, Vol. IIA, p. 43.
23. M. Goldman, J. F. Jacquinot, M. Chapellier, and Vu Hoang Chau, *J. Magn. Reson.*, 1975, **18**, 22.

Biographical Sketch

Maurice Goldman. *b* 1933. Diplôme d'Ingénieur Chimiste ESPCI, 1955, Doctorat d'Etat, 1967, University of Paris. Physicist, Commissariat à l'Energie Atomique (CEA), 1955–69. Vice-Director, College de France, 1969–83. Physicist, CEA, 1984–89. Research Director, CEA, 1989–93. Vice-President, ISMAR, 1992–present. Scientific Advisor, CEA, 1993–present. Approx. 100 publications, including three books. Research specialties: spin temperature and thermodynamics, nuclear magnetic ordering, relaxation in liquids and solids, and quantum theory of high-resolution NMR.

Maximum Entropy Reconstruction

Jeffrey C. Hoch and Alan S. Stern
Rowland Institute for Science, Cambridge, MA, USA

1	Introduction	1
2	Limitations of the DFT	1
3	Spectrum Analysis as an Inverse Problem	2
4	Solving the Inverse Problem Using Maximum Entropy Reconstruction	2
5	Numerical Algorithm	2
6	Analytic Solution	4
7	Example Applications	5
8	Quantification	7
9	Computational Cost	8
10	Concluding Remarks	8
11	Related Articles	8
12	References	8

1 INTRODUCTION

Efficient algorithms for computing the discrete Fourier transform (DFT) served as one of the enabling technologies behind the development of modern NMR spectroscopy.[1] While use of the fast Fourier transform (FFT) was widespread in science and engineering in the 1960s, it was nevertheless a fairly audacious proposal in 1965 to use the FFT to analyze time domain data as an alternative to conventional field or frequency swept experiments, since the marriage of a computer capable of performing the FFT to an NMR spectrometer had yet to be consumated. The implications turned out to be profound, of course, opening the way to the development of multidimensional NMR and magnetic resonance imaging. Yet while providing a crucial capability, the DFT is not without inherent limitations, some of which can be avoided by the use of alternative methods that would have been impractical in 1965, or even as recently as 1990.

2 LIMITATIONS OF THE DFT

The reasons for using the DFT are compelling, beyond even the efficiency of FFT algorithms. Among them are the linearity of the DFT (which simplifies quantification and error analysis and also permits applications such as difference spectroscopy) and the full weight of the theory behind the continuous Fourier transform.[2] A time series can be characterized as a finite sum of periodic functions, given by the inverse DFT

$$d_k = \frac{1}{\sqrt{N}} \sum_{n=0}^{N-1} f_n \mathrm{e}^{2\pi \mathrm{i} kn/N} \qquad (1)$$

where d_k is the value of the time series at time $k\Delta T$, ΔT is the interval between samples, f_n is the coefficient of the Fourier component with frequency $n/N\Delta T$, and N is the number of Fourier components (which is equal to the number of samples in the time series). The Fourier coefficients are computed by the forward DFT

$$f_n = \frac{1}{\sqrt{N}} \sum_{k=0}^{N-1} d_k \mathrm{e}^{-2\pi \mathrm{i} kn/N} \qquad (2)$$

Differences between the DFT and the continuous Fourier transform result from sampling and truncation, in both time and frequency. Sampling in the time domain can introduce artifacts in the spectrum, in which components with frequencies greater than $1/\Delta T$ appear at lower frequencies (aliasing). Truncation in the time domain introduces spurious spread of the components in the spectrum (leakage). Characterization of a time series beyond the sampled interval by means of Fourier coefficients computed from the interval (which is equivalent to estimating the spectrum with a digital resolution higher than $1/N\Delta T$) is correct only for periodic time series, since each Fourier component in equation (1) satisfies $\mathrm{e}^{2\pi \mathrm{i} kn/N} = \mathrm{e}^{2\pi \mathrm{i}(k+N)n/N}$.

Another difficulty associated with the DFT stems from the relationship between the number of data samples and the digital frequency resolution. The term digital frequency resolution is used to refer to the frequency difference between adjacent points in a discrete spectral estimate, and it should be distinguished from the resolution of the spectral estimate, which is a measure of the ability of a spectral estimate to distinguish between closely spaced frequency components. The digital resolution places a lower bound on the resolution of a spectral estimate. The spacing between points in the frequency domain is given by $1/N\Delta T$; therefore, to achieve high digital frequency resolution it is desirable to collect as long a data record as possible. In pulsed NMR experiments, however, the signal of interest usually diminishes with time. Thus collecting long data records to improve resolution rapidly leads to diminishing returns by degrading the signal-to-noise ratio (S/N) of the resulting spectrum. A technique for overcoming this degradation is to collect data for a short period of time and then append zeroes to the end (zero filling). This process also introduces discontinuities into the time series, resulting in leakage. The leakage can be severe if the signal of interest has not decayed sufficiently before the end of the sampled interval. Weighting functions (also referred to as apodization, window, or taper functions) can be applied to the time data, to minimize the extent of leakage by reducing the intensity of the signal near the end of the sampled interval, although this generally incurs an accompanying loss of resolution due to broadening of the spectral components. A virtual zoo of weighting functions exists, each function fulfilling a different goal (leakage reduction, resolution enhancement, sensitivity enhancement) or striking a compromise between various goals.[3] In particular the matched filter (which mimics the decay of the FID envelope), because of its theoretical properties, has long been employed to enhance sensitivity.[4]

One way to extend a time series in a more intelligent fashion than appending zeroes, is to extrapolate using linear prediction. Linear prediction is based on a model in which each value of a time series is assumed to be a linear combination of the preceding values. However, linear prediction is not

always appropriate. It is strictly correct only for exponentially decaying sinusoids, it requires a relatively high S/N, and it is only applicable to time series that have been sampled at uniform intervals. (See ***Fourier Transform and Linear Prediction Methods***.)

3 SPECTRUM ANALYSIS AS AN INVERSE PROBLEM

A more general approach, that avoids the limitations of the DFT and linear prediction, treats spectrum analysis of a time series as an inverse problem. Inverse problems are those in which the properties of interest can only be viewed indirectly. A famous example is Plato's allegory of the cave,[5] in which the problem is to infer the characteristics of an object from the shadows in the firelight it casts on the walls of a cave. In NMR spectrum analysis, the inverse problem can be stated as that of recovering the spectrum f_n of an ensemble of spins, when the only observations we have are the FID at various times (d_k), contaminated by noise (ϵ_k):

$$\hat{d}_k = d_k + \epsilon_k \tag{3}$$

We can approach this inverse problem by placing restrictions on the possible solutions f_n. The first restriction comes from the obvious requirement that f_n must be consistent with the experimental observations. The agreement can be quantified through the use of a constraint statistic that measures how well the reconstructed spectrum agrees with the available data. The statistic is determined by comparing a 'mock' FID, given by the inverse DFT of the reconstructed spectrum, with the actual data. When the noise and experimental error in the measured data are normally distributed, an appropriate statistic is the (unweighted) χ^2 statistic,

$$\chi^2 = \sum_{k=0}^{M-1} |m_k - \hat{d}_k|^2 \tag{4}$$

where M is the number of data samples collected, and m_k is the mock FID. Other forms of the constraint statistic, C, are possible, but χ^2 is the one generally used, because of its simplicity and the difficulty in justifying any other distribution of errors in the data. (A weighted χ^2 statistic can also be used, for example, if there is good reason to believe that some of the data points are more subject to error than others.) Whatever the form of C, the constraint that the reconstructed spectrum must be consistent with the measured data takes the form

$$C \leq C_0 \tag{5}$$

where C_0 is an upper bound on the allowed error. Given a prior estimate of the amount of noise in the data, C_0 should be comparable to the root-mean-square (RMS) noise level.

4 SOLVING THE INVERSE PROBLEM USING MAXIMUM ENTROPY RECONSTRUCTION

The constraint statistic alone does not provide enough of a restriction on the possible reconstructions to be of much use. In fact, any mock FID that matches the experimental FID to within C_0 for the first M points will satisfy the constraint. If we are to improve over the DFT, we need some additional criteria for regularizing the reconstructed spectrum, that will effectively constrain the values of the mock FID beyond M. One such criterion is the maximum entropy principle, which says that a reasonable reconstruction should add no new information beyond that contained in the experimental data. The principle originated in the work of Claude Shannon on the information-carrying capacity of circuits,[6] where he showed that the entropy of a probability distribution p, defined by

$$S(p) = -\sum_n p_n \log p_n \tag{6}$$

is a measure of the lack of information. There is a formal link between Shannon's entropy and the statistical entropy of an ensemble, and this link can be used to provide a constraint on possible spectrum reconstructions. On a more pragmatic level, the maximum entropy principle can be viewed simply as a means of obtaining a smooth, bounded reconstruction. The use of the maximum entropy principle to regularize the possible solutions to the spectrum analysis inverse problem is called maximum entropy (MaxEnt) reconstruction. [Maximum entropy reconstruction should be distinguished from the maximum entropy method (MEM) introduced by Burg,[7] which is more closely related to linear prediction.] Entropy is not unique as a regularizer, however, and there are other functionals that have similar properties.[8]

An important distinction between MaxEnt reconstruction and methods of spectrum analysis (such as those based on linear prediction) that implicitly assume Lorentzian lineshapes, is that MaxEnt reconstruction per se makes no assumptions about the signal to be recovered. Yet it is flexible enough to allow prior information to be incorporated into the reconstruction. A particularly simple means for incorporating prior knowledge is through a convolution kernel. Typical kernels might include exponential decay at some known rate, or J modulation at a known frequency. The reconstruction then yields the *deconvolved* spectrum having the highest entropy.

5 NUMERICAL ALGORITHM

The maximum entropy principle provides a formal basis for reconstructing the spectrum f_n, but some additional details must be addressed in order to apply MaxEnt reconstruction to NMR data. For modern NMR experiments, we need to be able to reconstruct complex spectra containing both positive and negative components. The Shannon formula [equation (6)] clearly does not apply to complex-valued spectra. A more suitable approach is to find the spectrum corresponding to a maximum entropy ensemble of spin-$\frac{1}{2}$ particles.[9] The resulting formula is

$$S(f) = -\sum_{n=0}^{N-1} \frac{|f_n|}{def} \log\left(\frac{|f_n|/def + \sqrt{4 + |f_n|^2/def^2}}{2}\right) - \sqrt{4 + |f_n|^2/def^2} \tag{7}$$

where *def* is a scale factor. The maximum entropy distribution prescribes the value of *def* (it depends on the spectrometer

response and the total number of spins in the sample). However, it is more convenient to treat *def* as an adjustable parameter.

The next detail that we are faced with is how to solve the constrained optimization problem, that is, the problem of maximizing $S(f)$ subject to the constraint that $C \leq C_0$. An equivalent unconstrained optimization problem is to maximize the objective function

$$Q = S - \lambda C \tag{8}$$

where λ is a Lagrange multiplier. The solution we seek corresponds to a critical point of Q, i.e., a point where $\nabla Q = 0$. In the general case there is no analytic solution to this problem, and we are forced to seek numerical solutions. For many problems of this type, a numerical search using the gradient of the objective function (steepest ascent or conjugate gradients) is a reasonably efficient method for finding the critical point. Unfortunately, an objective function constructed from two such dissimilar functionals as the χ^2 statistic and the entropy is quite difficult to maximize. Practical solution of the general MaxEnt reconstruction problem requires a fairly complex optimizer, and the most efficient algorithms require of the order of 100 (or more) times the computational effort of the FFT.

Since the entropy [given by equation (7)] and the constraint statistic [equation (4)] are both everywhere convex, there is a unique, global solution to the constrained optimization problem. Furthermore, this maximum satisfies $C = C_0$ provided that the trivial solution $f_n = 0$ does not also satisfy the constraint.

There have been several algorithms published for computing MaxEnt reconstructions. A particularly robust and efficient algorithm was described by Skilling and Bryan.[10] This method uses multiple search directions and a variable metric to determine the size of the step at each iteration. We describe here a variant we have found useful in our laboratory.

The algorithm begins with a flat trial spectrum equal to zero everywhere. At each iteration, a mock FID is computed from the current value of the trial spectrum. In the general case this involves inverse Fourier transformation and multiplication by a decay kernel, which is specified by the user as an input parameter. A decay does not need to be applied, but when it is, the reconstructed spectrum is an approximation of what would have been observed had the decay not been present. The first M points of the N point mock FID are used to compute the value of C, according to equation (4). The algorithm constructs a small set of direction vectors, and computes a quadratic approximation to the entropy in the subspace spanned by these vectors. Since the constraint is itself quadratic, it is possible to maximize analytically the entropy approximation subject to the constraint in this subspace. This results in the trial spectrum for the next iteration.

The quadratic approximation to the entropy is accurate only for small step sizes, so when the value of C for the mock FID is far from the desired value C_0, it is better to solve the analytic maximization using a constraint value C', intermediate between C_0 and the current value of C, rather than attempt one large step. Consequently the algorithm proceeds in two phases. In the first phase, C is larger than C_0 and the algorithm attempts to lower C. In the second phase, C_0 has been attained and the algorithm seeks to maximize the entropy.

This approach could be based on direction vectors that include ∇S, the gradient of the entropy (with respect to f). The problem is that the gradient can be dominated by small values of f, and the algorithm would spend more time adjusting values that are close to zero than adjusting signal peaks. The key insight of Skilling and Bryan was that the introduction of an 'entropy metric' produces an algorithm that more evenly weights the contributions of large and small values of the spectrum. Using the entropy metric amounts to replacing ∇S and ∇C (the gradient of the constraint with respect to the trial spectrum) with $\mathbf{H}^{-1}\nabla S$ and $\mathbf{H}^{-1}\nabla C$, where $\mathbf{H}$ is $-\nabla^2 S$, the negative of the Hessian (the matrix of second derivatives) of S. The matrix $\mathbf{H}$ is nearly diagonal, so its inverse is easy to compute. The search directions used during the first phase of the algorithm are:

$$\begin{aligned} &\nabla C \\ &\mathbf{H}^{-1}\nabla C \\ &\mathbf{H}^{-1}\nabla Q \\ &\mathbf{H}^{-1}(\nabla^2 C)\mathbf{H}^{-1}\nabla Q \\ &Q = S - \lambda C \end{aligned} \tag{9}$$

and λ is set to $|\nabla S|/|\nabla C|$. During the second phase, the second search direction is replaced by ∇Q. In the original algorithm of Skilling and Bryan, neither ∇C nor ∇Q are used as search directions. We found that including them speeds convergence. The major effort in computing these vectors stems from four discrete Fourier transformations (two each to compute ∇C and to apply $\nabla^2 C$) and multiplication by $\mathbf{H}^{-1}$.

With these direction vectors, a quadratic model for the entropy and the constraint can be constructed using a second-order Taylor expansion about the trial spectrum. A spectrum f' in the subspace spanned by the direction vectors can be represented by a vector of length four, $\bar{a}$; the correspondence is given by

$$f' = a_1 v_1 + a_2 v_2 + a_3 v_3 + a_4 v_4 + f_0 \tag{10}$$

where v_1 through v_4 are the direction vectors and f_0 is the current trial spectrum. The quadratic approximations then become

$$S(\bar{a}) \approx S(\ f_0) + \bar{B} \cdot \bar{a} + \tfrac{1}{2}\bar{a} \cdot \mathbf{M} \cdot \bar{a} \tag{11a}$$

and

$$C(\bar{a}) \approx C(\ f_0) + \bar{G} \cdot \bar{a} + \tfrac{1}{2}\bar{a} \cdot \mathbf{N} \cdot \bar{a} \tag{11b}$$

where vectors $\overline{B}$ and $\overline{G}$ are inner products of ∇C and ∇S with the direction vectors

$$\bar{B}_i = \nabla S \cdot v_i \tag{12a}$$

$$\bar{G}_i = \nabla C \cdot v_i \tag{12b}$$

Similarly, the 4×4 matrices $\mathbf{M}$ and $\mathbf{N}$ are the inner products of $\nabla^2 S$ and $\nabla^2 C$ with the direction vectors:

$$M_{ij} = v_i \cdot \nabla^2 S \cdot v_j \tag{13a}$$

$$N_{ij} = v_i \cdot \nabla^2 C \cdot v_j \tag{13b}$$

Computing these values requires several more Fourier transformations and large matrix products. The Lagrange condition $\nabla S - \lambda \nabla C = 0$ for the maximum of the objective function in the subspace becomes

$$(\bar{B} + \mathbf{M} \cdot \bar{a}) - \lambda(\bar{G} + \mathbf{N} \cdot \bar{a}) = \bar{0} \tag{14}$$

By a suitable change of coordinates in the subspace it is possible to simplify this equation by simultaneously diagonalizing **M** and **N**. The solution then is given by

$$a_i = \frac{B_i - \lambda G_i}{\lambda N_{ii} - M_{ii}} \tag{15}$$

λ can be found by using a binary search to determine the value for which $C(\bar{a})$ equals the target value C'.

Convergence criteria for determining when the trial spectrum is sufficiently close to the MaxEnt reconstruction derive from the Lagrange condition and the requirement that $C \approx C_0$. The Lagrange condition implies that ∇C and ∇S are parallel, so convergence can be monitored by computing the value

$$Test = \left| \frac{\nabla S}{|\nabla S|} - \frac{\nabla C}{|\nabla C|} \right| \tag{16}$$

The algorithm terminates when $C \approx C_0$ and $Test \ll 1$. In practice, we stop the algorithm when $Test < 10^{-3}$, or when a preset maximum number of iterations has been executed.

The value of C_0 can be estimated from the data by examining a portion of an FID that is essentially free of signal, or alternatively, by examining a signal-free region of the DFT spectrum. For MaxEnt reconstructions, C_0 should generally be somewhat larger than the estimate of the RMS noise level. Very large values of C_0 result in overly smooth reconstructions in which weaker components are washed out.

The other adjustable parameter, *def*, is rather more difficult to prescribe. *def* represents the scale at which the nonlinear effects of MaxEnt reconstruction become significant. A large value of *def* results in nearly linear reconstructions. When *def* is large and C_0 is zero, the resulting reconstruction is essentially the same as the DFT of the zero-filled FID. However, very low values of *def* can give rise to spurious artifacts. As a rule of thumb, we use values of *def* somewhat lower than the noise level. Fortunately, the results are not overly sensitive to the choice of *def*. We know of no algorithmic procedure for determining the best value.

6 ANALYTIC SOLUTION

While numerical solution is required in the general case, there is a special case of MaxEnt reconstruction that has an analytical solution. Though unrealistic in several respects, examination of this special case can give some insights into how MaxEnt reconstruction works. When N (the number of points in the reconstructed spectrum) is equal to M (the number of experimental data points), and when the relationship between the trial spectrum and the mock FID is given simply by the inverse Fourier transform (i.e. we are not trying to deconvolve a decay), the solution can be found analytically. Parseval's theorem, which states that the sum of the squared magnitudes of a vector is equal to the sum of the squared magnitudes of its Fourier coefficients, permits the constraint statistic to be computed in the frequency domain. Under these circumstances the Lagrange condition becomes

$$0 = \nabla Q = \nabla S - 2\lambda(f - F) \tag{17}$$

where F is the DFT of the data $\hat{d}$. The solution is given by

$$|f_n| = \delta_\lambda^{-1}(|F_n|) \tag{18a}$$

$$\text{phase}(f_n) = \text{phase}(F_n) \tag{18b}$$

where δ_λ is the function

$$\delta_\lambda(x) = x - s'(x)/2\lambda \tag{19}$$

and $s(x)$ is the contribution of a spectral component with magnitude x to the overall entropy S [see equation (7)]. This result corresponds to a nonlinear transformation, applied point by point to the DFT of the time domain data. The transformation depends on the value of λ, and has the effect of scaling every point in the spectrum down, but points closer to the baseline are scaled down more than points far above the baseline. Figure 1 illustrates $\delta_\lambda^{-1}(x)$ for various values of λ. As λ increases, the relative weight given to the constraint term in the objective function increases, and the transformation becomes more nearly linear.

This helps to explain the characteristic of MaxEnt reconstructions that noise near the baseline is suppressed more than noise away from the baseline (for example, superimposed on a broad peak). A further point to note is that there is a very important distinction between S/N and sensitivity. Sensitivity is the ability to distinguish signal from noise. Applying the same transformation to both the signal and the noise cannot improve this ability, since peaks that are comparable in height to the noise level will be reduced by the same amount as the noise. The ratio between the highest signal peaks and the noise

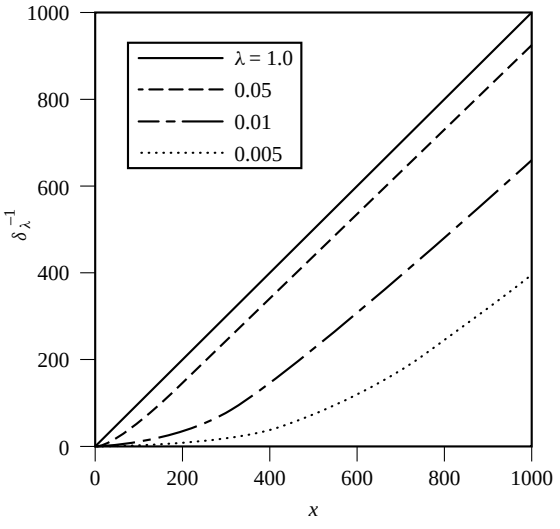

Figure 1 The nonlinear transformation $\delta_\lambda{}^{-1}(x)$ applied to the DFT spectrum that results in the MaxEnt reconstruction when $N = M$, for various values of the Lagrange multiplier λ

may increase, but small peaks will be just as difficult to distinguish as before. For linear operations (such as apodization), an improvement in S/N necessarily implies an improvement in sensitivity; for nonlinear operations (such as MaxEnt reconstruction) this is not so. In this special case, gains in S/N in the MaxEnt reconstruction are purely cosmetic. In the more general case, for example when an approximately known decay is deconvolved from the reconstructed spectrum, there may be real sensitivity gains. However, a prudent investigator will always question whether gains in S/N really correspond to gains in sensitivity.[11]

7 EXAMPLE APPLICATIONS

Armed with an efficient optimizer, the Cambridge Maximum Entropy group and their collaborators performed the earliest applications of MaxEnt reconstruction to NMR.[12] Properties of MaxEnt reconstruction depend on both the data and the parameters of the reconstruction, such as the decay kernel, and so are best illustrated by examples using typical NMR data. In addition to providing a concrete means of exploring the use of MaxEnt reconstruction for improving resolution or enhancing sensitivity, they provide a means of comparing the performance of alternate methods.

7.1 One-Dimensional

7.1.1 Resolution

Figure 2 illustrates the methyl and aliphatic region of spectra obtained for a sample of 20 mM L-Ala-L-Pro in D_2O at pD 6.0 and 25°C. Data consisting of 1024 complex points were collected at 400 MHz on a JEOL GX-400 spectrometer. Shown are the zero-filled (to 8192 points) DFT spectrum without (a) and with (b) windowing (60°-shifted sine-bell). Figure 2(c) is the DFT spectrum obtained by extrapolating from 1024 points to 8192 with linear prediction, using a filter order of 60 and reflecting roots of the characteristic polynomial that fall outside the unit circle to the inside. Figure 2(d) illustrates the MaxEnt reconstruction, computed using 1.0 for C_0 and 0.1 for *def*. All parts of Figure 2 are plotted using the same scale. The region near the methyl peaks (around 1.55 ppm, arising from both the *cis* and *trans* forms of the peptide bond) shows the artifacts due to truncation. Windowing the FID ameliorates the artifacts, at the expense of lower resolution due to broadening. More aggressive resolution enhancement (for example a 30°-shifted sine-bell) improves the resolution at the expense of more pronounced negative 'wings' surrounding the methyl peaks. Extrapolation by linear prediction [Figure 2(c)] dampens the artifacts somewhat; further reduction could be obtained by windowing the extrapolated FID. The MaxEnt reconstruction [Figure 2(d)] is virtually free of artifacts and has narrow lines; further line narrowing could be achieved by deconvolving the natural linewidth.

7.1.2 Signal-To-Noise Ratio

Figure 3 illustrates gains in S/N that can be achieved using MaxEnt reconstruction. Figure 3(a) contains the aliphatic

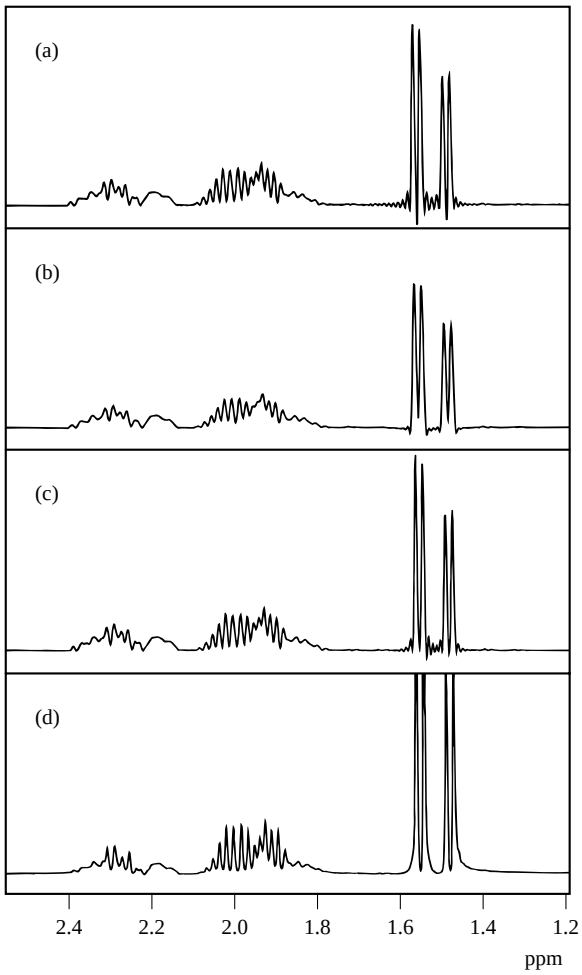

Figure 2 Aliphatic region of the ^1H spectrum of L-Ala-L-Pro, from 1024-point data: (a) zero filled to 8192 and Fourier transformed; (b) zero filled, apodized using a 60°-shifted sine-bell and Fourier transformed; (c) extrapolated to 8192 points using linear prediction and Fourier transformed; (d) MaxEnt reconstruction

region of the DFT spectrum for a sample of 0.1% ethylbenzene in deuterochloroform, using a single 90° observe pulse; 1024 complex points were zero-filled to 4096 and windowed using a 60°-shifted sine-bell prior to Fourier transformation. Figure 3(b) shows the DFT spectrum of data collected using a 7° observe pulse, and processed as in Figure 3(a). Figure 3(c) shows the MaxEnt reconstruction obtained using 2.8 for C_0 and 0.01 for *def*; no decay was deconvolved. Although striking, the improvement in S/N does not necessarily correspond to a real gain in sensitivity, as discussed earlier. Note that the multiplet structure of the peak near 3.25 ppm is not much more evident in (c) than in (b).

7.1.3 Robustness

A characteristic of MaxEnt reconstruction that distinguishes it from parametric methods, such as linear prediction, is that it makes no implicit assumptions about the nature of the data (although using MaxEnt reconstruction to perform deconvolution does presume the convolution kernel to be correct). Linear prediction, however, is strictly correct only for exponentially decaying sinusoids. MaxEnt is thus less

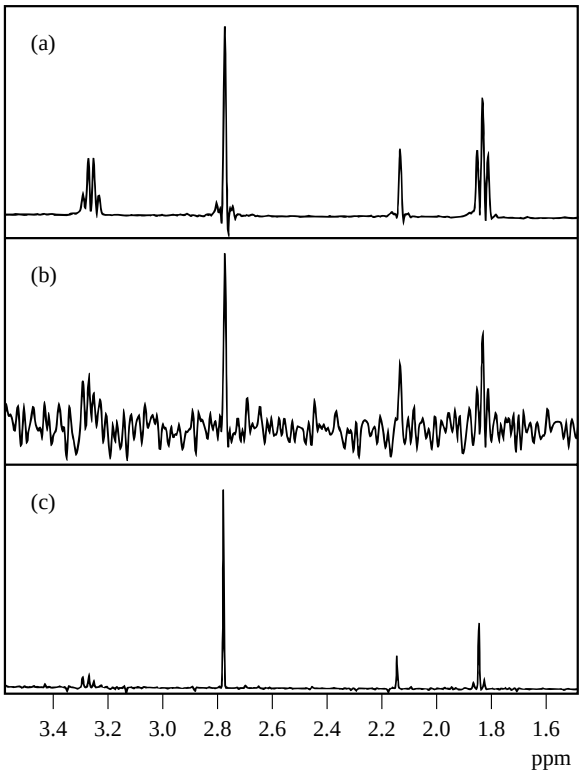

Figure 3 Aliphatic region of the ^{1}H spectrum of ethylbenzene: (a) obtained using a 90° observe pulse; (b) obtained using a 7° observe pulse followed by 60°-shifted sine-bell apodization, zero filling, and Fourier transformation; (c) obtained using a 7° observe pulse followed by MaxEnt reconstruction

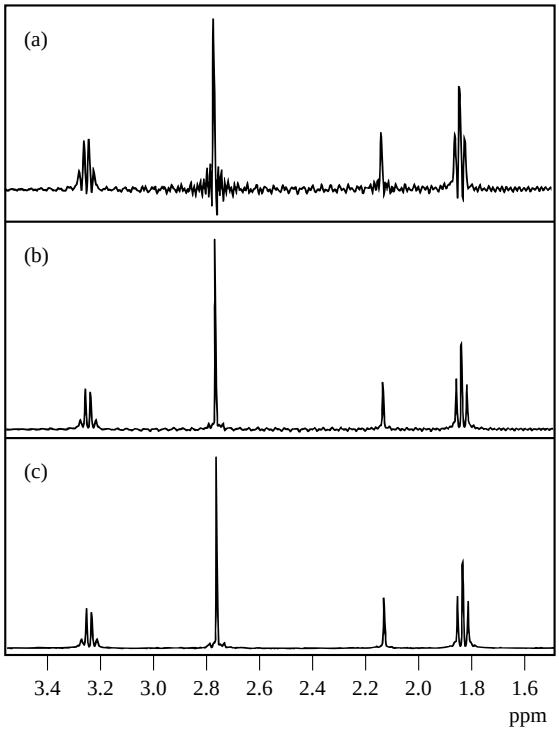

Figure 4 Spectra computed from data corrupted at two interior stretches of the FID using: (a) Fourier transformation, (b) MaxEnt reconstruction utilizing the entire data set, and (c) MaxEnt reconstruction excluding the corrupted data points

susceptible to bias when the signal has unusual characteristics such as markedly nonexponential decay, when the S/N is low, or when the data have been corrupted. It is quite common for points at the begining of a FID to be corrupted, which can result in distorted baselines. In these circumstances, backwards linear prediction can be used to correct the corrupted points. However, if the corrupted data points are in the middle of a FID, or distributed in some unusual fashion throughout the FID, linear prediction is less useful. MaxEnt reconstruction, however, does not require the data to be sampled at uniformly spaced intervals, and so can be applied quite easily to data that are corrupted in an irregular fashion. It is our own sad experience that points in the indirect dimensions of long multidimensional experiments are occasionally contaminated by intermittent instrument failure or environmental influences. Maximum entropy reconstruction provides a means of recovering useful spectra from such data.

To demonstrate the possibilities, we consider a contrived example, constructed by manually corrupting the one-dimensional FID used to generate Figure 3(a). The complex 1024-point FID was corrupted by setting to zero the real and imaginary parts of the points from 350 to 359 and 750 to 759. Figure 4(a) shows the DFT spectrum of the corrupted FID, zero-filled to 4096 points. Figure 4(b) and (c) are 4096-point MaxEnt reconstructions, using 1.0 for C_0 and 0.1 for *def*, and without deconvolving a decay. In Figure 4(b) all 1024 points of the FID were included in the computation of χ^2, while in Figure 4(c) the corrupted points were left out. Figure 4(b) illustrates that MaxEnt reconstruction is much more robust to data contamination than the DFT. Figure 4(c) shows the flexibility of MaxEnt reconstruction for treating data corrupted at arbitrary locations when the points of corruption are known.

7.2 Multidimensional

Maximum entropy reconstruction can also be applied to multidimensional data, and it is here that the ability to obtain high-resolution spectra from short data records offers the most significant benefits. Since the data collection time increases linearly with the amount of data collected in indirect dimensions of a multidimensional data set, resolution in these dimensions is often limited by practical considerations of the amount of experiment time available. An advantage of MaxEnt reconstruction over linear prediction for ameliorating those constraints is that the data samples need not be collected at uniform intervals, allowing data collection to be tailored to the type of experiment, sampling more frequently when the S/N is high and hence making more efficient use of available measuring time.

There are a number of ways MaxEnt reconstruction can be extended to multiple dimensions. The most general is simply to compute the entropy of the entire spectrum. As a practical matter, however, this can present a formidable computational challenge for large data sets, since each iteration of the reconstruction algorithm requires several transformations from the time to the frequency domain (and back). An alternative that is far less demanding is to apply MaxEnt reconstruction to each FID in one dimension independently. With this approach, MaxEnt reconstructions of large multidimensional data sets

can be performed efficiently on typical workstations. With a small modification to the algorithm, this approach using a series of one-dimensional reconstructions yields results that are nearly equivalent to the more general multidimensional reconstruction.

In one-dimensional MaxEnt reconstruction, one seeks the local maximum of the objective function for which $C = C_0$. This occurs for a specific value of λ. When computing MaxEnt reconstruction for the rows of a multidimensional data set, normal variations in the noise and the signal can result in different values of λ for each row. The consequences of this variation are often insignificant, but they can be important if they are large enough to perturb the lineshapes, or if quantification of the reconstructed spectrum is performed. Since the nonlinearity of MaxEnt reconstruction depends on the relative weights applied to the entropy and the constraint statistic, it is important to ensure that the same weight (value of λ) applies to each row. This is relatively easy to accomplish by choosing a typical row, estimating the noise, and computing a normal one-dimensional MaxEnt reconstruction. For the multidimensional data set, each row is then reconstructed using the value of λ obtained from the reconstruction of the trial row, instead of iterating to achieve $C = C_0$.

While the resolution of a spectrum determined by MaxEnt reconstruction is mainly determined by the time of the last data sample (as for the DFT), higher sensitivity for the same number of measurements can be achieved by tailoring the sampling schedule to the expected signal.[13–15] The optimal schedule depends on whether the signal is an exponentially damped sinusoid, is cosine modulated, or is stationary (such as that in a constant time experiment).

Figure 5 shows the methyl region of the two-dimensional ^{1}H–^{13}C HMQC spectra for a 10 mM sample of the 16-residue peptide α_1B in D_2O at pH 5.0 and 25°C, obtained with natural abundance of ^{13}C at 9.4 T. The data used to compute the spectra in (a) and (b) consisted of 1024 complex points in the ^{1}H dimension (t_2) and 128 complex points in the ^{13}C dimension (t_1). The spectrum in Figure 5(a) was computed by windowing with a 30°-shifted sine-bell, and zero filling to 2048 complex points prior to Fourier transformation in t_2, followed by linear prediction using a filter order of 10 to extrapolate the data to 512 points in t_1, windowing using a 45°-shifted sine-bell, zero filling to 1024 points and Fourier transformation. The data used to compute the spectrum in Figure 5(b) were obtained similarly to the data for (a) in t_2, but exponential sampling using an effective decay time of 30 ms was used to collect 128 complex points, selected from a linear schedule of 512 points. Processing in t_2 was performed as before, but MaxEnt reconstruction was performed in t_1, with values of 10 for *def* and 0.0554 for λ, and deconvolving a 20 Hz linewidth kernel. The data for Figure 5(c) consisted of 64 points exponentially sampled from a linear schedule of 256 points; the spectrum was computed as in (b). Comparison of (a) and (b) shows that nonlinear sampling in conjunction with MaxEnt reconstruction yields higher resolution than is achieved using conventional data acquisition and processing. In particular, the couplings between the leucine methyl protons and the γ proton are more clearly evident in (b). Comparison of (a) and (c) shows that exponential sampling can also be used to obtain resolution comparable to or better than conventional methods using less data. For long multidimensional experiments, even a reduction by a factor of 2 in experiment time can be significant.

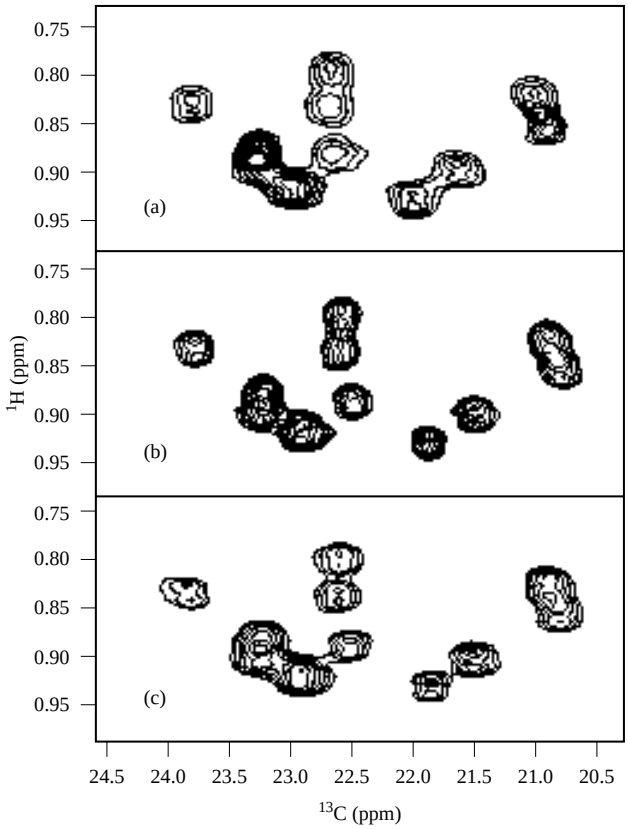

Figure 5 Methyl region of the ^{1}H–^{13}C HMQC spectra of α_1B: (a) computed from 128-point (in t_1) conventionally acquired data using linear prediction, extrapolation, windowing, and Fourier transformation, (b) using MaxEnt reconstruction of 128-point exponentially sampled t_1 data, and (c) using MaxEnt reconstruction of 64-point exponentially sampled t_1 data

7.3 Deconvolution

MaxEnt reconstruction can also be used to deconvolve an arbitrary modulation. One application is to deconvolve J modulation. Figure 6 shows the same region of the HMQC spectrum of α_1B as Figure 5, but MaxEnt reconstruction has been used in the ^{1}H dimension to deconvolve the 7 Hz coupling. This method is equally applicable to spectra exhibiting antiphase modulation; however, it is only capable of deconvolving a single, fixed modulation frequency.

8 QUANTIFICATION

The nonlinearity of MaxEnt reconstruction is an inherent characteristic, and is responsible for the method's ability to achieve noise suppression without sacrificing resolution to the extent associated with linear filtering (such as the windowed DFT). This nonlinearity has important implications in situations where quantification of peak intensities or volumes is required, such as nuclear Overhauser effect measurements or difference spectroscopy. For difference spectroscopy, it may be sufficient to compute the difference using the time domain data and compute the MaxEnt reconstruction of the difference. This assures that the same

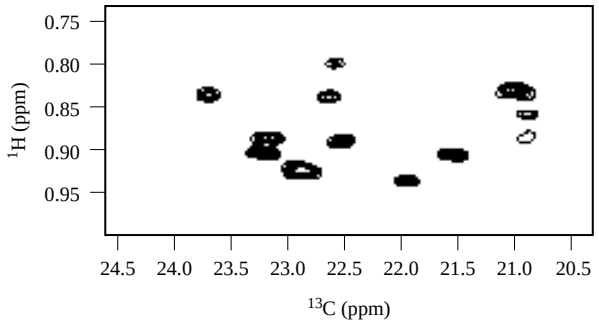

Figure 6 Methyl region of the ^{1}H–^{13}C HMQC spectrum of α_1B, with 7 Hz J modulation deconvolved in the ^{1}H dimension using MaxEnt reconstruction

nonlinearity applies to both experiments. When measuring nuclear Overhauser effects, or otherwise quantifying peak intensities, there are two possible approaches. One is to constrain tightly the reconstruction to match the data, which forces the reconstruction to be more nearly linear (although at the expense of noise suppression). Another is to inject synthetic signals of known relative intensity into the time domain data prior to reconstruction. A calibration curve can then be constructed by quantifying the intensities of the known signals.

The nonlinear nature of MaxEnt reconstruction also renders the S/N a poor estimate of sensitivity. Sensitivity estimates are perhaps best obtained by adding signals of known intensity to the data prior to reconstruction.

9 COMPUTATIONAL COST

The computational cost of MaxEnt reconstruction for one-dimensional spectra is typically 2 orders of magnitude greater than the cost of computing an FFT. For large, multidimensional reconstructions, the elapsed time is dominated by memory requirements, rather than the number of computations: the algorithm described above requires of the order of 16 times the size of the reconstructed spectrum for intermediate storage. While row-wise reconstruction can be used to ameliorate this requirement, fully multidimensional MaxEnt reconstructions remain the province of supercomputer-class machines with large amounts of high-speed random-access memory.

10 CONCLUDING REMARKS

Maximum entropy reconstruction is a powerful method for computing spectral estimates from time domain NMR data that avoids some of the limitations inherent in the discrete Fourier transform. It is more general than parametric methods, such as those based on linear prediction, that are restricted to Lorentzian signals, yet is capable of incorporating prior knowledge about the signal when it is available. The computational cost, while significantly greater than the FFT, is in a range that is practical on modern workstations, even for large data sets. Some of the power of the method stems from its nonlinearity, which dictates that the method must be used cautiously. Its ability to use nonlinearly sampled data provides a powerful tool for improving the resolution and sensitivity of multidimensional experiments. Used prudently, MaxEnt reconstruction can extend the limits of sensitivity and resolution in NMR, simplify analysis, and enable the study of larger molecules and molecules at lower concentrations than is feasible using the DFT.

11 RELATED ARTICLES

Data Processing; Fourier Transform and Linear Prediction Methods; Fourier Transform Spectroscopy.

12 REFERENCES

1. R. R. Ernst, in *Computational Aspects of the Study of Biological Macromolecules by Nuclear Magnetic Resonance Spectroscopy*, eds. J. C. Hoch et al., Plenum, New York, 1991.
2. E. O. Brigham, *The Fast Fourier Transform*, Prentice-Hall, Englewood Cliffs, NJ, 1974.
3. R. R. Ernst, G. Bodenhausen, and A. Wokaun, *Principles of Nuclear Magnetic Resonance in One and Two Dimensions*, Clarendon, Oxford, 1987.
4. R. R. Ernst, *Adv. Magn. Reson.*, 1966, **2**, 1.
5. Plato, *Republic*, Hacket, Indianapolis.
6. C. E. Shannon, *Bell Syst. Tech. J.*, 1948, **27**, 379.
7. J. P. Burg, in *Modern Spectrum Analysis*, ed. D. G. Childers, IEEE Press, New York, 1978.
8. D. L. Donoho, I. A. Johnstone, J. C. Hoch, and A. S. Stern, *Proc. R. Stat. Soc. B*, 1992, **54**, 41.
9. J. A. Jones and P. J. Hore, *J. Magn. Reson.*, 1991, **92**, 276.
10. J. Skilling and R. Bryan, *Mon. Not. R. Astron. Soc.*, 1984, **211**, 111.
11. D. L. Donoho, I. A. Johnstone, and A. S. Stern, *Proc. Natl. Acad. Sci. USA*, 1990, **87**, 5066.
12. S. Sibisi, J. Skilling, R. Brereton, E. Laue, and J. Staunton, *Nature (London)*, 1984, **311**, 446.
13. J. C. J. Barna, E. D. Laue, M. R. Mayger, J. Skilling, and S. J. P. Worrall, *J. Magn. Reson.*, 1987, **73**, 69.
14. M. Robin, M.-A. Delsuc, E. Guittet, and J.-Y. Lallemand, *J. Magn. Reson.*, 1991, **92**, 645.
15. P. Schmieder, A. S. Stern, G. Wagner, and J. C. Hoch, *J. Biol. NMR*, 1993, **3**, 569.

Acknowledgments

We are grateful to David Donoho, Ian Johnstone, Peter Schmieder, Gerhard Wagner, and Peter Connolly for many stimulating discussions and continuing fruitful collaborations on aspects of maximum entropy reconstruction in NMR. We also thank John Osterhout and Marcela Oslin for providing the sample of α_1B, and George Maalouf and Peter Connolly for collecting NMR data.

Biographical Sketches

Jeffrey C. Hoch. *b* 1954. A.B. Boston University, 1976; A.M. Harvard, 1978; Ph.D. Harvard, 1983. Introduced to NMR by M. Karplus and C. M. Dobson. Member of Rowland since founding in 1981. Approx. 30 publications. Director of NATO Workshop ‘Computational Aspects of

the Study of Biological Macromolecules by NMR Spectroscopy', and editor with C. Redfield and F. M. Poulsen of the published proceedings. Research interests include NMR data processing, analysis, and protein structure determination.

Alan S. Stern. *b* 1958. A. B. Harvard, 1979; Ph.D. U.C. Berkeley, 1984. Member of Rowland since 1988. Approx. 15 publications. Research interests include signal processing and mathematical logic.

Multiple Quantum Coherences in Extended Dipolar Coupled Spin Networks

Serge Lacelle
Université de Sherbrooke, Quebec, Canada

1	Background and Phenomenology	1
2	Ensemble Considerations	2
3	Quantum Mechanics of an N-Spin Subsystem	3
4	Quantum Statistical Mechanics of an Ensemble of N-Spin Subsystems	4
5	Development of Multiple Spin/Multiple Quantum Coherences in Dipolar Coupled Solids	5
6	Statistical Properties of Distributions of Dipolar Coupling Constants and Their Products in Large Spin Networks	7
7	Dynamical Scale Invariance in the Growth of Multiple Spin Correlations in Dipolar Coupled Solids	8
8	Related Articles	9
9	References	10

1 BACKGROUND AND PHENOMENOLOGY

In condensed matter, dipolar interactions among nuclear magnetic moments and their manipulation in multiple quantum (MQ) NMR experiments induce multiple spin correlations. The temporal and spatial development of these collective modes yield information about the structure and the dynamics of spin networks.[1–3] In this article, we examine the fundamental aspects of the growth of multiple spin/multiple quantum coherences in extended dipolar coupled spin networks driven by rf magnetic fields.

In MQ NMR, investigations of strongly dipolar coupled spin systems, such as rigid solids, the simplest relevant Hamiltonian needed to describe and understand experimental observations in a laboratory reference frame is given by

$$\hat{\mathcal{H}}(t) = \hat{\mathcal{H}}_{\mathrm{Z}} + \hat{\mathcal{H}}_{\mathrm{d}} + \hat{\mathcal{H}}_{\mathrm{rf}}(t) \tag{1}$$

The contributions to $\hat{\mathcal{H}}(t)$ in equation (1) include the interactions of the nuclear magnetic moments with a strong static magnetic field ($\hat{\mathcal{H}}_{\mathrm{Z}}$), with other nuclear magnetic moments through dipolar interactions ($\hat{\mathcal{H}}_{\mathrm{d}}$), and with time-dependent rf magnetic fields ($\hat{\mathcal{H}}_{\mathrm{rf}}$). Furthermore, $[\hat{\mathcal{H}}_{\mathrm{Z}}, \hat{\mathcal{H}}_{\mathrm{d}}] = 0$, and $[\hat{\mathcal{H}}_{\mathrm{Z}} + \hat{\mathcal{H}}_{\mathrm{d}}, \hat{\mathcal{H}}_{\mathrm{rf}}] \neq 0$.

In order to simplify the description and make connection with experiments, the Hamiltonian of equation (1) is transformed to a frame rotating about the z axis of the laboratory frame at the nuclear spin precession frequency. In this new reference frame, $\hat{\mathcal{H}}_{\mathrm{Z}}$ disappears. A further transformation to another noninertial frame, the rf toggling frame which 'follows' the directions of the rf fields during a pulse sequence, produces an effective Hamiltonian $\hat{\mathcal{H}}_{\mathrm{de}}(t)$. In this newest frame, $\hat{\mathcal{H}}_{\mathrm{de}}(t)$ results from the modulation of $\hat{\mathcal{H}}_{\mathrm{d}}$ by the time-dependent rf fields. The time average of $\hat{\mathcal{H}}_{\mathrm{de}}(t)$ over the period of a cycle of a multiple pulse excitation sequence yields, under appropriate conditions, a time-independent average Hamiltonian $\tilde{\hat{\mathcal{H}}}_{\mathrm{d}}$:

$$\tilde{\hat{\mathcal{H}}}_{\mathrm{d}} = \sum_{j>k} D_{jk}\, f(\hat{\boldsymbol{I}}_j, \hat{\boldsymbol{I}}_k) \tag{2}$$

where D_{jk} is a dipolar coupling constant between spins j and k

$$D_{jk} = \frac{\gamma^2\hbar^2(3\cos^2\theta_{jk} - 1)}{2r_{jk}^3} \tag{3}$$

and $f(\hat{\boldsymbol{I}}_j,\hat{\boldsymbol{I}}_k)$ is a function of bilinear operators involving the components of the spin angular momentum operators $\hat{\boldsymbol{I}}$, of spins j and k.

Formally, the geometrical interpretations of these transformations correspond to unitary transformations on the state of the spin system (i.e. the density operator) and its dynamical variables (i.e. the spin angular momentum and Hamiltonian operators). The resulting interaction pictures associate different parts of the time dependence of the physical system [i.e. the spins in the sample evolving under the Hamiltonian in equation (1)] to the state of the system and to the dynamical variables. This procedure is generic to all NMR experiments involving the manipulation of spin Hamiltonians. By a judicious choice of a reference frame, different portions of the Hamiltonian can be selected to appear to dominate the spin dynamics; hence, the possibility to discriminate among the various contributions in a spin Hamiltonian. Such an approach underlies the success of NMR spectroscopy. It is noteworthy that these transformations, from one frame to another, inertial or noninertial, do not necessarily preserve the invariance and conservation principles of physics. For example, spin energies measured in the laboratory frame are different from those measured in the rotating frame, while the spin quantum numbers, $I = \frac{1}{2}$ for protons, remain identical. However, observations restricted within a reference frame will be consistent with known laws of physics.

In pulsed NMR experiments, the evolution of the spin system is detected in the rotating frame. The time development of the spin system under $\tilde{\hat{\mathcal{H}}}_{\mathrm{d}}$ in the toggling frame is monitored directly, in multiple pulse line-narrowing sequences such as MREV-8, or indirectly, in MQ NMR, by stroboscopic observations when both the rotating and the toggling frames coincide.

A variety of rf multiple pulse sequences have been tailored to produce different average dipolar Hamiltonians $\tilde{\hat{\mathcal{H}}}_{\mathrm{d}}$. In MQ NMR experiments,[1–3] $[\hat{\mathcal{H}}_{\mathrm{Z}}, \tilde{\hat{\mathcal{H}}}_{\mathrm{d}}] \neq 0$. The spin portions [see equation (2)] $f(\hat{\boldsymbol{I}}_j,\hat{\boldsymbol{I}}_k)$ of these nonsecular average dipolar Hamiltonians include, among the bilinear spin operators, terms like $\hat{I}_{jz}\hat{I}_{k\pm}$, and $\hat{I}_{j\pm}\hat{I}_{k\pm}$, where $\hat{I}_+$ and $\hat{I}_-$ correspond to the raising and lowering (or ladder) spin angular momentum operators, respectively. These operators in $\tilde{\hat{\mathcal{H}}}_{\mathrm{d}}$ are responsible for the radiative coupling of Zeeman nuclear spin states with differing magnetic quantum numbers M_z by ±1 and ±2.

Evolution under $\bar{\mathcal{H}}_d$ for extended periods of time leads to nonstationary states with possibly larger differences in ΔM_z, as discussed in the next section. MQ NMR pulse excitation sequences for solids are specifically designed and optimized to generate multiple spin/multiple quantum coherences among the spins in a macroscopic sample.

The selection rules for the observation of transverse magnetization, or single spin/single quantum coherences, correspond to transitions with $\Delta M_z = \pm 1$. Thus, the creation and evolution of coherent superpositions of quantum states with $\Delta M_z \neq 1$ cannot be detected directly. Indirect piecewise mappings of multiple spin/multiple quantum coherences are accomplished through two-dimensional NMR methods as a function of the excitation and/or evolution times.[1–3] MQ NMR spectra obtained in this fashion reveal the presence of multiple spin/multiple quantum coherences with $\Delta M_z = n$, where n is the order of the coherences, in the sample during the excitation/evolution period (see Figure 1).

Figure 1 shows schematic MQ NMR spectra, obtained with time-resolved two-dimensional experiments, as a function of the excitation time. For a fixed excitation period, the spectral intensities decrease with increasing orders. With increasing excitation times, a redistribution of spectral intensities is observed to proceed or to 'flow' towards higher order coherences.

Understanding the behavior of the MQ NMR spectral intensity profiles of solids, as a function of order and excitation time, still poses an interesting challenge to NMR spectroscopists. Specifically, one would like to learn how the multiple spin dynamics depend on the lattice parameters and the space-filling properties of spin networks. Examples of the latter include spatial extent, morphologies, and effective dimensionalities of domain structures on mesoscopic length scales, i.e. in the range 1 nm to 1 μm, in condensed matter systems. More generally, the recognition of emergent properties, generic or universal behavior, amidst the complexities of this many-body problem with multiple scales, would deepen our understanding of the fundamental aspects of MQ NMR. These issues are addressed in the following sections, from the perspective of statistical mechanics.

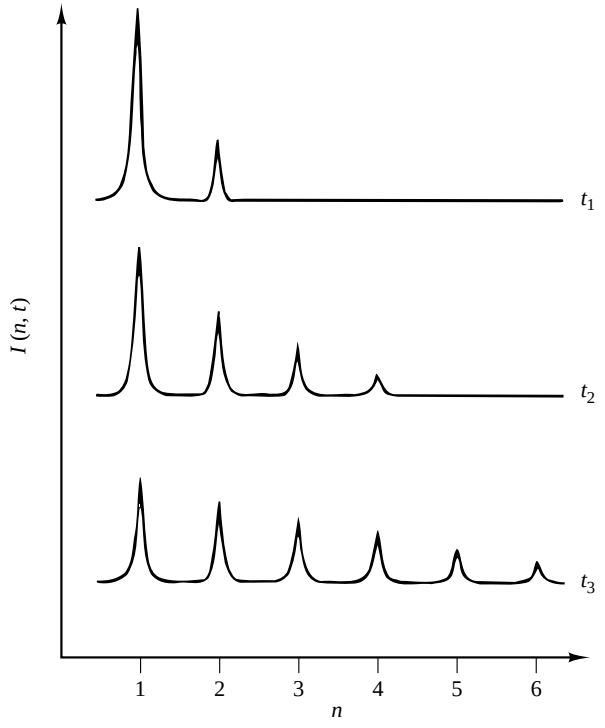

Figure 1 Typical MQ NMR spectra of a rigid solid: spectral intensities $I(n,t)$ as a function of order n and excitation time t, with $t_1 < t_2 < t_3$

2 ENSEMBLE CONSIDERATIONS

From a macroscopic point of view, in a MQ NMR experiment energy is pumped through rf magnetic fields produced by electronic devices into a solid sample residing in a strong static magnetic field. From a microscopic point of view, this injection of energy proceeds from individual nuclear magnetic moments, embedded in the lattice, to induce multiple spin correlations. Both the microscopic and macroscopic descriptions of the rf irradiation processes involve nonequilibrium driven systems: the macroscopic solid and the microscopic magnetic moments. As these experiments are performed in laboratories on a macroscopic scale, but interpreted microscopically, it is imperative to understand clearly how the macroscopic observables emerge from the numerous microscopic degrees of freedom.

A rigid solid is an aggregate of a large number of spatially fixed atoms. Various solids exist due to the nature of their constituents, which include atoms, ions, or molecules. In MQ NMR of rigid solids, ions and molecules lose their distinct identities on account of the through-space dipolar interactions among all magnetic moments. Hence, the spin network, consisting of the nuclear magnetic moments and their dipolar coupling constants, remains the only relevant and essential substratum onto which the microscopic degrees of freedom, the multiple spin coherences, evolve in MQ NMR experiments.

Solid samples used in MQ NMR investigations typically contain on the order of 10^{20} or more spins. The multiple spin correlations induced in spin networks by present-day MQ NMR methodologies involve coherences with up to possibly 10^2 spins. Consequently, the size difference between the sample and the multiple spin coherences suggests that the macroscopic observables, or responses, in MQ NMR experiments, arise from the random superposition of numerous multiple spin coherences. In other words, the sample could be viewed as an ensemble of loosely coupled subsystems.

Such a description of a macroscopic sample is certainly valid in liquid state NMR experiments, where under normal conditions, molecules behave as essentially independent subsystems. This outlook can also be extended to correlated molecular systems, as observed in critical fluctuations close to critical points.[4] For example, close to a consolute temperature, the intermolecular interactions among molecules in a critical binary fluid contrive and lead to composition fluctuations over length and timescales that can be quite large compared with those associated with the molecules, but still much smaller than those of the macroscopic sample. However, care must be exercised with such an analogy, since in critical phenomena systems are at equilibrium, while MQ NMR has to do with nonequilibrium driven systems. Possibly a more appropriate comparison for MQ NMR would be with the growth kinetics and processes of domain structures observed during phase

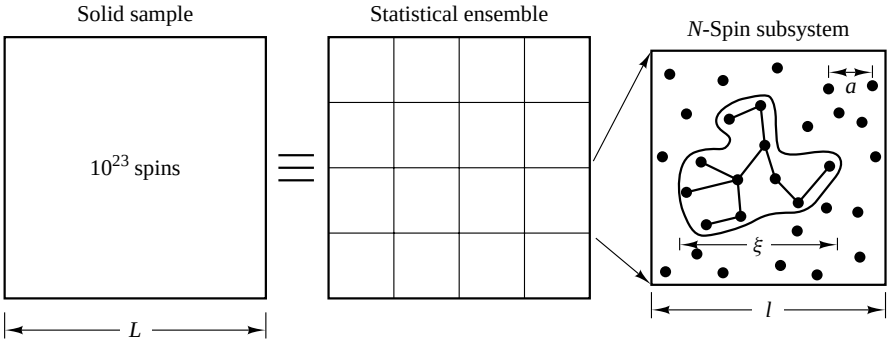

Figure 2 A macroscopic sample viewed as an ensemble of loosely coupled N-spin subsystems. Relevant length scales include: the lattice spacing a, the correlation length of a multiple spin coherence ξ, the extent of a subsystem l, and the sample size L, which satisfy $a < \xi < l \ll L$. Spins are denoted by •. An 11-spin coherence is also shown, with the lines representing the dipolar coupling constants appearing in the product, which multiplies the corresponding product operator term of the density operator

separation of binary fluids.[5] In this case, a similarity to critical phenomena exists; however, a richer behavior arises due to the nonequilibrium conditions and nonlinearity. In any event, the point at issue, that a macroscopic sample can be viewed, under certain conditions, as an ensemble of loosely coupled subsystems, where a subsystem can be one or several molecules, or even part of a spin network in a solid, would appear physically plausible.

Figure 2 shows a representation of a macroscopic sample as a statistical ensemble of N-spin subsystems. The number of spins N per subsystem is much smaller, by many orders of magnitude, than the total number of spins in the sample. The relevant length scales in this ensemble include the sample size L, the spatial extent of a subsystem l, the correlation length of the multiple spin coherences ξ, and the underlying lattice spacing a. This hierarchy of length scales satisfy the inequalities, $a < \xi < l \ll L$. Interaction energies between subsystems are assumed to be weak in comparison with interaction energies within the subsystems. This amounts to a neglect of surface effects for the MQ dynamics. Such approximation becomes more accurate in the limit when $\xi \ll l$. These effects are nevertheless necessary to achieve equilibrium or uniform spin temperature in the ensemble. The presence of the long-range dipolar interactions among the magnetic moments would appear to preclude or even invalidate this perspective of the sample as representing an ensemble of loosely coupled subsystems. However, as will be seen in Section 5, in time-resolved MQ NMR experiments, multiple spin coherences are 'weighted' by products of dipolar coupling constants. As it turns out, in spin networks, the distributions of dipolar coupling constants and their products are extremely wide. Since, at early excitation times, the MQ spin dynamics are dominated by the largest coupling constants and their products, the ensemble picture remains a good approximation for most experimental conditions. This approximation breaks down for mean field interpretations, e.g. MQ NMR experiments having infinite excitation periods.

Measurements performed over a short period of time on a macroscopic sample, made up of an ensemble of subsystems, correspond to averaging over the ensemble.[7] When a physical property of a macroscopic system is equal to this property averaged over the subsystems, spatial ergodicity exists. In statistical mechanics, the Gibbs canonical ensemble is composed of identical systems from the macroscopic point of view, i.e. they all have the same number of particles N, volume V, and temperature T. However, most systems are in different microscopic states. In the ensemble construction for a nonequilibrium driven macroscopic system, as described above, none of the subsystems need to be strictly identical. Instead, one assumes that statistical homogeneity is valid for the subsystems. On a subsystem scale, the statistical properties are stationary in space, i.e. a subsystem is statistically translationally invariant in space. Another feature of time-resolved MQ NMR measurements on such an ensemble, is the fact that, as the multiple spin coherences grow, so does their correlation length ξ. As the inequality $\xi < l$ must be satisfied for a consistent interpretation of the ensemble, this implies that the number of subsystems actually decreases as a function of time. This should be of no significant consequence, as long as $l \ll L$. Under present MQ NMR experimental conditions, these conditions are always satisfied, and the ensembles will consist of huge numbers of subsystems. Such ensembles yield asymptotic statistical states in experimental investigations.

Thus, a time-resolved MQ NMR measurement on a macroscopic solid is assumed to be equivalent to many independent measurements on the subsystems. Since the decomposition of the macroscopic sample into subsystems is not unique, the averaging process over the ensemble implied in a measurement is really a summation over the subsystems. As the spin dynamics are being probed on the scale of a subsystem, the response of the collective ensemble is taken to reflect the behavior of a typical subsystem. Underlying the spin dynamics are dipolar coupling constants and their products. Due to subtleties related to wide distributions and to averaging over products, the role of the couplings is more intricate than appears in the present discussion. For example, the distinction between average and typical behavior is very important in the MQ NMR of large spin networks.[6] We shall return to these issues in Section 6.

3 QUANTUM MECHANICS OF AN N-SPIN SUBSYSTEM

The focus on the spin dynamics within a subsystem and the subsequent averaging over a large collection of subsystems, yields a more tractable avenue to the understanding of

MQ NMR of solids, rather than treating a single spin system consisting of 10^{20} or more spins. Nevertheless, on the timescale of MQ NMR experiments, the spin dynamics within a subsystem still retain some of complexities of the many-body problem.

In a subsystem consisting of N spins I, there are $(2I + 1)^N$ stationary states of $\hat{\mathcal{H}}_Z$. For $I = \frac{1}{2}$, these 2^N energy levels can be classified according to the magnetic quantum numbers M_z given by

$$M_z = \sum_i^N m_{iz} \tag{4}$$

where m_{iz} is the eigenvalue ($m_z = \pm\frac{1}{2}$) of the ith spin. These Zeeman states, in the magnetic field $\boldsymbol{B}_0$, have corresponding energies

$$E_z = -\gamma\hbar B_0 M_z \tag{5}$$

and degeneracies

$$\Omega = \frac{N!}{(\frac{1}{2}N + M_z)!(\frac{1}{2}N - M_z)!} \tag{6}$$

The Zeeman manifolds are further broadened by homonuclear dipolar perturbations $\hat{\mathcal{H}}_d$. The resulting energy level diagram can be characterized, in principle, by the combined eigenvalues and eigenfunctions of $\hat{\mathcal{H}}_Z$ and $\hat{\mathcal{H}}_d$. However, due to the presence of bilinear spin operators in $\hat{\mathcal{H}}_d$, the combined eigenfunctions are constructed from direct products of $\hat{\mathcal{H}}_Z$ eigenfunctions. As a consequence, the m_{iz} eigenvalues are not good quantum numbers. In addition, the presence of large N rapidly makes this approach analytically intractable.

Therefore, as a first approximation, only the energy level diagram due to $\hat{\mathcal{H}}_Z$ is considered. This is justifiable, since the Zeeman splittings are usually of the order of tens to hundreds of megahertz as compared with tens of kilohertz for dipolar splittings. Radiative coupling of pairs of Zeeman levels leads to

$$\binom{2^N}{2} = 2^N(2^N - 1)/2 \tag{7}$$

possible transitions. The distinction between $+n$ and $-n$ coherences results in $2^N(2^N - 1)$ transitions. These transitions, or coherences, are classified according to their orders n. The number of coherences of order $n \neq 0$, Z_n, where $|n| \leq N$, is obtained from the constrained sum over the products of degeneracies of coupled Zeeman manifolds,

$$Z_n = \sum_{M_i - M_j = n} \binom{N}{\frac{1}{2}N + M_i}\binom{N}{\frac{1}{2}N + M_j} = \binom{2N}{N - n} \tag{8}$$

The number of coherences within a Zeeman manifold or with $n = 0$, Z_0, is given by

$$Z_0 \sum_{M_i = N/2+1}^{-N/2+1} \binom{N}{\frac{1}{2}N + M_i}\left[\binom{N}{\frac{1}{2}N + M_i} - 1\right] = \binom{2N}{N} - 2^N \tag{9}$$

Radiative coupling within a subsystem of N dipolar coupled spins $\frac{1}{2}$ can be rationalized, to a very good degree of approximation, on the basis of the possible $2^N(2^N - 1)$ transitions which connect the 2^N energy levels. The information content needed to describe this physical situation involves $2^N(2^N - 1)$ coherences and 2^N populations, or a total of 4^N parameters.

The 2^N eigenfunctions of $\hat{\mathcal{H}}_Z$, $|r\rangle$, for an N-spin-$\frac{1}{2}$ subsystem, constitute a complete basis set to characterize any spectroscopic experiments involving coherences and populations. As a consequence, any state $|\psi\rangle$ of a subsystem, can be expanded with the complete Zeeman basis set,

$$|\psi\rangle = \sum_{r=1}^{2^N} |r\rangle\langle r|\psi\rangle = \sum_{r=1}^{2^N} c_r|r\rangle \tag{10}$$

$$\langle r|\psi\rangle = c_r \tag{11}$$

Similarly, the observables or expectation values corresponding to any dynamical variables, such as the magnetization M_x, detected in a spectroscopic measurement on a subsystem, can be represented in this basis set with the corresponding operator $\hat{M}_x$ as,

$$\begin{aligned}\langle\psi|\hat{M}_x|\psi\rangle &= \sum_{r,s}\langle\psi|s\rangle\langle s|\hat{M}_x|r\rangle\langle r|\psi\rangle \\ &= \sum_{r,s} c_s^* c_r \langle s|\hat{M}_x|r\rangle\end{aligned} \tag{12}$$

where $c_r = \langle r|\psi\rangle$. The matrix elements $\langle s|\hat{M}_x|r\rangle$ are numbers related to the values of the dynamical variable M_x. The matrix elements, $c^*_s c_r$, are numbers describing the state $|\psi\rangle$ of the subsystem; there are 4^N such matrix elements. As a consequence, this matrix is isomorphic to, or has the same information content as, the description in terms of coherences and populations.[8,9] The diagonal elements are proportional to the probabilities of occupation of the energy levels, and consequently to the populations. The off-diagonal elements correspond to correlations between the values of the coefficients c_r. For time-dependent problems, as in spectroscopic measurements, these off-diagonal elements are related to coherent superpositions of the stationary states, i.e. coherences or transitions, present in a spin subsystem.

Different states $|\psi\rangle$ yield different values for the same observable, as can be seen from equation (12). The products, $c^*_s c_r$, vary according to the states $|\psi\rangle$, while the matrix elements $\langle s|\hat{M}_x|r\rangle$ remain invariant. It proves convenient to describe the state of the subsystem, with a projection operator for a single state, $\hat{P}_\psi = |\psi\rangle\langle\psi|$, in the Zeeman basis set:

$$\langle r|\hat{P}_\psi|s\rangle = c_s^* c_r \tag{13}$$

With this projection operator, the expectation value of $\hat{M}_x$ in a subsystem becomes [see equation (12)]:

$$\begin{aligned}\langle\hat{M}_x\rangle = \langle\psi|\hat{M}_x|\psi\rangle &= \sum_{r,s}\langle r|\hat{P}_\psi|s\rangle\langle s|\hat{M}_x|r\rangle \\ &= \mathrm{Tr}\{\hat{P}_\psi\hat{M}_x\}\end{aligned} \tag{14}$$

4 QUANTUM STATISTICAL MECHANICS OF AN ENSEMBLE OF N-SPIN SUBSYSTEMS

A measurement of M_x over an ensemble of subsystems is equivalent to averaging over $\langle \hat{M}_x \rangle$ in equation (14). As the state $|\psi\rangle$ or $c^*_s c_r$ of each subsystem will generally be different, while the dynamical variable will be identical, the averaging gives

$$\overline{\langle \hat{M}_x \rangle} = \sum_{r,s} \overline{\langle r|\hat{P}_\psi|s\rangle} \langle s|\hat{M}_x|r\rangle = \mathrm{Tr}\{\hat{\rho}\hat{M}_x\} \tag{15}$$

with $\hat{\rho}$, the density matrix of the ensemble,[8,9] defined as

$$\langle r|\hat{\rho}|s\rangle = \sum_\psi p_\psi \langle r|\hat{P}_\psi|s\rangle = \overline{\langle r|\hat{P}_\psi|s\rangle} = \overline{c^*_s c_r} \tag{16}$$

where p_ψ is the statistical weight of $|\psi\rangle$ in the ensemble.

For NMR experiments, the density matrix is represented by a density operator, corresponding to the Boltzmann weight of the canonical ensemble with the appropriate Hamiltonian operator defined with respect to some convenient reference frame,

$$\hat{\rho} = Q^{-1} \mathrm{e}^{-\hat{\mathcal{H}}/kT} \tag{17}$$

where Q is the ensemble partition function,

$$Q = \sum_{r=1}^{2^N} \langle r|\mathrm{e}^{-\hat{\mathcal{H}}/kT}|r\rangle \tag{18}$$

The description of any spectroscopic experiment will involve the time dependence, due to evolution under some Hamiltonian $\hat{\mathcal{H}}$ of $\hat{\rho}$ to characterize the ensemble, or $\hat{P}$ to represent a subsystem. In the Schrödinger picture, the time dependence is assigned to the state of the system, specifically, to the coefficients $c_r(t)$ of equation (11).[8,9] In MQ NMR experiments of solids, the relevant Hamiltonian corresponds to the time average of $\hat{\mathcal{H}}_\mathrm{d}$ in the rf toggling frame, $\tilde{\hat{\mathcal{H}}}_\mathrm{d}$ [see equation (2)], over a cycle of the rf excitation sequence. The equation of motion for $\hat{P}$ is obtained by inserting $|\psi\rangle$ into the time-dependent Schrödinger equation to yield[8,9]

$$\frac{\mathrm{d}\hat{P}}{\mathrm{d}t} = \frac{\mathrm{i}}{\hbar}[\hat{P}, \tilde{\hat{\mathcal{H}}}_\mathrm{d}] \tag{19}$$

The averaging of equation (19) over the ensemble of subsystems with identical $\tilde{\hat{\mathcal{H}}}_\mathrm{d}$ gives the equation of motion for $\hat{\rho}$:

$$\frac{\mathrm{d}\hat{\rho}}{\mathrm{d}t} = \frac{\mathrm{i}}{\hbar}[\hat{\rho}, \tilde{\hat{\mathcal{H}}}_\mathrm{d}] \tag{20}$$

Equation (20) is also known as the Liouville–von Neumann equation.

For a time independent average Hamiltonian, a formal solution to equation (20) is

$$\hat{\rho}(t) = \hat{U}\hat{\rho}(0)\hat{U}^{-1} \tag{21}$$

where the propagator $\hat{U}$ is defined as

$$\hat{U} = \exp\left(-\frac{\mathrm{i}}{\hbar}\tilde{\hat{\mathcal{H}}}_\mathrm{d} t\right) \tag{22}$$

The interpretation of equation (21) is of importance for understanding the development of multiple spin coherences in time resolved MQ NMR experiments. Insight in this many-body problem, as discussed in the next section, can be gained through a Taylor expansion of $\hat{\rho}(t)$ about $t = 0$:

$$\hat{\rho}(t) = \hat{\rho}(0) + \sum_{n=1}^{\infty} \frac{t^n}{n!} \frac{\mathrm{d}^n}{\mathrm{d}t^n} \hat{\rho}(t)|_{t=0} \tag{23}$$

From equations (21) and (22), one finds the derivatives of $\hat{\rho}(t)$, of which only the first two are given here:

$$\frac{\mathrm{d}\hat{\rho}(t)}{\mathrm{d}t} = \frac{\mathrm{i}}{\hbar}[\hat{\rho}(0), \tilde{\hat{\mathcal{H}}}_\mathrm{d}] \tag{24}$$

$$\frac{\mathrm{d}^2\hat{\rho}(t)}{\mathrm{d}t^2} = -\frac{1}{\hbar}[[\hat{\rho}(0), \tilde{\hat{\mathcal{H}}}_\mathrm{d}], \tilde{\hat{\mathcal{H}}}_\mathrm{d}] \tag{25}$$

Finally, by substituting equations (24) and (25) and all the other derivatives into equation (23), one obtains:

$$\hat{\rho}(t) = \hat{\rho}(0) + \frac{\mathrm{i}t}{\hbar}[\hat{\rho}(0), \tilde{\hat{\mathcal{H}}}_\mathrm{d}] - \frac{t^2}{2\hbar^2}[[\hat{\rho}(0), \tilde{\hat{\mathcal{H}}}_\mathrm{d}], \tilde{\hat{\mathcal{H}}}_\mathrm{d}] + \cdots \tag{26}$$

5 DEVELOPMENT OF MULTIPLE SPIN/MULTIPLE QUANTUM COHERENCES IN DIPOLAR COUPLED SOLIDS

The power series in time for $\hat{\rho}(t)$ in equation (26) describes the evolution of the spin dynamics in MQ NMR experiments. With the initial conditions corresponding to the spin system at equilibrium in a strong Zeeman field at a high temperature, equation (17) implies

$$\hat{\rho}(0) \propto \hat{I}_z = \sum_i \hat{I}_{zi} \tag{27}$$

As pointed out in Section 3, since $|\hat{\mathcal{H}}_\mathrm{Z}| \gg |\hat{\mathcal{H}}_\mathrm{d}|$, it is appropriate to neglect the contributions of $\hat{\mathcal{H}}_\mathrm{d}$ in the initial conditions. However, in the toggling reference frame, $\tilde{\hat{\mathcal{H}}}_\mathrm{d}$ is crucial for determining the evolution of the spin dynamics. By inserting $\hat{\rho}(0)$ and the nonsecular average Hamiltonian $\mathcal{H}_\mathrm{d}$ suitable for a particular MQ NMR experiment into equation (26), it is possible to examine the qualitative features of the growth of multiple spin/multiple quantum coherences in a solid.

With $\rho(0)$ corresponding to single-spin interactions and $\tilde{\hat{\mathcal{H}}}_\mathrm{d}$ to two-spin interactions, the ascending terms in the expansion of $\hat{\rho}(t)$ describe the sequential growth of multiple spin coherences due to the evolution under $\tilde{\hat{\mathcal{H}}}_\mathrm{d}$. In the first-order terms t^1, the commutators produces two-spin correlations of the form $\hat{I}_{i\alpha}\hat{I}_{j\beta}$, where the components α and β of the spin angular momentum operators are determined by the actual

details of $\hat{\mathcal{H}}_d$. The nested commutators in the second-order terms t^2 yield three-spin operators, $\hat{I}_{i\alpha}\hat{I}_{j\beta}\hat{I}_{k\gamma}$. The hierarchy of nested commutators from the higher order terms t^n generate $(n-1)$-spin operators. By introducing ladder (raising and lowering) operators in these product operators, the order n of the corresponding MQCs becomes explicit; the sum of raising operators minus the sum of the lowering operators in a product operator gives the order of the coherence. Thus, to observe an n quantum coherence it is necessary to have, at the minimum, a contribution of order t^{n+1}, implying the presence of an n-spin/n quantum operator in the expansion of $\hat{\rho}(t)$. Higher order terms can also produce n quantum coherences. The distinction between these different n quantum coherences comes from the number of spins participating in the correlations. Since multiple spin coherences contribute to equation (26) through the product of dipolar coupling constants (as discussed below and in Section 6), the lattice parameters r_{ij} and θ_{ij} will ultimately control and distinguish between the various n quantum coherences.

The interplay between the development of multiple spin coherences and the order of the resulting multiple quantum coherences depends on selection rules associated with the nature of $\hat{\mathcal{H}}_d$ and equation (26). With respect to the time development of the number of spins in multiple spin coherences, the bilinear spin operators of $\hat{\mathcal{H}}_d$ and the algebra of the nested commutators in equation (26) imply a cascade process in the growth of correlations. An n-spin coherence can only grow by sequentially incorporating one single spin at a time, one after another. The time development of multiple quantum coherences is constrained to pathways, in a K-spin/n quantum space, which depend uniquely on the nature of $\hat{\mathcal{H}}_d$.[2,10] The pulse excitation sequences for MQ NMR of solids produce generic classes of $\hat{\mathcal{H}}_d$ terms: 2-spin/0,2 quantum operators, 2-spin/1-quantum operators, and 2-spin/2 quantum operators. These excitation sequences achieve a redistribution of MQ NMR spectral intensities according to selections rules on ΔK and Δn. For example, with 2-spin/2 quantum operators in $\hat{\mathcal{H}}_d$, and an $\hat{I}_z$ initial condition, equation (26) and the selection rules $\Delta K = \pm 1$ and $\Delta n = \pm 2$, demonstrate that only even coherences develop; in addition, the evolution cannot generate 4-spin/4 quantum coherences. The redistribution of spectral intensities produced by the different $\hat{\mathcal{H}}_d$ terms is optimized according to the size or spatial distribution of the spins within a subsystem, e.g. for the detection of spin clusters, or extended spin networks.

One of the simplest models, the so-called statistical or Gaussian model,[1] used to interpret MQ NMR spectra of solids, consists of assuming that all the individual coherences possible in an N-spin subsystem have the same magnitudes with random phases, and that all have been excited at long excitation times in the sample or ensemble of subsystems. Time-reversal excitation produces transitions with identical phases within an order.[11] Hence, the assumption of a priori equal weight of the different coherences implies that the MQ NMR spectral intensities $I(n,t)$ are proportional to Z_n, [see equation (8)]. Stated differently, the distribution of coherences in the ensemble of subsystems is proportional to Z_n. For large N and small n, it is possible to transform Z_n in equation (8) with Stirling's approximation $y! \approx (2\pi y)^{\frac{1}{2}}\, y^y\, e^{-y}$ to give

$$Z_n \approx 4^N (\pi N)^{-\frac{1}{2}} e^{-n^2/N} \tag{28}$$

As a consequence, according to the statistical model, a MQ NMR spectral intensity profile as a function of order $I(n,t)$ should be Gaussian, as suggested by equation (28).

The time dependence of these profiles arises from the growth of the subsystem size $N(t)$. The variance $N(t)$ obtained from fitting $I(n,t)$ to a Gaussian function of n represents the effective number of dynamically coupled spins, in a typical subsystem, following an excitation period of duration t under $\hat{\mathcal{H}}_d$. In addition to spin counting with this variance, it has been suggested that the rate of change in $N(t)$ with time reflects on some of the space-filling properties, such as dimensionality effects, of spin networks.[1,1,12–14] Qualitatively, three generic classes of behavior have been observed for $N(t)$. Saturation in $N(t)$ implies the presence of isolated clusters of spins. Unbounded growth curves are observed in extended spin networks. Saturation behavior seen at early excitation times, followed by unbounded growth, indicates the occurrence of coupled clusters of spins.

The simplicity of the statistical model accounts for its widespread use in the MQ NMR literature of solids.[2,3] However, some questions have been raised concerning the validity of the assumption of the a priori equal weight of all coherences.[2,6] In addition, the convenience of the Gaussian model with the use of simple fitting procedures to analyze MQ NMR spectral intensity profiles is not successful with extended spin networks.[15] To appreciate the nature of these problems, and to understand the development of multiple spin/multiple quantum coherences in solids beyond the level of the statistical model, it is necessary to consider further fundamental aspects of the spin dynamics in MQ NMR.

As discussed in previous sections, the interpretation of MQ NMR experiments of solids relies on the spin dynamics within a subsystem, followed by averaging over an ensemble of subsystems. The density operator $\hat{\rho}$ in equation (17) and its equation of motion [equation (26)] reflect this two-fold averaging: a quantum mechanical averaging or the determination of expectation values in a subsystem [equation (14)], and a statistical averaging over the expectation values due to the distribution of subsystem states in the ensemble [equations (15) and (16)].

It is possible to construct a statistical ensemble of diagrams or graphs, including evolution, which is completely isomorphic with the density operator formalism used to describe MQ NMR.[2] This approach provides complementary physical insights into MQ NMR spin dynamics, averaging, and measurements. The diagrams include vertices corresponding to spins, and edges or links to delineate dipolar coupling constants between spins. The weight of an edge is proportional to the absolute value of the dipolar coupling constant. The state of a spin is represented by a color. For a spin $\frac{1}{2}$ there are three colors, $\hat{I}_x$, $\hat{I}_y$, and $\hat{I}_z$; generalization to higher spins is possible.

The decomposition of the density operator proceeds by examining an N-spin subsystem, under rigid lattice conditions and without any symmetry elements. In such an N-spin subsystem, the number of distinct subsets n_i each containing i spins is given by the binomial coefficient:

$$n_i = \binom{N}{i} \tag{29}$$

For example, the number of pairs of spins or dipolar coupling constants in a single subsystem is n_2. The subsets can range in size from $i = 1$ to N. The sum over all possible subsets is:

$$n_{\mathrm{T}} = \sum_{i=1}^{N} n_i = \sum_{i=1}^{N} \binom{N}{i} = 2^N - 1 \tag{30}$$

In equation (30), n_{T} is the sum of all possible spin correlations in the spin subsystem. By including the states of the spins or colors within the spin correlations, one obtains

$$n_{\mathrm{T}}^{\mathrm{c}} = \sum_{i=1}^{N} n_i 3^i = \sum_{i=1}^{N} \binom{N}{i} 3^i = 4^N - 1 \tag{31}$$

where $n_{\mathrm{T}}^{\mathrm{c}}$ is the total number of distinct colored subsets, and is equal to the number of elements (coherences and populations) of the normalized density operator in an N-spin-$\frac{1}{2}$ subsystem.

The growth of multiple spin/multiple quantum coherences is described by equation (26). From the interpretation of this equation, the coherences were seen to grow sequentially by adding one spin after another with increasing time. It is clear that this description is valid for the density operator, either in the product operator formalism or in the ensemble of colored spin correlations described above.

However, there is an essential feature related to the growth processes and the averaging over the subsystems, which becomes more obvious with the diagrams. Consider a generic term of $(n + 1)$th order in the Taylor expansion of equation (19) for the time dependence of the projection operator $\hat{P}_\psi$. The resulting equation is analogous to equation (26) with $\hat{P}_\psi$ replacing $\hat{\rho}$. The product of spin operators will include n-spin operators corresponding to different spins in the subsystem. As $\hat{\mathcal{H}}_{\mathrm{d}}$ is present in the nested commutators, there will also be products of $(n - 1)$ dipolar coupling constants which multiply the n-spin product operators. For example, a 3-spin coherence involving spins i, j, and k, will have a corresponding product operator of the form $\hat{I}_{i\alpha}\hat{I}_{j\beta}\hat{I}_{k\gamma}$, multiplied by a product of dipolar coupling constants $D_{ij}D_{jk}$. Hence, in general, the contributions or weights of n-spin coherences in the equation of motion are determined by products of $(n - 1)$ dipolar coupling constants. A diagram, consisting of n vertices connected with $(n - 1)$ edges is called a tree; no loops are permitted in such a graph. The number of ways to connect n vertices, with $(n - 1)$ edges chosen among $\binom{n}{2}$ distinct edges, corresponds to the number of distinct trees given by

$$n^{n-2} \tag{32}$$

Equation (32) also gives the number of products of n dipolar coupling constants for a particular n-spin coherence. In an N-spin subsystem, the total number of products of n dipolar coupling constants for n-spin coherences is

$$\binom{N}{n} n^{n-2} \tag{33}$$

The averaging over an ensemble of subsystems, in order to obtain $\hat{\rho}$, as discussed in Section 4 and in NMR texts,[8,9] proceeds by assuming that the Hamiltonians are identical for all subsystems [see equations (19) and (20)]. This is certainly true for a hypothetical representative ensemble, or approximately true for a sample viewed as an ensemble of loosely coupled subsystems, as presented in Section 2. However, when the averaging is done over a nonequilibrium ensemble for a finite sample, care must be taken to distinguish between the sum in the Hamiltonian [see equations (2), (19) and (20)] and the realizations of multiple spin correlations (with corresponding product operators) present in the ensemble. As an example, consider a 25-spin subsystem. In this subsystem, there is only a single MQ coherence of order 25 represented by a product operator consisting of 25 raising operators. According to equation (26), the 25-spin/25 quantum coherence is weighted by a product of 24 dipolar coupling constants. Among these spins, there are $\binom{25}{2} = 300$ distinct dipolar coupling constants. The number of distinct products of 24 dipolar coupling constants corresponds to the number of trees, in this case $25^{23} \approx 10^{32}$ realizations. It should be clear that a macroscopic sample consisting of 10^{20} spins will not have enough 25-spin subsystems to represent all trees or possible realizations of the 25-MQ coherence. An MQ NMR measurement on a macroscopic sample, consisting of an ensemble of subsystems, is really an average over the subsystems [see equation (16)]. The average over multiple spin coherences is really performed over the distribution of corresponding trees present in the ensemble, i.e. over products of dipolar coupling constants. To appreciate the intricacies of such a measurement or averaging procedure, we now examine the distributions of dipolar coupling constants and their products in spin networks.

6 STATISTICAL PROPERTIES OF DISTRIBUTIONS OF DIPOLAR COUPLING CONSTANTS AND THEIR PRODUCTS IN LARGE SPIN NETWORKS

Consideration of equation (26) demonstrated that different multiple spin coherences contribute to the evolution of ρ according to the values of the products of dipolar coupling constants. Thus, for a finite excitation time, coherences cannot be treated equally, as is assumed in the Gaussian statistical model.[1] Only in the limit of an infinite excitation time will all the coherences contribute equally to the spin dynamics.[6] The recognition that in spin networks the distributions of dipolar coupling constants and their products are characterized by asymmetry associated with extreme widths is important for understanding MQ NMR spin dynamics.[6] Difficulties encountered with the interpretation of equation (26), due to the presence of multiple length- and timescales, actually arise from these broad and peculiar distributions.

In three-dimensional solids, lattice sums of dipolar coupling constants can be replaced by a continuum approximation involving integrals such as

$$\sum_{i\rangle j}^{N} D_{ij} \propto \int_r (1/r^3) r^2 \, \mathrm{d}r \propto \ln r \tag{34}$$

For an infinite sample, the lattice sum diverges, while for finite spin networks the sum is conditionally convergent, i.e. it depends on the sample shape. Some approaches, such as the Ewald summation and the Lorentz cavity method, have

been devised to study these distributions in samples of general shapes.

In one-dimensional solids, the lattice sums can be performed analytically. Consider an infinite crystalline one-dimensional chain of spins with lattice parameter r oriented perpendicular to the Zeeman field. The average dipolar coupling constant per spin $\langle D \rangle_s$ is

$$\langle D \rangle_s = 2 \sum_{k=1}^{\infty} \tfrac{1}{2} \gamma^2 \hbar^2 (kr)^{-3} \approx 1.20 \gamma^2 \hbar^2 / r^3 \qquad (35)$$

In this case, 83% of the average is determined by the value of two nearest neighbor couplings out of an infinity of couplings!

Figure 3 shows a schematic distribution of the absolute values of dipolar coupling constants and their logarithms for a large spin subsystem. One should note that the distribution in Figure 3(a) is really a caricature, since in large networks the width essentially cannot be observed on linear scales.[6] Several statistical features are illustrated by Figure 3. The average $\langle |D| \rangle$ is determined by the coupling constants in the tail of the distribution, while the most probable value $|D|_{\mathrm{MPV}}$ is sensitive to the small and numerous long-range couplings. The transformation of the distribution on a logarithmic scale demonstrates the huge dynamic range of the distribution. For example in a two-dimensional square lattice of $10^2 \times 10^2$ spins, the distribution of coupling constants covers over 10 orders of magnitude. Differences between $\langle \ln |D| \rangle$ and $\ln \langle |D| \rangle$ are important to reconcile with measurements on an ensemble. The value of $\langle |D| \rangle$ is sensitive to the largest coupling constants, while $\langle \ln |D| \rangle$ is more sensitive to the details of the overall distribution. Such distinctions are significant in the physics of

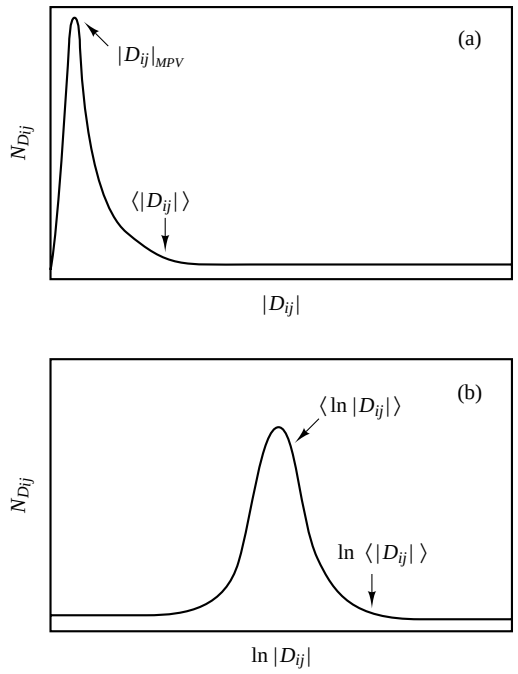

Figure 3 (a) Schematic distribution of the absolute values of dipolar coupling constants in an N-spin subsystem. (b) Schematic distribution of the logarithm of the absolute values of dipolar coupling constants in the same subsystem. Note the difference between $\langle \ln |D_{ij}| \rangle$ and $\ln \langle |D_{ij}| \rangle$. The analogous distributions, involving products of dipolar coupling constants, show similar behavior, but with wider distributions

disordered systems.[16,17] Products of dipolar coupling constants show similar features; however, the distributions are even wider.[6]

Probably the most interesting feature of these distributions arises from the scaling behavior of the statistical properties as a function of N, the number of spins. The relative fluctuations RF,

$$\mathrm{RF} = \frac{(\langle |D|^2 \rangle - \langle |D| \rangle^2)^{\frac{1}{2}}}{\langle |D| \rangle} \qquad (36)$$

measure the relative spread about the mean. In the limit of large spin networks,

$$\mathrm{RF} \propto N^{+\frac{1}{2}} \qquad (37)$$

This result implies that the distributions become wider as N increases, i.e. there is no self-averaging. The ratio of the most probable value to the first moment can be shown to scale as $N^{+\frac{3}{2}}$. The product of dipolar coupling constants shows a similar behavior with the same scaling exponents.[6] Such behavior is highly counterintuitive, since in random additive processes, within the central limit theorem, the relative fluctuations scale as $N^{-\frac{1}{2}}$, and the most probable value coincides with the first moment in the thermodynamic limit.

Some implications of these results for the growth of multiple spin coherences/multiple quantum coherences are beginning to emerge.[2,18] For example, anisotropy effects in the growth process should be determined by the products of the angular contributions of dipolar coupling constants. In a measurement on an ensemble of subsystems, the realizations of multiple spin coherences which are detected should be those with the largest products of dipolar coupling constants. However, these products are the least numerous but still dominate the dynamics due to their large weights. This last result would suggest that a single subsystem, where a multiple spin coherence with the largest possible product has been excited, could eventually dominate a macroscopic measurement. The statistical properties of the distributions of dipolar coupling constants and their products should also be relevant for other aspects of strongly dipolar coupled spin systems; examples include problems associated with FIDs[19] and the lineshapes,[20] spin diffusion,[21] and spin temperature.[22]

7 DYNAMICAL SCALE INVARIANCE IN THE GROWTH OF MULTIPLE SPIN CORRELATIONS IN DIPOLAR COUPLED SOLIDS

Dilation or scaling symmetry, observed under certain conditions in some physical systems, is a generalization of the concept of similarity among geometrical objects. In geometry, the properties of two circles with different radii are similar to one another by simple transformations of scales. In physical sciences, the practical aspects of scaling involve the determination of the relevant scaled variables to describe a phenomenon, such that all data acquired under a range of conditions collapse onto some single universal plot. Thus, scaling reveals an invariance or a kind of unification among the relevant scaled variables, which was not obvious

in the original unscaled variables. Understanding the physical reasons underlying scaling symmetry usually leads to deeper insights into the phenomenon.

Some scaling arguments have been applied to various aspects of the growth of multiple spin/multiple quantum coherences in solids.[1,2,15,23] In the context of the Gaussian statistical model, studies have focused on the behavior of the variance $N(t)$ in dilution effects[1] and power law growth[2] in spin networks, and dimensional analysis of growth curves.[23] A more elaborate scaling analysis of MQ NMR spectral intensity profiles, as a function of order and excitation time, demonstrated non-Gaussian behavior in extended spin networks.[15] These studies also provided additional support for the case of exponentially decaying intensity profiles. Behind these approaches lies the belief that the physics of the growth processes should be invariant or scale free, for some range of length- and timescales.

Baum et al.[1] have studied the effects of dilution of spin networks with MQ NMR. With increasing dilution, the growth curves $N(t)$ were shifted to longer excitation times. When the excitation time was multiplied by a scaling factor, all growth curves for the diluted systems could be collapsed onto the data of the undiluted or 'pure' spin network. In this case, the scaling symmetry demonstrates the invariance of the physics of the growth processes in the pure and diluted spin networks. A simple dilution in time relates these different systems. The scaling factor was observed to be a function of dilution; no serious attempts were made to understand this phenomenology.

Lacelle[2] has studied the growth curves $N(t)$ of a large variety of solid samples. All the data were seen to follow power law behavior,

$$N(t) \propto t^{\alpha} \tag{38}$$

where α is a growth exponent characteristic of the samples and the growth mechanism. The presence of power law growth indicates a scale invariant process, such that the functional

$$N(\lambda t) = \lambda^{\alpha} N(t) \tag{39}$$

exists for any values of the scaling factor λ. The solution of equation (39), i.e. equation (38), is obtained by setting $\lambda = 1/t$ in equation (39). In order to determine the physics behind the growth exponents, several models were considered. For example, in diffusive growth, the length scale ξ of the multiple spin correlations should follow

$$\xi \propto t^{\frac{1}{2}} \tag{40}$$

The space-filling properties of a homogeneously embedded solid in D dimensions imply that

$$N \propto \xi^{D} \tag{41}$$

Equations (40) and (41) yield

$$N \propto t^{D/2} \tag{42}$$

from which the growth exponent $\alpha = D/2$ is deduced for a diffusive growth mechanism. None of the models developed could account successfully for all the observed growth exponents. However, a classification of the spin networks could be achieved with the long time behavior of the growth rates

$$\frac{\mathrm{d}N}{\mathrm{d}t} \propto t^{\alpha-1} \tag{43}$$

When $\alpha < 1$, the growth rates converge to zero at long excitation times, implying the presence of clusters of spins. When $\alpha > 1$, a divergence in the growth rates should occur, which indicates the presence of an extended network. The case of $\alpha = 1$ corresponds to the threshold between these regimes. In a sense, α serves as a localization/delocalization criterion for multiple spin coherences.

Scruggs and Gleason[23] have examined the growth curves of different simple crystalline materials. By assuming that the growth processes were only determined by a relevant time-independent scale, the inverse of the square root of the second moment of the dipolar linewidths, the different growth curves collapsed onto a single universal curve for early excitation times. Their assumption for this empirical scaling is implicitly equivalent to assuming that the growth processes are dominated by nearest neighbor couplings, since Van Vleck's second moment is also dominated by such couplings.

One could argue about the quality and the quantitative aspects of the fitting procedures with the Gaussian approximation in these studies.[1,2,23] However, the value of such studies really lies in the efforts made to explore the possible facets of scaling in the growth processes of multiple spin/multiple quantum coherences. To ascertain any quantitative aspects of scaling, for example, growth exponents, under these circumstances it is clear that many more experiments involving high quality data will be required.

Lacelle et al.[15] have developed some scaling arguments in order to test the validity of the Gaussian statistical model. In particular, they strived to observe the scaling of MQ NMR spectra, as a function of order and excitation times, in extended spin networks. The Gaussian dependence suggested for the spectral intensity profiles $I(n,t)$ in equation (28) is actually a generalized homogeneous equation. With the time dependence of the variance $N(t)$ corresponding to a random walk model in product operator space,[1,10] the expected scaling, $I(n,t)/t^{-\frac{1}{2}}$ versus $n/t^{\frac{1}{2}}$, should have collapsed all MQ NMR spectra for a sample onto a single universal spectrum. The lack of scaling clearly demonstrated non-Gaussian behavior. Instead, consideration of the multiplicative nature of the coupling constants associated with product operators in equation (26) led to a heuristic argument predicting exponential decaying intensity profiles. The ensuing scaling analysis collapsed MQ NMR spectra, obtained at different excitation times, onto a single universal spectrum, thereby demonstrating dynamical scale invariance in the growth process of multiple spin/multiple quantum coherences. Such an approach reveals some aspects of the complexities, richness, and subtleness of multiple spin dynamics in MQ NMR of solids.

8 RELATED ARTICLES

Average Hamiltonian Theory; Double Quantum Coherence; Multiple Quantum Coherence in Spin-1/2 Dipolar Coupled Solids; Multiple Quantum NMR in Solids; Spin Diffusion in Solids.

9 REFERENCES

1. J. Baum, M. Munowitz, A. N. Garroway, and A. Pines, *J. Chem. Phys.*, 1985, **83**, 2015.
2. S. Lacelle, *Adv. Magn. Opt. Reson.*, 1991, **16**, 173.
3. K. K. Gleason, *Concepts Magn. Reson.*, 1993, **5**, 199.
4. H. E. Stanley, *Introduction to Phase Transitions and Critical Phenomena*, Oxford University Press, New York, 1971, Chap. 9
5. J. D. Gunton, M. San Miguel, and P. S. Sahni, in *Phase Transitions and Critical Phenomena*, ed. C. Domb and J. L. Lebowitz, Academic, London, 1983, Vol. 8, Chap. 3
6. S. Lacelle and L. Tremblay, *J. Chem. Phys.*, 1993, **98**, 3642.
7. D. Chandler, *Introduction to Modern Statistical Mechanics*, Oxford University Press, New York, 1987, Section 3.1.
8. C. P. Slichter, *Principles of Magnetic Resonance*, 3rd edn., Springer, Berlin, 1990, Section 5.4.
9. M. Goldman, *Quantum Description of High-Resolution NMR in Liquids*, Oxford University Press, New York, 1988, Section 4.1.
10. M. Munowitz, A. Pines, and M. Mehring, *J. Chem. Phys.*, 1987, **86**, 3172.
11. Y. S. Yen and A. Pines, *J. Chem. Phys.*, 1982, **78**, 3579.
12. D. H. Levy and K. K. Gleason, *J. Phys. Chem.*, 1992, **96**, 8125.
13. B. E. Scruggs and K. K. Gleason, *Chem. Phys.*, 1992, **166**, 367.
14. G. Cho and J. P. Yesinowski, *Chem. Phys. Lett.*, 1993, **205**, 1.
15. S. Lacelle, S. J. Hwang, and B. C. Gerstein, *J. Chem. Phys.*, 1993, **99**, 8407.
16. B. Derrida, *Phys. Rep.*, 1984, **103**, 29.
17. S. Redner, *Am. J. Phys.*, 1990, **58**, 267.
18. S. Lacelle and L. Tremblay, *Bull. Magn. Reson.*, 1994, in press.
19. I. J. Lowe and R. E. Norberg, *Phys. Rev.*, 1957, **107**, 46.
20. J. H. Van Vleck, *Phys. Rev.*, 1948, **74**, 1168.
21. N. Bloembergen, *Physica*, 1949, **15**, 386.
22. M. Goldman, *Spin Temperature and Nuclear Magnetic Resonance in Solids*, Clarendon, Oxford, 1970.
23. B. E. Scruggs and K. K. Gleason, *J. Magn. Reson.*, 1992, **99**, 149.

Biographical Sketch

Serge Lacelle. *b* 1955. B.Sc., Ottawa, 1978; Ph.D., Iowa State, 1984. Introduced to NMR by B. C. Gerstein. Faculty, Chimie Université de Sherbrooke, 1985–present. Research interests: the development and understanding of NMR methods to probe mesoscopic length scales (1 nm to 1 μm) in condensed matter; statistical mechanics of spin networks; multiple quantum NMR of solids; phase separation and critical phenomena; fluid mechanics; and pattern formation.

Multiple Quantum NMR in Solids

Karen K. Gleason

Massachusetts Institute of Technology, Cambridge, MA, USA

1	Introduction	1
2	MQ Coherence Intensities	1
3	MQ Excitation by $\hat{\mathcal{H}}_{yx}$	2
4	Measuring MQ Intensities	3
5	Small Dipole Coupled Networks	4
6	Large Dipole Coupled Networks	5
7	Dimensionality of a Nuclear Spin Distribution	6
8	Relaxation and Effect of Molecular Motion	8
9	Related Articles	9
10	References	9

1 INTRODUCTION

Multiple quantum (MQ) NMR can provide unique insight into the distribution and motion of nuclei in solids. In this article, we consider multiple quantum coherences associated with homonuclear dipolar coupling among spin-$\frac{1}{2}$ nuclei in solids. Therefore, we consider nuclei with high natural isotopic abundance and a high gyromagnetic ratio. ^{1}H MQ NMR has been applied to study organic solids,[1–3] amorphous semiconductors,[4–7] and adsorbates on catalysts[8–14] and chromatography columns.[15] In addition, ^{19}F MQ NMR has been used to study bulk salts,[16] photosensitive salt/polymer mixtures,[17–19] and bulk polymers.[20] MQ NMR of ^{31}P in solids has also been demonstrated.[21] Several review articles and textbook chapters on MQ NMR experiments and their applications are available.[21–29]

The rate of MQ coherence development depends on the strength and time dependence of each pairwise homonuclear dipolar coupling as well as the number of such pairs. For a network of N equivalent nuclei, the second moment M_2 of the distribution of all the pairwise homonuclear dipole couplings can be related to the geometry of the spin distribution through the van Vleck equation:[30]

$$M_2 = \tfrac{3}{4}\gamma^4\hbar^2 \frac{I(I+1)}{2} \sum_{i<j}^{N-1} \frac{(1-3\cos^2\theta_{ij})^2}{r_{ij}^6} \qquad (1)$$

Thus, many combinations of internuclear distances r_{ij} and the total number of pairs in the summation $N-1$ can give rise to identical M_2. Using MQ NMR, the number and distribution of dipolar couplings can be investigated independently, thus allowing the distribution of nuclei in a solid to be explored.

Observation of MQ coherence development in solids is accomplished interferometrically via a two-dimensional NMR technique.[1,29] By incrementing the MQ preparation time τ, the presence of finite clusters of nuclei can be distinguished from nuclear distributions which are homogeneous on the 1–2 nm length scale of this experiment.[2,3] Coherences arising from a cluster of nuclei will saturate with increasing MQ excitation time, because no additional nuclei are available for correlation in the surrounding region. In contrast, the number of nuclei coupled together in a large homogeneous dipole network will increase monotonically with time until relaxation occurs.

Furthermore, a simple scaling exists for the growth of MQ coherences among many bulk materials.[16,31] This behavior allows homogeneous three-dimensional distributions of nuclei to be differentiated from one- and two-dimensional distributions.[31–33] Identification of two-dimensional distributions is particularly valuable for determining whether a given nuclear species, such as ^{1}H, ^{19}F, or ^{31}P, is segregated at a surface,[31,34] such as a grain boundary in a polycrystalline material. A model which expands the density matrices in terms of average product operators allows these differences to be evaluated numerically.[31]

More complex distributions of nuclei can also be analyzed using MQ NMR. For example, both isolated salt molecules and large aggregates of salt have been observed simultaneously within polymeric matrices.[17–19] Finally, MQ NMR and its relaxation may serve as a valuable probe of molecular reorientation in solids which modulate the dipolar coupling network at frequencies in the kilohertz range.[20,35,36]

2 MQ COHERENCE INTENSITIES

Analysis of MQ intensities is the underlying principle for using MQ NMR as a 'spin-counting' technique, allowing the number of dipole coupled nuclei in a isolated cluster to be determined.[3] Although only two possible states, α and β, exist for an individual spin-$\frac{1}{2}$ nucleus, when N of these nuclei are dipole coupled there are 2^N possible product states. Thus, a $2^N \times 2^N$ density matrix is required to represent fully the time development of MQ coherence intensity among N dipolar coupled spin-$\frac{1}{2}$ nuclei. A schematic representation of ρ for $N = 3$ is shown in Figure 1, where the indices of the matrix are the eight possible product states. Diagonal elements can be used to calculate the populations of the product states, while the off-diagonal elements indicate the MQ coherences between two different states.

The MQ coherence order, n, is equal to the difference in m_z between the two states. Since the z component of angular momentum m_z of an individual spin state is $\pm\frac{1}{2}$, m_z for the product states ranges from $-N/2$ to $+N/2$. Thus, MQ orders can be positive, negative, or zero, provided that $|n| \leq N$. This limitation provides a very elegant way of determining the number of dipole coupled spins in a spatially isolated cluster. However, there is only one way to achieve such an $n = N$ coherence, making it statistically difficult to observe intensity in highest MQ order for large N. Fortunately, the number of density matrix elements Z_n for lower order coherences ($|n| < N$) also depends on the number of coupled nuclei:

$$Z_n = \sum_{i<j} \delta_{[(m_{zi}-m_{zj}),n]} = \binom{2N}{N-|n|} \qquad (2)$$

In this equation, Z_0 includes both off-diagonal elements with $n = 0$, representing true zero quantum coherence (0Q), and diagonal elements representing self-correlation among the

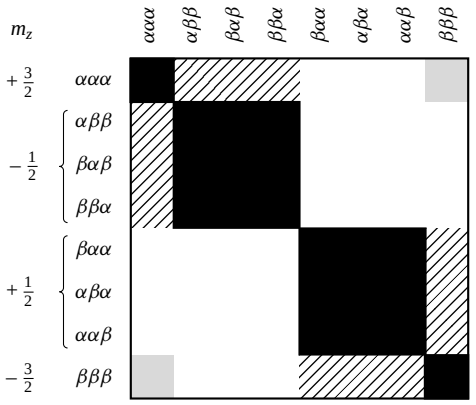

Figure 1 Schematic representation of ρ for $N = 3$. The 2^3 product states are sorted by m_z so that elements corresponding to even MQ coherences ($n = 0$, black; $|n| = 2$, striped) appear in the upper left and lower right quadrants. The remaining elements correspond to odd MQ orders ($|n| = 1$, white; $|n| = 3$, grey)

states, as no difference is resolved between these two types of element by most MQ experiments.

Each element in Figure 1 is shaded according to the absolute value of its corresponding MQ order. Note that the first $4^N/2$ indices in Figure 1 represent the states with $m_z = (N - k)$, where k is an integer. Thus, elements corresponding to even order MQ coherences will appear only in the upper left and lower right quadrants of the density matrix. The remainder of the elements in the upper right and lower left quadrants correspond to odd order MQ coherences. If only even order MQ coherences are excited, this density matrix will be block diagonal with only $4^N/2 = 32$ possible nonzero elements. For $N = 3$, the number of elements contributing to the even orders will be $Z_0 = 20$ and $(Z_2 + Z_{-2}) = 12$.

At equilibrium, the density matrix is proportional to I_z. Thus, only the diagonal elements are nonzero. As MQ excitation begins, intensity develops in density matrix elements of low MQ order. Longer excitation times are required for growth of high-order MQ coherences. The n quantum intensity at any time τ after MQ excitation is begun $I_n(\tau)$, contains contributions from all Z_n density matrix elements comprising that order:[37]

$$I_n(\tau) = \sum_{i<j} \delta_{[(m_{zi}-m_{zj}),n]} |\rho_{ij}(\tau)|^2 \tag{3}$$

Thus, calculation of MQ dynamics requires following the time evolution of the density matrix under the influence of the Hamiltonian corresponding to the MQ excitation sequence during the experiment.

The Liouville von Neumann equation of motion can be used to calculate $\hat{\rho}(\tau)$ explicitly:

$$\frac{\mathrm{d}\hat{\rho}(\tau)}{\mathrm{d}\tau} = \mathrm{i}[\hat{\rho}(\tau), \tilde{\hat{\mathcal{H}}}] \tag{4}$$

where $\hat{\mathcal{H}}$ is the Hamiltonian applied to the system for a duration τ in order to develop MQ coherences. If average Hamiltonian theory can be applied, the solution of equation (4) is

$$\hat{\rho}(\tau) = \exp(-\mathrm{i}\tilde{\hat{\mathcal{H}}}\tau)\rho(0)\exp(\mathrm{i}\tilde{\hat{\mathcal{H}}}\tau) \tag{5}$$

For small numbers of spins ($N \leq 9$), the development of $I_n(\tau)$ has been calculated explicitly using equations (3) and (5).[32,37,38]

However, tracking the time development of the 4^N density matrix elements is a large task for any significant number of coupled spins. For $N = 95$, the number of density matrix elements exceeds the number of hydrogen atoms in the Earth's sun! Thus for a large N, statistical limit behavior is often assumed, in which all MQ coherences have equal probability, allowing the magnitude of all density matrix elements to become equal at long excitation times.

The assumption of a statistical limit[37] greatly simplifies the analysis of MQ coherence intensities since the intensity of an n quantum coherence depends only on the number of elements of that order Z_n:

$$I_n = \frac{C Z_n}{4^N} \tag{6a}$$

The inverse of the constant C represents the fraction of density matrix elements where nonzero intensity could be excited. This fraction depends upon the selectivity of the Hamiltonian applied to the system. When nonselective excitation is used, all MQ orders are excited and $C = 1$. However, selective MQ excitation is often used. For instance, if only even MQ orders are excited, $C = 2$. Since equation (2) shows that Z_n is a function of n and N only, the distribution of $I_n(\tau)$ allows N to be determined. When $N \geq 6$, the right-hand side of equation (6a) can be approximated by a Gaussian distribution:

$$I_n \simeq \frac{C}{\sqrt{N\pi}} \exp(-n^2/N) \tag{6b}$$

Equations (6a) and (6b) are valid for all positive, negative and zero integer values of n, and are normalized such that

$$\sum_{n=-\infty}^{\infty} I_n = 1 \tag{7}$$

In addition, note that the MQ intensity distribution is symmetric, $I_n = I_{-n}$, and that I_0 contains both populations and true 0Q coherences. Furthermore, higher order coherences are statistically more difficult to achieve than lower order coherences. As will be shown below, I_0 tends to deviate more from the predicted values than the positive orders; only the latter are generally utilized to determine N. Statistical limit behavior is often a poor assumption for very small groups of spins, due to presence of symmetry forbidden transitions.

3 MQ EXCITATION BY $\hat{\mathcal{H}}_{yx}$

One of the most desirable Hamiltonians for exciting MQ coherences in solids is $\hat{\mathcal{H}}_{yx}$:

$$\tilde{\hat{\mathcal{H}}}_{yx} = -\frac{1}{2}\sum_{i<j} R_{ij}(\hat{I}_{i+}\hat{I}_{j+} + \hat{I}_{i-}\hat{I}_{j-}) \tag{8}$$

Other Hamiltonians such as $\hat{\mathcal{H}}_{zx}$ have been used for exciting MQ coherences. However, higher orders develop more quickly under $\hat{\mathcal{H}}_{yx}$,[38] maximizing the number of spins that can be correlated before relaxation effects become significant.

The bilinear raising and lowering operators $\hat{I}_{+i}\hat{I}_{+j}$, and $\hat{I}_{-i}\hat{I}_{-j}$ allow only even-order MQ coherence intensity to evolve when $\hat{\mathcal{H}}_{yx}$ is utilized in conjunction with an equilibrium initial density matrix $\rho(0)$ that is proportional to $\hat{I}_z$. When only half of all possible orders are excited, the intensity of each is twice that of a nonselective experiment [equation (6)]. The increased intensity is particularly important for detecting high-order coherences, which are statistically less likely than lower order coherences. Odd order and nonselective excitation using $\hat{\mathcal{H}}_{yx}$ results when prepulses create an initial density matrix proportional to the single quantum operator $\hat{I}_x$ or it can be made nonselective if $\rho(0)$ is a mixture of $\hat{I}_z$ and $\hat{I}_x$, respectively.[40]

For spin counting applications it is important to note that the selection rules for $\hat{\mathcal{H}}_{yx}$ from an initial density matrix proportional to $\hat{I}_z$ result in the inability to create $n = N$ quantum coherence. Obviously, N quantum coherence cannot be developed when N is odd. More surprisingly, N quantum coherence cannot be achieved among $N = 4k$ dipole coupled spins, where k is a positive integer.[40] Thus, four quantum coherence cannot develop among an isolated cluster of four coupled nuclei. While these limitations appear problematic, the ability to achieve N quantum coherence via other MQ propagators can be even more restrictive. For instance, under $\hat{\mathcal{H}}_{zx}$ the N quantum order can never be achieved when starting from the equilibrium density matrix. The restrictions on creating N quantum coherence are only significant for size determination among very small clusters of nuclei. In larger dipole coupled networks, the signal-to-noise ratio of the highest order MQ coherence is generally below the detection limit, rendering the ability to achieve this coherence insignificant.

To carry out the MQ experiment in the laboratory, the phase ϕ of $\hat{\mathcal{H}}_{yx}$ is generally varied.[1,2] One or more repetitions of the eight-pulse cycle shown below have been used to create $\hat{\mathcal{H}}_{yx}(\phi)$:

$$(\Delta/2) - 90^\circ_\phi - (\Delta') - 90^\circ_\phi - (\Delta) - 90^\circ_\phi - (\Delta') - 90^\circ_\phi - (\Delta) - 90^\circ_{\phi+180^\circ} - (\Delta') - 90^\circ_{\phi+180^\circ} - (\Delta) - 90^\circ_{\phi+180^\circ} - (\Delta') - 90^\circ_{\phi+180^\circ} - (\Delta/2)$$

where $\phi = 0^\circ$ corresponds to an x pulse. The relationships between the delays is $\Delta' = 2\Delta + t_p$, where t_p is the pulse length. The average Hamiltonian, $\tilde{\hat{\mathcal{H}}}_{yx}(\phi)$ is then

$$\tilde{\hat{\mathcal{H}}}_{yx}(\phi) = -\frac{1}{2}\sum_{i<j} R_{ij}[\hat{I}_{i+}\hat{I}_{j+}\exp(2i\phi) + \hat{I}_{i-}\hat{I}_{j-}\exp(-2i\phi)] \quad (9)$$

Considering $0^\circ \le \phi < 360^\circ$, $\tilde{\hat{\mathcal{H}}}_{yx}(\phi) = \hat{\mathcal{H}}_{yx}$ at $\phi = 0^\circ$ or 180° and $\tilde{\hat{\mathcal{H}}}_{yx}(\phi) = -\hat{\mathcal{H}}_{yx}$ at $\phi = 90^\circ$ or 180°. During the mixing period, the value of ϕ is fixed at 90°, corresponding to $-\hat{\mathcal{H}}_{yx}$.

In the presence of heteronuclear couplings, the $\hat{\mathcal{H}}_{yx}$ sequence can be used to examine the distribution of I spins without irradiation of the S spin frequency or reduction of the $I-S$ couplings by isotopic exchange.[16] This is particularly important when both ^{19}F and ^{1}H are present in the sample of interest.

As in any multiple pulse NMR experiment, deviations from perfect delta pulses, finite pulse cycle times with respect to the inverse frequences of the interactions in the sample, and off-resonance effects can lead to undesirable effects.[42] The sensitivity to chemical shift offset has recently been exploited to measure the correlation length of the chemical shift shielding tensor in polycrystalline solids.[43] This increased sensitivity of higher order coherences to magnetic field gradients has also been exploited to enhance the spatial resolution of NMR imaging of solids.[44] In the future, excitation using shaped rf pulses has the potential for improving experimental implementation of the MQ experiment.[45] In practice, rectangular pulses with $t_p \le 3\,\mu$s and eight-pulse cycle times t_c, of $30-72\,\mu$s are generally employed, and the experiment is carried out on resonance.

4 MEASURING MQ INTENSITIES

Although MQ coherences have sometimes been detected directly by CW NMR,[22] MQ coherences cannot be detected directly by FT NMR. Since MQ intensities are nonlinear under CW experiments, two-dimensional NMR experiments are currently employed for this purpose. Only an overview of the required experimental procedure is provided below. Additional descriptions can be found in Yen and Pines,[1] Baum et al.,[2] Baum and Pines,[3] and Gleason.[21]

As in most two-dimensional NMR experiments, there are four distinct periods: preparation, evolution, mixing, and detection. During the preparation period, of length τ and phase ϕ, MQ coherences are excited as a result of homonuclear dipole couplings, and nonzero intensity is developed in the off-diagonal elements of the density matrix [equation (9)]. However, no observable magnetization from these elements can be detected experimentally. These coherences evolve during t_1, the evolution period time. The mixing period of length τ (identical to the preparation period length) and phase $\phi = 90^\circ$, converts MQ coherences in the off-diagonal elements back into diagonal elements, corresponding to z magnetization. Finally, the detection period is used to create observable signal $S(\phi, \tau)$.

In order to resolve the various n quantum coherences, the phase of the preparation period ϕ is changed from 0 to 360° in increments of $\Delta\phi$, while the preparation period length, the mixing period length, and the phase of mixing period are held fixed. Fourier transformation of this series of $S(\phi,\tau)$ at constant τ with respect to ϕ yields the intensities of the n quantum orders $I_n(\tau)$. At least $2n$ phase shifts must be performed when detectable n quantum intensity is present. Fewer phase shifts will alias high-order coherence intensity to lower values of n. Most commonly, $\Delta\phi$ is set at 5.6° or 2.8°, allowing detection of $|n| \le 16$ and 32, respectively.

In order to determine the local distribution of nuclei within a sample, $I_n(\tau)$ is measured for a series of τ. Generally,

$\tau = n_c t_c$ which corresponds to changing the integer number of repetitions n_c, of the basis eight-pulse MQ subcycle for $\hat{\mathcal{H}}_{yx}$. In a given sample, longer τ values correspond to probing the dipolar network over increasing distances.

The length of the evolution period t_1 can also be incremented, allowing MQ coherences to evolve under the internal Hamiltonian of the spin system, yielding the n quantum coherence lineshapes.[1] However, for many applications, only the integrated intensity of the coherence is required. Thus, the evolution period time t_1 is often set to zero,[5,46] maximizing the final signal intensity and significantly decreasing acquisition time. This also eliminates the effects of couplings linear in $\hat{I}_z$ such as chemical shift and heteronuclear dipole coupling during the evolution period.

When $t_1 = 0$ and relaxation effects are neglected, the density matrices at times 0 and 2τ are identical when $\phi = 0^\circ$ or 180°, so called 'time reversal'. At other ϕ some transverse magnetization will also be present at the end of the mixing period and the magnitude of z magnetization will be reduced. Thus, prior to the detection period, a delay which is long compared to T_2 but short compared to T_1 allows for decay of any transverse magnetization transients. Then, a $\pi/2$ pulse can be applied to detect $S(\phi,\tau)$. Spin locking with periodic sampling can be employed during the detection period to enhance the signal-to-noise ratio of $S(\phi,\tau)$.

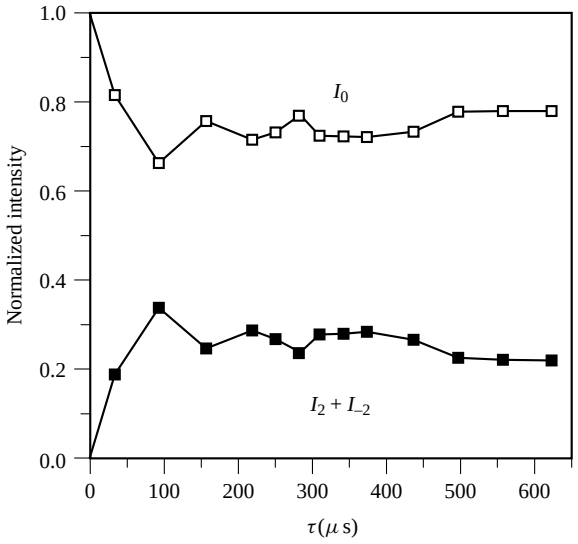

Figure 2 The ^{19}F zero quantum and +2 and −2 quantum intensities from an even-selective experiment on 2 wt.% NH_4+$CF_3SO_3^-$ in poly(*p*-hydroxystyrene). The salt is well dispersed in the polymer, and thus its CF_3 group behaves as expected for $N = 3$. Oscillations are distinct at early τ and destructive interference leads to steady-state values at long τ. (Reproduced by permission of the American Chemical Society from Limb et al.[19]

5 SMALL DIPOLE COUPLED NETWORKS

Even when the number of dipole coupled spins is small, the dynamics of MQ coherence growth can become quite complicated. The simplest possible system to consider is isolated pairs ($N = 2$) of spin-$\frac{1}{2}$ nuclei with identical internuclear separations and orientations with respect to the external magnetic field. Thus, all intrapair dipole coupling constants R are identical and much stronger than any interpair coupling. Then, even order selective excitation by $\hat{\mathcal{H}}_{yx}$ allows only the zero quantum and ± 2 quantum intensity to develop as given by the analytical solution to equation (5):

$$I_2(\tau) = I_{-2}(\tau) = \tfrac{1}{2}[1 - I_0(\tau)] = \tfrac{1}{2}[1 - \cos(R\tau)] \quad (10)$$

In the absence of relaxation, the oscillatory exchange of MQ coherence intensity between the orders will continue indefinitely.[38]

In a macroscopic NMR sample, such as a single crystal or a liquid crystal, identical orientations of internuclear vectors with respect to the external magnetic field can occur. By contrast, polycrystalline powders are the most commonly used samples for MQ NMR. Even for isolated pairs with identical internuclear spacings, the angular dependence of the dipolar coupling interaction leads to destructive interference among the characteristic frequencies which contribute to the MQ intensity development, leading to steady state values of I_n at long τ.

The appearance of oscillations which are damped at long times is characteristic of the powder average of a small number of coupled spins.[41] Figure 2 shows the ^{19}F MQ coherence development for sodium triflate salt ($NH_4^+CF_3SO_3$) well dispersed in polyhydroxystyrene.[19] Only the $n = 0$, 2, and −2 quantum orders have nonzero intensity under the even-selective MQ excitation employed. This is the same behavior expected for an isolated network of three dipole coupled ^{19}F nuclei, where only even MQ orders with $|n| \leq 3$ develop. This result indicates that the average spacing between the salt anions is large, allowing its CF_3 group to act as an isolated $N = 3$ cluster. Note that this configuration can be represented by the density matrix shown in Figure 1. Furthermore, the development of ± 2 quantum coherence intensity indicates that the time average of the intraion dipole couplings is nonzero. Thus, the triflate anion is not reorienting rapidly and isotropically within the polymeric matrix.

Clear oscillations in the MQ intensities are initially observed in Figure 2, while steady state is approached at $\tau >$ 500 ms. The observed long time values are 0.78 for the zero quantum coherence and 0.22 for the sum of the +2 and −2 quantum coherences. These values differ significantly from the predictions of equation (6a), utilizing $N = 3$ and $C = 2$, of 0.625 and 0.375, respectively. This difference shows that the statistical limit has not been achieved, a problem that was anticipated for very small numbers of coupled spins due the presence of symmetry disallowed MQ transitions. Thus, it is desirable to determine N for very small networks by detecting the highest order coherence present, rather than by assuming that the statistical limit holds.

For larger groups of spins, good agreement with the statistical limit behavior has been found. The liquid crystal, *p*-hexyl-*p*′-cyanobiphenyl ($C_{19}H_{21}N$) is a finite cluster of dipole coupled spins, since translation and anisotropic rotation serve to destroy intermolecular dipole couplings, while intramolecular dipole couplings maintain nonzero values. As expected, the positive order MQ coherences grow with τ until all the protons on the liquid crystal molecule are coupled on the experimental timescale. No further increase occurs as the preparation time increases further. The distribution of the steady state MQ intensities is well described by equation (6b)

with $N = 20 \pm 1$. This result is in excellent agreement with the known structural formula.[3]

Thus, MQ NMR gives quantitative information on the number of nuclei in a limited network of dipole, when the structure is unknown. For instance, the size of small hydrogenated defects in amorphous semiconductors has been determined.[4–7] The clustering of molecules inside zeolites[9,11–14] and the distribution of molecules on catalysts[8,10,29] and on chromatographic supports[15] have also been investigated using the MQ spin counting technique.

6 LARGE DIPOLE COUPLED NETWORKS

Although the MQ dynamics of spin systems for which the dipole coupling network extends beyond the typical 1–2 nm length scale of a MQ NMR experiment are nearly impossible to calculate exactly, similar development of $I_n(\tau)$ is observed in many samples. Figure 3 shows the development of positive even-order MQ coherence intensity for CaF_2 powder for increasing τ created from integral multiple repeats of t_c between 30 and 60 μs. The smooth MQ development in Figure 3 is a result of the distribution of dipole coupling present in this polycrystalline sample. Significant oscillations in $I_n(\tau)$ can be seen in a single crystal CaF_2 with its (111) direction oriented perpendicular to the applied magnetic field (Figure 4). For this configuration, all internuclear vectors to the nearest ^{19}F neighbors are at either 54.7°, the magic angle, or (54.7 + 180)°. Thus, all four dipole couplings between nearest neighbors are zero for this configuration. The strongest couplings in this system are actually between next nearest neighbors. The lack of angular dispersion and relative weak dipole couplings lead to only slow damping of the oscillation of the MQ coherences which arises from the even weaker dipolar coupling to neighbors in other shells. The small dipolar couplings in the (111) oriented crystal also lead to slower growth of positive MQ intensities than is observed for the powdered CaF_2 sample.

The observed distributions of $I_n(\tau)$ for polycrystalline powders are often described empirically as a Gaussian distribution, as can be seen in Figure 5 for powdered CaF_2 and GaP, where the solid lines are given by equation (7). The slow development of MQ coherence intensity in GaP allows the comparison to be made for low $N(\tau)$ while CaF_2 provides information at higher $N(\tau)$ values. This description is convenient, as the single parameter $N(\tau)$ can be used to describe an entire MQ spectrum.[2] However, the interpretation of $N(\tau)$ via equation [6,7]6 is not straightforward, since the number of coupled spins is ill defined in this situation. Materials with the highest dipolar couplings also display the fastest growth of $N(\tau)$. Thus $N(\tau)$ has been considered as a parameter that is dependent on the size, structure, and motion of the dipolar coupling network.

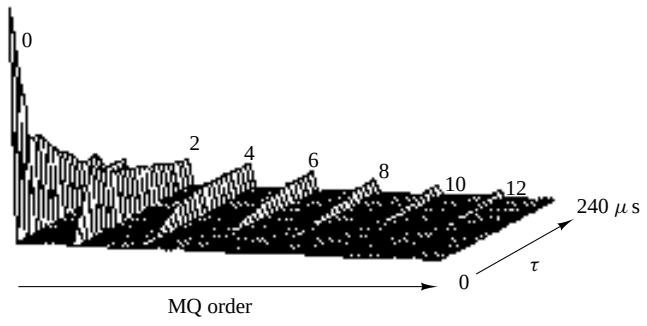

Figure 3 Even-order selective ^{19}F MQ spectra of a polycrystalline powder of CaF_2. As τ increases, high-order coherence intensities grow monotonically

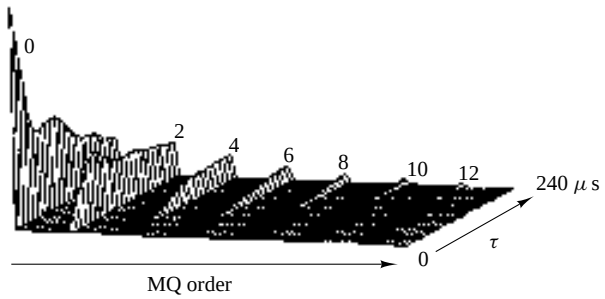

Figure 4 Even-order selective ^{19}F MQ spectra of a single crystal of CaF_2 oriented with its (111) direction along the external magnetic field. The lack of angular orientation distribution, as compared to the powder (Figure 3), leads to oscillatory growth of the zero and two quantum coherences, while the smaller magnitude of the dipole couplings in this sample leads to slower higher order coherence growth

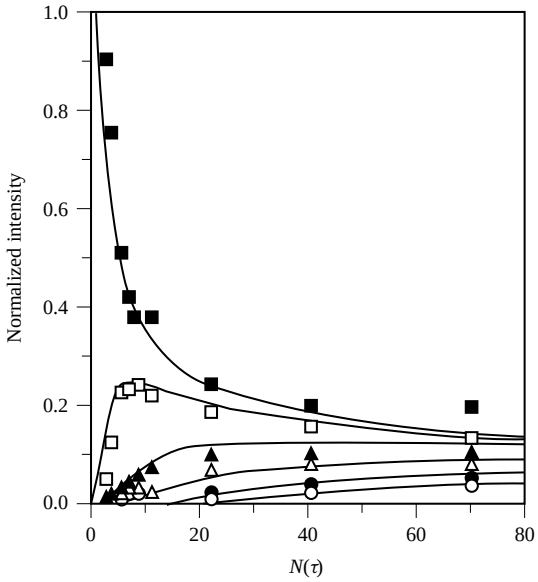

Figure 5 Gaussian distribution (——) and experimentally measured intensities versus $N(\tau)$ for two large dipole coupled networks, $Ca^{19}F_2$ (squares) and $Ga^{31}P$ (other symbols), showing reasonable agreement for $N(\tau) < 70$: (■) I_0, (□) I_2, (▲) I_4, (△) I_6, (●) I_8, (○) I_{10}

Non-Gaussian behavior of the distribution of positive MQ orders for infinite spin systems at long τ has been noted, usually becoming significant when $N(\tau)$ is greater than about 70. In addition, a least-squares fit to equation (6) underpredicts the intensity of the nonzero orders while overpredicting the zero quantum intensity. This may indicate relaxation of intensity in the off-diagonal density matrix elements back to diagonal elements. These effects are not seen in the 21-spin system, liquid crystal *p*-hexyl-*p*′-cyanobiphenyl ($C_{19}H_{21}N$), experiments at similar τ, and thus cumulative pulse errors cannot be the sole cause of the deviation. Experimentally,

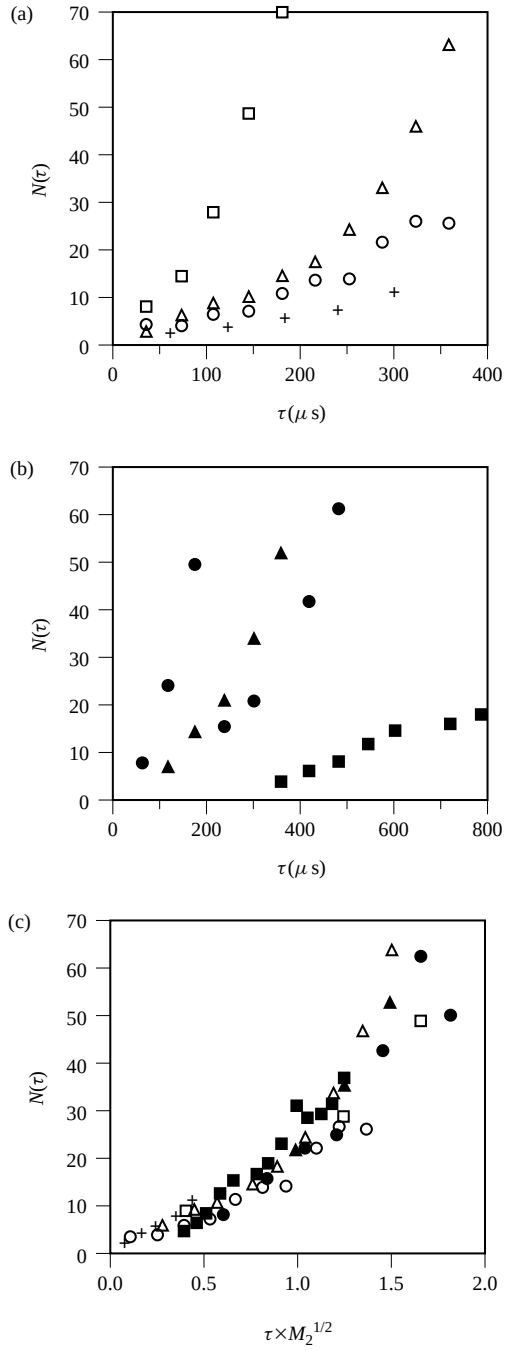

Figure 6 Effective number of correlated nuclei, $N(\tau)$ as function of τ for three-dimensional distributions (a): (□) CaH_2 (^{1}H),[31] (△) adamantane (^{1}H),[31] (○) sodium bicarbonate (^{1}H),[31] (+) Ga P (^{31}P).[21] (b) All ^{19}F:[16] (+) CaF_2, (▲) $NaAsF_6$, (●) CsF, (■) $(C_6F_5)_3SAsF_6$. (c) A universal MQ growth curve is seen for all the samples in (a) and (b), when a nondimensional time axis is created by multiplying τ by $M_2^{1/2}$ (equation (1))

the zero quantum intensity deviates from Gaussian behavior at the smallest number of correlated spins, making it a strong indicator of the onset of relaxation effects.

However, as shown in Figure 6(a) and 6(b) for $N(\tau) < 70$, $N(\tau)$ does grow as the MQ excitation time τ increases. This development of $N(\tau)$ can be described by a universal growth curve when a dimensionless MQ excitation time is created by multiplying τ by $M_2^{\frac{1}{2}}$.[18,21,31] The result of this scaling is shown in Figure 6(c), where $M_2^{\frac{1}{2}}$ has been calculated from equation (1) using the known crystal structures of the materials. The solids represented in Figure 6 fall into one of two catagories. In both categories the dipolar field at each nucleus in a three-dimensional crystal lattice is equivalent and time independent on the MQ timescale. For the first class of materials, no translation or rotation occurs on the NMR timescale. Examples of this category include Ca^1H_2, $Ca^{19}F_2$, and $Ga^{31}P$. In the second class, rapid isotropic rotation exists in the absence of translation, allowing only intermolecular dipole couplings to survive. Examples of such behavior are ^{1}H in adamantane or ^{19}F in salts containing hexafluoroarsenate anions (AsF_6^-). For this second category, the high concentration of NMR active nuclei with relatively low dipole couplings allows larger numbers of spins to be correlated before relaxation effects become significant.

The MQ dynamics of many molecular solids do not follow the universal growth curve, since these solids possess a variety of short internuclear spacings and motion which is neither fast nor isotropic. Sometimes, lowering the sample temperature can eliminate such undesirable motion. In addition, some nuclear distributions are inherently nonuniform, and non-Gaussian intensity distributions are observed even at short τ. For example, both isolated salt molecules and salt aggregates can exist within the same salt/polymer mixture.[17,19] The fraction of each environment can be quantitated by treating the observed MQ spectra as a linear combination of the two MQ intensity distributions. Treatment of MQ coherence growth from nuclei within tightly coupled clusters in addition to slower intercluster growth has also been used to analyze proton distributions in amorphous hydrogenated semiconductors[4–7] and to characterize the distribution of molecules absorbed in zeolites.[11,12]

7 DIMENSIONALITY OF A NUCLEAR SPIN DISTRIBUTION

Certain deviations from the MQ universal behavior [Figure 6(c)] for large dipole coupled networks cannot be accounted for by the presence of molecular motion. Such deviations may indicate that the nuclear distribution is not three dimensional. Hydrogen existing on the surface of a treated natural diamond powder is an example of a two-dimensional distribution.[31] For the diamond powder, the $N(\tau)$ versus τ curve exhibits a concave upward shape, unlike $N(\tau)$ for the 21-spin liquid crystal, which saturates at large preparation times. Thus, the diamond powder represents a large dipole coupled network. However, its MQ growth does not follow the universal scaling behavior of the three-dimensional model compounds. Even greater deviation from the universal curve was found for the initial MQ growth among protons in hydroxyapatite which provides a pseudo-one-dimensional distribution of spin-$\frac{1}{2}$ nuclei.[33]

To predict the influence of dimensionality on the rate of MQ coherence in large dipolar networks, a solution to equation (4) is required. For this purpose $\hat{\rho}(\tau)$ is expanded in terms of product operators, as an alternative to tracking the time development of each of the 4^N individual elements.[41] These product operators are formed from the multiplication

of individual spin operators ($\hat{I}_{iz}$, $\hat{I}_{i+}$ or $\hat{I}_{i-}$) from M of the N nuclei in the dipole network. For example, $\hat{I}_{5z}\hat{I}_{6-}\hat{I}_{7+}\hat{I}_{8z}$, represents $M = 4$ possible product operators when $N \geq 8$.

Two simplifications[31] allow $\hat{\rho}(\tau)$ to be approximated by an expansion requiring only N coefficients:

$$\hat{\rho}(\tau) \approx \sum_{M=1}^{N} C_M(\tau)\hat{P}_M \tag{11}$$

Here, $\hat{P}_M$ is a time independent average product operator, representing all the possible product operators containing M spins. Thus, the time evolution of the MQ coherence and multiplicity of all possible product operators with respect to M is contained in the coefficients $C_M(\tau)$.

When $\hat{\rho}(0) = \hat{I}_z$, only $C_1(0)$ has nonzero intensity. Intensity develops in C_M for $M > 1$ with increasing τ through the commutator obtained when equation (11) is substituted into equation (4) under excitation by $\hat{\mathcal{H}}_{yx}$:

$$\sum_M \left(\frac{\mathrm{d}C_M}{\mathrm{d}\tau}\hat{P}_M\right) = \frac{-\mathrm{i}}{4}\sum_M C_M\left\{\sum_i^N\sum_{i\neq j}^N R_{ij}[\hat{P}_M, (\hat{I}_{i+}\hat{I}_{j+}\hat{I}_{i-}\hat{I}_{j-})]\right\} \tag{12}$$

This summation represents only N coupled differential equations, thus significantly reducing the volume of calculation required compared to the exact solution. Information on the order of the MQ coherences has been averaged away. However, approximating the effective spin correlation size $N(\tau)$ as the center of mass of the distribution of C_M over M allows the results of the average product operator model to be compared directly with experimental measurements of $N(\tau)$.[31]

To emphasize that the rate of MQ coherence development through equation (12) is strongly dependent on the geometry of the dipole coupled network, only two values of R_{ij} will be considered. All nearest neighbor dipole couplings are taken to be equal to the root-mean-square value over the powder average for the nearest neighbor separation, and all R_{ij} for all non-neighboring nuclei are set equal to zero. This is a stepwise approximation to the true decay in the magnitude of dipole coupling constants with internuclear distance cubed.

Because R_{ij} is nonzero only for nearest neighbors, only product operators representing M spins occupying a contiguous region of space will contribute to the average product operator $\hat{P}_M$. For simplicity, lines, squares, and cubes are the shapes assumed to be associated with $\hat{P}_M$ for nuclei distributed uniformly over one-, two-, and three-dimensional lattices, respectively. A schematic drawing of P_9 for a two-dimensional (surface) distribution of nuclei is shown in Figure 7. In order to compute MQ dynamics, the commutator in equation (11) must be evaluated. Only adjacent i,j spin pairs need to be considered because only these have nonzero values of R_{ij}. Thus, the larger the number of nearest neighbors, the greater the possibilities for high-order MQ development. As shown in Figure 7, the spin pair i,j and the M spins comprising $\hat{P}_M$ will have zero, one, or two of their spins in common; these cases correspond to pairs external to, at the surface of, or internal to $\hat{P}_M$, respectively. The commutator for external pairs is identically zero, resulting in no change in the size of the MQ coherence. Products of $M + 1$ and $M - 1$ spin operators result from commutators involving surface and internal pairs, respectively.

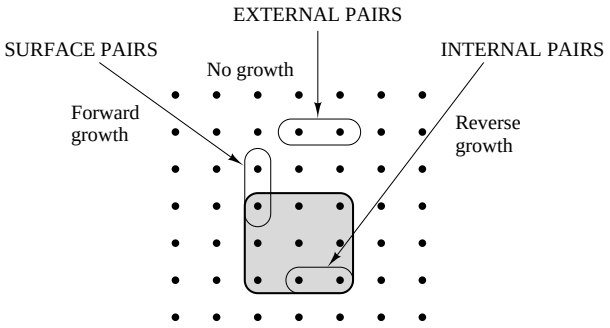

Figure 7 Schematic drawing of $\hat{P}_M$, the average product operator for nine spins on a two-dimensional square lattice. Surface pairs lead to forward MQ growth, while internal pairs reduce the coherence size. Faster MQ coherence growth rates are anticipated as the dimensionality of the lattice increases, since the ratio of surface pairs to internal pairs increases

The $\hat{P}_{M+1}$ operators represent forward growth of the MQ coherence size, while the $\hat{P}_{M-1}$ operators correspond to reverse growth, allowing equation (12) to be simplified to

$$\sum_M (\mathrm{d}C_M/\mathrm{d}\tau)\hat{P}_M = \frac{-\mathrm{i}}{4}\sum_M C_M \times (W^{\mathrm{f}}_{M+1}\hat{P}_{M+1} + W^{\mathrm{r}}_{M-1}\hat{P}_{M-1}) \tag{13}$$

Note that the $\Delta M = \pm 1$ selection rule for product operator evolution under $\hat{\mathcal{H}}_{yx}$ is evident from this equation. The forward and reverse growth rate coefficients W^{f}_M and W^{r}_M depend on the number of pairs at the surface of and internal to $\hat{P}_M$. Since the surface-to-volume ratio for $\hat{P}_M$ depends on its dimensionality, higher MQ growth rates are anticipated for homogeneous distributions of nuclei of increasing dimensionality.

Thus, using average product operators, an N-spin system can be represented by a set of N simultaneous differential equations, allowing the MQ dynamics of large numbers of spins, arranged in varying morphologies, to be easily simulated. Figure 8 shows the growth of $N(\tau)$ predicted by the average product operator model using only nearest neighbor couplings of 1.0 kHz. The analytical formulae used to calculate W^{f}_M and W^{r}_M in equation (13) are given in Levy and Gleason.[31] The three curves were obtained by considering 2500 nuclei arranged uniformly on linear, square, or cubic lattices. As expected, the three-dimensional configuration of nuclei yields the fastest MQ growth. The linear geometry yields slow linear growth of $N(\tau)$. The model can be used to simulate the MQ dynamics of various types of spin distribution and has been extended to nuclear distributions having more than one characteristic nearest neighbor dipole coupling.[31]

The model and experimental data can be compared by scaling the time axis in Figure 7. The experimental data for CaH_2 and for hydrogenated diamond powder given in Figure 9 are in good agreement with the computer simulations of MQ coherence growth for two- and three-dimensional nuclear distributions based on the average product operator

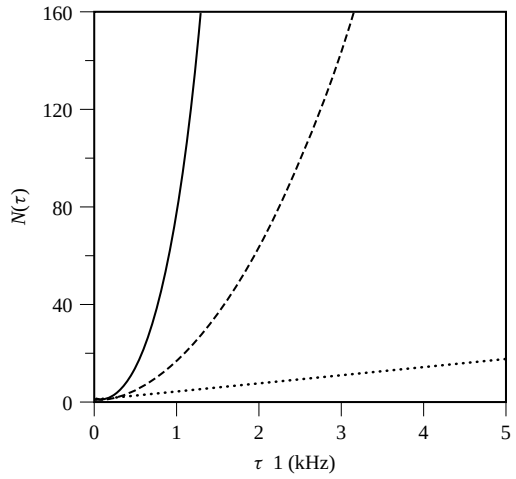

Figure 8 Values of $N(\tau)$ predicted by the average product operator model for spin-$\frac{1}{2}$ nuclei evenly spaced on a line, square lattice, or cubic lattice. In each case, the nearest neighbor dipole coupling was fixed at 1 kHz. The most rapid growth of $N(\tau)$ results for the cubic lattice which has the largest number of nearest neighbors, while the linear arrangement, with the lowest number of nearest neighbors, yields the slowest development of $N(\tau)$. (Reproduced by permission of NMR Concepts from Gleason[21]

model with only one adjustable parameter. In addition, the initial MQ growth of the pseudo-one-dimensional distribution of protons in hydroxyapatite has been found to agree with the slow, nearly linear growth predicted by the results of the product operator calculation for the one-dimensional distribution of nuclei.[33]

8 RELAXATION AND EFFECT OF MOLECULAR MOTION

MQ relaxation rates have been considered in detail by Ernst in terms of the Redfield formalism.[35] The zero quantum and

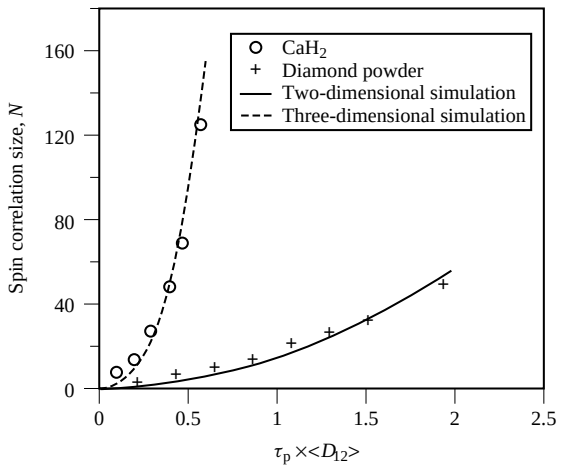

Figure 9 Comparison of MQ dynamics predicted by average operator theory and experimental data for infinite two- and three-dimensional systems. (Reproduced by permission of the American Chemical Society from Levy and Gleason[30]

$n \geq 2$ MQ relaxation rates provide information on the spectral densities of autocorrelation and cross-correlation functions which is not obtainable from the more traditionally measured single quantum relaxation rates. Since the sensitivity to static magnetic field inhomogeneity is proportional to the MQ order, this effect can be problematic when measuring higher order MQ relaxation rates. However, zero quantum relaxation rates have the desirable property of not being influenced by such gradients. This exact theoretical treatment of MQ relaxation has been applied to the external paramagnetic relaxation of two spin-$\frac{1}{2}$ nuclei in a liquid[35] and of an oriented CH_3 group in a liquid crystal.[36] However, application of this exact theory becomes increasingly difficult as the size of the coupled spin-$\frac{1}{2}$ network increases and when the results must be averaged over many possible orientations. Thus, although general considerations have been addressed,[23,28] the measurement and quantitive analysis of MQ relaxation in polycrystalline solids have been limited to date.

Empirically it has been observed that the total signal present in the detection period after MQ excitation of a rigid solid decreases with τ, often becoming negligible for $\tau > 1$ ms. The largest number of spins correlated is thus generally limited to between 100 and 1000, corresponding to a 1–2 nm length scale in a bulk three-dimensional solid. In addition, models for the growth of MQ coherence are difficult to validate because spin correlation data are generally only available for relatively very short τ.

Additional effects are observed when molecular motion modulates the dipolar couplings in solids through variations in internuclear distances and/or the orientation of the internuclear vectors with respect to the applied magnetic field.[20] When the timescale for motion is comparable to τ, complete time reversal of the preparation period is not achievable during the mixing period. Thus, the fraction of magnetization which is actually refocused by the MQ experiment f_{MQ} will generally be < 1. However, efficient refocusing can occur if the frequency of the molecular motion and the MQ experiment are matched correctly. Since τ is generally between 30 μs and 1 ms, motions with frequencies between 1 and 33 kHz can be probed. Since MQ coherences can involve anywhere from 2 to >100 nuclei, the correlated motion for atomic groups of various sizes can be probed, rather than tracking the motion of a single site.

As temperature is monotonically increased and the MQ preparation time is fixed, the frequency of motion can take on several of these special refocusing frequencies, interspersed by defocusing frequencies. Thus, a series of oscillations in f_{MQ} with temperature is expected. In addition to identifying the frequency of motion, the shapes of these oscillations are signatures of the underlying mechanism of molecular motion, e.g. multisite hops versus continuous rotations. Only motions which restore the relative positions of the nuclei after the MQ experiment will cause refocusing. Motions, such as translational diffusion, which do not restore the initial configuration of the nuclei will not produce refocusing under any condition.

Figure 10 shows the temperature dependent ^{19}F f_{MQ} for two polytetrafluoroethylene samples of different crystallinity.[19] Each line indicates a fixed value of the MQ preparation period τ. The overall decrease in f_{MQ} with increasing τ indicates that relaxation is not associated with molecular motion. However, at each fixed τ, oscillations in f_{MQ} can be seen. Oscillations in

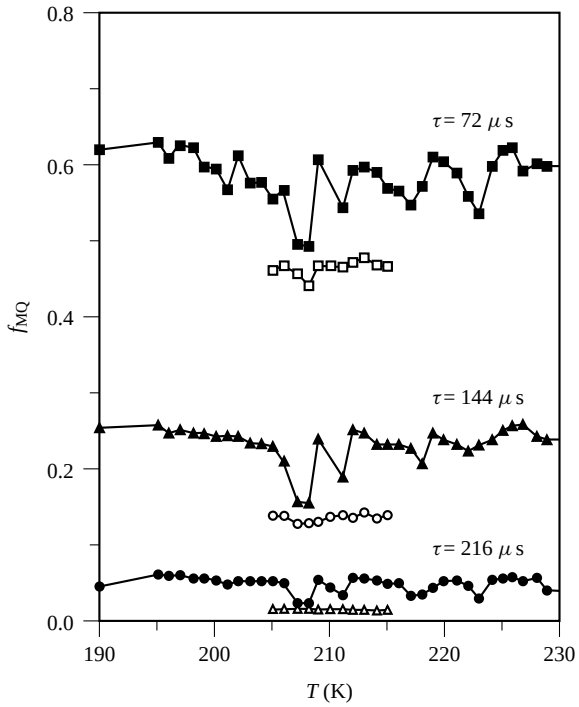

Figure 10 The fraction of refocused magnetization, f_{MQ} at three different values of τ as a function of temperature for *as*-polymerized (■, ▲, ●, ——) and melt-crystallized (□, ○, △, ------) polytetrafluoroethylene. Oscillations are seen only in the *as*-polymerized polymer, corresponding to the motion of a point defect

f_{MQ} are observed from 208 to 230 K for the 98% crystalline sample, while this ratio is constant over the same temperature range for the 64% crystalline sample. These oscillations may be associated with paracrystalline defects found only in the first sample. Thus, the MQ refocusing experiment is able to differentiate clearly between polymer samples which have different thermal histories. The sharpness of the MQ refocusing features and their variations in magnitude, shape, and sign with temperature are signatures of the molecular level details of the underlying dynamics which produce them.

9 RELATED ARTICLES

Amorphous Silicon Alloys; Average Hamiltonian Theory; Diamond Thin Films; Double Quantum Coherence; Liquid Crystals: General Considerations; Molecular Sieves: Crystalline Systems; Multiple Quantum Coherence in Spin-1/2 Dipolar Coupled Solids; Multiple Quantum Coherences in Extended Dipolar Coupled Spin Networks; Multiple Quantum Spectroscopy in Liquid Crystalline Solvents; Multiple Quantum Spectroscopy of Liquid Samples; Polymer Dynamics and Order from Multidimensional Solid State NMR.

10 REFERENCES

1. Y.-S. Yen and A. Pines, *J. Chem. Phys.*, 1983, **78**, 3579.
2. J. Baum, M. Munowitz, A. N. Garroway, and A. Pines, *J. Chem. Phys.*, 1985, **83**, 2015.
3. J. Baum and A. Pines, *J. Am. Chem. Soc.*, 1986, **108**, 7447.
4. J. Baum, K. K. Gleason, A. Pines, A. N. Garroway, and J. A. Reimer, *Phys. Rev. Lett.*, 1986, **56**, 1377.
5. K. K. Gleason, M. A. Petrich, and J. A. Reimer, *Phys. Rev. B*, 1987, **36**, 3259.
6. M. A. Petrich, K. K. Gleason, and J. A. Reimer, *Phys. Rev. B*, 1987, **36**, 9722.
7. S. Mitra, K. K. Gleason, H. Jia, and J. S. Shinar, *Phys. Rev. B*, 1993, **48**, 2175.
8. P.-K. Wang, C. P. Slichter, and J. H. Sinfelt, *Phys. Rev. Lett.*, 1984, **53**, 82.
9. R. Ryoo, S. B. Liu, L. C. de Menoval, K. Takegushi, B. Chmelka, M. Tresoshe, and A. Pines, *J. Phys. Chem.*, 1987, **91**, 6575.
10. S. J. Hwang, T. S. King, and B. C. Gerstein, *Catal. Lett.*, 1991, **8**, 367.
11. B. F. Chmelka, J. G. Pearson, S. B. Liu, R. Ryoo, L. C. de Menorval, and A. Pines, *J. Phys. Chem.*, 1991, **95**, 303.
12. J. G. Pearson, B. F. Chmelka, D. N. Shykind, and A. Pines, *J. Phys. Chem.*, 1992, **96**, 8517.
13. S. B. Hong, H. M. Cho, and M. E. Davis, *J. Phys. Chem.*, 1993, **97**, 1622.
14. S. B. Hong, H. M. Cho, and M. E. Davis, *J. Phys. Chem.*, 1993, **97**, 1629.
15. W. V. Gerasimowicz, A. N. Garroway, J. B. Miller, and L. C. Sander, *J. Phys. Chem.*, 1992, **96**, 3658.
16. B. E. Scruggs and K. K. Gleason, *J. Magn. Reson.*, 1992, **99**, 149.
17. B. E. Scruggs and K. K. Gleason, *Macromolecules*, 1992, **25**, 1864.
18. B. E. Scruggs and K. K. Gleason, *J. Magn. Reson.*, 1992, **99**, 149.
19. S. J. Limb, B. E. Scruggs, and K. K. Gleason, *Macromolecules*, 1993, **26**, 3750.
20. D. A. Lathrop and K. K. Gleason, *Macromolecules*, 1993, **26**, 4652.
21. K. K. Gleason, *Concepts Magn. Reson.*, 1993, **5**, 199.
22. G. Bodenhausen, *Prog. NMR Spectrosc.*, 1981, **14**, 137.
23. D. P. Weitekamp, *Adv. Magn. Reson.*, 1983, **11**, 111.
24. M. Munowitz and A. Pines, *Science*, 1986, **233**, 525.
25. S. Lacelle, *Adv. Magn. Opt. Reson.*, 1991, **16**, 173.
26. M. Mehring, *Principles of High Resolution NMR in Solids*, Springer, Berlin, 1983, pp. 233–259.
27. M. Munowitz, *Coherence and NMR*, Wiley, New York, 1988, pp. 123–124, 200–218.
28. T. J. Norwood, *Prog. Nucl. Magn. Reson. Spectrosc.*, 1992, **24**, 295.
29. B. C. Gerstein, M. Pruski, and S. J. Hwang, *Bull. Magn. Reson.*, 1993, **15**, 211.
30. A. Abragam, *The Principles of Nuclear Magnetism* Clarendon, Oxford, 1961.
31. D. H. Levy and K. K. Gleason, *J. Phys. Chem.*, 1992, **96**, 8125.
32. B. E. Scruggs and K. K. Gleason, *Chem. Phys.*, 1992, **166**, 367.
33. G. Cho and J. P. Yesinowski, *Chem. Phys. Lett.*, 1993, **205**, 1.
34. B. E. Scruggs and K. K. Gleason, *J. Phys. Chem.*, 1993, **97**, 9187.
35. A. Wokaun and R. R. Ernst, *Mol. Phys.*, 1978, **36**, 317.
36. J. Tang and A. Pines, *J. Chem. Phys.*, 1980, **72**, 3290.
37. J. B. Murdock, W. S. Warren, D. P. Weitekamp, and A. Pines, *J. Magn. Reson.*, 1984, **60**, 205.
38. M. Munowitz, *Mol. Phys.*, 1990, **71**, 959.
39. D. Suter, S. B. Liu, J. Baum, and A. Pines, *Chem. Phys.*, 1987, **114**, 103.

40. Y. Ba and W. S. Veeman, *Isr. J. Chem.*, 1992, **32**, 173.
41. M. Munowitz, A. Pines, and M. Mehring, *J. Chem. Phys.*, 1987, **86**, 3172.
42. B. C. Gerstein and C. R. Dybowski, *Transient Techniques in NMR of Solids*, Academic, Orlando, 1985, Chap. 5
43. L. M. Moran and J. P. Yesinowski, *Chem. Phys. Lett.*, 1994, **222**, 363.
44. A. N. Garroway, J. Baum, M. G. Munowitz, and A. Pines, *J. Magn. Reson.*, 1984, **60**, 337.
45. C. J. Lee, N. Murali, and N. S. Warren, *Adv. Magn. Reson.*, 1990, **14**, 241.
46. S. Emid, *Physica B*, 1985, **128**, 79.

Biographical Sketch

Karen K. Gleason. *b* 1960. B.S., 1982, M.S., 1982, MIT; Ph.D., University of California, Berkeley, 1987. Introduced to NMR by J.A. Reimer. Faculty, Chemical Engineering, MIT, 1987–present. Approx. 50 publications. Research interests: application of NMR to thin films and interfaces, particularly for detecting low concentrations of hydrogen, and development of multiple quantum NMR spectroscopy.

Nuclear Spin Properties and Conventions for Chemical Shifts (IUPAC Recommendations 2001†)

Robin K. Harris,[1]* Edwin D. Becker,[2] Sonia M. Cabral de Menezes,[3] Robin Goodfellow,[4] and Pierre Granger[5]

[1] *Department of Chemistry, University of Durham, South Road, Durham, UK*
[2] *National Institutes of Health, Bethesda, MD, USA*
[3] *PETROBRAS/CENPES/QUÍMICA, Ilha do Fundão, Cidade Universitária, Rio de Janeiro, Brazil*
[4] *School of Chemistry, University of Bristol, Cantock's Close, Bristol, UK*
[5] *Institut de Chimie, Université Louis Pasteur de Strasbourg, 1 rue Blaise Pascal, Strasbourg, France*

1	Introduction	5
2	Nuclear Spin Properties	5
3	Chemical Shifts	10
4	Summary of Recommendations	17
5	Appendix	18
6	Related Article in this Volume	18
7	References	18

ABSTRACT: A unified scale is recommended for reporting the NMR chemical shifts of *all* nuclei relative to the ^{1}H resonance of tetramethylsilane. The unified scale is designed to provide a precise ratio, Ξ, of the resonance frequency of a given nuclide to that of the primary reference, the ^{1}H resonance of tetramethylsilane (TMS) in dilute solution (volume fraction, $\varphi < 1\%$) in chloroform. Referencing procedures are discussed, including matters of practical application of the unified scale. Special attention is paid to recommended reference samples, and values of Ξ for secondary references on the unified scale are listed, many of which are the results of new measurements.

Some earlier recommendations relating to the reporting of chemical shifts are endorsed. The chemical shift, δ, is redefined to avoid previous ambiguities but to leave practical usage unchanged. Relations between the unified scale and recently published recommendations for referencing in aqueous solutions (for specific use in biochemical work) are discussed, as well as the special effects of working in the solid state with magic-angle spinning. In all, nine new recommendations relating to chemical shifts are made.

Standardized nuclear spin data are also presented in tabular form for the stable (and some unstable) isotopes of all elements with non-zero quantum numbers. The information given includes quantum numbers, isotopic abundances, magnetic moments, magnetogyric ratios and receptivities, together with quadrupole moments and linewidth factors (where appropriate).

1 INTRODUCTION

A distinguishing feature of nuclear magnetic resonance (NMR) is that signals are isotope-specific. In other words each signal can be firmly linked to a particular element and nuclide. Two features follow: Firstly there is a close connection with chemistry and, in particular, with the Periodic Table, since almost all elements can be studied; secondly, the spin properties of each isotope need to be clearly tabulated and firmly understood. It is a principal purpose of this document to provide such information.

Any scientific discipline relies for its effectiveness upon communication of ideas and results, which can only occur if there is an agreed basis for the meaning of the terminology used. The process of communication is greatly eased if there are universally-recognized conventions for measurement and reporting of quantities with their units and symbols. The aim of this document is to set down such a set of meanings and conventions in relation to chemical shifts (and shielding) and to list resonance frequencies for reference signals for each magnetically active nucleus.

Within IUPAC, Commission I.5 has been responsible for Molecular Structure and Spectroscopy. Until now, this Commission has produced only three reports[1–3] specifically relating to NMR. The two earlier ones of these refer to chemical shifts. The more recent of these two publications is 25 years old, and the NMR world has changed beyond recognition since then. Recently, however, conventions for chemical shifts of five nuclei of wide biochemical interest have been included in *Recommendations for the Presentation of NMR Structures of Proteins and Nuclei Acids*[4] by Commission I.7, Biophysical Chemistry. The current document addresses the same issue for general chemical usage and extends the conventions to the entire range of active nuclei, providing a more comprehensive guide to the factors important in chemical shift referencing. A unified list of properties of NMR-observable nuclei is also included herein.

2 NUCLEAR SPIN PROPERTIES

The phenomenon of NMR is based upon the magnetic properties of various isotopes of elements in the Periodic Table. It is therefore important to have an accessible unified list of these properties. These are contained in Tables 1–3 of this article which include the following for each stable isotope and each long-lived radioactive isotope with non-zero spin:

* To whom correspondence should be addressed: *E-mail*: r.k.harris@durham.ac.uk

† The original article may be freely accessed at (and reproduced from): http://www.iupac.org/publications/pac/2001/7311/7311×1795.html. Membership of the relevant IUPAC Commission during the preparation of the report is listed therein.

Table 1 The Spin Properties of the Spin-1/2 Nuclei[a]

Isotope[b]	Natural abundance,[c] x/%	Magnetic moment,[d] μ/μ_N	Magnetogyric ratio,[d] $\gamma/10^7$ rad s^{-1} T^{-1}	Frequency ratio,[e] Ξ/%	Reference compound	Sample conditions[f]	Literature for Ξ	Relative receptivity[g] D^p	Relative receptivity[g] D^C
^{1}H	99.9885	4.837 353 570	26.752 2128	100.000 000[h]	Me_4Si	$CDCl_3$, $\varphi = 1\%$	–	1.000	5.87×10^3
^{3}H[i]	–	5.159 714 367	28.534 9779	106.663 974	Me_4Si-t_1	[j]	**10**	–	–
^{3}He	1.37×10^{-4}	−3.685 154 336	−20.380 1587	76.179 437	He	gas	**11**	6.06×10^{-7}	3.56×10^{-3}
^{13}C	1.07	1.216 613	6.728 284	25.145 020	Me_4Si	$CDCl_3$, $\varphi = 1\%$	**12,13**	1.70×10^{-4}	1.00
^{15}N	0.368	−0.490 497 46	−2.712 618 04	10.136 767	$MeNO_2$	neat/$CDCl_3$[k]	**9**	3.84×10^{-6}	2.25×10^{-2}
^{19}F	100	4.553 333	25.181 48	94.094 011	CCl_3F	[j]	**14**	0.834	4.90×10^3
^{29}Si	4.6832	−0.961 79	−5.3190	19.867 187	Me_4Si	$CDCl_3$, $\varphi = 1\%$	**15**	3.68×10^{-4}	2.16
^{31}P	100	1.959 99	10.8394	40.480 742	H_3PO_4	[j]	**16**	6.65×10^{-2}	3.91×10^2
^{57}Fe	2.119	0.156 9636	0.868 0624	3.237 778	$Fe(CO)_5$	C_6D_6[l]	**9**	7.24×10^{-7}	4.25×10^{-3}
^{77}Se	7.63	0.926 775 77	5.125 3857	19.071 513	Me_2Se	neat/C_6D_6[k]	**9**	5.37×10^{-4}	3.15
^{89}Y	100	−0.238 010 49	−1.316 2791	4.900 198	$Y(NO_3)_3$	H_2O/D_2O[m]	**9**	1.19×10^{-4}	0.700
^{103}Rh	100	−0.1531	−0.8468	3.186 447[n,o]	$Rh(acac)_3$[p]	$CDCl_3$, sat.	**18**	3.17×10^{-5}	0.186
(^{107}Ag)	51.839	−0.196 898 93	−1.088 9181	4.047 819	$AgNO_3$	D_2O, sat.	**9**	3.50×10^{-5}	0.205
^{109}Ag	48.161	−0.226 362 79	−1.251 8634	4.653 533	$AgNO_3$	D_2O, sat.	**9**	4.94×10^{-5}	0.290
(^{111}Cd)	12.80	−1.030 3729	−5.698 3131	21.215 480	Me_2Cd	neat[j]	**19**	1.24×10^{-3}	7.27
^{113}Cd[q]	12.22	−1.077 8568	−5.960 9155	22.193 175	Me_2Cd	neat[j]	**19**	1.35×10^{-3}	7.94
(^{115}Sn)	0.34	−1.5915	−8.8013	32.718 749	Me_4Sn	neat/C_6D_6[k]	**9**	1.21×10^{-4}	0.711
(^{117}Sn)	7.68	−1.733 85	−9.588 79	35.632 259	Me_4Sn	neat/C_6D_6[k]	**9**	3.54×10^{-3}	20.8
^{119}Sn	8.59	−1.813 94	−10.0317	37.290 632	Me_4Sn	neat/C_6D_6[k]	**9**	4.53×10^{-3}	26.6
(^{123}Te)	0.89	−1.276 431	−7.059 098	26.169 742	Me_2Te	neat/C_6D_6[k]	**9**	1.64×10^{-4}	0.961
^{125}Te	7.07	−1.538 9360	−8.510 8404	31.549 769	Me_2Te	neat/C_6D_6[k]	**9**	2.28×10^{-3}	13.4
^{129}Xe	26.44	−1.347 494	−7.452 103	27.810 186	$XeOF_4$	neat[j]	**20,21**	5.72×10^{-3}	33.6
^{183}W	14.31	0.204 009 19	1.128 2403	4.166 387	Na_2WO_4	D_2O, 1 M	**11**	1.07×10^{-5}	6.31×10^{-2}
^{187}Os	1.96	0.111 9804	0.619 2895	2.282 331	OsO_4	CCl_4, 0.98 M	**22**	2.43×10^{-7}	1.43×10^{-3}
^{195}Pt	33.832	1.0557	5.8385	21.496 784[n]	Na_2PtCl_6	D_2O, 1.2 M	**9**	3.51×10^{-3}	20.7
^{199}Hg	16.87	0.876 219 37	4.845 7916	17.910 822	Me_2Hg[r]	neat	**11**	1.00×10^{-3}	5.89
(^{203}T1)	29.524	2.809 833 05	15.539 3338	57.123 200[s]	$T1(NO_3)_3$	[j]	**24**	5.79×10^{-2}	3.40×10^2
^{205}T1	70.476	2.837 470 94	15.692 1808	57.683 838	$T1(NO_3)_3$	[j]	**25**	0.142	8.36×10^2
^{207}Pb	22.1	1.009 06	5.580 46	20.920 599	Me_4Pb	neat/C_6D_6[k]	**9**	2.01×10^{-3}	11.8

[a] A complete list for stable nuclei, but excluding the lanthanides, the actinides and most radioactive isotopes.
[b] Nuclei in parentheses are considered to be not the most favorable of the element concerned for NMR.
[c] Data are 'representative isotopic compositions', taken from Rosman et al.,[8]. For the error limits, see Rosman et al.[8]
[d] Data derived from the compilation in Mills et al.,[6] pp. 98–104, which lists values of $\mu_{max}/\mu_N = \gamma\hbar I/\mu_N$. For the error limits, see Mills et al.[6]
[e] Ratios of the resonance frequency of the reference to that of the protons of TMS at infinite dilution (in practice at $\varphi = 1\%$) in $CDCl_3$.
[f] M ≡ molarity in mol dm^{-3} (solution); m ≡ molality in mol kg^{-1} (solvent). Some results from Ref.[9] were initially referenced[7] to a TMS concentration of 4.75 m in $CDCl_3$, but the values are corrected to refer to a dilute ($\varphi = 1\%$) solution of TMS in $CDCl_3$.
[g] D^p is the receptivity[5] relative to that of ^{1}H whereas D^C is relative to ^{13}C.
[h] Value by definition (see the text).
[i] Radioactive (half-life 12 y).
[j] See literature cited.
[k] Small amount of lock substance ($\varphi < 10\%$) in neat liquid.
[l] $\varphi = 20\%$ of C_6D_6 in $Fe(CO)_5$.
[m] H_2O/D_2O solution, concentration not reported.
[n] Alternatively, the precise values 3.160 000 MHz and 21.400 000 have been suggested[17] as the references for ^{103}Rh and ^{195}Pt, respectively.
[o] Subject to considerable variation with temperature.
[p] acac ≡ acetylacetonato.
[q] Long-lived radioactive isotope.
[r] The high toxicity of this compound means its direct use should be strongly discouraged.[23]
[s] Deduced from Refs.[24,25]

Table 2 The Spin Properties of Quadrupolar Nuclei[a]

Isotope[b]	Spin[c]	Natural abundance,[c] x/%	Magnetic moment,[d] μ/μ_N	Magnetogyric ratio,[d] $\gamma/10^7$ rad s^{-1} T^{-1}	Quadrupole moment,[e] Q/fm^2	Frequency ratio,[f] Ξ/%	Reference sample	Sample conditions[g]	Literature for Ξ	Line-width factor,[h] ℓ/fm^4	Relative receptivity[i]	
											D^p	D^C
^{2}H[j]	1	0.0115	1.212 600 77	4.106 627 91	0.2860	15.350 609	$(CD_3)_4Si$	$CDCl_3$, $\phi = 1\%$	**15**	0.41	1.11×10^{-6}	6.52×10^{-3}
^{6}Li	1	7.59	1.162 5637	3.937 1709	−0.0808	14.716 086	LiCl	D_2O, 9.7 m	**9**	0.033	6.45×10^{-4}	3.79
^{7}Li	3/2	92.41	4.204 075 05	10.397 7013	−4.01	38.863 797	LiCl	D_2O, 9.7 m	**9**	21	0.271	1.59×10^{3}
^{9}Be	3/2	100	−1.520 136	−3.759 666	5.288	14.051 813	$BeSO_4$	D_2O, 0.43 m	**9**	37	1.39×10^{-2}	81.5
^{10}B	3	19.9	2.079 2055	2.874 6786	8.459	10.743 658	$BF_3{\cdot}Et_2O$	$CDCl_3$[k]	**29**	14	3.95×10^{-3}	23.2
^{11}B	3/2	80.1	3.471 0308	8.584 7044	4.059	32.083 974	$BF_3{\cdot}Et_2O$	$CDCl_3$[k]	**29**	22	0.132	7.77×10^{2}
^{14}N[j]	1	99.632	0.571 004 28	1.933 7792	2.044	7.226 317	CH_3NO_2	neat/$CDCl_3$[l]	**9**	21	1.00×10^{-3}	5.90
^{17}O	5/2	0.038	−2.240 77	−3.628 08	−2.558	13.556 457	D_2O	neat	**9**	2.1	1.11×10^{-5}	6.50×10^{-2}
^{21}Ne	3/2	0.27	−0.854 376	−2.113 08	10.155	7.894 296[m]	Ne	gas, 1.1 MPa	**9**	140	6.65×10^{-6}	3.91×10^{-2}
^{23}Na	3/2	100	2.862 9811	7.080 8493	10.4	26.451 900	NaCl	D_2O, 0.1 M	**9**	140	9.27×10^{-2}	5.45×10^{2}
^{25}Mg	5/2	10.00	−1.012 20	−1.638 87	19.94	6.121 635	$MgCl_2$	D_2O, 11 M	**9**	130	2.68×10^{-4}	1.58
^{27}Al	5/2	100	4.308 6865	6.976 2715	14.66	26.056 859	$Al(NO_3)_3$	D_2O, 1.1 m	**9**	69	0.207	1.22×10^{3}
^{33}S	3/2	0.76	0.831 1696	2.055 685	−6.78	7.676 000	$(NH_4)_2SO_4$	D_2O, sat.	**9**	61	1.72×10^{-5}	0.101
^{35}Cl	3/2	75.78	1.061 035	2.624 198	−8.165	9.797 909	NaCl	D_2O, 0.1 M	**9**	89	3.58×10^{-3}	21.0
^{37}Cl	3/2	24.22	0.883 1998	2.184 368	−6.435	8.155 725	NaCl	D_2O, 0.1 M	**9**	55	6.59×10^{-4}	3.87
^{39}K	3/2	93.2581	0.505 433 76	1.250 0608	5.85	4.666 373	KCl	D_2O, 0.1 M	**9**	46	4.76×10^{-4}	2.79
(^{40}K)	4	0.0117	−1.451 3203	−1.554 2854	−7.3	5.802 018	KCl	D_2O, 0.1 M	**31**	5.2	6.12×10^{-7}	3.59×10^{-3}
(^{41}K)	3/2	6.7302	0.277 396 09	0.686 068 08	7.11	2.561 305[n]	KCl	D_2O, 0.1 M	**31**	67	5.68×10^{-6}	3.33×10^{-2}
^{43}Ca	7/2	0.135	−1.494 067	−1.803 069	−4.08	6.730 029°	$CaCl_2$	D_2O, 0.1 M	**32**	2.3	8.68×10^{-6}	5.10×10^{-2}
^{45}Sc	7/2	100	5.393 3489	6.508 7973	−22.0	24.291 747	$Sc(NO_3)_3$	D_2O, 0.06 M	**9**	66	0.302	1.78×10^{3}
^{47}Ti	5/2	7.44	−0.932 94	−1.5105	30.2	5.637 534	$TiCl_4$	neat[p]	**9**	290	1.56×10^{-4}	0.918
^{49}Ti	7/2	5.41	−1.252 01	−1.510 95	24.7	5.639 037	$TiCl_4$	neat[p]	**9**	83	2.05×10^{-4}	1.20
(^{50}V)[q]	6	0.250	3.613 7570	2.670 6490	21.0	9.970 309	$VOCl_3$	neat/C_6D_6[l]	**9**	17	1.39×10^{-4}	0.818
^{51}V	7/2	99.750	5.838 0835	7.045 5117	−5.2	26.302 948	$VOCl_3$	neat/C_6D_6[l]	**9**	3.7	0.383	2.25×10^{3}
^{53}Cr	3/2	9.501	−0.612 63	−1.5152	−15.0	5.652 496	K_2CrO_4	D_2O, sat.	**9**	300	8.63×10^{-5}	0.507
^{55}Mn	5/2	100	4.104 2437	6.645 2546	33.0	24.789 218	$KMnO_4$	D_2O, 0.82 m	**9**	350	0.179	1.05×10^{3}
^{59}Co	7/2	100	5.247	6.332	42.0	23.727 074	$K_3[Co(CN)_6]$	D_2O, 0.56 m	**9**	240	0.278	1.64×10^{3}
^{61}Ni	3/2	1.1399	−0.968 27	−2.3948	16.2	8.936 051	$Ni(CO)_4$	neat/C_6D_6[l]	**33**	350	4.09×10^{-5}	0.240
^{63}Cu	3/2	69.17	2.875 4908	7.111 7890	−22.0	26.515 473	$[Cu(CH_3CN)_4][ClO_4]$	CH_3CN, sat.[r]	**9**	650	6.50×10^{-2}	3.82×10^{2}
^{65}Cu	3/2	30.83	3.074 65	7.604 35	−20.4	28.403 693	$[Cu(CH_3CN)_4][ClO_4]$	CH_3CN, sat.[r]	**9**	550	3.54×10^{-2}	2.08×10^{2}
^{67}Zn	5/2	4.10	1.035 556	1.676 688	15.0	6.256 803	$Zn(NO_3)_2$	D_2O, sat.	**9**	72	1.18×10^{-4}	0.692

(*continued overleaf*)

Table 2 (*Continued*)

Isotope[b]	Spin[c]	Natural abundance,[c] x/%	Magnetic moment,[d] μ/μ_N	Magnetogyric ratio,[d] $\gamma/10^7$ rad s^{-1} T^{-1}	Quadrupole moment,[e] Q/fm^2	Frequency ratio,[f] Ξ/%	Reference sample	Sample conditions[g]	Literature for Ξ	Line-width factor,[h] ℓ/fm^4	Relative receptivity[i]	
											D^p	D^C
(^{69}Ga)	3/2	60.108	2.603 405	6.438 855	17.1	24.001 354	$Ga(NO_3)_3$	D_2O, 1.1 m	**34**	390	4.19×10^{-2}	2.46×10^2
^{71}Ga	3/2	39.892	3.307 871	8.181 171	10.7	30.496 704	$Ga(NO_3)_3$	D_2O, 1.1 m	**34**	150	5.71×10^{-2}	3.35×10^2
^{73}Ge	9/2	7.73	−0.972 2881	−0.936 0303	−19.6	3.488 315	$(CH_3)_4Ge$	neat[s]	**35**	28	1.09×10^{-4}	0.642
^{75}As	3/2	100	1.858 354	4.596 163	31.4	17.122 614	$NaAsF_6$	CD_3CN, 0.5 M	**9**	1300	2.54×10^{-2}	1.49×10^2
(^{79}Br)	3/2	50.69	2.719 351	6.725 616	31.3	25.053 980	NaBr	D_2O, 0.01 M	**9**	1300	4.03×10^{-2}	2.37×10^2
^{81}Br	3/2	49.31	2.931 283	7.249 776	26.2	27.006 518	NaBr	D_2O, 0.01 M	**9**	920	4.91×10^{-2}	2.88×10^2
^{83}Kr	9/2	11.49	−1.073 11	−1.033 10	25.9	3.847 600[t]	Kr	gas	**36**	50	2.18×10^{-4}	1.28
(^{85}Rb)	5/2	72.17	1.601 3071	2.592 7050	27.6	9.654 943	RbCl	D_2O, 0.01 M	**9**	240	7.67×10^{-3}	45.0
^{87}Rb[q]	3/2	27.83	3.552 582	8.786 400	13.35	32.720 454	RbCl	D_2O, 0.01 M	**9**	240	4.93×10^{-2}	2.90×10^2
^{87}Sr	9/2	7.00	−1.209 0236	−1.163 9376	33.5	4.333 822	$SrCl_2$	D_2O, 0.5 M	**37**	83	1.90×10^{-4}	1.12
^{91}Zr	5/2	11.22	−1.542 46	−2.497 43	−17.6	9.296 298	$Zr(C_5H_5)_2Cl_2$	CH_2Cl_2, sat.[r]	**9**	99	1.07×10^{-3}	6.26
^{93}Nb	9/2	100	6.8217	6.5674	−32.0	24.476 170	$K[NbCl_6]$	CH_3CN, sat.[u]	**9**	76	0.488	2.87×10^3
^{95}Mo	5/2	15.92	−1.082	−1.751	−2.2	6.516 926	Na_2MoO_4	D_2O, 2 M[v]	**9**	1.5	5.21×10^{-4}	3.06
(^{97}Mo)	5/2	9.55	−1.105	−1.788	25.5	6.653 695	Na_2MoO_4	D_2O, 2 M[v]	**9**	210	3.33×10^{-4}	1.95
^{99}Tc[q]	9/2	–	6.281	6.046	−12.9	22.508 326	NH_4TcO_4	D_2O[w]	**9**	12	–	–
^{99}Ru	5/2	12.76	−0.7588	−1.229	7.9	4.605 151	$K_4[Ru(CN)_6]$	D_2O, 0.3 M	**9**	20	1.44×10^{-4}	0.848
^{101}Ru	5/2	17.06	−0.8505	−1.377	45.7	5.161 369	$K_4[Ru(CN)_6]$	D_2O, 0.3 M	**9**	670	2.71×10^{-4}	1.59
^{105}Pd	5/2	22.33	−0.760	−1.23	66.0	4.576 100	K_2PdCl_6	D_2O, sat.	**22**	1400	2.53×10^{-4}	1.49
(^{113}In)	9/2	4.29	6.1124	5.8845	79.9	21.865 755	$In(NO_3)_3$	D_2O, 0.1 M[x]	**34**	470	1.51×10^{-2}	88.5
^{115}In[q]	9/2	95.71	6.1256	5.8972	81.0	21.912 629	$In(NO_3)_3$	D_2O, 0.1 M[x]	**34**	490	0.338	1.98×10^3
^{121}Sb	5/2	57.21	3.9796	6.4435	−36.0	23.930 577	$KSbCl_6$	CH_3CN, sat.[u]	**9**	410	9.33×10^{-2}	5.48×10^2
(^{123}Sb)	7/2	42.79	2.8912	3.4892	−49.0	12.959 217	$KSbCl_6$	CH_3CN, sat.[u]	**9**	330	1.99×10^{-2}	1.17×10^2
^{127}I	5/2	100	3.328 710	5.389 573	−71.0	20.007 486	KI	D_2O, 0.01 M	**9**	1600	9.54×10^{-2}	5.60×10^2
^{131}Xe[j]	3/2	21.18	0.893 1899	2.209 076	−11.4	8.243 921[y]	$XeOF_4$	neat		170	5.96×10^{-4}	3.50
^{133}Cs	7/2	100	2.927 7407	3.533 2539	−0.343	13.116 142	$CsNO_3$	D_2O, 0.1 M	**9**	0.016	4.84×10^{-2}	2.84×10^2
(^{135}Ba)	3/2	6.592	1.081 78	2.675 50	16.0	9.934 457	$BaCl_2$	D_2O, 0.5 M	**9,38**	340	3.30×10^{-4}	1.93
^{137}Ba	3/2	11.232	1.210 13	2.992 95	24.5	11.112 928	$BaCl_2$	D_2O, 0.5 M	**9,38**	800	7.87×10^{-4}	4.62
^{138}La[q]	5	0.090	4.068 095	3.557 239	45.0	13.194 300	$LaCl_3$	D_2O/H_2O[z]	**39**	120	8.46×10^{-5}	0.497
^{139}La	7/2	99.910	3.155 6770	3.808 3318	20.0	14.125 641	$LaCl_3$	D_2O, 0.01 M	**11**	54	6.05×10^{-2}	3.56×10^2
^{177}Hf	7/2	18.60	0.8997	1.086	336.5	(4.007)[A]	–	–		1.5×10^4	2.61×10^{-4}	1.54
^{179}Hf	9/2	13.62	−0.7085	−0.6821	379.3	(2.517)[A]	–	–		1.1×10^4	7.45×10^{-5}	0.438
^{181}Ta	7/2	99.988	2.6879	3.2438	317.0	11.989 600[B]	$KTaCl_6$	CH_3CN, sat.	**40**	1.4×10^4	3.74×10^{-2}	2.20×10^2

(^{185}Re)	5/2	37.40	3.7710	6.1057	218.0	22.524 600[B]	$KReO_4$	D_2O, 0.1 M	**40**	1.5×10^4	5.19×10^{-2}	3.05×10^2
^{187}Re[q]	5/2	62.60	3.8096	6.1682	207.0	22.751 600[B]	$KReO_4$	D_2O, 0.1 M	**40**	1.4×10^4	8.95×10^{-2}	5.26×10^2
^{189}Os[j]	3/2	16.15	0.851 970	2.107 13	85.6	7.765 400[B]	OsO_4	CCl_4, 0.98 M	**22**	9800	3.95×10^{-4}	2.32
(^{191}Ir)	3/2	37.3	0.1946	0.4812	81.6	(1.718)[A]	–	–		8900	1.09×10^{-5}	6.38×10^{-2}
^{193}Ir	3/2	62.7	0.2113	0.5227	75.1	(1.871)[A]	–	–		7500	2.34×10^{-5}	0.137
^{197}Au	3/2	100	0.191 271	0.473 060	54.7	(1.729)[A]	–	–		4000	2.77×10^{-5}	0.162
^{201}Hg[j]	3/2	13.18	−0.723 2483	−1.788 769	38.6	6.611 583[C]	$(CH_3)_2Hg$[D]	neat	**41**	2000	1.97×10^{-4}	1.16
^{209}Bi	9/2	100	4.5444	4.3750	− 51.6	16.069 288	$Bi(NO_3)_2$	$HNO_3/D_2O/H_2O$[E]	**9**	200	0.144	8.48×10^2

[a] Excluding the lanthanides, the actinides and most radioactive isotopes.
[b] Nuclei in parentheses are considered to be not the most favorable of the element concerned for NMR.
[c] Data are 'representative isotopic compositions', taken from Rosman et al.,[8]. For the error limits on the natural abundances, see Rosman et al.[8]
[d] Data derived from the compilation in Mills et al.,[6] pp. 98–104, which lists values of $\mu_{max}/\mu_N = \gamma\hbar I/\mu_N$. For the error limits, see Mills et al.[6]
[e] Data from Mills et al.,[6] pp. 98–104 (taken mostly from Pyykko[26] and Raghavan[27]) and updated from Pyykko.[28] It should be noted that reported values of Q may be in error by as much as 20–30%. For the error limits, see Pyykko.[28]
[f] Ratio of the resonance frequency of the reference to that of the protons of TMS at infinite dilution (in practice at $\varphi = 1\%$) in $CDCl_3$.
[g] M ≡ molarity in mol dm^{-3} (solution); m ≡ molality in mol kg^{-1} (solvent). Some results from Ref.[9] were initially referenced[7] to a TMS concentration of 4.75 m in $CDCl_3$, but the values are corrected to refer to a dilute ($\varphi = 1\%$) solution of TMS in $CDCl_3$.
[h] $\ell = (2I + 3)Q^2/I^2(2I - 1)$ (Ref.[5]). The values are quoted, arbitrarily, to 2 significant Figures.
[i] D^p is the receptivity[5] relative to that of ^{1}H whereas D^C is relative to ^{13}C. The values are given to three significant figures only.
[j] A useful isotope of $I = 1/2$ exists.
[k] 15% by volume of $BF_3{\cdot}Et_2O$ in $CDCl_3$.
[l] Small amount of lock substance ($\varphi \leq 10\%$) in neat liquid, except for ^{61}Ni (where φ = ca. 20% of C_6D_6 is involved).
[m] Ξ In reasonable agreement with a value deduced from a ratio given in Ref.[30]
[n] Ξ Deduced from data in Ref.[31]
[o] Ξ Deduced from a ratio given in Ref.[32]
[p] Plus C_6D_{12} ($\varphi = 10\%$) for field/frequency lock purposes.
[q] Radioactive, with a long half-life.
[r] Containing a little C_6D_6 ($\varphi < 10\%$).
[s] With conversion factors applied by Granger.
[t] The data in Ref.[36] are only accurate to 4 decimal places. The proposal herein is that Ξ (^{83}Kr) is defined to the 6 decimal places given.
[u] In CH_3CN/CD_3CN for ^{93}Nb, ^{121}Sb and ^{123}Sb.
[v] Plus a small quantity of NaOH.
[w] Semi-saturated in H_2O/D_2O.
[x] Plus 0.5 M DNO_3.
[y] Calculated from the value for ^{129}Xe via the ^{129}Xe : ^{131}Xe frequency ratio.
[z] For the solution conditions, see the reference.
[A] Value calculated from literature data on nuclear magnetic moments.
[B] The proposal herein is to define to 6 decimal places, but linewidths are generally such that this is unnecessarily accurate.
[C] Deduced from the ^{201}Hg : ^{199}Hg ratio given in Ref.[41]
[D] The high toxicity of this compound means its direct use should be strongly discouraged.[23]
[E] Saturated in conc. HNO_3, then diluted with an equal volume of D_2O.

(i) The nuclear spin quantum number, I, of the ground state of the nucleus.* This defines the magnitude of the spin angular momentum vector (and hence magnetic dipole moment – see below). The z-component quantum number is then denoted by m_I.

(ii) The standard isotopic natural abundance, x, expressed as a mole fraction in %.

(iii) The magnetic dipole moment, μ, of the nuclide, in terms of the nuclear magneton, μ_N. It should be noted that we have chosen to use the full vector magnitude of μ, given by:

$$|\mu|/\mu_N = |\gamma|\hbar[I(I+1)]^{1/2}/\mu_N \quad (1)$$

where γ is the magnetogyric ratio and $\hbar$ is the Planck constant divided by 2π. Many lists prefer to give only the maximum value of the z-component of μ, namely $\mu_z = \gamma\hbar I$, frequently without explicitly stating this fact. The sign of μ given in Tables 1–3 refers to its direction compared to the related spin angular momentum vector.

(iv) The magnetogyric ratio, γ (sometimes called the gyromagnetic ratio). The SI base units of this quantity are (angular frequency)/(magnetic induction), normally given as rad s^{-1} T^{-1}.

(v) The receptivity, of a nucleus in natural abundance, which influences the NMR signal strength. A common definition[5] involves the proportionality of receptivity to $\gamma^3 x I(I+1)$. In practice it is useful to list such receptivities relative to those of the commonly-used nuclei ^{1}H (proton) and ^{13}C, giving receptivity ratios D^p and D^C respectively. Both these quantities are given in Tables 1 and 2.

(vi) The quadrupole moment, Q, for nuclei with spin quantum number $I > 1/2$ (Tables 2 and 3 only). These data fall naturally in the region of 10^{-30} m^2, i.e., fm^2. However quadrupole moments are often expressed in units of 10^{-28} m^2, called a barn, where 1 barn = 100 fm^2.

(vii) The line-width factor, ℓ, for quadrupolar nuclei. This is defined[5] by:

$$\ell = Q^2(2I+3)/[I^2(2I-1)] \quad (2)$$

When taken in conjunction with the relative receptivity (e.g., as D^C/ℓ), this quantity gives a guide to the ease with which spectra can be obtained for different quadrupolar nuclei in solution for similar site symmetries and molecular mobilities. However, in practice, both symmetry and mobility may vary widely, thus introducing variations that may amount to several powers of ten.

Table 1 gives the data for the spin-1/2 nuclei in the Periodic Table, whereas Table 2 refers to quadrupolar nuclei. These two tables omit the lanthanide and actinide nuclei, which are separately listed in Table 3. Many of the data in Tables 1–3 have been taken from the IUPAC 'Green Book',[6] but additional information is included (particularly on resonance frequencies and quadrupole moments). A version of Tables 1–3 has been published.[7] However, the tables given here contain revised resonance frequencies for consistency with the recommended primary reference, as described in Section 3.5. In addition, some new measurements of resonance frequencies are reported in Tables 1–3, and information about solution conditions and relevant references has been added.

* NMR is entirely concerned with the nuclear spin in the lowest-energy nuclear state, though Mössbauer spectroscopy involves values of I in higher-energy nuclear states.

3 CHEMICAL SHIFTS

3.1 Background

Since the discovery of the chemical shift in 1950, NMR spectroscopy has become of vital importance to chemistry and related disciplines. The term chemical shift refers to a difference in resonance frequency (conventionally expressed as a fraction – see below) between nuclei in different chemical sites (or for samples under different physical conditions). Such effects are caused by variations in shielding by the electronic environment of the nuclei in question, and the concept of chemical shift is described by equation (3):

$$\nu = \frac{\gamma}{2\pi} B_0(1-\sigma) \quad (3)$$

In this equation, the resonance frequency ν (normally in the radiofrequency region) is related to the applied magnetic flux density B_0 by the magnetogyric ratio of the nucleus and the shielding constant σ. In the SI, ν is expressed in hertz, Hz, (and is normally in the range of tens or hundreds of MHz), B_0 is in tesla, T, and σ is a dimensionless fraction (generally reported in parts per million, ppm). Equation (3) is usually applied to the situation in isotropic media (liquids, solutions and gases), for which σ can be represented as a scalar quantity. However, the value of σ depends on molecular orientation in the applied magnetic field and can be represented by a scalar quantity only because of the averaging caused by rapid isotropic molecular tumbling. Therefore, σ is a second-rank tensor and must be used in that form for many situations in the solid state and in liquid crystals (and their solutions).

Whereas frequencies can be measured very precisely, the same cannot be said of B_0. Thus, although in principle chemists would like to know the absolute value of σ, it has long been recognized that only relative values can normally be obtained with precision. Therefore, from the early days of NMR the concept of a standard reference signal has been developed. This requires a number of choices, among which are:

(i) whether to base chemical shifts on resonance frequencies or on shielding

(ii) which compound to use as a reference

(iii) what further conditions to specify for the reference situation

(iv) whether to use separate references for different nuclei or to attempt to link them.

These matters will be dealt with in detail below.

In the early days of NMR, resonance was normally achieved by varying the applied field B_0. It therefore seemed natural for positive chemical shifts to refer to situations where the sample resonated at higher field than that of the reference. Equation (3) shows that this corresponds to greater shielding for the sample than for the reference – a convention that was popular with theoreticians, who are principally concerned

Table 3 The spin properties of lanthanide and actinide nuclei[a]

Isotope	Spin	Natural abundance x/%	Magnetic moment μ/μ_N	Magnetogyric ratio $\gamma/10^7$ rad s^{-1} T^{-1}	Quadrupole moment[b] Q/fm^2	Frequency ratio[c] Ξ/%
^{141}Pr	5/2	100	5.0587	8.1907	−5.89	(30.62)
^{143}Nd	7/2	12.2	−1.208	−1.457	−63.0	(5.45)
^{145}Nd	7/2	8.3	−0.744	−0.898	−33.0	(3.36)
^{147}Sm[d]	7/2	14.99	−0.9239	−1.115	−25.9	(4.17)
^{149}Sm	7/2	13.82	−0.7616	−0.9192	7.4	(3.44)
^{151}Eu	5/2	47.81	4.1078	6.6510	90.3	(24.86)
^{153}Eu	5/2	52.19	1.8139	2.9369	241.2	(10.98)
^{155}Gd	3/2	14.80	−0.332 08	−0.821 32	127.0	(3.07)
^{157}Gd	3/2	15.65	−0.435 40	−1.0769	135.0	(4.03)
^{159}Tb	3/2	100	2.600	6.431	143.2	(24.04)
^{161}Dy	5/2	18.91	−0.5683	−0.9201	250.7	(3.44)
^{163}Dy	5/2	24.90	0.7958	1.289	264.8	(4.82)
^{165}Ho	7/2	100	4.732	5.710	358.0	(21.34)
^{167}Er	7/2	22.93	−0.63 935	−0.77 157	356.5	(2.88)
^{169}Tm	1/2	100	−0.4011	−2.218	–	(8.29)
^{171}Yb	1/2	14.28	0.855 06	4.7288	–	17.499 306[e]
^{173}Yb	5/2	16.13	−0.804 46	−1.3025	280.0	(4.821)
^{175}Lu	7/2	97.41	2.5316	3.0552	349.0	(11.404)
^{176}Lu[d]	7	2.59	3.3880	2.1684	497.0	(8.131)
^{235}U[d]	7/2	0.7200	−0.43	−0.52	493.6	1.841 400[f]

[a]These nuclides are sufficiently little used that values for linewidth factors and relative receptivities are not listed here. However, for ^{169}Tm, $D^p = 5.70 \times 10^{-4}$ and $D^C = 3.35$, while for ^{171}Yb, $D^p = 7.89 \times 10^{-4}$ and $D^C = 4.63$.
[b]For the limits of accuracy, see Ref.[28]
[c]Values in brackets are approximate (calculated from the magnetogyric ratios).
[d]Long-lived radioactive isotope.
[e]Reference: Yb(η-$C_5Me_5)_2$(THF)$_2$, 0.171M in THF solution (THF ≡ tetrahydrofuran).[42]
[f]Reference: UF_6(with $\varphi = 10\%$ of C_6D_6).[43]

with σ. The first clear consensus on an experimental reference compound for proton NMR (by far the most popular nucleus at the time because of its high sensitivity) was tetramethylsilane (TMS), introduced in 1958 by Tiers.[44] However, both for proton NMR and for other nuclei various chemical shift scales were used, with some increasing in the direction of increasing magnetic field and others increasing in the direction of decreasing field (which corresponds to increasing frequency).

The convention recommended by IUPAC in the 1972 document,[1] which mostly concerned proton NMR, was that given in equation 4:

$$\delta_{X,sample} = \left(\frac{\nu_{X,sample} - \nu_{X,reference}}{\nu_{X,reference}} \right) \times 10^6 \qquad (4)$$

in which the chemical shift of a resonance for nucleus X is defined. For protons referenced to TMS this convention gives positive values with increasing frequency, and most proton chemical shifts then turn out to be positive. A second IUPAC report[2] in 1976 extended the recommendations to include nuclei other than protons, always with a high-frequency-positive convention.

Of course, since σ is, in principle, a tensor quantity, so is δ. However, the present document deals only with the isotropic average value of δ, which is the usual value of relevance for solution-state NMR. The tensor properties of σ and δ may be the subject of a later document.

3.2 Recommendations Endorsed

At this point it is appropriate to list those recommendations of the previous two IUPAC reports on NMR which relate to chemical shifts[1,2] (including presentation of spectra) and which we endorse, with one exception noted under item 6. These relate to notational matters and are particularly directed at publications in chemical journals. In several places we use different wording from the original reports and in some cases extended meanings:

1. The nucleus giving rise to the spectrum concerned should always be explicitly stated in full or in abbreviation (e.g., ^{10}B NMR or boron-10 NMR). The isotopic mass number should be given except in cases without ambiguity. In the case of hydrogen NMR the *de facto* usage is proton NMR, deuterium NMR or tritium NMR, in spite of the inconsistency of the wording. Abbreviations such as PMR for proton NMR are strongly discouraged. The term multinuclear NMR is clumsy (a repeated word 'nuclear') and so is also to be discouraged. Where reference to a variety of nuclei is required, multinuclear magnetic resonance should be written in full.
2. The graphical presentation of spectra should show frequency increasing to the left and positive intensity increasing upwards.
3. The dimensionless scale for chemical shifts should be tied to a reference, which should be clearly stated. The procedures used must be carefully defined.

4. The dimensionless scale factor for chemical shifts should generally be expressed in parts per million, for which ppm is the appropriate abbreviation. The radiofrequency of the reference, appropriate to the nucleus in question and to the spectrometer in use, should always be quoted, with sufficient accuracy in relation to the numerical values of shifts listed. Unfortunately, older software supplied by manufacturers to convert from frequency units to ppm in FT NMR sometimes uses the carrier frequency in the denominator instead of the true frequency of the reference, which can lead to significant errors.
5. The chemical shift scale should be defined with respect to resonance frequencies, with the appropriate sign convention (i.e., a positive sign should imply the sample resonates to high frequency from that of the reference). In order to avoid ambiguities of sign, the term 'chemical shift' should *not* be used to describe variations in shielding.
6. The symbol δ (lower case Greek delta) should be used for chemical shift scales with the sign convention given above. Such a symbol should *never* be used to refer to shielding. These recommendations cohere with the definition of the δ-scale adopted in References.[1,2] The definition of δ in equation 4 leads to a value with no units, and the 1972 document recommended that 'ppm' be not stated explicitly (e.g., $\delta = 5.00$, *not* $\delta = 5.00$ ppm). However, this convention is widely ignored. Therefore we do *not* endorse the omission of 'ppm' in reporting values of δ (see Section 3.3).
7. The nucleus in question should be indicated as a subscript or in brackets, e.g., δ_C or $\delta(^{13}\mathrm{C})$, unless there is no ambiguity.
8. As far as possible full information should be given in publications regarding any factor that might influence chemical shifts, such as:

   (i) The physical state of the sample (solid, liquid, solution or gas), with additional relevant facts where necessary.
   (ii) For solutions, the name of the solvent and the concentration of solute.
   (iii) The nature of the referencing procedure, e.g., internal, external (coaxial tubes or substitution), absolute frequency. (This aspect is discussed in detail in later sections of this article.)
   (iv) The name of the secondary reference compound local to the nucleus in question and its concentration. Note, however, that no reference compound needs to be added to the sample if the unified scale described in Section 3.5 is used, though a chemical shift value with respect to a recommended secondary reference compound, obtained via the unified scale, may still be quoted. In exceptional cases, where an isotope-specific secondary reference compound must be used in the experimental measurement, a clear description of the referencing procedure should be given.
   (v) The temperature and (if different from ambient) the pressure of the sample.
   (vi) Whether oxygen and other gases have been removed from the sample.
   (vii) Any chemicals present in the sample, in addition to the solvent and the compound under investigation, and details of their concentrations.

3.3 Definition and Reporting of δ Scales

As mentioned above, the IUPAC Recommendation[1] dating from 1972 defined the proton chemical shift scale in such a way that δ has no quoted units but is presumed to be in ppm. However, this recommendation not to use 'ppm' has *not* received acceptance in practice. It is a simple matter to rewrite equation 4 in a general way that can lead validly to the units of ppm. We now *define* the chemical shift (for any nucleus X, using its local reference substance) by equation 5:

$$\delta_{\mathrm{X,sample}} = (\nu_{\mathrm{X,sample}} - \nu_{\mathrm{X,reference}})/\nu_{\mathrm{X,reference}} \qquad (5)$$

that is, *without* the factor of 10^6. This leads, in general, to a very small number, $M \times 10^{-n}$. Normal practice has been and will doubtless continue to be to use $n = 6$ and thus to express δ in ppm. With equation 5 as the *definition* of δ, equation 6 provides a simple procedure for *calculating* the value of δ in ppm from measured frequencies:

$$\delta_{\mathrm{X,sample}}/\mathrm{ppm} = \frac{(\nu_{\mathrm{X,sample}} - \nu_{\mathrm{X,reference}})/\mathrm{Hz}}{\nu_{\mathrm{X,reference}}/\mathrm{MHz}} \qquad (6)$$

where the factor of 10^6 difference in the units of numerator and denominator is appropriately represented by the units ppm.

This re-definition allows values to be quoted also in parts per billion, ppb $= 10^{-9}$, (as is appropriate for some isotope effects) by expressing the numerator in equation 6 in millihertz (mHz). Alternatively, the units of equation 6 could be altered to give % (relevant for some heavy-metal chemical shifts), but ppm will undoubtedly remain as the most common usage. *IUPAC therefore recommends that the chemical shift δ be defined by equation 5 and that δ normally be expressed in ppm.*

3.4 Referencing Procedures

Accurate and consistent referencing is easy to visualize but hard to implement. For mobile isotropic media (liquids, solutions and gases) there are several possible methods:

(a) *Internal referencing*, where the reference compound is added directly to the system under study. This method is used almost universally for ^{1}H and ^{13}C NMR. However, it is clearly limited by the solubility, miscibility or mutual reactions of the sample components and may be difficult to implement for many samples in which a variety of nuclei are studied.
(b) *External referencing*, involving sample and reference contained separately in coaxial cylindrical tubes. A single spectrum is recorded, which includes signals from both the sample and the reference compound.
(c) *Substitution method*: The use of separate cylindrical tubes for the sample and reference compound, with (in principle) spectra recorded individually for each. It is similar to external referencing in that sample and reference materials are not mixed, but there are significant differences in the two procedures, as described later, which arise because of the common use of precise field/frequency locking (usually *via* the ^{2}H signal of a deuterated solvent). If locking is not used, the magnet should not be re-shimmed between running the sample and reference solutions, since this changes the applied magnetic field.

(d) Referencing *via* direct measurement of the absolute frequency of the field/frequency lock signal, usually provided by the ^{2}H resonance of an internally-contained deuterated compound (frequently the solvent). This method is discussed more fully in Section 3.6.
(e) Application of magic-angle spinning, usually with the substitution method, but also conceivably with coaxial tubes – see Section 3.8.

These methods all have various advantages and disadvantages. For (a) the shielding of the reference nucleus depends, to a greater or lesser extent, on the solvent, on the solute under study, and on the concentration of both solute and reference because of the effects of intermolecular interactions. These effects may be minimized by a judicious choice of solvent and reference compound, but they cannot be eliminated. External reference procedures (b) generally require corrections arising from differences in bulk magnetic susceptibility between sample and reference. These corrections depend on the geometry employed for the sample containers. For the usual coaxial cylindrical arrangement, the correction is[45]

$$(\delta_{\text{true}} - \delta_{\text{obs}}) = k(\kappa_{\text{sample}} - \kappa_{\text{reference}}) \tag{7}$$

where κ refers to the relevant volume magnetic susceptibility (in rationalized units) and ideally $k = +1/6$ for a tube perpendicular to B_0, $k = -1/3$ for a tube parallel to B_0 (as is usual for a superconducting magnet), and $k = 0$ for a tube inclined at the magic angle. These theoretical factors are calculated for infinite cylinders. In practice they depend on the length of the liquid column and other geometrical factors which are not always under control. No correction is needed for spherical samples, but the production of a truly spherical sample cell is generally not feasible. (Equation 7 is consistent with SI notation. A corresponding expression in the cgs system would substitute $k_{\text{cgs}} = 4\pi k_{\text{SI}}$ along with a $\Delta\chi_V$ term numerically equal to $\Delta\kappa/4\pi$. Many listings of susceptibility data give χ_V rather than κ.)

The substitution method uses the fact that, with the advent of stable, internally solvent-locked spectrometers, it has become feasible to obtain accurate data by measuring the spectra of sample and reference in two separate experiments. If the sample and the reference compound are each dissolved in the same solvent at low concentration (which, where feasible, we recommend), the substitution method is equivalent to use of an internal reference except that the reference substance does not contaminate the sample or interact with it, chemically or physically. If the reference compound is a nearly neat liquid with only a small amount of the deuterated 'solvent' to serve as a lock, the measured chemical shifts may be slightly different from those obtained with an internal reference because of differing molecular interactions. It might appear that a magnetic susceptibility correction would be needed if the susceptibilities of sample and reference differ, but this is not the case. With the field/frequency lock established via the deuterated solvent, the applied magnetic field simply shifts slightly to maintain the magnetic induction inside the sample tube constant so as to keep the ^{2}H nuclei on resonance. There is thus a distinct difference between the commonly used *internally locked* system, in which the magnetic induction B_0 is maintained constant and an *unlocked* (or *externally locked*) system in which the applied field H_0 is constant.

If the lock signal of the sample differs from that of the reference, a lock correction may need to be applied according to:

$$\delta_{\text{true}} = \delta_{\text{measured}} + \left(\delta^{\text{lock}}_{\text{sample}} - \delta^{\text{lock}}_{\text{reference}}\right) \tag{8}$$

Except for very strongly hydrogen-bonded systems,[46–48] no primary isotope effects between proton and deuterium have been firmly established, and none are expected on theoretical grounds. Hence, the difference between deuterium lock frequencies in equation (8) may be obtained from a table of proton chemical shifts. However, when polyhydrogenated groups are involved, corrections may be needed for secondary isotope effects[46] arising from $^1\text{H} \rightarrow {}^2\text{H}$ replacement. When high precision is required, the measurement of the shift difference between the locks may be obtained via direct observation of the deuterium spectrum of the two solvents, placed in coaxial tubes.

However, for most modern spectrometers the manufacturers have incorporated compensating procedures for lock changes, largely for the users' convenience of retaining the spectral window in the same position on the screen or chart. Unfortunately these procedures vary between manufacturers and between spectrometers of different ages from the same manufacturer, so no completely general comments on this question can be made here. NMR spectroscopists must refer to the relevant operating manual for details. In most cases with modern instruments the effect is to keep the magnetic field inside the samples constant when different lock compounds are used. In such situations the correction term in brackets in equation 8 is not necessary. Of course, the accuracy of the result clearly depends on what the manufacturers use for the term in brackets, generally present in a 'look-up' table in the spectrometer software. *We recommend that manufacturers give clear, explicit and accurate guidance on their procedures in this matter and quote their 'look-up' tables prominently.*

Another situation where isotope shifts have some effect is when signals of the reference compound are affected, for instance for ^{19}F measurements. In this case the signal is split into four lines with intensities approximately 27 : 27 : 9 : 1 because the natural-abundance isotopic ratio $^{35}\text{Cl} : {}^{37}\text{Cl}$ is ca. 3 : 1. Since $CFCl_3$ is firmly accepted as the local reference for ^{19}F, it is not reasonable to suggest a new alternative. It is recommended that the reference signal is that of $CF(^{35}Cl)_2(^{37}Cl)$.

Earlier IUPAC documentation[1,2] did not suggest any specific composition for the reference sample, or choice of solvents. Ideally, for most referencing methods, a non-polar solvent consisting of nearly spherical molecules should be used, and measurements should be extrapolated to zero reference concentration. Clearly such procedures are not generally feasible, so that caution always needs to be exercised when comparing shift data from different sources.

3.5 A Unified Scale

As NMR studies of various nuclei were initiated, each was, of necessity, treated independently, with some substance containing the nuclide being studied selected as a reference compound. The result is a vast collection of data in the literature for multinuclear magnetic resonance based on a large array of reference compounds. The proliferation of

reference substances is, however, unnecessary and in some ways unhelpful. In a given magnetic field all resonance frequencies form a single spectral range, and it is only because different nuclides resonate at markedly different frequencies that use of separate references has arisen. With modern instruments, in which all frequencies are derived from a single source, it is therefore possible to relate the observed frequencies of all nuclides in a particular sample to that of a single primary reference – preferably the proton resonance of TMS.[#]

There are, however, two reasons for wishing to retain the concept of a separate reference for each nucleus: (i) It is convenient to speak of, say, an aromatic ^{13}C resonance at x ppm from the ^{13}C line of TMS, rather than always quoting a frequency to many significant figures, and (ii) many data tabulations are available with values only expressed relative to separate heteronuclear references. Thus, for a unified scale to be of practical use, there must be agreed frequency relations between a set of commonly used secondary (heteronuclear) references and the primary reference. Measurements of such relations have been reported sporadically since the time of early double-resonance experiments,[49] and it has been proposed to relate the separate reference frequencies to a primary standard originally defined for a magnetic field such that the ^1H TMS signal is at exactly 100 MHz. These frequencies have been given[49] the symbol Ξ (capital Greek xi), and some tabulations have been presented.[5,14,50–52] However, it is clearer and more appropriate for users of modern high-field NMR spectrometers simply *to define Ξ as the ratio of the secondary (isotope-specific) frequency to that of ^1H in TMS in the same magnetic field. Therefore, it is convenient to express Ξ as a percentage* by the use of equation 9:

$$\Xi/\% = 100(\nu_X^{obs}/\nu_{TMS}^{obs}) \quad (9)$$

where ν_{TMS}^{obs} is the measured ^1H frequency of TMS. The use of percentage ensures that values of Ξ with this recommendation are numerically identical to those based on the earlier[49] definition.

Recently, the question of a unified reference has been addressed for multinuclear studies in biomolecular NMR: Wishart et al.[53] surveyed the relevant literature, pointed out inconsistencies in existing practices, and proposed the use of a single internal reference – for their purposes, one that is highly soluble in water (sodium 2,2-dimethyl-2-silapentane-5-sulfonate, DSS[#], preferably deuterated at the CH_2 positions). Operationally, as discussed in the following sections, it is often easier to obtain the necessary heteronuclear frequency data directly via the lock signal than to make additional measurements with various reference materials for different nuclei.

IUPAC recommends that a unified chemical shift scale for all nuclides be based on the proton resonance of TMS as the primary reference. This recommendation is in line with the *Recommendations for Presentation of NMR Structures of Proteins and Nucleic Acids*, recently promulgated[4] by IUPAC in conjunction with the International Union of Biochemistry and Molecular Biology and the International Union of Pure and Applied Biophysics, which include recommended Ξ values for several nuclei of importance in such studies for aqueous solutions, but which uses the proton resonance of DSS as the primary standard because of its solubility in water (see Section 3.9).

In conformity with other areas in physical chemistry, it would be desirable to define a precise standard state – for example, pure liquid TMS or TMS at infinite dilution in $CDCl_3$ at 293 K and 1 bar. [Indeed, in principle a better standard might be ^3He or ^{129}Xe in the gaseous state at a very low pressure (see Ref.[55] and references therein), but this is not practicable.] However, in this document we concentrate on aspects that are of immediate practical utility.

Temperature and pressure effects on chemical shifts for solutions and solid samples are sufficiently small for the lighter elements to be generally ignored for most chemical usage of NMR (largely carried out at ambient probe temperature and pressure), so we make no detailed recommendations regarding these parameters. References[55,56] contain some data on the temperature dependence of ^1H and ^{13}C resonances for TMS. Variation of solvent and/or change in sample concentration are known to have important effects on many chemical shifts, but they are relatively small for a symmetrical, non-polarizable molecule like TMS.

To assess the magnitude of the concentration effect, measurements have been obtained[12] of the proton chemical shift for TMS in solutions of volume fractions, $\varphi = 0.01\%$, 1% and 80% in $CDCl_3$ (see the Appendix). The ^1H NMR frequency of TMS ($\varphi = 1\%$) in chloroform is essentially at the infinite dilution level, the value for a $\varphi = 0.01\%$ solution differing by of the order of $10^{-7}\%$ in Ξ, which is normally reported to only $10^{-6}\%$. However, for a $\varphi = 80\%$ solution Ξ is $9 \times 10^{-6}\%$ larger than for a $\varphi = 1\%$ solution. *Therefore, for the primary reference in multinuclear magnetic resonance we recommend a dilute solution (approximately $\varphi = 1\%$ or less) of TMS in $CDCl_3$.* This recommendation does not preclude the use of TMS in other solvents as an alternative internal reference for ^1H NMR, and it is consistent with the use of DSS in aqueous solution (see Section 3.7).

These recommendations should not be taken in any way to preclude the design and implementation of experiments to measure specific properties, such as very high precision relative frequency measurements and special sample arrangements designed to minimise certain molecular interactions. Data will continue to be reported in the most effective way for the purpose at hand, but we believe that adoption of the unified chemical shift scale will facilitate comparison of the vast majority of NMR frequency measurements. The choice of the base reference as the proton signal of TMS is in accord with the virtually universal use of this signal as a reference for proton NMR.[#]

[#] TMS has a low boiling point (28 °C), which can be advantageous in facilitating removal from non-volatile samples after use, but can in other circumstances be a severe disadvantage. To overcome this problem, a substance such as $[(CH_3)_3Si]_4C$ (m.p. 267 °C), can be used as a reference[54] and the results converted to the TMS standard.

[#] The name sodium 3-(trimethylsilyl)propane-1-sulfonate is strictly the correct one for this compound.

[#] With hindsight it might have been better to choose the ^{29}Si signal of TMS since that is arguably even less susceptible to outside influence than the ^1H resonance (silicon being at the symmetry center of the molecule). However, because of the large amount of literature based on the proton signal, we recommend that the primary reference remain the ^1H signal of TMS.

If the recommendation for use of a unified scale is widely adopted, future measurements should be reported as Ξ values. However, to assure consistency with data already in the literature, it is important to have a set of Ξ values of sufficient accuracy to permit conversion between the primary TMS reference and at least one secondary homonuclear reference for each nuclide (other than ^{1}H). Tables 1–3 list values of Ξ for a number of commonly used secondary references, which are hereby recommended for further use. These values come from a number of sources, as indicated in the tables. However, it should be noted that a number of these compounds are hazardous (for example: Me_2Se, Me_2Te, $Ni(CO)_4$ and, especially, Me_2Hg). The unified scale has the advantage that its use avoids direct handling of any secondary references (see Section 3.6). For most of the nuclides listed in Table 3, there are few data available, and the values of Ξ are simply approximations based on magnetogyric ratios.

However, for Tables 1 and 2, values of Ξ are stated for almost all nuclides to 10^{-6}%. For 69 of the most commonly studied nuclides, careful measurements of Ξ have been made specifically for the purpose of this tabulation. The frequencies of ^{13}C and ^{29}Si were determined for samples of TMS in dilute solution in $CDCl_3$.[12,13,15] The remaining 67 measurements were made[9] by the substitution method (as described in the Appendix). Since all observation frequencies and the ^{2}H lock frequency are derived from a single source, the measured frequencies (Ξ) are reproducible to better than 10^{-7}% and are reported to 10^{-6}%. Experimental details are given in the Appendix. Values of Ξ for the remaining 30 nuclides in Tables 1 and 2 are taken from published values, which have been converted to be consistent with the choice of the ^{1}H signal for TMS in very dilute solution as the primary reference. The literature cited should be consulted for details of the experimental procedure and for estimates of experimental precision and accuracy.

For ^{1}H and ^{13}C NMR, internal referencing has been used almost exclusively, primarily to avoid bulk magnetic susceptibility effects, which can be of the same magnitude as some chemical shift differences that are interpretable with regard to chemical structure. The recommended reference for these nuclides is therefore TMS in a dilute solution in $CDCl_3$, and for consistency this reference is recommended also for ^{29}Si. For most other nuclides, magnetic susceptibility effects are small relative to chemical shift differences, and many of the published data have been reported relative to an external or replacement reference, often a neat liquid where feasible. To provide maximum utility, most of the entries in Tables 1 and 2 refer to such neat liquids or concentrated solutions, usually with a minimum amount of deuterated substance added to provide a stable lock. Of course, a very large number of such reference materials and lock substances could be used, but as described in Section 3.6, it is relatively simple to convert from one to another if necessary.

Values of Ξ can generally be determined to 10^{-6}%, which represents resonance measurement differences of only 0.01 ppm for nuclides with large values of γ to 0.5 ppm for nuclides with very low γ values (an imprecision which is usually negligible compared with their generally large chemical shift ranges). Under the unified scale, chemical shifts can thus be reported to a precision that is often dependent on linewidth or other sample-related factors, rather than instrumental factors. Since literature data for a number of nuclides are usually referred to a secondary reference and hence are often of considerably lower precision, small discrepancies in values of Ξ are of little practical consequence in most instances.

3.6 Practical Application of the Unified Scale

Modern NMR spectrometers invariably include field/frequency locking and frequency synthesizers, so that all frequencies are reliably interrelated by locking to a master clock frequency. There are two ways in which this fact can be used to determine chemical shifts, either directly on the Ξ scale or with respect to a recognized reference for the nucleus in question. These two ways are equivalent to the use of the conventional internal reference and substitution methods, respectively. In the former case, if a nucleus X is to be studied, and the sample can be prepared with a small amount of TMS, then two direct frequency measurements made whilst maintaining the same ^{2}H locking conditions will provide the chemical shift of X on the unified scale according to equation 9. If this procedure is applied to a series of samples, the effect is to replace 'medium effects' on the shielding of X (given by measurements using a reference compound containing the nuclide X) by 'medium effects' on the shielding of ^{1}H in TMS. In general, this should result in a reduction of 'medium effects' due to the referencing procedure, which is desirable. Clearly, the substitution method can be used similarly and is particularly valuable when it is not convenient to add TMS to the sample. Equation (9) is still pertinent. However, as noted in Section 3.4, medium effects may vary to some extent if different concentrations of sample and reference are used.

In the future, reporting of chemical shift data as Ξ values may become more common and acceptable. Conversion of Ξ values to conventional chemical shifts relative to a reference of an X-containing compound requires only subtraction of the Ξ value of a suitable homonuclear reference, as given in Tables 1 and 2, followed by division by the Ξ value of the homonuclear reference. Thus:

$$\delta_X/\text{ppm} = 10^6(\Xi_{X,\text{sample}} - \Xi_{X,\text{reference}})/\Xi_{X,\text{reference}} \qquad (10)$$

The widespread use of a ^{2}H lock for NMR measurements on isotropic samples suggests a modification of the substitution approach, since the relevant reference frequency should not vary with time. Thus the chemical shifts of the X nuclei can, in principle, be determined on the unified (TMS-based) scale merely by measuring the resonance frequency of the sample and using a predetermined reference frequency for the nuclide in question. Thus only one (sample) tube is required and no reference substance needs to be added. The predetermined reference frequency is obtained by measuring the proton resonance of TMS under similar conditions to the sample (i.e., with the same lock compound) in a single experiment for the spectrometer being used. Then the frequency of the usual secondary reference for the X nucleus can be calculated using the pre-determined value of ν_{TMS}:

$$\nu_{\text{reference}} = \nu_{TMS} \times \Xi_{\text{reference}}/100\% \qquad (11)$$

where $\Xi_{\text{reference}}$ takes the appropriate value given in Tables 1–3. Thence the chemical shift (or the value of Ξ_X) for the sample can be readily derived. If the lock substance in

the sample solution is not the same as that of the reference solution, a lock correction must be applied (equation (8)).

As an example, suppose that a ^{77}Se resonance has been measured on a compound dissolved in acetone-d_6, resulting in a value:

$$\nu_{\text{sample}} = 76\,344\,378\,\text{Hz}$$

On this spectrometer, the ^{1}H resonance of a $\varphi = 1\%$ solution of TMS in $CDCl_3$ has been found at 400 103 342 Hz when the spectrometer was installed. The reference frequency of selenium is then, from Table 1:

$$400\,103\,342\,\text{Hz} \times 19.071\,513 \div 100 = 76\,305\,761\,\text{Hz}$$

The proton chemical shifts of the resonances of the lock compounds are:

$$\delta_{\text{H}}(\text{CHCl}_3) = 7.27\,\text{ppm and } \delta_{\text{H}}(\text{acetone}) = 2.17\,\text{ppm}$$

Then:

$$\delta_{\text{Se,sample}} = (76\,344\,378 - 76\,305\,761)/76.305\,761 + (2.17 - 7.27) = 501.0\,\text{ppm}$$

Since this is still basically a substitution method, an error will arise if the ^{2}H frequency of the solvent has been influenced by the particular sample used. For many samples which consist of dilute solutions the error is small, and for many nuclei with large chemical shift ranges the error introduced in this way is probably smaller than would occur if a homonuclear (X) reference were used in the conventional manner.

Reporting of Ξ_{X} and δ_{X} measurements in future heteronuclear magnetic resonance studies will ultimately lead to a large set of consistent data, provided that values of $\Xi_{\text{X,ref}}$ are established and used consistently in all future work. Therefore, particularly for comparison with chemical shifts reported relative to a homonuclear (X) reference via conventional internal referencing procedures, it is essential that the values of Ξ in Tables 1 and 2 represent the accepted values for the substances listed (which are the 'best' available at the present time). *We therefore recommend that the defined local chemical shift scale zero values are established as those listed in Tables 1 and 2, and that such definitions are not subject to future change arising from remeasurement even where this results in increasing accuracy for the reference compound in question.* However, the values of Ξ for 'rare earth' nuclei in Table 3 should be regarded as provisional, pending more accurate measurement.

The Unified Scale offers many advantages over other methods of referencing. However, serious errors can occur in reading and displaying frequencies in some spectrometers unless care is taken. The software in NMR spectrometers is continually evolving, and even some spectrometers of relatively recent vintage are configured to display frequencies that are rounded off or that appear with many digits that do not correctly represent the frequency of a peak indicated by the cursor. The correct information is available in the appropriate parameter tables, but the authors of this document have found that in instruments which are several years old it may be necessary to seek the correct file and not rely on what appears to be an 'obvious' display. Although the situation has improved with the latest version of commercial instruments, *we strongly recommend that each user verify that his/her own instrument correctly determines one or more values of Ξ as given in Tables 1–3.*

3.7 Alternative Reference Compounds

Many of the elements have more than one proposed reference compound for the chemical shift scale mentioned in the literature. The majority are secondary reference standards chosen for convenience. Although our recommendation stands for the compounds listed in Tables 1 and 2, there are some situations where an alternative reference has to be used. One of these cases occurs when ^{1}H, ^{13}C, ^{15}N, ^{29}Si and other nuclei have to be referenced in highly polar solvents such as water, where TMS is only very sparingly soluble. For those situations, DSS or its partially deuterated form, $Me_3SiCD_2CD_2CD_2SO_3Na$, is the recommended primary reference.[53,57] [Sodium 3-(trimethylsilyl)propanoate (TSP) is another salt that has been suggested.[58]] When DSS is used as a reference, it has been recommended[4] that ^{1}H chemical shifts be denoted by the symbol δ_{DSS} to distinguish them from those referenced to TMS. However, the resonances of DSS and TMS, *both dissolved in the same solvent*, are very close: On the scale with TMS as zero, DSS has a chemical shift of $\delta = 0.0173$ ppm in dilute aqueous solution, while in dilute solution in di[($^2H_3$)methyl] sulfoxide (DMSO-d_6), the chemical shift of DSS is $\delta = -0.0246$ ppm[4]. For most purposes these differences are negligible (falling well below the anticipated range of solvent effects), and *data from the TMS and DSS scales may be validly compared without correction for the different ^{1}H reference*.

Table 4 repeats the recommended values of Ξ from Reference,[4] along with data for additional references proposed in the literature for nitrogen, and compares them with our recommendations in Tables 1 and 2. For ^{13}C studies in aqueous solution, Reference[4] recommends using the ^{13}C methyl resonance of DSS, rather than that of TMS, as the secondary reference. Carbon-13 chemical shifts based on DSS and TMS differ by about 2 ppm, which can cause confusion if not clarified. *We recommend that when ^{13}C chemical shifts are referenced to DSS, that point should be made clear by using a notation such as $\delta_{\text{DSS}}(^{13}\text{C})$.*

Reference[4] recommends use of trimethyl phosphate (internal) as a secondary reference for ^{31}P studies in aqueous solution, whereas Table 1 recommends 85% phosphoric acid (external), which has been used more widely, particularly for chemical systems where use of an internal reference is not feasible. The two secondary references differ by about 3 ppm, so *it is important to specify which is being used.*

Several reference compounds have been used historically for nitrogen NMR, partly resulting from the very different properties and natural abundances of the two nuclides (^{14}N and ^{15}N). Nitromethane as either an internal or external reference has been the most widely used for ^{14}N and to some extent for ^{15}N, while liquid ammonia has been a popular external reference for ^{15}N. Ammonium and tetramethylammonium salts have been used as internal references for both ^{14}N and ^{15}N. Reference[4] recommends liquid NH_3 as a secondary reference for ^{15}N in aqueous solutions, since most biochemical applications of ^{15}N NMR have used this reference. In Tables 1 and 2 *we recommend nitromethane as a reference*, in line with common usage in many other applications. The values of Ξ

Table 4 Alternative Secondary References

Isotope	Alternative secondary references				Recommended Secondary references[a]		
	Reference compound	Sample conditions	Frequency ratio	Literature Ξ/%	Reference compound	Sample conditions	Frequency ratio
^{1}H	DSS	Internal	100.000 000	**4**	TMS	Internal[b]	100.000 000
^{2}H	DSS	Internal	15.350 608	**4**	TMS	Internal[b]	15.350 609
^{13}C	DSS	Internal	25.144 953	**4**	TMS	Internal[b]	25.145 020
^{31}P	$(CH_3O)_3PO$	Internal	40.480 864	**4**	H_3PO_4 (85%)	External	40.480 742
^{15}N	NH_3 (liquid)	External	10.132 912	**4**	CH_3NO_2	External	10.136 767
^{15}N	$[(CH_3)_4N]I$	Internal[c]	10.133 356	**59,60**			
^{14}N	$[(CH_3)_4N]I$	Internal[c]	7.223 885	**59**	CH_3NO_2	External	7.226 317

[a]See Tables 1 and 2.
[b]Volume fraction $\varphi = 1\%$ in $CDCl_3$.
[c]0.075 M in DMSO-d_6.

for different nitrogen reference compounds are presented in Table 4, along with those for tetramethylammonium iodide, which has been suggested as an internal reference for both ^{14}N and ^{15}N since the tetrahedral geometry results in sharp lines for both isotopomers.

For most of the nuclei listed in Tables 1 and 2, Ξ values are listed for only one homonuclear reference, since conversions to other reference compounds can be readily made from literature values.

3.8 Magic-angle Spinning

It has been shown[61–63] that in theory bulk isotropic magnetic susceptibility effects are eliminated by spinning an infinitely-long cylindrical sample with its axis at the magic angle (54.7°) to the static magnetic field of an NMR spectrometer. Therefore, in principle, magic-angle spinning (MAS) can be used in the external referencing method to obtain chemical shifts free from bulk susceptibility problems. Whereas this technique was proposed in the context of solid-state NMR (see below), its utility applies equally well to the solution state.[64,65] In practice an infinitely long cylinder is not necessary to reduce bulk susceptibility effects on chemical shifts to an acceptable level. Strictly speaking, to correct for *isotropic* bulk magnetic susceptibility effects, it is also not necessary to spin at the magic angle, but merely to orient the cylinder containing the sample at the magic angle (see equation (7)). However, spinning may narrow the lines significantly and so is normally essential for accurate chemical shift measurement.

3.9 Solids

Sample-handling procedures differ substantially for solids from those appropriate for solutions, and there are clear advantages to using suitable solids as secondary references. This is almost always done using sample replacement. However, the spectrometers are generally used without field/frequency locking, so that the resulting chemical shifts are inevitably less accurate than those for solutions. This is not a significant problem, because linewidths are usually substantially greater than those for solutions and they impose an upper limit to accuracy. High-resolution NMR of solids almost invariably relies on magic-angle spinning, and, as discussed in Section 3.8, this eliminates the effects of differences in bulk isotropic magnetic susceptibilities. Early papers[61,62] addressed this matter, and a recent review by VanderHart,[45], which refers to both liquids and solutions, further discusses the influence of MAS for referencing spectra. Unfortunately, the situation is simple only for systems with isotropic magnetic susceptibility. VanderHart[45] discusses the case of anisotropic susceptibility, but there has been to date little experimental work in this area. However, in general it may be taken that, within the accuracy of measurement, referencing by sample replacement under MAS conditions in an unlocked but stable spectrometer is to a good approximation equivalent to the substitution method as described in Section 3.5.

Several papers[66–68] take advantage of the MAS technique to suggest secondary solid standards for practical use in solid-state NMR. For example the ^{13}C signals of solid adamantane, glycine, hexamethylbenzene and $[(CH_3)_3Si]_4Si$ have been referenced to those for liquids and solutions using MAS, and data were reported to accuracies in the region of 0.004–0.04 ppm.

Chemical shift referencing for solid-state NMR is not yet at the stage where much further discussion is warranted here, so the only recommendation that we make is for referencing procedures to be always clearly and carefully stated in publications.

4 SUMMARY OF RECOMMENDATIONS

In addition to the endorsements of earlier Recommendations stated in Section 3.2 above, IUPAC recommends the following:

(a) Equation (5) should be used to define chemical shift scales, with symbol δ and with ppm (or ppb or %, as appropriate) explicitly stated after the numerical values. Equation (6) provides a simple way to calculate chemical shift values in ppm.
(b) The ^{1}H signal of tetramethylsilane in dilute solution (ca. volume fraction $\varphi = 1\%$ in $CDCl_3$) should be used as the primary *internal* or substitution reference for the resonance frequencies (and hence chemical shifts) for *all* nuclei. However, for aqueous solutions the recommendations of Ref.[4] are supported.
(c) The secondary references listed in Tables 1 and 2 may be used for the nuclei of the various elements, with their Ξ taking the fixed values given (not subject to revision).
(d) Internal referencing may be used for solutions but its limitations should be recognized.

(e) For solution-state measurements, referencing via an internal ^{2}H lock signal may be used, either to give the value of Ξ directly or to calculate the chemical shift with respect to the relevant secondary reference (via equation (8) where relevant).
(f) Referencing by the substitution method with field/frequency lock spectrometers may also be used for solutions.
(g) External referencing for either liquids or solids may be carried out with magic-angle spinning.
(h) External referencing by means other than (f) and (g) is to be discouraged unless corrections are applied for bulk magnetic susceptibility effects.
(i) In all circumstances, and especially where strict adherence to these Recommendations is not feasible, details of experimental procedures should be given clearly so that results may be validly intercompared.

Acknowledgements

We thank H. J. C. Yeh (National Institutes of Health), A. M. Kenwright (University of Durham) and B. Ancian (Université de Paris VII) for measurements of Ξ for ^{13}C and ^{29}Si in solutions of TMS in $CDCl_3$. Other special measurements of Ξ have also been made by C. Brevard, R. Hoffman, J. Raya, M. Bourdonneau, T. Meersmann, B. Ancian and L. Helm. We are also grateful to W. Bremser, who participated in some of the early discussions on the topic of these recommendations, and to J. Kowalewski and G. Martin for comments and encouragement. Specific comments were received from members of IDCNS (W. V. Metanomski, K. Hatada, A. D. Jenkins, J. W. Lorimer, W. H. Powell, S. E. Schwartz, A. J. Thor, H. A. Favre, T. Cvitaš) and a wide range of NMR experts and others (A. D. McNaught, D. L. Van der Hart, D. T. Burns, M. Duteil, J. R. Everett, B. E. Mann, W. McFarlane, P. S. Pregosin, B. Mandava, W. von Philipsborn, T. D. W. Claridge, C. Ye, D. Neuhaus, P. Jonsen, G. Hägele, J. C. Lindon, P. E. Meadows, B. Wrackmeyer, D. L. VanderHart, K. Mizuno, T. Richert); we are very grateful for their assistance and guidance. P. Pyykko very helpfully supplied details of his review of quadrupole moments in advance of publication, and R. Hoffman not only supplied data for Ξ on several nuclei but also made many pertinent and useful suggestions.

5 APPENDIX

As noted in the body of this document, a number of new experimental measurements have been made to verify values of Ξ for various nuclides. Experimental details are given here.

Concentration dependence of δ_H (TMS).[12] Measurements were made with a Varian VXR-500S spectrometer, sample at ambient probe temperature (about 23 °C), locked onto the signal for $CDCl_3$. Measured ^{1}H frequencies were as follows:

$$\varphi = 0.01\% : 499.872\,5048\ \text{MHz}$$

$$\varphi = 1\% : 499.872\,5054\ \text{MHz}$$

$$\varphi = 80\% : 499.872\,5495\ \text{MHz}$$

Ξ for ^{13}C and ^{29}Si. Three measurements were made of Ξ (^{13}C) for TMS in $CDCl_3$ at $\varphi = 1\%$, all at ambient probe temperature using the following spectrometers: – Varian VXR-500S,[12] $\Xi = 25.145\,0188\%$; Varian Unity-300,[13] $\Xi = 25.145\,0202\%$; and Varian Inova-500,[13] $\Xi = 25.145\,0196\%$. The reported value[15] (Table 1) of Ξ (^{29}Si) for TMS in $CDCl_3$ at $\varphi = 1\%$ was obtained at ambient probe temperature using a Bruker Avance-400 spectrometer.

Other values of Ξ. Most of the remaining 67 new measurements presented in Tables 1 and 2 were made by the substitution method (as described above) with a Bruker Model MSL spectrometer, operating at a nominal frequency of 300 MHz for ^{1}H, and with corrections applied for the lock signals (see equation 8).[9] However, Ξ was measured for the following nuclei using a Bruker Avance-400 spectrometer: ^{2}H, ^{17}O, ^{45}Sc, ^{47}Ti, ^{49}Ti, ^{55}Mn, ^{75}As, ^{81}Br, ^{87}Rb, ^{127}I, ^{131}Xe, ^{133}Cs, ^{135}Ba, and ^{137}Ba. The ^{21}Ne value was measured[9] using a Chemagnetics Infinity 600 spectrometer. All 67 measurements were made at ambient probe temperature, approximately 298–300 K. The replacement reference samples used were either a concentrated solution ($m = 4.75\,\text{mol kg}^{-1}$, $\varphi = 80\%$) of TMS in $CDCl_3$, or a $\varphi = 1\%$ solution of TMS in $CDCl_3$. In the former case, the values have been converted to refer to TMS ($\varphi = 1\%$) in $CDCl_3$ (see above).

6 RELATED ARTICLE IN THIS VOLUME

Parameters and Symbols for Use in Nuclear Magnetic Resonance (IUPAC Recommendations 1997). The reader should note that together these two articles in this volume, Nuclear Spin Properties and Conventions for Chemical Shifts (IUPAC Recommendations 2001) and Parameters and Symbols for Use in Nuclear Magnetic Resonance (IUPAC Recommendations 1997), essentially replace the article Nuclear Spin Properties and Notation in volume 5 of the Encyclopedia. In fact some of the numbers in the tables have been changed from that article by updating and because the primary standard has been rebased from 4.75 m in $CDCl_3$ to 1% in $CDCl_3$.

7 REFERENCES

1. Recommendations for the Presentation of NMR Data for Publication in Chemical Journals, *Pure Appl. Chem.*, 1972, **29**, 627.
2. Presentation of NMR Data for Publication in Chemical Journals – B. Conventions relating to Spectra from Nuclei other than Protons, *Pure Appl. Chem.*, 1976, **45**, 217.
3. R. K. Harris, J. Kowalewski, and S. C. de Menezes, Parameters and Symbols for Use in Nuclear Magnetic Resonance, *Pure Appl. Chem.*, 1997, **69**, 2489.
4. J. L. Markley, A. Bax, Y. Arata, C. W. Hilbers, R. Kaptein, B. D. Sykes, P. E. Wright, and K. Wüthrich, Recommendations for the Presentation of NMR Structures of Proteins and Nucleic Acids, *Pure Appl. Chem.*, 1998, **70**, 117.
5. 'NMR and the Periodic Table', eds R. K. Harris and B. E. Mann, Academic Press: 1978.
6. I. Mills, T. Cvitas, K. Homann, N. Kallay, and K. Kuchitsu, 'Quantities, Units and Symbols in Physical Chemistry', 2nd edn., published for IUPAC by Blackwell Scientific Publications: 1993.
7. R. K. Harris, in 'Encyclopedia of NMR', eds D. M. Grant and R. K. Harris, Wiley: Chichester, 1996, vol. 5, p 3301.
8. K. J. R. Rosman and P. D. P. Taylor, *Pure Appl. Chem.*, 1998, **70**, 217.
9. P. Granger, J. Raya, M. Bourdonneau, L. Helm, and T. Meersmann, measurements previously unpublished in the primary literature. See the Appendix for details.
10. J. P. Bloxsidge, J. A. Elvidge, J. R. Jones, R. B. Mane, and M. Saljoughian, *Org. Magn. Reson.*, 1979, **12**, 574.
11. R. Hoffman, private communication.

12. H. J. C. Yeh, previously unpublished work.
13. A. M. Kenwright, previously unpublished work.
14. S. Brownstein and J. Bornais, *J. Magn. Reson.*, 1980, **38**, 131.
15. B. Ancian, previously unpublished work.
16. H. T. Edzes, *Magn. Reson. Chem.*, 1992, **30**, 850.
17. P. L. Goggin, R. J. Goodfellow, and F. J. S. Reed, *J. Chem. Soc. Dalton*, 1974, 576; S. J. Anderson, J. R. Barnes, P. L. Goggin, and R. J. Goodfellow, *J. Chem. Res. (M)*, 1978, 3601.
18. R. Benn and A. Rufinska, *Angew. Chem., Int. Ed. Engl.*, 1986, **25**, 861.
19. J. D. Kennedy and W. McFarlane, *J.C.S. Perkin II*, 1977, 1187.
20. M. Gerken and G. J. Schrobilgen, *Coord. Chem. Rev.*, 2000, **197**, 335.
21. G. A. Schumacher and G. J. Schrobilgen, *Inorg. Chem.*, 1984, **23**, 2923.
22. C. Brevard, previously unpublished work.
23. M. B. Blayney, J. S. Winn, and D. W. Nierenberg, *C & E News*, May 12, 7 1997; T. Y. Yoribara, T. W. Clarkson, and D. W. Nierenberg, *C & E News*, June 16, 6 1997; D. Live, *C & E News*, July 14, 7 1997; R. K. Harris, *C & E News*, July 14, 7 1997.
24. J. F. Hinton, G. L. Turner, G. Young, and K. R. Metz, *Pure Appl. Chem.*, 1982, **54**, 2359.
25. J. F. Hinton and R. W. Briggs, *J. Magn. Reson.*, 1977, **25**, 555.
26. P. Pyykko, *Z. Naturforsch.*, 1992, **47A**, 189.
27. P. Raghavan, *At. Data Nucl. Data Tables*, 1989, **42**, 189.
28. P. Pyykko, *Mol. Phys.*, 2001, **99**, 1617.
29. J. D. Kennedy, in 'Multinuclear NMR', ed J. Mason, Plenum Press, Ch. 8, p 221, 1987.
30. J. T. LaTourrette, W. E. Quinn, and R. F. Ramsey, *Phys. Rev.*, 1957, **107**, 1202.
31. W. Sahm and A. Schwenk, *Z. Naturforsch.*, 1974, **29a**, 1754.
32. O. Lutz, A. Schwenk, and A. Uhl, *Z. Naturforsch.*, 1975, **30a**, 1122.
33. N. Hao, M. J. McGlinchey, B. G. Sayer, and G. J. Schrobilgen, *J. Magn. Reson.*, 1982, **46**, 158.
34. J. Kodweiss, O. Lutz, W. Messner, K. R. Mohn, A. Nolle, B. Stütz and D. Zepf, *J. Magn. Reson.*, 1981, **43**, 495.
35. J. Kaufmann, W. Sahm, and A. Schwenk, *Z. Naturforsch.*, 1971, **26A**, 1384.
36. D. Brinkman, *Helv. Phys. Acta*, 1968, **41**, 367.
37. W. Sahm and A. Schwenk, *Z. Naturforsch.*, 1974, **29a**, 1763.
38. O. Lutz and H. Oehler, *Z. Physik A*, 1978, **288**, 11.
39. O. Lutz and H. Oehler, *J. Magn. Reson.*, 1980, **37**, 261.
40. C. Brevard and P. Granger, 'Handbook of High Resolution Multinuclear NMR', Wiley: 1981.
41. G. Wu and R. E. Wasylishen, *Magn. Reson. Chem.*, 1993, **31**, 537.
42. A. G. Avent, M. A. Edelman, M. F. Lappert, and G. A. Lawless, *J. Am. Chem. Soc.*, 1989, **111**, 3423.
43. H. LeBail, C. Chachaty, P. Rigny, and R. Bougon, *C.R. Acad. Sci.*, 1983, **297**, 451.
44. G. V. D. Tiers, *J. Phys. Chem.*, 1958, **62**, 1151.
45. D. L. VanderHart, in 'Encyclopedia of NMR', eds D. M. Grant and R. K. Harris, Wiley: Chichester, 1996, vol. 5, p 2938.
46. P. E. Hansen, *Prog. Nucl. Magn. Reson. Spectrosc.*, 1988, **20**, 207.
47. D. F. Evans, *J.C.S. Chem. Commun.*, 1982, 1226.
48. L. J. Altman, D. Laungani, G. Gunnarson, H. Wennerström, and S. Forsen, *J. Am. Chem. Soc.*, 1978, **100**, 8264.
49. W. McFarlane, *Proc. R. Soc. (London) A*, 1968, **306**, 185 and references therein.
50. W. McFarlane, *Annu. Rev. NMR Spectrosc.*, 1968, **1**, 135.
51. R. K. Harris and B. J. Kimber, *J. Magn. Reson.*, 1975, **17**, 174.
52. D. Canet, C. Goulon-Ginet and J. P. Marchal, *J. Magn. Reson.*, 1976, **22**, 537.
53. D. S. Wishart, C. G. Bigam, J. Yao, F. Abildgaard, H. J. Dyson, E. Oldfield, J. L. Markley, and B. D. Sykes, *J. Biomol. NMR*, 1995, **6**, 135.
54. N. N. Zemlyanskii and O. K. Sokolikova, *Russ. J. Anal. Chem.*, 1981, **36**, 1421.
55. C. J. Jameson, A. K. Jameson, and S. M. Cohen, *J. Magn. Reson.*, 1975, **19**, 385.
56. F. G. Morin, M. S. Solum, J. D. Withers, and D. M. Grant, *J. Magn. Reson.*, 1982, **48**, 138.
57. G. V. D. Tiers and A. Kowalewsky, paper presented to the Division of Physical Chemistry, 137th National Meeting ACS, Cleveland, Ohio, 1960, Abstracts, p. 1712; G. V. D. Tiers and R. I. Coon, *J. Org. Chem.*, 1961, **26**, 2097.
58. G. V. Tiers and A. Kowalewsky, Division of Physical Chemistry, 137th ACS National Meeting, Cleveland, Ohio, 1960; L. Pohl and M. Ecke, *Angew Chem., Int. Ed. Engl.*, 1969, **8**, 381; D. H. Live and S. I. Chan, *Org. Magn. Reson.*, 1973, **5**, 275.
59. E. D. Becker, *J. Magn. Reson.*, 1971, **4**, 142.
60. E. D. Becker, R. B. Bradley, and T. Axenrod, *J. Magn. Reson.*, 1971, **4**, 136.
61. D. Doskočilová and B. Schneider, *Macromolecules*, 1972, **5**, 125.
62. D. Doskočilová, D. D. Tao, and B. Schneider, *Czech. J. Phys. B*, 1975, **25**, 202.
63. W. L. Earl and D. L. VanderHart, *J. Magn. Reson.*, 1982, **48**, 35.
64. A. N. Garroway, *J. Magn. Reson.*, 1982, **49**, 168.
65. S. Hayashi, M. Yanagisawa, and K. Hayamizu, *Anal. Sci.*, 1991, **7**, 955.
66. S. Hayashi and K. Hayamizu, *Bull. Chem. Soc. Jpn.*, 1989, **62**, 2429.
67. S. Hayashi and K. Hayamizu, *Bull. Chem. Soc. Jpn.*, 1991, **64**, 685.
68. S. Hayashi and K. Hayamizu, *Bull. Chem. Soc. Jpn.*, 1991, **64**, 688.

Probe Design and Construction

F. David Doty
Doty Scientific Inc., Columbia, SC, USA

1	Introduction	1
2	General Classes of NMR Probes	1
3	Historical Perspective on NMR Probes	2
4	Radiofrequency Engineering—Basics	2
5	Signal-to-Noise Ratio and B_1	4
6	Double Resonance	6
7	Construction Materials and Techniques	7
8	Thermal Engineering	8
9	Gradient NMR Probes	8
10	Related Articles	9
11	References	9

1 INTRODUCTION

From the early days of NMR, the word probe (or probehead) has been used to refer to the complete piece of equipment intimately associated with the sample (except the sample tube). For the simplest experiments, the probe consists of the mechanical structure required to hold the sample in the 'sweet spot' of the magnet, a coil surrounding the sample, a tuning capacitor, and an rf transmission line. However, most chemical problems of interest require control over the sample environment (temperature, electromagnetic irradiation, pressure, orientation, and re-orientation), and apparatus associated therewith becomes a part of the NMR probe.

The modern NMR probe is a complex piece of apparatus designed to accommodate all of the environmental requirements of the NMR experiment. The radiofrequency (rf) portion often includes (a) an rf 'observe' channel optimized for highest signal-to-noise-ratio (SNR, or S/N, also called sensitivity) at the X nucleus frequency, (b) a less efficient rf channel for heteronuclear decoupling (usually ^{1}H, except for indirect detection), and (c) another low-efficiency channel for magnetic field lock (usually ^{2}H). Variable temperature (VT) control is achieved with a resistive heater in a gas stream that flows over the sample. In high-resolution liquids probes, slow sample spinning (10–200 revolutions per second, Hz) about the $\boldsymbol{B}_0$ axis to average out azimuthal inhomogeneity in $\boldsymbol{B}_0$ is usually accomplished with a pneumatic system external to the probe, but high-speed sample spinning apparatus (200–26 000 Hz) for solids averaging techniques is an integral part of a solids probe.

One of the most demanding technical aspects of liquids probes is the requirement of extremely high $\boldsymbol{B}_0$ field homogeneity (as high as several parts per billion), but sometimes it is advantageous to be able deliberately to spoil the field homogeneity over precise time periods by applying field gradients. When very high gradients and fast switching are required, as in diffusion measurements or solids microscopy magnetic resonance imaging (MRI), the gradient coils must be as small as possible and incorporated into the probe. However, for most MRI work with samples larger than 40 mm, the gradient coils are external to the probe.

Another challenging technical requirement is often that of minimizing NMR background signals from construction materials that contain trace amounts of the nuclide of interest—particularly for highly sensitive proton (^{1}H) experiments. Other technical complications may stem from provisions for optical or microwave irradiation and operation at extreme temperatures.

Addressing the often conflicting requirements of high sensitivity, high resolution, large spectral bandwidth, low background signals, wide VT range, high-speed sample spinning, intense irradiation, and uniform field gradients requires careful attention to a number of problems in materials science, physics, electrical engineering, and mechanical engineering. The engineering effort often makes the price of a probe comparable to the price of a new sports car.

2 GENERAL CLASSES OF NMR PROBES

2.1 Liquids Probes

Approximately 80% of NMR experiments are performed on high-resolution liquids probes designed for samples in axially aligned glass tubes in superconducting magnets using saddle-shaped rf coils or slotted resonators for signal reception. They are often required to achieve a spectral resolution of several parts per billion on slowly spinning samples. A small fraction of their usage has been for in vivo experiments on small living animals or ex vivo or in vitro experiments on surgically removed tissues kept alive for short periods of time by perfusion with nutrients in saline solutions furnished by a flow system in the probe. Most multinuclear liquids probes have provided proton decoupling with multinuclear observe and deuterium lock, but recently many have been designed for inverse experiments (proton detection with X-nucleus decoupling). At present, high-resolution liquids probes are commercially available for experiments from $-180\,^\circ$C to $380\,^\circ$C.

2.2 Gradient Probes

Pulsed field gradient (PFG) and microscopy MRI probes are usually similar to conventional liquids probes with the addition of gradient coils for one or three axes respectively. PFG probes are used for the measurement of diffusion coefficients, solvent suppression, or selection of specific coherences. Their usage has grown very rapidly in the past several years because of the time savings they provide in two-dimensional NMR. Microscopy in vivo probes may include surface coils for improved localized signal reception.

2.3 Solids Probes

The original (and simplest) probe for NMR of solid samples is the wideline probe, which is normally characterized as being able to generate 90° pulse lengths less than $3\,\mu$s (spectral excitation bandwidths greater than 80 kHz) by withstanding

peak rf coil voltages in excess of 3 kV. Often they are double tuned (DT) to permit cross polarization (CP) with high-power decoupling for increased sensitivity and resolution. High-speed magic angle spinning (MAS) of the sample is added in the CP MAS probe for line narrowing of spin-$\frac{1}{2}$ nuclei, and dynamic angle spinning (DAS) and double rotation (DOR) may be provided for quadrupolar nuclei. When sufficiently large single crystals of the sample can be grown, high-resolution spectra and the chemical shift tensor can be obtained using a single crystal probe that includes a suitable goniometer and crystal orientation mechanism.

3 HISTORICAL PERSPECTIVE ON NMR PROBES

Through the late 1960s 'NMR' implied 'proton NMR of liquids' unless specifically stated otherwise, and multinuclear probes were unheard of. There was a rather widespread misconception that sensitivity increased linearly with coil inductance, even though the early classic treatments[1,2] were sound. High-inductance solenoids (1–50 μH, compared with 40–200 nH for modern probes) wound around the sample tube could be used for efficient reception in the transverse field of the electromagnet, but audio field-modulation coils were needed to shift the detection frequency above the $1/\nu$ noise region of the phase-sensitive video detector. The orthogonal Helmholtz transmit coils could be driven with low-power (milliwatt) oscillators for most continuous wave (CW) techniques, and the transmit/receive coils were carefully isolated using Faraday shields and tuning paddles. Since low-impedance preamplifiers with low noise figures were not available, it was best to include the first stage of the preamplifier in the probe and match it (usually 300–2000 Ω) directly to the receive coil.

Although many time domain pulsed NMR experiments were performed in the first two decades of NMR for relaxation studies, the explosion of NMR techniques awaited the application of Fourier transform (FT) by Richard Ernst in 1966 to the time domain data to obtain the complete frequency domain spectra in a single free induction decay (FID). The increase in sensitivity was comparable to the ratio of the total spectral width to the narrowest line in the spectrum—often two or three orders of magnitude.[3,4] (See also ***Fourier Transform Spectroscopy***.)

Field shimming (homogenizing) was extremely crude and tedious prior to Golay's development of the theory and practice of orthogonal shim coils.[5] With the advent of FT NMR came more incentive to obtain higher resolution because of its dramatic impact on sensitivity. Ultrahigh purity (99.9995%) copper receive coils with precision magnetic compensation and Varian's sample spinner mounted on top of the probe quickly became standard. An external lock employing a sealed sample and separate coil (usually tuned to ^{19}F or ^{2}H) beside the sample coil was used to stabilize the field.[6]

The probe rf circuitry was also quickly impacted by FT NMR. To excite the entire spectral width with large Helmholtz coils at 60 MHz required 10–100 W and generated several kV across the coil, so impedance matching to the transmit circuit became important. The increase in sensitivity from FT NMR opened up the field of multinuclear MR—especially ^{13}C and ^{31}P.[7] The advantages in resolution and sensitivity provided by proton decoupling required double resonance circuits, which made it more difficult to use separate transmit/receive coils, and double-tuned single-coil circuits with transmit/receive duplexers began to appear.[8,9] It is fair to say that modern NMR probe technology was ushered in by David Hoult in 1976 with his transparent analysis of S/N based on the obscure concept of reciprocity.[10] Today, separate transmit/receive coils survive only in single resonance MRI where the high rf homogeneity afforded by a large transmit coil is beneficial and small surface coils are optimum for reception.

Probe technology has matured over the past two decades, and major advances in most probe specifications are not expected. Nonetheless, probe technology will retain its pivotal role in NMR progress because even small improvements can contribute a lot to total system performance.

4 RADIOFREQUENCY ENGINEERING—BASICS

Basic rf engineering has been treated in a number of elementary texts[11,12] and introductory review articles,[13,14] but the probe engineer also needs a working understanding of some of the more advanced concepts in electromagnetic field theory.[15,16] NMR signal reception is different from (and simpler than) antenna theory, in that antennas are designed to receive electromagnetic waves in the far-field limit whereas NMR probes are designed to sense magnetic fields in the near-field limit.[17] While the rf circuits in NMR probes can usually be approximated with simple circuits and analyses, the critical importance of the probe to the total spectrometer performance justifies a level of detailed field and efficiency analysis seldom encountered outside of NMR probes. A number of articles[10,18–25] and a textbook[26] have presented excellent treatments of general NMR probe design problems over the past two decades. A summary of basic NMR probe electronics follows.

4.1 Capacitance

Capacitance (farads) is defined as electric charge per volt (Q/V), and capacitive energy storage is equal to $CV^2/2$. Stray capacitance can often be estimated to sufficient accuracy from the expression for the parallel plate capacitor C_p of area A (m^2), separation distance d (m), and dielectric constant k_d,

$$C_\mathrm{p} = \frac{k_\mathrm{d}\varepsilon_0 A}{d} \tag{1}$$

or from the expression for the low-frequency capacitance of a coaxial capacitor[21] of length h, dielectric o.d. d_o, and dielectric i.d. d_i,

$$C_\mathrm{c} = \frac{2\pi k_\mathrm{d}\varepsilon_0(h + d_\mathrm{o})}{\ln(d_\mathrm{o}/d_\mathrm{i})} \tag{2}$$

where ε_0 is the permittivity of free space, 8.84 pF m^{-1}. Parallel capacitors add algebraically, ($C_\mathrm{T} = C_1 + C_2 + \ldots$), while series capacitors add reciprocally ($C_\mathrm{T}^{-1} = C_1^{-1} + C_2^{-1} + \ldots$).

4.2 Inductance

The simplest definition of inductance L (henrys) comes from Faraday's law of induction—the induced voltage divided

by the rate of change in current di/dt. For inductance calculations, the most practical 'definition' follows from the energy equation

$$U = i_T^2 L/2 \tag{3}$$

where U is the total energy in the magnetic field (the integral of $B^2/2\mu\mu_0$ over all space) and i_T is the current *at the pair of terminals* generating the magnetic field $\boldsymbol{B}$. [We follow popular usage of denoting the magnetic flux density or induction field $\boldsymbol{B}$ (T) as the 'magnetic field' and $\boldsymbol{H} = \boldsymbol{B}/\mu\mu_0$ as the field intensity (A m^{-1}) where μ is the relative permeability of the material.] For all NMR probes, μ is always unity. The permeability of free space μ_0 equals $4\pi \times 10^{-7}$ H m^{-1}.

The inductance of the finite, multiturn, single layer rf solenoid of Figure 1 with a constant pitch, an integral number of turns, and a high surface coverage is given in nH, for dimensions in mm, by the following expression:

$$L_S = \frac{4n^2r^2(1 - 0.2/n)}{h + 1.2r^{0.9}} \quad \text{[mixed]} \tag{4}$$

where n is the number of turns (Figure 1 has five turns), h is the *overall* axial length, and r is the effective inside radius, which for round wire is approximately equal to the inside coil radius plus 20% of the wire radius. The last term in the numerator corrects for the fact that the helix makes the effective coil length a little less than the overall length. The above expression is correct to within several per cent for $h/r > 0.2$. For the loop-gap resonator[27,28] (a single-turn solenoid, also called a split ring), the helix correction term is dropped, and the coefficient changes to 3.9 to correct for current concentrating at the ends of the ring. Higher order corrections for multiturn coils with low surface coverage can be added.

Lead (parasitic) inductance is usually best estimated by calculating the inductance of a loop-gap resonator having a length equal to the diameter of the lead wire and $r^2 = A_C/\pi$, where A_C is the area enclosed by the loop formed by the leads. Sometimes lead inductance is better estimated from the expression for the inductance L_C of a coaxial transmission line:

$$L_C = \frac{\mu_0 h}{2\pi} \ln\left(\frac{d_o}{d_i}\right) \tag{5}$$

Clearly from equation (5), series inductors add like resistors ($L_T = L_1 + L_2 + \ldots$); likewise, parallel inductors add reciprocally ($L_T^{-1} = L_1^{-1} + L_2^{-1} + \ldots$).

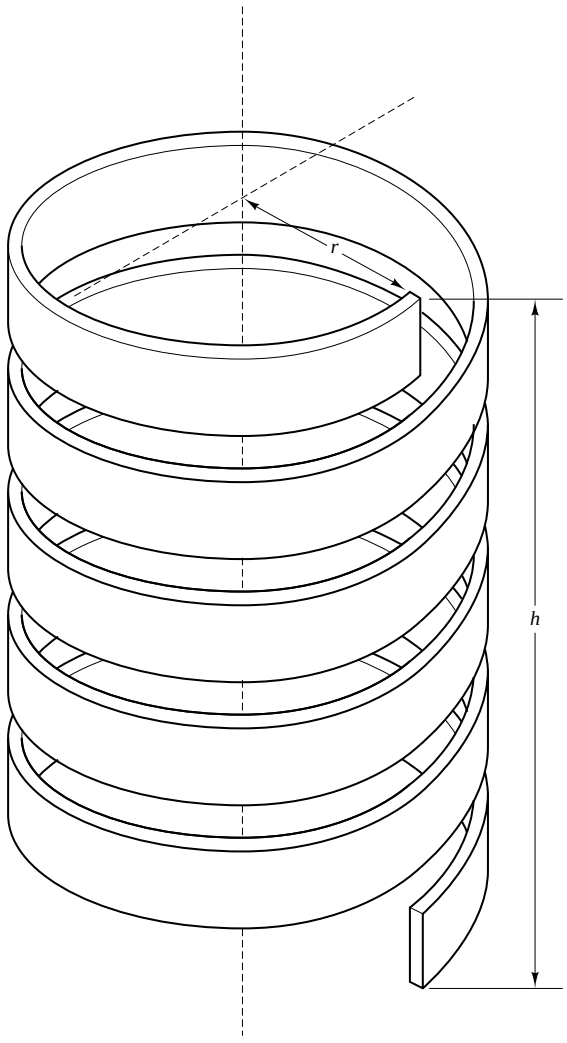

Figure 1 A five-turn solenoid

4.3 Single Resonance Circuits

4.3.1 Power

Figures 2 and 3 illustrate the basic *RLC* series and parallel circuits, respectively. The losses in the series *RLC* circuit of Figure 2 are best represented by the total effective series resistance R_s (from the coil, capacitor, leads, etc.). For the parallel circuit of Figure 3, the losses may be represented more conveniently by a total effective parallel resistor R_p. In both cases, the basic equations from ac circuits apply for rms power P and peak power P_P. (Power is assumed to be rms unless denoted otherwise.)

$$P = \frac{P_P}{2} = \frac{i_P^2 R_s}{2} = \frac{V_P^2}{2R_p} \tag{6}$$

Power ratios are often expressed in dB, $10 \log(P_2/P_1)$, and power is often expressed in dBm—defined as dB relative to a milliwatt:

$$\text{dBm} \equiv 10 \log(1000P) \tag{7}$$

In practice, peak-to-peak voltages ($2V_P$) are usually measured on an oscilloscope, and the measurements are significantly influenced by harmonic distortion, VSWR (Voltage

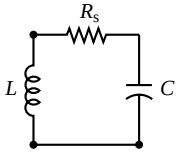

Figure 2 Series *RLC* circuit

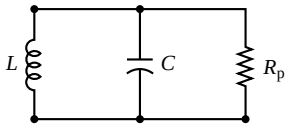

Figure 3 Parallel *RLC* circuit

Standing Wave Ratio), loading, and oscilloscope bandwidth. Most conventional liquids probes are excited with 100 W pulses of 10–80 μs at the observe frequency (usually the low frequency, LF) at duty cycles below 0.1% while they are driven with 10 W at the decouple frequency (usually ^{1}H, the high frequency, HF) at duty cycles below 50%. Solids probes typically see LF pulses of 200–400 W with duty cycles up to 1% while irradiating with HF power of 50–200 W at duty cycles below 30%. Whole body MRI probes are usually driven with 1–10 kW at duty cycles below 0.5%.

4.3.2 Resonance

Since charge (q) equals CV and $i = \mathrm{d}q/\mathrm{d}t$, a capacitor reaches a steady-state (monochromatic) reactance X_C (analogous to resistance, V/i) of $1/\mathrm{i}\omega C$ after several RC time-constants, where i is the imaginary unit, $\sqrt{-1}$. Likewise, since $V = -L\ \mathrm{d}i/\mathrm{d}t$, an inductor has reactance $X_L = \mathrm{i}\omega L$ and time constant L/R. For the normal high-Q condition ($Q = \omega_0/\Delta\omega_{\frac{1}{2}}$), resonance occurs when the inductive reactance X_L plus the capacitive reactance X_C equals zero. (Often the phase is omitted for convenience, but it must be remembered that the voltage phase in the inductor leads by 90° while in the capacitor it lags by 90° relative to that in the resistor.) Hence,

$$\omega_0 = \frac{1}{\sqrt{LC}} \tag{8}$$

At resonance, the series impedance of the series RLC circuit is R_s (since $X_L + X_C = 0$) and the parallel impedance of the parallel RLC circuit is R_p [since $(X_L X_C)/(X_L + X_C) = \infty$]. The 3 dB width $\Delta\omega_{1/2}$ of the resonance defines the quality factor of the unloaded (and unmatched) RLC circuit, and the following relationships are readily derived:

$$R_\mathrm{p} = QX_L \tag{9}$$

$$R_\mathrm{s} = X_L/Q = R_\mathrm{p}/Q^2 \tag{10}$$

4.3.3 Matching

Since X_L is typically 20–200 Ω, R_s is usually less than 1 Ω and R_p is greater than 2000 Ω. For efficient coupling to the transmitter and preamplifier, the resonant circuit, transmission lines, preamplifier, and transmitter must all be matched to approximately the same impedance, although mismatches of up to a factor of two are often unimportant. The international standard is 50 Ω (except in the television industry, where it is 75 Ω). Figures 4 and 5 illustrate the two basic methods of impedance matching: shunt inductor and series capacitor.

The inductive matching technique has the advantage of not requiring a second high-voltage capacitor, but the matching range is limited by the difficulty of adjusting very small inductors. The required shunt inductor (for $R_\mathrm{p} \gg Z_0$) is

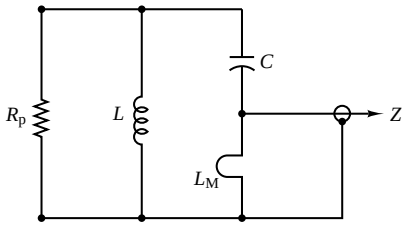

Figure 4 Shunt inductive matching circuit

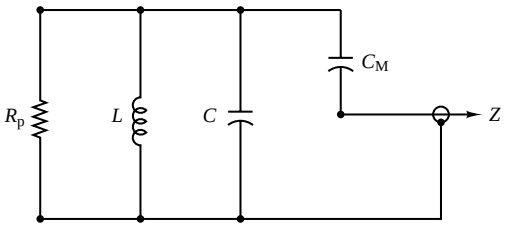

Figure 5 Series capacitive matching circuit

$$L_\mathrm{M} = L_\mathrm{T}\sqrt{Z_0/R_\mathrm{p}} \tag{11}$$

where L_T is the total series inductance ($L_\mathrm{s} + L_\mathrm{M}$ + leads) and Z_0 is the transmission line characteristic impedance—normally 50 Ω. The resonant frequency is calculated from L_T and C.

The capacitive matching circuit simplifies multinuclear (broadband) tuning requirements as high-voltage (HV) variable capacitors are readily available. The required match capacitance (again, for $R_\mathrm{p} \gg Z_0$) has reactance X_{CM} given by

$$X_{CM} = \sqrt{R_\mathrm{p} Z_0} \tag{12}$$

and rms current equal to that in the transmission line, $\sqrt{P/Z_0}$. In practice, some combination of capacitive and inductive matching is often used, and capacitive voltage division is often employed to reduce the demands on the matching variable capacitor.[29] Properly 'pruned' transmission lines can also be used to transform impedance (see ***Probes for Special Purposes***).

5 SIGNAL-TO-NOISE RATIO AND B_1

5.1 Magnetization and the NMR Signal

The NMR voltage signal S from a sample with susceptibility χ, with nuclear spins precessing at angle ϕ in magnetic field $\boldsymbol{B}_0$ at angular frequency ω, detected by a coil that generates a circularly polarized (rotating) transverse field $\boldsymbol{B}_1(\boldsymbol{r})$, over the sample volume V_S for current i, may be shown from the principle of reciprocity[10,26] to be

$$S = \frac{\chi B_0 \omega}{\mu_0 i} \int_S \sin\phi\, B_1(\boldsymbol{r})\, \mathrm{d}V \tag{13}$$

Simply put, the receiver coil need only be analyzed as a $\boldsymbol{B}_1$ transmitter. For a uniform $\boldsymbol{B}_1$ generated by a current i,

immediately following a 90° pulse,

$$S = \frac{\chi B_0 \omega B_1 V_S}{\mu_0 i} \tag{14}$$

The equilibrium magnetization $\boldsymbol{M}_0$ is given by[1,6]

$$\boldsymbol{M}_0 = \frac{\chi \boldsymbol{B}_0}{\mu_0} = \frac{n_s \gamma^2 \hbar^2 I_x (I_x + 1) \boldsymbol{B}_0}{3 k_B T_S} \tag{15}$$

where n_s is the number of spins at resonance per unit volume, γ is the magnetogyric ratio, I_x is the spin quantum number, k_B is Boltzmann's constant, T_S is the sample temperature, and $\hbar = h/2\pi$, where h is Planck's constant.

5.2 Thermal Noise

The Johnson (thermal) rms noise N from a resistor R_E for filter bandwidth $\Delta\nu$ (not ν/Q) is[1,2]

$$N = (4 R_E k_B T_R \Delta\nu)^{1/2} \tag{16}$$

where T_R is the temperature of the resistor. (For R_E = 50 Ω, N = −168 dBm $Hz^{-1/2}$.) The effective series resistance (X_L/Q) of the loaded circuit is best determined by measuring Q. Other noise sources (interference, triboelectric, spurious, shot, microphonic, preamplifier) can usually be made negligibly small with careful engineering.[23]

5.3 B_1 in the Rotating Frame

A linearly polarized oscillating magnetic field $2B_1$ (as in a solenoid) may be decomposed into the sum of two oppositely rotating circularly polarized fields, each of magnitude B_1. One of these components can be used to drive NMR precession within a bandwidth approximately equal to its magnitude (in Hz) if it is transverse to $\boldsymbol{B}_0$; the other has no effect on NMR precession, as its frequency in the rotating frame is -2ω. From the Biot–Savart law,[15] B_1 at the center of a solenoid is given by

$$B_1 = \frac{\mu_0 n i}{2h\sqrt{1 + 4(r/h)^2}} \tag{17}$$

Using equations (3), (6), and (10), it may be shown that $U = PQ/\omega$, and B_1 may be expressed as follows for the infinite solenoid:

$$B_1 = \left[\frac{\mu_0 P Q}{2\omega V_C}\right]^{1/2} \tag{18}$$

where V_C is the coil volume. [Adding the term $1 + 4(r/h)^2$ in the denominator inside the brackets of equation (18) improves the accuracy for typical solenoids.]

The unloaded Q_0 of the typical multiturn solenoid (well below self-resonance and with high surface coverage) is, in mixed units, approximately

$$Q_0 \approx 6\sqrt{hrf} \quad [\mathrm{MHz}^{1/2}\ \mathrm{mm}^{-1}] \tag{19}$$

Saddle coils (commonly, but incorrectly, called Helmholtz coils;[15] more properly they could be called Ginsberg[30] or Golay[5] coils) and slotted resonators[19,25] are better suited for liquids NMR in superconducting magnets, as they generate a transverse $\boldsymbol{B}_1$ while allowing axial access. Moreover, their axial symmetry makes it easier to obtain high $\boldsymbol{B}_0$ homogeneity. The coefficient in equation (19) is reduced to a value of 2 for saddle coils with medium surface coverage, as is necessary for orthogonal double resonance operation.

The loaded circuit quality factor Q_L will be lower than that of the coil because of losses in capacitors, shields, and sample. A convenient method of measuring Q_L is with a reflectance bridge, where the appropriate Δf value is measured at −7 dB return loss, which may be calibrated with a 21 Ω or 119 Ω load on a 50 Ω line.[23] (Q_L is not lowered much by 'matching' to the preamplifier if its noise figure is less than ∼1 dB.)

For *any* coil, *average* B_1 in gauss over the usable volume may be expressed in mixed units by the following:

$$\langle B_1 \rangle = \beta \left[\frac{\eta_E P Q_L}{f V_C}\right]^{1/2} \quad \text{[mixed]} \tag{20}$$

where β is a dimensionless function of coil geometry, f is in MHz, V_C is in mL, and η_E is the rf efficiency—the fraction of the power delivered to the rf coil and sample.[21] The rf efficiency η_E is usually greater than 0.9 for single resonance circuits at low fields, but it may be less than 0.2 for double resonance at high fields. In practice, it is always necessary to measure rather than calculate Q_L, which then includes the capacitor losses. The above equation is still valid if η_E is then defined as $1 - \eta_L$, where η_L is the fraction of the power dissipated in inductors not generating B_1 (leads and coils added for multiple resonances).

For special high-resolution applications of solenoidal rf coils, the optimum h/r value is 2, and $\beta \approx 2.4$. For very lossy samples, the optimum h/r is the largest permitted by space constraints, and $\beta = \sqrt{10}$ for the infinite solenoid. For MAS, the optimum h/r is 3, and β = 2.1 when the coil is at the magic angle. For saddle coils and slotted resonators, β ranges from 0.8 to 1.4, depending on surface coverage, subtended angle, and the ratio of height to diameter.

A magnetic filling factor η_f may be defined by

$$\eta_f = \frac{\int B_1^2 \, dV}{\mu_0 U} \tag{21}$$

where the integration is over the sample volume V_S. From equations (3), (10), (20), and (21) comes a very practical (and exact) definition of the filling factor:

$$\eta_f = \frac{\beta^2}{20} \frac{V_S}{V_C} \tag{22}$$

5.4 S/N

From the above, the S/N from a single 90° pulse with an optimum filter [$1/(\pi\Delta\nu) = T_2$, the spin–spin relaxation time, and $\Delta\nu < \omega/2\pi Q_L$] can be written as follows:

$$\text{S/N} = \frac{S}{2N} = \left[\frac{\hbar^2\sqrt{\pi\mu_0}}{12k_B^{3/2}}\right]\left[\frac{n_s\gamma I_x(I_x+1)\sqrt{T_2}}{T_S\sqrt{T_R}}\right](\eta_E\eta_f Q_L V_S)^{1/2}\omega^{3/2} \tag{23}$$

The extra factor of 2 in the denominator arises because S is the initial peak signal voltage that decays with time-constant T_2 and N is the rms noise voltage. The product of the two bracketed terms is $1.65 \times 10^{-5}\,\text{s}^{3/2}\,\text{m}^{-3/2}$ for protons in water with $T_2 = 0.1$ s and $T_S = T_R = 300$ K.

A useful simplification of equation (23) is the following for given NMR conditions (sample, γ, $\boldsymbol{B}_0$, T_S, T_2, technique):

$$\text{S/N} \propto \frac{V_S}{\tau_{90}\sqrt{P}} \tag{24}$$

where τ_{90} is the mean 90° pulse width obtained over sample volume V_S with power P.

5.5 Minimizing Losses

For small samples, the Q_L is usually dominated by coil resistance. However, above 400 MHz it may be dominated by capacitor losses unless extreme care is taken in their selection, and it may be necessary to parallel a number of low-value capacitors for sufficiently low capacitor losses. For large, lossy samples, Q_L and T_R are dominated by sample losses. Dielectric losses from electric fields in the sample may be reduced by decreasing the coil inductance and increasing the capacitance.[20,31] Usually, the only ways to reduce power P_S deposited by the inductive mechanism in a sample of uniform resistivity by a rotating $\boldsymbol{B}_1$ are to maximize the $\boldsymbol{B}_1$ homogeneity and to maximize the rms flux path length ξ for a given volume, but sometimes it is possible to use insulating films to suppress currents in the sample.[32] The presence of skin, fat, and bones in MRI can make the estimate of P_S as much as an order of magnitude too large when using a worst-case tissue resistivity ρ_S of 1.2 Ω m.

$$P_S \approx \frac{B_1^2\omega^2 V_S^2}{16\pi\rho_S\xi} \tag{25}$$

Equation (25) is equivalent to the low-frequency limit given by Carlson[24] for a sphere, but the inclusion of ξ improves loss predictions for nonspherical samples. The loaded Q_L may be estimated from the unloaded Q_0 and the sample Q_S:

$$Q_L = \frac{Q_0 Q_S}{(Q_0 + Q_S)} \tag{26}$$

For reasonably uniform, *linear* B_1, Q_S is approximately

$$Q_S \approx \frac{32\pi\rho_S\xi V_C}{\mu_0\eta_E\beta^2\omega V_S^2} \tag{27}$$

The numerical coefficient in equation (27) is increased to 64 for circular polarization.

The ratio Q_0/Q_L has frequently been used as a figure-of-merit for coils in MRI, but this does not properly consider the dielectric losses nor the major effects of $\boldsymbol{B}_1$ inhomogeneity in surface coils.[33] equation (24) provides a better figure-of-merit, but it still does not adequately evaluate homogeneity.

The 'birdcage' resonator of Edelstein et al. made quadrature coils practical for generating a single rotating $\boldsymbol{B}_1$.[22,34] Liquids and solids NMR find few applications for quadrature rf coils, as coil losses usually dominate. However, in MRI, when inductive sample losses dominate, quadrature coils offer up to a 40% improvement in S/N. For an advanced treatment of the birdcage resonator, the reader is referred to the article by Tropp.[35] (See also ***Birdcage Resonators: Highly Homogeneous Radiofrequency Coils for Magnetic Resonance***.)

A proper calculation of L, B_1, and Q_0 requires a knowledge of the surface current distribution in the conductors—especially in single-turn resonators.[25] The so-called 'proximity effect' is ambiguous. A better method of determining current distribution in large conductors is to iterate on Biot–Savart integration, letting the currents move around in the conductors to a minimum inductance ($2U/i_T^2$) configuration. The current usually prefers to take the shorter paths (inside surface) and tends to concentrate near regions of high flux curvature (end edges) and high flux density (nearby shields). The normal component of the rf magnetic field always vanishes near the surface of conductors, and the current penetrates only to a depth given by the classical skin depth:

$$\delta = \left(\frac{2}{\omega\mu_0\sigma}\right)^{1/2} \tag{28}$$

where σ is the electrical conductivity. For copper at 300 K, δ = 6.4 μm at 100 MHz. Nonuniform surface current density is responsible for Q_0 being lower by a factor of 3–8 than would occur for uniform surface current density. In some cases, Q_0 may be improved by the use of Litz wire (woven wire, using individually enameled strands as fine as 0.03 mm).

6 DOUBLE RESONANCE

Two saddle coils, rotated 90° about the $\boldsymbol{B}_0$ axis provide a convenient method of doing double resonance NMR with good isolation. However, only the innermost coil can have the optimum filling factor, and sometimes it is beneficial to have the same spatial distribution of the two rf fields, $\boldsymbol{B}_1$ and $\boldsymbol{B}_2$. Also, triple- or quadruple-resonance NMR experiments are often useful. Thus, it is often desirable to double-tune or triple-tune a single sample coil, although Anderson described in 1973 a clever method of using three orthogonal, single-tuned coils.[36]

The number of modes in a resonant circuit will generally be equal to the number of unique inductors or capacitors, whichever is fewer. (Resonant transmission lines may count as either.) It is sometimes necessary to add additional inductors or capacitors (producing extraneous modes) to improve isolation or to achieve balance at the frequencies of interest, although this can complicate tuning.[37,38] The most common double-tuned circuit, shown in Figure 6, has been analyzed by several authors.[21,23,39] It has an HF parallel mode and an LF series mode. The efficiency at the HF is increased by *decreasing* L_S/L_H, where L_S is the sample coil inductance and L_H is the HF tuning coil inductance. On the other hand, efficiency

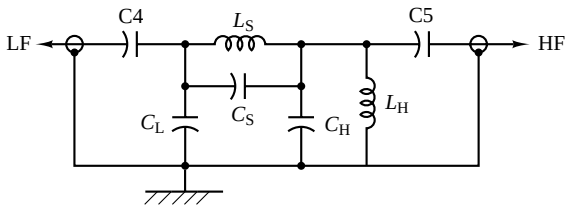

Figure 6 Double resonance circuit

at the LF is increased by *increasing* L_S/L_H. In principle, if the losses in L_H and the tuning capacitors can be made vanishingly small compared with sample losses, the efficiency can approach 100% at both frequencies.[40] Rise time, however, will be degraded (because the total Q_L must increase), but this is seldom significant for in vivo experiments. For 8-mm sample coils, efficiencies at HF and LF are typically 40% and 75% respectively (when Q_L includes capacitor losses, as in the referenced analyses). From equations (20) and (23), B_1 and S/N are degraded only as the square root of the efficiency.

7 CONSTRUCTION MATERIALS AND TECHNIQUES

Although $\boldsymbol{B}_0$ homogeneity specifications sound frighteningly stringent, the capability of orthogonal shim systems is such that only in the immediate vicinity of the sample is magnetic susceptibility critical. Austenetic stainless steels (with SI volume susceptibility $\chi_V = \mu - 1 \approx 0.02$) can often be used for thin-walled Dewars surrounding the sample region and for Dewared transfer lines, although glass is preferred if space permits. It is, of course, desirable to minimize the amount of shimming effort required when the probe is changed, so low-susceptibility construction materials and thin sections are preferred. The magnetic susceptibilities of the components immediately above and below the sample region (in the B_z direction) are more significant, and axial and azimuthal symmetry are both important.[41,42]

The common aluminum alloys[43] 6063-T6 (0.7% Mg, 0.4% Si, up to 0.3% Fe) and 6061-T6 (1% Mg, 0.6% Si, 0.3% Cu, 0.3% Cr, up to 0.7% Fe) are usually acceptable for thin shield cylinders and support structure since the iron is usually in a nonmagnetic phase ($FeAl_3$ or Fe_2Al_7),[44] but they often present acoustic ringing problems below 15 MHz.[45] Jewelry bronze [copper alloy C22600, 87.5% Cu, 12.5% Zn, 0.005% (max.) Fe] is usually a better choice for shields and support structure because of its lower magnetism, much higher acoustic absorption, good electrical conductivity, high strength, and excellent finishing and joining properties. Iron content is also rather carefully controlled in the more readily available phosphor–tin bronzes, such as C51000 [94.8% Cu, 5% Sn, 0.2% P, 0.1% Fe (max.)]. Aluminum, silicon, and zinc bronzes (or brasses) have to be checked carefully if they are to be used within $r_b/3$ of the sample, where r_b is the bore radius, as iron contents can exceed 0.5%. Copper-rich iron compounds are not stable, and the solubility of iron in copper at 200 °C is only 13 ppm,[44] thus copper alloys are likely to be ferromagnetic unless the iron is bound up in iron-poor compounds (such as $FeAl_3$ or $FeSi_2$), in which case it is still strongly paramagnetic ($\chi_V \sim 2$ for Fe_2O_3). For B_0 above 2.16 T, the ferromagnetic components saturate with a high-field χ_V of 2.16 T/B_0.

The critical importance of high-integrity ground connections throughout multiple resonance probes cannot be overemphasized, especially as the wavelength becomes comparable to or shorter than four times the maximum dimension of the electronics region. Welding, press-fits, and solder joints are preferred over silver-filled epoxy and silver paint.[23] The external shield cylinders are often anodized for an aesthetically pleasing finish that also helps eliminate variability in grounds. Figure 7 illustrates three typical NMR probes: a high-resolution liquids narrow bore probe, a CP MAS wide bore probe, and a single crystal probe with a goniometer.

Quartz is usually selected for coil forms in high-field magnets because of its lower dielectric loss, even though its magnetic, mechanical, and acoustic properties are inferior to those of Pyrex. Acoustic ringing in quartz, Macor, and ceramic capacitors may cause problems at frequencies up to 50 MHz. Zirconia has often been used in MAS probes for solids because of its superior mechanical properties.

One of the best engineering thermoplastics is polyether ketone (PEK) because of its low dielectric loss and excellent chemical, thermal, and dimensional stability at modest cost, but other insulating materials (Kel-f, Teflon, Macor, Vespel, zirconia) are often chosen for specific background or thermal considerations. Fiberglass reinforced composites are also widely used, but they must be cleaned well after machining to

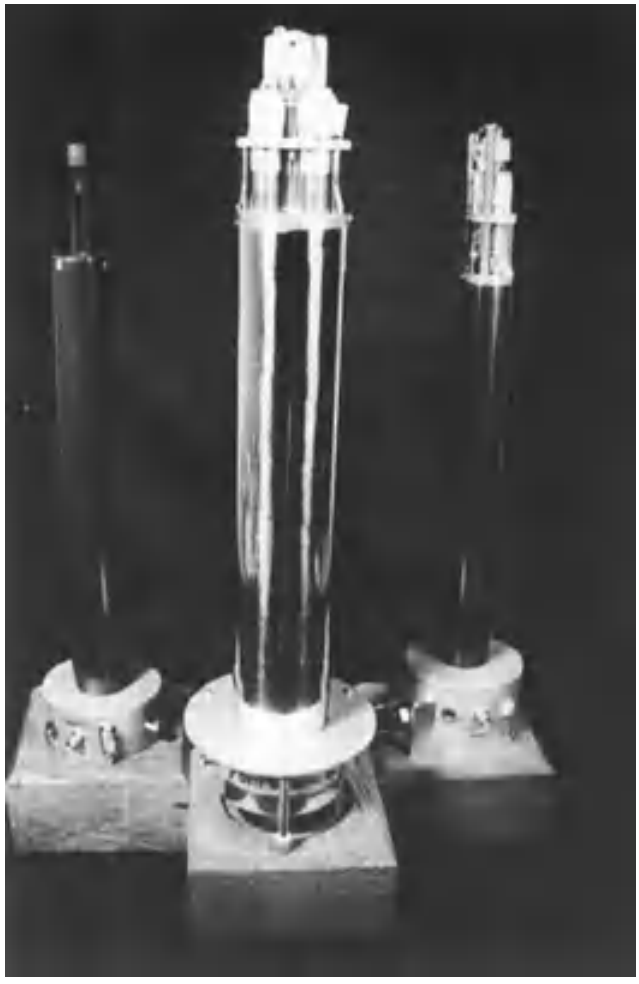

Figure 7 Three typical NMR probes

remove traces of steel from the tools, and the glass fibers may produce aluminum and silicon background signals. Excellent epoxies are available for securing components and mounting coils—such as Epo-Tek 354, 360, and 377 from Epoxy Technology, Inc., Billerica, MA, USA. Several brands of Kel-f and heat-shrink Teflon have sufficiently low hydrogenous content for critical proton applications, but experimentation and careful control are necessary.

8 THERMAL ENGINEERING

Linewidth and lineshape are often critically dependent on temperature control and stability.[46] Most commercial probes are intended to operate from −100 °C to +120 °C, but special liquids probes are commercially available for operation from −170 °C to +380 °C, and solids probes are available to cover the range 35–900 K. Temperatures are usually regulated by using a dc resistive heater (designed for minimal magnetic interaction) to heat a stream that is directed past the sample.

First-order heat-transfer calculations and simple power balance analysis are generally sufficient in the probe design. The heater power P_H required to increase the temperature of the gas by δT with specific heat C_p (1000 J kg^{-1} K^{-1} for N_2) and flow rate G (typically 1–2 g s^{-1} for MAS probes) is

$$P_H = GC_p\delta T \tag{29}$$

The gas temperature is usually measured with a copper–constantan thermocouple shortly before it reaches the sample, but optical sensors have also been used.[47] Platinum resistors (RTDs) are best in the range from 20–75 K and above 700 K, but in the intermediate range they are not as accurate as a thermocouple unless small magnetic-field-dependent corrections are made. They are often used to sense the heater temperature for protection in the event of inadvertent loss of gas flow. The control problems are more difficult than usually encountered elsewhere because of the requirement for precision temperature control of a stream of low specific heat that may encounter large fluctuations in flow rate. Standard PID (proportional-integral-derivative) control algorithms have been incorporated within the past several years by all manufacturers with vast improvements over the simple PI algorithms used previously. Dynamic control stability can be further improved by adding a power estimate that is a function of temperature and flow rate, and fuzzy logic may have advantages. Lead shot has occasionally been used for a thermal ballast because of its high volumetric specific heat and low Debye temperature (105 K).

Heat-transfer calculations are often limited to simple conduction calculations through thin sheets:

$$P_T = k_T A\delta T/d \tag{30}$$

where P_T is the thermal conduction power (W), k_T the thermal conductivity (W m^{-1}) of the material, A the area perpendicular to the direction of heat transfer, δT the temperature difference between the two surfaces, and d the thickness in the direction of heat transfer. The other common conduction problem is through a thick-walled tube with i.d. d_i, o.d. d_o, and length h:

$$P_T = \frac{2\pi k_T h\delta T}{\ln(d_o/d_i)} \tag{31}$$

The high Reynolds numbers (often greater than 10^5) that are seen in Dewared transfer lines result in a very high heat transfer through the bare glass or metal joints unless they are lined internally with plastic tubing, in which case the above equation can be used to estimate the losses.

The extreme temperatures that are often desired[48–50] can make differential thermal expansion responsible for stresses that exceed the rupture limit of one of the components in the probe if not properly designed. However, most of the materials used in NMR probes have high strength. The exceptions, Macor and glasses, tolerate high compressive stresses. Hence, even these materials can often be used with plastics in properly designed situations even though their thermal expansions differ widely. Macor is the only commonly used material that is likely to rupture from internal steady-state thermal stresses, as its maximum thermal stress temperature ($T_T = S/b_T E$, where S is tensile strength, b_T thermal expansion coefficient, and E the Young's modulus of elasticity) and thermal conductivity are both very low.

9 GRADIENT NMR PROBES

By applying magnetic field gradients in three orthogonal directions ($\delta B_z/\delta x$, $\delta B_z/\delta y$, $\delta B_z/\delta z$), it is possible to use NMR to image macroscopic structures, and indeed this has made clinical magnetic resonance imaging (MRI) an important medical diagnostic technique.[51,52] Obtaining spatial resolution below 1 mm on liquid-like samples requires gradients above the 10 m T m^{-1} available in most clinical MR machines. Higher gradients are easily obtained by reducing the size of the gradient coils or improving their efficiency. MR microscopy generally involves incorporating the gradient coils into wide-bore or narrow-bore probes along with small rf coils so that spatial resolution down to 10 μm can be obtained on liquid-like samples. Limited imaging experiments are also then possible on solid samples.[53]

Single axis gradients ($\delta B_z/\delta z$) based on Maxwell pairs (sometimes called anti-Helmholtz coils) are much easier to implement in small spaces and are very useful for diffusion experiments using pulsed field gradients (PFG).[54] Similar probes (with lower gradient coefficients, to keep digital-to-analog convertor and amplifier drift requirements more manageable) have recently become very popular for gradient enhanced spectroscopy (GES), as the run time is often dramatically reduced for 2D NMR.

Rapid switching of large gradient coils requires high-power audio amplifiers (up to 500 kW). Hence, the switching efficiency η_s is very important:

$$\eta_s = \frac{\alpha^2 d_S^4 h_S}{\mu_0 L} \tag{32}$$

where α is the gradient coefficient (T A^{-1} m^{-1}), d_S the sample diameter, h_S the sample length, and L the gradient coil inductance. (The gradient coefficient is sometimes called the 'efficiency', but the above dimensionless definition is more consistent with other efficiency definitions.) The 'fingerprint'

design of Schenck et al.[55] achieves much higher η_s values than earlier Golay coils, but new proprietary designs achieve even higher efficiency.

Image linearity has often been described in terms of field linearity—the relative difference between the gradient field and a linear field at the edge of the sample. A better definition of image linearity is rms local deviation of the gradient from its mean value throughout the sample volume. This has also been called differential linearity. It is sometimes desirable to use highly nonlinear local gradients (more than 40% local deviation) and image distortion correction software so that higher gradients can be achieved,[56] but local deviation below 10% is usually preferred.

When the gradients are switched, eddy currents are induced in the cold radiation shield of the magnet that have long decay times because of the ultralow resistivity of copper below 40 K. Active shielding of the gradients greatly reduces the external fields generated by the gradients and permits rapid pulse techniques without excessive cryogen boiling or high-order compensation techniques.[57,58] Acoustic resonances in the gradient coils are then likely to limit gradient decay time, particularly at very high fields, but novel coil geometries are becoming available that greatly reduce this electromechanical or acoustic efficiency.

10 RELATED ARTICLES

Gradient Coil Systems; Instrumentation for the Home Builder; Probes for High Resolution; Radiofrequency Systems and Coils for MRI and MRS; Sensitivity of Whole Body MRI Experiments; Solid State Probe Design; Spectrometers: A General Overview; SQUIDs; Surface Coil NMR: Detection with Inhomogeneous Radiofrequency Field Antennas.

11 REFERENCES

1. A. Abragam, *The Principles of Nuclear Magnetism*, Oxford University Press, Oxford, UK, 1961.
2. W. G. Clark, *Rev. Sci. Instrum.*, 1964, **35**, 316.
3. R. R. Ernst and W. A. Anderson, *Rev. Sci. Instrum.*, 1966, **37**, 93.
4. R. R. Ernst, in *Advances in Magnetic Resonance*, ed. J. S. Waugh, Academic Press, New York, 1966, Vol. 2, pp. 1–135.
5. M. J. E. Golay and N. J. Rumson, US Pat. 3 569 823, 1971.
6. H. D. W. Hill and R. E. Richards, *J. Phys. E, Ser. 2*, 1968, **1**, 977.
7. D. G. Gillies, in *Nuclear Magnetic Resonance*, ed. R. K. Harris, Chemical Society, London, 1972, Vol. 1, pp. 176–180.
8. J. D. Ellett, M. G. Gibby, U. Haeberlen, L. M. Huber, M. Mehring, A. Pines, and J. S. Waugh, in *Advances in Magnetic Resonance*, ed. J. S. Waugh, Academic Press, New York, 1971, Vol. 5, pp. 117–176.
9. D. D. Traficante, J. A. Simms, and M. Mulcay, *J. Magn. Reson.*, 1974, **15**, 484.
10. D. I. Hoult and R. E. Richards, *J. Magn. Reson.*, 1976, **24**, 71.
11. M. J. Wilson, *The ARRL Handbook for the Radio Amateur*, ARRL, Newington, CT, USA, 1987.
12. *Basic Electronics*, US Navy Bureau of Naval Personnel, Dover, NY, 1973.
13. R. E. Gordon, *Phys. Med. Biol.*, 1985, **30**, 8, 741.
14. D. D. Traficante, *Concepts Magn. Reson.*, 1989, **1**, 73.
15. J. R. Reitz and F. J. Milford, *Foundations of Electromagnetic Theory*, Addison-Wesley, Palo Alto, 1967.
16. J. D. Jackson, *Classical Electrodynamics*, 2nd edn., Wiley, New York, 1975.
17. D. I. Hoult, *Concepts Magn. Reson.*, 1989, **1**, 1.
18. D. I. Hoult, *Prog. NMR Spectrosc.*, 1978, **12**, 41.
19. H. J. Schneider and P. Dullenkopf, *Rev. Sci. Instrum.*, 1977, **48**, 68.
20. D. I. Hoult and P. Lauterbur, *J. Magn. Reson.*, 1979, **34**, 425.
21. F. D. Doty, R. R. Inners, and P. D. Ellis, *J. Magn. Reson.*, 1981, **43**, 399.
22. C. Hayes, W. Edelstein, J. Schenck, O. M. Mueller, and M. Eash, *J. Magn. Reson.*, 1985, **63**, 622.
23. F. D. Doty, T. J. Connick, X. Z. Ni, and M. N. Clingan, *J. Magn. Reson.*, 1988, **77**, 536.
24. J. W. Carlson, *J. Magn. Reson.*, 1988, **78**, 563.
25. G. J. Kost, S. E. Anderson, G. B. Matson, and C. B. Conboy, *J. Magn. Reson.*, 1989, **82**, 238. (Improved methods of treating nonuniform surface current distributions have recently been developed: S. Crozier, K. Luescher, L. K. Forbes, and D. M. Doddrell, *J. Magn. Reson., Ser. B*, 1995, **109**, 1.)
26. C.-N. Chen and D. I. Hoult, *Biomedical Magnetic Resonance Technology*, Adam Hilgar, New York, 1989.
27. W. N. Hardy and L. A. Whitehead, *Rev. Sci. Instrum.*, 1981, **52**, 213.
28. M. F. Koskinen and K. R. Metz, *J. Magn. Reson.*, 1992, **98**, 576.
29. F. D. Doty, US Pat. 4 710 719, 1987.
30. D. M. Ginsberg and M. J. Melchner, *Rev. Sci. Instrum.*, 1970, **41**, 122.
31. D. W. Alderman and D. M. Grant, *J. Magn. Reson.*, 1979, **36**, 447.
32. H. Kugel, *J. Magn. Reson.*, 1991, **91**, 179.
33. J. J. H. Ackerman, *Concepts Magn. Reson.*, 1990, **2**, 23.
34. W. A. Edelstein, J. F. Schenck, O. M. Mueller, and C. E. Hayes, US Pat. 4680548, 1987.
35. J. Tropp, *J. Magn. Reson.*, 1989, **82**, 51.
36. W. A. Anderson, US Pat. 3 771 055, 1973.
37. S. M. Holl, R. A. McKay, T. Gullion, and J. Schaefer, *J. Magn. Reson.*, 1990, **89**, 620.
38. F. D. Doty, US Pat. 5 162 739, 1992.
39. E. Najim and J.-P. Grivet, *J. Magn. Reson.*, 1991, **93**, 27.
40. J. R. Fitzsimmons, H. R. Brooker, and B. Beck, *Magn. Reson. Med.*, 1989, **10**, 302.
41. H. D. Hill and A. P. Zens, US Pat. 4 517 516, 1985.
42. H. D. Hill, US Pat. 4 563 648, 1986.
43. J. R. Davis (ed.), *Metals Handbook*, 10th edn., ASM International, New York, 1990, Vol. 2.
44. M. Hansen (ed.), *Constitution of Binary Alloys*, 2nd. edn., McGraw-Hill, New York, 1989.
45. M. L. Buess and G. L. Petersen, *Rev. Sci. Instrum.*, 1978, **49**, 1151.
46. A. Allerhand and S. R. Maple, *J. Magn. Reson.*, 1988, **76**, 375.
47. H. J. Williams, Y. Gao, A. I. Scott, M. H. Gross, and M. H. Sun, *J. Magn. Reson.*, 1988, **78**, 338.
48. F. D. Doty, J. B. Spitzmesser, and D. G. Wilson, US Pat. 5 202 633, 1993.
49. M. S. Conradi, *Concepts Magn. Reson.*, 1993, **5**, 243.

50. J. F. Stebbins, E. Schneider, J. B. Murdoch, A. Pines, and I. S. E. Carmichael, *Rev. Sci. Instrum.*, 1986, **57**, 39.
51. P. Mansfield and P. G. Morris, in *Advances in Magnetic Resonance*, ed. J. S. Waugh, Academic Press, New York, 1982, Vol. 12, Suppl. 2.
52. D. G. Taylor, R. Inamdar, and M.-C. Bushell, *Phys. Med. Biol.*, 1988, **33**, 6, 635.
53. D. G. Cory, J. W. M. van Os, and W. S. Veeman, *J. Magn. Reson.*, 1988, **76**, 543.
54. P. T. Callaghan and Y. Xia, *J. Magn. Reson.*, 1991, **91**, 326. (Important improvements in the original technique have recently been developed: D. Wu, A. Chen, and C. S. Johnson, *J. Magn. Reson., Ser. A*, 1995, **115**, 260.)
55. J. F. Schenck, M. A. Hussain, and W. A. Edelstein, US Pat. 4 646 024, 1987.
56. P. Roemer, US Pat. 4 926 125, 1990.
57. P. Mansfield and B. Chapman, *J. Magn. Reson.*, 1986, **66**, 573. (Force cancellation has recently been described: R. Bowtell and P. Mansfield, *Magn. Reson. Med.*, 1995, **34**, 494.)
58. J. J. Van Vaals and A. H. Bergman, *J. Magn. Reson.*, 1990, **90**, 52.

Biographical Sketch

F. David Doty. *b* 1950. B.A., Physics, 1972, Anderson University, IN, USA, Ph.D., 1983, Physics, University of South Carolina. Began work in NMR under Paul Ellis, 1979. President of Doty Scientific, Inc., 1982–present. Approx. 20 publications and 15 patents. Research interests include rf electronics, NMR probe technology, electromagnetism, manufacturing, turbomachinery, energy conversion cycles, ceramics engineering, acoustics, economics, and religions.

Quantum Exchange

Kurt W. Zilm
Yale University, New Haven, CT, USA

1	Introduction	1
2	Experimental Observations	1
3	Theory	1
4	Examples	7
5	Summary	8
6	References	9

1 INTRODUCTION

By the late 1950s, all of the physics important to high-resolution solution NMR seemed to have been identified. The basic interactions of chemical shift and scalar or J couplings, as well as the dynamics leading to spin relaxation and chemical exchange, were understood—at least in principle. It seemed that all of the relevant terms in the Hamiltonian that applied to NMR in isotropic solutions were known. Advances in NMR theory focused on the details of dealing with complex spin systems and their manipulation by pulse trains, or how the spins reflected molecular dynamics, as exemplified in this Encyclopedia. This article deals with the recent recognition of an additional term in the solution NMR Hamiltonian, namely, that for nuclear–nuclear exchange coupling, and the dramatic effects it can have on solution NMR spectra. The purpose is to provide the reader with as intuitive and physical a picture of this purely quantum mechanical effect as possible. More rigorous treatments of the details of the underlying physics may be found in the references.

2 EXPERIMENTAL OBSERVATIONS

The discovery of nuclear–nuclear exchange couplings or quantum exchange couplings in solution NMR spectroscopy[1–3] grew out of NMR studies of transition metal polyhydrides in the 1980s. Kubas at Los Alamos National Laboratory had discovered a class of transition metal complexes that bind H_2 as an intact ligand, rather than oxidatively adding the H_2 to the metal center.[4] This prompted a great deal of activity among inorganic chemists in the synthesis of new hydride and dihydrogen complexes, as well as the reinvestigation of many previously known systems. At the time, the synthetic chemists also postulated that species such as H_3^+ might also be stabilized as ligands in transition metal complexes. Solution NMR spectroscopy of ^{1}H was usually the structural method of choice in these investigations, and the classic signature of an H_2 complex became a measurable value for $^1J(^1\mathrm{H}, ^2\mathrm{D})$ in the HD isotopomer, usually of the order of 20–35 Hz. It was widely assumed that a large value of $^1J(^1\mathrm{H}, ^1\mathrm{H})$ would be found in any H_3 complex.

In the late 1980s, Heinekey at Yale and Chaudret at Toulouse independently[5,6] made some somewhat startling observations in the ^{1}H NMR of several transition metal trihydrides. In these systems, the spectra indicated that $^1J(^1\mathrm{H}, ^1\mathrm{H})$ could be over 200 Hz. Since the coupling in molecular H_2 itself is only 280 Hz as inferred from the NMR of HD, these large values for ^1J were at first glance evidence for the putative H_3^+ complexes. However, it soon became clear that these systems were not to be explained so simply. During the next few years, Heinekey carried out a set of classic experiments that formed the basis on which it is now accepted that these splittings are exchange couplings.

One of the first indications that the observed splittings were not due to the usual Fermi-contact mediated scalar coupling mechanism was their extreme sensitivity to temperature. Early on, the apparent J couplings seemed to be field-dependent. However, careful experiments by Heinekey showed that this apparent B_0 dependence arose from slight variations in the probe temperature on different instruments. The splittings in fact did not depend upon field, but instead were hypersensitive to temperature. Many alternate models were considered for explaining these observations at the time. Some invoked chemical equilibria involving an unusual thermally accessible state that would have unprecedently large J couplings. Several tunneling-type mechanisms were also considered, but these seemed difficult to resolve with the observation of these splittings in fluid media at close to ambient temperatures. (For a review of previous experimental observations, other models eliminated, and pertinent references, see Zilm and Miller.[7]) Heinekey then carried out some very important experiments employing ^{2}D substitution. The resulting pattern of isotope shifts and the isotopic variations on the apparent values of $^1J(^1\mathrm{H}, ^1\mathrm{H})$ in the remaining protons ruled out any sensible model involving chemical equilibrium.[2] Unfortunately, the spectra of the partially deuterated isotopomers themselves did not provide convincing evidence for the involvement of tunneling. While no $^1J(^1\mathrm{H}, ^2\mathrm{D})$ couplings were observed, this observation could be explained just as convincingly by self-decoupling due to the rapid ^{2}D relaxation in concert with chemical exchange as by a tunneling mechanism. The key experiment to perform became clear. The NMR of a partially tritiated isotopomer would have none of the complications encountered with deuterium. Given the difficulties in handling radioactive samples, this experiment was more than difficult to perform. The results were well worth Heinekey's efforts: a coupling that started as over 500 Hz in a perprotio molecule was reduced to a $^1J(^1\mathrm{H}, ^3\mathrm{T})$ of less than 30 Hz at the same temperature.[1] This was the first conclusive evidence obtained in favor of the exchange coupling mechanism for these large temperature dependent couplings. The initial report[1] of this result and a theoretical framework for quantitatively accounting for these couplings and their temperature dependence was soon published. Simultaneously with this report, Jones and Weitekamp[8] also proposed an exchange coupling mechanism in these systems, which utilized symmetry arguments, but with no additional experimental data.

3 THEORY

Exchange interactions among electrons are familiar to any student of solid state physics or quantum chemistry. They are central to the quantum mechanical description of bonding in

molecules and the mechanism of phenomena such as high-temperature superconductivity. The appearance of $J\boldsymbol{I}_1\cdot\boldsymbol{I}_2$ type couplings in ESR spectra of triplet biradicals is a well-known spectroscopic manifestation of the electron–electron exchange interaction. For nuclei, quantum mechanical exchange interactions are less familiar, and until recently they were not known to affect high-resolution magnetic resonance spectra in any manner. (For references on quantum exchange in solid ^{3}He and in related electronic structure problems, see Zilm and Miller.[7]) The best-known example of heavy particle quantum exchange is in solid ^{3}He. In this system, diffusion rates and other properties are known in large part to be determined by ^{3}He–^{3}He exchange interactions. NMR spectra of tunneling methyl groups at low temperature also display features related to rotational tunnel splittings, but these have not usually been considered as manifestations of an exchange interaction per se. Given that quantum effects such as these have typically been considered as purely low-temperature phenomena, it is not surprising that quantum exchange involving nuclei has not until recently been recognized as having any role in solution NMR spectroscopy.

Any theory accounting for quantum exchange must consider the total wavefunctions for the nuclei being observed, spanning both spin and spatial coordinates. In this respect, quantum exchange is quite distinct from the other terms in the NMR Hamiltonian. A typical NMR interaction can usually be written as a product of a spin operator and an interaction constant or tensor, which is an expectation value of the rest of the system Hamiltonian over all coordinates except spin. In quantum exchange, however, the spin coordinate and the spatial coordinate are correlated, and such a separation is not possible. To illustrate this, we shall consider a simple two-spin system where the spins occupy chemically inequivalent sites.

3.1 Molecular Dynamics

To understand quantum exchange in the context of NMR spectroscopy, we must first consider the quantum mechanics governing the Cartesian displacements of the NMR active nuclei, i.e., their orbital wavefunctions, and then see how this is coupled to their spin coordinates, i.e., the spin functions. For a start, we shall consider a simple two-particle quantum mechanics problem that is often somewhat misunderstood. Although our treatment will be quite similar to a number of familiar problems in tunneling (see, e.g., Atkins[9]), we should like to emphasize now that quantum exchange does not in fact imply that tunneling motions occur. This point will be clarified in the following discussion.

The molecular systems in which quantum exchange has been observed by NMR all are of the form (**1**)

(1)

where the other ligands collectively denoted by L_3 are typically another hydride, a cyclopentadienyl, and a phosphine. Single crystal neutron diffraction studies[3] indicate that the hydrides are typical terminal hydrides having a single bond to the central transition metal atom M. Although the M–H linkages are significantly more 'floppy' than C–H bonds, these hydrides are basically localized at their binding sites. To a very good approximation, the potential well that each of these hydrides experiences can be approximated by the harmonic oscillator potential as depicted in Figure 1(a).

A complete quantum mechanical treatment of the pair of hydrides under consideration would involve a six-dimensional potential energy surface describing the energy of all configurations of the two hydrides as they are moved relative to each other and to the metal center. As long as the hydrides remain outside each other's van der Waals radii, the potential experienced by either is still roughly harmonic. If the hydrides do not have any appreciable interaction with one another, the problem reduces to that of two uncoupled harmonic oscillators.[7]

As a simple model for this system, consider two hydrides bound to a surface, each in locally harmonic single particle potentials, (**2**) and (**3**).

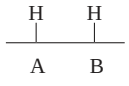

(2)

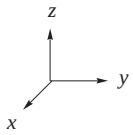

(3)

If the interaction between the two protons is sufficiently weak, their displacements are approximately harmonic except for the symmetric displacement towards one another. In this instance, each hydride feels a repulsive force, which rises rapidly as they near one another. The hydrides are also attracted to the potential minimum at the other binding site. It is the displacement of the hydrides along this type of coordinate that we shall focus upon.

A good model potential for displacements along this exchange coordinate is a double well potential such as that in Figure 1(b). Movement along this coordinate exchanges the two hydrides between the two wells. The reaction coordinate is a two-particle potential, and is necessarily somewhat complicated. If the hydrides simply each moved along the y axis towards one another, there would be an essentially infinite barrier separating the two configurations. The model we want to consider instead takes the coordinate to be a minimum energy type of path along which exchange is possible. At the barrier the two particles must move out of each other's way along a path that takes them out of the (y, z) plane.

It worthwhile to note what is, and what is not, important in the choice of this potential energy curve. The double well model is only one approach to connecting the two different possible ground state configurations of the hydrides. Displacement on a periodic rotational coordinate would also produce the type of effects to be discussed.[10] The required features are only that the potential has two wells representing two distinct configurations and that there be a finite barrier separating them.

Having reduced the two-particle problem to a single internal reaction coordinate in a double well makes the problem fairly simple. We shall only consider the vibrational ground state in this potential, since we know that the hydrides are basically bound fairly tightly to their binding sites. This places them in one of the two configurations representing the double well minima. Near the bottom of either well, the potential is close to harmonic, and a good approximate two-particle ground state

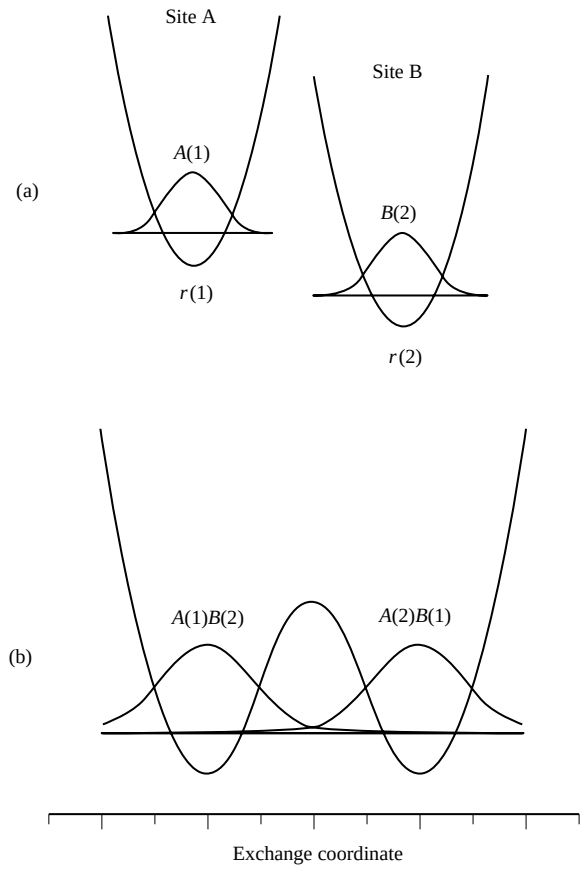

Figure 1 (a) Depiction of two harmonic potentials at two different sites, with vibrational ground state wavefunctions. This is a reasonable description of two largely uncoupled M–H vibrators in a transition metal hydride. The coordinates are the displacements of the individual hydrides. (b) A model two-particle potential describing the change in potential energy as the two hydrides in the two sites shown in (a) are exchanged between the two sites. The coordinate is the reaction coordinate along which the exchange takes place. The wavefunctions shown are two-particle wavefunctions for the two degenerate configurations

wavefunction would be a Gaussian centered in either of the two wells. We define $\psi(\mathrm{L})$ as the configuration where the protons 1 and 2 were at sites A and B, respectively. This configuration can be written as a product of one-particle wavefunctions, i.e., $A(1)B(2)$, where $A(1)$ and $B(2)$ are the Gaussians representing the one-particle ground state vibrational wavefunctions in the single particle potentials representing the two binding sites. The other side of the double well would then be represented by the two-particle wavefunction $\psi(\mathrm{R})$=$A(2)B(1)$ [see Figure 1(b)].

It is tempting to apply what we know about the quantum mechanics of a single particle in a double well directly to this two-particle problem, since the mathematical formulation is now the same at this point (see, e.g., Atkins[9]). Because the wells are a finite distance apart, the wavefunctions for the two ground state basis configurations we have chosen overlap each well. This produces an off-diagonal element in the matrix for the system Hamiltonian $\hat{\mathcal{H}}_{\mathrm{L}}$ that includes the interaction of the particles with both wells and each other. To get the best possible description of the ground state within this restricted basis set, we must diagonalize this matrix. If

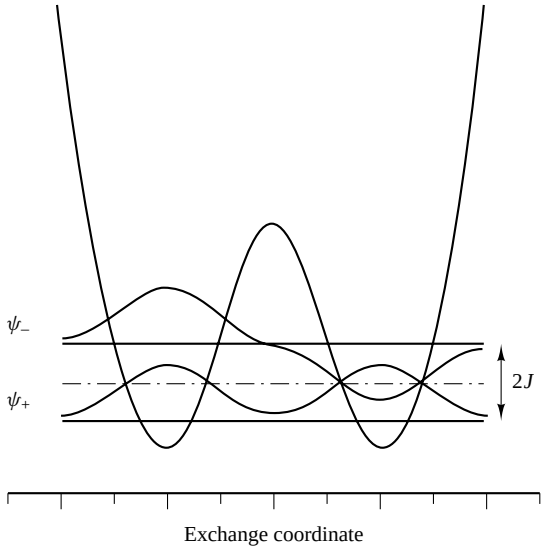

Figure 2 Model double well exchange potential showing the two lowest energy eigenfunctions ψ_+ and ψ_-. The energies of these two states are split by $2J$ symmetrically about the energy of the two degenerate localized basis states

the two sides of the double well have the same depth, the basis states are degenerate. No matter how small the off-diagonal term, the two basis set wavefunctions will be mixed. As every student of quantum mechanics knows, in the single particle case the symmetric and antisymmetric combinations of the two Gaussians are then good approximations to the proper wavefunctions. The eigenenergies of the two eigenstates $\psi_\pm = \frac{1}{2}[\psi(\mathrm{L}) \pm \psi(\mathrm{R})]$ for the symmetrical potential are $E_\pm = E \pm J$ (see Figure 2). E is the unperturbed energy of either of the degenerate configurations given by

$$\int\int [A(1)B(2)]^* \hat{\mathcal{H}}_{\mathrm{L}} A(1)B(2)\,\mathrm{d}\tau_1\,\mathrm{d}\tau_2 \qquad (1)$$

and J is the value of the off-diagonal matrix element

$$\int\int [A(1)B(2)]^* \hat{\mathcal{H}}_{\mathrm{L}} A(2)B(1)\,\mathrm{d}\tau_1\,\mathrm{d}\tau_2 \qquad (2)$$

In the case of a single particle in the double well, the energy difference $2J$ is a tunnel splitting. The wavefunctions indicate that the particle is equally likely to be in either well. This is interpreted to mean that the particle is 'delocalized' over both sides of the potential. If a localized state is prepared by a superposition of ψ_+ and ψ_-, it will evolve in time according to the usual rules of time-dependent quantum mechanics. The picture that emerges is one of the maximum in the probability density oscillating between the two wells at a frequency $2J/h$. One usually describes the particle as coherently tunneling from one well to the other at this rate. On the other hand, when the two wells are of differing depths, the particle quickly becomes localized. As long as the difference in the energies of the two states $\psi(\mathrm{L})$ and $\psi(\mathrm{R})$ is larger than the off-diagonal term J, these remain good states to first order in the perturbation treatment.

The mapping of the two-particle case onto this reduced one-particle description contains some subtleties. If the two

sites are energetically the same, i.e. the one-particle potentials at the two binding sites are identical, the configurations $A(1)B(2)$ and $A(2)B(1)$ will clearly have the same energies. The degeneracy will again be lifted by any finite matrix element connecting the functions $A(1)B(2)$ and $A(2)B(1)$, and there will be two states separated by a tunnel splitting. In the molecules we are considering, however, the hydrides are chemically inequivalent. This means that the local one-particle potentials are different, if only slightly so on a cm^{-1} scale. However, this does necessarily break the symmetry of the two-particle potential along the exchange coordinate. If the two particles are identical, the basis configurations $A(1)B(2)$ and $A(2)B(1)$ representing $\psi(\mathrm{L})$ and $\psi(\mathrm{R})$ will still have the same energies. Exchange of identical particles can then be described by a mirror-symmetric two-particle potential in the exchange coordinate. If the hydrides are not identical (e.g., a proton and a triton), this symmetry will be broken, since the two basis configurations will have different energies. The eigenstates will then be localized, and no tunneling will occur. In this case of two distinguishable particles, the two sites would have to be identical for the exchange potential to remain symmetric.

The appearance of a potential for particle exchange with mirror symmetry is then a prerequisite for exchange splittings to appear in the energy level diagram for this two-particle system. Many familiar systems have this type of symmetry, but not all can display quantum exchange. For example, consider the umbrella mode of ammonia, or the chair-to-chair inversion of cyclohexane. In the gas phase, both displacements can be described by mirror-symmetric double wells. Placing these molecules into a condensed phase, however, breaks this symmetry. When either molecule inverts, it moves from one region of space to another. The presence of an anisotropic solvent shell around each site gives the configurations distinct energies. This is not the case for the transition metal polyhydrides we are considering, or other systems such as rotating methyl groups. In the transition metal hydrides, the configuration before and after the exchange of two hydrides occupies the same region of space. Rotation of a methyl group by 120° likewise results in a new configuration that occupies the same space as before the rotation. These displacements are then always instantaneously described by mirror-symmetric potentials, and thus will have exchange-type splittings appearing in their energy level structure. It should be emphasized that whether particles are identical or not depends only on the nature of the particles and not on their location in the molecule or lattice. However, whether a molecular rearrangement that exchanges identical particles is a truly degenerate rearrangement energetically depends on the relation of the molecule to the lattice at the beginning and the end of the rearrangement.

The above treatment of the two-particle exchange problem as a single pseudoparticle in a double well is only partially correct. This is because the two-particle wavefunctions have additional constraints. One must remember that the spatial portion of a wavefunction describes the probability of a particle's location. When several particles are described by a single wavefunction, the probabilities can only be ascribed individually to particles that are distinguishable. For indistinguishable particles, the identity (e.g., particle number) is irrelevant.[11] The wavefunction for a pair of identical particles can then only give the probability of finding a particle of that type at any position. It cannot tell us the probability for finding a particular particle there.

Our interpretation of $\psi_\pm$ in the one- and two-particle cases, then, is somewhat different. For the single particle in the double well, the equal probability amplitudes on the left and right sides is taken as an indication that the particle is 'delocalized' over both sides. This notion is reinforced by the time-dependent behavior of a single particle in this potential if the initial state is localized as just discussed. On the other hand, the two-particle wavefunctions $\psi_\pm$ do not imply delocalization of the two particles, or of the configuration. These functions now simply state that the system is most likely in a configuration with one particle on the left and one on the right, but the identity of the configuration is indeterminate. We may not ask about the location of individual particles, since they are identical, and as such their labels are simply irrelevant. Thus, we see in the two-particle case that the indeterminacy as to which particle is on the left or on the right has replaced the delocalization that arises in the one-particle problem.

This statistical interpretation of the two-particle wavefunctions requires that any relabeling of the particle identities must leave the probability densities unchanged. Thus, the wavefunction must be the same, or at most change sign, when the particle labels are permuted. In accord with the well-known symmetrization postulate, wavefunctions for identical bosons are symmetric or remain the same, while those for identical fermions are antisymmetric or change sign, under particle label exchange. With this in mind, we return to the problem of two particles in the double well. Consider the case where the particles are of zero spin and are therefore bosons. The function ψ_+ has the proper symmetry, while ψ_- does not. The ground state can then only exist as ψ_+, since ψ_- is an unacceptable wavefunction. The consequence of this is that a 'localized' state cannot be constructed by combining ψ_+ and ψ_-. The picture we arrived at in the one-particle state of an initially localized state periodically moving between the two wells is then inappropriate. The system can only remain in the ground state ψ_+. This is most easily interpreted as the system being localized in one of the two possible indistinguishable configurations.

3.2 Including the Spin Coordinate

When the spin functions are included in the two-particle problem, the symmetry of the total wavefunction including spin must be considered. One place to start is to write the individual spatial and spin functions as separate symmetrized sets. For a pair of spin-$\frac{1}{2}$ nuclei the symmetrized functions are the symmetric triplet functions T_0, T_{-1}, T_{+1}, and the antisymmetric singlet spin function S_0. The total wavefunction for identical fermions must be antisymmetric with respect to exchange, and therefore ψ_+S_0, ψ_-T_0, ψ_-T_{-1}, and ψ_-T_{+1} are the only acceptable combinations. Now that spin has been introduced, the system can have an energy of either $E + J$ or $E - J$, depending upon the spin state of the nuclei. Any additional small interaction of the magnetic field would not be expected to change the situation with respect to the energy associated with the orbital or lattice terms of the Hamiltonian. On the other hand, magnetic interactions will mix the singlet and triplet spin manifolds. Any spin flip that occurs must also make up any difference in lattice energy accompanying the transition. The appearance of the exchange energy in an

NMR transition is then a consequence of the correlation of the spin states with the orbital energies associated with the displacements of the NMR active nuclei.

In general, the above type of prescription for determining properly symmetrized total spin + spatial wavefunctions is cumbersome. The resulting functions can be recast in a more physical and convenient basis, which we call the site spin basis.[11] Rather than deriving the site spin basis, we shall develop it directly from some basic symmetry considerations. Let us start by considering a pair of protons in chemically equivalent sites that comprise an AX spin system. Normally we ignore the complications brought on by the coordinate or orbital part of the wavefunction, and simply write the spin eigenfunctions as $|+\ +\rangle$, $|+\ -\rangle$, $|-\ +\rangle$, and $|-\ -\rangle$, where the labels refer to m_S for particles 1 and 2 in that order. These two-particle product basis spin functions themselves, however, do not have the proper symmetry with respect to particle exchange, i.e., $|+\ -\rangle \neq \pm|-\ +\rangle$. This at first sight seems perplexing, since every NMR spectroscopist knows that these wavefunctions are what are always used for an AX spin system. The answer is that in actuality the spin labels do not refer to the particle identities. Instead, the functions are of the form $|m_S(\mathrm{A}), m_S(\mathrm{B})\rangle$, i.e., the labels are according to the site identity, not the particle numbers. The function $|+\ -\rangle$ says the particle in site A is in the + state, and the particle in site B is in the − state. What the function does not tell us is which particle is in which site. Therefore, the spin functions labeled according to the m_S in each site are automatically symmetric with respect to particle exchange. To differentiate the product basis labeled according to sites, we shall write these kets as $[+\ -\rangle'$.

In using this site labeling convention, we must also relabel our spin Hamiltonian.[11] For instance, the Zeeman plus chemical shift term in frequency units for two spins would be written as

$$\hat{\mathcal{H}}_{\mathrm{cs}} = -\nu_{\mathrm{A}}\hat{I}_{z\mathrm{A}} - \nu_{\mathrm{B}}\hat{I}_{z\mathrm{B}} \tag{3}$$

The resonance frequencies and spin operators are thus identified with the molecular site instead of a particle number. In most instances, this is in fact how NMR problems are typically handled, even though one may have the impression that one is using particle labels instead of site labels.

The overall symmetry of the total site spin basis function $\psi_{\mathrm{site}} = \psi_{\mathrm{orbital}}\psi_{\mathrm{spin}}$ is then determined solely by the symmetry of the orbital wavefunction. For this pair of spin-$\frac{1}{2}$ nuclei, ψ_{orbital} must always be the antisymmetric function ψ_-, since ψ_{spin} is always symmetric with this site labeling convention. The total wavefunction for the $[+\ -\rangle'$ spin state is then $\sqrt{\frac{1}{2}}[A(1)B(2) - A(2)B(1)][+\ -\rangle'$ (the normalization is only approximate, since we have ignored the small overlap term). As a shorthand, these site spin basis functions will be written as $[m_S(\mathrm{A}), m_S(\mathrm{B})\rangle$, dropping the prime notation to imply the inclusion of the orbital portion. Remember that the labeling of the spin portion is according to site A and B, not particle 1 and 2, in these functions with the '[' notation. In order to calculate a spectrum, it is instructive first to explicitly calculate a few matrix elements. We shall use the sum of the coordinate Hamiltonian for the particles, $\hat{\mathcal{H}}_{\mathrm{L}}$, and $\hat{\mathcal{H}}_{\mathrm{cs}}$ as an example.

First consider $\langle+-]\hat{\mathcal{H}}_{\mathrm{cs}}[+-\rangle$. Using the site labeling convention, this is evaluated as $\frac{1}{2}(\nu_{\mathrm{B}} - \nu_{\mathrm{A}})$ in the usual fashion. The integral over the particle coordinates is unity, since the orbital function is normalized. To calculate $\langle-]\hat{\mathcal{H}}_{\mathrm{L}}[+-\rangle$, we must expand $[+\ -\rangle$ in terms of functions with particle labels:

$$[+-\rangle = \tfrac{1}{2}[A(1)B(2)|+-\rangle - A(2)B(1)|-+\rangle] \tag{4}$$

Since the spins have particle number designations on the right-hand side, the + and − labels have been arranged to keep the + spin in the A site and the − spin in the B site. The quantity $\langle+-]\hat{\mathcal{H}}_{\mathrm{L}}[+-\rangle$ can be written as a sum of products of integrals over spin and space separately:

$$\begin{aligned}
&\langle+-]\hat{\mathcal{H}}_{\mathrm{L}}[+-\rangle \\
&= \tfrac{1}{2}\langle+-\,|\,+-\rangle \int\int [A(1)B(2)]^*\hat{\mathcal{H}}_{\mathrm{L}}A(1)B(2)\,\mathrm{d}\tau_1\,\mathrm{d}\tau_2 \\
&\quad +\tfrac{1}{2}\langle-+\,|\,-+\rangle \int\int [A(2)B(1)]^*\hat{\mathcal{H}}_{\mathrm{L}}A(2)B(1)\,\mathrm{d}\tau_1\,\mathrm{d}\tau_2 \\
&\quad -\tfrac{1}{2}\langle-+\,|\,+-\rangle \int\int [A(2)B(1)]^*\hat{\mathcal{H}}_{\mathrm{L}}A(1)B(2)\,\mathrm{d}\tau_1\,\mathrm{d}\tau_2 \\
&\quad -\tfrac{1}{2}\langle+-\,|\,-+\rangle \int\int [A(1)B(2)]^*\hat{\mathcal{H}}_{\mathrm{L}}A(2)B(1)\,\mathrm{d}\tau_1\,\mathrm{d}\tau_2
\end{aligned} \tag{5}$$

Note again that the spin labels on the left refer to sites A and B, while those on the right refer to particle numbers 1 and 2. The first two integrals each give $\frac{1}{2}E$, and the last two are zero because of the vanishing integral over the spin coordinate. The net value of the element $\langle+-]\hat{\mathcal{H}}_{\mathrm{L}}[+-\rangle$ is then the lattice energy E. Now consider the element $\langle-+]\hat{\mathcal{H}}_{\mathrm{L}}[+-\rangle$. In a similar fashion, the integral can be expanded as

$$\begin{aligned}
&\langle-+]\hat{\mathcal{H}}_{\mathrm{L}}[+-\rangle \\
&= \tfrac{1}{2}\langle-+\,|\,+-\rangle \int\int [A(1)B(2)]^*\hat{\mathcal{H}}_{\mathrm{L}}A(1)B(2)\,\mathrm{d}\tau_1\,\mathrm{d}\tau_2 \\
&\quad +\tfrac{1}{2}\langle+-\,|\,-+\rangle \int\int [A(2)B(1)]^*\hat{\mathcal{H}}_{\mathrm{L}}A(2)B(1)\,\mathrm{d}\tau_1\,\mathrm{d}\tau_2 \\
&\quad -\tfrac{1}{2}\langle+-\,|\,+-\rangle \int\int [A(2)B(1)]^*\hat{\mathcal{H}}_{\mathrm{L}}A(1)B(2)\,\mathrm{d}\tau_1\,\mathrm{d}\tau_2 \\
&\quad -\tfrac{1}{2}\langle-+\,|\,-+\rangle \int\int [A(1)B(2)]^*\hat{\mathcal{H}}_{\mathrm{L}}A(2)B(1)\,\mathrm{d}\tau_1\,\mathrm{d}\tau_2
\end{aligned} \tag{6}$$

In this case, the first two integrals are zero, and the second pair give contributions of $-\frac{1}{2}J$ for a total value of $-J$.

The reader may already see that these matrix elements can be evaluated on inspection following a few simple rules. When dealing with the NMR or spin Hamiltonian, we proceed as normally, using spin operators, interaction coefficients, and spin functions labeled according to site. The coordinate part seems trickier, but can be simply treated as a permutation operator over the spin. For a term $\langle ij]\hat{\mathcal{H}}_{\mathrm{L}}[kl\rangle$, a value of E is returned if $i = k$ and $j = l$. If $i = l$ and $j = k$, a contribution of $-J$ is obtained. The additional terms that the exchange interaction brings to the NMR Hamiltonian can then be recognized as having the same form as the classical exchange matrix familiar to students of dynamic NMR lineshape analysis.

Table 1 Hamiltonian Matrix in the Site Spin Basis for a Simple AX Spin System

	$\|+\,+\rangle$	$\|+\,-\rangle$	$\|-\,+\rangle$	$\|-\,-\rangle$
$\langle++\|$	$-\frac{1}{2}\nu_A - \frac{1}{2}\nu_B + E - J$	0	0	0
$\langle+-\|$	0	$-\frac{1}{2}\nu_A + \frac{1}{2}\nu_B + E$	$-J$	0
$\langle-+\|$	0	$-J$	$+\frac{1}{2}\nu_A - \frac{1}{2}\nu_B + E$	0
$\langle--\|$	0	0	0	$+\frac{1}{2}\nu_A + \frac{1}{2}\nu_B + E - J$

For our simple AX spin system, the full Hamiltonian matrix in the site spin basis can then be written on inspection as in Table 1. Since the orbital energy E only adds to the diagonal, it just represents a shift of the energy scale and can arbitrarily be set to zero. If the chemical shift difference $|\nu_A - \nu_B| \gg |J|$ then the off-diagonal terms will be truncated, and the NMR transitions will give two doublets centered at ν_A and ν_B with splittings of $-2J$. This Hamiltonian then gives the same spectrum as that for an AX spin system with an effective J coupling of $-2J$. Since the matrix element that J represents is inherently negative, the apparent coupling in the spectrum is positive. For spin-$\frac{1}{2}$ nuclei, it can be shown that any pairwise exchange interaction gives rise to a term that behaves just as if there were a scalar coupling $-2J$ between those two sites. Higher-spin systems, however, cannot be described by such a simple effective spin Hamiltonian.[11]

One could incorrectly infer from the energy level structure of this simple example that the identity of the particles can somehow be made known by the fact that they experience different chemical shifts at the two different sites. A question that might be asked is how often the spins can change places by tunneling. The answer turns out to be that one cannot tell. The probability that a spin in site A has exchanged with a spin in site B becomes a maximum when their spin quantum numbers are identical. In other words, the spins can tunnel when one cannot tell them apart, even by their spin. Therefore, the most straightforward interpretation is that the spins remain localized, but which spin is localized where is something that cannot be known, since the particles are indistinguishable.

The advantage of the site spin basis approach to treating exchange coupling in NMR spectroscopy is that it is very easily extended to more complicated permutations or exchanges of spins, and is easily applied to problems involving nuclei of arbitrarily large I. The general form of the exchange Hamiltonian in the site spin basis can be shown[11] to be

$$\hat{\mathcal{H}}_{ex} = \sum_i \xi^{p(i)} J_i \hat{\mathcal{P}}_i(k, l, m, \ldots) \tag{7}$$

where $\xi = e^{2\pi i I}$ and I is the spin quantum number of the nucleus in question. The permutation of the spins among the sites k, l, m, ... is represented by the operator $\hat{\mathcal{P}}_i(k, l, m, \ldots)$, which acts on the spin labels within the site spin basis functions. Each site spin basis function has the same orbital function implied. For fermions, this is formed using a Slater determinant for the orbital states for each site. If the nuclei are bosons, an antideterminant is used instead. The exchange matrix element is given by J_i. It is calculated by taking the matrix element of $\hat{\mathcal{H}}_L$ between an orbital state for one configuration and that of the configuration resulting from the permutation. For example, consider a three-site problem (e.g., a methyl group). A starting configuration would be $A(1)B(2)C(3)$. If the three particles are subjected to a cyclic permutation, this state would become $A(3)B(1)C(2)$. The value of J_c would be

$$J_c = \int\int\int [A(1)B(2)C(3)]^* \hat{\mathcal{H}}_L A(3)B(1)C(2)\, d\tau_1\, d\tau_2\, d\tau_3 \tag{8}$$

Different permutations have different parities. For bosons, this is irrelevant. However, for fermions, permutations of even parity produce negative elements, and those of odd parity give positive exchange integrals. This is handled by the $\xi^{p(i)}$ term. If the nuclei are fermions with spin $I = n + \frac{1}{2}$ then $\xi = -1$. If they are bosons then $\xi = +1$. For fermions, a single pairwise permutation has odd parity, and $p(i) = 1$, which produces a negative sign for the exchange matrix element. On the other hand, a permutation that can be written as the product of two pairwise permutations has even parity, and $p(i) = 2$. These permutations give positive exchange coupling elements in the Hamiltonian matrix. One can show by straightforward but tedious calculations that the results of this prescription are to reproduce the matrix elements that would be obtained by expanding the site spin basis functions as products of properly symmetrized orbital functions and spin functions with particle labels, and performing the integration explicitly.

In practice, one simply associates a different J value with each particular topological rearrangement or permutation of the nuclei between the different locations in a molecule. High barrier permutations give low J values, and facile permutations give larger ones. The states that are connected are those where the permutation operation shuffles the spin labels so that they match those of the state to which it is coupled. The procedure is exactly the same as filling an exchange matrix for a classical chemical exchange lineshape problem. The signs of the elements are determined by whether the spins are fermions or bosons, and whether the permutation has even or odd parity. These elements are added to the rest of the standard NMR Hamiltonian, and the spectrum is determined by finding the eigenstates and determining the transition moments in the usual fashion.

A convenient starting point for computer simulation of exchange-coupled spectra in the presence of chemical exchange is to start with any of the many programs for dynamic NMR lineshape simulation. One simply duplicates the code for calculating the elements of the classical exchange matrix, and uses it to add exchange coupling elements to the Hamiltonian matrix. In this manner, we have been able to computer-simulate exchange-coupled NMR spectra for systems of up to four chemically exchanging protons or deuterons.

3.3 Temperature Dependence

Our main purpose so far has been to provide a physical picture of how exchange interactions produce splittings in

NMR spectra. The theory accounts for the disappearance of exchange couplings between different isotopes of the same element, for the persistence at ambient temperatures of an effect that is similar to tunneling, and for the different spectral patterns that are observed for spin-$\frac{1}{2}$ and spin-1 systems (see below). Accounting for the size of these splittings and their temperature dependence is another matter. Several models have been proposed, and probably all are correct to some extent. A definitive calculation of the exchange coupling would require an accurate $3N$-dimensional potential energy surface for N identical nuclei. This is at present out of reach, so the models are either approximate analytical or computational attempts to focus on key features of the exchange process.

The model we have favored most is based on a treatment of exchange in solid ^{3}He by Landesmann.[2,7] Landesmann has analytically calculated the ground state exchange splitting for two atoms in harmonic wells and repelled by a hard sphere potential. To account for the temperature dependence, thermal excitations that place the molecules in higher vibrational states are involved. Since these vibrationally excited states are more delocalized, there is more overlap of the individual particles with the neighboring sites, and the size of J goes up with vibrational quantum number. In the double well description, the splittings of the higher states increase exponentially as one moves beyond the ground state. In solution, the vibrational states are short-lived, and the NMR experiment measures a Boltzmann population weighted average of the splittings over the vibrational ladder. The spin state is conserved in these transitions, and the sign of J remains the same; therefore, the weighted average of J increases with temperature. We have shown that the sum over vibrational states can be effectively accomplished by first calculating a Boltzmann population weighted overlap function.[7] This can be shown to be approximated by a Gaussian of increasing width with increasing temperature. As Landesmann's ground state calculation used a Gaussian basis set, this result can then be applied to the averaged splitting as a function of temperature also. The final expression obtained is

$$J(T) = \frac{-3\hbar a}{8\pi m\delta(T)^3}\sqrt{\frac{3}{\pi}}\exp\left[-\frac{3}{4}\frac{a^2+\lambda^2}{\delta(T)^2}\right] \qquad (9a)$$

where

$$\delta(T)^2 = \frac{3h}{4\pi m\nu}\coth\left(\frac{h\nu}{2kT}\right) \qquad (9b)$$

Here a is the inter-hydride equilibrium distance, λ is a hard sphere radius (usually taken as 10 nm), ν is the bending frequency of the M–H bonds, and m is the proton mass. When deuterium or tritium is involved, the mass and bending frequency are adjusted accordingly.

Equation (9a) can be used to fit J versus T data, and both a and ν determined. The values found in a large number of fits are quite close to the distances a found by single crystal neutron diffraction and the few ν bending frequencies that have been measured.[2] For systems with very large ^{1}H–^{1}H exchange interactions, this equation has correctly predicted the size of the ^{2}D–^{2}D exchange couplings when they can be measured. This equation also explains why exchange couplings are not observed in organic molecules. The exchange coupling decreases about two orders of magnitude for every 100 cm^{-1} increase in ν. Since C–H bends are of the order of 600 cm^{-1} higher than M–H bends, the exchange couplings in organic systems are about 10^{12} smaller and thus unobservable.

Jones and Weitekamp have developed a similar model using numerical diagonalization of model double well potentials.[12] The behavior of J versus T is calculated by a sum over the thermally populated states. One difficulty with this approach is making a connection between the model reaction coordinate and the molecular structure. Harris and co-workers[13] have studied exchange using muffin-tin-type potentials. They are also able to account for the observed data, and have offered some insight into the types of reaction coordinates that may play an important role.

Limbach[10] has proposed an alternative model to these that is most different in the assumed exchange coordinate. This is a rotational model that produces an exchange splitting from a periodic exchange potential. In the rotational tunneling problem, the tunnel splittings alternate in sign with increasing rotational quantum number. One might then expect that the exchange coupling would have to decrease with temperature in this model instead of increasing as is observed. To circumvent this problem, Limbach proposes that in the ground state the hydrides have no appreciable rotational tunnel splitting. Thermal excitations then allow the system to access a state that is a nascent H_2 complex. The H_2 ligand in this state has a substantial tunnel splitting, which produces the appearance of the exchange coupling. The temperature dependence arises from the thermal population of essentially just the lowest rotational state of the H_2 complex. Such a model can also be used to fit all of the experimental data collected on perprotio systems to date. The main difficulty with this model is rationalizing the existence of an H_2 complex that must lie only 4–8 kJ mol^{-1} above the ground state trihydride structure. In addition, the barrier to rotation of the H_2 ligand in the thermally excited state must be well over 40 kJ mol^{-1} to properly account for the apparent tunnel splitting in the lowest rotational state of this nascent H_2 complex.

Differentiation of how well these and other models describe these systems is being tested by several computational groups at present.[14,15] Potential energy surfaces are calculated for a model system, and the Hamiltonian is then numerically diagonalized. A Boltzmann population-weighted average over the calculated exchange splittings is computed for comparison to the experimentally observed variation of J with temperature. Such calculations can be made to reproduce the trends observed experimentally. However, it remains to be seen how high a level of calculation will be needed to do a better job than the approximate analytical theories.

4 EXAMPLES

A large number of transition metal hydride systems that display exchange couplings have been discovered or rediscovered. One of the most striking is the $Cp^*(CO)IrH_3^+$ cation. At 500 MHz, spectra similar to the simulations shown in Figure 3 are observed.[16] This is a deceptively simple AB_2 spectrum, which at first glance is a single line. On closer inspection, one sees that the central line is flanked by two broader lines with integrated intensities of approx. one-tenth of the central peak. This is an example of a dynamically broadened spectrum with a very large $J(^1H,^1H)$. The apparent

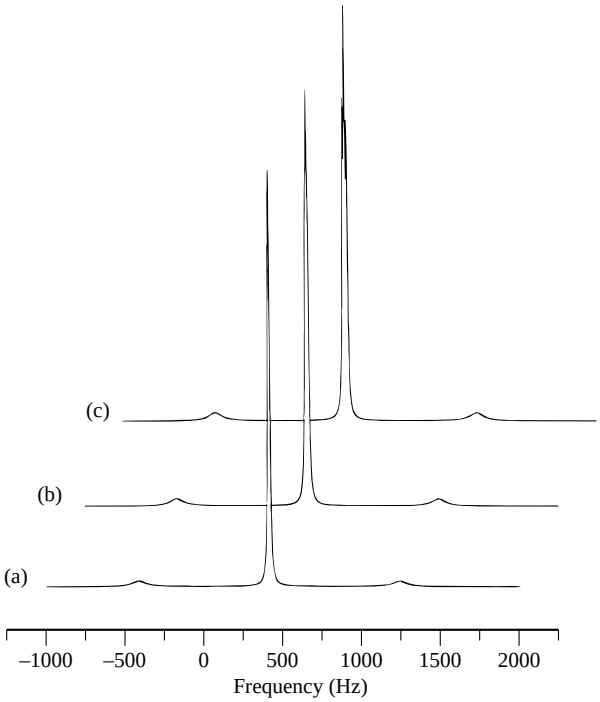

Figure 3 Simulated AB_2 dynamic ^1H NMR spectra similar to what are observed at 500 MHz and about 140 K for the $Cp^*(CO)IrH_3^+$ cation.[16] $J = -2J$ in these simulations is (a) 50 kHz, (b) 25 kHz, and (c) 18 kHz. The central line appears at the weighted average of the A and B chemical shifts. One of the dynamically broadened wings appears at the A-site chemical shift. In comparison with the experimental spectra, only simulations with $J = -2J > 50$ kHz produce a narrow enough central peak. In such cases where $|\nu_A - \nu_B| \ll J$, the central line does not broaden as the decoalescence temperature is reached—rather, only the outer wings narrow. This can lead to the impression that such a molecule is fluxional when in fact it is not

$J = -2J$ must be over 50 kHz as judged from comparison of these simulations with the experimental spectra. This large J lead us to predict that the exchange interaction in the perdeutero system would be of the order of 30–60 Hz and thus observable. Figure 4 shows an example of ^2D–^2D exchange coupling observed in this molecule. Simulation of this spectrum requires an exchange coupling. This is because, for spin $I = 1$, the Hamiltonian no longer has the same symmetry as a scalar coupling; therefore, these data cannot be simulated using a scalar coupling network. From the dependence of J on T, one can extract the parameters a and ν, which predict that $J(^1H,^1H)$ should be approx. 75 kHz, in accordance with the observed ^1H spectra. In future, it will be important to find systems in which both the ^1H and ^2D exchange interactions can be accurately measured as a test of exchange coupling theories.

As a final example, Figure 5 displays some calculated ^2D exchange-coupled spectra for AB_2 spin systems with various ratios of exchange coupling to the chemical shift difference. A D_B–D_B scalar coupling has also been included. Note that the scalar coupling between two magnetically equivalent nuclei is now seen to have an effect upon the spectrum! This result is expected, since the D_A–D_B exchange interactions do not commute with the D_B–D_B scalar coupling Hamiltonian, making it possible now to observe it in the spectra.

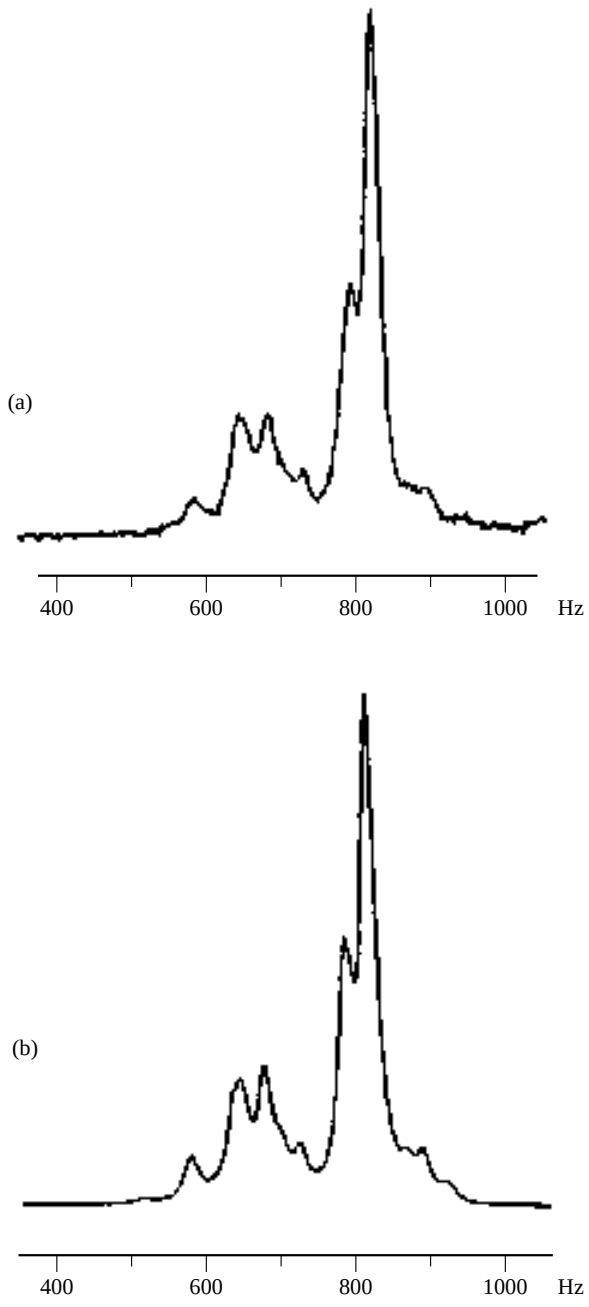

Figure 4 (a)Experimental ^2D NMR spectrum of a mixture of deuterated isotopomers of the $Cp^*(CO)IrH_3^+$ cation (approx. 60% D) at about 145 K. (b) Simulated spectrum giving a D–D exchange coupling between the A and B sites of approx. 40 Hz. Such spectra cannot be fitted using a scalar coupling network

5 SUMMARY

Exchange couplings in solution NMR spectra are manifestations of a purely quantum mechanical effect on the energy levels of sets of identical nuclei in molecules. These effects are related to rotational tunnel splittings in systems such as H_2 or methyl groups, and have the same origins as quantum exchange in solid ^3He. The unique feature of exchange coupling in transition metal polyhydride systems is that it persists to relatively high temperatures in the solution phase, making it possible to observe very small exchange splittings by

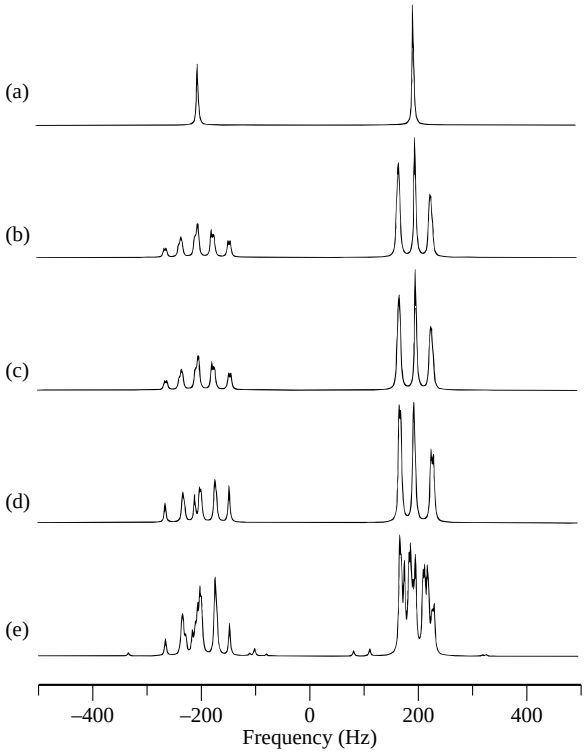

Figure 5 Calculated ^{2}D NMR spectra for an AB_2 spin system with scalar and exchange couplings (the chemical shift difference has been set at 400 Hz): (a) no couplings; (b) scalar couplings J(A, B) = 30 Hz, J(B, B) = 0; (c) scalar couplings J(A, B) = 30 Hz, J(B, B) = 100 Hz; (d) AB exchange coupling $|-2J|$ = 30 Hz, scalar J(B, B) = 0; (e) AB exchange coupling $|-2J|$ = 30 Hz, scalar J(B, B) = 100 Hz. Note that in (c) the inclusion of J(B, B) = 100 Hz has no visible effect, while the spectrum in (e) is dramatically different from that in (d) when J(B, B) is introduced

high-resolution NMR. While these splittings are related to tunnel splittings, they do not imply that coherent tunneling motions occur. Rather, they are a consequence of shifts in the orbital energies of the nuclei that are correlated with their spin states. This correlation of spatial and spin variables results in the exchange energy appearing in the transition frequencies observed in NMR spectra.

6 REFERENCES

1. K. W. Zilm, D. M. Heinekey, J. M. Millar, N. G. Payne, and P. G. Demou, *J. Am. Chem. Soc.*, 1989, **111**, 3088.
2. K. W. Zilm, D. M. Heinekey, J. M. Millar, N. G. Payne, S. P. Neshyba, J. C. Duchamp, and J. Szczyrba, *J. Am. Chem. Soc.*, 1990, **112**, 920.
3. D. M. Heinekey, J. M. Millar, T. F. Koetzle, N. G. Payne, and K. W. Zilm, *J. Am. Chem. Soc.*, 1990, **112**, 909.
4. G. J. Kubas, *Acc. Chem. Res.*, 1988, **21**, 120.
5. D. M. Heinekey, N. G. Payne, and G. K. Schulte, *J. Am. Chem. Soc.*, 1988, **110**, 2302.
6. T. Arliguie, B. Chaudret, J. Devillers, and R. Poilblanc, *C. R. Hebd. Seances Acad. Sci., Ser. 2*, 1987, **305**, 1523.
7. K. W. Zilm and J. M. Millar, *Adv. Magn. Opt. Reson.*, 1990, **15**, 163.
8. D. H. Jones, J. A. Labinger, and D. P. Weitekamp, *J. Am. Chem. Soc.*, 1989, **111**, 3087.
9. P. W. Atkins, *Molecular Quantum Mechanics*, 2nd edn., Oxford University Press, Oxford, 1983, pp. 314–316.
10. H. Limbach and B. Chaudret, *Angew. Chem., Int. Ed. Engl.*, 1992, **31**, 1369.
11. S. J. Inati and K. W. Zilm, *Phys. Rev. Lett.*, 1992, **68**, 3273.
12. C. R. Bowers, D. H. Jones, N. D. Kurur, J. A. Labinger, M. G. Pravica, and D. P. Weitekamp, *Adv. Magn. Opt. Reson.*, 1990, **14**, 269.
13. E. M. Hiller and R. A. Harris, *J. Chem. Phys.*, 1993, **98**, 2077.
14. A. Jarid, M. Moreno, A. Lledos, J. M. Lluch, and J. Bertran, *J. Am. Chem. Soc.*, 1993, **115**, 5861.
15. O. Eisenstein and P. Daudey, to appear.
16. D. M. Heinekey, personal communication.

Acknowledgments

My work in this area has benefited from many interactions with NMR spectroscopists, inorganic chemists, and theoreticians interested in transition metal hydride chemistry. Especially important to me has been my close and very enjoyable collaboration with Professor D. Michael Heinekey and his group. Without his careful attention to experimental detail, the phenomenon of exchange coupling in solution NMR spectra would probably still remain undiscovered.

Biographical Sketch

Kurt Z. Zilm. *b* 1955. B.S., 1976, Ph.D., 1981, University of Utah, USA. Introduced to NMR by D. M. Grant. Faculty in Chemistry Yale University, 1983–present. Approx. 80 publications. Research interests: theory and development of NMR techniques for solving problems of chemical interest, studies of transition metal polyhydrides, supported metal catalysts, matrix-isolated organic intermediates and metal clusters, applications of optical pumping in gas phase NMR, tunneling in NMR, dipolar demagnetizing field effects in NMR and development of new solids NMR techniques for structural studies in polymers and organic geochemistry.

Quantum Optics: Concepts of NMR

Erwin L. Hahn
University of California, Berkeley, CA, USA

1	Introduction	1
2	The Resonance Equations	2
3	Radiation Damping	4
4	Optical FID and the Photon Echo	5
5	Principal Effects Common to NMR and Quantum Optics	7
6	Conclusions	8
7	Related Articles	8
8	References	8

1 INTRODUCTION

The purpose of this review is to outline a few NMR concepts and relationships that carry over into the realm of quantum and laser optics. It is natural that the semiclassical physics of resonance excitation in two quantum level systems should be common to both quantum optics and NMR. Solutions of the Bloch–Maxwell equations serve as a model for analogs of NMR experiments that occur in quantum optics. The resemblances to NMR of effects in quantum optics cannot have a strict one-to-one relationship in every property, but they do exist in varying degrees. There is no intent here to present a comprehensive review of these analogs, but rather to focus upon principles of coherent macroscopic emission of dipole radiation. Although a number of NMR conditions and effects may be conceived in the domain of quantum optics, they are not always easy and routine to demonstrate, because the required experimental parameters in quantum optics are often more difficult to implement.

There are obvious differences between NMR and quantum optics. The effects of spontaneous emission and wave propagation are absent or negligible in NMR, but dominate in quantum optics. For this reason, there are numerous quantum optical effects that have no counterpart in NMR. Conversely, there are unique conditions and experiments in NMR that do not have analogs in quantum optical systems. For example, there is no simple direct optical analog of a NMR dipolar reservoir to be distinguished from the Zeeman reservoir. The validity of an optical electric 'dipolar reservoir' temperature in a coupled optical electronic two level system in the rotating frame of reference has not so far been demonstrated. In solids, strong exchange electric interactions of optical dipoles among themselves, or with the host lattice, prevent the distinction between an optical electric dipolar and a 'two level internal splitting' (analogous to Zeeman splitting) reservoir. In NMR, the weakly interacting nuclear moment permits the definition of isolated spin reservoirs to a high degree. Therefore, decoupling of spin–spin magnetic dipole–dipole interactions from externally controlled spin Zeeman interactions can be achieved over long relaxation times. In quantum optics, short lifetimes of excited states are associated with strongly interacting internal atomic electric degrees of freedom. Transitions are often broadened or rapidly transformed by complex mechanisms that are difficult to analyze and are not amenable to the predictions of the relatively simple Hamiltonians so useful in NMR. Pulsed coherent laser experimental techniques have not yet reached the stage of sophisticated high-resolution pulsed NMR spectroscopy, utilizing elaborate pulse sequences and double resonance methods, made possible by the persistence of coherent nuclear precession over relaxation times ranging widely from microseconds to many seconds.

As NMR is a predecessor of quantum optics, the molecular beam magnetic resonance method should be recognized as the predecessor of NMR. After space quantization of spin was confirmed by the Stern–Gerlach molecular beam deflection experiment,[1] a series of nonresonant type of molecular beam deflection experiments followed. Spins were measured directly, and magnetic moments were measured indirectly by combining laboriously acquired beam deflection data with theory known at the time. Of special interest was the effect of the apparent rotating magnetic field seen by an observer moving at the velocity of magnetic moments in a molecular beam as it passes through a static inhomogeneous field. For those molecules in the Maxwell spectrum that have just the right velocity, the static inhomogeneous field appears to rotate in partial synchronism with the Larmor frequency of spin precession determined by the main magnetic field. Therefore, the synchronism acts as a partial resonance and flips the spin. Rabi published the theory for this effect,[2] and in principle defined a magnetic resonance. The application of radiowave resonance excitation was not carried out by Rabi's Columbia group immediately after Rabi's paper was published. C. J. Gorter visited Columbia in 1937, and suggested to Rabi that it would be more efficient to apply a rotating radiofrequency field produced by an oscillator-driven inductance rather than rely on field inhomogeneity. This suggestion stimulated Rabi and his collaborators in 1937 to apply radiofrequency magnetic excitation to a beam of LiCl, and the magnetic resonance spectrum of the Li nucleus was obtained[3] as the first coherent spectroscopic measurement in the history of physics, followed by a series of many ground-breaking resonance experiments. Although line broadening effects such as time of flight and field inhomogeneity did initially reduce the precision of molecular beam resonance spectroscopy, this first demonstration showed that spin resonance electromagnetic energy could be concentrated into a single coherent frequency by an oscillator, and led to the development of precision magnetic resonance and laser spectroscopy as it exists today.

For a number of years after the Bloch and Purcell groups[4,5] initiated the science of NMR, it was not anticipated that the dynamic Bloch equations of NMR could describe as well the transient and steady state behavior of optical electric dipole resonance. Measurements of nuclear spins and magnetic moments were an early preoccupation. Studies were and still are focused upon lineshape, relaxation times, and high-resolution NMR spectra where the spins serve as probes of molecules, local fields, and fluctuations of the medium. Because the applied field energies and intensities usually far exceed total spin coupling energies and NMR signal intensities, applied rf fields are taken as constant. Therefore the direct role of cavity coupling to the spins in the resonance equations is

not a major consideration, although this coupling is necessary in order to observe NMR signals in the first place. In order to take into account the alteration of applied electric fields and free precession signals due to radiation damping caused by coupling with the cavity or the Poynting flux in free space in quantum optics, however, radiation damping must be considered of primary importance.

Tuned circuit cavity–spin coupling effects show up during free precession of the macroscopic nuclear magnetization in terms of coherent radiation damping.[6] Slight effects of radiation damping of free induction signals are evident in magnetic resonance imaging, where magnetic fields are very homogeneous and relaxation times are long. Radiation damping in NMR is essentially 'coherent overdamping'. The rate at which the cavity resistively dissipates power absorbed from the precessing magnetization usually far exceeds the rate at which power is emitted by the magnetization as it precesses about a reaction field H_1 in the rotating frame of reference. Radiation damping occurs only over the signal coherence lifetime T_2 (including the effect of inhomogeneous broadening as well as natural broadening), which is usually much shorter than the radiation damping time τ_r of the magnetization. Therefore the magnetization tips back by a slight amount toward alignment with the polarizing magnetic field. The radiation damping rate[6] is given by $1/\tau_r = 2\pi Q\gamma M_0\xi$. Suppose the cavity losses become less and less, and the emission from the two-level system becomes greater and greater. Let any or all of the terms in the product of cavity figure of merit Q, magnetization M_0, gyromagnetic ratio γ, and filling factor ξ be made large enough so that, instead of the usual condition $T_2 \ll \tau_r$, the approximate equality $\tau_r \approx T_2$ holds. This is the threshold condition that would make possible spontaneous NMR oscillations, applicable as well to the laser when translated into parameters of macroscopic electric dipole radiation. The final requirement is to maintain an inverted population of the two-level system, and the maser or laser is therefore invented with benefit of hindsight. The parameters expressed by $1/\tau_r$ reappear upon manipulation of optical Bloch–Maxwell equations, outlined later. The above conditions for laser oscillations indeed became the basis for the maser–laser principle, finally realized[7] by Townes and by Basov and Prokhorov in 1954.

In 1954, Dicke[8] stressed the idea of radiation coherence from an ensemble of phased electric dipole moments, applicable to the prediction of the dipole pattern of radiation from two-level systems other than magnetic spins. Formally, the incoherent spontaneous emission rate, proportional to N dipoles, can be distinguished from the coherent emission rate, proportional to N^2, by inspecting the rules of angular momentum that apply to collective Bose states. Dicke pointed out that coherent superpositions of atomic two-level states attained by radiation-driven initial states could be prepared, just as in pulsed NMR, and that these states give rise to coherent dipole radiation. Following this work, a semantic trend developed in the literature in which the term 'superrradiance' was applied to almost every process of coherent radiation from phased dipole arrays, particularly in coherent laser optics. Perhaps this happened because the direct application of optical Bloch equations had not yet been made, and it appeared as though the generation of coherent optical radiation was a unique phenomenon. However, it is standard knowledge from the Maxwell equations that coherent dipole source terms emit power in proportion to N^2, which 'is' superradiance, and is absolutely necessary, for example, to detect ordinary NMR signals. It would seem reasonable not to rename an old Maxwell phenomenon just because 'superradiance' rolls off the tongue so impressively. It is more à propos to apply the term to those special effects in which the initial incoherent spontaneous emission of power, proportional to N, finally evolves into the coherent emission condition[8,9] where the power becomes proportional to N^2.

From above, the obvious conclusion is that all NMR phenomena as we know them involve an enormous number of N dipoles prepared in phased arrays, where $N^{1/2} \ll N$. Likewise, many optical analogs of NMR are governed by this condition. There is therefore no need to supplement the semiclassical approach with quantum field theory in the majority of experiments involving macroscopic behavior, although it may be desirable in certain circumstances to deal with subtle aspects of fluctuations and spontaneous emission. Instead, spontaneous emission is introduced as a phenomenological damping term, just as the spin–lattice relaxation time T_1 appears in the Bloch equations.

In 1957, Feynman, Vernon, and Hellwarth[10] showed that electric dipole transitions in a two-level system could be formulated using equations that were the analogs of the Bloch torque equations, originating from the density matrix. Although the discussion in their paper was restricted to a particular maser problem, they utilized the semiclassical method in which the atoms are quantized, but the radiation and applied fields become classical self-consistent solutions of the Maxwell and Schrödinger equations. The works of Jaynes[11] and Lamb[12] extended the semiclassical method to quantum maser and laser analysis. A number of treatments and reviews have appeared with the express purpose of clarifying and justifying the assumptions of the semiclassical approach. In a monograph by Bloembergen[13] on nonlinear optics, the density matrix formulation commonly used in NMR is spelled out so that it may be applied more universally to optical systems, extending as well to multilevel systems. Allen and Eberly[14] treat a number of topics in greater depth, some of which are briefly outlined in this article, particularly with regard to radiation damping as it pertains to photon echoes[15] and self-induced transparency.[16] The book by Shen[17] covers modern topics in quantum optics, including transient phenomena related to NMR.

The discussion of NMR foundations in quantum optics that follows will not attempt to hew to the line of notation different from NMR introduced in the original papers and monographs referred to above. A one-to-one notation conventional in NMR will be carried over into a presentation of the optical Bloch–Maxwell equations. From them, certain parametric and phenomenological relationships between NMR and quantum optics will be pointed out.

2 THE RESONANCE EQUATIONS

The optical picture of NMR absorption was first introduced by the Harvard group.[4] The Bloch equations[5] of the Stanford group at first emphasized the nuclear induction dynamics of macroscopic nuclear polarizations, but of course these two approaches lead to the same interpretation of NMR. The rate equation for the population difference $n = N_1 - N_2$ between

the number of spins N_1 in the ground state and the number N_2 in the excited state is given by

$$\frac{\mathrm{d}n}{\mathrm{d}t} = \frac{n_0 - n}{T_1} - 2nR_{12} \tag{1}$$

In the high-temperature approximation $n_0/N \ll 1$ for spin $I = \frac{1}{2}$, the equilibrium population difference is given by $n_0 = N\hbar\omega_0/2kT$, where $N = N_1 + N_2$ is the total number of spins, $\omega_0 = \gamma B_0$, $\gamma = 2p/\hbar$ is the gyromagnetic ratio, and B_0 is the applied polarizing magnetic field. Note that coherence cannot be described by equation (1). The rate[18] of rf absorption, expressed from standard perturbation theory,

$$R_{12} = \tfrac{1}{2}\pi\gamma^2 H_1^2 g(\delta) \tag{2}$$

tends to equalize the populations, while the spin–lattice relaxation rate T_1^{-1} tends to restore a population difference toward thermal equilibrium. The off-resonance parameter $\delta = \omega_0 - \omega$ appears in the normalized (assumed to be Lorentzian) lineshape function

$$g(\delta) = \left(\frac{T_2}{\pi}\right)\frac{1}{1 + \delta^2 T_2^2} \tag{3}$$

where ω_0 is the Larmor frequency and ω is the applied frequency of the rotating rf field modulus H_1.

Equation (1) can now be modified so that it speaks the language of optics, useful later in devising the optical Bloch–Maxwell equations. The energy of the two level ensemble is first defined as $W = -\frac{1}{2}n\hbar\omega_0$, so that equation (1) becomes

$$\dot{W} = \frac{W_0 - W}{T_1} - 2WR_{12} \tag{4}$$

Substitution of $g(\delta) = T_2/\pi$ from equation (2) into equation (3), for $\delta = 0$, gives for the last term in equation (4),

$$2WR_{12} = \omega_0 H_1 v \tag{5}$$

The absorption component of magnetization $v = np\gamma H_1 T_2$ can be identified as a slowly varying solution at resonance for the linear unsaturated driven magnetization of the Bloch equations in the rotating frame of reference, transverse to the applied rotating field H_1. The slowly varying longitudinal magnetization $M_z = np$ is directed along the polarizing field $\boldsymbol{B}_0$. In the Bloch equations, the v and W terms as written are time-dependent and valid on or off resonance. This generality may be adopted, and therefore the restricted on-resonance quasisteady state interpretations of v and W in equation (4) may be dropped. Instead, equation (4) becomes one of the coherence-dependent Bloch equations:

$$\dot{W} = -\omega_0 H_1 v + \frac{W_0 - W}{T_1} \tag{6}$$

valid for any δ, expressed in terms of the energy

$$W = -M_z B_0 = -\frac{M_z\omega_0}{\gamma},$$
$$W_0 = -M_0 B_0 = -n_0 p \tag{7}$$

2.1 Optical Bloch–Maxwell Equations

At this point, a jump in the interpretation of the Bloch equations can be made from the NMR of a two-level system to the resonance description of a two-level optical system. Now the polarizations representing absorption (v) and dispersion (u) are to be interpreted as electric source term functions of time t and distance z in the Maxwell equations of propagation. A pseudoelectric polarization may be defined as $P_z = -(\kappa/\omega_0)W$, with P_z replacing M_z, the 'gyro-electric' ratio $2p_o/\hbar = \kappa$ replacing γ, and the electric field modulus $\mathcal{E}$ replacing H_1. The polarizations v and u are defined in the frame of reference rotating at the applied optical frequency ω of a plane wave

$$E(z, t) = 2\mathcal{E}(z, t)\cos[\omega t - kz + \phi(z, t)] \tag{8}$$

In the slowly varying wave approximation $\partial\mathcal{E}/\partial z \ll k\mathcal{E}$, $\partial\mathcal{E}/\partial t \ll \omega\mathcal{E}$, the field modulus $\mathcal{E}(z, t)$, u, v, W, and the phase shift $\phi(z, t)$ now appear as slowly varying parameters.

The optical analogue of the NMR torque equation in the rotating frame reads

$$\frac{\mathrm{d}\boldsymbol{P}}{\mathrm{d}t} = \boldsymbol{P} \times [\boldsymbol{u}_0\kappa\mathcal{E}(z, t) + \boldsymbol{z}_0(\delta\omega + \dot{\phi}(z, t)] - \frac{\boldsymbol{u}_0 u + \boldsymbol{v}_0 v}{T_2} - \frac{\boldsymbol{z}_0(W - W_0)}{T_1} \tag{9}$$

where $\boldsymbol{P} = \boldsymbol{u}_0 u + \boldsymbol{v}_0 v + \boldsymbol{z}_0 P_z$ is the total macroscopic electric polarization vector, and $\boldsymbol{u}_0$, v_0, and $\boldsymbol{z}_0$ are the unit vectors of the axes in the rotating frame. The effective frequency and propagation terms are given by $\omega_e = \omega + \dot{\phi}(z, t)$ and $k_e = k + \partial\phi(z,t)/\partial z$, respectively. Instead of the pseudopolarization component P_z, the energy $W = -\frac{1}{2}n\hbar\omega_0$ is often the appropriate physical term to be used in the optical Bloch equations. In the absence of damping, the conservation condition

$$N^2 p_0^2(u^2 + v^2) + \frac{\kappa^2}{\omega_0^2}W^2 = \frac{\kappa^2}{\omega_0^2}W_0^2 \tag{10}$$

applies, and, with damping, the optical Bloch equations are written out completely as

$$\dot{u} = v(\delta\omega + \dot{\phi}) - \frac{u}{T_2} \tag{11a}$$

$$\dot{v} = -u(\delta\omega + \dot{\phi}) + \frac{\kappa^2}{\omega_0}\mathcal{E}W - \frac{v}{T_2} \tag{11b}$$

$$\dot{W} = -v\mathcal{E}\omega_0 + \frac{W_0 - W}{T_1} \tag{11c}$$

The relaxation time T_1 here is assumed to be the inverse spontaneous emission rate. At equilibrium, the excited state of the optical two-level system is empty, and therefore the ground state population is $n_0 = N$ at the equilibrium condition $\hbar\omega_0 \gg kT$, in contradiction to the high-temperature approximation $n_0/N \ll 1$ applied in equation (1). However, the form of equation (11c) remains valid because the rate of change of population difference due to spontaneous emission in equation (4) can be written as

$$\frac{\mathrm{d}n}{\mathrm{d}t} = 2R_{\mathrm{spon}}N_2 = R_{\mathrm{spon}}(N - n) \tag{12}$$

so that the identity

$$\frac{W_0 - W}{T_1} = \tfrac{1}{2} R_{\text{spon}}(N - n)\hbar\omega_0 \tag{13}$$

may be retained in equation (11c) where $W_0 = -\frac{1}{2}N\hbar\omega_0$, $W = -\frac{1}{2}n\hbar\omega$, and $1/T_1 = R_{\text{spon}}$.

Equations (11a)–(11c) are time-dependent at a given position z, and include the effect of frequency modulation in the term $\dot{\phi}(z, t)$. They are then connected with the Maxwell wave equation

$$\frac{\partial^2 E(z,t)}{\partial z^2} = \frac{\eta^2}{c^2}\frac{\partial^2 E(z,t)}{\partial t^2} + \frac{4\pi}{c^2}\frac{\partial^2 P_{u,v}(z,t)}{\partial t^2} \tag{14}$$

by assuming the slowly varying wave approximation expressed earlier, with the definition $P_{u,v} = (u + iv)\exp\{i[\omega t - kz - \phi(z, t)]\}$. Therefore combining equations (11a)–(11c) with equation (14) yields

$$\frac{\partial \mathcal{E}(z,t')}{\partial z} = \frac{-2\pi\omega}{\eta c}\int_{-\infty}^{\infty} v g(\delta)\,\mathrm{d}\delta \tag{15}$$

and

$$\mathcal{E}\frac{\partial \phi(z,t')}{\partial z} = \frac{2\pi\omega}{\eta c}\int_{-\infty}^{\infty} u g(\delta)\,\mathrm{d}\delta \tag{16}$$

in the retarded frame of reference, where the retarded time $t' = t - \eta z/c$. Equations (11a)–(11c), (15), and (16) may apply to either sign of circular polarization (positive as shown) of the rotating $\mathcal{E}$ field modulus, satisfying the transition selection rule $\Delta m = \pm 1$. Oppositely rotating magnetizations excited by a linearly polarized field $\mathcal{E}_x(z, t)$, expressed by equation (8), involves the selection rule $\Delta m = 0$, and the magnetizations sum to produce a linearly polarized magnetization along the x axis in the laboratory frame as follows:

$$\begin{aligned} P_x &= P_{u,v}(+) + P_{u,v}(-) \\ &= u\cos\psi(z,t) - v\sin\psi(z,t) \end{aligned} \tag{17}$$

where $\psi(z, t) = \omega t - kz - \phi(z, t)$. The Bloch–Maxwell equations above can be generalized to cases where the two-level system is degenerate[16] and not necessarily characterized by one dipole matrix element. In that case, u and v are replaced by sums $\sum_i u_i$, $\sum_i v_i$ corresponding to sums over the i matrix elements.

If equation (14) is applied without the slowly varying wave approximation, extra smaller terms of the type $\ddot{u}$, $\ddot{v}$, $omègaú$, and $\omega\dot{v}$ would appear in equation (15) and (16) along with $\omega^2 u$ and $\omega^2 v$, which dominate. The smaller higher-order terms are of the same order of magnitude as the off-resonance response contribution by dipole matrix elements in the atom involving transitions to quantum levels other than the two-level system at or on resonance. Although other levels are not included, they must contribute in a formal sense, as dictated by the sum rule for optical response. Unless other levels are taken into account, it is quite possible to arrive at unrealistic conclusions concerning optical pulse propagation effects using extremely sharp and powerful laser pulses.

3 RADIATION DAMPING

The mechanism of radiation damping is essential for the detection of free precession signals in NMR and quantum optics. The coupling of precessing spin magnetization to the cavity (*LCR* tuned circuit) in NMR allows the spin system to radiate coherently into a cavity volume V_c with a single mode confined to a bandwidth $\Delta\nu = \nu/Q$, where the wavelength λ is much greater than the cavity and sample dimensions. The density of states is therefore $\rho_c = (V_c\ \Delta\nu)^{-1}$ whereas, with no cavity present, the magnetic dipole system would radiate incoherently because of vacuum field fluctuations $\boldsymbol{B}_{\text{vac}}$ at an infinitesimally small Einstein emission rate, given by

$$\frac{1}{\tau_E} = \frac{2\pi}{\hbar^2}\langle\, \boldsymbol{P}\cdot\boldsymbol{B}_{\text{vac}}\rangle\rho_F = \frac{32\pi^3 p^2}{\hbar\lambda^3} \tag{18}$$

where the free space density of states is $\rho_F = 8\pi\nu^2/c^3$. The connection between incoherent spontaneous emission rate of the dipole moment in free space to that in the NMR cavity is made by replacing the density of states ρ_E by $\rho_c = (V_c\ \Delta\nu)^{-1}$ in equation (18); i.e.,

$$\frac{1}{\tau_r} = \frac{NV_s}{\tau_E}\frac{\rho_c}{\rho_E} = 2\pi M_0\gamma Q\xi \tag{19}$$

The NMR coherent emission rate in a cavity is enhanced by factors of NV_s coherent spins and the cavity density of states ρ_c (which is much larger than ρ_E). In the *LCR* circuit, spin energy is dissipated under the condition $\gamma H_1 \gg R/L$, where $Q = \omega/\Delta\nu$, and the sample filling factor is $\xi = V_s/V_c$. The power emitted by the spins in terms of the voltage V_{ind} is given by

$$M_0 B_0 V_S\frac{\mathrm{d}(\cos\theta)}{\mathrm{d}t} = \frac{V_{\text{ind}}^2}{2R} = \frac{(4\pi M_0\omega N_t\xi\sin\theta)^2}{2R} \tag{20}$$

where N_t is the number of turns in the inductance $L = 4\pi \times (N_t/l)^2 V_c$ of length l and volume $V_c = Al$, and $\Delta\nu = R/L$. From equation (20), the radiation damping equation is expressed as

$$\begin{aligned} \gamma H_1(t) &= -2\pi M_0\gamma Q\xi\sin\theta = \dot{\theta} \\ &= -\frac{\sin\theta}{\tau_r} = -\frac{1}{\tau_r}\mathrm{sech}\left(\frac{t+t_0}{\tau_r}\right) \end{aligned} \tag{21}$$

Following a θ_0 pulse at $t = t_0$, the magnetic moment M_0 precesses about the cavity reaction field $H_1(t)$ in the frame of reference rotating at frequency ω, and is tipped toward the external magnetic field direction at a later time to a smaller angle $\theta(t)$. If the spins remain in phase for a short time $T_2 \ll \tau_r$ after an applied $\theta_0 = \frac{1}{2}\pi$ pulse ($t = -t_0$), the spin energy $W_s = -M_0 B_0\Delta\theta$ is given up to the cavity after a small decrease in angle $\Delta\theta \approx \gamma H_1 T_2 \approx T_2/\tau_r$. Therefore the emitted spin precession power immediately after the $\frac{1}{2}\pi$ pulse is

$$P_{\max} = \frac{M_0 B_0\Delta\theta}{T_2}V_S = \frac{M_0 B_0}{\tau_r}V_S = 2\pi Q M_0^2\omega_0\xi V_S \tag{22}$$

3.1 NMR Maser and Optical Laser Threshold Condition

Equation (21) can be adapted to a steady state interpretation of an NMR maser by postulating that $M_0 \to -M_0$, and the

spin population is maintained in an inverted steady state. The field $H_1 = \dot{\theta}/\gamma$ is now time-independent instead of a transient, and the steady state condition at resonance for the transverse magnetization in equation (21) requires the conversion

$$-M_0 \sin\theta \rightarrow v = \frac{-M_0 \gamma H_1 T_2}{1 + (\gamma H_1)^2 T_1 T_2} \tag{23}$$

obtained from the steady state solution of the Bloch equations, which includes the saturation denominator. Substitution of equation (23) in place of $M_0 \sin\theta$ in the first equality of equation (21), yields the relation $H_1 = v/\gamma\tau_r M_0$, and therefore

$$(\gamma H_1)^2 T_1 T_2 = \sqrt{-1 + T_2/\tau_r} \tag{24}$$

This very simple macroscopic relation shows that the NMR 'maser' field H_1 can only be sustained as a real quantity when the condition $T_2/\tau_r \geq 1$ applies at threshold. Obviously, equation (24) cannot take into account statistical properties at threshold due to noise, nor does it properly take into account the gain in H_1^2 when the condition $T_2/\tau_r > 1$ is obeyed. In a qualitative sense, this threshold condition defines a phase transformation boundary between the incoherent spontaneous emission phase and coherent emission phase.

In terms of optical parameters, equation (24) satisfies the threshold condition as well for laser action. For later reference, the optical Bloch equation, equation (11c), is now written using optical parameters:

$$\dot{W} = -\omega\kappa\tau_{ro} P_o \mathcal{E}^2 - \frac{W - W_0}{T_1} \tag{25}$$

where

$$\mathcal{E} = \frac{P_o \sin\theta}{P_o \kappa \tau_{ro}} = \frac{v}{P_o \kappa \tau_{ro}} \tag{26}$$

and the optical damping time τ_{ro}, now governed by feedback in an optical cavity, replaces τ_r. The definition equation (26) is analogous to $H_1 = v/\gamma\tau_r M_0$ expressed by equation (23) in the case of NMR. Note that $\mathcal{E}$ can only be interpreted as a reaction field in equation (25) and not an applied field. In the weak perturbation limit, the saturation denominator in v is absent, and any dependence of $\mathcal{E} = v/P_o\kappa\tau_{ro}$ on T_1 is included only by its effect on T_2. In the next section, the damping time τ_{ro} will pertain to optical coherent emission in the absence of cavity feedback.

4 OPTICAL FID AND THE PHOTON ECHO

In terms of the tranverse polarization v, a sample of radiating electric dipoles is prepared in cooperative phase by a traveling wave short pulse (or two pulses in succession to obtain a photon echo), and thereafter emits an optical FID signal. The sample length l is much shorter than the linear absorption length

$$\alpha^{-1} = \left(\frac{8\pi N p_0^2 \omega T_2}{\hbar \eta c}\right)^{-1} \tag{27}$$

This restriction avoids the possibility of nonlinear propagation effects such as self-induced transparency,[16] in which case the applied pulse itself is modified in shape, amplitude, and velocity as it transmits through the sample. [The absorption coefficient α is obtained from equation (11c) and (15) in the homogeneous line limit by combining the relations $(\eta c/4\pi)\partial\mathcal{E}^2/\partial z = \dot{W}$ and $v = Np_0\kappa\mathcal{E}T_2$, and dropping the last term in equation (11c) in the weak pertẆurbation limit that $W \approx W_0$. Here the the field $\mathcal{E}$ is interpreted as an applied field.] The reaction field $\mathcal{E}$ in equation (25) is now interpreted as the electric FID signal radiated by the polarization v that remains in phase for a coherence time t_p, shorter than T_1. Because the cooperative emission rate is enhanced over the spontaneous rate term $(W - W_0)/T_1$ in equation (25), this term is dropped. The conservation relation

$$\frac{nc}{4\pi}\mathcal{E}^2 = \dot{W} l \approx \mathcal{E}^2 \omega \kappa \tau_{ro} P_o l \tag{28}$$

now defines the flux per unit area passing out of a sample of length l. This flux represents a power loss analogous to the radiation damping Ohmic loss in the NMR case of radiation damping. Coherent radiation is directed along l, and the emission rate $1/\tau_{ro}$ is defined from the identity equation (29) as

$$\frac{1}{\tau_{ro}} = 2\pi P_o \kappa \omega \frac{2l}{\eta c} = \frac{1}{\eta \tau_E} N V_{coh} \tag{29}$$

This rate depends on the free space spontaneous emission rate $1/\tau_E$ given by equation (18). There is no cavity feedback, but there is emission enhancement by a factor of the number of phased dipoles contained in a coherence volume defined by $V_{coh} = \lambda^2 l/2\pi$. In the case of NMR, the wavelength is large compared with the sample dimensions, and therefore the coherence volume is given by the entire sample volume $V_s = \xi V_c$ as it appears in equation (19). In the optical FID case, the wavelength is much less than the sample dimensions, and therefore the radiation rate is determined by a much smaller coherence volume V_{coh} instead of V_s.

Before Hartmann and his collaborators[15] obtained photon echoes, there was a period of time when the coherent FID emission rate was predicted to be much too large. This resulted because the sample volume V_s was used in place of the coherence volume V_{coh} in equation (29). The optical FID pulse burst of power or 'optical bomb'[8] was expected to be as short as 10^{-13} s or shorter—a number intimidating enough to make experimentalists believe that the FID would be just about impossible to observe. The much longer observed times of photon echo bursts extend from about 10^{-8} s to 10^{-6} s.

Laser pulse coherent transient experiments often require pulses shorter than spontaneous emission times, of order 10^{-9}–10^{-8} s, so that the initial tipping angle $\theta_0 \approx \theta(t) \ll 1$ must be small if laser output power is limited. Also, the optical line is usually inhomogeneously Stark electric or Doppler broadened, and only a small fraction ($\approx T^*_2/t_p$) of the N atoms in the line is excited spectrally, where t_p is the pulse width. Therefore the number of dipoles actually excited is given by $n \approx N\theta(t)T^*_2/t_p$. These dipoles contribute from an optical spectral width of about $1/t_p$ within the optical line, and the emitted electric field in equation (25) appears in the form of a transient FID or a photon echo[15] lasting about t_p. Using equation (26), equation (28), may be rewritten to express the FID pulse power emitted by a volume Al of the sample:

$$\dot{W}Al = \frac{v^2}{\hbar P_o \kappa \tau_{ro}} Al \tag{30}$$

The number of photons $N_{ph,A}$ emitted per unit area by an electric dipole FID lasting for t_w from n dipoles in coherent superposition is given by

$$N_{ph,A} = lt_w \dot{N}_{ph} = \frac{lt_w \dot{W}}{\hbar\omega_0} = \frac{v^2}{\hbar P_o \kappa \tau_{ro}} \frac{lt_w}{\hbar\omega_0} = \frac{8\pi^2 p_o^2 l^2 n^2 t_w}{\eta\hbar\lambda} \tag{31}$$

$$N_{ph,A} \approx \frac{8\pi^2 p_o^2 l^2 N^2}{\eta\hbar\lambda} \frac{T_2^{*2}\theta^2}{t_w} \tag{32}$$

Note that the coherence volume V_{coh} in equation (29) appears naturally in the application of the optical Bloch equations, and does not have to be introduced explicitly.

4.1 Role of the Reaction Field During Linear Propagation

The concept of the reaction field is connected with induced absorption and emission during steady state propagation. Consider linear absorption (no saturation denominator in v) through a two-level medium where the propagating beam intensity is given by $\mathcal{E}^2(z) = \mathcal{E}^2(z = 0)e^{-\alpha z}$. The reduction in field amplitude over a short distance $\Delta z = l$ at position z is given by $\Delta\mathcal{E} \approx -\frac{1}{2}\mathcal{E}\alpha z$. Substitution of α from equation (27) and $\mathcal{E} = v/P_o\kappa T_2$ into this expression for $\Delta\mathcal{E}$ shows that it is is identical to the reaction field given by equation (26), where $1/\tau_{ro}$ is given by equation (29). If the incoming driving field $\mathcal{E}$ that induces the steady state polarization v is cut off abruptly then v will radiate an initial FID field $\Delta\mathcal{E}$ identical to the reaction field that existed before $\mathcal{E}$ was cut off. The $\Delta\mathcal{E}$ fields add in phase over the entire sample to provide a total optical FID signal at the exit end of the sample. Similarly, if the two-level system is maintained in the inverted state, acting as a traveling wave amplifier, $\Delta\mathcal{E}$ will represent a gain in field amplitude, with the FID signal shifted in phase by 180° following the abrupt cut-off.

4.2 Two-Pulse Photon Echo Phase Matching Condition

The two-pulse photon echo is obtained in practice after a first θ_1, $\boldsymbol{k}_1$ pulse, propagating in the $\boldsymbol{z}$ direction, is followed by a second θ_2, $\boldsymbol{k}_2$ pulse applied in a slightly different direction by a small angle ξ. The $\boldsymbol{k}$ propagation directions now play an important role. It will be seen that the photon echo signal[15] is emitted and detected in a third $\boldsymbol{k}_{echo}$ direction, deviating by small angle 2ξ with respect to $\boldsymbol{z}$. This property conveniently avoids saturation of the optical detector by the applied laser pulses along the $\boldsymbol{k}_1$ and $\boldsymbol{k}_2$ directions. In a given volume element $A\Delta z$ at z, the rotating electric laser modulus $\mathcal{E}$ is shifted in phase angle by $\vartheta = (k_1 - k_2)z$ relative to its alignment in the rotating frame during the first pulse. In the NMR case for a two-pulse echo, if the θ_2 pulse is applied at a rf phase shift ϕ with respect to the phase of the θ_1 pulse then the phase shift of the echo signal is 2ϑ relative to the echo that occurs when both pulses are in phase.[19]

The photon echo is now described only with regard to its z dependence as it propagates. Integration must be carried out over all the signals emitted from given volume elements $A\Delta z$ extending from $z = 0$ to $z = L$, the length of the sample. Phase dependences $k_1 z$, $k_{echo}(L - z)$, and $2\phi = 2(k_1 - k_2)z$ account respectively for the phased array set up along $\boldsymbol{z}$ by the first pulse, the phase change of the echo emitted from volume element $A\Delta z$ at z to L, and the phase shift caused by the shifted direction of the second pulse. The result for $\xi \ll 1$ is

Table 1 Effects and Concepts From NMR That Occur in Quantum Optics

Linear and nonlinear absorption and dispersion; saturation, hole burning, and spectral and spatial diffusion
Homogeneous and inhomogeneous broadening
Radiation damping; coherent reaction field dynamics
Rabi flop; precession about the effective field in the rotating frame (optical nutation)
Adiabatic following and inversion
Photon echo, rotary photon echo, three-level echoes, transfer of coherence, single pulse free precession (FID)
Stimulated echo pulse holographic memory storage in rare earth crystals
Coherent quantum beats; stimulated heterodyne coherent Raman beats, coherent Raman scatering
Self-induced transparency
Two-photon transition phenomena; AC Stark effect; multiple quantum transitions
Electric rotary saturation
Double resonance
Two-level laser theory and operation
Optical four-wave mixing, stimulated echo, backward-wave echo
Optical phase conjugation
Fourier transform spectroscopy
Optical pulse chirping, frequency modulation
Relaxation dynamics, motional narrowing, dipole–dipole coupling
Autler Townes effect; dressing of atomic levels, fast driven precession averaging
Holography, grating scattering
Nuclear polarization by optical pumping, spin exchange

$$E_{\text{echo}}(L) \propto \int_0^L e^{2i(k_1-k_2)z - ik_1 z - ik_{\text{echo}}(L-z)}\, dz$$
$$= \frac{\sin\{\frac{1}{2}[k_{\text{echo}} - (2k_2 - k_1)]L\}}{\frac{1}{2}[k_{\text{echo}} - (2k_2 - k_1)]L} \qquad (33)$$

Since the magnitudes of the two-pulse $\boldsymbol{k}$ vectors ($|\boldsymbol{k}_1| = |\boldsymbol{k}_2|$) are the same in the usual experiment, the phase matching condition above cannot be satisfied exactly, given that the direction of $\boldsymbol{k}_2$ is chosen at a small angle ξ with respect to the $\boldsymbol{z}$ direction of $\boldsymbol{k}_1$. If ξ were not small, the phase factor in the integrand in equation (33) should be written as $\exp\{i[\boldsymbol{k}_{\text{echo}} - (2\boldsymbol{k}_2 - \boldsymbol{k}_1)] \cdot \boldsymbol{r}\}$, which in principle would require integration over all dipoles at points over $\boldsymbol{r}$ in the sample. Since we ignore diffraction from a strip of dipoles along $\boldsymbol{r} = \boldsymbol{z}$, it is seen for $\xi \ll 1$ that $[\boldsymbol{k}_{\text{echo}} - (2\boldsymbol{k}_2 - \boldsymbol{k}_1)] \cdot \boldsymbol{r} \approx (k_1 - |2\boldsymbol{k}_2 - \boldsymbol{k}_1|)z \cos 2\xi$, where the maximum photon echo amplitude is emitted at an angle of approximately 2ξ with respect to the $\boldsymbol{r} = \boldsymbol{z}$ direction when $\boldsymbol{k}_{\text{echo}}$ is parallel to $2\boldsymbol{k}_2 - \boldsymbol{k}_1$. However, because $|\boldsymbol{k}_1| = |\boldsymbol{k}_2|$, the propagation vector triangle cannot form an exact closed triangle, and the intensity of the photon echo is therefore reduced by a very small factor. The important point is that the photon echo is emitted in the $\boldsymbol{k}_{\text{echo}}$ direction at an angle of approximately 2ξ with respect to the $\boldsymbol{k}_1$ direction along $\boldsymbol{z}$ in order to avoid the blanking effect of the applied laser pulses.

There is a connection between the various types of photon echo production in the time domain and steady state nonlinear optical effects[17] such as four-wave mixing and phase conjugation. Propagating phonon backward-wave acoustic echoes observed by Shiren[20] are identically phase-conjugated echoes. The phase-conjugated echo represents an apparent reversal in time, because δ is effectively changed in sign in the precession phase δt. In addition, the sign of the $\boldsymbol{k}$ vector in the propagation phase kz is reversed, and the echo travels in the reverse z direction instead of the usual forward direction of applied pulses. These effects occur because pulse echoes are caused by nonlinear transformations imposed upon the Bloch vectors during applied pulses. As laser pulse sequences are conceived to merge with one another into the steady state, considerations of nonlinearity[17] persist, but in a different form.

5 PRINCIPAL EFFECTS COMMON TO NMR AND QUANTUM OPTICS

A number of the most important NMR effects and concepts that appear in quantum optics can be listed (Table 1). However, it is sometimes difficult to make clear one-to-one relationships between the two fields. The basic physics of the Bloch–Maxwell equations, together with general application of the density matrix to more than two quantum levels, encompass a large number of phenomena in both fields. Many items are not listed that involve spontaneous emission, certain propagation effects, and some multilevel Raman processes, all having only remote connections to NMR. Parametric conversion effects are also omitted. No doubt there are some topics overlooked that deserve listing; or, vice versa, some

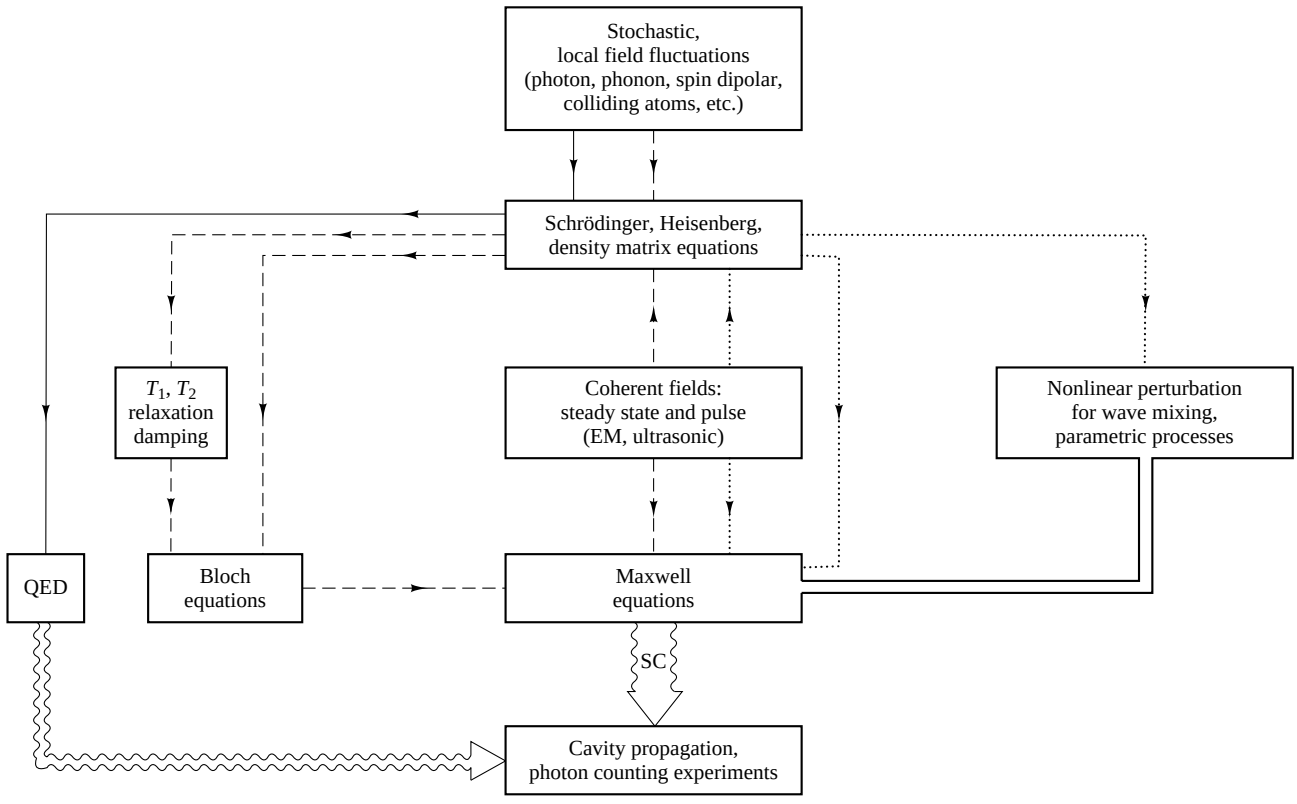

Figure 1 Various routes of analysis in quantum optics, including quantum electrodynamics (QED). The semiclassical (SC) method connects the Maxwell equations to various polarization source terms. The Bloch–Maxwell equations are designated by coupling the Maxwell equations to the optical Bloch equations adapted from NMR

items appearing may not deserve recognition in the opinion of some people. Rather than give references for each item, the reader is referred to standard reviews in the literature. For examples, books by Shen,[17] Yariv,[21] Sargent, Scully, and Lamb,[22] Bagguley,[23] and Allen and Eberly[14] treat many modern topics in quantum optics.

6 CONCLUSIONS

This brief review has covered only a few fundamental concepts of spontaneous coherent dipole radiation that connect NMR to quantum optics. The block diagram of Figure 1 suggests how the Bloch–Maxwell equations tie in with various routes of analysis that cover a broad number of topics in the literature. The figure shows the path of a frequently used perturbation approach, carried out without employing the Bloch equations, by taking the $\cdots\cdots\gg$ route. Instead of using the Bloch equations directly on a par with the Maxwell equations, perturbation terms are inserted directly into the Maxwell equations. However, by taking the $---\gg$ route, all orders of perturbation in principle are included simultaneously from these equations when they are directly coupled to the Bloch equations. Although full theoretical rigor is not always satisfied when the Bloch–Maxwell equations are used, they are helpful in providing phenomenological predictions. Figure 1 includes diagrammatically the role of other degrees of freedom and mechanisms involved in quantum optics, and indicates how experiments analyzed using quantum electrodynamics (QED) take a different route.

7 RELATED ARTICLES

Laser Devices in NMR: Routes to Chaos; Multiple Quantum NMR in Solids; Optically Enhanced Magnetic Resonance; Radiofrequency Pulses: Response of Nuclear Spins; Ruby NMR Laser; Ultrasonic Irradiation and NMR.

8 REFERENCES

1. O. Stern, *Z. Phys.*, 1921, **7**, 249; W. Gerlach and O. Stern, *Ann. Phys. (Leipzig)*, 1924, **74**, 673.
2. I. I. Rabi, *Phys. Rev.*, 1937, **51**, 652.
3. I. I. Rabi, J. R. Zacharias, S. Millman, and P. Kusch, *Phys. Rev.*, 1938, **53**, 318.
4. N. Bloembergen, E. M. Purcell, and R. V. Pound, *Phys. Rev.*, 1948, **73**, 679.
5. F. Bloch, W. W. Hansen, and M. E. Packard, *Phys. Rev.*, 1946, **69**, 474; F. Bloch, *Phys. Rev.*, 1946, **70**, 460.
6. N. Bloembergen and R. V. Pound, *Phys. Rev.*, 1954, **95**, 8.
7. J. P. Gordon, H. J. Zeiger, and C. H. Townes, *Phys. Rev.*, 1954, **95**, 282; N. G. Basov and A. M. Prokhorov, *Soviet Phys. JETP*, 1954, **27**, 43.
8. R. H. Dicke, *Phys. Rev.*, 1954, **93**, 99; in *Proceedings of 3rd International Conference on Quantum Electronics*, eds. P. Grivet and N. Bloembergen, Columbia University Press, New York, 1964, p. 35.
9. M. S. Feld and J. C. MacGillivary, in *Coherent Nonlinear Optics*, ed. M. S. Feld and V. S. Letokhov, Springer-Verlag, Berlin, 1980.
10. R. P. Feynman, F. L. Vernon, and R. W. Hellwarth, *J. Appl. Phys.*, 1957, **28**, 49.
11. E. T. Jaynes and F. W. Cummings, *Proc. IEEE*, 1963, **51**, 89.
12. W. E. Lamb, *Phys. Rev.*, 1964, **134**, A1429.
13. N. Bloembergen, *Nonlinear Optics*, Benjamin, New York, 1965, 3rd Printing, 1976.
14. L. Allen and J. H. Eberly, *Optical Resonance and Two-Level Atoms*, Wiley, New York, 1975.
15. I. D. Abella, N. A. Kurnit, and S. R. Hartmann, *Phys. Rev.*, 1966, **141**, 391.
16. S. L. McCall and E. L. Hahn, *Phys. Rev. A*, 1970, **2**, 861.
17. Y. R. Shen, *The Principles of Nonlinear Optics*, Wiley, New York, 1984.
18. A. Abragam, *The Principles of Nuclear Magnetism*, Clarendon Press, Oxford, 1961, p. 28.
19. E. L. Hahn, *Phys. Rev.*, 1950, **80**, 580.
20. N. S. Shiren and T. G. Kazyaka, *Phys. Rev. Lett.*, 1972, **28**, 1304.
21. A. Yariv, *Quantum Electronics*, Wiley, New York, 1975.
22. M. Sargent III, M. O. Scully and W. E. Lamb, *Laser Physics*, Addison-Wesley, Reading, MA, 1974.
23. D. M. S. Bagguley (ed.), *Pulsed Magnetic Resonance: NMR, ESR, and Optics*, Clarendon Press Oxford, 1992.

Acknowledgments

The author thanks the National Science Foundation for support.

Biographical Sketch

Erwin Louis Hahn. *b* 1921. B.S., 1943, Juniata College, USA; Ph.D., 1969, University of Illinois. Postdoctoral Fellow, Physics Instructor, Stanford University, 1950–52. Research Physicist, IBM Thomas J. Watson Laboratory, New York, 1952–55. Physics Faculty, University of California, 1955–91. Professor Emeritus, 1991–present. Research interests: pulsed NMR and nonlinear laser phenomena, spin coupling effects in NMR, NQR and quantum optics, double resonance, and nuclear quadrupole resonance spectroscopy.

Radiofrequency Pulses: Response of Nuclear Spins

Alex D. Bain

McMaster University, Hamilton, Ontario, Canada

1	Introduction	1
2	Basic Interactions	1
3	Continuous Wave Radiofrequency	2
4	Pulsed Radiofrequency	3
5	Conclusions	6
6	Related Articles	6
7	References	6

1 INTRODUCTION

Radiofrequency pulses are the major tool in modern nuclear magnetic resonance. In the simplest case, they are used to excite a free induction decay, which is then Fourier transformed to provide a spectrum. Even when there is no interest in the dynamics of the spins and all we want is a simple spectrum, this has many advantages over the classic continuous wave (CW) NMR. Sensitivity is increased owing to the fact that we observe all the spectrum all the time (see ***Fourier Transform Spectroscopy***). Also, a pulse experiment gives us an instantaneous picture of the whole spectrum, so that we can follow kinetics and relaxation. Except when the cost of the instrument is an important factor, pulse spectrometers are always used to acquire spectra.

Pulses can do much more. The routine acquisition of spectra is just one example of the response of spin systems to rf pulses. The normal one-dimensional spectrum is only a small part of the information about a spin system. Because of the coherent nature of NMR, the spectrum can be manipulated by a series of pulses to produce a wide range of experiments. Many of the experiments are multidimensional (see ***Multidimensional Spectroscopy: Concepts***). For example, chemical shift information can be passed from one nucleus to another for detection (see ***COSY Two-Dimensional Experiments*** and ***Heteronuclear Shift Correlation Spectroscopy***), or chemical shifts can be separated from couplings (see ***Two-Dimensional J-Resolved Spectroscopy***). Spin systems have many unobservable multiple quantum transitions, and these can be measured by pulse techniques. The basis of all these experiments is the response of a nuclear spin system to rf pulses.

In this article, we start with the basic interactions and draw on some results from the Bloch equations. These can be used to predict transient response, but it is usually assumed that in a pulse spectrometer, the rf magnetic field dominates all the other magnetic interactions. In this case, an rf pulse is usually equivalent to a rotation of the frame of reference through some angle called the flip angle. In simple cases, this is equivalent to a vector picture of magnetizations in three-dimensional space. These vector pictures can be very useful, particularly for pulse sequences used in imaging. For scalar-coupled spin systems, the vector picture breaks down, and the actual behavior may be quite unexpected. For such systems, theory and simulations provide some insight into the behavior. Beyond these systems are those with strong interactions, such as quadrupolar nuclei, in which the rf does not dominate. Further complications arise in these cases. This article cannot cover all the responses of all spin systems to all types of pulses, but we follow the important and characteristic examples.

2 BASIC INTERACTIONS

Nuclear spins have magnetic moments, which interact with magnetic fields. This includes not only the static magnetic field in which NMR is done, but also any oscillating magnetic fields associated with electromagnetic radiation. In all cases, the interaction is given by the Hamiltonian

$$\mathcal{H} = -\boldsymbol{\mu} \cdot \boldsymbol{B} \tag{1}$$

where $\boldsymbol{\mu}$ is the nuclear magnetic moment and $\boldsymbol{B}$ is the magnetic field. Both of these are vector quantities, and the energy resulting from their interaction is the scalar product of the two vectors. This is the basic Hamiltonian.

The magnetic moment of a spin can be considered to arise from its angular momentum character. The physics of angular momentum means that the motion of the spins can be quite complex. In the simplest case when the magnetic field is static, or effectively so, the result of this interaction is that the spins will precess around the magnetic field. The frequency of this precession is ω_0, the Larmor frequency, which is given by

$$\omega_0 = \gamma B_0 \tag{2}$$

If the magnetic field is oscillating in a plane then it can be made effectively static by going to a frame of reference rotating at the oscillation frequency. If the field as a function of time is given by

$$\boldsymbol{B}_1(t) = \boldsymbol{B}_1 \cos(\omega t) \tag{3}$$

then this can be reexpressed as

$$\boldsymbol{B}_1(t) = \boldsymbol{B}_1(\mathrm{e}^{\mathrm{i}\omega t} + \mathrm{e}^{-\mathrm{i}\omega t})/2 \tag{4}$$

The oscillating magnetic field is replaced by the sum of two counter-rotating fields. If the oscillation is near resonance with the Larmor frequency then in the frame of reference rotating with the rf magnetic field, the spins experience a field that is almost static. More precisely, they interact with an effective magnetic field shown in Figure 1.

The effective field is given by the vector sum of the rf magnetic field $\boldsymbol{B}_1$ in the (x, y) plane and the magnetic field that corresponds to the difference between the frequency of the rf, ω, and the Larmor frequency, ω_0. In the rotating frame of reference, spins will precess around the effective magnetic field. Typical values for B_1 range from very small up to 10 mT. In terms of precession frequencies around $\boldsymbol{B}_1$, these values correspond to frequencies of less than 1 Hz up to the order of 100 kHz. For a spin-$\frac{1}{2}$ nucleus in a liquid, the $\boldsymbol{B}_1$ field is usually assumed to dominate other terms in the Hamiltonian, although

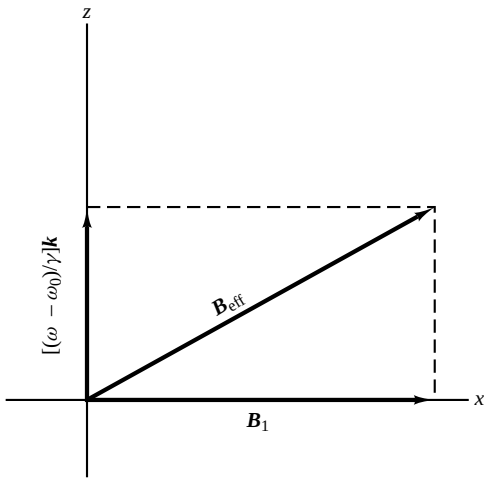

Figure 1 The effective field that spins experience in the rotating frame of reference. The field is the vector sum of the rf magnetic field $\boldsymbol{B}_1$ and the magnetic field corresponding to the difference in frequency between the Larmor frequency of the spin, ω_0, and the frequency of the rf, ω. (Here $\boldsymbol{k}$ is the unit vector along the z axis)

this is by no means always true. For solids and quadrupolar nuclei, this seldom holds, since dipolar and quadrupolar terms can be of the order of megahertz. However, the approximation that the rf can be represented as a static magnetic field in the (x, y) plane of a rotating frame of reference works very well in most cases.

Two cases of the interaction of spins with rf fields arise: the continuous irradiation (CW for continuous wave) case and the pulse response. This is an oversimplification, but it is convenient for our purposes here. In the first case we are mainly concerned with a steady state that the spin system achieves during irradiation, whereas the transient response to a pulse is most important in the second. One of the differences between the two cases is the treatment of spin relaxation. In the pulse case, relaxation is almost always ignored, whereas in the CW case, we are usually interested in the steady state achieved between the rf perturbation and the relaxation trying to reestablish equilibrium.

3 CONTINUOUS WAVE RADIOFREQUENCY

The critical parameter with CW NMR is whether or not the radiofrequency irradiation is saturating. If γB_1 is much smaller than the rate of spin relaxation $1/T_1$ then the field is nonsaturating. The rf power typically used in this case is quite low—of the order of milliwatts—and γB_1 is $1\,\text{s}^{-1}$ or less. This is the case under normal operating conditions in a CW NMR spectrometer.

The Bloch equations provide a description of spin behavior under rf irradiation. They give the equations of motion for the three components of the magnetization for a single spin-$\frac{1}{2}$ in the presence of an rf magnetic field. By convention, the z component is defined as M_z, but the x and y components in the rotating frame of reference are called u and v. The u mode (dispersion mode) is in phase with the rf, and v is $\frac{1}{2}\pi$ out of phase, and is called the absorption mode. The coupled differential equations defining these magnetization components are

$$\frac{\mathrm{d}u}{\mathrm{d}t} = (\omega_0 - \omega)v - \frac{u}{T_2} \tag{5}$$

$$\frac{\mathrm{d}v}{\mathrm{d}t} = -(\omega_0 - \omega)u + \gamma B_1 M_z - \frac{v}{T_2} \tag{6}$$

$$\frac{\mathrm{d}M_z}{\mathrm{d}t} = -\gamma B_1 v - \frac{M_z - M_0}{T_1} \tag{7}$$

In the steady state, the solution to the Bloch equations is

$$u = M_0 \frac{\gamma B_1 T_2^2(\omega_0 - \omega)}{1 + T_2^2(\omega_0 - \omega)^2 + \gamma^2 B_1^2 T_1 T_2} \tag{8}$$

$$v = M_0 \frac{\gamma B_1 T_2}{1 + T_2^2(\omega_0 - \omega)^2 + \gamma^2 B_1^2 T_1 T_2} \tag{9}$$

$$M_z = M_0 \frac{1 + T_2^2(\omega_0 - \omega)^2}{1 + T_2^2(\omega_0 - \omega)^2 + \gamma^2 B_1^2 T_1 T_2} \tag{10}$$

Note that this solution is valid for all values of B_1—whether or not the rf is saturating depends on whether the term $(\gamma B_1)^2 T_1 T_2$ is much greater than or much less than 1.

Under nonsaturating conditions, the magnetization is only slightly perturbed away from equilibrium, as shown in Figure 2. If the rf is assumed to lie along the x axis then it exerts a torque on the magnetization, forcing it away from the z axis towards y. This is counterbalanced by relaxation, which tends to take the magnetization back to z. The steady-state magnetization is tipped slightly away from equilibrium towards the y axis. The receiver picks up the xy component of the magnetization, which in this case is out of phase with the rf. This gives a faithful representation of the 'slow passage' spectrum. Provided the field is nonsaturating, the y component will increase linearly with the strength of the rf field. These are the classic results from the Bloch equations.

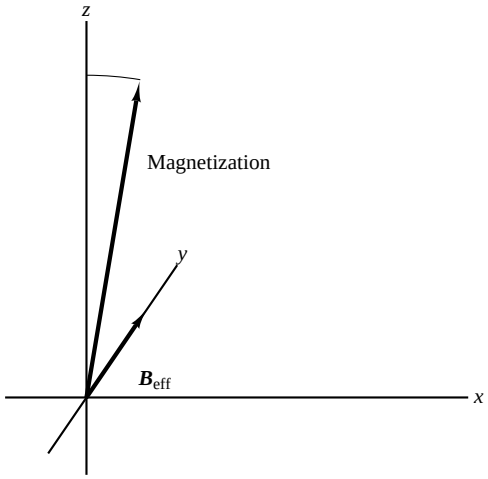

Figure 2 Schematic illustration of the steady state magnetization of a single spin during weak continuous irradiation, as described by the Bloch equations. The rf magnetic field exerts a torque on the magnetization, tilting it away from the z axis

On a modern pulse Fourier transform spectrometer with a single coil probe, we often want to apply continuous irradiation during acquisition, for decoupling of homonuclear systems. The irradiation cannot be left on during the actual acquisition, since it would swamp any observed signal. In practice, the homonuclear irradiation is time-shared with the sampling of the digital points. For each point of the FID, the signal is sampled, the receiver is gated off, and the irradiation is turned on for a small part of the dwell time between sampling points. Typically, the duty cycle for the decoupler is 10%. Therefore, this continuous irradiation is really an infinite series of short, weak pulses. Provided the flip angle of each individual pulse is much less than 1 rad, this is equivalent to continuous irradiation at the same average power.[1]

As well as the steady-state response to CW irradiation, there are transient effects that follow the change in rf power or frequency. Some examples are the ringing of a signal after the rf has swept past, the techniques of adiabatic rapid passage, and the observation of Torrey oscillations. The Bloch equations can also describe these effects, but the applications for which they are used are now better served by pulse methods.

4 PULSED RADIOFREQUENCY

4.1 Fundamentals

In this case, the rf power and the associated magnetic field are usually as large as possible. The aim here is usually to dominate all of the terms in the Hamiltonian, so that the main term is the precession about the rf magnetic field. Radiofrequency powers range up to a few kilowatts, and values of γB_1 are tens or hundreds of kilohertz. If the rf field is large enough, it will affect all of the spectrum uniformly. The spectrum will be distorted if different parts of the spectrum experience different effective fields.

The effect of a strong pulse is very simple. The Bloch equations show that the field induces a torque on the spins. A pulse rotates the frame of reference through some flip angle α. *Note that this is not the same as rotating the magnetizations through a flip angle of* $-\alpha$. For the simple case of a single line spectrum, this distinction is not important, and the usual simple vector picture can be used successfully to rationalize the behaviour of spin systems. For more complex homonuclear coupled spin systems, the behavior of the magnetizations when the frame of reference is rotated can be quite counterintuitive.

The complex behavior of coupled spin systems can be rationalized by saying that both the spin that is being observed and the spin that is causing the splitting are experiencing the rotation simultaneously. Not only is the observed magnetization being rotated, but also the interaction that splits the magnetization is changing with the rotation. Because the rf field dominates all the terms in the Hamiltonian, values of the coupling constants and chemical shifts are irrelevant to the pulse response. It is the fact that the different parts of the multiplet are separated and may have different intensities and phases that is important.

One example of this behavior is the case in which intensities within a multiplet are distorted,[2–4] as in Figure 3, or some CIDNP experiments (see ***Chemically Induced Dynamic Nuclear Polarization***). In a doublet due to homonuclear coupling, the two lines do not behave as two vectors. Rather, the pulse acts on the sum of the two lines and their difference. In particular, the differences amongst members of a multiplet usually offer the best means of manipulating a spin system. This is why many pulse sequences use delays of $1/2J$ to maximize the difference magnetization in a doublet. If we are looking at an equilibrium spectrum, it shows none of this flip angle dependence. This is because, as far as the pulse

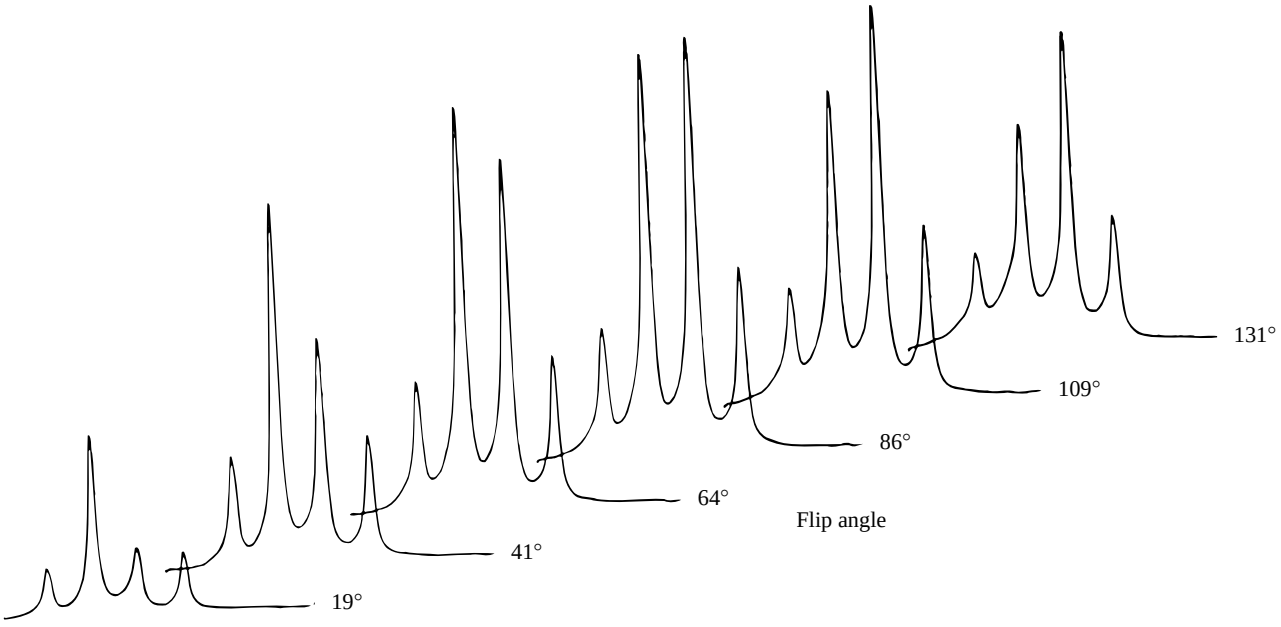

Figure 3 Illustration of flip angle effects on spectra when intensities within a multiplet are distorted. The diagram shows spectra of the methylene quartet in ethyl acetate as a function of flip angle. Prior to observation, the low-frequency inner peak of the quartet had been partially saturated. The small flip angle spectrum accurately reflects this, but the spectra with flip angles larger than $\frac{1}{2}\pi$ actually have the saturated line as apparently the most intense

is concerned, the equilibrium spectrum is a single density matrix element, no matter how complex the spectrum. It is the deviations from equilibrium that cause the flip angle dependence.

Because the exact behavior of a spin system can be obscure, several mathematical formalisms and simulation tools have been developed to help in our understanding.[5–7] These provide complete and rigorous ways of calculating the density matrix as a function of time. The density matrix can be regarded in many ways: an element can be thought of as a transition, a magnetization, an operator, or a quantum mechanical coherence. All are different ways of looking at the same quantity. A good mathematical description means that we can follow not only the observable magnetizations, but also the unobservable multiple quantum coherences that form important parts of many pulse experiments.

All the formalisms do essentially the same job of providing a solution to the equation of motion of the density matrix, and the differences are mainly in the approach to the problem. One powerful tool is the use of angular momentum properties of the spin system. These provide a basis for using spherical tensors, since spherical tensors are a natural and general way of describing what happens to a system when the frame of reference is rotated. The details of these formalisms are far beyond the scope of this article, but a simple example of the treatment of a system of spin-$\frac{1}{2}$ nuclei is as follows.

For a single spin-$\frac{1}{2}$ system, there are four spin operators that define the system: the unit operator $\hat{1}$ and $\hat{I}_x$, $\hat{I}_y$, and $\hat{I}_z$, representing the x, y and z components of the magnetization. For experiments that only involve pulses that are multiples of $\frac{1}{2}\pi$, the effect of a pulse on these operators is simple. A pulse along the x axis takes the z component $\hat{I}_z$ onto the y axis, takes $\hat{I}_y$ onto $-z$, and leaves $\hat{I}_x$ alone. For more complex spin systems, products of these spin operators, one for each nucleus, can be manipulated in the same way. For instance, the product operator $\hat{I}_z\hat{I}_y$ represents a coherence associated with the second spin. A pulse along x turns this into $\hat{I}_y\hat{I}_{-z}$, which is coherence on the first spin, so coherence has been transferred. This provides a quick and convenient way of analyzing pulse sequences.

In order to describe a general pulse, of any flip angle or phase, the spin operators can be combined as follows to create spherical tensors:

$$\left.\begin{aligned} |0) &= \frac{1}{\sqrt{2}}\hat{1} \\ |1_{+1}) &= -(\hat{I}_x + \mathrm{i}\hat{I}_y) \\ |1_0) &= \sqrt{2}\hat{I}_z \\ |1_{-1}) &= \hat{I}_x - \mathrm{i}\hat{I}_y \end{aligned}\right\} \qquad (11)$$

The notation $|M_m)$ means an angular momentum (superspin) with total angular momentum quantum number M, and z component m.[6] The utility of this approach is that the effect of any rotation about any axis is given by the appropriate Wigner matrix. For the three elements in equation (11) with superspin 1, the effect of a rotation about the y axis through an angle α is given by

$$\begin{bmatrix} \sin^2\frac{1}{2}\alpha & \sqrt{\frac{1}{2}}\sin\alpha & \cos^2\frac{1}{2}\alpha \\ \sqrt{\frac{1}{2}}\sin\alpha & \cos\alpha & -\sqrt{\frac{1}{2}}\sin\alpha \\ \cos^2\frac{1}{2}\alpha & -\sqrt{\frac{1}{2}}\sin\alpha & \sin^2\frac{1}{2}\alpha \end{bmatrix} \qquad (12)$$

In the simplest case, a z magnetization corresponding to $|1_0)$ is tipped down to form an xy magnetization proportional to $\sin\alpha$ and leaves a z magnetization proportional to $\cos\alpha$. More complex cases can then be described by products of Wigner matrices. This approach, using the angular momentum properties, also helps in calculating the effect of phase changes in the rf.

4.2 Phase of the Radiofrequency Pulse

The phase of an rf pulse defines the position of the rf magnetic field in the (x, y) plane (see ***Phase Cycling***). The phase angle is the azimuthal angle between $\boldsymbol{B}_1$ and a reference, say the x axis. The absolute phase is irrelevant, but the relative phases of rf pulses in a sequence are critical, as well as their individual flip angles. For instance, a $\frac{1}{2}\pi$ pulse around the x axis, followed by a $\frac{1}{2}\pi$ pulse around y, has quite a different effect on a vector than a pair of $\frac{1}{2}\pi$ pulses around x. Most pulse experiments employ some sort of phase cycling sequence—repeating the experiment with the same values of the flip angles but with different rf phases. Phase cycling plays a crucial role, since it offers a good way of selecting coherences that we need, and eliminating unwanted signals.[8,9] Until magnetic field gradients became common, phase cycling was the only way to do this.

Pulses are somewhat indiscriminate in their action, since there are no selection rules as to how many orders of multiple quantum coherence can be created. If there are N coupled spins $\frac{1}{2}$ then a density matrix element can have a coherence level (a number that counts the number of quanta involved in the associated transition) anywhere from $-N$ to $+N$ in integral steps. A general pulse acting on a general spin state will take coherence from anywhere in that range to anywhere else. Phase cycling tidies this up.

When an rf pulse is applied, it usually changes the coherence of a density matrix element. For instance, it will take z magnetization[8] (no coherence, coherence level 0) into xy magnetization (single quantum coherence, coherence level ± 1). In general, this change in coherence level is by an amount Δm. When the phase of the rf pulse is changed by an angle ϕ, then coherence is changed by a phase factor $\mathrm{e}^{\mathrm{i}\Delta m\phi}$.[10] One of the simplest examples is the P-type versus N-type peak selection in COSY. When, in a second acquisition, the mixing pulse is shifted by $\frac{1}{2}\pi$, the P type has a phase factor of +1, but the N type has a factor of -1. Subtraction of the two spectra cancels the P-type peaks. This is the simplest type of phase cycling, and, for experiments with many pulses, the complete phase cycling sequences can get much longer.

4.3 Weak Pulses

The next question that arises is what happens when the rf magnetic field no longer dominates the other terms in the Hamiltonian. For instance, a $10\,\mu$s pulse corresponds to

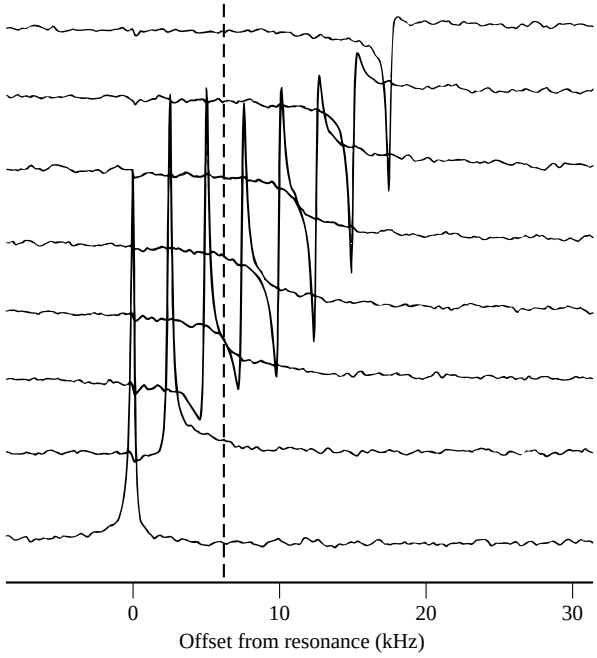

Figure 4 The effects of a weak pulse on a single line spectrum as a function of offset from resonance. The first spectrum on the left was acquired on resonance and phased for pure absorption. Successive spectra were acquired at 2500 Hz increments from resonance, and the same phase correction was used. The $\frac{1}{2}\pi$ pulse in this case was set to 40 μs, corresponding to a precession rate of 6250 Hz around the rf magnetic field. The dashed vertical line is at this value

γB_1 = 25 kHz, and it is not unusual for a line in the spectrum of a heavy element at high magnetic field to be 25 kHz off resonance. In such cases, the effective rf field is a long way from the (x, y) plane. However, as Figure 4 shows, the spectrum is remarkably little affected, despite the breakdown of the model of the pulse. The intensity of the line remains large out to offsets of $5\gamma B_1$, and the principal distortion is just the phase of the signal. In some sense, the effective field is self-compensating. As the signal moves off resonance, the effective field is tilted up out of the (x, y) plane, but it gets stronger because of the contribution of the offset from resonance. A flip angle of $\frac{1}{2}\pi$ on resonance becomes a flip angle of $\sqrt{\frac{1}{2}}\pi$ about an effective field that is tilted up by an angle of 45°. The net xy component of the magnetization has a similar magnitude in each case, but the phase is different.[11]

In order to achieve some sort of selective excitation, pulses are often deliberately made long and weak (see ***Shaped Pulses*** and ***Selective Pulses***). There is a temptation to think of the excitation profile of a pulse as the Fourier transform of the pulse shape, but this can be very dangerous. Because of the coherence in the system, the detailed response to a weak pulse must be calculated using density matrix treatments.

Off-resonance effects can be removed very efficiently by the use of sequences of pulses that correct for some of the inaccuracies (see ***Composite Pulses***). These are sequences of pulses with different phases, which can dramatically extend or shape the frequency response of the sequence. The design of these pulse sequences is quite sophisticated, and depends on the exact application. For instance, a sequence $(\frac{1}{2}\pi)_x$–$(\frac{4}{3}\pi)_y$–$(\frac{1}{2}\pi)_x$ is very good at taking z magnetization and inverting it, but it is not the best sequence for reversing an xy magnetization to create a spin echo.

4.4 Pulsed Spin Decoupling

For many nuclei, such as ^{13}C, it is convenient to remove proton couplings from the spectrum so that there is a single line for each carbon site in the molecule. Originally this was done with strong CW irradiation (see ***Double Resonance***) or with digital noise modulated rf. The aim is to quantize the protons perpendicular to the direction of the carbon quantization, so that the scalar coupling (which is the scalar product of the proton and carbon vectors) vanishes. Because of off-resonance effects, this works only over a narrow range.

Subjecting the spin to a continuous sequence of pulses works much better (see ***Decoupling Methods***). Several sequences have been developed, with acronyms such as MLEV, WALTZ, and GARP, based on the concepts of composite pulses and refocusing of errors. These provide much better decoupling over a wider range of parameters, and are now standard practice.

4.5 Pulses Acting on Quadrupolar Systems

For a single spin-$\frac{1}{2}$, there is a rigorous and very useful mapping between the observable magnetizations and the components of a vector. For quadrupolar nuclei, those with spin quantum numbers greater than $\frac{1}{2}$, the situation is much more complex, particularly in solids and other rigid systems.

For these nuclei, the interaction of the magnetic quadrupole with the electric field gradient must be considered (see ***Quadrupolar Interactions***). This interaction varies, depending on local symmetry at the nucleus, but it may be tens of megahertz. Therefore, the assumption that the rf field dominates all the interactions no longer holds. However, there are some limiting cases in which the interaction of the nucleus and the rf field can be made relatively simple.

The first case is that in which the quadrupolar interaction is relatively weak. This can occur when the electric field gradient is small, as in symmetric environments, or the quadrupole moment itself is small, as in ^{6}Li or ^{133}Cs. A very important example is the deuterium nucleus in a C–D bonded system, for which the quadrupolar interaction is approximately 150 kHz. For this case, a pulse is still equivalent to a rotation of the frame of reference, and the angular momentum methods used for spin-$\frac{1}{2}$ systems work very well.[12] However, the results are not as intuitively obvious as in the spin-$\frac{1}{2}$ case. For a spin-1 nucleus like deuterium, the echo sequence used is not the $\frac{1}{2}\pi - \pi$ Hahn echo sequence, in which the rf phases are not critical. Rather, the $(\frac{1}{2}\pi)_x$–$(\frac{1}{2}\pi)_y$ sequence is used, which is based on the solid echo sequence. For nuclei with larger spin quantum numbers, there may not even be a good echo sequence. Still, the basic principles of how a pulse affects a system with a small quadrupolar coupling are well-established.

When the quadrupolar interaction is large, there is no general solution. Angular momentum methods are not so useful, since a pulse is no longer equivalent to a rotation of the frame of reference. In many cases, numerical computations are necessary, and the results are difficult to interpret. An example of this is nutation spectroscopy, in which we look at the

response of a system to a pulse of regularly increasing length (see ***Nutation Spectroscopy of Quadrupolar Nuclei***). Some analytical results for spins $\frac{3}{2}$ and $\frac{5}{2}$ have been published,[13] but the general problem is still unsolved.

One case that can be analyzed is that of systems with half-integral spins and strong quadrupolar coupling. For these systems, most of the transitions are very broad and unobservable, but the $-\frac{1}{2} \rightarrow +\frac{1}{2}$ is not affected to first order by the quadrupolar coupling, and remains relatively sharp. This transition can be treated as a two-level system, using the fictitious spin-$\frac{1}{2}$ method. For this central line in a spin-I system, the rf pulse acts in the normal way, but the effective flip angle for a pulse is $\alpha(I + \frac{1}{2})$, rather than α.[14] This has the consequence that small flip angles ($\frac{1}{10}\pi$) are needed to get good quantitative spectra of quadrupolar nuclei such as ^{27}Al (see ***High Speed MAS of Half-Integer Quadrupolar Nuclei in Solids***).

5 CONCLUSIONS

The response of spins to rf fields is central to NMR. Modern pulse NMR consists in using combinations of pulses and delays to manipulate spin systems. The behavior during a delay is more familiar, since we observe this directly in an FID. What happens during a pulse is much less obvious.

The basics are very simple, but capable of provoking almost endless fascination. In most cases, the pulse is equivalent to a rotation of the frame of reference—but this is not necessarily equivalent to a rotation of a magnetization vector in the laboratory frame. What happens in detail to a coupled spin system during this rotation requires a mathematical description, usually based on angular momentum properties of the system. This combination of experiments, theory, simulations, experience, and educated intuition is needed to understand the response of nuclear spin systems to radiofrequency pulses.

6 RELATED ARTICLES

Chemically Induced Dynamic Nuclear Polarization; Composite Pulses; COSY Two-Dimensional Experiments; Decoupling Methods; Double Resonance; Fourier Transform Spectroscopy; Heteronuclear Shift Correlation Spectroscopy; High Speed MAS of Half-Integer Quadrupolar Nuclei in Solids; Multidimensional Spectroscopy: Concepts; Nutation Spectroscopy of Quadrupolar Nuclei; Phase Cycling; Quadrupolar Interactions; Selective Pulses; Shaped Pulses; Two-Dimensional J-Resolved Spectroscopy.

7 REFERENCES

1. A. D. Bain and G. J. Duns, *Bull. Magn. Reson.*, 1993, **15**, 64.
2. S. Schäublin, A. Höhener, and R. R. Ernst, *J. Magn. Reson.*, 1974, **13**, 196.
3. A. D. Bain and J. S. Martin, *J. Magn. Reson.*, 1978, **29**, 125.
4. A. D. Bain and J. S. Martin, *J. Magn. Reson.*, 1978, **29**, 137.
5. O. W. Sørensen, G. W. Eich, M. H. Levitt, G. Bodenhausen, and R. R. Ernst, in *Progress in Nuclear Magnetic Resonance Spectroscopy*, eds. J. W. Emsley, J. Feeney, and L. H. Sutcliffe, Pergamon Press, Oxford, 1983, Vol. 16, p. 163.
6. A. D. Bain, in *Progress in Nuclear Magnetic Resonance Spectroscopy*, eds. J. W. Emsley, J. Feeney, and L. H. Sutcliffe, Pergamon Press, Oxford, 1988, Vol. 20, p. 295.
7. S. Vega, *J. Chem. Phys.*, 1978, **68**, 5518.
8. A. D. Bain, *J. Magn. Reson.*, 1984, **56**, 418.
9. G. Bodenhausen, H. Kogler, and R. R. Ernst, *J. Magn. Reson.*, 1984, **58**, 370.
10. A. D. Bain, *J. Magn. Reson.*, 1980, **39**, 335.
11. P. Meakin and J. P. Jesson, *J. Magn. Reson.*, 1973, **10**, 290.
12. B. C. Sanctuary and T. K. Halstead, *Adv. Magn. Opt. Reson.*, 1990, **15**, 79.
13. P. P. Man, *Mol. Phys.*, 1993, **78**, 307.
14. I. Solomon, *Phys. Rev.*, 1958, **110**, 61.

Biographical Sketch

Alex D. Bain. *b* 1948. B.Sc., 1970, Toronto, Canada; M.Sc., 1972, University of British Columbia; Ph.D., 1975, Cambridge. First learned much NMR from Ph.D. supervisor, Ruth Lynden-Bell. After postdoctoral work, employed as Applications Spectroscopist by Bruker Spectrospin Canada for six years. Since 1987, Professor of Chemistry, McMaster University. Approx. 50 publications. Research interests: spin dynamics, relaxation, chemical exchange, statistical methods.

Relaxation Theory: Density Matrix Formulation

Alfred G. Redfield

Brandeis University, Waltham, MA, USA

1	Introduction	1
2	Review of the Literature	1
3	Strong Relaxation	2
4	Ensembles, Systems, Operators, and Representations	2
5	The Density Matrix and the Relaxation Matrix	3
6	Transition Rates	4
7	Linewidths and Off-Diagonal Elements	5
8	Effects of rf Fields: Spin Locking	5
9	Cross-Correlation Effects	5
10	Transverse Relaxation Rates and Dynamic Shifts	6
11	Derivation of the Relaxation Equation	7
12	Conclusions	7
13	Related Articles	8
14	References	8

1 INTRODUCTION

This article introduces nuclear spin relaxation primarily in the *weak limit*, by which we mean the kind of relaxation theory that is also called the perturbation limit, or the motionally narrowed limit. This is the most common form of relaxation in NMR.

Generally any theoretical treatment of relaxation divides the equations of motion of the spin system into two parts: first, a static or nearly static part consisting of the Zeeman energy, the spin–spin couplings (usually also including the dipolar energy between spins, and quadrupolar interactions, for rigid solids), and some other terms depending on the system; and second, a randomly time-varying part that produces relaxation. The latter can often be described approximately by two parameters: a size in energy units of $\hbar\omega_i$, and a time τ_c or 'correlation time', which is a characteristic time, usually the time that it takes for the random interaction to change by an amount that is unpredictable but is comparable to $\hbar\omega_i$. For example, when two nuclear spins in a molecule in solution relax mainly via the dipolar interaction between each other, ω_i is of the order of 10^5 s^{-1} for vicinal protons, decreasing as the inverse cube of the distance for further neighbors, and τ_c is of the order of the time for the interspin vector to rotationally diffuse by about one radian away from any initial direction. Neither ω_i nor τ_c can be defined precisely for every problem, although for some important problems they can be usefully defined. For large biopolymers, τ_c is of the order of 10^{-8} s, and it is roughly proportional to molecular weight.

The weak limit is almost always valid if $\omega_i\tau_c \ll 1$, but a more useful criterion is that the relaxation rate (such as ${T_1}^{-1}$ or ${T_2}^{-1}$), calculated using the weak limit formulas, be small compared to ω_i. A useful rule of thumb is that transverse relaxation times T_2 are of the order of ${\omega_i}^2\tau_c$ and longitudinal rates are of the order of ${\omega_i}^2\tau_c/(1 + \omega^2{\tau_c}^2)$, where ω is a nuclear spin frequency, or difference in nuclear spin frequencies, depending on the relaxation process under consideration. It is commonplace that $\omega\tau_c$ be greater than one for moderately large molecules, and it also can happen that $\omega_i\tau_c$ is greater than one, so that T_2 processes cannot be treated using the weak limit, whereas, in the same system, T_1 processes can be. In fact, T_1 processes can almost always be treated by the weak limit, with the exception of experiments, usually field cycling, performed at low field; and for conceptually similar experiments in the rotating frame such as studies of slow motions described in ***Ultraslow Motions in Solids***.

In the present article, we shall introduce this topic in as simple a way as possible, in the hope of demystifying it for the inexperienced reader. We do not attempt a thorough review or much discussion of the different classes of relaxation that can occur. Even setting up the main Hamiltonian and the smaller time-dependent Hamiltonian requires many assumptions and some intuition about the system. On the other hand, we shall mention a number of topics not found in general texts. We shall not discuss details of applications since these are treated elsewhere in this Encyclopedia. Fortunately, the list of relaxation interactions is not long: dipolar relaxation already mentioned; similar relaxation due to electron spin–nuclear spin interaction in paramagnetic materials; spin–rotation interaction, especially in gases but also in smaller molecules in solution; and, for nuclei other than spin-$\frac{1}{2}$, the fluctuating electric quadrupolar interaction.

The kind of theory we have been describing is called *semiclassical*, because the time dependence of the perturbing interaction is generally described by classical variables such as distances. Relaxation theories can be, and generally are, also set up completely quantum mechanically. Unfortunately, the character of the time dependences of most relaxation interactions cannot be calculated from first principles, so that most relaxation theories are semiclassical. An exception is relaxation by lattice vibrations in solids or electron spins in metals, although even in these cases theories are likely to be somewhat phenomenological. Quantum relaxation theory also helps to justify some apparently arbitrary assumptions of the semiclassical theory.

2 REVIEW OF THE LITERATURE

The original Bloch equations,[1] containing two relaxation times, hinted at the probable richness of information contained in relaxation theory. ${T_1}^{-1}$ was the rate at which energy changes would occur, and this more demanding process was expected to be slower than T_2 (line-broadening) processes, which do not require energy transfer in the absence of an rf field. The basic picture of nuclear relaxation was virtually completed with the masterful paper by Bloembergen, Purcell, and Pound (BPP), connecting transition rates between levels with spectral densities, and T_2 processes primarily with spectral densities at zero frequency.[2] By symmetry, T_1 and T_2 should be equal in the low-field limit and also, since T_2 must be a continuous function of B_0, $T_1 = T_2$ in the limit of short correlation time, $\omega_0\tau_c \ll 1$ (where ω_0 is the Zeeman frequency γB_0).

In early papers, it was assumed that the relaxation by spin–spin interactions in rigid solids would produce straightforward transverse relaxation, but this view was

incorrect. The dipolar spin–spin interaction has to be treated separately from weak relaxation mechanisms in a rigid solid, and it can participate in a wide variety of interesting phenomena.

The next important development was the introduction of the density matrix to describe the system to be relaxed, and the satisfactory calculation of T_1 and T_2 for a single spin, by Wangsness and Bloch. This treatment was then restated and generalized by various workers. Kubo and Tomita provided a theory based on the general theory of irreversible processes; Bloch treated relaxation in the rotating frame, among other things; and the present writer provided a version of the theory that may be useful to the novice reader. During this same period, Solomon was performing his important experiments on the HF molecule, providing a systematic basis for discussion of cross-relaxation theory (NOE) as treated in the papers of Solomon and Bloembergen. The topic has been treated in several texts, reviews, and monographs,[1–15] of which Abragam's may be the most lucid introduction to the operator version of the formalism.[3,6,14] In the present article, we use the notation of our own work[15] and of Slichter[4] as far as possible, while maintaining consistency with the other articles in this Encyclopedia. Excellent reviews of applications of weak and strong relaxation theories can be found in the books edited by Muus and Atkins[8] and by Tycko.[11]

A somewhat separate, more sophisticated and general approach has been developed by several theorists, based primarily on the work of Kubo and Tomita, and of Morita.[8,10,12,13] The reader should be aware that there is only one underlying theory, and that the independent formalisms of various workers mentioned are all valid, and differ only in sophistication and in suitability for different problems.

3 STRONG RELAXATION

Strong relaxation theories are not presented here, but we describe them briefly. Many such theories are generalizations of the early well-known treatment of McConnell and of Slichter in which the chemical shift of a single spin is assumed to change at a random rate between two definite values, as a model for a dynamic change between two major average conformations. Generally, weak mechanisms such as dipolar relaxation are grafted onto such a theory, and the entire spin-dynamic problem can be solved analytically, as described in ***Chemical Exchange Effects on Spectra***. Sometimes essentially the same kind of theory is set up with an infinite number of conformational states and shifts. An important example is the simulation of lineshapes for deuterium NMR in membranes and liquid crystals. The type of problem discussed in ***Ultraslow Motions in Solids*** is also in this class.

All such strong relaxation mechanisms can become weak in the limit where the correlation time becomes sufficiently short, as already implied.

Another class of strong relaxation mechanisms is that of the Orbach processes, in which excited electronic states are important.[8] This type of relaxation is not important for NMR problems, except perhaps for paramagnetic solids.

Finally we mention Anderson theory,[8] which was first used to describe the exchange narrowing[3] of electron spin resonances in solids. In NMR, it is adapted to estimate linewidths of dilute heteronuclei in solids,[3] and processes like solid state cross relaxation and magnetization (spin) diffusion for which perturbation theory is not applicable, but that are nevertheless slow.[7]

4 ENSEMBLES, SYSTEMS, OPERATORS, AND REPRESENTATIONS

We now describe the elements of models for relaxation theories. Here and throughout this article we only outline those topics that are relatively standard. The reader who is not familiar with topics mentioned is urged to refer to the literature surveyed above and to standard texts on quantum and statistical physics.

A typical relaxation theory treats the average behavior of an *ensemble* of systems. Most generally, each member of the ensemble is a replica of the NMR lab, according to Gibbs, but an almost equivalent view is that each member of the ensemble is represented by a single experiment on the same system, out of a large ensemble of experiments in which the sample is prepared as far as possible in the same way each time. A gentler version of an ensemble can be that it represents the average behavior of many pieces of a large sample of N particles ($N \approx 10^{23}$), each piece having fewer than N particles, but still a great many, say 10^{12}. Finally, it is useful sometimes, though not strictly correct, to view each member of the ensemble as one molecule out of the collection (ensemble) of molecules being studied. The latter view cannot be used for a rigorous treatment of intermolecular or collective effects such as intermolecular NOE or 'radiation damping'. In any case, it is most important to be entirely clear as to what system one is defining, before starting.

As already indicated, a starting point for any semiclassical weak relaxation theory is to write the Hamiltonian $\hat{\mathcal{H}}$ in the form

$$\hat{\mathcal{H}} = \hat{\mathcal{H}}_0 + \hat{K}(t) \tag{1}$$

where $\hat{\mathcal{H}}_0$ is the main Hamiltonian, and relaxation is produced by the randomly varying part $\hat{K}$. It is specifically assumed that $\hat{K}$ has zero value after being averaged over the ensemble: $\langle \hat{K}(t) \rangle = 0$, where the angular brackets always denote the ensemble average. It is important to remember that $\hat{K}$ is assumed to be different for each member of the ensemble.

It is useful to note explicitly that $\hat{K}$ can usually be written as the sum of more or less independent terms, each of which can be written (for one member of the ensemble) as a spin operator times a function of classical variables (usually internuclear distances, and angles defining directions of internuclear vectors):

$$\hat{K} = \sum_q H_q(t) \hat{K}^q \tag{2}$$

The H_q are ordinary real random functions of the time. They can be terms such as those of the dipolar interaction of BPP, for example $\hbar^2\gamma^2(1 - 3\cos^2\theta)/r^3$. The $\hat{K}^q$s corresponding to this H_q would be the operators $\hat{I}_{1z}\hat{I}_{2z}$ and $-\frac{1}{4}(\hat{I}_1{}^-\hat{I}_2{}^+ + \hat{I}_2{}^+\hat{I}_1{}^-)$. In this case, the classical variable H_q is random because θ and

r vary randomly, in solution. The elements of $\hat{K}^q$ may also be functions of the time for a time-dependent *representation* of the system, discussed below. For weak relaxation, it turns out that all we need to know about $\hat{K}$ are the auto- and cross-correlation of the functions $\langle H_q(t)H_{q'}(t+\tau)\rangle$. These will be discussed later.

The quantum Hamiltonian is an operator, and the thing on which it operates is a wavefunction:

$$\psi = c_n(t)u_n \tag{3}$$

where the c_n are complex numbers that generally vary with time, and the u_n are a complete set of *basis functions*. There are rules concerning how to set up such a complete set, and how they must change under transformations of various kinds. For spin problems, we mention four, out of many, ways to define them.

1. The u_n can be wavefunctions that specify the orientation (or m_z, for $S > \frac{1}{2}$) of each spin in the system. These are eigenfunctions of the Zeeman Hamiltonian and we call this the 'Zeeman' representation.
2. The u_n can be eigenfunctions of the entire main Hamiltonian $\hat{\mathcal{H}}_0$, with energy eigenvalues E_n. $\hat{\mathcal{H}}_0$ includes, in addition to the Zeeman Hamiltonian, spin–spin coupling for molecules in solution. Deriving these u_n from the Zeeman ones can be easy—or it can be very complicated—but nevertheless it is useful to talk about them. This is the 'Schrödinger' representation. The terms c_n generally depend on time in this representation, as exp (i$E_nt/\hbar$), modified by relaxation.
3. The u_n can be appropriate for a rotating frame transformation. For such a transformation, most of the Zeeman Hamiltonian is removed, and the u_n are the same as for case 1 except that the new u_n are equal to those of case 1 multiplied by exp $(-\mathrm{i}\omega_j t)$, where ω_j are the sums of, or differences between, nuclear resonance frequencies of relevant spins. This could be called the 'product operator' representation, since it is used for product operator theory.
4. The representation may be one in which the entire average Hamiltonian $\hat{\mathcal{H}}_0$ is transformed away. This is the 'Heisenberg' or 'interaction' representation. It is most convenient for setting up relaxation theory. In this representation, the c_n are time-independent except for the relaxing effect of $\hat{K}(t)$, and the new u_n are equal to those of the Schrödinger representation times exp $(-\mathrm{i}E_nt/\hbar)$. All operators such as $\hat{K}(t)$ are similar to their form in the Schrödinger representation, except that their off-diagonal elements are time-dependent.

The wavefunction ψ is completely specified by specifying the basis u_n and all the c_n. The latter set of numbers is viewed as a *vector in Hilbert space* in analogy to the set (x, y, z) of coordinates that represents the real-space position vector of a particle.

Before proceeding, we note that $\hat{\mathcal{H}}_0$ can include time-varying things such as rf pulses or field gradients. For the most part, we ignore such fields. Equation (1) also omits any semiclassical interaction that restores thermal equilibrium. The equation should include another friction term that will do so.[8,13,16] Otherwise, the energy of each system will increase continuously, toward infinite temperature. This is a consequence of the fact that $\hat{K}(T)$ does not have a temperature associated with it.

In fact, *nuclear spin relaxation theory is virtually identical to Brownian motion theory*. It deals with Brownian-like motion of vectors, in Hilbert space, that describe the spin system.[8,10] In each time of the order of the correlation time τ_c, an individual system wavefunction changes very little, in analogy to the effect of single collisions on a large particle undergoing Brownian motion. The interested reader should read the last chapter of Reif's text[17] to see how Brownian motion of relatively large particles is related to fluctuating forces of the surrounding medium—in particular to the spectral densities (see below) of these forces. The analogy to Brownian motion may reassure the novice reader that nuclear spin relaxation involves nothing really new. In particular, Brownian motion theory always contains a presumed force of friction, and Einstein showed how the friction coefficient must be related to the diffusion coefficient, which is a manifestation of the fluctuating forces of collisions. Frictional forces were not described as such in early papers.[15,16]

The statement in the above paragraph describes an *analogy*, which should not be confused with the important *applications* of NMR to the study of real diffusion. These include studies of translational diffusion, dating back to Hahn's original papers on spin echoes, and of rotational diffusion, starting with BPP (reviewed, for example, in ***Relaxation Effects of Chemical Exchange***).

5 THE DENSITY MATRIX AND THE RELAXATION MATRIX

The density matrix is defined by[4]

$$\sigma_{ij} = \langle c_i c_j^* \rangle \tag{4}$$

where * here denotes the complex conjugate. Notice that it is a matrix whose elements depend on what representation we are using, which has to be kept in mind during any discussion or calculation. The density matrix can be shown to transform in the same way as any standard quantum operator, under change of representation, so it can be thought of as an object $\hat{\sigma}$ that is represented in some particular representation by a matrix σ_{ij}. Thus $\hat{\sigma}$ is often referred to as the density operator, even though it does not seem to operate on anything.

The symbol $\hat{\rho}$ was originally used for the density matrix of an entire system, including coordinates of nonspin variables. The notation $\hat{\sigma}$ was introduced to denote a "reduced" density matrix that describes the nuclear spin system alone. Often, as for example in the product operator formalism, $\hat{\sigma}$ is written as a sum of products of spin operators; this is what we mean by an operator formalism. Use of this language implies that correlations between spin orientations and molecule or lattice variables are, on the average, not large. This assumption has to be dropped for strong relaxation theories. In the absence of relaxation, $\hat{\sigma}$ obeys the quantum version of the Liouville equation:

$$\frac{\mathrm{d}\hat{\sigma}}{\mathrm{d}t} = \frac{\mathrm{i}}{\hbar}[\hat{\sigma}, \hat{\mathcal{H}}_0] \tag{5a}$$

where $[\hat{\sigma}, \hat{\mathcal{H}}_0]$ denotes the commutator bracket $\hat{\sigma}\hat{\mathcal{H}}_0 - \hat{\mathcal{H}}_0\hat{\sigma}$.

The Schrödinger representation that we will use is not convenient for actual calculations, but is useful in developing and discussing the general theory. In this representation, the basis functions u_n are exact eigenvalues of $\hat{\mathcal{H}}_0$, as already mentioned. The diagonal element σ_{ii} of $\hat{\sigma}$ is simply the probability that the energy level E_i is occupied. As expected, the Liouville equation predicts that σ_{ii} will be time-independent, a consequence of the fact that $\hat{\mathcal{H}}_0$ is diagonal in this representation. The elements of $\hat{\sigma}$ represent the entire set of possible physical observables of the system. These are not the same things that we may observe in practice, and in NMR there is usually really only one quantity that we observe. It is the transverse magnetization in the fixed x direction, $\hat{M}_x$. Its expectation value is given by $\mathrm{Tr}(\hat{M}_x\hat{\sigma})$, where Tr means a sum over diagonal elements. It is the sum of many off-diagonal elements of $\hat{\sigma}$ in the Schrödinger representation, because $\hat{M}_x$ has many off-diagonal elements in this representation, for a system of several spins. From the Liouville equation, the time dependence of an off-diagonal element σ_{ij} is given by a constant times $\exp[\mathrm{i}(\omega_i - \omega_j)t]$. Each spectral line in a directly observed spectrum is a manifestation of a coherence represented by an off-diagonal density matrix element, damped, of course, by relaxation not included in equation (5a). However, typically $\hat{\sigma}$ has many more off-diagonal elements than are observed in this way; for a system of 10 protons, for example, it has only 1024 diagonal elements, but roughly a million off-diagonal elements. The vast majority of the latter are both uninteresting and difficult to study. Elements that are not directly observable in a simple free induction decay are called forbidden, and of these the most useful are the lower order (zero, double, triple, etc.) 'multiple quantum' coherences.[6]

As might be expected, the result of weak relaxation theory is an equation for $\hat{\sigma}$ that is a direct generalization of Bloch's equations:

$$\frac{\mathrm{d}\hat{\sigma}}{\mathrm{d}t} = \frac{\mathrm{i}}{\hbar}[\hat{\sigma}, \hat{\mathcal{H}}_0] + \hat{R}(\hat{\sigma} - \hat{\sigma}^0) \tag{5b}$$

where $\hat{\sigma}^0$ is the thermal equilibrium value of $\hat{\sigma}$, equal to a constant times $(\exp -\hat{\mathcal{H}}_0/RT)$. The extra term $\hat{R}(\hat{\sigma} - \hat{\sigma}^0)$ is shorthand for a matrix whose ij element is $\Sigma_{i'j'}R_{iji'j'}(\sigma_{i'j'} - \sigma_{i'j'}{}^0)$; thus the *relaxation matrix* $\hat{R}$ is a fourth-order matrix. We shall discuss it using the Schrödinger representation here. The elements of $\hat{\sigma}$ are analogous to the magnetizations in Bloch's equations, and the term $\mathrm{i}[\hat{\sigma}, \hat{\mathcal{H}}_0]/\hbar$ is analogous to $\gamma(\boldsymbol{B} \times \boldsymbol{H})$. The coefficients in $\hat{R}$ are extensions of Bloch's rates $T_1{}^{-1}$ and $T_2{}^{-1}$, and the term $\hat{\sigma}^0$ is similar to his M_0.

As already mentioned, frictional forces must exist that return the system to equilibrium, and the term $-\hat{R}\hat{\sigma}_0$ was arbitrarily inserted to account for these. As included in equation (5b), it ensures that $\mathrm{d}\hat{\sigma}/\mathrm{d}t$ is zero at equilibrium, when $\hat{\sigma} = \hat{\sigma}^0$. Friction forces are connected with the memory of the surroundings: for example, as a spin precesses in matter, the interaction represented as relaxation by $\hat{\mathcal{H}}_1(t)$ will slightly deform the matter to produce a small local field at the spin. The deformation is analogous to the deformation in a bed when you lie on it. As the spin moves, this deformation follows it, but not instantly. There is a small lag, and this produces a memory field that is exactly right to make the system approach equilibrium.[8] The $\hat{R}\hat{\sigma}^0$ term can also be fully justified by a quantum derivation,[16] or by taking spin interaction into account for the lattice's motion.[17]

6 TRANSITION RATES

The semidiagonal element R_{iijj} is simply the rate constant for the transition from level i to level j. The theory of these transition rates was already fully implied in BPP, not requiring a density matrix for its description. Thus we can redefine σ_{ii} as a probability p_i that level i is occupied, and R_{iijj} as a transition rate w_{ij} from level j to i, writing equations of the form

$$\frac{\mathrm{d}p_i}{\mathrm{d}t} = \sum_j w_{ij}(p_j - p_j^0) \tag{6a}$$

where $p_j{}^0$ is the thermal equilibrium value of p_j, proportional to $\exp(-E_j/kT)$. The form of equation (6a) is based on the relaxation equation, equation (5b), and the w_{ij} are symmetric: $w_{ij} = w_{ji}$, as defined in the original theory.[15] The w_{ij} are not identical to what are normally considered transition probabilities, which occur in the so-called master equation:

$$\frac{\mathrm{d}p_i}{\mathrm{d}t} = \sum_j (W_{ij}p_j - W_{ji}p_i) \tag{6b}$$

Here, detailed balance requires $W_{ij}/W_{ji} = \exp[-(E_i - E_j)/kT]$. Equation (6b) is also the equation for standard first-order chemical kinetics, if p_i is replaced by the molarity $[i]$ of systems in spin level i, and the W_{ij} are replaced with first-order rate constants usually denoted by k_{ij} or the equivalent.

Since the matrix w_{ij} is symmetric, whereas W_{ij} is not, equation (6a) is inconsistent with the more general equation, equation (6b), and with detailed balance. Apparently, the convenient form of relaxation theory described by equation (6a) *is valid only in the high-temperature approximation*, where $(E_i - E_j)/kT \ll 1$. Fortunately, this approximation is almost always obeyed for NMR experiments. In that case, it is reasonable to specify W_{ij} by

$$W_{ij} = w_{ij}\left(1 - \frac{E_i - E_j}{2kT}\right) \tag{7}$$

which preserves detailed balance within the high-temperature approximation. The problem with the semiclassical theory mentioned above can be avoided, when the high-temperature approximation is invalid, by either using the completely quantum version of the theory,[15] or by augmenting the semiclassical model of equation (1) with a memory, or friction term, as already mentioned.[13,16] A simple example of a memory effect is 'radiation damping' (see below).

For a large and important class of experiments such as NOESY, the situation is even simpler. With important exceptions such as methyl groups, there are no complicated correlations between spins, and the important evolution by relaxation is described by diffusion of magnetization among spins ('spin diffusion'). Relaxation is described by

$$\frac{\mathrm{d}m_i}{\mathrm{d}t} = \sum_j s_{ij}(m_j - m_j^0) - r_1(m_i - m_i^0) \tag{6c}$$

where m_i is the z component of magnetization of the ith spin species, m_i^0 is its thermal equilibrium value, r_i is the relaxation rate of the ith spin due to all mechanisms, and the s_{ij} are cross relaxation rates between spins. Note that s and r are often denoted by σ and ρ in the literature. Furthermore, the term 'relaxation matrix' is often used in the literature of these problems, to denote the collection of relaxation rates; it is not to be confused with the more complicated $\hat{R}$ matrix of the full theory.

An equation similar to equation (6c) can also describe the ROESY experiment, with redefinition of m_i as magnetization along the effective field of spin i. We shall briefly return to ROESY below.

All these versions of NMR kinetic theory are described by first-order differential equations, whose evolution can be described by sums of simple normal modes, each having a single relaxation time. These modes include in principle all the m_i (or possibly σ_{ii}) and are time consuming to calculate. Magnetization diffusion and relaxation viewed in terms of normal modes has been applied by T. L. James to macromolecules. However, an equivalent approach is to ask how a localized departure from equilibrium, at a single spin i, spreads to other spins as time passes. This 'Green's function' approach is perhaps more economical in computer time than the normal mode approach, and it may provide a rather direct and more intuitive model for the evolution of diagonal and cross peaks in NOESY and ROESY. Routines that can perform such a calculation are included in some NMR data analysis programs. The normal mode approach is more useful for problems having a high degree of symmetry.

7 LINEWIDTHS AND OFF-DIAGONAL ELEMENTS

In the Schrödinger representation, any element of σ_{ij} of $\hat{\sigma}$ varies as exp (i$\omega_{ij}t$), neglecting relaxation, where $\omega_{ij} = (E_i - E_j)/\hbar$. The elements of $\hat{R}$ are time-independent (only for this representation!). A *secular* term $R_{ii'jj'}$ is one for which $\omega_{ii'} = \omega_{jj'}$. All the rates in the previous section are thus secular, because all the ω_{ii} and ω_{jj} are zero. Likewise, terms of the relaxation matrix $\hat{R}$ terms R_{ijij}, which are rather direct analogs to Bloch's rate ${T_2}^{-1}$, are secular. The minimum full linewidth of a spectral transition between levels i and j is R_{ijij}/π, just as the full linewidth for Bloch's equations is $(\pi T_2)^{-1}$. Thus, if all relaxation terms of equation (5b) are ignored except R_{ijij} then σ_{ij} varies as a damped exponential, exp (i$\omega_{ij}t$ + $R_{ijij}t$). The sign of R_{ijij} is negative (see below).

Those terms of the relaxation matrix $\hat{R}$ that are not of the form R_{iijj} or R_{ijij} can mostly be ignored. That is fortunate, because $\hat{R}$ has roughly 10^{12} elements for a 10-proton problem, for example.

Specifically, any element $R_{ii'jj'}$ connecting any density matrix element $\sigma_{ii'}$ to another one $\sigma_{jj'}$ can often be ignored provided

$$|\omega_{ii'} - \omega_{jj'}| graphic |R_{ii'jj'}| \tag{8}$$

If equation (8) is strongly obeyed (if the equation is valid with $>$ replaced by $\gg$) then the element of $\hat{R}$ being considered is a time-independent relaxation term connecting two elements of $\hat{\sigma}$ that are varying rapidly compared with the element of $\hat{R}$. These terms are called 'nonsecular', and they are expected to perturb the final solution by an amount equal to the ratio of the right-hand to the left-hand side of equation (8), compared with secular terms of the same size. The name and idea of secular and nonsecular perturbations date back to classical mechanics, and were invoked by Van Vleck in truncating the dipolar Hamiltonian in order to calculate moments of resonance lines.

Terms in $\hat{R}$ for which equation (8) is only weakly obeyed, or corresponding terms in operator-based theories of relaxation,[14] should always be included in any solution of a relaxation problem. The effect of such terms can be dramatic, and can unexpectedly produce narrowing, and collapse of multiplets. A simple example is the non-observance of ^{14}N splitting of the proton resonances of NH groups, due to rapid electric quadrupole relaxation of the ^{14}N spin. The N–H J splitting is suppressed by rapid relaxation coupling of coherences of the product operator form $\hat{I}_z\hat{S}_x$, where I is ^{14}N and S is the NH proton. Of course, this example, like many, does not require density matrix relaxation theory in order to be understood. This kind of relaxation is called 'narrowing of the second kind'.[3]

8 EFFECTS OF RF FIELDS: SPIN LOCKING

The consideration of nonsecular terms in $\hat{R}$ became richer when it was realized that the elements of $\hat{\sigma}$ can have their time dependence altered by the presence of rf fields, such as in a spin lock experiment. Off-diagonal elements can be driven to have periodic variation at the rf frequency, rather than their natural frequencies, and elements of $\hat{R}$ that connect two elements of σ which have slightly different frequencies become secular. Thus, rf fields can alter the relaxation behavior, as first shown by Vold and Vold. Here it is assumed that $\hat{R}$ itself is not affected by the rf field. A commonplace example of this effect is in the ROESY (CAMELSPIN) experiment of Bothner-By. Magnetizations of different spins cross relax in this experiment because they are spin locked at the same rf frequency, and these magnetizations correspond directly to off-diagonal density matrix elements that would evolve at different frequencies, and not cross relax, in the absence of the spin lock. It must be emphasized, however, that the ROESY experiment was undoubtedly invented and analyzed independently of the theory outlined in the present article.

The phenomena described in the last paragraph are quite general. Another useful measurement can be made on systems that are expected to have dynamic, chemical, or conformational changes taking place on a timescale in the range of 10 ms or slower. Then it is of interest to study the variation in the transverse relaxation time with respect to the spin-locking rf field intensity $\omega_1 = \gamma B_1$. This relaxation time is generally called $T_{1\rho}$, since the process it describes resembles a T_1 process, but in the rotating frame. The theory of $T_{1\rho}$ can be treated using spectral densities and density matrix theory, following Bloch, or it can with equal validity be treated using the type of theory reviewed in ***Chemical Exchange Effects on Spectra***. In general, $T_{1\rho}$ starts to decrease below its value at zero B_1, (which is the same quantity as T_2) at field intensities where $\omega_1\tau_c$ approaches one. Here τ_c is the correlation time for the slow perturbation. Such a measurement yields an estimate of this correlation time, and also the general size of the shift ω_i associated with the perturbation.

9 CROSS-CORRELATION EFFECTS

An understanding of the effect of cross correlations between the random functions $H^q(t)$ in equation (2) can help to provide interesting information about a system from its linewidths or transition rates. This topic is reviewed in ***Relaxation Processes: Cross Correlation and Interference Terms***. An important example is the often-seen unequal linewidth of ^{13}C (or ^{15}N) multiplets, due to correlation and interference between the dipolar interaction and the CSA of the ^{13}C nucleus. A rough estimate of the CSA can be obtained from this effect.[5]

To understand the general usefulness of cross-correlation effects, consider the dipolar interaction in a hypothetical spin system ABC, where nuclei A, B, and C are nonequivalent protons and the distances A to B, and B to C, are assumed fixed and equal. If the angle ABC could vary randomly with equal probability for all angles then the spectrum of B would show an uninteresting multiplet due to the uncorrelated dipolar interactions between A and B, and B and C. If, instead, the system is rigid and linear, with the angle ABC equal to 180°, the dipolar interactions mentioned above are highly correlated. If spins A and C are oriented oppositely for the rigid linear case, their dipole fields at B will cancel; if spins A and C are both oriented in the same direction, the dipolar fields always add. Thus, the centerlines of B's multiplet will be narrow, and the outer lines will be four times as broad as in the uncorrelated case.

An interesting example of a correlation effect is 'radiation damping'. This is due to the rf fields, fluctuating and induced, from the probe pickup coil. The effect is misnamed, because no radiation is involved. It is a correlated effect, because the field felt at each spin is virtually the same as at every other spin. This means that these fields cannot directly change the magnitude of total nuclear magnetism, only its direction, if rf inhomogeneity of the probe coil is ignored.

10 TRANSVERSE RELAXATION RATES AND DYNAMIC SHIFTS

Let us focus on two levels i and j giving an observable signal, or a forbidden coherence, at a frequency $\omega_{ij} = (E_i - E_j)/h$, where E_i and E_j are the energies of the two levels. We shall not write down the form for the elements of $\hat{R}$ in general, which can be found in many texts, as well as in other articles in this Encyclopedia. However, it is of interest to write the expressions for elements of $\hat{R}$ that are most closely analogous to Bloch's relaxation rates as explained above. The term similar to $T_1{}^{-1}$ is R_{iijj}, given by

$$\tfrac{1}{2}\, T_1^{-1}\rangle R_{iijj} = J_{ijij}(\omega_{ij}) + J_{jiji}(\omega_{ji}) \qquad (9a)$$

Here $T_1{}^{-1}$ is the apparent rate that would be measured for the spectral line at ω_{ij} by a selective saturation–recovery experiment, and '>' indicates that the actual apparent rate could be shortened by relaxation to levels other than i and j. The factor of $\frac{1}{2}$ multiplying $T_1{}^{-1}$ is inserted because Bloch's $T_1{}^{-1}$ is twice the rate constant connecting two levels in a two-level master equation, as one can verify by writing and solving such a master equation for the recovery of M_z. The Js are Fourier transforms of correlation functions of $\hat{K}$. They are called spectral densities, and are given in general by

$$J_{iji'j'}(\omega) = \int_{-\infty}^{\infty} \mathrm{e}^{\mathrm{i}\omega\tau}\, \langle K_{ij}(t) K^*_{i'j'}(t+\tau)\rangle \,\mathrm{d}\tau \qquad (10)$$

with * here denoting the complex conjugate. The expressions within the ensemble-average brackets $\langle\ \rangle$ are cross-correlation functions, or autocorrelation functions if $i', j' = i, j$. These are assumed to be real and independent of t, and are also assumed to be even functions of τ (that is, unchanged by the substitution of τ by $-\tau$). From these assumptions, it is easy to show that the right-hand side of equation (9a) is real, as it has to be.

The term of $\hat{R}$ most closely similar to Bloch's $T_2{}^{-1}$ is

$$\begin{aligned} T_2^{-1}\rangle R_{ijij} = {} & 2J_{iijj}(0) - J_{iiii}(0) - J_{jjjj}(0) \\ & - J_{ijij}(\omega_{ji}) - J_{jiji}(\omega_{ji}) \\ & - \sum_{m\neq i,j} [J_{mimi}(\omega_{mi}) + J_{mjmj}(\omega_{mj})] \end{aligned} \qquad (9b)$$

This equation is much simpler than it appears, and can be obtained from the original equations for the $\hat{R}$ matrix given elsewhere[6] and in ***Dynamic Frequency Shift***; ***Relaxation Processes: Cross Correlation and Interference Terms*** and ***Relaxation Theory for Quadrupolar Nuclei*** by rearranging sums, and substitution of equation (9a).

The first three terms on the right-hand side of equation (9b) can be rewritten [by substitution with equation (10)] as

$$\begin{aligned} & 2J_{iijj}(0) - J_{iiii}(0) - J_{jjjj}(0) \\ & \quad = -\int_{-\infty}^{\infty} \langle \Delta_{ij}(t)\Delta_{ij}(t+\tau)\rangle \,\mathrm{d}\tau \end{aligned} \qquad (11)$$

where $\Delta_{ij}(t) = K_{ii}(t) - K_{jj}(t)$. The quantity Δ_{ij} is just the fluctuating part of the first-order extra splitting between levels i and j produced by the perturbation $\hat{K}(t)$ for a member of the ensemble, and equation (11) is the zero-frequency spectral density associated with this fluctuation, or its 'motionally averaged' relaxation rate. This *adiabatic* term usually dominates relaxation in large molecules. Equation (11) also provides an important refinement over the rule of thumb above that transverse relaxation rates are proportional to $\omega_{\mathrm{i}}{}^2\tau_{\mathrm{c}}$, where $\omega_{\mathrm{i}}{}^2$ is approximately the size of squares of elements of $\hat{K}$. For T_2 processes, it is the size of fluctuating *differences* between diagonal elements of $\hat{K}$ that matters. The adiabatic contribution to $T_2{}^{-1}$ is often denoted by $(T_2{}^*)^{-1}$ (here of course, * does not indicate the complex conjugate).

For example, in larger proteins, the dipolar interaction between ^{15}N and H, for NH groups of fully ^{15}N-labeled proteins, might be expected to dominate linewidths. However, for double quantum evolution, as in heteronuclear double quantum correlation experiments, the dominant $\hat{I}_z\hat{S}_z$ part of the dipolar interaction does not contribute to widths, because it affects the two levels connected in the zero, and the double, quantum coherences equally. Thus the double quantum transition connects levels $m_I = m_S = +\frac{1}{2}$ with levels $m_I = m_S = -\frac{1}{2}$, and the expectation value of the operator $\hat{I}_z\hat{S}_z$ is the same for both of these levels. The spacing between these two

levels does not fluctuate as the molecule tumbles, even though the energy of each level fluctuates; they fluctuate together (as far as this particular dominant interaction is concerned). Simple reasoning of this kind is often useful in thinking about linewidths.

The next two terms of equation (9b) are equal, and the sum of their real parts is identical to R_{iijj} [see equation (9a)]. The real part often dominates, and its presence in equation (9b) indicates that T_1 processes will always contribute to T_2 processes. However, comparing with equation (9a), the contribution is only half of the minimum value ${T_1}^{-1}$. The origin of the factor $\frac{1}{2}$ can be seen for a model system consisting of a single spin interacting with a fluctuating field $\boldsymbol{h}(t)$. T_1 processes (longitudinal spin flips) are produced by both of the transverse components of $\boldsymbol{h}(t)$, namely h_x and h_y. However, transverse relaxation of magnetization M_x, for example, cannot be produced by h_x, only by h_y, because h_x is along M_x. Transverse relaxation can also be produced by h_z, but this latter contribution is the adiabatic kind of relaxation discussed above, represented by the first terms in equation (9b).

The terms of equation (9b) discussed so far are often described in the older literature by the equation ${T_2}^{-1} = ({T_2}^*)^{-1} + \frac{1}{2}T_1$.

The real part of the last terms expresses the obvious fact that T_1 relaxation to other levels m, in a multispin or $S > \frac{1}{2}$ system, will also contribute to T_2. However, in contrast to equation (9a), the last five terms of equation (9b) are not arranged in pairs ensuring that their sum is real. In fact, if the magnitudes of ω_{ij}, ω_{jm} or ω_{im} are greater than τ_c, the imaginary parts of these terms can be greater than the real parts, a fact that was not properly recognized in the earlier theories of weak relaxation, and was first emphasized by Paul Hubbard.[15] These imaginary contributions to 'T_2' give rise to 'dynamic shifts' of resonances, and are reviewed in ***Dynamic Frequency Shift***.

These dynamic shifts are useful for making an estimate of the size of fluctuating parts of $\hat{K}$. They can also be derived quantum mechanically as the second-order perturbation of the spin–lattice interaction, represented above semiclassically by $\hat{K}(t)$, on the spin levels.[15] An important example of a dynamic shift is that of the resonance connecting the $\pm\frac{1}{2}$ levels of a quadrupolar spin, relaxed by a fluctuating electric field gradient. In this case, $\hat{K}$ does not connect these levels directly, and the first terms of equation (9b) are therefore small. The last terms are mainly imaginary provided $\omega_0\tau_c > 1$, where ω_0 is the Larmor frequency.

11 DERIVATION OF THE RELAXATION EQUATION

The general form of the terms of $\hat{R}$ is given in some of the other articles in this Encyclopedia. It is most easily derived in the time-dependent Heisenberg representation mentioned above, in which the time-average main Hamiltonian $\hat{\mathcal{H}}_0$ is transformed to zero, and each element of the perturbation $K_{ij}(t)$ is replaced by $e^{i\omega_{ij}t}K_{ij}(t)$. Lacking the perturbation $\hat{K}(t)$, each ensemble member would have a stationary wavefunction in this representation, and $\hat{\sigma}$ would be time-independent. Relaxation is treated by considering a time Δt that is somewhat larger than any correlation time τ_c, but shorter than any relaxation time. It is always possible to define such a Δt, by the definition of weak limit relaxation, when that limit applies. One then gets an equation of motion by calculating $\hat{\sigma}(t + \Delta t) - \hat{\sigma}(t)$ using a perturbation expansion, and dividing by Δt to get $\mathrm{d}\hat{\sigma}/\mathrm{d}t$. The evolution of the c_i is calculated to second order in the elements of $\hat{K}$, for a member of the ensemble. Then the density matrix is formed from the c_i by using equation (4), and terms that are of first order in the $K_{ij}(t)$ vanish because the $K_{ij}(t)$ are zero in the ensemble average. The lowest nonzero terms are the second-order terms, while terms of higher than second order are assumed negligible, and are dropped. Finally, the solution outlined involves double integrals of correlation functions (multiplied by oscillating $e^{i\omega t}$ terms) with limits between t and $t + \Delta t$; these limits are extended to $\pm\infty$ because the integrands are assumed nonzero over only a short range, of the order of τ_c. The mathematics is very simple for secular elements of $\hat{R}$, and the assumptions involved are explained in detail elsewhere.[4,15] For nonsecular terms, the situation is more complicated; the contribution to the change in $\hat{\sigma}$ for a given time is smaller than it is for secular terms, but this decrease in effectiveness appears to be entirely due to the fact that the elements of $\hat{\sigma}$ in the Schrödinger representation, connected by the elements of $\hat{R}$, have a different time variation. So it was proposed that these elements could be taken to be time-independent in the Schrödinger representation and have essentially the same form as the secular terms. This somewhat unsatisfactory reasoning seems to have withstood the test of time.

The spectral densities $J(\omega)$ of elements of $\hat{R}$ are usually smoothly varying functions that become small for $\omega\tau_c > 1$. If τ_c is small compared with the Larmor frequencies then all the Js can be replaced by their values at zero frequency, and the $\hat{R}\hat{\sigma}$ term can then be written as a pleasing double commutator of $\hat{K}$ with $\hat{\sigma}$. This operator expression is also applicable in a modified form for high-field NMR, where levels are grouped into collections having nearly the same energy.[3,6,14] However, it is probably prudent to avoid using approximations in these operator methods for more complicated problems.

12 CONCLUSIONS

Weak relaxation theory was born with NMR, already well developed in BPP, and mature by the 25th anniversary of NMR. It achieved a new lease on life with the advent of FT NMR and, later, multidimensional methods, providing access to relaxation phenomena that were not dreamed of when the subject was developed. It is now virtually certain that computers will have a strong impact on the field, being able to predict the behavior of complex spin systems, to analyze data, and eventually to suggest better ways to obtain data, rather than relying on complicated analysis.

Experimentally, new developments will undoubtedly come from new pulse methods. An obvious general development will be the combination of pulse methods with high-speed high-resolution field cycling in some form, to map out completely the frequency dependence of spectral densities in a way that has so far been done only for the water resonance (described in ***Dynamics of Water in Biological Systems: Inferences from Relaxometry***).

The theory we have described has had minor impact in other fields. Obviously, it is useful for electron paramagnetic

resonance. Theory equivalent to BPP has also been developed by Zusman and others to describe the nonadiabatic regime of electron transfer.[18] Other forms of spectroscopy do not have the interesting variety of phenomena that NMR does, and such a theory is not needed.

13 RELATED ARTICLES

Chemical Exchange Effects on Spectra; Coupled Spin Relaxation in Polymers; Deuterium NMR in Solids; Diffusion Measurements by Magnetic Field Gradient Methods; Diffusion in Solids; Dynamic Frequency Shift; Dynamic NMR in Liquid Crystalline Solvents; Dynamics of Water in Biological Systems: Inferences from Relaxometry; Fast Ion Conductors; Field Cycling Experiments; Gas Phase Studies of Chemical Exchange Processes; Gas Phase Studies of Intermolecular Interactions and Relaxation; Gases at High Pressure; Overhauser Effect Imaging of Free Radicals; Liquid Crystalline Samples: Relaxation Mechanisms; Magnetization Transfer and Cross Relaxation in Tissue; Magnetization Transfer between Water and Macromolecules in Proton MRI; Molecular Motions: T_1 Frequency Dispersion in Biological Systems; Motional Effects on Protein Structure: Acyl Carriers; NOESY; Nuclear Overhauser Effect; Paramagnetic Relaxation in Solution; Protein Dynamics from NMR Relaxation; Protein Dynamics from Solid State NMR; Protein Structures: Relaxation Matrix Refinement; Quantum Tunneling Spectroscopy; Relaxation: An Introduction; Relaxation of Coupled Spins from Rotational Diffusion; Relaxation Effects of Chemical Exchange; Relaxation Matrix Refinement of Nucleic Acids; Relaxation Mechanisms: Magnetization Modes; Relaxation Processes in Coupled-Spin Systems; Relaxation Processes: Cross Correlation and Interference Terms; Relaxation of Quadrupolar Nuclei Measured via Multiple Quantum Filtration; Relaxation Theory for Quadrupolar Nuclei; Relaxation of Transverse Magnetization for Coupled Spins; Relaxometry of Tissue; ROESY; Rotating Frame Spin–Lattice Relaxation Off-Resonance; Selective Relaxation Techniques in Biological NMR; Slow and Ultraslow Motions in Biology; Spin–Rotation Relaxation Theory.

14 REFERENCES

1. F. Bloch, *Phys. Rev.*, 1946, **69**, 1.
2. N. Bloembergen, E. M. Purcell, and R. V. Pound, *Phys. Rev.*, 1948, **73**, 679.
3. A. Abragam, *Principles of Nuclear Magnetic Resonance*, Oxford University Press, Oxford, 1961.
4. C. P. Slichter, *Principles of Magnetic Resonance*, 3rd edn., Springer-Verlag, Berlin, 1990.
5. M. Goldman, *Quantum Description of High-Resolution NMR in Liquids*, Oxford University Press, Oxford, 1988.
6. R. R. Ernst, G. Bodenhausen, and A. Wokaun, *Principles of Nuclear Magnetic Resonance in One and Two Dimensions*, Oxford University Press, Oxford, 1987.
7. D. Wolf, *Spin-Temperature and Nuclear-Spin Relaxation in Matter*, Oxford University Press, Oxford, 1979.
8. L. T. Muus and P. W. Atkins (eds.), *Electron Spin Relaxation in Liquids*, Plenum Press, New York, 1972.
9. J. McConnell, *The Theory of Nuclear Magnetic Relaxation in Liquids*, Cambridge University Press, Cambridge, 1987.
10. R. Lenk, *Brownian Motion and Spin Relaxation*, Elsevier, Amsterdam, 1977.
11. R. Tycko (ed.), *Nuclear Magnetic Resonance Probes of Molecular Dynamics*, Plenum Press, New York, 1994.
12. P. W. Atkins, *Adv. Molec. Relax. Processes*, 1972, **2**, 121.
13. D. Kivelson and K. Ogan, in *Advances in Magnetic Resonance*, ed. J. S. Waugh, Academic Press, New York, 1974, Vol. 7, p. 72.
14. S. Szymanski and G. Binsch, *J. Magn. Reson.*, 1989, **81**, 104.
15. A. G. Redfield, in *Advances in Magnetic Resonance*, ed. J. S. Waugh, Academic Press, New York, 1965, Vol. 1, p. 1.
16. A. G. Redfield, in *NMR Basic Principles and Progress*, eds. P. Diehl, E. Fluck, and R. Kosfeld, Springer-Verlag, Berlin, 1976, Vol. 13, p. 1.
17. F. Reif, *Fundamentals of Statistical and Thermal Physics*, McGraw-Hill, New York, 1965.
18. J. Tan, Z. Wang, and J. R. Norris, *J. Chem. Phys.*, 1993, **99**, 97.

Acknowledgments

I thank Dr. L. Werbelow for helpful suggestions and information.

Biographical Sketch

Alfred G. Redfield. *b* 1929. B.A., 1950, Harvard, USA; Ph.D., 1993, University of Illinois at Champaign-Urbana. Postdoctoral works with N. Bloembergen, 1953–55. IBM Watson Laboratory at Columbia University and Adjunct Member, Columbia Physics Department, 1955–72. Professor of Physics and Biochemistry, Brandeis University, 1972–present. Sabbatical visitor in the laboratories of A. Abragam, 1960–61, and D. Koshland, 1970–72. Principal research interests: superconductivity, transfer RNA, and small G-proteins.

Rotating Solids

Robert G. Griffin

Massachusetts Institute of Technology, Cambridge, MA, USA

1	Introduction	1
2	Early History	1
3	Hamiltonians, Rotational Echoes, and Spectra	2
4	Multiple Pulse NMR in Rotating Solids	5
5	Multidimensional MAS Experiments	7
6	Related Articles	10
7	References	10

1 INTRODUCTION

In the late 1960s and early 1970s, a number of experiments were developed that were aimed at performing 'high-resolution NMR in solids'. In general, these techniques are classified into two general categories:

1. multiple pulse (MP) experiments, aimed at attenuating the homonuclear dipolar couplings in strongly coupled spin systems typically found in protonated solids;
2. dilute spin double resonance/cross-polarization (CP) experiments, which detect signals from magnetically dilute nuclei such as ^{13}C and ^{15}N in the presence of strong dipolar decoupling.

However, in both cases, the resulting spectra consisted of powder patterns due to shift anisotropies, or rather broad lines in spectra of single crystals. Thus, while the resolution of solid state spectra was much improved, it was still not comparable to that observed in liquids.

This situation changed dramatically with the marriage of magic angle spinning (MAS), a 'partially successful' mechanical rotation technique also developed to attenuate dipolar couplings in solids, with CP and/or MP to yield a new class of hybrid solid state techniques. In these cases, homo- or heteronuclear decoupling removes the dipolar interactions, and MAS narrows the shift anisotropy. The resulting spectra exhibit resolution comparable to that observed in liquids, and, as a consequence, these techniques are currently widely utilized in a variety of forms to examine problems in biology, chemistry, physics, materials science, and a number of engineering disciplines.

The subject of this article is the early developments that led to these MAS techniques, and advances in MAS that have occurred in the last 15 years or so. We focus primarily on the spectra of dilute $I = \frac{1}{2}$ spins in 1D and 2D experiments, with a brief interlude where we consider the possibility of reintroducing the dipolar coupling of the dilute spins to ^{1}H (so-called DIPSHIFT experiments), since this was the initial MAS 'recoupling technique'. More recent advances in the area of homonuclear and heteronuclear recoupling (rotational resonance, DRAMA, RFDR, REDOR, TEDOR, etc.) are considered in other articles.

2 EARLY HISTORY

The initial MAS NMR experiments were performed in the late 1950s,[1,2] and were aimed at attenuating homonuclear dipolar interactions in NMR spectra of solids, thereby revealing the underlying chemical shifts and scalar spin couplings. The approach was successful in cases where the dipolar couplings $|\hat{\mathcal{H}}_{\rm d}|$ were not too large, and therefore the spinning rate $\omega_{\rm r}/2\pi$ satisfied the condition $\omega_{\rm r}/2\pi > |\hat{\mathcal{H}}_{\rm d}|$. Early results obtained on ^{23}Na in NaCl, on ^{31}P in PCl_5, and on ^{19}F in $KAsF_6$ demonstrated line narrowing, and resolution of chemical shifts and J couplings, respectively.[3,4] However, in the 1960s, NMR spectrometers utilized iron magnets and continuous wave (CW) observation techniques, and this in turn constrained researchers to observe primarily ^{1}H and ^{19}F, which generally yield spectra with dipolar breadths of 25–50 kHz. Since available spinning speeds were in the range of 5–10 kHz, the spectra could not in general be narrowed, a result connected with the fact that $\hat{\mathcal{H}}_{\rm d}$ is a *homogeneous* interaction.[5] For this reason, for most of the 1960s and early 1970s, MAS was viewed as an interesting but not very useful technique.

During this period, several developments occurred that eventually led to a renaissance in MAS. First, in 1968, J. S. Waugh and co-workers introduced MP techniques for attenuating homonuclear dipolar couplings in solids.[6] Since the cycle of four pulses in a WAHUHA experiment could be applied rapidly compared with the size of $|\hat{\mathcal{H}}_{\rm d}|$, this technique, and its subsequent refinements,[7–9] have been more successful than MAS in removing homonuclear dipolar couplings. In 1972, a second, very versatile approach to high resolution in solids emerged from Waugh's laboratory. At that time, FT spectroscopy[10,11] was developing as the preferred method of recording solution spectra, and reports describing spectra of less abundant nuclei (^{13}C, ^{15}N, etc.) were beginning to appear. It seemed reasonable that ^{13}C and ^{15}N spectra should also be observed in solids, and an approach for accomplishing this involving a Hartmann–Hahn[12] cross polarization and decoupling[13,14] was described by Pines et al.[15] While both MP and CP were very interesting developments, they both yielded spectra consisting of powder patterns or required single crystals; therefore, much of the high-resolution NMR community was unimpressed with the promise of the solid state NMR.

It was appreciated by at least a few individuals that an approach to narrowing these powder spectra was to incorporate MAS into the experiment.[16] Specifically, any second-rank tensor—dipolar, chemical shift, quadrupole, Knight shift, and indirect dipolar couplings—is narrowed by MAS. Ultimately, this led to the Schaefer and Stejskal[17] experiment, which demonstrated that high-resolution, 'liquid-like' spectra of solids could be obtained by combining dilute spin double resonance—cross polarization and decoupling—and MAS into what is now referred to as a CP MAS experiment. Later, Gerstein and co-workers[18] performed similar experiments with MP and MAS, a technique now referred to as CRAMPS (combined rotation at the magic angle and multiple pulse).

Initially, CP MAS experiments were performed at a ^{13}C frequency of about 22.6 MHz, and therefore a typical 150–200 ppm ^{13}C shift tensor was 3.75–5.00 kHz wide, and near the regime $\omega_{\rm r}/2\pi > \Delta\sigma$. Conventional wisdom dictated that line narrowing by MAS would not occur unless this condition was satisfied; therefore, spinning experiments should

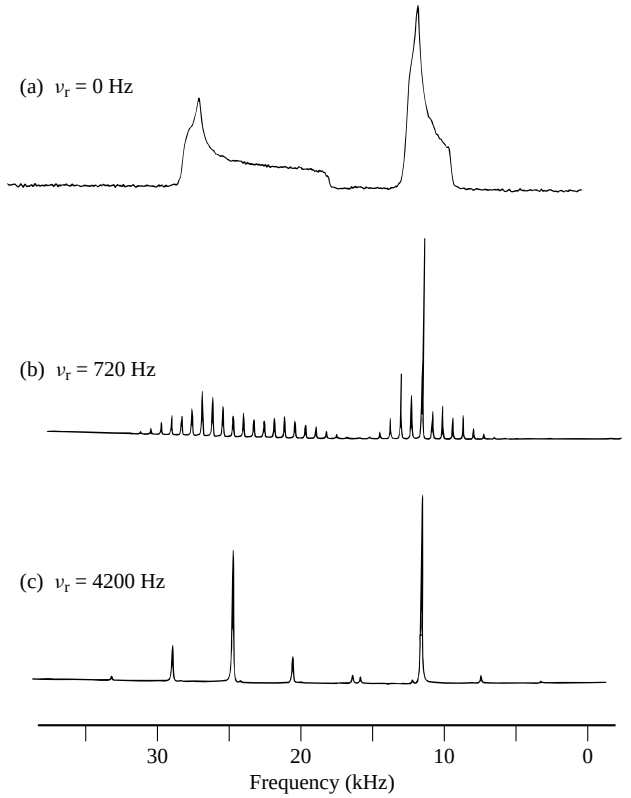

Figure 1 Static (a) and MAS (b, c) ^{13}C spectra of zinc acetate, showing the effect of MAS on chemical shift anisotropic powder patterns. The spectra were obtained with a standard CP sequence. The rotational sidebands observed in (b) and (c) are spaced at the spinning frequency. The breadths of the powder patterns are 10.2 and 3.2 kHz, respectively, for the $-CO_2^-$ and $-CH_3$ resonances. Note that the sidebands for the methyl pattern are completely attenuated at $\omega_r/2\pi$ = 4.2 kHz

be performed at low fields, and not in the superconducting solenoids that were becoming the standard polarizing field for NMR spectrometers. However, the results of performing MAS in the slow spinning regime, $\omega_r/2\pi < \Delta$, where Δ is the size of the interaction of interest, were already in the literature. In 1974, Andrew et al.[19] showed that the Knight shift observed in Cd metal narrows into a sharp centerband and sidebands when the spinning rate is less than the breadth of the pattern. Subsequently, several other groups[20–23] observed the same behavior for shift anisotropy powder patterns of ^1H decoupled spectra of $I = \frac{1}{2}$ nuclei: ^{13}C, ^{31}P, etc. Some examples of the type of spectra observed are shown in Figure 1, where ^1H-decoupled ^{13}C spectra of zinc acetate. H_2O (ZnAc) are illustrated as a function of spinning speed.

The CO_2^- and $-CH_3$ powder lineshapes are about 10.2 and 3.2 kHz wide, respectively, and evolve to a sharp centerband and sets of sidebands at spinning speeds of 4.2 kHz. These types of spectra are now routinely observed in the spectra of $I = \frac{1}{2}$ nuclei, and have brought solid state NMR into the realm of high resolution. Specifically, resolved centerbands and sidebands are observed for each magnetically inequivalent nucleus, and therefore MAS spectra can be used in much the same fashion as their high-resolution counterparts observed in solution. The remainder of this article will consider the shape of these spectra (i.e., the sideband intensities), new ways of utilizing and manipulating sidebands, and multidimensional experiments.

3 HAMILTONIANS, ROTATIONAL ECHOES, AND SPECTRA

3.1 MAS Hamiltonian

The generalized laboratory frame Hamiltonian for a nuclear spin interaction is

$$\hat{\mathcal{H}} = C\hbar \sum_{l=0,2} \sum_{m=-1}^{1} (-1^m) \hat{R}_{l-m} \hat{T}_{lm} \tag{1}$$

where C is a collection of constants, and $\hat{R}$ and $\hat{T}$ are second-rank tensor operators containing the spatial and spin dependences of the coupling, respectively.[24] In a principal axis system (PAS), the tensor $\boldsymbol{R}$ representing $\hat{R}$ is diagonal, with principal values R_{ii} ($i = x,y,z$). These lead to an isotropic component

$$R = \tfrac{1}{3}(R_{xx} + R_{yy} + R_{zz}) \tag{2}$$

an anisotropy

$$\delta = R_{zz} - R \tag{3}$$

and an asymmetry

$$\eta = \frac{R_{xx} - R_{yy}}{\delta} \tag{4}$$

with the diagonal elements ordered so that

$$|R_{zz} - R| \rangle |R_{xx} - R| \rangle |R_{yy} - R| \tag{5}$$

The mechanical system under consideration consists of a rotor inclined at an angle θ relative to the external field $\boldsymbol{B}_0$ and spinning at ω_r. The laboratory frame with $z \| \boldsymbol{B}_0$ is related to the PAS of a specific coupling tensor $\boldsymbol{R}$ by two sets of Euler angles. The first transformation takes the laboratory into the rotor frame with Euler angles (θ_m, $-\omega_r t$), and the second maps the rotor frame onto the PAS of the coupling tensor. Using the definitions above and some algebra, we obtain a compact form for the MAS Hamiltonian. Specifically, for the chemical shift $\hat{T}_{00} = \hat{I}_z B_0$ and $\hat{T}_{20} = \sqrt{\frac{2}{3}} \hat{I}_z B_0$, we obtain

$$\begin{aligned} \hat{\mathcal{H}}(t) &= \omega(t) \hat{I}_z \\ &= -\Delta\omega \hat{I}_z - \omega_1 [g_1 \cos(\omega_r t + \varphi_1) + g_2 \cos(2\omega_r t \\ &\quad + \varphi_2)] \hat{I}_z \end{aligned} \tag{6}$$

in which

$$\Delta\omega = \omega_1^0 + \omega_{off} = \tfrac{1}{3}\omega_0(\sigma_{11} + \sigma_{22} + \sigma_{33}) + \omega_{off} \tag{7}$$

$$\omega_1 = \omega_0(\sigma_{33} - \tfrac{1}{3}\mathrm{Tr}\boldsymbol{\sigma}) = \omega_0\sigma_{33} - \omega_1^0 \tag{8}$$

g_1 and g_2 depend on the Euler angles β and γ,

$$g_1 = \tfrac{1}{2}(\tfrac{1}{2}\sin 2\theta \sin\beta) \times[(\eta\cos 2\gamma + 3)^2\cos^2\beta + \eta^2\sin^2 2\gamma]^{1/2} \quad (9a)$$

$$g_2 = \tfrac{1}{2}(\tfrac{1}{2}\sin^2\theta_m)\{[\tfrac{3}{2}\sin^2\beta - \tfrac{1}{2}\eta\cos 2\gamma(1+\cos^2\beta)]^2 + \eta^2\cos^2\beta\sin^2 2\gamma\}^{1/2} \quad (9b)$$

The phase factors ϕ_1 and ϕ_2 are given by

$$\varphi_1 = \alpha + \varphi_1 \quad (10a)$$

$$\varphi_2 = 2\alpha + \varphi_2 \quad (10b)$$

where

$$\tan\varphi_1 = \eta\frac{\sin 2\gamma}{\eta\cos 2\gamma + 3}\cos\beta \quad (11a)$$

$$\tan\varphi_1 = \eta\frac{\cos\beta\sin 2\gamma}{\frac{3}{2}\sin^2\beta - \frac{1}{2}\eta\cos 2\gamma(1+\cos^2\beta)} \quad (11b)$$

for axially symmetric tensors $\eta = 0$ and

$$\varphi_1 = \alpha, \quad \varphi_2 = 2\alpha, \quad (12)$$

Similar expressions can be derived for the heteronuclear dipolar Hamiltonian with $\hat{T}_{00} = 0$ and $\hat{T}_{20} \approx \hat{I}_z\hat{S}_z$ [in equation (1)]. Note that a term proportional to $3\cos^2\theta_m - 1$ must be added to equation (6) when the spinning is off the magic angle. Recently, a new approach for expressing the anisotropy of NMR Hamiltonians has been suggested involving the span $\Omega = \sigma_{33} - \sigma_{11}$ and skew $k = (\sigma_{11} + \sigma_{33} - 2\sigma_{22})/(\sigma_{33} - \sigma_{11})$ of the interaction. These definitions are discussed in ***Sideband Analysis in Magic Angle Spinning NMR of Solids***.

3.2 Rotational Echoes

The spectra in Figure 1 result from the fact that the chemical shift interaction is *inhomogeneous*, a term used by Portis[25] to denote that a 'hole could be burned' into spectral patterns. In the absence of motion, continuous irradiation of one part of a powder pattern with a narrow frequency signal will saturate that part of the spectrum, and, because of the absence of coupling among the spins, that saturation will not diffuse through the spectral lineshape. In contrast, if the line is homogenously broadened, for instance, if a homonuclear dipolar coupling determines the lineshape, then irradiation at a narrow band of frequencies will diffuse through the spin reservoir and lead to saturation of the entire spectrum. Thus, solid state spectra can be decoupled with single frequency irradiation, whereas liquids require wideband (noise or composite pulse[26,27]) decoupling.[5] Another approach to this statement is to consider the average Hamiltonian $\langle\bar{\hat{\mathcal{H}}}\rangle$ for an MAS experiment:[22,24]

$$\langle\bar{\hat{\mathcal{H}}}\rangle = \sum_{\mu=0}^{\infty}\bar{\hat{\mathcal{H}}}^{(\mu)} \quad (13)$$

where the first two terms are

$$\bar{\hat{\mathcal{H}}}^{(0)} = \frac{\omega_r}{2\pi}\int_0^{2\pi/\omega_r}\hat{\mathcal{H}}(t')\,dt' \quad (14a)$$

$$\bar{\hat{\mathcal{H}}}^{(1)} = \frac{i\omega_r}{4\pi}\int_0^{2\pi/\omega_r}\int_0^{t''}[\hat{\mathcal{H}}_0(t'),\hat{\mathcal{H}}(t'')\,dt'\,dt'' \quad (14b)$$

Because of the oscillatory nature of the MAS chemical shift Hamiltonian [see equation (6)], the time-dependent terms vanish, and the zeroth-order term $\bar{\hat{\mathcal{H}}}^{(0)}$ is equal to the isotropic shift. Physically, this tells us that the system returns to its initial state after each revolution of the spinner. In general, the higher order correction terms like equation (14b) will be nonzero, and when $|\bar{\hat{\mathcal{H}}}|\tau_c\rangle 1$ (where τ_c is the cycle time), these terms interfere with the line narrowing. In the case of the 'homogeneous' homonuclear dipolar coupling, $\bar{\hat{\mathcal{H}}}^{(1)}$ is of substantial size, because the coupling between i and j does not commute with that between i and k, or j and k, etc. However, for the chemical shift, the commutator in equation (14b) vanishes, as do those in higher-order correction terms. For this reason, the chemical shift powder patterns are resolved into sideband patterns even in the slow spinning regime $\omega_r/2\pi < \delta$.

Finally, it should be mentioned that the heteronuclear dipolar and first-order quadrupolar couplings are also inhomogeneous, as is an isolated dipolar-coupled pair of like spins, and all of these cases will yield sideband spectra similar to those in Figure 1.[5] However, when a homonuclear dipolar coupling is present, in addition to two or more spins with noncoaxial chemical shift tensors, the result is a homogeneous interaction that will not narrow completely. Some interesting examples of this last case are discussed below.

The average Hamiltonian describes the state of the system modulo the rotor period, but it says nothing about the evolution during the rotor cycle. In fact, what occurs for slow spinning is that the signal is recovered after each rotation as an echo, and for systems with reasonable decay times, a train of echoes is observed. The vanishing of $\bar{\hat{\mathcal{H}}}^{(0)}$ means that each echo will have the same shape, an example being shown in Figure 2(a). The Fourier transform of this train yields a centerband/sideband spectrum similar to those illustrated in Figure 1. The linewidths of the centerband and sidebands are determined by the decay time of the entire echo train, while the shape of the sideband envelope is governed by the shape of the rotational echoes.[5]

Our intuitive understanding of the behavior of single spins in liquids is enhanced by the use of vector pictures, which are very useful for depicting FIDs, Hahn spin echoes, and a number of other phenomena. Similarily, vector pictures provide insight into formation of rotational echoes and other phenomena associated with MAS. In Figure 3, we illustrate spin packet trajectories for two crystallites under MAS for a rotor period, and we have shrunk the length of the vector during the rotor period to clearly show its path. The magnetization trajectories are shown for three cases: before a π pulse is applied [(a) and (b)], after a single π pulse [(c) and (d)], and after two π pulses [(e) and (f)]. In all cases, the motion is τ_r-periodic, so that vectors return to their initial positions after a rotor period. We shall return to a discussion of this figure when we consider echoes. It has been shown[28] that a powder average of these spin packets leads to formation of

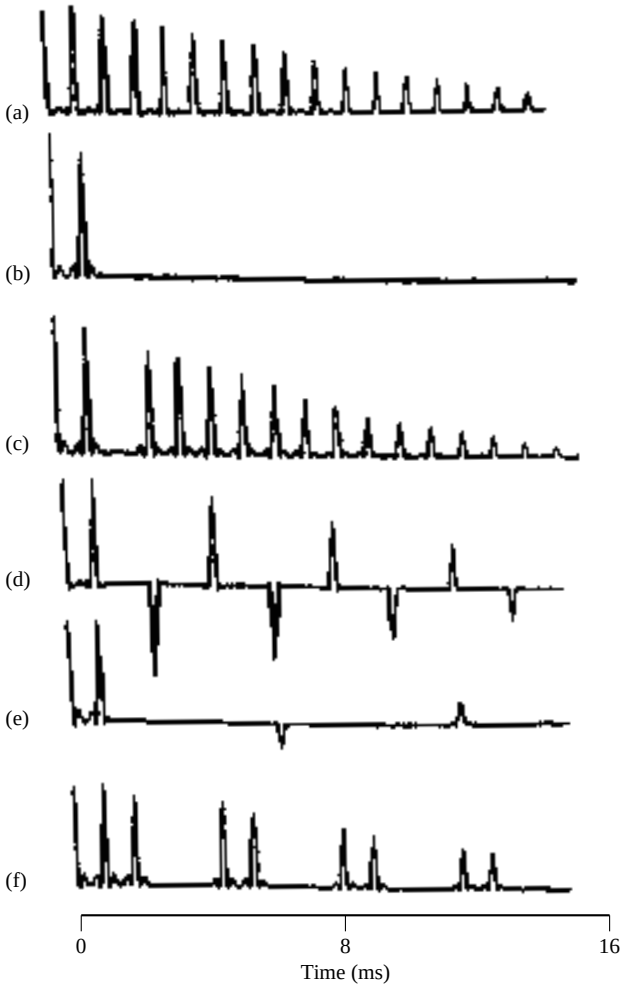

Figure 2 Rotational echo trains measured on a sample of [1-^{13}C]-glycine spinning at $\omega_r/2\pi$ = 1.03 kHz. The rf carrier frequency coincided with the isotropic chemical shift: (a) a train of unperturbed rotational echoes; (b) a single π pulse inserted at $\frac{3}{2}\tau_r$ results in the disappearance of the echo train; (c) two π pulses inserted at $\frac{3}{2}\tau_r$ and $\frac{5}{2}\tau_r$ result in the disappearance and reappearance of the echo train at $3\tau_r$; (d) multiple applications of $(-\pi_x-\tau_r-\pi_y-\text{echo})$ lead to the train with alternate echoes inverted; (e) echo train with $\tau_c = \frac{3}{5}\tau_r$ and alternating phases (0° and 90°) of the pulses; an inverted echo is recovered after $2n\tau_r = 6$ echoes and the intervening application of $2m\tau_r = 10$ π pulses; (f) echo train with $\tau_c = 2\tau_r$

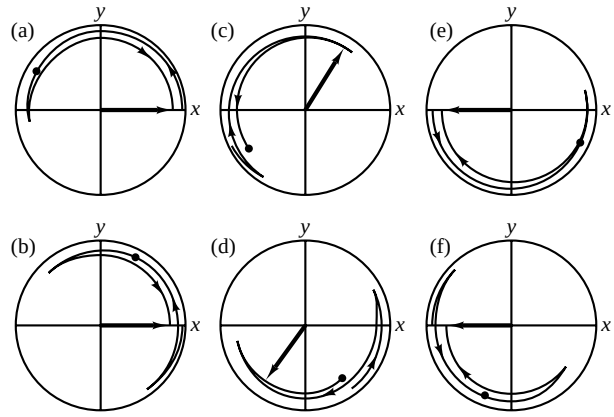

Figure 3 Spin packet trajectories in the rotating frame, showing the effect of π pulses on rotational echo formation. All calculations used $\omega_r/2\pi$ = 2.0 kHz, δ = 5.0 kHz, η = 0, and β = 60°. The position of the magnetization vector at $\frac{1}{2}\tau_r$ is represented by a dot, while the position of the vector at the end of the next rotor period is represented by a long arrow. The direction of motion of the vectors is indicated by arrowheads. The length of the vector was shrunk over time in order to make the paths clearer. (a) α = 60°: evolution from 0 to τ_r. (b) α = 20°: evolution from 0 to τ_r. (c) α = 60°: evolution from $\frac{1}{2}\tau_r$ to $\frac{3}{2}\tau_r$ after the first π pulse of phase 0° was applied at $\frac{1}{2}\tau_r$; a second π pulse of phase 90° was applied at $\frac{3}{2}\tau_r$. (d) α = 20°: same as in (c). (e) α = 60°: evolution from $2\tau_r$ to $3\tau_r$ after the application of the second π pulse of phase 90° at $\frac{3}{2}\tau_r$. (f) α = 20°: same as in (e)

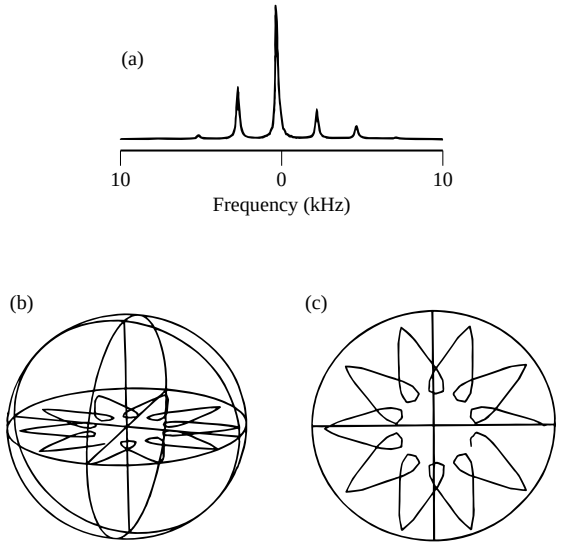

Figure 4 (a) MAS spectrum for δ = 5.4 kHz, η = 0 and spinning at $\omega_r/2\pi$ = 2.0 kHz, 200 Hz off resonance. (b, c) The magnetization path corresponding to the MAS spectrum shown in (a) and its (x, y) projection. The petals in the rosette pattern correspond to the formation of rotational echoes

the 'rosette pattern' illustrated in Figure 4. Here we show the path of the magnetization in a MAS experiment for a sample with δ = 5.4 kHz, η = 0, and $\omega_r/2\pi$ = 2.0 kHz, with a resonance offset of 200 Hz, and nine rotational echoes are apparent.

3.3 Spectra

There have now been many interesting applications utilizing these MAS spectra in biology, chemistry, physics, and materials science. These include studies of chemical exchange and other dynamic phenomena in solids, as well as studies of structure. In order to illustrate the explosive growth of MAS NMR in structural investigations, we present an illustration of the size of molecular system, which is often a limiting parameter in many magnetic resonance studies, that can be approached with this technique. Figure 5 shows spectra of a double ^{13}C-labeled membrane protein, [14-^{13}C]retinal-[ε-^{13}C]Lys-bacteriorhodopsin (bR), which has not been crystallized and which cannot be effectively studied with solution NMR techniques because of its size and aggregation. The top trace in the figure contains lines due to both the label and the natural abundance background, while the middle

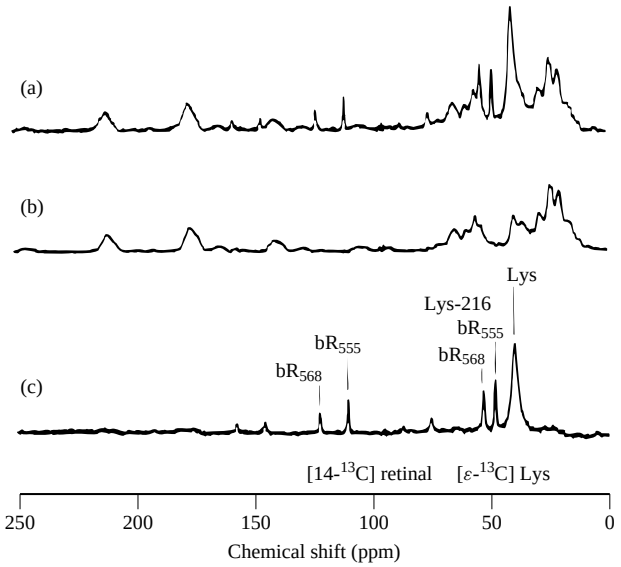

Figure 5 ^{13}C MAS spectra of dark-adapted bR collected at −80 °C with a sample spinning speed of 2.8 kHz: (a) [14-^{13}C]retinal-[ε-^{13}C]Lys-bR; (b) unlabeled bR; (c) the difference spectrum obtained upon subtraction of (b) from (a). The signals at 40, 48 and 53 ppm are due to the [ε-^{13}C]Lys label, and the signals in the 100−130 ppm range arise from the [14-^{13}C]retinal marker resonances. Rotational sidebands are observed 35 ppm upfield and downfield of the centerbands

trace shows only the natural abundance spectrum. The bottom trace illustrates the difference spectrum exhibiting only the ^{13}C labels. Dark-adapted bR contains a 60 : 40 mixture of 13-*cis*- and all-*trans*-retinal (referred to as bR_{555} and bR_{568}, respectively, where the numbers indicate the wavelengths of their absorption maxima). Therefore, there are two retinal and two Lys lines in the spectrum, together with a line due to six lysines not involved in the Schiff base linkage. bR has a molecular weight of 26.6 kDa, and the membrane is about 75 wt% protein, leading to an effective MW ≈ 35.5 kDa. Together, the two retinal and Lys Schiff baselines represent a single ^{13}C, and thus for the bR_{568} resonances, we are observing about 40% of a single ^{13}C, corresponding to a single ^{13}C in a protein of MW ≈ 88 kDa. Further, it is possible with recoupling techniques (rotational resonance and RFDR) to measure the distance between the retinal and lysine labels, and to determine the conformation about the retinal C=N bond in both bR_{555} and bR_{568}. Because of its ability to address protein problems of this size, MAS NMR will undoubtably continue to find applications in many different areas.

4 MULTIPLE PULSE NMR IN ROTATING SOLIDS

In this section, we describe the effects of MP trains on MAS spectra. We first consider the effects of single and multiple π pulse trains on rotational echoes, since these effects are important in designing other experiments. This is followed by a discussion of the TOSS and scaling experiments, which are used to manipulate sidebands in MAS spectra. Several features of these experiments, including intensity losses and rotor frequency lines, will emerge from the discussion. Finally, we describe the hybrid, TOSS/scaling experiment, which combines desirable features of each approach.

4.1 π Pulses and Rotational Echoes

The simplest multiple pulse (≥2 pulses) experiment possible is the addition of π pulse(s) following excitation (cross polarization or a 90° pulse) analogous to a Carr−Purcell experiment in liquids. Experimental results showing the effects of π pulses during a rotor period are shown in Figure 2(b)−(f).

In Figure 2(b), a π_x pulse is applied at the middle of a rotor period, in this case $\frac{3}{2}\tau_r$, and the signal vanishes. This effect is readily understood by examining the single crystallite magnetization trajectories shown in Figure 3, where we have plotted the path for before [(a) and (b)] and after [(c) and (d)] the π_x pulse for two crystallite orientations: α = 60°, β = 60° (a) and α = 20°, β = 60° (b). Following excitation, both vectors lie along the x axis, evolve on the trajectories shown, and return to the origin after each rotor period, resulting in the formation of an echo. The application of a π_x pulse in the middle of a rotor period (corresponding to the position of the dot on the trajectory) results in a reflection of the trajectory about the x axis of the rotating frame. Thus, while the pulse does not affect the periodicity of the crystallite's magnetization path, it does reorient each vector in a way that alters their phase relationship, and the signal disappears. A second π_x pulse at $\frac{5}{2}\tau_r$, again when the vector position is at the 'dot', restores the phase relation among the crystallites, and the echo train reappears [Figure 2(c)].

Another parameter of importance in echo phenomena is the relative phase of the rf pulses. In Figure 2(d), we show that the echo train may be inverted—in this case, multiple times from positive to negative to positive, etc.—by employing a 90° phase shift in the second of the two rf pulses. Specifically, instead of using $-\pi_x\tau_r\pi_x-$ for the refocusing, we use $-\pi_x\tau_r\pi_y-$. Thus, the initial 'scrambling' of the phases accomplished by the π_x pulse is reversed by a π_y pulse, but the refocusing occurs along the $\bar{x}$ rather than the x direction. This is easily understood by comparing Figures 3(c) and (d) with Figures 3(e) and (f), where the application of the π_y pulse results in refocusing along $\bar{x}$. Each new application of the $-\pi_x\tau_r\pi_y-$ sequence again reverses the sign of the subsequent echo, as shown in Figure 2(d).

As is discussed elsewhere,[29] there are many other combinations of π pulses that will yield echo trains, and the general conditions for echo formation in these trains have been studied. Specifically, for

$$\tau_c = \frac{n}{m}\tau_r \tag{15}$$

where τ_c is the cycle time, τ_r the rotor period, and n and m are integers, refocusing will occur only for odd m; after $2m$ π pulses, echo formation will occur at $2n\tau_r$. Some results using this formula are shown in Figure 2(e) for $\tau_c = \frac{3}{5}\tau_r$ (a string of ten π pulses yields an echo at $6\tau_r$) and Figure 2(f), where $\tau_c = 2\tau_r$.

4.2 TOSS and Chemical Shift Scaling

The sidebands in a MAS spectrum, which reflect the anisotropic chemical shift, contain information that can be invaluable in understanding molecular and electronic structure.[30,31] Nevertheless, in analytical applications of MAS,

the isotropic shift is the focus of attention, a fact that has provided the impetus to develop techniques to eliminate or attenuate sidebands. To date, there have been two approaches to the problem: the TOSS experiment, due originally to Dixon,[32] and its subsequent variations,[33–35] and scaling, due to Aue et al.[36,37] The methods are based on fundamentally different physical principles, and each has its advantages and disadvantages.

The original four π pulse version of the TOSS pulse sequence is illustrated in Figure 6, and some experimental spectra obtained from [1-^{13}C]glycine are shown in Figure 7. The top two spectra were taken at $\omega_r/2\pi$ = 3.20 kHz with MAS (a) and TOSS (b), and the TOSS experiment clearly suppresses the rotational sidebands. The physical basis for TOSS is spin packet alignment—the preparation pulses result in a situation where the centerbands have the same amplitude and phase, and therefore add constructively. In contrast, the sidebands have different phases, add destructively, and are canceled when a powder average is performed. There is, however, a problem with this process, which is evident in Figure 7. First, the spectral intensity that resides in the sidebands is not transferred to the centerband by the alignment process. More specifically, when TOSS was first proposed, it appeared that the behavior illustrated in the top half of Figure 7 would always prevail. However, it was soon noticed that substantial intensity losses occur when the tensor is large or when the spinning speed low—i.e., when $\delta/(\omega_r/2\pi) \gg 1$.[38] The spectra in the bottom half of Figure 7 dramatically illustrate this point, in that the centerband inverts when $\delta/(\omega_r/2\pi) \approx 8$. Calculations and experimental data show that for an $\eta = 0$ tensor, the centerband intensity is positive when $\delta/(\omega_r/2\pi) \leq 6$; however, for larger values of this parameter, the intensity approaches zero, and becomes negative for $\delta/(\omega_r/2\pi) > 8$. Thus, TOSS centerband intensities cannot be employed to 'count spins' in the same fashion as normal NMR spectra, and the signal-to-noise ratio of the experiment is decreased substantially. In addition, since the pulse sequence is spread over 1–4 rotor periods, TOSS is difficult to apply to samples with broad NMR lines. Finally, with weak rf fields, the pulses sometimes overlap.

Despite these limitations, the idea suggested by Dixon is an important addition to the repertoire of MAS experiments, and its features have been explored extensively. Equations for the timing of the pulses have been presented,[28,35,39] and have been solved analytically by Lang[40] and more recently by Levitt and co-workers.[34,41] New timings[42] and sequences have been explored, including the SELTICS sequence with continuous rf burst,[33] which suspends the chemical shift evolution. In addition, TOSS has been employed to examine

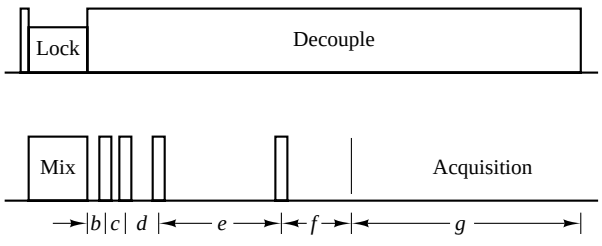

Figure 6 TOSS pulse sequence used to suppress rotational sidebands. The locations of the pulses and the initiation of sampling over two rotor periods are (in fractions of a rotor period) b = 0.1763, c = 0.6289, d = 0.8617, d = 1.2060, e = 1.6485, f = 1.8170, and g = 1.9326

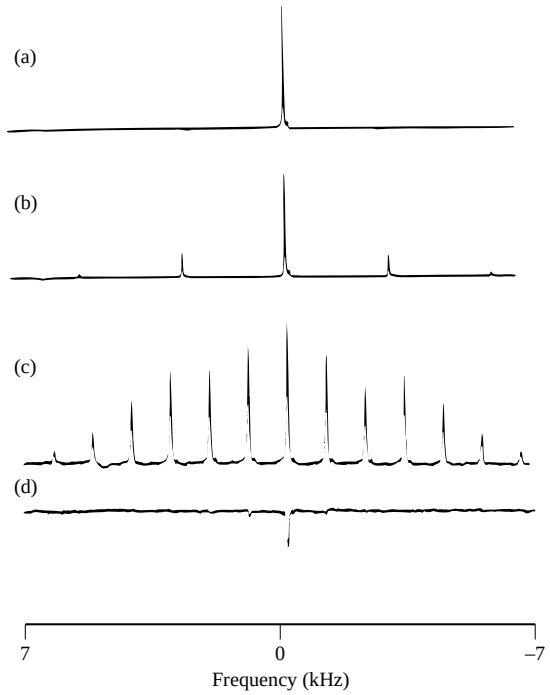

Figure 7 Experimental MAS and TOSS spectra of [1-^{13}C]glycine: (a) MAS at $\omega_r/2\pi$ = 3.2 kHz; (b) TOSS at $\omega_r/2\pi$ = 3.2 kHz; (c) MAS at $\omega_r/2\pi$ = 1.2 kHz; (d) TOSS at $\omega_r/2\pi$ 1.2 kHz. The same phase correction was employed for all spectra. Note that the sideband intensity was not transferred to the centerband in (b) and that the centerband inverts when $\Delta\sigma/(\omega_r/2\pi) > 4.5$, as shown in (d)

chemical exchange,[43–45] and can be usefully incorporated into 2D experiments to separate isotropic and anisotropic chemical shifts.[29]

The second approach to attenuating sidebands involves incorporation of a MP experiment into a MAS experiment to reduce the effect size of the shift anisotropy. If the scale factor q is sufficiently small then $q\ \Delta\sigma/\nu_r < 1$, and the spectrum will be dominated by centerbands. This is based on the well-known fact that all multiple pulse trains scale certain interactions to varying degrees. For example, WAHUHA and MREV-8, etc.[6,7] scale $\hat{\mathcal{H}}_d^{I-I}$ to zero and the chemical shift by 0.57 and 0.47, respectively. The first experiment explicitly designed to scale chemical shifts was that of Ellett and Waugh.[46] More recently, Aue et al.[47,48] developed improved scaling sequences, and used them to scale ^{13}C–^{1}H J couplings.

By itself, scaling will not reduce the sidebands in a MAS spectrum to zero, and therefore it is advantageous to combine scaling with TOSS in a hybrid experiment. The timings for the TOSS sequence must be adjusted to account for the scaling sequence,[49] but the result is a substantial increase in the signal strength of lines associated with large anisotropies. This is illustrated in Figure 8, where we show the MAS, TOSS, and TOSS/scaling spectra of alanine. A comparison of Figures 8(a) and (b) shows that, while TOSS does suppress sidebands, it does little to enhance the $-CO_2^-$ centerband intensity. However, as shown in Figure 8(c), the presence of a scaling sequence distills the intensity of the $-CO_2^-$ sidebands into the centerband so that the three lines are of approximately equal intensity, as expected. In the process, the intensity of

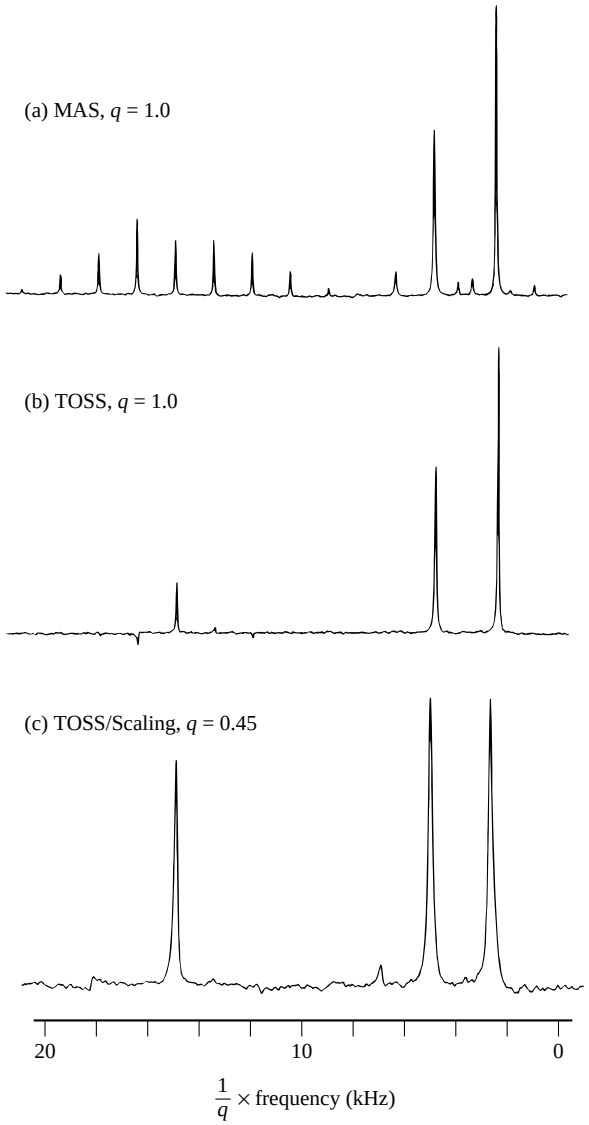

Figure 8 79.9 MHz ^{13}C spectra of natural abundance Ala obtained at $\omega_r/2\pi$ = 1.5 kHz. (a) MAS spectrum showing the numerous sidebands arising from the $-CO_2^-$ group and the narrow centerbands from the $-CH_3$ and α-CH carbons. (b) TOSS spectrum illustrating the attenuation of the sidebands and the loss of intensity that occurs for the $-CO_2^-$ centerband—i.e., it should be of equal intensity to the other lines in the spectrum. (c) TOSS/Scaling spectrum demonstrating that the signal intensity present in the rotational sidebands may be transferred to the centerband. The noise in the baseline has increased owing to the greater bandwidth used for the integrate-and-hold circuit that sampled the magnetization

the $-CO_2^-$ centerband increases by a factor of approximately five.

4.3 Rotor Frequency Lines and Powder Lineshapes

In a multiple pulse experiment, a factor responsible for limiting resolution is the (lack of) perfection of the pulse train. In fact, the development of pulse sequences that compensate for pulse errors has been a major industry in NMR. The effects of pulse errors also appear in MAS multiple pulse experiments—but in an unexpected manner. In many practical cases, a scaling or CRAMPS experiment with a scale factor of 0.5 will move the intensity to the centerbands, which are then readily identifiable. In addition, however, extra lines appear in the spectra at 0, $\pm n\omega_r/2\pi$, etc., which are referred to as *rotor frequency lines*.[28,36,37] These lines are also observed in ^1H CRAMPS spectra and appear and disappear as the resonance offset is changed.[36,37,50]

A theoretical explanation of these phenomena[28,50] is rather lengthy and involved. Physically, the origin of rotor lines is the presence of small pulse errors, which create components perpendicular to the average Hamiltonian and lead to a significant alteration in the paths of the magnetization vectors. For example, if a small (about 2%) pulse error is included in the calculation—the scaling is performed with 270°_x, $265^\circ_{\bar{x}}$ pulses rather than $270^\circ_{x(\bar{x})}$ pulses—then rotor frequency lines at 0 and $\pm n\omega_r/2\pi$ appear in the spectra. Concurrently, the intensity is reduced, since the signal goes into the rotor line rather than the real spectrum.

Finally, it should be mentioned that scaling, MREV-8, and other multiple pulse experiments function well as long as the cycle times of the experiments satisfy the condition $\tau_c < \tau_r$. In practice, this means there are three or more pulse cycles per rotor period. With fewer cycles, $\tau_c \approx \tau_r$ and a number of interesting phenomena occur. For example, when $2\tau_c = \tau_r$, powder patterns rather than sharp lines appear in the spectra, albeit in distorted forms.[20,36,37,51,52]

5 MULTIDIMENSIONAL MAS EXPERIMENTS

In this section, we review some of the early and simplest multidimensional MAS experiments employed for resolving and correlating various interactions in solid state NMR spectra. Our discussion will focus primarily on 2D experiments for

1. separation of isotropic and anisotropic chemical shifts;
2. separation of the heteronuclear dipolar interaction and chemical shifts;
3. heteronuclear chemical shift correlation spectroscopy;
4. 2D chemical exchange experiments.

This is currently a rapidly expanding area, and correlation experiments involving other homonuclear and heteronuclear dipolar interactions are discussed in ***Homonuclear Recoupling Schemes in MAS NMR*** and ***REDOR and TEDOR***.

5.1 Isotropic and Anisotropic Chemical Shifts

As discussed above, MAS NMR spectra sometimes display large numbers of sidebands, which degrade the resolution. Restoration of the resolution provided the impetus for the development of the TOSS, Scaling, and TOSS/Scaling experiments. However, since these experiments discard two-thirds of the information available in the spectra, it is useful to consider methods to restore these data. This problem was originally addressed with a 2D experiment with isotropic chemical shifts on one axis and isotropic and anisotropic on the second.[37] In order to extract the isotropic spectrum, the magnetization was sampled synchronously with the rotation in the $\omega_1/2\pi$ dimension, yielding the isotropic spectrum, and sampled without restriction in $\omega_2/2\pi$, which will contain both isotropic and anisotropic shifts. The difficulty

with synchronous sampling is the limited bandwidth in the $\omega_1/2\pi$ dimension (typically $\pm 2-4$ kHz), which is too small to accommodate the dispersion of isotropic ^{13}C shifts at superconducting fields (about 20 kHz). Therefore, the spectra will be aliased in this dimension, and, for example, lines from the $-CH_3$, $-CH_2-$ region of the spectrum will appear in the aromatic/carboxyl region. However, the $\omega_2/2\pi$ dimension contains *redundant* information—namely, both the isotropic and anisotropic shifts—and, for this reason, this sort of problem will not generally occur. Nevertheless, in certain situations, the 2D spectrum will not be completely resolved—in particular, when two resonances, δ_i and δ_j, satisfy the following two conditions: (i) $\delta_i - \delta_j = n\omega_r/2\pi$ and (ii) their shift anisotropies are sufficiently large that their sideband patterns overlap. Because the isotropic shifts are separated by $n\omega_r/2\pi$, they occur at the same frequency in $\omega_1/2\pi$, and their sideband patterns are then overlapped. However, by incorporating chemical shift scaling into the t_1 dimension, it is possible to circumvent this problem and to affect a complete resolution of the spectrum.[37]

A second solution to this problem is the TOSSOT experiment,[29] whose pulse sequence is shown in Figure 9, and will be recognized as forward and reverse TOSS. Initially, the TOSS sequence prepares magnetization to yield a t_1 period of isotropic evolution, while the time-reversed TOSS restores the anisotropic spectrum during t_2. The physical basis for the experiment is that the spin packet alignment resulting from TOSS can be restored at any time subsequent to its preparation by a mirror image sequence. However, TOSS must be initiated at the peak of a rotor echo to perform sideband suppression. Thus, in the present scheme, it is not possible to initiate TOSS at an arbitrary time in a rotor period. In addition, the TOSSOT scheme does show significant resonance offset effects, so care must be exercised in extracting anisotropies. Nevertheless, the experiment functions well in performing a 2D separation of isotropic shifts in $\omega_1/2\pi$ and isotropic plus anisotropic in $\omega_2/2\pi$. A 2D resolved spectrum of Tyr · HCl taken at $\omega_r/2\pi$ = 1.7 kHz illustrating the technique is shown in Figure 10. Note the substantial sideband manifolds present for the aromatic lines, which are clearly separated by their isotropic chemical shift. These lines are strongly overlapped in the 1D projection shown at the top.

The TOSSOT experiment has recently been employed by Geen and Bodenhausen[43,44] in studies of chemical exchange and in observation of isotropic chemical shifts.

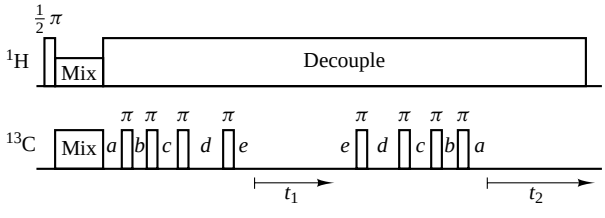

Figure 9 TOSSOT (TOSS/reverse TOSS) pulse sequence for 2D resolution of isotropic and anisotropic chemical shifts. The interpulse delays measured from the centers of the π pulses were (in fractions of a rotor period) a = 0.1226, b = 0.0773, c = 0.2236, d = 1.0433, and e = 0.7744

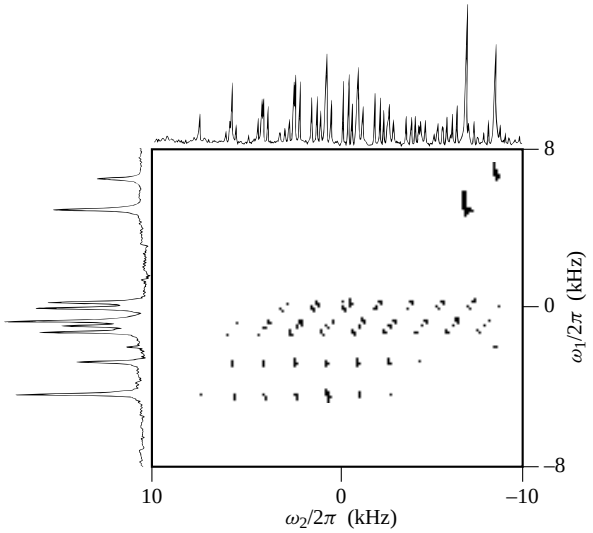

Figure 10 2D resolved ^{13}C TOSSOT spectrum of Tyr · HCl, $\omega_r/2\pi$ = 1.7 kHz. The normal MAS spectrum is given at the top and the ω_1 projection on the left. Slices in ω_1 with negative intensity were phase-reversed in the ω_1 projection. The ^{13}C pulse length was 8.0 s

5.2 Heteronuclear Dipolar and Chemical Shift

The heteronuclear dipolar coupling, like the chemical shift, is an inhomogeneous interaction, and will therefore yield sharp sidebands in a MAS experiment. Thus, if homonuclear couplings can be suppressed with an MP train, it is possible to separate the heteronuclear dipolar interaction and the chemical shift in a 2D correlation experiment. The Hamiltonian for this system is conveniently written as

$$\hat{\mathcal{H}} = a(\Omega,t)\hat{S}_z + b(\Omega,t)\hat{I}_z\hat{S}_z + c(\Omega,t)\sum_{i,j}(\hat{\boldsymbol{I}}_i \cdot \hat{\boldsymbol{I}}_j - 3\hat{I}_{iz}\hat{I}_{jz}) \qquad (16)$$

where we have collected the angular and temporal dependence in the coefficients $a(\Omega,t)$, $b(\Omega,t)$, and $c(\Omega,t)$. There are several pulse sequences that can be used to affect the desired separation, two of which are shown in Figure 11. The magnetization is prepared by cross polarization, and during t_1, the $a(\Omega,t)$ and $c(\Omega,t)$ terms are removed from equation (16) by application of a refocusing pulse and MREV-8, respectively. What remains during t_1 is the heteronuclear $\hat{I}_z\hat{S}_z$. During t_2, ^{1}H decoupling is applied, removing the $b(\Omega,t)$ and $c(\Omega,t)$ terms and leaving the chemical shift term $\hat{S}_z$. In addition, spectra are often recorded in the regime $\omega_r/2\pi < \Delta\sigma$, so we initiate sampling at the peak of a rotational echo to ensure the proper phase relationship among the sidebands in the chemical shift domain; t_1 thus runs from 0 to $N\tau_r$, and sampling commences at $2N\tau_r$.

The 2D dipolar/chemical shift (DIPSHIFT) spectra obtained from this experiment consist of a matrix of sidebands spaced at $\omega_r/2\pi$ in each dimension, which display two unusual features illustrated in Figure 12. The dipolar slices corresponding to chemical shift sidebands are asymmetric, and inverted sidebands are present in some of the slices. The origin of this effect has been discussed elsewhere,[53] and is due to the weighting of symmetric dipolar slices by the chemical shift,

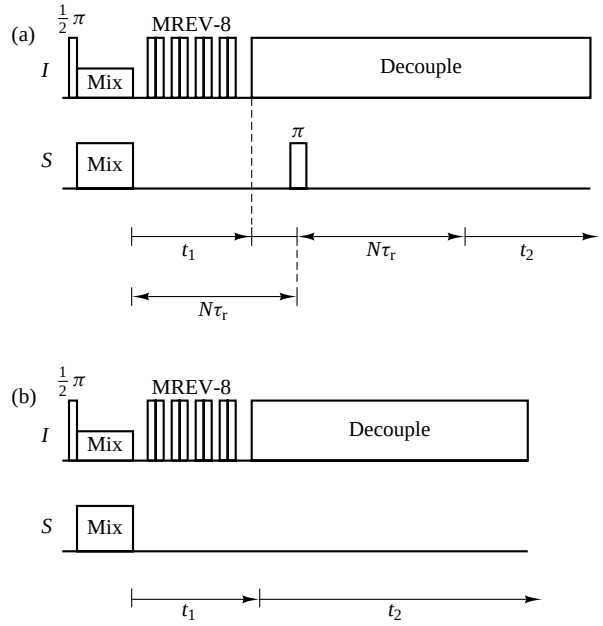

Figure 11 Pulse sequences for 2D dipolar–chemical shift spectroscopy. (a) The constant time experiment with a rotor synchronized π pulse to refocus isotropic chemical shifts at $N\tau_r$. Acquisition commences at $2N\tau_r$. (b) Simplified experiment where a shearing transformation is required to align the sideband manifolds

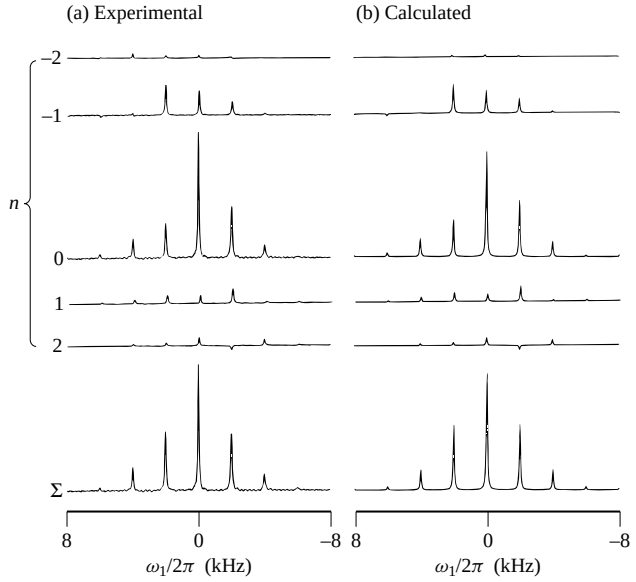

Figure 12 2D dipolar chemical shift spectra of ^{15}N-acetyl-DL-valine (NAV) $\omega_r/2\pi$ = 2.000 kHz. Slices were taken on points corresponding to sideband frequencies in ω_2. (a) Spectrum from the experiment of Figure 11 after shearing. (b) Simulation using the chemical shift tensor, the N–H bond length, and the nutual orientation of the chemical shift and dipolar tensors of NAV; σ_{11} = −64.7 ppm, σ_{22} = −39.7 ppm, σ_{33} = 104.4 ppm and r_{NH} = 105 pm. Polar angles of the NH bond in the principal axis system of the N shielding tensor are (θ, ϕ) = (22°, 0°). The multiple pulse scaling factor was κ = 0.480

leading to asymmetric and inverted sidebands. The dipolar slices corresponding to four sidebands and a centerband for the ^{15}N–^{1}H DIPSHIFT spectrum obtained from *N*-acetyl-DL-valine is shown in Figure 12, and the asymmetric intensities in the dipolar slices and inverted sidebands are apparent. When a full powder average is performed—i.e., when the dipolar and chemical shift spectra are projected onto the $\omega_1/2\pi$ and $\omega_2/2\pi$ axes, respectively—these two features disappear, as shown in Figure 12. The experimental spectrum and simulation of Figure 12 agree extremely well, and yield r_{NH} = 104.9 ± 0.3 pm and an angle between the σ_{33} element of the tensor and the NH direction of 22° in agreement with single crystal studies. Differences in tensor orientation as small as 5° lead to sideband intensities that are perceptively different.

The salient feature of the DIPSHIFT experiment is that it can locate protons in polycrystalline or amorphous solids. This cannot be done accurately with X-rays, and instead requires a neutron diffractometer and large single crystals. Furthermore, the NMR experiment is relatively easy to perform, and can yield proton-rare spin bond distances with a precision of better than 0.5% and relative orientations of tensors to less than 5°. This has been studied in an experimental comparison of neutron and NMR data,[54] and the NMR bond distances are consistently about 3.5 pm longer than the diffraction results owing to different vibrational averaging.[55] Otherwise, there is an excellent correlation between the two techniques, indicating that DIPSHIFT-type experiments can be used to obtain structural data on polycrystalline samples.

There have been a number of other versions and applications of DIPSHIFT experiments. For example, the sequence shown in Figure 11(b) yields the same spectra as Figure 11(a), but with improved signal-to-noise, since there is only a delay of t_1 prior to sampling. However, the slices in the chemical shift dimension must be corrected with a shearing transformation.[56]

In addition, sequences with scaling and double windows[57,58] have been described, as have measurements of bond distances in DNA[59] and studies of dynamics of aromatic rings in polymers.[60]

5.3 Heteronuclear Correlation Spectra

Another 2D experiment that is extremely useful in solution NMR is heteronuclear correlation spectroscopy,[61] where, for example, the ^{13}C spectrum is used to increase dispersion of the ^{1}H spectrum. Since resolution in the ^{1}H spectra of solids is relatively poor, it could possibly be improved with such a technique. The basic sequence for correlation spectroscopy has a preparation period consisting of a 90° pulse on ^{1}H, and during the evolution, a multiple pulse train is applied to ^{1}H while decoupling ^{13}C; thus, only ^{1}H chemical shifts persist. This is followed by a mixing period and detection of ^{13}C in the presence of ^{1}H decoupling. During the mixing period, several schemes can be employed to transfer coherence between the spin reservoirs. Some possibilities considered by Roberts et al.[62] were normal cross polarization, single pulse transfers, and pulse transfers involving MREV-8, while Caravatti et al.[63] proposed an interesting windowless isotropic mixing sequence (WIM) for this purpose. The optimal mixing technique depends somewhat on the sample being studied. For molecules like adamantane and *cis*-polybutadiene, the pulse transfer schemes work well, whereas for rigid solids the simultaneous MREV-8 cycles or the WIM sequence are preferable because of their selectivity. Burum and Bielecki[64] have further improved these schemes,

focusing on the homonuclear and heteronuclear decoupling during the evolution period.

5.4 Dynamic Processes in Solids

Over the last decade, several groups have employed MAS in 2D exchange experiments for solids.[65–68] Typically, these experiments have involved studies of intramolecular proton transfer processes or the dynamics of motion of aromatic rings or polymers.[45] In the fast spinning limit ($\Delta\sigma/\nu_r < 1$), the solid state experiment is a simple modification of Jeener's classic three-pulse sequence,[39] except that the first $\frac{1}{2}\pi$ pulse in Jeener's sequence is typically replaced by cross polarization, and ^{1}H decoupling is applied during t_1 and t_2. In the opposite high-field limit, where the 1D spectrum exhibits sidebands ($\Delta\sigma/\nu_r > 1$), the 2D spectrum will be complicated by 'self-cross peaks' between every sideband in a sideband family, even if that resonance is not undergoing exchange. Veeman and co-workers[66] demonstrated that an exchange spectrum may be observed when $\Delta\sigma/\nu_r > 1$, provided that the mixing period is synchronized with the rotor period.

Clearly, isotropic evolution during t_1 (or t_2) will eliminate self-cross peaks, and the exchanging signals will not be dispersed over sidebands in either dimension. In early experiments, this was accomplished by working at low fields or by inserting chemical shift scaling into t_1, which focused the intensity into the centerband. Thus, proton transfer in tropolone[65] and slow aromatic ring flips occurring with a time constant of about 4 s in *p*-nitroanisole were examined.[67] More recently, a variety of slow motions in polymers have been studied,[45] as well as intermolecular exchange processes involving proton transfers in oxalic acid dihydrate between the COOHs and H_2Os of hydration.[69] 2D ^{1}H spectra (obtained from ^{2}H-labeled samples to eliminate ^{1}H dipole broadening) showing cross peaks due to this exchange process are shown in Figure 13. The exchange has a rate constant of about $55\,s^{-1}$ at 17 °C and $E_a \approx 35.6\,kJ\,mol^{-1}$. The 2D experiment is also extremely useful in elucidating complicated exchange networks in solids, as shown by spectra of the complex of oxalic acid and ammonium hydrogen oxalate hydrate.[69]

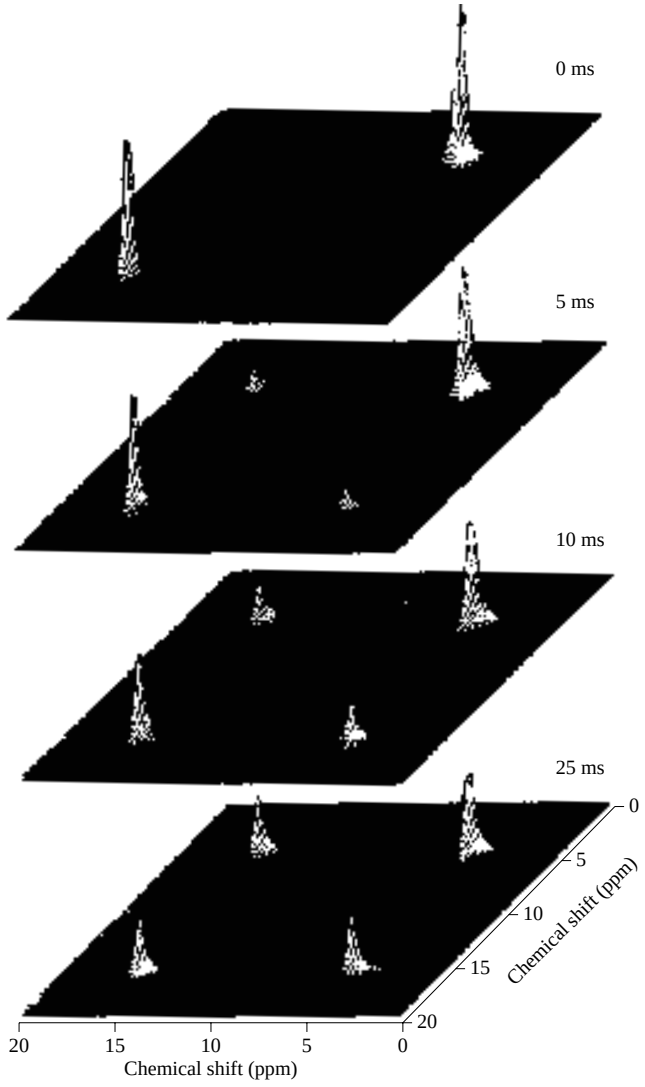

Figure 13 2D 400 MHz ^{1}H spectra of oxalic acid dihydrate (90% ^{2}H-labeled) obtained with the Jeener three-pulse (NOESY) sequences. Note the cross peaks due to proton transfer between the −COOH and H_2O moieties

6 RELATED ARTICLES

Average Hamiltonian Theory; CRAMPS; Double Rotation; Dynamic Angle Spinning; High Speed MAS of Half-Integer Quadrupolar Nuclei in Solids; Homonuclear Recoupling Schemes in MAS NMR; Magic Angle Spinning; Magic Angle Turning and Hopping; Probe Design and Construction; REDOR and TEDOR; Sideband Analysis in Magic Angle Spinning NMR of Solids.

7 REFERENCES

1. I. J. Lowe, *Phys. Rev. Lett.*, 1959, **2**, 285.
2. E. R. Andrew, A. Bradbury, and R. G. Eades, *Nature (London)*, 1958, **182**, 1659.
3. E. R. Andrew, L. F. Farnell, and T. D. Gledhill, *Phys. Rev. Lett.*, 1967, **19**, 6.
4. E. R. Andrew, M. Firth, A. Jasinski, and P. J. Randall, *Phys. Lett. A*, 1970, **31**, 446.
5. M. M. Maricq, and J. S. Waugh, *J. Chem. Phys.*, 1979, **70**, 3300.
6. J. S. Waugh, L. M. Huber, and U. Haeberlen, *Phys. Rev. Lett.*, 1968, **20**, 180.
7. P. Mansfield, *J. Phys. C*, 1971, **4**, 1444.
8. D. P. Burum and W.-K. Rhim, *J. Chem. Phys.*, 1979, **71**, 944.
9. D. P. Burum, M. Linder, and R. R. Ernst, *J. Magn. Reson.*, 1981, **44**, 173.
10. I. J. Lowe and R. E. Noreberg, *Phys. Rev.*, 1957, **107**, 46.
11. R. R. Ernst and W. Anderson, *Rev. Sci. Instrum.*, 1966, **37**, 93.
12. S. Hartmann and E. L. Hahn, *Phys. Rev.*, 1962, **128**, 2092.
13. L. Sarles and R. Cotts, *Phys. Rev.*, 1958, **111**, 853.
14. F. Bloch, *Phys. Rev.*, 1958, **111**, 841.
15. A. Pines, M. G. Gibby, and J. S. Waugh, *J. Chem. Phys.*, 1973, **59**, 569.
16. U. Haeberlen and J. S. Waugh, *Phys. Rev.*, 1968, **175**, 453.
17. J. Schaefer and E. O. Stejskal, *J. Am. Chem. Soc.*, 1976, **98**, 1031.

18. B. C. Gerstein, R. G. Pembleton, R. C. Wilson, and L. M. Ryan, *J. Chem. Phys.*, 1971, **66**, 361.
19. E. R. Andrew, W. S. Hinshaw, and R. S. Teffin, *J. Magn. Reson.*, 1974, **15**, 191.
20. E. Lippmaa, E. Alla, and T. Tuherm, in *Proceedings of 19th Ampère Congress, Heidelberg, 1976*, p. 113.
21. E. O. Stejskal and J. Schaefer, *J. Magn. Reson.*, 1977, **25**, 569.
22. M. M. Maricq and J. S. Waugh, *Chem. Phys. Lett.*, 1977, **47**, 327.
23. R. A. Haberkorn, *J. Am. Chem. Soc.*, 1978, **100**, 1296.
24. U. Haeberlen, *High Resolution NMR in Solids: Selective Averaging. Advances in Magnetic Resonance, Supplement No. 1*, Academic Press, New York, 1976.
25. A. Portis, *Phys. Rev.*, 1953, **91**, 1071.
26. M. H. Levitt, in *Progress in Nuclear Magnetic Resonance Spectroscopy*, ed. J. W. Emsley, J. Feeney, and L. H. Sutcliffe, Pergamon Press, Oxford, 1986, Vol. 18, p. 61.
27. J. S. Waugh, *J. Magn. Reson.*, 1982, **50**, 30.
28. E. T. Olejniczak, S. Vega, and R. G. Griffin, *J. Chem. Phys.*, 1984, **81**, 4804.
29. A. C. Kolbert and R. G. Griffin, *Chem. Phys. Lett.*, 1990, **166**, 87.
30. G. S. Harbison, S. O. Smith, J. A. Pardoen, J. M. L. Courtin, J. Lugtenburg, J. Herzfeld, R. A. Mathies, and R. G. Griffin, *Biochemistry*, 1985, **24**, 6955.
31. J. Hu, J. Herzfeld, and R. G. Griffin, *Proc. Natl. Acad. Sci. USA*, in press.
32. W. T. Dixon, *J. Chem. Phys.*, 1982, **77**, 1800.
33. J. Hong and G. S. Harbison, *J. Magn. Reson., Ser. A*, 1993, **105**, 128.
34. Z. Song, O. N. Antzutkin, X. Feng, and M. H. Levitt, *Solid State NMR*, 1993, **2**, 143.
35. D. P. Raleigh, E. T. Olejniejak, and R. G. Griffin, *J. Chem. Phys.*, 1988, **89**, 1333.
36. W. P. Aue, D. J. Ruben, and R. G. Griffin, *J. Magn. Reson.*, 1982, **46**, 354.
37. W. P. Aue, D. J. Ruben, and R. G. Griffin, *J. Chem. Phys.*, 1984, **80**, 8302.
38. D. P. Raleigh, E. T. Olejniczak, S. Vega, and R. G. Griffin, *J. Magn. Reson.*, 1986, **106**, 8302.
39. D. P. Raleigh, E. T. Olejniczak, S. Vega, and R. G. Griffin, *J. Magn. Reson.*, 1987, **72**, 238.
40. S. S. Lang, *J. Magn. Reson.*, 1993, **104**, 345.
41. O. N. Antzukin, Z. Song, X. Feng, and M. H. Levitt, *J. Chem. Phys.*, 1994, **100**, 130.
42. N. C. Nielsen, H. Bildsoe, and H. J. Jakobsen, *J. Magn. Reson.*, 1988, **80**, 149.
43. H. Geen and G. Bodenhausen, *J. Chem. Phys.*, 1992, **97**, 2928.
44. H. Geen and G. Bodenhausen, *J. Am. Chem. Soc.*, 1993, **115**, 1529.
45. A. Hagemeyer, Schmitt-Rhom, and H. W. Spiess, in *Advances in Magnetic Resonance*, ed. J. S. Waugh, Academic Press, New York, 1989, vol. 13, p. 85.
46. J. D. Ellett, Jr. and J. S. Waugh, *J. Chem. Phys.*, 1969, **51**, 2851.
47. W. P. Aue and R. R. Ernst, *J. Magn. Reson.*, 1978, **31**, 533.
48. W. P. Aue, D. P. Burum, and R. R. Ernst, *J. Magn. Reson.*, 1980, **38**, 375.
49. D. P. Raleigh, E. T. Olejniejak, and R. G. Griffin, *J. Magn. Res.*, 1991, **93**, 472.
50. S. Vega, E. T. Olejniczak, and R. G. Griffin, *J. Chem. Phys.*, 1984, **80**, 4832.
51. A. Bax, N. Szeverenyi, and G. E. Maciel, *J. Magn. Reson.*, 1983, **51**, 400.
52. Y. Yarmin-Agaev, P. N. Tutunjian, and J. S. Waugh, *J. Magn. Reson.*, 1982, **47**, 51.
53. M. G. Munowitz and R. G. Griffin, *J. Chem. Phys.*, 1982, **76**, 2848.
54. J. E. Roberts, G. S. Harbison, M. G. Munowitz, J. Herzfeld, and R. G. Griffin, *J. Am. Chem. Soc.*, 1987, **109**, 4163.
55. E. R. Henry and A. Szabo, *J. Chem. Phys.*, 1985, **82**, 4753.
56. A. C. Kolbert, M. H. Levitt, and R. G. Griffin, *J. Magn. Reson.*, 1989, **85**, 42.
57. M. G. Munowitz, W. P. Aue, and R. G. Griffin, *J. Chem. Phys.*, 1982, **77**, 1686.
58. M. G. Munowitz and R. G. Griffin, *J. Chem. Phys.*, 1983, **78**, 613.
59. J. A. Diverdi and S. J. Opella, *J. Am. Chem. Soc.*, 1982, **104**, 1761.
60. J. Schaefer, E. O. Stejskal, R. A. McKay, and W. T. Dixon, *Macromolecules*, 1986, **17**, 1479.
61. G. Bodenhausen and R. Freeman, *J. Magn. Reson.*, 1977, **28**, 471.
62. J. E. Roberts, S. Vega, and R. G. Griffin *J. Am. Chem. Soc.*, 1984, **106**, 2506.
63. P. Caravatti, L. Braunschweiler, and R. R. Ernst, *Chem. Phys. Lett.*, 1983, **100**, 305.
64. D. P. Burum and A. Bielecki, *J. Magn. Reson.*, 1991, **95**, 184.
65. N. M. Szeveranyi, M. J. Sullivan, and G. E. Maciel, *J. Magn. Reson.*, 1982, **47**, 462.
66. A. F. De Jong, A. P. M. Kentgens, and W. S. Veeman, *Chem. Phys. Lett.*, 1984, **109**, 337.
67. G. S. Harbison, D. P. Raleigh, J. Herzfeld, and R. G. Griffin, *J. Magn. Reson.*, 1985, **64**, 284.
68. J. Jeener, B. H. Meier, P. Bachmann, and R. R. Ernst, *J. Chem. Phys.*, 1979, **71**, 4546.
69. L. Zheng, K. W. Fishbein, R. G. Griffin, and J. Herzfeld, *J. Am. Chem. Soc.*, 1993, **115**, 6245.

Biographical Sketch

Robert G. Griffin. *b* 1942. B.S., 1964, University of Arkansas, USA, Ph.D., 1969, Washington University, St. Louis. Postdoctoral Fellow, Department of Chemistry, MIT 1969–72. Staff member, Francis Bitter National Magnet Laboratory, MIT, 1972–1989. Professor of Chemistry, MIT, 1989–present. Director, Francis Bitter National Magnet Laboratory, 1992 – present. Approx. 190 publications. Research interest include development of new methods for performing high-resolution NMR experiments in solids, high-frequency DNP and EPR, and applications of these techniques to problems in biological, chemical, and physical systems.

Rudimentary NMR: The Classical Picture

Bernard C. Gerstein
Ames Laboratory of the US DOE, Iowa State University, Ames, IA, USA

1	Introduction	1
2	Classical Mechanics of Precession: Magnetic Resonance	1
3	The Bloch Equations: Relaxation in the Classical System	2
4	The Rotating Frame	3
5	The Pulse NMR Experiment: Pulse and Fourier Transform NMR	5
6	Chemically Shifted Spectra	6
7	Related Articles	8
8	References	8

1 INTRODUCTION

The phenomenon of a *N*ucleus with a magnetic moment, placed in a *M*agnetic field, *R*esonating with a radiofrequency excitation (NMR), first reported[1,2] in 1946, has become one of the single most powerful quantitative and qualitative analytical tools for the physical scientist, materials scientist, biological scientist, geologist, and medical diagnostician.[3] In this section, we consider some simple ideas that may lead to an understanding of why such a strong statement is made. We shall just consider a classical picture of NMR for purposes of a simple introduction to the field. Both the classical and quantum pictures are provided in a more comprehensive treatment[4] not appropriate to this Encyclopedia.

Consider a child's top, which is initially lying at rest on the floor. The child grabs the handle, and excitedly proceeds to pump it up and down to set the top spinning. Here, at least four different phenomena may be observed. First is the vigorous action of the child in setting the top in motion; in this case, a 'pumping' of the handle, which imparts a circular motion to the top via a vertical up-and-down motion of the handle. Second is just the spinning. Soon, as the spinning axis becomes tipped from the perpendicular, i.e., from alignment of the spinning axis with the Earth's gravitational field, a wobble, or precession, is also seen. This precession is the natural consequence of the reaction of an angular momentum, in this case that of the spinning top, with its vector aligned along the spinning axis, to a noncollinear field, here the Earth's gravitational field perpendicular to the surface of the Earth. Finally, if left alone after the energy has been pumped into the top to set it spinning, the top will relax to its initial equilibrium position lying on the floor. So, we have excitation, precession, and relaxation. Exactly the same phenomena may be observed among some nuclei placed in a magnetic field, and pumped with radiofrequency energy. One of the intriguing aspects about nuclear magnetic resonance, which is fundamentally a quantum mechanical phenomenon, is that there are such easily understood classical analogs to many of the phenomena that may be observed in NMR. Let us look at some of these. In doing so, of course, we will invoke the fact that nuclei are really particles that must obey quantum mechanics, and therefore behave discretely.

2 CLASSICAL MECHANICS OF PRECESSION: MAGNETIC RESONANCE

The classical mechanics of the precessional motion of a spinning body in a field $\boldsymbol{g}$, say, is well understood: a spinning body with mass m at a distance $\boldsymbol{r}$ from the spinning axis possesses an angular momentum $\boldsymbol{L}$. There is a torque, i.e., a twisting force, upon the body. This torque, $\boldsymbol{G}$, say, is perpendicular with both the angular momentum $\boldsymbol{L}$ and the field $\boldsymbol{g}$, and so is proportional to their cross product: $\boldsymbol{G} = \Gamma \boldsymbol{L} \times \boldsymbol{g}$. Torque is the rate of change of angular momentum with time (similarly to the way in which force is the rate of change of momentum), and so we have the equation of motion

$$\boldsymbol{G} = \frac{\mathrm{d}\boldsymbol{L}}{\mathrm{d}t} = \Gamma \boldsymbol{L} \times \boldsymbol{g} \tag{1}$$

The resulting classical motion is obviously a precession of the angular momentum vector about the field, at angular velocity $\boldsymbol{\omega} = -\Gamma \mathbf{g}$ (i.e., with precession frequency $\omega = \Gamma g$), as illustrated for the top in Figure 1.

One picture that we have of the nucleus (e.g., of the proton, which is the nucleus of the hydrogen atom) is that of a spinning electric charge. The spinning imparts an angular momentum to the charge. The fact that it is a charge, e, that is spinning imparts a magnetic moment to this hydrogen nucleus, in the same manner in which we create a magnet by running a current through an inductor. The classical relation between a charge e of mass m circulating about an area A with linear velocity v, resulting in a current i and the magnetic field $\boldsymbol{B}$ created by this situation and aligned along the $\boldsymbol{k}$ direction (the z axis) in space corresponds to the existence of a magnetic moment

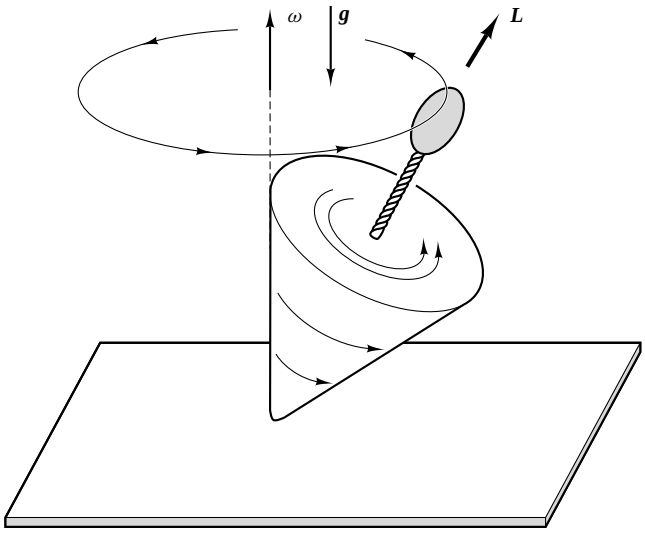

Figure 1 Motion of an angular momentum $\boldsymbol{L}$ in a field, as illustrated by the motion of a child's toy top in the Earth's field $\boldsymbol{g}$

$$\frac{\boldsymbol{M}}{4\pi} = \frac{\boldsymbol{k}iA}{c} = \boldsymbol{k}\frac{\mathrm{d}q}{\mathrm{d}t}\frac{A}{c} = \boldsymbol{k}\frac{m}{m}e\frac{v}{2\pi r}\frac{A}{c} = \boldsymbol{k}\frac{emv}{2mc\pi r}\frac{\pi r^2}{c}$$
$$= \boldsymbol{k}\frac{mvre}{2mc} = e\boldsymbol{r}\times\frac{m\boldsymbol{v}}{2mc} = \frac{e\boldsymbol{r}\times\boldsymbol{p}}{2mc} = \frac{e\boldsymbol{L}}{2mc} \equiv \gamma\boldsymbol{L} \quad (2)$$

We see, then, that we may expect the nucleus of a hydrogen atom to have a magnetic moment that is proportional to the nuclear angular momentum $\boldsymbol{L}$. Since nuclear angular momenta come quantized in units of $h/2\pi$, we write the nuclear angular momentum in terms of the quantum number I, with the total nuclear angular momentum being $\boldsymbol{L} = 2\pi\boldsymbol{I}$. So the magnetic moment is given by the magnetogyric ratio times the angular momentum: $\boldsymbol{\mu} = (e/2mc)\boldsymbol{L} \equiv \gamma\boldsymbol{L}$. The correct quantum mechanical result is a factor of two higher, namely, e/mc. The classical equation of motion of this moment in a magnetic field $\boldsymbol{B}$ is

$$\frac{\mathrm{d}\boldsymbol{\mu}}{\mathrm{d}t} = \gamma\boldsymbol{\mu}\times\boldsymbol{B} \quad (3)$$

and the classical motion is a precession of $\boldsymbol{\mu}$ about the field $\boldsymbol{B}$ with angular frequency $\boldsymbol{\omega} = -\gamma\boldsymbol{B}$. In quantum mechanics, of course, $\boldsymbol{I}$ becomes an operator $\hat{\boldsymbol{I}}$ with magnitude $[I(I+1)]^{1/2}$, and the allowed projections of $\hat{\boldsymbol{I}}$ along the z axis of quantization (as set by an external magnetic field) are given by the allowed quantized values of $\hat{I}_z$, the component of $\hat{\boldsymbol{I}}$ along the field, which range from $-I$ to $+I$ in steps of unity. For a proton, $I = \frac{1}{2}$, and the allowed expectation values of $\hat{I}_z$ are $-\frac{1}{2}$ and $+\frac{1}{2}$ in units of $h/2\pi$. With the classical energy of a magnetic moment $\boldsymbol{\mu}$ in a field $\boldsymbol{B}$ being

$$E = -\boldsymbol{\mu}\cdot\boldsymbol{B} = -\gamma\boldsymbol{L}\cdot\boldsymbol{B} \quad (4)$$

which corresponds to magnets aligning north–south, north–south beside each other, we see that a classical picture of a quantized moment $\hat{\boldsymbol{\mu}} = \gamma\hat{\boldsymbol{I}}$ in a magnetic field $\boldsymbol{B}$ corresponds to discrete energies

$$E_{1/2} = -\frac{1}{2}\gamma B_0 \equiv -\frac{1}{2}\omega_0 \quad (5a)$$

$$E_{-1/2} = \frac{1}{2}\gamma B_0 \equiv \frac{1}{2}\omega_0 \quad (5b)$$

in which the classical motion of the 'high' energy state, with energy $E_{-1/2}$, is a precession of the classical vector $\boldsymbol{\mu}$ about the field $\boldsymbol{B}$, with the component of $\boldsymbol{\mu}$ along the field being oriented in the same direction as the field, as shown in Figure 2. Similarly, the 'low' energy state, with energy $E_{1/2}$, corresponds to a classical motion in which $\boldsymbol{\mu}$ precesses about $\boldsymbol{B}$, but has direction aligned oppositely to that of $\boldsymbol{B}$, as would the energy of two bar magnets be minimized if they were aligned north–south, north–south, and maximized if they were aligned the other way.

In summary, we have the following.

1. Many nuclei have magnetic moments, with the relation between the classical moment and the quantized angular momentum being $\hat{\boldsymbol{\mu}} = \gamma\hat{\boldsymbol{I}}$.
2. In a magnetic field $\boldsymbol{B}$, the classical motion of these nuclei is a precession about $\boldsymbol{B}$.
3. Since the nuclear moments are quantized, only discrete precessional states are allowed, and these correspond to energies (in units of frequency) $-I\omega, -(I-1)\omega, \ldots, I\omega$.

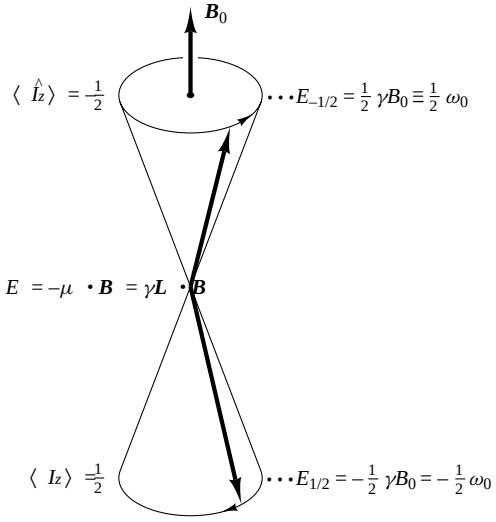

Figure 2 Energies of the two z components of the angular momentum of a spin-1/2 nucleus in a field $\boldsymbol{B}$

In the article ***Nuclear Spin Properties and Notation*** is given a table of the magnitudes of the magnetic moments of nuclei, and their precessional frequencies for a fixed field. For example, in a field of 2.3 T, the nuclide ^{13}C will precess at an angular frequency of $\omega = 2\pi \times 25 \times 10^6$ rad s^{-1}, corresponding to a frequency $\nu = 25$ MHz. Note the relation $2\pi\nu = \omega$.

An immediate translation of the above ideas is that when a nucleus (e.g., ^{1}H) with spin quantum number $I = \frac{1}{2}$, is in a magnetic field $\boldsymbol{B}_0$, its lowest energy state will be with its moment aligned against the field, and precessing happily at its Larmor frequency $\omega_0 = \gamma B_0$, corresponding to the vector picture $\boldsymbol{\omega}_0 = -\boldsymbol{B}_0$. The magnitude of the precessional frequency is familiar to those who listen to FM radio; it is in the radiofrequency range of tens to hundreds of megahertz. If, therefore, a frequency matching this precessional frequency is applied to this nucleus precessing in a field, a possibility is that the nucleus will 'resonate' with this precessional frequency, in much the same manner that a car wheel that is out of balance will cause a vibration of the car suspension system when the 'natural' vibrational frequency of the wheel's rotation and that of the suspension system match each other. The nucleus can absorb energy from the radiofrequency field, but, since it is a sufficiently small particle, it must obey quantum mechanics, and its energies are quantized—for a proton, by $\Delta E = E_{1/2} - E_{-1/2} = \omega_0$. This resonance of a nucleus being driven by a radiofrequency oscillation in a magnetic field is called NMR, nuclear magnetic resonance. Of course, once a system absorbs energy, if allowed sufficient time, it will relax to its initial equilibrium state, as did the child's top when it slowed, and finally rolled to a stop, which was its state before the child excited it by pumping the handle. In fact, both the absorption of energy to an excited state and the emission of energy accompanying relaxation to the equilibrium ground state involve relaxation processes—the first a 'relaxation' to the 'new' equilibrium state in the presence of a driving excitation, and the second to the old equilibrium state in the absence of the excitation. Let us look at this business of 'relaxation' in a bit more detail.

3 THE BLOCH EQUATIONS: RELAXATION IN THE CLASSICAL SYSTEM

Imagine an ensemble of nuclear spins $I = \frac{1}{2}$, for example, ^{1}H in H_2O(gas). Classical thermodynamics tells us that at equilibrium in the absence of fields (e.g., magnetic, gravitational, and electric fields) the number of macroscopic variables that completely specify the state of this system is $C + 2$, where C is the number of compounds or elements needed to prepare the system in the specified state. For example in the case of gaseous water, $C = 1$, since we need only take water from the tap to prepare the system as described. For H_2O(g), $C + 2 = 3$, and only three of the four total variables, which are the extensive variables n and V, and the intensive variables P and T, are needed to uniquely specify the state described by $PV = nRT$. Now let us place this water vapor, suitably contained in an NMR tube, in the magnetic field of, let us say, a magnet with static field 2.3 T, by putting the tube in the inductor of the tuned circuit (see ***Probes for High Resolution***) of an NMR probe that is in this 2.3 T magnet. Suddenly, the situation changes drastically. The nuclear moments $\boldsymbol{\mu}$, which previously could align themselves in any direction in space (ignoring the Earth's small magnetic field—but see ***Well Logging***), now find themselves in a highly anisotropic environment. In one direction (let us call it the z direction to conform with convention), there is a field vector $\boldsymbol{B}_0 = \boldsymbol{k}B_0$, while the other directions in the (x,y) plane have no field component at all. These moments suddenly find themselves in the situation that their quantized levels $E_{1/2}$ and $E_{-1/2}$ are being pried apart by the internal field vector $\boldsymbol{B} = \mu_0\boldsymbol{\mu}\cdot\boldsymbol{H} \equiv \mu_0(\boldsymbol{1} + \boldsymbol{\chi})\cdot\boldsymbol{H}$. Here $\mu_0 = 4\pi \times 10^{-7}$ H m^{-1}, and $\boldsymbol{\chi}$ is the rationalized volume susceptibility (see ***Magnetic Susceptibility and High Resolution NMR of Liquids and Solids***). Suddenly, the number of variables describing the equilibrium state of this system changes from $C + 2$ to $C + 5$ as $\boldsymbol{H}$ is added. The number is $C + 5$ because $\boldsymbol{H}$ has three vector components H_x, H_y, and H_z, leading to the internal field seen by the protons in this system being $B_x = 0$, $B_y = 0$, and $B_z = B_0$. The moments must relax to this new equilibrium situation, and clearly do so in an anisotropic manner, since now the z direction in space differs drastically from the x and y directions, which are equivalent for purposes of describing the anisotropy of the environment in this case.

We have seen that in a magnetic field, the equation of motion of a microscopic moment $\boldsymbol{\mu}_k$, an ensemble of which leads to a macroscopic moment $\boldsymbol{M} = \sum_k \boldsymbol{\mu}_k$, is given by equation (3). In the presence of relaxation processes, the equations of motion of the three components of the macroscopic magnetic moment are the cross product from equation (3) plus relaxation: $\mathrm{d}\boldsymbol{M}/\mathrm{d}t = \gamma\boldsymbol{M} \times \boldsymbol{B}$ + relaxation. (The details of this relaxation involve rather more quantum mechanics than there is room for here—and, indeed, are beyond the scope of this article—but for a simple example, see Chapter 2, Section IV of Gerstein and Dybowski.[4]) The simplest form of equations describing the kinetics of relaxation were first developed by Bloch, who assumed simple first-order kinetics, with rate constants $1/T_1$ for the z direction, and $1/T_2$ for the (x,y) plane. So, including relaxation, the equations of a moment in a field become

$$\frac{\mathrm{d}M_z}{\mathrm{d}t} = -\frac{M_z - M_z^{\mathrm{eq}}}{T_1} \tag{6a}$$

$$\frac{\mathrm{d}M_x}{\mathrm{d}t} = \gamma M_y B - \frac{M_x - M_x^{\mathrm{eq}}}{T_2} \tag{6b}$$

$$\frac{\mathrm{d}M_y}{\mathrm{d}t} = -\gamma M_x B - \frac{M_y - M_y^{\mathrm{eq}}}{T_2} \tag{6c}$$

where the superscript 'eq' indicates the equilibrium value. Equation (6a) is of the form $y = \mathrm{d}x/x$, and can be solved immediately to yield

$$M_z(t) = M_z^{\mathrm{eq}} + [M_z(0) - M_z^{\mathrm{eq}}\mathrm{e}^{-t/T_1}] \tag{7a}$$

The approach to equilibrium of the z component is a simple exponential. This immediately tells us that when we place our water vapor sample in the magnet, we must wait roughly $5T_1$ for the nuclei to polarize along the magnetic field to 99% of their full polarization. Since relaxation to the equilibrium value caused by the sudden introduction of a magnetic field involves alignment along the longitudinal z axis, such relaxation is sometimes termed 'longitudinal' relaxation. For reasons not obvious here, it is also termed 'spin–lattice' relaxation.

The x and y components form a coupled set of differential equations. These can be decoupled (for a general method for doing this, see page 77 of Gerstein and Dybowski[4]), to give

$$M_x(t) = \mathrm{e}^{-t/T_2}[M_x(0)\cos\gamma Bt + M_y(0)\sin\gamma Bt] \tag{7b}$$

$$M_y(t) = \mathrm{e}^{-t/T_2}[-M_x(0)\sin\gamma Bt + M_y(0)\cos\gamma Bt] \tag{7c}$$

These solutions may be verified by substitution. If the boundary conditions are that the transverse magnetization at time zero is $\boldsymbol{M}_0$ and the angle between $\boldsymbol{M}_0$ and the x axis at time zero is ϕ_0 then

$$M_x(t) = M_0\mathrm{e}^{-t/T_2}\cos(\gamma Bt - \phi_0) \tag{8a}$$

$$M_y(t) = -M_0\mathrm{e}^{-t/T_2}\sin(\gamma Bt - \phi_0) \tag{8b}$$

The form of these results is shown in Figure 3. The x and y components are exponentially damped monotonic oscillations that are 90° out of phase with each other.

4 THE ROTATING FRAME

NMR signals are detected not in the laboratory coordinate system, but in a system rotating at roughly the Larmor frequency ω_0. Recall that NMR frequencies in modern laboratories are in the FM radio range—the range from a few to a few hundred megahertz. Let us think about FM radio for just a moment. We use radio to produce signals in the audio range of frequencies, to which our ears are sensitive—a few tens of hertz to a few kilohertz, the higher frequency depending upon our age (our ears become less sensitive to the higher frequencies as we get older). But when we tune in an FM station, we are tuning to frequencies in the megahertz range. What is going on here? A very simple explanation is that the 'information' in the audio range is 'carried' by a frequency

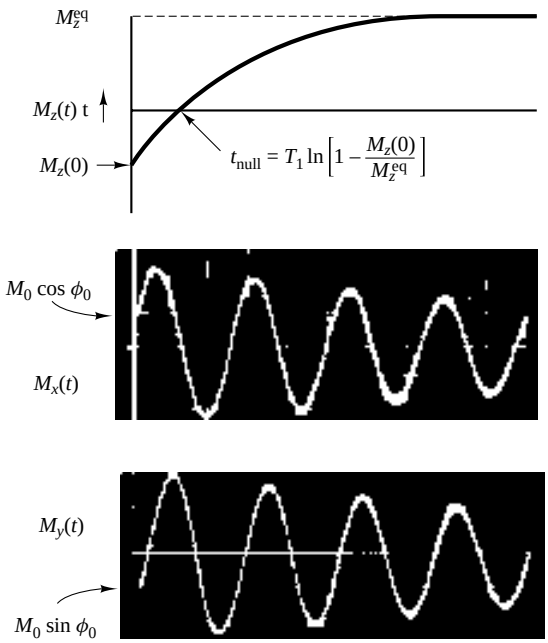

Figure 3 Bloch relaxation in a field along the z axis. The initial state is magnetization in the (x, y) plane

in the megahertz range by a process of modulation of the higher frequency with the lower, so that both frequencies are carried over the airwaves. When the signal that is broadcast from the radio station is received by our radio, we 'tune it in', which is in effect 'demodulating' the carrier from the kilohertz frequencies that are the interesting and desired information. An analogy might be a child seeing a group of children playing on a merry-go-round, but being unable to see what they are really doing because the merry-go-round is going around too fast. The children on the merry-go-round are simply a blur to the child on the ground. However, if the stationary child hops on the merry-go-round, he is in sync with the other children, and can easily see all they do without the complication of the rotation of the playground instrument. An exactly similar situation applies to demodulating a megahertz carrier from the carrier-plus-kilohertz information. The motion of the carrier is removed from the view of the system by demodulation, i.e., by transformation to the frame of the merry-go-round—the 'rotating frame'. Let us develop the classical rule for this transformation with the help of some simple diagrams and a little calculus.

Consider a vector $\boldsymbol{A}$ fixed in a coordinate system (cs) rotating with angular velocity ω (in rad s^{-1}) about the z axis of the laboratory frame, as indicated in Figure 4 (for example, $\boldsymbol{A}$ might be a line painted on a top). The angular velocity vector ω is therefore parallel to the z axis of the laboratory frame. Let x, y, z label the laboratory cs, and x', y', z' the cs rotating about z with angular velocity ω such that in any time period δt the angular change is $\delta\phi = \omega\, \delta t$. As indicated in Figure 4, if $\boldsymbol{A}$ is fixed at an angle θ to the axis of rotation, as indicated in Figure 4(b), then the magnitude of the change in $\boldsymbol{A}$, $\delta\boldsymbol{A}$, is given by

$$|\delta \boldsymbol{A}| = |\omega|\,|\boldsymbol{A}| \sin\theta \delta t \tag{9}$$

So, relative to a fixed laboratory cs,

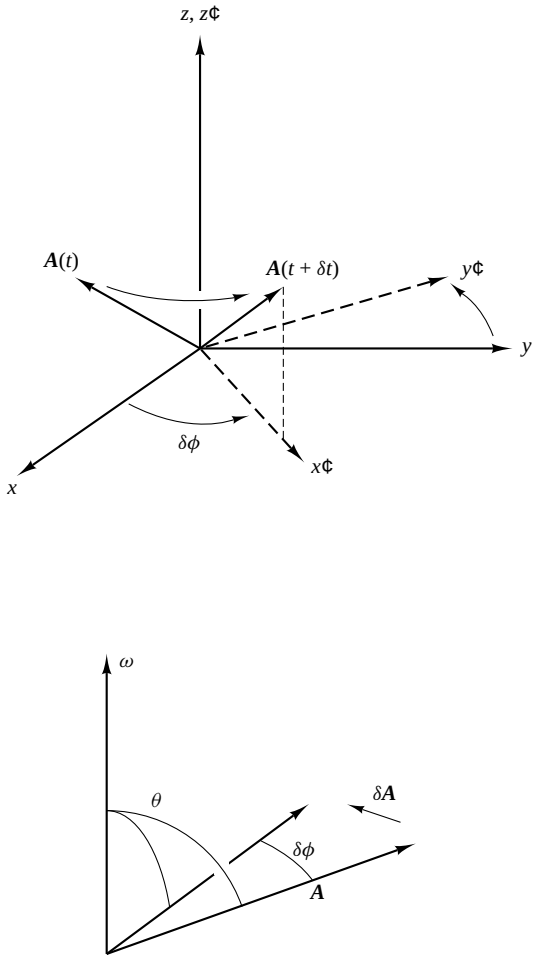

Figure 4 Geometrical representation of the transformation to the rotating frame

$$\lim_{\delta \to 0} \frac{\delta \boldsymbol{A}}{\delta t} = \frac{\mathrm{d}\boldsymbol{A}}{\mathrm{d}t} = \boldsymbol{\omega} \times \boldsymbol{A} \tag{10}$$

Note that equation (10) sets the direction of $\boldsymbol{\omega}$ relative to the direction of rotation.

Now suppose that $\boldsymbol{A}$, instead of being fixed in the cs that is rotating within the laboratory, is moving with respect to this rotating cs. For example, the rotating cs might be fixed in a child's top that is turning, and the vector $\boldsymbol{A}$ might be fixed to an ant that happened to be on the top when it is set spinning, and is walking around on the top while it is spinning. Suppose this ant is walking on the top with velocity relative to the top $\mathrm{D}\boldsymbol{A}/\mathrm{D}t$. Then, relative to the room in which the top is spinning,

$$\frac{\mathrm{d}\boldsymbol{A}}{\mathrm{d}t} = \frac{\mathrm{d}\boldsymbol{A}}{\mathrm{d}t} + \boldsymbol{\omega} \times \boldsymbol{A} \tag{11}$$

The total motion is just the superposition of the two motions. Identifying the vector $\boldsymbol{A}$ as the magnetic moment $\boldsymbol{M} = \gamma \boldsymbol{L}$, we see that

$$\frac{\mathrm{d}\boldsymbol{M}}{\mathrm{d}t} = \frac{\gamma\, \mathrm{d}\boldsymbol{L}}{\mathrm{d}t} = \gamma \boldsymbol{M} \times \boldsymbol{B}_0 \tag{12}$$

or the rate of change in the rotating cs is

$$\frac{\mathrm{D}\boldsymbol{M}}{\mathrm{D}t} = \boldsymbol{M} \times (\gamma \boldsymbol{B}_0 + \boldsymbol{\omega}) \tag{13}$$

Equation (14) has two important consequences: first, transforming to the rotating frame replaces $\boldsymbol{B}_0$ with an 'effective' field $\boldsymbol{B} = \boldsymbol{B}_0 + \boldsymbol{\omega}/\gamma$. The second, critical to this discussion, is that if $\boldsymbol{\omega} = -\gamma \boldsymbol{B}_0$ then $\mathrm{D}\boldsymbol{M}/\mathrm{D}t = 0$, i.e., there is no motion relative to the rotating cs. An equivalent statement is that, relative to the fixed frame, the moment is precessing about the z axis with angular velocity ω_0. This is just the result we inferred before: a magnetic moment in a field will precess about the field with Larmor precession frequency $\omega_0 = \gamma B_0$. It is easy to see that transformation to the rotating frame accomplishes two ends. First, the equation of motion in that frame is simplified; the moment is static in this frame. Second, it becomes clear inferentially that motion relative to the laboratory frame is precession about $\boldsymbol{B}_0$, a fact perhaps not immediately detectable from first observation of equation (3).

5 THE PULSE NMR EXPERIMENT: PULSE AND FOURIER TRANSFORM NMR

As we indicated in Section 4, the NMR signal is generated by a carrier operating at ω_0, generally in the frequency range of tens of to hundreds of megahertz. The information content, which develops as a modulation on the carrier, is obtained by demodulating the carrier from the total signal. In pulse operation, a simple schematic of how this is done is shown in Figure 5. S is a switch, controlled by a pulse programmer. D is a signal divider. A mixer mixes signals at ω_1 and ω_2, and produces a mixed signal at frequencies $\omega_1 \pm \omega_2$.

An idea of how this apparatus allows us to look at the response of the net magnetization associated with an ensemble of nuclear spins in a magnetic field, polarized initially in the z direction, parallel to the static magnetic field, and acted upon by a transient radiofrequency pulse is now discussed. To start, let us indicate schematically how we view the situation

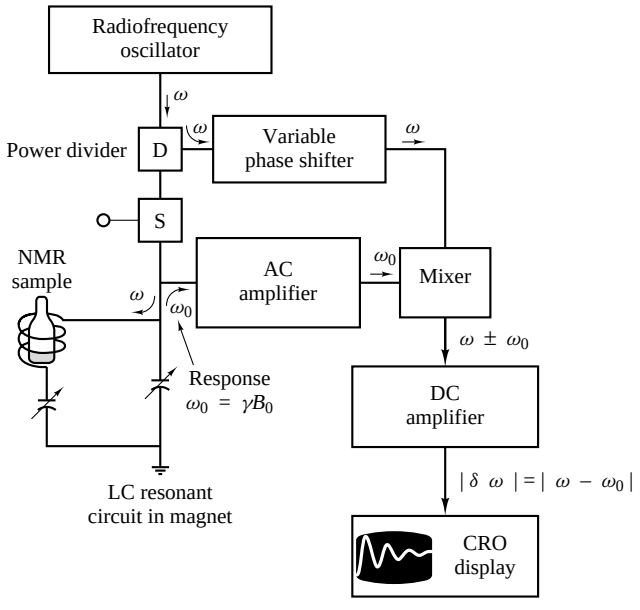

Figure 5 Simple schematic of a pulsed NMR spectrometer

in the rotating frame, the frame of the demodulated signal, in which we mix the carrier frequency ω_0 with the carrier plus the information content, $\omega_0 + \delta$, to observe the signal oscillating at frequency δ from the frame of our observation. By adjusting the phase shifter in the reference phase arm of the spectrometer, we may swing our view around in the rotating frame to look anywhere in the (x,y) plane. Let us look in the y direction, as indicated in Figure 7(a) below.

At this point, it is necessary to consider the relation between the time and frequency domains in NMR. The reason for having to deal with this duality is that many modern NMR experiments utilize transient excitations to cause NMR, with the result that the observable is a transient magnetization varying with time: $I(t)$ (cf. Figure 3), an intensity versus time; i.e., a signal observed in the time domain. For many purposes—and most familiar to those who routinely deal with NMR as a tool for identifying chemical shifts—the most common representation of the desired information is a plot of intensity versus frequency. Therefore we must become a little familiar with how signals in the time and frequency domains relate to each other. A simple way to see this relation is to consider a simple sine wave $I(t) = \cos \omega_0 t$. A plot of this function appears as shown in Figure 6(a). Now, think for a moment what this signal must look like as a function of ω. This function is monotonic in the frequency ω_0. It is a delta function at $\omega = \omega_0$. There is only one frequency in this signal, that of ω_0. This plot of $I(\omega)$ versus ω is shown in Figure 6(b). The mathematical operation that transforms $I(t)$ to $I(\omega)$ is called a *Fourier transform.* We may symbolically write $I(\omega) = \mathcal{F}I(t)$. The inverse statement would be $I(t) = \mathcal{F}^{-1}I(\omega)$. At this point, it is not important what specific mathematical form is represented by the operator $\mathcal{F}$. It is only important to know that it exists and that, as we have seen above in thinking about how a sine wave is represented in the time and frequency domains, as a mathematical operator it is a lot less complex than the left hemisphere of our brain. The formalism of Fourier transforms and their physical applications is nicely discussed by Champeney.[5]

Now let us consider an ensemble of nuclear moments $\boldsymbol{\mu}_k$, which sum together to form a macroscopic moment $\boldsymbol{M}$. Since we are creating a classical description of NMR and the pulse experiment, we adopt the model that this moment at equilibrium in a static field $\boldsymbol{B}_0$ in the z direction is parallel to the z axis as shown in Figure 7(a). (For one treatment of

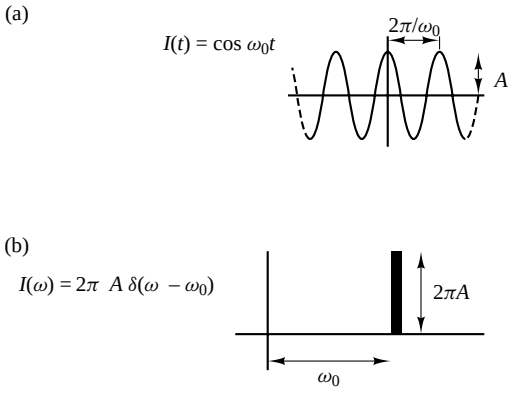

Figure 6 Relation between the time and frequency domain signals of a simple monotonic oscillation

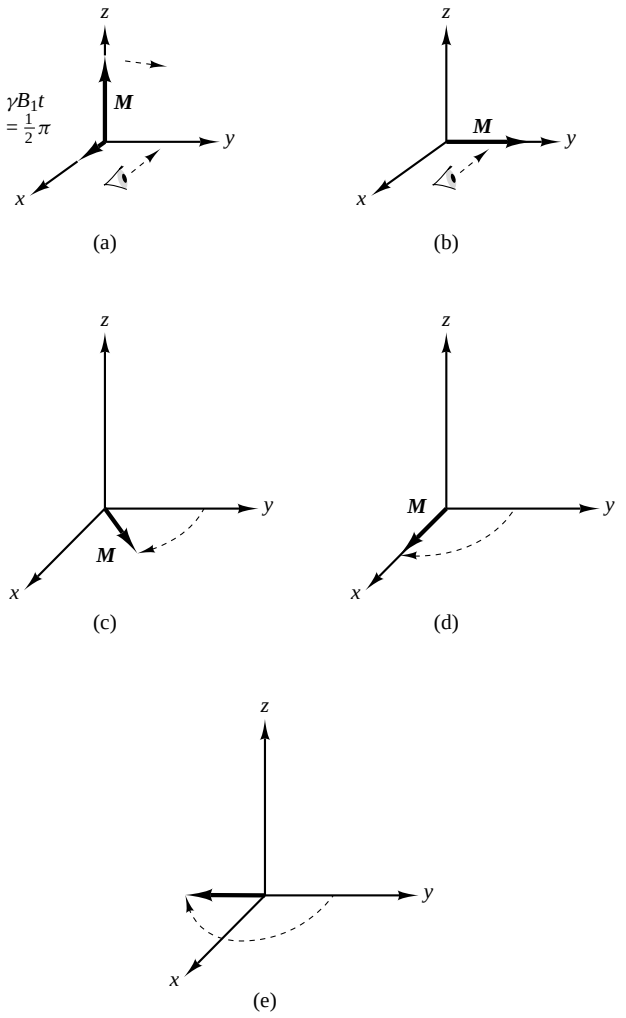

Figure 7 The pulse NMR experiment: observation of the magnetization of the moment after a 90°_x pulse with observation along y in the rotating frame

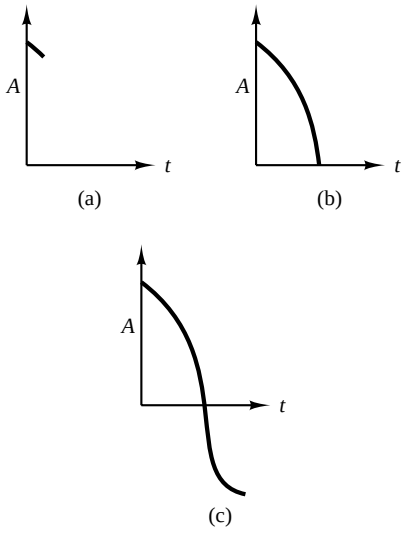

Figure 8 Time domain signal corresponding to observation illustrated in Figure 7

the quantum mechanical description, see Chapter 2 of Gerstein and Dybowski.[4])

We are now going to perform a pulse NMR experiment. First, we set the phase detector so that we are looking along the y axis. Then, as indicated in Figure 7(a), we apply a magnetic field $\boldsymbol{B}_1$, along the x axis for a time t_p such that the moment, which will precess about the new field $\boldsymbol{B}_1$ with precession frequency $\omega_1 = \gamma B_1$, precesses by an angle $\omega_1 t_p = 90^\circ$, called the 'tip angle'. (For a discussion and a graphical illustration of the setting of the reference phase and of the pulse width t_p, see Chapter 5 of Gerstein and Dybowski.[4]) Note carefully the distinction between the phase angle, which we have designated by saying we are 'looking' along the x axis, and the tip angle. At the end of the time t_p, therefore, the moment has precessed about the x direction to finally lie along the y axis, as shown in Figure 7(b). At this point, it realizes that it is a nonequilibrium position *vis-á-vis* the static field, $\boldsymbol{B}_0$, so it proceeds to precess about $\boldsymbol{B}_0$ as indicated in Figures 7(c)–(e).

Now, in the interest of clarity, we have been just a little bit too simplistic in our description at this point. There are some things that need to be said more carefully. For one thing, we have not specified that we are in the rotating frame, so the vector $\boldsymbol{B}_1$, which in the laboratory is rotating about $\boldsymbol{B}_0$ at frequency $\omega_0 = \gamma B_0$, is *relatively* motionless with respect to the x axis of the rotating frame. If we were to specify that we have set the carrier at exactly the Larmor frequency ω_0, then at all times the x axis and the rf field vector $\boldsymbol{B}_1$ would be parallel. However, if, as indicated in Figures 7(c) and (d), the carrier frequency is set at some small *offset* δ from the Larmor frequency of the nuclei in question then the axis of the rotating frame of the carrier frequency will rotate at δ with respect to the moment $\boldsymbol{M}$. It is this rotation that is depicted in Figures 7(c)–(e). In addition, we have not said that during the application of the pulse, there will be some rotation of $\boldsymbol{M}$ about $\boldsymbol{B}_0$. If the frequency ω_1 is sufficiently large compared with the offset δ then we can neglect this rotation for the purposes of the present discussion—which we do. Then the NMR signal in the time domain is as shown in Figure 8. It will be an oscillation with period $2\pi/\delta$. A photo of such a signal due to protons in water is shown in Figure 9(a). If the resonance offset δ is set to zero, and we detect along the negative y axis, we will see the signal shown in Figure 9(b). The decay in amplitude of the signal with time is that associated with transverse relaxation, with time constant $1/T_2$, as discussed in Section 3.

6 CHEMICALLY SHIFTED SPECTRA

We finally come to the most commonly used fingerprint of the nucleus in an NMR experiment by a physical scientist, that of the *chemical shift.* Of course, these days, the most commonly used fingerprint of the nucleus familiar to the public is just its presence, as detected by NMR in the magnetic resonance imaging (MRI) scanning used by the medical profession to complement the use of the more biologically invasive X rays in medical imaging. It is an interesting side note that 'MRI' is not 'NMRI', because of the lack of education on the part of the public about the fact that 'nuclear' does not necessarily mean biologically damaging radiation of the type coming from the use of radioactive materials, and one of the major hazards experienced in the development of

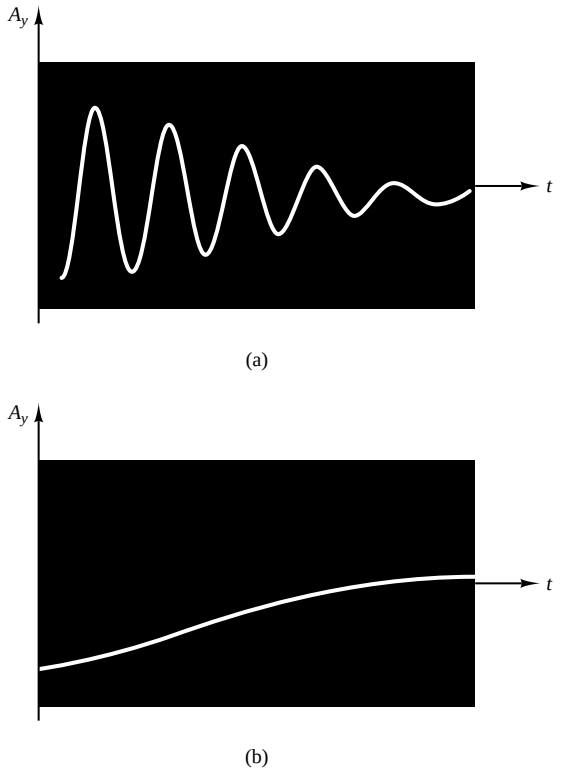

Figure 9 Time domain signal of protons in water: (a) off resonance; and (b) on resonance after a 90°_x pulse with observation along $-y$ in the rotating frame

nuclear weapons. All matter consists of nuclei and electrons, among other particles, and most of them are not radioactive! So the 'nuclear' in NMR must not be confused with the implications to health that come along with the 'nuclear' of nuclear reactors! NMR does not mean 'radioactive'. There *is* radiation in the NMR experiment, as we discussed above, in the FM radio range, but this radiation is like oak trees along the river bottoms in Iowa—common, and not hazardous to our health as applied in the NMR experiment.

The phenomenon of NMR, discovered in 1945 on protons, remained a physicists' curiosity until 1950, when Procter and Yu[6] noticed that in a solution of ammonium nitrate, NH_4NO_3, there were two signals observed for the nuclide ^{14}N. These two resonances were incredibly close together in terms of the fractions with which we deal in our every day life. We think that if we can measure a weight to 0.1%, we are doing about as well as an analytical chemist can do. But the differences in resonance frequencies of nuclei in different chemical environments in molecules, e.g. the 'ammonium' chemical functionality compared with the 'nitrate' chemical functionality, is of the order of 0.000 01%, i.e., of the order of parts per million (ppm), rather than thousands of parts per million. In fact, in modern NMR spectrometers, we are able to detect differences of the order of thousandths of ppm, which is about equivalent to being able to see two cats sitting a foot apart on the Moon when viewed from the Earth. This is an incredibly delicate fingerprint in terms of the usual accuracy and precision of measurement in physical science, and has since its development commercially in the 1950s been the workhorse of quantitative and qualitative analysis for the working chemist dealing with liquid solutions. As just a simple example of the power of the technique, we consider the protons in methanol, CH_3OH. Here there are two distinct chemical functionalities of hydrogen: those in the methyl group, CH_3, and those in the hydroxyl group, OH. Recall the relation $\omega_0 = \gamma B_0$. In a molecule, a nucleus will experience not only the field $\boldsymbol{B}_0$ from the magnet used in NMR, but also a *shift* in this field, designated as δ, the *chemical shift*, due to the different chemical electronic environments of the nuclei in methyl and in hydroxyl groups. For the protons in methanol, this shift will be about 5 ppm. Chemical shifts of hydrogen in organic molecules in solution commonly have a range of about 15 ppm of the resonance frequency. For example, protons in common organic molecules in a spectrometer operating at 500 MHz for ^1H will exhibit a chemical shift range of about $15 \times 500 = 7500$ Hz. Scalar couplings (see below) to other hydrogens and to carbons are characteristically around a hundred hertz. Resolution in commercial liquid state spectrometers is of order of a few tens of hertz, so hydrogen NMR on molecules in the liquid state supplies an easily detectable, well-resolved, and sensitive fingerprint for routine analysis.

In terms of what we can expect from the pulse NMR experiment, e.g. on ^1H in methanol, think a moment about what has just been said about chemical shifts. The two protons in methanol resonate about 5 ppm apart. Therefore, in a magnetic field, it is impossible to set the carrier frequency to be 'on resonance' with 'protons'. If one sets the carrier to be on resonance with the methyl protons, one will be 'off resonance' by an amount δ from the hydroxyl protons, which will resonate, it turns out, at a higher frequency than the methyl protons. So an easy escape from this dilemma of where to set 'resonance' is just to choose a reference molecule, and refer all resonances to the nuclide of interest in that molecule. For hydrogen, this molecule is tetramethylsilane, $(CH_3)_4Si$ (TMS), and we say that nuclei resonate at so many ppm with respect to TMS. Since TMS also has carbon in the form of the NMR-active (not radioactive!) nuclide ^{13}C, and the NMR-active nuclide ^{29}Si, it is also the reference molecule now commonly used for NMR of both carbon and silicon.

So a pulse NMR experiment, for example on the two protons in CH_3OH, will result in two different sets of magnetic moments precessing about the static field. This means that now, instead of one frequency being observed in the time decay, we shall see two. A superposition of two frequencies is well known to 'beat' against each other, as is commonly heard in the tuning of a guitar by using harmonics. An example of such a beat signal is shown in Figure 10. This time domain signal contains two frequencies, so of course in the frequency

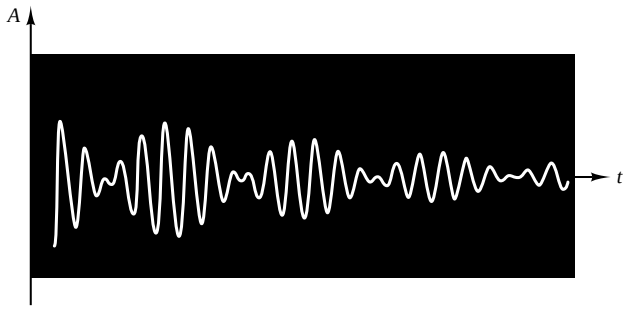

Figure 10 Slow beat pattern for chemically shifted protons observed in the rotating frame at a carrier frequency off resonance from both

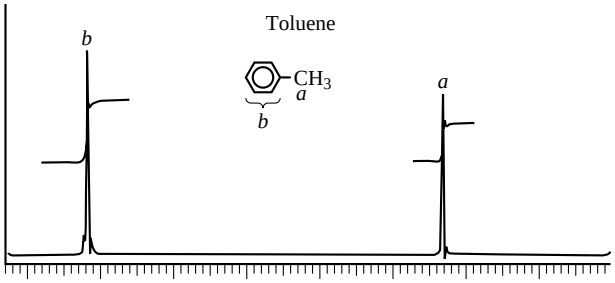

Figure 11 NMR spectrum of two sets of chemically shifted protons; for example, the aromatic ring protons and the aliphatic ring protons in toluene, $C_6H_5CH_3$

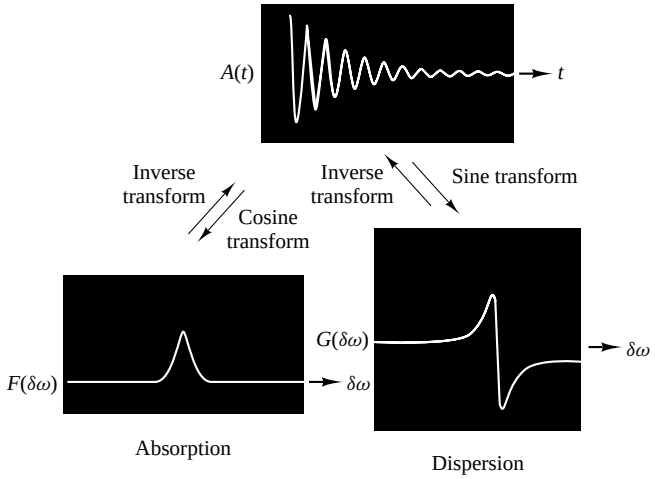

Figure 12 Illustration of the relation between signals in the time and frequency domains. The width of the signal in the frequency domain is related to the damping constant T_2 in the time domain by fwhm = $1/\pi T_2$

domain, there will be two peaks in the plot of $I(\omega)$ versus ω. The signal in the frequency domain is shown in Figure 11 for the aromatic and aliphatic protons in toluene. The general relation between the time and frequency domains is shown in Figure 12. Because of relaxation via processes associated with transverse and longitudinal relaxation, with time constants T_2 and T_1, the time signal will not be an infinitely long oscillatory signal, as was first discussed in comparing time and frequency domains, but will be a damped oscillation. If the damping constant is, for example, T_2 then for many liquid samples, the relation between the damping in the time domain characterized by T_2 (meaning that the time signal will decay to 1/e of its value in a time T_2) and that in the frequency domain is that the *width* of the signal in the frequency domain will be fwhm = $1/\pi T_2$. So a signal in the time domain decaying to a third of its initial intensity in a time of 10 ms will have a linewidth in the frequency domain of fwhm = 1/0.03 = 33 Hz. If this signal is due to nuclei resonating 5 ppm apart at a frequency of 500 MHz, then the resonances will be $5 \times 500 = 2500$ Hz apart, which is pretty far compared with the linewidth of 33 Hz. We see, therefore, that under these conditions, two signals 60 Hz apart could be resolved, which is a resolution of 60/500 = 0.1 ppm—and even this is not considered terribly good in really high-quality liquid state machines!

Not even mentioned in this brief review of the basics of the NMR experiment are fingerprints other than the chemical shift, fingerprints in the time domain, solids, quadrupolar nuclei, ... Thus, one can begin to understand why NMR is such an incredibly powerful and rich tool, both for the theorist and experimentalist, and for those outside of the immediate 'hard science' of the technique.

7 RELATED ARTICLES

Magnetic Susceptibility and High Resolution NMR of Liquids and Solids; Nuclear Spin Properties and Notation; Probes for High Resolution; Well Logging.

8 REFERENCES

1. F. Bloch, W. W. Hansen, and M. Packard, *Phys. Rev.*, 1946, **70**, 474.
2. E. M. Purcell, H. C. Torrey, and R. V. Pound, *Phys. Rev.*, 1946, **69**, 37.
3. B. C. Gerstein, *Nuclear Magnetic Resonance*, Encyclopedia of Science and Technology, Academic Press, Orlando, FL, 1987.
4. B. C. Gerstein and C. R. Dybowski, *Transient Techniques in NMR of Solids: An Introduction to the Theory and Practice*, Academic Press, Orlando, FL, 1986.
5. D. C. Champeney, *Fourier Transforms and Their Physical Applications*, Academic Press, New York, 1973.
6. W. G. Proctor and F. C. Yu, *Phys. Rev.*, 1950, **77**, 717.

Biographical Sketch

Bernard C. Gerstein. *b* 1932. B.S., 1953, Purdue, USA; Ph.D., 1960, Iowa State. Introduced to NMR by R.W. Vaughan. Faculty in Chemistry, Iowa State University, 1962–present. Approx. 150 publications. Research interests include the theory and practice of learning, and applications of solid state NMR to problems in the physics and chemistry of materials, fossil fuels, and heterogeneous catalysis.

Solid State Probe Design

F. David Doty

Doty Scientific Inc., Columbia, SC, USA

1	Introduction	1
2	High-Power Capacitors	1
3	Sample Coils for Solids	3
4	WideLine	5
5	Magic Angle Spinning	5
6	Goniometers and Slow MAS	7
7	Variable Temperature (VT)	8
8	Dynamic Angle Spinning (DAS)	9
9	Double Rotation (DOR)	9
10	Related Articles	10
11	References	10

1 INTRODUCTION

Obtaining detailed structural information from NMR of solid samples is more complex than for liquids because of the absence of molecular tumbling in solids to average line-broadening interactions; hence, much greater probe bandwidths are required.[1–4] The wideline probe usually has spectral excitation bandwidth greater than 80 kHz (i.e., able to generate 90° pulses less than 3 μs). To do this, it normally must withstand peak rf voltages in excess of 3 kV. Often wideline probes are double-tuned (DT) to permit cross polarization (CP) and high-power decoupling for increased sensitivity and resolution. If $\pi/2$ pulse lengths below 2 μs can be generated, multiple pulse line-narrowing techniques may be used to remove dipolar broadening,[3] but this is generally possible only in single resonance probes where low inductance coils can be used effectively.

The most common solids probe is the cross polarization/magic angle spinning (CP MAS) probe, which adds high-speed sample spinning at the magic angle to the other capabilities of the DT wideline probe for effective averaging of the chemical shift anisotropy (and perhaps dipolar broadening at very high speeds), thereby greatly improving resolution for spin-$\frac{1}{2}$ nuclei.[5] Single resonance MAS probes can generate the short pulses needed for the combined rotation and multiple pulse spectroscopy (CRAMPS) line-narrowing technique for ^{1}H or ^{19}F. Large volume MAS rotors can achieve the rotational spin rate stability needed for slow MAS, where pulses are applied at precise rotor orientations to average out the anisotropic chemical shift broadening as with high-speed MAS, although sensitivity may be reduced. Commercially available extended variable temperature (X-VT) CP MAS probes permit experiments from 35 K to 650 °C.

When sufficiently large single crystals of the sample can be grown, high-resolution spectra and the chemical shift tensor can be obtained using a single crystal probe,[6] which is similar to a wideline probe but includes a goniometer and crystal orientation mechanism for rotating the sample about three perpendicular axes.

Table 1 Dielectric Properties

Dielectric	k_d	tan δ[a]
Teflon, PE, PP	2.0–2.2	0.0002+
Kel-F	2.5	0.001
PMMA	2.8	0.03
PEK	3.4	0.003
Vespel	3.5	0.004
Epoxy	3.6	0.03
Quartz	3.8	0.0001
Macor	5.5	0.005
Porcelains	5–8	0.0002+
Si_3N_4[b]	8	0.001+
MgO	9.65	0.0005
Al_2O_3 (sapphire)	9.9	0.0002
PSZ (ZrO_2–MgO)	22	0.005+
BaO	34	0.001
COG	65–95	0.001
TiO_2	90	0.001
$SrTiO_3$	330	0.002+

[a]Loss tangent is approximate at 300 K, 30 MHz, and increases with temperature and frequency, especially in plastics and high-k dielectrics.
[b]High purity, high density, with minor Y–Al–Mg–O glass phase.

Quadrupolar interactions require more complex motions for effective averaging.[7] The dynamic angle spinning (DAS) probe allows the spinning axis to be changed rapidly while spinning the sample at high speeds. In another approach, known as double rotation (DOR), the sample is placed in a small spinner inside a larger spinner and spun about two intersecting axes simultaneously.

The short T_2 values (and often long T_1 values) in solids make sensitivity much lower than in liquids, and the requirement for high-power decoupling requires attention to efficiency at the proton frequency. In liquids probes, it is the sample coil that is most critical. For solids, it is the capacitors.

2 HIGH-POWER CAPACITORS

The special requirements of capacitors for NMR probes include the following: ultra-low magnetic susceptibility, high Q, high voltage, high current, ultra-low piezoelectric effects, and dielectrics devoid of unwanted NMR background signals. Losses in rf capacitors at a given frequency may be indicated by a capacitor quality factor Q_c, an effective series resistance [ESR = $(\omega C Q_c)^{-1}$], a loss tangent (tan $\delta \cong \pi/Q_c$), or a loss factor, k_d tan δ, where k_d is the dielectric constant (relative permittivity). Direct current losses may be specified by a leakage resistance, but this usually has no relationship to R_P (the effective parallel resistance of a tuned circuit) above 1 MHz. Table 1 lists typical permittivity and loss properties of dielectrics frequently encountered in NMR probes.[8–12]

Solids probes are usually designed for peak voltages of 2.5–4 kV, compared with ~1 kV for most liquids probes. Voltage breakdown strengths often tabulated for dielectrics are best ignored unless two important parameters are also specified: test material thickness and frequency. The frequency dependence is not easily characterized, but dc ratings of rf capacitors are typically four times the short-pulse rf ratings at 100 MHz. For very short pulses where heating is not much of a factor, the voltage rating at 10 MHz is typically only twice that

Table 2 Typical Dielectric Breakdown Voltages

Thickness (mm)	V_B, $k_d > 30$ (V)	V_B, $k_d < 10$ (V)
0.1	500	1000
0.5	1200	2200
3.0	3000	5400

at 500 MHz, but with long pulses the voltage derates at least as the $\frac{3}{2}$ power of the frequency above a cutoff that is a function of Q_c/C. Table 2 shows typical rf breakdown voltages, V_B, for several thicknesses of low-k and high-k dielectrics at 30 MHz. Above 50–100 V, V_B is a square root function of thickness and shows relatively little variation within the two classes of rf dielectrics listed.[11] Dry air has an ionization V_B comparable to that of high-k dielectrics, but arc voltage in monatomic gases (He, Ne, Ar) is less by a factor of at least five (more for large gaps) because of the absence of low-energy rotational and vibrational relaxation modes.[13] The additional rotational modes in polyatomic gases usually increase the breakdown voltage, except in the case of ionic gases such as H_2O.

2.1 Ceramic Capacitors

The standard COG (ceramic oxide glass) rf capacitor specification (formerly type NPO) requires a temperature coefficient of less than ± 30 ppm and tan δ below 0.001 for the range $-55\,^{\circ}$C to $125\,^{\circ}$C. For moderate-power applications up to 300 MHz, the COG formulation usually consists of fine-grained baria–neodymia–titania systems or magnesium titanate prefired with 6 mol% calcium titanate, but they are also made from mixtures of neodymium carbonate, titania, and barium titanate. A two-stage firing is generally required for multilayer capacitors so that the final firing temperature can be kept below $1150\,^{\circ}$C to allow the use of Pd–Ag electrodes. The ceramic precursors are prefired at a high temperature, then reground and mixed with a powdered glass binder with matched thermal expansion such as 36% CdO, 23% Bi_2O_3, 25% PbO, 5% ZnO, 5% B_2O_3, 5% SiO_2, 1% Al_2O_3.[9] Alternate layers of ceramic/glass and metallization slurry are built up by a screening or spraying process.

Porcelains (magnesium–aluminum–silicates) are often used in the UHF range for high-power capacitors below 15 pF. Corning Pyroceram 9606 consists mostly of cordierite ($2MgO–2Al_2O_3–5SiO_2$), with lesser amounts of cristobalite and various magnesium titanates. Its low thermal expansion can cause problems with the metallization. Forsterite ($2MgO \cdot SiO_2$) is electrically almost as good as Pyroceram, easier to produce, and easy to metallize, but has poor thermal shock resistance.

UHF high-power capacitors above 30 pF are usually based on strontium titanate, which is not piezoelectric but may contain piezoelectric barium titanate impurities. High-power rf capacitors are often coated with a sealing glass such as $2PbO \cdot SiO_2$ ($550\,^{\circ}$C) to keep out moisture,[8] as it facilitates silver migration in the presence of an electric field.

The magnetic properties of ceramic capacitors are unpredictable, as most ceramics are slightly diamagnetic (bismuth compounds are very diamagnetic), palladium is extremely paramagnetic, and ferromagnetic nickel barriers are sometimes used in the terminations. A number of manufacturers are by now quite familiar with the stringent requirements of NMR/MRI capacitors and offer 'nonmagnetic' chip capacitors with 500–1000 V rating (a 2.5–3 mm cube), but it is always necessary to screen them for magnetism using a small magnet (a 2-mm cube of high-energy neodymium–boron–iron) suspended from a string. Also, nearly 1% of new capacitors may be noisy in a double resonance circuit as a result of microgaps between the electrodes or terminations and the dielectric.[14] Premature breakdown may be initiated by surface tracking and moisture in solder rosin.

At least four manufacturers (JFD, ATC, Murata Erie, and Tansitor Electronics) offer 3-kV multilayer ceramic rf capacitors in roughly a $3.5 \times 10 \times 11\,mm^3$ package. The JFD capacitors have generally been found to have the highest Q, but the difference is often not important. Some of the best NMR ceramic capacitors (when available, but once discontinued) are the 2-kV UV10 and UV17 series ($3.3 \times 6 \times 8\,mm^3$) by Murata Erie, as they have very low magnetic susceptibilities and a 2-kV rating in a small package. Moreover, for typical circuit values (reactance above 100 Ω), Q_c is usually greater than 3000 for capacitance below 150 pF at frequencies at least up to 50 MHz, and Q_c is usually greater than 1000 up to 500 MHz.

2.2 Piezoelectric Acoustic Ringing

While acoustic ringing is seldom a problem in liquids probes because of the longer T_2s and the effectiveness of the Patt acoustic suppression sequence,[15] piezoelectric-induced acoustic ringing[16] of capacitors can obscure signals in solids probes requiring short recovery times. Subjecting a capacitor with ferroelectric impurities to a dc electric field in excess of $1\,kV\,mm^{-1}$, as may occur in a voltage withstanding test or from asymmetric rf breakdown, causes domain alignment and imparts a net crystallographic piezoelectric orientation to the ceramic. The ferroelectric is said be 'poled', and may exhibit acoustic ringing. The polarization of ferroelectrics can be annealed out by heating above the Curie temperature ($130\,^{\circ}$C for $BaTiO_3$; 180–$300\,^{\circ}$C for lead–magnesium–niobates), but they can easily become poled again.

Grain size is usually under $4\,\mu$m for rf power COG capacitors in the 10–30 pF range, in which case Rayleigh scattering will normally keep acoustic decay times under a few μs above 30 MHz. However, grain size may exceed $100\,\mu$m in high-voltage (HV) capacitors above 150 pF and occasionally in low-valued capacitors, resulting in reduced acoustic absorption and acoustic decay times greater than $10\,\mu$s at frequencies as high as 45 MHz. On the other hand, acoustic ringing in bulk metals from the Lorentz interaction is seldom a problem above 15 MHz.[17]

2.3 Variable Capacitors

The double rotation (DOR) probe shown in Figure 1 illustrates the use of three common types of variable capacitors (air, quartz, and pressurized gas) and 3-kV ceramic chip capacitors (attached to the left of the quartz variable near the center of the photo). The Johanson 5000-series nonmagnetic, air-dielectric, trimmer capacitor (one is mounted on the upper circuit board near the center of Figure 1, just to the right of the central support post) is typical of that used in most liquids NMR probes and the high-frequency (HF) channel in solids probes with capacitive voltage division. It consists

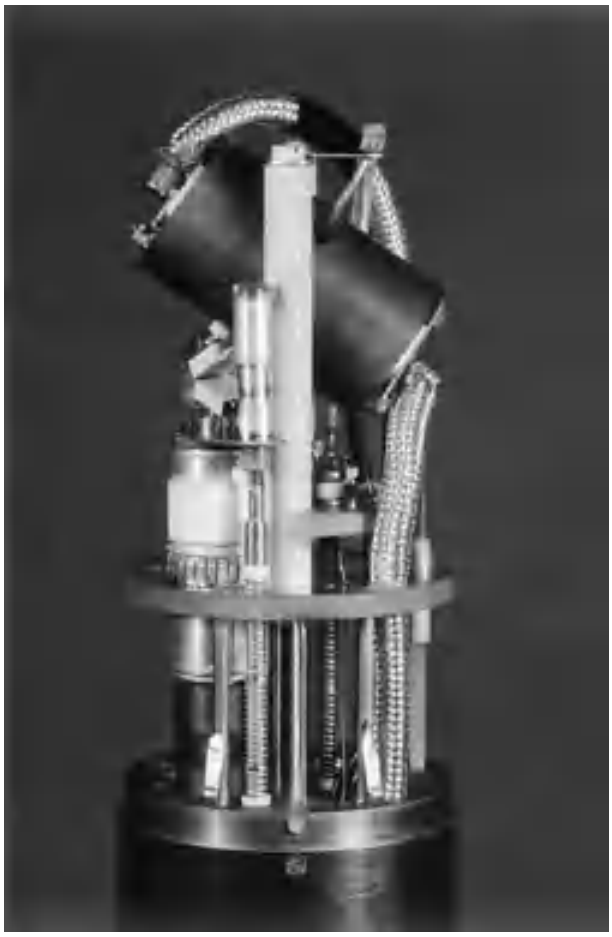

Figure 1 DOR WB probe (Doty Scientific, Inc.)

of an alumina ceramic housing supporting several concentric, silver plated brass cylinders at the 'hot' end; a precision screw mechanism adjusts a similar intermeshing arrangement at the mount end. The minimum radial air gap is under 0.1 mm, and breakdown occurs at 500–700 V when new. With use, alignment deteriorates, and the voltage rating decreases. Care must be taken to avoid dissolving the internal lubricants (which are essential for an acceptable lifetime) with cleaning solvents. The capacitors may be sealed, but this is inconvenient; hence, their voltage rating also decreases with altitude and humidity or high concentrations of monatomic gases. These variable capacitors are manufactured using 300 °C Pb–Ag solder between the alumina and brass body parts, and they tolerate repeated overvoltages.

Also shown in Figure 1 (near the center, on top of a gas variable capacitor, just left of the central support post) is the JMC 7584, quartz-dielectric, 0.8–10 pF, variable capacitor. Its 2.5-kV rf capability allows five-times the tuning range of the above air variables, as tuning range is generally proportional to $(CV^2)^{\frac{1}{2}}$. Defective silver plating on the piston or sleeve has occasionally been found to produce noise at lower voltages in double resonance circuits.[14] Impurities in the brass base and piston of the JMC capacitor are not controlled as carefully as in a similar capacitor by Voltronics, but the JMC capacitor is more robust which simplifies certain capacitive voltage division arrangements,[18] and the magnetism is acceptable unless it must be very close to the sample. These capacitors have been used successfully up to 400 MHz. They may lock up at high temperatures from the piston expanding or at low temperatures from the lubricants freezing.

The single component most synonymous with solids NMR probes is the Jennings CHV1 N-45 gas variable capacitor—the 22-mm diameter ceramic cylinder on the left side of the main circuit board in Figure 1. It is pressurized with about six atmospheres of CO_2 and SO_2 in its minimum capacitance position and may be adjusted from 1.5 pF to 45 pF using a pushrod mechanism. It has a peak breakdown voltage V_B of about 3.5 kV near the low end of its range (∼10 pF) but V_B increases to about 5 kV near the high end as the gas becomes more compressed. The ceramic-to-metal seals are slightly magnetic, but this is seldom a problem as they are normally more than 20 mm from the sample. These variables have been used successfully for tuning purposes up to 220 MHz. With proper layout, they are usable on the low-frequency (LF) channels of multituned circuits with 500 MHz HF. These capacitors tolerate repeated overvoltages and are usable from −20 °C to 100 °C. If the external mechanical stop is not set properly, they may be easily damaged by pushing the adjustment rod beyond the specified limit.

Teflon variables with very low magnetism are available from Polyflon and Voltronics in a variety of sizes and ratings similar to the three described above, but Teflon does not tolerate the brief, inadvertent overvoltages which are unavoidable in most laboratories.

3 SAMPLE COILS FOR SOLIDS

Almost all solids probes use solenoidal rf coils for higher filling factor and Q than saddle coils. Standard oxygen-free, high-conductivity (OFHC) electronic-grade copper wire (C10100, 99.99%) has acceptably low iron content (less than 25 ppm, typically 4 ppm) for most solids coils at high fields. Optimum space between wires is half the wire diameter[19] or perhaps a little less. An enamel coating does not usually cause a background problem with carbon experiments, but it should be removed using warm sulfuric acid if proton experiments are planned.

High-Q circuits are usually preferred—except perhaps for wideline. Coil length-to-diameter ratio is not critical, but values between 1.0 and 1.4 (depending on available wire sizes) are usually best, except for MAS. Larger ratios (1.4–3.0) give better S/N for MAS (more sample for a given speed and lower dielectric losses), but some manufacturers use short coils to achieve shorter pulse lengths and higher decoupling fields. Coil forms help stabilize tuning but reduce both filling factor and maximum voltage before the onset of arcing. If used, they should be of low-permittivity dielectrics for minimal electric field gradients and arcing.

Special or custom wire may be obtained from MWS Wire Industries, Westlake Village, CA. Gold flash (0.3-μm plating) is often applied to prevent copper sulfates and chlorides (which have a large positive susceptibility due to antiferromagnetism) from forming on the wire surface, but it is critical to specify that the common practice of first applying a nickel strike (to minimize diffusion into the copper) be omitted or the wire will be very magnetic. The gold flash degrades the Q by about 1%. Silver plating does not improve Q (because of unavoidable defects) and does not provide the same degree of

Table 3 Properties of NMR Probe Materials at 300 K

(a) Conductors

Material	Density	Young's modulus	Poisson ratio	Yield strength	Electrical conductivity	Thermal conductivity	Thermal expansion	Specific heat	Magnetic susceptibility
Symbol	d	E	r	S	σ	k_T	b_T	C_p	χ_v
Units	kg m^{-3}	GPa		MPa	(MWm)$^{-1}$	W mK^{-1}	10^6 K^{-1}	J (kg K)$^{-1}$	10^{-6}
Aluminum	2700	69	0.33	30	36.6	230	22	900	21
Copper	8950	122	0.34	150	58.0	400	16.5	490	−9.8
Gold	19 300	78	0.42	20	44.0	315	14.2	128	−34
Hafnium	13 090	110	0.34	300	2.9	22	5.9	145	69
Iridium	22 500	440	0.27	1200	19.8	147	6.8	130	38
Molybdenum	10 200	320	0.3	300	18.1	138	5.2	276	120
Palladium	12 020	115	0.38	250	9.3	76	11.8	245	840
Rhodium	12 440	330	0.29	800	20.9	150	8.3	247	168
Silver	10 500	78	0.38	100	61.4	428	19	235	−24
Tungsten	19 250	410	0.28	1000	18.4	173	3.8	133	80
Zirconium[a]	6506	99	0.35	200	2.3	21	5.85	295	160
Al-6061T6[b]	2700	69	0.33	214	25	180	23.6	896	20
H. C-22[c]	8690	206	0.3	400	0.9	10	12.4	414	650
J-bronze[d]	8780	115	0.34	200	23.5	173	18.6	380	−10
P-bronze[e]	8860	110	0.35	200	11.5	84	17.8	380	−9.2
60/40PbSn	9700	30	0.4	40	6.3	45	24	176	∼5
SS304[f]	8000	193	0.31	300	1.4	16	17	500	∼3000

(b) Insulators

Material	Density	Young's modulus	Poisson ratio	Yield strength	Electrical conductivity	Thermal conductivity	Thermal expansion	Specific heat	Magnetic susceptibility
Symbol	d	E	r	S	k_d	k_T	b_T	C_p	χ_v
Units	kg m^{-3}	GPa		MPa	(MΩm)$^{-1}$	W mK^{-1}	10^6 K^{-1}	J (kg K)$^{-1}$	10^{-6}
99.5Al_2O_3	3950	390	0.22	240	9.9	35	8	780	−18
A-JGN3030[g]	1560	10	0.35	130	3.7	0.3	∼35	960	−5
HIPd-Si_3N_4[h]	3250	310	0.26	710	7	25	3.2	740	−20
Kel-f	2100	1.3	∼0.45	20	2.5	0.21	60	800	−10.6
Macor[i]	2520	64	0.28	80	5.9	1.7	9	750	∼−15
99.5%MgO	3400	250	0.2	100	9.6	20	13.5	955	
PEK	1300	3.8	∼0.4	70	3.3	0.24	54	1500	∼−8
PSZ[j]	5700	200	0.25	500	23	3	9.5	490	−8
Pyrex-7070	2500	70	0.2	60	4.0	1.3	3.3	800	−11
Quartz[k]	2250	74	0.16	50	3.8	1.4	0.5	700	−16
Silica foam[l]	770	∼20	–	∼5	∼1.5	∼0.1	0.5	700	−3.5
Teflon	2200	0.4	∼0.45	12	2–2.2	0.25	120	750	−9.8
Vespel[m]	1430	3.1	0.41	86	3.5	0.33	54	1130	−9
Water	997	0	–	0	80	0.6	–	4182	−9.06

Note: Volume susceptibility χ_v in SI is related to cgs molar susceptibility χ_m by: $\chi_v = 4\pi d\chi_m/(\text{M.wt.})$.
[a]Commercially pure zirconium, grade 702: 96Zr, 3Hf, 0.1Cr, 0.1Fe.
[b]97Al, 1Mg, 0.6Si, 0.4Fe.
[c]Haynes C-22: 60Ni, 22Cr, 13Mo, 5W + Co.
[d]C22600: 88Cu, 12Zn, 0.005Fe.
[e]C51000: 95Cu, 5Sn, 0.1Fe.
[f]68Fe, 19Cr, 9Ni, 2Mn, 1Si.
[g]Aurum PI resin, 30% glass fiber.
[h]98Si_3N_4, 2Y_2O_3, HIPd.
[i]Al–B–Si–Mg–F ceramic glass, Corning.
[j]94ZrO_2, 3HfO_2, 3MgO.
[k]Fused silica, electronic grade.
[l]Fused silica foam, industrial grade.
[m]Dupont polyimide SP-1.

protection against corrosion—even when the plating thickness is increased to 3 μm. Silver and its compounds are quite diamagnetic but often contain paramagnetic impurities.

High-purity copper coils for high resolution are often plated with the proper thickness of iridium or rhodium to cancel the diamagnetism of copper.[20] Palladium can also be used for this purpose if it is plated only on the side that will be the external surface of the coil (where there is little current flow) so that the Q is not spoiled. Table 3 lists various properties, including volumetric magnetic susceptibility χ_v, for materials commonly

found in NMR probes. The desired plating thickness for foil is that for which the algebraic sum of the product of thickness and χ_v for the different layers is zero.

4 WIDELINE

The initial instrumentation for solids NMR borrowed extensively from radar and UHF transmitter technology, using fixed-frequency transmission lines as circulators and magic-Ts to isolate the multikilowatt transmitter from the low-noise preamplifier.[2,3] However, it was soon determined that it was not difficult to deal with the phase transients from Qs of 50–200—an order of magnitude higher than initially thought. Pulse rise times could be as much as one-third the pulse length without serious difficulties.[21] Hence, several hundred watts were sufficient except perhaps for low-γ nuclei. The cost savings of moderate power transmitters and the shift from transmission line traps to lumped elements facilitated the commercial solids probe,[22] which is usually required to be multinuclear and reasonably user friendly.

For proton NMR it is still beneficial to damp the Q to about 100 by coating the coil with tin–lead solder (as proton linewidths are large and sensitivity is enormous) but care must be taken not to trap rosin in the coating, or backgrounds will be seen. Also, experiments on other nuclides with very broad lines may benefit from moderate Q-damping if samples larger than 0.1 mL are being used, since the increased bandwidth simplifies data collection. A number of accelerated ringdown schemes have been proposed,[2,23] but the method seeing more use today appears to be overcoupling[24,25] because of noise, reliability, and magnetism problems associated with other methods. Moreover, the recent availability of linear prediction often obviates the need for active damping (see ***Fourier Transform and Linear Prediction Methods***).

The unbalanced, capacitively matched DT circuit (see ***Probe Design and Construction***, Figure 6) is usually used for wideline probes to simplify multinuclear tuning. The HF tuning coil L_H (which may be a capacitively shortened $\lambda/4$ coaxial transmission line) is chosen to have an inductance such that its untuned reactance would be between 25 Ω and 60 Ω at the HF. Lead inductance is minimized subject to VT, high voltage, and multinuclear constraints. The total series lead inductance is then typically 25–40 nH.[14] Maximum B_1/V_T, where V_T is the maximum total circuit voltage, is obtained for coil inductance L_S half of the total circuit inductance, but a somewhat higher value is usually selected for improved LF sensitivity with some sacrifice in HF efficiency and a slight reduction in maximum B_1.

Minimum 90° pulse lengths have typically been 3 μs, but recent successful demonstrations of wideline ^{2}H Hadamard NMR[26] may have a major impact on single resonance solids NMR. In Hadamard NMR, the spin system response to the application of a large number of pseudorandom pulses with flip angles as small as 0.1° (mW, μs pulses) at periods on the order of tens of microseconds can be transformed into the equivalent NMR response from a single high-power pulse. A Hadamard wideline probe should benefit from a low-Q (∼5) saddle excitation coil in combination with a moderate-Q (∼100) solenoid receive coil. SNR for Hadamard appears comparable to Fourier transform (FT). (See also ***Stochastic Excitation***.)

5 MAGIC ANGLE SPINNING

In 1958, Raymond Andrew[27] and co-workers showed that high-speed sample spinning at the 'magic' angle of 54.7° could be an effective tool in averaging out dipolar broadening. However, the required rotational rates for abundant dipolar nuclei (35 kHz for ^{1}H) appeared impossible, and the technique was largely ignored[28] for nearly two decades until Stejskal and Schaefer[4,5] showed that more realistic rotational rates (3–5 kHz), capable of averaging chemical shift anisotropy, combined with high-power decoupling to remove the ^{1}H dipolar broadening, could be extremely effective in obtaining high-resolution ^{13}C spectra from solid samples.

Andrew used a conical bearing/drive surface which eventually achieved speeds in excess of 10 kHz using helium gas.[29] This spinner was based on the classic ultracentrifuge work by Beams[30] and depended on the Bernoulli effect to hold the sample spinner close to the drive jets. The stiffness of such a bearing is extremely low, which results in low-frequency oscillations, precession, and instabilities. Moreover, angular accuracy of 0.3° is sometimes required in MAS, which is an order of magnitude beyond the capability of the conical Bernoulli–Beams bearing. Lippmaa,[31] Veeman, Pines, Eckman, and others introduced the double bearing cylindrical rotor to circumvent these problems, and Doty and Ellis presented an approximate analysis of the cylindrical air bearing optimization.[32] [Note that typographical errors resulted in equations (9) and (12) in the referenced article[32] appearing twice. The second equation in each case is correct. The first should be deleted.]

The high-strength ceramics[8] that have recently become available are required to obtain high sensitivity (from high filling factor) and high spinning speeds simultaneously. Silicon nitride[33] has the highest strength-to-mass ratio of any available ceramic, which allows the highest surface speeds with low-density samples; but zirconia has higher strength, better toughness, and fewer defects, making it the preferred material for heavier samples—except perhaps at very high fields or high temperatures. Most commercial MAS rotors and stators are ground and lapped (using precision diamond tooling) from partially stabilized zirconia (PSZ) or hot isostatic pressed (HIPd) Si_3N_4. As a consequence, these items are rather expensive. The press-fit turbine caps are usually machined from Vespel, as polyether ether ketone (PEEK) has poor wear resistance despite its other desirable properties. Zirconia turbines may be attached to a zirconia rotor by thermal interference fit. Other high-strength plastics and ceramics as listed in Table 3 are also used for special thermal or background considerations. Fiber-optics spin-rate detection is normally provided to allow precise, synchronous pulsing for the total suppression of sidebands (TOSS) technique.[34]

5.1 High-Speed Air Bearings

The high mass of ceramic rotors requires more attention to rotor resonances than was required in the earlier designs using plastic rotors.[35] For stability throughout a wide speed range, it is advantageous to have the high bearing stiffness that comes from tight radial clearances. However, as the clearance is reduced, bearing frictional heating becomes more severe; moreover, the possibility of a 'crash' increases. A crash may

occur in a hydrostatic bearing when the rotor moves close enough to the stator to cause extreme choking around the perimeter of the bearing nozzles on the proximal side, at which point the stiffness changes sign and the rotor is driven into the stator. Pockets or recesses at the orifice exit may eliminate this crash mechanism,[36] but the reduced response time adversely affects stability at very high speeds unless the pockets are very small.[37]

Highest spinning speeds have been obtained with the design illustrated in Figure 2, which has achieved surface speeds in excess of the speed of sound at room temperature for rotor diameters from 5–14 mm. Half of the bearing gas exits over the ends of the rotor forming an axial thrust bearing at each end, while half exits out the center of the stator. Allowing the gas to flow axially inward as well as outward (nearly) doubles the bearing stiffness (by nearly doubling effective area) and was probably the most significant innovation in the spinner by Langer et al.[38] which achieved a 40% increase in surface speed over previous designs.

Optimum bearing radial clearance for controlling Taylor vortices[39] in the air bearing at moderate speeds is proportional to $(\mu^2 d/c^2\rho^2)^{\frac{1}{3}}$, where μ is the gas viscosity, d is the rotor diameter, c is the velocity of sound, and ρ is the gas density. Optimum clearance r_c for the control of whirl instabilities with minimum friction at high speeds fits the following empirical equation for typical NMR spinners:

$$r_c \cong kT^{0.25}d^{0.4} \text{ (mixed units)} \quad (1)$$

where T is the gas temperature (K), d is the rotor diameter in mm, and k has an approximate numerical value of 0.0027 for nitrogen and 0.0035 for helium with units of $K^{-0.25}$ $mm^{0.6}$; it is necessary to take into account the strain that will occur even in ceramic rotors at top speeds: 0.1% and 0.15% for silicon nitride and zirconia, respectively. Smaller clearances than given by equation (1) may be used if the additional heating can be tolerated, and larger clearances may be used with large rotors if other measures are taken to control whirl instabilities. Optimum bearing hole size is such that bearing

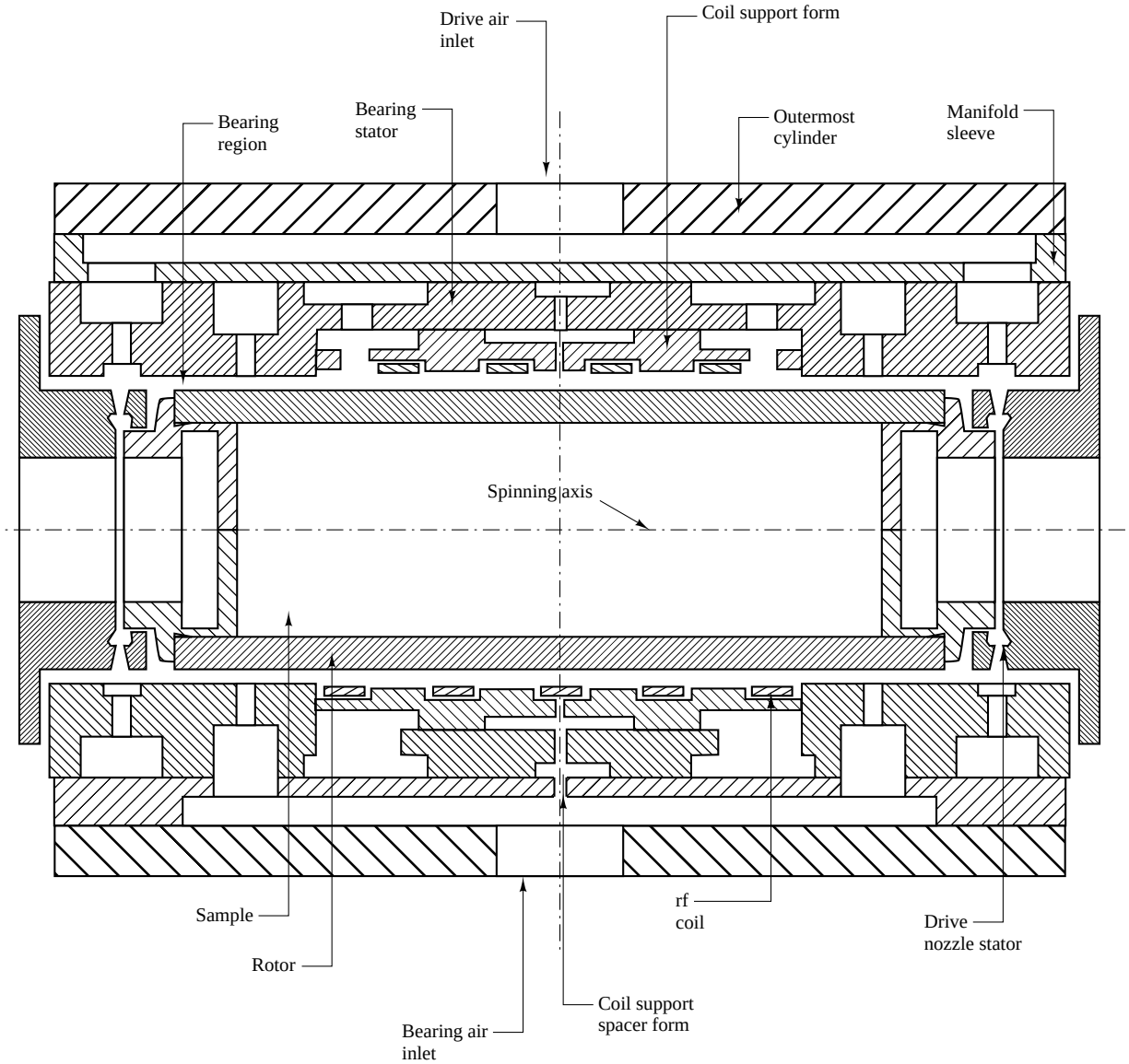

Figure 2 Supersonic sample spinner (Doty Scientific, Inc.)

mass flow at 0.3 MPa with the rotor in place is 60%–85% of the mass flow with the rotor removed. Short bearing hole sizes normally range from 0.13 mm for 3.5-mm rotors to 0.28 mm for 14-mm rotors, but slightly larger long bearing holes work better for VT.

With very small rotors, the bearing clearance becomes extremely critical—partly for manufacturing reasons and partly for fundamental reasons. To appreciate the fundamental limitation, consider the conical resonance frequency,[32] which is approximately proportional to the square root of the quotient of the bearing stiffness and the rotor mass near the end of the rotor. In order for this resonance to scale as $1/d$, the stiffness must be linear with diameter (since the mass is cubic with diameter), which requires the radial clearance to be proportional to the diameter if the pressure is constant. But clearance cannot be linear with diameter or frictional power density on the rotor surface becomes unmanageable with small rotors. Hence, Nature does not like small rotors, and it is in fact fortuitous that 5-mm rotors can achieve supersonic surface speeds (21 kHz) under optimum conditions with nitrogen bearing pressures of 0.5 MPa. While 3.5-mm Si_3N_4 rotors have occasionally reached 27 kHz, they are fraught with instabilities above 24 kHz which are exacerbated by the large, axial Bernoulli effects from poor turbine efficiency.

5.2 Radial-Inflow Microturbines

To achieve surface speeds above 240 m s^{-1} it is necessary to use microturbines in a symmetrical fashion so that axial reaction forces are precisely balanced at all speeds (unless helium drive gas is used), since the load capacity of the axial thrust bearings is quite limited.[40] The reduced-diameter radial-inflow microturbines used in Figure 2 achieve order-of-magnitude higher isentropic efficiency that the earlier Peltier microturbines by (a) controlling flow separation over the blades, (b) operating at lower tip speed, and (c) reducing exhaust swirl.[41] Inlet and exit angles are not particularly critical, but axial clearance over the blades is—unless the turbine is designed for a very low reaction ratio. A vaneless radial-inflow supersonic diffuser may be used with the larger sizes to obtain supersonic, nonseparated flow at the rotor entrance. The microturbines on a 14-mm rotor have 28 blades with 10-mm tip o.d. and produce 25 W shaft power each at 40% isentropic efficiency at 6 kHz. The 2.5-mm o.d. microturbines on the 3.5-mm rotor have only 12 blades and achieve approximately 10% efficiency at 22 kHz. Unlike large turbines, substantial efficiency losses occur in the nozzles (even with the 14-mm spinners) because of boundary layer effects. For an excellent treatment of turbine theory and design, the reader is referred to the text by Wilson.[42]

5.3 Radiofrequency Circuits

Most MAS work requires CP and/or high-power decoupling. Hence, the circuit is essentially identical to that described earlier for the DT wideline probe except that lead inductance may be a little larger,[14] necessitating somewhat higher sample coil inductance for high sensitivity. Maximum $\boldsymbol{B}_1$ is usually 30% less than expected of a similar DT wideline probe, but many wideline experiments are still possible with an MAS probe. For large samples at high fields, it can be beneficial to balance the HF channel for more efficient decoupling—especially at high temperatures. A modified form of the standard ^1H–^2H high-resolution balanced decoupler/lock circuit may be adapted to the high-power requirements of solids.[43]

Wu and Zilm[44] showed that high rf homogeneity is much more important than originally recognized for efficient CP at high speeds and that variable amplitude proton $\boldsymbol{B}_2$ can greatly improve CP efficiency in the presence of large rf inhomogeneity. Leifer[45] recently presented an elegant method of optimizing rf homogeneity for six- and 10-turn solenoids. Many software packages using numerical methods are now available for general field calculations and optimizations, and a few are capable of properly handling nonuniform surface current distributions.[46]

Single resonance circuits can efficiently use very low inductance coils (e.g., two-turn, 6-mm, 18-nH coils) to achieve the short $\pi/2$ pulse lengths (1.5 μs) needed for multiple pulse techniques to average dipolar interactions of abundant ^1H or ^{19}F nuclei.[4] When combined with sample spinning at several kHz to average chemical shift anisotropy, the technique is called combined rotation and multiple pulse spectroscopy (CRAMPS). High resolution in CRAMPS requires extremely high $\boldsymbol{B}_1$ homogeneity. Since wide conductors and leads are required with low-inductance coils (to limit lead voltage, if not losses), the current locations are not known and the method of Leifer and related analytical methods cannot be used to homogenize the field. However, the most difficult technical problem in making CRAMPS probes is usually that of eliminating proton background signals from hydrogenous contaminants in Teflon and even Kel-F.

Triple resonance circuits have been used occasionally for more than a decade,[47] but the development of the powerful rotational echo double resonance (REDOR) technique[48] for accurate distance determinations from weak dipolar couplings has recently resulted in a large demand for triple resonance MAS probes. The circuit shown in Figure 3 uses an inductively coupled HF tank to permit multinuclear tuning at both the middle and the low frequency with high efficiency and excellent isolation on all ports.[49] It has been used successfully for ^1H up to 500 MHz, and can easily be extended to quad resonance experiments such as RETRO.[50] Fixed frequency triple resonance MAS probes for REDOR experiments are expected to be available soon at 750 MHz.

6 GONIOMETERS AND SLOW MAS

The earliest applications of NMR to solids involved the study of single crystals, as relatively narrow lines are observed without multiple pulse or high-speed spinning techniques. These studies are necessarily limited to materials that can be obtained in single crystals of sufficient size (usually several mm^3) for acceptable S/N. The method requires the ability to slowly and precisely rotate the crystal about three orthogonal axes while observing the anisotropic chemical shift. The standard method for the past two decades has involved gluing a small crystal into a three-sided, 4-mm 'semicube'.[6] (Similar probes with larger coils have rotated sealed tubes to study oriented liquid crystals.) The sample may then be inserted into a precision holder inside the sample coil for 360° rotation

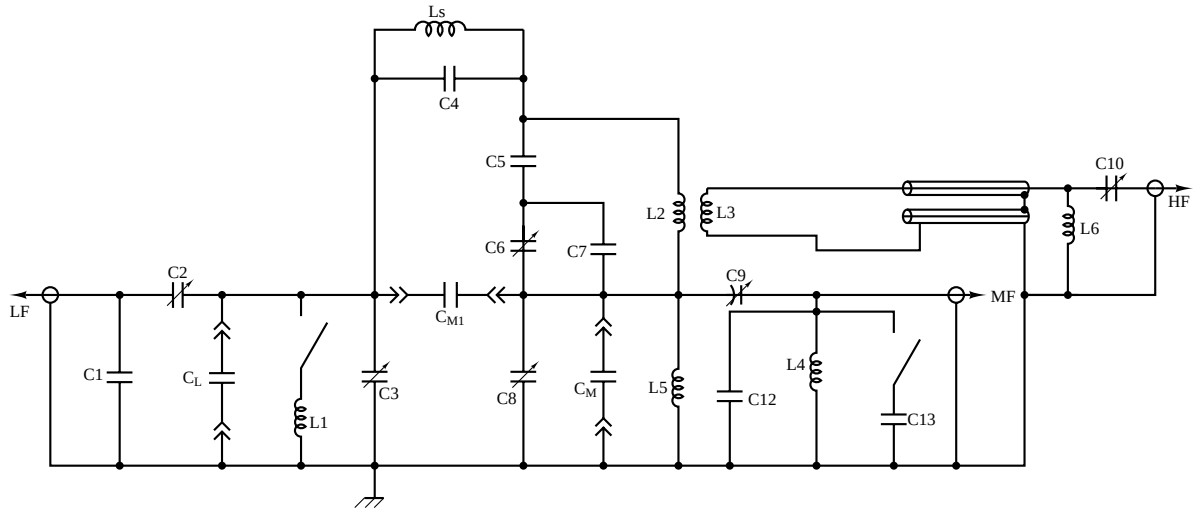

Figure 3 Doubly broadband, triple resonance circuit (Doty Scientific, Inc.)

about an axis perpendicular to $\boldsymbol{B}_0$ in small increments at which spectra are collected. The semicube is then removed and reinserted for rotation about a second axis, and the process is repeated again for the third axis. The crystal orientation with respect to the semicube holder is determined using X-ray crystallographic techniques.

The sample holder axis may be inclined at the magic angle to permit slow MAS, which is a method of addressing the spinning sideband problem by applying pulses precisely at 0°, 120°, and 240°. There is renewed interest in this technique for obtaining high-resolution spectra from large samples of dilute systems. (See ***Magic Angle Turning and Hopping***.)

Rotation has usually been accomplished using precision aluminum or brass bevel gears, but worm gears, belts, and flexible shafts have also been used. The early versions used a manual goniometer, but a stepper motor under computer control is now common. A DT multi-X circuit is usually used.

7 VARIABLE TEMPERATURE (VT)

Most CP MAS probes operate from −120 °C to +160 °C, but XVT CP MAS probes are available for wider temperature ranges, and several methods[51] have been used to cool the drive gas and circumvent liquefaction problems in pressurized nitrogen. Gay[52] optimized the conventional high-resolution sample tube spinner to obtain rotational rates sufficient for many MAS applications (over 3 kHz for 5-mm tubes) with the advantages of greater independence of the sample temperature and spinning characteristics and the ability to spin long, sealed glass tubes at the magic angle. The MAS design of Bartuska et al.[53] also provides clear separation between the VT and the bearing gas.

One manufacturer (Doty Scientific) uses a low-temperature and a high-temperature CP MAS probe, as pictured in Figure 4 along with a standard CP MAS probe, to cover the range from 35 K to over 900 K. In these probes, the electronics are maintained near room temperature and positioned close to the sample to allow multinuclear tuning without excessive lead losses, although lead inductance is increased by about 30 nH over the standard probes. Another manufacturer (Bruker) offers a gas-levitated, laser-heated wideline probe for experiments to 1200 °C.[54] Attempts to provide CP MAS down to 6 K have proven too difficult for commercial success thus far, but a number of research groups[55,56] have performed wideline NMR experiments in the 0.03−3 K range.

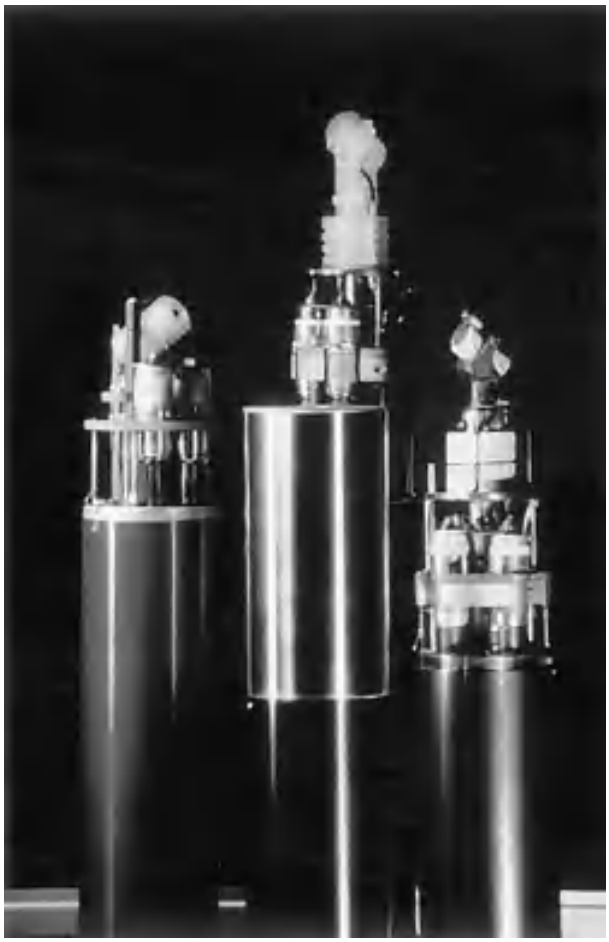

Figure 4 VT CP MAS, low-temperature CP MAS, and high-temperature CP MAS probes

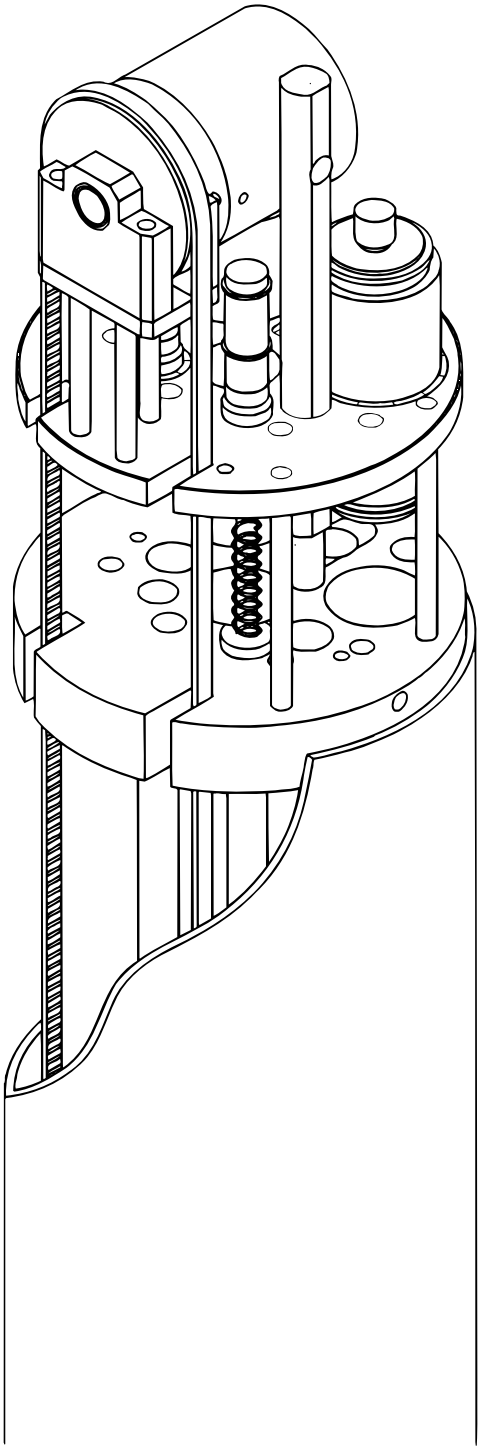

Figure 5 DAS probe with fixed coil and belt-drive spinner reorientation

8 DYNAMIC ANGLE SPINNING (DAS)

High-resolution NMR spectra can be obtained from quadrupolar nuclei if the sample spinning axis can be dynamically reoriented such that the time average of the second and fourth spherical harmonic functions vanishes.[7] The dynamic angle spinning (DAS) probe allows the spinning axis to be rapidly changed while spinning the sample at high speeds to accomplish the required averaging. One early design used a pneumatic system to switch between two fixed angles, but a high-performance servo motor and precision encoder are now standard, as programming flexibility is needed to experiment with the various 'magic angle pairs' such as [0°, 63.43°], [30.56°, 70.12°], and [37.38°, 79.19°].[57]

Two basic approaches have been used: moving coil and fixed coil. The moving coil design has the rf coil mounted on the spinner stator and attached with flexible leads or sliding contacts.[58] The fixed coil design uses a small spinner assembly that can be rotated perpendicular to its spinning axis inside a large rf coil that is perpendicular to the external field and coaxial with the reorientation axis.[59] The first commercial DAS probes used a moving coil, but it was abandoned in favor of the fixed coil because of lead failures, as most DAS experiments are two-dimensional and require millions of flips. The fixed-coil design has inherently poor filling factor, but special spinners and coils are being developed to minimize this drawback.

High-torque, low-inertia servo motors with optimized linkage should permit axis reorientation under 5 ms if the air bearings supporting the sample rotor have sufficient stiffness and load capacity; but control limitations, linkage compliance, and structure vibrations have often resulted in settling times of 25 ms or more.[59] The currently available commercial DAS probe shown in Figure 5 uses a 21-mm diameter rf coil, 8 mm long, and offers a choice of three interchangeable sample spinners: 8.6-mm diameter by 12 mm; 7-mm diameter by 13 mm; and 5-mm diameter by 14 mm. The shortest reorientation times thus far with 8.6-mm rotors are about 15 ms. Half that time may be possible with the 5-mm rotors, but the filling factor is very small. One of the factors contributing to the engineering difficulties is that the motor must be positioned well below the magnet to operate properly, which requires a rather long drive linkage that still must allow easy insertion of the probe into the magnet. The other major technical problem is that rotors with small aspect ratio (length-to-diameter ratio) are required for good filling factor, but a large aspect ratio is needed for bearing stability during rapid reorientation.

9 DOUBLE ROTATION (DOR)

In the DOR technique, the sample is placed in a small spinner inside a larger spinner and spun about two intersecting axes simultaneously to accomplish the time averaging needed to remove dipolar and quadrupolar interactions. It usually comes as a surprise to the uninitiated that such a feat would be possible at high speeds, even though most have observed a football traveling through the air executing free precession—spinning about two axes simultaneously with no significant external torques acting upon it.

The requirement for no net torques on the inner rotor is given by the following:

$$f_1 = \frac{f_2(I_T - I_A)\cos\theta_2}{I_A} \tag{2}$$

where f_1 is the frequency of the inner rotor, f_2 the frequency of the outer rotor, I_A the *axial* moment of inertia of the inner spinner (rotor, sample, caps), I_T the *transverse* moment of inertia of the inner spinner, and θ_2 is the angle of the inner rotor with respect to the axis of the outer rotor.[60]

In practice, the outer rotor is always inclined at the dipolar magic angle, 54.7°, and θ_2 is 30.56°. For stability, (a) f_1 must be a few per cent larger than given by the above, (b) the center of mass of the inner rotor must lie precisely on the axis of the outer rotor, and (c) the outer rotor must be dynamically balanced when the inner rotor is removed. The highest double rotation rates thus far are approximately 1800 Hz outer and 7000 Hz inner for 0.1-mL samples. The outer spinner assembly of a DOR spinner is shown in Figure 1, inclined at 54.7°. (The braid-reinforced lines entering each end of the assembly supply air to the inner spinner.)

10 RELATED ARTICLES

Ceramics Imaging; CRAMPS; Double Rotation; Dynamic Angle Spinning; Magic Angle Spinning; Probe Design and Construction; Probes for Special Purposes

11 REFERENCES

1. S. R. Hartmann and E. L. Hahn, *Phys. Rev.*, 1962, **128**, 2042.
2. P. Mansfield and J. G. Powles, *J. Sci. Instrum.*, 1963, **40**, 232.
3. J. S. Waugh, US Pat. 3 530 373, 1970.
4. R. W. Vaughan, *Annu. Rev. Phys. Chem.*, 1978, **29**, 397.
5. E. O. Stejskal, J. Schaefer, and J. S. Waugh, *J. Magn. Reson.*, 1977, **28**, 105.
6. R. S. Honkonen, F. D. Doty, and P. D. Ellis, *J. Am. Chem. Soc.*, 1983, **105**, 4163.
7. B. F. Chmelka and A. Pines, *Science*, 1989, **246**, 71.
8. S. J. Schneider (ed.), *Engineered Materials Handbook*, *Vol. 4, Ceramics and Glasses*, ASM International, Novelty, OH, 1991.
9. R. C. Buchanan (ed.), *Ceramic Materials for Electronics*, Marcel Dekker, New York, 1991.
10. J. Agranoff (ed.), *Modern Plastics Encyclopedia*, McGraw-Hill, New York, 1982.
11. J. J. O'Dwyer, *The Theory of Electrical Conduction and Breakdown in Solids Dielectrics*, Oxford University Press (Clarendon), London/New York, 1973.
12. D. R. Lide (ed.), *CRC Handbook of Chemistry and Physics*, 73rd edn., CRC Press, Boca Raton, FL, 1992.
13. J. D. Swift, in *The Encyclopedia of Physics*, 2nd edn., ed. R. M. Besancon, Van Nostrand Reinhold, New York, 1974, pp. 249–253.
14. F. D. Doty, T. J. Connick, X. Z. Ni, and M. N. Clingan, *J. Magn. Reson.*, 1988, **77**, 536.
15. S. L. Patt, US Pat. 4 438 400, 1984.
16. D. G. Hughes and L. Pandey, *J. Magn. Reson.*, 1984, **56**, 428.
17. M. L. Buess and G. L. Petersen, *Rev. Sci. Instrum.*, 1978, **49**, 1151.
18. F. D. Doty, US Pat. 4 710 719, 1987.
19. D. I. Hoult and R. E. Richards, *J. Magn. Reson.*, 1976, **24**, 71.
20. D. I. Hoult, *Prog. Nucl. Magn. Reson., Spectrosc.*, 1978, **12**, 41.
21. R. W. Vaughan, D. D. Elleman, L. M. Stacey, W. K. Rhim, and J. W. Lee, *Rev. Sci. Instrum.*, 1972, **43**, 1356.
22. F. D. Doty, R. R. Inners, and P. D. Ellis, *J. Magn. Reson.*, 1981, **43**, 399.
23. W. G. Clark and J. A. McNeil, *Rev. Sci. Instrum.*, 1973, **44**, 844.
24. G. C. Chingas, *J. Magn. Reson.*, 1983, **54**, 153.
25. D. I. Hoult, *J. Magn. Reson.*, 1984, **57**, 394.
26. M. Greferath, B. Blumich, W. M. Griffith, and G. L. Hoatson, *J. Magn. Reson., Ser. A*, 1993, **102**, 73.
27. E. R. Andrew, A. Bradbury, and R. G. Eades, *Nature (London)*, 1958, **182**, 1659.
28. J. D. Ellett, M. G. Gibby, U. Haeberlen, L. M. Huber, M. Mehring, A. Pines, and J. S. Waugh, in *Advances in Magnetic Resonance*, ed. J. S. Waugh, Academic Press, New York, 1971, Vol. 5, pp. 117–176.
29. E. Andrew, L. Farnell, M. Firth, T. Gladhill, and I. Roberts, *J. Magn. Reson.*, 1969, **1**, 27.
30. J. W. Beams, *J. Appl. Phys.*, 1937, **8**, 795.
31. E. T. Lippmaa, M. A. Alla, A. A. Salumyae, and T. A. Tukherm, US Pat. 4 254 373, 1981.
32. F. D. Doty and P. D. Ellis, *Rev. Sci. Instrum.*, 1981, **52**, 1868.
33. J. Adlerborn, M. Burstrom, L. Hermansson, and H. T. Larker, *Mater. Design*, 1987, **8**, 229.
34. W. T. Dixon, J. Schaefer, M. D. Sefcik, E. O. Stejskal, and R. A. McKay, *J. Magn. Reson.*, 1982, **49**, 341.
35. V. J. Bartuska and G. E. Maciel, *J. Magn. Reson.*, 1981, **42**, 312.
36. W. B. Rowe, *Hydrostatic and Hybrid Bearing Design*, Butterworths, London, 1983.
37. F. D. Doty, US Pat. 4 456 882, 1984.
38. V. Langer, P. Daugaard, and H. J. Jakobsen, *J. Magn. Reson.*, 1986, **70**, 472
39. D. Dowson (ed.), *Superlaminar Flow in Bearings*, MEP, London, 1975.
40. F. D. Doty, J. B. Spitzmesser, and D. G. Wilson, US Pat. 5 202 633, 1993.
41. F. D. Doty, B. L. Miller, G. S. Hosford, D. G. Wilson, W. Huanbo, and J. D. Jones, *Proc. IECEC-91*, 1991, Vol. 2, SAE, Warrendale, PA, p. 436.
42. D. G. Wilson, *The Design of High-Efficiency Turbomachinery and Gas Turbines*, MIT Press, Cambridge, 1984.
43. F. D. Doty, US Pat. 5 162 739, 1992.
44. X. Wu and K. Zilm, *J. Magn. Reson., Ser. A*, 1993, **104**, 154.
45. M. C. Leifer, *J. Magn. Reson., Ser. A*, 1993, **105**, 1.
46. G. J. Kost, S. E. Anderson, G. B. Matson, and C. B. Conboy, *J. Magn. Reson.*, 1989, **82**, 238.
47. S. Kan, M. Fan, and J. Courtieu, *Rev. Sci. Instrum.*, 1980, **51**, 887.
48. T. Gullion and J. Schaefer, in *Advances in Magnetic Resonance*, ed. W. S. Warren, Academic Press, San Diego, CA, 1989, Vol. 13, pp. 57–83.
49. F. D. Doty, 'Doubly Broadband Triple Resonance Circuit', US Pat. 5 424 645, 1995.
50. S. M. Holl, R. A. McKay, T. Gullion, and J. Schaefer, *J. Magn. Reson.*, 1990, **89**, 620.
51. R. D. Kendrick, S. Friedrich, B. Wehrle, H. H. Limbach, and C. S. Yannoni, *J. Magn. Reson.*, 1985, **65**, 159.
52. I. D. Gay, *J. Magn. Reson.*, 1984, **58**, 413.
53. V. J. Bartuska, D. H. Lewis, R. B. Lewis, and D. G. Dalbow, US Pat. 4 511 841, 1985.
54. D. Massiot, C. Bessada, P. Exchegut, J. P. Coutures, and F. Taulelle, *Solid State Ionics*, 1990, **37**, 223.
55. K. Carduner, M. Villa, and D. White, *Rev. Sci. Instrum.*, 1984, **55**, 68.
56. J. L. Weil, S. L. Tan, J. S. Waugh, and D. D. Osheroff, *J. Magn. Reson.*, 1987, **66**, 264.
57. B. Q. Sun, J. H. Baltisberger, Y. Wu, A. Samoson, and A. Pines, *Solid State NMR*, 1992, **1**, 267.
58. K. T. Mueller, B. Q. Sun, G. C. Chingas, J. W. Zwanziger, T. Terao, and A. Pines, *J. Magn. Reson.*, 1990, **86**, 470.
59. K. T. Mueller, G. C. Chingas, and A. Pines, *Rev. Sci. Instrum.*, 1991, **62**, 1445.
60. Y. Wu, B. Q. Sun, A. Pines, A. Samoson, and E. Lippmaa, *J. Magn. Reson.*, 1990, **89**, 297.

Biographical Sketch

F. David Doty. *b* 1950. B.A., 1972, physics, Anderson University, IN, USA, Ph.D., 1983, Physics, University of South Carolina. Began work in NMR under Paul Ellis, 1979. President of Doty Scientific, Inc., 1982–present. Approx. 20 publications and 15 patents. Research interests include rf electronics, NMR probe technology, electromagnetism, manufacturing, turbomachinery, energy conversion cycles, ceramics engineering, acoustics, economics, and religions.

Thermodynamics of Nuclear Magnetic Ordering

Maurice Goldman

Centre d'Etudes de Saclay, Gif-sur-Yvette, France

1	Introduction	1
2	Local Weiss Field. Prediction of Ordered Structures	2
3	Weiss Field and Beyond	3
4	Spin Waves and RPA	5
5	Related Articles	6
6	References	6

1 INTRODUCTION

Nuclear magnetic ordering (NMO), that is, the spontaneous transition of nuclear magnetic moments towards a magnetic ordered state under the effect of their mutual interactions, has long been a dream in the mind of reputably 'unrealistic' physicists. This 'unrealistic' goal has become a reality during the last few decades. The reason why such an endeavor has long been considered a chimera can be understood as follows. Let $\hbar\Delta$ be the typical energy span of the interspin interactions. As an order of magnitude, ordering will take place below a critical temperature T_c such that

$$k_B T_c \approx \hbar\Delta \tag{1}$$

In the case of electronic spins, their mutual interactions are often Heisenberg interactions, which are nonmagnetic in nature: they are simply the mathematical expression of the difference between the electrostatic energies of a spin pair in the (orbital) symmetric and antisymmetric states. By virtue of the Pauli principle, an orbital state of a given symmetry corresponds to a spin state of opposite symmetry, so that the total state is antisymmetric. This is the reason why this interaction of purely electric orbital origin can formally be expressed as an interaction between the electronic spins. For many electronic spin systems, this interaction is so large that the critical temperature T_c is in the range 10^2–10^3 K (it is a notorious fact that permanent magnets exist at room temperature). In the case when the electronic spin–spin interactions are purely magnetic dipole–dipole interactions, the critical temperature T_c is much lower: of the order of 1 K. Magnetic moments of light nuclei in insulators also experience purely magnetic dipole–dipole interactions. Since these interactions are proportional to the square of the magnetic moments, and since nuclear moments are roughly three orders of magnetic smaller than electronic moments, it can be surmised from the start that the critical temperature for the onset of nuclear magnetic ordering lies at best in the microkelvin range, a range that for a long time appeared desperately out of reach of experiment. Indeed, the span of orbital energies is so much larger than this energy range (remember that $1\,\mu\text{K} \sim 20\,\text{kHz} \sim 10^{-10}\,\text{eV}$) that the heat capacity of solids is negligibly small at such temperatures, which raises formidable problems for extracting heat from the sample so as to lower its temperature further, without even mentioning the problem of transferring the lattice temperature to the nuclear spins. The solution to this Gordian knot problem arose from the realization that, in order to produce nuclear magnetic ordering, it is not necessary to impart such low temperatures to the lattice: it is sufficient to cool the nuclear spins themselves. This implies that one can find conditions where spins and lattice may have different temperatures, and do not thermally mix over macroscopic time spans, and furthermore that one has means of imparting sufficiently low temperatures to the nuclear spins. There are two possibilities to meet these two conditions, which are described in ***Low Spin Temperature NMR***. In one of them, practised in our laboratory, one uses insulators composed of light nuclei and performs the nuclear cooling in two successive steps: dynamic nuclear polarization (DNP) followed by nuclear adiabatic demagnetization.[1,2] At low temperature (and in high field), the spin–lattice relaxation time T_1 is so long that waiting for nuclear thermal equilibrium would be exhaustingly time-consuming—whence the use of DNP—whereas this very length of T_1 ensures that, after demagnetization, the nuclear temperature can remain much lower than the lattice one over extended periods (a few minutes to several hours, depending on the samples), much longer than the time of order T_2 required to reach an internal equilibrium described by a spin temperature. As is well known in the NMR community, several options are open. One may demagnetize the spins to actual zero field, in which case the spin–spin interactions are the full dipole–dipole interactions. One may also demagnetize the spins in the rotating frame, by an ADRF (adiabatic demagnetization in the rotating frame), in which case the spin–spin interactions are the secular dipolar interactions, whose form depends on the orientation of the external field with respect to the crystal axes. Furthermore, the sign of the spin temperature may be chosen at will to be either positive or negative. The ordered state for $T \to +0$ is that of minimum energy, whereas that for $T \to -0$ is the state of maximum energy. The cooling of the nuclear spins by ADRF in high field has two consequences (advantages?). Firstly, the double freedom of field orientation and temperature sign makes it possible, with one and the same sample, to explore a whole series of different orderings—a bonus as regards physical interest. Secondly, the presence of the large external field makes it possible to study the system by NMR—a bonus for the 'Encyclopedia of NMR'. This approach enabled us to observe nuclear antiferromagnetism in CaF_2 in 1969,[3] as well as to perform many other NMO studies in the following years (see, e.g., Chapter 8 of Abragam and Goldman[4]).

The second method[5,6] of nuclear cooling has been practised with metals. In very high field and at very low temperature (in the millikelvin range), the thermal equilibrium nuclear polarization is high, and the efficient Korringa mechanism for spin–lattice relaxation enables the nuclear spins to reach thermal equilibrium in a reasonable time. In the subsequent adiabatic demagnetization (in two stages), the final metallic sample, on which NMO is to be produced and studied, is thermally isolated (by a surrounding vacuum and superconducting thermal barrier with preceding demagnetization stage). At very low temperature, the specific heat of the conduction electrons is so low that, although much hotter than the nuclear spins, the former are unable to heat the latter. NMO has been obtained in actual zero field in metals since 1979.[6,7] It turned out that in

most metals studied, the spins were 'frustrated' with respect to dipolar interactions, and that the ordering was determined in a large part by small RKKY interactions. This frustration, associated with the small value of the nuclear gyromagnetic ratios, resulted in very low critical temperatures, and it enabled the authors to beat 'the world record of low temperature'. In fact, as explained in ***Low Spin Temperature NMR***, what counts is not so much temperature as entropy. The spin frustration in metals resulted in 'world-beating records' of low transition entropy.

The purpose of this article is to give an overall description of the thermodynamic approximations used for the study of nuclear magnetic ordering. It is limited to those methods used in our laboratory to study pure dipolar magnetic ordering in high field. Rather than developing heavy calculations whose description can be found elsewhere,[4,8,9] we have chosen to insist on the principles and ideas behind these calculations.

2 LOCAL WEISS FIELD. PREDICTION OF ORDERED STRUCTURES

We consider for simplicity, and as a typical example, systems with equivalent nuclear spins, such as ^{19}F in CaF_2. The well-known form of the secular dipole–dipole Hamiltonian is

$$\hat{\mathcal{H}}'_{\mathrm{D}} = \frac{1}{2}\sum_{ij} A_{ij}(2\hat{I}^i_z\hat{I}^j_z - \hat{I}^i_x\hat{I}^j_x - \hat{I}^i_y\hat{I}^j_y) \tag{2}$$

where

$$A_{ij} = \tfrac{1}{2}(1 - 3\cos^2\theta_{ij})r_{ij}^{-3} \tag{3}$$

The essence of the mean field approximation is to neglect short-range correlations, that is to write

$$\langle \hat{I}^i_\alpha \hat{I}^j_\alpha\rangle \approx \langle \hat{I}^i_\alpha\rangle\langle \hat{I}^j_\alpha\rangle \tag{4}$$

The energy associated with the Hamiltonian of equation (2) can then be written as

$$\langle \hat{\mathcal{H}}'_{\mathrm{D}}\rangle = \frac{1}{2}\sum_{i,j} \boldsymbol{\omega}_i \cdot \langle \hat{\boldsymbol{I}}_i\rangle \tag{5}$$

where the local mean field has components

$$\omega_{iz} = \sum_j A_{ij} 2\langle \hat{I}^j_z\rangle \tag{6a}$$

$$\omega_{ix} = -\sum_j A_{ij}\langle \hat{I}^j_x\rangle \tag{6b}$$

$$\omega_{iy} = -\sum_j A_{ij}\langle \hat{I}^j_y\rangle \tag{6c}$$

This mean field (in a nonlocal form, as seen later) was introduced phenomenologically by Pierre Weiss to describe ferromagnetism. In most cases, it is due to Heisenberg interactions, and it is dubbed the 'molecular field'. In the present case, it is actually magnetic, and has nothing to do with molecules. This is why we prefer to call it the 'Weiss field'.

In this picture, the spins are treated as independent particles evolving in a self-consistent field, and their entropy has its standard form. For spin-$\frac{1}{2}$, for instance, it is

$$S/k_{\mathrm{B}} = \sum_i \{\ln 2 - \tfrac{1}{2}[(1+p_i)\ln(1+p_i) + (1-p_i)\ln(1-p_i)]\} \tag{7}$$

By maximizing

$$-\beta F = S - \beta\langle \hat{\mathcal{H}}'_{\mathrm{D}}\rangle \tag{8}$$

where

$$\beta = (k_{\mathrm{B}}T)^{-1} \tag{9}$$

is the 'inverse temperature', one obtains

$$|\langle \hat{\boldsymbol{I}}_i\rangle| = I B_I(|\beta\boldsymbol{\omega}_i|) \tag{10}$$

which, for spins $\frac{1}{2}$, yields, more precisely,

$$\langle \hat{\boldsymbol{I}}_i\rangle = -\frac{1}{2}\frac{\boldsymbol{\omega}_i}{|\boldsymbol{\omega}_i|}\tanh\left(\frac{\beta|\boldsymbol{\omega}_i|}{2}\right) \tag{11}$$

Remark. What one learns in thermodynamic courses and books is that the stable state of a system is that which minimizes its free energy

$$F = E - TS \tag{12}$$

The basic facts are, however, that
1. an isolated system has a constant energy,
2. its stable state is the most probable one—that is, that of maximum entropy.

From mathematics, we know that we can replace this problem of constrained maximum by an unrestricted one through the use of a Lagrange multiplier; that is, we look for the unrestricted maximum of $S - \beta E$, which is identical with equation (8)—an equation that can be used to define F. The multiplier β is later identified with inverse temperature. In usual systems, the temperature T and therefore β are always positive, so that if $-\beta F$ is maximum then the free energy F is minimum. For spin systems at negative temperature, stability corresponds to F maximum—a result that has often been found difficult to swallow by outsiders. NMR, spin temperature theory and nuclear magnetic ordering have compelled us not to content ourselves with standard formulas from standard books, but to return to the very roots of statistical thermodynamics.

There are two ways to proceed. The approach of Luttinger and Tisza[10] (or more precisely a 'trick' found in this reference) considers the case of zero temperature, a case where
1. the entropy vanishes, so that stability corresponds to E minimum or maximum, for $T \to +0$ or $T \to -0$, respectively;
2. all spins are fully polarized:

$$\forall i, \quad \langle \hat{\boldsymbol{I}}_i\rangle\langle \hat{\boldsymbol{I}}_i\rangle = I^2 \tag{13}$$

Again, we are confronted with an extremum problem with constraints, which can be solved by the method of Lagrange multipliers—as many as there are spins in the sample, say N. In this form, the problem is well nigh intractable. The 'trick'

of Luttinger and Tisza is to replace the N constraints by a single one:

$$\sum_i \langle \hat{\boldsymbol{I}}_i \rangle \langle \hat{\boldsymbol{I}}_i \rangle = N I^2 \tag{14}$$

which restricts the requirements to only one Lagrange multiplier λ. The solution turns out to be

$$\boldsymbol{\omega}_i = \lambda \langle \hat{\boldsymbol{I}}_i \rangle \tag{15}$$

Owing to the form in equations (6a)–(6c), for ω_i, it is evident that one must use Fourier transforms, that is

$$\boldsymbol{\omega}(\boldsymbol{k}) = \lambda \langle \hat{\boldsymbol{I}}(\boldsymbol{k}) \rangle \tag{16}$$

This system has N solutions, with values of λ associated with Fourier transforms $A(\boldsymbol{k})$ of the dipolar coefficients A_{ij} either $2A(\boldsymbol{k})$ for ordering parallel to Oz or $-A(\boldsymbol{k})$ for ordering perpendicular to Oz.

The stable solution at T positive (respectively negative) corresponds to the minimum (respectively maximum) value of λ. If the solution thus determined happens to satisfy the N constraints in equation (13), it can be shown that it is the correct solution.

In the approach of Villain,[11] one considers the immediate vicinity of T_c, where the polarizations are vanishingly small, so that one can use a linear expansion for the Brillouin function. Equation (10) is then of the same form as equation (15), with $\lambda \propto T_c$. It can be shown that the stable structure is that for which $|T_c|$ is maximum. This is the same criterion as for the Luttinger and Tisza method, and the solutions are the same. For the 'good' L–T solutions, all $|\langle \hat{\boldsymbol{I}}_i \rangle| = I$. The corresponding $|\langle \hat{\boldsymbol{I}}_i \rangle|$ near T_c are very small, but all equal; i.e., all Weiss field coefficients have equal modulus. It is likely that the solution at both ends, $T = T_c$ or $T = 0$, remains the same at intermediate temperatures, which has been backed up by experiment in all cases investigated. These kinds of solutions to the problem of the stable structure, where all $|\langle \hat{\boldsymbol{I}}_i \rangle|$ have equal temperature-dependent values, have been called 'permanent' solutions, because, to within a scaling of $|\langle \hat{\boldsymbol{I}}_i \rangle|$, they remain the same through the whole temperature range of ordering.

Things may be different when there are different kinds of spins: spins of different species, such as in LiF or LiH, or spins with different environments, such as ^{19}F in $KMgF_3$. The reason is that at zero temperature, it is natural to use different Lagrange multipliers λ_α for the different kinds of spins I_α, whereas close to the transition, there is one transition temperature common to all spins, so that the equations at both ends are not the same. If the stable states at $T = T_c$ and at $T = 0$ are not the same, one may expect a first-order transition at an intermediate temperature. This example shows that both approaches—Luttinger–Tisza and Villain—are useful, and complement each other.

There is a case where Villain proves better than L–T: it is for detecting stable quasi-permanent structures. A case at hand is that of the so-called 'ferrosandwich' in CaF_2, at negative spin temperature and with the field orientation in an angular domain around [111]. The maximum of λ (which determines the stable structure) corresponds to values of $\boldsymbol{k}$ that are small (i.e., k^{-1} much larger than the interatomic distance a), and parallel to Oz. However $\langle \hat{I}_z(\boldsymbol{k}) \rangle \neq 0$ corresponds to a sine modulation of the spin polarization—definitely not a permanent solution. Although it is acceptable near T_c, the question arises as to how it will evolve at lower temperature. The solution arose from the fact that $\lambda \langle \boldsymbol{k} \rangle$ is degenerate for all $\boldsymbol{k}$ in a given direction as long as their modulus is small. One can then combine small-$\boldsymbol{k}$ components parallel to Oz, until one obtains a ferromagnet with domains in the form of thin slices perpendicular to the external field, with polarizations alternatively parallel and antiparallel to the field. The limitation $ka \ll 1$ shows up in the fact that the transition between the domains is not infinitely sharp: the domain wall has a finite thickness, which should depend on temperature. Approximate models[9] show that this thickness should be small, which is substantiated by experiment. Historically, we began with the L–T approach and missed completely the prediction of this structure. It was the observation by W. Th. Wenckebach (then on a visit to our laboratory) and J. F. Jacquinot of a splitting of the ^{43}Ca NMR signal, after ADRF at $T < 0$ and with $\boldsymbol{B}_0 \parallel$ x[111], that let the light be and rendered evident the merit of the Villain method.[11]

3 WEISS FIELD AND BEYOND

3.1 The Weiss-Field Approximation

Once the stable, permanent structure has been determined by the above methods, one can use the Weiss-field approximation at temperatures intermediate between 0 and T_c, through its main result—the relation in equation (10) between spin polarization and Brillouin function—with, however, both a simplification and an extension. The simplification is that since in zero effective field all Weiss fields have the same modulus, there is only one Weiss field coefficient, and the number of equations required to analyze the properties of the ordered state is small. The extension is to the case when the ADRF is not stopped at exact resonance, and/or when an rf field is present, so that the spins experience both an effective field and a Weiss field.

The Weiss-field approximation can be combined with intuition to guess, and then check by calculation, the existence of more complex structures. We take as an example CaF_2 demagnetized at $T < 0$ with the field parallel to [100]. Theory predicts in zero field the occurrence of antiferromagnetism, with two sublattices of opposite polarizations. A distinctive property of antiferromagnets is that the lower the temperature (in absolute value), or else the lower the entropy, the lower is the parallel susceptibility. This means that in a longitudinal magnetic field (produced by adiabatic remagnetization), the bulk nuclear magnetization along the field remains small. There is no possibility of transition to a spin-flop phase as in Heisenberg antiferromagnets, because of the anisotropy of $\hat{\mathcal{H}}'_D$. Above a threshold magnetic field, it is more advantageous for the system (i.e., it increases its free energy—remember, $T < 0$!) to shift to a paramagnetic state with all spin polarizations parallel, so as to sacrifice Weiss-field energy at the benefit of Zeeman energy. That things behave differently can be surmised by the following intuitive argument. Whereas in the L–T approximation, the state of highest energy is the antiferromagnetic state referred to above, the next 'best solution' is the ferrosandwich, with thin slices of polarizations alternatively parallel and antiparallel to the external field. The

latter has a reasonably high parallel susceptibility. Whereas in zero effective field, the domains of opposite polarizations have equal widths and the bulk magnetization vanishes, in the presence of a longitudinal effective field, this magnetization can easily grow through the motion of the domain walls, so as to favor the domains with magnetization antiparallel to the field against those of opposite magnetization (This is what is actually observed in the ferrosandwich structures, and serves to ascertain their nature.) It would be nice to maximize the free energy by a compromise whereby neither the Zeeman energy nor the antiferromagnetic Weiss-field energy would be sacrificed, by a combination of best and second best solutions in the form of a structure consisting of thin slabs perpendicular to the field, retaining some antiferromagnetic character, but having different bulk polarizations. By trial-and-error Weiss-field-based calculations, the best solution consists of such a structure indeed, where one type of slices is antiferromagnetic with small parallel magnetization, and the other is paramagnetic with all individual spin magnetizations antiparallel to the effective field. The relative volumes of these two types of slices are functions of the field. This was experimentally investigated by following, as functions of field and entropy, the relative intensities of the two NMR lines of ^{43}Ca, differently shifted by the different mean fields at their sites in the two types of domains. The striking agreement of the results with theory proves that this guess was the good one.

All and all, the Weiss-field approximation yields on the average predictions in agreement with both experiment and logic—but only at sufficiently low entropy. Close to the transition, it is totally inadequate, and some account of short-range correlations is definitely required. We describe below some of the approximations that we have used.

3.2 The Heisenberg Approximation

It is probably the first attempt made to account partly for short-range correlation effects on ferromagnetism,[13] devised by Heisenberg (shortly after introducing exchange interactions, that provided the explanation for the huge molecular fields required in the Weiss model).

The idea of Heisenberg was to consider the subspace with total angular momentum S' for the N individual spins of the sample. It is easy to calculate within this subspace the first and second moments of the exchange energy. It is then assumed that, within this subspace, the density of states is a Gaussian function centered on the first moment, of width determined by the (reduced) second moment. This enables one to calculate the partition function, whence all properties of the system.

We have tried to modify this method slightly, so as to adapt it to such cases as antiferromagnetism, as follows. For an antiferromagnet with sublattices $\mathcal{A}$ and $\mathcal{B}$, we have calculated the first and second moments of the secular dipolar energy in a subspace with well-defined sublattice polarizations, i.e.,

$$\sum_{i\in\mathcal{A}} I_z^i = \tfrac{1}{2}NLp_{\mathrm{A}}, \quad \sum_{\mu\in\mathcal{B}} I_z^\mu = \tfrac{1}{2}NLp_{\mathrm{B}} \tag{17}$$

and we have similarly assumed a Gaussian density of states within this subspace. It should be noted that for ferromagnetism, this variant differs notably from the Heisenberg approach.

We never actually used this modified Heisenberg approximation, because we soon realized that the Kirkwood approximation, to be described next, was better: to the lowest order of short-range correlations, it yielded results identical with the present approach, but it also yielded a general procedure to push the approximation further.

3.3 The Restricted Trace Approximation

We illustrate the principle of the restricted trace approximation[14,15] for the case of an antiferromagnet of spins $\frac{1}{2}$. Each sublattice $\mathcal{A}$ and $\mathcal{B}$ has an equal number $\frac{1}{2}N$ of spins. All static properties of the system can be deduced from the knowledge of the partition function:

$$\mathcal{Z} = \mathrm{Tr}\{\exp(-\beta\hat{\mathcal{H}})\} \tag{18}$$

We choose as a basis the eigenstates of both:

$$\hat{I}_z^{\mathrm{A}} = \sum_{i\in\mathcal{A}} \hat{I}_z^i, \quad \hat{I}_z^{\mathrm{B}} = \sum_{\mu\in\mathcal{B}} \hat{I}_z^\mu \tag{19}$$

and we split the Hilbert space into subspaces corresponding to the different eigenvalues of $I_z{}^{\mathrm{A}}$ and $I_z{}^{\mathrm{B}}$:

$$\langle \hat{I}_z^{\mathrm{A}} \rangle = \tfrac{1}{4}Np_{\mathrm{A}}, \quad \langle \hat{I}_z^{\mathrm{B}} \rangle = \tfrac{1}{4}Np_{\mathrm{B}} \tag{20}$$

The trace in equation (18) is a sum of partial traces:

$$\begin{aligned} \mathcal{Z} &= \sum_{p_{\mathrm{A}},p_{\mathrm{B}}} \mathrm{Tr}'\{\exp(-\beta\hat{\mathcal{H}})\} \\ &= \sum_{p_{\mathrm{A}},p_{\mathrm{B}}} \mathcal{Z}'(\beta, p_{\mathrm{A}}, p_{\mathrm{B}}) \end{aligned} \tag{21}$$

We then assume that the restricted traces $\mathcal{Z}'(\beta, p_{\mathrm{A}}, p_{\mathrm{B}})$ exhibit sharp maxima for p_{A} and p_{B} equal to the sublattice polarizations in the ordered state. To within a correction of order $\ln N$, negligible compared with N in the limit as $N \to \infty$, we have

$$\ln \mathcal{Z}(\beta) \approx \ln \mathcal{Z}'(\beta, p_{\mathrm{A}}, p_{\mathrm{B}}) \tag{22}$$

The procedure is to calculate $\mathcal{Z}'(\beta, p_{\mathrm{A}}, p_{\mathrm{B}})$ and to choose the polarization values from the condition of maximization:

$$\frac{\partial}{\partial p_{\mathrm{A}}} \ln \mathcal{Z}' = \frac{\partial}{\partial p_{\mathrm{B}}} \ln \mathcal{Z}' = 0 \tag{23}$$

In practice, $\ln \mathcal{Z}'(\beta, p_{\mathrm{A}}, p_{\mathrm{B}})$ can be calculated in the form of a power expansion in short-range correlations within the $\{p_{\mathrm{A}}, p_{\mathrm{B}}\}$ subspace, proportional to increasing powers of β. Using such limited expansions in the rigorous relations (78) and (79) of ***Low Spin Temperature NMR*** yields approximations of various orders to the properties of the state. It can be shown that, to the lowest order of approximation for short-range correlations, this method yields results identical with those of the Heisenberg approximation of the preceding subsection.

The advantage of the restricted trace is that the extension of the approximation to higher orders is obvious, even if not easy in practice. We have used approximations up to the third order.

3.4 The 'Physical Model'

This home-made model was devised *à propos* the study of transverse rotating helical magnetic ordering[16,17] in CaF_2, at $T > 0$, and with the field orientation in the vicinity of the [111] direction. It is much simpler to explain it for the case of the ferrosandwich, which occurs for similar field orientations, but at negative temperature. Let us consider the case when the field is parallel to [111]. For such an orientation, the secular dipolar interaction of a given ^{19}F spin with its nearest neighbors vanishes, because $\cos\theta = \sqrt{\frac{1}{3}}$ in equation (3). It is possible to imagine a relative orientation of its next-nearest neighbors that would maximize the local field it experiences, but this structure is not translationally invariant. The 'frustrated' spins then take advantage of the long range of dipolar interactions: they sacrifice the mean field from close neighbors at the benefit of that originating from distant nuclei. Indeed, consider a thin pancake normal to $\boldsymbol{B}_0$ with all ^{19}F spin polarizations parallel to $\boldsymbol{B}_0$. We can draw a sphere around a given spin and compute the mean field it experiences as the sum of the contributions from the spins inside the sphere and those outside. The first one vanishes for the sc lattice of ^{19}F in CaF_2. As for the second one, it is indeed maximum for that particular domain shape, as is known from classical magnetostatics. The nature of the structure can be deduced by different, and more systematic means (Section 2), but the important lesson of present use is that the Weiss field is due to distant spins. It is known from general arguments that distant spins do not experience short-range correlations, i.e., that

$$\langle \hat{I}_z^i \hat{I}_z^j \rangle \approx \langle \hat{I}_z^i \rangle \langle \hat{I}_z^j \rangle \tag{24}$$

Let us now isolate by thought a sphere of homogeneous spin polarizations, of radius large enough compared with the interatomic spacing that surface effects are negligible. Then the mean field experienced by all spins of the sphere is due to distant spins for which equation (24) holds. As a consequence, the field does not differ qualitatively from that produced by an external magnet. This is the essence of the Physical Model: the properties of the spins in the sphere are the same as those of a paramagnet subjected to an external field, and it is possible to approximate them by a limited expansion in β, that is, limited to short-range correlations within the sphere, as described in ***Low Spin Temperature NMR***. Afterwards, when considering the whole sample, the 'Zeeman' energy associated with this field is multiplied by $\frac{1}{2}$, to account for the fact that it is a self-energy, and the value of the field, a function of the nuclear polarization, is determined self-consistently. To the same order of approximation, this method yields results similar to the restricted trace method described above. The unique virtue of the Physical Model is elsewhere: unlike the other approximations, it can be used to describe the *dynamic* properties of the system.

The main motivation for developing this model was to account for the shape of the NMR absorption signal of ^{19}F in the transverse rotating helimagnetic structure. In this structure, the nonvanishing spin component expectation values are in the plane normal to the external field, in a helical arrangement. (More precisely, the nonvanishing Fourier components correspond to $\boldsymbol{k} \parallel \boldsymbol{B}_0$ and $ka \ll 1$, but are otherwise degenerate.) This structure looks static in the rotating frame. As viewed from the laboratory frame, the transverse spin components are rotating in bulk around $\boldsymbol{B}_0$ at the Larmor frequency—whence the name of this type of ordering. It was observed that the (antisymmetric) absorption signal of ^{19}F consisted of two relatively narrow peaks flanked with bumps in the wings, whose importance depended strongly on the orientation of the field $\boldsymbol{B}_0$. The qualitative reason for this was soon realized. The condition $ka \ll 1$ makes it possible to isolate by thought in the sample a sphere of radius $R \gg a$ with practically homogeneously oriented transverse spin polarizations (which justifies the use of the Physical Model). The secular dipolar interactions, equation (2), are sums of components $\hat{T}_2{}^0(z)$ of spin tensorial operators, with respect to the direction Oz of the external field. In the sphere under consideration, it is natural to choose as the quantization axis the direction Ox of the spin polarization. With this choice, each tensor component $\hat{T}_2{}^0(z)$ is a sum of components $\hat{T}_2{}^0(x)$ and $\hat{T}_2{}^{\pm 2}(x)$. The latter mix states $|m_x\rangle$ with $|m_x \pm 2\rangle$. When an rf field is applied at frequency ω, it appears in the frame rotating at the Larmor frequency ω_0 as rotating at the frequency $\Delta = \omega_0 - \omega$. In the sphere under consideration, this rotating field can be decomposed into an oscillating component normal to Ox and an oscillating component parallel to Ox.

The former is able to induce transitions corresponding to $\Delta m_x = \pm 1$, and it accounts for the inner doublet. As for the longitudinal component, thanks to the state mixing described above, it is able to induce transitions corresponding to $\Delta m_x = \pm 2$, and it should account for the outer shoulders. Things are a little more complicated, because the transverse magnetization produced by the rf irradiation produces a transverse Weiss field on the other parts of the sample, which contributes to their own transverse response. The self-consistent calculation is rather complex. Performed within the Physical Model, it yielded a semiquantitative reasonable agreement with experiment.[16]

The validity of the Physical Model seems limited to structures where the mean field on a given spin originates from distant spins, and would seemingly exclude, say, antiferromagnetic structures. However, by analogy with the 'vertex renormalization' described briefly in ***Low Spin Temperature NMR***, it might possibly be proved that it is also valid in such cases. This is so far but wishful thinking.

4 SPIN WAVES AND RPA

One of the simplest and clearest description of these approximations is found in Anderson's 'Concepts in Solids'.[18]

The spin wave approximation was initially developed by Felix Bloch for describing the low-temperature properties of ferromagnets. In the ground state, all spins are, say, in their eigenstate $\hat{I}_z{}^i = -I$. At low temperature, there will be few excitations, limited mostly to states where $\hat{I}_z{}^i = -I + 1$ would contribute. It is then a good approximation to treat $\hat{I}_+{}^i$ and $\hat{I}_-{}^i$ as boson creation and annihilation operators $\hat{\alpha}_i{}^+$ and $\hat{\alpha}_i$. One then finds that the excitations correspond to the Fourier transform operators $\hat{\alpha}^+(\boldsymbol{k})$ acting on the ground state, considered as 'the vacuum'. The extension of this approximation to antiferromagnets has met with a little problem. For Heisenberg interactions of the form $J\hat{\boldsymbol{I}}^i \cdot \hat{\boldsymbol{I}}^j$, and also for secular dipolar interactions of the form of equation (2), an antiferromagnet where half the spins are in their eigenstates $\hat{I}_z{}^i = +I$ and the other half in their eigenstate $\hat{I}_z{}^\mu = -I$, corresponds to a state that is not an eigenstate of the Hamiltonian, because of the presence

of operators $\hat{I}_-{}^i\hat{I}_+{}^\mu$. This Hamiltonian has matrix elements between this trial ground state and excited states. As a result, the true ground state has an energy lower than the initial one. Formally, this true ground state is approximated in spin wave theory through a so-called Bogolyubov transformation on the initial pseudo creation and annihilation operators. This method has met with definite success at low temperature, much lower than T_c and out of reach of present studies of NMO. In NMO, we have made one successful qualitative use of spin wave theory, which can be described without any calculation. In CaF_2, at positive temperature and with $\boldsymbol{B}_0$ oriented in the vicinity of the axis [111], the L–T and Villain methods have two degenerate solutions for the ground state: a transverse helix described above, or a ferrosandwich with domains whose large dimension is parallel to $\boldsymbol{B}_0$, so as to minimize the energy—a requirement opposite to that at negative temperature. Discrimination between these possibilities can be obtained only by taking short range correlations into account. This is what is partly achieved by spin waves. The ferrosandwich is nearly an eigenstate of the Hamiltonian, except for the spins near the domain walls. The ground state energy is then close to that computed by the Weiss-field approximation. The existence of the domain walls is likely to increase it somewhat. As regards the transverse helix, it is definitely not an eigenstate of the Hamiltonian. As for the case of antiferromagnetism, the use of the spin wave approximation leads to the definition, through a Bogolyubov transformation, of a modified ground state, whose energy is lower than that of the initial state, i.e., that computed within the Weiss-field approximation. The qualitative result is that the (spin-wave amended) transverse helix has a ground state of energy lower than the ferrosandwich, and is therefore the stable ordered structure. The same conclusion has been reached at higher temperature through the restricted trace approximation, and it has been backed by experiment.

The random phase approximation (RPA), results in the definition of creation and annihilation operators of the same form as those in the spin wave approximation, with the difference that the energy of the excitations is 'renormalized': it is proportional to the ordered spin polarization. The theoretical approach may be similar to[18] or very different from[19] that of spin waves. Although expected to be an improvement over spin waves at not-too-low temperatures, RPA did not prove very useful for the study of NMO, except in one case that we describe qualitatively. It concerns the experimental evidence for the existence of transverse helimagnetism in CaF_2. This evidence was provided by an experimental 'paraphrase' of the Hartmann–Hahn method: the resonant polarization transfer between two spin systems subjected to rf irradiation when their respective effective frequencies in the rotating frame are equal. The idea was that in the state of transverse helimagnetic ordering, the ^{19}F spins experience a transverse Weiss field, which should play the same role as the external rf field in the Hartmann–Hahn experiment. We have therefore subjected the ^{43}Ca spins to rf irradiation and studied as a function of effective frequency their rate of polarization through thermal mixing with the ^{19}F spins in the absence of irradiation of the latter. This rate exhibited a sharp maximum at a nonzero ^{43}Ca effective frequency, thereby proving that the ^{19}F spins experienced a Weiss field not aligned with the external field, i.e., at least partly transverse.

On second thoughts, the preceding interpretation is too simplistic. An elementary process of energy exchange between ^{19}F and ^{43}Ca proceeds through a flip of a single ^{43}Ca spin, but not through a flip of a single ^{19}F spin. The ordered system of fluorine spins can change its energy only through the creation or annihilation of elementary excitations, which involve many spins. We have used the RPA model for these excitations: their spectrum, density of states, probability of flipping a calcium spin. The predicted curve of polarization rate versus ^{43}Ca effective frequency is in qualitative agreement with experiment. More revealing, however, is that the variation of its shape when changing the external field orientation (that is the form of $\hat{\mathcal{H}}'_D$) is also as observed. In these experiments, the transverse fluorine polarization was about 0.7, as deduced from the Hartmann–Hahn-like resonance—a polarization high enough for RPA still to be a reasonable approximation.

We have not attempted other approximations such as Green functions beyond the RPA level, spherical model, etc. The accuracy of the experiments did not justify such an effort.

5 RELATED ARTICLES

Low Spin Temperature NMR; Nuclear Ferromagnetism and Antiferromagnetism.

6 REFERENCES

1. A. Abragam, *C. R. Hebd. Séances Acad. Sci.*, 1960, **251**, 225.
2. A. Abragam, *C. R. Hebd. Séances Acad. Sci.*, 1962, **254**, 1267.
3. M. Chapellier, M. Goldman, Vu Hoang Chau, and A. Abragam, *C. R. Hebd. Séances Acad. Sci., Sér. B*, 1969, **268**, 1530.
4. A. Abragam and M. Goldman, *Nuclear Magnetism: Order and Disorder*, Clarendon Press, Oxford, 1982.
5. N. Kurti, F. N. H. Robinson, F. Simon, and D. A. Spohr, *Nature (London)*, 1956, **178**, 450.
6. P. J. Hakonen, O. V. Lounasmaa, and A. S. Oja, *J. Magn. Magn. Mater.*, 1991, **100**, 394.
7. P. J. Hakonen, R. T. Vuorinen, and J. E. Martikainen, *Phys. Rev. Lett.*, 1993, **70**, 2818, and references therein.
8. M. Goldman, M. Chapellier, Vu Hoang Chau, and A. Abragam, *Phys. Rev. B*, 1974, **10**, 226.
9. M. Goldman, *Phys. Rep.*, 1977, **32**, 1.
10. J. M. Luttinger and L. Tisza, *Phys. Rev.*, 1946, **70**, 954; see also D. H. Lyons and T. A. Kaplan, *Phys. Rev.*, 1960, **120**, 1580.
11. J. Villain, *Phys. Chem. Solids*, 1959, **11**, 303.
12. C. Urbina, J. F. Jacquinot, and M. Goldman, *J. Phys. (Orsay, Fr.)*, 1982, **43**, 1461.
13. W. Heisenberg, *Z. Phys.*, 1928, **49**, 619; see also J. H. Van Vleck, *The Theory of Electric and Magnetic Susceptibilities*, Oxford University Press, Oxford, 1932, p. 326.
14. J. G. Kirkwood, *J. Chem. Phys.*, 1938, **6**, 70.
15. M. Goldman and G. Sarma, *J. Phys. (Orsay, Fr.)*, 1975, **36**, 1353.
16. C. Urbina, J. F. Jacquinot, and M. Goldman, *J. Phys. C*, 1986, **19**, 2275.
17. M. Goldman, J. F. Jacquinot, and C. Urbina, *J. Phys. C*, 1986, **19**, 2299.
18. P. W. Anderson, *Concepts in Solids*, Benjamin, New York, 1963.
19. S. V. Tyablikov, *Methods in the Quantum Theory of Magnetism*, Plenum Press, New York, 1967.

Biographical Sketch

Maurice Goldman. *b* 1933. Diplôme d'Ingénieur Chimiste ESPCI, 1955, Doctorat d'Etat, 1967, University of Paris. Physicist, Commissariat à l'Energie Atomique (CEA), 1955–69. Vice-Director, College de France, 1969–83. Physicist, CEA, 1984–89. Research Director, CEA, 1989–93. Scientific Adviser, CEA, 1993–present. Vice-President, ISMAR, 1992–present. Approx. 100 publications, including three books. Research specialties: spin temperature and thermodynamics, nuclear magnetic ordering, relaxation in liquids and solids, and quantum theory of high-resolution NMR.

Abragam, Anatole: 'The Bible'

Anatole Abragam
Collège de France, Paris, France

Editor's Note: The following article, describing the writing of the classic work 'The Principles of Nuclear Magnetism', is taken from Professor Abragam's autobiography, 'Time Reversal', a charming, humorous and very informative book that was published in 1989. This excerpt is used with the permission of the author and the publisher, Oxford University Press.

I think it was in 1955 that Maurice Pryce told me that Oxford University Press (OUP) had asked him to write a book on magnetic resonance; but he did not have the time to do it, or did not feel like it, or both, and so he had mentioned my name to OUP and had been asked by them to sound me out for the job. 'It's just at the right moment', he said glibly. 'You have just completed a course on NMR and another on ESR: all you have to do is to translate it all into English and the trick is done'. I had no experience of the trade of book writing, I had only read a lot of them; but I understood that it would not be quite so simple.

What attracted and frightened me at the same time was that this book, which was yet to be written, would be part of the illustrious collection of the OUP Monographs. Before the war, it was with reverence that I used to contemplate their prestigious titles, written in letters of gold on the backs of their bottle-green bindings, standing on the shelves of the library of the Institut Henri Poincaré: *The Principles of Quantum Mechanics* by Dirac, the greatest physics book ever written, *The Theory of Atomic Collisions* by Mott and Massey, *The Quantum Theory of Radiation* by Heitler, *The Theory of Electric and Magnetic Susceptibilities* by Van Vleck, *The Principles of Statistical Mechanics* by Tolman—prestigious books, fountains of wisdom where I had quenched my thirst for knowledge. Could it be that my imperfect opus would stand next to them on the shelves?

I accepted timorously. A few weeks later I received two copies of a contract which, from the quality of the paper and of the typography, was more like a diplomatic treaty than a vulgar commercial agreement; OUP was already displaying the quality of its productions.

The contract was leonine: OUP reserved an exorbitant part of the television rights for itself, and declined all responsibility in case of prosecution for obscenity. Still, I accepted, asked Michel Trocheris to commit himself on my side by bearing witness to my signature, countersigned all the pages, and sent back one of the copies. *Alea jacta erat!*

Pryce had spoken lightly of some 300 pages to cover both ESR and NMR, while my lecture notes were already twice that size. I decided that I had to choose: ESR or NMR, that was the question. In 1955 I was far better known for my work on ESR than for my NMR; and I was advised by some friends to choose ESR where, I was told, I was an expert, rather than NMR where I was at best a beginner. I was not convinced: while I had hardly published anything on NMR, for five years I had read most of what was worth reading on the subject. Furthermore I foresaw possibilities for development in nuclear magnetism, many more than I saw in ESR. Finally, in my infant laboratory, there were lots of things to be done straight away in NMR, and nothing of the kind in ESR. I made my decision. The book would be on nuclear magnetism and, in the wake of Dirac, I dared to call it *The Principles of Nuclear Magnetism*.

Then followed four years of strenuous work. One may well ask how, during these four years, I managed to combine the writing of a book of 600 pages (we were a long way from the projected 300 pages for NMR plus ESR), with the setting-up and the running of a new laboratory, and with my personal research. The answer is that there was a symbiosis between these various pursuits; my ideas and those of my young co-workers, and the results of our experiments, were fed into the book even while they were being submitted to scientific journals. Conversely, the writing of the book was at the origin of some of our researches.

For example, dissatisfied with the current theory of spin diffusion, I 'ordered' a better formulation from Pierre-Gilles de Gennes and entered it into the manuscript of my book even before he had published it in a journal.

I also liked to imagine experiments, aimed at illustrating some points of the theory in a spectacular manner. Some far from trivial experiments, which were performed in the lab during that period, originated purely for that reason.

I seldom presented a calculation taken from published literature without attempting to make it shorter, clearer, or more rigorous. I have already spoken of my efforts to strip Bloch's theory of the master equation of its Wagnerian mantle. I performed a similar operation of cosmetic surgery (I am mixing my metaphors) on a very important work, which was profoundly original but almost unintelligible, by Alfred Redfield. I heard from some of my readers that they understood Redfield's ideas for the first time in my presentation of them.

I kept strictly to my rule of including no theory in my book to which I did not subscribe, no experimental fact that contradicted a theory to which I did subscribe wholeheartedly, no formula that I had not checked myself. I departed from the last rule twice, to regret it both times.

All those who write books intended for students know, or at least ought to know, that they owe them a great responsibility, which is greater the better the students. A good student who reads a scientific book, pen in hand, trusts its author, and, when he comes up against an error, will waste a lot of his time trying to understand or to rederive the incorrect result. I am not saying that it is harmless to accumulate errors in an original scientific publication, but at least there the experienced reader will recognize earlier, and perhaps not without some innocent pleasure, the errors of a colleague.

This is why I took great care to detect any errors. I remember a formula cited by Bloembergen and Anderson (neither a Nobel laureate yet), with a discrepancy by a factor of four (or perhaps eight), while I myself had found a third result. Before including my own version in the book I had consulted with Walter Kohn and de Gennes, who fortunately both agreed with me.

In spite of all these efforts, small errors did remain, which readers pointed out to me and which I have, I hope, weeded out through the many printings the book has known during its long existence.

I found some relaxation from my labors by inventing short epigraphs which were appropriate to the contents of the various chapters. It is thus that I honored Marilyn Monroe (very much alive then) by giving the chapter on spin temperature the title of her picture: *Some Like it Hot*. OUP frowned at it; I replied, however, that to my knowledge it was the title of an old nursery rhyme, and what else did they have in mind?

In the preface I warned the reader (and the authors) that: ' . . . in a book, in contrast to an article, no references need be given solely for credit . . . ' By so doing, I considerably reduced the volume of the bibliography and made a few enemies.

The success of the book exceeded all my expectations and my hopes. It was translated into French (by André Landesman), Russian and Japanese, received a record number of citations for the last 25 years in the notorious *Citation Index*, and last but not least, sold very well.

If I have written at such length about the genesis of this book, it is not only because I lived cheek by jowl with it during the four years it took me to write it. It is also because it gets on my nerves, with the shadow it casts on the other things I have done.

Conan Doyle was deeply annoyed by the prejudicial effect of Sherlock Holmes's success on some other works of his, which he considered at least as important. Well, I feel a little like that too. All those who had anything to do with NMR, and that's quite a crowd, know my name because of the book. Only a minority of them know that 10 years later Bleaney and I wrote an even thicker book on ESR, and still fewer know of my work after 1960 and of the book I published with Maurice Goldman in 1982, devoted to new developments in nuclear magnetism 'with most of them coming from my own laboratory'. But, to tell the truth, I also sometimes think that the recognition I got for these other achievements is quite reasonable and in keeping with their value; it is the success of the Principles which may be excessive. Nobody is ever pleased with his lot.

Biographical Sketch

Anatole Abragam *b* 1914. Grad. Sorbonne 1938, D.Phil. Oxon, 1950. Introduced to ESR by Maurice Pryce and Brebis Bleaney, to NMR by Robert Pound, Ed Purcell and Felix Bloch. Professor of Nuclear Magnetism at the Collège de France (Paris) 1959-1985. Main fields of interest: hyperfine structure in solid state, perturbed angular correlations, dynamic nuclear polarization (DNP), nuclear magnetic ordering, nuclear pseudomagnetism, Muon precession. Publications in ESR, NMR, and other subjects. Books: 'The Principles of Nuclear Magnetism' (OUP 1961) and others.

Abraham, Raymond J.: A Brief History of Proton Chemical Shifts

Raymond J. Abraham
University of Liverpool, UK

The most important single parameter in high-resolution NMR spectroscopy is the proton chemical shift, and the classic demonstration by Arnold, Dharmatti, and Packard[1] of the three separate proton resonance peaks in ethanol illustrated the immense potential of NMR in structural organic chemistry. This was almost immediately recognized by Harold Bernstein and Bill Schneider at the National Research Council of Canada. They purchased one of the first commercial NMR spectrometers (a Varian 40 MHz spectrometer) and also invited John Pople to the NRC for a number of visits during the summers of the late 1950s. Thus, by an organizational tour-de-force, Harold and Bill had obtained both the facility for the production of a whole new set of experimental data and the cooperation of one of the finest theoreticians available to interpret it.

In 1957 I was working with Harold Bernstein as a postdoctoral fellow at the NRC, and was a student of and an admirer of both the first class science which resulted from this collaborative effort, including their seminal book on high-resolution NMR[2] (of which I suspect I have the only autographed copy in existence), and also of the excellent, informal, nonbureaucratic organization of the NRC at that time. This was indeed at times almost life-saving as they allowed me to sleep in their air-conditioned laboratory, which provided instant relief from occasional serious attacks of asthma precipitated by the high pollen count and humidity of Ottawa in the summer (at least compared to the UK!).

At this time, Allred and Rochow[3] had shown conclusively how the proton chemical shifts of methyl derivatives (CH_3X) were linearly related to the electronegativity of X, and indeed used this relationship to define the electronegativities of some atoms and groups for which data were not available.

At the NRC, research into the fundamentals of proton chemical shifts proceeded in two separate directions. Spiesecke and Schneider[4] made a comprehensive study of the proton chemical shifts of some simple gases, an exceptionally difficult experimental investigation given the comparatively poor sensitivity and stability of NMR spectrometers at that time. They attempted to eliminate the effects of the medium on proton chemical shifts, and their work showed the large effects that hydrogen bonding interactions have on proton chemical shifts, effects which even today have no quantitative theoretical explanation.

Another major project at the NRC was the determination of the proton chemical shifts of aromatic molecules, partially inspired by another basic concept in proton chemical shifts, the aromatic ring current. The simple equivalent dipole model of the benzene ring current proposed by Pople[5] has been shown to be amazingly accurate. Despite subsequent more complex treatments,[6,7] this simple equation[8] is still the easiest method of accurately calculating the ring current field at any position external to the benzene ring. The most spectacular illustration of the aromatic ring current is the proton spectra of condensed aromatic molecules such as the porphyrins and an extension of this dipole model, the double dipole or network model has been used successfully by our group to calculate proton chemical shifts both external to and within the porphyrin nucleus.[9]

The early research thus appeared at first to provide a complete understanding of proton chemical shifts. One could say in the early 1960s that proton chemical shifts were due to the charge on the proton, as illustrated by the effects of electronegative atoms on methyl proton shifts, modified by the shielding effects of anisotropic groups, such as aromatic compounds, carbonyl groups, etc., and by medium/complexation effects (in particular, hydrogen bonding, both intra- and intermolecular). It looked as if everything was falling in place.

Unfortunately, as so often happens in science, the truth was rather more complex and less comprehensible than our simple explanations had implied. The linear relation of CH_3X proton chemical shifts with the electronegativity of X would imply that the partial atomic charge on the proton determines proton chemical shifts. This, however, was not confirmed by quantum mechanical calculations. Indeed, modern sophisticated ab initio calculations using the Mulliken population analysis predict that the positive charge on the protons of methyl fluoride is *less* than on the protons of methane. On the simple basis of charge versus proton chemical shift, the methyl fluoride chemical shift should be upfield of that of methane!

Furthermore, it was noticed that although the chemical shift difference $\delta(CH_3) - \delta(CH_2)$ of the protons in ethyl derivatives also correlated linearly with the electronegativity of the substituent, the actual shielding of the CH_3 protons *increased* with increasing substituent electronegativity, i.e., opposite to expectations.

Even worse, solvent effects on proton chemical shifts were found to be large[10] and could not be ignored in any quantitative calculation of proton chemical shifts even where hydrogen bonding was not involved.

And finally, even in simple hydrocarbons with no anisotropic or polar groups, large differences in proton chemical shifts were observed. The classic example was cyclohexane in which the axial and equatorial protons resonate at δ 1.19 and 1.68 ppm. This last result proved the final straw. The only acceptable explanation of this difference was that it was due to C–C bond anisotropy, but the major difficulty with this explanation was that the anisotropy had to be so large to obtain the experimental shift difference that the C–C bond would have to be paramagnetic in one direction!

So what happened then? NMR spectroscopists discovered FT NMR, noise decoupling, ^{13}C NMR, and subsequently a whole new world of multidimensional NMR. The interpretation of proton chemical shifts was left to undergraduate classes, and they fortunately do not usually ask any questions!

However, some researchers continued this by now unfashionable research topic. Steric effects were shown to be important in proton chemical shifts,[11] and advances in molecular modeling and our knowledge of molecular geometries meant that these could, for the first time, be calculated at least semi-quantitatively.

The effect of a vicinal methyl group on the proton chemical shift was shown to be a function of the C–C–C–H dihedral angle.[12] In a *gauche* orientation the methyl is shielding,

whereas in a *trans* orientation the methyl is deshielding, with a ca. cos ϕ dependence.

Also, in contrast to quantum mechanical calculations, semiempirical calculations of partial atomic charges gave remarkably good correlations with proton chemical shifts.[13,14] Does this mean that proton chemical shifts are a function of the partial atomic charge on the proton after all?

We have recently reinvestigated this question, and produced a simple scheme for calculating proton chemical shifts based on a semiempirical calculation of partial atomic charges together with an orientational dependence of electronegative substituents and including also steric effects.[15] To date this scheme has been applied successfully to hydrocarbons and simple acyclic molecules. On this scheme the axial versus equatorial chemical shift difference in cyclohexane is simply due to the orientational dependence of the vicinal carbon atom, the equatorial proton having two vicinal carbon atoms in an *anti* (*trans*) orientation, whereas the axial proton has the carbon atoms in a *gauche* orientation. Is this the true explanation, or will proton chemical shifts continue to baffle the theoretical chemist? As usual, only time will tell.

REFERENCES

1. J. T. Arnold, S. S. Dharmatti, and M. E. Packard, *J. Chem. Phys.*, 1951, **19**, 507.
2. J. A. Pople, W. G. Schneider, and H. J. Bernstein, *High Resolution Nuclear Magnetic Resonance*, McGraw-Hill, New York, 1959.
3. A. L. Allred and E. G. Rochow, *J. Am. Chem. Soc.*, 1957, **79**, 5361.
4. H. Spiesecke and W. G. Schneider, *J. Chem. Phys.*, 1961, **35**, 722.
5. J. A. Pople, *J. Chem. Phys.*, 1956, **24**, 1111.
6. C. E. Johnson, Jr. and F. A. Bovey, *J. Chem. Phys.*, 1958, **29**, 1012.
7. C. W. Haigh and R. B. Mallion, *Mol. Phys.*, 1971, **22**, 955.
8. R. J. Abraham, J. Fisher, and P. Loftus, *An Introduction to NMR Spectroscopy*, Wiley, Chichester, 1988, p. 20.
9. R. J. Abraham and I. Marsden, *Tetrahedron*, 1992, **48**, 7489.
10. A. D. Buckingham, T. Schaeffer, and W. G. Schneider, *J. Chem. Phys.*, 1960, **32**, 1227.
11. S. Li and N. L. Allinger, *Tetrahedron*, 1988, **44**, 1339.
12. D. Danneels and M. Anteunis, *Org. Magn. Reson.*, 1974, **6**, 612.
13. J. Gasteiger and M. Marsili, *Org. Magn. Reson.*, 1981, **15**, 353.
14. R. J. Abraham and G. H. Grant, *J. Comp.-Aided Mol. Des.*, 1992, **6**, 273.
15. R. J. Abraham, M. Edgar, L. Griffiths, and R. L. Powell, *J. Chem. Soc., Chem. Commun.*, **1993**, 1544.

Biographical Sketch

Raymond J. Abraham. *b* 1933. B.Sc., 1954, Ph.D., 1957 (supervisor David Whiffen), D.Sc., University of Birmingham, UK. Postdoctoral work at National Research Council of Canada, Ottawa with Harold Bernstein and Basic Physics Division, National Physical Laboratory, London with John Pople. Successively lecturer, senior lecturer, reader and professor at University of Liverpool, UK. Approx 250 publications. Current research specialties: NMR, conformational isomerism, and molecular modeling.

Ackerman, Joseph J. H.: Oxford Knights

Joseph J. H. Ackerman
Washington University, St. Louis, MO, USA

In the mid-1970s I was a physical chemistry graduate student in Gary Maciel's group in the Department of Chemistry at Colorado State University. My research life had been consumed with liquid and solid state multinuclear MR experiments particularly those involving metal nuclides. David Hoult came by to give a seminar. He talked about the marvelous high sensitivity ^{31}P NMR spectrometer he and his University of Oxford colleagues had put together under the aegis of the Rex Richards/George Radda research group. David showed beautiful new results demonstrating detection of the major phosphorus metabolites in intact isolated muscle tissue.

A few years later I found myself an NIH postdoctoral fellow in the same University of Oxford laboratory. Space was limited. I shared a desk along with Tom Grove, a NATO postdoctoral fellow, and Gordon Wong, a Rhodes Scholar. David Gadian, a bright young physicist, was now taking over the science reins from Rex Richards. Despite his time-consuming high level administrative duties as Warden of Merton and Vice Chancellor, Rex still dropped into the laboratory now and then to talk science and be brought up to date on recent developments. David Hoult had left for the NIH in Bethesda and spectrometer building and design were now in the very capable hands of Peter Styles, Rod Porteous and Nick Soffe.

A principal focus of the laboratory was on perfused organ ^{31}P NMR experiments with the Radda group exploring rat heart physiology and Gadian and co-workers pursuing frog skeletal muscle metabolism. Efforts focused on carefully excising the tissue or organ of interest and interfacing the sample to a perfusion support system. True to everyone's training in the dogma of high-resolution NMR, and as had been done for decades before, the sample was placed *inside* the NMR antenna coil. Prior to placing the tissue in the magnet the static field homogeneity was optimized by shimming on a test sample containing a concentrated phosphorus solution so as to give a strong ^{31}P free induction decay.

My first contribution was to introduce a technique taught to me by my close friend and mentor Jerry Dallas who had also been a graduate student in the Maciel group pursuing multinuclear MR. This was that one can often shim on the solvent ^{1}H free induction decay even if the antenna coil is frequency tuned and impedance matched for a nuclide at a different resonance frequency, say that of ^{31}P. Although this idea met with some disbelief at first among my Oxford co-workers, the ^{1}H tissue water signal was found to be very strong from the ^{31}P antenna coils used for perfused rat heart and other organs. One could now routinely shim directly on the tissue sample of interest.[1] The ^{31}P linewidth resolution improved significantly. For example, the intracellular and extracellular inorganic phosphate signals in perfused rat heart were now readily resolved. The respective pH values were determined from their chemical shifts.

Tom Grove and I became good friends. We also were pursuing perfused rat heart experiments.[2] Tom decided to explore the possibility of studying the tissue in situ by implanting the antenna coil about the heart with the entire rat, fully anesthetized and breathing on a respirator, then going into the magnet. This approach required rather radical surgery and taught me a great deal about antenna loading by lossy conductive samples. Nevertheless, the experiments worked well and were, I believe, perhaps the first localized in situ and in vivo ^{31}P measurements.[3]

Flush with this success, we joined with Gordon Wong—a budding molecular biologist trapped for a short while in an NMR laboratory—to repeat this approach with rat kidney. Gordon, under the guidance of David Gadian and Brian Ross, had been struggling mightily with a difficult perfused kidney preparation.[4] Tom and I thought the implanted coil offered perhaps a better idea.

It was not to be. Try as we might, the in vivo ^{31}P kidney spectra showed substantial levels of phosphocreatine, a compound essentially absent in renal tissue but not in the surrounding muscle tissue. Clearly the antenna coil so carefully designed to surround the kidney was exciting and detecting signals from outside the coil.

I remember well the repeated unsuccessful attempts to pack gauze pads about the coil in an attempt to push the surrounding tissue out of the antenna coil's transmission/reception range. It was 2 a.m., the jokes were getting stale and tempers a bit edgy, when I realized the all-too-simple lesson in front of us: samples don't have to be inside the antenna coil to be detected. I walked out of the spectrometer room and down the hall to our office. This cramped space also served as the coil-design electronics laboratory. The first surface coil was wound. A simple tank circuit frequency-tuned and impedance-matched the surface coil to ^{31}P—80 MHz at 4.2 T.

I returned to the spectrometer room to find even more gauze packed about the implanted kidney coil. Tom and Gordon were clearly fed up with the kidney experiment. They agreed to humor me. We put the surface coil on the rat thigh, the largest muscle group. One of us ventured that if we could just get enough ^{1}H tissue water signal to shim the field we might have a chance with the ^{31}P experiment. We were stunned, the ^{1}H FID was enormous. Shimming was remarkably easy. Tom, Gordon, and I quickly switched the spectrometer over to ^{31}P. Within minutes a beautiful muscle spectrum showing inorganic phosphate, phosphocreatine, and the α-, β-, and γ-phosphate resonances of ATP was in hand.

It seemed almost too easy. How quickly one forgets the years of training leading up to a 'simple' finding. We had all been used to continually struggling with complex and delicate organ perfusion systems. All of our NMR training had taken as a given that the sample was placed inside the antenna coil. Now, in one early morning experiment all that changed.

The next few weeks were a frenzy of activity. David Gadian worked out the antenna theory to explain just why surface coils were so sensitive and what their localization properties were. Tom, Gordon, and I repeated the muscle experiments and extended this approach to rat brain ^{31}P analysis. George convinced us that the name surface coil was better than any of the names I came up with. A manuscript was submitted to *Nature*.[5]

A few months later I left for Washington University in St. Louis. Two a.m. seems awfully early to me now.

REFERENCES

1. J. J. H. Ackerman, D. G. Gadian, G. K. Radda, and G. G. Wong, *J. Magn. Reson.*, 1981, **42**, 498.
2. J. J. H. Ackerman, P. J. Bore, D. G. Gadian, T. H. Grove, and G. K. Radda, *Philos. Trans. R. Soc. London, Ser. B*, 1980, **289**, 425.
3. T. H. Grove, J. J. H. Ackerman, G. K. Radda, and P. J. Bore, *Proc. Natl. Acad. Sci. USA*, 1980, **77**, 299.
4. J. J. H. Ackerman, M. Lowery, G. K. Radda, B. D. Ross, and G. G. Wong, *J. Physiol. (London)*, 1981, **319**, 65.
5. J. J. H. Ackerman, T. H. Grove, G. G. Wong, D. G. Gadian, and G. K. Radda, *Nature (London)*, 1980, **283**, 107.

Biographical Sketch

Joseph J. H. Ackerman. *b* 1949. B.A., 1972, Boston University, Ph.D., 1978, Chemistry, Colorado State University (with Prof. Gary Maciel). Postdoctoral work at Colorado State University (with Prof. Maciel) and University of Oxford (with Sir Rex Richards and George Radda). Faculty at Washington University, St. Louis, MO, 1979–present. Currently Professor and Chair, Department of Chemistry, Research Professor of Chemistry in Medicine, Department of Medicine, and Professor of Radiology, Department of Radiology, Washington University School of Medicine. Approx. 100 publications. Research specialties: multinuclear MR spectroscopy and imaging of living systems.

Ailion, David C.: The First Observations of Ultraslow Motions

David C. Ailion

University of Utah, Salt Lake City, UT, USA

I was a graduate student in the Physics Department at the University of Illinois in the late 1950s and early 1960s. Initially I thought that I wanted to be a theorist, but after having done some calculations for Jim Koehler for a year or so, I realized that I knew absolutely nothing about experimental methods. Since I didn't want to have such a gap in my education, I decided to try to work for a group that used a variety of different experimental techniques. Charlie Slichter's NMR group appeared to be such a group, and it also had a fine reputation for doing important physics.

In those days Charlie used the apprentice system—a new graduate student would work under a late-stage student and, in exchange for providing assistance, would 'learn the ropes'. My initial assignment was to assist Bill Simmons, who was interested in looking at metallic indium. Because of the skin depth it was important to obtain a powder sample, which was usually obtained by filing a chunk of the material manually and then passing the filings through a sieve to obtain small particles. As luck would have it, indium is very soft at room temperature, so filing it would be like filing butter. I constructed a holder which rigidly clamped one end of an indium bar and submerged the other end in liquid nitrogen. My 'baptism under fire' (as Charlie called it) consisted of spending several weeks filing this bar in liquid nitrogen. I never found out what happened subsequently to the powder or to the experiments planned with it.

There was a coffee pot in one of the labs, and Charlie would generally show up between 8.00 a.m. and 8.30 a.m. to get a cup of 'red-eye', as he called it. At that time he would be happy to talk with any of his students about their data from the night before. (Yes, we were expected to work at night!) Since Charlie was very busy, often this was the only opportunity that we would have to speak to him. It was also an extremely effective way for Charlie to get his students into the lab early.

Charlie hated to throw away anything that might be potentially useful; as a result, his labs were cluttered with equipment constructed by former students. Unfortunately, much of this equipment had already seen its best days and no longer worked. Charlie felt that a good way for a student to get started in electronics was to repair or otherwise make operational some of this older equipment, even though circuit diagrams often did not exist. He also believed that the best way for a student to master NMR equipment was to build it. This was a convenient philosophy since very little NMR equipment was commercially available then. Since it appeared likely that my thesis research would involve the measurement of relaxation times, Charlie asked me to construct a 'boxcar' circuit like that constructed years earlier by Holcomb and Norberg. Their circuit utilized vacuum tubes, as did most of the NMR equipment at that time, since transistors were beginning to be used more widely only towards the end of my graduate student days. After much wasted time, I finally persuaded Charlie to allow me to build a different kind of boxcar, one designed by R. J. Blume, which used expensive ($20 each!) ceramic diodes with a very favorable ratio of forward to back resistance. This circuit worked like a charm, and my construction of it did more to build up my self-confidence than anything I had done until then.

One of the fringe benefits of working in Slichter's lab at Illinois was that we would get visits from very famous scientists. Erwin Hahn would often grace us with his valuable insights and his funny jokes. Another frequent visitor was Al Redfield, who had in 1955 developed the concept of spin temperature in the rotating frame.[1] This idea was that a spin system subject to a very strong rf field $\boldsymbol{B}_1$ would form a canonical distribution among the Zeeman levels in the rotating frame of $\boldsymbol{B}_1$. In 1961 Charlie persuaded Bill Holton, who had just finished his Ph.D. thesis and was awaiting his exam, to attempt an experimental verification of Redfield's hypothesis by performing an adiabatic demagnetization experiment in the rotating frame.[2] This experiment consisted of transfering lab-frame Zeeman order to rotating-frame Zeeman order by simply slowly sweeping the static field $\boldsymbol{B}_0$ from way off-resonance to on-resonance. For several nights Charlie and Bill worked until the wee hours of the morning. The experiment was successful, and they had thereby demonstrated the possibility of performing a truly significant experiment in a very short time, if one has a sufficiently good idea. This experiment paved the way for my later work on ultraslow motions.

It was, of course, well known that atomic diffusion could result in a minimum in a plot of the temperature dependence of T_1. This minimum would occur when the atomic jump rate $1/\tau$ equals the Larmor frequency ω_0 ($= \gamma B_0$). Thus, if one could perform an experiment in a sufficiently small magnetic field, the T_1 minimum would come from much slower motions (a longer value of τ). The problem was how to perform an NMR experiment in a very small magnetic field without losing all the signal. In the mid-1950s Charlie and another illustrious student, Chuck Hebel, had measured T_1 in zero magnetic field in superconducting aluminum[3] by performing a laboratory frame demagnetization followed after a variable time by a remagnetization. By plotting the signal following the remagnetization as a function of time in the demagnetized state, T_1 in zero magnetic field could be measured. To perform such an experiment to detect very slow diffusion would require a demagnetization of several thousand gauss, which in turn would require several seconds to be adiabatic. During this time the normal T_1 processes would in most cases relax the magnetization, thereby preventing the observation of the slow motions. As a result of his familiarity with Redfield's hypothesis and his experiment with Holton, Charlie got the brilliant idea that this difficulty could be overcome by performing an adiabatic demagnetization in the rotating frame. The role of $\boldsymbol{B}_0$ in determining the T_1 minimum would then be played by B_1, in which case the minimum would occur when $\omega_1\tau = 1$, where $\omega_1 = \gamma B_1$. Since B_1 could be of the order of a few gauss instead of several thousand gauss, such an experiment could result in the detection of motions three orders of magnitude slower than those detectable by ordinary T_1 measurements. He suggested to me that the experimental verification of this idea by measuring the rotating-frame relaxation time $T_{1\rho}$ for a diffusing system would be a suitable topic for my Ph.D. research.

I then had two problems. One was to get the equipment to the point where I could perform the experiment, and the other was to understand the underlying physics. It was clear that even slower diffusion could be observed by performing a second adiabatic demagnetization in which B_1 is reduced to zero. One question was where would one expect the T_1 minimum to be in zero magnetic field. It was clear that at ω_0 or ω_1 equals zero the T_1 minimum couldn't be at $\tau = \infty$, since the Bloembergen, Purcell, and Pound (BPP) theory would not be valid in zero magnetic field. The BPP theory, which predicts that the minimum should occur when $\omega_0\tau = 1$, is a perturbation theory that assumes that the fluctuating dipolar Hamiltonian can be treated as a perturbation on the Zeeman levels. Such a theory would clearly break down at zero field since then there would be no Zeeman Hamiltonian. Accordingly, assuming that one could measure the relaxation due to diffusion in a very weak (or zero) magnetic field, a very different kind of theory would be required to relate τ to the measured relaxation time. After discussing this point with Peter Mansfield, who was at that time a postdoc attempting to do double resonance, I realized that, in zero field, the relaxation time minimum would occur when $\tau \approx T_2$. The second adiabatic demagnetization would transfer rotating-frame Zeeman order to dipolar order. Since there would then be a canonical distribution among the dipolar levels, with a splitting proportional to ω_d, the minimum of the zero-field T_1 (subsequently called the dipolar relaxation time T_{1d}) should occur when $\omega_d\tau = 1$ or $\tau \approx T_2$, which would be at the onset of motional narrowing. Only T_1 would limit the value of τ that could be detected. Since T_1 could be seconds to hours in length, motions could in principle be observed that were far slower than any that had been detected previously by NMR. We solved the theoretical problem of determining the jump time τ from the measured $T_{1\rho}$ or T_{1d} by developing a spin temperature theory[4] (the so-called *strong collision* theory) to replace the BPP perturbation theory. This theory is valid only in the 'rigid lattice' (where $\tau > T_2$), and thus complements the region of validity of BPP.

There was also work that I had to do to get the equipment ready to do the experiment. Most of the T_1 measurements performed prior to this work utilized short hard pulses. Since $T_{1\rho}$ or T_{1d} could be seconds or longer in length, it was necessary to modify the power amplifier so that it could generate very long pulses. (This turns out to be not always necessary for T_{1d} measurements, however.) In addition, a highly stable magnetic field was desirable to ensure that the magnetic field was exactly on resonance. The magnet available in the lab was a hand-made 12 in. electromagnet that had current regulation but no field stabilization. The field stabilization method that I developed was very primitive and consisted of a feedback loop of which the experimenter was part. I constructed a CW NMR spectrometer, a marginal oscillator containing a narrow-line sample (water), to monitor the field. A frequency counter was used to monitor and eliminate frequency drifts in the marginal oscillator. Prior to each measurement of $T_{1\rho}$, I readjusted the drifted magnetic field to its original value, so that all the measurements occurred at the same magnetic field.

The sample which we decided to look at for our initial experiment was metallic lithium powder. Holcomb and Norberg (HN) had performed T_1 and T_2 measurements in the alkali metals[5] and had shown that the onset of motional narrowing in lithium occurred at a convenient temperature (just below room temperature). Because of the skin depth, it was important to obtain a powder sample and, because of the reactivity of lithium with water, the sample was immersed in mineral oil.

On 12 June 1963, I performed the first $T_{1\rho}$ measurement on lithium powder and observed, much to my delight, that its value was orders of magnitude shorter than T_1 at the same temperature, suggesting that our ideas were correct and that we indeed should be able to study ultraslow motions by this technique. After taking the first data point, I had to leave the lab since it was my fiancee's birthday, and I had promised to take her out for dinner. However, later that night I sneaked back into the lab to take another data point, to make sure that my success was not a dream. It wasn't, and it was with great pleasure that I presented my results to Charlie over coffee the following morning.

Over the next several months we established this new method for studying ultraslow atomic motions. In particular, we confirmed the validity of the strong collision theory by showing that the values for τ obtained by applying the strong collision theory to our $T_{1\rho}$ results in the rigid lattice region agreed very well with an extrapolation of HN's values for τ obtained by applying BPP to their T_1 data.[6] (For a more complete discussion of the theoretical and experimental features of the ultraslow motion techniques, see ***Ultraslow Motions in Solids*** in this Encyclopedia.)

RELATED ARTICLES

Diffusion Measurements by Magnetic Field Gradient Methods; Field Cycling Experiments; Magnetization Transfer between Water and Macromolecules in Proton MRI; Rotating Frame Spin–Lattice Relaxation Off-Resonance; Ultraslow Motions in Solids.

REFERENCES

1. A. G. Redfield, *Phys. Rev.*, 1955, **98**, 1787.
2. C. P. Slichter and W. C. Holton, *Phys. Rev.*, 1961, **122**, 1701.
3. L. C. Hebel and C. P. Slichter, *Phys. Rev.*, 1959, **113**, 1504.
4. C. P. Slichter and D. C. Ailion, *Phys. Rev.*, 1964, **135**, A1099.
5. D. F. Holcomb and R. E. Norberg, *Phys. Rev.*, 1955, **98**, 1074.
6. D. C. Ailion and C. P. Slichter, *Phys. Rev.*, 1965, **137**, A235.

Biographical Sketch

David C. Ailion. *b* 1937. A.B., 1956, M.S., 1958, Ph.D., 1964, Physics, University of Illinois, USA, under supervision of C. P. Slichter. Faculty member (currently Professor of Physics) University of Utah, 1964–present. Fellow of American Physical Society, Guest Member of AMPERE Committee, Recipient of Humboldt Senior Research Award and University of Utah Distinguished Research Award. Approx. 150 publications. Current research specialties: magnetic resonance imaging of lungs, NMR of partially disordered systems (incommensurate insulators and glasses).

Aime, Silvio: A Taste of NMR in Inorganic Chemistry

Silvio Aime

Università degli Studi di Torino, Torino, Italy

It was by sheer chance that I encountered NMR. In the late 1960s organometallic chemistry was experiencing a particularly good period of development with the discovery of a number of interesting reactions. Among them, the oxidative addition of unsaturated substrates to transition metal carbonyl clusters was especially attractive for the senior research fellows in the Inorganic Chemistry group at the University of Torino. These reactions often promote the formation of hydrides, both terminal and bridging two or three metallic centers. None of the available techniques (IR, MS, X-ray diffraction) provided firm support for the occurrence of the metal–hydrogen bond. NMR spectroscopy did! Although the reason was not well understood at that time (and probably now as well) the hydride resonance was observed in a characteristic high-field region, about 10–20 ppm upfield from TMS. Since then NMR has become for us the technique of excellence for assessing the formation of hydride products in our organometallic reactions. Its powerful capability for elucidating the exotic structures of organometallic cluster derivatives quickly attracted everyone's interest to the new NMR technique.

Later, in the early 1970s, when we obtained an FT spectrometer we gratefully appreciated how unique NMR is for the investigation of stereochemical nonrigidity in metal carbonyls. It was very exciting to discover how many different exchange processes of carbonyl ligands were possible over the surface of metal clusters and how the exchange processes of different ligands could be concerted.

Organometallic chemistry owes much to NMR spectroscopy. Both the number of active nuclei usually present in organometallic compounds (metals, ^{1}H, ^{13}C, ^{15}N, ^{31}P ...) and the variety of exotic bonding schemes make organometallic molecules particularly suitable for NMR investigation.

Later our interest focused on the relaxation properties of organometallic compounds and we found that several structural and dynamic problems may be tackled by measuring longitudinal and transverse relaxation times, often as a function of temperature and magnetic field strength. For example, the position of hydride ligands bonded to heavy transition metals, a problem that normally requires neutron diffraction data, may be determined directly in solution from an analysis of the dipolar contribution to the longitudinal relaxation time. Furthermore, in the presence of chemical exchange we showed that the thermodynamic parameters of the exchange processes may be calculated by comparing T_1 and T_2 values for hydride ligands at different temperatures.

An improvement relevant to our studies of organometallic chemistry was achieved, more recently, by the availability in our laboratory of solid state NMR equipment. Particularly interesting applications, both with wideline and high-resolution techniques, were carried out in the VT investigations of the dynamic behavior of organometallic compounds containing cyclopentadienyls, arenes, and hydrides.

In 1986, when I moved from the Faculty of Science to the Faculty of Pharmacy, I was looking for some new research fields capable of linking inorganic chemistry with biomedicine and NMR spectroscopy in order to accomplish my new duties better and to attract more interest from new students. This led me to investigate the physicochemical properties of paramagnetic lanthanide complexes in view of their use as contrast agents for magnetic resonance imaging. On entering the fascinating world of paramagnetic systems, where the spectroscopic answer is so nicely amplified, someone used to the scale of diamagnetic species is initially shocked! Lanthanide(III) complexes may afford proton spectra covering hundreds of ppm, allowing then the discrimination of very minor structural differences in the surroundings of a given resonance. A relevant role in these studies was the discovery of the huge potential of relaxometry in describing the structural and electronic properties of Gd(III) complexes.

We are lucky enough to have in Italy (at the University of Florence) a fully automated field cycling spectrometer developed by S. H. Koenig and R. D. Brown, III (IBM, NY) that provides the best way to accomplish such studies.

I would like to conclude by saying that although nothing is very special in this 20-year story, the personal pathway sketched in this brief report may closely resemble the story of many (hundreds, thousands?) of researchers who had the fortune to meet the splendid armory of NMR spectroscopy early in their career.

Biographical Sketch

Silvio Aime. b 1948. Laurea, 1971, University of Torino. Postdoctoral work at University of East Anglia, UK (with Robin K. Harris). Successively assistant and associate professor. Currently Professor of General and Inorganic Chemistry at the Faculty of Pharmacy of the University of Torino, Italy. Approx. 160 publications. Research specialties: solution structures and dynamics of coordination and organometallic compounds, solid state NMR, relaxometry of paramagnetic complexes.

Anderson, Weston A.: Early NMR Experiences and Experiments

Weston A. Anderson
Varian Associates, Palo Alto, CA, USA

EARLY SCIENTIFIC INTERESTS OF THE AUTHOR

I have been told that at a very early age, before I learned to walk, I showed interest in lights and plugs. It somehow must have been born in me, but not directly inherited, as my father was a banker and my mother a nurse. As I grew into my boyhood I collected batteries, lights, motors, buzzers, and the like, and was fond of hooking them together. In my early teens an uncle taught me a lot about radio. During my high school years I experimented with radio and got both a commercial radio license and a radio ham license (W6API) which I have kept up to this day. In high school I took physics and chemistry which I greatly enjoyed. My teacher in these two subjects, Mr. Gilbert Ewan, was a graduate of Stanford University, and he encouraged me to go there. I lived at home for my first two years of college, attending Reedley Junior College (now Reedley College).

ON TO STANFORD

In 1948 I transferred to Stanford as a junior. I majored in physics with minors in electrical engineering and math, receiving a B.S. degree in 1950. I continued on at Stanford for a master's degree and finally a Ph.D. For my thesis I worked on nuclear magnetic resonance (NMR) under Professor Felix Bloch, who in 1952 shared the Nobel Prize with Edward Purcell of Harvard for their discoveries. The work that Bloch did for the prize was done before I came to Stanford.

Those were exciting times. When I started my thesis work, Jim Arnold was already in the process of building a permanent magnet for a new NMR spectrometer that (hopefully) would have very high magnetic field uniformity and time stability. This would enable him (and me) to study very small shifts and splitting that he and others had recently detected in various chemical compounds.[1] Using my earlier experience with radio, I built the rf transmitter and receiver for the experiments. When the magnet and electronics were finished, we found the magnetic field dropped off faster than anticipated. To compensate for this drop-off, Jim built a set of current shims that consisted of a spiral pancake of wire on each pole face, with many taps so the current in each section could be independently regulated. The linear transverse gradients were controlled by slightly changing the tilt of the pole pieces by adjusting a set of differential screws. It was often a tedious job to adjust the field homogeneity, because the controls were not independent. In addition, small temperature changes in the room caused the magnetic field to drift, so we became very adept at raising and lowering the windows and turning a small heater on and off.

Professor Bloch suggested[2] that if we could completely stir the sample rapidly within the sample tube, the effect of the magnetic field variations over the sample volume could be essentially eliminated. After many unsuccessful attempts to achieve complete mixing, we settled upon spinning the sample, which caused averaging over concentric circles centered on the axis of rotation. This partial averaging was a great improvement as it made the job of magnet shimming much easier.[3]

My thesis work dealt with taking the NMR spectra of various chemical compounds, and then analyzing spectra to derive the chemical shifts and spin coupling constants. Quantum mechanics was used to do the analysis, which I found fascinating. The title of my Ph.D. thesis was 'Nuclear Magnetic Resonance Spectra of Some Hydrocarbons'. Several years later, after publishing a paper with the same title,[4] a chemist friend told me that the molecules that I studied and analyzed were not hydrocarbons!

In the summer of 1954, Professor Bloch received an offer to become Director General of the newly formed European Centre for Nuclear Research (CERN). It was then temporarily headquartered in Switzerland at the University of Geneva. Bloch asked me to write my thesis on the work I had been doing. Because of the time pressure, I wrote it and had it accepted in approximately two weeks.

WORKING AT CERN

Professor Bloch thought it would be good to get some research work started at CERN. Up to that time the main activity had been planning and developing the site. He proposed that Jim Arnold and I go with him to CERN, take along some of our equipment, and do some experiments. We happily agreed.

We spent an interesting year in Geneva. We did some work,[5] too, but not a lot, and did some skiing on the weekends. That was a very pleasurable year, and I met some other fascinating physicists. Professor Anatole Abragam, who was at Saclay at that time, came periodically to visit CERN. We went out to concerts and other places with him. There's a story he reported in his book, *Time Reversal, An Autobiography*, that I've told often, and now he's told it on himself.

There was to be a meeting of the Faraday Society[6] in Cambridge, England, and Jim and I decided to report about our work at Stanford. I was going to give the talk, and Abragam told me, 'These are only 10-min talks, but if you have someone in the audience ask questions, then you have some extra time while answering the questions'. So we went through all of my material and picked out a slide that needed more elaboration, and he agreed to ask a question about it. In due time, we went off to the meeting and I gave my talk, after which he asked the agreed-upon question. Then the embarrassing moment came. In response to his question, I said, 'I'm sorry, I didn't have time to show that slide'. I don't know if he's ever forgiven me for that. He said later that he knew the material so well that he wasn't listening to what I said.

Originally, Bloch had planned to stay at CERN for two years, so Jim and I would have been there two years also, but after one year, Bloch had had enough of it. It was

more administration than he liked. He decided to go back to Stanford. Then I had to decide just what I wanted to do. In 1951, I had worked at Westinghouse Research Center in Pittsburgh during the summer quarter. In the summer of 1952, I worked at Varian Associates in San Carlos, at the original site where the company started. I had job offers from both companies, as well as an offer from Anatole Abragam to work at the French Atomic Energy Commission at Saclay. I was pleased that Professor Abragam had apparently forgiven me, and I think I would have gone to Saclay except the draft board contacted me and suggested that I come back to the States. Being a native Californian with the hope of keeping my roots in California and the chance to continue work in magnetic resonance led me to choose Varian.

Figure 1 First NMR signals, reported by Bloch, Hansen, and Packard. (From Ref. 8c)

VARIAN ASSOCIATES AND THE BLOCH–HANSEN PATENT

Before continuing with my story, let me step back and give some background of how Varian was founded and got into NMR. I give here only a bare outline; a rather complete version of the story can be found in the book *The Inventor and the Pilot* by Dorothy Varian.[7] Russell Varian (called Russ by his friends) is perhaps best known for his invention of the klystron tube, however he also made many important contributions to the field of NMR. His acquaintance with NMR started in mid-1946 when he returned to Stanford from Sperry on Long Island, New York, where he and several Stanford people had worked to perfect the klystron and incorporate it into the early radar systems. The discovery of NMR had taken place less than a year earlier at Stanford under Felix Bloch,[8] and at Harvard under Edward Purcell.[9] Russ immediately conceived the idea that NMR could have important applications as a method of chemical analysis. The only published NMR signal at that time was that of water, which is reproduced in Figure 1. On the basis of this spectrum and others like it, and from what was known about NMR at that time, it seems remarkable that Russ Varian believed it could become a useful tool for chemical analysis. At this time the chemical shift and the spin–spin couplings between nuclei were yet to be discovered. Russ told Felix Bloch and Bill Hansen about his ideas of chemical analysis and urged them to apply for a patent. Bloch felt the technique would be of interest only to a few academic physicists who might want to measure magnetic fields or magnetic properties of nuclei. Since Bloch showed little interest in applying for a patent, Russ offered to prepare a patent application and handle its filing in return for an exclusive license for himself and his brother, Sigurd, with the understanding that the license could be transferred to his company when it was established. They agreed, and Russ wrote a good part of the patent application with help from Bloch, Hansen, and his patent attorney, Paul Hunter. Russ incorporated the idea of chemical analysis in the claims and titled the patent *Method and Means for Chemical Analysis by Nuclear Induction*. The patent was filed in December 1946 and was issued in July 1951.[10]

Tellegen, who was at Philips Research Laboratory in Eindhoven, Holland, developed the mathematical concept of the gyrator. He described it as a new electric network element that violated the reciprocity relation but was consistent with the laws of physics. He published this work in 1948 and 1949.[11] Les Hogan, who was at Bell Labs, developed a practical gyrator using ferromagnetic materials, which depends upon the gyromagnetic properties of electrons. He applied for a patent in 1950, which was issued in 1951 and immediately put under security orders. When the order was lifted, Hogan immediately published his material in the *Bell Labs Technical Journal*.[12] In this paper, Hogan pointed out that the nuclear resonance phenomena observed by Bloch also satisfied the gyrator relationship.

Marvin Chodorow, a professor at Stanford, received a copy of the *Bell Labs Technical Journal* and realized that since the phenomena described by Hogan and Bloch were the same, there was a deficiency in the Bloch–Hansen patent application. By this time, the original Bloch–Hansen patent had been issued, so it was necessary to file for a reissued patent. The wording of the original patent was changed to include resonance of electrons as well as nuclei by inserting the words 'portions of atoms', where previously the words 'nuclei of atoms' had been used. New claims were also added that broadly covered the gyrator concept. The Bloch–Hansen patent was finally reissued in 1955.[13]

Varian Associates was incorporated in the state of California in April 1948. The name 'Varian' was used because it was the well-known name of the inventor of the klystron tube, and 'Associates' because the founders wanted to convey the idea that this was going to be an association of equals. The purpose of the company, as stated in the charter, was to conduct research in the fields of physical science of every kind or nature, including heat, sound, light, X-rays, charged particles, ionizing radiation, properties of solids, liquids and gases, chemistry, and to measure the gyromagnetic ratio of nuclei of atoms, and to use the gyromagnetic properties of atoms to measure magnetic fields or for other purposes. The Articles of Incorporation described a number of fields in which the company became a leader including NMR, linear accelerators, optical spectrometers, and microwave tubes.

RUSS VARIAN AND HIS MAGNETOMETER

After I arrived at Varian Associates in September 1955, I became involved with magnetometers. This got me deferred

from military service because the magnetometers had military applications, which included searching for land mines and hunting submarines. I worked on what is called a 'free precession magnetometer' that Russ Varian had invented.[14] Russ had conceived the idea in 1948, less than three years after NMR had been discovered. The idea of free precession formed an important part of what later became Fourier transform (FT) NMR. The concept of his magnetometer is quite simple. Protons in a bottle of water are polarized by sending a strong electrical current through a coil that surrounds the bottle, producing a strong magnetic field in the water sample. The coil is oriented so the strong magnetic field is approximately perpendicular to the Earth's magnetic field. After a few seconds the protons in the water become polarized, and a majority point in a direction of the strong magnetic field, i.e. along the axis of the coil, which is perpendicular to the Earth's magnetic field. Then the polarizing field is quickly turned off, and the protons are left in this position. They immediately start to precess about the Earth's magnetic field, and in doing so they induce a current in the coil which has a frequency that is proportional to the strength of the Earth's magnetic field. The coil is quickly switched to the input of a sensitive amplifier and a frequency meter. The measure of that frequency gives a very precise value for the Earth's magnetic field.

It's a simple device, but you have to be careful about several things. One of these is the current turn-off circuit. If you turn off the polarizing magnetic field too slowly, the proton nuclei will follow the changes in direction of the magnetic field, slowly swinging back until they point parallel to the Earth's field, and then they won't precess. If you turn off the current too rapidly, before dissipating the energy stored in the coil, a transient oscillatory magnetic field is produced and the protons become disoriented and do not remain perpendicular to the Earth's field. I developed a circuit that would turn off the field quickly and remove the energy that is stored in the coil without disrupting the orientation of the protons. I was also involved in developing coil configurations that would reduce or eliminate external interference arising from low frequency electromagnetic fields.[15]

In order to test the magnetometer at various values of the external field I built a set of coils to simulate the field changes that might occur naturally or occur in other parts of the world. The set, shown in Figure 2, consisted of four coils arranged so that the first uncorrected gradient was of 8th order.

A portable free precession magnetometer was developed and sold commercially. One application that generated a lot of publicity, but not much profit, was using the magnetometer to locate skiers buried in an avalanche. The skier would wear a small magnet obtained at the ski lift. Should the skier happen to be trapped by an avalanche, a search team with the magnetometer could quickly locate the magnet under many feet of snow and dig the person out.

Russ was a very clever guy and one of the things that I really enjoyed about the early years at Varian was the interaction with him. He would come around and talk; and he talked to everyone, not just me. That's one of the things that's changed from the early days at Varian. There are lots of stories about Russ. One I remember is about the time Russ had a visitor from India. Russ was bringing the visitor through the front door, and Pete, the janitor, was sweeping up there. Pete said, 'Hello, Russ'. And Russ said, 'Good morning, Pete', as they walked by. The Indian visitor was astonished that the janitor would address the president of the company by his first name.

Figure 2 Young Anderson with magnetic field biasing coils used to change the magnetic field at the bottle of water sensor of a free precession magnetometer

Figure 3 Photograph of Russell Varian taken in the mid-1950s

Russ was absent-minded, and another story about him was from the early days in San Carlos. He had recently moved into a new house. One day, forgetting that he had moved, he walked into his old house and surprised the people who were living there.

HIGH-RESOLUTION NMR EXPERIMENTS

Soon after starting my full time job at Varian, I also became involved in improving the performance of the NMR

spectrometers to make them more useful for chemical analysis. Martin Packard was the R&D manager, and Ralph Kane the group manager. The group was called Special Products, later called the Instrument Division, and currently called Nuclear Magnetic Resonance Instruments. At that time there was little structure and quite a bit of freedom. Jim Shoolery ran an NMR chemical applications lab, and he had an endless thirst for improvements of all kinds. We also got suggestions and feedback from customers visiting the applications laboratory and attending the NMR workshops. We were aware of where improvements could be made and that these improvements would lead to more applications. It wasn't a blind 'Let's try something and see if it goes'. We had a good idea of the importance of certain areas and where to put the emphasis. The emphasis was on higher magnetic fields, greater sensitivity, better resolution, field/frequency stability and double resonance.

I put a lot of effort on designing current shims to improve the resolution. Because of the rather long relaxation times found in liquids, it became obvious to us that we could improve the resolution if we could make the magnetic field more uniform. In order to make the shims independent, Ed Jaynes[16] had suggested winding them on the boundary of a sphere in a way that would make the shims correspond to the spherical harmonic mathematical expansion. This could be done easily for the proton free precession magnetometer where there was plenty of open space around the sample. However, in high-resolution spectrometers the sample was confined to a narrow region between two pole caps. After some thought, I designed and built a shim coil set that preserved the same mathematical relationship but would fit flat against the pole caps.[17] This was an extension and improvement of the coil set that Jim Arnold and I used at Stanford several years earlier.

Another area that required attention was magnetic field inhomogeneities due to the finite magnetic susceptibility of the rf probe coils. Up to that time copper wire had been used to wind the probe coils. Although copper has a small magnetic susceptibility, because of its closeness to the NMR sample it can introduce high order magnetic field gradients, which are difficult or impossible to compensate for by the use of current shims. We couldn't find a suitable material with zero susceptibility so we used two closely spaced materials, one with positive susceptibility, the other negative, to yield a combination that behaved like a material with zero or near-zero susceptibility.[18]

Taming the spectrometer to sweep smoothly through a spectrum was another project that took on some importance. It turned out Jim Shoolery wasn't interested in opening and closing windows, turning on and off heaters, or adjusting knobs to control the changing random drifts that were particularly troublesome when sweeping slowly through the very narrow lines of a high-resolution spectrum. A number of ideas were proposed and evaluated before a suitable solution was found. In 1956 a flux stabilizer, called a 'Superstabilizer', was introduced which removed the rapid random fluctuations of the magnetic field strength. Russ Varian came up with the concept that led to the ultimate solution to the stability problem.[19] His idea, shown in Figure 4, was to use one NMR line as a control to stabilize the field/frequency relationship of a sample group. He proposed using a control line as part of a feedback loop in an oscillator so its frequency would be determined by the resonance condition of that line. This frequency could then be used to stimulate the resonance of the sample group. Since the two samples were separated in space, a small field-sweep coil could be used to sweep through the resonance of the sample group. A number of related schemes were

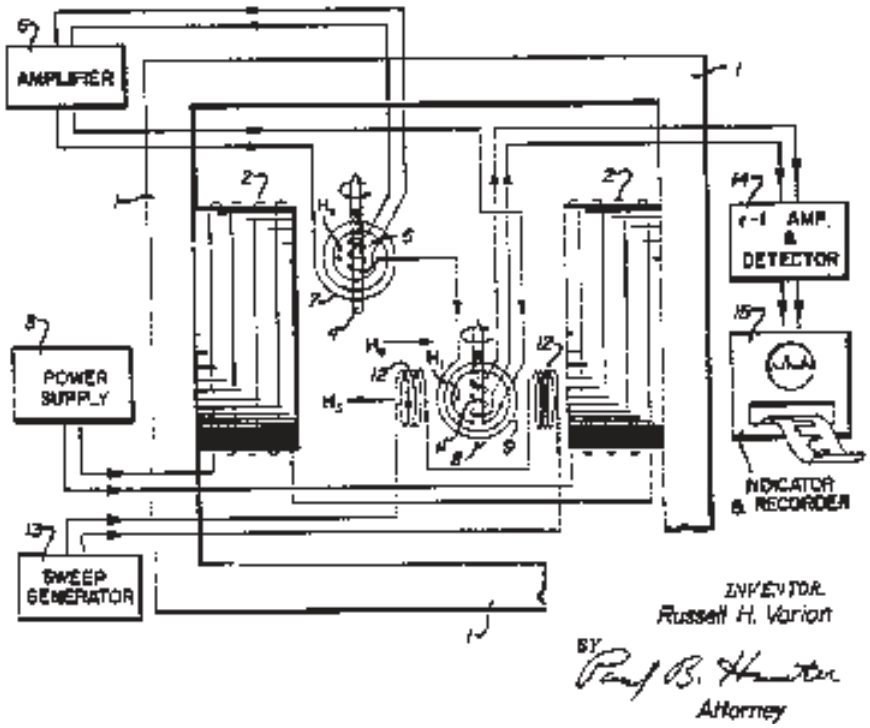

Figure 4 Drawing showing a method to stabilize the field/frequency relationship in an NMR spectrometer. (From Russell Varian, *US Pat. 3 109 732*; Ref. 19)

developed for achieving field/frequency stability that utilized a stabilizing control line either in the same sample or in a different sample.[20] In the late 1950s an accessory was offered to provide the field/frequency stabilization system to the high-resolution NMR spectrometers. One variation on Russ's NMR oscillator that I had developed, called the sideband oscillator,[21] was used in the Varian A-60 spectrometer. This was Varian's first analytical NMR spectrometer. It incorporated the use of precalibrated recorder chart paper and an integrator as standard features. The use of high-frequency field modulation also provides baseline stability which is particularly important when integrating NMR spectra.[21]

By going to higher values of magnetic field strength one gains both sensitivity and dispersion. During his graduate work at Stanford, Harry Weaver designed and built a 12-in. H-shaped electromagnet. His design formed the basis of the iron magnets that Varian sold and later incorporated into the early Varian NMR spectrometers. The first Varian high-resolution NMR spectrometers operated at a frequency of 30 MHz (approximately 0.7 T) and were designed for proton spectroscopy. Much effort was directed toward achieving higher magnetic field strengths using various pole cap materials, tapering the caps in various ways, narrowing the gap, and improving the current shims. By 1955 we were operating at 40 MHz. Then a project called SMOFF was started, which stood for Sixty Megacycles Or Fifty Five. Fortunately we met the 60 MHz goal in 1958. By the time we reached 100 MHz in 1962 we realized we were near the end of the line with iron magnets because of saturation of the iron.

After receiving his Ph.D. at Stanford, Harry Weaver spent two years at the University of Zürich and then in 1954 joined Varian in Palo Alto. Here he developed a high-resolution superconducting magnet system using a niobium–titanium alloy.[22] The result was the Varian HR-200, the HR-220, and later the HR-300 high-resolution NMR spectrometers. To achieve still higher fields, a niobium–tin alloy is used in the central core of the magnet. Using magnets purchased from Oxford Instruments, Varian has produced NMR spectrometers 400, 500, 600, and now 750 MHz (17.6 T). Figure 5 is a graph showing the highest spectrometer frequency plotted versus the year of introduction. It is interesting to note the slope of the curve is quite steep during the iron magnet period (1953–1962), somewhat flatter for the niobium–titanium alloy period (1964–1972) and still flatter for the more difficult niobium–tin alloys currently used. I might speculate that in future years we will see 1000 MHz and above, perhaps using the new high transition temperature superconducting materials (but still operating near liquid helium temperatures).

Double resonance studies provided a way to get more information than a single sweep spectrum.[23] Spin decoupling experiments demonstrated the usefulness for simplifying spectra. When Ray Freeman arrived at Varian in 1961, he was anxious to extend some of the techniques for determining relative signs of spin coupling constants that he and Whiffen had started.[24] We worked out the double resonance patterns expected for a number of different spin configurations.[25] One of the ideas we explored was that of indirect detection of naturally abundant ^{13}C nuclei by modulation techniques[26] or the small splitting on proton lines as a weak rf frequency was swept through the carbon spectrum.[27] These techniques provided the sensitivity of the proton resonance while detecting the position of the ^{13}C peaks. We also did the early experiments using multiple quantum transitions to help in high-resolution NMR spectra determinations.[28]

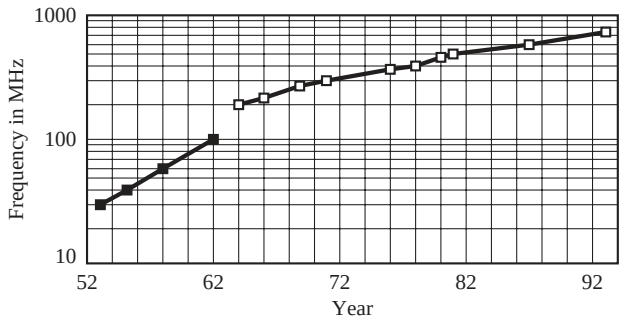

Figure 5 Plot of the maximum NMR spectrometer frequency versus year. The line segment at the left represents data for spectrometers with iron magnets; the right segment is for spectrometers with superconducting magnets

I also worked with Larry Piette, who was the Jim Shoolery of EPR, and Jim Hyde, who was my counterpart in EPR. Jim worked on EPR instrumentation, and Larry worked on the chemistry applications. Forrest Nelson was an electrical engineer who contributed to many NMR and EPR ideas. Richard Ernst joined the group in 1963 and Howard Hill in 1968. The strong interaction among the various members of the group as well as interactions with the applications laboratory people provided a very stimulating atmosphere. It was a good environment for exploring ideas that could improve NMR and EPR spectroscopy, and make them more useful to the scientific community.

FOURIER TRANSFORM NMR

Perhaps the most important development that I participated in was that of Fourier Transform NMR or FT NMR. It was this development that speeded up NMR data collection by a factor of 1000 or more. This is another area in which the initial suggestions came from Russ Varian. He proposed[29] using a wide band set of frequencies to increase the sensitivity of NMR spectrometers. His method was to excite all of the lines in the NMR spectrum with a wide band noise source (see Figure 6). The resulting signals would then be heterodyned down to the audiofrequency range and recorded on magnetic tape. After the recording was completed, an endless tape would be made by pasting the end of the tape to the beginning. The endless tape would then be played back many times, each time mixing it with a different frequency. The mixer output would then be fed through a narrow band filter and recorded. Basically, it was a crude Fourier analyzer. Different mixing frequencies would select different signal frequencies and different parts of the NMR spectrum. The output of the detector represented the amplitude of a particular frequency component. This was a non-real-time system; however, the spectrometer could be getting new data while the analysis was being carried out on the old data.

One of the ideas I had was to generate each frequency by a separate oscillator, rather than use a noise source to produce a wide band of frequencies. By using separate oscillators, the individual frequencies would be coherent so that the same

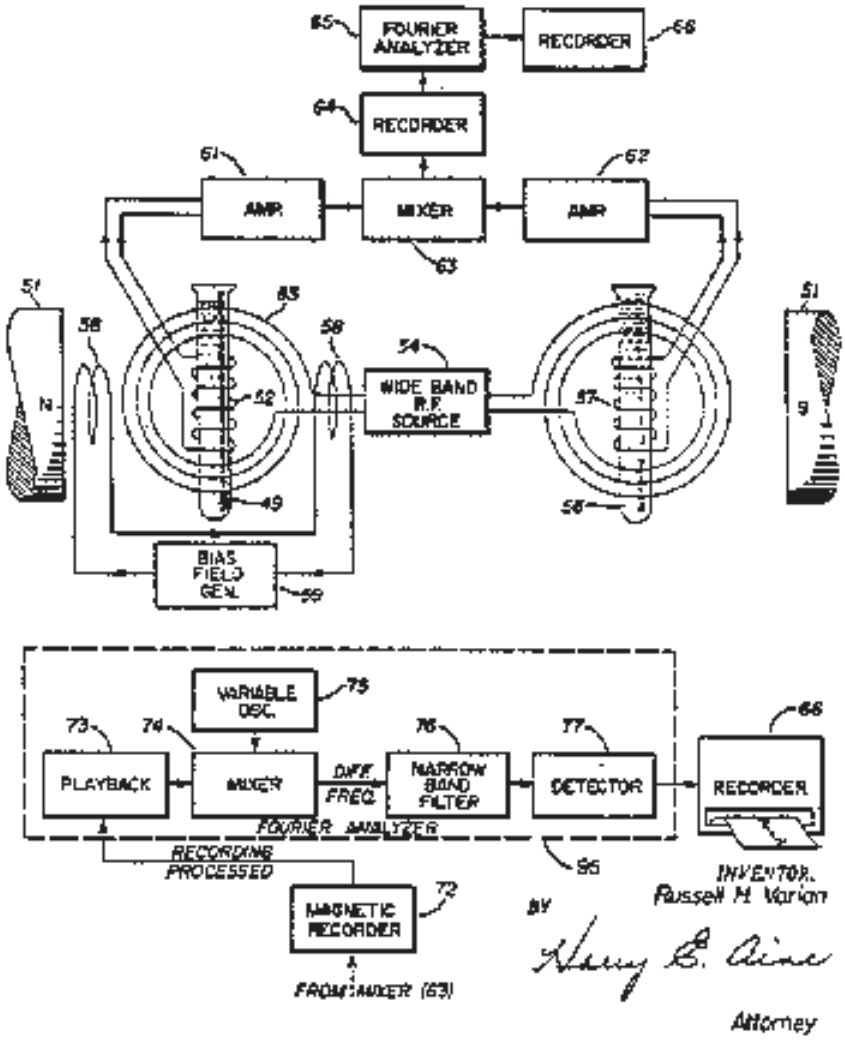

Figure 6 Drawing showing the concept of wide band excitation and a Fourier transform detection system to increase the sensitivity of a high-resolution NMR spectrometer. (From Russell Varian, *US Pat. 3 287 629*; Ref. 29)

oscillator could be used to phase-detect each frequency. I proposed a rather simple way to generate and detect all of the frequencies simultaneously with an optical chopper wheel, called a 'Wheel of Fortune' by some and a 'Prayer Wheel' by the skeptics (Figure 7). It was a plastic cylinder about 6 in. diameter and 8 in. high, which was slowly rotated by an electric motor. The wheel contained about 20 cylindrical segments, each with a slightly different diameter. On each segment was placed a strip of a Ronchi grating (a photographic film of light and dark bands) with about 40 bands per inch. A light was placed inside the cylinder. A lens placed outside the cylinder would direct the light passing through each cylindrical segment onto a common photoelectric detector. As the wheel turned, each cylindrical segment would chop the light at a slightly different frequency, so the output of the photoelectric detector would contain all of these frequencies. This signal would then be mixed with a suitable offset frequency and transmitted to the probe to stimulate any NMR resonance signals.

This same wheel was used to separate the received NMR signals. The received NMR signals would be brought back into the audio range by mixing them with the same offset frequency. The resulting audiofrequency would then be applied to a second light source within the wheel, but on the opposite side. This time the light would be demodulated by the series of light and dark bands on the wheel. After the light had passed through each segment, it would be collected on a separate photoelectric detector. The output of each photoelectric detector would then be fed to separate integrators, and the output of each integrator would correspond to one frequency component of the NMR spectrum. This system would operate in real time, with no delay for processing the signals.

Before this system was finished, a better idea came along of using pulses and computers instead of the wheel. Eventually, the chopper wheel was donated to the Smithsonian Institution as an example of one step in the evolution of an idea[30] (Figure 8).

The new idea was even closer to the original Fourier transform idea of Russ Varian. The wide band of frequencies is generated by a series of pulses applied to the transmitter frequency. The resulting frequencies, which are all coherent, are applied to the nuclei in the magnetic field to stimulate responses from the entire NMR spectrum. The stimulated resonances are brought into the audiofrequency range by

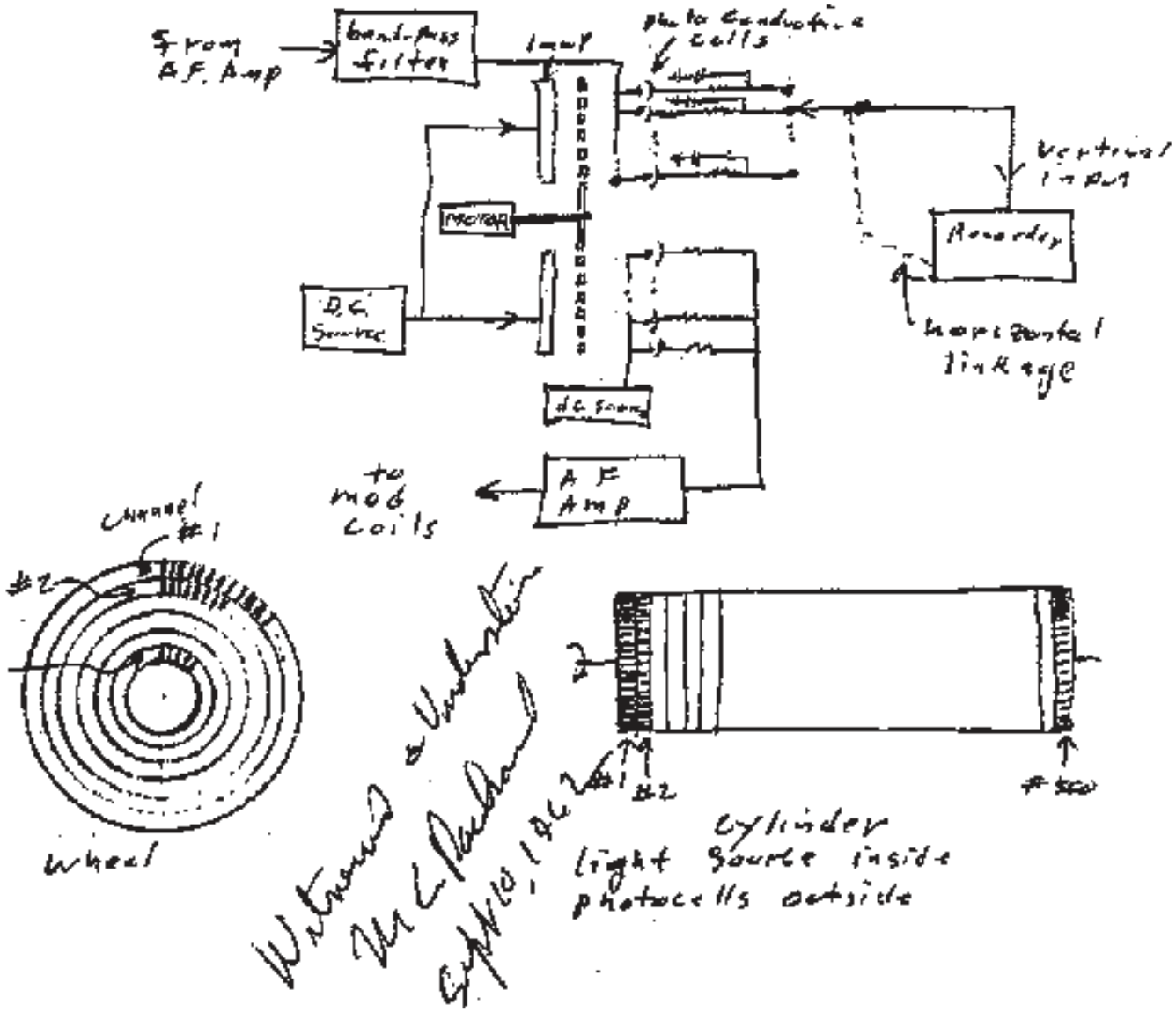

Figure 7 Excerpt from Anderson's notebook outlining the concept of the 'Prayer Wheel'

Figure 8 Anderson saying good-bye to the 'Prayer Wheel' as it departs for the Smithsonian

mixing them with the original rf frequency. The audio responses would then be digitized and stored by a computer of average transients (CAT) that was then commonly used to time-average NMR data (Figure 9). Richard Ernst built the apparatus and our first experiment gave us good data. However, using the technology of the day, we had to punch out the data on paper tape, convert the tape data to IBM cards, and take the cards to the Service Bureau Corporation on the other side of Palo Alto. Several days later, after waiting for payroll and factory inventory processing to be completed, the computer performed the Fourier transform step and plotted out the spectrum.[31]

As soon as possible, we ordered a minicomputer. By today's standards it was slow, and the 4000 bytes of memory trivially small; however, it enabled us to transform the data and plot it in a few minutes. With the advent of larger and faster computers and with the development of the Fast Fourier Transform (FFT) techniques by Cooley and Tukey, the transform has been speeded up considerably. Today even large

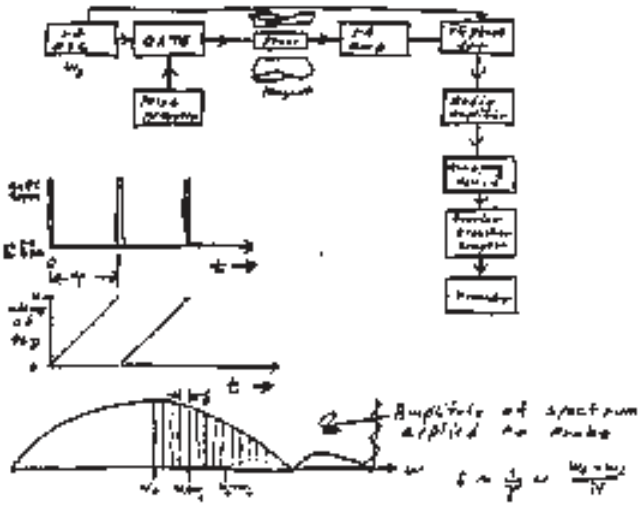

Figure 9 Excerpt from a page in Anderson's notebook outlining the idea of the FT NMR spectrometer

multidimensional transforms can be taken in seconds. Fourier transform changed the whole way of life in NMR. Varian offered an FT accessory for the HR-100 in 1968. Soon FT NMR almost completely replaced the former method of slowly scanning through the spectrum. From contributors throughout the world a whole new set of techniques have been developed to enhance further the capability of FT NMR.

THEN AND NOW

It is remarkable how far NMR has advanced during its 50 years of history. Much of the early progress can be traced to Russell Varian, from his early belief that NMR would be important to chemistry, his writing the original NMR patent, obtaining a licence under the patent, his insistence that his new company, Varian Associates, develop and commercialize NMR magnetometers and spectrometers, and because of the important technical contributions he made to the technique. He would be pleased to see how far NMR has developed in the intervening years since his death in July 1959. It has been exciting for me to play a small role in furthering the development of NMR instrumentation and to extend its usefulness.

In 1972 I was named Director of the Varian Systems and Techniques Laboratory and became involved in other research activities. My initial activity in this new laboratory was the development of ultrasound equipment for real time medical imaging of the human heart—but that's another story.

Improvements of NMR instruments continued, building upon the earlier work. In 1974 Richard Ernst, now back at the Federal Institute of Technology (ETH) in Zürich, followed a proposal of Jeener[32] to demonstrate a new two-dimensional (2D) technique.[33] A second frequency dimension was introduced and a second FT used to extract additional NMR data. In 1975, Ernst proposed an FT method of acquiring and reconstructing MRI data[34] that is analogous to the 2D spectroscopy method. For these two achievements and our earlier work with FT NMR he was awarded the 1991 Nobel Prize in Chemistry.

Today FT NMR is playing an indispensable role in medicine with MRI instruments and a crucial role in spectroscopy as a tool for chemists and biologists. All signs point to continued development leading to a still brighter future.

REFERENCES

1. J. T. Arnold, S. S. Dharmatti, and M. E. Packard, *J. Chem. Phys.*, 1951, **19**, 507; H. S. Gutowsky and D. W. McCall, *Phys. Rev.*, 1951, **82**, 748; M. E. Packard and J. T. Arnold, *Phys. Rev.*, 1951, **83**, 210; H. S. Gutowsky, D. W. McCall, and C. P. Slichter, *Phys. Rev.*, 1951, **84**, 589.
2. F. Bloch, *Phys. Rev.* 1954, **94**, 496.
3. W. A. Anderson and J. T. Arnold, *Phys. Rev.*, 1954, **94**, 497.
4. W. A. Anderson, *Phys. Rev.*, 1956, **102**, 151.
5. W. A. Anderson and J. T. Arnold, *Phys. Rev.*, 1956, **101**, 511.
6. W. A. Anderson and J. T. Arnold, *Discuss. Faraday Soc.*, 1955, **19**, 226.
7. D. Varian, *The Inventor and the Pilot*, Pacific Book Publishers, Palo Alto, CA, 1983.
8. (a) F. Bloch, W. W. Hansen, and M. E. Packard, *Phys. Rev.*, 1946, **69**, 127; (b) F. Bloch, *Phys. Rev.*, 1946, **70**, 460; (c) F. Bloch, W. W. Hansen, and M. E. Packard, *Phys. Rev.*, 1946, **70**, 474.
9. E. M. Purcell, H. C. Torrey, and R. V. Pound, *Phys. Rev.*, 1946, **69**, 37.
10. F. Bloch and W. W. Hansen, US Pat. 2 561 489 (Filed Dec. 23, 1946; Issued July 24, 1951).
11. B. D. H. Tellegen, *Philips Res. Rep.*, 1948, **3**, 81; ibid., 1948, **3**, 321; ibid., 1949, **4**, 31; ibid., 1949, **4**, 366.
12. C. L. Hogan, *Bell Sys. Tech. J.*, 1952, **31**, 1.
13. F. Bloch and W. W. Hansen, US Pat. Re 23 950 (Issued Feb. 22, 1955).
14. R. H. Varian, US Pat. 2 561 490 (Filed Oct. 21, 1948; Issued July 24, 1951); R. H. Varian, US Pat. Re 23 769 (Issued Jan. 12, 1954).
15. W. A. Anderson and J. M. Mathias, US Pat. 3 004 211 (Filed Oct. 14, 1957; Issued Oct. 10, 1961).
16. E. T. Jaynes, private communication and US Pat. 3 566 255 (Filed March 6, 1959; Issued Feb. 23, 1971).
17. W. A. Anderson, *Rev. Sci. Instrum.*, 1961, **32**, 241; W. A. Anderson, US Pat. 3 199 021 (Filed Dec. 19, 1960; Issued Aug. 3, 1965).
18. W. A. Anderson and J. N. Shoolery, US Pat. 3 091 732 (Filed June 5, 1958; Issued May 28, 1963).
19. R. H. Varian, US Pat. 3 109 138 (Filed Aug. 29, 1956; Issued Oct. 29, 1963).
20. W. A. Anderson, US Pat. 3 085 125 (Filed July 11, 1957; Issued April 9, 1963); W. A. Anderson, US Pat. 3 147 428 (Filed Oct. 16, 1958; Issued Sept. 1, 1964); W. A. Anderson, US Pat. 3 173 083 (Filed Nov. 23, 1960; Issued March 9, 1965).
21. W. A. Anderson, *Rev. Sci. Instrum.*, 1962, **33**, 1160; W. A. Anderson, US Pat. 3 173 084 (Filed Dec. 19, 1960; Issued March 9, 1965).
22. H. L. Marshall and H. E. Weaver, *J. Appl. Phys.*, 1963, **34**, 3175; H. E. Weaver, US Pat. 3 577 067 (Filed May 11, 1966; Issued May 4, 1971).
23. A. L. Bloom and J. N. Shoolery, *Phys. Rev.*, 1955, **97**, 1261.
24. R. Freeman and D. H. Whiffen, *Mol. Phys.*, 1961, **4**, 321; R. Freeman and D. H. Whiffen, *Proc. Phys. Soc. (London)*, 1962, **79** 794.
25. W. A. Anderson and R. Freeman, *J. Chem. Phys.*, 1962, **37**, 85.
26. W. A. Anderson, *J. Chem. Phys.* 1962, **37**, 1373; R. Freeman and W. A. Anderson, *J. Chem. Phys.*, 1965, **42**, 1199.
27. R. Freeman and W. A. Anderson, *J. Chem. Phys.*, 1962, **37**, 2053; R. Freeman and W. A. Anderson, *J. Chem. Phys.*, 1963, **39**, 806.

28. W. A. Anderson, *Phys. Rev.*, 1956, **104**, 850; W. A. Anderson, R. Freeman and C. A. Reilly, *J. Chem. Phys.*, 1963, **39**, 1518.
29. R. H. Varian, US Pat. 3 287 629 (Filed Aug. 29, 1956; Issued Nov. 22, 1966).
30. *Smithsonian Institution News*, Office of Public Affairs, Smithsonian Institution, Washington, DC, Nov. 26, 1990; *IEEE Center for the History of Electrical Engineering Newsletter No. 24*, Summer 1990.
31. R. R. Ernst and W. A. Anderson, *Rev. Sci. Instrum.*, 1966, **37**, 93; W. A. Anderson and R. Ernst, US Pat. 3 475 680 (Filed May 26, 1965; Issued Oct. 28, 1969).
32. J. Jeener, Presented at *AMPERE International Summer School, Basko Polje, Yugoslavia, 1971*.
33. W. P. Aue, E. Bartholdi, and R. R. Ernst, *J. Chem. Phys.*, 1976, **64**, 2229; R. R. Ernst, US Pat. 4 134 058 (Filed Nov. 28, 1977; Issued Jan. 9, 1979); R. R. Ernst, US Pat. 4 168 462 (Filed June 5, 1978; Issued Sept. 18, 1979).
34. A. Kumar, D. Welti, and R. R. Ernst, *Naturwissenschaften*, 1975, **62**, 34; A. Kumar, D. Welti, and R. R. Ernst, *J. Magn. Reson.*, 1975, **18**, 69; R. R. Ernst, US Pat. 4 070 611 (Filed April 13, 1977; Issued Jan. 24, 1978).

Biographical Sketch

W. A. Anderson, *b*. 1928. B. S., Stanford, 1950, Ph.D. (under Prof. Bloch on NMR) Stanford, 1955. Special Assistant to the Director of CERN, Geneva, Switzerland 1955–56; Varian Associates, Palo Alto, CA, 1955–present; member of Instrument Division Research Group, 1955–1963; Director of Research, Instrument Division, 1963–1972; Director of the Systems & Techniques Laboratory, Corporate Research, 1972–1987; Principal Scientist, 1987–present; Varian Fellow, 1988–present. Approx. 40 publications and 40 issued US Patents.

Ando, Isao: Structures and Electronic States of Polymers as Studied by High-Resolution NMR Spectroscopy Combined with Quantum Chemistry

Isao Ando

Tokyo Institute of Technology, Tokyo, Japan

Since Gutowsky et al.[1] observed the 18 MHz ^{1}H high-resolution NMR spectrum of uncured Heva rubber (polyisoprene) in CS_2 in 1957, high-resolution NMR spectroscopy has developed to become the most powerful method available for characterizing the structures and dynamics of synthetic polymers in the solution and solid states. Nishioka et al.[2] and Bovey et al.[3] separately determined the stereochemical structure of poly(methyl methacrylate) prepared by radical polymerization and anionic polymerization by means of high-resolution ^{1}H NMR spectroscopy. These studies have provided great influences in the research fields of structure and stereospecific polymerization in polymer science.[4] In addition, Schaefer et al.[5] have recently successfully measured the high-resolution solid state ^{13}C CP MAS (cross polarization/magic angle spinning) NMR spectra of polymers in the solid state. This leads to the elucidation of structure and dynamics of polymers in the solid state.

Nevertheless, in order to provide a deeper insight into molecular structures and electronic structures of polymers, more sophisticated approaches might be developed in high-resolution NMR spectroscopy. The NMR chemical shift should provide detailed information about the structure and electronic state of polymers in the solution state and the solid state if high-resolution NMR spectroscopy is combined with quantum chemistry.[6,7] The chemical shifts of the nuclei in polymers depend on their magnetic environment which depends on the stereochemical configuration and higher-order structure such as conformation and crystal structure of the polymer chains.

My co-workers and I have developed a methodology for obtaining stereochemical configuration and higher-order structure, and the electronic states of polymers both in the solution[6, 8–13] and solid state[7, 14–23] through a combination of the observation and calculation of NMR chemical shifts, and have applied this to various polymer systems. Theoretical calculations of NMR chemical shifts for polymer systems have been done mainly by two approaches. One is that model compounds such as the dimer, trimer, etc., as local structures of polymer chains, are used in the calculation by combining quantum chemistry and statistical mechanics.[6, 8–13] In particular, this approach has been applied to polymer systems in the solution state. However, in solid polymer systems it sometimes has to be recognized that the results of quantum chemical calculations on model compounds are not readily transferable to polymers because of differences in electronic structure, including long-range interactions such as intrachain interactions and interchain interactions. Electrons are constrained to a finite region of space in small molecules whereas this is not necessarily the case for polymers, and for this reason some additional approaches are required. Another approach is to employ the tight-binding molecular orbital (TB MO) theory,[24] which is well known in the field of solid state physics, to describe the electronic state of linear polymers with periodic structure within the framework of the linear combination of atomic orbitals approximation for the electronic eigenfunctions.[7, 14–23] These approaches have led to the determination of the structure and/or electronic state of polymer systems including polypeptides in the solution state and solid state. The essence of these two approaches will be described below.

APPROACH USING MODEL COMPOUNDS

A polymer chain can assume an enormous number of conformers because of the various possibilities of rotation around the chain bonds. Thus the factors governing the appearance of the NMR spectra include stereochemical configurations, the relative energies of the rotational isomers, the chemical shifts, and spin couplings. If molecular motion in the polymer chain is slow, the spectrum represents the superposition of the spectra for the various conformations. However, if the rotation around the chain bonds is very fast on the NMR timescale, the experimentally observable chemical shift for nucleus A is given as:

$$\langle \sigma_{\mathrm{A}} \rangle = \sum_{i=1}^{n} P_i \sigma_i \tag{1}$$

The numerical indices refer to the preferred conformers, and P_i and σ_i are the probability of occurrence and the chemical shift of the preferred conformer i, respectively. This indicates that the chemical shift of a given nucleus in a polymer chain in the solution state can be calculated by means of a combination of a quantum chemical method[25] and a statistical mechanical method[26] as described below. The chemical shift of an atom depends upon its electronic and molecular environments. The chemical shift for atom A can be estimated by a sum of the following terms:[25]

$$\sigma_{\mathrm{A}} = \sigma_{\mathrm{d}} + \sigma_{\mathrm{p}} + \sigma' \tag{2}$$

where σ_{d} is the diamagnetic term, σ_{p} is the paramagnetic term, and σ' is another term which comes from the magnetic anisotropy effect, polar effect, and ring current effect. For nuclei with 2p electrons such as ^{13}C, ^{15}N, etc., the relative chemical shift is predominantly governed by the second term, and for the ^{1}H nucleus by the first and third terms. The paramagnetic term is expressed as a function of excitation energy, bond order, and electron density according to the sum-over-state (SOS) method in the simplest form as follows:[25]

$$\sigma_{\mathrm{p}} = -C \sum \langle r^{-3} \rangle_{2\mathrm{p}} (E_m - E_n)^{-1} Q \tag{3}$$

where $E_m - E_n$ is the singlet–singlet excitation energy of the nth occupied and the mth unoccupied orbitals, and Q is a factor including the bond order and electron density.

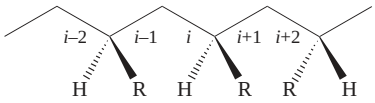

Figure 1 The planar conformation of any specified configuration of a vinyl polymer

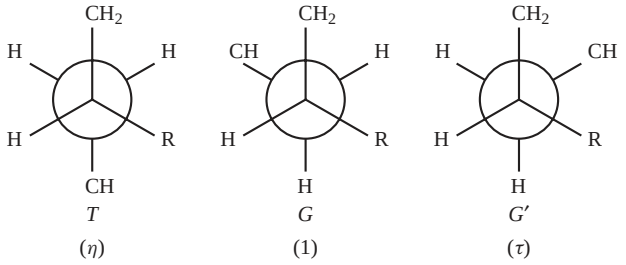

Figure 2 Newman projections of the rotational isomeric states about the $(i-1)$th bond in Figure 1. T depicts *trans*, G and G' two *gauche* conformations; η, 1 and τ are statistical weight factors

The quantity $\langle r^{-3}\rangle_{2p}$ is the spatial dimensions for a 2p electron while C is the coefficient incorporating the universal constants. In the estimation of σ_p the finite perturbation theory (FPT)[27] has frequently been used. The diamagnetic term is estimated from the calculated electron density. Using these procedures, the chemical shift σ_i of the model compound with any specified conformation is calculated. We sometimes have cases where solute–solvent interactions play an important role in an understanding of the chemical shift behavior. We have developed a method of calculating nuclear shielding by incorporating the FPT method and reaction field type solute–solvent interactions.[11, 28–30] This approach reasonably explains the experimentally observed solvent effects on chemical shift (and also the spin–spin coupling constant [31]).

The probabilities P_i of the preferred conformations in various configurations in vinyl polymers as a function of the racemic units necessary for the calculation of the averaged chemical shift $\langle\sigma\rangle$ is estimated by statistical mechanics for a polymer chain. For convenience, the planar conformation in any specified configuration of a vinyl polymer is shown in Figure 1. Newman projections of the rotational isomeric states about the $(i-1)$th bond are given in Figure 2.

The statistical weight matrices for the characterization of the array of chain conformations of vinyl polymers can be used.[26] The purpose of calculating the probability that the pairs of skeletal bonds within the kth dyad, the kth triad, and so on in a chain are in particular rotational states is that such statistical weights are used to construct statistical weight matrices $\mathbf{U} = \mathbf{U}'\mathbf{U}''$. In such matrices, rows are associated with rotational states about bond $i-1$ and columns with rotational states about bond i. The complete statistical weight matrices in the case of pairs of bonds adjoining CHR groups are designated $\mathbf{U}''$. These matrices are expressed as

$$\mathbf{U}' = \begin{pmatrix} \eta & 1 & \tau \\ \eta & \omega & \tau \\ \eta & 1 & \tau\omega \end{pmatrix} \tag{4}$$

for the first skeletal bond of a dyad and

$$\mathbf{U}''_{m} = \begin{pmatrix} \eta\omega & 1 & \tau\omega \\ \eta & \omega & \tau\omega \\ \eta\omega & \omega & \tau\omega^2 \end{pmatrix} \tag{5}$$

$$\mathbf{U}''_{r} = \begin{pmatrix} \eta & \omega & \tau\omega \\ \eta\omega & 1 & \tau\omega \\ \eta\omega & \omega & \tau\omega^2 \end{pmatrix} \tag{6}$$

for the second; the former matrix, equation (5), is for a *meso* dyad and the latter [equation (6)] for a racemic one. The statistical weight factors 1, η, and τ are defined in Figure 2. The configuration partition function Z for the entire chain can be expressed as the sum of the statistical weights for all molecular conformations of the chain consisting of n bonds or $x = 1/2\ n$ repeating units

$$Z = \mathbf{J}^*\left(\prod_{i/2=1}^{n/2-1} \mathbf{U}'_i\mathbf{U}''_i\right)\mathbf{J} \tag{7}$$

where $\mathbf{J}^* = (1\ 0\ 0)$ and $\mathbf{J}$ is the transpose of $(1\ 1\ 1)$. Let β and γ denote indices from the set T, G, and G'. The probability $P_{\beta\gamma:k'}$ that the pair of skeletal bonds within the kth dyad are in the rotational states β and γ, respectively, is the ratio of the sum of the statistical weights for all conformations. It is given by

$$P_{\beta\gamma:\,k''} = Z^{-1}\mathbf{J}^*\left(\prod_{h=1}^{k-1}\mathbf{U}'_h\mathbf{U}''_{h+1}\right)\left(\mathbf{U}'_k\mathbf{U}''_{(\beta\gamma)k}\right)\left(\prod_{i=k+1}^{x-1}\mathbf{U}'_i\mathbf{U}''_{i+1}\right)\mathbf{J} \tag{8}$$

in which $\mathbf{U}''_{(\beta\gamma)k}$ is the matrix representing the second bond of the kth dyad with all of the elements, except $\mathbf{U}''_{(\beta\gamma)}$, replaced by zero. $P_{\beta\gamma:k'}$ is estimated by generating Monte-Carlo chains. An averaged chemical shift is then obtained using the values obtained for $P_{\beta\gamma:k'}$ and σ_i.

Using this developed methodology, the structural behaviors of polyethylene and n-paraffins, vinyl polymers such as poly(vinyl chloride) and polypropylene, poly(L-alanine), etc. in the solution state have been successfully elucidated on the basis of their observed spectra.[6, 8–13] We demonstrated that such approaches for polymer systems in the solution state provide useful explanations of the observed spectra, conformational behavior, and assignments of resonances to the configurational structures such as a dyad, triad, tetrad, and so on.

In the crystalline state polymer chains assume a fixed conformation. In this case, the structural information obtained from the chemical shift corresponds to the fixed conformation. The calculation of ^{13}C chemical shifts for a dipeptide fragment of poly(L-alanine) has been attempted using the FPT INDO method in order to understand and predict the ^{13}C chemical shift behavior of polypeptides associated with a secondary structure such as an α-helix, β-sheet, etc., and the determination of secondary structure through the observation of the ^{13}C chemical shift.[32] The ^{13}C chemical shifts of the C_β carbon of an alanine residue in various peptides and polypeptides vary significantly depending on the conformation, which may be a right-handed α-helix, β-sheet, or other conformation. Such

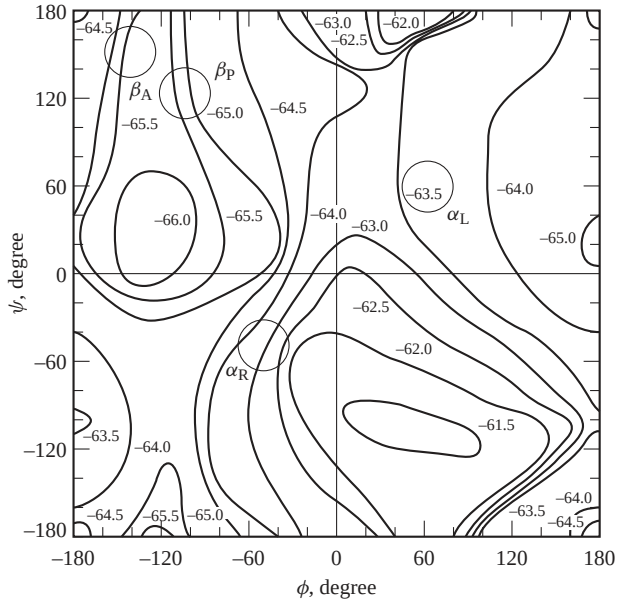

Figure 3 The calculated ^{13}C chemical shift contour map of C_β in N-acetyl-N'-methyl-L-alanine amide obtained using the FPT INDO method. The chemical shifts were calculated at 15 ° intervals for Φ and Ψ

sizeable displacements of the ^{13}C chemical shifts can be characterized by variations in the electronic states of the local conformation as defined by the dihedral angles (ϕ,ψ). The calculated contour map for the C_β carbon is shown in Figure 3. From this map, we can estimate the ^{13}C shielding for any specified conformation. It has been demonstrated from comparisons of the experimental data and the predicted values given by this contour map that the map successfully predicts the ^{13}C chemical shifts of alanine residues in polypeptides and proteins.[33,34] (It should be noted that the negative sign of the shielding constant σ indicates deshielding and so shielding variations can be compared with the observed chemical shift δ where a positive sign denotes deshielding.) Such calculations are very useful as a means of analyzing the structures of polymers.

Most recently, the linear relationship between the ^{13}C chemical shift and hydrogen bond length of the carbonyl carbon in glycine and alanine residues of peptides in the solid state has been clarified.[35–37] This result has been justified by FPT INDO calculations. The observation of the chemical shift of the glycine and alanine residue carbonyl carbons of peptides in the solid state allows a determination of the hydrogen bond length. Such experimental findings help to refine the hydrogen bond lengths in proteins as determined by X-ray diffraction.[37] Furthermore, ^{15}N NMR experiments provide very useful information about the structure of peptides and polypeptides in the solid state through the assistance of nuclear shielding calculations.[38]

APPROACH OF USING INFINITE POLYMER CHAINS

Sometimes the estimation of the electronic states of polymer chains necessitates the inclusion of long-range interactions and intermolecular interactions in the calculations. To do this, it is necessary to use a sophisticated theoretical method which can take account of the characteristics of polymers. In this context, the tight-binding molecular orbital (TB MO) theory from the field of solid state physics is used, in the same sense in which it is employed in the LCAO approximation in molecular quantum chemistry to describe the electronic states of infinite polymers with a periodic structure. In a polymer chain with linearly bonded monomer units, the potential energy of an electron varies periodically along the chain. In such a system, the wavefunction Ψ for electrons at a position r can be obtained from Bloch's theorem as follows:

$$\Psi(k) = N^{-1/2} \sum_{j=-(N-1)/2}^{(N-1)/2} \sum_{\nu=1}^{s} \mathrm{e}^{-\mathrm{i}kja} C_{\nu n}(k) \phi_\nu(r - ja) \quad (9)$$

where k is the wavenumber, n is the band index, ν is an orbital index in the jth cell, a is the unit vector of translational symmetry, N is the total number of cells, and l is the number of atomic orbitals in the cell. The term $\phi_\nu(r - ja)$ represents the νth atomic orbital in the jth cell and $C_{\nu n}(k)$ the expansion coefficient. The formulas needed to calculate the shielding of polymers using the TB MO theory incorporating the SOS method have been derived as a function of k as follows:[14,15]

$$\sigma_\mathrm{d}(k) = C \sum P(k) \langle \phi_\nu(r) | r^{-1} | \phi_\nu(r) \rangle \quad (10)$$

$$\sigma_\mathrm{p}(k) = -C' \sum \langle r^{-3} \rangle_{2\mathrm{p}} [E_m(k) - E_n(k)]^{-1} Q(k) \quad (11)$$

where C and C' are constants and $P(k)$ is the bond order as a function of wavenumber. The nuclear shielding is calculated as a function of k. In order to compare the calculated and experimental values of the nuclear shielding, it is necessary to average the calculated data over k, within the first Brillouin zone, as given by

$$\sigma = \int_{-\pi/b}^{\pi/b} \sigma(k) D(k) \, \mathrm{d}k \quad (12)$$

where $D(k)$ is the density of states, namely the number of states per unit amount of energy.

Using this methodology, the elucidation of conformation-dependent chemical shifts of various polymer chains such as polyethylene, polyacetylene, polypyrrole, polyoxymethylene, and polyoxyethylene in the crystalline state has been studied systematically.[7, 14–23] For example, a comparison of the experimental data and the TB INDO/S calculation of the ^{13}C chemical shift tensor of *cis*- and *trans*-polyacetylene in the solid state is shown in Figure 4. The directions of the principal axes are indicated at the bottom. These results agree well with the experimental data.

This shows that the TB MO calculation correctly predicts the origin of the chemical shift and electronic state associated with the structure of the polymers. Furthermore, TB INDO/S calculations have been carried out on the seven polyacetylene chains which take an orthorhombic form. From these results it has been demonstrated that the chemical shift is very sensitive to intermolecular interactions and the TB MO calculation provides useful information about the band structure. The TB MO calculation on the ^{15}N chemical shift of polypyrrole in the solid state allows useful information to be extracted from

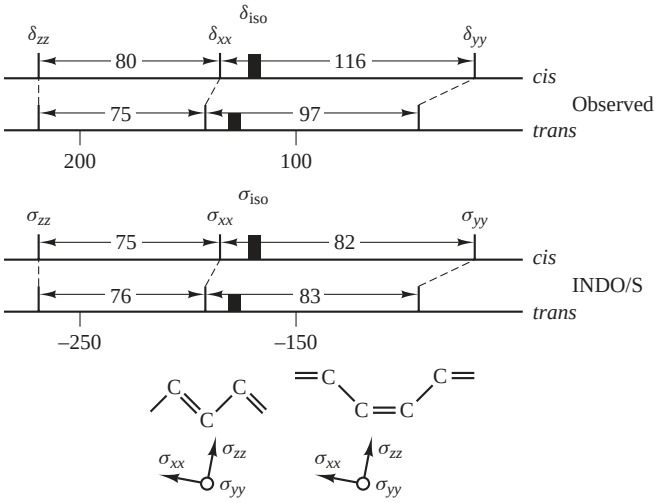

Figure 4 The observed and calculated components of the ^{13}C shielding tensors of *cis*- and *trans*-polyacetylene. The directions of the principal axes are indicated at the bottom (the angles between the C–H bond and the direction of σ_{zz} for *trans*- and *cis*-polyacetylene are 16 ° and 17 ° respectively)

the observed spectra, namely that the two peaks obtained are correctly assigned to the quinoid and aromatic structures.[24] (The quinoid structure is closely related to the electric conductivity.) A decrease in the band gap leads to a downfield shift. These results on conducting polymers demonstrate that the chemical shift behavior provides information about the band gap which, in turn, is a measure of the electrical conductivity. It can be said that TB MO calculations offer useful perspectives in interpreting the results of NMR nuclear shieldings in polymers, both in terms of the structure in the solid state and in understanding the effect of intermolecular interactions on nuclear shieldings. The latter are shown to operate through the electronic states of the polymers considered. The above-mentioned research work has already been presented in a number of review articles.

Finally, NMR in Japan should be mentioned. There are a number of research groups for NMR, the largest being the Research Group of NMR in Japan which organizes a domestic NMR symposium every autumn to which foreign speakers are invited. The Research Group of NMR in Japan was established in 1961 by the NMR spectroscopists Professors S. Fujiwara, A. Nishioka, A. Saika, and T. Yonezawa amongst others. The number of presentations is about 100 per meeting, and the number of participants is normally about 500. The field of these presentations is NMR techniques, NMR theory, organic chemistry, inorganic chemistry, physical chemistry, polymer science, natural products, biochemistry, solid state NMR, and NMR imaging. The NMR Research Group in the Society of Polymer Science, Japan was established in 1977. The number of members is about 100. Meetings are organized twice every year and about five speakers are invited. The number of participants is about 40. A workshop is open for NMR beginners every year, mainly drawn from the Institute of Industries. Recently, the development of NMR imaging has led to the establishment in 1981 of the Society of Magnetic Resonance, Japan associated with the field of medicine. The number of members is about 3000. Superconducting NMR instruments are available at many universities, public institutes, and industrial research centers in Japan. It is estimated that the number of superconducting NMR instruments is about 1200. The number of MRI machines found in hospitals is over 800. As a result, many NMR seminars are organized in Japan.

REFERENCES

1. H. S. Gutowsky, A. Saika, M. Takeda, and D. E. Woessner, *J. Chem. Phys.*, 1957, **27**, 537.
2. A. Nishioka, A. Watanabe, I. Yamaguchi, and H. Shimizu, *J. Polym. Sci.*, 1960, **45**, 232.
3. F. A. Bovey and G. V. D. Tiers, *J. Polym. Sci.*, 1960, **44**, 173.
4. I. Ando, T. Yamanobe, and T. Asakura, *Prog. NMR Spectrosc.*, 1990, **22**, 349.
5. J. Schaefer, E. O. Stejskal, R. A. McKay, and W. T. Dixon, *Macromolecules*, 1984, **17**, 1479.
6. I. Ando and T. Asakura, *Annu. Rep. NMR Spectrosc.*, 1979, **10A**, 81.
7. I. Ando, T. Yamanobe, H. Kurosu, and G. A. Webb, *Annu. Rep. NMR Spectrosc.*, 1990, **22**, 205.
8. I. Ando, A. Nishioka, and T. Asakura, *Makromol. Chem.*, 1975, **176**, 411.
9. I. Ando and A. Nishioka, *Makromol. Chem.*, 1975, **176**, 3089.
10. I. Ando, Y. Kato, and A. Nishioka, *Makromol. Chem.*, 1976, **177**, 2759.
11. I. Ando, Y. Kato, M. Kondo, and A. Nishioka, *Makromol. Chem.*, 1977, **178**, 803.
12. T. Asakura, I. Ando, and A. Nishioka, *Makromol. Chem.*, 1975, **176**, 1151; ibid., 1976, **177**, 1493.
13. T. Asakura, I. Ando, and A. Nishioka, *Makromol. Chem.*, 1977, **178**, 1111; ibid., 1977, **178**, 1521.
14. T. Yamanobe, R. Chujo, and I. Ando, *Mol. Phys.*, 1983, **50**, 123.
15. T. Yamanobe and I. Ando, *J. Chem. Phys.*, 1985, **83**, 3154.
16. T. T. Yamanobe, I. Ando, H. Saito, R. Tabeta, A. Shoji, and T. Ozaki, *Chem. Phys.*, 1985, **99**, 259.
17. T. Yamanobe, I. Ando, H. Saito, R. Tabeta, A. Shoji, and T. Ozaki, *Bull. Chem. Soc. Jpn.*, 1985, **58**, 23.
18. T. Yamanobe, T. Sorita, T. Komoto, I. Ando, and H. Sato, *J. Mol. Struct.*, 1987, **151**, 191.
19. H. Kurosu, T. Yamanobe, T. Komoto, and I. Ando, *Chem. Phys.*, 1987, **116**, 391.
20. T. Ishii, H. Kurosu, T. Yamanobe, and I. Ando, *J. Chem. Phys.*, 1988, **89**, 7315.
21. H. Kurosu, T. Yamanobe, and I. Ando, *J. Chem. Phys.*, 1988, **89**, 5216.
22. H. Kurosu and I. Ando, *J. Mol. Struct. (Theochem)*, 1991, **231**, 231.
23. M. Kikuchi, H. Kurosu, and I. Ando, *J. Mol. Struct.*, 1992, **269**, 183.
24. J. J. Ladik, *Quantum Theory of Polymers as Solids*, Plenum Press, New York, 1988.
25. I. Ando and G. A. Webb, *Theory of NMR Parameters*., Academic Press, London, 1983.
26. P. J. Flory, *Statistical Mechanics of Chain Molecules*., Interscience, New York, 1969.
27. J. A. Pople, J. W. McIver, Jr., and N. S. Ostlund, *J. Chem. Phys.*, 1968, **49**, 2960.
28. I. Ando, A. Nishioka, and M. Kondo, *J. Magn. Reson.*, 1976, **21**, 429.
29. I. Ando and H. S. Gutowsky, *J. Magn. Reson.*, 1978, **31**, 387.
30. I. Ando and G. A. Webb, *Org. Magn. Reson.*, 1981, **15**, 111.
31. M. Kondo, S. Watanabe, and I. Ando, *Mol. Phys.*, 1968, **15**, 435.
32. I. Ando, H. Saito, R. Tabeta, A. Shoji, and T. Ozaki, *Macromolecules*, 1984, **17**, 457.

33. H. Saito, R. Tabeta, A. Shoji, T. Ozaki, I. Ando, and T. Miyata, *Biopolymers*, 1984, **23**, 2279.
34. H. Saito, R. Tabeta, T. Asakura, Y. Iwanaga, A. Shoji, T. Ozaki, and I. Ando, *Macromolecules*, 1984, **17**, 1405.
35. S. Ando, I. Ando, A. Shoji, and T. Ozaki, *J. Am. Chem. Soc.*, 1988, **110**, 3380.
36. N. Asakawa, S. Kuroki, H. Kurosu, I. Ando, A. Shoji, and T. Ozaki, *J. Am. Chem. Soc.*, 1992, **114**, 3261.
37. N. Asakawa, H. Kurosu, I. Ando, A. Shoji, and T. Ozaki, *J. Mol. Struct.*, 1994, **317**, 119.
38. A. Shoji, S. Ando, S. Kuroki, I. Ando, and G. A. Webb, *Annu. Rep. NMR Spectrosc.*, 1993, **26**, 55.

Biographical Sketch

Isao Ando, *b* 1941. Ph.D., (supervisor Atsuo Nishioka) 1972, Polymer Chemistry, Tokyo Institute of Technology, Japan. Postdoctoral work at University of Illinois, Urbana (with Herb Gutowsky). Successively research associate, associate professor, and professor, Tokyo Institute of Technology. Approx. 250 publications. Research specialities: structures and electronic states of solid polymers, solid state NMR, and nuclear shielding calcuations.

Andrew, E. Raymond: Spinning the Spins: A Lifetime in NMR

E. Raymond Andrew

University of Florida, Gainesville, FL, USA

It happens that my professional life spans the first 50 years of NMR that we are celebrating in this volume. It is a most wonderful evergreen subject with a continual supply of new and exciting developments, and I have been most fortunate to have had the opportunity to participate in some of them.

I first heard about nuclear magnetic resonance in 1946 when I was a research student in the Cavendish Laboratory at Cambridge University, working for my Ph.D. on problems in superconductivity with Professor David Shoenberg. Whenever something of interest caught David's eye in the literature he would depute one of us to read it up and present a talk at the weekly low-temperature seminar. In this way I read the first publications of Bloch[1] and Purcell[2] and their colleagues. Then in 1947 Professor Bloch paid a visit and gave a fascinating talk and in 1948 Bloembergen and Pound came through. It was clear that NMR was an exciting new subject and when applying to the Commonwealth Fund for a postdoctoral fellowship, I proposed to work on NMR at Harvard.

The first British pioneer in NMR was Dr. Bernard Rollin at Oxford University, so before leaving Britain for my postdoctoral year in America, I visited him at the Clarendon Laboratory. Immediately after seeing the first NMR publications in early 1946, he had built a very simple and elegant NMR spectrometer of novel design, and by November 1946, he had published his first NMR paper in *Nature*[3] announcing detection of proton and fluorine NMR in a range of liquids and solids and had measured their relaxation times. The next year, 1947, he undertook the first low-temperature NMR, measuring T_1 and T_2 in liquid and solid hydrogen and other materials down to 1 K.[4] His work is less widely known than it deserves to be partly because he would never travel outside Oxford. In fact he would only speak at a conference if the conference was held in Oxford!

I was very fortunate to spend my postdoctoral year, 1948–49, working in the laboratory of Professor E. M. Purcell at Harvard University. He is a truly remarkable scientist with wide interests beyond NMR ranging from astrophysics (with his student Ewen he first discovered, in 1951, the 21-cm hydrogen hyperfine line from outer space) to biophysics (in 1984 he was jointly awarded with Howard Berg the APS Biological Physics prize for the elucidation of bacterial locomotion). He is also an extraordinarily pleasant person and, as I write in 1993, is still active, going daily to the Lyman lab at Harvard at the age of 81. Photographs of some scientists mentioned in the text, including E. M. Purcell, are given in Figure 1.

In my application to the Commonwealth Fund I had proposed to study the NMR linewidth at phase transitions in solids where specific heat measurements suggested the possible onset of molecular rotation. An alternative technique for the study of molecular reorientation in solids was dielectric dispersion, but that requires molecules with a permanent electric dipole moment which are inherently asymmetrical. It seemed to me that the beauty of NMR was that one could examine symmetrical molecules like benzene which were more likely to rotate in the solid state, even though the specific heat showed no anomaly. Unknown to me when I made my proposals, Herb Gutowsky and George Pake were completing theses at Harvard in Ed Purcell's lab on the ammonium halides and methyl groups, so my research proposals fell on very receptive ears. I spent a marvelous year in his laboratory working on NMR in solid long-chain paraffins, solid benzene, and various solid methylbenzenes.[5] Solid benzene, in particular, provided an excellent example of reorientation about its sixfold axis in the solid state.

I had a laboratory on the basement floor of the Lyman Laboratory and in the next lab was one of Ed Purcell's graduate students, Charlie Slichter, now a Professor at the University of Illinois. There was a large rectangular hole in the communicating wall about 1 m wide, 0.3 m high, put there by a previous occupant who needed a long light path. Charlie and I got to know each other well through that hole in the wall, and I'm very happy that our paths have crossed frequently in recent years as officers of ISMAR. My continuous-wave NMR spectrometer (see photograph in Figure 2) consisted of a permanent magnet, a General Radio signal generator, an rf bridge and preamplifier, a Hallikrafters receiver, an output meter, and an oscilloscope.

A condition of the Commonwealth Fund Fellowships, a far from irksome condition, was the requirement that we travel around the United States for three months and take back our experiences and impressions to Britain. During April to July of 1949, we covered 20 000 km in a pre-war Ford; I learnt a lot about cars as well as NMR that year. We visited NMR labs and low temperature labs. I had the great pleasure of meeting Henry Torrey at Rutgers, Felix Bloch at Stanford, and W. F. Giauque at Berkeley. I came to know Felix quite well over the years and visited him several times including 1983, shortly before his death. He obtained his doctorate at Leipzig and had a fund of stories about Heisenberg who was Professor of Theoretical Physics there, and about Boltzmann who previously held the same Chair. Just down the road at MIT I had several meetings with Francis Bitter who made some early contributions to NMR.[6] At Harvard itself there were many famous physicists at work, including Van Vleck,[7] who had just written his classic second and fourth moment paper, Bob Pound pioneering quadrupole interactions[8] in NMR, Bloembergen who had just returned from Leiden during my year, Ramsey setting up his new high-resolution atomic beam magnetic resonance system, and Bridgman still working in his retirement on physics at high pressures.

In 1949, I returned to Britain after this splendid year in America and took up an academic appointment as a lecturer at St. Andrews University, the oldest university in Scotland. With the enthusiastic encouragement of our Head of Department, Professor Jack Allen, we set about constructing an NMR spectrometer. Alwyn Rushworth and I designed a 0.6 T permanent magnet and had it built in Sheffield. At 2 tons it was the largest permanent magnet in Britain at the time. My first research student, Bob Eades, helped me build the NMR spectrometer. Our first projects centered on molecular dynamics in solids measuring spin–lattice relaxation times T_1 over a wide temperature range, supplemented by second

Figure 1 Some scientists mentioned in the text: (a) F. Bloch; (b) E. M. Purcell; (c) C. J. Gorter; (d) A. Kastler; and (e) E. K. Zavoisky.

moment analysis. We examined solid cyclohexane[9] and solid benzene[10] in depth, determining the kinetics of a variety of modes of reorientation and in solid cyclohexane finding the first unequivocal evidence of molecular diffusion in the solid state by NMR.

Soon after the publication of my first NMR paper in the *Journal of Chemical Physics*, a letter arrived from Professor Alfred Kastler in Paris. He had earlier measured the Raman spectrum of solid benzene and wondered how our work could be compatible with his. After all, if the molecules were rotating about their hexad axes, how could a Raman spectrum be found from hexad librations? He was most interested in my explanation that by NMR we measured the relatively infrequent reorientations of the molecules while he was measuring the rotational oscillations between these events. Soon afterwards he invited me to lecture in Paris, so beginning a long friendship until his death in 1984. He was awarded the Nobel prize in 1966 for discovering optical methods for studying radiofrequency resonances in atoms.

Not only does NMR give dynamical information concerning the solid state but it also gives structural information, especially about hydrogen atoms as George Pake had demonstrated in a classic experiment on hydrates.[11] NMR and X-ray diffraction complement each other. Hydrogen, the one element on which X-ray diffraction is silent, is the element on which NMR is most articulate. Urea was a molecule of substantial biophysical significance; its X-ray structure was known, giving the positions of the four heavier atoms in the molecule, but the placing of the four hydrogen atoms was a matter of controversy in the literature. Was the molecule planar or nonplanar?

Figure 2 (a) The author in his NMR laboratory at Harvard University, 1949. Note the hole in the wall to the laboratory of C. P. Slichter. (b) E. R. Andrew (President) and C. P. Slichter (Vice-President) at the ISMAR Conference in Rio de Janiero 1986.

My student, Dan Hyndman, patiently grew some single crystals and we were able to show unequivocally from the proton NMR spectra and second moments that the planar form was correct,[12] and we determined the bond lengths to 1% with evidence of hydrogen bonding to neighboring oxygen atoms. Later this structure was confirmed by neutron diffraction. We liked to point out how much cheaper it was to gain structural information by NMR than by neutron diffraction!

About this time in Oxford, Rex (now Sir Rex) Richards began his early pioneering applications of NMR in chemistry. This eventually developed into an important school of high-resolution NMR spectroscopy in chemistry and biochemistry. One of Rex's students, Ray Freeman, returned to Oxford after working for some years at Varian Associates in California and later become Professor of NMR Spectroscopy at Cambridge University.

While we were in St. Andrews we were delighted to hear that the 1952 Nobel Prize for Physics had been awarded to Professors Felix Bloch and Ed Purcell. Very shortly afterwards it was a pleasure to welcome Ed to St. Andrews, and we were also very happy to have a visit from Bob Pound. Another welcome visitor was a young Japanese theorist called Kazuhisa Tomita, who was then working on the famous relaxation paper by Kubo and Tomita;[13] we met from time to time over the years until his death in 1991. Our NMR work had begun to attract some attention and in 1952 I was very pleased to be elected a Fellow of the Royal Society of Edinburgh. This old-established society is the Academy of Arts and Sciences of Scotland and had been presided over in earlier years by Sir Walter Scott and Lord Kelvin.

Many physicists and chemists were now taking an interest in NMR and there was a need for a book on the subject. I wrote my book Nuclear Magnetic Resonance[14] in St. Andrews in 1953–54 and it was published by Cambridge University Press the following year. When my first royalty cheque for $50 arrived, I remember calculating that this represented a rate of pay of about sixpence (about 5 cents) per hour spent on the project! Happily as the sales built up, the rate became somewhat more respectable.

My stay in Scotland, the land of my grandfathers, was five years and in 1954, I moved to the University of Wales at Bangor as Professor of Physics and Head of Department. NMR was a good subject to pursue in a small department with limited financial resources but plenty of talent. Bob Eades rejoined me as a lecturer after postdoctoral work in Vancouver; we had a long collaboration and built an active NMR group. Among many international collaborators was Dr. (now Professor) Jacek Hennel, who visited us for a year from Krakow, Poland, the first of many mutual visits. We had visits too from Abragam from Paris and Hahn from Berkeley.

In Wales we became interested in quadrupole-split spectra and Kenneth Swanson[15] and I established a method for distinguishing quadrupolar from dipolar relaxation mechanisms in solids. David Tunstall and I derived the $2I$ relaxation times for nuclei of spin I for quadrupolar relaxation mechanisms in solids.[16] This analysis has turned out many years later to be useful in current work on the new high-temperature superconductors where several of the elements of interest have quadrupolar nuclei of high spin. As physicists we were aware that in crystals, even cubic crystals, most physical properties are anisotropic. This led us to establish the anisotropy of T_1 in a number of ionic crystals and to relate this anisotropy to relaxation theory.[17] We were also able to establish the anisotropy of chemical shift for ^{19}F in several molecular solids.

An important new interest emerged from our work in Wales which led us to discover magic angle spinning. It arose from the resolution of an NMR paradox. Molecular motion in a solid narrows the NMR spectrum and reduces its second moment to new plateau values as the temperature is raised. Yet according to Van Vleck's theory, the second moment should remain invariant. My solution to this paradox was that the reduced second moment came from the time-averaged dipolar Hamiltonian and that the time-dependent part generated weak unobservable satellite wings in the spectrum which, if included, maintained the invariance of the second moment. Detailed theoretical analysis confirmed this. However, it is never very satisfying to have to rely on something unobservable, so how could these weak satellites be made observable? It seemed to me that if we were to rotate a specimen rapidly we could simulate the effect of molecular motion on the dipolar interactions, but since all nuclear pairs would be rotating at the same rate the satellites would appear at the same frequency and be observable. Our first successful sample spinning experiment was reported in *Nature*[18] in

1958, confirming the invariance of the second moment and demonstrating the satellite lines (spinning sidebands). Analysis showed that this line narrowing by rapid rotation should follow a factor $|\frac{1}{2}(3\cos^2\beta - 1)|$, where β is the angle between the axis of spin and the main magnetic field. It follows that when $\cos^2\beta = \frac{1}{3}$, or $\beta = 54^\circ 44'$ (the magic angle), dipolar interactions should be removed entirely from the central spectrum. We reported our confirmation of this in *Nature*[19] in 1959. Unknown to us Irving Lowe[20] carried out a similar experiment independently in St. Louis, also reported in 1959. Later, in 1969, Irving came to spend a sabbatical year in Nottingham and he lived in my house while I was on leave at the University of Florida.

When we reported our first sample rotation results at the AMPERE Congress in Pisa in 1960, Professor Gorter of Leiden found the removal of the dipolar broadening of the NMR lines quite remarkable and referred to it as 'magic', so we called the technique 'magic angle spinning' after that. We showed theoretically that magic angle spinning removes broadening arising from any bilinear tensor interaction and we subsequently demonstrated this experimentally for dipolar and pseudodipolar interactions, for chemical shift anisotropy, and for quadrupolar interactions.[21] With this technique we resolved the first spin multiplets in solids,[22] in polycrystalline sodium hexafluoroarsenate and hexafluoroantimonate. We also resolved a number of chemically-shifted lines in solids. We went on to apply magic angle spinning to metals. The NMR lines of metals such as aluminum,[23] cadmium, and copper were narrowed by two orders of magnitude enabling the Knight shifts to be measured to a precision two orders of magnitude greater than hitherto. In copper we were able to measure the weak Ruderman–Kittel interactions,[24] normally obscured by the larger dipolar interaction, and to relate them to theory.[25]

Magic angle spinning required very high rotation speeds. When visiting Professor R. M. Davies at our sister college in Aberystwyth, I noticed that he was spinning an octagonal mirror fast with the aid of a simple air turbine made of steel. This gave me the idea to fashion an air turbine made of nylon or other strong polymeric nonmetallic material, enclosing a specimen chamber. Our rotors spun to 10 kHz routinely and occasionally to 15 kHz. The peripheral velocity of a 19-mm diameter rotor rotating at 10 kHz is 2000 km h^{-1}, which is supersonic. Consequently for the highest rotation rates the rotors were driven with compressed helium;[21] the velocity of sound in helium is 2.7 times higher than in air. The peripheral acceleration at 10 kHz is $4 \times 10^6 g$ and it was therefore necessary to use the strongest available materials to fashion the rotors. The world expert on high-speed rotation was Professor Jesse Beams of the University of Virginia. He invited me to visit his laboratory and I must confess I was pleased when he commented we had done well! Magic angle spinning has now become a standard feature of NMR spectrometers enabling chemists and others to obtain high-resolution NMR spectra from solid materials of all kinds. Nowadays spinning rates twice as fast as ours are obtainable using rotors of smaller diameter.

We had some tall people in the magic angle spinning team. Arnold Bradbury, 6 ft. 8 in., was one of the pioneer group; he joined the academic staff in the University of Wales and is still there. Geoffrey Jenks, 6 ft. 5 in., joined us soon after from Australia, after his Ph.D. returning to Melbourne. Gwynfor Williams, 6 ft. 3 in., was one of the invaluable workshop technicians who made precision rotors. The Physics Department had an outstanding basketball team at that time which carried all before them in the University championship.

As momentum gathered in the applications of magnetic resonance in physics and chemistry, a forum was needed to enable practitioners to discuss their progress, their methods and new results. In France the Groupement AMPERE had been founded in 1952 for such a purpose, but its proceedings were at that time wholly in French. So, in 1956, we launched the British Radiofrequency Spectroscopy Group at an inaugural meeting at the University of Wales in Bangor. I was Chairman of the BRSG for its first three years and 25 years later I was again asked to be Chairman and to organize a jubilee meeting in Nottingham in 1981. I am delighted to record that 38 years later the BRSG is still a very active organization with a regular program of meetings, which have been held in all parts of Britain and also in Dublin and Paris. BRSG not only covers nuclear magnetic resonance but also electron spin resonance and other branches of radiofrequency and microwave spectroscopy. ESR had been discovered a year earlier than NMR by E. K. Zavoisky[26] in Kazan, Russia, in 1944, quite astonishingly at the height of the Second World War. So ESR celebrated its 50th anniversary in 1994, a year ahead of NMR.

After 10 years in Wales, I accepted an invitation to return to England in 1964 as Lancashire–Spencer Professor of Physics and Head of the Department of Physics at Nottingham University. A large new physics building with much new equipment provided a wonderful opportunity. Several new academic appointments were possible and a strong NMR group was assembled, now all professors: Stanley Clough, who accompanied me from Bangor and later became Head of Department, Peter (now Sir Peter) Mansfield, Peter Allen, now Head of Applied Sciences in Medicine at the University of Alberta, and Bill Derbyshire now at Rank–Hovis–MacDougall. Dr. Bill Moore also joined our NMR activities later, before his move to Harvard, where very sadly he died in 1984.

The move to Nottingham in 1964 saw a change in our NMR methodology. Pulsed methods gave a new dimension to NMR measurement enabling relaxation to be investigated more readily with accurate determination of all NMR parameters T_1, $T_{1\rho}$, T_{1D}, T_2, M_2, D; the spin system evolves freely between excitations, and the free induction decay could be Fourier-transformed to give the NMR spectrum. The broad NMR spectra from solids, especially from ^{1}H and ^{19}F, meant that a 90 $^\circ$ pulse had to be as short as 1 μs and correspondingly of high intensity. A grant from the Science Research Council enabled us to purchase the first Bruker 1–100 MHz short pulse NMR spectrometer for solid state work in Britain. Very stable electromagnets were now available. The days when we designed and made our own spectrometers and magnets were now largely at an end.

In Nottingham my magic angle spinning research continued with Jim Carolan and Waldo Hinshaw and also my interest in molecular dynamics in solids, where I became fascinated with a new form of dynamic behavior, conformational motion.[27,28] In materials such as solid cyclobutane, rapid interconversion of conformers leads to NMR line narrowing and relaxation; at higher temperatures it can lead to conformational order–disorder and a specific heat anomaly. Conformational disorder is propagated in a manner analogous to spin waves

and the quasiparticle characterizing elementary excitation of conformational waves I called a conformon (1971). I suppose we would all like to discover a new elementary particle and if not a 'real' particle, then at least a quasiparticle. After all, a quasiparticle is not only the next best thing to a real particle, it is just about as fundamental as some real particles!

I had earlier been interested in the NMR of simple solid compounds of biological interest such as urea and the polymethylammonium ions. From 1970 onwards this became one of my more positive interests and we began to examine a wider group of compounds important in biology. We started with proton NMR relaxation investigations into the solid state of the whole family of 20 amino acids from which proteins are assembled.[29,30,31] We identified or confirmed their molecular form and determined the molecular dynamics of methyl, amino, and other groups. In this work I was fortunate to have the collaboration of Waldo Hinshaw, Michael Hutchins, and Rolf Sjöblom. For Rolf the year in my laboratory was part of his doctorate work for the University of Uppsala in Sweden. It led to my going to Uppsala the following year as his official 'opponent' at the public doctoral examination in the presence of his department, family, and friends and reminded me of the old medieval disputations.

From amino acids we moved on to the NMR relaxation study of polycrystalline dipeptides, tripeptides, and homopolypeptides. We were now poised to examine solid proteins[32] by NMR. The advantage of relaxation investigations in the solid state is that large molecules are rather immobile and one is therefore studying directly the intramolecular motions of groups and segments. In solution such motions are superimposed on the motion of the molecule as a whole and in analyzing the relaxation behavior it is difficult to disentangle the internal motions in a clear and unique manner. David Bryant and Eamonn Cashell joined me in examining lysozyme,[33] ribonuclease,[34] α-chymotrypsin,[33] and insulin,[35] three enzymes and a hormone. Using the knowledge gained from the precursors we could identify motions attributed to segmental motion, to methyl groups and side chains, to proline conformational motion, and to the motion of water molecules intrinsic to the structure.[36] Dr. Gaspar visited us from Hungary and by studying $T_{1\rho}$ and T_{1D} we were also able to investigate very slow molecular motions.[37] A year's visit by Professor Michael Hoch from Johannesburg in South Africa provided the opportunity also to investigate the proton dynamics in DNA and its component bases[38] in the solid state.

In 1979 changes in China brought our first visitors from that country for many years and were delighted to welcome Mr. Quin-An Meng from the Institute of Physics in Beijing, who came to work with us for two years. He contributed to our work on insulin and other proteins and also polyproline. He later arranged for me to visit well-equipped NMR centers in China at Beijing, Shanghai, Wuhan, and Fuzhou.

While all this work was going on a new chapter in NMR suddenly opened. Waldo Hinshaw, Bill Moore, and I attended the ISMAR meeting in Bombay in January 1974, where we heard Paul Lauterbur talk about NMR imaging, which he called Zeugmatography.[39] Waldo and Bill soon devised an alternative approach and on our return to Nottingham, Waldo, working in my laboratory with our Bruker spectrometer, was producing NMR images in a few weeks[40] and was able to present some very good images of small objects including a spring onion at the Nottingham AMPERE Congress in September 1974. The future potential of this technique in biology and medicine was clear, and Bill and I obtained a grant from the Medical Research Council to pursue NMR imaging on objects of larger size. Here was a procedure capable of giving excellent images of the interior of the body without the use of ionizing radiation. Waldo returned from America to rejoin the project and we were also joined by Neil Holland and an Australian research student, Paul Bottomley, who went on to make a name for himself in the subject in the United States.

With a magnet having a 13-cm aperture, good, geometrically faithful images were obtained in 1977 of a lemon and other fruit, and of the abdominal anatomy of a rat. We also obtained the first NMR images of a human hand,[41] wrist,[42] and forearm. The image of the lemon appeared on the front cover of *Nature* in 1977. The question then arose whether the radiofrequency fields needed for NMR would adequately penetrate human tissue for imaging the whole head and body. Paul Bottomley and I carried out a calculation[43] assuming a simple cylindrical model of the body and concluded that penetration would be almost complete at the frequencies to be used. It was a great pleasure to us that this paper, which was frequently quoted, became a Citation Classic. Then with support from the Wolfson Foundation a whole body NMR imaging system was constructed which gave images of the human head and body, both normal and diseased,[44,45] with the first clinical assessment of pathology. By now we needed clinical advice and we were fortunate to have the active interest and collaboration of Dr. Brian Worthington, Professor of Diagnostic Radiology at Nottingham University Medical School. Meanwhile a very successful parallel series of investigations was being carried out in the Department of Physics by Professor Peter Mansfield and his colleagues using somewhat different techniques.[46] Our early NMR images played a part in convincing medical instrument manufacturers to produce commercial NMR scanners, nowadays a huge industry, and it led to our becoming consultants first with EMI and then with GEC, working with Dr. Hugh Clow and Dr. Ian Young, who obtained the first human head images.[47]

Physicists are great conference people and love to get together and discuss their work with others in their field. In April 1976, we organized the first international conference on NMR imaging in Nottingham. Most of the activists in the world of magnetic resonance imaging of the day, about 25 in all, were there.

BRSG continued to provide magnetic resonance meetings at the national level in Britain and the Groupement AMPERE at the European level. It was Professor René Freymann of France who suggested that AMPERE's name provided an appropriate acronym: Atomes et Molecules Par Etudes Radio-Electriques, and we therefore often write it out in capital letters. The AMPERE Group originally catered for French speakers but as its popularity grew, papers in English were allowed and eventually English took over as the primary language. AMPERE Congresses, Colloques and Summer Schools were held in most European countries from Lisbon in the west to beyond the Urals in Novosibirsk and Shushenskoe in the east, from Turku in the north to Crete in the south. It provided an excellent vehicle for meeting magnetic resonance scientists in Europe despite the political divisions of those days. After organizing the 18th AMPERE Congress in Nottingham in 1974, I had the honor of being elected President of the

Groupement AMPERE and served till 1980. The Groupement AMPERE owes much to the dedicated service of its Secretary-General, Georges Béné, who served for 34 years till 1990. He is a wonderful person and a great friend. In 1994 the AMPERE congress went to Kazan to celebrate the discovery of ESR by Zavoisky[26] there 50 years ago. Besides these activities in Europe there was a need for worldwide meetings of magnetic resonance scientists and in 1971 at a meeting in Israel, the International Society of Magnetic Resonance (ISMAR) was founded, spearheaded by Professor Daniel Fiat, who was its Chairman till 1983. A new constitution was agreed in that year with a rotation of officers, and I served as the first President of ISMAR till 1986. In 1995 ISMAR will hold its triennial meeting in Sydney, Australia, and will celebrate the discovery of NMR 50 years earlier.

The years were passing and I began to notice without enthusiasm that the age of my compulsory retirement (65) at Nottingham University was approaching. So I was very delighted to receive an invitation to come to the University of Florida in 1983 as a Research Professor, without a specified date of retirement, and I accepted with great pleasure. Here in Florida I have joint appointments in the Physics Department and in the University Medical School, and I spend half my time in each. I had earlier spent a year of sabbatical leave working in Florida with my old friend, the late Tom Scott, whom I knew from Harvard days, and I am particularly grateful to old colleagues from that year, especially Jim Brookeman and Kate Scott, for this opportunity. Here the winters are warm, I have palm trees outside my office window, and we never have snow or ice or fog. I encourage my friends from cold places to visit us!

In the Physics Department I have been able to continue my NMR research on molecular solids. A long-standing exchange program with Poznan University in Poland has provided a series of excellent postdoctoral fellows from the laboratory of Professor Pajak. We have investigated molecular structure and dynamics in solid carbohydrates, sugars, cholesterol,[48] cortisone, progesterone, testosterone,[49] lactic acid and lactates, *t*-butylselenol,[50] AMP, ADP, and ATP. However, it has been remarked that life is lived in aqueous solution and with this in mind we have also investigated relaxation and relaxation mechanisms in these and other metabolites in aqueous solution for ^{1}H and ^{31}P using high-resolution NMR spectrometers in a renewed collaboration with Professor Gaspar from Hungary.[51,52] This knowledge is very useful in MRS investigations of quantitation, NOE, saturation transfer, dynamics, and exchange.

Shortly after my arrival in 1983, the University of Florida hospital acquired one of the first generation commercial 0.15 T whole body NMR imaging systems. It was manufactured by Technicare where Dr. Waldo Hinshaw was in charge of NMR technology. It served us well for several years and Technicare gave us a second system dedicated to research. These years witnessed a rapid development of MRI to become a regular clinical modality of radiological investigation and the method of choice for many disease situations. With the advances in superconducting technology we replaced these early systems and currently we have two 1.5 T systems and a 3 T system. So the University of Florida has extremely good NMR imaging facilities devoted primarily to patient care, but also providing excellent opportunities for MRI and MRS research.[53] We also have a 4.7 T 33-cm bore NMR imaging spectrometer for smaller scale and animal research, together with 7 T and 14 T high-resolution spectrometers suitable for NMR microscopic imaging. Besides taking advantage of these facilities, I have also been making contributions to magnet screening[54,55] and to novel field gradient systems.

I was glad to find I had not been totally forgotten in my home country when in 1984, I was elected to Fellowship of the Royal Society, the citation specifically mentioning contributions to NMR. Shortly afterwards I shared the Royal Society's Wellcome Medal and Prize with Jim Hutchison, John Mallard, and Peter Mansfield for our contributions to NMR imaging. We have happily stayed in the United States, continuing to work, but returning to Britain frequently. I was especially glad to be welcomed back to Nottingham in 1992 to a BRSG meeting held in honor of my 70th year. From Florida I was able to take sabbatical leave back to England in 1989, spending it in Cambridge as a Fellow of Christ's College, where I had been an undergraduate 50 years earlier, and I worked in Professor Laurie Hall's new NMR laboratory in the University Medical School, where MRI and NMR microimaging are a specialty.

In Florida a new horizon opened when I was asked to start the new journal *Magnetic Resonance in Medicine* as Editor-in-Chief. The journal was urgently needed in this burgeoning field and grew rapidly, reaching the top of the impact table in its group of 50 radiology journals. After 8 years, I retired from the editorship in 1991, and the Society of Magnetic Resonance in Medicine most kindly awarded me their Distinguished Service Medal.

The most recent magnetic resonance excitement in Florida comes from the new US National High Magnetic Field Laboratory created in Florida under grants from the National Science Foundation and the State of Florida. Begun in 1991, it is now complete and open for business. NMR at the highest magnetic fields is one of the many areas of science to be undertaken at the laboratory, along with ESR and ICR. Centered in Tallahassee, the NHMFL has outposts in Los Alamos and in Gainesville, and several of us at the University of Florida serve on the NHMFL planning committee and are active in prosecuting this exciting new venture.

Finally, I would like to say what a tremendous privilege it has been to work in this great subject of nuclear magnetic resonance for close on 50 years. It has been an inspiration to participate in this adventure over the years with many able colleagues including some 30 postdoctoral fellows and 40 graduate students, and I am most grateful to the pioneers of NMR who made this possible. The subject is still very active with new developments opening up continually. We can be confident of a very bright future for NMR.

REFERENCES

1. F. Bloch, W. W. Hansen, and M. Packard, *Phys. Rev.*, 1946, **69**, 127.
2. E. M. Purcell, H. C. Torrey, and R. V. Pound, *Phys. Rev.*, 1946, **69**, 37.
3. B. V. Rollin, *Nature*, 1946, **158**, 669.
4. B. V. Rollin and J. Hatton, *Nature*, 1947, **159**, 201.
5. E. R. Andrew, *J. Chem. Phys.* 1950, **18**, 607.
6. F. Bitter, N. L. Alpert, H. L. Poss, C. G. Lehr, and S. T. Lin, *Phys. Rev.*, 1947, **71**, 738.
7. J. H. Van Vleck, *Phys. Rev.*, 1948, **74**, 1168.

8. R. V. Pound, *Phys. Rev.*, 1950, **79**, 685.
9. E. R. Andrew and R. G. Eades, *Proc. Roy. Soc. A*, 1953, **216**, 398.
10. E. R. Andrew and R. G. Eades, *Proc. Roy. Soc. A*, 1953, **218**, 537.
11. G. E. Pake, *J. Chem. Phys.*, 1948, **16**, 327.
12. E. R. Andrew and D. Hyndman, *Faraday Soc. Disc.*, 1955, **19**, 195.
13. R. Kubo and K. Tomita, *J. Phys. Soc. Japan*, 1954, **9**, 888.
14. E. R. Andrew, *Nuclear Magnetic Resonance*, Cambridge University Press, Cambridge, 1955.
15. E. R. Andrew and K. M. Swanson, *Proc. Phys. Soc.*, 1960, **75**, 582.
16. E. R. Andrew and D. P. Tunstall, *Proc. Phys. Soc.*, 1961, **78**, 1.
17. E. R. Andrew, K. M. Swanson, and B. R. Williams, *Proc. Phys. Soc.*, 1961, **77**, 36.
18. E. R. Andrew, A. Bradbury, and R. G. Eades, *Nature*, 1958, **182**, 1659.
19. E. R. Andrew, A. Bradbury, and R. G. Eades, *Nature*, 1959, **183**, 1802.
20. I. J. Lowe, *Phys. Rev. Lett.*, 1959, **2**, 285.
21. E. R. Andrew, *Phil. Trans. Roy. Soc.*, 1981, **299A**, 505.
22. E. R. Andrew, L. F. Farnell, and T. D. Gledhill, *Phys. Rev. Lett.*, 1967, **19**, 6.
23. E. R. Andrew, W. S. Hinshaw, and R. S. Tiffen, *Phys. Lett.*, 1973, **46A**, 57.
24. E. R. Andrew, J. L. Carolan, and P. J. Randall, *Phys. Lett.*, 1971, **37A**, 125.
25. E. R. Andrew and W. S. Hinshaw, *Phys. Lett.*, 1973, **43A**, 113.
26. E. K. Zavoisky, S. A. Altshuler, and B. M. Kozyrev, *Zhur. Ekspt. i Theor. Fiz.*, 1944, **10**, 11.
27. E. R. Andrew, *Phys. Lett.*, 1971, **34A**, 30.
28. E. R. Andrew and J. R. Brookeman, *J. Magn. Reson.*, 1970, **2**, 259.
29. E. R. Andrew, W. S. Hinshaw, M. G. Hutchins, and R. O. I. Sjoblom, *Molec. Phys.*, 1976, **31**, 1479.
30. E. R. Andrew, W. S. Hinshaw, M. G. Hutchins, R. O. I. Sjoblom, and P. C. Canepa, *Molec. Phys.*, 1976, **32**, 795.
31. E. R. Andrew, W. S. Hinshaw, M. G. Hutchins, and R. O. I. Sjoblom, *Molec. Phys.*, 1977, **34**, 1695.
32. E. R. Andrew, D. N. Bone, D. J. Bryant, E. M. Cashell, R. Gaspar, Jr., and Q. A. Meng, *Pure Appl. Chem.*, 1982, **54**, 585.
33. E. R. Andrew, D. J. Bryant, E. M. Cashell, and Q. A. Meng, *Phys. Lett.*, 1982, **88A**, 487.
34. E. R. Andrew, D. J. Bryant, and E. M. Cashell, *Chem. Phys. Lett.*, 1980, **69**, 551.
35. E. R. Andrew, D. J. Bryant, E. M. Cashell, and Q. A. Meng, *FEBS Lett.*, 1981, **126**, 208.
36. E. R. Andrew, D. J. Bryant, and T. Z. Rizvi, *Chem. Phys. Lett.*, 1983, **95**, 463.
37. R. Gaspar, Jr., E. R. Andrew, D. J. Bryant, and E. M. Cashell, *Chem. Phys. Lett.*, 1982, **86**, 327.
38. M. J. R. Hoch and E. R. Andrew, *Chem. Phys. Lett.*, 1977, **48**, 377.
39. P. C. Lauterbur, *Nature*, 1973, **242**, 190.
40. W. S. Hinshaw, *Phys. Lett.* 1974, **48A**, 87.
41. E. R. Andrew, P. A. Bottomley, W. S. Hinshaw, G. N. Holland, W. S. Moore, and C. Simaroj, *Phys. Med. Biol.*, 1977, **22**, 971, errata 1291.
42. W. S. Hinshaw, E. R. Andrew, P. A. Bottomley, G. N. Holland, W. S. Moore, and B. S. Worthington, *Neuroradiology*, 1978, **16**, 607.
43. P. A. Bottomley and E. R. Andrew, *Phys. Med. Biol.*, 1978, **23**, 630.
44. R. C. Hawkes, G. N. Holland, W. S. Moore, and B. S. Worthington, *J. C. A. T.*, 1980, **4**, 577.
45. E. R. Andrew, *Phil. Trans. Roy. Soc. B*, 1980, **289**, 471.
46. P. Mansfield, P. G. Morris, R. J. Ordidge, I. L. Pykett, V. Bangert, and R. E. Coupland, *Phil. Trans. Roy. Soc. B*, 1980, **289**, 503.
47. H. Clow and I. R. Young, *New Scientist*, **1978**, 588 (23 November 1978).
48. E. R. Andrew and B. Peplinska, *Molec. Phys.*, 1990, **70**, 505.
49. E. R. Andrew and J. M. Radomski, *Solid State NMR*, 1993, **2**, 57.
50. E. R. Andrew, K. Jurga, and E. Szczesniak, *Molec. Phys.*, 1988, **65**, 1421.
51. R. Gaspar, Jr., W. S. Brey, A. Qiu, and E. R. Andrew, *Chem. Phys. Lett.* 1989, **156**, 619.
52. R. Gaspar, Jr., W. S. Brey, and E. R. Andrew, *Chem. Phys. Lett.*, 1991, **184**, 17.
53. E. R. Andrew, *Proc. Roy. Soc. B*, 1985, **225**, 399.
54. E. R. Andrew and E. Szczesniak, *Mag. Res. Med.*, 1989, **10**, 373.
55. E. R. Andrew, *Mag. Res. Med.*, 1991, **17**, 22.

Biographical Sketch

E. Raymond Andrew. *b*. 1921. B.A. (Physics), M.A., Ph.D., Sc.D., Cambridge University, UK, Hon. D.Sc. Turku, Poznan, Leipzig, FRSE and FRS. Postdoctoral fellow, Harvard with E. M. Purcell. Lecturer, St. Andrews University, Scotland. Professor of Physics, University of Wales, Bangor. Professor and Dean of Science, Nottingham University, England. Currently Research Professor, University of Florida, USA. President, Groupement AMPERE, 1974–80. President, ISMAR, 1983–86. Editor, *Magnetic Resonance in Medicine*, 1983–91. Four books: Nuclear Magnetic Resonance, Magnetic Resonance and Related Phenomena (jtly), Clinical Magnetic Resonance (jtly), NMR in High Magnetic Fields (jtly), 325 publications. Research interests: NMR in condensed matter, NMR imaging, MR in medicine.

Anet, Frank A. L.: A Lapsed Organic Chemist in the Wonderland of NMR

Frank A. L. Anet
University of California, Los Angeles, CA, USA

INTRODUCTION

I first heard about NMR in 1954 when I was a postdoctoral fellow in a natural products laboratory headed by Léo Marion at the NRC (National Research Council of Canada) in Ottawa. Close by was H. J. Bernstein's Raman spectroscopy laboratory. Communication between these two research groups on the social level was greatly helped by occasional evening bridge games. The organic chemists thus learned that H. J. Bernstein and W. G. Schneider were getting expensive instrumentation to do a new kind of spectroscopy. I remember well the talk amongst the postdoctoral fellows: what were the odds that this spectrometer would turn out to be a white elephant because applications to chemistry would prove to be limited and fleeting? No one, of course, knew the answer to this question or remotely guessed the revolutionary influence that NMR would have on so many areas of science (including organic chemistry). In this contribution I describe especially how I entered the field of NMR and my early research in this area. My interests gradually shifted from natural product chemistry to physical organic chemistry and conformational analysis by means of dynamic NMR, to instrumentation and relaxation aspects of NMR. All along I maintained a strong connection with my organic chemistry colleagues.

UNIVERSITY OF OTTAWA

In September 1954 I joined the fledgling bilingual University of Ottawa. Ray Lemieux was the Chairman of the new Department of Chemistry and was most helpful to my career, not least because he himself got involved in NMR (with his student Rudy Kullnig) in collaboration with the group at the NRC at a very early date.

As a result of intense efforts by Ray Lemieux, a 60 MHz NMR spectrometer was funded by the NRC and installed in early 1959 at the University of Ottawa. At the time, few universities had NMR spectrometers, and even fewer organic chemists had good access to an NMR spectrometer (J. D. Roberts at Caltech was a prominent exception). I was very lucky indeed.

I had become interested in obtaining NMR spectra on a new alkaloid even before the University of Ottawa had acquired its own 60 MHz NMR spectrometer. Harold Bernstein at the NRC ran a 40 MHz spectrum of an alkaloid that we knew contained a pyridine ring from its UV absorption, and the NMR spectrum immediately (and correctly) told us that it was a 2,3-disubstituted pyridine. From an unsplit methyl peak signal in the spectrum we concluded (incorrectly, as we showed later) that a methyl group was bonded to a quaternary carbon. We published these results in 1958 in my 20th paper[1] (and the first one to include NMR data); a reference to this paper found its way into Pople, Schneider, and Bernstein's classic book[2] on NMR, published in 1959. The appearance of an unsplit methyl signal in a CH_3-CH moiety, where the chemical shift difference was large compared to the vicinal coupling constant, expected to be about 7 Hz, subsequently impressed on me the importance of NMR spectral analysis. When I understood what was going on, I wrote a paper[3] which was published in 1961 on the nature of the signals of C-methyl groups, and this explained many anomalous 'coupling constants' involving methyl groups in steroids and other compounds; it anticipated later research by others on virtual coupling. Although spectral analysis is becoming almost a lost art in the midst of so-called 'modern NMR', it is in fact just as useful and necessary as it has ever been, in my own experience.

My interest in reaction mechanisms led me to study the spectra of the isomeric 2,3-dibromobutanes and this work,[4] published in 1959, also foreshadowed an important concept in the understanding and analysis of complex spectra, namely subspectrum analysis. Here again methyl signals that I had (naively) expected to be doublets instead showed six lines; a full paper was published in 1962.[5]

Work on the configuration of enzymatically produced deuterio-L-malic acid, the use of remote deuteration in spectral analysis, and the determination of the negative sign of the geminal coupling constant in CH_2DOH were published[6–8] in 1960–1962 and all involved deuterated compounds. The latter work employed a special irradiation scheme because the standard decoupling methods for relative sign determination were not applicable. I used the decoupling theory published by Bloom and Shoolery;[9] I was of course not aware of the extensive investigation on 'spin tickling' done by Anderson and Freeman[10] and submitted and published at almost exactly the same time as my article; as it turns out, I had unwittingly spin tickled CH_2DOH! The frequency stability of the decoupler (made by NMR Specialties) was actually too poor for spin tickling, but I found a simple way to stabilize it. This was my first venture into NMR hardware and I was so encouraged by its success that, despite knowing very little electronics, I later decided to build a whole spectrometer!

The use of deuterium to simplify spectra and later to investigate isotope effects on chemical shifts has been a recurring theme in my work. Other continuing topics have been conformational investigations of ring systems, restricted rotation, and atom inversion, and here also deuterium substitution combined with dynamic NMR has been vital. My first encounter with dynamic NMR was accidental and I did not immediately recognize it. In 1959, I measured the spectrum of an alkaloid, strychnospermine, which I had related chemically to strychnine as a part of my Ph.D. work with Sir Robert Robinson at Oxford University. The coalescence temperature for one of the protons at 60 MHz was close to room temperature and the signal was so broad as to be invisible (the alkaloid is an *N*-acetylindoline derivative); all the other signals were sharp. Our probe initially did not allow the temperature to be varied, and thus I did not realize what was happening until several years later.[11]

The importance of magnetic equivalence and nonequivalence and my interest in spectral analysis forced me to learn some group theory and to make use of quantum mechanics; I

developed a strong interest in symmetry properties which ultimately extended well beyond NMR. The breaking of symmetry in a molecule by isotopic substitution particularly fascinated me. For example, the boat-shaped 1,3,5,7-cyclooctatetraene in solution gives only a single line in its proton spectrum at all temperatures, even though the molecule has two different vicinal coupling constants. The bond shift process that exchanges the double bonds with the single bonds does not affect the spectrum. The ^{13}C satellites of this line show a dynamic NMR effect at about $-10\,^{\circ}C$, allowing the barrier to the bond-shift process to be measured. This, by the way, was a predicted encounter with dynamic NMR, a technique that fitted ideally with my aspiring physical organic interests. I promptly submitted a communication on the cyclooctatetraene work to the *Journal of the American Chemical Society* and soon received a signed referee report from Jack Roberts at Caltech. He informed me that he and his student, George Whitesides, had made similar observations, so it was fortunate that I had not delayed submitting a paper. It was published in 1962[12] with a mention of Roberts and Whitesides's work.

UNIVERSITY OF CALIFORNIA, LOS ANGELES

In 1962, I received a phone call from Saul Winstein asking me whether I would like to come to UCLA as a visiting professor for one semester and teach a graduate course in physical organic chemistry. I accepted and my wife and I spent the first half of 1963 in Los Angeles, where the winter temperatures are more like those in Sydney, where I had done my undergraduate work, than in Ottawa. This initial contact led to my joining UCLA in the summer of 1964.

At UCLA, my students and I used a 60 MHz Varian spectrometer with a 12-in. magnet and an internal lock and frequency sweep system that I had built in Ottawa and brought with me. Other organic chemistry students used the convenient new Varian A-60 spectrometer, which however lacked the decoupling and very low-temperature capability that we had added to the older spectrometer. A little later we also used a Varian HA-100 spectrometer that the department acquired.

The years 1963 and 1964, spent partly in Los Angeles and Ottawa, were quite productive on both the organic chemistry and NMR fronts. Ring processes in 1,3,5-cycloheptatriene,[13] deuterated cyclooctane[14] and cyclohexene,[15] restricted rotation in benzaldehyde,[16] and nitrogen inversion in aziridines[17] started a lasting interest in low-barrier dynamic NMR processes. We also used NMR extensively in our research on alkaloids,[18] to detect some unusually stable hydrogen-bonded dimers,[19] and in the first synthesis of a benzocyclopropene derivative.[20]

Tony Bourn, a postdoctoral student from Randall's laboratory, who had helped elucidate in Ottawa the ring-inversion and bond-shift processes in derivatives of cyclooctatetraene,[21] came with me to UCLA. He carried out a careful study of the ring inversion in cyclohexane-d_{11},[22] following earlier preliminary work.[23] Tony was also involved in a very important paper, the first use of the proton–proton NOE for structural purposes.[24] We were trying to detect a possible but undoubtedly small and unresolved coupling between two strongly sterically compressed protons. We irradiated one of the signals and immediately noticed that the height of the other signal had increased, but when we tried to measure the expected decrease in linewidth, we found that there was none! Clearly the area of the peak had increased. We then found that we could get a similar behavior in *N*,*N*-dimethylformamide, but only when the methyl group *cis* to the formyl proton was saturated. This kindled my interest in relaxation and resulted in many hours over the years spent with Abragam's book. While on the subject of relaxation, I might mention a short stay in 1971 at the General Electric Company visiting George Levy and working on ^{13}C relaxation problems.[25] Much later (1989) I spent a short time, together with my student Dan O'Leary, with Chuck Wade and Bob Johnson at the IBM laboratories in Almadén, where we found a ^{13}C resonance having a T_2*longer* than T_1.[26] During the late 1980s, the extraordinary relaxation properties of aromatic protons in viscoelastic micellar solutions were elucidated.[27,28]

Work at UCLA in the 10 years after I joined, some in collaboration with Chris Foote, Don Cram, Herb Kaesz, and Saul Winstein, was highly productive and was initially done on 60 and 100 MHz spectrometers. Maurice St.-Jacques, Mark Henrichs, Jim Sudmeier, Mary Brown, Jan Sandström, Geo Schenck, Larry Bock, Linda Sweeting, Duncan Mullis, Maurice Brookhart, François Leyendecker, and O. Abrams participated in this research, which is too extensive and varied to discuss here.

By 1964, Varian Associates had demonstrated the usefulness of superconducting solenoids for NMR and had built a 200-MHz prototype NMR spectrometer for DuPont. I applied to NIH for a grant to buy a superconducting solenoid from Varian and to build the rest of the (sweep) spectrometer myself. After some time the grant was funded, but then Varian announced they were stopping the production of solenoids until they had solved severe problems with unexpected quenching. After about six months Varian decided that they would only produce complete 220 MHz spectrometers, and not individual solenoids. I ultimately ordered a solenoid from Magnion, a company with no experience in NMR. Because of the delay, new niobium–titanium wire with a large amount of copper for stabilization had become commercially available and was far better behaved than the niobium–zirconium wire with only a thin copper coating that had to be used earlier by Varian. Another fortunate accident was that Magnion decided to make a solenoid with a bigger bore than Varian was using.

I built a very simple spectrometer from a 70 MHz frequency synthesizer and pulse generator (both from General Radio) and some Hewlett Packard double-balanced mixers for time sharing rf switches and phase detectors. Gwen Chmurny worked with me trying to find deuterium resonance at 38.4 MHz, which was hampered by the field homogeneity being a factor of 10 worse than the specification, and by the solenoid being far from persistent. We returned the solenoid to Magnion a couple of times, waited several months each time, but never received a satisfactory product.

Ned Baker at Dow Chemicals had also ordered the same kind of solenoid as we had from Magnion and was helpful to us. The welded superconducting joints made by Magnion were not persistent and were remade by Craig Bradley with a cold-welding machine lent to us by Ned. Craig built most of the spectrometer. We published our first two papers[29,30] on dynamic NMR processes that could only be poorly or not observed at lower frequencies while the spectrometer was still under construction. Craig's thesis,[31] which was submitted in early 1970 just before he joined Bruker, was on NMR

instrumentation (plus a few applications); he had originally wanted to work with me on natural products, a field that I decided not to pursue once at UCLA.

Another person who was helpful to us, especially in shim coil design, was Joe Dadok at Carnegie-Mellon. We soon added ^{13}C and ^{11}B capabilities to our spectrometer, which operated at 59 kG (5.9 T, 251 MHz proton frequency) in a time-shared frequency sweep mode. We managed to acquire a Data General Nova computer with 24 kbytes of memory, an ASR 33 teletypewriter, and a fast paper tape reader. Tony Cheng and I programmed the Nova in assembler language and Vladimir Basus built A/D and D/A interfaces to the spectrometer, to which a pulse capability was added. A little later we thankfully acquired a hard disk and more memory. Of course, in only a few years the hardware was almost obsolete, something that has not changed to this day.

Using the 251 MHz spectrometer, we determined the conformational properties of a large number of molecules, mostly by dynamic NMR in association with molecular mechanics calculations, and we did isotope effects and relaxation studies. The persons doing this work were: Tony Cheng, Vladimir Basus, Roy Easton, Lech Kozerski, Peter Degen, Jostein Krane, Gerald Buchanan, Armand Dekmezian, Issa Yavari, Mehran Ghiaci, Tarik Rowdah, Joseph Wagner, and Mike Squillacote.

I do not have space to recount here Jane Strouse's work with matrix shim coils or the design and winding of an Nb−Ti superconducting solenoid. A proton frequency greater than 400 MHz was reached, although we chose to operate the spectrometer at 396 MHz. We described our efforts at several ENC meetings in the late 1970s. This spectrometer was used in the next few years by myself, Dan Donovan, and Brad Bacon and regularly (once a week) by Fred Hawthorne's students at UCLA to obtain ^{11}B spectra of carboranes.

The departmental NMR facility at UCLA, which was then under the direction of Jane Strouse, had been using a JEOL FX-90Q and a Bruker WP-200 spectrometer for several years to which it added a Bruker AM-500 MHz spectrometer in 1984. These instruments were used by Xia-Hui Ji, Kaozheng Li, Zhihong Tan, and Jaemin Park in a variety of NMR projects. Max Kopelevich synthesized a chiral compound containing a $-CH_2D$ group where the two diastereotopic protons have observably different chemical shifts.[32] If the $-CH_2D$ group is replaced by a $-CHDT$ group, the two diastereomers that result have observably different ^3H chemical shifts, which were assigned in work done by Dan O'Leary in collaboration with Heinz Floss and co-workers at the University of Washington.[33] In our most recent work, done in collaboration with Martin Saunders and co-workers at Yale University, Darón Freedberg obtained ^3He NMR spectra of ^3He encapsulated inside the fullerenes C_{60} and C_{70}.[34]

I have mentioned in the text or references nearly all the persons who worked with me on NMR at the University of Ottawa or at UCLA; recent outside collaborators whose names I have not mentioned yet are: George Olah and Surya Prakash (University of Southern California), Kurt Mislow (Princeton), Jay Siegel (UCSD), Leo Paquette (Ohio State University), and Phil Williams (UCB). Thanks are due to all of them, to the granting agencies that supported our work, and to my predecessors and contemporaries in NMR for making NMR a wonderland for me.

REFERENCES

1. F. A. L. Anet, and C. R. Eves, *Can J. Chem.*, 1958, **36**, 902.
2. J. A. Pople, W. G. Schneider, and H. J. Bernstein, *High-Resolution Nuclear Magnetic Resonance*, McGraw-Hill, New York, 1959.
3. F. A. L. Anet, *Can. J. Chem.*, 1961, **39**, 2262.
4. F. A. L. Anet, *Proc. Chem. Soc., London*, **1959**, 327.
5. F. A. L. Anet, *J. Am. Chem. Soc.*, 1962, **84**, 747.
6. F. A. L. Anet, *J. Am. Chem. Soc.*, 1960, **82**, 994.
7. F. A. L. Anet, *J. Am. Chem. Soc.*, 1962, **84**, 1053.
8. F. A. L. Anet, *J. Am. Chem. Soc.*, 1962, **84**, 3767.
9. A. L. Bloom and J. Shoolery, *Phys. Rev.*, 1955, **97**, 1261.
10. R. Freeman and W. A. Anderson, *J. Chem. Phys.*, 1962, **39**, 1518.
11. F. A. L. Anet, *Can. J. Chem.*, 1963, **41**, 883.
12. F. A. L. Anet, *J. Am. Chem. Soc.*, 1962, **84**, 671.
13. F. A. L. Anet, *J. Am. Chem. Soc.*, 1964, **86**, 458.
14. F. A. L. Anet and J. S. Hartman, *J. Am. Chem. Soc.*, 1963, **85**, 1204.
15. F. A. L. Anet and M. Z. Haq, *J. Am. Chem. Soc.*, 1965, **87**, 3147.
16. F. A. L. Anet and M. Ahmad, *J. Am. Chem. Soc.*, 1964, **86**, 119.
17. F. A. L. Anet and J. M. Osyany, *J. Am. Chem. Soc.*, 1967, **89**, 352.
18. F. A. L. Anet, M. Z. Haq, N. H. Khan, W. A. Ayer, R. Hayatsu, S. Valverde-Lopez, P. Deslongchamps, W. Riess, M. Teruback, Z. Valenta, and K. Wiesner, *Tetrahedron Lett.*, **1964**, 751.
19. F. A. L. Anet and J. M. Muchowski, *Proc. Chem. Soc., London*, **1962**, 219.
20. R. Anet and F. A. L. Anet, *J. Am. Chem. Soc.*, 1964, **86**, 525.
21. F. A. L. Anet, A. J. R. Bourn, and Y. S. Lin, *J. Am. Chem. Soc.*, 1964, **86**, 3576.
22. F. A. L. Anet and A. J. R. Bourn, *J. Am. Chem. Soc.*, 1967, **89**, 760.
23. F. A. L. Anet, M. Ahmad, and L. D. Hall, *Proc. Chem. Soc., London*, **1964**, 145.
24. F. A. L. Anet and A. J. R. Bourn, *J. Am. Chem. Soc.*, 1965, **87**, 5250.
25. G. C. Levy, J. D. Cargioli, and F. A. L. Anet, *J. Am. Chem. Soc.*, 1972, **95**, 1527.
26. F. A. L. Anet, D. J. O'Leary, C. G. Wade, and R. D. Johnson, *Chem. Phys. Lett.*, 1990, **171**, 401.
27. F. A. L. Anet, *J. Am. Chem. Soc.*, 1986, **108**, 7102.
28. F. A. L. Anet and D. J. O'Leary, *J. Magn. Reson.*, 1990, **86**, 358.
29. F. A. L. Anet, C. H. Bradley, M. A. Brown, W. L. Mock, and J. H. McCausland, *J. Am. Chem. Soc.*, 1969, **91**, 7782.
30. F. A. L. Anet, J. C. Jochims, and C. H. Bradley, *J. Am. Chem. Soc.*, 1970, **92**, 2557.
31. C. H. Bradley, Ph.D. Thesis, University of California, Los Angeles, 1971.
32. F. A. L. Anet and M. Kopelevich, *J. Am. Chem. Soc.*, 1989, **111**, 3429.
33. F. A. L. Anet, D. J. O'Leary, J. M. Beale, and H. G. Floss, *J. Am. Chem. Soc.*, 1989, **111**, 8935.
34. M. Saunders, H. A. Jiménez-Vázquez, R. J. Cross, S. Mroczkowski, D. I. Freedberg, and F. A. L. Anet, *Nature (London)*, 1994, **367**, 256.

Biographical Sketch

Frank A. L. Anet. *b* 1926. B.Sc., 1949, M.Sc., 1950, University of Sydney, Australia, D. Phil., 1952, University of Oxford, UK.

Postdoctoral work at Oxford and the National Research Council of Canada, Ottawa. University of Ottawa, Ontario, Canada, 1954–64; University of California, Los Angeles, CA., 1964–present. Emeritus Professor of Chemistry. Approx. 220 publications. Research interests include conformations of organic molecules, dynamic NMR, molecular mechanics, isotope effects in NMR, relaxation phenomena, NMR instrumentation, and helium-3 NMR of fullerene–helium compounds.

Arata, Yoji: Early Days of NMR in Japan

Yoji Arata

University of Tokyo, Hongo, Tokyo, Japan 113

In 1959, when I became interested in NMR as a graduate student majoring in organic chemistry, only a few NMR instruments had been installed throughout the whole of Japan. Using a low magnetic field strength which gave the proton resonance at 56.44 Mc/s on a Varian instrument then in operation at the Japan Atomic Energy Research Institute, I had difficulties in analyzing the three-spin proton spectrum of acrylic acid which had been measured with the help of Ichiro Yamaguchi and Naohiro Hayakawa at the Institute. I had to face a number of difficulties in the spectral analysis. The first was the problem of a severe signal overlap encountered at the low magnetic field which was eventually overcome by making use of the solvent effect of benzene. This was followed by the more difficult problem of the spectral analysis of the strongly coupled three-spin system. Hiroshi Shimizu, who was a research associate in Professor Shizuo Fujiwara's laboratory at the University of Tokyo, and I developed a least-squares method for the spectral analysis of strongly coupled spin systems. However, at that time, numerical calculations could only be done using a hand calculator available from the Tiger Computer Company. I had to spend at least a week, if I was lucky, to reach a converged solution.

However, in 1961 the first digital computer in Japan became available to us. This was the Parametron PC-1 computer built by Professor Hidetosi Takahasi and his graduate student Eiichi Goto at the Physics Department of the University of Tokyo. Although the computer memory was only 256 words, one word being 24 bits, this was sufficient to allow a tremendous speeding up of the calculation. In most cases, one overnight calculation was sufficient to reach the refined sets of parameters for the three-spin system.

The calculation became even faster when Hidetosi Takahasi's group built their second computer PC-2 with 1024 words. With the help of Takao Iijima and Isao Suzuki, who were then at the Department of Chemistry, University of Tokyo, I was able to write a program in machine language for PC-2 for spectral analyses of the proton spectra of strongly coupled spin systems. I used the program for the analyses of the spectra of amino acids and published a series of papers in the *Bulletin of the Chemical Society of Japan* and the *Journal of Molecular Spectroscopy*. By that time Masatami Takeda and Oleg Jardetzky had already published a report on their successful attempt to use NMR for conformational analyses of some of the amino acids. This experience eventually led me to join Oleg Jardetzky's group at Stanford in 1971, where I started a proton NMR study of proteins. Since then I have spent more than 20 years engaging in multinuclear magnetic resonance molecular structural analyses of antibodies.[1]

Based on my experiences since the early days of my NMR career, I should like to make the following comments. One is related to the algorithm of fast Fourier transformation (FFT). The development of the FFT algorithm has a long and interesting history. The FFT algorithm dates back to 1903, when Runge exploited symmetry and periodicity to simplify the numerical calculation of Fourier transformation. In 1965, Cooley and Tukey published their well-known paper describing the FFT algorithm. Although the names of those associated with the history of FFT have been recorded, probably one exception only is that of Hidetosi Takahasi.

Many of us in the Japanese scientific community involved in numerical calculations using Fourier transformation know that Hidetosi Takahasi deposited his own FFT program in the library of the computer center at the University of Tokyo. Everyone who knows him well agrees that Hidetosi Takahasi is a virtuoso in physics. However, for those with the background of Western civilization he might appear an enigmatic person. He was not at all interested in what was going on outside his office, and in most cases was not interested in publishing what came to his mind either; it was his belief that physicists had to create everything on their own initiative. Toshiko Tochigi, a former associate of his, recalled that Hidetosi Takahasi was a quiet man who talked very little about what was in his mind. He showed her once his program for the computation of a Fourier transformation, and made some suggestions about the revision of his program. According to the record left in the computer center at the University of Tokyo, the final version of Hidetosi Takahasi's program was deposited on August 23, 1966. It is not my intention at all to claim that Hidetosi Takahasi was the first man in the world to have developed the FFT algorithm, but I should simply like to stress that as early as the mid-1960s an FFT program was being used successfully in Japan, independently of what was going on in the rest of the world.

Second, I should like to comment on the theoretical analysis of the effect of anisotropic Brownian motion of molecules on their nuclear relaxation. In virtually all papers published outside Japan, the work of D. E. Woessner is cited as the first report on this subject. This paper was published in the August 1, 1962 issue of the *Journal of Chemical Physics*. Very little, however, is mentioned even in Japan about Hiroshi Shimizu, who published his independent analysis of the effect of anisotropic Brownian motion in the August 15, 1962 issue of the same journal. My concern is that Shimizu's manuscript was received in the office of the Journal on June 6, 1961 and was printed more than one year later, whereas Woessner's manuscript was received on April 25, 1962. In addition to this important work, Hiroshi Shimizu has made a tremendous contribution to the theoretical analyses of nuclear magnetic relaxation; most of his work is summarized in his Ph.D. thesis (University of Tokyo, 1961). Unfortunately, before the dawn of FT NMR, experimental NMR techniques were at a very primitive stage and it was virtually impossible for Hiroshi Shimizu to perform any experimental study to follow what he had predicted on the basis of his theory. He left NMR soon after he finished his Ph.D. work and became interested in the theoretical treatment of irreversible processes in a more general sense. He is now the Director of The 'Ba' Research Institute, Kanazawa Institute of Technology and International Media Research Foundation, and has published a series of interesting pieces of work relating to the theory associated with analyses of irreversible processes in biological systems.

Before closing my brief recollections of the early days of NMR in Japan, I should like to mention the name of Kazuo Tori, who to our great shock passed away in 1982 at the age of 51 when he was Research Director, Division of NMR

Spectroscopy, at Shionogi Research Laboratories, Shionogi & Co., Ltd. His contribution to the development in Japan of the use of NMR in the field of organic chemistry was phenomenal. It is unfortunate that his days coincided with those of CW 100 Mc/s one-dimensional NMR. In view of his scientific achievements which amounted to more than 230 papers, I am certain that with modern multidimensional techniques he would have made a tremendous contribution to exploring the fascinating world of NMR in the field of organic chemistry.

This brief note is dedicated to the memory of the late Dr. Kazuo Tori. I thank Dr. Yoko Takayama, Shionogi & Co., Ltd. for giving me a chance to talk to her and recall the days when we both enjoyed discussions with Dr. Kazuo Tori. I also thank Dr. Hiroshi Ozawa and Toshiko Tochigi, Computer Center, University of Tokyo, and Professor Toshiyasu Kunii, Aizu University, for discussing the scientific achievements of the late Professor Hidetosi Takahasi. Discussions with Professor Masatsune Kainosho, Tokyo Metropolitan University, have always been encouraging and stimulating in continuing my NMR career.

REFERENCE

1. Y. Arata, K. Kato, H. Takahashi, and I. Shimada, *Methods Enzymol*., 1994, **239**, 440.

Biographical Sketch

Yoji Arata. *b* 1934. B.S., 1956, Ph.D., 1963, Chemistry, University of Tokyo. University of Electro-Communications, 1960–65; Department of Chemistry, University of Tokyo, 1965–82; Department of Biophysics and Biochemistry, University of Tokyo, 1982–86; Faculty of Pharmaceutical Sciences, University of Tokyo, 1986–94; Water Research Institute, 1994–present. Approx. 200 publications. Current research specialty: NMR structural analyses of larger proteins.

Arnold, James T.: Early Perceptions in Nuclear Magnetic Resonance (NMR)

James T. Arnold

P.O. Box 314, Los Altos, CA, USA

The purpose of these paragraphs is to try to recreate some of the atmosphere and the views and perceptions of the early days of NMR as I saw them. My point of view was that of a callow graduate student at Stanford University, a novice confronting other far more experienced graduate students and the very accomplished faculty of the Stanford University Physics Department. Standout names in the faculty included Paul Kirkpatrick (X-Rays), David Webster (Electromagnetism), Leonard Schiff (Theoretical Physics and Quantum Mechanics), William Hansen (Microwaves and NMR), Willis Lamb (Quantum Electrodynamics), and Felix Bloch (Theoretical Physics and NMR). The stature of these professors has been recognized in a notable array of distinctions, including two Nobel Prizes. It was my good fortune to be on the scene when there was room for another candidate in the NMR cadre. The first student to complete his NMR thesis, Martin Packard, was retained as a first year instructor, and I was attracted to his continuing work with Bloch. I was introduced to the NMR activity through low level screwdriver and soldering iron contributions to Packard's project at the time, and happily found myself accepted as a member of the NMR team when Professor Bloch gave me a most friendly and graceful interview.

There was no way to know at the time the extent to which application of NMR would expand to become a very productive contributor to the scientific community and to mankind. NMR was first an investigative method for physicists, delivering at the first instance a table of nuclear moments. It then became, second, a major means to elucidate molecular structures for chemists. Still later, it has come to furnish a powerful diagnostic tool for medicine, providing noninvasive tomographic imaging with views and contrast not previously available to X-ray shadow viewing or tomography.

The progress of NMR has also produced important advances in collateral technology. First, the art of producing very high magnetic fields of ultrahigh quality has been advanced beyond the most visionary expectations, beginning by pushing the advantage of iron as far as saturation properties permitted, and then progressing to an ascending series of cryogenic superconducting magnets.

Second, signal levels in NMR are painfully small, and from the beginning, it was necessary to improve the 'receiver' element's noise figure and other qualities as far as Nature would permit. To access the information content of the NMR signal requires acquisition of low level closely spaced radiofrequency spectral components. Stability of electronics was a crucial contributor to acquiring signals through integration over longer and longer periods of time.

Quite apart from the integrating time, extended to improve signal-to-noise in order to capture these spectral signals, the time required to sweep through each spectral component scanned necessarily increases as the reciprocal square of the fineness of the lines as resolution is improved. This condition grows out of the fact that the nuclei interrogated are gyrators whose motion continues after excitation, with substantial memory of the interrogation event. Probing the spectrum requires a time period to wait for that motion to relax for each spectral line passed, and this puts severe demands on the stability of the excitation frequency and the magnetic field that they remain stable during an experiment to a scale much finer even than parts per million. To help solve this problem, at a later date, a remarkable shortcut to acquire signals from all the spectral components simultaneously, superposed in the time domain, was brought to bear. The spectral information was present, albeit in an unfamiliar form as the Fourier transform of the familiar spectra in the frequency domain. This method was originally suggested by Russell Varian, long before the computation problems could be addressed with machines of sufficient power and speed. When it became possible with the development of better computers and electronics, the Fourier transform process produced useful analysis at a dramatically increased rate, and the development of transform methods under the demands of NMR has provided benefits in other areas of scientific application.

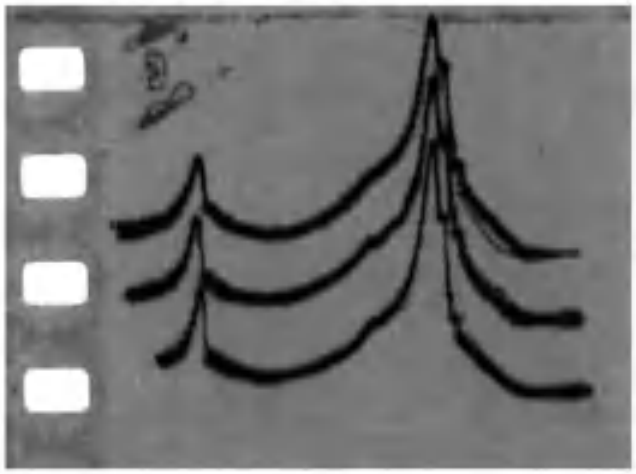

Figure 1 First record of chemical shift structure in proton NMR spectra. (a) Acetic acid; (b) ethyl alcohol (Reproduced by permission from *Journal of Chemical Physics*, 1951, **19**, 1608)

Looking back to the earlier days, I have been struck by the extent of progress and understanding achieved with relatively simple hardware, and with good fortune, as to some physical constants in the chemical aspects of NMR spectroscopy. Before my thesis was assigned, I participated with Packard and Dr. Shrinivas S. Dharmatti, a postdoctoral investigator visiting Stanford from the Tata Institute in India, in an experiment that demonstrated two separate chemical shifts of protons in the same molecule (acetic acid), see Figure 1. Credit for suggesting that an NMR 'spectrum' arising from distinguishable protons in a single molecule could be observed belongs to Dharmatti. The delicate separation of the chemically shifted lines is field dependent and amounts to just a few parts per million. It was only with very small samples and much empirical searching in the magnet for a 'homogeneous spot' that the separation of the spectral lines could be observed.

From acetic acid, we graduated almost immediately to ethyl alcohol (ethanol) and other alcohols as sample, observing in ethanol a gratifying set of three spectral lines corresponding to the three separate chemical groups, methyl, methylene, and hydroxyl that chemists describe to make up the structure of this molecule. The outcome of these experiments led to a publication in (appropriately enough) the *Journal of Chemical Physics*, (1951, **19**, 507). That publication was the springboard that propelled NMR into the world of organic chemistry, elucidating chemical structures by interpreting their proton NMR spectra. The NMR spectrum for ethanol, resolved as to the chemical shift, is also shown in Figure 1.

The magnet used for the experiment was a 12-in. electromagnet designed by Harry E. Weaver. The magnet produced a field of 7000 G (0.7 T), in a magnet gap of ca. 1.5 in. This field led to a proton resonance frequency of approximately 30 Mc/s. (I shall continue to use the names of units that were familiar to us at that time.) Although the poles were basically round with square edges, quasi Rose shims had been added to improve the homogeneity of the field in the center of the magnet. The difficulty of achieving a field of sufficient uniformity will be appreciated when one considers the fact that geometrical disturbances of the magnet pole caps must measure on a scale of parts per million multiplied by powers of the reciprocal ratio of the sample size to the gap width and the space wavelengths of the disturbances. In no way could the magnet parts be fabricated to the necessary precision, and much of the experimental effort was directed to discover the most favorable saddle points in the field. With luck, a sample of 1 mm diameter could be maneuvered to find a region with sufficient homogeneity to resolve the spectra sought.

I mentioned above the luck of some physical constants as they related to the spectra observed. First, the electron (diamagnetic) shielding that gives rise to the grosser spectral shifts of lines in the NMR spectrum (chemical shifts) is proportional to the magnetic field, and, in fields of a few thousand gauss, easily achieved in the laboratory, has a value significantly greater than the (then) apparent linewidths of the individual spectral components. Second, the time required at this stage of resolution to scan the spectrum was a few seconds or tens of seconds at most, and the magnetic field could be held with reasonable stability over this timescale. The luck that these two features fell into a range that could be reached with the experimental equipment achievable at that time evolved into a challenge to improve the apparatus further in order to probe deeper into the interactions that gave rise to the spectra. We observed, first in the Weaver magnet, some evidence that there might be a finer structure, not yet resolved, in the spectrum of ethanol. When conditions were just right, we actually observed indications of further splitting of the chemically shifted lines seen up to that time. The challenge which became my thesis topic was to construct apparatus that had the stability and resolution to reveal that structure with useful precision.

Throughout this early exploratory period and in the progressive steps that followed, we, the cadre of graduate students in NMR, benefited from the welcome encouragement and intellectual support, and the intuitive insight of Felix Bloch. His scientific stature and contributions were recognized in the fall of 1952, when his award (with Edward M. Purcell) of the Nobel Prize was announced for the work in NMR.

It is also appropriate to acknowledge that financial support for the project and the graduate students was, in part, derived from grants from the Office of Naval Research (ONR) and the Atomic Energy Commission (AEC). This support was not in the grand scale of later government grants to academic institutions, and we were always looking for means to save money by building our own equipment and adapting items from the rich legacy of military surplus that became available following World War II. (Part of the reason for choosing the frequency of about 30 megacycles per second grew out of the fact that the intermediate frequency amplifiers of many WWII radars centered on this frequency. These very high quality amplifiers could be bought for pennies on the surplus market.)

In supplement to the financial support derived from the ONR, an anonymous grant of $5000 was donated for use at Bloch's discretion. He announced to me that if I could design a permanent magnet (that should be much more stable in the short term than the electromagnets used up to that time for NMR), the $5000 fund was available to finance it. This was very exciting. After calculations and investigations we determined that if we chose available low-cost materials that could be handled in the Stanford Physics Department shop, we could construct a magnet of the sort we wanted within the budget available. The largest dollar investment would be to cover 18 bars of Alnico totaling about 1400 lb.

The detailed design of the magnet is described in an article in *Physical Review* (1956, **102**, 136); I will comment here on just a few features to emphasize the atmosphere in which the leading edge of physics often took place in the years just after WWII.

The frame of the magnet was constructed of yoke members each comprising 12 lamina of cold rolled steel (low carbon) 1×6 in. in section which could be manhandled in the shop and then bolted together. Planning of the project included a note that it would be necessary to magnetize the Alnico with a closed gap; it was therefore required to design the magnet with an adjustable gap, still maintaining considerable mechanical precision. The adjustable gap was provided by mounting one pole of the magnet on a precise roller arrangement carried on accurately machined rails mounted to the main yoke structure with provision for empirical micro adjustment. Since the magnetic forces would be quite large, more than 5 tons, a powerful mechanism had to be devised to adjust the gap opening. We settled on a hydraulic solution. The main hydraulic cylinders were surplus US Air Force B-17 aircraft landing gear shock struts purchased for $10 apiece. A surplus hydraulic pump was also acquired to supply the

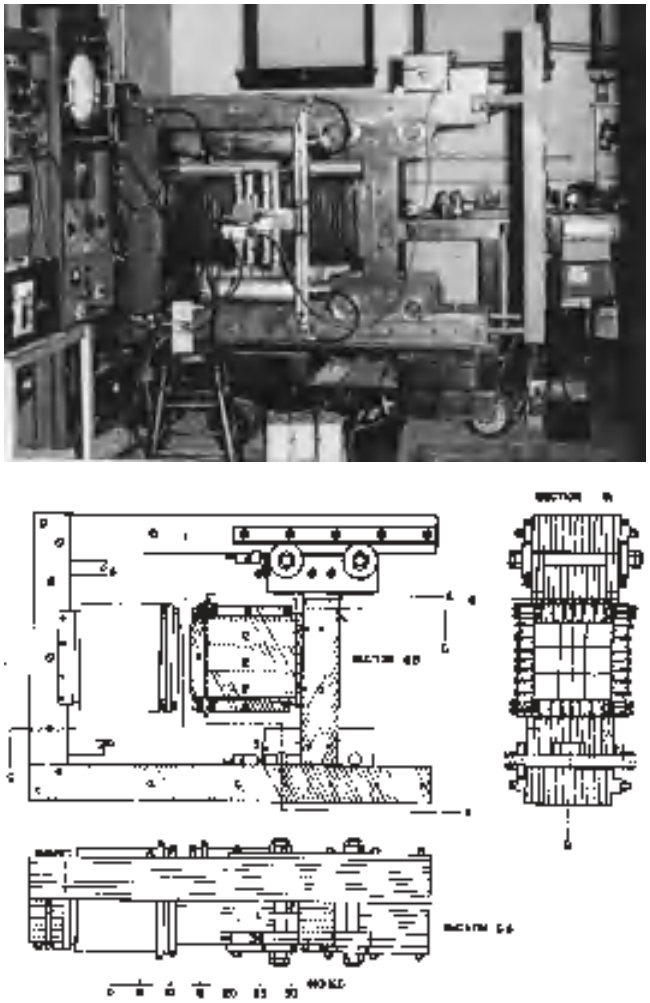

Figure 2 The Stanford permanent magnet for high-resolution NMR spectroscopy (Reproduced by permission from *Physical Review*, 1956, **102**(1), 136)

motive power. The entire magnet was mounted on a wooden cart of massive proportions which rolled on three wheels, again surplus, originally used as tail wheels for the Navy SB-2-C dive bomber ($4 each). A drawing and photograph of the magnet are shown in Figure 2.

The Alnico bars were seated in the respective poles, nine bars, each about 14 in. long and of 4 × 4 in. section, to each pole. We felt it essential to control the geometry of the Alnico faces as well as possible in order to achieve the best uniformity of field ultimately in the gap. To ensure the geometrical precision, it was necessary to grind the Alnico bars in place, and since we had no grinder available to do this we improvised an outboard grinder from a defunct milling machine. Patience delivered what we deemed a usable geometry. Alnico is very hard and subject to spalling, so patience was required to achieve the Alnico faces needed. Calculations of the field to be expected from the Alnico, and the need to provide smoothing of local perturbations of field on the Alnico faces, led us to provide pole caps shaped and tapered to reduce the area of the gap by about 10%. The caps were made of two slabs of heat treated very pure Armco 'ingot iron' which was said to be very uniform and magnetically soft, and could be expected to smooth out field irregularities occurring at the Alnico faces. The pole caps were carefully machined and were ground flat and parallel in an outside shop, this being the only 'outsourcing' that was undertaken in the magnet construction. Finally assembled and resting on its wooden carriage, the magnet was complete although not 'charged'.

The charging of the magnet was accomplished with a closed gap, using copper coil windings preassembled on the poles with a calculated minimum of copper and a maximum of current. Again, in the interests of holding costs down, the magnet was energized using local and borrowed facilities. The laboratory was near an electrical substation at Stanford where three-phase 60 cycle 4360 V power was available. To use this source, we benefited from the kindness of Varian Associates who loaned us six large ignitrons to rectify and switch power. The expected current would be about 400 A, giving a power level of nearly 2 MW. The magnetization was carried out at 1 a.m. so that the surge (and possible actuation of circuit breakers) would not be noticed by other members of the Stanford community. Energizing the magnet required application of current for less than 1 s to provide a magnetizing force sufficient to saturate the Alnico.

In order to confirm that sufficient magnetizing force had been applied, at the suggestion of Professor Bloch a single turn of wire had been thrown around the pole structure and connected to a 19th century ballistic galvanometer from one of the student laboratories. As the galvanometer delivered the expected reading, we were confident that magnetization was achieved and we disconnected the charging circuit. Later, when the gap was opened, measurements of the field produced very welcome numbers. The final field in a gap of about 1.5 in. was sufficiently above 7000 G that we could apply the prescribed stabilizing demagnetization, a step that brought the nominal field to a value suitable for 30 Mc/s proton resonances.

The performance of the magnet was very gratifying. Stability was considerably improved compared with the electromagnet earlier used, although we were beset with a livable but inconvenient long-term reversible variation resulting from temperature changes. Also, the properties of the magnet with the necessary long poles of low permeability Alnico did not provide as much magnetic shielding as would a comparable electromagnet with soft iron poles. To counter these two problems, we determined first the times when the temperature effects were minimum (very early in the morning) in order not to compromise the linearity of the very slow sweeps that were necessary as the lines became narrower. For the slowest sweeps, on occasion, we actually used the thermal drift which was extremely steady, if not altogether linear.

The harmful effect of diminished shielding was to admit fluctuations of the field when an operator moved in the laboratory, he carrying the usual burden of keys, shoe nails, belt buckles, pocket knives, tools, etc. The perturbation of the field resulting from the operator moving about was sufficient to displace lines in the spectrum by unacceptable amounts. When data for record were acquired, the operator (me) stripped (with a bit more than necessary drama) to underwear in order not to disturb the field.

To furnish the most uniform field in order to achieve high resolution of spectra, a number of measures were undertaken, some of which were rational and productive. The sample used was made as small as the low signal level would permit. The materials used in the NMR 'probe' comprising the housing of the crossed coils, the coils themselves, and all of the parts

that were anywhere near the sample had to be selected for complete absence of any ferromagnetic material and for the lowest possible magnetic susceptibility. Parts were cleaned in dilute HCl to digest any small particles of iron that might have been left from machining processes. The need for these precautions may be appreciated with the recollection that a 10 μm ferromagnetic particle saturated in a large magnetic field will produce a field gradient comparable to chemical shifts at 1 cm distance, and for 'nonmagnetic' materials, even diamagnetic susceptibilities are in the parts per million range and could influence the field adversely at the site of the sample when linewidths are less than one-tenth of this figure.

The disparity of the lowest possible susceptibility to be found in materials for the probe and the requirement for spectral resolution was resolved by observations of Professor Bloch and others (I particularly remember discussions with Harry Weaver and Martin Packard) to the point that in a magnetic field originally uniform, the introduction of a body of uniform susceptibility and circular (or ellipsoidal) geometry will provide that within the body the field will also be uniform, although slightly decreased for diamagnetic bodies. The field outside the body will be distorted to bring about this accommodation. At the point of this observation and onward, NMR probes were designed with religious observance of the need to surround the sample with nested sections conforming as far as possible to spheres or long cylinders.

Many other measures were undertaken to improve the quality of the spectra. Two stand out, one being a logical correction process to improve the quality of the magnetic field, namely, the introduction of adjustable 'current shims' which could add small changes to the local field gradients in order to bring about greater uniformity. The original shims were of crude geometry and haphazard operation. Current shims have since been very much refined, now being constructed according to an appropriate geometrical expansion of terms devised to furnish a nearly orthogonal set (less than complete) up to the fourth order. The original current shims, which were simply circular, did make it easier to maneuver the field and the location of the sample in the field, albeit with very tedious, nonconverging adjustments, to improve the lineshapes.

The second measure to improve the lineshape was an outcome of a leap of intuition on the part of Professor Bloch. He called me into his office one afternoon and said that if a means could be devised to stir up the sample in a time short compared to broadening of the line brought about by variations of the magnetic field (measured in units of the reciprocal proton frequency) the lines should be narrowed accordingly inasmuch as the nuclei would sense just the average magnetic field. As in all of the best inventions, once said, the logic of this concept was obvious, and I set to work immediately to make a tiny paddle wheel to stir up the sample (which at that time was held in a 4 or 5 mm tube). The paddle was made up of glass, possibly not the best choice of material in view of its necessarily unfavorable (noncircular) geometry and uncertain magnetic susceptibility. The little paddle was attached to a tiny turbine by a long glass shaft and was spun by a stream of argon gas. (We had a cylinder of argon that had been just a little used and was available. At our very low rate of consumption that abandoned resource lasted more than a year.)

By 11 p.m. I had the first results and observed notable improvement from the very first application. The greatest improvement was transient each time the turbine was turned on, although considerable improvement was sustained for as long as the stirring continued. We quickly understood that the initial kick of starting the turbine provided a more thoroughly random stirring of the entire sample, while the steady state provided only rotation. In the steady-state condition, there was no averaging of fields along the axis of rotation and the gradient in that direction brought about a residual broadening. Sample 'stirring' was accomplished in later versions just by spinning the sample tube itself, the geometry of the tube conforming to the required circular section, with no paddle inside to disturb the magnetic field. This approach provided very effective averaging in the azimuth of rotation, and the operation to improve lineshape was simplified to the extent, in this order, that only variations along the rotation axis needed to be adjusted or compensated.

The outcome of these moves, and a lot of patience, was a very satisfying exploration of the ethanol molecule. The luck of natural constants, expressed first in the value of the chemical shift perturbations, held further as we were able to resolve the interior structure of the three originally observed chemically shifted lines. The chemical shift originates in the local diamagnetism of electron orbital motion at the three chemically distinguishable sites in the molecule. A second perturbation, quantum mechanical in character and different from the chemical shift, gives rise to a discrete splitting of the chemically shifted components independent of the main magnetic field. This perturbation is called spin–spin interaction.

In the Hamiltonian description, this interaction can be expressed as a separate and different energy term involving the quantized angular momenta of the chemically shifted groups, and for ethanol (and many other organic samples) the energy of the perturbation is conveniently smaller than the chemical shift term (in the range of magnetic fields used at the time) by about an order of magnitude. Including the dominant term due to the moment of the protons in the primary magnetic field, there are three energy terms with successively decreasing values in the Hamiltonian description. This circumstance leads to a very convenient Hamiltonian analysis, using perturbation methods, of the spectral properties to be found in the experiment. When a Hamiltonian description is undertaken with the dominant interaction of nuclear moments in the main magnetic field, and with the two added terms representing chemical shift and spin–spin interaction, respectively, the finer displacements and multiplicity of the energy levels can be computed by perturbation theory. With the interaction with the main field described as the first-order solution, the results of the perturbation calculation conform very well in the number, locations, and amplitudes of peaks, to the best resolved spectra observed in experiment, with the calculation taken to the third order in the perturbation expansion.

In the first order of the spin–spin energy term (the second-order perturbation of the main term of the Hamiltonian), we expect, and see in the experiment, the component of the methyl group of protons to be split into a triplet, representing the three quantum mechanical combinations of spin of the two protons in the adjacent methylene group. The component of the spectrum due to the methylene group can be doubly split by the influence of the four combinations of spin of the three protons in the methyl group compounded with the two states of the proton in the hydroxyl group. Indeed, in the right circumstance, at this level of resolution eight lines can be seen

experimentally, along with the expected tripling in the group of lines due to the hydroxyl proton.

As higher resolution was achieved experimentally, additional splitting was revealed. For example, in the methyl group, the three peaks resolved in second order were themselves split, the central peak showing a doublet and the two side peaks showing triplets. This further structure conformed faithfully to the results of the next order of perturbation calculation with constants already determined from the first-order displacements observed. These aspects of the spectra furnish a very nice confirmation of the quantum mechanical behavior of the ethanol system in the NMR experiment.

The frequency interval of the splitting at this level was in the scale of a fraction of a cycle per second, and with the broadening of lines due to spin–lattice relaxation no further splitting or displacement could be resolved. In order to obtain spectra at this degree of resolution, very long sweep times (extending typically to 30 min) were used, and all of the tricks that we could devise to maintain stability and uniformity of field had to be invoked. Figure 3 shows ethanol spectra progressively better resolved along with the calculated values for the peaks taken to successively further order. Except for an artifact of a slightly nonlinear sweep at the highest resolution, agreement between the calculated and observed spectra is very good.

The study of ethanol yielded one additional dramatically significant observation. On occasion, when the resolution of the methyl group was very good the resolution of the methylene and hydroxyl groups seemed equivocal. In other experiments, the methylene group showed a reasonably sharp first-order splitting to only four lines, while the hydroxyl proton furnished a single sharp line. Experiments varying the 'pH' of the ethanol by adding very small amounts of HCl and NaOH and with slight dilution with water led to a graded series of spectra with second-order splitting into four components for the methylene group with a single hydroxyl proton line at one extreme, and with eight methylene components and the hydroxyl proton 'group' split into three components with nearly the same sharpness as the finest lines of the methyl group.

These phenomena were explained by presuming an exchange process for the hydroxyl proton at rates that were dependent on the chemical matrix surrounding the ethanol molecules, most pointedly expressed in the 'pH' of the sample. The model used in the explanation presumed that the hydroxyl proton of ethanol could exchange with free hydrogen ions in the matrix, originating either from water or from trace addition of acid or base, or even from dissociated ethanol. The rate of exchange would be proportional to the number of free ions in the matrix. In the 'purest' samples, the rate of exchange was less than the spin–spin splitting (defined in frequency units), and the hydroxyl protons of ethanol were associated sufficiently long to define the states leading to the structural features of the associated hydroxyl spectral group. When there were sufficient numbers of free ions in the matrix, on the other hand, exchange events were much more rapid, and the residence time of the hydroxyl protons was so short that their interaction was simply averaged over the ensemble of states in the methylene groups of the many ethanol molecules visited. Under these circumstances one would find the hydroxyl proton line discrete and narrow as in a free proton, and the corresponding spectral presentation of the methylene group would be found structured only as to the interaction with the methyl group permanently attached.

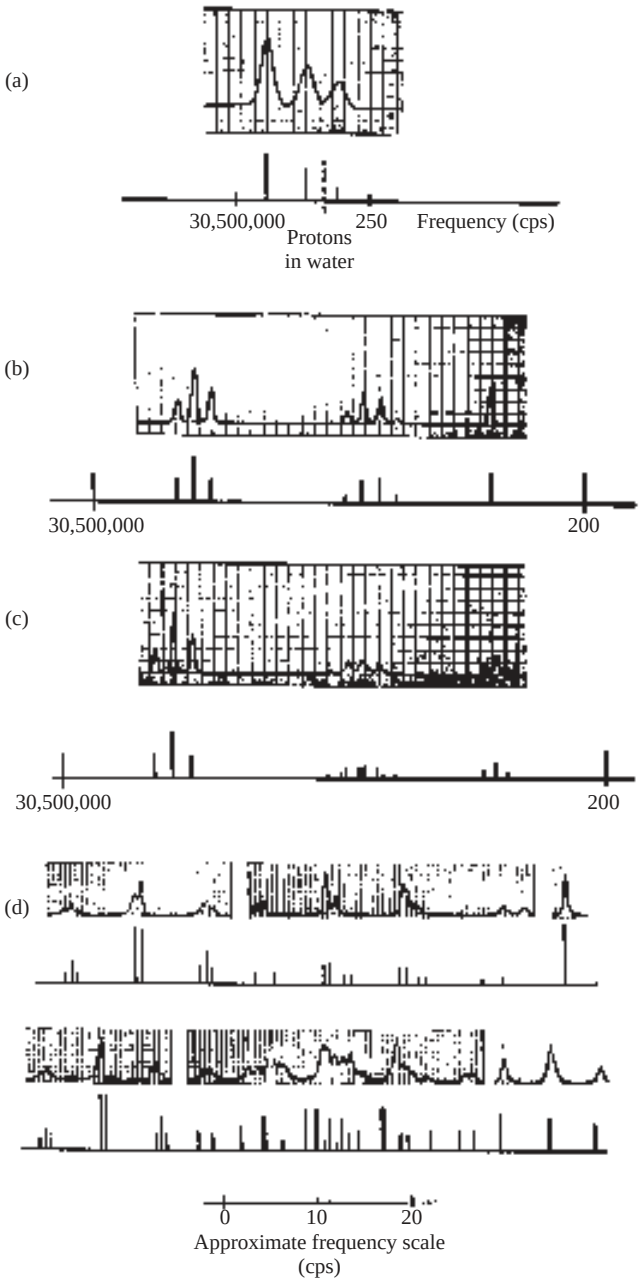

Figure 3 Spectral lines for ethyl alcohol in successive steps of resolution. (a) Resolved to first order (chemical shift) with calculated spectrum. (b) Resolved to second order showing the gross spin–spin splitting. The hydroxyl proton association time is short. (c) Second-order structures with association time sufficient to exhibit the interaction of methylene and hydroxyl proton. (d) Third-order structure resolution of the three chemically shifted groups with the positions and amplitudes of lines calculated to third order with the two extremes of hydroxyl proton association (Reproduced by permission from *Physical Review*, 1956, **102**(1), 136)

This observation of the exchange event could be carried through a range of association times, beginning with the longest (of the range 1 s or greater) in 'pure' ethanol with sharp lines, through samples that exhibited association times (in range a few tenths of a second) comparable to the reciprocal of

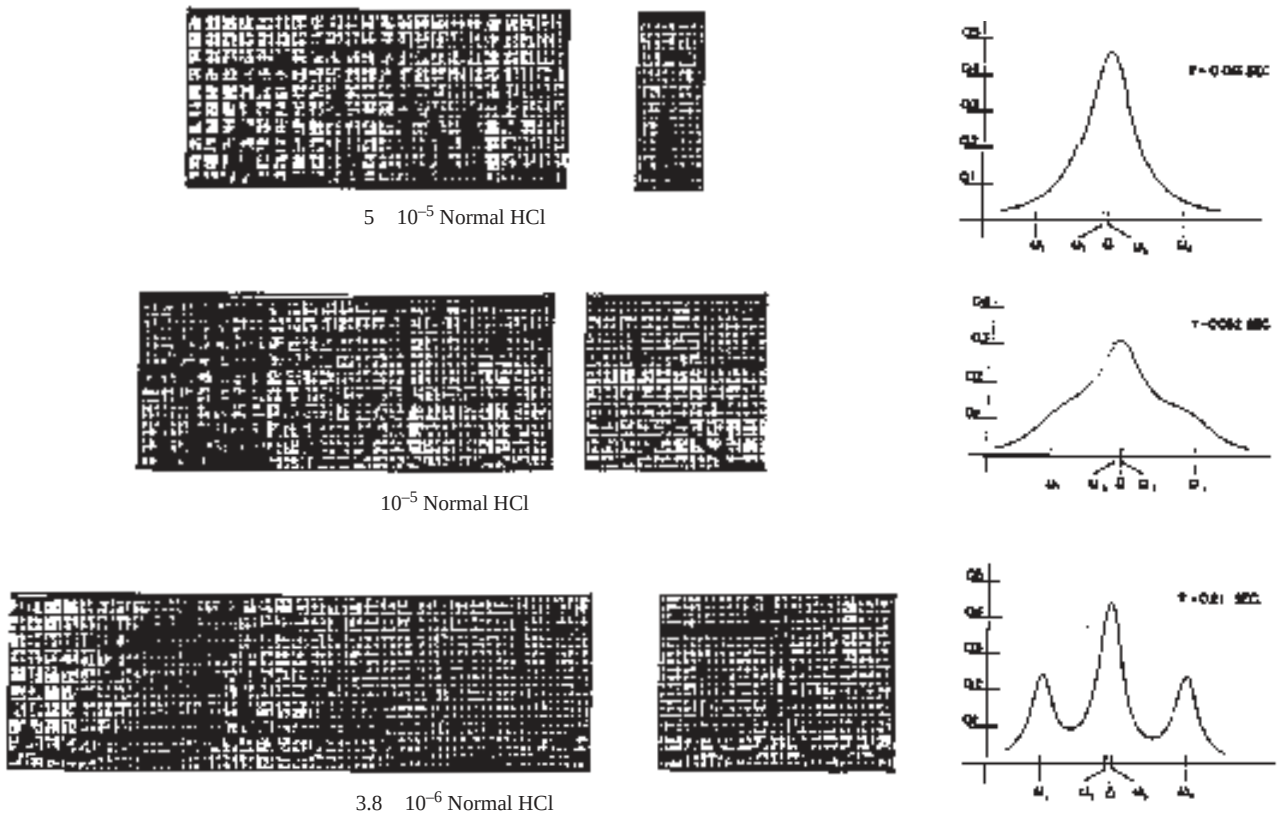

Figure 4 The effect of association time in the hydroxyl proton. Intermediate cases were calculated for comparison. In the third spectrum, the association time must be about 1 s (Reproduced by permission from *Physical Review*, 1956, **102**(1), 136)

the spin–spin interaction (expressed as frequency), ultimately to very rapid exchange times (above 10 per second). The sharp lines at the extremes have been described. At the intermediate range, the lines of the methylene and hydroxyl groups were actually broadened enough almost to obscure the splitting corresponding to the second-order (spin–spin interaction) calculation of energy levels, even though the lines in the methyl group showed good resolution of fine lines. At the extremes of fast exchange, the line structure of the methylene group showed the splitting corresponding to the second-order calculation split only by the adjacent methyl group. Figure 4 shows the theoretical and experimental spectra for the three cases.

The magnet used for these experiments had an interesting career. It was used for two additional Ph.D. theses under Professor Felix Bloch, one of which was the definitive standout work of Weston Anderson. In 1954, the European Centre for Nuclear Research (CERN) was inaugurated in Geneva, Switzerland. Professor Bloch was invited to be the first director, and, to maintain continuity for his students, he asked that two of us (Weston Anderson and myself) and the equipment for high-resolution NMR be transported to Geneva to continue the work. I had just finished my thesis, and Anderson was in the final processes of his work. When we were invited to accompany Bloch with the equipment, needless to say we accepted the opportunity with enthusiasm!.

Beginning in Geneva, and continuing thereafter at Stanford for something over two years, the magnet and the equipment were used for experiments extending the work on simple organic molecules. Examples were chosen to illustrate particular aspects of the energy relationships, with Anderson's particularly penetrating methods using multiple frequencies. Additional experiments in Geneva and later at Stanford with a variety of timed excitation sequences began to explore time domain NMR, explicitly not to say at this stage as yet anything resembling transform spectroscopy.

At Stanford University after the final graduate student, the magnet was retired. Shortly thereafter, Stanford received a request that it be turned over to the Smithsonian Institute where it now waits for possible inclusion in a historical display of 20th century scientific events.

In keeping with the narrative character of this writing, I have, for the most part, omitted literature references. Clearly the work that took place at the time was carried out at several institutions in a very open environment of communication and publication. I have focused on the work taking place at Stanford University. Additional groups were also very active, and much of the accomplishment of the times must be credited to the many other members of the NMR community as a whole.

It is most appropriate in closing, as I speak for myself and for other members of the Stanford NMR cadre, emphatically to express appreciation for Professor Felix Bloch as a person of graceful humanity, culture, and personal kindness, and to recognize his truly exceptional qualities as a great physicist. As a gifted scientist of truly outstanding stature he was known and appreciated by a wide range of professional fellows. We, his students, were a very privileged few.

Biographical Sketch

James T. Arnold. *b* 1920. B.A., 1942, Ph.D., 1954, Physics, Stanford University, USA. US Navy (aviator and qualified test pilot), 1942–47. Oberlin College, laboratory instructor. Introduced to NMR at Stanford University by Professor Felix Bloch. Assistant, CERN, 1954, Assistant Professor of Physics, Oregon State, 1957. Engineer and Senior Scientist, Varian Associates, 1958. Approx. 30 publications, 12 patents. Research specialties: NMR, optical pumping, mass spectrometry, cardiac diagnostic ultrasound.

Bain, Alex D.: Early Development of Homonuclear 2D NMR (From the Outside)

Alex D. Bain

McMaster University, Hamilton, Ontario, Canada

The central mystery of pulse and Fourier transform NMR has always been the effect of a pulse on a system of nuclear spins. Pulse sequences are made up of both pulses and delays, but the evolution during a delay is relatively straightforward. In the absence of any rf, the various transitions simply oscillate at their resonant frequency and decay. A pulse is more complex.

The development of 2D NMR required an understanding of a pulse. First of all, what does a pulse do, and second, how can you control it? What a pulse does can still be mysterious and counter-intuitive, even if the rf terms dominate all the others in the Hamiltonian (a 'hard' pulse). The simple vector picture often works, but it breaks down just when you need it. This later spawned many theoretical descriptions of the effects of a pulse.[1,2] The development of one of these, the superspin formalism,[2] was guided by two important papers, both from Ernst's group.[3,4] I think they laid many of the foundations of pulse and multidimensional NMR.

The first paper[3] discussed flip angle effects in Fourier transform spectra. In principle, FT spectra resemble the true spectrum only in the limit of small flip angles. Nobody used small flip angles, and the fact that your very new and very expensive Fourier transform spectrometer might not give the same spectrum as your old reliable CW machine was perhaps somewhat disturbing at the time. That particular problem was not serious, as it turned out, but this paper was one of the first to point out how much difference there is between the way a coupled spin system responds to a pulse and a delay. A doublet evolves as two lines during a delay, but during a pulse it is much better to think of a doublet as the sum of the two lines and the difference between the two lines. As we see from polarization transfer experiments, it is the differences amongst members of a multiplet that are the most interesting and which are responsible for the most important phenomena.

These flip angle effects provided an early case where the response to a pulse had to be considered correctly. A pulse is equivalent to a rotation of the frame of reference, but in the simple vector picture it does not much matter whether the magnetization is rotated one way or the frame of reference is rotated the other. For a coupled spin system, the distinction is crucial—it must be the frame that is rotated. This is because the spin that is being observed and the spin that is causing the splitting are both being rotated simultaneously. This is where angular momentum and spherical tensors come in. They provide an elegant and complete way, via Group Theory, to describe what happens to anything when the frame of reference is rotated. A spherical tensor description of NMR transitions is then a natural way to describe a pulse. Spherical tensors had already been introduced into NMR to simplify relaxation calculations,[5] but they turned out to be much more useful for spin dynamics because of their rotation properties.

The angular momentum arises because a transition between two spin states inherits the combination of the spin angular momentum of the initial and final states. This angular momentum of the transition was dubbed superspin,[2] by analogy with superoperators in Liouville space. It is an angular momentum like any other, with a length and a z component. This then provides a complete way of describing a pulse, with no restrictions on whether the spin system was weakly coupled or whether the pulse phase or flip angle were multiples of $\pi/2$.

The second important paper represents the first use of phase cycling in a nonintuitive way.[4] Phase cycling schemes such as CYCLOPS had been used for a long time, but these could be understood relatively easily with vectors. Even though COSY is implicit in the first papers on 2D, it is arguable that this paper on SECSY represents the first homonuclear shift correlation. While this paper was being published, homonuclear shift correlations had been observed, basically as artifacts in J-resolved spectra,[6] but there were two copies of the spectra which came to be known as P and N type peaks. The SECSY paper showed how one set could be eliminated by cycling the mixing pulse. Even though it is quite easy to show mathematically why this works,[7] it is difficult to have a good physical picture.

Phase cycling is a critical part of all pulse sequences. Still, however, there is no perfect way to design a phase cycle for a given pulse sequence. It is easy to put one together, based on some simple principles and experience. It is also straightforward to analyze whether it will work or not. However, there is usually some redundancy in these schemes and no clear way to get some sort of a minimal scheme. In general, however, phase cycling works very well in producing reliable, robust pulse sequences.

These two papers,[3,4] although not often cited, represent the real foundations of two-dimensional NMR, in my opinion. The combination of what a pulse does, along with what we can do to control it by phase cycling, provided all we needed to know.

REFERENCES

1. O. W. Sørensen, G. W. Eich, M. H. Levitt, G. Bodenhausen, and R. R. Ernst, *Prog. Nucl. Magn. Reson. Spectrosc.*, 1983, **16**, 163.
2. A. D. Bain, *Prog. Nucl. Magn. Reson. Spectrosc.*, 1988, **20**, 295.
3. S. Schäublin, A. Höhener, and R. R. Ernst, *J. Magn. Reson.*, 1974, **13**, 196.
4. K. Nagayama, K. Wüthrich, and R. R. Ernst, *Biochem. Biophys. Res. Commun.*, 1979, **90**, 305.
5. N. C. Pyper, *Mol. Phys.*, 1971, **21**, 1.
6. A. D. Bain, R. A. Bell, J. R. Everett, and D. W. Hughes, *J. Chem. Soc., Chem. Commun.*, **1980**, 256.
7. A. D. Bain, *J. Magn. Reson.*, 1984, **56**, 418.

Biographical Sketch

Alex D. Bain. *b* 1948. B.Sc., 1970, Toronto, M.Sc., 1972, U.B.C., Ph.D., 1975 Cambridge (Ph.D. supervisor, Ruth Lynden-Bell, who introduced him to NMR). After postdoctoral work, was employed as Applications Spectroscopist by Bruker-Spectrospin Canada for six years. Since 1986 has been Professor of Chemistry, McMaster University. Approx. 50 publications. Research interests: spin dynamics, relaxation, chemical exchange.

Balaban, Robert S.: Personal Perspective on the History of NMR

Robert S. Balaban
National Heart Lung and Blood Institute, National Institutes of Health, Bethesda, MD, USA

I began my involvement in NMR with a NATO fellowship in 1980 to work in Professor George Radda's laboratory at the University of Oxford. At that time George's laboratory was very active in renal biochemistry studies in collaboration with Brian Ross. This research related to my thesis work on optical spectroscopy studies on the kidney. Upon my arrival Joe Ackerman had just finished his work on the development of the surface coil, which truly opened the door to many in vivo NMR biological applications. The laboratory was a unique environment where physicists, chemists, biochemists, and myself, the lone physiologist, were trying to learn from each other in this highly multidisciplinary field. It was a marvelous scientific environment, which illustrated to me the importance of these multidisciplinary approaches in the biological sciences. During this time J. Waterton and D. Gadian were developing $\boldsymbol{B}_1$ field spectroscopic imaging techniques, and K. Thulborn was showing that the relaxation properties of water could be used to monitor blood oxygenation and flow in situ, a procedure that would take almost 10 years to be fully developed in humans. Numerous studies were being conducted on the perfused heart, including the measurements of the cardiac ATP synthetic rate by P. Matthews.

My own work was mostly learning the physics and hardware associated with NMR, as well as ^{31}P NMR studies concerning the energetics of isolated renal tubules and mitochondria (with Gordon Wong). We also had a lot of fun trying to combine optical and NMR spectroscopic studies of metabolism on simple systems. The magnet schedule (a wide bore 180 MHz prototype) was two 24-h blocks every two weeks. Thus, I would spend all day and all night making mitochondria or renal tubules to run on the magnet. Of significance in these studies was the determination of phosphate metabolite distribution in the mammalian kidney and the visibility of ATP in the mitochondrial matrix. One morning, after a particularly long 24 hours of liver mashing, we were approached by a maintenance man in the building politely requesting the return of his floor polisher from the newly energized 2 T wide-bore magnet down the hall . . . . It turned out to be an even longer day . . .

From this initial experience in George's lab, it became clear that you should not only keep the door locked to your spectrometer but that NMR would provide an extremely important tool in the study of physiology. Upon arriving at the NIH in 1981, the scientific director of the NHLBI, Dr. Jack Orloff, was also convinced of this potential and began the NHLBI biological NMR program by purchasing a wide-bore 360 MHz magnet for the Chemistry Laboratory. I still remember the looks of horror as Jim Ferretti and Bob Highet watched me place the first live rat in their treasured new instrument. This began a very productive collaboration with Jim Ferretti in the utilization of 2D NMR techniques in the evaluation of complex enzyme kinetics in vitro and in vivo even though Jim still entered the room only after the rat was in the magnet . . .

During this time the serendipity of the biological applications of NMR spectroscopy became very clear. In one of our earliest studies we performed a series of studies with ^{14}N NMR attempting to measure the concentration and distribution of urea in the intact kidney (with Mark Knepper). However, our studies revealed a very broad and not very useful urea ^{14}N resonance (exchange broadening), but an extremely sharp and intense resonance in the region of trimethylamines. After a week of library and telephone interviews it was clear that no-one knew what this compound was in the kidney in the 20–80 mM concentration! It turned out to be the oxidation product of choline, betaine, and its discovery started a new area of research in renal studies on the role and regulation of these organic osmolytes in the protection and function of the kidney. Another serendipitous result was the discovery that adenylate kinase produces quaternary adenosine phosphate under physiological conditions (with Jim Ferretti and V. Kuprianov). These results clearly demonstrated that the scanning nature of the NMR experiment is of great value to the biologist since it provides information on parameters he/she would not have had the prior knowledge to suspect to be an important parameter. This has the important implication of showing the investigators a new direction which could have not been predicted a priori.

Dr. Howard Kantor arrived in my lab as a clinical associate. After attending the first SMRM meeting, where the difficulties of obtaining localized spectra from the heart were discussed, Howard suggested that if a coil could be fabricated on the end of a catheter he could get it into the heart to collect the localized spectroscopic data. Indeed, the quote I remember from Howard was 'To tell the truth, a coil would not be a big deal, you should see what we put in patients' hearts'. After designing several different coils, we finally reached our design specifications after numerous visits to the local plastic shops trying to find the best insulator and a small 50 Ω nonmagnetic coaxial cable. Next we needed a high field magnet large enough to fit a dog. At this time there were very few wide bore magnets capable of making this type of spectroscopic measurement. Thankfully, Dr. Richard Briggs had a 2 T system at the Hershey Medical Center, two and one-half hours north of Washington, and he agreed to collaborate on this project if we provided the animals. This resulted in many enjoyable trips to the chocolate town with premeasured animals in tow which would fit in Richard's magnet. Despite Howard's claims, the placement of the coil was not trivial, and we spent many, many hours in the rather hot catheterization lab wearing very heavy lead aprons working on the catheter coil placement. I think my lower back suffers more from that experience than the foolish years of football earlier in life . . . . However, in the end a very simple and robust procedure was developed which resulted in some of the earliest ^{31}P NMR studies on the effects of cardiac work on high-energy phosphates in vivo.

With our successful dog experiments, the NIH lab was expanded to include a 30-cm bore 4.7 T system with imaging gradients, and a new laboratory, The Laboratory of Cardiac Energetics, was created. Many fellows working on spectroscopic applications came through the lab at this time, including Alan Koretsky, Larry Katz, Fred Heineman, Dave Kim, Tom Scholz, Teresa Kassera, Maren Laughlin, and Mike Portman. These studies involved numerous aspects of cardiac energetics,

including cardiac cycle studies, hormonal stimulation, development and metabolic substrate dependencies. Indeed, this program is still a very large part of our research program today, and as a brief survey of the physiological literature will currently reveal, NMR has in general become a standard tool in the evaluation of physiological function.

Imaging gradients in the 4.7 T system provided a new tool into performing metabolic imaging studies. Two medical students, Paul Hsieh and Steve Wolff, started in the lab with an intense interest in imaging and began our metabolic and functional imaging program. With our long-standing interest in enzymatic rate measurements, it was not surprising that our first work was the generation of creatine kinase activity maps in the intact rabbit leg using ^{31}P NMR imaging. This was quickly followed by one of the first 'functional images' of the body, when Steve demonstrated the three-dimensional topology and kinetics of sodium washout during diuresis in the in vivo kidney using ^{23}Na NMR.

Our success in this rate constant imaging resulted in a late night discussion of transferring these ideas to ^{1}H studies. Our preliminary studies showed that we could improve the signal-to-noise of ammonia or urea detection by ^{1}H NMR by factors in excess of 1000 by using saturation transfer techniques, monitoring the exchange of water with these metabolites. In a field where improvements in S/N are usually measured in terms of factors of two or less, we were very excited about the use of this approach in vivo. Steve's first in vivo experiments were very successful, and large reductions in the water resonance were observed when he irradiated at the NH_3 or urea chemical shifts in the in vivo kidney. The problem was that no matter where Steve irradiated, over almost a 40 kHz bandwidth, a strong saturation transfer effect was detected on the water resonance. Furthermore, the distribution of this interaction did not track the concentration of ammonia or urea in the kidney. After several weeks of confirming that this was not due to some bizarre artifact in our sometimes reliable spectrometer, we confirmed that this was a real phenomenon with a defined bandwidth and spin lattice relaxation effect on the water protons. We quickly realized that this effect was not due to the presence of numerous exchanging metabolites in tissue, but must be due to a magnetization transfer effect between the solvent water and restricted motion protons associated with the macromolecules of the cell. These studies eventually led to the development of magnetization transfer imaging techniques, where the signal intensity in an image is modified by the degree of dipolar coupling to the macromolecular matrix, resulting in magnetization transfer contrast. Several fellows beside Steve and Paul provided key insights into this area, including Toni Ceckler, John Eng, and Teresa Fralix. The almost immediate clinical application of this laboratory result was also a very rewarding as well as surprising event since, as most basic researchers, we never expect our studies to have such an immediate impact on clinical practice.

The numerous successes around the world in the biological applications of NMR at 4.7 T and higher fields suggested that high-field ($>$1.5 T) studies on humans might be feasible and perhaps desirable. Several of the manufacturers had reached the same conclusions and had begun 4 T projects, which in 1987 were ready for more application studies and less technical development. After Dr. Orloff and Dr. Claude Lenfant, Director of the NHLBI, secured funding to begin a 4 T program in the NHLBI, a whole body 4 T system was purchased. This system was installed at the NIH in 1990 and after significant technical modifications has shown that our initial impression concerning the advantages of high magnetic fields in humans was correct. These studies have included functional imaging of the human brain with Bob Turner and Peter Jezzard, as well as a whole host of spectroscopic studies on the biochemistry and composition of the human body. Clearly the advantages of high field greatly helped our understanding of human biochemical and physiological function. However, much is left unknown.

Biographical Sketch

Robert S. Balaban. *b* 1953. B.S., 1975, Ph.D., 1980, Physiology and Pharmacology, Duke University, USA. First experience in NMR during postdoctoral fellowship with G. Radda at University of Oxford (1981). Joined National Heart Lung and Blood Institute NIH in 1982. Currently Chief, Laboratory of Cardiac Energetics. Approx. 200 publications. Research specialties: macromolecule/water magnetization transfer, in vivo NMR applications, coil development, tissue energetics, mitochondrial respiratory control.

Barfield, Michael: Thirty-Three Years of NMR Parameters

Michael Barfield

University of Arizona, Tucson, AZ, USA

In 1957 I had an encounter with a 40 MHz Varian NMR spectrometer (while employed at General Dynamics in San Diego), but it was a few years later that I actually started using NMR. In 1960 I joined the research group of David M. Grant at the University of Utah. Dave had recently joined the Chemistry Department as an assistant professor after completing a postdoctoral fellowship with H. S. Gutowsky and Martin Karplus at the University of Illinois. A project of immediate interest to me was the H–C–H angle dependence of geminal H,H coupling constants. Based on the H,D coupling constants for a series of deuterated compounds, it soon became apparent that this type of coupling was more sensitive to the number and orientation of adjacent substituents than to the H–C–H angle. Our attempts to use semiempirical valence bond theory to understand these factors were not successful until it became obvious that these types of geminal coupling constants were negative in sign. This was demonstrated by the relative sign measurements of Frank Anet and others reported at the NMR meeting in Boulder, Colorado in the summer of 1962.

After completing the Ph.D. work at Utah in 1962, I joined John D. Baldeschwieler's group at Harvard University as a postdoctoral associate. This research was in the general area of nuclear magnetic double resonance (NMDR) and it presented the opportunity to learn more about the instrumental and phenomenological aspects of NMR. When I started to look for a job, some of the industrial interviews were cancelled because there appeared to be no obvious applications for NMDR techniques. At Shell Development Company in Emeryville, CA, the person making an offer said that if I accepted an assistant professor position at the newly created University of South Florida (USF) in Tampa, I would never be heard from again.

At USF my attention returned to the theory of nuclear spin–spin coupling. It appeared that the conformational dependence of long range H,H coupling constants could also be explained via valence bond (VB) methods. During this period there developed a correspondence with Martin Karplus, which was to continue for several years and which was concerned, in part, with the popular misconceptions of the factors affecting *J* couplings. These problems were especially apparent in the often used and misunderstood terms 'through space' and 'through bond', which we defined in terms of a VB bond order formulation.

In 1964 I came across a paper entitled 'The Spatial Correlation of Electrons in Molecules' by J. E. Lennard-Jones (*J. Chem. Phys.*, 1952, **20**, 1024) which stimulated my interest in using density matrix techniques to study NMR parameters and the effects of electron correlation on *J* couplings. Following a move to the University of Arizona (1965), density matrix techniques were used to simplify previous MO and VB derivations and to develop new procedures including a VB formulation with an explicit sum over triplets. These methods were used for a large number of our studies, especially for factors affecting long range H,H coupling constants, *J* anisotropies, and studies of hyperfine coupling constants. In the 1960s a considerable effort was put into modifying the old polyatom SCF–MO program for use on our local computer to perform ab initio calculations of *J* couplings (Joanne Reed, Ph.D., 1971). Our ab initio results were consistent with those of other groups in demonstrating inadequacies at the Hartree–Fock level, and were abandoned in favor of semiempirical methods.

In 1969 Sever Sternhell (University of Sydney) came to Tucson to discuss long-range coupling constants. This was the beginning of a more than 25 year collaboration. In the period 1970–71 Milton D. Johnston, Jr., a postdoctoral fellow (now at USF), developed techniques for describing solvent effects on nuclear spin–spin coupling constants. These models, which made use of coupled Hartree–Fock theory and semiempirical MO methods, went through increasing degrees of sophistication starting with a reaction field model, a cluster model, and then a rotating cluster model. In 1972 I returned to the laboratory to learn the intricacies of Fourier transform NMR. This quickly led to collaborations on $^{13}C–^{13}C$ coupling constants with David M. Doddrell (then at Griffith University, Brisbane) and James L. Marshall (North Texas State University). During the period 1974–76, with the encouragement of Dave Grant, we became interested in the theory of chemical shielding and chemical shielding anisotropies.

During my sabbatical in Australia (1976–77) and David Doddrell's sabbatical in Tucson (1977–78) we investigated, with the mathematical expertise of Hans P. W. Gottlieb (Griffith University), some aspects of relaxation in paramagnetic species and structural effects on deuterium quadruple coupling constants. Experimental and theoretical studies of NMR parameters in bicyclic compounds were part of collaborative efforts with Ernest W. Della (Flinders University, Adelaide) and N. Dale Ledford (University of South Alabama). These and other experimental ^{13}C NMR studies in Arizona were accomplished by some outstanding graduate students including Stephen R. Walter (Ph.D., 1982), Abdulla S. Babaqi (Ph.D., 1982), and Lung-Fa (Jeff) Kao (Ph.D., 1983). Another experimental program initiated in 1979 used ^{13}C NMR to investigate polymer microstructure, especially for unusual species having all cyclobutane rings in the backbone. Key players in these studies include H. K. Hall, Jr. of this Department, Jeff Kao, Ray J. H. Chan, and visiting scientist Yinghong Mou.

With the help of Julio C. Facelli (visiting scientist, now at Utah) we continued with studies of *J* couplings. Our most recent effort on *J* coupling (in collaboration with William B. Smith, Texas Christian University) concisely demonstrates the way in which vicinal H,H coupling constants depend on both H–C–C angles and dihedral angles.

Following a sabbatical year (1986–87) in Germany, the major new areas of interest have been concerned with ab initio MO studies of chemical shielding emphasizing conformational dependencies of ^{13}C chemical shifts. The ab initio MO studies of conformational effects for chemical shifts in lactams and peptides were accomplished with the help of Ding Jiao (Ph.D., 1993). We have also used local origin methods in trying to understand transition metal shielding, especially

for molybdenum compounds in collaboration with John H. Enemark and a postdoctoral associate Jaime E. Combariza.

Biographical Sketch

Michael Barfield. *b* 1934. B.A., 1957, Ph.D., Chemistry, University of Utah, USA, 1962 (advisor David M. Grant). Postdoctoral fellow, Harvard University, 1962–63 (with John D. Baldeschwieler). Assistant professor, University of South Florida, 1963–65. Assistant professor, Associate professor, professor, University of Arizona, 1965–present. Approx. 100 publications. Research specialties: studies of NMR parameters, especially nuclear spin–spin coupling and chemical shielding.

Bax, Ad: NMR of Ethanol and Interferon-γ

Ad Bax
Laboratory of Chemical Physics, National Institutes of Diabetes and Digestive and Kidney Diseases, National Institutes of Health, Bethesda, MD, USA

GETTING STARTED

Ever since NMR was first discovered, NMR spectroscopists have been battling the technological problems that present the major barrier between creativity and experimental results. In the early 1970s, Toon Mehlkopf in the Applied Physics Department at the Delft University of Technology, The Netherlands, got so frustrated by the technical limitations of commercial NMR equipment that he decided to design and build one himself, the so-called 300-MHz project. The system included four home-built synthesizers and was controlled by a Hewlett Packard 21/M20 computer with 32 kbyte of memory. It was designed to be capable of both CW and pulsed NMR, including such important techniques as spin tickling, rapid scan correlation spectroscopy, DEFT and SEFT experiments, and a long list of other experiments that have long since been forgotten. In 1975, I was lucky to be accepted by Toon to work as an undergraduate student on the development of the pulse programmer and the data acquisition software of his spectrometer. Indeed, once completed in 1977, this spectrometer was capable of performing virtually any experiment. It also could acquire FIDs of up to 300 k Word at speeds of up to 45 kHz and average those to data stored in double precision on the disk. It also could execute pulse sequences of arbitrary length and complexity.

In the summer of 1977 when our group leader, Jaap Smidt, returned from a conference where he had heard Richard Ernst speak about two-dimensional NMR, our spectrometer was put to the true test. The main hurdle, it turned out, was for me to understand what Aue, Bartholdi, and Ernst were talking about in their historic paper.[1] After it slowly started to dawn upon me, it was relatively little work to write the required pulse program and data matrix transposition routine. About four weeks after Smidt's return, we had our first homonuclear J-resolved 2D spectrum.

When the next spring Mehlkopf and Smidt suggested that I continue to work for a Ph.D., I was excited about this opportunity, as well as by the idea that this would postpone my national service by at least four years. My only fear was that 'all experiments had already been invented', so what was I supposed to work on?

My first two papers were the result of a two-day trip to Zürich, where I visited the labs of Richard Ernst and Kurt Wüthrich. After Alex Wokaun very patiently but in vain had tried to explain to me the principles of multiple quantum NMR, I got into a heated debate with Kuniaki Nagayama, then a postdoc with Wüthrich, about obtaining absorption mode homonuclear broadband decoupled spectra. According to Nagayama, and he was right of course, one cannot get such a spectrum from a skewed projection of a homonuclear J spectrum because of the 'cross section projection theorem'. Back in the Netherlands, and still frustrated about having been 'set straight' by a biochemist, I came up with a way around this theorem: constant time spectroscopy. By keeping the time between the initial 90° pulse and the first detected data point constant and shifting the position of a 180° pulse [$90^\circ - (T - t_1/2) - 180^\circ - (T + t_1/2) -$ Acq.], I obtained a homonuclear decoupled spectrum of ethanol, and my first paper.[2] Little did I realize at that time how useful this silly idea would become in heteronuclear NMR of ^{13}C-enriched proteins, where it is now widely used to eliminate ^1J(C,C) couplings.[3]

Another esoteric idea that would later prove useful occurred to me after I had been wrestling my way through a stack of re- and preprints that Alex Wokaun had given me on my Zürich visit: pulsed field gradients. Clearly it should be possible to separate the different orders of multiple quantum coherence by means of pulsed field gradients. It took Toon Mehlkopf and electronics engineer Tom Tiggelman less than two weeks to build a pulsed field gradient device (with lock interruption) and implement it on the home-built 300 MHz spectrometer. Although the idea worked,[4] eddy currents induced by the pulsed field gradients were a serious problem—self-shielded gradients had not yet been invented—and discouraged me from further pursuing it. Nowadays, in protein NMR there is virtually no experiment left that does not significantly benefit from the use of pulsed field gradients with self-shielded coils.

OXFORD BLUES

When Ray Freeman, frustrated by an antiquated CFT-20, heard about Mehlkopf's 300-MHz project, he promptly offered him a job. Fortunately for me, Toon was unable to accept and he suggested that I might be interested in conducting part of my Ph.D. work with Ray in Oxford. The next three years were tremendously exciting for me. Not only is Oxford considered a Mecca for oarsmen—one of my favorite sports—but it also proved to be a very exciting place to live, with long-reaching consequences for my future social life.

Ray's brilliant insight in NMR and his enthusiasm for science tremendously stimulated his research group and convinced me that science could be very enjoyable indeed. The coffee and tea breaks, which typically would take at least an hour, were the highlights of the day, to the great frustration of Gladys, the cafeteria manager, who never managed to close early and go home. My stay in Oxford coincided with that of Malcolm Levitt, Gareth Morris, Tom Frenkiel, David Max, Stewart Kempsell, A. J. Shaka, and James Keeler. Needless to say, that this was a most inspiring working environment.

When I arrived in Oxford, Stewart had just come back from a conference where he had seen organic chemists measuring ^{13}C–^{13}C coupling constants from the satellites in a ^{1}H-decoupled ^{13}C spectrum. There should be a better way to do this he argued, and as I was considered to be 'the' multiple quantum expert from my previous pulsed field gradient multiple quantum work, I was asked whether multiple quantum somehow could help. And that was how the INADEQUATE experiment was born.[5] Although the concept of multiple quantum filtration was developed independently by the Ernst group,[6] the INADEQUATE experiment stole the limelight, not in the least because of the acronym that Ray had come up with, which stands for Incredible Natural Abundance

Double Quantum Transfer Experiment. It was not clear at that time that the extemely lengthy 128-step phase cycle that we proposed was doing nothing else but eliminating the 'T_1 memory' of the spins. Because the delay between scans was not much longer than the ^{13}C T_1, the z magnetization of the next scan would 'remember' the rf phases used in the preceding scan and therefore cancellation of the signal from isolated ^{13}C nuclei was not complete. By sheer coincidence, the order of the steps in the 128-step phase cycle would cause such effects largely to cancel.[7] Unfortunately, our complex phase cycle led to the idea 'the more phase cycling, the better—no questions asked'.

THE MILE HIGH CLUB

On the recommendation of Ray I went on to do postdoctoral work with Gary Maciel in his 'Mile High Proton Enhanced Nuclear Induction Spectroscopy' laboratory in Colorado. I could not have made a better choice. Gary was extremely enthusiastic and supportive of my rather crummy attempts to apply some of the high-resolution ideas in solids, none of which happened to work out too well. I was lucky to be in Gary's group at the same time as Nick Szeverenyi, who had a true fascination with building gizmos. My original prototype of a magic angle hopping device consisted of rubber bands and Q-tips and required the operator to yank twice every scan on a nylon string. Nick's design and construction of a stepper-motor driven hopping probe made the experiment actually work.[8] Another one of his challenging accomplishments at that time was the design and construction of a 'magic angle flipping' probe[9] which would alter the orientation of the rotor axis between the magic angle and the xy plane, twice per scan. The anticipated problem, to keep the spinner going, posed no real difficulty for Nick. The main problem turned out to be that after every 100 000 flips or so, the leads connecting the coil to the tuning capacitors would succumb to fatigue. This 'flipping probe' allowed us to do a 2D experiment where the isotropic ^{13}C shifts are detected during t_2 and the associated CSA powder pattern, scaled by $-\frac{1}{2}$, in t_1. The first powder patterns of dimethoxybenzene measured this way were highly distorted and exhibited some very unusual nonpowder pattern features. In search of the cause of the bizarre appearance of these patterns, I desperately—Waugh, forgive me—even started questioning the generality of 'coherent averaging'. Only by chance did we finally discover that these distorted patterns would turn 'normal' if one packed the spinner very tightly; otherwise the centripetal force of the spinner would cause a nonrandom orientation of the individual crystallites inside the rotor.

While I was studying the principles of solid state NMR, next door in the NMR Center Richard Griffey was trying to correlate ^1H and ^{15}N chemical shifts by selective coherent ^{15}N decoupling and observing the collapse of the imino proton doublets in ^{15}N-enriched tRNA. When Bruce Hawkins, manager of the NMR Center, mentioned this to me I knew there should be better ways to do this. Although in principle Geoffrey's 'Overbodenhausen experiment' (aptly named that way by Ray Freeman during one of our tea breaks, but now better known as heteronuclear single quantum correlation, or HSQC) would permit ^1H detection of the ^{15}N resonances,[10] an additional problem was posed by the intense H_2O solvent signal; solvent presaturation was not possible because of rapid imino proton exchange. Heteronuclear multiple quantum coherence (HMQC) solved this problem and allowed us to do the experiment using only a single ^1H pulse which was adjusted to have a null in its excitation profile at the H_2O frequency. After discussing the pulse scheme with Bruce, he built an inverse ^{15}N channel literally overnight and the next day we obtained a 2D $^1H-^{15}N$ correlation spectrum, first try! Even in retrospect this experiment, conducted on an old 360 MHz Nicolet spectrometer and using only 3 mg of a 25 kD macromolecule in H_2O, was quite impressive.[11] Although the same HMQC pulse schemes, together with a large number of alternative schemes, were proposed independently by the Australian group of Bendall, Pegg, and Doddrell,[12] the application of our experiment to a biological macromolecule and to natural abundance peptides was probably the main reason for the surge in popularity of these HMQC experiments. For me it was my first encounter with a biological application of NMR, and I liked it.

WELCOME TO THE GOVERNMENT

Although I loved Colorado, besides Gary Maciel none of the faculty at Colorado State were particularly impressed by my NMR experiments and I had to look for employment elsewhere. To my honest surprise, the National Institutes of Health offered me a tenure-track job. How on earth they could imagine that NMR, particularly the type of work I was known for, could benefit the NIH program was totally beyond me. Obviously, Ted Becker (the editor of this volume), Bill Eaton, and their colleagues at NIH had more foresight.

The first excitement occurred when Donald Davis, who had joined me for a sabbatical year, was trying to use Aksel Bothner-By's CAMELSPIN experiment[13] to measure NOE interactions under spin-locked conditions in a cyclic peptide that gave miserable spectra with the regular NOESY method ($\omega\tau_c \sim 1$). This CAMELSPIN experiment later became better known as ROESY, for rotating frame Overhauser enhancement (ROE) spectroscopy. Yes, for many proximate ^1H pairs in the peptide we observed beautiful ROE cross peaks with opposite phase to the diagonal peaks. However, there were also a number of cross peaks in phase with the diagonal, in apparent conflict with Aksel's predictions. Most notably, the geminal nonequivalent C^δ protons of a proline residue in the peptide showed a very intense positive cross peak. Considering the short distance between the two C^δ protons (1.77 Å) we had expected a very intense ROE cross peak for this ^1H pair, so why would it be of the wrong sign and have an intensity that exceeded that of the diagonal? It was my solid state NMR experience that tipped us off to the real cause of these anomalous cross peaks: they were due to homonuclear Hartmann–Hahn cross polarization.[14] Two resonances that feel the same spin lock rf field and that are J coupled should be subject to J cross polarization, just as in the heteronuclear case. Changing the offset and spin lock field strength indeed confirmed that these artifactual peaks were due to Hartmann–Hahn cross polarization. At the time, Donald and I suggested minimizing the Hartmann–Hahn artifacts by judiciously choosing the carrier position and the rf field strength.[14] A much neater solution was later proposed by

A. J. Shaka, another Freeman pupil, which 'spin locks' the magnetization perpendicular to the rf field.[15]

Once we had recognized the origin of the Hartmann–Hahn artifacts, it was relatively straightforward to capitalize on them and use them for obtaining J connectivity. For maximum Hartmann–Hahn transfer the goal was to make the trajectories of the coupled spins as identical as possible. In retrospect therefore not surprisingly, our improved Hartmann–Hahn cross polarization schemes started to look more and more like heteronuclear decoupling schemes, where the objective is to make ^{1}H spins coupled to ^{13}C in the $|\alpha\rangle$ and $|\beta\rangle$ spin states undergo identical trajectories.[16] The fact that the chemical shift difference between two J-coupled protons is typically much larger than ^1J(C,H) makes the homonuclear Hartmann–Hahn (HOHAHA) cross polarization actually somewhat more demanding. Our initial attempt to publish the use of an MLEV16 mixing scheme was thwarted by a reviewer who argued, correctly, that the spectra had significant phase distortions and therefore were not all that useful. After a few more experiments it became clear that the artifacts were due to two distinctly separate effects. First, not only was the magnetization parallel to the y axis transferred from one spin to its coupling partner, but also the x-axis magnetization, albeit with a different efficiency. Second, even for a single noncoupled spin, for example the proton in chloroform, we found an offset dependent rotation about the z axis during the MLEV16 scheme, which at that time we naively attributed to pulse imperfections but which, as later shown by John Waugh,[17] is inherent to the MLEV16 scheme. In any case, both effects were easy to eliminate: trim pulses ensured that the x magnetization was effectively eliminated. Adding a 17th pulse along the y axis after each MLEV16 cycle caused the average Hamiltonian to be dominated by this term and transverse magnetization could no longer 'wander away' from y and, voila, MLEV17 was born.[18]

While trying to develop our homonuclear Hartmann–Hahn (HOHAHA) pulse schemes it became clear that the concept was not new. Lukas Braunschweiler and Richard Ernst had several years earlier proposed the use of isotropic mixing in the so-called TOCSY experiment[19] which accomplished magnetization transfer by means of a string of closely spaced 180 ° pulses. After its initial publication, this TOCSY experiment did not really 'catch on', probably because it did not work very well in practice. Although I am unaware of any detailed early studies on the efficiency of the TOCSY experiment, the general feeling at that time was that an experiment with so many 180 ° pulses should suffer from rf inhomogeneity and other pulse imperfections. However, the true reason for its poor performance can be seen by considering the string of 180 ° pulses as a homonuclear Hartmann–Hahn cross polarization. Due to the different offsets of the coupled protons, the rotation experienced by off-resonance protons is larger than that for on-resonance protons, causing a 'Hartmann–Hahn mismatch'. Although even now the original MLEV17 mixing scheme still finds widespread use, more efficient mixing schemes have since then been developed by A. J. Shaka[20] and others, whereas Richard Ernst and co-workers devised an elegant scheme to eliminate ROE effects from macromolecule HOHAHA/TOCSY spectra.[21]

PROTEINS ARE BIG

For the first few years at NIH, I was primarily interested in studying complex small molecules such as natural products and peptides. When Laura Lerner joined my group she convinced me to add carbohydrates to the list. However, when in 1986 Michael Summers and I had completed a detailed NMR study of coenzyme B_{12},[22] primarily thanks to our development of the HMBC experiment, I had the feeling that methodologically this area might be maturing and my interests started to shift from small molecules to proteins. I had always avoided proteins like the plague, not in the least because I was horrified by the idea of staring into a light box for many months in a row. However, when Dennis Torchia, also at NIH, had managed to over-express and purify isotopically enriched staphylococcal nuclease, a protein of about 17 kD, he easily talked me into trying some of our small molecule experiments on nuclease. Together with Dennis and a very enthusiastic postdoc, Vladi Sklenar, we actually managed to get some neat experiments done. However, the big step came in 1988 when Dominique Marion and Lewis Kay decided they wanted to do 3D NMR. Dominique had joked that he 'was tired of working on weekends' and wanted an experiment that would run for at least three or four days. Unfortunately for him, a full disk on our old Nicolet spectrometer needed to be unloaded every 7 h or so, days, nights, ... and weekends too. Right from the start it was obvious to us that heteronuclear 3D was the way to go and our first and successful attempt was to record a 3D ^{15}N-separated NOESY spectrum.[23]

At that point it appeared to me that protein NMR might have a future after all and it was easy to convince NIH that investing in protein NMR would be a useful move. For starting a dynamic protein NMR program it would be essential to have a critical mass and we were fortunate to attract Marius Clore and Angela Gronenborn to the NMR program, which formed the beginning of a close and very productive collaboration. We also managed to obtain a significant commitment from NIH for space and capital equipment. With the arrival of two new AM-type Bruker spectrometers we were set to go and make serious attempts at recording high quality 3D spectra. The first hurdle that needed to be overcome, however, was the Bruker itself. In the normal mode of operation the ASPECT computer would require up to about 10 s at the completion of each increment to recompile the pulse sequence and get going again. Considering that most 3D experiments require only very few transients per increment, this compilation time more than doubled the duration of our 3-day 3D experiment, causing us some serious headaches. Fortunately, Rolf Tschudin, our electronics engineer, hired away by Ted Becker from Varian some 15 years earlier, was able to solve our problem by designing and building a box that would interrupt the Bruker pulse programmer clock for a defined amount of time that would increment each time the 'Tschudin timer box' received a clock pulse. This invention greatly reduced the time needed for recompilation of the pulse sequence and made 3D into a practical approach on the AM systems.

TRIPLE FUN

After our initial excitement about being able to record high-quality ^{15}N-separated NOESY and HOHAHA spectra, reality

sank in. Making complete resonance assignments based on these two types of 3D spectra was going to be a very long and tedious process. The protein calmodulin that my new postdoctoral associate Mitsu Ikura had just started to work on was probably the best possible example for illustrating how difficult it could still be to make the sequential assignment following the well-established Wüthrich procedure.[24] Because of the very high degree of α-helix in this protein, the amide and H^{α} chemical shift dispersion was particularly poor.

At that time, my colleague Dennis Torchia was exploring the possibilities for using several variations of the Kainosho double-labeling approach[25] for making sequential assignments. By selectively ^{13}C labeling a certain amino acid type, A, in the carbonyl position and another type of amino acid, B, with ^{15}N in the amide position, only B-type amino acids that are immediately preceded by an A-type residue show a $^{1}J(N,C)$ splitting in a $^{1}H-^{15}N$ shift correlation spectrum. However, complete backbone assignment with this double-labeling approach required a large number of sample preparations and therefore a lot of work.

Dennis had the foresight to order a triple resonance probehead for his system; one that was optimized for proton detection but that also had a larger doubly tuned $^{13}C/^{15}N$ coil. I remember it took quite some effort to convince Bruker that this 'crazy' probe was what we wanted. With the capability to record 3D spectra already available, it was a relatively small step to come up with the so-called HNCO 3D experiment. This experiment ideally requires uniformly $^{13}C/^{15}N$-enriched protein, so every backbone amide ^{15}N is preceded by a ^{13}C carbonyl and generates a spectrum where every backbone amide proton gives rise to a single resonance, with ^{1}H, ^{15}N, and ^{13}CO shifts determining the position of the resonance in the F_3, F_2, and F_1 dimension. The ^{13}CO shift itself is not very informative, but by conducting a second 3D experiment (HCACO) that correlates H^{α}, C^{α}, and the ^{13}CO shifts we argued it should be possible to correlate H^{α}/C^{α} of one residue with the $^{15}N/^{1}H$ resonances of the next residue, as both would connect to the same ^{13}CO chemical shift. Again we were fortunate to have Rolf Tschudin in our lab who was able to build very rapidly a third rf channel that we could control from the Bruker pulse program and actually try out these 'Gedanken experiments'.

Primarily due to the creativity and persistence of Lewis Kay, we were finally able to make the triple resonance experiments work, and using the new 3D data Mitsu Ikura was able to complete his backbone calmodulin assignments shortly thereafter. Of course, we were tremendously impressed by our own accomplishments and were anticipating rave reviews when we submitted our results to the journal *Biochemistry*. To the contrary, the paper[26] was initially rejected. Such 'complicated experiments' requiring the very expensive ^{13}C labeling were deemed to be of no practical interest!

The next step in our structural study of calmodulin required making the side-chain assignments of calmodulin. Unfortunately, the presence of ^{13}C needed to disperse the $^{1}H-^{1}H$ correlations into a third dimension also causes severe broadening of the ^{1}H resonances due to the strong $^{1}H-^{13}C$ dipolar interaction. Regular $^{1}H-^{1}H$ COSY approaches therefore were not expected to yield useful data for proteins the size of calmodulin and larger. Instead, we chose the same solution as for the backbone assignments: transfer magnetization from one proton to another via one-bond heteronuclear J couplings, from ^{1}H to attached ^{13}C via $^{1}J(C,H)$, from ^{13}C to a second ^{13}C via $^{1}J(C,C)$, and back to the ^{1}H attached to this second ^{13}C. Despite the fact that magnetization in this so-called HCCH approach is transferred by three steps instead of one, such experiments are very efficient because each of the three steps transfers via a coupling that is larger than the pertinent linewidth.[27] Independent of our work Stephen Fesik, Erik Zuiderweg, and co-workers came up with an analogous solution which relied on isotropic mixing of ^{13}C magnetization with a MLEV17 scheme.[28] Both approaches are currently widely used.

Staring at all his ^{13}C assignments, Mitsu noted that there appeared to be a correlation between C^{α} chemical shift and the protein backbone conformation: all $^{13}C^{\alpha}$ carbons in α-helical residues showed a downfield shift relative to their random coil position. A subsequent more systematic analysis of the C^{α} and C^{β} shifts in four different proteins by Silvia Spera clearly demonstrated the generality of Mitsu's observation.[29]

WE CAN COUNT TO FOUR

In the same way as the idea of 3D NMR had been circulating for a long time before its real use was actually demonstrated, extending the dimensionality of the NMR spectrum to four was an obvious step to make. However, rather than proving that we indeed could count to four, we were looking for an application that would demonstrate its use. It was clear that spectral crowding is most pronounced in NOESY spectra and initially we wanted to focus on $^{13}C/^{13}C$ separated $^{1}H-^{1}H$ NOESY, an experiment that later would prove to be extremely challenging.[30,31] Instead, Marius Clore had a better idea that was much easier to implement: separate the ^{15}N-separated 3D NOESY into a fourth dimension, ^{13}C. This could be done with a minimal amount of phase cycling and Lewis Kay was able to obtain an impressive 4D spectrum for Marius's interleukin-1β.[32] Subsequent attempts to obtain a high quality $^{13}C/^{13}C$-separated NOESY spectrum proved that this was far more difficult and although we finally did manage to obtain such a spectrum only after the introduction of pulsed field gradients has this experiment become routine.[33]

The performance of many of the triple resonance experiments was significantly improved by Stephan Grzesiek when we were trying to study the protein interferon-γ, which with a total molecular weight of over 31 kD presented a formidable challenge to our methods. Short T_2 values were 'killing' a number of the triple resonance experiments. By departing from our old dogma that 'a good pulse sequence must have few pulses', Stephan was able to improve dramatically the performance of many of them.[3] The concept of 'constant time' was reintroduced, allowing dephasing and frequency encoding to occur simultaneously instead of sequentially, and with a few additional pulses Stephan also minimized the time that magnetization would be in the fast-relaxing antiphase state. Stephan also introduced a number of experiments that J-correlate the amino acid side-chain resonances with the backbone amides which made it possible for him to simplify dramatically the assignment process and complete the interferon-γ backbone assignments.[34]

In the fall of 1991 Geerten Vuister, a graduate student of Robert Kaptein, joined my lab. Among other experiments, he

developed a large number of ingenious schemes for measuring homonuclear and heteronuclear coupling constants, most of them based on the concept of what we refer to as 'quantitative J correlation'. In this approach, the experiment is designed in such a way that, for example, the intensity of a cross peak between nuclei A and B is directly related to their J coupling. This turns out to be very practical and widely applicable in protein NMR. For example, not only was Geerten able to use this approach for measuring J couplings between amide and H^{α} protons, which characterize the backbone angle ϕ, but he was also able to measure ^{3}J(N,C) couplings between side-chain $^{13}C^{\gamma}$ and backbone ^{15}N.[35] This latter coupling turned out to be very small, $\sim$2.2 Hz for *trans* and $\sim$0.5 Hz for *gauche*. Even in small molecules it had previously been difficult to measure such couplings, whereas with this new method we are now able to measure these values in proteins as large as 20 kD. Together with ^{3}J(C,C),[36] ^{3}J(C,N) defines the important χ_1 side-chain torsion angles and also aids in distinguishing the prochiral methyl groups in valine residues.

WHAT'S IN THE CRYSTAL BALL?

The introduction of stable isotopes in proteins by ourselves and others has extended tremendously the power of NMR for characterizing their structure. I anticipate that with further software development for automated assignment and for the analysis of the 4D NOESY spectra, determining a high-resolution structure for proteins up to a few hundred amino acids will become as routine as it is presently in crystallography. Undoubtedly, however, NMR will find increasing use in characterizing the dynamic features of a protein, which frequently are critical to its function and which may not easily be studied by other methods. The study of the dynamics of the linker region in calmodulin, carried out by Nino Barbato using the methodology that Lewis, Dennis, and I had developed earlier,[37] is an interesting example of such a study. In the crystalline state, the linker was found to be a rigid helix, giving the protein a dumbbell shape. In solution, at 35 °C and at physiological pH and salt concentration, five residues in the middle of the linker were clearly highly flexible as judged by their ^{15}N relaxation properties. Analysis of the relaxation rates for the amides in the small globular domains of the protein showed that these domains were subject to nearly isotropic rotational diffusion, in contrast to what would be expected for a rigid dumbbell.[38]

Thus, it came as no surprise when subsequently Ikura, with the help of Marius Clore and Angela Gronenborn, was able to show that upon binding to its target the two globular domains come together with the target clamped in between them.[39]

Present work is focusing on extending the size limit of proteins that can be studied by NMR by further improving the methodology. So far we have relied almost exclusively on ^{15}N and ^{13}C although it is clear that deuteration can also be tremendously useful.[40] An initial attempt by Stephan Grzesiek to combine both approaches showed encouraging results and yielded substantial line narrowing of the deuterated C^{α} carbons.[41] A large number of different types of approaches along similar lines can be envisaged and only time, and lots of experiments, will tell which ones will be of long-term value.

The prospects for protein NMR are roesy, equipment is no longer inadequate and there remains plenty of room for further development of crazed ideas.[42]

REFERENCES

1. W. P. Aue, E. Bartholdi, and R. R. Ernst, *J. Chem. Phys.*, 1976, **64**, 2229.
2. A. Bax, A. F. Mehlkopf, and J. Smidt, *J. Magn. Reson.*, 1979, **35**, 167.
3. S. Grzesiek and A. Bax, *J. Magn. Reson.*, 1992, **96**, 432.
4. A. Bax, P. G. de Jong, A. F. Mehlkopf, and J. Smidt, *Chem. Phys. Lett.*, 1980, **69**, 567.
5. A. Bax, R. Freeman, and S. P. Kempsell, *J. Am. Chem. Soc.*, 1980, **102**, 4849.
6. U. Piantini, O. W. Sørensen, and R. R. Ernst, *J. Am. Chem. Soc.*, 1982, **104**, 6800.
7. C. J. Turner, *J. Magn. Reson.*, 1992, **96**, 551.
8. A. Bax, N. M. Szeverenyi, and G. E. Maciel, *J. Magn. Reson.*, 1983, **52**, 147.
9. A. Bax, N. M. Szeverenyi, and G. E. Maciel, *J. Magn. Reson.*, 1983, **55**, 494.
10. G. Bodenhausen and D. J. Ruben, *Chem. Phys. Lett.*, 1980, **69**, 185.
11. A. Bax, R. H. Griffey, and B. L. Hawkins, *J. Magn. Reson.*, 1983, **55**, 301.
12. M. R. Bendall, D. T. Pegg, and D. M. Doddrell, *J. Magn. Reson.*, 1983, **52**, 81.
13. A. A. Bothner-By, R. L. Stephen, J. Lee, C. D. Warren, and R. W. Jeanloz, *J. Am. Chem. Soc.*, 1984, **106**, 811.
14. A. Bax and D. G. Davis, *J. Magn. Reson.*, 1985, **63**, 207.
15. T.-L. H. Wang and A. J. Shaka, *J. Am. Chem. Soc.*, 1992, **114**, 3157.
16. J. S. Waugh, *J. Magn. Reson.*, 1982, **50**, 30.
17. J. S. Waugh, *J. Magn. Reson.*, 1986, **68**, 189.
18. A. Bax and D. G. Davis, *J. Magn. Reson.*, 1985, **65**, 355.
19. L. Braunschweiler and R. R. Ernst, *J. Magn. Reson.*, 1983, **53**, 521.
20. A. J. Shaka, C. J. Lee, and A. Pines, *J. Magn. Reson.*, 1988, **77**, 274.
21. C. Griesinger, G. Otting, K. Wüthrich, and R. R. Ernst, *J. Am. Chem. Soc.*, 1988, **110**, 7870.
22. M. F. Summers, L. G. Marzilli, and A. Bax, *J. Am. Chem. Soc.*, 1986, **108**, 4285.
23. D. Marion, L. E. Kay, S. W. Sparks, D. A. Torchia, and A. Bax, *J. Am. Chem. Soc.*, 1989, **111**, 1515.
24. K. Wüthrich, *NMR of Proteins and Nucleic Acids*, Wiley, New York, 1986.
25. M. Kainosho and T. Tsuji, *Biochemistry*, 1982, **21**, 6273.
26. M. Ikura, L. E. Kay, and A. Bax, *Biochemistry*, 1990, **29**, 4659.
27. L. E. Kay, M. Ikura, and A. Bax, *J. Am. Chem. Soc.*, 1990, **112**, 888.
28. S. W. Fesik, H. L. Eaton, E. T. Olejniczak, E. R. P. Zuiderweg, L. P. MacIntosh, and F. W. Dahlquist, *J. Am. Chem. Soc.*, 1990, **112**, 886.
29. S. Spera and A. Bax, *J. Am. Chem. Soc.*, 1991, **113**, 5490.
30. G. M. Clore, L. E. Kay, A. Bax, and A. M. Gronenborn, *Biochemistry*, 1991, **30**, 12.
31. E. R. P. Zuiderweg, A. M. Petros, S. W. Fesik, and E. T. Olejniczak, *J. Am. Chem. Soc.*, 1991, **113**, 370.
32. L. E. Kay, G. M. Clore, A. Bax, and A. M. Gronenborn, *Science*, 1990, **249**, 411.
33. G. W. Vuister, G. M. Clore, A. M. Gronenborn, R. Powers, D. S. Garrett, R. Tschudin, and A. Bax, *J. Magn. Reson. B*, 1993, **101**, 210.
34. S. Grzesiek, H. Doebeli, R. Gentz, G. Garotta, A. M. Labhardt, and A. Bax, *Biochemistry*, 1992, **31**, 8180.

35. G. W. Vuister, A. C. Wang, and A. Bax, *J. Am. Chem. Soc.*, 1993, **115**, 5334.
36. A. Bax, D. Max, and D. Zax, *J. Am. Chem. Soc.*, 1992, **114**, 6923.
37. L. E. Kay, D. A. Torchia, and A. Bax, *Biochemistry*, 1989, **28**, 8972.
38. G. Barbato, M. Ikura, L. E. Kay, and A. Bax, *Biochemistry*, 1992, **31**, 5269.
39. M. Ikura, G. M. Clore, A. M. Gronenborn, G. Zhu, C. B. Klee, and A. Bax, *Science*, 1992, **256**, 632.
40. C. H. Arrowsmith, R. Pachter, R. B. Altman, S. B. Iyer, and O. Jardetzky, *Biochemistry*, 1990, **29**, 6332.
41. S. Grzesiek, J. Anglister, H. Ren, and A. Bax, *J. Am. Chem. Soc.*, 1993, **115**, 4369.
42. W. S. Warren, W. Richter, A. H. Andreotti, and B. T. Farmer, II, *Science*, 1993, **262**, 2005.

Biographical Sketch

Ad Bax. *b* 1956. Ph.D., Applied Physics, Delft University of Technology. Postdoctoral work at Colorado State University (on solid state NMR with Gary Maciel). National Institutes of Health, 1983−present, currently Chief of Biophysical NMR Spectroscopy Section, 230 publications. Current research specialty: biomolecular NMR.

Becker, Edwin D.: NMR at the NIH: Inception and Growth Over Four Decades

Edwin D. Becker

National Institutes of Health, Bethesda, MD, USA

I never planned to go into NMR, it just happened! As a graduate student in chemistry at the University of California at Berkeley in the early 1950s, I was working with George Pimentel in infrared spectroscopy. My Ph.D. thesis was largely devoted to testing a new method, 'matrix isolation' which permitted us to obtain infrared spectra of unstable molecules such as free radicals in a matrix of an inert solid material deposited from the gas phase (e.g. nitrogen or argon).[1] We also found the method useful for studying some aspects of hydrogen bonding,[2] a subject that I have pursued for many years, as I will describe.

MY FIRST INKLINGS OF NMR

During that period, none of this had anything to do with NMR (though matrix isolation came to be used in NMR studies many years later.) In fact, I don't think I had ever heard of NMR until 1954 when Felix Bloch gave a talk at Berkeley. As I recall, he talked about relaxation, motional narrowing, and his recently discovered method of sample spinning. It would be nice to be able to say that that talk changed my research direction, but it didn't. All this sounded like interesting physics, but it was not something that I could envisage for my own work. Later that year, Jim Shoolery gave a seminar at Berkeley and showed how Varian's new 'high-resolution NMR spectroscopy' could be used to determine the structures of certain molecules. Now that seemed at least more relevant to chemistry, but the molecules he was able to study and analyze were very limited, and NMR seemed to me to be far from a really useful tool in chemistry. Nevertheless, some seeds must have been planted by these talks. I still remember them 40 years later even though they had no immediate impact on my perspectives.

One other event at Berkeley turned out to be very important in my eventual journey into NMR. One of George Pimentel's other students, Charles Huggins, was studying the effect of hydrogen bonding on the frequency and intensity of infrared bands. George suggested (perhaps that's not the right word!) that Charles look into the use of NMR in a collaboration with Jim Shoolery. Some very useful results came from that work,[3] and I learned more about NMR from Huggins' reports back at our lab.

ON TO NIH

After receiving my Ph.D. in 1955, I came to the National Institutes of Health for what I thought would be a two to three year postdoctoral stint. NIH turned out to be a marvelous place to do research, so I spent my entire career here. I originally came to NIH to work with Urner Liddel, a physicist who had done some fundamental studies of hydrogen bonding by infrared methods in the 1930s, then served as a science administrator in government and in industry before returning to lab research at NIH. We were doing infrared studies, but both Urner and our Section Chief, Fred Brackett (who had discovered Brackett's Series in the spectrum of atomic hydrogen in 1922) were interested in the potential of NMR. In the fall of 1956 that interest, together with my slight acquaintance with Shoolery and the hydrogen-bonding work, led to my being sent for a week to Palo Alto to work with Shoolery and evaluate the potential of NMR for chemical analysis, but especially for hydrogen-bonding studies.

LIDDEL AND RAMSEY

Let me provide a sidelight here about Urner Liddel. He really didn't know much about NMR, but he had published the first paper on the effect of hydrogen bonding in NMR. According to Urner's account, that started one day in 1951 when Urner, then in the Office of Naval Research, visited Norman Ramsey's lab at Harvard. Ramsey had the structure of ethanol on his blackboard and explained that he was puzzling over some results from Stanford that showed the chemical shift of the OH peak in ethanol to be markedly temperature-dependent, while the CH_3 and CH_2 chemical shifts were temperature-independent.[4] Liddel commented that he had studied hydrogen bonding in ethanol many years earlier, and Ramsey inquired as to whether this hydrogen bonding would be temperature-dependent. Of course, replied Liddel, because of the equilibria involved, which would also be affected by diluting ethanol with a non-hydrogen-bonding solvent such as CCl_4. Liddel returned to his office in Washington, and not too long thereafter he received in the mail a manuscript, 'Temperature Dependent Magnetic Shielding in Ethyl Alcohol' by Liddel and Ramsey, which Ramsey had already sent to the *Journal of Chemical Physics*.[5] The role of hydrogen bonding is put forth as a plausible explanation for the temperature dependence, and a test of the explanation is proposed: dilute the ethanol in CCl_4. Arnold and Packard did just that and reported their results on the same journal page along with the Liddel–Ramsey paper.[6]

Liddel's second (and last) paper on NMR was my first—a quantitative study of hydrogen bonding in ethanol that I carried out with Jim Shoolery during that week at Varian in 1956.[7] We did a few other experiments as well, and my report to the NIH hierarchy on the potential for NMR was sufficient for our institute to purchase a 40 MHz spectrometer. I still continued to be more interested in vibrational spectroscopy than in NMR, but when the NMR instrument arrived in the summer of 1957 I was considered the local expert. After all, I had had a week at Varian, and that was 1 week's more experience than anyone else at NIH! I often regret never having had any formal training

in NMR, but sometimes one can manage just by plunging in. So I was put in charge of the new acquisition, which at $30 000 was our most expensive instrument. Ever since, I have divided my research time between vibrational spectroscopy and NMR, but with increasing emphasis on NMR as the field developed spectacularly.

EARLY NMR STUDIES

Most of my initial work in NMR was related to structure elucidation. It was marvelous to have an NMR spectrometer at that time. Organic chemists came to see whether 'that big machine' would tell them what compound they had isolated or synthesized. Sometimes it did! I was glad to help other investigators with their work, and I obtained access to a number of compounds that I could use to study more fundamental aspects of NMR. In the late 1950s many NMR spectroscopists had studied steroids, alkaloids, sugars, amino acids, peptides, and other classes of molecules, but no one had reported on porphyrins. Because of their importance in heme proteins, chlorophyll, and other important substances, I thought that we should investigate the NMR spectra of some simple, metal-free porphyrins. Several biochemists at NIH worked with porphyrins and seemed willing to provide samples. The problem was the quantity needed. When I said 10 mg would be adequate, there was usually a pause, then a statement, 'You must mean 10 μg'. No biochemist could believe the quantities we needed for NMR, but remember this was during the days of 60 MHz spectrometers and long before time averaging. In 1959 I finally found an adequate source of porphyrins: Cecil Watson, an expert in internal medicine at the University of Minnesota, had long studied the disease porphyria and had developed a strain of cows that excreted large amounts of porphyrins. He could (barely) provide the 10 mg samples needed. My associate Bob Bradley and I ran spectra of several of these compounds and published the first NMR papers on porphyrins.[8,9] By far the most surprising observation, as shown in Figure 1, was the position of the NH resonance, which was about 4 ppm *more* shielded than tetramethylsilane — one of the very few such 'high field' resonances that had ever been detected. The reason, of course, is that these protons lie *inside* the porphyrin ring, and the large ring current shields them, just as we should have expected on the basis of the Johnson–Bovey picture of π-electron circulation.[10]

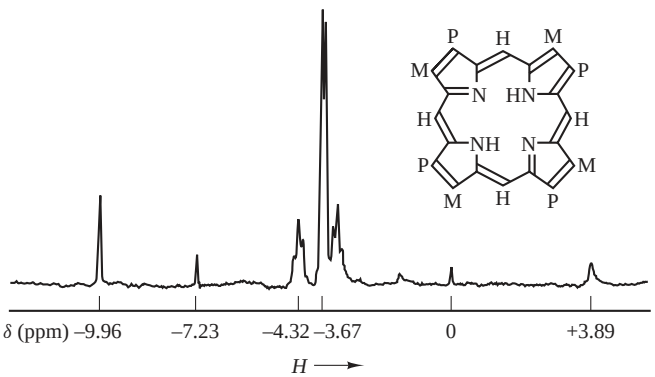

Figure 1 ^{1}H NMR spectrum (60 MHz) of coproporphyrin-1 methyl ester in $CDCl_3$ (0.05 M). M = CH_3; P = $CH_2CH_2COOCH_3$. The peak at δ + 3.89 ppm is due to the NH protons. Note the old sign convention for denoting chemical shifts which is opposite to currently accepted practice.

Hydrogen bonding continued to be one of my interests. In the 1960s I began to delve into the effect of H-bonding on the chemical shift of the hydrogen acceptor. Oxygen was not easy to study but ^{15}N offered some possibilities. We used and modified double resonance methods to allow us to study ^{15}N chemical shifts in enriched compounds with the sensitivity of ^{1}H, an essential requirement for the dilute solutions that we had to use for such studies.[11] Nowadays, of course, such studies can be carried out with ^{15}N in natural abundance by various inverse detection methods, but in the pre-Fourier transform days such techniques were beyond comprehension. Much later, with better methods, we made studies of chemical shifts[12] of ^{17}O and the effect of H-bonding on ^{13}C relaxation times.[13,14]

HIGHER FIELDS AND LARGER MOLECULES

Of course, we have upgraded NMR instruments over the years, with the initial 40 MHz to 60 MHz improvement coming only a year or two after our initial purchase. I think I made one important decision in the early 1960s *not* to follow the crowd in moving to 100 MHz. High homogeneity superconducting magnets were clearly on the horizon, so I preferred to conserve our financial resources and obtain one of the early 220 MHz instruments and later a 270 MHz spectrometer. For almost a decade we had the only superconducting NMR systems in the southeastern part of the country. Not only did they permit many investigators at NIH to make rapid advances in chemical and biochemical research, but we were able to provide instrument time to many people outside the NIH.

Todd Miles and others at NIH introduced me to problems in the structure and hydrogen-bonding interactions in nucleosides and nucleotides. We showed that the Watson–Crick base pairing is dominant for mononucleosides,[15] found the site of protonation in a number of cytosine derivatives,[16] and measured internal rotation in cytosine derivatives.[17,18] Tom Pinnavaia came from Michigan State University to spend his sabbatical in my lab in 1974–75. He discovered that guanosine-5′-phosphate (GMP) in neutral or basic solution self-associates by hydrogen bonding to give a stable structure in which the H-bonds exchange only slowly on the NMR timescale. We were able to interpret the NMR, along with ancillary infrared spectral data, in terms of an unexpected tetrameric structure (**1**).[19] We noticed a large 'hole' in the center which should tend to destabilize the structure, but Tom, an inorganic chemist, realized that a counterion such as Na^+ would fit neatly into the hole. In fact, as later shown by Cherie Fisk's study of GMP by ^{1}H and ^{13}C NMR, the structure is an octamer consisting of two stacked planes bound together by the Na^+.[20] Today the guanosine tetramer of Figure 2 is of great interest in the mechanism of chromosome replication.

FARRAR AND BECKER

During the 1960s I had the good fortune to meet Tom Farrar, who was then at the nearby National Bureau of Standards.

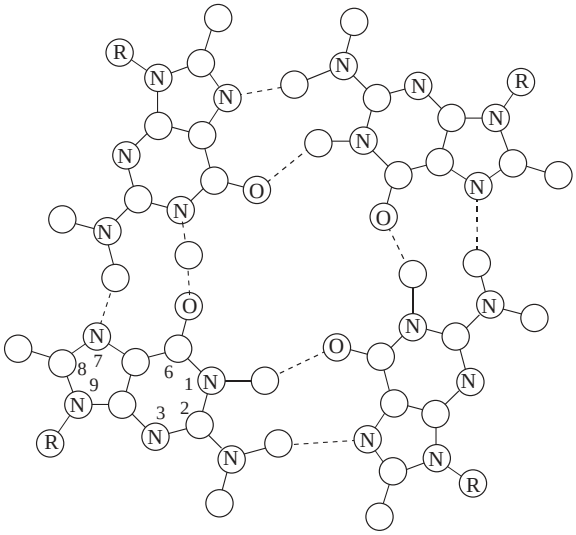

(1)

Figure 2 Tetrameric structure formed by self-association of GMP.

Tom was building pulse NMR apparatus and was interested in possible chemical applications. We began collaborations initially aimed at studies of rate phenomena, but this was soon bypassed by the idea of using Tom's pulse spectrometer to excite ^{13}C free induction decays that could be Fourier-transformed to yield spectra in a reasonable time. The first such spectra were obtained only with great difficulty, paralleling the cumbersome procedures used a few years earlier by Ernst and Anderson in their pioneering work on Fourier transform NMR of protons. Jim Ferretti, who was then in the Division of Computer Research and Technology at NIH, played a key role in taking data from Tom's lab on paper tape, bringing the tape to NIH, where one computer converted it to punched cards (!), which could then be fed into a second computer to do the Fourier transform. Such niceties as phase correction required an inordinate amount of further hands-on computation. But we did get ^{13}C spectra and eventually built better pulse spectrometers that could be interfaced to the then new minicomputers, such as the Nicolet 1080. Meanwhile, Gitte Shoup (later Vold), Tom, and I studied ^{13}C relaxation and clarified the relative importance of various relaxation mechanisms.[21] During this period I also thought up a pulse method for restoring magnetization to its equilibrium value more rapidly than T_1 processes and expected it to be useful for studying ^{13}C NMR. At my insistence that we provide a catchy acronym, Tom and I came up with the name Driven Equilibrium Fourier Transform.[22] The acronym DEFT had a very positive connotation. Unfortunately DEFT turned out not to be useful for ^{13}C studies[23] but many years later has found some applicability in NMR imaging. Soon after publishing, we were embarrassed to find that we had simply reinvented a pulse sequence reported eight years earlier by Streever and Carr in their paper on relaxation of ^{129}Xe.[24] I'm not sure whether to be pleased or dismayed that our acronym served as the basis for a plethora of acronyms for really useful techniques, e.g. WEFT, SEFT, and, especially, INEPT.

The collaboration with Tom certainly ranks as one of the high points in my NMR career. In addition to our research, we decided to organize a course at the NIH Graduate School on the then new pulse NMR methods, and that in turn led to our book Pulse and Fourier Transform NMR.[25] We decided to limit this book to a simple introduction that would be comprehensible to chemists and wrote it in six months. We persuaded the publisher (for whom I had already written a successful book on High Resolution NMR,[26]) to rush the book out in six months and to charge no more than $7.50, since we wanted it to be widely used. After 20 years this book still sells a few copies per year (at a now absolutely exorbitant price!). Its success probably stems largely from the fact that Tom and I were both feeling our way along with these methods that were then quite foreign to chemists, and our explanations were understandable because we were almost explaining it to ourselves.

FURTHER EVOLUTION OF NMR AT NIH

For me the 1970s was an exciting period, highlighted by continuing developments in Fourier transform methodology. We worked largely at optimizing pulse methods so they would be useful in practical applications.[27] Raj Gupta spent a year at NIH and spearheaded several investigations into the efficiency of measurements of relaxation times[28,29] and especially the practical development of the rapid scan correlation method[30] that had been devised by Dadok and Sprecher.[31] This method is still in use as an inexpensive alternative to pulse FT in 60 MHz instruments designed for analytical studies.

While I spent most of the 1980s dealing with administrative matters as an NIH associate director, I maintained contact with NMR. Fortunately we recruited Ad Bax, essentially as my successor, and his accomplishments are legendary. Soon we were able to bring Marius Clore and Angela Gronenborn to our lab to start a program on protein NMR studies. Meanwhile, in the 1970s Dennis Torchia had joined NIH, and we agreed to cooperate in sharing equipment and facilities. This combination of outstanding NMR investigators, together with excellent financial support, has made NIH a world-class facility for NMR studies of protein structure. Although NIH is organized into many small, independent research groups, we have always had excellent cooperation from all the NMR spectroscopists in maintaining an atmosphere that is conducive to collaboration and sharing of both instruments and ideas.

I have also been able to observe closely the advent of NMR imaging and in vivo spectroscopy, even though I have had only limited participation in these areas.[32] I remember a meeting in New York in late 1972, when Paul Lauterbur told me during an evening stroll about his first imaging experiments (published a few months later). Like many great ideas the concept seemed in retrospect almost obvious, but it was clear from the beginning that this technique would be of great importance. I followed developments in Paul's lab and elsewhere very closely and in 1977 was able to facilitate David Hoult's joining NIH to take up research in imaging. Later, in the 1980s, when imaging and in vivo spectroscopy were firmly established worldwide, I was fortunately able to combine my background in NMR with my broader administrative functions to organize the NIH In Vivo NMR Research Center, where scientists from many different labs at NIH are able to share equipment and facilities, and moreover to exchange ideas in developing and applying these fascinating techniques. We were able to recruit top-notch talent (e.g. Chrit Moonen and Jeff Alger) to join with other NIH investigators, such as Bob

Balaban, Jack Cohen, Andy Byrd, Bill Egan, and David Hoult, to establish the Center.

A FINAL NOTE

Editing this volume of the Encyclopedia is a real pleasure, especially since I have had the opportunity to be in close touch with the early (and not so early) giants in the development of NMR. For someone that never intended to go into NMR, I have found it a very rewarding career.

REFERENCES

1. E. D. Becker and G. C. Pimentel, *J. Chem. Phys.*, 1956, **25**, 224.
2. M. Van Thiel, E. D. Becker, and G. C. Pimentel, *J. Chem. Phys.*, 1957, **27**, 95.
3. C. M. Huggins, G. C. Pimentel, and J. N. Shoolery, *J. Chem. Phys.*, 1956, **60**, 1311.
4. M. E. Packard and J. T. Arnold, *Phys. Rev.*, 1951, **83**, 210.
5. U. Liddel and N. F. Ramsey, *J. Chem. Phys.*, 1951, **19**, 1608.
6. J. T. Arnold and M. E. Packard, *J. Chem. Phys.*, 1951, **19**, 1608.
7. E. D. Becker, U. Liddel, and J. N. Shoolery, *J. Mol. Spectrosc.*, 1958, **2**, 1.
8. E. D. Becker and R. B. Bradley, *J. Chem. Phys.*, 1959, **31**, 1413.
9. E. D. Becker, R. B. Bradley, and C. J. Watson, *J. Am. Chem. Soc.*, 1961, **83**, 3743.
10. C. E. Johnson, Jr. and F. A. Bovey, *J. Chem. Phys.*, 1958, **29**, 1012.
11. L. Paolillo and E. D. Becker, *J. Magn. Reson.*, 1970, **2**, 168.
12. L. Baltzer and E. D. Becker, *J. Am. Chem. Soc.*, 1983, **105**, 5730.
13. L. M. Sweeting and E. D. Becker, *J. Phys. Chem.*, 1984, **88**, 6075.
14. E. E. Tucker, T. R. Clem, J. I. Seeman, and E. D. Becker, *J. Phys. Chem.*, 1975, **79**, 1005.
15. R. R. Shoup, H. T. Miles, and E. D. Becker, *Biochem. Biophys. Res. Commun.*, 1966, **23**, 194.
16. E. D. Becker, H. T. Miles, and R. B. Bradley, *J. Am. Chem. Soc.*, 1965, **87**, 5575.
17. R. R. Shoup, H. T. Miles, and E. D. Becker, *J. Am. Chem. Soc.*, 1967, **89**, 6200.
18. R. R. Shoup, E. D. Becker, and H. T. Miles, *Biochem. Biophys. Res. Commun.*, 1971, **43**, 1350.
19. T. J. Pinnavaia, H. T. Miles, and E. D. Becker, *J. Am. Chem. Soc.*, 1975, **97**, 7198.
20. C. L. Fisk, E. D. Becker, H. T. Miles, and T. J. Pinnavaia, *J. Am. Chem. Soc.*, 1982, **104**, 3307.
21. T. C. Farrar, S. J. Druck, R. R. Shoup, and E. D. Becker, *J. Am. Chem. Soc.*, 1972, **94**, 699.
22. E. D. Becker, J. A. Ferretti, and T. C. Farrar, *J. Am. Chem. Soc.*, 1969, **91**, 7784.
23. R. R. Shoup, E. D. Becker, and T. C. Farrar, *J. Magn. Reson.*, 1972, **8**, 298.
24. R. L. Streever and H. Y. Carr, *Phys. Rev.*, 1961, **104**, 20.
25. T. C. Farrar and E. D. Becker *Pulse and Fourier Transform NMR*, Academic Press, New York, 1971.
26. E. D. Becker, *High Resolution NMR*, 2nd edn., Academic Press, New York, 1980.
27. E. D. Becker, J. A. Ferretti, and P. N. Gambhir, *Anal. Chem.*, 1979, **51**, 1413.
28. R. K. Gupta, J. A. Ferretti, E. D. Becker, and G. H. Weiss, *J. Magn. Reson.*, 1980, **38**, 447.
29. E. D. Becker, J. A. Ferretti, R. K. Gupta, and G. H. Weiss, *J. Magn. Reson.*, 1980, **37**, 381.
30. R. K. Gupta, J. A. Ferretti, and E. D. Becker, *J. Magn. Reson.*, 1974, **13**, 275.
31. J. Dadok and R. F. Sprecher, *J. Magn. Reson.*, 1974, **13**, 243.
32. C. T. W. Moonen, P. C. M. Van Zijl, J. A. Frank, D. Le Bihan, and E. D. Becker, *Science*, 1990, **250**, 53.

Biographical Sketch

Edwin D. Becker. *b* 1930. B.S., 1952, University of Rochester, Ph.D., 1955, Chemistry, University of California, Berkeley, USA. National Institutes of Health, 1955–present; Laboratory Chief (1972–80, 1988–present); Associate Director for Research Services (1980–88). Concurrent position on Faculty, Georgetown University, 1959–present. Books on NMR. Research interests and publications: hydrogen bonding, molecular structure elucidation, technique development in NMR and other areas of molecular spectroscopy.

Béné, Georges-J.: The Early Days of NMR Research in Geneva

Georges- J. Béné
Section de Physique, DPMC, Geneva, Switzerland

INTRODUCTION

A series of fortuitous events led the present author in the autumn of 1947 to take up research in a field which was entirely new in continental Europe, namely nuclear magnetic resonance.

I had completed several months beforehand my preparatory work at the University of Lyon for a Doctorat ès Sciences when serious family reasons prompted me to apply for a scholarship offered by the University of Geneva to a doctoral student from Lyon. My candidature was successful and on 30 October 1947 Jean Weigle, then the Director of the Institut de Physique at the University of Geneva, assigned the first tasks that were to lead to a doctorate. They involved the comparison of magnetic resonance frequencies of nuclei when the magnetic field $\boldsymbol{B}_0$ is produced by an electromagnet with ferromagnetic pole pieces and by an ironless coil in order to reveal a pure spin–spin interaction—if it existed—between the moments of the pole pieces and those of the sample's atoms as proposed by Stueckelberg.[1]

I should perhaps point out that Jean Weigle on returning from a short stay in the USA had brought back the very first publications of E. M. Purcell, F. Bloch, and their co-workers. This collection was complemented in 1948 by the famous article of N. Bloembergen, E. M. Purcell, and R. V. Pound on nuclear relaxation.

FIRST NMR DETECTION

Work started immediately with this (limited) material. The small team headed by Dr. R. C. Extermann as the project leader (he was to succeed J. Weigle as Professor and Director at the Institut de Physique) included P. Denis, another doctoral candidate who joined us several months later.

It is unnecessary to recall our difficulties in getting the research moving: the construction of an oscillator; tests of various types of bridges including that of Purcell; modifications of an old electromagnet whose homogeneity left much to be desired; the winding of crossed coils for a Bloch spectrometer. The equipment was finally almost complete at the end of June 1948 . . . , but there was still no proton signal.

By participating at the international conference 'Spectroscopy at Radiofrequencies' of the Physical Society held in Oxford at the end of July, my colleague R. Extermann and I were able to come into contact with the main exponents in the field present at the conference (Bloembergen, Rollin, Drain . . .). Above all, however, we found out many details from Drain on how his spectrometer worked. The entire team set to work assiduously when we returned to Geneva, and on the 14 August 1948 we observed the proton signal in a dilute solution of ferric nitrate using Bloch's method at a frequency of ν_0 = 10 MHz.

I was informed at this time that without adequate replenishment my scholarship dried up at the end of July 1948. G. Déjardin, my former 'patron' in Lyon who had been responsible for my finding a scholarship, worked extremely efficiently in helping me obtain support from the French CNRS, starting in October 1948.

On the scientific level, the observed resonance signal was made unusable by transients of various sorts; our first task was to identify and analyze all of them.

TOWARDS THE EARTH'S MAGNETIC FIELD

In order to detect the Stueckelberg effect, two conditions had to be fulfilled. One was the use of an ironless coil to generate the magnetic field. Ours, which had been made available by our colleagues at the University of Lausanne, comprised two coils in a Helmholtz configuration capable of being cooled with circulating water. With this we were able to observe the proton resonance at $\nu_0 \simeq 3$ MHz although stability problems obliged us to work at field strengths below 3.5×10^{-2} T. Resonances for ^{1}H and ^{19}F were thus detected at $\nu_0 \simeq 1.4$ MHz.

The Stueckelberg effect was not observed, but fortunately the Helmholtz coils permitted the inhomogeneity of the magnetic field at the center of symmetry to be calculated accurately for the analysis of transients. Our first publication, presented at the spring meeting of the Swiss Physical Society at Brienz on 7 May 1949, dealt with a thorough study of the 'beats' discovered and analyzed by Jacobsohn and Wangsness.[2] That communication was made a few weeks before the first publication on NMR made by the group from the Ecole Normale Supérieure (ENS) in Paris (30 May 1949). The converging objectives of the two groups became the basis for a close and fruitful collaboration, the only engagement of this type in NMR in continental Europe at the time.

The study of the effects of the speed at the resonance of the sweep field led us to reduce the amplitude of the B_0 static field and increase that of the alternating sweep field. In February 1954 we observed proton resonance in a purely alternating field with a frequency of ν_0 = 350 kHz. Unfortunately, the inhomogeneity of the B_0 field prevented the determination of the lineshapes or linewidths of the narrowest resonances. It was because of this that a proposal by Yves Rocard, then the Director of the Physics Laboratory at the ENS, attracted us. He offered technical assistance and financial support—provided we studied NMR in the Earth's magnetic field, B_T.

Collaboration with a doctoral student from Lausanne (Claude Manus) and with scientists from Paris (mainly J. Winter, B. Cagnac, and J. M. Rocard) allowed us in the spring of 1955 to observe proton resonance in the Earth's field. Our spectrometer was then set up in the middle of a forest where the proton linewidth in benzene did not exceed 1.5×10^{-10} T. Work carried out with this installation is described elsewhere in this Encyclopedia in a contribution entitled ***Terrestrial Magnetic Field NMR*** to which the reader can refer.

REFERENCES

1. E. C. G. Stueckelberg, *Phys. Rev.*, 1948, **73**, 808.
2. B. A. Jacobsohn and R. K. Wangsness, *Phys. Rev.*, 1948, **73**, 942.

Biographical Sketch

Georges-J. Béné. *b* 1919. Dr. Sc., 1951, University of Paris (F). Successively Attaché Chargé, Maître de Recherches CNRS (F) 1948–1957. Successively Professeur Associé, Extraordinaire, Ordinaire, University of Geneva (CH) 1956–1989. President Physics Section of Geneva University 1969–1977. General Secretary (1956–1989) and President (1970–72) of the AMPERE Group—Member of the Steering Committee (1966–68) and of the Council (1968–89) of the European Physical Society. Retired (Honorary Professor) since 1989. Approx. 250 scientific publications.

Bertini, Ivano: A Life with Paramagnetic Molecules

Ivano Bertini

Department of Chemistry, University of Florence, Italy

I come from the School of Inorganic Chemistry of the late Luigi Sacconi. In the early 1960s he was in competition with the School of R. H. Holm at MIT who was pioneering NMR applications to paramagnetic nickel(II) complexes. I therefore went to ETH Zürich to perform my first ^{1}H NMR spectra of paramagnetic bis-salicylaldiminatonickel(II) complexes. The instrument was a Varian HR-60, with no lock and field sweep. The calibration was obtained through sidebands. I joined in 1966 the club associated with the high-resolution NMR of paramagnetic compounds in solution.[1] The first instrument purchased by the University of Florence in 1967 was a Varian DA 60, with internal lock and frequency sweep. We implemented the instrument with an audiofrequency generator in order to modulate the sweeping radiofrequency with the aim of achieving large spectral widths. In this way we could go beyond the 100 ppm spectral width, although highly shifted signals usually suffered from excessive line broadening. The problem of spectral width was, and is, quite serious in the investigation of paramagnetic molecules.

When the FT instruments became available, the most versatile for this kind of problem were the Bruker CXP and then the MSL instruments because of the high power, short 90 $^\circ$ pulses, and short dead times. We could therefore afford to record the ^{1}H signals of high spin cobalt(II) proteins with a spectral width of 200 ppm and low concentration ($\approx$1 mM) of the macromolecule. The first spectrum, partly assigned, of a cobalt protein was that of cobalt-substituted carbonic anhydrase (MW 30 000).[2] Among other systems, I can recollect liver alcohol dehydrogenase (MW 80 000) which shows the β-CH_2 signals of coordinated cysteines between 200 and 300 ppm downfield.[3] Finally, we investigated a paramagnetic copper(II) protein (copper–zinc superoxide dismutase) by allowing copper to interact magnetically with cobalt through a bridging ligand. This is a uniquely successful example in which the electronic relaxation times of a metal ion (copper) have been changed with the aim of making a system suitable for NMR investigation.[4]

With the advent of 600 MHz instruments, it became clear (at least to me) that the magnetic field strength was the main quality of an instrument. Again, we faced the problem of the spectral width. Bruker had built for us a probe which could stand an unusually high power radiofrequency, featuring a proton 90 $^\circ$ pulse of 3.5 μs, with little loss of signal-to-noise. With this probe and a fast ADC we were able to measure spectra over 300 ppm and to perform 2D NOESY spectra on the same spectral width.[5]

If the spectral width has been a limit to overcome, another is the development of time-dependent spin Hamiltonians and suitable software. The problems addressed have been the development of strategies for the suppression of strong signals (e.g. solvent) in order to reduce dynamic range drawbacks. Such drawbacks are particularly serious for paramagnetic molecules which readily display low intensity broad signals. The most successful strategies for signal detection are those which exploit the different relaxation times. Hence NOE experiments were made feasible for fast relaxing nuclei thanks to improvements in spectrometer stability and to the optimization of pulse length, pulse phases, and pulse sequences. The latter have been developed to overcome artifacts which could be dramatic when fast relaxing signals are saturated or inverted.[6] Finally, the optimization of parameters has made possible 2D and 3D spectra for paramagnetic molecules.

During the development of these techniques we found a novel manifestation of cross correlation.[7] Nuclear relaxation in paramagnetic molecules may be due to the presence of a time-averaged electronic magnetic moment. The contribution due to nucleus–nucleus dipolar coupling may also be operative and the two mechanisms cross correlate. As a result, COSY spectra display cross peaks even in the absence of scalar coupling. Such cross peaks contain further structural information. We consider this to be a sign that the NMR of paramagnetic molecules has matured and deserves full recognition in the NMR community.

Simultaneously, I tried to understand further the effect of electron relaxation on nuclear parameters. I interacted in this area with S. H. Koenig formerly at IBM, Yorktown Heights, NY. I introduced zero-field splitting and hyperfine coupling with metal nuclei in the evaluation of nuclear relaxation. Finally, efforts were made to understand why magnetic coupled metal clusters may have such short electron relaxation times to be suitable for NMR characterization.[8]

I should also say that these achievements from the Florence laboratory were possible thanks to my former students, and now colleagues, Claudio Luchinat and Andrea Scozzafava and at a later stage to my pupil Lucia Banci. I am also indebted to Prof. W. DeW. Horrocks who has been one of my teachers.

REFERENCES

1. J. D. Thwaites, I. Bertini, and L. Sacconi, *Inorg. Chem.*, 1966, **5**, 1036.
2. I. Bertini, G. Canti,. C. Luchinat, and F. Mani, *J. Am. Chem. Soc.*, 1981, **103**, 7784.
3. I. Bertini, M. Gerber, G. Lanini, C. Luchinat, W. Maret, S. Rawer, and M. Zeppezauer, *J. Am. Chem. Soc.*, 1984, **106**, 1826.
4. I. Bertini, G. Lanini, C. Luchinat, L. Messori, R. Monnanni, and A. Scozzafava, *J. Am. Chem. Soc.*, 1985, **107**, 4391.
5. I. Bertini, C. Luchinat, L. Messori, and M. Vasak, *Eur. J. Biochem.* 1993, **211**, 235.
6. L. Banci, I. Bertini, C. Luchinat, and M. Piccioli, *FEBS Lett.*, 1990, **272**, 175.
7. I. Bertini, C. Luchinat, and D. Tarchi, *Chem. Phys. Lett.*, 1993, **203**, 445.
8. L. Banci, I. Bertini, and C. Luchinat, *Nuclear and Electron Relaxation*, VCH, Weinheim, 1991.

Biographical Sketch

Ivano Bertini. *b* 1940. Italian Doctor, 1964; free docent, (1969) lecturer (1965) and Professor of Chemistry (1975) at the University of Florence, Italy. More than 300 publications; with C. Luchinat the book (1986), NMR of Paramagnetic Molecules in Biological Systems,

Benjamin/Cummings, Menlo Park, CA, and with L. Banci and C. Luchinat the book (1991), Nuclear and Electron Relaxation, VCH, Germany. Research interests include the structure and dynamics of paramagnetic metalloproteins, nuclear relaxation, electron relaxation, protein chemistry, and environmental biotechnology.

Bible, Roy H. Jr.: NMR: An Organic Chemist's Dream Come True

Roy H. Bible, Jr.

G. D. Searle & Co., Skokie, IL, USA

My own interest in NMR as an analytical tool originated from my intense concern with the structures of organic molecules. I had worked at G. D. Searle & Co. as an organic chemist at the bench for 12 years before the first easily operated NMR instrument, the Varian A-60, became available in 1961. Prior to that time, we had only elemental analysis, UV, IR, and optical rotatory dispersion available as supplements to solubility tests, color reactions, and chemical derivatizations to assist us in the structure elucidation of molecules.

The first NMR spectrum which I received on a compound of my own was a 40 MHz proton spectrum determined at the Worcester Foundation for Experimental Biology and Medicine. At that time we were attempting to introduce a methyl group into a steroid, and were using the integration of the 7.25 μm infrared absorption band to determine if we had, in fact, achieved our goal. The NMR spectrum immediately gave the answer, and the analytical world has never been the same since.

From the organic chemist's viewpoint, the availability of the Varian A-60 spectrometer revolutionized NMR. Suddenly spectra were easily obtained and plotted on a precalibrated chart rather than on the strip recorder with markings generated by an audio signal generator. The field and frequency were locked together by use of an internal water sample. I first saw the A-60 in a hotel room in Chicago during an ACS meeting, where it was being demonstrated by NMR pioneers LeRoy F. Johnson and James N. Shoolery of Varian Associates.

My interest in the structure elucidation of organic compounds had already led me to become a consultant of sorts at G. D. Searle in the interpretation of IR and UV spectra. The availability of a Varian A-60 instrument at Searle rapidly led to my full-time involvement in the use of physical techniques for the elucidation of structures. Because the older techniques were primarily chemical, the new techniques were called 'physical methods' and in 1966 I became 'Head of Physical Methodology'.

My first exposure to a collection of proton spectra was an examination of the proof copy of the first Varian catalog by Shoolery, Bhacca, and Johnson, at one of the early Varian Workshops in Palo Alto, CA. I studied the spectra intensely, trying to relate the spectral characteristics to the structures. I recall that my traveling companions were on edge while I studied the spectra, because we were running late to catch a plane back to Chicago. Perhaps this pattern of my trying to gather the last bit of data before leaving the laboratory for a lecture or a trip still persists.

For my own mental enjoyment, I find it necessary to correlate all the small pieces of data into a larger picture. On arrival of our A-60 at Searle, I presented a seminar which summarized the major aspects of the interpretation of proton NMR data. To make the seminar as useful as possible, I assembled the discussion into a small spiral-bound pamphlet, which resulted in my being asked to give similar talks for various outside groups.

Charles Bell and Ludwig Bauer had decided that there was enough interest for a short course in NMR at the University of Illinois School of Pharmacy, and invited me to give a presentation there. My little booklet evolved further, and eventually I was the lead-off speaker at the short courses at the School of Pharmacy. In the 1-hour presentations I told everything I knew about the interpretation of proton spectra! The presentation expanded as my own knowledge base grew and, at the last short course, included a reasonable discussion of second-order effects in proton spectra.

I remember distinctly at one of the School of Pharmacy sessions that LeRoy Johnson had an HR-100 spectrometer. The magnet was powered by enormous vacuum tubes which glowed white-hot and generated a tremendous amount of heat.

Herman A. Szymanski heard me present my 1-hour summary of the interpretation of proton spectra, and had seen the booklet which I had prepared. He suggested that I write a book on the interpretation of proton spectra. I eagerly accepted his suggestion, and the book was published by Plenum Press in 1965.

As an organic chemist, I wanted to know how to use NMR. The theory was of interest to me, but the important thing was the use of NMR data to determine the structures of organic molecules. To make the contents of my book very clear, I entitled it The Interpretation of NMR Spectra—An Empirical Approach.

This small book was followed by a work-book which led the organic chemist by the hand through the interpretation of specific examples of NMR spectra. Both books were translated into Japanese. The first book was also translated into Russian, without permission of course. Surprisingly, both of these books were still being sold at a very moderate rate even in 1993.

I still believe that most of the use of NMR comes from an empirical application of observations rather than from the application of theory. Attesting to this, I think that there are very few practising NMR spectroscopists who really understand the Cooley–Tukey fast Fourier transform algorithm and its implementation in the computer.

In 1966, Varian, with the cooperation of the American Chemical Society, sponsored a short course in NMR at Pittsburgh airport. This location was, in fact, a center of operations for Varian. They had both an applications laboratory and a parts depot. There was a legendary service engineer, Cappy Joller, who, according to legend, had memorized all the schematics and critical voltage measurements and could recite the details on the spot.

The course taught at the Pittsburgh airport, which included the hands-on use of instruments, was led by LeRoy F. Johnson. In 1967, LeRoy Johnson asked me if I would be willing to help teach an ACS course on the interpretation of proton NMR spectra. He said that the empirical approach which I had taken in my book appealed to many of the participants. Thus began my teaching partnership with LeRoy Johnson, which has continued over the years and still actively goes on.

The course which we taught on the interpretation of proton spectra changed every time we taught it of course, and naturally I learned more from teaching it than the participants learned from taking the course. From our experience, we published an ACS audio course in 1978. We incorporated every advancement that came along, and at every course we would

show the spectra which we had obtained from the latest NMR instrumentation.

My teaching with LeRoy Johnson led to my involvement in other short courses: a series at Canisius College which was started by Herman Szymanski; a series at the University of New Hampshire organized by Robert E. Lyle; a series organized by John Grutzner of Purdue University; and currently a series originated by Harry C. Dorn and taught at Virginia Tech.

The Experimental NMR Conferences have played an important role in my own NMR education. George Slomp of Upjohn and I always sat in the front row and made audio tapes of nearly every talk. I remember Richard Ernst's presentation of his first Fourier transform experiments, and Paul Lauterbur showing images of an earthworm which he chose as a sample because it fitted in his 5-mm tube. I remember the detailed discussions by Castellano and Bothner-By on computer simulations of spin−spin coupling patterns and determinations of coupling constants to a hundredth of a hertz.

My own excitement in NMR has come from the tremendous amount of information made available to the organic chemist about how his molecule of interest is put together and how it behaves. My interests have been on the practical side, always eager to use theory where it would help to solve a problem, but in general emphasizing the most practical techniques which could be used to solve chemical and structural problems with the least effort. To one who initially had to integrate peaks by first tracing them on paper, then cutting them out and weighing the paper, it is very rewarding to see how NMR has evolved. I am sure that the fun and excitement have just begun!

Biographical Sketch

Roy H. Bible, Jr. *b* 1926. B.S., 1948, Virginia Tech., M.S., 1949, Ph.D., 1951, University of Illinois at Urbana. Successively medicinal chemist, Head of Physical Methodology, Assistant Director of Analytical Resources and Methods, Director of Physical Methodology, research fellow, and currently senior research fellow and Director of Physical Methodology. Two NMR texts and, with LeRoy Johnson, an ACS sponsored audio course on the interpretation of NMR spectra. Lecturer in many short courses. Research specialty: application of NMR techniques in organic chemistry, especially in structure determination.

Blinc, Robert: The AMPERE Society and the Development of Magnetic Resonance in Eastern Europe

Robert Blinc

University of Ljubljana, Ljubljana, Slovenia

Despite the fact that electron spin resonance had already been discovered in the radiofrequency region in 1944 in St. Petersburg by Zavoisky (and the corresponding article published in German in the *Phys. Zeitschrift der Sowiet Union*) the development of magnetic resonance in Eastern Europe—and also in most of Western Europe with the exception of Great Britain—was significantly slower than in the United States. This was the result of the destruction during the World War II, the emigration of a significant part of the European scientific elite to the USA before and after the war and the 'iron curtain' which was dividing Europe into two parts: western Europe which was slowly recovering with the help of the Marshall plan, and eastern Europe where, among other things, the dictatorial regimes imposed severe restrictions on the free exchange of goods, scientists, and scientific information. To stimulate magnetic resonance research in Europe and to overcome the general lack of equipment, literature, know-how, and many other resources in the field of radiospectroscopy, R. Freymann from Paris at a conference in Oxford in 1948 proposed the idea of creating a liaison bulletin to exchange information and to ask for government support to purchase surplus American equipment for joint use. With the help of Professors Alfred Kastler (who later won the Nobel Prize), Yves Rocard, and Pierre Grivet, Freymann's idea gained support and in 1952 the first AMPERE (= Atomes et Molécules par Etudes Radio-Electriques) conference was held in Paris. In 1953 the first issue of the Bulletin AMPERE was published by George Béné from Geneva. The AMPERE group was created as an association of scientists and laboratories, not of official national organizations—with a minimum of bureaucratic constraints. It was first a society of French speaking radiospectroscopists but the frontiers became more and more open at each subsequent meeting and in 1955 most magnetic resonance laboratories in western Europe participated. One of the important goals of the AMPERE group was to promote scientific contacts between scientists in eastern and western Europe in spite of all the political difficulties. In order to facilitate these contacts, Geneva in neutral Switzerland was chosen as the seat of the secretariat.

In Great Britain, Oxford and the British Radiospectroscopy Group were centers of excellence in magnetic resonance research with Professors Bleaney, Andrew, and Jack Powles. Professor Abragam from France had also been a prominent visitor to Oxford. In the Netherlands, France, Italy, and Belgium, magnetic resonance groups were working successfully. In East Germany, A. Lösche had started magnetic resonance research and had written the book Kerninduktion. In Switzerland, magnetic resonance centers in Geneva—Béné, Peter—and in Zürich—Känzig, Gränicher—had been established. In West Germany, Karl Hausser was essential in building up magnetic resonance research and H. Dehmelt—who later left for the USA—discovered nuclear quadrupole resonance (some years later he won the Nobel Prize for his measurements of the g-factor of the electron). Professor Laukien started the Bruker company. In the Soviet Union, the center of magnetic resonance research had moved to Kazan with Professor Altschüller, whereas important low-temperature work had been done by Borovik-Romanov in Moscow. Much later a very successful center was established in Estonia by Lippmaa. Magnetic resonance groups were also starting in Poland in Poznan and Krakow, in Romania in Cluj (Ursu) and in Zagreb and Ljubljana in Yugoslavia (at present in Croatia and Slovenia).

In 1956 the first scientist from eastern Europe, Professor A. Lösche from Leipzig, was invited to attend the Colloque AMPERE in Geneva and in 1961 the AMPERE Congress was held in Leipzig, i.e. in the same year as the Berlin Wall was built. In 1965, a year before the Congress AMPERE in Ljubljana, the AMPERE Society had already 550 member physicists from 12 western and eight eastern European countries. In 1972, at the AMPERE Summer School in Baško Polje on the Adriatic coast which was organized by the Ljubljana group, Jean Jeener first proposed the idea of 2D NMR. A student from Switzerland informed his advisor Richard Ernst about Jeener's proposal, resulting in the development of multidimensional NMR. John Waugh, Erwin Hahn, and many other scientists from the USA also took part at this event. They, as well as Alex Pines, became regular guests at subsequent AMPERE events, much to the benefit of the development of magnetic resonance in eastern and western Europe.

Biographical Sketch

Robert Blinc. *b* 1933. Ph.D., 1959, Physics, University of Ljubljana. Postdoctoral work with J. S. Waugh, MIT, Cambridge, MA. Faculty member (currently Professor of Physics), University of Ljubljana, J. Stefan Institute, 1969–present. President of AMPERE Society 1988–94. Approx. 450 publications and, with B. Žekš, the book 'Soft Modes in Ferroelectrics and Antiferroelectrics'; ISMAR prize, 1977. Research interests include NMR of phase transitions and disordered condensed matter.

Bloch, Felix: The Principle of Nuclear Induction

Felix Bloch
Stanford University, Stanford, U.S.A.

Nobel Lecture, December 11, 1952
© Le Prix Nobel, 1952

It is a tribute to the inherent harmony and the organic growth of our branch of science that every advance in physics is largely due to the developments that preceded it. The discovery for which Purcell and I have received the honor of the Nobel Prize award for the year 1952 is a typical example of this situation, and before describing the principle I shall therefore present an outline of its long and distinguished background.

Both the method and the object go back ultimately to spectroscopy, a field to which modern physics owes so much in other respects. Among the various aspects of this field there are two which are of particular importance here: the Zeeman effect for introducing magnetic fields as an essential element of spectroscopy, and the hyperfine structure of spectral lines for revealing the existence of nuclear moments. The correct interpretation of hyperfine structures was first given in 1924 by Pauli,[1] who proposed that atomic nuclei may possess an intrinsic angular momentum (spin) and, parallel to its orientation, a magnetic moment. The energy of interaction of this magnetic moment with the magnetic field H(O), produced by the atomic electrons at the position of the nucleus, depends upon the angle between them and leads thus to the observed small splitting of the energy levels. Conversely, it is possible under suitable conditions to determine from this splitting both the spin and the magnetic moment of the nucleus, and these two important quantities have indeed been determined in a great number of cases from the observation of hyperfine structures. The magnetic moments of the nuclei have been found, in all observed cases, to be of the order of the 'nuclear magneton' which one obtains by substituting in the formula for the atomic Bohr magneton the mass of the proton in place of that of the electron. Nuclear moments are thus about a thousand times smaller than atomic moments, and this is plausible in view of the fact that one deals here with protons instead of electrons as elementary charged constituents. There are, however, distinct disadvantages in the optical determination of nuclear moments. In the first place the accuracy is seriously limited due to the fact that the effect consists only in such a small splitting of spectral lines that one has to be concerned with their finite width. In the second place it is necessary for the determination of the nuclear magnetic moment from the observed hyperfine structure to have a knowledge of the field H(O) which is usually rather inaccurate since it involves complex electron configurations. In view of these limitations one is led to values of nuclear magnetic moments with an accurary of a few per cent at best. Finally, one is faced with the fact that hyperfine splittings tend to decrease with decreasing atomic number with the result that it is not possible, by optical means, to observe them in the case of the greatest fundamental importance, that of hydrogen.

A decisive step forward was made in 1933 by Stern,[2] who applied his method of molecular beams to the determination of the magnetic moments of the proton and the deuteron in hydrogen molecules. Instead of the emitted light, it is here the deflection of the molecule in an inhomogeneous magnetic field which is affected by the nuclear moments. Although the observed effect was close to the limit of observability it yielded the proton moment to within 10% with the most important result that instead of having the expected value of one nuclear magneton it is about 2.5 times larger. Of similar importance was the result that the magnetic moment of the deuteron was between 0.5 and one nuclear magneton, since it indicated from the simplest plausible considerations of the structure of this nucleus that one should ascribe a moment of about 2 nuclear magnetons to the neutron. I shall come back later to this point; it represents the start from which my own experimental work has followed in an almost continuous line.

Subsequent to Stern's work, a number of far-reaching further developments have been achieved by Rabi in the application of atomic and molecular beams to the measurement of nuclear moments and hyperfine structures. Without attempting completeness I want to mention some aspects of method in the brilliant series of investigations which he carried out with his collaborators. One of them is based upon a paper by Breit and Rabi,[3] which treats the variation of the magnetic moment of an atom for the different Zeeman levels of hyperfine structure under the influence of an external magnetic field and which was applied to atomic beams where the deflection gives a direct measure of the magnetic moment. Another important aspect lies in the passage of the beam through two and later three separate field regions which can be adjusted to give zero deflection so that one deals with a null method. These innovations, besides giving many other interesting results, allowed the measurement of the hyperfine structure in the ground state of light and heavy hydrogen atoms; since the previously mentioned field H(O), produced by the electron at the place of the nucleus, was given here, through a formula of Fermi[4] from the well-known theory of the hydrogen atom, this measurement resulted in the determination of the magnetic moments of the proton and the deuteron with an accuracy of a few per cent.

However, the most significant improvement in molecular and atomic beam techniques was the introduction of the magnetic resonance method. The beam here passes through a region where the magnetic field is homogeneous and constant with a weak alternating magnetic field superimposed at right angles to the strong constant field. Analogous to the resonance absorption of visible light, transitions occur here from one Zeeman level to another if the alternating field satisfies Bohr's frequency condition for the energy difference between the two levels. However, instead of optical frequencies one deals here normally with frequencies in the radio range so that this application of the magnetic resonance method, like our own, is properly labeled as belonging to the new field of radiofrequency spectroscopy. In the beam technique it has the great advantage of dispensing with a knowledge of the deflecting inhomogeneous fields, since the deflection is merely used now as an indicator for the occurrence of transitions in the homogeneous field region. A very much greater accuracy can thus be obtained; it led, for example, to the knowledge of the magnetic moments of the proton and the deuteron with an accuracy of about one part in a thousand and to the important

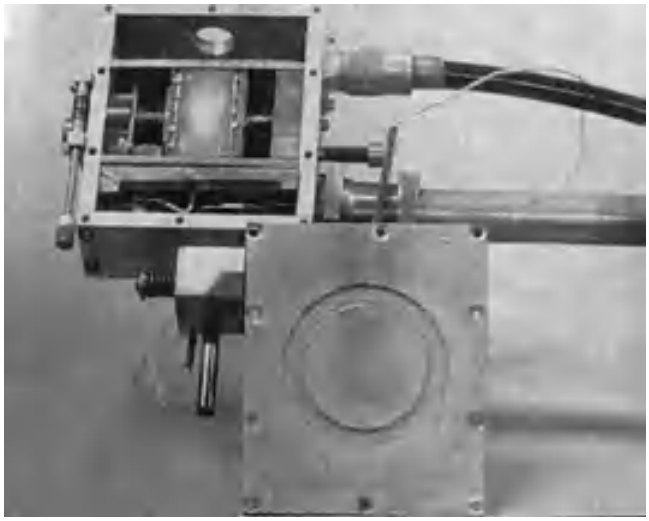

Figure 1 The 'head' of the crossed coil arrangement with the cover plate removed. The bottom tube to the right contains the leads to the transmitter coil, which is wound in two sections visible in black in the head. The black cable leads from the receiver coil to the amplifier; the receiver coil is wound with a vertical axis inside the hollow lucite piece between the two sections of the transmitter coil. The sample test tubes are placed in its interior through the circular hole at the top of the supporting frame

discovery of a small but finite electrical quadrupole moment of the deuteron[5] in 1939.

The first use of the magnetic resonance method was suggested in 1936 by Gorter[6] in an attempt to detect the resonance absorption of radio quanta through the heating of a crystal. While the results of this experiment were negative, Rabi[7] in 1937 has treated the transitions in a rotating field and has pointed out their use in atomic and molecular beams.

Coming from quite a different direction, I was led at that time to similar ideas. They originated from my preceding work which dealt with the magnetic moment of the neutron and which had been stimulated by Stern's previously mentioned measurement of the magnetic moment of the deuteron.[2] The idea that a neutral elementary particle should possess an intrinsic magnetic moment had a particular fascination to me, since it was in such striking contrast to the then only existing theory of an intrinsic moment which had been given by Dirac[8] for the electron. Combining relativistic and quantum effects, he had shown that the magnetic moment of the electron was a direct consequence of its charge and it was clear that the magnetic moment of the neutron would have to have an entirely different origin. It seemed important to furnish a direct experimental proof for the existence of a magnetic moment of the free neutron, and I pointed out in 1936[9] that such a proof could be obtained by observing the scattering of slow neutrons in iron. The very strongly inhomogeneous magnetic field in the neighborhood of each iron atom was shown to affect a passing neutron through its magnetic moment and thus to lead to an appreciable magnetic scattering effect; it was shown at the same time, that magnetic scattering would lead to the polarization of neutron beams. The existence of this effect was first clearly demonstrated in 1937 by a group of investigators at Columbia University,[10] and it opened up the possibility of further work with polarized neutron beams.

The most desirable goal to be reached here was that of accurately measuring the magnetic moment of the neutron. It occurred to me that resonance depolarization could be achieved by passing a polarized neutron beam through a region where a weak oscillating field is superimposed on a strong constant field, provided that the frequency of the former is equal to the frequency with which the neutron moment carries out a precessional motion around the direction of the constant field. A knowledge of this field and of the corresponding resonance frequency directly determines the magnetic moment under the safe assumption that the spin of the neutron is $\frac{1}{2}$, and the magnetic scattering effect enters in this arrangement merely as an indicator for the occurrence of resonance depolarization. The application to polarized neutron beams was also noted by Rabi[7] in his previously mentioned original paper on the magnetic resonance method. It was first achieved in 1939 by Alvarez and myself[11] with the use of the Berkeley cyclotron, and yielded a value for the magnetic moment of the neutron which was consistent with that of the deuteron if one assumed the latter to be additively composed of the moments of the proton and the neutron. The accuracy of this measurement amounted to about 1% and was partly limited by that with which the strength of the constant field could be determined. Another limit of accuracy arose from the smallness of the observed polarization effect, but a subsequent systematic investigation of neutron polarization,[12] carried out with the Stanford cyclotron, showed how this effect could be greatly increased.

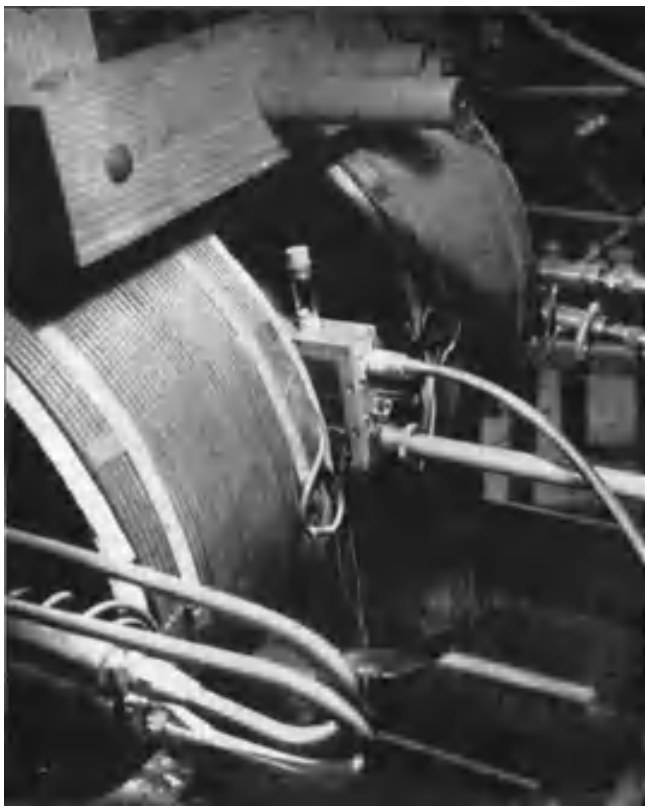

Figure 2 The same head as in 1, about to be inserted in the gap of an electromagnet and containing a sample test tube. The two protruding lucite rods between the leads reach into the interior of the head and carry small copper disks; a fine adjustment of the coupling is achieved by rotation of these 'paddles'

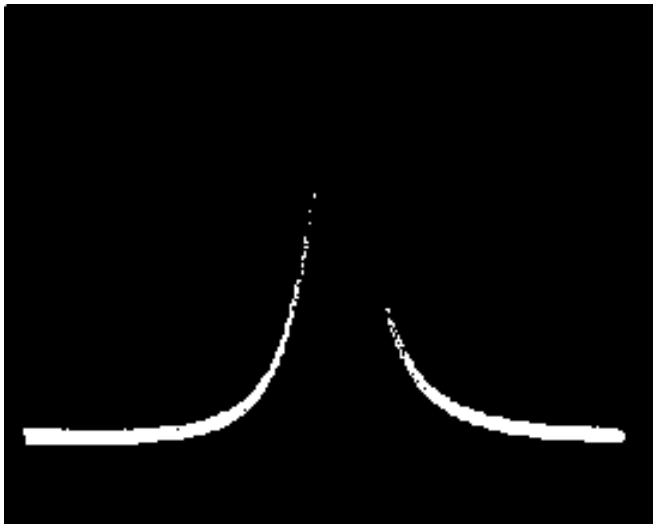

Figure 3 A resonance line of protons in water, containing $MnSO_4$ as a paramagnetic catalyst, and obtained from the phase component of the nuclear induction signal which corresponds to absorption. The photograph is that of the trace on a cathode-ray oscillograph with the vertical deflection arising from the rectified and amplified signal and the horizontal deflection corresponding to different values of the constant field

It was of considerable importance to improve the accuracy of the determination of the neutron moment to at least one part in a thousand in order to test small deviations from the additivity of the moments of the proton and the neutron, which could be expected in connection with the finite electric quadrupole moment of the deuteron, according to the theoretical work of Rarita and Schwinger.[13] The fact that higher accuracy hinged essentially upon that of a field calibration and the search for a suitable and convenient standard led me to new ideas when, toward the end of the last war, my thoughts turned back to the continuation of my previous work.

The essential fact of the magnetic resonance consists in the change of orientation of nuclear moments, and the methods to be employed in molecular and atomic beams as well as in neutron beams are primarily indicated by the different ways to detect this change. The acquaintance with radio techniques during the war suggested to me still another and much simpler way, that of detecting the reorientation of nuclear moments through the normal methods of radio reception. The signals to be detected would be due to the electromagnetic induction caused by nuclear reorientation and should appear as a voltage difference between the terminals of an external electric circuit. I believe that this is the most general and distinctive feature of our discovery, and it is for this reason that I chose for it the name of 'nuclear induction'. Purcell, whose independent approach was largely based on considerations of energy relations, has chosen to call it 'nuclear magnetic resonance absorption', but soon after our respective initial work and despite its apparent difference, it became clear that it was based upon the same principle.

In order to understand this principle, one can start from macroscopic quantities and describe the underlying phenomenon in classical terms. Consider for this purpose, as a typical example, about one cubic centimeter of water with the protons contained in it as the nuclei under investigation. Their magnetic moments are oriented in a completely random manner in the absence of an external magnetic field; after the sample has been brought into such a field, however, there will be established a new thermal equilibrium in which the magnetic moments are distributed with a slight surplus parallel to the field. Even in relatively strong fields of the order of 10 000 G this surplus will at room temperature amount to no more than about one part in a million. While its direct observation would be difficult, there thus exists a 'nuclear paramagnetism' in the sense that one deals with a finite macroscopic nuclear polarization which is both parallel and proportional to the applied external field. The establishment of thermal equilibrium demands the transfer of the energy released by the partial orientation of the nuclear moments into heat, and it can take place only through interaction of these moments with their molecular surroundings. The strength of this interaction determines the time interval required for the nuclear moments to adjust themselves to the equilibrium conditions; it is measured by the 'relaxation time', as in the analogous case of atomic paramagnetism. The role of the relaxation time is of basic significance for our experiments, and I shall soon come back to its discussion.

For the moment, we shall return to the equilibrium state, once it is established, and to the description of the nuclear polarization under the conditions of magnetic resonance. A simple mechanical consideration of the gyroscope shows that an alternating field at right angles to the constant field has the effect of tilting the direction of the polarization with respect to the constant field and that the polarization will

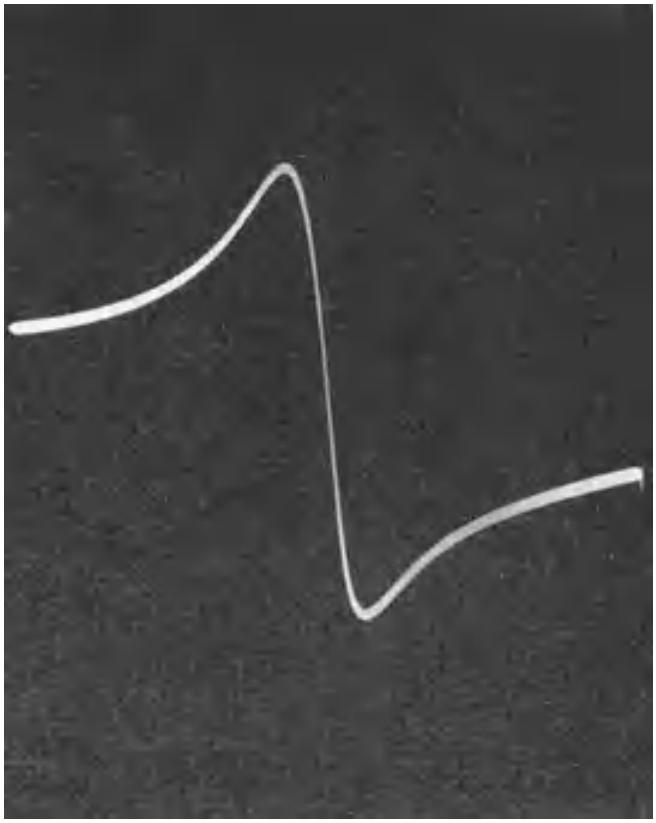

Figure 4 The only difference between this line and that of Figure 3 lies in the adjustment of the observed phase which is here that corresponding to dispersion

thereupon continue to perform a precessional rotation around this field. The angular frequency of precession is proportional to the field with a constant of proportionality which is called the 'gyromagnetic ratio' of the nuclei and which is equal to the ratio of their magnetic moment and their intrinsic angular momentum. From a perfectly macroscopic point of view, one thus deals with a situation in which the protons in our cubic centimeter of water have the effect of an invisible compass needle rotating in its interior. The 'invisibility' refers actually only to observation of optical frequencies; the rotation occurs in the range of radiofrequencies, and it can very well be observed by using Faraday's law of induction. Indeed, the rotation of our compass needle is accompanied by that of a magnetic field which possesses an alternating component perpendicular to the axis of rotation, and hence by an electromotive force, induced in a suitably wound coil of wire around the sample. From here on it is merely a matter of the standard techniques of radio reception to rectify and amplify this electromotive force so that it can be recorded on a voltmeter, displayed on a cathode-ray oscillograph, or made audible in a loudspeaker.

What amazed me most in my first calculations on this effect was the magnitude of the signals which one could expect from nuclear induction. In our example of a cubic centimeter of water in a normal field of a few thousand gauss they turned out to amount to the order of a millivolt. This magnitude is well above the noise which accompanies any radio receiver and which sets the ultimate limit of signal detection. It should be observed here that, being a phenomenon of fluctuations, the noise can always be reduced by averaging over sufficiently long times. This procedure was used later to very greatly increase the sensitivity of the method; it is characteristic of the present possibilities that my collaborators have succeeded in the last few years in detecting in natural water signals arising from deuterium and from the isotope of oxygen with atomic mass 17, despite their low abundances of 0.02% and 0.04%, respectively.

The existence and detection of a precessing nuclear polarization in a sample represents to my mind the basis of nuclear induction. It is, however, necessary to consider also the features which produce and counteract the tilt of the polarization with respect to the constant field. Magnetic resonance enters here as the most important means of producing the tilt, since it allows its achievement under the application of relatively weak oscillating fields. In fact, it is a common feature of every resonance phenomenon that relatively weak external forces can produce large effects if their frequency is equal to the natural frequency of the system to which they are applied. The natural frequency in question is, in our case, that with which the nuclear polarization precesses by itself around the constant field and the practical way to determine this frequency is to vary either that of the applied alternating field or the magnitude of the constant field until resonance conditions are established and detected by a maximum of the observed nuclear induction signal. The simultaneous knowledge of resonance field and frequency then directly yields, as in the use of magnetic resonance in molecular beams, the gyromagnetic ratio and, with a knowledge of the spin, the magnetic moment of the nucleus. Actually, it is also possible to determine the spin separately by using the additional piece of information contained in the intensity of the observed signal.

To follow the analogue of mechanical resonance we must now come back to relaxation, which can be seen to act like a friction, and which counteracts the tilt produced by the alternating field. If the friction is large, i.e., if the relaxation time is short, it will either reduce the effect for a given amplitude or require a correspondingly larger amplitude of the alternating field. It will, in either case, result in a relatively broad resonance line, thus diminishing the accuracy of the measurement. While from this point of view it is undesirable to have too short a relaxation time, it is equally undesirable to have it too long, since the very circumstance of producing its tilt diminishes the magnitude of the polarization so that it requires the refreshing influence of the relaxation mechanism to bring it back to its equilibrium value.

There was not much known about the magnitude of nuclear relaxation times when Purcell and I started our first experiments on nuclear induction, and the main doubt about their success arose from the possibility of insufficient relaxation. In fact, it seems, in retrospect, that the failure of Gorter's first attempt,[6] as well as of a second one, undertaken in 1942,[14] was primarily due to this circumstance. While E. M. Purcell, H. C. Torrey, and R. V. Pound,[15] toward the end of 1945, obtained their first positive results from protons in paraffin, the late W. W. Hansen, M. E. Packard, and I[16] found ours a few weeks later in water without either of the groups knowing anything about the work of the other. The relaxation time of paraffin has the convenient value of about 1/100 s, while pure water has a somewhat unfavorably long relaxation time of about 2 s. Neither of these two values had been foreseen, and I was fully prepared to find the relaxation time of pure water considerably longer and in fact too long for our method of observation. It was known, however, that the conversion of *ortho*- and *para*-hydrogen was accelerated by the presence of paramagnetic atoms and molecules; this mechanism has the common feature, with the attainment of the equilibrum polarization of protons, that it requires a random process of nuclear reorientation, and it had been understood to take place through the magnetic field of the paramagnetic catalyst acting upon the magnetic moment of the proton. An estimate showed that, depending upon the concentration of a paramagnetic salt dissolved in water, a wide range of relaxation times, going down to values of the order of 10^{-5} s, could be obtained. Before starting our observations we therefore had prepared solutions of the paramagnetic iron nitrate in water, and although the first weak signals were received from pure water we found, shortly afterward, considerably stronger signals from a solution with about 0.5 molar concentration of iron nitrate. The signals appeared as rather broad lines on the cathode-ray oscillograph because of insufficient homogeneity of the constant magnetic field.

Since the width of the resonance line determines the accuracy with which magnetic moments can be determined, we shall briefly consider the conditions necessary for obtaining sharp lines. In the first place, it is necessary that the constant field have the same value in all parts of the sample; in the second place, one must not choose an excessive amplitude of the alternating field, since this too would cause an excessive broadening. The ultimate limit is given by the natural width of the line and it is closely related to the relaxation time; it can be seen, in fact, that the relative accuracy of a measurement by nuclear induction, due to the natural linewidth, is limited to the

order of the number of cycles which the nuclear polarization carries out in its precession around the constant field during the relaxation time. As an example, we shall again consider protons in pure water and in a field of 10 000 G; the frequency of precession is here 42.5 Mc/s, so that about 10^8 cycles are performed during the relaxation time of approximately 2 s. This means that an accuracy of about 1 part in 100 millions could be, in principle, achieved here, provided that one had a sufficiently homogeneous field available. While this limit has not yet been reached, it is noteworthy that in water, alcohol, and other liquids, resolutions of one part in 10 millions have actually been achieved. It is indeed the possibility of coherent observation over a large number of cycles which allows the use of nuclear induction as a method of high precision measurements. In fulfillment of my original plans, it was applied by H. H. Staub, D. B. Nicodemus, and me to the magnetic moments of the proton, the neutron and the deuteron,[17] and it resulted not only in the verification of the previously mentioned deviation from additivity in the deuteron,[13] but in its measurement with an accuracy which is beyond the present scope of the theory of nuclear forces. It was particularly gratifying to me to obtain these results from experiments combining the polarization and magnetic resonance depolarization of neutrons with nuclear induction.

The description of nuclear induction which I have presented follows closely my own original thoughts on the subject but it can equally well be approached from other angles. The simplest one is probably that of Gorter[6] in his first attempt to detect nuclear magnetic resonance. We have seen before that the alternating field tilts the nuclear polarization against the constant field. This process requires a certain amount of work which, through relaxation, will reappear in the form of heat produced in the sample. The effect in fact does not involve induction but represents pure nuclear resonance absorption; however, it would be very slight and has not yet been established. A second attempt of Gorter,[14] carried out later, is based upon the fact that the nuclear paramagnetic susceptibility has a maximum for radiofrequencies, corresponding to magnetic resonance conditions; it would manifest itself in the frequency of an electric oscillator of which a coil, surrounding the sample, forms the self-inductance. This scheme is actually one of the many others which can be devised for the observation of nuclear induction and, if successful, would have represented the first demonstration of the effect. Purcell's first successful experiment involved the electrodynamical aspect of absorption insofar as its occurrence under resonance conditions was manifested through the increased loss of a cavity resonator; the cavity was replaced in his succeeding arrangements by more conventional circuit elements. A particularly suitable and convenient arrangement consists of a radiofrequency bridge, which contains in one arm a coil, surrounding the sample. As a consequence of nuclear induction there occurs, under resonance conditions, a change of the impedance of this coil and thereby a readily detectable change in the balance of the bridge. It should be remarked that the change of impedance is complex, with its real part corresponding to absorption, its imaginary part to dispersion. This fact can be traced back to the phase relation between the nuclear induction signal and the applied radiofrequency field, and the phase sensitivity of the bridge allows the observation of the effect either as absorption or as dispersion or as a combination of both.

Finally, I shall give a brief description of our own original arrangement which we still use in its principal features. The essential balance which Purcell has obtained by a bridge method is here to a large extent achieved geometrically by using two radiofrequency coils with their axes oriented at right angles to each other and to the constant field. One of them, the 'transmitter coil' produces the alternating field, while the other, the 'receiver coil', serves for detection of the nuclear induction signal (see Figures 1, 2). A small amount of coupling between the two coils is admitted to produce a voltage across the receiver coil, and its phase with respect to the superimposed voltage induced by the nuclei can be adjusted for the observation of either absorption or dispersion in similarity to the bridge method (see Figures 3, 4).

A considerable variety of other circuits has been introduced by different investigators. Except for the greater or lesser ease of avoiding instrumental difficulties, they lead to the same ultimate sensitivity and accuracy of the method, since they all observe the same basic phenomenon.

There is, however, one distinctive feature in the cross-coil arrangement, which automatically yields another significant piece of information. The two coils imply a sense of rotation around the constant field; depending upon whether the nuclear polarization precesses in the same or the opposite sense of rotation there results a phase difference of 180° between the voltage in the receiver coil due to coupling with the transmitter coil and the superimposed voltage due to nuclear induction. The action of the rectifier translates this phase difference into an inversion of the signal, which is directly displayed on the oscillograph or on the recording instrument. One obtains in this simple manner information about the sign of the magnetic moment of the nucleus, defined by its relative orientation to the angular momentum, since it is this sign which determines the sense of rotation of the nuclear polarization in a given field. The sign of nuclear moments represents an important clue to their interpretation in terms of nuclear structures; usually it is referred to the sign of the proton moment, which has been known for a considerable time to be positive. It has been determined in this manner for a number of nuclei where it was not previously known.

REFERENCES

1. W. Pauli, *Naturwiss.*, 1924, **12**, 741.
2. R. Frisch and O. Stern, *Z. Phys.*, 1933, **85**, 4; R. Frisch, I. Estermann and O. Stern, *Z. Phys.*, 1933, **85**, 17; I. Estermann and O. Stern, *Phys. Rev.*, 1934, **45**, 761.
3. G. Breit and I. I. Rabi, *Phys. Rev.*, 1931, **38**, 2082.
4. E. Fermi, *Z. Phys.*, 1930, **60**, 320.
5. J. M. B. Kellogg, I. I. Rabi, N. F. Ramsey, Jr., and J. R. Zacharias, *Phys. Rev.*, 1939, **55**, 318; 1940, **57**, 677.
6. C. J. Gorter, *Physica (The Hague)*, 1936, **3**, 995.
7. I. I. Rabi, *Phys. Rev.*, 1937, **51**, 652.
8. P. A. M. Dirac, *Proc. R. Soc. London*, 1928, **A117**, 610.
9. F. Bloch, *Phys. Rev.*, 1936, **50**, 259; 1937, **51**, 994.
10. P. N. Powers, H. G. Beyer, and J. R. Dunning, *Phys. Rev.*, 1937, **51**, 371.
11. L. W. Alvarez and F. Bloch, *Phys. Rev.*, 1940, **57**, 111.
12. F. Bloch, M. Hamermesh, and H. Staub, *Phys. Rev.*, 1943, **64**, 47.

13. W. Rarita and J. Schwinger, *Phys. Rev.*, 1941, **59**, 436.
14. C. J. Gorter and L. J. F. Broer, *Physica*, 1942, **9**, 591.
15. E. M. Purcell, H. C. Torrey, and R. V. Pound, *Phys. Rev.*, 1946, **69**, 37; N. Bloembergen, E. M. Purcell, and R. V. Pound, *Phys. Rev.*, 1948, **73**, 679.
16. F. Bloch, W. W. Hansen, and M. Packard, *Phys. Rev.*, 1946, **69**, 127; F. Bloch, *Phys. Rev.*, 1946, **70**, 460.
17. F. Bloch, D. Nicodemus, and H. H. Staub, *Phys. Rev.*, 1948, **74**, 1025.

Biographical Sketch

Felix Bloch. *b* 1905, *d* 1983. Ph.D., Physics, University of Leipzig, 1928. Research on theoretical solid state physics with Pauli, Kramers, Heisenberg, Bohr, and Fermi. Professor of Physics, Stanford University, 1933–83. Devised the procedure of nuclear induction and demonstrated it with W. W. Hansen and M. E. Packard in January 1946. Awarded the Nobel Prize in Physics in 1952.

Bloembergen, Nicolaas: My Early Years in NMR, 1946–48

Nicolaas Bloembergen

Pierce Hall,, Harvard University, Cambridge, MA, USA

I had the good fortune to arrive at Harvard University in February 1946, about six weeks after the discovery of nuclear magnetic resonance in condensed matter by Edward M. Purcell, Robert V. Pound, and Henry C. Torrey.[1] This volume contains a first-hand account of the facts surrounding this discovery written by Pound (***Pound, Robert V.: Early Days in NMR***).[2] He begins by describing the concentrated activity of scientists at the MIT Radiation Laboratory to advance radar techniques which played a vital role in the conduct of World War II.

I passed those war years in The Netherlands, occupied by Nazi forces. I studied physics at the University of Utrecht and passed my qualifying doctoral examination in April 1943 just a few weeks before the German authorities closed all Dutch universities. I survived the remaining two war years without significant scientific activity.

After the liberation of The Netherlands in May 1945 by the allied forces, the prospects for carrying out good physics research in Europe to obtain a Ph.D. degree in a reasonable time were dim. I therefore wrote to three universities in the United States, which I identified on the basis that the *Physical Review* in the years prior to 1942 had published a substantial number of papers originating from these institutions. Only Harvard University responded positively to my inquiry. The formalities of documentation required for admission to the Graduate School of Arts and Sciences, for a Dutch passport, for a US student visa, for a permit to exchange Dutch to US valuta, and obtaining passage on a liberty ship freighter from the destroyed port of Rotterdam to the United States took about eight months. My arrival at Harvard in the middle of February 1946 was determined by these external factors, but it turned out that I had arrived at a propitious place at a propitious time.

The contrast between the anemic state of academic affairs in the war-torn Netherlands and the exhilarating pulse of scientific research in Cambridge, Massachusetts, was bewildering at first, but members of the Harvard physics faculty were most helpful and sympathetic. I discussed the possibility of cosmic ray research with Professor J. C. Street and of NMR research with Professor E. M. Purcell. The latter topic appealed to me more, because it was a new experimental technique and it was somewhat related to Dutch work on magnetic relaxation which I had heard about. More important was the fact that Professor Purcell needed a pair of hands for a follow-up on the pioneering experiment,[1] while he, Pound, and Torrey were still engaged in writing chapters for the MIT Radiation Laboratory Series. The spring term 1946 at Harvard had an exceptionally large and gifted class of graduate students. Most of them had just returned from military service, had no previous laboratory experience, and were enrolled in a full-time course program. Fortunately I had brought with me a preprint of predoctoral research work carried out at the University of Utrecht.[3] It involved the development of a low-noise photoelectric amplifier coupled to a phase-sensitive a.c. galvanometer.[3] On this basis Purcell accepted me tentatively as his first graduate student and as a quarter-time laboratory assistant. He advised me that I should also take two graduate courses. I enrolled several weeks late in a course on electromagnetism given by Julian Schwinger and a course on statistical mechanics by E. C. Kemble. Since I had taken both subjects before with L. Rosenfeld in Utrecht, I had no trouble with either course and spent most of my time in the laboratory.

My first task was to make a mud pie of mineral oil and calcium fluoride powder and to stuff it through a small coupling hole into the cavity used in the first NMR experiment. A few days later I witnessed the detection of both the proton and fluorine NMR signals, as Pound controlled the electronic equipment and Purcell managed the magnet current.

My next task was to build a lock-in amplifier according to Dicke's design.[4] It would take many years before this item would become commercially available. I familiarized myself with RCA vacuum tubes, electronic components, chassis punches, etc. My craftsmanship was marginal. The lock-in performed reasonably during my 18 months at Harvard, but was relegated to the scrap heap soon after my departure. I also built a 30 Hz multivibrator oscillator and power amplifier to feed the modulation coils installed on the 1905 electromagnet from the Société Génévoise, which was to serve us in future experiments. The ponderous cavity was replaced by an LC circuit resonant near 30 MHz. The coil was placed in a shielded sidearm which fitted into the 1-in. wide gap between the pole pieces of about 5 in. diameter. The Q-value of the LC circuit was about one order of magnitude smaller than that of the cavity, and the sample volume was reduced by three orders of magnitude. The coil was about 1 cm long with a 0.5 cm inside diameter.

The stability of the magnetic field caused problems, because of low-frequency variations in the output of an old dc generator with a wobbly armature. I spent considerable time building a feedback amplifier to stabilize the current. This effort was not successful and it was decided to supply the magnet current from truck storage batteries. A jury-rigged rheostat consisting of clamp sliding along manganin strips adjusted the current. The research budget was extremely limited and 'string and sealing wax' techniques were widely used.

When I. I. Rabi visited Harvard in April 1946, balancing the radiofrequency bridge was still a tricky art. Purcell was disappointed that we were not able to show Rabi the proton NMR signal in water or mineral oil on the lock-in output meter. After they left, I tuned all controls from scratch and within an hour or so was able to get the signal back. I rushed upstairs to Purcell's office. Fortunately Rabi was still there and they were both happy to see the NMR signal.

I built a more symmetrical rf bridge with orthogonal adjustments of amplitude and phase, so that the in-phase and out-of-phase part of the nuclear magnetic susceptibility could be measured independently. We observed saturation of the NMR resonance when the rf power was turned up, while increasing the balance of the bridge so as to keep the input to the rf amplifier at a constant level.

At this time Purcell and Pound had returned from the MIT Radiation Laboratory and could devote more time to the project. When I once mentioned to Bob Pound that the

signal appeared to change in magnitude after reinsertion of the probe in the magnet gap, he immediately moved the probe around the gap in a systematic manner. We found the narrowest resonance with the largest peak signal at the location away from the center of the gap near the edge of a pole piece. This was caused by inhomogeneities in the magnet material. The minimum linewidth in water and some other fluid samples was about 0.14 G. At this 'sweet spot' of minimum inhomogeneity of the magnetic field, the resonance in a CaF_2 sample remained broad.

We decided we could measure the true width, proportional to ${T_2}^{-1}$, in a single crystal of CaF_2. We also realized that this width should show a marked anisotropy and would be a minimum when the magnetic field was pointed along the body diagonal of the cubic lattice. In this orientation the nearest neighbors would not contribute a static local field component parallel to the external field. It is the magic angle δ between the body diagonal and the cubic axis, for which $3\cos^2\delta = 1$. I spent a few days cutting a cylinder with its axis along a face diagonal out of a natural CaF_2 crystal. This cylindrical sample could be rotated inside the rf coil. Our observed linewidths were in agreement with a formula for the second moment of internal dipolar fields derived by Van Vleck. Purcell spent hours on a Marchant mechanical calculator to evaluate the dipolar lattice sums for a cubic lattice. This resulted in a joint publication with Purcell and Pound.[5]

Of more interest were the narrow lines in fluids. We realized that we could not measure their true width which was masked by the magnetic field inhomogeneity but we could measure the relaxation time T_1. Somehow the motion in the fluids 'averaged out' the local magnetic field variations produced by neighboring nuclear spins. Very soon the term 'motional narrowing' was coined, as the three of us moved our index fingers relative to one another in space to visualize the time dependence of dipolar interactions. The variations of the local field with time were the important clue to magnetic relaxation problems.

Purcell and Pound conceived an experiment on hydrogen gas. The local field, and therefore the Larmor precession frequency, would change during the collisions. The collision rate could be varied by changing the pressure. Pound[2] describes how he understood the process of averaging as a rapid random modulation of the resonant frequency. They built a cell which contained an rf coil and hydrogen gas at a variable pressure. It was found the relaxation time T_1 increased as the pressure was increased from 10 atm to 30 atm. The term 'pressure narrowing' was introduced, even though the magnetic field inhomogeneity prevented direct observation of the true width.[6] This behavior stands in sharp contrast to the 'pressure broadening' familiar in optical spectroscopy.

I concentrated my attention on the proper description of the time-dependent local field in liquids. Fortunately I had followed a seminar on Brownian motion and noise given by J. M. W. Milatz in 1942 at Utrecht. I had written the lecture notes for it which had been distributed in mimeographed form. I was therefore familiar with the concept of power spectral densities of random variables. Purcell made the valuable suggestion that the book by Debye entitled 'Polar Molecules' would be relevant.[7] He was obviously aware of the high frequency dielectric losses of polar liquids. The dielectric relaxation in polar liquids is caused by the random rotation of the electric dipole moments as described by Debye. During the fall of 1946 I worked out the spectral density of the various terms in the dipole–dipole interaction between two proton spins due to the random rotation of a water molecule. I also calculated the contributions to the local field spectral density of translational Brownian motion of spins in different molecules. I realized that the Fourier components in the local field at the Larmor frequency and twice the Larmor frequency were responsible for the longitudinal relaxation process and determined T_1. I remember I obtained explicit equations for T_1 in water between Christmas 1946 and New Year in my dormitory room, when a bad cold prevented me from going to the lab.

The transverse relaxation process described by T_2 also had a contribution from Fourier components near zero frequency. I correctly surmised that a self-consistent description required that motional narrowing starts when the local field spectral density has a correlation time shorter than T_2 for the static case. It need not be short compared to the resonant period.

These insights could of course be tested by varying the viscosity of the fluid samples. I prepared scores of samples with hydrocarbons from light to heavy oils, water–glycerin mixtures, and measured their viscosities. The experimental data for T_1 for these samples fitted the theory nicely.

All this experimental and theoretical activity took place during the last three months of 1946. During this period I evolved from a lab assistant to a full-fledged research partner. Purcell decided that I should present the results on NMR relaxation in liquids at the annual meeting of the American Physical Society in New York City in January 1947. The abstract was published in the *Physical Review*.[8] My mandate was to get the essential ideas of T_1 in fluids across in 10 min. Thanks to a rehearsal at Harvard before a critical audience consisting solely of Purcell and Pound, I was able to finish the presentation in accented English before a packed audience at Columbia University a few seconds before the chairman's bell rang.

The spring of 1947 was spent in rounding out the experimental data for my Ph.D. thesis. I realized that the cleanest way to check the dependence of T_1 on the correlation time τ_c of the fluid motion was to vary the temperature of a glycerin sample over a wide temperature range. At $-40\ ^\circ$C glycerin is almost glasslike. I soldered some copper tubing around the brass pipe containing the rf coil and put a can filled with acetone and dry ice above the magnet gap. I started a syphoning action by sucking some cold acetone which then dripped into another can below the magnet gap. The temperature of the sample was monitored with a thermocouple. Thus the smell of acetone was added to the acrid smell from the overnight battery recharging process in the basement room of the Lyman laboratory. Environmental regulations did not impede the pace of progress in NMR research in early 1947. I also realized that many solids including ice had sufficient internal motion to explain observed relaxation times T_1. The shortening of T_1 by paramagnetic ions in solution was quantitatively measured. A few additional experiments on the relaxation of ^{19}F and ^{7}Li in ionic solutions were also carried out.

I made the inhomogeneous broadening of the linewidth in water visible on the screen of an oscilloscope in the following way. I first turned off the current in the modulation coils. The rf field would then saturate the protons in that part of the sample where the resonance condition was satisfied. I next turned up the modulation current to a large value so as to sweep through

the whole resonance broadened by the field inhomogeneity. This resonance showed the saturation dip. I called it 'eating a hole out of the inhomogeneous distribution'. The dip filled up in a time of a few seconds. I was so excited by this observation made during a weekend that I immediately called Purcell at his home. A few days later we filmed the disappearance of the 'hole' with an 8-mm movie camera and determined that T_1 = 2.3 s in water. Of course, we also checked that the resonance in CaF_2 was homogeneously saturated and showed no dip.

I built another rf bridge at 4.8 MHz to extend the T_1 measurements to a lower frequency. The theoretical dependence of T_1 on $\omega\tau_c$ was verified. The lower frequency also permitted the detection of the deuteron magnetic resonance in heavy water with the magnet at our disposal. In a 50:50 per cent mixture of light and heavy water, I found the relaxation time of $\boldsymbol{D}$ to be much shorter than that of $\boldsymbol{H}$. I realized that the explanation should be found in terms of a time-dependent quadrupolar interaction, and I subsequently calculated the spectral density of the electric field gradient explicitly. This observation of the relaxation time in heavy water is an early manifestation of a nuclear quadrupole interaction in condensed matter.

While Purcell and Pound were regular participants in the experiments in the fall of 1946, their visits to the basement room in 1947 became infrequent. Pound had shifted his interest to the study of nuclear quadrupole interactions in solids, while Purcell was not only busy with teaching duties but also with preparing other research projects for additional graduate students. Already in 1946 he had designed a permanent magnet with a field of about 6000 Oe in a gap of about 2 cm. George Pake used this magnet to study the lineshape of NMR in a gypsum crystal. Pake worked in the basement room next door to mine and we conversed regularly through a hole in the wall. We decided to move the permanent magnet to the physics lecture hall to give a public demonstration of NMR at the Harvard Physics Colloquium in April 1947 where I had been invited to speak. By this time the experimental work for my thesis was essentially complete.

Professor C. J. Gorter from the University of Leiden was a guest lecturer at Harvard arriving in the summer of 1947. He gave a special course on paramagnetic relaxation based on his book written during the last years of the war.[9] I had not met him before in The Netherlands. He was of course much interested in the work on magnetism carried out at Harvard by J. H. Van Vleck and by Purcell's group. I explained to him that I would like to submit my Ph.D. thesis with him at Leiden, since I had already passed all my qualifying examinations in The Netherlands and I did not want to spend the time and money to repeat them at Harvard. Gorter was enthusiastic and immediately offered me a research position at Kamerlingh Onnes laboratory in Leiden. I was to start there in September 1947. Purcell was quite understanding and agreed to this arrangement. He and Van Vleck, who was then Chairman of the Physics Department, were however interested in my eventual return to Harvard. They arranged for me to be interviewed by the Senior Fellows of the Society of Fellows before my departure. I was to hear in 1948 in The Netherlands about the outcome of this interview.

I witnessed discussions between Gorter and Van Vleck about the influence of scalar spin exchange interactions in electron paramagnetic resonance. Gorter argued correctly that the rapid spin flip–flop exchanges would cause the equivalence of motional narrowing. This viewpoint appealed to me. Van Vleck argued, also correctly, that the scalar exchange interaction leaves the second moment of the resonance line invariant. He subsequently realized that the exchange interaction greatly enhances the fourth moment and that consequently the observed resonance would indeed exhibit exchange narrowing.[15]

During the summer of 1947 I completed the rough draft for my thesis which I discussed with Gorter and Purcell. The latter retained a copy of my handwritten notes which would serve as the basis for the comprehensive paper we planned to publish in the *Physical Review*.[10] It was also decided to communicate the essence of our results more quickly in a note in *Nature*.[11] This decision was probably spurred by the appearance in this journal of some related work by B. V. Rollin and others[12–14] at Oxford University.

Gorter and I were both keen on introducing NMR techniques to the European continent and extend the relaxation investigation to liquid helium temperatures. We decided that we could make a quick start by duplicating the Harvard setup. We therefore went to the Boston Radio Shack and bought all the electronic equipment and components needed. The Kamerlingh Onnes lab had of course good electromagnets and cryostats. I had the NMR setup going within one month after my arrival in Leiden. The machine shops there were supervised by highly professional master technicians and instrument makers. It was not appreciated, or even permitted, for scientists to do an amateurish job as I had done at Harvard. If one went through the established channels, however, beautiful gadgets were delivered on a surprisingly fast schedule. The liquefaction of hydrogen and helium was entirely in the hands of the technicians and no mortal scientist was allowed to touch a helium Dewar. Liquid helium was only available on Thursdays and my low-temperature experiments had to be scheduled well in advance.

Gorter, who was busy as Director of the large Kamerlingh Onnes Laboratory, left me complete freedom to proceed as I wished. I was most interested in understanding the NMR relaxation mechanism in solids without large-scale atomic motion. I knew that Waller's theory on the interaction of nuclear spins with phonons predicted extremely long relaxation times,[16] and I had confirmed this by calculating the change in local fields produced by the classical motion of vibrating atoms. Clearly paramagnetic impurities might play a role. They would have to produce local fields at the nuclear Larmor precession frequency and it occurred to me that the z component of the electron spin might produce such Fourier components, as it executed random transitions through the interaction with lattice vibrations in the paramagnetic relaxation process. For a quantitative test a series of potassium aluminum crystallites were grown, doped with concentrations of Fe^{3+} ions varying from a few ppm to a few per cent. The relaxation time in these samples was measured from room temperature to liquid helium temperature. The influence of these impurities in concentrations of a few ppm on the nuclear spin relaxation time was confirmed. I calculated, however, that at these low concentrations most nuclear spins would be too far away from the impurity to undergo rapid relaxation. I resolved this difficulty by introducing the concept of spin diffusion.[17]

The theory of Heitler and Teller[18] for nuclear spin relaxation in metals by interaction with conduction electrons predicted reasonably short values for T_1. I tested this experimentally in a sample of copper powder particles embedded in paraffin and

obtained results[19] in agreement with the Heitler–Teller model. Gorter asked me to measure the T_1 relaxation time of ^{7}Li in the identical LiCl crystal which he and Broer[20] had used in their attempt to detect NMR in 1942. I measured this time to be 10 min at 2.1 K, caused by some undetermined paramagnetic impurity. It is likely that they saturated this resonance on their first scan and consequently no reproducible signal could be found on subsequent traversals. They would have had a better chance if they had used a less pure crystal, or had observed the influence of dispersion on the resonant frequency with a marginal oscillator.

I was interested in showing that fast electron spin exchange, in a way similar to fast electron spin–lattice relaxation, would prevent excessive broadening of a nuclear spin resonance. I therefore grew a crystal of $CuSO_4{\cdot}5H_2O$. The proton resonance was readily observable at room temperature and its width was mostly determined by the local fields of other protons. When the crystal was cooled, the line broadened and assumed a complicated pattern at 20 K. At liquid helium temperatures the resonance was split into 10 well-resolved lines, extending over 400 G, corresponding to a variation of over 7%. These correspond to 10 distinctive proton positions in the unit cell, each with a different time-averaged local field produced by the average magnetization of the copper ions. These paramagnetic shifts[21] are large, but they attracted much less attention than the Knight shift in metals[22] caused by the temperature-independent paramagnetism of conduction electrons.

In May 1948 I defended my Ph.D. thesis 'Nuclear Magnetic Relaxation' in a grand public ceremony in the centuries-old aula of Leiden University, where I arrived in white tie and tails in a horse-drawn carriage according to an ancient ritual which has since succumbed to modern efficiency. I had 500 copies of the thesis printed. About half of them were distributed among the Dutch physics faculty and colleagues, family and friends. The remaining copies sold quickly through the offices of the publishing house Nyhoff in The Hague. During the 1950s my thesis was reproduced in various formats in Japan, in The Netherlands, and possibly elsewhere. It was republished in 1961 in the 'Frontiers in Physics' series.[23] Some comments and corrections were added in an appendix which relate our earlier work to subsequent developments and improvements. They are of some historical interest.

The article 'Relaxation Effects in Nuclear Magnetic Resonance Absorption' which was published[10] in *Physical Review* also received much attention. It is commonly referred to as BPP, an acronym of the names of the authors: Bloembergen, Purcell, and Pound. The paper belongs to the top half dozen physics papers which received most citations in the *Science Citation Index*[24] during the period 1945–1988. It attains this distinction as a Citation Classic,[25] undoubtedly because a large number of scientists outside of physics have referred to it over an extended period.

In the summer of 1948 I felt that the basic nuclear spin relaxation mechanisms in solids, liquids, and gases were understood. I was invited to speak about this topic at an international conference in Zürich, devoted to postwar advances in high energy and nuclear physics as well. The international renown of Bloch and Purcell was already high, but in 1948 transatlantic travel was still predominantly by ocean liner. Considerations of time and expense prevented them from attending. I was honored to introduce the emerging field of NMR to a critical audience, which included among others Heitler, Pauli, and Weisskopf. In the hallway I heard afterwards the comment that 'the experimenters had gotten ahead of the theoreticians'. This reinforced my view that a combination of these two aspects of physics is more than the sum of the separate parts.

I also traveled with Gorter to a low-temperature conference in Oxford, where I became acquainted with B. Bleaney and M. H. L. Pryce who worked on electron spin resonance at microwave frequencies. I also met for the first time with B. V. Rollin and J. Hatton whose work closely paralleled my own.[26] I had the impression that they considered NMR as an amateur sport. For me it was not only fun, but also a serious professional pursuit. Therefore our experimental and theoretical results were more systematic and quantitative and received subsequently much wider attention.

I had decided to accept the offer to become a Junior Fellow in the Society of Fellows, a position R. V. Pound had held earlier. I left Leiden and returned to Harvard in January 1949. This switch also marked my taking leave from NMR for several years. For better or for worse, I decided to become familiar with other aspects of physics. For starters, I wanted to acquire some first-hand experience with microwave techniques. I studied the electron spin resonance at the transition from ferromagnetic to paramagnetic resonance near the Curie point of nickel.[27] Next, I joined the Harvard cyclotron group to learn some nuclear physics. At the end of my term in the Society of Fellows I obtained a tenured faculty position in the Division of Engineering and Applied Physics at Harvard in July 1951. There was no vacancy in the Physics Department, where R. V. Pound, E. M. Purcell, and N. F. Ramsey already directed experimental research programs in magnetic resonance. Research in solid state physics was to be carried out in the Division, headed at that time by J. H. Van Vleck as Dean. I was glad to return to NMR and apply its techniques to the study of solids. Although the NMR enterprise had grown enormously during the intervening years 1949 to 1951, I found that many nuggets remained to be unearthed. It has remained a fertile field up to the present.

REFERENCES

1. E. M. Purcell, H. C. Torrey, and R. V. Pound, *Phys. Rev.*, 1946, **69**, 37.
2. R. V. Pound, Early Days in NMR, *Encyclopedia of NMR*, Wiley, Chichester, 1994, Vol. 1.
3. J. M. W. Milatz and N. Bloembergen, *Physica (The Hague)*, 1946, **11**, 449.
4. R. H. Dicke, *Rev. Sci. Instrum.*, 1946, **17**, 268.
5. E. M. Purcell, N. Bloembergen, and R. V. Pound, *Phys. Rev.*, 1946, **70**, 988.
6. E. M. Purcell, R. V. Pound, and N. Bloembergen, *Phys. Rev.*, 1946, **70**, 986.
7. P. J. W. Debye, *Polar Molecules*, Dover Publications, New York, 1945.
8. N. Bloembergen, R. V. Pound, and E. M. Purcell, *Phys. Rev.*, 1947, **71**, 466.
9. C. J. Gorter, *Paramagnetic Relaxation*, Elsevier, Amsterdam, 1947.
10. N. Bloembergen, E. M. Purcell, and R. V. Pound, *Phys. Rev.*, 1948, **73**, 679.
11. N. Bloembergen, E. M. Purcell, and R. V. Pound, *Nature (London)*, 1947, **160**, 475.

12. B. V. Rollin, *Nature (London)*, 1946, **158**, 669.
13. B. V. Rollin and J. Hatton, *Nature (London)*, 1947, **159**, 201.
14. B. V. Rollin, J. Hatton, A. H. Cooke, and R. J. Benzie, *Nature (London)*, 1947, **160**, 436.
15. J. H. Van Vleck, *Phys. Rev.*, 1948, **74**, 1168.
16. I. Waller, *Z. Phys.*, 1932, **79**, 370.
17. N. Bloembergen, *Physica (The Hague)*, 1949, **15**, 386.
18. W. Heitler and E. Teller, *Proc. R. Soc. London*, 1936, **A155**, 629.
19. N. Bloembergen, *Physica (The Hague)*, 1949, **15**, 588.
20. C. J. Gorter and L. J. F. Broer, *Physica (The Hague)*, 1942, **9**, 591.
21. N. Bloembergen, *Phys. Rev.*, 1949, **75**, 1326; *Physica (The Hague)*, 1950, **16**, 95.
22. W. D. Knight, *Phys. Rev.*, 1949, **76**, 1259.
23. N. Bloembergen, *Nuclear Magnetic Relaxation*, W. A. Benjamin, 1961.
24. E. Garfield, The Most-cited Papers of all Time, Science Citation Index 1945–1988, Parts 1 and 2, *Current Contents*, 1990, **30**, No. 7, 45 and No. 26, 227.
25. *Current Contents*, 1977, **17**, No. 18, 7.
26. B. V. Rollin and J. Hatton, *Phys. Rev.*, 1948, **74**, 346.
27. N. Bloembergen, *Phys. Rev.*, 1950, **78**, 572.

Biographical Sketch

Nicolaas Bloembergen. *b* 1920. Phil. Cand., 1941, Phil. Drs., 1943, University of Utrecht, Dr. Phil., 1948, University of Leiden, The Netherlands. Research for Ph.D. thesis entitled ‘Nuclear Magnetic Relaxation’ carried out at Harvard University under the guidance of E. M. Purcell. Postdoctoral work in Leiden, 1947–48. Junior Fellow, 1949–1951; Tenured Professor at Harvard University since 1951. Nobel Prize for Physics, 1981. Currently, Gerhard Gade University Professor, Emeritus. Approx. 350 publications, including two monographs. Research specialties: magnetic relaxation, masers and lasers, nonlinear optics.

Bloom, Myer: Personal Views of NMR History

Myer Bloom
Department of Physics, University of British Columbia, Vancouver, BC, Canada

McGILL UNIVERSITY (1949–50): NUCLEAR PHYSICS

I first heard of NMR in late 1948 while an undergraduate in the final year of the mathematics and physics program at McGill University. A speaker at the weekly colloquium, Karl Darrow, then Secretary of the American Physical Society, told us about the work of the Harvard and Stanford groups and predicted that NMR would ultimately become a major research area in its own right. Furthermore, he informed us that NMR experiments were being carried out at the McGill Radiation (Nuclear Physics) Laboratory. As a consequence, I spent a year doing an M.Sc. thesis in NMR. It may seem odd now that my introduction to NMR was in a nuclear physics laboratory, but the majority of NMR papers published in that era involved measurements of nuclear magnetic moments that are now listed in isotope tables. This subfield was used up in short order and has by now disappeared completely from the NMR culture.

Although I had the (mistaken) impression in 1950 that nuclear physics was going to be the most exciting subfield in physics for the next decade, I had learned as a summer student researcher at Chalk River (Canada's atomic energy laboratory) about the use of neutron diffraction to determine the positions of hydrogen atoms in crystalline solids. Having only one electron, hydrogen atoms are essentially invisible to X-rays in the presence of heavy atoms. The isotopes of hydrogen do scatter neutrons as well as heavy elements, better than most in fact, so that neutron diffraction renders them visible. By now, neutron diffraction has become a standard tool in crystallography but only a few people appreciated its potential value at that time. Having been sensitized by this experience, it is not surprising that my M.Sc. thesis[1] was based on the 1949 paper by the Harvard group[2] in which accurate estimates of proton–proton distances in solids were obtained from second moments of proton NMR lines. The rigorous interpretation of second moments underlying this type of crystallographic study had been established in Van Vleck's classic theoretical paper.[3]

UNIVERSITY OF ILLINOIS (1950–54)

I went to Illinois as a student in the Ph.D. program with the intention of studying nuclear physics, but adopted NMR as a research field for my Ph.D. thesis immediately after meeting Charlie Slichter. As a lowly 'Instructor', Charlie did not yet have sufficient seniority to supervise graduate students officially, but a lively group was already gathering about him. Richard Norberg was a worldly-wise, experienced graduate student who plays an important role in my narrative. Dick was by then well advanced in his experimental study of the hydrogen–palladium system, perhaps the first serious study of a solid state system carried out using NMR. He had actually overlapped with the legendary Erwin Hahn, recently departed for Stanford, and had many amusing stories to tell about the joyous approach to the study of natural phenomena personified by Hahn.

An important feature of the NMR scene in Urbana was the presence of Herb Gutowsky and his group in the Chemistry Department. Gutowsky and Slichter had known each other from their Harvard days, and their graduate students and visitors interacted in a completely natural way. This interaction proved to be important to my ultimate choice of a Ph.D. thesis topic.

FREE MAGNETIC INDUCTION IN PURE NUCLEAR QUADRUPOLE RESONANCE

Dave McCall, then a graduate student in Gutowsky's laboratory, was studying the recently discovered[4] 'nuclear quadrupole resonance' (NQR) signals of the ^{35}Cl and ^{37}Cl isotopes in solids. In this experiment, no static external magnetic field is used and the nuclear spin energy levels are due to the coupling of the nuclear quadrupole moment with the electric field gradient. McCall was using a horribly nonlinear, but sensitive, device characterized as a 'super-regenerative oscillator–detector'. This instrument had proven to be effective for the detection of NQR of nuclei such as ^{35}Cl and ^{37}Cl having small magnetic moments. Dave explained to me that the theory of the instrument[5] postulated that, under resonance conditions, a nuclear magnetic induction signal provided the initial condition for the onset of oscillations when the instrument was operated in a 'pulse–quench' mode. The theory had, however, only been established for NMR and Dave assumed that similar conditions obtained for NQR. This stimulated me to consider the theory for the magnetic induction signal for a spin-$\frac{3}{2}$ system in zero magnetic field, having a quadrupolar splitting and subjected to one or more rf pulses applied close to the quadrupolar splitting frequency. My calculations showed that the type of magnetic free induction and spin echo signals found by Erwin Hahn[6] in NMR should also be observable in NQR. That this should happen was not immediately obvious since the spin system is initially unpolarized in zero magnetic field when the $I_z = \pm m$ states are degenerate and equally populated. In modern terms, however, we would say that the difference in population between the pairs of states characterized by $I_z = \pm \frac{1}{2}$ and $\pm\frac{3}{2}$ causes a tensor polarization to be established at equilibrium. The application of rf pulses breaks the quadrupolar symmetry allowing tensor polarization to be transferred to vector polarization via precession induced by the quadrupolar interactions. The relevance of these symmetry considerations was pointed out to me by Slichter.

The first observation of an NQR spin echo was made shortly thereafter on the ^{35}Cl signal in $NaClO_3$ by Dick Norberg who had long since completed his Ph.D. thesis and had a broadband pulse spectrometer suitable for searching for such a signal. It turned out that, unbeknownst to us, Erwin Hahn and his student Bernie Herzog were also hot on the trail of NQR spin echoes; they detected the echoes at about the same time as we did as indicated by our concurrent publications.[7,8] I subsequently

carried out a systematic study of NQR spin echoes and the main results of my thesis[9] were published jointly with Hahn and Herzog.[10] In closing this section, I wish to express my appreciation to both Charlie Slichter and Dick Norberg, who contributed to the conceptual and practical aspects of detecting magnetic induction in NQR and who unselfishly insisted that they should not participate in the final paper which owed so much to them.

KAMERLINGH ONNES LABORATORIUM, UNIVERSITY OF LEIDEN (1954–56): LOW-TEMPERATURE PHYSICS

In 1954, I went to the Kamerlingh Onnes Laboratory in Leiden on a National Research Council of Canada Travelling Fellowship. The K.O. lab was a dominant force in low-temperature physics from 1908, when Kamerlingh Onnes first liquefied helium, to the mid-1950s. Its director in 1954 was Professor C. J. Gorter, known primarily as a leading figure in low-temperature research and also for his two valiant, though unsuccessful, attempts to detect NMR[11,12] and for his proposal of the 'Rabi method' of doing magnetic resonance in atomic and molecular beam experiments.[13] Professor Gorter induced Nicolaas Bloembergen, who is of Dutch origin, to present his Ph.D. thesis, based on work carried out at Harvard University, to the University of Leiden[14] and to do some postdoctoral research there. The results of Bloembergen's Leiden researches[15] are of considerable historical interest since they indicate that the failure of Gorter and Broer[12] to detect NMR can be attributed to the high purity of the alkali halide solids used in their search, resulting in extremely long spin–lattice relaxation times in the liquid helium temperature range that rendered the NMR signals invisible. For psychological reasons, these initial searches for NMR seem to have been carried out from the perspective of low-temperature physics, the mandate of the K.O. lab so to speak. Looking back, it appears to me that Gorter's failure to be the first to undertake a successful NMR experiment in a bulk sample was due to a combination of bad luck and the limitations of this low-temperature perspective.

Leiden was a wonderful place for a neophyte like myself to learn low-temperature physics. The Kamerlingh Onnes Laboratory had been designed around an instrument makers school and the teachers in this outstanding school were master technicians with the title *Meester* who worked directly with the low-temperature scientists. Visitors were treated with great courtesy by the *Meesters* who helped them immeasurably both in learning Dutch and acquiring the lore of low-temperature experimental methodology. I decided to participate in the ongoing research program by joining the group of Nico Poulis, who was using NMR effectively to study magnetic phase transitions in the liquid helium range. While helping the Poulis group, I would construct a pulsed spectrometer in order to introduce spin echo techniques to the K.O. lab. I wasn't quite sure what I planned to do with the pulse spectrometer and postponed that decision to a later day.

The day-to-day manner in which physics was done in the K.O. lab was totally different from anything in my previous experience. Almost all experiments involved the use of liquid helium, which was a precious commodity to be handled with care and in a systematic manner. It was a matter of pride that some of the procedures worked out by Kamerlingh Onnes and the *Meesters* were still being used! Helium was liquefied only on the specific day of each week set aside for measurements; the other days of the week were spent thinking carefully about the meaning of the last set of measurements and preparing for the next. The lab thus had a rhythm into which individual researchers had to fit the style and personality of their work. As a new Ph.D. from the newly-emerging NMR culture, this took some getting used to. I had become accustomed to having my own pulsed NMR rig with which I could do experiments or just fool around with whenever I felt like it.

Another cultural difference was the decoupling in Leiden between theory (in the Lorentz Institute) and experiment (in the K.O. lab). Though these were in adjoining buildings, it seemed that the experimental and theoretical physicists met each other only on the evening of the historical *Ehrenfest Colloquium*. An exception was Professor Gorter who had a well-developed theoretical intuition and interacted strongly with theoreticians (cf. his explanation with Van Vleck[16] of exchange narrowing in NMR). Compare this separation of theory and experiment with the American style of doing physics as characterized by Dyson's perceptive comments[17] on the famous Bloembergen, Purcell, and Pound paper:[18] 'It is one of the finest examples of the American style of physics, with experiment and theory working together as inexorably as a steam-roller and squashing a problem flat'. I came to appreciate the educational value of teaching 'living theory' to experimentalists, as was done in Illinois, only after starting to work in Leiden.

SPIN–LATTICE RELAXATION BY MAGNONS

My lack of appreciation of the importance and intensity of this difference in working styles led ultimately to some profound difficulties in my working relationships in the K.O. lab. During my first year in Leiden, the Poulis group had initiated a study of the temperature dependence of T_1 in the antiferromagnetic phase of $CuCl_2 \cdot 6H_2O$. They found an extremely strong variation of T_1 with temperature in the liquid helium temperature range, T_1 increasing by about three orders of magnitude (from a few ms to a few seconds) as the temperature was decreased from 4.2 K to 1.2 K.[19] This behavior generated lots of excitement and speculation in the lab but no progress was made over a period of months on its quantitative interpretation. The K.O. lab was closed over the Easter holiday period, but I didn't go on holiday and instead spent my time thinking hard about the T_1 results. I found that the temperature dependence of the relaxation rate $(1/T_1)$ correlated well with the *deviations* $\Delta M_{\pm} = M_0 - M_{\pm}(T)$ of the sublattice magnetizations from their saturation values, as inferred from the temperature dependence of the proton Larmor frequency measured carefully by the Poulis group over the previous year. Furthermore, I found that if I associated $\Delta M_{\pm}$ with magnetic particles traveling through the magnetic sublattices with a constant velocity derived from the hopping of spins between neighboring Cu atoms due to the exchange interaction, I obtained good quantitative agreement with the measured values of T_1 in the low-temperature regime. Needless to say, I was very excited by the ease with which I could deal with relaxation due to particles associated with spin waves (I believe that the term *magnon* had not yet been

invented for such particles at that time), more so as I only understood what I was doing in an intuitive manner. The first person to appear in the lab towards the end of the holiday was Professor Gorter and I immediately blurted out my 'great discovery'. He immediately recognized that I was proposing a type of spin wave model and urged me to visit a new staff member at the Lorentz, Jan van Kranendonk, who was working on a general theory of spin waves in ferro- and antiferromagnetic materials. This led ultimately to a theory of nuclear spin–lattice relaxation via coupling with magnons, formulated with characteristic elegance by van Kranendonk.[20] When the experimentalists returned, my excited presentation of the correlation between $\Delta M_{\pm}$ and $1/T_1$ was met to my dismay not with wild enthusiasm, but only in a polite, subdued manner. Then, when I revealed that I had begun talking to van K. about making a real theory, the roof fell in and I found myself excommunicated in the lab. As I learned later, this behavior was a reaction to previous interactions with theoreticians who had in the eyes of the experimentalists exploited them and their data without adequate acknowledgement.

MOLECULAR HYDROGEN—GAS, LIQUID, AND SOLID

Fortunately, I had nearly finished building my pulse spectrometer by then. The fast recovery 30 MHz (Mc/s in those days) amplifier that had given me some trouble and was being built by the electronics shop at Philips had arrived. I could now put everything together, test the spectrometer and prepare for some experiments at the beginning of my second year in September 1955. I needed an interesting problem, however, especially since I would have to go it alone and could no longer just fit myself into the experimental program of the NMR group in the K.O. lab. An idea for an experiment well suited to my pulse spectrometer emerged from a talk at the September 1955 Low Temperature Conference in Paris by B. V. Rollin [21] of Oxford University. Rollin reported motional narrowing experiments on solid H_2 and D_2 near their melting points which provided a measure of the temperature dependence of the molecular diffusion constants. It was clear that pulse techniques could give more reliable T_2 measurements over a wider temperature range than the linewidth measurements of Rollin and Watson.[21] An attractive aspect of the H_2 study to me was that liquid hydrogen was available in the K.O. lab any day (or night) of the week so that I could follow my own whims on when and how to work.

The study of self-diffusion in solid H_2 and HD did, in fact, ultimately lead to interesting physics.[22c] Of more long-term interest to me, however, was the unexpected observation of a strong NMR signal from the gas before we had condensed it into our sample holder. The nuclear magnetization of H_2 gas at 20 K is only about a factor of five smaller than H_2O at room temperature, so I should not have been surprised! The observation of this signal allowed me to study T_1 in the gas [22a] as well as the liquid [22b] and solid [22c] phases. In all of these measurements, T_1 was directly related to the rate of molecular reorientation and could be used to investigate the properties of the relatively weak anisotropic intermolecular interactions. Though this mechanism had been identified in the original BPP paper,[14,18] it had not been followed up to extract useful molecular information. After I returned to Canada, the study of T_1 in molecular gases led to a large program in our laboratory at the University of British Columbia over a period of more than 10 years.[23] This program allowed us to explore the nature of intermolecular interactions in a special way using NMR.

The significance of the experimental data was enhanced considerably by the development of a fundamental theory of spin–lattice relaxation which was due mostly to Irwin Oppenheim.[24,25] Oppenheim was a postdoctoral fellow (PDF) at the Lorentz Institute during my second year in Leiden and the idea of relating T_1 in molecular gases in a basic way to intermolecular interactions arose naturally from the many discussions we had after becoming friends in Leiden. The actual development of a theory took place after we had both returned to North America and was influenced by experimental studies of T_1 in molecular gases that I discuss later.

UNIVERSITY OF BRITISH COLUMBIA (1956–PRESENT DAY): MORE NQR—A GENERAL TWO-LEVEL SYSTEM

After my two years as a PDF in Leiden, I joined George Volkoff as a research associate at the University of British Columbia, where I have been ever since. I wanted to return to Canada and was aware of the work of Volkoff and his students on the measurement and analysis of NMR spectra under the combined effects of Zeeman and quadrupolar interactions for spins with $I \geq 1$ in single crystals. When I arrived, George and his Ph.D. student Lloyd Robinson were puzzled by the dependence of the intensity of ^{27}Al NMR lines in a spodumene single crystal on the magnitude and orientation of the external magnetic field. At certain crystal orientations and intermediate fields (i.e. when the Zeeman and quadrupolar interactions were of comparable magnitude), the intensities of certain transitions went through zero when the transition probability was predicted to be a maximum.[26] Crucial to the understanding of this apparently paradoxical result was the fact that Robinson was using a crossed coil spectrometer in these experiments. We finally realized that for any two-level, or pseudo two-level system such as a single pair of levels being resonated in the ^{27}Al ($I = \frac{5}{2}$) system, only three variables are required to characterize all measurements made on the system and one can derive a set of equations analogous to the Bloch equations to describe its most general dynamical behavior.[27] This feature of any two-level system is now known and understood by any beginning student in NMR who has learned the elements of the density matrix description of spin systems. However, density matrix theory had only just been developed by Al Redfield in 1957[28] and the words *density matrix* appear neither in our paper nor in the more general formulation of this property of two-level systems carried out independently at about the same time by Hellwarth et al.[29] We derived a set of Bloch equations for a general two-level system and were able to account for Robinson's experimental results[26] by showing[27] that, while the transition probability is proportional to $|\langle I_x \rangle|^2$, the detected signal is proportional to the product of $\langle I_x \rangle$ and $\langle I_y \rangle$ for transmitter and detector coils oriented along the x and y axes, respectively, in a crossed coil system. In general, the precession is elliptically polarized; zero signal occurs for linear

polarization when one of the coils is oriented perpendicular to the direction of polarization.

SPIN–LATTICE RELAXATION IN H_2 GAS

When I arrived at U.B.C., George Volkoff encouraged me to take some new initiatives and generously made his NRC operating grant available to me for whatever I chose to do. Since I had a lot of unfinished business to complete with pulsed spin echo techniques, I once more built a spin echo spectrometer to operate with a 7000 G permanent magnet that was available in the lab. I was joined soon by a Ph.D. student, Max Lipsicas, who had written to me after reading my Leiden papers on T_1 in H_2 gas, liquid, and solid[22] to propose a study of T_1 in H_2 gas as a function of the ratio of *ortho*- to *para*-H_2 over a wide temperature range. Max hoped that such measurements would provide a novel method of determining the anisotropic interactions between H_2 molecules responsible for collision-induced changes in molecular orientation in the gas phase. In fact, Max Lipsicas's measurements[30] turned out to be very interesting and stimulated a theory of T_1 in molecular gases in which the general theory of spin–lattice relaxation was integrated with a treatment of molecular collisions from first principles.[23,24] One of the surprising features of the initial measurements, which was explained in terms of the radial dependence of the various terms in the anisotropic intermolecular potential, was the qualitative difference in the temperature dependence of the average cross-section for molecular reorientation of *ortho*-H_2 molecules as a result of *ortho–ortho* and *ortho–para* collisions. This led to an accidental cancellation of the variation with temperature of the average cross-section between 100 K and 300 K for normal H_2, i.e. 75% *ortho*-H_2.[30]

Space does not allow me to go into detail on the subsequent studies of molecular reorientation in various gases of different molecular symmetry[23–25,31] as well as their extension to molecular liquids and solids.[32] These studies extended over a period of more than 15 years and were carried out by a large number of talented students and PDFs, some of whom have become well known for their work in NMR and other fields (e.g. Walter Hardy, Ron Dong, Peter Beckmann, and Elliott Burnell).

THE TRANSVERSE STERN–GERLACH EXPERIMENT

In the early 1960s, I was diverted into thinking about a different aspect of magnetic resonance as a result of a series of coffee-room discussions with a nuclear physicist colleague, Karl Erdman. He speculated on whether one could improve the accuracy of measurements of the g-factor of the free electron by somehow detecting resonant transitions at the frequency $\omega_L - \omega_c$ corresponding to the difference between the Larmor and cyclotron frequencies and thereby measuring $g - 2$. Upon looking into the selection rules for this type of transition, which involves a simultaneous change of spin and cyclotron quantum numbers, I found that the interaction required to produce the transitions was of the Stern–Gerlach type in the sense that it involved a magnetic field *gradient*! This led to a theoretical formulation of a generalization of the Stern–Gerlach experiment, which we called the *transverse Stern–Gerlach (TS–G) experiment*.[33] The theory demonstrated that, for neutral atoms, the application of a rotating *inhomogeneous* magnetic field near ω_L gives rise to 'space quantization', with the angular momentum being quantized along $\boldsymbol{H}_{\text{eff}}$, the 'effective field in the rotating reference frame'. (The term 'space quantization' here means that the Stern–Gerlach apparatus sets up a correlation between the momentum of the particles in the beam and the component of angular momentum of the particles along the direction of quantization.) The TS–G experiment thus demonstrates that $\boldsymbol{H}_{\text{eff}}$ is not only of pedagogical importance but also has an important operational significance in the quantum mechanical description of NMR.

The main motivation for exploring the TS–G experiment was that we perceived a possible advantage in doing magnetic resonance on beams of charged particles. We have never succeeded in doing such an experiment. In 1964–65, however, after a sabbatical leave at Harvard University spent partly with Norman Ramsey's group, I came to the conclusion that it would be interesting to illustrate the conceptual aspects of the TS–G experiment by doing an experiment on neutral atoms. Eric Enga, a gifted experimentalist, carried out this experiment in collaboration with Hin Lew at the National Research Council laboratories in Ottawa[34] and verified the predictions of the theory.[33]

The TS–G experiment can be regarded, in retrospect, as a special case of magnetic resonance using an interaction with a spatial gradient—in essence, the gradient gives rise to a force leading to momentum changes. In standard magnetic resonance experiments, the resonance is detected by magnetic induction rather than by force effects. Yet, aside from an experiment analogous to the TS–G experiment using oscillating, inhomogeneous electric fields,[34a] the additional freedom afforded by the possibility of using force detection remained unexplored from 1967 until just recently when several exciting developments have taken place. An optical S–G experiment, using the spatial gradient of a resonant, laser-produced electromagnetic field, has been successfully carried out on particle beams,[35] a trap of neutral atoms based on the TS–G force has been proposed and developed,[36] and the theory of magnetic resonance TS–G experiments on beams[37] and trapped ions has been explored.[38] Most exciting of all, however, and of great potential importance to workers in NMR is the proposal by Sidles[39] to detect NMR in solids using the techniques of atomic force microscopy (AFM). According to Sidles's calculations, there is no theoretical reason why it will not be possible, ultimately, to detect the NMR signal via AFM methods for a *single spin* in a solid! The basic principle of magnetic resonance detection via AFM has recently been verified by Nino Yannoni and Daniel Rugar at the IBM Almaden laboratory in an ESR–AFM experiment on a 30 ng sample of diphenylpicrylhydrazil;[40] the same group has recently detected an NMR signal from a sample of NH_4NO_3 with a sensitivity of about 2×10^{13} protons.[a] At the time of writing (November 1993), this field is moving rapidly and it is not clear what the the ultimate sensitivity of this method of NMR detection will be.

MEMBRANES

One pattern in my life that I have maintained with religious fervor has been to take a sabbatical leave from U.B.C. every seventh year. These breaks with normal routine have invariably generated unpredictable changes in my research activities which made life more interesting in the long term. The 1971–72 leave in France, partly with the Orsay Liquid Crystal Group, proved to be especially important to me. Pierre-Gilles de Gennes had generated an exciting atmosphere in Orsay in which people from different scientific backgrounds communicated with each other on problems related to liquid crystals. The ferment created by this environment led ultimately to the award of the 1991 Nobel Prize in Physics to De Gennes.

When I arrived in Orsay in the late summer of 1971, I was asked by the head of the NMR group (Claude Froidevaux) to share an office with Jean Charvolin, who was then a young researcher in the process of preparing his Ph.D. thesis. Charvolin had just completed a set of proton magnetic resonance (^{1}H NMR) experiments on soap–water solutions in collaboration with Paul Rigny of Saclay[41] and Claude hoped that I would act as a critic of the NMR data at the interpretative stage. The system being studied, potassium palmitate, forms liquid crystals whose symmetry depends on the concentration of potassium palmitate molecules in water. It had recently been discovered that biological membranes were fluid under physiological conditions and that the lamellar symmetry of the smectic A phase of the soap–water system was identical to that of membranes. For this reason, the soap–water system could be considered as a simple model for some structural features of model membranes.

The ^{1}H NMR properties of these systems are unusual. The 'powder lineshape' had been described as a *superlorentzian* because the lines are sharp but decrease more slowly in the wings than does a Lorentzian. In their definitive study, Charvolin and Rigny[42] showed that unlike NMR lines associated with isotropic fluids, the motionally averaged dipolar interaction $\langle H_{\rm dip}\rangle$ is not zero in a membrane-like system. From an NMR perspective this is the crucial feature of *anisotropic fluids* that distinguishes them from the more familiar isotropic fluids. In fact the main features of *superlorentzian* lines can be easily explained[43,44] in terms of a superposition of dipolar broadened lines having the property that $\langle H_{\rm dip}\rangle \propto (3\cos^2\theta - 1)$, where θ is the angle between the external magnetic field and the normal to the bilayer surface, the liquid crystal director.

Having learned about the physical properties of fluid membranes from a familiar NMR perspective, I was sensitized to the excitement in biological circles aroused by the growing realization that cell membranes were *universally* in a lamellar fluid ('liquid crystalline') phase under physiological conditions as proposed by Singer and Nicolson.[45] When I returned to Vancouver, I wondered whether to embark on some serious experimental studies of membranes. A perverse encouragement to move in this direction was an apparent lack of ease with nonzero average tensor interactions such as dipolar interactions that seemed to be present in some of the NMR studies of membranes that began to appear in the literature.

Eventually, with the help of an equipment grant from NRC and a special grant to develop interdisciplinary research from a Canadian foundation (Killam), we formed a group to work on membrane-related problems. I have often been asked by physicists how I managed to make the transition into such an enormous area of science as membrane research 'on my own'. Looking back, however, I am impressed by the size and range of expertise of our initial group and those that evolved from it during the following few years. The transition involved a lively and interesting group effort and was certainly not made 'on my own'. The initial group included my colleagues Elliott Burnell in chemistry and Gerald Weeks in microbiology; research associates Christine Nicol in microbiology, Tim Higgs in chemistry, and Marko Valic in physics; PDFs Jim Davis and Alex MacKay; vistiting professors Steve Roeder and Ken Jeffrey, followed later by Bruno Maraviglia, Ole Mouritsen, Paul Callaghan, Jerzy Blicharski, and Philippe Devaux. A number of important collaborative studies also developed with short term visitors as I mention below.

Our first effort involved the solution of a subtle and controversial motional averaging problem in the ^{1}H NMR of vesicular bilayer structures[46] in relation to the special nature of the origin of the superlorentzian shapes of dipolar broadened lines in powder dispersions of membranes.[43] The subtlety of this problem arises because of the scaling of $\langle H_{\rm dip}\rangle$ for all the protons in an individual lipid molecule with $(3\cos^2\theta - 1)$ as mentioned above. Under these conditions, the ^{1}H NMR lineshape resulting from modulation of θ due to isotropic vesicle tumbling is not given by the standard theory of motional averaging, i.e. a Lorentzian line does not obtain. Rather, each isochromat in the quasi-continuous ^{1}H NMR spectrum of an oriented bilayer is *separately* motionally averaged leading to a complex superposition of Lorentzian lines. The extraction of useful information about membranes from ^{1}H NMR requires great care.

A major advance in the study of membranes using NMR was the introduction of the quadrupolar echo method of doing ^{2}H NMR spectroscopy.[46] This was done by Jim Davis immediately after his arrival in our lab. We had been discussing how a decay of the *solid echo*, i.e. the echo following a $90_x - \tau - 90_y$ pulse sequence in the ^{1}H NMR signal of a dipolar-broadened membrane sample, required the influence of dipolar couplings between protons on different methylenes with its accompanying spin diffusion along the lipid chains, since the solid echo pulse sequence would refocus all the phase accumulated by the protons of isolated two-spin systems. Jim immediately appreciated that a consequence of this was that the influence of quadrupolar interactions of a nucleus having $I = 1$ could be *completely* refocused by the same pulse sequence. The use of the quadrupolar echo, though conceptually simple, was extremely important in that it opened up the possibility of producing distortion-free ^{2}H NMR spectra. For deuterons in lipid systems, the timescale for dipolar interactions is at least an order of magnitude greater than that of the quadrupolar interactions. As a result, the ^{2}H NMR spectrum can be represented, to a good approximation, as a superposition of *Pake doublets*.[47] Analysis of the spectrum of Pake doublet splittings, e.g. using the method of 'dePakeing',[48] provides a quantitative picture of membrane fluidity. This has proven to be crucial in obtaining useful information about such important questions as the nature of the interaction between lipids and biologically important molecules such as proteins, peptides, or cholesterol in membranes. As a consequence, ^{2}H NMR is now

recognized as a major technique in the determination of the physical properties of biological and model membranes.[49]

Space does not allow a detailed description of the role of ^{2}H NMR in membrane research. I should, however, mention the enrichment of our own work that resulted from collaborations with a number of outstanding biophysicists and biochemists from other institutions: Ian Smith of the National Research Council of Canada, Bob Cushley of Simon Fraser University, Rick Dahlquist of the University of Oregon, Philippe Devaux of the Institut de Biologie-Physico-Chimique in Paris, and Thomas Bayerl of the Technical University of Munich. Jim Davis's realization of how to use the quadrupolar echo as a means of doing distortion-free ^{2}H NMR attracted these people to our laboratory with proposals of specific experiments and with the capability of preparing and characterizing materials of interest in the study of membranes, a capability that we did not have. Some of our visitors came to us simply to learn broadline NMR. They soon had their own spectrometers and became independent, but they left us with much lore on membrane biophysics and biochemistry that is difficult to acquire by reading published papers.

We also attracted researchers from other departments of our own university: Pieter Cullis (biochemistry), David Godin (pharmacology), Neil Kitson (dermatology), Ian Taylor (botany), as well as PDFs and students with diverse backgrounds: Klaas-Pieter Datema, a physicist from the Netherlands; Michel Lafleur, a physical chemist from Quebec; Myrna Monck, a biochemist from U.B.C.; François Macquaire, a biophysicist from France; Peter Pauls, a botanist from Ontario; Michel Roux, a biochemist from France; Olle Söderman, a physical chemist from Sweden; Jenifer Thewalt, a biophysicist from Vancouver; Clare Morrison, Frank Nezil, and Ed Sternin, all U.B.C. Ph.D. students.

For me, the thrill of working on biologically oriented problems has been connected with the realization that Nature in 'designing its materials' via evolutionary processes has invariably optimized the physical properties of the materials for the survival of the organism. Appreciation of this optimization arose from NMR studies showing that cholesterol or equivalent sterol molecules are ubiquitous in the fluid, plasma (outer) membranes of eukaryotic cells and have had a definitive influence on their special physical properties.[50,51] The unusual, ultrasoft nature of most biological materials is related to membrane fluidity and makes NMR especially useful in their study. I have tried to explain elsewhere[52] the special interest of these soft materials in relation to projected future developments in the physics of condensed matter.

Finally, I mention the connections with modern medicine inevitably stimulated by the study of biological systems using NMR. Though only peripherally involved, I have found this area of research particularly rewarding. I am grateful to my friend Ian Smith for having introduced me to Dr. Carolyn Mountford, an Australian biophysicist who had developed a proton NMR method for diagnosing unusual aspects of cancer. As a result of spending part of my 1985–86 sabbatical year with Carolyn's group, I found an interesting application for some of our earlier proton NMR lineshape studies[43,45] in this medical area.[52] As important, perhaps, from a psychological perspective were the four months spent in the company of a tenacious, feminist, and competent group working on an important problem involving a complicated spin system. Since returning from Australia, I have noticed that my research group has also become feminist and tenacious, but this may be a coincidence.

REFERENCES

1. M. Bloom, '*Crystallographic Investigations Using the Shape of the NMR Line*', M.Sc. Thesis, McGill University, 1949.
2. H. S. Gutowsky, G. B. Kistiakowsky, G. E. Pake, and E. M. Purcell, *J. Chem. Phys.*, 1949, **17**, 972.
3. J. H. Van Vleck, *Phys. Rev.*, 1948, **74**, 1168.
4. H. G. Dehmelt and H. Kruger, *Z. Phys.*, 1951, **129**, 401.
5. C. Dean, Ph.D. Thesis, Harvard University, 1952.
6. E. L. Hahn, *Phys. Rev.*, 1950, **80**, 580.
7. M. Bloom and R. E. Norberg, *Phys. Rev.*, 1954, **93**, 638.
8. E. L. Hahn and B. Herzog, *Phys. Rev.*, 1954, **93**, 639.
9. M. Bloom, '*Magnetic Induction in Nuclear Quadrupole Resonance*', Ph.D. Thesis, University of Illinois, 1954.
10. M. Bloom, E. L. Hahn, and B. Herzog, *Phys. Rev.*, 1955, **97**, 1699.
11. C. J. Gorter, *Physica (The Hague)*, 1936, **3**, 995.; C. J. Gorter and R. de L. Kronig, *ibid.*, 1952, **3**, 1009.
12. C. J. Gorter and L. J. F. Broer, *Physica (The Hague)*, 1942, **9**, 591.
13. C. J. Gorter, Bad Luck In Attempts To Make Scientific Discoveries, *Phys. Today*, January 1967, pp. 76–81; April 1967, p. 13.
14. N. Bloembergen, *Nuclear Magnetic Relaxation*, W. A. Benjamin, New York, 1961. This publication of Professor Bloembergen's 1948 thesis is interesting also for the 'Comments and Corrections' added by the author, which connects the early Harvard work and the way it was described to the NMR culture in 1961. In addition, this book contains the paper in ref. [15] and comments on it.
15. N. Bloembergen, *Physica (The Hague)*, 1949, **15**, 386.
16. C. J. Gorter and J. H. Van Vleck, *Phys. Rev.*, 1947, **72**, 1128.
17. F. J. Dyson, *Phys. World*, August 1993, pp. 33–38.
18. N. Bloembergen, E. M. Purcell, and R. V. Pound, *Phys. Rev.*, 1948, **73**, 679.
19. G. E. G. Hardeman, N. J. Poulis, and W. E. v. d. Lugt, *Physica (The Hague)*, 1956, **22**, 48.
20. J. van Kranendonk and M. Bloom, *Physica (The Hague)*, 1956, **22**, 545.
21. B. V. Rollin and E. Watson, *Suppl. Bull. Inst. Froid*, **1955**, 474.
22. M. Bloom, (a) *Physica (The Hague)* 1957, **23**, 237; (b) *ibid*, **23**, 378; (c) *ibid*, **23**, 767.
23. M. Bloom in *MTP International Review of Science, Physical Chemistry, Series One*, ed. C. A. McDowell, Butterworths, London, 1972, Vol. 4, pp. 1–42.
24. I. Oppenheim and M. Bloom, *Can. J. Phys.*, 1961, **39**, 845.
25. M. Bloom and I. Oppenheim, *Adv. Chem. Phys.*, 1967, **12**, 549.
26. L. B. Robinson, *Can. J. Phys.*, 1958, **36**, 1295.
27. M. Bloom, L. B. Robinson, and G. M. Volkoff, *Can. J. Phys.*, 1958, **36**, 1286.
28. A. G. Redfield, *IBM J. Res. Dev.*, 1957, **1**, 19.
29. R. P. Feynman, F. L. Vernon, Jr., and R. W. Hellwarth, *J. Appl. Phys.*, 1957, **28**, 49.
30. M. Lipsicas and M. Bloom, *Can. J. Phys.*, 1961, **39**, 881.
31. M. Bloom, F. Bridges, and W. N. Hardy, *Can. J. Phys.*, 1967, **45**, 3533.
32. J. A. Morrison and M. Bloom, Orientational Order and Disorder in the Solid Isotropic Methanes, in *Surface and Defect Properties in Solids* ed. J. M. Thomas, The Chemical Society, London, 1973., Vol. 2, pp. 140–149.
33. M. Bloom and K. L. Erdman, *Can. J. Phys.*, 1962, **40**, 179.
34. M. Bloom, E. Enga, and H. Lew, *Can. J. Phys.*, 1967, **45**, 1481.

34a. R. M. Hill and T. F. Gallagher, *Phys. Rev.*, 1975, **A12**, 451.

35. T. Sleator, T. Pfau, V. Balykin, O. Carnal, and J. Mlynek, *Phys. Rev. Lett.*, 1992, **68**, 1996.

36. T. E. Barrett, N. G. Woodard, and G. P. Lafyatis, *Phys. Rev. Lett.*, 1992, **69**, 422.
37. L. J. Mueller and D. P. Weitekamp, *Bull. Magn. Res.*, 1993, **15**, 187.
38. P. J. Pizarro and D. P. Weitekamp, *Bull. Magn. Res.*, 1992, **14**, 220.
39. J. A. Sidles, *Phys. Rev. Lett.*, 1992, **68**, 1124.
40. D. Rugar, C. S. Yannoni, and J. A. Sidles, *Nature (London)*, 1992, **360**, 563.
40a. D. Rugar, O. Züger, S. Hoeu, C. S. Yannoni, H.-M. Vieth and R. D. Kendrick, *Science*, 1994, **264**, 1560.
41. J. Charvolin and P. Rigny, *J. Chem. Phys.*, 1973, **58**, 3999.
42. J. Ulmius, H. Wennerström, G. Lindblom, and G. Arvidson, *Biochim. Biophys. Acta*, 1975, **389**, 197.
43. M. Bloom, E. E. Burnell, S. B. W. Roeder, and M. I. Valic, *J. Chem. Phys.*, 1977, **66**, 3012.
44. S. J. Singer and G. L. Nicolson, *Science*, 1972, **175**, 720.
45. M. Bloom, E. E. Burnell, A. L. MacKay, C. P. Nichol, M. I. Valic, and G. Weeks, *Biochemistry*, 1978, **17**, 5750.
46. J. H. Davis, K. R. Jeffrey, M. Bloom, M. I. Valic, and T. P. Higgs, *Chem. Phys. Lett.*, 1976, **42**, 390.
47. G. E. Pake, *J. Chem. Phys.*, 1948, **16**, 327.
48. M. Bloom, J. H. Davis, and A. L. MacKay, *Chem. Phys. Lett.*, 1981, **80**, 198; E. Sternin, M. Bloom, and A. L. MacKay, *J. Magn. Reson.*, 1983, **55**, 274.
49. M. Bloom, E. Evans, and O. G. Mouritsen, *Q. Rev. Biophys.*, 1991, **24**, 293.
50. M. Bloom and O. G. Mouritsen, The Evolution of Membrane, in *Handbook of Physics of Biological Systems*, ed. R. Lipowsky, Elsevier, New York, 1994, 1, pp. 89–119; see also, *Can. J. Chem.*, 1988, **66**, 706.
51. M. Bloom, The Physics of Soft, Natural Materials, *Phys. Canada*, 1992, **48**, 7.
52. M. Bloom, K. T. Holmes, C. E. Mountford, and P. G. Williams, *J. Magn. Reson.*, 1986, **69**, 73.

Biographical Sketch

Myer Bloom. *b* 1928. B.Sc., 1949, M.Sc., 1950, McGill University, Canada, Ph.D., 1954, Physics, University of Illinois, USA (with Charles Slichter). National Research Council of Canada Postdoctorate Travelling Fellow, 1954–56 at the University of Leiden, Holland (with C. J. Gorter). Research associate, 1956–57 (with George Volkoff) and Faculty in Physics, University of British Columbia, 1957–present. Approx. 150 publications. Research specialties: nuclear quadrupole resonance, nuclear spin relaxation and molecular motions in gases, liquids, and solids, the transverse Stern–Gerlach experiment, structure and dynamics of model and biological membranes.

Bodenhausen, Geoffrey: Traveling through the World of Magnetic Resonance in the 1970s

Geoffrey Bodenhausen
Université de Lausanne, Lausanne, Switzerland

As an undergraduate at ETH in Zürich between 1970 and 1974, I had plenty of opportunities to hear about magnetic resonance. Initially, I was not so much attracted by the physicochemical aspects of NMR, but rather by its applications to analytical chemistry. I was greatly impressed by Wilhelm Simon's charisma, and by his fascinating weekly sessions where analytical puzzles ('Probleme der Woche') were eagerly debated in a large auditorium. A set of IR, UV, MS, and NMR spectra were distributed at the outset, and anyone, from undergraduates to senior researchers, could try his or her talent and suggest molecular structures that appeared to be compatible with the spectral evidence. NMR was clearly the richest and most intriguing source of information. In my third undergraduate year, I had my first hands-on encounter with an NMR spectrometer in the analytical teaching laboratory, but this turned out to be disappointing. We tried to carry out some tickling experiments—in vain, because the stability of the machine was not sufficient for such delicate double-resonance methods. To make matters worse, we were constantly interrupted by graduate students who kept rushing into the lab with samples that they had just cooked up, which they insisted should be put immediately into the NMR spectrometer. Needless to say, we did not approve of the way these mundane measurements were taking precedence over our intellectual endeavor. This episode may have contributed to my attitude to synthetic chemists, and also turned my attention away from NMR, for I was equally fascinated by fluorescence, electrochemistry, ion-selective electrodes, in fact anything that would allow one to probe the mysteries of matter. To be truthful, Richard Ernst's lectures on Fourier transforms and data processing appeared a bit dry. Yet I could not resist the appeal of magnetism, and asked to join his group during my last undergraduate term ('Diplomarbeit'). Richard suggested that I should look into Overhauser effects. He provided a list of ideas dated January 20th 1974, which I'll attempt to translate literally: '*The problem:* One should consider the possibility of systematically determining the relaxation parameters of a coupled spin system through a complete set of Overhauser experiments. *Detailed problems*. Formal analysis of the coupled set of equations for special and general cases. Formal structure. Number of independent equations. Possibilities for determining the parameters. Determination of measurement errors. Calculation of relaxation parameters for a chosen molecule. Proposals for organizing the measurements. Experimental tests and interpretation of the results.' For the benefit of today's reader, I should explain that the 'complete set of Overhauser experiments' referred to all (!) possible single-, double- and multiple-irradiation experiments. The 'coupled set of equations' refers to the master equation with a $2^N \times 2^N$-dimensional matrix containing the transition probabilities between the 2^N eigenstates of a system of N spins with $I = \frac{1}{2}$. Needless to say, I did not quite manage to run through all of these ideas in the eight weeks of a summer term. In fact, I'm still working on this job nearly 20 years later: our recent efforts to quench spin diffusion[1] may be regarded a partial attempt to fulfill Richard's expectations as he wrote them out back in 1974.

Why did I embark on a seemingly endless Odyssey through the NMR community rather than stay at ETH for a Ph.D.? To be sure, I largely failed to appreciate the depth of Richard's research. In retrospect, I realize that Fourier imaging was developed there right before my eyes, on the blackboard, when Richard came back from a meeting in the US. He must have heard Paul Lauterbur speak of 'Zeugmatography', the early version of NMR imaging, which originally relied on the back-projection method. Richard asked around his group for volunteers who would be willing to develop Fourier imaging, and Anil Kumar and Dieter Welti came forward.[2] This must have been one of the key moments of NMR history, but, to be honest, I did not perceive anything particularly exciting. I was much more preoccupied with the duration of a typical Ph.D. thesis in Zürich. In fact, when I returned there in 1980, after three years in Oxford, a year in San Diego, and nearly two years in Massachusetts, I met a former classmate who had remained in Zürich for all those years, and who was about to begin writing up his thesis. At that point, I felt immensely grateful that I'd seen some of the world, and I still believe that mobility is worthwhile.

Why did I choose to move to Oxford? The initial idea came after an eloquent lecture that Rex Richards gave in Zürich in 1974. He talked about resolving protein structure with the help of paramagnetic ions, which allowed him 'to peel the molecule like an onion'. He also mentioned phosphorus NMR as an intracellular pH meter. The very next day I wrote to Professor Richards to ask him whether I could join his Oxford group. He promptly replied that he had no space available, but that a young man was just starting up a new group across the road in physical chemistry. This young man was Ray Freeman. He may have been young from Rex's perspective (Ray had been one of his D.Phil. students), but when I first met him in the summer of 1974, I was mightily impressed. Ray must have been 42 in 1974, which happens to be my age at the time of writing these lines. I initially called him 'Sir', not knowing that 'Dr. Freeman' would have been more appropriate, and completely failing to perceive that he would have preferred to be called 'Ray'. In spite of my insecurity about manners and language, I was delighted about Oxford. However, once in the lab, in January 1975, I was perturbed by the lack of structure and the absence of guidelines. Gone were Richard Ernst's long lists of instructions. There was, in fact, an 'idea book' in the lab where anyone could enter his fantasies, but ideas were rarely handed down from the top. It took me years to adjust. In this period, I greatly benefitted from the stimulation provided by people such as Gareth Morris and David Turner. Though I was tempted to look down on them for what I perceived as a lack of formal training (they'd never heard of convolution integrals!), I marveled in secrecy at their independence. I slowly came to realize that intellectual autonomy is harder to acquire than a knowledge of calculus. I also began to perceive that research can actually be *fun*, and need not be a calvinistic exercise

in self-discipline. Ray appeared to spend more time looking for cartoons than writing papers. (How can one be so light-hearted!) I could never quite fathom the source of his playful creativity. Some outsiders seem to believe that Ray does not understand quantum mechanical systems. I would rather say that Ray has such a deep, intuitive grasp of energy levels, transitions, coherences, and all the rest, that he simply *doesn't need* to dress them up in mathematical terms. Ray has no use for unitary transformations to work out his coherence transfer pathways, no more than a pro tennis player needs a pocket calculator to master the trajectories of his passing shots.

The last year of my stay in Ray's laboratory was the beginning of the great epoch of acronyms. We were very proud of our first phase cycling recipe,[3] which allowed us to remove artifacts that Ray had affectionately dubbed 'phantoms' and 'ghosts'. At that time, the movie theaters featured a film called 'The Exorcist', so that we naturally came to christen our invention 'Exorcycle'. I hoped Ray might dress up as a priest (after all, he had to wear a college gown on occasions), and ride a bicycle while sprinkling holy water. He never agreed to enact this fantasy.

Phase cycling provided a guiding thread for my intellectual endeavor for many years. In retrospect, it seems a very thin thread, but there it was. To exploit this idea, I had to modify various spectrometers to shift radiofrequency phases. I built a digital phase shifter for Ray's CFT-20 in Oxford, and an improved version for Bob and Gitte Vold's homebuilt machine in San Diego. When I moved to the Francis Bitter National Magnet Laboratory at MIT in 1979, Dave Ruben built another phase shifter, with mysterious analog components such as splitters and combiners that I never quite trusted. After my return to ETH, Markus Hintermann built a fast digital device, supposedly under my direction, though I could never quite fathom how it actually worked. But it did, and allowed us to select 'coherence transfer pathways' more or less at will. In the meantime, that expression had become the 'buzz word' of the trade, and given some respectability to the rather mundane world of phase cycling.[4] As always, once a subject becomes transparent it ceases to be an object of active research. Until someone invents another buzz word. I've recently heard that one should 'project the density operator onto the receiver phase'. Perhaps that sounds good enough to bring new life to phase cycling?

From time to time, research can be a source of frustration. One episode from which I learned a great deal was the invention of INADEQUATE,[5] which Ray presented at the Experimental NMR Conference (ENC) in Tallahassee, Florida, in 1979. We had invented *exactly* the same sequence, but our applications to proton spectra of nucleotides[6] must have appeared quite mundane compared to Ray's spectacular unraveling of carbon–carbon couplings in samples with natural isotopic abundance. I gave a muddled, overcrowded talk at ENC, no match for Ray's sharp sense of presenting a 'single selling proposition'. Worst of all, while Ray gleefully talked about his Incredible Natural Abundance Double Quantum Transfer Experiment, I simply didn't have any acronym at all! I really should have dropped out of the field of NMR right there in Tallahassee. . . .

In a sense, my involvement with magnetic resonance is marked by a series of failed opportunities. In 1974, when I joined Richard Ernst's group as undergraduate I opted for the Overhauser project outlined above. In doing so I actually turned down another suggestion which might have been far more exciting: Richard offered me an opportunity to get involved in the very early stages of two-dimensional correlation spectroscopy. But this didn't happen and I got bogged down in Overhauser effects for much of my career. I missed another opportunity when I left Ray's lab at the end of 1977. We had been playing with variants of heteronuclear correlation spectroscopy, largely inspired by the work of Maudsley and Ernst.[7] To be truthful, we found it hard to break new ground. But within weeks of my departure from Oxford, Gareth Morris and Ray Freeman came up with their famous INEPT method (Insensitive Nuclei Enhanced by Polarization Transfer).[8] Today there is hardly any flashy three- or four-dimensional NMR sequence which doesn't incorporate a few INEPT building blocks. Once I had arrived at UCSD in 1978 I again missed an opportunity: I should have listened carefully to Bob and Gitte Vold's teaching on relaxation theory. But I was too much absorbed by the technicalities of coherence transfer to get the overall picture. In recent years, we have made many efforts in Lausanne to develop new approaches to the measurement of relaxation phenomena. Basically, I feel that after all those years I am still driven by a desire to catch up with my failure to penetrate the secrets of relaxation during my stay at UCSD. After moving to MIT in 1979, the same scenario repeated itself: my involvement with solid state NMR was so superficial that I really did not develop much appreciation of the theory. It was long after I left MIT that I came to realize how convenient it would have been to listen more carefully to Bob Griffin's advice. Again, the efforts that we have undertaken in Lausanne in the field of solid state NMR may be regarded as an attempt to catch up with the lost paradise. Perhaps Richard Ernst was most successful in stopping my natural tendency to disperse my attention. When I joined his lab in 1980 as a postdoc, I tried to convince him to start what I thought to be an exciting project (I believe it had to do with phase cycling, for a change). Richard listened carefully, understood the implications and limitations, and commented that my idea would make a nice footnote. . . .

The world of magnetic resonance is wonderfully rich, not simply because of the extraordinary wealth of intriguing ideas, but primarily because of the presence of so many talented people. It is most rewarding to see that this community is constantly being rejuvenated by the arrival of bright and demanding newcomers. Let us hope that their Odysseys will be as rewarding and stimulating as ever.

REFERENCES

1. C. Zwahlen, S. J. F. Vincent, L. Di Bari, M. H. Levitt, and G. Bodenhausen, *J. Am. Chem. Soc.*, 1994, **116**, 362.
2. Anil Kumar, D. Welti, and R. R. Ernst, *J. Magn. Reson.*, 1975, **18**, 69.
3. G. Bodenhausen, R. Freeman, and D. L. Turner, *J. Magn. Reson.*, 1977, **27**, 511.
4. G. Bodenhausen, H. Kogler, and R. R. Ernst, *J. Magn. Reson.*, 1984, **58**, 370.
5. A. Bax, R. Freeman, and S. P. Kempsell, *J. Am. Chem. Soc.*, 1980, **102**, 4849.
6. G. Bodenhausen and C. M. Dobson, *J. Magn. Reson.*, 1981, **44**, 212.

7. A. A. Maudsley and R. R. Ernst, *Chem. Phys. Lett.*, 1977, **50**, 368.
8. G. A. Morris and R. Freeman, *J. Am. Chem. Soc.*, 1979, **101**, 760.

Biographical Sketch

Geoffrey Bodenhausen. *b* 1951. Diploma, 1974, Chemistry, ETH, Zürich, D.Phil., 1977, Oxford University (Supervisor Ray Freeman). Postdoctoral research, University of California, San Diego (with Robert and Regitze Vold), 1978; Francis Bitter National Magnet Laboratory (with Robert Griffin), 1979–80; ETH Zürich (with Richard Ernst), 1980–85. Associate professor, University of Lausanne, Switzerland, 1985–1994. Professor, Florida State University, and Director, NMR Program, National High Magnetic Field Laboratory, Tallahassee, Florida, 1994–present.

Bothner-By, Aksel A.: Computer Analysis of High-Resolution NMR Spectra

Aksel A. Bothner-By

Carnegie Mellon University, Pittsburgh, PA, USA

In 1959, Cecile Naar-Colin and I embarked on a study of the high-resolution proton resonance spectra of simple organic molecules with a view to finding out something about their structures, especially their rotameric populations. The top spectrometer frequency then available was 60 MHz and almost all the spectra we recorded were strongly non first order, since the chemical shifts between coupled nuclei were usually just a few times larger than the spin–spin coupling constants. This meant that one could not simply read off the shifts and coupling constants from the observed spectra, and there was an urgent need to be able to compute their values somehow from the observed line positions.

The basic method of calculating what the line positions and intensities should be, given a set of shifts and coupling constants, had been set forth by Hahn and Maxwell,[1] Gutowsky, McCall, and Slichter,[2] and McConnell, McLean, and Reilly[3] in the early 1950s; our guide on how to do this was the beautiful exposition by Pople in the classic book High-Resolution Nuclear Magnetic Resonance.[4]

The successive steps in the calculation can be represented by equations **(1)–(5)**:

$$\mathbf{H} = \sum_{i=1}^{i=n} \nu_i I_{zi} + \sum_{i=1}^{i=n-1} \sum_{j=i+1}^{n} J_{ij} \boldsymbol{I}_i \cdot \boldsymbol{I}_j \tag{1}$$

$$\Lambda = e^{-1}\mathbf{H}e \tag{2}$$

$$\boldsymbol{A} = e^{-1}\left(\sum_{i=1}^{i=n} I_{+i} \right) e \tag{3}$$

$$\nu_{kl} = \lambda_{kk} - \lambda_{ll} \tag{4}$$

$$s_{kl} = A_{kl}^2 \tag{5}$$

In the first step a square Hamiltonian matrix is constructed which gives the energies and interaction energies of a set of basis states of the nuclei as though each were independently quantized. For protons and other spin-$\frac{1}{2}$ nuclei, the states are symbolized α and β, which designate states (or spin coordinates, or spin functions, or spin wavefunctions) in which the nuclear spin axis is specified to be parallel or antiparallel to the magnetic field. For two spins, the four possible states would be symbolized $\alpha\alpha$, $\alpha\beta$, $\beta\alpha$, and $\beta\beta$. For the two-spin case, the upper left-hand element in the 4×4 matrix, at the intersection of the row and column each associated with the state $\alpha\alpha$, would have the value $H_{\alpha\alpha,\alpha\alpha} = \nu_A(\frac{1}{2}) + \nu_B(\frac{1}{2}) + J_{AB}(\frac{1}{2})(\frac{1}{2})$. The only basis states which interact are $\alpha\beta$ and $\beta\alpha$, and for these, $H_{\alpha\beta,\beta\alpha} = H_{\beta\alpha,\alpha\beta} = J_{AB}/2$.

In the second step, the matrix **H** is diagonalized to get Λ. The process may be thought of as a rotation to a new set of coordinates, and the form of equation (2) is that of a similarity transformation, i.e. expression of the same entity in a new coordinate framework. The term Λ is thus also a Hamiltonian, but expressed in terms of the spin states which do not interact. Only the elements λ_{11}, λ_{22}, λ_{33}, and λ_{44} are nonzero. The eigenvector matrix e specifies the coordinate transformation required.

Thirdly, the transition amplitude matrix, **A**, between the eigenstates is found by applying the same coordinate transformation to the amplitude matrix calculated for the basis states. This amplitude is unity if exactly one spin flips from α to β in going from one basis state to another, and is zero otherwise.

Finally the transition frequencies, ν_{kl}, and transition intensities, s_{kl}, are obtained by subtracting λ_{ll} from λ_{kk}, and by squaring A_{kl}.

The only nontrivial part of this calculation is the diagonalization. For simple spin systems, such as the AB case, where no basis state interacts with more than one other basis state, the determination of the eigenstates and eigenvectors requires only the solution of a quadratic equation of the form $(H_{kk} - \lambda)(H_{ll} - \lambda) - H_{kl}^2 = 0$. The roots are λ_{kk} and λ_{ll}. Using this fact, Pople was able to provide general algebraic solutions giving the frequencies and intensities of the expected lines for many simple systems such as A_2, AB, ABX, A_2X_2. If the system contains groups of spin-$\frac{1}{2}$ nuclei which are magnetically equivalent (i.e. which all have the same chemical shift and which are all equally spin-coupled to each other nucleus in the system), it turns out that the coupling between the spins in the magnetically equivalent group does not affect the appearance of the spectrum, so that it can be arbitrarily taken as zero. This expands the kinds of systems for which closed algebraic solutions can be found to AB_n, A_mB_n, $A_mB_nX_p$, etc. E. Bright Wilson published an elegant exposition[5] of how group theory could be applied to take advantage of the symmetries in spin systems such as that of 1,3,5-trifluorobenzene, and to reduce the interactions to pairwise ones. These solutions provided a ready means to analyze the spectra of many simple systems, and to extract the shifts and coupling constants from the observed spectra.

Even with the algebraic solutions in hand, the task of tabulating all the line frequencies and intensities and finding the values of shifts and coupling constants giving a spectrum agreeing with the observed one was tedious, error-prone, and time-consuming. The availability of an IBM 650 through the newly-formed Department of Computer Science at the Carnegie Institute of Technology appeared to offer a fast and convenient way to tabulate these spectra, and we set out to write a few programs for specific cases, such as the $X_3AA'X_3'$, applicable to the case of the 2,3-dihalobutanes, which we were then studying. From Alan Perlis, the Director, we received a set of instructions on how to prepare a program for the computer in a language called IT. After a couple of weeks of puzzling, we

produced what we thought would be a working program and brought it to be run. Unfortunately, IT had become obsolete in the interim, and a new language, AT, was now in use. Our second attempt also took about two weeks to write, and, predictably, was also out of date when we got it there. Back, to rewrite in GAT. This time we were barely in time, and, amazingly, to us, it worked. The computer gave us a list in about 2 minutes that it would have taken us 2 days to crank out on a Monroe. We were able to use it for the intended analyses.[6]

Most of the systems we wanted to look at, however, did not fit into the categories for which closed algebraic solutions were available. For systems with three or more interacting states, the algebraic solutions were of formidable complexity, and did not then appear to be practically useful. On the other hand, if the actual values of the shifts and coupling constants are introduced into **H**, the diagonalization problem becomes a purely numerical one. Numerical methods for the iterative diagonalization of large symmetric real matrices have long been known. One such, the Jacobi method, simply treats the interaction elements in succession, nulling each one by a coordinate transformation as though it were the only one. After each coordinate rotation, the other interaction energies are mixed, but eventually they are all reduced to less than any arbitrarily set limiting value.

It was a straightforward task to write a program which would read in a set of values for shifts and coupling constants, evaluate the numerical Hamiltonian according to equation (1), perform the diagonalization by the Jacobi method, and produce a list of frequencies and intensities for the expected spectrum. With the help of Carl Saalbach, our first program, FREQINT, was completed. It worked without problems, but it did not meet the central need. The difficulty was that it calculated the spectrum from the shifts and coupling constants, and what was needed was the reverse calculation, shifts and coupling constants from the spectrum.

It was not at all obvious how to get the calculation to go in the opposite direction. The difficulty was centered in the diagonalization step; how could one find a recipe for finding the eigenvectors in the reverse direction? The only way we could see to do this was to guess at a set of shifts and coupling constants, calculate the spectrum, compare it with the experimental spectrum, change the shifts and coupling constants in what seemed like a reasonable direction to bring the calculated transition frequencies closer to the observed ones, and calculate again. One then repeated this until no better agreement could be obtained, or fatigue terminated the effort. The adjustments to the parameters, shifts, and coupling constants, were made by first order, i.e. if the observed separation between lines that looked like a doublet arising from spin−spin splitting was too large by 0.1 Hz, then J was reduced by 0.1 Hz. Satisfactory analyses of the spectra of propene, butene-1, and hexene-1 were obtained using this procedure.[7]

An improvement on this method of iterating was worked out by Delores Geisel. It would clearly be possible to make better corrections to the trial parameters if the change in line position caused by a change in parameter value $\Delta\nu_{ij}/\Delta\rho_{\mathrm{m}}$ were available. Then the error in line position would be just the product of this differential and the correction to the parameter, ρ_{m}. To get the differentials, we calculated the trial spec-trum and extra spectra with each parameter changed by a small amount. For each line, the finite differentials were calculated, then corrections were applied using the least-squares criterion:

$$\begin{aligned}(\Delta/\Delta p_m)\sum_l(\nu_{\mathrm{obs}}-\nu_{\mathrm{calc}})^2\\ =-2\sum_l(\nu_{\mathrm{obs}}-\nu_{\mathrm{calc}})(\Delta\nu_{\mathrm{calc}}/\Delta p_m)=0\end{aligned} \tag{6}$$

In matrix notation, the equations which one wished to solve were the equations of condition

$$\mathbf{D}\Delta\boldsymbol{p}=\Delta\boldsymbol{\nu} \tag{7}$$

and the normal equations giving the least-square solution,

$$\mathbf{D}^{\mathrm{T}}\mathbf{D}\Delta\boldsymbol{p}=\mathbf{D}^{\mathrm{T}}\Delta\boldsymbol{\nu} \tag{8}$$

where **D** is the matrix of differentials, $\Delta\nu_{ij}/\Delta\rho_m$, $\mathbf{D}^{\mathrm{T}}$ is its transpose, $\Delta\boldsymbol{p}$ is the desired vector of corrections to the parameters, and $\Delta\nu$ is the vector of discrepancies in the line positions. Again, numerical methods for inverting real symmetric matrices, such as $\mathbf{D}^{\mathrm{T}}\mathbf{D}$, were readily available, and the method was readily implemented. It worked quite well.[8]

There was one real difficulty with it. In order to evaluate the matrix **D**, the computer produced a multicolumn output of frequencies, one column for each parameter varied. Occasionally, when a parameter was incremented, the frequencies of two lines would cross, so incorrect differentials would be generated. The only way to detect this was to sit with the multicolumn output and examine it, row by row, following the changes across the page, and identifying suspicious movements in the wrong direction or unusual changes in intensity. Using a pencil to connect the entries belonging to the same line generated a plot which looked like an array of mostly parallel but sometimes intertwined snakes. The kinks were removed by re-entering the frequencies in their correct positions. This experience impelled us to name the program LAOCOON, after the famous statute in the Vatican museum of the Trojan priest and his sons, Thymbraeus and Antiphas(!) attacked by serpents (Figure 1). We justified this name as an acronym for Least-squares Adjustment of Calculated On Observed NMR spectra.

Other groups had encountered and were attacking this problem as well. In 1960 Charles Reilly and Jerry Swalen reported an analysis of the spectra of some substituted epoxides, and described a systematic iterative method for correcting the trial parameters.[9] The method involved applying the similarity transformation obtained in calculating the trial spectrum in the reverse direction to the set of energy levels deduced from the experimental spectrum.

Since the eigenvectors change more slowly than the Hamiltonian, this gave an improved trial Hamiltonian from which improved trial parameters could be obtained. The method worked well (although occasionally it did not converge), and they incorporated the method into a pair of programs, NMREN, which calculated the best fitting energy levels from the frequencies of an assigned experimental spectrum, and NMRIT, which performed the iterative procedure improving the trial parameters.

Ragnar Hoffman very shortly[10] also contributed the suggestion that the iteration could be performed by applying the similarity transformation in the forward direction to a small

Figure 1 Laocoon, reproduced with permission of the Vatican museum

correction Hamiltonian on the trial Hamiltonian, and applying perturbation theory to evaluate the correction Hamiltonian.

All of the methods above relied exclusively on matching the frequencies of the lines, and did not take account of the intensities. Intensities were useful in confirming the validity of the parameters in the trial spectrum, but since they could be measured with much less precision than the frequencies it was felt reasonable not to include them. Still, they were available, valid pieces of information, and Yoji Arata[11] in 1962 proposed a method in which they were included in the iterative scheme.

In 1962, our group was joined by Salvatore Castellano who had performed a prodigious task in analyzing the three-spin problem algebraically, while he was at MIT working with John Waugh.[12] There were several important insights that came out of this work. A very important one was the demonstration that the frequencies observed in a three-spin spectrum were often compatible with more than one set of shifts and coupling constants (quite aside from the trivial change of sign of all the coupling constants). This underscored the absolute necessity of setting trial parameters for iterative calculations which produced the correct assignment of all the transitions in the experimental spectrum. In a short time, he had written a computer program, EXAN, which used his analysis to obtain the possible sets of parameters directly from the transition frequencies in a three-spin spectrum, and this program was indispensable in the analysis of a variety of spectra such as the 3-fluoropropenes.[13]

One day in the spring of 1964 he came in with a piece of paper with these equations written on it:

$$\Lambda = e^{-1}\mathbf{H}e \tag{9}$$

$$\begin{aligned}\frac{\partial \Lambda}{\partial p_m} &= \frac{\partial e^{-1}}{\partial p_m}\mathbf{H}e + e^{-1}\frac{\partial \mathbf{H}}{\partial p_m}e + e^{-1}\mathbf{H}\frac{\partial e}{\partial p_m} \\ &= \frac{\partial e^{-1}}{\partial p_m}e\Lambda + e^{-1}\frac{\partial \mathbf{H}}{\partial p_m}e + \Lambda e^{-1}\frac{\partial e}{\partial p_m}\end{aligned} \tag{10}$$

He had found the way for getting the differentials exactly and had banished the snakes. As he pointed out, the matrix products $(\partial e^{-1}/\partial p_m)e$ and $e^{-1}(\partial e/\partial p_m)$ are skew symmetric (their sum is just $\partial e e^{-1}/\partial p_m$ or $\partial \mathbf{1}/\partial p_m$), and their products with Λ, which is itself diagonal, can only have zeros on the diagonal. Thus $\partial\Lambda/\partial p_m$ is equal to the diagonal elements of $e^{-1}(\partial \mathbf{H}/\partial p_m)e$. In addition, the differentials for the transitions ν_{kl} are just the differences $\partial\lambda_{kk}/\partial p_m - \partial\lambda_{ll}/\partial p_m$. Since e and e^{-1} are obtained in the diagonalization process, everything is available to get not just the finite differentials, but the exact differentials of all the transition frequencies.

When this process was built into LAOCOON, renamed LAOCOON II, it worked marvelously, and LAOCOON II and its descendants, LAOCOON III, LAOCN, and others became very widely used.[14] It was also quickly improved and expanded in many ways: C. W. Haigh[15] added the capability to handle groups of magnetically equivalent spins, and improved the efficiency in his program, LAME. He also improved the efficiency in calculating AB..XY.. type spectra by using factorization in his program LACX. Tom Flautt and his colleagues[16] added the capability to include direct dipolar couplings in the Hamiltonian, so that spectra of molecules oriented in liquid crystals might be analyzed. Several groups, including ours, added the capability to include nuclei with spins greater than $\frac{1}{2}$, and to include quadrupole couplings in the Hamiltonian. An excellent version, incorporating many of the improvements, is PANIC, the program distributed by Bruker, Inc. A quite separate development was the series of DNMR programs, produced by Gerhard Binsch.[17] These were aimed at the analysis of spectra from systems undergoing dynamic exchanges or rearrangements. DNMR2 and DNMR3 were simulation programs,[18] allowing calculation in the forward direction, while DNMR5 was an iterative program,[19] allowing refinement of the NMR and dynamic parameters, in the spirit of LAOCOON II.

In spite of the great success of these programs, and their very widespread and diverse applications, there remained one annoying problem. All of them (except EXAN) required the spectroscopist to produce an initial assignment or an initial guess at the NMR parameters which would lead to a calculated spectrum sufficiently resembling the observed spectrum that one could identify corresponding lines. For highly non-first-order spectra, this could be frustratingly difficult. That so many successful analyses were performed was a tribute to the ingenuity, dogged persistence, and luck, of the investigators. The first versions of LAOCOON went out to the users with the suggestion that the initial trial assignment might be obtained by 'shrewd guess, accident, divine inspiration, or examination of the entrails of freshly slain pigeons'. This recipe, patiently

followed, led to success in 99% of the cases we addressed, but occasionally even a prolonged and arduous effort failed to produce a recognizable match.

This problem was finally solved by Gerhard Binsch and David Stephenson[20] in 1980. Their program, DAVINS, accepts as input a digitized spectrum; both transition frequencies and intensities guide the program towards a final set of parameters. Falling into a local minimum and converging to an incorrect assignment and parameter set is avoided by an ingenious scheme which smooths the least-square surface to the extent that only one minimum exists. During the iteration, the smoothing is gradually reduced until the iteration is concluded with an unsmoothed surface. While convergence is not always achieved, trials indicate that it is successful in more than 90% of the cases, even with highly non-first-order spectra.

What of the present and the future? More powerful and comprehensive programs are being written at an accelerating pace—for simulation and analysis of 2D spectra, for simulation of spectra obtained during irradiation with rf, for simulation of spectra with the inclusion of relaxation processes. With the advent of ever faster, larger, and more versatile computers, there appears to be no limit on the reach and span of computer-aided analysis.

REFERENCES

1. E. L. Hahn and D. E. Maxwell, *Phys. Rev.*, 1952, **88**, 1070.
2. H. S. Gutowsky, D. W. McCall, and C. P. Slichter, *J. Chem. Phys.*, 1953, **21**, 279.
3. H. M. McConnell, A. D. McLean, and C. A. Reilly, *J. Chem. Phys.*, 1955, **23**, 1152.
4. J. A. Pople, W. G. Schneider, and H. J. Bernstein, *High-Resolution Nuclear Magnetic Resonance*, McGraw-Hill, New York, 1959, Chap. 6
5. E. B. Wilson, Jr., *J. Chem. Phys.*, 1957, **27**, 60.
6. A. A. Bothner-By and C. Naar-Colin, *J. Am. Chem. Soc.*, 1962, **84**, 743.
7. A. A. Bothner-By and C. Naar-Colin, *J. Am. Chem. Soc.*, 1961, **83**, 231.
8. A. A. Bothner-By, C. Naar-Colin, and H. Guenther, *J. Am. Chem. Soc.*, 1962, **84**, 2748.
9. C. A. Reilly and J. D. Swalen, *J. Chem. Phys.*, 1960, **32**, 1378.
10. R. A. Hoffman, *J. Chem. Phys.*, 1960, **33**, 1256.
11. Y. Arata, H. Shimizu, and S. Fujiwara, *J. Chem. Phys.*, 1962, **36**, 1951.
12. S. Castellano and J. S. Waugh, *J. Chem. Phys.*, 1961, **34**, 295.
13. A. A. Bothner-By, S. Castellano, and H. Guenther, *J. Am. Chem. Soc.*, 1965, **87**, 2439.
14. S. Castellano and A. A. Bothner-By, *J. Chem. Phys.*, 1964, **41**, 3863.
15. C. W. Haigh, *Annu. Rep. NMR Spectrosc.*, 1971, **4**, 311.
16. P. J. Black, K.D. Lawson, and T. J. Flautt, *J. Chem. Phys.*, 1969, **50**, 542.
17. G. Binsch and H. Kessler, *Angew. Chem.*, 1980, **92**, 445.
18. D. A. Kleier and G. Binsch, *Quantum Chemistry Program Exchange*, 1970, program 165.
19. D. S. Stephenson and G. Binsch, *J. Magn. Reson.*, 1978, **32**, 145.
20. D. S. Stephenson and G. Binsch, *J. Magn. Reson.*, 1980, **37**, 409.

Biographical Sketch

Aksel A. Bothner-By. *b* 1921. B.Chem., 1943, Ph.D., 1949 (with R. B. Woodward, Harvard), Brookhaven Natl. Lab. 1949-1952. ETH Zürich, 1952-1953. Harvard, 1953-1958. Mellon Institute, then Carnegie Mellon U. 1958-1992. Began study of NMR in 1954. ~150 publications. Research specialties: molecular geometry by high-resolution NMR; Overhauser effects, longitudinal and transverse; molecular orientation by high magnetic field.

Bottomley, Paul A.: The Development of High-Field NMR Imaging: 0.12 T to 1.5 T

Paul A. Bottomley

GE Research and Development Center, Schenectady, NY, USA

In 1984 the Medical Systems Division of the General Electric Company (GEMS) in Milwaukee shipped six of its first NMR imaging product, a high-field, 1.5 Tesla (T), whole-body NMR system based on a prototype research scanner developed at the Corporate Research and Development Center (CRD) in Schenectady. The system represented a major advance over contemporary commercial offerings and existing whole-body research scanners: its field strength was about four or more times higher, its signal-to-noise ratio was better, and it uniquely combined NMR imaging and NMR spectroscopic capabilities in a single instrument. The system rapidly gained and dominated the market for high-performance NMR scanners, and nine years later, the total number of these systems shipped exceeded 1350.

Yet in the early 1980s whole body NMR imaging was not generally considered practical above about 10 MHz (∼0.3 T) for two reasons: problems with rf penetration into the body,[1] and the inability to make high-frequency body rf coils.[2] I was partly to blame for the penetration argument, having published an earlier analysis while at Nottingham, showing significant penetration effects.[3] That paper identified phase variation in the transmitted field as the main problem and suggested that the use of the 'power spectrum' would solve it, as it does. It did not rule out high-field imaging. The coil argument was based on the idea that phase variations must be kept minimal around the coil.[2] That idea didn't hold up for long: the standard solution is to allow a 2π phase variation around the coil.[4] Anyway, at the time I thought the two arguments non-prohibitive. If the magnet existed and a coil could be made, I had no misgivings about attempting an imaging experiment, quietly.

I interviewed at CRD on April 30 1980. My first contact was with John Schenck who said they wanted to hire researchers for a whole body NMR program. I had been a research associate in Don Hollis's group at the Department of Physiological Chemistry at the Johns Hopkins Medical Institutions in Baltimore since 1978. I was trying to use imaging gradients to localize ^{31}P spectra within perfused hearts, but the group was disintegrating. Don Hollis had resigned, while the rest of us were supported by his grants. We had built a 3-cm aperture imager for an existing 180 MHz (4.1 T) spectrometer,[5] the highest field imager at the time, but abandoned it in 1980 in favor of surface coils. These were new,[6] and tuning them for the heart in those days involved groveling around the floor with a soldering iron, chip capacitors, and a heart beating sticky perfusate all over the place. I was doing just that on the afternoon of my interview, and tore off a sheet of spectra as I dashed for the plane.

I thought GE's interest was whole body imaging, so I focused my interview talk on NMR imaging work I had done at Johns Hopkins and Nottingham.[7] I was astounded to learn that their interest was localized spectroscopy. Red Redington, my future boss, wanted a whole body NMR system to study phosphate metabolism in people and their hearts. They could get no support from GEMS for NMR imaging, and so decided to pursue metabolism using corporate assessed funds. Years earlier, GE had concluded that NMR imaging could never compete with X-ray computed tomography in terms of signal-to-noise ratio per unit time. I produced the sheet of heart spectra and described our latest ^{31}P NMR experiments on regional ischemia[8] with glee.

The day in August that I started at CRD, I sat in a meeting with Intermagnetics General Corporation. They, along with Oxford Instruments, were bidding for a high-field, high homogeneity, 1-m bore, whole body superconducting electromagnet for the spectroscopy project: neither had made one before. Oxford Instruments was ultimately chosen. The target field was 2 T but due to uncertainty about whether the design specifications could be met in practice, a minimum acceptable field was also set. This was 1.5 T.

In September, Bill Edelstein arrived from Aberdeen, equipped with the spin-warp NMR imaging method[9] and experience from constructing a 0.04-T whole body imager. We exchanged stories of strife in our former Aberdeen and Nottingham laboratories. Bill offered: 'Well Paul, I'm not sure whether this spectroscopy thing is going to amount to anything, but if you want to work on that, I'd rather work on NMR imaging'. I responded 'I don't know whether spectroscopy is going anywhere either, but I certainly believe that it is imaging that is more likely to succeed'.

The 1.5−2 T magnet wasn't due until late 1981 or 1982. Bill and I sat in a succession of temporary offices for a month or two waiting for someone to tell us what to do (not that we'd do it, anyway). Nothing happened, so we decided to build a low-field imaging system. We knew we'd need imaging technology for localized spectroscopy anyway. Red got $100K from GEMS to buy a 0.12-T resistive electromagnet. We'd build and ship this system to the Hospital of the University of Pennsylvania (HUP) for patient studies before the high-field system came. The group at this time comprised Bill Edelstein and myself full-time, and Bill Leue, Howard Hart, and John Schenck part-time, managed by Red. I did the gradient and rf coils, and put together bits of the rf spectrometer. We had images for the October 1981 NMR imaging meeting in Winston-Salem,[10] which I recall as the all-time best NMR meeting for innovations per unit time. The 0.12-T system went to HUP in August 1982.

By early 1982, at last, GEMS had become concerned about the rise of NMR imaging and its potential impact on its X-ray CT product. 'Luminary' customers were looking elsewhere to purchase NMR systems, and GEMS had nothing on NMR at their all-important technical exhibit at the Radiological Society of North America (RSNA) meeting in Chicago in December 1981. This was in the face of major exhibits by Picker-EMI, Technicare, Siemens, Philips, and some smaller companies. GEMS reversed strategies and asked us to turn down our high-field magnet for a 'short' spate of imaging. I figured I could make an NMR coil set that worked at about 20 MHz, and had a body coil in March. The plan then was to obtain a few spectra at high field when the magnet arrived, then turn it down to 0.5 T. This was presented at a meeting with GEMS on April

7. Meanwhile GEMS was also seriously considering offering a commercial resistive system like our 0.12-T one.

The high-field magnet was installed by the end of May 1982. It barely made it to 1.5 T and was reluctant to stay there: its field drifted down at a rate of about 2 ppm h^{-1}. Sometime thereafter I made a head imaging coil which worked at 54 MHz. Very excited, I showed Red: 'Looks like we won't have to turn the field down, after all'. I was concerned that once the field came down, given the way imaging was hotting up, it would never go up again. I was affronted when my suggestion was transformed into a command from on high a week or so later: 'Thou shalt make images at 1.5 T'.

GEMS, increasingly anxious over imaging, foisted an extra manager on us, and a team of program planners who descended in July to make us make images more quickly. They came to make charts with boxes of tasks with surrealistic completion dates. We were interrogated for hours but I divulged nothing: 'It'll be done when it's done'. Finally, Red got fed up with the fuss and threw them out. I took over the NMR coils and spectrometer with help from L. S. Smith and O. Mueller. John Schenck with Bill Edelstein came up with new distributed current gradient coils. Bill Leue did the computer and interface, and Howard Hart looked after the magnet.

By October I had a head saddle coil that self-resonated at 86 MHz and a slotted-tube resonator that would work at 1.5 T. I acquired surface coil ^{31}P spectra of metabolites in the legs, head, and torso. During this period, Bill Edelstein and I were also regular trippers to HUP, to maintain the 0.12-T system. Finally, late in the evening of November 22, Howard Hart and John Schenck made the first 1.5-T images of the head and limbs using the saddle coil.

The image quality and resolution of these images wasn't good. We had one week before the 1982 RSNA meeting to do better, but our 5-kW rf power amplifier was broken. Red had one flown in from GEMS. We were walking back from lunch the day it arrived: the crowd outside the NMR building was ominous. There was the power amplifier, all right, stuck in the magnet! It had apparently taken off while being wheeled too close: the mover was in hospital with hand injuries. We tried winching it out, but the Dewar broke: the magnet turned into a snowball, and we were wiped out until the end of January (Figure 1). GEMS ran with the images and spectra that we had, however, printing green leaflets announcing our high-field imaging/spectroscopy capability as a breakthrough at the 1982 RSNA meeting. This generated a storm of interest, and undoubtedly stalled many NMR purchases to await GEMS's offering, as was hoped.

Late on February 1, 1983 with the magnet fixed and Howard's head inside the slotted tube resonator, I began obtaining fantastic images with 256 × 256 resolution in 4-mm slices and 100 s scan times. I was ecstatic. My notebook that day is scrawled with expletives next to the polaroid prints. There was no one to show (Howard was magnet-bound). I dragged in the cleaner: 'Isn't this the most incredible picture you've ever seen?' We published in the *Lancet*.[11] We knew the images were better than anything else around at the time.

GEMS's competitors were committed to low-field systems and some ugly accusations flew amongst marketeers: 'they faked the pictures', 'they can't do whole body imaging', 'the increased rf power is hazardous', 'their work was rejected as unscientific'. The most vocal were from the Radiologic Imaging Laboratory in South San Francisco who claimed

Figure 1 The 5 kW rf power amplifier, complete with dolly cart, being winched from the bore of the whole-body 1.5-T imaging system, at full field in November 1982 (picture courtesy W. A. Edelstein)

that the signal-to-noise ratio decreased above 0.3 T and that the switch-over time between imaging and spectroscopy was 2–14 h.[12] We hunkered down: Bill Edelstein made a 1.5-T body coil and started getting body images in March.[13] The forces faced-off at the meeting in August 1983 of the Society of Magnetic Resonance in Medicine in San Francisco. Bill's retort at the session paraphrased a song: 'If you don't have the field you love, you love the field you have'. For my part, GEMS gave me a scrapper award, 'for ultimate defense of high-field strength'.

REFERENCES

1. P. Mansfield and P. G. Morris, *NMR Imaging in Biomedicine*, Academic Press, New York, 1982, pp. 174, 187–191, 264.
2. D. I. Hoult, in *NMR Imaging*, eds. R. L. Witcofski, N. Karstaedt, and C. L. Partain, Bowman Gray School of Medicine, Winston-Salem, 1982, pp. 33–39.
3. P. A. Bottomley and E. R. Andrew, *Phys. Med. Biol.*, 1978, **23**, 630.
4. C. E. Hayes, W. A. Edelstein, J. F. Schenck, O. M. Mueller, and M. Eash, *J. Magn. Reson.*, 1985, **63**, 622.
5. P. A. Bottomley, *J. Phys. E: Sci. Instrum.*, 1981, **14**, 1081.
6. J. J. H. Ackerman, T. H. Grove, G. G. Wong, D. G. Gadian, and G. K. Radda, *Nature (London)*, 1980, **283**, 167.

7. W. S. Hinshaw, P. A. Bottomley, and G. N. Holland, *Nature (London)*, 1977, **270**, 722.
8. R. L. Nunnally and P. A. Bottomley, *Science*, 1981, **211**, 177.
9. W. A. Edelstein, J. M. S. Hutchison, G. Johnson, and T. Redpath, *Phys. Med. Biol.*, 1980, **25**, 751.
10. *NMR Imaging*, eds. R. L. Witcofski, N. Karstaedt, and C. L. Partain, Bowman Gray School of Medicine, Winston-Salem, 1982, pp. 139–145.
11. P. A. Bottomley, H. R. Hart, W. A. Edelstein, J. F. Schenck, L. S. Smith, W. M. Leue, O. M. Mueller, and R. W. Redington, *Lancet*, July 30 1983, 273.
12. L. Kaufman, L. Crooks, and A. Margulis, *Diagnostic Imaging*, Jan. 1984, 36.
13. W. A. Edelstein, O. M. Mueller, P. A. Bottomley, H. R. Hart, J. F. Schenck, L. S. Smith, M. O'Donnell, W. M. Leue, and R. W. Redington, *Magn. Reson. Med.*, 1984, **1**, 145.

Biographical Sketch

Paul A. Bottomley. *b* 1953. B.Sc. Hon., 1974, Monash University, Australia, Ph.D. (NMR imaging), 1978, University of Nottingham, UK, with E. Raymond Andrew and Waldo Hinshaw. Physicist, General Electric (GE) Research and Development Center, Schenectady New York, 1980–1994. Presently Russell H. Morgan Professor of Radiology, Johns Hopkins University, Baltimore, USA. Approx. 120 publications, 110 conference reports, 25 patents. Gold Medal, Society of Magnetic Resonance in Medicine, 1989; GE Coolidge Medal and Fellow, 1990. Research specialties: in vivo NMR imaging, spectroscopy, and tissue relaxation times.

Bovey, Frank A.: NMR of Polymers

Frank A. Bovey

AT&T Bell Laboratories, Murray Hill, NJ, USA

When polymers in solution were first observed by high-resolution NMR some 30 years ago, almost nothing was known about the subject. Previous work at Bell Laboratories, by D. W. McCall and W. P. Slichter,[1] had been confined to the solid state. Proton resonances were too broad to reveal any structural information and it was primarily *chain motion* that was of interest. There was in fact somewhat the same feeling about solution spectra as about solid state spectra — namely, that they would be too broad and too complicated to be of any interest for the determination of structure. Happily, when the experiment was actually tried this proved not to be the case, and the rest is history.

The chemical shifts and proton J couplings of random coil macromolecules are closely similar to those of small molecules of analogous structure. In Figure 1 the spectrum of ethyl orthoformate (**1**) is compared with that of poly(vinyl ethyl ether) (**2**).

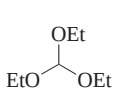

(1)

(2)

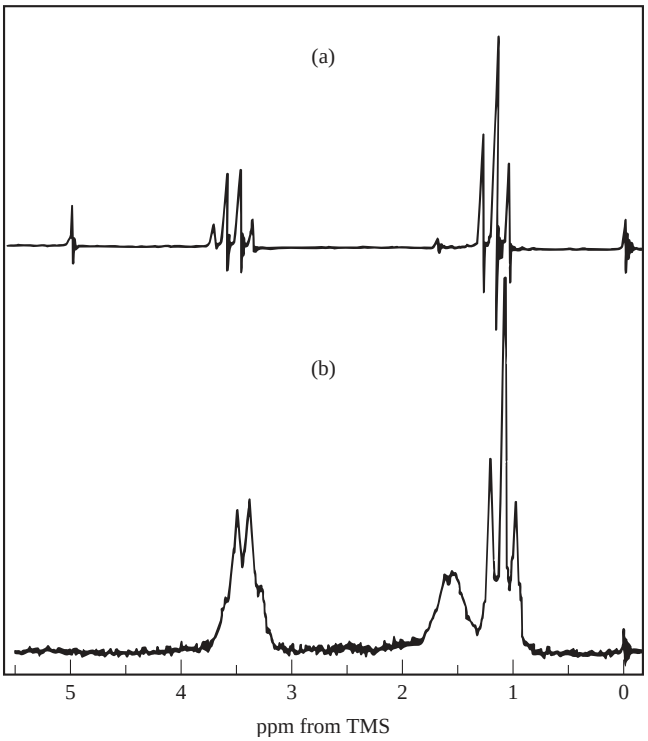

Figure 1 60 MHz ^{1}H NMR spectra of (a) ethyl orthoformate and (b) poly(vinyl ethyl ether)

The polymer exhibits the same ethyl proton resonances and, in addition, those of the main chain β-protons, appearing at 1.5 ppm, and of the α-protons, appearing under the CH_2 quartet. The broadening of the polymer lines is in part due to the slower motions of the large molecules but is mainly due to overlapping resonances arising from steric sequences (vide infra). In general, linewidth is only weakly dependent on molecular weight or the macroscopic viscosity of polymer solutions.

NMR is very informative concerning the stereochemical configuration of vinyl and diene polymer chains. In Figure 2 are shown 500 MHz proton spectra of (a) syndiotactic and (b) isotactic poly(methyl methacrylate). Polymer (a) was prepared with a free-radical initiator and polymer (b) with fluorenyllithium in toluene, an anionic initiator. To interpret these spectra let us consider the chain in terms of sequences of two monomer units or *dyads*. There are two possible types of dyads and they have different symmetry properties. The syndiotactic or racemic (r) dyad has a twofold axis of symmetry and consequently the two methylene protons are in equivalent environments on a time average over the chain conformations, which are not necessarily in the planar zigzag form shown in the projection formulas (**3**) and (**4**). These protons therefore have the same chemical shift and appear as a singlet despite strong two-bond or geminal coupling between them. The isotactic or *meso (m)* dyad has a plane of symmetry but no twofold axis and so the two protons are nonequivalent and have different chemical shifts. When there is no vicinal coupling to neighboring protons, as is the case in poly(methyl methacrylate), the syndiotactic sequences should exhibit a methylene singlet while the isotactic form should give two doublets, each with a spacing equal to the geminal coupling, ca. 15 Hz. We see in Figure 2 that the methylene spectrum of the anionic polymer (b) is almost exclusively a pair of doublets (ca. 1.6 and 2.3 ppm); quantitative assessment shows that this polymer is 95% isotactic. The methylene spectrum of the free-radical polymer (a) is more complex, but the principal resonance (at ca. 1.9 ppm) is a singlet, showing that this polymer is predominantly syndiotactic but more irregular than (b). This is generally the case for vinyl polymers prepared with free-radical initiators. (The other resonances are discussed below.)

(3) *r*

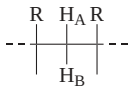

(4) *m*

Planar zigzag conformation

We see that proton NMR can provide absolute stereochemical information concerning polymer chains without recourse to X-ray or other methods. Somewhat more detailed, but not absolute, information can be gained from the methyl proton resonances near 1.2 ppm. (The ester methyl resonances at ca. 3.6 ppm, which are not shown, are less sensitive to stereochemistry.) In both spectra we note three peaks—or, more correctly, groups of peaks (vide infra)—appearing in similar positions but with greatly different intensities. These correspond to the α-methyl groups in the center monomer unit of the three possible triad sequences: isotactic (**5**), syndiotactic (**6**), and heterotactic (**7**). These may be more simply and

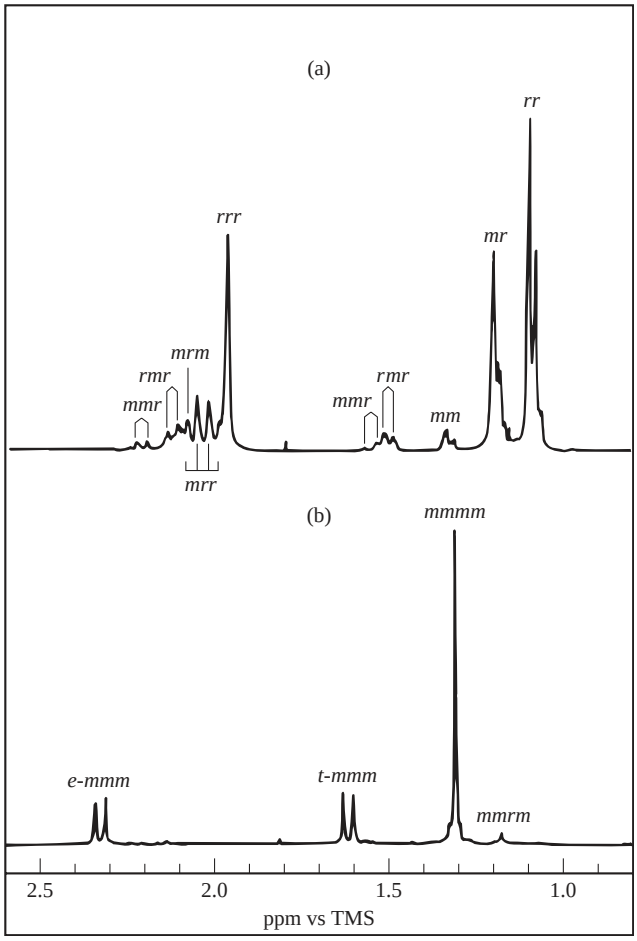

Figure 2 500 MHz ^{1}H NMR spectra of (a) syndiotactic and (b) isotactic poly(methyl methacrylate)

appropriately designated by the *m* and *r* terminology, as indicated. Measurement of the relative intensities of the *mm*, *mr*, and *rr*α-methyl peaks, which appear from left to right in both spectra in this order, gives a valid statistical representation of the structure of each polymer.

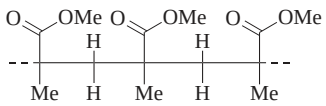

(5) Isotactic, *mm*

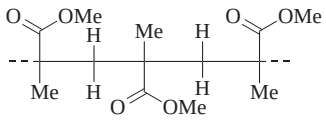

(6) Syndiotactic, *rr*

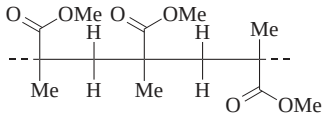

(7) Heterotactic, *mr* (or *rm*)

From the triad data one may gain considerable insight into the mechanism of propagation. This is one of the principal uses

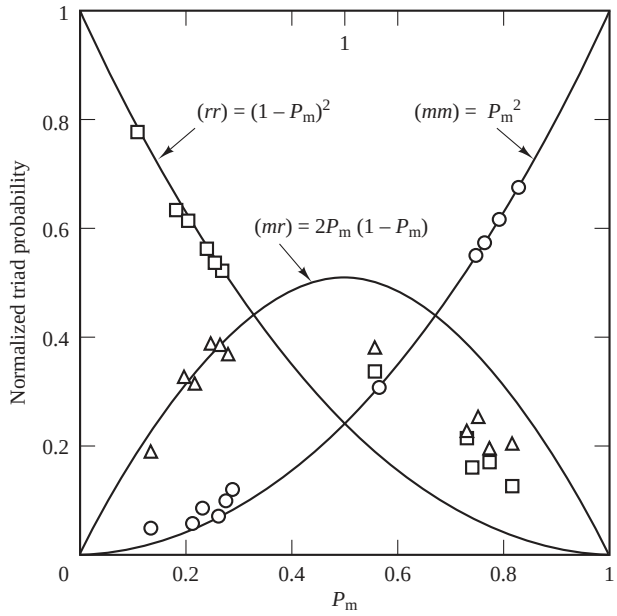

Figure 3 Probabilities of various triads formed in a Bernoulli propagation process

of such information. Let us designate by P_m the probability that the polymer chain will add a monomer unit to give the same configuration as that of the last unit at its growing end, i.e. that an *m* dyad will be generated. We assume that P_m is independent of the stereochemical configuration of the growing chain. The generation of the chain is a Bernoulli-trial process; it is like reaching into a large jar of balls marked *m* and *r* and withdrawing a ball at random. The proportion of *m* balls in the jar is P_m. Since two monomer additions are required to form a triad sequence, it is readily evident that the probabilities of their formation are

$$[mm] = P_m^2 \tag{1}$$

$$[mr] = 2P_m(1 - P_m) \tag{2}$$

$$[rr] = (1 - P_m)^2 \tag{3}$$

The heterotactic sequence must be given double weighting because both directions *mr* and *rm*—observationally indistinguishable—must be counted. A plot of these relationships is shown in Figure 3. It will be noted that the proportion of *mr* (heterotactic) units rises to a maximum when P_m is 0.5, corresponding to a strictly random or atactic configuration for which $[mm]/[mr]/[rr]$ will be 1:2:1. For any polymer, if Bernoullian, the $[mm]$, $[mr]$, and $[rr]$ sequence intensities will lie on a single vertical line in Figure 3, corresponding to a single value of P_m. Spectrum (a) in Figure 2 corresponds to these simple statistics, P_m being 0.25 ± 0.01. The polymer corresponding to spectrum (b) does not. The propagation statistics in this case can be interpreted to indicate that the probability of isotactic placement is dependent upon the stereochemical configuration of the growing chain and cannot properly be expressed by a single parameter such as P_m. Free radical and

Table 1 Stereoregular Sequences in Poly(Methyl Methacrylate)

	Designation	α Substituent projection	Bernoullian probability		Designation	β -CH_2 projection	Bernoullian probability
Triad	Isotactic, *mm* (*i*)		P_m^2	Dyad	*meso*, *m*		P_m
	Heterotactic, *mr* (*h*)		$2P_m(1-P_m)$		racemic, *r*		$(1-P_m)$
	Syndiotactic, *rr* (*s*)		$(1-P_m)^2$	Tetrad	*mmm*	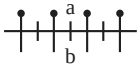	P_m^3
Pentad	*mmmm* (isotactic)		P_m^4		*mmr*	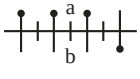	$2P_m^2(1-P_m)$
	mmmr		$2P_m^3(1-P_m)$		*rmr*	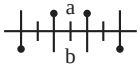	$P_m(1-P_m)^2$
	rmmr		$P_m^2(1-P_m)^2$		*mrm*	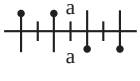	$P_m^2(1-P_m)$
	mmrm		$2P_m^3(1-P_m)$		*rrm*	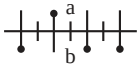	$2P_m(1-P_m)^2$
	mmrr		$2P_m^2(1-P_m)^2$		*rrr*	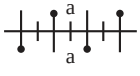	$(1-P_m)^3$
	rmrm (heterotactic)		$2P_m^2(1-P_m)^2$				
	rmrr		$2P_m(1-P_m)^3$				
	mrrm		$P_m^2(1-P_m)^2$				
	rrrm		$2P_m(1-P_m)^3$				
	rrrr (syndiotactic)		$(1-P_m)^4$				

cationic propagations always give predominantly syndiotactic chains. Anionic initiators may also do so if strongly complexing ether solvents such as dioxane or glycol dimethyl ether are employed rather than hydrocarbon solvents as with the polymer depicted in Figure 2(b).

It is evident that in the spectra of Figure 2, there is fine structure in both the methylene and methyl regions which we have not discussed. In spectrum (a) this corresponds principally to residual resonances of the stereoirregular portions of the chains; in (b) such residual resonances are less conspicuous. These arise from sensitivity to longer stereochemical sequences than dyad and triad. In Table 1 are shown planar zigzag projections of such sequences, together with their frequency of occurrence as a function of P_m, assuming Bernoullian propagation. The tetrads, and all 'even-ads', refer to observations of β-methylene protons (or β-carbons), while the 'odd-ads' refer to substituents on the α-carbons (or α-carbons themselves). Resonances for tetrad sequences or higher 'even-ads' should appear as fine structure in the dyad spectra, while pentad sequences or higher 'odd-ads' should appear as fine structure on the triad resonances.

It may be noted that *r*-centered tetrads, e.g. *mrr*, do not necessarily appear as singlets if the sequence as a whole lacks a twofold axis.

The numbers of observationally distinguishable configurational sequences, or *n*-ads, designated $N(n)$, obey the following relationship

n	2	3	4	5	6	7	8	9
$N(n)$	2	3	6	10	20	36	72	136

or in general

$$N(n) = 2^{n-2} + 2^{m-1} \tag{4}$$

where $m = n/2$ if n is even and $m = (n-1)$ if n is odd. Discrimination of these longer sequences is unlikely to be possible beyond $n = 6$ (hexads) or $n = 7$ (heptads). The

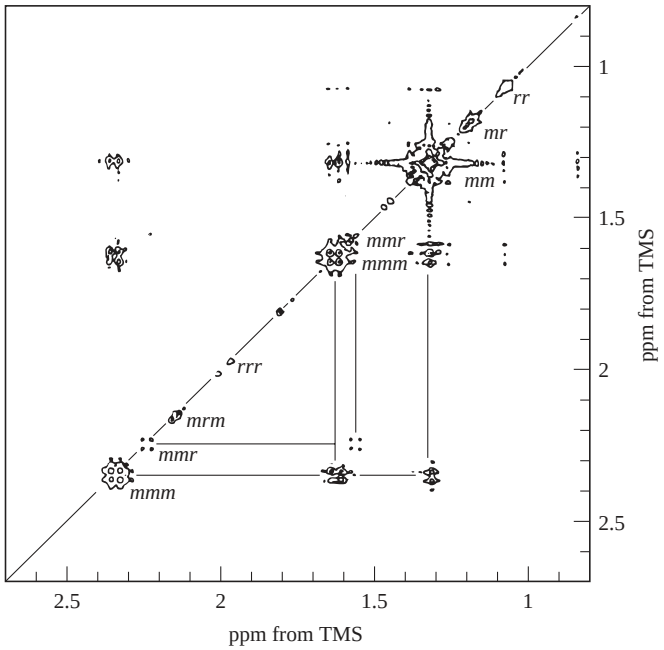

Figure 4 ^{1}H 2D COSY spectrum at 500 MHz of poly(methyl methacrylate)

observation of such sequences permits rather searching tests of polymerization mechanisms.

Let us now observe isotactic poly(methyl methacrylate) in the 2D proton NMR mode, also at 500 MHz. The spectrum shown in Figure 4 is an example of correlated 2D NMR, in which the correlation is provided by J coupling, Along the diagonal is the 1D spectrum in contour form. This of itself provides no new information, but the off-diagonal resonances or cross peaks connect J-coupled protons. This supplies the whole network of connectivities at a glance. In the present case the crosspeaks confirm the geminal coupling in the *meso* methylene dyads. The methylene proton which projects on the same side of the planar zigzag as the ester groups in the *trans–trans* conformation is designated as *erythro*, the other being *threo*. Rather unexpectedly, we see a cross peak between the α-methyl resonance and the *erythro* methylene proton but not the *threo* proton. This correlation is brought about by very weak four-bond couplings of the order of 1 Hz and tells us that the preferred conformation of the isotactic chain is *trans–trans*. In this conformation only the *erythro* proton is capable of forming with an α-methyl proton (one-third of the time for each) a 'W'-shaped four-bond path of the kind generally thought to be favorable for such long-range coupling. Expressed somewhat differently, the methyl group and the *erythro* proton exhibit in the *trans–trans* conformation the 180° dihedral angle corresponding to maximum coupling according to the correlation of Barfield, whereas the *threo* proton is near a minimum. This correlation is also observed for methyl methacrylate oligomers and is in agreement with energy calculations indicating a strong *trans* preference.

REFERENCE

1. W. P. Slichter, *Adv. Polym. Sci.*, 1958, **1**, 35.

Biographical Sketch

Frank A. Bovey. *b* 1918. B.S., 1940, Harvard, Ph.D., 1948, Physical Chemistry, University of Minnesota. Polymer research, Minnesota Mining and Manufacturing Co., 1948–62. Bell Laboratories, 1962–94. Research specialties: physical chemistry of polymers, NMR of polymers.

Brey, Wallace S.: The First 40 Years Should Be the Hardest

Wallace S. Brey
University of Florida, Gainesville, FL, USA

MY INTRODUCTION TO NMR

My first contact with nuclear magnetic resonance came in the year 1951–52. The Philadelphia Section of the American Chemical Society sponsored several series of Continuing Education lectures for chemists, and one of these series, arranged by Adalbert Farkas, was devoted to heterogeneous catalysis. Not only did I help to manage these programs, but my industrial experience and doctoral research at the University of Pennsylvania had been in this field. One of the lecturers was P. W. Selwood, who described some of the extensive studies he had made of the magnetic susceptibilities of supported metal catalysts, the results of which were taken as a measure of the extent to which the metal atoms were dispersed over the surface rather than aggregated into clumps. Indeed, during my earlier graduate days at Penn, I had participated in a physical chemistry seminar in which we worked through Selwood's newly published book.

During the course of his talk, Selwood did not mention NMR, but at the beginning of the question period there was a great deal of excitement among a number of the members of the audience who were chemists employed in the petroleum industry. They wanted to know 'the story about all this business of looking at protons', of which they had heard rumors. Selwood obliged with a 20-min introduction to NMR, representing the precessing and flipping nuclei with a long pointer conveniently at hand. The questioners were referring to what was probably the first application of NMR to heterogeneous catalysis. Selwood had sent one of his students to use the NMR apparatus at Harvard to investigate the effects of paramagnetic catalyst systems on the relaxation times of organic liquids in which they were immersed,[1,2] and the results for the amount of exposed metal surface were consistent with the results from susceptibility measurements.

Two more associations with NMR occurred after I moved to the University of Florida in 1952. One was a Sigma Xi tour lecture by Felix Bloch, devoted to the principles of NMR and a few of the early applications. The second was in 1954 at an instrument exposition at the Commercial Museum, adjacent to Convention Hall in Philadelphia, which I attended on the way to an ACS meeting in New York City. Each registrant was able to choose two from a list of instrument types, one for the morning and one for the afternoon. Some eight or so sections were curtained off in the exhibit hall and each was assigned to an instrument manufacturer. I attended the General Electric session on mass spectrometry, but my real interest lay in the Varian session on NMR.

The Varian representatives had set up an operating spectrometer. The magnet was of course an electromagnet, with a field strength corresponding, as well as I can recall, to 30 MHz. The item of great pride on the part of the Varian representatives was the introduction of sample spinning, which enabled the quartet–triplet structure in the spectrum of ethanol, displayed on a small round oscilloscope screen, to be resolved.

As I look back, I am still amazed at the quality of the Varian staff who participated in this session: they were the people responsible at the highest level for the design of the instrument. Most impressive was the presence of one of the Varian brothers himself, a person most striking in physical appearance. During the course of the lectures, attention was turned away from the instrument for some time, and then someone noticed that the spectrum has disappeared from the screen—as one might expect, considering the rise in temperature in a confined space, for a spectrometer without a lock. In an instant, three or four of the 'inventors' of NMR instrumentation converged on the console, reaching for the switches that would reverse the field drift.

NMR SPECTROMETERS IN THE UNIVERSITY OF FLORIDA DEPARTMENT OF CHEMISTRY

In 1958, Harry H. Sisler, Chairman of the Department, convinced of the power of NMR as a tool in chemistry, collected money from various pockets to purchase a spectrometer and I was put in charge, partly because I shared with Arthur M. Buswell, earlier a pioneer in the use of infrared spectroscopy, an NIH grant on water structure. One of the most significant applications of this instrument was in the structural analysis of fluorinated organic compounds produced by the half dozen research groups active in this area for a period of years at the University of Florida.

The Varian DP-60 (for 'dual-purpose 60 MHz') spectrometer was operated in field sweep mode, with a fixed frequency for each nucleus, controlled by a crystal oscillator. Our instrument was among the first to be manufactured. There was no lock, and the way one determined peak positions accurately was to sweep the field back and forth 5 to 10 times, with audiofrequency sidebands applied, tediously measure relative distances on the continuous chart paper, and average the results. Initially, the magnet had no shim coils. The procedure for optimizing homogeneity was to 'squeeze' the magnet yoke with a ratcheted screw working against a metal flange attached to the magnet support and to move the probe around near the middle of the field to find, by trial and error, the best location. Further, when the magnet was first brought up to field, it was necessary to 'overcycle' it, raising the field by a definite amount above the operating value and then lowering it. This served to reduce the domed contour of the field near the magnet axis. This system did have a 'Superstabilizer', a galvanometer with optical beam falling between two photocells arranged to compensate for transients in the magnetic field.

Very soon x, y, z, and radial shims were added to the magnet, along with insulation about the yoke to reduce the temperature variation. The magnet was cooled by tap water circulating through copper tubing wound along with the conductors. After a few years, this small tubing was blocked up and the magnet could only be operated at reduced field—nice proton spectra at 15 or even 24 MHz could be obtained. Despite valiant efforts by relays of students pouring

phosphoric acid solution into the coils, they remained blocked and were eventually replaced, along with the addition of a heat exchanger.

Early studies on recalcitrant nuclei, such as carbon-13, were based on fast passage, dispersion mode resonances, which do not saturate. A neat sample of low molecular weight material at natural isotopic abundance gives a satisfactory resonance under these conditions, permitting evaluation of the chemical shift.

Our research interests in the structure of liquids containing fluorocarbons, the binding of substrates to catalysts, and the hydration of proteins led to the use of relaxation rate measurements. At first these were done by a combination of saturation studies for T_1 and linewidth determinations for T_2. Later a set-up based on pulses was assembled by Vincent Heuring by combining a series of Tektronix pulse generator units. In the surface studies, the wideline function of the dual-purpose spectrometer was extremely useful. The hardware was essentially the same as that in Varian EPR units and comprised a motor-driven field-scanning mechanism and a source of modulation of the field at variable intensity and at a selected frequency. The sensitivity of this scheme was very good, but care had to be exercised to adjust the modulation level for the linewidth of the resonance. For example, when we first followed the linewidth variation for protons in adsorbed methanol to temperatures well below room temperature, it appeared that the line first widened and then narrowed as -90 $^{\circ}$C was approached. A little reflection led to the realization that the resonance of the hydroxyl proton was continuing to broaden as the temperature was lowered, becoming so broad that the modulation was not covering a wide enough field to pick up the peak with reasonable sensitivity, and that only the somewhat narrower resonance of the methyl group was evident at low temperatures.

In the mid-1960s, the Department acquired two A-60 spectrometers, along with a 'computer of average transients', better known as a CAT. The latter could be used with the DP-60 and with EPR instruments as well as with the A-60s to enhance sensitivity. In 1968, matching grants enabled us to acquire a 100 MHz instrument. The first unit was a DA-100 with 12-in. vertical yoke, iron magnet. The magnet was shortly replaced by a 15-in. magnet with tilted yoke, giving access to the samples from directly above. The power supply for this magnet was based upon a mechanically driven set of brushes in a variable transformer set-up. These soon began to arc and the supply was replaced, just as the warranty period expired, by an electronically regulated supply. Multinuclear capability was provided by new probes along with the retuning of several rf units from the DP-60.

An interesting sidelight to the acquisition of this spectrometer is related to my visit to Palo Alto to inspect the available equipment. I was proudly shown, among other items, Ray Freeman's set-up for measuring relaxation times which had been christened the 'Freelaxer'. The magnet for this instrument was enclosed in both an inner and an outer housing of transparent plastic, and was equipped with a two-stage field stabilization circuit. There was also a pulse sequence generator, prearranged to give the proper sequences for various types of measurement. After I was filled with the best Palo Alto Chinese food, I was taken by Martin Packard in his Packard convertible to his house on the hills with a wonderful view overlooking the bay. The conversation there led to questions about my views on the future of NMR, the most specific of which was whether there was likely to develop any general interest in the determination of relaxation times, to which I answered bravely an emphatic 'Yes!' However, before the Freelaxer could reach commercial production, pulsed FT NMR appeared on the horizon.

The HA-100 console was traded in for an XL-100 in 1970. Again, our instrument happened to be among the first dozen produced. All the components arrived just in time for the 12th ENC at Gainesville in 1971, the first ENC to be held away from Pittsburgh. This instrument had a fully equipped decoupler module, enabling irradiation at any frequency over an extremely wide range, and its 12-mm probes afforded high sensitivity for less receptive nuclei, although observation was limited to hydrogen, fluorine, phosphorus, boron, and carbon. The output of the decoupler was not nearly sufficient to decouple fluorines over the range of some 100 ppm, but applied between acquisitions, the rf provided a very useful Overhauser sensitivity enhancement for observation of ^{13}C. There was also an external lock, particularly useful for studying very reactive fluorinated molecules in sealed tubes.

The design of the XL-100 console was rather interesting because there were on the back quite a few connectors of high pin count which had no apparent function. It developed that the designers had foreseen the application of computers and had provided these for digital inputs to control the decoupler and observe offset frequencies, a function which became somewhat superfluous with pulsed FT methods. In 1978, the addition of a Nicolet multinuclear unit incorporating a PTS synthesizer and provided with an 18-mm probe for low frequencies greatly increased the versatility of this instrument, permitting, for example, acquisition of ^{43}Ca spectra in natural abundance.

An NT-300 system with wide bore Oxford magnet was delivered in 1981. At this stage of development, designers avoided multinuclear decoupling and concentrated on proton irradiation, a situation unfortunate for the study of ^{13}C in fluorocarbons. This system was subsequently upgraded with a Phoenix disk drive, a coprocessor board for the computer, and a raster-scan monitor. Probes include a custom-made Jakobsen solid state MAS probe.

SOME CONTRIBUTIONS FROM THE FLORIDA LABORATORY

Several of the more significant contributions from students in the NMR research group at the University of Florida may be mentioned. K. C. Ramey found very interesting behavior of the coupling constants between fluorine nuclei as the temperature was lowered to below -90 $^{\circ}$C.[3] In a similar vein, K. D. Lawson showed that wideline results for alcohols absorbed on thorium oxide reflected successive freezing out of the mobility of various molecular units as the temperature is lowered.[4]

M. E. Fuller showed that the activation energies for the motion of water molecules bound to solid proteins pass through a minimum at about the amount of water equivalent to one molecule per polar functional group.[5] In collaboration with Hans Jakobsen of the University of Aarhus, L. W. Jaques and P. J. Kanyha extended selective polarization transfer methods and applied them to the determination of the signs of coupling constants.[6,7]

Much of our work has been devoted to the study of fluorinated molecules. In addition to spectra of new compounds synthesized within the university, many thousands of spectra were run for products of Peninsular ChemResearch, now PCR, Inc. Perhaps the most interesting of the latter were those concerned with the development of the production process for 5-fluorouracil by a direct fluorination procedure, rather than by a complex, highly expensive multistep synthesis. In the days before NMR spectrometers were so universally available, we also ran samples for a group from Dewey and Almy Chemical Co., in a project to develop a safer fluorinated anesthetic, and for Air Products and Chemicals. We still provide NMR service for the fluorine chemists in the Air Force Laboratories at Dayton, Ohio.

With the widespread application of multidimensional experiments, we can look back on what were possibly the first three-dimensional experiments to be reported, in which COSY and *J*-resolved segments were combined.[8] Michael Cockman did the programming required to keep track of scale factors and other details during the processing and he and H. Daniel Plant carried out the experiments using a Hawk disk drive which required a series of cartridge withdrawals and insertions to do all the processing.

THE JOURNAL OF MAGNETIC RESONANCE

About 1964, I received a call from an editor at Academic Press, who stated that he was taking a poll to find out whether it was the feeling of NMR scientists that a journal devoted to the field was needed. The answer was no and I thought nothing more about the matter for several years. In 1968, my answer changed to yes when I was asked a similar question. A bit later, Thomas Lanigan of Academic Press called and asked to arrange to meet me at an American Chemical Society meeting in Atlanta. The gravity of his voice led me to suspect what the subject of the meetings was to be, and I was ready with a positive answer when he suggested that I undertake the editorship of the new journal.

We did not know that another periodical devoted to NMR was being planned in England at the same time. Although the original idea of the Academic Press editors was related to the increased use of NMR in organic chemistry, I was, fortunately, given complete freedom by the publishers to define the scope of the *Journal* and so it was made very broad, including all aspects of magnetic resonance, for all phases of matter, all types of nuclei as well as electrons, and encompassing both theoretical and practical points of view.

At the beginning of publication, from 1969 on, the pages of the *Journal* were composed and printed in Britain because of economic reasons, and copies intended for North America were flown across the Atlantic in bulk and mailed from New York. Considerable difficulty resulted when the compositor decided to convert to computerized typesetting and underestimated by a large margin the time required for the transition. Consequently, the *Journal* dropped several months behind publication schedule until these difficulties were finally overcome.

Throughout the ensuing years, there has been a steady expansion in the number of manuscripts submitted, and the number of pages published per year has been correspondingly increased. In 1991, it became evident that the amount of material concerning biological applications was increasing so rapidly that difficulty in accommodating all the significant papers could be anticipated. Consequently, in 1993, a separate series of the *Journal* was begun in which this area is emphasized.

DEDICATION

In view of the critical role that computers have played in the development of modern NMR, it is appropriate to conclude with an acknowledgment, of both a professional and personal nature, to John W. Mauchley who conceived and built the first operating electronic digital computer. I had the great pleasure and benefit of working with him as an undergraduate assistant at Ursinus College, and the honor of having my contributions cited in two of his publications. Most of what I know about the physics on which NMR techniques are based derives from his teaching in lectures or his personal instruction in the laboratory.

REFERENCES

1. R. B. Spooner and P. W. Selwood, *J. Am. Chem. Soc.*, 1949, **71**, 2184.
2. P. W. Selwood and F. K. Schroyer, *Discuss. Faraday Soc.*, 1950, **8**, 337.
3. K. C. Ramey and W. S. Brey, *J. Chem. Phys.*, 1964, **40**, 2349.
4. W. S. Brey and K. D. Lawson, *J. Phys. Chem.*, 1964, **68**, 1474.
5. M. E. Fuller and W. S. Brey, *J. Biol. Chem.*, 1968, **243**, 274.
6. W. S. Brey, L. W. Jaques, and H. J. Jakobsen, *Org. Magn. Reson.*, 1979, **12**, 243.
7. H. J. Jakobsen, P. J. Kanyha, and W. S. Brey, *J. Magn. Reson.*, 1983, **54**, 134.
8. H. D. Plant, T. H. Mareci, M. D. Cockman, and W. S. Brey, *Abstr. 27th Exp. NMR Conf., Baltimore, MD, 1986*, A23.

Biographical Sketch

Wallace S. Brey. *b* 1922. B.S., Ursinus, 1942, M.S., Pennsylvania, 1946, Ph.D., 1948. Faculty at DePauw Univ., 1948–49, St. Joseph's University, 1949–52; University of Florida, 1952 to date. Approximately 85 publications. Author of three textbooks in physical chemistry; Editor of the volume 'Pulse Methods in 1D and 2D Liquid-Phase NMR' 1987; Editor, *Journal of Magnetic Resonance*, 1969–present. Research interests: heterogeneous catalysis and adsorption, structure and interactions of proteins, ^{19}F, ^{27}Al, ^{29}Si, and ^{31}P NMR in liquids and solids.

Budinger, Thomas F.: Perspectives on Reconstruction Tomography and Magnetic Field Physiological Effects

Thomas F. Budinger
University of California, Berkeley, CA, USA

The inverse problem of determining in three dimensions a process or constitutive property of matter by multiple observations from different angles had its practical applications in geophysics, astrophysics, and biological molecule structural analysis long before magnetic resonance was discovered as a method of probing the state of matter. The ideas of back projection into a 'smoke filled' a posteriori space were used by crystallographers in the mid-1900s, with the first practical back projection images performed by Kuhl and Edwards in nuclear medicine applications in 1963 and the first Fourier projection theorem reconstruction of phage tail structure by deRosier and Klug in 1968. One of the simplest approaches to reconstruction was undertaken in 1956 by myself for the problem of determining iceberg shape and volumes using sextant, compass, and radar. Ronald Bracewell advanced astrophysics through Fourier techniques in the 1970s. By 1974 we had succeeded in overcoming the 'intractable mathematical problem' of the attenuated radon transform by incorporating a priori information regarding the variable attenuation coefficient in the emission tomography problem.[1] This work caught the attention of Paul Lauterbur with whom I have worked since. At the same time Peter Mansfield sent me a manuscript on echo planar reconstruction mathematics which I found fascinating but a challenge to understand well enough to teach until a few years later. Through the encounters with these two great innovators and the galley proofs of Kumar, Welti, and Ernst's seminal paper, which Raymond Damadian asked me to explain to him, I became interested in the problem of magnetic resonance applications to the study of the human body.

Because my interest in brain stimulation by electric and oscillating magnetic fields was known to Paul Lauterbur, he asked me to analyze the effects of the magnetic resonance experiment on human physiology. The deadline for the analysis was June 1979 for an IEEE conference. So I squeezed literature, good and bad, and my own experiments with some cautious predictions[2] which were reiterated a few years later in an expanded paper in 1991.[3] During the last 20 years of advancement in magnetic resonance imaging of human subjects the fears of health effects have been expressed in scientific debate ranging from a chaired professor at the University of Pennsylvania saying that one day my 'brain might click off while walking down the street' to predictions that blood flow will be seriously retarded in high (e.g. 4 T) fields. None of these predictions is of concern now.

During this last 20 years, however, the hunt for effects on human physiology has ranged from evaluation of 40 T static field exposure of a musician's hands for years at the MIT Francis Bitter Magnet Laboratory to oscillating magnetic field exposure at various frequencies from $3000\,\mathrm{T\,s^{-1}}$ in animals to $100\,\mathrm{T\,s^{-1}}$ in man, in Germany. The search for rf heating effects has ranged from evaluation of hyperthermia physiology of human exposures to 42.5 °C in experiments by me with Robert Pettigrew and by me in Scotland to actual measurements of energy absorption in humans undergoing MRI protocols by swallowed and even surgically implanted probes in Ohio using pulse sequences which challenged 1986 vintage rf amplifiers. Fortunately, the power at 50–60 Hz around the contemporary NMR environment is low and we avoided the power-line electromagnetic field hysteria of the early 1990s.

The reason so much effort was placed on the measurement of physiological effects of static and oscillating magnetic fields is that advances in magnetic resonance applications to medical science depend on improvements in temporal and spatial resolution as well as improvement in signal-to-noise, particularly for carbon-13, sodium-23, potassium-39, nitrogen-15, and even chlorine and rubidium. Applications depend on rapidly switching magnetic fields and increases in static fields beyond 4 T. Known effects are neuromuscular stimulation from E-fields induced by rapidly oscillating magnetic fields of $60\,\mathrm{T\,s^{-1}}$ at 1 kHz and body heating associated with rf power deposition.

Goals such as human cortex 3D isotropic imaging at 300 μm resolution and short T_2 potassium concentration studies in $8\,\mathrm{cm^3}$ volumes are possible and can be safely accomplished at fields beyond 4 T. These are only two of a multitude of safe projections which lead to the prediction that this methodology will provide fundamental knowledge on the biochemical bases of mental and behavioral disorders, as well as knowledge on the mechanisms of cancer, atherosclerosis, and aging.

REFERENCES

1. T. F. Budinger and G. T. Gullberg, *Phys. Med. Biol.*, 1974, **19**, 387.
2. T. F. Budinger, *IEEE Trans. Nucl. Sci.*, 1979, **NS26**, 2821.
3. T. F. Budinger, H. Fischer, D. Heutschel, H. E. Reinfelder, and F. Schmitt, *J. Comp. Ass. Tomog.*, 1991, **15**, 909.

Biographical Sketch

Thomas F. Budinger. *b* 1932. B.S., 1954; M.S., 1957, Oceanography, University of Washington; M.D., 1964, University of Colorado; Ph.D., 1971, Physics, University of California, Berkeley. Professor of Electrical Engineering and Computer Science, UC Berkeley, 1976–present. Head, Center for Functional Imaging, Lawrence Berkeley Laboratory. Professor of Radiology and Director, Magnetic Resonance Science Center and Research PET, UC San Francisco. Approx. 300 publications. Research specialties: high-resolution PET and SPECT instrumentation and magnetic resonance for studies of mental disorders, cancer and heart disease.

Bydder, Graeme M.: Magnetic Resonance at Hammersmith Hospital

Graeme M. Bydder
Hammersmith Hospital, Royal Postgraduate Medical School, University of London, London, UK

When I joined the EMI-Hammersmith NMR imaging group on 1 January 1981 the prospects appeared exciting. The world's first cryomagnetic-based magnetic resonance system had been installed just before Christmas 1980 and was already producing images. It was the first such system to be placed inside a hospital and patients' studies were eagerly awaited. The group was well aware that the first X-ray computed tomography (CT) scan of a patient performed at Atkinson-Morley's Hospital on 1 September 1971 had shown a left frontal lobe tumor. This had been such a remarkable event that immediately following it those most reserved of men, James Ambrose and Godfrey Hounsfield, had jumped up and down like football players who had just scored a winning goal.[1] The success of the technique had seemed assured from that point on. Likewise, using the first commercial body CT scanner, Louis Kreel at Northwick Park Hospital had diagnosed a cancer of the pancreas in the first patient examined on 1 July 1975. Body CT had also gone on to become a great success.

There were a number of problems with NMR imaging though. Although Godfrey Hounsfield had received the Nobel Prize for CT in 1979, Electrical and Musical Industries Ltd, (EMI) had since moved out of medical imaging. They had sold their interests in CT and were looking for a buyer for their NMR imaging research group. There were also difficulties between the EMI team and the Hammersmith Hospital group. The Department of Health, which had helped fund the construction of the NMR imaging system, was in effect using the hospital group to test whether or not the system met its specifications. From the EMI research team's point of view the hospital group was perceived as people who did not help with the development of the system but criticized it to one of their principal paymasters.

There were other difficulties. The Department of Radiology was not only installing a new NMR system but also a CT system and there was no radiologist in the department with any clinical experience with either technique. The new CT system was bought from a rival company (Siemens) and was providing very high quality images of greater spatial resolution than the NMR system. The NMR machine itself was single slice only, and each of these slices took 7 min to reconstruct (the CT system took only 5 s). It was difficult to see how it would be possible to complete even a single examination of the head (16 slices) with NMR in less than 3 h. The patient handling of the NMR system was acutely uncomfortable, the water-cooled valve amplifiers were highly unreliable, and the sole copy of the operating manual went missing soon after installation and was never found again.

Patient studies began on 25 March 1981 and, unlike the situation with both head and body CT, the diagnosis was missed in each of the first three cases studied (multiple sclerosis, hemosiderosis, and a posterior fossa lesion). Soon after, the clinical director of NMR research, Professor Frank Doyle, suffered a major stroke which left him severely aphasic and hemiplegic. The Hammersmith Hospital physicist left, and so did the visiting professor from Yale who had been advising on the project. This left the hospital group with only two people. On the clinical side it soon became apparent that Hammersmith Hospital, which had no neurosurgery and very little neurology, was in no position to supply suitable patients for clinical evaluation of NMR imaging in neurological disease.

We also knew that the Nottingham clinical group headed by Brian Worthington had published the first series of brain patients in September 1980[2] and had received over 1000 reprint requests. Frank Smith in Aberdeen was energetically studying patients and had published results in both the *British Medical Journal*[3] and the *Lancet*.[4] We also knew that the San Francisco group (headed by Larry Crooks and Leon Kaufman) had published animal studies and were due to receive the next whole body cryomagnet from Oxford Instruments after ours. They were bound to make a success of their clinical work. Unlike all of these groups, we were banned from publishing by the EMI management who wished to keep their work in NMR a commercial secret. This was in spite of the fact that they had issued a press release announcing the world's first NMR image of the head over two years before, in November 1978.[5]

There was also greater interest in spectroscopy than imaging at that time, and visitors to the UK would generally travel down the A40 to visit George Radda's NMR spectroscopy unit at Oxford without finding it necessary to stop and view the imaging at Hammersmith Hospital on the way. Brian Ross had already shown remarkable findings in McArdles syndrome using their system.[6]

At about this time the magnet quenched and had to be warmed up. It was out of commission for five weeks. Although there were very few clinical results to show and our group seemed to be way behind the UK and international competition, there were some rays of hope. Gordon Higson and John Williams from the Department of Health seemed able to perceive some encouraging signs even if others could not. The physicists and engineers in the EMI group under the leadership of Ian Young had stuck to their task remarkably well and totally supported the clinical work. They would arrive within minutes of any machine breakdown and members of the group such as Alasdair Hall seemed more devoted and concerned with helping patients than the medical staff. Jackie Pennock was a versatile and remarkably able researcher and Professor Robert Steiner was an astute head of department. The patients also seemed prepared to put up with any amount of discomfort and inconvenience in the interests of research.

Forty-six volunteers and 48 patients had been examined prior to the magnet quench and there were insufficient data for any significant papers, but this period allowed a time for regrouping and establishing new targets for the three months prior to the Winston-Salem meeting on 1–3 October 1981. This was billed as a back-to-back showdown between the UK and US groups. The previous NMR meeting in 1980 at Nashville had not been a success because of lack of clinical results, but it was clear that a number of groups were now getting them and there was a pecking order to be established.

It was also becoming clear that while the T_1-weighted inversion recovery was slow, it showed a remarkable level

of gray white matter contrast in the brain and there was often an amazing level of contrast between abnormal and normal soft tissue. Sometimes the contrast difference was so high it was difficult to display the images.

When the show down came at Winston-Salem it soon became apparent that other groups in the UK and US had had their difficulties too.[7] In fact, Bill Oldendorf in his commentary on the meeting suggested that the poor showing of the US groups relative to those in the UK was due to excessive numbers of US physicists working in defense to the detriment of medical research.[8] By this time we had sent off six papers[9–14] and Picker International had bought the system from EMI.

At the Winston-Salem meeting it was clear that there was a considerable prize for whoever first performed the definitive NMR imaging study on the brain. The Massachusetts General Hospital group had the inside running with an operating system and great strengths in neurology and neurosurgery as well as the leading neuroradiologist in the world, Professor Juan Taveras. We thought this target worth pursuing and David Thomas (neurologist) and Christopher Pallis actively sought suitable patients while we made arrangements to study them at any hour of the day or night.

By the following January we had over 100 patients with conditions that included most of the common headings in neurology, but we then had a windfall. David Bailes had resurrected the spin echo sequence which previously had failed to show disease in its short echo time form and increased the echo time to 40, 80, and then 120 ms. This caused a wide range of lesions in the brain to shine out with high contrast (Figure 1). We had been fortunate enough to stumble on the most valuable screening sequence in NMR imaging—the heavily T_2-weighted spin echo. Over a two-week period we recruited a further 30 patients and included these in two papers which were published in July[15] and August 1982, the second of which described 140 cases.[16] The largest published clinical series up until this time had been 10 cases.

By this stage we had begun studying infants and children and were able to show normal and delayed myelination[17] as well as a wide range of disease.[18] The logistics and practical problems in examining infants were overcome by Lilly Dubowitz, Linda De Vries, Frances Cowan, and Mary Rutherford. They proved remarkably patient with machine difficulties.

Although we had turned the corner in 1981 our reprieve was relatively short-lived. We lost ground in the second half of 1982 to other groups with multislice systems, including particularly that from San Francisco under Alex Margulis. In addition, most other groups were using two-dimensional Fourier transfer or the spin warp[19] which was tolerant of motion and bad fields (rather than projection reconstruction which we were using). In the beginning of 1983, we changed to the spin warp system and, in response to a move from Technicare, to high resolution (256 $\times$ 256 matrix size). One of the secrets which made this possible was the use of tightly coupled coils in the form of helmets covering the head, collars around the neck, and corsets around the body.[20,21] These low bandwidth techniques, Michael Burl's rf system, and David Gilderdale's display, enabled us to produce good quality high-contrast and high-resolution images on a routine basis using our low field (0.15 T) system (Figure 2).

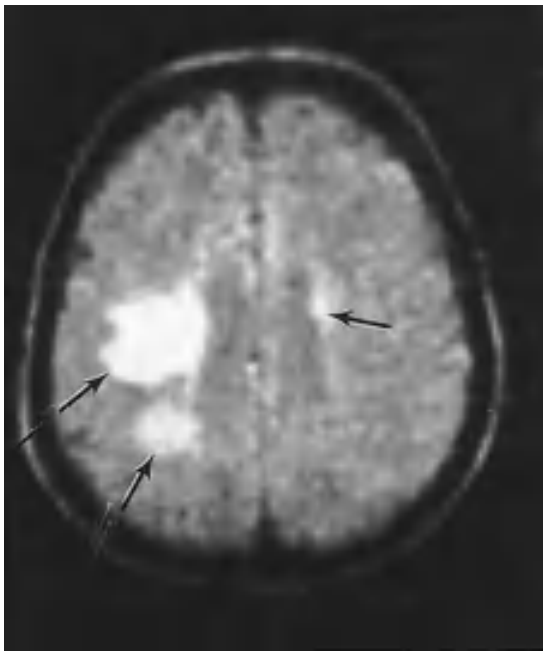

Figure 1 Multiple sclerosis, February 1982: T_2-weighted spin echo (SE1080/80) image of the brain. The lesions are highlighted (arrows)

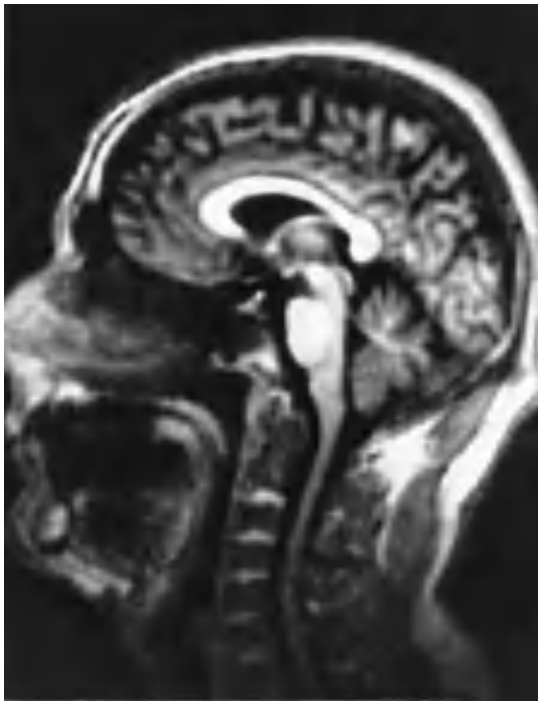

Figure 2 Normal brain, March 1983: Sagittal IR1400/10/400 sequence. High contrast is seen between gray and white matter. The anatomical detail in the brainstem is well seen

We knew that the next Society of Magnetic Resonance in Medicine (SMRM) meeting in San Francisco in August 1983 would be a showdown between low-field and high-field systems. General Electric had launched their 1.5-T system and anticipated a very large increase in signal-to-noise ratio with it. If this proved to be the case, their system would completely

outclass all existing low-field and mid-field machines. On the opening day of the meeting, Ian Young produced a series of high-resolution images taken at 0.15 T and the expected demise of low field did not happen. In fact, the meeting became somewhat disorderly with hints that Ian Young was being less than honest about the time he was taking and the techniques he was using to acquire his remarkably good images. This same argument was replayed in the 1984 SMRM meeting in New York with more disorderly scenes and Ian Young almost stealing the show completely with a spectacular cervical spine image of syringomyelia. The gain in signal-to-noise with high field turned out to be much less than had been at first anticipated and could only be realized with a lot of hard work.[22]

In the meantime David Bryant had successfully employed a phase sensitive technique for measuring flow.[23] He was later to implement 4D chemical shift imaging[24] as well as ^{13}C spectroscopy on our 1.5-T spectroscopy system. Donald Longmore was later to transform this early flow work and made the dream of successful cardiac imaging a reality.

By the end of 1983, Schering had developed gadolinium-DTPA and begun volunteer studies with Roland Felix in Berlin. Ulrich Speck and Hans Pieter Niendorf were kind enough to provide us with this agent for clinical trials. While the first patient ever studied showed no change, the second was a spectacular success (Figure 3). Ten of the first 12 patients showed enhancement.[25]

Walter Curati and Moshe Graif examined benign and malignant tumors with enhancement and performed detailed sequence comparison and time course studies.[26] The spinal cord studies were also a success.[27] With John Brown's help we obtained considerable mileage from this contrast agent before it was released more widely in the US and elsewhere in Europe.

After this, we again drifted behind the play, but made a special effort in 1985. Ian Young was the principal organizer for the SMRM Barbican meeting in London in 1985 and we wished to make an impression at this meeting since it was on our home territory. For this we implemented the field echo sequence with an echo time of 22 ms at 0.15 T to cancel red marrow and provide high contrast lesions of the bone marrow.[28] David Bailes and Alan Collins implemented respiratory ordered phase encoding to provide control of motion artifact in the abdomen.[29] The most spectacular images, however, were provided by the short inversion time inversion recovery (STIR) sequence with its fat suppression and very high lesion contrast.[30] It subsequently proved to be of considerable value in the musculoskeletal system, bone marrow, and the body as a whole, including oncology. Bruce Porter,[31] Paul Goddard, Don Schnaff, and Alina Greco performed excellent studies with this technique.

The spectroscopy system which was designed and built by David Bryant and Alasdair Hall was installed in 1987. Clinical applications of the liver were initially developed by David Menon and refined by Simon Taylor-Robinson. These proved successful and the use of proton spectroscopy in birth asphyxia was developed by Carol Peden and taken further by Frances Cowan. Jane Cox provided the organizational framework and impetus for much of the work as well as for studies of scrapie in mice. Richard Iles provided help when it was acutely needed and Janet Sargentoni made an invaluable contribution on the clinical side. Jimmy Bell proved remarkably adept at in vitro

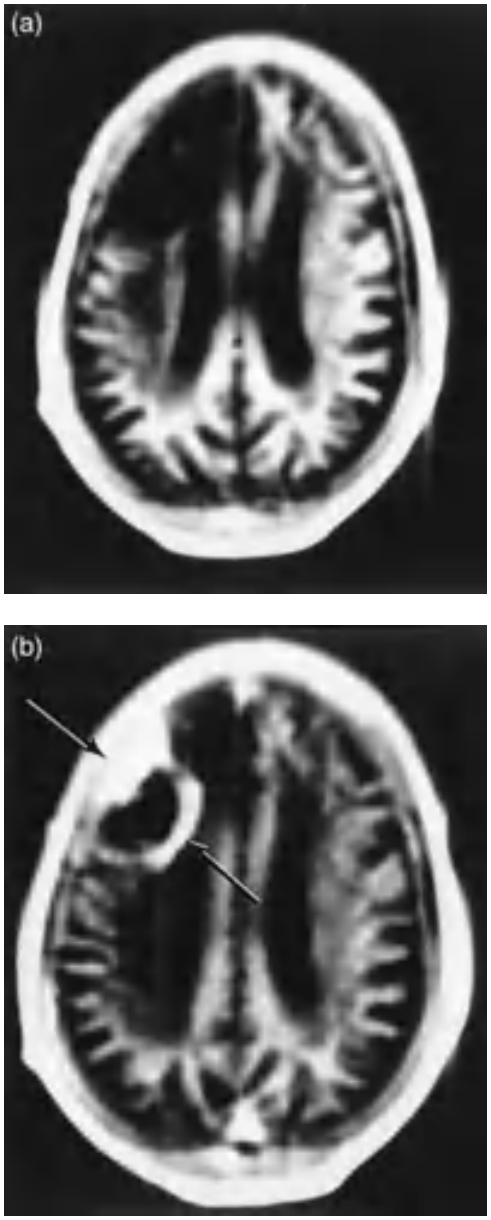

Figure 3 Brain metastases, December 1983: Inversion recovery (IR1400/5/400) sequence without (a) and with (b) intravenous gadolinium-DTPA. Ring enhancement is obvious in (b) (arrows)

animal and carbon studies, and provided the focus of much of the research work. Coil development for this system was taken on to a new plane by David Gilderdale, Reg Harman, and Michael Burl.

The development of the long echo time field echo provided high contrast imaging of cerebral hemorrhage at low field contrary to theoretical predictions based on 1.5 T work.[32,33] This apparent miracle dealt with the issue of low-field systems being incapable of demonstrating the various phases of hemorrhage at the Montreal SMRM meeting in 1986.

Christine Baudouin undertook the development of internal coils and this was later taken over by Nandita deSouza.[34,35] The images of the uterine cervix and ear were remarkable. Interventional studies starting with laser ablation of the prostate were begun under Nandita deSouza and Glyn Coutts's

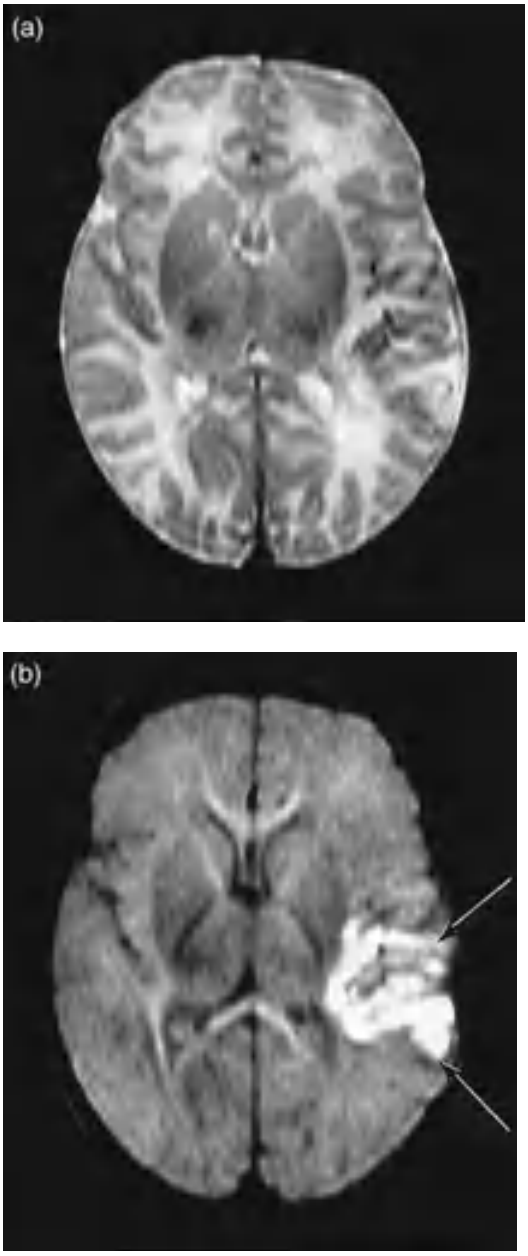

Figure 4 Diffusion-weighted imaging in acute neonatal infarction, January 1994: T_2-weighted spin echo (SE3000/120) (a) and diffusion-weighted image (SE pulse rate/200, through plane sensitization b = 600 s mm^{-2}) (b). The lesion is poorly seen in (a) but is very obvious in (b) (arrows)

direction and with Rakesh Puni's help. This type of study may point the way to many future applications of MR imaging.

In 1992 Joseph Hajnal implemented another high contrast sequence, the fluid attenuated inversion recovery and it proved effective not only for lesions of the brain[36] and spinal cord[37] but also, under David Harris's direction, for detecting brain swelling in post-operative patients.[38] Diffusion weighted imaging developed by Joseph Hajnal and Angela Oatridge and applied by Frances Cowan, Jackie Pennock, and Jane Schwieso proved particularly suitable for the acute diagnosis of hypoxic ischemia injury in infants (Figure 4).[39,40]

Joseph Hajnal's thorough analysis of the activation experiment set a new standard of image interpretation.[41] At the present time the former EMI group and the Hammersmith clinical groups remain together. Nadeem Saeed and Joseph Hajnal have implemented a precise registration program which appears likely to have widespread application in detecting small changes in the size of the brain and other organs on serial examinations. Approaches to imaging the cortex including the doubly attenuated inversion recovery sequence and techniques for unfolding it are under way.

We benefited greatly from the excellent organization of Ann Case, Di Spencer, and Christine Soleimanpour who all subsequently ran their own units. We learned a lot about patient management and the conduct of clinical research from Eve Johnson and David Owens. We also learnt about efficient organization from Mary Ann Johnson, Susan Brothers Peterman, Beatrice De Coene, and Margarete Hayward.

We were greatly encouraged by Bill Bradley in Los Angeles and Peter Rinck in Europe who inspired us with their enthusiasm and took every chance to support our group. George Radda from Oxford also recognized the possibilities in imaging at an early stage and provided considerable help. Ian Isherwood from Manchester was another stalwart supporter over a long period. We also admired the Aberdeen group of John Mallard, Jim Hutchison, Meg Foster, Tom Redpath, and David Lurie, who achieved an enormous amount with a minute budget.

There were other lessons. We held on to our original prototype 0.15-T system for too long (1980–93). While it earned its place in the Science Museum (London), we should have changed to a commercial system much earlier. We became preoccupied by the high field–low field argument and stayed with our low-field system with its antiquated computer. As a result, we lost out on fast imaging, angiography, and close integration with Picker International systems.

From our earlier experiences we developed a fixation on the spectacular image which would transform the practice of MRI overnight. In 1981 and 1982, display of such an image at a conference would be greeted by 'oohs' and 'ahs' as well as a shower of camera clicks. We were able to achieve this with the T_2-weighted spin echo, high-resolution images, contrast enhancement, STIRs, FLAIRs, diffusion-weighted, and other images, and these were of obvious diagnostic value. However, we pursued high contrast images of this type at the expense of other targets such as a reduction in imaging time and quantitative studies which might have been as, or more, productive.

We also operated from too narrow a funding base. While the Department of Health, Medical Research Council, and Picker International were all very helpful, we found the funding of new technological advances difficult and did not pursue other sources of funding with the necessary persistence.

The teaching was rudimentary and the balance between independent research and proper supervision always seemed wrong whatever way we played it. We also took a long time to come to understand and work with Picker International. In fact, it was not until Surya Mohapatra took control that the relationship with the company really improved.

For the first five years while we were the only clinical MR unit in London there was no problem in obtaining patient referrals from other hospitals in any clinical group, but once

other hospitals obtained their own systems this became more difficult and our clinical studies suffered.

At the end of 14 years of development two particular memories remain. One is of a large number of people completing patient examinations, papers, grant applications, machine developments, and other essential tasks against deadlines at all hours of the day and night. This included most people in the unit but particularly Patricia Hamilton and Dulcie Rodrigues. The other is of many people such as Jaume Gili, Iain MacKay, Giovanni Di Chiro, Max Andre Hopf, Steven McKinstry, Ros Dietrich, William Yuh, and Josef Assheuer who gave us their unstinting help.

REFERENCES

1. J. Ambrose, *Semin. Roentgenol.*, 1977, **12**, 7.
2. R. C. Hawkes, G. N. Holland, W. S. Moore, and B. S. Worthington, *J Comput. Assist. Tomogr.*, 1980, **4**, 577.
3. F. W. Smith, J. M. S. Hutchison, J. R. Mallard, G. Johnson, T. W. Redpath, R. D. Selbie, A. Reid, and C. C. Smith, *Br. Med. J.*, 1981, **282**, 510.
4. F. W. Smith, J. R. Mallard, A. Reid, and J. M. S. Hutchison, *Lancet*, 1981, **i**, 963.
5. Anon., *New Scientist*, 1978, **80**, 588.
6. B. D. Ross, G. K. Radda, D. G. Gadian, G. Rocker, M. Esiri, and J. Falconer-Smith, *N. Engl. J. Med.*, 1981, **304**, 1338.
7. R. L. Witcofski, N. Karstaedt, and C. L. Partain (eds.), *NMR Imaging*, The Bowman Gray School of Medicine of Wake Forest University, Winston-Salem, NC, 1982.
8. W. H. Oldendorf, *J. Comput. Assist. Tomogr.*, 1982, **6**, 429.
9. F. H. Doyle, J. C. Gore, J. M. Pennock, G. M. Bydder, J. S. Orr, R. E. Steiner, I. R. Young, M. Burl, H. Clow, D. J. Gilderdale, D. R. Bailes, and P. E. Walters, *Lancet*, 1981, **ii**, 53.
10. I. R. Young, M. Burl, G. J. Clarke, A. S. Hall, T. Passmore, A. G. Collins, D. T. Smith, J. S. Orr, G. M. Bydder, F. H. Doyle, R. H. Greenspan, and R. E. Steiner, *Am. J. Roentgenol.*, 1981, **137**, 895; and *Am. J. Neuroradiol.*, 1981, **2**, 487.
11. I. R. Young, A. S. Hall, C. A. Pallis, N. J. Legg, G. M. Bydder, and R. E. Steiner, *Lancet*, 1981, **ii**, 1063.
12. I. R. Young, G. J. Clarke, D. R. Bailes, J. M. Pennock, F. H. Doyle, and G. M. Bydder, *J. Comput. Assist. Tomogr.*, 1981, **5**, 543.
13. I. R. Young, D. R. Bailes, M. Burl, A. G. Collins, D. T. Smith, M. J. McDonnell, J. S. Orr, L. M. Banks, G. M. Bydder, R. H. Greenspan, and R. E. Steiner, *J. Comput. Assist. Tomogr.*, 1982, **6**, 1.
14. F. H. Doyle, J. M. Pennock, L. M. Banks, M. J. McDonnell, G. M. Bydder, R. E. Steiner, I. R. Young, G. J. Clarke, T. Pasmore, and D. J. Gilderdale, *Am. J. Roentgenol.*, 1982, **138**, 193.
15. D. R. Bailes, I. R. Young, D. J. Thomas, K. Straughan, G. M. Bydder, and R. E. Steiner, *Clin. Radiol.*, 1982, **33**, 395.
16. G. M. Bydder, R. E. Steiner, I. R. Young, A. S. Hall, D. J. Thomas, J. Marshall, C. A. Pallis, and N. J. Legg, *Am. J. Roentgenol.*, 1982, **139**, 215.
17. M. I. Levene, A. Whitelaw, V. Dubowitz, G. M. Bydder, R. E. Steiner, C. P. Randell, and I. R. Young, *Br. Med. J.*, 1982, **285**, 774.
18. M. A. Johnson, J. M. Pennock, G. M. Bydder, R. E. Steiner, D. J. Thomas, R. Hayward, D. J. Bryant, J. A. Payne, M. I. Levene, A. Whitelaw, L. M. S. Dubowitz, and V. Dubowitz, *Am. J. Neuroradiol.*, 1983, **4**, 1013; *ibid.*, *Am. J. Roentgenol.*, 1983, **141**, 1005.
19. W. A. Edelstein, J. M. S. Hutchison, G. Johnson, and T. Redpath, *Phys. Med. Biol.*, 1980, **25**, 751.
20. G. M. Bydder, P. R. Butsen, R. R. Harman, D. J. Gilderdale, and I. R. Young, *J. Comput. Assist. Tomogr.*, 1985, **9**, 413.
21. G. M. Bydder, W. L. Curati, D. G. Gadian, A. S. Hall, R. R. Harman, R. R. Butsen, D. J. Gilderdale, and I. R. Young, *J. Comput. Assist. Tomogr.*, 1985, **9**, 987.
22. I. R. Young, *Br. Med. Bull.*, 1984, **40**, 139.
23. D. J. Bryant, J. A. Payne, D. N. Firmin, and D. B. Longmore, *J. Comput. Assist. Tomogr.*, 1984, **8**, 588.
24. D. R. Bailes, D. J. Bryant, H. A. Case, A. G. Collins, I. J. Cox, A. S. Hall, R. R. Harman, S. Khenia, P. McArthur, B. D. Ross, and I. R. Young, *J. Magn. Reson.*, 1988, **77**, 460.
25. D. H. Carr, J. Brown, G. M. Bydder, H.-J. Weinmann, U. Speck, D. J. Thomas, and I. R. Young, *Lancet*, 1984, **i**, 484.
26. M. Graif, G. M. Bydder, R. E. Steiner, H.-P. Niendorf, D. G. T. Thomas, and I. R. Young, *Am. J. Neuroradiol.*, 1985, **6**, 855.
27. G. M. Bydder, J. Brown, H. P. Niendorf, and I. R. Young, *J. Comput. Assist. Tomogr.*, 1985, **9**, 847.
28. G. M. Bydder and I. R. Young, *J. Comput. Assist. Tomogr.*, 1985, **9**, 1020.
29. D. R. Bailes, D. J. Gilderdale, G. M. Bydder, A. G. Collins, and D. N. Firmin, *J. Comput. Assist. Tomogr.*, 1985, **9**, 835.
30. G. M. Bydder and I. R. Young, *J. Comput. Assist. Tomogr.*, 1985, **9**, 659.
31. B. A. Porter, A. F. Shields, and D. O. Olson, *Radiol. Clin. North Am.*, 1986, **24**, 269.
32. I. R. Young, S. Khenia, D. G. T. Thomas, C. H. Davis, D. G. Gadian, I. J. Cox, B. D. Ross, and G. M. Bydder, *J. Comput. Assist. Tomogr.*, 1987, **11**, 2.
33. G. M. Bydder, J. M. Pennock, R. Porteous, L. M. S. Dubowitz, D. G. Gadian, and I. R. Young, *Neuroradiology*, 1988, **30**, 367.
34. C. J. Baudouin, W. P. Soutter, D. J. Gilderdale, and G. A. Coutts, *Magn. Reson. Med.*, 1992, **24**, 196.
35. N. M. deSouza, J. C. Hawley, J. E. Schwieso, D. J. Gilderdale, and W. P. Soutter, *Am. J. Roentgenol.*, 1994, **163**, 607.
36. B. De Coene, J. V. Hajnal, P. Gatehouse, D. B. Longmore, S. J. White, A. Oatridge, J. M. Pennock, I. R. Young, and G. M. Bydder, *Am. J. Neuroradiol.*, 1992, **13**, 1555.
37. S. J. White, J. V. Hajnal, I. R. Young, and G. M. Bydder, *Magn. Reson. Med.*, 1992, **28**, 153.
38. D. N. F. Harris, S. M. Bailey, P. L. C. Smith, K. M. Taylor, A. Oatridge, and G. M. Bydder, *Lancet*, 1993, **342**, 586.
39. J. V. Hajnal, M. Doran, A. S. Hall, A. G. Collins, A. Oatridge, J. M. Pennock, I. R. Young, and G. M. Bydder, *J. Comput. Assist. Tomogr.*, 1991, **15**, 1.
40. F. M. Cowan, J. M. Pennock, J. D. Hanrahan, K. P. Manji, and A. D. Edwards, *Neuropaediatrics*, 1994, **25**, 172.
41. J. V. Hajnal, R. Myers, A. Oatridge, J. E. Schwieso, I. R. Young, and G. M. Bydder, *Magn. Reson. Med.*, 1993, **31**, 283.

Biographical Sketch

Graeme M. Bydder. *b* 1944. M.B., Ch.B., 1969, Medicine, University of Otago, New Zealand (NZ). House surgeon and physician, NZ, 1970–71. Registrar, Otago Medical School NZ, 1972–78. Nuffield Fellow in X-ray computed tomography and research fellow, Clinical Clinical Research Centre, Northwick Park Hospital, 1978–80. Research fellow and senior lecturer, 1981–89 and Professor of Diagnostic Radiology, Royal Postgraduate Medical School, Hammersmith Hospital, 1989–present. Approx. 300 publications. Research interests: clinical applications of imaging and spectroscopy.

Callaghan, Paul T.: From γ-Rays to Gradients

Paul T. Callaghan

Massey University, Palmerston North, New Zealand

I am part of that generation which inherited nuclear magnetic resonance, having been born nearly two years after its discovery in 1945. I have no heroic tales to tell of the early days. I am simply one of those who followed after, who made a scientific life in this domain of the nuclear spin, and felt kindly treated by the experience. That experience is unremarkable except in one respect. Some explanation must be found for the persistence of nuclear magnetic resonance. It has survived for 50 years as an exciting field of research, not just because its applications are so vast in number, but because it is a subject which is scientifically rich and personally rewarding.

I began in magnetic resonance in a very odd way. As a graduate student in Oxford's Clarendon Laboratory I used to implant or diffuse radioactive nuclei into ferromagnetic host metals and then cool them down to milliKelvin temperatures using adiabatic demagnetization. The purpose was to measure nuclear hyperfine interactions. My thesis supervisor was Nick Stone, while my scientific 'grandparents' were Nicholas Kurti, Michael Grace, and Brebis Bleaney. Even then I was following the route laid down by others. My work involved using CW radio waves to detect magnetic resonance via disturbance to the nuclear γ-emissions as the spin sublevel populations were equalized. Hence I was able to measure the nuclear magnetic dipole moments of quite a number of unstable nuclei. During this time we learned of some remarkable anomalies in adiabatic passage experiments on ^{60}Co discovered by Geoff Wilson at Monash University in Australia. My fellow student, Peter Johnston, and I were lucky enough to discover the reason for this. It turned out that small quadrupole interactions in this high-spin nucleus caused successive pairwise inversion which, instead of reversing the spin magnetization, caused a cyclic permutation of populations. This led to dramatic effects in the γ-ray emission anisotropy and, ultimately, an unusual form of audio-modulated spectroscopy (MAPON) for measuring exceedingly delicate quadrupole splittings in the presence of overwhelming inhomogeneous line broadening.

The point of the story is simply this. I learned then the pleasure of thinking about spin gymnastics, and in enjoying what I call the 'instant gratification' experiment. The wonderful thing about nuclear magnetic resonance is that it allows exotic spin manipulations, in which one can test predictions against the immediate result, if not today, then at least within the month. That suits me perfectly.

My first contact with 'proper NMR' was a revelation. I was sent by Nick Stone to report our adiabatic passage results to the first specialized Colloque AMPERE, held in Krakow in August 1973. I listened to Erwin Hahn, Raymond Andrew, Myer Bloom, John Waugh, and Alex Pines. I was simply astonished by the range and complexity of NMR *detected without γ-rays*. Peter Mansfield spoke on NMR diffraction in solids, one of his first reports of imaging, and a young woman graduate student from Robert Blinc's group, Metka Luzar, spoke about pulsed gradient spin echo (PGSE) NMR. Although I didn't know it at the time, her talk was to be one of the most important influences in my scientific career. It was to be 20 years before I met Dr. Luzar again and could tell her this.

In 1974, I returned to my native New Zealand to take up a post as a physics lecturer at the newly formed Massey University. I wanted to get back to nuclear spins and one of my chemist colleagues, Ken Jolley, was kind enough to share his new 1.4 T NMR system with me. I decided to build a pulsed gradient spin echo diffusion attachment, aided by graduate student Craig Trotter. Remarkably, the apparatus worked so well that it opened up the possibility of studying a host of diffusion phenomena relating to molecular organization and semilocal motions in polymers, liquid crystals, emulsions, colloids, and just about every soft material considerate enough to contain protons with T_2 values longer than 1 ms. It turned out that we had solved, by sheer accident, some problems of instrumental artifacts which led to echo instabilities in PGSE NMR, and which had plagued attempts at using the method since its first demonstration by Stejskal and Tanner in 1965. I had stumbled on a productive 'niche' in magnetic resonance.

The use of magnetic field gradients led, inevitably, to imaging. Most of the emphasis in MRI had been on scaling apparatus up for whole body tomography and it was clear that by scaling down it was possible to take advantage of improved sensitivity and larger magnetic field gradients. This time I was helped by a remarkably talented graduate student, Craig Eccles, who built our first NMR microscope. The trick with NMR microscopy, whose resolution is really rather poor, is to find the right contrast. The amalgamation of PGSE NMR and imaging has led to a host of diffusion- and velocity-mapping applications, as diverse as the imaging of in vivo fluid transport in plants and rheometric studies of colloidal and polymeric fluids under shear. Imaging has also had a reciprocal impact on PGSE NMR where the application of Fourier diffraction approaches has provided us with some remarkable insight regarding restricted diffusion, in which the echo attenuation exhibits many of the properties of both elastic and inelastic scattering structure factors.

For all my fun with pulsed magnetic field gradients, my most concentrated lessons in NMR came from reading Abragam's book and by spending a year working in Myer Bloom's laboratory in Vancouver. Beyond those two individuals I could name a hundred more who have taught me so much. I learn best by listening to others speak or write with enthusiasm about their work. How fortunate I have been to work in a field in which so many wonderful scientists have participated. Charles Slichter told the 1993 Gordon Conference on magnetic resonance how writing his book gave him so much pleasure because he became, in the process, so familiar with the work of others. I share that feeling.

I believe that science is an intensely personal and creative activity which may be practised in many ways. Along with many of my nuclear magnetic resonance colleagues, I do my best work by dreaming up new tricks to play on the molecules via the nuclear spins, and then waiting with excitement for the result. To the younger scientist intent on joining NMR in its second half century I would say, find the approach which best suits your temperament and be alert for the role of chance and serendipity. There are more niches waiting to be discovered.

Biographical Sketch

Paul T. Callaghan. *b* 1947. B.Sc., 1970, Physics, Victoria University of Wellington, New Zealand, D.Phil., 1974 (radiative detection of NMR in oriented nuclei at milliKelvin temperatures), University of Oxford, UK, D.Sc., 1995, University of Oxford, UK. Lecturer, Senior Lecturer in Physics 1975–1983, Professor of Physics, 1984–present, Massey University, New Zealand. Approx. 120 publications. Author of book Principles of Nuclear Magnetic Resonance Microscopy, published by Oxford University Press, 1991. Research specialties: pulsed gradient spin echo NMR and NMR microscopy, molecular translational dynamics in porous media, in polymers and in other complex fluids.

Carr, Herman Y.: Early Years of Free Precession Revisited

Herman Y. Carr

Rutgers University, New Brunswick, NJ, USA

In early November 1949 the bulletin for the Chicago meeting of the American Physical Society arrived in Cambridge at an opportune time for me. It was the beginning of my second year as a Harvard graduate student, and with the guidance of Edward Purcell I had just begun to read about nuclear magnetic resonance. That bulletin contained the abstract[1] of Erwin Hahn's contributed paper to the Thanksgiving meeting—the historic announcement of the phenomenon of 'spin echoes'! Purcell suggested that I read the abstract and try to understand this fascinating effect. Thus began an exciting three-year period for me as one of Purcell's graduate students in a new and rapidly developing area of physics.

Many of the results which developed from that research were published in two papers. The first paper[2] reported the observation of an indirect electron-coupled nuclear spin–spin interaction in HD gas. Purcell and Norman Ramsey[3] had predicted the existence of such an interaction as they successfully sought to explain the recently discovered high-resolution and field-independent J coupling.

The second paper[4] emphasized many of the experimental procedures which evolved from our research both at Harvard and during my first two years at Rutgers. These technologies included the use of 90° and 180° pulses in free precession experiments, a method for measuring the transverse spin–spin relaxation time T_2 even in the presence of diffusion through the magnet inhomogeneity, the inversion recovery method for measuring the longitudinal spin–lattice relaxation time T_1, and the intentional application of field gradients to study spatial effects (diffusion and flow).

In the following commentary I focus not so much on the technical description of the results already reported in the above two papers, but more on several episodes related to the birth of ideas preceding the results. Most of these episodes were reported in my 1952 Harvard thesis.[5] The thesis provided more opportunity for describing the unfolding of new ideas than did the shorter papers.

ECHOES IN THE NIGHT AND AT LUNCH

In his experiments at the University of Illinois, Hahn[6] used two equal rf pulses to induce his spin echoes. These echoes were not easy to understand. Hahn explained them using a model involving only equatorial components of precessing nuclear moments. But Purcell suggested using a three-dimensional model, and although this greatly simplified the understanding, the explanation of the various echoes induced by two equal pulses still was quite challenging. Indeed, in a letter to Hahn on December 14, 1949, Purcell wrote 'I see how the dimple-sphere comes about; last night while lying awake I was able, in a particularly lucid moment, to flop the cones around mentally and trace what happens . . . '

During the Christmas recess while attending a student conference at Urbana, I left the political activity of the conference one afternoon and visited Erwin Hahn in his cramped laboratory at the top of a high stairwell. It was exciting for me to see spin echoes for the first time and to hear details of their discovery. In the spring term Purcell and I decided to pursue our interest in free precession techniques and to plan for the necessary apparatus. Like Hahn who had worked with pulse apparatus in the Navy during World War II, I had worked with pulse apparatus in the Air Force. This was a great help. Our Harvard apparatus, however, differed from that in Illinois in a special way—we incorporated several independently variable pulse gates for an important reason.

It was during lunch one day, while explaining spin echoes to another graduate student, that I realized the explanation could be further simplified by considering two unequal pulses—a 90° pulse followed by a 180° pulse. Moreover it was easy to understand how a sequence of echoes could be induced by following one initial 90° pulse with a sequence of 180° pulses. Later that afternoon after a departmental seminar I told Purcell about this idea. I still recall and appreciate his delighted response, 'Elegant!' A similar response which I have long remembered came from Ramsey about two years later near the conclusion of my graduate work. After weeks spent searching for the predicted J coupling in the HD molecule—including many nights of discouragement—I finally found the predicted modulation of the free induction decay following a 90° pulse, first for the proton signal and then for the deuteron signal. Ramsey was away from Cambridge for that part of the summer recess. When I telephoned him with the news, his delighted response was, 'Best news all summer!' It was good to experience so vividly the fact that discouragement does not last forever!

These memories also remind me how important it is for faculty members to share their delight and enthusiasm with students and other colleagues.

SAMPLE SPINNING AND A NEW TYPE OF ECHO

The spinning of samples to reduce the effect of magnetic field inhomogeneity in high-resolution experiments had its origin in the development of a new kind of spin echo. The idea for rotating the sample came from an analogy with the sequence of 180° rf pulses and echoes described above. These spin echoes could be explained as in Figure 1 by the way a 180° rf pulse tips the equatorial plane of incremental magnetic moments associated with the various parts of a sample located in an inhomogeneous field. After each 180° tip the previously dispersing moments start to recluster and eventually form an echo after a time spent reclustering that is exactly equal to the time spent dispersing before the 180° tip.

There is another way, however, to obtain such reclustering without resorting to the forced nutation from a 180° pulse at the resonance frequency. This was particularly easy to predict

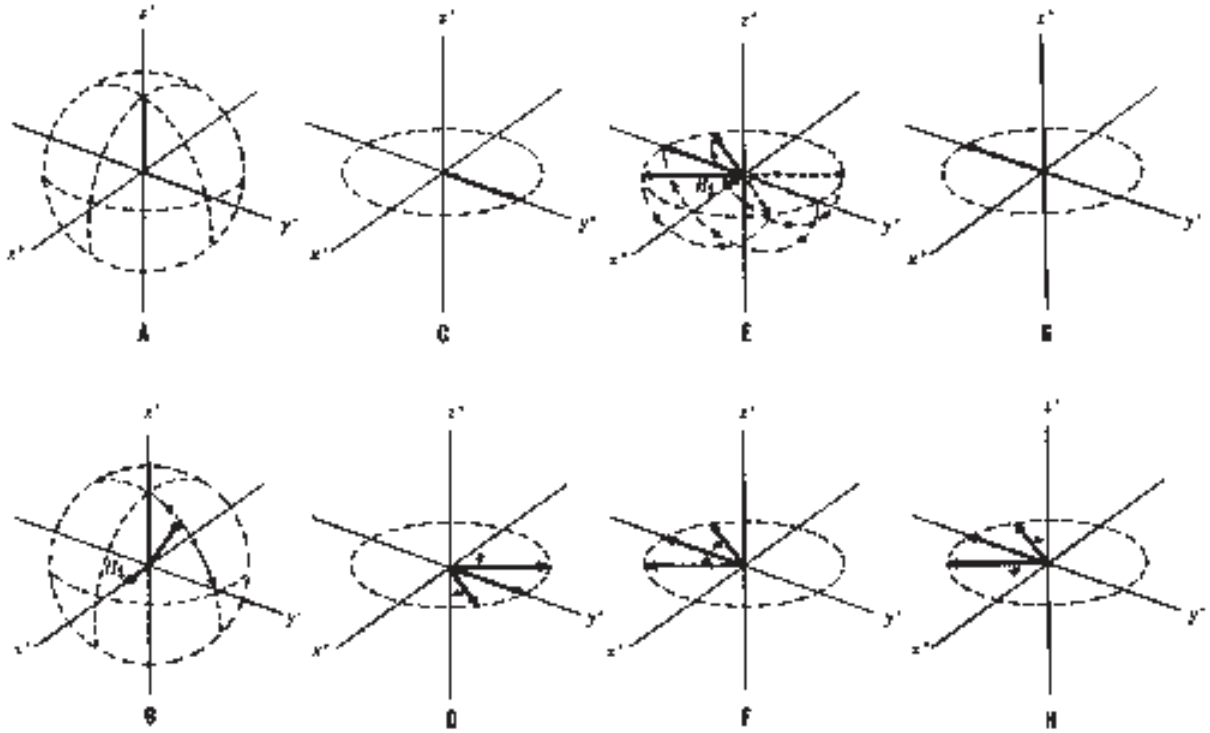

Figure 1 The formation of an echo (from Ref. 4). Initially the net magnetic moment vector is in its equilibrium position (a) parallel to the direction of the strong external field. The rf field $\boldsymbol{H}_1$ is then applied. As viewed from the rotating frame of reference the net magnetic moment appears (b) to rotate quickly about $\boldsymbol{H}_1$. At the end of a 90 ° pulse the net magnetic moment is in the equatorial plane (c). During the relatively long period of time following the removal of $\boldsymbol{H}_1$, the incremental moment vectors begin to fan out slowly (d). This is caused by the variations in $\boldsymbol{H}_z$ over the sample. At time $t = \tau$, the rf field $\boldsymbol{H}_1$ is again applied. Again the moments (e) begin to rotate quickly about the direction of $\boldsymbol{H}_1$. This time $\boldsymbol{H}_1$ is applied just long enough to satisfy the 180 ° pulse condition. This implies that at the end of the pulse all the incremental vectors are again in the equatorial plane. In the relatively long period of time following the removal of the rf field, the incremental vectors begin to recluster slowly (f). Because of the inverted relative positions following the 180 ° pulse and because each incremental vector continues to precess with its former frequency, the incremental vectors will be perfectly reclustered (g) at $t = 2\tau$. Thus maximum signal is induced in the pickup coil at $t = 2\tau$. This maximum signal, or echo, then begins to decay as the incremental vectors again fan out (h)

if the inhomogeneity of the static field comes from a uniform gradient in one direction across the sample. Sometime shortly after an initial 90° rf pulse, one simply rotates the sample 180° about an axis along the length of the cylindrical sample, so that each nucleus that previously experienced a field larger than the axial field by a certain amount now experiences a field that is smaller than the axial field by the same amount. Just as for the previous echoes which were induced by 180° rf pulses, the incremental magnetic moments which were previously dispersing begin to recluster. And after the time spent reclustering is equal to the time spent dispersing, all the incremental moments will coincide with the incremental moment associated with the axial field. The sample *rotation* has produced an echo! The phase of this echo, however, is the same as the phase of the free induction decay (FID) following the original 90° rf pulse. This is in contrast to an rf-induced echo which would be 180° out of phase with the FID, assuming that the rf phase of the 180° pulse is the same as for the 90° pulse.

This new type of echo, no longer induced by the forced nutation associated with an rf pulse at the resonance frequency, was subsequently obtained by others by simply reversing the sign of the static field gradient.[7] At the time the echo is formed the incremental moments previously dispersing in too large (or small) a static field will have spent exactly the same time reclustering in too small (or large) a static field. Persons working with such echoes in today's imaging experiments often call them 'gradient' echoes in contrast to the previous 'spin' echoes. But this is a misnomer—all these echoes are 'spin' echoes associated initially with dispersion and then reclustering from a 'gradient'. The significant difference is that the original type of spin echo is induced by the forced nutation from rf pulses at the resonance frequency. Thus, changes in the populations of the Zeeman energy levels occur. For the new type of echo with no rf pulses at the resonance frequency, there are no such changes. A sequence of the resonance-induced echoes can experience forced saturation. In contrast, a sequence of the new nonresonance-induced echoes is only associated with relaxation, but not forced saturation. This is a crucial distinction in applications such as fast imaging.

The new type of echo can be induced by changing the sign of the gradient either abruptly or steadily, and similarly by rotating the sample either abruptly or steadily. In the original 1951 Harvard experiments the sample was rotated steadily on the end of the long wooden shaft from the motor shown in Figure 2. The motor was located outside the magnet gap so that no metal parts moved in the strong magnetic field. The

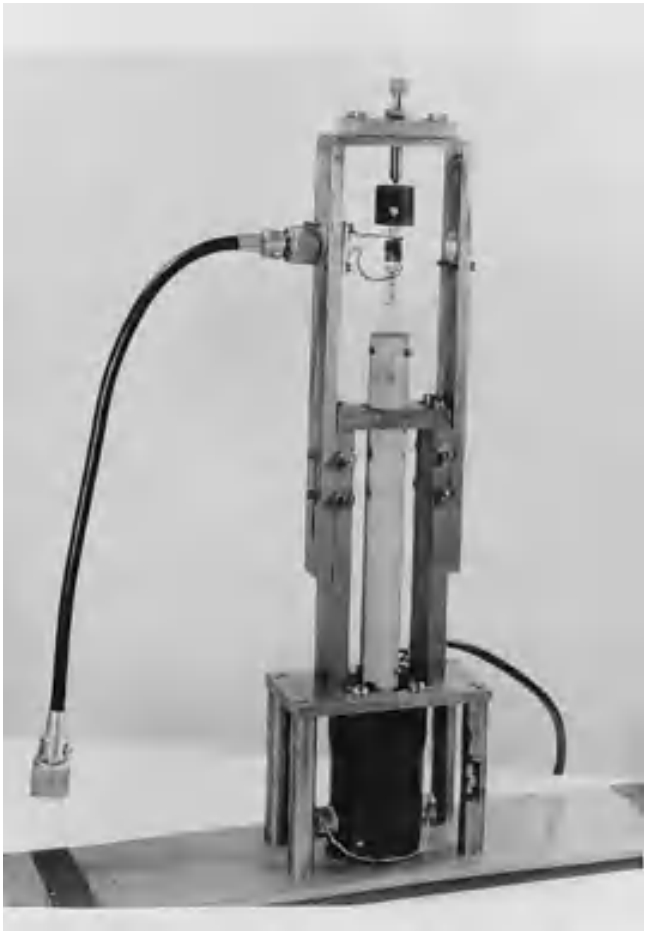

Figure 2 Motor used to induce nonresonance mechanical echoes. From Ref. 5

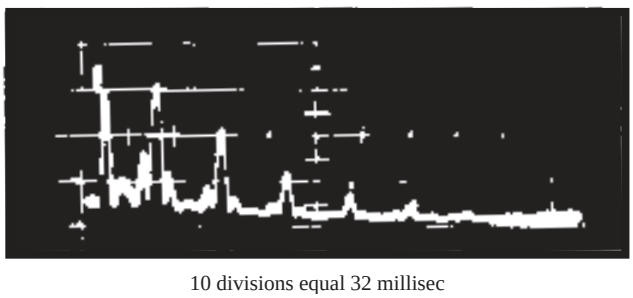

Figure 3 A sequence of nonresonance-induced echoes using motor in Figure 2. From Ref. 5

observed echoes shown in Figure 3 altered their spacing as a function of motor speed exactly as predicted.

It was this sequence of nonresonance-induced echoes that enabled us to see the previously discovered fine structure or chemical shift in ethyl alcohol.[8] Our Harvard magnet was too inhomogeneous to reveal fine structure easily. We saw no chemical shift modulation on the FID following a single 90° rf pulse—the rapid dispersion of the incremental moments associated with the inhomogeneity of the magnet came much faster than the slow dispersion from the relatively small inhomogeneity associated with the nonequivalent nuclear locations in the ethyl alcohol molecules. Nor did the original type of resonance-induced echoes produce evidence of the chemical shift—these pulses reclustered the dispersion from both the external inhomogeneity of the magnet and from the internal inhomogeneity of the different locations in the molecules. However, for the new type of echoes, the reclustering was associated only with the external magnet not with the different locations within a molecule. Thus the modulation of the envelope of our new type of echoes as in Figure 4 revealed the existence of the chemical shift. This proved to be very important for high-resolution spectroscopy. By increasing the rotational speed of the motor, we were able to observe this modulation without the typical echo effect. The individual echoes simply merged together. This FID—actually, a merger of echoes—following the initial 90° rf pulse was equivalent to the FID obtained from the same sample at rest in a much more homogeneous field. The sample spinning procedure is now commonly used in high-resolution spectrometers to reduce the effect of magnet inhomogeneity.[9]

Not all of our samples were candidates for such spinning. For precarious high-pressure gas samples sealed in glass tubes—for example, the HD samples—we used electric currents in the shim coils shown in Figure 5 to reduce the inhomogeneity, a technique also now commonly used in high-resolution spectrometers.[10]

IMAGING AND 'MENTAL' FOURIER TRANSFORMS

The Fourier transform relating (a) the time dependence of the FID following a pulse and (b) the frequency or field

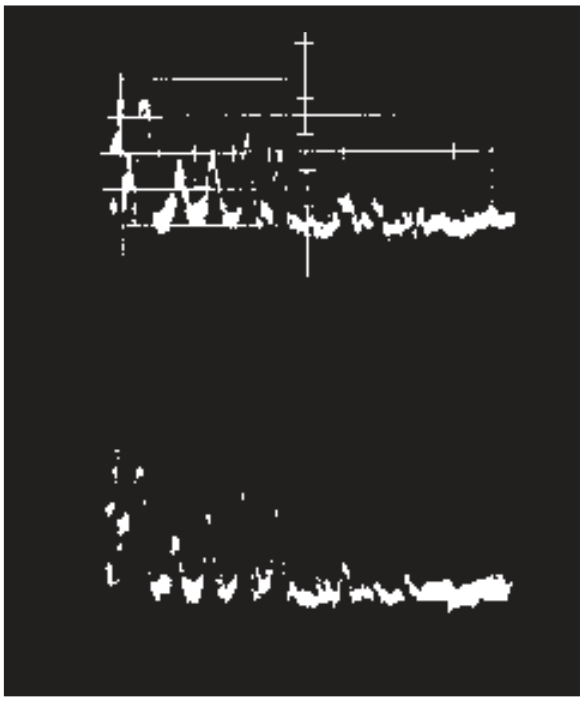

Figure 4 Nonresonance-induced ethyl alcohol echoes using motor in Figure 2; the modulation of the echo envelope reveals the chemical shift. From the research notebook of H. Y. Carr, 1950–52

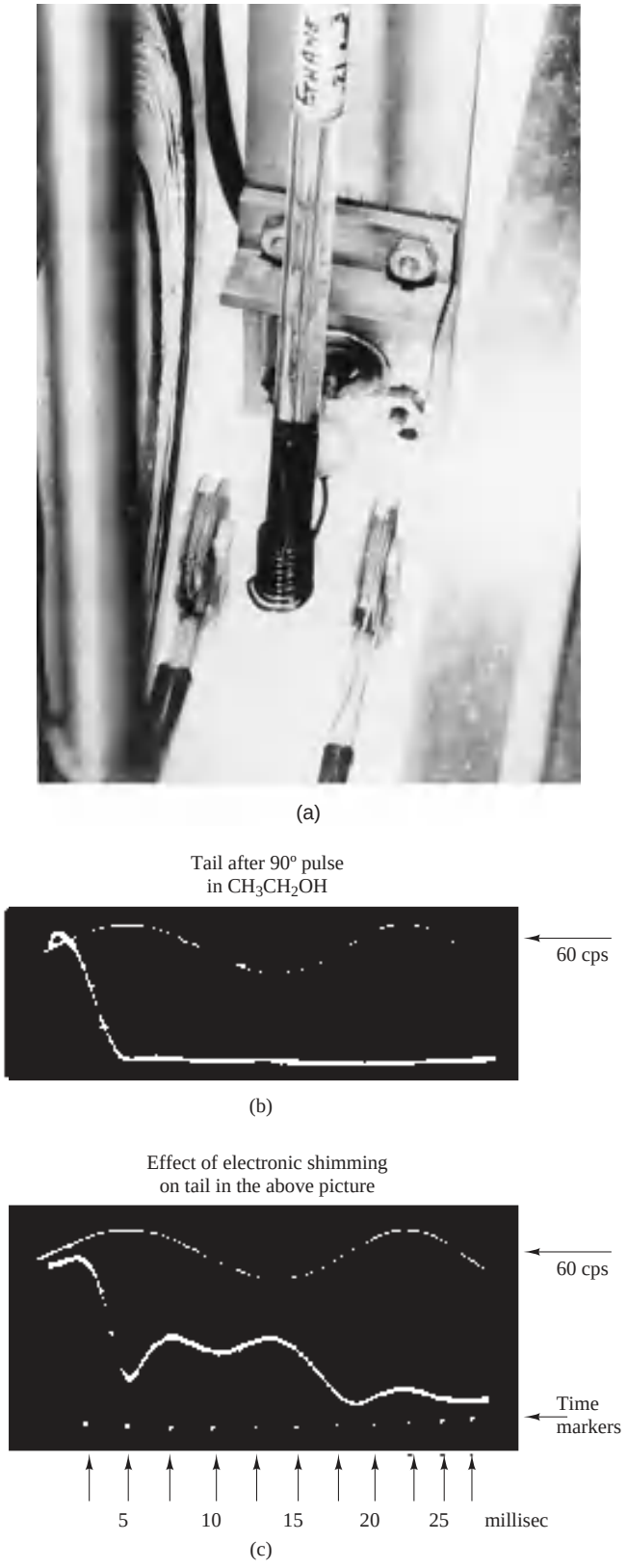

Figure 5 (a) Current carrying shim coils used to improve homogeneity of static field. FID of ethyl alcohol (b) without shim current and (c) with shim current. From Ref. 5

distribution of the molecules was recognized very early in our work. Initially this relationship was used to determine the lineshapes in our relatively inhomogeneous magnet. More interesting applications came after we began to improve magnet homogeneity by both sample spinning and the use of electric shims. These improvements made it possible to use our magnet to observe as in Figure 4 and Figure 5 more complicated FIDs caused by chemical shifts and indirect spin–spin couplings.

Some may think that fast Fourier transforms (FFTs) were not a part of free precession work until after the development of fast computers or 'electronic brains'. Not so! Very early we used our own brains to make speedy Fourier transforms of at least the simpler FIDs we were observing. The simplest FID—for example, the deuteron signal from our HD gas—consisted of a pure sinusoidal beat signal which we immediately recognized to be the Fourier transform of a distribution consisting of two lines of equal intensity. This was precisely the Ramsey–Purcell prediction[3] for an indirect spin coupling between H and D. Essentially half of the deuterons have proton neighbors with nuclear spin up, while the remaining half have proton neighbors with spin down.

Slightly more complicated was the modulation observed on the proton FID from acetic acid, CH_3COOH. Here the minima between the peaks of the modulated envelope of the beat signal in the FID did not go to zero, but only down to half the intensity observed at the peaks. Even without knowing the chemical structure for acetic acid, we could mentally transform this FID to a field distribution consisting of two lines—but now with one line having an intensity three-times larger than the other. The magnitude ratio for the peak intensities of the beat modulation becomes $(3 - 1)/(3 + 1) = \frac{1}{2}$ instead of the $(1 - 1)/(1 + 1) = 0$ ratio for the above deuteron signal from HD gas. The different field values for acetic acid correspond to different diamagnetic shielding at the nonequivalent locations of the protons—the first field at the locations of the three equivalent protons in the CH_3 group and the second field at the location of the one proton in the COOH group. The sensitivity of the above FIDs to changes of the external field value helped identify the type of shift—the indirect nuclear spin coupling was field independent while the chemical shift was field dependent.

The 'mental' Fourier transforms were not too difficult even when three spin groups were involved, especially when—as for the proton resonance in HD gas where the neighboring deuterons had spin 1—the three lines had *equal* intensity. But when the intensities of the three lines were *unequal*, and when the number of lines increased, the 'mental' Fourier transforms became quite difficult. Fortunately for NMR spectroscopy, and for MRI, the development of fast computers came to the rescue! Richard Garwin who had experience studying helium using NMR free precession techniques at IBM provided the crucial stimulation for Tukey and Cooley to develop their fast Fourier transform (FFT), published in 1965.[11] This stimulation did not originate in a study of line structure—simple helium lines have no fine structure. It arose from the coincidence of Garwin's time-consuming calculations concerning the alignment of nuclear spins in solid helium and his participation in a 1959 meeting concerned with the detection of underground nuclear explosions! This unique coincidence set the stage for Garwin's encounter with Tukey and Cooley.[12] Both NMR

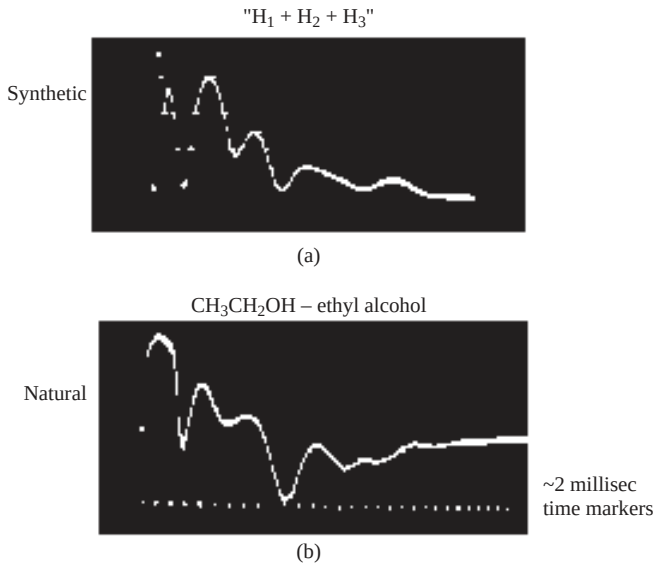

Figure 6 Comparison of FIDs from ethyl alcohol phantom (synthetic) and from a sample of real ethyl alcohol (natural). H_3, H_2, and H_1 are signals from the small rubber samples cut in the volume ratios 3:2:1. From Ref. 5

and MRI—and, indeed, nearly all fields of science—have benefited enormously from this coincidental encounter!

Our increasing difficulty with 'mental' Fourier transforms as the NMR line structure became somewhat more complicated, and the total absence of FFTs in 1951, led me to a one-dimensional imaging experiment. Visitors to our laboratory had little trouble understanding the above relatively simple FIDs from the protons in HD or CH_3COOH. But the much-discussed FID from ethyl alcohol, CH_3CH_2OH, gave a lot of trouble. The recently discovered chemical shift in ethyl alcohol involved three proton lines with intensities in the ratio 3:2:1. About this time we were intentionally superimposing a uniform gradient onto the main homogeneous magnetic field in connection with our diffusion studies. The gradient provided information on spatial location—each position corresponded to a different resonance frequency. Therefore, in order to help visitors understand the origin of the rather strange ethyl alcohol FID in Figure 5(c), I constructed a phantom—in the 1952 thesis I called it 'synthetic alcohol'. The phantom consisted of an rf coil stretched out along the uniform gradient of the static field. Three small pieces of rubber which had a strong proton resonance were placed in the coil at positions such that the ratio of the differences of the separations of the pieces, and therefore the ratio of the differences of their resonance frequencies, was approximately the same as for the ratio of frequency differences associated with the three lines of the real ethyl alcohol resonance. Moreover the volumes of the three small pieces of rubber were cut in the ratios 3:2:1 to correspond to the alcohol line intensities. To observe the FID in the time domain, we simply applied a 90° rf pulse. As expected, the phantom FID shown in Figure 6(a) looked very much like the real alcohol FID in Figure 6(b). This experiment had two results. Implicitly, it demonstrated crucial steps of the imaging concept: the use of the *Fourier transform* to relate the signal intensity in the time domain to the signal intensity distribution in the frequency and field domain, and the use of the *uniform gradient* to relate the signal intensity distribution in the frequency and field domains to the inhomogeneous spin distribution of the sample in the spatial domain. Explicitly, however, it enabled the visitors to 'look' at the phantom in the magnet and at the FID on the oscilloscope screen, and thus convince themselves that this relatively complicated FID does indeed come from this spatially inhomogeneous sample—three small *separate* pieces of uniform rubber with nuclei numbers in the ratio 3:2:1.

A word of caution comes from this phantom demonstration. When only the macroscopic external uniform gradient and the macroscopic structure of the phantom produce the signal intensity distribution in the frequency or field domain, the FID can be used to deduce the macroscopic structure of the phantom. But for the real ethyl alcohol sample in a homogeneous external field, the chemical structure of the signal intensity distribution in the frequency and field domains originates from the internal inhomogeneity within each molecule. Therefore the Fourier transform of the alcohol FID reveals the chemical shift, not macroscopic spatial structure. The simultaneous presence of a detectable chemical shift and an external gradient may complicate the spatial imaging. This complication has been exploited to improve some modern medical images.

FLOW AND MYSTERIOUS EVEN-NUMBERED ECHOES

A discussion of the effects of coherent molecular motion—convection and flow—was included in our 1954 paper. The even echo rephasing—or more precisely the odd echo dephasing—was used to establish that convection was not present when we used the new NMR technique to measure the diffusion coefficient of water.

The experimental results for diffusion and flow reported in the 1954 paper were obtained at Rutgers in 1953 using Henry Torrey's excellent new electromagnet shown in Figure 7. To the best of my knowledge, it was the first magnet commercially designed and built for NMR work. At Rutgers the intentionally superimposed uniform gradient came from two coaxial current loops shown in Figure 8 with current flowing in opposite directions. The gradient is uniform over the largest volume when the square of the diameter of each circular loop is equal to $\frac{4}{3}$-times the square of the loop separation. I called them 'anti-Helmholtz' coils. Later I learned that James Clerk Maxwell, while writing about a three-coil galvanometer,[13] considered two such loops. They have been called a *Maxwell gradient pair*, the next most elementary circular current configuration following *Ampere's loop* and a *Helmholtz field pair*.[14] The sample at Rutgers was water flowing steadily through a plastic tube that threaded the rf coil.

My first encounter with a flow effect, however, occurred at Harvard in 1951 under vastly different conditions. Initially I observed relaxation times for fluid samples. At one point, however, we thought it would be interesting to look at the relaxation in a solid sample. So I froze one of my ethane samples by immersing it in liquid nitrogen and then moved it quickly into the rf coil. Thus I had a brief opportunity to observe the echoes before, while, and just after the sample

Figure 7 The 1947 electromagnet built by General Electric for Rutgers, specifically designed for magnetic resonance use: 0–1.5 T magnetic field, 18.0 in. diameter pole faces, 3.5 in. gap width with variations less than ± 0.001 in. The yoke consisted of two major pieces, each weighing 4500 lb; the two coils each contained 700 lb of copper

melted. Obviously there were huge temperature gradients present. What I observed is described in some detail in the 1952 thesis. One effect in particular was mysterious and almost unbelievable. The second echo shown in Figure 9 was larger than the first! How could the echo midway between the second and third 180° pulses be more intense than an earlier echo between the first and second 180° pulses? This was contrary to all our usual experience and understanding of echo formation!

After some days of puzzlement we became more aware that in our previous thinking about echoes we almost always made certain implicit assumptions. One was that each molecule in the inhomogeneous magnet experienced exactly the same static field while dispersing before the 180° pulse as it experienced while reclustering after the pulse.

Clearly we had to modify our analysis to account for convection and for steady flow. The new analysis was reported in both the 1952 thesis[5] and the 1954 paper.[4] The even-echo rephasing shown in Figure 10 was finally well understood. Moreover, an improved understanding of the effect of diffusion evolved from these new insights into the effect of coherent flow. Although Hahn and Charles Slichter had correctly analyzed the effect of diffusion on the FID following the initial rf pulse, the expression in Hahn's 1950 paper[6] did

Figure 8 *Maxwell gradient pair* for obtaining uniform gradient: 2.0-in. diameter coils with separation distance adjustable from approximately 1.0 in. to 2.0 in. (to fit easily into the 3.5 in.-gap of the magnet in Figure 7). Knurled nut at bottom center was used for experimental adjustment of ideal diameter to separation ratio to correct for finite thickness of wire and number of turns in each coil. Constructed by master machinist Ralph V. H. Campbell of Rutgers Physics Machine Shop

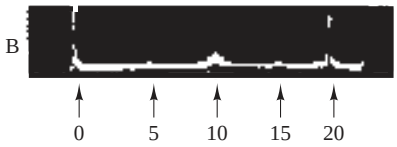

Figure 9 Mysterious second echo (at 20 time units) with intensity larger than that of first echo (at 10 time units). Sample was melted ethane. Harvard, 1951. From Ref. 5

not fully account for the effect of diffusion when a second rf pulse induced an echo. In particular, Hahn's analysis did not account for the ability of the Carr–Purcell pulse sequence to circumvent the effect of diffusion on echoes when more 180° pulses were interspersed between the 90° pulse and the final echo. Assuming a random walk model for diffusion through the inhomogeneous field, Purcell used two examples to consider a final echo intensity after eight random walk steps in the uniform gradient of an inhomogeneous field. In the first example an echo after the eighth step came in response to a single 180° pulse after the fourth step. In the second example an echo also came after the eighth step, but now in response to two 180° pulses—the first 180° pulse after the second step and the second 180° pulse after the sixth step. Another echo, of course, appeared after the fourth step. As he suspected, Purcell's tabulations for the phase distribution function of

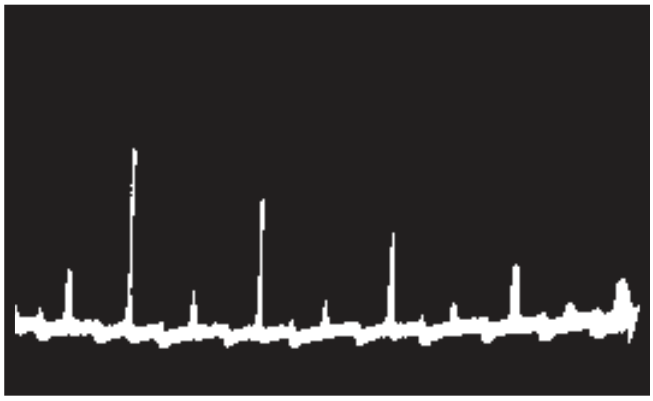

Figure 10 Even echo rephasing in flowing water. Rutgers, 1953. From Ref. 4

the first example with only *one* 180° pulse revealed a less intense echo after the eighth step than did the tabulations for the second example with *two* 180° pulses. Clearly the 180° pulses had the ability to eliminate part of the decay caused by diffusion!

Using Purcell's eight-step analysis as an incentive, and with the help of a lunchtime discussion with fellow graduate student Richard Milburn, I extended the analysis to an arbitrarily large number of steps, interspersed with an arbitrary number of 180° pulses. The result confirmed the Hahn–Slichter analysis for the behavior of the FID following a 90° pulse, and at the same time fully accounted for all our new experimental observations for the echoes.[4] Several years later in a very beautiful paper[15] Henry Torrey, by modifying the Bloch equations to include diffusion terms, confirmed the results of our random walk analysis.[4]

That fleeting glimpse of what appeared at first to be a mysterious even-numbered echo opened the door to applications beyond all our expectations. The new understanding of the effect of coherent motion on the phase of the NMR signal eventually pointed the way to the development of phase contrast magnetic resonance angiography (MRA) now commonly used in clinical work.

EPILOGUE

Space does not permit me to comment on more of the events during those three years at Harvard and the many additional benefits I received from the insight of other graduate students and faculty, especially Fred Reif, George Benedek, and Robert Pound. Nor is there space to describe in any detail the enjoyable and exciting times, despite some faulty starts and discouraging moments, I have had in subsequent years at Rutgers. Again I have benefited from many wonderful colleagues—students, postdoctoral fellows, faculty, and staff.

During the past 40 years, NMR in our laboratory has been less a field of study in itself and more an experimental technology that enriches other fields of study. To be sure, occasionally new techniques were added to those developed in the earlier years at Harvard. I find it fascinating that some of these Rutgers techniques—for example, nondestructive measuring[16] (now known as driven equilibrium) and steady-state free precession[17] were in large measure devised to help graduate students complete in a reasonable amount of time the measurements needed for their dissertations. The time needed to study slow-relaxing dilute xenon gas was undoubtedly the greatest challenge—the time needed for those measurements had to be reduced from years to months! Today these same techniques, along with the multiecho Carr–Purcell sequence (both resonance- or non-resonance-induced echoes), contribute to the development of fast imaging in medical applications. But now the time change is from hours to minutes or even seconds!

The central focus of my research at Rutgers, however, has been a study of fluids—a challenging state that lacks both the dilute gas simplification of extreme randomness and the solid state simplification of immense order.

An important part of our early research in fluids was the discovery made with Ralph Streever of a strong density-dependent local magnetic field shift in xenon.[16] Although some do, I prefer not to call this a chemical shift—its origin is *inter*molecular not *intra*molecular.

This shift played a crucial role when later our studies extended to the liquid–vapor critical region—a rich meeting place for experiment and theory. We used the local field shift to measure density. Perhaps our most important contribution to the renaissance of critical point studies was the experimental determination[18] with Larry Stacey and Barry Pass that, even in the absence of gravitational complications, the shape of the liquid–vapor coexistence curve accessible to experiment near the critical point clearly could not be described by a pure-power law with a single critical exponent. Later, a temperature quenching technique[19] was developed in our laboratory. This enabled us to work even closer to the critical point despite the complications always associated with gravitationally induced density gradients. Using this technique, Cecil Hayes and I made an NMR determination of the leading correction term to the power law describing the liquid–vapor coexistence curve.[19] The result was in agreement with the renormalization group prediction.

Our current research includes MRI studies of temperature quenching near the liquid–vapor critical point. NMR free precession between the forced nutation during pulses still continues to be an essential part of our explorations. It has been and continues to be a lot of fun! And the applications—beyond all our expectations—are deeply gratifying. It seems that almost each month brings new excitement from the excellent NMR and MRI work currently being done by what surely must by now be many thousands of innovative biologists, chemists, engineers, physicians, physicists, and others.

REFERENCES

1. E. L. Hahn, *Bull. Am. Phys. Soc.*, 1949, **24**, 13.
2. H. Y. Carr and E. M. Purcell, *Phys. Rev.*, 1952, **88**, 415.
3. N. F. Ramsey and E. M. Purcell, *Phys. Rev.*, 1952, **85**, 143.
4. H. Y. Carr and E. M. Purcell, *Phys. Rev.*, 1954, **94**, 630.
5. H. Y. Carr, '*Free Precession Techniques in Nuclear Magnetic Resonance*', Ph.D. Thesis, Harvard University, Cambridge, MA, 1952.
6. E. L. Hahn, *Phys. Rev.*, 1950, **80**, 580.
7. W. A. Edelstein, J. M. S. Hutchison, G. Johnson, and T. Redpath, *Phys. Med. Biol.*, 1980, **25**, 751.

8. J. J. Arnold, S. S. Dharmatti, and M. E. Packard, *J. Chem. Phys.*, 1951, **19**, 507.
9. G. A. Williams and H. S. Gutowsky, *Phys. Rev.*, 1956, **104**, 278.
10. J. T. Arnold, '*The Magnetic Resonances of Protons in Ethyl Alcohol*', Ph.D. Thesis, Stanford University, Palo Alto, CA, 1954.
11. J. W. Cooley and J. W. Tukey, *Math. Comp.*, 1965, **19**, 297.
12. J. W. Cooley, R. L. Garwin, C. M. Rader, B. P. Bogert, and T. G. Stockham, Jr., *IEEE Trans. Audio. Electroacoust.*, 1969, **AU-17**, 66.
13. J. C. Maxwell, *A Treatise on Electricity and Magnetism*, republication of 3rd edn., Dover, New York, 1954, Vol. II, Sect. 715.
14. M. W. Garrett, *J. Appl. Phys.*, 1951, **22**, 1091.
15. H. C. Torrey, *Phys. Rev.*, 1956, **104**, 563.
16. R. L. Streever and H. Y. Carr, *Phys. Rev.*, 1961, **121**, 20.
17. H. Y. Carr, *Phys. Rev.*, 1958, **112**, 1693.
18. L. M. Stacey, B. Pass, and H. Y. Carr, *Phys. Rev. Lett.*, 1969, **23**, 1424.
19. C. E. Hayes and H. Y. Carr, *Phys. Rev. Lett.*, 1977, **39**, 1558.

Biographical Sketch

Herman Y. Carr. *b* 1924. A.B., 1948, Ph.D., 1953, Physics, Harvard University, USA. Faculty in Physics, Rutgers University, USA, 1952–87, Professor Emeritus, 1987–present. Guggenheim Fellow and visiting scientist, Cornell University, USA, 1967–68. Visiting scientist, Van der Waals Laboratory, University of Amsterdam, NL, 1983. Current research specialty: Liquid–vapor critical phenomena.

Clough, Stanley: NMR and Quantum Tunneling Rotation

Stanley Clough

University of Nottingham, Nottingham, UK

When the first NMR observations of the quantum tunneling rotation of hindered methyl groups were made in 1952 it could not have been anticipated that they would lead to a scientific puzzle involving a fundamental aspect of quantum theory, only unraveled 40 years later. Already in 1952, motional narrowing and spin–lattice relaxation of rotating methyl groups were nicely explained by the classical model of random hopping rotation. When the NMR line of some methyl-containing materials failed to broaden at low temperatures it was correctly attributed to quantum tunneling, the stationary states of the group being orientationally delocalized. Since the same samples obeyed the orientationally localized hopping model at high temperatures, it was natural to envisage a continuous evolution from the delocalized stationary states to the localized hopping states such as occurs in the band-to-hopping transition in linear transport. Early attempts to construct a continuous theory looked promising but soon came up against an impasse. The quantum theory of molecular rotors was incompatible with the hopping theory.

My involvement in tunneling spectroscopy began in 1966 with EPR studies of free radicals containing methyl groups. With the advantage of resolved hyperfine structure and different spectra at low and high temperature, we were able to study details of the continuous evolution between tunneling and hopping. The results disagreed radically with expectations based on the theory of spin symmetry species, suggesting where the solution to the theoretical problem would ultimately be found. ENDOR brought the first measurement of a tunneling frequency. Weak tunneling sidebands of EPR and NMR spectra were predicted and found by single and double resonance techniques. Experiments detecting internal resonances between tunneling frequencies and the electron Larmor frequency of paramagnetic impurities introduced level crossing methods to tunneling spectroscopy and field cycling techniques. Similar resonances were soon discovered with nuclear Larmor frequencies. High-field NMR studies of tunneling were hampered because of weak transitions. Low-field NMR though turned out to be unexpectedly powerful, as did tunneling spectroscopy in the rotating frame. The techniques to which many people contributed opened a succession of frequency windows on tunneling spectroscopy from a few kHz to tens of GHz. As the spectroscopy became routine, our thoughts turned during the 1980s to the next phase. With the development of NMR as a model, it was natural to consider the time domain and the evolution of superpositions of methyl tunneling states. Having the form of rotating wavepackets, these are a coherent version of the hopping rotation, and they similarly modulate the dipole–dipole interaction with interconversion of rotational and spin angular momentum and energy. When the conversion is described by incoherent transitions, nuclear spin thermodynamics are extended to include molecular rotation with a rotational reservoir and temperature. When treated coherently, rotational and spin dynamics are unified. Throughout this period the theory remained broken-backed. There was one theory for low temperature data and one for high temperatures.

The theoretical puzzle concerns the labels used to identify fermions in quantum mechanics. In classical mechanics identical particles are identified by their trajectories. A particle may only be referred to as ‘the particle in trajectory *j’*, not as ‘particle *j’*. These are respectively trajectory and particle labels. Superficially they may appear the same, the distinction between them being quite subtle. The conversion of *a(i)b(j)* to *a(j)b(i)*, where *a* and *b* are trajectories, occurs with the exchange of particles if *i* and *j* are particle labels and with the exchange of the meanings of the *i* and *j* if they are trajectory labels. Quantum mechanics borrows terms for the interactions of identical particles from classical mechanics and these are naturally expressed using trajectory labels. Quantum mechanical statefunctions, however, are written in terms of the illegal particle labels, compensated by imposing a constraint on the statefunction requiring it to be antisymmetric with respect to exchange of the labels. The inconsistent use of labels and the dynamical constraint are the source of many problems of which the reconciliation of quantum and classical theories of methyl rotation is only one. The general problem is resolved by formulating quantum mechanics using only trajectory labels. Then antisymmetrization of a trial statefunction only involves meaning exchanges. By revealing when two or more of the fermion trajectories are identical, a condition forbidden by the exclusion principle, it enables allowed eigenstates to be selected. With this role it imposes no dynamical constraint and is compatible with classical mechanics. With the excitation of wavepacket states the trajectory labels introduce the rotation and other coordinates which feature in classical theories and provide a description of particle dynamics which parallels the spin dynamics of NMR.

The removal of the constraint also makes the theory of quantum rotation transformable between rotating reference frames. This ensures that the relativity principle is satisfied and is also an important step in the unification of rotation with spin dynamics in which the use of rotating frames plays a vital role. A single theory can be devised encompassing both the high-temperature hopping model and the low-temperature tunneling states, while at low temperatures rotational wavepackets evolve coherently under the influence of the dipole–dipole interaction in a unified rotation and spin dynamics. All of the concepts of NMR can be extended to this wider field. Since rotational relaxation times are very long at low temperatures, time domain experiments can be envisaged in which spin order and rotational order are interchanged, opening a new field of coherent lattice dynamics for ingenious experimentalists. The intimate relationship of NMR and quantum tunneling rotation has been long obscured by conceptual problems. With these out of the way the future could be richer than the past.

Biographical Sketch

Stanley Clough. *b* 1932. B.Sc., 1952, Ph.D., 1963. Industrial scientist, 1952-9, initiating NMR and EPR at ICI in 1956. Lecturer, University of

Wales, Bangor 1959-63. University of Nottingham since 1963, Professor since 1975. Approx 150 publications, focusing since 1968 on NMR and EPR studies of methyl tunneling, the quantum-classical transition and combined coherent spin and particle dynamics at low temperatures.

Codrington, Robert S.: Comments on NMR Instrument Development

Robert S. Codrington
Los Altos Hills, CA, USA

When my thesis work started at Notre Dame in the fall of 1948 it was intended that I would investigate phase changes in polymers by high-frequency dielectric measurements. Before work actually started however, Felix Bloch stopped at the university to visit his friend and my thesis adviser Gene Guth. Bloch questioned us about why we weren't using NMR in the study of phase transitions rather than dielectric constant, since the polar groups in polymers were usually associated with the backbone or more rigid sections of the polymer molecules whereas the phase transitions were often governed by the motion of the end or terminal side groups of the molecule. He suggested that we talk to Herb Gutowsky and Herman Marks about it and shortly thereafter my thesis subject was changed to NMR in polymers. Earlier training as a radar specialist had provided me with an ideal background for designing NMR instrumentation, and it was not just a coincidence that all the inventors of NMR had played an important role in radar development.

In 1951 I joined the Physics Department at Rutgers University working for Henry Torrey on a project for the Office of Naval Research to investigate the use of magnetic resonance in submarine detection. Torrey had published his paper on the transient solutions of the Bloch equations using the Laplace transform methods and my work with him proved to be very useful for later work with Fourier transform systems. By the fall of 1952 I was sharing an office with Herman Carr who had come to Rutgers to complete his thesis and use their large homogeneous magnet for some of the new spin echo experiments which he and Purcell wished to carry out. Discussions with Carr as well as my involvement in testing the Navy's magnetometers, including the Russell Varian/Martin Packard free induction system, gave me a good introduction to transient NMR instrumentation.

The Schlumberger Corporation wished to apply the submarine magnetic resonance techniques to the detection of oil in geological formations and in 1954 I was hired to work with their consultant Nicolaas Bloembergen in trying to improve the sensitivity of NMR detection for this application. We designed a number of CW and pulsed NMR systems, one of which became a commercial instrument, and although the oil well instruments were never completely successful they did anticipate future developments in NMR imaging. In the period 1957–62 I became associated with the Navy missile programs and had access to the new digital systems which later had application to NMR designs. The Schlumberger NMR products were sold to Varian in 1961 and I joined the company in 1962.

My first job at Varian was getting the new A-60 spectrometer into production. It was an external lock system with a calibrated chart display for high-resolution spectra and became widely used for routine organic chemical analysis. The advantages of the lock and calibrated charts were so helpful to the chemists that the older research spectrometers were upgraded to include them. A time-averaging computer, which digitized and stored the CW data, was also added to the product line. By the late 1960s work in the Varian laboratories by Wes Anderson and Richard Ernst in time-averaging time domain (FID) data, by Harry Weaver in using a higher field supercon magnet, by Ray Freeman in obtaining very high resolution performance, and by Jim Shoolery in developing tools for molecular conformation studies made it evident that a new type of research NMR spectrometer would be needed in the 1970s. Unfortunately, the costs of the different components needed for such a spectrometer were at that time just too expensive for use in a commercial instrument, and manufacturers compromised by selling hybrid CW/Fourier transform systems such as the Varian XL-100.

By the early 1970s rapid changes were occurring in the electronic and computer industries, all of which would have an impact on the design of NMR spectrometers. The improved noise figure of transistors resulted in much better receivers and higher frequency components made it possible to mix at gigahertz frequencies in synthesizers used to generate the three basic NMR frequencies (observe, lock, and decouple), thus avoiding the harmonic mixing ghosts that had plagued earlier synthesizers. Lower cost computers became available which used RAM memory in combination with fast i/o hard disk storage rather than magnetic core memory. Faster ADCs with larger dynamic range and low cost microprocessors also became available. The quality and stability of superconducting wire improved significantly and new designs of the magnet Dewar systems increased the liquid helium hold time by more than 10 times. Additionally, the use of new structured programming languages such as Pascal and C increased the speed and efficiency of developing large software packages needed for multidimensional NMR and new pulse sequences. Varian was able to utilize all this new technology in the XL-200 spectrometer (1978), and by 1980 all commercial research NMR spectrometers were incorporating most of it in their designs.

In the mid-1970s, Ernst and Packard as well as Derek Shaw and Felix Wehrli in Europe had encouraged Howard Hill and myself to keep up with developments in the MR imaging field. In 1983 we began the development of a series of spectrometers combining both NMR spectroscopy and NMR imaging in fields up to 7 T for use with smaller animals. By 1991 the latest system in this series, a whole body (1-m bore) 4 T unit developed in cooperation with Siemens, was completed. Recent results on this system and the new very high field spectrometers have demonstrated that if a breakthrough could be made in high-temperature superconductors it would open up new horizons in NMR applications.

Biographical Sketch

Robert S. Codrington. *b* 1924. B.A., 1946, M.A., 1948, University of British Columbia, Ph.D., 1951, University of Notre Dame, all in physics. Assistant, Rutgers University, 1951–54. Technical Director, Schlumberger Corp., 1954–62. Various positions including Director of R & D, Varian Instrument Division and Varian Imaging Systems, 1962–92. Approx. 50 publications and 20 patents. Current specialties: in vivo imaging and spectroscopy of the brain and extremities.

Cohen, Jack S.: Recollections of Early NMR Applications to Proteins and Cells

Jack S. Cohen

Georgetown University Medical Center, Washington DC, USA

In 1966 I arrived in the US for the first time, as a postdoctoral fellow at Oleg Jardetzky's laboratory at Harvard Medical School in Boston. Until then I had mainly done nucleotide chemistry and ^{31}P NMR,[1] but I had decided that I wanted to learn more about proteins, specifically using NMR methods.

When I arrived, I met John Markley and Donella (Dee) Meadows, who were both just finishing their graduate work in the lab on NMR of polypeptides. A paper had recently appeared[2] from the laboratory of Harold Scheraga at Cornell, in which three pH-dependent signals were reported in the downfield region of the proton spectrum of Ribonuclease A at 60 MHz. The spectra were terribly noisy, however, and the analysis seemed confused, since RNase has four histidine (His) residues. Dee Meadows, who had a wonderful touch with the old Varian HR-60 machine in the basement of the Medical School, ran some spectra of Ribonuclease A at very slow scan rates and managed to see four resonances at certain pH values.

Very soon after I arrived, Oleg had decided to move to Merck Research Labs in New Jersey, where they had a Varian HA-100 that was equipped with an analog computer of average transients (CAT) to improve signal-to-noise. We immediately began running the spectra of several proteins to look for their histidine imidazole signals. Initially Dee studied RNase, John chose staphylococcal nuclease, and I focused on lysozyme.

Lysozyme was a much studied protein because it is readily available (from hen egg whites) and is extremely stable. One other point that particularly attracted me was that it had only one histidine residue, at position-15 in the amino acid sequence. Since the origin of the signals seen in the RNase spectrum was controversial, I thought that if I could see one titrating resonance, that would clarify the issue.

In fact I did see one titrating resonance, and was able to assign this to the imidazole ring C-2 (or C-ϵ) proton of His-15. Thus, this was the first individually resolved proton in a protein NMR spectrum that was unequivocally assigned. This, as well as the observation of four titrating resonances at some pH values in RNase and *Staph*. nuclease, was sufficient to show that one should expect one signal per His residue, and that the pK represented not an aggregate pK value but rather reflects the local protein microenvironment. The results were published in a paper that had a dramatic effect on the development of the field of macromolecular applications of NMR.[3]

In order to confirm this observation I looked for other lysozymes, and found that human lysozyme had then become available. This also had one His residue, so I obtained samples and ran spectra, and found that while there was also only one such titrating resonance, the pK obtained (7.1) was very much higher than that for HEW lysozyme (pK = 5.8), as a result of very different microenvironments for these residues.[4]

In 1969 I joined NIH, where Ted Becker had acquired one of the first 220 MHz spectrometers. Although I was employed in the computer division, I carried out NMR studies of proteins in collaboration with Chris Anfinsen's laboratory. We did one of the first computer curve-fitting analyses of protein NMR data,[5] and we used NMR and the four His residues of *Staph*. nuclease[6] to show that individual residues in a protein can exhibit different denaturation midpoints.[7] We analyzed[8] and unequivocally assigned[9] all the four His resonances of RNase, and we also reported the first ^{13}C NMR titration curves of carboxy groups in proteins.[10]

After several years of studying protein NMR signals and analyzing their relationship to protein conformation, I saw that major developments were occurring in biological NMR. But, with only 220 MHz and 270 MHz NMR spectrometers with narrow bore magnets available, potential applications were limited. We did some successful studies on chromaffin granules,[11] but I wanted to study intact cells. However, following some of the pioneering work of Navon et al.[12] on cell suspensions proved difficult, and the results were very variable. We decided that the reasons were two-fold: first, sedimentation of the cells (unlike the granules that remained suspended), and second, loss of ATP signals in the cells due to the depletion of glucose and oxygen, as well as the acidification due to lactate build-up. In order to overcome these problems, a perfusion system was needed to supply fresh nutrients and remove catabolites. But how to prevent the cells from moving with the perfusate, and use only a standard NMR tube?

At first we tried various kinds of fibers, but they were not good due to the back-pressure and the very slow perfusion/diffusion rates. We also tried microspheres, but they also had major disadvantages not least the loss in sensitivity.[13] Finally we decided to embed the cells in a gel,[14] but a gel block was not good. So we tried to cut the gel into small pieces and we also tried to mould the gel into small beads. After some experimentation, however, we found that the best means was to make a very fine gel thread by extruding the liquid gel (mixed with cells) through a cooled capillary.[15,16] This had the advantages that the gel could be packed with cells (thus retaining signal-to-noise ratio) and the small diameter of the thread (0.5 mm) allowed effective access to the nutrients, as we showed by extensive diffusion studies.[17] This method has now been applied for 10 years and many successful studies of cancer cell metabolism have been published.[18]

REFERENCES

1. G. M. Blackburn, J. S. Cohen, and Lord Todd, *Tetrahedron Lett.*, **1964**, 2873.
2. J. H. Bradbury and H. A. Scheraga, *J. Am. Chem. Soc.*, 1966, **88**, 4240.
3. D. H. Meadows, J. L. Markley, J. S. Cohen, and O. Jardetzky, *Proc. Natl. Acad. Sci. USA*, 1967, **58**, 1307.
4. J. S. Cohen, *Nature (London)*, 1969, **223**, 43.
5. J. S. Cohen, R. I. Schrager, M. McNeel, and A. N. Schechter, *Biochem. Biophys. Res. Commun.*, 1970, **40**, 144.
6. J. S. Cohen, R. I. Shrager, M. McNeel, and A. N. Schechter, *Nature (London)*, 1970, **228**, 642.
7. H. Epstein, A. N. Schechter, and J. S. Cohen, *Proc. Natl. Acad. Sci. USA*, 1971, **68**, 2042.

8. J. S. Cohen, J. Griffin, and A. N. Schechter, *J. Biol. Chem.*, 1973, **248**, 4305.
9. H. Shindo, M. B. Hayes, and J. S. Cohen, *J. Biol. Chem.*, 1976, **251**, 2644.
10. H. Shindo and J. S. Cohen, *Proc. Natl. Acad. Sci. USA*, 1976, **73**, 1979.
11. H. Pollard, H. Shindo, C. E. Creutz, C. J. Pazoles, and J. S. Cohen, *J. Biol. Chem.*, 1979, **254**, 1170.
12. G. Navon, S. Ogawa, R. G. Shulman, and T. Yamane, *Proc. Natl. Acad. Sci. USA*, 1977, **74**, 87.
13. J. S. Cohen, ^{31}P NMR Studies of Cell Metabolism, in *Magnetic Resonance in Biology and Medicine*, Tata McGraw-Hill, New Delhi, India, 1985, pp. 77–100.
14. L. Jacobson and J. S. Cohen, *Biosci. Rep.*, 1981, **1**, 141.
15. D. L. Foxall and J. S. Cohen, *J. Magn. Reson.*, 1983, **52**, 346.
16. D. L. Foxall, J. S. Cohen, and J. B. Mitchell, *Exp. Cell Res.*, 1984, **154**, 521.
17. R. C. Lyon, P. J. Faustino, and J. S. Cohen, *Magn. Reson. Med.*, 1986, **3**, 663.
18. O. Kaplan, P. C. M. van Zijl, and J. S. Cohen, NMR Studies of Metabolism of Cells, and Perfused Organs, in *In Vivo Magnetic Resonance Spectroscopy. III. In-Vivo MR Spectroscopy: Potential and Limitations*, eds. I. Seelig and M. Rudin, Springer Verlag, Heidelberg, 1992, Vol. 28, pp. 4–52.

Biographical Sketch

Jack S. Cohen, *b* 1938. B.Sc., 1961, London University, UK, Ph.D., 1964, Chemistry, Cambridge University, UK. Introduced to NMR during graduate work in Cambridge University by Michael Blackburn. Involved in NMR research at NIH for 20 years. Since 1990 Professor of Pharmacology at Georgetown University, Washington DC, USA. Approx. 240 publications. Biological applications of NMR, especially to oligonucleotides and cancer cell metabolism.

Mildred Cohn: Peregrinations of an Enzymologist in NMR

Mildred Cohn

University of Pennsylvania Medical School, Philadelphia, PA, USA

In the 1950s, Washington University was a center of magnetic resonance with George Pake and Dick Norberg in the Physics Department and Sam Weissman in the Chemistry Department, and news of the developments were transmitted to me by my husband, Henry Primakoff, a member of the Physics Faculty. My research interests at that time focused on the reactions of adenosine triphosphate (ATP), first on the specificity of the obligatory divalent metal ion, e.g. Mg versus Ca, and second on the specificity of the bond cleavage, i.e. what determined whether cleavage occurred on the γ-P of ATP (phosphoryl transfer) or the α-P of ATP (adenyl transfer). Metal ion specificity could be ascribed to metal-dependent structural differences in the metal nucleotide complexes (M · ATP) and enzyme-dependent bond cleavage specificity might be ascribed to involvement of different phosphate groups of ATP in the enzyme–metal–ATP complexes (E · M · ATP).

I had failed to answer these questions by ESR spectroscopy of the Mn(II) complexes[1] and it occurred to me while on sabbatical at Oxford in 1955 that ^{31}P NMR should be able to distinguish the three P atoms of ATP and consequently define the structure of enzyme-bound M·ATP. When I returned to St. Louis in February 1956, I was disappointed to learn that the home-made NMR spectrometer at Washington University was limited to the detection of protons. Consequently I contacted Varian and inquired whether I could try to observe the ^{31}P spectrum of ATP in their Applications Laboratory in Palo Alto. Their reply was most enthusiastic, inviting me to come any time. Due to family obligations, I decided it was not feasible for me to go off to California for an extended period. Two years later in 1958, we planned to spend the summer quarter at Stanford. I wrote to Varian informing them that I was still interested in the problem, inquiring whether I could pursue it that summer. Their reply was grudgingly in the affirmative. In the two years that had elapsed Varian had developed a reliable, stable instrument, increased the magnetic field by 50% (HR-60) and had demonstrated its unique usefulness in determining structures of organic compounds. The Applications Laboratory was overwhelmed by requests from organic chemists for feasibility studies. The biochemists, except for the pioneering work of Oleg Jardetzky on amino acids and dipeptides,[2] had not yet discovered NMR.

The first Sunday we were at Stanford, we visited our friends the Hofstadters, where I met Felix Bloch. During the visit, Bloch asked what I planned to do that summer and I told him that I hoped to make some NMR measurements at Varian. Whereupon he said I am going to Varian tomorrow, would you like to come with me? Overwhelmed by my good fortune, I answered with alacrity I'd be delighted. On the adventurous trip in his convertible the next day (Bloch's driving habits were hardly reassuring), he told me that he no longer worked in NMR—it was now chemistry.

In spite of my introduction to Jim Shoolery by Bloch, I did not get to do ^{31}P NMR until six weeks after that initial visit. I did the ^{1}H NMR of ATP the first week, but the Applications Lab was very busy demonstrating the potency of proton NMR to prospective customers, and with only one HR-60 spectrometer available to them they were understandably loath to switch from a ^{1}H probe to a ^{31}P probe. Finally I was granted a day and I brought three incredibly viscous solutions, 1 M ATP, 1 M MgATP, and 1 M MnATP, the concentration necessary to observe ^{31}P in a single scan at 24.3 MHz in a 5-mm tube. That day, I was most grateful to Varian, feasibility of the approach was demonstrated; the spectrum of ATP revealed three well-resolved peaks which shifted with Mg, particularly the β-P resonance, and Mn(II) obliterated all three peaks.

Full of enthusiasm to pursue the problem systematically when I returned to St. Louis, I fortunately learned that the Chemistry Department at the University of Illinois had recently acquired an HR-60 spectrometer with a ^{31}P probe. Through friends at Washington University and at Illinois, arrangements were made enabling me to have the use of the spectrometer on weekends. It was not an easy commute but it was manageable on an interim basis. I extended my original experiments and found, as expected, that the α-P of ADP and ATP had similar shifts and the β-P of ADP and the γ-P of ATP shifts were similar and highly pH-dependent; the unusually high upfield shift of the β-P of ATP confirmed the original observation. Unlike the chemical shifts in proton NMR, there was no theory available to explain the shifts in ^{31}P NMR.

In the meantime, Sam Weissman had been asked to apply for a grant from NIH to purchase a Varian spectrometer for the Washington University Chemistry Department and he invited my participation in the proposal, generously offering me one-fourth time on the instrument. Sometime in 1959, the DP-60 spectrometer duly arrived and Tom Hughes, a physics graduate student, was put in charge. Considerable delay was encountered not only because Hughes was a perfectionist, but because Varian had neglected to include a temperature control for the magnet (temperature changes may not have been a problem in Palo Alto, but in St. Louis the temperature could easily vary by 20 °C in the course of a day). A spectrum of 0.5 M ATP recorded in a single scan on this spectrometer is shown in Figure 1;[3] easily resolving the doublet for γ-P, the doublet for α-P broadened by the unresolved coupling to ^{1}H-5′ of the ribose and the apparent triplet of β-P, allowing the coupling constants of $\alpha-\beta$ and $\beta-\gamma$ to be determined. To increase the sensitivity, Hughes applied an ingenious method, the opposed sideband technique,[3] and succeeded in observing the three peaks of ATP at 0.09 M with good signal-to-noise, albeit in 12-mm thin-walled plastic tubes (containers of Hughes' Havana cigars). Although our ^{31}P probe could maximally accommodate a 12-mm diameter tube, no spinner was available and the nonspinning peaks were very broad. The pH dependence of the chemical shifts of ADP and ATP were determined,[3] and we proceeded to study the effects of metal ions.

In preparation for the metal complex experiments, I removed the sodium from the commercial ATP and substituted the tetramethylammonium ion on an ion-exchange column. Much to my surprise and chagrin, the spectrum of this preparation differed greatly from that of sodium ATP, the β- and γ-P

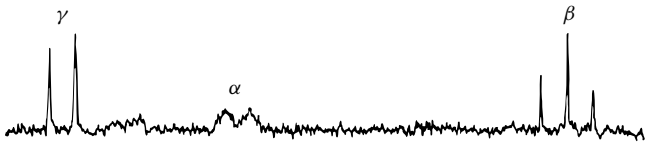

Figure 1 High-resolution ^{31}P NMR spectrum of tetramethylammonium salt of ATP (0.5 M) at pH 10.0. The splitting due to spin−spin interaction is 19.3 ± 0.5 c/s for all the peaks. The two small peaks following the γ doublet are artifacts due to baseline instability and were not observed in subsequent experiments (Ref. 3)

resonances were very broad and the α-P resonance was sharper and enhanced in height. Disturbed, I consulted my chemist friends and Dave Lipkin said, *It looks like a paramagnetic effect*. Whereupon I investigated the history of the resin and found that it had been sized through a brass sieve, the usual procedure at that time. The unlikely supposition that copper had been picked up by the resin during sizing and had been removed by the ATP was indeed confirmed by ashing the ATP sample and analyzing for copper. Because Cu(II) can only form square-planar complexes, only the β-P and γ-P resonances were broadened and the narrowing of the α-P represented the collapse of the unresolved α-P doublet due to the greatly increased relaxation rate of the β-P (the poor man's decoupling technique). In the diamagnetic ion complexes of ADP and ATP (Mg, Ca, Zn), the largest change in chemical shift for all three ions was again the β-P resonance of ATP (3 ppm) with only minor differences among the ions. An attempt to observe an effect of the enzyme hexokinase failed because, as I found many years later, the effect was much too small with such a low ratio of E·MgATP/MgATP.

Upon the urging of Sam Weissman, I submitted a preliminary communication co-authored with Tom Hughes to the *Journal of the American Chemical Society* on the ^{31}P spectrum of ATP and the effect of metal ions thereon. The manuscript was rejected. One referee stated that no chemist would be interested because we had used a commercial instrument and the second referee commented that no biochemist would understand it and suggested that it be expanded into a full paper. I took the latter's advice and published two papers in the *Journal of Biological Chemistry*, one on the pH effect[3] and another on the metal ion effects.[4]

In July 1960, I moved from Washington University to the Johnson Research Foundation/Biophysics Department of the University of Pennsylvania. When I arrived I found that there was no NMR spectrometer on campus. I was not too disappointed because I had already come to the conclusion that high-resolution ^{31}P NMR was too insensitive, both in required concentration and magnitude of chemical shifts, to be useful in establishing the structures of metal nucleotide−enzyme complexes. There was an ESR spectrometer in our department and an electrical engineering student, Jack Leigh, under the direction of Britton Chance, was constructing a pulsed NMR instrument which would be suitable for measuring relaxation times of water as developed by Hahn.[5]

The concentration of one component of enzymatic reaction systems, namely water, lends itself readily to NMR measurements and the insensitive chemical shift parameter could be replaced by the highly sensitive effect of Mn(II) on the proton relaxation rates, $1/T_1$ and $1/T_2$, (PRR) of water; 1 M Mn(II) increases the PRR of water approximately 10 000-fold. Mn can substitute for Mg as the obligatory divalent activator in all enzymatic reactions of ATP. Thus it became possible to measure an NMR parameter of enzyme systems at concentrations in the range of 10^{-4} to 10^{-5} M in 0.1 mL volumes. I expected to determine the number of water molecules remaining in the first coordination sphere of Mn from the decrease in $1/T_1$ as the substrates and enzyme displaced the water ligands in $Mn(H_2O)_6$, as occurred when small molecules complexed with Mn(II). Much to my surprise, we observed a large increase in $1/T_1$ in Mn−enzyme complexes. I had to re-examine my naive assumptions.

The following equations describe the dependence of $1/T_{1p}$, the paramagnetic contribution to the longitudinal relaxation rate, on n, the number of water molecules in the first coordination sphere of the paramagnetic ion, on τ_c, the correlation time, and on the frequency ω_I:

$$1/T_{1p} = np/(\tau_M + T_{1M}) \quad (1)$$

where τ_M is the residence time, T_{1M} the longitudinal relaxation time in the first coordination sphere of the metal ion; p is the ratio of the concentration of paramagnetic ions to that of water. For macromolecular manganous complexes, the Solomon−Bloembergen equation for $1/T_{1M}$ simplifies to:

$$1/T_{1M} = B/r^6[3\tau_c/(1 + \omega_I^2\tau_c^2)] \quad (2)$$

where B is a product of physical constants determined by the electron spin of Mn(II) and the magnetogyric ratio of the proton, r is the ion−proton internuclear distance, ω_I is the angular precession frequency of the nucleus, and τ_c is given by:

$$1/\tau_c = 1/\tau_r + 1/\tau_e \quad (3)$$

where τ_r is the rotational correlation time of the water in the hydration sphere and τ_e is the electron spin relaxation time. Eisinger et al.[6] observed increases of PRR by factors of five to 10 in DNA solutions with Mn(II), Cu(II), and Cr(III); Ni(II) and Co(II) showed no such enhancement (ϵ). Only for Mn(II), Cu(II), and Cr(III) with their long spin relaxation times does τ_r determine τ_c. If the ion is bound to a macromolecule, the rotation of the remaining water in the hydration sphere of the ion is hindered, τ_r increases, τ_c increases and the PRR is enhanced.

The first instrument constructed in conjunction with the ESR spectrometer (0.6 T) had a Varian ^{31}P probe (24.3 MHz) which was borrowed from the Chemistry Department's newly acquired 60 MHz NMR spectrometer. The oscilloscope was perched on a box about 2 ft. above floor level and it could be observed only in a squatting position. This feature was eventually remedied after I complained that I was getting too old for that sort of experimental technique. Polaroid camera photographs of the oscilloscope screen showing signals obtained by the 180°–90° null method of Carr and Purcell were used to determine T_1. Our later models of the pulsed NMR spectrometer with a 1.4-T Varian magnet were capable of variable frequency and temperature measurements and a readout of the null point.

When we measured PRR in enzyme systems,[7] we found that for enzymes which bound Mn(II) at the active site, the values of ϵ in the metal−protein complexes increased more than an

order of magnitude. Furthermore, each ternary or quaternary complex had a unique value of ϵ. We initiated a two-pronged study over the next 15 years to (1) explain the physical basis of the PRR enhancement and (2) understand the implications of the PRR enhancement values for enzyme mechanisms. The first goal was accomplished by studying the PRR as a function of frequency and temperature, and it was found that, in the Mn(II) macromolecular complexes, τ_r becomes so long that τ_c is now determined by τ_e of Mn(II). These measurements were complemented by ESR spectroscopy of the Mn(II)–enzyme complexes as developed by George Reed. The aspects of enzyme mechanisms which could be derived from these measurements were (1) the determination of binding constants and number of binding sites, (2) the differentiation between those enzymes which bind the metal in a binary complex and those which bind the metal ion via a substrate bridge, and (3) after determining τ_c, the number, n, of water molecules remaining in the first coordination sphere of Mn(II) which were in rapid exchange with the bulk water could be calculated for each complex. The generalization which resulted was that as each successive ligand (substrate or product) was added to the enzyme, n decreased, implying that the active site became less and less accessible to solvent. The applications to various enzyme systems have been reviewed.[8–10]

With the improvement of commercially available spectrometers, the Varian HR-60 was followed by the HR-100, and biochemists began to use high-resolution proton NMR spectroscopy, particularly for structure determination of molecules of biological interest. By the end of 1963, when Arthur Kowalsky and I reviewed applications of NMR in biochemistry,[11] there were 140 relevant papers in the literature, almost all published between 1960 and 1963. In the mid-1960s through the 1970s, we began exploring once again the possibilities of using high-resolution NMR to elucidate enzyme mechanisms. For example, Mildvan and Leigh initiated the mapping of ligand geometry at active sites of kinases by determining distances from Mn(II) to various atoms in the enzyme-bound substrates from the effect of paramagnetic Mn on the relaxation rates of the nuclei of those atoms; narrowing of proton resonances in macromolecules was attempted. In the 1970s, the stereochemistry of the enolase reaction was determined by combined ^{31}P and ^{13}C measurements; an intermolecular NOE effect between a ligand proton and a lysyl residue on creatine kinase was observed; and the proton NMR of the enzyme adenylate kinase was investigated at 220 MHz.

Finally we returned to the original problem, and Nageswara Rao investigated the changes in the ^{31}P spectra of MgATP and MgADP upon binding to stoichiometric concentrations of enzymes and in equilibrium mixtures of enzyme-bound substrates and products. The most striking finding was that regardless of the value of the equilibrium constant of the overall reaction which, for the kinase reactions investigated, ranged over four orders of magnitude, the equilibrium constant for the central complexes $E \cdot S_1 \cdot S_2 \rightleftharpoons 2; E \cdot P_1 \cdot P_2$, was always close to 1. From lineshape analysis, the rate of this step could also be determined and it could be established whether it was the rate-determining step in the overall reaction. The results of this series of experiments have been reviewed.[12] Other aspects of enzyme mechanisms were examined with ^{31}P NMR by substitution of ^{16}O in phosphate groups by either ^{18}O[13] or by sulfur.[14]

In recent years there has been an unforeseen explosion in applications of NMR in biomedical research resulting from spectacular technological developments. High-resolution proton spectroscopy at 500–600 MHz is the most informative method for studying protein structures in solution, ^{31}P is the nucleus of choice for most in vivo studies, and PRR of water is the most used parameter of MRI.

REFERENCES

1. M. Cohn and J. Townsend, *Nature (London)*, 1954, **173**, 1090.
2. M. Takeda and O. Jardetzky, *J. Chem. Phys.*, 1957, **26**, 1346.
3. M. Cohn and T. R. Hughes, Jr., *J. Biol. Chem.*, 1960, **235**, 3250.
4. M. Cohn and T. R. Hughes, Jr., *J. Biol. Chem.*, 1962, **237**, 176.
5. E. L. Hahn, *Phys. Rev.*, 1950, **80**, 580.
6. J. Eisinger, R. G. Shulman, and W. E. Blumberg, *Nature (London)*, 1961, **192**, 963.
7. M. Cohn and J. S. Leigh, *Nature (London)*, 1962, **193**, 1037.
8. A. S. Mildvan and M. Cohn, *Adv. Enzymol.*, 1970, **33**, 1.
9. M. Cohn and J. Reuben, *Acc. Chem. Res.*, 1971, **4**, 214.
10. M. Cohn and G. H. Reed, *Annu. Rev. Biochem.*, 1982, **51**, 365.
11. A. Kowalsky and M. Cohn, *Annu. Rev. Biochem.*, 1964, **33**, 45.
12. B. D. Nageswara Rao, in *Phosphorus-31 NMR Principles and Applications*, ed. D. G. Gorenstein, Academic Press, Orlando, FL, 1984, Chap. 3.
13. M. Cohn, *Annu. Rev. Biophys. Bioeng.*, 1982, **11**, 23.
14. M. Cohn, *Acc. Chem. Res.*, 1982, **15**, 326.

Biographical Sketch

Mildred Cohn. *b* 1913. B.A., 1931, Ph.D., 1938, Chemistry, Columbia University, USA. Research associate, Biochemistry, Cornell Medical College, 1938–46. Research associate, then Associate Professor, Biochemistry, Washington University School of Medicine 1946–60 where she was introduced to NMR by Sam Weissman. Faculty, Biophysics and Biochemistry, University of Pennsylvania 1960–82, Professor Emeritus, 1982–present. Approximately 150 publications. Research specialties: ^{31}P NMR, paramagnetic effects on relaxation rates applied to enzyme systems.

Corio, Paul L.: High-Resolution NMR at Columbia University

Paul L. Corio

University of Kentucky, Lexington, KY, USA

I began my second year of graduate study working with Richard Noyes on a problem in chemical kinetics, my first task being the synthesis of a cyclic compound containing two adjacent sulfur atoms. After some disquieting experiences with superheated steam coursing angrily through a crudely constructed still, I obtained about 50 mL of product, a clear, viscous liquid, which polymerized overnight. I rolled the pliable polymer between my palms into a sphere and, bouncing it, discovered that it had a remarkably high coefficient of restitution. A few days later, however, a persistent, irritating rash erupted on both hands, rendering further chemical research impossible. I thought about physics or mathematics, but a friend persuaded me to speak to Ben Dailey, who had just spent a summer working with Jim Shoolery at Varian Associates in Palo Alto. Dailey was enthusiastic about NMR, and wanted to build a spectrometer, starting with a few pieces of commercial equipment and some circuit diagrams provided by Varian—but no magnet! With gloves protecting my bandaged hands, we built the simpler components. Someone at the Watson Laboratories of IBM graciously consented to let us use a Varian 12 in. magnet, so we hauled our nondescript creation over to the laboratories on 115th Street where, to my astonishment, it worked.

There were several notable physicists associated with the Watson Laboratories at the time: Llewellyn H. Thomas, Leon Brillouin, Erwin Hahn, and, somewhat later, Alfred Redfield. Hahn gave some lectures on magnetic resonance which were quite good, but that was a judgement I was only able to make on looking over my notes long after the course was over. Hahn's students were doing spin echo experiments, unfortunately at the same frequency as our high-resolution experiments, and their rf pulses cut through our spectra like a chain saw. The only solution was to work evenings, which had the further advantage that the line voltage settled down. One afternoon, however, I stepped into the laboratory and discovered Hahn behaving very strangely. He stooped before the 12 in. magnet and, still stooping, waddled up to the magnet like a duck, all the while twirling a small, metallic loop with his forefingers, rotating one finger about the other. When he reached the magnet, he stopped for a moment, then, still stooping, waddled backward, this time reversing the twirling motion of his fingers. I decided that it would be wise to leave, when Hahn stood up and, noting my evident dismay, hastily explained he was trying to demagnetize his watch by taking it through a hysteresis loop. When my watch was subsequently magnetized, I tried Hahn's procedure—late at night, when no one was about. It didn't work. I don't believe Hahn ever had the right time.

Dailey and I started looking at the spectra of monosubstituted benzenes, and though our interpretations were qualitatively correct, improvements in resolution were so remarkable within a few months that I couldn't bear to look at spectra that once seemed beautiful. Field inhomogeneity was the principal problem, and Ben got the money for a new 12 in. Varian magnet, which had to be hoisted to the eighth floor of the Chandler Chemistry Laboratories. A pulley system was rigged upon the roof, and a winch in the back of a small pick-up truck started hoisting the magnet skyward. As the magnet rose, so did the tail end of the truck, to an angle of 30 ° when the magnet was four stories high. The lift was not successfully accomplished until a half-dozen workmen mounted the rear of the truck.

After we were established in our own laboratory, resolution improved markedly, and I became interested in understanding the fine structure we were observing. The papers from which I profited most were those of Hahn and Maxwell,[1] Gutowsky, McCall, and Slichter,[2] and Anderson.[3] The papers by Hahn and Maxwell gave the first exact calculations for what are now known as the AB and A_2B systems. The calculations were simple examples of matrix mechanics, and I began an assiduous study of the problem, interrupted only when Dailey arranged for me to spend some time at Varian Associates, where I met Wes Anderson and Jim Shoolery, and, at Stanford, Jim Arnold (whose permanent magnet set an extraordinary standard for resolution) and Felix Bloch. Wes Anderson was working on the application of the moment method to high-resolution spectra, and I calculated the moments of *o*-dichlorobenzene for him with a planimeter. I've always thought the moment method was the most elegant approach to spectral analysis; unfortunately, error accumulation in the determination of the higher moments is considerable. When I returned to Columbia, I worked out the details of the method and gave a seminar on it, using a strongly coupled three-spin system as an example. The method was subsequently published by Anderson and McConnell,[4] but the development I gave in a review article[5] is essentially Anderson's original version.

The most useful results of my work on high-resolution spectra were the proofs of a few theorems, the first use of computers in the analysis of spectra,[5] and the decomposition of a complex spectrum into the superposition of the spectra of its irreducible components,[6,7] leading to the complete or partial analyses of some spectra by inspection.

Later, at the Paulsboro Laboratories of the Mobil Oil Corporation, Irving Weinberg and I set up an extremely stable high-resolution system operating at 40 MHz. We installed an independent water supply to the magnet and used a motor generator to provide a stable line voltage. A large, wooden box with a door of transparent plastic enclosed the magnet, and had small circulating fans inside the box to eliminate temperature gradients. With this system, together with cycling magic and humble invocations, we were able to resolve line spacings between 0.2 and 0.3 Hz, before the advent of superstabilizers.

REFERENCES

1. E. L. Hahn and D. E. Maxwell, *Phys. Rev.*, 1951, **84**, 1246; *ibid.*, 1952, **88**, 1070.
2. H. S. Gutowsky, D. W. McCall, and C. P. Slichter, *J. Chem. Phys.*, 1953, **21**, 279.
3. W. A. Anderson, *Phys. Rev.*, 1956, **102**, 151.
4. W. A. Anderson and H. M. McConnell, *J. Chem. Phys.*, 1957, **26**, 1496.
5. P. L. Corio, *Chem. Rev.*, 1960, **60**, 363.

6. P. L. Corio, *Structure of High-Resolution NMR Spectra*, Academic Press, New York, 1966.
7. P. L. Corio and R. C. Hirst, *J. Chem. Educ.*, 1969, **46**, 345.

Biographical Sketch

Paul L. Corio. *b* 1928. US Navy, 1946–47; A.B., 1953, Columbia College, A.M., 1954, Ph.D., 1957, Columbia University, preceptor, B. P. Dailey. Research associate, Mobil Oil Corporation, 1957–70; Professor of Chemistry, University of Kentucky, 1970–present. Research specialties: nuclear and electron spin resonance, theory of reaction mechanisms, theoretical chemistry.

Cotts, Robert M.: Historical Recollections

Robert M. Cotts

Cornell University, Ithaca, NY, USA

Two main themes in my experimental work in NMR have been (1) translational diffusion and (2) metal–hydrogen systems. These are compatible in that, because of its low mass and relatively small size, hydrogen has a high mobility in metals. Because of space limitations this article covers primarily these two themes with regrettable omissions.

Walter D. Knight introduced me to NMR when I joined his research group early in 1952 at the University of California, Berkeley. In addition to learning to use their CW NMR spectrometer, built around a Pound–Knight marginal oscillator, I built a similar spectrometer for looking at 'pure nuclear quadrupole resonance', NQR. There was considerable interest in perovskite ferroelectrics, and I found the ^{93}Nb (I = 9/2) resonances and measured the NQR interaction parameters in two solid state phases of $KNbO_3$, including observing the transition to its nonferroelectric cubic phase.[1]

I then joined Felix Bloch's group as an Instructor in Physics at Stanford University. With George Pake there on leave from Washington University, and a short visit from E. Raymond Andrew from the UK, line narrowing processes were frequently discussed. Graduate student Lynn R. Sarles and I did a spin decoupling experiment on solid NaF, looking at the ^{23}Na NMR at low power using a marginal oscillator while driving the ^{19}F spins with a 100 W, modified military rf transmitter operating at 17 MHz. Emphasis was on the second moment of the Na resonance.[2] All second moments were obtained by double integration (by hand) from the first derivative of the lineshape on chart paper.

After my move to Cornell University in 1957, graduate student David H. Smith built another CW spectrometer and he grew some good single crystals of thiourea, $SC(NH_2)_2$, an organic ferroelectric for a study using ^{14}N NQR and ^{1}H NMR. A second student, David S. Schreiber, started a project on NMR of lanthanum metal and its alloys to measure Knight shifts in normal and superconducting states. Pure La was hard to obtain. In tracking down the reason for observing a second, shifted La resonance line, he identified it as an impurity, LaH_x. We found this hydride so interesting that it became the project and yielded an abundance of evidence on H atom siting, Knight shifts, a metal–insulator transition, and the effects of H atom motion on both the ^{1}H and ^{139}La NMR lineshapes and relaxation rates.[3] Schreiber built a 1 kW pulsed spectrometer based on the one well-designed and developed at Cornell by W. Gilbert Clark, a student in Donald F. Holcomb's group. In addition to analyzing ^{14}N NQR in thiourea, Smith used the pulse rig to observe a deep T_1 minimum in ^{1}H due to molecular reorientation, and demonstrated cross relaxation between ^{1}H and ^{14}N systems by field cycling experiments.[4] The pulse rig became a laboratory work horse and made many new NMR experiments possible.

I was attracted to the sensitivity of NMR and its use to study atomic motion. David Zamir came on a postdoc from Israel, and in studying diffusion effects of H in NbH_x, he found that at high temperatures the transverse relaxation rate, ${T_2}^{-1}$, did not equal ${T_1}^{-1}$ as it should.[5] From Carr–Purcell pulse trains, the additional rate was identified as attenuation of the ^{1}H spin echo due to H atom diffusion in field gradients caused by susceptibility broadening in the necessarily small metal particles.[6] Thinking about diffusion in small volumes triggered Richard C. Wayne's studying effects of 'reflecting' planar boundaries on diffusion coefficient measurements made using constant magnetic field gradients. As his working substance he used gaseous methane at about 6 MPa.[7] This work stimulated Baldwin Robertson's calculations on restricted diffusion[8] and C. H. Neuman to publish his useful analytic approximations.[9]

James S. Murday built a current source for pulsed field gradients (PFG) and measured the diffusion isotope effect in liquid lithium. He extended Neuman's restricted diffusion theory to the PFG experiment and used the results to correct his data to compensate for finite-sized Li spheres. He also developed means to correct for systematic errors due to background gradients.[10] Of course, visitor Olgierd J. Zogal had no such corrections to make on his D measurements on a 6-mm diameter single crystal of $NbH_{0.6}$.[11] Based on these developments, plant science student Darryl G. Stout devised a way to use PFG echo dependence on gradient strength under highly restricted diffusion conditions to measure the water permeability of membranes of the spherical, small cells of *Chlorella vulgaris*.[12]

Continued concern about systematic errors from background gradients in metal hydride particles led W. David Williams and our collaborator Edward F. W. Seymour from the UK to invent a way to eliminate the nuisance 'cross term' in PFG echo analysis by finding a way to insert the PFG pulses into Carr–Purcell echo trains.[13] Later at Pittsburgh, R. F. Karlicek and I. J. Lowe (KL) found a better way using bipolar gradient pulses. They persuaded us, so Philip E. Mauger built a bipolar pulser of his design and a new pulse rig to measure H diffusion in Group V transition metal hydrides.[14] Elena Sevilla used the KL technique to show the importance of crystal structure in that diffusion parameters are about the same for H in bcc Ti as for other bcc host lattices.[15] Because of the T_2 shortening, the stimulated echo has advantages in PFG experiments, and here with the Johannesburg visitor Michael J. R. Hoch's help, several schemes for reducing and eliminating the 'cross term' were developed and demonstrated.[16]

We developed growing interest in more accurate[11] calculations for determining the mean residence time, τ_d, from relaxation rate measurements. With reliable τ_d values, and independently measured D values from PFG experiments, one could see whether the 'step length' was consistent with an assumed diffusion mechanism. Larry D. Bustard measured both D and τ_d of H in cubic TiH_x to settle an issue over whether H atoms indeed jumped to the nearest neighbor site. Bustard independently developed his Monte-Carlo simulation of atoms hopping on a simple cubic lattice to calculate the pair correlation functions needed to determine τ_d from relaxation data, and he showed that H jumps are to nearest neighbor sites.[17] In a test of such detailed understanding, postdoc Nouha Salibi experimentally confirmed the $\omega^{1/2}$ dependence of ${T_1}^{-1}$ at low NMR frequencies.[18] My last student, Andrew F. McDowell, substantially extended the Monte-Carlo simulation to H in the metallic glass $NiZr_2H_x$, to see how a realistic distribution of site and/or barrier energies affect the NMR relaxation peak curves, and

in comparing these to his experimental data, demonstrated the special importance of barrier energies.[19]

REFERENCES

1. R. M. Cotts and W. D. Knight, *Phys. Rev.*, 1954, **96**, 1285.
2. L. R. Sarles and R. M. Cotts, *Phys. Rev.*, 1958, **111**, 853.
3. D. S. Schreiber and R. M. Cotts, *Phys. Rev.*, 1963, **131**, 1118.
4. D. H. Smith and R. M. Cotts, *J. Chem. Phys.*, 1964, **41**, 2403.
5. D. Zamir and R. M. Cotts, *Phys. Rev.*, 1964, **134**, A666.
6. D. Zamir and R. M. Cotts, in *Proceedings of the XIIIth Colloque AMPERE*, ed. L. Van Gerven, North Holland, Amsterdam, 1965, p. 276; D. Zamir, R. C. Wayne and R. M. Cotts, *Phys. Rev. Lett.*, 1964, **12**, 327.
7. R. C. Wayne and R. M. Cotts, *Phys. Rev.*, 1966, **151**, 264.
8. B. Robertson, *Phys. Rev.*, 1966, **151**, 273.
9. C. H. Neuman, *J. Chem. Phys.*, 1974, **60**, 4508.
10. J. S. Murday and R. M. Cotts, *J. Chem. Phys.*, 1968, **48**, 4938; *ibid.*, *Z. Naturforsch.*, 1971, **26a**, 85.
11. O. J. Zogal and R. M. Cotts, *Phys. Rev. B*, 1975, **11**, 2443.
12. D. G. Stout, P. L. Steponkus, L. D. Bustard, and R. M. Cotts, *Plant. Physiol.*, 1978, **62**, 146.
13. W. D. Williams, E. F. W. Seymour, and R. M. Cotts, *J. Magn. Reson.*, 1978, **31**, 271.
14. P. E. Mauger, W. D. Williams, and R. M. Cotts, *J. Phys. Chem. Solids*, 1981, **42**, 821; A. F. McDowell, P. E. Mauger, and R. M. Cotts, *J. Less-Common Met.*, 1991, **172–174**, 624.
15. E. H. Sevilla and R. M. Cotts, *Phys. Rev. B*, 1988, **37**, 6813.
16. R. M. Cotts, M. J. R. Hoch, T. Sun, and J. T. Markert, *J. Magn. Reson.*, 1989, **83**, 252.
17. L. D. Bustard, R. M. Cotts, and E. F. W. Seymour, *Phys. Rev. B*, 1980, **22**, 12; L. D. Bustard, *Phys. Rev. B*, 1980, **22**, 1.
18. N. Salibi and R. M. Cotts, *Phys. Rev. B*, 1983, **27**, 2625.
19. A. F. McDowell and R. M. Cotts, *Z. Phys. Chem.*, 1994, **183**, 65.

Biographical Sketch

R. M. Cotts. *b* 1927. B. S., University of Wisconsin, 1950, Madison, Ph.D., 1954, University of California, Berkeley. Introduced to NMR by W. D. Knight. Faculty in Stanford University, 1954–57; Cornell University, 1957–present. Approx. 55 publications. Research interests: study of physics in condensed matter, including applications of NMR and NQR, translational diffusion in solids and liquids, and motion and siting of hydrogen in transition and rare earth metals.

Crooks, Lawrence E.: Field Strength Selection for MR Imaging

Lawrence E. Crooks
University of California, San Francisco, CA, USA

INTRODUCTION

I joined the University of California San Francisco's Radiology Department in 1976 to work on NMR imaging (later MR imaging). The first task was to get a new Varian 4-in. gap electromagnet working and produce rat images. The magnet was designed to operate at 0.35 T for its specified homogeneity. This magnet was similar to one used by Hinshaw at Nottingham to produce animal and wrist images[1–3] at 0.7 T. He used ac gradients to produce sensitive points and lines. These sensitive point and line scans were my first choice of technique since I had inherited a continuous wave (CW) system. Although the CW nature of the ac gradient imaging was a good match, the ac gradients were incompatible with the field modulation required by the lock-in-amplifier output section of the receiver. I eventually used a sensitive point technique like Damadian's[4,5] to image phantoms and a rat by moving them through the sensitive point.[6] These crude images were sufficiently impressive that the laboratory director, Leon Kaufman, convinced Pfizer Medical Systems to support our development of a whole body imager.

I began the simultaneous design and construction of a pulsed FT electronics package and the search for a suitable human-sized magnet. My experience was with electromagnets at 0.23 T (with J.R. Singer) and the Varian unit above. I detested the field drift of these units and considered a field stabilizer in the presence of pulsed gradients to be a tougher problem than I wanted to solve. The typical human-sized imaging magnets of the time were four coil resistive air core units. Lauterbur was using one, the Aberdeen group was building one, and one group at Nottingham had one on order. These covered the 0.05–0.15 T field range.

CONCEPTUAL LIMITS ON FIELD STRENGTH

In guiding our choice of field strength we had Hoult and Lauterbur's paper[7] on signal-to-noise ratio (S/N) versus field strength as a start. It indicated a 10 MHz maximum (0.23 T) for body imaging. Next was Bottomley's paper[8] on rf penetration into uniform conducting cylinders. Its graphs indicate rapidly increasing penetration loss between 10–30 MHz. My experience at 10 MHz and 15 MHz was positive and a head-sized saddle coil we built would tune at 15 MHz with reasonable capacitors. We thus decided to attempt 0.35 T with the thought that we could reduce the field strength if it was too high.

MAGNET SELECTION

We began our search with Varian, who proposed an iron core electromagnet (like the animal imager turned on its side) scaled to human size. Their first thought was that their usual Rose shim would require a 56-in. diameter pole tip to achieve the same homogeneity (in ppm) as our animal imager over a head size volume. They considered this too large to handle and would investigate better shimming methods. Fortunately we never pursued this any further.

At this time I attended the 19th ENC in Blacksburg, VA (April 1978) to hear reports on progress by Damadian, Hoult, Lauterbur, and Mansfield. During the meeting I met Richard Woods from Intermagnetics General Corporation. Mr. Woods was an enthusiastic proponent of superconducting magnets for imaging. IGC had built a 2 T monkey-size magnet for Joe Battocletti's blood flow research. Although our size and homogeneity requirements were much better than that magnet, he thought both were achievable and our field strength rather modest. When I asked about field stability, the persistent superconductor was exquisite compared to any other magnet type. At that year's Gordon Research Conference (August) I met Derek Shaw from Oxford Instruments, Oxford. Dr. Shaw was much more conservative about superconductive magnets since Oxford was working on four coil resistive air core designs. After returning to England he later contacted us with a superconductive design proposal.

Our contacts at Pfizer Medical Systems were pleased with the superconducting magnet idea. One thought it sounded so sexy that no doctor would pass it up. The usual concern we encountered within our radiology department was 'You're going to have cryogens in the hospital!?' That did not seem to concern Pfizer and we proceeded to visit Oxford and IGC to review the designs and so that Pfizer could assess the companies. Based on business and technical aspects, Pfizer decided to order a magnet from Oxford for placement in our laboratory. Oxford at the same time built a similar magnet for EMI that was placed in Hammersmith Hospital. It worked before ours, but at 0.15 T.

During the year and a half construction and installation period, we used our pulsed FT system to image rat populations with induced diseases in the Varian magnet. We measured T_1 and T_2 of normal and abnormal tissue to begin quantifying the disease detection characteristics of MR imaging.[9–11] We refined imaging techniques and electronics in anticipation of the arrival of the bigger magnet.

Once the magnet was working, we had the challenges of getting the Oxford gradient power supplies to behave and then compensate the eddy currents, and getting rf coils to work effectively. We still have today the copper mesh screen room we built to house the imager. The room included the gradient power supplies since that was easier then building filters that removed rf from the gradients but would not make the power supplies oscillate.

IMAGING RESULTS

Our first head image was a line scan on 7 March 1981. We had concentrated on line scanning because of Leon Kaufman's concern that 'reconstruction' methods would suffer the nasty motion artifacts prevalent in X-ray CT at that time. The S/N

advantage of two-dimensional Fourier transform (2D FT) MR imaging[12,13] and its wider contrast range than X-rays turned out to hide these artifacts. I converted to 2D FT imaging with a 10-times gain in S/N.

These were good images compared to what others were achieving.[14–19] Measuring gray and white matter relaxation times provided refinements to image contrast. Human abdominal imaging used the relaxation times from our rats. Ongoing improvements in rf shielding and coils, and eddy current performance got us to great image quality level by November 1981.[20,21]

Our demonstration of the lack of rf penetration problems and effective head and body coils at 15 MHz with superior S/N began a race to ever higher field strengths. Increasing field strength gained S/N as rf coil performance improved. However, changing relaxation times and chemical shift detract from the image quality so that the actual improvement is less than expected. These topics have been actively debated.[22–26]

CONCLUSIONS

Today the most common field strength is 1.5 T with 0.5 T gaining in popularity. Head imaging at 3 T and 4 T is gaining interest for functional brain imaging[27] due to the dependence on magnetic susceptibility. At these frequencies, rf penetration and dielectric resonances are appearing, so we are encountering some of the expected limits. Instead of going to higher field strengths, our laboratory moved down to 0.065 T. This gave a less expensive more open imager.[28] The challenge is to extract the most S/N and take advantage of the shorter T_1 relaxation times of tissue to improve disease detection.

The high-field race occurred in an environment of performance at any price. Today health care reform is increasing the emphasis on economics. This may slant the choice of imagers to lower field strengths that are today as diagnostically effective as higher field imagers were a few years ago.

REFERENCES

1. E. R. Andrew, P. A. Bottomley, W. S. Hinshaw, G. N. Holland, W. S. Moore, and C. Simaroj, *Phys. Med. Biol.*, 1977, **22**, 971.
2. W. S. Hinshaw, P. A. Bottomley, and G. N. Holland, *Nature (London)*, 1977, **270**, 722.
3. W. S. Hinshaw, E. R. Andrew, P. A. Bottomley, G. N. Holland, W. S. Moore, and B. S. Worthington, *Br. J. Radiol.*, 1979, **52**, 36.
4. R. Damadian, L. Minkoff, M. Goldsmith, M. Stanford, and J. Koutcher, *Science*, 1976, **194**, 1430.
5. R. Damadian, M. Goldsmith, and L. Minkoff, *Physiol. Chem. Phys.*, 1977, **9**, 97.
6. L. E. Crooks, T. P. Grover, L. Kaufman, and J. R. Singer, *Invest. Radiol.*, 1978, **13**, 63.
7. D. I. Hoult and P. C. Lauterbur, *J. Magn. Reson.*, 1979, **34**, 425.
8. P. A. Bottomley and E. R. Andrew, *Phys. Med. Biol.*, 1978, **23**, 630.
9. G. Hansen, L. E. Crooks, P. Davis, J. DeGroot, R. Herfkens, A. R. Margulis, C. Gooding, L. Kaufman, J. Hoenninger, M. Arakawa, R. McRee, and J. Watts, *Radiology*, 1980, **136**, 695.
10. P. L. Davis, L. Kaufman, L. E. Crooks, and T. R. Miller, *Invest. Radiol.*, 1981, **16**, 354.
11. R. Herfkens, P. Davis, L. Crooks, L. Kaufman, D. Price, T. Miller, A. R. Margulis, J. Watts, J. Hoenninger, M. Arakawa, and R. McRee, *Radiology*, 1981 **141**, 211.
12. A. Kumar, D. Welti, and R. R. Ernst, *J. Magn. Reson.*, 1975, **18**, 69.
13. L. Crooks, *Progr. Abs. 22nd Exp. NMR Conf.*, 1981, VII-4.
14. J. Hutchison, W. A. Edelstein, and G. Johnson, *J. Phys. E*, 1980, **13**, 947.
15. J. A. O. Besson, A. I. M. Glen, E. I. Foreman, A. MacDonald, F. W. Smith, J. M. S. Hutchison, J. R. Mallard, and G. W. Ashcroft, *Lancet ii*, 1981, 923.
16. R. C. Hawkes, G. N. Holland, W. S. Moore, and B. S. Worthington, *J. Comput. Assist. Tomogr.*, 1980, **4**, 577.
17. G. N. Holland, R. C. Hawkes, and W. S. Moore, *J. Comput. Assist. Tomogr.*, 1980, **4**, 429.
18. I. R. Young, M. Burl, G. J. Clark, A. S. Hall, T. Pasmore, A. G. Collins, D. T. Smith, J. S. Orr, G. M. Bydder, F. H. Doyle, R. H. Greenspan, and R. E. Steiner, *Am. J. Roentg.*, 1981, **137**, 895.
19. I. R. Young, D. R. Bailes, M. Burl, A. G. Collins, D. T. Smith, M. J. McDonnell, J. S. Orr, L. M. Banks, G. M. Bydder, R. H. Greenspan, and R. E. Steiner, *J. Comput. Assist. Tomogr.*, 1982, **6**, 1.
20. L. Crooks, M. Arakawa, J. Hoenninger, J. Watts, R. McRee, L. Kaufman, P. L. Davis, A. R. Margulis, and J. De Groot, *Radiology*, 1982, **143**, 169.
21. L. E. Crooks, D. A. Ortendahl, L. Kaufman, J. Hoenninger, M. Arakawa, J. Watts, C. R. Cannon, M. Brant-Zawadzki, P. L. Davis, and A. R. Margulis, *Radiology*, 1983, **146**, 123.
22. P. A. Bottomley, W. A. Edelstein, H. R. Hart, J. F. Schenck, L. S. Smith, W. M. Leue, O. Mueller, and R. W. Redington, *Sci. Progr. 2nd Annu. Meet. Soc. Magn. Reson. Med.*, 1983, 55.
23. L. E. Crooks, M. A. Arakawa, J. C. Hoenninger, B. McCarten, J. C. Watts, and L. Kaufman, *Sci. Progr. 2nd Annu. Meet. Soc. Magn. Reson. Med.*, 1983, 100.
24. W. A. Edelstein, *Sci. Progr. 3rd Annu. Meet. Soc. Magn. Reson. Med.*, 1984, 202.
25. L. Kaufman and L. Crooks, *Sci. Progr. 3rd Annu. Meet. Soc. Magn. Reson. Med.*, 1984, 403.
26. L. E. Crooks, M. Arakawa, J. Hoenninger, B. A. McCarten, J. Watts, and L. Kaufman, *Radiology*, 1984, **151**, 127.
27. K. K. Kwong, J. W. Belliveau, D. A. Chesler, I. E. Goldberg, R. M. Weisskoff, B. P. Poncelet, D. N. Kennedy, B. E. Hoppel, M. S. Cohen, R. Turner, H.-M. Cheng, T. J. Brady, and B. R. Rosen, *Proc. Natl. Acad. Sci. USA*, 1992, **89**, 5675.
28. L. Kaufman, M. Arakawa, J. Hale, P. Rothschild, J. Carlson, K. Hake, D. Kramer, W. Lu, and J. Van Hetern, *Magn. Reson. Q.*, 1989, **5**, 283.

Biographical Sketch

L. E. Crooks. *b* 1949. B.S., 1971, M.S., 1973, and Ph.D., 1978, Electrical Engineering and Computer Science, University of California, Berkeley. Introduced to NMR by J. R. Singer. Faculty in Radiology, University of California, San Francisco, 1976–present. More than 100 papers and 14 patents on MR imaging. Research interests are the use of MR for medical imaging and the associated instrumentation.

Dadok, Josef: High-Field NMR Instrumentation

Josef Dadok

Carnegie Mellon University, Pittsburgh, PA, USA

INTRODUCTION

In 1957 I entered the field of NMR instrumentation while working at the Institute for Scientific Instruments of the Czechoslovak Academy of Sciences in Brno, Czechoslovakia. There I headed a group engaged in building a microwave spectrometer for the 1.25 cm K-band. At that time it was very difficult to obtain components for the K-band in Czechoslovakia (they were on the embargo list) and therefore my deputy O. Chramosta and I both welcomed the proposal by Otto Knessl of the Institute of Organic Chemistry and Biochemistry of the Czechoslovak Academy of Sciences in Prague, to switch to building an instrument for which the resources were available at home. Using the literature and a few ideas of our own, we went through the usual sequence of troubles and frequencies and we were able to produce high-resolution spectra at 30 MHz in 1960, at 40 MHz in 1962, at 60 MHz in 1964, and at 80 MHz in 1967. The technical documentation was given to a company named TESLA BRNO and Czechoslovakia became the only supplier of high-resolution NMR spectrometers for countries in eastern Europe.

We had many amusing experiences during that time, but one of them is perhaps noteworthy. After we observed the first spectra of ethyl alcohol on the screen, it was obvious that the stability of the magnetic field was not as good as the stability of the current we supplied to the magnet. Very soon we started to suspect the line of a trolley bus in our street. Quick calculations revealed that one bus alone could not produce the size of the observed variations and that probably a common cable for more lines had to be there. The supervisor of the city network denied this and therefore we decided to find the source ourselves. Equipped with a big coil with many thousands of turns and with a sensitive galvanometer, we stepped out into the streets and followed the source of magnetic fluctuations. After about half a mile, we ran into a control station for the trolley system and there on the wall we found a diagram that confirmed our suspicion. Obviously, we had talked before to the wrong person. We fixed the problem in two ways: first, we moved to a new location which was at least 200 meters away from another streetcar line and second, we built a flux superstabilizer using a chopper stabilized dc amplifier. Even then we could tell when a train left the closest station by observing the change in the bucking coils current.

SOME 'NEW' IDEAS

At the start of our effort, an external field/frequency lock was being used for long term stabilization and it occurred to me that an internal lock would do better. Using the theory of modulation techniques, I designed an original scheme of homonuclear internal field/frequency lock, only to find out later that Primas,[1] and probably many others, had the same idea.

In the early 1960s I started to work on my Ph.D., thesis concentrating on the factors that limited the sensitivity and resolution of an NMR spectrometer. I studied the lineshape in an inhomogeneous field and, to my surprise, I found an analytical solution for the distribution function of the resonant frequencies of a cylindrical sample in a field with a fourth-order inhomogeneity.[2,3] In combination with the finite length of the receiver coil, it was possible to explain exactly the origin of the so-called 'satellite' at the side of a strong single line which often troubled us during shimming. Around about that time I was trying to visit the USA and participate in the ENC conference in Pittsburgh, but I was never able to obtain an exit visa. It was therefore very rewarding to meet Jim Shoolery, who visited Prague in 1964 and who, of course, was fully qualified to evaluate our work.

In 1965 I sent two abstracts to the ENC but again in vain. Finally in 1966 with some help from the President of the Academy, I was allowed to come to Pittsburgh and that changed my whole life. Three other developments were responsible for that change: Harry Weaver's success in building the first NMR magnet using superconducting wire, my meeting Aksel A. Bothner-By, and then later the Soviet invasion of Czechoslovakia.

HIGH-FIELD NMR AT 250 MHZ

The introduction of superconducting magnets into high-resolution NMR shifted the 'high-field' border above 100 MHz for protons.[4] The need for cryogenics was obvious and it happened that Czechoslovakia was manufacturing helium liquefiers designed originally by the Soviet scientist Kapitsa. I was somewhat discouraged when I saw it, because the liquefier was a big monster. Nevertheless, we started to build a low-temperature laboratory at our institute in Brno (there were plans to use superconducting coils in another major project: electron microscopy) and I was supposed to return to the USA to learn about superconducting magnets for NMR. In October 1967 the political situation was heading toward 'Prague's Spring 68', and I went for a 1 year fellowship to the Mellon Institute in Pittsburgh. As it turned out, I never made it back.

A. A. Bothner-By was heading an NIH NMR facility at MI and wanted to build a high-field spectrometer for 'other' nuclei. It was supposed to be the first shared high-field instrument serving Mellon Institute, University of Pittsburgh, and Carnegie Institute of Technology. He was not able to purchase a suitable superconducting magnet anywhere at that time and decided to take an offer from Westinghouse, where superconductivity was a major R&D project. I was given the task of designing the spectrometer and Richard Sprecher joined us in the overall effort. It turned out that Westinghouse did not have the expertise in high homogeneity magnets and so I found myself very soon not only involved in the mapping of the field, but also in redesigning the main coil and in the design of the superconducting shim coils.[5]

The result was a relatively small persistent magnet for a 250 MHz spectrometer and it was equipped with four superconducting shim coils. After adding 10 room-temperature

Figure 1 The first 250 MHz high-resolution NMR spectrometer with persistent superconducting magnet and removable current leads

shim coils and an internal field/frequency lock system, we actually ended with a high-resolution spectrometer with resolution better than 0.1 Hz. This was in 1969 and we proudly presented it at the 11th ENC (1970) as the highest operating frequency spectrometer in the world.[6] Only hours later Varian announced their first results at 300 MHz.

During the work on the 250 MHz system we had a very nice collaboration with Frank Anet from UCLA, who was building a 251 MHz system (magnet from Magnion) and with Rex Richards from Oxford University, who was building a 7 T system for ^{31}P spectroscopy (magnet built by Oxford Instruments). Both systems were eventually brought to operation and this probably marked the beginning of the domination of the superconducting NMR magnet market by Oxford Instruments.

Besides the design of the shim coils, based on ideas published by W. Anderson,[7] I also applied in a more extensive way the time sharing pulse modulation introduced originally by Arnold.[8] A set of exchangeable receiver coils of our design and a set of exchangeable filters provided the multinuclear capability. Rich was trying to optimize the dimensions of our magnet leads and he found (not surprisingly) that the best leads are no leads at all. He therefore designed the first removable leads in an NMR magnet and we started to operate the facility quite routinely. With 0.1 L of liquid He needed per hour, we had to refill once every 4 days.

The spectrometer (Figure 1) was a success and many scientists from around the world came to use it. With the built-in (sometimes too much) flexibility, we could provide spectra of almost any nucleus. It was still the time of predominantly CW techniques but the writing was already on the wall.

SPECTRUM CONTAINING ONLY SPINNING SIDEBANDS

Because of our extensive use of a single receiver coil system, and because of the less than ideal homogeneity of our rf and static fields, we observed some unusual behavior of the spinning sidebands. By more detailed analysis[9] we were able to show, that in the presence of $\boldsymbol{B}_0$ and $\boldsymbol{B}_1$ inhomogeneity, one inhomogeneity can actually compensate for the other. We could then state that the best nonspinning lineshape does not give the smallest spinning sidebands and that the shape of spinning sidebands depends on the direction of spinning and on the sign of the magnetogyric ratio, γ. To check the ideas we then proposed an experiment in which the center band disappears after the spinning of the sample is started. This was achieved by orienting a saddle-shaped coil with B_1 along the z axis in an electromagnet. The only NMR signal generated in that way comes from the x component due to B_1 inhomogeneity and it is almost 100% modulated during spinning of the sample. Many of our colleagues were puzzled and amused when confronted with this experiment.

RAPID SCAN CORRELATION NMR

During the late 1960s, pulsed FT NMR was taking over and it was obvious to us that we needed our own computer. Thanks to the cancellation of another project at Purdue, NIH gave us, in 1971, a modern small mainframe computer, an XDS SIGMA 5. It probably was the first 32-bit computer dedicated fully to NMR. The memory was of a somewhat limited size (64 kb) but it had a relatively fast floating point processor. At that time a digital computer was somewhat opaque to me, but Rich was able to handle it with ease and soon we were trying our first pulsed FT experiment. R. Ernst had just published a paper on stochastic excitation in NMR[10] and Rich thought that we should try it. We immediately ran into a problem: our analog hardware was built for CW and therefore it was narrow-banded. I was browsing through the mathematics of the general Fourier transform theory, realizing that to the first approximation we were looking for the transfer function of a quasilinear system. According to textbooks, this can be done in practice either by slow frequency sweep, pulse excitation followed by FT, or by noise excitation using cross correlation.[11] Theoretically any excitation will do, if it has the proper spectral density function. By intuition I felt that a rapid frequency sweep could have some advantages, but to my surprise I could not find any references in the available literature. I mentioned this 'Gedankenexperiment' to some of my colleagues, but except for Richard Ernst, I mostly met with doubts.

I tried to go through the exact mathematics of such an experiment, but before finding the full analytical expression I saw that cross correlation of two Lorentzian lines recorded with identical sweep rates with 'wiggles'[12] will give a new Lorentzian line without wiggles and of a linewidth given by the sum of the original two lines. Rich promptly wrote the necessary software and in February 1972 we were recording

the first rapid scan correlation spectra at 250 MHz using a chloroform line as the reference. In the next step Rich calculated the theoretical reference line by integrating the Bloch equations. We presented this at the 13th ENC[13] and started to refine the technique while slowly preparing the publication. By digging deeper into the description of the action of the synchronous detector under the rapid scan, I was able to provide Rich with the expression for the zero-width reference line in the frequency domain:

$$R(\omega) = \mathrm{e}^{-j\frac{\omega^2}{2a}\operatorname{sgn}\omega} \tag{1}$$

where a is the sweep rate. This of course simplified the calculation and we continued to add other refinements like resolution enhancement, difference spectroscopy, and others. We learned in the meantime that G. A. Petersson used a line with wiggles for optimum filtering and for sensitivity or resolution enhancement in his thesis.[14] We did not know that after the 13th ENC another group at NIH was intensively working on the detailed theory of the rapid scan experiment[15] and, only after we found out, submitted our communication in a hurry.[16] After that, we used the rapid scan technique extensively and solved along the way many small problems connected with digital frequency sweep, sampling, filtering, homonuclear lock, etc.

To eliminate some truncation problems, we later chose to calculate the theoretical reference line from the time domain response of an infinitely narrow line to rapid scan, which is given by the Fourier transform of equation (1):[17]

$$r(t) = \sqrt{\frac{a}{\pi}}\left[\cos\frac{1}{2}at^2\left(\frac{1}{2} + \operatorname{sgn} t \times C_2\left\{\frac{1}{2}at^2\right\}\right) + \sin\frac{1}{2}at^2\left(\frac{1}{2} + \operatorname{sgn} t \times S_2\left\{\frac{1}{2}at^2\right\}\right)\right] \tag{2}$$

Here C_2 and S_2 are Fresnel integrals. A similar formula was first derived by Bitter et al.[18] from the Bloch equations.

Using this technique for 1D spectra offers some advantages such as low rf transmitter power, very selective tailored excitation and simple water signal suppression, but for 2D spectroscopy the pulse technique is without competition. There were attempts to incorporate the rapid scan correlation technique into commercial spectrometers, but not with much success. Only Hitachi is using it now in a simple field sweep 60 MHz instrument. We were using it exclusively at 250 MHz and are using it routinely even now at 620 MHz for some experiments.

HIGH-FIELD NMR AT 600 MHZ

While the 250 MHz spectrometer was in intensive use from 1969 to 1978, we were thinking about a new project, possibly at higher fields. As sometimes happens, at the same time General Electric was looking for some new applications of their recently developed Nb_3Sn superconducting tape. In September of 1970, their market development manager Paul Swartz sent us a letter with a piece of Nb_3Sn tape attached to it, and informed us that they could build a nonpersistent superconducting magnet for us with a field of 11.75 T. At that time the commercially available NMR magnet was 7.05 T. When we confronted Paul with the demands for homogeneity and stability of an NMR magnet, he admitted that this was too much for them at that time. But he was back two years later as the vice president of the GE spin-off called Intermagnetics General Corporation (IGC) with a proposal for a magnet, where the stability problems would be handled by a superconducting cylinder in the bore. It would provide some sort of flux stabilization while using a current supply of high stability and an NMR feedback. In the meantime a 360 MHz Bruker system with an Oxford Instruments NbTi persistent magnet was in operation at Stanford and therefore we proposed to raise the field as high as possible.

IGC agreed to move the field up to 14.1 T (600 MHz for protons) and in the summer of 1975 we were able to get the first phase of the funding from NSF. This was a surprise to some members of the NMR community, because they were convinced that there was no way to achieve the necessary stability and homogeneity for high-resolution NMR with a superconducting magnet utilizing Nb_3Sn tape.

In the following three years IGC provided the tape and magnet technology (Dennis Markiewicz, Ed Mains, and Mike Hennessy) and we helped with the problems of homogeneity and stability. We also supplied an improvised 600 MHz NMR spectrometer for testing at the IGC site. The flexibility of our 250 MHz system was then a big advantage.

The IGC magnet was made of 32 pancakes, each pancake containing two ribbon-wound coils with two leads on the outside (Figure 2). The tape itself was superconducting but

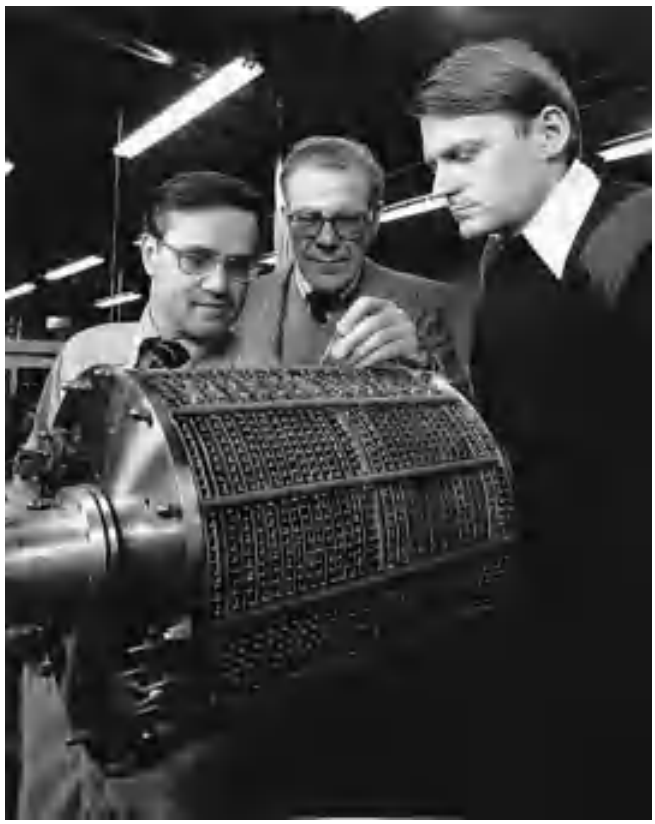

Figure 2 The IGC team checking the coils of the 14 T nonpersistent magnet (Reproduced by permission of Intermagnetics General Corporation)

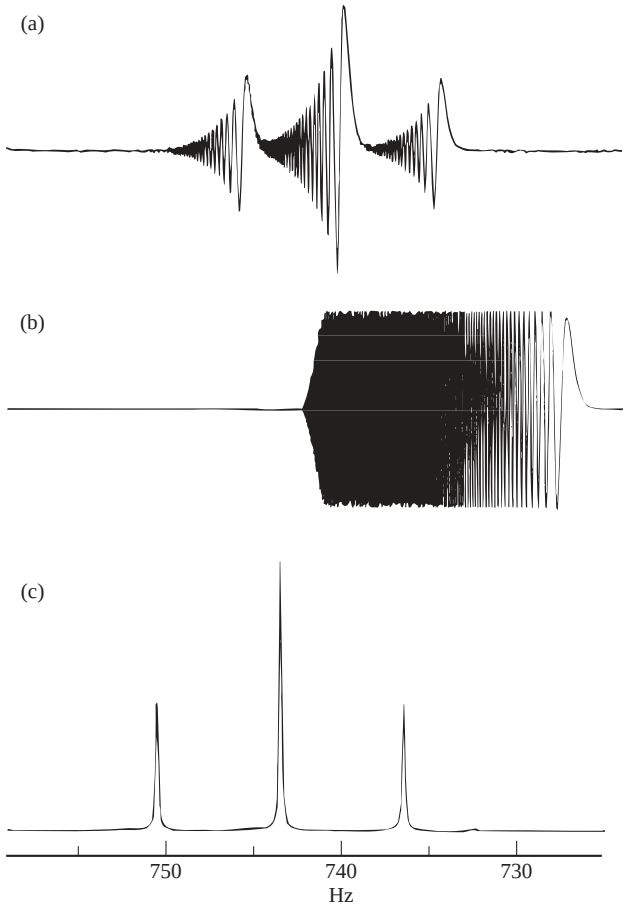

Figure 3 Resolution and short-term stability test at 600 MHz using the rapid scan correlation technique: (a) signal from the CH_3 triplet in 1% ethylbenzene under rapid scan at 1 Hz s^{-1}; (b) reference line calculated from equation (2) but truncated to prevent violation of the sampling theorem; and (c) spectrum resulting from cross-correlation between (a) and (b)

the many joints were not. The flux stabilization using the superconducting cylinder did not perform sufficiently well because of the mechanical stresses on the cylinder, and therefore we decided to go the classical way known from electromagnets. We monitored the voltage across the magnet and through electronic feedback suppressed the changes of the total magnetic flux. The superconducting shimming of the magnet was difficult, especially for the transverse gradients due to the reaction currents in the tape, and hence we abandoned it completely. The homogeneity was adjusted by changing the calculated separation of the pancakes and by the fine tuning of the small central gap. The remaining inhomogeneity was then corrected by a set of room temperature shim coils. By making the receiver coil relatively short (and paying the price of somewhat lower sensitivity), we were able to get quite good resolution. The first spectrum was recorded in April 1977 on the factory floor using a ^{31}P sample at 243 MHz.[19]

The first proton spectra at 600 MHz were recorded in December 1977,[20] and in 1978 we presented the results at two international NMR conferences, in England[21] and in Japan.[22] In York, J. W. Emsley introduced us as the winners of the 600 MHz race. In Nara, Kurt Wüthrich introduced Aksel and me to Felix Bloch and told him what we were doing. His quick comment was: 'I always thought, why don't they go to higher fields?'. By that time the commercial persistent magnets had moved up to 400 MHz.

The final stages of refinement and transfer into a new Dewar were made in 1978 and we moved the magnet to Pittsburgh in February 1979. We started to offer routine spectra at 600 MHz very shortly after that. The resolution (0.15 Hz) and stability were excellent (Figure 3) although we would have enjoyed better sensitivity and smaller spinning sidebands. The conversion from 250 MHz to 600 MHz was done by frequency shifting, using mixers and filters, and in the first two years we operated in the rapid scan correlation mode.[23] In December of 1979 we presented the results and the capability of our instrument to the NMR community at a symposium where users shared their own experiences. Bruker used this opportunity to show the first FT spectra taken at 500 MHz utilizing the latest Oxford Instruments persistent magnet.[24] Our first FT system was put together using an old Bruker WH-90 console with the Aspect 2000 computer. Obviously our first IF frequency was 90 MHz and in 1981 we joined the 2D community.[25]

At that time Mellon Institute suffered many power failures and even a short failure would bring the field down. We therefore designed protective circuitry which would place a short across the magnet and produce a time constant of many hours. Once we installed the protection, Murphy's law stepped in and the power failure occurred only twice during the next 10 years.

The price for the nonpersistency was liquid helium consumption of 0.95 L h^{-1} and with our 65 L reserve it meant filling three times a week. In 1982 we installed our own helium recycling hardware which I liked to call 'an inexhaustible source of entertainment and education', but we were able to cut the cost of operation substantially. With the production rate of 4 L h^{-1} we ran it for three days per week. It is obvious that a persistent magnet has many advantages (low liquid He consumption and easier use for long *n*-dimensional experiments) and consequently besides Oxford Instruments there were other efforts to build them. John Williams at the Francis Bitter National Magnet Laboratory at MIT had solved the problem of persistent joints for high fields among others and eventually built 500 MHz (1979) and 600 MHz (1989) NMR magnets while operating at somewhat reduced temperature (3 K and 2.5 K). It seemed to us, however, that for achieving the highest possible field at a given time the nonpersistent magnet had an edge, and we were able to show that it can be used successfully for high-quality, high-resolution NMR.

In 1985 we bought a Varian 4000 data acquisition console with a Zeta plotter. The new software was more flexible and allowed us to run phase sensitive 2D.[26] For the off-line processing we chose later a Sun Sparcstation computer with the Hare Research Felix program and a 600 dpi laser printer. All the time the laboratory was operating under the name 'NMR Facility for Biomedical Studies' and was supported by NIH until 1990.

For more than eight years this was the only 600 MHz NMR spectrometer in the world. It served in a similar way as the 250 MHz instrument before it, i.e. by providing access to high-field NMR for many scientists from around the country (and some from overseas) who were willing to come to Pittsburgh or at least to send us their samples. A large number of collaborative projects developed, mainly in biochemistry

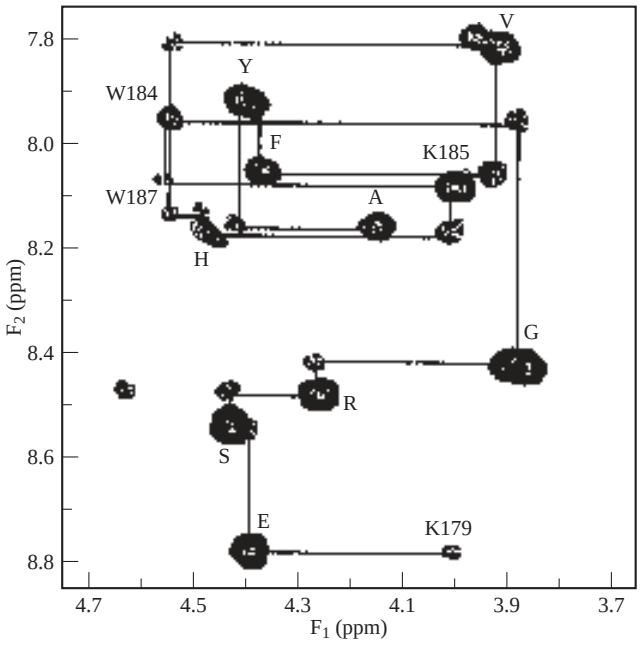

Figure 4 Portion of the 620 MHz COSY (solid contours) and NOESY (dashed contours) spectra, showing sequential assignment for the choline receptor peptide fragment KESRGWKHWVFYA (from a collaborative effort with B. Low)

(Figure 4). A number of new techniques were also introduced in our lab. The most important was CAMELSPIN, conceived by Aksel A. Bothner-By.[27] In connection with the observation of high-field orientation effects,[28] we developed precise measurements of very small and poorly resolved splittings by cosine division or by tailored resolution enhancement,[29] and precise measurement of large (^{13}C, ^{1}H) splittings by cross correlation of spectral segments. In 1984, in collaboration with C. A. Fyfe, we recorded the first ^{29}Si and ^{27}Al MAS spectra of zeolites at 14 T.[30] In 1986 we increased the operating frequency to 620 MHz and actually observed slightly better homogeneity. In the same year Bruker Instruments demonstrated the first commercial 600 MHz spectrometer with a persistent Oxford Instruments magnet. In 1991 we recorded a few spectra at 630 MHz and we think that we could go up to 650 MHz, but the risk of a possible damaging quench makes such a move questionable.

During the 15 years of operation we had only two accidents where we were forced to de-energize the magnet. Both happened during the first years, before we put a fence around our magnet. In one of them a technician offered the magnet a pair of cutting pliers in his rear pocket. The pliers stopped close to the center of the bore after piercing a 10-mm Teflon plate.

THE 900 MHZ PROJECT

While the 620 MHz system operation was underway, we started to plan the next stage. Bert Wang from Lawrence Livermore National Laboratory (LLNL) had just started his private enterprise and he was willing to try to go up with the field to 21 T. We submitted a joint proposal to NIH in 1984, but it was turned down. In 1985 we tried again with IGC (Dennis Markiewicz) and with LLNL (John Miller, Don Slack), and in 1987 the first phase of a 900 MHz system development was under way. The goal was to develop superconducting wire for a 21.15 T magnet which would operate at 1.8 K, and to perform a test on a scaled-down coil. If successful, we would build the final version of the magnet and electronics during the second phase. The wire development called for doping the Nb_3Sn multifilament wire with tantalum, and it ran into a series of difficulties. The test on the small coil was delayed, but thanks to intensive cooperation of IGC and LLNL the coil was finally built in 1990 and in September we were able to perform the test successfully. The coil was placed into a 1.8 K Dewar inside a huge 10-T superconducting magnet at LLNL, and was then energized. The test was monitored from a big control room and the atmosphere was similar to that of a rocket launch; everybody was quite tense and there were congratulations after the final quench. We reached a maximum field of 20.4 T as planned[31] and the remaining 0.6 T would be achieved by a small reduction of the operating current density.

Unfortunately we were not able to obtain funding for the second phase, i.e., for the building of the whole 900 MHz system. It can be expected that other groups in the future will try to move up to an operating frequency of 900 or even 1000 MHz. In the meantime, Oxford Instruments and Bruker Instruments have both announced persistent magnets for 750 MHz. The proton spectra displayed at the 34th ENC (1993) have confirmed again that there is no substitute for NMR at high field and that the upper limit in operating frequency is still far away.

REFERENCES

1. R. Ernst and H. Primas, *Discuss Faraday Soc.* 1962, **34**, 43.
2. J. Dadok, Ph.D. Thesis, Institute for Scientific Instruments, Brno, Czechoslovakia, 1963.
3. J. Dadok, *7th ENC*, Pittsburgh, PA, 1966.
4. F. A. Nelson and H. E. Weaver, *Science*, 1964, **146**, 223.
5. J. Dadok, *10th ENC*, Pittsburgh, PA, 1969.
6. J. Dadok, R. F. Sprecher, A. A. Bothner-By and T. Link, *11th ENC*, Pittsburgh, PA, 1970.
7. W. A. Anderson, *Rev. Sci. Instrum.*, 1961, **32**, 241.
8. W. A. Anderson, *Rev. Sci. Instrum.*, 1962 **33**, 1160. Reference [15] of this paper attributes the pulse modulation technique to J. T. Arnold.
9. J. Dadok, *12th ENC*, Gainsville, FL 1970.
10. R. R. Ernst, *J. Magn. Reson.*, 1970, **3**, 10.
11. K. G. Beauchamp, *Signal Processing*, Wiley, New York, 1973.
12. B. A. Jacobsohn and R. K. Wangsness, *Phys. Rev.*, 1948, **73**, 942.
13. J. Dadok and R. F. Sprecher, *13th ENC*, Asilomar, CA, 1972.
14. G. A. Petersson, Ph.D. Thesis, California Institute of Technology, 1970.
15. R. K. Gupta, J. A. Ferretti, and E. D. Becker, *J. Magn. Reson.*, 1974, **13**, 275.
16. J. Dadok and R. F. Sprecher, *J. Magn. Reson.*, 1974, **13**, 243.
17. M. Abramowitz and A. I. Stegun, *Handbook of Mathematical Functions*, Dover Publications, New York, 1968.
18. F. Bitter, N. L. Alpert, C. G. Lehr, S. T. Lin, and H. L. Poff, *MIT Res. Lab. Electron., Quart. Progr. Rep.*, 1947, p. 26.
19. J. Dadok and A. A. Bothner-By, Poster, *18th ENC*, Asilomar, CA, 1977.
20. J. Dadok and A. A. Bothner-By, *19th ENC*, Blacksburg, VA, 1978.

21. J. Dadok, A. A. Bothner-By, W. D. Markiewicz, M. Hennessy, and P. Swartz, *4th Int. Meet. NMR Spectrosc., York, UK, 1978*.
22. J. Dadok, A. A. Bothner-By, W. D. Markiewicz, M. Hennessy, and P. Swartz, *VIIIth Int. Conf. NMR in Biol. Systems, Nara, 1978*.
23. A. A. Bothner-By and J. Dadok, *NMR Spectroscopy: New Methods and Applications*, *ACS Symposium Series*, 1982, 191, 31.
24. F. W. Wehrli, *NMR Spectroscopy: New Methods and Applications*, ed. G. C. Levy, Am. Chem. Soc., Washington, DC, 1982, p. 7.
25. J. T. J. Lecomte and M. Llinas, *Biochemistry*, 1984, **23**, 4799.
26. A. A. Bothner-By and J. Dadok, *Recent Advances in Organic NMR Spectroscopy*, ed. J. B. Lambert and R. Rittner, Norell Press, Landisville, NJ, 1987; K. L. Constantine, A. De Marco, M. Madrid, C. L. Brooks, III, and M. Llinas, *Biopolymers*, 1990, **30**, 239.
27. A. A. Bothner-By, R. L. Stephens, J. M. Lee, C. D. Warren, and R. W. Jeanloz, *J. Am. Chem. Soc.*, 1984, **106**, 811.
28. A. A. Bothner-By, P. J. Domaille, and C. Gayathri, *J. Am. Chem. Soc.*, 1981, **103**, 5602.
29. A. A. Bothner-By and J. Dadok, *J. Magn. Reson.*, 1987, **72**, 540.
30. C. A. Fyfe, G. C. Gobbi, G. J. Kennedy, J. D. Graham, R. S. Ozubko, W. J. Murphy, A. A. Bothner-By, J. Dadok, and A. S. Chesnick, *Zeolites*, 1985, **5**, 179.
31. W. D. Markiewicz, G. M. Giansetta, A. W. Grandin, D. W. Hazelton, D. S. Slack, M. R. Chaplin, S. S. Shea, A. A. Bothner-By, and J. Dadok, *Adv. Cryog. Eng.*, 1991, **37a**, 361.

Biographical Sketch

J. Dadok. *b* 1926. M.S., 1951, Technical University Brno, Czechoslovakia, Ph.D. 1963, Institute for Scientific Instruments of the Czechoslovak Academy of Sciences, Brno. Headed a group responsible for the development of high-resolution NMR spectrometers in Czechoslovakia (1957–67). Involved in design and operation of high-field NMR spectrometers with superconducting magnets in collaboration with A. A. Bothner-By at Carnegie Mellon University in Pittsburgh, PA, 1967–present. Faculty member in Chemistry Department, 1972–present. Research specialties: shimming of superconducting magnets and lineshape analysis, stabilization of nonpersistent superconducting magnets for very high fields, rf probe design, processing of NMR signals by computer. Proposed a new technique for the efficient accumulation of NMR spectra known as rapid scan correlation NMR spectroscopy.

Diehl, Peter: NMR at the Physics Department of the University of Basel, Switzerland (1949–96)

Peter Diehl

Physics Department, University of Basel, Switzerland

When, in autumn 1950, I arrived as a young student at the University of Basel, NMR was already five years old, being used mainly by physicists as a method for measuring unknown spins and magnetic moments of nuclei, although the nitrogen chemical shift had already been observed by Proctor and Yu.[1] In Basel, two people, Alder and Halbach, had just finished the construction of a low-resolution NMR spectrometer and were busy looking for the signals of the ^{175}Lu and ^{176}Lu nuclei as well as for the spin of ^{53}Cr. Alder had previously been working for a year with Bloch's research group at Stanford. In 1953 I had my first contact with NMR, helping to measure the effects of low-frequency field modulation on the signal shape. By then the chemical shift as well as spin–spin coupling were well-established phenomena, and when I started my thesis in 1954 I suggested entry into the field of high-resolution NMR to the director of the Physics Department. He was not very enthusiastic because Alder and Halbach had in the meantime left the Department. His decision was that either I should do research in nuclear physics as all my colleagues, or that as part of my thesis I should construct the spectrometer singlehandedly. Luckily I was naive enough to accept the condition, and started first slowly to improve the magnet field homogeneity winding coils and also fixing thin nickel foils on the pole shoes. As a byproduct, and because the linewidth was still considerable, I studied the quadrupole relaxation of ^{35}Cl in liquids and published my first research paper on this subject in 1956.[2]

The construction of the spectrometer was not easy, particularly because I had to use available electronic parts, e.g. the crystals for the transmitter and for the intermediate frequency amplifier were US army surplus material. The frequencies did not fit so that I had to adjust them by polishing the crystals manually, measuring the polishing time with a stop watch, because I had tested how many kilocycles of frequency increase could be 'rubbed off' per minute.

In 1955, when Bloch was Director General of CERN at Geneva, I visited his research group. Arnold and Anderson showed me their permanent magnet spectrometer system, which having been shipped from Stanford to Geneva never again reached its earlier resolution. They introduced me to the idea of spinning the sample, showing me a large-scale model of a rotating sample tube containing water and aluminum powder.

When the construction of the spectrometer electronics was finished, the magnet was still of insufficient quality for high resolution. It was then decided to buy a Varian magnet and combine it with the home-built 34.2 MHz proton frequency spectrometer.

I vividly remember the moment in 1956 when I first ran the whole system. I had filled the sample tube with wine, of which I had found a few bottles hidden and left below the wooden floor which had to be removed in order to construct the concrete magnet base which was sitting directly on the underlying ground. To my great surprise I immediately saw the water line as well as the famous ethyl alcohol peaks. The time stability of the magnet was still poor, however, and spectra had to be registered either on a wax-paper Sanborn fast recorder or had to be photographed from the oscilloscope screen.

I immediately started to study the influence of hydrogen bonding on the hydroxyl proton shift with my spectrometer[3] and because the shifts were larger and more easily measured I looked at the ^{19}F resonance of BF_3 complex formation with water and organic molecules. This led me to analyze spectra affected by chemical exchange. The results were published as my thesis in 1958.[4] During the period of my thesis we had visitors who stayed in Basel for a year, Proctor and Ogg, who brought considerable NMR experience with them and certainly enriched my NMR knowledge.

After my doctorate I remained at the Physics Department, although what I did was at least halfway between physics and chemistry. The financing of physics research was easier, however, because in these early years the title '*nuclear* magnetic resonance' opened the door to funds for nuclear research.

My thesis had convinced the Director of the Physics Department, as well as some physical chemists active in the local chemical industry, that NMR could be used to solve chemical problems. Consequently, in 1958 money was provided to add a Varian spectrometer to the existing Varian magnet to be run at 56.4 MHz for fluorine and protons.

Using this spectrometer to look at the spectra of substituted benzenes, I was fascinated by the drastic solvent effects, particularly those of benzene; i.e., ASIS.[5] However, precise measurement was impossible, because analysis programs only became operative a few years later.

In 1960 I had a chance to visit the NMR research groups of Richards at Oxford for a few months, where I also met Buckingham, and of Pople at the National Physical Laboratory at Teddington. At Oxford I found a rich collection of *meta*- and *para*-disubstituted benzenes which had earlier been used for IR spectroscopy and which I now reused in order to study the additivity of substituent[6] and solvent effects[7] on the proton shifts. There was also a computer program available for calculating the spectra. So I applied the substituent effects to the prediction of the fluorobenzene spectrum. I spent two months waiting in the 'queue' to use the computer, but the resulting spectrum was disappointingly different from that observed. At Teddington, where I met Abraham, Freeman, and Schäfer, I was fascinated by an idea which Pople had used to simplify the description of a particular spectrum, and was able to prove that the same idea could be generalized for all spectra containing at least one group of weakly coupled nuclei.[8] This was the beginning of subspectral analysis.[9]

Back in Basel I was contacted by a group of organic chemists who were interested in ^{17}O NMR which had already been shown to be feasible. Together with a student, I started working in this field and we soon published the ^{17}O shifts of over 100 compounds.[10]

In 1962 I had a chance to visit the USA for the first time, being invited by the American Chemical Society to a meeting on high-resolution NMR spectroscopy at Boulder, CO. I particularly remember the evenings when, sitting at a round

table drinking large quantities of low alcohol content beer, I had a chance for fascinating NMR discussions with Pople, Schneider, Bernstein, Dailey, Sheppard, Becker, Lustig, and many others.

The probehead which we had bought for running ^{17}O spectra induced me to initiate the field of high-resolution ^{2}D spectroscopy[11] because the Larmor frequencies of the two nuclei are quite close. In our first publication we discussed all the various aspects of the method, i.e. sensitivity, chemical shifts, simplification of spectral analysis, quadrupole relaxation, dipole relaxation by paramagnetic ions, proton decoupling from deuterons by paramagnetic relaxation difference, solvent and isotope effects, the study of selective solvation, as well as kinetic studies.

In 1964 I had another chance to go abroad for a few months in order to cooperate with the research group of Bernstein at the National Research Council, Ottawa. There I applied my method of subspectral analysis to the *sym*-trifluorobenzene molecule whose spectrum had resisted analysis for over a year.[12] In general, subspectral analysis kept me busy until 1967.

Since 1963 I had heard and read about the NMR of molecules oriented in nematic solvents. In addition, I had had the possibility of discussing the method with Saupe in Freiburg and Englert who had taken a job with a pharmaceutical company in Basel. Although the spectroscopy looked rather complex and had been applied almost exclusively to molecules of high symmetry, I entered the field in 1968 together with Khetrapal who had come to Basel as a postdoctoral fellow. Our work advanced rapidly and we were able to publish approximately 1 paper per month on all aspects of this new spectroscopy. We discussed the dependence of the spectra on temperature, concentration, and spinning speed of the sample,[13] and the use of direct and moment methods for their analysis. We analyzed spectra of molecules with low symmetry, detected isotope effects on the molecular orientation, and measured quadrupole coupling constants. We wrote about the existence of the deceptive simplicity in spectra of oriented molecules and, finally, used an electric field to rotate the liquid crystal optic axis in the magnetic field.[14] At that time we were ‘famous’ in the Physics Department for our permanent ‘smell’ of liquid crystals and for our yellow hands. Practically all the available liquid crystals at that time had a yellow color and had to be subjected to considerable heat treatment to become isotropic and dissolve the solute. Heating had to be undertaken in 5-mm glass tubes and usually the samples boiled over.

Our 14th paper on the NMR of oriented molecules was an article which later became a Citation Classic[15]. It was published in the series ‘NMR, Basic Principles and Progress’ (by Springer Verlag), which Fluck, Kosfeld, and I had started in 1969 and which has grown to about 30 volumes in the meantime.

I should not forget to mention that in the 1960s and 1970s the annual Colloquia on NMR Spectroscopy organized in Aachen by Kosfeld, as well as the Experimental NMR Conferences at Pittsburgh, where I met Shapiro, Bothner-By, and Castellano, were very important for the permanent exchange of ideas with other NMR research groups.

In 1968 we modified the LAOCOON program so that it could be applied to spectra of oriented molecules,[16] and in 1971 we demonstrated that the NMR of oriented molecules can be used to study intramolecular motion and barrier heights.[17] The latter paper has been cited over 170 times during the last 20 years.

In 1974, together with Sykora and Vogt, I began to look into the possibility of analyzing spectra automatically by computer. This idea had fascinated me for a long time, especially having experienced together with Burnell the rather tedious work of assigning about 600 transitions in the spectrum of *o*-xylene in order to find out whether the two methyl groups moved in geared motion.[18] We investigated two related strategies. In one we compared the least-squares fit with the problem of finding the deepest crater in the deepest valley of the moon by rolling a sphere on the lunar surface. Obviously, to avoid getting caught in the thousands of relative minima these had to be filled with sand, i.e. the sharp transitions had to be broadened artificially. This basic approach was later on taken up and realized by Binsch.[19] In the second strategy we started from the idea that for automatic analysis a spectrum had to be transformed into a set of mutually independent figures, each describing a specific property of the spectrum. Obviously, the only possible such set had to be integral transforms of the spectrum. After many trials we arrived at the conclusion that Fourier transforms were ideal. In the iterative automatic least-squares fit an increasing number of such transforms were used in combination with a few spectral moments for centering the system at the correct position. In this way the program worked like an analysis by hand, fitting at first the rough features of the spectrum and subsequently the finer details. Although it took a whole year to get our program[20] working, we enjoyed this period of hard work very much and amused ourselves by testing the ‘stupid’ skill of the program which was even able to fit a cross section through the Swiss Alps as a four-spin system.

In 1976 we introduced the study of ^{13}C and ^{15}N satellites in proton spectra of oriented molecules in order to determine not only proton but also carbon and nitrogen positions.[21]

In 1977 we obtained our first Fourier transform 90 MHz spectrometer from Spectrospin-Bruker.

Our next achievement in 1979 was a program [VIBR] for the correction of direct couplings for vibrational motion. These corrections turned out to be particularly important for the determination of C–H bond lengths which, when compared with different methods, had usually turned out to be too long in the spectra of oriented molecules.[22]

There was still one unsolved problem in this field: the apparent structures of molecules were solvent dependent. We attributed this dependence to a correlation between the structure and orientation of the dissolved molecules. The same process had been suggested earlier to explain the direct couplings observed in tetrahedral molecules where the static coupling must be zero.

Already in 1974 I had tried a correlation model in which the molecule existed in two complexed forms with slightly different structures, and showed that the true deformation is usually amplified in the measured spectrum to an unusually large extent.[23] In a more complex approach, in 1975 we interpreted the difference between the observed and vibration corrected structure of benzene and the theoretical hexagon as being due to the continuous deformation of the molecule as a function of its angle of orientation with respect to the liquid crystal director.[24] Finally, with the help of Lounila, we developed a generally valid deformation model[25] and in 1986 constructed the program MASTER.[26] This is able to

derive the solvent-independent molecular geometry, as well as the interaction tensors between the individual molecular bonds and the anisotropic liquid crystal potential which are responsible for the deformation and degrees of order of the solute simultaneously. This actually brought the method of structure determination of oriented molecules into a final form.

In 1987 we obtained a Bruker superconductive 250 MHz spectrometer. During a visit to the Indian Institute of Science in Bangalore in 1989 I started, in cooperation with Khetrapal, to study the interactions of ions with molecules dissolved in liquid crystal solvents.[27] We also tried to deduce the complex geometry from the observed changes in the degrees of order, i.e. from changes in the interaction tensor.[28]

It was again molecular deformation by the liquid crystal which 'pushed' me into an entirely different field of research which at present still keeps us busy. I started with the idea that because tetrahedral molecules are deformed in the liquid crystal, an even 'simpler' charge cloud should also be deformed. The cloud was chosen to be the noble gas ^{131}Xe and the deformation was measured via the quadrupole splitting of the Xe signal.[29] As a by-product of this study, performed in cooperation with Jokisaari and his research group from Oulu, Finland, we noticed the extreme sensitivity of the Xe shift which clearly indicated phase transitions as well as the nature of the liquid crystal phase.[30] This, in turn, led to the question of shift-sensitivity and the solvent effects of noble gases in general i.e. Xe, Kr, Ne and, finally, He. We found a surprising linear relationship between the solvent effects of all the noble gases.[31]

Finally, as a typical example of how research often works by looking for something but finding something else which may be even much more interesting, I mention our latest results on ^{3}He which, by coincidence, we observed not only as a signal from the sample volume but also as a separate signal from the gas diffusing through the glass wall.[32] This means that the well-known shift-sensitive but relatively large probe-nucleus ^{129}Xe, which is used for characterizing the solid state properties of, for example, clathrates and zeolites, has a considerably smaller 'brother', ^{3}He, which is not shift-sensitive but can contribute information via its relaxation behavior and as a probe for measuring local magnetic fields.

NMR studies in the Physics Department of the University of Basel are planned to end in 1996 when I will go on pension. The Department will at last get rid of a permanent 'foreign body' which for the physicists was too chemically oriented, for the chemists too physical, and for physical chemists located in the wrong department. In contrast, I believe that this 'outlaw position' made it possible really to enjoy the freedom of research and I hope that some of our pioneering contributions will permanently survive in this beautiful and endlessly fascinating spectroscopy.

REFERENCES

1. W. G. Proctor and F. C. Yu., *Phys. Rev.*, 1950, **77**, 717.
2. P. Diehl, *Helv. Phys. Acta*, 1956, **29**, 219.
3. P. Diehl, *Helv. Phys. Acta*, 1957, **30**, 91.
4. P. Diehl, *Helv. Phys. Acta*, 1958, **31**, 685.
5. P. Diehl and I. Gränacher, *Helv. Phys. Acta*, 1959, **32**, 288.
6. P. Diehl, *Helv. Chim. Acta*, 1961, **44**, 829.
7. P. Diehl, *Helv. Chim. Acta*, 1962, **45**, 568.
8. P. Diehl and J. A. Pople, *Mol. Phys*, 1960, **3**, 557.
9. P. Diehl, *Helv. Chim. Acta*, 1965, **48**, 567.
10. H. A. Christ, P. Diehl, H. R. Schneider, and H. Dahn, *Helv. Chim. Acta*, 1961, **44**, 865.
11. P. Diehl and Th. Leipert, *Helv. Chim. Acta*, 1964, **47**, 545.
12. P. Diehl, R. G. Jones, and H. J. Bernstein, *Can. J. Chem.*, 1965, **43**, 81.
13. P. Diehl and C. L. Khetrapal, *Mol. Phys.*, 1967, **14**, 283.
14. P. Diehl, C. L. Khetrapal, H. P. Kellerhals, U. Lienhard, and W. Niederberger, *J. Magn. Reson.*, 1969, **1**, 527.
15. P. Diehl and C. L. Khetrapal, *NMR, Basic Principles and Progress*, Springer-Verlag, Berlin, 1969, Vol. 1.
16. P. Diehl, C. L. Khetrapal, and H. P. Kellerhals, *Mol. Phys.*, 1968, **15**, 333.
17. P. Diehl, P. M. Henrichs, and W. Niederberger, *Mol. Phys.*, 1971, **20**, 139.
18. E. E. Burnell and P. Diehl, *Mol. Phys.*, 1972, **24**, 489.
19. D. S. Stephenson and G. Binsch, *J. Magn. Reson.*, 1978, **32**, 145.
20. P. Diehl, S. Sykora, and J. Vogt, *J. Magn. Reson.*, 1975, **19**, 67.
21. P. Diehl, H. Bosiger, A. S. Tracey, and R. Ader, *Org. Magn. Reson.*, 1976, **8**, 17.
22. S. Sykora, J. Vogt, H. Bösiger, and P. Diehl, *J. Magn. Reson.*, 1979, **36**, 53.
23. P. Diehl, S. Sykora, W. Niederberger, and E. E. Burnell, *J. Magn. Reson.*, 1974, **14**, 260.
24. P. Diehl, H. Bosiger, and H. Zimmerman, *J. Magn. Reson.*, 1979, **33**, 113.
25. J. Lounila and P. Diehl, *Mol. Phys.*, 1984, **52**, 827.
26. R. Wasser, M. Kellerhals, and P. Diehl, *Magn. Reson. Chem.*, 1989, **27**, 335.
27. P. Diehl, H. R. Wasser, G. A. Nagana Gowda, N. Suryaprakash, and C. L. Khetrapal, *Chem. Phys. Lett.*, 1989, **159**, 199.
28. N. Suryaprakash, R. Ugolini, and P. Diehl, *Magn. Reson. Chem.*, 1991, **29**, 1024.
29. P. Diehl and J. Jokisaari, *Chem. Phys. Lett.*, 1990, **165**, 389.
30. J. Jokisaari, P. Diehl, and O. Muünster, *Mol. Cryst. Liq. Cryst.*, 1990, **188**, 189.
31. R. Seydoux, P. Diehl, R. K. Mazitov, and J. Jokisaari, *J. Magn. Reson.*, 1993, **A101**, 78.
32. R. K. Mazitov, P. Diehl, and R. Seydoux, *Chem. Phys. Lett.*, 1993, **201**, 543.

Biographical Sketch

Peter Diehl. *b* 1931. Ph.D., 1958, Physics, University of Basel, Switzerland. Postdoctoral work at Oxford (with Rex Richards), Teddington (with John Pople), and Ottawa (with Harold Bernstein). Research Professor, University of Basel, 1964–present. Approximately 200 publications, including 3 books. Research specialties: ^{17}O spectroscopy, spectral analysis, ^{2}D spectroscopy, oriented molecules in liquid crystals, noble gas NMR.

Doddrell, David M.: An Historical Perspective of Research Based Upon Misguided Advice

David M. Doddrell

University of Queensland, Brisbane, Australia

I have often wondered just how a scientific discovery is made; after 27 years as an active researcher I still don't know. Our understanding of the cognitive processes in the brain are so poor that little solitude can, in my view, be obtained by turning to the neuropsychologists to provide a satisfactory explanation. I have always been surprised at the important contribution of serendipity, along with the added ingredient of being at the right place at the right time.

I began research in magnetic resonance in 1967; I had been advised then not to enter the field as it had no future! This is about as good advice as I gave in a lecture at Caltech in 1970 when I stated that I thought that Fourier transform methods in NMR did not have much promise. Predoctoral student days at Indiana University in 1967–70 were exciting times; Art Clouse, an electronics engineer retired from the US Navy, taught me how to set up ^{13}C NMR with ^{1}H decoupling. An old Navy reject frequency source (frequency variation about 100 Hz min^{-1}) provided the proton channel with noise decoupling induced via a double-balanced mixer; off-resonance noise decoupling to count nonprotonated carbons was the outcome of this research,[1] the product of having such an unstable frequency source. Of course, Jack Roberts' group at Caltech had already done these experiments[2] and more, but they had a frequency synthesizer! All this work was done with field or frequency modulation methods not FT techniques. In 1971, I was lucky to be Adam Allerhand's first postdoc. He and Clouse had built an FT spectrometer for ^{13}C NMR and my task was to help measure and understand ^{13}C T_1 and NOE values. Our fear was that they may be uselessly long (we guessed tens of seconds for protonated carbons—thus my comment in 1970 about FT methods). Of course history proved that we were up to a factor of 100 too long in our guess; the major result of this work was that we had developed a simple method of studying solution molecular dynamics which is still in use today.[3] I also consequently understood Solomon's 1955 paper on dipolar relaxation.[4]

In 1979, Morris gave me a copy of his paper[5] with Freeman on INEPT. I was in Canada at the time. On returning to Australia Jim Field and I implemented this pulse sequence; Field built the hardware and I 'played'. It was clear that not only did one get the polarization transfer enhancement as Freeman and Morris claimed, but by changing the appropriate delays CH, CH_2 and CH_3 proton-decoupled carbon signals could be easily distinguished via their phase variation.[6] Overnight, off-resonance decoupling methods were made obsolete. We, at least here in our group when I was at Griffith University, all found the Freeman/Morris explanation of INEPT unsatisfying. David Pegg, a theoretical physicist, came up with the concept of spins rotating in the doubly-rotating frame as a general approach to multipulse methods (we had unwittingly invented another name for multiple quantum effects) and complex vector diagrams were the order of the day.[7] These diagrams did allow Robin Bendall to predict the EPT pulse sequence[8] that was designed to give a proton-decoupled ^{13}C CH subspectrum exclusively. It did, but while pulse programming it I made an error in setting the 'multiple quantum' proton read pulse angle (we did not call it that in 1981) and the DEPT pulse sequence was born.[9] The variation of signal phase dependent on the proton multiple quantum read pulse angle was classic serendipity; we knew what we had done but no simple vector diagram could ever have predicted the result. The theory at the time had to be cast in terms of computing the time evolution of the spin system during the pulse sequence,[10] as with the vector description, not a particularly useful predictive approach to multipulse NMR. In 1982, while on study leave at Cambridge, Ruth Lynden-Bell taught me about product operator algebra.[11] Of course, Packer[12] and Sørensen et al.[13] published different constructions of this algebra and it could be argued that the development of product operator methods was one of the most important advances in NMR in the 1980s. Although DEPT was serendipitous in its genesis but simply understood retrospectively using operator methods, not so with the POMMIE pulse sequence. Mark Bulsing and I reasoned that if polarization transfer could be induced via a multiple quantum read pulse of parametric angle (DEPT) then a 90° pulse with parametric phase must also work. The pulse sequence we published is correct[14] but the original theory as published is wrong; this was subsequently corrected in a later paper.[15]

My education in NMR took a new tack in 1985. I started to learn about pulsed field gradients: we had bought a horizontal magnet system. Whereas the introduction of operator algebra made the understanding of solution state multipulse methods straightforward, pulsed field gradients seemed to defy logic. They induce that curse of NMR spectroscopists, eddy currents. Oh, the ideas were simple, but the 'in practice' implementation of a field gradient pulse sequence in a magnet is a different matter. Even today with shielded gradients there is still a degree of art in setting preemphasis, cross preemphasis, and $\boldsymbol{B}_0$ correction. Sometimes the trimming procedure of a gradient sequence appears to be illogical but achieves the best results. In 1985, Bill Brooks and I started to 'play' with shaped rf pulses; for a sinc pulse we noted the 'well known' linear phase roll with frequency offset and that it could be refocused with a hard 180° pulse; the SPACE image-guided volume selection method was born.[16] The short T_2 encoding of this method allows the observation of the signal from many brain metabolites with better sensitivity than using other volume-selection 'echo' methods; the human spectroscopic applicability of the SPACE method remains problematical, however. Of course, if we had read Fernbach and Proctor's 1955 paper[17] on a phase memory device, SPACE would have been obvious; so might have been slice selection in magnetic resonance imaging.

It was of course natural to attempt 2D NMR in vivo; we had noted that gradients were very effective for water suppression and naturally incorporated them into our volume-selected 2D sequence. We were amazed that we could induce ω_1 quadrature selection without phase cycling. Hurd published similar results[18] for solution state NMR but Freeman had published a gradient enhanced COSY in 1985.[19] But why did gradients induce ω_1 quadrature detection? I simply did

not believe the results and I made Stuart Crozier repeat the experiment using a 'read' gradient of different polarity. Sure enough N or P type selection could be induced simply by changing the gradient polarity.[20] We incorporated gradients into the product operator description of the COSY sequence and the results were readily explainable. While in France in 1990 I did some algebra in my head and proposed a heteronuclear gradient-enhanced experiment.[21] It worked, but not in the way that I had guessed. It took Ian Brereton and me a number of months to sort out that mess; moral — don't take everything for granted, but do guess.

I often reflect on the original advice given in 1967 that NMR had no future. Its inaccuracy has taught me to be guarded in counseling my own students and I look back over the past 27 years and wonder what I would have done if I had listened in 1967. The answer of course is indeterminable.

One last comment. I am often asked the unfair question, 'Except for the discovery of the technique, what was the most important conceptual advance in NMR spectroscopy?' My answer is that Erwin Hahn has a lot to answer for.

REFERENCES

1. E. Wenkert, A. O. Clouse, D. W. Cochran, and D. M. Doddrell, *J. Am. Chem. Soc.*, 1969, **91**, 6897.
2. H. J. Reich, M. Jautelat, M. T. Messe, F. J. Weigert, and J. D. Roberts, *J. Am. Chem. Soc.*, 1969, **91**, 7445.
3. A. Allerhand, D. M. Doddrell, and R. Komoroski, *J. Chem. Phys.*, 1971, **55**, 189.
4. I. Solomon, *Phys. Rev.*, 1955, **99**, 559.
5. G. A. Morris and R. Freeman, *J. Am. Chem. Soc.*, 1979, **101**, 760.
6. D. M. Doddrell and D. T. Pegg, *J. Am. Chem. Soc.*, 1980, **102**, 6388.
7. D. T. Pegg, M. R. Bendall, and D. M. Doddrell, *J. Magn. Reson.*, 1981, **44**, 238.
8. M. R. Bendall, D. T. Pegg, and D. M. Doddrell, *J. Chem. Soc., Chem. Commun.*, **1982**, 872.
9. D. M. Doddrell, D. T. Pegg, and M. R. Bendall, *J. Magn. Reson.*, 1982, **48**, 323.
10. D. T. Pegg, D. M. Doddrell, and M. R. Bendall, *J. Chem. Phys.*, 1982, **77**, 2745.
11. R. M. Lynden-Bell, J. M. Bulsing, and D. M. Doddrell, *J. Magn. Reson.*, 1983, **55**, 128.
12. K. J. Packer and K. M. Wright, *Mol. Phys.*, 1983, **50**, 797.
13. O. W. Sørensen, G. W. Eich, M. H. Levitt, G. Bodenhausen, and R. R. Ernst, *Prog. NMR Spectrosc.*, 1983, **16**, 163.
14. J. M. Bulsing, W. M. Brooks, J. Field, and D. M. Doddrell, *J. Magn. Reson.*, 1984, **56**, 167.
15. J. M. Bulsing and D. M. Doddrell, *J. Magn. Reson.*, 1985, **61**, 197.
16. D. M. Doddrell, W. M. Brooks, J. M. Bulsing, J. Field, M. G. Irving, and H. Baddeley, *J. Magn. Reson.*, 1986, **68**, 367.
17. S. Fernbach and W. G. Proctor, *J. Appl. Phys.*, 1955, **26**, 170.
18. C. H. Sotak, D. M. Freeman, and R. E. Hurd, *J. Magn. Reson.*, 1988, **78**, 355.
19. P. Barker and R. Freeman, *J. Magn. Reson.*, 1985, **64**, 334.
20. I. M. Brereton, S. Crozier, J. Field, and D. M. Doddrell, *J. Magn. Reson.*, 1991, **93**, 54.
21. J. M. Tyburn, I. M. Brereton, and D. M. Doddrell, *J. Magn. Reson.*, 1992, **97**, 305.

Acknowledgements

In a short essay such as this, it is impossible to acknowledge all the co-workers who have made the research possible. There are two exceptions; my wife, Pauline, and Jim Field. My wife's understanding over the years has been remarkable, and Field's ability with a soldering iron unsurpassed.

Biographical Sketch

David M. Doddrell. *b* 1944. B.Sc., 1966, University of Queensland, Ph.D., 1969, Indiana University, D.Sc., 1977, Griffith University. Introduced to NMR by A. Clouse, E. Wenkert, and A. Allerhand. Faculty positions at Griffith University 1974–86, University of Queensland 1986–present. Approximately 220 publications. Research interests: multipulse NMR liquid state applications, in vivo NMR spectroscopy, magnetic resonance imaging, and hardware developments.

Doskočilová, Danica & Schneider, Bohdan: Development of Magic Angle Rotation for the Narrowing of Proton NMR Lines in Organic Materials

Danica Doskočilová & Bohdan Schneider

Academy of Sciences of the Czech Republic, Prague, Czech Republic

In introductions to scientific papers, the state of the art is invariably described together with clearly defined aims. To show how things sometimes actually work, let us tell the story of our development of the magic angle spinning method for applications in proton NMR.

At Christmas time of 1962 we were lucky to install the first commercial NMR spectrometer (JEOL JNM−3−60) in the then Czechoslovakia in the Spectroscopy Department of our institute which was engaged in studies of synthetic polymers. It was equipped both for classical ^{1}H broadline measurements and for ^{1}H high-resolution work in liquids. It was without lock, of course, but it had easy switching from broadline to high-resolution regimes and a very good variable temperature outfit.

By that time the basis of CW ^{1}H high-resolution work in liquids had already been conveniently summarized in the classical book by Pople, Schneider, and Bernstein, and we quickly proceeded to apply it to structural studies of polymers and especially of their model compounds. The weird observation that the PVC dimer model compound—*meso*-2,4-dichloropentane—a molecule with only a mirror plane of symmetry, exhibited equal vicinal coupling constants, $J_{AX} = J_{BX}$, in its ABX_2 spectral pattern led us to realize the existence of rapid conformational interconversions in polymer model compounds, and ultimately in the polymer molecules themselves. For some years subsequently we concentrated on a study of the conformational structure of polymer model compounds by a combination of vibrational and ^{1}H high-resolution NMR spectroscopy, thus establishing a basis for both experimental and theoretical studies of polymer conformation and configuration.

Nevertheless, it quickly became clear that our dear JNM−3−60 was becoming obsolete for high-resolution work in liquids. Moreover, many synthetic polymers do not dissolve in NMR solvents and, even when they do, for most practical purposes they are applied as solids and therefore should be studied as such. Looking around for a way to utilize the remaining excellent properties of our JNM−3−60, the imagination of one of us (B.S.) was caught by the 'magic' of rotational line narrowing (MAR), described by E. R. Andrew and I. J. Lowe in the late 1950s for some inorganic solids. According to theoretically versed physicists, the odds were against us for ^{1}H NMR work: in rigid samples the large dipolar broadening would require virtually inaccessible spinning speeds, whereas in samples with naturally narrowed NMR signals (such as polymers) further line narrowing would be prevented by the existing internal motional frequencies. Nevertheless, we would not be dissuaded from our MAR gadget and actually our first turbine, machined directly from methacrylate glass and spun about a central wire, did give some kind of effect.

During a short visit to Professor Andrew in Nottingham in 1967, B.S. inspected his spinning mechanism with a lower conical bearing and discussed with him all contemporary views of the success (or failure in the case of ^{1}H) of MAR. Agreeing on the fact that a good theoretician should always find an explanation for a positive experiment, they parted as friends. Meanwhile in Prague, in collaboration with our electronics engineer Z. Růžička and the head of the Institute workshop J. Babka, by making use of the excellent skills of the workshop mechanics we built[1] within seven months an apparatus suitable for proton MAR NMR. The probe could be inclined continuously from 90° to 53° with respect to the magnetic field, and permitted direct transition from broadline to high-resolution measurement which was important in our preliminary experiments and attempts at theoretical interpretations. The nitrogen gas propelled turbines were suspended in two conical dynamic gas bearings and reached spinning speeds of up to 10 kHz when machined directly from a suitable solid polymer. We also developed[2] hollow glass turbines which could be spun up to 5 kHz for the measurement of liquids in suspensions or sorbed on powders. To achieve a field homogeneity necessary for high-resolution work at the sample site, the probe housing and gas jet construction were built from nonmagnetic materials. With our very limited conditions at that time, this was only possible thanks to the very profound knowledge and love of exotic materials of Z. Růžička, so that almost anything could be found in his garage (but no car!). At perfect magic angle setting, we could reach a resolution of 3 Hz. Within a short time the apparatus was also modified for operation at variable temperature.[3] To this day, spinning assemblies of very similar type are used in all modern solid state high-resolution NMR spectrometers.

Already in our first communication on the subject,[1] most prospective applications of ^{1}H NMR line narrowing by magic angle rotation had been listed and the criterion for a positive line narrowing effect was stated in terms of the good old theory of Gutowsky and Pake:[4] to obtain line narrowing by magic angle rotation at practically attainable spinning speeds, the static linewidth must be partially narrowed by internal motion which is anisotropic in space, with residual static dipolar interactions. The resulting residual linewidth in the MAR NMR spectrum is limited by the frequency of the internal motion which causes partial narrowing of the static spectrum. The applications included studies of the phase structure in solid polymers, motional frequencies of various proton groups in liquid crystalline polymer solutions, and the structure of swollen cross-linked polymer gels, the latter two applications thanks to the construction of the turbine allowing the measurement of more or less liquid samples.[5] In later developments it was shown that by combining the information from MAR NMR spectra with static lineshape analysis, information could be obtained both on the dynamics of internal motions and on the degree of their spatial anisotropy.[6]

In this work, we were traveling a very lonely path. We made mistakes. We did not patent our apparatus abroad, only in Czechoslovakia, and even that at a rather late date (1971).

In the late 1970s, the advent of pulsed ^{13}C NMR was followed by an explosive interest in the magic angle spinning method (from then on called MAS), and its success quenched any interest in ^{1}H MAR. Having at that time no suitable ^{13}C NMR spectrometer we did not participate in that boom, though some of our previous experience was almost tacitly absorbed in it.

REFERENCES

1. D. Doskočilová and B. Schneider, *Chem. Phys. Lett.*, 1970, **6**, 381.
2. B. Schneider, D. Doskočilová, and J. Jakeš, *Abstr. XXth Congress AMPERE, Tallinn, 1978*, p. 57.
3. B. Schneider, D. Doskočilová, J. Babka, and Z. Růžička, *J. Magn. Reson.*, 1980, **37**, 41.
4. H. S. Gutowsky and G. E. Pake, *J. Chem. Phys.*, 1950, **18**, 162.
5. D. Doskočilová and B. Schneider, *Adv. Colloid. Interface Sci.*, 1978, **9**, 63.
6. D. Doskočilová and B. Schneider, *Pure Appl. Chem.*, 1982, **54**, 575.

Biographical Sketch

Danica Doskočilová. *b* 1925. RNDr., 1949 (electrochemistry), Charles University, Prague, M.Sc., 1948 (physical chemistry), University of Minnessota, Ph.D., 1961 (vibrational spectroscopy), Institute of Antibiotics, Prague. Chief Research Fellow, Institute of Macromolecular Chemistry, Czechoslovak Academy of Sciences, 1961–present. Approx. 100 publications. Research specialties: NMR work, mostly in the polymer field.

Bohdan Schneider. *b* 1927. B.S., 1950, Ph.D., 1954 (theory of vibrational spectra), D.Sc., 1966 (molecular spectroscopy in the polymer field), Institute of Physical Chemistry, Czechoslovak Academy of Sciences. Chief Research Fellow, Institute of Macromolecular Chemistry, Czechoslovak Academy of Sciences, 1960–present. Approx. 250 publications. Research specialties: correlation of NMR results (mostly solid state) with those of vibrational spectroscopy.

Doty, F. David: A Random Walk Toward High-Speed Sample Spinning

F. David Doty

Doty Scientific, Columbia, SC, USA

My introduction to ESR and NMR began under Charlie Poole[1] in the graduate Physics Department at the University of South Carolina. There I became rather well known throughout both the Physics and Chemistry Departments as being unafraid to walk into any instrumentation laboratory and start dismantling equipment. This brazen behavior was tolerated because I would put the instruments back together with improved gadgets I had made (usually without permission) in the machine shop and electronics laboratories.

One spring day in 1979, (***Ellis, Paul D.: Multinuclear MR Experiments, the Surrogate Probe Strategy, and Other Fun & Games***) came looking for me. He needed some kilowatt UHF transmitters and a high-speed sample spinner that really worked to perform his solid state NMR experiments. At the time I was more confident with the transmitters, being well versed in the witchcraft of microwave and rf from ESR and years of TV repair experience. But I had also been rebuilding automobile and tractor engines since early childhood and was keenly interested in turbomachinery—with visions of the Brayton cycle achieving 65% energy conversion efficiency dancing in my brain.

After completing the transmitters and struggling for a few months with the Andrew–Beams spinners, I came to the conclusion that the problems with low-frequency torsional modes (several hundred Hz) and frequent instabilities above 2 kHz could only be solved by going in the general direction that Lippmaa, Veeman, Pines, and others were going: double cylindrical air bearings (see ***Solid State Probe Design***). Paul wanted to look at natural abundance ^{13}C in surface-adsorbed species, so it was necessary to explore the use of high-strength ceramic rotors for improved filling factor (see ***Probe Design and Construction***). We found operation at moderately high spinning speeds to be much more difficult than the early papers seemed to imply—at least with the higher density ceramic rotors. Catastrophic explosions from materials defects were common, so I became very experienced in the precision diamond grinding of hard ceramics. On more than one occasion I would work through the night in the machine shop (my wife Judy would sometimes relieve me at the lathe) so that the NMR experiments could continue the next day.

However, we could not blame all the crashes on ceramics defects, so it was necessary to do a more careful study of gas bearings and microturbines. It was encouraging to find calculated optimum bearing hole size and radial clearance reasonably close to experimentally determined optima, but that didn't make it any easier to eliminate systematic and statistical measurement errors or to reproduce the required dimensions.

Simple calculations eventually convinced us that we were often limited by the 'whirl instabilities' previously reported in gas bearings for dental drills. In church choir one Sunday, while half-dozing and half-listening to the resonant bass from the organ, I worked out the increase in the conical whirl mode that could be expected simply by changing the turbine caps from Lippmaa's design (internally hollowed and filled with sample) to externally hollowed and empty.[2] The improvement proved to be greater than I had expected because of the additional beneficial effect on damping. After another year of constructive criticism from Ruth Inners, Paul Ellis, and J. B. Spitzmesser, my CP MAS probes appeared to be ready for a small commercial venture. In the spring of 1982, a physics colleague Bruce Sofge succeeded in convincing a wealthy friend to loan us approximately $100 000. Judy, J. B., Bruce, and I started Doty Scientific, Inc. So it began.

In June 1986 at the EENC in Bad Aussee, Vagn Langer and Preben Daugaard upset the status quo by demonstrating the design they had developed for Varian with reproducible spinning at surface speeds above 70% of the speed of sound.[3] Vagn was concerned that Varian would now put me out of business. I assured him that he needn't worry. The key difference was obvious upon casual inspection: the gas from Vagn's air bearings was allowed to exit axially in both directions, nearly doubling the area of the effective hydrostatic bearing and hence the radial stiffness. Indeed, this had been done by others before (so no problem with patents), but I wasn't doing it. A few months later, our high speed model emerged, and we were spinning routinely at 75% of the speed of sound. Vagn was relieved—Varian was dismayed.

My earlier work in energy conversion had introduced me to one of the great turbine engineers, David Gordon Wilson.[4] In the spring of 1990, I called him up and asked him if he would be interested in collaborating on the development of an efficient microturbine. The ensuing relationship was one of the more rewarding of my business career. Most of the final supersonic spinner design details were worked out and communicated back to the plant by fax during the EENC in Veldhoven that May, and within weeks we had a manufacturable design approaching 90% of the speed of sound. A few months later we were achieving supersonic surface speeds and isentropic turbine efficiencies above 30% for 7-mm rotors (compared with 8% for our previous 7-mm microturbines), but scaling to smaller sizes proved to be nontrivial. The following summer while discussing with David the difficult resonances in our 5-mm spinner, we found time for a pleasant evening of singing old English madrigals with his wife around the grand piano in his living room in Cambridge. It was to take two more years and hundreds of failed experiments by my patient colleague Jerry Hacker during difficult recessionary times before we were to recognize several nonlinear scaling laws and the importance of the Bernoulli effects over the ends of the turbine blades and achieve routine spinning above 24 kHz with 3.5-mm rotors.

REFERENCES

1. C. P. Poole, *Electron Spin Resonance*, Interscience, New York, 1976.
2. F. D. Doty, US Pat. 4 456 882, 324/321, 1984.
3. P. Daugaard, V. Langer, and H. Jakobsen, US Pat. 4 739 270, 324/321, 1988.
4. D. G. Wilson, *The Design of High-Efficiency Turbomachinery and Gas Turbines*, MIT Press, Cambridge, 1984.

Biographical Sketch

F. David Doty. *b* 1950. B.A., 1972, Physics, Anderson University, Indiana, USA, Ph.D., 1982, Physics, University of South Carolina. Began work in NMR under Paul Ellis. President of Doty Scientific, Inc., 1982 to present. Approx. 20 publications and 15 patents. Research interests include rf electronics, NMR probe technology, electromagnetism, manufacturing turbomachinery, energy conversion cycles, ceramics engineering.

Dwek, Raymond A.: From Antibodies to Glycobiology

Raymond A. Dwek
University of Oxford, Oxford, UK

My career in magnetic resonance started in 1963 with Professor Sir Geoffrey Allen at Manchester University. Under his guidance, I completed my M.Sc. which dealt with using NMR to monitor keto–enol tautomerism. Learning that exciting things were happening at Oxford, in 1964 I joined the group of Sir Rex Richards, one of the pioneers of NMR in the UK. There, in 1966 I completed my D.Phil. My thesis topics involved nuclear electron double resonance. In Rex's lab, I obtained a very sound grounding of theoretical concepts and principles and also came into contact with many of the other leading figures in the NMR world. I stayed on for my postdoctoral studies with Rex Richards and was given an opportunity to develop several inorganic applications of NMR. These involved mainly studying the paramagnetic properties of transition metal ions and measuring the exchange rates of the molecules in the first coordination sphere.

A visit to the Institute For Exploratory Research at Fort Monmouth (1968), where I worked on other aspects of nuclear electron double resonance, convinced me that the use of NMR in the life sciences was really where the future growth was going to be. This was reinforced by a short visit to Professor Z. Luz at the Weizmann Institute in Israel the following summer. By this time, my interests in biochemical problems were known to Rex and shortly after my return to Oxford I was offered a position in the Biochemistry Department in Oxford under the Nobel Laureate, Rodney Porter.

Rex Richards and his group were still housed in the Physical Chemistry Laboratory in Oxford— I continued to use his equipment and collaborate with him. In the Biochemistry Department, I began a long collaboration with Professor George Radda and his group, in which we used paramagnetic probes and spin labels as reporter groups in phosphorylase A and B. At the same time, I was working on fluorinated sugars made by Paul Kent's group in conjunction with Professor R. J. P. Williams and one of his research students, A. V. Xavier. In 1971 I was elected to the newly formed Oxford Enzyme Group, which was under the chairmanship of Rex Richards, and developed a series of collaborations with many of the members mainly using techniques involving paramagnetic ions. These included I. O. Walker, A. Peacock, G. K. Radda, R. E. Richards, R. J. P. Williams, and my colleague Iain Campbell with whom I wrote Biological Spectroscopy in 1984. I collaborated with David Phillips and Louise Johnson on many structural aspects of substrates binding to lysozyme in solution and in this our joint research student Stephen Perkins played a major role.

By 1972 the advance in instrument design and particularly the use of Fourier transform spectroscopy had greatly improved the sensitivity of spectrometers. People were already talking about using NMR to solve the three dimensional structures of biologically important molecules, but there were also many other applications of NMR in biological systems. In 1973 I collected some of these together in my book— 'Nuclear Magnetic Resonance in Biochemistry: Application to Enzyme Systems'. The book was well reviewed, I remember one letter in particular from David Phillips in which he said that he 'admired the way in which you have brought out the immediate importance to biology of what might seem a somewhat esoteric development!'

In 1973, after what I thought was a particularly excellent seminar by one of my postdoctoral workers on phosphofructo kinase, Professor Porter called me to his office to discuss the seminar. He pointed out that simply 'monitoring' conformational changes in large proteins using reporter groups might be interesting mechanistically, but without detailed 3D studies he did not consider it to be at the cutting edge. What was needed he said was a major assault on the antibody problem! With his guidance began an exciting and exhilarating time in which I switched my interests towards the antibody molecule. Professor David Givol from the Weizmann Institute came over and together we started what was to be a nine year collaboration studying antibody combining sites. In the early days, I thought that the problem was tremendously difficult. I prepared a series of feasibility studies for Rodney Porter in which I did not rate our chances highly. What made the combining site problem soluble was mainly that the addition of a hapten (a small molecule) to an antibody combining site only perturbed those resonances in and around the combining site. Difference spectroscopy then enabled us to obtain subspectra of the combining site. I had some wonderful colleagues in Oxford, and with them we actually solved the combining site of the myeloma protein MOPE 315 which bound dinitrophenyl haptens. In 1976, we published the structure of this binding site in *Nature* and it was gratifying in 1988 to find that somebody had finally crystallized it in David Phillips's laboratory and that the structure reported was very similar, if not identical, to that determined by NMR. Our approach to the antibody combining site had been to gamble in 1973 that the fold of all antibodies would essentially be conserved. We built our amino acid residues onto the fold and then refined the model using NMR data, spin label data, and a whole host of other complementary physical techniques. We observed very large ring current shifts of the hapten when it was in the combining site and this necessitated a recalibration of the Johnson–Bovey ring current tables. Our connections with our colleagues Louise Johnson and David Phillips enabled Steve Perkins to complete these studies and recalibrate the ring current tables based on the crystal structures of lysosyme.

My interest in paramagnetic ions had, of course, continued. With Dennis Burton in Sture Forsén's lab in Lund, I continued a collaboration on proton/deuteron relaxation enhancement. When Dennis Burton came to England to do his postdoctoral work in my laboratory, we continued to use a variety of nuclear magnetic resonance techniques as we turned our attention towards the Fc portion of the antibody molecule. This is the portion of the molecule that is concerned with the elimination functions of the antibody— once it has bound the antigen. Our interests widened and with the aid of Professor J. Novotny and colleagues, we predicted the Clq receptor site on the antibody Fc region on the basis of sequence conservation, accessibility, and other studies. It was, however, these interests in the effector functions of antibody, mediated by receptors binding to the Fc, that led to the question whether the conserved carbohydrate in the Fc domain IgG molecule played an important role. This led to the challenge of studying the

carbohydrate structures of antibodies and led me into the area of ‘glycobiology’

Biographical Sketch

Raymond A. Dwek. *b* 1941. M.Sc., 1963 (Manchester), D.Phil., 1966 (Oxford), M.A. D.Sc., 1985 (Oxford). C.Chem. F.R.S.C. Research at Manchester University 1963–4, Oxford University 1964–9. Departmental demonstrator, University of Oxford, 1969–74. University lecturer, and Professor of Glycobiology and Director of the Glycobiology Institute, 1976–present. Approx. no. of publications, 400. Research specialties: effector functions of the antibody molecule and study of attached carbohydrates.

Dybowski, Cecil: Bob Vaughan and Solid State NMR at Caltech in the 1970s

Cecil Dybowski

University of Delaware, Newark, DE, USA

The first time I met Bob Vaughan was in Chuck Wade's office at the University of Texas. Bob had given a seminar at Texas and I felt fortunate to have a few minutes to talk with him. It was late 1972 and I was finishing the work on my dissertation. While the bulk of my work had been watching flashes on an oscilloscope to measure T_1 values, one of Chuck's other students, John Bowell, had built a pulse sequencer. We tried some multipulse sequences with our Magnion spectrometer, but it was obviously more difficult than I had at first thought. Here was the opportunity to talk with someone who had done this experiment. What a generous and open person he seemed to be in this first meeting—entirely open about his work and extremely interested in what we had been trying.

In February 1973, Bob called me because Won-Kyu Rhim had gotten a position at JPL. He asked me to come to Caltech as a postdoctoral fellow. What an opportunity!! I would be able to work on pulse sequences which was the thing to study at that time in NMR, following the seminal work in Waugh's group at MIT. By summer I was at Caltech, with both awe and trepidation.

At Caltech the experiments were done in an old Varian magnet Bob had gotten, I believe, from Roberts. Its vintage was indicated by a single-digit serial number. Averaging was limited by the time we could maintain its stability, at the most about 8 h. The PDP-8 computer was loaded from paper tape, and when loaded all except two bytes of computer memory were used. There was no storage outside computer memory, so one took a spectrum, transformed it, and plotted it. There could be no mistakes or the whole process had to be repeated.

Despite the modest setup, the laboratory was tremendously impressive. Perhaps the most significant facet of the lab was the elaborate care taken to produce uniform, controlled radiofrequency excitation. At Caltech at that time, the actual experiments were a minor part of the time one spent in the lab; most of the work was spectrometer setup. Bob was a master of the art, from rudimentary settings to the most subtle details. For example, he could lean on the spectrometer console and the tuning would change, and he knew why and by how much it would change. This attention to detail was the key to being able to do experiments few others could do.

Bob had been a student of Harry Drickhamer at Illinois and, to my knowledge, did not do significant amounts of work in NMR spectroscopy as a graduate student. I attribute Bob's success not just to his rather gigantic intellect, but also to the fact that he came to NMR experiments with no preconceived notions about them. Rather, he went about them in an extremely logical way with no shortcuts or presumptions about the way things 'should' operate. Every detail mattered to him and every adjustment was made while mimicking spectrometer operation during the experiment.

I met Drickhamer once when he visited Bob at Caltech. I realized immediately many of Bob's traits, including his global view of problems and his detailed approach to experimentation, were direct spinoffs of Drickhamer's approach to scientific problems.

As a postdoctoral fellow at JPL, Vaughan was tremendously influenced by Dan Elleman. He, Rhim, and Elleman had collaborated on multipulse NMR experiments before I arrived at his lab, and I could feel the great respect Bob held for Elleman. It seemed to me that he, Elleman, and Rhim formed an excellent team, each with unique strengths to contribute to the overall effort.

The year before I arrived, Bernie Gerstein was a visiting professor in Bob's lab. When I arrived, he was finishing the sabbatical there and was preparing to return to Iowa State, where later he would independently make major contributions to solid state NMR such as CRAMPS. Bernie and I were office mates for a month and became close friends in a way few do—a friendship that has endured for 20 years. I continue to be amazed that such a strong bond was forged in such a short time, but I am happy to be the beneficiary of its strength.

The years I spent at Caltech saw a dramatic change in the Vaughan laboratory. The number and variety of students increased from two (Schreiber and Lau) to something like a half dozen, from chemistry, chemical engineering and physics. This diversity produced a lively atmosphere I have found nowhere else. The strengths of each person seemed to be enhanced by others in the group, each working independently, yet relying on the others for philosophical, and practical, support. The result was a way of learning independently about one's project by interacting with others.

In addition to the graduate students, postdoctoral fellows, and faculty, various distinguished visitors would frequently visit Caltech. David Grant spent a year as a Sherman Fairchild Scholar. During that year, he actively participated in the Vaughan group seminars and added to the lively debate in those multihour marathons. I also vividly remember Ed Stejskal's talk on magic angle spinning and Hans Spiess's visit to Caltech. After we had had dinner, I remember Bob telling me 'There's a guy to watch. He is really good'. In addition to his keen understanding of the technology and science, Bob obviously had the ability to recognize talent in others and admit it freely.

The graduate and undergraduate students were excellent. For example, we were putting together the first system in a superconducting magnet after I arrived. Doug Carson had the job of working on the new PDP computer to make it control the experiment, and I remember how he struggled with its idiosyncracies. My part was the rf. It was exceptionally difficult to adjust the probe tuning at first, since we had only a vector impedance meter that went to 108 MHz, and the probe was to be tuned at 200 MHz. I remember how relieved I was with the arrival of a new vector voltmeter, for I could then adjust the tuning and measure the result easily.

After I finally got the probe adjusted to my satisfaction, I began to use the spectrometer to search for the proton resonance. Of course, I saw no signal where the Bruker engineer had when he brought the magnet up with his probe weeks earlier. I worked for a week doing various things, and still saw nothing. Then one of the really fine students,

Mike Stoll, joined in the search. Each day we would start at the frequency where the proton signal had been found in the Bruker probe and lower the frequency, reasoning that the magnet might have a slightly lower field than when first brought up (why? I don't know). Mike, on one of the many days, noticed a tiny blip in the spectrum which he concluded was the signal folded over many times. I wouldn't believe it. He pulled out paper, pencil, and calculator and calculated the expected attenuation by folding. With these calculations in hand, he made the bold prediction that the actual resonance was at higher frequency. To placate him, I moved the frequency up, and the signal increased by just the amount he calculated. We continued this process and, in short order, had a gigantic signal. Apparently because of slight differences in the probe I had built and the Bruker probe, the resonance was actually at *higher frequency* in our probe. Thanks to Stoll's faith in the laws of physics, we finally found the water signal.

Having a superconducting magnet meant more than just a second spectrometer; the increased sensitivity and stability gave us a real opportunity to investigate adsorbed phases—Bob's passion. Bob had been unjustly criticized by some for not moving more swiftly toward the study of adsorbed materials, but it was obvious to us that one had to deal with the development of technology first; the applications came later. After I left the lab, students like Mike Duncan would develop the study of surface species with NMR spectroscopy, although Schreiber had done some elegant preliminary studies in the old Varian magnet on the proton resonance of the surface hydroxyls of silica-aluminas.

Bob had another passion that surfaced at morning coffee. He and I would be at Chandler Dining Hall for coffee at 8 a.m., despite the fact that we had worked until 12 midnight or 1 a.m. the night before. We'd talk about lots of things dealing with NMR spectroscopy. I had decided to look at relaxation under multipulse sequences, and that was always among the topics we started out on as I added cream and sugar to the coffee.

During these daily routines, we'd often be joined by George Gavalas and John Seinfeld. NMR ceased (under duress) to be the topic of conversation on those occasions. It was at those times that Bob's other passion, money and the economy, appeared. He had very definite ideas about the subject, on which he would gladly speak whenever there was a willing audience. It was in these moments that you could see that Bob was a dyed-in-the-wool laissez faire capitalist! Not too surprising for a boy from Macalester, Oklahoma!

Speaking of Oklahoma, I had the worst run of luck during my time at Caltech. Being a graduate of the University of Oklahoma, Bob was always ready to place a gentleman's bet on the outcome of the Texas–Oklahoma football game. Fortunately for Bob (and unfortunately for me), those were the halcyon days of Oklahoma football. Needless to say, I had to buy the beer every October while I was at Caltech, thanks to the Texas and Oklahoma football teams.

There were many other incidents that showed the uniqueness of the time and place that was Vaughan's lab in the early 1970s—a place that was stimulating, innovative, and humane, not pretentious or overblown in its claims. However, ultimately my tenure there had to end, and I moved on to Delaware. I was very fortunate, because the DuPont Company had the wisdom to make Bob a consultant, and I saw him frequently after I moved to Delaware. We spent many evenings in pleasant conversation (after he had spent a full day at DuPont!) talking about the latest experiment one of us was trying.

When I came to Caltech, Vaughan's lab was a small operation concentrating on the technology of one NMR experiment. During my time there, I saw a transformation that really came to fruition after I had moved to Delaware. Those people not only expanded the technology of NMR in many ways, they were engaged in an ever-widening array of unique NMR experiments. Indeed, they really brought to fruition the studies I thought I'd come to Caltech to pursue, but never really was able to 'get into'—NMR of adsorbed materials.

I talked to Bob last about a week before his death, when he was again at DuPont. We discussed the upcoming meeting in Menton, France, to which we were both going. Bob seemed at ease because many of his problems were behind him and, both personally and professionally, his star was rising quickly. We agreed to meet in Paris before continuing to the Riviera.

The day of his death I called his office to talk about meeting in Paris before proceeding to Nice. His secretary, Sharon Vigario, told me Bob was in Chicago, that he would be home that evening, and she would have him call me the next morning. It happened that on the TV news that evening, when they talked about the air disaster on the Chicago to Los Angeles flight, a list of victims' names was put on the screen. I was relieved not to find his name there. After all, there were lots of flights from Chicago to Los Angeles.

As it happened, Bob pulled his usual trick of booking a late flight, returning on standby on an earlier one. He was on the flight! Even after 15 years, I still see in my mind the newspaper photo of the hapless airliner, and I realize how unsympathetic and cold death is.

What was the legacy of Vaughan's brief, illustrious career? The scientific papers speak clearly of intellect and curiosity and the scientific innovation that Vaughan engendered in others around him. They run the gamut, from highly theoretical projects, such as the proof of the spinor properties of nuclei, to very applied, such as studies of the nature of various catalytic surfaces.

I shall always consider him one of the three great scientific mentors in my life. He taught me science, patience, and kindness. His lasting legacy is really a single generation of scientists and engineers who have contributed to the improvement of NMR spectroscopy, science and the world through their own work and that of their students. I often wonder how many subsequent generations there would have been if only he had missed that plane from Chicago, and what the 1980s and 1990s would have been like at Caltech had he lived on.

Biographical Sketch

Cecil R. Dybowski. *b* 1946. B.S. (Chemistry), 1969, Ph.D. (Chemical Physics), 1973, University of Texas at Austin, USA. Research fellow in Chemical Engineering, California Institute of Technology, 1973–76. Faculty of Chemistry, University of Delaware, 1976–present. Visiting scientist, E. I. du Pont de Nemours and Company, 1982–83, Professeur Associé, Université P. et M. Curie, 1989. Approx. 120 publications. Research specialties: multinuclear MR of solids and molecules at surfaces; NMR of solid polymers; adsorption and catalytic reactions.

Ellis, Paul D.: Multinuclear MR Experiments, the Surrogate Probe Strategy, and Other Fun & Games

Paul D. Ellis

Battelle Pacific Northwest Laboratories, Richland, WA, USA

I am not old enough to do this, but given the nature of this Encyclopedia, I feel it is important to be able to recognize the colleagues that I have had the privilege to work with over the years during my tenure at the University of South Carolina (USC). I received my Ph.D. in 1970 at the University of California at Davis working with Professor Gary Maciel. I left Davis to go to USC just before Gary moved from Davis to Colorado State University in Fort Collins Colorado. Before I joined the faculty at USC Gary gave me some sage advice. He basically warned me that ^{13}C NMR was becoming too easy and hence popular (thanks to groups headed by Jake Stothers, David Grant, Gary's, and Jack Roberts) and it was going to be easy to get 'lost' given all of those efforts. Basically, he was pointing me to the remainder of the Periodic Table. A lesson I was not to forget. I left USC in early 1993 to move to Battelle's Pacific Northwest Laboratory. Here we are setting up an ultra high frequency (UHF) magnetic resonance lab for solids and liquids, e.g. a spectrometer based upon a 23 T magnet. My group is part of a larger effort in Environmental Molecular Sciences. The main effort of the laboratory (EMSL) is to provide molecular level understanding to the complex environmental problems which plague the world today. However, the main thrust of this note will be a summary of some of the early efforts to get Fourier transform multinuclear MR experiments going and the application of that method to metal sites in metalloproteins.

In the 1960s and early 1970s it was common for manufacturers of NMR spectrometers to build the spectrometer around specific nuclei rather than being broadbanded. Hence, if you purchased your spectrometer with ^{1}H, ^{13}C, and ^{31}P observe capabilities you would get three transmitters, three local oscillators, three preamps and, depending upon the manufacturer, three probes. It was a great marketing tool designed to bring in a gazillion dollars per spectrometer but a poor way to do science. This picture started to change when Dan Traficante[1] learned how to 'fake' a spectrometer into thinking it was performing a ^{13}C NMR experiment, when it was really looking at ^{29}Si. Basically what was involved was stepping up (or down) the transmitter frequency to excite the nucleus in question, utilizing a properly tuned probe, then stepping the transmitter down (or up) to detect the signal. Dan used a Bruker HFX-90 spectrometer for these modifications. Our group was using a Varian XL-100. Working with Charlie Peters of Varian Associates and Harold Walsh from the USC Chemistry support staff, we[2] put together a prototype of what would later become known as Varian's 'Gyrocode Observe Option', the first commercially available multinuclear observe accessory. These modifications provided a basis for us to perform NMR experiments on a wide variety of inorganic and bioinorganic systems. Utilizing modern spectrometers, these exercises are not needed since the operator simply needs to dial up the nucleus of interest and proceed with the experiment.

With this capability, we sought to develop NMR spectroscopy as a means of characterizing metal sites in zinc- and calcium-dependent proteins. This work was initiated in collaboration with Professor Jerry Odom of USC and Professor David Behnke when he was at USC. The overall objective of this research is to develop NMR methods to a point where they can be used to study the metal sites in diamagnetic metalloproteins. The metals of initial interest have been zinc and calcium. In the past 20 years, we[3] and others[4] have developed and utilized Cd^{2+} via ^{113}Cd NMR spectroscopy as a 'spin spy' to study the Zn^{2+} and Ca^{2+} sites in metalloproteins. The reasoning behind this strategy is the fact that Zn^{2+} and Ca^{2+} have such poor spectroscopic properties. Consequently, a viable alternative is to employ a surrogate probe as a means of studying these metals in this important class of biological systems. In every case studied to date, the surrogate strategy has worked, i.e. it has provided results which are consistent with the known chemistry of the system of interest. This progress has come about as a result of single-crystal measurements[3] g where a comparison between structure and shielding can be examined. It is the combination of solid- and liquid-state NMR methods which has made ^{113}Cd NMR a valuable structural probe.[4]

Currently, we are taking our qualitative structural correlations obtained from our single-crystal investigations[3] g of ^{113}Cd shielding tensors and investigating the utility of recent ab initio theories of chemical shielding[5] in predicting these experimental trends.

REFERENCES

1. D. D. Traficante and J. A. Simms, *Rev. Sci. Instrum.*, 1972, **43**, 1122; D. D. Traficante, J. A. Simms, and M. Mulcay, *J. Magn. Reson.*, 1974, **15**, 484. For those discerning readers, this is the same Traficante as the famous 'Lawn Mower' Traficante of Merck Suite fame.
2. P. D. Ellis, H. C. Walsh, and C. S. Peters, *J. Magn. Reson.*, 1973, **11**, 426; C. S. Peters, R. Codrington, H. C. Walsh, and P. D. Ellis, *J. Magn. Reson.*, 1973, **11**, 431.
3. (a) A. D. Cardin, P. D. Ellis, J. D. Odom, and J. W. Howard, *J. Am. Chem. Soc.*, 1975, **97**, 1672; (b) P. D. Ellis, *Science*, 1983, **221**, 1141; (c) P. D. Ellis, *J. Biol Chem.*, 1989, **264**, 3108; (d) E. Rivera, M. A. Kennedy, R. D. Adams, and P. D. Ellis, *J. Am. Chem. Soc.*, 1990, **112**, 1400; (e) E. Rivera, M. A. Kennedy, and P. D. Ellis, *Adv. Magn. Reson.*, 1989, **13**, 257; (f) P. S. Marchetti, R. S. Honkonen, and P. D. Ellis, *J. Magn. Reson.*, 1987, **71**, 294; (g) R. S. Honkonen and P. D. Ellis, *J. Am. Chem. Soc.*, 1984, **106**, 5488; (h) P. S. Marchetti, P. D. Ellis, and R. G. Bryant, *J. Am. Chem. Soc.*, 1985, **107**, 8191.
4. M. F. Summers, *Coord. Chem. Rev.*, 1988, **86**, 43.
5. T. D. Bouman and A. E. Hansen, '*RPAC Molecular Properties Package, Version 8.6*', Southern Illinois University at Edwardsville, 1990; A. E. Hansen and T. D. Bouman, *J. Chem. Phys.*, 1985, **82**, 5035; K. Wolinski, J. F. Hinton, and P. Pulay, *J. Am. Chem. Soc.*, 1990, **112**, 8251.

Acknowledgements

During my years at USC I enjoyed the support of many of my colleagues, faculty, postdoctorals, and graduate students, and I wish

to thank them for this. Further, this work could not have been accomplished without the financial support of the National Science Foundation and the National Institutes of Health. For their support I am forever grateful.

Biographical Sketch

Paul D. Ellis. *b* 1944. B.S., 1966, Ph.D., 1970, Chemistry, University of California at Davis. Assistant, associate, and George H. Bunch, Sr. Professor of Chemistry, University of South Carolina, 1970–93; Associate Director, Macromolecular Structure and Dynamics Group, Battelle Pacific Northwest Laboratories, 1993–present. Approx. 150 publications. Current research interests: heterogeneous catalysis, structural biology.

Emsley, James W.: Having Fun with Liquid Crystals

James W. Emsley

University of Southampton, Southampton, UK

In the end is my beginning. This is probably true for most scientists in that our ideas have developed continuously from our postgraduate work to what is currently occupying our minds. The closeness of the end to the beginning can suggest an absence of development, but this would be to ignore the richness of the journey. I started research in Leeds in 1956 as a postgraduate student supervised by John Smith, who had recently moved there from Oxford where he had been a student of Rex Richards, doing some of the first applications of NMR in chemistry. My doctoral work involved proton NMR of single crystals of thiourea, urea, and formamide, and the particular interest was to characterize the bond rotational motion in these amides. These studies impressed upon me the usefulness of the dipolar interaction for characterizing molecular motion, particularly if single crystal samples are used. I am still exploiting the dipolar interaction, but now with liquid crystalline samples, and here too the most important contribution that NMR can make is in characterizing the internal modes of motion. Summarized in this way it seems a small step from studying solid crystals to liquid crystals, but the route has been both more challenging and stimulating.

Those early experiments were done on a homebuilt spectrometer, operating at 16 MHz in a field of 0.3 T, and all the analysis of the data was done with planimeters to measure spectral moments and mechanical calculators to fit these to those predicted by models of the motion. Electronic computers became available in Leeds in about 1957 and it then became relatively easy to solve Schrödinger's equation for groups of interacting spins. I can still recall how exciting the future prospects for the application of NMR seemed, which until this advance was limited to analyzing the spectra only of very simple spin systems.

When I left Leeds in 1960 it was at the beginning in Britain of the advent of high-resolution liquid state NMR. Commercial spectrometers were appearing, and I went to Liverpool where Les Sutcliffe had been exploring applications in chemistry with a Varian spectrometer, operating at 40 MHz, which was high field in those days, and about to be upgraded to 60 MHz. It was here that I met Jim Feeney, who had just completed his Ph.D. and who was a newly appointed assistant lecturer, and Neville Boden, who was just starting as a research student. I was to spend almost two years in Liverpool, and the most important outcome was the writing of the book High Resolution NMR Spectroscopy. The book originated in an approach to Les Sutcliffe by Pergamon Press, the new publishing house founded by Robert Maxwell. The writing had commenced before I arrived in Liverpool, involving Jim Feeney and Joe Lee, who had preceded me as a postdoc. and who had left to take up a lectureship at UMIST. Joe eventually decided not to continue and I was asked to take his place. It was a daunting task and I was very conscious of my inadequate background for writing a text to cover the whole of this relatively new subject. It was, however, extremely stimulating and a wonderful way of learning about the capabilities of NMR then apparent. The book was started by the three of us in about 1961 and was finally published in 1965, three years after I had left Liverpool and was in Durham. It had been initiated by Les and he was largely responsible for ensuring that it did appear eventually. Les was also the initiator of our review series, *Progress in NMR Spectroscopy*, suggesting that this would provide a continuing source of authoritative articles on NMR. The first seven volumes appeared at approximately annual intervals and provided another invaluable learning experience, not least in that authors almost always underestimate the time it takes to write a review and completing volumes can be an editor's nightmare. We solved this problem by going to the present system of publishing in parts, in effect, becoming a review journal, although a formal change to a subscription-based periodical came later. The series was in an excellent position to benefit from the expansion in the applications in NMR which started in the 1970s, and now we produce six issues per year, having published 25 volumes and over 150 articles by the end of 1993.

I have been extremely lucky in being a participant in two major scientific developments: NMR and liquid crystals. My interest in liquid crystals started in 1963 when I read the paper by Englert and Saupe describing the first high-resolution proton spectrum from a liquid crystalline sample, that of benzene dissolved in a nematic solvent. This brought together the advantages of solid state NMR, in providing structural information via dipolar interactions, and the narrow linewidths of liquid-state NMR. The possibilities seemed very exciting and I resolved to teach myself how to obtain these spectra. I made virtually no progress until moving to Southampton in 1967, where I acquired a Varian HA-100 spectrometer, a postdoc, Tony Storey, who had been trained as an organic chemist and so could make the liquid crystalline compounds, and a colleague Geoffrey Luckhurst, who had been introduced to liquid crystals whilst an undergraduate at Hull, where George Gray was doing his pioneering work which has had such an influence on electrooptic devices. Our first tasks were to learn how to obtain well-resolved proton spectra from liquid crystalline samples, and how to analyze them by modifying LAOCOON. Tony Storey made several liquid crystals to use as solvents and also showed a quite unexpected flair for writing computer programs, so much so that he has spent the rest of his career in the computer industry.

Our work had a tremendous boost when John Lindon came as a postdoc. He had done a year with Ben Dailey at Columbia and so had experience of recording and analyzing spectra. John stayed for five years which were very productive scientifically, especially as he taught me and my students so much; a part of that continuing learning experience which is such an enjoyable part of the life of a scientist. After we had been working together for a couple of years we decided to write a book, NMR Using Liquid Crystalline Solvents, which was published in 1975. John left to go to a post at the Wellcome Foundation Research Laboratories, where he has established a reputation in quite different aspects of NMR. We have, however, started once more to do science together and I will return to this later.

The proton spectra from liquid crystalline samples become very complex as the number of interacting spins increases, and in those early days we could not analyze spectra with more than about eight protons but even then the spectra often defied analysis. It was obvious that the range of application

of proton LCNMR would remain limited to small molecules unless this limitation could be overcome. It seemed to me that the spectra could be simplified by partially deuterating and removing the $^1H-^2H$ dipolar interactions by irradiating the deuteron resonances. The deuteron spectra are dominated by the quadrupolar interaction and are essentially doublets for each group of nonequivalent nuclei, with splittings of typically several kHz. Anderson and Nelson in 1963 had suggested that in such cases decoupling was more efficient if the irradiating signal was modulated so as to produce sidebands at the doublet frequencies. I persuaded a colleague in the Department of Electronics, Trevor Wilmshurst, to design and build a modulator and he suggested that we use phase rather than amplitude modulation. The experiment worked and we sent a note to *Chemical Communications* in July 1971 showing a simple example. In August I attended the 4th ISMAR Meeting in Israel and learned from Saul Meiboom that they had also done a successful deuterium decoupling experiment, but without using modulation. They had simply irradiated at the center of the ^2H spectrum and the good decoupling achieved was attributed to the excitation of double quantum transitions. They had also in fact done a cleverer experiment in another sense. They took 98% deuterated cyclohexane so that decoupling the deuterons gave a proton spectrum consisting of a single line from $C_6D_{11}H$ and doublets from the 18% of the molecule which contain just two protons. This experiment has proved extremely useful. Single frequency decoupling with modern probes is now quite easy, and we regularly obtain well-resolved spectra from eight or even more coupled spins. It is also now much easier to do the modulated decoupling experiment, but using frequency switching rather than phase modulation.

The other major development which has proceeded alongside the experimental improvements has been in our understanding of how dipolar and quadrupolar couplings are related to the structure and orientational order of molecules which have some form of internal motion. In the early days, the view of those using NMR to study dissolved molecules was that the orientational order of a flexible molecule could be described by a single matrix, and that the number of nonzero independent elements reflected an effective symmetry produced by the internal motion, if this was faster than the overall, molecular reorientational motion. Burnell and de Lange convincingly demonstrated inconsistencies in this approach and in its place they proposed a theory which still invoked the kinetics of the molecules. It seemed to Geoffrey Luckhurst and me that this was a complicated way of approaching the problem. We published an alternative theory in 1980 which used equilibrium statistical mechanics to describe the averaging of such interactions as the dipolar and quadrupolar couplings, and this approach seems to have become the accepted way of looking at this problem. The consequence of this theory is that to average dipolar coupling requires a model for predicting how the orientational order is coupled to the internal degrees of freedom in the molecule. Our own approach was developed from the work of Marcelja, who had published a seminal paper in 1974 describing a model for the ordering of alkyl chains in liquid crystals which used a potential of mean torque, U, constructed by adding contributions from the alkyl C–C bonds to that from an aromatic core of the molecule. In fact, the idea of additive contributions to U had also been proposed by Saupe and Nehring as early as 1969 for rigid molecules.

Our early work on flexible molecules was concerned with pure liquid crystals, and at that time the only practical way of studying such complex molecules was to use deuterium NMR. The use of deuterium NMR to study liquid crystals dates from 1965 and a paper by Rowell, Phillips, Melby, and Panar. It was only in the 1970s, with the advent of pulse FT NMR, that ^2H became an easily studied nucleus and then there was a rapid increase in the applications to liquid crystals.

Our own early work used a Varian XL-100, which had a $50\,\mu s$ 90° pulse for ^2H, a spectral width limited to 25 kHz, and no disk system. In 1979, however, I acquired a Bruker CXP-200 and this made ^2H NMR a much easier nucleus to study. The CXP also had a disk and a programmable temperature controller, making it possible to explore the temperature dependence of orientational order or relaxation rates. The year 1979 also marked the arrival in Southampton of David Turner, and his expertise in FT and 2D techniques enabled us to explore some new applications of NMR to liquid crystalline samples. I was also fortunate in having a graduate student, Tony Avent, who had spent a year working with Ray Freeman. Together we had great fun trying out new experiments. One of the more successful was to use a $90^\circ-\tau-180^\circ-\tau$ echo sequence with single point acquisition to obtain proton spectra of deuterated samples which were free from proton–deuterium spin coupling: 'decoupling' without irradiating at the nonresonant nuclear frequency. Moreover, coupling to all nonresonant nuclei was removed and so spectral simplification could be achieved, for example, in samples containing protons, fluorine, and deuterium. The major disadvantage of this method, however, was the time taken to obtain a spectrum, which was typically several hours.

Our second year with the CXP coincided with Peter Beckmann spending a sabbatical in my lab. Peter had been a graduate student with Myer Bloom and had several years experience of solid state NMR, particularly with measuring and interpreting relaxation rates. We decided to see what new things could be done for liquid crystals. I had been tremendously impressed by the work done by Bob and Gitte Vold and David Grant on measuring spectral densities on small molecules dissolved in liquid crystalline samples, and it seemed to me that it would be fun to try similar experiments on the deuterated liquid crystals which we had used in our studies of orientational order. We were able to demonstrate that Jeener–Brockaert experiments could be applied to obtain $J_1(\omega_0)$ and $J_2(2\omega_0)$ for each site containing deuterium, which was simply repeating what had been done for small molecules, but also that selective inversion–recovery experiments were an alternative way to obtain these data. The interpretation of the large data sets obtained was far more problematic since the relaxation rates depend upon whole molecule reorientational motion, internal motion, and possibly on collective modes of motion, known as director fluctuations. Our first attempt to understand our newly acquired data ignored director fluctuations as a relaxation mechanism and showed that a simple model of superimposed motions, which Peter Beckmann had used in studies of solids, accounted for the main trends in the data. We were always conscious that our neglect of director fluctuations was probably not justified, but we could not see a simple way of accounting for its effects in these complex molecules. The theories available at the time had been developed for rigid, cylindrically-symmetric molecules and extending them to flexible molecules with no

symmetry has still not been attempted. This venture into relaxation has been immensely rewarding for me in that it not only introduced me to some fascinating problems, but I have also come to know such lively people as Bob and Gitte Vold, Pier-Luigi Nordio, Ron Dong, Jack Freed, and Frederick Noack. More recently, it has stimulated me to learn about computer simulation techniques, particularly from Dominic Tildesley, and with him and Bill Palke, who spent a sabbatical in Southampton in 1989–90, to investigate how they can be used to study molecular dynamics and hence to test the analytical theories of relaxation processes.

The 1980s were very productive years for the NMR of liquid crystals. Many labs acquired access to new equipment and the interest in the subject expanded in parallel with an explosion of interest in liquid crystals generally. In Southampton we explored new applications of NMR to these materials, our particular interest being to show how experiments could be used to test molecular theories. Geoffrey Luckhurst, with his wide-ranging interests and knowledge of liquid crystallinity, was a constant source of ideas and together with some excellent students we had an exciting time showing how NMR can give unique insights into the behavior of the molecules in these phases. The availability of high-field spectrometers enabled us to demonstrate how field-induced quadrupolar splittings of deuterium can be used to study pretransitional phenomena in the isotropic phase of nematogens, and we also demonstrated how electric field-induced splittings can be monitored by NMR. We were like children discovering new, untouched playgrounds, with many toys with which to excite our imaginations. We ventured into the use of pressure as a variable, showing the advantages of using deuterium to obtain site-specific data with which to test theories. The pressure probe was built by 'Tim' Timimi, a refugee from Saddam's Iraq, a gifted experimentalist who also played a key role in bringing social cohesion to a diverse research group.

To conclude, I want to relate the story of the Italian connection which has been such a stimulating and successful collaboration. It started when Gian Franco Pedulli came to Southampton from Bologna in about 1968 to work with Geoffrey Luckhurst on ESR. Franco then encouraged a student, Claudio Zannoni, to do a Ph.D. with Geoffrey. Meanwhile, I met a colleague of Franco's, Ludovico Lunazzi, at the ISMAR Meeting in Israel in 1971, and he suggested that we should collaborate on some NMR studies of solutes with the aim of determining their structures. Ludovico is an organic chemist with considerable expertise in both ESR and NMR, and the collaboration made good sense. We obtained a NATO grant and for the next few years spent a week or two each year in each other's labs. Through Ludovico I met Carlo Alberto Veracini who works in Pisa, and I added another lab to my Italian connection and became familiar with a second, beautiful Italian city. A former student of Alberto's, Marcello Longeri, then obtained a fellowship to enable him to spend a year in Southampton and he arrived with his wife Grazia in 1977. Marcello has an uncanny ability for analyzing impossibly complex NMR spectra. He wrote improved versions of our old spectral analysis programs, combining magnetic equivalence with reflection symmetry so that larger spin systems could be analyzed on the available computers. He works in Calabria, the toe of Italy, and over the last 16 years we have maintained a close collaboration; more recently this has also involved Giorgio Celebre and Pina De Luca. In recent years our work has concentrated on attempts to use NMR to characterize the bond rotational potentials within molecules via the dipolar couplings. This has proved to be particularly interesting, and has involved Claudio Zannoni in Bologna as well as Alberto Veracini's group in Pisa. John Lindon, my old colleague, is also involved, not only directly in doing experimental work, but also in being the industrial partner in a CASE project which partially supports a graduate student, Lizzy Foord, who is exploring the use of this method to study molecules with therapeutic properties.

In 1984 Alberto Veracini and I organized a NATO ASI at San Miniato on the NMR of liquid crystals at which Claudio Zannoni gave a series of lectures on how to describe the orientational order in rigid and flexible molecules. He mentioned too that it should be possible to obtain a conformational distribution directly from the experimental data, such as dipolar couplings, D_{ij}, by using the maximum entropy principle. He and Alberto, together with Claudia Forte and Lorenzo Di Bari from Pisa, demonstrated this idea on the D_{ij} value obtained for 3-phenylthiophene dissolved in a liquid crystalline solvent. This maximum entropy (ME) method can be thought of as 'model-free', compared with the methods developed at Southampton and elsewhere which I describe as additive potential (AP) methods and which are model-dependent. In recent years the groups in Pisa, Calabria, and Southampton have explored the relationship between AP and ME, at first by seeing if the same conformational distribution is obtained by the two methods from the same data, and very recently by showing in a joint publication in the *Journal of Physical Chemistry* how the two methods are related.

This Anglo–Italian collaboration demonstrates how science is about people interacting, testing out ideas on one another, and synthesizing new ideas as a result. It also shows the truly international nature of science.

Biographical Sketch

J. W. Emsley. *b* 1934. B.Sc., 1956, Ph.D., 1960, University of Leeds, (supervised by J. A. S. Smith). ICI Research Fellow, University of Liverpool, 1960–62; research assistant and then lecturer, University of Durham, 1962–67. Since 1967 at Department of Chemistry, University of Southampton, currently as a reader. Research interests center on NMR of liquid crystalline samples. Editor of *Progress in NMR Spectroscopy* with Jim Feeney; about 150 scientific publications.

Engelhardt, Günter: Silicon-29 NMR of Silicates: From Liquids to Solids. An Historical Perspective

Günter Engelhardt

University of Stuttgart, Stuttgart, Germany

The history of the application of silicon-29 NMR to silicates began as early as 1956 when Holzman et al.[1] published the ^{29}Si chemical shifts of an impressive variety of solid and liquid silicon compounds, including quartz, cristobalite, amorphous silica, silicate glasses, and a sodium silicate solution. However, owing to the poor spectral resolution and the low sensitivity of the NMR equipment available at that time, the potential of ^{29}Si NMR in silicate research was not further exploited until, in the early 1970s, the pulse Fourier transform technique was developed and applied in commercial high-resolution NMR spectrometers. In 1973, our group at the Academy of Sciences of the GDR in Berlin-Adlershof was happy to receive a brand-new JEOL FT NMR spectrometer and as soon as the instrument was running we first started ^{29}Si FT NMR experiments on various types of silicon compounds, liquids or solutions, since at that time chemical applications of high-resolution FT NMR were restricted to the liquid phase.

In addition to organosilicon compounds and silicone polymers, we also studied several aqueous sodium silicate solutions and it was quite a surprise to observe numerous sharp and well-resolved resonances in the spectra of some of the solutions. This observation was of particular interest since evidence from other techniques such as Raman spectroscopy, paper chromatography, trimethylsilylation, and reaction with molybdic acid strongly suggested the presence of a distribution of oligomeric silicate anion species in aqueous silicate solutions. However, the structural characterization of individual anion types by these techniques appeared to be difficult. Further systematic studies, carried out in close cooperation with W. Wieker and D. Hoebbel from the Institute of Inorganic Chemistry of the Academy, soon revealed that the various resonances in the ^{29}Si FT NMR spectra of a series of sodium silicate solutions of different composition arise from distinct $Q^n(\equiv(SiO)_nSi(O)_{4-n})$ groups in a variety of oligomeric silicate anions.

The results of these early studies were published in 1974[2] and, most notably, two further papers on the same topic but from two other groups appeared in the same year.[3,4] In subsequent years, numerous detailed ^{29}Si NMR studies of silicate solutions were carried out by various authors which established the identities of a large variety of oligomeric silicate anions of different structures. In particular, Harris and Knight[5] were able to identify 19 anionic structures in ^{29}Si isotope-enriched potassium silicate solutions, and Knight[6] confirmed these structural assignments and identified four new silicate species by two-dimensional COSY experiments. Moreover, the dependency of the anion distribution on the chemical composition of the silicate solutions, the specific structure-directing effects of various cations, the dynamic exchange processes of SiO_4 tetrahedra between distinct silicate anions, the condensation reactions of silicic acids, the formation of dissolved aluminosilicate anions, and other interesting features of the solution chemistry of silicates were investigated in detail. Altogether, an exciting wealth of new information on the structure, reactivity, and dynamics of silicate anions not amenable by other techniques could be derived from the ^{29}Si FT NMR studies of silicate solutions[7] which even nowadays attracts considerable interest.

Since most of the silicates occurring in Nature and used in a wide range of technical applications are solids, it was obvious from the very beginning of the above mentioned liquid state ^{29}Si NMR studies that the high potential of ^{29}Si NMR in providing detailed information on silicate structure should be extremely useful if it could also be applied to solid silicates and aluminosilicates. However, although the principles of magic angle spinning and cross-polarization techniques were already known to be effective means for line narrowing and sensitivity enhancement in solid state NMR spectra, high-resolution NMR of solids in general, and that of ^{29}Si in particular, was not yet well developed in the early 1970s. At that time we had already had for several years a very fruitful cooperation with the group of Endel Lippmaa at the Estonian Academy of Sciences in Tallinn on the application of multinuclear liquid-state FT NMR to various organic, elementorganic, and inorganic compounds, including ^{29}Si NMR of organosiloxanes and silicates. Encouraged by the first successful experiments of the Tallinn group with the combination of MAS and CP techniques in measurements of high-resolution solid state ^{13}C NMR spectra of powder samples,[8] we decided in 1977 to carry out systematic studies on the general applicability of these methods to organic and elementorganic solids and, in particular, to solid silicates.

For the initial experiments, a 0.94-T large-gap electromagnet and a homebuilt air-driven MAS turbine with 10-mm o.d. glass rotors, rotated at speeds up to 4 kHz in a double-tuned crossed-coil probe with adjustable angle of the spinning axis, was used in Tallinn. The rf pulse sequences were generated by a modified NIC-293 input–output device, connected to a NIC-1085 computer which was also used for signal accumulation and the fast Fourier transform. While this equipment worked well for ^{13}C CP MAS NMR of organic solids, first attempts to measure ^{29}Si CP MAS NMR spectra were not successful. However, after several months of cumbersome work improving the performance of the spectrometer and the mechanics of the MAS probe, we succeded in the summer of 1977 in measuring the first highly resolved ^{29}Si CP MAS NMR spectra of solid silicates and organosilicon compounds.[9] This success was mainly due to the skilful activities of the late Mädis Alla, of Tiit Tuherm and of other members of the Tallinn group in the development of the MAS equipment and the high-power spectrometer electronics.

A considerable step ahead was the installation in Lippmaa's laboratory of a Bruker CXP-200 solid state high-resolution spectrometer equipped with a superconducting 4.7-T wide-bore magnet and a MAS probe for conical Andrew-type rotors manufactured from Delrin. Using this instrument the ^{29}Si MAS NMR and CP MAS NMR spectra of an extended series of solid silicates and aluminosilicates of natural and synthetic origin were measured in 1979,[10] followed by a detailed investigation of a number of aluminosilicate zeolites in 1980/81.[11] These studies clearly demonstrated that the main

characteristics of the ^{29}Si NMR spectra of silicate solutions can also be applied to the interpretation of the spectra of solid silicates, and that additional information can be derived on specific structural features of the solids such as the distribution of silicon and aluminum in aluminosilicates, and the presence of crystallographically inequivalent Si sites. Starting from this pioneering work in the years 1980–81, high-resolution solid state ^{29}Si NMR has emerged rapidly as an extremely useful and widely applied tool for the structural characterization of a wide range of crystalline and amorphous silicates and related materials.[7] This progress is demonstrated in more detail by the following related articles in this Encyclopedia, see ***Silicon-29 NMR of Solid Silicates***, ***Amorphous Silicon Alloys***, ***Silica Surfaces: Characterization*** and ***Geological Applications***.

REFERENCES

1. G. R. Holzman, P. C. Lauterbur, J. H. Anderson, and W. Koth, *J. Chem. Phys.*, 1956, **25**, 172.
2. G. Engelhardt, H. Jancke, D. Hoebbel, and W. Wieker, *Z. Chem.*, 1974, **14**, 109.
3. H. C. Marsmann, *Z. Naturforsch. B.*, 1974, **29**, 495.
4. R. O. Gould, B. M. Lowe, and N. A. Macglip, *J. Chem. Soc., Chem. Commun.*, **1974**, 720.
5. R. K. Harris and C. T. G. Knight, *J. Chem. Soc., Faraday Trans. 2*, 1983, **79**, 1525, 1535.
6. C. T. G. Knight, *J. Chem. Soc., Dalton Trans.*, **1988**, 1457.
7. G. Engelhardt and D. Michel, *High-Resolution Solid-State NMR of Silicates and Zeolites*, Wiley, Chichester, 1987.
8. E. T. Lippmaa, M. Alla, and T. Tuherm, in *Magnetic Resonance and Related Phenomena*, Proc. 19th Congr. AMPERE, eds. H. Brunner, R. Hausser, and D. Schweitzer, Heidelberg/Geneva, 1976.
9. E. T. Lippmaa, M. A. Alla, T. J. Pehk, and G. Engelhardt, *J. Am. Chem. Soc.*, 1978, **100**, 1929.
10. E. Lippmaa, M. Mägi, A. Samoson, G. Engelhardt, and A.-R. Grimmer, *J. Am. Chem. Soc.*, 1980, **102**, 4889.
11. E. T. Lippmaa, M. Mägi, A. Samoson, M. Tarmak, and G. Engelhardt, *J. Am. Chem. Soc.*, 1981, **103**, 4992.

Biographical Sketch

Günter Engelhardt. *b* 1936. Dipl.-Chem., 1960. Dr.rer.nat., 1963, Technical University of Dresden, East Germany (supervisor Heinrich Kriegsmann), Dr. habil., 1969, Humboldt University Berlin, East Germany. Central Institute of Physical Chemistry, Academy of Sciences of the GDR, Berlin-Adlershof, East Germany, 1963–86. Faculty of Chemistry, University of Konstanz, West Germany, 1987–92. Institute of Chemical Technology I, University of Stuttgart, Germany, 1992–present. Approx. 180 publications, and, with D. Michel, the book High-Resolution Solid-State NMR of Silicates and Zeolites (Wiley, 1987). Current research specialty: multinuclear solid state MR and its application to zeolite catalysts and other inorganic materials.

Ernst, Richard R.: The Success Story of Fourier Transformation in NMR

Richard R. Ernst

Eidgenössische Technische Hochschule, Zürich, Switzerland

This chapter could also be entitled: How to be successful by borrowing clever ideas. During my undergraduate studies at the Swiss Federal Institute of Technology in Zürich (ETH Zürich) from 1952–56, the term nuclear magnetic resonance was never even mentioned, and when I started my thesis with Professor Hans H. Günthard in 1958 after some healthy military training I knew nothing about my beloved future companion NMR. It was, so to say, a marriage arranged by my thesis advisor. Fortunately, an extraordinarily gifted, truly ingenious scientist, Hans Primas, was just in the course of finishing the construction of the first Swiss high-resolution NMR spectrometer. I had the enormous luck to work under his guidance on my Ph.D. thesis for the following 4 years.

Figure 1 Professor Hs.H. Günthard, the spinning nucleus of the research group in 1958

HANS PRIMAS AND HIS NMR SPECTROMETERS

Professor Hans H. Günthard, at that time Associate Professor in the Laboratorium für Organische Chemie, later Head of the Laboratorium für Physikalische Chemie, was an enormously enterprising and stimulating leader (Figure 1). He set out to introduce all powerful modern spectroscopic tools into the Swiss university chemistry. It should also be mentioned here that he was strongly encouraged by Professor Leopold Ruzicka who was heading the Laboratorium für Organische Chemie with much foresight. At the early date of 1953, Professor Günthard asked Hans Primas to pioneer the construction of a high-resolution NMR spectrometer useful for chemical applications (Figure 2). During a brief stay at the University of Zürich in 1953 with Professor Hans Staub, who was a former co-worker of Felix Bloch at Stanford, and with his associate Ernst Brun, Hans Primas was exposed for the first time to the practical aspects of NMR, here in the hands of enterprising solid state physicists.

The 25 MHz proton resonance spectrometer that Primas and Günthard constructed used a 0.6 T permanent magnet (Figure 3), spherical sample containers to improve the magnetic field homogeneity,[1–4] and a field flux stabilizer.[5] It was an important event when in 1956, Günthard and Primas convinced the Swiss company Trüb-Täuber, with its scientific director Dr. L. Wegmann, to manufacture and commercialize this spectrometer under the name KIS I.[6] Several instruments of this type were sold in Europe during the following years.

Hans Primas decided to continue his engineering ventures by designing a high-field instrument working at 75 MHz proton

Figure 2 Professor Hans Primas working on his electronic design for the 25 MHz NMR spectrometer in 1958

resonance, and he developed a new concept of shaped pole caps for electromagnets to achieve high-field homogeneity by avoiding local saturation.[7] This spectrometer was also commercialized as KIS II, operating at a proton resonance frequency of 90 MHz.

The company Trüb-Täuber was dissolved in 1965, and its NMR spectroscopy division became the germ for the well-known Swiss company Spectrospin AG in Fällanden, which is a member of the Bruker group. In some sense, the instruments built by Hans Primas are the ancestors of the modern high-resolution Bruker-Spectrospin spectrometers. Besides numerous instrumental innovations, Hans Primas also contributed during this time to new theoretical concepts such

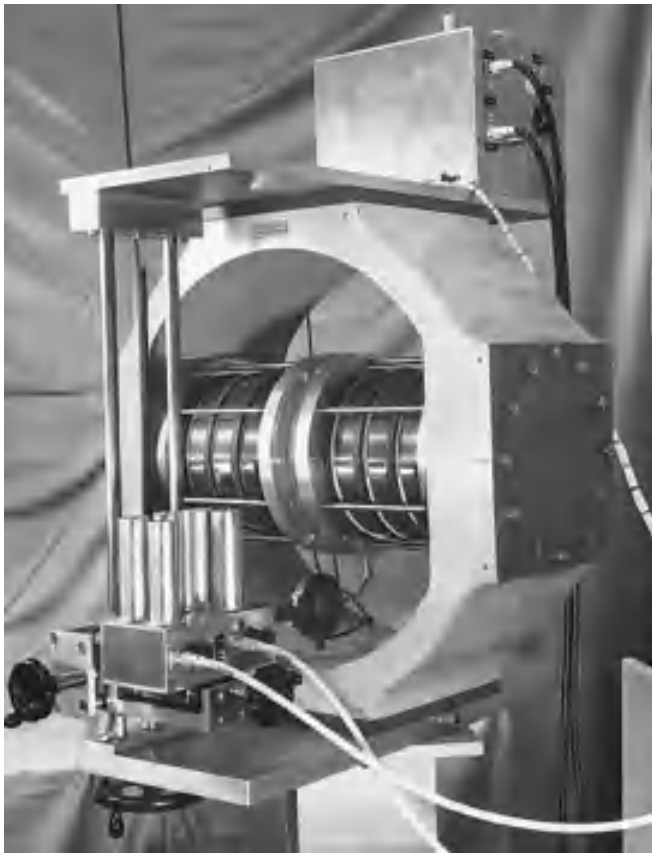

Figure 3 The 6 kG permanent magnet for the 25 MHz proton magnetic resonance spectrometer in 1958. The coils for the magnetic flux stabilizer are visible on the pole pieces. The probe assembly is directly attached to the preamplifier. The radiofrequency transmitter stands on top of the magnet

as a generalized perturbation theory in operator form[8] and superoperator concepts for calculating NMR spectra.[9,10]

FIRST VENTURE IN STOCHASTIC RESONANCE

I never even started my first thesis subject posed by Professor Günthard in 1958, i.e. a group theoretical analysis of NMR spectra. After extensive ventures into electronics and the construction of NMR probe assemblies, frequently burning my fingers with solder and high voltages, I finished my graduate studies in 1962 with a purely theoretical investigation of stochastic magnetic resonance. The pertinent ideas for this study came from Hans Primas, who at that time was working on the theory of quantum mechanical systems with a stochastic Hamiltonian,[11] inspired by the work of Norbert Wiener[12] and others.

The application of stochastic excitation for obtaining spectral information with an inherent multiplex advantage was not considered at that time. Rather, stochastic excitation was intended for decoupling purposes. By a broadband excitation of all spins except for one within a homonuclear spin system, broadband spin decoupling of this selected spin was attempted. Sweeping a broadband frequency source with a narrowband hole in its spectrum through the entire spectral range should lead to a completely decoupled homonuclear spectrum, which could be observed with a weak coherent irradiation in the center of the hole. It was disappointing for us to recognize that the principle only functions for weakly coupled spin systems, a situation that needed, in our view, anyway no further simplication. Weak coupling was too simple to appeal to us, and we missed the possibility of inventing stochastic heteronuclear decoupling. No wonder that we never did a stochastic resonance experiment. Our aim was more a theoretical excursion to explore the nonlinear stochastic response of a quantum mechanical system by means of an example.[13]

THE SENSITIVITY DEFECT OF NMR

Anyone who performed NMR experiments in the 1950s will remember the exceedingly low sensitivity of NMR at that time. A signal-to-noise ratio of 5:1 for the spectrum of a 1% ethylbenzene solution was considered to be excellent. Indeed, nobody could envision the 1000-fold increase that would happen in the next 30 years. We thought a lot at that time about sensitivity enhancement techniques. Special \hbox{low-noise} preamplifiers using ceramic tubes of the type 7077-G-E-60-17, optimized probe assemblies, and electronic filtering techniques were considered.[14] Noise calculations of probes and of complete spectroscopic experiments were a daily routine in the laboratory of Professor Günthard. This was normally the last resort for completing a Ph.D. thesis if the constructed spectrometer did not perform properly. However, this taught us more about response theory, Fourier transforms, and noise figures than any working spectrometer would have done.

This was the time of the computer of averaged transients, CAT, which helped to improve sensitivity by the coaddition of slow passage spectra.[15] At that time we advanced the idea of using one ultraslow passage instead of repeated scanning through the same spectrum. In this way we missed some important facts that became clear to me only after my arrival in the fall of 1963 at Varian Associates in Palo Alto for my postdoctoral years.

Under the guidance of Dr. Weston A. Anderson, I started extensive investigations of rapid scan performance conditions based on numerical solutions of the Bloch equations. They revealed the possibility of significantly enhancing the sensitivity per unit time by rapid and repetitive scanning through the spectrum,[16–18] facts that were already well known to scientists such as Bitter[19] and Jacobsohn and Wangsness.[20] However, at that time nobody recognized the possibility of using computers to remove the distortions which the rapid scan introduced into the spectrum.

FOURIER TRANSFORM NMR SPECTROSCOPY

I remember in the spring of 1964, when the calculations of performance conditions were in full progress, Wes Anderson

Figure 4 Dr. Weston A. Anderson and his Little Devil Prayer Wheel which he constructed for multiple channel NMR spectroscopy in 1963

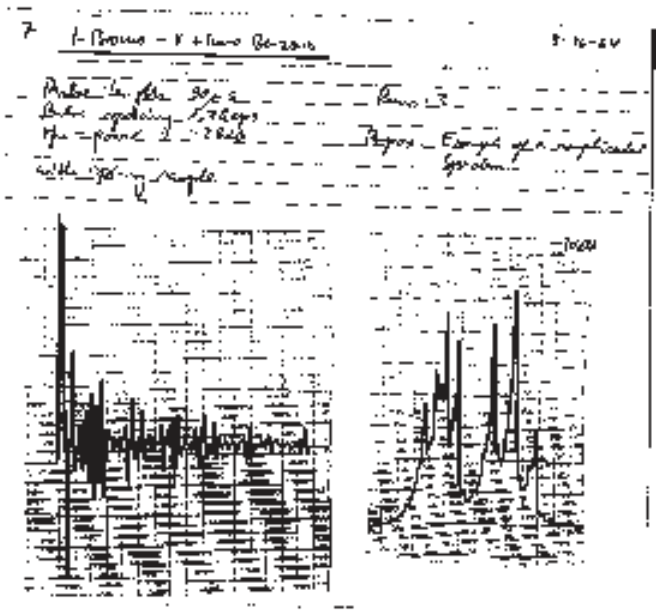

Figure 5 Early experiments performed on 16 September 1964. After a few experiments on benzene, a complicated spin system, 1-bromo-4-fluorobenzene, was also treated on the first day. The figure shows the FID and a CW spectrum. The Fourier transform of the FID has been lost

Figure 6 The author in front of the modified DP-60 NMR spectrometer on which the first Fourier transform NMR experiments were performed at Varian Associates, Palo Alto, CA, in 1965. The author is acting as a human interface between the time averaging computer C1024 and an IBM card punch

came to me and mentioned the possibility of applying repetitive pulses for the simultaneous excitation of all nuclear resonances and using a computer to analyze the response. I was asked to sign, as a witness, the important notebook pages by Wes Anderson that contained the principles of pulse Fourier spectroscopy. I was not very aware at that time of Wes's previous work on the Wheel of Fortune (Figure 4); in fact, I never saw it. I do not remember whether Wes showed me at the same time or slightly later the highly important patent application by Russell Varian[21] which already contained the basic idea.

There was no rf pulse equipment available at Varian at that time as everybody was fully devoted to continuous wave spectroscopy. However, as a result of masterly support by the electronic engineer William Siebert, within two months a proton-pulse spectrometer with 300 W pulse power using a fluorine field/frequency lock without any magnetic field modulation was assembled.

The crucial first experiments were performed during the summer months of 1964 while Wes Anderson was on an extensive journey abroad (Figure 5). When he came home, I was able to hand him the first successful results that surprised me as much as him. However, there was no reason to be overenthusiastic and we certainly did not think in terms of a champagne party. When one considers the cumbersome treatment of the data acquired in a time averaging CAT 400 computer, into paper tape, being converted into punched cards at IBM San Jose, then converted to magnetic tape at the Service Bureau Corporation, Palo Alto, Fourier-transformed on an IBM 7090, and plotted on a Calcom plotter, nobody could have been convinced by us of a time-saving advantage! Later, we had our own card punch to shorten the data pathway (Figure 6).

Nevertheless, we decided to publish the work in the *Journal of Chemical Physics*. However, we had no success; the paper was rejected twice, being considered too technical and not of sufficient originality. We then submitted the paper to *Review of Scientific Instruments* on 9 July 1965 where, after further revision, it was finally accepted on 16 September 1965.[22]

I also discussed the subject at the 6th Experimental NMR Conference in Pittsburgh, 25–27 February 1965. In general the response was not overwhelming, except from a few people with foresight like Oleg Jardetzky. The Varian management was also not too excited. With little enthusiasm, an accessory was developed for the HR-100 spectrometer; however, that never performed properly. Even the newly developed XL-100 concept, which was worked out in the following years, was designed with a field-modulation system that prohibited the implementation of pulse Fourier transform spectroscopy. Ultimately, it was the competitive German company Bruker Analytische Messtechnik with Toni Keller and Professor Günther Laukien which demonstrated and sold the first properly designed Fourier transform equipment in 1969. With much foresight, they brought the first Fourier-transform-only spectrometer HX 90 onto the market in 1971.

HETERONUCLEAR NOISE DECOUPLING

Being out of better ideas for the time being, it was tempting in May 1965 to try some of the ideas left over from my thesis,[14] thus justifying post mortem my otherwise spoiled best years. Broadband spin decoupling indeed appeared to be a worthwhile goal to me, especially for heteronuclear spin systems. The first experiments concentrated on a flourine–proton system. The necessary binary random noise was taken initially from the even/odd character of the last digits in the Palo Alto telephone directory, modulated onto the radiofrequency carrier, and applied to the protons, observing the fluorine resonance at the same time.[23] This led to the initial pseudonym phone-book resonance. Only later was I informed by R. Whitehorn (Varian Associates) that binary noise could be generated in a more convenient and predictable manner by shift register generators[24] that were used from September 1965 onwards.

Numerous further modulation schemes such as repetitive 180 ° and other pulses were used and it was found that primarily the spectral properties had a significant effect, but otherwise the type of sequence was immaterial. There was no indication whatsoever in my experiments for the dramatic improvement that was discovered much later by Malcolm Levitt and Ray Freeman[25] using composite pulse sequences.

COMPUTERIZED SPECTROSCOPY

Until 1966, Varian Associates did not possess even a single computer, and all the Fourier NMR experiments I undertook at Varian used off-company data processing. Finally, in October 1966, the first PDP8 computer with 4096 words of 12-bit memory arrived, and I interfaced it with the help of William Siebert to the most widely used routine NMR spectrometer, the A-60. This prohibited the use of pulse Fourier transform experiments for which the A-60 is unsuited by design. Numerous other applications were programmed and tried in a rapid sequence in view of a presentation at the 8th ENC, 2–4 March 1967, in Pittsburgh.

The experiments included signal averaging with automatic drift compensation by searching for the TMS line, resolution enhancement by convolution, spectra analysis by multiplet identification, coding of spectra for a subsequent automatic library search, automatic 2D shim mapping, and automatic shimming by use of the simplex search algorithm. Except for the automatic shimming procedure,[26] this work was not published at that time as it was felt to be of little originality. A later account can be found in Ref. 27.

RETURN TO THE HOMELAND

My return to Switzerland in the spring of 1968 proved to be a scientific disadvantage. Unsuitable equipment and the lack of support at the Laboratorium für Physikalische Chemie, ETH Zürich, made progress difficult. I had to supervise an ill-suited Varian 220 MHz spectrometer that was strictly limited to continuous wave operation without a field/frequency lock system. With a streetcar line in the neigborhood, this turned out to be a disaster. Despite a homemade lock system, the spectrometer never performed satisfactorily. Scientific output was low, and after two years of struggling I was affected by a nervous breakdown in 1970.

Looking back, I am tempted to rate my years from 1968 to 1974 as the dark Middle Ages after the productive and inspiring classical years in Palo Alto. We tried numerous new approaches, but none with an epoch-making breakthrough. (Personally, I became interested in the mysterious and fascinating Tibetan art during this time period.)

With my first graduate student, Thomas W. Baumann (thesis 1969–74), we ventured on our first exploratory excursion into solid state NMR, constructing a 1.5-T solid state spectrometer. We devoted much time on cross polarization in the laboratory frame ($^{35}Cl \rightarrow {}^{1}H$) and in the rotating frame ($^{1}H \rightarrow {}^{13}C$). Our time-consuming solid state activities became more exciting in 1973 with the work of Luciano Müller which will be described later.

My second graduate student, Dieter Welti (1970–76), together with Max Linder, explored the use of paramagnetic shift and relaxation reagents in NMR, using borneol and 1-propanol as model compounds. The question of accurate structure determinations using the multifaceted shift and relaxation effects was our primary interest.[28]

Just to keep our obstinate HR-220 Varian spectrometer busy, we started a series of investigations on simple molecules dissolved in a nematic phase. After the study of a few four-ring compounds by Christian Oertli, we explored, together with Alexander Frey, the distortion of cubic molecules by liquid crystalline solvents.[29] Again the determination of molecular structures was our main interest.

I was still interested in the slowly emerging Fourier transform spectroscopy, and I studied some subtle effects of pulse excitation such as the equivalence of slow passage and pulse spectroscopy,[30] saturation effects in Fourier spectroscopy, together with my first postdoc Robert E. Morgan,[31] and the causality principle in Fourier spectroscopy, together with my third graduate student Enrico Bartholdi.[32] Motivated by the notorious field instability in Zürich, we also proposed at that time the usage of difference-frequency measurements to avoid the need for a field/frequency lock system.[33,34]

Another series of studies was devoted to the application of pulse spectroscopy to chemically induced dynamic nuclear

polarization (CIDNP). It appeared to us very natural to investigate time-dependent phenomena with time-resolved measurement techniques. This was the subject of the thesis of Stefan Schäublin (1971–76). For a short period he was supported by Alexander Wokaun.[35,36] This work also led to the recognition of the important intensity problems when investigating nonequilibrium populations by pulse experiments.[37] Later, these studies were extended to stopped flow experiments by René O. Kühne and Thierry Schaffhauser.[38]

STOCHASTIC RESONANCE

Pursuing my old love and motivated by a correspondence with Wes Anderson, in June 1968 I started the first attempts to compute and measure NMR spectra via stochastic noise excitation of the sample and by Fourier transforming the cross-correlation function that relates input and output noise.[39] The first experiments already used shift register sequences as sources of binary pseudorandom noise.[24] At virtually the same time, Reinhold Kaiser also proposed stochastic resonance for recording spectra, but using Gaussian noise to excite the spin system.[40]

Subsequently, the theory of stochastic resonance was worked out in great detail in the thesis of Enrico Bartholdi (1971–75) and by Alexander Wokaun.[41] Experiments have been performed by Kurt A. Meier and Marco Genoni.

Although the properties of higher correlation functions were well known to us at that time, we did not recognize that they contain multidimensional information that could be used and displayed in the form of 2D spectra. This became obvious to us however, in the course of the early calculations of Enrico Bartholdi in 1972 in the context of two-pulse 2D Fourier spectroscopy.[42]

Figure 7 Professor Jean Jeener, the inventor of two–dimensional Fourier transform NMR

Figure 8 Thomas Baumann (right) and the author trying to understand the notes of the AMPERE Summer School on the two-pulse experiment proposed by Jean Jeener in 1971. In the background is the modified DP-60 Varian NMR spectrometer on which the first two-dimensional NMR experiments were performed

THE DAWN OF TWO-DIMENSIONAL SPECTROSCOPY

The participation of Thomas W. Bauman at the AMPERE Summer School in Basko Polje, Yugoslavia, in September 1971 was an extremely fortunate event. Being a meticulous scientist, he brought home a careful script of the lectures, among them one by Jean Jeener that attracted my attention immediately: a simple two-pulse experiment that produced revealing 2D spectra by 2D Fourier transformation of a 2D set of response signals (Figure 7 and 8).

This was exactly the technique I had been waiting for. I had been thinking for some time about systematic computer-controlled double resonance experiments, but appreciated the complexity of the resulting 2D spectra should they follow the shape of the famous Anderson–Freeman plots.[43] The Jeener two-pulse experiment appeared not to have this disadvantage.

Enrico Bartholdi, who had just started his graduate studies, was willing to perform some analytical calculations on two-pulse experiments, taking relaxation into account. He confirmed the principal usefulness of the experiment and studied its features in detail. We did not plan to perform experiments for two reasons. First we considered 2D spectroscopy as Jeener's property and waited for his results to be published. Second, we thought that our computing equipment, with 16 000 words of memory, was inadequate for two-dimensional data storage and processing. We had some correspondence with Jean Jeener on the experiment in 1973, and he showed us a rough draft of an unfinished paper on this subject which, unfortunately, was never published.

In 1974, I attended the 15th Experimental NMR Conference (ENC) and heard on 30 April 1974 an exciting lecture by Paul Lauterbur entitled Zeugmatography–Spatial Resolution of NMR Signals. He discussed the attainment of images by the projection–reconstruction method using continuous wave experiments. I immediately recognized that time domain experiments with switched magnetic field gradients in complete analogy to 2D spectroscopy would be the method of choice. This led to the concept of Fourier zeugmatography or Fourier imaging with a patent filed orginally on March 18, 1975, and issued on January 24, 1978. As I was acting

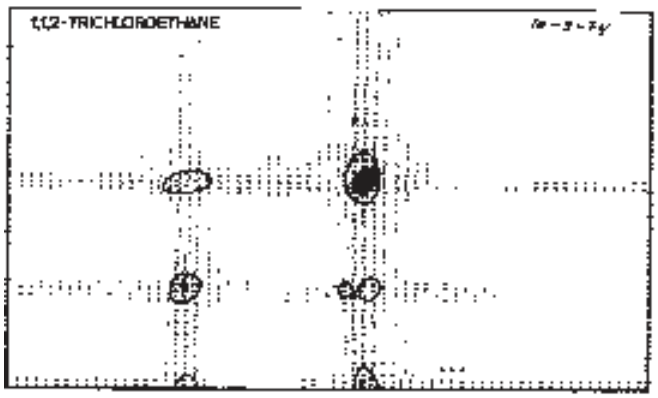

Figure 9 Early 2D spectrum of 1,1,2-trichloroethane recorded on 10 September 1974 with the Jeener two-pulse sequence on the spectrometer illustrated in 8. The absolute value spectrum using letter-coded intensities in a contour representation shows two strong diagonal peaks, two cross peaks, and two axial peaks

Figure 10 One of the very first 2D Fourier images of two coaxial water-filled sample tubes, recorded by Anil Kumar on 10 July 1974 on a modified Bruker SPX4-100 spectrometer. The plot uses letter-coded intensities

at that time as a consultant, I assigned it to Varian Associates.

I was now sufficiently motivated to perform 2D spectroscopic and imaging experiments. At the same time, I was also asked by Kurt Wüthrich to present some introductory remarks, possibly on our own work, at the VIth International Conference on Magnetic Resonance in Biological Systems, Kandersteg, 16–21 September 1974, which we organized together with Joachim Seelig. As I did not have anything biological to talk about, I decided to perform rapidly the first 2D and Fourier imaging experiments, both with biological applications in view. I undertook the initial 2D experiments myself on a modified Varian DA-60 spectrometer equipped with a Varian 620i computer with 16 000 memory words (16 bits) using my own software (Figure 9). Using a teletype for letter-coded contour maps, I obtained the first halfway decent spectra on 1 July, 1974. The Fourier imaging experiments were performed together with Anil Kumar on a Bruker SPX4-100 spectrometer equipped with a Varian 620/L-100 computer with 12 000 memory words, using the x- and y-shim coils of the Varian 15 in. magnet for the switched field gradients[44,45] (Figure 10). It was little wonder that my rapidly concocted contribution was rated as premature at the Kandersteg conference! Sometimes, however, even prematurely born children survive and excel.

This was indeed the end of my dark middle ages. We had been freed from our one-dimensional narrow-mindedness and had again room to move in new dimensions. Modern times had started without being noticed at that instant. We had some difficulty in appreciating the future as far as these new horizons were concerned, but we very much enjoyed playing with a novel toy that produced fascinating 2D plots and images. We felt at this moment more like graphic artists and playboys than scientists.

PLAYING WITH A NEW TOY

We were indeed fascinated by the wealth of new possibilities offered by the 2D spectroscopy concept. Numerous homonuclear schemes were explored in the thesis work of Walter P. Aue (1974–79): the detection of multiple quantum transitions,[42] homonuclear broadband decoupling and J-resolved NMR spectroscopy together with Jiri Karhan,[46] and phase separation techniques together with Peter Bachmann and Luciano Müller.[47] Heteronuclear experiments were performed by Luciano Müller in his thesis work (1973–77), partially together with Anil Kumar.[48–51] Andrew Maudsley showed for the first time the possibility of indirect detection of low-γ nuclei,[52,53] and Alexander Wokaun expanded the techniques and applications of multiple quantum spectroscopy[54–57] in his thesis (1974–78). He showed for the first time the possibility of phase cycling for the selection of individual orders of multiple quantum coherences,[55] and demonstrated the usefulness of multiple quantum relaxation.[56]

Competition was not yet a real problem during these early years. Few scientists believed in the future of 2D spectroscopy—with one exception: Ray Freeman and his extremely talented graduate student Geoffrey Bodenhausen (who did his earlier studies in our research group in Zürich). In the design of powerful heteronuclear 2D experiments, in particular, they were very strong,[58–60] and merit much of the credit for the initial phase in the development of 2D NMR spectroscopy.

The second major 2D spectroscopy technique, 2D exchange spectroscopy, originated from a discussion with Jean Jeener at the Gordon Conference on Magnetic Resonance in 1978. He confessed on this occasion that the three-pulse scheme of 2D exchange spectroscopy was in fact the first that came to his mind before proposing the two-pulse experiment at the AMPERE Summer School in Basko Polje in 1971. With the small molecules to which we were limited in our laboratory, it proved difficult to detect cross-relaxation cross peaks, but Beat H. Meier found it quite easy to observe chemical exchange cross peaks.[61,62] The special features of this important experiment were worked out subsequently in great detail by Slobodan Macura, Yong-Ren Huang, and Dieter Suter.[63–68]

Also, at the same time several solid state 2D experiments were investigated, but this work will be summarized later.

EXPLORING THE WEALTH OF MODIFIED 2D TECHNIQUES

While the previous development of 2D spectroscopy had been more or less sequential, the following period rather resembled little Max in Paradise who does not know which fruit to pick and eat first. Development during this time had, in essence, two goals: (i) to increase the information content of 2D spectra; and (ii) to decrease their complexity. I had little personal impact on these developments. A group of extraordinarily creative co-workers determined the direction of our future research efforts. I became more an organizer and trouble shooter.

The first step in increasing the information content was the introduction of a relayed homonuclear coherence transfer step by Geoffrey Bodenhausen together with Günther Eich[69,70] where a two (or more) pulse sequence leads to a multistep coherence transfer, important for the elucidation of crowded NMR spectra. Similar heteronuclear procedures were proposed by Philip H. Bolton almost simultaneously.[71]

The next development was total correlation spectroscopy (TOCSY) in the rotating frame tested for the first time by Lukas Braunschweiler.[72] Here all the resonances of a coupled spin system are connected by cross peaks. This allows the easy recognition of complete families of coupled spins. Subsequently, considerable work in our group has been devoted to rotating frame experiments, as well as extending the important work of Axel Bothner-By on ROESY.[73] Christian Griesinger has introduced procedures for the elimination of frequency-offset effects[74] and of cross-relaxation effects by Clean TOCSY.[75] He introduced the invariant trajectory approach for the description of radiofrequency-perturbed experiments.[76] Jacques Briand further improved Clean experiments by the introduction of Clean CITY,[77] and Rafael Brüschweiler suggested a novel cross-relaxation measurement technique called T-ROESY.[78]

Another neat experiment, called Accordion spectroscopy and worked out by Geoffrey Bodenhausen,[79] increases the information content of 2D spectra by incorporating exchange-type information into the 2D peak shape. The resulting spectra effectively represent projected 3D spectra.

An even larger class of experiments allows the simplification of overcrowded 2D spectra for facilitating their analysis. The most successful and general type of simplification scheme is multiple quantum filtering, introduced by Ole W. Sørensen[80,81] with contributions from Malcolm H. Levitt.[82,83] The techniques of multiple quantum spectroscopy[84] and coherence-transfer-pathway selection[85] are related. In this context Geoffrey Bodenhausen, together with Lukas Braunschweiler and Herbert Kogler, have made a very significant contribution. Further filtering procedures, mainly due to Ole W. Sørensen, are J-filters[86] and Z-filters.[87]

The names of Christian Griesinger and Ole W. Sørensen are nowadays closely connected with exclusive correlation spectroscopy or ECOSY,[88–90] a technique that leads to simplified multiplet patterns in 2D spectra and allows ready determination of J coupling constants. The ultimate forms of ECOSY are bilinear and planar COSY experiments, introduced by Thomas Schulte-Herbrüggen, Zoltan L. Mádi, and Ole W. Sørensen.[91] In this context, the symmetry features of 2D spectra, worked out again in contributions by Ole W. Sørensen and Christian Griesinger together with Claudius Gemperle, Serge Boentges, and Beat U. Meier,[92–94] are important.

A very drastic simplification of 2D (or 1D) is achieved by spin topology filtration, investigated by Malcolm H. Levitt and Christian Radloff.[95–99] Here, the coupling network topology is used as a criterion for peak rejection.

In parallel to these predominantly homonuclear experiments, heteronuclear experiments have also been worked out by Ole W. Sørensen.[81,100–102] His work in this area is summarized in Refs. 103 and 104.

It is not surprising that Malcolm H. Levitt also left in Zürich some composite pulse traces.[105–108]

Instead of simplifying 2D spectra to allow their manual analysis, it is often possible to devise computer routines for their automatic analysis. Major contributions in this field have been made by Geoffrey Bodenhausen, Beat U. Meier, Zoltan L. Mádi, and Serge Boentges.[109–113]

It is not possible to mention all the contributions of an astonishingly creative group of enthusiastic co-workers here nor is it possible to make well-deserved cross references to other highly productive research groups.

COLLABORATION WITH KURT WTHRICH AND THE APPLICATIONS OF 2D SPECTROSCOPY TO MOLECULAR BIOLOGY

At the end of 1975, the high-field NMR center with the Varian HR-220 spectrometer under our supervision was replaced by a new high-field NMR center with a Bruker HMS-360 spectrometer under the supervision of Kurt Wüthrich. It was desirable at this point for both sides to continue and intensify the collaboration that had existed in a loose form since the inauguration of the high-field NMR center in 1969. It was easy to select 2D spectroscopy as the subject of mutual interest, as it became clear that its application to molecular biology could be fruitful if only the enormous technical difficulties could be solved.

In December 1976, a joint project was started with Peter Bachmann, a very experienced spectroscopist and computer programmer, and Kuniaki Nagayama, a brilliant young Japanese scientist. This was the beginning of an extremely fruitful series of joint projects lasting for 101/2 years. Initially, the projects were supported by ETH Zürich. However, due to a financial bottleneck in the school, the later phases were financed by Spectrospin AG and the Kommission zur Förderung der wissenschaftlichen Forschung.

The initial studies concentrated on the simplification of biomolecular NMR spectra by 2D J-resolved NMR,[114–117] and by the use of selective spin decoupling.[118,119] The first correlation spectra were recorded in the spin-echo-correlated (SECSY) mode to save performance time and computer memory by restricting the ω_1 domain.[120]

A major breakthrough in 1980 was achieved by Anil Kumar, who had joined the project during his second stay in Zürich. He demonstrated that cross relaxation in macromolecules can be detected surprisingly well with the experiment presently known under the acronym NOESY.[121] This is the 2D version of the 1D transient NOE experiment that Gordon and Wüthrich had previously introduced for studies of proteins.[122] It is the same experiment that had earlier been used by Jean Jeener, Beat H. Meier, and Peter Bachmann for the exploration of chemical exchange networks.[61,62] Together with the correlation experiment in the original form proposed by Jeener and known as COSY, Kurt Wüthrich, Gerhard Wagner, and co-workers had all the required tools in their hands in 1980 to develop their ingenious highly successful sequential assignment procedure for biopolymers,[123] a task they had already pursued previously using more cumbersome one-dimensional NMR techniques.[124]

Further work undertaken in this series of joint projects concerned quantitative comparisons of 1D and 2D NOE measurements,[125] strong coupling effects,[126] an extension of previous 1D NOE build-up rate studies[122,127] to 2D NMR,[128] triangular multiplication,[129] and symmetrization.[130] The successor to Anil Kumar, Slobodan Macura, was an expert on 2D exchange studies and contributed significantly to the suppression and separation of J cross peaks in NOESY spectra.[131,132] Further important improvements by multiple quantum filtering and multiple quantum spectroscopy were achieved by Mark Rance.[87, 133–136] Norbert Müller worked out the rules for the appearance of forbidden relaxation-induced cross peaks in 2D spectra,[137,138] and of cross peaks in multiple quantum filtered spectra.[139] Finally, Michael H. Frey contributed to more applied projects.[140,141]

EXTENSION TO THREE DIMENSIONS

For a long time, 3D spectroscopy appeared to be out of reach because of performance–time and storage–space limitations. The first attempts by Christian Griesinger and Ole W. Sørensen in this direction, partially in collaboration with the research group of G. Marius Clore and Angela M. Gronenborn, therefore used selective excitation techniques.[142–144] Later, however, it was found that nonselective 3D experiments are also quite feasible.[145] This parallels the work by other research groups, in particular by R. Kaptein and A. Bax.

CONFORMATIONAL DYNAMICS OF BIOMOLECULES

During the course of the past five years, our interest has shifted away from the design of pulse sequences for the manipulation of multidimensional spectra. We have become more interested in the study of the intramolecular dynamics of biomolecules. This is a field where much progress is still needed before the motional modes relevant for biological activity can be sufficiently well characterized. To date, much of our work has concentrated on the cyclic decapeptide antamanide, and relevant contributions have been made by Christian Griesinger, Zoltan L. Mádi, Rafael Brüschweiler, Martin Blackledge, Jürgen Schmidt, Matthias Ernst, Ping Xu, and Tobias Bremi in collaboration with the research groups of Martin Karplus and Wilfred van Gunsteren.[146–152]

ACTIVITIES IN SOLID STATE NMR

Since my return from California in 1968, our involvement in solid state NMR has been considerable. I often mentioned that although about 70% of our efforts went into solids about 70% of our results came from liquid-state NMR. Solids have proved to be harder and more brittle in our hands than liquids!

After some initial exploratory studies by Thomas Baumann from 1969 to 1974 which have been mentioned earlier, Luciano Müller together with Anil Kumar and Thomas Baumann produced results in 1974 for our very first *Physical Review Letter*,[153] describing a particularly neat example of transient oscillations in cross-polarization experiments together with a simple explanation.[154] We have not always been so lucky. A somewhat related, but not uninteresting paper on cross polarization with a pulsed radiofrequency field, received a devastating comment from a referee and was never published.

After the success of 2D spectroscopy in liquids, and following some very early work by the research group of John S. Waugh,[155,156] we also tried to explore possibilities in liquid crystals[157] and in solids.[158] Perhaps the most relevant contribution in this context was the orientation of tensorial interactions based on ridge patterns in 2D powder spectra obtained by Max Linder (thesis 1979–82) and Alfred Höhener.[158] Taking advantage of the newly developed windowless dipolar decoupling multiple pulse sequences by Doug Burum and Max Linder,[159] heteronuclear high-resolution correlation experiments in solids were also explored by Pablo Caravatti, Geoffrey Bodenhausen, and Lukas Braunschweiler.[160,161]

After the closure of the high-field NMR center in 1975, we converted the HR-220 spectrometer into a solid state ^{14}N apparatus to observe resolved ^{14}N double quantum spectra in the hope of developing applications to biomolecules. This turned out to be more difficult than expected. However, these experiments did allow Peter Brunner and Michael Reinhold to explore the mechanism of cross polarization of double quantum transitions.[162,163]

The attempts of Thierry Schaffhauser to study the one-dimensional organic conductor bis(tetrathiotetracene) triiodide by proton and carbon-13 resonance in collaboration with Bruno Hilti of Ciba-Geigy AG also turned out to be more difficult than we had thought.[164,165] Firstly, it was difficult to obtain sufficiently large single crystals, and secondly, their conductivity led to disastrous arcing.

Two focal points characterize our more recent solid state NMR research under the guidance of Beat H. Meier: hydrogen-bond dynamics in carboxylic acid dimers,[166–174] and the investigation of spin diffusion in disordered solids combined with theoretical considerations about spin order transfer.[174–188]

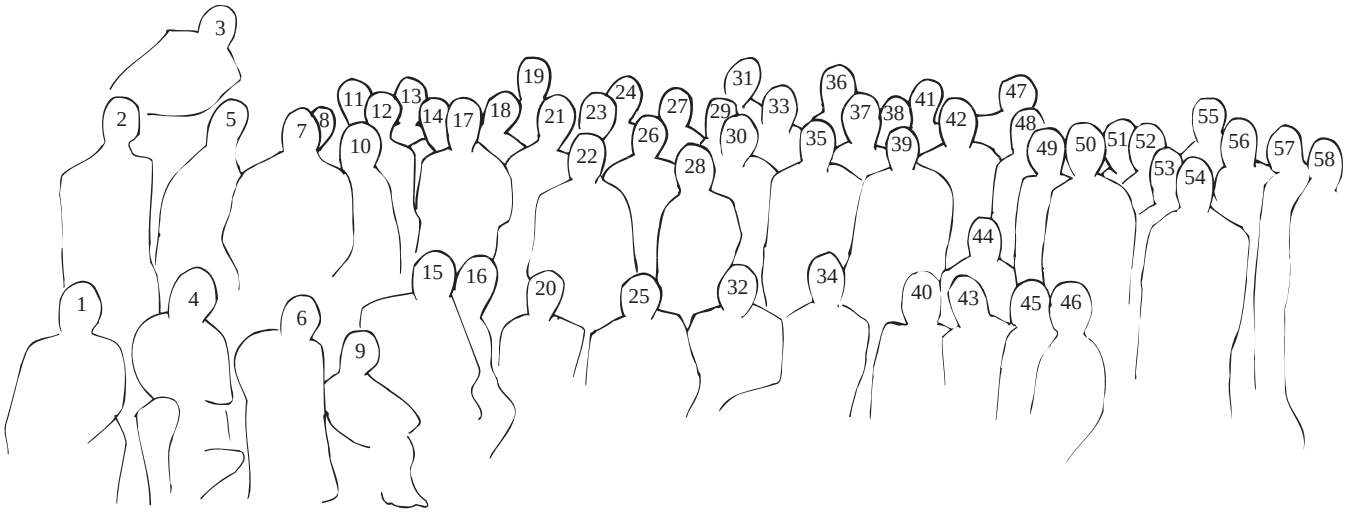

Figure 11 (a) Group photograph of present and many former co-workers at the Nobel Prize Symposium, March 1992, Centro Stefano Francini, Ascona, Switzerland. The persons, numbered in sketch (b), can be identified from the following list. 1 Nagayama, Kuniaki 2 Wokaun, Alexander 3 Jeener, Jean; Prof. (guest) 4 Ernst, Richard R. 5 Robyr, Pierre 6 Aue, Walter 7 Macura, Slobodan 8 Blackledge, Martin 9 Müller, Irène 10 Klein, Jeannette 11 Bodenhausen, Geoffrey 12 Schaffhauser, Thierry 13 Meier, Beat H. 14 Rance, Mark 15 Kessler, Horst; Prof. (guest) 16 Müller, Luciano 17 Griesinger, Christian 18 Gemperle, Claudius 19 Schweiger, Arthur 20 Sierra, Gustavo 21 Brüschweiler, Rafael 22 Höhener, Alfred 23 Mádi, Zoltan 24 Schulte-Herbrüggen, Thomas 25 Kumar, Anil 26 Reinhold, Michael 27 Signer, Paul 28 Pastore, Annalisa 29 Bachmann, Peter 30 Schäublin, Stefan 31 Wacker, Thomas 32 Linder, Max 33 Sebbach, Jochen 34 Kreis, Roland 35 Counsell, Christopher 36 Schmidt, Jürgen 37 Boentges, Serge 38 Baumann, Thomas 39 McCoy, Mark 40 Radloff, Christian 41 Schick, Martin 42 Kogler, Herbert 43 Xu, Ping 44 Müri, Marcel 45 Xi-Li, Wu 46 Levante, Tilo 47 Welti, Dieter 48 Forrer, Jörg 49 Karhan, Jiri 50 Sørensen, Ole W. 51 Müller, Norbert 52 Schönenberger, Christian 53 Levitt, Malcolm H. 54 Zhang, Shanmin 55 Baldus, Marc 56 Stöckli, Armin 57 Meier, Beat U. 58 Suter, Dieter

Our interest in the dynamics of hydrogen bonds has been spurred by Federico Graf who joined our group in 1979 after completing a Ph.D. in EPR with Hans H. Günthard and a postdoctoral period at IBM San Jose. We wanted to gain more insight into the proton transfer dynamics in a simple double-minimum system and in the contribution of tunneling to the dissipative transfer. The experimental NMR and neutron-diffraction measurements are associated with Beat H. Meier, first in his thesis work from 1978–84;[166–169], [189] and later through his supervision of the work of Armin Stöckli[170,172] and Pierre Robyr.[174] Of great importance to the success of this project was the support given by Rolf Meyer,[171–173] one of the unrivalled experts in the computation and analysis of intramolecular dynamics,[190] as well as the support by Albert Furrer, Peter Fischer and their team regarding the use of neutron diffraction.[167–170] Hydrogen-bond dynamics turned out to be a critical test case for our understanding of nuclear spin relaxation in solids.

The transfer of spin order through the network of dipolar interactions appeared to us to be one of the most important, interesting, and useful features of NMR in solids. Being a typical many-body problem, it is difficult to treat theoretically. Attempts in this direction have been made by Dieter Suter[175,178] and Malcolm H. Levitt[179] in our group. On the other hand, spin diffusion has turned out to be an ideal tool for studying local order in macroscopically disordered materials, such as polymers, polymer blends, and glasses. After some initial demonstration examples treated by Pablo Caravatti, Janos A. Deli, and Geoffrey Bodenhausen,[176] the work of Pablo Caravatti (thesis 1981–86) concentrated on polymer blends investigated by proton spin diffusion[177,191] in collaboration with the polymer expert Peter Neuenschwander.

The limited achievable resolution of proton resonance was soon recognized to be a grave drawback, and the desire to use carbon-13 instead was only logical. However, in natural abundance ^{13}C spin diffusion can be exceedingly slow and isotopic enrichment is not always possible. This motivated Beat H. Meier to start an extensive program on techniques to accelerate spin diffusion for dilute spin systems. Thanks to his and his co-workers' efforts, we have today several possibilities in hand to increase the spin-diffusion rate, such as rotor-driven spin diffusion as developed by Marco G. Colombo and Thomas Burmeister,[180,181] radiofrequency-driven spin diffusion as explored by Pierre Robyr,[182] and the use of xenon-129 probes as investigated by Marco Tomaselli.[186]

The question of the reversibility of spin-diffusion dynamics has been addressed by Shanmin Zhang.[183] He has also proposed indirect measurement techniques for spin diffusion.[184,185] This work on spin dynamics has been well summarized and extended in a recent review by Beat H. Meier (in press).

Finally, a short but exciting excursion in the lowlands of zero-field resonance should also be mentioned. Following the footsteps of Alex Pines and his team,[192,193] Roland Kreis and Albert Thomas have further explored the possibilities of this fascinating technique.[194,195]

CONCLUSIONS

To be honest, we have made a living not only by borrowing clever ideas. Particularly in the later phases, numerous new concepts have been created in-house by a number of incredibly

gifted co-workers. Thus our research group has been lucky in two respects, the influx of brilliant ideas and of even more brilliant individuals (Figure 11).

This essay certainly provides a one−sided view of NMR history. Because of lack of space, it is impossible to do justice to all former co-workers and even less to other research groups.

REFERENCES

1. H. Primas, *Helv. Phys. Acta*, 1957, **30**, 297.
2. H. Primas and Hs. H. Günthard, *Helv. Phys. Acta*, 1957, **30**, 315.
3. H. Primas and Hs. H. Günthard, *Helv. Phys. Acta*, 1957, **30**, 331.
4. H. Primas, R. Arndt, and R. R. Ernst, *Z. Instrumentenkde*, 1959, **67**, 293; 1960, **68**, 8; 1960 **68**, 21; 1960, **68**, 55.
5. H. Primas and Hs. H. Günthard, *Rev. Sci. Instrum.*, 1957, **28**, 510.
6. L. Wegmann, *DECHEMA-Monogr.*, 1958, **35**, 84.
7. A. Huber and H. Primas, *Nuclear Instrum. Methods*, 1965, **33**, 125.
8. H. Primas, *Rev. Mod. Phys.*, 1963, **35**, 710.
9. H. Primas, *Proceedings of the Conference on Molecular Spectroscopy*, eds. R. Thornton and H. W. Thompson, Pergamon Press, London, 1959, p. 19.
10. C. N. Banwell and H. Primas, *Mol. Phys.*, 1963, **6**, 225.
11. H. Primas, *Helv. Phys. Acta*, 1961, **34**, 36.
12. N. Wiener, *Nonlinear Problems in Random Theory*, Wiley, New York, 1958.
13. R. R. Ernst and H. Primas, *Helv. Phys. Acta*, 1963, **36**, 583.
14. R. Ernst, Thesis, ETH Zürich, 1962.
15. O. Jardetzky, N. G. Wade, and J. J. Fischer, *Nature (London)*, 1963, **197**, 183; M. P. Klein and G. W. Barton, *Rev. Sci. Instrum.*, 1963, **34**, 754; L. C. Allen and L. F. Johnson, *J. Am. Chem. Soc.*, 1963, **85**, 2668.
16. R. R. Ernst, *Rev. Sci. Instrum.*, 1965, **36**, 1689.
17. R. R. Ernst and W. A. Anderson, *Rev. Sci. Instrum.*, 1965, **36**, 1696.
18. R. R. Ernst, *Adv. Magn. Reson.*, 1966, **2**, 1.
19. F. Bitter et al., *MIT Res. Lab. Electron. Quart. Progr. Rep.*, 15 July 1947, p. 26.
20. B. A. Jacobsohn and R. K. Wangsness, *Phys. Rev.*, 1948, **73**, 942.
21. R. H. Varian, US Pat. 3 287 629, 1966.
22. R. R. Ernst and W. A. Anderson, *Rev. Sci. Instrum.* 1966, **37**, 93.
23. R. R. Ernst, *J. Chem. Phys.*, 1966, **45**, 3845.
24. S. W. Colomb, *Shift Register Sequences*, Holden-Day, San Francisco, 1967.
25. M. H. Levitt and R. Freeman, *J. Magn. Reson.*, 1981, **43**, 502.
26. R. R. Ernst, *Rev. Sci. Instrum*, 1968, **39**, 998.
27. R. R. Ernst, Without Computers—No Modern NMR, in *Computational Aspects of the Study of Biological Macromolecules by Nuclear Magnetic Resonance Spectroscopy*, eds. J. C. Hoch, F. M. Poulson, and C. Redfield, Plenum Press, New York, 1991, p. 1.
28. D. H. Welti, M. Linder, and R. R. Ernst, *J. Am. Chem. Soc.*, 1978, **100**, 403.
29. A. Frey and R. R. Ernst, *Chem. Phys. Lett.*, 1977, **49**, 75.
30. R. R. Ernst, W. P. Aue, E. Bartholdi, A. Höhener, and S. Schäublin, *Pure Appl. Chem.*, 1974, **37**, 47.
31. R. R. Ernst and R. E. Morgan, *Mol. Phys.*, 1973, **26**, 49.
32. E. Bartholdi and R. R. Ernst, *J. Magn. Reson.* 1973, **11**, 9.
33. R. R. Ernst, *J. Magn. Reson.*, 1971, **4**, 280.
34. R. R. Ernst, *J. Magn. Reson.*, 1971, **5**, 398.
35. S. Schäublin, A. Wokaun, and R. R. Ernst, *Chem. Phys.*, 1976, **14**, 285.
36. S. Schäublin, A. Wokaun, and R. R. Ernst, *J. Magn. Reson.*, 1977, **27**, 273.
37. S. Schäublin, A. Höhener, and R. R. Ernst, *J. Magn. Reson*, 1974, **13**, 196.
38. R. O. Kühne, T. Schaffhauser, A. Wokaun, and R. R. Ernst, *J. Magn. Reson.*, 1979, **35**, 39.
39. R. R. Ernst, *J. Magn. Reson.*, 1970, **3**, 10.
40. R. Kaiser, *J. Magn. Reson.*, 1970, **3**, 28.
41. E. Bartholdi, A. Wokaun, and R. R. Ernst, *Chem. Phys.*, 1976, **18**, 57.
42. W.P. Aue, E. Bartholdi, and R. R. Ernst, *J. Chem. Phys.*, 1976, **64**, 2229.
43. W. A. Anderson and R. Freeman, *J. Chem. Phys.*, 1962, **37**, 85.
44. A. Kumar, D. Welti, and R. R. Ernst, *Naturwissenschaften*, 1975, **62**, 34.
45. A. Kumar, D. Welti, and R. R. Ernst, *J. Magn. Reson.*, 1975, **18**, 69.
46. W. P. Aue, J. Karhan, and R. R. Ernst, *J. Chem. Phys.*, 1976, **64**, 4226.
47. P. Bachmann, W. P. Aue, L. Müller, and R. R. Ernst, *J. Magn. Reson.*, 1977, **28**, 29.
48. L. Müller, A. Kumar, and R. R. Ernst, *J. Chem. Phys.*, 1975, **63**, 5490.
49. L. Müller, A. Kumar, and R. R. Ernst, *J. Magn. Reson.*, 1977, **25**, 383.
50. A. Kumar, W. P. Aue, P. Bachmann, J. Karhan, L. Müller, and R. R. Ernst, *Abs XIXth Congr. AMPERE*, Heidelberg, 1976, p. 473.
51. L. Müller and R. R. Ernst, *Mol. Phys.*, 1979, **38**, 963.
52. A. A. Maudsley and R. R. Ernst, *Chem. Phys. Lett.*, 1977, **50**, 368.
53. A. A. Maudsley, L. Müller, and R. R. Ernst, *J. Magn. Reson.*, 1977, **28**, 463.
54. A. Wokaun and R. R. Ernst, *J. Chem. Phys.*, 1977, **67**, 1752.
55. A. Wokaun and R. R. Ernst, *Chem. Phys. Lett.*, 1977, **52**, 407.
56. A. Wokaun and R. R. Ernst, *Mol. Phys.*, 1978, **36**, 317.
57. A. Wokaun and R. R. Ernst, *Mol. Phys.*, 1979, **38**, 1579.
58. G. Bodenhausen, R. Freeman, and D. L. Turner, *J. Chem. Phys.*, 1976, **65**, 839.
59. G. Bodenhausen, R. Freeman, R. Niedermeyer, and D. L. Turner, *J. Magn. Reson.*, 1976, **24**, 291.
60. G. Bodenhausen, R. Freeman, G. A. Morris, and D. L. Turner, *J. Magn. Reson.*, 1977, **28**, 17.
61. B. H. Meier and R. R. Ernst, *J. Am. Chem. Soc.*, 1979, **101**, 6441.
62. J. Jeener, B. H. Meier, P. Bachmann, and R. R. Ernst, *J. Chem. Phys.*, 1979, **71**, 4546.
63. S. Macura and R. R. Ernst, *Mol. Phys.*, 1980, **41**, 95.
64. S. Macura, Y. Huang, D. Suter, and R. R. Ernst, *J. Magn. Reson.*, 1981, **43**, 259.
65. S. Macura and R. R. Ernst, *Period Biol.*, 1981, **83**, 87.

66. Y. Huang, S. Macura, and R. R. Ernst, *J. Am. Chem. Soc.*, 1981, **103**, 5327.
67. S. Macura, R. R. Ernst, A. Kumar, and K. Wüthrich, *Bull. Magn. Reson.*, 1981, **2**, 293.
68. S. Macura, Y. Huang, and R. R. Ernst, *Bull. Magn. Reson.*, 1981, **2**, 316.
69. G. Eich, G. Bodenhausen, and R. R. Ernst, *J. Am. Chem. Soc.*, 1982, **104**, 3731.
70. H. Kessler, M. Bernd, H. Kogler, J. Zarbock, O.W. Sørensen, G. Bodenhausen, and R. R. Ernst, *J. Am. Chem. Soc.*, 1983, **105**, 6944.
71. P. H. Bolton and G. Bodenhausen, *J. Magn. Reson.*, 1982, **46**, 306.
72. L. Braunschweiler and R. R. Ernst, *J. Magn. Reson.*, 1983, **53**, 521.
73. A. A. Bothner-By, R. L. Stephens, J. Lee, C. D. Warren, and R. W. Jeanloz, *J. Am. Chem. Soc.*, 1984, **106**, 811.
74. C. Griesinger and R. R. Ernst, *J. Magn. Reson.*, 1987, **75,** 261.
75. C. Griesinger, G. Otting, K. Wüthrich, and R. R. Ernst, *J. Am. Chem. Soc.*, 1988, **110**, 7870.
76. C. Griesinger and R. R. Ernst, *Chem. Phys. Lett.*, 1988, **152**, 239.
77. J. Briand and R. R. Ernst, *Chem. Phys. Lett.*, 1991, **185**, 276.
78. R. Brüschweiler, C. Griesinger, and R. R. Ernst, *J. Am. Chem. Soc.*, 1989, **111**, 8034.
79. G. Bodenhausen and R. R. Ernst, *J. Am. Chem. Soc.*, 1982, **104**, 1304.
80. U. Piantini, O. W. Sørensen, and R. R. Ernst, *J. Am. Chem. Soc.*, 1982, **104**, 6800.
81. H. Kessler, H. Oschkinat, O. W. Sørensen, H. Kogler, and R. R. Ernst, *J. Magn. Reson.*, 1983, **55**, 329.
82. M. H. Levitt, O. W. Sørensen, and R. R. Ernst, *Chem. Phys. Lett.*, 1983, **94**, 540.
83. O. W. Sørensen, M. H. Levitt, and R. R. Ernst, *J. Magn. Reson.*, 1983, **55**, 104.
84. L. Braunschweiler, G. Bodenhausen, and R. R. Ernst, *Mol. Phys.*, 1983, **48**, 535.
85. G. Bodenhausen, H. Kogler, and R. R. Ernst, *J. Magn. Reson.*, 1984, **58**, 370.
86. H. Kogler, O. W. Sørensen, G. Bodenhausen, and R. R. Ernst, *J. Magn. Reson.*, 1983, **55**, 157.
87. O. W. Sørensen, M. Rance, and R. R. Ernst, *J. Magn. Reson.*, 1984, **56**, 527.
88. C. Griesinger, O. W. Sørensen, and R. R. Ernst, *J. Am. Chem. Soc.*, 1985, **107**, 6394.
89. C. Griesinger, O. W. Sørensen, and R. R. Ernst, *J. Chem. Phys.*, 1986, **85**, 6837.
90. C. Griesinger, O. W. Sørensen, and R. R. Ernst, *J. Magn. Reson.*, 1987, **75**, 474.
91. T. Schulte-Herbrüggen, Z. L. Mádi, O. W. Sørensen, and R. R. Ernst, *Mol. Phys.*, 1991, **72**, 847.
92. O. W. Sørensen, C. Griesinger, and R. R. Ernst, *Chem. Phys. Lett.*, 1987, **135**, 313.
93. C. Griesinger, C. Gemperle, O. W. Sørensen, and R. R. Ernst, *Mol. Phys.*, 1987, **62**, 295.
94. S. Boentges, B. U. Meier, C. Griesinger, and R. R. Ernst, *J. Magn. Reson.*, 1989, **85**, 337.
95. M. H. Levitt and R. R. Ernst, *Chem. Phys. Lett.*, 1983, **100**, 119.
96. M. H. Levitt, C. Radloff, and R. R. Ernst, *Chem. Phys. Lett.*, 1985, **114**, 435.
97. M. H. Levitt and R. R. Ernst, *J. Chem. Phys.*, 1985, **83**, 3297.
98. M. H. Levitt, C. Radloff, and R. R. Ernst, Simplification of 2D Spectra by (a) Topology-selective Multiple-Quantum Filtration or (b) by Linear Mixing, in *Advanced Magnetic Resonance Techniques in Systems of High Molecular Complexity*, Birkhäuser, Boston, 1986, Vol. 2, p. 49.
99. C. Radloff and R. R. Ernst, *Mol. Phys.*, 1989, **66**, 161.
100. O. W. Sørensen, and R. R. Ernst, *J. Magn. Reson.*, 1983, **51**, 477.
101. O. W. Sørensen and R. R. Ernst, *J. Magn. Reson.*, 1983, **54**, 122.
102. O. W. Sørensen and R. R. Ernst, *J. Magn. Reson.*, 1983, **55**, 338.
103. O. W. Sørensen and H. J. Jakobsen, in *Pulse Methods in 1D and 2D Liquid-phase NMR*, ed. W. S. Brey, Academic Press, New York, 1988.
104. O. W. Sørensen, *Progr. NMR Spectrosc.*, 1989, **21**, 503.
105. M. H. Levitt and R. R. Ernst, *J. Magn. Reson.*, 1983, **55**, 247.
106. M. H. Levitt and R. R. Ernst, *Mol. Phys.*, 1983, **50**, 1109.
107. M. H. Levitt, D. Suter, and R. R. Ernst, *J. Chem. Phys.*, 1984, **80**, 3064.
108. C. Counsell, M. H. Levitt, and R. R. Ernst, *J. Magn. Reson.*, 1985, **63**, 133.
109. P. Pfändler, G. Bodenhausen, B. U. Meier, and R. R. Ernst, *Anal. Chem.*, 1985, **57**, 2510.
110. Z. L. Mádi, B. U. Meier, and R. R. Ernst, *J. Magn. Reson*, 1987, **72**, 584.
111. B. U. Meier, Z. L. Mádi, and R. R. Ernst, *J. Magn. Reson.*, 1987, **74**, 565.
112. Z. L. Mádi and R. R. Ernst, *J. Magn. Reson.*, 1988 **79**, 513.
113. B. U. Meier and R. R. Ernst, *J. Magn. Reson.*, 1988, **79**, 540.
114. K. Nagayama, K. Wüthrich, P. Bachmann, and R. R. Ernst, *Biochem. Biophys. Res. Commun.*, 1977, **78**, 99.
115. K. Nagayama, K. Wüthrich, P. Bachmann, and R. R. Ernst, *Naturwissenschaften*, 1977, **64**, 581.
116. K. Nagayama, P. Bachmann, K. Wüthrich, and R. R. Ernst, *J. Magn. Reson.*, 1978, **31**, 133.
117. R. R. Ernst, L. Müller, K. Nagayama, and K. Wüthrich, *Recherche*, 1978, **9**, 1124.
118. K. Nagayama, P. Bachmann, R. R. Ernst, and K. Wüthrich, *Biochem. Biophys. Res. Commun.*, 1979, **86**, 218.
119. K. Wüthrich, K. Nagayama, and R. R. Ernst, *Trends Biochem. Sci.*, 1979, **4**, 178.
120. K. Nagayama, K. Wüthrich, and R. R. Ernst, *Biochem. Biophys. Res. Commun.*, 1979, **90**, 305.
121. A. Kumar, R. R. Ernst, and K. Wüthrich, *Biochem. Biophys. Res. Commun.*, 1980, **95**, 1.
122. S. L. Gordon and K. Wüthrich, *J. Am. Chem. Soc.*, 1978, **100**, 7094.
123. G. Wagner, A. Kumar, and K. Wüthrich, *Eur. J. Biochem.*, 1981, **114**, 375; G. Wagner and K. Wüthrich, *J. Mol. Biol.*, 1982, **155**, 347; K. Wüthrich, *NMR of Proteins and Nucleic Acids*, Wiley-Interscience, New York, 1986.
124. A. Dubs, G. Wagner, and K. Wüthrich, *Biochem. Biophys. Acta.*, 1979, **577**, 177.
125. Ch. Bösch, A. Kumar, R. Baumann, R. R. Ernst, and K. Wüthrich, *J. Magn. Reson.*, 1981, **42**, 159.
126. G. Wider, R. Baumann, K. Nagayama, R. R. Ernst, and K. Wüthrich, *J. Magn. Reson.*, 1981, **42**, 73.
127. G. Wagner and K. Wüthrich, *J. Magn. Reson.*, 1979, **33**, 675.
128. A. Kumar, G. Wagner, R. R. Ernst, and K. Wüthrich, *J. Am. Chem. Soc.*, 1981, **103**, 3654.

129. R. Baumann, A. Kumar, R. R. Ernst, and K. Wüthrich, *J. Magn. Reson.*, 1981, **44**, 76.
130. R. Baumann, G. Wider, R. R. Ernst, and K. Wüthrich, *J. Magn. Reson.*, 1981, **44**, 402.
131. S. Macura, K. Wüthrich, and R. R. Ernst, *J. Magn. Reson.*, 1982, **46**, 269.
132. S. Macura, K. Wüthrich, and R. R. Ernst, *J. Magn. Reson.*, 1982, **47**, 351.
133. M. Rance, O. W. Sørensen, G. Bodenhausen, G. Wagner, R. R. Ernst, and K. Wüthrich, *Biochem. Biophys. Res. Commun.*, 1983, **117**, 479.
134. G. Wider, S. Macura, A. Kumar, R. R. Ernst, and K. Wüthrich, *J. Magn. Reson.*, 1984, **56,** 207.
135. G. Bodenhausen, G. Wagner, M. Rance, O. W. Sørensen, K. Wüthrich, and R. R. Ernst, *J. Magn. Reson.*, 1984, **59**, 542.
136. M. Rance, O. W. Sørensen, W. Leupin, H. Kogler, K. Wüthrich, and R. R. Ernst, *J. Magn. Reson.*, 1985, **61**, 67.
137. N. Müller, G. Bodenhausen, K. Wüthrich, and R. R. Ernst, *J. Magn. Reson.*, 1985, **65**, 531.
138. N. Müller, G. Bodenhausen, and R. R. Ernst, *J. Magn. Reson.*, 1987, **75**, 297.
139. N. Müller, R. R. Ernst, and K. Wüthrich, *J. Am. Chem. Soc.*, 1986, **108**, 6482.
140. M. H. Frey, G. Wagner, M. Vasák, O. W. Sørensen, D. Neuhaus, E. Wörgötter, J. H. R. Kägi, R. R. Ernst, and K. Wüthrich, *J. Am. Chem. Soc.*, 1985, **107**, 6847.
141. M. H. Frey, W. Leupin, O. W. Sørensen, W. A. Denny, R. R. Ernst and K. Wüthrich, *Biopolymers*, 1985, **24**, 2371.
142. C. Griesinger, O. W. Sørensen, and R. R. Ernst, *J. Magn. Reson.*, 1987, **73**, 574.
143. C. Griesinger, O. W. Sørensen, and R. R. Ernst, *J. Am. Chem. Soc.*, 1987, **109**, 7227.
144. H. Oschkinat, C. Griesinger, P. J. Kraulis, O. W. Sørensen, R. R. Ernst, A. M. Gronenborn, and G. M. Clore, *Nature (London)*, 1988, **332**, 374.
145. C. Griesinger, O. W. Sørensen, and R. R. Ernst, *J. Magn. Reson.*, 1989, **84**, 14.
146. Z. L. Mádi, C. Griesinger, and R. R. Ernst, *J. Am. Chem. Soc.*, 1990, **112**, 2908.
147. R. Brüschweiler, M. Blackledge, and R. R. Ernst, *J. Biol. NMR*, 1991, **1**, 3.
148. R. R. Ernst, M. Blackledge, S. Boentges, J. Briand, R. Brüschweiler, M. Ernst, C. Griesinger, Z. L. Mádi, T. Schulte-Herbrüggen, and O. W. Sørensen, *Molecular Dynamics of Peptides and Proteins Investigated by NMR, Proteins: Structure, Dynamics, Design*, eds. V. Renugopalakrishnan, P. R. Carey, I. C. P. Smith, S.-G. Huang, and A. C. Storer, Escom, Leiden, 1991, p. 11.
149. R. Brüschweiler and R. R. Ernst, *J. Chem. Phys.*, 1992, **96**, 1758.
150. R. M. Brunne, W. F. van Gunsteren, R. Brüschweiler, and R. R. Ernst, *J. Am. Chem. Soc.*, 1993, **115**, 4764.
151. J. M. Schmidt, R. Brüschweiler, R. R. Ernst, R. L. Dunbrack, Jr., D. Joseph, and M. Karplus, *J. Am. Chem. Soc.*, 1993, **115**, 8747.
152. M. J. Blackledge, R. Brüschweiler, C. Griesinger, J. M. Schmidt, Ping Xu, and R. R. Ernst, *Biochemistry*, 1993, **32**, 10 960.
153. L. Müller, A. Kumar, Th. Baumann, and R. R. Ernst, *Phys. Rev. Lett.*, 1974, **32**, 1402.
154. L. Müller, A. Kumar, Th. Baumann, and R. R. Ernst, *Abs. 18th Congr. AMPERE*, Nottingham, 1974, p. 557.
155. R. K. Hester, J. L. Ackerman, B. L. Neff, and J. S. Waugh, *Phys. Rev. Lett.*, 1976, **36**, 1081.
156. E. F. Rybaczewski, B. L. Neff, J. S. Waugh, and J. S. Sherfinski, *J. Chem. Phys.*, 1977, **67**, 1231.
157. A. Höhener, L. Müller, and R. R. Ernst, *Mol. Phys.*, 1979, **38**, 909.
158. M. Linder, A. Höhener, and R. R. Ernst, *J. Chem. Phys.*, 1980, **73**, 4959.
159. D. P. Burum, M. Linder, and R. R. Ernst, *J. Magn. Reson.*, 1981, **44**, 173.
160. P. Caravatti, G. Bodenhausen, and R. R. Ernst, *Chem. Phys. Lett.*, 1982, **89**, 363.
161. P. Caravatti, L. Braunschweiler, and R. R. Ernst, *Chem. Phys. Lett.*, 1983, **100**, 305.
162. P. Brunner, M. Reinhold, and R. R. Ernst, *J. Chem. Phys.*, 1980, **73**, 1086.
163. M. Reinhold, P. Brunner, and R. R. Ernst, *J. Chem. Phys.*, 1981, **74**, 184.
164. T. Schaffhauser, R. R. Ernst, B. Hilti, and C. W. Mayer, *Chem. Scr.*, 1981, **17**, 27.
165. T. Schaffhauser, R. R. Ernst, B. Hilti, and C. W. Mayer, *Phys. Rev. B*, 1981, **24**, 76.
166. B. H. Meier, F. Graf, and R. R. Ernst, *J. Chem. Phys.*, 1982, **76**, 767.
167. B. H. Meier, R. Meyer, R. R. Ernst, P. Zolliker, A. Furrer, and W. Hälg, *Chem. Phys. Lett.*, 1983, **103**, 169.
168. B. H. Meier, R. Meyer, R. R. Ernst, A. Stöckli, A. Furrer, W. Hälg, and I. Anderson, *Chem. Phys. Lett.*, 1984, **108**, 522.
169. P. Fischer, P. Zolliker, B. H. Meier, R. R. Ernst, A. W. Hewat, J. D. Jorgensen, and F. J. Rotella, *J. Solid State Chem.*, 1986, **61**, 109.
170. A. Stöekli, A. Furrer, Ch. Schönenberger, B. H. Meier, R. R. Ernst, and I. Anderson, *Physica (The Hague)*, 1986, **136B**, 161.
171. R. Meyer and R. R. Ernst, *J. Chem. Phys.*, 1987, **86**, 784.
172. A. Stöckli, B. H. Meier, R. Kreis, R. Meyer, and R. R. Ernst, *J. Chem. Phys.*, 1990, **93**, 1502.
173. R. Meyer and R. R. Ernst, *J. Chem. Phys.*, 1990, **93**, 5518.
174. P. Robyr, B. H. Meier, and R. R. Ernst, *Chem. Phys. Lett.*, 1991, **187**, 471.
175. D. Suter and R. R. Ernst, *Phys. Rev. B*, 1982, **25**, 6038.
176. P. Caravatti, J. A. Deli, G. Bodenhausen, and R. R. Ernst, *J. Am. Chem. Soc.*, 1982, **104**, 5506.
177. P. Caravatti, P. Neuenschwander, and R. R. Ernst, *Macromolecules*, 1985, **18**, 119.
178. D. Suter and R. R. Ernst, *Phys. Rev. B*, 1985, **32**, 5608.
179. M. H. Levitt, D. Suter, and R. R. Ernst, *J. Chem. Phys.*, 1986, **84**, 4243.
180. M. G. Colombo, B. H. Meier, and R. R. Ernst, *Chem. Phys. Lett.*, 1989, **146**, 189.
181. B. H. Meier, M. G. Colombo, T. Burmeister, and R. R. Ernst, *Abs. 24th Congr. AMPERE*, Poznan, Poland, 1988, p. 825.
182. P. Robyr, B. H. Meier, and R. R. Ernst, *Chem. Phys. Lett.*, 1989, **162**, 417.
183. S. Zhang, B. H. Meier, and R. R. Ernst, *Phys. Rev. Lett.*, 1992, **69**, 2149.
184. S. Zhang, B. H. Meier, S. Appelt, M. Mehring, and R. R. Ernst, *J. Magn. Reson. Ser. A*, 1993, **101**, 60.
185. S. Zhang, B. H. Meier, and R. R. Ernst, *Solid State NMR*, 1992, **1**, 313.
186. M. Tomaselli, B. H. Meier, P. Robyr, U. W. Suter, and R. R. Ernst, *Chem. Phys. Lett.*, 1993, **205**, 145.
187. S. Hediger, B. H. Meier, and R. R. Ernst, *Chem. Phys. Lett.*, 1993, **213**, 627.

188. M. Tomaselli, B. H. Meier, P. Robyr, U. W. Suter, and R. R. Ernst, *Chem. Phys. Lett.*, 1993, **214**, 1.
189. B. H. Meier and R. R. Ernst, *J. Solid State Chem.*, 1986, **61**, 126.
190. R. Meyer, *J. Mol. Spectrosc.*, 1979, **76**, 266.
191. P. Caravatti, P. Neuenschwander, and R. R. Ernst, *Macromolecules*, 1986, **19**, 1889.
192. D. P. Weitekamp, A. Bielecki, D. Zax, K. Zilm, and A. Pines, *Phys. Rev. Lett.*, 1983, **50**, 1807.
193. A. Bielecki, J. B. Murdoch, D. P. Weitekamp, D. B. Zax, K. W. Zilm, H. Zimmermann, and A. Pines, *J. Chem. Phys.*, 1984, **80**, 2232.
194. R. Kreis, D. Suter, and R. R. Ernst, *Chem. Phys. Lett.*, 1985, **118**, 120.
195. R. Kreis, A. Thomas, W. Studer, and R. R. Ernst, *J. Chem. Phys.*, 1988, **89**, 6623.

Acknowledgments

Without generous funding by the Swiss Federal Institute of Technology (ETH Zürich), by the Swiss National Science Foundation, by the Kommission zur Förderung der wissenschaftlichen Forschung, by Varian Associates, and by Bruker Analytische Messtechnik and Spectrospin AG, I would not have been asked to write a contribution for this volume.

Biographical Sketch

Richard R. Ernst. *b* 1933. Dipl. Ing. Chem., 1956, Ph.D., 1962, Chemistry, ETH Zürich, Switzerland. Scientific co-worker, Varian Associates, Palo Alto, CA, USA, 1963–68. Currently Professor of Physical Chemistry, ETH Zürich. Wolf Prize, Horwitz Prize, Nobel Prize in Chemistry, 1991. Research activities: methodological developments in liquid and solid state NMR, intramolecular dynamics.

Farrar, Thomas C.: Historical Reminiscences of Some NMR Experiences

Thomas C. Farrar

University of Wisconsin, Madison, WI, USA

I arrived in Urbana, Illinois on 21 August 1954, a naive young man from the dusty plains of Wichita, Kansas. I had decided to work for Professor Herbert S. Gutowsky even before I left Wichita. A neighbor, David McCall, had recently finished his Ph.D. work with Professor Gutowsky and he told me and some of my other undergraduate colleagues about what an absolutely splendid fellow Gutowsky was and how this new field of research in nuclear magnetic resonance was truly going to revolutionize chemistry. I have often wondered if he realized back in 1953 how true his prophesy would be!

On arriving in Urbana, I was a bit disappointed to learn that Herb was away on sabbatical leave and did not plan on returning until the summer of 1955. But, as is usually the case with beginning graduate students, I was so busy taking classes and teaching in the first two semesters that I had very little time for research. I dutifully took the suggested classes and scheduled interviews with all members of the Physical Chemistry Division and remained firm in my wish to work in this new field of NMR spectroscopy. Herb returned in the late spring of 1955 and I had my first taste of real NMR research in the summer of 1955.

There were so many things happening in those early days that it is difficult, 40 years later, to remember the exact chronology. It is quite easy to remember, however, one of the initiation rites of new Gutowsky graduate students, the task of mapping the field of the permanent magnets and using a piece of fine emery paper to sand down the high spots in the pole faces in order to obtain a more homogeneous magnetic field. Since the magnet pole faces all had a sharp, raised, outer circumference, the task of pole face polishing usually resulted in a case of badly skinned knuckles. New Gutowsky graduate students were easy to spot because they were the ones that went around for the first month or two with Band-Aids on all or most of their knuckles. That first summer was also interesting because Herb had received a very nice package in the mail from Rex Richards, who at that time was Professor of Physical Chemistry at Oxford. In the package were two beautiful pieces of embroidery. The embroidered art-work consisted of two circular pieces of silk, each about 8 in. in diameter. In the central part of the circles was a rather complex pattern, sewn with fine copper wire. The patterns were designed in accord with some calculations which had recently been completed by Marcel Golay. The idea was that if one placed these embroidered circles on the pole faces of the magnet and then put the proper amounts of current through the various copper patterns, this would result in a magnetic field of greatly improved homogeneity. The silk circles were mounted on the magnet pole faces in the prescribed manner and the loose pieces of fine copper were attached to some simple variable current power supplies. Several of the members of our research group then tried for a week or two to improve the magnetic field using these early shim coils. In the end we gave up and went back to skinned knuckles!

Several months after this unsuccessful effort to use shim coils, we tried another new idea which had been received from the West Coast. Bloch had tried to stir an NMR sample in order to average out magnetic field inhomogeneities. This did not work very well, but Wes Anderson then came up with the idea of rotating the NMR sample tube and this worked very well indeed. The radial magnetic field inhomogeneities were averaged and the sharpness of the spectral lines was greatly improved. This idea we tried and for us, too, it worked very well. This was a really very important step forward because sensitivity and resolution in those days were not very impressive.

There were two permanent magnets used in the Gutowsky group at that time, and a year later a commercial electromagnet was added. The larger permanent magnet had a pole face diameter of about 8 in. and a field strength of about 0.7 T (a proton resonance frequency of about 28 MHz) and was used primarily for wideline studies of solids and polymer samples. The smaller one had a pole face diameter of about 6 in. (as I recall) and a magnetic field strength of about 0.5 T (a proton frequency of about 17.5 MHz); it had much better homogeneity than its larger brother. The smaller magnet was used for high-resolution studies. The high-resolution spectrometer itself was essentially a radiofrequency (rf) bridge with the sample being placed in the coils which served as the inductance in a tuned circuit of one part of the bridge. As the magnetic field was swept and a resonance condition was reached for some particular group of protons they absorbed energy. This caused the bridge to become unbalanced and the relative degree of unbalance was proportional to the relative number of protons at resonance.

The spectra were recorded on a Sanborn recorder which had a very fast response (these Sanborn recorders were the same ones that were frequently used in a number of early medical instruments), but resulted in spectra which came out on curly rolls about 15 in. long and 3 in. high. The paper used on these rolls was designed in such a way that lying flat was a very high energy configuration; the low energy configuration was to curl up into a tight roll. The rf bridge consisted of a rat's nest of wires, capacitors, resistors, and inductors, all of which were stuffed into an old shoe box. Of course, the shoe boxes made 40 years ago were very substantial and sturdy, not the flimsy affairs which are used these days. The lid of a metal coffee can, which was about 7 in. in diameter, was attached to the shaft of the tuning capacitor in order to allow more precise tuning of the rf bridge. Although the spectrometer looked rather crude it often out-performed the new 40 MHz commercial spectrometer which had been recently installed down the hall in the Noyes Laboratory.

Spectral resolution was always a problem in those early days. One very frustrating problem was that good homogeneity was a bit like the weather. It often changed from good to bad rather abruptly and was rather unpredictable. At one point a large box was constructed (not out of the usual cardboard, but out of sheets of very substantial 3/4-in. plywood) and placed around the high-resolution magnet, its temperature being controlled as precisely as was possible in those days. When the magnet was in good form and the homogeneity was really outstanding, samples were run as rapidly as possible and

students often worked around the clock in order to get their spectra before the homogeneity took a turn for the worse.

Gutowsky's research group was quite large in the early days (17 to 20 people) and there were three major areas of research, wideline studies of solids and polymers, high−resolution NMR (both experimental and theoretical), and pulsed NMR work (both experimental and theoretical). The theoretical work was rather interesting since much of it involved the use of the Illiac computer. This machine was really awesome. In those days, of course, one had only vacuum tubes. The heat output of the Illiac was, as I recall, about 50 kW! It had 1024 words of memory and each word consisted of 40 binary bits. There was no floating point arithmetic available and all calculations had to be scaled such that no number was greater than one. Addressing was also fixed, so great care was needed if a program had to be modified by adding an additional instruction or an additional piece of data. Input was via punched paper tape and all programming was in machine language, i.e. hexadecimal numbers. Access to the computer was via debug sessions each morning and each afternoon. No more than about 5 min per person was allowed for the debug sessions. Even with all the difficulties, however, the Illiac could do an awesome amount of calculating once a program was up and running.

One of the problems I worked on at Urbana had to do with the measurement of the proton−proton spin coupling constant in methane. The problem I had really started to work on was an experimental test of some calculations which had been done by Ed Stejskal on the rotational energy barrier of the methyl group in methylchloroform. I thought I might try to make d_1-methylchloroform, since Ed's theory predicted that its barrier should be quite different from isotopically normal methylchloroform and we might be able to distinguish the difference between a tunneling model and an activation model. My copy of 'Organic Chemistry' by Fieser and Fieser indicated that if one added DCl to vinyl chloride, the result should be d_1-methylchloroform. The synthesis seemed to work as indicated and in order to check the purity we decided to look at the high-resolution proton NMR spectrum. Much to our surprise we got quite a mixture of compounds ranging from no deuteration to d_3-methylchloroform. We were also delighted to observe that we had obtained the proton−deuteron spin coupling constant, which was about 1.7 Hz, indicating that the proton−proton spin coupling constant was about 12 Hz. This was most interesting because a recent molecular orbital calculation on methane came up with the result of about 200 Hz. We didn't really think that the difference between methylchloroform and methane could be so great, but I decided to synthesize d_1-methane anyway. Again, the proton−deuteron coupling constant was found to be about 1.7 Hz. This was the beginning of a long and productive collaboration with Martin Karplus on the calculation of spin−spin coupling constants. But that is another story.

Another interesting observation about the proton spectrum in the methane sample (which was a gas at about 10 atm pressure in a 5-mm NMR tube; boy did we love to live dangerously in the old days!) was that the lines were rather broad. We had a number of interesting theories about the reason for the broad lines, including one which postulated that since the sample was gaseous perhaps the gas molecules remained stationary as the sample tube was spun. We even constructed an NMR tube with glass partitions to ensure that the gas molecules were being averaged over the radial field inhomogeneities; this helped not a bit. It was not until several years and many experiments later that other members of Gutowsky's group tumbled to the fact that spin rotation relaxation caused the relaxation times to be very short, which in turn led to the broad lines.

In about my last year in Urbana, Martin Karplus got the great idea that I should go to Cambridge to work with Frank Boys who had come up with a brilliant new way of calculating the multicenter integrals which are required in ab initio quantum mechanical calculations. I was fortunate enough to be awarded an NSF postdoctoral fellowship and did go to Cambridge to work with S. F. Boys. When I arrived in Cambridge, Professor Longuet-Higgins tried very hard to convince me that working with Dr. Boys was a terrible mistake and a waste of time. I did some work with Longuet-Higgins, but then decided that working with Dr. Boys would be more interesting and challenging. I was involved with him and members of his research group in the development of Gaussian-59. The calculations were done on the Edsac-2 computer. It had 1024 words of 40-bit memory (RAM) and an additional 1024 words of stored programs (ROM). Both Edsac-2 and the Illiac were designed by David Wheeler, but the Edsac had a large number of advances over the Illiac. Edsac-2 had floating point arithmetic and address modifier registers. And, most importantly, it had four magnetic tape drives for storing overlay programs and data. One of the first molecules we studied when the programs were finally all up and working properly was N_2. It took about 30 min to do the calculation; it had taken Daniel Kaestler (a graduate student with Roothaan at the University of Chicago) several years to calculate the same integrals by hand! Unfortunately, it would be many years before computer hardware was advanced enough to carry out accurate calculations of chemical shift tensors and other interesting NMR parameters.

After a brief go at academia in Eugene, Oregon, I accepted a job at the National Bureau of Standards in Washington, D.C. Since pulse NMR spectrometers were not available in 1963, we decided to have one built at NBS. After about a year the electronics shop delivered to us a spectrometer, but it didn't work. So, armed with a copy of the bible according to the AARRL (The American Amateur Radio Relay League), we set to work fixing the problems. Much of the early work was concerned with relaxation time measurements in liquids and solids. During some of the lectures that Ted Becker and I were giving at an NIH continuing education course, Gitte Vold suggested that we try some Carr−Purcell experiments to measure chemical exchange rates. That sounded like a great idea, but by the time we had improved the sensitivity and the stability of the spectrometer to the point that we could make meaningful T_2 measurements, we realized that it was also stable enough to obtain good pulse high-resolution FID (free induction decay) signals. The spectrometer was an eclectic mixture of new and old, the old being the external fluorine lock which used an rf bridge very similar to the one used by Bloembergen, Purcell, and Pound. This led us into the area of high-resolution pulse NMR spectroscopy.

At a meeting of the Society for Applied Spectroscopy in Anaheim, California (Disneyland) in 1970, we showed some of the first carbon-13 FT NMR spectra. Tony Keller was also at the meeting and he too had just obtained some nice ^{13}C FT NMR spectra. The improvements in sensitivity for ^{13}C

were so impressive that everyone was very keen to start doing such experiments. The collaborative work between NIH (Ted Becker and his group) and NBS (my research group) used our homemade spectrometer and a Fabri-Tek model 1064 signal averager. The 1064 had 4096 words of 20-bit memory and the output was in the form of punched paper tape. FID spectra were output on the punch paper tape and when we had a laundry basket full of tape we would drive 10 miles down the road to NIH to carry out the data reduction. The data reduction at NIH involved several computers since the computer which could read the punched paper tape had no plotter or graphics; it was used to convert the paper tape to punched cards which were then carried to another computer where the Fourier transformation and plotting were done. After a year of this tedious process we convinced Dick Cushing of Fabri-Tek (which later became Nicolet Instruments) to build a very simple computer into the signal averager. My group at NBS purchased model #1. It worked beautifully from the first day it was installed and was still working a few years ago. Dave VanderHart tells me that it is no longer being used. One of the early attempts to improve sensitivity involved pulse sequences similar to those now used in DEPT and other experiments. We called our experiment the DEFT experiment (driven equilibrium Fourier transform). We had originally thought about calling it the LEFT (longitudinal equilibrium Fourier transform), but the McCarthy days were still fresh in everyone's mind and the US government was not wildly enthusiastic about LEFTist activities.

Those were wonderful years in Urbana and in Washington. There are wonderful memories of the excitement of many new discoveries and of stimulating, challenging, and productive seminars and discussions with Charlie Slichter and the members of his research group, who were just across the street in the physics building. What really amazes me is the rate at which new experiments and new discoveries continue to be made in the field of NMR spectroscopy. Dave McCall was indeed correct; NMR has very much changed forever the field of chemistry.

Biographical Sketch

Thomas C. Farrar. *b* 1933. B.Sc., 1954, Chemistry and Mathematics, Wichita State University, Ph.D., 1959, Physical Chemistry, University of Illinois-Urbana, (Supervisors H. S. Gutowsky and Martin Karplus). NSF Postdoctoral fellowship in theoretical chemistry, Cambridge University, UK (with S. F. Boys) 1959–61. Assistant Professor of Chemistry, University of Oregon-Eugene, 1961–63. National Bureau of Standards, 1963–71 (Chief of Magnetism Section). JEOL, Ltd. Director of Research and Development, 1971–75. National Science Foundation, Director of Chemistry Instrumentation Program, 1975–79. University of Wisconsin, Professor of Chemistry, 1979–present. Research interests include high-resolution, pulse and solid state NMR spectroscopy, study of structure and dynamics in liquids, hydrogen bonding, NMR relaxation time theory and experiments.

Feeney, James: Personal Reminiscences on NMR

James Feeney

National Institute for Medical Research, London, UK

In July 1957 I received a letter from Les Sutcliffe explaining that I had been allocated to work with him during the final year of my chemistry degree course at Liverpool University. He wrote 'I have decided that your research problem will be in nuclear magnetic resonance spectroscopy. This is an excellent opportunity because this subject is one of the newest and most promising in Chemistry'. What a prophetic statement and what amazing good fortune for me! Earlier that year, Les Sutcliffe had taken delivery of one of the first NMR commercial spectrometers in the UK, a 40 MHz Varian instrument. By the time I arrived he had already decided that the original purpose for which it was bought, namely to support his ongoing studies on metal redox reactions, was not going to be feasible at the low sensitivity available and that studies of molecular conformations in fluorinated molecules via ^{19}F NMR would be a much more fruitful area. Looking back on those days, I recall that a great deal of time was spent on 'finding resonance' (the electromagnet was usually switched off overnight) and then searching for homogeneity 'hot-spots' in the field to give good resolution. Occasionally, when everything was just right, we would record superb spectra on our compounds which almost always revealed something new and interesting! Much time was spent on constructing and testing 'home-built' variable temperature units and probes for the conformational work. During these studies we detected and characterized the large geminal F, F coupling constant (~290 Hz) and other longer range couplings in fluorinated cyclohexanes.[1] In those days it was fashionable to carry out detailed spectral analysis on second-order spectra and our compounds provided many such examples (for example, SF_5X compounds were analyzed with Jim Emsley and Neville Boden as AB_4 spin systems).[2]

In January 1961 I met Warren Proctor at a conference in Bradford (my first public NMR lecture) and I like to think that this chance meeting subsequently led to my joining Varian in 1964. Those Varian days were exciting with excellent equipment and stimulating colleagues, such as Jim Shoolery, Leroy Johnson, and Attilio Melera. I can still remember visits to the laboratory by eminent organic chemists reexamining compounds they had synthesized, sometimes 20 years earlier, and being amazed at the structural details revealed by the new NMR technology. At that time, the application of double and triple resonance and early NOE measurements, mainly on the HA-100, were all part of the 'modern' approach to structural NMR work. One of our experiments, dating from 1969, showed that gated double resonance could be used to enhance the sensitivity of nondecoupled ^{13}C spectra by retaining $\{^1H\}^{13}C$ NOE information after the decoupler was switched off;[3] this was the forerunner of many variations of such gated decoupling experiments.

During my time at Varian I became increasingly aware of the potential use of NMR in biology—stimulated largely during visits by Arnold Burgen. He was convinced of the powerful role that NMR would eventually play in monitoring protein–ligand interactions. In 1970 I eventually joined Arnold Burgen and his colleagues (Jim Metcalfe, Gordon Roberts and, later, Berry Birdsall) in his newly established MRC Molecular Pharmacology Unit in Cambridge, which later transferred to the National Institute for Medical Research at Mill Hill. In the early days we managed to get useful information by concentrating on NMR studies of isotopically labeled ligands bound to proteins. These studies allowed us to characterize the multiple conformational states that frequently exist in protein–ligand complexes and also the dynamic processes involved in the protein–ligand interactions during the lifetime of the complex. Some of our experiments have proved to be of general use. For example, in 1974 (with Poul Hansen) we found that the β-CH_2 protons in peptides could be assigned stereospecifically and rotamer populations determined by considering both ^3J(H,H) and ^3J(C,H) coupling constants.[4,5] In another experiment we drew attention to the potential of NOE difference spectroscopy and showed how this could be used to follow pseudo INDOR effects (1973).[6] Our initial protein ^1H NMR experiments were at 100 MHz on proteins such as dihydrofolate reductase (M.W. 18 300) and these yielded very few assigned signals. Of course, nowadays, modern 2D and 3D experiments on the isotopically labeled protein at 600 MHz give us essentially all the resonance assignments. In the late 1970s, during some magnetization transfer experiments, we were surprised to observe negative intramolecular NOE effects between protons in a free ligand examined in the presence of its protein–ligand complex (with Jean Pierre Albrand). These NOE effects were transferred to the free ligand by exchange between the bound and free species and allowed us to obtain the conformation of the bound ligand from NOE observations on the free ligand.[7] We also participated in the search for solvent suppression methods and suggested the use of data shift accumulation methods for overcoming the dynamic range problem (in 1979 with Klaus Roth and Barry Kimber).[8]

The phenomenal progress in protein structure determination using NMR has ensured that the promise predicted for the technique by the early workers has been fully realized and there is no doubt that activity in this area will continue to expand.

REFERENCES

1. J. Feeney and L. H. Sutcliffe, *J. Phys. Chem.*, 1961, **65**, 1894.
2. N. Boden, J. W. Emsley, J. Feeney, and L. H. Sutcliffe, *Trans. Faraday Soc.*, 1963, **59**, 620.
3. J. Feeney, D. Shaw, and P. J. Pauwels, *Chem. Commun.*, **1970**, 554.
4. J. Feeney, P. E. Hansen, and G. C. K. Roberts, *J. Chem. Soc., Chem. Commun.*, **1974**, 465.
5. P. E. Hansen, J. Feeney, and G. C. K. Roberts, *J. Magn. Reson.*, 1975, **17**, 249.
6. J. Feeney and P. Partington, *J. Chem. Soc., Chem. Commun.*, **1973**, 611.
7. J. P. Albrand, B. Birdsall, J. Feeney, G. C. K. Roberts and A. S. V. Burgen, *Int. J. Biol. Macromol.*, 1979, **1**, 37.
8. K. Roth, B. J. Kimber, and J. Feeney, *J. Magn. Reson.*, 1979, **41**, 302.

Biographical Sketch

James Feeney. *b* 1936. B.Sc., (Chemistry), Ph.D., (supervisor Les Sutcliffe), D.Sc., University of Liverpool. Lecturer in Chemistry, University of Liverpool, 1961–64. Varian Associates 1964–69 (final position, Director, European Laboratories). 1969–present, British Medical Research Council (Cambridge 1969–72, National Institute for Medical Research, Mill Hill, 1972–present). Currently Centre Controller, MRC Biomedical NMR Centre and Head, Laboratory of Molecular Structure, NIMR. Visiting Professor at University of Surrey since 1985. Approx. 250 publications. Research interest: NMR studies of protein–ligand interactions.

Ferguson, Raymond C.: William D. Phillips and Nuclear Magnetic Resonance Spectroscopy at DuPont

Raymond C. Ferguson
Formerly Central Research Department, E. I. duPont de Nemours & Co., Wilmington, DE, USA

This article was originally assigned to Bill Phillips, but he had only completed the following before his death in 1993:

In 1951 I completed requirements for my Ph.D. in Physical Chemistry at the Massachusetts Institute of Technology (MIT) and accepted an offer of employment at the Corporate Research Laboratory of DuPont in Wilmington, DE. My thesis work had been in the area of vibrational spectroscopy (infrared and Raman) and, although I was never again to utilize seriously this powerful tool in research, vibrational spectroscopy with its group frequencies and symmetry-based selection rules provided a basis (emotional as well as technical) for entry into the relatively virgin territory of NMR of molecules in late 1953. My first victory in NMR came with the assignment of the two AB doublets in the ^{19}F spectra of a series of substituted tetrafluorocyclobutanes that had been submitted to Varian Associates in the course of negotiations between Varian and DuPont for the purchase of a spectrometer.

In due course, a Varian 30-MHz spectrometer was delivered to Wilmington in early 1954. Unfortunately, the magnet had been shipped with water left in the magnet cooling coils. In trucking the magnet from Palo Alto, CA, to Wilmington, the water in the cooling coils had frozen, expanded, and left the magnet totally inoperable. In short order, however, the magnet was replaced, the rf unit was upgraded to 40 MHz, and provision was made for sample spinning. By mid-1954, we had a functioning NMR spectrometer capable of obtaining ^{1}H and ^{19}F spectra at 40 MHz.

I first met Phillips in 1954, but was not directly involved with his work until 1964. I did, of course, follow his work closely, and occasionally met with him to discuss problems of mutual interest. Phillips was always an enthusiastic promoter of NMR and other spectroscopic and physical methods. He was always helpful to me and others who were working in these fields.

In this article, I review his contributions, guided by his own summary of major scientific contributions, written earlier. I have added discussion of my own work. The time period covered is from 1953 to the mid-1970s. Neither of us was directly involved in NMR at DuPont thereafter. Space limitations make it impossible to discuss the work of other colleagues in various departments at DuPont, many of which were significant.

The Central Research (then Chemical) Department of DuPont was the first industrial laboratory to acquire a high-resolution NMR spectrometer. Howard S. Jarrett had been doing EPR with a Varian Associates spectrometer. His supervisor, Monroe Sadler, learned of the NMR development and visited Varian to get more information, and provided samples for study. DuPont ordered a spectrometer.

Phillips (I am told) reluctantly agreed to take charge of the work, with the promise that he would not have to get bogged down with electronics problems (he always wanted to concentrate on fundamental physical chemistry, and was aware of the electrical problems Jarrett had encountered in his work).

However, this assignment worked out well. His wife, Esther, has told me that the early days in NMR were the most exciting of his career, and I would say, also of my own. My wife referred to 'my' first NMR spectrometer as 'his new toy'. Everything we did then was new, unique, and exciting.

Phillips was clearly a pioneer in the application of NMR to the structural, dynamic, and electronic properties of molecules. While at DuPont he published nearly 70 papers, mostly on high-resolution NMR, but also using ESR, IR, and other methods. He continued NMR work as he advanced in research management. His first DuPont paper confirmed restricted rotation in amides[1] and the last was a biochemical paper on the mechanism and kinetics of allene reduction by *Azotobacter* nitrogenase.[2]

The large chemical shift dispersion of ^{19}F NMR resonances and substantial research programs in fluorine chemistry at DuPont made fluorine work particularly attractive, and led to significant early discoveries, particularly involving the stereochemistry and analysis of spin–spin splitting patterns.

Phillips continued the ^{19}F work on tetrafluorocyclobutanes which had been started at Varian. He published spectra, chemical shifts, and spin–spin (J) coupling constants of a series of 17 tetrafluorocyclobutanes substituted unsymmetrically with respect to the plane of the cyclobutane ring.[3]

Nonequivalence of the two fluorines bonded to a common ring carbon atom produced four-line patterns which were not the expected pair of doublets separated by the chemical shift difference. This may have been the first recognized example of 'strong coupling'. Phillips introduced the appropriate AB spin system analysis, which continued to be important in continuing work on asymmetric systems.

Another major contribution was the earliest application of NMR to studies of hindered rotation in organic molecules.[4] He confirmed hindered internal rotation about the C–N bond in amides, which had been postulated, but never before confirmed experimentally.[1] He mentioned the significance of this result with respect to the structures of protein molecules, perhaps anticipating his later interests.

Due to conjugation of the double bond, *N*,*N*-dimethyl formamide, $(CH_3)_2–N–C{=}O$, has a nearly planar structure which places the methyl groups in magnetically nonequivalent environments. He observed two methyl resonances in the ^{1}H spectra. Temperature dependence and coalescence of the methyl resonances at elevated temperatures allowed estimation of the rotational barriers.

Proton NMR and infrared work on a series of nine nitrosoamines, $R'R''N–N{=}O$, demonstrated nearly planar structures and temperature dependence due to restricted internal rotation around the N–N bond. Similar work on six alkyl nitrites, $R–O–N{=}O$, revealed restricted rotation around the N–O bond.

The effects of asymmetry were further demonstrated by ^{19}F NMR evidence of restricted rotation about the C–C bond in four substituted *gem*-difluoroethanes.[5] Absolute rotational configurations were assigned on the basis of spin–spin splittings and temperature dependencies of the spectra.

Early on, Phillips recruited Harlan Foster, an experienced organic chemist, to take over the increasing demand for 'service work', mainly organic structure analysis. Foster became one of the finest practitioners of that art that I know of.

This was a clever move by Phillips, because he was then able to be more selective in his own research, and to branch into other forms of spectroscopy and physics. He became head of a group working on special projects using NMR, ESR, Raman, infrared spectroscopies, and other physical methods.

He and Earl L. Muetterties used ^{19}F in studies of structures and fluorine-exchange processes in inorganic fluorides of the type MF_n, where n = 3, 4, 5, 6, such as SF_4, ClF_3, and fluoroarsenates.[6]

He investigated other nuclei, most successfully ^{11}B. He and his co-workers reported the ^{11}B chemical shifts and $^{11}B-^{1}H$ J coupling constants for 30-odd representative examples of boron-containing compounds.[7] Conclusions regarding bonding were made and temperature dependence studies undertaken on selected samples. This and other work on organo-inorganic and organometallic systems in cooperation with Muetterties and others produced significant and useful results for research efforts at DuPont.

The discovery of an apparently anomalous effect of paramagnetic ions on the magnetic resonance absorption of alcohols[8] led Phillips later to use paramagnetic ions to elucidate the structural and electronic properties of transition metal chelates and of paramagnetic proteins such as cytochrome-*c* and plant and bacterial ferredoxins.

In a series of papers beginning in 1960, he and co-workers used isotropic contact proton hyperfine interactions to determine the configurations and magnetic properties of paramagnetic bis-nickel(II) chelates of aminotroponeimines.[8] Spin densities from Ni transmitted through N, O and S atoms connecting conjugated ligands produced large high- and low-frequency chemical shifts of the protons on the ligands. Synthesis and study of compounds with various ligands allowed the determination of spin densities of a large number of aromatic, cyclic 7-carbon, alkyl, and fluorine substituents.[9] Similar studies were made on nickel(II) salicylaldimines.

In the late 1950s, Phillips realized that modern physical methods had great potential for biological research, and a future for chemical and physical research and development in the chemical industry. He took leave of absence to go to MIT for postdoctoral work in biochemistry for the academic year 1962–63.

This was a significant break from his early emphasis on fundamental electronic and structural properties of inorganic, organic, and organometallic compounds. He published around 30 papers, mostly NMR and ESR, on the earlier work. Collaborators who made significant contributions included J. J. Drysdale, C. E. Looney, E. L. Muetterties, H. C. Miller, H. Foster, D. B. Chesnut, R. E. Benson, D. R. Eaton, D. R. Josey, and R. E. Merrifield.

In the meantime, other DuPont research laboratories were moving into NMR. I first heard about nuclear induction or nuclear magnetic resonance while at Harvard University in 1950–53. Daniel Kivelson, a fellow graduate student in chemistry, gave a seminar about the Purcell and Pound work. He covered their broadline work on solids, including natural rubber and gypsum. I do not recall any mention of high-resolution work on liquids.

When I joined DuPont at the Jackson Laboratory, Organic Chemicals Department in 1953, I was assigned to a group developing synthetic polyurethane elastomers for which my thesis on gas-phase microwave spectroscopy was not helpful. William Remington, my division head, discussed the Purcell and Pound paper with me, but questioned their interpretation of the effects of sulfur curing on natural rubber. We were both unaware of any high-resolution work and agreed that NMR would probably not be helpful to us.

However, Rudolph Pariser, my group leader, had better information and a more optimistic view. He sent me to see Phillips, who acquainted me with high-resolution NMR on liquids and solutions, illustrated with his results on organic compounds

I became a believer and helped prepare a project proposal to acquire our own NMR spectrometer. The proposal was rejected, partly because the largely organic and dye chemistry management was not quite sure about physical chemists, and perhaps more importantly, about unproved expensive instrumentation. They, and perhaps we, did not fully appreciate the revolutionary impact NMR and other developing instrumental methods would have on organic chemistry.

Nevertheless, I was assigned liaison with Phillips and provided him with research samples of mutual interest, including some polymers. The first was poly(tetramethylene ether glycol), a component of our polyurethane elastomer. This was a viscous liquid of about 1000 molecular weight which we were able to run neat. We observed two methylene and a hydroxyl resonance with unresolved fine structure. A few weeks later, Phillips repeated a scan of the sample and found changes in the pattern, which we learned were due to oxidative degradation. Sample stability was then, and forever, a problem. It was an indication of Phillips's alertness to any unusual result that he immediately called me.

Shortly after our unsuccessful proposal to acquire an NMR spectrometer, John D. Roberts (MIT) and Melvin Calvin (University of California), highly regarded consultants, visited Jackson Laboratory within a week or two of each other. They persuaded our management that NMR had great potential for support of organic chemistry, which was the major focus of Jackson Laboratory research. The directors then asked for a proposal which Remington and Pariser submitted, diplomatically failing to mention the earlier one.

I am reliably informed that Roberts was introduced to Phillips at DuPont, and that Phillips introduced Roberts to high-resolution NMR. At any rate, Roberts continued as a consultant and I saw him frequently. I often felt that we taught him more than we learned, but the relationship was symbiotic. He was very helpful in keeping us and our managements informed about significant developments in NMR in the outside world, and went to bat on our behalf with our managements.

Jackson Laboratory acquired a 40-MHz spectrometer equipped for ^{1}H, ^{19}F, and ^{13}C in late 1954 or early 1955. Our riggers dropped the magnet, fortunately on the yoke, so the only significant damage was to the floor. I have heard that

Varian had many other difficulties in getting their electromagnets delivered safely.

The original Varian 30- and 40-MHz spectrometers were electromagnet/continuous wave (CW) radiofrequency (rf) systems and had no field/frequency control. Spectra were recorded by sweeping the magnetic field. The systems were so unstable that spectra could only be observed by rapid scan oscilloscope display or recorded on a fast-writing Sanborn recorder. Tuning for resolution and examining multiplet structure were done mainly on the oscilloscope. We were usually able to distinguish singlets, doublets, triplets, quartets, and 'multiplets'. External magnetic perturbations were a serious problem, and made plumbers, construction workers, delivery carts, and swining metal doors enemies of progress.

Varian developed a 'Superstabilizer' which sensed the magnetic field through pick-up coils around the magnet poles, and used an optical galvanomenter feedback system to correct the fluctuations. This was a significant improvement. Later, the development of field/frequency lock on the line of an internal reference compound was an even better solution.

With the acquisition of our own instrument, I began providing service work at Jackson Laboratory, mainly for structural analysis and purity estimations on organic compositions, including fluorocarbons and fluoropolymers. In those days, with fixed rf frequency, we had to change the magnetic field to study other nuclei. Thus, most of the early work was done on proton resonance.

Some of my work involved interesting proton spectra of substituted tetrahydrofurans, with one or more alkyl groups attached to the $(CH_2CH_2)_2O$ ring. Asymmetric substitution across the plane produced nonequivalence of the sets of methylene protons and complex spectra such as observed for the tetrafluorocyclobutanes. In addition, the samples were often mixtures, making the analysis more difficult. I spent considerable time on this work, until the head of the synthesis group found out that my NMR charges were breaking his budget. We were, however, able to identify the structures and estimate purities — work that would have been difficult, costly, or impossible by conventional characterization methods.

The ^{19}F work was exciting because of the large chemical shift range and magnetic inequivalence effects, such as those seen by Phillips. My first NMR paper was on the compositional and structural analysis of vinylidene fluoride/hexafluoropropylene copolymers with a range of mole ratios.[10] The 40-MHz ^{19}F NMR spectra had resolved patterns for four basic sequences, $CH_2CF_2CF_2CF(CF_3)-$, $-CH_2CF_2CF(CF_3)CF-$, $-CH_2CF_2CH_2CF_2-$, and $-CH_2CF_2CF_2CH_2-$. The mole ratios of the monomers and the fractions of the above sequences could be determined from intensity measurements. There were no hexafluoropropylene–hexafluoropropylene dyads, consistent with the inability to homopolymerize this monomer or to incorporate it in the copolymers at greater than 50% molar concentration.

In 1958 I was assigned to the Elastomer Chemicals Department and moved into other projects. In 1960 we moved to a new laboratory at the experimental station, and I was assigned to the infrared laboratory and to liaison for NMR work being done for us in the Central Research Department. They had by then, or shortly thereafter, acquired a Varian spectrometer operating at 100 MHz for protons and 94.1 MHz for fluorine.

We acquired a Varian A-60 spectrometer and I began work on monomers and polymers. The NMR spectrum of an all-*cis*-polychloroprene prepared by a stereospecific route confirmed the *cis* structure. Additional studies of typical free radical-initiated polychloroprenes (neoprenes) revealed greater structural complexity than had been known previously.[11]

Chloroprene, $CH_2{=}CCl{-}CH{=}CH_2$, typically polymerizes mainly 1,4 to produce *cis*- and *trans*-2-chloro-2-butylidene-1,4 $-CH_2-CCl{=}CH-CH_2-$units, and also polymerizes 1,2 and 3,4 to produce minor amounts of $-CH_2-CCl(CH{=}CH_2)-$and $-CH_2-CH(CCl{=}CH_2)-$units, respectively. The methylene region of the proton spectra revealed that the basic 1,4-polymerization units were attached to each other head-to-tail in about 70%–80% of the pairs, but had 15%–10% each of head-to-head and tail-to-tail attachments.

The spectra of some of the monomers and model compounds related to this work led me into computer fitting of more complicated spectra. I worked with Donald Marquardt, a mathematician/statistician in our engineering department, using their Univac computer. We chose to follow the magnetic equivalence factoring method introduced by Swalen and Reilly.[12] This was an iterative approach in which trial spectra were calculated using estimated parameters. Tentative line assignments to the observed frequencies were made, then the program produced the statistically best fit to the energy levels. These were then applied in a second step to calculate the best parameter estimates. We applied the method to the proton spectra of propane, isobutane, 4-chloro-1,2-butadiene and other compounds.[13,14]

Perhaps my most significant contribution was in getting Marquardt involved. His statistical procedures, which later became known as the Marquardt/Levenberg algorithms (widely used in multiregression analysis), were later incorporated into more sophisticated computer programs which fit lineshapes and intensities, rather than frequencies alone.

I later wrote a program for simulating many-spin spectra, specifically designed for trial fitting of polymer spectra.[15] This was applied to computer simulations of the 220 MHz spectra of polypropylene and other synthetic polymers. The basis was to input subspectra for the various stereoregular sequences, which were combined with appropriate probabilities to match the observed patterns.[16]

When Phillips returned to DuPont as an Assistant Director of Basic Science, he formed a research group which included a number of disciplines, including his chosen field, biophysics. NMR projects were his major interest, but because of administrative duties collaborators did most of the work. Nevertheless, he kept in close touch with the work. I learned that the best time to talk with Phillips was about 7 a.m., when he would be in his office reviewing the previous day's (or night's) NMR results, even before reading the *Wall Street Journal*.

In 1964, the maximum field strength of conventional magnet systems having been reached, Varian Associates approached DuPont with a proposal to build a 300-MHz superconducting solenoid spectrometer. Phillips was particularly interested because of difficulties in resolving the proton spectra of biopolymers at 100 MHz. I transferred to Central Research Department to take charge of the operation of this new spectrometer. Varian loaned us a 200 MHz prototype during fabrication of our spectrometer.

Because of limitations in wire technology, Varian was unable to reach the target field, and finally produced a 220-MHz ^{1}H spectrometer which we accepted. I came later somewhat to regret this because it was a difficult system to operate and maintain. It had a liquid helium hold time of about 48 h, which required someone to come in on weekends and/or holidays to top up the Dewars. Fortunately, we were running a two-shift operation, including weekend work by enthusiastic visiting scientists. Spectrometer time was divided between biophysics and other research, somewhat disproportionately in favor of the former.

The system was prone to spontaneous quenches (collapse of the field) and because it was difficult to establish field and resolution from a 'warm' start, we kept it at field continuously. It also had poorer resolution and worse spinning sidebands than the later 220- and 300-MHz spectrometers Varian made. Nevertheless, it was used very effectively for several years, and was only replaced when spontaneous quenches became too frequent.

With this spectrometer Phillips and his co-workers revealed the large and characteristic differences in the spectra of proteins in the reversibly denatured (biologically inactive) and the folded (biologically active) states. The differences were attributed to proximity effects (ring current shifts, hydrogen bonding, etc.) that occurred in the folded form of the protein and were absent in the unfolded form. They demonstrated that the spectra of denatured (unfolded) proteins were well represented by the sum of the individual amino acid resonances, while the proteins had significantly different spectra in their natural (folded) state.[16] The differences were due to hydrogen bonding and interactions with other groups in close proximity in the folded state.

It was further demonstrated that, at the higher resonance fields provided by the superconducting solenoid, inequivalent hydrogen atoms of native proteins could be resolved and, in favorable circumstances, uniquely assigned to hydrogen atoms of the protein. These and subsequent studies provided necessary underpinning to the remarkable work of others who have developed NMR into a unique tool for the elucidation of the three-dimensional structure of proteins in solution.[16]

I regret that I cannot give a better account of the biopolymer work, consisting of nearly 40 papers. However these contributions have been better discussed by Jardetzky and Roberts,[17] and others. Among the collaborators in the biopolymer work were C. C. McDonald, J. Lazar, J. D. Glickson, M. Poe, J. F. Weiher, R. G. Bartsch, W. Lovenberg, R. F. W. Hardy, and R. C. Burns.

In 1974 Phillips accepted a transfer to England as Technical Manager of a mycoprotein venture at The Lord Rank Research Centre. This was a joint venture with DuPont, targeted toward manufacturing synthetic food for human consumption. When DuPont dropped out of this venture he returned to Wilmington in 1976 to become an Assistant Director of Research in the Polymer Department. However, these assignments took him away from his primary interests in science, so in 1977 he went to Washington University in St. Louis, MO, and later on to other posts.

My work at the higher frequency was devoted principally to the structural analysis of synthetic polymers, including the tacticity of polypropylene and poly(methyl methacrylate), monomer sequences in copolymers, and branch and end-group studies.[16, 18]

In the mid-1970s I was assigned other work and, though I used NMR, I was not actively involved in operating the equipment. Like Phillips, I spent most of my NMR career in the CW world, mainly on proton and fluorine resonance. We were getting out just as Fourier transform NMR was opening up new applications of carbon-13 and other less sensitive nuclei, and multiple pulse techniques were further revolutionizing the field. This was perhaps fortunate for me, as I was always uncomfortable in the 'rotating frame', and the very elegant multiple pulse experiments being introduced convinced me that it was time to move aside for younger and more agile minds. Still, it would have been great fun to start all over again.

REFERENCES

1. W.D. Phillips, *J. Chem. Phys.*, 1956, **25**, 949.
2. R. C. Burns, R. W. F. Hardy and W. D. Phillips, *Nitrogen Fixation by Free-living Micro-organisms*, ed. W. D. P. Stewart, International Biological Program, New York, 1975, Vol. 6, p. 38.
3. W. D. Phillips, *J. Chem. Phys.*, 1955, **25**, 1363.
4. W. D. Phillips, *Ann. N. Y. Acad. Sci.*, 1958, **70**, 817.
5. J. J. Drysdale and W. D. Phillips, *J. Am. Chem. Soc.*, 1957, **79**, 319.
6. E. L. Muetterties and W. D. Phillips, *J. Am. Chem. Soc.*, 1959, **81**, 1084.
7. W. D. Phillips, H. C. Miller and E. L. Muetterties, *J. Am. Chem. Soc.*, 1959, **81**, 4496.
8. W. D. Phillips and R. E. Benson, *J. Chem. Phys.*, 1960, **33**, 607.
9. D. R. Eaton, W. D. Phillips, and D. J. Caldwell, *J. Am. Chem. Soc.*, 1963, **85**, 397.
10. R. C. Ferguson, *J. Am. Chem. Soc.*, 1960, **82**, 2416.
11. R. C. Ferguson, *J. Polym. Sci.*, 1964, **A2**, 4735.
12. J. D. Swalen and C. A. Reilly, *J. Chem. Phys.*, 1962, **37**, 21.
13. R. C. Ferguson and D. W. Marquardt, *J. Chem. Phys.*, 1964, **41**, 2087.
14. R. C. Ferguson, *J. Phys. Chem.*, 1964, **68**, 1594.
15. R. C. Ferguson, *J. Magn. Rescon.*, 1973, **12**, 296.
16. R. C. Ferguson and W. D. Phillips, *Science*, 1967, **157**, 257.
17. O. Jardetzky and G. C. K. Roberts, *NMR in Molecular Biology*, Academic Press, New York, 1981.
18. R. C. Ferguson, *Kautsch. Gummi, Kunstst.*, 1965, **18**, 823.

Biographical Sketches

Raymond Craig Ferguson. *b* 1922. B.S., 1948, Chemistry, M.S., 1950, Analytical Chemistry, Iowa State University (Ames), Ph.D., 1953, Physical Chemistry, Harvard University, USA. Research at E. I. duPont de Nemours & Co., 1953–85. Introduced to NMR by William D. Phillips in 1954 and continued NMR work until 1974. Approximately 30 publications. Research specialties: molecular spectroscopy (gas-phase microwave, infrared, high-resolution NMR) of organic compounds and synthetic polymers, computer analysis of spectra, polymer characterization, polymer physics.

William Dale Phillips. *b* 1925. A.B., 1948, University of Kansas, Ph.D., 1951, Physical Chemistry, Massachusetts Institute of Technology. Research and research management, finally Associate Director of Basic Science, Central Research Department, E. I. duPont de Nemours (USA), 1951–74. Technical Manager, mycoprotein venture, The Lord Rank Research Centre, England, 1974–76. Assistant Director of Research & Development, Plastic Products & Resins Department, E. I. duPont de Nemours, 1976–78. Charles Allen Thomas Professor of Chemistry and

Chairman of Department, School of Medicine, Washington University, St. Louis, MO, 1977–84. Director, Center for Biotechnology, 1982–84. Senior Vice President, Science & Technology, Mallinckrodt, 1984–90. Associate Director, Office of Science & Technology Policy, 1990–91; deceased, 1993. Research specialties: physical chemistry, molecular spectroscopy, particularly NMR, ESR and IR, biophysics, molecular and electronic structure of organic and inorganic compounds, polypeptides, nucleic acids and proteins.

Fiat Daniel: The International Society of Magnetic Resonance (ISMAR). Landmarks and Highlights

Daniel Fiat

University of Illinois at Chicago, Chicago, IL, USA

OBJECTIVES

The aims of the International Society of Magnetic Resonance are: to advance and disseminate knowledge of magnetic resonance and its applications in physics, chemistry, biology, and medicine among scientists and research institutions throughout the world; to foster interactions among scientists in different fields of magnetic resonance; to encourage interdisciplinary explorations; to organize schools, local and international symposia on magnetic resonance; and to publish articles and periodicals on this subject.

HISTORICAL BACKGROUND

In September 1965 an international symposium on nuclear magnetic resonance was held in Tokyo, Japan, chaired by Shizuo Fujiwara. This meeting was followed by a second international meeting held in Sao Paulo, Brazil, in July 1968 and organized by Leonard Reeves, E. Geisbrecht, and S. Mathias. A third meeting followed, held in Clayton, Victoria, Australia, in 1969. This meeting was organized by Clive K. Coogan.

At the closing session of the Clayton meeting, the participants recommended the formation of an International Society of Magnetic Resonance and elected myself as chairman for the purpose of founding the society.

In August 1971 the fourth international meeting on magnetic resonance, which I organized, was held in Rehovot and Jerusalem, Israel. This meeting marked the 25th anniversary of the discovery of nuclear magnetic resonance. Following the opening session the first award of the society—the ISMAR Prize—was presented to Erwin L. Hahn by Felix Bloch for the discovery of the spin echo phenomena and his many outstanding contributions to the field.

The International Society was formally founded following the 4th meeting and its constitution adopted by its founders: E. Raymond Andrew, Nottingham; Robert Blinc, Ljubljana; A. David Buckingham, Bristol; Clive K. Coogan, Clayton; Daniel Fiat, Rehovot; Shizuo Fujiwara, Tokyo; Karl H. Hausser, Heidelberg; Leonard W. Reeves, Waterloo; and John S. Waugh, Cambridge. These founders formed the Executive Committee. The Council consisted of the Executive Committee and the following members: George J. Béné, Geneve; Felix Bloch, Stanford; Jacques Danon, Rio De Janeiro; Sture Forsén, Lund; Herbert Gutowsky, Urbana; Jacek Hennel, Krakow; Valdemar Kowalewski, Buenos Aires; D. Arthur Losche, Leipzig; A. K. Saha, Calcutta; Jacob Smidt, Delft; Ionel Solomon, Paris; and Ioan Ursu, Bucharest.

The Council recommended holding future ISMAR meetings triennially. Subsequently ISMAR meetings were held in 1974 in Bombay, 1977 in Banff, 1980 in Delft, 1983 in Chicago, 1986 in Rio de Janeiro, 1989 in Morzine, and 1992 in Vancouver. The 1995 meeting will be held in Sydney, Australia.

An attempt has been made to hold each meeting in a different continent to bring together scientists from the different fields of magnetic resonance: nuclear magnetic resonance, electron spin resonance, and nuclear quadrupole resonance; also to bring together scientists involved in the development of magnetic resonance techniques with those involved in the applications of the techniques in physics, chemistry, biology, and medicine.

ISMAR held International Schools and sponsored series of Specialized International Symposia in NMR, ESR, and NQR, oriented towards specific topics and applications that reflected the most recent and advanced developments. Schools were held jointly with the Groupment AMPERE in Yugoslavia. Schools in Italy were organized by the ISMAR sponsored scientific organization in Italy, GDRM.

The *Bulletin of Magnetic Resonance* is the quarterly review'journal of ISMAR. Its first editor was J. Howard Bradbury, Canberra; its present editor is David Gorenstein, Purdue.

It is not possible to cover here all of the important developments in magnetic resonance and its applications; however, certain events at ISMAR meetings that demonstrate the great advances in magnetic resonance stand out in my mind. I would like to mention a few. I remember John Waugh in 1968, at the Sao Paulo meeting, eagerly awaiting a call from his students in regard to a novel method that would allow high-resolution studies of solids by a unique pulse sequence. The novel approach of John and his students led to developments of the utmost importance in nuclear magnetic resonance and its applications. The method was later combined with the high-resolution method developed earlier by Raymond Andrew, thus opening the way for detailed high-resolution studies of solids, leading to the development of many other novel techniques by the same investigators as well as inspiring important developments by others.

Among the many distinguished scientists at the small but intimate Clayton meeting in 1969 was J.H. Van Vleck, who participated and inspired most illuminating scientific discussions.

In 1971, at the Rehovot–Jerusalem meeting three large parallel sessions took place: one in physics, the second in chemical applications, and the third in biological and clinical applications of magnetic resonance. Lectures covered developments in nuclear magnetic resonance, electron spin resonance, and nuclear quadrupole resonance.

At the Bombay meeting, in 1974, the ISMAR Prize was awarded to Herbert Gutowsky for his outstanding achievements in the field of magnetic resonance and its applications to chemistry. Another major highlight of the meeting was the presentation by Paul Lauterbur of NMR 'Zeugmatography'. As we well know, this innovative method provided the impetus for the development of magnetic

resonance imaging which has been found invaluable in the clinical field and has additional applications of utmost importance in the biological sciences and in studies of the physics and chemistry of solids.

At the Banff meeting, in 1977, the ISMAR Prize was awarded posthumously to E. K. Zavoiski, for his discovery in 1945, in Kazan, of electron paramagnetic resonance, and to Robert Blinc for his distinguished contributions in the applications of nuclear magnetic resonance to studies of collective motion near phase transitions, and for the development of a distinguished school in nuclear magnetic resonance in Yugoslavia.

The 1980 meeting in Delft was a large meeting, jointly held with the Groupment AMPERE, and brought together the European scientific community with the international community-at-large. It was a great success.

At the opening of the Delft meeting, ISMAR Prizes were awarded to Hans Dehmelt and to Gunther Laukien. The prize to Hans Dehmelt was awarded for his distinguished contributions to magnetic resonance and rf spectroscopy including his codiscovery with his doctoral advisor H. Kreuger, in 1949 in Göttingen Germany, of the nuclear quadrupole resonance phenomenon for the development, in Seattle, of techniques for studying atomic particles at rest in free space, resulting in the most precise determination of the electron *g* factor in free electron traps in 1976, and in 1979 for the most precise studies of magnetic properties of a single positron, the best test obtained so far of quantum electrodynamics. The ISMAR Prize for the industrial development of magnetic resonance instrumentation was presented to Gunther Laukien.

An active participant and a source of inspiration in the Rehovot–Jerusalem, Bombay, Banff, and Delft meetings, Felix Bloch contributed significantly to the scientific contents of the meetings. He was heavily involved in society matters in preparation for the Chicago meeting in August 1983. Unfortunately, the physics and magnetic resonance community suffered a great loss when Felix Bloch died on September 10 of that year.

The number of participants at the Chicago meeting was large, about 1000. At the meeting magnetic resonance physics, techniques, and applications in chemistry, biology, and medicine were presented and discussed. A very illuminating talk describing the development of magnetic resonance was given by Norman Ramsey. The ISMAR Prize was awarded to B. Bleaney, Oxford, for developing the field of electron spin resonance.

Charles P. Slichter was awarded the ISMAR Prize at the Rio de Janeiro meeting (1986) in recognition of his pioneering work in nuclear magnetic resonance and its applications in solid state and surface physics. The Rio de Janeiro meeting was a great success, the participants included many of the pioneers in magnetic resonance as well as students and younger investigators.

John S. Waugh was awarded the ISMAR Prize at the Morzine meeting (1989) in recognition of his pioneering work in nuclear magnetic resonance and for teaching us all that spins can be made to do almost everything. Among the many important scientific contributions to the meeting were the lectures presented by Erwin L. Hahn, Richard R. Ernst, Charles Slichter, Ray Freeman, and Alexander Pines.

Paul Lauterbur and Peter Mansfield were awarded the ISMAR Prize at the Vancouver meeting (1992) in recognition of their important contributions to the fundamentals of nuclear magnetic resonance and its applications, especially their inventions of practical means of forming images which make it possible to determine and display the spatial variation of important physical, chemical, and biological properties of matter.

The absence of many of the pioneers of magnetic resonance and the participation of many younger investigators at this meeting marked the change of times. It was very moving to see Charles P. Slichter and Ray Freeman going from group to group discussing science with the new generation.

Biographical Sketch

Daniel Fiat. *b* 1930. D.Sc., 1960, Physical Chemistry, Israel Institute of Technology. Princeton University, 1960–61; University of California, Berkeley, 1961–64; Weizmann Institute of Science, Israel, 1964–75; University of Illinois, Chicago, 1975–present. Chairman ISMAR, 1969–83; Founding Chairman ISMAR, 1983–present. Approx. 200 publications. Current research: determination of $rCMRO_2$, rCBF, and rCBV in the human by ^{17}O MRI and MRS, ^{17}O NMR of solutions and solids.

Forsén, Sture: 'Saturation Transfer' and 'TSI'—Early Days and Nights of NMR in Sweden

Sture Forsén
University of Lund, Lund, Sweden

An enterprising young woman from Thame
Took a trip in the rotating frame
She returned the next day
Most contented and gay
With no signs of repent or of shame.

(Late night poetry from the Forsén and Hoffman labs; AD 1962)

The first two commercial NMR spectrometers (Varian, 40 MHz) arrived in Sweden in early and mid-1957. One was procured by Prof. Kai Siegbahn, a few years earlier appointed to the prestigious Chair in Physics at Uppsala University. The other was obtained by Dr. Erik Forslind, Associate Professor of Physical Chemistry at the Royal Institute of Technology ('KTH') in Stockholm. These instruments were actually not the first NMR spectrometers in Sweden. Dr. Gunnar LindstrÖm at the Nobel Institute of Physics in Stockholm had, around 1950, built his own instrument. His magnet was of such good quality that he actually was one of the first, if not the first, to report ^{1}H NMR chemical shifts—between water and CH_2/CH_3 groups in mineral oil.[1] Lindström's spectrometer was later modified by a Swedish medical doctor, Dr. Erik Odeblad, who used it for his pioneering biomedical NMR applications in the mid-1950s—the truly first in vivo experiments.[2] I am not quite sure for what purpose Kai Siegbahn had intended to use his Uppsala spectrometer. Possibly he had in mind originally to determine accurate values of nuclear magnetic moments—but the damned chemical shifts became an irritating obstacle and I think his interest faded gradually. Anyway, he had the good inspiration to send a young gifted graduate student, Ragnar Hoffman, to an introductory NMR course at Varian in Palo Alto in early 1957. At Palo Alto Ragnar learned about all the wonderful things that NMR could do in chemistry—knowledge that he brought back to his Physics Department colleagues who, however, now seemed all into atomic beams rather than messy liquids.

The instrument at the Royal Institute of Technology was originally intended for one particular research project: to elucidate the molecular properties of water in hydrogels, notably cement. The spectrometer thus had a 'wideline' attachment as well as the standard high-resolution parts. In early 1956 I had been enlisted as a teaching assistant at the Physical Chemistry Division and had come to know Dr. Forslind. After my M.Sc. in Chemical Engineering in mid-1956, I was snatched away into compulsory military service and was eventually transferred to the National Defense Research Laboratories in Stockholm. One day in early 1957 I received a phone call from Dr. Forslind who asked me to join him as his first ever graduate student and in charge of the NMR instruments. With some hesitation—my knowledge of NMR was rudimentary and I had seen pictures of spectrometer consoles that looked scaringly like the gadget-crowded cockpits of commercial airliners—I accepted. During my free time I then started spending many hours in the library of the National Defense Research Laboratories reading early NMR articles and teaching myself quantum chemistry. In mid-1957 I was a civilian again, and joined Forslind's group in time to see the heavy Varian electromagnet being lifted in through the windows of the Physical Chemistry labs on the second floor.

Meanwhile in Uppsala, Ragnar Hoffman had established contacts with the Organic Chemistry Department, especially with Assoc. Prof. Salo Gronowitz, an enthusiastic and successful expert on thiophene chemistry. He soon provided Ragnar with a number of mono- and disubstituted furans and thiophenes with interesting AB, ABC, and ABX spectra. The Hoffman–Gronowitz collaboration was very fruitful, a number of publications resulted and became the core of Ragnar's Ph.D. thesis that he defended in late 1960—with Dr. Forslind and myself as opponents. Nearly the entire Swedish NMR community gathered in one room!

Assimilating the basis of NMR in those days was totally based on self-studies. The early monograph by E. R. Andrew (1958) was in many ways most valuable, but gave little insight on high-resolution NMR on liquids. So it was a struggle through the published literature—articles by Gutowsky, Pople, Schneider, Bernstein, McConnell, etc.—trying to learn as one went along. Ragnar, with his solid background in theoretical physics, had little problem with the spin Hamiltonian and soon became a master of analyzing ABC, ABX, AA′BB′, etc. spectra. I myself was for a long time occupied trying to make sense of the wideline spectra of Forslind's hydrogels and performing crude quantum chemical calculations using analytical expressions (fitted using slow desk top calculators!) of numerical Hartree–Fock wavefunctions. Eventually I managed to swing my thesis towards experimental studies of hydrogen–bonding in liquids—a subject that fascinates me to this day. I also started collaborating with graduate students in the Organic Chemistry Division which under Prof. Holger Erdtman was largely directed toward studies of natural products from the plant kingdom. Erdtman was then known for his scepticism against the use of spectroscopic methods for structure elucidations. IR was just about acceptable. All that changed completely after a lecture at the Royal Institute of Technology by Sir Derek Barton in which he beautifully demonstrated the enormous benefits of ^{1}H NMR for structure elucidations of steroids, terpenes, etc.—studies mostly made in collaboration with Lloyd Jackman. Erdtman was completely converted to ^{1}H NMR from that very day, to my great benefit.

In 1959, after some dissension with my supervisor, I wrote up a licentiat thesis (old Swedish degree, more like a Ph.D. of today) on my hydrogen-bonding studies and left for a job at the Atomic Power Department of ASEA in Västerås—a town some 160 km west of Stockholm. I could, however, not abandon the NMR field—for a long time I was traveling back and forth between the Royal Institute and Västerås, running spectra on late evenings and weekends. Eventually I got a generous offer from Erdtman and Forslind to return to Stockholm with a lot of freedom to carry out my own NMR

research, as long as I kept the organic chemists happy with a spectral service. After an intense year of work, I defended my Ph.D. thesis (old system) in late 1962. The same autumn I met Ragnar Hoffman at an NMR meeting in Oxford. We soon discovered a common childish streak in our personalities and had a hilarious time trying to outsmart the ignorant and slightly xenophobic scouts at Balliol College—our place of lodging. We decided that we must start to collaborate—the question was merely on what. Double resonance was then one of the excitements of the day with the possibilities of determining the relative signs of spin coupling constants as pioneered by D.F. Evans, Ray Freeman, and David Whiffen. We decided to explore this and on our return to Sweden things moved swiftly. At the Royal Institute we had some hardware parts, e.g. an audiooscillator, that made it natural to do the experiments there. We worked enthusiastically and hard. Ragnar thought of experiments in terms of spin Hamiltonians and doubly rotating frames, while I tended to think in terms of energy level diagrams and of the chemical aspects of the molecules we looked at. We found that there were some variants of the double resonance technique that had not yet been explored—for example, selectively inverting the populations of the levels corresponding to a particular transition in a multispin system. This we introduced as 'TSI', i.e. transitory selective irradiation - an early NMR version of a 'soft' selective 180° pulse.[3] We used the TSI method extensively for characterizing the coupling parameters in complex spin systems.

One day in early 1963, during a coffee break in Uppsala, I asked Ragnar semi-seriously what would happen if one were to irradiate an NMR signal from a proton that was not spin coupled to but in chemical exchange with another proton with a different chemical shift. Would anything happen at all? Ragnar hesitated, 'I am not sure. Let us do an experiment!' How to find a suitable chemical system? My previous experience with hydrogen-bonded organic molecules now came in handy. After some trial and error we had several candidates. One could for example mix a bulky aliphatic alcohol, like *t*-butanol, with a molecule with an intramolecular hydrogen bond, like 2-hydroxyacetophenone, and get two well-separated OH NMR signals. Also by gradually adding small amounts of an amine, one could increase the rate of chemical exchange between the two types of OH groups to the point of coalescence. So we could certainly test the new double resonance experiment at different exchange rates if need be.

Very late one night in May 1963 the experiment was tried out—a shot in the dark, literally! A modulated sideband was set on one OH signal while the intensity of the other was monitored by a rapidly repeated 'Phantastron' sweep—and lo and behold the observed signal gradually decreased in intensity to a new low value! Great excitement!! We eventually decided that the experiment was indeed reproducible and OK. Childish happiness and dancing on the lab floor ensued. One week later everything was wrapped up. The theory of the new 'magnetization or saturation transfer' method of determining moderately slow chemical exchange rates was developed mainly by Ragnar, and the first short communication was sent off.[4] We soon carried out more experiments on different exchanging systems and wrote two detailed accounts of the method.[5,6] Thanks to John Baldeschwieler, we were also given an opportunity to present the new method as a late entry at the 1963 ENC in Pittsburgh.

The collaboration between Ragnar and myself was very intense for the following three years and in a way culminated in a rather extensive review on double and multiple resonance for the first issue of the new series *Progress in NMR Spectroscopy*.[7] In 1966 I was appointed to the new Chair in Physical Chemistry at the University of Lund, some 600 km south of Stockholm and became rather busy with building up the new division and with teaching duties. Ragnar went for a sabbatical with John Waugh at M.I.T. and wrote a learned review article on the development of a very general matrix inversion formalism for calculating NMR lineshapes.[8] In 1969 we decided to write a 'down-to-earth' and useful textbook on the analysis of high-resolution NMR spectra. During this work Ragnar started showing clear signs of strain and weariness. I understood that in order to obtain a tenured position as university lecturer in physics at Uppsala University he had to take courses in relativity theory, astronomy, and what not. Conscientious as he was, and despite the fact that he already must have been more than qualified for such a position, he vigorously committed himself to these studies. This, on top of his extremely heavy teaching loads and his strong desire to be an ever present family father, took a heavy toll on his health.

Ragnar passed away unexpectedly in early 1970, mourned by friends and colleagues near and far. I miss him tremendously. We had a great time exploring the rotating frame. I often wonder what great things he would be doing now.

REFERENCES

1. G. Lindström, *Phys. Rev.*, 1950, **78**, 817.
2. E. Odeblad and G. Lindström, *Acta Radiol.*, 1955, **43**, 469.
3. R. A. Hoffman, B. Gestblom, and S. Forsén, *J. Chem. Phys.*, 1963, **39**, 486.
4. S. Forsén and R. A. Hoffman, *Acta Chem. Scand.*, 1963, **17**, 1787.
5. S. Forsén and R. A. Hoffman, *J. Chem. Phys.*, 1963, **39**, 2892.
6. S. Forsén and R. A. Hoffman, *J. Chem. Phys.*, 1964, **40**, 1189.
7. R. A. Hoffman and S. Forsén *Prog. NMR Spectrosc.*, 1966, **1**, 15.
8. R. A. Hoffman, *Adv. Magn. Reson.*, 1970, **4**, 87.

Biographical Sketch

Sture Forsén. *b* 1932. M.Sc. (Chem. Eng.), 1956, Dr. Techn., 1962, Teaching Assistant Physical Chemistry, Royal Institute of Technology, Stockholm, Sweden. Associate Professor of Chemical Physics and acting Professor of Physical Chemistry, Royal Institute of Technology 1963–66. Chair in Physical Chemistry, University of Lund, Sweden 1966–present. Approx. 300 publications. Research interests have gradually moved from basic NMR spectroscopy and the study of chemical kinetics to the application of NMR in structure/function studies of proteins—particularly Ca^{2+} binding molecules.

Fraenkel, Gideon: Reminiscence of NMR

Gideon Fraenkel

Ohio State University, Columbus, OH, USA

University of Illinois, 1951. Herb Gutowsky taught us physical chemistry. Little did we know he had just discovered the chemical shift, a household word for future generations of chemists.

Harvard, 1955: NMR seemed a safe topic for the graduate student organic seminar, so obscure that a professor couldn't understand why the transition energies should depend on magnetic field. Not only had most organic chemists never heard of the Zeeman effect, they knew precious little about chemical physics in general. NMR changed all that. It became the conduit between organic chemistry and chemical physics.

Caltech days: After my rather structured experience at Harvard, I couldn't believe the no less intellectually demanding, informal atmosphere at Caltech. Everybody's door was open and everything seemed designed to facilitate the progress of research. I went there originally to work with Carl Nieman on enzyme kinetics. Instead, I literally got drawn to the NMR machine in Church Laboratory, then a Varian HR-40. Carl suggested we might learn something useful by looking at the NMR of amino acids. Unfortunately, the Jardetskys had just done that. Nieman was very supportive. He encouraged me to choose my own problems. This is how I got into the amide business.

It had always been assumed, but never proved, that amides protonate on oxygen, (**1**).

One day I had a mental image that in *N*-protonated DMF (**2**) there would be free rotation about the $C_{CO}-N$ bond, whereas the *O*-protonated species (**1**) should show a barrier around this bond at least as large as that measured by Herb Gutowsky's group. So one would expect that (**1**) would exhibit nonequivalent methyls in the ^1H NMR spectrum at room temperature; needless to say this turned out to be the case. Amides were a favorite subject at Caltech, especially among Pauling's structure colleagues, and I became a popular person. The department gave me a Noyes Fellowship, so I continued to explore various physical organic problems, mainly via NMR.

One morning my lab mate Bob Carter (now at Astra Hassle) asked me if the cyclopentadienyl anion had fivefold symmetry. I assured him this was so but search the literature as we might, no crystallographic data were to be found. So we ran proton NMR on different salts, subtracted out the assumed ring current contribution (Pauling's formula), and then I looked at other symmetrical species (tropylium, benzene). Thus was born the linearity of sp^2 proton shift with charge. Around that time I was introduced to Andrew McLachlan who had recently justified from theory the linearity of hyperfine splitting with electron spin density. It seemed to him that our result could be handled in a similar fashion. We published a paper together. How did this all happen? It was the people and the atmosphere. Everybody went to coffee. I met Cafiero Franconi who worked with me further on amides. Aharon Lowenstein told me about kinetics from signal averaging. Because of Aharon, I eventually met and worked with Jerry Kaplan, the patron saint of density matrix theory applied to NMR signal averaging. People make a department. Jack Roberts really showed us by example that pretty complicated chemistry could be elucidated with NMR, Roberts more than anyone else.

First Gordon Conference on Magnetic Resonance: just boiling over with excitement, starting in the train from Boston; all the (now and later) famous names—Gutowsky, Bloembergen, Abragam, Hahn; people talking late into the night, new results just pouring out. I got to present the *O*-protonated amides. It turned out three other groups, Phillips (du Pont), Saunders (Yale), and Meiboom (Weizmann) had the same idea. But we were first. Next time around, the physicists wanted to scrap the conference. After all, everything had been worked out, correctly—the nuclear spin Hamiltonian, the Ramsey equation for chemical shifts, and the principal mechanisms for spin relaxation. Fortunately, calmer minds prevailed. Technical advances and the complexities of molecules have driven the field ever since. And Sputnik.

Biographical Sketch

Gideon Fraenkel. *b* 1932. B.S., 1952, University of Illinois, Ph.D., 1957, Harvard University. Research fellow and Noyes Fellow California Institute of Technology; introduced to NMR by John Roberts and Harden McConnell. Faculty in Chemistry, Ohio State University, 1960–present. Approx. 150 publications; research areas: reaction mechanisms, ion-pairs, dynamic NMR, carbanion chemistry.

Frahm, Jens: Toward Rapid NMR Imaging

Jens Frahm

Max-Planck-Institut für Biophysikalische Chemie, Göttingen, Germany

This article presents a personal view of our development of STEAM and FLASH NMR techniques in 1984 and 1985 at the Max-Planck-Institut für biophysikalische Chemie in Göttingen, Germany. To facilitate the understanding of the steps leading to rapid NMR imaging sequences, it will be helpful to start with some background information on NMR imaging as developed up to 1983–84 when we were first able to carry out experimental work on our own. Following some comments upon how the Göttingen project was set up, I will discuss our work on stimulated echo imaging sequences that led directly to the design of rapid low flip angle gradient echo imaging.

NMR IMAGING IN 1984

In 1984, the development of medical magnetic resonance imaging appeared to have reached a natural end. Following Lauterbur's original work[1] on the use of frequency-encoding magnetic field gradients for spatial discrimination of NMR signals in conjunction with a projection reconstruction algorithm for calculation of an NMR image, the onset of industrial development of the machinery by medical manufacturers around 1978–79 had led to considerable instrumental progress including the availability of 1-m bore superconducting magnets. Medical applications had focused on studies of the central nervous system and promised great sensitivity to detect abnormalities in a large number of disease states of the brain.

Even the image quality had become quite acceptable by combining several advances achieved between 1975 and 1981. Firstly, the preferred form of image reconstruction had been shifted from projection reconstruction to two-dimensional Fourier transformation (2D FT). This had been proposed by Kumar, Welti, and Ernst[2], who replaced the rotating frequency-encoding gradient of the Lauterbur experiment by a fixed frequency-encoding gradient and a variable phase-encoding gradient that probed the spatial distribution of spins along a second orthogonal dimension. Image calculation by 2D FT was in complete analogy to 2D NMR experiments for high-resolution structure elucidation such as 2D J-resolved or shift-correlated spectroscopy. Secondly, for practical implementations the spin warp modification of the phase-encoding gradient as described by Edelstein, Hutchison, Johnson, and Redpath[3] provided technical simplicity and robustness with regard to image artifacts. Thirdly, plane definition by slice selection had been successfully accomplished by combining a frequency-selective shaped 90 ° rf pulse with a slice selection gradient. Following a controversy between Mansfield[4] and Hoult,[5] agreement was reached on the necessity to refocus the dephasing effect of the slice selection gradient during the second half of the rf pulse by gradient reversal after the end of the rf pulse. And fourthly, an important step forward had been made by two research groups led by Young[6] and Edelstein[7] in adopting Hahn's spin echo rf pulse sequence[8] for NMR imaging. The spin echo version overcame severe signal losses and instabilities that arose from magnetic field inhomogeneities due to technical limitations of the early wide-bore magnets and in vivo tissue susceptibility differences.

In view of the aforementioned accomplishments, a typical summary of the state-of-the-art in NMR imaging in 1984 might have been as follows. The spatial resolution of the images was considered acceptable for many medical applications and the accessible soft tissue contrast based on differences in T_1 and T_2 relaxation times turned out to be excellent. Foreseeable improvements were to be expected in technical areas such as the quality of hardware components (rf coils, preamplifiers, computers, etc.), the reduction of eddy currents associated with gradient switching, and the design of slice-selective 180° refocusing pulses that compensate for the nonlinearity of the Bloch equations borne out by long pulses and strong off-resonance effects in the presence of a gradient. Other issues concerned the handling and user-friendliness of the instruments and included multislice and oblique imaging procedures as well as respiratory and EKG-triggering and gating.

However, there was agreement that no major change was to be expected for the #1 problem in NMR imaging, i.e. the relatively long measuring times of the order of minutes. While typical repetition times were 500–2000 ms to ensure sufficient signal recovery, the reconstruction of a high-resolution image required at least 128–256 acquisitions with different phase-encoding gradients. Thus, the temporal resolution in NMR imaging appeared to be determined by physical limitations such as T_1 relaxation times and the principle of image formation. This problem was central to many applications and in a sense overshadowed the usefulness of NMR imaging as a whole when compared with competing modalities in diagnostic imaging. Obviously, long imaging times cause motion problems for cardiac and abdominal examinations as well as for less cooperative patients, and generally do not allow dynamic studies with a time resolution of seconds typical for many physiological processes. They also preclude the use of 3D NMR imaging studies since pertinent acquisition times would easily reach several hours. In this context Mansfield's development of echo planar imaging[9] as a high-speed method was not considered to be an alternative for 'plain' imaging, due to a lack of image quality and limited spatial resolution as determined by the rapid decay of transverse magnetization from tissue water in most organ systems.

It was in this atmosphere that our small group of researchers at the Max-Planck-Institut für biophysikalische Chemie in Göttingen, Germany described a new concept for rapid scanning that marked a breakthrough in NMR imaging and led to a still growing number of new applications.

THE GÖTTINGEN PROJECT

My personal acquaintance with and first practice of NMR dates back to the mid-1970s when my scientific teacher Hans Strehlow offered me work on a diploma thesis where NMR T_1

relaxation differences were exploited to measure the kinetics of rapid chemical exchange reactions.[10] The equipment I had to use was an old-fashioned 60 MHz Bruker electromagnet connected to a 'pulse spectrometer'. However, the lack of any Fourier transform analysis and the enthusiasm of Hans Strehlow gave me an excellent introduction into basic pulsed NMR experiments. Although our emphasis was solely on dynamic and kinetic aspects with applications in physical chemistry, the original experiments of Hahn,[8] Gutowsky,[11] Carr and Purcell,[12] Woessner,[13] Stejskal,[14] Tanner,[15] and many others involved in the development of 'zero-dimensional' NMR without chemical shift discrimination formed the ground for our later work in the in vivo field.

In the second half of the 1970s the Max-Planck-Institut für biophysikalische Chemie was an exciting place where many scientists trained as physicists or chemists started using their expertise to look into biological systems. Manfred Eigen developed the concept of the hypercycle as a model for biological evolution at the molecular level, Fritz Schäfer helped to turn the laser into a multipurpose instrument for biological research, and Erwin Neher and Bert Sakmann worked on electrophysiological recordings of single cells, to name only a few. In this environment a young scientist had to be attracted by the way discipline-crossing research was carried out. In fact, even a quick look into NMR immediately indicated its potential role in biology with noninvasive investigations of cells, excised organs, or even small laboratory animals.

At that time the 'ruling' NMR community showed only little interest in the future capabilities of NMR imaging and its need for serious scientific research to promote further developments and applications. Very little was known about those involved and their 'suspicious' contacts to industry or their 'dubious' collaborations with such disciplines as medicine or radiology. However, without prejudice I felt ready to make my own decisions in a critical postdoctoral phase of my scientific career and I was therefore very much influenced by the clear and positive messages of Lauterbur, Damadian, Mansfield, and Radda, who all lectured at the 1979 European Experimental NMR Conference in Autrans, France. Firstly, there was no doubt that access to 'spatial resolution' would be available to NMR researchers dealing with imaging or high-resolution spectroscopy, and secondly, the newly formed in vivo NMR community represented a fascinating melting pot for physicists, biologists, clinicians, and manufacturers who opened the way into a field where basic and applied research frequently fail to be distinguishable.

Although it took until early 1982 before we submitted a grant application to the Deutsche Forschungsgemeinschaft (DFG), it was still the first proposal for a research project that dealt with NMR imaging in Germany. The group of enthusiasts comprised Wolfgang Hänicke, a mathematician, who had worked with me on theoretical issues such as slice selection and time-variable frequency-encoding gradients in NMR imaging;[16,17] Dietmar Merboldt, a physicist who was my first Ph.D. student and who had just finished a thesis on water proton NMR relaxation in ternary systems as a very simple model of heterogeneity in biological cells; Dieter Matthaei, a clinician from the University hospital of Göttingen with a background in internal medicine and Axel Haase, another physicist from the Max-Planck-Institut who had just received a Ph.D. for his work on membrane-bound pH indicators which involved NMR experiments to characterize the exact location of the dye molecules. Provided DFG financial support was granted, Axel Haase had promised to join after his postdoctoral stay in Radda's lab in Oxford where he worked on surface coils and rotating frame imaging.

The DFG application focused on 'quantitative parametric' NMR imaging techniques that ought to be developed with use of an experimental 2.35-T 40-cm bore magnet. Unfortunately, the project was not only delayed by the DFG, who invited all German radiologists to contribute applications for NMR imaging, but was subsequently turned down by giving preference to two clinical applications based on 1.5-T whole body units: just another example of how bias in research funding and reviewing may affect scientific progress, particularly in countries that preclude proper outside refereeing by applications not being available in the English language. The reason why this article can be written is only due to the technical understanding and the personal courage of Friedrich Unz, who at that time was responsible for research grants from the German government, i.e. the Bundesminister für Forschung and Technologie (BMFT), and thus participated in the DFG decision as an observer. He decided to grant BMFT financial support for more or less the same proposal within a period of only three months, which then allowed us to start the project in July 1983.

In February 1984 a Bruker imaging and spectroscopy system was installed in Göttingen. At that time the manufacturing of high-field wide bore magnets was still a critical experiment and so there was no real surprise that the 2.35-T, 40-cm bore magnet had to be replaced only a couple of weeks later because of a significant field drift following a quench (as far as I remember it was finally up to 1 kHz h^{-1}). However, since then we have successfully worked with a second magnet, while the rest of the system has been upgraded several times. During the first weeks and months we worked through spin echo imaging and image reconstruction techniques, and rapidly learned that the practical reliability of some of the theoretical concepts was clearly limited by technological constraints such as rf power restrictions and magnetic field gradient eddy currents. However, we also identified a lack of investment in more sophisticated techniques as a potential source of some scientific and clinical disappointment in NMR imaging. Or in other words, the real problems were in physics and biology rather than in data handling and postprocessing. We therefore decided to focus on new methods that would enhance the specificity of the image information by providing better access to contrasts beyond spin density, T_1, and T_2.

Our first target was the loss of chemical shift information. Even for the simple case of water and fat components contributing to an object, no attempt was made to retrieve the chemical information for imaging. With the availability of shaped rf pulses and magnetic field gradients as required for imaging, however, a spectroscopic separation of water and fat proton NMR signals was easily accomplished by a suppression of the unwanted chemical shift component prior to data acquisition. The CHESS (chemical shift selective) technique simply excites the unwanted resonance with use of a frequency-selective rf pulse and then dephases ('spoils') the resulting transverse magnetization prior to the application of a subsequent imaging or spectroscopy experiment.[18] The same principle is now commonly applied for water-suppressed

localized proton NMR spectroscopy or for solvent suppression in high-resolution NMR.

STEAM . . .

Another area of interest was the NMR access to molecular dynamic information that might be adopted for imaging. Maps of microscopic mobility or 'diffusion' would not only be of scientific value in complex biological systems, but also serve diagnostic purposes in disease states. In fact, diffusion-weighted NMR imaging now seems to be the method of choice for the early detection of infarction zones in patients after a cerebral stroke. In the classical literature the stimulated echo sequence comprising three rf pulses had been demonstrated by Tanner[15] to be particularly suitable for the investigation of systems with long T_1 and short T_2 relaxation times, as in proton NMR studies of biological tissue. In NMR imaging stimulated echoes had only occurred as artifacts originating from imperfect 180° rf pulses in multiecho sequences. In early 1984, Wolfgang Hänicke and Dietmar Merboldt therefore started to focus on NMR imaging experiments based on stimulated echoes. Computer simulations with variable numbers of slice-selective 90° rf pulses and different predephasing and rephasing strategies were rapidly followed by the implementation of basic STEAM (stimulated echo acquisition mode) imaging sequences on the Bruker scanner. The first positive results enforced a detailed theoretical and practical evaluation of the sequences' compatibility with imaging, i.e. slice selection, spatial encoding, and spoiling of unwanted spin echoes and FID signals. For example, we identified the complete dephasing of any transverse magnetization before the application of the second rf pulse as a prerequisite for ensuring maximum intensity of the stimulated echo. Interestingly, this was not properly claimed in Hahn's elegant paper on 'Spin Echoes',[8] which in retrospect may be explained by the very short T_2* relaxation times in the fairly inhomogeneous magnets available in 1950.

The relatively easy and successful development of a completely new imaging concept stimulated our optimism considerably about further substantial progress in NMR imaging, which in 1984 was partly in contrast to published suggestions by industrial researchers and clinicians. In our group almost every day somebody came up with a new idea on how to improve the versatility of the STEAM imaging sequence.[19] Dozens of modifications and variants were developed between the summer and fall of 1984 and filed as a German patent application on December 14, 1984. Although diffusion imaging[20] was the original impetus, applications extended to new forms of bolus-tracking flow imaging,[21] CHESS imaging,[22] and even localized spectroscopy[23] which later became a major tool in our efforts to study human brain metabolism. In addition, we recognized the potential of measuring T_1 relaxation processes by varying the middle interval *Tm* between the second and third rf pulse rather than by changing the repetition time. This form of T_1-weighted imaging was somewhat similar to measuring T_2 relaxation by an echo train. In fact, multiple readout points with different *Tm* intervals could be obtained within a single STEAM sequence by subdividing the available longitudinal magnetization with the use of several low flip angle read pulses. This series of pulses replaced the single 90° rf pulse in the third position of the basic stimulated echo sequence. By iteration it was possible to calculate the flip angles of any given number of pulses that created equal amounts of transverse magnetization, each of which was then differently T_1-weighted according to the actual *Tm* value.

We realized as an important aspect of the STEAM T_1 imaging sequence[24] that it distinguishes between two types of longitudinal magnetization created during the course of the sequence. This refers to the pre-encoded longitudinal magnetization originating from the first two rf pulses that refocusses as a stimulated echo and to the longitudinal magnetization recovered from T_1 relaxation during the sequence. The latter magnetization contributes to the FID signal excited by any third read pulse. Thus, even large numbers of low flip angle read pulses followed by short stimulated echo acquisition intervals would not lead to a complex overlap of intermingling coherences. These considerations gave birth to the high-speed STEAM imaging idea. All we needed to do was to phase-encode differently a sequential series of frequency-encoded stimulated echoes that were created by two leading 90 ° rf pulses and a series of slice-selective low flip angle read pulses.[25]

. . . AND FLASH

Our first high-speed STEAM images had imaging times of 200–1200 ms and created tremendous excitement. However, despite the fact that more recent implementations have demonstrated considerable potential for rf refocused high-speed cardiac imaging[26] and motion-insensitive diffusion-weighted imaging,[27] the sequence exhibits limited signal-to-noise because of its partitioning of (half of) the initially excited equilibrium magnetization into small portions for data acquisition. Instead of wasting the recovered longitudinal magnetization, it would be much more advantageous to exploit its feedback by T_1 relaxation with the use of multiple *excitation* pulses. Thus, as soon as the potential of multiple low flip angle *read* pulses in STEAM had been recognized, we thought of applying the concept directly to the equilibrium magnetization. This would eliminate the leading two 90 ° rf pulses in the high-speed STEAM sequence and then require phase- and frequency-encoding the spatial information into a gradient-recalled echo rather than into an rf refocused stimulated echo. Although the schematic rf pulse and gradient switching scheme was rapidly drawn on a sheet of paper, its actual implementation was somewhat slowed down due to discussions about potential coherence transfer problems that might occur during the rapid imaging process. Nevertheless, we finally decided to run an experimental trial since the amount of any residual transverse magnetizations would be very small due to both the small tip angles used and the short T_2* relaxation times encountered in living tissues.

It was on a Friday morning around 10 a.m. that all members of the group gathered together to implement a low flip angle gradient echo sequence with a short repetition time. Of course, with regard to its simplicity, it could have been done within 30 min. However, the implementation was carried out piece by piece with some kind of aesthetic care and suspenseful slowness. It was quite obvious that everybody knew that we were close to a major breakthrough in NMR imaging

and everybody wanted to experience fully the excitement at the end. At noon we had our first results, i.e. FLASH (fast low angle shot) images of a water-filled beaker and—a few minutes later—of a human hand that demonstrated a tremendous gain in signal-to-noise ratio when compared with high-speed STEAM images. The measuring times were 1.92 s using a 128 × 128 data matrix and a repetition time of 15 ms. Over the weekend multiple versions were developed including dynamic scanning by sequential acquisitions and rapid three-dimensional imaging. And we agreed upon the acronym 'FLASH'.[28–31]

In contrast to high-speed STEAM and echo planar imaging, the measuring time of a FLASH sequence is not limited by physical properties such as the duration of a relaxation time. The new concept offered an unrestricted and user-dependent choice of spatial and temporal resolution so that speed may be traded-off for resolution and image quality (signal-to-noise). Although *subsecond* FLASH imaging has found some useful applications,[32–34] the main potential seems to lie in the fast scan domain where cross-sectional images of conventional quality may be acquired within seconds, while three-dimensional data sets need measuring times of minutes.

On February 12, 1985 we filed a German patent application. It was also decided to submit Abstracts to the 1985 Annual Meetings of the Society of Magnetic Resonance in Medicine (SMRM) in London and the Radiological Society of North America in Chicago. To maximize the expected 'big bang' in NMR imaging we thought it worthwhile not to publish journal articles prior to our oral presentation of 'NMR movies' at the SMRM in August. Unfortunately, the planned surprise failed completely since we felt safe in disclosing our information on FLASH scanning shortly before the SMRM meeting to manufacturers involved in the industrial development of medical NMR imaging. We simply forgot about the ease of implementation of the sequence and the speed of modern communications. For example, Derek Shaw of General Electric immediately recognized the potential of the FLASH concept during his visit to Göttingen a week before the SMRM. He transferred the information to Milwaukee where Gary Glover implemented the sequence on a 1.5-T scanner and obtained good quality FLASH images of the human abdomen. Without knowing about these experiments we were therefore quite shocked upon arrival at the Barbican Centre in London, where last minute posters announced '2-s images' as General Electric's most recent achievement just imported from Milwaukee. In fact, we had a hard week in defending our invention against the publicity of a big manufacturer, in particular since the SMRM program committee had scheduled our presentation on the last day of the 5 day meeting. Nevertheless, the first NMR movie showing the dynamic flow pattern in a water beaker after stirring and the inflow of a paramagnetic contrast agent into the kidneys of an anaesthetized rabbit was a great success in demonstrating the new dimension the FLASH concept had added to NMR imaging. And without access to a whole body machine in 1985, we were extremely pleased by the quality of FLASH images obtained on commercially available medical NMR imaging systems.

Of course, many extensions and improvements have followed the early work. Among these are at least two areas that are based on FLASH sequence properties that were originally considered as disadvantages in giving rise to unwanted image artifacts. The first is NMR angiography, which exploits the sensitivity of FLASH images to a continous inflow of unsaturated spins from water protons within blood for a noninvasive delineation of the vasculature, while the second more recent application is based on the sensitivity of the gradient echo to magnetic field inhomogeneities or tissue susceptibilities. The latter effect may be used for functional NMR imaging of brain activation, since regional increases of cerebral blood flow associated with task performance result in a decrease of the concentration of paramagnetic deoxyhemoglobin in red blood cells.

In summary, the advent of rapid scanning NMR imaging has not only improved our access to high-resolution anatomy but opened the way to physiological insights into the human body.

REFERENCES

1. P. C. Lauterbur, *Nature (London)*, 1973, **242**, 190.
2. A. Kumar, D. Welti, and R. R. Ernst, *J. Magn. Reson.*, 1975, **18**, 69.
3. W. A. Edelstein, J. M. S. Hutchison, G. Johnson, and T. Redpath, *Phys. Med. Biol.*, 1980, **25**, 751.
4. A. N. Garroway, P. K. Grannell, and P. Mansfield, *J. Phys. C: Solid State Phys.*, 1974, **7**, L457; P. Mansfield, A. A. Maudsley, P. G. Morris, and I. L. Pykett, *J. Magn. Reson.*, 1979, **33**, 261.
5. D. I. Hoult, *J. Magn. Reson.*, 1977, **26**, 165; *ibid.*, 1979, **35**, 69.
6. I. R. Young, D. R. Bailes, A. G. Collins, and D. J. Gilderdale, Image Options in NMR, in *NMR Imaging: Proceedings of an International Symposium on Nuclear Magnetic Resonance Imaging, October 1–3, 1981, Winston-Salem, NC*, eds. R. L. Witcofski, N. Karstaedt, and C. L. Partain, Bowman Gray School of Medicine, Wake Forest University, 1982, p. 93.
7. W. A. Edelstein, P. A. Bottomley, H. R. Hart, W. M. Leue, J. F. Schenck, and R. W. Redington, NMR Imaging at 5.1 MHz: Work in Progress, in *NMR Imaging: Proceedings of an International Symposium on Nuclear Magnetic Resonance Imaging, October 1–3, 1981, Winston-Salem, NC*, eds. R. L. Witcofski, N. Karstaedt, and C. L. Partain, Bowman Gray School of Medicine, Wake Forest University, 1982, p. 139.
8. E. L. Hahn, *Phys. Rev.*, 1950, **77**, 297; *ibid.*, 1950, **80**, 580.
9. P. Mansfield, *J. Phys. C: Solid State Phys.*, 1977, **10**, L55; P. Mansfield and I. L. Pykett, *J. Magn. Reson.*, 1978, **29**, 355.
10. H. Strehlow and J. Frahm, *Ber. Bunsenges. Phys. Chem.*, 1975, **79**, 57.
11. H. S. Gutowsky and D. W. McCall, *Phys. Rev.*, 1951, **82**, 748; H. S. Gutowsky and A. Saika, *J. Chem. Phys.*, 1953, **21**, 1688.
12. H. Y. Carr and E. M. Purcell, *Phys. Rev.*, 1954, **94**, 630.
13. D. E. Woessner, *J. Chem. Phys.* 1961, **34**, 2057.
14. E. O. Stejskal and J. E. Tanner, *J. Chem. Phys.*, 1965, **42**, 288.
15. J. E. Tanner, *J. Chem. Phys.* 1970, **52**, 2523; *ibid.*, 1972, **57**, 3586.
16. J. Frahm and W. Hänicke, *J. Phys. E: Sci. Instrum.*, 1984, **17**, 612.
17. J. Frahm and W. Hänicke, *J. Magn. Reson.*, 1984, **60**, 320.
18. A. Haase, J. Frahm, W. Hänicke, and D. Matthaei, *Phys. Med. Biol.*, 1985, **30**, 341.
19. J. Frahm, K. D. Merboldt, W. Hänicke, and A. Haase, *J. Magn. Reson.*, 1985, **64**, 81.
20. K. D. Merboldt, W. Hänicke, and J. Frahm, *J. Magn. Reson.*, 1985, **64**, 479.

21. K. D. Merboldt, W. Hänicke, and J. Frahm, *J. Magn. Reson.*, 1986, **67**, 336.
22. A. Haase and J. Frahm, *J. Magn. Reson.*, 1985, **64**, 94.
23. J. Frahm, K. D. Merboldt, and W. Hänicke, *J. Magn. Reson.*, 1987, **72**, 502.
24. A. Haase and J. Frahm, *J. Magn. Reson.*, 1985, **65**, 481.
25. J. Frahm, A. Haase, D. Matthaei, K. D. Merboldt, and W. Hänicke, *J. Magn. Reson.*, 1985, **65**, 130.
26. J. Frahm, W. Hänicke, H. Bruhn, M. L. Gyngell, and K. D. Merboldt, *Magn. Reson. Med.*, 1991, **22**, 133.
27. K. D. Merboldt, W. Hänicke, H. Bruhn, M. L. Gyngell, and J. Frahm, *Magn. Reson. Med.*, 1992, **23**, 179.
28. A. Haase, J. Frahm, D. Matthaei, W. Hänicke, and K. D. Merboldt, *J. Magn. Reson.*, 1986, **67**, 258.
29. J. Frahm, A. Haase, and D. Matthaei, *Magn. Reson. Med.*, 1986, **3**, 321.
30. J. Frahm, A. Haase, and D. Matthaei, *J. Comp. Assist. Tomogr.*, 1986, **10**, 363.
31. J. Frahm, M. L. Gyngell, and W. Hänicke, Rapid Scan Techniques, in *Magnetic Resonance Imaging*, eds. D. D. Stark and W. G. Bradley, 2nd edn., Mosby, St. Louis, MO, 1992, p. 165.
32. A. Haase, *Magn. Reson. Med.*, 1990, **13**, 77.
33. J. Frahm, K. D. Merboldt, H. Bruhn, M. L. Gyngell, W. Hänicke, and D. Chien, *Magn. Reson. Med.*, 1990, **13**, 150.
34. D. Chien, K. D. Merboldt, W. Hänicke, H. Bruhn, M. L. Gyngell, and J. Frahm, *Magn. Reson. Imaging*, 1990, **8**, 829.

Biographical Sketch

Jens Frahm, *b* 1951. Dipl.Phys., 1974, Ph.D., 1977, Physical Chemistry, University of Göttingen, Germany. Introduced to NMR by Hans Strehlow, research assistant at the Max-Planck-Institut für biophysikalische Chemie in Göttingen, 1977-1992, Head of Biomedical NMR Group, 1982-1992, Head of Biomedizinische NMR Forschungs GmbH, 1993–present. Approx. 165 publications. Research specialty: NMR studies of living systems; anatomic, metabolic, and functional aspects of intact organ systems; NMR imaging, localized NMR spectroscopy. Current interests: biochemical and physiological studies of the living human brain, functional organization, cerebral metabolism, brain disorders.

Fraissard, J.: A Look at Solid Catalysts by NMR

J. Fraissard

Université Pierre et Marie Curie, Paris, France

After beginning my higher education in the rather too sunny climate of Algiers, I came to the University of Paris and, perhaps because of the less disturbing climate, passed out of the Sorbonne in 1957 as top student of that year. Thanks to this result I went to the Laboratory of General Chemistry of the Faculty of Paris as a postgraduate to do thesis work, under Boris Imelik, on the study of the structure and properties of silica gels. Boris Imelik was at the time one of the most outstanding French experts on catalysis and surface chemistry. Although he ended his career as Director of the highly prestigious Institut de Recherche sur la Catalyse (IRC) in Villeurbanne, his international reputation was not what it might have been, probably because of his reluctance to travel and to speak in public.

The techniques used at the time for the study of solid catalysts were X-ray diffraction for the structure, IR spectroscopy and specific chemical reactions for the nature of surface hydroxyls. I naturally continued with this type of research. I think I was the first to show that IR spectroscopy could also be very useful in studying microstructures when the particles are too small to give X-ray diffraction diagrams. Above all, although solid state NMR was in its infancy, I realized in 1958 the interest of this technique for obtaining unique information about the nature and the distribution of the constitutive water of silica gels, as well as about the mobility of the protons at the surface of these solids. These characteristics are in fact all-important for understanding the behavior of solid catalysts with Brønsted acidity. I then went to work with I. Solomon in the already famous laboratory of Professor A. Abragam. I hope you will forgive the young scientist because I did not realize until much later how much science and intelligence it housed. There was, above all, Anatole Abragam, whose 80th birthday has just been celebrated in Paris by the entire international NMR community. But also, in no particular order, José Ezratty, Jean Combrisson, André Landesman, Jacques Winter, Charles Ryter (later to become an astrophysicist), Maurice Gueron (now a biologist at the Ecole Polytechnique), Maurice Goldman (who later took over as head of the laboratory) whose knowledge, patience, and modesty are always very impressive, and, of course, Ionel Solomon, nicknamed by Abragam 'the long-legged spinner', now Professor at the Ecole Polytechnique, who made me understand the power of NMR and to whom I owe my taste for spectroscopy. I was also able to rub shoulders with many eminent visitors, such as Richard Bersohn, Ray Freeman, Ralph Livingstone, Robert Pound, Warren Proctor, Alfred Redfield, et al.

The signal of the protons of silica gels was at that time very difficult to detect because of their low concentration, their relatively long relaxation times, the width of the lines, and the low sensitivity of NMR at frequencies below 16 MHz. However, by using strong radiofrequency fields in the dispersion mode, I was able to obtain signals with an adequate signal-to-noise ratio and to distinguish quite clearly for the first time the characteristics of the OH groups of xerogels and aerogels, both from the point of view of the distribution and of the mobility of the superficial protons.[1] These results earned me the French Chemical Society prize in 1962.

Then, starting from Redfield's and Solomon's theories, I carried out a theoretical study of the variation of the NMR dispersion signal for a set of nuclear spins. This was achieved using both the spin relaxation times T_1 and the modulation period T_m of the sinusoidal magnetic field of low amplitude which was superposed on the field $\boldsymbol{B}_0$ when the signal was amplified using the 'lock in' detection of the old spectrometers. The curves vary with the relative values of T_1 and T_m. Using the general signal equation, I was able to show how these curves could be used to determine the parameters of the nuclear spin considered.[2]

These results were then applied to many solid catalysts provided it was possible to obtain a decent NMR signal. Comparison of the theoretical and experimental signals allowed me to observe that the distribution of the surface OH groups depends on the nature of the solid and on the preparation of the sample. In certain cases the hydroxyls are distributed in small zones with a maximum local density; dehydration is moreover very inhomogeneous, the elimination of OH proceeding zone by zone. In other cases the hydroxyls are distributed statistically over the surface, regardless of the treatment temperature. NMR also makes it possible to determine the exact role of the different faces of the microcrystallites: some are absent or dehydrated during the formation of the solid, others have contiguous OH zones up to high temperatures.[1,3–5]

I have for more than 20 years been the director of a large laboratory whose activity is mainly concerned with the study of the surface properties of solids, of gas–solid interactions, and of the mechanisms of heterogeneous catalysis. I shall only mention here a few of these original research projects based on the use of NMR.

I was also the first, as early as 1959–60, to show that high-resolution NMR could provide interesting information about the structure of activated complexes. The spectrum of an adsorbed molecule presents a certain number of perturbations as compared with that of the isolated molecule: certain lines are broadened, others are shifted. These variations in the chemical shifts depend on the adsorbant and on the adsorbate and its various functional groups. They relate to the change in the electronic configuration of the molecule upon adsorption and therefore allow one to determine the electronic configuration of the complex formed. For example, the spectrum of formic acid adsorbed on an insulator such as silica gel or alumina shows only one line due to the CH group. The OH group is the seat of the adsorption phenomenon and the characteristic line becomes too broad to be detected by conventional high-resolution NMR.[6] In the same way, NMR enabled me to reveal four successive structures of butenes chemisorbed on silica–aluminas and then to determine the mechanism of the isomerization of butenes on these solids.[7]

It should be remembered that the chemical shifts of adsorbed phases can only be measured with respect to internal references. I showed, by ^{1}H NMR study of the physical adsorption of certain gases, how the necessary corrections can be made, in particular by determining the volume susceptibility of a powder with an accuracy, expressed in chemical shift, of about 0.3 ppm. This technique, which is now used by

everyone, makes it possible to classify the chemical shifts of heterogeneous systems with respect to the classical references of homogeneous systems.[8]

Modern high-resolution techniques for solids have confirmed my results, but have also led to a dramatic increase in the application of NMR to the study of heterogenous gas–solid systems. However, the new techniques cannot always be used. For example, paramagnetic systems are generally studied by EPR. I have, however, shown that in many cases the amount of information provided by NMR is much greater: value and sign of the electron–nucleus coupling, distribution of the electron spin densities on the various nuclei of the chemisorbed complex, etc. For example, the large but opposite chemical shifts of the C and H of the CH group of HCOOH chemisorbed on slightly reduced TiO_2 demonstrate that there is a transfer of positive electron spin density (and, in this case, of electronic charge) from the solid to the antibonding π orbital of the COOH group. This transfer explains the catalytic power of the surface electron-donating Ti^{3+} in the dehydration of this acid.[9] It should be remarked that the signals of these chemisorbed complexes are very broad. They cannot be narrowed by modern high-resolution NMR techniques. Only the technique of rapid exchange of physisorbed and chemisorbed molecules, developed in my laboratory, allows the determination of the chemical shifts characteristic of the chemisorbed complex.

I have also involved myself in the study of the Brønsted acidity of solids. Techniques used before 1970 (IR spectroscopy, colored indicators, etc.) were incapable of giving a precise comparison of the acid strength of solids. I was the first to suggest (later shown to be incorrect) that the acidity of an OH group depends on its polarization and may therefore be characterized by the chemical shift of the hydrogen. At that time, in the absence of any high-resolution NMR technique (MAS, CRAMPS), the chemical shift of the protons of solids could not be measured directly because of the large dipolar broadening of the signals. I showed that in the case of OH groups located on the surface of catalysts it was possible to narrow the proton signals by rapid exchange with adsorbed molecules and to calculate from these signals the shift, δ^{H}_{OH}, of the OH group, provided the molecules adsorbed had two detectable spins (e.g., ^{15}NH, $^{31}PH_3$, etc.); from the value of δ^{H}_{OH}, it was then possible to deduce the electronic environment of the H atoms.[10] The values of these shifts were checked much later by ^{1}H MAS NMR (Pfeifer's team). Unfortunately, measurement of δ^{H}_{OH} values in the absence of any adsorbed phase cannot possibly characterize the intrinsic acidity of the OH group. The perturbations (such as hydrogen bonds) due to their natural environment are far from negligible. Furthermore, the acid strength of O–H groups depends not only on the polarization of this bond but also on its polarizability. Hence the need to study it in the presence of an adsorbate.

This is why I have recently proposed a new procedure for at last defining a true acidity scale for solids. I have replaced the interactions of the OH groups with their ill-defined environment by a specific OH–B (basic molecule) interaction, where the adsorbed molecule B is H_2O, in order to bring the problem closer to that of aqueous solutions. To eliminate the fast exchange of protons between the different species, the spectra are recorded at 4 K and the dipole interactions are capable of defining the equilibria

$$OH + H_2O \rightleftharpoons OH\cdot\cdot O\begin{matrix}H\\H\end{matrix} \rightleftharpoons H_3O^+ + O^- \qquad (1)$$

The software for the simulation of the spectra corresponding to the dipolar interactions of these species and of their mixture has been written. By using a powerful computer it is then possible to search for the several parameters (sometimes 10) required to simulate the spectra and hence to demonstrate quantitatively the various surface species and, in particular, to determine the dissociation constant of OH.[11]

I have also proposed many other techniques for studying solid catalysts, in particular those which use probes which can be detected by NMR. Let me give two examples.

(a) The ^{1}H NMR study of hydrogen adsorbed on metals: the physical and electronic properties of metal particles, in particular their magnetism, depend on their size, at least when they are sufficiently small. NMR could therefore prove to be an interesting technique for studying these properties. As Slichter showed for platinum, the detection of the supported metal can provide precise data about its dispersion. However, this leads to considerable theoretical and experimental problems which prevent it being used as a routine technique. For this reason I proposed, well before Slichter's work,[10] studying metal surfaces by NMR, but with the help of a gas such as hydrogen which can be chemisorbed by all metals and therefore used as a universal probe. Hydrogen has the advantage of high sensitivity of detection and of being one of the gases most used in catalysis. The main results obtained are as follows.

1. The chemical shift of hydrogen adsorbed on a metal is very high (Knight shift), and is positive or negative depending on the metal.
2. At 25°C, for a given metal, the value of δ extrapolated to zero concentration depends on the particle size and the temperature of chemisorption. It is often even possible to detect several signals corresponding to sets of particles of sufficiently distinct size. This result is particularly interesting when the particles are too small to be detected by electron microscopy.[12]
3. In the case of palladium, NMR is capable of distinguishing the α- and β-hydrides in equilibrium with the adsorbed phase.[13]
4. During the preparation of bimetallic catalysts, Pt–Au for example, this technique allows the reduction of the first metal to be followed, then the second, then (or at the same time) the formation of the small alloy particles. This technique has since been used by many researchers on various metals and alloys.

(b) The study of microporous solids by ^{129}Xe NMR of adsorbed xenon: The fundamental idea of this new research was to find a chemically inert molecule which was particularly sensitive to physical interactions with its environment and which could be used as a probe to determine the special properties of zeolites and, more generally, of microporous solids. This probe should, moreover, be NMR detectable since this technique is particularly well adapted to the study of the electronic perturbations of molecules undergoing rapid movement. I found that xenon is an ideal probe in this respect. Thus it is an inert gas, monoatomic, with a very

large, spherically symmetrical electron cloud. Any distortion of the latter is felt directly at the level of the nucleus and is consequently expressed as a variation of the chemical shift. From the NMR point of view the ^{129}Xe isotope is particularly suitable: it has a spin of $\frac{1}{2}$, its natural abundance is 26%, and its detection sensitivity is good (10^{-2} compared to that of the proton).

I have shown that the chemical shift of xenon situated in any system is always the sum of terms corresponding to the various perturbations to which it is subjected:[14]

$$\delta = \delta_{\text{ref}} + \delta_{\text{S}} + \delta_{\text{Xe}} + \delta_{\text{SAS}} + \delta_{\text{E}} + \delta_{\text{M}} \qquad (2)$$

δ_{ref} is the reference. For a solid with no electric charge, δ_{S} (δ extrapolated to zero concentration) depends on the mean free path, I, of the xenon imposed by the structure of the zeolite. The quantity I depends on the dimensions of the cages and the channels and on the ease of diffusion of the xenon in the crystallites. The term δ_{Xe} expresses the influence of the Xe–Xe interactions, δ_{SAS} represents the influence of strong adsorption sites (which are generally cations, more or less charged, and sometimes paramagnetic), and δ_{E} and δ_{M} correspond to the effects of the corresponding electric and magnetic fields, respectively.

By means of this technique it is possible to determine the dimensions and form of the internal free volumes of zeolites without knowing their structures; to reveal structure defects produced, for example, by dealumination, and to determine their characteristics; to calculate the short-range crystallinity, as opposed to that determined by X-rays; to follow the mechanism of the synthesis and crystallization of zeolites during their preparation; to locate cations in the zeolite structure and to follow their migration or the change in their environment depending on various factors; to locate any 'encumbering' species, for example, adsorbed molecules, extraframework species, coke formed during catalytic cracking reactions, etc.; to determine the dispersion of metals (particularly when the particles are too small to be seen by electron microscopy) and the distribution of the molecules adsorbed on the particles (as opposed to the mean coverage); and to compare the diffusion of species as a function of the size of the zeolite 'windows'.

This technique can also be applied to any microporous system[15,16] (amorphous solid, polymer, clay, etc.). This list of applications is certainly not exhaustive. The power of this technique explains why it is currently used by most of the biggest companies which synthesize or employ zeolites and microporous solids.

REFERENCES

1. J. Fraissard, I. Solomon, R. Caillat, J. Elston, and B. Imelik, *J. Chim. Phys.*, **1963**, 676.
2. J. Kermarec, J. Fraissard, and B. Imelik, *J. Chim. Phys.*, **1967**, 911.
3. J. Kermarec, J. Fraissard, and B. Imelik, *J. Chim. Phys.*, **1968**, 920.
4. M. A. Enriquez, C. Doremieux-Morin, and J. Fraissard, *Application of Surface Science*, 1980, **5**, 180.
5. M. A. Enriques, C. Doremieux-Morin, and J. Fraissard, *J. Solid State Chem.*, 1981, **40**, 233.
6. J. Fraissard, R. Caillat, J. Elston, and B. Imelik, *J. Chim. Phys.*, **1963**, 1017.
7. J. Fraissard, S. Bielikoff and B. Imelik, *C.R. Acad. Sci. Ser. C*, 1970, **271**, 897.
8. J. L. Bonardet and J. Fraissard, *J. Magn. Reson.*, 1976, **22**, 543.
9. B. Bigot, M. A. Enriquez and J. Fraissard, *J. Catalysis*, 1982, **74**, 84.
10. J. L. Bonardet, L. C. de Menorval, and J. Fraissard, *Proceedings of the VIth International Congress on Catalysis*, London, July 1976, eds. G. Bond, P. Wells, and F. C. Tompkins, The Chemical Society, London, 1977, 633.
11. P. Batamack, C. Doremieux-Morin, R. Vincent, and J. Fraissard, *J. Phys. Chem.*, 1993, **97**, 9779, and references cited therein.
12. L. C. de Menorval and J. P. Fraissard, *Chem. Phys. Lett.*, 1981, **77**, 309.
13. M. Polisset and J. Fraissard, *Colloids and Surfaces A: Physicochemical and Engineering Aspects*, 1993, **72**, 197.
14. J. Fraissard and T. Ito, *Zeolites*, 1988, **8**, 350, and references cited therein.
15. W. C. Conner, E. L. Weist, T. Ito, and J. Fraissard, *J. Phys. Chem.*, 1989, **93**, 4138.
16. J. L. Bonardet, J. B. Moffat, and J. Fraissard, *Colloids and Surfaces*, 1993, **72**, 191.

Biographical Sketch

J. Fraissard. *b* 1934. Maîtrise ès Sciences, 1957, Doctorat ès Sciences, 1961, Paris. Introduced to NMR by I. Solomon. Centre National de la Recherche Scientifique 1960–63; University of Paris, 1963–present. Approx. 180 publications; five books including 'Thermodynamics and Kinetics' and, with R. Mahé, 'Chemical Equilibria in Aqueous Solutions'. Co-editor of four NATO ASI Series on Magnetic Resonance Applications: 'Colloid and Interface Science, Fossil Energy' and 'Acidity of Solids'. Research interests: applications of solid state NMR to problems of gas–solid interactions and catalysis.

Freeman, Ray: Double Resonance Methods in High-Resolution NMR

Ray Freeman
Cambridge University, Cambridge, UK

When magnetic resonance methods were first introduced, they differed from other contemporary spectroscopic techniques in two important respects. The radiation was *coherent*, and in this sense NMR and ESR were leading the way, demonstrating what laser spectroscopy would accomplish many years later. They also offered the possibility of double resonance experiments long before they were dreamed of in optical or infrared spectroscopy. This idea that one could *manipulate* NMR spectra seemed new and attractive, a tiny hint of the forthcoming explosion of 'spin gymnastics' experiments that have made modern NMR so exciting. There were already some pioneering double resonance experiments by F. Bloch,[1] V. Royden,[2] A. L. Bloom and J. N. Shoolery,[3] and W. A. Anderson.[4] In 1959, I set out to try my hand at proton decoupling[5] on a Varian 60 MHz spectrometer using Robert Pound's idea that modulation sidebands could be used for the excitation of NMR signals.[6,7]

Bloom and Shoolery's paper on $^{19}F-^{31}P$ double resonance[3] seemed to hold the key to the theory, but when we tried to extend these calculations to predict the observed frequency dependence in proton–proton decoupling experiments, things did not seem to fit. The head of the ESR group of our laboratory, David Whiffen, was able to resolve the dilemma overnight. My mistake had been to assume that sweeping the field was equivalent to sweeping the radiofrequency. However, in double resonance experiments there is a significant difference, since a magnetic field sweep is equivalent to sweeping the frequencies of both B_1 (the observation field) and B_2 (the perturbing field), keeping a fixed separation between them. A true frequency sweep double resonance experiment would keep the frequency of B_2 fixed while scanning the frequency of B_1.

To check these ideas on the spectrometer was not straightforward since at that time there were no facilities for frequency sweep high-resolution experiments. However, Hans Primas[8] in Switzerland had just suggested a revolutionary idea for field/frequency control using the *internal* reference compound, tetramethylsilane, and this seemed to offer the way to test the new double resonance predictions that David Whiffen had worked out. So we introduced yet another modulation sideband[9] to excite the dispersion-mode response of tetramethylsilane and derive an error signal to feed to the galvanometer of the Varian 'superstabilizer'. If the field drifted one way this error signal would be positive, if the other way it would be negative. The TMS signal was monitored as a Lissajous figure on an oscilloscope. You can imagine our joy when, on closing the switch, the Lissajous figure stayed rock solid, indicating that the field/frequency ratio was stable within a few parts in 10^{10}, something we had never imagined possible. We were able to demonstrate that field sweep and frequency sweep proton–proton double resonance experiments did indeed give quite different results, in accord with the calculations. Later, of course, 'internal lock' became the universally accepted method of stabilization and is still used today, with deuterium, rather than protons, as the reference signal.

SELECTIVE DECOUPLING

So far we had a cure looking for a suitable disease. What could one actually do with double resonance? A colleague from my graduate student days at Oxford provided one interesting application. Dennis Evans[10] had been studying the proton NMR spectrum of the thallium diethyl cation, where the Tl–H couplings are so large that they are comparable with the chemical shifts, giving two methyl resonances and two methylene resonances, all well separated from each other. Dennis realized that it was not at all certain which methyl resonance went with which methylene, but that he could determine this by a selective decoupling experiment in which only one of the methyl resonances was irradiated. We can think of this as asking a 'Maxwell demon' to separate molecules with ^{205}Tl in an α spin state from those with ^{205}Tl in a β spin state so that the proton spectra of the two ethyl groups can be displayed separately. The 'effective proton chemical shifts' involve the magnitudes and *signs* of the Tl–H coupling constants, so here was a new method for determining relative signs of J couplings.

When Dennis Evans described this elegant experiment to David Whiffen, we realized that similar measurements of relative signs of coupling constants could be performed for *any* three-spin system, for example three protons, if only the irradiation could be made sufficiently selective. One proton (M) of an AMX spin system remains passive in the experiment, simply generating weak local fields at the A and X protons. This creates two AX subspectra, and we perform a decoupling experiment in one subspectrum with minimal perturbation of the other, thus distinguishing the 'α molecules' from the 'β molecules', just as if our Maxwell demon had been at work. Figure 1 shows the proton spectrum of 2,3-dibromopropanoic acid with A and X transitions assigned to α and β spin states of the passive spin M *assuming* opposite signs of J_{AM} and J_{MX}. In the lower trace a selective decoupling experiment confirms this assumption. Two decades later it became possible to obtain similar results from two-dimensional correlation spectra[11] where the presence of the passive spin M in an AMX

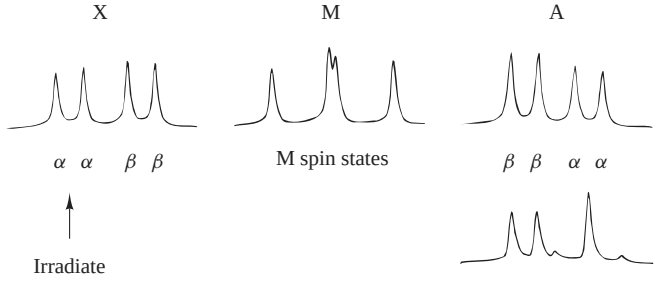

Figure 1 Selective decoupling of protons in 2,3-dibromopropanoic acid. The spin states of the passive spin M have been assigned *on the assumption* that J_{AM} and J_{MX} have opposite signs; this is borne out by the double resonance experiment (lower trace)

system determines the form of the AX cross peaks, giving the relative signs by inspection.

After some initial reluctance, chemists began to use selective decoupling to identify proton resonances that were related by a spin–spin coupling. Today we would call this 'chemical shift correlation'. The additional equipment required for homonuclear double resonance was minimal—a stable audiofrequency oscillator usually sufficed. Several tricky assignment problems were resolved by these simple homonuclear decoupling experiments. With the advent of two-dimensional NMR, selective decoupling has been superseded by correlation (COSY or TOCSY) spectroscopy.[12,13] In the abstract of his notes for a summer school, Jeener[12] comments that two-dimensional spectroscopy provides the same information as double resonance, but does it more efficiently. Indeed, most present-day two-dimensional experiments are essentially more sophisticated manifestations of earlier double resonance techniques.

SPIN TICKLING

I had always admired Wes Anderson's work at Varian Associates, so given the opportunity to take sabbatical leave I joined his group in late 1961. At that time there were several excellent physicists working in the Varian Instrument Division, and their enthusiasm was such that they held evening seminars in various scientists' homes, with slide projector, coffee, and cakes provided. I had only been in California a few days when, as the newcomer, I was 'railroaded' into giving the next evening seminar. I described David Whiffen's calculations and showed the frequency sweep double resonance spectra we had obtained in England. During question time, one of the Varian scientists, Harry Weaver, pointed out that the spectra obtained at low irradiation levels appeared to show evidence of 'spin tickling' effects. This was an expression that several people had used without really *defining* exactly what it meant, but the essence was to set the B_2 level so low that only a single NMR transition was affected. This contrasted with spin decoupling, where an entire spin multiplet was irradiated. Looked at in this light, the frequency sweep double resonance spectra on my slides did seem to show tickling effects, and Wes Anderson and I decided to explore this idea further, exploiting the enhanced stability that could be obtained with the new internal field/frequency lock scheme.

It turned out to be an interesting phenomenon.[14] Tickling a given NMR transition splits several other transitions into doublets. These are the 'connected' transitions, those that share an energy level with the irradiated line. The observed splitting is equal to $\gamma B_2/2\pi$(Hz), and this provides a convenient calibration of the irradiation field intensity B_2. If the irradiation field is not quite set to exact resonance, the observed doublet becomes asymmetric, one component getting weaker (eventually becoming a forbidden transition) while the other gets stronger (eventually reverting to the normal, allowed transition). Clearly we were dealing with an energy level noncrossing rule similar to that governing Fermi resonance in infrared spectroscopy.

At first we were puzzled to find that some doublets appeared to be better resolved than others in the same spin tickling spectrum. It turned out that the effect was real and that the explanation was rather subtle. Two transitions can be connected in two different ways; they can be *progressive* or *regressive* (Scheme 1).

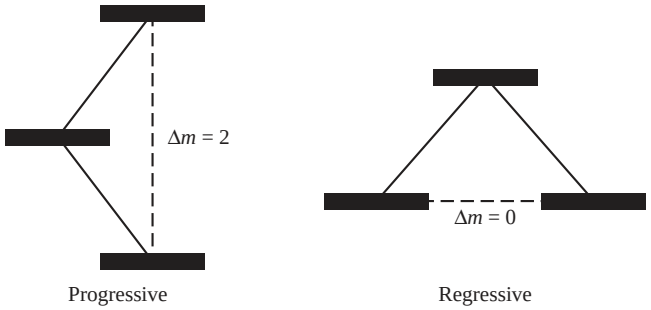

Scheme 1

Note that the progressive configuration is associated with a double quantum transition $\Delta m = 2$ whereas the regressive case involves the zero quantum transition $\Delta m = 0$. The tickling doublets arise from a quantum-mechanical mixing of allowed and forbidden transitions, such that both become equally allowed at exact resonance for the irradiation field, just as in Fermi resonance. The doublets with some double quantum character (the progressive case) are poorly resolved since the broadening by magnet field inhomogeneity is aggravated under these conditions, whereas the doublets with some zero quantum character (the regressive case) have the field inhomogeneity effect partly compensated and are better resolved. Thus the observation of a spin tickling doublet establishes that two transitions are connected and also indicates whether the configuration is progressive or regressive. Figure 2 shows the first spin tickling results obtained with the two-spin system 2-bromo-5-chlorothiophene, demonstrating a well-resolved and a poorly-resolved doublet.

For regressively connected transitions, when the B_2 field intensity is turned down even further, it is possible to 'burn a hole' by double resonance.[15] The frequency selectivity is so high that only a localized region of the sample is saturated, while other parts (in slightly different applied magnetic fields) are too far from resonance to be significantly affected. If the frequency of B_2 is moved to another point on the profile of a chosen transition, the corresponding 'hole' in a regressively connected transition moves in concert. This turns out to be one of the most accurate methods for measuring frequency separations in high-resolution NMR; the observed line profiles are sensitive to as little as 0.001 Hz changes in the irradiation frequency.

In the early 1960s, when there were many cases of strongly coupled proton spectra, the first step of computer analysis was the assignment of observed transitions to the appropriate energy level diagram. Spin tickling was therefore a very useful assignment aid. It also picked out the subspectra that indicated the relative signs of coupling constants. With the new high-stability field/frequency lock, it was possible to reverse the spin tickling experiment, holding the observing field B_1 at the peak of a chosen transition and sweeping the perturbing field B_2 through the spectrum to search for connected transitions, where there would be a dip in the monitored signal. This 'INDOR' technique[16] is useful for locating weak or hidden transitions.

Quite by accident, Jim Ferretti at Berkeley discovered an interesting variant of the INDOR experiment. He used an *intense* $\boldsymbol{B}_1$ field, such that the monitored line was

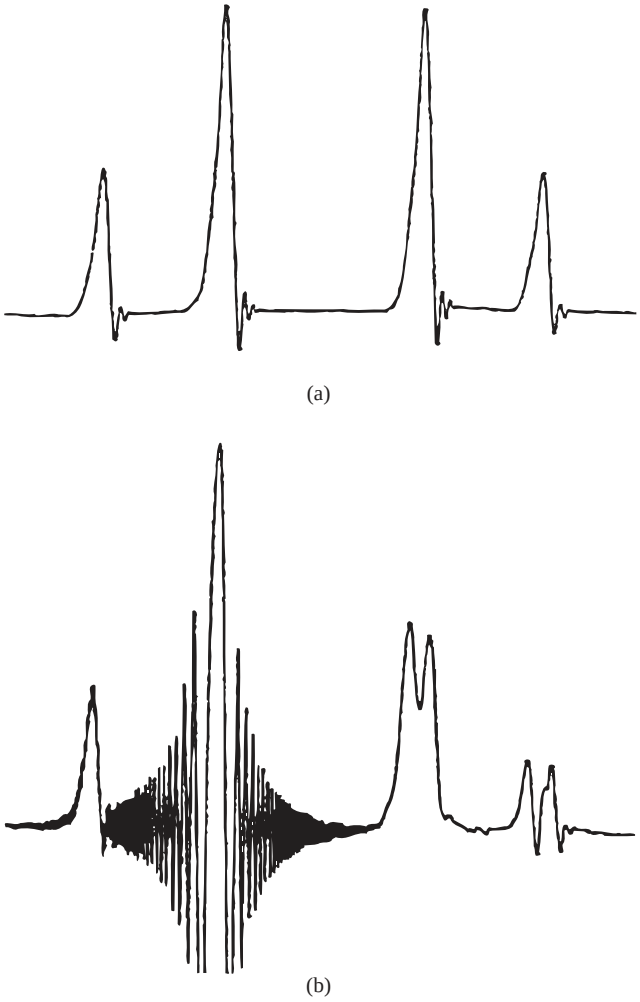

Figure 2 Spin tickling of protons in 2-bromo-5-chlorothiophene. The zero-beat pattern (b) indicates where the B_1 observing field sweeps through the fixed B_2 irradiation field. Note that one of the new doublet splittings is poorly resolved (progressive case) and the other is well resolved (regressive case). (Reproduced from Freeman and Anderson[14])

saturated. When $\boldsymbol{B}_2$ was swept through a connected transition under adiabatic fast passage conditions, there was a sudden population inversion which was picked up on the monitored line as a 'transient nutation' having a very characteristic pattern.[17] A progressive transition gives a positive-going oscillation whereas a regressive transition gives a negative-going oscillation. Figure 3 shows an example from the 60 MHz proton spectrum of the three-spin system in 2-chlorothiophene.[18]

SLOW CHEMICAL EXCHANGE

Forsén and Hoffman[19] introduced an entirely new application of double resonance that has assumed increasing importance over the years and is now one of the standard applications of two-dimensional spectroscopy. If two chemical species exchange slowly in comparison with their chemical shift separation, it is possible to follow the actual transfer of spins from one site to the other by labeling them with

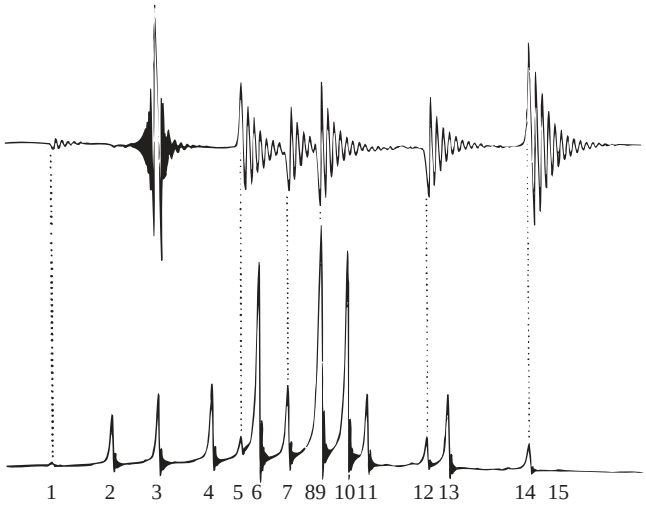

Figure 3 The 60 MHz proton spectrum of 2-chlorothiophene (lower trace). When the constant-frequency observing field (B_1) saturates line 3 and the perturbing field (B_2) is swept through the spectrum under adiabatic fast passage conditions, the population disturbance is transferred to the connected transitions, inducing positive-going transient nutations for the progressive case (lines 5 and 14), negative-going for the regressive case (lines 1, 7, 8, and 12). (Reproduced from Ferretti and Freeman[18])

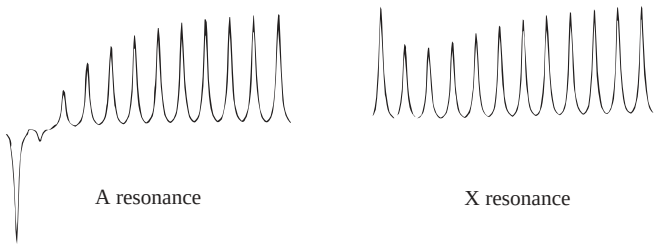

Figure 4 Simulation of the effect of inverting the spin population of a site A when there is slow chemical exchange with site X. Inverted spins are carried from A to X, reducing the intensity of the X spin signal. At later times, spin–lattice relaxation returns the populations to Boltzmann equilibrium

a population disturbance. Forsén and Hoffman used selective saturation, but it is more convenient to employ a population inversion brought about by a selective 180° pulse. A sudden population inversion of site A gives an inverted NMR signal for A and then a gradual loss of intensity at site X, as inverted spins are transferred from A to X. Later, spin–lattice relaxation returns the intensity at both sites to normal (Boltzmann equilibrium). Analysis of the time development of the A and X intensities gives the rate of chemical exchange. Figure 4 shows a simulation of the time-dependence of the A and X signals for this experiment.

NUCLEAR OVERHAUSER EFFECT

When the Overhauser effect[20] was first predicted, many well-known magnetic resonance scientists were reluctant to believe that such a large NMR signal enhancement could be achieved by saturating the electron spin resonance. It

was soon demonstrated by experiment. The analogous effect between two dipolar-coupled nuclear spins is much smaller in magnitude, being given by the formula:

$$S_Z/S_0 = 1 + \eta = 1 + 0.5\gamma_I/\gamma_S \qquad (1)$$

where γ_I and γ_S are the gyromagnetic ratios of the irradiated spin and the observed spin, respectively. Thus for proton–proton interactions ($\gamma_I = \gamma_S$) the maximum enhancement is 50%. The full effect is only observed if the S spin relaxation is exclusively determined by dipolar interaction with the I spin. This is hardly a method for sensitivity enhancement but it has proved extremely useful as a diagnostic of proximity, since the nuclear Overhauser effect (NOE) falls off as the inverse sixth power of the internuclear distance. The early experiments were performed by selective double resonance and were usually aimed at determining molecular configuration.[21] More recently, two-dimensional methods [22] have been used to extend NOE measurements to biological macromolecules where there are literally thousands of protons exhibiting dipolar interactions, each observed Overhauser enhancement imposing a 'distance constraint' on the structure.

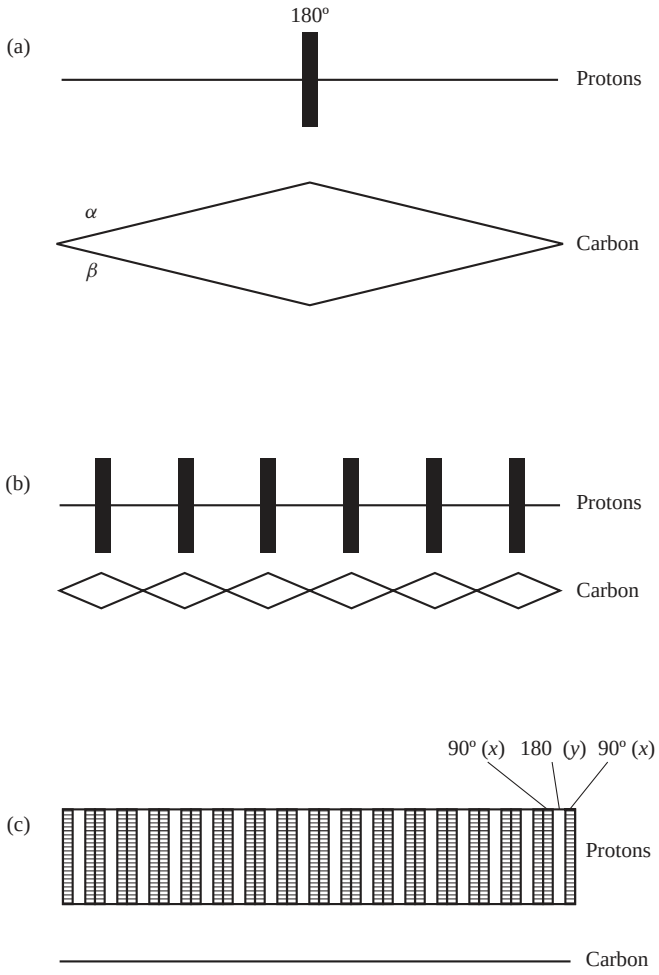

Figure 5 (a) A 180° proton pulse during the evolution period of a two-dimensional experiment refocuses the α and β carbon-13 vectors. (b) Multiple refocusing of the α and β vectors. (c) Multiple refocusing with composite 180° pulses, with no windows for free precession

BROADBAND DECOUPLING

When the technology became available to study carbon-13 spectroscopy in natural abundance, it became clear that there was a considerable advantage to be gained by proton decoupling. First of all, this greatly simplified the carbon-13 spectrum and gathered the multiplet intensities into single lines. Secondly, it gave up to a threefold enhancement of sensitivity through the nuclear Overhauser effect. To be generally applicable, this required *broadband decoupling* in which all protons were effectively decoupled, independent of their chemical shifts. Richard Ernst provided the breakthrough with noise decoupling[23] where the second radiofrequency source (B_2) was modulated with a pseudorandom sequence of phase inversions in order to render it incoherent. At that time pseudorandom noise generators were hard to come by, so his initial experiments used 'random' numbers taken from the Palo Alto telephone directory. Noise decoupling was the universally accepted method for many years. The chemist simply switched on the decoupler at the appropriate frequency (the center of the proton spectrum) and set the B_2 intensity as high as possible, compatible with an acceptable level of radiofrequency heating of the sample.

Yet there is always something slightly unsatisfactory about the application of noisy or random processes in magnetic resonance. One suspects that it might be possible to devise an ordered 'dance' for the spins that would be more effective than this uncontrolled jiggling motion. This concept of 'spin choreography' evolved from multipulse experiments in solid state NMR and from ideas current in two-dimensional spectroscopy.[12,13] It eventually led to a method of broadband heteronuclear decoupling that was effective in high-field superconducting spectrometers, where the proton spectra span a much wider frequency range. Noise decoupling can involve excessive radiofrequency heating and can 'cook' some delicate biochemical materials. We lost a priceless sample of a rare snake venom neurotoxin in just this fashion.

The germ of the idea for the new decoupling methods can be traced back to some early two-dimensional experiments aimed at correlating proton and carbon chemical shifts.[24] To simplify these spectra and to eliminate correlations through long-range CH couplings, a 180° pulse was introduced into the evolution period so that diverging CH magnetization vectors were partially refocused. If the two carbon-13 vectors are labeled α and β according to the proton spin states, the 180° proton pulse interchanges these labels and brings the two vectors to a focus (or near-focus) at the end of the evolution period [Figure 5(a)]. The corresponding CH splitting is eliminated (or scaled down) in the F_1 dimension of the correlation spectrum.

We began to wonder whether refocusing might not be used more generally to decouple protons in conventional carbon-13 spectroscopy. This 'spin-flip decoupling' would employ a *repeated* train of 180° proton pulses, with the acquisition of the carbon-13 free induction decay synchronized with the focus points between proton pulses.[25] The scheme is set out in Figure 5(b). One could liken this to freezing the motion of a disco dancer by using stroboscopic lighting of the appropriate

frequency. The carbon spins would be tricked into 'thinking' that they had no coupling to protons. Unfortunately this sets a quite low upper limit on the digitization rate for carbon-13 signals and any attempts to increase the proton pulse rate soon leads to excessive power dissipation.

It was Malcolm Levitt who provided the solution to this problem. The reason we need *intense* 180° pulses is that the refocusing must be effective for all proton resonance offsets. During his first year as a graduate student at Oxford, Malcolm Levitt came up with the brilliant idea of the composite 180° pulse—a sandwich of three pulses $90^\circ(x)$ $180^\circ(y)$ $90^\circ(x)$ which automatically compensates the imperfections of the individual pulses.[26,27] This concept has much in common with the invention of the compensated pendulum, which essentially eliminated the temperature variations of the timekeeping of mechanical clocks. With composite 180° proton pulses, refocusing of carbon-13 magnetization vectors could be achieved with far lower radiofrequency levels, and therefore at much higher pulse repetition rates. Indeed it became quite feasible to assemble the composite 180° pulses into a continuous 'windowless' sequence [Figure 5(c)]. This allows us the freedom to set any desired acquisition rate for the carbon-13 signal, not necessarily synchronous with the proton pulsing.

There was still a fly in the ointment. Such a long repeated sequence of pulses inevitably builds up cumulative errors, even if the individual imperfections are very small. A simple phase alternation of the 180° pulses is not effective in this situation; it merely aggravates the effects of resonance offset. It was again Malcolm Levitt who saw the solution—a 'magic cycle' of the form $RRR\overline{R}$ where R is a composite 180° pulse and $\overline{R}$ is its phase-inverted counterpart.

This MLEV-4 cycle[28] proved to be significantly more effective than the existing methods of broadband decoupling. This can be quantified in terms of a figure of merit Ξ defined as the ratio of effective decoupler bandwidth to decoupler field intensity:

$$\Xi = 2\Delta B_{\max}/B_2 \tag{2}$$

where $\Delta B_{\max}$ is the proton offset at which the carbon-13 signal falls to 80% of its maximum intensity. Noise decoupling achieves a figure of merit $\Xi \simeq 0.3$, while MLEV-4 has $\Xi \simeq 1.0$. It soon emerged that 'supercycles' could be designed [29] by combining cyclically permuted versions of MLEV-4 into a longer sequence. These more elaborate decoupling sequences have wider effective bandwidths, for example MLEV-64 has a figure of merit $\Xi \simeq 1.8$, and more uniform decoupling efficiency across the band.

There were nevertheless some disturbing features when the experimental results were examined in detail. The decoupling efficiency appeared to be very sensitive to the exact phase shift between the 'x' and 'y' pulse channels; indeed the sequences appeared to work slightly better if this phase shift was not quite equal to 90°. These and other curious new phenomena were explained by a theory advanced by John Waugh.[30,31] Hitherto the favored treatment had been average Hamiltonian theory. The new approach considered the cyclic nature of the proton motion in the time domain and permitted a direct calculation of the form of the decoupled carbon-13 spectrum as a function of decoupler offset. Essentially this predicted a very small residual splitting of the carbon-13 line which varied with offset. The aim was to devise a pulse sequence that made these residual splittings so small that they were always hidden within the instrument linewidth.

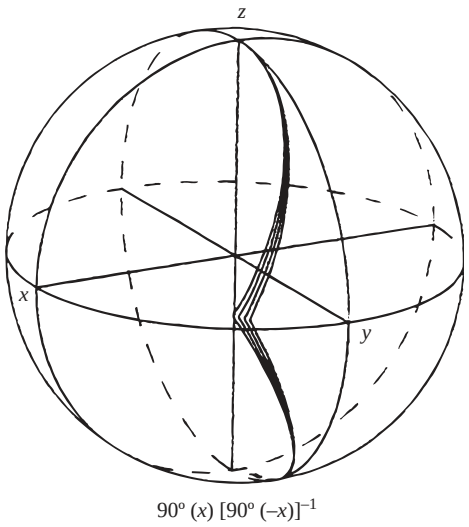

Figure 6 Off-resonance trajectories for the combination $90^\circ(x)[90^\circ(-x)]^{-1}$. Deviations due to off-resonance effects are largely compensated and the trajectories terminate near the $-z$ axis (Reproduced from Shaka et al.[33] by permission of Academic Press)

The Waugh theory explained why cyclic permutation and phase inversion were of paramount importance in the construction of decoupling supercycles. It also predicted that sequences involving combinations of 'x' and 'y' pulses would be particularly sensitive to the precise value of this phase shift and showed why the optimum would not be exactly 90°. At this point A. J. Shaka made a seminal contribution to the decoupling saga by inventing an entirely new family of decoupling sequences[32,33] based on the principles laid down by John Waugh. These new sequences involve only 0° and 180° radiofrequency phases, thus avoiding the difficulties with orthogonal radiofrequency channels.

Again it was Malcolm Levitt, on a short visit to our laboratory, who suggested one of the key ideas. A 90° pulse is to some extent self-compensating, in that it brings magnetization from the $+z$ axis into the xy plane for a wide range of offsets. If this could be followed by a pulse that generated mirror-image trajectories then this would carry these vectors to the $-z$ axis, a good approximation to the ideal compensated inversion pulse (Figure 6). This may be represented as:

$$R = 90^\circ(x)[90^\circ(-x)]^{-1} \tag{3}$$

where $[90^\circ(-x)]^{-1}$ is a 'reversed precession pulse' about the $-x$ axis. The latter is a *hypothetical* pulse for which resonance offset acts in the opposite sense to Nature. Now the combination $270^\circ(-x)$ $270^\circ(x)$ is a close approximation to an exact cycle. We may write this as

$$270^\circ(-x)270^\circ(x) \approx E \tag{4}$$

where E is the identity operation. Malcolm Levitt suggested that this implied

$$180^\circ(-x)270^\circ(x) \approx [90^\circ(-x)]^{-1} \tag{5}$$

that is to say we have a practical way to implement the hypothetical 90° reversed precession pulse. The compensated 180° pulse would then be

$$R = 90^\circ(x)180^\circ(-x)270^\circ(x) \qquad (6)$$

This may be written in the shorthand notation $1\bar{2}3$, where '1' represents a 90° element and the overbar a phase inversion. Assembling four of these elements in the sequence $RRR\bar{R}$ gives the decoupling scheme $R = 1\bar{2}3\ 1\bar{2}3\ \bar{1}2\bar{3}\ \bar{1}2\bar{3}$. This was given the acronym WALTZ-4. Expansion of this sequence through cyclic permutation of a 90° element followed by global phase inversion generates the supercycle WALTZ-16. This widely used decoupling sequence, which has a figure of merit $\Xi \simeq 2.0$, involves much smaller residual splittings than WALTZ-4, and is user-friendly since it is relatively insensitive to pulse miscalibration and to errors in the radiofrequency phase shift.

In certain situations, for example at very high fields or in experiments where carbon-13 (or nitrogen-15) has to be decoupled during proton observation, even broader decoupling bands must be covered. This may be achieved by slightly relaxing the demand for extremely small (unresolved) residual splittings. It is then possible to design sequences, for example GARP,[34] with a figure of merit as high as $\Xi = 4.8$.

CONCLUSIONS

Double resonance thus covers the entire range from extremely weak irradiation fields that are just sufficient to burn a hole in a single line, to intense, broadband irradiation that affects all the spins of a given nuclear species, irrespective of chemical shift. Most double resonance applications described above—assignment, correlation, decoupling, chemical exchange, multiple quantum effects, nuclear Overhauser enhancement—are now carried out by multidimensional spectroscopy, although the basic principles remain the same.

REFERENCES

1. F. Bloch, *Phys. Rev.* 1954, **93**, 944.
2. V. Royden, *Phys. Rev.*, 1954, **96**, 543.
3. A. L. Bloom and J. N. Shoolery, *Phys. Rev.*, 1955, **97**, 1261.
4. W. A. Anderson, *Phys. Rev.*, 1956, **102**, 151.
5. R. Freeman, *Mol. Phys.*, 1960, **3**, 435.
6. R. V. Pound, *Rev. Sci. Instrum.*, 1957, **28**, 966.
7. R. Freeman and R. V. Pound, *Rev. Sci. Instrum.*, 1960, **31**, 103.
8. H. Primas, *Abstr, 5th Eur. Congr. Mol. Spectrosc., Amsterdam*, 1961.
9. R. Freeman and D. H. Whiffen. *Proc. Phys. Soc. London*, 1962, **79**, 794.
10. D. F. Evans and J. P. Maher, *Proc. Chem. Soc. London*, **1961**, 208.
11. A. Bax and R. Freeman, *J. Magn. Reson.*, 1981, **45**, 177.
12. J. Jeener, *Abstr. AMPERE International Summer School*, Basko Polje, Yugoslavia, 1971.
13. W. P. Aue, E. Bartholdi, and R. R. Ernst, *J. Chem. Phys.*, 1976, **64**, 2229.
14. R. Freeman and W. A. Anderson, *J. Chem. Phys.*, 1962, **37**, 2053.
15. R. Freeman and B. Gestblom, *J. Chem. Phys.*, 1968, **48**, 5008.
16. E. B. Baker, *J. Chem. Phys.*, 1962, **37**, 911.
17. H. C. Torrey, *Phys. Rev.*, 1949, **76**, 1059.
18. J. A. Ferretti and R. Freeman, *J. Chem. Phys.*, 1966, **44**, 2054.
19. S. Forsén and R. A. Hoffman, *J. Chem. Phys.*, 1963, **39**, 2892.
20. A. W. Overhauser, *Phys. Rev.*, 1953, **92**, 411.
21. J. H. Noggle and R. E. Schirmer, *The Nuclear Overhauser Effect: Chemical Applications*, Academic Press, New York, 1971.
22. K. Wüthrich, *NMR Spectra of Proteins and Nucleic Acids*, Wiley, New York, 1986.
23. R. R. Ernst, *J. Chem. Phys.*, 1966, **45**, 3845.
24. G. Bodenhausen and R. Freeman, *J. Magn. Reson.*, 1977, **28**, 471.
25. R. Freeman, S. P. Kempsell, and M. H. Levitt, *J. Magn. Reson.*, 1979, **35**, 447.
26. M. H. Levitt and R. Freeman, *J. Magn. Reson.*, 1979, **33**, 473.
27. M. H. Levitt and R. Freeman, *J. Magn. Reson.*, 1981, **43**, 65.
28. M. H. Levitt and R. Freeman, *J. Magn. Reson.*, 1981, **43**, 502.
29. M. H. Levitt, R. Freeman, and T. Frenkiel, *J. Magn. Reson.*, 1982, **47**, 328.
30. J. S. Waugh, *J. Magn. Reson.*, 1982, **49**, 517.
31. J. S. Waugh, *J. Magn. Reson.*, 1982, **50**, 30.
32. A. J. Shaka, J. Keeler, T. Frenkiel, and R. Freeman, *J. Magn. Reson.*, 1983, **52**, 335.
33. A. J. Shaka, J. Keeler, and R. Freeman, *J. Magn. Reson.*, 1983, **53**, 313.
34. A. J. Shaka, P. B. Barker, and R. Freeman, *J. Magn. Reson.*, 1985, **64**, 547.

Biographical Sketch

Ray Freeman. *b* 1932. M.A., D.Phil., (1958) Chemistry, Oxford University, (supervisor Rex Richards). Postdoctoral research with Robert Pound and A. Abragam at the Centre d'Etudes Nucléaires de Saclay, France 1957–59. Senior Scientific Officer, National Physical Laboratory, England, 1959–63. Instrument Division research, Varian Associates, Palo Alto, CA, 1963–73. University Lecturer, Oxford University, 1973–87. D.Sc. (1975) Oxford University. Fellow of the Royal Society. Currently Professor of Magnetic Resonance, Cambridge University. President, International Society of Magnetic Resonance, 1989–92. Approx. 220 publications. Research specialties: NMR double resonance, relaxation times, coupling constants, spin echoes, coherence transfer, multidimensional spectroscopy, multiple quantum spectroscopy, selective excitation.

Fujiwara, Shizuo: Early Development of the Study of NMR in Japan

Shizuo Fujiwara

The University of Tokyo, Urawa, Japan

NMR studies in Japan were begun in 1951 at the Physics Department of Osaka University by Prof. Jyunkiti Itoh and his colleagues, who performed structural analyses of the double halides of potassium mercury chlorides and other compounds.[1] In 1952, at the University of Electro-Communications, I applied NMR techniques to the precise measurement of nuclear magnetic moments.

Soon after World War II, the General Headquarters of the Allied Armies (GHQ) strictly controlled the introduction of foreign scientific literature into the country. Under these conditions, the initial NMR studies took rather dramatic turns.

Before World War II, two groups in Japan were engaged in nuclear science research using cyclotrons, one at Osaka led by Prof. Seishi Kikuchi, and the other at RIKEN, the scientific research institute in Tokyo, led by Dr. Yoshio Nishina. These two cyclotrons were destroyed by GHQ when the war ended. However, Japanese scientists remained hopeful of continuing the study of nuclear science.

The physicists at Osaka University learned about the discovery of NMR because the library of the American Center in Osaka was located in the building next to the Physics Department. When Dr. Itoh and Dr. Teinosuke Kanda read Purcell's paper, they began their own investigation of NMR with the encouragement of Prof. Kikuchi.

I learned about NMR through a conversation with a classmate who was working for the US Army as a translator. At that time, I was working on high-frequency chemical analysis.[2] He told me that US scientists had discovered a method of measuring nuclei by radio waves, and I realized from the US discovery that I should incorporate a magnetic field into my high-frequency chemical analysis. Therefore, without any written guidelines, I constructed an NMR spectrometer. The aim was to apply nuclear measurements to the field of analytical chemistry. The entire spectrometer, including the electromagnet, was handmade. I received considerable guidance on instrumentation from Mr. Shoichi Hayashi and on theory from Dr. Kenjiroh Kambe.

Hayashi and I could measure nuclear magnetic moments very precisely by using a standard wave of 100 kHz; at the time the Japanese Government encouraged scientists to use a standard wave in all studies involving radiofrequency techniques. Thus, we obtained very accurate nuclear magnetic moments for the nuclei ^{1}H, ^{19}F, ^{23}Na, ^{63}Cu, ^{65}Cu, ^{79}Br and ^{81}Br.[3] Because the US did not have good data on copper, our data were registered at the Oak Ridge National Laboratory.[4] Meanwhile, in 1954, a paper by Profs. Ryogo Kubo and Kazuo Tomita was well received by NMR researchers as a broad outline of NMR dynamics.[5]

I went to the laboratory of Prof. H. S. Gutowsky at the University of Illinois in 1953 for further study of high-resolution NMR. While there, I participated in the construction of a high-resolution NMR machine. It used a permanent magnet and operated at 28 MHz. In January 1955, good resolution was obtained, largely due to the new technique of sample spinning. At the suggestion of Prof. Gutowsky, I tried to determine whether the proton signal of monofluorobenzene showed a composite multiple structure. Prof. Gutowsky was particularly interested in obtaining information about the localization of π electrons in aromatic rings in connection with the molecular orbital theory of Prof. Mulliken of the University of Chicago. The spectrum obtained at that time showed a simple doublet structure.

I returned to Japan in October 1955. With the warm approval of Prof. Gutowsky, I constructed a duplicate of the NMR machine at Illinois using research funds from the Japanese Ministry of Education. With Mr. Hiroshi Shimizu, I remeasured the NMR spectrum of monofluorobenzene and obtained a spectrum with a multiplet structure, which suggested a localized π-electron distribution. The spectrum was quantum-mechanically analyzed as an AB_2C_2X system. The results of the analysis gave nonuniform distributions of the π electrons at the *o*-, *m*-, and *p*-hydrogens. Furthermore, the data showed that the resolution of our machine was about 0.2 Hz, as compared with that of the Illinois instrument of ca. 0.5 Hz. For the analysis of the spectrum, we used the Parametron computer, PC-1, at the University of Tokyo. Unfortunately, publication of our results was delayed,[6] and thus did not contribute directly to the growth of molecular orbital theory.

The first NMR meeting sponsored by the Chemical Society of Japan was held in the fall of 1960 in Tokyo. I am pleased to have organized the First International Conference on NMR in Tokyo in 1965. Among the participants were such pioneers as Drs. E. R. Andrew, S. Alexander, J. Baldeschwieler, A. L. Bloom, R. R. Ernst, R. Freeman, D. M. Grant, H. S. Gutowsky, O. Jardetzky, W. D. Knight, G. E. Maciel, L. W. Reeves, C. Reilly, R. U. Lemieux, M. T. Rogers, J. N. Shoolery, C. P. Slichter, J. S. Waugh, and others from abroad, as well as Drs. J. Itoh, K. Kambe, Y. Kakiuchi, T. Kanda, R. Kubo, K. Tomita, and others from Japan. This conference was the first international meeting in which physicists and chemists, both theoreticians and experimentalists, could interact. Subsequent meetings in this series led to the formation of the International Society of Magnetic Resonance, which continues to hold meetings every three years.

The Japan Electron Optics Co., JEOL, was founded in 1947 by Mr. Kenji Kazato to develop electron microscopes. When I returned home in October 1955, JEOL was just starting the development of an NMR machine, and an active interest in NMR was growing in Japan. JEOL built a 32 MHz machine with an electromagnet in 1956, and then developed 40, 60, 100, and 90 MHz machines. The all-transistorized product JNM-C-60HL and later the minisized 'Minimer' JNM-MH-60 and MH-100 were welcomed by users worldwide. The MH-100 received the IR-100 award from the *Journal of Industrial Research* in 1967.

Meanwhile, the introduction of Varian and Bruker spectrometers, initially continuous wave and later using the Fourier transform mode, contributed greatly to the development of NMR in Japan. Tom Farrar and Gary Samuel played key roles in designing and constructing the first FT NMR machine in this country. Rapid scan correlation NMR spectroscopy was described by Ted Becker on a visit to Japan in 1974. Prof.

Yoji Arata and Dr. Hiroshi Ozawa quickly developed a similar system, which resulted in a productive activity in NMR and led to the currently available 60 MHz Hitachi rapid scan correlation instrument.

Since the 1960s an active interest has grown in Japan as in other countries in the application of NMR in bioscience, and in 1978 I organized the 9th International Conference of Magnetic Resonance on Biological Systems (ICMRBS) in Nara.

I began NMR and ESR measurements on the whole bodies of live silk worms in 1969[7] and gave a detailed report at the Seventh International Conference of MRBS in New York in 1973.[8] That work represented the beginning of the gross study of live samples in Japan. Dr. Findeis of NSF then invited me to speak in Washington DC, and I told the audience that I would like funds to construct an NMR magnet that could encompass an entire human body. In May of that year Professor Lauterbur told me that he could obtain the funds, which pleased me greatly. At that time the state of the art of computer science in Japan was insufficient for the study of imaging. Today, however, both NMR and ESR imaging studies are flourishing in Japan, as they are in the rest of the world.

It has been extremely gratifying to be involved in the field of magnetic resonance since its beginnings.

REFERENCES

1. J. Itoh, R. Kusaka, Y. Yamagata, R. Kiriyama, H. Ibamoto, T. Kanda, and Y. Masuda, *J. Phys. Soc. Jpn.*, 1953, **8**, 287.
2. S. Fujiwara and S. Hayashi, *Anal. Chem.*, 1953, **26**, 239.
3. S. Fujiwara, *Bull. Chem. Soc. Jpn.*, 1951, **24**, 116.
4. H. E. Walchli (ed.), *Tables of Nuclear Moment Data*, Oak Ridge National Laboratory, Oak Ridge, TN, 1964, Supplement II, Physics.
5. R. Kubo and K. Tomita, *J. Phys. Soc. Jpn.*, 1954, **9**, 888.
6. S. Fujiwara and H. Shimizu, *J. Chem. Phys.*, 1960, **32**, 1636.
7. S. Fujiwara, H. Tadano, and M. Nakajima, *Bull. Chem. Soc. Jpn.*, 1970, **43**, 3023.
8. S. Fujiwara and M. Nakajima, *Ann. N.Y. Acad. Sci.*, 1973, **222**, 677.

Biographical Sketch

Shizuo Fujiwara. *b* 1920. B.S., 1994, Dr.Sc., 1949, University of Tokyo. Assistant Professor at the University of Electro-Communications, 1949–53. Post-doc at University of Illinois (1953–55) with Prof. H. S. Gutowsky. Professor of Analytical Chemistry University of Tokyo (1960–81). After retirement, Chemistry Professor at Chiba University, founding Dean of Faculty of Science, and founding Director of Research Institute of Information and Knowledge of Kanagawa University, Approx. 500 publications. Present research interest: origin of chirality, oxygen complex with an eutectic compound of sodium chloride and water.

Gadian, David G.: From Brawn to Brain

David G. Gadian

Institute of Child Health, London, UK

Towards the end of my undergraduate course in physics, my attention naturally focused on potential topics for a doctorate. I was interested in applying my physics in the biological sciences, and it was fortunate that the head of my Oxford college was Rex Richards, who had recently moved his NMR group from the Department of Physical Chemistry to the Biochemistry Department. Despite knowing little about NMR, and even less about biochemistry, I joined Rex's group in October 1971. This, it turned out, provided a wonderful opportunity to participate in a multidisciplinary research program, for strong links had already been forged with the biochemists, and in particular with George Radda and his group.

My D.Phil. research in Oxford proceeded in fairly typical fashion. I learnt a lot, I enjoyed the research, and for two years I produced little in the way of publishable material. But in those days there seemed to be relatively little concern about publications. My research was concerned primarily with ^{31}P spectroscopy of the glycolytic enzyme phosphoglucomutase, and the work went reasonably well, albeit with little in the way of excitement. I showed that it was possible to assay the enzyme by monitoring the ^{31}P signals of substrate and product (glucose 1-phosphate and glucose 6-phosphate). However, this did not seem terribly exciting either, as the enzyme could be assayed rather more cheaply and with a great deal more sensitivity using standard biochemical techniques.

Then, close cooperation and discussion between Rex's and George's groups led to a series of seemingly logical developments. We showed that we could use ^{31}P NMR to monitor enzyme-catalyzed reactions not just in the presence of a simple enzyme but also with multienzyme systems, in particular in the presence of glycogen particles and muscle homogenates. It was not very long before we showed that we could detect metabolites in intact muscle (see ***Hoult, D. I., Biomedical NMR Instrumentation–A Personal Viewpoint***, for further memories). The excitement was high (although I was perhaps a little too young and naive to appreciate many of the potential implications), publications ensued, my D.Phil. thesis was a lot more interesting than it might have been, and I stayed on for postdoctoral research . . . for a further eight years! During this subsequent period, the group attracted numerous talented scientists. I had a memorable collaboration with Doug Wilkie and Joan Dawson of University College, London, and many young(ish) scientists joined from overseas, including Alan McLaughlin, Pieter Cullis, Bob Balaban, Jo Ackerman, Richard Briggs, Keith Thulborn, Craig Malloy, and Axel Haase. Surface coils evolved, clinical spectroscopy emerged, and I believe that these developments, many of which in retrospect seem so obvious, reflected the unique nature of our team: namely the close liaison between physicists, chemists, biochemists, and physiologists, who may have regarded each other with some suspicion at times, but who worked on an equal basis with a high degree of mutual respect for each other's talents and knowledge.

In 1983, I moved to London to set up a new group at The Royal College of Surgeons. I was keen to establish a similar type of multidisciplinary environment, and while I do not have the space to dwell on this in any detail it is a great pleasure to see how the team has developed and progressed. Our team of basic scientists has now become the Royal College of Surgeons Unit of Biophysics, based at the Institute of Child Health and Hospital for Sick Children, Great Ormond Street, and it is good to see the basic scientists working together with clinical teams, using both imaging and spectroscopy to understand more about brain function and dysfunction, and to see how these NMR methods can now contribute to the clinical management of children with brain disease. It is also gratifying to see the increasing interaction of imaging with spectroscopy; for example, the close relationship between changes in diffusion-weighted images and energy metabolites in acute stroke models opens up the possibility of visualizing the effects of energy failure in stroke patients with the spatial resolution of imaging, rather than the much coarser resolution of spectroscopy. And the excitement continues! While we were certainly not the first to carry out functional magnetic resonance imaging of the brain, it was nevertheless a remarkable experience when we first saw regions of the brain 'light up' in response to visual and motor tasks. It was even more remarkable when we found that we could use functional magnetic resonance imaging to visualize seizure activity in a child with epilepsy, a study that I am sure we shall look back upon with a great deal of satisfaction.

These are some highlights. But of course there have been some difficult times; there have been times when experiments have failed. There was the time when, during the course of my D.Phil. research in Oxford, I was 'baby-sitting' the magnet over the Christmas period and, to my horror, I came in one morning to see it iced up. It wasn't long before I discovered that it did not attract the metal rule in quite the usual fashion, and that it had quenched because I had forgotten to switch off the power supply to the superconducting shim coils (we were having problems with the shimming) and as a result the cryogens had boiled off. I was really depressed. I remember telephoning my girl friend Rosemary and saying to her that I might just give up science altogether and become a crofter in Scotland. But Rex knew the magnet well. He came in, dismantled the cryogen system, discovered that one of the superconducting shim coils was not wired up correctly, and a couple of weeks later the magnet was working better than ever before. And within two months, we used the magnet to obtain the first high-resolution spectra of intact tissue!

Biographical Sketch

David G. Gadian. *b* 1950. B.A., 1971, Physics, D.Phil., 1975, University of Oxford, UK (supervisor Rex Richards). Postdoctoral research with Rex Richards and George Radda in Oxford. Moved in 1983 to the Royal College of Surgeons in London. Currently Rank Professor of Biophysics and Head of the RCS Unit of Biophysics and of the Radiology and Physics Unit at the Institute of Child Health, London. Approx. 140 publications. Research interests: development and application of magnetic resonance techniques for noninvasive investigation of brain metabolism and physiology.

Garroway, Allen N.: Origins of MRI—A Personal View

Allen N. Garroway
Washington, DC, USA

This is a narrow view of the origins of magnetic resonance imaging (MRI). In retrospect, I see substantial but unheeded foreshadowings of NMR imaging in my own professional education. I obtained my Ph.D. in condensed matter physics at Cornell University. Before beginning their research, physics graduate students at Cornell University would sign up for Physics 510, an advanced physics laboratory. One purpose of this course was to provide experimental physicists with a flavor for different disciplines. To this end, there were brief tours to various research groups at Cornell. I clearly recall the demonstration given by Professor Robert M. Cotts. He asked for a volunteer from the assembled Physics 510 students to stick a finger into the Varian wideline NMR probe so that the spectrometer could be tuned on the hydrogen resonance of the water in the finger. Of course, none of us stepped forward: there was no telling what those magnetic fields, both dc and rf, might do to the human body.

A 1966 summer job with Dr. Larry Bennett at the National Bureau of Standards (now the National Institute for Science and Technology) further introduced me to NMR and I subsequently joined Professor Cotts's NMR group as a research assistant in 1967. My thesis work involved the nature of concentrated metal–ammonia solutions. By determining the respective self-diffusion coefficients for hydrogen and the alkali metal nuclei with the pulsed magnetic field gradient methods of Stejskal and Tanner, we established that, over the timescale of the diffusion experiment, lithium is solvated by four ammonia molecules, while sodium is solvated by six molecules in these concentrated solutions.

Calibration of the strength of the magnetic gradient pulse is central to accurate determination of diffusion coefficients. Techniques that were well known in this field and used in our lab included measuring the time of the 'zero crossing' of the proton free induction decay (FID) of a test tube of water in the presence of a gradient perpendicular to the axis of the tube; I believe this was first reported by Herman Y. Carr. It was well appreciated that the Fourier transform of the spatial profile gave the FID, and vice versa. And, of course, all our discussions of the method of pulsed gradient diffusion measurement invoked the physical explanation that 'the magnetic gradient labels the spatial position with the frequency variable'. Still, the potential of NMR imaging was not clear in my mind.

I recall when Dr. Raymond Damadian's 1971 *Science* article[1] appeared on the determination of spin–lattice relaxation in cancerous growths. I was rather perplexed at the paper's unphysical assumption that the complex relaxation behavior of a heterogeneous tissue could be characterized by a single T_1 value. At the time, I did not foresee the potential for in vivo measurement.

In February 1972 I joined Dr. Peter Mansfield's group at Nottingham University as a postdoctoral fellow. I was interested in the multiple pulse line-narrowing techniques that he was developing to suppress the dipolar coupling in strongly coupled homonuclear systems so that the more subtle effects of the chemical shift could be recovered in solids. In the group at that time were research students Denis Stalker and Peter Grannell. Grannell continued in the group as a postdoc, working on resolution and signal enhancement methods for NMR observation of rare spins in solids.

One day, in the early summer of 1972, as Grannell and I were having morning coffee in the Physics tea room, Peter Mansfield pulled up a chair and said, in essence: 'I've had this really crazy idea. It seems that one could measure atomic separations in crystalline materials by imposing a magnetic field gradient and observing the resulting NMR diffraction pattern'. Grannell rolled his eyes. From my experience in pulsed gradient diffusion, I volunteered that the required magnetic gradients would need to be immense and, further, that the alignment and the perfection of the crystal would need to be of the order of crystal lattice dimensions. I may have also suggested that the basic idea of using a gradient to obtain spatial information had already been demonstrated. We three batted ideas around for a while. When I returned at tea time, Mansfield and Grannell were still in extended conversation.

Mansfield and Grannell vigorously pursued this diffraction idea. However, Grannell's 'rare spin' spectrometer was not appropriate to demonstrate NMR diffraction. So Stalker, Grannell, and I performed a rudimentary 'imaging' experiment illustrating the aspects of diffraction. We imaged not a liquid but rather a solid, camphor—a plastic crystal in which intermolecular proton dipolar couplings are attenuated by rapid molecular reorientation. We employed one of Mansfield's line-narrowing sequences, now called MREV-8, to reduce dipolar couplings, and displayed the one-dimensional interferogram (pseudo FID) of a series of slabs of camphor to a resolution better than 1 mm.

That first Nottingham imaging work[2] was presented in a talk by Peter Mansfield at the First Specialized AMPERE Colloquium in Krakow, Poland, in August 1973. While I was sitting in the back row with Peter Grannell during that talk, the pieces finally fell into place for me, and in that epiphany I saw that magnetic resonance imaging was indeed going to impact medical science.

After Mansfield's AMPERE talk, a questioner from the audience, Professor John S. Waugh of MIT, asked if this approach was related to Professor Paul C. Lauterbur's (State University of New York at Stony Brook) 'zeugmatography' just reported in *Nature*.[3] At the time none of us had seen that work. I seem to remember that Waugh in his remarks alluded to a 'zeitgeist': when ideas are 'ready', they seem to spring spontaneously and independently from many sources.

On their return to Nottingham after the Krakow meeting, Grannell and Mansfield continued their imaging work while Stalker and I pursued understanding the limitations on the experimentally obtained resolution in the line-narrowing experiments. In February 1974 some of us physics postdocs took a short holiday to Moscow. On the trip was my friend Dr. Waldo S. Hinshaw, at the time a postdoc with Professor E. Raymond Andrew at Nottingham. Hinshaw and (the late) William Moore had just returned from an ISMAR (International Society for Magnetic Resonance) meeting in Bombay and, on hearing Lauterbur's presentation there, were fired up about the prospects for NMR imaging. In my talks

with Hinshaw in Moscow, I too became more interested in imaging.

Back at Nottingham I thought further about the possibilities of NMR imaging and realized it could be used to image flow fields in liquids, both the spatial variation of the velocity field and also the velocity distribution function. One simple imaging demonstration[4,5] I first presented at the 1974 AMPERE meeting in Nottingham showed the parabolic profile expected for laminar flow in a cylindrical tube. I destroyed magnetization in a restricted region with a $\pi/2$ pulse and then waited a further time before 'imaging' with a magnetic field gradient perpendicular to the tube axis. This way one sees signal only from the fresh spins that move into that region; the number of fresh spins and hence their signal is proportional to the local velocity in the laminar flow field.

In that flow experiment, the region was restricted quite crudely: I wrapped copper foil around the tube to (somewhat) shield those regions from the rf field, and left unwrapped the region of the tube to be interrogated.

Were there any better ways to excite spins in one region of space and leave others unperturbed? I had just read of the method of 'selective irradiation' by Tomlinson and Hill[6] that used weak pulses to excite only a part of an inhomogeneously broadened line. I realized that such a method could then be used in NMR imaging to excite only a portion of the overall sample, inhomogeneously broadened by the applied magnetic field gradient.

I immediately implemented such a selective irradiation approach on our line-narrowing spectrometer, a homebuilt system operating at a proton frequency of 9 MHz (!) controlled by a Honeywell 316 computer with 4 K [sic] of memory. (Within this 4 K of memory, I could generate rather elaborate multiple pulse sequences, acquire up to 1 K of data, and perform a 1 K fast Fourier transform.)

My naive notion was to define a region by applying a pulse sequence that was essentially the Fourier transform of the desired region. This is not a bad approximation provided the effective nutation angles are less than $\pi/2$. I wrote a machine language program to Fourier transform an arbitrary spatial profile, and then to generate automatically the machine language code that provided the correct pulses and delays to the transmitter.

I was extremely pleased with those first results,[7] showing a narrow selectively irradiated slice excited from the semicircular profile of a test tube of water, the same geometry I had used at Cornell to measure magnetic field gradients for the diffusion measurements.

Just as I was doing these selective irradiation experiments, Mansfield and Grannell had some imaging experiments they wanted to try out on the 9 MHz spectrometer. Indeed they had also realized that some sort of spatial restriction was quite useful if one wished to image a fully three-dimensional object. Their approach was to use saturation methods, i.e. a train of weak pulses, to destroy magnetization in unwanted regimes in contrast to the selective excitation.

Grannell, Mansfield, and I recognized we were all taking the same basic approach to slice up an object for imaging. That approach[7] which we pioneered, selective rf irradiation to excite specific regions of a sample, finds substantial application in modern MRI.

I left Nottingham in October 1974 for a postdoctoral position at the Naval Research Laboratory. After Nottingham's initial demonstration on solids imaging, almost everyone moved to the medical applications. In the 1980s I elected to explore further some aspects for NMR imaging in materials with possible applications to nondestructive evaluation of polymeric systems. My colleagues and I at the Naval Research Laboratory continue to maintain that general interest: perhaps Mansfield's initial crazy notions about solid state imaging were not so crazy.

Here I have conveyed only my own first-hand perspective of the very early work at Nottingham; I have not described the many significant contemporaneous contributions of others. I feel a great kinship to co-workers at Nottingham and to other early workers at Stony Brook, Aberdeen, and Zurich.

There are also lessons that one might draw from these early days of MRI about the convoluted way that new ideas spring forth when the time is right; how new ideas are implemented; and how, or indeed whether, that evolution can be 'nurtured', 'managed', or 'programed' by beneficent funding organizations. But that is another topic.

REFERENCES

1. R. Damadian, *Science*, 1971, **171**, 1151.
2. P. Mansfield, P. K. Grannell, A. N. Garroway, and D. C. Stalker, *1st Specialized Colloque AMPERE, Krakow*, 1973, p. 16.
3. P. C. Lauterbur, *Nature (London)*, 1973, **242**, 190.
4. A. N. Garroway, *Proceedings of the 18th AMPERE Conference, Nottingham*, 1974, p. 435.
5. A. N. Garroway, *J. Phys. D: Appl. Phys.*, 1974, **7**, L159.
6. B. L. Tomlinson and H. D. W. Hill, *J. Chem. Phys.*, 1973, **59**, 1775.
7. A. N. Garroway, P. K. Grannell, and P. Mansfield, *J. Phys. C: Solid State Phys.*, 1974, **7**, L457.

Biographical Sketch

Allen N. Garroway. *b* 1943. B.S., 1965, Physics, Rensselaer Polytechnic Institute, Ph.D., 1972, experimental solid state physics, Cornell University (supervisor Robert M. Cotts). Postdoctoral research at University of Nottingham (Peter Mansfield) and US Naval Research Laboratory (Henry A. Resing). Research Physicist, Chemistry Division, US Naval Research Laboratory, 1976–present. Research specialties: solid state NMR imaging, polymer properties and dynamics, non-traditional applications of NQR.

Gerstein, B. C.: The Vaughan Days, CRAMPS, and Transient Techniques in NMR

B. C. Gerstein

Ames Laboratory of Iowa State University, Ames, IA, USA

I want to share our experience with the development of high-resolution solid state NMR of strongly homonuclear dipolar coupled solids. Necessarily, a large part of this history will involve Bob Vaughan.

My training in chemistry was as a low-temperature thermodynamicist. We were interested in linear magnetism in inorganic solids as studied by low-temperature initial susceptibilities, and low-temperature heat capacities. It became clear early on that the number of interesting problems in that field was too limiting for my taste. About 1970 I became interested in heterogeneous catalysis. I sought a faculty improvement leave from Iowa State University at a location where I might learn something of catalysis and the most modern techniques which could be used for such studies. I contacted Harry Gray at Caltech, and he recommended 'a really bright new chemical engineer, who is using this new solid state NMR multipulse business to look at catalytic processes.' This was Bob Vaughan, whom I called, and asked if he would consider having a senior (I was 39, and Bob 30) person working with him for a year. Bob, who did an enormous amount of traveling, replied that he would like to stop and visit my laboratory. He wanted to see, I suppose, if this fellow Gerstein was someone who had fallen asleep, or someone who could fit into his dynamic new research effort. After visiting my laboratory, he made a positive decision. He called me from Caltech saying that George Hammond had arranged half salary for me (my university covered the other half), and I could come the next year. I said 'Bob, I hope you realize that I want to come and learn your new technique, steal it, and bring it to Ames'. He said 'come along!'.

It was a strange, tense, and exciting year. Bob took quite a chance in allowing me to come and work with him, his first graduate student Loren Schreiber, and Won-Kyu Rhim, a former postdoc of John Waugh's, then a scientist at JPL. Bob was a dynamic, personally kind, and brilliant man. My wife and I became close personal friends with Bob and Sharon.

Bob's NMR was homebuilt around a 1 T old Varian iron core magnet. A PDP-11, with paper tape feed for the programs, was used for experimental control, and manipulations of data. My first day in the lab was spent in replacing the Variac in the power supply of the magnet, Bob and I working and sweating together in the August heat of Southern California to pull the heavy beast from the frame, and replace it with another Bob had saved from an old supply. I rapidly realized that in Vaughan there existed a remarkable combination of chemical physicist, chemical engineer, electrical engineer, and mathematician.

Work in the Vaughan lab went on seven days and seven nights a week. I generally took Sunday off to be with my family in Santa Monica, jogging there, or racing a Thistle Class sloop down at Balboa with three of my five children as crew. They ranged in age from 9 to 11, and together all four of us weighed a whopping 350 pounds, considered a very light crew for a Thistle. We did very well in light air.

I could always depend on Bob being in the lab any evening of the week. He would generally arrive about 8.30 a.m., and was there when I ran out of steam about midnight. When I would say 'Bob, I have to go home, I'm making too many mistakes,' he would reply 'Oh, you've had a long day. Let's quit for the night', and after I left, he went home and prepared lectures until well into the early hours of the morning. I guess he slept about five hours a night.

During that year the MREV-8 sequence was developed in the Vaughan lab (as well as earlier in Peter Mansfield's laboratory at Nottingham, although I didn't know of it at the time), and I had the marvelous opportunity to use it for the first time to determine the shielding tensor of the protons in trichloroacetic acid. I can't count how many times that probe was disassembled, a fried resistor or capacitor replaced, and reassembled, but it was enough to give me the confidence that I could go home and build a machine like Bob's, with the circuit diagrams Bob gladly supplied me, and John Yehle's kind help.

Another important feature of that year was the Vaughan group weekly seminars. During these, by either Bob or Won-Kyu Rhim, the theory behind the homonuclear decoupling experiments was developed, and I had my first taste of average Hamiltonian theory. The real beginnings of my understanding of the formalism began one weekend near the end of my stay at Caltech when my wife and I, and Bob and Sharon took a trip down to San Miguel, a little fishing village just north of Ensenada. I vividly recall my being confused about how spin operators transform under rotations. While Bob and I were walking on that marvelous six mile long sparkling sand beach just south of Ensenada, Bob said, 'no, you have to remember the order', and in the sand with his finger he traced

$$\hat{\mathcal{H}}_{\text{int}} = U_{\text{rf}}^{-1}\hat{\mathcal{H}}_{\text{int}}U_{\text{rf}} \tag{1}$$

and then pointed out that the inverse rotation operator is a product of the inverse rotation operators in inverse order. For the first time I began to see how Bob and Rhim were thinking about the design of pulse sequences, and how one might, in principle, come up with a MREV-8 oneself. Of course there are quite formal general ways of thinking about this matter that Peter Mansfield had published, of which I was not aware at the time. During the Vaughan group seminars, I took careful notes, worked them up immediately after each lecture, and consulted Bob, who was always available when questions arose. I began to appreciate the beauty of what we were doing, in that there was so tight a connection between theory and experiment that an idea conceived one day could be verified by experiment the next. Such was the case with second averaging the chemical shift by an offset[1] that Vaughan and Dybowski published shortly thereafter.

Regarding Dybowski, that winter Bob brought me a file of an application for a postdoctoral position from this fellow Dybowski, who did his graduate work with Wade at the University of Texas. It was characteristic of Bob that he sought advice from a wide range of people, and he asked me to look carefully at the file, and help him decide if we should have

him in the group. Dybowski's file looked pretty good to me, even though a 6 ft. 2 in. Texan with flaming red hair and a ponytail seemed a bit strange at first sight. Dybowski arrived in the spring, and he and I became fast friends as I quickly realized he was a superb chemical physicist with a fine pair of hands, and a lover of Mexican food. We both gained quite a bit of weight that summer as we toured the restaurants, especially 'Ernies' in Pasadena.

In September of 1973 I returned from Pasadena, and proceeded with the help of ISU's Ames Lab electronics' shop to recreate Bob's pulse spectrometer, incorporating state-of-the-art improvements in the pulse programmer as devices came on the market. We had an old 1 T Varian electromagnet like Bob's, donated to Iowa State by Dow Chemical, which was used by Baker and Burd for their pioneering field/frequency locked spectrometer and for Baker's early INDOR experiments. A very bright young electrical engineer named Doug Adduci was assigned to help build the pulse programmer, and with the advent of microswitches and Merrimac adjustable phase shifters, we were able to create a four phase rf switch with 25 possible pulses on which our first homonuclear decoupling pulse experiments were made. The Vaughan group rf switch employed picturesque sliding trombone phase trimmers protruding from the console like a device out of Star Wars. We lost a bit of culture when we went to the Merrimacs. Subsequently, since about that time the microprocessor was developed, Adduci designed a microprocessor-based pulse programmer[2] which gave us an enormous increase in versatility for that period.

I believe I had read somewhere (but I cannot trace the source, although John Waugh tells me he was aware of the idea at the time[9]) that magic angle spinning might be coupled with homonuclear pulse decoupling to produce liquid-like lines of protons in strongly homonuclear coupled solids. Perhaps the idea came from Ray Andrew's papers in which he said that both shielding anisotropy and homonuclear dipolar coupling could be removed by magic angle spinning. In any event, we proceeded to review the techniques of Jesse Beams which he used in his collaboration with The Svedberg on the ultracentrifuge to make high velocity rotors. I blush to admit that our first rotors were made of phosphor bronze. A graduate student named Larenzo Ryan, who visited me from Arizona when I was at Caltech to see if he wanted to work with me at ISU, was working on getting the MAS going. He used ideas from the papers by Andrew and by Lowe, and referred back to Beams's RSI paper that was published the year I was born. We could spin a Kel-F™ DuPont rotor of Beams's design to a kilohertz or so, but no more. A personal call to Beams resulted in the use of a ballast volume to take the surges out of our compressed air line, and a speed of 3 kHz on a good day.

A postdoctoral student by the name of Chee Chow, who had worked with Rog Willett at Washington State, had just come to work with me. We had found an old Rhodes–Schwartz tube type frequency synthesizer in a scrap heap in the Physics Department at ISU, and used it to obtain our first NMR signals. A retired IFI 500 distributed amplifier system, used previously by Gerry Pearson on ENDOR experiments, was the transmitter. Chow was a bit wild, and when resonance could not be found at one frequency, he began varying the frequency all over the ball park, resulting in the Lowe–Tarr scheme quarter-wavelength stubs which protected the receiver failing to do so, and the first two Avantek amplifiers in the receiver were 'fried' as Vaughan would say. It was a fortunate accident. When Doug Adduci heard of our tragedy, he asked me if I was interested in rapid recovery. '**YES!**', I replied. Doug had just seen an ad for Spectrum-Microwave receivers that boasted a 1 μs recovery after a 5 V overload. With these, and with Dave Torgeson and Doug's careful design of the receiver chain,[3] we were able to obtain a recovery of less than 2 μs after a 500 W pulse at 56 MHz, and a cycle time for the MREV-8 sequence of about 22 μs on a good day.

One event that made the construction of our spectrometer possible was that the State of Iowa had funded ISU for $5 million to study coal cleaning. Iowa has lots of coal, but much of it is high sulfur content, some as much as 15% due to chunks of pyrite as large as my fist. The Ames Laboratory Director at the time, Bob Hansen said 'Bernie, why don't you apply for some of those funds and see if this new technique you have a gleam in your eye for can do some new analysis on coal?' We obtained enough to buy our first PRD frequency synthesizer, and our first publication using NMR was on the nondestructive determination of hydrogen in coal.[4]

By that time, Rich Wilson had come from Rollie Myers' group at Berkeley as a postdoctoral, and Bob Taylor, Bob Pembleton, and Larenzo Ryan were students. One winter morning in 1976 was posted on my door the first CRAMPS[5] spectrum obtained in our group. Our CRAMPS paper was published the next year, with Ryan coining the acronym, inspired by Alex Pines' use of his name in one.

Of course, at the same time, in Jena, Hans Rosenberger and Gerd Scheler were working on the same technique with similar success in the more difficult higher frequency region using superconducting magnets. I had the pleasure of visiting their lab during the trip to Poland in 1983 for the symposium Alex Gutsze organized on 'NMR in Surface and Colloid Science'. That was the trip during which I was arrested for being a spy, but that is another story.

Dybowski stayed at Caltech for a couple of years, and then accepted a faculty position at the University of Delaware. Before leaving Caltech, he asked me if I was interested in making a book from the Vaughan group seminar notes. I immediately sent him the first two chapters which I had written for my own group seminars, and after some agonizing collaboration at a distance we finalized the manuscript working together from morn to eve during a grueling two week stint in the Pocono Mountains. We stayed on speaking terms. 'Transient Techniques in NMR of Solids'[6] was published by Academic Press in 1985.

I will never forget that terrible day in 1979 when Sunney Chan called me and said 'Bernie, I am afraid I have some bad news for you. Bob Vaughan was on that DC 10 which went down in Chicago on Friday.' For years after that I had dreams that Bob was still alive, and that it was all an awful mistake. I have not had one of those for a while now. We still see Sharon and her second husband when we visit California.

I must also mention the enormous contributions made to our group by Paul Murphy, who succeeded in achieving our first cross polarization experiments, using a receiver that looked like a rat's nest, and had to be breathed upon properly to prevent feed-thru of the proton signal, and the subsequent applications that students such as Murphy and Po-Jen Chu made to fossil fuels, polymers, inorganic solids, and materials such as amorphous silicon hydride.

Finally there came to our group from Poland as a result of my visit there in 1983 a young man named Marek Pruski, who is presently the group leader, and deservedly so, of the research group that once I directed. Pruski, with training under Gutsze as a physicist, thoroughly modernized the equipment in the group, and with his keen criticality and marvelous creativity made our collaboration with Terry King a stunning example of the power of modern NMR in the study of heterogeneous catalysis (see Pruski, ***Supported Metal Catalysts***), and is proceeding to cut his own path on the world scene of NMR.

One of the most incredible experiences I had was that of meeting Maurice Goldman in 1987. Alex Pines and I were the two Americans invited by Joseph Virlet to talk at a French NMR school in Les Houches. Alex lectured on multiple quantum NMR among other subjects, and I didn't understand it. After the lecture, I asked Maurice, whom I had admired from afar for years if he understood this subject. He said, 'I think so. Come to my room this evening'. Well, for that evening and two more, I was in Maurice's room, and he wrote with the speed of light, developing the theory of the development and detection of multiple quantum NMR in spin- 1/2 dipolar coupled solids. It was stunning! The spin dynamics he carried in his head was simply a marvel to witness. He was enormously kind, and unbelievably patient with my slow understanding of his lightning-like thinking. I was on leave at that time and spent the next month enjoying Wiebren Veeman's hospitality in Nijmegen. Wiebren gave me a desk and only asked that I give his group some lectures on this theory of multiple quantum NMR, which he, as another lecturer at Les Houches, had also heard. After two weeks, I understood the production from reading Maurice's notes, and gave a three hour lecture on that. After another two weeks, and some phone calls to Maurice, I understood the detection well enough to talk about that. Dave Cory, who was a postdoc with Wiebren at the time, immediately built a probe for the experiment and proceeded to begin to try to get some multiple quantum spectra. He didn't have the capability of fast digital phase shifting which we developed after I returned to the US the next spring,[7] but what he did with what he had was simply amazing!

After returning to the US, I wrote these lectures into what became a publication[8] with the last truly brilliant student to work with me, Son-Jong Hwang, a three-year Phillips Fellow, and awardee of the ISU Alpha Chi Sigma award for outstanding doctoral research.

NMR has been kind to me. I have met and enjoyed the hospitality of people who have suffered through my pizza; Cecil and Mary Dybowski, Chuck and Kim Wade, Bob and Marcia Bryant, Bob and Helene Pearson, Don and Joan Wilson, Dave and Mary VanderHart, Nino and Sue Yannoni, Gary and Maxine Maciel, Dave and Reva Grant, Alex and Dietza Pines, Ken and Christine Packer, Jose' and Carol Fripiat, Harry and Christina Pfeifer, Dieter and Crystal Michel, Jacques and Mimi Fraissard and Jacques's entire warmly hospitable group, especially Robert and Danielle Vincent and Claudine Dore'mieux-Morin, Michel and Claudette Guelton, Jean-Paul and Patricia Amoureux, Lechek and Anna Stefaniak, Bogdan Kamienski, and Alex Gutsze, only some of the many lovely people who are friends and have made life richer.

REFERENCES

1. C. R. Dybowski and R. W. Vaughan, *Macromolecules*, 1975, **8**, 50.
2. D. Adduci and B. C. Gerstein, *Rev. Sci. Instrum.*, 1979, **50**, 1403.
3. D. J. Adduci, P. A. Hornung, and D. R. Torgeson, *Rev. Sci. Instrum.*, 1976, **47**, 1503.
4. B. C. Gerstein and R. G. Pembleton, *Anal. Chem.*, 1977, **49**, 75.
5. B. C. Gerstein, R. G. Pembleton, R. C. Wilson, and L. M. Ryan, *J. Chem. Phys.*, 1977, **66**, 361.
6. B. C. Gerstein and C. R. Dybowski, *Transient Techniques in NMR of Solids; An Introduction to the Theory and Practice*, Academic Press, Orlando, FL, 1985.
7. B. C. Gerstein, Jin-Woo Han, Son-Jong Hwang, Pan Hong-Jun, and Harold Skank, *Rev. Sci. Instrum.*, 1990, **61**, 2349.
8. Son-Jon Hwang and B. C. Gerstein, *Bull. Magn. Reson.*, 1994, **15**, 213.
9. Note added in proof. Bob Griffen supplied me with the reference as being U. Haeberlen and J. S. Waugh, *Phys. Rev.*, 1968, **175**, 453.

Biographical Sketch

B. C. Gerstein. *b* 1932. B.S., 1953, Purdue, Ph.D., 1960, Iowa State. Introduced to NMR by R. W. Vaughan. Faculty in Chemistry, Iowa State University, 1962−present. Approx. 150 publications, and, with H. F. Franzen the text 'Rudimentary Thermodynamics', and with C. R. Dybowski, the book 'Transient Techniques in NMR of Solids; An Introduction to the Theory and Practice'. Research interests include the theory and practice of learning, and applications of solid state NMR to problems in the physics and chemistry of materials, fossil fuels, and heterogeneous catalysis.

Goldman, Maurice: The Time when Spin Temperature was Hot Stuff

Maurice Goldman

CEA-Saclay, Gif-sur-Yvette, France

Spin temperature theory underwent its 'big bang' in the late 1950s and early 1960s. I was privileged to be at that time in one of the hot spots where these developments took place, both as a witness and a partial contributor. My view of what happened is therefore from the observation point of Anatole Abragam's Laboratoire de Résonance Magnétique at Saclay, France.

When I joined this lab in 1956, I knew about the funny results observed by Purcell and Pound in the demagnetization/remagnetization of LiF, but my first real introduction to spin temperature was at the return of Abragam from a trip to the United States in early 1957: he had had an idea which he told us with great excitement. The slow demagnetization down to zero field in the Pound and Purcell experiment corresponded to an evolution of the spin system which was adiabatic in the *thermodynamic* sense, not in the Ehrenfest sense: it was meaningful to speak of a spin temperature which evolved from Zeeman to dipolar and whose evolution could be calculated. Thanks to the nature of the energy spectrum and the slow relaxation of the nuclear spins, this temperature could differ from that of the lattice and be either positive or negative. If this was true, the nuclear polarizations after slow magnetization should be the same whether the system in low or zero field had been cooled by adiabatic demagnetization or by contact with a helium bath. Warren Proctor, who was then visiting us, was invested with implementing the experiment, which he did successfully together with a few others, the set of which is rightly considered as a historical landmark for spin temperature. I was honored with the task of calculating the local field.

At about the same time, I read a preprint by Alfred Redfield about a slower saturation for dispersion than for absorption in copper and aluminum, together with an attempt at a physical explanation. Ionel Solomon asked me afterwards: 'What did you get out of it?' My reply: 'Not much'. This could have been said by anybody else in the world (except Alfred). It was simply the discovery, in 1955, of spin temperature in the rotating frame. Most of the concepts Abragam had had the idea of were there, plus some extra, under more complex conditions. It was the great merit of Abragam to decipher this work and make his understanding of it available to the scientific community in his famous book of 1961, 'The Principles of Nuclear Magnetism'.

After the interlude of my military service, I read this book in preprint form in the summer of 1960. All of us in the lab have had the advantage of learning there about spin temperature roughly one year before the rest of the world. Shortly after reading the chapter on spin temperature I had a bizarre idea: induce chlorine transitions in low field, in *p*-dichlorobenzene, go to zero field and remagnetize, in a cyclic fashion. I expected to get in that way a proton polarization nearly 10-times larger than that corresponding to the Boltzmann ratio for the chlorine quadrupole splitting. I told this to Ionel Solomon, whose reply was: 'No! All of us have been taken off-guard by Overhauser's prediction, but now it is digested. We even understand the polarization in solids (reference to the solid effect, newly discovered by Abragam), but too much is too much, and you will never make me swallow that you can get more than the solid effect'. He turned out to be wrong. I started working on this 'rotten' idea with André Landesman, initially so that he could help me use a 35 MHz oscillator he had built. We saw nothing (I found the effect later, after realizing there were problems with mixing and relaxation times). One day, while rf irradiation in zero field near the quadrupole frequency of ^{35}Cl had been on, André absent-mindedly put the magnetic field on and we saw an ENORMOUS proton signal on the run. We started working feverishly to determine the qualitative features of the effect, which were surprising. Proton polarization was positive or negative when the irradiation in zero field was below or above chlorine quadrupole resonance. Solomon: 'It's ridiculous! When you irradiate in zero field, how do the protons know in which directions to polarize when the field is put on?' These were exciting days where, in the rush of new exploratory experiments, we had visits from Abragam and Solomon several times a day, with frantic brain-storming sessions. It was Solomon who first got the right interpretation: it was a matter of Redfield-like spin temperature. What determined the polarization direction was the sign of the dipolar spin temperature in zero field. He extended the idea to dynamic polarization through paramagnetic impurities, and introduced the notion that the nuclear Zeeman reservoir can get mixed with the electronic spin–spin reservoir, a process distinct from the solid effect proper, which turned out to be correct and of great importance for the production of polarized targets. Alfred Redfield, who came a few months later for a one-year visit, tried to fit this with his baby, the rotating frame. It was not obvious for a quadrupole splitting and he tried to imagine a frame that would be simultaneously rotating in two opposite directions. The final answer was formulated by André and myself: forget about geometrical pictures and use an interaction representation. During the course of discussions, Alfred made several remarks which we did not understand. There are some points associated with our work we understood only about two years later, and then we realized that Alfred had understood them from the start from these remarks that had flown over our heads.

Alfred Redfield is somebody quite remarkable. In one work, described in his article of 1955, he had invented spin temperature in the rotating frame, understood sudden and fast passage, mastered the concept of local field, and derived the complete theory of relaxation in the rotating frame. In my contacts with him I have been struck by the rapidity and profoundness of his understanding of physical problems. These qualities are combined with a rare gift for obscurity. It took me a long time to understand why, until I heard him give a lecture at a summer school on his NMR work on superconductors. This talk was luminously clear! It is because he knew his NMR audience was not fluent in superconductivity. The root of his being obscure is genuine modesty: when talking NMR to a NMR man, it would be insulting to describe in too much detail what is obvious (what he thinks is obvious).

I worked for several more years alone on this subject. I had the surprise to see our first big article *Thermal mixing in low*

fields cited in a bibliographical compilation on geology (under the title *Thermal mining in low fields*). These were years of frantic experimental explosions by a small international group of spin temperature addicts to test all consequences of the spin temperature concept, both in the laboratory and in the rotating frame, and to invent new methods for the benefit of NMR in solids. To cite but a few of them: besides the gods Abragam and Redfield, there were Charles Slichter with Judy Franz, Hebel, Holton, Lurie, Schumacher, and Ailion, Erwin Hahn with Anderson, Hartmann, Strombotne, Irving Lowe, and Walter Goldburg plus S. Clough later on, Bloembergen and Sorokin, R. Walstedt, Jean Jeener with Broekaert, Eisendraht, and Van Steenwinkel, the Soviet schools with Provotorov (about whom I will have more to say), Atsarkin, Mefed, and Rodak in Moscow, and Khutsishvili and Buishvili in Tbilissi, and, in France, Solomon and Ezratty, and Jerome in our lab, Sapoval and Lepine, Minier and Berthier, plus a number of others. Among the subjects investigated were the sudden and adiabatic variations of the Hamiltonian, the effect of pulses, the role of spin−spin interactions in cross polarization, nuclear relaxation in low field, actual or effective, all kinds of thermal mixings, cases when there are several constants of the motion, the validity of spin temperature for dilute systems of electronic spins, etc ... . Several ideas were in the air. Once I told Abragam about an idea for detecting slow motion. He replied that Redfield had had the very same idea one year earlier, but finally the fastest on the draw were Ailion and Slichter. Likewise, Jeener and I simultaneously made similar studies on the adiabatic modulation of the local field in the rotating frame. There are other examples.

In the spring of 1962, Ionel Solomon talked at our weekly seminar about an article by Goldburg where he had found faster rf saturation off-resonance than on-resonance, in accordance with a theory of an unknown Soviet physicist named Boris Provotorov. Abragam took over to describe this theory from a preprint in Russian that this Provotorov had handed to him. It dealt with the dynamics of the establishment of a spin temperature in the rotating frame when the rf field was much smaller than the local field. The theory turned out to be fundamental for understanding CW NMR in solids. It was extended by Provotorov to cross polarization where it proved equally important. I had taken careful notes (at the date of May 28, 1962) and for a while I became the Provotorov expert in the lab, whom everybody consulted whatever his or her problem. One of them was Jacqueline Poitrenaud, who wanted to study the correlations of conduction electrons at nearby nuclear sites in metals from the ratio of Zeeman to dipolar relaxation times. The theory was from Redfield and the experimental method from Solomon and Ezratty, with lock-in signals. Her problem was that the results made absolutely no sense. I succeeded in finding out why by using Provotorov's theory to describe the saturation of lock-in signals in solids. Under her conditions (modulation period shorter than relaxation times), what she saw was not what she expected. A test of the theory was that the lock-in signals had to saturate more slowly in the absorption mode than in the dispersion mode, which she verified. I published the theory together with a simplified formulation of Provotorov's theory in French, and outside France it was virtually only noticed by the Russians. A number of other applications of the Provotorov theory of direct practical usefulness for NMR work were discovered later.

A few years later, Abragam thought of writing a new edition of his book on nuclear magnetism, not alone but in collaboration with three people in the lab: Jacques Winter, André Landesman, and myself. I would be in charge of the chapter on spin temperature. This project did not come off, and my chapter ended up as a book. At that time the cognoscenti of spin temperature were considered to be a small, exclusive (and snobbish?) club whose esoteric language was opaque to outsiders. Having experienced the usefulness of this theory, I tried very hard to be as clear as possible so as to turn the small snobbish group into a large snobbish group. It was then part of the folklore of the lab that to be exposed to explanations of mine turned anybody dizzy, and Abragam feared that I would lack clarity. He took the pain of reading each chapter several times (as many times as I rewrote them after the grinding mill of his criticisms). Really he should be considered a co-author, and in retrospect I think he was right: without him it might have been terribly obscure. I tried to follow the policy of Abragam in his book on nuclear magnetism: cite as fairly as possible the authors of what I was talking about, but avoid giving people's names to phenomena or equations. This could be considered questionable as regards Alfred Redfield, but I may possibly have been right after all. He established so many basic equations, each of which is referred to as 'the Redfield equation' in the literature, that if I had done the same in the restricted space of one or two chapters, I fear complete confusion would have ensued. I made just one exception to this rule, for Provotorov, for the following reason. At the time of sending the manuscript to the editor, I met at a congress Mrs Rodak, who told me that my article in *Journal de Physique* had been of definite help to Provotorov in dressing his theory with western respectability, at a time when some of his colleagues claimed that this theory was nonsense and he himself was insane. I decided that giving some advertisement to Provotorov in my book could do no harm.

At about the time of publication of the book, Rhim, Pines, and Waugh at MIT made their 'magic sandwich' experiment showing that after all spin temperature might not be as leakproof as then believed. John Waugh told me later he hoped I would receive the preprint while celebrating the publication of my book with a glass of champagne in hand. Firstly there was no champagne celebration, and secondly what I received was an empty envelope. John swore it was his secretary who forgot to put a preprint in it, but I keep being convinced that something Freudian must have been involved. This magic sandwich business proved important. Firstly it compelled us to re-examine critically the concept of temperature, and it proved that the concept of macroscopic irreversibility simply reflects the limitation of our means of handling of large systems, in contrast to NMR which is richer than other disciplines in that respect. Secondly, in the hands of Alex Pines and his students, it opened the way to the study of multiple quantum coherence in solids, so fundamentally and practically useful at present in NMR.

It was in 1965, while I was on a one-year visit to Dick Norberg's lab in Saint Louis, that Abragam asked me that on my return I direct an investigation of nuclear magnetic ordering (NMO) following the principle he had published: polarize dynamically the nuclei and then demagnetize them either in the lab or in the rotating frame. I started at the end of 1965 with Maurice Chapellier and a Ph.D. student, Vu Hoang Chau. Nuclear magnetic ordering had long been a dream

and a challenge, because of the extremely low temperature it required, in the microkelvin range. Thanks to Abragam's scheme, it would only be a spin temperature. We chose to work in the rotating frame where the form of the secular dipolar interactions could be modified by rotating the sample in the field, and where we could use NMR for observation. The field was entirely virgin. On the one hand we had to choose the proper system and put into it the proper paramagnetic centers so as to obtain large dynamic polarization, and on the other hand we had to learn the approximate theories of magnetic ordering so as to predict which structures would be produced with which properties. Getting help from professional theorists of magnetism proved hopeless: they lost balance as soon as did the rotating frame. The third hand was devoted to imagining which methods could be used to measure these properties. Necessity compelled us to exhibit still more hands. For the practical purpose of measuring the rf amplitude, calibrating the nuclear polarization, calibrating the receiver gain, understanding and minimizing losses due to the adiabatic demagnetization or CW signal observation, we had to rederive the whole of NMR theory so as to devise new methods and then implement them experimentally. Our previous NMR baggage which was restricted to the high-temperature approximation was of limited help. There was also the need to master cryogenics then in relative infancy, practice EPR at then indecent wavelengths, i.e. 4 mm and then 2 mm, and understand in depth (in order to tame them) dynamic polarization, electronic relaxation, phonon bottleneck, nuclear Zeeman, and dipolar relaxation at low temperature (still not understood).

We stayed in this field for over two decades, with a number of collaborators: J. F. Jacquinot, V. Bouffard, S. Cox, Y. Roinel, W.Th. Wenckebach, C. Urbina, S. Leibler, C. Fermon, J. Gregg, F. Bonamour, plus P. Roubeau for the cryogenics and P. Meriel, G. L. Bacchella, and M. Pinot for the neutron diffraction. We performed clean and elegant studies on ferro- and antiferromagnetism and rotating helimagnetism on a number of compounds: CaF_2, LiF, LiH, $TmPO_4$, $KMgF_3$. We used both NMR and neutron diffraction (it was Abragam who found this was possible, against the views of all neutron specialists). I think we did a good job, but it was very difficult and the yield of results per unit time very low. Few have followed us, except Tom Wenckebach after a one-year visit to our lab. Other studies of NMO many years later were of a different nature and, although very interesting, were much more remotely connected with the NMR brand of spin temperature.

Other, more human (i.e. high-temperature) developments of spin temperature were scant during that period. They consisted mostly of checking its validity for effective Hamiltonians in multipulse sequences. Such studies were undertaken by Pines and Waugh in 1974, Rhim, Burum, and Elleman in 1976, and Quiroga, Virlet, and myself in 1982.

NMR in solids has evolved towards the generalized use of pulses, sample spinning, and Fourier transforms, with strong emphasis on physicochemical applications, and spin temperature theory has become of much more limited use than we had anticipated.

What remains is that spin temperature theory stands as a beautiful body of knowledge which gave rise to an astonishing number of diverse experiments of great elegance and of fundamental character in the general frame of thermodynamics. What is particularly remarkable is its twofold character. On the one hand, the concept of spin temperature proves valid down to temperatures where a symmetry breaking takes place in the form of magnetic ordering, and on the other hand it can also be proved that spin systems are definitely not stochastic, through the selective refocusing of the off-diagonal elements of the density matrix by clever spin manipulations.

The historical development of spin temperature has followed the typical pattern of all scientific endeavors. Its evolution did not follow logic, complex things appeared before simple ones, and simple ones looked complicated for not being properly understood. Progress does not proceed along the majestic path of induction–deduction imagined by Descartes, but mostly through the laborious elimination of misconceptions and prejudices. The emergence of a new idea, however simple, is definitely unnatural and painful. The awareness that the theory had become mature came to me when, after reading my book on spin temperature, a Ph.D. student of mine said: 'Well, it's all evident!'

It seems appropriate, as a conclusion, to stress how incredibly lucky we have been that spin temperature theory has developed at all. There are at least two circumstances that could have caused its abortion. It was the observation that dispersion did not saturate, in contradistinction to absorption, which led Redfield to the conception of a spin temperature in the rotating frame. He worked with copper and aluminum and looked at the lock-in signals. It so happens that in these metals the relaxation times are not long, compared with the periods of the field modulations he used, and what he saw was close to the derivative of the CW steady-state signals. Had he worked with an insulator, or used a faster modulation, he would have observed the opposite: a normal saturation of the dispersion signal (at resonance) and a much slower saturation of the absorption signal. Who knows where this would have led him? The second circumstance was the discovery of the 'magic sandwich'. It seemed to disprove spin temperature at a time when innumerable experiments had already quantitatively verified its predictions. Thus, there could be no question of rejecting it flatly, but we were led to scrutinize anew the foundations of the temperature concept. The mathematical description of this experiment is extremely simple and it could have been done much earlier by anyone of the patricians of NMR. The result would probably have been that nobody would have accepted the mere idea of a spin temperature. The great merit of Rhim, Pines, and Waugh is not only to have discovered the magic sandwich, but not to have discovered it too early. To borrow an expression from Arthur Koestler, I take these as further proof that scientists are definitely sleepwalkers.

Biographical Sketch

Maurice Goldman. *b* 1933. Diplôme d'Ingénieur Chimiste ESPCI, 1955, Doctorat d'Etat, 1967, University of Paris. Physicist at Commissariat à l'Energie Atomique (CEA), 1955–69. Vice-Director at the College de France, 1969–83. Physicist at CEA, 1984–89. Research Director at CEA, 1989–93. Scientific adviser at CEA, 1993–present. Vice-President of ISMAR, 1992–present. Approx. 100 publications and three books. Research specialties: spin temperature and thermodynamics, nuclear magnetic ordering, relaxation in liquids and solids, quantum theory of high-resolution NMR.

Gorenstein, David G.: Developments in ^{31}P NMR

David G. Gorenstein

University of Texas Medical Branch, Galveston, TX, USA

Unlike almost all other fields of science, the theory and application of nuclear magnetic resonance has been on an exponentially rising curve of interest for the past 50 years. ^{31}P NMR has shared similar success from the first spectra in 1951 by Dickinson[1] and Gutowsky and co-workers.[2] Normally in science we expect an exciting new field to draw initially many new participants to it (the 'bandwagon' phenomenon) with a resulting explosion of new discoveries. However, once many of the major questions are answered, ultimately as the field passes from favor (fewer grant funds!), many participants migrate to the next exciting development in science. The vitality of the field is often characterized by a bell-shaped time curve.

The lifetime of a field in science is often disturbingly short, 15 to 25 years. However, this has not been the case with nuclear magnetic resonance, where we find that even after these past five decades we still are on the rising exponential portion of the curve. The reason for the difference of course is that there have been numerous ways of inventing new and exciting applications and understanding of magnetic resonance. As in almost all areas of nuclear magnetic resonance, including ^{31}P NMR, we have seen wave after wave of new scientific disciplines utilizing the rich information provided; with physicists, chemists, biochemists, and medical specialists entering the field. I don't believe that any of the early visionaries of magnetic resonance would have thought that ^{31}P NMR, with such relatively low sensitivity, could ever be used for understanding the detailed structure and dynamics of macromolecules such as DNA. ^{31}P magnetic resonance imaging and spectroscopy now constitute the latest phase of this explosion. Each of these waves has brought ever more diverse and creative scientists into the field.

The development of commercial multinuclear MR spectrometers by 1955, primarily through the efforts of Varian Associates, greatly expanded the application of ^{31}P NMR as an important analytical tool for structure elucidation. By 1956, chemical shifts on several hundred phosphorus compounds had been reported in the literature; the concept of spin–spin coupling which evolved from the pioneering studies of Gutowsky and co-workers on such molecules as PF_3 was also elucidated. Efforts to correlate structure with the theory of chemical shift and coupling constants also evolved from some of these early ^{31}P studies (see leading references in Gorenstein, 1984).[3]

Early spectrometers generally required neat samples in large nonrotating tubes (8–12 mm o.d.). In the middle 1960s more sensitive, higher field electromagnets, and signal averaging led to further rapid growth in the number of reported ^{31}P spectra and the publication of the first monograph devoted to this field.[4] With the introduction by 1970 of Fourier transform (FT) and high-field superconducting magnet NMR spectrometers, ^{31}P NMR spectroscopy expanded from the study of small organic and inorganic compounds to biological phosphorus compounds. Mildred Cohn's original continuous wave ^{31}P NMR spectrum of adenosine triphosphate in 1958 set the stage for the explosion of later biological applications.[5]

In my own laboratory, we began some of the first ^{31}P NMR studies of protein complexes. Our early studies on the binding of mononucleotides to bovine pancreatic ribonuclease A[6] were attempted in the continuous wave mode on a Bruker HFX-90 spectrometer (90 MHz ^{1}H). The ^{31}P signal at mM level concentrations of the mononucleotides in the presence of enzyme were often discouragingly buried within the baseline noise. Even CW CAT averaging on a specially constructed data acquisition system was highly irreproducible. With our acquisition around 1970 of a Nicolet 1080 FT data system which we added to our Bruker HFX-90/B-KR 322 S pulsed spectrometer, we could finally reliably see the enzyme complex signal. Early on we realized that instrumentation alone was not our only experimental problem. Variable amounts of trace paramagnetic metal ions often broadened and shifted the signals. Treatment of the samples with a new multivalent metal ion chelating agent (Chelex-100) saved the day. Today of course these are very simple experiments.

Few would have thought that NMR of whole cells could provide any useful high-resolution spectra until the groundbreaking ^{31}P studies of red blood cells by Moon and Richards.[7] It was soon recognized that these spectra provided information on whole cell metabolism and allowed characterization of heart disease and cancerous tumors.[8] These ^{31}P studies on isolated tissues and perfused whole organs were followed by localized magnetic resonance spectroscopy and even limited ^{31}P imaging on whole bodies.

With the tremendous increase in sensitivity in modern FT NMR spectrometers, biological and medical applications of ^{31}P NMR spectroscopy grew dramatically during the 1970s, 1980s and continue into the 1990s. A number of monographs[3, 9–11] entirely devoted to ^{31}P NMR, covering theory and applications to organophosphorus, phosphorus–metal complexes, and biological and medical aspects of the field have been published.

OTHER IMPORTANT ^{31}P MILESTONES

One of the first demonstrations of an ^{18}O isotope shift on a directly bonded nucleus was demonstrated for ^{31}P NMR.[12, 13] This ^{18}O isotope shift provided a convenient monitor of ^{18}O isotope incorporation into phosphorus compounds undergoing hydrolysis, since integration of the ^{18}O signals relative to the ^{16}O–^{31}P signal yields directly the percentage ^{18}O incorporation. Separate signals are also observed for each of the multiple ^{18}O-labeled species. Cohn and Hu[14] also showed that a rough linear correlation exists between the magnitude of the ^{18}O isotope ^{31}P shift and the bond order between phosphorus and the isotopically-substituted atom. This dependence on bond order was used in my and John Gerlt's laboratories[15, 16] to establish the stereochemistry of the ^{18}O label in a prochiral phosphate diester (chiral by virtue of oxygen isotopic differences). This important methodology provided information on the stereochemistry of hydrolysis of a phosphate ester. Indeed, pro-prochiral phosphate monoesters were later synthesized in chiral form by substitution of

the three nonester oxygens by the three stable isotopes of oxygen.[17] This made it feasible to study the stereochemistry of the enzymatic and nonenzymatic hydrolysis of monophosphate esters and anhydrides. In this case use was also made of the quadrupolar broadening of the ^{31}P signal by a directly bonded ^{17}O atom.[18]

^{31}P NMR has also developed as a powerful probe of the structure and dynamics of nucleic acids in solution. Synthetic methods have now been developed where defined deoxy- (and more recently ribo- and backbone modified) oligonucleotides can be routinely produced in multimilligram quantities. The concomitant development of sequence-specific 2D ^{1}H/^{1}H and 2D and 3D ^{1}H/^{31}P NMR assignment methodologies has made the assignment of the ^{31}P NMR spectrum of modest size oligonucleotides (8–14 base pairs) possible (see D. G. Gorenstein, ***Nucleic Acids: Phosphorus-31 NMR***).

One of the main reasons for assigning ^{31}P resonances of oligonucleotides is to obtain information on the conformation of the phosphodiester backbone.[3,19] The internucleotide linkage is defined by six torsional angles from one phosphate atom to the next along the DNA backbone. Theoretical studies first showed that the conformation of two of the six torsional angles (α: O3′–P–O5′–C5′ and ζ: C3′–O3′–P–O5′) appear to be most important in determining ^{31}P chemical shifts. Molecular dynamics calculations, X-ray diffraction, and 2D NMR spectroscopy have also shown that the phosphate ester conformation is the most variable part of nucleic acid structure.[19] ^{31}P chemical shifts and ^{1}H–^{31}P coupling constants have been able to provide valuable information on the conformation and dynamics of the phosphodiester backbone in nucleic acids and protein–nucleic acid complexes.

CONCLUSIONS

^{31}P NMR has become an indispensable tool in studying the chemistry and biochemistry of phosphorus compounds. ^{31}P magnetic resonance spectroscopy and imaging hold great noninvasive diagnostic promise for the future. Newer NMR instrumentation and experiments have enormously enhanced the application of ^{31}P NMR in biology and medicine. It is quite likely that further developments will be seen in the next 50 years.

REFERENCES

1. W. C. Dickenson, *Phys. Rev.*, 1951, **81**, 717.
2. H. S. Gutowsky and D. W. McCall, *Phys. Rev.*, 1951, **82**, 748.
3. D. G. Gorenstein, in *Phosphorus-31 NMR: Principles and Applications*, ed. D. G. Gorenstein, Academic Press, Orlando, FL, 1984, pp. 1–604.
4. M. M. Crutchfield, C. H. Dungan, L. H. Letcher, V. Mark, J. R. VanWazer, M. Grayson, and E. F. Griffin, in *Topics in Phosphorus Chemistry*, Wiley-Interscience, New York, 1967, pp. 1–487.
5. M. Cohn and T. R. Hughes, Jr., *J. Biol. Chem.*, 1960, **235**, 3250.
6. D. G. Gorenstein and A. M. Wyrwicz, *Biochem. Biophys. Res. Commun.*, 1973, **54**, 976.
7. R. B. Moon and J. H. Richards, *J. Biol. Chem.*, 1973, **248**, 7276.
8. B. Chance and G. K. Radda, in *NMR in Biochemistry: a Symposium Honoring Mildred Cohn*, eds. S. J. Opella and P. Lu, Marcel Dekker, New York, 1994, pp. 269–281.
9. L. D. Quin and J. G. Verkade, in *Phosphorous-31 NMR Spectroscopy in Stereochemical Analysis*, VCH Publishers, Deerfield Beach, FL, 1987, pp. 1–717.
10. C. T. Burt, in *Phosphorus NMR in Biology*, CRC Press, Boca Raton, FL, 1987.
11. L. D. Quin and J. G. Verkade, in *Phosphorus-31 NMR Spectral Properties in Compound Characterization and Structural Analysis*, VCH Publishers, New York, 1994,
12. M. Cohn and A. Hu, *Proc. Natl. Acad. Sci. USA*, 1978, **75**, 200.
13. G. Lowe and B. S. Sproat, *J. Chem. Soc., Chem. Commun.*, **1978**, 565.
14. M. Cohn and A. Hu, *J. Am. Chem. Soc.*, 1980, **102**, 913.
15. D. G. Gorenstein and R. Rowell, *J. Am. Chem. Soc.*, 1980, **102**, 6165.
16. J. A. Gerlt and J. A. Coderre, *J. Am. Chem. Soc.*, 1980, **102**, 4531.
17. S. L. Buchwald and J. R. Knowles, *J. Am. Chem. Soc.*, 1980, **102**, 6601.
18. M. D. Tsai, in *Methods in Enzymology*, ed. D. L. Purich, 87th edn., Academic Press, New York, 1982, pp. 235–279.
19. F. J. M. van de Ven and C. W. Hilbers, *Eur. J. Biochem.*, 1988, **178**, 1.

Biographical Sketch

David G. Gorenstein. *b* 1945. B.S., 1966, Ph.D., 1969, Chemistry, Harvard University, USA (with Frank Westheimer). Assistant, associate, and full professor, University of Illinois at Chicago, USA. Professor of Chemistry and Director of Purdue Magnetic Resonance Laboratory, Purdue University, USA (1985–1994). Currently Professor of Human Biological Chemistry and Genetics, and Director of NMR Center, University of Texas Medical Branch, USA. Senior Fulbright Fellow, Oxford University (1977–8), Oxford, UK and Guggenheim Fellow at University of California at San Francisco, USA (1986). Approx. 160 publication. Current research specialty: NMR, structure and dynamics of biological macromolecules.

Govil, Girjesh: Nuclear Magnetic Resonance in India: A Historical Sketch

Girjesh Govil

Tata Institute of Fundamental Research, Bombay, India

Magnetic resonance activities were initiated in a big way in India in the early 1950s by Prof. S. S. Dharmatti, known for his work on the ^{1}H NMR of ethyl alcohol.[1] He started an active school at the Tata Institute of Fundamental Research (TIFR), Bombay, which was devoted to areas of solid state NMR, high-resolution NMR spectroscopy, and ESR. Some of the early members of Prof. Dharmatti's team were Profs. C. R. Kanekar, Balu Venkataraman, and R. Vijayaraghavan. Almost simultaneously, Saha and Das started an active group at the Saha Institute of Nuclear Physics, Calcutta. Their book 'Theory and Applications of Nuclear Induction' was one of the early texts which covered all facets of NMR spectroscopy.[2] In the early 1950s, Suryan at the Indian Institute of Science (IISc) pioneered novel experiments on flow studies and sensitivity in NMR experiments.[3,4] In the initial years, there was an emphasis on the building of indigenous spectrometers and most of the studies were carried out with homebuilt spectrometers. High-resolution experiments were initiated with one of the earliest models built by Varian, a 30 MHz NMR spectrometer.

A number of young people in the late 1950s and early 1960s came back after postgraduate training in western countries and set up NMR centers in India. Special mention should be made of Prof. P. T. Narasimhan who was also responsible for laying the foundations of the Association of Magnetic Resonance Spectroscopists of India. In 1962, the council of the Tata Institute of Fundamental Research decided to appoint Prof. Felix Bloch as an honorary Fellow of the Institute, an honor so far given to only 33 very eminent persons who have helped the growth of this famous institution in India. Prof. Bloch visited India twice and delivered lectures at the TIFR. During this period, NMR became an integral part of chemistry laboratories and chemical industries in India as elsewhere in the world.

Today the culture of NMR has spread all over the country and there are a number of active centers working on various aspects of NMR. However, due to the high cost of present day spectrometers, our efforts may be relatively modest by US standards. Most of the NMR machines are supported by the Government as national or regional facilities and are meant for use by a broad range of academic researchers and industries. There are two major centers which have remained in the forefront of NMR research ever since activity started in India. One is at the TIFR, whose major contributions are in the field of biomolecular NMR, cellular and tissue studies, and in solid state physics. The other is at the Indian Institute of Science, which is known for the development of new pulse techniques and the use of liquid crystals for the determination of molecular structure. In addition, there are several sophisticated NMR facilities spread over all corners of India, catering to the needs of general NMR users. Recently, good facilities for biomedical research have been set up at the All India Institute of Medical Sciences, New Delhi. NMR has also been applied to agricultural research in India.

India has hosted two major world conferences in the field of NMR. The fifth ISMAR conference was held in Bombay in January 1974. It was during this conference that Prof. Lauterbur announced his results on NMR zeugmatography. Interestingly, this contribution was originally meant to be a short presentation. However, realizing the importance of this area, the organizers decided to give it the status of a plenary presentation. The XIth International Conference on Magnetic Resonance in Biological Systems was held in Goa in 1984. The use of NMR for probing the stereodynamics of biological molecules came into focus during this conference. In addition, a number of schools have been conducted. Prof. Richard Ernst has been the principal speaker at two of these schools.

The international community is generally familiar with the work of Indian scientists. Details of some of the books and monographs published by Indian authors are given in References 5–9.[5–9]

REFERENCES

1. J. T. Arnold S. S. Dharmatti, and M. E. Packard, *J. Chem. Phys.*, 1951, **19**, 507.
2. A. K. Saha and T. P. Das, *Theory and Applications of Nuclear Induction*, Saha Institute of Nuclear Physics, Calcutta, India, 1957.
3. G. Suryan, *Phys. Rev*., 1950, **80**, 119.
4. G. Suryan, *Proc. Indian Acad. Sci*., 1951, **A33**, 107.
5. N. Chandrakumar and S. Subramanian, *Modern Techniques in High-Resolution FT-NMR*, Springer-Verlag, 1987.
6. C. L. Khetrapal and A. C. Kunwar, *Adv. Magn. Reson.*, 1977, **9**, 301.
7. G. Govil and R. V. Hosur, *Conformation of Biological Molecules: New Results from NMR*, Springer-Verlag, 1982.
8. G. Govil, C. L. Khetrapal, and A. Saran (eds.), *Magnetic Resonance in Biology and Medicine*, Tata McGraw-Hill, 1985.
9. C. L. Khetrapal and G. Govil (eds.), *Magnetic Resonance: Current Trends*, Springer-Verlag/Narosa, 1991.

Biographical Sketch

Girjesh Govil. *b* 1940. Ph.D., 1963, Tata Institute of Fundamental Research (TIFR), Bombay, where he was introduced to NMR by S. S. Dharmatti. Post-doctoral work at National Physical Laboratory, Teddington, UK (with Prof. D. H. Whiffen) and National Research Council of Canada, Ottawa (with Dr. H. J. Bernstein). At TIFR 1959–present, currently Senior Professor and Dean; Chairman, ICMRBS, 1993–94; Secretary, Indian National Science Academy (1988–92) and member, IUPAB Council (1990–date). Approx. 170 publications and three books. Research specialties: magnetic resonance in biomolecules and intact cells, and biomolecular electronics.

Grant, David M.: Carbon-13 Magnetic Resonance—An Exquisite NMR Garden of Surprises

David M. Grant
University of Utah, Salt Lake City, UT, USA

Carbon, carbon quite contrary, how does your garden grow?
With chemical shifts, coupling constants, and spin relaxation
standing in a row.

INTRODUCTION TO NMR AT THE UNIVERSITY OF ILLINOIS

In 1957 I finished a thesis with Randall Hamm on dimerization kinetics in dioldioxalatochromium(III) complexes and, shortly thereafter, accepted a DuPont Instructorship in Chemistry at the University of Illinois. The freedom to pursue any area of interest led me into NMR which, at the time, was advancing rapidly into the world of chemistry. Illinois was already a premier NMR chemistry center with Herb Gutowsky at the lead and Martin Karplus providing many of the new theoretical foundations in this exciting field. Also contributing extraordinary NMR luster to Illinois was Charles Slichter and his group in physics.

As a graduate student I had been fascinated with quantum chemistry, taught by Henry Eyring, but the simplicity and elegance of spin wavefunctions seemed almost preternatural in their ability to account for every NMR spectral detail and intricacy. It was clear that quantum theory and NMR were harmonious disciplines. Herb and Martin graciously allowed me full access to their research groups, and we soon were involved in both an experimental and a quantum chemical study of geminal couplings in CH_2 groups.[1] Martin also suggested a theoretical analysis of scalar couplings between selected magnetic nuclei and their directly bonded protons.[2]

Geminal couplings, to be observed, require magnetic nonequivalent hydrogens achievable either with deuterium substitution of one methylene hydrogen or symmetry breaking features such as found in many A_2B_2 coupled systems. The intricacies and deceptively simple spectra that can result in second-order A_2B_2 systems were incompletely appreciated in 1958 even though the A_2X_2 spin system had been discussed in 1955 by McConnell. My first graduate student Charles Hirst finished the A_2B_2 analysis initiated at Illinois.[3] Sufficient experimental examples soon existed to confirm our theoretical results on the HCH angular dependence of geminal coupling constants.[1] A gifted associate, Michael Barfield, later described the π-electron hyperconjugative enhancement of geminal couplings along with other structurally dependent features affecting scalar couplings.[4]

The directly bonded couplings of protons with boron and nitrogen by Ogg[5] and the ^{13}CH couplings in methane and ethylene, provided respectively by Lauterbur and by Muller, were theoretically analyzed. Bond charge distributions and electron hybridization explained the variations in these directly bonded couplings.[2] The theoretical work on ^{13}CH couplings initiated for me a lifetime of fascination with the ^{13}C magnetic nuclide and provided the motivation to pursue the resonance of this important but low abundant magnetic nucleus.

The ^{13}C seed had been planted in promising though rocky soil!

CARBON-13 RESONANCE AT THE UNIVERSITY OF UTAH

My daughter, Heidi, born in Illinois, was hospitalized during much of her early life with a serious asthmatic condition due to the midwest climate. This prompted our return west in the fall of 1958 when I was invited to establish an NMR facility at Utah. With our new Varian DP-60 spectrometer, we also obtained Varian's first proton decoupler and dual-frequency probe for observing ^{13}C. The ^{13}C adiabatic rapid passage work of Lauterbur[6] and an unpublished 1962 continuous wave ^{13}C spectrum by Shoolery provided assurance that naturally occurring ^{13}C resonances could be observed, thereby encouraging Ed Paul with his inordinate persistency, to struggle with the experimental difficulties of this low abundant ^{13}C magnetic spin. Early progress was gradual, but as circumstance would have it the proton decoupler became the crucial component in our first ^{13}C observations in 1960. Significantly, the ^{13}C singlets were enhanced by the collapse of proton splittings, but to our delight an additional increase in intensity was realized also from a proton induced NOE.[7]

A rather robust ^{13}C seed had sprouted and was growing steadily!

With rudimentary ^{13}C spectroscopic tools now in place, a group of very talented graduate students and postdoctoral associates (Terry Alger, Terry Brown, Vern Cheney, Don Dalling, Alan Jones, Bill Litchman, Ronald Pugmire, Werner Woolfenden) worked diligently to establish an early ^{13}C NMR presence at Utah. In these early days the ^{13}C principal investigators (Paul Lauterbur, Endel Lippma, Gary Maciel, Jack Roberts, Jake Stothers, and others) were comparatively few, but they were an inordinately able group and the competition was formidable. These workers are legends in the field and their outstanding accomplishments, upon which our own progress also depended, were crucial to the early development of ^{13}C NMR. Among our promising early results was the striking dependence of ^{13}C shifts upon molecular conformations[8,9] and upon aromatic properties in benzenoid and nitrogen heterocyclic systems. Many other important structural correlations of ^{13}C chemical shifts, too numerous for discussion in this brief article, also surfaced during the 1960s.

Carbon-13 seedlings, with both fragrance and nectar, began beautifying the chemical world!

NEW CONSTANT FIELD ^{13}C INSTRUMENTS

Jack Roberts, elsewhere in this volume (***Roberts, John D., A Personal NMR Odyssey***), has described his purchase of a digital frequency sweep spectrometer; we followed promptly in 1967 with an analog frequency sweep instrument (Varian

AFS-60) which, with time-averaging capabilities, significantly increased the signal-to-noise ratio due to repetitive ^{13}C spectral acquisitions. As our first constant field instrument, the AFS-60 also greatly simplified the simultaneous double irradiation of both ^{13}C and ^{1}H nuclei, a condition essential for multiplet collapse and for manifestation of the beneficial NOE. With the AFS-60 Karl Kuhlmann was able to measure quantitatively the proton-induced NOE in ^{13}C labeled formic acid,[10] see Figure 1, in which the maximum threefold ^{13}C NOE was first confirmed. Favorable NOE enhancements had been anticipated over a decade earlier in the seminal work of Solomon.[11] Experimental benefits, due to multiplet collapse and NOE, greatly improved both the quantitative measurements and spectral throughput for the less receptive ^{13}C nucleus. We obtained an XL-100 FT spectrometer shortly after its announcement in 1970. This FT instrument, with its improvements in ease of operation and in ^{13}C signal-to-noise ratio, was developed by prominent workers (i.e. Ray Freeman, Howard Hill, Vern Burger among others) at Varian. Fourier transform instruments of this type released the ^{13}C genie from its lamp, and presently routine ^{13}C spectra became available to practicing chemists.

Explosively, the ^{13}C blooms were spreading across the NMR chemical landscape.

Our early research had been governed by the principle, *survey large fields, but cultivate small plots*, and with the significant improvements in ^{13}C spectrometers we focused on some of the exciting smaller ^{13}C *plots*. Extending Kuhlmann's results, Robin Harris[12] published with us a paper on the NOE and its relation to the dipolar spin relaxation.[13] The prognosis for the future of ^{13}C transient properties was encouraging and during the ensuing two decades a group of outstanding co-workers (Terry Alger, Richard Bertrand, Ed Black, Kenner Christensen, Scott Collins, Don Dalling, Luis Diaz, Paul Fagerness, David Hamill, Ken Ladner, Jim Lyerla, Fred Morin, Zu Wen Qiu, Mark Solum, Michele Williams) concentrated on ^{13}C relaxation studies. Various ^{13}C relaxation mechanisms (i.e. ^{13}CH dipole–dipole, scalar coupling, spin rotation, and chemical shift anisotropy, etc.) were delineated and their chemical applications exploited.[14] During my 1972–73 sabbatical leave at the California Institute of Technology, the influence of organic structure and motional dynamics on both ^{13}C and ^{15}N relaxation rates were examined with members of Jack Roberts's excellent research group (Stefan Berger, Frtiz Kreissl, Ian Armitage, Donald Giannini, Harry Pearson). Jens Led explained the paramagnetic relaxation of ^{13}C in Mn and Zn amino acid complexes of histidine, work that estimated the distance between unpaired metal electrons and the relaxing carbon nuclei.[15] A consistent dynamical picture began to emerge linking ^{13}C relaxation and molecular motions. For example, the common ^{13}CH dipole–dipole mechanism describes a number of motional features: anisotropic rotation of rigid molecules, internal methyl rotation, methylene pseudorotation, motion of molecules in cavities such as molecular sieves and cyclodextrins, etc.

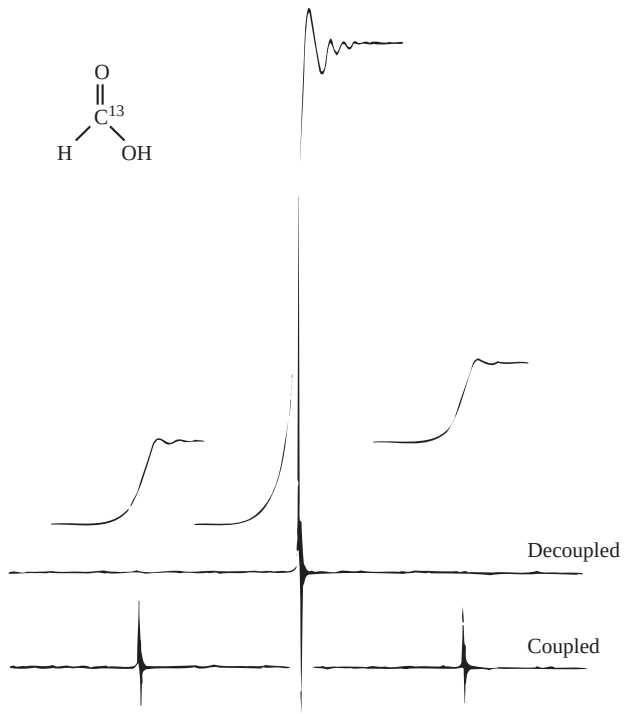

Figure 1 The coupled and decoupled ^{13}C spectra of 23% enriched formic acid exhibit a 2.98 nuclear Overhauser enhancement in peak heights and integrated intensities. The integrals, obtained at slower sweep rates and at expanded sweep widths, were used to measure this factor quantitatively. (Reproduced by permission of The American Chemical Society from Ref. 10)

COUPLED SPIN OR MULTIPLET RELAXATION METHODS

Early in the 1970s it became clear that the proton decoupler used to obtain ^{13}C singlets was obscuring valuable relaxation information contained in proton-induced ^{13}C multiplets. Charles Mayne, a very careful spectroscopist and able mathematical analyst, measured the multiplet relaxation responses of coupled spins in CH_2I_2 with a variety of hard and soft preparation pulses.[16] The multiple exponential character of coupled relaxation, from Mayne's initial work, is obvious in Figure 2. Even the simple $^{13}CH_2$ moiety requires up to 12 different interlevel transition probabilities to characterize the relaxation processes contributing to multiple exponential responses. This information-rich approach yields spectral power densities for a variety of second-rank (i.e. dipolar, chemical shift anisotropy, etc.) and first-rank (i.e. spin rotation, free electrons, etc.) mechanisms along with cross-correlated relaxation terms between interactions of the same rank and symmetry. An able and energetic group of colleagues (Don Alderman, Jean-Marie Bernassau, Ed Black, Mark Brown, Marie-Therese Chenon, Michael Fuson, Fang Liu, Charles Mayne, Richard Newmark, Wenping Wu, Zhiwen Zheng) provided the experimental foundations and many of the theoretical insights for these advances. In the mid-1970s Larry Werbelow, a premier coupled spin theorist, and an outstanding faculty colleague, Jim Wang,[17] provided a theoretical extravaganza for the group's experimental efforts in multiplet relaxation. The basic formulation of coupled-relaxation principles was largely complete by the late 1970s and summarized accordingly.[18]

Extensive data analysis is needed to interpret transient behavior in spectral multiplets as they respond to a variety

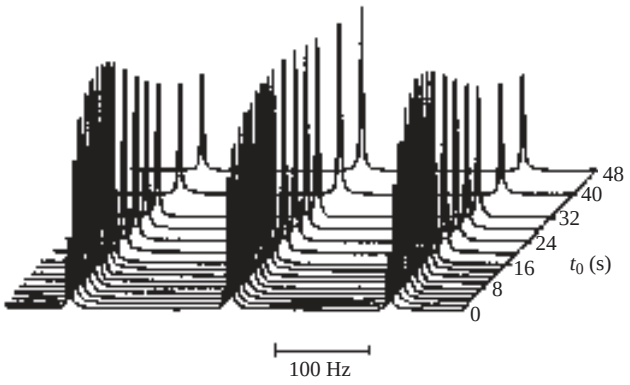

Figure 2 Examples of ^{13}C FT NMR spectra of methylene iodide obtained at various times t_0 following the inversion of both proton lines with a hard π pulse. (Reproduced by permission of The American Institute of Physics from Ref. 16.)

of spin polarizations and induced multiple spin orders. Furthermore, these studies are becoming increasingly complex at higher magnetic fields where larger chemical shift anisotropy contributes to the relaxation. Fortunately, the analysis is stable and computer software exists for the simultaneous extraction of many independent relaxation parameters that may be converted with statistical mechanical methods into details on molecular rotation and diffusion and, when present, on the internal motions in flexible molecules.

Since the late 1970s multiplet relaxation studies[19] have focused on applications that extend the tumbling motion of rigid molecules to the internal motions in flexible paraffinic chains such as found in alkanes, in synthetic polymers, and more recently in biological molecules. For example, ^{13}C-labeled methylenes, placed at various positions in nonane[20] and in decanol-1, provided a dynamical map of continuous paraffin chains. These data by Mark Brown and Fang Liu on flexible molecules were correlated nicely with theoretical Brownian dynamical models, developed in concert with Glen Evans, Michael Fuson, and Tian-xiang Xiang. Multiplet relaxation methods are being extended and applied presently to amino acids and ^{13}C-labeled peptides by Russ Brown with the anticipation that the differential motional features will eventually provide dynamical maps of important biological molecules. Recent coupled relaxation work by Shi Bei and Craig Taylor in supercritical fluids (SCF) spans the range of densities between gases and liquids and portends high potential for studies in SCF media.

Multiplet relaxation work involves the stimulation of multiple spin orders, similar to those used in multidimensional spectral methods. Thus, these two NMR fields, important to dynamics and structure, have much in common, and the information is complementary. Multidimensional spectral methods produce biomolecular structural maps, while multiplet relaxation methods provide a dynamical map for flexible molecules.

Structural and motional blossoms were becoming increasingly abundant in the ^{13}C garden.

SIMILARITIES BETWEEN ^{13}C AND OTHER LESS RECEPTIVE NUCLEI

The ^{2}H and ^{15}N nuclides have many of the challenges associated with the ^{13}C nuclide, i.e. all three are low in natural abundance and all have reduced gyromagnetic ratios. These similarities suggested that many ^{13}C methods should be directly portable to ^{2}H and ^{15}N spectroscopies. For example, the naturally abundant ^{2}H singlets, obtained by Janet Curtis with proton-decoupling, produce very simple ^{2}H spectra when compared with the complexity and banding found in many proton spectra. Similar to ^{13}C shifts, these ^{2}H shifts also have been shown to depend intimately on molecular conformations.[21] Mary Francis Leopold and Bill Epstein found that variations in naturally occurring $^{2}H/^{1}H$ isotopic ratios are able to characterize pathways for terpene biosynthesis in plant materials.[22] Similar to ^{13}C results, Karen Anderson's ^{15}N shift tensors exhibited a dependence on molecular electronic effects in aromatic nitrogen bases. Her ^{15}N work on solid NH_4NO_3 provides a splendid example of motional averaging of NMR parameters in the solid state.[23]

With ^{13}C cultivation methods, hybrids of ^{2}H and ^{15}N also may adorn the garden of spins!

THE DIRECTLY BONDED ^{13}C–^{13}C INADEQUATE EXPERIMENT

The INADEQUATE experiment, involving ^{13}C–^{13}C scalar couplings at the 1% natural abundance level, suffers from the incredibly low signal-to-noise ratio associated with the 1 in 10 000 molecules of two adjacent ^{13}C nuclei. This serious limitation in sensitivity reduces the impact of the INADEQUATE experiment which otherwise has the potential to be the preeminent organic NMR structural method by providing a complete molecular graph of all directly bonded carbon nuclei. Hence, extensive attention has been given to mitigating the low INADEQUATE sensitivity for complex molecules and their mixtures. Reinhardt Dunkel developed a very powerful automatic software routine to recognize INADEQUATE patterns in spectral signals obscured by noise.[24] For fairly large molecules, approaching 10 000 daltons, Reinhardt's software provides all of the direct ^{13}C–^{13}C bond connectivities and the associated scalar coupling constants and chemical shifts. This software also characterizes the line intensities and linewidths. The automated INADEQUATE experiment is especially useful with natural products (e.g. a set of botanical and marine samples collected by Paul Cox, Chris Ireland and their associates were run by Noel Owens, Du Li, Charles Mayne et al.)[24] Such automatic pattern recognition methods also portend well for other 2D NMR methods with highly constrained response functions.

Alas, INADEQUATE but delicate ^{13}C flowers sparkle brilliantly under computer magnification!

^{13}C CHEMICAL SHIFT TENSORS AND CRYOGENIC TEMPERATURES

Our early interests in ^{13}C chemical shifts were revived in an experiment, conducted by Kurt Zilm and assisted by Josef Michl's group, on molecules trapped in a cryogenic matrix.[25] Carbon-13 powder patterns from molecules immobilized in nonreactive inert gas media exhibit chemical shift tensors for small molecules that are normally gases at room temperature. The inert gas matrix also approximates closely the environment of molecules isolated in a vacuum, a condition presumed for most quantum chemical calculations. Thus, cryogenic tensor data are especially amenable for theoretical study. A group of key associates (Anita Orendt, Mark Solum, Al Beeler, Henri Strub) expanded on the initial cryogenic work to understand an extensive collection of tensors for small molecules. Our recent emphasis stresses shift tensors for highly reactive intermediates that exist only at cryogenic temperatures. Spectra of ^{13}C doubly-labeled molecules in solid argon matrices exhibit the expected ^{13}C–^{13}C Pake doublets. The splittings depend on the internuclear distances and on the orientation of the C–C bond vector in the principal ^{13}C shift axes.[26] In reactive or low molecular weight molecules without an easily available single crystal, dipolar spectra often offer the only convenient way to designate the orientation of principal shift axes.

Amazingly, a wild strain in the ^{13}C garden flourished even under cryogenic conditions!

CHEMICAL SHIFT TENSORS FROM POWDER SAMPLES AT AMBIENT TEMPERATURES

Tensor data from 1D overlapping powder patterns, whether extracted at cryogenic conditions or ambient temperatures, are limited to simple molecules of only two or three unique ^{13}C atoms. While one may resort to ^{13}C-labeled molecules of any size to achieve the required spectral simplicity, as done by Arlen Soderquist to observe the three unique α-carbons in phenanthrene, three other avenues have been pursued successfully at Utah to unscramble overlapping spectral bands. These methods include a 1D VAS approach, a 2D orientational correlation method, and a new 2D slow magic angle turning (MAT) experiment. Tensor data from these experiments have been extracted using a POWDER approach[27] for frequency fitting and a time fitting approach developed initially by Bill Heeschen.[28] Both the POWDER and FID methods are combined with least-square minimization routines to provide accurate tensor spectral parameters.

With a VAS probe, similar to the one designed by Jacque Courtieu[29] for controlling the director orientation in nematic liquid crystals, Naresh Sethi[30] found that it was possible to scale the width of overlapping tensor bands about their isotropic shifts. Spinning at the magic angle produces a solid state spectrum of ^{13}C singlets for each unique resonance. By varying the spinning axis on each side of the magic angle, tensor patterns emerge with widths that depend on the spinning angle. The shape and width of each overlapping band varies about its own isotropic shift, in such a way that a computer is able to extract tensor values for seriously overlapping carbon resonances providing sufficient spinning angles are analyzed simultaneously.

The 2D orientational correlation approach based on a flipper probe, similar to that of Spiess, has been used by Craig Hughes[31] and Mao-Lin Hsu to provide the correlated orientational information essential to obtain tensor quantities. By spreading the spectral information in 2D, the resolving power of the experiment is enhanced and very similar principal shift values are more readily identified. This method is especially attractive for polymers and other amorphous solids not amenable for single crystal study and has been used to determine the degree of crystallinity and molecular ordering in polyethylene and related polymers. Recent 2D correlation work on a naphthalene pitch, obtained from the pyrolysis of naphthalene, also indicates promise for the method.

The elegant MAT experiment proposed by Gan[32] is generically related to the magic angle hopping experiment of Bax, Szeverenyi, and Maciel.[33] Refined and enhanced by Jian Zhi Hu and others,[34] this new MAT method portrays, without detrimental overlap of tensor bands, both the ^{13}C isotropic shifts and their tensor powder patterns for relatively large molecules. The method applies a set of repetitive 90 $^{\circ}$ pulses properly spaced with a one-third periodicity over the rotor cycle. Properly processed, the spectrum exhibits both the isotropic shifts and tensor powder patterns along mutually perpendicular directions in a 2D solid state spectrum. Distinct tensors for carbons whose isotropic shifts differ by little more than 1 ppm have been extracted from the two closest vertical slices shown in Figure 3 for two methyl carbons in 1,2,3-trimethoxybenzene. These vertical slices from Figure 3 provide powder patterns of a unique ^{13}C tensor without overlap problems. Significant future uses are anticipated for this promising new 2D method because of the wealth of shift information that may be obtained on powder samples.

Novel NMR methods and new applications are bracing as fresh spring flowers!

NMR APPLICATION OF POWDER METHODS IN FOSSIL FUELS

The solid state NMR methods discussed above, including MAS, have been especially powerful in the analysis of structural moieties present in complex fossil fuels. This work with Prof. Ronald Pugmire, a long-time colleague and a close associate from Utah's Chemical Engineering and Fuels Department, has provided innumerable NMR challenges that have their origin in the industrial world. The complexities of applied science, with its attendant economic and societal benefits, often stimulate basic spectroscopic developments of considerable value. Pugmire's unlimited energies and enthusiasm for the latest NMR applications in a number of significant energy-related problems have been assisted by the careful experimental work of outstanding associates (Mark Solum, Larry Alemany, Anita Orendt, Mike Wilson, Yi-Jin Jiang, and others). For example, NMR data characterize the origins and degrees of maturation of various coals. Specific chemical features found in coal include the average size of fused aromatic rings, the chemical nature of bridging groups between the aromatic clusters, and the types of side chains. Such NMR chemical information, with percolation lattice

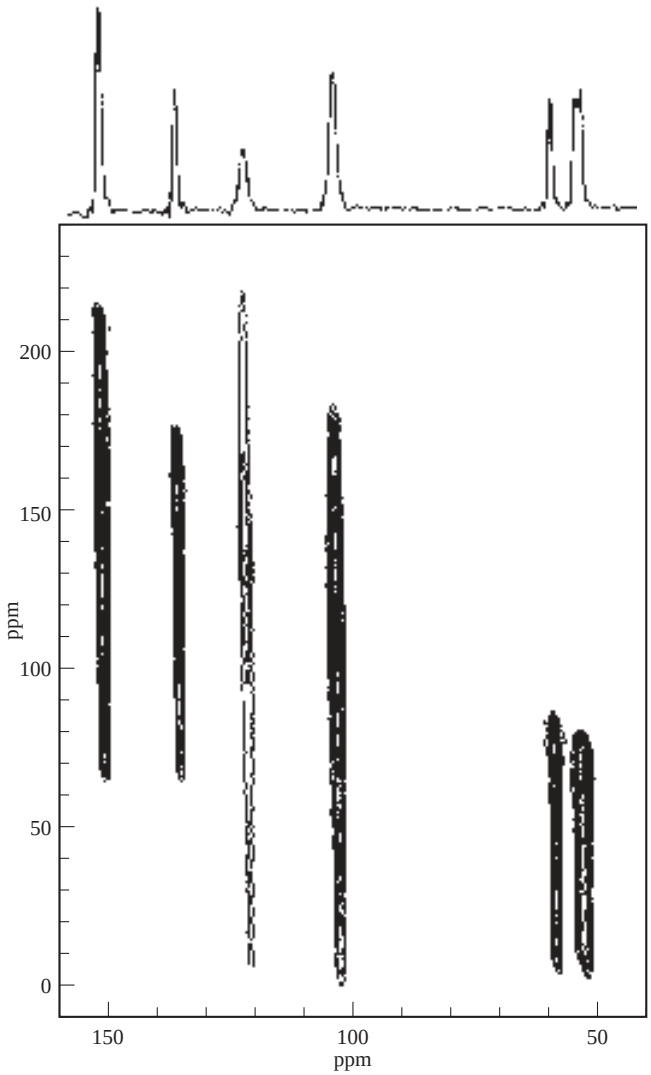

Figure 3 Fully refocused triple echo MAT spectrum 1,2,3-trimethoxybenzene with the isotropic projection shown at the top. Vertical slices provide high quality tensor powder patterns without serious overlap. (Reproduced by permission of Elsevier Science Publishers B. V. from Ref. 34)

statistics, led to a devolatilization (CPD) submodel critical to our understanding of coal combustion;[35] talented co-workers in the CPD development were Ronald Pugmire, Tom Fletcher, Alan Kerstein, Matthew Pugmire, and Mark Solum. While the chemical aspects of coal combustion are much too complex to be explained in every detail by this macroscopic CPD model, the approach works much better than might be expected because the distributed NMR shifts in carbonaceous solids represent faithfully many of the diverse chemical features that affect coal devolatilization.

THE SINGLE CRYSTAL MECHANICAL FLIPPER PROBE

Our interests in chemical shift tensors found their culmination in a new 2D solid state flipper probe designed by Don Alderman, Carl Carter,[36] and Mark Sherwood[37] for single crystals. Don, with extraordinary experimental talents and a propensity for novel physical insights, has been an essential member of the Utah ^{13}C laboratory for many years and much of our progress has depended on this able and creative scientist. The single crystal flipper mechanism provides the correlated orientational information critical to the determination of the shift tensor and its orientation in a crystal's unit cell and consequently in the molecular frame. Traditionally, single crystal work required that the crystal be mounted three times in a single axis goniometer and observed by stepping through small angular displacements (about 5°). Unfortunately, less than 20 unique carbon atoms per unit cell can be indexed conveniently in this traditional manner. By flipping between two orientations associated with the time-evolution axes in a 2D spectrum, orientational correlation information may be obtained that addresses ambiguities arising from closely positioned 1D peaks. Figure 4 shows an early example of the 2D single crystal spectrum of 1,2,3-trimethoxybenzene with 36 peaks.[38] Note the correlated orientational information and the superior resolution of the 2D spectrum compared with the traditional 1D spectral projections.

Recent single crystal work by Fang Liu and Rob Iuliucci, respectively, has advanced the technique to yield spectra with 56 and 72 resolved peaks. It is estimated that this 2D single crystal method has the potential for indexing considerably more than 100 separate carbon resonances at higher magnetic fields. Single crystal methods determine the principal values of the shift tensor but also give directly the orientation of principal axes in the molecular frame. These experimental data, six numbers for each magnetically unique carbon in a crystal, provide an information-rich representation of the three-dimensional electronic structure of organic molecules. Admittedly, this method requires relatively large single-crystal prisms, a nontrivial indexing of hundreds of tensor values (e.g. 432 tensor values for a 2D spectrum of a unit cell with 72 magnetic nuclei) and a challenging assignment procedure to

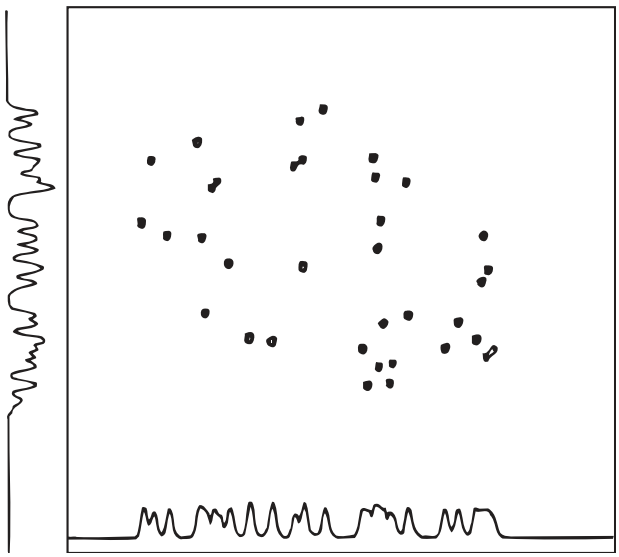

Figure 4 Two-dimensional NMR spectrum of a single crystal of 1,2,3-trimethylbenzene showing the resolution of all 36 lines. A rotation of 45 ° between orientations was utilized. (Reproduced by permission of The Royal Society of Chemistry from Ref. 38)

relate the large number of tensor shifts and their orientations with specific molecular structural features. However, the wealth of electronic and molecular structural information obtained by this approach more than compensates for these efforts.

As with the first fruit of summer, the 2D single crystal results were indeed delectable!

THE THEORETICAL ANALYSIS OF CHEMICAL SHIFT TENSORS

With an increasing availability of experimental shift tensors, it became more important to have good theoretical methods for analyzing the molecular and electronic origins of these tensors.[39] Whereas isotropic shifts in liquids have enjoyed great correlative value in designating molecular structure, the six parameters in experimental ^{13}C shift tensors provide sufficient new electronic details that the associated molecular features may be specified in much greater depth.[40] The help of a close and valued associate Julio Facelli and of other theoretical colleagues (Tom Bouman, John Downing, Aage Hansen, Werner Kutzelnigg, Josef Michl, Cu Phung and Michael Schindler) has been essential to our understanding of the experimental shift tensors. We also recognize the use of new GAIO software provided by Peter Pulay, Jim Hinton, and their associates. Theoretical correlation between experiment and theory is now at the point where the calculations are accurate enough to reflect limitations in the diffraction data on which the theoretical wavefunctions depend.[41] Diffraction errors, as they propagate through the wavefunctions into limitations in theoretical shift tensors, are relatively larger than the corresponding experimental shift errors. Thus, it is tempting to look into the future when chemical shift measurements along with improved quantum mechanical treatments of molecular crystals will have the capacity to refine diffraction-based molecular structures.

Theoretical illumination of ^{13}C shifts reflects the bounteous harvest of a golden autumn!

REFERENCES

1. H. S. Gutowsky, M. Karplus, and D. M. Grant, *J. Chem. Phys.*, 1959, **31**, 1278.
2. M. Karplus and D. M. Grant, *Proc. Natl. Acad. Sci. USA*, 1959, **45**, 1269.
3. D. M. Grant, R. C. Hirst, and H. S. Gutowsky, *J. Chem. Phys.*, 1963, **38**, 470.
4. M. Barfield and D. M. Grant, *Adv. Magn. Reson.*, 1965, **1**, 149.
5. R. A. Ogg, Jr., *J. Chem. Phys.*, 1954, **22**, 1933; R. A. Ogg, Jr. and J. D. Ray, *J. Chem. Phys.*, 1957, **26**, 1515.
6. P. C. Lauterbur, *Ann. N. Y. Acad. Sci.*, 1958, **70**, 841.
7. E. G. Paul and D. M. Grant, *J. Am. Chem. Soc.*, 1963, **85**, 1701; 1964, **86**, 2977.
8. D. M. Grant and E. G. Paul, *J. Am. Chem. Soc.*, 1964, **86**, 2984. Featured in 'Citation Classics', see *Current Contents/Eng. Technol. Appl. Sci.*, 1984, **15**, 16.
9. D. K. Dalling and D. M. Grant, *J. Am. Chem. Soc.*, 1967, **89**, 6612. Featured in 'Citation Classics', see *Current Contents/Phys. Chem. Earth Sci.*, 1983, **23**, 22.
10. K. F. Kuhlmann and D. M. Grant, *J. Am. Chem. Soc.*, 1968, **90**, 7355.
11. I. Solomon, *Phys. Rev.* 1955, **99**, 559.
12. The high regard I have for Robin Harris started at this juncture in our careers and contributed to our joining efforts on this *Encyclopedia of Nuclear Magnetic Resonance*.
13. K. F. Kuhlman, D. M. Grant, and R. K. Harris, *J. Chem. Phys.*, 1970, **52**, 3439.
14. J. R. Lyerla, Jr.and D. M. Grant, *MTP International Review of Science, Series One*, Butterworths/University Park Press, London/Baltimore, 1972, Vol. 4, p. 155.
15. J. J. Led and D. M. Grant, *J. Am. Chem. Soc.*, 1975, **97**, 6962; *J. Am. Chem. Soc.*, 1977, **99**, 5845.
16. C. L. Mayne, D. W. Alderman, and D. M. Grant, *J. Chem. Phys.*, 1975, **63**, 2514; *J. Chem. Phys.*, 1976, **65**, 1684.
17. C. H. Wang and D. M. Grant, *J. Chem. Phys.*, 1976, **64**, 1522.
18. L. G. Werbelow and D. M. Grant, *Advances in Magnetic Resonance*, ed. John Waugh, Academic Press, New York, 1977, vol. 9, p. 189.
19. D. M. Grant, C. L. Mayne, F. Liu, and T.-X. Xiang, *Chem. Rev.*, 1991, **91**, 1591.
20. M. S. Brown, D. M. Grant, W. J. Horton, C. L. Mayne, and G. T. Evans, *J. Am. Chem. Soc.*, 1985, **107**, 6698.
21. J. Curtis, D. K. Dalling, and D. M. Grant, *J. Org. Chem.*, 1986, **51**, 136.
22. M. F. Leopold, W. W. Epstein, and D. M. Grant, *J. Am. Chem. Soc.*, 1988, **110**, 616.
23. K. A. Anderson-Altmann and D. M. Grant, *J. Phys. Chem.*, 1993, **97**, 11096.
24. R. Dunkel, C. L. Mayne, R. J. Pugmire, and D. M. Grant, *Anal. Chem.*, 1992, **64**, 3133; R. Dunkel, C. L. Mayne, M. P. Foster, C. M. Ireland, D. Li, N. L. Owen, R. J. Pugmire, and D. M. Grant, *Anal. Chem.*, 1992, **64**, 3150.
25. K. W. Zilm, R. T. Conlin, D. M. Grant, and J. Michl, *J. Am. Chem. Soc.*, 1978, **100**, 8038.
26. K. W. Zilm and D. M. Grant, *J. Am. Chem. Soc.*, 1981, **103**, 2913.
27. D. W. Alderman, M. S. Solum, and D. M. Grant, *J. Chem. Phys.*, 1986, **84**, 3717.
28. W. A. Heeschen, D. W. Alderman, and D. M. Grant, *J. Phys. Chem.*, 1988, **92**, 6504.
29. J. Courtieu, D. W. Alderman, D. M. Grant, and J. P. Bayles, *J. Chem. Phys.*, 1982, **77**, 723.
30. N. K. Sethi, D. M. Grant, and R. J. Pugmire, *J. Magn. Reson.*, 1987, **71**, 476.
31. C. D. Hughes, M. H. Sherwood, D. W. Alderman, and D. M. Grant, *J. Magn. Reson., A*, 1993, **102**, 58.
32. Z. Gan, *J. Am. Chem. Soc.*, 1992, **114**, 8307.
33. A. Bax, N. M. Szeverenyi, and G. E. Maciel, *J. Magn. Reson.*, 1983, **52**, 147; N. M. Szeverenyi, A. Bax, and G. E. Maciel, *J. Magn. Reson.*, 1985, **61**, 440.
34. J. Z. Hu, A. M. Orendt, D. W. Alderman, R. J. Pugmire, C. Ye, and D. M. Grant, *Solid State NMR*, 1994, **3**, 181; J. Z. Hu, W. Wang, F. Liu, M. S. Solum, D. W. Alderman, R. Pugmire, and D. M. Grant, *J. Magn. Reson., A*, 1995, **113**, 210.
35. D. M. Grant, R. J. Pugmire, T. H. Fletcher, and A. R. Kerstein, *Energy Fuels*, 1989, **3**, 175.
36. C. M. Carter, D. W. Alderman, and D. M. Grant, *J. Magn. Reson.*, 1985, **65**, 183; *J. Magn. Reson.*, 1987, **73**, 114.
37. M. H. Sherwood, D. W. Alderman, and D. M. Grant, *J. Magn. Reson. A*, 1993, **104**, 132.
38. C. M. Carter, J. C. Facelli, D. W. Alderman, and D. M. Grant, *J. Chem. Soc., Faraday Trans. 1*, 1988, **84**, 3673.
39. J. C. Facelli and D. M. Grant, *Topics in Stereochemistry*, eds. E. L. Eliel and S. H. Wilen, Wiley, New York, 1989, Chap. 19

40. D. M. Grant, J. C. Facelli, D. W. Alderman, and M. H. Sherwood, *NATO Workshop, July 1992*; *Nuclear Magnetic Shielding and Molecular Structure*, ed. J. Tossell, Kluwer, Dordrecht, The Netherlands, 1993, p. 367.
41. J. C. Facelli and D. M. Grant, *Nature (London)*, 1993, **365**, 325.

Biographical Sketch

David M. Grant *b* 1931. *m*. Reva L. Carlow, 1953. B. S., 1954, Ph.D., 1957, Chemistry, University of Utah, USA. DuPont Instructor, University of Illinois, 1957–58, introduced to NMR by Herb Gutowsky and Martin Karplus. Faculty in Chemistry, University of Utah since 1958, presently Distinguished Professor. Over 300 publications. Awards: 1969 Calif. Section Gold Medal (ACS); 1973 Utah ACS Section Award; 1973–74; Sherman Fairchild Distinguished Scholar, Cal. Inst. Tech.; 1987 Univ. of Utah Rosenblatt Prize; 1991 ACS Award in Petroleum Chem.; 1992 Utah Governor's Medal for Science. Current research specialties: methods and theoretical foundations of carbon-13 NMR, coupled spin relaxation and molecular motions, chemical shifts in liquids and solids with emphasis on carbon-13 shift tensors and their origins in electronic and molecular structure.

Griffin, Robert G.: Perspectives of Magnetic Resonance

Robert G. Griffin

Massachusetts Institute of Technology, Cambridge, MA, USA

EDUCATION

My first contact with NMR occurred fortuitously in my junior year in high school. That year, 1958–59, the Little Rock schools were closed because of the 'integration crisis' and I was forced to attend a Pulaski County school, Fuller High School, in Sweet Home, AR. I was fortunate enough to have an excellent chemistry teacher, Dr. Ed Barron, a recent medical school graduate waiting to start an internship, who inspired us in many ways and was constantly suggesting stimulating extra credit projects. One of these, from the *Scientific American* amateur scientist column, turned out to be the construction of an ^{1}H NMR spectrometer. It was appealing since it involved assembly of a 4.2 MHz radiofrequency oscillator (something that I was familiar with from being an amateur radio operator), a 'powerful' 1 kG permanent magnet, and an oscilloscope. The system required a great deal of effort to construct, but in the end my colleague and I detected a signal from a large sample of H_2O.

Following this initial encounter with magnetic resonance, I moved (in both high school and college) into more conventional science of the early 1960s—acid–base equilibria in immiscible solvents and electrochemistry in mixed solvents.[1,2] However, during my senior year at the University of Arkansas (UA) it seemed clear that, for a person with my interests in physical chemistry and physics, spectroscopy was the natural avenue for the future. This thinking was stimulated further by a molecular spectroscopy course where we discussed a new area, NMR, and what it could tell us about the structure of solids (it was about to replace X-rays as a means to locate protons) and liquids. I found this amusing since I had built one of these instruments as a high school junior. In a chance conversation, the department chair at UA told me that the university where he received his Ph.D.—Washington University (St. Louis) (WU)—had a number of excellent people in magnetic resonance, and suggested that I consider WU for graduate work. I followed his advice without much thought as to other possible graduate schools.

After a semester of courses, I joined the research group of S. I. Weissman. Although Sam was most famous for his research in EPR, he nevertheless had an occasional student performing NMR experiments, and in those years that happened to be me. I was assigned a project to measure the electron transfer rate between the radical ion of trimesitylboron and its diamagnetic precursor by observing the broadening of the ^{1}H NMR resonances due to exchange. Since the line broadening went as a^2, where a is the electron nuclear hyperfine coupling constant, I also had to perform EPR experiments to determine a. We succeeded in this endeavor by analyzing a very complicated EPR spectrum (14 630 lines) via a combination of NMR and EPR.[3]

As I had been promised, WU had a rich and expanding tradition in NMR and EPR. George Pake spent his early years in St. Louis, and assembled an active faculty in magnetic resonance in the Physics Department. This included Richard Norberg, from whom I took a first course in magnetic resonance, and Maurice Goldman, who had just completed his post-doctoral work as I arrived. The research in physics involved low temperatures, acoustic resonance, EPR of semiconductors, and a topic called magic angle spinning (MAS) on which a student, Horst Kessemier, had just completed a thesis. I remember being told that MAS experiments were possible only because of the abilities of a talented machinist named Otto who could build Kessemier/Norberg rotors. And, as a chemist, I should be interested in these techniques since they had the potential to permit measurement of chemical shifts and J couplings in solids.

Among the seminars I attended as a student, four have remained in my memory. The first was a talk by Raymond Andrew on MAS where I initially saw ^{31}P spectra of PCl_5 and ^{19}F spectra of $KAsF_6$ illustrating the resolution of chemical shifts and J couplings in solids—as promised by my physics colleagues. He also discussed rotor design (to ~10 kHz) and the possibility of using a rotating field rather than a rotating sample. Later Erwin Hahn presented a talk on detection of 'bundant' nuclear species with 'abundant' spins via destruction of the latters' signal. This was Erwin's version of what we now know as cross polarization in solids. In addition, Jake Schaefer visited from Monsanto and presented a theoretical seminar (I had previously met Jake on visits to Monsanto to use their HA-100). Finally, John Waugh spoke at a local ACS symposium on his newly invented multiple pulse line narrowing techniques.

Because of the prior interest in MAS and high-resolution NMR in solids at WU, Waugh's talk and his papers, which were appearing regularly in *Phys. Rev.* and *J. Chem. Phys.*, stimulated a great deal of excitement. As a result, Sam Weissman recruited a student to work in physics to continue Kessemier's experiments, and he also went to Holland to see if something called a 'spiral groove bearing' could be used for an improved rotor. Everyone was convinced that MAS would be competitive with multiple pulse experiments if only the strength of materials problem associated with high speed rotors could be solved.

Finally, I completed enough electron transfer studies to write a thesis and I began to look for a postdoctoral position. At the time the exciting areas on the horizon were laser light scattering, optically detected magnetic resonance of photoexcited triplets, biological magnetic resonance (which was just beginning to become feasible), and NMR in solids. Following a brief flirtation with laser scattering, I arrived at John Waugh's laboratory at MIT in May 1970.

POSTDOCTORAL YEARS

Upon my arrival at MIT, Waugh introduced me to his research group which consisted of three postdocs—Michael Mehring, Won-Kyu Rhim, and Dave Ellett—and half a dozen graduate students including Alex Pines, Mike Gibby, Hong-Ning Yeung, and Sam Kaplan. The first problem I encountered in the lab was the overpowering array of homebuilt equipment.

This problem was eventually solved by collaborating with Michael Mehring, who explained pulsed spectrometers to me. Michael is an excellent experimentalist and was responsible for many of the innovations in rf transmitter and probe design of that era. Shortly before I arrived, he had completed an excellent 1 kW amplifier featuring a pair of 4CX250s for the original 54 MHz WAHUHA machine. In addition, Pines and Gibby had finished a new high power broad-band pulse spectrometer with the first computerized pulse programmer interfaced to a DEC PDP-12. Thus, we no longer had to hard wire new pulse sequences, but could simply write a new pulse program! The utility of the programmer had just been demonstrated by performing Won-Kyu's complicated magic echo sequences. The WAHUHA machine had an elderly Varian iron magnet on it, and the new spectrometer was awaiting delivery of a high field (250 MHz) superconducting magnet from Oxford Instruments. Since the supercon had not arrived, Pines and Rhim had strung cables ~50 ft. down the hall so that they could use the iron magnet and Michael's transmitter at night and on weekends. The problem with this arrangement was that Alex's new computerized pulse programmer would regularly malfunction, causing Mehring's transmitter to emit a continuous 1 kW burst which would destroy the 4CX250s and other selected parts of the transmitter and probe! Ultimately, the superconducting magnet did appear, and, after Dave Ellett and I wrote a machine language FT program for a PDP-8/I (which occupied all 4096 words of 12-bit memory), we separated the spectrometers. Unfortunately, the Oxford magnet never made it much above 100 MHz, but we did not let this impede the science.

After about two weeks of discussion with people in the lab, I settled on a research project for detecting chemical shift anisotropies using MP techniques. We decided to examine ^{19}F spectra because the tensors were supposed to be large (~ 200 ppm). Since motional averaging might be a problem, it seemed important to build a low temperature (LT) probe. I also had to do something about shortening the expected long T_1 values of rigid solids. After a few false starts I doped fluoranil, $C_6F_4O_2$, with a paramagnetic NO· radical, we repaired a minor dc offset problem in the audio section of the new spectrometer console, and Mehring and I managed to observe the first shift anisotropy powder pattern with a WAHUHA experiment.[4] Subsequently, I built an LT system capable of reaching ~10 K and we studied the narrowing of the powder pattern of a CF_3 group from $\eta \approx 1$ to $\eta \approx 0$ due to the threefold hopping with increasing temperature, as well as a number of other ^{19}F shift anisotropies.[5] This was followed by single crystal studies of ^{19}F shift tensors,[6,7] and Dave Ellett and I performed a careful examination of ring inversion in C_6F_{12} in the solid.[8]

With the 'original' WAHUHA machine, MP NMR was difficult even on good days, and the double resonance experiments that Alex Pines and Mike Gibby were performing were appealing because of their simplicity—cross polarize and decouple. Thus, in the latter part of my postdoc, I became involved in ^{15}N and ^{13}C spectroscopy,[9] and, in addition, we observed high-resolution ^{14}N–^{13}C dipolar couplings in single crystals of glycine[10] and acetonitrile.[11] I travelled to an ISMAR conference in Israel and to an NMR summer school in Basko Poljé, Yugoslavia where Jean Jeener introduced the world to 2D NMR. There were many exciting discoveries in Waugh's lab during this period—average Hamiltonian theory, magic echoes, shift anisotropies, spin decoupling in solids, cross polarization, etc—and I felt fortunate to be part of such a stimulating environment.

In 1972 I began to search for permanent employment and eventually accepted a position at the MIT Francis Bitter National Magnet Laboratory (FBNML), where Leo Neuringer, a low temperature physicist, was trying to start an NMR program. Thus, I moved across campus and began to build a spectrometer with the part-time assistance of Dave Ruben, who was finishing his Ph.D. in gas-phase microwave spectroscopy. After completing his Ph.D., Dave spent about three years at Berkeley, prior to returning to MIT. We have remained at the FBNML since that time, and the NMR program has expanded enormously in terms of the number of spectrometers and the number of students and postdocs. The remainder of this paper consists of a description of research at the FBNML since 1972 in a number of different areas.

THE FRANCIS BITTER NATIONAL MAGNET LABORATORY

My first task at the FBNML was to assemble a functioning 'high-field' NMR spectrometer. The end result was a broad-band heterodyne double resonance instrument operating at 300 MHz for ^1H. We built a hardwired pulse programmer capable of performing a few special sequences, power amplifiers delivering 1 kW, and a probe with a goniometer for single crystal studies. Dave Ruben designed the computer interface and wrote the spectrometer software on a PDP-11/20, which we borrowed from the plasma physicists at the FBNML. We have continued the tradition of fabricating much of our own instrumentation since that time—computerized pulse programmers, low level rf components, probes, and a few superconducting magnets. Much of this has been accomplished by Ruben, and more recently, Chris Turner, as well as our long term technicians—Peter Allen, Ajay Thakker, and more recently, Jeff Bryant.

Our first paper was a single crystal study of the $^{13}CO_2^-$ and $^{13}CO_2H$ tensors in an oxalate.[12] At that time 'high-resolution' NMR in solids consisted of creating new schemes for multiple pulse NMR and studies of powders and single crystals. We therefore performed a number of these investigations,[13] including studies of ^{13}C, ^{31}P, and ^{15}N chemical shifts, ^{13}C–^{14}N,[14] ^{13}C–^{13}C,[15] and ^1H–^{14}N[16] dipole couplings, and ^2H[17] and ^{14}N[18,19] quadrupole couplings and chemical shifts.

LIPID AND MEMBRANE NMR

The 'dynamic structure' of lipid bilayers and membranes has been a topic of continuing interest to the biophysics community for the last 20 years. As we demonstrated with our early study of a CF_3 group,[5,6] the narrowing of a chemical shift powder pattern with temperature told us a great deal about the dynamics of a molecule, and we thought the same would be true for lipids and membranes. Thus, as our entree to 'biological NMR' we started to examine powder spectra of lipids, first the ^{31}P spectra associated with the head group,[20,21] then ^{13}C spectra of $^{13}C{=}O$ labeled lipids,[22] and finally the ^2H spectra of chain labeled species[23] provided by Sunil Das Gupta. The goal of this work was to elucidate the

structure and dynamic properties of pure and mixed systems. When we initiated this work the standard approach was to employ 'order parameters' to interpret these spectra, as exemplified by the early work of Eric Oldfield and the beautiful experiments of Joachim Seelig with specific ^{2}H labeling in polymethylene chains. Our goal was different—specifically, to calculate the powder lineshapes based on a reasonable model for the motion. Dick Wittebort produced the first results by successfully simulating the ^{13}C=O spectra of lipids as they passed through the $L_{\beta'} \rightarrow L_\alpha$ phase transition.[24] These same ideas and Wittebort's computer programs were used by Alfred Blume[25,26] and Tai-Huang Huang[23] in studies of gel phase lipids and glycolipids, respectively, and most recently in an elucidation of the phase diagram of the cholesterol/phosphatidylcholine system.[27] David Rice also used ^{2}H spectra to characterize the rate of 180° flips of aromatic rings,[28] and Kebede Beshah the threefold hopping rate of CD_3 groups.[29] Ed Olejniczak, stimulated by the work of Dennis Torchia and Attila Szabo, added T_1 calculations to Wittebort's programs so that the T_1 anisotropy, as well as the ^{2}H lineshapes, could be used to examine dynamics.[30] Barbara Lewis studied mixed lipid systems,[31] and Carolyn Lee recorded and simulated the spectra of trehalose–lipid mixtures.[32]

One of the long-term goals of our research was to calculate the ^{13}C, ^{2}H, etc. spectra of lipid bilayers in their biologically relevant liquid crystalline phase. Unfortunately, the L_α phase spectra of bilayers exhibit 'fast limit' lineshapes on the ^{2}H timescale, and therefore the spectra are not sensitive to dynamics. Thus, in order to understand the dynamics, we required a probe sensitive to motion on the 10^8–10^{10} s^{-1} regime, and thus the T_1 anisotropy seemed an obvious choice. In two initial searches of pure bilayer systems the expected T_1 anisotropy of ^{2}H spectra of bilayers was not detected due to an unfortunate choice of the position of the ^{2}H label; however it had been observed by David Siminovitch and Marty Ruocco in cholesterol-containing systems.[33] Nevertheless, Julia Speyer and Ralph Weber found a large T_1 anisotropy in pure glycolipids and were able to calculate the lineshapes in great detail.[34] Thus, the axial diffusion rate and the *gauche–trans* isomerization rate at each position of the chain were available from the anisotropy of the spin–lattice relaxation. Interestingly enough, the anisotropy changed sign and was therefore almost zero at the 4 position of the lipid chains where the previous workers had placed their label. In any case, these experiments accomplished a major goal of our research effort. We are continuing our studies of dynamics in solids and membranes.

RETINAL PROTEINS

In the late 1970s Judy Herzfeld initiated our efforts to perform solid state NMR on bacteriorhodopsin (bR), the single protein of the purple membrane of halobacteria, and was enthusiastically advocating MAS experiments for this purpose. MAS as we know it today did not exist, and in addition to isotopically labeling the protein, we had to develop the probes and techniques to perform the spectroscopy. When Gerry Harbison, Judy's biophysics graduate student from Harvard, joined the lab in 1979, he was encouraged to pursue this problem. In 1983 Gerry succeeded in recording spectra of Judy's ^{15}N-lysine labeled bacteriorhodopsin (bR) using Andrew–Beam rotors in MAS experiments.[35] His results showed that the Schiff base linkage was protonated, settling a controversy. More importantly, he demonstrated that MAS NMR could be used to examine large membrane proteins not accessible to solution NMR, and that interesting biophysical information could be gleaned from the spectra. Almost immediately Harbison decided that it would be a great idea to look at the retinal in bR, and did a thorough study of retinals and retinal derivatives as background.[36] On a seminar trip to Berkeley I met Rich Mathies, who told me that his colleague Johan Lugtenburg in Leiden had synthesized a large number of ^{13}C-labeled retinals; a collaboration was immediately formed, and Harbison was soon taking spectra of ^{13}C-retinal labeled proteins. Rich, Johan and their colleagues continue to be important collaborators in our retinal protein studies—being involved in essentially all of the experiments. Our first ^{13}C experiments focused on the middle of the chain[37] and also on the C=N bond conformation,[38] which chemical shifts suggest was *syn* and *anti* in bR_{555} and bR_{568}, respectively. In addition, Gerry noted a large downfield shift ($\sim$ 10 ppm) in the isotropic shift of the 5-^{13}C position of retinal, and analysis of the sideband intensities indicated the change resided in the σ_{22} component. We interpreted these results in terms of a perturbed 6-*s*-*trans* chromophore, the perturbation being due to a 'point charge'.[39]

The next generation of researchers involved with bR were Huub de Groot and Steve Smith. Huub focused on blue membrane, bR_{605}, and showed that the ^{15}N resonance was shifted farther downfield in this species and developed the idea of a hydrated complex, rather than a single, Schiff base counterion, and a very weak hydrogen bond.[40,41] Much to our satisfaction, the electron diffraction model of bR, which appeared subsequently, showed a cluster of three residues—Asp-85, -212, and Arg-82 positioned with space for the water around the Schiff base—de Groot's complex counterion. Huub also built a spinning speed controller and developed difference spectroscopy.[42] Steve did the first work on trapping the M_{412} photointermediate of bR and showed that the retinal was C=N *anti* in a least one of the M_{412}s.[43] In addition, he and Dan Raleigh began to search for the tyrosinate ion that the optical spectroscopist thought was present in bR and its photointermediates. We looked at 4′-^{13}C labeled tyrosine where deprotonation has a large effect, and saw a 12 ppm shift with deprotonation in the model compounds. Later Ann McDermott and Margaret Farrar observed no shifts in the protein,[44,45] suggesting that Tyr was not present. The optical spectroscopy now concurs with this position.

More recently, Ann, Francois Creuzet, Lynmarie Thompson, Michele Auger, and K. V. Lakshmi have been measuring distances in bR and its photointermediates with rotational resonance, confirming some of our interpretations of chemical shifts and extending others.[46–48] Janet Griffiths, Andrew Bennett, and K. V. Lakshmi have also recently obtained our initial 2D spectra of bR using rf-driven recoupling techniques.[49] Finally, Jinqua Hu has shown that the 'opsin shift' in bR can be explained by a synergistic coupling of Gerry Harbison's 6-*s*-*trans* chromophore and the weak complex counterion proposed by Huub de Groot.[50] Thus, we now believe we understand one of the major problems in retinal proteins—the 'opsin shift'. We are still working on the mechanism of proton translocation in bR and Ling Zheng

has recently demonstrated the possibility of observing proton exchange directly in solids.[51]

We have also investigated a number of other large proteins with various MAS experiments. Valerie Copié examined Ala racemase,[52] thermolysin,[53] and Steve Smith examined rhodopsin.[54] Smith also looked at α-lytic protease[55] and Ann McDermott and Francois Creuzet studied D-Ala-D-Ala ligase with R^2 experiments.[56] Rick Spencer and Michele Auger[57] initiated a study of β-amyloid in collaboration with Peter Lansbury and Bruce Tidor, currently in progress.

MAS—SINGLE SPINS

Our original motivation for beginning MAS experiments was to obtain high-resolution spectra of model and biological membranes (including bR) without resorting to sonication or detergent solubilization. Because every 'well-educated NMR spectroscopist' knew spinning would not work well in the slow spinning regime (at high fields and/or slow spinning speeds), I was not optimistic about the success of these endeavors. Nevertheless, Judy Herzfeld was determined and convinced me to visit Raymond Andrew's lab during the 1974 AMPERE Congress in Nottingham. I returned with a handful of Andrew–Beam rotors which Judy used as models to design our initial spinners and rotors. Ron Haberkorn completed the probe and recorded the first spectra of lipid bilayers.[58] In addition, Ron also recorded the spectrum of barium diethyl phosphate (BDEP), illustrating the resolution of a powder pattern into a center band and manifold of sidebands which have appeared in a number of textbooks. These spectra and others led to the Herzfeld–Berger analysis of sideband intensities to extract shift anisotropies. Concurrently, we initiated our efforts to observe spectra of membrane proteins like bR, but progress was slow because of sensitivity and since Andrew–Beam rotors would not spin reliably with wet samples.

Our next MAS project addressed the problem of separation of sidebands due to isotropic/anisotropic chemical shifts. Walter Aue arrived from Ernst's lab, built a new MAS probe, and recorded 2D spectra of BDEP using synchronous sampling and chemical shift scaling in the isotropic dimension.[59,60] The scaling ideas were later incorporated into DIPSHIFT experiments (see below), and also combined with TOSS by Dan Raleigh and Ed Olejniczak. In performing scaling experiments Walter quickly encountered 'rotor lines' which are due to pulse errors and occur in any MAS multiple pulse experiment.[60,61] An explanation of these effects based on Floquet theory was later formulated by Olejniczak and Shimon Vega,[62] who spent his sabbatical at MIT.

During Shimon's sabbatical we worked on several topics, the most prominent of which was a vector picture of MAS. We developed plots of the magnetization during rotor cycles, and by examining individual and collections of crystallites we were able to demonstrate the formation of rotational echoes.[63] In addition, we investigated the effects of π pulses on an echo train and showed the manner in which the echo train could be canceled and recalled. This stimulated a subsequent study of the conditions for echo formation in MAS experiments by Andrew Kolbert and Dan Raleigh.[64] π Pulses also led to Dixon's TOSS experiment, and we wrote down a set of equations for the timings of the pulses and proposed a mechanism to explain how TOSS functions in the case of axially symmetric shift tensors.[65] TOSS experiments were combined with scaling by Dan Raleigh and Ed Olejniczak[66] and Andrew Kolbert suggested the TOSSOT experiment (TOSS/reverse TOSS) to separate isotropic and anisotropic chemical shifts.[67] Finally, Jim Roberts and Shimon Vega collaborated on $^{13}C-^{1}H$ shift correlation experiments.[68]

MAS—RECOUPLING EXPERIMENTS

In the closing days of my postdoctoral appointment in John Waugh's lab, Alex Pines and I recorded ^{13}C single spectra of glycine and observed ^{14}N dipolar couplings.[10] Although I had come to Waugh's lab imbued with the idea of suppressing dipolar interactions in solids, I began to wonder if it were possible to (in the words of Mike Munowitz) 'reintroduce these couplings in a manner consistent with the goal of high resolution' — to perform high-resolution dipolar recoupling experiments. Ruth Stark and Ron Haberkorn did several experiments on $^{13}C-^{14}N$, $^{13}C-^{13}C$, and $^{1}H-^{14}N$ dipole spin pairs in single crystals, [13] but we clearly needed a more generally applicable approach to perform structural studies in solids.

In 1979 a 'separated local field' experiment for static solids was reported, and shortly thereafter I was reading a reprint by Waugh on MAS and realized it should be possible to combine the SLF idea with spinning. Specifically, since the heteronuclear coupling is inhomogenous, we should obtain dipolar sidebands from which we could measure heteronuclear distances. I discussed this with Geoffrey Bodenhausen, who was at the FBNML at that time, and we decided that it would be important to synchronize the experiments with the rotor, since there would otherwise be phase distortions of the sidebands (we now appreciate this problem can be corrected with a shearing transformation[69]). Thus, we arrived at a scheme which included Geoffrey's favorite refocusing pulse at $n\tau_r$ with sampling initiating at $2n\tau_r$, a pulse sequence identical to that which Geoffrey and Ruth Stark had used in $^{1}H-^{14}N$ single crystal studies.[19] WAHUHA was used to remove homonuclear dipole couplings during t_1 leaving only heteronuclear couplings, and the t_2 dimension had only the chemical shift. We referred to this experiment as the dipolar/chemical shift (DIPSHIFT) experiment. Initially Mike Munowitz, Chris Dobson's 'solid state student' from Harvard, tried this experiment on $Ca(CHO_2)_2$[70] using a new spinning probe constructed by Tai-Huang Huang. It functions well for strong couplings found in $^{1}H-X$ systems, and Mike analyzed the dipolar sideband patterns for several versions of DIPSHIFT in great detail for his thesis. [71–73] Versions of DIPSHIFT have been employed by Jake Schaefer to study dynamics and by Stan Opella to measure bond distances in DNA. DIPSHIFT was the first successful *dipolar recoupling* experiment in MAS.

It was clear that molecular structure determinations would require that weak dipolar couplings—between $^{13}C-^{14}N$, $^{13}C-^{13}C$, and $^{13}C-^{31}P$—would have to be measured. Andrew Kolbert attempted to employ pulse trains to enhance sideband amplitudes in DIPSHIFT experiments[74] and while these schemes were successful they were only applicable to directly bonded systems. What was needed were techniques applicable to weak couplings not arising between directly bonded spin pairs.

At the time there was a double ^{13}C labeled glycine sample around the laboratory, left over from measurements of double quantum spectra in solids.[75] Dan Raleigh performed a MAS experiment with this sample and happened to observe a pronounced broadening of the ^{13}C resonances at a spinning speed equal to one-third of the isotropic shift difference. We had rediscovered rotational resonance (R^2), a phenomenon initially reported by Raymond Andrew in 1963/65. We described the broadening in glycine and other spectra in a short paper and pointed out that this was a recoupling effect which could provide internuclear distances.[76] For long distances or weak couplings the lineshape effects were too small to be useful, so I proposed a magnetization exchange experiment at R^2 for such cases to Dan and Malcolm Levitt. Malcolm remarked that the magnetization would oscillate between the spins, Dan confirmed this result on ZnAc, and Malcolm wrote the first program to simulate the exchange.[77,78] Francois Creuzet had just arrived in the lab and built a new high-speed spinning probe which he and Dan used to explore experimentally a number of R^2 phenomena and showed that they could measure distances up to $\sim$ 5 å in TEE.[79] Subsequently, Francois and Ann McDermott performed the first R^2 distance measurements on a protein.[56,80] We and others are continuing to explore R^2 and apply it to different systems—for instance the β-amyloid protein. R^2 phenomena have been studied by Beat Meier in Richard Ernst's lab, by Zhou Gan in David Grant's lab, and by Charles McDowell and co-workers. Shimon Vega and Asher Schmidt wrote a theoretical description based on Floquet theory.

The problem with R^2 (and REDOR in its present form) is that it measures one distance at a time. Thus, it is difficult to accumulate enough data to determine a structure quickly. Broadband multidimensional experiments (which we refer to as rf driven recoupling) addressing this problem were initially considered in our lab by Jong Ok and most recently by Andrew Bennett[81] and Dan Sodickson[82] along with Levitt and Vega. The experiments consist of longitudinal mixing schemes with one π pulse per rotor period to perform the recoupling. At the latest ENC there were about a dozen papers on this topic, so it is an area of active research. One of these was by Boqin Sun and Phil Costa and relies on rotor synchronized spin locking fields to produce a DRAMA-like Hamiltonian for recoupling in an experiment which we call MELODRAMA. It is also amusing to witness the full circle that this area of NMR has executed. In 1948 George Pake told us that NMR could measure distances in solids by examining dilute spin pairs, but in the 1950s and 1960s we discovered that spin pairs were not too common via broadline solid state NMR spectra. In the 1970s, thanks to John Waugh, we recovered the chemical shift, and now in the 1990s we are routinely reintroducing dipolar couplings among pairs of spins in high-resolution spectra.

HIGH FIELD DNP AND EPR

In 1985 David Singel arrived at Harvard University and we began to discuss a number of problems in magnetic resonance. We had been performing MAS experiments at the FBNML for what seemed like an eternity and I was looking for a new and completely different research topic. In addition, we had developed a number of dipolar recoupling experiments in the lab, and we were constantly faced with the realization that these experiments would benefit enormously from an increase in the signal-to-noise ratio. David had just completed a postdoc at IBM with Nino Yannoni and had assembled a spectrometer for dynamic nuclear polarization (DNP) NMR. A few years earlier Dan Raleigh and I, stimulated by Robert Wind's 40 GHz DNP experiments, had talked extensively about the possibility of using DNP to enhance signals in MAS spectra. We came to the realization that suitable high-frequency, high-power microwave sources were the major stumbling block to DNP experiments at higher fields. Rick Temkin, a colleague in the MIT Plasma Fusion Center, suggested the answer to our problems was a gyrotron, a high-power, high-frequency microwave source which employs a superconducting magnet, rather than a slow wave structure, to generate the microwaves. As a result David, Rick and I submitted for an NIH grant to build a 140 GHz (2 mm) gyrotron and a 210 MHz DNP/NMR spectrometer to go with it. The grant was funded and we began construction in 1987.

In recent years, DNP experiments by Robert Wind, Nino Yannoni, and Jake Schaefer and Ed Stejskal have been performed at 40 GHz but the EPR spectrum was not examined. However, we suggested it was also important to perform high field EPR, since the EPR spectra would change dramatically with a factor of 15 increase in field strength, and we would need to know where in the spectrum we were irradiating. Thus, Ralph Weber joined us from Leiden and began ordering parts for the EPR. He was succeeded by Thomas Prisner who, together with Sun Un and Ann McDermott, performed our initial CW and pulsed EPR experiments. Ann started to assemble the NMR and Sun Un initially was in charge of the gyrotron. Ken Fishbein and Brenden Bellew were the two students involved in the spectrometer construction.

The 140 GHz EPR worked first. We therefore recorded spectra of several model test systems and photosystem-I, and we did pulsed EPR experiments with a pulsed EIO borrowed from PFC.[83,84] Slightly later we finished the NMR and used the pulsed EIO for our initial DNP experiments in which we saw enhancements of $\sim$ 10.[85]

After much work, Lino Becerra finally brought the gyrotron into operation and we obtained our initial DNP results with it as the microwave source.[86] Gary Gerfen, Brenden Bellew, and our technician Jeff Bryant have improved the EPR immensely with cylindrical resonators which we are also using for DNP. High field EPR spectra of paramagnetic proteins, contrary to the expected wisdom, are thus far very impressive.[87] Late in 1993 we obtained our first 140 GHz microwave switches and have performed pulsed EPR and some more pulsed DNP experiments. Recently we have achieved enhancements of 185 in a water/glycerol/TEMPO mixture and transferred this polarization to the carbon-13s in a solute, glycine.[88] These enhancements translate to reductions in signal averaging times of $>10^4$ or reductions in sample size of $>10^2$. We are still improving the instrumentation, and new scientific problems appear regularly.

THE FUTURE

Most of the research topics mentioned above are still under investigation by the current group of students and postdocs in the laboratory. Joanna Long, John Gross, and Sunil Das Gupta are probing the dynamics of lipid bilayers and seeking new

methods for performing spectroscopy. Joanna, Doug Maus, Jinqua Hu, Boqin Sun, Janet Griffiths, and Ani Petkova are working on bR and retinal proteins. Phil Costa and Janet are working on the structures and spectroscopy of peptides and amyloid proteins. Boqin, Phil, and Andrew Bennett are heavily involved in new MAS methodology. Dennis Hall, Brenden Bellew, Souhiel Inati, Gary Gerfen, and Lino Becerra are performing high-frequency DNP and EPR experiments. Three new students—Chad Rienstra, Henry Spindler, and David Rovnyak—recently joined the group and have yet to select thesis topics. With this group of individuals and research topics, the future will be as exciting as the past.

REFERENCES

1. J. R. Bard, J. O. Wear, R. G. Griffin, and E. S. Amis, *J. Electroanal. Chem.*, 1964, **8**, 419.
2. R. G. Griffin, E. S. Amis, and J. O. Wear, *J. Inorg. Nucl. Chem.*, 1966, **28**, 548.
3. R. G. Griffin and H. van Willigen, *J. Chem. Phys.*, 1972, **57**, 86.
4. M. Mehring, R. G. Griffin, and J. S. Waugh, *J. Am. Chem. Soc.*, 1970, **92**, 7222.
5. M. Mehring, R. G. Griffin, and J. S. Waugh, *J. Chem. Phys.*, 1971, **55**, 746.
6. R. G. Griffin, J. D. Ellett, Jr., M. Mehring, J. G. Bullit, and J. S. Waugh, *J. Chem. Phys.*, 1972, **57**, 2147.
7. R. G. Griffin, H. N. Yeung, M. D. Laprade, and J. S. Waugh, *J. Chem. Phys.*, 1973, **59**, 777.
8. J. D. Ellett, Jr., R. G. Griffin, and J. S. Waugh, *J. Am. Chem. Soc.*, 1974, **96**, 345.
9. M. G. Gibby, R. G. Griffin, A. Pines, and J. S. Waugh, *Chem. Phys. Lett.*, 1972, **17**, 80.
10. R. G. Griffin, A. Pines, and J. S. Waugh, *J. Chem. Phys.*, 1975, **63**, 3676.
11. S. Kaplan, A. Pines, R. G. Griffin, and J. S. Waugh, *Chem. Phys. Lett.*, 1974, **25**, 78.
12. R. G. Griffin, and D. J. Ruben, *J. Chem. Phys.*, 1975, **63**, 1272.
13. R. G. Griffin, G. Bodenhausen, R. A. Haberkorn, T.-H. Huang, M. Munowitz, R. Osredkar, D. J. Ruben, R. E. Stark, and H. van Willigen, *Phil. Trans. R. Soc. London*, 1981, **A299**, 547.
14. R. A. Haberkorn, R. E. Stark, H. van Willigen, and R. G. Griffin, *J. Am. Chem. Soc.*, 1981, **103**, 2534.
15. H. van Willigen, R. G. Griffin, and R. A. Haberkorn, *J. Chem. Phys.*, 1977, **67**, 5855.
16. R. E. Stark, R. A. Haberkorn, and R. G. Griffin, *J. Chem. Phys.*, 1978, **68**, 1996.
17. H. van Willigen, R. A. Haberkorn, and R. G. Griffin, *J. Chem. Phys.*, 1977, **67**, 917.
18. E. K. Wolff, R. G. Griffin, and C. Watson, *J. Chem. Phys.*, 1977, **66**, 5433.
19. G. Bodenhausen, R. E. Stark, D. J. Ruben, and R. G. Griffin, *Chem. Phys. Lett.*, 1979, **67**, 424.
20. R. G. Griffin, *J. Am. Chem. Soc.*, 1976, **98**, 851.
21. R. G. Griffin, L. Powers, and P. S. Pershan, *Biochemistry*, 1978, **17**, 2718.
22. R. J. Wittebort, C. F. Schmidt, and R. G. Griffin, *Biochemistry*, 1981, **20**, 4223.
23. T. -H. Huang, R. P. Skarjune, R. G. Wittebort, R. G. Griffin, and E. Oldfield, *J. Am. Chem. Soc.*, 1980, **102**, 7377.
24. R. J. Wittebort, A. Blume, T. -H. Huang, S. K. Das Gupta, and R. G. Griffin, *Biochemistry*, 1982, **21**, 3487.
25. A. Blume, D. M. Rice, R. J. Wittebort, and R. G. Griffin, *Biochemistry*, 1982, **21**, 6220.
26. A. Blume, R. J. Wittebort, S. K. Das Gupta, and R. G. Griffin, *Biochemistry*, 1982, **21**, 6243.
27. T.-H. Huang, C. W. B. Lee, S. K. Das Gupta, A. Blume, and R. G. Griffin, *Biochemistry*, 1993, **32**, 13 277.
28. D. M. Rice, R. J. Wittebort, R. G. Griffin, E. Meirovitch, E. R. Stimson, Y. C. Meinwald, J. H. Freed, and H. A. Scheraga, *J. Am. Chem. Soc.*, 1981, **103**, 7707.
29. K. Beshah, E. T. Olejniczak, and R. G. Griffin, *J. Chem. Phys.*, 1987, **86**, 4730.
30. R. J. Wittebort, E. T. Olejniczak, and R. G. Griffin, *J. Chem. Phys.*, 1987, **86**, 5411.
31. B. A. Lewis, S. K. Das Gupta, and R. G. Griffin, *Biochemistry*, 1984, **23**, 1988.
32. C. W. B. Lee, J. S. Waugh, and R. G. Griffin, *Biochemistry*, 1986, **25**, 3737.
33. D. J. Siminovitch, M. J. Ruocco, E. T. Olejniczak, S. K. Das Gupta, and R. G. Griffin, *Chem. Phys. Lett.*, 1985, **119**, 251.
34. J. B. Speyer, R. T. Weber, S. K. Das Gupta, and R. G. Griffin, *Biochemistry*, 1989, **28**, 9569.
35. G. S. Harbison, J. Herzfeld, and R. G. Griffin, *Biochemistry*, 1983, **22**, 1.
36. G. S. Harbison, P. P. J. Mulder, J. A. Pardoen, J. Lugtenburg, J. Herzfeld, and R. G. Griffin, *J. Am. Chem. Soc.*, 1985, **107**, 4809.
37. G. S. Harbison, S. O. Smith, J. A. Pardoen, P. P. J. Mulder, J. Lugtenburg, J. Herzfield, R. Mathies, and R. G. Griffin, *Biochemistry*, 1984, **23**, 2662.
38. G. S. Harbison, S. O. Smith, J. A. Pardoen, C. Winkel, J. Lugtenburg, J. Herzfeld, R. Mathies, and R. G. Griffin, *Proc. Natl. Acad. Sci. USA*, 1984, **81**, 7106.
39. G. S. Harbison, S. O. Smith, J. A. Pardoen, J. M. L. Courtin, J. Lugtenburg, J. Herzfeld, R. A. Mathies, and R. G. Griffin, *Biochemistry*, 1985, **24**, 6955.
40. H. J. M. de Groot, S. O. Smith, J. M. L. Courtin, E. van der Berg, C. Winkel, J. Lugtenburg, R. G. Griffin, and J. Herzfeld, *Biochemistry*, 1990, **29**, 6873.
41. H. J. M. de Groot, G. S. Harbison, J. Herzfeld, and R. G. Griffin, *Biochemistry*, 1989, **28**, 3346.
42. H. J. M. de Groot, V. C. Copié, S. O. Smith, P. J. Allen, C. Winkel, J. Lugtenburg, J. Herzfeld, and R. G. Griffin, *J. Magn. Reson.*, 1988, **77**, 251.
43. S. O. Smith, J. Courtin, E. van der Berg, C. Winkel, J. Lugtenburg, J. Herzfeld, and R. G. Griffin, *Biochemistry*, 1989, **28**, 237.
44. J. Herzfeld, S. K. Das Gupta, M. R. Farrar, G. S. Harbison, A. E. McDermott, S. L. Pelletier, D. P. Raleigh, S. O. Smith, C. Winkel, J. Lugtenburg, and R. G. Griffin, *Biochemistry*, 1990, **29**, 5567.
45. A. E. McDermott, L. K. Thompson, C. Winkel, M. R. Farrar, S. Pelletier, J. Lugtenburg, J. Herzfeld, and R. G. Griffin, *Biochemistry*, 1991, **30**, 8366.
46. F. Creuzet, A. McDermott, R. Gebhard, K. van der Hoef, M. B. Spijker-Assink, J. Herzfeld, J. Lugtenburg, M. H. Levitt, and R. G. Griffin, *Science*, 1991, **251**, 783.
47. L. K. Thompson, A. E. McDermott, J. Raap, C. M. van der Wielen, J. Lugtenburg, J. Herzfeld, and R. G. Griffin, *Biochemistry*, 1992, **31**, 7931.
48. K. V. Lakshmi, M. Auger, J. Raap, J. Lugtenburg, R. G. Griffin, and J. Herzfeld, *J. Am. Chem. Soc.* 1993, **115**, 8515.
49. J. M. Griffiths, K. V. Lakshmi, A. E. Bennett, J. Raap, C. M. van der Wielen, J. Lugtenburg, J. Herzfeld, and R. G. Griffin, *J. Am. Chem. Soc.*, 1994, **116**, 10178.
50. J. Hu, R. G. Griffin, and J. Herzfeld, *Proc. Natl. Acad. Sci. USA*, 1994, **91**, 8880.
51. L. Zheng, K. W. Fishbein, R. G. Griffin, and J. Herzfeld, *J. Am. Chem. Soc.*, 1993, **115**, 6254.
52. V. Copié, W. S. Faraci, C. T. Walsh, and R. G. Griffin, *Biochemistry*, 1988, **27**, 4966.
53. V. Copié, A. C. Kolbert, D. H. Drewry, P. A. Bartlett, T. G. Oas, and R. G. Griffin, *Biochemistry*, 1990, **29**, 9176.
54. S. O. Smith, I. Palings, M. E. Miley, J. Courtin, H. J. M. de Groot, J. Lugtenburg, R. A. Mathies, and R. G. Griffin, *Biochemistry*, 1990, **29**, 8158.

55. S. Farr-Jones, S. O. Smith, C. A. Kettner, R. G. Griffin, and W. W. Bachovchin, *Proc. Natl. Acad. Sci. USA*, 1989, **86**, 6922.
56. A. E. McDermott, F. Creuzet, R. G. Griffin, L. E. Zawadzke, Q. Z. Ye, and C. T. Walsh, *Biochemistry*, 1990, **29**, 5767.
57. R. G. S. Spencer, K. J. Halverson, M. Auger, A. E. McDermott, R. G. Griffin, and P. T. Lansbury, *Biochemistry*, 1991, **30**, 10 382.
58. R. A. Haberkorn, J. Herzfeld, and R. G. Griffin, *J. Am. Chem. Soc.*, 1978, **100**, 1296.
59. W. P. Aue, D. J. Ruben, and R. G. Griffin, *J. Magn. Reson.*, 1982, **46**, 354.
60. W. P. Aue, D. J. Ruben, and R. G. Griffin, *J. Chem. Phys.*, 1984, **80**, 1729.
61. E. T. Olejniczak, J. E. Roberts, S. Vega, and R. G. Griffin, *J. Magn. Reson.*, 1984, **56**, 156.
62. S. Vega, E. T. Olejniczak, and R. G. Griffin, *J. Chem. Phys.*, 1984, **80**, 4832.
63. E. T. Olejniczak, S. Vega, and R. G. Griffin, *J. Chem. Phys.*, 1984, **81**, 4804.
64. A. C. Kolbert, D. P. Raleigh, and R. G. Griffin, *J. Magn. Reson.*, 1989, **82**, 483.
65. D. P. Raleigh, E. T. Olejniczak, and R. G. Griffin, *J. Chem. Phys.*, 1988, **89**, 1333.
66. D. P. Raleigh, E. T. Olejniczak, and R. G. Griffin, *J. Magn. Reson.*, 1991, **93**, 472.
67. A. C. Kolbert, and R. G. Griffin, *Chem. Phys. Lett.*, 1990, **166**, 87.
68. J. E. Roberts, S. Vega, and R. G. Griffin, *J. Am. Chem. Soc.*, 1984, **106**, 2506.
69. A. C. Kolbert, M. H. Levitt, and R. G. Griffin, *J. Magn. Reson.*, 1989, **85**, 42.
70. M. G. Munowitz, R. G. Griffin, G. Bodenhausen, and T.-H. Huang, *J. Am. Chem. Soc.*, 1981, **103**, 2529.
71. M. G. Munowitz, and R. G. Griffin, *J. Chem. Phys.*, 1982, **76**, 2848.
72. M. Munowitz, W. P. Aue, and R. G. Griffin, *J. Chem. Phys.*, 1982, **77**, 1686.
73. M. Munowitz, and R. G. Griffin, *J. Chem. Phys.*, 1983, **78**, 613.
74. A. C. Kolbert, D. P. Raleigh, M. H. Levitt, and R. G. Griffin, *J. Chem. Phys.*, 1989, **90**, 679.
75. E. M. Menger, S. Vega, and R. G. Griffin, *J. Am. Chem. Soc.*, 1986, **108**, 2215.
76. D. P. Raleigh, G. S. Harbison, T. G. Neiss, J. E. Roberts, and R. G. Griffin, *Chem. Phys. Lett.*, 1987, **138**, 285.
77. D. P. Raleigh, M. H. Levitt, and R. G. Griffin, *Chem. Phys. Lett.*, 1988, **146**, 71.
78. M. H. Levitt, D. P. Raleigh, F. Creuzet, and R. G. Griffin, *J. Chem. Phys.*, 1990, **92**, 6347.
79. D. P. Raleigh, F. Creuzet, S. K. Das Gupta, M. H. Levitt, and R. G. Griffin, *J. Am. Chem. Soc.*, 1989, **111**, 4502.
80. C. W. B. Lee, S. K. Das Gupta, J. Mattai, G. G. Shipley, O. H. Abdel-Mageed, A. Makriyannis, and R. G. Griffin, *Biochemistry*, 1989, **28**, 5000.
81. A. E. Bennett, J. Ok, R. G. Griffin, and S. Vega, *J. Chem. Phys.*, 1992, **96**, 8624.
82. D. K. Sodickson, M. H. Levitt, S. Vega, and R. G. Griffin, *J. Chem. Phys.*, 1993, **98**, 6742.
83. T. F. Prisner, A. E. McDermott, S. Un, J. R. Norris, M. C. Thurnauer, and Griffin, R. G. *Proc. Natl. Acad. Sci. USA*, 1993, **90**, 9485.
84. T. F. Prisner, S. Un, and R. G. Griffin, *Isr. J. Chem.*, 1992, **32**, 357.
85. S. Un, T. Prisner, R. T. Weber, M. J. Seaman, K. W. Fishbein, A. E. McDermott, D. J. Singel, and R. G. Griffin, *Chem. Phys. Lett.*, 1992, **189**, 54.
86. L. R. Becerra, G. J. Gerfen, R. J. Temkin, D. J. Singel, and R. G. Griffin, *Phys. Rev. Lett.*, 1993, **71**, 3561.
87. G. J. Gerfen, B. F. Bellew, S. Un, J. M. Bollinger, J. Stubbe, R. G. Griffin, and D. J. Singel, *J. Am. Chem. Soc.*, 1993, **115**, 6420.
88. G. J. Gerfen, L. Becerra, D. A. Hall, R. G. Griffin, R. J. Temkin, and D. J. Singel, *J. Chem. Phys.*, 1995, **102**, 9494.

Biographical Sketch

Robert G. Griffin. *b* 1942. B. S., 1964, University of Arkansas, Ph.D., 1969, Washington University (St. Louis), Post-doctoral Fellow, Dept. of Chemistry, MIT 1969–72; staff member Francis Bitter National Magnet Laboratory, MIT, 1972–1989; Professor of Chemistry, MIT, 1989–current; Director, Francis Bitter National Magnet Laboratory, 1992–current. Approximately 210 publications. Research interests include development of new methods for performing high-resolution NMR experiments in solids, high-frequency DNP and EPR, and applications of these techniques to problems in biological, chemical, and physical systems.

Günther, Harald: From Organic Chemistry to NMR—A Personal Experience of Magnetization Transfer

Harald Günther

University of Siegen, Germany

My first encounter with NMR was in the late 1950s while I was still a graduate student of chemistry at the University of Heidelberg, during a visit to the ACHEMA, the international exhibition of chemical instrumentation at Frankfurt, where a presentation of the Swiss manufacturer Trüb & Täuber displayed a formidable instrument. I still remember the dark red color of the cabins with the electronic parts, exclusively valves at that time, and a friend, several years older than myself, told me that in his department somebody had just delivered a seminar about a new technique dealing with nuclear magnetism. This episode had no immediate consequences. However, as my Doktorvater, Georg Wittig, several years later, when I was about finishing my Ph.D. work in his laboratory, suggested I should take up a postdoctoral position at the Mellon Institute with Aksel A. Bothner-By in order to get acquainted with a new physical method for the investigation of chemical structures, known as nuclear magnetic resonance; a decision was taken which has determined my further career and indeed my whole life.

When I came to Pittsburgh in 1961, the Mellon Institute had just received the first Varian A-60 NMR spectrometer and Barry Shapiro was in charge of this instrument. I joined Aksel's research group which was working at that time on rotational isomerism in olefins. My immediate duty was to synthesize a number of substituted propenes and only later was I initiated into the secrets of operating the A-60 and introduced to the analysis of ^{1}H NMR spectra. In addition to the private seminars in Aksel Bothner-By's office, where Barry Shapiro and I sat on one of those low leather sofas while Aksel explained energy level diagrams at the board, the books by John D. Roberts on applications of NMR to organic chemistry[1] and on spin–spin coupling[2] as well as Jackman's monograph[3] guided the beginner, who now and then had the courage to look into Pople, Schneider, and Bernstein.[4]

The art of NMR spectral analysis started to develop at that time and the Pittsburgh group had established the program FREQINT IV, which allowed the calculation of stick spectra from trial parameters. No iterative process was available and the analysis proceeded by visual comparison of the calculated and observed spectra. From the observed differences one had to derive changes in the initial parameters which, hopefully, would improve the fit. In most cases they did not. Computer time was available for our group at a private computer center in downtown Pittsburgh and an afternoon on the IBM 704 high-speed computer was easily invested in a number of trial and error attempts with the spectrum of 3-chloropropene (**1**) and those of related compounds.[5] This was the first time I learned that research also costs money. Real progress was then made after an iterative procedure for parameter improvements was added to the program which from then on was called LAOCOON. The final version emerged after Salvatore (Turi) Castellano joined the group in 1962 and became available later as the famous LAOCOON II package.[6]

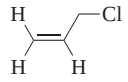

(1)

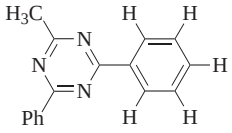

(2)

At that time quite a number of substituent effects were unknown in proton NMR spectra and with Turi we worked on a project which originated from an unexpected chemical shift effect. Vinicio Mini, an Italian postdoc working with W. Grundmann in the field of heterocyclic chemistry, had synthesized methyldiphenyl-*s*-triazine (**2**) and the ^{1}H NMR spectrum of this compound was routinely measured with the A-60. With this instrument the spectrum was usually scanned in the ^{1}H chemical shift range of 0–8 ppm, and low-field regions were investigated only in rare cases. To his surprise, Mini missed two proton resonances of the phenyl rings which were later found—quite unexpectedly for such a structure—at fairly low field. Several mechanisms were recognized consequently as the origin of this unusual deshielding for phenyl protons.[7]

While our work was thus completely confined to proton NMR with perhaps a ^{19}F spectrum now and then, in another laboratory at the institute, Paul Lauterbur was trying hard to find ^{13}C signals in natural abundance, an esoteric enterprise at that time.[8] As I heard later, one day he was visited by the FBI. With his 8.5 MHz transmitter he had hit the local FBI frequency network and they located the uninvited participant. Across from my lab, Harold Conroy, originally a natural products chemist at Yale and one of the fathers of the Karplus–Conroy curve,[9] worked on the exact solution of the Schrödinger equation. Organic research fellows like Satoru Masamune or Eugene LeGoff provided interesting compounds for NMR studies.

Back in Germany, my original plans to start research in the field of mechanistic organic chemistry at Heidelberg changed. Emanuel Vogel at Cologne University invited me to join his institute as assistant in charge of the newly acquired A-60. This turned out to be a unique opportunity to continue with NMR and, together with Detlef Wendisch as my first Ph.D student (now an NMR spectroscopist with Bayer AG at Leverkusen), we investigated rotational isomerism in vinylcyclopropanes (**3**).[10] Analysis of the ^{1}H NMR spectra of these systems required extensive calculations and we were relieved when Aksel Bothner-By on a visit to Cologne in 1964 provided us with the final version of the LAOCN III program. At that time the University of Cologne had no computer center and our spin analyses were run at the nearby University of Bonn which was in possession of an IBM 7090 computer. So, several afternoons in the week we went to Bonn by train and came back in the evening with the r.m.s. error reduced by a few millihertz. Nevertheless, the work eventually established the three-well potential for internal rotation in vinylcyclopropane.

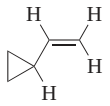

(3)

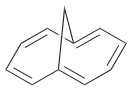

(4)

Apart from this project, my interest was caught by the compounds coming from Vogel's group. In October 1963, shortly after I arrived at Cologne, they succeeded in preparing 1,6-methano[10]annulene (**4**), which proved to be the start to a chapter of fascinating syntheses of bridged annulenes.[11] These systems were, of course, nicely tailored for spectral analysis with the A-60 and apart from ring current effects, which were exciting chemists in the 1960s, gave interesting relationships between bond properties and proton spin−spin coupling constants.[12] During my time at Mellon I had already had a brief glimpse of this field as Lloyd Jackman gave a seminar where he reported the peculiar NMR behavior of Sondheimer's [18]annulene.[13]

One of the most exciting molecules at that time was oxepine, synthesized in Vogel's group for the first time. Walter Böll, who was engaged in the successful synthesis of oxepine, first noted the strong solvent dependence of the UV spectrum of this compound and my ^{1}H NMR work revealed peculiar chemical shifts for the α-protons and a strong temperature and solvent dependence of these resonances.[14] Clearly, an oxepine−benzene oxide equilibrium (**5** $\rightleftharpoons$ **6**) was indicated; however, the respect for the aromatic character of benzene was so strong among organic chemists that it was difficult for them to believe that benzene oxide should be a stable compound. Obviously, low-temperature NMR measurements were necessary to settle the question and since the A-60 available at Cologne was limited to measurements down to −60 °C, I had to go to Freiburg where Horst Friebolin, who was in charge of the NMR equipment at the Fraunhofer-Institut headed by R. Mecke, had offered me the opportunity to run some low-temperature spectra. So, one day I took the Loreley express, one of the fast trains going south, a Dewar filled with dry ice containing the NMR tube with oxepine prepared by Walter Böll in my bag and went to Freiburg. What followed was an exciting afternoon and evening at Friebolin's DP-60 spectrometer and when much later I returned to my hotel, I spent a few hours more looking at the spectra where we had recorded the line broadening at low temperature and which finally showed the splitting into two separate signal sets for the two isomers[15]—a truly memorable and exciting moment. In this context it should be mentioned that the whole field of degenerate valence isomerizations could not have been developed without NMR, and the pioneering work of Doering and Roth[16] on homotropylidene and Schröder[17] as well as Saunders[18] on bullvalene are true landmarks in this field.

(5) (6)

While working on oxepine, I frequently visited Freiburg which was an active NMR center at that time. In addition to Friebolin's work on conformational analysis,[19] Dischler and Englert had developed direct methods for the analysis of AA′BB′ systems[20] and Saupe and Englert had discovered the alignment of small molecules in liquid crystals.[21] While visiting Alfred Saupe one day, he showed me his beautiful 50-line spectrum of benzene dissolved in a mixture of liquid crystals.[22]

As time went on, the NMR frequencies increased and we acquired a Varian HA-100 at Cologne. This improved our low-temperature work, gave the basis for real double resonance experiments, and for the first time allowed us to study small molecules oriented in liquid crystals.[23] Being an optimist, I had also ordered a probe for ^{13}C NMR which was, however, never used. It was only after the invention of the Fourier transform technique that we entered this field and my first spectra were run in 1970 during the evenings at an NMR workshop organized by Robert Kosfeld at Aachen. After finishing my seminars on proton NMR and chemical structure, I ran down to the basement of the institute where Toni Keller of Bruker was operating the first 15 MHz ^{13}C FT NMR spectrometer. During the meeting we finished a project on norcaradiene−cycloheptatriene isomerism, (**7**) and (**8**), which lent itself to ^{13}C analysis because of the large chemical shift difference existing between the 1,6-carbons in both structures.[24] My complete ignorance of computer techniques led to an error in the chemical shifts we recorded, because instead of using multiples of 2^{10}, I converted the digitized data for the line positions by decimal numbers which gave an error of several ppm for the high frequencies. However, I shortly became acquainted with ^{13}C FT NMR as we purchased at Cologne a Bruker HX-90 spectrometer equipped with a Nicolet 1080 computer. On starting to measure proton decoupled ^{13}C spectra, the quantum mechanical know-how about spin analysis soon faded away in my group and after a few months my students completely ignored the HA-100.

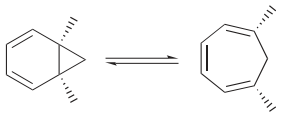

(7) (8)

Working in an institute for organic chemistry, my contact with NMR groups was confined exclusively to workshops and international meetings. The 13th Colloque AMPERE at Leuven 1964 was the first conference I attended and I still remember an impressive lecture by Solomon. At the 8th European Congress on Molecular Spectroscopy which took place in 1965 at Copenhagen, a larger number of high-resolution NMR contributions were presented. To my own surprise I was asked to chair one of the sessions, with the most famous speaker during the afternoon being Ray Freeman.[25] A red lamp had been installed on the front table in the lecture hall in order to remind the speakers of the time-table which was quite naturally rather crowded because posters had not yet been invented. When Freeman's time ran out, he gave no indication that he would come to an end. I was probably convinced that everybody should be treated alike and after a few minutes I pushed the button. Freeman was not at all impressed. Instead he took a box which was on the table, put it over the lamp and continued. The loud peal of laughter from the audience showed me that I certainly did not know enough about this speaker.

In Germany, meetings on NMR which dealt with applications in chemistry only became a regular practice after an NMR

Discussion Group was founded in 1974. The initiative for this came from Ernest Lustig who had returned to Germany shortly before. The first meeting was organized in Frankfurt by Horst Kessler, and during our fifth meeting, arranged by the late Gerhard Binsch in 1978 at Kloster Ettal south of Munich, the NMR Group applied for membership in the Society of German Chemists (GDCh). Since then, regular meetings have been held every year and the group has now, after German reunification, more than 400 members.

In 1977 I moved from Cologne to Siegen, one of the newly founded universities in the state of Nordrhein-Westfalia. This provided the basis for acquiring a high-field spectrometer, and in May 1979 we charged our 400 MHz superconducting magnet. The world of NMR would soon become even more exciting as the newly developed two-dimensional techniques entered the laboratories and multinuclear experiments became routine. In addition the enormous breadth of NMR nowadays, which has gone far beyond the borders of physics and chemistry, and its fascinating applications in chemistry make it still one of the most attractive areas in modern science.

REFERENCES

1. J. D. Roberts, *Nuclear Magnetic Resonance—Applications to Organic Chemistry*, McGraw-Hill, New York, 1959.
2. J. D. Roberts, *An Introduction to the Analysis of Spin–Spin Splitting in High-Resolution Nuclear Magnetic Resonance Spectra*, W. A. Benjamin, New York, 1961.
3. L. M. Jackman, *Applications of Nuclear Magnetic Resonance Spectroscopy in Organic Chemistry*, Pergamon Press, Oxford, 1959.
4. J. A. Pople, W. G. Schneider, and H. J. Bernstein, *High-resolution Nuclear Magnetic Resonance*, McGraw-Hill, New York, 1959.
5. A. A. Bothner-By, C. Naar-Colin, and H. Günther, *J. Am. Chem. Soc.*, 1962, **84**, 2748; A. A. Bothner-By and H. Günther, *Discuss. Faraday Soc.*, 1962, **34**, 127.
6. S. Castellano and A. A. Bothner By, *J. Chem. Phys.*, 1964, **41**, 3863.
7. S. Castellano, H. Günther, and S. Ebersole, *J. Phys. Chem.*, 1965, **69**, 4166; H. Günther and S. Castellano, *Ber. Bunsenges. Phys. Chem.*, 1966, **70**, 913.
8. P. C. Lauterbur, *J. Am. Chem. Soc.*, 1961, **83**, 1838.
9. M. Karplus, *J. Chem. Phys.*, 1959, **30**, 11; H. Conroy, in *Advances in Organic Chemistry*, Interscience, New York, 1960, Vol. 2, p. 265.
10. H. Günther and D. Wendisch, *Angew. Chem.*, 1966, **78**, 266; *Angew. Chem., Int. Ed. Engl.*, 1966, **5**, 251.
11. E. Vogel and H. D. Roth, *Angew. Chem.*, 1964, **76**, 145; *Angew. Chem., Int. Ed. Engl.* 1964, **3**, 228.
12. H. Günther, *Z. Naturforsch.*, 1965, **20b**, 948; D. Cremer, and H. Günther, *Liebigs Ann. Chem.*, 1972, **763**, 87.
13. L. M. Jackman, F. Sondheimer, Y. Amiel, D. A. Ben-Efraim, Y. Gaoni, R. Wolovsky, and A. A. Bothner-By, *J. Am. Chem. Soc.*, 1962, **84**, 4307.
14. E. Vogel, W. A. Böll, and H. Günther, *Tetrahedron Lett.*, **1965**, 609.
15. H. Günther, *Tetrahedron Lett.*, **1965**, 4085.
16. W. v. E. Doering and W. R. Roth, *Tetrahedron*, 1963, **19**, 715.
17. G. Schröder, *Angew. Chem.*, 1963, **75**, 722; *Angew. Chem., Int. Ed. Engl.* 1963, **2**, 481.
18. M. Saunders, *Tetrahedron Lett.*, **1963**, 1699.
19. H. Friebolin, R. Mecke, S. Kabuss, and A. Lüttringhaus, *Tetrahedron Lett.*, **1964**, 1929.
20. B. Dischler and G. Englert, *Z. Naturforsch.*, 1961, **16a**, 1180.
21. A. Saupe and G. Englert, *Phys. Rev. Lett.*, 1963, **11**, 462.
22. A. Saupe, *Z. Naturforsch.*, 1965, **20a**, 572.
23. J. B. Pawliczek and H. Günther, *J. Am. Chem. Soc.*, 1971, **93**, 2050.
24. H. Günther and T. Keller, *Chem. Ber.*, 1970, **103**, 3231
25. R. Freeman, *C^{13} Nuclear Magnetic Resonance Spectra Studied by Slowly Pulsed Double Resonance, Abstracts of papers presented to the 8th European Congress on Molecular Spectroscopy, Copenhagen, August 14–20, 1965, Abstr. No. 55*.

Biographical Sketch

H. Günther, *b* 1935. Studied chemistry at the Universities of Stuttgart and Heidelberg, Ph.D., 1961, Heidelberg with G. Wittig. Research fellow at Mellon-Institute, Pittsburgh 1961–63; introduced to NMR by A. A. Bothner-By. 1963–77 Staff member at the Institute of Organic Chemistry, University of Cologne; Habilitation 1968 with E. Vogel; Associate Professor 1970; since 1977 Full Professor at the University of Siegen. 1973 Chemistry Award of the Academy of Sciences, Göttingen; 1973 Award of the Fonds der Chemischen Industrie, Frankfurt; 1995 Member of the Academy of Sciences of Nordrhein-Westfalia; ca. 200 publications; author of NMR textbook (German, English, Russian, Polish, French editions). Editor-in-Chief of *Magnetic Resonance in Chemistry* since 1992. Research interests include applications of high-resolution and solid state NMR in organic and organometallic chemistry.

Gutowsky, Herbert S.: The Coupling of Chemical and Nuclear Magnetic Phenomena

Herbert S. Gutowsky
University of Illinois, Urbana, IL, USA

INTRODUCTION

If nuclear magnetic resonance had not been discovered by Purcell[1] and Bloch,[2] chemists would have had to invent it, because without NMR the world's understanding and use of chemistry today would not be nearly as profound or as extensive as it has become. Some evidence of this is given in Figure 1, taken from a review article that Jiri Jonas and I published in 1980.[3] It shows the number of scientific articles per year with NMR key words in *Chemical Abstracts* over the 1970s. Since then the number has continued to grow and is now approaching 10 000 per year.

This remarkable utility of NMR has two main sources. First, NMR observables are affected by a wide range of interactions between magnetic nuclei and their chemical surroundings, i.e. within a few Å. Second, our technology, principally ultra-high-resolution superconducting solenoids and computers, makes it feasible to observe even very small chemical/nuclear interactions on microgram samples. I had the rare good fortune to be the first chemist to explore the synergistic coupling of chemical and NMR phenomena. This is an account[4] of some of my early experiences and impressions along the way.

In their initial NMR experiments, the physicists were not seeking a novel way to study chemistry. They were motivated mainly by interest in a simpler method for determining nuclear moments and spins. At that time the methods of choice used very difficult atomic and molecular beam techniques. The first attempts to detect nuclear magnetism in bulk samples were

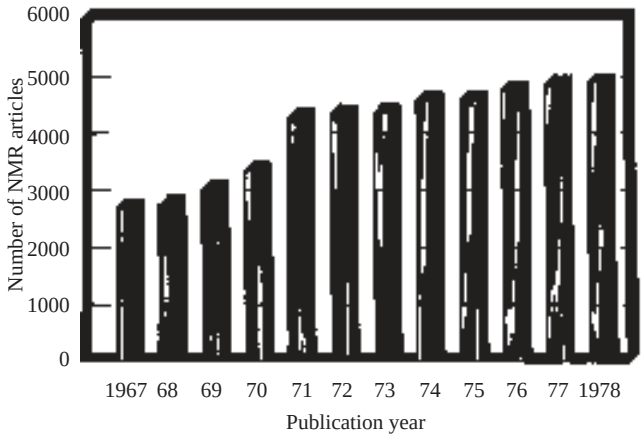

Figure 1 NMR articles per year contained in *Chemical Abstracts* for the period 1967–78[3]

those of C. J. Gorter in the Kamerlingh Onnes Laboratory at Leiden in 1936 and again in 1942.[5,6] They were unsuccessful, probably because of a poor choice in the chemical state of the samples.

Gorter used KF or LiCl powder in the tank coil of an rf oscillator. The sample was kept at low temperatures to improve the Boltzmann factor and signal strength, and the static magnetic field was swept slowly through the probable resonance regions for F and Li. The 1936 experiments[5] attempted to detect a rise in temperature of the sample at the resonance condition and the 1942 experiments[6] looked for a change in inductance of the coil and in oscillator frequency. We now know that the desired effects were weakened by the large dipolar broadening of the resonance in solids, by saturation due to the long spin–lattice relaxation time (T_1) in solids at low temperatures, and by inhomogeneity broadening from the applied magnetic field.

Why were Purcell and Bloch successful in detecting magnetic resonance and Gorter not? From conversations with them I learned it wasn't because they knew any better what they were doing, but because they tried the right things for the wrong reasons. Both sought to detect the resonant absorption of radiofrequency energy by magnetic nuclei at ambient temperature. Purcell wanted a high concentration of strongly magnetic nuclei. He had become familiar with paraffin wax as a proton-rich neutron shield in cyclotron research during World War II. So he chose 850 cm^3 of the 'solid' wax[1] as his sample. The unconsidered high molecular mobility in the wax at room temperature gave a strong, somewhat motionally narrowed proton resonance with a shortened T_1 and was relatively easy for them to detect.

Bloch wanted to avoid samples with a long T_1 which would saturate too readily and thereby give a weak signal. So he used a water sample doped with paramagnetic ions to shorten T_1 and also looked for the proton resonance. Here too the molecular mobility of liquid water led to a narrow, strong signal which was readily detected.[2] In both instances the key to success was the narrowness and shortened T_1 of the resonance due to the motional averaging of the dipole–dipole interactions.

DIPOLAR BROADENING AND MOTIONAL NARROWING AT HARVARD

The way I became aware of NMR and started research on it has some anomalous aspects. While Purcell and Bloch were making their discoveries at MIT and Stanford in late 1945, I was a graduate student at Berkeley finishing a master's degree in chemistry with Ken Pitzer. The quickest way for me to get into NMR would have been to go across the Bay Bridge from Berkeley to Stanford and work with Bloch. Instead, in February 1946, I went to Harvard where in the fall of 1947 I ended up working with Purcell and George Pake as a student of George Kistiakowsky.

In practice, my introduction to NMR resulted from an unlikely chain of events. My M.S. thesis work with Pitzer was on the electron-deficient dimers formed by Group III compounds such as the aluminum alkyls and borane as illustrated in Figure 2. At that time the nature of the bonding responsible for the dimerization was highly speculative. Two

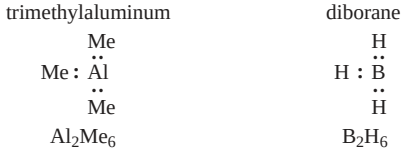

Figure 2 Group III electron-deficient molecules that dimerize

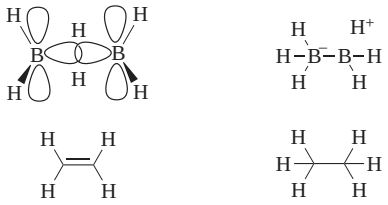

Figure 3 Ethylene-bridge and ethane-like structures proposed for diborane

structural models were in vogue and it was a matter of choosing between them. In the classical case of diborane, the two structures are the ethylene-bridge and ethane-like types shown in Figure 3. My cryoscopic study of the dimerization of the aluminum alkyls did not shed much light on the nature of the bonding. It encouraged me, however, to give a group seminar on diborane at Harvard and perform a couple of unsuccessful experiments on its chemistry.

My initial Ph.D. research problem with Kistiakowsky at Harvard was to obtain an infrared spectrum of the methyl radical as a means of learning something about its structure. It was a significant problem but technically very difficult. It proved to be beyond me and in fact wasn't completed successfully until 15 years later, by someone else with new technology. So I found myself knowing how to run E. Bright Wilson's homemade infrared spectrometer[7] and having on hand a supply of dimethylmercury which I'd prepared as a source of methyl radicals. I hated to see the effort I'd put in on the problem be entirely wasted, so I checked the literature and found that the vibrational spectrum had not been reported for dimethylmercury. This led me to run the Raman as well as the infrared spectrum of the compound, and do a frequency assignment and normal coordinate analysis of the results. Later I did the same for the zinc and cadmium homologs.

By the middle of 1947, I had completed most of these tasks, admittedly of a fairly pedestrian nature. However, Kistiakowsky wasn't about to grant me a Ph.D. from Harvard on the basis of the infrared and Raman studies alone. So we cast about for something else to keep me busy. At this point serendipity entered in a major way. One day in early September Kisty had lunch with Ed Purcell at the Harvard faculty club, where Purcell told him about the NMR technique which a graduate student of his, namely George Pake, was using to determine the proton–proton distance in the water molecules of solid gypsum, $CaSO_4{\cdot}2H_2O$.[8] The proton lineshape of a powder sample is shown in Figure 4.

The only magnetic nuclei in the sample are the protons which occur in close pairs. The strong, magnetic dipole–dipole interactions in the pairs lead to the very broad Pake doublet pattern in the figure, at the bottom of which is the first derivative observed for the NMR absorption while the top gives the integrated lineshape. The dependence upon the inverse cube of the interproton distance of what is now called

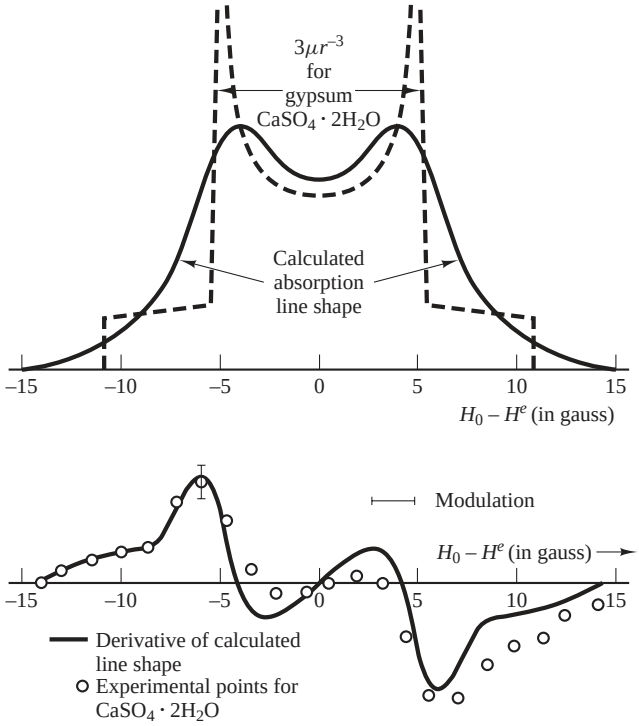

Figure 4 The broad proton lineshape of powdered gypsum, $CaSO_4{\cdot}2H_2O$. The first derivative is at the bottom and the integrated lineshape at the top[8]

the Pake splitting led Kisty to suggest that the proton NMR spectrum of diborane might differentiate between the ethylene-bridge and ethane-like structures. The two protons in the bridge should be closer than the two protons in the terminal BH_2 groups, whereas in the ethane-like structure the three protons at each end would have the same separation. In turn, one might expect a large and a small dipolar splitting for the ethylene-bridge structure and only one splitting for the ethane-like structure.

So, on September 19, 1947, after an enthusiastic conference with Kistiakowsky and a meeting between myself and George Pake, I began my initiation into NMR. My initial tasks in the collaborative exercise were those appropriate to a chemist. I was to synthesize the compound. My other task was to build some sort of cryostat which would freeze the sample so that the proton–proton dipolar interactions weren't narrowed by the molecular mobility in the liquid. This job was complicated by the fact that the permanent magnet being used by Pake had only a 0.75 in. gap. The result was not a thing of beauty nor a technological triumph, but it worked. The sample was placed in a 0.375 in. o.d. Pyrex tube and inserted into a hollowed-out copper block which conducted heat into an insulated brass can containing liquid nitrogen.[9] The main problem with the cryostat was the high rate at which it consumed liquid nitrogen, then relatively expensive and hard to get, which Kisty provided. The rate of consumption was about 5 L h^{-1} and for years afterward, whenever I visited Harvard, he would remind me of the large amount of liquid nitrogen George Pake and I boiled off in the experiments.

On February 21, 1948, Pake and I made our first low-temperature run on the proton resonance of diborane. This was done with an rf bridge system, using 30 cycle modulation

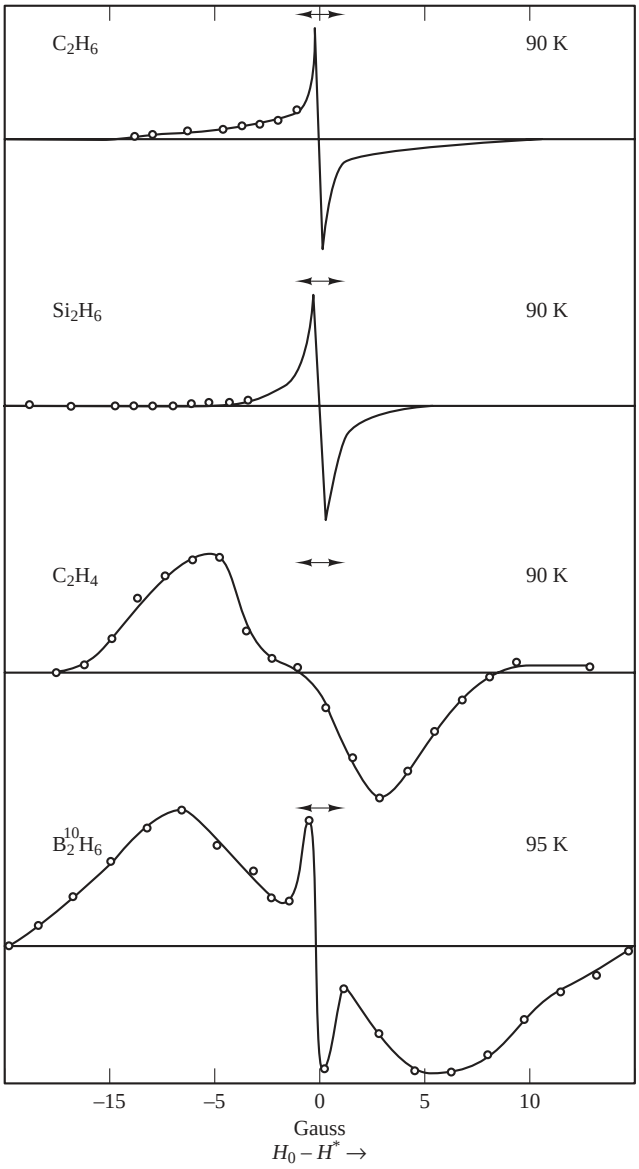

Figure 5 Derivatives of the proton magnetic resonance lines observed at 29.0 MHz in polycrystalline ethane, disilane, ethylene, and diborane at 90–95 K[9]

of the magnetic field with a lock-in detector.[8] The main field of the permanent magnet was swept manually via a rheostat which adjusted the dc current through a set of biasing coils, and the first derivative of the absorption was recorded by watching an output meter and writing down its value on a point-by-point basis. George did the field sweeping while I monitored the liquid nitrogen and the temperature and did the writing. What we hoped to see was the derivative of an absorption line bearing some resemblance to that of the proton doublet found by Pake for the water of crystallization in powdered gypsum.

What we actually observed bore little resemblance to this; the results are shown at the bottom of Figure 5. It is the derivative of a broad line, featureless except for a small spike in the center. My disappointment at seeing nothing resembling a doublet structure was compounded by confusion about the origin of the sharp spike at the line's center. The melting point of diborane is only 108 K, so for some time we thought that part of the sample might still be liquid because of the crudity of the cryostat which gave a sample temperature of 90–95 K. However, after spending several days transferring the sample to a larger tube and otherwise improving its thermal contact with the liquid nitrogen, it became apparent that the spike was attributable to the solid.

The absence of a doublet structure left us with no basis for determining what the structure of diborane was. Later, after Van Vleck's theory for the second moment was published,[10] we were able to use it to analyze our data and provide some support thereby for the bridge structure. But at the time I saw my thesis project going up in fog with the liquid nitrogen. So I did what chemists have been doing for generations. I made a comparative study of related compounds, ethylene and ethane in this case. Their lineshapes are given in Figure 5. That for ethylene is quite similar to diborane while that for ethane is very narrow. However, our lowest cryostat temperature was at the melting point of ethane (90 K), so to be sure of our results I synthesized some disilane, the silicon analog of ethane which has a m.p. of 141 K, 50 degrees above that of ethane.

Nonetheless disilane also gave a narrow, liquid-like resonance, shown in Figure 5. Up to that time, narrow lines were expected in liquids and broad lines in solids.[11] At this stage, however, we finally realized we were seeing a new phenomenon—an averaging out of the dipolar broadening by the hindered molecular motions in a 'plastic' solid. So I switched directions and we started studying the motions. Figures 6 and 7 are a good example of the sort of things we found.[12] Figure 6 compares the width of the proton resonance (lower curve) with the heat capacity in solid 1,2-dichloroethane as a function of temperature. We see that an anomaly in C_p corresponds with a major change in the proton linewidth.

Figure 7 gives the proton lineshapes in the solid at temperatures above and below the heat capacity anomaly. The lineshapes are very similar except that the one at higher temperature is about half as broad as that at lower temperature. A theoretical analysis shows that this corresponds to the proton pairs in $-CH_2Cl$ undergoing restricted rotation about an axis perpendicular to the intrapair axis, which no doubt is the *trans*-Cl–C–C–Cl axis. Moreover, the narrowing requires that the reorientations be fast on what is now called the NMR timescale. That is, the reorientation frequency needs to be

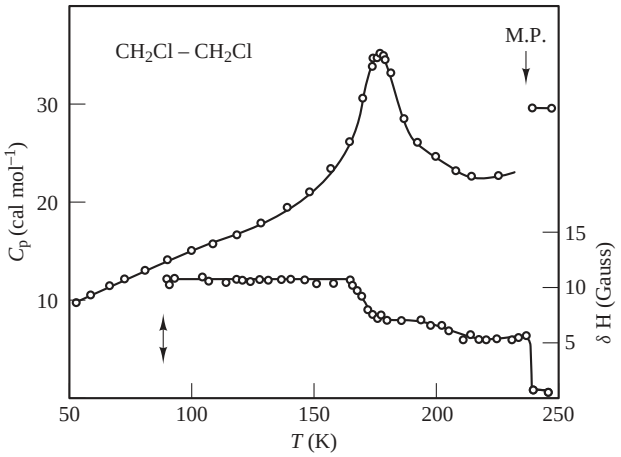

Figure 6 Comparison of proton linewidth and heat capacity versus temperature curves for 1,2-dichloroethane[12]

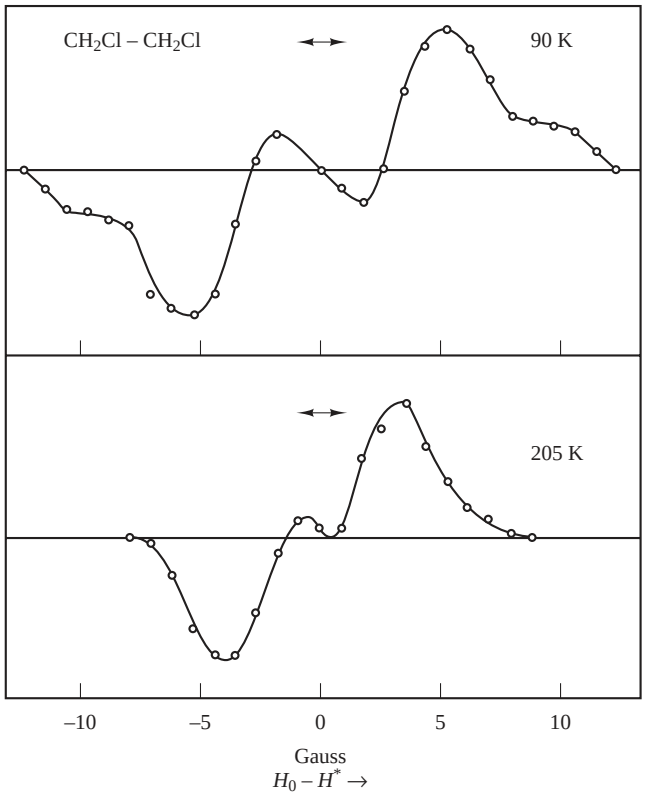

Figure 7 Derivatives of the proton magnetic resonance line observed at 29.0 MHz in solid 1,2-dichloroethane at 90 and 205 K[9]

comparable with the dipolar broadening in frequency units being averaged out. This requires that the correlation time τ_c for the motion be shorter than $\sim 10\ \mu$s at the C_p anomaly.

In this way I ended up with the second half of my Ph.D. thesis. It was not primarily an NMR determination of the structure of diborane. Instead we discovered a broad range of circumstances where magnetic dipole interactions are strongly coupled to the dynamic state of the chemical species containing the nuclei.[9,12,13] Also, we showed that dipolar broadening in the 'rigid lattice' at low temperatures could give accurate structural information, in particular a value of 1.025 Å for the N–H distance in the ammonium ion.[9]

STARTING OUT AT ILLINOIS

My joining the faculty at Illinois in September, 1948 was also accidental in character. I wasn't appointed because of the bright future of NMR, but because Roger Adams, the head of the Chemistry Department, needed someone to be responsible for the operation of an infrared spectrometer which the organic chemists had adopted as an essential research service. The instrument was the eighth single-beam infrared spectrometer produced by the Perkin-Elmer Co. during the Second World War, and it and the technician running it required periodic encouragement. My experience with Bright Wilson's homemade spectrometer[7] overqualified me for the task. So I accepted the appointment at Urbana as an instructor in physical chemistry but with the understanding that NMR would be my main research effort.

At the time I, of course, had no real appreciation of what the future of NMR would bring. I did know enough about physical chemistry, however, to realize that basic new phenomena are not discovered very often. Also, not very many persons have the good fortune to be on the scene at the time of such discoveries. So, blessed with that much good sense, and not inhibited by any real knowledge of electronics or of magnetic theory, I set out to build a broadline NMR spectrometer, such as that which Pake set up at Harvard, but better. Starting up a research program then wasn't too different from what it is now. I had to prepare a proposal and submit it for funds to the University of Illinois Graduate Research Board. They quickly granted me the $5000 requested, but with the stipulation that I also submit the proposal to Research Corporation. If I received a grant from them, the Research Board funds were to be returned! So I asked for and got $7500 from Research Corporation and returned the $5000 to Illinois.

The main item needed was a large magnet. I never seriously considered an electromagnet for the purpose, because I knew it was beyond me and the rudimentary shop facilities then available in chemistry at Illinois, and I wanted to avoid the added operating complexity. These reasons, along with the cryogenic limitations of the 0.75 in. gap in Pake's spectrometer led me to decide on a permanent magnet with a 2 in. gap. Even more important, though I didn't know it at the time, were the efforts I made to attain a homogeneous magnetic field. I did this to avoid problems in locating a good spot for the sample in the field and also to minimize any inhomogeneity corrections to the second moments of the broad lines which were to be studied. So the pole tips were designed with a Rose-type shim to correct for the fall-off in field at the edge of the gap, and high-quality, carefully heat-treated steel was used for the pole tips.[14]

My location at the University of Illinois proved advantageous in designing and acquiring the permanent magnet, because two manufacturers of Alnico V permanent magnets were within 200 miles of Urbana. Arnold Engineering Co. in northern Illinois built our first magnet, with a field of 6365 G, which turned out very well. The main problem we had with it was because I had placed no tolerances on the coaxiality of the pole tips in the rectangular, horizontally mounted yoke. The vertical adjustment was fine, because the tips were supported from the bottom of the gap, but the horizontal adjustment proved to be 0.125 in. out of line. We discovered this quite late in the game after spending a couple of months trying to improve the field homogeneity by manually polishing the pole tips, with mixed results. But that's getting ahead of the story.

The magnet was delivered in early October 1949 with a field reported to be 6050 G. On October 20 we saw our first proton resonance in a water sample at 27.1 MHz. However, my original plans to continue studying the motional narrowing of the broad resonances in solids ran into two snags. Our homemade electronics, especially the lock-in amplifier and the preamplifier just after the rf bridge we were using, didn't have the sensitivity needed. Moreover, my initial efforts at designing and building an all-metal cryostat weren't very successful, in spite of having a 2 in. gap in which to place it. Fortunately, Knight's report[15] of the resonance shifts in metals appeared at that time and it included the observation of ^{31}P shifts in several compounds. Later, in early 1950, Proctor and Yu reported chemical shifts between the ^{14}N resonances in the NH^+_4, CN^- and $NO_3{}^-$ ions,[16] and Dickinson found shifts for fluorine in

several compounds.[17] These effects were viewed as a nuisance by the physicists who wanted to make accurate measurements of nuclear moments. But they attracted our attention because, first of all, we could observe NMR in liquids, and, second, I felt the shifts must depend in some way on the chemical species involved. So we turned our interests to chemical shifts in fluorine compounds and the beginnings of high-resolution NMR.

HIGH-RESOLUTION NMR

At first we looked at whatever compounds we could lay our hands on. Then we began to see if we could resolve the fluorine resonances from structurally nonequivalent nuclei in the same molecule and on April 26, 1950 we looked at the fluorine resonance in a benzene derivative with a CF_3 group and three fluorines on the ring, and were able to resolve them. This encouraged us greatly and led me to think about how the shifts are related to molecular structure.[18] Chemists learn very early to look for periodicities in the chemical and physical properties of compounds, or they don't stay in chemistry very long. We deal with such a large number and wide variety of systems that we have to oversimplify their diversity to be able to remember them. Moreover, in my senior year at Indiana University I was exposed to Linus Pauling's book, 'The Nature of the Chemical Bond', which is a masterpiece of such oversimplifications. In any case, it seemed to me that the chemical shift, as an electronic phenomenon, should be related in some way to the nature of the chemical bonds. This in turn depends upon the nature of the atoms bonded together, so I chose to study the simple binary fluorides, which was a very happy choice.

I was encouraged in this approach, because at about that time I acquired my first graduate student, Charles Hoffman, who was interested in and very good at inorganic synthesis. He undertook to synthesize the fluorides needed for the study, many of which were difficult, and he measured their fluorine shifts. At this juncture, in May 1950, good fortune favored me again. I found exceptionally able help with our electronics problems from R. E. McClure a senior in electrical engineering, who worked part-time with my group while he finished his bachelor's and master's degrees.

Bob was an immediate help, not only in maintaining, designing, and constructing our apparatus, but in running many of the early experiments. With his able help, we set out to see if we could find shifts in proton resonances. We convinced ourselves of them on June 30, 1950, when Bob found small but reproducible shifts, several times larger than experimental error, between the protons in benzene, mineral oil, and aqueous solutions of strong acids.[18] At this stage, we started a major effort on improving the homogeneity of the magnetic field by plotting it and hand-polishing the pole tips in those areas where the field was high. And later, we broadened the shift study to include the simple hydrides. A block diagram of the sort of early high-resolution spectrometer we used in these measurements is given in Figure 8.

The shifts found for the fluorides are shown in Figure 9 where they are plotted against the electronegativity of the atom bonded to the fluorine.[14] There is an approximate linearity, with ionic fluoride the most highly shielded and the most covalent fluorine (F_2) the least shielded. I later challenged

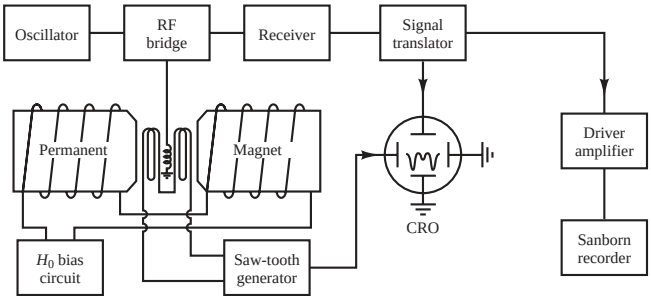

Figure 8 Block diagram of an early (1951) high-resolution NMR spectrometer

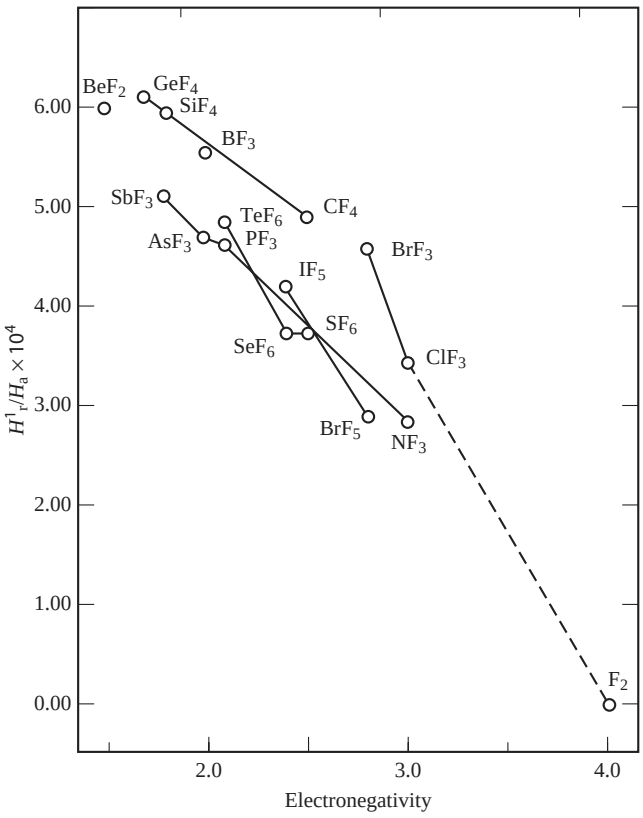

Figure 9 Fluorine chemical shifts in binary covalent compounds versus the electronegativity of the atomic species bonded to the fluorine.[14] Larger values of δ are upfield shifts

Apollo Saika, a student from Japan, to account for this strong correlation and he and Charlie Slichter came up with their elegant paper[19] attributing it to the second-order paramagnetic term of Ramsey's theory[20] and its dependence upon the p-electron bonding orbital of the fluorine. The shifts for protons are more complex, as may be seen in Figure 10, depending markedly on the Group of the partner element. Also, their range is 60-fold smaller than for fluorine. Both differences stem from the s-electron bonding for hydrogen and p-electron for fluorine.

In our study of the fluorine shifts we came upon a new phenomenon—the indirect coupling of nuclear spins or the spin–spin coupling as it is often called. Independent work by several groups was needed for its unraveling.[16,21–30] The story is an interesting illustration of just how difficult it is

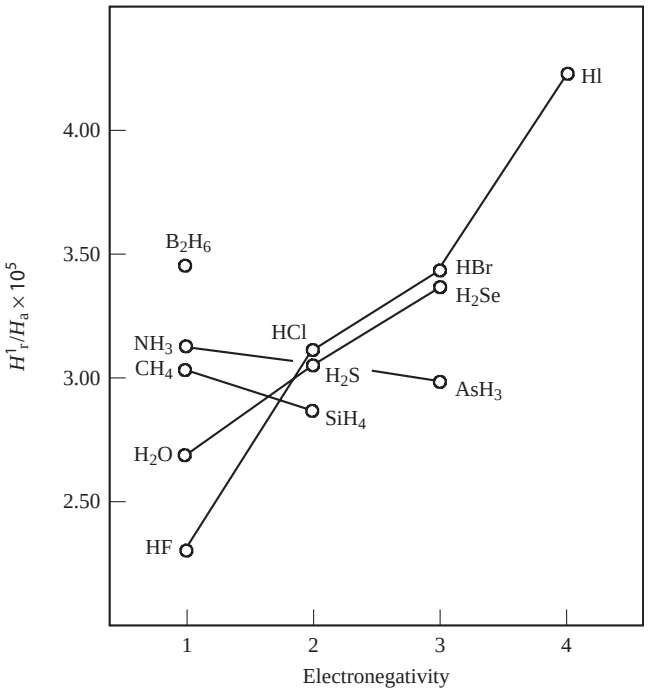

Figure 10 Proton chemical shifts in binary covalent hydrides versus the electronegativity of the atomic species bonded to the proton (Ref. 14). Larger values of δ are upfield shifts

to accept something really new even when you see it. In my lab, the first observation of the effect was by Charlie Hoffman on September 8, 1950. In measuring the fluorine resonance of the small sample of PF_3 he had synthesized, we found two close lines of comparable intensity. They were attributed to what we knew, to a chemically shifted impurity, probably $PClF_2$ or PCl_2F from the preparation. Hoffman repurified the sample, but the second line wouldn't go away. So another preparation route was tried but the new product gave the same fluorine doublet. During this period PF_5 was synthesized and the fluorine resonance was found to be a double line. This time we could not ignore the equal intensities of the two lines and attribute them to a chemical shift between the three equatorial and two apex fluorines of the trigonal bipyramidal structure, which it wasn't. The effect remained a mystery for four months.

It wasn't until March 1951 that it became completely clear we were really seeing something entirely new. At that time I encouraged a beginning graduate student, Dave McCall, to look at some phosphorus shifts in several fluorochloro phosphorus compounds of known purity, which I scrounged from Don Martin then on the inorganic faculty. When the ^{31}P resonance in the $POCl_2F$ compound exhibited a 1–1 doublet structure, it finally dawned on me that we had been observing a new type of spin–spin interaction. In it the splitting of the fluorine resonance depends on the number of different phosphorus spin states (2) while splitting of the phosphorus resonance depends on the number of different fluorine spin states (also 2).[22] It was a great thrill for Dave and me when shortly thereafter we first saw a ^{31}P resonance such as that reproduced in Figure 11 for Me_3OPF_2, a 1–2–1 triplet caused by the two equivalent fluorines, as predicted.

In the meantime Erwin Hahn had observed 'slow beats' in the spin echo envelope for nonequivalent protons.[24] This led

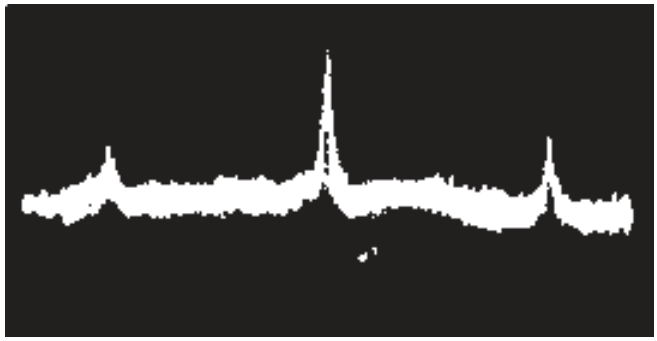

Figure 11 Oscilloscope photograph of the phosphorus resonance observed in liquid Me_3OPF_2 at 25.5 MHz[30]

me and Charles Slichter's group to explore the relationship between the steady-state multiplets and the modulation of the spin echo envelope. We found that the fluorine spin echo envelopes of BrF_5 and IF_5 (tetragonal pyramids) exhibited a slow beat frequency corresponding to the steady-state (first-order) multiplet splitting of the apex and equatorial fluorines.[25] Comparison by Hahn of the proton spin echo modulation[26] with the steady-state splittings[27] was more difficult because of second-order effects caused by the small proton shifts. But it later led[24] to the same conclusion—only one interaction was involved.

Thoughts about the nature of that interaction started with the familiar. The first 'multiplet' was published by Proctor and Yu.[16] They reported the ^{121}Sb and ^{123}Sb resonances in an aqueous HF solution to be symmetrical multiplets and suggested the cause might be the Sb–F magnetic dipole–dipole interactions, incompletely averaged out by hindered rotation.[12] Andrew[21] made a theoretical analysis of this model. This was tested in a repeat of the experiment.[29] The results were incompatible with hindered rotation but in agreement with the 'multiplet rules'.

Along the way it was recognized[23,26] that the mathematical form of the interaction must be $A_{12}\mu_1 \cdot \mu_2$ with A_{12} a coupling constant related to the electronic structure of the molecule. A general theory was developed by Ramsey and Purcell[28] for the coupling constant, attributing it to an indirect interaction between the nuclear spins via their magnetic polarization of the electrons. Slichter showed that this approach predicted coupling constants in reasonable agreement with our early experimental results, primarily on phosphorus compounds with P–H and P–F splittings.[30]

Motional narrowing, chemical shifts, and the spin–spin coupling are the phenomenological basis of high-resolution NMR. It remained to be discovered how useful it is. A major step in this direction was taken by Lee Meyer in 1952 with a new high-resolution spectrometer built by our group.[31] Lee made a survey of the extent to which proton shifts are characteristic of the various functional groups in different organic compounds. This approach, in which he was later joined by Apollo Saika, reflected my supervision of the Perkin-Elmer infrared spectrometer which was the cause of my being hired at Illinois. In the course of that service work, I had become impressed by the extent to which various functional groups absorbed at characteristic vibrational frequencies in the infrared region and I thought it important to try the same thing for proton shifts. I presented the results at a meeting of the American Chemical Society in Chicago in the fall of

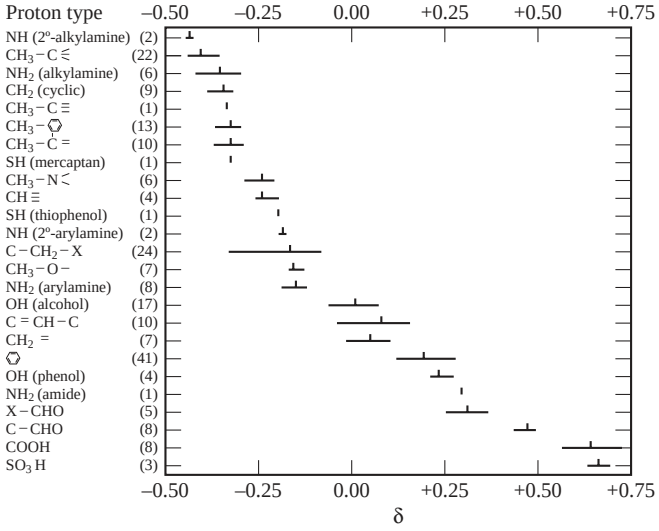

Figure 12 A chart of the proton chemical shifts observed for various functional groups in different compounds[31]

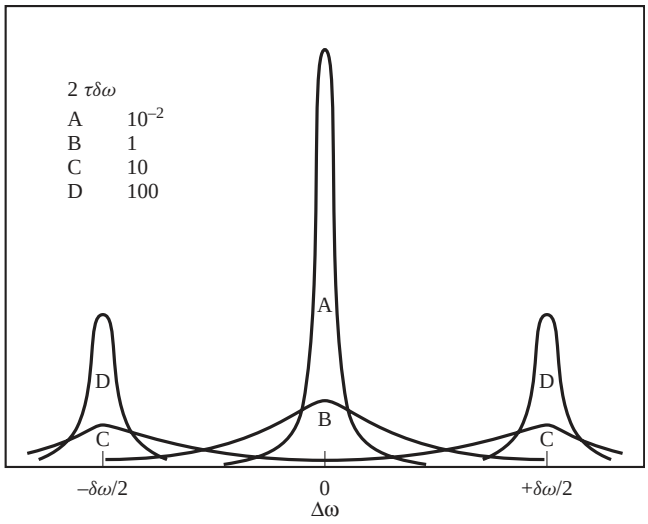

Figure 13 High-resolution NMR lineshapes as a function of exchange lifetime, τ, between two equally populated sites separated by $\delta\omega$ in the absence of exchange[32]

1953. They are summarized in Figure 12.[31] The horizontal bars indicate the range of shifts found for each functional group, the number of compounds observed for each group being given after the group's formula.

By that time Varian Associates had built two or three high-resolution spectrometers on special order for several of the oil companies, but the market was then very limited. In fact, Martin Packard confided to me much later that at the time of the Chicago meeting Varian Associates was about ready to drop their NMR program as unprofitable, or at least the high-resolution part of it. Whatever the case, the results shown in Figure 12 did foreshadow some of the promise which high-resolution NMR has since fulfilled and encouraged Varian to continue the development of applications.

EXCHANGE AVERAGING IN HIGH-RESOLUTION SPECTRA

During the course of characterizing the spin–spin coupling we became aware of the fact that 'fast' chemical exchange can average out the splittings. For example we found a fluorine doublet in solutions containing the PF_6^- anion but not in HF. Another case was that of aqueous HBF_4, in which the proton and fluorine resonance widths were instrumentally determined, at about 0.01 G, while that of ^{11}B may have been somewhat larger. ^{11}B has a large g-value, so we expected to resolve a splitting of the fluorine resonance as in aqueous HPF_6. But we didn't. After a great deal of debate, we attributed the absence to chemical exchange of fluorines among the BF_4^- ions. This led Charlie Slichter to develop a mathematical treatment, based upon the Bloch equations, of the exchange effects.[30]

The results prompted a more deliberate search for definitive examples of the phenomenon. The first of such studies was by Apollo Saika, who in 1952 looked at the concentration dependence of the proton shifts in aqueous strong acids.[32] The fast proton transfer in such systems puts them in the fast exchange limit, so exchange rates could not be measured, only the concentration-dependent average shift. In addition, Apollo calculated (by hand in those days) a set of lineshapes in the intermediate region between fast and slow exchange for the equally populated two-site case. The results are given in Figure 13 as a function of τ, the exchange lifetime. In the slow exchange limit, the resonance is a doublet; in the fast exchange limit, a central singlet.

These lineshapes led me to suggest that rather short chemical lifetimes in the range of 10^{-2}–10^{-4} s could be measured by such an approach. I even was bold enough to propose[32] that 'a combination of temperature and magnetic field changes in the transition region would permit evaluation of the activation energy for the exchange'. Reduction of this to practice was delayed by the difficulty of finding suitable systems with exchange rates in the right region. At that time there just weren't other methods for measuring reactions with halflives in the millisecond range, so no known suitable examples were available for us to study via the proposed new method.

Moreover, the discovery of an appropriate system for study was delayed for several years because at first it wasn't recognized as such. This is of course the now classic example of the *N*,*N*-dimethylamides (**1**) and (**2**), which when pure have at room temperature a close doublet from the two *N*-methyl groups. The structure is as shown below. One of the methyls is *cis* to the C–O group at the other end of the molecule, while the second methyl is *trans*, so they have chemically shifted lines. Furthermore, the partial double-bond character of the central N–C bond hinders internal rotation about that bond and prevents exchange narrowing of the shift at room temperature.

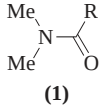

(1)

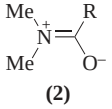

(2)

Lee Meyer in the survey of proton shifts did observe a double *N*-methyl resonance in *N*,*N*-dimethylformamide.[31] However, it wasn't a very 'clean' doublet, perhaps because

traces of acid and base catalyze the exchange and tend to average it out. In any case, a chemically shifted doublet was not expected by Lee and when a poor one appeared it was shrugged off as an instrumental and/or impurity effect. But a couple of years later, after Phillips reported seeing it at room temperature,[33] the compound impressed me as a very likely candidate for a temperature-dependent rate study by NMR methods. A graduate student, Chuck Holm, became interested in this possibility and, after improving the spectrometer, he made a successful study of the internal rotation rate in amides as a function of temperature, through the coalescence transition from slow to fast exchange. His results[34] are crude by today's standards but they did give reasonable values for the exchange rates and enabled the activation energy to be determined. They were good enough to encourage the use of NMR in a wide variety of exotic conformational exchanges.

CONCLUSION

The initial decade of NMR, from 1945–55, was a tremendously exciting period of discovery in magnetic resonance, not only in NMR but also in ESR and pure quadrupole resonance. Moreover, the numbers of scientists then engaged in such research was small, so it was possible to keep up with what was going on. There was a club-like atmosphere to the field. It was great to be a participant in some of the more chemically oriented research during this period.

As a chemist I was accustomed to looking at different chemical species. And in those days it seemed that every new compound you tried turned up a new phenomenon. In reminiscing about the good old days, I've tried to describe how subjective and personal factors can change the course of science and also, how important it is to determine whether the unexpected result is an artifact, a nuisance, or something really significant. And for the newcomer, looking for yet another exotic phenomenon in the field, I quote from the 1980 review article[3] which still holds, 'NMR is a true evergreen'.

REFERENCES

1. E. M. Purcell, H. C. Torrey, and R. V. Pound, *Phys. Rev.*, 1946, **69**, 37.
2. F. Bloch, W. W. Hansen, and M. Packard, *Phys. Rev.*, 1946, **69**, 127.
3. J. Jonas and H. S. Gutowsky, *Annu. Rev. Phys. Chem.*, 1980, **31**, 1.
4. Portions of this chapter have been reprinted by permission of the publisher from 'Chemical Aspects of Nuclear Magnetic Resonance' by H. S. Gutowsky in *J. Magn. Reson.*, 1975, **17**, 281. Copyright 1975 by Academic Press, Inc.
5. C. J. Gorter, *Physica (The Hague)*, 1936, **3**, 995; C. J. Gorter and R. de L. Kronig, *Physica (The Hague)*, 1936, **3**, 1009.
6. C. J. Gorter and L. J. F. Broer, *Physica (The Hague)*, 1942, **9**, 591.
7. H. Gershinowitz and E. B. Wilson, Jr., *J. Chem. Phys.*, 1938, **6**, 197.
8. G. E. Pake, *J. Chem. Phys.*, 1948, **16**, 327.
9. H. S. Gutowsky, G. B. Kistiakowsky, G. E. Pake, and E. M. Purcell, *J. Chem. Phys.*, 1949, **17**, 972.
10. J. H. Van Vleck, *Phys. Rev.*, 1948, **74**, 1168.
11. N. Bloembergen, E. M. Purcell, and R. V. Pound, *Phys. Rev.*, 1948, **73**, 679.
12. H. S. Gutowsky and G. E. Pake, *J. Chem. Phys.*, 1950, **18**, 162.
13. H. S. Gutowsky and G. E. Pake, *J. Chem. Phys.*, 1948, **16**, 1164.
14. H. S. Gutowsky and C. J. Hoffman, *J. Chem. Phys.*, 1951, **19**, 1259; 1952, **20**, 200.
15. W. D. Knight, *Phys. Rev.*, 1949, **76**, 1259.
16. W. G. Proctor and F. C. Yu, *Phys. Rev.*, 1950, **77**, 717.
17. W. C. Dickinson, *Phys. Rev.*, 1950, **77**, 736.
18. H. S. Gutowsky and C. J. Hoffman, *Phys. Rev.*, 1950, **80**, 110; H. S. Gutowsky and R. E. McClure, *Phys. Rev.*, 1951, **81**, 276.
19. A. Saika and C. P. Slichter, *J. Chem. Phys.*, 1954, **22**, 26.
20. N. F. Ramsey, *Phys. Rev.*, 1950, **78**, 699.
21. E. R. Andrew, *Phys. Rev.*, 1951, **82**, 443.
22. H. S. Gutowsky, C. J. Hoffman, and R. E. McClure, *Phys. Rev.*, 1951, **81**, 305; H. S. Gutowsky and D. W. McCall, *Phys. Rev.*, 1951, **82**, 748.
23. H. S. Gutowsky, D. W. McCall, and C. P. Slichter, *Phys. Rev.*, 1951, **84**, 589.
24. E. L. Hahn, *Phys. Rev.*, 1950, **80**, 580; E. L. Hahn and D. E. Maxwell, *Phys. Rev.*, 1952, **88**, 1070.
25. E. B. McNeil, C. P. Slichter, and H. S. Gutowsky, *Phys. Rev.*, 1951, **84**, 1245.
26. E. L. Hahn, personal communication; E. L. Hahn and D. E. Maxwell, *Phys. Rev.*, 1951, **84**, 1246.
27. M. E. Packard and J. T. Arnold, *Phys. Rev.*, 1951, **83**, 210.
28. N. F. Ramsey and E. M. Purcell, *Phys. Rev.*, 1952, **85**, 143.
29. S. S. Dharmatti and H. E. Weaver, Jr., *Phys. Rev.*, 1952, **87**, 675.
30. H. S. Gutowsky, D. W. McCall, and C. P. Slichter, *J. Chem. Phys.*, 1953, **21**, 279.
31. L. H. Meyer, A. Saika, and H. S. Gutowsky, *J. Am. Chem. Soc.*, 1953, **75**, 4567.
32. H. S. Gutowsky and A. Saika, *J. Chem. Phys.*, 1953, **21**, 1688.
33. W. D. Phillips, *J. Chem. Phys.*, 1955, **23**, 1363.
34. H. S. Gutowsky and C. H. Holm, *J. Chem. Phys.*, 1956, **25**, 1228.

Biographical Sketch

H. S. Gutowsky. *b* 1919. A.B., Chemistry, 1940, Indiana University, M.S. 1946, University of California at Berkeley (with K. S. Pitzer), Ph.D., 1949, Harvard University (with G. B. Kistiakowsky). Faculty in Chemistry, University of Illinois at Urbana-Champaign, 1948–present. Approx. 300 publications primarily developing NMR methods for studying chemical problems. Current research on rotational spectroscopy of small, weakly bonded clusters.

Haeberlen, Ulrich: The Early Days of Multiple Pulse NMR

Ulrich Haeberlen
Max-Planck-Institut für Medizinische Forschung, Heidelberg, Germany

In the summer of 1967 I received a fellowship from the Deutsche Forschungsgemeinschaft to undertake postdoc work with John S. Waugh at MIT. After having crossed the Atlantic by ship(!), I arrived in Cambridge, MA in the fall and when I arrived it was already there. The idea. The idea that and how the line broadening in solids caused by homonuclear dipolar couplings of the spins could be suppressed. The witchcraft to accomplish that feat were sequences of rf pulses of special, well-defined phases and delays. No doubt it was John's idea. Clearly, it was something fundamentally different from spin locking. It was going to retain *spectral* information.

It required a pulse spectrometer capable of firing 90 ° pulses in rapid succession. 'Rapid' on the timescale of the decay time T_2 of the free induction decay (FID) of a solid meant 20–30 μs. Within T_2, four pulses with mutually orthogonal rf phases and spaced by delays $\tau - 2\tau - \tau - 2\tau$, etc. should hit the sample, the extra condition being that the NMR should be picked up between the pulses on the flight. Lee Huber was working hard to build a spectrometer to satisfy these requirements. The central piece of his equipment was an (always drifting) Varian '60 MHz' high-resolution 12-in. magnet. It was sitting in the center of a basement room of the MIT Chemistry Department. In those days NMR labs were always banished to basement rooms because of the weight of the magnet.

John didn't know much about me except that as part of my Ph.D. thesis I had built a pulse spectrometer and that I boasted it had one of the shortest, if not *the* shortest, recovery time of any current pulse spectrometer. A short recovery time was urgently needed for the new experiment. So, logically, John suggested I should assist Lee. He assigned me a desk in the room with the 12-in. magnet. On 'my' desk there was naturally (as I now know) a heap of junk. The first thing I did, naturally enough in my opinion, was to find another place where I could pile up all the junk, and to clean up and to clean my desk (it was also full of dust). When John noticed that he beamed and remarked: Aha, Germans need Lebensraum. He said 'Lebensraum' in German. Obviously I had just acted like a Bilderbuch German.

In those days a pulse NMR spectrometer was quite different from what it is today. The signal detection path consisted usually of only an rf amplifier and an oscilloscope which served for displaying the FID or the spin echo. There was no computer and, ipso facto, no software [which is now considered by many as the most important part of the spectrometer—original quotation (1985) of a Varian representative]. Remember the famous Ernst–Anderson paper on Fourier transform NMR had only appeared in the preceding year and neither mini- nor microcomputers existed as yet. A typical pulse spectrometer was then designed to perform FID and the Carr–Purcell–Gill–Meiboom echo train and, perhaps, spin-locking experiments. For this reason it comprised two rf channels with a mutual 90 ° phase shift and a pulse programmer that could generate a 'preparation' pulse and then a burst of radiofrequency or a sequence of other pulses whose width and spacing could be adjusted. With such a spectrometer one could not undertake the 'line-narrowing' four-pulse experiment we had in mind, but the extensions needed were straightforward: instead of two rf channels we needed four, and the pulse programmer was required to generate not only one but two separate delays in a ratio of 2 : 1. On the detection side it was clearly not sufficient to observe the NMR signal directly at the Larmor frequency. A *phase sensitive detection* was called for. Thinking back, I now find it strange that phase sensitive detection did not strike me as a kind of revelation—I, who until then had always observed FIDs and echoes either directly at the Larmor frequency or by diode detection. As far as I recall, it really did not. Actually it was simple to implement because Hewlett Packard had just started to market double balanced mixers which could do the job in an elegant manner. Building the pulse programmer was particular fun because it gave us the opportunity to play with the newly introduced integrated circuits—the DTL logic family! (No mistake, DTL, *not* TTL.)

In any event it did not take long before Lee and I got the spectrometer ready for the first line-narrowing multiple pulse (mp) experiment. Again, I now find it strange that there was absolutely no discussion about the kind of sample we should take for trying it out. Of course it had to be a single crystal of calcium fluoride, CaF_2, oriented such that its (111) crystal axis pointed along the applied field $\boldsymbol{B}_0$. In those days CaF_2 was *the* NMR *drosophila* for all experiments testing propositions about homonuclear dipole–dipole interactions. We knew that for (111) along $\boldsymbol{B}_0$ the fluorine FID of CaF_2 had a first zero crossing at 52.3 μs. [For (100) along $\boldsymbol{B}_0$ it occurs after 19 μs.] In the beginning we could make τ equal to 6 μs, but not shorter. A full 'cycle' lasted 6τ, i.e. 36 μs and we knew that this time, called the 'cycle time', had to be much shorter than T_2. Now, 36 μs is not *really* much shorter than 52.3 μs and this latter time is not for T_2 but for the first zero crossing! Hence we were quite anxious about whether or not the experiment would work.

It worked. It worked remarkably well, so well that before the end of the year we had submitted a letter to *Phys. Rev. Letters*. It appeared in the issue of 29 January 1968. With a sample-and-hold circuit and a Fabri-Tek 1062 signal averager we had 'sampled' the NMR signal once per cycle during an mp train of about 200 cycles. We had punched the record of samples into IBM punch cards—one sample per card—and had it Fourier transformed in the MIT computer center. We had added to the sample of CaF_2 a small amount of liquid $C_6H_5CF_3$ to demonstrate that 'our' sequence was able to resolve chemical shifts (albeit scaled down by a factor of $1/\sqrt{3}$). While preparing this article I looked again at this first mp Fourier-transform spectrum. I now recognize that it must have been the *power* spectrum of our mp record of samples. I wonder whether back in 1967 I was aware of the difference between a *power* and an *absorption* spectrum. John was, I am sure. Nowadays I disdain power spectra. No matter whether it was a power spectrum or not, it marked the coming into existence of *high-resolution NMR in solids*.

Of course there were precursors. G. Siegle in Stuttgart (1966) and the British NMR groups around J. G. Powles, P. Mansfield, and J. H. Strange (1962, 1963) had produced

spin echoes from strongly dipolar coupled solids. Their pulse sequences differed from the Hahn echo sequence in two respects: the second pulse had a phase shift of 90° with respect to the first one and, for producing the largest possible echo, it had to be a 90° pulse. An echo appeared *only* if the second pulse was fired *before* the FID generated by the first had decayed to virtually zero. These experiments had demonstrated that the fast decay of the transverse magnetization of a dipolar coupled solid is not a totally irreversible process. Ostroff and Waugh (1966) and Waugh and Huber (1967) had taken another important step forward: they had subjected the spin system to a whole string of pulses and had followed its time evolution 'in one shot'. They had also formulated the eventual goal of line-narrowing mp spectroscopy: measuring small chemical shifts in the presence of strong dipolar couplings. Their sequence allowed them just to touch this goal: when, as a result of the chemical shift, the magnetization had nutated by roughly 90°, the mechanism of suppressing the dipolar line broadening ceased to be effective. Then there was the famous, often-quoted Lee–Goldburg experiment (1965). It had demonstrated that by setting up an effective field $\boldsymbol{B}_{\mathrm{eff}}$ in the rotating frame which subtends the 'magic angle' with the applied field $\boldsymbol{B}_0$, it is possible to keep alive the precessing magnetization of a solid for a much longer time than T_2.

All these precursors of line-narrowing mp spectroscopy have their due place in the history book of NMR, nevertheless they all remained experiments which, in essence, were undertaken only once. They never took the decisive step of becoming a *method*, a method for *measuring something*. Another important precursor, the magic angle sample spinning (MASS) experiment of Andrew, Bradbury, and Eades (1958), and Lowe (1959) eventually took this step after having had a dormant phase of nearly two decades and having undergone a metamorphosis during which abundant ^{23}Na and ^{31}P had transformed into rare ^{13}C and ^{29}Si nuclei.

The unique *something* which the mp line-narrowing method promised to make amenable to measurement—and eventually did—was the shielding tensor of protons and ^{19}F nuclei. This was clear to us from the very beginning, but it took us almost a full year before at last we could record an mp spectrum from a solid with two separate resonances and with one of them displaying even a feature which the loving eye could recognize as a chemical shift anisotropy powder pattern. Actually we were not very proud of it and John thought we had better hide it in *Polymer Letters*. By that time Lee had received his Ph.D. and Dave Ellett had joined the team. Rather than looking for real applications we spent our time on 'inventing' and analyzing variants of the four-pulse sequence and on developing a theory suitable for describing these 'experiments' (as we called them). The theory is now known as *Average Hamiltonian Theory* and it is a pleasure for me to take this opportunity to acknowledge its first germ: it is W. A. B. Evans's Report 881 issued by the Materials Science Center of Cornell University. He wrote on 'Some Applications of the Magnus Expansion in NMR'. In February 1968 John had received a typewritten preprint which he showed me. It is this paper which acquainted me with the Magnus expansion.

The predominance of theory and the development of new line-narrowing mp sequences over actual measurements of shielding tensors lasted until the early 1970s. In the meantime the Nottingham and the Caltech NMR groups around P. Mansfield and A. N. Garroway, and R. W. Vaughan, W.-K. Rhim, and D. D. Elleman (and, somewhat later, D. Burum), respectively, had joined the MIT group in its efforts in developing high-resolution NMR in solids. Soon the group in Jena around G. Scheler, H. Rosenberger, and B. Schnabel joined the mp NMR club. We were all friends and, frankly speaking, at the same time fiercely jealous competitors. Jealousy has died away over the years, friendship survives. We all mourn the tragic deaths of our friends Robert Vaughan (25.5.1979) and Hans Rosenberger (9.3.1989).

In September 1969 I returned to the old continent by plane. Ocean liners were out of business. Karl Hausser—I am still very much obliged to him—had offered me the opportunity to set up an mp NMR lab in his department at the Max-Planck-Institut für Medizinische Forschung in Heidelberg.

When I arrived it was already there. The minicomputer. It was a French model, un ordinateur CII 10010, and had cost the German taxpayer a fortune, about the equivalent of a comfortable home including the garden. It had a magnetic core memory of 16 kbytes and no operating system whatsoever. It came with an assembler which had to be loaded from a punched paper tape. The loading with a teletype took 20 min. Every syntax error led to a fatal crash and the assembler had to be reloaded. It was completely useless and Alfred Döhring eventually did all the programming in machine language.

The 10010 had two wonderful features. The first was the direct memory access. By pulling (asynchronously) one line, called CYEX, it would hand over to the external device the control of the address and data lines within at most three clock cycles of 500 ns, i.e. within 1.5 μs. I still wonder how the 10010 did it because it implied suspension even of running microprograms—they continued properly after the external device had returned the control to the machine. A response time of 1.5 μs was fast enough for acquiring mp data with just a sample-and-hold circuit and an 8 bit, 1 megasamples s^{-1}, 7000 DM analog-to-digital converter between the spectrometer proper and the 10010. The other feature which I greatly appreciated was that I always knew in which physical core a given data bit was stored. When after about 10 years we sent the 10010 into retirement, it took me a long time to accept that such a mysterious thing as an operating system could be trusted to handle the data storage.

Apart from the minicomputers, the early 1970s brought another important change to the mp field: inventing and analyzing pulse sequences gradually moved to the back of the stage and 'real' applications came to the limelight. In 1971, M. Mehring, R. Griffin, and J. S. Waugh recorded and published ^{19}F mp powder spectra of a number of perfluorinated compounds. These spectra allowed the reliable determination for the first time of the principal components of ^{19}F shielding tensors. In the same year L. M. Stacey, R. W. Vaughan, and D. D. Elleman reported the first single crystal measurements of complete shielding tensors including the principal directions.

By 1973, the time had come for applying the mp line narrowing technique to the measurement of proton shielding tensors (Haeberlen and Kohlschütter, 1973). This is the point at which, to recall that, in 1969, D. C. Haddix and P. C. Lauterbur had measured in a straightforward way the proton shielding tensor in trichloroacetic acid using a 100 MHz spectrometer. At this frequency and in this particular compound, the proton shift anisotropy is larger than the dipolar linewidth. For proton mp spectroscopy, we in Heidelberg had an advantage over our competitors at MIT, Caltech and Nottingham: our spectrometer

was operating at 90 MHz, whereas the MIT and Caltech groups still worked at 54 MHz while the Nottingham group did its mp research at 'only' 9 MHz.

The first occasion where members of all the mp NMR groups met and reported on the state-of-the-art in their labs was the 1st Specialized Colloque AMPèRE in Krakow in 1973.[1] High-resolution NMR in solids was the dominating theme and also the title of the opening lecture delivered by E. R. Andrew. John Waugh and Alex Pines spoke about the PENIS experiment, and Paul van Hecke presented the mp work of MIT. He showed spectra and chemical shift rotation patterns of single crystals of anhydrous oxalic acid, $(COOH)_2$, and explained how the proton shielding tensors could be extracted from such data. It is important to remember what a judicious choice anhydrous oxalic acid was: the compound contains protons as the only magnetic species (forget the rare ^{13}C nuclei); all the protons are crystallographically equivalent; the proton shielding anisotropy is 'large' ($\simeq$20 ppm); and crystals can easily be grown. (Later on Paul spent a year in Heidelberg and did a beautiful experiment on KHF_2 with simultaneous homo- and heterodecoupling.)

I was particularly anxious about what Bob Vaughan was going to report, because shortly before the conference his group (*R*him, *E*lleman, *V*aughan, 1973) had introduced the line-narrowing sequence which is now known as the MREV sequence. The 'M' in the acronym stems from Peter *M*ansfield who, in a notation which nobody except himself understood at the time, had already proposed it in 1971. I was anxious because I knew that Bob had just obtained fantastically long-lasting mp decays from CaF_2 with that sequence. In his talk, however, Bob went so hastily over these intriguing results that people suspected he was not quite sure of them. As a matter of fact only recently have I come to feel that after all they may have been real.[2] In any event the climax of Bob's talk was a proton mp spectrum of a powder sample of trichloroacetic acid. It demonstrated a down-to-earth spectral resolution.

I reported on measurements of the proton shielding tensors in oriented single crystals of malonic acid. I was particularly proud of the data from the CH_2 group because that group was considered a difficult case—strong dipole–dipole couplings and a small shielding anisotropy. U. Haubenreisser and B. Schnabel from Jena had investigated the shielding anisotropy of the crystal water in kieserit, $MgSO_4 \cdot H_2O$ and M. Mehring, then in Dortmund, and his student H. Raber demonstrated what a true solid state physicist and NMR spectroscopist should do: apply the newly discovered technique to metals. They had refined the values of the Knight shifts in aluminum and beryllium. And Peter Mansfield, what did he talk about? He began with reflection symmetry in mp sequences but soon turned to NMR diffractometry. In retrospect he talked and speculated about spin imaging and actually showed pictures of phantoms! Literally nobody took him seriously. What a mistake.

Back to mp NMR. It continued to mature and soon became *the* method for measuring proton shielding tensors. In 1977 I was invited to give a talk at the NMR Gordon Conference. I chose the title: 'Harvesting Time in Multiple Pulse NMR'.

In 1975 I had written a chapter on 'High Resolution NMR in solids; Selective Averaging' for *Advances in Magnetic Resonance*.[3] It was too long for a chapter so it became a separate volume and Supplement 1 of this series. John was kind enough to write a foreword. He expressed his belief that this volume represents the last word on the subject. I feel proud of this assessment but likewise I am happy that John turned out to be wrong. The ideas developed along with the advance of mp spectroscopy have greatly influenced other and unforeseen areas of research. I restrict myself to mentioning the creation and detection of multiple quantum coherences. Line narrowing by mp sequences combined with magic angle sample spinning, a technique now known as CRAMPS, has become the method of choice when solid state proton NMR is used for *analytical* purposes. This possibility was initially mentioned in our *Phys. Rev. Letter* in 1968. After the great success of NMR imaging in medicine, people naturally turned to NMR imaging of solids and of course used mp sequences for narrowing the resonances. But even mp spectroscopy in the narrow sense of the word had not come to an end in 1976.

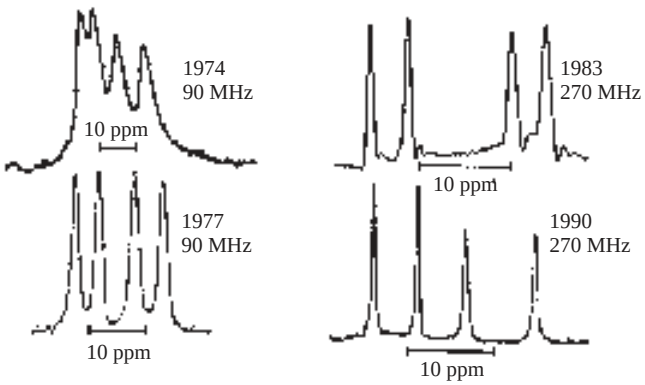

Figure 1 Progress in mp NMR. ^1H spectra of a single crystal of malonic acid. The full width at halfheight of the two resonances on the left of the 1990 spectrum is 45 Hz, corresponding to 0.4 ppm

In 1979 D. P. Burum and W.-K. Rhim introduced their 24 and 52 pulse cycles.[4] While the latter is too long to be practical, the former has become one of the standard mp sequences. In a recent article[2] we wrote that its line-narrowing capacity has probably never been fully exhausted in actual experiments. The resolution of state-of-the-art mp spectra is no longer limited by residual dipolar broadening. Progress must now come from seemingly trivial matters such as sample handling.

In Figure 1 we present a series of mp spectra for a single crystal of malonic acid which documents the progress of mp spectroscopy with time. The three older spectra appeared initially in 19855 and M. Munowitz was kind enough to reproduce them in his book entitled 'Coherence and NMR'.6

We are glad we can now add a fourth. Ralf Prigl recorded it in 1990. In 1994, Bernd Tesche has studied crystals which give rise to as many as 12 lines in the proton mp spectrum and he claims to be able to measure the components of proton shielding tensors to within $\pm$0.1 ppm.

REFERENCES

1. J. W. Hennel (ed.), *Proceedings of the 1st Specialized Colloque AMPèRE*, Kraków, 1973.
2. R. Prigl and U. Haeberlen, *Adv. Magn. Opt. Reson.*, 1994, in press.
3. U. Haeberlen, High Resolution in Solids; Selective Averaging, *Adv. Magn. Reson.*, Suppl.1, Academic Press, New York, 1976. This supplement contains all references to earlier work.

4. D. P. Burum and W.-K. Rhim, *J. Chem. Phys.*, 1979, **71**, 944.
5. U. Haeberlen, *Magn. Reson. Rev.*, 1985, **10**, 81.
6. M. Munowitz, *Coherence and NMR*, John Wiley, New York, 1988.

Biographical Sketch

Ulrich Haeberlen. *b* 1934. Dipl. Phys., 1962, Ph.D., 1966, Physics, University of Stuttgart, Germany. Postdoctoral fellow and research associate with J. S. Waugh at MIT, 1967–69. Max-Planck-Institut für Medizinische Forschung, Heidelberg, 1969–present. Professor of Physics, University of Heidelberg, 1975. Research specialties: line narrowing multiple pulse NMR, shielding- and quadrupole-coupling tensors of protons/deuterons, motions in molecular crystals.

Hägele, Gerhard: Analysis and Simulation of High-Resolution 1D NMR Spectra. Some Steps Closer to Automation

Gerhard Hägele

Heinrich-Heine-Universität, Düsseldorf, Germany

Intuitive understanding of complex second-order spectra and the computational analysis and simulation of high-resolution 1D NMR spectroscopy has intrigued us for many years. This interest was encouraged by R. K. Harris in Norwich when we studied the ^{1}H and ^{31}P NMR spectra of symmetrical phosphorus compounds such as $[CH_3(C(CH_3)_3)P(X)]_2Y$ (X = :, O, S; Y = —, O, S). Algebraic equations for transition frequencies and intensities of $[AR_tX_n]_2$ spin systems and the programs DOK178 and DOK177 were developed to simulate the R_t and X_n or A spectra. Later on a more general treatment for spin systems holding n_g groups in

$$\left[A\sum_{i=1}^{n_g}X_{n_i}^{i}\right]_2$$

was derived.

For analyzing the ^{1}H and ^{19}F NMR spectra of $CH_2FCHFCO_2CH_2CH_3$ (superpositions of ABCXY and ABC_3), LAOCOON and UEANMR programs for single spins and composite particles consisting of spins $I = \frac{1}{2}$ were used. Decoupling the protons of cyclobut-1-ene-1,2-bis(phosphonic acid) tetramethyl ester (**1**) by $^{19}F\{^{1}H\}$ and $^{31}P\{^{1}H\}$ led to an $[A[X]_2]_2$ spectrum involving the chemical equivalence of single spins in a twofold symmetry which was tackled with LACX. The nondecoupled ^{1}H, ^{19}F, and ^{31}P NMR spectra of this compound bear the full complexity of the combined chemical and magnetic equivalence in $[AM_6[X]_2]_2$ systems with spins $I = \frac{1}{2}$ and were dealt with by NUMAR and NUMARIT programs. (A review of program development and references up to 1987 are given in Ref. 1)

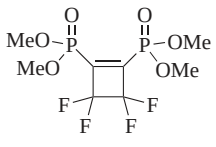

(1)

My interests concentrated on fluorine compounds and corresponding spin systems, e.g. pentafluorophenylsilanes $(C_6F_5)_nSi(CH_3)_{4-n}$ (n = 1–4) (approximately $[A[BC]_2]_n X_{3(4-n)}$), 1,3,5-trifluorobenzene $[AX]_3$, and octafluoronaphthalene ($[AB]_4$), which created demands for spectral simulators and iterators capable of higher symmetries for fast calculations of greater spin systems. Based on the projection operator technique, the most general forms of chemical and magnetic equivalence were combined in simulators DSYMPLOT[1] and DCYMPLOT[1] (QCPE), two FORTRAN IV programs for mainframe computers. Iterative versions were not based on the explicit line assignment technique of Castellano/Bothner-By/Braillon since the total lineshape approach was more appropriate. The iterative core of G. Binsch's DAVINS was extracted, modified for faster convergence and supported by simulators DSYM and DCYM to yield a set of programs[1] SPECPREP, DAVSYM1, DAVSYM2, DAVCYM1, and DAVCYM2 (QCPE). Streamlined FORTRAN versions were combined in to a package DAISY,[1] available for mainframe computers and workstations, e.g. the Bruker X.32 computer.

With the advent of PCs and the descent of computing centers, it was imperative to develop fast algorithms and the easy-to-handle menu-driven programs DSYMPC[2] and DCYMPC[2] for simulations on PCs. Early DOS limited the systems to 8 spins and the Lorentz plots to 2k data points. Iterations on PCs still proved to be slow at this stage. A major breakthrough came from several points of view: algorithms for QM calculations and Lorentz generation were thoroughly reformulated and implemented in C++. Easy data input was achieved via WINDOW techniques. In particular, the input of the symmetry description was simplified to set up permutational operators automatically. A novel and efficient iteration concept was introduced in cooperation with C. Witsch, B. Neeb, and H. W. Höffken (Mathematics, Düsseldorf). These sources were designed to run on PCs 486 under WINDOWS as WIN-DAISY using WIN-NMR (Bruker). The program WINDAISY[3] is able to handle composite particles of spins $I \geq \frac{1}{2}$ in isotropic and anisotropic phases. The full Hamiltonian was installed involving intra- and intercomposite particle dipolar coupling constants. The ^{19}F NMR spectrum of $Hg(CF_3)_2$[3] in nematic solution including the ^{199}Hg satellites was dealt with successfully.

Due to dynamic programming, the maximum number of spins n_s in the system is limited for 32-bit computers to $n_s! \leq 2^{31} - 1$. Future 64 bit computers will allow $n_s! \leq 2^{63} - 1$. At present a maximum of 12 spins in 10 groups is allowed, e.g. $A_3BCDEFGHIJ$. Further progress is achieved by 'chemical factorization' of isolated 'spin islands'. For example, benzoic acid phenyl ester may be handled using two different concepts: (a) as a 10-spin spectrum with zero inter-ring coupling constants or (b) as two overlapping five-spin spectra obtained from two consecutive simulations. Model (a) requires 5 min and (b) 2 s for calculations, which corresponds to an acceleration factor of 150. This MEGASIM principle might be useful for overlapping spectra, e.g. in peptide chemistry. Iterations of a singular phenyl $A[BC]_2$ spectrum require 2 min while 10-spin problems need about 28 h.

The method of total lineshape analysis has solved many intricate spin systems with start parameters reasonably far from the final data, but no mathematical method exists to predict reliably the iterability of specific problems. There are 'bad' cases, especially when very sharp lines with an insufficient number of data points per halfwidths occur. In addition, if essential information is hidden in frequencies connected with low intensities, then explicit line assignment, preferably supported by R. Laatikainen's automation in PERCH,[4] may help. On the other hand, the line assignment will fail in a

multiline system with an overlap of broad lines. Consequently, future developments will combine both optional approaches supported by structural and numerical data banks to obtain reasonable start parameters for fast iterations.

To support the analysis and simulation of HR 1D NMR spectra, auxiliary programs have been designed: MINILA[2] (teaching QM in NMR), NMDR[2] (Double Resonance) and SPINA-AT.[2] The latter program covers the classical literature on explicit solutions for transition frequencies and intensities given for two to four spins and some composite particle problems. The input of experimental frequencies (in some cases intensities) will yield results from direct and subspectral analysis. The parameters obtained may be iterated on-line to yield optimized data. Finally, a brute force method of spectral analysis was developed: NMRFILM.[2] A simulator is placed inside nested DO loops varying frequencies and coupling constants from lower to upper limits and producing a film-like sequence of NMR spectra on the PC monitor. Ocular inspection leads to the best parameter combination.

REFERENCES

1. (a) G. Hägele, M. Engelhardt, and W. Boenigk, *Simulation und automatisierte Analyse von Kernresonanzspektren*, VCH Verlag, Weinheim, 1987. (b) G. Hägele, P. Reinemer, and M. Grzonka, *Workshop Computer in der Chemie, Software-Entwicklung in der Chemie* 1988, vol. 2, p. 241, Springer Verlag, Berlin.
2. (a) S. Goudetsidis and G. Hägele, *Workshop Computer in der Chemie, Software-Entwicklung in der Chemie* 1990, vol. **4**, p. 233. (b) G. Hägele, S. Goudetsidis, H. W. Höffken, Th. Lenzen, R. Spiske, and U. Weber, *Phosphorus, Sulfur and Silicon*, 1993, **77**, 262.
3. (a) U. Weber, R. Spiske, H.-W. Höffken, G. Hägele, and H. Thiele, *Bruker Manual* 1993. (b) V. N. Zinin, A. V. Il'yasov, H. Thiele, G. Hägele, and U. Weber, *Appl. Magn. Reson.*, in press, 1994. (c) V. N. Zinin, A. V. Il'yasov, U. Weber, G. Hägele, and H. Thiele, *J. Fluorine Chem.*, 1995, **70**, 289.
4. R. Laatikainen (a) *J. Magn. Reson.*, 1988, **78**, 127. (b) *J. Magn. Reson.*, 1991, **92**, 1. (c) *QCPE Bull.*, 1992, **12**(**1**).

Acknowledgements

Thanks are due to dedicated work from the Düsseldorf group: V. Lueg, W. Boenigk, H. Dolhaine, M. Engelhardt, M. Grzonka, K. Strang, W. Wagner, U. Weber, Ch. Witsch, B. Neeb, H. W. Höffken, R. Spiske, Th. Lenzen, R. Fuhler, and A. Hottgenroth.

Hahn, Erwin L.: Pulsed NMR—A Personal History

Erwin L. Hahn
University of California, Berkeley, CA, USA

INTRODUCTION

The personal history which follows is concerned with a limited number of my researches in pulsed NMR. It outlines some of the circumstances, early ideas, and false starts which led to the final result. Because of space limitations, my account includes only those individuals and institutions locally connected with the described experiments. I regret that I have had to omit extended reference to many other of my students and colleagues who have had great influence on me. I am indebted to them, as well to those appearing in this history, for all that I have learned in pursuing my researches.

UNIVERSITY OF ILLINOIS, 1946–50

As a beginning physics graduate student in 1946 at the University of Illinois, I was a research assistant to the betatron development program headed by D. W. Kerst. I entered this program with some background experience in radar and sonar electronics as a technician in the Naval Reserve during World War II. Not particularly enamored of participating in big machine physics, I decided in 1948 to change to another field for a thesis subject. Prof. James H. Bartlett, a theoretical physicist, suggested that I should switch to 'small science physics' and start by reading the pioneering NMR papers by the Bloch[1] and Purcell[2] groups at Stanford and Harvard. There was no NMR specialist in the Illinois Physics Department faculty at that time who could guide a thesis in this new field. However, with the umbrella support of an ONR Physics Department block grant, I was allowed to forge ahead on my own with the help of a skilled technician to build a copy of the Harvard CW NMR rig. I remember with gratitude the benevolent support of Physics Department Chairman F. W. Loomis, who appropriated funds for me to visit the Harvard NMR laboratory of Pound, Bloembergen, and Purcell and to talk with them.

In the beginning I had no idea about what I wanted to measure with my newly constructed apparatus. I was happy just to see a signal from protons. About the same time, Herb Gutowsky came from Harvard and joined the staff of the Illinois Chemistry Department. With the NMR experience acquired at Harvard, Gutowsky carried out pioneering NMR experiments which initiated the field of structural chemical analysis. Charlie Slichter also came from Harvard and joined the Physics Department about a year later. In particular the NMR doublet and lineshape work by George Pake[3] and the technique of linewidth analysis by the Van Vleck method[4] of diagonal sums came out of Harvard as new developments, very important for CW solid state and chemical analysis.

As I remember, I interacted only casually with Herb, not close enough to follow or really understand in depth what he was doing. I felt I was an ignorant peasant graduate student, preoccupied with learning the rudiments of NMR. Herb asked me what I was going to do with the rig I built for my physics thesis. By the time of his query I had cooked up a vague idea that perhaps I could follow the progress of a chemical reaction, maybe by looking at the changes in relaxation times in liquid systems. I decided I needed experience first by measuring relaxation times in the time domain using a pulse saturation method. Why did I choose of all things the heretical subject of measuring the 'progress of a chemical reaction' for a graduate physics thesis? The reason: my undergraduate degree was in chemistry, so that was about the only original thing I could think of at the time.

Spin Echoes

After reading the published thesis[5] of Nico Bloembergen, which contained an analysis by J. Schwinger of the nutation effect, often referred to as the 'Rabi flop',[6] I dropped the fuzzy idea of measuring a chemical reaction and decided to measure instead the nutation dynamics of protons in the rotating frame. Spin nutations had never been seen directly by NMR in condensed matter. The experiment appealed to me because it required the application of rf pulses. Pulse techniques were familiar to me as a former radar technician and instructor in the US Navy. These pulses would also be useful for carrying out saturation in order to measure spin–lattice relaxation times. Little did I know at the time that Henry Torrey[7] had already succeeded in measuring nutations at Rutgers by applying rf pulses which remained on for long time periods in order to record as many nutation oscillations as possible. Unfortunately for Torrey, his pulse lengths and time sequences were too long to allow the discovery of free precession and echo signals. Luckily for me, it will be seen next that I was destined to discover free induction and spin echoes by accident because I turned on rf pulse power over shorter time periods, using pulse sequences in pairs in order to measure relaxation times.

After I wrote my thesis which dealt with measurements of nutations, spin–lattice relaxation times,[8] and adiabatic fast passage effects, I remained another year (1949–50) at Illinois as a postdoc. Through the summer of 1949 I continued further investigations of nutations and was about to write up my results in detail. However, I gave up when Torrey came out with his nutation paper[7] which scooped me completely. I only went as far as publishing an abstract[9] and continued instead to do more nutation measurements with increased rf pulse power, thinking that the larger amplitude and higher frequency nutation signals might be a useful way of achieving better NMR sensitivity. That was a naive idea of no value, but the experimental setup provided conditions for the accident by which I discovered spin echoes.

My use of pulses permitted measurements of short spin–lattice relaxation times in the millisecond domain. The scheme was as follows: when an rf pulse was turned on, it lasted long enough for a 60 cycle one-half sine wave of magnetic sweep field to pass through nuclear resonance at the middle of the pulse. The pulse voltage was balanced to a sufficient null by a bridge circuit so that the receiver was not saturated and could detect the absorption 'v mode' signals

which appeared on top of a pedestal, a small leakage of the pulse itself due to a slight bridge unbalance. Starting at thermal equilibrium with a first pulse, the signal at the top of the pedestal due to that pulse was compared, after a known time delay with no rf excitation, to a smaller 'v mode' signal on top of a second delayed pedestal caused by an applied second pulse. The second signal amplitude relative to the first one indicated spin–lattice relaxation recovery of magnetization following the saturation caused by the first pulse. By varying known times between first and second pulses, spin–lattice relaxation times were determined in proton samples such as glycerine and water.[8] All signals were synchronized with 60 cycles. In a sweep time of one period of 60 cycles, the oscilloscope face displayed a single 'v mode' signal on top of each pedestal, and zero signal during sweeps with time delay and no rf pulse excitation.

Finally one day the weird signal appeared. For no good reason, except maybe to measure as many points as possible, I increased the pulse power and narrowed the pulse width considerably, to a time of the order of a millisecond or less. The result—a 'v mode' type of signal which looked strangely symmetric—appeared on the oscilloscope in the absence of a pulse and its corresponding pedestal. But I did not admit to that observation at the time as a genuine signal, and cursed at it as an annoying glitch. I twiddled the pulse width knob back to a wider pulse and the glitch went away. Off-handedly, on the day of that observation (late summer 1949), I blamed the glitch on an erratic misfiring of a multivibrator gate.

A week went by and luckily I fooled with the pulse width knob again. Up popped the signal with no pulse to account for it. The signal, of course, was the spin echo, and this time I nursed and cajoled the then mysterious blip with various maneuvers. I realized that the 60 cycle modulation was an annoyance and removed it. The symmetric signal had a definite amplitude dependence on pulse intensity and pulse width. After displaying the two pulse sequence in one slow single sweep (from protons in glycerine), all the standard characteristics of echo behavior fell out in front of my astonished eyes like a cornucopia from Mother Nature.

I stuck a screwdriver in the magnet and the echo width narrowed because of the increase in field inhomogeneity. Later I looked at the echo decay envelope of protons in water, and it was startlingly different. Compared to glycerine the water decay envelope no longer looked exponential, but was rather Gaussian in character. This was the signature of self-diffusion, a deduction which took me a while to realize only after I noticed that the Gaussian decay depended on the strength of the field gradient. In short order, all of the characteristics of damping and various echoes with their delays showed up with more than two pulses.[10] Although the pulses were narrow enough to permit the formation of an echo, they were at first too wide to allow perceptible FID signals until the pulses were made even narrower. The FID told me immediately that I had free precession, but to figure out the various echoes from three pulses, including the very interesting stimulated echo, I had to sit down with Bloch's equations and figure out first why two equal pulses produced an echo. This effort would have been simplified considerably if I had first conceived of the 90–180 ° pulse echo pancake model demonstrated later[11] by Carr and Purcell. I devised my own more complicated two-dimensional vector models for primary and stimulated echoes which follow after the application of two and then three identical pulses. After I announced the discovery of the echo, I was honored by a letter of congratulations from Ed Purcell in which he sketched his three-dimensional 'eight-ball' picture of the 90–90 ° spin echo. To say the least, so many new effects came out in such a short time that I was bewildered and shaky with excitement. It was only a few days after I confirmed the signal as genuine that I happened to look at the echoes from the protons in alcohol and saw the mysterious beat modulation of the echo envelope. That was too much! I had a lot of explaining to do!

I had the good fortune to overlap with Charlie Slichter for about a year after he arrived from Harvard. He just finished his Ph.D. as a student of Ed Purcell. I profited from his presence as the first member of the Illinois Physics Faculty in NMR who helped me enormously. An important example: Charlie advised me about the correct statistical mathematical approach to analyze the effects of spin diffusion on the damping of echo signals. Charlie was the first outside denizen of NMR with whom I was in constant contact and who I feel was the first of the Physics Faculty to sense the significance of my discoveries. Dick Norberg, who was Slichter's first graduate research student, shared lab space with me in the so-called 'Physics Penthouse Loft' on the top floor of the old physics building. Dick was a beneficial stimulus in bringing up all sorts of interesting questions, and encouraging me not to delay further the writing of a major paper[12] because I was trying solve all the mysteries at once before doing so.

I should mention here that Arnold Nordsieck became my nominal thesis advisor after James Bartlett went on sabbatical leave, just as I was beginning my thesis project. Nordsieck did not follow what I was doing nor was he interested when I told him later about the echoes. He was so preoccupied with the design and construction of an analog computer that he absolutely avoided all distractions. Nevertheless I owe my thanks to Nordsieck. As a theoretician who at one time had worked with Felix Bloch, Nordsieck convinced Bloch to take me on as a postdoc fellow at Stanford when it became time for me to leave Illinois. I was very fortunate to win a one year National Research Council Fellowship (not easy to get in those days). So off to Stanford I went in the fall of 1950.

STANFORD, 1950–52

Indirect Spin–Spin Interaction

When I first arrived at Stanford, I remember vividly my first contact with Felix Bloch. He was sitting on a lab stool in the basement of the old 'Physics Corner' hunched over a chart recorder, inspecting NMR signals newly obtained by his students huddled around him. The Stanford group specialized in hunting and confirming new spins and magnetic moments. In the course of making spectroscopic searches, the effects of chemical shifts and indirect spin–spin interactions fell out of their data. At first they considered these as a nuisance, complicating their spectroscopy. Earlier the group at Stanford reported the observation[13] of a field-independent splitting of ^{121}Sb in the SbF^{-}_{6} ion. The physical origin of the splitting, quite different from the chemical shift, was not confirmed. Martin Packard and colleagues had first displayed the celebrated proton chemical shift spectrum of alcohol, later

accompanied by the field-independent fine structure splitting with improved resolution.[14] This spectrum turned out to be the steady-state counterpart of the mysterious echo envelope beats I first saw[12] in alcohol.

In retrospect, my first days with Felix Bloch were a precious and privileged experience. Soon after my arrival Bloch took off several afternoons and grilled me about my spin echo results. I outlined the mystery of the echo envelope beats, and Bloch agreed that I should build an echo rig and track down the cause of the beats. I discussed with him at length a model involving first-order interactions between two groups of spins, coupled to one another, distinguished by different chemical shifts. However the model, often applied to simple chemical reactions, is only dissipative and would not predict beats. This idea did come in handy later however, when it was realized how chemical exchange would modify or average out '*J* coupling', by virtue of proton spin exchange which I observed in methyl and ethyl alcohol.

I really did not know how to manipulate the quantum mechanics of spins in a genuine facile manner when I began my research at Stanford. I learned from Bloch how to calculate echo pulse sequences quantum mechanically, beginning with a pertinent Hamiltonian, rather than just to rely on his macroscopic equations. There was no way to predict the envelope beats from modified Bloch equations. Gutowsky et al. reported splittings[15] in liquids, which appeared to be the remnant (as a brief speculation discounted by them[16]) of the magnetic dipole–dipole interaction because of hindered rotation. After noting certain empirical results from their data, they confirmed[16] that the $J\ \mathbf{I}_1 \cdot \mathbf{I}_2$ exchange term would account for their observations, and described them in detail later in a major paper.[17] Independently, I found it necessary to choose the same term in order to explain echo modulation beats. Since the Illinois measurements were made in the steady state and mine were in the transient regime, I had the wrong impression at first that my experiment elicited an effect that could only occur in the time domain. In the steady state, if the NMR splittings of spins were caused by local fields of nonresonant coupled foreign spin species, they did not show up in terms of echo envelope beats. Apparently my magnetic field inhomogeneity was too large at first to resolve the beat oscillations (within a single echo or FID) due to coupled foreign spins.

I first thought of the exchange interaction in terms of the overlap of nuclear wavefunctions, a mechanism infinitesimally small which we never took seriously and out of the question unless one believes in cold fusion. I simply cut my teeth by carrying out a quantum mechanical echo calculation which incorporated into the Hamiltonian chemical shift terms which distinguish one proton species from its coupled neighbor; knowing about the form of the exchange operator from Heisenberg's model for ferromagnetism, I added the $J\ \mathbf{I}_1 \cdot \mathbf{I}_2$ exchange term. This calculation showed that at least two chemically inequivalent spin species (such as the CH_3 and CH_2 groups in alcohol) had to be excited simultaneously by the two-pulse sequence in order to display echo envelope beats. The mystery in my mind was then solved as to why echo envelope *J* coupling beats would not result if the spins were all equivalent.

Don Maxwell was assigned to me as my first graduate thesis student. In our major paper[18] we presented the experiment and theory for various cases of proton spin couplings in molecules. The paper discusses some ideas using rate equations about the influence of chemical exchange on the attenuation of envelope beats, and presents the results of damping in the time domain rather than translating them into the frequency domain. Slichter and McConnell[19] presented related and clearly more useful interpretations of reactions and line narrowing in the frequency domain.

After we published our initial proton echo envelope results in a letter side-by-side with a letter by MacNeil et al.[20] of the Illinois group (they reported results concerning their measurements of fluorine echo envelope 'slow beats'), Ramsey and Purcell identified[21] the physical origin of the '*J*' coefficient as the effect of indirect exchange, caused by nuclear hyperfine interactions. At the news of this explanation, Bloch called me into his office and literally apologized to me. He said he should have thought of this idea himself because he was well aware of the nuclear hyperfine interaction. In fact later as a joke, after Don Maxwell and I wrote our paper and acknowledged the advice and encouragement of Bloch at the end of the paper, Bloch read it and chortled 'You should have acknowledged me for my constant discouragement!'

It was clear to me why Bloch didn't think of the origin of the interaction. In his view all of these effects were 'chemical' and not sufficiently fundamental. Many times Bloch indicated he would not be caught up in the morass of solving problems related to chemical structure and worry about the mystery of the field-independent splitting. On one occasion when Dick Norberg visited Stanford, and he and I were telling Felix at length about our results, finally Bloch said 'Hahn, you should be a chemist, and Norberg, you should be a metallurgist!' (Norberg was studying the NMR of hydrogen adsorbed in platinum and palladium.) Later, when NMR proved to be extremely important for chemical analysis and MRI, Bloch changed his views and indeed he was very interested.

As a junior citizen, my sojourn at Stanford came to an end. It was the policy of the Stanford Physics Department at that time to hire 'at the top' and not to promise a ladder appointment to young upstarts like me. Sid Drell, who graduated with me at Illinois, was also at Stanford at the same time and had the same fate. I should mention that Drell gave me very helpful advice about theory; and of course Felix Bloch inculcated in me many concepts without which I would not have succeeded in rounding out my understanding of my research results at Stanford. In 1952 I took a research position at IBM Watson Laboratory in New York City, and Drell went to MIT. Eventually I went to Berkeley and Drell returned to Stanford.

IBM WATSON LABORATORY, 1952–55

I was hired as a research physicist by the IBM Watson Computing Lab at Columbia and entered a new research group. In hiring me, IBM expressed an interest in the possibility that spin echoes might be useful for digital memory in computers. I took a dim view of their interest for fear that I would be channeled into doing applied research. I took the job on the basis that there was to be no obligation on my part to lead a research program in spin echo memory, that I would serve only as a consultant. Even at that time one could sense that spin echo memory would be too slow and of low capacity, which proved to be the case.

Spin Echo Memory

On the subject of how the practicality of the spin echo method was viewed in those early days, it should be pointed out that while I was at Stanford, Russell Varian advised me to write up a patent[22] on the applications of pulsed nuclear induction. Chemical analysis appeared to be its main use. With the support of the Varian patent staff I wrote up the patent. In order to do this however I had to ask the ONR, and subsequently the University of Illinois, to release the patent rights to me, which they did. As a good example of how small-scale research results can be immediately viewed with utter boredom and no foresight by higher authority, the President of the University of Illinois sent me a formal letter of release of their patent rights, which stated ' ... the spin echo is a phenomenon of Nature ... ', with words to the effect that it would be of no use. (On the contrary, the spin echo is absolutely an 'unnatural phenomenon'! Ludwig Boltzmann would have said the same thing!) Stuck somewhere in that patent written for Varian was the suggestion, as well as in one of my papers, that there might be a possible application to computer memory. When the University of Illinois heard that IBM was interested in spin echo memory they regretted their decision to release the spin echo patent and tried to renege.

Spin echo memory for computing proved to be of no use. The outcome of IBM spin echo memory research consisted of a few IBM patents written by my research colleagues who contributed a number of original ideas. A very interesting summarizing paper[23] was published which confirmed the behavior of inverse order multiple transverse echo pulse memory and direct order multiple longitudinal stimulated echo pulse memory. These memories could be separated from one another by the application of magnetic field gradient pulses, thus eliminating the interference of any nonlinear higher order echoes. This paper introduced several ideas about manipulations and pulse sequences which later found their way into magnetic resonance imaging (MRI) and photon stimulated echo pulse memory experiments in rare earth crystals.[24]

Zero-Field NQR Echoes

At IBM Watson Laboratory, I was given the status of an associate in the Columbia University Physics Department and taught a course in atomic physics. I took on Bernard Herzog as a beginning graduate thesis student and we worked on the problem of detecting zero-field ^{35}Cl nuclear quadrupole spin echoes using the 'workhorse' crystal of sodium chlorate. Zero-field CW NQR had been discovered[25] by Dehmelt and Kruger, and it was natural to look for spin echoes in this novel nuclear quadrupole coupled regime. Meyer Bloom, Slichter's student at Illinois, was doing the same experiment for his thesis, unknown to us at first. There was some question at the time about how one should expect to see a signal from crossed coils, beginning from thermal equilibrium, when the zero net spin angular momentum of the spin ensemble results from the spin degeneracy of the quadrupole moments in zero field. Admittedly after some fumbling and bumbling we finally got a signal, which could only be picked up from the same coil that was excited with an rf pulse. We realized only later that the application of a small magnetic field would permit a modulation signal to be seen even in a cross coil at right angles to the excited coil. Meyer Bloom apparently saw his signal shortly before we did at Watson laboratory, but he kindly agreed that we publish a paper[26] together. In that paper Bloom contributed an interesting echo envelope modulation effect which occurs when the two-pulse echo is generated within the FID lifetime following the second pulse. Also in that paper, although not recognized as such because it was not in the language of the density matrix, we presented a formulation of the pseudo two-level spin system from which we devised a vector model.

The 'workhorse' crystal, sodium chlorate, which made its debut with zero-field NQR echoes, served later as a model two-level system that displayed the effects of SEDOR,[27] cross spin polarization transfer,[28] spin noise,[29] and finally nuclear quadrupole induced atomic electric dipole oscillations[30] (the inverse of the Stark effect in NQR).

SEDOR—Spin Echo Double Resonance

The $J\ \mathbf{I}_1 \cdot \mathbf{I}_2$ interaction in liquids indicated to me that the turnover of a spin would alter the precession phase of the spin echo of its neighbor because of the magnetic dipole–dipole interaction in a solid. This property led to the following experiment: a separate rf resonance pulse was applied to flip the sodium spin neighbors of ^{35}Cl in sodium chlorate during the application of the second pulse of a two-pulse sequence to obtain the ^{35}Cl spin echo at its own precession frequency. The resonance of sodium is therefore detected indirectly when the scrambling of phases due to local dipolar fields of sodium at the ^{35}Cl sites causes a maximum reduction in the ^{35}Cl echo amplitude. Hence the SEDOR (Spin Echo Double Resonance) method was adopted as the thesis of Bernard Herzog. Measurements of the attenuation of the echo envelope were carried out as a function of the extent of phase scrambling caused by the SEDOR process. A model[27] based upon stochastic predictions of the Fokker–Planck equation was applied to fit the data.

UNIVERSITY OF CALIFORNIA, BERKELEY, 1955–91

Cross-Relaxation Polarization Transfer

After settling down in Berkeley I pursued further SEDOR spectroscopy and relaxation experiments, which finally constituted the graduate theses of Kaplan and Emschwiller.[31] At the same time I mused a great deal over ways one could increase the double resonance sensitivity, if only the time for scrambling phases could be significantly increased. However phase scrambling was not a good approach because the echo memory relaxation time of 'T_2' for echoes in solids is at best no longer than a few milliseconds. Could a longer time of the order of the spin–lattice relaxation time 'T_1' be exploited instead? Here is where Sven Hartmann came into the picture—a very perceptive thesis student who was a match for an entirely new kind of experiment.

The so-called Hartmann–Hahn cross-relaxation experiment[28] evolved from hints contained in Al Redfield's famous paper.[32] These hints were to be found in his discussion of 'rotary saturation' and in his concept of spin temperature in

the rotating frame. Rotary saturation was first practised by applying an external longitudinal oscillating field parallel to the polarization direction of nuclear spins, in order to cause resonance saturation of a spin ensemble in the rotating frame. I was intrigued by the idea of flipping (nutating) a spin in a solid so that it would produce an internal 'local longitudinal dipolar field' which would cause rotary saturation of a neighboring spin characterized by an entirely different Larmor frequency. I first thought in terms of imitating the spin–lattice relaxation mechanism, by imagining that one replaces the Fourier component of lattice noise at the ^{35}Cl resonance frequency by a specific rotary saturation frequency component. This component would be produced by a neighboring Na spin, resonant with ^{35}Cl. But how could that be done? An intense rf field, impossible to produce, would be required to flip the Na spins in order to 'relax' the observed ^{35}Cl ensemble at its resonance frequency of 30 MHz?!! Of course, one had to prepare the ^{35}Cl system in the rotating frame. The rotary saturation frequency would be much lower and the rf field could be generated. Sven Hartmann reminded me about Solomon's spin-locking technique.[33] That was the way to do it, and along with the rotating frame came the necessity of thinking in terms of spin temperature, expounded further by Lurie and Slichter.[34]

It is interesting to point out that the method of 'dynamic nuclear polarization', introduced earlier[35] by Anatole Abragam and Carson Jeffries, can be treated as though it is a case of Hartmann–Hahn cross relaxation. In the rotating frame, electron spins acquire a low absolute spin temperature (with negative or positive polarization) and a Larmor frequency which closely matches the Larmor frequency of coupled nuclear spins at a higher spin temperature in the laboratory frame. This particular cross-relaxation process requires intense microwave electron spin excitation because a small fraction of the electron spin 'magnetic heat capacity' is utilized.

Directly following the work with Hartmann, a series of investigations involving variations of double resonance spectroscopy were carried out by Dick Slusher,[36] Russ Walstedt, and Dave McArthur,[37] and Gil Leppelmeier.[38] The dynamics of the double resonance process were studied in particular by Walstedt and McArthur, who very carefully and with great skill measured the fluctuation spectrum of the ^{19}F–^{43}Ca spin–spin coupling operator in CaF_2. This spectrum is characterized by a still-unexplained exponential function of the rotating frame ^{43}Ca Zeeman splitting over a wide range of cross-relaxation rates. Also the transient regime of spin population cross-coupling oscillations was measured and analyzed. The transient is a version of the oscillations observed earlier between coupled dipolar and Zeeman reservoirs brought suddenly into contact in the laboratory frame.[39]

Self-Induced Transparency

Some time before Sven Hartmann obtained photon echoes,[40] I was curious about what effect zero-field NQR resonant absorption of ^{35}Cl might have on rf pulses matched to a transmission line filled with powdered $NaClO_3$ crystals. The experiment was attempted surreptitiously, because I suspected it would fail from the start. The transmission line had to be too long in order to see a significant effect. Jim Kemp, who came over from the Electrical Engineering Department to collaborate on a pulsed EPR experiment, suggested that we try to look at the change in the properties of a propagating EPR pulse when it is tuned to the electron spin resonance of two ferrite spheres separated down the line from one another in a wave guide. The excitation of the first sphere by the pulse would cause the sphere to reradiate and drive to some extent the second sphere down the guide. Finally, the output pulse was expected to be some sort of superposition of driving and reradiated signals. We certainly saw signals, but they were too messy to interpret because of a combination of wave guide reflections and multiple spin wave modes excited in the spheres.

Again the propagation game was abandoned and resumed once more, this time after the photon echo[40] was revealed by Sven Hartmann at Columbia. Logically, in concentrating on the dynamics of newly found optical echoes, Hartmann made the approximation that laser pulses remained unaffected while propagating through a short length of ruby crystal. This was a setup suitable now for Sam McCall (a superb new thesis student) and me to look for propagation effects on a traveling wave laser pulse at resonance with ruby. By choosing a crystal long enough to include a sufficient number of absorption lengths, we confirmed experimentally what had been predicted in a small way by an ignored computer empirical analysis we published earlier as an abstract.[41] Finally, thanks to Sam's computer and theoretical expertise, we were able to formulate a general description of self-induced transparency[42] based upon analytical semiclassical solutions of the Bloch–Maxwell equations. Self-induced transparency was the first clear experimental example of soliton behavior in the form of optical traveling wave pulses.

The description of two-level systems in the Bloch–Maxwell model of the self-induced transparency experiment contains many ideas borrowed from the description of coherent transients in NMR. A number of pulsed laser experiments then followed over the years which demonstrated analogs[43] of pulsed coherent NMR transient phenomena. Of greatest utility were the results[44] concerning two-photon and Raman response of three-level systems, formulated in terms of the density matrix by Dick Brewer and myself. As a result of my collaboration with Dick Brewer at IBM over a number of years, his researchers inspired a number of laser thesis topics which I carried out with my students at Berkeley.

IN RETROSPECT

Several transient signal effects under conditions of driven rf excitation were reported in the early NMR literature. It seems to me that these transient effects provided sufficient information that could easily have led to the prediction and production of a FID signal. Perhaps the spin echo would not have been immediately predicted, but it would have been discovered eventually, if not by me, then by somebody else. In his first paper,[1] Bloch mentioned that free precession would result after the sudden reorientation of spins by a nonadiabatic dc field pulse. Jacobsohn and Wangsness reported[45] the measurements and theory of an NMR transient called the 'wiggles'. This is a beat phenomenon often seen in CW NMR when a small sweep magnetic field passes through the resonance condition, and the nuclear spins are tipped slightly to produce a transverse precessing magnetization. The Larmor frequency of this magnetization tracks with the externally

swept dc field, and beats with the fixed driving rf field after the resonance condition is traversed. In Torrey's paper[7] on nutations, he mentions explicitly that no one had yet seen free nuclear induction signals. Inexplicably, neither he nor anyone else followed up that statement by applying a short rf pulse at resonance to see if a predicted FID could be detected. It was left for me to find it by accident! Volumes can be written about numerous cases of this sort in the annals of science.

REFERENCES

1. F. Bloch, *Phys. Rev.*, 1946, **70**, 460.
2. N. Bloembergen, E. M. Purcell, and R. V. Pound, *Phys. Rev.*, 1948, **73**, 679.
3. G. E. Pake, *J. Chem. Phys.*, 1948, **16**, 327.
4. J. H. Van Vleck, *Phys. Rev.*, 1948, **74**, 1168.
5. N. Bloembergen, *Nuclear Magnetic Relaxation*, Martinus Nijhoff, The Hague, 1948.
6. I. I. Rabi, *Phys. Rev.*, 1937, **51**, 652; J. Schwinger, *Phys. Rev.*, 1937, **51**, 648.
7. H. C. Torrey, *Phys. Rev.*, 1949, **76**, 1059.
8. E. L. Hahn, *Phys. Rev.*, 1949, **76**, 145.
9. E. L. Hahn, *Bull. Am. Phys. Soc.*, 1949, **24**, 16.
10. E. L. Hahn, *Phys. Rev.*, 1950, **77**, 297.
11. H. Y. Carr and E. M. Purcell, *Phys. Rev.*, 1954, **94**, 630.
12. E. L. Hahn, *Phys. Rev.*, 1950, **80**, 580.
13. W. G. Proctor and F. C. Yu, *Phys. Rev.*, 1951, **81**, 20.
14. M. E. Packard and J. T. Arnold, *Phys. Rev.*, 1951, **83**, 210; J. T. Arnold, S. Dharmatti, and M. E. Packard, *J. Chem. Phys.*, 1951, **19**, 507.
15. H. S. Gutowsky and D. W. McCall, *Phys. Rev.*, 1951, **82**, 748.
16. H. S. Gutowsky, D. W. McCall, and C. P. Slichter, *Phys. Rev.*, 1951, **84**, 589.
17. H. S. Gutowsky, D. W. McCall, and C. P. Slichter, *J. Chem. Phys.*, 1953, **21**, 279.
18. E. L. Hahn and D. E. Maxwell, *Phys. Rev.*, 1952, **88**, 1070.
19. C. P. Slichter, *Principles of Magnetic Resonance*, 3rd edn., *Springer Series in Solid State Sciences 1*, Springer Verlag, Berlin, 1990, Appendix F; H. M. McConnell, *J. Chem. Phys.*, 1958, **28**, 430.
20. E. B. MacNeil, C. P. Slichter, and H. S. Gutowsky, *Phys. Rev.*, 1951, **84**, 1245; E. L. Hahn and D. E. Maxwell, *Phys. Rev.*, 1951, **84**, 1246.
21. N. F. Ramsey and E. M. Purcell, *Phys. Rev.*, 1952, **85**, 143.
22. US Pat. 2 705 790 (April 5, 1955). E. L. Hahn, *Spin Echo Technique and Apparatus*
23. A. G. Anderson, R. L. Garwin, E. L. Hahn, J. W. Horton, G. L. Tucker, and R. M. Walker, *J. Appl. Phys.*, 1955, **26**, 1324.
24. M. Mitsunaga and N. Uesugi, *Opt. Lett.*, 1990, **15**, 195.
25. H. G. Dehmelt and H. Kruger, *Naturwissenschaften*, 1950, **37**, 111; 1951, **38**, 921.
26. M. Bloom, E. L. Hahn, and B. Herzog, *Phys. Rev.*, 1955, **97**, 1699.
27. B. Herzog and E. L. Hahn, *Phys. Rev.*, 1956, **103**, 148.
28. S. R. Hartmann and E. L. Hahn, *Phys. Rev.*, 1962, **128**, 2042.
29. T. Sleator, E. L. Hahn, C. Hilbert, and J. Clarke, *Phys. Rev.*, 1987, **B36**, 1969.
30. T. Sleator, E. L. Hahn, M. B. Heaney, C. Hilbert, and J. Clarke, *Phys. Rev.*, 1988, **B38**, 8609.
31. M. Emshwiller, E. L. Hahn, and D. Kaplan, *Phys. Rev.*, 1960, **118**, 414.
32. A. G. Redfield, *Phys. Rev.*, 1955, **98**, 1787.
33. I. Solomon, *C. R. Acad. Sci.*, 1959, **248**, 92.
34. F. M. Lurie and C. P. Slichter, *Phys. Rev.*, 1964, **133**, A1108.
35. A. Abragam and W. G. Proctor, *C. R. Acad. Sci.*, 1958, **246**, 2253; C. D. Jeffries, *Phys. Rev.*, 1957, **106**, 164; A. Abragam, *The Principles of Nuclear Magnetism*, Oxford University Press, Oxford, 1961, Chap. 9
36. R. E. Slusher and E. L. Hahn, *Phys. Rev.*, 1968, **166**, 332.
37. D. A. McArthur, E. L. Hahn, and R. E. Walstedt, *Phys. Rev.*, 1969, **188**, 609.
38. G. W. Leppelmeier and E. L. Hahn, *Phys. Rev.*, 1966, **142**, 179.
39. R. L. Strombotne and E. L. Hahn, *Phys. Rev.*, 1964, **133**, A1616.
40. I. D. Abella, N. A. Kurnit, and S. R. Hartmann, *Phys. Rev.*, 1966, **141**, 391.
41. S. L. McCall and E. L. Hahn, *Bull. Am. Phys. Soc.*, 1965, **10**, 1189.
42. S. L. McCall and E. L. Hahn, *Phys. Rev.*, 1969, **183**, 457.
43. E. L. Hahn, Heritage of the Bloch Equations in Quantum Optics, *Felix Bloch and 20th Century Physics. A Festschrift*, Rice University Press, Texas, 1980.
44. R. G. Brewer and E. L. Hahn, *Phys. Rev.*, 1975, **A11**, 1641.
45. B. A. Jacobsohn and R. K. Wangsness, *Phys. Rev.*, 1948, **73**, 942.

Biographical Sketch

Erwin L. Hahn. *b* 1921. B.S., 1943, Juniata College; US Naval Reserve, 1944–46; Ph.D., research associate, University of Illinois, 1949–50. Instructor, postdoctoral worker, Stanford University, 1950–52; IBM Watson Laboratory, 1952–55; Professor of Physics, University of California, Berkeley, 1955–present. Research specialties: pulsed NMR and laser phenomenology, spin–spin coupling, double resonance, nuclear quadrupole resonance.

Hall, Laurance D.: NMR Studies of Carbohydrates

Laurance D. Hall

University of Cambridge, Cambridge, UK

My involvement in nuclear magnetic resonance spectroscopy was the result of a traumatic experience. One Friday in 1959 I had obtained the last elemental microanalysis to show that I had completed the synthesis of a series of furanose carbohydrates. By the following Monday I had convinced my supervisor, Les Hough, that all was well and on Tuesday afternoon I went to the library of the Chemistry Department of Bristol University to write my first paper. Browsing through the latest issue of the *Journal of the Chemical Society* to gain some sense of the appropriate style, I was appalled to find a paper by L. N. Owen of Imperial College which described my work! Fortunately I had made both the D- and L-series of derivatives, and was able to publish[1] the work in full; nevertheless I was so upset that I decided there and then that I would find my own Ph.D. topic, remote from the interests of others. Late that same evening, unable to work, I returned to the library and started to browse through the new monographs that were kept on a separate shelf by the entrance door. One of these, 'High Resolution NMR' by Pople, Schneider, and Bernstein,[2] attracted my attention for no particular reason. Yet within minutes I was riveted; one section showed the proton NMR spectra of fully acetylated pyranose sugars, the work of Lemieux, Kullnig, Bernstein, and Schneider.[3] I did not understand how the spectra had been obtained nor the meaning of the terms 'chemical shift' or 'coupling constant', yet it was absolutely clear to me that here was the technique which would revolutionize structural analysis of carbohydrates; more importantly, I had a wonderful collection of furanose sugars and it appeared that nobody had yet studied such substances; it also occurred to me that since the H-1:H-2 coupling constants of pyranose sugars varied with the relative stereochemistry of the C-1:H-1 and C-2:H-2 bonds, I might be able to work out the shapes of my furanose sugars and thereby understand the stereospecific dependencies of their reactions; furthermore, since I had systematically varied the substituents attached to O-3 of my glycofuranose sugars I would be able to demonstrate the specific chemical shift changes induced by functional groups, something at that time unknown, but potentially important.

By now it was early morning, too late to go home, so I stayed in the library until Les Hough came into the lab, and I told him that I had decided to abandon my synthesis work and take up NMR spectroscopy instead! In retrospect, and having since supervised a huge number of my own Ph.D. research students, Les could have attempted to dissuade me; indeed, he did point out that Bristol University had no NMR spectrometer, that he knew nothing about the method, and that the prudent thing to do was to get my Ph.D. first and then learn about NMR as a postdoctoral fellow elsewhere. Of course, I would have none of this, and went off to read all I could about NMR; this involved me in the *Journal of Chemical Physics* and the *Canadian Journal of Chemistry*, which were far removed from organic synthesis. I also talked to all and everyone about my ideas; again in retrospect my behavior must have verged on the noxious, but I was blissfully unaware of this at that time. Then came the second of a series of lucky breaks; I was a teaching assistant to an undergraduate inorganic chemistry laboratory supervised by E. W. Abel and discovered that he had been a postdoctoral fellow at Imperial College, London and that he actually knew something about NMR (at that time he was the only one in Bristol who did!). I must have made life hell for him since I bombarded him with questions: one day he made an offer; on Friday he was to go to Imperial College; he would take three samples and try to persuade someone to run their spectra; the deal was that until I had interpreted them I would not talk to him or anyone else about my ideas for NMR! Little did I know that that promise was to mean that I was to be in purdah for nine months. In any event, the following week he returned with three envelopes each containing narrow strips of thermal sensitive paper with black squiggles on them and some strange hieroglyphics such as 'SSB' or 'ASB,100'. None of that mattered since I could see that one of the spectra contained nearly as many separate peaks as there were different protons in the molecule . . . something that was quite different from the spectra published by Lemieux and co-workers. I eventually persuaded the departmental photographer to make some photographic enlargements of those spectra so I could calibrate them, learned that 'ASB' was 'Audiomodulation Sideband' and 'SSB' was 'Spinning Sideband' and was in business.

Nine months later I was able to hold an intelligent discussion with Eddie Abel, but was still unable to understand my spectra fully because there were too many 'doublets' and not enough 'quartets'. Then came my second break, with the publication[4] by M. Karplus of his '$\cos^2\theta$' interpretation of the stereospecific dependence of coupling constants. Now I could see that my furanose sugars must be in a conformation in which one of the pairs of C–H bonds had a dihedral angle of 90 ° and hence a zero coupling constant, something that had never been seen before. My problem was that I still could not assign the individual resonances; I needed more spectra! Then came my third break, because I remembered that when I had worked one summer for ICI Dyestuffs Division at Manchester I had been shown an NMR spectrometer, something I had completely forgotten up to that point. I wrote immediately to Mrs. Neil, their academic liaison officer, telling her my story, and to my delight received from her the offer of spectra for any 12 samples of my choice. Those were sent off the next day, and several weeks later I received the results with a covering letter from Jack Becconsall who had run them, to the effect that some of them looked interesting. Elatedly I rushed off to tell my then flatmate and friend Les Rigby . . . and hence to the next stroke of luck. He was being visited by Keith McLauchlan who had been a student at Bristol, and who I discovered was now a postdoctoral fellow at the National Physics Laboratory at Teddington working with John Pople; he not only had access to an NMR spectrometer, but was working with Ray Abraham on the shape of another set of five-membered rings, those of hydroxyproline derivatives. The following week Keith returned to say that he and Ray were willing to run my samples; my reply was 'I want to go with the samples'. In due course it was agreed that he would take those of my samples he had chosen and that a month later I could go to Teddington for a one-day visit, no longer. When I arrived there was some gloom since all the samples they had run had given overlapping resonances.

That did not surprise me because I had already decided that the samples Keith had chosen were not the best suited to the project . . . I had those in my pocket! It turned out that one of the other scientists was going on holiday that next week and Ray Abraham suggested that, although the project was likely to fail, perhaps I might like to run some samples myself. After an introduction as to how to crank a magnet pole face to improve the field homogeneity and how one could track the sweet spot by moving the probe within the magnet to improve the resolution (this was before we had either shim coils or baseline stabilization) I was ready for my first spectrum (3-*O*-acetyl-1,2-*O*-isopropylidene-α-D-glucofuranose); everyone gathered round and kept still whilst the chart recorded a spectrum with seven completely resolved proton resonances, each with close to baseline resolution. By then I knew enough about chemical shifts to say with reasonable confidence which was which.

After that there was no question about abandoning the work, nor even of my returning to Bristol; simply I was going to push this as hard as I could. Of course, there were some logistical problems to overcome, such as my undergraduate lab demonstration duties in Bristol, Les Hough my supervisor, and how I could pay to live in London. In the event, I stayed with my parents and spent three hours each day commuting diagonally across London and started writing papers.[5] I also listened carefully to the other members of Pople's group which at that time included Tom Connor and Ray Freeman. Tom was from Chris Reid's laboratory at the University of British Columbia and he taught me how to make dry, ethanol-free chloroform (stand it over silica gel) and how to measure H–O–C–H couplings and then 'decouple them' by adding a trace of trifluoroacetic acid; I put that to good use for my sugars. Ray Freeman and I soon found that we shared a common lack of interest in cricket, something which put us both somewhat apart from the rest of Pople's group. So, whilst the others played cricket in the sun, he and I sat in the shade and I talked to him about my hopes whilst he listened patiently. One Wednesday morning he told me that he had just built a new machine and that he would use it to assign all my proton resonances, and if I would make up a solution he would run the experiment that morning. After coffee we went to the lab and Ray went through his routine of rewiring the Varian DP-60 spectrometer to what was then the world's first 'frequency sweep' spectrometer; this involved taking from a clothes hanger behind the lab door, a bundle of cables with banana plugs on each end, and using them to connect two small metal boxes to the DP-60. The dials were unlabeled and nobody but Ray had any idea of how the apparatus worked. However, on that day everyone trooped into the lab for the first demonstration of Ray's latest toy. He put me on the spot by asking me which pairs of resonances were coupled (remember that there was a zero coupling); within a few minutes he had proved that my previous assignments based on chemical shifts were correct, and by lunchtime we had completed the full cycle of decoupling experiments. After lunch, while all the others went off to cricket, Ray and I wrote a paper which was sent off to the Chemical Society the following afternoon.

By now it was clear that my thesis was to include a great deal of NMR spectroscopy and that I was unlikely to spend much time at Bristol, so Les Hough was invited to come for a visit and a deal was struck whereby I would visit Bristol a week every month to fulfill my lab demonstrating activities (having swapped with my friends so that my duties were bunched together). In due course (January 1962) I returned to Bristol to write up my Ph.D. thesis, which was subsequently examined by Peter Schwarz from Edinburgh; after 10 minutes, during which he made several excellent suggestions about my chemistry, he closed the examination and asked me to spend the next two hours explaining to him how NMR worked. I was then 'invited back' to Bristol to give a lecture on my work; this was unprecedented, but I can still remember how that, my first formal lecture, felt . . . I feel the same before any major lecture. By then I had had offers of postdoctoral fellowships from Frank Anet at Ottawa University and from Lloyd Jackman who was moving from Imperial College to Melbourne. I decided to go to Ottawa since that was also where Bernstein and Schneider were. There were other distractions too; such as being offered a job by Frank Rose to set up an NMR machine for ICI Pharmaceuticals at Alderley Edge (a job which Geoff Bedford did far better than I could ever have done); such as going to my first international symposium (on carbohydrates at Birmingham), where I first learned that some abstracts claim more that the lecture presents; and getting married.

My move to Ottawa in August 1962 brought about a mixed set of developments. The bad news was that Frank Anet had decided to go on sabbatical within a few weeks of my arrival; so once again I was left without a supervisor, but this time in charge of a lab full of graduate students, one of whom was 15 years older than myself. The good news was that I had access to a 60 MHz spectrometer and was an honorary member of the NRC lab where Bill Schneider and Harold Bernstein worked. Furthermore, both Margaret and I enjoyed Canada; our first daughter, Gwendolen, was born in May 1963, and I decided to try to make a career in Canada instead of returning to England. So in March 1963 I went to Pittsburgh to my first ENC meeting, at which I made friendships which have lasted my lifetime. On my return I found invitations to visit Queen's University and also the University of British Columbia. I arrived in Vancouver on a beautiful sunny day, fell in love with the scenery, gave a stimulating lecture and was eventually offered a post of 'Instructor II', which I later found was even lower than Assistant Professor. A memorable drive across Canada in August 1963 then started 25 years at UBC which was only terminated by the machinations of Joachim Burhenne, then Head of Radiology, who wished to control magnetic resonance imaging in Vancouver. During those years at UBC I learned how to run a research group, build NMR machines, and also that my love of my science was probably stronger than was compatible with a balanced life; however I run ahead of myself.

Based on my own experience and that of Lemieux, it was clear to me that carbohydrates provided an ideal skeleton for studying the stereospecific dependencies of NMR parameters; thus the pyranose ring was generally conformationally rigid, and by using appropriate substitution it was feasible to obtain essentially first-order spectra, even at 60 MHz. My first research involved the synthesis of a wide variety of specifically fluorinated carbohydrates; those enabled us to delineate the stereospecific dependencies of $^{19}F-^{1}H$ and $^{19}F-^{19}F$ coupling constants,[6] and the intrinsic chemical shift differences between the axial and equatorial orientations. Subsequent studies involved phosphorus-31,[7] mercury-199,[8] and thallium-203.[9]

My interest in conformational analysis of carbohydrates also prompted me to explore the possible use of lanthanide

shift reagents, but this was not a convenient procedure. However, our studies[10] of the spin–lattice relaxation rates of the protons of sugars was a far more rewarding area. It was possible to prove rigorosly that their relaxation was entirely via the intramolecular dipole–dipole mechanism.[11] Furthermore, methods were developed whereby specific interproton relaxation contributions could be measured quantitatively; these involved use of specific deuteration,[12] or of selective proton T_1 measurements.[11] Undoubtedly the most important discovery was the interproton relaxation between the H-1 proton on one ring and those on the adjacent ring;[13] in the form of specific interring nuclear Overhauser enhancement measurements this is now widely used in oligosaccharide conformational analysis.

During the early 1970s it became clear that the increased spectral dispersion produced by superconducting solenoid magnets would revolutionize the ease with which proton spectra could be assigned. Sadly, the Canadian NRC had decided that they would not provide such devices for any Canadian university, so I decided to assemble my own. Thus a 60 MHz Bruker console was purchased from the fledgling company Nicolet and upgraded to 270 MHz operation by the electronics shop in the UBC Chemistry Department. A 270 MHz magnet was purchased from Oxford Instruments, a crude proton-only probe constructed (no mean feat at a time when probes were regarded as being black magic), and we had access to high-quality spectra. It was fortunate both that Dave Dalrymple, then at Nicolet, had written software for processing the then new class of two-dimensional NMR spectra, and that I had an outstandingly able graduate student, Subramanian Sukumar. That combination soon enabled us to describe for the first time how the proton 2D J resolved spectroscopic technique could be used to unravel complex carbohydrate spectra,[14] that was followed by the use of NOESY and COSY spectroscopy. We were then joined by Gareth Morris from Ray Freeman's group, who built our first $^{13}C-^{1}H$ probe and demonstrated the power of 2D heteronuclear correlation spectroscopy[15] as a tool for the carbohydrate chemist. I remember the elation I felt when I realized that that method gave us the effective resolving power of a 10 000 MHz proton spectrometer; the chemical shift sensitivity of ^{13}C is 40-times that of the equivalent proton resonances. Our work in 2D NMR was hugely aided by the fact that we had a second Nicolet computer set up as a data-processing station; that was regarded as being a luxury at that time!

Exciting as it was, the development of that 270 MHz spectrometer was to be the nemesis for my carbohydrate spectroscopy, since by 1980 the performance of our homebuilt instrument was no longer competitive with the new spectrometers available commercially. Rather than abandon the instrument, Sukumar and I decided to convert it to an 'NMR microscope'. We found that this was straightforward, and that the Nicolet 2D software could be used to plot out in contour format the results from imaging of simple objects.[16] Those exciting developments enabled us to be the first in Canada to study NMR imaging. Inexorably, I found myself drawn from the 'Laboratory' to the 'Hospital' where by 1983 I had installed the first MRI scanner in Canada. Inexorably too, I was dragged into the jungle of local medical politics; the imaging went well, the politics equally badly and job offers abounded; in 1984 I accepted the invitation to be the first holder of the Herchel Smith Chair of Medicinal Chemistry at Cambridge University. This is a clinical chair and has enabled me to fulfill at least some of the hopes which prompted my move into MR imaging. Having built the Institute I am now returning to my interests in carbohydrates, this time to polysaccharides; two examples will suffice to explain what can be achieved. Since the NMR properties of water are influenced by dissolved polysaccharides, it is possible to develop MRI protocols to map in space and time the location of polysaccharides; for example, we have shown[17] that when calcium alginate is formed from sodium alginate and calcium chloride, the resultant gel is not homogeneous, rather there is a higher concentration of alginate at the outside of the gel structure. More importantly, we have demonstrated[18] that MRI can be used to study cartilage structure and composition in the articular joints of man. Changes in cartilage due to osteoarthritis are of great importance to the pharmaceutical industry, and we now have the most promising method for detecting the early onset of that disease and for monitoring not only the natural progression but, possibly, the efficacy of new drug treatments.

It has been an interesting experience to write this article, since the feelings of 1959 are as vivid now as they ever were. I now have about 12 years to go before I am forced from my research chair and I fully intend to use them to explore the wonderful synergy between 'carbohydrates' and 'NMR'. The fortunate experiences of 1959 have dominated both my scientific career and my private life, and I have no regrets about continuing to explore the creative opportunities which connect those two scientific disciplines.

REFERENCES

1. L. D. Hall, L. Hough, and R. A. Pritchard, *J. Chem. Soc.*, 1961, **302**, 1537.
2. J. A. Pople, W. G. Schneider, and H. J. Bernstein, *High Resolution NMR*, McGraw-Hill, Toronto, 1959.
3. R. U. Lemieux, R. K. Kullnig, H. J. Bernstein, and W. G. Schneider, *J. Am. Chem. Soc.*, 1958, **80**, 6098.
4. M. Karplus, *J. Chem. Phys.*, 1959, **30**, 11.
5. R. J. Abraham, K. A. McLauchlan, L. D. Hall, and L. Hough, *Chem. Ind. (London)*, **1962**, 213; R. J. Abraham, L. D. Hall, L. Hough, and K. A. McLauchlan, *J. Chem. Soc.*, **1962**, 3699; R. J. Abraham, R. Freeman, L. D. Hall, and K. A. McLauchlan, *J. Chem. Soc.*, **1962**, 2080.
6. L. D. Hall, J. F. Manville, and N. S. Bhacca, *Can. J. Chem.*, 1969, **47**, 1; L. D. Hall, and J. F. Manville, *Can. J. Chem.*, 1969, **47**, 19; L. D. Hall, R. N. Johnson, J. Adamson, and A. B. Foster, *Chem Commun.*, **1970**, 463; L. D. Hall, R. N. Johnson, J. Adamson, and A. B. Foster, *Can. J. Chem.*, 1971, **49**, 118; L. D. Hall, R. N. Johnson, A. B. Foster, and J. H. Westwood, *Can. J. Chem.*, 1971, **49**, 236; E. M. Bessel, A. B. Foster, J. H. Westwood, L. D. Hall, and R. N. Johnson, *Carbohydrate Res.*, 1971, **19**, 39; A. D. Barford, A. B. Foster, J. H. Westwood, L. D. Hall, and R. N. Johnson, *Carbohydrate Res.*, 1971, **19**, 49; A. B. Foster, R. Hems, J. H. Westwood, and L. D. Hall, *Carbohydrate Res.*, 1972, **23**, 316; A. B. Foster, J. H. Westwood, B. Donaldson, and L. D. Hall, *Carbohydrate Res.*, 1972, **25**, 228.
7. L. D. Hall, and R. B. Malcolm, *Can. J. Chem.*, 1972, **50**, 2092; L. D. Hall, and R. B. Malcolm, *Can. J. Chem.*, 1972, **50**, 2102; L. Evelyn, L. D. Hall, P. R. Steiner, and D. H. Stokes, *Org. Magn. Reson.*, 1973, **5**, 141; L. Evelyn, L. D. Hall, L. Lynn, P. R. Steiner, and D. H. Stokes, *Carbohydrate Res.*, 1973, **27**, 21.
8. V. G. Gibb, and L. D. Hall, *Carbohydrate Res.*, 1976, **50**, C3; V. G. Gibb, and L. D. Hall, *Carbohydrate Res.*, 1977, **55**, 239.
9. V. G. Gibb and L. D. Hall, *Carbohydrate Res.*, 1978, **63**, C1.

10. L. D. Hall and C. M. Preston, *Carbohydrate Res.*, 1973, **29**, 522; C. M. Preston and L. D. Hall, *Carbohydrate Res.*, 1974, **37**, 267.
11. R. Freeman, H. D. W. Hill, B. L. Tomlinson, and L. D. Hall, *J. Chem. Phys.*, 1974, **61**, 4466; L. D. Hall, K. F. Wong, and H. D. W. Hill, *J. Chem. Soc., Chem. Commun.*, **1979**, 951.
12. L. D. Hall, K. F. Wong, W. E. Hull, and J. D. Stevens, *J. Chem. Soc., Chem. Commun.*, **1979**, 953.
13. L. D. Hall, and C. H. Preston, *Carbohydrate Res.*, 1976, **49**, 3; J. M. Berry, L. D. Hall, D. W. Welder, and K. F. Wong, *Carbohydrate Res.*, 1977, **54**, C22.
14. L. D. Hall, S. Sukumar, and G. R. Sullivan, *J. Chem. Soc., Chem. Commun.*, **1979**, 292; L. D. Hall, and S. Sukumar, *J. Am. Chem. Soc.*, 1979, **101**, 3120; L. D. Hall, G. A. Morris, and S. Sukumar, *Carbohydrate Res.*, 1979, **76**, C7; M. A. Bernstein, L. D. Hall, and S. Sukumar, *Carbohydrate Res.*, 1982, **103**, C1; M. A. Bernstein, and L. D. Hall, *J. Am. Chem. Soc.*, 1982, **104**, 5553.
15. L. D. Hall, G. A. Morris, and S. Sukumer, *J. Am. Chem. Soc.*, 1980, **102**, 1745; G. A. Morris and L. D. Hall, *J. Am. Chem. Soc.*, 1981, **103**, 4703; G. A. Morris and L. D. Hall, *Can. J. Chem.*, 1982, **60**, 2431.
16. L. D. Hall and S. Sukumar, *J. Magn. Reson.*, 1982, **50**, 161; L. D. Hall and S. Sukumar, 'Device and Method for Nuclear Magnetic Resonance Imaging Formation', US Patent 488 414, April 23, 1983; L. D. Hall and S. Sukumar, 'Nuclear Magnetic Resonance Spectrum at a Point Within a Sample', US Patent 488 415, April 25, 1983; L. D. Hall and S. Sukumar, *J. Magn. Reson.*, 1984, **56**, 179; L. D. Hall S. Sukumar, and S. L. Talagala, *J. Magn. Reson.*, 1984, **56**, 275; L. D. Hall and S. Sukumar, *J. Magn. Reson.*, 1984, **56**, 314; L. D. Hall and S. Sukumar, *J. Magn. Reson.*, 1984, **56**, 326.
17. K. Potter, N. J. Herrod, T. A. Carpenter, and L. D. Hall, *Carbohydrate Res.*, 1993, **239**, 249; K. Potter, T. A. Carpenter, and L. D. Hall, *Carbohydrate Res.*, 1993, **246**, 43.
18. R. J. Hodgson, T. A. Carpenter, and L. D. Hall, and in *Articular Cartilage Osteoarthritis*, eds. K. E. Keuttner, R. Schleyerbach, J. G. Peyron, and V. C. Hascall, Raven Press, New York, 1992, Chap. 45

Biographical Sketch

Laurance D. Hall. *b* 1938. B.Sc., 1959, Ph.D., 1962, Chemistry, University of Bristol, UK. Postdoctoral fellow, Ottawa University (with Frank Anet). Successively Instructor II, assistant, associate, and full Professor, University of British Columbia, Canada. Currently first holder of the Herchel Smith Chair of Medicinal Chemistry, University of Cambridge, UK. Approx. 400 publications. Research specialties: all aspects of magnetic resonance imaging.

Harris, Robin K.: Chemical Magnetic Resonance goes Multinuclear

Robin K. Harris
University of Durham, Durham, UK

INTRODUCTION

In the early days of NMR, when it was exclusively the realm of physicists, a variety of nuclei were studied. Thus, the chemical shift phenomenon, which was to prove such a boon to chemists, was first discovered[1–3] for ^{14}N, ^{19}F, and ^{59}Co. However, it soon became evident that the highest resolution was only achieved for spin-$\frac{1}{2}$ nuclei.

THE PROTON, FLUORINE-19, AND PHOSPHORUS-31

I first came into contact with NMR during my undergraduate days at Cambridge. At that time (1956–59) chemical NMR in the UK was in its infancy, and the teaching of it had only just been included in the Cambridge curriculum. It seemed an exciting area and I decided to study for a Ph.D. in NMR under Norman Sheppard, who was responsible for the newly-acquired Varian 40 MHz spectrometer. I was introduced to the delights of field cycling and yoke-bending of the magnet to achieve good $\boldsymbol{B}_0$ homogeneity. The spectrometer was only really suitable for examining nuclei with high natural abundance, and so chemical applications of ^{1}H and ^{19}F field sweep NMR became the subject of my thesis.

One consequence was that homonuclear indirect spin–spin coupling was of importance, and it frequently led to the occurrence of second-order spectra. Spectral analysis was a growth industry at the time. Much was, of course, already understood, and the seminal monograph by Pople, Schneider, and Bernstein[4] had just been published. However, many wrinkles remained to be discovered. Others in Norman Sheppard's group were, for example, engaged[5] in analyzing '^{13}C satellites'. It was interesting for me to be involved in the early use of computers to examine ABC and ABCX spectra. Having just read the paper by Whitman et al.[6] on the 'composite particle' method of viewing groups of magnetically-equivalent nuclei, I happened to notice some interesting ^{19}F spectra being obtained by a research student, Ken Packer, in the Inorganic Chemistry Department, and I recognized these to be classic examples of the AB_4 type I had been thinking about.[7] Analysis was attractive since a computer was unnecessary, only 2×2 submatrices being involved. The full spectra could be readily broken down into independent parts, and the concept of 'subspectral analysis', subsuming some earlier concepts and examples, was seen to have general validity, especially by Peter Diehl in Basel, with whom I collaborated to produce a review article.[8]

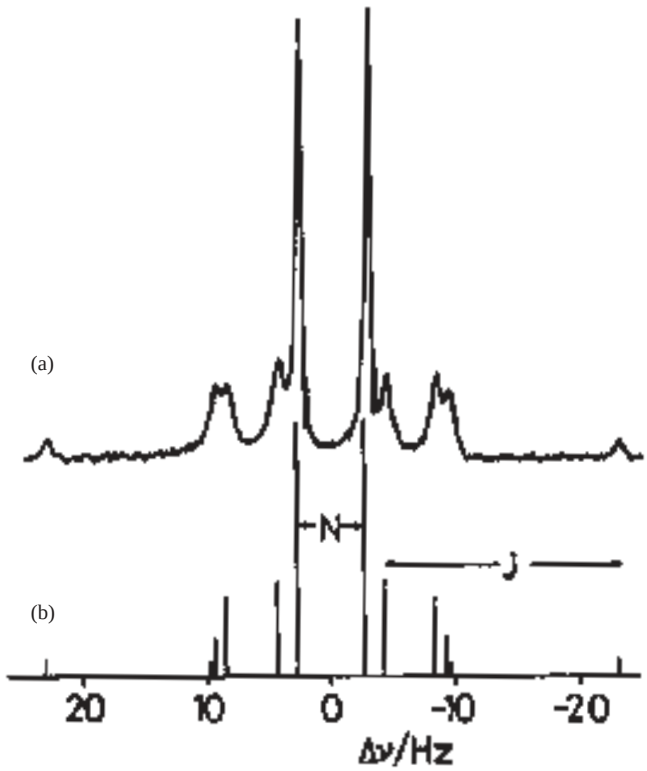

Figure 1 Observed (a) and calculated (b) 60 MHz ^{1}H spectra of tetramethyldiphosphine disulfide in solution in $CDCl_3$. [Spectrum redrawn from Ref. 9.] The zero on the scale is the chemical shift (δ_H = 1.96 ppm)

On finishing my Ph.D. I went to the Mellon Institute, Pittsburgh, where, after a year in vibrational spectroscopy, I joined Aksel Bothner-By's group, the home of the famous LAOCOON spectral analysis computer program (produced by Aksel with Salvatore Castellano). Here I again benefited by seeing someone else obtaining interesting spectra (on the marvelous Varian A60)—in this case R. G. Hayter who was looking at $(CH_3)_2P(:S)P(:S)(CH_3)_2$. This has a symmetrical spin system of the type $[X_3A]_2$, and the spectra (Figure 1) could be interpreted[9] very simply once one understood the theoretical basis. This type of case turned out to be very common in coordination chemistry and had the nice twist that $|J(P,P)|$ was obtainable by simple inspection of the proton spectrum (Figure 1). Back in the UK in 1964, at the new University of East Anglia, I was able to exploit the spectral analysis concepts, helped by students such as Elliot Finer and Tony Cunliffe, and to apply them to a wide range of problems in phosphorus–fluorine chemistry (especially in collaboration with German inorganic chemists Reinhard Schmutzler and Gerhard Hägele) and other areas. Such studies are now, however, frequently bypassed by sophisticated experimental procedures.

CARBON-13 AND SILICON-29

In the mid-1960s attention was turned by a few pioneers, such as Jake Stothers and Dave Grant, to the possibility of observing the 'dilute' nucleus ^{13}C (still with continuous wave

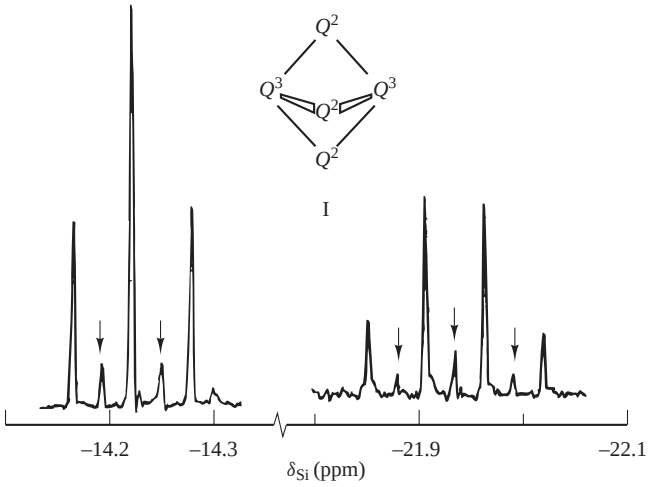

Figure 2 Expansion of part of the 99.36 MHz ^{29}Si spectrum of an aqueous potassium silicate solution, with enrichment of ^{29}Si to 95.3%. At least 20 species are in dynamic equilibrium in the solution, and the partial spectrum illustrated can be assigned to the novel cage structure I (in which Q^2 and Q^3 indicate silicate environments involving two and three siloxane bridges, respectively). The arrows indicate peaks arising from molecules containing ^{28}Si sites. [Spectrum redrawn from Ref. 12]

methods of course), and I was pleased to spend my first sabbatical leave (five months in 1968–69) at the University of Utah with Dave Grant to learn about this area. Just about that time, use of the Fourier transform principle, pioneered by Richard Ernst,[10] 'transformed' the NMR of insensitive nuclei, and back home the University of East Anglia was soon able to acquire a commercial FT spectrometer. The rush, worldwide, into ^{13}C NMR was considerable (ironically for me, no second-order spectral analysis was generally needed for proton-decoupled spectra). Although I joined in, this concentration on ^{13}C seemed to me to ignore other possibilities, and I was attracted to using the ^{29}Si nucleus, as a handful of other groups were doing. Barry Kimber was the first person in my group to study ^{29}Si NMR and he showed that the technique is invaluable for examining polymeric silicones,[11] since excellent dispersion of signals can be obtained. The quotation at the beginning of Barry's Ph.D. thesis is one of the most piquant I have come across:

> ... 19 Down: It sounds foolish to study this element (7). The Times Crossword Puzzle No. 13 231.

However, the quotation was arguably more appropriate for alkaline silicate solutions, the absence of coupling being a considerable hindrance to assigning the plethora of signals. The answer lay in the use of ^{29}Si isotopic enrichment with which we obtained the first spectra. At one point, I believe we purchased the total supply (at least in the UK) of ^{29}Si-enriched silica—which is one way to stymie any competition! Soon we progressed to the first very-high-field ^{29}Si spectrum (Bruker WM500, courtesy of Bill Hull in their applications laboratory in Karlsruhe) of such samples. With the ^{29}Si enrichment, coupling became important, and in his Ph.D. with me Chris Knight used both first-order and second-order spectra to yield the first unequivocal structural determination of many species present in the solutions (Figure 2).

OXYGEN-17 AND SULFUR-33

With few exceptions, the large linewidths often found for quadrupolar nuclei (because of the short transverse relaxation times) made them substantially less popular than the spin-$\frac{1}{2}$ cases. This was particularly so for ^{17}O and ^{33}S, which are the only magnetically-active nuclei of these chemically-important elements, since they also suffer from low natural abundance (0.037% and 0.76%, respectively). Sensitivity is therefore a big problem, and there are additional difficulties associated with the relatively long dead-times for the electronics of high-resolution solution state spectrometers. Oxygen-17 studies were of interest to Norman Sheppard and Ioannis Gerothanassis at the University of East Anglia in the mid-1970s. They were aided by the availability of isotopically-enriched $H_2{}^{17}O$. Sulfur enrichment is far less common, and I became interested (with Peter Belton of the nearby Food Research Institute) in the extent to which ^{33}S could be used at natural abundance in chemical applications. Together with a Ph.D. student, Jane Cox, we made some contributions[13] to the general debate in this area, though it became clear that such ^{33}S NMR is only attractive for a few specific chemical types.

AND THE REST

During the first half of the 1970s, many groups were exploring the chemical applications of a variety of nuclei. The problems of low magnetic moments (and hence both low resonance frequency and low sensitivity), low natural abundance, and high quadrupole moments inhibited developments for some nuclei for a while, but it became clear that nearly all the elements were accessible. Since it seemed the ideal time to survey the whole area, I collaborated with Brian Mann to plan and edit the book 'NMR and the Periodic Table'.[14] At that time only seven elements with suitable nuclei (Ni, Zr, Ru, Pd, Hf, Ir, and Au), apart from the lanthanides and radioactive cases, had *not* been the subject of chemical NMR studies, and most of these found use shortly afterwards.

AND SO TO SOLIDS: REVISITING ^{13}C, ^{29}Si, ETC.

Up to 1976 I had only been dealing with solutions. However, the work of John Waugh's group on cross polarization[15] opened up new vistas, and I had some interesting discussions with Ken Packer on this area which resulted in us making a joint application to the UK Research Council for a grant. Ken had, coincidentally, been appointed to the permanent academic staff at the University of East Anglia the same year that I had, and he had developed research in broadline and relaxation NMR. The combination of his experience and of my own in pulsed FT NMR seemed ideal for CP work on solids, and we collaborated in this area until we both left East Anglia in 1984. In the middle of preparing our application, the first article[16] on the CP MAS combination appeared and led us to alter our application considerably. It was successful, and our group (especially Barry Say and Giovanni Balimann) soon constructed the first suitable spectrometer in the UK. We concentrated on ^{13}C at first (especially on polymers and pharmaceutical polymorphs), with Alan Kenwright exploring

both areas in his Ph.D. work—and thereby missed a trick in not repeating the quick transition to ^{29}Si of my solution state FT studies (though we did give some advice to John Thomas and Jacek Klinowski in their pioneering work on zeolites in collaboration with Colin Fyfe).

However, there were plenty of other aspects to work on, and we produced, inter alia, some of the early results[17] on the splittings in spin-$\frac{1}{2}$ MAS spectra arising from residual dipolar interactions with quadrupolar nuclei, which has remained one of my interests.[18] More recently, my group (especially Matthew Leach and David Apperley) has become involved in using MAS for looking at ceramic materials. Cross polarization is inapplicable in most cases because of the absence of protons, and long ^{13}C and ^{29}Si relaxation times ($T_1 \sim 1$ h!) can cause problems, but the spectra yield much useful information. Moreover, isotopic enrichment again yields dividends, especially for ^{17}O and ^{15}N NMR,[19] which can give information on crystallographic order in situations where X-ray diffraction studies encounter problems.

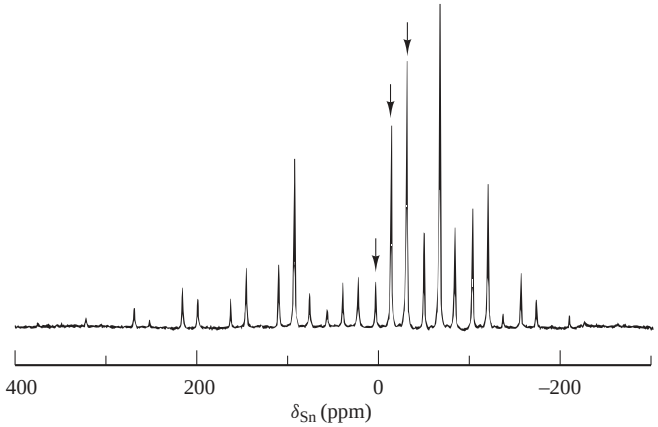

Figure 3 Tin-119 cross-polarization magic angle spinning spectrum of triisobutyl fluoride at 74.63 MHz, with high-power proton decoupling. The three centerband peaks indicated by arrows show the tin is five-coordinate in the solid state (coupled to two fluorine nuclei). Spinning sideband analysis exploiting the interplay between dipolar, shielding, and indirect coupling tensors gives detailed information. [Spectrum taken from Ref. 19b.]

HEAVY-METAL SPIN-$\frac{1}{2}$ NUCLEI

Although slow to see the potential of ^{29}Si NMR for solids, we did start to look further down the Periodic Table and became particularly interested[20] in ^{119}Sn, ^{207}Pb, ^{199}Hg, ^{195}Pt, and ^{113}Cd, with Pat Reams's Ph.D. work providing some early examples. These nuclei are very suitable for solid state NMR and very informative chemically, especially because of the frequently large shielding anisotropies encountered. Ken Packer and I were persuaded by Bob Griffin (in a restaurant in London during a Royal Society meeting in 1980) that spinning sidebands are more of a blessing than a bane, and my group has utilized them (as have others) for new types of spectral analysis—for instance looking at the interplay between dipolar coupling, indirect coupling and shielding tensors[21] (Figure 3). Solid state tin-119 NMR has been a special interest in my group since I moved to the University of Durham in 1984, reinforced by Angelika Sebald spending a couple of years in the group. Prior to our experiments, there was only one mention of its use,[22] but there are some fascinating facets, and it is now a technique of choice for insoluble tin compounds.

It seems to be time for a monograph on 'NMR of solids and the Periodic Table', especially since techniques[23,24] such as DOR, DAS, and SINMR make observation of resonances from quadrupolar nuclei more informative.

AND BACK TO SQUARE ONE: ^{1}H, ^{19}F, AND ^{31}P (IN SOLIDS)

The techniques for high-resolution spectra of abundant spins in solids, i.e. combined rotation and multiple pulse spectroscopy (CRAMPS), which were introduced by Gerstein and co-workers[25] and independently by East Germans,[26] have proved to be more difficult to implement than CP MAS methods for dilute spins. However, much is to be gained from their application, especially for studies of hydrogen bonding and of fluoro polymers, both of which are of interest to us in Durham,[27,28] as demonstrated particularly by Geoff Nesbitt, Larry Merwin, and Pete Jackson in their Ph.D. work. Of course, as we have shown[29] for ^{31}P, multiple pulse methods can be combined with CP MAS to give better resolution at modest spinning speeds, though usually acceptable spectra can be obtained without such complications. We have also proved that ^{1}H $\rightarrow$ ^{19}F CP MAS with high-power proton decoupling is feasible.[30]

POSTSCRIPT

For chemical applications, NMR is undoubtedly now the most generally useful technique available, partly because it can be applied to all phases of matter, but also because it is element-specific, and thirdly because nearly all elements in the Periodic Table contain useful nuclei. It has been a rewarding experience for me to watch these matters develop to full fruition over the past 35 years. As with all academics, the research in which I have been involved has only been possible because of the participation of research students, postdoctoral fellows, visiting scientists, and collaborators at other institutions. Space restrictions prevents mention of most of their names here.

REFERENCES

1. W. G. Proctor and F. C. Yu, *Phys. Rev.*, 1950, **77**, 717.
2. W. C. Dickinson, *Phys. Rev.*, 1950, **77**, 736.
3. W. G. Proctor and F. C. Yu, *Phys. Rev.*, 1951, **81**, 20.
4. J. A. Pople, W. G. Schneider, and H. J. Bernstein, *High-resolution Nuclear Magnetic Resonance*, McGraw-Hill, New York, 1959.
5. N. Sheppard and J. J. Turner, *Proc. R. Soc. London, Ser. A*, 1959, **252**, 506.
6. D. R. Whitman, L. Onsager, M. Saunders, and H. E. Dubb, *J. Chem. Phys.*, 1960, **32**, 67.
7. R. K. Harris and K. J. Packer, *J. Chem. Soc.*, **1961**, 4736; *ibid.*, **1962**, 3077.
8. P. Diehl, R. K. Harris, and R. G. Jones, *Prog. NMR Spectrosc.*, 1967, **3**, 1.

9. R. K. Harris, *Can. J. Chem.*, 1964, **42**, 2275; R. K. Harris and R. G. Hayter, *ibid.*, 1964, **42**, 2282.
10. R. R. Ernst and W. A. Anderson, *Rev. Sci. Instr.*, 1966, **37**, 93.
11. R. K. Harris and B. J. Kimber, *J. Organomet. Chem.*, 1974, **70**, 43.
12. R. K. Harris and C. T. G. Knight, *J. Chem. Soc., Faraday Trans. 2*, 1983, **79**, 1525; *ibid.*, 1983, **79**, 1539.
13. P. S. Belton, J. Cox, and R. K. Harris, *J. Chem. Soc., Faraday Trans. 2*, 1985, **81**, 63.
14. R. K. Harris and B. E. Mann, *NMR and the Periodic Table*, Academic Press, London, 1978.
15. A. Pines, M. G. Gibby, and J. S. Waugh, *J. Chem. Phys.*, 1973, **59**, 569.
16. J. Schaefer and E. O. Stejskal, *J. Am. Chem. Soc.*, 1976, **98**, 1031.
17. C. J. Groombridge, R. K. Harris, K. J. Packer, B. J. Say, and S. F. Tanner, *J. Chem. Soc., Chem. Commun.* **1980**, 174.
18. R. K. Harris and A. C. Olivieri, *Prog. NMR Spectrosc.*, 1992, **24**, 435.
19. R. K. Harris, M. J. Leach, and D. P. Thompson, *Chem. Mater.*, 1992, **4**, 260.
20. R. K. Harris, P. Reams, and K. J. Packer, *J. Mol. Struct.*, 1986, **141**, 13; R. K. Harris and A. Sebald, *Magn. Reson. Chem.*, 1987, **25**, 1058.
21. (a) R. K. Harris, K. J. Packer, and A. M. Thayer, *J. Magn. Reson.*, 1985, **62**, 284; (b) H. Bai and R. K. Harris, *J. Magn. Reson.*, 1992, **96**, 24.
22. E. T. Lippmaa, M. A. Alla, T. J. Pehk, and G. Engelhardt, *J. Am. Chem. Soc.*, 1978, **100**, 1929.
23. A. Samoson, E. Lippmaa, and A. Pines, *Mol. Phys.*, 1988, **65**, 1013; A. Llor and J. Virlet, *Chem. Phys. Lett.*, 1988, **152**, 248.
24. J. Homer, P. McKeown, W. R. McWhinnie, S. U. Patel, and G. J. Tilston, *J. Chem. Soc., Faraday Trans. 2*, 1991, **87**, 2253.
25. B. C. Gerstein, R. G. Pembleton, R. C. Wilson, and L. M. Ryan, *J. Chem. Phys.*, 1977, **66**, 361.
26. B. Schnabel, U. Haubenreisser, G. Scheler, and R. Müller, *Proceedings of the 19th Congress AMPERE, Heidelberg*, 1976, p. 441
27. R. K. Harris, P. Jackson, L. H. Merwin, B. J. Say, and G. Hägele, *J. Chem. Soc., Faraday Trans. 1*, 1988, **84**, 3649.
28. R. K. Harris and P. Jackson, *Chem. Rev.*, 1991, **91**, 1427.
29. R. K. Harris, P. Jackson, P. J. Wilkes, and P. S. Belton, *J. Magn. Reson.*, 1987, **73**, 178.
30. S. A. Carss, R. K. Harris, P. Holstein, B. J. Say, and R. A. Fletton, *J. Chem. Soc., Chem. Commun.*, **1994**, 2407.

Biographical Sketch

Robin K. Harris. *b* 1936. B.A. (Nat. Sci.), Ph.D., (supervisor Norman Sheppard), Sc.D., University of Cambridge, UK. Postdoctoral work at Mellon Institute, Pittsburgh, PA (with Aksel Bothner-By). Successively lecturer, senior lecturer, and professor, University of East Anglia, UK. Currently Professor of Chemistry, University of Durham, UK. Secretary-General of ISMAR, 1986–92. Approx. 350 publications. Current research specialty: solid state NMR and its applications in materials chemistry.

Hennel, Jacek W.: Poland. Early NMR

Jacek W. Hennel

Niewodniczanski Institute of Nuclear Physics, Krakow, Poland

The start of NMR research in Poland was strongly affected by the conditions which arose in the country as a result of World War II. A few years had elapsed since the discovery of NMR before the experiment could be repeated in Poland. The reason was the state of destruction in which the Polish scientific community found itself at the end of the war. A great number of scientists had lost their lives, most of them murdered in accordance with Nazi and Soviet policy to exterminate Polish intelligentsia. Polish universities had remained closed from the autumn of 1939 until January 1945. Laboratories were destroyed, and even teaching at the grammar school level was strictly forbidden by the German invaders. During the war only a fraction of young people (like the author of this note) were able to benefit from the secret school system organized under the auspices of the Polish Government in Exile in London. Academic staff, especially professors, not only lost their jobs but even had to disguise themselves as uneducated people in order to survive.

At the end of the war, the organization of teaching and the rebuilding of laboratories were the most urgent tasks of Polish physicists. In spite of formidable obstacles such as the postwar economy of the country, lack of educated people, and Communist restrictions, academic life was rapidly recovering from the destruction. The old universities which found themselves in the new Polish state were immediately opened, a number of new ones were founded, young people were hired, scientific journals subscribed to, and libraries modernized. There was also some help from abroad. A great number of young people were admitted to the universities in 1945 and the following years to study physics.

In 1948 the Soviet authorities imposed a system of strict Communism and Stalinist terror on Poland. For science this meant an end to freedom of speech and isolation from abroad, both east and west. These heavy restrictions lasted a few years. The symbol of their removal was the International Conference 'Atoms for Peace' held in Geneva in 1955 in which a few Polish scientists were allowed to take part.

At the Jagiellonian University at Krakow (the oldest Polish university, founded in 1364) a special chair for nuclear physics was established in 1946 and given to Henryk Niewodniczanski, who had been Professor of Atomic Optics at the King Batory University in Vilna before the war. That old Polish university could not be restored after the war and hence Prof. Niewodniczanski moved to Krakow together with a small number of collaborators. As a relatively new branch of nuclear physics not demanding expensive equipment, NMR was just the right subject of research for the new laboratory. The initiative was taken by one of Niewodniczanski's former Vilna students, Andrzej Z. Hrynkiewicz. He and two other newly graduated members of the staff, Jacek W. Hennel (the present author) and Olgierd K.-Daszkiewicz, started construction of an NMR apparatus about 1951 and obtained, in 1953, the first NMR signal observed in Poland.

There were no people acquainted with NMR in Poland and, since personal contacts abroad were forbidden, we had to depend solely on the literature. The paper by Bloembergen, Purcell, and Pound (BPP)[1] turned out to be our major source. The apparatus consisted of an electromagnet of 15-cm pole face diameter fed from a large stationary battery set, a simple amateur radio signal generator (a Czechoslovakian product), a Soutif–Gabilard high-frequency bridge, a German radio receiver tuned to 28 MHz and a German oscilloscope. Equipment left by the defeated German army (Wehrmacht) was at that time the main source of electronic supplies available to the Polish physical laboratories. The magnet, the bridge, and the Helmholtz coils for modulation were made by ourselves. The sample was water in a vial.

Although it was very primitive, our apparatus had at that time quite a good scientific capability. It was immediately used for the investigation of NMR in water flowing through a tube. The first idea was to study the influence of spin–lattice relaxation on the signal,[2] the second was to demonstrate nonadiabatic passage in liquids[3] since this phenomenon was known only in solids, and the third was to mark the exact volume of the flowing water by such a passage and differentiate between laminar and turbulent flow on the basis of the shape of the signal.[4] After considerable reconstruction by G. Zapalski, the apparatus was also used for measurements of spin–lattice relaxation times T_1 in different liquids. An original method of T_1 measurement was developed.[5] It was based on fast adiabatic transitions. The signal was recorded on photographic paper with the use of a mirror oscillograph. The problem studied was the temperature dependence of the function $T_1 h/T$ (where h is the viscosity and T the absolute temperature). According to the theory of BPP this function should be constant. We found that it decreases with temperature.[6] The first achievements were reported at the Colloque AMPERE in Paris in 1958. This was possible because the restrictions on foreign travel had been relaxed by then.

Hrynkiewicz withdrew from NMR research in 1960 because of his involvement in gamma spectroscopy. Leadership of his group was taken over by Hennel. Daszkiewicz specialized in the construction of spin echo apparatus. His first model was finished in 1955 and the second one with a digital programmer in about 1960. This second model was suited for CPMG experiments and served for relaxation research in protein solutions.[7] During the next few years a number of new young people joined the group, among them K. Krynicki who later emigrated to England and collaborated there with Professor J. G. Powles in the study of NMR in liquids, J. Blicharski, who discovered the interference effect of interactions in relaxation,[8] and a few years later by A. Jasinski, who more recently initiated NMR imaging research in Poland.

A few years after the first NMR signal was obtained in Krakow, other physical laboratories in Poland started to work on NMR. In January 1957 an NMR signal was observed by K. Antonowicz at the Copernicus University in Torun. His scientific interest was NMR in flowing liquids, mainly relaxation.[9] A strong NMR group was created at the Mickiewicz University in Poznan by Professor A. Piekara. His young students, J. Stankowski and J. Angerer, built NMR apparatus for the investigation of flowing liquids in 1959 and at the same time another of his students, Z. Pajak, was sent to Paris for a year to work on high-resolution NMR[10]

under the supervision of Professor Rene Freyman. Pajak and Stankowski formed two separate NMR groups in Poznan, one at the university and one at the Institute of Molecular Physics.

In about 1960 commercial spectrometers became available, enabling chemists to apply NMR to their problems. Nowadays there are three NMR superconducting magnets working in physical laboratories and six in chemical ones.

Development of NMR research in Poland would not have been possible without international contacts. In this respect an important role was played by the European learned society known as the Groupement AMPERE and by Professor E. R. Andrew, the famous British pioneer of NMR who over the past 35 years has invited many Polish physicists to collaborate with him in Bangor, Nottingham, and Gainesville.

REFERENCES

1. N. Bloembergen, E. M. Purcell, and R. V. Pound, *Phys. Rev.*, 1948, **73**, 679.
2. A. Z. Hrynkiewicz and T. Waluga, *Acta Phys. Pol.*, 1957, **16**, 381.
3. A. Z. Hrynkiewicz, T. Waluga, and G. Zapalski, *Arch. Sci.*, 1958, **11**, 190.
4. A. Z. Hrynkiewicz, *Acta Phys. Pol.*, 1958, **17**, 353.
5. J. W. Hennel and A. Z. Hrynkiewicz, *Arch. Sci.*, 1958, **11**, 238.
6. J. W. Hennel, A. Z. Hrynkiewicz, K. Krynicki, T. Waluga, and G. Zapalski, *Arch. Sci.*, 1958, **11**, 243.
7. O. K.- Daszkiewicz, J. W. Hennel, B. Lubas, and T. W. Szczepkowski, *Nature (London)*, 1963, **200**, 1006.
8. J. S. Blicharski, *Phys. Lett.*, 1967, **24A**, 608.
9. K. Antonowicz, *Bull. Acad. Pol. Sci.*, 1957, **5**, 813.
10. Z. Pajak, *C. R. Acad. Sci.*, 1959, **249**, 1211.

Biographical Sketch

Jacek W. Hennel. *b* 1925. M.Sc., 1950, Ph.D., 1960, Jagellonian University of Krakow. Research fellow, University College of North Wales, Bangor 1959–60 where he worked under the supervision of Professor E. R. Andrew. Successively assistant and professor, Niewodniczanski Institute of Nuclear Physics, Krakow, Poland. Currently Head of the Department of Nuclear Radiospectroscopy, Niewodniczanski Institute of Nuclear Physics. Research field: solid state NMR. Books: 'Introduction to the Theory of NMR' (in Polish) (1966) and 'Fundamentals of NMR' (1993) with J. Klinowski as co-author.

Hinshaw, Waldo: Notes on the History of MR Imaging from my Perspective

Waldo Hinshaw
Imatron, Inc., South San Francisco, CA, USA

The following notes describe the advent of clinical MR imaging from the point of view of someone who had the uncommon luck to be there when it happened. I leave it to others to present a balanced and documented history; this is what I remember.

I selected Paul Hubbard as my thesis advisor at the University of North Carolina, despite the warnings of my fellow graduate students that NMR had nothing interesting in its future. Professor Hubbard had studied under Edward Purcell. In fact, until the arrival of MRI, everyone working in NMR could trace his or her academic lineage back to either Purcell or Bloch, the originators of NMR.

The Physics Department of the University of Nottingham was very active in NMR when I went there as a postdoc in late 1971. Its reputation in the field was due to Professor E. Raymond Andrew, the department chairman. As I worked with him, we searched for biological applications of NMR. We used NMR to study the properties of crystalline amino acids. Others, at Nottingham and elsewhere, were looking at the NMR properties of animal tissue. Bill Derbyshire at Nottingham was looking at the relaxation times of fish muscle to determine, among many other things, if a violent death affected its NMR properties and its taste. Professor Andrew showed me a short article describing relaxation measurements of a tumor on the tail of a mouse. As I remember, they had dropped the small tumor, while still attached to the live mouse, into a standard NMR spectrometer. This paper, and an earlier paper arguing that T_1 could be used to diagnose cancer,[1] did not suggest any useful application to us since we saw no way to make organ-specific measurements in humans without removing the tissue.

In 1973, during one of the religiously observed free-discussion times known as morning coffee and afternoon tea, Peter Mansfield mentioned that he wanted to apply a strong enough gradient to a solid to resolve the interaction between adjacent spins. We discussed what other applications such a technique could have since the NMR spectrum in the presence of a gradient reflects the distribution of the sample along the direction of the gradient. We tried, without success, to come up with biological applications for looking at one-dimensional distributions.

Later in 1973, I attended an NMR meeting in Krakow, Poland. At the meeting, Mansfield presented a short paper that contained three separate ideas. One was the suggestion of applying a strong gradient to show crystal structure in one dimension. John Waugh of MIT stood up during the question period and asked Mansfield if he knew of Paul Lauterbur's recent paper[2] which presented the idea of using NMR to form images. This work was unknown to both Mansfield and me and, as far as I could tell, everyone else in the audience.

I did not spend much time thinking about Lauterbur's idea until hearing him lecture on the subject at an NMR meeting in Bombay in January 1974. After his lecture, I went up and introduced myself. His enthusiasm for the idea was infectious.

The paper I presented at that Bombay meeting described spinning the NMR sample very rapidly in order to reduce the broadening of the spectral lines. As part of this work, I had been looking at the various broadening mechanisms, including that of externally applied inhomogeneous fields, or gradients. A passing idea was to keep the sample stationary and 'spin' the gradient in order to narrow the spectral lines. This was the basis of the early 'sensitive point' method of imaging. Rotating the gradients allows the portion of the sample on the axis to experience a static field while the remainder of the sample experiences an oscillating field. Applying another oscillating gradient in the direction of this axis made the field oscillatory everywhere except at one point. By properly applying the rf field, you could saturate the spins everywhere except at that one point. Then by scanning this point through the sample, it would be possible to obtain an image. Rapid and rock-steady rf pulses are applied. The pulse amplitude is adjusted for maximum signal strength, which usually occurred at less than 90 °. The signal refocuses and forms an echo that peaks at each rf pulse. This interesting rf technique is called 'steady-state free precession'.

I flew back from Bombay with Bill Moore, a member of the Nottingham Physics Department. He and I passed the time by discussing moving gradients as a way of localizing the magnetic resonance signal. By the time the long flight was over, the ideas were well enough formulated to allow some laboratory work to start.

One constraint we had in developing an imaging method was the lack of a computer. I did have access to Andrew's pulsed NMR spectrometer, which had an analog output—and everything else in the lab was analog. I spent evenings and weekends assembling clock motors and potentiometers and coils. Bill provided constant encouragement. By April of 1974, we had produced the first images. With this work, we were the first group after Lauterbur to produce magnetic resonance images. Bill and I applied for and were awarded the first patent on MRI or, as we called it then, 'NMR spin-mapping'.[3]

During this time (in 1974), my good friend Al Garroway, a postdoc with Peter Mansfield, would stop by my cubicle after morning coffee and ask all sorts of questions about how to do imaging, what the problems were, etc. Then, suddenly, he stopped asking. I learned later that he had started working on MRI in his laboratory. He applied weak rf pulses in the presence of a field gradient in order to achieve spatial selectivity.

Next door to where Al was working, Mansfield and another of his postdocs were quietly developing a related method. They were attempting to saturate all of the sample except for the selected region of spins. As I understand the story, one day Mansfield showed Garroway a manuscript, or patent application, that he had prepared on his work. Garroway showed him what he had been doing. The issue was finally resolved by combining both efforts in the patent and publications.

In late 1974, I accepted a position with Professor Irving Lowe at the University of Pittsburgh. During my stay there, Professor Andrew and Bill Moore applied for and were awarded a grant from the Medical Research Council to develop an NMR imaging system. So I returned to Nottingham and, for the next couple of years, worked flat-out to put together

Figure 1 Participants at the First International Meeting on Magnetic Resonance Imaging, University of Nottingham, April 1976

an imaging system for 3-in. diameter samples. I remember working the usual 12 h one Christmas day. Every computer instruction, including, for example, those for handling the cassette tape drive, was loaded by hand using a set of toggle switches on the front panel of the Data General minicomputer.

As initially configured, the system used a sensitive line, as described above. A static gradient was applied along the line and then the signal was Fourier-transformed to obtain the distribution of the sample along the line. The steady-state free precession pulse method produces a comb of discrete spectral signals. The data collection and Fourier transformation are done so that each point in the transformed spectrum corresponds to one of the discrete signals. The sensitive line was swept slowly through the sample to form an image of a slice of the object.

At the beginning of the project we considered using several different magnets, including permanent magnets, superconducting magnets, and resistive electromagnets. We chose a then current Varian iron-core electromagnet with modified pole faces that gave us something like a 3-in. diameter working volume.

Early in the project, Neil Holland joined us. He later became the principal NMR scientist and engineer for Picker. Paul Bottomley joined the effort as a Ph.D. student. He later became an important scientist in the NMR imaging effort of General Electric (GE). Peter Allen, a member of the Physics Department staff, became active later in the project.

Professor Andrew organized the first international MR imaging meeting at Nottingham in April 1976 (Figure 1). Earlier scientific meetings had included presentations on MRI, but this was the first meeting dedicated exclusively to the subject. All of the groups working on MRI projects, with one exception, were represented. Although important work was being done in applying NMR to biological problems, it was not included in this meeting.

- Paul Lauterbur, the originator of the field, was there.
- Richard Ernst was there—his major contribution to imaging had occurred the previous year.
- Jim Hutchison was there. He was developing a small and very innovative whole body imaging system at the University of Aberdeen. I always enjoyed talking to Jim; he always had good ideas. Once, when I visited his lab, Bill Edelstein, who would later go to GE, was there. The personality difference between Jim and Bill was so great that it was difficult to get a chance to listen to Jim.
- Peter Mansfield and his students Andrew Maudsley, Ian Pykett, and Peter Morris were there.
- Hugh Clow from EMI was there. Under his direction, the EMI engineers put together an imaging system with a magnet and coils large enough for imaging the human head. There was no one in his initial group who knew NMR. When they turned the system on, no image appeared. After obtaining advice from some Nottingham scientists, they produced the first image of the human head using the original Lauterbur method.
- Locher and Creyghton, who were working with Philips, were there.

Bottomley, Holland, and I wrote up and published the initial results from our work.[4] That issue of *Nature* had a cross-sectional magnetic resonance image of a lemon on the cover. The article, which contained a clear thin-slice image through Bottomley's wrist, was important in that it provided the first convincing evidence that MRI would become clinically useful.

As a result of the increasing stress between the different imaging groups within the Nottingham Physics Department, and since the goal of the MRC grant had been achieved, I left Nottingham to accept a position with GEC Medical outside London. After several months of trying to get an MRI program started, I resigned and began a long and fruitful association with the Harvard Medical School, The Massachusetts General Hospital, and the Johnson & Johnson company.

Jack McConnell was an executive with Johnson & Johnson and was responsible for finding and evaluating new technology for the company. He came to Nottingham to visit us during the very early days. It was never clear what Jack was trying to do, but I came to believe that he made at least a partial attempt to gain control of the emerging technology for Johnson & Johnson. He also placed an order with Oxford Instruments for a superconducting magnet suitable for MRI of a human in late 1977 or early 1978. After

resigning from GEC, I became a consultant for him, starting in late 1978, and helped establish the specifications for the magnet. We requested a superconducting magnet with a 1-m diameter room-temperature bore and an operating field of 1.8 T. However, the specifications, which were accepted by Oxford Instruments, were too ambitious. It would be several years before Oxford Instruments could build such a magnet.

At about this time I received a visit from what I came to think of as the 'gang of four', Gerry Pohost, Joanne Ingwall, Mark Silverman, and Eric Fossel. Enabled by their friendship and support, I returned to the USA in the late fall of 1978 and accepted a position with Juan Taveras, head of the Radiology Department at the Massachusetts General Hospital (MGH). For the next year, with the full support of the 'gang of four', I worked as a facilitator in negotiating a technology development agreement between MGH and Johnson & Johnson. The negotiations included the heads of the departments of surgery, radiology, cardiology, internal medicine, and neurology on one side, and Jack McConnell on the other. The successful agreement was, I understand, the first of its kind for the Harvard Medical School system in that it exchanged access to intellectual property developed within the program for significant financial support. Since that time, other and much larger agreements of the same type have been put in place with other companies.

During that year, the initial steps were taken at the MGH to establish the Society of Magnetic Resonance in Medicine. Gerry Pohost was the initial driving force. Joanne Ingwall, Paul Lauterbur, and later Tom Budinger worked closely with him. I was on the initial board of directors and was head of the program committee for the second annual meeting. I remember discussions about which radiologist to invite to be on the board. The society has been very successful and influential in promoting the technology and it currently has about 4000 members.

After the MGH and Johnson & Johnson agreement was in place, it became clear that the hospital environment was not ideal for developing a complex imaging system. So, in late 1979, I moved to Solon, OH, and began working within Technicare (a recently purchased and wholly owned subsidiary of Johnson & Johnson) while retaining my appointments at Harvard and MGH. I expected to return to the MGH with the initial system to explore clinical applications. However, the development program at Technicare acquired such momentum that I never did go back.

During those early days, not many groups were working on MRI. We all knew each other, liked each other, and enjoyed sharing ideas. The first US meeting dedicated to MRI was hosted by the Vanderbilt Radiology Department in Nashville. The second meeting was at the Wake Forest Medical School in North Carolina. The list of attendees gives a clear picture of who was interested in the subject at the time.

In late 1980 and early 1981, a few of us from Technicare flew to England (on Concorde) to negotiate with Thorn EMI for the purchase of their MRI program. This group was in the process of installing a whole-body 0.3 T system in the Hammersmith Hospital. At the time we were there, the system was beginning to produce images of the head. On our third trip there, they told us that they had already done a deal with someone else.

At about the same time, we visited Leon Kaufman's lab in South San Francisco. His MRI work had been funded until then by Pfizer, but they had decided to get out of the business. I urged the Technicare management to 'buy' the group. Just after we made an initial visit, we learned that they had become associated with Diasonics and were no longer available.

Technicare was a very aggressive engineering-driven medical imaging company and was the ideal environment for the rapid development of an MRI product. We put together a team of about 14 engineers and, within 9 months, had a small system producing images at 1.5 T. We had the mistaken idea that it would be easier to develop a small system first. We also wanted to explore as early as possible the clinical utility of spectroscopy. This 'small animal' system went to the MGH and enabled the team there to publish several early papers.

Our initial two-dimensional imaging method used steady-state free precession together with oscillating gradients to select the slice and back-projection to obtain the two-dimensional image within the slice. (One of the many invaluable inputs from the MGH group was that the motion sensitivity of this method was too great for most clinical applications.) Another early method used three-dimensional back-projection with reconstruction of slices in any desired orientation after the data were collected. This three-dimensional acquisition had the advantage of simplicity. The reconstruction kernel, or the back-projection filter, was localized, unlike the filter for two-dimensional back-projection. Also, rapidly switched gradients were not required. We felt that, since the new technology was inherently three dimensional, it would pay to exploit its strength. However, radiologists preferred the images that could be obtained from a set of separately acquired slices. So we soon began using selective irradiation to define the slices and, within the slice, phase and frequency encoding followed by a two-dimensional Fourier transform to obtain the image.

We put together systems using the best magnets we could obtain. We had a standing order with Oxford Instruments to send us their latest and best magnet. The first large magnet from them was a whole body resistive water-cooled magnet operating at 0.15 T. They shipped it full of cooling water which froze while crossing the Atlantic. We had to pull it apart and machine out the split copper water pipes that were embedded in the aluminum plates. Within a few days, we had it reassembled and working.

Later, we designed, manufactured, and shipped several of our own water-cooled whole body magnets using a quite different design. The first one went to the MGH and was used there for several years. These first resistive systems had just two imaging modes, called 'a' and 'b'. At the early users-meetings, the first clinical users thoroughly enjoyed debating which mode was best. Then, in about 1983, we gave the user the ability to design his own protocol, to select the slice thickness, slice spacing, pulse timings, and the like. This innovation perhaps loaded too much responsibility, and even confusion, onto the radiologists.

We soon accepted delivery of Oxford Instruments' first whole body sized superconducting magnet. We built systems based on 0.3, 0.5, and 0.6 T (and, much later, 1.5 T) superconducting magnets. They were able to get their first meter-bore superconducting magnet only up to 0.3 T and, even then, it went through repeated quenches to get there. We continued to push for higher fields and insisted that we receive every magnet they built. After shipping us two or three at 0.5 and 0.6 T, they came to us and said the next one would go only to 0.35 T. After considerable internal discussion, we decided to

reject it. It probably is a coincidence that Diasonics introduced its product at 0.35 T.

Technicare made a big product announcement and introduction of resistive and superconducting systems at the 1981 RSNA (Radiological Society of North America), the huge annual meeting of radiologists. The product we introduced there, the Teslacon, was listed by *Fortune* magazine as a 'Product of the Year'.

My experience was with only one of the teams that developed the early systems. I assume the other teams were similar. It was a very exciting time, and we saw the inside of humans in a brand new way. For example, we saw the first sagittal slices of the human brain, the view of the brain that is now everywhere. We saw clear tumors and radiation damage in the brain of the first patient we put in our prototype system. We worked flat-out, adding features, solving problems, and immediately installing our improvements in the systems being used on patients.

John Keller and Russ Compton were the principal engineers. Each of them was more productive than any other ten people I know. David Kramer and Hong Yeung were the principal scientists. They, and their key team members, were trained as chemists. The chemists and the engineers worked well together. While physicists incorrectly view themselves as 'super' engineers and insist on being involved in designing the system, the chemists were interested only in its performance.

We were significantly ahead of the academic groups. We would go to meetings and be quietly amused as the academic groups took credit for techniques and ideas that we already had in use with patients. As a result of this experience, I have wondered how often a new technology was actually developed within a company even though history has it being developed within academia.

We did not publish in the scientific literature; we were having too much fun and were too busy. Furthermore, despite the wise and persistent requests of the Johnson & Johnson management, we did not patent much of what we did. Prior to MRI, the tradition among the medical imaging companies was for each company to obtain a few patents and then quietly to ignore everyone else's patents. None of the players wanted to start a patent war. Battles are now being fought, however, over some of the early patents.

We developed a lot of new technology. Even though it serves no purpose to try to list it here, I will mention a couple of things we worked on. We looked at all sorts of ways, including spirals, to move around in k-space during data collection. We looked at rectangular back-projection. We developed many innovative pulse sequences (including interleaving, multislice, and multiple echo), sequences with the higher moments balanced for motion compensation, half Fourier acquisition, flow and chemical shift imaging, fluorine imaging, and the like. We built all our own hardware, including the complete acquisition system, data handling and reconstruction hardware, gradient power supplies, and a solid low-noise potted gradient coil with distributed windings. Some of the first special-purpose rf coils we developed were for breast imaging.

We kept the early customer shipments as quiet as possible. We did not want to frighten our competitors. We manufactured and placed perhaps about 15 systems before receiving clearance from the US Food and Drug Administration (US FDA) to market the products. Technicare and Diasonics received the first clearance at the same time. The submission to the US FDA was based on clinical data obtained from the 0.15 T system at the MGH, and the higher field systems operating in Cleveland. We worked closely with the US FDA to help them understand what to worry about and how to evaluate a system.

On 9 April 1986, Johnson & Johnson announced that Technicare was closed. The engineering team was in the early stages of a major upgrade to the magnetic resonance product. We were allowed to finish the upgrade. We collected a team of 270 of the best people from throughout the company, finished the project, and handed it over to a GE manufacturing team by the end of the year.

By the end of 1986, MRI was a well established and growing business.

POSTSCRIPTS

Many of the scientists contributing to MRI have been publicly recognized. However, those who have quietly turned the scientists' ideas into products, products that significantly improve the quality of our health care, have not been recognized. Those without recognition have been working within companies—the engineers, manufacturers, and businessmen. To a large degree, the development of MRI as a clinical reality is due to businessmen with vision.

Although individuals in several companies deserve credit, my interaction was with Technicare and Johnson & Johnson. Joe Teague, President of Technicare, and J. B. Richey, Head of the Technicare's New Ventures Division, provided the unique and necessary environment for rapid product development. Jim Burke, Chief Executive Officer of Johnson & Johnson, had the remarkable vision and bravery to pour substantial money into a development program that had great promise but no guarantee. I believe Burke deserves credit for making MRI a clinical reality. Without the early effort of Technicare, the other companies may not have made the commitment to invest the required resources to take the technology out of the lab and into the hospitals.

No discussion of the early days of MRI would be complete without mention of Raymond Damadian. Unfortunately, any mention of Damadian creates controversy. Damadian's belief that T_1 and T_2 measurements could be used to detect cancer may have motivated several people to take MRI more seriously than they otherwise would have. However, I believe that his idea did not affect the development of the field of MRI. Nothing could be done until Lauterbur showed how gradients could be used to make images, and once that was done, Damadian's early observations did not affect anyone's actions. Furthermore, as far as I know, no one has ever detected or diagnosed cancer by measuring relaxation times. Damadian was invited to present his work at the first one or two MRI meetings in the USA. At those meetings, he astonished the attending scientists by showing a slide of his patent on detecting cancer[5] and disclosed little about his research efforts.

The one person who came up with the fundamental idea that is the basis of MRI is Paul Lauterbur. His publication[2] was the first to suggest MRI, and in fact described it adequately enough for someone 'skilled in the art' to do it. The publication clearly states the potential clinical applications. It is unusual

for the initial publication in a new technology to be so clearly identifiable.

In addition to making the seminal invention, Lauterbur was tireless in advocating MRI. He nurtured the field until it attained a life of its own. He visited our lab several times while I was working in England. He paid for me to visit his lab in Stony Brook. He was open with his ideas and full of encouragement. He made sure, through these efforts, that the early developers stayed in touch and were friends.

Once, in an intemperate moment (Paul and I used to enjoy our intemperance whenever we got together), I asked Lauterbur why he did not obtain a patent. His article in *Nature*,[2] with a little work by a patent attorney, would have been the controlling patent for the entire field of MRI. He clearly suffered as he told me that the university bureaucracy got in the way and, in fact, maintained that such a patent would have no value.

REFERENCES

1. R. Damadian, *Science*, 1971, **171**, 1151.
2. P. C. Lauterbur, *Nature (London)*, 1973, **242**, 190.
3. W. S. Hinshaw, *J. Appl. Phys.*, 1976, **47**, 3709.
4. W. S. Hinshaw, P. A. Bottomley, and G. N. Holland, *Nature (London)*, 1977, **270**, 722.
5. R. Damadian, US Patent 3 789 832; filed March 17, 1972, issued February 5, 1974.

Houlт, D. I.: Biomedical NMR Instrumentation—A Personal Viewpoint

D. I. Houlт
Institute for Biodiagnostics, National Research Council, Winnipeg, Canada

INTRODUCTION

The problems facing the researcher who attempts to cross disciplinary boundaries can be quite daunting. Not only is there a new vocabulary to be learnt, but new lore, concepts, and even thought processes often conspire to present a considerable barrier to the interloper. Equally, the analytical tools and knowledge that one carries into a new arena may be objects of incomprehension and even suspicion by the local residents. Communication becomes of paramount importance; patience and respect valuable commodities. However, in 1968, with a new degree in physics, and a passionate interest in electronics—I was an amateur radio enthusiast—I knew nothing of such subtleties as I started my doctoral studies with Professor (later Sir) Rex Richards in the Physical Chemistry Department at Oxford University. I was initially to investigate the subject of field homogeneity, a topic that has exercised me on and off ever since, but a year later, when he announced his intention of resigning the professorship and moving into the Biochemistry Department, I had learnt enough to be, along with the rest of his research group, apprehensive. I was being marched from *terra externa* into *terra incognita* and was not sure I liked it.

Probably partly out of reaction to an alien environment and partly from a need completely to understand a subject to feel secure therein, I delved very deeply into the instrumental requirements of the then-new technique of Fourier transform (FT) spectroscopy. With my expertise in electronics, I felt on safe ground there and Rex, as was his wont, gave me free reign. Biochemistry passed me by and I put all my efforts into helping build the best quadrature FT spectrometer that we could. As my understanding increased, I was able fairly easily to cope with problems such as receiver deadtime, dynamic range, and radiofrequency (rf) leakage, but two difficulties loomed large: how to improve the sensitivity of our 7.5 T superconducting instrument, and how to remove 'ghost' lines in a quadrature spectrum caused by imperfect quadrature detection.[1]

SENSITIVITY AND CYCLOPS

In the early 1970s, the theory of NMR signal reception was rooted in continuous wave (CW) spectroscopy performed with resistive electromagnets. Thus the emphasis was upon absorption of rf energy by a sample in a solenoidal receiving coil, and of particular importance was the 'filling factor' of the coil. Strictly speaking, if a current I is passed through a coil of inductance L so that magnetic energy $E = LI^2/2$ is stored therein, the filling factor η is the ratio of the energy E_s stored in the magnetic field passing through the sample, to the total stored energy, i.e. $\eta = E_s/E$. However with a solenoidal coil it can be shown that about half the energy is consistently stored within the confines of the coil, regardless of its exact winding details. Thus the term 'filling factor', as the appellation implies, came to be understood as half the fraction of the space inside the receiving coil occupied by the sample. However, when I applied formulas developed by my predecessor in the group, Dr. Howard Hill, to the probes I had built, I consistently obtained predictions of signal-to-noise ratio that were two to three times too large.

To my chagrin, I later discovered that my error was in using the popular, rather than the exact, definition of filling factor, and this mistake alerted me most forcefully to a danger ever-present in science—that of applying a well-known and trusted theory to a situation that is subtly different from that envisaged by the proponents of the theory. A superconducting magnet employs of necessity a saddle-shaped rather than a solenoidal receiving coil, and the open geometry ensures that the fraction of the magnetic energy stored in the confines of the sample is heavily dependent upon that geometry. For example, if a very thin conductor is used, most of the energy is stored round the conductor and the filling factor can be as small as 0.05. I now believe that the way to avoid making such mistakes is to take the time and effort to understand a subject, *on one's own terms*, from the most fundamental level upwards. With my failure to explain the observed signal-to-noise ratio, I was forced to ask two very basic questions: from whence comes the signal and from whence the noise? The respective answers were simple but revealing: from electromagnetic induction of a voltage in the receiving coil, caused by the precessing nuclear magnetic moments (i.e. an alternator!), and from the generation of random voltages—a measure of which was the coil's resistance—by Brownian motion of the coil's electrons. The rest of the paper that Rex Richards and I wrote on the subject is an embellishment of these two principles—the consequence of a new view taken *de profundis*.[1,2] The ideas of quadrature detection in the laboratory frame with two receiving coils to increase the signal strength, and of lowering the temperature of those coils to decrease the Brownian motion,[1] came as a natural consequence of that new view. The former has found extensive use in imaging, while Styles and colleagues have demonstrated with elegant engineering how profitable a probe temperature reduction can be for ^{13}C spectroscopy.[3]

The solution to the problem of quadrature 'ghosts' came about in a different manner. I understood the difficulty completely, but was at a loss as to how to resolve it. For example, the gains of the two outputs X and Y of a quadrature receiver might differ, and exaggerating the error we might write for the two free induction decays (FIDs):

$$X_0 = 1 \cos \omega t \exp\{-t/T_2\} \tag{1}$$

$$Y_0 = 0.9 \sin \omega t \exp\{-t/T_2\} \tag{2}$$

or

$$X_0 + \mathrm{i}Y_0 = [(1 + 0.05\mathrm{i}) \exp\{\mathrm{i}\omega t\} - 0.05\mathrm{i} \exp\{-\mathrm{i}\omega t\}] \times \exp\{-t/T_2\} \tag{3}$$

where i = $\sqrt{-1}$. From equation (3) it is clear that in addition to a small change in the main signal, a 'ghost' term with frequency $-\omega$ is introduced by the error.

I prowled round the problem trying to probe it from various angles, and among the many possibilities I explored was that of averaging: whether there was any way to generate from equation (1) and equation (2) two signals that each had an amplitude of 0.95. I could find no simple method, but dealing with quadrature detection the idea of a 90 ° phase shift was never far away, so it was perhaps not surprising that I also considered the consequence of changing the transmitter phase by 90 °. This gives two new signals:

$$X_{90} = 1\cos(\omega t + \pi/2)\exp\{-t/T_2\} = -\sin\omega t\exp\{-t/T_2\} \quad (4)$$

$$Y_{90} = 0.9\sin(\omega t + \pi/2)\exp\{-t/T_2\} = 0.9\cos\omega t\exp\{-t/T_2\} \quad (5)$$

and I immediately saw that I could realize my idea of averaging, for:

$$(X_0 + Y_{90})/2 = 0.95\cos\omega t\exp\{-t/T_2\} \quad (6)$$

$$(Y_0 - X_{90})/2 = 0.95\sin\omega t\exp\{-t/T_2\} \quad (7)$$

The combination regenerates perfect quadrature signals. Generalizing the idea, it was found that errors of quadrature phase were also corrected, while the accuracy of correction was insensitive to the precision of the transmitter phase shift. Thus was born CYCLOPS,[1] a CYCLically Ordered Phase Sequence in which the phase of successive transmitter pulses, and hence of FIDs, was incremented by 90 °, while the computer was used to perform the 'data routing' and averaging of equation (6) and equation (7). My approach in this instance could not be dignified with any Latinism—it resembled more a 'search and destroy' mission in which I boringly and systematically explored possibilities.

POSTPRANDIAL SERENDIPITY AND SLICES

The top floor of the Biochemistry Department commands a fine view of Oxford's 'dreaming spires' and its library and common room are situated there. It is the custom for work to pause at about 3.45 p.m. for tea, biscuits, and the view, and one day in 1974 my colleagues (in particular, David Gadian) and I were so doing while chatting with members of George Radda's biochemistry group (in particular, Steve Busby and John Seeley). At that time, our spectrometer was tuned to ^{31}P NMR to observe phospholipids and to our surprise we discovered that the biochemists were assaying phosphorus in excised rat muscles by a mysterious technique that sounded vaguely reminiscent of a medieval torture—'freeze clamping'. Naturally, the thought occurred to everyone that it might be possible to observe phosphorus metabolites by NMR. I knew that our instrument could detect phosphorus in 0.5 mM solution and so was enthusiastic concerning our chances of detecting metabolites in the millimolar range. David and John became equally enthused, but enthusiasm waned when the thought arose that a muscle would spoil the field homogeneity. I disagreed strongly and remember remarking that the homogeneity would be fine so long as the muscle was in water. (About the only thing I knew about muscle was that it was mostly water!) John quickly doused the proposal, objecting that the muscle would have to be bathed in Ringer's solution. I had no idea what Ringer's solution was, but hearing the magic word 'solution' and knowing that the susceptibility of most liquids was similar to that of water I pushed very hard for the experiment to be done. David and John went off to work out the details; I surreptitiously went to the library to discover what on earth Ringer's solution was, and realized that I was going to have to learn at least a little biochemistry. I descended to the laboratory to my first encounter with rats. I expected gore but not the smell, and noticed that I was not the only one to leave the room quite frequently. In honor of the occasion, David had selected a new 8 mm NMR tube, and a hind leg muscle was inserted together with the solution. The result is a well-known paper in *Nature* that heralded the field of in vivo spectroscopy.[4] Less well known is that the paper was at first rejected by the referee on the grounds that ^{31}P NMR was not novel, and that the experiment failed the second and third times. The failure was traced to the use of old NMR tubes that had been re-cut, and had in consequence rough edges that scratched the muscles as they were inserted. Various theories, ranging from induced contraction to release of enzymes, were put forward to explain the failure but were not explored; there was too much success in the air.

This was my first encounter with serendipity in science and I have often dwelt since on the wisdom of having new NMR tubes, communal tea breaks, small conferences in relaxed surroundings, and the urgent need for a modicum of interdisciplinary education. In retrospect, our progress into the world of biochemistry would have been much more rapid if we had had some basic formal course work therein.

Not surprisingly, 'my' instrument was soon lost to me, inundated with biological experiments, and in particular David Gadian started a very fruitful collaboration with Doug Wilkie and Joan Dawson of (then) University College, London. However, I felt bereft, and having read Paul Lauterbur's classic paper in *Nature*,[5] was intrigued with the prospect of imaging animals and people. My interest became urgent when I read in short order papers by Lauterbur and Garroway concerning pulses for slice selection, and realized with intuitive certainty that they were wrong![1] For me, that realization remains a classic example of how a different viewpoint can lead to radically different understanding and interpretation. The two papers described how in a sample whose spectrum was broadened by a field gradient a long, low-power pulse could selectively flip on-resonance magnetization, supposedly giving thereby signal only from those spatial regions (a slice) whose frequency was not significantly disturbed by the gradient.

However, I viewed the experiment differently. I saw the spectrometer as a 'black box' with transfer function $H(\omega)$ (the spectrum) into which one fed a time-dependent driving function $T(t)$ with a certain spectral density function $T(\omega)$ (the selective pulse), and from which there issued a time-dependent output $S(t)$ (the NMR signal) with spectral density function $S(\omega)$ determined by $T(\omega)$ and $H(\omega)$. In other words, assuming

to a first approximation a linear response theory:

$$S(\omega) \approx H(\omega)T(\omega) \tag{8}$$

But, I reasoned, when a strong field gradient is applied to a sample such as a tube of water, the spectrum $H(\omega)$ is essentially flat over a large bandwidth; in other words, $H(\omega)$ can be assumed with good accuracy to be a constant h. Thus:

$$S(\omega) \approx hT(\omega); \quad S(t) \propto T(t) \tag{9}$$

and the spectrometer functioned in effect as a very expensive attenuator, the output $S(t)$ being a small replica of the input $T(t)$. However, in contrast to an attenuator, an NMR instrument is turned off when the transmitter is on, and I therefore felt that the only signal one should see should be due to the breakdown with large flip angle pulses of the linear theory of equation (8). To prove my point experimentally, I set up a simple on-resonance experiment with a sample of phosphoric acid. (There was no chance of using another nucleus by this time!) With a homogeneous main field, I applied a 2 ms 30 $^\circ$ pulse, thereby keeping the experiment in an approximately linear regime, and obtained a strong, on-resonance FID of known phase. I then applied a field gradient with the z shim and watched the signal become shorter and shorter as I turned the potentiometer until its duration became less than the dead-time of the spectrometer—it disappeared. Not surprisingly, I discovered that a signal, a mirror image of the pulse, could be recovered with the aid of an echo, and thus was born the slice selection technique that is in common use in imaging. Having studied the nonlinear properties of the NMR system for inclusion in my doctoral thesis, I was not surprised to discover that a small *negative* FID followed a 90° selective pulse and that a large negative signal followed a selective 180° pulse—presumably the signals seen by Lauterbur and Garroway. However, while I proved my point experimentally fairly easily, a mathematical proof took me considerably longer, and as a result controversy raged for some time. Incidentally, the engineering and rotating frame points of view are easily reconciled when the *phases* of the flipped isochromats are taken into account.

IMAGING

Some months later, Paul Lauterbur passed through Oxford and we had an enjoyable discussion about spinning samples during which he produced the aphorism that 'nuclei are slippery little things' and do not change their angular momentum just because the sample does. I explained to him my ideas concerning the origins of the signal-to-noise ratio and how I felt they could be extended to formulate a theory for imaging. I also showed him my results concerning slice selection. When I had finished he looked at me quizzically and, imitating my British English, said 'You're telling me I've been a bloody fool!' I think I blushed from head to toe as I miserably said 'Yes'. He pondered the arrogance of a young postdoctoral researcher and then suggested a collaboration on imaging sensitivity.

Again the black box concept was useful as I envisaged measuring resistance to predict the Brownian noise. If all an engineer had available to him were two terminals projecting from a black box wherein was a large coil, he would measure the resistance indirectly from measurements of Q factor and inductance. If, unbeknownst to him, a person's head were then placed in the coil, all he would notice would be a sudden change of Q factor, which he would interpret as increased resistance r_m and hence increased noise (originating from the Brownian motion of electrolytes in the human body). Thus, I realized it was possible to extend my theory of signal-to-noise ratio simply by calculating the additional resistance r_m. The task was relatively simple for regular shapes and we were both pleased with the resulting theoretical paper,[1,6] but less pleased when we had heard nothing from the journal many months after submission. The paper had disappeared in the mail and was eventually published much later than we had hoped.

It was clear that in vivo spectroscopy would be the dominant NMR topic for many years in the Oxford Biochemistry Department, and as I was by now thoroughly 'hooked' on imaging, I moved at Ted Becker's instigation to the National Institutes of Health (NIH) in Maryland in 1977. I was determined that I would not 'lose' another machine that I built and so, with the complicity of Ching-Nien Chen who came to me as a postdoctoral worker from Lauterbur's group, the imaging system for babies that was conceived there never quite came to gestation. Instead, it served as a test-bed for ideas such as shimming an imaging magnet with pieces of steel. In the early days of imaging there was considerable fear that the slightest amount of steel in the environment could wreck the magnet's field homogeneity. However, there was little hard information on how serious the problem was and we attempted to gain some by placing steel plates at various distances from our magnet. It was clear that the field generated by any steel's magnetization could, as usual, be analyzed in a spherical harmonic basis set. The problem was to quantify the effects and assign amplitudes to the harmonics. Working with a French mathematician, Françoise Roméo, who was a guest in my laboratory, we realized that the mathematics were tractable for elementary volumes of magnetized steel, provided we knew the direction of the field at those volumes, but that a full computation for an arbitrary volume and location was much more difficult. However, when one remembers that if steel *is* present, one's primary objective is to remove its deleterious effects, it was but a short conceptual step to the realization that elementary volumes could be placed *inside* the magnet to perform this task. There, they would saturate in a strong, known field of given direction z and would generate accurately quantifiable fields—which could be used to cancel fields produced by steel without. We could fight steel with steel! We tested the idea on our home built baby system with ball bearings and cut plate, and along with a review of field correction techniques sent the results to the fledgling *Magnetic Resonance in Medicine* for the first issue.[1,7]

A severe test of the method, that resulted in its adoption by industry and the overturning of objections to NMR units being sited within hospitals, came a little later when a commercial imager was installed in the NIH Radiology Department. The weight of the whole-body, superconducting magnet was taken by a strengthened steel I-beam in the floor which reduced the homogeneity to 1.2 parts per thousand: the specification was 10 ppm. The magnet manufacturers had attempted to shim the magnet with over 400 kg of steel on the outside, and to

the consternation of many, Picker engineer, Dooey Lee and I stripped it off. So began three weeks of frantic activity, shimming the magnet not with elementary volumes of steel within—they were too weak—but with steel rods of various shapes and sizes for which we scoured half of Maryland. The theory developed as we progressed,[1] but finally with about 10 kg of steel we obtained the desired specification in a systematic manner, though not without drama. We were both very tired towards the end of the exercise, and one morning while carrying a steel rod I tripped and fell. Poor Dooey was kneeling in the magnet and the rod flew with great speed and precision directly between his legs without touching him. I thought he was going to pass out in the magnet from shock!

CONCLUSION

NMR imaging and in vivo spectroscopy are now mature topics from the point of view of instrumentation development. However, NMR has provided exceedingly fertile ground for transplanted physical engineers such as myself, and will hopefully continue to do so. The complexity and diversity of this 50-year old tool leave room for fresh viewpoints and continue to challenge understanding and ingenuity. My fear is that because it *is* a mature topic, the continuing need for instrumentation research in an academic environment will neither be recognized nor catered for financially. Much has been accomplished; much remains to be achieved.

REFERENCES

1. C. N. Chen and D. I. Hoult, *Biomedical Magnetic Resonance Technology*, Adam Hilger, Bristol, 1989.
2. D. I. Hoult and R. E. Richards, *J. Magn. Reson.*, 1976, **24**, 71.
3. P. Styles, N. F. Soffe, and C. A. Scott, *J. Magn. Reson.*, 1989, **84**, 376.
4. D. I. Hoult, S. J. W. Busby, D. G. Gadian, G. K. Radda, R. E. Richards, and P. J. Seeley, *Nature (London)*, 1974, **252**, 285.
5. P. C. Lauterbur, *Nature (London)*, 1973, **242**, 190.
6. D. I. Hoult and P. C. Lauterbur, *J. Magn. Reson.*, 1979, **34**, 425.
7. D. I. Hoult and F. Roméo, *Magn. Reson. Med.*, 1984, **1**, 44.

Hurd, Ralph E.: A Brief History of Gradients in NMR

Ralph E. Hurd
GE Medical Systems, Fremont, CA, USA

The history of field gradients in NMR begins in 1950 with Hahn's treatise on spin echoes.[1] This work described the relationship between echo intensity, molecular diffusion, and spatial variations in $\boldsymbol{B}_0$. The measurement of molecular diffusion is improved by the introduction of a static field gradient coil as described by Carr and Purcell in 1954.[2] Only a year later, Anderson et al.[3] reported the first application of pulsed field gradients. This article introduced the idea of using a gradient pair to avoid spurious echoes from imperfect rf refocusing. Gradient selection of stimulated echoes was also described. These early pulsed gradient applications are still used in contemporary NMR, especially in imaging and localized spectroscopy, where they have taken on names such as *primer–crusher pairs*, *crushers*, and *spoiler* gradients. Oddly enough, this was one of a pair of papers in 1955 that focused on the potential for NMR-based storage memory. In the other, Fernbach and Proctor[4] used a static gradient to encode and read out the frequency response from selective rf excitation. Over the next 10 years little progress was made toward routine use of gradients in NMR. Almost a notable exception is a 1960 epistle to the geophysics community in which Hahn described the potential use of gradients to encode coherent motion—the velocity of sea water.[5] A major advance came in 1965 with Stejskal and Tanner's introduction of pulsed gradients for the measurement of molecular diffusion.[6] In a 1968 paper which marks the rebirth of interest in gradient methods unrelated to motion, Vold et al.[7] extended the use of spoiler gradients to avoid the effects of imperfect rf inversion. Shortly thereafter, a number of groups reported the benefits of using spoiler gradients, often referring to them as *homospoil pulses*.

The use of field gradients to obtain images, as first demonstrated by Paul Lauterbur in 1973,[8] led to profound changes in the history of gradients and in the development of NMR. In 1974, Garroway et al.[9] reported the use of tailored rf in the presence of a gradient for slice selection. As with the development of the diffusion measurement, NMR imaging was first accomplished using static field gradients. The use of pulsed gradients for imaging followed quickly as described by Kumar et al. in 1975 for Fourier imaging[10] and by Mansfield in 1977 for echo planar methods.[11] The spatial selectivity of most modern MRI uses a combination of frequency encoding, phase encoding, and slice selection. With a few exceptions, the development of localized spectroscopic methods has followed in the footsteps of imaging. In addition to their spatial encode function, the use of gradients to avoid artifacts is an ubiquitous part of MRI and in vivo spectroscopy. The important applications of flow and diffusion imaging use gradients to encode both space and motion, and have developed in sophistication along with the rest of MRI.

In 1977, Wokaun and Ernst[12] described the relationship between coherence order and the effect of a gradient pulse. The idea of using gradients for coherence pathway selection was further developed in several key papers.[13–16] In early studies, the potential benefits of using pulsed gradients were often overshadowed by drawbacks such as long gradient recovery times, increased phase instability, peak shape distortion and for high-resolution applications, disturbance of the field/frequency lock system. Preemphasis and improvements in gradient amplifiers helped, but the development that had the biggest impact was the introduction of actively shielded gradients.[17,18] This was important for the development of imaging and localized spectroscopy, especially on small horizontal bore systems equipped with maximum diameter gradient coils. For us, the inspiration to pursue high-resolution applications of shielded gradients came from surprisingly undistorted in vitro results used in the development of in vivo lactate imaging.[19] The work that led to the introduction of gradient enhanced spectroscopy[20] in 1990 convinced us that the benefits of pulsed gradients in high-resolution NMR would eventually eclipse the drawbacks. The decision to develop shielded gradient technology for high-resolution NMR was also supported by concurrent studies, especially the work on diffusion-weighted water suppression by Van Zijl and Moonen[21] and the demonstration of single shot heteronuclear coherence pathway selection by Knüttel et al.[22]

Since 1990, application and development of NMR methods incorporting gradients has grown dramatically. High-resolution and in vivo NMR now benefit from all of the basic applications of gradients; the encoding of space, motion and coherence order, and the spoiling of unwanted magnetization.

REFERENCES

1. E. L. Hahn, *Phys. Rev.*, 1950, **80**, 580.
2. H. Y. Carr and E. M. Purcell, *Phys. Rev.*, 1954, **94**, 630.
3. A. G. Anderson, R. L. Garwin, E. L. Hahn, J. W. Horton, G. L. Tucker, and R. M. Walker, *J. Appl. Phys.*, 1955, **26**, 1324.
4. S. Fernbach and W. G. Proctor, *J. Appl. Phys.*, 1955, **26**, 170.
5. E. L. Hahn, *J. Geophys. Res.*, 1960, **65**, 776.
6. E. O. Stejskal and J. E. Tanner, *J. Chem. Phys.* 1965, **42**, 288.
7. R. L. Vold, J. S. Waugh, M. P. Klein, and D. E. Phelps, *J. Chem. Phys.*, 1968, **48**, 3831.
8. P. C. Lauterbur, *Nature (London)*, 1973, **242**, 190.
9. A. N. Garroway, P. K. Grannell, and P. Mansfield, *J. Phys. C: Solid State Phys.*, 1974, **7**, L457.
10. A. Kumar, D. Welti, and R. R. Ernst, *J. Magn. Reson.*, 1975, **18**, 69.
11. P. Mansfield, *J. Phys. C: Solid State Phys.*, 1977, **10**, L55.
12. A. Wokaun and R. R. Ernst, *Chem. Phys. Lett.*, 1977, **52**, 407.
13. A. A. Maudsley, A. Wokaun, and R. R. Ernst, *Chem. Phys. Lett.*, 1978, **55**, 9.
14. A. Bax, P. G. deJong, A. F. Mehlkopf, and J. Smidt, *Chem. Phys. Lett.*, 1980, **69**, 567.
15. P. Barker and R. Freeman, *J. Magn. Reson.*, 1985, **64**, 334.
16. C. J. R. Counsell, M. H. Levitt, and R. R. Ernst, *J. Magn. Reson.*, 1985, **64**, 470.
17. P. B. Roemer, W. A. Edelstein, and J. S. Hickey, *Abs. Soc. Magn. Reson. Med.*, **1986**, 1067.
18. P. Mansfield and B. Chapman, *J. Phys. E.*, 1986, **19**, 540.
19. R. E. Hurd and D. M. Freeman, *Proc. Natl. Acad. Sci. USA*, 1989, **86**, 4402.
20. R. E. Hurd, *J. Magn. Reson.*, 1990, **87**, 422.
21. P. C. M. van Zijl and C. T. W. Moonen, *J. Magn. Reson.*, 1990, **87**, 18.

22. A. Knüttel, R. Kimmich, and K. H. Spohn, *J. Magn. Reson.*, 1990, **86**, 526.

Biographical Sketch

Ralph E. Hurd. *b* 1950. B.A., 1973, Chemistry, CSUSB, Ph.D., 1977, Biochemistry, University of California, Riverside (advisor Brian R. Reid). Joined Nicolet Magnetics in 1980 (working with LeRoy Johnson on HR applications of NMR); 1983, manager CSI Applications, GE Medical Systems (formerly Nicolet Magnetics); 1989, manager Combined CSI and HR Applications; since 1990, manager Spectroscopy Research and Development. Approx. 60 publications, 4 patents. Current research: clinical MR spectroscopy.

Hyde, James S.: The NMR/EPR Interface at Varian, ENDOR, and notes on Zavoisky

James S. Hyde
Medical College of Wisconsin, Milwaukee, WI, USA

I was at Varian from 1959 to 1975. W. A. Anderson was my immediate supervisor, as he was for R. Ernst and R. Freeman. In turn, M. E. Packard was Anderson's superior. My assignment was to develop EPR, and these notes reflect on the interface between EPR and NMR at that time.

An early memory is of muted and serious discussions about whether or not the Bloch–Hansen patent[1] could withstand challenge because of the prior publication of the first EPR paper by Ye. K. Zavoisky. The Bloch–Hansen patent was filed on December 23, 1946. Zavoisky's dissertation was written in 1944, and the first paper appeared in 1945.[2] My understanding is that the challenge would be particularly serious if a copy of the Soviet journal could be found to exist anywhere in the US in 1946, but that none could be found.

I visited Zavoisky's colleague, S. A. Al'tshuler, in 1971 in Kazan. I can report that he told me that he and Zavoisky felt that they had seen an NMR signal in 1939 but that they were unable to make the resonance 'stand still'. He said that Zavoisky deliberately switched to electrons when he returned to research in 1942 or 1943 because of the larger moment. A sentence from the Al'tshuler and Kozyrev book[3] catches some sense of their feeling for history:

> 'The discovery of an analogous effect in atomic nuclei, made by Purcell and Bloch et al. within two years after publication of Zavoisky's work, was a natural sequel to the study of paramagnetic resonance of electrons.'

I met Zavoisky at the meeting celebrating the 25th anniversary of the discovery of EPR held in Kazan in 1969. He delivered an interesting paper on ion cyclotron resonance in the gas phase. Somebody told me that he was involved in research on power generation using thermonuclear fusion.

I chose to try to advance the candidacy of Zavoisky for a Nobel Prize by speaking to a few key Swedish scientists. I came to understand that he had been seriously considered but that the failure to follow up the initial discovery by a sustained series of publications was considered detrimental.

Academician N. M. Emanuel kindly managed to supply a copy of Zavoisky's dissertation to Varian, and I recall looking it over. I know no Russian, but the equations, equipment drawings, and spectra were more or less familiar.

The debate on who was first in NMR no longer seems so important. A few years ago I challenged Martin Packard directly with the question, 'Is it true that you were the first person on the planet to see an NMR signal?' His reply was a mild, 'It's possible'. My question was based on the speculation that Packard, an experimentalist and Bloch's student, probably had the experiment working before showing it to his mentor.

In looking over other early Varian patents, I came across 3 068 399, 'Gyromagnetic Resonance Methods and Apparatus'.[4] The first paragraph reads:

> 'This invention will be explained and described with reference to a nuclear resonance spectrometer system, but it should be understood that this invention is broadly applicable to atomic quantum systems in general, including those involving atom portions other than nuclei, for example, electrons.'

This is the spin-decoupling patent. As far as I know, no one has yet carried out an analogous EPR experiment.

My first EPR patent six years later[5] was also entitled 'Gyromagnetic Resonance Methods and Apparatus', and starts out with a similar first paragraph. Efforts to write patents that are simultaneously applicable to NMR and EPR continue to this day.

The first true NMR experiment in which I was involved was electron nuclear double resonance (ENDOR) in liquids—detecting NMR signals indirectly by observation of EPR signals. G. Feher discovered ENDOR in 1956 when I was in the midst of graduate studies.[6] A. H. Maki, who was a visitor at Varian in 1963, and I decided to see if ENDOR was possible for free radicals in the fluid phase. Earliest success occurred in a narrow window in time each day between 5 and 5.30 p.m. when for some reason our power lines were unusually quiet. I recall one very good week when the signal-to-noise ratio improved by a factor of 2 each day for five days in a row. Maki was in transit between Harvard and UC Riverside at the time. His parting words as I prepared to write up the first communication[7] were, 'Make it sound important'.

Other early ENDOR experiments include ENDOR in unordered solids and on the ligands of copper complexes with G. Rist,[8] and on a protein with L. E. G. Eriksson and A. Ehrenberg.[9] Ehrenberg invited me to talk about ENDOR at the Second International Conference on Magnetic Resonance in Biological Systems held in Stockholm in 1966. At that exciting conference, W. D. Phillips reported the first NMR experiments on proteins, using the Varian 220 MHz superconducting magnet and spectrometer. H. E. Weaver, who had developed the first commercial EPR spectrometer in about 1956 based around the Varian wideline NMR spectrometer, switched back to NMR to lead the development team for the spectrometer used by Phillips.

Richard Ernst, in his Nobel Prize address, acknowledged W. A. Anderson for the seminal role he played in these early days. I too would like to acknowledge his role and, in particular, the appendices of his dissertation paper.[10] Here he describes magnetic field modulation in rigorous fashion in terms of double sums over modulation sidebands and intermodulation sidebands. In another appendix, the effect of two CW irradiating radiofrequency fields is discussed. Thirty-five years later, these two appendices served as the basis for experiments on multiquantum EPR.[11]

We recently reported liquid phase ENDOR by detection of the effect of inducing an NMR transition on an EPR intermodulation sideband that is produced when two equally intense microwave frequencies that lie within a homogeneous line irradiate an EPR transition.[12] I suggest that this fairly elaborate spin physics had its origins in the heady environment of the early NMR days at Varian.

REFERENCES

1. F. Bloch and W. W. Hansen, US Pat. 2 561 489 (Dec. 23, 1946).
2. Ye. K. Zavoisky, *J. Phys. USSR*, 1945, **9**, 245.

3. S. A. Al'tshuler and B. M. Kozyrev, *Electron Paramagnetic Resonance*, Academic Press, New York, 1964.
4. F. Bloch, M. E. Packard, and J. N. Shoolery, US Pat. 3 068 399 (Sept. 7, 1954).
5. J. S. Hyde, US Pat. 3 100 280 (Oct. 25, 1960).
6. G. Feher, *Phys. Rev.*, 1956, **103**, 834.
7. J. S. Hyde and A. H. Maki, *J. Chem. Phys.*, 1964, **40**, 3117.
8. G. H. Rist and J. S. Hyde *J. Chem. Phys.*, 1968, **49**, 2449.
9. A. Ehrenberg, L. E. G. Eriksson, and J. S. Hyde, *Biochim. Biophys. Acta*, 1968, **167**, 482.
10. W. A. Anderson, *Phys. Rev*., 1956, **102**, 151.
11. H. S. Mchaourab and J. S. Hyde, *J. Chem. Phys.*, 1993, **98**, 1786.
12. H. S. Mchaourab, T. C. Christidis, and J. S. Hyde, *J. Chem. Phys.*, 1993, **99**, 4975.

Biographical Sketch

James S. Hyde. *b* 1932. B.S., 1954, Ph.D., 1959, MIT. Senior scientist, Varian Associates, 1959–75. Professor of Biophysics, Medical College of Wisconsin, 1975–present. Approx. 300 publications, 25 patents. Research interests: methodology of electron paramagnetic resonance and magnetic resonance imaging, spin physics and relaxation processes.

Jackman, Lloyd M.: NMR in Organic Chemistry–the Fabulous Fifties

Lloyd M. Jackman

The Pennsylvania State University, University Park, PA, USA

'Have we ever thought of writing a book?', asked Professor Derek Barton, who had just walked into my office in Imperial College. I recognized the editorial 'we', and with what was perhaps excessive enthusiasm told him that indeed I was just beginning one on the mechanisms of oxidation and reduction reactions.

'Ah, an important subject', he replied. 'But one only writes a book to make one's fame or fortune and a book on oxidation will do neither. Why don't we write one on NMR spectroscopy?'

And so it was that I came to chronicle the explosion of NMR spectroscopy into the field of organic chemistry that occurred in the 1950s.

Most of us had already adopted IR and UV/visible spectroscopy for functional group analysis and were therefore immediately receptive to this new technique. For some, however, it created difficulties. For example, one eminent chemist on reviewing a structure I had derived from its NMR spectrum pronounced it 'interesting' but added that he thought they would 'do a little chemistry'. I suspect that he really accepted my structure but wistfully realized that the beautiful structure proofs based on series of chemical degradations that had constituted the high arts of organic chemistry were about to leave the stage.

Organic chemists were dazzled by the early spectrometers with their massive electromagnets and huge power supplies. My first views were provided by color slides of a Varian HR-40 (yes! 40 MHz) presented in a lecture by Prof. Jack Roberts who later provided me with my first NMR spectrum. Subsequently, Prof. Wilkinson purchased this instrument for the Inorganic Chemistry Department at Imperial College and kindly allowed me access to it. It was installed for us by Dr. Warren Proctor, one of the pioneers in the field. By locating the probe just outside the pole faces of the magnet he picked up a signal from a sample of diphenylpicrylhydazyl and pointed out that we had also purchased an ESR spectrometer. Finally, he gave us a lecture on spin Hamiltonians.

These early spectrometers were quite outside the experience of organic chemists. Shimming was accomplished by a mysterious mixture of cycling the magnet current and mechanically distorting the magnet itself. Field/frequency locks had not been commercially developed and so precalibrated spectral charts could not be used. Calibration was accomplished by introducing audiofrequency sidebands into spectra and the frequency separations of signals were obtained by averaging data from several spectra. Integration was generally performed by 'cutting and weighing' the peaks in the spectra.

The application of NMR in organic chemistry depends mainly on two phenomena, the chemical shift and spin–spin coupling. The pioneering work of Gutowsky and others at the beginning of the decade thus set the stage for the entry of NMR into organic chemistry. In particular, a 1953 paper of the Gutowsky group in which they listed 150–200 proton chemical shifts for protons in various chemical environments clearly demonstrated the enormous potential of NMR. Shortly thereafter two valuable compilations of proton chemical shifts made by Drs. N. F. Chamberlain and G. D. V. Tiers became available to many in the NMR community and these contributed greatly to the development of the subject. Unfortunately, during this period much confusion reigned regarding both the method of referencing spectra and the definition of the proton chemical shift scale. Bothner-By and Glick pointed out the fallacy of using an external reference contained in a coaxial capillary tube and it was left to George Tiers to suggest the ideal internal reference, namely tetramethylsilane. Even then, there was controversy whether the ppm scale should increase or decrease with increasing shielding. Eventually the latter was adopted to be consistent with the scales used for other nuclides.

During the latter part of the decade, NMR spectroscopists were devoting much attention to the analysis of the spectra of complex spin systems. Since access to computational methods was somewhat limited, clever techniques, such as subspectral analysis, which avoided quantum mechanical calculations, were developed. The utility of spin decoupling experiments was recognized but the commercial spectrometers did not yet offer the capability of double irradiation. During this period, many organic chemists became comfortable with unraveling first-order spectra although 'virtual coupling' and 'deceptively simple spectra' caused some confusion.

The 1950s was also a period of intense interest in conformational analysis. The appearance of the 'Karplus equation' relating the magnitude of the vicinal coupling constant to the dihedral angle was therefore greeted with great enthusiasm. Here was a powerful, new method for establishing conformation and relative stereochemistry, particularly in alicyclic systems.

By the end of the decade, proton NMR spectra of representatives of most of the major groups of natural products had appeared in the literature and NMR spectroscopy had contributed significantly to proofs of the structure and/or the stereochemistry of carotenoids, alkaloids, terpenoid substances, plant phenolics, mold metabolites, and carbohydrates. It is hard to convey the exhilaration which many of us felt when we succeeded in establishing a structure that we knew would have taken a lengthy series of experiments to achieve or that, for reasons of sample limitation, could not easily be tackled by chemical methods. Just as exciting was to see organic chemists come to recognize that NMR trivialized many simple problems and that it could be employed to monitor many reactions used in synthetic organic chemistry.

The decade closed with the appearance of the Varian A-60 spectrometer, which operated with a field/frequency lock and could therefore record spectra on precalibrated chart paper. NMR was now a 'hands-on' tool for the bench organic chemist. Its impact was immediate and enormous.

Perhaps some of us felt the excitement was over. We knew that 100 MHz spectrometers were coming but we could not envision 750 MHz. We believed that one day routine ^{13}C NMR might somehow be possible, but our crystal ball certainly did not reveal FT NMR and the multiplicity of $(1 + n)D$ techniques it has brought with it. We knew of the nuclear Overhauser enhancement but few, if any, recognized that it would take

its place alongside the chemical shift and spin–spin coupling constant as a key parameter for the elucidation of structure and stereochemistry. And imaging. Impossible!

Biographical Sketch

Lloyd M. Jackman. *b* 1926. B.Sc., 1945, Ph.D., 1951, Chemistry, University of Adelaide, Australia. Postdoctoral work at Imperial College of Science and Technology, University of London (with Sir Patrick Linstead and E. A. Braude). Successively lecturer, senior lecturer, and reader at Imperial College, Professor of Organic Chemistry at University of Melbourne, Professor of Chemistry at The Pennsylvania State University. Currently Professor Emeritus at Penn. State. Approx. 160 publications including book 'Applications on Nuclear Magnetic Resonance Spectroscopy in Organic Chemistry'. Current research specialty: structures, reaction mechanisms, and NMR spectroscopy of organic lithium compounds.

Jakobsen, Hans J.: A Retrospect on the Development of High-Speed Sample Spinners for Solids since 1980

Hans J. Jakobsen

University of Aarhus, Aarhus, Denmark

Although the method of magic angle spinning (MAS) for obtaining high-resolution NMR spectra of solids was established long before 1980, it was at that time still considered a technique for the specialists. One reason for the long-awaited breakthrough of the methodology was the commercial inaccessibility of stable and routinely spinning MAS probes. The painful struggle to obtain decent spinning by carefully packing/repacking rotors undoubtedly prevented many newcomers from entering the field at that time. Before 1980, the most widely used spinner designs were those after Andrew[1] employing a conical surface with a single air-bearing and drive source. However, cylindrical rotors with separate bearing and drive systems also emerged at that time (e.g. by Lippmaa et al and by Veeman et al.).[2] Around 1980 the maximum attainable spinning frequency was generally considered to be $\nu_r = 4-5$ kHz.

During 1978–83, our laboratory was heavily engaged in collaborative research projects with Paul D. Ellis, University of South Carolina (USC). Following a sabbatical in John Waugh's lab (1976–77), Paul was very excited about setting up instrumentation for solid state NMR at USC. I became infected by Paul's enthusiasm and decided to introduce high-resolution solid state NMR in Denmark when purchasing our new spectrometer.

One of Paul's graduate students engaged in designing the USC solid state NMR equipment was David Doty. During a visit to USC in December 1979, I witnessed Dave working hard on having a prototype MAS spinner operating before Christmas. At a students' Christmas party at Paul's house, Dave and his wife Judy were the last to arrive. When entering the room Dave and Judy were each blowing an air hose and the rotor was actually spinning in Dave's first cylindrical spinner assembly. Improvements of the design resulted in an 8-mm spinner assembly with a maximum $\nu_r \approx 5$ kHz and the Doty and Ellis review[2] of their design. The successful development of NMR equipment at USC during these years undoubtedly convinced Dave to found his own company, Doty Scientific, Inc., in 1982 (see ***A Random Walk Toward High-Speed Sample Spinning***) and Doty 5-kHz MAS probes were soon on the market.

Following the installation of a Varian XL-300 liquids/solids spectrometer at University of Aarhus (UAa) in 1983, a decision was made one year later to improve the spinning performance of the original Varian pneumatic MAS probe by designing our own spinner assembly. The objective was routinely to spin inhomogeneously packed samples in a 7-mm cylindrical rotor at 5–6 kHz. The basic idea was a stiff air-bearing system, an experience gained from USC,[2] however using an otherwise new design. Following a year of 'ups and downs' in design/construction, we (Vagn Langer, Preben Daugaard, and myself) finally recorded our first 5-kHz MAS spectra in early 1985. A period of competition for pushing the limit of 'high-speed spinning' started right away. By early 1986 our spinner assembly was considerably improved and we routinely recorded 10-kHz MAS spectra using 7-mm rotors.[3] A collaboration on high-speed MAS probes was initiated with Varian Associates following the patent of our design.

At the 8th European ENC, Spa, Belgium in June 1986, our spinner system was presented live to the scientific community. Furthermore, at that conference, Doty Scientific for the first time presented its products in Europe. Considering the efforts in starting up a new company, Dave had carried out few improvements in high-speed spinning since he left USC. Watching our 7-mm rotor perform at $\nu_r = 10$ kHz, Dave got excited and said quietly, 'I need to go back to the workshop'. Some months later Dave phoned us back, 'I have 10 kHz for my 7-mm rotor'.

During the same time period, developments of high-speed spinner systems were being performed at the University of Colorado by Dec, Wind, and Maciel. In 1986 this group published MAS spectra for 4.5-mm o.d. rotors spinning at 17 kHz using air.[4] Thus the competition on high-speed spinning kept going.

It did not take long for the UAa lab to modify our spinner assembly for 5-mm o.d. rotors[5] (maximum $\nu_r = 16.4$ kHz) which was presented at the 28th ENC, 1987. This was followed by the introduction of a 4-mm o.d. rotor system with a maximum $\nu_r = 20.6$ kHz at the 31st ENC, 1990. Comparable improvements were achieved by Doty Scientific during these years.

The maximum attainable ν_r values for our various rotor sizes are determined by the largest outer diameter of the rotor/end-cap system, for which a speed equal to the speed of sound (346 m s^{-1} at 25°C) can be observed in all cases. For our rotor design, the diameters for the end-caps are all larger than the rotor o.d., e.g. 9.80, 6.75, and 5.00 mm for the 7, 5, and 4 mm rotors. These rotors yield maximum ν_r values of 11.4, 16.4, and 20.6 kHz, corresponding to speeds of 353, 348, and 324 m s^{-1} for the end-cap o.d.s, i.e. about the speed of sound but not above.

During recent years the possibility of supersonic MAS has been investigated both at Doty Scientific and in our lab. For example, $\nu_r = 26$ kHz has observed for a 3.5-mm rotor at Doty Scientific. At UAa we have increased the rotor speeds by (i) reducing the largest o.d. for the end-cap and (ii) modifying the drive jets. For example, for the 7-mm rotor with an 8.2-mm o.d. end-cap and new drive design, we have observed $\nu_r = 14.5$ kHz corresponding to a speed for the largest diameter of 374 m s^{-1}, i.e. supersonic above 13.5 kHz. Provided our future efforts further to reduce the end-cap o.d.s to that of the rotors are equally successful, we should obtain spin rates of 17, 24, 30, and 34 kHz for 7, 5, 4, and 3.5 mm rotors, respectively. An exciting prospect for the future of MAS NMR.

REFERENCES

1. E. R. Andrew, L. F. Farnell, M. Firth, T. D. Gladhill, and I Roberts, *J. Magn. Reson.*, 1969, **1**, 27.

2. F. D. Doty and P. D. Ellis, *Rev. Sci. Instrum.*, 1981, **52**, 1868, and references cited therein.
3. V. Langer, P. Daugaard, and H. J. Jakobsen, *J. Magn. Reson.*, 1986, **70**, 472; US Pat. 4 739 270 (April 19, 1988).
4. S. F. Dec, R. A. Wind, G. E. Maciel, and F. E. Anthonio, *J. Magn. Reson.*, 1986, **70**, 355.
5. H. J. Jakobsen, P. Daugaard, and V. Langer, *J. Magn. Reson.*, 1988, **76**, 162.

Biographical Sketch

H. J. Jakobsen. *b* 1940. B.S., 1961, Ph.D., 1964, University of Aarhus. Introduced to NMR by K. Schaumburg, 1962. Faculty in Department of Chemistry, University of Aarhus, 1964–present. Approx. 145 publications. Research interests: practice and theory of high-resolution, solid state NMR, and applications to chemistry and materials research.

James, Thomas L.: Time for Preparation and Evolution. But what is the Mechanism for Relaxation?

Thomas L. James

University of California, San Francisco, CA, USA

I first learned of the potential application of NMR to problems of biochemical interest while in my first year (1965–66) of graduate school in the Biochemistry Department at the University of Wisconsin, Madison, where I had matriculated following graduation from the University of New Mexico. Loren Anderson, the instructor in the introductory biochemistry class, was properly excited by the then-unpublished studies of R. U. Lemieux and J. D. Stevens on sugar conformations. While I retained an underlying interest in biochemical processes, at that time my limited perception was that biochemistry as a discipline was too empirical. So I switched to the Chemistry Department at Wisconsin in that first year and began graduate research looking at protonation via NMR in the lab of Asst. Prof. Richard J. Kula, who had recently obtained his Ph.D. from the University of California, Riverside, in the labs of Donald Sawyer and Sunney Chan. In my second year of graduate school, Rich announced he was returning to California, specifically the greener hills of Berkeley and the greener pastures promised by the study of law. As I had also acquired an NIH predoctoral fellowship providing a small amount of research money in addition to my salary by then, I had an unusual situation for a graduate student: I had nearly complete freedom to devise a thesis project on my own, a little'experience, and a strong interest in a field only in its infancy—biological NMR. By that time, I had read the few pioneering papers by Mildred Cohn, Oleg Jardetzky, William Phillips, and Robert Shulman, and found those relating NMR relaxation to biochemical problems to be particularly interesting. With so little prior literature, I simply leafed through my biochemistry textbook, picked four subjects I thought appropriate for study via NMR relaxation, and worked out a plan for one: use of ^{23}Na NMR relaxation to examine aspects of the active transport of sodium across biological membranes. With this plan, I approached Joe Noggle whom I was told was acquiring a pulsed NMR spectrometer. Joe accepted me into his lab and enthusiastically encouraged me to pursue the project. As there was little prior work with ^{23}Na NMR studies of complexes, I carried out some studies of other sodium ion complexes, but eventually was able to study the interactions of sodium ion with the Na–K transport ATPase, which purportedly was involved in membrane transport.

After a two-year hiatus in the chemical industry in Texas studying aspects of heterogeneous catalysis without a single NMR experiment, I longed for the challenge of NMR, biochemistry, and academe. I was able to join Mildred Cohn's lab in the Johnson Research Foundation (Biophysics) at the University of Pennsylvania, where mostly I used NMR to study aspects of enzymology. I also found time on the side in my first year there to do some self-diffusion studies in biological tissue. Mildred taught those in her lab to focus on the scientific question, not on the technique, i.e. NMR. I have tried to adhere to this focus with modest success ever since. (I have learned that this view is strongly shared by most NIH study sections as well.)

At the time of my postdoctoral work, i.e., early 1970s, many others were starting work in biological NMR or were interested. Several people asked me where they could learn sufficient NMR to conduct biochemical studies. Physics books on NMR were considered too daunting, and chemistry books typically skirted relaxation which was so important for biochemical and biological applications. Consequently, I wrote the book 'NMR in Biochemistry' at nights and weekends during the second year of my postdoc. However, I had acquired a faculty position in the Pharmaceutical Chemistry Department at the University of California, San Francisco, before the book was in print.

In my latter months at Penn, I used intermolecular NOE experiments to examine the interaction of a ligand with specific amino acyl residues at an enzyme active site. After a frustrating first year at UCSF without access to a decent NMR instrument, I continued with further NOE studies on the high-field spectrometer at Stanford. We were subsequently successful in funding our first research-grade instrument at UCSF. Not long after, the emphasis of my research shifted to DNA with a lower level of activity remaining with proteins. Relaxation remained a major interest with studies of molecular motion later being displaced by structural studies centered around measurements of internuclear distances via complete relaxation matrix analysis of 2D NOE spectral intensities.

Although studies of sickle cell disease with erythrocytes in NMR tubes were initiated with Irwin D. (Tack) Kuntz soon after my arrival in San Francisco, developments in magnetic resonance imaging by colleagues at UCSF and in vivo NMR in general elsewhere brought numerous local colleagues to my door to inquire how NMR might be useful for their research interests. Three such inquiries on one particular day convinced me that I should either get seriously involved with in vivo NMR or change my phone number—I chose the former. Consequently, I became involved in several projects with local collaborators utilizing systems ranging from cell cultures to perfused organs, to animals, and to humans.

My research has profited immensely from the intellectual milieu of UCSF; in particular, the molecular studies have benefited from long-term interactions with Vladimir J. Basus, Peter A. Kollman, Tack Kuntz, and Richard H. Shafer, and the in vivo NMR studies have benefited from a long term interaction with Lawrence Litt. I have also had the privilege of having several talented postdocs and graduate students in my lab, most of whom have now left to pursue successful careers elsewhere.

Biographical Sketch

Thomas L. James. *b* 1944. B.S., 1965, Chemistry, University of New Mexico, Ph.D., 1969, Chemistry, University of Wisconsin, Madison, with Joseph H. Noggle. Postdoctoral work, 1971–73, Biophysics, at University of Pennsylvania with Mildred Cohn. Faculty at University of California, San Francisco, 1973–present. Currently, Professor of Chemistry, Pharmaceutical Chemistry and Radiology. Approx. 230 publications. Current research interests: biochemical and biological applications of NMR.

Jameson, Cynthia J.: Early Work on the Ranges of Chemical Shifts and Signs of Coupling Constants

Cynthia J. Jameson

University of Illinois at Chicago, Chicago, IL, USA

When I came to the University of Illinois at Urbana-Champaign as a graduate student, Herb Gutowsky's group had the only computer program in existence for the computation of high-resolution NMR spectra of a general six-spin system. It was written by Geneva Belford and ran on that marvelous machine (for its time) the Illiac I. I was using it to compute the proton spectrum of the $-CH_2CH_2-$groups in [2.2] metacyclophane (in which the methylene groups are locked in virtually symmetrical staggered positions, with tetrahedral bond angles), an AA′BB′ spectrum which at 60 Mc s^{-1} looked almost of the A_2X_2 type. The quality of the spectra, calibrated by the usual audiofrequency sideband method, was such that even at this high field I could distinguish between sets of chemical shift and coupling constant parameters by focusing on the relative intensities and splittings between two sets of small peaks. I came to the conclusion that it was impossible to fit the spectrum using uniformly positive coupling constants. Jim Shoolery at Varian Associates kindly ran a low-field spectrum for us (15.083 Mc s^{-1}) and this was definitely AA′BB′. There was excellent agreement with the assignment J_{trans} = +12.3, J_{gem} = − 12.0, J_{gauche} = +4.0, and $J_{gauche'}$ = +3.2 Hz and, of course, with the other set in which all the signs are reversed. The key finding was that J_{trans} and J_{gem}, the two largest coupling constants were opposite in sign.[1]

I was convinced that I had logically exhausted all the possible combinations of the parameters to test against the spectra, but Herb did not have confidence in my results at that time. After all, Martin Karplus (with Anderson, Farrar, and Gutowsky) had calculated these coupling constants in CH_4 and the H−C−C−H fragment in two classic papers,[2,3] the latter being the original paper about what was to become known as the Karplus relationship. Both papers were considered to be in good agreement with experiment, and in CH_4 itself the calculated magnitude of the coupling constant was right on. My results went into a hole for several months until Herb (with Dave Grant) started looking into the nature and analysis of A_2B_2 and A_2X_2 spectra in general, and became convinced that I was right after all. The implications of this finding were unfortunate, or so we said then, for it meant that one of the two calculations was in error. It turned out that it would be decades later before the J_{gem} value could be calculated properly, but the H−C−C−H fragment calculation lives on.

The synthesis of the xenon fluorides generated a lot of excitement during this time and there was a great deal of speculation about the nature of the bonding in these molecules. Tom Brown told Herb about the ^{129}Xe chemical shifts that he and Whipple obtained indirectly by INDOR on the ^{19}F well before the paper came out in *Science*.[4] The shifts were very large, Xe was deshielded by 5785 ppm in XeF_4 compared to the Xe in xenon gas, for example, and among the three fluorides XeF_2, XeF_4, and $XeOF_4$ the spread was very nearly 2000 ppm. Were the shifts as large as they were because the bonding in these new compounds was highly unusual, i.e. drastically different from ordinary compounds? Herb asked me to 'explain' the very large Xe chemical shifts. I figured that I could not 'explain' the large magnitudes of the chemical shifts of Xe in these compounds in isolation. It would only be a credible explanation if at the same time I could explain why some nuclei have large chemical shifts while others were much smaller in the regular compounds for which the nature of the bonding was not in question. After collecting the entire chemical shift data known at that time (a mere handful of nuclei) and putting the ranges of their chemical shifts in the Periodic Table, I thought I could see a Z-dependence that might possibly be periodic. I look back on the very fragmentary information on which I based this leap of faith and think that it's amazing how graduate students have no fear. What could be causing this periodic behavior? If I could find a logical reason for the chemical shifts to behave that way then there is no problem with Xe, for I could almost see the rising trend in going from left to right in a row of the Periodic Table and within a group, from top to bottom, so that Xe would logically be at a peak in the row and also in the column of rare gas nuclei.

Well, I did not find the answer immediately. I got married and left to join my husband out east. While browsing around in the library in Columbia University, looking at the paper on chemical shifts of xenon in the gas phase at high pressures by Carr and the explanation of the relaxation of ^{129}Xe in xenon gas by Torrey, I happened upon the paper by Barnes and Smith in the same volume of the *Physical Review* (with computerized information retrieval this would never have happened). This paper was entitled 'Electric Field Gradients of Atomic p Electrons'.[5] Off-hand one would not think that this had anything to do with chemical shifts, but I was just browsing. So I read about the determination of the spin−orbit coupling constants for the atoms from the term energies and the calculations of the average value of $1/r^3$ for the p electron from these constants. And there it was, the periodicity that I was looking for. The $1/r^3$ term that appears in the operator for the paramagnetic part of the nuclear magnetic shielding in Ramsey's formulation has an average value for the free atoms that was periodic in the way that I imagined the ranges of chemical shifts were periodic. It did not take long after I made this serendipitous discovery to write it up and send it off to Herb, and we polished it up during a two-week visit I made to Urbana.[6] Of course, now that most nuclei in the Periodic Table have been observed extensively, the ranges of the chemical shifts of the nuclei show the periodic behavior very beautifully, tracking the periodic behavior in the average values of $1/r^3$ for the atoms.[7]

REFERENCES

1. H. S. Gutowsky, and C. S. Juan *J. Chem. Phys.*, 1962, **37**, 120.
2. M. Karplus, D. H. Anderson, T. C. Farrar, and H. S. Gutowsky, *J. Chem. Phys.*, 1957, **27**, 597.
3. M. Karplus, *J. Chem. Phys.*, 1959, **30**, 11.
4. T. H. Brown, E. B. Whipple, and P. H. Verdier, *Science*, 1963, **140**, 178; *J. Chem. Phys.*, 1963, **38**, 3029.

5. R. G. Barnes and W. V. Smith, *Phys. Rev.*, 1954, **93**, 95.
6. C. J. Jameson and H. S. Gutowsky, *J. Chem. Phys.*, 1964, **40**, 1714.
7. C. J. Jameson and J. Mason, in *Multinuclear NMR*, ed. J. Mason, Plenum Press, New York, 1987.

Biographical Sketch

Cynthia J. Jameson. *b* 1937. B.S., University of the Philippines, Ph.D., 1963, University of Illinois at Urbana-Champaign. Introduced to NMR by Herb Gutowsky. Faculty in Chemistry, University of Illinois at Chicago, 1968–present. Approx. 130 publications. Research interests include theoretical and experimental studies of the chemical shift, in simple systems in the gas phase and in molecules absorbed in microporous solids, with particular emphasis on intramolecular and intermolecular shielding surfaces and averages therein; also, spin relaxation in gases and their connection with the anisotropy of intermolecular potentials and molecular dynamics.

Jardetzky, Oleg: NMR in Molecular Biology—A History of Basic Ideas

Oleg Jardetzky

Stanford University, Stanford, CA, USA

Attempts to apply NMR to biology did not lag far behind the first applications in chemistry. Even in 1954, Jacobson, Anderson, and Arnold[1] had tried to measure the hydration of DNA via the intensity of the NMR water signal in DNA solutions. The reported observation was later shown to have been an instrument artifact, but a beginning had been made.

My own involvement with NMR began at about the same time. As a graduate student interested in Na^+ transport across biological membranes and discouraged by the fashion of treating the membrane as a black box, I was looking for a new approach to the problem. One of my advisors, the chemist Bill Lipscomb, suggested NMR as a possibility. The other, the physiologist Maurice Visscher, said wisely: 'the unexplored is always tempting—see what you can do'. An Na^+ resonance had not been seen before, but John Wertz raised the funds to construct a 7.9 MHz oscillator for Na^+ at 7 kG. Hence my thesis became the first NMR study of the interactions of Na^+ ions in solution and the first published detection of an NMR signal in living matter. We did not learn much about transport, but something about complexing of Na^+ with intracellular proteins and a variety of metabolites (Figure 1).[2]

The inspiration for a systematic investigation of the potential of NMR in molecular biology came from the first comprehensive review of the NMR literature by John Wertz in 1955.[3] Wertz likened the resonating nuclei to the radio transmitters of spies reporting what the surrounding atoms were doing. At the time, the Watson–Crick DNA double helix was barely two years old and, for lack of conclusive evidence, by no means universally accepted. Protein crystallography was at a hopeful rumor stage. The prospect of studying biological macromolecules at atomic resolution was tantalizing.

We began our systematic study of protein and nucleic acid building blocks—amino acids, small peptides, then mono- and oligonucleotides—in 1956.[4] When the first NMR spectrum of a protein (ribonuclease) was recorded by Saunders, Wishnia, and Kirkwood in 1957,[5] we were in the position to account for its general shape from the spectra of constituent amino acids.[6] The initial result was disappointing. Instead of detailed reports, only messages scrambled by overlap-jammed airwaves. One observation of lasting value did emerge from a few additional experiments: mobile regions in biopolymers could be distinguished from the compact structure by their narrow lines. This prompted us to develop a relaxation method for the study of molecular interactions.[7] Among our first findings was that the aromatic substituent on penicillin, rather than the penicillanic acid moiety, was responsible for its binding to serum albumin. The method still finds some use today and was recently reinvented, without reference to the original work.[8] Estimates of expected widths for amino acid lines (of known chemical shift) in 'rigid' proteins led as early as 1961 to the conclusion that the observed broad envelopes were due only in part to the high molecular weight, but in part also to chemical shift nonequivalence.[9] This meant hope.

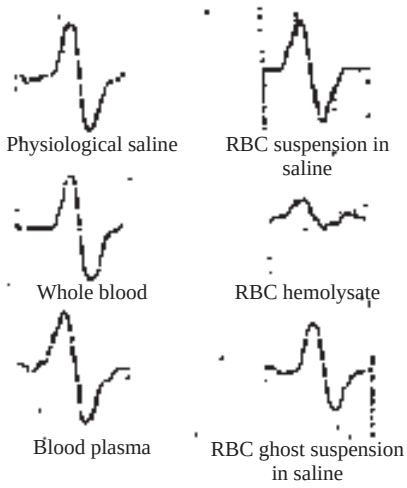

Figure 1 ^{23}Na resonance in blood and blood fractions. (Taken from Jardetzky, *Ph.D. Thesis*, 1956[2])

The classes of problems in molecular biology that NMR could solve were clear from prototype experiments by the time we wrote our first review on the subject in 1961: '(a) *primary structure*, (b) *conformation* or *secondary* and *tertiary structure*, (c) *rate processes* and *molecular motion* and (d) *interactions* between molecules'.[9] The agenda has remained the same since, but specific information within it has grown explosively over 30 years.

The major obstacles standing in the way of detailed structural studies on proteins and nucleic acids by NMR were rapidly recognized as those of *sensitivity*, *resolution*, and *rules of interpretation.*

The problem of *sensitivity* was solved first. In 1962, inspired by radioastronomers, we instituted signal averaging, for the first time attaching a small computer (CAT, computer of average transients) to the NMR spectrometer. This achieved a roughly 100-fold improvement in signal-to-noise ratio.[10] In 1963, similar experiments were reported by Klein, Allen, and Laszlo, but it still took nearly two years before the CAT became part of a commercial spectrometer. The menagerie of averaging methods grew rapidly, including the DOG (very slow sweep) and the MOUSE (a simple capacitor circuit). However, CAT NMR became the standard method of the 1960s. This was ironic, because the better—now universally used—solution had been conceived almost simultaneously. Discussing our initial results at a 1962 Gordon Conference (more precisely, swimming in Webster lake), Richard Ernst suggested that it may be more efficient to average in the time rather than in the frequency domain. This idea became the basis of modern Fourier transform (FT) spectroscopy. It took four years to bring to fruition[11] and it was 1970 before FT spectrometers became generally available. A variety of technical advances has improved sensitivity by an additional factor of 20–30 since the introduction of signal averaging, yet the practical gain in macromolecular spectroscopy has been much less. It was then possible to look at millimolar solutions of proteins—and it is now still necessary to look at millimolar solutions. The relative 'loss' of sensitivity is, of course, due to the fact that in the 1960s one was looking at the main spectral

lines, while at present one is deriving information from the much less intense cross peaks in multidimensional spectra.

The problem of *resolution* in macromolecular spectra can at present be regarded as essentially solved by the development of three technologies: (1) high-field magnets, allowing frequencies above 500 and now up to 750 MHz; (2) 2D and later multidimensional FT spectroscopy; and (3) isotopic spectral editing. Now the spectra of small proteins and oligonucleotides (MW < 10 kD) can often be assigned by spectroscopic experiments alone. However, at higher molecular weights simplification of spectra by isotopic labeling has proved indispensable. The solution emerged in stages over a 20-year period and in reverse of the order listed.

The highest frequency spectrometer available in the mid-1960s—based on the first Varian superconducting magnet designed by Harry Weaver—operated at 220 MHz. In the hands of W. D. Phillips and his colleagues at DuPont it gave promising, but not sufficient, improvements in the resolution of protein spectra.[12] Based on our knowledge of chemical shift differences observed in peptides and the amino acid composition of several proteins, it was possible to estimate that even at fields of 1000 MHz a complete resolution of the proton NMR spectra of proteins of moderate size (MW 17–20 kD) could not be expected. At the historic NMR meeting in Tokyo, organized in 1965 by Shizuo Fujiwara, himself a pioneer of amino acid and peptide NMR, I therefore proposed that to extract detailed information on individual residues it would be necessary to simplify protein NMR spectra by selective deuteration.[13] We made a detailed list of desirable criteria for the protein to be studied—a single chain, moderate molecular weight, bacterial origin, ease of preparation, knowledge of the primary sequence, etc.—and through a serendipitous encounter with Chris Anfinsen, who had recently isolated and sequenced staphylococcal nuclease, we found an ideal system.

The proposal was implemented by 1968 by Markley, Putter, and Jardetzky[14] with a dramatic and informative simplification of the nuclease spectrum (Figure 2) and by Crespi, Rosenberg, and Katz for phycocyanin,[15] for which, however, no structural studies were reported. In the case of staphylococcal nuclease, spectral editing allowed the first detailed NMR study of the structure and dynamics of an enzyme–inhibitor complex.[16] The use of ^{13}C for spectral editing was proposed in 1970 by Paul Lauterbur and the use of ^{15}N in 1976 by Aviva Lapidot. Spectral editing was used sporadically through the years for assignment and simplification, but did not really come into its own until the late 1980s when it became generally recognized that even multidimensional proton spectroscopy would not allow a complete spectral assignment for larger proteins. Since that time many ingenious labeling schemes described elsewhere in this work have been invented and have become an indispensable component of protein structure determination by NMR. To tackle the largest structures thus far solved by NMR—the *trp* repressor (25 kD) and its DNA complex (37 kD)—we had to use a combination of heteronuclear 3D *and* selective deuteration.[17] It can be expected that this combination will be essential for the NMR study of larger structures in general.

The most dramatic of the three methodological contributions to the solution of the resolution problem for macromolecular spectra has been first two-dimensional and later multidimensional FT spectroscopy. Following up on the initial suggestion

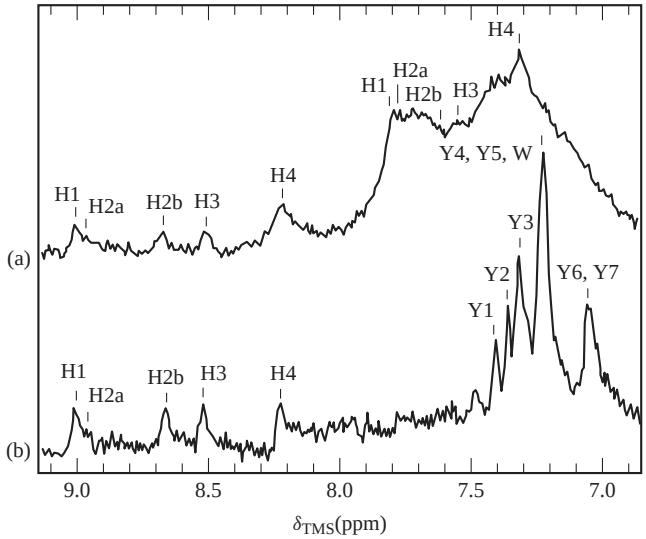

Figure 2 Comparison of the aromatic region of the NMR spectra of (a) staphylococcal nuclease and (b) a selectively deuterated analog. Assignments: His, H1, H2a, H2b, H3 and H4 (the low-field peaks are C-2 and the high-field peaks C-4 imidazole protons): Tyr, Y1-7 (2,6-protons); Trp, W (C-2 ring proton). (Taken from Putter et al., 1969[14])

by Jean Jeener in 1971, the development of the theory of the method and of many key experimental techniques has for the most part been the monumental contribution of Richard Ernst and his school, summarized in their 1987 book[18] and elsewhere in this volume. Applications to proteins emerged rapidly in several laboratories—particularly at Oxford, Stanford, and Zurich.[19] As long as attention was focused on very small proteins, it appeared that nothing else was needed to solve all problems of protein NMR spectroscopy. The fact that we now know this not to be true in no way detracts from the enormous value of multidimensional spectroscopy, even if its success depends on high-frequency spectrometers and its most important contributions are bound to be in its isotope edited form.

The development of high field magnets played a decisive role in the development of protein and nucleic acid NMR. Instrumental resolution has improved by a factor of 15–20, compared to the 40 MHz ribonuclease spectrum in 1957. The contributions of many individuals lie behind this development and these are described elsewhere in this volume. Landmarks of progress were the 270 MHz instrument at Oxford in 1971, the 360 MHz at Stanford in 1974, the 600 MHz at Pittsburgh in 1979, and the 750 MHz at Oxford in 1992.

The *interpretation* of NMR findings on macromolecules must still be regarded as an incompletely solved problem, even though some of the fundamentals are well understood. The basic question: What kind of information about protein structure does an NMR spectrum contain?, had not been answered by the early finding of chemical shift dispersion among chemically identical residues in the spectra of native proteins. Was this dispersion due to primary structure effects of nearest neighbors? To secondary structure? To tertiary folding? A series of investigations on model systems and on protein denaturation, largely in our laboratory and that of W. D. Phillips, answered these questions by 1967. It was shown that in linear peptides and random coil polymers, primary sequence effects were small. The 1964 proposal by M. Sheinblatt to use NMR for the sequencing of proteins

proved applicable only to very short peptides, where titration shifts of the N- and C-terminal residues could be detected. Markley, Meadows, and Jardetzky[20] first demonstrated that the formation of α-helices was accompanied by a + 0.4 ppm shift of the α-CH resonances. This and other regularities in peptide spectra were summarized by Nakamura and Jardetzky.[21] Crucial were the denaturation experiments of Cohen and Jardetzky[22] and McDonald and Phillips[23] which showed that the spectrum of a denatured protein was, to a good first approximation, the sum of the spectra of the constituent amino acids. In particular, our study of lysozyme denaturation revealed differences between the native, partially denatured (still disulfide-linked) and fully denatured (reduced) forms of the enzyme. The partially denatured form—now called the molten globule—has become a favorite object in studies of protein folding. Denaturation studies on selectively deuterated staphylococcal nuclease provided additional decisive evidence.[16] It was thus clearly established that the protein NMR spectrum contained information on the secondary and tertiary structure of the native protein.

From the beginning, an important task was to identify specific questions that NMR could answer in protein chemistry and to design prototype experiments to demonstrate feasibility. Spectroscopists often tend to forget that only a small fraction of the techniques they invent are relevant to the study of macromolecules—and that the selection process is not straightforward. The technique must be matched to the biological question. Most important for protein function was a description of conformational transitions and of the behavior of ligands at active sites—neither easily studied by crystallography. At the relatively low spectrometer resolution and high cost of isotopic spectral editing, a complete structural analysis of a protein by NMR remained beyond reach in the 1960s and 1970s. Our own efforts therefore centered on the study of partial structures—the structures of drug and enzyme inhibitor complexes. Relaxation measurements were used to define the geometry of small molecular weight ligands such as penicillin,[24] the sulfonamides,[25] or acetylcholine derivatives[26] in a protein binding site. More complete structures of the complexes of nucleotide inhibitors with pancreatic ribonuclease[27] and staphylococcal nuclease[16] could be deduced from the patterns of chemical shift changes in both the ligand and in protein side chains. A reliable geometry could be obtained only with prior knowledge of the crystal structure of the free protein. Nevertheless, the structures deduced were shown to be correct by subsequent crystallographic and structural NMR studies. In the case of ribonuclease they provided us with a solid structural basis for proposing a detailed mechanism of enzyme action[28] which predicted subsequent kinetic results[29] and stood the test of time.

The importance of relaxation parameters for defining the geometry of macromolecules and their complexes was clearly understood as early as 1964. In my article in the *Advances in Chemical Physics*[7] it was pointed out that in contrast to chemical shifts and coupling constants, relaxation parameters ranked as 'the potentially most informative measurements', that cross relaxation between two protons could be measured, and the internuclear distances could be used to define geometry. This is now standard practice, but the degree to which it was considered unrealistic even six years later can best be conveyed by citing verbatim an exchange which took place at the Ciba Foundation Symposium in London in 1970 during the discussion of my paper on the structure of the nucleotide–staphylococcal nuclease complex:[30]

> F. M. Richards: Without reference to other techniques, how much information could you specify ... ? Are you able to specify distances and orientations to the other groups whose signals you can measure, or put certain limits on them?
>
> O. Jardetzky: ... In principle you can get this information if you measure relaxation times and the dependence of relaxation times on each neighbor in the vicinity.
>
> H. M. McConnell: That is an exaggeration!
>
> O. Jardetzky: It is (only) an exaggeration in the sense that it is a diabolically difficult undertaking. It is a very hard thing to do, but if you did have just two protons, you could make a good guess about the distance between them. Admittedly nobody has tried to do this.

Everyone was doing it 20 years later.

To acknowledge reality, the 1964 article[7] not only summarized the principles of obtaining structural information but also defined the difficulties of interpreting NMR parameters measured on macromolecules. These difficulties are still with us. The relaxation equations proposed then for the study of proteins and protein complexes for the first time included individual spectral density functions for each internuclear vector, and internuclear distances averaged over time, to take into account internal mobility and the resulting averaging of geometric parameters. The formulation made it clear that interpretation of relaxation measurements on molecules with many degrees of internal motional freedom is a severely underdetermined problem. Calculating distances from relaxation parameters—be they T_1, T_2, or NOE—is treacherous, because each parameter is a function of *both* an unknown distance and an unknown time function. Averaging brings with it additional uncertainties, and we pointed these out in 1980.[31]

Discoveries of internal motion, evident not only in relaxation parameters but also in the averaging of chemical shifts, began accumulating rapidly. The free rotation of tyrosine rings in the interior of globular proteins was first discovered in the isotope edited spectra of staphylococcal nuclease in 1968. The phenomenon was carefully studied by Campbell, Dobson, and co-workers in 1975[32] and subsequently by many others. In 1974 we were able to draw a distinction between librations and 'ring flipping' by comparing ^{13}C relaxation measurements and chemical shift averaging in parvalbumin, leading us to point out that placing a cage of six relatively rigid α-helices onto a quivering hydrophobic core conveyed conformational flexibility to an otherwise rigid molecule.[33] In the late 1970s we also demonstrated flexibility in the RNA-binding region of tobacco mosaic virus, the DNA binding region of the *lac*-repressor, and in myosin.[34] Similar observations were soon made on the pyruvate dehydrogenase multienzyme complex.[35] The general importance of dynamics, especially in nucleic acid binding regions, has only recently become apparent, as numerous additional examples began appearing in the literature.

Structural work on small proteins in the 1980s largely ignored dynamics, treating proteins and oligonucleotides as rigid spheres. The success of this first approximation for defining the protein fold has been remarkable, but the inaccuracy introduced remains undetermined. For more complex proteins, problems of structure and dynamics have to be solved simultaneously. To determine an NMR structure, we have to understand its dynamics—and to understand the

dynamics we must know the structure. This clearly requires information from methods other than NMR.

Nonetheless, efforts to obtain complete 3D structures began in the early 1970s. The 'lanthanide method' advanced by R. J. P. Williams and his colleagues[36] attracted considerable attention as it promised to provide all the distance and angular information needed for a complete protein structure determination by measuring the paramagnetic shifts and relaxation effects of lanthanide ions bound at specific sites on the protein. The method provided some useful information on the structure of calcium-binding proteins, but generally failed because of the prevalence of nonspecific ion binding sites and for theoretical reasons discussed by us in 1981.[1]

Deriving information from unperturbed protein spectra appeared more promising generally. A significant conceptual advance was the paradigm developed by W. Gibbons in 1975, combining coupling constant and NOE measurements to obtain a sequential assignment of resonances in a peptide.[37] The assignment of an NH and α-CH (and other groups) within the same residue was made from CH−CH and CH−NH coupling constants, and the proximity between NH (i) and NH (i + 1) as well as CH (i + 1) was established by a NOE, allowing for calibration of distances and assessment of the secondary structure. The Gibbons paradigm became generally known as the 'sequential assignment method' (usually cited without reference to its inventor) and proved to be the method of choice for assignment and definition of secondary structure in small proteins (MW $<$ 6−10 kD). It breaks down when overlap is too extensive or when coupling becomes unobservable at higher molecular weights. In favorable cases it can be replaced by a NOE-based paradigm, which we have devised more recently,[17] or by the heteronuclear 3D and 4D techniques developed in particular by the groups of Bax,[38] Laue,[39] and Oschkinat.[40] Still, the initial impact of NMR protein structure determination in the early 1980s was due largely to the widespread successful use of the Gibbons paradigm.

By the time Gordon Roberts and I completed our 'NMR in Molecular Biology' in the spring of 1981,[1] it was possible to formulate the general rules for NMR studies of protein structure and dynamics. Delepierre et al. had calibrated NOEs reflecting the tertiary structure of lysozyme.[41] Earlier, Kuntz et al. had pointed out that a sufficient number of imprecise distances can be a powerful constraint on possible structures.[42] Later in 1981 we proposed the first folded protein structure ever proposed solely on the basis of NMR data—that of the *lac*-repressor headpiece.[43] By 1980 we had established that the headpiece was about 70% helical and were then able to define the contact between the N- and C-terminal helices on the basis of long-range NOEs. The middle remained ill-defined until Zuiderweg et al. applied the Gibbons paradigm and achieved a complete sequential assignment and definition of the secondary structure in 1983.[44] This allowed us to complete the model which was published in 1984.[45] In 1985, Kaptein et al. published the refinement of a similarly handbuilt model by restrained molecular dynamics, unfortunately with no reference to our prior work.[46] The new fashion was to regard model building as an inadequate method for defining NMR structures. However, when a careful comparison was made between the handbuilt model and structures calculated by other methods (in part provided by the Kaptein group), the backbone folds were identical and the average RMSD of atomic position between any of them was less than 2.5 Å—a typical scatter for modest data sets attainable at that time.[47] The lesson to be learned from this is that computational methods may improve the fit within the structure, but the essential step in deriving a structure from NMR distance constraints is model building.

The 1980s will probably go down in history as the gold rush era of protein NMR, with boundless enthusiasm, confusion of basic concepts, rediscovery of known facts, and aggressive staking of personal claims. The impression became widespread that 'the NMR method for protein structure determination' has just been invented and allows a 2D FT spectrum to be almost automatically transformed into a structure of crystallographic quality by simple algorithms. Yet the fundamental difference between X-ray crystallography and NMR remains standing. In crystallography one can *calculate* a structure from the diffraction pattern by Fourier transformation. In NMR no such transformation exists. Subjective judgments on the relationship between the NOE, the internuclear distance, and the relevant spectral density function must precede all model building. It is the indeterminacy of these relationships that prompted me to point out at the outset of the structure determination era[45] that in a strict sense a *determination* of a structure from spectroscopic data was impossible in principle. Still, remembering that one is dealing with approximate structures derived from approximate data, on the basis of a set of subjective assumptions, the approximation can be very good.

While the determination of small protein structures by NMR became commonplace in the mid-1980s, our attention shifted to the two major unsolved problems: (1) the development of methods for defining the structure and function of larger, functionally more interesting protein systems and (2) defining the accuracy of NMR structures. For the first we chose the *trp*-repressor (25 kD)−operator (12 kD) system from *E. coli*, controlled by the amino acid tryptophan. It was the smallest complete allosteric system available and was given to us by its discoverer, Charles Yanofsky. We could predict that the then existing methods—spectroscopic as well as computational—would fail for larger structures. The limitations of spectroscopy were overcome by resorting to extensive isotopic spectral editing. The computational problems proved more formidable. To add to the already existing distance geometry methods, originally introduced by Havel, Crippen, and Kuntz[48] and restrained molecular dynamics, introduced almost simultaneously by the groups of van Gunsteren and Karplus,[49] we developed PROTEAN and the use of optimal filtering.[50] The philosophy of PROTEAN differed from the preceding two in that it was based on an exclusion paradigm—systematically generating a set of structures and retaining all that satisfied a given set of constraints, without optimization. This has the advantage of reducing optimization bias, which for small structures may be inconsequential, but can significantly distort larger structures through the accumulation of errors, unless one begins with a reasonably accurate starting structure. To evaluate accuracy, we compared the performance of all three types of methods.[51] All three types of methods can reproduce the fold of a 'gold standard' structure to a first approximation equally well. But the mean structures calculated by different methods differed by an RMSD of about ±1 Å from each other, even though the precision of the family of structures calculated by any given method was of the order of 0.5−0.7 Å. Clearly, each method introduces its own bias and more comparisons of this type are

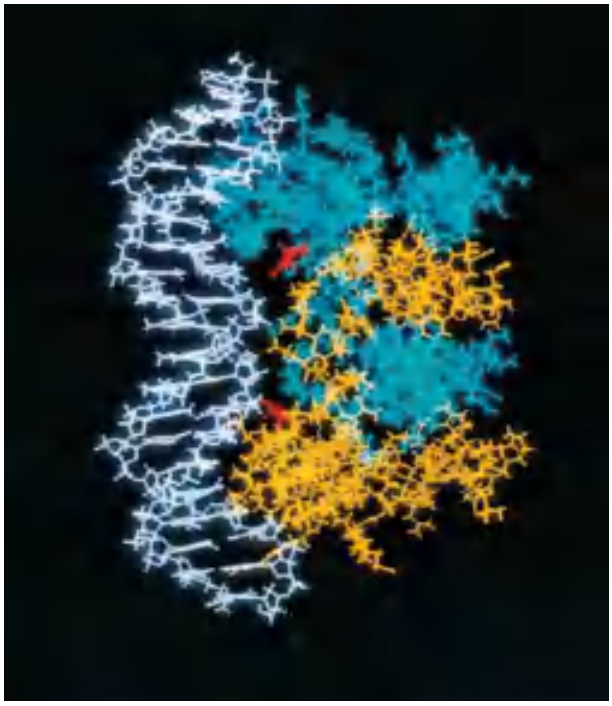

Figure 3 A three-dimensional structure of the *E. coli trp*-repressor/ODNA complex calculated from NMR experimental constraints

needed. In the meantime, we cannot claim a greater *accuracy* for NMR structures than ± 1 Å even if the *precision* appears greater.

The study of the *trp*-repressor system also brought home the old dilemma—that one must understand the dynamics of the protein before one can determine its structure by NMR, and vice versa. The protein is a dimer of two chains, consisting of six α-helices each. It binds to DNA in the presence of the corepressor tryptophan, but the ternary complex dissociates if the tryptophan ligand is removed. Only the first three and the last helices in the two chains are well defined by NMR in the free protein.[17] The fourth and fifth are well defined only in the DNA complex, where they form a helix-turn helix with most of the contacts responsible for DNA sequence recognition. Detailed study of backbone proton exchange and relaxation behavior led us to a more complicated picture. The structure of the free protein is relatively unstable. Binding of *trp* stabilizes it and especially the DNA-binding helix-turn helix, which however still remains relatively unstable—being about 90% of the time in helical and 10% in an unfolded form. Binding to DNA stabilizes it further, but the lifetime of the DNA complex remains on the same timescale as the lifetime of the helices in the DNA binding domain. The structure of the complex, the largest structure thus far determined by NMR, is shown in Figure 3. The long path from the 1957 ribonuclease spectrum to this result has justified itself.

The interplay between protein structure and protein dynamics and the potential functional role of dynamics are only now beginning to be investigated and understood. As molecular dynamics (MD) simulations of proteins became feasible in the mid-1970s, it became clear that *in principle* they could provide all the information necessary to calculate all relaxation parameters on proteins and characterize all conformational states and conformational averaging. This would allow more accurate estimates of internuclear distances on which all NMR structure determinations rest and correctly account for all averaged NMR parameters. Yet it also became increasingly clear that *in practice* this would require potentials far more accurate than any available even now and computations longer by about six orders of magnitude than any that can be carried out on the most modern computers. Clearly, *in practice*, MD will not give us an answer in the foreseeable future. The problem of structural interpretation of NMR data has therefore also been solved only in so far as motional problems and averaging can be ignored.

The best correction for fast motions we found is an empirical estimate of the spectral density functions for vectors of known length (e.g. from ^{13}C measurements for CH bonds). These could then be used for the calculation of unknown distances in the surroundings. Not quite correct, but it is better than ignoring dynamics.[52] We had explored the use of this approach in the early 1970s in our T_1, T_2, and NOE studies of carp parvalbumin.[33] The approach can be exploited to its fullest now that a complete set of sequential assignments and *experimental* values of spectral density functions can be obtained by the strategy of Peng and Wagner.[53]

It is now also becoming possible to begin to account for such experimentally determined individual spectral density functions correctly.[54] The inadequacy of simple models for describing protein or nucleic acid dynamics has been repeatedly demonstrated in the 1970s.[1] One relaxation parameter always yields a single correlation time, but seldom could one find a combination that would simultaneously account for all three—T_1, T_2, and NOE. The model-free formalism King and I introduced in 1978 rigorously defined the information content of a set of relaxation parameters, but proved unappealing because the set of calculated frequencies and normalized amplitudes could not be simply related to motional parameters without introducing information extraneous to NMR. In 1982 Lipari and Szabo[55] proposed that the first two terms of our expansion could be given physical meaning by assuming that only isotropic tumbling and fast internal motions mattered. The latter could then be described by an effective correlation time and an order parameter. Although still called model-free, this was in fact a very restrictive model. With a limited number of relaxation measurements this 'model-free' model enjoyed some initial success—but as more extensive relaxation measurements became possible, its inadequacy became evident.[54,56] Realistic specific models of protein motions based on searches of the conformational space by MD and Monte Carlo techniques can now be constructed, and a more accurate picture is beginning to emerge.

The *trp*-repressor system—where ^{1}H exchange and ^{1}H relaxation data indicate that the DNA-binding helices are unstable on the millisecond timescale and ^{15}N relaxation data indicate that on the nanosecond scale they are *not* unstable, where NOE data suggest that the helices are disordered and chemical shift data indicate that they are *not* disordered—well illustrates the complexity of NMR findings we can expect as the method becomes applicable to larger proteins with more complex functions than small globular structures or protein fragments. It may well serve as a paradigm for future work.

NMR is today a mature technology for the study of macromolecular structure and dynamics, alongside X-ray diffraction, as envisioned three decades ago. After nearly a

decade of overstatements about NMR as a structural tool at the expense of dynamics, we are returning to the basic insights about its role expressed in our book in 1981: ' ... in structural investigations of molecules in solution NMR should be regarded as a method that defines a class of possibilities more often than it permits the proof of a single structure. Interpretation of NMR findings is as much a matter of judgment as a matter of calculation. ... NMR does not derive its importance as a method in molecular biology from being a technique in which one can routinely proceed from the measurement by straightforward calculation to a definite answer. ... The importance of NMR rests rather on the fact that it provides a much greater wealth of clues on questions of structure, *dynamics and function* than other methods.'

REFERENCES

1. Full citations for this and other references given in the text by name and year only to save space can be found in O. Jardetzky and G. C. K. Roberts, *NMR in Molecular Biology*, Academic Press, New York, 1981.
2. O. Jardetzky, *A Study of Interactions of Aqueous Sodium Ion by Nuclear Spin Resonance*, Ph.D. Thesis, University of Minnesota, 1956; J. E. Wertz and O. Jardetzky, *J. Chem. Phys.*, 1956, **25**, 357; O. Jardetkzy and J. E. Wertz, *Am. J. Physiol.*, 1956, **187**, 608; O. Jardetzky and J. E. Wertz, *Arch. Biochem. Biophys.*, 1956, **65**, 569.
3. J. E. Wertz, *Chem. Rev.*, 1955, **55**, 829.
4. M. Takeda and O. Jardetzky, *J. Chem. Phys.*, 1957, **26**, 1346; C. D. Jardetzky and O. Jardetzky, *J. Am. Chem. Soc.*, 1960, **82**, 222.
5. M. Saunders, A. Wishnia, and J. G. Kirkwood, *J. Am. Chem. Soc.*, 1957, **79**, 3289.
6. O. Jardetzky and C. D. Jardetzky, *J. Am. Chem. Soc.*, 1957, **79**, 5322.
7. O. Jardetzky, *Adv. Chem. Phys.*, 1964, **7**, 499 and references therein.
8. Y. Fraenkel, G. Navon, A. Aronheim, and J. M. Gershoni, *Biochemistry*, 1990, **29**, 2617.
9. O. Jardetzky and C. D. Jardetzky, *Methods Biochem. Anal.*, 1962, **9**, 235 and references therein.
10. O. Jardetzky, N. G. Wade, and J. J. Fischer, *Nature (London)*, 1963, **197**, 183.
11. R. Ernst, in *Computational Aspects of the Study of Biological Macromolecules by NMR Spectroscopy*, ed. J. C. Hoch, et al., Plenum Press, New York, 1991, pp. 1–25.
12. C. C. McDonald and W. D. Phillips, *J. Am. Chem. Soc.*, 1967, **89**, 6332.
13. O. Jardetzky, *Proc. Int. Conf. Magn. Reson., Tokyo, Japan, 1965*, N-3-14.
14. J. L. Markley, I. Putter, and O. Jardetzky, *Science*, 1968, **161**, 1249; I. Putter, A. Barreto, J. L. Markley, and O. Jardetzky, *Proc. Natl. Acad. Sci. USA*, 1969, **64**, 1396.
15. H. L. Crespi, R. M. Rosenberg, and J. J. Katz, *Science*, 1968, **161**, 795.
16. J. L. Markley and O. Jardetzky, *J. Mol. Biol.*, 1970, **50**, 223. Other papers of this series are cited in the review by G. C. K. Roberts and O. Jardetzky, *Adv. Protein Chem.*, 1970, **24**, 447.
17. D. Zhao, C. H. Arrowsmith, X. Jia, and O. Jardetzky, *J. Mol. Biol.*, 1993, **229**, 735.
18. R. R. Ernst, G. Bodenhausen, and A. Wokaun, *Principles of Nuclear Magnetic Resonance in One and Two Dimensions*, Clarendon Press, Oxford, 1987.
19. See, for example, O. Jardetzky, W. W. Conover, G. R. Sullivan, and V. J. Basus, in *Proc. XXth Congress AMPERE, Tallinn, USSR, 1979*, and other references cited in Ch. VII of O. Jardetzky and G. C. K. Roberts, *NMR in Molecular Biology*, Academic Press, New York, 1981.
20. J. L. Markley, D. H. Meadows, and O. Jardetzky, *J. Mol. Biol.*, 1967, **27**, 25.
21. A. Nakamura and O. Jardetzky, *Proc. Natl. Acad. Sci. USA*, 1967, **58**, 2212.
22. J. S. Cohen and O. Jardetzky, *Proc. Natl. Acad. Sci. USA*, 1968, **60**, 92.
23. C. C. McDonald and W. D. Phillips, *Biochem. Biophys. Res. Commun.*, 1969, **35**, 43; C. C. McDonald and W. D. Phillips, *J. Am. Chem. Soc.*, 1969, **91**, 1513.
24. J. J. Fischer and O. Jardetzky, *J. Am. Chem. Soc.*, 1965, **87**, 3237.
25. O. Jardetzky and N. G. Wade-Jardetzky, *Mol. Pharm.*, 1965, **1**, 214.
26. A. S. V. Burgen, O. Jardetzky, J. C. Metcalfe, and N. Wade-Jardetzky, *Proc. Natl. Acad. Sci. USA*, 1967, **58**, 447.
27. D. H. Meadows, G. C. K. Roberts, and O. Jardetzky, *J. Mol. Biol.*, 1969, **45**, 491 and references therein.
28. G. C. K. Roberts, E. A. Dennis, D. H. Meadows, J. S. Cohen, and O. Jardetzky, *Proc. Natl. Acad. Sci USA*, 1969, **62**, 1151.
29. G. G. Hammes and P. B. Roberts, *J. Am. Chem. Soc.*, 1969, **91**, 1812.
30. R. Porter and M. O'Connor (eds.), *Molecular Properties of Drug Receptors, CIBA Foundation Symposium*, J. & A. Churchill, London, 1970.
31. O. Jardetzky, *Biochim. Biophys. Acta*, 1980, **621**, 227.
32. I. D. Campbell, C. M. Dobson, and R. J. P. Williams, *Proc. R. Soc. London, Ser. B*, 1975, **189**, 503; I. D. Campbell and C. M. Dobson, *Methods Biochem. Anal.*, 1979, **25**, 1.
33. S. J. Opella, D. J. Nelson, and O. Jardetzky, *J. Am. Chem. Soc.*, 1974, **96**, 7157.
34. O. Jardetzky, K. Akasaka, D. Vogel, S. Morris, and K. C. Holmes, *Nature (London)*, 1978, **273**, 564; N. Wade-Jardetzky, R. P. Bray, W. W. Conover, O. Jardetzky, N. Geisler, and K. Weber, *J. Mol. Biol.*, 1979, **128**, 259; S. Highsmith, K. Akasaka, M. Konrad, R. Goody, K. Holmes, N. Wade-Jardetzky, and O. Jardetzky, *Biochemistry*, 1979, **18**, 4238.
35. R. N. Perham, H. Duekworth, and G. C. K. Roberts, *Nature (London)*, 1981, **292**, 474.
36. I. D. Campbell, C. M. Dobson, R. J. P. Williams, and A. V. Xavier, in *Electron Spin Resonance and Nuclear Magnetic Resonance in Biology and Medicine and Magnetic Resonance in Biological Systems*, eds. S. E. Lasker and P. Milvy, *Ann. N.Y. Acad. Sci.*, 1973, **222**, 163.
37. W. A. Gibbons, D. Crepaux, J. Delayre, J.-J. Dunand, G. Hajdukovic, and H. R. Wyssbrod, in *Peptides: Chemistry, Structure and Biology*, eds. R. Walter and J. Meienhofer, Ann Arbor Sci., New York, 1976, p. 127.
38. L. E. Kay, M. Ikura, R. Tschudin, and A. Bax, *J. Magn. Reson.*, 1990, **89**, 496; L. E. Kay, M. Ikura, G. Zhu, and A. Bax, *J. Magn. Reson.*, 1991, **91**, 422.
39. W. Boucher, E. D. Laue, S. L. Campbell-Burk, and P. J. Domaille, *J. Biomol. NMR*, 1992, **2**, 631; S. L. Campbell-Burk, P. J. Domaille, M. A. Starovasnik, W. Boucher, and E. D. Laue, *J. Biomol. NMR*, 1992, **2**, 639.
40. H. Oschkinat, C. Griesinger, P. J. Kraulis, O. W. Sorensen, R. R. Ernst, A. M. Gronenborn, and G. M. Clore, *Nature (London)*, 1988, **332**, 374; H. Oschkinat, T. A. Holak, and C. Cieslarx, *Biopolymers*, 1991, **31**, 699.
41. M. Delepierre, C. M. Dobson, J. C. Hoch, E. T. Olejniczak, and F. M. Poulsen, in *Abs. 9th Int. Conf. Magn. Reson. Bio. Syst.*, 1980, p. 46.
42. I. D. Kuntz, G. M. Crippen, and P. A. Kollman, *Biopolymers*, 1979, **18**, 939.
43. A. A. Ribeiro, D. Wemmer, R. P. Bray, and O. Jardetzky, *Biochim. Biophys. Res. Commun.*, 1981, **99**, 668.

44. E. R. P. Zuiderweg, R. Kaptein, and K. Wüthrich, *Eur. J. Biochem.*, 1983, **137**, 279.
45. O. Jardetzky, in *Progress in Bioorganic Chemistry and Molecular Biology*, ed. Yu. A. Ovchinnikov, Elsevier Science, Amsterdam, 1984, p. 55.
46. R. Kaptein, E. R. P. Zuiderweg, R. M. Scheek, R. Boelens, and W. F. van Gunsteren, *J. Mol. Biol.*, 1985, **182**, 179.
47. R. B. Altman, R. Pachter, and O. Jardetzky, *J. Appl. Magn. Reson.*, 1993, **4**, 441.
48. I. D. Kuntz, J. F. Thomason, and C. M. Oshiro, in *Nuclear Magnetic Resonance, Part B: Structure and Mechanisms, Methods of Enzymology 177*, eds. N. J. Oppenheimer and T. L. James, Academic Press, New York, 1989, p. 159.
49. R. M. Scheek, W. F. van Gunsteren, and R. Kaptein, in *Nuclear Magnetic Resonance, Part B: Structure and Mechanisms, Methods of Enzymology 177*, eds. N. J. Oppenheimer and T. L. James, Academic Press, New York, 1989, p. 204.
50. R. B. Altman and O. Jardetzky, in *Nuclear Magnetic Resonance, Part B: Structure and Mechanisms, Methods of Enzymology 177*, eds. N. J. Oppenheimer and T. L. James, Academic Press, New York, 1989, p. 218.
51. Y. Liu, D. Zhao, R. Altman, and O. Jardetzky, *J. Biomol. NMR*, 1992, **2**, 373.
52. O. Jardetzky and A. Lane, in *Physics of NMR Spectroscopy in Biology and Medicine*, ed. B. Maraviglia, North-Holland Physics, Amsterdam, 1988, p. 267.
53. J. W. Peng and G. Wagner, *J. Magn. Reson.*, 1992, **98**, 308.
54. Z. Zheng, J. Czaplicki, and O. Jardetzky, *Biochemistry*, 1995, **34**, 5212.
55. G. Lipari and A. Szabo, *J. Am. Chem. Soc.*, 1982, **104**, 4546.
56. R. Powers, G. M. Clore, S. J. Stahl, P. T. Wingfield, and A. Gronenborn, *Biochemistry*, 1992, **31**, 9150; O. Jardetzky, *Chemtracts: Biochem. Mol. Biol.*, 1992, **3**, 301.

Biographical Sketch

Oleg Jardetzky. *b* 1929. B.A., 1950, Chemistry & Biology, Macalester College, St. Paul MN, M.S., 1953, Physiology & Physical Chemistry, M.D., 1954, Medicine, Ph.D., 1956, Physiology & Physical Chemistry, University of Minnesota, St. Paul, MN. National Research Council Fellow, Department of Chemistry, Caltech, 1956–57; Associate in Pharmacology, 1957–59, Assistant Professor of Pharmacology, Harvard Medical School, 1959–66; Director, Department of Biophysics & Pharmacology, Merck, Sharp & Dohme, 1966–68; Executive Director of Basic Medical Science, Merck Institute for Therapeutic Research, 1968–69; Professor of Pharmacology, 1969– present, Director, Stanford Magnetic Resonance Laboratory, Stanford University, 1975–present. Approx. 230 publications. Current research interests: structure dynamics and function of proteins involved in regulatory processes; the mechanism of action of *trp*-repressor; use of high-resolution NMR spectroscopy and other physical methods to define mechanisms of conformational transitions and protein folding.

Jeener, Jean: Reminiscences about the Early Days of 2D NMR

Jean Jeener

Université Libre de Bruxelles, Brussels, Belgium

When I started an NMR research group in Brussels in the early 1960s, my aim was to perform clear experiments in connection with the major theoretical effort of the Prigogine group (also in Brussels) on the statistical mechanics of irreversible processes. For this purpose, we started looking at NMR (and pure NQR) in 'simple' solids (LiF, CaF_2, gypsum, Pb, $NaClO_3$ ...) using coherent pulse techniques, and spent much time building spectrometers and working on spin thermodynamics and spin–spin coupling energy. Our favorite techniques were to transform the order available under complete equilibrium conditions (Zeeman or pure quadrupolar) into spin–spin order via a pair of pulses (appropriately timed and phase-shifted: the 'Jeener–Broekaert' sequence), and to look at the state of the spin system somewhat later on by means of a third pulse and quadrature detection of the FID.[1–3]

In the late 1960s, many experiments had been performed in different laboratories on liquids and solids in which the spin response was studied after a sequence of two (or more) pulses, with the variable separation between these pulses (or the duration of a pulse) as the essential parameter. A well-known early example of such an experiment with a strong flavor of today's 2D NMR is the observation of J couplings in liquids by Hahn and Maxwell in 1952.[4] With this in mind, one may wonder why the double Fourier transform was not used earlier as a systematic tool for processing the data from experiments involving multiple time delays. First, there were the difficulties which slowed down the development of 'single' Fourier transform methods: no phase sensitive detection in early pulse spectrometers (hence, nonlinear detection), long dead times, slow ADC, no computer in the laboratory, etc. Also, multiple pulse experiments seemed so complicated, particularly in solids, that one was tempted to treat the various delays separately whenever possible.

Two souvenirs come back to my mind, illustrating the generally incomplete intuitive understanding of Fourier spectroscopy at a time where this was already the accepted technique in high-resolution NMR. The first begins with a lecture which I gave at the Waterloo (Ontario) NMR Summer School, in 1969 or 1971, advocating the use of quadrature detection in solid NMR, in which I casually mentioned that quadrature detection would improve the signal-to-noise ratio by a factor of $\sqrt{2}$ in high-resolution FT NMR. The next Sunday evening, at the opening of the NMR Gordon Conference, I was caught in a circle of excited NMR friends who strongly opposed this latter 'Waterloo' statement on the mistaken ground (as I recall) that the same noise was fed to both phase sensitive detectors, hence the corresponding outputs had to be strongly correlated. At this point, I realized the difficulty of 'proving' something which looked obvious to me, and I was glad to feel the moral support of people like Hahn, Waugh, and Redfield, watching the event from a distance, while I was struggling to defend my views. The second is the surprising unwillingness of the instrument manufacturers to provide quadrature detection on their NMR pulse spectrometers for many years, in spite of strong insistence from many physicists.

At that time I became interested in extending our work on protons in gypsum[5] into a study of molecular motion in liquid crystals by measurements of the relaxation matrix (mainly spin–lattice relaxation). For this purpose I tried to cook up a pulse scheme which would give results of the type presently given by NOESY, making dreams resembling stochastic NMR. This led to the design and construction of a fancy digitally controlled pulse generator, but was otherwise in vain except for the impression that if a suitable scheme emerged it would be plagued by the coherent response caused by the multiple pulses. Almost in despair, I started investigating this latter problem with the help of Gerrit Alewaeters,[6,7] initially on the simple case of the standard AB spectrum in liquids. This soon led to the general proposal of 2D FT NMR spectroscopy in the simple case of homonuclear COSY without phase cycling. We tried to observe the effect experimentally on ethylbenzene, spending weekends working with the rather primitive FT spectrometer available in organic chemistry at our university. Due to the bad phase stability of this spectrometer and to our total lack of practice of high-resolution NMR, Gerrit Alewaeters could only observe some of the strongest cross peaks of the 2D spectrum with a signal-to-noise ratio just high enough to confirm that our quantum mechanical predictions were correct (not really a surprise ...), but too low to make the new technique look very usable. Formal publication was deferred until cleaner experimental confirmation would be available, but I kept spreading the idea by personal contacts, lectures (probably for the first time at the AMPERE Summer School in Baško Polje in 1971), and by circulating 'unpublished' notes written in November 1971.[8] Soon, Richard Ernst let me know that his co-worker Baumann had brought the 2D FT idea back from Baško Polje to Zürich, and that the Zürich group intended to work on it. As it turned out, one of our recurrent delights in Brussels for a number of years has been receiving news from Zürich about the progress of 2D NMR, both experimental and theoretical. It was also a pleasure to learn about the new 2D FT ideas developing in many other groups.

In 1977, Richard Ernst was describing the many different ways of using 2D NMR in such a clear and systematic presentation that it soon struck me that my original goal, investigating spin–lattice relaxation, was absent from the list but could be implemented 'easily' (by the method now called NOESY, much simpler than my original dreams). I mentioned this to Ernst at the NMR Gordon Conference. He asked whether we intended to develop the method in Brussels; the answer was 'no' for lack of practice and of suitable instrumentation, and I was delighted to accept the proposal of developing NOESY as a joint project between Zürich and Brussels.[9]

Since that time, I have always kept a part-time interest in 2D NMR and its variants. I learned the 'superoperator' technology in an attempt to provide a suitable tool for 2D peak-shape analysis,[10] and Marianne Koenig demonstrated that this is indeed a viable method for the study of the rate of chemical reactions under favorable circumstances.[11] More recently, I have become interested in the collective effects of radiation damping and dipolar field in 2D NMR, and I

am participating in the present controversy about the suitable theoretical presentation of these effects.

REFERENCES

1. J. Jeener and P. Broekaert, *Phys. Rev.*, 1967, **157**, 232.
2. P. Broekaert and J. Jeener, *Phys. Rev.*, 1977, **B15**, 4168.
3. C. Segebarth and J. Jeener, *Phys. Rev.*, 1984, **B29**, 1176.
4. E. L. Hahn and D. E. Maxwell, *Phys. Rev.*, 1952, **88**, 1070.
5. H. Eisendrath, W. Stone, and J. Jeener, *Phys. Rev.*, 1978, **B17**, 47; H. Eisendrath and J. Jeener, *Phys. Rev.*, 1978, **B17**, 54.
6. G. Alewaeters, *Licenciaat Verhandeling*, Vrije Universiteit Brussel, 1969 (unpublished).
7. G. Alewaeters, *Thesis*, Vrije Universiteit Brussel, 1976 (unpublished).
8. J. Jeener, The unpublished Baško Polje (1971) lecture notes about two-dimensional NMR spectroscopy in *NMR and more, in the honour of Anatole Abragam*, Les Editions de Physique, Paris, 1994.
9. J. Jeener, B. H. Meier, P. Bachmann, and R. R. Ernst, *J. Chem. Phys.*, 1979, **71**, 4546.
10. J. Jeener, *Adv. Magn. Reson.*, 1982, **10**, 1.
11. Marianne Koenig and J. Jeener, *J. Chem. Phys.*, 1989, **90**, 2959.

Biographical Sketch

Jean L. Jeener. *b* 1931. D.Sc., 1958, Chemistry, University of Brussels (supervisor I. Prigogine). Postdoctoral work at Harvard University (with N. Bloembergen). Professor of Physics, University of Brussels, 1960–present. Approx. 32 publications. Current research topics: dipolar field and radiation damping in high-resolution liquid NMR, pulse spectroscopy with fully quantized field, dynamical and statistical aspects of solid state NMR.

Johnson, Charles S. Jr.: The Evolution of Ideas about Optical Analogies to PFGNMR and the Visualization of PFGNMR Experiments

Charles S. Johnson, Jr.

University of North Carolina, Chapel Hill, NC, USA

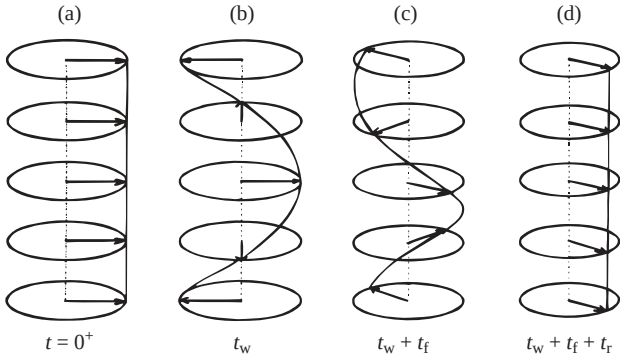

Figure 1 Magnetization helices. The isochromats (vectors) represent the magnetization of evenly spaced layers of the sample in the direction of the gradient. (Taken from Ref. 6)

In the period 1974–84 we were concerned primarily with dynamic light scattering (DLS) and holographic relaxation spectroscopy (HRS) for the measurement of diffusion and electrophoretic drift. The HRS experiments are particularly easy to visualize.[1] Concentration patterns (or gratings) of photoproducts are created by photoexcitation with crossed laser beams, and the patterns are smeared out by diffusion and translated by flow. The time evolution of a pattern is detected directly by monitoring the efficiency with which it diffracts light from a weak probe laser beam. However the experiments are not easy and the amount of information obtained is limited. Furthermore, photochemical reactions often complicate the interpretation of data.[2]

We also worked with complementary pulsed field gradient NMR (PFGNMR) experiments,[3] but we did not make use of the underlying similarities between DLS and PFGNMR. Of course, I had seen Mansfield's paper on NMR diffraction and microscopy,[4] and I knew that the magnitude of the optical scattering vector $\boldsymbol{q}$ and the area of the gradient pulse ($\gamma g \delta$) played similar roles; but my grasp of the optical NMR analogy was far from complete. What was needed was time for reflection. It was fortunate that I was able to begin a sabbatical leave in January 1985 in the laboratory or R. R. Vold and R. L. Vold (Bob and Gitte) at La Jolla. In that pleasant atmosphere I spent half of my time writing papers on HRS and the other half on computer simulations of PFGNMR experiments involving flow.

A particularly important instance for me occurred when Alex Pines invited me to Berkeley to give a seminar on HRS. He picked me up at the Oakland airport, and we talked about light scattering and NMR on the way back to Berkeley. I clearly remember him commenting that a spin echo is analogous to a diffraction spot. We talked about short T_2 storage experiments and stimulated echoes. I am not sure that I actually learned anything new in that conversation, but it focused my thoughts on the connections between PFGNMR, NMR imaging, and optical diffraction.

Meanwhile back in Chapel Hill, Tim Saarinen started work on PFGNMR as the, somewhat isolated, NMR person in my light scattering laboratory. The goal of his thesis project was to combine electrophoresis with PFGNMR to develop electrophoretic NMR (ENMR). This experiment was expected to be similar to electrophoretic light scattering (ELS) but with the advantage of selectivity based on chemical shifts. The ENMR project went slowly because we did not have a dedicated NMR spectrometer; and we had to share the departmental Bruker WM-250, an instrument that seemed to have more down time than up time. Tim finally resorted to carrying his gradient probe and current driver to a spectrometer 15 miles away at the Research Triangle Institute.

This was an exciting (and frustrating) time in the laboratory as Tim designed and tried to interpret gradient experiments while learning the theory of PFGNMR. He had a new idea almost every day, and he forced me to think hard about gradients and NMR. We often argued about theory and interpretation, and discovered that the new idea was an old idea in disguise, e.g. z magnetization gratings (new) and the stimulated echo experiment (old). However, a very useful picture of the PFGNMR experiment evolved. This picture was based on the idea that magnetization gratings can be created that are analogous to the concentration gratings in HRS. In fact, Tim obtained an image of a magnetization grating and used it to calibrate a magnetic field gradient. I do not remember the exact sequence of events, but I believe that Tim was the first to talk about magnetization ribbons composed of isochromats for different layers of a sample after a 90 ° rf pulse, and the twisting of the ribbons into helices by constant magnetic field gradients. He presented the transient magnetization gratings (TMG) for the measurement of diffusion and flow at the 1987 ENC[5] and we published the details in 1988.[6]

An illustration of the winding and unwinding of magnetization helices from that paper is shown in Figure 1. The sample is prepared by a 90 ° rf pulse at $t = 0$. This is followed by a gradient pulse of duration t_w that sensitizes the magnetization to translational motion of the spins. Diffusion and flow during the time interval t_f produce attenuation and translation of the helix, and sometime during this interval a 180 ° rf pulse changes the signs of the phase angles. A second gradient pulse then refocuses the isochromats to form an echo at time $t_w + t_f + t_r$. The Fourier transform of the echo signal with respect to t_r produces an image of the magnetization grating.[6] The *spatial manipulation of magnetization* (SPAMM) method now used in MRI for the measurement of flow is an important application of TMGs.[7]

The winding up of helices and the effects of diffusion and flow on helical magnetization patterns captures the essence of PFGNMR, and provides a better illustration for constant gradients (linear magnetic field change) than the spherical plots traditionally used in this field. This intuitive picture of helices or spirals is also useful. For example, Paul Callaghan

told me that he thought of *modulus addition through spatially separated echo spectroscopy* (MASSEY) after seeing the pictures of helices being unwound.[8] In fact, the magnetization ribbons and their behavior under the influence of rf pulses and gradients provide insight about the essential features of all gradient experiments.

It turns out that the stimulated echo (STE) experiment with a constant gradient is directly analogous to diffraction by a transmission grating.[9] The first two 90 ° rf pulses in the presence of a magnetic field gradient prepare a spatial grating of the z components of nuclear magnetization. The third 90 ° rf pulse then converts the z grating into a grating of transverse magnetization. It is this planar cosinusoidal pattern that is twisted by a gradient to produce the stimulated echo, and the vector addition of isochromats to form the echo[10] is similar to the addition of electric field vectors to produce a diffraction spot.[11] The wonderful thing about PFGNMR is that all of the lines in the NMR spectrum can be unraveled from the echo to reveal their associated diffusion coefficients and flow rates.[12] This forms the basis of 2D ENMR[13,14] and the more recent diffusion-ordered 2D NMR (DOSY)[15] that were outgrowths of the transient gradient idea in this laboratory.

I hasten to add that the diffraction analogy was stressed by Mansfield in his first paper on NMR imaging[16] and optical analogies have influenced many others working in magnetic resonance imaging (MRI).[17] The idea that a single rf pulse can produce an echo for a layered sample was clear from imaging experiments. Also, in retrospect, the pioneering work of Tanner and Stejskal,[18] especially as it related to restricted diffusion, is filled with analogies to diffraction. However, I am not aware of the use of gratings and helices in the interpretation of PFGNMR diffusion and flow experiments prior to Saarinen's work. Of course, all of this appears obvious and even trivial now. It really is remarkable that NMR imaging was not discovered until 20 years after Hahn's papers on free induction and spin echoes.[19,20]

RELATED ARTICLES

Diffusion and Flow in Fluids; Diffusion Measurements by Magnetic Field Gradient Methods; Electrophoretic NMR

REFERENCES

1. H. J. Eichler, P. Gunter, and D. W. Pohl, *Laser-induced Dynamic Gratings*, Springer-Verlag, Berlin, 1986.
2. K. W. Rhee, D. A. Gabriel, and C. S. Johnson, Jr., *J. Phys. Chem.*, 1984, **88**, 4010.
3. L. S. Lever, M. S. Bradley, and C. S. Johnson, Jr., *J. Magn. Reson.*, 1986, **68**, 335.
4. P. Mansfield and P. K. Grannell, *Phys. Rev.*, 1975, **B12**, 3618.
5. T. R. Saarinen and C. S. Johnson, Jr., *Abs. 28th Exp. NMR Conf., Asilomar, Pacific Grove, CA, 1987*, WF78.
6. T. R. Saarinen and C. S. Johnson, Jr., *J. Magn. Reson.*, 1988, **78**, 257.
7. L. Axel, and L. Dougherty, *Radiology*, 1989, **171**, 841.
8. P. T. Callaghan, *J. Magn. Reson.*, 1990, **88**, 493.
9. J. E. Tanner, *J. Chem. Phys.*, 1970, **52**, 2523.
10. C. S. Johnson, Jr., in *NMR Probes of Molecular Dynamics*, R. Tycko, Kluwer, Dordrecht, The Netherlands, 1994, p. 454.
11. R. P. Feynman, *QED: The Strange Theory of Light and Matter*, Princeton University Press, Princeton, NJ, 1985.
12. T. L. James and G. G. McDonald, *J. Magn. Reson.*, 1973, **11**, 58.
13. C. S. Johnson, Jr.and Q. He, *Adv. Magn. Reson.*, 1989, **13**, 131.
14. K. F. Morris and C. S. Johnson, Jr., *J. Am. Chem. Soc.*, 1992, **114**, 776.
15. K. F. Morris and C. S. Johnson, Jr., *J. Am. Chem. Soc.*, 1993, **115**, 4291.
16. P. Mansfield and P. K. Grannell, *J. Phys. C*, 1973, **6**, L422.
17. P. T. Callaghan, *Principles of Nuclear Magnetic Resonance Microscopy*, Oxford University Press, Oxford, 1991.
18. J. E. Tanner and E. O. Stejskal, *J. Chem. Phys.*, 1968, **49**, 1768.
19. E. L. Hahn, *Phys. Rev.*, 1950, **77**, 297.
20. E. L. Hahn, *Phys. Rev.*, 1950, **80**, 580.

Biographical Sketch

Charles S. Johnson, Jr. *b* 1936. B.S., 1958, Georgia Institute of Technology, Ph.D., 1961, Massachusetts Institute of Technology (supervisor John Waugh). NAS-NRS Postdoctoral fellow and Instructor at Illinois (with Herb Gutowsky). Faculty member Yale University 1962–67, University of North Carolina, Chapel Hill, 1967–present. Research interests include dynamic light scattering (DLS), electrophoretic NMR, diffusion-ordered 2D NMR, and applications of DLS and NMR to complex liquid mixtures.

Johnson, LeRoy F.: My Early Days in NMR Spectroscopy

LeRoy F. Johnson
Cupertino, CA, USA

My career in NMR began in July 1957 when I was hired by Varian Associates in Palo Alto. I was to be an applications chemist working for Jim Shoolery in Martin Packard's instrument division research group. By then, Varian had developed the NMR product line to the level of an HR-40 instrument, which consisted mainly of a water-cooled electromagnet with 1.5 kV, 1 A current-regulated power supply, galvanometer/flux-stabilizer system, slow-sweep unit, rf unit, spinning sample tube probe, and a 6-in. strip chart recorder. Not having the benefit of field shim coils or even a ratchet magnet bender, resolution was optimized by moving the probe in/out and up/down using a two-axis screw drive probe holder. This optimizing became a daily chase in search of the 'sweet spot' as the room temperature made its diurnal change in the non-air-conditioned lab.

The HR-40 grew into the HR-60 and refinements such as magnet cooling water temperature control, magnet thermal insulation, and field shim coils improved long-term stability and provided a higher level of performance with greater sample throughput.

Short-term stability was still a problem, and it was not until the A-60 came into existence in 1961 that a new level of performance was achieved with the use of an NMR lock signal. An external sample of water in the A-60 probe provided a signal which could be used to tie together magnetic field and rf frequency fluctuations. This field/frequency lock provided a very great increase in spectrometer stability, and for the first time permitted scans to be plotted on precalibrated chart papers using a flat-bed recorder.

The new level of stability also provided some improvement in sensitivity, since it was now possible to sweep more slowly through the spectrum while using more rc filtering to remove higher frequency noise components. However, owing to the presence of what amounts to baseline wander, it was not possible to gain much sensitivity with the slow sweep method.

In the summer of 1962, Dr. Leland Allen of Princeton University Chemistry Department visited the Varian applications lab in order to try out a new method for sensitivity improvement. He proposed to increase the signal-to-noise ratio by using repetitive scans through a spectral region using normal sweep rates or even somewhat faster than normal. Results from each scan would be converted from the voltage that was normally sent to the plotter to counts through use of a voltage-to-frequency converter. It was necessary then to separate the spectral region into discrete channels, and somehow to store the counts obtained from each scan. The NMR signals would *coherently* add as counts from each scan were added into each channel. Random noise would also add, but *incoherently*. The result would be an increase in signal-to-noise proportional to the square root of the number of scans.

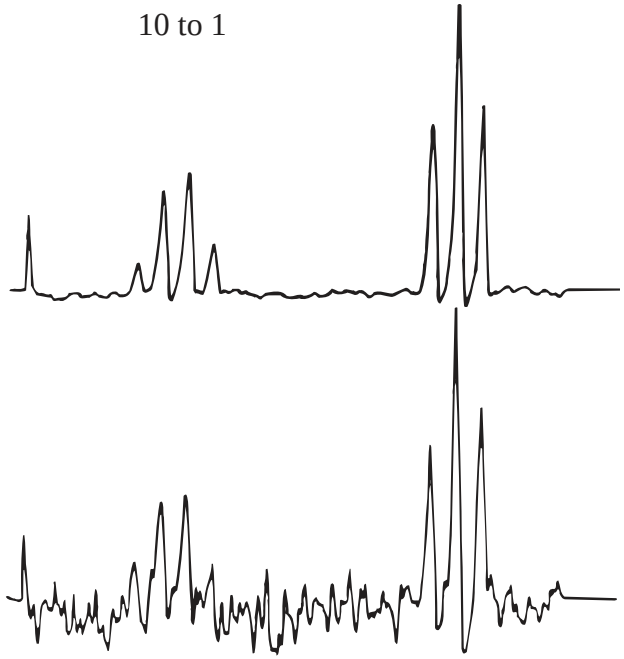

Figure 1 Top: Normalized sum of 100 sweeps of 0.2% ethylbenzene in CCl_4. Bottom: A single 4-min trace with a Varian A-60 spectrometer

A device well-suited to the task was then available from the Mnemotron Company, a subsidiary of Technical Measurements Corp. The CAT (computer of average transients) model 400 combined a voltage-to-frequency converter, 400 channel analyzer, timing circuits, a digital-to-analog converter, and a small oscilloscope display in one package. Repetitive sweeps through the spectral region of interest were made by appropriately setting the A-60 sweep width, sweep rate, and offset adjustments and then repeating the forward scan and quick back scan functions by using microswitches which would be tripped as the recorder arm moved and generated the sweep. In order to initiate data accumulation reliably a sideband from a TMS signal was generated by a tunable audio oscillator which would be triggered off as soon as data accumulation started. Part of my contribution to the project was the design and construction of the triggering circuitry to control all this, resulting in what came to be known as the CAT box. Counts stored in each channel were converted back to voltage suitable for output to the small oscilloscope or to the A-60 plotter by the digital-to-analog converter.

We were able to demonstrate that as much as a factor of 50 in signal-to-noise improvement could be achieved using overnight data accumulations. Figure 1 is taken from our communication describing the method.[1]

The method was refined and led to the development of the Varian C-1024 time averaging computer with 1024 channels and built-in voltage sweep ramp with adjustable fly-back rate. This accessory was ultimately connected to different makes and models of NMR spectrometers, and chemists were soon exploiting the benefit of digitized NMR spectra.

Digitization of free induction decays generated by pulsed rf excitation followed by Fourier transformation was yet to come.

REFERENCES

1. L. C. Allen and L. F. Johnson, *J. Am. Chem. Soc.*, 1963, **85**, 2668.

Biographical Sketch

LeRoy F. Johnson. *b* 1933. B.S., 1954, M.S., 1956, Chemistry, Oregon State University. Applications chemist and manager, Applications Laboratory, Varian Associates, 1957–72. Vice-President, Research, Nicolet Magnetics Corp., 1972–83. Senior scientist and Manager, Analytical NMR, GE NMR Instruments 1983–92. Analytical NMR Manager, Bruker Instruments, Inc., Fremont, CA, 1992–94. Currently, NMR Consultant, Cupertino, CA. Approx. 80 publications dealing with a wide variety of NMR applications.

Jonas, Jiri: NMR and High Pressure

Jiri Jonas

University of Illinois at Urbana-Champaign, Urbana, IL, USA

Looking at the title of this article, one could conclude that I want to discuss the highly competitive way we do NMR research these days. In spite of a strong temptation to do so, however, I will describe instead my attempts to use pressure as an experimental variable in NMR experiments. Before I start my story, I would like the reader to know that my initial motivation to enter the magnificent field of NMR was not completely pure. We have to go back to 1959 in Czechoslovakia to understand the situation. I figured that, because no respectable high-resolution NMR was then done in the former Soviet Union and other Eastern-bloc countries, NMR spectroscopy would be my ticket to the West and preferably to the mecca of all displaced persons—the United States. It really did work!

Thanks to a prominent organic chemist from the University of Illinois, Roger Adams, who visited our neophyte NMR laboratory in Prague, I was lucky to land in Herb Gutowsky's laboratory at the University of Illinois at Urbana-Champaign in 1963 and started to do NMR spectroscopy seriously. I enjoyed myself very much, as I was contemporary with Adam Allerhand, Nevil Boden, Joe Deck, Bill Derbyshire, Dave Vanderhart, Bob Vold, and many other great students and postdoctoral students in Gutowsky's group. I still remember the NMR course given by Charlie Slichter in the Department of Physics and, I may add, this course is even now, after 30 years, required for my own graduate students. My very first NMR experiments[1–3] were carried out on high-resolution NMR Varian spectrometers, models A-60 and DP-60. In particular, the shimming of the DP-60 was sometimes quite an adventure. I can well recall the struggles to achieve the best resolution on the DP-60. The use of 'magnet cycling', especially the use of a mechanical field trimmer, was an art that required a lot of practice to master. These procedures for attaining a good resolution on an electromagnet are well described in a 1960 monograph published by Varian Associates.[4]

After several years of doing high-resolution NMR spectroscopy, I was looking for an industrial job, but to my surprise was offered a position as an assistant professor in the Department of Chemistry at the University of Illinois in 1966. I still remember when the Head of the Department of Chemistry and Chemical Engineering, Herb Carter, offered me the position. As a start-up package there was no NMR instrument dedicated for my use, but I was offered a sum of $8000. Carter told me not to use these funds for a summer salary and also advised me not to spend it all in one place! After some soul searching, I purchased a Tektronix storage oscilloscope and the departmental electronic shop built a trapezoidal sweep generator for me; I was on my way to measuring relaxation times via the adiabatic fast passage (AFP) technique.[5] For my work I was using a departmental Varian DP-60 high-resolution NMR spectrometer either at night or on weekends, whenever this instrument was not used for routine service.

For the benefit of the current generation of NMR researchers, I may add that extracting a single T_1 value represented a laborious process. First, I had to calibrate the H_1 field and the sweepwidth and determine whether the AFP conditions were satisfied.[5] Then I had to record several oscilloscope traces for different settings of the waiting time. In spite of the lengthy procedures to generate the T_1 data, I succeeded with the help of an undergraduate student, Tom Digenarro, in finishing several NMR studies of the dynamics of motion in polyatomic molecular liquids.[6–8]

These studies dealt with anisotropic reorientation of selectively deuterated methylacetylenes[8] and phenylacetylenes[7] in the liquid state. Of particular interest was the finding that for methylacetylene-d_1 the dipole–dipole interactions provide the dominant relaxation mechanism for methyl proton relaxation at lower temperatures, whereas at higher temperatures the contribution of the spin–rotation interactions could be detected. This finding led us to systematic experiments on liquids where the spin–rotation interactions represent a major relaxation mechanism.[9–13] The reason for my interest in spin–rotation interactions in liquids was related to the fact that, by studying nuclei relaxed by spin–rotation interactions, one can learn about angular momentum correlation times, which together with the knowledge of reorientational correlation times permit a more detailed characterization of the nature of molecular motions in liquids; for example, one can find out whether one is dealing with a small-step or large-step rotational diffusion.

Since I intended to carry out systematic studies of the dynamic structure of liquids, I realized that any serious experimental attempts to characterize the molecular dynamics in a liquid must include the separation of the effects of density and temperature on molecular motion. Most NMR studies of liquids have used temperature as the only experimental variable, while pressure was left constant, usually at atmospheric pressure. Such studies probe only a narrow region of the liquid state since, for any given temperature, a liquid can exist over a range of densities. The use of pressure provides another dimension over which to investigate the liquid system. It is important to realize that changing the temperature at constant pressure affects molecular motion in two distinct ways: not only is the average kinetic energy of the molecule changed, but there is always an accompanying change in the average volume available for the motion of the molecule. If one uses both pressure and temperature as experimental variables in an NMR experiment, only then can one separate the effects of density and temperature on molecular motion.

At first it would appear that the change in density for a liquid over the typical experimental range ($\sim$100°C) is insignificant; however, for a molecular liquid, an increase of 30°C requires the pressure to be increased approximately 40 to 60 MPa (1 bar = 0.1 MPa) to maintain a constant density. Very often the temperature effects on the dynamics of molecular motions are much smaller than the combined density–temperature effects, and in many cases volume effects play the dominant role in influencing motions in the liquid state. This is physically quite reasonable because the molecules are so closely packed in the dense liquid that the forces between particles rise almost exclusively from the harsh short-ranged repulsive forces between nearest neighbors. Therefore, even small changes in density can produce a considerable change in the molecular dynamics of the system.

To my surprise I found out that several high-pressure NMR studies had already appeared. These early high-pressure NMR studies of solids, liquids, and gases were reviewed by Benedek[14] in his brief monograph dealing with NMR at high pressure. In addition, McCall et al.[15–17] reported the pressure dependence (up to 70 MPa) of the self-diffusion coefficient in several liquids at room temperature, using the spin echo method. However, these early studies used equipment with no provision to keep the samples oxygen free, nor did they allow high-resolution operation.

Since my goal was to carry out systematic studies of various NMR relaxation times in molecular liquids, it was important that I develop a high-pressure NMR probe with the following performance features: (a) wide pressure and temperature ranges; (b) large sample volume; (c) reliable high-pressure rf feedthroughs; (d) contamination-free sample cell; (e) ease of assembly; and (f) high-resolution capability. The original design[18,19] proved quite versatile as in later years we used its modified versions to carry out high-pressure NMR experiments on solids and polymers,[20–22] high-pressure experiments at high temperature,[23] and experiments up to 1 GPa (1 GPa = 10 kbar); we were even able to introduce a mixing device for the study of homogeneous catalytic reactions.[24] The modified version of the original NMR probe[19] is used even now in our high-pressure NMR studies of biochemical systems.[25]

A major change in my research lifestyle occurred in August 1970 when I purchased from Varian Associates the high-resolution magnet system consisting of the V-3800-1 electromagnet with 3.8-in air gap and all accessories such as a heat exchanger and a flux superstabilizer. The wide gap of this 1.4 T electromagnet provided us with enough working space so that we could optimize the design of high-pressure NMR probes. In addition, the acquisition of the high rf power pulsed NMR spectrometer made by NMR Specialties, Inc. was another major improvement of our experimental capabilities.

Between 1967 and 1973 I was fortunate to have quite a number of excellent graduate students such as Roger A. Assink, Tom E. Bull, Jack DeZwaan, Yunko Lee, Nan-I Liu, Sam Seymour, and David J. Wilbur. In 1970, Bull and I published our very first high-pressure NMR study of liquid acetone.[26] We were able to follow the effects of pressure on the intramolecular and intermolecular dipolar relaxation in this liquid by using isotopic dilution T_1 experiments on acetone in acetone-d_6 at elevated pressures. This initial experiment was followed by other studies dealing with pressure effects on anisotropic reorientation in liquids,[27] on spin–rotation interactions,[10] and on reorientational motions in several selectively deuterated liquids[28] and by high-resolution FT NMR studies of fluids at high pressure.[29] All these studies were reviewed in my article[30] which appeared in 1973 in *Advances of Magnetic Resonance*, edited by John Waugh.

Instead of discussing in detail all the various results we obtained by using pressure as an experimental variable in our NMR experiments, I shall focus on several specific studies whose results led to significant developments in later years. For example, Wilbur and I reported[29] that it is possible to achieve a high homogeneity of the magnetic field over the nonspinning sample (0.8 cm diameter) at high pressure (500 MPa). As a result, for the first time we were able to use the Fourier transform technique to obtain high-resolution spectra of various liquids or liquid solutions at high pressure.[29–32] In addition, we predicted the promising future of this FT high-pressure and NMR approach in other fields. However, the main applications[25,33,34] were delayed until high homogeneity super-conducting magnets equipped with superconducting and room-temperature shims became available commercially.

This high-pressure FT NMR technique,[29] together with the general results of our systematic experiments[35–38] dealing with the applicability of hydrodynamic equations at the molecular level, allowed us to carry out a series of experiments[39,40] that for the first time provided the experimental evidence of the so-called Kramer's turnover for reactions in liquid solutions. The technique also resulted in observation of the energy-controlled regime for organometallic systems,[41] thus demonstrating the existence of the so-called heavy metal atom bottleneck effect[42] which reduces the intramolecular energy transfer. In this connection, let me stress the importance of using pressure as an experimental variable in the studies of dynamical solvent effects on reaction rates, because the collision frequency that reflects the coupling of the reaction coordinate to the medium can be related through simple hydrodynamic arguments to shear viscosity. In most studies, shear viscosity is changed by using different solvents, but in high-pressure experiments viscosity can be changed by changing the pressure. Viscosity represents only an approximate measure of the degree of coupling of the reaction coordinated to the reaction medium. Consequently, by changing solvents one may influence the reaction rate by different molecular shape, size, or strength of the intermolecular interactions of the solvent molecule used. Therefore, different solvents of the same shear viscosity may not have the same effect on the reaction rate measured. Clearly, using the same solvent and changing its viscosity by pressure represents a much cleaner experiment. Because most of the studies of simple isomerization reactions involve laser spectroscopic techniques, let me also comment on the relative merits of the NMR technique. There are several advantages in using NMR to study isomerization and hindered rotation in liquid solutions. The system chosen can be very simple and the molecule can be studied in its ground state. For example, the chair–chair isomerization of cyclohexane[40] is a relatively simple process that can be characterized by two degrees of freedom.

Another good example of an early high-pressure NMR study whose results motivated further successful research efforts was the study of the density effects on the dynamic structure of liquid D_2O.[43] These results led to systematic studies of the applicability of the Debye and Stokes–Einstein equations in H_2O and D_2O over a wide range of pressures (up to 1 GPa),[44] including subzero temperatures[45] and the compressed supercritical H_2O and D_2O.[46] As a matter of fact, the general conclusions we arrived at are helpful for us even now in our studies of pressure-induced reversible unfolding of proteins,[47] because the pressure dependence of the water–water interactions and water–protein interactions plays the dominant role in this process.

The study of the pressure dependence up to 400 MPa of the proton T_1 value in solid adamantane[48] at various temperature is yet another example of an experiment that led to new developments. Specifically, the large difference between the T_1 value of the orientationally disordered rotor phase of adamantane and the T_1 value for the ordered (brittle) solid phase of adamantane can be used to obtain information about the kinetics of the phase transition.[49] At a much later date,

we used an analogous approach to study the pressure effects on crystallization kinetics of polyethylene,[22] a problem of technological relevance.

Brief though it is, this historical sketch of my early years in NMR covers the period 1963 through 1973. In subsequent years, I have been very fortunate in continuing to take advantage of the fact that 'NMR in chemistry is a true evergreen'.[50] For a general impression of the NMR studies performed in my research group after 1973, the reader may wish to peruse several key reviews that have appeared since then.[51–56]

REFERENCES

1. J. Jonas and H. S. Gutowsky, *J. Chem. Phys.*, 1965, **42**, 140.
2. J. Jonas, A. Allerhand, and H. S. Gutowsky, *J. Chem. Phys.*, 1965, **42**, 3396.
3. J. Jonas, W. Derbyshire, and H. S. Gutowsky, *J. Phys. Chem.*, 1965, **69**, 1.
4. F. Nelson, in *NMR and EPR Spectroscopy*, by the NMR–EPR staff of Varian Associates, Pergamon Press, New York, 1960, p. 81.
5. R. G. Parker and J. Jonas, *Rev. Sci. Instrum.*, 1970, **41**, 319.
6. J. Jonas, *J. Chem. Phys.*, 1968, **49**, 4232.
7. J. Jonas and T. M. DiGenarro, *J. Chem. Phys.*, 1969, **50**, 52.
8. J. Jonas and T. M. DiGenarro, *J. Chem. Phys.*, 1969, **50**, 2392.
9. T. E. Bull and J. Jonas, *J. Chem. Phys.*, 1970, **52**, 1978.
10. T. E. Bull, J. S. Barthel, and J. Jonas, *J. Chem. Phys.*, 1971, **54**, 3663.
11. N.-I. Liu and J. Jonas, *J. Chem Phys.*, 1971, **55**, 463.
12. R. G. Parker and J. Jonas, *J. Magn. Reson.*, 1972, **6**, 106.
13. R. A. Assink and J. Jonas, *J. Chem. Phys.*, 1972, **57**, 3329.
14. G. B. Benedek, *Magnetic Resonance at High Pressure*, Wiley, New York, 1960.
15. D. W. McCall, D. C. Douglass, and E. W. Anderson, *Phys. Fluids*, 1959, **2**, 87.
16. D. W. McCall, D. C. Douglass, and E. W. Anderson, *J. Chem. Phys.*, 1959, **31**, 1555.
17. D. C. Douglass, D. W. McCall, and E. W. Anderson, *J. Chem. Phys.*, 1961, **34**, 152.
18. J. Jonas, T. E. Bull, and C. A. Eckert, *Rev. Sci. Instrum.*, 1970, **41**, 1240.
19. J. Jonas, *Rev. Sci. Instrum.*, 1972, **43**, 643.
20. N.-I. Liu and J. Jonas, *Chem. Phys. Lett.*, 1972, **14**, 555.
21. T. Eguchi, C. Marinos, J. Jonas, B. G. Silbernagel, and A. H. Thompson, *Solid State Commum.*, 1981, **38**, 919.
22. D. R. Brown and J. Jonas, *J. Polym. Sci., Polym. Phys. Ed.*, 1984, **22**, 655.
23. T. H. DeFries and J. Jonas, *J. Magn. Reson.*, 1979, **35**, 111.
24. D. G. Vander Velde and J. Jonas, *J. Magn. Reson.*, 1987, **71**, 480.
25. J. Jonas, P. Koziol, X. Peng, C. Reiner, and D. M. Campbell, *J. Magn. Reson.*, 1993, **102B**, 299.
26. T. E. Bull and J. Jonas, *J. Chem. Phys.*, 1970, **52**, 2779.
27. T. E. Bull and J. Jonas, *J. Chem. Phys.*, 1970, **53**, 3315.
28. H. J. Parkhurst, Jr., Y. Lee, and J. Jonas, *J. Chem. Phys.*, 1971, **55**, 1368.
29. D. J. Wilbur and J. Jonas, *J. Chem. Phys.*, 1971, **55**, 5840.
30. J. Jonas, *Adv. Magn. Reson.*, 1973, **6**, 73.
31. D. J. Wilbur and J. Jonas, *J. Magn. Reson.*, 1973, **10**, 279.
32. D. J. Wilbur and J. Jonas, *J. Chem. Phys.*, 1975, **62**, 2800.
33. J. Jonas, D. L. Hasha, W. J. Lamb, G. A. Hoffman, and T. Eguchi, *J. Magn. Reson.*, 1981, **42**, 169.
34. J. Jonas, C.-L. Xie, A. Jonas, P. J. Grandinetti, D. Campbell, and D. Driscoll, *Proc. Natl. Acad. Sci. USA*, 1988, **85**, 4115.
35. R. A. Assink, J. DeZwaan, and J. Jonas, *J. Chem. Phys.*, 1972, **56**, 4975.
36. H. G. Parkhurst, Jr., and J. Jonas, *J. Chem. Phys.*, 1975, **63**, 2698.
37. H. G. Parkhurst, Jr., and J. Jonas, *J. Chem. Phys.*, 1975, **63**, 2705.
38. M. Fury and J. Jonas, *J. Chem. Phys.*, 1976, **65**, 2206.
39. D. L. Hasha, T. Eguchi, and J. Jonas, *J. Chem. Phys.*, 1981, **75**, 1571.
40. D. L. Hasha, T. Eguchi, and J. Jonas, *J. Am. Chem. Soc.*, 1982, **104**, 2290.
41. X. Peng and J. Jonas, *J. Chem. Phys.*, 1990, **93**, 2192.
42. V. Lopez and R. A. Marcus, *Chem. Phys. Lett.*, 1982, **93**, 232.
43. Y. Lee and J. Jonas, *J. Chem. Phys.*, 1972, **57**, 4233.
44. D. J. Wilbur, T. DeFries, and J. Jonas, *J. Chem. Phys.*, 1976, **65**, 1783.
45. T. DeFries and J. Jonas, *J. Chem. Phys.*, 1977, **66**, 5393.
46. J. Jonas, T. DeFries, and W. J. Lamb, *J. Chem. Phys.*, 1978, **68**, 2988.
47. S. D. Samarasinghe, D. M. Campbell, A. Jonas, and J. Jonas, *Biochemistry*, 1992, **31**, 7773.
48. N.-I. Liu and J. Jonas, *Chem. Phys. Lett.*, 1972, **14**, 555.
49. M. Fury, S. G. Huang, and J. Jonas, *J. Magn. Reson.*, 1979, **33**, 211.
50. J. Jonas and H. S. Gutowsky, *Annu. Rev. Phys. Chem.*, 1980, **31**, 1.
51. J. Jonas, *Science*, 1982, **216**, 1179.
52. J. Jonas, *Acc. Chem. Res.*, 1984, **17**, 74.
53. J. Jonas, *NATO ASI, Series C*, 1987, **197**, 193.
54. J. Jonas, *NMR Basic Principles and Progress*, 1991, **24**, 85.
55. J. Jonas and Y. T. Lee, *J. Phys.: Cond. Matter*, 1992, **4**, 305.
56. J. Jonas and A. Jonas, *Annu. Rev. Biophys. Biomol. Struct.*, 1994, **23**, 287.

Biographical Sketch

Jiri Jonas *b* 1932. B.Sc., 1956, Ph.D., 1960, Chemistry, Czech. Acad. Sci., Prague, Czechoslovakia. Postdoctoral work 1963–66 at the University of Illinois with Herb Gutowsky. Professor of Chemistry, University of Illinois, Urbana, IL, USA, 1966–present. Approx. 280 publications. Research specialties: NMR spectroscopy at high pressures; dynamic structure of liquids, biochemical systems, and disordered solids.

Kaplan, Jerome I.: Chemical Exchange in Various Guises

Jerome I. Kaplan

Indiana University Purdue University Indianapolis (IUPUI), IN, USA

I graduated in theoretical solid state physics from the University of California, Berkeley in 1954 and immediately took a position at the Naval Research Lab (NRL), Washington, DC. Some time in 1955, C. Pekeris of the Weizmann Institute gave a talk at NRL. Someone at the lab heard that I had expressed an interest in visiting Israel, so it was arranged that I would drive C. Pekeris back to the train station. On the way it was arranged that on application I would be able to obtain a Louis Lipsky fellowship to The Weizmann Institute.

I left NRL in the spring of 1955, hitchhiked around Europe for three months—ending up in Naples. From there I took a boat to Israel. At the Weizmann Institute I lived in housing on the campus and ate at the campus cafeteria (this monastic existence allowed me to save money for my subsequent trip through Asia). There was no Physics Department at that time, so I was listed as a member of the Applied Math Department and assigned to work with Saul Meiboom—the NMR guru.

My only memory of the working environment was a large room with a magnet and racks of electronics. The various switches on the electronics were unmarked, and I was told by Saul Meiboom that those using the equipment knew what each switch did and those who did not know should keep their hands off. I did though get an opportunity to finger-rotate the sample holder, which miraculously lengthened the FID. The lab practice was to obtain the 'same' result by using a windshield wiper motor.

Saul Meiboom shortly after I arrived gave me the problem I was to work on. The Hamiltonian for the nuclear spin system of molecule A is given as

$$\hat{\mathcal{H}}_{\mathrm{A}} = \sum \omega_{0i} \hat{S}_i^z + \sum J_{ij} \hat{\boldsymbol{S}}_i \cdot \hat{\boldsymbol{S}}_j \qquad (1)$$

In the weak coupling limit (where the J values are small relative to the differences in the ω_{0i} values) H_{A} can be approximated by

$$\hat{\mathcal{H}}_{\mathrm{A}} = \sum \omega_{0i} \hat{S}_i^z + \sum J_{ij} \hat{S}_i^z \hat{S}_j^z \qquad (2)$$

The theory for chemical exchange in the weak coupling limit had been worked out by Gutowsky, McCall, and Slichter (GMS). My problem was to develop a general theory for chemical exchange for strong coupling. I remember immersing myself in this problem for about a month without any feeling that I was getting closer to its solution. Being very frustrated, I decided to take a day off and sit around the lab watching the on-going experiments. While passing the time, I glanced at a journal article. Something there was the missing clue, for I suddenly realized I knew how to formulate chemical exchange for strongly-coupled systems.[1]

I worked on two other NMR problems while I was at the Weizmann Institute: one was a mathematical description of how the sample holder rotation modified the FID[2] and the other was the calculation of the double quantum absorption. Here one obtains the double photon absorption peak midway between the two single photon peaks, $\omega_{0\mathrm{A}}$ and $\omega_{0\mathrm{B}}$. I worked out the theory and Saul Meiboom verified the effect experimentally.[3]

In the lab over most of my stay were three graduate students—Shlomo Alexander, David Gil, and Aharon Lowenstein. They spoke intimately of the War for Independence 1948 and, if memory serves me right, of someone being a classmate of Anne Frank. I traveled a lot about Israel—I had a small Fiat car—but the trips I remember best were trips to Masada—a mesa near the Dead Sea which was the final resting place for a Jewish sect which had held out against the Roman army, and a trip to Eilat—a seashore area near the Red Sea. On these trips we had lots of student company and traveled well armed so as to provide protection against possible terrorist attacks (fedayeen).

There was a short war during my stay during which I was air raid warden of my building (slept through the night while my roommate next door, a Japanese survivor of the bombing of Tokyo, sat out the night in our air raid shelter), dug slit trenches for a local kindergarten, and went with David Gill and another student into the Israeli-temporarily-occupied Gaza Strip by crossing over an unguarded dry river bed. This of course was illegal and we got properly rebuked by the border guard when we left through a normal check point (the Gaza Strip was returned to Egypt the next day).

I left Israel in the fall of 1956 and traveled through Asia for three months. My memory is cloudy but I believe I met H. McConnell in California, where he told me he had put the GMS theory into a Bloch equation form. Thus, when a friend suggested that I quickly send in an abstract to an upcoming meeting, I modified the strong coupling exchange paper written in Israel so it could be expressed in 'Bloch' form, and this ended my Weizmann Institute experience.[3,4]

It was over 10 years after my second paper on chemical exchange that I again became involved with NMR. I had been at the Battelle Institute, Columbus, OH about a year when I called Gideon Fraenkel (Department of Chemistry, Ohio State University) to see if he would give a seminar talk at Battelle. He asked if I were the Kaplan who had written papers on chemical exchange. We immediately got together and collaborated. Our major result was a simplified procedure to obtain the density matrix equations for chemical exchange which we called 'permutation of indices'.[5] Exactly who made the suggestion that we write a book on chemical exchange is lost in time (my wife claims she was the instigator). It took us almost two years to complete the book as we had to cover a number of topics not previously described.[6]

I then left Columbus, OH for Indianapolis, IN, where I was employed in a tripartite arrangement: one-third at the Krannert Institute of Cardiology, one-third at the Indianapolis Center For Advanced Research (working mostly on solar energy and medical devices), and one-third in the Physics Department of IUPUI (Indiana University/Purdue University at Indianapolis). My task in the Cardiology Institute was to obtain heart mapping using NMR.

Starting in 1975 we began a search to find an NMR parameter which would distinguish ischemic muscle tissue from normal muscle tissue. Initially we decided to see if T_2 could provide the differentiation, but because of experimental

difficulties we gave this up and switched to T_1 differentiation. We submitted the results to *Science* in July 1977, but the paper was not accepted for technical reasons. A revised write-up was submitted in 1979 to *Journal of Nuclear Medicine* and accepted for publication in 1980.[7] We found that there existed approximately a 10% difference in water concentration of ischemia as compared with normal tissue. It thus became apparent that to achieve a significant normal ischemic discrimination we would need to work with the T_1 differences rather than the water density differences.

With this in mind, I developed the idea of the inversion recovery procedure. A description of the inversion recovery procedure was given in a manuscript dated August 20, 1979, as received by the *Journal of Magnetic Resonance*. The manuscript was not published. I don't have a record as to why. Subsequently the ideas in the manuscript were published as a US Patent.[8,9]

Our attempts to obtain good experimental images in our laboratory were not successful, so I cast about for some other laboratory which would permit me to run the inversion recovery procedure. I first contacted Waldo Hinshaw; he was agreeable but could not get approval from Massachusetts General. I then contacted Johns Hopkins, but the group there was temporarily closing down. Finally I contacted Larry A. Crooks at the Nuclear Imaging Laboratory, University of California, San Francisco. He said he could run the procedure.

Thus in the summer of 1980 I went out to the University of Washington, and during the month of August traveled down to San Francisco and during a nail biting two days (August 18 and 19) (equipment was down the first day) was able to obtain one good run.

The samples were first pseudo density sensitized by the inversion recovery procedure and then mapped using the Nuclear Imaging Laboratory standard mapping procedure. I was overjoyed both by the results as well as the surprised looks on the faces of the Nuclear Imaging Laboratory personnel who did not expect to see so much contrast.

The results have not been previously reported as a research contribution because a morphological comparison was never made by the Nuclear Imaging Laboratory, University of California. The image using the inversion recovery procedure is shown in Figure 1 and in Figure 2 is shown the mapping without the inversion recovery procedure.

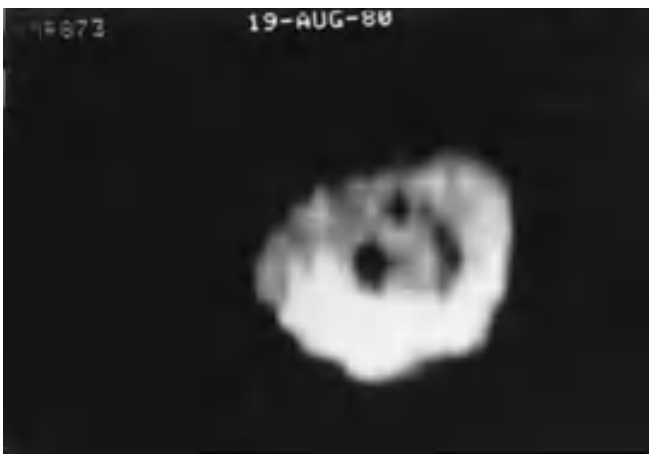

Figure 1 Image using inversion recovery procedure

Figure 2 Mapping without inversion recovery procedure

It was clear that for heart mapping we needed a much faster method for mapping than was then available. Through an extended period I mulled over a concept from my childhood of summer camp groups spread out on the main floor of Grand Central Station, New York City, who would signal to the station master that they were ready to disembark by singing their camp song. Thus, I imagined mapping could be done by having a unique series of frequencies to be established at each point in two- or three-dimensional space. I developed these ideas and was invited by General Electric to give a talk on the subject in Milwaukee on July 13, 1983. At the end of the talk I was handed a patent by Likes—a General Electric employee—which disclosed how to obtain the unique series of frequencies at each point but failed to disclose how to use this information to obtain an image. I then went ahead and obtained a patent on this concept.[10]

Because of circumstances outside of my control, I had no further interaction involving MRI at IUPUI or the Radiology Department of the Indiana Medical School which is on the IUPUI campus.

In 1981, I was invited by Al Garroway to come to the Naval Research Laboratory, Washington, DC, where we worked on MRI imaging of epoxy compounds and on a comparison of the theoretical signatures for homogeneous and inhomogeneous distribution of correlation times for chemical exchange.[11] The lack of what I felt was a valid theory for the stretched exponential used in this paper was then the impetus when I came back to IUPUI to formulate 'A Proposed Mechanism for Nonexponential Chemical Exchange'.[12]

REFERENCES

1. J. I. Kaplan, *J. Chem. Phys.*, 1958, **28**, 278.
2. J. I. Kaplan, *J. Chem. Phys.*, 1957, **27**, 1426.
3. J. I. Kaplan and S. Meiboom, *Phys. Rev.*, 1957, **106**, 499.
4. J. I. Kaplan, *J. Chem. Phys.*, 1958, **29**, 462.
5. J. I. Kaplan and G. Fraenkel, *J. Am. Chem. Soc.*, 1972, **94**, 2907.
6. J. I. Kaplan and G. Fraenkel, *NMR of Chemically Exchanging Systems*, Academic Press, New York, 1980.
7. E. S. Williams, J. I. Kaplan, F. Thatcher, G. Zimmerman, and S. Knoebel, *J. Nucl. Med.*, 1980, **21**, 449.
8. 'Nuclear Magnetic Resonance Spatial Mapping', US Pat. 4 383 219 (May 10, 1983).

9. In a careful literature search we found that the first reference to the inversion recovery approach was given in a short note: 'Imaging of Macroscopic Objects of NMR Fourier Zeugmatography', A. Kramer, D. Welti, and R. R. Ernst, *Naturwissenshaften*, 1975, **62**, 34.
10. 'Methods for Two Dimensional Nuclear Magnetic Resonance Imaging', US Pat. 4 642 567 (Feb. 10, 1987).
11. J. I. Kaplan and A. N. Garroway, *J. Magn. Reson.*, 1982, **49**, 464.
12. J. I. Kaplan, *J. Magn. Reson.*, 1991, **91**, 39.

Biographical Sketch

Jerome I. Kaplan. *b* 1926. B.S. University of Michigan, Ann Arbor, 1950; Ph.D., University of California, Berkeley, 1954. Research Scientist, Naval Research Laboratories, Washington, DC 1954–58; Louis Lipsky Fellow, Weizman Institute, Israel, 1956–57; research associate, 1958–61 and then Assistant Professor of Physics, Brandeis University, 1961–62; Fulbright Lecturer, University College of Rhodesia and Nyasaland 1962–63; Associate Professor of Research, Brown University, 1963–67; research scientist, Battelle Institute, Columbus, Ohio, 1967–73; staff scientist, Krannert Institute of Cardiology, Indianapolis, 1974–80; Center Fellow, Indianapolis Center for Advanced Research, 1974–83; currently Professor of Physics at Indiana University–Purdue University at Indianapolis. Research interests are in solid state physics, biophysics, and solar energy.

Kaptein, Robert: The Early Days of CIDNP

Robert Kaptein

Utrecht University, Utrecht, The Netherlands

The years 1967–68 were a very exciting period. The first reports on chemically induced dynamic nuclear polarization (CIDNP) had just appeared[1–4] and it was clear that the new phenomenon could be extremely useful for the study of free-radical reactions in solution. However, it was also clear that the first explanations offered[2,4] could not be correct or at least were incomplete. In particular, the so-called multiplet effect, which denotes the simultaneous occurrence of positive and negative intensities within the multiplet of a spin-coupled nucleus, defied explanation in terms of the dynamic nuclear polarization (DNP) theory,[2,4] which is analogous to the Overhauser effect. So, there we had these enormously enhanced NMR lines, which could be easily generated by running free-radical reactions in the NMR tube, and for several years nobody had a clue as to how they arose. In the following article I shall give a personal account of the early development of CIDNP and in particular of the birth of what is now called the radical pair theory (for early reviews see Refs. 5 and 6).

The first observation of CIDNP dates long before the 1967 publications. In fact, countless discoveries and rediscoveries have been made, often dismissed as artifacts. An example is that from the laboratory of Prof. Th. J. de Boer of the University of Amsterdam. NMR spectra of a cyclopropyl compound in $CDCl_3$ had the chloroform line in emission or absorption depending on the operator who ran the spectrum. It turned out that one operator had the habit of shaking the NMR tube before recording the spectrum, while the other had not! The slight amount of oxygen mixed in the solution oxidized the labile cyclopropyl compound, which resulted in polarized $CHCl_3$ as one of the products of a radical recombination reaction. Since the chloroform proton has a T_1 value of 60 s or so, it is a particularly favorable molecule in which to store nuclear polarization.

The first to observe the CIDNP effect and realize it was not an artifact was probably Joachim Bargon, a graduate student in Darmstadt in 1964. He made an NMR study of polymerization reactions initiated by benzoyl peroxide and discovered a strong negative polarization for benzene. In the hierarchical German system he would never have published these findings on his own, but he had also great difficulty in convincing his supervisor or others that he had hit upon something important. Finally he got Hanns Fischer interested and this led to the first publications of the Darmstadt group.[1,2] An interesting aspect of the second paper[2] describing the DNP-like theory was that it seemed so plausible and even quantitatively correct. This led many people to believe that things were basically understood and that only the multiplet effect present in the Ward and Lawler paper[3] needed some small modification. It is indeed somewhat surprising that in radical reactions the DNP mechanism has never been seen to contribute, all the polarization effects being due to the stronger radical pair mechanism.

Another even earlier observation should be mentioned, namely that of electron polarization (CIDEP) by Fessenden and Schuler[7] in 1963. The ESR spectrum of hydrogen atoms generated by pulse radiolysis showed one hyperfine line in emission and the other in absorption. This was a single observation that did not receive much attention until it was followed up by similar findings by Smaller and co-workers.[8]

My own involvement with these polarization phenomena started immediately after the first reports of CIDNP[1–4] in 1967. At the time I was a graduate student in the department of Professor L. J. Oosterhoff at the University of Leiden. It was a curious department, certainly by today's standards. Research projects covered an extremely broad range of subjects, from theoretical and physical chemistry to various kinds of spectroscopy, of which magnetic resonance was only one of many. It was fairly big (ca. 40 people), but Oosterhoff was there only two days per week as he also had a job at the Shell laboratory in Amsterdam. One would therefore not see much of him. In any case, in his opinion a supervisor should give his students almost absolute freedom, which suited me very well. I had started an NMR study of stable free radicals, which were observable at high concentrations in solution, because electron exchange would narrow the NMR lines. I had therefore become familiar not only with NMR but also with the properties of free radicals (hyperfine coupling, electron exchange, etc.). This gave me an excellent background to tackle the problem of the new polarization phenomena, which I took up as a bigger challenge. An experimental study of a number of diacyl peroxide decompositions[9] showed for the first time polarization sign reversals depending on the type of product formed. Products from radical pair combination showed one sign, while those from radical scavenging reactions the opposite (this was later termed 'recombination' and 'escape' polarization). This led me to believe that radical pair interactions were somehow important, rather than processes in single free radicals as the DNP theory would suggest. After many unsuccessful attempts the answer was finally provided by a quantum mechanical description of the spin effects during birth and subsequent reactions of a radical pair.[10,11] The surprising result was that the reaction probability of a radical pair depends to some extent on the spin state of its nuclei that are hyperfine coupled to the electron spins. This arises through the role of the hyperfine interactions in mixing singlet and triplet electronic states of a radical pair. These energetically tiny interactions are nevertheless very efficient in this mixing process, because the singlet and one of the triplet states (T_0) become degenerate shortly after formation of a radical pair in solution (i.e. the electron exchange interaction drops rapidly with distance). I had first treated the CIDEP effect in this way[10] and had given an explanation of the NMR multiplet effects using cross relaxation from polarized electron states (so strong was the DNP paradigm at that time!). However I soon realized that the same mechanism could account for the nuclear spin multiplet effects as well. This also explained the sign reversals depending on product type that were called 'spin selection' (α-nuclei and up in one type of product, β-nuclei in the other). This notion that nuclear spins direct the course of a chemical reaction to some extent, was probably the most novel aspect of the new theory.

At the same time, Gerhard Closs at the University of Chicago, who died in 1992, had formulated essentially the same theoretical ideas.[12] He was looking at photochemical reactions by NMR and had noted polarization sign reversals

in reaction products depending on the initial electronic state, singlet or triplet, of the precursor molecules.[13,14] This had led him to develop a very similar theory based on hyperfine coupling induced S–T mixing. Although his initial treatment was in terms of stochastic, relaxation-like transitions,[12] he soon adopted the fundamentally more correct description as a coherent, quantum mechanical superposition of states with an inherent oscillatory behavior. It is interesting to note that these oscillations or 'quantum beats' have indeed been observed experimentally.[15]

Once the ground rules had been laid out, the following period saw some extensions and improvements of the theory. The combined effect of hyperfine coupling and g-factor differences explained net polarization effects.[16] A more appropriate treatment of the re-encounter probability of a diffusing radical pair[17–19] also made the theory in quantitative agreement with experiments. A short paper[20] that presented simple rules for the qualitative prediction of CIDNP effects gave me great personal satisfaction. These sign rules contain all the sign reversals of the radical pair theory and apart from a few exceptions[21] are still valid today. High-powered theoreticians came in and developed more formal versions of the theory (for a review see for instance Ref. 22; it is sad to note, however, that in this review the original papers[10–12] are not mentioned).

In the meantime CIDNP had become a powerful tool in mechanistic organic chemistry and photochemistry. It also became clear, however, that apart from CIDNP and CIDEP the radical pair mechanism could account for various other phenomena. For instance, in optical spectroscopy it lies at the basis of 'delayed fluorescence'[23] and 'reaction yield detected magnetic resonance' (RYDMR).[24] Also, an interesting consequence of the radical pair mechanism is the magnetic isotope effect,[25,26] which could be used as an isotope separation tool.

In the late 1970s I became interested in the emerging field of biomolecular NMR. An application of CIDNP to proteins[27,28] made the change of fields for me an adiabatic one. In this so-called 'laser photo-CIDNP method', one irradiates a protein solution containing a flavin dye in the NMR probe. Reversible electron or hydrogen atom transfer reactions cause the protons of aromatic residues (His, Tyr, and Trp) to become polarized, when these residues are surface-accessible. The obtainable information is not as complete as that of a full structural study using NOEs and coupling constants, but a virtue of the method is that it is very quick and it provides useful information, in particular on protein–ligand interaction sites.

Thus, nuclear and electron polarization and related phenomena are now firmly established in (bio)physical chemistry. I remember vividly the excitement of the early days and it has been very gratifying to be able to contribute to the development of the field. I am greatly indebted to my supervisor Professor Oosterhoff, not only for the freedom I enjoyed as a graduate student, but also for his encouragement and the stimulating environment he created. With his broad knowledge and deep insight into theoretical chemistry he was able to put some of my immature ideas into a broader perspective.

REFERENCES

1. J. Bargon, H. Fischer, and U. Johnsen, *Z. Naturforsch.*, 1967, **22a**, 1551.
2. J. Bargon and H. Fischer, *Z. Naturforsch.*, 1967, **22a**, 1556.
3. H. R. Ward and R. G. Lawler, *J. Am. Chem. Soc.*, 1967, **89**, 5518.
4. R. G. Lawler, *J. Am. Chem. Soc.*, 1967, **89**, 5519.
5. G. L. Closs, in *Advances in Magnetic Resonance*, ed. J. S. Waugh, Academic Press, New York, 1974, Vol. 7, p. 157.
6. R. Kaptein, in *Advances in Free Radical Chemistry*, ed. G. H. Williams, Elek Science, London, 1975, Vol. 5, p. 319.
7. R. W. Fessenden and R. H. Schuler, *J. Chem. Phys.*, 1963, **39**, 2147.
8. B. Smaller, J. R. Remko, and E. C. Avery, *J. Chem. Phys.*, 1968, **48**, 5174.
9. R. Kaptein, *Chem. Phys. Lett.*, 1968, **2**, 261.
10. R. Kaptein and L. J. Oosterhoff, *Chem. Phys. Lett.*, 1969, **4**, 195.
11. R. Kaptein and L. J. Oosterhoff, *Chem. Phys. Lett.*, 1969, **4**, 214.
12. G. L. Closs, *J. Am. Chem. Soc.*, 1969, **91**, 4552.
13. G. L. Closs and L. E. Closs, *J. Am. Chem. Soc.*, 1969, **91**, 4549.
14. G. L. Closs and A. D. Trifunac, *J. Am. Chem. Soc.*, 1969, **91**, 4554.
15. O. A. Anisimov, V. L. Bizyaev, N. N. Lukzen, V. M. Grigoryants, and Yu. N. Molin, *Chem. Phys. Lett.*, 1983, **101**, 131.
16. G. L. Closs and A. D. Trifunac, *J. Am. Chem. Soc.*, 1970, **92**, 2183.
17. F. J. Adrian, *J. Chem. Phys.*, 1970, **53**, 3374.
18. R. Kaptein, *Chemically Induced Dynamic Nuclear Polarization*, Doctoral Thesis, Leiden, 1971.
19. R. Kaptein, *J. Am. Chem. Soc.*, 1972, **94**, 6251.
20. R. Kaptein, *Chem. Commun.*, **1971**, 732.
21. P. J. Hore, S. Stob, J. Kemmink, and R. Kaptein, *Chem. Phys. Lett.*, 1983, **98**, 409.
22. J. H. Freed and J. B. Pedersen, *Adv. Magn. Reson.*, 1976, **8**, 1.
23. K. Schulten, H. Staerk, A. Weller, H. J. Werner, and B. Nickel, *Z. Phys. Chem.* 1976, **101**, 371.
24. E. L. Frankevich, A. I. Pristupa, and V. I. Lesin, *Chem. Phys. Lett.*, 1977, **47**, 304.
25. A. L. Buchachenko, *Russ. Chem. Rev.*, 1976, **45**, 375.
26. N. J. Turro and B. Kraeutler, *Acc. Chem. Res.*, 1980, **13**, 609.
27. R. Kaptein, K. Dijkstra, and K. Nicolay, *Nature (London)*, 1978, **274**, 293.
28. R. Kaptein, in *Biological Magnetic Resonance*, ed. L. J. Berliner, Plenum Press, New York, 1982, Vol. 4, p. 145.

Biographical Sketch

R. Kaptein. *b* 1941. M.S., 1965, Ph.D., Leiden, 1971. Postdoctoral fellow with Ray Freeman, Varian, Palo Alto, CA, 1971–72; Shell Research Laboratory, Amsterdam, 1972–75; Groningen University, 1975–87; Professor of Chemistry, Utrecht University, 1987–present. Approx. 250 publications. Research interests: biomolecular structure determination, NMR methodology, protein–DNA interaction.

Karplus, Martin: Theory of Vicinal Coupling Constants

Martin Karplus

Harvard University, Cambridge, MA, USA

My studies of vicinal coupling constants began as a problem in theoretical chemistry. After finishing my Ph.D. (1953) at the California Institute of Technology with Linus Pauling, I went to Oxford University to work as a postdoctoral fellow with Charles Coulson. I was only 23 years old at the time and having worked hard all the way through graduate school, I was eager to have my stay in Europe provide experiences beyond science. I benefited from one of the first NSF postdoctoral fellowships. Its generous (at the time) salary of $3000 per year permitted me to do some traveling. Consequently, I spent more time thinking about chemical problems than actually solving them. My aim was to find areas in chemistry where theory could make a useful contribution. I did not want to spend my life doing calculations whose results were of interest only to other theoretical chemists.

Reading the literature and listening to physics lectures in Oxford convinced me that magnetic resonance was an important developing area. At that time, chemical applications of nuclear magnetic resonance were just beginning. It seemed to me that nuclear magnetic resonance, in particular, was a field where theory and experiment could make mutually beneficial contributions to chemistry. The measurements could provide a means of testing the theoretical results but, more important, theory could be used to aid in interpreting the experimental results, as well as in suggesting new measurements.

As I was finishing my postdoctoral years in Oxford (1953–55) and looking for a place to begin my academic career, I decided it would be good to find an institution that had experimental programs in magnetic resonance. Fortunately, the University of Illinois had a number of openings at that time because the Department of Chemistry was undergoing a radical renovation. Several people had retired, and new people were being hired. Pauling recommended me to the University of Illinois. The department offered me a job without an interview and I accepted without visiting the department, something difficult to imagine today with the extended courtships that seem to have become an essential part of the hiring process. A major reason for going was that Charles Slichter and Herbert Gutowsky were working there. They had done some of the pioneering work in applying nuclear magnetic resonance to chemical problems. It thus seemed the perfect opportunity to combine my burgeoning interests in magnetic resonance with a position in a good department. At that time the University of Illinois offered instructorships as the starting position and the salary was $5000 per year. As far as I can remember they offered nothing in addition, and I did not think of asking for research support before accepting the position. I felt that the University of Illinois, although a very good institution, was located in an area where I could not imagine spending more than five years. However, having had such a good time as a postdoctoral fellow visiting various parts of Europe, it was time to get to work and Urbana seemed like a place where I could work with few distractions. Up to the time I was hired, there had been no Jews on the chemistry faculty, but with the departmental reorganization that had taken place, four Jewish instructors (Rolf Herber, Aron Kupperman, Robert Ruben, and I) were hired at the same time. This group, plus other young scientists on the faculty such as Lynn Belford, E. J. Corey, and Doug Applequist, led to a very active interactive and congenial atmosphere during my stay.

On arriving in Urbana, I decided to focus part of my research on theoretical methods for relating nuclear magnetic resonance parameters to the electronic structure of molecules. The first problem I examined was concerned with proton–proton coupling constants which were known to be dominated by the Fermi contact interaction. What made coupling constants of particular interest was that for nonbonded protons, the existence of a nonzero value indicated that there was an interaction beyond that expected from localized bonds. In the valence bond framework, which I used in part because of my training with Pauling, the nonzero coupling constant provides a direct measure of the deviation from the perfect pairing approximation.

D. H. Anderson, a graduate student working with Gutowsky, treated the proton–proton coupling in methane with a theoretical model that I had developed and obtained results in excellent agreement with experiment.[1,2] The calculated value was 12.5 c/s versus the measured value of 12.4 $\pm$ 0.6 c/s; as is usual in most calculations on many-electron systems, the theoretical result had no error bars. Encouraged by this success, we went on to extend the coupling constant theory to other problems. Examples are the calculation of the HCH′ angular dependence of the proton–proton coupling in methylene groups[3] and the interpretation of the directly bonded coupling between a heavy atom (^{13}C, ^{15}N) and a proton in terms of the hybridization and ionic character of the bond involved.[4]

Some time later the apparent ‘excellent’ agreement of the original calculation for methane was shown to be an illusion. A number of papers appeared in 1961 that demonstrated experimentally that the geminal and vicinal proton coupling constants had opposite signs, whereas theory predicted them to have the same sign. I was very upset by this development. It is never pleasant publishing something that is wrong and it is particularly unpleasant to do so at the beginning of one’s career. I went back to reexamine the theory and concluded that it was the geminal coupling constant which was wrong because the final result depended on several terms with opposite signs that nearly canceled.[5] Further, I suggested an experiment[5] which could be used to measure the sign of the coupling constant so as to test my conclusion. Subsequent measurements confirmed the analysis, which indicated that vicinal coupling constants were positive and that, therefore, geminal coupling constants were negative.

There are two reasons for describing the problem with the geminal coupling calculation, even though I am probably one of the few people who still remembers it. First, the vicinal coupling theory, which is the reason for this chapter, would probably not have been developed if I had not believed that the geminal coupling constant result was so good. Second, like many a young faculty member, I was concerned about making some ‘distance’ between Gutowsky and myself. He was known worldwide for his research in NMR. I wanted to show that the calculations were ‘my’ work, though there is no question that I profited greatly from discussions with him and from access to

his students like Dave Anderson and Tom Farrar. After some discussion, we agreed that we would divide up the geminal and vicinal coupling work. Gutowsky would appear on papers describing one of the two and not on those concerned with the other. For various reasons, including that I had done the vicinal coupling calculation by myself, I picked that. It was a lucky choice.

As in the case of methane, I used valence bond theory to calculate the value of the vicinal proton–proton coupling constant in the HCC′H′ fragment as a function of the dihedral angle. The formal theory of coupling constants[2,3] and other second-order properties[6] had been developed already so that the problem was one of its application. Because the proton–proton interaction corresponds to a second-order perturbation theory contribution, it requires evaluation of a sum over excited states. This was difficult to do accurately at the time because of the slow convergence of the sum. To avoid the excited state summation problem, the so-called 'average energy approximation' was introduced. It leads to the following expression for the vicinal coupling constant $J(\mathrm{H,H'})$:

$$J(\mathrm{H,H'})(\mathrm{c/s}) = -\frac{1.210 \times 10^{-45}}{\Delta \mathrm{E(eV)}} \left\langle \psi \left| \sum_{\mathrm{j,k}} \delta(\boldsymbol{r}_{\mathrm{jH}}) \delta(\boldsymbol{r}_{\mathrm{kH'}}) S_j \cdot S_k \right| \psi \right\rangle \quad (1)$$

in a standard notation. The average energy approximation could introduce problems because the coupling constant involves two different perturbations.[7] However, there was no alternative and it seemed necessary to apply an approximation that might not be fully justified so as to be able to treat systems of interest with the methods and resources that were available. A more recent case of this type is the application of molecular dynamics simulation methods to proteins. They were used first when the potential functions were not accurate enough and the computers permitted only simulations that were too short. In spite of this, the original work[8] was instrumental in introducing a dynamic view of proteins. Since then, the utility of such simulations has been demonstrated repeatedly and many people are now using them with better potentials and longer simulations to study a wide range of problems.[9,10]

Although the HCC′H′ fragment is a relatively simple system consisting of six electrons with the neglect of inner shells, and can be described approximately by including only five covalent valence bond structures, the calculations for a series of dihedral angles were sufficiently time consuming that it seemed worthwhile to develop a computer program. This was not as simple in 1958 as it would be now. Fortunately, the University of Illinois had built the ILLIAC, a large scale computer at that time. If I remember correctly, it had a 1000 words of memory, which was sufficient for my simple program. The actual program was written by making little holes in a paper tape. If you made a mistake, you filled in the incorrect holes with nail polish so that you could continue the program. The output appeared on spools of paper, some of which I still have today. Probably the most important aspect of having a program was that once it was known to be correct, a large number of calculations could be done without having to worry about arithmetic mistakes.

Just as I finished the work on vicinal coupling constants,[11] I heard a lecture by R. V. Lemieux on the conformations of acetylated sugars.[12,13] I do not remember why I went to the talk because it was on organic chemistry. Lemieux reported results for vicinal coupling constants and noted that there appeared to be a dihedral angle dependence, although the details of the behavior were not clear. However, it was evident that these experimental results confirmed the theory, even before it was published.

Having completed the vicinal coupling constant theory and found that it yielded results in reasonable agreement with experiment, my feeling was that the project was done although I continued to explore the insights that such an approach could give concerning the electronic structure of molecules.[6,14] I soon became interested in other problems, including the theory of chemical reactions.[15,16] As in magnetic resonance, my interest in this field was stimulated by the development of new experimental techniques. Most important was the introduction of crossed molecular beams for the study of the collisional aspects of chemical reactions.[17]

E. J. Corey, who was at that time an assistant professor at Illinois and later became a colleague at Harvard, was one of the people with whom I had dinner on a fairly regular basis at the Tea Garden, a passable restaurant in Champaign-Urbana. We often discussed recent work that we thought might be of mutual interest and one day I described the studies that I had made of vicinal coupling constants. Corey immediately recognized the possibility of using the results for structure determination and shortly published what is probably the first application in organic chemistry.[18] Shortly after, the theory appeared in a comprehensive review of the use of nuclear magnetic resonance in organic structure determinations.[19] Someone introduced the name 'Karplus equation' for the relationship I had developed—a mixed blessing which was to haunt me for many years. Many people attempted to apply the equation to determine dihedral angles in organic structures and, of course, since it was a qualitative relationship, found deviations of the measured coupling from the predicted dihedral angle dependence for known structures. All of this came to a head when several papers were published[20] pointing out that the equation was not as accurate as many chemists seemed to have assumed it to be.

Most people who use the 'Karplus equation' appear not to have read the original paper[11] and so did not know the limitations of the theory cited there. They assumed that because the equation had been used to estimate vicinal dihedral angles, the theory said that the coupling constant depends *only* on the dihedral angle. By 1963, I had learned that important organic chemists write and read only Communications to the *Journal of the American Chemical Society* and so I decided to publish such a Communication,[21] in which I described various factors, other than the dihedral angle, that are expected to affect the value of the vicinal coupling constant; they include the electronegativity of substituents, the valence angles of the protons (HCC′ and CC′H′) and bond lengths.[21] The main point of the paper was not to provide a more accurate equation but rather to make clear that caution had to be used in applying the equation to structural problems. My closing sentence, which has often been quoted, was the following: 'Certainly with our present knowledge, the person who attempts to estimate dihedral angles to an accuracy of one or two degrees does so at his own peril'.

In spite of this caution, the use of the equation has continued and the original paper[11] is one of the *Current Contents* 'Most

Cited Papers in Chemistry'. In addition, there have been many empirical 'extensions' of the equation; perhaps the most complex published form is given in Ref. 22, where a 12-term expression is introduced. Equations have been developed also for vicinal coupling constants involving a variety of nuclei[23] (e.g. ^{13}C−CC−H, ^{15}N−CC−H) and they have been applied in areas ranging from inorganic through organic to biochemistry. One of the more recent uses is as part of the data employed in the structure determination of proteins by NMR.[24,25]

The vicinal coupling constant model, which I developed to understand deviations from perfect pairing, has been much more useful than I would have guessed (obviously I am very pleased with this) and refinements based mainly on empirical fits have been found helpful in obtaining improved results. In many ways my feeling about the uses and refinements of the 'Karplus equation' is that of a proud father. I am very pleased to see all the nice things that the equation can do, but it is clear that it has grown up and now is living its own life.

REFERENCES

1. M. Karplus, D. H. Anderson, T. C. Farrar, and H. S. Gutowsky, *J. Chem Phys.*, 1957, **27**, 597.
2. M. Karplus and D. H. Anderson, *J. Chem. Phys.*, 1959, **30**, 6.
3. H. S. Gutowsky, M. Karplus, and D. M. Grant, *J. Chem. Phys.*, 1959, **31**, 1278.
4. M. Karplus and D. M. Grant, *Proc. Natl. Acad. Sci. USA*, 1959, **45**, 1269.
5. M. Karplus, *J. Am. Chem. Soc.*, 1962, **84**, 2458.
6. M. Karplus, *Rev. Mod. Phys.*, 1960, **32**, 455.
7. M. Karplus, *J. Chem. Phys.*, 1960, **33**, 941.
8. J. A. McCammon, B. R. Gelin, and M. Karplus, *Nature (London)*, 1977, **267**, 585.
9. C. L. Brooks, III, M. Karplus, and B. M. Pettitt, *Proteins: A Theoretical Perspective of Dynamics, Structure, and Thermodynamics, Vol. LXXI, Adv. Chem. Phys.*, John Wiley & Sons, New York, 1988.
10. M. Karplus and G. A. Petsko, *Nature (London)*, 1990, **347**, 631.
11. M. Karplus, *J. Chem. Phys.*, 1959, **30**, 11.
12. R. U. Lemieux, Karl Folker Lecture, University of Illinois, 1958.
13. R. U. Lemieux, R. K. Kullnig and R. Y. Moir, *J. Am. Chem. Soc.*, 1958, **80**, 2237.
14. M. Karplus, *J. Phys. Chem.*, 1960, **64**, 1793.
15. M. Karplus, R. N. Porter, and R. D. Sharma, *J. Chem. Phys.*, 1964, **40**, 2033.
16. M. Karplus, in *Structural Chemistry and Molecular Biology: A Volume Dedicated to Linus Pauling by his Students, Colleagues, and Friends*, eds. A. Rich and N. Davidson, W. H. Freeman & Co., San Francisco, 1968, pp. 837–847.
17. D. R. Herschbach, in *Les Prix Nobel en 1986*, The Nobel Foundation, Stockholm, 1987.
18. W. H. Bradshaw, H. E. Conrad, E. J. Corey, I. C. Gunsalus, and D. Lednicer, *J. Am. Chem. Soc.*, 1959, **81**, 5507.
19. H. Conroy, *Adv. Org. Chem.*, 1965, **2**, 265.
20. See, for example, (a) K. L. Williamson, *J. Am. Chem. Soc.*, 1963, **85**, 516; (b) O. L. Chapman, *J. Am. Chem. Soc.*, 1963, **85**, 2014; G. V. Smith and H. Kriloff, *J. Am. Chem. Soc.*, 1963, **85**, 2016; P. Laszlo and P. von R. Schleyer, *J. Am. Chem. Soc.*, 1963, **85**, 2018.
21. M. Karplus, *J. Am. Chem. Soc.*, 1963, **85**, 2870.
22. K. Imai and E. Osawa, *Tetrahedron Lett.*, **1989**, 4251.
23. S. Karplus and M. Karplus, *Proc. Natl. Acad. Sci. USA*, 1972, **69**, 3204.
24. A. D. Kline, W. Braun, and K. Wüthrich, *J. Mol. Biol.*, 1988, **204**, 675.
25. D. F. Mierke, T. Huber, and H. Kessler, *J. Comp. Aided Mol. Design*, 1994, **8**, 29.

Biographical Sketch

Martin Karplus. *b* 1930. B.S. 1950 (Harvard), Ph.D. (California Institute of Technology, supervisor Linus Pauling). Postdoctoral fellow, Oxford University, 1953–55 (with Charles Coulson); instructor, assistant professor, associate professor, University of Illinois, 1955–60; professor, Columbia University, 1960–66; professor, Harvard University, 1966–present; Theodore William Richards Professor of Chemistry, Harvard University, 1979–present; Professeur Associé, Université de Paris-Sud, 1972–73, 1980–81; Professeur, Université de Paris VII, 1974–75; Professeur, Collège de France, Paris, 1980–81, 1987–88; Professeur Associé, Université Louis Pasteur, Strasbourg, 1992, 1994–95; Professeur Conventionné, Université Louis Pasteur, Strasbourg, 1995–present. Approx. 500 publications. Research interests: theoretical chemistry, including the electronic interpretation of NMR and ESR spectra of molecules, the development of techniques for the evaluation of molecular properties, and the formulation of detailed models for chemical reactions. Recent work is concerned with molecules that play an important role in living systems.

Keller, Tony: The Development of the First Multinuclear Fourier NMR Spectrometers

Tony Keller

Bruker Analytische Messtechnik, Rheinstetten, Germany

In the late 1960s heteronuclear NMR spectroscopy began to stimulate the interest of many spectroscopists. Our goal at Bruker was to design spectrometers that could meet the many challenges this application posed. Heteronuclear field/frequency lock (first ^{1}H, then ^{19}F and ^{2}H) and time averaging with a multifrequency CW spectrometer had been developed, but a big problem remained—sensitivity. Long nights of data accumulation with a 'CAT' (computer for accumulating and time-averaging analog signals) were needed for ^{13}C NMR of very concentrated samples, and you were lucky just to see peaks emerging out of the 'grass'. Some exotic possibilities for improving sensitivity, such as the simultaneous use of a multitude of transmitter and detector frequency channels, were contemplated but these possibilities could not be realized with the technology of the day. It was like experiencing a beautiful sunrise when I first heard about the Fourier spectroscopy results obtained by Anderson and Ernst. However, many pessimists considered the odds to be slim that FT methods would ever become practical for several reasons: limited applications, excessively long T_1 relaxation times were expected (e.g. for ^{13}C), complexity and expense of the method with only minor benefits expected for day-to-day spectroscopy.

For me, it was clear that I just had to give it a try. It is always challenging to find out if the signs of the time are right. It was obvious that the 'lorry approach' of Ernst and Anderson (data transfer to a mainframe computer via truckloads of punchcards) would not be very popular with our customers, whose acceptance of any new method is our measure of success. However, our supplier of data acquisition processors, Fabritek, revealed that they could combine their averaging system with a PDP-8 computer.

Our CW multinuclear spectrometer was already a success and it needed only minor modifications. We had just finished developing a transmitter/receiver time-sharing system in order to get rid of drifting baselines during long accumulations with the traditional modulation scheme. This pulsed mode for frequency sweep spectroscopy utilized a wideband receiver system that was appropriate for Fourier techniques. At the time, while living in the United States, I was also working with a group of engineers in Germany to develop a new broad-band proton decoupler. At once, our design goal became a combined broadband ^{1}H and multinuclear power transmitter.

Many trips across the Atlantic were necessary until in the summer of 1969 two transmitters arrived in Elmsford, NY, Bruker's US headquarters in those years. At the same time a brand-new PDP-8/Fabritek 1074 combination started to work. The first experiments with ^{1}H detection were only marginally successful; the ^{19}F lock was not very stable under the influence of the strong ^{1}H pulses that were being applied to our high-resolution instruments for the first time. Therefore, I decided to have a go at the really tough challenge—broadband ^{1}H-decoupled ^{13}C FT NMR—giving me the chance to check out our new BB decoupler at the same time. I had already decided that noise modulation would not provide efficient decoupling, so I developed a 180° phase modulation scheme with an adjustable sawtooth ramp for the modulation frequency. In fact, this BB method, especially in its later optimized digital form, proved to be the most efficient scheme available until composite pulse methods were introduced in the 1980s. Anyway, back in 1969 the time for serious NMR measurements was usually just after midnight, and when the first ^{13}C test started the screen was filled immediately with what looked like hideous rf interference or cross talk. But wait a moment, *this looks like a free induction decay and it's growing*! Now the time for strong nerves had come: Fourier transformation of a 1k spectrum took 5–10 *minutes*. Then, for the first time, I was looking at a BB-decoupled ^{13}C spectrum with S/N > 100.

A few days later, the Anaheim conference on ^{13}C NMR spectroscopy was to be held, and, of course, I wanted to show the first spectra made with my FT system. So I frantically performed FT NMR spectroscopy day and night on every substance I could get my hands on. It was just so beautiful to be able to measure NMR signals that had never been seen before. I was so excited about turning out spectral 'masterpieces' one after the other that I nearly missed the plane to Los Angeles. One of the first to see my treasures was Tom Farrar. He was so excited himself that he gave me five minutes of his lecture time to present my data (Thanks, Tom!). When the most famous ^{13}C spectroscopist of the CW era stepped into our hospitality suite, he pondered my decoupled ^{13}C spectra hanging on the wall and asked, 'Do you also have ^{13}C data?' It took me a long time to convince him that, in fact, he had ^{13}C spectra before his incredulous eyes (Figure 1).

In the following weeks I learned the basics of FT NMR spectroscopy and ran the first FT spectra of ^{31}P, ^{29}Si, ^{119}Sn, ^{11}B, and several other nuclei. Of course, I was confronted with a number of new problems that required new solutions in order to make the technique as easy to use as CW spectroscopy. Even ^{1}H NMR was increasingly being done with FT methods (only the 'oldtimers' can appreciate how much we missed those beautiful wiggle beats), and I finally found a solution to one of the burning issues for proton FT NMR: *homonuclear* decoupling. All the traditional ways of generating an irradiation sideband failed. As always, when

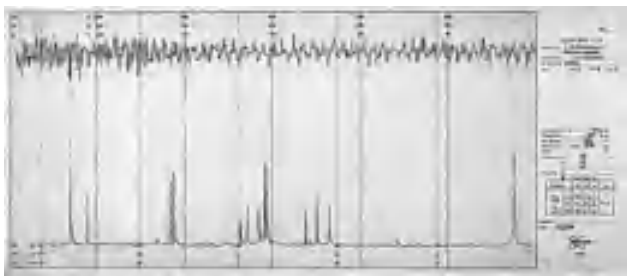

Figure 1 FID and spectrum from one of the first ^{13}C FT NMR experiments. As one can clearly see the spectral paper was the kind we used for ^{13}C CW spectroscopy

Figure 2 ^{13}C FT NMR works, and children have to fetch their goodnight kiss at the spectrometer

NMR knowhow did not help, I had to rely on my electronics background and radar experience, which told me that I should generate the sideband with a fast, repeating pulse (long before DANTE entered the scene). The NMR specialists with whom I consulted were very skeptical of the new idea, which required the synchronization of the decoupler pulse train with the data acquisition dwell time. In the end, pulsed homonuclear decoupling was indeed successful. After a relatively short development time, we proudly exhibited the first FT-only NMR spectrometer at the Pittsburgh conference in 1972.

Biographical Sketch

Tony W. Keller. *b* 1937. Employed with Trüb Täuber AG, Switzerland, NMR division as a service engineer, 1960. Transfer of NMR activities of Trüb Täuber to Spectrospin AG, Switzerland, later appointed as one of the directors, 1965. Establishment of Bruker Group representation in the USA, development of first commercial FT-NMR system, 1969. Employed with Bruker Physik AG being responsible for the NMR division, 1973. Appointed Managing Director, Bruker Analytische Messtechnik GmbH, 1979. Honorary doctorate of the Technical University, Berlin for achievements in the development of NMR, 1989. Author and co-author of numerous patents.

Kessler, Horst: Dynamics by NMR

Horst Kessler

Technical University München, Garching, Germany

In the early 1960s NMR spectroscopy became a popular method for elucidating the structures of organic compounds. Working on my thesis in Tübingen under the guidance of Eugen Müller, I reacted diazomethane catalytically with aromatic compounds yielding norcaradienes or cycloheptatrienes. NMR was ideally suited for identifying the structure of the reaction products. I was soon collecting NMR spectra for the whole group using our 56.4 MHz Varian spectrometer, later with an A-60. The observation of broad lines in several spectra fascinated me and I began to study exchange processes. At that time only a few of these processes were known. Exchange rates which were too fast to allow the isolation of isomers were not accessible. It was a golden age for organic chemists to look at such processes and study substituent effects to elucidate the details of internal mobility.

Substituent effects were used to increase barriers to allow separation, e.g. the first *N*-monosubstituted amide rotamers could be separated in 2,4,6-tri-*tert*-butylacetanilide and the equilibration observed by NMR.[1] Substituent effects have also been used to facilitate rotations about carbon–carbon double bonds via biradical or push-pull stabilized polar transition states. We found several new examples of hindered rotation, e.g. about single bonds and partial double bonds.[2] A particular interest at that time was to prove the mechanism of the *syn–anti* isomerization of imines and related compounds. Substituent effects of X, Y, Z strongly favored the inversion mechanism over single-bond rotation. In particular, stereochemical arguments relating to guanidines with prochiral groups in the *ortho* position provided strong evidence for the preference of the inversion pathway (Scheme 1).[3] We later investigated barriers for ion recombination to covalent species.[4] Free enthalpies of activation of 10 kcal mol^{-1}, for the dissociation and recombination between triphenylchloromethane and the triphenylmethyl cation/chloride anion, for example, were a big surprise to us as solvation effects were ignored at that time.

When the field of DNMR (dynamic NMR) had been established, we turned to peptide conformations which appeared to be of biological relevance. We soon realized that the flexibility of these substances limits and averages the conformational data that can be obtained and hence conformational restrictions provided by cyclization must be utilized.[5] Hence, small cyclic peptides were our primary target in synthesis and for conformational investigation. The advantage of constraints via cyclic modifications of linear bioactive peptides is that higher activity and receptor selectivity can be obtained whereby the bioactive conformation of the recognized peptide sequence can be locked in.[5] Our speculation that small recognition areas should be found in the loop regions of proteins was established in several cases and small cyclic peptides turned out to be the best way for proving the spatial orientation of pharmacophors in peptides (see, for example, for RGD-containing cyclopeptides for the inhibition of cell–cell adhesion).[6] One

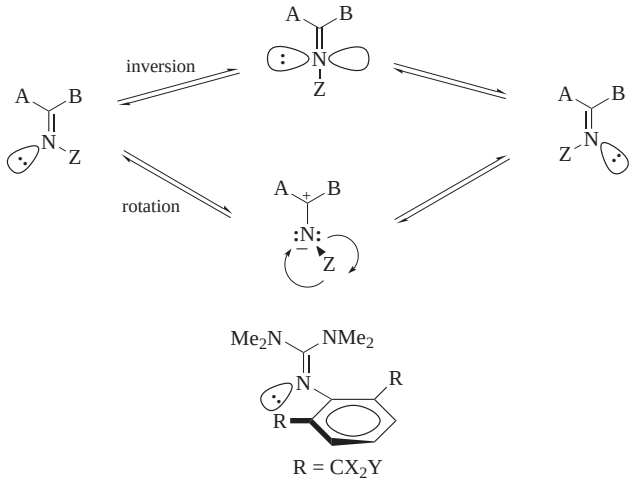

Scheme 1 Inversion and rotation pathways in guidelines

of our patients turned out to be a potent and selective inhibitor for angiogenesis in tumors and may lead to a new concept of tumor therapy.[16] From the viewpoint of an NMR spectroscopist, restriction may force the molecule into a preferred conformation which can be determined experimentally. We also became aware that the preferred conformation does not necessarily coincide with the conformation in the crystal[7] or at the receptor. Hence as many restrictions as possible have to be incorporated into peptides to allow conclusions about the bioactive conformation.

Sensitivity to environmental effects and the lack of sufficient experimental data led us to the 'all-atom approach', whereby ^{15}N and ^{13}C NMR parameters, in addition to those of ^{1}H, are included for structure determination.[8] To avoid circular conclusions, constitutional assignments have to be separated, if possible, from spatial structure determinations. As a consequence we prefer heteronuclear long-range couplings over NOEs for the sequential assignments of a peptide. Restrained molecular dynamics, and later distance geometry calculations, were used to derive an experimentally based structure model compatible with our experiments. This need not be *the* single 'true' structure, if such a thing exists at all. However, many other conformations can be excluded by this procedure.

If sufficient data are available, internal inconsistencies between the experimental NMR parameters can be identified which often indicate conformational flexibility. Rapid conformational equilibria may be detected by analyzing J coupling constants[9] or via NOEs.[10] Recently J coupling constants have also been used as restraints in distance geometry and ensemble calculations.[11]

The most important help for our approach came from the development of multidimensional NMR spectroscopy. We came into this field at the end of the 1970s. The exchange of co-workers with Ray Freeman (Regina Schuck, Hartmut Oschkinat) and Richard Ernst (Herbert Kogler, Christian Griesinger) greatly sped up our ability to use the new methodology. Within a short time we were able to develop or modify the pulse sequences needed for the work mentioned above. To name a few: improved heteronuclear correlations (COLOC as constant time hetero COSY[12]), concatenation of π pulses in H,H,C-relayed COSY,[13] nonsynchronous π pulses for scaling down J coupling in a fixed delay,[14] 1D analog

of 2D experiments by selective Gaussian or half-Gaussian excitation,[15] improvements of some 3D heteronuclear triple resonance experiments, and some methods for extracting coupling constants from multidimensional spectra. In 1986, when Hartmut Oschkinat and Christian Griesinger worked on the 'soft analog' of the relay spectrum, we performed a 2D analog by incrementing the relay–delay yielding 'half a 3D spectrum'[15] which we called the 'one-and-a-half-D' in our lab slang. Later on when Christian went to Richard Ernst, he developed 3D spectroscopy, still in collaboration with Hartmut, who was working with Geoffrey Bodenhausen in Lausanne at that time. What began as playing with ideas turned out to be an important extension of 2D into higher dimensions.

In summary, we have always been interested in the structure and dynamics of molecules as a means of understanding their physicochemical and biological properties. The development of NMR during the last 30 years has sharpened our perception of the structural variety and interconversions between the large number of conformations on different timescales. In this respect, NMR has contributed significantly to the modern view of dynamic structures and their relevance for understanding molecular behavior and molecular recognition.

REFERENCES

1. H. Kessler and A. Rieker, *Liebigs Ann. Chem.*, 1967, **708**, 57.
2. H. Kessler, *Angew. Chem., Int. Ed. Engl.*, 1970, **9**, 219.
3. H. Kessler and D. Leibfritz, *Chem. Ber.*, 1971, **104**, 2143.
4. H. Kessler and M. Feigel, *Acc. Chem. Res.*, 1982, **15**, 2.
5. H. Kessler, *Angew. Chem., Int. Ed. Engl.*, 1982, **21**, 512.
6. M. Gurrath, G. Müller, H. Kessler, M. Aumailley, and R. Timpl, *Eur. J. Biochem.*, 1992, **210**, 911.
7. H. Kessler, G. Zimmermann, H. Förster, J. Engel, G. Oepen, and W. S. Sheldrick, *Angew. Chem., Int. Ed. Engl.*, 1981, **20**, 1053.
8. H. Kessler, H. R. Loosli, and H. Oschkinat, *Helv. Chim. Acta*, 1985, **68**, 661.
9. F. A. A. M. de Leeuw, C. Altona, H. Kessler, W. Bermel, A. Friedrich, G. Krack, and W. E. Hull, *J. Am. Chem. Soc.*, 1982, **105**, 2237.
10. H. Kessler, C. Griesinger, J. Lautz, A. Müller, W. F. van Gunsteren, and H. J. C. Berendsen, *J. Am. Chem. Soc.*, 1988, **110**, 3393.
11. D. F. Mierke, T. Huber, and H. Kessler, *J. Comp.-Aided Mol. Des.*, 1994, **8**, 29.
12. H. Kessler, C. Griesinger, J. Zarbock, and H. R. Loosli, *J. Magn. Reson.*, 1984, **57**, 331.
13. H. Kessler, M. Bernd, H. Kogler, J. Zarbock, O. W. Sørensen, G. Bodenhausen, and R. R. Ernst, *J. Am. Chem. Soc.*, 1983, **105**, 6944.
14. H. Kessler, C. Griesinger, and G. Zimmermann, *Magn. Reson. Chem.*, 1987, **25**, 579.
15. H. Kessler, H. Oschkinat, C. Griesinger, and W. Bermel, *J. Magn. Reson.*, 1986, **70**, 106.
16. P. C. Brooks, A. M. Montgomery, M. Rosenfeld, R. A. Reisfeld, T. Hu, G. Klier, and D. A. Cheresh, *Cell*, 1994, **79**, 1157.

Biographical Sketch

H. Kessler *b* 1940. Ph.D. 1966, Chemistry, Leipzig and Tübingen. Habilitation, 1969, Tübingen. Full Professor of Organic Chemistry, J. W. Goethe University, Frankfurt/Main, 1971–1989. Technical University of Munich, 1989–present. Approx. 325 publications. Foundation and first Chairman of the Fachgruppe Magnetic Resonance Spectroscopy of the German Chemical Society. Research specialties: design of bioactive peptides based on conformation, development and application of new multidimensional NMR techniques, chemical synthesis of peptidomimetics, DG and MD calculations including more experimental parameters and with explicit solvents.

Khetrapal, C. L.: Development of NMR of Oriented Systems

C. L. Khetrapal

Indian Institute of Science, Bangalore, India

The utility of anisotropic NMR parameters, particularly the direct dipolar and quadrupolar couplings, in the precise determination of molecular structure has been well recognized since the early days of NMR. In practice, such interactions have been observed in the solid state and utilized for the study of the structure of crystals since the 1950s. However, the presence of intermolecular interactions in the solid state drastically limits the precision of the derived information. Hence, a well defined goal of NMR spectroscopists was to discover a technique whereby such interactions could be observed and measured from the line-frequency separations rather than the linewidths. Several ideas such as the use of an electric field, the adsorption of molecules in polymers with subsequent stretching, and embedding the molecules in zeolite crystal channels were tried initially, but not much success was achieved until 1963 when Saupe and Englert for the first time prescribed the use of liquid crystals as solvents for such a purpose. This gave birth to the new field of NMR spectroscopy of oriented molecules. Since then the field has developed rapidly, particularly for the determination of relative internuclear distances and bond angles. Though the potentials and promises of the technique become apparent from the principles underlying the phenomena, the actual developments have several interesting stories associated with them.

Soon after their discovery, both Saupe and Englert left Freiburg, Germany, where the discovery was made. Saupe moved to the Liquid Crystal Institute, Kent, OH, USA while Englert joined a pharmaceutical company in Basel, Switzerland. The physical separation of the two was a blessing in disguise for the development of the field. Saupe continued his main research work in the area of liquid crystals per se with some interest in the field of NMR of oriented molecules, particularly in the study of small molecules with high symmetry. Englert in Basel, being in a pharmaceutical company, could not devote a proper share of his time to nursing his own baby but was alert to the potential and utility of the discovery. He, therefore, used to have frequent discussions with Peter Diehl from the Physics Department of the University of Basel. Diehl became keenly interested in exploring and developing this area as a routine method for the study of molecular geometries in the liquid phase. Around the same time, an active group emerged at the Bell Telephone Laboratories headed by Meiboom and Snyder and in Columbia University under the supervision of Dailey with Yannoni as a collaborator. Another active group emerged in England with Buckingham as the leader and Burnell and de Lange as younger colleagues who joined subsequently; they mainly concentrated on the use of the method for the determination of chemical shielding anisotropy. The Bell Lab group, on the other hand, provided the motional constants approach for describing molecular order. The main interest of the group at Columbia was towards the use of the method for the study of chemical shift anisotropies and the structure of highly symmetric molecules such as cyclobutadiene iron tricarbonyl.

It was at this stage in 1967 that I joined Diehl's group in Basel. Though we realized the bright future of the subject, we were slightly discouraged by the warnings of others already in the field. In addition, overall knowledge on the subject was close to nil at that time. The goal, however, was clear. In order to open up the field to practical NMR scientists, the group in Basel studied the dependence of the spectra on the temperature, concentration, and spinning speed of the samples. The use of direct and moment methods for the analysis of such spectra was also developed. Extension to molecules with lower symmetry and to larger molecules was attempted. Studies on intramolecular motions, isotopic effects on molecular structure and order, and quadrupole coupling constants were undertaken. The existence of deceptively simple spectra under various conditions was pointed out. The use of electric fields to rotate the liquid crystal director in the magnetic field was demonstrated. It became obvious during 1968–69 that the spectra of molecules oriented in nematic liquid crystalline phases were, in general, strongly coupled unless heteronuclei were involved. This apparently restricted the utility of the method for the determination of molecular structure and function of systems with more than about six chemically different interacting nuclei. Furthermore, the work on oriented systems utilized nematic phases at high temperatures. At this stage, I left Basel and thus the group bifurcated with the creation of another group at the Tata Institute of Fundamental Research, Bombay, India.

Lyotropic liquid crystals formed by C_8 or C_{10} alkyl sulfates with the corresponding alcohols, sodium sulfate, and water were discovered as orienting media between 10–75°C by Black and others in Cincinnati around 1967–68. The advantage of such media was that they were usable at ambient temperatures and the spectra in general were 'weakly' coupled, and hence amenable to simpler analysis procedures. Subsequently many new lyotropic liquid crystals were discovered and extensively utilized by Reeves and Tracey in Canada, Long and Goldstein in the US and our group in Bombay.

Our group has been involved in the extension of the method to larger spin systems with lower symmetries and organometallic compounds. On the other hand, the Basel group has concentrated mainly on the development of automatic analysis procedures and iterative computer programs for the interpretation of the derived dipolar couplings in terms of molecular structure.

The decade starting in 1970 was the golden age for developments in the field of oriented molecules. The discovery of room temperature thermotropic nematic liquid crystals during this period has been significant in advancing this field. In addition, the use of lyotropic liquid crystals for the study of the dynamic properties of membranes and model systems was proposed by Charvolin in France and Seelig in Basel. Both techniques have been extensively utilized by various active groups such as those of Smith and Bloom in Canada.

The use of specifically deuterated materials followed by proton decoupling as a technique for the simplification of complicated proton spectra proposed by Meiboom, Snyder, and Luz in 1971–73 was a landmark. The use of perdeuterated

systems as an aid to the analysis of complicated proton spectra is a corollary of the above and has been extensively employed. At this stage, Luz moved over to Israel and established a group there. This group has been most active in developments relating to spectral simplifications, dynamical studies, and smectic and discotic liquid crystals. Simultaneously, I visited Kent for about a year and collaborated with Saupe in solving various structural and conformational problems of chemical interest.

Subsequently, the Bombay group in India shifted to Bangalore to establish an active group there. Efforts were still concentrated towards developing techniques for spectral simplifications, since none of the above-described methods could provide a routine technique for such a purpose. The pioneering work of Alex Pines and his colleagues in Berkeley in the use of multiple quantum and zero field spectroscopies in the late 1970s and early 1980s were steps forward in this direction. Various two-dimensional NMR techniques have been proposed and extensively exploited for such purposes by the groups of Emsley in Southampton, myself and Anil Kumar in Bangalore, and Fung in Oklahama. Emsley and his offshoots in Italy became active in the interpretation of ultracomplicated spectra. They claim that they should be able to analyze the spectrum of any molecule however complex it may be.

In the meantime, magic angle spinning methods became available commercially. I proposed in 1979–80 that the use of near magic angle sample spinning could be employed for the simplification of the spectra of oriented molecules. This was achieved experimentally by Grant and his colleagues around 1981.

At this stage, Ted Becker of the National Institutes of Health, USA became deeply interested in exploring the utility of the technique for biologically important problems. He invited me to collaborate with him in this area. This resulted in many significant developments in the field of NMR of oriented biologically important molecules, such as substituted imidazoles, model peptide systems, and substituted uracils, etc.

Another breakthrough in the technique towards new applications took place in Bangalore in 1981–82 where the use of liquid crystals of opposite diamagnetic anisotropies was proposed. In view of the utility of such experiments, an independent chapter on this topic is included in this Encyclopedia (***Liquid Crystals: Mixed Magnetic Susceptibility Solvents***).

Other active groups which emerged in the 1980s are those of Bucci, Veracini, Longeri, and Chidichimo in Italy. They have specialized in maximum entropy approaches and flexible molecules. During the same period an active group under the supervision of Jokisaari developed in Oulu in Finland in collaboration with Diehl in Basel. This group specialized in the study of structural and conformational problems of various types, such as those in spherical molecules, rare gases, and the use of mixed liquid crystals of opposite diamagnetic anisotropies.

In 1989, Diehl visited Bangalore, and we initiated work on the study of metal-ion ligand interactions in thermotropic liquid crystals and discovered induced smectic phases in mixtures of nematics using NMR.

In the current decade, the state-correlated two-dimensional NMR experiments proposed by Akasaka and his team in Japan appear to be potentially valuable for spectral analysis purposes.

The use of an electric field for orienting the molecules has been developed by MacLean and his colleagues in the Netherlands, essentially in the 1980s. The use of a magnetic field for similar purposes is a future hope when spectrometers operating at ultrahigh magnetic fields become available.

Biographical Sketch

C. L. Khetrapal. *b* 1937. M.Sc., 1959, Allahabad, Ph.D., 1965, Bombay. Introduced to NMR by S. S. Dharmatti. Worked at Tata Institute of Fundamental Research, Bombay, 1959–73 in various positions, the last one being reader; Raman Research Institute, Bangalore, 1973–84, as Associate Professor and Indian Institute of Science, Bangalore, 1984–present, as Professor and Head, Sophisticated Instruments Facility. Nearly 200 publications and several reviews, books, and monographs. Research interests include NMR of oriented systems with emphasis on molecular structure and function, developments of novel techniques, and applications of NMR imaging and in vivo spectroscopy to problems of agricultural interest.

Klein, Melvin P.: Recollections of 40 Years of Magnetic Resonance at Berkeley

Melvin P. Klein
Lawrence Berkeley Laboratory, University of California, Berkeley, CA, USA

My introduction to magnetic resonance derived from the great activity in Berkeley during the early 1950s because of the presence of the experimentalists Erwin Hahn, Carson Jeffries, Walter Knight, and Arthur Kip, all of whom were prodded on by the theorist Charles Kittel. George Feher was also a graduate student and it was in kibitzing his experiments on EPR in the alkali metals at 100–300 MHz that I first saw a resonance curve traced out.

The need for a good magnetic field measurement obliged me to get some hands-on experience with magnetic resonance and also to become acquainted with the spins and moments of many nuclides other than protons. This led subsequently to the measurements of the abundance ratio of the lithium isotopes in collaboration with B. E. Holder.[1] Measurement of the chemical shifts of nitrogen followed.[2]

One of our colleagues, the late G. E. Barton, Jr., was performing mass spectroscopy with data acquisition by ion counting into a pulse height analyzer. The nuclear physics community had developed these devices to measure the energy-intensity distribution of γ-rays. In these devices an analog-to-digital converter measures the height of the light pulse produced by a scintillator–photomultiplier and converts it into an address, adding one count to the register corresponding to that address. Barton's mass spectrometer was arranged to map the magnetic field intensity, corresponding to a given e/m ratio, onto an address in the analyzer and to add a count for each ion reaching the detector. We had often discussed that such a scheme would be very useful for our NMR and EPR measurements, if we could find some clever way of digitizing the outputs of these spectrometers.

These feelings were reinforced during a sabbatical at Bell Labs where I often passed by a Mössbauer apparatus dutifully accumulating ^{57}Fe counts as a function of the velocity of the sample. Shortly after my return to California we learned of the newly developed voltage-to-frequency converter. Barton and I immediately acquired one of these devices, connected it to a borrowed pulse height analyzer, and in a relatively short time demonstrated signal averaging. Our most impressive achievement at that time was to acquire the signal of deuterium in natural abundance in absorption, without a lock-in.[3]

It is surely not my intention to review all of our activities but a few areas do stand out in my memory.

As sensitivity and signal-to-noise ratio seem to have been a preoccupation, I fondly recall the measurement of the NMR in an excited state of a short-lived radionuclide. In this experiment the technique of perturbed angular correlation was employed. A parent nucleus decays by two successive γ-rays with a common intermediate state. The angular correlation between the γ-rays was measured and then the effects of a radiofrequency field on this time correlation function determined. We were able to detect essentially the NQR of this state with some 200 000 counts.[4]

The excitement of the Fourier transform spectroscopy introduced by Ernst and Anderson did not take long to cross San Francisco Bay. We acquired FIDs in a primitive signal averager which was in turn connected to a paper tape punch. Data were carried from the campus to Lawrence Berkeley Laboratory, where the computers we used were located together with some program elements that Richard generously supplied. Surely, the FTs worked. One day John Waugh called and suggested that we do T_1 measurements by FT methods for complex spectra. That, too, worked nicely.[5] The technical endeavors of John Despotakis who built the first computer based (PDP-8) data acquisition system for performing FT NMR are warmly remembered.

It was during this period that Himan Sternlicht, then in the Berkeley Chemistry Department, became convinced that ^{13}C NMR would become an enormously useful tool. He began his work using indirectly detected resonance, but knew exactly the benefits to be derived from pursuing the Fourier methods. He began such work in Berkeley but unfortunately left the field.[6] His prescience is amply justified by the impact that ^{13}C spectroscopy has had in the chemical and biological sciences.

Another Berkeley colleague, J. B. Neilands, had isolated a series of small natural iron chelators which he called siderophores, principally the ferrichromes. These compounds with a molecular weight of about 1 kD were of broad interest. The EPR signals of the high spin Fe^{3+} were among the first of the well-studied g = 4.3 species.[7] The Mössbauer spectra of these molecules were the first to exhibit and have relaxation effects explained.[8] The Fe^{3+} ion could be replaced by Al^{3+} and Ga^{3+}. Thus they became amenable for study by high-resolution NMR in our then state-of-the-art 220 MHz spectrometer. Our student Miguel Llinas carried structural interpretations far beyond anything we believed possible at the outset.[9] It was on these molecules that the first FT double resonance experiments were performed on ^{15}N-substituted molecules.[10] Had we looked and thought more carefully about these spectra, we might have stumbled onto 2D heteronuclear NMR before it was first suggested by Jeener.[11]

Our activities in proton and ^{31}P NMR in model and true membranes with Rick Horwitz, Danny Michaelson, and Sue Kohler[12] were followed by Kohler's measurements on single crystals of model phosphorus-bearing compounds, the aim of which was to provide the full shift-tensor information.[13] The motionally-averaged spectra could then be used to infer correlation times of the motion of phospholipids in the membranes. Much later, ^{31}P data became important for in vivo spectroscopy and Sun Un was able to use MAS spectra to derive information on the forms of ATP in tissue.[14]

The early endeavors by two students, Greg Karczmar and Alan Koretsky, into in vivo NMR spectroscopy have led them to very productive careers.[15] The excellent experiments and interpretations on ammonium ions in the solid phase by Tom Pratum also stand out.[16]

Finally, our introduction of ^{3}H NMR as a highly useful addition to the toolbox of biological NMR is recalled with pleasure. This activity was inspired by my colleague R. M. Lemmon who had begun the synthesis of tritiated compounds for the purposes of tracing the pathways of molecules in the photosynthetic conversion of CO_2 to carbohydrates under

Melvin Calvin's urging. It was possible to know the specific activity of the labeled compound, but the distribution of the label in the compound could only be guessed from the synthetic routes. As the chemical shifts of ^{3}H and ^{1}H are identical on a ppm scale, aside from some very subtle isotope effects, a tritium NMR (TMR) spectrum would be directly interpretable. The National Tritium Labeling Facility at LBL was subsequently established and uses TMR in a routine fashion.[17]

I have enjoyed and benefited enormously from the interactions with colleagues in the magnetic resonance com-munities. Most especially, I acknowledge the contributions and friendship of the students, postdoctoral fellows, sabbatical visitors and other colleagues with whom I have had the privilege of working. They are: W. A. Anderson, W. E. Blumberg, R. D. Britt, A. Bothner-By, M. Calvin. P. J. Carson, S. I. Chan, V. J. DeRose, J. Despotakis, S. L. Dexheimer, J. D. Ellett, R. E. Ernst, K. E. Falk, R. Freeman, D. M. Grant, M. Guéron, E. L. Hahn, J. A. Happe, B. E. Holder, W. J. Horsley, A. F. Horwitz, J. S. Hyde, C. D. Jeffries, G. S. Karczmar, S. J. Kohler, A. P. Koretsky, J. C. Lagarias, M. Llinas, W. Lubitz, J. L. Markley, A. E. McDermott, E. Matthias, D. M. Michaelson, W. B. Mims, K. Möbius, C. M. Oshiro, M. E. Packard, D. E. Phelps, A. Pines, A. M. Portis, T. K. Pratum, I. Salmeen, J. C. Schoolery, W. C. Shih, D. A. Shirley, G. E. Smith, D. Stehlik, H. Sternlicht, D. M. Teaney, M. Tomkeiwicz, R. L. Vold, C. G. Wade, R. L. Ward, J. S. Waugh, M. W. Weiner, D. E. Wemmer, H. H. Wickman, P. G. Williams, D. M. Wilson, K. Wüthrich, and V. K. Yachandra.

REFERENCES

1. M. P. Klein, and B. E. Holder, *Phys. Rev.*, 1955, **106**, 837.
2. B. E. Holder and M. P. Klein, *J. Chem. Phys.*, 1955, **23**, 1956.
3. M. P. Klein and G. W. Barton, Jr., *Rev. Sci. Instrum.*, 1963, **34**, 754.
4. E. Mathias, D. A. Shirley, M. P. Klein, and N. Edelstein, *Phys. Rev. Lett.*, 1966, **16**, 974.
5. R. L. Vold, J. S. Waugh, M. P. Klein, and D. E. Phelps, *J. Chem. Phys.*, 1968, **48**, 3831.
6. W. J. Horsley, H. Sternlicht, and J. S. Cohen, *Biochem. Biophys. Res. Commun.*, 1969. **37**, 47.
7. H. H. Wickman, M. P. Klein, and D. A. Shirley, *J. Chem. Phys.*, 1965, **42**, 2113.
8. H. H. Wickman, M. P. Klein, and D. A. Shirley, *Phys. Rev.*, 1966, **152**, 345.
9. M. Llinas, M. P. Klein, and J. B. Neilands, *J. Mol. Biol.*, 1970, **52**, 399.
10. M. Llinas, W. J. Horsley, and M. P. Klein, *J. Am. Chem. Soc.*, 1976, **98**, 7554.
11. J. Jeneer. AMPèRE Summer School, Basko Polje, Yugoslavia, 1971.
12. A. F. Horwitz, M. P. Klein, D. M. Michaelson, and S. J. Kohler, *Ann. N. Y. Acad. Sci.*, 1973, **222**, 468.
13. S. J. Kohler, J. D. Ellett, Jr., and M. P. Klein, *J. Chem. Phys.*, 1976, **64**, 4451.
14. S. Un and M. P. Klein, *J. Am. Chem. Soc.*, 1989, **111**, 5119.
15. G. S. Karczmar, A. P. Koretsky, M. J. Bissell, M. P. Klein, and M. W. Weiner, *J. Magn. Reson.*, 1983, **53**, 123.
16. T. K. Pratum and M. P. Klein, *J. Magn. Reson.*, 1989, **81**, 350.
17. R. D. Newmark, S. Un, P. G. Williams, P. J. Carson, H. Morimoto, and M. P. Klein, *Proc. Natl. Acad. Sci. USA*, 1990, **87**, 583.

Biographical Sketch

Melvin P. Klein. *b* 1921. A.B., 1952, University of Colorado, Denver, Ph.D., 1958, University of California, Berkeley. Employed at Lawrence Berkeley Laboratory, University of California, 1952–present. Approx. 200 publications. Current research specialties: X-ray absorption spectroscopy, CW and time domain EPR to study structure and function of photosynthetic oxygen-evolving complex.

Klinowski, Jacek: Historical Sketch: Molecular Sieves

Jacek Klinowski
University of Cambridge, Cambridge, UK

The development of magic angle spinning (MAS) NMR by Andrew and his colleagues[1,2] at the University College of North Wales, Bangor, and by Lowe[3] at Washington University, St. Louis, initiated a new era in the structural study of solids. The technique has greatly enhanced our knowledge of a wide range of materials used in chemical, physical, biological, and earth sciences, and in the technology of glass and ceramics. The term 'magic angle spinning' was coined by Gorter in 1960 when he heard Andrew's results presented at the AMPERE congress in Pisa.

It took nearly 20 years for MAS to become a routine tool for structural investigation. The reasons were the difficulty of spinning the sample at the very high speeds required and the insufficiently high magnetic fields. However, the introduction of Fourier transform NMR, cross polarization, and superconducting magnets during the 1960s and 1970s greatly improved the sensitivity of the spectra. Schneider, Pivcova, and Doskočilová used ^{1}H MAS NMR for the study of polymers,[4] and Schaefer and Stejskal[5] were the first to combine MAS and cross polarization for the ^{13}C NMR of organics.

The field of molecular sieves has particularly benefited from the introduction of MAS. Molecular sieves are a family of porous open-framework solids which includes zeolites as well as materials derived from aluminum phosphate. Zeolites are built from corner-sharing SiO_4 and AlO_4 tetrahedra linked by the apical oxygen atoms to form frameworks of high internal surface area with regular channels and cavities of molecular dimensions. Their microporous structure enables zeolites to be used as sieves (as they can only adsorb molecules of certain size), cation exchangers, and catalysts for cracking, hydrocracking, oxidation, and isomerization of hydrocarbons. Most synthetic molecular sieves are microcrystalline and thus difficult to study by conventional methods of structural elucidation.

I had been working on molecular sieves at Imperial College, London since 1969 with R. M. Barrer, the pioneer in the field. In late 1979 the first high-resolution ^{29}Si MAS NMR spectra of zeolites measured jointly by groups led by Lippmaa (Tallinn, Estonia) and Engelhardt (Berlin) were shown as a poster at an obscure conference in the then East Germany.[6] I had just moved to Cambridge, and was greatly excited by these results. The head of my Department, Professor (now Sir) John Meurig Thomas suggested to C. A. Fyfe, then at the University of Guelph, Canada, that we embark on a joint project. We began work on 9 January 1981. Several other research groups, notably those at EXXON (led by Melchior), Shell-Amsterdam, Leipzig (Pfeifer and Freude), Namur (Derouane and Nagy), Nijmegen (Veeman), and Paris (Fraissard) embarked on their own investigations. I have been interacting with many of these workers and was privileged to witness the rapid development of the field at first hand.

MAS NMR opened a completely new layer of insight into the structure of molecular sieves, and for several months one could simply take a sample off the shelf to obtain results which were novel, fascinating, and important. Framework Si in zeolites is four-coordinate, and thus there are five different possible environments of a silicon atom: $Si(OAl)_4$, $Si(OAl)_3(OSi)$, $Si(OAl)_2(OSi)_2$, $Si(OAl)(OSi)_3$, and $Si(OSi)_4$. Accordingly, the ^{29}Si MAS spectra are normally composed of up to five signals corresponding to these structural units.[7–11] The Si/Al ratio of the zeolitic framework can be calculated from the spectra, and the distribution of Si and Al atoms in the structure, which has important catalytic consequences, can be determined.[8] By comparing $(Si/Al)_{NMR}$ values with the results of chemical analysis, which gives bulk composition, the amount of extraframework aluminum in chemically modified zeolites can be determined.[9,10] The fact that the ^{29}Si chemical shift is related to the T–O–T angles and mean Si–O bond distances in zeolitic frameworks is also useful for structural studies.[12,13]

The situation in highly siliceous zeolites, such as silicalite/ZSM-5, is very different, because there is little or no aluminum present. ^{29}Si MAS NMR spectra are composed of $Si(OSi)_4$ signals corresponding quantitatively to nonequivalent sites for silicon.[14] In the case of silicalite as many as 22 of the 24 inequivalent silicons can be distinguished by NMR. The fine structure of the spectra depends on the temperature and is also affected by the presence of adsorbed organics.[15,16] Thus NMR monitors subtle local rearrangements of atoms in the structure, an effect which cannot be readily studied by X-ray diffraction.

^{27}Al MAS NMR spectra of many natural and synthetic zeolites were measured soon after, providing new insights into the chemical status of aluminum. At first, the spectra were in apparent disagreement with the combined results of ^{29}Si MAS NMR and chemical analysis, but it was soon shown that ^{27}Al spectra must be measured at high fields and with very short radiofrequency pulses in order to be quantitatively reliable. ^{27}Al MAS NMR distinguishes between four- and six-coordinate aluminum (the latter is present in chemically treated zeolites), while quadrupole nutation NMR allows different Al species to be monitored.[17]

The Brønsted acidity of zeolites, responsible for their catalytic activity, arises from the presence of accessible hydroxyl groups associated with framework aluminum ('structural hydroxyls'). The acidic protons are relatively far apart which considerably reduces their dipolar interaction and important information on the chemical status of hydroxyl groups in dehydrated zeolites has been obtained by ^{1}H NMR, mainly by the Leipzig group. Extensive ^{1}H MAS NMR measurements of zeolites[18] have led to the assignment of the various proton resonances. ^{1}H NMR of static samples can also probe the geometry of the Brønsted acid site using the moment method.

^{13}C MAS NMR spectra of organic molecules intercalated in zeolites established that the templating tetrapropylammonium cations in zeolite ZSM-5 are located at channel cross sections in such a way that two hydrocarbon chains extend into the straight channels and two into the zigzag channels.[19] ^{13}C MAS NMR spectra identify 29 different organic species in the intracrystalline space of zeolite ZSM-5 during the catalytic conversion of methanol to gasoline and monitor their fate as a function of time and temperature; demonstrate the reality of product shape selectivity in a zeolite and the presence of a new type of shape selectivity; and distinguish between mobile and attached species.[20,21]

There has been much interest in the use of ^{129}Xe (spin $I = \frac{1}{2}$ and 26.4% natural abundance) as a probe for investigating microporous materials.[22,23] The technique can monitor sample crystallinity and is sensitive to the size and content of the cavities and channels.

A new challenge for NMR came in 1982 with the discovery of the $AlPO_4$ molecular sieves, porous equivalents of aluminum phosphate built from alternating AlO_4 and PO_4 tetrahedra. Incorporation of an Si source into the synthetic gel results in the formation of silicoaluminophosphates, SAPO, and the incorporation of a metal into $AlPO_4$ and SAPO gives the MeAPO and MeAPSO sieves, respectively. VPI-5, containing 18-membered rings of Al and P atoms, has considerable potential for the separation and catalytic cracking of large molecules. Cloverite, a gallophosphate with 20-membered rings, is the most porous molecular sieve prepared so far.

The $AlPO_4$ sieves are a challenge to solid state NMR, given the wide variety of new crystal structures and the presence of two kinds of 100% abundant nuclei (^{31}P and ^{27}Al) in close proximity.[24] Also, some Al atoms in $AlPO_4$ may be five or six-coordinate, which makes possible a wide range of structures. Another challenge is the strong quadrupolar interactions of ^{27}Al. In the last decade $AlPO_4$ sieves have been studied in many countries. ^{27}Al double rotation (DOR), a technique in which the sample is rotated around two different axes simultaneously, can monitor the structure of these materials,[25] and spin echo double resonance (SEDOR) can establish the relative spatial disposition of spins.

I am confident that advanced methods, such as 2D solid state NMR and laser-assisted techniques, will soon be employed to resolve many hitherto inaccessible problems of molecular sieve chemistry. The field is certain to flourish in the years to come.

REFERENCES

1. E. R. Andrew, A. Bradbury, and R. G. Eades, *Nature (London)*, 1958, **182**, 1659.
2. E. R. Andrew, *Int. Rev. Phys. Chem.*, 1981, **1**, 195.
3. I. J. Lowe, *Phys. Rev. Lett.*, 1959, **2**, 285.
4. B. Schneider, H. Pivcova, and D. Doskocilova, *Macromolecules*, 1972, **5**, 120; D. Doskocilova and B. Schneider, *Macromolecules*, 1972, **5**, 125.
5. J. Schaefer and E. O. Stejskal, *J. Am. Chem. Soc.*, 1976, **98**, 1031.
6. G. Engelhardt, D. Kunath, A. Samoson, M. Tarmak, and E. Lippmaa, *Workshop on the Adsorption of Hydrocarbons in Zeolites, Berlin-Adlershof, GDR, 19–22 November* 1979.
7. E. Lippmaa, M. Mägi, A. Samoson, G. Engelhardt, and A.-R. Grimmer, *J. Am. Chem. Soc.*, 1980, **102**, 4889; E. Lippmaa, M. Mägi, A. Samoson, M. Tarmak, and G. Engelhardt, *J. Am. Chem. Soc.*, 1981, **103**, 4992.
8. J. M. Thomas, C. A. Fyfe, S. Ramdas, J. Klinowski, and G. C. Gobbi, *J. Phys. Chem.*, 1982, **86**, 3061; J. Klinowski, S. Ramdas, J. M. Thomas, C. A. Fyfe, and J. S. Hartman, *J. Chem. Soc., Faraday Trans. 2*, 1982, **78**, 1025.
9. J. Klinowski, J. M. Thomas, C. A. Fyfe, and G. C. Gobbi, *Nature (London)*, 1982, **296**, 533.
10. I. E. Maxwell, W. A. van Erp, G. R. Hays, T. Couperus, R. Huis, and A. D. H. Clague, *J. Chem. Soc., Chem. Commun.*, **1982**, 523.
11. M. T. Melchior, D. E. W. Vaughan, and A. J. Jacobson, *J. Am. Chem. Soc.*, 1982, **104**, 4859; M. T. Melchior, D. E. W. Vaughan, R. H. Jarman, and A. J. Jacobson, *Nature (London)*, 1982, **298**, 455.
12. J. V. Smith and C. S. Blackwell, *Nature (London)*, 1983, **303**, 223.
13. J. M. Thomas, J. Klinowski, S. Ramdas, B. K. Hunter, and D. T. B. Tennakoon, *Chem. Phys. Lett.*, 1983, **102**, 158; S. Ramdas and J. Klinowski, *Nature (London)*, 1984, **308**, 521.
14. C. A. Fyfe, G. C. Gobbi, J. Klinowski, J. M. Thomas, and S. Ramdas, *Nature (London)*, 1982, **296**, 530.
15. G. W. West, *Aust. J. Chem.*, 1984, **37**, 455.
16. H. Strobl, C. A. Fyfe, G. T. Kokotailo, C. T. Pasztor, and D. M. Bibby, *J. Am. Chem. Soc.*, 1987, **109**, 4733; C. A. Fyfe, G. J. Kennedy, C. T. DeSchutter, and G. T. Kokotailo, *J. Chem. Soc., Chem. Commun.*, **1984**, 541.
17. K. F. M. G. J. Scholle, A. P. M. Kentgens, W. S. Veeman, P. Frenken, and G. P. M. van der Velden, *J. Phys. Chem.*, 1984, **88**, 5.
18. D. Freude, M. Hunger, H. Pfeifer, and W. Schwieger, *Chem. Phys. Lett.*, 1986, **128**, 62.
19. G. Boxhoorn, R. A. van Santen, W. A. van Erp, G. R. Hays, R. Huis, and D. Clague, *J. Chem. Soc., Chem. Commun.*, **1982**, 264.
20. M. W. Anderson and J. Klinowski, *Nature (London)*, 1989, **339**, 200; *J. Am. Chem. Soc.*, 1990, **112**, 10.
21. B. R. Richardson, N. D. Lazo, P. D. Schettler, J. L. White, and J. F. Haw, *J. Am. Chem. Soc.*, 1990, **112**, 2886.
22. L.-C. de Menorval, J. P. Fraissard, and T. Ito, *J. Chem. Soc., Faraday Trans. 1*, 1982, **78**, 403.
23. P. J. Barrie and J. Klinowski, *Prog. NMR Spectrosc.*, 1992, **24**, 91.
24. P. J. Barrie, *Adv. Spectrosc.*, 1993, **22**, 151.
25. R. Jelinek, B. F. Chmelka, Y. Wu, P. J. Grandinetti, A. Pines, P. J. Barrie, and J. Klinowski, *J. Am. Chem. Soc.*, 1991, **113**, 4097.

Biographical Sketch

Jacek Klinowski. *b* 1943. M.Sc., 1965, Dr.Rer.Nat., 1968, Jagiellonian University, Kraków (Cracow), Poland, Ph.D., University of London, 1973, Diploma of Imperial College, 1973, M.A., University of Cambridge, 1988. Assistant Director of Research, University of Cambridge. 262 Publications and, with Jacek Hennel, the book 'Fundamentals of Nuclear Magnetic Resonance'. Editor-in-Chief, *Solid State Nuclear Magnetic Resonance*. Current research specialty: all aspects of solid state NMR.

Knight, Walter D.: The Knight Shift

Walter D. Knight
University of California, Berkeley, CA, USA

INTRODUCTION—HOW TO FIND A THESIS

I received the M.A. degree in physics at Duke University in 1943, and completed course requirements for the Ph.D. Then there was an interruption during 1944–45 when I joined the US Navy, saw small parts of the world on radar screens, and learned a lot about electronics. Subsequently I accepted a position as an Assistant Professor at Trinity College, Hartford, to work under Professor F. W. Constant, who had been one of my teachers and M.A. thesis supervisor at Duke. In seeking a way to complete the doctorate, I consulted Norman Ramsey who was Head of the Physics Department at Brookhaven National Laboratory. He pointed out that molecular beam magnetic resonance (MBMR) had been the preferred method for measuring nuclear moments[1] because of the high accuracy obtainable. However, the new methods based on the nuclear magnetic resonance techniques of Bloch and Purcell had the combined advantages of accuracy, simplicity, and sensitivity for bulk solid or liquid materials.

My conversations with Ramsey resulted in a summer (1948) position for me in the newly established Nuclear Moments Laboratory at Brookhaven. Bill Cohen, who like Ramsey had been a student of Rabi, was running the nuclear moments program. Bill suggested that I visit Bob Pound's lab at Harvard to learn about his marginal oscillator-detector, which was tunable over the wide frequency ranges needed to search for nuclear magnetic resonances. At the time, interest in nuclear moments was stimulated by the recently developed nuclear shell model. The problem was interesting and I decided to work along these lines hoping that a specific thesis topic would emerge.

In the rest of this article I will concentrate primarily on some related pieces of work which were intimately known to me during the 1950s and 1960s. Some of this is of course out of date, but it is of historical interest. References 1, 4, 6 and 16, which cover that period of time, give extensive coverage of the problems to be discussed, and may be consulted for details and further references.

SEARCHING FOR A RESONANCE

Bill Cohen designed and oversaw the construction of a suitable electromagnet, and I constructed a marginal oscillator based on Pound's circuit, with generous assistance from Bob on details. Thanks to plenty of training in electronics in the Navy radar programs, I found the construction easy and we found a proton resonance on our first attempt. However, it was difficult to maintain stable oscillation and sensitivity over wide frequency ranges, and so I decided to try a simpler circuit based on the cathode-coupled oscillator. Later, I explained the new oscillator to Pound, who liked it and put his student George Watkins to work analyzing it and constructing an improved version, which came to be known in the trade as the 'Pound Box'.[2] The summer was soon over, and I returned to teaching at Trinity College. During the college year I spent many weekends traveling to Brookhaven improving the NMR system, returning to Hartford in time to teach Monday morning classes. The following summer (1949) I resumed the search for nuclear magnetic resonances at Brookhaven.

The first search was for resonances in antimony, which has two isotopes ^{121}Sb and ^{123}Sb having different nuclear spins and magnetic moments—hopefully, we could bag two birds in one search! The first run was on a sample of antimony trichloride.

A good signal appeared to the delight and excitement of all in the lab, but unfortunately the observed resonance occurred nowhere near the frequency expected from the spectroscopic magnetic moments. Could it be an impurity? ... we dumped the sample and ran the empty test tube ... the signal persisted ... what is in Pyrex glass? ... boron! ... sure enough, the observed frequency was close to that expected for boron ... for a double check we removed the test tube entirely, which eliminated the boron signal ... then a previously unseen signal appeared near the frequency which Pound had reported for ^{63}Cu signals originating within the rf skin depth of the copper resonance coil ... but our observed frequency was about 20 kHz higher than what is expected from the standard tables of nuclear moments ... were there any other known moments close to copper? ... no ... was there an error in the tables? ... no ... In order to be sure of the effect we constructed a sample mixture of dry powders of copper metal and cuprous chloride. The resulting experimental resonance profile showed two well-resolved peaks, with the resonance for the pure metal appearing approximately 20 kHz above the resonance for the nonmetallic salt, around a 10 MHz average frequency. The measured relative shift was 0.23%.

Later that day Sam Goudsmit, who was Director of Brookhaven at the time, came by the lab to see the new results. I asked his advice whether I should pursue the search for new magnetic moments or continue studying the shift. He replied that naturally new physics should be more productive than another moment in the tables, and we returned to the experiments this time to determine what was shifting and why. In a flurry of activity in the next few weeks we investigated several other metals, including sodium, aluminum, and liquid gallium, each with its unique shift, and determined that isotopic pairs such as ^{63}Cu and ^{65}Cu possess equal shifts and that the fractional frequency shift was independent of the resonance field.[3]

A THEORY TO MATCH THE EXPERIMENT

Charlie Townes had moved to Columbia, and was spending time at Brookhaven that summer. He mentioned some of his recent work on hyperfine structure in molecules, and suggested that the NMR shift in metals might result from a hyperfine interaction between the magnetically polarized metal conduction electrons and the magnetic moments of atomic nuclei. The hyperfine field should augment the applied field and shift the resonance to a higher frequency. He suggested I try to estimate the magnitude of the effect in terms of the Pauli

electronic paramagnetism and the contact term for s-electron hyperfine interaction. I studied up on hyperfine structure, located Goudsmit's formula for the contact interaction, and got a result which agreed quite well with the experimental shift for sodium. In further discussions, Charlie took me to the article of Sommerfeld and Bethe in the 'Handbuch der Physik' and explained how the atomic hyperfine structure differs from the corresponding average for electrons at the Fermi surface of a metal. The average contact hyperfine field at the nucleus for an electron at the Fermi surface is[4–6]

$$\Delta B = (8\pi/3)[\chi_{\mathrm{p}} V_0 B] P_{\mathrm{F}} \qquad (1)$$

where χ_{p} is the Pauli susceptibility per unit volume, V_0 is the atomic volume, and B is the applied magnetic field. The quantity P_{F} is the probability density for the s electron at the nucleus, averaged over electrons at the Fermi surface. The relative frequency shift, $K = \Delta f/f = \Delta B/B$, and the above equation may be used in several ways, depending on what quantity is to be obtained. For example, in metals where χ_{p} can be measured directly, P_{F} may be calculated from equation (1).

Having established that all the other metals studied showed comparable shifts of a few tenths of a percent, we were surprised to find no measurable effect in beryllium. Charlie arranged a consultation with Conyers Herring,[5] who had recently published an article with Hill on the electronic structure of Be. Herring believed that the hyperfine field, equation (1), is low because of the strong p character (low P_{F}) of the wavefunction and also an abnormally low density of states (low χ_{p}) at the Fermi level.

In early investigations we studied the metals Li, Be, Na, Al, V, Cu, liquid Ga, and nonmetallic white phosphorus.[3] The shift in white P compared to the nonmetallic phophorus trichloride was approximately 0.1%. Ramsey[1] recognized that the observed nonmetal (chemical) shifts were caused mainly by Van Vleck orbital paramagnetism, which produces a smaller hyperfine field than does the contact interaction. Later[1] Bill Dickinson reported shifts depending on solution concentration, and Warren Proctor et al. reported shifts in several chemical compounds.

THE NUCLEUS AS A NONINVASIVE STRUCTURAL PROBE

While I was completing my thesis during the spring of 1950, I made several trips to New York to consult with Charlie Townes, who continued to be my informal adviser providing me with strong support. Charlie told me that he had given a talk in about 1949 with a title something like 'The Nucleus as a Probe of Structures'. Understanding that 'structures' include molecular and crystalline structures and electronic structures as well, the probe idea became the main theme of NMR experiments. The NMR and quadrupole coupling energies are in most cases negligible in comparison with atomic and molecular binding energies. Consequently the resonance experiments can be used to measure local internal fields in materials, without disturbing the basic structure of the system under study.

The NMR lineshift K in metals, named 'Knight shift' by Bloembergen,[6] is a phenomenon unique to the metallic state since it depends on conduction electrons, and it enables a practical analytical technique for probing systems endoscopically. The Knight shift has been used in many studies, including the melting of metals, metal–insulator transitions, normal–superconducting transitions, and phase transitions and magnetic couplings in metal alloy systems.

ANALYSIS OF ELECTRONIC AND GEOMETRICAL STRUCTURES

When I moved from Hartford to Berkeley in 1950, the Physics Faculty, particularly Owen Chamberlain, Emilio Segre, and Charlie Kittel (who arrived about the same time as me), were generous in their support for a new young colleague. Bob Brode gave me a couple of research labs, and I received for start-up a few kilobucks, which was around 1% of present custom. Most of this provided for construction of a permanent magnet and materials. I built the electronics.

I was also greeted by three graduate students who were all fired up and ready to join the exciting new game of NMR physics. We planned projects for the three students to work on Knight shifts in alkali metals, in metallic alloys, and chemical shifts in phosphorus. We organized a seminar on NMR, including some interested chemists. For a while, the seminar consisted mainly of a series of presentations by Al Overhauser on electron interactions in metals and the 'Overhauser effect', the enhancement of the nuclear polarization by interaction with the much larger conduction electron polarization. It was exciting to be led, chapter by chapter, through Al's thinking in the early stages. Actually there was considerable skepticism about the effect, and as usual most of the community waited for a successful experiment, which required prior observation of the electron spin resonance in a simple (alkali) metal. This took place in Art Kip's lab down the hall in Berkeley. Frank Abell suggested they should look for the ESR of sodium. I encouraged Frank to give them one of our ultrasonically produced fine particle sodium samples. This he took to Kip, and shortly after that Kip and Griswold found the ESR in sodium. Later the Overhauser effect was observed in lithium by Carver and Slichter at Illinois.

Following the study of pure metals, we explored effects in well-known alloys, e.g. CuAl, both constituents of which possessed known Knight shifts. The preliminary results in Al-rich alloys showed two Cu resonances with shifts which were assigned respectively to known metallurgical phases. However, the Cu NMR in the Cu-rich region did not show the variation expected for a changing average electron density. This was later explained by Bloembergen and Rowland,[6] who assumed that in the Cu-rich regions the electronic structure varied only locally in regions near Al impurities. The affected Cu nuclei would have occupied noncubic sites, with resonance lines greatly quadrupole broadened and not observed. The observed Cu nuclei showed the normal shift.

Referring to the Cu-rich region of CuAl, the Al NMR shift was greatly reduced compared with pure Al, and showed little dependence on concentration. The same was true of Ga in CuGa. In view of their quadrupole moments, it appears that the observed resonances of Ga and Al originated with atoms lying in a cubic environment, the electronic structure of which is

governed by Cu, with the further implication that the trivalent atom contributes but one electron to the conduction band.

PHASE TRANSITIONS, LATTICE DYNAMICS, AND QUADRUPOLE COUPLING

Pound's[7] pioneering work showed how quadrupole splitting of the NMR resonance peak gives detailed information about the magnitude of the quadrupole coupling and the crystal axis orientations in aluminum oxide. Later, Bob Cotts,[8] studying single crystals of ferroelectric potassium niobate, identified the cubic, tetragonal, orthorhombic, and rhombohedral phases and the transition temperatures, and compared the results with X-ray, optical, and dielectric measurements. The pure quadrupole resonance (NQR) of Nb was also observed.

The importance of lattice dynamics appeared in a study of NaTl-type intermetallic compounds, in particular LiAl.[9] The absence of Knight shifts confirmed that the compound is nonmetallic. The NMR linewidths and intensities of both nuclei were strongly temperature dependent as a result of the rapid diffusion of the small Li ions whose thermal motion was facilitated by an approximately constant density of vacancies in the Al 'defect lattice', which includes slightly less than the stoichiometric half of the total number of atoms. The narrowing of the NMR line results when the thermal motion averages out the Li–Li and Li–Al quadrupole couplings, analogous to NMR linewidth narrowing seen in alkali metals by Holcomb and Norberg.[6]

It was unclear what to expect for quadrupole couplings in metals. Molecular calculations corresponded well with experiment,[10] but how to estimate the effects of the conduction electrons in metals? The first observation was of quadrupole satellites[11] astride the NMR in polycrystalline Be metal. Mel Pomerantz and T. P. Das[12] invented a simple band structure method for determining the effective charge at the metal lattice points, and calculated the appropriate lattice sum for Be. We developed an interpolation based on Townes[10] method and applied it to crystalline Ga metal. The observed NQR frequencies for the two isotopes turned out to be very close to the calculated values.[13] Subsequently, Bob Hammond[14] investigated the NQR of metallic Ga in the superconducting state, and found a small frequency shift as well as an enhancement of the relaxation rate[15] just below the superconducting transition temperature.

It is evident that the probing nucleus is a versatile instrument, considering both the magnetic and quadrupole moments. It is also interesting to reflect on the importance of sample preparation for NMR experiments. The problems become increasingly difficult as smaller particle sizes are studied, as will be seen below in the case of superconductors.

SPIN-REVERSING SCATTERING AND SUPERCONDUCTIVITY

The BCS theory of superconductivity is based on conduction electron spin pairing, and implies a zero Knight shift at zero temperature. This raised a lot of questions and provoked a lot of discussion.[16] Fred Reif[17] performed a beautiful set of experiments showing that the shift K_s in superconducting Hg approaches approximately two-thirds of the normal state value K_n as $T \rightarrow 0$. Theoretical arguments were developed[18,19] showing that a nonzero value of K was to be expected. In particular, the spin-reversing scattering introduces a statistical spin coupling so that complete pairing at low temperatures has a low probability. While this was going on, we tried Reif's experiment on a specimen of mercury of particle size smaller than Reif 's and got a result more like $K_s/K_n \rightarrow 2/10$, which further confused a difficult question. That experiment was not repeated because we didn't know how to make a uniform size distribution of small mercury particles. Instead we developed a method for producing quite uniform ~100 Å tin platelets deposited by evaporation on Mylar sheets which were folded into a many-layer 'Dagwood' sandwich of tin particles. We then measured K as a function of temperature with the result $K_s/K_n \rightarrow \sim 3/4$ as $T \rightarrow 0$,[20] implying that Reif 's result was right in the first place. Later, when the experiments were extended to investigate the spin–orbit scattering lengths for several superconducting metals of different particle size and purity, the experimental results[21] for K_s/K_n turned out to be in reasonable agreement with the relevant theoretical treatments.[18,19] Abrikosov and Gorí'kov[22] developed a general theoretical framework involving a parameter which is based on the ratio of the inverse spin lifetime to the superconductor energy gap. Like other treatments of spin-reversing scattering it implies an indirect size dependence for the shift K_s in the superconductor, because of the effects of boundary as well as impurity scattering. Unfortunately, the experimental results for the very interesting case of aluminum were in disagreement.[23,24] By this time the theorists knew what was right and lost interest in the experimental morass. Afterward the problems multiplied in the studies of type II and high T_c superconductors.

It appears that NMR experiments have been of unique importance in studying superconductivity, not necessarily by directly answering the crucial questions, but rather by generating further questions which will ultimately lead to improved understanding.

THE PENULTIMATE SHRINK—TRAVELING IN LILLIPUT

In the foregoing we have chosen a series of NMR problems to illustrate the wide range of fundamental situations which can be treated by employing the nucleus to probe electronic and geometrical structures. The order of choice has been partly related to the size of the object under study. Critical dimensions have depended on parameters such as rf skin depth in metals (microns), and superconducting penetration depth (hundreds of ångstroms). The size realm closest to atomic dimensions is inhabited by the metal clusters containing up to thousands of atoms with critical dimensions depending on the Fermi wavelength (nanometers).

Following our adventures in superconductorland, we became interested in effects of pure smallness which had previously been considered by Fröhlich[25] and Kubo.[26] My interest in the small particle effects was reinforced by a visit to Nico Bloembergen, who told me about the recent work of Kubo.

The effect of spin-reversing scattering in nonsuperconducting metals can be described in the Abrikosov–Gor'kov[22]

framework, with the basic parameter modified by replacing the superconductor energy gap with the average energy level spacing in the small particles. Experiments on copper[27] included specimens with diameters ranging between 25 Å and 110 Å. The observed decrease in the copper Knight shift, with decreasing temperature and particle size, indicates the existence of spin-reversing scattering. The larger copper particles were early examples of the recently discussed mesoscopic structures in which, depending on scattering lengths, quantum interference effects become important.[28,29]

Recently, we have found[30] that the metal clusters (nanostructures) have a periodic table of their own, with magic numbers signifying special stability, analogous to the rare-gas atoms and magic-number nuclei. The existence of elaborate and complex electronic structures in these smallest metallic systems promises still further developments in the fundamental understanding of metals.

The preceding discussions represent a long series of fundamentally related experiments which lead logically to next steps in the continuing exploration of the behavior of microscopic metal particles. Predictably, NMR studies of mesoscopic structures[27,31] will merge with NMR and optical studies of clusters,[30] allowing further exploration of these neighboring microscopic size realms.

REFERENCES

1. N. F. Ramsey, *Nuclear Moments*, Wiley, New York, 1953.
2. R. V. Pound and W. D. Knight, *Rev. Sci. Instrum.*, 1950, **21**, 219.
3. W. D. Knight, *Phys. Rev.*, 1949, **76**, 1259.
4. W. D. Knight, *Solid State Phys.*, 1956, **2**, 93.
5. C. H. Townes, C. Herring, and W. D. Knight, *Phys. Rev.*, 1950, **77**, 851.
6. T. J. Rowland, *Prog. Metal Phys.*, 1961, **9**.
7. R. V. Pound, *Phys. Rev.*, 1950, **79**, 685.
8. R. M. Cotts and W. D. Knight, *Phys. Rev.*, 1954, **96**, 1285.
9. H. E. Schone and W. D. Knight, *Acta Metall.*, 1963, **11**, 179.
10. C. H. Townes and B. P. Dailey, *J. Chem. Phys.*, 1949, **17**, 782.
11. W. D. Knight, *Phys. Rev.*, 1953, **92**, 539.
12. M. Pomerantz and T. P. Das, *Phys. Rev.*, 1960, **119**, 70.
13. W. D. Knight, R. R. Hewitt, and M. Pomerantz, *Phys. Rev.*, 1956, **104**, 271.
14. R. H. Hammond and W. D. Knight, *Phys. Rev.*, 1960, **120**, 762.
15. L. C. Hebel and C. P. Slichter, *Phys. Rev.*, 1959, **113**, 1504.
16. D. E. MacLaughlin, *Solid State Phys.*, 1976, **31**, 1.
17. F. Reif, *Phys. Rev.*, 1956, **102**, 1417.
18. R. A. Ferrell, *Phys. Rev. Lett.*, 1959, **3**, 262.
19. P. W. Anderson, *Phys. Rev. Lett.*, 1959, **3**, 325.
20. G. M. Androes and W. D. Knight, *Phys. Rev.*, 1961, **121**, 779.
21. F. Wright, Jr., W. A. Hines, and W. D. Knight, *Phys. Rev. Lett.*, 1967, **18**, 115; W. A. Hines and W. D. Knight, *Phys. Rev.*, 1971, **B4**, 893.
22. A. A. Abrikosov and L. P. Gor'kov, *Zh. Eksp. Teor. Fiz.* 1962, **42**, 1088 (*Sov. Phys.–JETP*, 1962, **15**, 752).
23. R. H. Hammond and G. M. Kelly, *Phys. Rev. Lett.*, 1967, **18**, 156.
24. H. L. Fine, M. Lipsicas, and M. Strongin, *Phys. Lett.*, 1969, **29A**, 366.
25. H. Fröhlich, *Physica (The Hague)*, 1937, **4**, 406.
26. R. Kubo, *J. Phys. Soc. Jpn.*, 1962, **17**, 975.
27. P. Yee and W. D. Knight, *Phys. Rev.*, 1975, **B11**, 3261.
28. B. L. Altshuler, P. A. Lee, and R. A. Webb (eds.), *Nanostructures and Mesoscopic Systems*, Elsevier, Amsterdam, 1991.
29. K. B. Efetov and V. N. Prigodin, *Phys. Rev. Lett.*, 1993, **70**, 1315.
30. W. A. deHeer, W. D. Knight, M. Y. Chou, and M. L. Cohen, *Solid State Phys.*, 1987, **40**, 93.
31. S. Kobayashi, T. Takahashi, and W. Sasaki, *J. Phys. Soc. Jpn.*, 1971, **31**, 1442.

Biographical Sketch

Walter D. Knight. *b* 1919. A.B., 1941, Physics, Middlebury College. M.A., 1943, Ph.D., 1950, Physics, Duke University, NC (informal supervisor, Charles H. Townes). Instructor in physics, Trinity College, Hartford, 1946–50. Assistant, associate, and professor, Physics Department, University of California, Berkeley, 1950–90, Dean, College of Letters and Science, 1967–72, Professor Emeritus, 1990–present. Member, National Academy of Sciences, American Academy of Arts and Sciences. Approx. 90 publications. Research specialties: NMR in metals, properties of metal clusters.

Kochelaev, Boris I.: Discovery of Electron Spin Resonance

Boris I. Kochelaev

Kazan State University, Kazan, Tatarstan, Russia

In May 1944 Eugeny K. Zavoisky submitted for approval his doctor's thesis, which contained the initial successful measurements of electron spin resonance in condensed matter.[1] The road to this discovery consisted of three stages: the development of a very sensitive method for measuring the energy absorption of radiowaves in substances; the search for nuclear magnetic resonance; and measurements of ESR itself.

These pioneering experiments were performed at Kazan University, one of the oldest universities of Russia, located in the city of Kazan on the Volga river.

METHOD FOR MEASURING A WEAK RADIOWAVE ABSORPTION

During his graduate and postgraduate work, Zavoisky studied peculiarities of high frequency (hf) radiowave generators. After 1933 his main interest shifted to the study of a substance by means of radiowaves. The first steps were connected with an investigation of hf field absorption in liquids by measurements of their heating. The sensitivity of this method did not satisfy Zavoisky and he was stimulated to use his own experience in radiophysics.

In 1936 Zavoisky suggested a very sensitive electronic method for measuring the energy absorption of radiowaves in condensed matter as an alternative to the existing calorimetric method.[2] The idea was based on the detection of variations in the working regime of the generator due to the absorption of its energy by the sample under investigation placed in the alternating field of the generator. Earlier Zavoisky had demonstrated by special experiments the linear relationship between changes of grid or anode circuit currents and the watt load on the generator, provided the load changes were small in comparison with the generator power. The change in grid current was recorded at first by a galvanometer connected in a bridge circuit; later a multicascade amplifier of constant or alternating current was used. The first estimations of the sensitivity of this 'grid current method' (GCM) led Zavoisky to the value of the order 50 nW per scale division for a frequency of 10 MHz. The first applications of GCM by Zavoisky were connected with measurements of the ionization potentials of molecules in liquids and gases.

ATTEMPTS TO DETECT NMR

In 1940 the research activity of Zavoisky took a new direction. He was impressed by the great precision of nuclear magnetic moment measurements performed by Rabi in molecular beams using the magnetic resonance phenomenon. Zavoisky anticipated that his highly sensitive method could be used to make similar measurements in solids and liquids despite Gorter's failure to do so. He involved colleagues from the Physics and Chemistry Departments—the theorist S. A. Al'tshuler and the physical chemist B. M. Kozyrev—in this work. This team was well prepared to solve the problem. The main scientific interests of Al'tshuler at that time were connected with the mechanical and magnetic moments of nuclei and their interactions. In particular, he had published a paper previously with I. E. Tamm in which the existence of the magnetic moment of the neutron and its value and sign had been predicted correctly.[3] Kozyrev had participated earlier in Zavoisky's measurements of the electrical absorption of radiowaves in liquids.

They decided to search for the proton magnetic resonance in water. It was not absolutely clear whether the spin relaxation of protons was effective enough to transfer the radiowave energy to the thermal bath. Theoretical estimations of the nuclear spin relaxation time given by Heitler and Teller predicted a value of many years, which did not provide much optimism. Zavoisky and his colleagues thought of special tricks to avoid this difficulty: they undertook measurements of concentrated solutions of both copper and manganese salts instead of pure water and in addition they used flowing water. A shortening of the proton relaxation time was expected due to interactions with paramagnetic ions.

Zavoisky was able to detect the proton magnetic resonance in May/June 1941. However, he did not achieve good reproducibility for the results at that time. This corresponded with the arrival of World War II in the former USSR and most of the institutions of the Academy of Sciences had to move from Moscow and Leningrad to Kazan University. Zavoisky's laboratory closed down and Al'tshuler joined the army as a volunteer. It is a pity that they did not have several months more to complete their task.

At this stage, it is perhaps pertinent to ask why these first NMR measurements were not stable? The answer is not quite clear, but it is certainly connected with difficulties in detection of the resonance signal using a galvanometer without constant magnetic field modulation. The latter was devised by Zavoisky two years later for his ESR measurements. Al'tshuler and Kozyrev also mentioned later the inhomogeneity of the external magnetic field. Zavoisky never discussed this question himself. Zavoisky looked through the papers of Purcell and Bloch and their colleagues, where the observation of NMR was reported, in the presence of Al'tshuler. According to his evidence, these publications did not cause any displeasure to Zavoisky. On the contrary, he was pleased with the fact that their techniques were approximately the same as his own.

THE FIRST MEASUREMENTS OF ESR

Zavoisky was only able to resume his research work in 1943. He did not continue the search for NMR but instead began studies of paramagnetic relaxation in orthogonal fields. It is not clear whether these experiments were conducted with the intention of detecting ESR. In fact, in the paper describing the first results of this study,[4] submitted for publication on 4 February 1944, we find other arguments: 'Taking into consideration that the paramagnetic relaxation in perpendicular fields was investigated not enough and having in mind further

measurements of the nuclear magnetic moments, we have decided to repeat the mentioned above Gorter's experiments ... using the method to measure the high frequency field absorption, which is much more sensitive then any calorimetric one.' It seems that NMR measurements were still attractive. At first they wanted to test the sensitivity of GCM. In fact, the technique was essentially the same. The grid current of the hf generator (35 MHz) was still measured by means of a compensated galvanometer. The static magnetic field of up to 1300 Oe was created by the electromagnet. Powdered samples of manganese, chromium, and copper salts were placed in the field using a quartz or glass test tube. Measurements were performed at 81 K and 219 K. The reported results were very similar to Gorter's findings concerning paramagnetic relaxation in perpendicular fields. Not a single word can be found about ESR.

At the end of 1943 Zavoisky introduced very important modifications to his methodology. By using a solenoid instead of the electromagnet he provided a smooth variation of the constant magnetic field at low values. Additional modulation of this field allowed the use of multicascade amplifiers for the output and registration of the absorption signal by means of an oscillograph. One should bear in mind that the electron Larmor frequency of 35 MHz corresponds to the magnetic field $B_0 \sim$ 12 Oe, i.e. the region of the rest fields of the electromagnet. The wavelength of the generator could also be varied from 200 to 18 m (1.5 to 17 MHz). Evidently Zavoisky was preparing to search for electron spin resonance.

Very soon absorption peaks were detected in manganese and copper sulfates, and in anhydrous chromium chloride. Measurements of the magnetic field at the absorption maximum versus the generator frequency gave a strict linear relationship between them. The position of the maximum was independent of the temperature from 300 K to 90 K, whereas the ordinates of the curve were proportional to $1/T$. The absorption peak disappeared when the constant field became parallel to the alternating field. The same results were obtained for aqueous solutions of manganese salts. All these findings demonstrate the existence of electron spin resonance or, according to Zavoisky, 'magnetospin resonance'. However, the resonance position could not be measured correctly at these low frequencies, and in the same year Zavoisky undertook new measurements at wavelengths of 32 and 65 cm (approximately 0.5 and 1.0 GHz). One of the curves obtained for the absorption derivative for copper sulfate at room temperature is shown in Figure 1 These results were presented in the supplement to his thesis[1] in October 1944.

In January 1945 Zavoisky repeated his experiments in the Institute of Physical Problems in Moscow by invitation of P. L. Kapitza. The results of ESR measurements in anhydrous copper chloride at a frequency of 133 MHz for temperatures in the range 20–300 K were published for the first time in a short paper.[5] These experiments helped to overcome the skepticism of some Moscow physicists. Later transition to 10–14 cm wavelengths made the ESR signal much more pronounced.[6] The resonant absorption curve for manganese sulfate at 2.75 GHz is shown in Figure 2.

Zavoisky's next step was the detection of the paramagnetic resonant dispersion curve using the 'crossed coils' induction method.[7] The nature of ESR line broadening due to spin–spin interactions was correctly interpreted in collaboration with Al'tshuler and Kozyrev.[8] Zavoisky also managed to observe

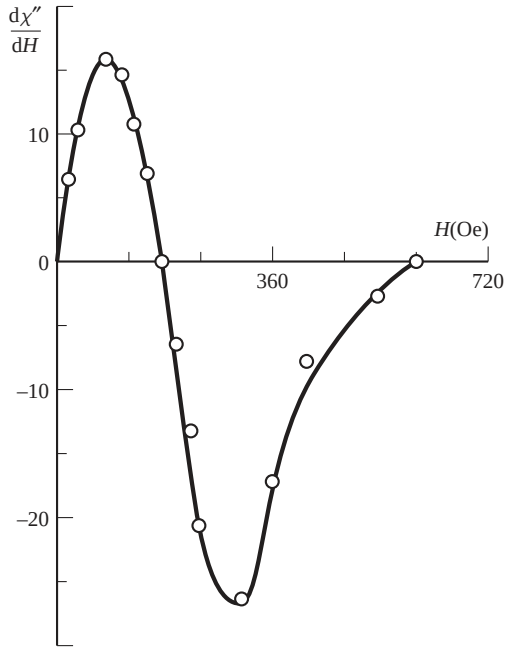

Figure 1 One of the first ESR signals, $CuSO_4 \cdot 5H_2O$ at 300 K and 0.46 GHz. (Redrawn from E. K. Zavoisky, 'Magnetic Radiowave Spectra of Paramagnets', Supplement to *Thesis*,[1] Kazan University, October 1944)

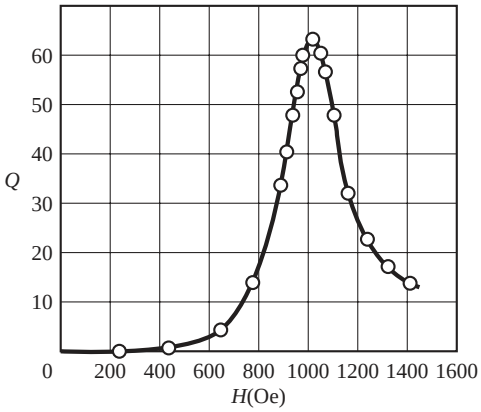

Figure 2 ESR signal at 2.75 GHz for $MnSO_4$, at a temperature of 300 K. (Redrawn from E. K. Zavoisky, *J. Phys. USSR*, 1946, **10**, 197)[6]

'forbidden' ESR lines corresponding to transitions between spin levels with changes in the magnetic quantum number Δm = 2, 3, 4 for the Mn(II) ion.[9] It is also worth mentioning that all the spectrometers employed by Zavoisky (including the generators) were constructed by his own hands.

In 1947 Zavoisky moved to Moscow and, at first, together with other colleagues developed methods to measure superfast processes with time resolutions in the range 10^{-12} to 10^{-14} s. After 1958 he was mainly interested in plasma physics in connection with the problem of controlled thermonuclear fusion. The 'resonance ideology' of Zavoisky was also displayed in this new field. He suggested the use of a magnetoacoustic resonance method for heating the plasma and EPR methods for its characterization.

REFERENCES

1. E. K. Zavoisky, *Paramagnetic Absorption in Orthogonal and Parallel Fields for Salts, Solutions and Metals*, Thesis, Kazan University, 1944.
2. E. K. Zavoisky, *Zh. Eksp. Teor. Fiz.*, 1936, **6**, 37.
3. S. A. Al'tshuler and I. E. Tamm, *Dokl. Akad. Nauk SSSR*, 1934, **1**, 455.
4. S. Al'tshuler, E. Zavoisky, and B. Kozyrev, *Zh. Eksp. Teor. Fiz.*, 1944, **14**, 407.
5. E. K. Zavoisky, *J. Phys. USSR*, 1945, **9**, 245.
6. E. K. Zavoisky, *J. Phys. USSR*, 1946, **10**, 197.
7. E. K. Zavoisky, *Zh. Eksp. Teor. Fiz.*, 1947, **17**, 155; *J. Phys. USSR*, 1947, **11**, 184.
8. S. A. Al'tshuler, E. K. Zavoisky, and B. M. Kozyrev, *Zh. Eksp. Teor. Fiz.*, 1947, **17**, 1122.
9. E. K. Zavoisky, *Dokl. Akad. Nauk SSSR*, 1947, **57**, 887.

Biographical Sketch

Boris I. Kochelaev. *b* 1934. Diploma, Cand.Sci. (supervisor S. A. Al'tshuler), Kazan University, Russia. Visiting scientist, Harvard University (with N. Bloembergen), 1963–64. Dr., 1968, Professor of Theoretical Physics at Kazan University, 1970–present. Fullbright Fellow at UCLA, 1979. Member of AMPERE Committee, 1984–present. Approx. 110 publications. Research specialty: spin kinetics in solids.

Koenig, Seymour H.: I. I. Rabi, F. Bloch, E. M. Purcell, and the History of NMR and Relaxometry

Seymour H. Koenig
Dartmouth-Hitchcock Medical Center, Hanover, NH, USA and Relaxometry, Inc., Mahopac, NY, USA

INTRODUCTION: RABI AND NMR IN ATOMIC AND MOLECULAR BEAMS

The instructions for contributors to these volumes note that this 'encyclopedia will take advantage of the fact that 1945 saw the first successful NMR experiments (published in 1946)'. The reality, of course, is that the Nobel Prize for Physics was awarded to I. I. Rabi the previous year, in 1944, 'for his discovery of a resonance method for recording the magnetic properties of atomic nuclei'. The initial publication,[1] in 1938, a letter titled 'A New Method of Measuring Nuclear Magnetic Moment', was followed shortly by a long paper[2] on 'The Molecular Beam **Resonance** Method for Measuring **Nuclear Magnetic** Moments' (emphasis mine).

In a radio broadcast which, because of wartime conditions, substituted for the Nobel ceremony, E. Hulthén noted that the Rabi technique—which clearly could be applied to electronic and molecular magnetic moments as well—was 'as simple as it was brilliant'. Rabi's approach involved beams of atoms or molecules in a vacuum. By introducing inhomogeneous magnetic fields[2] along the beam path, the specific trajectory of each particle as it traverses a long evacuated chamber becomes a function of its spatial quantization state. Inducing a transition in this quantization mid-course, by application of a resonant radiofrequency field, alters the particle trajectory and decreases the beam intensity (detectable by a variety of methods depending on the particular atom or molecule under study).

BLOCH, PURCELL, AND NMR IN CONDENSED MATTER

What was discovered in 1945 was NMR in condensed matter: Bloch et al.[3] in liquid water (doped with ferric nitrate)[4] and Purcell et al.[5] in rigid paraffin. However, much of the necessary 'cultural baggage' was already in place. As noted at the 1952 Nobel ceremony for Bloch and Purcell, again by Hulthén, the Nobel Prize had recently been awarded to Rabi for his invention of NMR. Indeed, both Bloch and Purcell cite the beam method in their original publications.[3–5] In addition, the magnitude of the proton magnetic moment was known, from beam methods,[6] to six-place accuracy; Gorter[7] (using calorimetry for detection) and Bloch (quoted by Rabi[1]) had already attempted, albeit unsuccessfully, to find the proton resonance in solids, and use of the rotating frame for discussing gyromagnetic motion was common.[8–10] Indeed, all this had been accomplished before 1940, before World War II interrupted the normal evolution of scientific discovery but enhanced the advance of technology.

From 1940 to 1945, Rabi was Associate Director of the MIT Radiation Laboratory, concerned with the development of microwave radar. Bloch came east in 1944, from Los Alamos to the Harvard Radio Research Laboratory, indeed, in time to attend the celebration in Cambridge of Rabi's prize. Purcell had been at the MIT 'Rad Lab' since 1940. Thus, both he and Bloch were immersed in the developments of the most sophisticated electronics of the time, including radiofrequency and microwave techniques and low noise detectors. As Rabi told it (private discussion, 1986), it was quite clear that—technically—the proton resonance could be detected in condensed matter, and that Bloch and Purcell could scarcely wait for the end of the war, each to try his own method—at opposite sides of the continent—to observe the proton moment. The major uncertainty was the magnitude of the proton spin–lattice relaxation time, since early estimates suggested that it might be so long that saturation effects would limit the rate at which the proton ensemble would absorb energy and thereby frustrate its detection. The Rabi beam method does not involve relaxation times; irradiated atoms and molecules are continually replaced by 'new' particles, much as in present-day measurements of blood flow in MRI (magnetic resonance imaging), experiments that are in a sense the condensed matter, high-resolution NMR, analog of the original Rabi beam experiment.

Bloch chose liquid water, reducing the solvent proton relaxation time by adding trace amounts of the paramagnetic solute ferric nitrate[4] (thus foreshadowing the use of such solutes as agents for altering contrast in MRI), and detecting the dispersive (transverse) component of the proton signal in the 7–11 MHz range. He named the method 'Nuclear Induction'. Purcell chose solid paraffin and the absorptive mode, using a sensitive radiofrequency bridge to measure changes in Q, i.e., the dissipation in the paraffin core of a cavity resonant near 30 MHz. The bridge was driven with a weak source, in expectation of a relaxation time of several hours. He referred to the method, not quite naming it, as resonance absorption.

What Bloch and Purcell contributed were nondestructive methods for the *precision* measurement of nuclear moments in condensed matter, on both an absolute and relative basis. It was certainly appreciated at the time that accurate determinations of nuclear moments would revolutionize the study of nuclear physics. Indeed, that the proton moment is ~2.8-times the nuclear magneton was just one more anomaly in the nature of nuclear forces, along with their short range and the existence of a magnetic moment for the (uncharged) neutron. What was not anticipated, at the time, was the phenomenal contribution that precision measurements of nuclear moments, now called 'high-resolution NMR', would make; initially to chemistry, and, later, to biochemistry and clinical medicine. Indeed, Rabi noted (private discussion) that the emphasis at the Columbia University Physics Department during the 1950s would have been much different had he foreseen the ultimate applications of the discoveries of Bloch and Purcell.

ESR IN BEAMS, NMR IN WATER, AND THE ANOMALOUS ELECTRON g-VALUE

My personal involvement, starting at Columbia University in 1949, was with the first experiment to combine the Rabi and Bloch–Purcell NMR approaches, together with the Rabi analog of condensed matter ESR (electron spin resonance).[11,12] It was known that the hyperfine splitting of atomic hydrogen was slightly larger than the value computed using the Dirac (relativistic) theory of the electron, and Breit[13] had recently suggested that an 'anomalous' addition to the magnetic moment of the electron, ∼0.1%, could account for this discrepancy. Moreover, initial low-order computations of the 'self-energy' contribution to the electronic moment, a term arising from the motion of an electron through its own electric field, agreed quite well with the hyperfine anomaly. These were the first results of the new Feynman–Schwinger–Tomonaga quantum electrodynamics, and the good agreement of the low-order results made both measurements and computations to higher order desirable. P. Kusch, a student and early collaborator of Rabi,[1] confined to bed for some time because of vertigo associated with scarlet fever, conceived of an experiment to measure the electron g-value to high precision, and offered it to me as a thesis.[12] It was to win the Nobel Prize for Kusch in 1955, shared with W. E. Lamb, Jr. The concept was, in part, a Rabi magnetic resonance experiment, in which microwave transitions in a beam of *atomic* hydrogen (generated in an electric discharge) were to be measured at ∼0.15 T; this is, in essence, an ESR experiment on a beam of free radicals. But it was more: the magnitude of the magnetic field was to be measured by the new Purcell NMR technique. A. Sachs had just joined the faculty at Columbia, bringing from Harvard the circuit of the 'Pound Box', a marginal oscillator with an output that was very sensitive to the Q of its resonance circuit. (This replaced the rf bridge used earlier.[5]) I was to build one and find the proton resonance in a sample of water, doped with manganese sulfate, contained in a vacuum-tight glass holder with a shape that approximated the beam geometry in the microwave transition cavity. Since Gardner and Purcell[14] had recently measured the electron cyclotron frequency (proportional to the Bohr magneton) in a field calibrated by proton NMR, a combination of the two results would give the electronic moment in terms of the Bohr magneton (the electron g-value), precisely the quantity desired. The experiment clearly worked; after corrections to the proton resonance frequency for shape and susceptibility factors, and to the electronic transition for a range of relativistic effects, the electron g-value was now known with new precision. More than one decade later (1965), Feynman, Schwinger, and Tomonaga shared the Nobel Prize in (experimental) Physics for explaining the anomaly measured by Koenig et al.,[11,12] an experiment initially conceived to test these very calculations.

RELAXOMETRY AND RELAXOMETERS

It was not until 15 years later, after having studied low-temperature electrical transport and inelastic neutron scattering in solids, that I saw another proton signal. This was during the renaissance in protein research that followed the discoveries of Watson and Crick. The question was whether there was some means of detecting changes of conformation of solute protein (then a nebulous concept) by a physical technique. The answer was (particularly in retrospect) to measure solvent proton magnetic relaxation rates in solutions of protein, both diamagnetic and paramagnetic. One reference then in the literature[15] indicated a solvent proton relaxation rate that was a nonlinear function of the paramagnetism (oxidation state) of ceruloplasmin, a Cu-containing blood-plasma protein, indicating (to me) the existence of a cooperative effect within each protein molecule, i.e., a conformation change. All that was necessary was to develop the appropriate instrumentation, find a set of good problems, and extend the theory of relaxation to these macromolecular systems!

It should be recalled that, in the early days of NMR, before it could be used to study small solutes with high precision, particularly those containing paramagnetic metal ions, measurement of the influence of solute on solvent relaxation was a standard approach, starting with the classic work of Bloembergen et al.[16] In time, this approach was used anew, and became the method of choice for investigating large solute molecules as the techniques of high-resolution NMR improved and dominated the study of smaller solutes. It remains the best approach for the study of complex macromolecular systems, including tissue.[17]

Over the years, with the collaboration of many—and the timely invention of MRI (which depends for its efficacy almost entirely on tissue-dependent relaxation rates of the protons of mobile tissue water)—all this has come together. The combination of activities is now a recognized field, named 'relaxometry' so named by me at an NIH workshop about a decade ago. The specialized instruments to measure relaxation rates as a function of field and temperature were named 'relaxometers'.

R. D. Brown III, a long-time associate, has worked steadily through the years to develop a relaxometer appropriate for our studies, which are mostly on liquid-like rather than solid state samples. The relaxometer is based on early 'field cycling' ideas of A. G. Redfield.[18] A major improvement came in the mid-1970s when the relaxometer was first attached to a large main-frame computer, not only for data-logging but for automated control of the experiments. This gave a 10-fold improvement in the rate of data acquisition and analysis, and a concomitant improvement in accuracy, allowing the first demonstration of a major conformation change that related to protein function. The protein was concanavalin A,[19] a bean lectin with a strong, but selective, affinity for certain sugars. We showed that, near equilibrium, the protein could exist in two conformations, distinguished by a *cis–trans* isomerization. One conformer carried the sugar-affinity but required the binding of two metal ions to make this conformer have the lower energy. It took four months of running time with the improved relaxometer to obtain data that yielded the equilibrium binding constants for metals and sugar to the two conformers. It took additional time to measure, using the automated instrumentation, the kinetics of metal-ion and sugar binding and, above all, the kinetics of the newly discovered conformation change. In addition to elucidating the structure–function relationships of transport and storage proteins, relaxometry has helped clarify the mechanisms of enzyme action in many systems, a particular case being carbonic anhydrase,[20] a protein that appeared to hydrate carbon dioxide at a rate faster that the limitations imposed by the diffusion of substrate.

With the advent of MRI, there were new demands for relaxometry measurements and for relaxometers. The advent of personal computers about a decade ago made it possible for Brown to develop a stand-alone version of our relaxometer, clones of which are now in Mons (Belgium), Florence (Italy), University of Illinois (Urbana), Dartmouth (Hanover), and NY Medical College (Valhalla). These instruments not only serve the entire pharmaceutical industry in their developments of magnetic contrast-enhancing agents for MRI, but are the means through which the molecular basis of tissue-specific contrast in MRI has finally been elucidated.[17,21]

REFERENCES

1. I. I. Rabi, J. R. Zacharias, S. Millman, and P. Kusch, *Phys. Rev.*, 1938, **53**, 318.
2. I. I. Rabi, S. Millman, P. Kusch, and J. R. Zacharias, *Phys. Rev.*, 1939, **55**, 526.
3. F. Bloch, W. W. Hansen, and M. Packard, *Phys. Rev.*, 1946, **69**, 127.
4. F. Bloch, W. W. Hansen, and M. Packard, *Phys. Rev.*, 1946, **70**, 474.
5. E. M. Purcell, H. C. Torrey, and R. V. Pound, *Phys. Rev.*, 1946, **69**, 37.
6. J. M. B. Kellogg, I. I. Rabi, N. F. Ramsey, Jr., and J. R. Zacharias, *Phys. Rev.*, 1939, **56**, 728.
7. C. J. Gorter, *Physica (The Hague)*, 1936, **3**, 995.
8. J. Schwinger, *Phys. Rev.*, 1937, **51**, 648.
9. I. I. Rabi, *Phys. Rev.*, 1937, **51**, 652.
10. F. Bloch and I. I. Rabi, *Rev. Mod. Phys.*, 1945, **17**, 237.
11. S. H. Koenig, A. G. Prodell, and P. Kusch, *Phys. Rev.*, 1951, **83**, 687.
12. S. Koenig, A. G. Prodell, and P. Kusch, *Phys. Rev.*, 1952, **88**, 191.
13. G. Breit, *Phys. Rev.*, 1947, **72**, 984.
14. J. H. Gardner and E. M. Purcell, *Phys. Rev.*, 1949, **76**, 1262.
15. W. E. Blumberg, J. Eisinger, P. Aisen, A. G. Morell, and I. H. Scheinberg, *J. Biol. Chem.*, 1963, **238**, 1675.
16. N. Bloembergen, E. M. Purcell, and R. V. Pound, *Phys. Rev.*, 1948, **73**, 679.
17. S. H. Koenig and R. D. Brown III, *Magn. Reson. Med.*, 1993, **30**, 685.
18. A. G. Redfield, W. Fite II, and H. E. Bleich, *Rev. Sci. Instr.*, 1968, **39**, 710.
19. R. D. Brown III, C. F. Brewer, and S. H. Koenig, *Biochemistry*, 1977, **16**, 1977.
20. S. H. Koenig, R. D. Brown III, I. Bertini, and C. Luchinat, *Biophys. J.*, 1983, **41**, 179.
21. S. H. Koenig, *Biophys. J.*, 1995, **69**, 1.

Biographical Sketch

Seymour H. Koenig. *b* 1927. B.S., 1949, M.A., 1951, Ph.D., 1952, Physics, Columbia University, USA. IBM Research, 1952–93. Presently, Research Professor, Radiology, Dartmouth-Hitchcock Medical Center, NH, USA and President, Relaxometry, Inc., Mahopac, NY, USA. Approximately 200 publications. Research specialties: atomic beams, solid state electrical transport, phonons and neutron scattering, laser-light scattering, and relaxometry, including protein structure and function, water proton relaxation in protein solutions and in tissue, and magnetic contrast-enhancing agents for MRI.

Kowalewski, V. J.: Tribulations of a Young Physicist with a New Phenomenon

V. J. Kowalewski

University of Buenos Aires, Buenos Aires, Argentina

Having obtained my Ph.D. degree in physics in 1948, I was appointed to the University of LaPlata as 'Adjoint Professor' (that means just a helper) to Professor A. Balseiro (whose name nowadays adorns the best physics institute of our country).

The Physics Department of this Faculty was at that time in the charge of a distinguished German professor, Dr. Richard Gans. He specialized in magnetism, having been an expert in this field at the AEG Company. When the moment arrived to talk about my research obligations, he told me that 'It is already time to begin the study of nuclear magnetism,' and he told me to read 'a certain paper by Felix Bloch' and to give a seminar on the subject. This was achieved after quite a short time (since I found Bloch's paper easy to understand), but I was then required to try to repeat his experiment.

Having also read Purcell's paper, I found Purcell's circuit simpler to build than Bloch's 'paddle' device. So I built an rf bridge in a simple aluminum box (the only trouble was to find a differential capacitor).

Of course, the main problem was the magnet. At that time there was a nice 8-in. magnet in the Institute, but it was used for Zeeman effect studies. So I had to content myself with an old, Dubois magnet, barely 3 in. in diameter. I am still amazed that I was eventually able to see an NMR signal with such a magnet!

The next step was to obtain the electronics. Having made a preliminary field measurement of the electromagnet (which was'powered by a pair of car batteries), I decided to work at 15 MHz. The Radio Department of the Faculty lent me a nice communications receiver and a standard rf generator, built for receiver calibration purposes. It took me about six months to get the system working. (At that time I was not yet a full-time professor.)

The bridge behaved nicely as a microphone. I could hear my voice in the receiver speaker when the bridge was attenuated below 80 db, but there was no NMR signal. Besides, when the bridge was adjusted in this way, I got a nice 'figure eight' Lissajous pattern on the scope!

I measured the noise figure of the receiver. I wrote to Prof. Torrey for advice which I got in plenty, but to no avail! My conclusion was that the 'figure eight' was due to the 100 Hz sidebands of the rf generator, which had its power supply filtered adequately for radio work, but not enough for my purposes.

I informed my Director, telling him about the necessity of improving somehow the power supply of the generator. The answer I got was (as to be expected): 'Try again'.

I was desperate.

Then, on a certain Saturday, a friend of mine came to look at my work and asked me what was I doing. I told him I was just cursing this . . . . apparatus on which, instead of a 'resonance' curve I only got an 'eight'. And I showed him the 'eight'. Suddenly he asked me: 'What is that?' We both saw a small absorption signal running back and forth along the 'eight' when the magnet current was swept. It was the signal I was looking for!

Now I was determined to get rid of the 'eight'. So I went to the Radio Department for advice, and they gave me more than that. At that time there were still some big 90 V batteries for country use available. They had three of those, which they gave me. It was an easy matter to disconnect the 'well filtered' 300 V power supply and to put the 270 V battery instead.

Then, at last, I got a beautiful NMR signal! My Director was very pleased!

Corollary: A new political government decided that neither my Director nor I were necessary in the Faculty. So I went to work in our Atomic Energy Commission . . . . under the same government!

P.S. I am now in charge of a 500 MHz supercon.

Biographical Sketch

Valdemar J. Kowalewski. *b* 1920. B.S. (Physics), 1946; Ph.D., 1948, Faculty of Exact and Natural Sciences, University of Buenos Aires (Argentina). Postdoctoral work, University of Uppsala (Sweden). Successively assistant professor, associate professor, professor, and since 1986, professor emeritus at the same Faculty. Three terms member of the ISMAR Council. Approximately 40 publications. Specialties: instrumentation, INDOR and signs of J couplings.

Kumar, Anil: Development of Two-Dimensional NMR—My Perception

Anil Kumar

Indian Institute of Science, Bangalore, India

The development of both one- and two-dimensional FT NMR created a revolution in the practice of NMR and provided a turning point in the methodology and applicability of NMR to complex systems such as biomolecules. Whereas the former made it possible to record the spectra of large molecules at low concentrations, the latter also made it possible to assign the spectra to individual nuclei and to obtain information on internuclear distances, leading to structure determination. Even though conceptually both are straightforward, each took several years to materialize. The Fourier relation between the spectrum and the free-induction decay had been known from the early days of NMR, but it was only in 1965 that Richard Ernst showed that it is faster (and better) to undertake time domain spectroscopy. Similarly one could easily think of two-dimensional Fourier analysis, but the idea had to wait several years for its germination and utilization.

It was at a summer school at Pulé, Yugoslavia in 1971 that Jean Jeener of Belgium proposed the rather esotoric idea of two-dimensional Fourier analysis of a two-pulse experiment. Jeener seems to have put the idea aside and never published it. I joined Ernst's group in Zürich in 1973 and started cross-polarization experiments in solids. Sometime during 1973 Ernst wondered whether to start on Jeener's idea, and finally decided to pursue it but, initially, for an entirely new purpose.

In 1973, Paul Lauterbur described a technique for obtaining images by NMR, using steady field gradients and projection reconstruction. In 1974, Ernst came up with the most outstanding idea of not only using Fourier spectroscopy in one dimension but with the idea of pulsed and switched gradients in two or three dimensions and the use of multidimensional Fourier analysis. Ernst wrote a few subroutines, Dieter Welti wrote others and I did the experiment. The gradients were applied by switching off the current in the linear shim coils of an electromagnet. A crude 64×64 matrix image of two tubes of water was printed on a teletype by digitizing the intensity into blanks, dots and alphabets. We laughed at the experiment and published it without patenting. This Fourier image is the first documented two-dimensional spectrum. After this we turned our attention to two-dimensional (2D) spectroscopy. Enrico Bartholdi worked on the theory, Walter Aue on protons, and Luciano Müller and I on carbon–proton experiments.

The first experiment was a simple one, resolving the ^{13}C spectrum of *n*-hexane into one coupled in one dimension and decoupled in the other. The spectrum, with the data plotted in stacked-plot form with the overlap of the back traces blanked out using white ink, had an immediate appeal. Kurt Wüthrich, on seeing the spectrum, immediately sat down with his head in his hands. The potentials of the technique seemed to have hit him. He later collaborated with Ernst in exploiting 2D NMR for biomolecular studies and, as a result, accelerated its subsequent growth.

Several modifications were undertaken to the initial 2D-resolved experiment, first by removing the carbon-13 chemical shift from one of the dimensions by the use of a spin echo and later removing strong coupling artifacts by using only one-half of the echo period for J evolution. We called these experiments (i) and (ii). Later Ray Freeman and Geoffrey Bodenhausen also invented the same experiments but named them appropriately as 'spin echo' and 'gated decoupler' 2D spectroscopy. The experiments are now known by these names. The importance of appropriately naming an invented technique led to the 'naming-game' in 2D spectroscopy, a game already started by John Waugh for studies in solids.

The complete theoretical framework for 2D spectroscopy was developed and is contained in a comprehensive paper by Aue, Bartholdi, and Ernst (1976). This paper contains a detailed analysis of intensities, phases, connectivity of transitions, lineshapes, flip angle dependence, strong coupling effects, relaxation and field inhomogeneity effects, and most original ideas on multiple quantum transitions, their excitation in pulsed spectroscopy, and indirect detection using a 2D algorithm, all supported with detailed experiments. The foundation of 2D spectroscopy was thus firmly laid and the paper has become a Citation Classic, just as the 1D FT paper.

There had been other schools which contributed significantly to 2D spectroscopy. John Waugh's group at MIT gave the algorithm for separated local field 2D spectroscopy in solids and Ray Freeman's group at Oxford contributed to liquid state 2D NMR almost from the begining.

At Zürich, 2D-resolved spectroscopy was extended to proton–proton systems and one could, for the first time, obtain self-decoupled proton spectra using a 45° projection of a spin echo 2D spectrum. As I was just getting involved with the influence of strong couplings in such spectra, I left Zürich and joined the Indian Institute of Science, Bangalore in 1977. I completed the analysis of the strong coupling effects in 2D spin echo spectra at Bangalore and confirmed them experimentally.

In the meantime, back at Zürich, work was going on at a hectic pace. Correlation spectroscopy was extended to heteronuclear systems, basic ideas of coherence transfer and sensitivity enhancement were established, and multiple quantum spectroscopy was studied in greater detail. A crucial collaboration started between Ernst and Wüthrich with the aim of applying 2D NMR to biomolecules. Kuniaki Nagayama from Japan provided the initial impetus to this project by applying resolved spectroscopy to the study of biomolecules and by inventing spin echo correlated spectroscopy. In 1979, I joined this project for a year. I was fascinated by the way the nuclear Overhauser effect (NOE) was being exploited in Wüthrich's laboratory for the study of biomolecules. They were literally doing hundreds of 1D difference NOE experiments. I noticed a preprint by Ernst, Jeener, and others describing a new three-pulse 2D experiment for the study of chemical exchange. This was too important for me to ignore as I was convinced that that was also the 2D experiment for the study of NOE in biomolecules. I launched a fullscale effort to try to make it successful. There were many hurdles which form an interesting side story of their own. Finally it worked and its success was phenomenonal. The 1D difference experiments were immediately given up and everyone wanted a 2D NOE spectrum of his biomolecule. The COSY experiment was rejuvenated and gave rise to NOESY–COSY diagrams. I remember the 1980 ENC meeting at Tallahasse, Florida where

ours was perhaps the only poster containing contour plots. A few years later one could hardly find a poster in an NMR meeting without a contour plot. The development of the 2D NOE experiment was perhaps the most important turning point in the development and applications of 2D NMR. It fueled a large-scale application of 2D techniques to the study of biomolecules, which in turn necessitated development of newer 2D techniques and their improvement.

The various developments and applications of 2D NMR during the 1980s resulted in the maturing of this field into fully-fledged practice and its acceptance as a viable tool for the structure determination of biomolecules in solution. The success of this algorithm has also been responsible for the development of higher frequency spectrometers and for NMR studies of molecules of a kind unimaginable up to the 1970s. Large computers and work stations have become integral parts of NMR hardware and NMR is now an accepted tool in biomolecular study, just as NMR imaging has become an integral part of radiology. We now await, rather look forward to, the next revolution.

Biographical Sketch

Anil Kumar. *b* 1941. M.Sc., 1961, Agra, Ph.D., 1969, Indian Institute of Technology, Kanpur (supervisor, B. D. N. Rao). Postdoctoral research at Georgia Tech., Atlanta, GA (Sidney Gordon) 1969–70, University of North Carolina, Chapel Hill, NC (Charles Johnson) 1970–72, and ETH. Zürich, Switzerland (Richard Ernst) 1973–76. Faculty of Physics, Indian Institute of Science, Bangalore, 1977–present. Sabbatical leave at ETH. Zürich with Kurt Wüthrich, 1979–80. Approx 100 publications. Research interests: methodology of NMR, two-dimensional techniques, relaxation studies, applications to structure determination of biomolecules, and characterization of molecular motions.

La Mar, Gerd N.: NMR of Paramagnetic Proteins

Gerd N. La Mar

University of California, Davis, CA, USA

The prevailing 'wisdom' has always been that integral paramagnetic molecules do not yield well-resolved or useful solution NMR spectra. The initial report of a solution NMR spectrum of an intact paramagnetic molecule occurred in 1957.[1] By the early 1960s there were appearing remarkable articles by the DuPont group of Phillips and Eaton defining the conjugation properties of a variety of organic functional groups in Ni(II) complexes. As a second year graduate student at Princeton in 1962, I was interested in theoretical aspects of hyperfine coupling constants when it was suggested that we instead measure such couplings by NMR, since this would yield both magnitude and sign. However, in order not to 'contaminate' with unpaired electrons the departmental Varian A-60, and because the fixed 2 kHz modulation introduced the cursed sidebands in the middle of the spectra, it was arranged with Bob Shulman that I would collect my spectra at Bell Labs. There I met Ernie Anderson who educated me on the virtues of a PAR lock-in amplifier and convinced me that the zero dB attenuation button for transmitter power on a DP 60 did, after all, have a practical use. Although by the middle 1960s the complexes of a variety of metal ions had been shown to yield well-resolved and informative NMR spectra, the NMR community continued to consider each successful report as just another exception, if not the last example.

The 1960s produced a spate of fruitful studies on inorganic transition metal complexes for which available synthetic methods allowed the necessary assignments. Biological applications were just starting, either with Mn^{2+}-induced relaxivity, or on the hemin complexes which yielded a wealth of information on the electronic structure of the isolated chromophore from hemoproteins. The relatively minor biological as compared to inorganic interest in these NMR studies was reflected in the first monograph on the subject in 1973, which devoted only ~10% of its coverage to biological applications.[2] However, it quickly became apparent that there was a distinct advantage for studying paramagnetic proteins, in that the hyperfine shifts for the prosthetic group afforded resolution not accessible on the available low-field spectrometers. The initial report of the NMR spectrum of a paramagnetic protein, ferricytochrome-*c*, was by Kowalsky in 1965, and was quickly followed by more extensive investigations on these and related hemoproteins by the research groups of Shulman, Wüthrich, and Redfield, and on iron–sulfur proteins by Phillips and co-workers.

The intrinsically high information content of hyperfine shifts was recognized early. However, with mounting piles of data on proteins, it also became clear that the assignments needed to interpret the data were elusive. The full realization of the experimental problems to attaining assignment resulted in a significantly waning interest in NMR of paramagnetic proteins, although not before a key report showed isotope labeling of the heme in myoglobin was practical. With the development of steady-state and time-dependent NOEs in diamagnetic proteins in the late 1970s, the lone representative of the paramagnetic metalloproteins whose NMR spectra benefited from these advances was the class of ferricytochromes, investigated primarily in Wüthrich's lab,[3] where the standard assignments in diamagnetic ferrocytochrome were carried over to paramagnetic ferricytochrome by saturation transfer. The broad-based success of this approach and the wealth of information on the control of the orbital ground state, however, while never so stated, left the impression that multipulse NMR methods were not applicable directly to a paramagnetic protein.

Our own entry to NMR of paramagnetic metalloproteins in 1977 was prefaced by a lengthy apprenticeship in elucidating the NMR properties of heme model compounds in order to lay the groundwork for interpretive bases for the protein spectra, followed by extensive isotope labeling of intact *b*-type hemoproteins that provided crucial assignments for testing multipulse methods. The first report of NOE within a paramagnetic molecule appeared by Redfield and Gupta in 1971, but was a relatively minor point in a study of magnetization transfer between the two oxidation states of cytochrome-*c*. The broad utility of NOE studies of paramagnetic metalloproteins was suggested to us in 1980, when we found that nonselective T_1 values are seldom single-exponential in paramagnetic proteins, implying that cross relaxation contributes significantly to the relaxation. With this impetus, we embarked on systematic studies of steady-state and time-dependent NOEs in both weakly and strongly paramagnetic proteins, using our previous isotope labeling work as a starting point to test the methods.[4] While the initial studies focused on small proteins such as myoglobin and cytochrome (13–18 kDa), successful studies were eventually extended up to a 155 kDa peroxidase. While heme proteins served as important test cases for the methodology, similar studies were subsequently extended to all classes of paramagnetic proteins which exhibit well-resolved NMR spectra.

The last major hurdle to bringing paramagnetic proteins into mainstream NMR studies, the application of 2D methods, came more slowly and coincided with obtaining a suitable NMR spectrometer in 1989. The earliest 2D experiments involving a paramagnetic protein, as was the case for 1D NOE experiments, entailed extension of the assignments from ferro- to ferricytochromes by magnetization transfer. However, shortly thereafter we demonstrated that the NOESY experiment could directly yield assignments for ferricytochrome b_5, and cyano metmyoglobin. Because of the strong increase in cross relaxation with molecule size, profitable studies were eventually extended to both large (44 kDa) and strongly paramagnetic ($S = \frac{5}{2}$) proteins. The extension to spin correlation experiments followed quickly, and it is now accepted that 2D NMR will yield quantitative molecular structural, as well as unique electronic structural information on a variety of small to intermediate sized paramagnetic metalloproteins.[4] In fact, by the beginning of the 1990s, the study of paramagnetic metalloproteins by modern NMR methodology, after a long tenure as a misunderstood orphan, has emerged as a fully fledged member of the arsenal of solution structural approaches to biopolymers.

REFERENCES

1. H. M. McConnell and C. A. Holm, *J. Chem. Phys.*, 1957, **27**, 314.

2. G. N. La Mar, W. D. Horrocks, Jr., and R. H. Holm (eds.), *NMR of Paramagnetic Molecules*, Academic Press, New York, 1973.
3. R. M. Keller and K. Wüthrich, in *Biological Magnetic Resonance*, ed. L. J. Berliner and J. Reuben, Plenum Press, New York, 1981, Vol. 3, pp. 1–42.
4. G. N. La Mar and J. S. de Ropp, in *Biological Magnetic Resonance*, ed. L. J. Berliner and J. Reuben, Plenum Press, New York, 1993, Vol. 13, pp. 1–78.

Biographical Sketch

Gerd N. La Mar. *b* 1937. B.S., 1960, Ph.D., 1964, Chemistry, Princeton University, USA. Postdoctoral student, 1964–65, University of Copenhagen; 1965–67, ETH, Zürich. Worked as research chemist for Shell Oil Company 1967–71. Faculty in Chemistry, University of California, Davis, 1971–present. Approx. 300 publications, Current research specialty: NMR of paramagnetic proteins, structure function relationship of hemoproteins and iron–sulfur cluster proteins.

Lambert, Joseph B.: The First Observation of Nitrogen-15 Nuclear Magnetic Resonances

Joseph B. Lambert

Northwestern University, Evanston, IL, USA

In 1962, when I began graduate studies with John D. Roberts, Caltech balanced the liberal requirement of no courses in one's major with the draconian requirement of three full year courses in a minor from a different department. After briefly flirting with astrophysics (quasars had just been discovered there), I settled on the more practical field of biochemistry, which at Caltech is a separate department. In the spring of 1963 I was sleeping my way through a year-long course on biophysics, having successfully survived light scattering and ultracentrifugation, when we finally reached spectroscopy. Professor Robert Sinsheimer got my attention, when in his lectures on NMR he mentioned how useful ^{15}N, with its spin of $\frac{1}{2}$, would be for biological systems. Moreover, he said that Roberts planned to initiate a program on the subject, since no ^{15}N resonance had ever been observed. When I asked Roberts's assistant Marjorie Caserio about it (I am sure that J.D.R. was out of town as usual), she mentioned that they had purchased a custom-made radiofrequency (rf) transmitter–receiver unit from Varian, but no one had ever used it. I found the V-4311 gathering dust on a shelf and decided to see if I could find a ^{15}N resonance. The frequency was 6.08 MHz for the 1.41 T magnet (14 100 G then).

By midsummer, George Whitesides was wrapping up his thesis work, so I had time on the HR-60 to set up the rf unit in place of the one we used for ^{1}H and ^{19}F. There was no procedure for finding resonances of entirely unstudied nuclei, but there was a procedure for finding the ^{1}H signal after the magnet had been turned off for cycling. It consisted of bringing the magnet to full power, turning on an oscilloscope with the spectrum condensed to a spot on the screen, and altering the magnetic field with a rheostat until the spot bounced. The bounce was the resonance whizzing by. If I stopped rotating the rheostat instantly upon seeing the spot, conversion of the oscilloscope from a spot display to a screen-wide display would reveal the resonance in all its glory. When Ken Servis and I tried this procedure with the ^{15}N unit and saw the spot bounce, my heart performed an analogous motion. The sample I used was commercial 8.57 M nitric acid containing 96.1% ^{15}N, in a 9.85 mm o.d. nonspinning tube. It was July 24, 1963, and this comprised the first observation of a ^{15}N resonance.

Advances came quite rapidly. Proper tuning and building a spinner assembly brought the linewidth from 10 Hz down to 1 Hz (cps then) with excellent ringing. I set about to synthesize a sequence of labeled molecules to survey chemical shifts, and within six months had studied nitrobenzene, aniline, acetamide, azobenzene, ammonia, azoxybenzene, potassium cyanide, and hydrazobenzene, among others. Protonation of the bases amongst these molecules led to an understanding of how the lone pair affects the chemical shift. I managed to rig an audiooscillator at the ^{1}H frequency and observe the first proton-decoupled ^{15}N spectrum, by collapsing the quintet of NH_4^+ to a singlet. In early efforts I observed some odd negative peaks. As the nuclear Overhauser effect was unknown at the time (the gyromagnetic ratio of ^{15}N is negative), a wonderful opportunity slipped by. I originally used the nitric acid sample as the chemical shift standard, but the constancy of the resonance position of dry ammonia and its high field location led me to settle on it as the chemical shift standard, and it is still used as such today. All these exciting results were bundled up and sent to the *Journal of the American Chemical Society* as a communication, which was promptly rejected as being too mundane. Imagine biological NMR today without ^{15}N (apparently the referees could)! We published it in the *Proceedings of the National Academy of Sciences*.[1]

The azoxybenzene sample had enabled me to measure the first coupling between two ^{15}N nuclei, 13.7 Hz over one bond.[2] A variety of systems with protons on nitrogen led to a relationship between the one-bond ^{15}N–^{1}H coupling constant and the s character of the N–H orbital,[2] $s = 0.43J + 6$. Over the next year the development of chemical shifts and coupling constants continued.[3] Gerhard Binsch began work on ^{15}N–^{13}C couplings[2] and Bryan Roberts on more biological systems.[4] My last studies were on dynamic systems with proton exchange[5] and systems containing oxygen as well as nitrogen, including nitrites, nitrates, and nitroso compounds.[6] The examination of nitrosobenzene was inspired by Rex Richards's plot of ^{14}N chemical shifts versus the wavelength of the lowest energy electronic transition. The λ_{max} of nitrosobenzene at 755 nm suggested a really low field chemical shift, which by synthesis was realized at δ 913, still possibly the low field ^{15}N extreme.[6] I had made one valiant effort to observe ^{15}N at natural abundance, using 90% nitric acid, without success. Natural abundance observations had to await the new generation of spectrometers in the late 1960s based on frequency sweep and finally became routine in the 1970s with Fourier transform systems.

REFERENCES

1. J. B. Lambert, G. Binsch, and J. D. Roberts, *Proc. Natl. Acad. Sci. USA*, 1964, **51**, 735.
2. G. Binsch, J. B. Lambert, B. W. Roberts, and J. D. Roberts, *J. Am. Chem. Soc.*, 1964, **86**, 5564.
3. J. B. Lambert, B. W. Roberts, G. Binsch, and J. D. Roberts, in *Nuclear Magnetic Resonance in Chemistry*, ed. B. Pesce, Academic Press, New York, 1965, pp. 269–275.
4. B. W. Roberts, J. B. Lambert, and J. D. Roberts, *J. Am. Chem. Soc.*, 1965, **87**, 5439.
5. J. B. Lambert, W. L. Oliver, and J. D. Roberts, *J. Am. Chem. Soc.*, 1965, **87**, 5085.
6. J. B. Lambert and J. D. Roberts, *J. Am. Chem. Soc.*, 1965, **87**, 4087.

Biographical Sketch

Joseph B. Lambert, *b* 1940. B.S., 1962, Yale University, Ph.D., 1965, California Institute of Technology with John D. Roberts. Faculty of Northwestern University, 1965–present, currently Clare Hamilton Hall Professor of Chemistry, 260 papers and 8 books. Research specialties: conformational analysis, reaction mechanisms, main group chemistry, electronic interactions.

Laszlo, Pierre: Getting Acquainted with a Spin-3/2 Nucleus

Pierre Laszlo
Université de Liège, Liège, Belgium; Ecole Polytechnique, Palaiseau, France

'Nobody can ever speak for anybody but himself—and even then in doubt and great confusion'

Gavin Ewart, 'No Fool Like an Old Fool', Gollancz, London, 1976, p. 71.

I received a call from the University of Liège and moved there from Princeton in 1970. There was an old Varian HA-100 machine, but shortly thereafter, the university acquired a Bruker HFX-90 Fourier transform spectrometer. For our 'Organic Spectroscopy' book, published in 1970, Peter Stang and I had obtained from David Grant a few early carbon-13 spectra. They had made me familiar with ^{13}C NMR. For a couple of years we sheepishly stayed on that bandwagon. At the University of Liège, regardless of expertise, NMR was firmly in the hands of the physicists. Professeur Henri Brasseur, who had been entrusted with the purchase of the new spectrometer, was an X-ray crystallographer. An on-going collaboration with Pierre Tarte, a silicate chemist, made him equip the HFX-90 with a sodium-23 probe and channel. These had never been used. At some point, because of the above-mentioned turf war—these are endemic in universities, who are we to blame the Yugoslavs!—in which I had willy-nilly become embroiled, I made a snap decision to blitzkrieg the sodium-23 territory. A brainstorming session with my co-workers defined the exploratory experiments we would do. We had no more than two months, we felt, to acquire competence and make a successful contribution, visible enough to ensure local respect.

The literature, besides showing us Paul Lauterbur's footsteps—he did pioneering work in this area as in so many others—showed a range of chemical shifts of some 40–100 ppm after preparation of the sodium anion by J. L. Dye.[1] We also found that a sodium chloride external reference in a capillary would do, with a small correction for the difference in magnetic susceptibilities. After a few years of work, our bibliographical equipment was markedly improved, if indirectly, by a copy of Lindman and Forsén's book on halide ion NMR.[2] It told us all we needed to know about quadrupolar nuclei with nonintegral spin numbers.

A graduate student, Christian Detellier, had spent several years working on the ion-paired systems formed by iodine and triphenylarsine in organic solvents, much complicated by formation of polyiodides. Overnight we switched his attention to sodium salts, dissolved in ether and polyether solvents. Our goals were to define solvation numbers for Na^+, to determine equilibrium constants for complex formation with such coordinating ligands, as well as with the then relatively novel crown ethers and cryptands. From the start, perfectionism and a desire to achieve as full an understanding as feasible gave us the following imperatives: not to content ourselves with empirical correlations between the chemical shift and the desired parameters—relaxation rates were equally important: basing our conclusions firmly on consideration of both observables; and, in order to extract reliable kinetic and thermodynamic parameters from the data, making accurate computer simulations.[3] Solvation and ion pairing could thus be studied both in inorganic and in bioinorganic systems.[4]

Our reliance upon joint consideration of linewidths and chemical shifts made us realize that the two types of observables were intimately related. This made us resurrect Deverell's outstanding electronic distortion model.[5,6] This last contribution capped a couple of years of an exemplary collaboration as three close friends, of Freddy Delville, a mathematician, André Gerstmans, a chemical technician, and the aforementioned Christian Detellier.

At the onset of our ^{23}Na work, we shied away from studies of binding to large biomolecules. Our timidity found support in reports that univalent ions, such as sodium cations, associated only weakly to them and did not stay very long in the married state. A single sentence will serve to convey the stale flavor of the field at the time: 'Because of short lifetimes of the macromolecular complexes of sodium, the relaxation rate of ^{23}Na cannot be used in studies of macromolecular dynamics in solution'.[7] There are now whole papers devoted to precisely such studies![8–11]

The next step was to look at pieces of meat—my then wife, a physician, had suggested this to me in the early 1960s, and I had then told her that only a broad featureless absorption would result! The ^{23}Na resonance in biological tissue was peculiarly non-Lorentzian. It consisted of two overlapping lines, a narrow one superimposed on a broader one. The immediate temptation was to deconvolute: one would invariably find 40% of the narrow component and 60% of the other. Accordingly, quite a few people, following the intrepid and uncritical lead from Freeman Cope[12] rushed into print the conclusion of the coexistence of 40% sodium ions in the free state and of 60% in a bound state, affixed to biological macromolecules. Bob Hirst, then at Goodyear in Akron, whom I knew from our joint time at Princeton and from our common delight in a rather arcane 19th century book of exploration, 'Voyage au Pays des Mormons', saved my neck: he knew the literature. Indeed, the two $[\pm\frac{3}{2}, \pm\frac{1}{2}]$ and $[+\frac{1}{2}, -\frac{1}{2}]$ transitions, corresponding to the broad and the narrow component lines, respectively, differ in their spectral densities. Thus, each submagnetization has its intrinsic relaxation rate outside of extreme narrowing.[13]

Various experimental approaches, such as the measurement of the dispersion of the relaxation rates at various Larmor frequencies, allowed accurate determination of the spectral densities and of the attendant correlation times. In this manner, sodium ions with an ionic radius identical to that of the divalent calcium ions could be used (sheep in wolves' garb) to explore calcium binding sites on biomolecules. Using this approach, Jean Grandjean and I studied a series of calcium-binding proteins.[14] A fringe benefit was utilization of the observed correlation time, in favorable instances when the residence time of sodium on the protein was of the same order as the reorientational correlation time of the complex,[15] to determine the full binding kinetics and thermodynamics. I was even able to convince a senior co-worker, André Cornélis, a staunch synthetic organic chemist to go on an NMR excursion, from which we brought back information about the ion-conducting membrane channels formed by gramicidin A.[16]

Our main effort, however, was directed to the formidable problem posed by the self-assembly of the 5′-GMP nucleotide, an all-important biological process since the G-rich regions of DNA are responsible for the pairing of chromosomes during meiosis as Felix Gilbert at Harvard was later to show. ^{23}Na NMR was an important asset in establishing some of the main feature of this structures held by noncovalent bonds only.[17,18]

We had learned a lot, and not only about NMR of quadrupolar nuclei. To operate in commando manner and stake out a new field, to ignore dogmatic statements, to choose our own way far from the madding crowd, and to experience the delight of discovery. When the President of Liège University, Professor Betz, had the guts to award to us alone a new superconducting magnet spectrometer, rather than to a competing group of half-a-dozen fellow chemists, when he thus chose competence over politics, we felt totally vindicated in having gone it alone.

REFERENCES

1. See J. L. Dye and M. G. DeBacker, *Annu. Rev. Phys. Chem.*, 1987, **38**, 271.
2. B. Lindman and S. Forsén, *NMR Basic Principles and Progress*, 1976, **12**, 1.
3. P. Laszlo, in NMR Spectroscopy: New Methods and Applications, *ACS Symp. Ser.*, 1981, **191**, 63.
4. P. Laszlo, *Angew. Chem., Int. Ed. Engl.*, 1978, **17**, 254.
5. C. Deverell, *Mol. Phys.*, 1969, **16**, 491.
6. A. Delville, C. Detellier, A. Gerstmans, and P. Laszlo, *J. Magn. Reson.*, 1981, **42**, 14.
7. J. Reuben, in *Metal–Ligand Interactions in Organic Chemistry and Biochemistry*, ed. B. Pullman and N. Goldblum, Reidel, Dordrecht, 1977, Vol. 2, p. 325.
8. H. Grasdalen and B. J. Kvam, *Macromolecules*, 1986, **19**, 1913.
9. M. Hald and J. P. Jacobsen, *Biophys. Chem.*, 1991, **41**, 113.
10. C. W. R. Mulder, J. d. Bleijser, and J. C. Leyte, *Chem. Phys. Lett.*, 1980, **69**, 354.
11. L. Nordenskiold, D. K. Chang, C. F. Anderson, and M. T. Record, Jr., *Biochemistry*, 1984, **23**, 4309.
12. F. W. Cope, *Proc. Natl. Acad. Sci. USA*, 1965, **54**, 225; F. W. Cope, *J. Gen. Physiol.*, 1967, **50**, 1353.
13. P. S. Hubbard, *J. Chem. Phys.*, 1970, **53**, 985.
14. J. Grandjean and P. Laszlo, in *Dynamics of Solutions and Fluid Mixtures by NMR*, ed. J. J. Delpuech, Wiley, Chichester, Chap. 5, 1995.
15. P. Laszlo, *Progress in Nuclear Magnetic Resonance Spectroscopy*, 1980, **13**, 257.
16. A. Cornélis and P. Laszlo, *Biochemistry*, 1979, **18**, 2004.
17. M. Borzo, C. Detellier, P. Laszlo, and A. Paris, *J. Am. Chem. Soc.*, 1980, **102**, 1124.
18. C. Detellier and P. Laszlo, *J. Am. Chem. Soc.*, 1980, **102**, 1135.

Biographical Sketch

P. Laszlo. *b* 1938. B.S., 1961, D.Sc., 1965, University of Paris, Sorbonne. Self-taught in NMR from Pople–Schneider–Bernstein and the Abragam lectures at Collège de France, 1961–62. Postdoctoral research, Princeton University, 1962–63. Assistant Professor, Princeton University, 1966–70; Professor, University of Liège, 1970–present; Professor, Ecole Polytechnique, 1986–present. Taught NMR courses at Hamburg, Cornell University, and University of Kansas, and NMR workshops in Europe, the United States, and Japan. Approx. 200 publications and among 14 books, ‘Organic Spectroscopy’ with Peter Stang in 1970 and editing of ‘NMR in Newly Accessible Nuclei’ (two volumes) in 1983. Current research specialty: NMR studies of molecular interactions and motions in chemical and biochemical systems.

Lauterbur, Paul C.: One Path out of Many—How MRI Actually Began

Paul C. Lauterbur

University of Illinois, Urbana, IL, USA

The invention of NMR imaging (MRI) can be traced back through a variety of specific incidents to a set of underlying interests developed in my childhood. This pathway does not represent the only route to the final result; many others would have converged to the same eventual result from other initial conditions, but this history does show that it is often impossible to predict the hidden ideas to be revealed at the end of a research journey. Knowledge of what we do not know is the beginning of wisdom. The story of what actually happened is told below.

Two particular ideas that were woven together during precollege days survived, with a little stimulus from science fiction, to become sources of future research activities: biology and organosilicon chemistry. Could there be a biology based wholly or partly on silicon, instead of or in addition to carbon? Those interests, led me, after graduation with a B.S. in chemistry from the Case Institute of Technology, to take a job with a Dow Corning-supported group at the Mellon Institute that synthesized and tested organosilicon compounds and polymers. Although I was unsure about graduate work, it was possible to study for a Ph.D. at the University of Pittsburgh without paying tuition, so that with a little extra effort I could have it all, as I straddled the worlds of industry and academia. Three especially seminal events occurred in those first years. Two of them came about because I was working on silicone elastomers, trying to understand cross-linking reactions involving Si−H groups and also the sources of the 'filler effect', the strengthening of silicone rubber by small particles (such as fused silica, strangely enough the equivalent of carbon black in carbon-based rubbers). The first question, the mechanism of the cross-linking reaction, led again to the question of free radical participation, sparking my interest in the recently discovered electron spin resonance method for detecting unpaired electrons. The second question also led to magnetic resonance, this time of the nuclear variety, through my interest in the physics of rubber elasticity and how particles interacting noncovalently with polymer chains could have drastic effects on the elastic modules, tear resistance, etc., of rubber. A paper on NMR relaxation times in such systems was published just then, and I gave a physical chemistry seminar on it at Pitt.

The third intrusion of magnetic resonance on my consciousness during 1952−53 was a seminar by Herbert Gutowsky, of the University of Illinois, on the proton NMR chemical shifts of substituted methanes and their use to deduce electron densities. Here at last was the ideal tool with which to develop clear insights into the difference between silicon and carbon chemistry! I proposed to Gutowsky that I would send him samples of a variety of substituted silanes (not readily available commercially) and that he and I would then try to work out what the comparative NMR data meant. He agreed.

It was the time of the Korean War, however, and my deferments ran out. I was drafted and eventually ended up at the Army Chemical Center, where my 'experience' with NMR got me a transfer and assignment to help set up the Varian NMR machine (40 MHz proton and ^{19}F, 17 MHz ^{31}P) which they purchased to support chemical warfare research. There I actually learned something about NMR and even published a few papers. After Army service two options developed: go to Illinois as a graduate student with Gutowsky, or persuade the Mellon Institute to buy an NMR spectrometer. The Institute itself declined, but the Dow Corning group took the plunge, at least partly because I claimed that useful ^{29}Si spectra would be possible. I chose that option, visited Varian and confirmed that ^{29}Si spectra could be seen (with an 8.5 Mc s^{-1} rf unit) and immediately decided that ^{13}C would be even more interesting. I soon published the first paper on ^{13}C NMR spectra.[1] The rest is another branch of personal and scientific history, except that ^{13}C led to interest in spin decoupling and biological polymers, which were both to become essential links in the chain of events leading to 'zeugmatography', as I originally called magnetic resonance imaging. Before that, however, I carried out research on NMR spectroscopy of a number of elements and on several outstanding questions in the field, and then completed a Ph.D. thesis on applications of ^{13}C NMR spectroscopy to studies of the electronic structures of molecules. When the industry-supported group at Mellon Institute began to seem too restrictive an environment, I accepted a faculty position in the Department of Chemistry at the new State University of New York at Stony Brook.

Two of the areas that began to interest me at Stony Brook led toward imaging. One was computer-aided acquisition and processing of spectra, and the other was biological applications. In pursuit of the latter I went to Stanford for a 1969−70 sabbatical, associated with John Baldeschweiler's group in chemistry, but also working with a Medical Center laboratory on ^{13}C labeling of proteins, and with Syntex on tritium NMR. For the latter we borrowed a retuned 100 MHz rf unit from Varian and found that we could see the tritium signals from labeled steroids (one turned out to be labeled in an unexpected location) and I later helped set up a National Institutes of Health (NIH) Research Resource for such work at Stony Brook. The other project generated the first ^{13}C NMR spectrum of a protein, from work with LeRoy Johnson on an early superconducting spectrometer at Varian,[2] but the more ambitious projects with ^{13}C labeled proteins were still incomplete at the end of the sabbatical year. Nevertheless, I was well on my way to developing a program for using isotopic labeling to study proteins, and getting excited about the other opportunities in biology.

A funny thing happened, however, as I did more preliminary work and tried to get some grant support, which was certainly delayed because of the incomplete preliminary protein-labeling experiments at Stanford. I had helped a small company to get started, during my Mellon Institute days, to build spin decouplers for double resonance experiments, after Varian had discontinued their production just when I desperately needed one for ^{13}C spectroscopy. When that company decided to start making superconducting NMR spectrometers I arranged to buy one for biopolymer work, including a plan to study enzymes by replacing calcium with cadmium. Then, in May 1971, events accelerated. At a hastily called board meeting it was revealed that the company's financial condition was not what the board,

the bank, the investors, and the customers had been led to believe. The banker threatened to throw the company into bankruptcy and close it down that day unless someone could be found to take over the company while an attempt was made to turn it around. Classes were over, I faced a summer without a grant or summer salary, and my superconducting system might never be finished if I didn't do something. Despite the need to commute to western Pennsylvania from Long Island, I agreed to take on the job.

There is a book to be written about that summer, but for present purposes the important event was a visit by a postdoc, Leon Saryan, from Don Hollis's laboratory at Johns Hopkins to attempt to follow up the studies reported earlier that year by Damadian[3] on water T_1 and T_2 in tumor tissues. The possibility of observing interactions of water with living tissues had attracted occasional investigators over the years. Perhaps the most indefatigable of these was Odeblad,[4] who was fascinated by the opportunities for characterizing the properties of human cells and secretions, and by the technical problems of observing NMR signals from small biological samples. Other early investigations included those on blood flow by Singer[5] and studies of muscle by Bratton and co-workers.[6] A remarkable anticipation of later research is to be found in an unpublished thesis by Ligon,[7] who measured NMR relaxation times in the arms of living human subjects. The first NMR signals from entire living animals were published shortly thereafter by Jackson and Langham[8] in 1968. A surge of interest in such studies became evident in 1971 when several papers on muscle appeared,[9–11] but the attention of the medical community was first attracted by the report of Damadian that some animal tumors have remarkably long water proton NMR relaxation times.[3]

Efforts to reproduce these results and to explore their significance were soon underway in other laboratories,[12] but it was the measurements, referred to above, that I observed Saryan carrying out in September 1971 that caught my attention.[13] Damadian's measurements had been done on the company's demonstration pulsed NMR spectrometer earlier that year, but I had not paid much attention, thinking that the controls were inadequate and the publicity overdone. The Hopkins studies were another matter, however. I watched them being done, including the sacrifice of the rats, specimen dissection, and the NMR measurements and was struck by the consistent differences obtained among various normal and malignant tissues. I knew, however, that biopsies were commonly done and examined by histologists, and I believed that NMR relaxation time measurements on tissue specimens were unlikely to contribute much to the rich variety of information available from optical microscopy.

All of this information about the tissues was apparently there, however, within the living organism. Was there any way that one could tell exactly which location an NMR signal was coming from within a complex object? That same evening I realized that inhomogeneous magnetic fields labeled signals according to their spatial coordinates, and made a leap of faith to the conclusion that the information could be recovered in the form of pictures (we would now say that the inverse problem could be solved). I was so sure of this that I immediately went out and bought a notebook and had the idea witnessed.

Why was I so certain? I remembered from my graduate student work that iterative solutions could be found for otherwise intractable problems using continuous functions represented by a grid or network of points, and I knew that there were already so-called 'shim' controls on NMR spectrometers that could shape the static magnetic field in known ways, allowing in principle a solution to the problem in the form of an image constructed from one-center harmonic representations. However, a much simpler idea came to me during the next several days. Sets of linear gradients oriented in different directions could uniquely encode each of a finite number of points representing the object, and I thought that an iterative comparison of the 'projections' thus generated with those from images, progressively refined to minimize the differences, could converge on a correct solution. Mathematicians and computer scientists whom I consulted disagreed on whether it would work, so I just went ahead and calculated some simple examples by hand, finding that the method worked easily and well. Only after that had been done was my attention called to a report by Gordon and Herman[14] containing an essentially identical algorithm for 'reconstruction from projections'. As I also discovered later, Hounsfield was bringing computerized axial tomography from X-rays (CAT scanning) to practical usefulness at about the same time.[15]

While working out the mathematics I asked myself two other important questions: would there be enough water proton signal-to-noise ratio for large objects in low magnetic fields to support useful resolution in practical acquisition times, and could large magnets with good enough homogeneity be built? The answer to the first question was easily calculated from equations in Abragam's standard book on nuclear magnetism. Those simple calculations revealed that physics allowed an adequate signal-to-noise ratio, and I had confidence that whatever physics allowed engineers could achieve. Next, there were examples of fairly large resistive magnets with fairly uniform fields in the literature, but more importantly there were also papers describing how to design them. It looked quite easy (and was), so almost everything had fallen into place to justify my instant faith that I had stumbled across an idea that was worth spending most of my time on for the foreseeable future, instead of carrying on with molecular structure studies.

The word 'almost' above is because I still did not know exactly *how* it would be useful in medicine to have a method for making three-dimensional pictures of the body, since I knew nothing about medical science or clinical practice. I therefore went to the new medical library at Stony Brook, skimmed innumerable books and journals on radiology, nuclear medicine, cardiology, oncology, and related subjects, and picked up the vocabulary I needed in order to talk to physicians. Very soon everything had fallen into place and I decided that I more-or-less knew what I was doing. After failing to convince various people and institutions that it was a good enough idea to patent, I started doing experiments, writing papers, preparing grant proposals (mostly rejected), and giving talks, starting in 1972 at Stony Brook and Brookhaven and at an American Physical Society meeting in January 1973. My first paper on this subject was published in *Nature* in early 1973.[16]

So that is how biology and silicon, simple mathematical techniques, a broad knowledge of NMR, the design of NMR shim coils, experiments on cancer tissue, the collapse of a small instrument company, and general contrariness threw up a new and unprecedented technique for medical and other imaging. I have left out many things that could have, but to

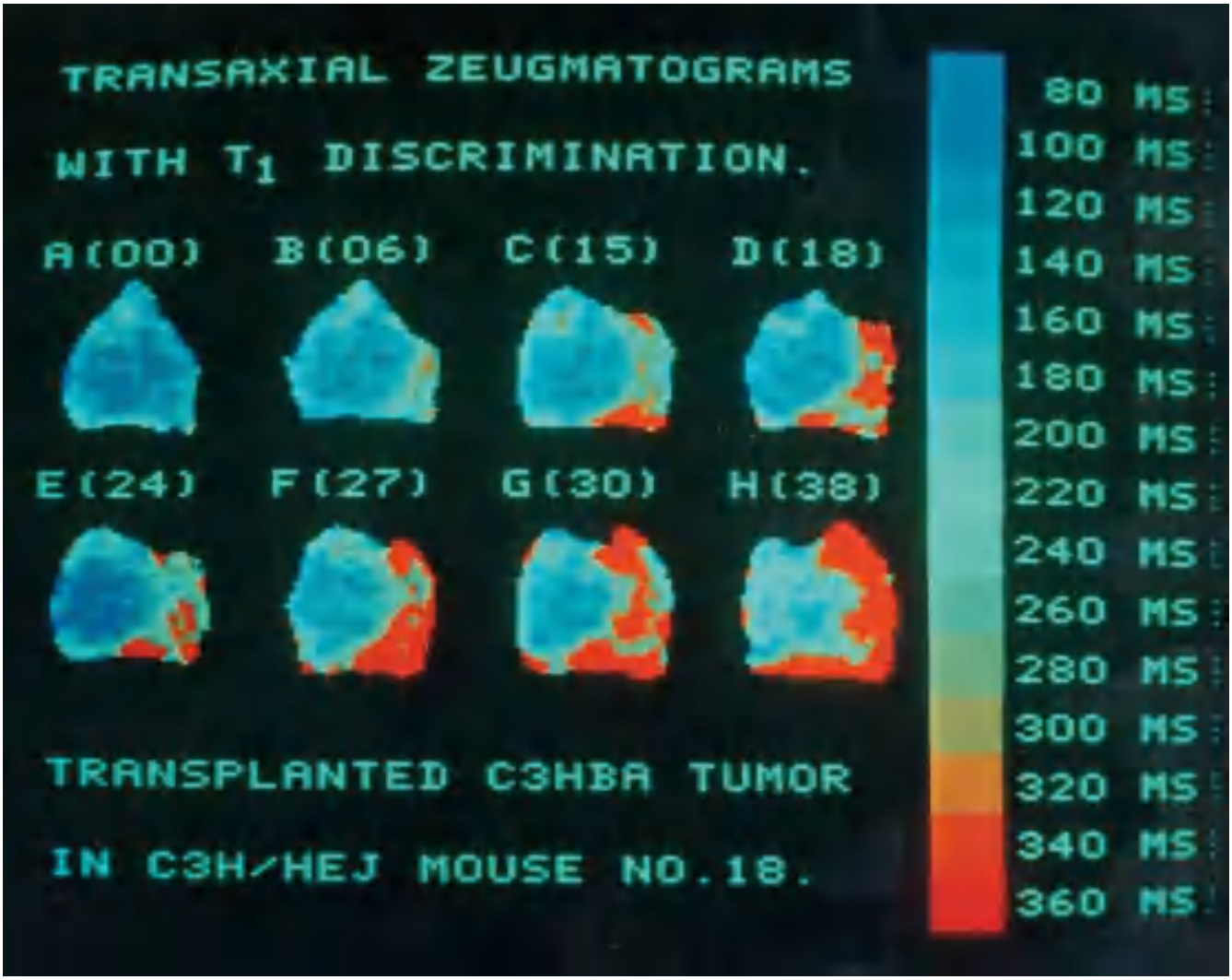

Figure 1 T_1 images showing the growth of an implanted tumor over a period of 38 days in a single mouse. Each two-dimensional picture, reconstructed from 12 projections, represents a thick section (ca. 3–4 cm) determined by the sensitivity profile of the rf coil

the best of my knowledge did not, influenced my conception of NMR imaging because I did not initially know about them. These include the NMR work of Gabillard,[17] the one-dimensional NMR experiments of Fairbank and others on ^{3}He,[18] and a speculative patent application by Damadian.[19] Only later did I become aware of much of the relevant mathematical literature, including a then little-known paper by Radon,[20] work by Bracewell[21,22] and Cormack,[23,24] and related ideas in medical imaging by Kuhl and Edwards,[25] in electron microscopy by DeRosier and Klug,[26] and the papers by Ramachandran.[27,28]

In my laboratory at Stony Brook, we soon set out to apply the imaging method to the study of living organisms. The first animal imaged, in the 5-mm space then available, was a 4-mm clam. An image showing the soft body of the clam within its shell was reconstructed from four projections.[29] When a larger standard spectrometer could be suitably modified, it became possible to make images of a variety of objects up to 3 cm in diameter, including a living mouse.[30] Those experiments led to the first attempts to image malignant tumors in living animals. These continued, with gradual refinement of the techniques, during the following 2 years. A special technique for the measurement of the spin–lattice relaxation time T_1 was worked out, using an intermittent CW scan. After calibration with known samples, and rather elaborate corrections for nonlinearities in the gradients, we reconstructed color images to show the growth of an implanted mouse tumor over weeks (see Figure 1). Thus, it was beginning to seem plausible that at least some cancers should be detectable by NMR imaging techniques in human patients.

Meanwhile, other publications on NMR imaging, beginning with the work of Mansfield and Grannell,[31] had started to appear.[32–40] Investigations on humans began,[41–43] and further studies of animal tumors were carried out.[37–44] In our own laboratory, work proceeded on a number of technical and medical aspects of NMR imaging. Chemical shift imaging of proton signals was described in 1975,[45] and paramagnetic contrast agents were introduced in 1978.[46] Three-dimensional projection reconstruction was largely developed between 1977 and 1981,[47–50] and then applied and demonstrated in a number of applications.[51–57] These included the first human breast imaging with a special breast coil,[52] the first surface coil imaging,[53] rapid three-dimensional human head imaging,[54] and three-dimensional image display.[56] A human whole body

system for three-dimensional imaging was constructed,[52] and studies of specimens removed during cancer surgery were carried out.[55,57]

Most descriptions of the tangled processes of scientific discovery are cartoons, so oversimplified as to be useless for any purpose other than providing apparent evidence for preconceived notions, polemical disputes, and the justification of budgets. Here I have told a tale of work that was not *initially* socially responsible, guided by perceived national needs, or particularly accountable to superiors or sources of funding. It is a story of striving for the most interesting and significant goals that seemed to be accessible from a given point in space and time, considering the available facilities, knowledge, skills, and interest, and a flexibility of research agendas shaped by a belief that science is so strongly interconnected that it is usually not a good idea to butt one's head against a brick wall in the direct path to a goal when the general advance in knowledge and techniques is likely to allow it to be reached indirectly in due course. The exceptions are situations driven by specific military, medical, or commercial emergencies, but those thrusts use up inordinate amounts of resources, both human and financial, and are made possible only by the broad range of knowledge, skills, and experience developed in less frantic contexts, and by the unexpected breakthroughs that grow in the fertile soil of 'curiosity-driven' research (which might often be better described as 'opportunity driven'), the most cost-effective kind in the long run.

REFERENCES

1. P. C. Lauterbur, *J. Chem. Phys.* 1957, **26**, 217.
2. P. C. Lauterbur, *Appl. Spectrosc.*, 1970, **24**, 450.
3. R. Damadian, *Science*, 1971, **171**, 1151.
4. E. Odeblad, B. N. Bhar, and G. Lindstrom, *Arch. Biochem. Biophys.*, 1956, **63**, 221.
5. J. R. Singer, *Science*, 1959, **130**, 1652.
6. C. B. Bratton, A. L. Hopkins, and J. W. Weinberg, *Science*, 1965, **147**, 738.
7. T. R. Ligon, M.S. Thesis, Oklahoma State University, 1967.
8. J. A. Jackson and W. H. Langham, *Rev. Sci. Instrum.*, 1968, **39**, 510.
9. R. Cooke and R. Wien, *Biophys. J.*, 1971, **11**, 1002.
10. J. R. Hansen, *Nature (London)*, 1971, **230**, 482.
11. C. F. Hazlewood, B. L. Nichols, D. C. Chang, and B. Brown, *Johns Hopkins Med. J.*, 1971, **128**, 117.
12. I. D. Weisman, L. H. Bennett, L. R. Maxwell, M. W. Woods, and D. Burk, *Science*, 1972, **178**, 1288.
13. D. P. Hollis, L. A. Saryan, and H. P. Morris, *Johns Hopkins Med. J.*, 1972, **131**, 441.
14. R. Gordon and G. T. Herman, *Commun. ACM*, 1972, **14**, 759.
15. G. N. Hounsfield, *Br. J. Radiol.*, 1973, **46**, 1016.
16. P. C. Lauterbur, *Nature (London)*, 1973, **242**, 190.
17. R. Gabillard, *C.R. Acad. Sci. Paris*, 1951, **232**, 1551.
18. G. K. Walters and W. M. Fairbank, *Phys. Rev.*, 1956, **103**, 262.
19. R. Damadian, US Patent 3 789 832, filed 17 March 1972, issued 5 February 1974.
20. J. Radon, *Akad. Wiss. Leipzig*, 1917, **69**, 262.
21. R. N. Bracewell, *Aust. J. Phys.*, 1956, **9**, 198.
22. R. N. Bracewell and A. C. Riddle, *Astrophys. J.*, 1967, **150**, 427.
23. A. Cormack, *J. Appl. Phys.*, 1963, **34**, 2722.
24. A. Cormack, *J. Appl. Phys.*, 1964, **35**, 2908.
25. D. E. Kuhl and R. A. Edwards, *Radiology*, 1963, **80**, 653.
26. D. J. DeRosier and A. Klug, *Nature (London)*, 1968, **217**, 130.
27. G. N. Ramachandran, *Proc. Ind. Acad. Sci.*, 1971, **73A**, 14.
28. G. N. Ramachandran and A. V. Lakshminarayanan, *Proc. Natl. Acad. Sci. USA*, 1971, **68**, 2236.
29. P. C. Lauterbur, in *Proceedings of the First International Conference on Stable Isotopes in Chemistry, Biology and Medicine*, eds. P. D. Klein and S. V. Peterson, Argonne National Laboratory, Argonne, IL, 1973, pp. 255–260.
30. P. C. Lauterbur, *Pure Appl. Chem.*, 1974, **40**, 149.
31. P. Mansfield and P. K. Grannell, *J. Phys. C*, 1973, **6**, L422.
32. W. S. Hinshaw, *Phys. Lett. A*, 1974, **48**, 87.
33. P. Mansfield and P. K. Grannell, *Phys. Rev. B*, 1975, **12**, 3618.
34. A. Kumar, D. Welti, and R. R. Ernst, *Naturwiss.*, 1975, **62**, 34.
35. A. Kumar, D. Welti, and R. R. Ernst, *J. Magn. Reson.*, 1975, **18**, 69.
36. W. S. Hinshaw, *J. Appl. Phys.*, 1976, **47**, 3709.
37. R. Damadian, L. Minkoff, M. Goldsmith, M. Stanford, and J. Koutcher, *Science*, 1976, **194**, 1430.
38. J. M. S. Hutchison, in *Medical Images: Formation, Perception and Measurement* ed. G. A. Hay, Wiley, New York, 1977, pp. 135–141.
39. E. R. Andrew, P. A. Bottomley, W. S. Hinshaw, G. N. Holland, W. S. Moore, and C. Simaroj, *Phys. Med. Biol.*, 1977, **22**, 971.
40. L. E. Crooks, T. P. Grover, L. Kaufman, and J. R. Singer, *Invest. Radiol.*, 1978, **13**, 63.
41. W. S. Hinshaw, P. A. Bottomley, and G. N. Holland, *Nature, (London)*, 1977, **270**, 722.
42. R. Damadian, M. Goldsmith, and L. Minkoff, *Physiol. Chem. Phys.*, 1977, **9**, 97.
43. P. Mansfield, I. L. Pykett, P. G. Morris, and R. E. Coupland, *Br. J. Radiol.*, 1978, **51**, 921.
44. I. L. Pykett and P. Mansfield, *Phys. Med. Biol.*, 1978, **23**, 961.
45. P. C. Lauterbur, D. M. Kramer, W. V. House, and C.-N. Chen, *J. Am. Chem. Soc.*, 1975, **97**, 6866.
46. P. C. Lauterbur, M. H. Mendonca Dias, and A. M. Rudin, in *Frontiers of Biological Energetics*, eds. P. O. Dutton, J. S. Leigh, and A. Scarpa. Academic, New York, 1978, pp. 752–759x.
47. C.-N. Chen, Ph.D. Dissertation, State University of New York, Stony Brook, 1980.
48. P. C. Lauterbur and C.-M. Lai, *IEEE Trans. Nucl. Sci.*, 1980, **NS-27**, 1227.
49. C.-M. Lai and P. C. Lauterbur, *Phys. Med. Biol.*, 1981, **26**, 851.
50. R. B. Marr, C.-N. Chen, and P. C. Lauterbur, in *Mathematical Aspects of Computerized Tomography*, eds. G. T. Herman and F. Natterer, Springer, Berlin, 1981, pp. 225–240.
51. D. M. Kramer, J. S. Schneider, A. M. Rudin, and P. C. Lauterbur, *Neuroradiology*, 1981, **21**, 239.
52. H. E. Simon, *Proc. Soc. Photo-Opt. Instrum. Eng.*, 1981, **273**, 41.
53. M. L. Bernardo, Jr, A. J. Cohen, and P. C. Lauterbur, *IEEE Comput. Soc. Press*, **1982**, 277.
54. M. L. Bernardo, Jr, and P. C. Lauterbur, *Eur. J. Radiol.*, 1983, **3**, 257.
55. M. H. Mendonca Dias, W. J. Mann, J. Chumas, M. L. Bernardo, Jr, and P. C. Lauterbur, *Biosci. Rep.*, 1982, **713**, 717.
56. G. T. Herman, J. K. Udupa, D. M. Kramer, P. C. Lauterbur, A. M. Rudin, and J. S. Schneider, *Opt. Eng.*, 1982, **21**, 923.
57. W. J. Mann, M. H. Mendonca Dias, and P. C. Lauterbur, *Am. J. Obstet. Gynecol.*, 1984, **148**, 91.

Biographical Sketch

Paul C. Lauterbur. *b* 1929. B.S., 1951, Ph.D., 1962, Chemistry, University of Pittsburgh, USA. Research Associate, Mellon Institute, 1951–63. Faculty, State University of New York, Stony Brook, 1963–85. Professor, University of Illinois, 1985–present. NMR research includes: initial work in carbon-13, silicon-29 and other nuclei; conception and development of NMR imaging. Numerous awards in chemistry, physics, and biomedical sciences.

Led, Jens J.: Aspects of NMR Studies of Paramagnetic Metal Complexes of Biological Relevance. A Historical Sketch

Jens J. Led

University of Copenhagen, Copenhagen, Denmark

In the late 1960s and the early 1970s much attention was focused on the application of NMR to the study of paramagnetic metal complexes of biomacromolecules and biological systems, such as metalloenzyme–substrate systems. In those premultidimensional NMR days the dramatic and often specific effect on the NMR spectra, caused by the interaction of the observed nuclei with the unpaired metal electrons (see ***Electron–Nuclear Hyperfine Interactions***), offered a unique method of extracting detailed information from the complex NMR spectra of such molecules and systems. This includes information about the structure, dynamics, and specific interactions of the biological systems, obtained from the changes of the relaxation and chemical shifts of the ligand nuclei. Excellent reviews by Mildvan and Cohn[1,2] cover, through 1970, paramagnetic relaxation effects in biochemical molecules with particular emphasis on enzymatic mechanisms, while an equally thorough review[3] by Phillips covers the influence of the paramagnetic metal ions on the chemical shifts of biomacromolecules.

The theoretical models for the paramagnetic relaxation (see ***Paramagnetic Relaxation in Solution***) of the nuclei given by the Solomon–Bloembergen–Morgan (SBM) theories,[4–6] are complex. This often makes a complete unraveling of the experimental data in terms of information about the structure and dynamics difficult, while the unraveling requires a considerable amount of experimental data. Because of this inherent difficulty, certain assumptions were often made as to the nature of the relaxation mechanisms involved, or to the magnitude of the associated parameters, in order to reduce the complexity of the interpretation and accommodate it to a limited amount of experimental data. Although this procedure could be justified in some cases, in others it led to clear inconsistencies between the experimental data and the applied model. Thus, both the time modulation and the magnitude of the zero-field splitting that cause the paramagnetic relaxation seemed incompatible with the SBM theories. Also the point-dipole approximation of these theories appeared to be violated. In most cases these inconsistencies were ascribed to deficiencies of the theoretical model rather than errors in the assumptions.

During a sabbatical leave from 1971 to 1973 that I spent in David Grant's laboratory at the University of Utah, we set out to investigate to what extent experimental NMR data of the paramagnetic Mn^{2+} and Ni^{2+} complexes of amino acids and nucleic acids can in fact be described by the SBM theories for relaxation if a data set is applied that is sufficiently large to allow an independent determination of all the parameters involved. The amount of data necessary for this analysis was substantial and included R_1 and R_2 relaxation rates and chemical shifts obtained at two magnetic field strengths and covering a wide temperature range. The observed nuclei were ^{13}C and ^{31}P. These nuclei were chosen because of their large chemical shift dispersions and because they allow a simpler theoretical model to be applied.

The result of the analysis was encouraging. Thus we found that the relaxation of the ^{13}C and ^{31}P nuclei in a series of representative binary and ternary Mn^{2+}- and Ni^{2+}-complexes[7–9] of amino acids and nucleic acids conforms closely to the SBM theories for the nuclei and electron relaxations, and that the parameters obtained were in general accord with the basic assumption of the theories.

Further development in the application of paramagnetic metal ions in the studies of biological systems was made by the establishment of the activity of the Mn^{2+} derivative of carbonic anhydrase[10,11] (see ***Carbonic Anhydrase***) in the catalysis of the reversible CO_2/HCO_3^- hydration-dehydration reaction, $CO_2 + H_2O \leftrightarrows HCO_3^- + H^+$, and the experimental verification of the central pentacoordinated metal complex in the catalytic pathway previously suggested by Lindskog. These results were achieved by a combined measurement of the paramagnetic relaxation and chemical exchange of the ^{13}C nuclei in the two substrates, CO_2 and HCO_3^-, in a magnetization transfer experiment (see ***Enzyme-Catalyzed Exchange: Magnetization Transfer Measurements***). A central issue in this study was the use of sets of *complementary* magnetization transfer experiments, as shown in Figure 1. Thus it was demonstrated, both theoretically and experimentally, that only by using such sets of experiments was it possible to achieve an amount of experimental information sufficiently large to allow an independent determination of the three involved rate constants, i.e. the R_1 relaxation rates of ^{13}C in the two sites, and the rate constant for the catalytic exchange between these sites.

REFERENCES

1. A. S. Mildvan and M. Cohn, *Adv. Enzymol.*, 1970, **33**, 1.
2. M. Cohn, *Q. Rev. Biophys.*, 1970, **3**, 61.
3. W. D. Phillips, in *NMR of Paramagnetic Molecules*, ed. G. N. La Mar, W. D. Horrocks, Jr., and R. H. Holm, Academic Press, New York, 1973, Chap. 11
4. I. Solomon, *Phys. Rev.*, 1955, **99**, 559.
5. N. Bloembergen, *J. Chem. Phys.*, 1957, **27**, 572.
6. N. Bloembergen and L. O. Morgan, *J. Chem. Phys.*, 1961, **34** 842.
7. J. J. Led and D. M. Grant, *J. Am. Chem. Soc.*, 1975, **97**, 6962.
8. J. J. Led, *Mol. Phys.*, 1980, **40**, 1293.
9. J. J. Led, *J. Am. Chem. Soc.*, 1985, **107**, 6755.
10. J. J. Led, H. Gesmar, and F. Abildgaard, *Methods Enzymol.*, 1989, **176**, 311.
11. J. J. Led, E. Neesgaard, and J. T. Johansen, *FEBS Lett.*, 1982, **147**, 74.

Biographical Sketch

J. J. Led. *b* 1938. M. S., 1963, Chemistry, The Technical University of Denmark, Ph.D., 1968, Sc.D., 1988, University of Copenhagen. Faculty

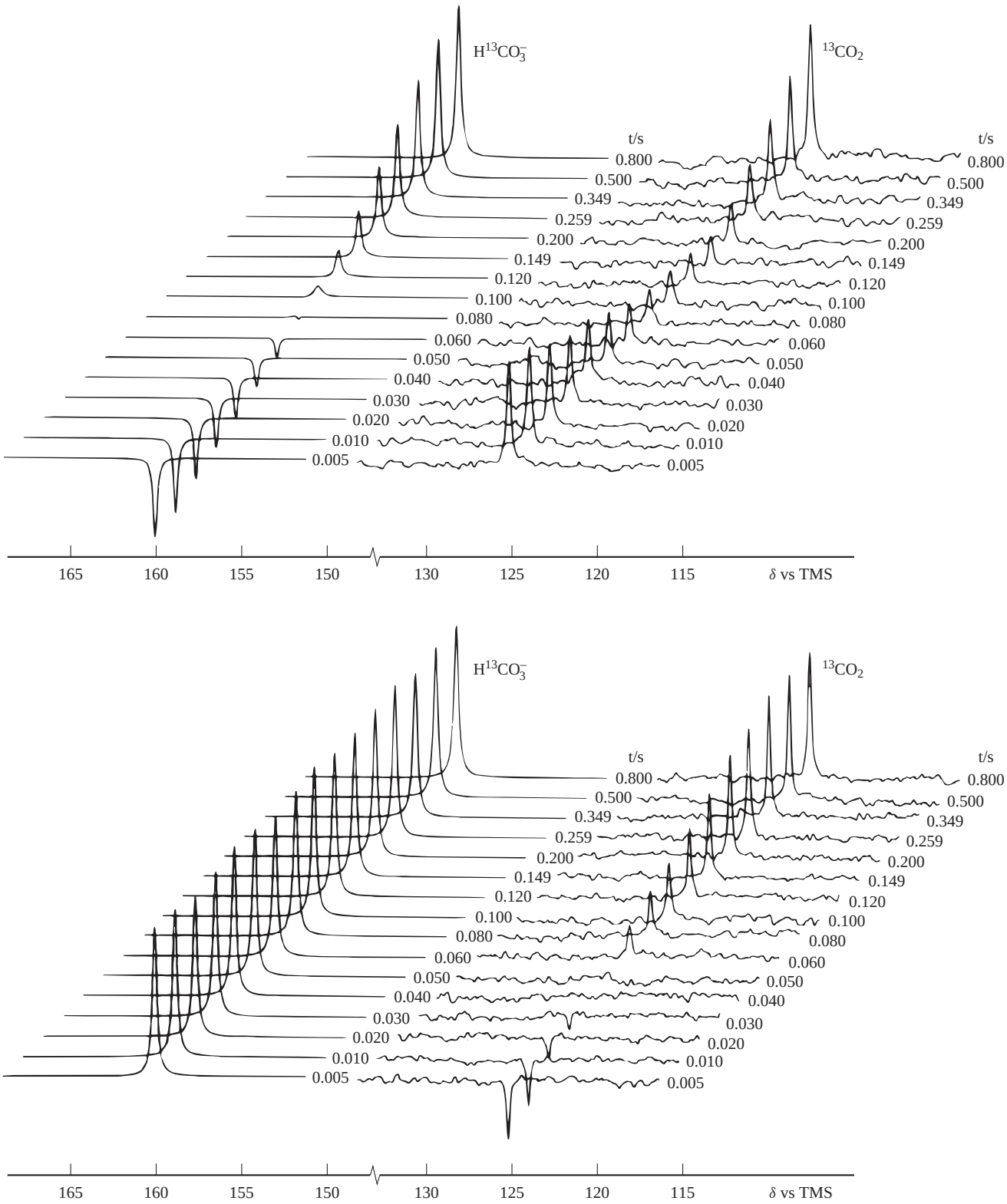

Figure 1 Sets of complementary magnetization transfer ^{13}C NMR spectra at 67.89 MHz of $H^{13}CO^-_3$ (100 mM) and $^{13}CO_2$ (0.38 mM) at chemical equilibrium in 50 mM tris-sulfate buffer at pH 8.7 and in the presence of Mn(II)–human carbonic anhydrase (8.8 μM). (Reproduced by permission of Elsevier/North-Holland from J. J. Led, E. Neesgaard, and J. T. Johansen, *FEBS Lett.*, 1982, **147**, 74)

in Chemistry, University of Copenhagen, 1969–present. Research associate, University of Utah, 1971–73. Approx. 60 publications. Introduced to NMR by Børge Bak, University of Copenhagen and David M. Grant, University of Utah. Current research specialties: NMR studies of protein structure and function, NMR signal analysis.

Lemieux, Raymond U.: First Observations: The Dependence on Torsion Angle of the Magnitude of the Coupling Constant for Vicinal Hydrogens and its Sign Compared to that for Geminal Hydrogens

Raymond U. Lemieux

University of Alberta, Edmonton, Alberta, Canada

While visiting the National Research Council of Canada (NRC) soon after I had moved to the University of Ottawa in the summer of 1954, I learned from my colleagues in organic chemistry that there existed a new spectroscopic method, based on the magnetic moment of the hydrogen nucleus, that allowed a nondestructive determination of the hydrogen content of an organic compound. This was highly intriguing. A few months later I returned to attend a physicist's lecture on the chemical shifts of the hydrogen atoms in fused-ring aromatic systems (published in 1957[1]). My attendance was strictly curiosity-driven. Little did I realize that I was about to gain the privilege of participating in the development of a revolutionary force for the advancement of chemical knowledge. This good fortune came to me because of my close proximity to NRC, which had recently acquired one of the very first Varian Associates HR-40 NMR spectrometers, and the expertise that was brought to a collaboration which I established with leaders in the still budding field of NMR spectroscopy, namely, Bill Schneider and Harold Bernstein.[2]

In his lecture, Chris Reid[1] demonstrated that chemically similar hydrogens in fused-ring aromatic molecules were chemically shifted when their immediate environments were different. This finding caused me to wonder whether or not NMR would also differentiate chemically similar hydrogens that differed in their environments because of their orientation on six-membered rings; that is, whether the orientation was axial or equatorial. It was on the basis of this idea that I approached my friends at NRC. The generous access to the machine and the expert guidance they provided to my Ph.D. student, Rudolf Kullnig, led to a joint communication in 1957 entitled: 'Configurational Effects in the Proton Magnetic Resonance Spectra of Acetylated Carbohydrates'.[3] The details and further observations were reported in the following year.[4] This latter paper became a Citation Classic.[5]

As hoped for, differences in chemical shift occurred and it turned out that an equatorial hydrogen normally produced a signal at substantially lower field than a 'chemically equivalent' hydrogen in axial orientation. On its own, this was a truly exciting discovery. However, with the improvement brought to the NMR experiments by spinning the sample tube and using a superstabilizer, the signal-to-noise ratio was increased to the extent that it could be concluded that the magnitude of a coupling constant for vicinal hydrogens was three- to four-times larger when the relationship was antiperiplanar than when it was synclinal. This was a true discovery, in the sense that it had not been anticipated by theoreticians, that has received an enormous number of applications starting with our paper entitled 'The Configuration of 3-Methoxycyclohexene Oxides. A Novel Application of Proton Magnetic Resonance Spectroscopy for the Determination of Structure and Configuration'.[6] The Karplus equation[7] for relating the torsion angle of vicinal hydrogens to the magnitude of their coupling constant together with Eliel's expression[8] for interpreting time-averaged chemical shifts and, soon thereafter, time-averaged coupling constants in terms of conformational equilibria, opened many new avenues for research, especially since the tenets of conformational analysis as developed by Barton[9] were firmly in place. My chief personal reward was that NMR allowed an unequivocal proof for the existence of a stereoelectronic contribution to bond strength which I termed the anomeric effect and which has since found widespread application. In fact, it was a preoccupation with the puzzle posed by the anomeric effect that caused my early involvement with NMR.[10a]

Since the requirements for a meaningful examination of the conformational equilibria for five-membered ring compounds appeared available, we undertook a study of the conformational properties of monosubstituted 1,3-dioxolanes.[11] These compounds were chosen because only three hydrogens are coupled to each other; namely, a pair of geminal hydrogens that is vicinal to a single hydrogen atom. Bob Fraser's initial attempts to establish the values for three positive coupling constants for the ABC-type system did not produce acceptable simulations of the observed spectra. However, fine simulations were achieved when the geminal coupling constant was made negative.[12] The *Journal of Chemical Physics* refused to publish our report presumably because our conclusions were contrary to published theoretical expectations. My colleague, Frank Anet, established that it is in fact the geminal coupling constant that has the negative sign.[13]

The subjects of this article are reviewed in greater detail in my autobiography published by the American Chemical Society in 1990.[10b]

REFERENCES

1. C. Reid, *J. Mol. Spectrosc.*, 1957, **1**, 18.
2. J. A. Pople, W. G. Schneider, and H. J. Bernstein, in *High-Resolution Nuclear Magnetic Resonance*, McGraw-Hill Book Company, Inc., New York, 1959, pp. 390–399.
3. R. U. Lemieux, R. K. Kullnig, H. J. Bernstein, and W. G. Schneider, *J. Am. Chem. Soc.*, 1957, **79**, 1005.
4. R. U. Lemieux, R. K. Kullnig, H. J. Bernstein, and W. G. Schneider, *J. Am. Chem. Soc.*, 1958, **80**, 6098.
5. R. U. Lemieux, *Citation Classic: Current Contents*, 1980, **26**, 10.
6. R. U. Lemieux, R. K. Kullnig, R. Y. Moir, *J. Am. Chem. Soc.*, 1958, **80**, 2237.
7. M. Karplus, *J. Chem. Phys.*, 1959, **30**, 11.
8. E. L. Eliel, *Chem. Ind. (London)*, **1959**, 568.
9. D. H. R. Barton, *Experientia*, 1950, **6**, 316.
10. R. U. Lemieux, *Explorations with Sugars. How Sweet it Was. Profiles, Pathways, and Dreams. Autobiographies of Eminent Chemists*, ed. J. I. Seeman, Am. Chem. Soc., Washington, DC, 1990, (a) pp. 75–110, (b) pp. 27–33.

11. R. U. Lemieux, J. D. Stevens, and R. R. Fraser, *Can. J. Chem.*, 1962, **40**, 1955.
12. R. R. Fraser, R. U. Lemieux, and J. D. Stevens, *J. Am. Chem. Soc.*, 1961, **83**, 3901.
13. F. A. L. Anet, *J. Am. Chem. Soc.*, 1962, **84**, 3767.

Biographical Sketch

Raymond U. Lemieux. *b* 1920. B.Sc., 1943, Ph.D., 1946, Organic Chemistry, McGill University, Montreal, Canada. Postdoctoral fellow, Ohio State University, 1946–47; lecturer, University of Saskatchewan, 1947–49; research officer, National Research Council, Saskatoon, 1949–54; Professor, University of Ottawa 1954–61; Professor, 1961–85 and University Professor Emeritus, University of Alberta, 1985–present. Approx. 260 publications. Research specialties: reactions and conformational analyses of carbohydrates, syntheses of complex oligosaccharides, molecular recognition—enzymes, antibodies, and lectins.

Levitt, Malcolm H.: A Cyclic Evolution In Spin Space

Malcolm H. Levitt

University of Stockholm, Stockholm, Sweden

I was recently on a boat in central Finland, and was impressed by the complex topology of the waterways. Wide island-studded lakes are joined by narrow channels, leading by circuitous detours, sometimes back to the starting point, sometimes to new vistas. Contemplating this article, I was struck with the analogy to my experience of science. The conceptual space we traverse is unpredictable and complex. Even now, 50 years after the discovery of our particular lake, new channels still turn up, within earshot of familiar waters churned by water-skiers and tourists. Sometimes the channels are dead ends, sometimes they only return to the beginning, but in any case, the view always changes.

My research experience started in 1979 when I joined Ray Freeman's group in Oxford as an undergraduate 'Part II' student. I immediately found NMR much to my taste as a mathematical field with a human, geometrical, face. I would doodle endlessly with vector pictures of echo formation. Geoffrey Bodenhausen taught me to write pulse programs in octal machine code. I was awed by the control of radiofrequency fields by mere sequences of ones and zeros. Geoffrey interested me in a (forgotten) experiment based on a train of many π pulses. Perhaps fortuitously, that particular experiment proved impractical on our primitive 80 MHz instrument, since the radiofrequency field was very nonuniform. This made me think about a way of compensating the radiofrequency field distribution by some sort of echo. I soon came up with a self-compensating three-pulse sequence. To my surprise, the idea survived the scrutiny of Gareth Morris, the acknowledged guardian of scientific rigor in the group at the time. Ray Freeman, with inimitable knack, came up with a name, and the composite pulse was born.[1]

Much of NMR can be interpreted in terms of rotations, so I had hit upon an idea with a bright future. For a long time I was to teach myself chunks of NMR purely by pushing composite pulses into some area. Ray Freeman stressed one particular line. He was intuitively convinced that the unsolved problem of broadband heteronuclear decoupling would eventually yield to the composite pulse, and never ceased pressing me to look into it. The breakthrough was Aue and Ernst's paper on J scaling.[2] This put the missing theoretical tools in my hands, and with some headscratching the first composite pulse broadband decoupling sequence was a reality.[3] Demonstrating it, however, still required reams of octal machine code. I could not count beyond seven for weeks.

The next step was to generalize the construction principles. I came up with a scheme based on phase shifts and cyclic permutations.[4] This was suggested by my experience as an electric guitarist in a jazz-fusion band, where we were using permutations to generate unusual musical effects. John Waugh had the same idea independently,[5] presumably with a different source of inspiration.

After a spell in Shimon Vega's lab in Israel, I joined Richard Ernst's group. In this vital environment I soon gained experience in many different fields, such as composite pulses in solids[6] and excitation of high-order multiple quantum coherences in liquids.[7] I could witness important developments such as the invention of product operator techniques by Sørensen,[8] and the treatment of phase cycling by Bodenhausen.[9] At last I broke with my beloved rotations, and moved into an entirely different area: spin dynamics and thermodynamics in solids. By a trivial mistake in a pulse program, I hit upon a remarkable effect: synchronous phase switching of the spin locking fields in a cross-polarization experiment can compensate for Hartmann–Hahn mismatch.[10] It took Dieter Suter and myself over two years before we even had a half explanation. I still consider the 'quasi-equilibrium' involved in this experiment as one of the biggest mysteries in routine NMR. Why does an apparently infinite spin system 'get stuck' in some nonequilibrium, nonuniform, polarization state? In my view there is much to be learnt here about the relationship of quantum mechanics to thermodynamics.

In 1985 I joined the Francis Bitter Magnet Laboratory in Cambridge, MA and collaborated closely with Bob Griffin and his group. My experience of cross polarization was useful for treating the interesting phenomenon of rotational resonance. Dan Raleigh had noticed a curious spectral broadening when doubly ^{13}C-labeled samples are spun in the magnet at just the right frequency.[11] This could be interpreted in terms of nuclear spin transitions induced by the sample rotation, suggesting the existence of rotation driven cross relaxation, and thereby a solid state analog of the nuclear Overhauser effect in liquids.[12] Rotationally resonant nuclear magnetization transfer is indeed gaining popularity as a method for determining molecular structures in the solid, or near-solid, state.

But with strange persistence, those simple sequences of π pulses keep coming back. Lorenzo Di Bari and I have been examining a curious *long-term* effect of π pulse trains. Like most, I would have expected that a long train of strong π pulses, lasting for many times T_1, would eventually saturate the spin system, destroying all order. Nevertheless, we have now shown that in the presence of certain relaxation mechanisms, the π pulses can actually *generate* spin order, leading to a correlated spin configuration (two-spin order).[13] This unusual effect is explained most easily by a reformulation of the 'master equation', striking at the heart of our usual conception of NMR experiments. It is characteristic of NMR that in the midst of well-traveled waters, we find an unexpected byway, leading in this author's case back to his very first experiences in scientific research.

REFERENCES

1. M. H. Levitt and R. Freeman, *J. Magn. Reson.*, 1979, **33**, 473.
2. W. P. Aue and R. R. Ernst, *J. Magn. Reson.*, 1978, **31**, 533.
3. M. H. Levitt and R. Freeman, *J. Magn. Reson.*, 1981, **43**, 502.
4. M. H. Levitt, R. Freeman, and T. A. Frenkiel, *Adv. Magn. Reson.*, 1983, **11**, 47.
5. J. S. Waugh, *J. Magn. Reson.*, 1982, **49**, 517.
6. M. H. Levitt, D. Suter, and R. R. Ernst, *J. Chem. Phys.*, 1984, **80**, 3064.
7. M. H. Levitt and R. R. Ernst, *J. Chem. Phys.*, 1985, **83**, 3297.
8. O. W. Sørensen, G. W. Eich, M. H. Levitt, G. Bodenhausen, and R. R. Ernst, *Prog. NMR Spectrosc.*, 1983, **16**, 163.

9. G. Bodenhausen, H. Kogler, and R. R. Ernst, *J. Magn. Reson.*, 1984, **58**, 370.
10. M. H. Levitt, D. Suter, and R. R. Ernst, *J. Chem. Phys.*, 1986, **84**, 4243.
11. D. P. Raleigh, G. S. Harbison, T. G. Neiss, J. E. Roberts, and R. G. Griffin, *Chem. Phys. Lett.*, 1987, **138**, 285.
12. M. H. Levitt, D. P. Raleigh, F. Creuzet, and R. G. Griffin, *J. Chem. Phys.*, 1990, **92**, 6347.
13. M. H. Levitt and L. Di Bari, *Phys. Rev. Lett.*, 1992, **69**, 3124.

Biographical Sketch

Malcolm H. Levitt. *b* 1957. B.A., 1978, D.Phil., 1981 (supervisor, Ray Freeman), Oxford University, UK. Postdoctoral work at Weizmann Institute, Israel, 1981–82 (with Shimon Vega) and ETH, Zürich, 1982–86 (with Richard Ernst). Research associate at Francis Bitter Magnet Laboratory, MIT, 1986–90; Royal Society Research Fellow, Interdisciplinary Research Centre for Superconductivity, Cambridge University, UK, 1990–91. Presently Lecturer in the Physical Chemistry Division, Stockholm University. Approximately 80 publications. Current research specialty: principles and methodology of NMR in both solid and liquid phases.

Levy, George C.: Recollections: Computers in the Early Days of ^{13}C NMR and 25 Years of Growth in NMR Computing

George C. Levy
Infomatrix, Inc., Ann Arbor, MI, USA

1968–70

While there were major advances in experimental NMR between its discovery in the 1940s and the late 1960s, nothing prior to that time compared with the revolution afforded by the advent of pulse Fourier transform experiments and the availability of heteronuclei lock and broadband ^{1}H decoupling channels. It is hard for us today to remember the earliest days when David Grant, J. D. Roberts, and a few other pioneers needed *more than 1 g of a low molecular weight molecule* to get a ^{13}C NMR spectrum. Initial Fourier transform ^{13}C NMR experiments gained about a factor of 20 in sensitivity through rapid time averaging of free induction decays (FIDs).[1] Improvements in probe and receiver designs, and operation at ever higher magnetic fields, eventually extended NMR sensitivity such that today's ^{13}C NMR sample can be smaller than those used for ^{1}H NMR in the 1960s. There were many things we needed to learn back then, and a lot of tricks we used to make experiments work. To set the scene, let's describe the situation in most research NMR laboratories at the end of the 1960s.

Most NMR instruments of the time were based on electromagnets having field strengths as high as 2.3 T (100 MHz for ^{1}H or 25.1 MHz for ^{13}C). An attached computer was rare, and when present it was usually a hard-wired signal averager with little or no additional capability. Bruker and then Varian began to manufacture FT NMR instruments with dedicated programmable computers. At the time, I was at the General Electric Corporate Research and Development Laboratory in Schenectady. I had been hired to continue and expand upon early NMR research and services established by John Bush, who was heading into management (John later became Vice President of Research & Development at Gillette). I went shopping and selected the newly announced Varian XL-100, accepting delivery of the first FT XL-100 delivered in the USA. (For months after delivery my XL-100 was a continuous wave (CW) instrument and then Varian field-installed the FT accessories.)

The system computer was a Varian 620i computer with 16 384 16-bit words of core memory and a paper tape punch/reader on its Teletype user I/O device. There was no magnetic storage—disk or tape. Every time we had a glitch or (heavens!) software failure, the computer had to be reloaded by hand toggling a starter program and then loading several paper tapes at 110 baud (about 12 characters per second). The very limited computer memory only allowed minimal NMR data acquisition and processing software, and only a single FID of 8k data points could be acquired and stored. In a few months we added an additional 16 kbyte stack of core memory at about $0.70 per 16-bit word, over a *million times the cost* of much smaller and much faster modern memory chips. (At the time of this writing, single chip memories of up to 64 megabits—8 Megabytes—are available.)

Our spanking new FT NMR spectrometer was great, but there were a few surprises. For example, we were all held hostage to our plotter pens. Since the computer could not store more than the single spectrum being acquired, it was necessary to plot that spectrum before proceeding to acquire another. I was interested in applying ^{13}C and other nuclei spin relaxation measurements to obtain an understanding of molecular motions and interactions between groups, molecules, solvent, counterions, and so on. Typical ^{13}C inversion–recovery T_1 measurements could then be acquired in an hour or so, and a complete experiment (10–12 spectra with varying τ values) would go overnight. Unfortunately, two problems often arose: (1) If the spectrometer/computer amplitude settings and spectrum plot offset were not carefully set, some of the spectral peaks could go off-scale and not be measurable. (2) Even if all settings were O.K., the plotter liquid ink pen might clog and not show the spectrum. Varian used a 'woodpecker' routine to tap the pen on the paper and try to start ink flow. In retrospect, it is amazing that it took quite a while for most of us to realize that we could replace the whole pen assembly with a more reliable ball-point or fiber tip pen. On weekends, I beat a regular trail to and from the lab, to change experiments and plotter paper, if the pen had written.

Because most of our experiments required multiple plots, after a short time we bought a digital magnetic tape unit and interfaced it to the XL-100 computer. Charley Peters, our Varian engineer, modified the NMR program to support dumping spectra to the tape. Life was better after that.

During the next few years, we were able to learn much about anisotropic molecular tumbling,[2,3] internal group motions,[4] solvent-restricted molecular dynamics,[5] and specific steric and electronic effects in largely rigid and inflexible molecules.[6] Subsequent inclusion of ^{29}Si and ^{15}N spin relaxation studies provided insight into organosilicon and nitrogen-containing molecules.[7–9] In the mid-1970s we discovered the potential of multifield ^{13}C spin relaxation measurements for learning about cooperative motions in micelles,[10] synthetic polymers,[11] and DNA.[12]

1976

A great many changes took place in NMR instrument computers during the next half-decade. The newest systems had disk memories of a few megabytes and NMR data acquisition and processing software gained flexibility through the use of computers having more than 64 kbyte of random access memory (although most machines at that time still had a 64 kbyte address limitation, which was a challenge to the instrument company programmers, who had carefully to design program overlay structures). It was at this time that we realized that software provided by the instrument manufacturers limited some of the things we needed to do. Also, we wanted to be

able to process and analyze our NMR data offline, so as to maximize the throughput of the spectrometer.

At that time the spectrometer computers could only deal with one activity at a time, thus offline processing allowed the instrument to begin another experiment immediately, without losing time while the operator processed, examined, and plotted the latest experimental data. Finally, the NMR instrument computers of the mid-1970s did not support then-standard computing technologies: efficient floating point computation, large random access memories, good language compilers with program development tools, etc. Use of a 1977 general purpose minicomputer enabled us to have all of these capabilities, and supported two simultaneous users!

Thus was born the project to network our NMR laboratory, using microcomputers to acquire and transfer data, and a Data General Eclipse computer for centralized processing, plotting, archiving, etc. The 8-bit parallel computer network, developed by graduate student Dan Terpstra, was named WARPATH[13] (Widespread Accurate Rapid Parallel Asynchronous Transfer Handler); the initial name for our one-dimensional NMR data processing software, developed by a team headed by then-student Charles Dumoulin, was ORACLE (Optimized Real-time Analysis for the Chemical Laboratory Environment). (After a while, we received a letter from a little-known database management company telling us that they had reserved the name ORACLE.) This software[14] eventually became known as NMR1 (NMR2 was developed for two-dimensional NMR).

1982–85

By 1982, NMR1 had gained several capabilities that were not available in other processing software. The program was getting large and complex, and our ideas outstripped our ability to write and maintain code. With support and encouragement from the Syracuse University administration, we decided to form a company to develop and support enhanced, comprehensive software products for processing and analysis of NMR data. I remember well the day a few of us had a beer and pizza party in my living room to name the new company.

I said that the new company would some day develop software for methods other than NMR spectroscopy, so we shouldn't restrict the name by directly using the acronym for nuclear magnetic resonance. But I wanted to have easy name recognition for the company. My wife, Linda, came up with the answer: New Methods Research, Inc.; abbreviated NMRi.

NMRi went on to achieve a number of firsts, including the first demonstration and commercial offering of NMR software on workstation computers (Apollo and Sun, by 1984), network-style data transfers with file conversion to a published universal NMRi datafile format for NMR data from all of the instrument manufacturers, high-level 'smart' algorithms to replace most direct user manipulation of spectral phasing, etc., and a high degree of automation for tasks such as curve fitting complex, overlapped bands. Early on, we recognized the wisdom of using *standards*. In particular, we moved to the emerging X-windows graphics standard, years before Sun and other workstation companies fully supported X. This did present its share of problems, and it delayed our software releases more than once, as we worked with the computer vendors to get X-windows working on their new systems.

1995

On the 50th anniversary of NMR, much is different in computer technology and NMR data processing. Personal computers have 1000-times the computing power of those 1970s NMR instrument computers; graphics workstations used for NMR processing are *more powerful* than Cray supercomputers, at a *thousandth* of the cost.

And the end is not in sight. By the year 2000, supercomputers will have yet another two orders of magnitude in speed; PCs may be comparable to today's fastest supercomputers. This may be used profitably. Tomorrow's multidimensional NMR datasets may contain 10^{10} data points. Totally automated data processing may include tasks that today require hours to weeks of careful analysis by spectroscopists. Automated preparation of accurate peak tables would support totally automated spectral assignment for a majority of molecules—including accurate assessment of three-dimensional structures.

We just have to wait a bit, but these things will happen before NMR spectroscopy gets past middle age.

REFERENCES

1. G. C. Levy and G. L. Nelson, *Carbon-13 Nuclear Magnetic Resonance for Organic Chemists*, Wiley-Interscience, New York, 1972; second edition, with Robert Lichter and Gordon Nelson, published in 1980.
2. G. C. Levy, J. D. Cargioli, and F. A. L. Anet, *J. Am. Chem. Soc.*, 1973, **95**, 1527.
3. G. C. Levy, *Acc. Chem. Res.*, 1973, **6**, 161.
4. G. C. Levy and G. L. Nelson, *J. Am. Chem. Soc.*, 1972, **94**, 4897; G. C. Levy, *Tetrahedron Lett.*, **1972**, 3709; G. C. Levy, *J. Am. Chem. Soc.*, 1973, **95**, 6117.
5. G. C. Levy, R. A. Komoroski, and J. A. Halstead, *J. Am. Chem. Soc.*, 1974, **96**, 5456; G. C. Levy, T. Holak, and A. Steigel, *J. Am. Chem. Soc.*, 1976, **98**, 495.
6. J. R. Lyerla, Jr.and G. C. Levy, *Top. Carbon-13 NMR Spectrosc.*, 1974, **1**, 79; D. A. Wright, D. E. Axelson, and G. C. Levy, *Top. Carbon-13 NMR Spectrosc.*, 1979, **3**, 103.
7. G. C. Levy, J. D. Cargioli, P. C. Juliano, and T. D. Mitchell, *J. Am. Chem. Soc.*, 1973, **95**, 3445.
8. G. C. Levy, J. J. Dechter, and J. Kowalewski, *J. Am. Chem. Soc.*, 1978, **100**, 2308.
9. G. C. Levy, C. E. Holloway, R. C. Rosanske, J. M. Hewitt, and C. H. Bradley, *Org. Magn. Reson.*, 1976, **8**, 643.
10. G. C. Levy, M. P. Cordes, J. S. Lewis, and D. E. Axelson, *J. Am. Chem. Soc.*, 1977, **99**, 5492.
11. G. C. Levy, D. E. Axelson, R. Schwartz, and J. Hochmann, *J. Am. Chem. Soc.*, 1978, **100**, 410.
12. G. C. Levy, P. R. Hilliard, Jr., L. F. Levy, R. L. Rill, and R. Inners, *J. Biol. Chem.*, 1981, **256**, 9986; G. C. Levy, P. S. Marchetti, A. Ejchart, L. F. Levy, A. Kumar, P. R. Hilliard, and R. L. Rill, *Biomol. Stereodyn.*, 1983, **1**, 795.
13. D. Terpstra and G. C. Levy, in *Computer Networks in the Chemical Laboratory*, ed. G. C. Levy and D. Terpstra, Wiley-Interscience, New York, 1981.
14. C. L. Dumoulin and G. C. Levy, *J. Mol. Structure*, 1984, **113**, 299.

Biographical Sketch

George C. Levy. *b* 1944, A.B., 1965, Ph.D., 1968, Chemistry, U.C.L.A., USA. General Electric Corporate R & D staff, 1968–73, Faculty member Florida State University, 1973–81. Faculty member and Science and Technology Professor, Syracuse University, 1981–94. In 1983, founded New Methods Research, Inc., the first company to develop and market NMR data processing and NMR laboratory networking software based on general purpose computers and workstations. Approximately 240 publications. Co-authored with Gordon Nelson the first published ^{13}C NMR book. Research specialties: ^{13}C NMR, data processing methods for one- and multidimensional NMR, utilization and commercialization of technology.

Lösche, Artur: The Beginnings of NMR in Leipzig

Artur Lösche

Formerly University of Leipzig, Leipzig, Germany

In the fall of 1940 I began my studies of physics at the University of Leipzig. Approximately a dozen years before, Pauli had suggested the existence of nuclear moments, a hypothesis to explain the hyperfine structure of spectral lines. It was the time when Rabi, Millman, and others observed the first transitions between nuclear Zeeman levels in molecular beams by resonance. Our physical discussions were dominated, however, by the experiments of Otto Hahn and Fritz Strassmann, and the possibilities of the fission of uranium by neutrons. In Leipzig, Heisenberg and Döpel prepared some investigations of this effect in bulk matter, which succeeded in 1942. At that time, however, I was far away as a consequence of World War II.

In 1945, when I came back, the Physical Institute was in a bad state (see ***Pfeifer, Harry, Leipzig, Summer 1951***); 80% of the buildings were destroyed, the experimental equipment was deficient, and the supply of new information incomplete. Much work had to be done to reinstall education in fundamental physics. Some fields of research were forbidden by law of the Allied Forces (valid until about 1955). Research work in physics was not only a problem of new ideas, it was also determined by the reduced possibilities we could realize under such circumstances.

In 1949–50, I read in the *Physikalische Blätter* a paper by Braunbek entitled 'Kerninduktion' (nuclear induction), which was a report on experiments undertaken by Bloch, Purcell, and co-workers five years previously: transitions between nuclear Zeeman levels were observed in condensed matter. I became interested in this method, because a few months before I had some preliminary thoughts on how to demonstrate the rotation of molecules. Nuclear induction seemed to be a suitable method for us. This was promoted by the fact that none of us had had any experience with possible technical problems. By a fluke I took advantage of participation in a meeting of the Nordwestdeutsche Physikalische Gesellschaft in Münster and read the original papers by Bloch, Purcell, and others in *Physical Review*. Finally, in the summer of 1950, we had the opportunity to obtain the fundamental journals in physics from 1946 onwards and could satisfy our lack of information.

I proposed to some students that they should work in this field. One of them was Harry Pfeifer. He was the first in Leipzig to observe proton NMR signals in water with a superregenerative oscillator in the middle of 1951; his paper gives more details about his success. About the same time, Hans Lippmann and Karl-Heinz Weber explored the Bloch method with two coils perpendicular to each other and a twin T bridge, respectively.

Our first aim was to obtain some experience in experimental methods and in the theory of rf spectrometers. For this reason Horst Winkler, supported by Werner Helmert, looked for spin echoes which they found in 1954. Autodyne detectors were also used. In the spring of 1956 I had the opportunity to report on our experimental results during the 5th Colloque AMPERE in Geneva.

In 1951–52, a small group of students at the Physical Institute of the Humboldt University in Berlin constructed a proton NMR spectrometer; Prof. F. X. Eder, the head of this institute, participated regularly in our seminars. After a short period, however, this work was stopped.

In the mid-1950s we began the next period, working in two directions:

(1) We tested additional methods, such as EPR and double resonance effects (Overhauser and 'Underhauser' effects, ENDOR spectroscopy and others). Furthermore, a magnetometer to measure the Earth's magnetic field of the Packard Varian type was constructed and used for geophysical prospecting.

(2) We looked for possibilities of solving structural problems in liquids and solids using NMR parameters such as relaxation times, line shifts, splittings, and others. For this purpose it was necessary to separate these data from technical effects, e.g. field inhomogeneities and coupling between the spin system and the rf coil.

In our search for applications of NMR, we have tested since about 1956 a large field of physical phenomena, which can only be summarized here in a very brief way: the influence of different ions on proton relaxation in water, orientational behavior in liquid crystalline phases, special processes during the nematic–isotropic transition, structural phase transitions in ferroelectric crystals, polymerization process in epoxy resins, radiation damage in polymers, frequency shifts in semiconducting crystals, high-resolution NMR in organic compounds and in lyotropic phases, and the adsorption of molecules on solid surfaces. The results of these experiments on a trial basis are being expanded in today's working groups.

It should be remembered that the first two decades of NMR were dominated by the CW technique with its limited sensitivity. As a result of this situation, I believed that the further development of NMR would be restricted. In my inaugural lecture during the 13th Colloque AMPERE in Louvain in 1964, I expressed the opinion that the NMR boom would finish in the near future. This proved to be quite wrong.

Since that time pulse and computer techniques have made great strides. A short time after that, fast Fourier transform spectroscopy was possible. This development from the CW technique to pulse spectroscopy with all its consequences was not only due to new physical knowledge but also to new technical possibilities. In general, I have the opinion that progress in science depends mainly on the cooperation of different disciplines.

Acknowledgements

I wish to thank Prof. Harry Pfeifer and Prof. Horst Winkler for helpful discussions.

Biographical Sketch

Artur Lösche. *b* 1921. *d* 1995. Dipl.-Phys., 1948, Dr.phil., 1949, Dr.phil.habil., 1953, Dr.rer.nat.h.c., 1986. Formerly Professor of Experimental Physics, University of Leipzig, Faculty of Mathematics and Science, Institute of Physics; retired 1987; deceased 1995. Approx. 140 publications. Research field: structure of molecular systems (e.g. ferroelectrics, liquid crystals), rf spectroscopy and its applications.

Lowe, Irving J.: My Life in the Rotating Frame

Irving J. Lowe
University of Pittsburgh, Pittsburgh, PA, USA

PREAMBLE

I joined George Pake's magnetic resonance group in the Physics Department of Washington University (St. Louis) during the summer of 1952. I was attracted to magnetic resonance because of the tradition that experimentalists often did a lot of theory as well. Also, the happiest of my fellow graduate students were those working with Pake. Shortly thereafter Donald Maxwell, Erwin Hahn's first graduate student from Stanford, joined the Physics Department and I was assigned to help him design and build a pulsed NMR spectrometer. Don left after two years, before we had a chance to do much experimental work with the completed spectrometer. Pake had also gone, and I continued my research under the direction of Richard Norberg who had recently joined the Washington University Physics Department.

RIGID LATTICE LINESHAPES AND THE FT THEOREM

In February of 1956, I was busy measuring the free induction decay (FID) shapes, echo envelopes, and spin–spin, and spin–lattice relaxation times (T_2 and T_1) of fluorine in Teflon and protons in polyethylene samples as a function of temperature and manufacturing techniques. The purpose of the experiments was the measurement of the motion of the long polymer chains and of the percentages of amorphous and crystalline regions of the samples. My spectrometer was very primitive by today's standards, consisting of an incoherent pulsed oscillator as an rf source, a simple diode square-law detector (whose nonlinearities had to be corrected for) and a 0.68 T permanent magnet with a 1.9-cm air gap. Around the rf coil was a styrofoam cup for insulation and temperature control. The detected NMR signal was displayed on an oscilloscope face and photographed with a polaroid camera for data storage and measurement.

I had already taken many hundreds of photographs that would have to be digitized by reading the traces with a grid; the data then had to be corrected for nonlinearities, plotted, and analyzed. This was a tedious task that I had been putting off and which I wasn't looking forward to. I had one more set of experiments to do, that of measuring the FIDs of the rigid lattice of my polymer samples. To do this, one evening I poured liquid nitrogen into the styrofoam cup around the NMR coil and sample to cool them to 77 K where molecular motion is very slow. Much to my surprise, the FID I observed was not monotonic but displayed several 'beats' or oscillations. The liquid nitrogen boiled away in about 10 min and the sample began warming up; the FID got longer and the 'beats' disappeared and the FID was again monotonic. I measured the FIDs of a number of other polymer samples at 77 K that evening and they all displayed a similar beat structure that disappeared as the sample warmed up. I was excited by these results, but was also bothered by them. I was well aware that Van Vleck[1] in his monumental paper on moments of NMR absorption lines had rigorously calculated the second and fourth moments (M_2 and M_4) for the rigid lattice case. He concluded that for $S = \frac{1}{2}$, for a set of equivalent spins in a cubic lattice that $[M_4/3M_2^2]^{1/4}$ was 0.95 for the applied magnetic field $\boldsymbol{B}_0$ along the [100] crystal axes, and about 0.99 for $\boldsymbol{B}_0$ along the [110] and [111] axes. This ratio is 1.0 for a Gaussian lineshape, and a Gaussian FID is monotonic and has no beats. Further, Pake and Purcell had measured M_2 and M_4 of ^{19}F in CaF_2 and obtained results[2] in good agreement with Van Vleck's calculations.

The next morning, I showed these peculiar results to Norberg, and to Pake who was visiting Washington University. They thought that the measurements were interesting and should be pursued. I was able to borrow a CaF_2 crystal from my classmate Bob Bruce, who was remeasuring M_2 and M_4 to obtain a more accurate value for them.[3] The FIDs of ^{19}F in CaF_2 also displayed a similar 'beat' structure (as seen in Figure 1) at room temperature, and the 'beat' structure depended upon the orientation of the crystal axes relative to the magnetic field, $\boldsymbol{B}_0$. After photographing a set of FIDs for CaF_2 with $\boldsymbol{B}_0$ along the [100], [110], and [111] crystal axes, I turned off my spectrometer and started to calculate a formula for the general shape of FIDs for $I = \frac{1}{2}$ nuclei in a rigid lattice. Had I been less naive, I might not have attempted it, but I had the encouragement of Norberg and access to Henry Primakoff, a superb and helpful theoretician.

At that time, density matrices and time-ordered expansions were not popularly used in NMR calculations. In formulating the calculation of the FID shape $f(t)$, and then evaluating it, I developed my own version of each. Only after completing the calculations did I learn of density matrices from Primakoff and recast my calculations into that language without having to change any results. An important byproduct of these calculations was the suggestion and general proof of the theorem that the Fourier transformation of the shape function $g(\omega)$ of the NMR absorption lineshape was equal to the NMR free induction decay shape $f(t)$ to within a multiplying constant for solids, liquids, and gases for a completely general interacting Hamiltonian.

The calculation of $f(t)$ for any spin system starts with

$$f(t) = \frac{\mathrm{Tr}\{\hat{I}_x(0)\hat{I}_x(t)\}}{\mathrm{Tr}\{\hat{I}_x^2(0)\}} \tag{1}$$

where $\hat{i} = \sum_j \hat{i}_j$ is the total spin angular momentum operator, $\hat{i}_j$ the angular momentum operator for the jth nucleus, and

$$\hat{I}_x(t) = \exp\left(-\mathrm{i}\frac{t\hat{\mathcal{H}}_{\mathrm{DD}}}{\hbar}\right)\hat{I}_x(0)\exp\left(\frac{\mathrm{i}t\hat{\mathcal{H}}_{\mathrm{DD}}}{\hbar}\right) \tag{2}$$

where $\hat{\mathcal{H}}_{\mathrm{DD}}$ is the truncated dipole–dipole interaction Hamiltonian

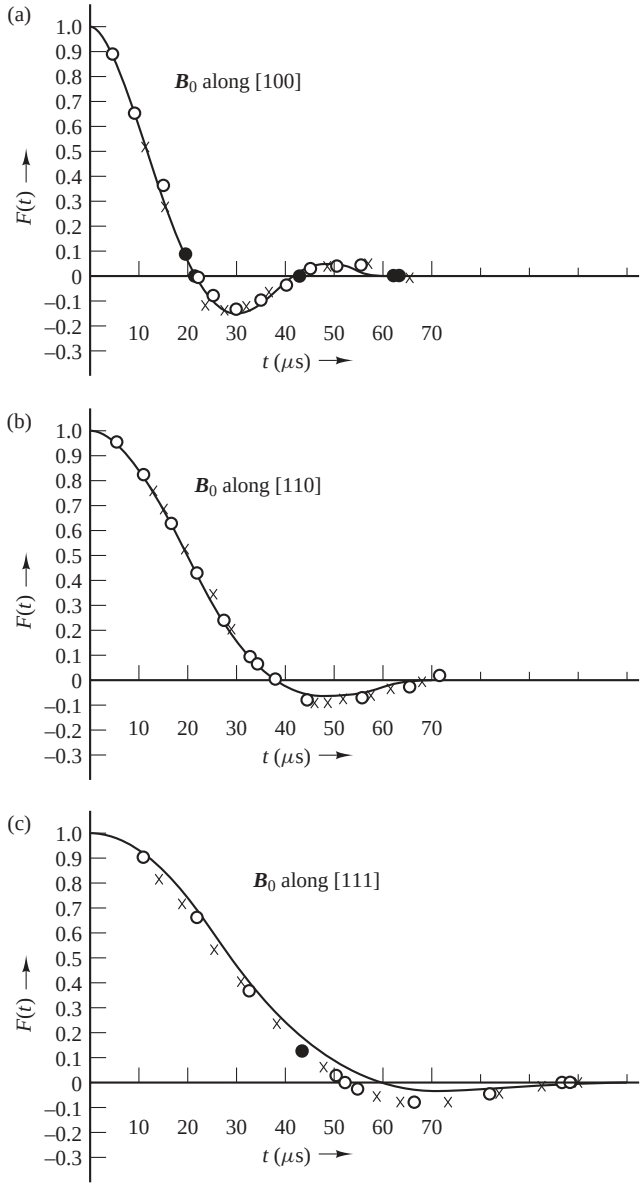

Figure 1 Free induction decay plots of ^{19}F in CaF_2 single crystals. (a) $\boldsymbol{B}_0$ along the [100] crystal axis; (b) $\boldsymbol{B}_0$ along the [110] crystal axis; (c) $\boldsymbol{B}_0$ along the [111] crystal axis. Crosses indicate observed FID amplitudes. Circles show Fourier transform of Bob Bruce's data[3] for the same crystal. The solid curve is the shape predicted by (65) in Ref. 5 (taken from Ref. 5)

$$\hat{\mathcal{H}}_{\mathrm{DD}} = \hbar(\hat{\alpha} + \hat{\beta}); \quad \hat{\alpha} = \frac{1}{2\hbar}\sum_{j\neq k} A_{jk}\hat{\boldsymbol{I}}_j \cdot \hat{\boldsymbol{I}}_k;$$

$$\hat{\beta} = \frac{1}{2\hbar}\sum_{j\neq k} B_{jk}\hat{I}_{jz}\hat{I}_{kz} \tag{3}$$

$$B_{jk} = -3A_{jk} = -\frac{3}{2}\frac{\gamma^2\hbar^2}{\boldsymbol{r}_{jk}^3}(3\cos^2\theta_{jk} - 1) \tag{4}$$

where $\boldsymbol{r}_{jk}$ is the vector connecting the jth and kth nuclei, θ_{jk} is the angle $\boldsymbol{r}_{jk}$ makes with the magnetic field $\boldsymbol{B}_0$ (which is in the z direction), and γ is the magnetogyric ratio of the nuclear species. The quantity $\hat{\alpha}$ does not commute with $\hat{\beta}$ which made evaluation of equation (2) difficult. It does commute with $\hat{i}$ which means that it will only contribute to $f(t)$ through terms containing $[\hat{\alpha}, \hat{\beta}]$. The terms making up $\hat{\beta}$ all commute and were easy to evaluate exactly; indeed, evaluation of equation (1) for just the $\hat{\beta}$ terms showed a beat structure. I spent several more months evaluating terms dependent upon $[\hat{\alpha}, \hat{\beta}]$ and also Fourier transforming Bob Bruce's measured lineshapes for CaF_2 to compare with my measured FIDs. These results[4,5] are also shown in Figure 1. The details of the calculations and theory are described in painful detail in my thesis[4] and Ref. 5. I wrote my thesis over the summer of 1956 and never again opened the drawer containing all the hundreds of photographs of data on polyethylene and Teflon.

MAGIC ANGLE SPINNING AND RF NARROWING

In February of 1958, George Theiss, an undergraduate student at Washington University, started a senior project with me. I was still intrigued with lineshapes in solids, and thinking about motional narrowing in solids[6] where the internal motion decreases the sample's observed NMR linewidth and apparent second moment M_2. Van Vleck's[1] expression for the second moment M_2 predicted that it should be invariant to internal motions and rotations of the sample because the motional part of the Hamiltonian commuted with the total spin operator. The motional modulation of the resonance line certainly narrowed the observed lineshape but it should also produce sidebands which added to the wings of the line to keep M_2 constant. The motional contribution to the wings usually is too weak to be observed however, because the internal motion has a broad frequency spectrum and the sideband contribution to the wings has a broad frequency range. I reasoned that the NMR lineshape for a solid, rotating at angular speed ω_s, should show sharp sidebands at frequencies related to ω_s.

The Hamiltonian for the spin system is the same one listed in equation (3), except that when the sample is rotated at an angle θ_H with respect to $\boldsymbol{B}_0$, the addition theorem for Legendre polynomials yields the result

$$\begin{aligned}(3\cos^2\theta_{jk} - 1) = {} & \frac{1}{2}(3\cos^2\theta_H - 1)(3\cos^2\theta_{jk} - 1) \\ & + \frac{3}{2}\sin(2\theta_H)\sin 2\theta'_{jk}\cos(\phi'_{jk} - \omega_s t) \\ & + \frac{3}{2}\sin^2\theta_H \sin^2\theta'_{jk}\cos[2(\phi'_k - \omega_s t)]\end{aligned} \tag{5}$$

where θ'_{jk} is the angle between $\boldsymbol{r}_{jk}$ and the axis of rotation. For $\theta_H = 0$, only the first term is nonzero and $f(t)$ is independent of the spinning speed of the sample. For $\theta_H = 90°$, the first term becomes $-\frac{1}{2}$ $(3\cos^2\theta'_{jk} - 1)$, and the partially narrowed line would then display the same shape as the nonrotating case but of one-half the linewidth and have sidebands at multiples of $2\omega_s$. For $\theta_H = \cos^{-1}(1/\sqrt{3}) \approx 54.7°$, the first term vanishes, the line should fully narrow, and $g(\omega)$ would only have sidebands at multiples of ω_s.

With this theory in mind, George and I started working on a mechanical technique to rotate the sample fast enough

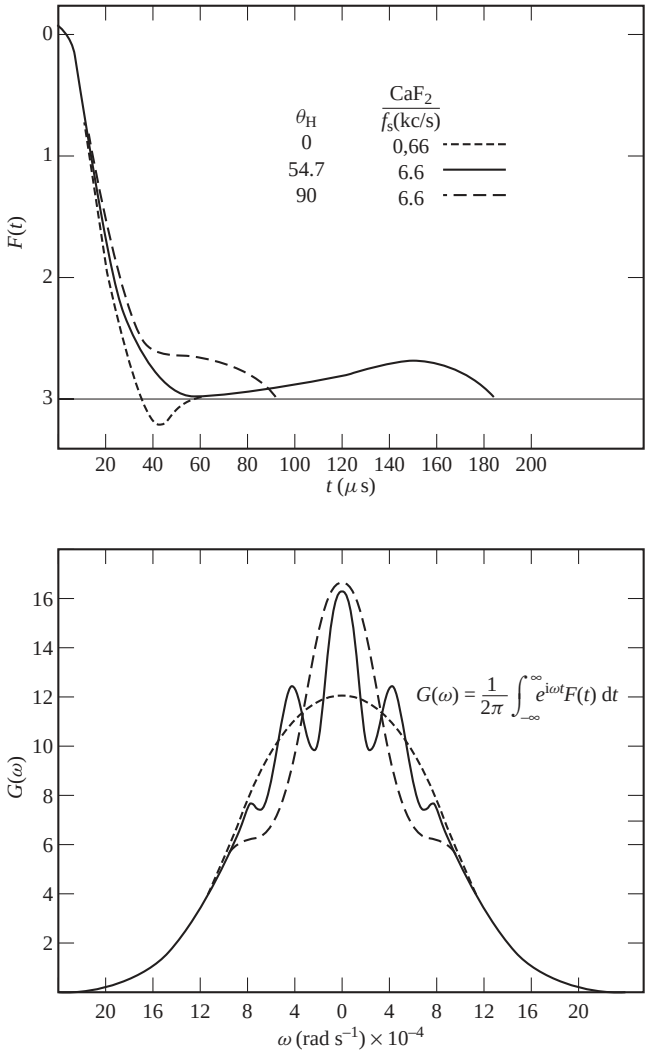

Figure 2 Free induction decays for spinning and nonspinning samples of powdered CaF_2 and their Fourier transforms (taken from Ref. 7)

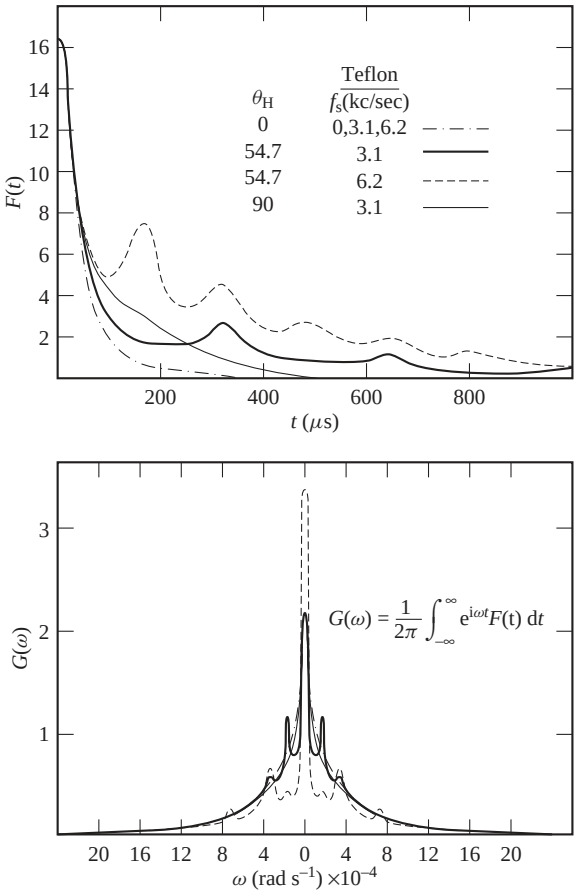

Figure 3 Free induction decays for spinning and nonspinning samples of Teflon and their Fourier transforms (taken from Ref. 7)

to see these effects. We were unable to do so by the time he graduated in May, 1958. About then, I was having some dental work done and saw a new air turbine drill that my dentist used. I decided to try to spin the sample by blowing air past it. A gifted machinist (Jim Boyle) and I made up some NMR samples that were cylinders 7 mm wide, 7 mm in diameter, had nylon bearings, and spun on thin phosphor bronze wires as axles. I found that spinning speeds were limited only by the strength of the sample and that speeds up to 7 kHz were easily obtainable. I put the spinner into my NMR probe, found that I could narrow the line of both Teflon and CaF_2, and was so excited that I worked for the next 48 hours taking data, stopping only when I had spun all my prepared samples to destruction. The next day, I woke up with a very high fever that was diagnosed as hepatitis a few days later when I turned a nice bright yellow. The dentist who was my source of inspiration for the spinning technique was also probably the source of my hepatitis infection. I was incapacitated for the next two and a half months, and two graduate students (Horst Kessemeier and Bill Yen) in the Norberg NMR group helped with analyzing the data of the FIDs and taking their Fourier transforms. The results[7] in Figures 2 and 3 indeed show that the spinning motion narrows the NMR lineshape and M_2 is seen to remain constant since the initial behavior of the FID is invariant to the rotation. Independently, and unknown to me, Andrew, Bradbury, and Eades[8] also showed that spinning motion narrowed NMR lineshapes. The invariance of M_2 to internal rotational motion was demonstrated[9] by my student, Ching Yao.

In 1962, I was at the University of Pittsburgh using a homemade phase coherent pulsed NMR spectrometer that boasted of linear-phase sensitive detection and several excitation pulses with adjustable phases. These luxuries allowed my students and me to study lineshape behavior and spin–lattice relaxation in the rotating frame.

For a spin system acted upon by a rotating magnetic field $\boldsymbol{B}_1$, rotating at angular speed ω, the effective magnetic field $\boldsymbol{B}_{\text{eff}}$ in the rotating coordinate system is

$$\boldsymbol{B}_{\text{eff}} = B_1 \boldsymbol{y} + \left(B_0 + \frac{\omega}{\gamma} \right) \boldsymbol{z} \tag{6}$$

where $\boldsymbol{y}$ and $\boldsymbol{z}$ are unit vectors in the y and z directions, respectively

By making a transformation to the coordinate system rotating about $\boldsymbol{B}_{\text{eff}}$ at angular speed $\omega_{\text{eff}} = \gamma B_{\text{eff}}$, one obtains a

new magnetic Hamiltonian whose time-independent terms are

$$\hat{\mathcal{H}}'_{\mathrm{DD}} = \frac{1}{2}(3\cos^2\theta - 1)\left(\frac{1}{2}\sum_{j\neq k} B_{jk}\left(\hat{I}'_{jz}\hat{I}'_{kz} - \frac{1}{3}\hat{I}'_j \cdot \hat{I}'_k\right)\right) \tag{7}$$

where $\theta = \tan^{-1}(B_1/(B_0 + \omega/\gamma))$.

Equation (7) demonstrates that the time-independent terms vanish for $\theta = \cos^{-1}(1/\sqrt{3})$, the so-called magic angle. This is similar to the rotating sample technique described earlier. For $\theta = 90^\circ$, $\hat{\mathcal{H}}'_{\mathrm{DD}}$ is just $-\frac{1}{2}\hat{\mathcal{H}}_{\mathrm{DD}}$ and the FID should evolve at exactly one-half the rate as in the laboratory frame, as my student Dennis Barnaal and I demonstrated.[10] At the same time, Walter Goldberg and Moses Lee, also at the University of Pittsburgh, demonstrated the magic angle case.[11]

RELAXATION IN THE ROTATING FRAME

At about the same time, my student, David Look, and I were studying slow internal motions in solids and being frustrated by materials that would undergo phase transitions before reaching a T_1 minimum where their correlation time τ_c could be measured. We reasoned and then showed that for $B_1 \gg B_{\mathrm{loc}}$ magnetization $M_y(t)$ that was spin-locked along a rotating magnetic field B_{1y} would relax to zero in a fashion similar to $M_z(t)$ relaxing to its equilibrium value M_0 in the magnetic field $B_0\boldsymbol{z}$. Since $B_1 <<< B_0$, the spin-locked magnetization relaxation rate, $T_{1\rho}$ would be much more sensitive to long τ_c values. We derived[12] a formula for $T^{-1}{}_{1\rho}$ whose dominant term in the long-time region is proportional to the spectral density function of $\hat{\mathcal{H}}_{\mathrm{DD}}$ in equation (3), evaluated at $2\omega_1$. When evaluated for specific models of motion, the formula contains terms of the form $\tau_c/(1 + \omega_1^2\tau_c^2)$. These formulas were tested[12] (see Figure 4) for T_1 and $T_{1\rho}$ in gypsum where the details of the flipping of the H_2O molecules are very well defined. Similar ideas for studying slow motions by measuring relaxation rates in the rotating frame were independently developed by Slichter and Ailion.[13,14]

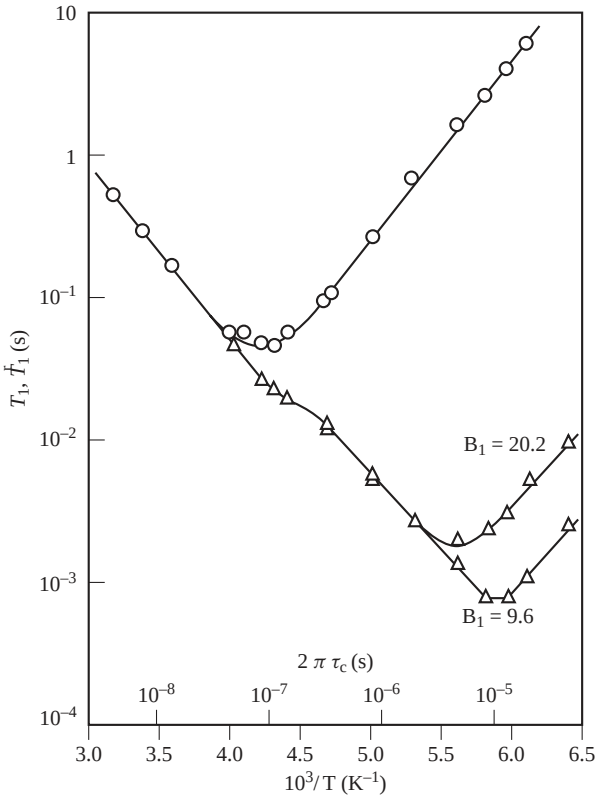

Figure 4 Proton spin–lattice relaxation times in gypsum along the static and rotating magnetic fields as a function of inverse temperature. The quantity τ_c is calculated from the T_1 curve using Eq. 40 from Ref. 12. The computed activation energy is 5.8 kcal mol^{-1}. ○ are T_1 data; ▲ are $T_{1\rho}$ data (taken from Ref. 12)

EPILOGUE

This article has described one limited but connected area of my work in NMR. Its imposed briefness has prevented me from referencing many of my other students and collegues who have greatly influenced me. My years in magnetic resonance have been even more exciting and fun than I had imagined possible back in 1952.

REFERENCES

1. J. H. Van Vleck, *Phys. Rev.*, 1948, **74**, 1168.
2. G. E. Pake and E. M. Purcell, *Phys. Rev.*, 1948, **74**, 1184.
3. C. R. Bruce, *Phys. Rev.*, 1957, **107**, 43.
4. I. J. Lowe, *Bloch Decays in Solids*, Ph.D. Thesis, University of Washington, 1957.
5. I. J. Lowe and R. E. Norberg, *Phys. Rev.*, 1957, **107**, 46.
6. H. S. Gutowsky and G. E. Pake, *J. Chem. Phys.*, 1950, **18**, 162.
7. I. J. Lowe, *Phys. Rev. Lett.*, 1959, **2**, 285.
8. E. R. Andrew, A. Bradbury, and R. G. Eades, *Nature (London)*, 1958, **182**, 1659.
9. C. Yao, *A Study of Motional Narrowing in Ammonium Selinate*, Ph.D. Thesis, University of Pittsburgh, 1980.
10. D. Barnaal and I. J. Lowe, *Phys. Rev. Lett.*, 1963, **11**, 258.
11. W. I. Goldburg and M. Lee, *Phys. Rev. Lett.*, 1963, **11**, 255.
12. D. C. Look and I. J. Lowe, *J. Chem. Phys.*, 1966, **44**, 2995.
13. C. P. Slichter and D. Ailion, *Phys. Rev.*, 1964, **135A**, 1099.
14. D. C. Ailion and C. P. Slichter, *Phys. Rev.*, 1965, **137A**, 235.

Biographical Sketch

Irving J. Lowe. *b* 1929. B.E.E., 1951, Cooper Union, Ph.D., 1956, Physics, Washington University (St. Louis). Thesis advisors were (in order) George Pake, Donald Maxwell, Richard Norberg. Sloan fellow at Washington, University 1956–58. University of Minnesota, 1958–62. University of Pittsburgh, 1962–present. Research specialties: NMR theory, solid state NMR, NMR instrumentation, magnetic resonance imaging.

Lunazzi, Lodovico: Conformers and Enantiomers, Rotations and Stereomutations: an NMR Playground for an Organic Chemist

Lodovico Lunazzi

University of Bologna, Bologna, Italy

My love affair with NMR began more than 30 years ago in the fall of 1962. I was preparing my doctoral thesis in the lab of one of the most distinguished Italian organic chemists (Professor F. Montanari, now at the University of Milan) when the head of the institute (the late Professor Mangini) acquired one of the first high-resolution NMR spectrometers to be seen in Italy (a Varian DP-60). Along with the spectrometer, there came back to Italy a research associate (now Professor F. Taddei, University of Modena) who had spent some time in London, at University College and at Imperial College, learning how to use the new device. Fascinated by the results offered by this technique, I asked permission to modify my project and so had the privilege of being allowed to play with the new toy. Since then I have remained faithful to NMR and, subsequently, I even became addicted to its half-brother, ESR. The instruments of those times were not so easy to use as no lock was available and the spectrum had to be chased (and was sometimes lost) along a drifting magnetic field. Sidebands had to be employed for calibration and shimming had often to be performed by mechanically moving, with a gear, the poles of the magnet. So a simple ^{1}H spectrum required a few hours to be properly recorded: fortunately at that time Saturday was a full working day in our institute.

With Taddei, I applied NMR to measure the $^{13}C-^{1}H$ coupling constants from the satellites of the proton signals in a variety of organic derivatives (some of them, like fluoroacetylene, were explosive and so dangerous to handle within the probe of the spectrometer that so far no one has measured these couplings again) and also learnt how to analyze second-order spectra. As no electrical computing devices were available, I did all the work with a mechanical one whose efficiency was determined by the rate at which I could rotate the handle (subsequently I was helped by a very muscular student who was able to rotate the handle even faster).

In 1967 I obtained a Canadian National Research Council (NRC) postdoctoral fellowship and moved to Ottawa to work with Syd Brownstein. There I became familiar with dynamic NMR as a tool to investigate exchange processes, a subject which is still one of my research interests: the series 'Conformational Studies by Dynamic NMR' which I started in 1972 has now reached its 50th paper. The work in Ottawa went quite well and the results of our investigation on the exchange kinetics between a carbonium ion and its parent molecule were eventually published in *J. Am. Chem. Soc.* in 1969. During that period I had the privilege of meeting Vladimir Bystrov, a Russian physicist who was also undertaking postdoctoral work with Syd and who obtained worldwide recognition later for his NMR work on the conformation of peptides and natural biomolecules. We became very good personal friends and kept visiting each other in our labs in Moscow and Bologna over a period when it was not so easy for Russian scientists to have contact with foreigners. In addition to being an excellent scientist, Vladimir was a person of great thoughtfulness and humanity: his sudden, untimely death in 1989 has been mourned by all the NMR community.

In the NRC library I also came across a review by Geoffrey Luckhurst (whom I had already met in the Varian lab in Zürich) about the use of liquid crystalline solvents to obtain NMR spectra very different from those one is accustomed to observing in isotropic liquids. When I returned to Bologna I began to apply this technique to investigate the conformation of flexible organic molecules. At that time people were debating whether biphenyl, known to be planar in the solid and twisted in the gas phase, was planar or twisted in solution. By making use of a conveniently synthesized chloro derivative, we could convincingly demonstrate by NMR that the twisting angle was about 35° in a liquid crystalline solvent. The model I had employed for the analysis was quite approximate and was subsequently refined in joint work with Peter Diehl of the University of Basel. Many more examples were later published by Sternhell in *J. Am. Chem. Soc.*, nicely confirming the correctness of our results. I continued to investigate many simple flexible molecules by this method working with a postdoc from Milan (Giovanni Fronza) and with colleagues from Pisa (C. A. Veracini) and Southampton (J. W. Emsley). I had met Jim in 1971 at the ISMAR meeting in Israel and a NATO grant helped us to visit each other and publish many papers, together including those on two isomers of bipyridyl which were, for those times, a real 'tour de force' because of the complexity of the partially oriented 8-spin systems which had to be analyzed.

During my visits in England I also met Ed Randall, from Queen Mary College, London who persuaded me to write a chapter on the application of liquid crystal NMR (he suggested the acronyms LXNMR) for the sixth volume of the series 'Determination of Organic Structures by Physical Methods' he was editing for Academic Press. It was a lot of work but I do not regret it for, although it is now certainly outdated, it was quite useful at that time for newcomers in the field, particularly from a practical point of view. This task gave me the opportunity of benefiting from learned discussions with Claudio Zannoni, a student who was then doing his Ph.D. in Southampton with Geoffrey Luckhurst. He later became a colleague of mine in Bologna (as well as a close personal friend) and is now recognized worldwide as one of the leading experts of the liquid crystalline state.

Meanwhile I had the possibility of using a 100 MHz FT spectrometer with a good variable temperature device, which enabled me again to start investigations of dynamic processes. Fascinated by the pioneering work of F.A.L. Anet, I repeated, now using ^{13}C, his classical ^{1}H study on the restricted rotation of benzaldehyde. Later on, with the help of a very able technician, Dante Macciantelli, I studied the internal motions of a variety of simple organic molecules that, despite their fundamental importance, had not yet been investigated, probably because of the technical difficulties involved in reaching the required low temperatures (often ranges between

−120 °C and −160 °C were needed) in solution. Thus we measured accurate barriers for the rotation of *N*-methylaniline, isomeric pyridine and thiophene aldehydes, nitrosobenzene, phenylhydrazine, etc. These studies were pursued until quite recently when, using more sophisticated instrumentation, we could directly detect by ^{13}C NMR the amount of the minor conformer (as low as 0.8% at −140 °C) of furan-3-aldehyde. Some of these spectra were nice enough to be reproduced in a number of books, including that on 'Dynamic NMR' by Jan Sandström.

In 1975, with the help of a Sardinian post-doc (Gianni Cerioni), we enlarged our field of interest by studying more complex molecules exhibiting the so-called gear effect: we were even able to determine the first X-ray structure of one of the 'gear conformers' we had observed at low temperature by NMR.

Of course the more complex molecules we kept synthesizing exhibited a variety of internal motions, and in 1981 we were lucky enough to detect a quite unique feature in a molecule that, at −140 °C, exists in a coplanar as well as in an orthogonal conformation as shown in Scheme 1.

The different symmetries of these two species allowed their unambiguous identification by ^{13}C NMR and their relative ratio at equilibrium could even be reversed by an appropriate change of solvent.

In 1973 I again spent some time at NRC in Ottawa (this time in the lab of Keith Ingold to do some ESR experiments), and on his suggestion once back in Bologna I tackled the conformational analysis of the simple, fundamental hydrocarbon tetramethylethane. We were able to show that at −180 °C the *gauche* and *anti* conformers yield different ^{13}C spectra (the intensity ratio of the two forms being 2:1) and we could measure the corresponding interconversion barrier (4.1 kcal mol^{-1}). For this experiment I made use of the 360 MHz Bruker spectrometer in Fallanden, Switzerland (at that time the highest field available) and I still remember how frightened the technicians were when I forced the temperature of such a precious instrument down to −180 °C; they did not allow me to repeat the experiment a second time. The paper eventually appeared in *J. Am. Chem. Soc.* in 1977 and has always been a source of great satisfaction to me since it has been quoted even in stereochemistry textbooks.

The year 1983 marked the arrival in my lab of a young research associate, Daniele Casarini, with whom I started to investigate dynamic processes in chiral environments, thus making conformational enantiomers detectable by NMR. We observed, for instance, that the *N*-methyl ^{1}H signals of Me_2NCH_2Me become anisochronous at −90 °C in the presence of a chiral agent, owing to the slow N-inversion process. The otherwise NMR invisible barrier could thus be measured by lineshape analysis. I still keep as a cherished souvenir the letter of Jean-Marie Lehn who congratulated us for this achievement. Again with Daniele (who had spent one year with Robin Harris in Durham to learn solid state NMR), I applied the CP MAS technique as a help for assigning *meso* and racemic conformers, taking advantage of the symmetry breaking of the NMR patterns in the solid with respect to the solution. The results satisfactorily matched the corresponding X-ray findings.

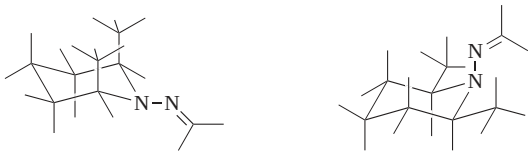

Scheme 1 Coplanar and orthogonal conformations

Since 1986 I have also started a fruitful cooperation (with the help of a NATO grant) with Edgar Anderson of the University College, London. By combining MM calculations with dynamic NMR we studied a variety of internal motions in conformers of quite complex trialkylamines: we even detected as many as four different dynamic processes within a single molecule and measured the corresponding barriers. Once, to unravel a particularly complicated case, we had to resort to a 600 MHz spectrometer (installed in Florence by Ivano Bertini) where we recorded spectra down to −120 °C which was then one of the lowest temperatures attained for such a large magnetic field. This scientific cooperation with Edgar also gave rise to a long lasting friendship, which was subsequently shared by our wives and even by our children.

The activity in the NMR field enabled me to join people from all over the world in common projects and it is quite amusing that I could publish papers even before having met my foreign co-workers. This happened with a project I was pursuing in Bologna with a colleague of mine (Giuseppe Placucci): at a certain point in the work we wrote to a Japanese scientist (Renji Okazaki, University of Tokyo) whom we only knew from his papers, seeking a particular compound. Thus we started a common project (later also Gaku Yamamoto joined us) which was carried out by letter, telex, and eventually by fax. The results, concerning motional couplings in the rotational processes of a very hindered hydrocarbon, were obtained and discussed without a single personal meeting between the two groups. Only after publication in 1990 of our joint paper in the *J. Am. Chem. Soc.* did I meet Renji, with whom I have developed a very friendly personal relationship.

At the moment I am interested in studying conformational chirality in collaboration with a colleague from Rome (Francesco Gasparrini). Using dynamic NMR, we measure the lifetimes of conformational enantiomers and use this information to set up low-temperature chiral chromatographic columns that enable the physical separation of enantiomers which interconvert with barriers as low as 18 kcal mol^{-1}. It has even been possible to measure the corresponding circular dichroism spectra, thus assigning an absolute chiral configuration to these elusive species.

In conclusion, NMR keeps showing such a variety of useful and fascinating new aspects to the organic chemist as to seem an endless source of wonder: after more than 30 years I am not yet tired of playing with such a versatile toy.

Note added in proof: After completion of this short biography my beloved wife Anna died suddenly in November 1994. To her, who always helped, assisted and comforted me, this article is gratefully dedicated.

Biographical Sketch

Lodovico Lunazzi. *b* 1940. Doctoral degree, 1963, Industrial Chemistry, University of Bologna, Italy. Postdoctoral work 1967–68 at the National Research Council, Ottawa, Canada (Syd Brownstein). Subsequently Assistant Professor and Professor (1975) at the University of Bologna. Approx. 160 publications. Current research specialties: conformational analysis of organic molecules and organic free radicals by NMR and ESR techniques.

Lutz, Otto: Heteronuclear Magnetic Resonance

Otto Lutz

University of Tübingen, Tübingen, Germany

As a graduate student I had the chance to participate in the Nobel Laureate Meeting at Lindau (in the Bavarian part of Lake Constance) in 1962. One of the aims of the Lindau meetings was to promote contact between laureates and students. It was therefore deeply impressive to hold personal discussions with scientists whose work was well known from lectures and the literature. I would like to mention in this connection I. I. Rabi, E. M. Purcell and W. E. Lamb, who are seen together with H. Urey in the snapshot (Figure 1).

During this period I performed experiments on the lifetime of the excited atomic states of strontium using the optical-radiofrequency double resonance method. In 1963 I changed to the field of nuclear magnetic resonance. At that time the so-called less common nuclei or heteronuclei had not been investigated very well. For this reason, magnetic moments, chemical shifts, and linewidths were of great interest, especially since as a result of cooperation with Siegfried Penselin (Bonn) and Victor W. Cohen (Brookhaven) it was possible to evaluate absolute magnetic shielding constants for the alkali isotopes, for example.[1] This work was performed with a homemade spectrometer and probes and a Varian magnet externally stabilized at 1.8 T using a ^{7}Li NMR method introduced and implemented by Andreas Schwenk.[2] In the late 1960s and early 1970s a multitude of nuclei were investigated[3] mainly in aqueous solution, especially when a Bruker B-Kr 322 s pulse spectrometer working in the Fourier mode replaced our homemade apparatus.

In 1975 we obtained a grant from the Deutsche Forschungsgemeinschaft with which to purchase our MONALISA, at that time an unusual combination of an externally stabilized 2.1-T Bruker SXP 4−100 pulse spectrometer and internally deuterium-stabilized high-resolution equipment (MONALISA was the solution of the problem of finding an appropriate girl's name which would fit as far as possible all the NMR-active isotopes, reading forth and back: 15). With this spectrometer (which is still working!), together with lots of homemade probes for different frequencies and purposes, further less-sensitive nuclei could be observed[4−6] and the list of observable isotopes could be expanded to more than 50.

Figure 1 Nobel Laureate Meeting, Lindau 1962: W. E. Lamb, E. M. Purcell, H. Urey, I. I. Rabi (from left)

During this period we started examinations of biologically interesting nuclei such as ^{25}Mg and ^{43}Ca,[7] and it was at the famous VIth International Conference on Magnetic Resonance in Biological Systems, Kandersteg, Switzerland, September 1974 when our cooperation with Peter Kroneck of Konstanz started, resulting in basic NMR studies on copper,[8] vanadium,[9] and molybdenum. The results on the latter element[10] are still obviously of interest, as can be seen from a 1993 paper by Xie et al.[11] on the calculation of the ^{95}Mo shielding in $(MoO_nS_{4-n})^{2-}$ anions.

A typical result with MONALISA was the detection of the ^{34}S−^{32}S mass-induced isotopic effect on the shielding of ^{95}Mo in the MoS2 −/4 ion from a high-resolution spectrum of this quadrupole nucleus.[12]

In the late 1970s we changed to heteronuclear magnetic resonance experiments in solids. Shielding constants and indirect and direct spin−spin couplings[13] for various nuclei have been evaluated. A typical example was the evaluation of the shielding tensor and the eigenvectors of ^{207}Pb in the crystallographically interesting $Pb(NO_3)_2$ single crystal by Alfons Nolle.[14] He showed in 1976 that a second-order quadrupole splitting can be reduced by sample spinning,[15] observing the ^{95}Mo NMR signal in solid $Mo(CO)_6$.

In the 1980s we changed more and more to the fields of in vivo magnetic resonance imaging and localized spectroscopy, since the University of Tübingen obtained a 1.5-T imager in 1985. Sophisticated imaging methods[16,17] and localization sequences[18] have been implemented and applied in studies with volunteers and patients.[19] Follow-up studies of leukemic and bone-marrow-transplanted patients are examples.[20] A further field of interest, experimentally and theoretically, is the problem of coupled spins in localized ^{1}H or ^{31}P in vivo spectroscopy.[21] The whole body imager at the Max Grundig Klinik (near Baden-Baden) is supplemented with a ^{13}C channel, so ^{13}C human in vivo investigations can be undertaken. Finally, magnetic resonance imagers can be used with heteronuclei for large sample spectroscopy at low concentrations[22] as well as for imaging; the recent ^{129}Xe gas image at atmospheric pressure[23] is one example.

REFERENCES

1. O. Lutz, *Z. Naturforsch., A*, 1968, **23**, 1202.
2. J. Kaufmann and A. Schwenk, *Z. Angew, Physik*, 1966, **21**, 527.
3. H. Krüger, O. Lutz, A. Nolle, and A. Schwenk, *Z. Phys., A*, 1975, **273**, 325.
4. B. W. Epperlein, H. Krüger, O. Lutz, A. Nolle, and W. Mayr, *Z. Naturforsch., A*, 1975, **30**, 1237.
5. P. Kroneck, O. Lutz, and A. Nolle, *Z. Naturforsch., A*, 1980, **35**, 226.
6. O. Lutz, in *The Multinuclear Approach to NMR Spectroscopy*, eds. J. B. Lambert and F. G. Ridell, D. Reidel, Dordrecht, 1983, pp. 297, 389.
7. O. Lutz, A. Schwenk, and A. Uhl, *Z. Naturforsch., A*, 1975, **30**, 1122.
8. P. Kroneck, O. Lutz, A. Nolle, and H. Oehler, *Z. Naturforsch., A*, 1980, **35**, 221.

9. O. Lutz, W. Messner, K. R. Mohn, and P. Kroneck, *Z. Phys., A*, 1981, **300**, 111.
10. O. Lutz, A. Nolle, and P. Kroneck, *Z. Naturforsch., A*, 1977, **32**, 505.
11. X. Xie, Z. Liu, and H. Liu, *J. Magn. Reson.*, 1993, **A 102**, 351.
12. O. Lutz, A. Nolle, and P. Kroneck, *Z. Phys., A*, 1977, **282**, 157.
13. R. Balz, M. Haller, W. E. Hertler, O. Lutz, A. Nolle, and R. Schafitel, *J. Magn. Reson.*, 1980, **40**, 9.
14. O. Lutz and A. Nolle, *Z. Phys., B*, 1980, **36**, 323.
15. A. Nolle, *Z. Phys., A*, 1977, **280**, 231.
16. M. Braun, W.-I. Jung, O. Lutz, and R. Oeschey, *Z. Naturforsch., A*, 1987, **42**, 1391.
17. F. Schick and O. Lutz, *J. Magn. Reson.*, 1993, **B 102**, 35.
18. W.-I. Jung and O. Lutz, *J. Magn. Reson.*, 1992, **96**, 237.
19. F. Schick, H. Bongers, S. Kurz, W.-I. Jung, M. Pfeffer, and O. Lutz, *Magn. Reson. Med.*, 1993, **29**, 38.
20. F. Schick, H. Einsele, H. Bongers, W.-I. Jung, M. Skalej, S. Duda, G. Ehninger, and O. Lutz, *Annals Hematology*, 1993, **66**, 3.
21. W.-I. Jung, K. Straubinger, M. Bunse, S. Widmaier, F. Schick, K. Küper, G. Dietze, and O. Lutz, *Magn. Reson. Med.*, 1993, **30**, 138.
22. O. Lutz and M. Pfeffer, *Z. Naturforsch., A*, 1992, **47**, 637.
23. M. Pfeffer and O. Lutz, *J. Magn. Reson.*, 1994, **A 108**, 106.

Biographical Sketch

Otto Lutz, *b* 1935. Dipl.-Phys., 1963, Dr.rer.nat., 1968, Habilitation, 1972, Physics, University of Tübingen, Germany. Professor für Experimentalphysik, Faculty of Physics, University of Tübingen, 1974–present. Approx. 140 publications. Research specialty: heteronuclear magnetic resonance in gases, liquids and solids; shielding constants, systematics of NMR parameters, nuclear quadrupole resonance, in vivo human NMR imaging and spectroscopy.

Luz, Zeev: The Early Days of NMR in Israel

Zeev Luz

The Weizmann Institute of Science, Rehovot, Israel

I first joined the Weizmann Institute (WI) in 1957 as a graduate student in the group of Saul Meiboom. I was actually preparing myself to become a science teacher in an agricultural high school (my own alma mater); however, after completing undergraduate studies in chemistry at the Hebrew University (HU) I had a few months left before reporting to work. Aharon Loewenstein (himself an alumnus of the same high school) urged me to start a Ph.D. and continue it concurrently with my teaching job; so I yielded. In those days chemistry students at the HU had very little exposure to modern science; quantum mechanics was not required and mathematics was taught in huge classes together with all life science students at a high school level. On the other hand, the chemistry students had to struggle through two extensive years of qualitative and quantitative inorganic chemistry. When I joined Meiboom's group it was at its prime, producing extremely interesting work in the forefront of NMR research; double quantum transition and radiation damping were observed, radiofrequency phase control was introduced to pulse sequences, strongly coupled spectra were interpreted and fast chemical processes were investigated by spectral lineshape analysis. Even the first application of the density matrix formalism to dynamic NMR was made there at the time. All these activities were directed by Meiboom, who although appearing shy and reserved, was the main driving force behind the operation. He provided encouragement, guidance, and ideas with a natural instinct to identify meaningful problems. My background was simply not sufficient to join in the excitement, but I was learning and watching. My account will therefore be predominantly that of an observer, describing the work of friends and colleagues, mainly during the period 1954–61, which could well be termed 'the early days of NMR in Israel'. The account is based on my own recollections, talks with colleagues, and written memoirs done especially for this article. For completeness it should be mentioned that in the late 1950s, Jan Grunzweig (Genosar) at the Israel Institute of Technology (Technion) in Haifa and his (then) student, David Zamir built an NMR spectrometer based on a Pound marginal oscillator and used it for solid state studies of quadrupole nuclei. I shall, however, limit my account to the high-resolution NMR work at the WI.

Felix Bloch was a member of the Board of Governors of the WI and would come to Rehovot almost every year for the Board meeting. As a scientist governor he was expected to advise the institute on scientific matters and in this capacity he persuaded its chiefs to establish a 'nuclear induction' laboratory (as NMR was referred to in those days in Stanford). At that time (1953) high-resolution NMR was in its very infancy; chemical shift and spin–spin interaction had just been discovered, but their potential impact on chemistry was not yet appreciated. In Bloch's laboratory, J. T. Arnold had recently completed the construction of a 7 kG high-resolution proton NMR spectrometer with probably the best magnetic field homogeneity of the time. Bloch suggested that a capable scientist be sent to his laboratory and replicate the apparatus. Chaim L. Pekeris, the head of the Department of Applied Mathematics, suggested Saul Meiboom, a co-worker in his department who was involved at the time in analyzing seismic signals from underground detonations as part of a geophysical oil prospecting project. Meiboom was born in Belgium and studied physical engineering in Delft (The Netherlands). He arrived in Jerusalem at the outbreak of World War II and participated in the war effort by designing and building electronic devices for military communication. After the war he joined the Department of Applied Mathematics at the WI, and in addition to the geophysical project he also pursued semiconductor research: together with Benjamin Abeles he studied the band structure of germanium and silicon, based on the Hall effect and magnetoresistance measurements. Part of this work became the thesis for his Ph.D., which he submitted to the HU. It was at this stage that Pekeris urged him to go to Stanford. So during the first half of 1954 Meiboom spent several months in Bloch's laboratory, after which he returned with blueprints of Arnold's spectrometer, as well as yet unpublished high-resolution spectra of ethanol, obtained by W. Anderson, in which higher-order splittings were observed for the first time.

Meiboom's first student in the field of NMR was Shlomo Alexander. In the summer of 1954 Alexander was about to finish his undergraduate studies at the HU and was looking for a place to do a Ph.D. in experimental physics. On the recommendation of his father, Ernst Alexander, the senior experimental physicist in Israel at the time, and William Low, who already ran an electron spin resonance laboratory at the HU, Alexander met with Meiboom to discuss possible topics for a thesis. By then Meiboom had already sent out orders for the necessary components for an NMR spectrometer, so they agreed that the construction of the spectrometer would constitute the first part of Alexander's thesis.

In 1954–55 Israel was still under rationing. Import of components involved a lot of red tape and took ages. The country had very little electronic and technological capabilities and was focused on its main concern: the absorption of huge waves of immigrants, mostly unskilled, who flooded the country and needed jobs. The Stanford spectrometer on the other hand was top technology. The success in replicating it under the prevailing conditions was due foremost to Meiboom's skill and drive, but also to the farsightedness of the WI directors, who provided support and help. Construction of the spectrometer started in November 1954 and within six months the first high-resolution spectra were recorded.

The magnet was ordered from a local factory near Petach Tikva (Magen Chetwood, which specialized in producing safe deposit boxes and had the heavy machines and lifting equipment needed for the job, see Figure 1). Its frame consisted of a ⌐¯-shaped yoke, closed with an I-shaped movable cart, both made of forged iron. The magnet poles, held horizontally inside the yoke, consisted of two sets of nine square Alnico rods, capped with soft iron pole pieces. Special attention was given to polishing these pole pieces in order to obtain maximum homogeneity. They were annealed in a hydrogen atmosphere and Meiboom and Alexander perfected their surfaces to optical flatness (as checked by Newton rings) by rubbing them against each other (Figure 2). In doing so they discovered that it was absolutely necessary to start with three pole pieces and rub them pairwise until

Figure 1 The not yet magnetized iron yoke being loaded at the Magen Chetwood factory for delivery to the Weizmann Institute

two were flat enough. The magnet poles were wound with 14 electric coils and used a three-phase Thyratron rectifier. The magnetizing current lasted a few seconds and resulted in burning out the main fuses of the whole WI. It was, however, sufficient to reach the desired field of 7 kG. Homogeneity was further improved by shim coils and sample spinning, or sample wobbling. The field drifted with time and compensating currents drawn from an automobile battery were required to minimize the effect. Because of the thermal expansion of the iron yoke the magnetic field also had a slow seasonal drift: the proton resonance frequency was 31.65 MHz in midwinter and 31.60 MHz in midsummer. The main modification compared with the original Arnold spectrometer was the introduction of a single coil probehead, instead of the Stanford cross-coil configuration. The rf irradiation was applied with coherent (1 kHz) weak pulses while during the time between pulses the coil served as a receiver. This greatly simplified the construction of the probehead, suspended the need to use 'leakage paddles' and eliminated baseline problems. The electronics were based entirely on vacuum tubes which were assembled on a big chassis with a soldering iron (Figure 3). There were very few 'black boxes' and the experiments could readily be controlled and modified by rewiring the electronic circuits. On the other hand there was an irritating dependence on the spectrometer's unpredictable mood and, of course, many of today's capabilities were not even thought of in those days. Much of the subsequent electronic modifications were made by Moshe Sasson, an electronic technician from the Israeli Air Force who joined the group in 1956. Excellent services were also provided by Bernard Feldman, a European-trained mechanical engineer who was hired by Chaim Weizmann in the early 1930s and produced unique fine mechanical devices until his death in 1991 at the age of 84 years.

Figure 2 Saul Meiboom (left) and Shlomo Alexander (right) rubbing a pair of pole pieces against each other to optical flatness

When in a good mood, the spectrometer produced beautiful high-resolution, T_2-limited spectra which, because of the low field, exhibited higher-order splitting of the type Anderson had already seen in ethanol and interpreted by second-order perturbation theory. Soon after the spectrometer became operational, Israel Dostrovsky, the head of the Isotope Research Department, showed up in the lab with a few hydrocarbon samples which he wanted to check by NMR. Some of them were vinyl derivatives which showed complex spectra due to the strong coupling between the three olefinic

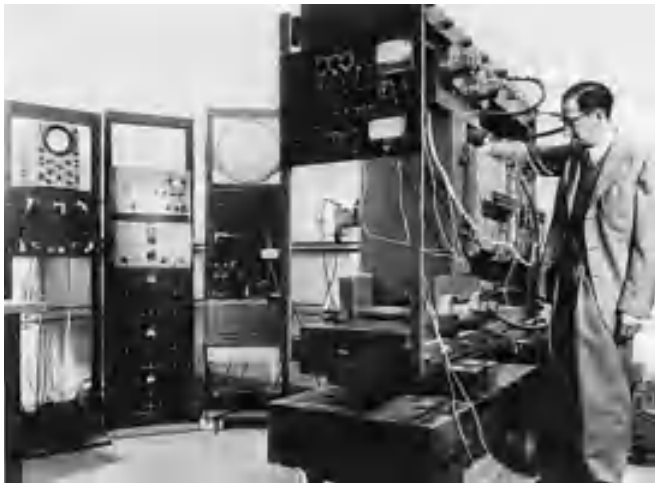

Figure 3 Saul Meiboom and the NMR spectrometer. To the right is the magnet with the shimming knobs on the front panel. The four stacks to the left side contain from right to left, a Sanborn strip recorder (which used a hot wire and temperature-sensitive wax paper strips), a CRT screen for displaying the spectra (obtained from military surplus), a Tektronix oscilloscope for controlling the pulse sequences, and a panel for controlling the rf source and the field sweep

protons. Second-order pertubation was not enough to explain the structure and a complete diagonalization of the spin Hamiltonian was necessary. This and the quantum chemical interpretation of the spin–spin couplings became the second part of Alexander's Ph.D. thesis. Fortunately Pekeris and his group had already completed the construction of the WEIZAC computer, the first digital computer in Israel and one of the first in the world outside the USA.[1] It was constructed from vacuum tubes, required 50 μs to perform an addition, had a total memory of 4000 numbers and was programmed in elementary machine language. Help was provided by Philip Rabinowitz, who was the only person in the institute with previous experience in programming. With this monster Alexander numerically diagonalized the 3 $\times$ 3 matrices of the ABC spin systems and interpreted the vinyl spectra. To his surprise he could only fit the spectra if one of the three spin–spin couplings had an opposite sign to the other two.[2] Opposite signs of couplings involving hydrogen and fluorine were already known from Gutowsky's work, but were not thought possible between hydrogens. This result contradicted the standard molecular orbital picture and demonstrated the importance of the correlation effects between electrons in different orbitals. Intrigued by the result, Alexander constructed an elegant valence bond theory based on the Dirac vector model to provide a satisfactory explanation of the observed couplings.[3] Nowadays with 10- to 20-fold higher magnetic fields, such complex spectra are rarely observed and at any rate are considered a nuisance for the experimentalists whose main interests lie in analytical and structural investigations.

Chemical applications of NMR started in Meiboom's laboratory with the arrival of Ernie Grunwald. He was a professor of chemistry at Tallahassee (Florida) and an accomplished physical organic chemist. In the summer of 1955 he came to spend a sabbatical year with Dostrovsky at the WI and soon realized the opportunities offered by NMR. Grunwald was interested in acidity functions of nonaqueous media and expected to be able to measure these from chemical shift changes induced by strong acids. Being physically limited at the time because of a car accident, he needed help with the bench work. So Aharon Loewenstein, who had just finished his M.Sc. at the WI, was invited to join the group as a Ph.D. student and carry out the experiments. His first task was to prepare and measure the proton NMR spectra of dilute ethanol solutions in sulfuric acid–water mixtures, but no S-shaped chemical shift dependence on the sulfuric acid concentration, as predicted by Grunwald, was found. To save the honor of chemistry, Grunwald suggested switching to aqueous media and proposed titrating solutions of methylammonium salts whose pK_a values were well established. This time the characteristic S-shape function showed up very clearly, but far more interesting were the effects on the spectral structure whereby the spin–spin multiplets would coalesce and resplit as a function of pH. These titration experiments led to the discovery of methods for studying the kinetics of acid- and base-catalyzed proton-transfer reactions in solutions. They resulted in a series of landmark papers[4–6] in which detailed kinetic analysis of the various protolytic processes in alkylammonium salt solutions were made.

Dynamic effects on NMR multiplets were already known at the time and analyzed by the method of Gutowsky, McCall, and Slichter (GMS), and subsequently by the much simpler method of McConnell. The spectra were analyzed using so-called 'lineshape parameters' which were dimensionless quantities such as the ratios of peak to trough in exchange broadened multiplets, or linewidth in units of the spin–spin coupling in the fast exchange regime. These parameters were obtained from simulated exchange broadened spectra (using the WEIZAC) but, since no plotters existed, the data were first hand plotted and then used to obtain the theoretical lineshape parameters. For each spin multiplet, exchange mechanism and natural linewidth (field inhomogeneity), a different lineshape parameter versus rate plot was made and subsequently used in the analysis of the experimental spectra. The field inhomogeneity was checked before and after each series of experiments by recording the free induction decay of a reference signal. These decay signals were measured using 'T_2 rulers' which consisted of transparent rectangular plastic pieces on which different exponential decay curves were marked. The rulers were moved over the recorded free induction decay signals until a good fit to a single exponential was obtained.

Another visitor in Meiboom's laboratory in those days was Jerry Kaplan. He graduated from Kittel's group in Berkeley and took a position at the Naval Research Laboratory (NRL) in Washington, DC, immediately after receiving his Ph.D. In 1955 Pekeris passed by the NRL and gave a talk. Someone in the lab knew that Kaplan was interested in visiting Israel and arranged that he would drive Pekeris to the train station. During this trip it was agreed that after appropriate application Kaplan would be awarded a Louis Lipsky Fellowship to the Weizmann Institute. He arrived in the summer of 1956 by boat from Naples, after hitchhiking for several months through Europe. Since there was no physics department at the WI in those days, he was assigned to Meiboom's group.

Chemical exchange studies were well under way in the group when Kaplan arrived. The quantitative analysis of the NMR lineshapes was based on the GMS theory which assumed weak coupling between the nuclei. This was not always an appropriate approximation and so Meiboom suggested that Kaplan extend the theory to the more general case. Kaplan, after a month wandering without getting anywhere, was suddenly struck by the idea of using the density matrix formalism. He combined it with the GMS method into a general theory for calculating dynamically broadened spectra.[7] He demonstrated the formalism by applying it to the case of a strongly coupled pair of protons, one of which was exchanging with another proton. When Kaplan returned to the USA at the end of 1956 he met H. McConnell who told him about his new way of including exchange phenomena in the Bloch equation. Kaplan incorporated this formalism into a second exchange paper which he wrote shortly after returning to the USA.[8] An extension of the formalism was subsequently made by Alexander, who when already at Bell Laboratories, was asked by Meiboom about the form that the linewidth equations should take for a spin–spin multiplet in the fast exchange regime. Alexander, who was unaware of Kaplan's second paper, developed the full density matrix analog of the Bloch–McConnell equations for both mono- and bimolecular reactions. Two papers emerged[9] which are Citation Classics to this day. Ironically it took a few years until they were appreciated by the NMR community: a minor typographic error in the example provided in the paper (the numeral one was substituted for the letter i in two places in the final equations) resulted in incomprehensible lineshapes. C.S.

Johnson and M. Saunders (from Yale) were diligent enough to go through the derivation and detected the error. They made good use of the theory afterwards.

Another problem that Kaplan worked on was the double quantum effect. On reading the Wangness–Bloch paper he realized that a double quantum transition should be observed under strong rf irradiation and he calculated its transition probability. Meiboom then confirmed the theory by experiments on ethanol where a double quantum peak indeed appeared midway between the methyl and methylene signals. They submitted the results for publication[10] in January 1957 and then discovered that two months earlier a note by W. Anderson[11] mentioned the observation of the effect in chlorobromothiophene. Kaplan and Meiboom recognized that the 'interpretation of complex multiplet structure may be facilitated by finding the double quantum transition',[7] an idea that many years later was effectively exploited by Alex Pines.

To achieve homogeneity it was customary to spin the samples by air turbines. This worked well with glass tubes. In an attempt to improve the homogeneity even more, sample holders with spherical cavities were also employed. These were constructed of two Rexolyte rods, each ending with a hemisphere hole. When put together these hemispheres formed a spherical cavity in which the liquid sample was placed, but the combined Rexolyte twin rod would not spin properly. So instead it was wobbled back and forth by a string connected to a car windshield motor. This drove Kaplan to perform a theoretical analysis of the effectiveness of the different motions on line narrowing. He concluded[12] that a periodic rotation was generally more effective, so the Rexolyte sample holders and the windshield motor were abandoned.

The next student to join the group was David Gill, a physicist with a chemical engineering background. He started his research work by measuring transverse relaxation in aqueous solutions of paramagnetic ions, but his main project was to explain the T_2 anomaly of water, namely the observation that the proton transverse relaxation rate (but not T_1) is enhanced at around pH 7. The possibility that the effect was due to oxygen-17 was rejected at the time because it was not believed possible that a rare isotope with a natural abundance of 4×10^{-4} could have any effect. Instead, the phenomenon was interpreted in terms of fast exchange between two types of chemically shifted protons: hydrogen bonded and non hydrogen bonded. If the breaking and reforming of hydrogen bonds were catalyzed by H^+ and OH^- ions, a minimum in the exchange rate and a corresponding minimum in T_2 should result at around pH 7 where their concentration is lowest. Unfortunately the only result still valid from the publication[13] in which the effect was announced is the very useful equation for T_2 in the fast exchange limit. Used in many applications, this equation gives the width of a coalesced line involving exchange between two chemically shifted sites with arbitrary relative populations. After permanently moving to Bell Laboratories in 1958, where he used a 60 MHz spectrometer, Meiboom discovered that the T_2 anomaly (which according to the original model should have increased quadratically with the field) was not due to chemical shift after all. Instead he showed[14] that the anomaly was indeed due to spin–spin coupling with oxygen-17, modulated by acid- and base-catalyzed proton exchange between water molecules. Meiboom even determined the proton–oxygen-17 coupling constant which was subsequently confirmed (by J. Ruben and D. Samuel at the WI) by direct measurements. Ironically, the WI was the world's main producer of oxygen-17 (and oxygen-18) enriched water. Gill needed only to borrow a sealed vial of oxygen-17 enriched water and observe an enormous broadening of the proton signal. In fact Dostrovsky, who 10 years earlier built the oxygen isotope separation plant at the WI, realized quite early the potential importance of oxygen-17 NMR. In the late 1950s he assigned Charles Braude to build an NMR spectrometer dedicated to oxygen-17; however, the project never got off the ground. In the early and mid-1960s a first commercial NMR spectrometer (a Varian DP60) was purchased by the WI. Daniel Fiat and his (then) students (including Jacques Ruben, Alexander J. Vega and Abraham Achlama) made extensive use of the availability of oxygen-17 for NMR studies, particularly for hydration problems. Somewhat later Brian Silver and I used it for ESR studies of oxygen-17 labeled radicals in solution and in solids.

Gill had difficulties in measuring long T_2 decays using the Carr–Purcell train scheme. At high pulse repetition rates the results became quite sensitive to the adjustment used: echo decays which ideally should be exponential often exhibited beats and other irregularities, although on rare occasions beautiful exponential decays were also observed. Gill realized that the effect could be due to phase errors accumulated as a result of imperfections in the widths of the 180° pulses. He first thought of correcting the error by inverting the phase of every other π pulse in the sequence. However, Meiboom soon realized that the much simpler experiment of shifting by 90° the phase of only the first 90° pulse in the sequence gives the same result. This modified sequence results in self-correcting phase errors, unlike the original Carr–Purcell scheme which results in an unstable state with accumulating errors. In the modified scheme, beautiful exponential decays were observed that were quite insensitive to the pulse width adjustment. As of now this so-called Carr–Purcell–Meiboom–Gill (CPMG) sequence is still the preferred method for measuring T_2 in liquids. The paper describing the experiment[15] is recognized as the first in which the importance of maintaining specific phase relations in pulse experiments was emphasized. It had a tremendous effect on the development of pulse techniques and is today one of the most quoted in the NMR literature.

Another experiment related to the 'rotating frame' picture which was conceived at the WI but actually implemented at Bell Laboratories, became the forerunner of many 'solvent supression' methods. Meiboom, in one of his rare letters to the group in Rehovot, mentioned that in order to measure the transverse relaxation rate of the methyl and hydroxyl signals in methanol separately, he was using 'weak pulses'. When Alexander met Meiboom at Bell Laboratories, he complimented him on the 'clever idea' of tilting one magnetization without affecting the other. After a short discussion they realized that they understood the term 'weak pulses' quite differently. While Meiboom simply implied that $\gamma B_1 < |\Delta\nu|$, Alexander thought of an experiment in which a 90° pulse was applied to one signal at resonance, $\gamma B_1 \tau_p = \frac{1}{4}$, while the other signal, $\Delta\nu$ Hz away, made a full rotation about its own effective field, $\tau_p[(\gamma B_1)^2 + (\Delta\nu)^2]^{1/2} = 1$. They immediately tried the experiment, obtaining beautiful CPMG decay echoes for one peak of methanol without the interference effect of the other.[16]

In 1957 three new students joined the group: Abraham Szöke, a physicist, and Mati Sheinblatt and myself, both chemists. We three closed the list of Meiboom's students at the WI since a year later he left permanently for Bell Laboratories. Szöke worked on two practical problems related to high-resolution NMR. His main project was to confirm and determine quantitatively earlier theoretical predictions on the coupling between the precessing magnetization and the receiver coil. The coupling was regulated by an amplifier which was fed with measured doses of both positive and negative feedbacks (Q-multiplier). At high Q very dramatic radiation damping of the FID signal was observed following a 90° pulse, while a 180° pulse yielded beats due to two level maser emission.[17] The effect was sufficiently impressive for A. Abragam (who visited the WI at the time that these experiments were performed) to reproduce a picture from Szöke's work in his 1961 book entitled 'The Principles of Nuclear Magnetism'. Szöke also designed and successfully operated field-locking NMR oscillators. Many designs worked but the winners in commercializing the device were others.

Sheinblatt and I were fascinated by the ability of NMR to measure fast chemical processes. Here one could calmly sit next to a spectrometer and measure processes, at equilibrium, having mean lifetimes as short as milli- and even microseconds. Sheinblatt extended Loewenstein's work to amino acids and later to peptides and oligopeptides, with the purpose of developing methods for sequencing. In that he certainly was one of the pioneers in applying NMR to biological research. I chose to work on proton exchange in hydroxylic solvents but after Meiboom's departure I joined forces with Brian Silver to work on the NMR of phosphorus compounds.

After Meiboom's departure for Bell Laboratories, Low would arrive weekly from Jerusalem to supervise Meiboom's orphans. However the day-to-day guidance was provided by Alexander, although he had just finished his Ph.D. At that time Szöke experimented with double irradiation and Gill attempted to build an NMR magnetometer for the detection of ground anomalies that could be used for example in archeological survey. Sasson and Bruno Bienenfeld (who later moved to Hewlett Packard in Palo Alto) provided excellent electronic services for these projects.

At the end of 1961 I finished my Ph.D. and joined Meiboom at Bell Laboratories as a postdoctoral fellow. At the same time I also discontinued my occupation as a high school teacher. Among the pupils in the last class that I taught was a 16 year old youngster by the name of Alex Pines. He will often be mentioned in this Encyclopedia. Meiboom had just explained the oxygen-17 induced T_2 anomaly of water, and together we extended the study to aqueous solutions of buffers in order to determine the average number of water molecules participating in single proton-transfer steps (the so-called Grotthus mechanism). In one of these studies we used an idea of Meiboom's to measure the CPMG echo decay as a function of the pulse repetition rates.[18] The experiment allowed the determination of exchange rates in the fast limit even when the interaction parameters were not known: they were obtained together with the kinetic parameters from the dependence on the pulse repetition rate. The method was rediscovered several times and, although not very widely used, it found some useful applications in polymer and membrane research. It would have probably become more popular had Meiboom invented an acronym for it!

To get away from proton-transfer processes, I started to study relaxation effects in solutions of paramagnetic ions. Just when I was beginning to understand what was happening, the famous paper by Swift and Connick appeared (I remember Bob Shulman, who showed interest in my work, entering my room with the latest issue of the *Journal of Chemical Physics*, asking 'Have you seen this?'). It provided a complete explanation of the oxygen-17 T_1 and T_2 relaxation in aqueous solutions of paramagnetic ions in terms of the exchange parameters between the bulk and the hydration shell molecules and the magnetic parameters of the ions. The signal of the hydration shell was, however, not observed at the time because of its excessive width caused by the electron–nuclear hyperfine and dipolar interactions and by the chemical exchange. On reading the article I was of course quite frustrated, but recovered after a few days when I realized that by switching to methanol as a solvent I should be able to extend the study and see even more. Since methanol solutions can be cooled down to almost $-100\,^{\circ}\mathrm{C}$, the exchange of solvation shell molecules could be frozen out, allowing their direct observation by NMR. This turned out to be very fruitful: solvation numbers could be determined, the magnetic properties of the solvation molecules could be directly studied, and the effects of mixed ligands on the solvation shell structure were clearly seen.[19] The period (1963) was the beginning of the biological application of NMR. 'Solvent relaxation enhancement' by paramagnetic active sites in enzymes was a favorite subject and these direct quantitiative studies of the solvation shells provided much insight for the biological work.

Eight years later I spent another year with Saul Meiboom at Bell Laboratories, collaborating on NMR in liquid crystals, a field of research that he pursued at the time with L. Snyder. He continued to study liquid crystals using a variety of other experimental methods and eventually shifted to theoretical calculations on the structures of the cholesteric blue phases, until his retirement in 1986. Shlomo Alexander who spent a postdoctoral period with P. W. Anderson at Bell Laboratories returned to the WI where for several years he ran an experimental laboratory in pure quadrupole resonance spectroscopy. In 1968 he moved to the HU to become a theorist in condensed matter physics. Twenty years later he returned to the WI. Ernie Grunwald followed Meiboom to Bell Laboratories and after several years moved to Brandeis University where he continued his studies in physical organic chemistry until his retirement in 1990. Aharon Loewenstein went as a postdoctoral student to J. D. Roberts at Caltech and then to B. Dailey at Columbia University. He later accepted a position at the Technion in Haifa working mainly on quadrupole nuclei and liquid crystals. Jerry Kaplan left Rehovot in the fall of 1956 and traveled through Asia to California. He then worked for many years at Battelle Institute and later settled in Indiana University. Mati Sheinblatt spent a postdoctoral training period with H. S. Gutowsky in Urbana and later with E. D. Becker at the NIH. Shortly after returning to Israel he accepted a position in the newly established Tel Aviv University and continued to work on the NMR of peptides. He passed away in 1989. Moshe Sasson became the first professional Bruker representative in Israel, but he too died very young in 1988. Abraham Szöke went for postdoctoral training to MIT where under A. Javan he switched to laser physics. He then joined Tel Aviv University but later moved to Livermore, California until his retirement in 1993.

David Gill, after a postdoctoral period with N. Bloembergen at Harvard, joined the HU and then spent several long periods in the United States. He became a biophysicist and in 1974 joined Ben Gurion University in Beer Sheva. Sonja Stollman, the able bilingual Hebrew–English secretary who cheerfully did all of Meiboom's paper work and typed the Ph.D. theses, left for the United States in 1959 and has since been living in New York City.

In 1964 I returned from my postdoctoral training to the WI where I have continuously held the torch of magnetic resonance. Many excellent NMR spectroscopists spent extended periods at the WI throughout the years including Daniel Fiat, Jacques Reuben, Mordechai Shporer, Abraham Achlama, Eva Meirovitch, and others. In the early 1990s NMR research has been pursued in essentially all universities and scientific institutions in Israel. The largest group is still at the WI where the activities range from solid state and theoretical NMR to biological application and imaging, with an enthusiastic group of scientists which includes Jacob Anglister, Peter Bendel, Hadassa Degani, Daniella Goldfarb, Irina Kustanovich, Aviva Lapidot, Michal Neeman, Raphi Poupko, Shimon Vega, and many young students.

REFERENCES

1. B. G. Estrin, *Annals Hist. Comput.*, 1991, **13**, 317.
2. S. Alexander, *J. Chem. Phys.*, 1958, **28**, 358.
3. S. Alexander, *J. Chem. Phys.*, 1961, **34**, 106.
4. E. Grunwald, A. Loewenstein, and S. Meiboom, *J. Chem. Phys.*, 1957, **27**, 630, 641.
5. A. Loewenstein and S. Meiboom, *J. Chem. Phys.*, 1957, **27**, 1067.
6. S. Meiboom, A. Loewenstein, and S. Alexander, *J. Chem. Phys.*, 1958, **29**, 969.
7. J. I. Kaplan, *J. Chem. Phys.*, 1958, **28**, 278.
8. J. I. Kaplan, *J. Chem. Phys.*, 1958, **29**, 462.
9. S. Alexander, *J. Chem. Phys.*, 1962, **37**, **967**, 974.
10. J. I. Kaplan and S. Meiboom, *Phys. Rev.*, 1957, **106**, 499.
11. W. A. Anderson, *Phys. Rev.*, 1956, **104**, 850.
12. J. I. Kaplan, *J. Chem. Phys.*, 1957, **27**, 1426.
13. S. Meiboom, Z. Luz, and D. Gill, *J. Chem. Phys.*, 1957, **27**, 1411.
14. S. Meiboom, *J. Chem. Phys.*, 1961, **34**, 375.
15. S. Meiboom and D. Gill, *Rev. Sci. Instrum.*, 1958, **29**, 688.
16. S. Alexander, *Rev. Sci. Instrum.*, 1961, **32**, 1066.
17. A. Szöke and S. Meiboom, *Phys. Rev.*, 1959, **113**, 585.
18. Z. Luz and S. Meiboom, *J. Chem. Phys.*, 1963, **39**, 366.
19. Z. Luz and S. Meiboom, *J. Chem. Phys.*, 1964, **40**, **1058**, 1066, 2686.

Biographical Sketch

Zeev Luz. *b* 1932. M.Sc., 1957, Hebrew University, Jerusalem, Ph.D., 1961, The Weizmann Institute of Science, Rehovot. Post-doctoral training at Bell Telephone Laboratories (with Saul Meiboom), 1961–64. Since 1964, at The Weizmann Institute of Science. Successively scientist, senior scientist, associate, and full professor. Oxford University, 1966–67; Bell Laboratories, Murray Hill, 1971–72; University of California, Berkeley, 1976–77; DuPont, Wilmington, 1984–85; MPI f. Poly. Research, Mainz, 1990–91. Approx. 220 publications. Research specialties: dynamic NMR, liquid crystals, solid state.

Lynden-Bell, Ruth M.: Reminiscences of Early Days of NMR

Ruth M. Lynden-Bell

The Queen's University, Belfast, UK

When I started my Ph.D. at the Chemical Laboratory in the University of Cambridge in 1959, nuclear magnetic resonance was a new spectroscopic technique. I joined Norman Sheppard's research group at the same time as Robin Harris; the other students working on NMR were Jim Turner and Colin Banwell.

The spectrometer that we used was a large 40 MHz Varian instrument that lived in the basement. It had an electromagnet which was over 1 m in diameter whose power supply occupied a large rack of electronic equipment and included the biggest valves I had ever seen. One realizes the enormous changes that computers have made to spectroscopy when one looks back at the way the instrument operated. In 1959 there were no computers attached to spectrometers, FT spectra were unknown in NMR and everything was one-dimensional. Each spectrum was a single scan of the magnetic field which came out on a narrow strip of heat-sensitive paper, and was burnt on the paper with a hot pointer. We were interested in measuring chemical shifts and spin–spin coupling constants of small molecules accurately and for this one selected each line or a few lines in turn, added frequency markers by generating sidebands of the standard (usually TMS) and then scanning slowly back and forth many times. One then measured the peak positions with a ruler.

To get the best—that is the most uniform—field from the spectrometer was a skilled operation. The technician in charge of the instrument, Eric Liddell, was adept at this. The power was shut off over the weekend and every Monday morning he powered up the electromagnet and then cycled it through a series of hysteresis loops. At first the field would be dome-shaped, bigger in the center of the magnet than at the sides, and after each cycle it would be more uniform and the lineshapes sharper and more symmetric. However one needed to know when to stop. If the cycling process was continued once too often the field would become dished, with a minimum at the center, giving broad asymmetric lines. This problem was greatly helped when, a few years later, Golay coils were added. These were used to generate small correcting fields to give sharp lines.

The spectrometer had been purchased for organic and inorganic chemists and Norman Sheppard employed to run a service. Most of the spectrometer time was spent on this service. Eric Liddell ran the spectra, which then went to Norman Sheppard for interpretation as in those days most chemists were quite unfamiliar with NMR spectra. By far the largest number of spectra run were proton spectra, but we did have ^{19}F and ^{31}P probes and a low-temperature probe. Those of us in the research group ran our own spectra.

Our research group was friendly and we learnt much from each other. We were in a special position as spectroscopists in a department of organic, inorganic, and theoretical chemistry; at that time the physical chemists were a separate department. Pople, Schneider, and Bernstein had published their comprehensive book on NMR[1] earlier in 1959 and that was where we learnt about the principles of the subject. Years later John Pople told me that they had included every reference up to the date of submission of the manuscript, which shows how young the technique was in 1959. The book is excellent and still provides most of the theory needed by NMR spectroscopists.

The main research interests of the group at that time were to measure accurate values of spectral parameters so that theories could be developed, and to use NMR spectroscopy to investigate conformational equilibria. My original problem was to measure the spin–spin coupling in tritiated hydrogen, HT. The tritium nucleus has spin-$\frac{1}{2}$ and quite a high magnetogyric ratio, so that one should have been able to measure the splitting in the proton spectrum accurately. This project came to nothing as my attempts to dissolve H_2 in a solvent under pressure to get a signal failed. I was more successful in the next stage of the project which was to use ^{13}C substitution to obtain all the coupling constants in acetylene, ethylene, and ethane. The source of ^{13}C was substituted $BaCO_3$ and I practised the syntheses many times before opening the bottle of precious labeled material. Luckily the syntheses all went well and I had my samples and could measure the ^{1}H spectra.[2] We had no ^{13}C probe, but the following year I visited Varian in California where Jim Shoolery ran the ^{13}C spectra of my samples. In fact the only additional information about coupling constants that one could obtain from the ^{13}C spectra was the relative sign of the HH and CC coupling in ethylene.

In order to analyze our spectra, which were rarely first order, we set up the secular equations using symmetry where relevant. It was all a most pleasing application of quantum mechanics and when the predicted and measured spectra agreed one felt really satisfied. We often needed to diagonalize matrices which were bigger than 2×2 and for that we used a computer. In 1959 computers were very different from those we use in 1993. Most universities had no computer, but at Cambridge we had EDSAC2, which was available to any research student or member of staff. One wrote programs in machine code and the total power was probably about the same as a modern calculator. It was very much a hands-on machine. Once one had written one's program and typed it onto punched tape, one joined the test queue. This was a queue of people waiting at the console and it ran for 15 min three times a day. When one reached the front of the queue one put in one's tape and switched a switch. Ideally the tape should have run through and the results come out on another tape. Programming was just the same then as now—programs didn't work first time. One frequent error was for the machine to get into an endless loop. There was a loudspeaker attached to the computer and when this happened it changed its tune. One switched off the computer, removed one's tape, rushed round to the back, edited the tape, and rejoined the test queue. Once one's program was working one submitted it to the job queue. The job queue was a pegboard with hooks on which one hung one's reel of paper tape for the operators to run at times when the test queue was not running. Library subroutines were available—we used a matrix diagonalization subroutine. These were on rolls of colored paper tapes, and one added a copy of the relevant one to one's own white reel.

NMR was fun in those days, and although I have since completely changed the field of my research, I am sure that NMR is still fun today.

REFERENCES

1. J. A. Pople, W. G. Schneider, and H. J. Bernstein, *High Resolution Nuclear Magnetic Resonance*, McGraw-Hill, New York, 1959.
2. R. M. Lynden-Bell and N. Sheppard, *Proc. R. Soc. London*, 1962, **A269**, 385.

Biographical Sketch

Ruth M. Lynden-Bell. *b* 1937. M.A., Ph.D., Sc.D., University of Cambridge, UK. Fellow and college lecturer, New Hall, University of Cambridge 1962–65; Lecturer, University of Sussex, 1965–72; Fellow and college lecturer, New Hall, University of Cambridge, 1972–1995; Professor of Condensed Matter Simulation, The Queen's University of Belfast, 1955–present. Approx. 100 publications. Current research interests: the study of molecular motion and local structure in solids, surfaces, and liquids using computer simulation.

Maciel, Gary E.: A Little Polarization Can be Good for You

Gary E. Maciel
Colorado State University, Fort Collins, CO, USA

THE MIT YEARS, 1960–61

My first awareness of NMR, as I recall, came about when I was an organic chemistry graduate student at MIT about 1958–59. I took a course in statistical thermodynamics presented by a very impressive young assistant professor, named John Waugh, who was engaged, according to graduate student scuttlebutt, in an elegant new (to chemists) phenomenon called nuclear magnetic resonance. During that period, my research supervisor was Frederick D. Greene III, a physical organic chemist, who called my attention to an exciting new book by John D. Roberts on NMR for organic chemists. Many organic chemists seemed to accept the proposition that, if Jack Roberts was interested in NMR, it was probably going to be important in organic chemistry. The eventual decisive manifestation of that proposition is perhaps a good calibration on Jack Roberts's insights and on the wisdom of organic chemists in paying attention to his interests. Jack Roberts's little book was aesthetically appealing, filled with beautiful vector diagrams (including red coloration, which was unusual in technical books at that time), and was quite seductive to an impressionable young chemist.

One of the hot areas in NMR research at the time was the analysis of second-order spectra, e.g., AB, ABC, etc., spin systems and the Roberts book gave a hint of the joy involved in the back-of-the envelope (sometimes a large envelope) quantum mechanical calculations involved in these spectral analyses. I was delighted to learn that John Waugh was involved in this kind of research, so I decided that it would be fun and educational for a physical organic chemist to spend a year in John Waugh's lab, learning about NMR—and, hence, getting some experience in quantum mechanics. To the extent permitted by the time constraints while finishing my Ph.D. thesis (concerned with the bromination of bibenzyl with ***N***-bromosuccinimide—no NMR there!), I became an occasional 'NMR groupie' in the Waugh lab, and was suitably impressed by students and visitors of the quality of Richard Fessenden (now at Notre Dame) and Robert Blinc (whose affiliation then, as now, was Ljubljana in what was then Yugoslavia). I remember one occasion, when John Waugh was trying to convince the Dean that the NMR lab was overcrowded and needed additional space (John had previously escaped from his initial cave under a stairwell). John asked me, along with a few other 'ringers' to pack his lab during the Dean's visit. The effort was a success.

The National Science Foundation accommodated my desire to spend a postdoctoral period in John Waugh's lab by awarding me a much-appreciated fellowship. My time in John Waugh's group (1960–61) was enormously educational for me, if not spectacularly productive for John (he *insisted* that students and postdocs call him by his first name; this was my first experience with this kind of informality among university faculty). I quickly learned that one should not be too intimidated by commercially provided instrumentation (e.g., NMR probes); if something built by *man* (even specialists at Varian, which was in many respects the center of the NMR universe at that time) was taken apart or even broken by man, it could always be repaired or rebuilt by another mortal man (there were no women in the Waugh group at that time, and very few in the entire MIT Chemistry Department).

During the period 1960–61, state-of-the-art in NMR spectrometers was a Varian HR-60, a field sweep high-resolution CW instrument. Just before I joined the Waugh group, one of the major technical problems in the lab originated in the water cooling system for the electromagnet; the NMR lab was directly below a men's restroom, and sometimes during a change of classes, enough toilets would be flushed at the same time to reduce the water pressure sufficiently to cause the pressure sensor of the magnet circulation system to shut down the magnet. Very annoying! This problem was, or course, solved by the introduction of a closed-circuit water cooling system.

John Waugh's laboratory at MIT was an enormously stimulating environment for a young scientist (even a physical organic chemist) to begin learning about NMR, not only because of John himself, but also because of some excellent students. I worked closely with Charles Johnson (now at the University of North Carolina), who impressed me greatly without trying, and from whom I learned a great deal. Fred Mannis, who went to DuPont upon completion of his Ph.D. thesis, was also very helpful and knowledgeable. In those days, smoking was much more common, even in the laboratory, and I have visions of Joe Gavin (a joint Waugh–Stockmayer student who later took jobs at the CIA and Perkin-Elmer, presumably not simultaneously) leaning over the Harvey-Wells magnet while he set up and observed his self-diffusion measurements (based on field gradients generated by the current from a bank of car batteries), cigarette dangling from his mouth, and smoke effectively screening the desired observations from his view. This smoke obviously caused his eyes great distress; but, he maintained, it was worth it! During this period I became acquainted with Gary Mennitt, who joined the faculty of the City University of New York after leaving the Waugh laboratory. Many years later (1980–81) Gary spent a sabbatical year with us in Colorado, during which we had some fun exploring ^{113}Cd chemical shifts in the solid state.

My 18 months in John Waugh's laboratory were a real learning experience for me, and mercifully NSF picked up the tab for my support. I dabbled in a few areas, which included obtaining and analyzing some relatively complicated high-resolution ^{19}F NMR spectra, an area in which we collaborated with Dietmar Seyferth. During that same period we collaborated with Gordon Hammes, then on the MIT faculty, on the first (I think) study of what subsequently became a very popular subject, the NMR investigation of interactions between metal ions and ATP.

Probably my favorite 'miniproject' at MIT, the one which allowed (forced) me to delve into the instrumentational side of NMR (e.g., those marvelous tube-based, analog Tektronix waveform/pulse generators), was based on John Waugh's recognition that the Fourier transform of the transient

signal from a *J* multiplet, following a pulse, would contain high-'resolution information regarding the multiplet structure. Furthermore, he recognized that if this experiment were carried out in a spin echo mode, one could avoid most of the problems associated with magnetic field inhomogeneity (a substantial issue in 1960). I left MIT before this project bore fruit, but I personally benefited greatly from the experience.

One terrific piece of luck in the timing of my postdoctoral period in John Waugh's group was the fact that Charles Slichter of the University of Illinois was spending a leave at the 'little red schoolhouse' down the street from MIT (this is how we affectionately referred to Harvard University), and was presenting a special course on nuclear magnetic resonance. This was a beautiful set of lectures and resulted, I believe, in the terrific book from which so many of us have profited since that time.

While it was Roberts' early books that attracted my attention to NMR initially, it was the magnificent book by Pople, Schneider, and Bernstein that I, and many others, really used to begin *learning* NMR. Initially it seemed like *everything* was in there, but I finally began to realize that there was much more to learn when John secured a copy (in 'blue ditto' form, as I recall) of the manuscript for the NMR bible by Abragam. That manuscript, which was in French, was circulated covetously through the group in a manner that reminded me of French postcards in high school.

THE UNIVERSITY OF CALIFORNIA, DAVIS YEARS, 1961–70

It seems almost impossible for me to believe now that I spent nearly 10 years in Davis, a period during more than half of which my wife, Maxine, had to put up with the difficulties of living with the typical insecurities of an untenured faculty member. I went to Davis in 1961, somewhat of an impostor as a physical chemist, with the intention of developing ^{13}C NMR as an approach for studying the structures of organic compounds, e.g., carbon connectivities, in liquid samples (we hadn't yet started dreaming about solid samples). Paul Lauterbur (then at the Mellon Institute) and C. H. Holm (Shell Development) had just produced two or three publications that clearly indicated to any organic structure oriented NMR researcher the enormous potential of ^{13}C NMR, even if one considered the daunting difficulties of obtaining ^{13}C spectra at that time. An impressive new Varian HR-60 spectrometer was awaiting me when I arrived in Davis, and the Department of Chemistry had equipped it at my request with a probe and rf unit (my assistant professor start-up package!) that was capable (in favorable cases) of detecting ^{13}C resonances. This equipment, which substantially predated field/frequency lock capabilities, was quite suitable for rapid passage/field sweep techniques (in which the peak maximum for one sweep direction was not at exactly the same place as the peak minimum for the other sweep direction—but an average value gave a good measure of the chemical shift). It was this crude approach that we, as well as Dave Grant's group at the University of Utah and Jake Stothers at the University of Western Ontario, used to explore the relationships between ^{13}C chemical shifts and molecular structure.

During this period I was very fortunate to be joined in this ^{13}C NMR effort at Davis by George Savitsky, who had started as an assistant professor in the department at the same time I started, although he was about 10 years older than me. George, who was a superb researcher and a brilliant teacher, had come to Davis by way of Princeton (postdoctoral research in infrared spectroscopy with Donald Hornig), the University of Florida (Ph.D. studies in physical chemistry), the Dominican Republic and Honduras (soil scientist with the United Fruit Company), the Phillipines (a displaced persons' camp), and China (born, raised, educated in the expatriate Russian community, and then forced to leave at the time of the Communist revolution in 1949). George Savitsky was trained as an infrared spectroscopist; but when he arrived in Davis and learned that there was no research-grade IR equipment, he decided to take advantage of the only state-of-the-art spectroscopic equipment in the building—the HR-60 spectrometer. Hence, George and I pooled our ideas and resources and collaborated closely (although we were advised that, for tenure reasons, we should also develop some independent ideas and publications). George was enormously innovative, and was one of the key figures in establishing and correlating the constitutive and additivity properties of ^{13}C chemical shifts. After about five years at Davis he moved to Clemson University (from which he recently retired) where he again used the equipment available to him (no ^{13}C NMR facility)—initiating a successful research program on the study and use of deuterium quadrupolar interactions for the determination of molecular correlation functions.

George had two graduate students working under his supervision at Davis, and hence closely with our group. Keishi Namikawa earned an M.S. degree and went back to Japan, after making a substantial contribution to the study of constitutive effects on ^{13}C chemical shifts. Bob Pearson was much more independent in his research than most of our students; he went on to Kaiser Chemical Corp., where he became a pioneer in the use of NMR for on-line process control, a subject that he now pursues as a principal in Tri-Valley Research, Inc.

During the period while George Savitsky and I were working close together and sharing the HR-60 spectrometer, the Davis campus was undergoing a major transformation, from primarily an agricultural campus to a general campus. As part of that transition, the old Crocker cyclotron was (at least nominally) being moved to Davis, rebuilt and installed in a magnificent new building. Part of the apparatus being moved to Davis was an old NMR console/probe system, used for calibrating magnetic fields, and the physicists at Davis brought it over to our laboratory to calibrate it with the HR-60 magnet. While this calibration was being carried out, I noticed that the manufacturer's label was 'Varian Associates' and the apparatus was marked 'Serial No. 1'.

During my first few years in Davis in the early 1960s, Stan Burdick,* of whom I have lost track (Stan, please call if you see this!), Charles Carmen (who went on to an outstanding research career at B. F. Goodrich), and John Natterstad (who is now in the instrumentation industry in the northwest) were M.S. students in the group and got things started. John carried out some of our first ^{13}C experiments on the effects of substituents, hydrogen bonding, and protonation on carbonyl groups. Soon after George Savitsky left Davis (in about 1965), we moved into a spacious new building, which came equipped with a Varian HA-100 spectrometer (now, at last, a field/frequency lock system!). About the time we acquired the HA-100, Don Hofer and George Gray joined the group,

Don working on ^{19}F chemical shifts in fluoride solutions and George measuring $^{13}C-^{13}C$ J couplings in dilabeled compounds that *he synthesized*. After a time at the University of Illinois and the University of Arizona, Don moved to IBM, where he works at the Almaden laboratory. George Gray spent a few years as one of the first faculty members of the newly established Oregon Graduate Center (now the Oregon Graduate Institute of Science and Technology), before joining Varian, where he is an applications scientist.

One thing that livened up our Davis laboratory, and enhanced our productivity, was the fact that we had several long-term visits by Dan Traficante, who now has 'his own series' and is on the faculty of the University of Rhode Island, but was then an Air Force lieutenant at the Frank Seiler Laboratory of the Air Force Academy, and had earlier been an organic chemistry lab-mate at MIT. Dan had, I suppose, convinced the Air Force that ^{13}C NMR was essential to the security of the free world, so they allowed him to visit us for weeks or months at a time, during which he would feverishly synthesize needed compounds (especially ^{13}C-labeled ones) and obtain their ^{13}C NMR spectra. As had happened to me a few years earlier, Dan was irreversibly infected at Davis by the NMR virus (from which there is seldom a full recovery before death).

Our venture into truly *high-resolution* ^{13}C NMR, with spectra that looked almost as good as those organic chemists obtain routinely today (in much, much less time), depended on computer time averaging (based on a CAT, for computer of average transients), which was made possible originally by our development of a field/frequency lock technique for the HA-100 based on the signal of ^{13}C-enriched carbon disulfide, and ultimately was made much easier by the efforts of Tom Nakashima (who has been on the staff of the University of Alberta for many years) and Vic Bartuska (who recently retired from Chemagnetics), who developed a ^{19}F field/frequency lock system for the HA-100 spectrometer. Although their Ph.D. thesis projects were much more chemically oriented, they both found that they enjoyed working with electronic instrumentation. Vic had been an organic chemist focusing on carbohydrates before joining our group. (He occasionally reminds me that he joined our group only because the carbohydrate chemist in the department stopped accepting students.) He found that instrumentation was more fun than chemistry and subsequently made his career in the NMR instrumentation industry. I'll never forget how Vic 'trained' the field/frequency lock system, based on audio modulation at 2–3 kHz, to respond to his whistling. He could walk into the spectrometer room and cause the spectrometer to lose lock, and then relock by whistling appropriately.

During the Davis period, we were very much influenced in our ^{13}C work in the early to mid-1960s not only by Lauterbur's seminal papers, but also by extremely important papers by Spiesecke and Schneider on substituent effects on ^{13}C chemical shifts, and by the theoretical (molecular orbital) treatments of ^{13}C chemical shifts by John Pople and Martin Karplus, and their co-workers. During the 1967–68 academic year, I was able to indulge my interest in ^{13}C chemical shift theory with a sabbatical leave split between Karplus's group at Harvard University, where I mainly studied formalism, and Pople's group at Carnegie-Mellon University, where I got serious about computational theory, mainly INDO calculations of J couplings, and developed a collaborative arrangement with postdoc James McIver, who subsequently joined the faculty at SUNY, Buffalo. I took the enthusiasm and essential computer routines for perturbed molecular orbital calculations of second-order properties (e.g. J coupling and chemical shifts) back to Davis and thoroughly infected my students with this enthusiasm, especially Paul Ellis (who recently moved from the faculty of the University of South Carolina to the Pacific Northwest Laboratory, PNL, in Richland, WA). Jim McIver collaborated with Paul and myself on ^{13}C chemical shift theory at the INDO level, which we found to be surprisingly successful (although not as accurate as later ab initio calculations). In Paul's natural mode of operation, he was soon running the campus computer and also had a substantial amount of time on one of the computers at the Lawrence Livermore Laboratory.

In addition to Paul Ellis, we were fortunate in the late 1960s in having a series of very good students, some of whom moved with me in 1971 to Colorado State University. These included: Harry Dorn, now a professor at Virginia Polytechnic Institute; Tom Nakashima; Larry Simeral, who went on to Ethyl Corporation, now Albemarle Co.; Mark Bacon, who spent a few years on the faculty at the University of Nevada in Reno and at Decatur University in Illinois, before settling into the electronics industry; and Kim Summerhays, who has been on the faculty of the University of San Francisco for several years.

During the Davis years, our group had its first 'real postdoc', Dieter Lauer, from Germany, who joined us in our detailed study of substituent effects (including deuterium isotope effects) on ^{13}C chemical shifts. Jointly with Ken Musker, an inorganic chemistry faculty member in the department, I also advised a student, Roger Scholl, who went to work for the Sierra Club after completing his Ph.D. studies. Roger carried out one of the first detailed experimental studies of structure–shift relationships in ^{29}Si NMR spectra of organosilanes. An old friend (he's *much older* now) and undergraduate classmate in the 1950s in Berkeley, Professor Edwin Motell of San Francisco State University, worked with us periodically at Davis on a variety of ^{13}C chemical shift studies, and continued to collaborate with us after we moved to Colorado State University (CSU) in 1971.

THE CSU YEARS, 1971–PRESENT

Spurred on by the inspiring academic initiatives of Ronald Reagan, who was Governor of California at the time, we moved from the University of California, Davis to CSU in 1971. One of the things that made the decision to move to Colorado a little less impulsive and less crazy than it may have appeared was the fact that CSU had waiting for me a new Bruker HFX-90 spectrometer, bought originally for Alan Jones, who had left CSU before having a chance really to use the new spectrometer (he was a British citizen, who was not able to solve his visa problem, so he moved to Alberta and eventually to Australia). The HFX-90 was a state-of-the-art CW spectrometer and there were funds available for an FT data system to add to the spectrometer.

When we arrived in Fort Collins, the HFX-90 stood silent in a dark, dusty room in a musty basement of the old chemistry building, covered by a plastic tarp. Tom Nakashima and Harry Dorn soon had it purring, and a new age of spectrometer

capabilities was upon us. A few months later, we moved the HFX-90, complete with its 9000 lb magnet, to a new chemistry building across campus. I was enormously impressed when the students were obtaining spectra of reasonably good quality just two hours after the movers set the magnet in place in the new laboratory.

At this time, the only commercially available FT NMR spectrometer was a Bruker HFX (or HX) system with a DEC PDP-8 minicomputer for Fourier transformation and a Fabritek (later Nicolet) signal averager. Digilab offered the only other stand-alone FT NMR accessory, based on a Data General minicomputer with a disk for storage, and we soon had a Digilab system installed on the Bruker spectrometer. This was, I believe, one of the first five or six FT NMR spectrometers in the world. It allowed us to not only continue our work in ^{13}C NMR, but also to branch out conveniently to a variety of other nuclides. The students were aided enormously by the appearance at about this time of the beautiful and timely little book by Farrar and Becker on pulse and Fourier transform NMR.

In addition to the Davis graduate students mentioned above (Harry Dorn, Tom Nakashima, Larry Simeral, Mark Bacon, and Kim Summerhays), there were two students I had met in California when they were undergraduates who moved to CSU to join our group—Jerry Dallas, who subsequently spent several years at GE NMR and is now doing protein NMR at Berlex Biosciences, and Rich Elliott, who left CSU after a couple of years for Wisconsin, where he went to medical school, eventually becoming a psychiatrist. Using the FT version of the HFX-90 spectrometer, Jerry Dallas carried out extensive work on ^{207}Pb NMR, and Marie Borzo (now at Hoechst-Celanese) explored ^{113}Cd and ^{199}Hg chemical shifts, as well as some theoretical aspects of nuclear Overhauser effects. Larry Simeral worked on ^{25}Mg and ^{67}Zn NMR in aqueous solutions, and Joe Ackerman (now a professor at Washington University) studied ^{109}Ag, ^{67}Zn, and ^{113}Cd chemical shifts from the point of view of solution structure. Tom Orr (now at Procter and Gamble) participated in ^{113}Cd studies of Cd(II) complexation, along with leading our subsequently aborted effort in ion cyclotron resonance. Most of the students during this period, especially Harry Dorn and Tom Nakashima, also participated actively in ^{13}C NMR, and some of them continued our computational–theoretical work on ^{13}C chemical shifts and J coupling, along with Don Miller (a postdoc, since then on the chemistry faculty of Washburn University). On the theoretical side, Kim Summerhays emphasized a molecular orbital trick that we called the 'pseudo atom effect' for examining substituent effects from a point of view based more-or-less on popular concepts in physical organic chemistry, and Kurt Seidman (now a professor at Randolf Macon Women's College) examined conformation and medium effects on ^{13}C chemical shifts; later Mary Severson (now a patent attorney in Atlanta, after a few years as a faculty member at Mercer University) continued theoretical studies of certain structural effects on ^{13}C chemical shifts and J couplings. During the past few years, our efforts in chemical shift theory have been extended to ab initio methods, mainly by Joe Iwamiya (now at Lockheed) and Dong-Hee Kim (a sabbatical visitor from Kunsan National University, Korea). During the 1970s, only Michael Heller (a joint student with Anthony Tu in our Biochemistry Department) broke our pattern of largely missing out on the revolution in NMR applications to the determination of protein and polynucleotide structures.

During the late 1970s and early 1980s, we continued working on a variety of high-resolution multinuclear MR projects on liquid samples, and also continued to dabble in little instrumentation developments and tricks, mainly in electronics. The liquid-sample studies included some ^{7}Li, ^{23}Na, and ^{27}Al studies of ionic interactions by Wrocklaw Kolodzieski (a postdoc, now with J. Klinowoski in Cambridge) and Joel Gray (who recently left Coors after many years in the analytical laboratory), and our first attempt at NMR-based quality control, the determination of sucrose in sugar beet juice, in the work of Doug Lowman (who has been at Tennessee Eastman for many years). During this same period there were major developments that dramatically reorientated our research emphasis toward solid samples, and impacted my career in very important ways. The cross polarization (CP) paper by Pines, Gibby, and Waugh had a profound influence on the way I thought about NMR, and, like many other NMR spectroscopists, I began considering the possibilities of working with solid samples. Also during the 1970s, Schaefer and Stejskal at Monsanto were reviving interest in magic angle spinning (MAS), and married CP with MAS. The prospect of obtaining high-resolution ^{13}C NMR spectra of solids almost routinely was terribly exciting. Having recently moved to Colorado, which was ostensibly on the verge of a major industrial impact based on oil shale, I thought it would be nice, for a change, to do some research that I could explain, or justify, even to my neighbors. ^{13}C CP (and eventually CP MAS) studies of oil shale seemed like the appropriate opportunity to become 'useful' to Colorado.

Three other developments came in confluence with my desire to reorient our research group toward solid state NMR studies. One was the emergence at NIH and subsequently at NSF of the concept of NMR Centers. I had already, unsuccessfully, tried to obtain funds from NIH to establish an NMR Center at CSU as part of a Colorado Regional Cancer Center; I was also planning to apply to NSF to establish a center when they eventually announced a broad-based program. During the mid-1970s the establishment of some kind of center seemed to me to be the only possible way of *ever* bringing a 'high-field' spectrometer (i.e., one based on a superconducting magnet) to CSU, and to establish an NMR Center with a major solid sample component seemed increasingly attractive to me.

The second development referred to above was that Vic Bartuska, who had spent time at Bruker in Karlsruhe and then at JEOL in Cranford, NJ, after leaving Davis, was unhappy professionally and looking for new horizons. He and I agreed that he should perhaps move to Fort Collins and play a major role in initiating the program I was planning in solid state NMR. This plan would certainly involve extensive instrumentation development, which he found appealing. Although funding was in short supply and very uncertain, we believed that something long term would work out for him so that he and Bettie could raise their family in Fort Collins. The long-term professional possibility that appealed most to Vic was managing the NMR Center we hoped to establish at CSU. As a fall-back position, in case nothing attractive appeared, we agreed that we could establish a small NMR-oriented company of some sort (e.g. NMR accessories) to provide a modest salary and professional challenge for him.

Accordingly, he moved his family to Fort Collins and in 1975 started working on modifying an old HR-60 spectrometer for solid state NMR experiments. His early MAS efforts, which included marginally successful experiments with the 'barrel' design being used at that time by Schaefer and Stejskal, were aided substantially by their generous cooperation. Vic's development of the 'bullet' MAS rotor, aided in the design stages by his observation of the flow patterns of cigarette smoke that he skillfully exhaled to strategic locations of his prototype systems, made it possible for us to venture into a variety of applications of CP MAS NMR—e.g. coal and oil shale (initially in collaboration with Fran Miknis of the Laramie Laboratory now known as the Western Research Institute).

The establishment of a federally-funded NMR Center at CSU did not happen soon enough to provide the position that Vic needed to stay in Fort Collins, so Chemagnetics, Inc. was established, with Vic and Bettie Bartuska, and Maxine and me as partners. Initially the company existed, and indeed prospered, by providing CP MAS probes (made by Vic, with help later by Robin Lewis) to JEOL for its FX-60 spectrometer. With profits from these probe sales, the company expanded its activities, technology base, and human resources (e.g., Dave Dalbow, a biologist turned magnet designer, instrumentation specialist and manufacturing ace; and David Lewis, a whiz at optimizing and implementing mechanical designs). Superconducting magnet technology was acquired initially from Craig Bradley, then extended by Dave Dalbow and Dean Sindorf, and by about 1983 the company was poised to think about building complete spectrometers. This was made possible by investments, initially from a New England group and later from family sources, and a parallel entity called Magnechem was established. With Steve Freeland developing a data system, Allen Palmer a probe, and with substantial input from Dale McKay (now at Quantum Magnetics), Dean Sindorf and, of course, Vic, the A-200 was introduced. Although not a huge success commercially, the A-200 (for which the Varian Gemini-200 eventually validated the concept) paved the way for subsequent spectrometers, mainly solids oriented—the M series, the CMC series, and the CMX series.

Chemagnetics grew during the 1980s, adding key people like Joe DiVerdi (from Opella's group) and David Hughes (from Varian). While never a resounding financial success during the 1980s, the company reached a point where 'mom and pop' financing was no longer viable (every month the bank would look at the Maciel and Bartuska homes with ever-increasing intensity). Hence, after an unsuccessful two-year search for suitable American financing, partnership, or purchase, controlling interest in Chemagnetics was sold to Otsuka at the end of 1989, and they subsequently purchased total ownership. My own role in the company had been primarily as a consultant and member of the Board of Directors, and that involvement ended a year or so after the 1989 purchase by Otsuka.

The third major development in my professional life during the late 1970s was the establishment of an NSF-funded regional instrumentation facility at CSU in October 1978. Although the CSU NMR Center was not formally part of our research group, the affiliation was close, and both entities benefited greatly from the association. Not only did the NSF funding provide exciting new facilities (spectrometers), but it also made it possible to assemble an outstanding technical staff—initially Bruce Hawkins (who is still at CSU, as a computer specialist, and has a side business in process control NMR) as manager, Jim Frye (now at Chemagnetics), and Dale McKay (who moved to Chemagnetics in about 1985, and subsequently moved to Quantum Magnetics). The Center brought modern NMR capabilities, especially for solids, to a large number of scientists, and successfully survived competitive renewal cycles in 1982 and 1986. The staff, with Dale McKay replaced in 1985 by Chuck Bronnimann (after he finished his Ph.D. project next door), not only provided valuable service to outside Center users, but also dramatically enhanced the overall technical expertise in our laboratory and were enormously helpful to the students. When NSF funding for the Center dried up in 1989–90, because of changing NSF policies, the saddest reality that we faced was the possibility (eventually the certainty) that an outstanding team could not be kept together. Both Jim Frye and Chuck Bronnimann moved to Chemagnetics in 1991.

During the same period when the NMR Center was being established and flourishing, our research group's activities in solid state NMR were growing. A substantial effort in the area of coal and oil shale studies was under way, an effort that has involved several people during the past 17 years: Nick Szeverenyi (a postdoc, now on the faculty at the Health Science Center, Syracuse, New York), Mark Sullivan (now at Hercules), Pat Hatcher (then a graduate student at the University of Maryland, and now a faculty member at Pennsylvania State University), Larry Dennis (a postdoc, now at Exxon R & D in Texas), Allen Palmer (a postdoc, now at Chemagnetics), Richard Bryson (deceased), Gaye and Oktay Erbatur (collaborators from Çukurova University in Turkey), Mark Davis (now at the National Renewable Energy Laboratory in Golden, CO, after a period on the staff of the NMR Center), Chuck Bronnimann, Robert Wind (now at PNL, after a couple of years at Chemagnetics), Greg Quinting (a postdoc, now at Sherwin-Williams), Ming Zhang (now in the import–export business in Chicago), H. Vicky Pan, Jincheng Xiong, and Antoni Jurkiewicz (originally a Fulbright Fellow from Poland, who has been a major influence in our coal research program for several years, and recently moved to PNL).

Another area of solid state NMR application in which our efforts began in the late 1970s and continue to the present is in the study of surfaces, especially silicas and derivatized silicas. Dean Sindorf (now at Chemagnetics) was the first to demonstrate, in the silica system, how $^{1}H \rightarrow X$ cross polarization can be used as a surface-selective technique. Dean's extensive work on silicas, their dehydration and rehydration, and their silylation was based on the ability of ^{29}Si NMR to distinguish among $(Si{-}O{-})_2\mathbf{Si}(OH)_2$ sites, $(Si{-}O{-})_3\mathbf{Si}OH$ sites, $(Si{-}O)_4\mathbf{Si}$ sites and $(SiO{-})\mathbf{Si}{\equiv}R$ sites on silicon surfaces, and was followed by related studies by several people in our laboratory, including Bruce Hawkins, Jim Frye, Steve Caravajal (now at Procter and Gamble), Walt Rudzinski (a frequent collaborator in the earlier days of these studies, from Southwest Texas State University), Bob Zeigler (now at Himont), Dave Kinney (now at ARCO), Ellen Keiter (a sabbatical visitor from Southern Illinois University), I-Ssuer Chuang, and Mike Shatlock (now at PPG, in Pittsburgh), who carried out early ^{113}Cd experiments on cadmium oxides analogous to ^{29}Si experiments on silica. I-Ssuer has been the key researcher in this area in recent years. Just as Dean Sindorf

found that ^{29}Si chemical shifts distinguish among various types of silicon sites at silica surfaces, Chuck Bronnimann, in his extensive development of CRAMPS techniques and applications, found that ^{1}H CRAMPS-based experiments could distinguish between hydrogen-bonded and isolated OH groups on a surface. N. R. Jagannathan (a postdoc, now on the faculty of the University of Madras) carried out some related experiments, and H. Vicky Pan and Changhau Liu are now studying some key structural issues of silica surfaces via ^{29}Si, ^{1}H, and ^{13}C NMR techniques.

Other surface-related NMR studies in our laboratory have been based on basic small-molecule probes of acidic surface sites. These studies have involved primarily I-Ssuer Chuang, Jim Haw (a postdoc, now on the Texas A & M faculty), Bruce Hawkins, Xaiohui Ji (now in the import–export business in Hong Kong), Laima Baltusis (a postdoc, now at Varian), and Jim Frye.

Our research group also has a long-term involvement in the application of solid state ^{13}C (and in some cases, ^{1}H or ^{31}P) NMR in the characterization of plant-related materials, e.g., cellulose, lignin, seeds (including germination), biomass issues, wood chemistry, and wood rotting. Participants in this work have been primarily Vic Bartuska and Dean Sindorf (our earliest efforts in this area), Dan O'Donnell (a postdoc, now at Phillips Petroleum), Jim Haw, Galen Hatfield (now at W. R. Grace), Maziar Sardashti (now at Phillips Petroleum), Mark Davis (in collaboration with Herbert Schroeder of the Department of Forest and Wood Science), and Cynthia Ridenour (now at Chemagnetics).

Scientifically intermediate, in a sense, between coal studies and plant-related studies have been a series of studies of humic and sediment samples. This work has been carried out mainly by people listed above in relationship to coal and plant-derived samples, some of it in collaboration with scientists of the US Geological Survey.

During the 1980s and 1990s, our research group has also extensively studied synthetic organic resins, principally phenolic resins, urea–formaldehyde resins, and furfuryl alcohol resins. The primary participants in this work have been I-Ssuer Chuang (throughout our work from 1982 to the present), Tom Early (a postdoc, now at GE Schenectady), Galen Hatfield, Rich Bryson, and Dave Duff (now at Varian).

In addition to the above-mentioned emphasis on solid state NMR applications to organic samples and silicas during the 1980s and 1990s, there has also been substantial NMR activity in our laboratory on inorganic systems (e.g., cadmium compounds, phosphoranes, ceramics, high-T_c superconductors, minerals) based on a variety of nuclides (e.g., ^{11}B, ^{17}O, ^{23}Na, ^{27}Al, ^{31}P, ^{89}Y, ^{113}Cd). The primary participants in this work have been Vic Bartuska (our earliest efforts), Mike Shatlock, Gary Mennitt (on sabbatical leave from Brooklyn College), Larry Dennis, Jim Frye, Steve Dec (who served on the Center staff until moving to the staff of the University of Connecticut), Bruce McGarvey (on sabbatical leave from the University of Windsor), John Fitzgerald (on sabbatical leave from South Dakota, and subsequently a frequent and valuable collaborator), Satoshi Shinozaki (on sabbatical leave from Chiba University), Paul Marchetti (a postdoc, now on the staff at the University of Arizona), and Joe Iwamiya, as well as Leonard Interrante and Wayde Schmidt (frequent collaborators from Rensselaer Polytechnic Institute).

Pervading our solid state NMR research during the 1980s and 1990s has been a continuing thread of technique development, much of it associated with mechanical developments, e.g., ultra high-speed spinning (mainly by Steve Dec, with the help of Robert Wind), and ultralarge MAS rotors (mainly by Ming Zhang), and/or gadgetry. Included in this last category are the imaginative developments of angle-flipping (the technical precursor of DAS) and magic angle hopping (the precursor of Gan's slow spinning) by Ad Bax (a postdoc here, now at NIH) and Nick Szeverenyi. The roughly two-year period between 1981 and 1983 when these two incredibly innovative individuals were here simultaneously as postdocs was a magical period for our laboratory. In and out of the laboratory, this pair was 'a couple of wild and crazy guys' (ref: *Saturday Night Live*). I have been told that Nick and Ad, both bachelors at the time, 'cut a swath' through Larimer County socially. These two were responsible for getting our group into the habit of thinking in terms of two-dimensional strategies (e.g. for determining chemical shift anisotropies) and in terms of incorporating mechanical trickery, when it is advantageous. This baptism led to later developments like the stop-and-go (STAG) technique (Bob Zeigler and Robert Wind), the slow-and-go (SLAG) technique (Steve Dec), and the GRASSHopper (gas reactor and solid state hopper, Steve Dec), as well as techniques for optimizing CP efficiency (Mazi Sardashti), and chemical shift-selective CSA determinations (Joe Iwamiya and Mark Davis). Nick Szeverenyi was also responsible for our entry into solid state NMR imaging, an area in which we have used only homebuilt equipment. This amateur (i.e. financially unsupported) effort has encompassed even MAS techniques, has yielded several publications, and has involved the part-time efforts of several group members—Mark Davis, Dave Duff, Herman Lock, Yahong Sun, Marian Buszko (a postdoc, now on the staff of the University of Florida), and Takao Shinozaki (on sabbatical leave from the KAO corporation).

Another technique in which Nick Szeverenyi was 'instrumental' in its implementation in our laboratory is dynamic nuclear polarization (DNP). This technique experienced a huge boost in our laboratory when Robert Wind came here in 1986 from Delft for about four years. Our DNP applications have included amorphous silicon, coal, chars, doped polymers, diamond films, and silicon nitride precursor materials; and DNP technique developments have included imaging and DNP in the nuclear rotating frame. The main participants, in addition to Robert Wind, have included Mark Davis, Liyun Li (on leave from the Wuhan Institute of Physics), Nick Zumbulyadis (a collaborator from Kodak), Russ Lewis, Randy Hall (now at Chemagnetics), Jan Wooten (on sabbatical leave from Philip Morris), Junji Kobayashi (on sabbatical leave from Mitsubishi Electric), and Herman Lock. In addition, there has been very useful cooperation with Chaohiu Ye of the Wuhan Institute of Physics.

Our latest 'thrust' directions are: (1) the use of modern NMR techniques to study in detail the chemical fate of pollutants in soil/groundwater systems; (2) the synthesis and characterization of novel polysiloxane systems; and (3) the generation and characterization of aromatic carbocations on surfaces. The main participants to date in the first of these three areas have been Antoni Jurkiewicz and I-Ssuer Chuang, with students David Keeler and Mark Seger also involved. The second area is being investigated by Issa El-Nahhal (a Fulbright Fellow from the Islamic University of Gaza), and

Jane Yang. The third area is being studied by Ting Tao. I hope that in these, and in any other future research directions, I am as fortunate as in the past in terms of the quality of the people who have worked with me and their scientific productivity.

NOTE

*Throughout this article the mention of a person's name without an indication of some other status (e.g., postdoc or collaborator) implies that the person was (or is) a graduate student in our research group.

Biographical Sketch

Gary E. Maciel. *b* 1935. B.S., 1956, Chemistry, University of California, Berkeley, USA, Ph.D., 1960, Massachusetts Institute of Technology (MIT), USA. Postdoctoral work at MIT (with John S. Waugh), 1960–61, his first hands-on experience with NMR. Assistant professor, associate professor, and professor at the University of California, Davis, 1961–70. Professor of Chemistry, Colorado State University, 1971–present. Approx. 320 publications. Research specialties: development and application of NMR techniques, especially for solids and surfaces, and currently for environmental studies.

Mansfield, Peter: A Personal View of My Involvement in the Development of NMR and the Conception and Development of MRI

Peter Mansfield

University of Nottingham, Nottingham, UK

INTRODUCTION

I graduated with First Class Honours in physics in 1959 from Queen Mary College, University of London. I had been involved at an undergraduate level with the design and construction of an Earth's field NMR magnetometer, a project set by the then Dr. J.G. Powles (now Emeritus Professor of Physics at the University of Kent at Canterbury, England).

The success of this project led to an invitation from Jack Powles for me to join his NMR research group in order to tackle the challenging problem of pulsed NMR in solids. This work started in October 1959 and lasted the usual three year Ph.D. study period for UK students. A piece of high-power pulsed NMR equipment was constructed[1] and during the second year of my Ph.D. studies experimental results were obtained on a number of solids. The apparatus relied on an incoherent high-power anode modulated oscillator. The experiments were concerned with applying 90° rf pulses to a range of polymers in order to measure their relaxation characteristics.

SOLID ECHOES

During the course of these experiments, a second 90° rf pulse was applied and because of the fast recovery nature of the apparatus it was possible to place two 90° pulses in close sequence to within 3 or 4 μs. When this was done an effect which looked very much like an NMR spin echo occasionally occurred following the second pulse. The signal sometimes vanished completely and the intermittent and unexpected nature of this effect created some scepticism among other students in the lab and also with Jack Powles himself. I was asked to go back and look again to make sure that the signal echo effect was not a receiver artifact due to possible transient gain changes through overloading. Since I had already satisfied myself beforehand that this was not the case, I sat down to try to fathom out the possible origin of such an effect.

The book Principles of Nuclear Magnetism by Abragam[2] had just been published in 1961 and I was struggling to understand the application of density matrix theory on which the book relied so heavily. To my surprise I found a statement in the book which seemed categorically to rule out the possibility of a spin echo in solids, yet here in the lab I was observing something which looked very much like a spin echo. In performing calculations I convinced myself that spin echoes in solids, far from being disallowed, would indeed occur and their presence would be highly dependent on the relative phase between the two excitation pulses. This meant that with an incoherent pulse rig the presence of a spin echo would fluctuate according to the random nature of the phase shift. The calculations were presented to Jack Powles who was able to refine them, and I was later able to demonstrate unequivocally using the isolated proton pairs within calcium sulfate that we were indeed seeing a real effect which could be confirmed theoretically.[3]

THE AMERICAN ADVENTURE

Following my Ph.D. studies I went in 1962 to join Professor C.P. Slichter's group in Urbana, Illinois where I learned among other things about NMR in metals. It was an extremely exciting and productive period for Charlie Slichter's group since he was heavily engaged in the development of nuclear double resonance and also in pioneering relaxation time studies in the rotating frame. I was greatly impressed by the ease with which everyone in his group seemed to be able to master the intricacies of density matrix theory, a topic which had given me so much difficulty one year earlier. However, my efforts were rewarded by being able to understand very quickly what others were achieving in the lab and I found the whole experience most exhilarating.

At the back of my mind were niggling questions concerning the work that I had left behind in London, and I continued to spend time on aspects of this while working in Urbana.[4] Of particular interest to me in that two-year period was the question what would happen if further 90° pulses were applied in a solid? Of course it was well known what would happen in a liquid from Erwin Hahn's pioneering work on the discovery of spin echoes, and also with Bloembergen, Purcell, and Pound's work, and Carr and Purcell's work using 180° pulse trains. Unfortunately the facility in Urbana was not sufficiently powerful or sufficiently well developed to study or even see responses from the short 90° pulses so this work had to wait until I returned to England.

MULTIPULSE EXPERIMENTS

In 1964 I joined the University of Nottingham as a lecturer in Physics. I was fortunate to attract a research student immediately and together with an SRC grant was able to design and build a high-power pulsed NMR spectrometer which had the capability of producing sustained rf pulse trains. The research student who joined me was Donald Ware who had decided to come to England from UBC where he had received an M.Sc. in NMR under the supervision of Basil Dunell. Within a year or so we had built a pulse rig and obtained some of our first results. In particular we had tried sustained 90° pulse trains and to our surprise and delight had observed an effective lengthening of the FID in calcium fluoride. I was bursting with excitement to announce this and prepared a draft letter for publication in the journal *Physics Letters*.[5] During

this time my ex-supervisor, Jack Powles, visited Nottingham (I believe as a colloquium speaker) and was able to see the effect on our machine. I remember that he looked pensive and said that he thought he had seen something very similar when visiting John Waugh's lab recently at MIT. I was, of course, unaware of any other activity in the field and nothing had been published so we went ahead with our paper which was published shortly after Ostroff and Waugh's paper on the same subject. This was in 1965 but began a period of sometimes stormy and acrimonious rivalry between me and John Waugh. This rivalry continued through the 1960s to the early 1970s and covered an extremely productive period from both the Nottingham and MIT groups, leading to generalizations of the multipulse line-narrowing theory of solids as we called it and the development of sophisticated pulse sequences such as the MREV-8 sequence which is still used today.[6,7] Incidentally, the MREV stands for Mansfield, Rhim, Elleman, and Vaughan. In fact Bob Vaughan's group in Pasadena rediscovered the eight-pulse sequence some two years after it was first described by me in the *Journal of Physics*.[8] Nevertheless, Bob Vaughan made some important contributions to the development of the subject and to the understanding of some of the intricacies in applying such techniques. The new rivalry with the Pasadena group was very much a gentlemanly and friendly one. It was therefore with great shock and sadness that we learned of Bob's untimely death in 1980 due to an aircraft crash at O'Hare Airport in Chicago.

Other Nottingham names associated with the development of multipulse techniques in this period were former research students Ken Richards, Dennis Stalker, Martin Orchard, Peter Morris, and Peter Grannell.

HOLE-BURNING EXPERIMENTS

Another episode which was later to have a bearing on the development of magnetic resonance imaging at Nottingham involved a research project funded by the Royal Radar Establishment at Malvern. This involved Raymond Andrew as cosupervisor with Alwyn Finney as our research student. We had been asked to look into the possible application of NMR as a means of information storage. The path that we chose to follow involved resurrecting some ideas on information storage originally proposed by Erwin Hahn, which relied upon hole-burning experiments in inhomogeneously broadened lines in liquids. Amongst other things we proposed and tried storing pulse trains by the simple mechanism of irradiating a suitably broadened liquid line with the pulse train, then reading out the information using a swept CW technique which revealed as hoped a hole-burnt spectrum which was close in shape and spacing to the Fourier transform of the pulse train spectrum. The line broadening in this work was achieved by applying a linear magnetic field gradient. This work was started in 1966 and a final report submitted in 1969.[9] The ideas developed in this project were to play an important part in my thinking later on after I had conceived the idea of NMR imaging which I now relate.

NMR IMAGING: THE IMMACULATE CONCEPTION

In 1971 I made plans to spend a sabbatical year in Heidelberg working in Karl Hausser's group. He had recruited Ulrich Haeberlen from John Waugh's lab to set up a multipulse facility. Meanwhile at Nottingham, Allen Garroway, formerly from Bob Cotts's group in Ithaca joined my group as a postdoc to learn about multipulse experiments in solids. The plan was that he would run my group during my absence. He became heavily involved in the implementation of fast Fourier transforms and during the course of the winter of 1972 together with Dennis Stalker produced some nice results in a number of fluorinated solids showing chemical shift anisotropy. The line-narrowing capability of the homebuilt spectrometer (constructed by Terry Baines) allowed effective linewidths down to 5–10 Hz in calcium fluoride and was something of a record at the time.[10]

In May or June 1972, while discussing our results with Allen Garroway and Peter Grannell over a cup of coffee the question arose as to what other possibilities there were to utilize the line-narrowing capability of the spectrometer. What followed was greatly influenced by work I had been doing on the calculation of lineshapes in solid calcium fluoride.[11] During this work I had been greatly impressed by a paper on Green's functions by Tomita and Tanaka[12] who had applied the technique to calculations in ferromagnetism. I was attempting to use a similar analytical approach and was intrigued by their use of spatial Fourier transforms of the dipolar interaction terms. I had been thinking how nice it would be if the spatial terms in the dipolar interaction could be unraveled to yield the lattice constants. This was of course a pipe dream in that particular context. However, during this coffee discussion it suddenly clicked in my mind that by applying a linear field gradient to a solid in which the dipolar interaction had, in effect, been removed we could achieve spatial Fourier transformations in solids, thereby evaluating the internal structure of a solid. My recollection is that Allen was somewhat sceptical and Peter Grannell was more receptive to the idea. In any event, I went away to perform some simple calculations and gave a copy of these to Peter Grannell and suggested that we might mount some simple experimental evaluation of the idea in a model lattice system. Unfortunately he was approaching the end of his three-year Ph.D. research period and was naturally more concerned about finishing off his research on time. The idea therefore languished during the summer of 1972. I was also making preparations to depart for Heidelberg.

SABBATICAL IN HEIDELBERG

My arrival in Heidelberg in October 1972 saw the start of an intense period of regular correspondence between me and Peter Grannell, and to a lesser extent with Allen Garroway. I was anxious that Peter should press on with the imaging experiments now that he had completed his Ph.D. studies. By November 1972 he had made some progress which he casually mentioned to Raymond Andrew during the autumn term of 1972. Peter slowly made further progress in 1973 to the point where he had demonstrated NMR diffraction effects in a model one-dimensional lattice. I returned to Nottingham in July 1973

and promptly wrote up the work as a letter for the *Journal of Physics*.[13]

PRESENTATION IN KRAKOW

I had already submitted an abstract for my invited talk at the 1st Specialized Colloque AMPERE which was to be held in Krakow, Poland in September 1973. This abstract[14] included a description of the one-dimensional imaging experiments. So far as we were concerned, my subsequent announcement of NMR diffraction in Krakow would be the first mention of this novel effect. At the end of my presentation, John Waugh, who was in the audience, said something to the effect that he thought that what I had just described was similar to a proposal by Paul Lauterbur. I did not know Paul Lauterbur at that time and was unaware of any similar work that he may have done. I was of course intrigued by Waugh's comment and as soon as we returned to Nottingham I looked up Lauterbur's paper.[15] I was struck by the stark contrast between our two approaches to NMR imaging. In my pulsed approach I had formally proposed the optical analogy of plane-wave scattering through a mathematical framework where reciprocal lattice space or k-space was introduced and in which the k vector was proportional to the product of time and gradient vector. The concept of k-space in MRI, of course, plays an important role these days in categorizing different imaging sequences in terms of the k-space trajectory.

SLICE SELECTION

My involvement with the development of MRI continued in 1974 with the introduction of rf slice-selection techniques.[16] This work was done in collaboration with Allen Garroway and Peter Grannell. I had come to the conclusion that rf pulses in combination with switched linear gradients could be used to define an active slice of magnetization within a larger specimen based on the experience gained in the late 1960s with Alwyn Finney's work. Allen Garroway had independently arrived at a similar conclusion influenced by a paper by Tomlinson and Hill,[17] in which frequency selective pulse sequences were proposed for irradiating inhomogeneously broadened spectral lines for spin decoupling experiments. Allen's approach was, therefore, to concentrate on pulse sequences comprising short constant amplitude high-power pulses with variable pulse spacing and rf phase. We quickly realized that the easier and cleaner approach to slice selection was simply to modulate a continuous rf pulse, the modulation being designed to create a nearly rectangular slice of active spin magnetization.

We quickly adapted tailored rf excitation methods to produce a fast line-scan imaging technique. This was used by Andrew Maudsley to produce the first NMR images demonstrating live human anatomy, albeit on one of his fingers.[18]

ECHO PLANAR IMAGING

In 1976 I introduced the ultra-high-speed echo planar imaging technique.[19] This arose out of a growing concern of mine at the time that if NMR imaging were ever to be of clinical value, imaging times, then measured in many tens of minutes, would have to be drastically reduced. At the time of its conception EPI was difficult to implement by virtue of the extreme requirements of gradient amplitude and fast switching rates. Nevertheless, an early version of EPI was implemented by Ian Pykett in 1977.[20] He succeeded in obtaining crude snap-shot images of a test-tube phantom and later a live human finger. With the benefit of hindsight, it is clear to see that EPI and the whole concept of ultra-high-speed imaging and spectroscopic imaging were ahead of their time by some 15 years or so.

Except at Nottingham, EPI languished worldwide but received a slight impetus when Ljunggren published his paper in 1983 on the comparison of NMR imaging methods using the rediscovered k-space approach.[21] By then the major MRI companies had launched a series of medical scanners based on slower imaging methods and were clearly not of a mind to upgrade machine specifications for the implementation of EPI before recouping their investments. Thus it was that EPI languished for a further 10 years.

In this intervening period, newcomers to the business began to rediscover low rf angle techniques and applied them to the process of speeding up the slower MRI methods. This class of fast imaging, known as FLASH imaging, was preferred by manufacturers who saw it as a stepwise approach to the implementation of high and hopefully ultra-high-speed imaging.

Also, in this intervening period, two former research students of mine, Ian Pykett and Richard Rzedzian, emigrated to the USA and formed a company in Boston called Advanced NMR Systems with the object, according to the company's prospectus, of building and marketing an EPI machine. Although several prototype machines were produced and installed at various sites, EPI never really took off in a big way commercially during that period.

ACTIVE SCREENING OF GRADIENT COILS

Back at Nottingham in the mid-1980s, we acquired a superconductive 0.5-T whole body magnet. It was clear to me, even before we received the magnet, that if EPI were to function correctly within the close confines of the magnet, something had to be done to decouple the rapidly switched gradient fields from the metal structures comprising the magnet cryostat. Work started on gradient screening in 1984 and culminated in the concept of active magnetic screening during the course of 1985.[22,23] Active magnetic screening of gradient coils was quickly taken up by General Electric and other major manufacturers, and now forms part of the standard range of features offered on all imaging machines.

The solution of gradient decoupling has had other benefits, especially with regard to magnetic resonance spectroscopy. The fact that active screening forms an integral part of modern MR imagers has, I believe, also helped in bringing to fruition the launch of commercial EPI machines announced in November 1993 by General Electric and by Siemens.

ACTIVE ACOUSTIC SCREENING OF GRADIENT COILS

Having solved the magnetic coupling problems associated with rapidly switched gradient coils, we were soon faced with another potentially hazardous situation when trying to implement EPI or indeed echo volumar imaging (EVI) at 3.0 T. This new problem arises from the very large levels of acoustic noise emitted from the gradient system when being pulsed with the very high current levels and fast switching rates associated with EPI and EVI. Some degree of acoustic attenuation can be provided by the use of ear defenders but similar protection cannot easily be provided for animal studies or indeed for human fetal studies in utero.

These considerations have therefore led us to introduce an active acoustic screening strategy,[24] which tackles the source of the acoustic problem rather than treats the symptoms. Active acoustic screening can also be combined with active magnetic screening and we predict that this approach will be widely adopted in the design of future scanners.

The reduction of acoustic vibrations in the probe assembly will also confer advantages in biological and nonbiological NMR microscopy performed at very high fields. In such situations, probe movement can vitiate the achievable spatial resolution. Active acoustic screening will help to reduce this kind of induced motion artifact.

REFERENCES

1. P. Mansfield and J. G. Powles, *J. Sci. Instrum.*, 1963, **40**, 232.
2. A. Abragam, *The Principles of Nuclear Magnetism*, Oxford University Press, Oxford, 1961.
3. J. G. Powles and P. Mansfield, *Phys. Lett.*, 1962, **2A**, 58.
4. P. Mansfield, *Phys. Rev.*, 1965, **137**, A961.
5. P. Mansfield and D. Ware, *Phys. Lett.*, 1966, **22A**, 133.
6. P. Mansfield, M. J. Orchard, D. C. Stalker, and K. H. B. Richards, *Phys. Rev. B*, 1973, **7**, 90.
7. W.-K. Rhim, D. D. Elleman, and R. W. Vaughan, *J. Chem. Phys.*, 1973, **59**, 3740.
8. P. Mansfield, *J. Phys. C*, 1971, **4**, 1444.
9. E. R. Andrew, A. Finney, and P. Mansfield, RRE Research Report No PD/24/026/AT. (1970).
10. A. N. Garroway, P. Mansfield, and D. C. Stalker, *Phys. Rev.*, 1975, **B11**, 121.
11. P. Mansfield, *Phys. Rev.*, 1966, **151**, 199.
12. K. Tomita and M. Tanaka, *Prog. Theor. Phys.*, 1963, **29**, 528.
13. P. Mansfield and P. K. Grannell, *J. Phys. C*, 1973, **6**, L422.
14. P. Mansfield, P. K. Grannell, A. N. Garroway, and D. C. Stalker, *Proc. 1st Specialized Colloque AMPERE*, Krakow, Poland, 1973, pp. 16–27.
15. P. C. Lauterbur, *Nature (London)*, 1973, **242**, 190.
16. A. N. Garroway, P. K. Grannell, and P. Mansfield, *J. Phys. C.*, 1974, **7**, L457.
17. B. L. Tomlinson and H. D. W. Hill, *J. Chem. Phys.*, 1973, **59**, 1775.
18. P. Mansfield and A. A. Maudsley, *Proc. 19th Congress AMPERE*, Heidelberg, 1976, p. 247; *ibid, Brit. J. Radiol.*, 1977, **50**, 188.
19. P. Mansfield, *J. Phys. C*, 1977, **10**, L55.
20. P. Mansfield and I. L. Pykett, *J. Magn. Reson.*, 1978, **29**, 355.
21. S. Ljunggren, *J. Magn. Reson.*, 1983, **54**, 338.
22. P. Mansfield and B. Chapman, *J. Magn. Reson.*, 1986, **66**, 573.
23. P. Mansfield and B. Chapman, *J. Phys. E, Sci. Instrum.*, 1986, **19**, 541.
24. P. Mansfield, P. Glover, and R. Bowtell, *Meas. Sci. and Technol.*, 1994, **5**, 1021.

Acknowledgments

To all those, past and present, who have helped me in the development of NMR and MRI, may I offer my sincere thanks and appreciation. The list of people is too long to reproduce here. I am especially grateful to my wife and family who have been a constant source of support throughout my career.

Biographical Sketch

Sir Peter Mansfield FRS. *b* 1933. B.Sc., 1959, Ph.D., 1962 (supervisor Jack Powles), University of London. Research associate, Urbana, Illinois, under Charlie Slichter, 1962–64. FRS, 1987. Knighted, January 1993. Currently Emeritus Professor of Physics, Magnetic Resonance Centre, University of Nottingham. Approx. 240 publications. Current research specialty: magnetic resonance imaging and its applications in medicine and biology.

Maraviglia, Bruno: A Personal Perspective about NMR Evolution

Bruno Maraviglia
Università di Roma 'La Sapienza', Rome, Italy

'LA SAPIENZA', ROME (1962–68): QUANTUM FLUIDS

My introduction to NMR came after an important period of research on superfluid helium. After obtaining my initial degree at the University of Florence, in 1962 I joined Giorgio Careri's group which had been carrying out attractive investigations in low temperature physics at 'La Sapienza' since 1960. Being thoroughly involved in quantized vorticity by means of second sound[1] and ionic currents,[2] I came across experimental NMR via friends who were searching for the expected phase transition in ^{3}He using nuclear suspectibility measurements; this transition was destined to be discovered about 10 years later at Cornell University[3] via an NMR experiment whose role, in my opinion, is wider than currently believed. I will come back to this point later.

DUKE UNIVERSITY (1969–70): QUANTUM SOLIDS

At the beginning of 1969 I went on leave, as a NATO Fellow, to the Physics Department of Duke University where I was appointed Assistant Professor of Optics and Spectroscopy. The invitation came from Horst Meyer and, although not planned in advance, determined my transition to NMR. In fact, when at Duke, I had time to decide whether to join the research activities of Henry Fairbank on superfluidity or that of Horst on quantum solids. By choosing the fascinating field of solid hydrogen, I also satisfied my attraction towards NMR whose role in condensed matter was continuously growing.

I started working with Fred Weinhaus (Ph.D. student) on solid D_2, which has a slower *ortho–para* transition rate than H_2 in addition to the possibility of observing the $J = 0$ molecules by NMR ($I = 0,2$), which cannot be detected in H_2. After constructing a ^{3}He cryostat, a systematic series of 'Pake doublets' of the antiferrorotational cubic phase was measured at different temperatures and *ortho–para* concentrations. The first 'surprise' was that the $J = 0$ molecules also become ordered, with an order parameter which is about 1/10th that of the $J = 1$ molecules;[4] the second result was the accurate determination of the zero point motion of the rotational angular momentum in a pure $J = 1$ system, together with the orientational order parameter as a function of the *ortho–para* concentration.[5]

Longitudinal relaxation times were also determined both in solid and liquid D_2. Liquid measurements showed complete decoupling of the $J = 0$ and $J = 1$ molecules providing a composite signal with two relaxation times, substantially different at $T_1 \sim 50$ ms ($J = 1$) and $T_1 \sim 3200$ s ($J = 0$), with a concentration ~98% of $J = 0$ molecules. This is probably the widest (and the most tiring) range of relaxation times in a pure liquid.[6]

'LA SAPIENZA', ROME (1971–76): QUANTUM SOLIDS AND LIQUIDS

On returning to Rome my plans were first to establish an NMR lab in order to carry on research on quantum solids and, at the same time, continue collaboration with Horst Meyer, and secondly I hoped that my deep interest in biophysics would generate some new research line. Although a pulsed Bruker spectrometer was obtained only in 1973, in the meantime research on superfluid helium was still carried on.[7]

Solid CH_4 and solid CH_4/Kr mixtures were the quantum systems studied. The first librational band of the ordered CH_4 molecule was measured,[8] from a study of relaxation time, and found to be in agreement with the theoretical prediction.[9] Disordering of the CH_4 ordered sublattices was also investigated as a function of Kr concentration and in relation to spin conversion.[10]

UNIVERSITY OF BRITISH COLUMBIA (1977–78): BIOLOGICAL MEMBRANES

The results of Myer Bloom's group in Vancouver had reconciled biological subjects with a quantitative physical approach and this attracted me so much that I decided to join his group in Vancouver.

Intense activity, aimed at the structure and dynamics of membranes, was going on at the University of British Columbia with excellent interaction between NMR physicists and biologists. In view of the fact that the erythrocyte membranes provided systems which had been studied extensively and that they play an important role in their structural correlation with diseases, I proposed to start research on such membranes. The results obtained with the crucial contribution of Jim Davis, allowed us to conclude that the erythrocyte membrane has a very wide thermal range of fluidity.[11]

On returning to Rome I finally determined to continue work on the physics of biological systems, including the use of spatially resolved NMR, which seemed well suited to the study of heterogeneous living organisms.

'LA SAPIENZA', ROME (1979–PRESENT DAY): SPATIALLY RESOLVED NMR

I had carefully followed the 'birth' of NMR imaging in the early 1970s mainly as an outsider since my direct involvement only began in 1979. In fact among the general skepticism (until 1980) regarding the possibility of producing quality images, there were frequent dramatic arguments as to who was the 'inventor' of NMR imaging. At this point I would like to remark on one experiment which anticipated the work of Paul Lauterbur[12] and Peter Mansfield and P. K. Grannell[13] in this field. This important publication, which I have already mentioned[3] for its important discovery of the magnetic and statistical properties of ^{3}He, produced, with the help of a linear

magnetic gradient, a one-dimensional image (they called it a profile) of a heterogeneous sample containing both solid and liquid ^{3}He. The authors also clearly expressed (on p. 921) the logic of selective irradiation, widely used today in NMR imaging. This paper was published before any other now currently regarded as NMR imaging work. Personally, from a knowledge of the authors of that work and the great impact of their discovery for the physics of condensed matter, I believe that they considered their imaging procedure a 'trivial tool'. Of course this is not meant to detract from the importance of the clear-cut thinking of Paul Lauterbur on this subject, who through the use of the projection reconstruction method demonstrated the way to produce images of biomedical interest.

The work on NMR imaging at 'La Sapienza' began in 1979 with the aim of building a small size imager as a first prototype. Close collaboration with Nottingham, i.e. with Raymond Andrew and Peter Mansfield, and frequent exchanges with Paul Lauterbur, gave us experience in the several approaches to imaging which were being tested at that time. In early 1981 the prototype was operating[14] and a whole body machine was immediately planned. The whole body system produced its first spin warp images in early 1982. The role of Francesco De Luca and Francesco Vellucci in this project was crucial. In fact, Vellucci later moved to Esaote Biomedica with others to start industrial production. My collaboration with Esaote is still active today. More fundamental aspects were then investigated such as the maximum entropy approach to NMR imaging[15] and some line-narrowing procedures which would lead to the imaging of solids.

Our studies of the development of NMR imaging of solids began in 1985 in connection with the work which Mefed and Atsarkin had been undertaking since 1977.[16] Although the initial results were promising[17] some fundamental improvements were obtained first by introducing a spin echo imaging sequence at audiofrequency in the rotating frame[18] and later by using an indirect rotating frame imaging approach.[19] The contribution of Francesco De Luca in this field was fundamental.

Another important subject of interest was functional imaging, which we studied using an original double resonance procedure[20] which allows indirect imaging of nucleus A, J coupled to proton P, with a gain in signal-to-noise of about $(\gamma_P/\gamma_A)^{11/4}$. The contribution of F. De Luca and R. Campanella in this field has been quite important.

In vivo spectroscopy[21] and other research lines closer to medical applications have also been developed[22] in collaboration with M. A. Macrì and C. Cametti.

REFERENCES

1. L. Bruschi, B. Maraviglia, and P. Mazzoldi, *Phys. Rev.*, 1966, **143**, 84.
2. L. Bruschi, B. Maraviglia, and F. E. Moss, *Phys. Rev. Lett.*, 1966, **17**, 682; S. Cunsolo and B. Maraviglia, *Phys. Rev.*, 1969, **187**, 292.
3. D. D. Osheroff, W. J. Gully, R. C. Richardson, and D. M. Lee, *Phys. Rev. Lett.*, 1972, **29**, 920.
4. B. Maraviglia, F. Weinhaus, H. Meyer, and R. L. Mills, *Solid State Commun.*, 1970, **8**, 815.
5. B. Maraviglia, F. Weinhaus, H. Meyer, and R. L. Mills, *Solid State Commun.*, 1970, **8**, 1683; H. Meyer, F. Weinhaus, B. Maraviglia, and R. I. Mills, *Phys. Rev.*, 1972, **B6**, 1112.
6. B. Maraviglia, H. Meyer, and S. M. Myers, *Phys. Rev.*, 1971, **A4** 1679.
7. P. Calvani, B. Maraviglia, and C. Messana, *Phys. Lett.*, 1972, **39A**, 123.
8. G. Briganti, P. Calvani, F. De Luca, and B. Maraviglia, *Can. J. Phys.*, 1978, **56**, 1182.
9. T. Yamamoto, Y. Kataoka, and K. Okada, *J. Chem. Phys.*, 1977, **66**, 2701.
10. P. Calvani, C. Casieri, F. De Luca, and B. Maraviglia, *Phys. Lett.*, 1981, **86A**, 490.
11. J. H. Davis, B. Maraviglia, G. Weeks, and D. V. Godin, *Biochim. Biophys. Acta*, 1979, **550**, 362; B. Maraviglia, J. H. Davis, M. Bloom, J. Westerman, and K. W. A. Wirtz, *Biochim. Biophys. Acta*, 1982, **686**, 137.
12. P. C. Lauterbur, *Nature (London)*, 1973, **242**, 190.
13. P. Mansfield and P. K. Grannell, *J. Phys. C*, 1973, **6**, L422.
14. F. De Luca, B. C. De Simone, and B. Maraviglia, *Magn. Reson. Imaging*, 1982, **1**, 205.
15. B. C. De Simone, F. De Luca, and B. Maraviglia, *Magn. Reson. Med.*, 1987, **4**, 78; B. C. De Simone, F. De Luca, and B. Maraviglia, *Magn. Reson. Med.*, 1988, **8**, 332.
16. A. E. Mefed and V. A. Atsarkin, *Sov. Phys–JETP*, 1978, **47**, 378.
17. F. De Luca and B. Maraviglia, *J. Magn. Reson.*, 1986, **67**, 169; F. De Luca, C. Nuccetelli, B. C. De Simone, and B. Maraviglia, *J. Magn. Reson.*, 1986, **69**, 496.
18. F. De Luca, C. Nuccetelli, B. C. De Simone, and B. Maraviglia, *Solid State Commun*, 1989, **70**, 797; F. De Luca, B. C. De Simone, N. Lugeri, B. Maraviglia, and C. Nuccetelli, *J. Magn. Reson.*, 1990, **90**, 124.
19. F. De Luca, N. Lugeri, B. C. De Simone, and B. Maraviglia, *Solid State Commun.*, 1992, **82**, 151; N. Lugeri, F. De Luca, B. C. De Simone, and B. Maraviglia, in *Nuclear Magnetic Double Resonance*, ed. B. Maraviglia, North-Holland, Amsterdam, 1993, pp. 449–466.
20. F. De Luca, R. Campanella, A. Bifone, and B. Maraviglia, *J. Magn. Reson.*, 1991, **93**, 554; F. De Luca, G. Raza, and B. Maraviglia, *J. Magn. Reson*, 1994, **A107**, 243; F. De Luca, G. H. Raza, M. Romeo, C. Casieri and B. Maraviglia, *J. Magn. Reson.*, 1995, **B107**, 74.
21. M. A. Macrì, R. Campanella, G. Garreffa, M. Occhigrossi, F. De Luca. E. Arrigoni Martelli, and B. Maraviglia, *Magn. Reson. Imaging*, 1992, **10**, 769.
22. C. Cametti, F. De Luca, A. D'Ilario, M. A. Macrì, B. Maraviglia, F. Bordi, L. Lenti, R. Misasi, and M. Sorice, *Biochim. Biophys. Acta*, 1992, **1111**, 197.

Biographical Sketch

Bruno Maraviglia. *b* 1938. M.Sc., 1962, University of Florence, Ph.D., 1964, Physics, University of Rome 'La Sapienza', Hab., 1968, Physics of Condensed Matter. Assistant professor, Duke University, NC, 1969–70 (introduced to NMR by Horst Meyer); Professor of Experimental Physics, University of Rome 'La Sapienza', 1971–present; Visiting professor, University of British Columbia, 1977–78. Approx. 140 publications. Current research specialties: NMR imaging in solids, double resonance imaging, spectroscopic methodologies.

Margulis, Alexander R.: How NMR was Started at the University of California, San Francisco (UCSF)

Alexander R. Margulis

University of California, San Francisco, CA, USA

The year was 1975. During the postgraduate course given by the UCSF Department of Radiology at the Fairmont Hotel in the middle of March, several presentations dealt with computed tomography of the brain with the wondrous EMI CAT scanner. Dr. Leon Kaufman, a physicist in our nuclear medicine section, who had been spending much of his energy on creating the germanium camera for nuclear medicine, asked for a one-half hour appointment on September 3, 1975. What he presented that day sounded extremely challenging. Get involved in developing and exploring a new technique of imaging: nuclear magnetic resonance. He drew on a piece a paper that he picked up from my desk a sketch outlining the basic physics of this approach. It all sounded mystifyingly complicated, particularly when he described how the signal caught by the receiving coil worked similarly to CAT scanners to produce images. Asked how good they were, he answered that they were not very good as yet but there was tremendous potential for improvement. I feel and felt strongly that the function of radiologic research is to bring physicists, engineers, radiobiologists, physiologists, clinical specialists, and radiologists together to develop the best imaging approaches that will depict the normal and abnormal anatomy and physiology of the body and its organ systems. The ultimate goal, perhaps unachievable, is to obtain as much information as possible at the level of basic biochemistry.

Leon was much more conservative in his expectations, but nevertheless, quite enthusiastic about the potential of this new imaging approach. He told me that a professor at Berkeley, Dr. Jay Singer, was a pioneer in research in this discipline and was willing to help us. I asked what I needed to do to help Leon get started; he suggested the sum of $40 000 to borrow a magnet, install it, and hire a young scientist with NMR experience. The meeting concluded with my promise to help. The next day, September 4, 1975, I received a hand-delivered letter which is reprinted here in its entirety.

‘September 4, 1975
Dr. Alexander Margulis
Department of Radiology
380-M
Dear Dr. Margulis:

Following our conversation to the effect, I would like to propose that we initiate an active research program leading to the development of a diagnostic imaging technique using nuclear magnetic resonance (NMR).

Briefly, the principle of NMR involves the following: all odd mass number atomic nuclei (those with an even number of protons and odd number of neutrons, or vice versa) behave as if they were small magnets. Placed in an external magnetic field they will align their spin with the field. The spin direction (or axis of rotation of the nucleus) can be flipped or turned around with radio waves of an exact energy. In returning to the normal state the nucleus will radiate back these radio waves. The energy of radiation, or wavelength, will depend on the nucleus being flipped as well as on its chemical state. The location of the radiating spot can be determined by purely electronic scanning (no physically moving parts). The potential thus exists for imaging the chemistry of the body. Since hydrogen is the most abundant odd mass number nucleus in the human body (naturally occurring O, C and N are almost fully even mass number nuclei), the easiest thing to do with NMR is to map the H density. Notice that this differs from electron density as measured by the EMI scanner. Also notice that while the EMI scanner needs information from *all* parts of the scanned region to resolve density by mathematical reconstruction techniques, the measurement of H density is unique at each spot. Thus, motion and algorithm artifacts become much less serious in NMR.

The second thing that can be done is to differentiate H in water from H in other tissues, thus obtaining a water map. Furthermore, blood can be differentiated from muscle, leading to the possibility for measuring myocardial and brain perfusion, two vexing clinical problems on which we have little or no diagnostic handle. More intriguing yet, we could possibly measure the chemical state of the H, maybe finding areas where certain fats accumulate, or where radicals are present. Also, certain atoms may be differentiated. For instance, phosphorus is known to strongly label any area of increased cell division. Natural P has an odd mass number and is detectable by NMR. Although natural calcium is mostly of even mass number, some is odd. Maybe calcifications (even diffuse ones not seen in X-rays) can be localized by NMR.

Clearly the payoffs are large, but the risk of failure is commensurate. For us to enter this area of research now will be extremely timely. I have found out that similar research is ongoing at Brookhaven, but this should not discourage us. There is an analogy with the germanium camera work, where we entered a technically difficult research area that was being studied in three other institutions. Thanks to the quality of the groups we are collaborating with, we managed, in less than two years, to become leaders in the field. In a similar vein, we learned a lesson from the search for support of the germanium camera: we were turned down three times because of skepticism as to our expertise and ability to solve this problem. After the School of Medicine, Academic Senate, grant tailings, and Livermore groups seeded the project and initial results were presented, funding was obtained for it.

The disadvantages of going to the NIH for funding at this time are two-fold. We will likely be turned down for lack of track record, and it will take a year to find out that we were turned down. I would propose that we proceed as follows:

1. Establish collaborative ties with an expert group. I have been directed to Professor J. Singer of the EE Department in Berkeley. He has an impressive publication record in the field, a long standing interest in biomedical applications (including a collaborative project with the obstetricians on this Campus), and is interested in collaborating with us.

2. Hire, for a year, a full-time researcher with experience in NMR, offering an Adjunct Assistant Professor position. Dr. Singer has recommended a recent Ph.D. student of his who

knows both the technique and the equipment, and who is able to build some of the specialized equipment himself.

3. Borrow, for a year, some of the most expensive equipment needed (magnet and power supply) and obtain appropriate space on Campus for this work. The size of what we can image depends on the magnet, but the larger the magnet the more the constraints on space. There are magnets at the Lawrence Berkeley Laboratory with useful areas as large as 29 × 36 in, but they weigh 50 000 lb and it may take six months to obtain good regulated power for them. A magnet with a useful volume of many cubic inches could be borrowed from Dr. Singer and put into operation quickly. We will get what we pay for. We should probably plan for both approaches simultaneously, so that we may get immediate results and look at the long term as well.

4. We need $20 000 for specialized major components. Dr. Singer estimates that this is reasonable for what we are trying to do.

5. We will also have to shift to this project (on a part-time basis) some of our research personnel and facilities.

I wish to emphasize that you should look at this as a poor risk loan. At worst, we will have lost $40 000 (note that a scintillation camera sells for $70 000, and EMI scanners are bargains at $400 000–$700 000 a piece). If things go well this investment will return the amount many times over. It is a gamble, but we have to look at diagnostic radiography not only in terms of the next year or two. Rather, we now have to lay the foundations for the next 10 years. I have no qualms that we are doing this in nuclear medicine, but it is clear that in the field of x-ray diagnostic developments we are lacking in hardware innovation. We have now a chance to provide a significant contribution.

Sincerely,

Leon Kaufman, Ph.D.'

I took $20 000 from the departmental professional fund reserves and obtained a loan for another $20 000 to be repaid when possible from the UCSF School of Medicine, Dean Julius Krevans. Julie emphasized that he had faith in Leon Kaufman. Leon proceeded and kept me informed about the progress of the project. Dr. Thomas Grover was hired to start the project and a small core magnet was bought and installed in the Earl Miller Laboratory in the basement of the East Tower Research Building on the UCSF campus. Dr. Grover moved soon to Colorado and the program really started going with Lawrence Crooks who had obtained a Ph.D. with Dr. Jay Singer at the University of California, Berkeley. As another $50 000 was needed to proceed and pay for Larry and the freshly purchased 0.35 T-0.30 cm core magnet, Leon, through a friend, negotiated an arrangement with Pfizer Medical Systems for a matching grant of $25 000 to proceed with the project. The first image of a rat's heart was published in 1978.[1] From then on the images got better and better and Larry, Leon, and I decided that it would be important to learn as much as possible about correlating imaging techniques to anatomy and physiology. A number of papers resulted reporting the application of Hahn's spin echo sequence into imaging, obtaining what is now called T_1, T_2, and proton density weighted images.[2] A correlation of frozen rat slices with corresponding MR image slices was published in another article in 1980[3] as also was a paper on the physiological applications of NMR imaging showing what was later called the 'flow void' by comparing the image of the aorta and the IVC in the living with that of the dead rat. An editorial that I wrote to accompany these articles in *Radiology* stated that we have a new technique which will revolutionize radiology. It was rejected as being too optimistic. Pfizer ordered for what now is the Radiologic Imaging Laboratory (RIL), housed at Oyster Point, a 0.35 T large core cryogenic magnet from Oxford Magnets which arrived in early 1981. While animal experiments continued on the small magnet teaching us about the MR imaging properties of implanted rat tumors[4] and inflammatory diseases,[5] we started imaging volunteers. We were fortunate to obtain, after many false starts, images of high quality just as Pfizer decided to get out of the imaging business and the new subsidiary of Diasonics, NMR Diasonics, was formed with venture capital investors. Another fortunate incident was obtaining the first body images on a volunteer with Dr. Kaufman who filled the body coil, rather than with the slender Dr. Crooks. The excellent multislice images of the head and abdomen produced universal admiration at the 1981 Radiological Society of North America meeting. The year 1982 saw the formation of the Society for Magnetic Resonance in Medicine by a small group composed of Drs. Lauterbur, Pohost, Budinger, Chance, and myself. The first meeting in Boston, incidentally a smashing success, had a number of clinical papers presented based on cooperative work between basic scientists, engineers and subspecialists in radiology at UCSF. This started the era of radiologic subspecialties in MR imaging.

REFERENCES

1. L. E. Crooks, T. P. Grover, L. Kaufman, and J. R. Singer, *Invest. Radiol.*, 1978, **13**, 63.
2. L. Crooks, J. Hoeninger, M. Arakawa, L. Kaufman, R. McRee, J. Watts, and J. R. Singer, *Radiology*, 1980, **136**, 701.
3. G. Hansen, L. E. Crooks, P. Davis, J. DeGroot, R. Herfkens, A. R. Margulis, C. Gooding, L. Kaufman, J. Hoenninger, M. Arakawa, R. McRee, and J. Watts, *Radiology*, 1980, **136**, 695.
4. P. L. Davis, L. Kaufman, L. E. Crooks, A. R. Margulis, and T. R. Miller, *Invest. Radiol.*, 1981, **16**, 354.
5. R. Herfkens, P. Davis, L. Crooks, L. Kaufman, D. Price, T. Miller, A. R. Margulis, J. Watts, J. Hoenninger, M. Arakawa, and R. McRee, *Radiology*, 1981, **141**, 211.

Biographical Sketch

Alexander R. Margulis. *b* 1921. M.D., 1950, Harvard University, USA, Professor & Chair, Department of Radiology, University of California, San Francisco 1963–1989. Associate Chancellor UCSF and Director MR Science Center at UCSF 1989–1993. Emeritus Professor of Radiology, UCSF, 1993–present. Specialty gastrointestinal radiology, abdominal MRI. Over 200 publications, multiple books.

Marshall, Alan G.: Ion Cyclotron Resonance Mass Spectrometry: a Brief History

Alan G. Marshall

Florida State University, Tallahassee, FL, USA

How does an NMR spectroscopist end up in mass spectrometry? When I joined John Baldeschwieler's research group at Stanford in 1965, he had just acquired the first commercial ion cyclotron resonance mass spectrometer from Varian. He realized that both NMR and ICR could be performed by marginal oscillator detection of power absorption at constant frequency and swept magnetic field, and his original intent was somehow to apply to ICR the NMR double resonance techniques (see below) which he had recently comprehensively reviewed.[1] My own Ph.D. research began with theoretical and experimental analyses of the NMR of quadrupolar halide nuclei as probes of accessibility and flexibility of specific mercury-labeled sites on chymotrypsin.[2,3] However, once immersed in a research group populated by several ICR mass spectroscopists, I soon began to notice parallels between the two techniques, and was able to show how to extract ion–molecule reaction rate constants from ICR lineshapes.[4,5]

Melvin Comisarow joined Baldeschwieler's group as a postdoc during my last year there as a graduate student. I left for a faculty position at the University of British Columbia in 1969 and Comisarow joined me there two years later (also as a faculty member). Mel spent the next two years building a field-scanning continuous wave ICR instrument, and in 1973 we collaborated in the invention and reduction to practice of Fourier transform ICR (see below). I maintained an active role in NMR until the late 1980s[6] and am now concentrating exclusively on FT-ICR mass spectrometry.

Pulsed excitation with Fourier transform data reduction is not the only common feature of NMR and ICR. In fact, there are ICR analogs to the following NMR phenomena: Larmor precession, T_1, T_2, rotating frame, sample spinning, spin lock, adiabatic rapid passage, Bloch equations, 180° pulse, double- and multiple-quantum coherences, shaped and stored waveform pulses, correlation NMR, crossed-coils versus single-coil modes, $\boldsymbol{B}_0$ shimming, $\boldsymbol{B}_1$ shimming, chemical exchange, population transfer, nuclear Overhauser effect, phase encoding by time delay, two-dimensional NOESY, T_1 noise, Hadamard excitation, phase cycling, dipolar versus quadrature excitation/detection, spinning sidebands, spin echo, dispersion versus absorption, various mode-coupling effects, direct versus heterodyne detection, decoupling, spin tickling, double resonance, and laser CIDNP. Finally, although ICR is usually analyzed classically, there is an alternative formalism based on cyclotron energy quanta. I shall now present a brief historical introduction to ICR, in the hope that at least some of its common heritage with NMR will be apparent.

In the absence of an electric field, an ion of mass m and charge q moving at velocity v in a plane perpendicular to a homogeneous static magnetic field $\boldsymbol{B}$ executes a circular motion of radius r at a 'cyclotron' frequency ω_c:

$$\omega_c = \frac{v}{r} = \frac{q\boldsymbol{B}}{m} \text{(SI units)} \qquad (1)$$

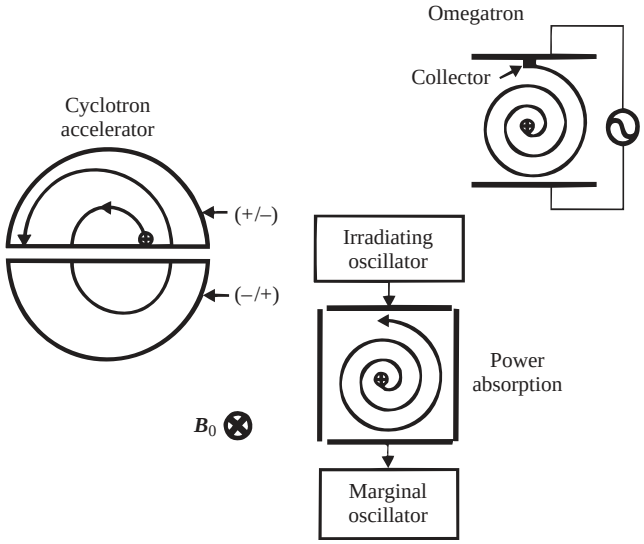

Figure 1 Schematic representations of the principle of operation of three devices based on the cyclotron principle. Left: cyclotron accelerator: each time an ion passes between two D-shaped electrodes, an electric field pulse (produced by alternately charging the electrodes to high voltage) speeds up the ion, which on entering the other D-electrode travels at the same cyclotron frequency but at larger cyclotron radius. Top right: omegatron, in which ions are accelerated continuously to larger cyclotron radius until they strike a collector electrode. Bottom right: power absorption measurement (with a marginal oscillator) during simultaneous resonant excitation; a mass spectrum is obtained by slowly varying the magnetic field at fixed excitation/detection frequency

The first of many clever methods and uses for exciting and detecting such motion was the invention and development by Lawrence and Livingston of the cyclotron accelerator in the early 1930s.[7] Ions were accelerated by electric field pulses, timed to coincide with the passage (twice per cyclotron orbit) of an ion packet between two D-shaped electrodes [Figure 1(left)]. The history of the cyclotron accelerator development era is summarized in a recent book.[8]

The first 'chemical' cyclotron designed to detect (rather than simply accelerate) ions according to their mass-to-charge ratio, m/z (in which m is ion mass in u and z is the number of elementary charges per ion) was the 'omegatron' developed by Sommer and Hipple in about 1950 [see Figure 1(top right)]. Their device used resonant excitation produced by applying a *continuous* (rather than pulsed) spatially uniform differential rf voltage between two opposed flat electrodes to excite ions in an orbit of increasing radius (i.e., a spiral path); the resonantly excited ions were detected by the current produced when the ions eventually struck a collector plate. A small dc potential was also applied to prevent ions from escaping along the **B** direction.

The next major innovation was, by analogy to NMR, detection of cyclotron motion by use of a marginal oscillator to measure *power absorption during excitation* [see Figure 1(bottom)], based on slowly scanning the applied magnetic field strength at fixed frequency for excitation and detection.

This idea seems to have been developed independently in the early 1960s by Leont'ev in Russia as a device to measure magnetic field strength[9] and by Wobschall in the USA as a mass spectrometer.[10,11] In the first commercial version developed by Llewellyn, an additional dc voltage was applied to induce the ions to drift from the ionization region (where the presence of a continuous electron beam disrupts attempts to excite and detect the ions directly) into a second region for resonant cyclotron excitation and detection.[12] Interestingly, in a paper largely unknown to most others in the field at the time, Genequand conceived and demonstrated excitation on one pair of opposed plates and (simultaneous) detection on an orthogonal pair of opposed plates, in the same spirit as 'crossed-coils' excitation and detection in continuous wave NMR of the 1960s.[13]

'Chemical' applications of ion cyclotron resonance (ICR) may be said to have begun with the Stanford group's introduction of what they called 'double resonance' (again by analogy to NMR), in which 'parent' ions of one *m/z* ratio were excited to higher kinetic energy, leading to ion–molecule reactions which were rendered observable by detection of a change in the abundance of 'product' ions of a different *m/z* value.[14] This general approach, now generally known as 'MS/MS' or 'tandem' mass spectrometry,[15] is one of the most powerful analytical tools for the analysis of mixtures, determining ion structure, and identifying ion–molecule reaction pathways, kinetics, equilibria, and energetics.

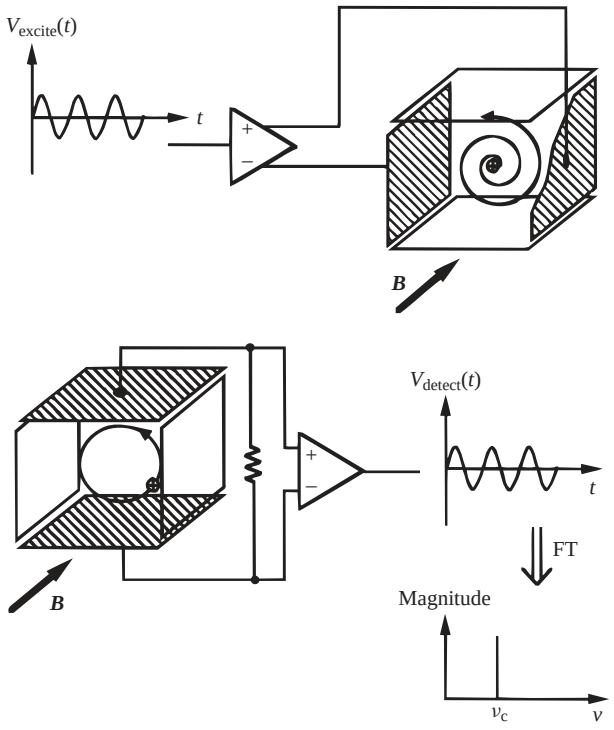

Figure 2 Schematic representation of a Fourier transform ICR mass spectrometer. Top: a small packet of ions is excited out to a particular cyclotron radius. Bottom: the excitation is removed, and the coherently orbiting ion packet induces a charge on opposed detector electrode plates; that time domain current signal is converted to a voltage, digitized, and Fourier-transformed to yield a frequency domain spectrum which is then converted to a mass spectrum

As for carbon-13 NMR, the advance which made ICR feasible for a wide range of applications was the introduction by Comisarow and Marshall in 1974 of pulsed[16] and frequency sweep (chirp)[17] excitation, followed by broadband detection of an induced transient signal (see Figure 2), followed by Fourier transformation (FT) to yield the whole mass spectrum in the time formerly required to scan through a single peak.[18] The FT experiment made it possible to obtain a full-range mass spectrum in ~1 s compared with ~0.5 h with scanning instruments. A typical experimental event sequence (~1 s) for the study of ion–molecule reactions is shown in Figure 3, along with the more familiar names given to the corresponding condensed-phase experiments. Because the magnetic field was now static rather than swept, magnetic field homogeneity was much improved and because detected ions traveled in a circle (like spinning the sample in NMR[19]) rather than a spiral (as in prior instruments), the mass resolving power improved (by a factor of up to 10^6).

Since FT-ICR frequency-domain linewidth varies directly with ion–neutral molecule collision frequency[20] (which in turn varies directly with gas pressure), FT-ICR excitation/detection is best performed at low pressure ($\leq 10^{-8}$ torr). However, most methods for ionizing neutral molecules require high pressure (up to atmospheric pressure of ~760 torr in some cases). In such cases, it has proved useful to perform the ionization and excitation/detection functions in chambers separated by a 'conductance limit' with a small (~2–3 mm diameter) hold to allow ion passage. The chambers may both be in a strong magnetic field (Littlejohn and Ghaderi's 'dual-trap'[21]), or the ion source may be outside the magnet, with ions guided into the excitation/detection region by rf[22] and/or dc.[23–25] electric lenses or as a highly collimated beam from a supersonic jet expansion.[26] Internal and external ion sources have allowed for FT-ICR mass analysis of ions formed by virtually any technique: electron ionization, chemical ionization, laser desorption/ionization (matrix-assisted or not), field desorption, fast neutral beam, glow discharge, fast atom bombardment, ^{252}Cf plasma desorption/ionization, surface-induced dissociation, fast ion bombardment, electrospray.[27]

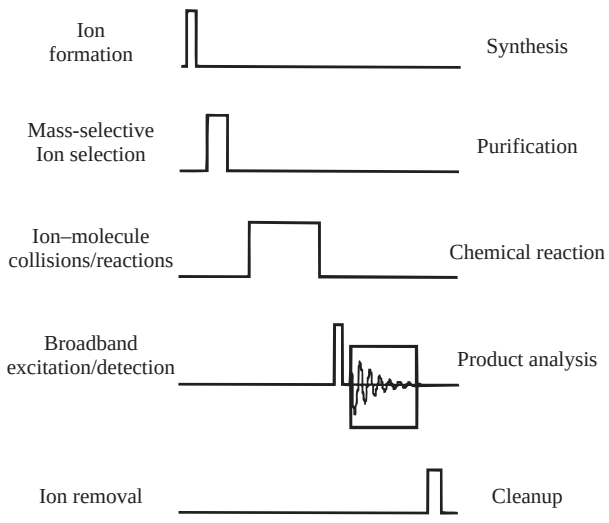

Figure 3 Generalized FT-ICR experimental event sequence for study of ion–molecule reactions (left), corresponding to similar condensed-phase chemical manipulations (right)

Optimal ICR performance demands spatially uniform static and rf electric field. The static electric 'trapping' field may either be shimmed to zero by use of grounded screens[28] or to near-perfect quadrupolar symmetry with segmented electrodes.[29] The rf electric field may be shimmed to near-perfect uniformity with guard rings.[30–32] It is also now possible to linearize *both* excitation and detection (i.e. eliminate harmonics and sidebands) by exciting and detecting with the same array of segmented electrodes.[33]

Unlike NMR, ICR detection (even without rf shimming) is quite linear (i.e. amplitude of response is proportional to amplitude of excitation); Marshall et al. therefore were able to show that one could synthesize any desired excitation versus frequency profile by performing a discrete inverse FT to generate the corresponding time domain waveform (stored-waveform inverse FT, or SWIFT[34]). SWIFT excitation allows for highly selective broadband mass-selective excitation and ejection (by exciting ions to a radius so large that the ions strike the sides of the container and are lost), for (for example) isolation of ions of particular *m/z* value(s) from a mixture or even two-dimensional (Hadamard/FT[35] or FT/FT[36]) experiments for MS/MS multiplexed with respect to both parent ion and product ion masses.

The addition of a (typically quadrupolar) electrostatic trapping potential (to confine ions and prevent their escape along the $\boldsymbol{B}$ direction) shifts the cyclotron frequency and introduces two additional motional modes (magnetron rotation and trapping oscillation).[37] A host of ion trap configurations[27] and operating modes[38] has been devised to select individual or particular combinations of these ion motional frequencies. For example, it is possible to trap positive and negative ions simultaneously[39,40] and distinguish between them by circularly polarized quadrature excitation.[41] Perhaps the most useful recent innovation is the use of resonant quadrupolar rf excitation, which (in the presence of the damping effect of ion–neutral molecule collisions) effectively 'shrink-wraps' ions into a small packet at the center of the trap,[42,43] for order-of-magnitude improvements in signal-to-noise ratio and mass resolving power, as well as in the efficiency of ion remeasurement, MS/MS, and external ion injection.

Because the ICR relaxation time (analogous to T_2 in NMR) varies inversely with pressure, it is possible to obtain ultrahigh FT-ICR mass resolving power by acquiring an undamped time-domain transient ICR signal for several seconds or longer: for example, FT-ICR mass resolving power of $m/\Delta m \simeq 400\ 000\ 000$ at *m/z* 18 (H_2O^+)[44] and $m/\Delta m \simeq 2\ 000\ 000$ for ubiquitin ions of mass 8565 Da[45] have been reported. Even higher precision is possible for closely-spaced mass doublets, as in a recent FT-ICR determination of the mass of $^{20}Ne^+$ at ppb accuracy.[46]

Finally, although the room-temperature detection limit for broadband FT-ICR/MS is about 150 ions,[47] it is possible to detect a *single* multiply-charged ion (e.g. a DNA molecule of 100 000 000 Da). Alternatively, Penning trap techniques based on SQUID detection at 4.2 K can detect an individual singly-charged ion.[48]

The present summary is intended to provide a brief overview of ion cyclotron resonance development to its current state. More than 160 FT-ICR systems have been installed worldwide, and the number is increasing rapidly with recent demonstrations of detection and sequencing of DNA and proteins of 30 000 Da and higher.[49] For further details and examples, the reader is referred to other reviews on the early development of continuous wave magnetic field-scanned instruments,[50–52] early development of FT-ICR,[53] and numerous recent summaries of the vast potential of FT-ICR/MS for analytical, biological, and chemical applications.[27,54–68]

Acknowledgements

The author gratefully thanks S. Guan for many helpful comments and discussion. This work was supported by NSF (CHE-94-96243), NIH (GM-31683), and the National High Magnetic Field Laboratory at Florida State University.

REFERENCES

1. J. D. Baldeschwieler, and E. W. Randall, *Chem. Rev.*, 1963, **63**, 81.
2. A. G. Marshall, *Biochemistry*, 1968, **7**, 2450.
3. A. G. Marshall, *J. Chem. Phys.*, 1970, **52**, 2527.
4. A. G. Marshall and S. E. Buttrill Jr., *J. Chem. Phys.*, 1970 **52**, 2752.
5. A. G. Marshall, *J. Chem. Phys.*, 1971, **55**, 1343.
6. A. G. Marshall and J. Wu, In *Biological Magnetic Resonance*, ed. L. J. Berliner and J. Reuben, Academic Press, New York, 1990, Vol. 9, pp. 55–118.
7. E. O. Lawrence and M. S. Livingston, *Phys. Rev.*, 1932, **40**, 19.
8. J. L. Heilbron and R. W. Seidel, *Lawrence and His Laboratory: A History of the Lawrence Berkeley Laboratory*, University of California Press, Berkeley, CA, 1989, Vol. 1.
9. N. I. Leont'ev, *Instrum. Exp. Tech. USSR.*, 1960, **2**, 275.
10. D. Wobschall, J. R. Graham, Jr., and D. P. Malone, *Phys. Rev.*, 1963, **131**, 1565.
11. D. Wobschall, *Rev. Sci. Instrum.*, 1965, **36**, 466.
12. P. M. Llewellyn, US Pat. 3 390 265 (25 June, 1969).
13. P. P. Genequand, *Z. Angew. Math. Phys.*, 1971, **22**, 951.
14. L. R. Anders, J. L. Beauchamp, R. C. Dunbar, and J. D. Baldeschwieler, *J. Chem. Phys.*, 1966, **45**, 1062.
15. F. W. McLafferty (ed.), *Tandem Mass Spectrometry*, Wiley, New York, 1983.
16. M. B. Comisarow and A. G. Marshall, *Chem. Phys. Lett.*, 1974, **25**, 282.
17. M. B. Comisarow and A. G. Marshall, *Chem. Phys. Lett.*, 1974, **26**, 489.
18. M. B. Comisarow and A. G. Marshall, US Pat. 3 937 955 (14 February, 1976).
19. M. B. Comisarow, *Adv. Mass Spectrom.*, 1978, **7**, 1042.
20. A. G. Marshall, M. B. Comisarow, and G. Parisod, *J. Chem. Phys.*, 1979, **71**, 4434.
21. D. P. Littlejohn and S. Ghaderi, US Pat. 4 581 533 (8 April, 1986).
22. R. T. McIver Jr., US Pat. 4 523 235 (13 August, 1985).
23. R. E. Smalley, *Anal. Instrum.*, 1988, **17**, 1.
24. P. Kofel and T. B. McMahon, *Int. J. Mass Spectrom. Ion Process.*, 1990, **98**, 1.
25. P. A. Limbach, A. G. Marshall, and M. Wang, *Int. J. Mass Spectrom. Ion Process.*, 1993, **125**, 135.
26. S. Maruyama, L. R. Anderson, and R. E. Smalley, *Rev. Sci. Instrum.*, 1990, **61**, 3686.
27. A. G. Marshall and L. Schweikhard, *Int. J. Mass Spectrom. Ion Process.*, 1992, **119**, 37.
28. M. Wang and A. G. Marshall, *Anal. Chem.*, 1989, **61**, 1288.
29. H. S. Kim, R. Chen, and A. G. Marshall, in *Proc. 41st Am. Soc. Mass Spectrom. Ann. Conf. Mass Spectrom. Allied Topics*, Am. Soc. Mass Spectrom., San Francisco, CA, 1993, pp. 448a,b.
30. H. Sommer, H. A. Thomas, and J. A. Hipple, *Phys. Rev.*, 1951, **82**, 697.

31. M. Wang and A. G. Marshall, *Anal. Chem.*, 1990, **62**, 515.
32. C. D. Hanson, M. E. Castro, E. L. Kerley, and D. H. Russell, *Anal. Chem.*, 1990, **62**, 520.
33. P. B. Grosshans, R. Chen, and A. G. Marshall, *Int. J. Mass Spectrom. Ion Process.*, 1994, **139**, 169.
34. A. G. Marshall, T.-C. L. Wang, and T. L. Ricca, *J. Am. Chem. Soc.*, 1985, **107**, 7893.
35. E. R. Williams, S. Y. Loh, F. W. McLafferty, and R. B. Cody, *Anal. Chem.*, 1990, **62**, 698.
36. C. W. Ross III, S. Guan, P. B. Grosshans, T. L. Ricca, and A. G. Marshall, *J. Am. Chem. Soc*., 1993, **115**, 7854.
37. L. S. Brown and G. Gabrielse, *Rev. Mod. Phys.*, 1986, **58**, 233.
38. L. Schweikhard and A. G. Marshall, *J. Am. Soc. Mass Spectrom.*, 1993, **4**, 433.
39. M. V. Gorshkov, S. Guan, and A. G. Marshall, *Rapid Commun. Mass Spectrom.*, 1992, **6**, 166.
40. Y. Wang and K.-P. Wanczek, *Rev. Sci. Instrum.*, 1993, **64**, 883.
41. S. Guan, M. V. Gorshkov, and A. G. Marshall, *Chem. Phys. Lett.*, 1992, **198**, 143.
42. G. Savard, S. Becker, G. Bollen, H.-J. Kluge, R. B. Moore, T. Otto, L. Schweikhard, H. Stolzenberg, and U. Wiess, *Phys. Lett. A*, 1991, **158**, 247.
43. L. Schweikhard, S. Guan, and A. G. Marshall, *Int. J. Mass Spectrom. Ion Process.*, 1992, **120**, 71.
44. F. Laukien, in *Proc. 35th Am. Soc. Mass Spectrom. Conf. Mass Spectrom. Allied Topics*, Am. Soc. Mass Spectrom., Denver, CO, 1987, pp. 781–782.
45. S. C. Beu, M. W. Senko, J. P. Quinn, F. M. Wampler II, and F. W. McLafferty, *J. Am. Soc. Mass Spectrom.*, 1993, **4**, 557.
46. M. V. Gorshkov, S. Guan, and A. G. Marshall, *Int. J. Mass Spectrom. Ion Process.*, 1993, **128**, 47.
47. P. A. Limbach, P. B. Grosshans, and A. G. Marshall, *Anal. Chem.*, 1993, **65**, 135.
48. R. M. Weisskoff, G. P. Lafyatis, K. R. Boyce, E. A. Cornell, R. W. Flanagan, Jr., and D. E. Pritchard, *J. Appl. Phys.*, 1988, **63**, 4599.
49. M. W. Senko, S. C. Beu, and F. W. McLafferty, *Anal. Chem.*, 1994, **66**, 415.
50. J. D. Baldeschwieler, *Science*, 1968, **159**, 263.
51. J. L. Beauchamp, *Annu. Rev. Phys. Chem.*, 1971, **22**, 527.
52. T. A. Lehman and M. M. Bursey, *Ion Cyclotron Resonance Spectrometry*, John Wiley, New York, 1976.
53. A. G. Marshall, *Acc. Chem. Res.*, 1985, **18**, 316.
54. D. M. Lubman (ed.), *Lasers in Mass Spectrometry*, Oxford University Press, New York, 1990.
55. N. M. M. Nibbering, *Acc. Chem. Res.*, 1990, **23**, 279.
56. B. S. Freiser, in Bonding Energetics in Organometallic Compounds, *Am. Chem. Soc., Symposium Series*, 1990, **428**, 55.
57. A. G. Marshall and P. B. Grosshans, *Anal. Chem.*, 1991, **63**, 215A.
58. B. Asamoto and R. C. Dunbar, *Analytical Applications of Fourier Transform Ion Cyclotron Resonance Mass Spectrometry*, VCH, New York, 1991.
59. L. M. Nuwaysir and C. L. Wilkins, in *Proc. SPIE Appl. Spectrosc. Mater. Sci.*, Int. Soc. Opt. Eng., Bellingham, WA, 1991, pp. 112–123.
60. J. E. Campana, in *Proc. SPIE Appl. Spectrosc. Mater. Sci.*, Int. Soc. Opt. Eng., Bellingham, WA, 1991, pp. 138–149.
61. R. C. Dunbar, *Mass Spectrom. Rev.*, 1992, **11**, 309.
62. C. Köster, M. S. Kahr, J. A. Castoro, and C. L. Wilkins, *Mass Spectrom. Rev.*, 1992, **11**, 495.
63. J. P. Speir, G. S. Gorman, and I. J. Amster, in *Mass Spectrometry in the Biological Sciences: A Tutorial*, ed. M. L. Gross, Kluwer, Dordrecht, 1992, pp. 199–212.
64. K. M. Stirk, L. K. M. Kiminkinen, and H. I. Kenttämaa, *Chem. Rev.*, 1992, **92**, 1649.
65. N. M. M. Nibbering, *Analyst*, 1992, **117**, 289.
66. C. B. Jacoby, C. L. Holliman, and M. L. Gross, in *Mass Spectrometry in the Biological Sciences: A Tutorial*, ed. M. L. Gross, Kluwer, Dordrecht, 1992, pp. 93–116.
67. M. V. Buchanan and R. L. Hettich, *Anal. Chem.*, 1993, **65**, 245A.
68. J. T. Brenna, W. R. Creasy, and J. A. Zimmerman, *ACS Symp. Ser.*, 1993, **236**, 129.

Biographical Sketch

Alan G. Marshall. *b* 1944. B.A., 1965, Chemistry, Northwestern University, Ph.D., 1970, Physical Chemistry, Stanford University (with John Baldeschwieler). Successively instructor II, asst. professor and assoc. professor, University of British Columbia, Vancouver, B.C., Canada, 1969–80; Professor of Chemistry and Biochemistry and Director, Campus Chemical Instrument Center, Ohio State University, 1980–93; Professor of Chemistry at Florida State University and Director of ICR Program at National High Magnetic Field Laboratory, Tallahassee, FL, 1993 to present. Approx. 200 publications. Prior research areas: nuclear magnetic relaxation and NMR determination of RNA secondary structure. Current research specialty: Fourier transform ion cyclotron resonance mass spectrometry.

Martin, Gérard J. Maryvonne L.: Ode to Ethanol

Gérard J. Martin & Maryvonne L. Martin

Université de Nantes-CNRS, Nantes, France

Probably because of its social connotations, ethyl alcohol has always been a favorite analytical probe of research workers. In its earliest days, NMR rapidly succumbed to its charm. Did it not inspire Arnold in 1951 to record the first proton spectrum of an organic species[1] (Figure 1)? This particular molecule has always held a privileged place in France, and not least amongst French physicists. Convinced of the importance of tracking down the specific properties of the ethanol molecule, one of us entered the world of research by exploring the potential of NMR spectroscopy to study hydrogen bonding in water/alcohol mixtures. One of the first ^{1}H NMR spectrometers to be acquired in France in 1957 therefore consumed quite a considerable amount of ethanol. The nominal frequency of this primitive spectrometer (Trüb-Taüber, Zürich) was 25 MHz, and in order to observe a spectrum the 0.6 T magnetic field was swept through the resonances in the absence of a locking device. The whole spectrometer system, which would have needed at least a 30 m^2 room, was installed in a dark cupboard in Prof. R. Freymann's laboratory—under the stairs of the venerable Sorbonne! The operator had a narrow gap, 1-m wide, in which to rush backwards and forwards between the various knobs of the machine, chasing the magnetic field which had an irrepressible tendency to escape from its resonance conditions. Here, there was neither the need nor room for a chair!

Unfortunately, in spite of the efforts of the most brilliant NMR specialists, we had to wait nearly 20 years before it was technically possible to run our first ^{2}H NMR spectrum of alcohols. The frequency stability of our electromagnet spectrometer, a WH-90 Bruker equipped with an external locking device, was only of a few hertz per hour but, despite this, natural abundance deuterium was accessible in Nantes (a region known for its Muscadet wine).

It was whilst investigating chemical mechanisms that we noticed a rather intriguing behavior pattern of the relative intensities of the methyl and methylene ^{2}H NMR signals. These were measured on ethyl acetate obtained from ethyl bromide samples and differed according to whether the latter had been purchased from Prolabo or from Aldrich. Taking into account the sensitivity and resolution available at that time, we put this 'supplier' effect down to impurities and electronic deficiencies. This proves that, despite having an ethyl group in common with ethanol, these chemicals do not have its power to inspire further investigation. It was nearly two years later that our interest in ^{2}H NMR was revived, following an advertisement published in the daily press by the French Treasury Department. This dealt with the highly sensitive problem of wine chaptalization and offered a prize of 1 million FF to the person(s) who could, by analyzing the finished wine, detect whether sugar had been added to the grape must before fermentation. Unauthorized chaptalization

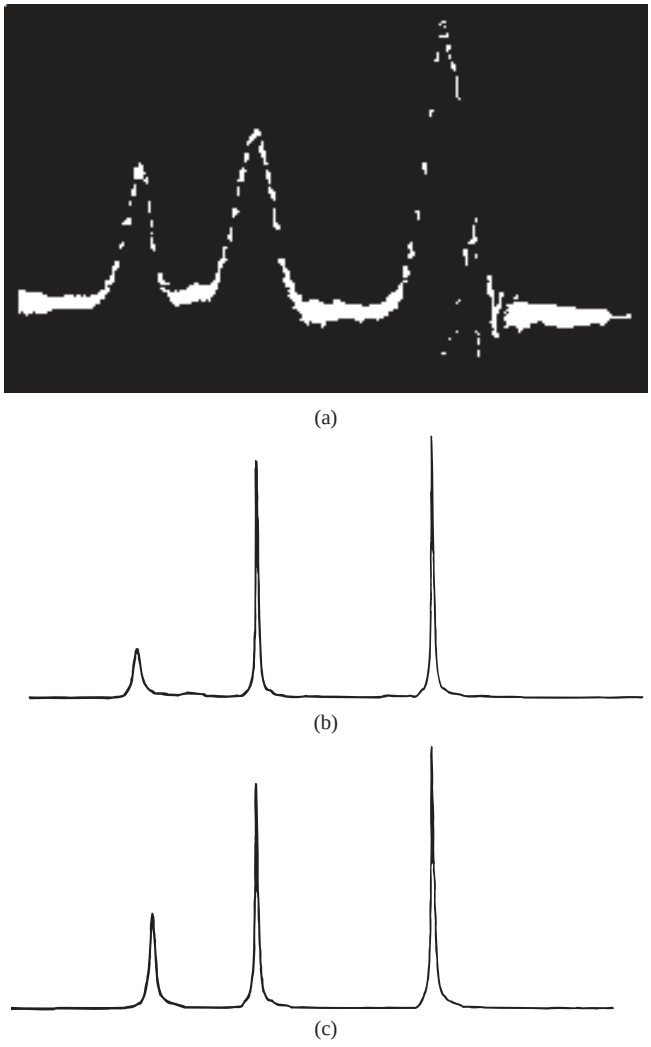

Figure 1 After more than 40 years the three lines of ethanol observed by Arnold[1] in ^{1}H NMR at 32.4 MHz (a) have lost nothing of their enticement. Now observed in natural abundance ^{2}H NMR at 61.4 MHz (b, c,) they have even gained in elegance. They show that pure ethanol is not identical according to whether it is obtained from wine (c) or from beet sugar fermentation (b). Consequently ethanol from chaptalized wine will differ from ethanol formed purely from grape sugars. Therefore (c) is an NMR quality label of the Bordeaux wine under investigation. Since only 50 to 300 mL of wine are necessary for the NMR experiment, interesting sensory parameters can also be determined on the same bottle!

is a serious financial problem, not only for France but for the European Union as a whole, contributing rather too efficiently to the overproduction of wine. In 1980, 7×10^9 L of wine were produced in France from about 11×10^9 m^2 of vineyards. The lowest quality or table wines, most of which were bought by the state for distillation on the basis of their alcoholic grade, made up more than 65% of the overall production. The finest quality wines, VQPRD, on the other hand, represented only 22%. Unofficial estimates showed that more than 10^5 tons per year of sucrose were being illegally used for wine enrichment. Fermenting this sucrose mountain would produce a 'wine' lake of 0.5×10^9 L in France alone. With the help of the rest of Europe's sucrose, a sizeable increase in this lake's volume would certainly be obtained.

Most previous studies on chaptalization had concentrated on the detection of minor components normally absent from wine and whose presence could be attributed to added sucrose. However these strategies failed with the progress in sugar-refining methods. Since, from the chemist's point of view, wine can be reduced, somewhat irreverently, to mainly water and ethanol, we decided to investigate ethanol with the following questions in mind: is deuterium statistically distributed on the different molecular sites and, if not, does the natural deuterium distribution depend on the botanical origin of the sugar precursor? This was the beginning of an exciting research project. NMR revealed that Nature is in fact a fascinating laboratory where isotopomeric molecules are biosynthesized in perfectly reproducible conditions for a given botanical species grown in a given environment. If the deuterium content in the methyl position of ethanol is arbitrarily given the statistical value 3, the methylene site is characterized by a factor which not only deviates strongly from the statistical value of 2, but also differs significantly for ethanols derived from grape ($\simeq$2.55) and beet ($\simeq$2.75) for instance (Figure 1). A method based on the NMR investigation of 'labeling without enrichment' was born.[2] To keep up with fashionable practice in an evocative spirit (wines have 'spirits'* don't they?), we chose the acronym SNIF-NMR for 'Site-specific Natural Isotope Fractionation studied by NMR' (and left it up to those less serious to add the second 'F' for factors).

With technical improvements in the performances of the commercial NMR spectrometers, in the theoretical algorithms for quantitative determination, and in the statistical procedures of data analysis, precisions of up to 0.2% in the isotopomeric contents of ethanol (for instance!) are now accessible. Possibly combined with isotope ratio mass spectrometry, SNIF-NMR transforms natural or synthetic end-products into rich sources of information on their disappeared precursors and on the whole history of their elaboration.[3] It renders possible the determination in a one-pot experiment of all primary and secondary kinetic isotope effects involved in a given chemical reaction. It also provides simultaneous determination of all primary and secondary thermodynamic isotope effects in chemical equilibria and gives access, in the same experiment, to the liquid–vapor fractionation factors of different isotopomers. It enables chemical or biochemical mechanisms to be inferred from the isotopic distribution measured on the products alone and information can even be obtained on the stereospecificity of reaction steps which introduce methylenic hydrogens in the course of biosyntheses in natural media.

Although a wide variety of molecules is accessible to SNIF-NMR, fermentation ethanol is certainly the most universal probe for tracing back the fate of any kind of carbohydrate and therefore for inferring the botanical, geographical, and temporal origin of plant products.[3] The consumption of ethanol by NMR has increased enormously in the last few years since the different official laboratories of the EU are now equipped to characterize several thousands of wines every year. The possibility of setting up a business offshoot of this research field was explored by the CNRS, and Eurofins S.A., created in 1987 in Nantes, was the first company to carry out and develop the SNIF-NMR concept. All the analytical steps involved in an authentication diagnosis of various food products, beverages, aromas, etc. are now fully automatized and computer-controlled. A data bank of several thousand authentic samples has been built up.

Ethanol still occupies a distinguished place in our NMR work and, even after all these years, not only have we not been discouraged by the monotony of its three ^{2}H lines but we are still amazed by the wealth of information contained in such a simple spectrum—on the physiological behavior of a plant precursor, on the weather which prevailed during the photosynthesis and the elaboration of fruits, and on the 'treatment' by man of authentic natural products.

NOTE

* Spirits: volatile compounds easily obtained by distillation.

REFERENCES

1. J. T. Arnold, S. S. Dharmatti, and M. E. Packard, *J. Chem. Phys.*, 1951, **19**, 507.
2. G. J. Martin and M. L. Martin, *Tetrahedron Lett.*, **1981**, 3525.
3. M. L. Martin and G. J. Martin, *NMR Basic Principles and Progress*, 1990, **23**, 1.

Biographical Sketches

Gérard J. Martin. *b* 1932. Ph.D., 1959, Organic Chemistry, University of Paris, Sorbonne. Assistant professor, 1964–71, Professor of Chemistry, University of Nantes, 1972–present; Head of Department of Chemistry, University of Nantes, 1968–74. Approx. 240 publications and patents; 3 books. Research interests: stable isotope analysis of metabolic pathways in natural environments; site-specific natural isotope fractionation studied by NMR.

Maryvonne L. Martin. *b* 1935. Ph.D., 1961, Chemical Physics, University of Paris, Sorbonne. Lecturer, University of Paris, Sorbonne, 1961–64, CNRS researcher, 1964–69, assistant professor, 1969–75, Professor of Chemistry, University of Nantes, 1978–present; Vice-President of the University of Nantes, 1984–89. Approx. 145 publications and 3 books. Research interests: physical chemistry of bio-products; site-specific natural isotope fractionation studied by NMR.

McConnell, Harden M.: Spin Chemistry

Harden M. McConnell

Stanford University, Stanford, CA, USA

My graduate research at the California Institute of Technology during 1947–50 under the supervision of Norman Davidson would be described as 'physical inorganic chemistry' today. Then and now, one cannot carry out chemical research without developing an interest in atomic and molecular electronic structure. As a graduate student I developed a special curiosity about the quantum mechanics of electron spin as it relates to electronic structure. For example, I was impressed by Slater's rules for multiplet splittings in atomic spectra and included some of my own 'back-of-the-envelope' calculations on multiplet splittings in diatomic hydrides in an addendum to my Ph.D. thesis. Even today, almost 50 years later, I clearly remember a lecture by Linus Pauling on electron spin correlations in the valence state of carbon in methane. As a National Research Fellow in the laboratory of Robert Mulliken, I worked on charge-transfer molecular complexes, but remained titillated by problems involving spin. For example, while at the University of Chicago I wrote a short letter to the *Journal of Chemical Physics* dealing with the catalysis of *cis/trans* isomerization of ethylene by paramagnetic substances, again involving a problem in molecular spin quantum mechanics.

On leaving Chicago in 1950 to take a position as a research chemist at Shell Development Company in Emeryville, California, my fascination with theories of molecular electronic structure had become tempered by the realization that (in 1950) it was virtually impossible to calculate anything of chemical interest theoretically with even semiquantitative accuracy. Thus, there was no way to test the then current and sometimes competing theories of molecular electronic structure, such as valence bond theory or molecular orbital theory. Fortunately, this depressing situation was about to undergo a dramatic change, through the developments of electron and nuclear magnetic resonance spectroscopy.

The first NMR spectrum that I ever saw was that of $CF_2{=}CH_2$, brought to me as a paradoxical problem by Charles Reilly, also a research chemist at Shell. For one who was interested in spin problems, the analysis of this spectrum was 'a piece of cake'. It was also straightforward to extend this analysis to molecules with other point group symmetries.[1] But my principal interest in this spectrum came from the fact that the various molecular spin–spin coupling constants depended on electron spin correlations within the molecule, a subject I explored theoretically in a rather large number of publications.[2–4] A major subsequent development was the discovery by C. A. Hutchinson, Jr. and S. I. Weissman that (electron spin)–(proton spin) hyperfine coupling constants in organic free radicals in solution could be observed in electron spin magnetic resonance spectroscopy. These free radicals, as well as organic free radicals in crystals, provided a direct, powerful means to determine electron spin distributions in molecules, and to test theories of molecular electronic structure.[5] There are now numerous publications describing such comparisons. One pleasant surprise in these comparisons was the finding that the molecular orbital theory of alternate π-electron hydrocarbons developed by H. C. Longuet-Higgins provided an excellent first approximation to the spin distributions in these molecules, and that valence bond theory led to negative spin densities on certain carbon atoms as observed experimentally.[6,7] From the point of view of determining spin distributions in molecules, there is no fundamental difference between electron and nuclear magnetic resonance. Hyperfine splittings, and thus spin distributions, can be determined from splittings in electron magnetic resonance spectra, as well as from paramagnetic shifts in nuclear magnetic resonance spectra.[6–8]

The above interplay of problems involving electron and nuclear spin systems has continued in my laboratory even when problems of molecular electronic structure were not involved. Examples include measurements of the rates of electron-transfer reactions,[9–11] molecular diffusion in biological membranes,[12,13] and studies of the structures and compositions of antibody combining sites.[14–17]

Today, in 1994, high-speed computers have brought about a true revolution in the techniques available for determining molecular electronic structure, as well as for developing and applying sophisticated magnetic resonance techniques. In this era of big computers, big machines, and big budgets, I have found it expedient to retreat into more primitive areas of science.

In retrospect, I cannot judge what impact these magnetic resonance studies during the period 1950–65 had on the chemists' view of molecules, but they certainly removed the anguish I felt in 1950 concerning molecular electronic structure theory.

REFERENCES

1. H. M. McConnell, A. D. McLean, and C. A. Reilly, *J. Chem. Phys.*, 1955, **23**, 1152.
2. H. M. McConnell, *J. Chem. Phys.*, 1955, **23**, 2454.
3. H. M. McConnell, *J. Chem. Phys.*, 1956, **24**, 460.
4. H. M. McConnell, *J. Mol. Spectrosc.*, 1957, **1**, 11.
5. H. M. McConnell and D. B. Chesnut, *J. Chem. Phys.*, 1958, **28**, 107.
6. H. M. McConnell and C. H. Holm, *J. Chem. Phys.*, 1957, **27**, 314.
7. H. M. McConnell and D. B. Chesnut, *J. Chem. Phys.*, 1957, **27**, 984.
8. H. M. McConnell and C. H. Holm, *J. Chem. Phys.*, 1958, **28**, 749.
9. H. M. McConnell and S. B. Berger, *J. Chem. Phys.*, 1957, **27**, 230.
10. H. M. McConnell, *J. Chem. Phys.*, 1958, **28**, 430.
11. H. M. McConnell and H. E. Weaver, Jr., *J. Chem. Phys.*, 1956, **25**, 307.
12. R. D. Kornberg and H. M. McConnell, *Proc. Natl. Acad. Sci. USA*, 1971, **68**, 2564.
13. P. Devaux and H. M. McConnell, *J. Am. Chem. Soc.*, 1972, **94**, 4475.
14. J. Anglister, T. Frey, and H. M. McConnell, *Biochemistry*, 1984, **23**, 1138.
15. T. P. Theriault, G. S. Rule, D. J. Leahy, M. Levitt, and H. M. McConnell, *J. Mol. Biol.*, 1991, **221**, 257.
16. T. P. Theriault, A. K. Singhal, G. S. Rule, and H. M. McConnell, *J. Phys. Chem.*, 1993, **97**, 3043.

17. M. Martinez-Yamout and H. M. McConnell, *J. Mol. Biol.*, 1994, **244**, 301.

Biographical Sketch

Harden M. McConnell. *b* 1927. B.S., 1947, George Washington University, Ph.D., 1951, California Institute of Technology (supervision Norman Davidson). Professor of Chemistry and Physics, Caltech, 1956–64. Professor of Chemistry at Stanford University, 1964–present. Approx. 390 publications. Research specialties: membrane immunology, antibody structures, and lipid monolayers.

McDowell, Charles A.: Four Decades of Chemical NMR at the University of British Columbia (UBC)

Charles A. McDowell

University of British Columbia, Vancouver, British Columbia, Canada

Nuclear magnetic resonance studies in the Department of Chemistry began in the mid-1950s with the construction of a broadline NMR spectrometer. The apparatus used phase sensitive detection and was built round a 6 in. Varian model V-4007 magnet. B. A. Dunell and his graduate student R. Grant, used it to study motion in stearic acid and some of its salts. The department acquired its first commercial spectrometer in 1956, a Varian high-resolution 40 MHz machine. Later I persuaded our Dean to provide funds to convert it into a dual-purpose Varian V4200/4300B spectrometer, probably the first such facility in Canada. A homemade variable temperature probe assembly provided a versatile spectrometer which was much used by faculty and graduate students, for liquid- and solid state NMR studies. The spectrometer was upgraded to perform at 60 MHz in 1961. The first solid state studies using the 40 MHz dual-purpose spectrometer were carried out by D. F. R. Gilson, a graduate student, now at McGill, and myself in 1957–58 on hydrocarbon/urea and thiourea inclusion compounds.[1] Using deutero-urea and deutero-thiourea as host matrices to reduce the proton–dipolar interactions between guest and host, it was clearly demonstrated for the first time by NMR that the guest molecules rotated about their long axes, or executed other motional behavior in urea inclusion or supramolecular compounds. These conclusions were confirmed later by others and particularly by deuterium spin echo studies. The early studies also included investigations of molecular motion of several enclathrated molecules and charge-transfer complexes.

L. W. Reeves, who had an extensive background in NMR having done postdoctoral work with W. G. Schneider at the National Research Council, Ottawa, and R. E. Connick at Berkeley joined the department in 1958. Reeves quickly started a research program on relaxation processes and chemical-exchange phenomena. Soon, with students and a postdoctoral fellow, E. J. Wells who had done his Ph.D. studies at Oxford with R. F. Richards, he built a spin echo apparatus, the first pulse spectrometer in the department. This equipment was used for extensive studies on spin–lattice effects and two- and multiple-site chemical-exchange reactions. Later Reeves and his group, including P. Englefeld, E. Krawkower, and K. Shaw, because of the need for sophisticated digital data collection, built a more elaborate pulse spectrometer around a Varian 12 in. magnet.

The 1960s saw the addition of many faculty members with research interests in preparative chemistry. Amongst those was L. D. Hall, a carbohydrate chemist who had been a postdoctoral fellow with F. A. L. Anet, then at the University of Ottawa. Hall made extensive use of CW and methods like INDOR. In addition, later, after the arrival of the Bruker BKR-322 S spectrometer, his group used pulsed proton NMR in his structural studies on carbohydrates. In the late 1960s there were added Varian A-60 and HA-100 spectrometers, a JEOL C-60 with a JLA-5 computer, a Varian T-60, and in 1972 a Varian XL-100 high-resolution FT instrument. In 1974 we acquired a Varian CFT-20 machine for proton and ^{13}C determinations.

The group of faculty members interested in solid state and condensed matter NMR studies was augmented by the appointment of E. E. Burnell in 1968. He had completed his Ph.D. studies under A. D. Buckingham, and gained postdoctoral experience with M. Bloom at UBC and in Basel with P. Diehl. That same year C. A. Fyfe joined me as a postdoctoral fellow and began his introduction to solid state NMR studying molecular motion. Because of the continuing need for more facilities, particularly for the study of solid state and condensed matter phenomena, the department obtained a Bruker BKR-322 S pulsed spectrometer. Elliott Burnell, B. A. Dunell, I, and our students continued to use this instrument for about 15 years. Of course, it was upgraded from time to time. Later when employed for deuterium-echo studies, an Oxford superconducting magnet was added. The spectrometer was later interfaced to an Intel 8080 microprocessor and a Nicolet 1280 computer. E. Burnell and his students made many significant studies of membranes and liquid crystals with this equipment. B. A. Dunell and his students, particularly, J. A. Ripmesster, and a postdoctoral fellow C. A. Ratcliff, both now at the National Research Council, Ottawa, studied molecular motion in solids. It was also extensively used by my students P. Raghunathan, A. W. Khanazada, and D. S. Williams, in addition to the existing Varian dual-purpose spectrometer, to study molecular motion of organic compounds as guests in deutero-clathrate hydrates and charge-transfer complexes. Dr. P. S. Allen, a visitor from the laboratory of E. R. Andrew (Nottingham), and now at the Faculty of Medicine (Edmonton), contributed notably to these studies. This group also carried out an extensive study of the temperature dependence of spin–lattice relaxation processes in those systems.

Spin–rotational relaxation measurements at various temperatures from 80–400 K were made by R. Ikeda, a postdoctoral fellow from Nagoya, and myself on polycrystalline NH_4ClO_4 which showed that above 200 K spin–rotational interactions were predominant in proton spin–lattice relaxation. To extend the studies to 4.2 K, a new spectrometer was built incorporating a modified Robinson oscillator operating at low rf powers to observe wideline proton spectra at these low temperatures. Weak signals were enhanced by accumulating spectra with a Varian C-1024 time-averaging computer. It was shown that the anomalous lineshapes observed occurred because of the quantum-mechanical tunneling rotations of the NH_4^+ ions. Later studies by Z. T. Lalowicz, a postdoctoral fellow from Poland, P. Raghunathan, and myself showed composite motions occurred involving coupling of the rotor states with lattice phonons.

Early in the 1970s, A. G. Marshall, who had completed his Ph.D. with J. D. Baldeschweiler at Stanford, joined us. Soon he and M. B. Comisarow invented and built the first Fourier transform ion cyclotron mass spectrometer. Particularly with his student L. G. Werbelow, Marshall also established a noteworthy research program in liquid state NMR. By this time there was very active research in practically

all aspects of chemical NMR. There was a great need for higher resolution spectra, so in about 1975 it was decided to build a high-field spectrometer. Using funds mainly from UBC sources, a 270 MHz superconducting magnet was bought from Oxford Instruments. We were fortunate to obtain an obsolete Bruker/Nicolet pulse FT spectrometer console which our electronic workshops most skilfully upgraded to perform at 270 MHz. L. D. Hall was notably involved in the evolution of this machine, which was probably the first high-resolution NMR superconducting magnet spectrometer built in Canada. It was soon heavily used for high-resolution spectra for the preparative chemists on the faculty, but mostly by L. D. Hall and his students who, later, with G. A. Morris, a postdoctoral fellow who had completed his Ph.D. with R. Freeman at Oxford, carried out some of the early applications of 2D NMR studies on carbohydrates. Subsequently, Hall used this equipment in his initial foray into chemical aspects of NMR imaging.

Though, as early as 1968, attempts had been made to obtain grants from NRC to purchase a Varian 220 MHz spectrometer, it was not until 1976 that I was successful in obtaining the long-sought financial support from NRC. Augmenting this grant with funds from UBC sources, by 1978 we had obtained a Bruker WH-400 high-resolution spectrometer and a WP-80 machine for routine studies. Also a Bruker CXP-200 solid state spectrometer for solid state and condensed matter NMR studies was delivered in 1979. The Bruker CXP-200 spectrometer proved versatile and has continued to be used about 24 h daily. Several additional probes were constructed including specially designed ones equipped with a goniometer for single-crystal NMR studies, and a specially designed variable temperature probe for studies on solids with quadrupolar nuclei.

The CPX-200 spectrometer was used later mainly by my group starting with A. Naito, K. Akasaka, a visitor from Kyoto, and S. Ganapathy, who first studied the $^{13}C-^{14}N$ dipolar–quadrupolar interactions in the NMR spectra of single crystals of l-alanine.[2] They gave a quantum mechanical interpretation of the experimental observations which proved to be seminal. This work was soon followed by CP MAS studies and equally successful theoretical interpretations, spectral simulations, and evaluations of the magnitudes and orientations of the spin parameters of several amino acids and related compounds. Extensive studies in collaboration with R. Barker, K. Takegoshi and D. L. Sastry of single crystal NMR, including 2D exchange spectra, yielded accurate values for the principal values and their orientations of chemical shift tensors and quadrupole coupling tensors in a host of amino acids and other organic compounds.[3] Studies of the orientational dependencies of spin–lattice relaxation and spin diffusion were also carried out.

By 1986, C. A. Fyfe returned to join the faculty. He brought with him a Bruker CXP-100 and an MSL 400 spectrometer, together with a Doty microscopic NMR imaging probe. He quickly reestablished his very active research programstudying the CP MAS spectra mainly of zeolites and polymers. About that same time the department was able to obtain an NSERC grant to purchase a Bruker MSL-200 console which was combined with a 200 MHz superconducting magnet already available. The addition of Doty MAS and DAS probes gave us greater access to much needed additional solid state NMR facilities. Making good use of these new opportunities, my group, which over time included A. Root, A. Kubo, R. Challoner, and T. Nakai, expanded the range of our activities to include MAS studies of spin diffusion processes[4] and spin–lattice relaxation processes and thus rediscover Andrew's rotational resonance, spin–spin interactions in two-spin systems, and two-dimensional exchange phenomena. We also investigated many new multiple pulse sequences. In addition the group contributed many theoretical innovations including novel applications of Floquet theory to interpret the NMR manifestations of rotating solids.[5]

The department in the late 1980s added several faculty members with research interests in biological aspects of chemistry and there was a demand for higher field spectrometers. Thus were added Varian XL-300, Bruker AM-300, AC-200, AMX-500 and most recently a Varian UNITY-500, high-resolution spectrometers. We probably now have the greatest concentration of NMR spectrometers with superconducting magnets of any chemistry department in Canada.

REFERENCES

1. D. F. R. Gilson and C. A. McDowell, *Nature (London)*, 1959, **183**, 1183.
2. A. Naito, S. Ganapathy, K. Akasaka, and C. A. McDowell, *J. Chem. Phys.*, 1981, **74**, 3190.
3. A. Naito, P. B. Barker, and C. A. McDowell, *J. Chem. Phys.*, 1984, **81**, 1583; C. A. McDowell, A. Naito, D. L. Sastry, and K. Takegoshi, *J. Magn. Reson.*, 1986, **69**, 283.
4. A. Kubo and C. A. McDowell, *J. Chem. Soc., Faraday Trans. 1*, 1988, **84**, 3713.
5. T. Nakai and C. A. McDowell, *Mol. Phys.*, 1992, **77**, 569.

Biographical Sketch

Charles A. McDowell. *b* 1918. B.Sc., 1941, M.Sc., 1942, D.Sc., 1955, Queen's University of Belfast, UK; D.Sc., honoris causa, University of British Columbia, Canada, 1984. National service, 1941–45; lecturer, University of Liverpool, UK, 1945–55; Professor and Head, Department of Chemistry, University of British Columbia, 1955–81; University Professor, 1981–84. Currently University Professor Emeritus, Department of Chemistry, University of British Columbia, Canada. Approx 380 publications. Current research specialties; mainly in solid state NMR.

McLauchlan, Keith A.: NMR Memories

Keith A. McLauchlan
University of Oxford, Oxford, UK

At the National Physical Laboratory in 1960, Ray Freeman, Ray Abraham, and I shared the first high-resolution 60 MHz spectrometer in Europe, under the direction of John Pople and David Whiffen. It was continuous wave, and field homogeneity ('shim') coils and field/frequency locking were still to be invented. A flux-sensing device ('superstabilizer') provided reasonable stability, but to obtain sufficient resolution was tedious.

Each morning the magnet was 'cycled', by increasing the field to a higher value than the resonance one for a time before reducing it. Hysteresis then produced, one hoped, a 'flat' field profile. Its effectiveness depended on the procedure used, and it was a continuous source of friction that we used different techniques, thereby 'ruining' the field for the next user. After cycling came the systematic tracking of the probe about the center of the magnet on a grid pattern, until a 'good spot' was discovered, detected by the observation of extensive 'ringing' in the rapidly-scanned spectrum of acetaldehyde. This procedure often took several hours, and the good spot usually appeared late in the evening.

This changed with the invention of shim coils by Golay, which also broke the domination of Varian patents in NMR, being introduced by Perkin-Elmer. We were obsessed by the mathematics of their orthogonality, but found them easy to use once we stopped trying to *calculate* which should be changed.

David Whiffen returned from a visit to Zürich where he had been shown the world's first field/frequency locked spectrometer in the laboratory of Hans Primas, who was also behind the development of a very remarkable commercial spectrometer (Trüb-Taüber) which employed three locked frequency sources. It was years ahead of its time, sold mainly in eastern Europe, and became very familiar to all of us who traveled there and found ourselves trying to fix it. Within half a day of Ray Freeman hearing of his achievement, he had locked our own spectrometer, using an audiofrequency sideband technique, and making the lock-in detectors himself. This opened new opportunities, and we moved immediately to field and frequency-swept double resonance studies, first homonuclear and then heteronuclear. We had so many different frequencies applied to the system that beats proliferated, and you really had to understand what you were doing to get anywhere. Ray left for a year at Varian, whence the first commercial field/frequency locked spectrometer, the A-60, soon resulted. It provided the major advance of precalibrated charts, all spectra having been previously calibrated by the generation of audiofrequency sidebands. Ray returned, and we performed a triple resonance experiment together which required very high resolution (he recognized and exploited the slow sweep condition) and immense stability. We ran the same spectrum without any adjustments to the spectrometer for hours on end, waiting until all the oscillators used happened to be at the right frequencies at the same time; this caused Varian some difficulties from others who expected their spectrometers *always* to be as stable. A little later the HA-100 appeared, providing field/frequency locking to an internal sample; its principle was not widely understood, and for years I was telephoned by service engineers from all over Europe to diagnose faults.

Our work was centered largely on the measurement of the relative signs of coupling constants, needed to determine which possible analysis of a spectrum was the correct one. It relied upon the ensemble nature of NMR spectroscopy, which allowed experiments to be performed inside subensembles in the sample. This was always a sticking point in lecturing on the subject. These experiments represented the leading edge of research and thanks to Ray produced the first trivial term in NMR, 'spin tickling'.

Another method then arose for getting the new information: multiple quantum spectroscopy. As the radiofrequency power of the spectrometer was increased the NMR signal was known to broaden and saturate. I realized that the observed pattern actually contained sharp transitions, which were completely reproducible, and David Whiffen told me what they were. Although M. Bloom and J. N. Shoolery had reported a double quantum transition before, this was their first use in analysis, and was the forerunner of multiple quantum coherence experiments.

We then turned to the absolute signs of coupling constants, which were believed to be impossible to measure since the spectrum was invariant to a complete sign change. David Buckingham suggested a new principle: we should make the nuclear dipolar interaction nonzero in a way which told us its sign and see whether the observed splitting in the spectrum, now given by the sum of the dipolar and scalar couplings, increased or decreased from its value in isotropic solution. This was the first experiment on partially-oriented molecules. Initially we oriented polar molecules inside a strong electric field inside the spectrometer, and suffered many explosions; the experiment was performed much more carefully by A. D. McLean later, but the same result was obtained. We also played with orientation by crystal lattices, in clathrates and zeolites, and in stretched polymer films. But then A. Saupe and G. Englert published the first spectra in liquid crystalline solvents, and it became obvious where the future lay.

In 1965 I left for Oxford, and it seemed to me that the interesting phase of NMR was over. I still believed it when after giving a lecture in Pittsburgh an unknown young man in the audience stood to ask a question. It was my first meeting with Richard Ernst, who may just have been right in thinking the whole field still had more of interest in it than I did.

Soon after, Rex Richards and I combined with Oxford Instruments to design the first genuinely high-resolution superconducting magnet with top sample loading, which was married to Bruker electronics to produce a 270 MHz spectrometer. It was designed specifically for biochemical studies. Another era of applications of NMR had begun, but apart from a brief flirtation with chemically induced dynamic nuclear polarization, this was my last contribution to NMR.

Biographical Sketch

Keith A. McLauchlan. *b* 1936, BSc., 1956, Ph.D., 1959, M.A., 1965, FRS, 1992, Physical Chemistry, University of Oxford, UK and Hertford College, Oxford. Postdoc at NRC Ottawa 1959–60, Senior Scientific

Officer, National Physical Laboratory London 1960–65 where he started his NMR work under John Pople and David Whiffen, Oxford 1965–present. Approx.160 publications. Current research specialties: ESR of transient radicals, chemically induced dynamic electron spin polarization (CIDEP), reaction yield detected magnetic resonance (RYDMR), effects of magnetic fields in chemistry, biochemistry and biology, including human health.

Mehring, Michael: Advent and Evolution of High-Resolution NMR in Solids: A Personal View

Michael Mehring

Universität Stuttgart, Stuttgart, Germany

In standard spectroscopy the intensity of a signal (absorption, transmission, number of particles, etc.) is measured for different frequencies (wavelength, wavenumber, etc.) using a frequency selective (dispersive) device. In fact, standard NMR spectroscopy proceeded for quite some time along the same lines where the magnetic field was swept. A qualitatively different approach to spectroscopy was introduced by the spin echo of Erwin Hahn and co-workers.[1] It demonstrated for the first time that spin interactions could be 'manipulated' by radiofrequency (rf) pulses. A wealth of multiple pulse experiments and finally high-resolution solid state techniques evolved from this.

Another important 'manipulation' of spin interactions was achieved by 'magic angle spinning' (MAS) introduced by Andrew[2] and Lowe[3] and co-workers. This technique achieved high-resolution right away by 'averaging' all second-rank tensor interactions which otherwise give rise to line broadenings. If all second-rank tensors can be averaged to zero by MAS, what about doing the same in spin space? Exactly this was achieved by the Lee–Goldburg[4] experiment where a strong rf field was applied at the magic angle in the rotating frame. This did not lead to very high resolution in solids however, although it achieved a lengthened decay which corresponded to a narrowed NMR line.

Later John Waugh and co-workers[5] designed a four-pulse sequence based on 'average Hamiltonian' theory[6] which was also capable of reducing higher-order correction terms, resulting in true highly resolved NMR spectra in solids.[7,8] I am very grateful for having been present in the Waugh group at that time and taking part in those fascinating experiments. There was a very particular atmosphere in the Waugh lab where I was together with David Ellett, Mike Gibby, Bob Griffin, Alex Pines, and Won-Ku Rhim. Average Hamiltonian theory[6] had paved the way for an easy proposal of new pulse sequences and for performing exciting experiments like the 'magic sandwich'.[9] The atmosphere was highly creative with John Waugh guiding every co-worker individually, either by an approving smile or a smart remark. It was the same time when Alex Pines proposed together with Mike Gibby and John Waugh an experiment based on the permutation of his name which turned out to be very useful in the end.[10] It is this experiment, namely 'proton-enhanced nuclear induction spectroscopy' which is still mostly used today when high resolution in solids is required. Soon after, monographs appeared which reviewed and summarized these techniques.[11,12]

It became evident at the beginning that one major benefit of high-resolution techniques applied to solids was the observation of shift anisotropies which are otherwise masked by dipolar interactions.[8] Starting with ^{19}F nuclei,[8,13] these were soon followed by ^{13}C nuclei,[10,14] and finally high-resolution spectra of protons were observed.[15,16] My personal interest was always in applying these novel techniques to solving special solid state physics problems. I therefore found it very fascinating to resolve very small Knight shifts in ordinary metals[17] and organic conductors.[18,19] An example of the first ^{13}C and ^{1}H Knight shifts in organic conductors is shown in Figures 1 and 2.

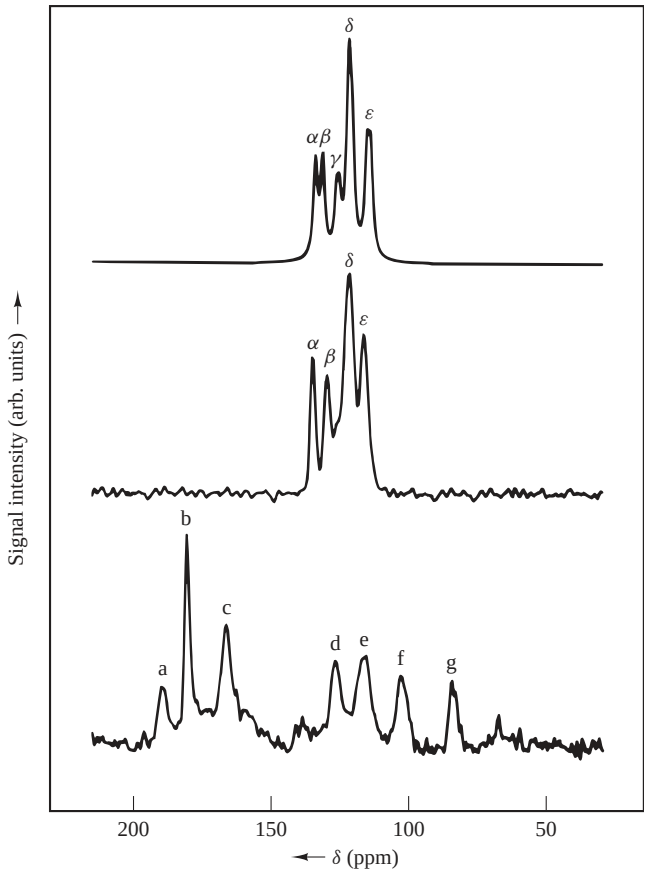

Figure 1 Room-temperature ^{13}C NMR magic angle spinning spectra ($\omega_{0n}/2\pi$ = 45 MHz) of solid fluoranthene (middle) and of the one-dimensional conductor (fluoranthenyl)$_2SbF_6$ (bottom). The spectrum of fluoranthene in liquid solution (top) is included for comparison.[18a] (Reproduced by permission of the American Physical Society)

The basic experiments discussed here were later extended into two-dimensional versions[20] and were combined with magic angle spinning and specially designed multiple pulse sequences. Major extensions to these 'classical' high-resolution techniques were introduced by Alex Pines and his co-workers in the area of multiple quantum[21] and double rotation NMR.[22] Bob Griffin and co-workers[23] applied high-resolution techniques to biological materials and developed MAS methods in order to measure distances between nuclear spins, based on the dipole–dipole interaction, very precisely. Using simpler techniques, Nino Yannoni and co-workers[24] also used this interaction in order to determine ^{13}C–^{13}C nuclear distances in basic materials like polyacetylene and C_{60}.

I have not tried to review the field but rather give a personal view on how I saw the subject developing.

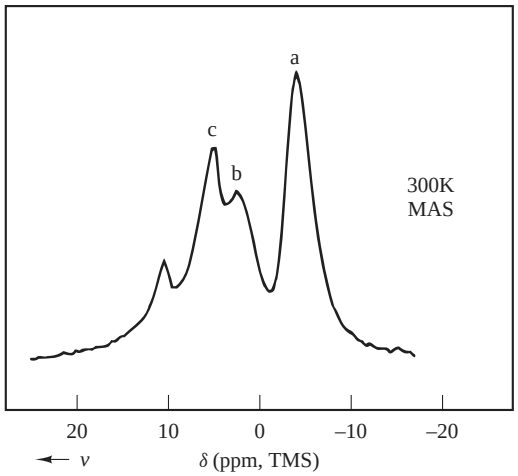

Figure 2 Proton Knight shift spectra of (fluoranthenyl)$_2$AsF$_6$ ($\omega_{0n}/2\pi$ = 180 MHz) at room temperature obtained by MAS combined with the MREV-8 multiple pulse sequence.[19a] (Reproduced by permission of the American Physical Society)

REFERENCES

1. E. L. Hahn, *Phys. Rev.*, 1950, **80**, 580.
2. E. R. Andrew, A. Bradbury, and R. G. Eades, *Nature (London)*, 1958, **182**, 1659; *ibid.*, 1959, **183**, 1802.
3. I. J. Lowe, *Phys. Rev. Lett.*, 1959, **2**, 301.
4. M. Lee and W. I. Goldburg, *Phys. Rev. Lett.*, 1963, **11**, 255; *Phys. Rev.*, 1965, **140**, A1261.
5. J. S. Waugh, L. M. Huber, and U. Haeberlen, *Phys. Rev. Lett.*, 1968, **20**, 180.
6. U. Haeberlen and J. S. Waugh, *Phys. Rev.*, 1968, **175**, 453.
7. J. D. Ellett Jr., U. Haeberlen, and J. S. Waugh, *J. Am. Chem. Soc.*, 1970, **92**, 411.
8. M. Mehring, R. G. Griffin, and J. S. Waugh, *J. Am. Chem. Soc.*, 1970, **92**, 7222; *J. Chem. Phys.*, 1971, **55**, 746.
9. W.-K. Rhim, A. Pines, and J. S. Waugh, *Phys. Rev. Lett.*, 1970, **25**, 218; *Phys. Rev.*, 1971, **B3**, 684.
10. A. Pines, M. G. Gibby, and J. S. Waugh, *J. Chem. Phys.*, 1972, **56**, 1776; *Chem. Phys. Lett.*, 1972, **15**, 373.
11. U. Haeberlen, High Resolution NMR in Solids: Selective Averaging, Supplement No. 1 to *Advances in Magnetic Resonance*, Academic Press, New York, 1976.
12. M. Mehring, *Principles of High Resolution NMR in Solids*, Springer-Verlag Berlin, 1st ed., 1976, 2nd revised ed., 1983.
13. R. G. Griffin, J. D. Ellett, Jr., M. Mehring, J. G. Bullitt, and J. S. Waugh, *J. Chem. Phys.*, 1972, **57**, 2147.
14. A. Pines, M. G. Gibby, and J. S. Waugh, *J. Chem. Phys.*, 1973, **59**, 569.
15. U. Haeberlen and U. Kohlschütter, *Chem. Phys.*, 1973, **2**, 76.
16. H. Raber, G. Brünger and M. Mehring, *Chem. Phys. Lett.*, 1973, **23**, 400.
17. M. Mehring, and H. Raber, *Solid State Commun.*, 1973, **13**, 1637.
18. (a) M. Mehring and J. Spengler, *Phys. Rev. Lett.*, 1984, **53**, 2441; (b) D. Köngeter and M. Mehring, *Phys. Rev.*, 1989, **B39**, 6361; (c) A. Vainrub, S. Vija, E. Lippmaa, V. Prigodin, R. Beha, and M. Mehring, *Phys. Rev. Lett.*, 1992, **69**, 3116; (d) F. Rachdi, T. Nunes, M. Ribet, P. Bernier, M. Helmle, M. Mehring, and M. Almeida, *Phys. Rev.*, 1992, **B45**, 8134; (e) G. Zimmer, A. C. Kolbert, M. Mehring, F. Rachdi, P. Bernier, and M. Almeida, *Phys. Rev.*, 1993, **B47**, 763.
19. (a) F. Hentsch, M. Helmle, D. Köngeter, and M. Mehring, *Phys. Rev.*, 1988, **B37**, 7205; (b) A. C. Kolbert, G. Zimmer, F. Rachdi, P. Bernier, M. Almeida, and M. Mehring, *Phys. Rev.*, 1992, **B46**, 674.
20. R. K. Hester, J. L. Ackerman, B. L. Neff, and J. S. Waugh, *Phys. Rev. Lett.*, 1976, **36**, 1081.
21. (a) A. Pines, D. J. Ruben, S. Vega, and M. Mehring, *Phys. Rev. Lett.*, 1976, **36**, 110; (b) W. S. Warren, S. Sinton, D. P. Weitekamp, and A. Pines, *Phys. Rev. Lett.*, 1979, **43**, 1791.
22. A. Samoson, E. Lippmaa, and A. Pines, *Mol. Phys.*, 1988, **65**, 1013.
23. (a) G. S. Harbison, S. O. Smith, J. A. Pardoen, J. M. L. Courtin, J. Lugtenburg, J. Hertzfeld, R. A. Mathies, and R. G. Griffin, *Biochemistry*, 1985, **24**, 6955; (b) B. A. Lewis, G. S. Harbison, J. Hertzfeld, and R. G. Griffin, *Biochemistry*, 1985, **24**, 4671; (c) A. C. Kolbert, D. P. Raleigh, R. G. Griffin, and M. H. Levitt, *J. Magn. Reson.*, 1990, **89**, 133.
24. (a) C. S. Yannoni and T. C. Clarke, *Phys. Rev. Lett.*, 1983, **51**, 1191; (b) C. S. Yannoni, P. P. Berbnier, D. S. Bethune, G. Meijer, and J. R. Salem, *J. Am. Chem. Soc.*, 1991, **113**, 3190.

Biographical Sketch

M. Mehring. *b* 1937. Diploma, 1964, University Münster, Dr. rer. nat., 1968, University Münster, Dr. habil., 1971, University Münster. Research Associate, MIT (Waugh), 1969–71; Professor, University Dortmund, 1972–82; Professor, University Stuttgart, 1982–present. Approx. 160 publications. Research interests include theory and applications of high-resolution NMR techniques, in particular multiple-pulse, double-resonance, and multiquantum NMR to solid state physics problems. Of particular interest are organic conductors and superconductors, conducting polymers, electron-transfer processes, and molecular electronics.

Mildvan, Albert S.: Early Applications to Enzymes of Paramagnetic Effects on Nuclear Relaxation

Albert S. Mildvan

Johns Hopkins University, Baltimore, MD, USA

Although my training was medical, I became committed to basic biochemical research early, inspired by excellent teachers of chemistry in high school, as an undergraduate at the University of Pennsylvania (Penn), and as a medical student at Johns Hopkins where, in 1953, ours was one of the first classes to hear lectures in biochemistry by the new Chairman, Albert L. Lehninger. My summers were spent in research in enzymology, the most exciting field in biochemistry, in the laboratories of Britton Chance at Penn and Albert Lehninger at Hopkins. In the 1950s one could easily monitor the velocity of enzyme-catalyzed reactions. However, the intermediate enzyme–substrate complexes were elusive. Inspiring work by Chance, combining rapid mixing with spectrophotometry had detected enzyme–substrate intermediates with peroxidase and catalase, and had elucidated all of the rate constants for their formation and disappearance.[1] However, nothing was known of the atomic structures of enzyme–substrate complexes or of the chemical basis for their unusual reactivity, resulting in overall enzymatic rate accelerations of chemical reactions by factors ranging from 10^6- to 10^{16}-fold.

After completing a medical internship, I returned to enzyme chemistry via postdoctoral training. Coincidentally, in 1960 while I was a postdoctoral fellow in Cambridge, UK with G. D. Greville, the first high-resolution X-ray structures of the proteins metmyoglobin and methemoglobin were being solved by Kendrew and Perutz at the nearby MRC Unit.[2,3] Although not enzymes, these structures demonstrated the power of a method which resolved individual atoms of a molecule. At that time I had also read several papers by Mildred Cohn who, in pioneering studies, had begun to apply NMR methods to enzymes, substrates, and their complexes. As Cohn pointed out, NMR, like X-ray, was a method with atomic resolution, with the advantage of being in solution. Using a Varian 60 MHz NMR spectrometer she reported in 1960 the first phosphorus spectrum of 0.5 M ATP showing separate, well-resolved resonances of the α, β, and γ phosphorus atoms.[4] By selective changes in chemical shifts induced by protonation or by Mg^{2+} coordination, and by paramagnetic broadening with transition metal ions,[5] she could tell which of the three phosphoryl groups of ATP were complexed. The sensitivity of NMR was still too low to study enzyme-bound ATP. However, Cohn was able to study enzyme–Mn^{2+}–substrate complexes indirectly by monitoring changes in the paramagnetic effects of bound Mn^{2+} on the longitudinal relaxation rate ($1/T_1$) of water protons.[6] Eisinger, Shulman, and Blumberg had shown earlier that complexation by DNA enhanced the paramagnetic effects of Mn^{2+} on $1/T_1$ of water protons due to an increase in the correlation time for dipolar interaction between Mn^{2+} and its residual water ligands.[7] Using this approach, Cohn and Jack Leigh obtained evidence for a substrate-bridge complex (E–ADP–Mn^{2+}) with the enzyme creatine kinase since enhanced water proton relaxation required all three components to be present. With enolase, a metal-bridge complex (E–Mn^{2+}–2-phosphoglycerate) was suggested since the enzyme and Mn^{2+} alone gave enhanced water proton relaxation, and this enhancement decreased on subsequent substrate binding, probably due to replacement of water ligands on Mn^{2+} by the substrate.[6] Based on this exciting work, I wrote to Mildred Cohn at the University of Pennsylvania and was fortunate in 1962 to obtain a postdoctoral position in her group.

As used by Cohn, the enhancement of $1/T_1$ by enzyme-bound Mn^{2+} was a qualitative method. Hence, my first project in her laboratory was to make the method quantitative, so that it might be used to measure dissociation constants, binding stoichiometries, and ultimately to count the number of residual water ligands on Mn^{2+} in binary and ternary complexes with enzymes and substrates. Because bovine serum albumin was stable, readily available in pure form, and was known from the literature to bind Mn^{2+} tightly, I started with this protein, titrating it with Mn^{2+}, and measuring $1/T_1$ of water protons on Jack Leigh's homebuilt pulsed NMR spectrometer which incidentally shared a magnet with an elderly Varian V4280A EPR spectrometer. As a check value, at each point in the titration, I used the EPR spectrometer to measure the free Mn^{2+} concentration. Gratifyingly, the binding stoichiometries and dissociation constants of Mn^{2+}–serum albumin obtained by both the enhancement of $1/T_1$ and independently by EPR agreed, establishing the $1/T_1$ method as a quantitative tool.[8] In addition, a new parameter ϵ_b, the enhancement factor due to bound Mn^{2+} was defined and directly evaluated which was 11.5-fold for the one tightly bound Mn^{2+} on serum albumin. This parameter, which reflected both the residual number of water ligands on Mn^{2+} and the correlation time, changed dramatically in response to changes in pH, and with the addition of denaturants. However, serum albumin was not an enzyme and did not form ternary complexes. Hence, I enthusiastically began a study of pyruvate kinase, a glycolytic enzyme which required a divalent cation and catalyzed the reversible enolization and phosphorylation of pyruvate by ATP to form phosphoenolpyruvate and ADP. I purified the enzyme from rabbit muscle using a procedure worked out by Tietz and Ochoa[9] and titrated the enzyme with Mn^{2+}. Like bovine serum albumin, and enolase, and unlike creatine kinase, pyruvate kinase bound Mn^{2+} tightly in the absence of substrates to form a binary complex with an unprecedentedly high enhancement factor (ϵ_b) of 30-fold.[10] Next, titration of the pyruvate kinase–Mn^{2+} complex with the substrate phosphoenolpyruvate resulted in a marked decrease in enhancement, with a clear endpoint at an enhancement factor of 2.2, suggesting the formation of a ternary enzyme–Mn^{2+}–phosphoenolpyruvate bridge complex. The other substrates, pyruvate, ATP, and ADP also decreased the enhancement but to a lesser degree.[11]

Importantly, the dissociation constants of Mn^{2+} and of each substrate from their enzyme complexes, determined by titrations measuring $1/T_1$, agreed with their respective K_M values, determined by the methods of enzyme kinetics, thus establishing active-site binding for Mn^{2+} and for each substrate. The $1/T_1$ data thus established the random order binding of substrates to the enzyme–Mn^{2+} complex and suggested the

formation of an enzyme–Mn^{2+}–phosphoenolpyruvate bridge complex. However, substrate coordination by the enzyme-bound Mn^{2+} was not directly proven since we had looked only at water protons rather than at the substrate itself. In 1966, a direct look at the paramagnetic effects of pyruvate kinase-bound Mn^{2+} on $1/T_1$ of phosphoenolpyruvate by continuous wave NMR was not easy. While continuous wave proton NMR was sensitive enough, the vinyl protons of this substrate would probably be too far from the bound Mn^{2+} to establish the structure of the ternary complex, and continuous wave ^{31}P NMR and ^{13}C NMR were certainly not sensitive enough. However, Tietz and Ochoa had shown that, in a side-reaction, pyruvate kinase also catalyzed the phosphorylation of the fluoride ion (F^-) by ATP to yield fluorophosphate (FPO_3^{2-}) and ADP.[9] Since fluoride was a substrate analogous to pyruvate, and fluorophosphate was analogous to phosphoenolpyruvate, a realistic experiment presented itself, namely to determine by ^{19}F NMR the effects of pyruvate kinase–Mn^{2+} on $1/T_1$ of fluoride and of fluorophosphate.[12]

Accordingly, I first carried out kinetic and binding studies with F^- and FPO_3^{2-} by $1/T_1$ measurements of water to facilitate the design of the ^{19}F NMR experiments. In the ^{19}F NMR experiments, carried out on a Varian HA-60 spectrometer, T_2 was measured by linewidth and the product $T_1 \times T_2$ was measured by rf power saturation, a method long forgotten in NMR but still occasionally used in EPR spectroscopy. In control experiments, the paramagnetic effects of Mn^{2+} on $1/T_1$ and $1/T_2$ of F^- and FPO_3^{2-} were measured. Using the $1/T_1$ values, Jack Leigh and I independently calculated Mn^{2+} to fluorine distances in the binary Mn^{2+}–F and Mn^{2+}–O_3PF complexes, using the dipolar term of the Solomon–Bloembergen equation, and obtained values of 2.1 Å and 4.4 Å, respectively. The agreement of these distances with those obtained from X-ray crystallographic data in the literature was so good that I repeatedly rechecked the units in our calculations to make certain that they were indeed Å rather than meters. We thereby became convinced that $1/T_1$ was indeed a powerful structural tool.[12]

With pyruvate kinase, our results were also clear cut. While Mn^{2+} alone profoundly increased $1/T_1$ and $1/T_2$ of F^-, the presence of pyruvate kinase deenhanced these effects by competing for the Mn^{2+}, thus arguing against an enzyme–Mn^{2+}–F^- bridge complex. On the other hand, pyruvate kinase significantly enhanced the effects of Mn^{2+} on the ^{19}F relaxation rates of FPO_3^{2-} qualitatively demonstrating an enzyme–Mn^{2+}–O_3PF bridge complex. A similar Mn^{2+} to fluorine distance on the enzyme as off was calculated, thus defining the structure of the complex as pyruvate kinase–Mn^{2+}–O_3PF.[12] The $1/T_2$ value of enzyme-bound FPO_3^{2-} was exchange-limited, yielding the rate constant for the dissociation of FPO_3^{2-} from the E–Mn^{2+}–FPO_3^{2-} complex. Since this rate was 10^3-fold faster than catalysis, we were indeed observing a kinetically competent complex. Thus NMR was not only a structural tool but also a kinetic tool, hence ideal for enzyme studies.

Eleven years later, after the introduction of higher magnetic fields and Fourier transform methods, the structure of the pyruvate kinase–Mn^{2+}–O_3PF complex was confirmed by ^{31}P-relaxation rate measurements by Thomas Nowak,[13] a former postdoctoral fellow in my laboratory, and an enzyme–Mn^{2+}–phosphoenolpyruvate bridge complex was detected by X-ray diffraction.[14] As an independent investigator, I extended these methods to many other enzymes. In addition to substrate bridge (E–S–M) and metal-bridge (E–M–S) complexes, enzyme-bridge (M–E–S) and second-sphere complexes [E–M(H_2O)S] were detected.[15,16]

Until 1969 paramagnetic effects on T_1 were limited to metal-ion requiring enzymes, which constitute only about one-third of all known enzymes. In 1965, Harden McConnell introduced the use of stable, paramagnetic nitroxides or spin labels as covalent EPR probes of macromolecular motion.[17] At that time it seemed obvious to me that with T_1 measurements, a spin-labeled substrate could be used like Mn^{2+} for binding studies to an enzyme and for the measurement of intersubstrate distances on an enzyme which had no metal requirements. In 1968, as a visiting lecturer at Purdue University, I met Henry Weiner who had synthesized tempo-ADP, a spin-labeled analog of NAD^+ and had shown it to be a competitive inhibitor of alcohol dehydrogenase with respect to NAD^+. At my invitation, Weiner came to Philadelphia, and together we showed that when alcohol dehydrogenase bound tempo-ADP, it enhanced the paramagnetic effects of the spin label on $1/T_1$ of water protons by as much as 80-fold. The enhancement factor was decreased on the subsequent binding of the other substrate, ethanol, to the enzyme, indicating the formation of a ternary enzyme–tempo-ADP–ethanol complex, and suggesting proximity between the two substrates.[18] By measuring the effects of the enzyme-bound nitroxide on $1/T_2$ of the protons of ethanol itself we were able to estimate the intersubstrate distance on this enzyme as ~4 Å,[19] a proximity confirmed 13 years later by X-ray diffraction.[20] These relaxation techniques have since been extended to many enzymes which do not require metal ions.

REFERENCES

1. B. Chance, *Biochem. J.*, 1967, **103**, 1.
2. R. E. Dickerson, J. C. Kendrew, and B. E. Strandberg, *Acta Crystallogr.*, 1961, **14**, 1188.
3. H. Muirhead, J. M. Cox, L. Mazzarella, and M. F. Perutz, *J. Mol. Biol.*, 1967, **28**, 117.
4. M. Cohn and T. R. Hughes, *J. Biol. Chem.*, 1960, **235**, 3250.
5. M. Cohn and T. R. Hughes, *J. Biol. Chem.* 1962, **237**, 176.
6. M. Cohn and J. S. Leigh, *Nature (London)*, 1962, **193**, 1037.
7. J. Eisinger, R. G. Shulman, and W. E. Blumberg, *Nature (London)*, 1961, **192**, 963.
8. A. S. Mildvan and M. Cohn, *Biochemistry*, 1963, **2**, 910.
9. A. Tietz and S. Ochoa, *Arch. Biochem. Biophys.*, 1958, **78**, 477.
10. A. S. Mildvan and M. Cohn, *J. Biol. Chem.*, 1965, **240**, 238.
11. A. S. Mildvan and M. Cohn, *J. Biol. Chem.*, 1966, **241**, 1178.
12. A. S. Mildvan, J. S. Leigh, and M. Cohn, *Biochemistry*, 1967, **6**, 1805.
13. T. Nowak, *Arch. Biochem. Biophys.*, 1978, **186**, 343.
14. H. Muirhead, D. A. Clayden, D. Barford, C. G. Lorimer, L. A. Fothergill-Gilmore, E. Schiltz, and W. Schmitt, *EMBO J.*, 1986, **5**, 475.
15. A. S. Mildvan and M. Cohn, *Adv. Enzymol.*, 1970, **33**, 1.
16. A. S. Mildvan, *Adv. Enzymol.*, 1979, **49**, 103.
17. T. J. Stone, T. Buckman, P. L. Nordio, and H. M. McConnell, *Proc. Natl. Acad. Sci. USA*, 1965, **54**, 1010.
18. A. S. Mildvan and H. Weiner, *Biochemistry*, 1969, **8**, 552.
19. A. S. Mildvan and H. Weiner, *J. Biol. Chem.*, 1969, **244**, 2465.
20. H. Eklund, B. V. Plapp, J.-P. Samama, and C.-I. Branden, *J. Biol. Chem.*, 1982, **257**, 14 349.

Biographical Sketch

Albert S. Mildvan. *b* 1932. A.B., Chemistry, University of Pennsylvania, M.D., Johns Hopkins School of Medicine. Postdoctoral work at NIH, Cambridge University, UK, and University of Pennsylvania. Faculty, University of Pennsylvania and staff member, Institute for Cancer Research Fox Chase. Professor of Biological Chemistry/Chemistry, Johns Hopkins School of Medicine. Approx. number of publications, 218. Current research specialties: application of kinetic and magnetic resonance methods to studies of mechanism of enzyme action.

Morris, Gareth A.: The Origins of DANTE

Gareth A. Morris

University of Manchester, Manchester, UK

My introduction to NMR research came as an undergraduate at Oxford, where chemistry students enjoy a fourth (Part II) year devoted to research, in the autumn of 1975. Having taken an interest in electronics and computers while at school, and having enjoyed being taught by Ray Freeman, I chose to join Ray's NMR group for my Part II. At that stage Geoffrey Bodenhausen was grappling with instrumental obstacles to the measurement of T_2 values, and David Turner was measuring T_1 values. Our only instrument was a Varian CFT-20, a carbon-13 FT spectrometer which was too unstable to be used for proton NMR. Its great virtue was a computer system which offered almost complete control over the spectrometer; new experiments could be tried out quickly and easily by modifying the software. This was something of an art, as modifications had to be made in 16-bit machine code, within the 6000 words of memory allocated to the control program.

Ray suggested some projects involving spin locking and transient nutations, both of which required a high pulse duty cycle, so I set out to build a new radiofrequency power amplifier. At the same time I was trying to get to grips with the basics of pulsed NMR. Having read about Fourier series while at school, I was keen to see how much of pulse FT NMR could be explained using Fourier transforms. Since the CFT-20 could only produce rectangular pulses, a logical place to start was to try to predict the behavior of a regular train of pulses. The Fourier transform of such a sequence is a series of equally spaced sinc functions, so this suggested the idea of using a train of pulses to achieve frequency selective excitation. When I discussed the idea with Ray he was a little sceptical, so the idea remained untried until events took over.

By the end of February 1976 I was becoming restive, as the Oxford Part II system requires students to submit a thesis at the beginning of June and I had very little material. A visitor to the laboratory, Aharon Loewenstein, offered cold comfort: 'Cheer up', he said, 'Nothing in NMR happens on a timescale of less than five years'. Finally at the end of February 1976 my rf amplifier was completed, so at 11 o'clock one night I ran the first tests. Unfortunately a capacitor in the final stage arced, leaving me with a dead amplifier and no thesis material. The next morning I came into the laboratory and decided that it was time to put the ideas about selective excitation to the test.

We already had a CFT-20 program suitable for generating trains of pulses (this was for an ill-starred experiment[1] involving the use of transient nutations to identify spins with $T_2 < T_1$), so it took only a short time to set up a simple test. At that time our favorite sample was ^{13}C-enriched methyl iodide, since this gave strong signals even at low field. The pulse sequence (later named DANTE) did indeed give frequency-selective excitation, exciting just one of the four lines of the proton-coupled methyl iodide quartet. By this stage Geoffrey Bodenhausen had arrived in the laboratory, and he suggested gating on the proton decoupler at the start of the free induction decay, causing the excited signal to change frequency. This led naturally to the idea that by gating the decoupler on during excitation and off during data acquisition, the technique could be used to excite proton-coupled carbon-13 multiplets selectively, allowing overlapping spectra to be disentangled.

The application to 'real' molecules proved straightforward[2,3] (although one of our chosen examples, menthone,[3] proved to be a severe case of virtual coupling), and I was able to produce a satisfactory thesis from a few weeks' work. We subsequently[4] went on to examine in detail the relationship between the linear response approximation and the Bloch picture, and demonstrated a number of other applications for pulsed selective excitation including selective spin locking, hole burning, and saturation transfer. By this time, however, most of our attention had shifted to a far more important topic, two-dimensional NMR. Surprisingly, DANTE is still in widespread use despite the advent of improved soft pulse instrumentation and techniques. Its prime advantages are its predictability and ease of use, and the fact that it produces selective excitation which is phase coherent with normal hard pulses. Recent uses in medical NMR, for example cardiac tagging, also exploit the characteristic multiple sidebands.

The most difficult part of the whole exercise was agreeing a suitably pithy name for the experiment. I had been reading the *Divine Comedy* (in translation, after a brief and unequal struggle with Dante's Italian) and had been struck by the parallel between the path taken by Dante and his guide Virgil through Purgatory and the trajectories of nuclear magnetizations during our experiments. Dante's Purgatory consists of a series of seven successive circular ledges running around a mountain, one for each of the seven deadly sins (arranged approximately in order of interest, with Pride at the bottom and Lust at the top). Souls progress heavenwards by circumnavigating each ledge before moving on to the next, just as our magnetizations alternately precessed during delays and were nutated by pulses. Ray was convinced by the analogy when he discovered diagrams in books on Dante that matched our simulated magnetization trajectories almost exactly, so we settled on the acronym DANTE (Delays Alternating with Nutations for Tailored Excitation) for our pulse sequence.

REFERENCES

1. R. Freeman, *Chem. Rev.*, 1991, **91**, 1397.
2. G. Bodenhausen, R. Freeman, and G. A. Morris, *J. Magn. Reson.*, 1976, **23**, 171.
3. G. A. Morris and R. Freeman, *J. Magn. Reson.*, 1978, **29**, 433.
4. R. Freeman, G. A. Morris, and M. J. T. Robinson, *J. Chem. Soc., Chem. Commun.*, **1976**, 754.

Biographical Sketch

Gareth A. Morris. *b* 1954. M.A. (Nat.Sci.), Ph.D., 1978 (supervisor Ray Freeman), Oxford University, UK. Fellow by Examination, Magdalen College, Oxford, 1978–81; Izaak Walton Killam Postdoctoral Fellow, University of British Columbia (with Laurie Hall) 1978–79. Lecturer (1982–89) and reader (1989 to date) in Chemistry, University of Manchester. Approx. 100 publications. Current research interests: development and application of novel NMR techniques to problems in chemistry, biochemistry, and medicine.

Nagayama, Kuniaki: The First Protein Two-Dimensional (2D) NMR

Kuniaki Nagayama

The University of Tokyo, Komaba, Tokyo, Japan

In the middle of April 1977, two professors had been awaiting my return from spring vacation. In the office of Kurt Wüthrich, my cheerfulness after a family tour to Mürren rapidly diminished on hearing the determined voice of Ernst saying, 'Oxford may be very close to the development of 2D NMR for proteins. We must work rapidly not to be beaten by that group'. Until that time, I had been watching as an unconcerned spectator while the competition between the Zürich group directed by Richard Ernst and the Oxford group directed by Ray Freeman continued in the development of 2D NMR. Now, however, I really understood my own personal position in this situation. Wüthrich ordered me to complete the current work and to produce the world's first 2D NMR spectrum of a protein as soon as possible. His voice was stern and he would not accept refusal, and I realized then that I would be facing one of the hardest times ever in the coming few weeks.

Nonstop writing of 2D NMR software began immediately and the Nicolet 1180 minicomputer occupied exclusively by me became covered by the printouts dumped from the Teletype roller. The circumstances in 1977 for software development were poor compared with current conditions, but the computer system with its 12-in. disk cartridge (DIABLO) was rather modern for those days. I utilized any useful resources at hand, such as my 24-h (overnight work every other day) utility softwares from Nicolet and custom programs used for 1D NMR from Bruker. I tried to make a small program satisfying the minimum requirements for performing the desired 2D *J* spectroscopy of proteins. When I was almost buried in paper at the end of April, my software development was finished and I was left with five thousand lines of code written by ASSEMBLER. A pretest was then made to check my program with a mixed solution of five amino acids: alanine, isoleucine, histidine, methionine, and tyrosine. I then asked Gerhard Wagner to use his protein, BPTI (basic pancreatic trypsin inhibitor), as the first sample for the 2D NMR program. I had already understood that the quality of *J* spectroscopy was critical for the resolution and, therefore, required sharp resonances. The BPTI solution was then prepared in high concentration (10 mM), placed in the HXS-360 NMR (Bruker 360 MHz), which was equipped with a newly designed cavity probe to avoid the troublesome $\boldsymbol{B}_1$ inhomogeneity, and measured at a high temperature (60°C). The *J* spectrum of BPTI clearly resolved the fine structures and exhibited very neat *J* coupling constants for all 20 methyls in the second dimension. It was May 5, 1977, two weeks after the start of my sleepless nights and five weeks after my attendance at the British Biophysical Society Meeting on NMR held at Oxford. There I had been a stranger just becoming acquainted with Geoffrey Bodenhausen and David Turner who were working on 2D NMR in Oxford. The well-resolved 2D *J* spectrum of 20 methyls in BPTI was immediately reported to *FEBS Letters* and soon rejected due to the lack of any biological relevance. With our angry sentiments it was sent to *Biochem. Biophys. Res. Commun.* and promptly accepted in July.[1]

At the end of November 1976, I had come to Zürich as the first postdoc invited by Wüthrich and Ernst to join in a research project emerging between the two professors that continued for 10 years thereafter. It was just one year after I had seen Wüthrich at the Taniguchi Symposium on Biophysics held in Kyoto. He told me that he remembered well my presentation on the helix−coil transition of polypeptides in the 6th International Biophysical Congress in Moscow in 1972 and offered me a position in the joint project. I became obsessed with the idea that I could study near the genius who had opened up the new NMR world by his FT revolution. So, with no hesitation, I decided to accept his offer even if I sacrificed my position as a research associate in the University of Tokyo. In May 1976, Wüthrich informed me that their research proposal had finally been formulated and asked me to study a 2D NMR paper[2] sent under a separate cover. My first reaction to the preprint full of density matrices and the new notion was a mixture of wonder and bewilderment. I convinced myself that there was something completely new there, but I could not understand what it was; then I simply reported to Wüthrich that I had tried to understand the paper as a simplification of NMR by taking an analogy with another paper[3] sent in the same mail.

My success with the software development and the NMR experiment, where I was able to shorten the period of my task from two months to two weeks, was not only a credit to the encouragement of Ernst and Wüthrich but also due heavily to the proper software training by Peter Bachmann who had been employed by Ernst in the project. Bachmann gave me personal lessons in how to manage the programming with the machine language ASSEMBLER. All persons concerned and unconcerned had been quite fascinated by the beautifully stacked 2D NMR plot of BPTI[1] and firmly believed that we would see a prosperous future for 2D NMR and a new age in protein NMR. We then extended *J* spectroscopy to spin echo correlated spectroscopy (SECSY),[4] which was used to take the first 2D correlation NMR of proteins. From the beginning of my encounter with FT NMR, the mathematical harmony behind it had been always my enchanting driving force and above all led me to the application of several mathematical tools, such as the cross-section projection theorem,[5] delayed acquisition and the similarity theorem,[6] and time reversal and frequency inversion.[7] I had thought that the spin engineering required to develop pulse sequences useful in particular applications of 2D NMR was not my business but that of the Ernst group. Now, the main stream of 2D NMR and protein NMR is provided by the perfect combination of COSY and NOESY,[8] and my work flashed over the *J* spectroscopy of proteins is destined to fade away into the shadows of history. On the other hand, the development of my 2D NMR software with a command interpreter and a disk system was more blessed. The program was extended twice and implemented on Aspect 2000 Bruker computers by Bachmann. It has also been extended to workstations where it can show the beauty of 2D or 3D NMR spectra with color graphics. When we see

modern NMR systems where 1 Mbyte of 2D data are Fourier-transformed within a few seconds, I always remember my time at Zürich where the J spectrum of BPTI with 1 million data points was obtained after an overnight run on a Nicolet 24 bit minicomputer.

REFERENCES

1. K. Nagayama, K. Wüthrich, P. Bachmann, and R. R. Ernst, *Biochem. Biophys. Res. Commun.*, 1977, **78**, 99.
2. W. P. Aue, E. Bartholdi, and R. R. Ernst, *J. Chem. Phys.*, 1976, **64**, 2229.
3. I. D. Campbell, C. M. Dobson, R. J. P. Williams, and P. E. Wright, *FEBS Lett.*, 1975, **57**, 96.
4. K. Nagayama, K. Wüthrich, and R. R. Ernst, *Biochem. Biophys. Res Commun.*, 1979, **90**, 305.
5. K. Nagayama, P. Bachmann, K. Wüthrich, and R. R. Ernst, *J. Magn. Reson.*, 1978, **31**, 133.
6. K. Nagayama, Anil Kumar, K. Wüthrich, and R. R. Ernst, *J. Magn. Reson.*, 1980, **40**, 321.
7. K. Nagayama, *J. Magn. Reson.*, 1986, **66**, 240.
8. Anil Kumar, R. R. Ernst, and K. Wüthrich, *Biochem. Biophys. Res. Commun.*, 1980, **95**, 1.

Biographical Sketch

Kuniaki Nagayama. *b* 1945. B.Sc., 1968, M.Sc., 1970, Ph.D., 1974, Physics, University of Tokyo. Research associate, Department of Physics, University of Tokyo, 1973–83; Postdoctoral research, Institute for Molecular Biology and Biophysics, ETH, Zürich, Switzerland, 1976–79; General Manager, Biometrology Laboratory, JEOL Ltd., Tokyo, 1983–93; Professor of Physics, College of Arts and Sciences, University of Tokyo, 1993–present. Approx. number of publications 160. Current research interests: structural analysis, stability analysis and synthesis of simple proteins and protein assemblies.

Nakanishi, Koji: First Encounter with NOE in Natural Products—the Ginkgolides

Koji Nakanishi

Columbia University, New York City, NY, USA

I have been engaged in structural studies of natural products throughout my career, including our current interests in ligand/receptor interactions. The emphasis has been to apply and develop various spectroscopic methods for structural studies, our present efforts being centered on the exciton coupled CD method. The emphasis in developing spectroscopic methods has even led us to advance structures which we suspect may have to be revised later, simply because spectroscopic interpretations led to the suggested structure and we were unable to find any rationale to dispute the result.

My first encounter with NMR was around 1957 when working on the triterpenoid antibiotic pristimerin (**1**); several groups in the UK and India were also working on its structure because of its use in folk medicine (India and China) and bright orange–red color. In 1955–56 we reported[1] that the Kuhn–Roth oxidation method showed the presence of a minimum of three methyl groups; in pre-NMR days, the number of methyl groups used to be estimated from the number of moles of acetic acid produced by vigorous oxidation. Soon thereafter, the tiny narrow strip chart depicting the 30 MHz NMR of pristimerin measured at Varian showed seven methyl singlets, an enormous help in determining the final structure.[2]

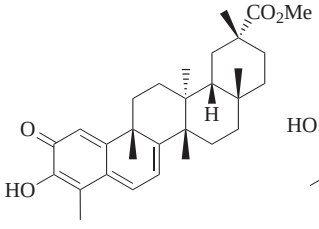

(1) Pristimerin

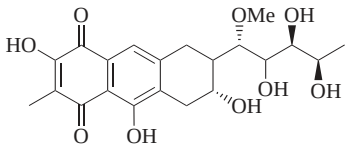

(2) Chromomyciquinone

A case demonstrating the immense power of NMR was encountered during studies of chromomycin A_3, an anticancer agent which was being used clinically. In the early 1960s, thanks to the generous support of Martin Packard and Jim Shoolery of Varian, the company supported two scientists to run the 100 MHz instrument at Tohoku University, where I was from 1963 to 1969. One of them, Norman Bhacca (now at Louisiana State University) performed one of the most exhaustive double and triple resonance experiments in those days on chromomyciquinone (**2**), a key compound in the structural studies of chromomycin A_3.[3] Not only did NMR clarify the connectivities leading to structure (**2**), but to our surprise it also showed that (**2**) contained one unexpected extra carbon.

An exciting event was the 'discovery' of intramolecular NOE by Dr. Vyn Woods (a Varian postdoc, now deceased) and Iwao Miura (he later moved to Columbia University and became a legendary NMR structural person in the Chemistry Department there; currently at Otsuka Pharmaceutical Co.). We were working on the structure of the ginkgolides, a group of diterpenes isolated from the 'fossil tree' *Ginkgo biloba*. We had 10–20 g of the various ginkgolides, GA (ginkgolide A), GB, GC, and GM, prepared about 50 derivatives, and encountered many interesting chemical reactions, rearrangements, and photochemistry during intensive structural studies. The group, led by Masao Maruyama (currently at Miyagi Kyoiku University) worked day and night for several years and had great fun. This was the last of the romantic and classical structural studies I did which involved many chemical degradations and derivatization reactions (Figure 1).[4] As far as we know, they are still the only natural products containing a *t*-butyl group, the unusual biosynthesis of which was studied by callus incorporation experiments.[5] Although no biological activity could be found for these aesthetically pleasing cage compounds with six five-membered rings including three γ-lactones, a spiro carbocycle, and a five-membered ether ring, subsequently the ginkgolides were found to be potent inhibitors of the platelet activating factor,[6] with over-the-counter annual sales exceeding $700 million.

The NMR of GA is too simple because the quaternary carbons and four lactones divide the protons into several groups with no connectivities [Figure 1(a)]. In order to gain more information, the lactones were reduced with lithium aluminum hydride (LAH). Upon accidental heating in an oven, the product octaol cyclized back to give the original pentacyclic cage(!), GA triether, the only difference being that now the three lactones had been replaced by ether rings. The triether exhibited a far more complex spectrum [Figure 1(c)] because of the proton connectivities arising from the new proton peaks designated cc′, ee′, and ff′. The similarity in the NMR of GA and GA triether-d_6, prepared by using LAD instead of LAH, shows that the original cage structure is retained in the triether [Figures 1(a) and (b)].[4]

During exhaustive decoupling experiments on the triether, Vyn and Iwao found that irradiation of the *t*-Bu peak led to 10%–33% enchancement in certain peak areas without an appreciable decrease in the halfbandwidth. Instead of dismissing this as an integrator error, they repeated the measurements and concluded that it was a new phenomenon. Vyn and Iwao suspected that it might be related to the Overhauser effect, where irradiation of unpaired electrons leads to enhancement of nearby proton signals,[7] and interpreted their observation as being due to an intramolecular Overhauser effect (spring 1966); this greatly facilitated our ginkgolide structural investigations. Around this time the first paper on NOE dealing with β,β-dimethylacrylic acid and a cage compound by Anet and Bourn appeared in the literature.[8] Vyn and Iwao's stubborn and uncompromising attitude had led to the finding of the NOE, unknown at that time in the natural products field. One of the first examples in our lab is shown in Figure 2. I presented a talk on NOE and the ginkgolide structure at the 4th IUPAC Symposium on Natural Products in Stockholm in June 1966,[9] and the NMR paper was submitted in the fall[10] together with four other communications leading to the final structure of the ginkgolides. We did not grasp the full implications of NOE when we first submitted our findings,[10] and hence the title was simply 'Some Aspects of their NMR Spectra'. However, its immense potential in structure determination

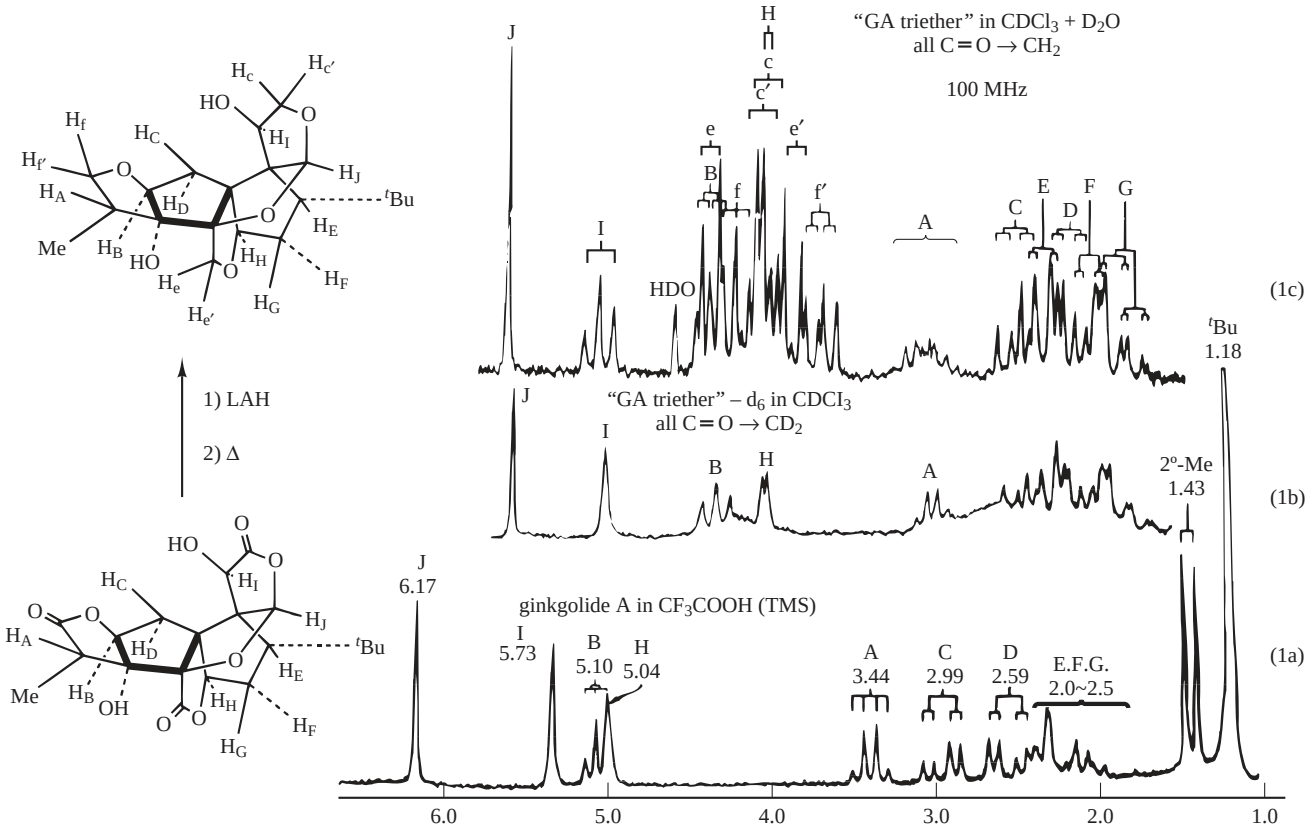

Figure 1 Proton NMR of ginkgolide A (GA) and derivatives at 100 MHz. (a) Bottom trace. GA in TFA. A, B, C, etc. denote the protons shown in the structure of GA. (b) Middle trace. 'GA triether'-d_6 obtained upon LAD reduction followed by pyrolysis, NMR in $CDCl_3/D_2O$. All lactonic carbonyls in GA are replaced by CD_2; differences in proton shifts between Figure 1(a) and (b) reflect difference in anisotropic effects. (c) Upper trace. 'GA triether' obtained upon LAH reduction followed by pyrolysis, NMR in $CDCl_3/D_2O$. All lactonic carbonyls in GA are replaced by CH_2, leading to a far more complex spectrum

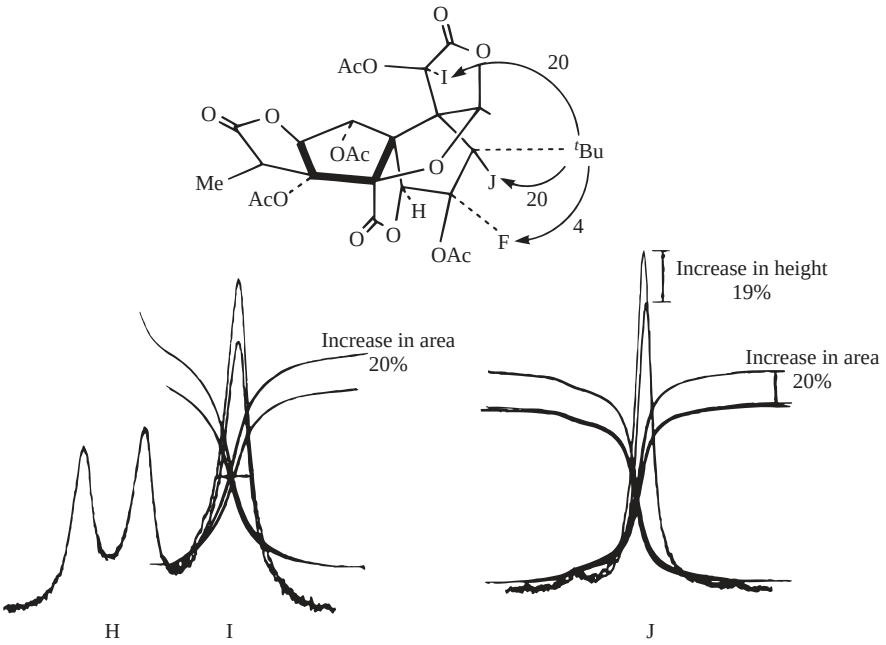

Figure 2 Effect of irradiating the *t*-butyl group in GC tetraacetate in TFA at 100 MHz. Traces show superimposed spectra with and without irradiation. Proton H, which is remote from the *t*-butyl group, shows no change in peak shape, whereas the signals of protons I and J, which are close to the *t*-butyl group, both undergo a ca. 20% increase in integrated area; although an increase in peak heights is seen, no appreciable decrease occurs in the halfbandwidths ($W_{1/2}$). A 4% NOE was also observed with proton F (not shown)

was soon realized and the next paper was more appropriately titled 'The Nuclear Overhauser Effect, a Unique Method of Defining the Relative Stereochemistry and Conformation of Taxane Derivatives'.[11]

REFERENCES

1. K. Nakanishi, H. Kakisawa, and Y. Hirata, *J. Am. Chem. Soc.*, 1955, **77**, 3169; K. Nakanishi, H. Kakisawa, and Y. Hirata, *Bull. Chem. Soc. Jpn.*, 1956, **29**, 7.
2. R. Harada, H. Kakisawa, S. Kobayashi, M. Musya, K. Nakanishi, and Y. Takahashi, *Tetrahedron Lett.*, 1962, 603.
3. M. Miyamoto, K. Morita, Y. Kawamatsu, S. Noguchi, R. Marumoto, K. Tanaka, S. Tatsuoka, K. Nakanishi, Y. Nakadaira, and N. S. Bhacca, *Tetrahedron Lett.*, 1964, 2355.
4. M. Maruyama, A. Terahara, Y. Itagaki, and K. Nakanishi, *Tetrahedron Lett.*, 1967, 299; M. Maruyama, A. Tetahara, Y. Itagaki, and K. Nakanishi, *Tetrahedron Lett.*, 1967, 303; M. Maruyama, A. Terahara, Y. Nakadaira, M. C. Woods, and K. Nakanishi, *Tetrahedron Lett.*, 1967, 309; M. Maruyama, A. Terahara, Y. Nakadaira, M.C. Woods, Y. Takagi, and K. Nakanishi, *Tetrahedron Lett.*, 1967, 315.
5. K. Nakanishi and K. Habaguchi, *J. Am. Chem. Soc.*, 1971, **93**, 3546.
6. P. Broquet (ed.), *Ginkgolides—Chemistry, Biology, Pharmacology and Clinical Aspects*, J. R. Prous Science Publishers, Barcelona, 1988, Vol. 1, p. 794.
7. A. W. Overhauser, *Phys. Rev.*, 1953, **92**, 411; A. Abragam, *Principles of Nuclear Magnetism*, Oxford Science Publications, Oxford, UK, 1961, p. 364.
8. F. A. L. Anet and A. J. R. Bourn, *J. Am. Chem. Soc.*, 1965, **87**, 5250.
9. K. Nakanishi, *Pure Appl. Chem.*, 1967, **14**, 89.
10. M. C. Woods, I. Miura, Y. Nakadaira, A. Terahara, M. Maruyama, and K. Nakanishi, *Tetrahedron Lett.*, 1967, 321.
11. M. C. Woods, H. C. Chiang, Y. Nakadaira, and K. Nakanishi, *J. Am. Chem. Soc.*, 1968, **90**, 522.

Biographical Sketch

Koji Nakanishi. *b* 1925. B.S., 1947, Ph.D., 1954, Nagoya University. Assistant Professor, Dept. of Chemistry, Nagoya University 1955–58; Professor, Dept. of Chemistry, Tokyo Kyoiku University 1958–63; Professor, Dept. of Chemistry, Tohoku University 1963–69; Professor, Dept. of Chemistry, Columbia University, 1969–80; Centennial Professor, Dept. of Chemistry, Columbia University, 1980–present; Chairman, Dept. of Chemistry, Columbia University, 1987–90; Director of Research, The International Centre of Insect Physiology and Ecology in Kenya, 1969–77; Director, Suntory Institute for Bioorganic Research in Osaka, 1978–91. Approx. 600 publications. Research interests include isolation, structural and bioorganic studies of bioactive compounds, retinal proteins, interaction between ligands and neuroreceptors, structural studies of oligosaccharides, and application of various spectroscopic methods, especially circular dichroic spectroscopy.

Norberg, Richard E.: NMR in Urbana and St. Louis

Richard E. Norberg
Washington University, St. Louis, MO, USA

UNIVERSITY OF ILLINOIS

I entered the University of Illinois as a physics graduate student in the fall of 1946. After some service as a teaching assistant I received research assistant support through to my Ph.D. by working with Arnold Nordsieck in the construction and testing of his compact synchro-driven analog differential analyzer. In addition to being a gifted theorist, Nordsieck was a master machinist. In a 1948 colloquium lecture Nordsieck described the Stanford and Harvard bulk sample NMR experiments. I decided to follow Erwin Hahn (a year ahead of me) into NMR research and in the spring of 1949 I began to share a lab with Erwin under the eaves on the top floor of the physics building. We had the support of two splendid electronics technicians, Howard Knoebel and Lynton Kypta. Much of the equipment either was homemade or World War II surplus. In daily conversations and lectures Erwin led me as I worked through the Stanford and Harvard papers and then as he proceeded with his own famous work on spin echoes. James Bartlett, a theorist who had encouraged Hahn, agreed to serve as my nominal thesis advisor and to authorize the modest necessary expenditures from the ONR contract which supported much of the departmental research.

Charles Slichter arrived from Harvard to join the faculty at Illinois in the fall of 1949. He at once took an interest in my work and I became his first graduate student, although he was not yet officially able to direct graduate theses. Between Hahn and Slichter I had unique mentors in NMR. During a splendid fall 1949 solid state physics course taught by Fred Seitz, I first learned something about the hydrogen in palladium system and its systematic variation of bulk magnetic susceptibility as the hydrogen concentration is changed and the 3d band filled. This struck me as a potentially interesting solid system for NMR investigation and, with encouragement from Seitz, Nordsieck, and Slichter, I set to work on a steady-state proton NMR investigation of shifts and relaxation times in HPd. I chose to work with protons within the 30 MHz 1.5-mil rf skin depth of 30 mil Pd wire which I had loaded in an H_2 atmosphere following glow discharge surface preparation. The thesis experiments were a bit eerie since the Pd rf coil appeared to be empty. Some measurements used a short segment of H-loaded Pd wire as the terminating stub of a nearly quarter wavelength rigid coaxial line. When Erwin Hahn discovered spin echoes late in 1949, I quickly converted my apparatus to pulsed spin echo investigations of the HPd system. I reduced transient coil disease for the free-standing Pd rf coils by potting the coil assembly with molten sulfur. As I completed my January 1951 thesis, I discovered that Henry Torrey's group at Rutgers had also been using proton NMR to study HPd.

Figure 1 shows the pulsed NMR apparatus used for my HPd work[1] and (with the addition of a pulsed boxcar integrator) for subsequent alkali metal studies with Slichter[2] and with his student Don Holcomb.[3] The dc field was provided by a D-shaped electromagnet constructed in 1938 for mass spectrographic work and powered by a Navy surplus selenium rectifier and parallel arrays of storage batteries. A frequency-modulated transitron oscillator NMR detector operating in a shimmed region of the pole face regulated the magnetic field. The panel at the lower left of Figure 1 shows the handle of a carbon pile resistor fine control on the magnet current. Above this are rack panels associated with the CW and pulsed rf crystal oscillators. In front on the table is the twin-T rf bridge with its dummy arm and the coax leading to the sample coil in the magnet. The signal from the bridge output went to a Wallman cascode preamplifier or to a surplus radar if strip and thence to a communications receiver with its if stages broadbanded to 30 kHz. The three oscilloscopes in the picture included one (bottom right) which could accept an external trigger and be conveniently used for pulsed NMR displays. The central rack panel controlled magnet regulation and a field modulation capability. On the right is a rack with a surplus frequency meter for field calibration and two communications receivers—one for detection of the transitron field control signal, and one for reception of the pulsed NMR free induction decays and spin echoes. Before we introduced the use of a boxcar integrator (a long time constant gated integrator and a dc amplifier), the data had to be recorded photographically from the oscilloscope and then measured mechanically. Warm-sample temperature control up to 75°C was achieved with a noninductively wound electrical heater inserted in a ceramic tube and placed within the Pd coil. Colder temperatures between 30°C and −60°C were achieved with a copper trough containing CS_2 or turpentine. Around the trough, copper tubing carried acetone from a reservoir containing a mixture of acetone and Dry Ice. The recycling pump and flow valve regulator consisted of a colleague and beaker. It all worked to within ±1°C.

Figure 1 Pulsed NMR equipment at Urbana, fall 1950

After my thesis defense in January 1951, I took the Nordsieck differential analyzer to the Radiation Laboratory at Berkeley for a LINAC design problem in W. Panofsky's group. After my return to Urbana in the spring of 1951, Slichter and I did spin echo studies of ^{23}Na motional narrowing in metallic sodium.[2] From mid-1951 to the summer of 1954 I had a University of Illinois appointment in physics and in

the Control Systems Laboratory (CSL), where I worked on computer–radar interface problems. During this time I worked on two novel pulsed nuclear resonance experiments. One was to continue work on alkali metals at night and on weekends with Slichter and with Don Holcomb. This work used our new pulsed boxcar integrator, which had been constructed to improve the limited signal-to-noise ratio which characterized the earlier HPd measurements. Since we were not yet using phase sensitive detection, it was necessary to calibrate the unipolar boxcar output for nonlinear diode detector response. The alkali metal work benefitted greatly from the help of Herb Gutowsky and Tom Carver.

A second new experiment arose from discussions about NQR with Charles Slichter and Myer Bloom. At CSL I had built another pulsed NMR rig to investigate the possible utility of digitally-encoded spin echoes and stimulated echoes for computer memory use. The computer memory idea did not work out, but I was able to use the 30 MHz pulse rig in a search for pulsed pure quadrupole echoes that had been predicted by Bloom. After some troubles with piezoelectric transients, I found the NQR echoes in $NaClO_3$ powder and then in a single crystal. After a few weeks the pulse rig was trucked over to the physics building and NQR was up and running there within a few hours. In another of those early coincidental efforts, it turned out that Erwin Hahn, then at the IBM Watson Lab, was not only working on an attempted spin echo computer memory but had also discovered pulsed NQR, so we published[4,5] adjoining NQR papers.

WASHINGTON UNIVERSITY

In August 1954 I came to Washington University as a visiting faculty member to replace George Pake, who was on leave at Stanford. Things worked out well and I remained at Washington University. From Pake and from Don Maxwell I inherited a small group with AFOSR support and graduate students C. Robert Bruce, James Burgess, and Irving Lowe. I was already familiar with the George Pake/Sam Weissman magnetic resonance groups since the Illinois and St. Louis groups quite regularly exchanged visits to each other's laboratories.

At Washington University I found faculty research collaborators in George Pake, Jack Townsend, Sam Weissman (in chemistry), and Barry Commoner (in botany). Eugene Feenberg and Henry Primakoff were the leading Physics Department theorists and they both maintained an interest in the NMR work. In St. Louis, as in Urbana, most of the magnetic resonance equipment was homemade. The single pulsed NMR apparatus had been assembled by Maxwell and Lowe. There were several modest electromagnets and permanent magnets. The latter included one permanent magnet whose field had been homogenized for high-resolution work by the heroic efforts of Bob Bruce. He used a micromanipulator and CW proton NMR from a small mineral oil sample to map contours of constant field in various gap planes. Then he shimmed the field by using the field plot templates and emery cloth to remove iron plated onto two brass discs to be mounted on the magnet pole faces. After homogenization, the magnet provided a resolution of about one part in 10^7 for a static proton liquid sample of 12 μl. Thermal stabilization of the magnet was required since the 27 MHz proton resonance frequency changed by 6 kHz per °C.

In a 1955 collaboration with Sam Weissman,[6] Bruce used his homogeneous magnet and high-resolution proton NMR to make the first NMR measurement of an electron exchange rate too slow to study with ESR. In 1956 Bruce, George Pake, and I pointed out[7] that radiation damping could significantly affect CW high-resolution NMR spectra. Bruce had observed radiation damping in his thesis work. Although the topic was discussed by others, it remained somewhat obscure until the growth of commercial high-resolution NMR.

Beginning from studies of ^{1}H and ^{19}F NMR in polymers, Irving Lowe and I became interested in the lineshapes of simple dipolar-coupled rigid lattice arrays of nuclear spins $\frac{1}{2}$. Lowe discovered that the free induction decays in cold polyethylene and Teflon were nonmonotonic but rather showed a distinct beat structure. Lowe set out to undertake single crystal studies and CaF_2 was an obvious choice because of its 100% abundant simple cubic array of ^{19}F spins and negligible abundance of ^{43}Ca. In addition, George Pake[8] and Bob Bruce[9] had studied the angular variation of the ^{19}F CW absorption line in CaF_2 and found good agreement with the second moment calculations of Van Vleck.[10] It was obvious that the Lowe beats reflected a lineshape somewhat more rectangular than a Gaussian and so we set to work to examine the Fourier transform relation between the free induction decay and the steady-state lineshape. Another connection with Illinois occurred when Bruce used the Nordsieck differential analyzer at Urbana to integrate his first derivative CW lineshapes and obtain the absorption lines published[9] and compared (via our Fourier transform theorem[11]) with Lowe's free induction decays. I believe that Lowe's subsequent work on the ^{19}F line in CaF_2 has made it by far the best-determined lineshape in any spectroscopy. Leonard Bowen, our early colleague in some of the polymer work, was a postdoctoral associate who returned to Australia and set up the first pulsed NMR apparatus on that continent.

Working with Irving Lowe was a delightful experience. Each day we would discuss some spin quantum mechanics and then early the next morning Lowe would arrive at my office to see if I had discovered the errors in the previous day's efforts. George Pake recommended me for an Alfred P. Sloan Fellowship and the award of that money allowed Lowe to stay on as a postdoc following his fall 1956 degree. During that time Lowe invented magic angle spinning[12] as a method for the pulsed NMR of rigid lattice solids. In another of the many coincidences in NMR, Raymond Andrew independently was developing MAS in CW experiments. My new students William Yen and Horst Kessemeier analyzed the first MAS results on CaF_2 and Teflon. The published transform spectra[12] were the results of tedious transformations using a mechanical desk calculator. Kessemeier went on to do the first FT examination of MAS-resolved chemically shifted lines in a solid spectrum.[13] Mg_3P_2, Zn_3P_2, and AlP were chosen for their large internuclear separations and consequent narrow rigid lattice lines. Arden Sher saw our first ^{129}Xe signals and Mario Engelsberg did a beautiful study[14] of the interference of pseudodipolar and dipolar interactions for ^{31}P in InP. Yen did the first pulsed NMR studies of self-diffusion in a rare gas solid (^{129}Xe in solid xenon).[15] Yen's ^{129}Xe work led to a series of rare gas measurements[16] on ^{131}Xe (William Warren, Don Cowgill, and Harry Ringermacher);

^{21}Ne (Rodney Henry and Bruce Sirovich); and ^{83}Kr (Don Cowgill, Eric Madaras, Jose Vithayathil, and Matt Commens). Warren's ^{131}Xe work led to the observation of a resolved composite solid echo–quadrupole echo in solid xenon. The ^{83}Kr work, in particular, led to a continuing collaboration with Peter Fedders, in which appreciation of the effects of intraspin cross relaxation[17] was crucial to understanding the NMR results. In solid neon and krypton, the rotating frame $T_{1\rho}$ methods of Slichter and Ailion[18] and of Look and Lowe[19] were essential for precise determinations of diffusion parameters and of spectral diffusion rates.

K. Luszczynski arrived in St. Louis from Great Britain in 1959 and we set out to do low-temperature pulsed NMR of quantum fluids. With James Opfer, James Gaines, and David Biegelsen we investigated spin–lattice relaxation, diffusion, spin diffusion, and magnetic susceptibility of ^{3}He in gas and liquid in ^{3}He–He(II) solutions.

In the summer of 1969, I met a St. Louis area high school student named Mark Conradi. He entered Washington University as a freshman in 1970 and at once began to work as an NMR electronics technician and laboratory wizard. Mark stayed on for his graduate work and later returned as a tremendous addition to our faculty. Conradi's Ph.D. thesis work[20] on dilute *ortho*- H_2 (o-H_2) in rare gas solids and liquids opened a research avenue which has continued to this day via the work of Carl Edwards, Gregory Mohr, Joseph Ganem, Jonghun Lyou, and Zhen Yan. Here again collaboration with Peter Fedders has been essential. The Raman-driven quadrupolar phonon transitions among the J = 1 o-H_2 molecular m_J states relax the protons and give rise to the characteristic power law temperature variations of T_1. This signature permitted us to recognize[21] the presence of molecular hydrogen in hydrogenated amorphous silicon. A decade of work followed on host-bonded hydrogen, H_2, HD, and D_2 in amorphous semiconducting films, where collaborations with James Boyce (Xerox PARC) and William Paul (Harvard) have been very fruitful. Dan Leopold made the first of our deuteron magnetic resonance structural measurements in amorphous semiconductors. He has been followed by Vincent Bork, Martin Volz, Plinio Santos, Yong Wah Kim, Robert Corey, Jeffrey Bodart, Pei Hsuon Chan, and Mary Jane Kernan.

The semiconductor work also led to the discovery of deuteron multiple echoes[22] for HD and o-D_2 physisorbed and trapped on internal surfaces in semiconductors and on MgO and BN.[23] The multiple echoes provide unique signatures for the first physisorbed layer and for HD/H_2 and o-D_2/HD isotopic separation. Other collaborations with Conradi have produced such results as the successful application of NMR to high-pressure studies in a diamond anvil cell[24] and current work on metal hydrogen systems with David Baker, Robert Bowman, Richard Barnes, and David Torgeson. This has extended earlier metal hydride work by Nouha Salibi, Bico Ting, Harry Ringermacher, Vincent Bork, and Martin Volz.

Over the many years, I have been particularly fortunate in the many excellent colleagues with whom I have worked.

REFERENCES

1. R. E. Norberg, *Phys. Rev.*, 1952, **86**, 745.
2. R. E. Norberg and C. P. Slichter, *Phys. Rev.*, 1951, **83**, 1074.
3. D. F. Holcomb and R. E. Norberg, *Phys. Rev.*, 1955, **98**, 1074.
4. M. Bloom and R. E. Norberg, *Phys. Rev.*, 1954, **93**, 638.
5. E. L. Hahn and B. Herzog, *Phys. Rev.*, 1954, **93**, 639.
6. C. R. Bruce, R. E. Norberg, and S. I. Weissman, *J. Chem. Phys.*, 1956, **24**, 473.
7. C. R. Bruce, R. E. Norberg, and G. E. Pake, *Phys. Rev.*, 1956, **104**, 419.
8. G. E. Pake and E. M. Purcell, *Phys. Rev.*, 1948, **74**, 1184.
9. C. R. Bruce, *Phys. Rev.*, 1957, **107**, 43.
10. J. H. Van Vleck, *Phys. Rev.*, 1948, **74**, 1168.
11. I. J. Lowe and R. E. Norberg, *Phys. Rev.*, 1957, **107**, 46.
12. I. J. Lowe, *Phys. Rev. Lett.*, 1959, **2**, 285.
13. H. Kessemeier and R. E. Norberg, *Phys. Rev.*, 1967, **155**, 321.
14. M. Engelsberg and R. E. Norberg, *Phys. Rev. B*, 1972, **5**, 3395.
15. W. M. Yen and R. E. Norberg, *Phys. Rev.*, 1963, **131**, 269.
16. R. E. Norberg, *Springer Tracts in Modern Physics*, Springer Verlag, Heidelberg, 1984, Vol. 103, p. 59.
17. P. A. Fedders, *Phys. Rev. B*, 1977, **15**, 3297.
18. C. P. Slichter and D. Ailion, *Phys. Rev.*, 1964, **135**, A1049.
19. D. C. Look and I. J. Lowe, *J. Chem. Phys.*, 1966, **44**, 2995.
20. M. S. Conradi, K. Luszczynski, and R. E. Norberg, *Phys. Rev. B*, 1979, **20**, 2594.
21. M. S. Conradi and R. E. Norberg, *Phys. Rev. B*, 1981, **24**, 2285.
22. M. P. Volz, P. Santos-Filho, M. S. Conradi, P. A. Fedders, R. E. Norberg, W. Turner, and W. Paul, *Phys. Rev. Lett.*, 1989, **63**, 2582.
23. E. K. Jeong, B. Ouyang, R. E. Norberg, P. A. Fedders, and M. S. Conradi, *Phys. Rev. Lett.*, 1992, **69**, 2983.
24. S. H. Lee, K. Luszczynski, R. E. Norberg, and M. S. Conradi, *Rev. Sci. Instrum.*, 1986, **58**, 415.

Biographical Sketch

Richard E. Norberg. *b* 1922. B.A., 1943, Ph.D., 1951, Physics, University of Illinois, USA, where he was introduced to NMR by Charles Slichter and Erwin Hahn. Postdoctoral work, University of Illinois, 1951–54. Faculty in Physics, Washington University, 1954–present. Approx. 100 publications. Research specialties: NMR at high pressure, for physisorbed species, in amorphous semiconductors, in condensed rare gases, in metal–hydrogen systems, for matrix isolated H_2, HD, and D_2.

Oldfield, Eric: NMR Adventures in Chemistry and Biology

Eric Oldfield

University of Illinois at Urbana-Champaign, Urbana, IL, USA

After undergraduate research on gibberellin glycosides (with Jake MacMillian) and on lipid bilayer structure (with Geoffrey Eglinton) at Bristol, I moved to Sheffield to work with Dennis Chapman on the development of new methods to study membranes. We began with an analysis of wideline pulsed NMR,[1] but it soon became clear that ^{1}H NMR methods were going to be difficult in that one had to settle either for low resolution (on multilayers, or intact membranes), or high resolution on less-than-intact systems. We also disliked the spin-label method, since knowing where the label was or how it might distort its local environment always seemed problematic. Fortunately, we had on hand some chain deuterated lipid (which had been made by Unilever to aid in their ^{1}H wideline assignments), Bill Derbyshire at Nottingham had a wideline deuterium probe (for studying $^{2}H_2O$ in meat), and I had an idea.

We obtained the first ^{2}H NMR spectra of membranes in early 1971, and were pleased to see that gel and liquid crystalline spectra were very different and that cholesterol caused large spectral changes—an increase in quadrupole splitting from ~27 kHz to 50 kHz above the pure lipid-phase transition temperature and an essentially identical spectrum below T_c[2]—indicating that the ^{2}H NMR method was going to be a useful new, nonperturbing probe of lipid and membrane structure. We then biosynthetically incorporated ^{2}H labeled fatty acids into real cell membranes, from *Acholeplasma laidlawii* B, and found surprisingly large amounts of gel phase lipid at the growth temperature.[3] The ^{2}H NMR method was then further developed by many groups, and at present appears to be one of the best spectroscopic techniques with which to study the structure of lipids and membranes. At Sheffield, we also began (in 1971) an exploration of ^{1}H magic angle sample-spinning of membranes with D. Doskočilová and B. Schneider in Czechoslovakia[4]—but it took about another 10 years for the technology to catch up with our needs, and in the 1980s we reported the first truly high-resolution (500 MHz) ^{1}H MAS spectra of lipids,[5] work which was successful because of the special 'inhomogeneous' nature of the dipolar interactions involved.[5] A natural outgrowth of this work was to investigate further the ^{13}C lipid and membrane systems we had struggled with in the early 1970s,[6,7]—such as lecithin–cholesterol and myelin[8,9]—which now give spectacular resolution.

After graduate school, I moved in 1972 'temporarily' to the United States to work with Adam Allerhand. Adam had the best ('homebuilt') ^{13}C NMR spectrometer available, and we all badly wanted to see individual ^{13}C sites in proteins—a feat accomplished with the 20-mm probe.[10] We used to cram 2–3 g of protein into the tube, and wait—but the spectra were extremely nice[11]—although generally restricted to nonprotonated carbons.[12] Of course, these days such amounts of protein seem absurd—although with labeling the numbers of ^{13}C spins are about the same!

The results obtained in 1972–74 clearly showed the excellent spectral resolution of ^{13}C NMR, where chemical shift nonequivalencies due to folding of >6 ppm were seen. These chemical shifts remained mysterious for about 20 years, even though without them modern higher dimensional studies of protein structure would be impossible. So after several attempts at explaining ^{13}C shifts empirically, we eventually tried the quantum chemistry approach.[13] It worked.[14] Thus, if a good starting structure is available, it is now possible to predict ^{13}C, ^{15}N, and even ^{19}F chemical shifts in proteins, an observation which should have significance for future use in structure prediction and structure refinement—both in solution and also in the solid state.

After several years at Illinois working on topics such as lipid–protein interaction ('boundary lipid') via ^{2}H NMR,[15,16] on analyzing phospholipid and glycolipid structure via ^{2}H NMR,[17] as well as developing the sideways-spinning probe for sensitivity enhancement,[18] we moved our interests into the area of inorganic chemistry and the materials sciences. In particular, we began to investigate the much neglected nonintegral spin quadrupolar nuclei.[19] Although MAS NMR of such systems had been reported much earlier by Andrew, the higher field strengths of the 1980s reduced second-order broadening such that very many nuclei (not just ^{133}Cs or cubic solids) became accessible. Also, we found that line narrowing of the central $(\frac{1}{2}, -\frac{1}{2})$ transition was much more effective at angles other than the magic angle, and variable-angle sample spinning began.[20,21] However, MAS NMR was the preferred modality, and we began a decade-long exploration of (primarily) ^{17}O NMR in inorganic solids, ranging from zeolite catalysts[22] to mineral phases,[23] and using static samples from heme-proteins[24] to high-temperature superconductors.[25,26] For the high-T_c materials, we used the method of magnetic ordering previously used in our ^{2}H NMR studies of heme proteins,[27] and obtained exceptionally highly resolved spectra—19 out of 20 peaks resolved in $YBa_2Cu_3O_{7-x}$.[25]

Our studies of quadrupolar nuclei eventually led to investigations of spin–spin relaxation, which we found was usually dominated by homonuclear and heteronuclear dipolar interactions.[28] This recently led to a useful technique for 'editing' out industrial catalyst binder (e.g. γ-Al_2O_3) resonances, which normally swamp the minor (but active) zeolite signals. We also recently introduced new methods using weak or selective pulse excitation, which enables quadrupole–quadrupole nucleus cross polarization, as well as the *quantitative* analysis of quadrupolar nuclei in solids, using weak-pulse spin echo excitation methods.[29]

When taken together, these developments, as well as those of Lippmaa, Fyfe, Thomas, and others have opened up the whole world of inorganic chemistry and materials science to investigation by means of solid state NMR. However, it is remarkable how little *analysis* of the plethora of chemical shift and quadrupole coupling constant data has actually been performed—a situation remarkably akin to the protein chemical shift problem noted above. Thus, there is now no shortage of data,[30,31] and it can be anticipated that new analyses of shielding and field gradient results will go hand-in-hand with price/performance improvements in computational hardware, over the next few years.

This leads to my final comment related to the general problem we have been posed by the editors: how did NMR develop? I think that it is fairly clear that not unlike the

Industrial Revolution, pure science drives technology and we all benefit from the technological developments. The discovery of NMR utilized World War II rf and magnet technology. Signal averaging and FT NMR used new computers, just as now we use the newest computers to perform dynamics trajectories or shielding calculations. The trick, of course, is to apply the new technologies in interesting new ways. Here, we often have to acknowledge the role of serendipity. This would probably be unsurprising to, for example, the discoverer of penicillin or lysozyme, or the first observers of spin echoes in liquids or multiple echoes in solids, but is perhaps not fully appreciated by new researchers. The '99% perspiration, 1% inspiration' axiom is probably about right.

Acknowledgement

This work was supported by the United States Public Health Service, the US National Science Foundation, the American Heart Association, the Illinois Heart Association, the US Department of Energy, the University of Illinois, the Alfred P. Sloan Foundation, the United Kingdom Science Research Council, the Mobil Foundation, Universal Oil Products, Texaco, Engelhard Corporation, and the Shell Oil Company.

REFERENCES

1. E. Oldfield, J. Marsden, and D. Chapman, *Chem. Phys. Lipids*, 1971, **7**, 1.
2. E. Oldfield, D. Chapman, and W. Derbyshire, *FEBS Lett.*, 1971, **16**, 102.
3. E. Oldfield, D. Chapman, and W. Derbyshire, *Chem. Phys. Lipids*, 1972, **9**, 69.
4. D. Chapman, E. Oldfield, D. Doskočilová, and B. Schneider, *FEBS Lett.*, 1972, **25**, 261.
5. J. Forbes, C. Husted, and E. Oldfield, *J. Am. Chem. Soc.*, 1988, **110**, 1059.
6. E. Oldfield and D. Chapman, *Biochem. Biophys. Res. Commun.*, 1971, **43**, 610.
7. K. M. Keough, E. Oldfield, D. Chapman, and P. Beynon, *Chem. Phys. Lipids*, 1973, **10**, 37.
8. E. Oldfield, J. L. Bowers, and J. Forbes, *Biochemistry*, 1987, **26**, 6919.
9. J. Forbes, J. Bowers, X. Shan, L. Moran, E. Oldfield, and M. A. Moscarello, *J. Chem. Soc., Faraday Trans. 1*, 1988, **84**, 3821.
10. A. Allerhand, R. F. Childers, and E. Oldfield, *Biochemistry*, 1973, **12**, 1335.
11. E. Oldfield and A. Allerhand, *Proc. Natl. Acad. Sci. USA*, 1973, **70**, 3531.
12. E. Oldfield, R. S. Norton, and A. Allerhand, *J. Biol. Chem.*, 1975, **250**, 6381.
13. R. Ditchfield, *J. Chem. Phys.*, 1972, **56**, 5688; K. Wolinski, J. F. Hinton, and P. Pulay, *J. Am. Chem. Soc.*, 1990, **112**, 8251.
14. A. C. de Dios, J. G. Pearson, and E. Oldfield, *Science*, 1993, **260**, 1491.
15. E. Oldfield, R. Gilmore, M. Glaser, H. S. Gutowsky, J. C. Hshung, S. Y. Kang, T. E. King, M. Meadows, and D. Rice, *Proc. Natl. Acad. Sci. USA*, 1978, **75**, 4657.
16. S. Y. Kang, H. S. Gutowsky, J. C. Hsung, R. Jacobs, T. E. King, D. Rice, and E. Oldfield, *Biochemistry*, 1979, **18**, 3257.
17. R. Skarjune and E. Oldfield, *Biochemistry*, 1982, **21**, 3154.
18. E. Oldfield and M. Meadows, *J. Magn. Reson.*, 1978, **31**, 327.
19. M. D. Meadows, K. A. Smith, R. A. Kinsey, T. M. Rothgeb, R. P. Skarjune, and E. Oldfield, *Proc. Natl. Acad. Sci. USA*, 1982, **79**, 1351.
20. E. Oldfield, S. Schramm, M. D. Meadows, K. A. Smith, R. A. Kinsey, and J. Ackerman, *J. Am. Chem. Soc.*, 1982, **104**, 919.
21. S. Ganapathy, S. Schramm, and E. Oldfield, *J. Chem. Phys.*, 1982, **77**, 4360.
22. H. K. C. Timken, G. L. Turner, J.-P. Gilson, L. B. Welsh, and E. Oldfield, *J. Am. Chem. Soc.*, 1986, **108**, 7231.
23. H. K. C. Timken, S. E. Schramm, R. J. Kirkpatrick, and E. Oldfield, *J. Phys. Chem.*, 1986, **91**, 1054.
24. E. Oldfield, H. C. Lee, C. Coretsopoulos, F. Adebodun, K. D. Park, S. Yang, J. Chung, and B. Phillips, *J. Am. Chem. Soc.*, 1991, **113**, 8680.
25. E. Oldfield, C. Coretsopoulos, S. Yang, L. Reven, H. C. Lee, J. Shore, O. H. Han, E. Ramli, and D. Hinks, *Phys. Rev. B*, 1989, **40**, 6832.
26. L. Reven, J. Shore, S. Yang, T. Duncan, D. Schwartz, J. Chung, and E. Oldfield, *Phys. Rev. B*, 1991, **43**, 10466.
27. T. M. Rothgeb and E. Oldfield, *J. Biol. Chem.*, 1981, **256**, 1432.
28. J. Haase and E. Oldfield, *J. Magn. Reson., Ser. A*, 1993, **101**, 30.
29. J. Haase and E. Oldfield, *J. Magn. Reson.*, 1993, **104**, 1.
30. E. Oldfield and R. J. Kirkpatrick, *Science*, 1985, **227**, 1537.
31. E. Oldfield, in *Encyclopedia of Inorganic Chemistry*, ed. R. Bruce King, John Wiley & Sons, Chichester, 1994, 5, 2645.

Biographical Sketch

Eric Oldfield. *b* 1948. B.Sc., 1969, University of Bristol, Ph.D., 1972 (supervisor Dennis Chapman), University of Sheffield, D.Sc., 1982, University of Bristol, UK. Postdoctoral work at Indiana University, Bloomington (with Adam Allerhand) and Massachusetts Institute of Technology, Cambridge (with John S. Waugh). Professor, University of Illinois at Urbana-Champaign, 1975–present. Approx. 200 publications. Research specialties: inorganic and biochemical applications, especially proteins, membranes, and heterogeneous catalysts.

Opella, Stanley J.: NMR Spectroscopy and Structural Biology

Stanley J. Opella

University of Pennsylvania, Philadelphia, PA, USA

PERSONAL PERSPECTIVE

It is an extraordinary privilege to be Professor of Chemistry at a major research university in the United States of America. The freedom to choose research goals and the responsibility to utilize public support wisely and creatively in pursuit of these goals, while training students in the ways of science, make this a unique and rewarding endeavor. The overall goals of my research program, which is in the Department of Chemistry at the University of Pennsylvania, are to develop NMR methods and instrumentation for the study of proteins and to apply NMR spectroscopy to determine the structures and describe the dynamics of proteins, especially those that are difficult or impossible to characterize by conventional approaches to structural biology. In practice, these research goals typically evolve into finding ways to master the correlation time problem, which results from large proteins and proteins in complexes reorienting so slowly that their resonances are too broad and weak for high-resolution studies.

From the day I first learned that structural biology existed, I have felt that it was the most important thing to understand and I wanted to be part of it. Structural biology is emerging as a comprehensive scientific method for describing, predicting, and altering biological organisms, including humans. It is truly contemporary science, based on the intellectual and technical revolutions that occurred in the fields of biophysics, molecular biology, and computation during the last decade. And it is one of the reasons that the 1990s are a wonderful time to participate in scientific research. For the first time it will be possible to understand how the macroscopic characteristics of life, such as reproduction and thought, are determined by the arrangements of atoms in polypeptides. I find it difficult to understand why so many students find fields firmly rooted in the past, such as literature, law, or finance, so attractive when contemporary chemistry and biology beckon.

Devastating hereditary diseases, such as sickle cell anemia or cystic fibrosis, provide dramatic illustrations of how enormous changes in biological function result from substituting a few atoms out of the several thousand in an individual protein. In contrast, much larger changes are tolerated without apparent consequences in some other proteins. This selectivity, which can only be understood through structural studies of proteins, provides opportunities for biomedical intervention in diseases as well as for the biotechnology industry to alter biological functions in ways thought to guarantee profits.

Of course, when I first heard of structural biology as an undergraduate chemistry major at the University of Kentucky, it was called bioorganic or biophysical chemistry. My understanding was that when the most powerful chemical and physical methods were used to study proteins and other biopolymers, their structural and functional properties could be analyzed in atomic detail. I was fully convinced as a junior in college that by utilizing the most sophisticated instruments and methods of spectroscopy, it would be possible to understand biological phenomena at the same level of detail as chemistry and physics. I knew I wanted to do NMR spectroscopy as soon as I learned that it enabled biopolymers to be probed with sophisticated instruments and techniques in the laboratory of Stanford L. Smith at the University of Kentucky during an undergraduate research project. At that time I learned a lot about research from many informal discussions in the department, especially with Joseph Wilson.

I was fortunate to be a graduate student at Stanford in the early 1970s when the Chemistry Department was at the forefront of interdisciplinary studies. This enabled me to obtain a Ph.D. in physical chemistry under the aegis of Harden McConnell while working on solution NMR studies of proteins in the laboratory of Oleg Jardetzky. I learned valuable lessons from these two pioneers of biological magnetic resonance, who differ so much in style. At that time NMR studies of proteins were severely limited by the technical capabilities of commercial NMR spectrometers, especially their low magnetic fields. I performed my graduate research on one of the first continuous wave spectrometers converted to pulsed Fourier transform operation by Transform Technology, Inc. This enabled me to convert from the era of continuous wave to that of pulsed spectroscopy just as it moved from development to application laboratories, and I benefited tremendously in this from having the opportunity to work closely with Roy Johnson as the instrumentation and software were developed. My initial approach to overcoming the limitations of ^{1}H NMR studies of proteins in solution was to observe other nuclei, especially with ^{13}C and labeled-site ^{19}F NMR experiments.[1] Later on ^{14}N and ^{15}N were to become favorite nuclei for interrogation.[2–4]

As I was completing my graduate research at Stanford, I started to focus on what kind of research and training to pursue next. The day-to-day limitations of NMR spectroscopy of proteins were so severe that the outstanding goal was simply to get past the barriers of the technique so that you could start thinking about proteins. Even then, prior to the development of convenient cloning and expression systems, new proteins were being isolated regularly, but it was numbing for every discussion about a protein to start with its molecular weight and solubility rather than its function. In order to reconcile my belief that NMR spectroscopy was the best way to study proteins with its inability to work effectively with most proteins, I was determined to attack its limitations head on. Solid state NMR spectroscopy appeared to offer this opportunity, since here the methods were actually improved by immobilization of the sample rather than made worse as is the case for solution NMR spectroscopy. The attractiveness of this approach was apparent in the dramatic results emerging from John Waugh's laboratory at MIT, and it was a great opportunity for me to work in his laboratory as a postdoctoral fellow in 1975 and 1976. I read the initial papers on high-resolution solid state NMR spectroscopy very carefully, and came to the conclusion that this type of spectroscopy was going to revolutionize the way proteins were studied. After all, the first paper on proton-enhanced nuclear induction spectroscopy did say 'Studies of chemical shift anisotropy of rare species

(e.g. metals bound to *proteins*) or the dipolar structure of rare spin groups . . . could be of value in structural studies'.[5]

As I began to write postdoctoral fellowship applications, I tried to systematize my ideas for protein NMR spectroscopy. I wanted to choose a protein system based on its biological importance, yet it still had to be tractable for spectroscopic experiments that were at an early stage in their development. The main issue certainly was size, but there are really two parts to this; the mass of the actual species in the sample tube since that determines the effective correlation time, and the complexity of the polypeptide chain that determines the number of resonances to resolve. The ideal system to start with for solid state NMR spectroscopy would have a large overall size due to many identical subunits that are symmetrically arranged. This would result in the situation where only a single polypeptide chain had to be studied, once the spectroscopic methods dealt with the correlation time problem. It would also have to be bacterial so that it could be both made in large amounts and labeled with stable isotopes.

I quickly decided on studying the coat proteins of bacteriophages. I first looked into the possibilities for the coat proteins of icosahedral viruses, but could find none with suitably short polypeptides. And then I learned about the filamentous bacteriophages because I was doing a lot of reading in the biochemistry library at Stanford and right at that time there was considerable activity in that department studying M13, a prototypical filamentous phage. I recall assuring several funding agencies that I could describe the coat protein in the virus particles in some detail during the two-year period of a postdoctoral fellowship. Of course, here it is 20 years later and I am still working on the problem. Considerable progress has been made in the last few years in describing the structure[6] and dynamics[7] of the coat proteins in the bacteriophage.

I joined the Department of Chemistry at the University of Pennsylvania as an assistant professor in 1976. At that time the department was still in the early stages of what was to become a spectacular development program initiated by David White, the Chairman who recruited and nurtured many of us. The greatest benefit of working in this department is the opportunity to work with the many talented and highly motivated undergraduate, graduate, and postdoctoral students who are here.

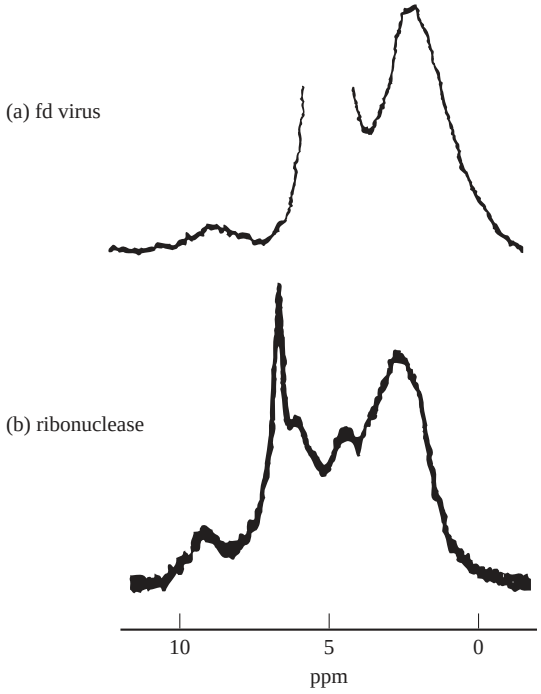

Figure 1 A comparison of high resolution ^{1}H NMR spectra of two proteins: (a) fd coat protein in virus particles in solution in a high-field spectrometer;[9] (b) ribonuclease in solution in a low-field spectrometer.[8] The spectra were scanned from the original articles and their width and alignment adjusted in a computer. Hence the scale is appropriate only for qualitative comparisons.

RESEARCH PERSPECTIVE

NMR Spectroscopy of Proteins

Even the earliest applications of NMR spectroscopy to proteins sought to identify spectral parameters that could be associated with the three-dimensional folding of proteins, primarily through the influence of the local protein environment on the chemical shifts of ^{1}H resonances. The first published NMR spectrum[8] of a protein is presented in Figure 1(b). It is my favorite because it provides optimism. By recognizing that this spectrum could be turned into the multidimensional masterpieces of today with every ^{1}H, ^{13}C, and ^{15}N resonance resolved and assigned, it is possible to be hopeful about almost any spectrum that might be acquired. For example, the spectrum in Figure 1(a) is a conventional one-dimensional ^{1}H NMR spectrum of fd bacteriophage.[9] Even though the predominant species is a 50-residue coat protein, the lines are very broad and weak, remarkably similar to those in the spectrum in Figure 1(b). This comparison illustrates one of the primary objects of my research, and that is to develop instrumentation and methods so that a spectrum like that in Figure 1(a) can be the starting point for detailed structural studies. The spectrum in Figure 1(a) was obtained under conditions that yield quite high-resolution spectra for the types of samples that were used to obtain the spectrum in Figure 1(b); since the breadth of its resonances reflects the slow reorientation of the protein complex, it is an entirely different task to turn this spectrum into something usable.

Rapid isotropic reorientation of proteins in solution is essential for the use of instrumentation, methods, and interpretations based on isotropic chemical shifts, spin–spin couplings, and through-space dipole–dipole interactions that result in nuclear spin relaxation, and when that is missing spectra such as that in Figure 1(a) result. In some cases, specific, selective, and uniform labeling with ^{15}N and/or ^{13}C aid in the resolution and assignment of complex spectra. These, and other labeling strategies, especially with ^{2}H, extend solution NMR methods to somewhat more slowly reorienting proteins. However, none of these methods are usable with proteins that are immobilized by virtue of their being part of supramolecular structures in solution, such as virus particles, membrane bilayers, or in the crystalline or amorphous solid state. This is the domain of solid state NMR spectroscopy, even if the samples are actually solutions.

THE DEVELOPMENT OF SOLID STATE NMR SPECTROSCOPY OF PROTEINS

The most important reason for developing solid state NMR spectroscopy as a general method for determining the structures of proteins is that it will extend the range of proteins that can be described at atomic resolution to include membrane proteins. Both X-ray crystallography and multidimensional solution NMR spectroscopy are highly effective methods for determining the structures of proteins. However, they are restricted for practical reasons to a single class of proteins—water-soluble, globular proteins with well-defined tertiary structures that tend to crystallize but not aggregate—and only a minority of biological properties are expressed by the globular proteins of the cytoplasm and the periplasm. There are other important classes of proteins, including structural proteins and membrane-bound proteins, that have very few examples with their structures determined. Additional reasons for developing high-resolution solid state NMR spectroscopy of proteins include its ability to give an alternative view of these structures, its ability describe their structure and dynamics in an integrated manner, and its relaxed sample requirements compared with the standard methods for protein structure determination. In addition, there is no intrinsic size limitation for the polypeptides that can be studied by solid state NMR spectroscopy.

Although solid state NMR spectroscopy was established as an independent method for determining molecular structure at atomic resolution in 1948,[10] only recently has it been used to obtain structural information that is completely independent of X-ray diffraction results, primarily because of the need to devise experimental methods capable of yielding spectra with sufficient sensitivity and resolution for observing resonances from individual sites in complex molecules like proteins. The basic physical properties of the various spin interactions are so well understood that spectroscopic interpretations have not been a limiting factor in applying solid state NMR spectroscopy to the study of proteins. A combination of biochemical and spectroscopic manipulations makes it possible to obtain spectra of proteins where resonances are resolved, assigned, and have spectral parameters from one of the spin interactions expressed in a defined way. The large amplitude, rapid motions of protein in solution average the chemical shift, dipolar, and quadrupolar spin interactions to their isotropic values, and only the indirect effects of their fluctuations through relaxation phenomena yield spatial information in the form of relative proximities. In contrast, in immobile proteins the rigid lattice values, as well as their angular dependencies, are directly observed.

The solid state NMR approach to determining the structures of peptides and proteins in oriented samples that we are most intensively involved in developing relies on the spectral simplifications that result from uniaxial sample orientation parallel to the direction of the applied magnetic field.[11] The spin interactions at individual sites yield single resonance lines characterized by their resonance frequencies or doublets (or triplets) characterized by the magnitudes (and asymmetry) of their splittings. The observed values of the frequencies and splittings depend on the orientations of the principal axes of the spin-interaction tensors present at each site relative to the direction of the applied magnetic field. Since the directions of sample orientation and the applied magnetic field are the same, they define a frame of reference for the evaluation of the orientational information. The orientations of many spin-interaction tensors have been established in their molecular frames of reference, enabling angular factors to be determined from the experimental data.

The development of solid state NMR spectroscopy as a method for determining the structures of oriented macromolecules began in 1975–76 with the observation of high-resolution spectra from a polymer fiber oriented parallel to the direction of the applied magnetic field, and the determination of the angles between the C–H bonds and the fiber axis using separated local field spectroscopy to measure heteronuclear dipole–dipole couplings.[12] This initial study of a synthetic polymer demonstrated the feasibility of structural studies of biopolymers that could be prepared with uniaxial orientation.

THE APPLICATION OF NMR SPECTROSCOPY TO PROTEINS

Filamentous Bacteriophages

Much of the development of the method for determining the structures of oriented proteins by solid state NMR spectroscopy has utilized the favorable properties of the filamentous bacteriophages, the overall requirements of the proteins being immobile on the appropriate NMR timescales (10^3–10^6 Hz) and uniaxially oriented along the direction of the applied magnetic field. Filamentous bacteriophage coat proteins are particularly well suited for this approach, since the structured residues of the major coat protein are immobilized by interactions within the protein subunit, and the virus particles are so large and elongated that they do not reorient on NMR timescales. Remarkably, these virus particles orient spontaneously with their filament axis aligned with the direction of the applied magnetic field.

All of the structural studies of the filamentous viruses planned when the laboratory was being established at the University of Pennsylvania starting in 1976–79 were designed to take advantage of the fact that these nucleoprotein complexes could be oriented either as fibers, or later as solutions in the magnetic field of the spectrometer. By 1982–83 the implementation of selective ^{15}N labeling of both backbone and sidechain sites and magnetic orientation of virus solutions enabled the high-resolution structural information to be obtained on a protein in a supramolecular structure, the 10^7 kilodalton virus particles. Subsequently, ^{13}C and ^{15}N NMR experiments were used to obtain data from a sufficient number of sites to yield a model of the fd coat protein in the bacteriophage.[6]

Membrane Proteins

Membrane proteins are responsible for many of the properties and functions of biological systems. Determining the structures of membrane proteins is one of the most important challenges in the field of structural biology at the present time. Because of the continuing difficulty in crystallizing these proteins, it is essential that NMR spectroscopy be able to

study these proteins. Many of the technical difficulties associated with NMR studies of proteins in membrane environments can be overcome with a concerted approach, combining the methods of high-resolution solid state NMR spectroscopy on samples of membrane proteins in bilayers with those of multidimensional solution NMR spectroscopy on samples of membrane proteins in micelles. In this approach, the secondary structure of the protein is determined on the basis of internuclear distance measurements in micelle samples and the arrangement of the major elements of secondary structure is derived from measurements of angular parameters in oriented bilayer samples.[13]

REFERENCES

1. S. J. Opella, D. J. Nelson, and O. Jardetzky, *J. Am. Chem. Soc.*, 1974, **96**, 7157.
2. R. Tycko, P. L. Stewart, and S. J. Opella, *J. Am. Chem. Soc.*, 1986, **108**, 5419.
3. T. A. Cross, J. A. DiVerdi, and S. J. Opella, *J. Am. Chem. Soc.*, 1982, **104**, 1759.
4. M. J. Bogusky, P. Tsang, and S. J. Opella, *Biochem. Biophys. Res. Commun.*, 1985, **127**, 540.
5. A. Pines, M. G. Gibby, and J. S. Waugh, *J. Chem. Phys.*, 1972, **56**, 1776.
6. S. J. Opella, P. L. Stewart, and K. G. Valentine, *Q. Rev. Biophys.*, 1987, **19**, 7.
7. S. J. Opella, in *Methods in Enzymology*, ed. C.H.W. Hirs, Academic Press, New York, 1985, Vol. 131, p. 327.
8. M. Saunders, A. Wishnia, and J. G. Kirkwood, *J. Am. Chem. Soc.*, 1957, **79**, 3289.
9. T. A. Cross, C. M. Gall, and S. J. Opella, in *Progress in Clinical and Biological Research*, ed. M.S. Dubow, Liss, New York, 1981, Vol. 64, p. 457.
10. G. E. Pake, *J. Chem. Phys.*, 1948, **16**, 327.
11. S. J. Opella and P. L. Stewart, in *Methods in Enzymology*, eds. N. J. Oppenheimer and T. L. James, Academic Press, New York, 1989, Vol. 176, p. 242.
12. S. J. Opella and J. S. Waugh, *J. Chem. Phys.*, 1977, **66**, 4919.
13. S. J. Opella and P. A. McDonnell, in *NMR of Proteins*, eds. A. M. Gronenborn and G. M. Clore, MacMillan Press, London, 1993, p. 159.

Acknowledgements

I thank all of the undergraduate and graduate students, postdoctoral fellows, and collaborators who have been involved in my research program for their ideas, enthusiasm, and hard work. My research program has been supported primarily by the National Institutes of Health. Additional sources of support for the program have included the University of Pennsylvania, the National Science Foundation, the American Chemical Society, the A. P. Sloan Foundation, the American Cancer Society, Smith, Kline and French Laboratories, Sogetal, Inc., Asahi Chemical Company, Silicon Graphics, Inc., and Symphony Pharmaceuticals. Graduate students and postdoctoral fellows in my group have been supported by fellowships from the National Institutes of Health, the National Science Foundation, the Damon Runyon–Walter Winchell Cancer Fund, the Cancer Research Institute, the National Science and Engineering Research Council (Canada), the European Molecular Biological Organization, and Conselho Nacional de Desenvolvimento Cientifico e tecnologico (CNPq) (Brazil).

Biographical Sketch

Stanley J. Opella. *b* 1947. B.S., 1969, Chemistry, University of Kentucky (undergraduate research with S. L. Smith), Ph.D., 1974, Chemistry, Stanford University (with O. Jardetzky and H. McConnell). Postdoctoral fellow, 1975–76, MIT (with J. S. Waugh). University of Pennsylvania, 1976–present, currently Professor of Chemistry. Approx. 125 publications. Research interests: development and application of NMR spectroscopy for the study of proteins, especially protein structure determination by solid state NMR spectroscopy.

Overhauser, Albert W.: Dynamic Nuclear Polarization

Albert W. Overhauser
Purdue University, West Lafayette, IN, USA

INTRODUCTION

New ideas generally spring from cultivated soil, a state of readiness formed by the efforts and inspirations of mentors and colleagues. The discovery described below would not have occurred had Charles Kittel not assigned me a thesis topic to study all mechanisms that cause conduction-electron spins in metals to relax towards equilibrium. Spin-flip scattering induced by the orbital motion or spins of (other) conduction electrons, by lattice vibrations, by paramagnetic impurities, and by nuclear spins were all investigated.[1] Of minor importance was the last mechanism, caused by the Pauli hyperfine coupling between electron and nuclear spins.

My postdoctoral efforts at the University of Illinois were focused on radiation-induced defects in solids, a comprehensive program due to Frederick Seitz. However by 1951, Illinois had become a hotbed of magnetic resonance. Research activities of C. P. Slichter, R. E. Norberg, and H. Gutowsky kept alive my interest in spin dynamics which, perforce, had become a sideline.

Calculations of spin–lattice relaxation rates usually assume that all other components of the system remain nearly in thermal equilibrium. This approximation is frequently satisfactory, but any part of a system which is out of equilibrium will also drive other parts to deviate. Such phenomena were well studied by L. Onsager. Intuition suggests that if one component is out of equilibrium by, say, a per cent, other components will be forced out of equilibrium by a similar, small amount. It was quite surprising then to discover that if conduction-electron spins were driven out of equilibrium by 1%, the nuclear spin polarization could be enhanced by ~2000%.

One technique for disrupting electron-spin equilibrium is ESR, i.e. driving the spin resonance towards saturation. With a static field B_0 in the z direction and an rf field $2B_1 \cos \omega t$ in the x direction, the absorbed power P increases with increasing B_1, but ultimately approaches a limiting value $P_{\max}$.

$$P = s P_{\max} \tag{1}$$

where the saturation factor s is

$$s = \frac{\gamma_e^2 B_1^2 T_1 T_2}{1 + \gamma_e^2 B_1^2 T_1 T_2} \tag{2}$$

The quantity γ_e is an electron's gyromagnetic ratio, $-2\mu_B/\hbar$ and T_1 and T_2 are the longitudinal and transverse relaxation times. At complete saturation (s = 1), up and down electron-spin populations become equal.

A nuclear spin $\boldsymbol{S}$ interacts with each conduction-electron spin $\boldsymbol{\sigma}$ through the Pauli hyperfine coupling, $\sim \boldsymbol{S} \cdot \boldsymbol{\sigma}$. This interaction conserves the total spin. Thus an out-of-equilibrium electron spin trying to flip down will occasionally do so by flipping a nuclear spin up. The induced steady-state polarization of nuclear spins, having gyromagnetic ratio γ_n, attains a value in the field $\boldsymbol{B}_0$ as if the nuclei had an effective gyromagnetic ratio,[2]

$$\gamma_{\text{eff}} = \gamma_n + s|\gamma_e| \tag{3}$$

This remarkable result, derived below, predicts that for $s \sim 1$, the induced nuclear polarization will be ~2000-times larger than expected.

A discussion of this prediction was given at the Washington, DC meeting of the American Physical Society in April, 1953. The presentation went over like a lead balloon. A. Abragam, who was there, records the following account in his autobiography:[3]

> To finish up with NMR at Harvard, I wish to mention another event which was to play an important part in my future activities: the Overhauser effect. Albert Overhauser, a young theoretician from the University of Illinois, had made the following prediction: in a metal, where the conduction electrons are known to be responsible for the nuclear relaxation, the saturation of the ESR resonance of these electrons should lead to an enormous increase in the nuclear polarization. I am not going to explain the meaning of this sentence here, for I will come to this problem later in the book. Right now I'll say two things. First, that this work provoked a delayed reaction in me which directed my thoughts on to a topic that was to preoccupy me for many years—namely "dynamic nuclear polarization". Secondly, that Overhauser's audience at the meeting of the American Physical Society—where he had (in ten minutes) presented the calculations which had led to his amazing conclusion—was immediately split into two parts, which, however, overlapped: those who did not understand a single word of his demonstration, and those who did not believe a single word of his conclusions. In the first row of the sceptics who did not believe his conclusions shone all the stars of magnetic resonance: Bloch and Purcell, Rabi and Ramsey. Bloembergen was of two minds and so was I. As for the presentation itself, I will repeat what Van de Graaff had told me of de Broglie's defense of his thesis in Paris in 1924. "Never had so much gone over the heads of so many".
>
> The real question was of course: "Was Overhauser right?" He was: the proof of the pudding was given the same year by Charles Slichter, a physicist from Illinois, and his student, Carver. They saturated the resonance of conduction electrons in metallic lithium and saw the enhancement of the nuclear polarization predicted by Overhauser.

Most nuclei have positive γ_n. For these, equation (3) predicts an effective nuclear spin temperature smaller than ambient by ~1/2000. However for nuclei with negative γ_n, equation (3) implies that the nuclear spin temperature is first driven to infinity, and then deeply into the negative, 'hotter than hot' temperature regime.

CROSS RELAXATION

For clarity and simplicity the treatment which follows employs nuclei with $S = \frac{1}{2}$. Furthermore, the electron

concentration will be taken to be sufficiently small so that Fermi–Dirac factors (which recognize the exclusion principle) can be neglected. The general theory without these simplifications leads to dynamic nuclear polarization given by equation (3).[4]

Longitudinal (spin–lattice) relaxation of electron spins can be written,

$$\frac{\mathrm{d}p_\mathrm{e}}{\mathrm{d}t} = -\frac{p_\mathrm{e} - p_{\mathrm{e}0}}{T'_{1\mathrm{e}}} - \frac{p_\mathrm{e} - p_{\mathrm{e}0}}{T_{1\mathrm{e}}p} \tag{4}$$

where p_e is the fractional spin polarization, $(n_{\mathrm{e}\downarrow} - n_{\mathrm{e}\uparrow})/n$; $p_{\mathrm{e}0}$ is its equilibrium value. Relaxation caused by the Pauli $\boldsymbol{S}\cdot\boldsymbol{\sigma}$ hyperfine interaction with nuclear spins, $1/T_{1\mathrm{e}}p$, has been separated from $1/T'_{1\mathrm{e}}$, caused by all other mechanisms. The $\boldsymbol{S}\cdot\boldsymbol{\sigma}$ term would be considered negligible in most contexts. Here, however, it is the only important term. The relevant effect of the dominant term, $1/T'_{1\mathrm{e}}$ in equation (4) is merely to increase the required rf power needed for ESR saturation. With conduction electrons present, nuclear spin relaxation arises from the Pauli hyperfine coupling.[5]

$$\frac{\mathrm{d}p_\mathrm{n}}{\mathrm{d}t} = -\frac{p_\mathrm{n} - p_{\mathrm{n}0}}{T_{1\mathrm{n}}p} \tag{5}$$

It is convenient here to introduce out-of-equilibrium variables, D_e and D_n,

$$D_\mathrm{e} = n_\mathrm{e}(p_\mathrm{e} - p_{\mathrm{e}0}) \tag{6a}$$

$$D_\mathrm{n} = n_\mathrm{n}(p_\mathrm{n} - p_{\mathrm{n}0}) \tag{6b}$$

which are both zero in thermal equilibrium. Cross relaxation between the electron and nuclear spin systems is easily introduced. For electron-spin relaxation,

$$\frac{\mathrm{d}D_\mathrm{e}}{\mathrm{d}t} = -\frac{D_\mathrm{e}}{T'_{1\mathrm{e}}} - \frac{D_\mathrm{e}}{T_{1\mathrm{e}}p} + \alpha D_\mathrm{n} \tag{7}$$

and for nuclear-spin relaxation,

$$\frac{\mathrm{d}D_\mathrm{n}}{\mathrm{d}t} = -\frac{D_\mathrm{n}}{T_{1\mathrm{n}}p} + \beta D_\mathrm{e} \tag{8}$$

where α and β are cross-relaxation coefficients, which arise from the Pauli $\boldsymbol{S}\cdot\boldsymbol{\sigma}$ coupling.

Since the $\boldsymbol{S}\cdot\boldsymbol{\sigma}$ interactions conserve total spin, the rates of change of the z components must be equal and opposite:

$$-\frac{D_\mathrm{e}}{T_{1\mathrm{e}}p} + \alpha D_\mathrm{n} = -\left(-\frac{D_\mathrm{n}}{T_{1\mathrm{n}}p} + \beta D_\mathrm{e}\right) \tag{9}$$

which after a mere rearrangement requires,

$$\left(\alpha - \frac{1}{T_{1\mathrm{n}}\,p}\right) D_\mathrm{n} = \left(\frac{1}{T_{1\mathrm{e}}\,p} - \beta\right) D_\mathrm{e} \tag{10}$$

Since this identity is valid for all, arbitrary values of both D_e and D_n, the cross-relaxation coefficients can only be:

$$\left.\begin{aligned}\alpha &= \tfrac{1}{T_{1\mathrm{n}}p}\\ \beta &= \tfrac{1}{T_{1\mathrm{e}}p}\end{aligned}\right\} \tag{11}$$

The relaxation of nuclear spins is now

$$\frac{\mathrm{d}D_\mathrm{n}}{\mathrm{d}t} = -\frac{D_\mathrm{n}}{T_{1\mathrm{n}}p} + \frac{D_\mathrm{e}}{T_{1\mathrm{e}}p} \tag{12}$$

For any nonequilibrium steady state, e.g. during a continuous ESR excitation, equation (12) must equal zero. Accordingly,

$$D_\mathrm{n} = \frac{T_{1\mathrm{n}}p}{T_{1\mathrm{e}}p} D_\mathrm{e} \tag{13}$$

The importance of this result is evident. It reveals the out-of-equilibrium nuclear polarization D_n resulting from any imposed value of D_e.

NUCLEAR POLARIZATION BY ESR SATURATION

The ratio of the two relaxation times appearing in equation (13) can be calculated, for example, by golden-rule perturbation theory. The spin-flip rate of a nuclear spin is,

$$\frac{1}{T_{1\mathrm{n}}p} = \frac{2\pi}{\hbar}|M|^2\rho_\mathrm{f} n_\mathrm{e} \tag{14}$$

where M is the appropriate matrix element of the $\boldsymbol{S}\cdot\boldsymbol{\sigma}$ interaction and n_e is the number of electron spins with which each nucleus interacts. Similarly,

$$\frac{1}{T_{1\mathrm{e}}p} = \frac{2\pi}{\hbar}|M|^2\rho_\mathrm{f} n_\mathrm{n} \tag{15}$$

All common factors cancel when equation (15) is divided by equation (14). Accordingly,

$$\frac{T_{1\mathrm{n}}p}{T_{1\mathrm{e}}p} = \frac{n_\mathrm{n}}{n_\mathrm{e}} \tag{16}$$

which with equation (13) implies,

$$\frac{D_\mathrm{n}}{D_\mathrm{e}} = \frac{n_\mathrm{n}}{n_\mathrm{e}} \tag{17}$$

The fractional polarizations, p_e and p_n, can now be restored from equation (6).

$$p_\mathrm{n} = p_{\mathrm{n}0} + p_\mathrm{e} - p_{\mathrm{e}0} \tag{18}$$

Now, the rf power P absorbed by the electron spins is converted into heat by the electron-spin relaxation. From equation (1),

$$s = \frac{P}{P_\mathrm{max}} = \frac{p_{\mathrm{e}0} - p_\mathrm{e}}{p_{\mathrm{e}0}} \tag{19}$$

equations (18) and (19) show that,

$$p_\mathrm{n} = p_{\mathrm{n}0} - s p_{\mathrm{e}0} \quad (\gamma_\mathrm{n}\,\text{negative}) \tag{20}$$

The equilibrium polarizations $p_{\mathrm{e}0}$ and $p_{\mathrm{n}0}$, defined to be positive, are (for high T) proportional to the gyromagnetic ratios γ_e and γ_n. Equations (6b) and (9) involved an implicit

assumption that γ_e and γ_n had the same sign. If γ_n is positive, equation (20) is replaced by

$$p_n = p_{n0} + s p_{e0} \quad (\gamma_n \text{ positive}) \tag{21}$$

Equations (20) and (21) agree with equation (3). However, the derivation just given is (unnecessarily) restricted to small deviations and high T.

It is necessary of course to examine the detailed mechanisms which cause the polarization enhancement in a way like that just presented. However it is not clear from such a treatment why the effect is so large. The fact that one electron-spin flip involves an energy change sufficient to flip $|\gamma_e/\gamma_n|$ nuclear spins does not by itself provide conviction. Kittel found an intuitive route which leads to equation (3) without any calculation whatsoever.[6]

The Boltzmann factors of a canonical ensemble, $\exp(-E/k_B T)$, arise from the entropy differences of the thermal reservoir. For nuclear spin up versus down, the reservoir energy differs by only a nuclear Zeeman splitting. However if a nuclear-spin flip occurs only in conjunction with an electron-spin flip, and the latter is immediately reversed by the saturating rf field driving the ESR, an electron's Zeeman energy, $2\mu_B B_0$, is effectively delivered (from the rf source) to the reservoir. Consequently the statistical weight of the reservoir is changed according to the sum of the Zeeman splittings, and the relative nuclear-spin populations respond accordingly.

Nonitinerant electrons, such as free radicals or paramagnetic ions can also be used for dynamic nuclear polarization.[7] The important spin–spin coupling is then a (magnetic) dipole–dipole interaction. This interaction does not conserve total spin, so the maximum polarization enhancement is smaller by about a factor of three.

VERIFICATION

The first confirmation of the theory was an intellectual one. During the summer of 1953 I received the following letter from Ramsey:

> July 27, 1953
>
> Dear Dr. Overhauser:
>
> You may recall that at the Washington Meeting of the Physical Society, when you presented your paper on nuclear alignment, Bloch, Rabi, Pearsall, and myself all said that we found it difficult to believe your conclusions and suspected that some fundamental fallacy would turn up in your argument. Subsequent to my coming to Brookhaven from Harvard for the summer, I have had occasion to see the manuscript of your paper.
>
> After considerable effort in trying to find the fallacy in your argument, I finally concluded that there was no fundamental fallacy to be found. Indeed, my feeling is that this provides a most intriguing and interesting technique for aligning nuclei. After considerable argument, I also succeeded in convincing Rabi and Bob Pound of the validity of your proposal and I have recently been told by Pound that he subsequently converted Pearsall shortly before Pound left for Europe.
>
> I hope that you will have complete success in overcoming the rather formidable experimental problems that still remain. I shall be very interested to hear of what success you have with the method.
>
> Sincerely,
>
> Norman F. Ramsey

Forty years later I found this letter in my file. I sent a copy to Ramsey as a remembrance of the encouragement he had provided to a young novice. His reply provides additional insight.

> April 20, 1993
>
> Dear Al:
>
> I greatly appreciate your thoughtful remarks about the letter I wrote you forty years ago. Although I clearly remember surprising some of my friends by writing a very favorable referee report, I had forgotten that I also had written you a letter.
>
> You might be interested in how I came to get the matter straight and avoid the lifelong embarrassment of being responsible for the rejection of a great pioneering paper.
>
> After the APS meeting I did not understand your paper and was thoroughly convinced by the vigorous arguments of Bloch, Rabi, and others that a radiofrequency field always produces heating. I was consequently annoyed when I was asked to referee the paper and therefore would have to find exactly what was wrong. I started my study with strong prejudices against you but I then remembered that in high school physics I had always had trouble remembering how a Servel (gas) refrigerator worked. I decided that I could not write a negative referee report until I understood once again how the Servel worked. By the time I understood that, I had lost my prejudice against your paper and on further study was convinced you were right. Incidentally the easiest way for me to remember how in principle a gas refrigerator can work without violating thermodynamics is to remember one could use the heat of the gas flame to operate a steam engine which in turn could operate a mechanical refrigerator
>
> Sincerely yours,
>
> Norman F. Ramsey

The most direct experimental test of dynamic nuclear polarization utilizes double resonance. One must select a static field B_0 for which rf excitation of the ESR and measurement of the NMR can occur simultaneously. This difficult experiment was first attempted by Carver and Slichter in metallic lithium.[8] They selected $B_0 = 30.3$ G, which required an NMR frequency of only 50 kHz. The ESR frequency was 84 MHz. Without the 84 MHz oscillation, no ^{7}Li NMR signal was visible. However with $B_1 = 5$ G (for the 84 MHz excitation), a large ^{7}Li NMR resonance appeared. On comparing the signal amplitude to the NMR of protons in glycerin (also at 50 kHz), the ^{7}Li NMR enhancement was estimated to be $\sim$100.

Hecht and Redfield later carried out precision measurements of the NMR enhancements in lithium and sodium.[9] They worked at 1.5 K, where NMR relaxation times were long ($\sim$29 s in Li). The nuclei were first polarized in a small field, $B_0 = 10.4$ G. Subsequently B_0 was adiabatically increased to several hundred gauss, where the nuclear polarization could be accurately measured. Nearly complete polarization, according to the prediction of equation (3), was observed.

Dynamic nuclear polarization by ESR saturation has been studied extensively in nonmetals: liquid and solid diamagnetics, paramagnetic salts, semiconductors, alkali halide crystals, and alkali ammonia solutions.[10]

ESR FREQUENCY SHIFT

Polarization of nuclei in metals can also be confirmed by measuring the ESR frequency shift caused by the polarization.[4] The Pauli paramagnetism of a metal produces an NMR frequency shift, i.e. $\nu_n = \nu_{n0}(1 + K)$, on account of

the hyperfine interaction between conduction electrons and nuclei.[11] The quantity K is the Knight shift. Values range from a fraction of a per cent to 2%. for lithium K = 0.0249%. The same hyperfine interaction will cause an ESR frequency shift as the nuclei become polarized.

$$\nu_e = \nu_{e0} + Dp_n \tag{22}$$

where p_n is the fractional nuclear polarization. For lithium D = 217 G. One must work at low temperatures to maximize the shift Dp_n.

An interesting optical bistability is associated with this phenomenon. Suppose one sweeps the ESR frequency slowly upwards. As the ESR becomes excited, the center of the resonance shifts upwards as the nuclei become polarized. The maximum shift will of course depend on the rf power and temperature. When the maximum shift according to equation (22) has been reached, further increase in ν will cause the rf to cross over the ESR peak. Subsequently the dynamic polarization will be lost, and p_n will relax back to p_{n0}. The shifted resonance, equation (22), is attained only if ν is swept positively. A negative sweep will not encounter the resonance until it approaches ν_{e0}. All of these effects have been verified by Ryter.[12]

ESR saturation in a metal counteracts the Pauli paramagnetism and thereby suppresses the Knight shift. Pake has suggested that the ESR shift, equation (22), be called the 'day shift' since it dawns as the Knight shift subsides.[13]

REFERENCES

1. A. W. Overhauser, *Phys. Rev.*, 1953, **89**, 689.
2. A. W. Overhauser, *Phys. Rev.*, 1953, **91**, 476.
3. A. Abragam, *Time Reversal, an Autobiography*, Oxford University Press, Oxford, 1989, p. 164; by permission of Oxford University Press.
4. A. W. Overhauser, *Phys. Rev.*, 1953, **92**, 411.
5. J. Korringa, *Physica (The Hague)*, 1950, **16**, 601.
6. C. Kittel, *Phys. Rev.*, 1954, **95**, 589.
7. A. Abragam, *The Principles of Nuclear Magnetism*, Oxford University Press, Oxford, 1961, Chap. IX.
8. T. R. Carver and C. P. Slichter, *Phys. Rev.*, 1953, **92**, 212.
9. R. Hecht and A. G. Redfield, *Phys. Rev.*, 1963, **132**, 972.
10. G. R. Khutsishvili, *Sov. Phys. Usp.*, 1960, **71**, 285.
11. W. D. Knight, *Solid State Physics*, eds. F. Seitz and D. Turnbull, Academic Press, New York, 1956, Vol. 2, p. 122.
12. Ch. Ryter, *Phys. Rev. Lett.*, 1960, **5**, 10.
13. G. E. Pake, *Solid State Physics*, eds. F. Seitz and D. Turnbull, Academic Press, New York, 1956, Vol. 2, p. 91.

Biographical Sketch

Albert W. Overhauser. *b* 1925. B.A., 1948, Ph.D., 1951, University of California, Berkeley (supervisor Charles Kittel), Sc.D. (honorary), University of Chicago, 1979. Postdoctoral work at the University of Illinois. Assistant and associate professor, Cornell University; Manager, Assistant Director, and Director for Physical Sciences, Ford Motor Co., Scientific Laboratory; currently Stuart Distinguished Professor of Physics, Purdue University. National Medal of Science, awarded by the President of the United States, 1994. Research specialties: solid state theory, many-electron theory, broken symmetry in metals, neutron interferometry, superconductivity.

Packard, Martin E.: Nuclear Induction at Stanford and the Transition to Varian

Martin E. Packard
Varian Associates, Palo Alto, CA, USA; Institute for Genetic Disease Control in Animals, Davis, Davis, CA

Figure 1 The magnet and probe assembly of the first nuclear induction apparatus used by Bloch, Hansen, and Packard at Stanford, circa January 4, 1946. The knob turned the 'paddle' to balance out the leakage. The clamps held the laminated pole pieces

THE BEGINNING—EARLY JANUARY 1946

We glimpsed our first nuclear induction signal one chilly night in early January 1946. The term 'nuclear induction' was coined because we were looking for a small voltage induced in the receiver coil by the precessing nuclei. The 'we' were Professors Felix Bloch, William W. Hansen, and the graduate student, Martin E. Packard. It was chilly because the experiment was set up in the cyclotron laboratory which was in a leaky, unheated, glassed-over light well in the basement of the original sandstone quad of Leland Stanford Junior University.

The glimpse followed a fruitless two hours of adjustment as we tried to optimize the equipment and parameters to match the expected conditions for resonance. The experimental conditions were set on the assumption that the thermal relaxation time, T_1, would be very long, perhaps days, and the transverse relaxation, T_2, would be very short, corresponding to the dipole–dipole interaction of the neighboring protons.

For these reasons, the sample of ordinary water was 'presoaked', i.e. polarized for 24 h in a special outrider gap of the fringe field of the cyclotron, and the radiofrequency (rf) level in the probe adjusted to be a few gauss. The strength of the magnetic field was adjusted for resonance at a value corresponding to the rf frequency of 7.76 megacycles. The 4 or 5-in. magnet was connected in series with the cyclotron magnet, thus using the cyclotron power supply and regulator. The 60 cycle sweep was broad enough amply to cover the putative linewidth of about 5 G. The radiofrequency (rf) level in the probe was adjusted to be a few gauss and set to the resonant frequency by means of a surplus US Army frequency meter.

The sample was removed by Bloch from the fringe field of the cyclotron magnet and placed in the nuclear induction probe which was centered in the gap of the small magnet (Figure 1). Nothing was seen. As a last ditch attempt, the current through the cyclotron and small magnet was taken much higher than expected for resonance and allowed to drift downward at the slow rate determined by the time constant of the cyclotron magnet.

I was watching the oscilloscope screen and saw a weak signal move across the screen, much as one would expect a radar signal to do. The lineshape of the signal was unique in that it was positive on the right-hand side of the screen and negative on the left-hand side. The pattern was repeated, thus releasing the euphoria which comes to researchers when they finally succeed. Thus in a few brief minutes we were compensated for the work and disappointments of the previous three months.

It was quite clear that our earlier estimate of the thermal relaxation time was several orders of magnitude too high. During the next day or two Bloch reviewed his equations and had the explanation for what we had seen; he named the condition as adiabatic rapid passage. He understood the role of the rapid tumbling of the water molecules in reducing the thermal relaxation time, although he did not anticipate the beautiful description later developed by Nicholas Bloembergen.[1] Bloch often stressed how treacherous was the theory of liquids as contrasted to solids and gases. We were all happy that ordinary water had been the sample of choice.

A short letter to the Editor[2] was prepared and appeared in *Physical Review*, along with the results of Professor Edwin M. Purcell, Henry C. Torrey, and Robert V. Pound.[3] The Nobel committee correctly overlooked this small priority of two weeks, as the two experiments were really conceived and implemented independently. The 1951 Nobel Prize in Physics was jointly awarded to Bloch and Purcell.

We might have been perhaps a week earlier had I not chosen to drive to Oregon to visit my parents over Christmas. I had not seen them for some time because of World War II.

PROLOGUE

The work of assembling the apparatus was started in late September 1945. However that was not the start of the project. Felix (we usually used his first name) told us the idea came to him during a concert which he attended while working with Professor Frederick Terman[4*] at the Harvard Radiation Lab, not the MIT lab. A project he was working on involved finding a coating that would absorb rather than reflect radar signals; the precursor of the Stealth Bomber of the 1990s.

A question which is often asked is what is the origin of an idea. In Bloch's story we will start with Professor Isador I. Rabi's[5] classical experiments. For several years Bloch had been focusing on measuring the value of the magnetic moment

of the neutron. He and Professor Luis W. Alvarez[6] of the University of California at Berkeley carried out a measurement of the neutron moment in terms of the proton cyclotron frequency. The extension of this method to several nuclei required an accurate and less cumbersome way to measure the magnetic field.

Bloch, of course, was familiar with Professor Rabi's[7] classical measurement of proton and deuteron moments in a molecular beam apparatus and with Professor C. J. Gorter's[8] unsuccessful attempt to observe resonance in a very pure solid. Felix Bloch pioneered the method of polarizing thermal neutrons[9] by passing them through a slab of magnetized iron. I was not aware of his early work in magnetism and the elucidation of the 'Bloch wall' until the arrival of the semiconductor age. Bloch's insight led him to a simple way of measuring magnetic fields by observing resonance in matter of 'normal density' as contrasted to the molecular beams of Rabi, an important step in expanding the measurement of nuclear moments. Conversations with Bill Hansen, while they were both at Harvard and later at Stanford, showed the feasibility of the idea and provided the practical basis for the apparatus.

Shortly after the Japanese capitulation in the summer of 1945, I was introduced to Professor Bloch by my Westinghouse supervisor and Stanford physics alumnus, Dr. Daniel Alpert. Our group had been sent from Pittsburgh to work on improving the mass spectrometer separation of uranium-235 for the Manhattan project. Our laboratory was next to the 184-in. cyclotron magnet in the hills above the University of California at Berkeley.

After listening to Professor Bloch explain his nuclear induction idea, I made an immediate decision to join his group, i.e. Bloch and Hansen. A week later my wife, Barbara, and I moved to Palo Alto and I was a graduate student and teaching assistant at Stanford. The admission procedure was more streamlined at that time.

The distribution of tasks was rather simple and required very little interaction between us.

Bloch prepared the magnet, starting with a small clumsy C-shaped lecture demonstration magnet. Laminated pole pieces were attached to allow the use of a large sinusoidal sweep for display of the signal. The magnetic field was measured with a conventional galvanometer and flip coil, the area of which could only be estimated to a few per cent.

Hansen designed and supervised the construction of the rf receiver portion of the system. This included the probe, the diode detector, and audio preamplifier. This was all contained in a brass box with an appendage, which we called the probe, that allowed the transmitter, receiver coils, and the sample to be placed between the pole pieces of the magnet. He also conceived and implemented the famous cross-coil configuration.

Bill Hansen was a genius in designing systems that would move but were not overconstrained, like linear motion using ball bearings in one V groove and a flat. He called this approach 'kinematic design'. His experience with the orthogonal nature of fields in microwave cavities and the decoupling needed in Doppler radar systems led him to decouple the transmitter and the receiver coil by making them orthogonal. Even at that he chose to use a diode detector without any rf amplification, to avoid saturation.

His first configuration, which used wires for constraints, allowed for rotation, but was sensitive to vibration and hence was too noisy. A redesign with the 'paddle' for flux steering was the solution (Figure 2).

Figure 2 This first nuclear induction probe was constructed by Hansen. The crossed wires provided kinematic constraints on rotation to achieve a geometric balance. The design proved to be noisy and was superseded by the 'paddle'

My task was to design and construct the rf source, the audio amplifier, and the display, which was a DuMont 5-in. oscilloscope.

The jargon which developed came from our individual experience in the radar business. The techniques which we used were well known. We were familiar with the detection of weak signals in the presence of a strong source and the use of orthogonal decoupling. The sweep field reduced the $1/f$ noise by shifting from the dc region. The signal-to-noise ratio was derived from a calculation of the Johnson[10] noise in the resonant receiver coil and the nuclear magnetization determined from the Boltzmann factor.

THE LULL AFTER THE FIRST SUCCESS

We moved the system into a room adjacent to the cyclotron and reassembled the system, without immediate success. Bloch was to present a talk on the experiment at the local weekly Physics Department colloquium. It seemed like a nice idea to show how simple the nuclear induction effect was by providing a demonstration as part of the talk. That was a mistake; I was unable to make it work, much to my embarrassment. Bloch in his usual nice way compensated for my confusion and lack of success.

THE BLOCH VERSUS PURCELL METHOD

At Stanford we viewed the phenomenon as one of expectation values which could be handled by classical mechanics and electrical theory, while Purcell viewed the phenomenon as a spectroscopic one with transitions taking place between the Zeeman levels.

The balance of the cross-coil system left only a quadrature leakage which selected for the out-of-phase component of the signal; thus we viewed the dispersion component. The balanced bridge of Purcell and co-workers favored the

absorption component. The initial experiments of Bloch and Purcell appeared to many to be quite different, whilst in reality the signals observed by the two groups were of the same phenomenon but only in quadrature to each other.

Strangely, this misconception persisted for a very long time.[11] Even 30 years after the initial experiments, I was challenged by a foreign visitor with the myth about the Bloch method and the Purcell method.

Bloch's equations proved to be the most useful approach for us in understanding the details of the nuclear resonances, particularly for steady state and pulses in the rotating frame.[12] However, the effects of spin–spin coupling required the spectroscopic approach to explain the observed splitting of the lines.

THE SCIENTIFIC DIRECTION OF THE LABORATORY

A review of many of the projects provides insight as to the main thrust of the laboratory and serves to identify the many able graduate students who obtained their Ph.D. degrees under Bloch.

Although the work of the laboratory was never highly organized and very few group meetings were held, Bloch had a simple objective and projects were selected to further that goal. He felt that the values of the nuclear moments of the isotopes would be important in understanding nuclear forces.

Neutron Measurements

In the paper with Luis W. Alvarez[†] prepared in 1939 on the neutron magnetic moment, the authors wrote: 'The now rather accurately known values ... of the magnetic moments of proton, neutron, and deuteron are of considerable interest for nuclear theory.' At that time, the deuteron moment was known to an accuracy of 1% to be the sum of the proton and the neutron moments. The accuracy was not high enough to test the theories rigorously. Higher accuracy would require a more accurate magnetic field determination, which Bloch later achieved with his nuclear induction method.

One of the first applications of nuclear induction was to improve the accuracy of the neutron moment measurement in terms of the proton. This measurement was done with the Stanford cyclotron by Professor Hans Staub, F. Bloch and Dr. D. Nicodemus.[13] The magnet field was automatically stabilized accurately at the proper value for neutron resonance by a nuclear induction magnetic field controller[14] which I devised and constructed.

The neutron experiments at Stanford and Berkeley had their genesis in the magnetic polarizing techniques proposed in 1936 by Bloch.[9] One of the earliest neutron experiments was by Dr. Edward Fryer whose Stanford dissertation was on the cross-section of moderated neutrons.[15] Ed Fryer was later to join Varian as manager of its Quantum Electronics Division, where he worked with magnetometers and frequency standards.

Emery Rogers, who later played a key role at Varian in building market acceptance by the chemists for the use of nuclear magnetic resonance (NMR), measured the sign of the moment of the neutron and proton using the Stanford cyclotron.

The Nuclear Magnetic Moment Spectrometer of Hansen

Bill Hansen designed a spectrometer which was to automate the search for magnetic moments. Its most prominent feature was a table-top Bitter magnet, named after its designer, Professor Francis Bitter of the Massachusetts Institute of Technology. The automated nuclear induction spectrometer was dropped in favor of the individual creativity and labors of graduate students.

Warren Proctor's initial assignment was to work on the spectrometer. Warren eased himself out of this approach and went on to discover the nitrogen chemical shift with Dr. Fu Chun Yu[16a,b] and to report on the magnetic moments of many isotopes. Bill Hansen[‡] devoted his remaining energy and life to demonstrating the electron linear accelerator. He had worked before the war on producing high voltages for an X-ray source. The rhumbatron, which was the heart of the klystron, was first demonstrated as part of a device for producing high voltages.[17]

The linear electron accelerator became the basis of SLAC. Dr. Henry Kaplan of the Stanford Medical School demonstrated its use for cancer treatment.[18] Dr. Edward L. Ginzton at Varian Associates commercialized the small accelerator as the modality of choice for radiation cancer therapy.

Hansen died on May 23, 1949 at a young age from emphysema which many of us felt was caused by vapors produced while welding beryllium.

The Chemical Shift of Nitrogen

Warren Proctor and Fu Chun Yu[§] used a dissolved sample of ammonium nitrate as a source of nitrogen in their measurement of the nitrogen moment.[16b] The resonance was found, but to our surprise and mild dismay consisted of two peaks, one for the NH_4^+ and the other for NO_3^-. This effect was quickly attributed to a diamagnetic shielding which was explained by Lamb,[19] and later as a paramagnetic shift by Professor Norman Ramsey.[20]

This chemical effect, which was to become the most important aspect of NMR for the chemists, forced a shift in the basic strategy of the laboratory. If the value of the magnetic moments was to be useful in nuclear force theory, the effect of the chemical shift must be removed.

Erwin Hahn and Spin Echoes

Dr. Erwin Hahn brought his beautiful spin echo technique [21a–c] to Stanford from Urbana with the puzzle about the structure in the echo when observing organic liquids. Felix worked closely with Erwin on the theoretical aspects of the chemical structure in the echoes. Although the spin echo technique was elegant, it was not widely used until the advent of magnetic resonance imaging (MRI) which is now an important imaging modality in medicine.

Erwin's pulse technology pointed the way for observing NMR by the use of pulses to tip the spins. Russell Varian's proton free precession idea[22a,b] was an alternative method of tipping the spins. Both concepts were preludes to Weston Anderson and Richard Ernst's pulsed Fourier transform methods.[23] The Fourier transform brought increased sensitivity and flexibility which was so important to the chemists and later for MRI. Richard Ernst received the Nobel Prize in Chemistry in 1991 for his work with Fourier transforms, which he started while at Varian Associates in 1962.

Other Moments and Graduate Students

Elliot Leventhal measured the magnetic moment of deuterium precisely in terms of the proton.[24] This experiment was the first to use a double tuned receiver and transmitter coil which allowed the use of two rf frequencies set to resonate simultaneously the nuclei of light and heavy water. Irradiating the sample with two frequencies become important to the chemist for magnet stability, calibration, and to control and identify spin–spin interactions.

Over the years, many nuclear magnet moments were observed by the graduate students. Proctor's early work was with nitrogen, but he reported on many other isotopes.[16a,25a–c] Harry E. Weaver reported on 12 other isotopes.[26a–d] Carson Jeffries measured the proton cyclotron frequency in terms of the proton moment,[27,28] thus providing the link to the earlier neutron measurements of Alvarez and Bloch.

This interest in magnetic moments of other isotopes continued for several years even after several of us joined Varian. Dr. Arnold Bloom, who joined Varian in 1953 from the University of California at Berkeley, provided the values for the early compilation of nuclear moments in the 'CRC Handbook of Chemistry and Physics'. Following Bloom's departure in 1966 for spectra physics, the listing was extended by Weston Anderson and Dr. Kenneth Lee. The current table contains 115 isotopes that have been determined by nuclear induction.

One of Varian's early products was a variable tuned spectrometer for observing wideline NMR signals in many isotopes. Harry Weaver became the product champion for this technology as well as Varian Associates' entry into electron paramagnetic resonance (EPR or ESR as it is known to many chemists). A stringent test for the sensitivity of the wideline nuclear magnetic moment spectrometer was to measure the deuterium in ordinary water. The deuterium signal is nearly a million-times weaker than the hydrogen signal in ordinary water, as both the magnetic moment and the natural abundance are smaller.

One special case was our work with Mel Klein of the Livermore Laboratory on measuring the ratio of ^{6}Li to ^{7}Li in enriched samples.[29]

The Tritium Experiment at Los Alamos

Professor Bloch arranged for us to measure the magnetic moment of tritium. This was during the winter of 1947, at which time small samples of triply heavy water were classified and available only at the National Laboratories. My earlier Q clearance came in handy.

We loaded all of our apparatus into a truck and moved it to Los Alamos. The principal piece of equipment was the large C-shaped magnet, which was borrowed from UC Berkeley. This was the same magnet, or at least the coils, used by Ernest O. Lawrence in his early cyclotron experiments.

The apparatus had to be modified, which I was in no rush to do, as our six weeks stay in Los Alamos was very pleasant. The laboratory had not yet begun to take on its modern shape. We stayed in the original Fuller Lodge, and my wife Barbara had time enough to learn about the culture of the Pueblo Indians of Santa Clara and San Ildefonso. She collected many art objects which include several pieces of Maria Martinez's now famous black pottery.

Felix managed to spend one weekend skiing with us, where I appreciated his mastery of the European telemark turn.[30] On the trip back from the ski slope, I stopped and took a 16-mm movie of the beautiful scenery. A young soldier guard spotted me. I had some trepidation that this might have been a serious infraction of security, but nothing happened.

The actual experiment was simple and done quickly as we needed only to adjust the rf to provide for simultaneous display of the signals. The frequencies were measured with a surplus US Army frequency meter.[31a–c] After the experiment was completed, R. Spence, the chemist, reported that the pressure, due to beta decay, in the fractional sample was higher then he had expected. I still wonder what would have happened if the experiment had been delayed and the sample ruptured. Al Graves was heavily irradiated by the accident which occurred when two ^{235}U samples were gingerly moved together by hand to test criticality. We were not oblivious to the risks of radioactive materials and were careful, but not paranoid.

Sensitivity

The need for increased sensitivity was always present and remained a challenge. David Garber[32] worked on a photographic technique for averaging multiple sweeps to reduce low frequency noise. The concept was sound but it was not applied until much later when Varian introduced the all-digital C-1024. At that time I was Division Manager at Varian and forecast that only 10 units would be sold. In actuality, hundreds were bought and used by the chemists.

Lineshapes

The accurate measurement of the resonant frequency required that we set the resonant condition well within the linewidth. As the resolution increased, we saw that the absorption lineshape was not a simple Lorentzian but asymmetric and followed by 'wiggles'. My solution was to follow our experience from the radar field and use a sine wave sweep and set on the center of symmetry. I

suggested this approach to Felix, who thought a moment and agreed.

The solution of the Bloch equations for the steady-state condition was trivial, but a real challenge for other conditions. Dr. Boris Jacobsohn and Rowald Wangsness[33] developed an analytical solution which included the wiggles. Years later Dr. Arnold Bloom tried to solve the equations using the big analog computer at Stanford, with no results. The machine lacked the necessary stability.

THE BEGINNING OF HIGH RESOLUTION

The sensitivity and the resolution improved steadily over the first years. Two of the standard experiments which were used to impress visitors were to observe the signal from a finger placed in the probe and to demonstrate one's strength by pressing on both sides of the C-configured magnet to cause the signal to shift across the oscilloscope screen.

Bloch's hope was that the true value of the magnetic moments could be determined by applying a calculated correction of the chemical shift. This seemed possible for the lighter isotopes but the precision had to be very high.

The All-New 12 in. Electromagnet

Harry Weaver was assigned the job of designing a magnet which would have larger pole pieces for homogeneity, a higher field for sensitivity, and a full yoke for stability. The windings were high impedance as the current was regulated using surplus modulators which had eight 304TL vacuum tubes.

This basic magnet design was used by Varian in all the high-resolution research NMR spectrometers until the advent of the superconducting magnet[34] which was also Harry's contribution to the chemist.

Helium-3

It was natural to try to measure the magnet moment of ^{3}He as part of the effort to reduce or remove the effect of the chemical shift. Again it was hoped that calculations, particularly of the lighter isotopes, would allow a correction to give the true magnetic moment.

Bloch obtained a very small sample of ^{3}He. I blew the glass for the sample-handling system and prepared the sample vial filled with FeO_2[35] as a means of reducing the relaxation time. The sample vial was evacuated and the helium transferred. It remained for H. L. Anderson[36] to provide the value, as we saw no signal. Whether this was due to the very small sample or to a flaw in the relaxation process we never knew.

Harry Weaver's big 12 in. electromagnet was placed in service sometime during 1950. James T. Arnold, a graduate student, and I set out to utilize its size and field strength to improve sensitivity and resolution to measure the magnet moments of the light isotopes better and to correct for the effect of the surrounding electrons.

With these narrow lines, hence low rf fields and better decoupling between the transmitter and receiver coils, we chose to use an rf amplifier. The leakage was adjusted to present the absorption mode. The operating frequency was chosen to be 30 Mc s^{-1} (MHz) because that was the frequency of the surplus radar intermediate frequency (if) strips. Stanford science benefitted from the mountain of surplus gear which was scattered about the old and condemned dormitory, Sequoia Hall. Thirty megahertz and 7000 G became the de facto standard for several years.

The pole pieces of the magnet were not finely machined or polished, which was somewhat of a blessing. Jim Arnold became a master at moving the probe within the gap to find a local region of high homogeneity. We tried some rudimentary electric shimming to improve the homogeneity. It remained for Dr. Edwin Jaynes[37] to provide the theoretical basis for the orthogonal electric shims and for others to make them practical by moving them from a spherical geometry to the flat pole pieces.[38a–d]

Another major improvement in homogeneity came with the spinning sample idea of Bloch's which was successfully demonstrated by Arnold and Anderson.[39a–c] Bloch reported that the idea came to him as he was stirring a cup of tea midday at home!

HIGH RESOLUTION IN ORGANIC COMPOUNDS

The Alcohol Experiment

Although we were able to measure the shifts, for example, between water and mineral oil, the standard of groups in the East,[40] this was set aside following the suggestion of Dr. Shrinvas Dharmatti, a postdoc from the Tata Institute in Bombay. He asked what would happen if we looked at an organic liquid.

We first tried ethyl alcohol, which was one of our favorite substances, and were rewarded with the view of three separate peaks. This led us to publish a comparison of the area under the peaks in various alcohols. This paper, although not important in itself, attracted considerable attention.[41a–d] It was this picture which later brought Dr. James Shoolery[42] to Varian, an event which contributed so much to the development of NMR spectroscopy for and by the chemists.

Felix Bloch did not choose to place his name on the seminal high-resolution paper of organic compounds even though it would have been appropriate. Although he never objected to our foray into chemistry, that was not his major interest.

The spectrum shown in the first alcohol paper was deliberately broadened by selecting an inhomogeneous spot in the magnet, but with great care we could observe three lines in the methyl group and four in the methylene group. The hydroxyl group remained only one peak (Figure 3). This splitting was the result of the spin–spin coupling which turned out to be so important to the chemists as it provided information about the number and closeness of near neighbors.

Hydrogen Bonding of the Hydroxyl Group in Alcohol

An important demonstration of the intermolecular exchange was noted by Jim Arnold who observed that the separation between the hydroxyl and methylene peak was temperature dependent. This we did not understand and decided to publish a short letter describing the effect. We were very quickly

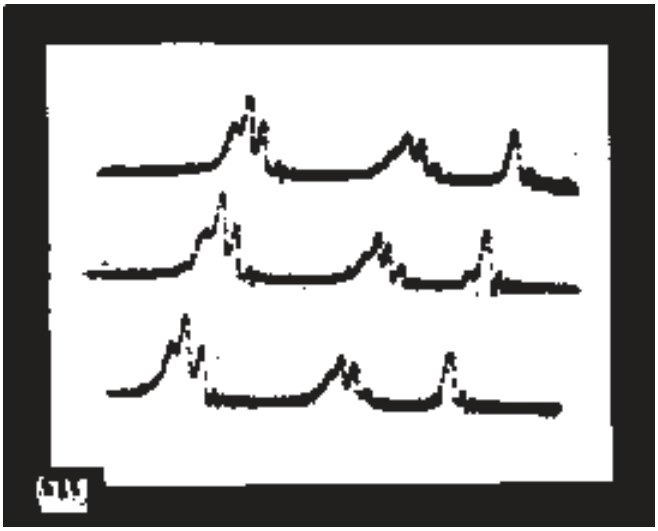

Figure 3 An early slide of the NMR spectrum of ethanol showing the splitting of the peaks caused by the spins of the adjacent protons. The sweep was repeated to reduce artifacts and was reversed from contemporary standards. The 'wiggles' following the peaks are the free precession transients due to a too fast sweep

rewarded with the answer by U. Liddel and Norman F. Ramsey that the effect was explained by the hydrogen bonding between the hydroxyl groups of the alcohol molecules.[41b,c] Norman Ramsey contributed to the art of cesium and hydrogen frequency standards. He was later elected to the Board of Varian Associates.

This simple explanation of hydrogen bonding for the temperature effect prompted Bloch to show me how a two peak pattern becomes one under conditions of rapid exchange. The split powder peak of George Pake** became one line with molecular motion.[43] This averaging effect provided the insight basic to the spin–spin decoupling methods,[44–46] and even the spinning sample method of line narrowing.

Second-Order Splitting

Jim Arnold single handedly built a large permanent magnet to provide better short time stability. With this magnet he observed and calculated the spectra using second-order perturbation theory. Weston Anderson joined Arnold and determined several organic spin coupling constants and chemical shifts by fitting them to an exact quantum mechanical model.[47a–c]

This magnet was taken to CERN, where Arnold and Anderson joined Bloch who served one year as its Director General. The magnet now reposes in the Smithsonian's large collection of early NMR artifacts.

Acceptance by the Chemists

Even though we were physically close to the Stanford Chemistry Department, our work attracted little attention on the campus. Professor Richard Ogg was our principal visionary supporter of the embryonic technique.[48a–c] This is not to say that the chemists were not cooperative. We relied on the chemistry store room and occasional help with chemistry which was beyond our capabilities. Professor Harry Mosher remembers preparing an exotic compound for Erwin Hahn to use in testing some proton-exchange ideas.[49]

RUSSELL VARIAN AND THE PATENT

From time to time I had discussions with Russell Varian, whom I knew as the inventor of the klystron. I knew about klystrons from my radar days and of Stanford's role because I inherited a corner of the old empty upstairs klystron lab in which to build the nuclear induction apparatus.

Although I was not aware of it at the time, Russell was preparing a patent application which was subsequently to be one of the cornerstones of the start-up company, Varian Associates. Russell's belief in and understanding of patents stemmed from his early work and perhaps was influenced by his uncle who was a patent attorney. Russell and his brother, Sig, started a research laboratory, the products of which were to be practical inventions.[50] Russell had gained wide experience over the years in preparing patents. He prepared some patents on geophysical equipment while working at Humble in Houston, he contributed to the klystron patent at Stanford, and he honed his claim-writing expertise while at Sperry. The klystron patent was to return money to the Varian brothers and to Stanford. The Varian Physics Building at Stanford had its genesis from Varian's share of the klystron royalties.

The inventors of nuclear induction, Professors Bloch and Hansen, were of the school that believed that science was done for science's sake. It was reported later that both Bloch and Hansen laughed at the idea of patenting the nuclear induction experiment. At that time, conflict of interest between industry and universities was not of great concern. Nevertheless, Russell's efforts, buttressed by Ed Ginzton, prevailed, and the patent was filed and assigned to the nascent Varian Associates. Without this modicum of monopoly, it would have been financially unrewarding for Varian to develop the instruments needed by the chemists.

Russ was experienced and effective in writing claims. The patent was contested by a major instrument firm only on the basis of prior art, citing Zavoisky's publication in Russia. Depositions were taken from Bloch, me, and others, but the case never went to the courts.

Although it was thought by the founders of Varian Associates that nuclear induction could be the company's main product, it turned out otherwise. The founders had considerable experience with klystrons, both theoretical and practical. The timing was right to obtain government and commercial contracts for new and rugged klystrons, both small and very large. Without this financial support the history of NMR might have been much different.

EPILOGUE

Support by the Office of Naval Research (ONR)

After the initial experiment, the laboratory was generously and wisely supported by the Office of Naval Research (ONR). At that time the research could only have been classified

as basic research with no foreseeable use by the Navy. In fact this was not the case. The high-resolution technology which stemmed from the early work on nuclear forces was of inestimable value to the Navy in solving chemical problems. We were grateful that Professor Walter Meyerhof, who had newly joined the Stanford Physics Department, shielded us from the administrative chores of the ONR contract.

The ONR support continued at Varian as the more fundamental ideas were applied to practical problems. Thus, Russell Varian's invention of the proton free precession magnetometer led to the standard Navy magnetometer for antisubmarine warfare (ASW) applications. The final version used the optical pumping of Professor Hans Dehmelt of the University of Washington and the helium improvement of Professor Peter Franken. Optical pumping is also the basis of atomic frequency standards used for applications such as the global positioning system (GPS).

We were grateful to the ONR experts, who had the vision to support very basic research and were rewarded with many practical solutions to society's needs.

Confluence of Ideas, People, and Environment

The period following the end of World War II in 1945 was unusual. The universities were just beginning to get back into action, the students and professors were well trained in the latest technologies coming from the war effort, and were highly motivated.

Stanford was an attraction for many because of the impressive intellectual and physical environment. These were the conditions which spawned what became known as Silicon Valley. Small entrepreneurs started companies to exploit the ideas presented by the academic community. The relationship between Stanford and Varian was a classic example. Varian prospered on three ideas from Stanford, the klystron, NMR, and the linear accelerator.

Technology Transfer

Technology transfer was achieved, long before it became articulated and fashionable, by the movement of students from the university laboratories to industry.

My role as a physicist working with NMR continued when I went to Varian in the fall of 1951. I had remained as an instructor at Stanford after achieving my Ph.D., as well as our first born, in the summer of 1949. My duties involved both research and the teaching of advanced courses, which I enjoyed. The Physics Department had a wise policy that restricted the addition of recent Stanford Ph.D.s to the staff. I had to make a decision between leaving for academia or industry. I choose Varian Associates, a decision which I never regretted.

My opportunity at Varian was to develop, under ONR sponsorship, another of Russ's ingenious ideas. This we called the 'black box' because it was classified by the Navy. It was to be a moving target filter for doppler radar. The concept of using quantum mechanical systems for circuit applications was sound, but the NMR signal-to-noise ratio was not high enough to make it practical. Nevertheless, the task stretched our technology which was then applied to other problems.

Figure 4 Martin Packard and Russell Varian with the first free precession Earth's field magnetometer. This provided an accurate measurement of the Earth's total field in terms of a frequency. The proton sample is the bottle of water in the foreground

Subsequently, I worked with Russ on still another of his ideas, the free precession magnetometer (Figure 4). This idea led Varian Associates into geophysics, oil-well logging, airborne and ground-based magnetometer surveys, antisubmarine warfare (ASW), and stable atomic frequency sources used in satellite-based navigation systems.

The knowledge of basic magnet resonance was effectively transferred from Stanford and other universities to the marketplace by the movement of graduate students to Varian. Although I have written primarily about the Stanford students, the contribution of students from other universities was equally important (Figure 5).

The Chemists Take Over

The physicists at Stanford made their contribution to the art of NMR but were in no position to bring the ideas to the marketplace where the technique could be used to solve problems arising in other disciplines, chemistry, biology, and medicine.

The glimpse of molecular configuration in the alcohols demonstrated the potential of the method, but would not be useful to the chemists without further development. Its development required a multidisciplinary approach, with the physicists continuing to develop the technology, the chemist

Figure 5 Technology was transferred from the university laboratories through the graduate students. From left to right, Martin Packard from Stanford, Richard Sands from the University of Michigan, and Professor Bloch discuss a topic at the workshop held by Varian for visiting scientists

Figure 6 Forrest Nelson, a Varian Engineer, shares his expertise with workshop participants. Forrest was responsible for many of the innovative ideas

providing the applications, and the engineers building the instruments, either singly or serially (Figure 6).

The year 1951 was the time for the chemists to take over from the physicists. However, at that time we never could have predicted that three decades later a chemist, Professor Paul Lauterbur,[51] would turn the technology over to the medical clinicians for noninvasive imaging.

Nature was Most Benevolent

Nature was most helpful in supplying the ubiquitous hydrogen nucleus with spin-$\frac{1}{2}$ and a large magnet moment.

Man's intellect in developing the basic mathematics and computers, and his insatiable curiosity and drive to make use of Nature's gifts, led to developments of great use to mankind throughout the world.

Very few scientific concepts have had such a long period of new and important applications as has nuclear induction, known as nuclear magnetic resonance (NMR) to the chemist, and magnetic resonance imaging (MRI) to the physician.

NOTES

*Professor Terman's contributions to the Stanford Industrial Park and what came to be known as 'Silicon Valley' are discussed in Ref. 4.

†Alvarez facetiously but proudly told me that Bloch's knowledge of experimental techniques came from his readings during the experiment.

‡Hansen has been quoted by Pieff Panofsky and others for his famous 1947 one-line quarterly report: 'We have accelerated electrons'.

§At the time of writing (1994), Professor Yu is still active although retired from the Physics Department of Beijing University. Science in the Physics Department at Stanford was truly international in its participation.

**George Pake was to become the chairman of the Stanford Physics Department and later to direct the Xerox Laboratory at Palo Alto, which spawned the mouse and the Macintosh computer concept.

REFERENCES

1. N. Bloembergen, *Nuclear Magnetic Relaxation*, Martinus Nijhoff, The Hague, 1948.
2. F. Bloch, W. W. Hansen, and M. Packard, *Phys. Rev.*, 1946, **69**, 127.
3. E. M. Purcell, H. C. Torrey, and R. V. Pound, *Phys. Rev.*, 1946, **69**, 37.
4. H. Lowood, *From Steeples of Excellence to Silicon Valley: the Story of Varian Associates and Silicon Valley*, Stanford University Libraries, Stanford, CA; Varian Associates, Palo Alto, CA, 1987.
5. I. I. Rabi, J. R. Zacharias, S. Millman, and P. Kusch, *Phys. Rev.*, 1938, **53**, 318; 1939, **55**, 526.
6. L. W. Alvarez and F. Bloch, *Phys. Rev.*, 1940, **57**, 111.
7. J. M. B. Kellogg, I. I. Rabi, N. F. Ramsey, Jr., and J. R. Zacharias, *Phys. Rev.*, 1939, **56**, 728.
8. C. J. Gorter and L. J. F. Broer, *Physica (The Hague)*, 1942, **9**, 591.
9. F. Bloch, *Phys. Rev.*, 1936, **50**, 259.
10. J. B. Johnson, *Phys. Rev.*, 1928, **32**, 97.
11. J. S. Rigden, *Rev. Mod. Phys.*, 1986, **58**, 433.
12. F. Bloch and A. Siegert, *Phys. Rev.*, 1940, **57**, 522.
13. F. Bloch, D. Nicodemus, and H. Staub, *Phys. Rev.*, 1948, **74**, 1025.
14. M. E. Packard, *Rev. Sci. Instrum.*, 1948, **19**, 435.
15. E. M. Fryer, *Phys. Rev.*, 1946, **70**, 235; this work was done in 1941 or 1942, but was classified.
16. (a) W. G. Proctor and F. C. Yu, *Phys. Rev.*, 1950, **77**, 716. (b) W. G. Proctor and F. C. Yu, *Phys. Rev.*, 1950, **77**, 717.
17. E. L. Ginzton, W. W. Hansen, and W. R. Kennedy, *Rev. Sci. Instrum.*, 1948, **19**, 89.
18. E. L. Ginzton, K. Mallory, and H. Kaplan, *Stanford Medical School Bulletin*, 1957, **15**, 123.
19. W. E. Lamb, *Phys. Rev.*, 1941, **60**, 817.
20. N. F. Ramsey, Jr., *Phys. Rev.*, 1950, **78**, 699.

21. (a) E. L. Hahn, *Phys. Rev.*, 1949, **76**, 145. (b) E. L. Hahn, *Phys. Rev.*, 1950, **77**, 297. (c) E. L. Hahn, *Phys. Rev.*, 1950, **80**, 580.
22. (a) R. E. Varian, *US Pat. Re* 23769 (1954) (b) M. E. Packard and R. H. Varian, *Bull Am. Phys. Soc.*, **1953**, 28.
23. R. R. Ernst and W. A. Anderson, *Rev. Sci. Instrum.*, 1966, **37**, 93.
24. F. Bloch, E. C. Levinthal, and M. E. Packard, *Phys. Rev.*, 1947, **72**, 1125.
25. (a) W. G. Proctor, *Phys. Rev.*, 1949, **75**, 522. (b) W. G. Proctor and F. C. Yu, *Phys. Rev.*, 1949, **76**, 1728. (c) W. G. Proctor, *Phys. Rev.*, 1950, **79**, 35.
26. (a) S. S. Dharmatti and H. E. Weaver, Jr., *Phys. Rev.*, 1951, **84**, 843; (b) S. S. Dharmatti and H. E. Weaver, Jr., *Phys. Rev.*, 1952, **85**, 927; (c) S. S. Dharmatti and H. E. Weaver, Jr., *Phys. Rev.*, 1952, **86**, 259; (d) H. E. Weaver, Jr., *Phys. Rev.*, 1953, **89**, 923.
27. F. Bloch and C. D. Jeffries, *Phys. Rev.*, 1950, **80**, 305.
28. C. D. Jeffries, *Phys. Rev.*, 1951, **81**, 1040.
29. B. E. Holder and M. P. Klein, *Phys. Rev.*, 1955, **98**, 265.
30. M. Packard, *Bull. Magn. Reson.*, 1985, **7**, 90.
31. (a) F. Bloch, A. C. Graves, M. Packard, and R. W. Spence, *Phys. Rev.*, 1947, **71**, 373. (b) H. L. Anderson and A. Novic, *Phys. Rev.*, 1947, **71**, 372. (c) F. Bloch, T. C. Graves, M. Packard, and R. W. Spence, *Phys. Rev.*, 1947, **71**, 551.
32. F. Bloch and D. H. Garber, *Phys. Rev.*, 1949, **76**, 585.
33. B. A. Jacobsohn and R. K. Wangsness, *Phys. Rev.*, 1948, **73**, 942.
34. H. L. Marshall and H. E. Weaver, Jr., *J. Appl. Phys.*, 1963, **34**, 3175.
35. F. Bloch, *Phys. Rev.*, 1951, **83**, 1062.
36. H. L. Anderson, *Phys. Rev.*, 1949, **76**, 1460.
37. E. Jaynes, *US Pat.* 3 566 255 (1959).
38. (a) M. J. E. Golay, *Rev. Sci. Instrum.*, 1958, **29**, 313. (b) W. A. Anderson, *Rev. Sci. Instrum.*, 1961, **32**, 241. (c) W. A. Anderson, *US Pat.* 3 199 021 (1960). (d) R. R. Ernst, *Rev. Sci. Instrum.*, 1968, **39**, 998.
39. (a) F. Bloch, *Phys. Rev.*, 1954, **94**, 496; (b) W. A. Anderson and J. T. Arnold, *Phys. Rev.*, 1954, **94**, 497. (c) F. Bloch, *US Pat.* 2 960 649 (1960).
40. H. S. Gutowsky and R. E. McClure, *Phys. Rev.*, 1951, **81**, 276.
41. (a) J. T. Arnold, S. S. Dharmatti, and M. E. Packard, *J. Chem. Phys.*, 1951, **19**, 507. (b) U. Liddel and N. F. Ramsey, Jr., *J. Chem. Phys.*, 1951, **19**, 1608. (c) J. T. Arnold and M. E. Packard, *J. Chem. Phys.*, 1951, **19**, 1608. (d) M. E. Packard and J. T. Arnold, *Phys. Rev.*, 1951, **83**, 210.
42. J. N. Shoolery, *Am. Lab.*, 1988, **20**(**10**), 49.
43. G. E. Pake, *J. Chem. Phys.*, 1948, **16**, 327.
44. V. Royden, *Phys. Rev.*, 1954, **96**, 543.
45. A. L. Bloom and J. N. Shoolery, *Phys. Rev.*, 1955, **97**, 1261.
46. F. Bloch, M. E. Packard, and J. N. Shoolery, *US Pat* 3 068 399 (1962).
47. (a) W. A. Anderson and J. T. Arnold, *Discuss. Faraday Soc.*, 1955, **19**, 226. (b) J. T. Arnold, *Phys. Rev.*, 1956, **102**, 136. (c) W. A. Anderson, *Phys. Rev.*, 1956, **102**, 151.
48. (a) E. C. Levinthal, E. H. Rogers, and R. A. Ogg, Jr., *Phys. Rev.*, 1951, **83**, 182. (b) R. A. Ogg, Jr., *Phys. Rev.*, 1954, **94**, 767. (c) J. Kelly, J. Ray, and R. A. Ogg, Jr., *Phys. Rev.*, 1954, **94**, 767.
49. E. L. Hahn and D. E. Maxwell, *Phys. Rev.*, 1952, **88**, 1070.
50. D. Varian, *The Inventor and the Pilot*, Pacific Books, Palo Alto, CA, 1988.
51. P. C. Lauterbur, *Nature (London)*, 1973, **242**, 190.

Biographical Sketch

Martin E. Packard. *b* 1921. B.A., 1942, Physics, Oregon State University, Ph.D., 1949, Physics, Stanford University. Westinghouse Research, 1942–45; Stanford University, 1945–51; Varian Associates, 1951–88; Institute for Genetic Disease Control in Animals, 1989–present. Current research specialties: the study of genetics as applied to the control of genetic diseases in dogs.

Packer, Ken: Connections (or One Thing Leads to Another)

Ken Packer

University of Nottingham, Nottingham, UK

In 1960, whilst pursuing preparative inorganic chemistry research for my doctorate, I made a new compound. In establishing that the structure of this was SF_5OSO_2F I had the ^{19}F NMR spectrum run on the department's Varian 40 MHz V4300 spectrometer. The spectrum was complex and, as I knew little of NMR at the time, I turned to Norman Sheppard. He realised that this spectrum was an excellent example of an AB_4X spin system. The theory of these spin systems was being worked on by one of his students, Robin Harris, and our collaboration in analyzing these spectra[1] kindled my enthusiasm for NMR and, of course, set the scene for further collaboration with Robin later in our careers whilst at the University of East Anglia (UEA). A postdoctoral fellowship at DuPont, with the late Earl Muetterties, generated the ^{19}F and ^{93}Nb NMR spectra of the NbF_6^- ion[2] which got me interested in relaxation processes. Soon after returning to a post at UEA I realised that sharing a high-resolution spectrometer with preparative chemists was not going to allow me to pursue my developing interests in the more physical aspects of NMR. I was fortunate enough to pursuade those controlling the funding of research that a pulsed NMR spectrometer was just what I needed so, in 1965, I found myself the proud owner of a Magnion pulsed NMR spectrometer which I combined with a 4 tonne AEI electromagnet.

In telling this personal story I hope to demonstrate how different aspects of one's research experience often interconnect. One of the areas which fascinated me at this early stage was the use of gradients in magnetic fields to allow transport processes such as diffusion and flow to be characterized.[3] This is still an active interest today. Our early work on flow had as a goal the design of a pulse sequence which would determine the flow character in a single shot. Carr and Purcell had shown that flow through a gradient only gave rise to effects on odd echoes of their multipulse echo sequence, which made it like a series of sequential two-pulse echo sequences. After much deliberation I realised, from an analysis of the phase shifts, that the phase of the magnetization had to be reversed more frequently which led to the $90^\circ - t - (180^\circ - t')_n$ sequence.[4] In a lecture at the 8th International NMR Colloquium held in Aachen in 1971 I recall presenting this work, including an analysis of the alternating rf phases required for the 180° pulses to minimize cumulative errors. As I was describing this aspect, which had taken me considerable effort to work through, I happened to glance at John Waugh, sitting in the front row, who made a gesture indicating the solution to this problem, solved I imagine as I spoke!

The demonstration by Ed Stejskal and John Tanner of the effectiveness of pulsed gradient experiments encouraged me to explore the area of restricted diffusion and the quantitative determination of droplet sizes in emulsions. In our paper in 1972 we noted that the long-time limiting behavior should allow the determination of the droplet size distribution through variation of the gradient pulse area.[5] This was noted by colleagues in Unilever and we subsequently developed an approach based on this suggestion.[6] The point of this story, however, is that at that stage we certainly did not recognise that there was a straightforward analogy of this behavior with optical scattering and diffraction with the gradient pulse area playing the role of a wavevector. Although the relationship between NMR in a gradient and diffraction was pointed out by Peter Mansfield in 1975, it was only when we commenced modeling the response of the pulsed field gradient spin echo experiment to the diffusion of molecules through porous media that the analogy became clear. Collaboration with Paul Callaghan on both theory and experiment added to our understanding of this phenomenon which is now widely recognised.[7] In retrospect it is interesting to note how 20 years of thinking about this experiment made it hard to accept that the echo signal could increase as the gradient pulse area increased!

My involvement with diffusion measurements led to work on biological tissues, but that's another story. However, this led to an interest in NMR of dynamically ordered systems and it was in this context that I learnt an important lesson. Satapah Ahmad was a new student from Malaysia. As a project, I suggested that he measure the T_2 behavior for D_2O in an oriented system for which the ^2H spectrum was a simple doublet and indicated that he should use the Ostroff–Waugh sequence, $90^\circ_x - t - (-90^\circ_y - 2t -)_n$, as this should refocus the secular quadrupolar interaction at each echo. After some time Satapah came to me and showed me his results which indicated that $T_2 > T_1$. Naturally, I was not impressed! After several repeats by him of the measurements with the same outcome I carried out the experiments myself and got the same results! Clearly, a lot of knowledge is a dangerous thing! We subsequently developed a density matrix theory treatment which explained this behavior and, in addition, showed how it was possible to obtain all three spectral densities determining the relaxation behavior in such a system despite it being in extreme narrowing.[8] A further outcome of my interest in this area was the development, with Kevin Wright, of a single spin operator formalism with which to describe the response of small spin systems with secular couplings to general pulse sequences.[9] It was on a plane journey from Melbourne to Canberra that I learnt from Geoffrey Bodenhausen that Richard Ernst's group had also been developing a similar approach. This was both good and bad news simultaneously! Our description of the generalized behavior of the AX spin system in the form of a topological framework was a particular pleasure to me.

Of course, the ultimate in terms of secular spin couplings are those in a many-spin rigid solid. When Gibby, Pines, and Waugh and Schaefer and Stejskal showed the way, Robin Harris and I recognized that our complementary experiences placed us in a strong position to contribute to this, then emerging area of high-resolution NMR in solids. Thus began a decade of challenging and fascinating research taking us from spectrometer building, engineering of cylindrical gas bearings for sample spinning and a range of new NMR phenomena, into a wide range of applications in chemistry and materials.[10]

In finishing this brief retrospective I recall some advice I was given when I was considering moving into NMR research as a graduate student who thought he had 'seen the (NMR)

light'. This was to the effect that NMR was pretty well developed and understood and did not have much more to offer a keen young researcher. That was in 1960! Predicting the future was never easy!

REFERENCES

1. R. K. Harris and K. J. Packer, *J. Chem. Soc.*, 1961, 4736; 1962, 3077.
2. K. J. Packer and E. L. Muetterties, *J. Am. Chem. Soc.*, 1963, **85**, 3035.
3. K. J. Packer, C. Rees, and D. J. Tomlinson, *Adv. Mol. Relaxation Processes*, 1972, **3**, 119.
4. K. J. Packer, *Mol. Phys.*, 1969, **17**, 355.
5. K. J. Packer and C. Rees, *J. Colloid Interface Sci.*, 1972, **40**, 206.
6. J. C. van den Enden, D. Waddington, H. van Aalst, C. G. van Kralingen, and K. J. Packer, *J. Colloid Interface Sci.*, 1990, **140**, 105.
7. P. T. Callaghan, A. Coy, T. P. J. Halpin, D. MacGowan, K. J. Packer, and F. O. Zelaya, *J. Chem. Phys.*, 1992, **97**, 651.
8. S. B. Ahmad and K. J. Packer, *Mol. Phys.*, 1979, **37**, 47, 59.
9. K. J. Packer and K. M. Wright, *Mol. Phys.*, 1983, **50**, 797.
10. G. E. Balimann, C. J. Groombridge, R. K. Harris, K. J. Packer, B. J. Say, and S. F. Tanner, *Phil. Trans R. Soc. London*, 1981, **A299**, 643.

Biographical Sketch

Ken J. Packer. *b* 1938. B.Sc., 1959, Chemistry, Imperial College, London, Ph.D., 1962, Cambridge University. Introduced to NMR by making a new compound and collaborating with fellow graduate student (Robin Harris) in the analysis of its spectrum. Reinforced by a postdoctoral year with Earl Muetterties at the duPont Experimental Station, Wilmington. 1963–84, School of Chemical Sciences, University of East Anglia; 1984–93, BP Research, Chief Research Associate in Spectroscopy and latterly Chief Scientist. Currently, Research Professor in Chemistry, Department of Chemistry, University of Nottingham. Approx 120 publications including book 'NMR of Solid Polymers' with V. J. McBrierty. Current research interests: NMR/MRI applied to heterogeneous catalysts, solid polymers, and fluid transport processes in porous solids.

Pake, George E.: A Graduate Student and Young Faculty Physicist Wanders into NMR: 1946–53

George E. Pake

Institute for Research on Learning, Palo Alto, CA, USA

Enrolling as a graduate student in the Harvard Physics Department in 1946 was a piece of extraordinary good fortune that arose from several chance decisions at forks in my personal educational road. It was extreme good luck because I happened into Harvard just as Edward Purcell and his colleagues Bob Pound and Nicolaas Bloembergen were launching their pioneering research program in NMR, and I became one of the first Harvard graduate students to join Purcell's research group. In fact, I believe I was the first; Bloembergen, whose thesis research with Purcell preceded mine, was in fact a University of Leiden student doing his doctoral research at Harvard because European universities were only just beginning to restore normal graduate programs in early 1946. American universities had been less severely disrupted by World War II and could resume graduate operations much more rapidly.

I had received my M.S. in Physics from Carnegie Institute of Technology (now Carnegie–Mellon University) in April 1945, and I then took up employment during those wartime years at the Westinghouse Research Laboratories in East Pittsburgh, developing microwave components for airborne radar systems. With World War II in full swing at the time (although the imminent defeat of Germany was evident, from all the news reports of the Nazi war machine being crushed between the Atlantic Allies' forces from the west and the Soviet hordes from the east), there were few if any truly active academic Ph.D. programs in Physics. The sensible procedure for an aspiring physicist at that time was to join the war effort in a way that used my physics training up to that point, awaiting the conclusion of hostilities to resume graduate study.

Although the decision to take a research position with Westinghouse was geographically convenient, it also turned out to be a real boost to my physics education. Microwave physics had not previously been mentioned in my studies, and I arrived at the Westinghouse labs to find a marvelously lucid set of lecture notes ('Principles of Microwave Radio', 1944, unpublished) by Edward Condon, then Associate Director of the Westinghouse Research Laboratories. I was given these notes and a development task to specify and test the design of an X-band (3-cm wave) directional coupler for an airborne radar. Further, I was urged to design and build an apparatus for measuring breakdown potentials of microwave gas discharges. From these tasks I learned several concepts and techniques which were later to be of value to me as a graduate student taking up research on NMR.

Other than some help that I provided in the low-temperature laboratory for Prof. I. Estermann at Carnegie during my masters degree studies, the microwave work at Westinghouse was one of my earliest laboratory research experiences, and building the gas discharge apparatus represented my first independent experimental effort. The apparatus was just producing its first gas discharges (but no measurements yet) in August 1945 as the Pacific war ended. I immediately wrote to graduate physics departments to apply for admission to a Ph.D. program. With advice from my Carnegie Department Chairman, Prof. Fred Seitz, I applied both to Princeton and Harvard, planning at that time to pursue a thesis in theoretical physics. Activity in my Westinghouse Laboratory was stymied by a strike and a picket line of laboratory technicians, so my gas discharge apparatus was unavailable to me for several weeks, until suddenly it was time to leave for Harvard (my choice because it offered me a teaching fellowship, and I had no funds otherwise to support my further graduate study).

Also influencing my selection of Harvard was a handwritten letter from J. H. Van Vleck, then chairman of the Harvard department, warmly inviting me to come to Harvard under a teaching fellowship. I arrived in Cambridge in late January 1946 and began with a heavy dose of graduate courses.

During that semester, I attended two physics colloquia that captured my interest: one (in February, I think) by Ed Purcell, just returned to Harvard as Associate Professor of Physics, on the Purcell–Torrey–Pound experiment which in late 1945 had just detected nuclear magnetic resonance absorption in bulk matter (paraffin). A little later (I guess in April, in close association with an American Physical Society meeting in Cambridge), W. W. Hansen of Stanford gave a Harvard physics colloquium on the Bloch–Hansen–Packard nuclear induction experiment.

Purcell's talk was deeply inspirational to me. Here was an experimental physicist who demonstrated real appreciation of theory and of the consequences of his research for all of physics, both theory and experiment. I thought to myself, 'Why confine one's interest to theoretical physics if one can join a group that operates within the entire sphere of physics, both experiment and theory?' The Purcell–Torrey–Pound experiment also appealed to my recent microwave experience, as the paraffin proton resonance was detected in a resonant cavity (of course, at 30 MHz, not exactly in the microwave range, but using concepts familiar to me from my Westinghouse work).

There were other attractions: Purcell exhibited his characteristic lucidity and deep insight into physics as he spoke. And, of course, I felt some of the excitement of being 'in on the ground floor' of a new technique in physics. I was also imbued, like many of my graduate student colleagues, with a sense that with the war over we should all pitch in to develop an understanding of the nucleus and nuclear forces comparable to our post-World War I understanding of the atom. With the capability of NMR to provide a rich set of measured nuclear spins and magnetic moments, I saw it at first as a tool for nuclear physics. In the summer of 1946, most of the course work for my Ph.D. being completed, I applied to and was accepted into Purcell's research group.

I was assigned a laboratory room in the basement of the Lyman Laboratory, adjoining the room in which Nico Bloembergen was using a large electromagnet to pursue for his thesis project with Ed Purcell the pioneering investigation of nuclear magnetic relaxation in liquids. That research became, of course, the basis for the world famous BPP paper in the *Physical Review*.[1]

Because the NMR lines could be very sharp, it was desirable to have a stable magnetic field. Purcell had decided to try out the efficacy of a fairly large permanent magnet. After it was magnetized with Purcell's help, this magnet became the central piece of my research apparatus. As I began to assemble a 30 MHz spectrometer for use in my experiments (by this time we were using lumped parameter resonant circuits, not cavities), I also engaged in serious planning for what my experiment should be. This of course involved numerous conferences with Purcell as my supervising professor, and I also had several informal discussions with Bob Pound and Nico Bloembergen.

Bob Pound at that time was pursuing his own researches on NMR line splitting in crystals, focusing particularly on nuclei of spin $I > \frac{1}{2}$ and their electric quadrupole splittings due to interaction with the gradient of the crystalline electric field. Pound was widely regarded as the group's electronics wizard. Whereas he surely had those skills in abundance, one should not overlook his deep comprehension of physics generally. As I was planning my thesis project, Bob Pound provided me with several valuable insights on nuclear magnets within crystal structures, which of course were the objects of his NMR studies of nuclear quadrupole interactions. Whereas Bloembergen and I operated fixed frequency rf spectrometers and swept the $\boldsymbol{H}_0$ field in small excursions through the NMR resonance, Pound kept his magnetic field fixed and, using a clock motor to drive a variable capacitor, systematically swept the frequency of his marginal oscillator resonance detector over a wide range encompassing the sometimes rather large quadrupole splittings. These pioneering experiments were described in his *Physical Review paper*.[2]

I also had many talks with Nico Bloembergen, who was readily available to me in the laboratory adjoining mine. A special feature of the common wall between our laboratories was a large hole about 1.5 ft. by 3–4 ft. through which I could shout questions at Nico whenever I needed experimental guidance or, often times, just to discuss physics.

Bloembergen was progressing in his investigations of nuclear relaxation in liquids, and he had quickly observed that the lines were sharp, with their width being determined by the spatial inhomogeneity over the small ($\sim$1 cm^3) volume of the samples he used. This seemed to imply early on that the relative motions of the protons in water, for example, were averaging away the local dipolar magnetic fields which at any given instant ought, by calculation, to be several gauss. In discussing this with Nico, the idea arose: why not look in solids, such as the crystalline hydrates, to see what the linewidths are for protons of water molecules rigidly bound into the lattice? After discussion with Purcell, I pursued this line of investigation seeking to understand in detail the factors determining NMR linewidths in crystalline solids. The next question was: which solid hydrate(s) should I investigate?

The most frequently encountered crystalline hydrate in my science education up to that point was $CuSO_4 \cdot 5H_2O$, which every student seemed to deal with in freshman chemistry as a source for the blue cupric ion in aqueous solutions. Also, it was relatively easy to grow single crystals from solution. However, for my purposes, the incomplete electron shells of the cupric ions render them paramagnetic, and the 2000-times larger Cu^{2+} ion magnetic moment would greatly perturb the tiny nuclear magnetic moments in its vicinity, making copper sulfate a poor candidate for studies of purely internuclear magnetic interactions.

Never having had any formal instruction in geology, I picked up an introductory text and looked for a likely naturally occurring hydrate crystal. One immediately caught my attention: gypsum, $CaSO_4 \cdot 2H_2O$. By virtue of the fact that even–even nuclei have zero nuclear spin in their ground states, the abundant isotopes of Ca, S, and O are all magnetically inert in gypsum, leaving only the pairs of water molecule protons to interact with each other and with neighboring pairs. This seemed ideal for my projected studies, but I had no idea how easily I could obtain a suitable single crystal. Upon crossing Oxford Street from the Lyman Laboratory to visit the Harvard Department of Mineralogy and Petrography, I found myself standing next to a gypsum crystal perhaps a meter long!

A kindly professor gave me a smaller gypsum single crystal from which I cut two samples about the size of my little finger. The cleavage planes were readily identifiable and there was little problem in establishing the unit cell axis directions using the known crystal structure.

Upon searching for the proton resonance in the gypsum crystal, I found immediately that the linewidth was strongly dependent upon crystal orientation in the external magnetic field, $\boldsymbol{H}_0$. From the presumed hydrogen nuclear positions based upon the structure as determined from X-ray diffraction (which permitted only educated inference of the likely hydrogen atom positions, as there is no electronic X-ray scattering from the protons), I was able to cut a crystal that, upon rotation in the magnetic field, permitted me to align $\boldsymbol{H}_0$ either perpendicular to the line joining partner protons in the H_2O molecule, or nearly parallel to it. Systematic recording of the proton resonances versus crystal orientation showed resolvable pairs of resonance lines, presumably arising from the two alternative orientations (spin up or down) of the partner proton in each H_2O molecule. A crude semiclassical estimate of the local magnetic field component experienced at each proton from its partner's magnetic moment aligned along or against the external magnetic field led me to estimate a splitting between the pair of resonance lines to be

$$(\Delta H)_{\text{est.}} = (\mu/r_0^3)(3\cos^2\theta - 1) \qquad (1)$$

where μ is the proton magnetic moment, r_0 the interproton distance in the water molecule, and θ the angle between $\boldsymbol{H}_0$ and the interproton line.

However, a quantum calculation allowing for the indistinguishability of the two magnetically equivalent proton spins within the spin triplet state gives the angular dependence and the magnitude of the splitting of the pair of resonance lines. This quantum perturbation calculation found that equation (1) underestimates the magnitude of the splitting and that a factor $\frac{3}{2}$ should be supplied to the right-hand side of the equation to give the correct splitting. This was a great relief to me, in as much as the observed splittings if interpreted using the uncorrected equation (1) would lead to a value of r_0 that seemed quite unreasonably small in view of the existing knowledge of the H_2O molecular structure in the gaseous state.

When I first did the perturbation calculation, I had just been learning about unitary transformations in a class with Prof. J. Schwinger, and I was apparently obsessed with unitary transformations. Beginning with the spin functions corresponding

to eigenstates for $m = +\frac{1}{2}$ and $m = -\frac{1}{2}$ along the external magnetic field $\boldsymbol{H}_0$, I formed the symmetric combinations for spin triplets, and then used unitary transformations to rotate axes through angle θ to the direction of the interproton line. Using these new functions and treating the magnetic dipole–dipole interaction between partner protons as a perturbation, I laboriously worked out the energy level shifts and obtained the splitting of equation (1) with the correct $\frac{3}{2}$ factor. This was a very 'round-about' and needlessly cluttered approach to the problem.

The next day I went over my tedious 12 or 14 pages of handwritten algebra with Ed Purcell, who the following morning showed me an operator identity from which the correct splitting could be deduced in about two lines of calculation: perhaps one-third of a page in total.

About four or five months later, Purcell came to my laboratory with a short visitor, introduced as Prof. E. Fermi of Chicago. Asked to explain my experiment to the visitor, I began with the crude semiclassical estimate of the partner proton magnetic field, whereupon Fermi glanced at the ceiling, muttered something about equivalent protons and, after a few seconds of thought, said, 'of course, the actual splitting will be $\frac{3}{2}$ of the semiclassical estimate'. To this day, I regard that experience as a somewhat accurate calibration of Pake's relative theoretical ability: Fermi, 10 seconds; Purcell, less than half a page; Pake, 12 or 14 tedious pages. No; I am sure those ratios overestimate Pake's ability by an order of magnitude or two. And they are unfair to Purcell, who doubtless only needed his one-third of a page in order to explain to me a calculation he made almost instantaneously.

Once I understood the gypsum single crystal splittings, I looked at a number of other hydrates, some of which I was only able to obtain in powdered form. This led me to deduce the obvious consequences of summing the resonance patterns of numerous randomly oriented microcrystals each exhibiting proton pair splittings that varied as $3\cos^2\theta - 1$. The resulting lineshape distribution is a characteristic doublet that is just barely resolvable in consequence of the broadening of each pair's pattern by the effects of the more distant neighboring pairs.[3]

Because the gypsum research project went so smoothly, I found myself with a nearly completed thesis in February or March of 1948, with my degree award scheduled for June Commencement. In the meantime, through conversations that Ed Purcell had with Prof. George Kistiakowsky in Chemistry, I was introduced to one of Kisty's students, Herbert S. Gutowsky, and together that spring and summer we used a copper-block cooling apparatus as a kind of cryostat for studying proton resonances in molecular van der Waals solids. These solids, even at temperatures near 100 K or 150 K, exhibited proton line narrowing that was evidence of hindered rotations either of whole molecules or of single-bonded radical groups attached thereto. From the amount of dipolar linewidth narrowing, we were able to interpret the nature of some of these rotations. We reported this research in a series of papers.[4–6] These experiments, for me, nicely filled a gap between my thesis project and beginning to organize my own laboratory as I took up my first faculty position in the autumn of 1948 at Washington University in St. Louis.

In late July 1948, I drove from Cambridge to St. Louis and began to build up my magnetic resonance laboratory at Washington University. The Physics Department under A. L. Hughes had an interesting and nearly unique policy of assigning each incoming graduate student immediately to a research group, which provided a sense of belonging and an early immersion in a research environment. As a consequence, after I had completed my thesis defense exam at Harvard and motored to St. Louis, I found myself called upon to transform from graduate student to research professor for seven graduate students. These eager young men were of great assistance as we began tooling up for research in the new field of magnetic resonance—although these students had noticeably less time for the lab once graduate course instruction reached full momentum that fall. There was, however, one major problem: the research field of NMR was so new in 1948 that no textbooks or treatises yet existed, and first-year graduate students typically had an inadequate background to read and comprehend the few published research papers, which in any case tended to be not very complete. While awaiting delivery of newly-ordered equipment for our laboratories-to-be, my students and I held a series of seminars in which I set forth background material for NMR research—being mindful that I could not yet assume a real working knowledge of quantum mechanics. These lectures I wrote up into a longish review article later published in the *American Journal of Physics* in two parts.[7,8]

I was continually besieged with reprint requests, inasmuch as these beginning-level articles seemed to meet a clear need for individuals worldwide who wished to learn about this new technique. Because I quickly exhausted my supply of *AJP* reprints—and because xerographic technology was only just about to be, but not yet, marketed—I arranged with the American Institute of Physics for Washington University to do a half-scale photo-offset reprinting of these articles. As I recall, we distributed somewhere between 2000 and 5000 of these reprint sets in response to requests.

These articles even attracted some rather recent attention when Prof. Robert H. Romer, Editor of the *American Journal of Physics*, nominated them for a listing of outstanding *AJP* articles over the past several decades (see *Am. J. Phys.*, 1991, **59**, 201).

With my fledgling group of graduate students at Washington University, we made some progress on applying NMR to a number of areas of interest in physics. Here I would note as follows: the electric quadrupole moment of ^{6}Li [9] and the spin of ^{9}Be,[10] measurements by N. A. Schuster; early application of NMR to the study of polymers[11] by Charles W. Wilson III; radiofrequency measurements of relaxation times for electron spin resonances in free radicals[12] by J. P. Lloyd.

This first mention of free-radical molecules is an indicator of a change in direction for my research interests, largely a consequence of collaborations begun with Prof. S. I. Weissman of the Washington University Chemistry Department. While I was launching my NMR researches at Washington University in 1948 and 1949, Sam Weissman would often appear at my office or laboratory to discuss the potential of magnetic resonance as a technique for studying stable free-radical molecules. I was intrigued, inasmuch as I had not even heard of these stable molecules having unpaired electrons in nonconformance to the simple rules I had learned in my elementary chemistry classes. Since these electronic magnetic moments were much larger than the nuclear moments studied heretofore in my research, free-radical experiments would often require higher frequencies in the microwave range. The

more Weissman and I talked, the more promising these avenues of research seemed, and we enlisted Dr. Jack Townsend who built several spectrometers for our early free-radical studies. Weissman and his students went on to pursue an active and stellar program of magnetic resonance studies of free radicals.

One particular free radical supplied to my own researches by Weissman's group enabled some experiments that were, for me, quite aesthetically pleasing. These involved the peroxylamine disulfonate ion, $ON(SO_3)_2^{2-}$, in solution. Note that the abundant nuclear isotopes of this ion are all, except for ^{14}N, even–even and therefore have zero nuclear moment. This leaves just the ^{14}N nucleus of spin 1 to interact magnetically with the unpaired electron whose wavefunction is somehow draped over the ion. Surely enough, as expected, the microwave electron paramagnetic resonance in moderately large laboratory magnetic fields is a triplet corresponding to the three nuclear spin orientations accessible to ^{14}N, with the hyperfine coupling being about 54 or 55 MHz.

What I found so appealing about this ion is that, with its radiofrequency hyperfine coupling, we had in a small sample tube of ions in solution the magnetic analog of the atomic magnetic moment as studied in the early molecular beam experiments. To the extent that the analogy was valid, the energy levels of our free radical ion system in a magnetic field should be governed by the Breit–Rabi calculation,[13] upon which rested interpretation of many of the historic molecular beam experiments, which had themselves helped to inspire the invention and detection of NMR. I therefore found enormous satisfaction in our radiofrequency investigation of the low magnetic field absorption spectrum of the $ON(SO_3)_2^{2-}$ ion,[14] which neatly fitted the Breit–Rabi energy levels for an unpaired electron in hyperfine interaction with a ^{14}N nuclear moment having hyperfine coupling $\Delta\nu = 54.7$ MHz.

In a way that I found irresistibly appealing, my personal sojourn through the early years of NMR had brought me full circle to Breit–Rabi, upon which so much of molecular beam physics had rested, and which therefore provided the foundations for NMR and electron paramagnetic resonance (EPR)—the fields upon which my own research career had been focused.

REFERENCES

1. N. Bloembergen, E. M. Purcell, and R. V. Pound, *Phys. Rev.*, 1948, **73**, 679.
2. R. V. Pound, *Phys. Rev.*, 1950, **79**, 685.
3. G. E. Pake, *J. Chem. Phys.*, 1948, **16**, 327.
4. H. S. Gutowsky and G. E. Pake, *J. Chem. Phys.*, 1948, **16**, 1164.
5. H. S. Gutowsky, G. B. Kistiakowsky, G. E. Pake, and E. M. Purcell, *J. Chem. Phys.*, 1949, **17**, 972.
6. H. S. Gutowsky and G. E. Pake, *J. Chem. Phys.*, 1950, **18**, 162.
7. G. E. Pake, *Am. J. Phys.*, 1950, **18**, 438.
8. G. E. Pake, *Am. J. Phys.*, 1950, **18**, 473.
9. N. A. Schuster and G. E. Pake, *Phys. Rev.*, 1951, **81**, 157.
10. N. A. Schuster and G. E. Pake, *Phys. Rev.*, 1951, **81**, 886.
11. C. W. Wilson III and G. E. Pake, *J. Polym. Sci.*, 1953, **10**, 503.
12. J. P. Lloyd and G. E. Pake, *Phys. Rev.*, 1953, **92**, 1576.
13. G. Breit and I. I. Rabi, *Phys. Rev.*, 1931, **38**, 2082.
14. J. Townsend, S. I. Weissman, and G. E. Pake, *Phys. Rev.*, 1953, **89**, 606.

Biographical Sketch

George E. Pake. *b* 1924. B.S. and M.S., 1945, Carnegie Institute of Technology. Ph.D., 1948, Harvard University. Faculty of Physics, Washington University, St. Louis, MO, 1948–56; Professor of Physics, Stanford University, 1956–62; Provost of Washington University, 1962–69; Vice President and Manager, Xerox Palo Alto Research Center, 1970–78; Group Vice President, Xerox Corporate Research, 1978–86; Director, Institute for Research on Learning, Palo Alto, 1987–91; Director Emeritus, 1991–present.

Pfeifer, Harry: Leipzig, Summer 1951

Harry Pfeifer
Universität Leipzig, Leipzig, Germany

The first nuclear magnetic resonance experiments performed at the University of Leipzig in the summer of 1951 were stimulated by events that took place 24 years before. In the fall of 1927 Peter Debye had moved from the Swiss Federal Institute of Technology at Zürich (ETH) to Leipzig where he became Director of the Institute of Experimental Physics and where he had persuaded Werner Heisenberg to accept the Professorship for Theoretical Physics (Figure 1). It was not surprising, therefore, that Leipzig became an attractive place for young scientists and students of physics. Among them the most prominent was apparently Felix Bloch, who writes in his 'Reminiscences of Heisenberg and the Early Days of Quantum Mechanics':[1] ' ... in October 1927 before the beginning of the winter semester, I left my nice home town (Zürich) for the first time to arrive on a cold gray morning in that rather ugly city of Leipzig ... As soon as I had completed the simple formality of registering as a student of the University in the center of the city I went to the Physics Institute, which was located near the outskirts. It was an old building opposite a cemetery on one side and adjoining the garden of a mental institution on the other, but occupied by people who were far from being either dead or crazy ... Debye had the Director's villa in a side wing, and for young bachelors like Wentzel and also Heisenberg upon his arrival there were small but comfortable apartments under the roof ... . These men were so entirely devoted to their science and their work spoke so clearly for itself that there was really no room or reason for any pretence, be it in the form of grand manners or false modesty ... ' In the following months Felix Bloch became the first doctorand of Werner Heisenberg, and he finished his thesis on 'The Quantum Mechanics of Electrons in Crystal Lattices' in 1928. After one year as an assistant to Pauli in Zürich and another year as Lorentz Fellow in Holland, Felix Bloch came back to Leipzig as Heisenberg's assistant in the fall of 1930 until Hitler succeeded in 1933 in forming a new Germany in his own frightful image.

After the war, in October 1947 when I came as a student for the first time to Leipzig University, the famous Institute of Physics 'located near the outskirts' in the Linnéstrasse 5 was only a ruin (Figure 2). The large auditory, the Director's villa, the large store rooms of scientific apparatus and most laboratories were completely destroyed. As a result, lectures were delivered at the Institute of Mathematics about one mile away where some rooms were also placed at the disposal of physicists including the Director's office and the library. Fortunately, nearly 80% of the scientific books and journals were saved since the Physics Library was housed in the tower of the Institute which survived the bombs due to its internal stability. In the ruin however, rain was destroying more and more of the remaining laboratories and the mechanical workshop, and I remember that in spite of the fact that all electrical equipment had been switched off, we observed a permanent electrical current of nearly 10 A at the main line supplying the ruin.

Nevertheless it was an exciting time of renewal, and at the end of the 1940s we received all the issues of *Physical Review* which could not be delivered before due to the war and afterwar problems. About that time Artur Lösche (*b* 1921) had finished his thesis on birefringence induced by mechanical rotation of polar liquids and became an assistant at the Institute of Physics. Being responsible for the library, he organized a systematic study of these journals. During this study he became aware of the exciting experiments of the former Leipzig scientist Felix Bloch, and in the summer of 1950 A. Lösche suggested the search for nuclear induction signals including preliminary experiments as a suitable topic for a diploma thesis. At this time I was students' assistant for the lectures in experimental physics delivered by the Director of the Institute, Professor Waldemar Ilberg, a physicist who had changed after the war from the electronic industry to university. He proposed the study of the light efficiency of gas discharge lamps since this would be a problem of special importance for an industry which was beginning to start at this time from a very low level in Germany. As a young student, it was not very easy for me to come to a decision but finally I chose the 'entirely useless' search for signals stemming from the Zeeman energy of hydrogen nuclei. There were two further students, Hans Lippmann and Karl-Heinz Weber, who also followed the suggestion of Dr. Lösche, so that we three started separately in September 1950 to find the nuclear induction signals which were described for the first time in 1946 independently by Felix Bloch et al. and E. M. Purcell et al. in the January issue of the *Physical Review*.[2,3] For my studies I used an old electromagnet that had survived the bombardments of the institute (December 4, 1943, February 19, 1944, and April 6, 1945) and with the direct current supply commonly available in Leipzig at this time it was possible to achieve a magnetic field of about 0.8 T with a gap width of 2 cm. Stimulated by a paper by A. Roberts[4] I decided to build a superregenerative detector and in this connection to study the nonlinear theory of electric oscillations established more than 20 years previously by van der Pol.[5] As a result of the latter studies it could be shown theoretically[6] why harmonic electric oscillations can be generated in the case of parallel resonant circuits only through a combination with a device whose negative differential electric resistance is achieved from the positive values via infinity, while for the other type of resonant circuits where the capacitor is in series with the inductance, the differential electric resistance must be zero at the transition from plus to minus. These considerations, however, did not help as much as some hints that I received from A. Roberts as a response to a letter that I wrote to him concerning practical aspects of the superregenerative detector. At the end of June 1951—I do not know the exact date, but I remember that it was in the late evening—I was looking at an oscilloscope at the output of the detector and listening simultaneously to a loudspeaker parallel to it. Suddenly I heard a growl when I varied the magnetic field around a certain value. Apparently it was caused by the 50 Hz modulation of the direct current of the electromagnet and, as it should, the growl ceased immediately after removing the small glass tube containing a dilute aqueous solution of iron chloride from the magnet: it was the first nuclear magnetic resonance signal at that place which Felix Bloch had left in 1933. Unfortunately, when the Director of the Institute, who had heard of the experiment, came to the ruin at the Linnéstrasse 5 to see the

Figure 1 The Physics Institute of the University of Leipzig before the war. The view is from the Linnéstrasse. On the right-hand side, the villa of the Director (1927, Peter Debye) can be seen; on the left-hand side is the large auditory and behind it the tower that housed the Physics Library

NMR signal, I could not reproduce it. I was very ashamed, but fatherlike with a slight smile on his face he said, 'Oh, I do know this effect very well, we called it several years ago the "Vorführeffekt" (demonstration effect)'. Of course a few days later I observed the NMR signal again and started a systematic study that finally led to my diploma thesis.[7] In the following year, the other two students also succeeded (diploma theses of H. Lippmann 1952 and of K.-H. Weber 1953), and Dr. Lösche published the first original paper on NMR in German with the title 'Kernparamagnetismus und Hochfrequenztechnik'.[8] In the same year the first publication reporting on successful NMR experiments performed at the Charles University, Prague by Pekárek and Urbanec appeared[9] and also a theoretical paper by Chuzishvili from the Georgian Academy of Sciences in Tbilisi concerning the interaction between spins and lattice vibrations in crystals.[10] The results of the first NMR studies performed in the former Soviet Union were published by Gvozdover and co-workers from Moscow[11,12] and by Kozyrjev and Rivkind from Kazan.[13] In 1953 another review by A. Lösche was published[14] and two original papers appeared in German about proton magnetic relaxation in liquids by Krüger from Stuttgart[15] and about the measurement of the intensity of the Earth's magnetic field by NMR.[16] One amusing point is that in the latter paper the editor had changed the symbol ø for the unit Oersted to the abbreviation Dmr for diameter so that the author and the readers of the paper were surprised to find that the total intensity of the Earth's magnetic field at Leipzig had been measured by NMR to be 0.475 ± 0.078 'diameters'. In 1954 the first paper on NMR studies performed in Hungary was published by Farago et al.,[17] and a short note by W. Müller-Warmuth from the University of Frankfurt/Main appeared about an electronic device of the bridging type for measuring NMR signals.[18] Since then, as in other countries, the number of NMR papers from Germany has increased substantially and a complete survey can be found in the book 'Kerninduktion' which was published by A. Lösche[19] in 1957, being the third monograph on nuclear magnetic resonance spectroscopy that appeared after the well-known books of Andrew[20] and Grivet.[21] From March 31 to April 2, 1960 the first German conference on rf spectroscopy was organized at Leipzig, and in 1961, only a few weeks after the wall was built in Berlin, the Tenth Colloque AMPERE (after Paris 1952, Grenoble 1953, Paris 1954, Paris 1955, Geneva 1956, St. Malo 1957, Paris 1958, London 1959, Pisa 1960) took place in Leipzig, with A. Lösche as chairman of the organizing committee.

The present position of nuclear magnetic spectroscopy in the Department of Physics of the University of Leipzig is characterized by the application of NMR methods in five main directions of research:

(1) *Liquid Crystals.* These studies go back to H. Lippmann and K.-H. Weber, the former students of A. Lösche who had already published a paper on this topic in 1957.[22] A review of the more recent results in this field is given by Grande et al.[23]

Figure 2 The Physics Institute after the war. The view is parallel to the Linnéstrasse. In the ruin on the right-hand side, in front of the tower, the first NMR signals in Leipzig were observed in the summer of 1951

(2) *Polymers.* Initiated by W. Holzmüller who after the war in 1952 returned to Leipzig from the Soviet Union. Polymer science was for many years one of the main areas of research at the Institute of Experimental Physics. At present, mainly polymeric layers[24] and polymer solutions[25] are being investigated.

(3) *Lipid Membranes.* These systems have been studied in Leipzig as models for biological membranes since the end of the 1970s by NMR and also by X-ray, neutron diffraction, infrared spectroscopy, and calorimetric methods (see, for example, Klose et al.[26,27]).

(4) *Structural Phase Transitions in Solids.* In close cooperation with the University of Saarbrücken (J. Petersson) these investigations have been undertaken on single crystals of dielectrics and ferroelectrics as well as with systems of incommensurate phases.[28] In addition to NMR methods, various techniques of electron spin resonance including transient ESR have also been applied to these systems.

(5) *Solid Surfaces and Adsorbed Molecules.* After the initial investigations which were concerned with nuclear magnetic relaxation of molecules adsorbed on silica[29] and on γ-alumina,[30] the present studies are based on more informative NMR methods such as, for example, solid state high-resolution measurements[31,32] and pulsed field gradient techniques[32,33] including infrared spectroscopy and inelastic neutron scattering. The systems under study are exclusively porous *crystals*, i.e. solids with a definite and well-known surface structure, such as zeolites or molecular sieves which have found widespread application in science and industry. The usefulness of NMR spectroscopy in this field was recognized by the presentation at the Seventh International Zeolite Conference in Tokyo 1986 of the Donald W. Breck Award to the Leipzig group,[34] this award having been established by the International Zeolite Association in 1983 to be presented for the most significant contribution to molecular sieve science and technology during the previous three years.

REFERENCES

1. F. Bloch, *Physics Today*, Dec. 1976, **29**, 23.
2. E. M. Purcell, H. C. Torrey, and R. V. Pound, *Phys. Rev.*, 1946, **69**, 37.
3. F. Bloch, W. W. Hansen, and M. Packard, *Phys. Rev.*, 1946, **69**, 127.
4. A. Roberts, *Rev. Sci. Instrum.*, 1947, **18**, 845.
5. B. van der Pol, *Proc. Inst. Radio Eng.*, 1934, **22**, 1051.
6. H. Pfeifer, *Z. Angew. Phys.*, 1954, **6**, 508.
7. H. Pfeifer, *Diploma Thesis, Universität Leipzig*, 1951.

8. A. Lösche, *Nachrichtentech. Elektron.*, 1952, **2**, 144.
9. L. Pekárek and J. Urbanec, *Czech. J. Phys.*, 1952, **1**, 78.
10. G. R. Chuzishvili, *Zh. Eksp. Teor. Fiz.*, 1952, **22**, 382.
11. S. D. Gvozdover and A. A. Maganzik, *Zh. Eksp. Teor. Fiz.*, 1950, **20**, 705.
12. S. D. Gvozdover and N. M. Pomeranzev, *J. Moscow State Univ.*, 1953, **6**, 85; 1953, **9**, 79.
13. B. M. Kozyrjev and A. I. Rivkind, *Zh. Eksp. Teor. Fiz.*, 1954, **27**, 69.
14. A. Lösche, *Exp. Tech. Phys.*, 1953, **1**, 19, 69, 128.
15. H. Krüger, *Kolloid-Z.*, 1953, **134**, 93.
16. H. Pfeifer, *Nachrichtentech. Elektron.*, 1953, **3**, 371.
17. P. S. Farago, M. Gecs, and J. Mertz, *Acta Phys. Hung.*, 1954, **3**, 329.
18. W. Müller-Warmuth, *Naturwissenschaften*, 1954, **1**, 368.
19. A. Lösche, *Kerninduktion*, Deutscher Verlag der Wissenschaften, Berlin, 1957.
20. E. R. Andrew, *Nuclear Magnetic Resonance*, Cambridge University Press, Cambridge, UK, 1955.
21. P. Grivet, *La Résonance Paramagnétique Nucléaire. Moments Dipolaires et Quadrupolaires*, Paris, 1955.
22. H. Lippmann and K.-H. Weber, *Ann. Phys. (Leipzig)*, 1957, **20**, 265.
23. S. Grande, St. Limmer, H. Schmiedel, and R. Stannarius, in *Selected Topics in LC Research*, ed. H. D. Koswig, Akademie-Verlag, Berlin, 1990.
24. D. Geschke and P. Holstein, *Prog. Colloid Polym. Sci.*, 1989, **80**, 71.
25. G. Fleischer, O. E. Zgadzai, V. D. Skirda, and A. E. Maklakov, *Colloid Polym. Sci.*, 1988, **266**, 201, 208.
26. G. Klose, A. Möps, and K. Haage, *Chem. Phys. Lipids*, 1990, **55**, 1.
27. G. Klose, B. König, V. I. Gordelij, and G. Schulze, *Chem. Phys. Lipids*, 1991, **59**, 137.
28. K.-P. Holzer, J. Petersson, D. Schüssler, R. Walisch, U. Häcker, and D. Michel, *Phys. Rev. Lett.*, 1993, **71**, 89.
29. J. R. Zimmerman, B. G. Holmes, and J. A. Lasater, *J. Phys. Chem.*, 1956, **60**, 1157.
30. H. Winkler, *Kolloid-Z*, 1958, **161**, 127.
31. G. Engelhardt and D. Michel, *High-Resolution Solid-State NMR of Silicates and Zeolites*, J. Wiley & Sons, Chichester, 1987.
32. H. Pfeifer, in *NMR Basic Principles and Progress*, Springer-Verlag, Berlin/Heidelberg, 1994, Vol. 31.
33. J. Kärger and H. Pfeifer, in *NMR and Catalysis*, eds. A. Pines and A. Bell, Marcel Dekker, New York, 1993.
34. Donald W. Breck Award to H. Pfeifer, D. Freude, J. Kärger, and M. Bülow, for *NMR Investigations of Acidity and Molecular Transport in Zeolites*, Tokyo, August 21, 1986.

Acknowledgements

I wish to thank Prof. Emeritus Artur Lösche, Prof. Dieter Michel, and Prof. Emeritus Horst Winkler for many helpful comments.

Biographical Sketch

Harry Pfeifer. *b* 1929. Dipl.-Phys., 1951., Dr.rer.nat., 1953, Dr.habil., 1956, Dr.h.c., 1989. Professor of Experimental Physics, University of Leipzig, 1960–present; Guest Professor, Univ. Pierre et Marie Curie, Paris, 1981, and Univ. Central de Venezuela, Caracas, 1983. Approx. 300 publications. Current research specialty: application of NMR spectroscopy to the study of surface phenomena.

Pines, Alexander: Solid State NMR: Some Personal Recollections

Alexander Pines

University of California at Berkeley, Berkeley, CA, USA

I was born in 1945, the same year as NMR. I grew up in Rhodesia and then went to Israel to pursue my undergraduate studies in mathematics and chemistry at the Hebrew University of Jerusalem.

In 1968 I journeyed to the United States and entered the Massachusetts Institute of Technology (MIT) as a graduate student. There I was fortunate to work under the tutelage of John Waugh in the Department of Chemistry and the Research Laboratory of Electronics. It was an exciting time to be at MIT, and Waugh as well as postdoctoral co-workers from those days—among them Robert Griffin, Ulrich Haeberlen, Michael Mehring, and Won-Kyu Rhim—have remained my colleagues and friends for more than 25 years.

The MIT group's primary efforts at that time were directed toward the new area of multiple pulse and high-resolution NMR spectroscopy in solids. Waugh's accomplishments in average Hamiltonian theory and line narrowing were establishing much of the basis and the very language of modern pulsed NMR. The idea was to manipulate the spins by trains of pulses in order to average the spin interactions selectively—for example to eliminate dipole–dipole couplings while retaining the underlying chemical shifts, a sort of spin alchemy.

Participating in the study of coherent averaging and the challenging experimental techniques of multiple-pulse spectroscopy, including the magic sandwich time-reversal experiments (which appeared to violate the spin temperature hypothesis), was a stimulating educational experience for me, but it was natural to wonder if there might be an alternative way to observe chemical shifts in solids. An appealing prospect was the organic chemists' nucleus, carbon-13, which offered the possibility of resolved Fourier transform spectra in solids, owing to the isotope's low natural abundance and correspondingly weak dipole–dipole couplings. There would be no need for the demands of homonuclear multiple pulse sequences, and high power proton spin decoupling would suffice to eliminate the relevant heteronuclear couplings, but we anticipated that sensitivity might pose a problem. Here, however, we could capitalize upon the double resonance scheme of Hartmann and Hahn, whereby two different resonant frequencies are matched in the rotating frame, allowing the exchange of magnetization between different spin species. The process of cross polarization (CP) from abundant hydrogen to dilute carbon-13 combined with spin decoupling would allow us to enhance the sensitivity and resolution of the directly observed carbon signal.

The idea seemed promising, and we proceeded to design and construct a double resonance spectrometer with a PDP-12 controlled pulse programmer and data system. The experiments also required a novel probe that would allow cross polarization and direct observation of the enhanced carbon-13 signal in the presence of high power proton spin decoupling. What we needed now was an appropriate model sample. It so happened that the late Henry Resing (known affectionately as Mr. Adamantane because of his work on plastic crystals) was visiting, and I asked him what would be an inexpensive compound (solid at room temperature) with at least two inequivalent carbon sites, but with the molecules reorienting rapidly and isotropically (in order to eliminate the chemical shift anisotropy) to yield laboratory and rotating frame spin–lattice relaxation times of about one second. He suggested adamantane.

Indeed, we were elated to observe resolved isotropic carbon-13 chemical shifts in solid adamantane, with ample signal/noise. We subsequently obtained resolved spectra allowing the measurement of carbon-13 chemical shift anisotropy in solid benzene and many other compounds, as well as signals from other dilute isotopes such as nitrogen-15 and silicon-29, leading some innocent bystanders to believe that high resolution solid state NMR of dilute spins might actually become useful in chemistry. We termed the technique proton-enhanced nuclear induction spectroscopy (proton-enhanced NMR for short) as a salute to the early foundations of nuclear induction laid by physicists. Combined with magic angle spinning (MAS), a legacy of Andrew, Lowe, and co-workers, incorporated by Schaefer and Stejskal soon after, the cross polarization/magic angle spinning (CP MAS) procedure was subsequently implemented and used on commercial spectrometers. Recent applications of CP MAS have included the possibility of measuring carbon-13 isotropic–anisotropic shift correlations through variable angle correlation spectroscopy (VACSY) as well as the measurement of carbon–carbon and carbon–hydrogen dipolar correlations for the purposes of distance and structure determination in solids.

On completing my Ph.D. in 1972 I was awarded a Miller Fellowship in physics sponsored by Erwin Hahn at the University of California, Berkeley. Shortly afterwards, however, the Berkeley Chemistry Department offered me a faculty position, which I accepted, but not without some regret at passing up the opportunity to work directly with Hahn. Happily, Hahn, together with Mel Klein, has remained a mentor, colleague, and friend for more than two decades.

Over the years, our group at Berkeley (the so called Pinenuts) has been concerned with fundamental phenomena in NMR and chemical physics, hoping to develop techniques of some use in condensed matter chemistry and physics. Our work has involved a combination of concepts, theory, techniques, instrumentation, and applications to a variety of chemical systems and materials. Advances in spectral resolution, sensitivity and selectivity have remained consistent goals. I have been fortunate to work with, and learn from, a group of extremely talented and creative co-workers at Berkeley, including graduate students, postdoctoral fellows, and sabbatical visitors, some of whom are listed in Table 1; they were the ones who did the research and my story is largely theirs. In addition to research, I have devoted much time and effort to teaching. Beginning in the 1970s with advanced courses in physical chemistry, I was later persuaded by my colleague George Pimentel to take over the introductory general chemistry class which I have taught, on and off over the years, to many thousands of students. Both the freshmen and my research group, with their broad curiosity and their drive to understand the principles and beauty of science, have kept me alert and have enriched my academic experience. We

Table 1 Co-Workers at Berkeley

Staff Scientist: Gerard Chingas	*Administrative Assistant:* Dione Carmichael		
Doctoral and Postdoctoral Students			
Eric Abramson	Hideaki Fujiwara	Shigeru Matsui	Klaus Schmidt-Rohr
Jerome Ackerman	Holly Gaede	Thomas Meersman	Erika Schneider
Madis Alla	Sheryl Gann	Peter Meier	Athan Shaka
Stuart Allison	Joel Garbow	John Millar	Thomas Shatuck
Jay Baltisberger	Miriam Gochin	Karl Mueller	Jay Shore
Geoffrey Barrall	Philip Grandinetti	Luciano Mueller	David Shykind
Jean Baum	John Harwood	Michael Munowitz	Steven Sinton
Anthony Bielecki	Alfred Hohener	Eric Munson	Yiqiao Song
Angelo Bifone	Mei Hong	James Murdoch	Larry Sterna
Bruce Black	Shan Hsi	Alon McCormick	Boqin Sun
Russell Bowers	Hans Huber	Daniel Nanz	Dieter Suter
Stefano Caldarelli	Deidre Hugi-Cleary	Peter Neidig	Kiyonori Takegoshi
Daniel Caplan	Martin Hurliman	John Pearson	Jau Tang
James Chang	Thomas Jarvie	Zheng-Yu Peng	Ann Thayer
Jih-Wen Chang	Raz Jelinek	Dominique Petit	Karl Thier
Bradley Chmelka	Jonathan Jones	Tanja Pietrass	Malaine Trecoske
Herman Cho	Paul Jonsen	Marie Quinton	Robert Tycko
Chuck Connor	Marianne Koenig	Daniel Raftery	Shimon Vega
George Davenport	Andrew Kolbert	Linda Reven	Warren Warren
Charles de Menorval	Juergen Kritzenberger	Toomas Room	Daniel Weitekamp
Susan DePaul	Bernard Lamotte	Mark Rosen	David Wemmer
Gary Drobny	Russell Larsen	David Ruben	Ulrike Werner
Margaret Eastman	Chang-Jae Lee	Steven Rucker	Wrenn Wooten
Richard Eckman	Young Lee	Ryong Ryoo	Yue Wu
Hommo Edzes	Shang-Bin Liu	Joseph Sachleben	Yu-Sze Yen
Lyndon Emsley	Antoine Llor	Ago Samoson	David Zax
Matthias Ernst	Henry Long	Kurt Schenker	Marcia Ziegeweid
Lucio Frydman	Gunter Majer	Claudia Schmidt	Kurt Zilm
			Josef Zwanziger
Sabbatical Visitors			
Yakir Aharonov	Jozef Kowalewski	Hiroshi Moriyama	Robert Vold
Ray Dupree	Raphael Levine	Shaul Mukamel	Jin-Feng Wang
Soemi Emid	Ze'ev Luz	Zbigniew Olejniczak	Chaohui Ye
Allen Garroway	Metka Luzar	Dietmar Stehlik	Dieter Ziessow
Gina Hoatson	Michael Mehring	Takehiko Terao	Herbert Zimmermann

have continued to remind each other to refrain from the narrow path, not to hesitate to ask why and how, and never to accept simply on authority that something is impossible.

Our work at Berkeley in the early 1970s continued to deal with theoretical and experimental aspects of spin dynamics and solid state NMR, in particular the question of total adiabatic polarization transfer, the measurement of chemical shift tensors in single crystals, and the effects of symmetry-restricted motion on carbon-13 lineshapes in solids. The experiments required a homebuilt spectrometer (this time under the control of a new generation PDP-8 based pulse programmer and data system) as well as considerable effort in completing the superconducting joints, shim coils, and cryogenics of our primitive magnet. We also became intrigued by liquid crystals, for which we were able to use the carbon-13 tensors to study molecular ordering and phase transitions.

During that time, my colleague Charles Harris was also involved in magnetic resonance experiments that exploited the enormous sensitivity of optical detection to observe continuous wave electron paramagnetic resonance (EPR) microwave spectra in excited triplet states of molecular crystals. Because of the different rates of phosphorescence from the three triplet sublevels to the single ground state, microwave generated transitions between the sublevels could generate a change in the phosphorescence signal by rearranging the sublevel populations, in analogy to continuous wave electron–nuclear double resonance (ENDOR). The detection of time domain signals, however, was a different matter—it was considered to be impossible because triplet sublevel coherences did not affect the populations and were therefore invisible to the phosphorescent emission; indeed, the detection of free induction decays and spin echoes in excited triplet states was traditionally performed only by direct microwave detection, with limited sensitivity. After pondering the possibility of applying optical detection to observe the spin coherence, we hit upon a solution that involved an additional read pulse, with which we were able to detect electron spin free induction decays and spin echoes through their effect on the optical emission. It was an early example of coherence transfer by transformation of the off-diagonal elements of the density matrix in order to map out the evolution of a perhaps invisible or hidden coherence, point by point.

What we learned from these experiments soon proved useful in the multiple quantum NMR experiments that followed. Our original intention was to study hydrogen NMR in solids, to provide an alternative to homonuclear multiple pulse sequences, this time by diluting protonated samples with deuterium. The idea was reminiscent of the approach

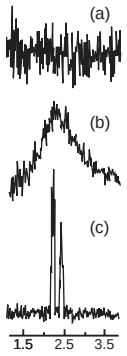

1. CP Adamantane

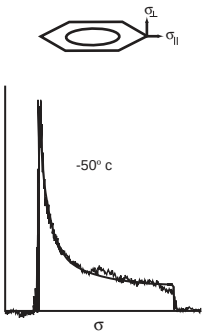

2. Benzene

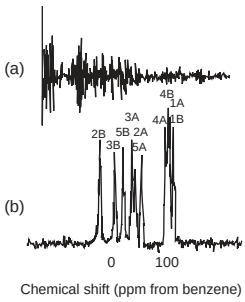

3. Durene Crystal

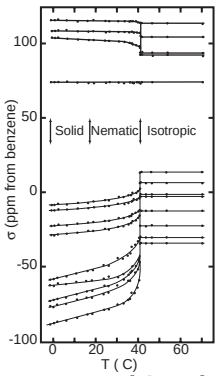

4. Liquid Crystal

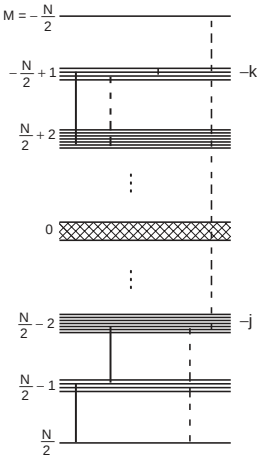

5. MQ Spectroscopy

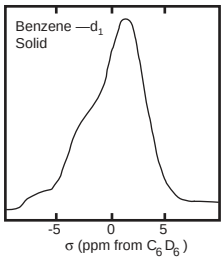

6. DQ Spectrum

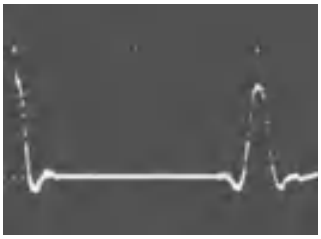

7. Magic Sandwich Echo

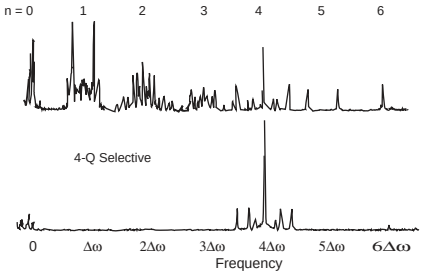

8. Benzene-LC MQ Spectra

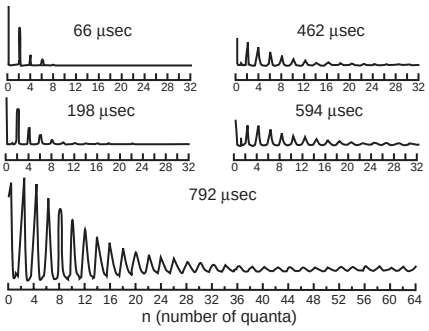

9. MQ Solids

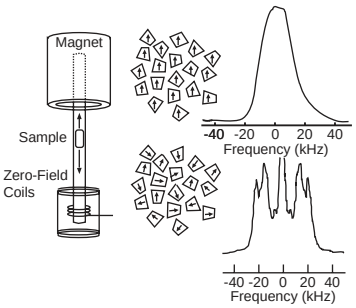

10. Zero-Field NMR

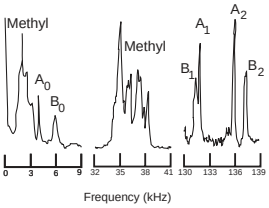

11. Deuterium Zero-Field

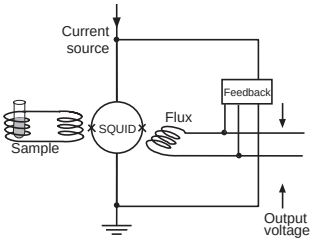

12. SQUID Spectrometer

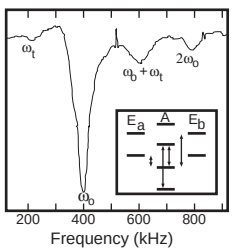

13. SQUID Methyl Tunneling

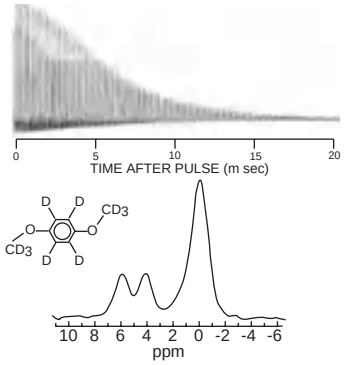

14. Deuterium MAS

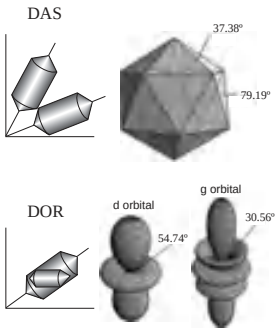

15. Quadrupolar Nuclei

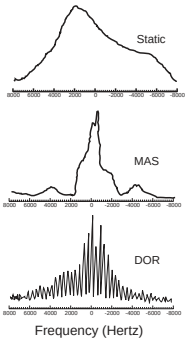

16. Sodium-23

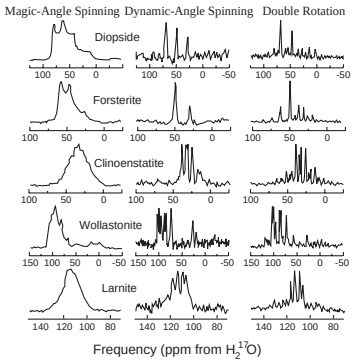

17. Oxygen-17

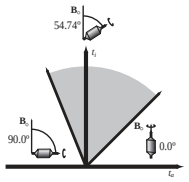

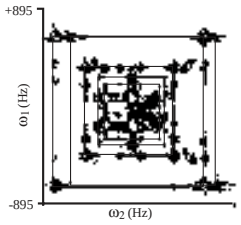

19. Dipole-Dipole Correlations

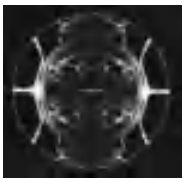

21. Iterative Sequence

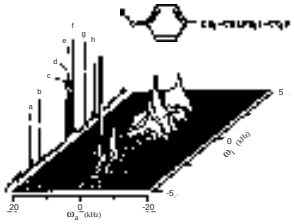

18. VACSY

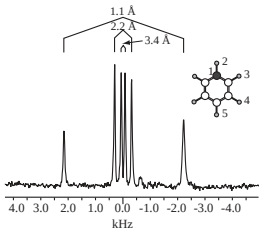

20. Resolved Local Fields

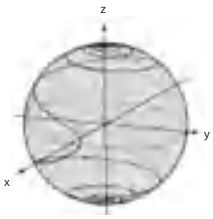

22. Sech π Pulse

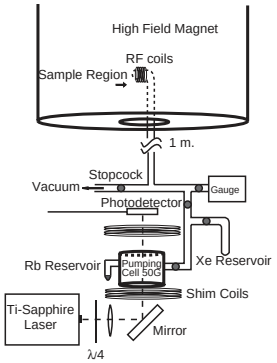

23. Optical Pumping Spectrometer

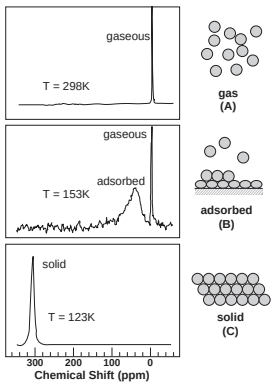

24. OP Xenon-129 Surface

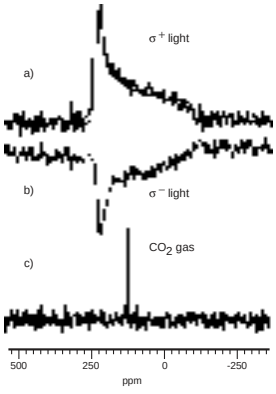

25. OP CP ^{129}Xe - $^{13}CO_2$

taken earlier with carbon, and here again there was a heteronuclear interaction that needed to be decoupled. The hydrogen–deuterium coupling, however, seemed futile to average because the wide, quadrupolar broadened deuterium line would require prohibitive radiofrequency power, but it was conceivable that we could exploit double quantum decoupling which had recently been used by Meiboom and co-workers in liquid crystals. Indeed, narrowband irradiation of the (+1, −1) transition of the deuterium with modest power yielded a resolved hydrogen spectrum, and in this way we could observe the chemical shift anisotropy of hydrogen in ice —a notoriously difficult system for homonuclear multiple-pulse techniques. This approach has also been useful for obtaining resolved hydrogen dipole–dipole couplings and, combined with MAS, is an alternative approach to high-resolution hydrogen NMR in solids.

The next question, which emerged from our double quantum decoupling work and our previous experience with indirect detection of invisible microwave coherences, involved the possibility of preparing and observing, in the time domain,

the forbidden deuterium double quantum transition. Related work was being done independently by Hashi and co-workers. Having developed an appropriate spin-1 formalism involving fictitious spin-1/2 operators, we learned how to excite and detect the seemingly invisible two quantum coherence, point by point, by means of soft double quantum pulses (or pairs of hard pulses) combined with coherence transfer read pulses. Since the double quantum superposition should evolve independently of the quadrupole coupling, its spectrum would, in principle, reveal the deuterium chemical shift buried beneath the enormous quadrupolar broadening. By sidestepping rather than attempting to average the quadrupolar coupling, we were thus able to measure the chemical shift anisotropy of hydrogen in solid benzene. Various manifestations of double quantum coherence followed directly, including double quantum spin locking, cross polarization, spin diffusion, and magic angle spinning.

The spin-1 theory and experiments revealed the two-fold sensitivity of double quantum coherence to resonance offsets and radiofrequency phase shifts—double quantum spin locking, for example, was accomplished with a forty-five degree phase shift. Shortly thereafter, we provided an extension, namely the n quantum phase shift, to multiple quantum coherences in coupled spin-1/2 systems; this allowed a number of developments, including the separation of coherence orders (beginning with the progressively simplified spectra of orders zero through six in oriented benzene) by time proportional phase incrementation (TPPI), selective excitation of n quantum spectra (despite the arguments of some authorities that selective excitation was not possible), iterative multiple quantum sequences, multiple quantum filtering, imaging, relaxation and diffusion schemes, heteronuclear multiple quantum coherence experiments, bilinear rotation decoupling (BIRD), scalar (isotropic) recoupling, and total coherence transfer. The use of time-reversal sequences made it possible to produce two-dimensional schemes with symmetrized (conjugate) preparation and mixing propagators, yielding pure in-phase signals and allowing the observation of high n quantum spectra (sometimes in excess of one hundred quanta) and spin counting in liquid crystals and solids. We were delighted to see many of the multiple quantum ideas incorporated into high-resolution multidimensional liquid spectroscopy as well. For N spins, the high order ($N-1$ and $N-2$) spectra turned out to be particularly useful for the determination of molecular structures and conformations. Some of the experiments required the application of thousands of pulses, bringing to my mind the comment of Hahn when he heard about the original dipole–dipole time-reversal experiments—With that many pulses I could bring back the Messiah.

Three other areas that occupied our attention during the early 1980s were the magnetic isotope effect (through which we were enable to obtain noticeable enrichments of carbon-13), broadband and selective excitation schemes involving iterative sequences and hyperbolic secant modulations, and the development of time domain zero-field NMR. Our long-standing interest in resolution and sensitivity led us to develop a pulsed version of nuclear quadrupole resonance (NQR) field cycling, by which it was possible to remove the orientational broadening from a powder spectrum while retaining resolved quadrupole and dipole–dipole couplings. The further development of Fourier transform zero-field spectroscopy included various (sometimes surprising) analogs of multiple pulse techniques, spin decoupling, time reversal, spin diffusion, two-dimensional correlations, and chemical exchange. Eventually, too, we used a superconducting quantum interference device (SQUID) to detect the nuclear magnetic flux directly in zero field. Direct detection eliminated the restrictive requirements of field cycling and made it simple to obtain nitrogen-14 spectra and to study other low-frequency phenomena such as quantum tunneling in zero and low magnetic fields.

In the late 1980s, we were concerned with two aspects of the geometry of quantum mechanics and spin dynamics. On the one hand, the concepts of Berry's phase and holonomy made it possible to answer fundamental questions about quantum evolution without recourse to explicit solutions of the Schroedinger equation. Geometric concepts and gauge symmetry were sufficient to explain a number of effects that arise in systems undergoing cyclic evolution. Nuclear spins provided an ideal arena for the demonstration of geometric phases and related phenomena, and the behavior was consistent with a unification of other systems and phenomena as diverse as light, Jahn–Teller molecules, and the reorientation of falling cats.

Geometry and symmetry were also at the heart of our approach to averaging second-order anisotropic broadening effects in NMR, for example those due to quadrupolar couplings. Although MAS was very useful for the averaging of anisotropic interactions of spin-1/2 nuclei such as hydrogen, carbon-13, nitrogen-15, fluorine-19, silicon-29, and phosphorus-31, a long-standing problem in the field was what to do about the obviously important quadrupolar nuclei such as oxygen-17, sodium-23, and aluminum-27. In the presence of quadrupole couplings, the resolution was limited by second-order broadening, which is incompletely averaged by MAS.

The solution, for which we developed both the theory, with independent work by Llor and Virlet, and demonstrated the initial experiments (with the indispensable support of Berkeley's machine shop), involved motional averaging through sample spinning about two axes. Two techniques emerged—dynamic angle spinning (DAS) and double rotation (DOR)—which brought to quadrupolar nuclei the kind of resolution previously reserved for spins-1/2. During this period our laboratory often felt like a dental clinic, with the whizzing and whining sounds and rich harmonics of dynamic-angle and double rotor probes.

Whereas the geometry of MAS could be considered a dynamic implementation of cubic symmetry, an appropriate approximation to the sphere for the purpose of averaging second rank tensors, the new spinning techniques involved the next approximation to the sphere, namely icosahedral symmetry, necessary for the averaging of spherical harmonics or tensors up to fourth rank. The first experimental results were obtained for sodium-23, soon followed by high resolution spectra of boron-11, oxygen-17, aluminum-27, and rubidium-87. Applications of DAS and DOR have recently been demonstrated in a number of materials including polymers, minerals, oxides, zeolites, catalysts, and glasses, and commercial probes are now available from the instrument companies.

The most recent work in our laboratory concerns the possibility of surface NMR in samples with low surface area, a relevant interface between NMR and the realm of surface chemistry and catalysis. This poses a prominent challenge in terms of selectivity and sensitivity because of the low

concentration of surface spins in the sample. Our approach was inspired by the work of Happer and co-workers who spin-polarized xenon by means of optical pumping. We used laser-polarized xenon as a sensitive NMR spy of the surface, exploiting the sensitivity of xenon chemical shifts to chemical environment, as demonstrated by Fraissard and co-workers. The spin-polarized xenon was condensed onto the surface of a polycrystalline sample in high magnetic field where surface-specific NMR signals were observed with high signal/noise. In subsequent experiments it has been possible to transfer, by cross polarization, the high xenon spin polarization to adjacent spins, including hydrogen and carbon-13, giving rise to surface-selective and enhanced NMR spectra. With these experiments we appear to have come almost full circle—back to the original ideas of cross polarization and solid state NMR of dilute spins.

Over the last 25 years I have had the privilege of witnessing three of the major developments in NMR: magnetic resonance imaging, multidimensional spectroscopy, and high-resolution solid state NMR. Solid state NMR has progressed from the days of wideline NMR, a curiosity for chemists, to the realm of modern high-resolution spectroscopy. These remain exciting times for solid state NMR as theory and experiments are further developed and used in many laboratories for chemistry and materials science; I look forward to the next generation of developments and surprises.

SELECTED PUBLICATIONS

Papers that illustrate our work in more detail and provide references to the relevant literature are listed below.

1. Time-Reversal Experiments in Dipolar-Coupled Spin Systems, W. K. Rhim, A. Pines, and J. S. Waugh, *Phys. Rev. B*, 1971, **3**, 684–696
2. Quantitative Aspects of Coherent Averaging: Simple Treatment of Resonance Offset Processes in Multiple-Pulse NMR, A. Pines and J. S. Waugh, *J. Magn. Reson.*, 1972, **8**, 354–365.
3. Proton-Enhanced Nuclear Induction Spectroscopy. A Method for High Resolution NMR of Dilute Spins in Solids, A. Pines, M. G. Gibby, and J. S. Waugh, *J. Chem. Phys.*, 1972, **56**, 1776–1777.
4. Proton-Enhanced NMR of Dilute Spins in Solids, A. Pines, M. G. Gibby, and J. S. Waugh, *J. Chem. Phys.*, 1973, **59**, 569–590. A. Pines, Citation Classic in *Current Contents*, 1991, **22**(32) 10.
5. Optically Detected Electron Spin Echoes and Free Precession in Molecular Excited States, W. G. Breiland, C. B. Harris, and A. Pines, *Phys. Rev. Lett.*, 1973, **30**, 158–161.
6. Carbon-13 Nuclear Magnetic Resonance in Solid Ammonium Tartrate, A. Pines, J. J. Chang, and R. G. Griffin, *J. Chem. Phys.*, 1974, **61**, 1021–1030.
7. Molecular Ordering and Even–Odd Effect in a Homologous Series of Nematic Liquid Crystals, A. Pines, D. J. Ruben, and S. Allison, *Phys. Rev. Lett.*, 1974, **33**, 1002–1005.
8. New Approach to High Resolution Proton NMR in Solids: Deuterium Spin Decoupling by Multiple-Quantum Transitions, A. Pines, D. J. Ruben, S. Vega, and M. Mehring, *Phys. Rev. Lett.*, 1976, **36**, 110–113.
9. Fourier Transform Double-Quantum NMR in Solids, S. Vega, T. W. Shattuck, and A. Pines, *Phys. Rev. Lett.*, 1976, **37**, 43–46.
10. Operator Formalism for Double Quantum NMR, S. Vega and A. Pines, *J. Chem. Phys.*, 1977, **66**, 5624–5644.
11. NMR Double Quantum Spin Decoupling in Solids, A. Pines, S. Vega, and M. Mehring, *Phys. Rev. B*, 1978, **18**, 112–125.
12. Fourier Transform Multiple Quantum Nuclear Magnetic Resonance, G. Drobny, A. Pines, S. Sinton, D. Weitekamp, and D. Wemmer, in *Faraday Division of the Chemical Society Symposium*, 1979, **13**, 49–174.
13. Experimental Results on Deuterium NMR in the Solid State by Magic Angle Spinning, J. L. Ackerman, R. Eckman, and A. Pines, *Chem. Phys.*, 1979, **42**, 423–428.
14. Double Quantum Cross Polarization NMR in Solids, S. Vega, T. W. Shattuck, and A. Pines, *Phys. Rev. A*, 1980, **22**, 638–661.
15. Theory of Selective Excitation of Multiple-Quantum Transitions, W. S. Warren, D. P. Weitekamp, and A. Pines, *J. Chem. Phys.*, 1980, **73**, 2084–2099.
16. Viscosity and Temperature Dependence of the Magnetic Isotope Effect, L. Sterna, D. Ronis, S. Wolfe, and A. Pines, *J. Chem. Phys..*, 1980, **73**, 5493–5499.
17. NMR Study of Molecular Reorientation under Fivefold Symmetry: Solid Permethylferrocene, D. E. Wemmer, D. J. Ruben, and A. Pines, *J. Am. Chem. Soc.*, 1981, **103**, 28–33.
18. Determination of Dipole Coupling Constants Using Heteronuclear Multiple Quantum NMR, D. P. Weitekamp, J. R. Garbow, and A. Pines, *J. Chem. Phys.*, 1982, **77**, 2870–2883.
19. Bilinear Rotation Decoupling of Homonuclear Scalar Interactions, J. R. Garbow, D. P. Weitekamp, and A. Pines, *Chem. Phys. Lett.*, 1982, **93**, 504–509.
20. Total Spin Coherence Transfer Echo Spectroscopy, J. R. Garbow, D. P. Weitekamp, and A. Pines, *J. Chem. Phys.*, 1983, **79**, 5301–5310.
21. Multiple-Quantum NMR Study of Molecular Structure and Ordering in a Liquid Crystal, S. W. Sinton, D. B. Zax, J. B. Murdoch, and A. Pines, *Mol. Phys.*, 1984, **53**, 333–362.
22. Zero Field NMR and NQR, D. B. Zax, A. Bielecki, K. Zilm, A. Pines, and D. P. Weitekamp, *J. Chem. Phys.*, 1985, **83**, 4877–4905.
23. Fixed Point Theory of Iterative Excitation Schemes in NMR, R. Tycko, A. Pines, and J. Guckenheimer, *J. Chem. Phys.*, 1985, **83**, 2775–2802.
24. Multiple-Quantum Dynamics in Solid State NMR, J. Baum, M. Munowitz, A. N. Garroway, and A. Pines, *J. Chem. Phys.*, 1985, **83**, 2015–2025.
25. Broadband and Adiabatic Inversion of Two-Level Systems by Phase Modulated Pulses, J. Baum, R. Tycko, and A. Pines, *Phys. Rev. A*, 1985, **32**, 3435–3447.
26. Multiple Quantum NMR Spectroscopy, M. Munowitz and A. Pines, *Science*, 1986, **233**, 525–531.
27. Multiple Quantum Dynamics: A Directed Walk through Liouville Space, M. Munowitz, A. Pines, and M. Mehring, *J. Chem. Phys.*, 1987, **86**, 3172–3182.
28. Effect of Correlated Proton Jumps on the Zero Field NMR Spectrum of Solid *p*-Toluic Acid, T. P. Jarvie, A. M. Thayer, J. M. Millar, and A. Pines, *J. Phys. Chem.*, 1987, **91**, 2240–2242.
29. Recursive Evaluation of Interaction Pictures, D. Suter and A. Pines, *J. Magn. Reson.*, 1987, **75**, 509–512.
30. Observation of Spin Diffusion in Zero Field Magnetic Resonance, D. Suter, T. P. Jarvie, B. Sun, and A. Pines, *Phys. Rev. Lett.*, 1987, **59**, 106–108.
31. Theory of Lineshapes for Zero Field NMR in the Presence of Molecular Motion, P. Meier, G. Kothe, P. Jonsen, M. Trecoske, and A. Pines, *J. Chem. Phys.*, 1987, **87**, 6867–6876.
32. Direct Detection of Aluminum-27 Resonance with a SQUID Spectrometer, J. Chang, C. Connor, E. L. Hahn, H. Huber, and A. Pines, *J. Magn. Reson.*, 1989, **82**, 387–391.
33. Double Rotor for NMR of Solids, A. Samoson and A. Pines, *Rev. Sci. Instrum.*, 1989, **60**, 3239.
34. Oxygen-17 NMR in Solids by Dynamic-Angle Spinning and Double Rotation, B. F. Chmelka, K. T. Mueller, A. Pines,

J. Stebbins, Y. Wu, and J. W. Zwanziger, *Nature (London)*, 1989, **339**, 42–43.
35. Some Developments in Nuclear Magnetic Resonance of Solids, B. F. Chemlka and A. Pines, *Science*, 1989, **246**, 71–77.
36. Dynamic Angle Spinning of Quadrupolar Nuclei, K. T. Mueller, B. Q. Sun, G. C. Chingas, J. W. Zwanziger, T. Terao, and A. Pines, *J. Magn. Reson.*, 1990, **86**, 470.
37. NMR in Physics, Chemistry and Biology: Illustrations of Bloch's Legacy, in *Proceedings of the Bloch Symposium*, ed. W. Little, World Scientific, 1990.
38. Two-Dimensional NMR Studies of Flexible Molecules in Liquid Crystals: Orientational Order and Conformational Probabilities of n-Hexane, M. Gochin, A. Pines, M. E. Rosen, S. P. Rucker, and C. Schmidt, *Mol. Phys.*, 1990, **69**, 671–695.
39. Berry's Phase, J. W. Zwanziger, M. Koenig, and A. Pines, *Ann. Rev. Phys. Chem.*, 1990, **41**, 601–646.
40. High Resolution ^{27}Al Double-Rotation NMR in VPI-5, Y. Wu, B. F. Chmelka, A. Pines, M. E. Davis, P. J. Grobet, and P. A. Jacobs, *Nature (London)*, 1990, **346**, 550–552.
41. High Field NMR of Adsorbed Xenon Polarized by Laser Pumping, D. Raftery, H. Long, T. Meersmann, P. J. Grandinetti, L. Reven, and A. Pines, *Phys. Rev. Lett.*, 1991, **66**, 584–587.
42. Scaling and Time Reversal of Spin Couplings in Zero-Field NMR, A. Llor, Z. Olejniczak, J. Sachleben, and A. Pines, *Phys. Rev. Lett.*, 1991, **67**, 1989–1992.
43. Variable-Angle Correlation Spectroscopy in Solid-State NMR, L. Frydman, G. C. Chingas, Y. K. Lee, P. J. Grandinetti, M. A. Eastman, G. A. Barrall, and A. Pines, *J. Chem. Phys.*, 1992, **97**, 4800–4808.
44. SQUID-NQR of Nitrogen-14 in Amino Acids and Small Peptides, U. Werner, B. Black, M. Ziegeweid, and A. Pines, *Chem. Phys. Lett.*, 1993, **209**, 17–21.
45. High Field Cross Polarization NMR from Laser Polarized Xenon to a Polymer Surface, H. W. Long, H. C. Gaede, J. Shore, L. Reven, C. R. Bowers, J. Kritzenberger, T. Pietrass, A. Pines, P. Tang, and J. A. Reimer, *J. Am. Chem. Soc.*, 1993, **115**, 8491–8492.
46. NMR Study of Xenon Dynamics and Energetics in Na-A Zeolite, R. G. Larsen, J. Shore, K. Schmidt-Rohr, L. Emsley, H. Long, A. Pines, M. Janicke, and B. F. Chmelka, *Chem. Phys. Lett.*, 1993, **214**, 220–226.
47. Lectures in Pulsed NMR, L. Emsley and A. Pines, in *Proc. Int. School of Phys., Enrico Fermi, Course CXXIII 1992*, 2nd edn, ed. B. Maraviglia, World Scientific, 1993, pp. 123–266.
48. Multiple-Pulse NMR of Optically-Pumped Xenon in Low Magnetic Field, D. Raftery, H. W. Long, D. Shykind, P. J. Grandinetti, and A. Pines, *Phys. Rev. A*, 1994, **50**, 567.
49. NMR Measurement of Resolved Heteronuclear Dipole Couplings in Liquid Crystals and Lipids, K. Schmidt-Rohr, D. Nanz, L. Emsley, and A. Pines, *J. Phys. Chem.*, 1994, **98**, 6668–6670.
50. Three-Dimensional Variable-Angle Nuclear Magnetic Resonance Exchange Spectroscopy without Rotor Axis Hopping, Y. K. Lee, L. Emsley, R. G. Larsen, K. Schmidt-Rohr, M. Hong, L. Frydman, G. C. Chingas, and A. Pines, *J. Chem. Phys.*, 1994, **101**, 1852.

Acknowledgements

The figures in this article have been adapted from the following sources: **1**: A. Pines, M. Gibby, and J. S. Waugh, *J. Chem. Phys.* 1972, **56**, 1776; **2**: M. G. Gibby, A. Pines, and J. S. Waugh, *Chem. Phys. Lett.*, 1972, **16**, 296; **3**: M. G. Gibby, A. Pines, and J. S. Waugh, *J. Chem. Phys.*, 1973, **59**, 591; **4**: A. Pines and J. J. Chang, *Phys. Rev. A*, 1974, **10**, 946; **5**: W. S. Warren, D. P. Weitekamp, and A. Pines, *J. Chem. Phys.*, 1980, **73**, 2084; **6**: A. Pines, S. Vega, D. J. Ruben, T. W. Shattuck, and D. Wemmer, Magnetic Resonance in Condensed Matter—Recent Developments, 1977, University of Ljublijana Press, ed. R. Blinc and G. Lahajanr, 127; **7**: W.-K. Rhim, A. Pines, and J. S. Waugh, *Phys. Rev. B*, 1971, **3**, 684; **8**: W. S. Warren, D. P. Weitekamp, and A. Pines, *J. Chem. Phys.*, 1980, **73**, 2084; **9**: J. Baum, M. Munowitz, A. N. Garroway, and A. Pines, *J. Chem. Phys.*, 1985, **83**, 2015; **10**: A. M. Thayer and A. Pines, *Acc. Chem. Res.*, 1987, **20**, 47; **11**: D. B. Zax, A. Bielecki, K. Zilm, A. Pines, and D. P. Weitekamp, *J. Chem. Phys.*, 1985, **83**, 4877; **12**: J. W. Chang, C. Connor, E. L. Hahn, H. Huber, and A. Pines, *J. Magn. Reson.*, 1989, **82**, 387; **13**: C. Connor, J. W. Chang, and A. Pines, *Rev. Sci. Instr.*, 1990, **61**, 1059; **14**: J. Ackerman, R. Eckman, and A. Pines, *Chem. Phys.*, 1979, **42**, 423; **15**: E. W. Wooten, K. T. Mueller, and A. Pines, *Acc. Chem. Res.*, 1992, **25**, 209–214; **16**: A. Samoson, E. Lippmaa, and A. Pines, *Mol. Phys.*, 1988, **65**, 1013; **17**: K. T. Mueller, Y. Wu, B. F. Chmelka, J. Stebbins, and A. Pines, *J. Am. Chem. Soc.*, 1991, **113**, 32; **18**: L. Frydman, G. C. Chingas, Y. K. Lee, P. J. Grandinetti, M. A. Eastman, G. A. Barrall, and A. Pines, *J. Chem. Phys.*, 1992, **97**, 4800; **19**: S. Rucker, Ph.D. Thesis, 1991, LBL-31122; **20**: K. Schmidt-Rohr, D. Nanz, L. Emsley, and Pines, *J. Phys. Chem.*, 1994, **98**, 6668–6670; **21**: H. Cho, J. Baum, and A. Pines, *J. Chem. Phys.*, 1987, **86**, 3089; **22**: J. Baum, R. Tycko, and A. Pines, *Phys. Rev. A*, 1985, **32**, 3435; **23** and **24**: D. Raftery, H. Long, T. Meersman, P. J. Grandinetti, L. Reven, and A. Pines, *Phys. Rev. Lett.*, 1991, **66**, 584; **25**: C. R. Bowers, H. W. Long, T. Pietrass, H. C. Gaede, and A. Pines, *Chem. Phys. Lett.*, 1993, **205**, 168–170.

Biographical Sketch

Alexander Pines. *b* 1945. B.Sc., 1967, Ph.D., 1972, Chemistry, M.I.T. (supervisor John Waugh). Faculty, University of California, Berkeley, and Materials Science, Lawrence Berkeley Laboratory, 1972–present, currently Professor and President's Chair, president ISMAR 1992–1995. Research specialty: solid state NMR theory and experiment.

Poole, Charles P. Jr.: The Dance of the Nucleons

Charles P. Poole, Jr.
University of South Carolina, Columbia, SC, USA

My choice of magnetic resonance as a vocation, like many things in life, was fortuitous. My undergraduate training at Fordham University was in premed, and when I did not get into medical school I obtained an M.S. in physics from Fordham. My first job designing radar components and antennae at Westinghouse was entered into in June of 1952 without much forethought. This was my engineering career. While I was there I studied microwave transmission and radiation, and soon realized that I really did not know very much about electromagnetic theory. Accordingly in September 1953 I enrolled in the physics doctoral program at the University of Maryland. Soon thereafter John Davis and I were entreated by Professor Roy Anderson to join his research project to help build an electron spin resonance spectrometer, John being an expert in electronics, and myself having microwave experience. Thus my first randomly chosen job at Westinghouse determined the whole course of my future life.

Toward the end of my Maryland tenure I gave a series of lectures to my fellow graduate students, and then I wrote an extended version of the lectures called 'The Dance of the Nucleons'. The title page of the lecture notes read:

THE DANCE OF THE NUCLEONS
Every spring the protons and electrons
assemble on the magnetic field and dance
around the quadrupole to the resonating rhythm
and modulating melodies of Larmor's lullabies.
This monograph is an exposé thereof.

I thought that this was clever at the time, and now it is finally in print after a delay of 40 years! What I did not know was that 'The Dance of the Nucleons' was the beginning of my writing avocation. Most of the material in the lecture notes eventually found its way into chapters or books.

After obtaining my doctorate in 1958 I spent six years in the catalysis division at Gulf Research near Pittsburgh, and I learned a great deal from my association with Don O'Reilly. This was my chemistry career, studying the NMR of aluminum nuclei in silica–alumina catalysts, and various gases and reactants absorbed on the surface. While there I felt at a disadvantage because I never did figure out what an acid site on a catalyst surface was all about, but this was compensated by the fact that I understood quantum mechanics better than the chemists. At the end of my stay at Gulf I wrote, in conjunction with Don MacIver, a 97 page review article on the spectroscopy and crystallography of chromia alumina catalysis for *Advances in Catalysis*. Bill Kehl had done the crystallography. I found writing this first review a very exciting learning experience.

While at Gulf it became clear that much of the microwave knowledge that I acquired earlier at Westinghouse had never appeared in the magnetic resonance literature, and I also found out that the copyright of the 28 volume Radiation Laboratory series of radar books had expired, which made the books part of the public domain. This caused me to start writing an ESR instrumentation book which reproduced several dozen figures and parts of many tables from the Radiation Laboratory series. It included the acknowledgment in the preface: 'I wish to express my appreciation to my wife, Kathleen, for her diligent typing of the first draft of the manuscript, and to my daughter Elizabeth whose birth during this period did not unduly delay the proceedings'.

The emphasis at Gulf was on improving catalysts and other aspects of petrochemical research. Many chemists and chemical engineers supplemented their income by applying for patents on various applications in these fields. I never submitted a patent proposal; the only patent that I obtained was the design of a high-temperature microwave cavity described in an article written for the *Review of Scientific Instruments* which had its publication held up by the legal department while a patent was applied for. Eventually I realized that my interests were more academic, and that I belonged in a university. The experience at Gulf was, nonetheless, a very worthwhile one.

I arrived at the University of South Carolina in July of 1964 for my third and last scientific job, with the emphasis on physics. My first doctoral student was Frank Griffith who already had an M.S. degree from Howard Shields of Wake Forest, and Howard himself had received his doctorate under Walter Gordy of Duke. My advisor Roy Anderson had also been a Gordy product, which made me an academic grandson of Gordy, and my first student was both a grandson, and through me a great grandson of Professor Gordy. Over the years I have helped to direct three other grandchildren of Gordy. It is indeed a small world!

While a graduate student at the University of Maryland I subscribed to the *Journal of Chemical Physics*, which was then the main source for important articles in magnetic resonance. I remember eagerly awaiting the arrival of the next issue of the journal, and often being disappointed because there was no article to read. In those days there was no trouble in reading most of the literature, and I used to send for reprints of everything that was published. Things are really different now.

Over the years I have always appreciated the chemistry and biology background that I acquired in my premed undergraduate major, because NMR and especially ESR were always on the border between chemistry and physics, and a knowledge of both helps. In contrast to many of my physics colleagues, I could always tell the difference between the aldehydes and the ketones.

A year after arriving in South Carolina my colleague Horacio Farach joined our faculty and we began an almost 30-year long collaboration which has led to the publication of several books and many research articles. I have been very fortunate to have him as a collaborator for these three decades. During the last five years it has been stimulating getting involved in the exciting new field of high-temperature superconductivity.

Biographical Sketch

Charles P. Poole, Jr. *b* 1927. M.S., 1952, Fordham University, Ph.D., 1958, University of Maryland. Physicist, Westinghouse Electronic

Corp., 1952–53, Gulf Research Corp., 1958–64. Associate professor of Physics, University of South Carolina, 1964–66, Professor of Physics, University of South Carolina, 1966–present. Approx. 115 publications, including seven books, Editor, *Magnetic Resonance Review*. Research interests: solid state physics, superconductivity, magnetic resonance, Clifford algebras.

Pound, Robert V.: Early Days in NMR

Robert V. Pound

Harvard University, Cambridge, MA, USA

Academic scientific research, especially in physics, was almost completely suspended between 1940 and 1945, with the creation of specialized laboratories dedicated to the development of instruments of war. In the United States, the Radiation Laboratory at the Massachusetts Institute of Technology (MIT), was devoted primarily to microwave 'radar', which called heavily upon the world of academic physics. The unprecedented bringing together of scientists from widely different backgrounds, brought about lasting cross fertilization of areas of scientific interest among the participants. This, as well as the experience of large-scale funding, had many consequences on the direction of research activities after World War II.

As the war was winding down in the summer of 1945, leading to VJ Day, August 14, we, at the Radiation Laboratory at MIT, naturally began thinking again about fundamental physics and how our advancement of many electronic techniques for the radar program might be applied to more basic research. Microwave spectroscopy was an obvious possibility. An impressive measurement of the inversion spectrum of ammonia at 1.25 cm had been made way back in 1933.[1] It could be explored far more thoroughly with our new technology. A couple of other examples had been pursued for wartime purposes within our laboratory. These were the absorption spectrum of molecular oxygen in the region of 5 mm wavelength[2] and the absorption of water vapor, the H_2O molecule,[3,4] in the region of 1.25 cm, at which wavelength the K-band radar had been designed to operate. Microwave spectroscopy offered especially important research possibilities to physical chemists. The frontier of physics research was largely in the study of nuclei, and it seemed less easy to transfer our novel technology into that field, except for new forms of accelerators. Most Radiation Laboratory members had for some time been making plans for their postwar careers, many returning to the institutions from which they had come. My own future had already been set in May of 1945 with my election to a three year term as a 'Junior Fellow' in Harvard's Society of Fellows, from July 1, 1945. Until this honor came to me, I expected to continue my formal study in physics as a graduate student. The Society of Fellows, founded in 1933, offered to a few who were recognized early by their achievements a less formal entrance into a research career than had become the norm in Ph.D. programs.

With the end of the war, the administration of the Radiation Laboratory asked several members of the soon to be disbanded laboratory to stay until as long as June 30, 1946, to contribute to a series of books which would preserve the advances, made mainly under tight military security during the five years, for the wider engineering and scientific communities. The longevity of many of the resulting 28 volumes testifies to the worth of that enterprise. Among the members asked to stay on for that purpose was Edward M. Purcell, leader of the 'Fundamental Development Group', Group 41. Purcell delayed his return to his faculty position in physics at Harvard from which he had been on leave-of-absence since January, 1941. Two others were Henry C. Torrey who headed the work of Group 53 on crystal rectifiers, and the present author who had been responsible for the design of crystal mixers, the microwave structures that employed crystal diodes and local oscillators to convert incoming microwaves to more conventional frequencies. The writing project led to my spending the first year of my membership in the Society of Fellows on a leave-of-absence.

One hot day in September, Henry Torrey and I invited Ed Purcell to join us for lunch at the small restaurant in Central Square, Cambridge, where we frequently went. On this particular occasion Purcell had been recently writing for the volume on propagation, the story of the absorption of K-band microwaves by atmospheric water vapor. He was particularly impressed that two, in this case among many, molecular states whose difference corresponded to the energy of the K-band photons, with a magnetic dipole transition connecting them, caused such absorption. Ed asked Torrey, who had done his Ph.D. thesis research in the molecular beam laboratory at Columbia under I. I. Rabi, 'Couldn't one detect the resonant absorption of nuclei, say protons, when placed in a magnetic field that would split the magnetic substates of the spin-$\frac{1}{2}$ protons by an amount corresponding to the energy of a radiofrequency photon?' Applying an rf magnetic field transverse to the magnetizing field then should result in such an absorption, detectable as a drop in the impedance or of the transmission of the circuit involved in applying the rf. I recall Henry's initial response being that he remembered there having been some talk about such a question at Columbia in the early days. He didn't remember just why it had been thought to be unworkable. He recalls, however, feeling he had given a pessimistic response to the proposition.

One of the things that had brought the attention of the physics community, and particularly of Purcell, to the resonance techniques of the atomic and molecular beam group at Columbia was the fact that the leader of that work had been I. I. Rabi, who became a founding member of the Radiation Laboratory, and headed Division 4 under which Purcell's Group 41 operated. We were surrounded by other veterans of the Columbia team, including the head of our rf group, Jerrold Zacharias, and, until he left for the Los Alamos project, Norman Ramsey, not to mention the continuing collaboration with the parallel Radiation Laboratory at Columbia, staffed mainly by Rabi's former colleagues. Rabi had been awarded the Nobel Prize for Physics for 1944, at a unique special ceremony in New York.

Torrey vividly recalls[5] thinking that evening about the question Purcell had put, and making some calculations. This changed his mind and he became excited. He went to Purcell's office first thing next morning, apologized for his pessimism of the previous day, and described his calculations that made him think that detection should be possible. Purcell said 'let's do it'. I was included in the project from the beginning.

We undertook the project as a side line to our main responsibilities on the book writing project. A critical component needed for the experiment was a large magnet able to provide about 7000 G, to render protons resonant at about 30 MHz, a frequency chosen because it was the intermediate frequency of most of our radars, and we had available the least noisy preamplifiers yet developed. Purcell undertook to find such a

magnet, and failing to find one we could use at MIT, he was happy to report to us that J. Curry Street agreed to our use of the large magnet in his cosmic ray research shed at Harvard. The magnet had not been operated since 1940 because Curry Street had also joined the Radiation Laboratory at the beginning. The main yoke of the magnet had been extracted from a large generator that had been discarded by the Boston Elevated Railway (now the MBTA). It had provided the field to bend tracks in a large cloud chamber with which Street and Stevenson had determined the mass of the muon,[6] a component of cosmic rays then on center stage. The magnet current was provided by a large dc generator in the basement of the contiguous Cruft Laboratory, and was controlled remotely by a rheostat on a wall panel in the cosmic ray shed. Our 30-MHz circuit took the form of a bridge with the sample containing protons filling a resonant cavity in one arm and with the signal transmitted through it balanced to a low level by a second arm having adjustable phase and amplitude. The bridge should suppress noise from the signal generator, should avoid overload of the amplifiers and allow observation of small fractional changes of the transmission. An output diode, added to the Hallicrafters S 36 communications receiver that followed the preamplifier, which had been a part of my apparatus for studying mixer performance, indicated the amplified residual signal and attendant noise. The choice of a cavity resonator for the sample testifies to our immersion in microwave technology for the previous four years. Most of the assembly of the apparatus took place in the evenings, except for the construction of the cavity which was machined from our drawings by Charles Rowe, a technician assigned to me at the Radiation Laboratory for several years. By later standards, the cavity and its sample volume were enormous, being an 8-cm length of shorted coaxial transmission line brought to open-ended resonance at the 10 m wavelength by a capacitive plate insulated from a lid by a thin mica sheet. With a diameter of about 12 cm, the space around the center conductor was filled with a primarily magnetic rf field when resonated at 30 MHz. When placed in the magnet with the axis of the coax parallel to the static field, the circumferential rf field was transverse. The rf was coupled in and out by small loops in that space. Most of the equipment, except for the magnet, was taken up to the Harvard laboratory from my MIT lab, but a General Radio 805B signal generator to provide the driving signal was borrowed by Purcell from the Harvard Psycho-Acoustic Laboratory of Professor S. Stevens.

As the plans went forward, Torrey and I, who shared an office for our writing enterprise, frequently discussed our 'moonlight' project. Henry realized he had assumed in his calculations that the two energy states of the protons would be in thermal equilibrium at room temperature, which would result in a very small excess population of the lower relative to the upper state. This would be a necessary condition for absorption because the rf would induce downward as well as upward transitions with equal probabilities, and no net absorption would result unless the populations were unequal. In thermal equilibrium, Boltzmann statistics at laboratory temperature and 30 MHz result in a difference of a few parts in a million. As Henry began to wonder what mechanism might bring about such an equilibrium, we raised the question with Ed Purcell. Torrey undertook to try to find some relevant ideas in the literature. He found an early paper of I. Waller[7] on the interaction between lattice phonons and electronic spins in a paramagnetic crystal. Henry adapted the calculation to apply to nuclei. Another paper, by Heitler and Teller,[8] also found by Henry, actually carried out just such a scaling of Waller's mechanism to nuclei in 'diamagnetic substances' and concluded the relaxation time would be as long as 10^6 years. Heitler and Teller, however, had only evaluated the so-called first-order effect in which the interaction is directly with lattice phonons of the resonant frequency, of which there are very few compared with those at higher frequencies. Henry found that Waller's second-order process was much stronger, whereby, through the nonlinearity of the dipole–dipole interaction, phonons of all frequencies participate by scattering into phonons differing by the resonance frequency. He concluded that the 'relaxation time' from the second-order process might be as short as several hours at room temperature. Our large sample and the low rf power we would apply would allow us to observe absorption for several hours without much reducing the population difference if once relaxation to equilibrium in the field had taken place.

Several evenings were spent at the Harvard lab, clearing out five years worth of cobwebs. We brought down from an undergraduate electricity laboratory a long period galvanometer and mutual inductance with which to calibrate the field versus current and evaluate its uniformity over the radius of our cavity. Purcell designed pole caps for the magnet that were planned to make the field more uniform. These were machined in the Harvard Physics Department shop by its foreman, Carl Johnson. We expected that the dipole–dipole interaction among the concentrated protons in our planned paraffin wax sample would lead by itself to a broadening of the resonance to as much as 10 G, so, after some modifications, we felt the uniformity of the magnetic field was adequate.

Finally we were able to make a determined search for the resonance on the evening of Thursday, December 13, 1945. Ed had brought in some home canner's paraffin wax from the small grocery shop, and we melted a couple of pounds and poured the cavity full. We balanced our bridge down to receiver noise, increased the input power, and rebalanced, until we could no longer reduce the meter reading to that of pure receiver noise because of the presence of noise at 30 MHz from the GR 805B signal generator, not further reducible because the two arms of the bridge transmitted a band of frequencies differently. We watched the meter for evidence of a change in balance as we passed back and forth through the region of 73 A of magnet current that our calibration indicated for the proton resonance, given the magnetic moment as reported by the Columbia group.[9] We scanned between about 65 and 80 A to allow for perhaps 10% error in the calibration but nothing was seen. Stare as we would at the output meter there was no movement that correlated with the changes in the magnet current. At about 4 a.m. Friday morning, somewhat discouraged, we shut down, with the agreement to try again Saturday. Ed Purcell proposed coming at about 7 a.m. and turning on the magnet. Our search would resume in the afternoon, when Henry Torrey and I would join after putting in our expected appearances at MIT. The idea was to allow the system to cook, or relax, in the field for seven or so hours, in case the relaxation time was comparable to that. The fact that the night time effort had taken a similar number of hours reduced the promise of this step.

As arranged we began the same kind of search in the afternoon of Saturday, December 15. After several hours of twisting the rheostat controlling the magnet current, watching

the output meter, and occasionally rebalancing the bridge, again nothing resembling the hoped-for resonance was seen. Late in the afternoon we decided to shut down and to think over what we might do next. All our calculations indicated that a resonance ought to double our detector meter reading, knowing that the *Q* value of the cavity was nearly 1000. In our minds was the idea of greatly increasing the sensitivity by going into a differential method with a modulated field and a coherent lock-in detector. During the course of shutting down, we ran the generator up to its 100 A top value and came down slowly. As we passed through 83 A, the meter kicked exactly as we had been hoping. That response proved repeatable for approach from either direction. We shut the magnet off completely and quickly brought it back; the signal was still present. We removed the cavity from the magnet and replaced it without affecting the signal. It looked as if the relaxation took place in less time than any of these maneuvers required. Our previous failures resulted from our not recognizing the degree by which the magnet iron was saturating in providing the field in so large a gap. It turned out that our calibration was only 2% optimistic, not bad for the old style flip coil, galvanometer, and mutual inductance, but it took 15% more current to gain that needed 2%. This factor allowed us to estimate a linewidth of a few gauss, when the current difference between the sides of the line were found to be about 0.5 A. We certainly should have recognized the problem sooner, because my notebook of the calibration data shows that even 102 A produced a field only a few hundred gauss greater than one of 73 A. How embarrassing it would have been if we had not accidentally discovered our error. So we were off and running with a new research tool. I was especially happy to think I had an easy way into nuclear physics, not withstanding my limited experience with the special techniques more usual in that field.

In the course of the development we heard that a project of similar intent was underway at Stanford, under Felix Bloch and W. W. Hansen. I understand that I. I. Rabi described to them our activities on a visit there in December. We also learned of the two previous unsuccessful efforts by C. J. Gorter[10] and Gorter and Broer[11] in Amsterdam. The first of these is probably the basis of Torrey's recollections from Columbia, because Gorter visited there in 1937 and discussed his effort at some length. Incidentally, Torrey[12] has told of Rabi's giving him, early on, a very pessimistic view of the expectations of our project. We ran our experiment a couple of more times and then wrote the letter to the *Physical Review*, which is dated as received there on December 24, 1945.[13] Bloch, Hansen, and Packard reported success soon after in a letter to the *Physical Review* that is dated January 29, 1946.[14] They had begun the project on 'Nuclear Induction' considerably earlier than we but seem to have completed their design later. Bloch and Hansen had returned to full-time academic life and begun their experiment in the spring of 1945.

We were all anxious to begin a more serious pursuit of this new field, but were still committed to the writing project. Nicolaas Bloembergen came to Harvard from the Netherlands as a graduate student and undertook to work as an assistant in the spring of 1946. We quickly began developing more sophisticated instrumentation. However, before setting aside our cavity, we filled it with a mixture of mineral oil and powdered CaF_2 in which we were able to detect both the proton and the ^{19}F resonances. Henry Torrey[15] and I[16] each read a 10-minute paper, authored by the three of us, describing the theory and our experiment at the annual spring meeting (the Washington meeting) of the American Physical Society, held in Cambridge in 1946 to mark the importance of the work in Cambridge in the war years. Felix Bloch came from California and gave the two papers[17,18] his group had submitted expanded to a single half-hour talk. This provided evidence of the differences as well as the similarities of the two methods.

With Bloembergen involved, and with both Purcell and myself at last moving to Harvard in July of 1946, our project intensified. Henry Torrey, after finishing his writing assignment, accepted a position at Rutgers University, where he became the first to explore transient effects produced by rf pulses.[19] At Harvard we took over a smaller magnet originally made in Switzerland in 1913 for Zeeman optical spectroscopy. It had poles of only about 6 in. diameter. We supplied the current from some large storage batteries, after finding that our small motor-generator had poor stability. We continued to use a bridge circuit, but abandoned the cavity in recognition of the evidence that relaxation times could be short enough to work with small samples contained in rf coils. The system observed derivatives of resonance lines, using a small 30-Hz modulation of the field with a lock-in amplifier, and a 30 MHz preamplifier feeding a new National Co. HRO communication receiver.

One of our first investigations was of the proton resonance in hydrogen gas, H_2. So as to provide sufficient density of protons we constructed a cell that could contain tank hydrogen in a pressure range up to 30 atm. The complex structure of the resonance reported by the Columbia molecular beam group[9] was known to us and, in advance, I supposed the line might be broad, reflecting the various internuclear and molecular interactions reported in the beam studies. Our first observation was at the end of the day, when we found a proton resonance, only 0.25 G wide, as narrow as any we had seen in our magnet, and consistent with the determining factor being the nonuniformity of our magnetic field. That evening when thinking about that result, I asked myself how the frequent collisions between molecules in the compressed gas would change things as compared with free molecules in a beam. I usually thought in terms of Fourier spectra of time-varying radiofrequencies, and, supposing that the collisions would switch the molecules from one substate to another, each having a differently shifted frequency, I related that effect to frequency modulation of a CW carrier at a rate rapid compared with the shifts themselves. I knew that in frequency modulation this case develops negligible intensity in sidebands, leaving the main carrier almost unaffected. Applying this model to our molecular hydrogen indicated that the interactive structure would be averaged out, a first recognition of 'pressure narrowing'. In addition to explaining the small width, the fluctuations of the interaction also provided a mechanism of spin–lattice relaxation, and measurements showed the relaxation time became proportional to pressure. The more rapid the collisions the lower the component of the fluctuations at the resonance frequency. These results were described in a letter[20] and thus there began the more detailed study of relaxation effects in liquids that became the widely recognized work known as BPP,[21] which also became Nicolaas Bloembergen's Ph.D. thesis submitted to Leiden University in 1948. We realized, at last, why our initial use of paraffin wax brought us a far shorter relaxation time than Torrey's estimate

had predicted for a rigid crystal, which paraffin clearly was not.

Another study performed in those early days was the measurement of the linewidth of the ^{19}F resonance in a single crystal of calcium fluoride, as a function of its orientation in the magnetic field,[22] confirming the quantitative analysis of our colleague, J. H. Van Vleck for the 'second moment' of the lineshape function,[23] as produced by the dipole–dipole interactions in the rigid lattice. A second graduate student, George Pake, soon undertook a research project with E. M. Purcell, and he made lineshape studies in rigid crystals. His thesis was based on his study of the lineshape of the proton resonance of the water of crystallization in single crystals of gypsum,[24] $Ca_2SO_4 \cdot 2H_2O$, which marked the start of a widespread application of NMR to problems in crystal structure. I still liked to think that NMR was a way into nuclear physics, and finding resonances for nuclei with relatively uncertain moment values seemed to be such a route. Bloembergen and I spent some unrewarding hours sweeping the field by sliding our crude current control resistance while staring at the fluctuations of our output meter on the lock-in amplifier, trying to detect the resonance of bromine isotopes, among others.

I. I. Rabi paid a visit and spoke about his Columbia group's work with molecular beams at our departmental colloquium in February, 1947. He included the description of effects from nuclear electric quadrupole moments in molecules and described resonances in low magnetic fields in which the frequencies were entirely determined by the nuclear quadrupole splittings. Rabi emphasized that extraction from the spectra of a quantity for the nuclear quadrupole moment was hard, because the electronic field gradient to which the splitting was proportional was too difficult to evaluate reliably. It occurred to me that a similar effect should exist in ionic crystals of lower than cubic symmetry, and I supposed that there, since ions are generally of closed shell, noble gas structure, the field gradient might be simply calculable from the structure parameters, assuming each ion to act as a point charge. To pursue this idea, I needed a spectrometer that could search in frequency, and our bridges or the crossed-coil device of the Stanford group seemed too difficult to convert to frequency scanning, requiring many tracking controls. This was the driving force behind my development of the regenerative, or controlled marginally oscillating, detector,[25] often spoken of as the Pound Box, with which I initially planned to try to find some magnetic resonant absorption at frequencies determined by quadrupole splitting without a magnetic field. My initially preferred candidate was hexagonal HgS, cinnabar, which I naively supposed to be ionic. With the spectroscopists' value for the quadrupole moment, and a simple estimate of the crystalline field gradient, I hoped to predict a frequency. However I soon found the slow convergence of the lattice sum for the field gradient made the evaluation difficult. I realized that this search was not likely to succeed, and I went back to using a magnet and applied my simple spectrometer to determine a few g-factors, as a contribution to nuclear physics. These included the two bromine isotopes,[26] the two copper isotopes,[27] the two gallium isotopes, and phosphorus ^{31}P.[28] The bromine isotopes are of almost identical natural abundance, but I was able to assign the nuclear magnetic resonances to the individual isotopes by using the fact that the relaxation in the liquid state was caused by the fluctuating quadrupole interaction, the broader line thus going with the isotope of larger quadrupole interaction, as already known from microwave spectra. Chemists studying rotational spectra of molecules with microwaves were reporting nuclear spins and quadrupole interactions, and I supposed that molecular interactions would be similar for such molecules in the solid state. However, demonstrating that didn't seem to me as rewarding as studying ionic crystals, because the problem of evaluating the field gradient in molecular crystals would be even more difficult than in the diatomic molecules described by Rabi.

The scanning spectrometer was successfully applied to the detection of electric quadrupole splittings in crystals with light nuclei such as ^{7}Li, ^{27}Al, and ^{23}Na. In these cases the quadrupole interaction, being smaller than the magnetic one even in my small magnet of only 3 kG, was treated as a perturbation of the magnetic structure. In the case of the aluminum resonance in corundum, Al_2O_3, I carried the perturbation calculation to the third order to give an adequate fit. One of the more novel experiments described in the extensive paper on these efforts[29] was the first example of double resonance. I applied saturating rf to one of the three well-resolved quadrupole split lines of the spin-$\frac{3}{2}$ ^{23}Na in a single crystal of $NaNO_3$ and recorded the resulting change in strength of the other lines. The results agreed with a detailed balance calculation that used the matrix elements of the quadrupole interaction in the relaxation assuming a modified Waller mechanism. Relaxation by magnetic interactions via impurities, as seemed to be the case for spin-$\frac{1}{2}$ nuclei, would not fit. My simplistic ideas on quadrupole interactions in ionic crystals were rather dashed when Rudolph Sternheimer showed[30] that distortions of the electron shells of the atoms and ions had enormous influences. He derived shielding and antishielding factors amounting to many hundreds for some atoms. Little hope remained for important data for nuclear physics from the quadrupole interactions in crystals.

Although I had not initially been attracted to the possibility of studying the interactions in molecular crystals containing, for example, bound halogens for which interaction strengths were already reported from gaseous molecular spectroscopy, I realized in 1949 that in some cases the interactions could be large compared with thermal energies at low temperature and would thus result in nuclear alignment,[31] which had possible interest for nuclear physics. Thus I began again an effort to detect the so-called 'pure quadrupole resonance', this time of ^{127}I in molecular solid iodine, which I believed would be easily found, although in the then electronically awkward frequency region of 1500 MHz. Before I was successful, Dehmelt and Kruger reported detecting pure quadrupole resonance in solids for the example of chlorinated ethylene[32] in the more conventional frequency region of 30 MHz.

Among several rather pure crystals I acquired from the Harshaw Chemical Company was one of LiF. I was surprised to discover that the relaxation time of the ^{7}Li at room temperature was as long as 5 min, varying somewhat with its orientation in the field. By probing the resonance periodically with the oscillating detector I was able to display on the chart recorder the build up of the magnetization after initially inserting the crystal cemented to the end of a wooden dowel. Immediately came to mind the question that had arisen in our first experiment with paraffin; once magnetized, what happens if the crystal is removed and then replaced in the

field? By doing so, I found that even in the Earth's field the crystal retained its reduced entropy, apparently becoming adiabatically demagnetized to a low absolute spin temperature and recovering its magnetization at high field if not kept out too long. In fact, by measuring the loss as a function of the time out of the magnet, I concluded that the relaxation time in zero field (actually the Earth's field) was about 15 s. Trials showed that the remagnetization was independent of any gyrations and rotations one made while out of the magnet. I published a letter describing this observation,[33] and soon after was joined by E. M. Purcell in an effort to trick the spins into some other condition while in the weak field. At first there was the thought that, since the spins could only reorient at a rate slower than their rate of precession in the weak field, a change of direction of such a field faster than that rate could not be followed. I was sure, however, that in the demagnetized state the field at each spin is the dipolar field of the neighbors and the macroscopic polarization is lost. A field large enough to retain the polarization would be needed and any quick transit through weaker fields should be fast compared with a 'spin–spin relaxation time' closely related to the linewidth caused by the dipole–dipole interaction.

We built a device using a small permanent magnet providing about 100 G, and a small solenoid in that field through which we could discharge a capacitor. The current rose and reversed the field in less than a microsecond but a series resistance slowed the return to the field of the small magnet to take more than a millisecond. Moving the magnetized crystal from the resonance magnet, placing it in the coil near the small magnet producing the discharge and returning the crystal to the NMR magnet, all in a few seconds, resulted in an inverted NMR signal. Such a signal corresponded to emission rather than absorption. It decayed through zero and back up as an absorption, with the same 5-min time constant already noted. We emphasized that the crystal suffered demagnetization to essentially zero field not only in transferring to the flipping gadget but again on the return when it was in this unnatural state. We termed its condition a 'spin system at a negative temperature'. The concept can be shown to be well based in thermodynamics and statistical mechanics and has entered many textbooks. Simpler inversions are easily produced in the liquid state, for example by fast passage, but there is no mechanism there producing internal equilibrium at a rate faster than the spin–lattice relaxation. In the rigid lattice the spin–spin interaction causing mutual flip-flops among like nuclei maintains a statistically probable state in the isolated spin system, even when fully demagnetized and inverted. The inversion is a way to put more energy into the spin system than corresponds to infinite temperature, so higher levels must become more populated than the lower ones. There is no way to obtain this condition from a normal thermal state and it can only be produced in a system with a bounded number of energy levels, like the spins. Our letter[34] stirred up controversy among thermodynamicists, but the concept slowly became generally accepted. Unfortunately the term 'negative temperature' has frequently been applied to such inversions as are invoked to produce lasers, but there no internal equilibrium exists. In quite another way we did influence the development of lasers and masers. Our description of the role of stimulated emission has been credited by C. H. Townes with playing a role in his conception of the first maser.[35]

These are some of my recollections of my involvements in the first five years of NMR. My effort to emphasize the nuclear physics aspect of the subject found little reward as results instead led to a wide range of applications in condensed matter physics, followed by chemistry, then biology, and perhaps most impressively of all, to medicine. I am grateful to my friends and collaborators, E. M. Purcell, H. C. Torrey, and, N. Bloembergen for helpful comments on this manuscript at several stages.

REFERENCES

1. C. E. Cleeton and N. H. Williams, *Phys. Rev.*, 1934, **45**, 234.
2. R. Beringer, *Phys. Rev*., 1946, **70**, 53.
3. G. E. Becker and S. H. Autler, *Phys. Rev.*, 1946, **70**, 300.
4. R. H. Dicke, R. Beringer, R. L. Kyhl, and A. B. Vane, *Phys. Rev.*, 1946, **70**, 340.
5. Private correspondence with H. C. Torrey, 1987.
6. J. C. Street and E. C. Stevenson, *Phys. Rev.*, 1937, **52**, 1003.
7. I. Waller, *Z. Phys.*, 1932, **79**, 370.
8. W. Heitler and E. Teller, *Proc. R. Soc. London.*, 1936, **A155**, 629.
9. J. M. B. Kellogg, I. I. Rabi, N. F. Ramsey, Jr., and J. R. Zacharias, *Phys. Rev.*, 1939, **56**, 728.
10. C. J. Gorter, *Physica (The Hague)*, 1936, **3**, 995.
11. C. J. Gorter and L. J. F. Broer, *Physica (The Hague)*, 1942, **IX**, 591.
12. Private communication with H. C. Torrey.
13. E. M. Purcell, H. C. Torrey, and R. V. Pound, *Phys. Rev.*, 1946, **69**, 37.
14. F. Bloch, W. W. Hansen, and M. Packard, *Phys. Rev.*, 1946, **69**, 127.
15. H. C. Torrey, E. M. Purcell, and R. V. Pound, *Phys. Rev.*, 1946, **69**, 680.
16. R. V. Pound, E. M. Purcell, and H. C. Torrey, *Phys. Rev.*, 1946, **69**, 681.
17. F. Bloch, W. W. Hansen, and M. Packard, *Phys. Rev.*, 1946, **69**, 680.
18. M. Packard, W. W. Hansen, and F. Bloch, *Phys. Rev.*, 1946, **69**, 680.
19. H. C. Torrey, *Phys. Rev.*, 1949, **76**, 1059.
20. E. M. Purcell, R. V. Pound, and N. Bloembergen, *Phys. Rev.*, 1946, **70**, 986.
21. N. Bloembergen, E. M. Purcell, and R. V. Pound, *Nature London*, 1947, **160**, 475; *Phys. Rev*., 1948, **73**, 679.
22. E. M. Purcell, N. Bloembergen, and R. V. Pound, *Phys. Rev.*, 1946, **70**, 988.
23. J. H. Van Vleck, *Phys. Rev.*, 1948, **74**, 1168.
24. G. E. Pake, *J. Chem. Phys*., 1948, **16**, 327.
25. R. V. Pound, *Phys. Rev*., 1947, **72**, 527; R. V. Pound and W. D. Knight, *Rev. Sci. Instrum*., 1950, **21**, 219; G. D. Watkins and R. V. Pound, *Phys. Rev*., 1951, **82**, 343.
26. R. V. Pound, *Phys. Rev.*, 1947, **72**, 1273.
27. R. V. Pound, *Phys. Rev.*, 1948, **73**, 523.
28. R. V. Pound, *Phys. Rev.*, 1948, **73**, 1112.
29. R. V. Pound, *Phys. Rev.*, 1950, **79**, 685.
30. R. Sternheimer, *Phys. Rev*., 1950, **80**, 102; 1951, **84**, 244.
31. R. V. Pound, *Phys. Rev.*, 1949, **76**, 1410.
32. H. G. Dehmelt and H. Kruger, *Naturwissenschaften*, 1950, **37**, 111.
33. R. V. Pound, *Phys. Rev.*, 1951, **81**, 156.
34. E. M. Purcell and R. V. Pound, *Phys. Rev.*, 1951, **81**, 279.
35. C. H. Townes at a Special Panel Discussion at the *14th Annual Precision Time and Time Interval Meeting held at NASA Goddard Space Flight Center, Greenbelt, MD, December 2, 1982*, in connection with the opening of the Atomic Clocks Exhibit at the Smithsonian Museum of American History.

Biographical Sketch

Robert V. Pound. *b* 1919. B.A., 1941, Physics, Univ. of Buffalo, M.A. (Hon.), 1951, Harvard, D.Sc., 1994, SUNY at Buffalo. MIT Radiation Laboratory, 1942–46, collaborator with E. M. Purcell and H. C. Torrey in first successful detection of NMR in condensed matter, December, 1945. First double resonance experiment, study of nuclear quadrupole interactions, oscillating detector spectrometers. With E. M. Purcell, introduced concept of negative spin temperature. With A. Abragam, explained effect of nuclear quadrupole interactions on directional correlations of successive nuclear radiations. Developed nuclear γ-ray resonance of ^{57}Fe to prove effect of gravity on photons. Mallinckrodt Professor of Physics, Emeritus, Harvard University since 1989.

Powles, Jack: Reminiscences of the Early Days of NMR

Jack Powles

University of Kent, Canterbury, UK

This is a personal account of my memories of NMR from 1952. I am no historian and my memory for facts and dates and people may not be very accurate 40 years on. If there are errors of commission or omission, especially when I name individuals and their doings, I must ask the kind indulgence of those people and the readers of this volume.

From 1945 to 1951 I worked on dielectric relaxation in liquids and solids with Willis Jackson in Manchester and Imperial College, London, with Edmond Bauer and Michel Magat in Paris, with Herbert Frohlich in Liverpool and with Charlie Smyth in Princeton. This gave me a lifelong interest in *relaxation* processes in a great variety of materials. I was a bit tired of dielectrics by 1951 and in the Princeton library I came across, by accident, the BPP paper[1] and Bloch's paper[2] and it was immediately clear to me that this novel method of spectroscopy was a new and powerful method of studying molecular motion in Nature and rate in condensed matter. Indeed it is much more powerful than dielectric spectroscopy since no electric dipole is necessary, just some suitable nuclei. Among these, for one, the most attractive to me was the proton since I had a longstanding interest in ice and water, the solid hydrogen halides, and methyl groups in particular. So, being quite good on electronic circuitry, statistical mechanics, and quantum mechanics, I thought I could change techniques quite easily. The opportunity presented itself and I became a research fellow with Herb Gutowsky in the fall of 1952 in Urbana, IL.

There was, in Herb's lab, a broadline spectrometer in working order. I churned out a mass of results[3–5] on samples of tetrasubstituted methanes (CCl_4, CCH_3Cl_3, etc. and mixtures thereof) of which I had studied the dielectric relaxation in Princeton and which Charlie Smyth kindly lent me. These were very nice things to learn on since they had a variety of line-narrowing processes, methyl reorientation, molecular partial reorientation, molecular isotropic reorientation, and molecular translation. The phase diagrams were quite complicated [4] and were materially quantified and explored by the sudden linewidth changes at phase transitions—perhaps the first instance of this use of NMR. This added to the very few studies of NMR in organic solids up to that time. We also found an effect novel to NMR at the time. It was familiar to me from earlier dielectric work.[6–8] I refer to the reorientation of methyl groups about the C_3 axis by a tunneling mechanism.[5] The apparent activation barriers were far too low, about 2 kcal mol^{-1} instead of 6 kcal mol^{-1}, and this was very neatly explained by a rather crude but adequate analysis of the reorientation by tunneling. Unfortunately, it could not be unequivocally established by deuteration as it had in HBr/DBr,[7,8] but it was surely correct. Of course tunneling, especially of methyl groups, is now a big industry, especially the work of Stan Clough in Nottingham, and many weird and wonderful offences against the pristine beauty of our nice simple experiment have been committed.

It should be mentioned that at this time in the laboratory next door, Herb and his students, Len Meyer and Dave McCall, were establishing the values of the proton chemical shifts for vast numbers of organic liquids scrounged from throughout the Noyes Laboratory. It is well known this is the basic information[9] and the beginning of the major industry of chemical analysis by nuclear magnetic resonance spectroscopy. Being a physicist I thought it was the most boring series of experiments I had ever heard of and I took little notice! This is an example of the commercial and technical application of NMR being excruciatingly dull as far as science is concerned, but the chemists went crazy over it. One advantage was that people soon started making decent magnets commercially and a lot of good science was done on these.

One great advantage of being in Urbana at that time was that in physics there was Charlie Slichter and his students, Myer Bloom and Don Holcomb. Norberg had just gone to St. Louis and Erwin Hahn to Stanford. This group was much oriented to pulsed NMR[10] and it seemed to me that the future lay in that direction, especially for the study of molecular motion. However, I was not able to do that for some time, it was too novel for the people with the money and power to understand. The chemists were particularly skeptical I remember—'What is a Fourier transform?'!

On returning to England, to Newcastle, in 1954, for a year, I managed to get a half-decent magnet and a chart recorder and built a broadline spectrometer which worked. I was just wondering what to do with it when I was visited by a party from ICI Plastics of Welwyn Garden City who were intrigued by this new technique. We were on the same wavelength because they were very knowledgeable about the dielectric relaxation in polymers and in fact knew my widely-quoted work on dielectric relaxation in polythene.[11] They were mainly concerned with mechanical relaxation. Most polymers are sold for their mechanical properties to this day. I was rash enough to claim to be able to predict mechanical relaxation from NMR, especially if I could do T_1 as well as T_2 measurements. In fact, to everyone's astonishment, including mine, I did actually manage to do this and so we were very early into NMR in polymers closely followed by Bill Slichter and Dave McCall at Bell Laboratories. This lasted some 15 years until ICI had a financial crisis and sacked all its most useful, and cheapest employees, their consultants, a commercial idiocy about the use of science in British industry which keeps us poor to this day. It was astonishing how quickly this field developed as witnessed by a review article I wrote in 1960,[12] from which one can see that NMR in polymers was already a major study by that time.

However, I moved to Queen Mary College, London in 1955, and at last was able to get support to do pulsed NMR. I had some excellent students to help me in this. John Luszczynski observed what must have been the first spin echoes to be seen outside the US.[13] Peter Mansfield built an even better pulse apparatus[14] and did a series of very nice measurements of T_1 and Bloch decays in all sorts of materials. Doug Cutler observed the first electron spin echo, in sodium/ammonia.[15] I think we were the first to use rf phase shifted pulse trains, 90_0, τ, 90_{90}, etc.,[16,17] which was the first attempt to remove the dipolar interaction in solids by pulse trains, which we

called ‘solid echoes’. These are I believe discussed in more detail by my former student John Strange elsewhere in this volume (***Strange, John H.: Echoes of the Past***). Similar work was being done, as we discovered later, by John Waugh at MIT quite independently. This developed into the elaborate and complex pulse trains which were developed subsequently by John Waugh and by Peter Mansfield when he went to Nottingham. It was amusing to be yet again measuring the solid hydrogen and deuterium halides, in 1968 this time by NMR.[18] We systematically showed that anything that could be done by steady-state spectroscopy could be done, usually faster and more easily, by spin echoes, for example the measurement of J coupling.[19]

I thought this was getting just too technical and elaborate for me, what with the rotating frame and multiple quantum transitions and what not. I felt that by 1970 or so NMR was getting too ‘mature’ and I looked around for something more exciting and with fewer able competitors! This was shortly before magic angle spinning and magnetic resonance imaging began really to get going! But I do not regret it; I am primarily interested in molecular motion and relaxation processes in condensed matter and one technique like NMR, powerful though it may be, is not enough. Indeed a narrow view using NMR only is often quite misleading.[20] On the other hand, I find one gets little credit for being knowledgeable in several fields. My advice to young people is, do not be interdisciplinary, be narrowminded but collaborate.

So I moved over to neutron scattering in 1971[21] and to computer simulation of liquids, my principal interest ever since, in 1973.[22] I look with wonder and awe at the remarkable things which are now done with NMR—but without any regrets, it was fun while it lasted!

REFERENCES

1. N. Bloembergen, E. M. Purcell, and R. V. Pound, *Phys. Rev.* 1948, **73**, 679.
2. F. Bloch, W. W. Hansen, and M. Packard, *Phys. Rev.*, 1946, **69**, 127.
3. J. G. Powles and H. S. Gutowsky, *J. Chem. Phys.*, 1953, **21**, 1695.
4. J. G. Powles and H. S. Gutowsky, *J. Chem. Phys.*, 1953, **21**, 1704.
5. J. G. Powles and H. S. Gutowsky, *J. Chem. Phys.*, 1955, **23**, 1692.
6. J. G. Powles, *Nature (London)*, 1950, **165**, 686.
7. J. G. Powles, *C. R. Acad Sci., Paris*, 1950, **230**, 836.
8. J. G. Powles, *J. Phys.*, 1952, **13**, 121.
9. L. H. Meyer, A. Saika, and H. S. Gutowsky, *J. Am. Chem. Soc.*, 1953, **75**, 4567.
10. E. L. Hahn, *Phys. Rev.*, 1950, **80**, 580.
11. J. G. Powles and W. G. Oakes, *Nature (London)*, 1946, **157**, 840.
12. J. G. Powles, *Polymer*, 1960, **1**, 219.
13. K. Luszczynski and J. G. Powles, *J. Sci. Instrum.*, 1959, **36**, 57.
14. P. Mansfield and J. G. Powles, *J. Sci. Instrum.*, 1963, **40**, 232.
15. D. Cutler and J. G. Powles, *Proc. Phys. Soc. (London)*, 1962, **89**, 130.
16. J. G. Powles and P. Mansfield, *Phys. Lett.*, 1962, **2**, 58.
17. J. G. Powles and J. H. Strange, *Proc. Phys. Soc. (London)*, 1963, **82**, 6.
18. M. Norris, J. H. Strange, J. G. Powles, M. Rhodes, K. Marsden, and K. Krynicki, *J. Phys. C.*, 1968, **1**, 422.
19. J. G. Powles and J. H. Strange, *Discuss. Faraday Soc.*, 1962, **34**, 1.
20. J. G. Powles, *Ber. Bunsenges. Phys. Chem.*, 1976, **80**, 259.
21. P. A. Egelstaff, D. I. Page and J. G. Powles, *Mol. Phys.*, 1971, **20**, 881.
22. P. S. Y. Cheung and J. G. Powles, *Mol. Phys.*, 1975, **30**, 921.

Biographical Sketch

Jack G. Powles. *b* 1924. B.Sc., 1945, Ph.D., 1948, Electrical Engineering, Manchester University, UK, D. ès Sc., 1951, Sciences Physiques, University of Paris. Introduced to NMR in 1953 by Herb Gutowsky and Charlie Slichter. Foundation Professor of Physics University of Kent, UK, 1964–1991. Now Emeritus but still active! More than 230 published papers, all worth reading. Main interest, computer simulation of liquids.

Proctor, Warren G.: When You and I Were Young, Magnet

Warren G. Proctor
Humlebaek, Denmark

I began my graduate studies early in January of 1946, the beginning of the winter trimester at Stanford University. Stanford, in 1946, was indeed the 'farm', a large sandstone quad and a few other buildings set amid grassy fields and trees. The Physics Department occupied one corner of the quad—I suppose the departments might have been arranged alphabetically because psychology was next to physics. There were about 15 beginning graduate students in physics. The faculty at that time was also quite small, but it is important to mention that Professors Felix Bloch and W. W. Hansen were among the half-dozen faculty members.

A memorable thing, related to the Physics Department colloquia held on Thursday afternoons, happened to me almost immediately. The first talk I heard was given by Professor Bloch who described the success of Professor Hansen, a graduate student named Martin Packard, and himself in observing nuclear magnetic resonance, which at that time he called nuclear induction. I must admit that I failed to grasp the significance of the discovery. I was fascinated by the instruments which had been carried up from the Physics Department basement to the lecture platform, where young Packard, while Professor Bloch was speaking, unsuccessfully attempted for an hour to show us a proton signal. I thought that all colloquia would be similar—each professor in turn describing to us the various interesting things he had observed in recent weeks.

Professor Bloch's ideas on magnetic resonance (he told me later) had been quietly worked out at home during the war years that he had spent at Harvard University. This made it possible to perform the experiment within a few months after his return to Stanford at the end of the war. The brilliance of his concept was clouded by only one thing: he had neglected to anticipate the narrowing of the lines in liquids due to their thermal motions, as explained by Bloembergen, Purcell, and Pound in their classic paper a year or so later. Until word of line narrowing reached Stanford, each time that a nuclear magnetic resonance signal was seen, the broad line that had been observed was always thought to have been its natural linewidth, in keeping with Bloch's simple dipole–dipole broadening mechanism. It was, in truth, due to the inhomogeneities of the magnets available in the Stanford Physics Department in those years.

For me, there was a period of about two years totally devoted to class work. One certainly heard about NMR in the department, and I remember two further colloquia which exposed me to the subject. One was given by Packard himself, an enjoyable talk from an experimentalist's point of view. Another talk was given somewhat later by Professor Bloch who had, with Packard, worked for several months at Los Alamos to measure the magnetic moment of tritium from a sample of the compressed gas. The emphasis at this time was the measurement of nuclear magnetic moments, and no doubt it was hoped that a precise measurement of many moments would provide some key to the understanding of nuclear structure.

The way I began working with NMR was the following. I was earning a little money correcting homework and examination papers for Professor Hansen, who was giving a course on microwaves. Professor Hansen came into the room where I was working one day and said that one of his graduate students had become much more interested in one of his new ideas—a linear electron accelerator—than he was in NMR. Hansen then asked me if I would be willing to take on the work that Richard Post would like to drop. Post had been given the thesis problem of building an automatic instrument that was to search for the magnetic resonances of all reasonably accessible stable isotopes. At this point I should say that my early wanderings in the physics basement taught me one thing: do NOT, I repeatedly had told myself, consider for a moment any research problem where vacuum was involved. This condition satisfied and having liked what I heard about nuclear induction, I accepted at once.

So I took over a very polished and complex apparatus that included a method of phase detection able to detect the U and V modes without having to tune for them at the probe. The reason for this was that the probe was simply inaccessible. The magnet had been built by a weird-looking fellow named Russell Varian. At one point I was bold enough to ask Professor Hansen why this fellow, who seemed to do little else but wander around, was hired by the Physics Department. I still remember Hansen's reply: 'You don't think he is doing anything, my boy, but the wheels are going around, the wheels are going around.' It was this thinker who constructed the magnet after a general design by Bitter. He realized that some magnetic moments would be very small, hence the highest possible fields would be necessary. Russell Varian consequently built a magnet which was totally enclosed, that is to say the magnet had complete cylindrical symmetry about a line running through the center of its poles. When looking at it one was simply faced by a large cylinder of steel, and there was no apparent access to the gap. Instead of opening a window at one side, as one would presumably do today, Varian felt it to be more sensible to have long holes drilled through the pole pieces and the pole caps for access into the gap since, NMR lines being broad, homogeneity was not a problem, but field strength was!

Only once during this time when the idea of motional narrowing reached us did I hear Felix Bloch express himself about it. I do not remember his words, some of them being possibly unprintable, but he was clearly furious with himself for not having thought of it.

Professor Bloch insisted for a number of years that the phenomenon be known as nuclear induction. I remember wondering about how this was all going to turn out until one day, in the basement, he called us all together. Who was there? Packard, Arnold, Dharmatti, Yu, Levinthal, Rogers, Jeffries? 'I have had a meeting with Purcell', he explained. 'It is important to be consistent with the nomenclature generally used in physics. It will be known as nuclear magnetic resonance', he concluded.

However, it was with this instrument that my practical introduction to NMR began. Moving to a large nearby magnet, it did not take me long to learn that the remaining part of

this magnificent apparatus was, for reasons I have forgotten, equally unsuited for the job that it was built for. During this time of construction and experimentation, problems of a practical type frequently arose. Who should one consult but one's thesis adviser? An electronic problem had arisen one day that baffled even this experienced seat-of-the-pants radio amateur, so I turned with my question to Professor Bloch. He invited me to the blackboard where I was horrified to see him beginning to write down Maxwell's equations! But, in the end, with a spectrometer consisting of a simple tracking transmitter and receiver, and a good magnet, I was ready to work and needed an easy target.

Poss had just observed ^{205}Tl but had failed to see the weaker resonance from ^{203}Tl. I decided to give it a try and was successful. I blush to remember my ridiculous pride as I sat in the audience nervously waiting to have my paper called at the Stanford Winter Meeting of the American Physical Society: my first professional appearance, describing to a bored audience the exciting news of a more precise value of the magnetic moment of thallium-203.

In the fall of 1949 Professor Bloch told me that he had invited Dr. F. C. Yu to work with me. Dr. Yu, he explained, wanted to learn about NMR, having completed his dissertation in another field at Ohio State. The following year proved scientifically exciting and personally rewarding, for Fu Chun Yu has remained a life-long friend. Of the many impressions I have of him at that time, I shall recall only one here: the basement NMR gang had driven for lunch to a Chinese restaurant located in a rickety building near the railway tracks in Mountain View. I had not been there before with Fu Chun and was surprised when he led us all through the dining room, through the kitchen, and into a small room with a large table in the back. A young man with pad and pencil arrived. Fu Chun took these and wrote some oriental symbols on the pad. 'What did you order for us, Fu Chun?' I asked. 'All we can eat for one dollar apiece,' he said. We worked together for one year during which time we found 18 new resonances and probably made the first observations of the chemical shift and spin–spin coupling.

The observation of the chemical shift was a classical case of an accidental discovery. The magnetic moment of ^{14}N was known fairly well but we wished to measure its magnetic moment more precisely. I remember going into the little Chemistry stockroom and searching for a compound which would give us the strongest possible resonance. I fell upon the bottle marked NH_4NO_3 because it was obviously very soluble in water and furthermore had two nitrogens per molecule. Downstairs we made up a concentrated solution and set it in the instrument. Fu Chun and I were facing each other, leaning on the magnet, anticipating the resonance as the small clock motor slowly changed the frequency of the spectrometer. As expected, a lovely resonance appeared on the recorder tape and, as we watched it, we were astounded to see the first resonance followed by a second one of equal amplitude. We repeated this measurement several times to make sure that there was no possible instrumental error and took the traces upstairs to Professor Bloch's office. He became very excited and we discussed possible reasons for the double resonance. There could be two reasons—one far more interesting than the other, namely that there were stable nuclear isomers with slightly different properties! We were hoping that we had made such a discovery. The second reason could be, of course, that it was some nasty chemical phenomenon, most probably a difference in the diamagnetic shielding due to different electron densities around the nitrogen nucleus. It was at this conference that Professor Bloch explained to us for the first time the next perturbation, the Van Vleck paramagnetism, which we decided later must contribute. A few days later he told us that he had arranged for Dr. Emilio Segre of the University of California to send us a sample of liquid ammonia, enriched in ^{15}N, because, as we later wrote about the presumed 'chemical effects': 'It seemed particularly important to us to verify that they were indeed of a chemical origin and not connected with questions of nuclear structure.'

I can still almost feel the agony of waiting several weeks for the enriched sample—such a spectacular observation could easily be observed and reported by someone else! Now here is where fact and fancy separate themselves. The 40 some years since that time have romanticized these events. Had I not taken the trouble to reread our publications, I would have written here that we agonizingly waited for the enriched sample before publishing, in order to be absolutely sure that the two resonances were of molecular origin. Consequently our letter was delayed ... to be published in an issue which also contained Dickenson's description of the chemical shifts he had observed for ^{19}F. Now, years later, looking up these old papers in the cellars of a modern university library, where ancient publications are stored, I have been shocked to learn that our first announcement of the chemical shift did not mention any measurements at all on ^{15}N. We did, indeed, rush into print without being absolutely sure that nuclear isomers were not involved, and my memory of the agony of waiting for the ^{15}N sample from Berkeley has been shown to be the stuff of good drama.

Dr Yu and I were also fortunate to discover, as far as I know, the first example of the spin–spin interaction: the very pretty multiplet observed for the resonance of ^{121}Sb in the ion SbF_6^-. This time we were astounded to see a multiplet of five lines. (Weaver later showed that there were seven.) This, of course, was manifestly impossible unless the SbF_6^- ions were impeded in their rotation. I remember sitting down and working out the pattern of magnetic fields one would expect to find at the antimony nucleus if one had a random but static distribution of the ions, taking into account the complexities of the spin distribution. The incredible thing was that this calculation gave a fairly satisfactory description of the multiplet we had observed. I remember being fairly happy with the explanation, but I remember equally well being unable to convince more experienced physicists of it. Indeed, I offered this explanation at the departmental colloquium at the University of California at Berkeley about this time and was greeted with loud shouts more characteristic of the British parliament than of a physics colloquium. This did not, however, prevent Dr. Yu and myself from describing this unusual interpretation in print. We were supported in our views when Prof. E. R. Andrew later suggested a mechanism that could explain the impeded motion: long chains of alternating hydrogens and SbF_6^- ions. However, it was about a year after this that Slichter and Hahn at Illinois noticed these interactions in hydrogen spectra and proposed the now well-known scalar interaction.

These days of discovery were exciting. What new nuclear or chemical mysteries were to be revealed with the next

nucleus? Sample inserted, field and frequency set for an all-night search, I bicycled through the early morning sunshine of Palo Alto to the Physics corner basement to examine eagerly the large heap of chart paper lying on the floor, sometimes on a very wet floor because the magnet had leaked overnight. A weak resonance could best be seen by pulling the paper straight and sighting along it from one end, suspicious areas to be reexamined during the course of the morning: a new resonance..a triumphant cup of coffee with Fu Chun . . . happy discussions with Bloch . . . the newer students Harry Weaver and Weston Anderson standing nearby.

But these years soon came to an end. Erwin Hahn and I, at an afternoon departmental coffee, in the late summer of 1952, he to leave for IBM and I to the University of Washington, wondered what we were to do next. We had no ideas. NMR is dead, we concluded.

How wrong we were! At the University of Washington I decided to start working on nuclear quadrupole resonance without having a clear idea where it might lead. As a young instructor I was given a roomy corner laboratory on the ground floor of the physics building, completely empty, and a miserable departmental allowance for purchases. Nuclear quadrupole resonance was built for a situation like this—no magnet necessary, elementary electronics, and the Minerology Department for samples. With several students the quadrupole resonances of boron and aluminum were studied in the hope of contributing to the partially known structures of the minerals involved. I should point out that NQR is really NMR—magnetic dipole transitions between energy states given, of course, by the interaction of the quadrupole moment with the internal crystalline field gradients.

I wish it were possible for me now to recall how the idea came, but come it did: how truly to make quadrupole transitions between quadrupolar energy states, pure quadrupole resonance indeed. It was a simple idea—modulate the quadrupolar interaction with ultrasonic waves at the transition frequency in a direction such that off-diagonal matrix elements were involved. Walter Tantilla had at that time asked about a thesis problem and he got this one. We wanted only to demonstrate that transitions took place and so took the easy way out: we would monitor the population differences by NQR with and without sonic waves. We chose to use $NaClO_3$ because single crystals could be easily grown and the resonant frequency of chlorine was conveniently high, around 30 MHz. I shall never forget the letters we received after our letter was published. One from Bloch, congratulating us on ‘catching such a pretty little fish’. And two further letters, one from Al’tschuler and one from Kastler, both kindly pointing out that they had proposed such an experiment in earlier papers. Other experimenters made the short life of nuclear acoustic absorption, as the field was called, into something useful. For example, by monitoring the resonant absorption on the ultrasonic transducer itself one was able to study the otherwise inaccessible quadrupolar interactions in the interior of metallic crystals. Perhaps the future will find a new need for NAA—who knows?

Biographical Sketch

Warren George Proctor. *b* 1920. Graduated 1942, Electrical Engineering, California Institute of Technology. M.I.T. Radiation Laboratory, 1942–45. Postgraduate year at the University of Basle and Stanford. Assistant Professor at the University of Washington, returning to Basel as Guest Professor in 1955. Joined Varian Associates, and later Managing Director, 1956–75. University of Helsinki and the Technical University of Denmark, 1975–86. Retired 1986. Research specialties, semi-conductor physics.

Purcell, Edward M.: Research in Nuclear Magnetism

Edward M. Purcell

Harvard University, Cambridge, MA, USA

Nobel Lecture December, 11, 1952
© Les Prix Nobel, 1952

Professor Bloch has told you how one can detect the precession of the magnetic nuclei in a drop of water. Commonplace as such experiments have become in our laboratories, I have not yet lost a feeling of wonder, and of delight, that this delicate motion should reside in all the ordinary things around us, revealing itself only to him who looks for it. I remember, in the winter of our first experiments, just seven years ago, looking on snow with new eyes. There the snow lay around my doorstep—great heaps of protons quietly precessing in the Earth's magnetic field. To see the world for a moment as something rich and strange is the private reward of many a discovery. But I'm afraid it has little bearing on the sober question we must, as physicists, ask ourselves: what can we learn from all this about the structure of matter? It is my privilege to tell you now of some of the things that can be learned.

Let us begin with the most direct application of nuclear induction methods, the measurement of nuclear magnetic moments. The basis for this is the resonance condition

$$f = \frac{\mu H_0}{Ih} \tag{1}$$

in which f is the frequency of precession of the axis of nuclear spin in a magnetic field of strength H_0, and μ is the magnetic moment of the nucleus. The number I is the nuclear spin quantum number, an integer or half-integer, and h is Planck's constant. Now H_0, except for a certain slight correction, is simply the field of the magnet in which the substance has been put, and it can be measured. The frequency of precession, once it is detected, is easily measured with high accuracy, and thus one can determine the quantity μ/Ih. However, for practical reasons, it is hard to measure the strength of a magnetic field very precisely. This difficulty is avoided if one is content to measure the *ratio* of the magnetic moments for two different nuclear species. We could, for example, compare the precession frequencies f_{H} and f_{D} for protons and deuterons exposed to the *same* magnetic field H_0. A mixture of light and heavy water, H_2O and D_2O, might serve as our sample. Then $f_{\mathrm{D}}/f_{\mathrm{H}}$ is the ratio of the magnetic moment of the deuteron to that of the proton, apart from the simple factor $I_{\mathrm{D}}/I_{\mathrm{H}}$, which is the ratio of the spins, in this case 2. In this way the magnetic moments of many different nuclei have been measured, relative to the moment of the proton, with great precision.

To show what accuracy can be achieved, let me describe one example, a very recent experiment by F. T. Wimett in the laboratory of Professor Bitter of the Massachusetts Institute of Technology. The ratio of the deuteron moment to the proton moment had been carefully determined before by Anderson and Smaller at Chicago, and by K. Siegbahn and Lindström here at the Nobel Institute. Wimett has now refined this measurement still further using as his sample the gas HD. This substance has a certain advantage: the two different nuclei are not only in the same vessel, but in the same molecule, so there is no doubt that the magnetic field at each is the same. Figure 1 shows simultaneous traces of the proton resonance and the deuteron resonance in a field of about 15 000 G. You will notice at once that the resonances are not simple. The proton resonance is a triplet line, almost fully resolved, while the deuteron resonance is a cleanly resolved doublet. This has an interesting explanation, to which I shall return near the end of my lecture, but it has no direct bearing on this experiment except to emphasize the extraordinary resolution. The separation of the deuteron doublet is only 0.07 G, 1 part in 200 000 of the applied field. By carefully lining up the central proton peak with each deuteron peak, in turn, a measurement reliable to about 1 part in 10 million can be made. The determination of the exact frequency ratio is accomplished by an elaborate scheme of harmonic multiplication. Wimett's result, which he kindly gave to me just a few days before I left Cambridge, is

$$\frac{\mu(\mathrm{D})}{\mu(\mathrm{H})} = 0.307\,012\,189 \pm 0.000\,000\,030. \tag{2}$$

The results of four earlier experiments of this sort are listed in Table 1 Of course the neutron experiment is a very special one, and Professor Bloch has already described his elegant method for detecting the neutron precession frequency. The other values were obtained by various investigators[1] in the way I have just indicated. These numbers provide a very stringent test of any theory of nuclear structure. A wholly satisfactory theory ought to be able to predict them. As you know, we are very far from having such a theory now. But even so, the high accuracy is not all wasted. The moment of the deuteron is not *quite* equal to the sum of the moments of its separate parts, the neutron and proton. Thanks to the extreme precision of the experimental values, this small but significant discrepancy is itself fixed quite accurately.

As we leave the simplest nuclei and proceed through the Periodic Table, the situation changes a little. The experimental precision is just as high, but one must apply to the measured frequency ratios a small correction to take account of

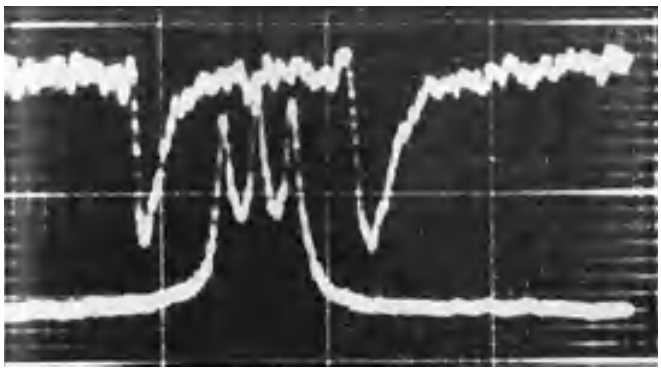

Figure 1 Simultaneous display of deuteron and proton resonances in HD. The proton trace is inverted. (T. F. Wimett, Massachusetts Institute of Technology)

Table 1 Magnetic Moments of the Neutron (n), Deuteron (^{2}H), Triton (^{3}H), and ^{3}He, Relative to the Moment of the Proton (^{1}H)

$\frac{\mu(\mathrm{n})}{\mu(^1\mathrm{H})} = -0.685\ 001$	$\frac{\mu(^2\mathrm{H})}{\mu(^1\mathrm{H})} = 0.307\ 012\ 25$
± 3	± 10
$\frac{\mu(^3\mathrm{H})}{\mu(^1\mathrm{H})} = 1.066\ 636$	$\frac{\mu(^3\mathrm{He})}{\mu(^1\mathrm{H})} = -0.761\ 815\ 0$
± 10	± 12

the magnetic shielding effect of the atomic electrons. This correction increases rapidly with atomic number. Until better atomic wavefunctions are available, it cannot be calculated reliably enough to support the six figure accuracy of the resonance measurement. There is one important exception. For two isotopes of the same element, the correction cancels out. Accurate moment ratios for isotopic pairs are of considerable interest, especially if the hyperfine structure interval for the two isotopes can be determined. A. Bohr and Weisskopf[2] have shown that such a comparison can reveal something about the internal structure of the nucleus.

Perhaps the greatest present need, through most of the Periodic Table, is for spin values and only moderately precise moment values, to help test the promising shell theories of nuclear structure. Nuclear induction methods will surely continue to contribute to this task. Spin determinations in particular, which depend on careful intensity measurements, are likely to receive more attention.

The experimental physicist often needs to measure the intensity of a magnetic field. Until recently a precise magnetic field measurement has been a formidable undertaking, but it is such no longer. At the National Bureau of Standards in Washington, Hipple and his collaborators[3] have measured the proton precession frequency and, at the same time, have measured in absolute units the intensity of their magnetic field. All the resources of the Bureau were brought to bear on the latter measurement, and an accuracy of 1 part in 40 000 was achieved. Knowing their result, an experimenter anywhere in the world can determine absolute magnetic intensities to the same precision, using equipment no more elaborate than an ordinary radio receiver. He need only determine the proton precession frequency in the field in question. Few physical quantities are as easy to measure accurately as a radiofrequency, thanks to modern electronic techniques and the availability, in most countries, of standard-frequency broadcasts.

Already a number of experiments have been performed in which the nuclear resonance has served as a standard of reference. Certain ones are of special interest because they have improved our knowledge of the fundamental atomic constants. In each of these experiments two *different* magnetic resonance phenomena have been observed at the same time in the same magnet. The phenomena involved are indicated in Figure 2. The precession of the proton moment [Figure 2(a)] we have already described; it is detected and measured in a nuclear induction experiment. The electron has an intrinsic spin and magnetic moment and also precesses in a magnetic field [Figure 2(b)]. For the same field strength, the electron's spin-precession frequency is about 700-times greater than the proton precession frequency. A bare proton, moving in a magnetic field, revolves in a circular orbit with a certain frequency [Figure 2(c)]. This is the familiar principle of the cyclotron and we might name the associated frequency the

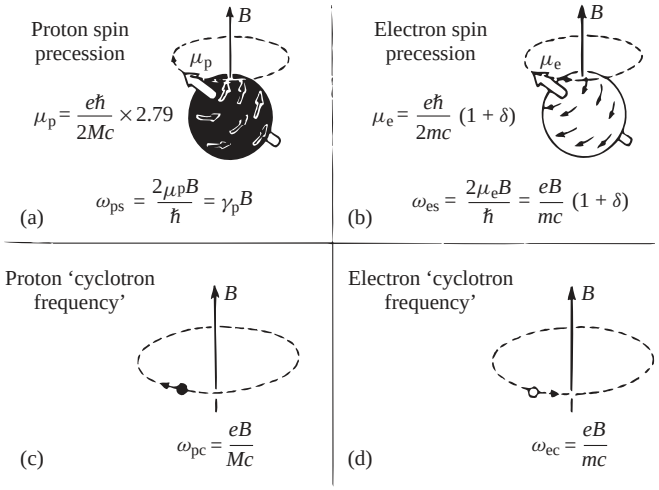

Figure 2 Four elementary magnetic resonance phenomena

'proton cyclotron frequency'. A free electron in a magnetic field likewise revolves in a circular orbit, with a frequency that we may call the 'electron cyclotron frequency'. These 'cyclotron frequencies' are governed simply by the particle's charge-to-mass ratio. If any pair of these resonance phenomena are compared, in the same magnetic field, the field strength cancels out and we are left with a relation between certain atomic constants. The experiment is thus reduced to the measurement of a frequency *ratio*.

The ratio of the proton spin-precession frequency to the proton cyclotron frequency has been determined by Hipple,[4] and by Bloch,[5] in ways very different but equally ingenious. (The direct result of this measurement is the value of the proton moment in nuclear magnetons.) In my laboratory we have measured the ratio of the proton precession frequency to the cyclotron frequency of free electrons.[6] The precession of the spin of a truly free electron has not been observed, but Kusch and his collaborators at Columbia, by combining the techniques of atomic beams and nuclear induction, have determined very precisely the ratio of the proton's precession frequency to that of the spinning electron in the hydrogen atom.[7] The results of these experiments have in one way or another improved the accuracy of the following constants of atomic physics: the Faraday, F; the specific charge of the electron, e/mc; the ratio of the mass of the proton to that of the electron, M/m; the dimensionless *fine-structure constant*, $2\pi e^2/hc$. They have also helped to test the new theoretical advances in quantum electrodynamics led by Schwinger.

We turn now to a very different subject, one whose rapid growth was surely not anticipated at the beginning of this work. That is the study of nuclear magnetism for the light it can throw on problems of molecular structure and molecular motion, problems rather close to physical chemistry. Indeed certain branches of this work are now being pursued in chemical laboratories. We are interested not in the mere occurrence of nuclear resonance at a particular frequency but in its finer details. The variety that we find is suggested by Figure 3. Here are shown several lineshapes typical of the proton magnetic resonance in a few simple substances. One way to record such a spectrum is to hold the applied magnetic field constant while slowly varying the frequency of observation. In every case the center of the resonance absorption occurs

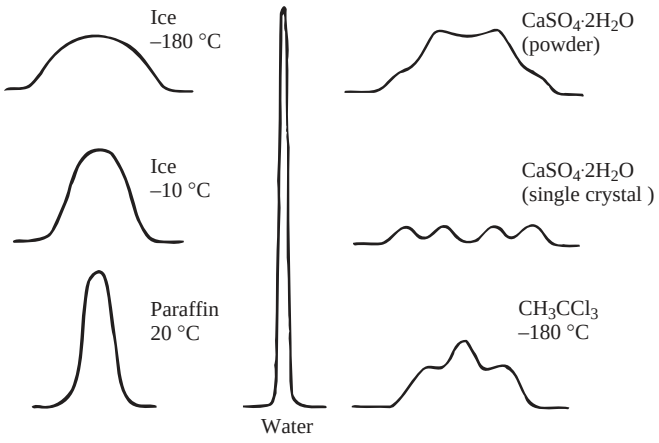

Figure 3 Lineshapes typical of the proton resonance in various substances. The line in water is not drawn to scale; it is actually much narrower and more intense than indicated

at very nearly the same frequency, in these substances. The linewidth, on the other hand, varies from some 50 kc s^{-1}, in the case of ice at low temperature, to less than a few c s^{-1}, in the case of a liquid like water. (The true width of the resonance in water is too small to be shown properly in the diagram.)

The effects shown here can all be traced to the action of the nuclear magnets on one another. In ice, each hydrogen nucleus is subjected not only to the field of our magnet, which might be several thousand gauss, but to the small magnetic field caused by each nearby proton in the crystal. Each nearest neighbor produces a field of a few gauss, more or less random in direction, with the result that the resonance absorption for the crystal as a whole is spread out over a corresponding interval in frequency. These 'local magnetic fields' are present in water, too, but their effectiveness is destroyed by the rapid molecular diffusion characteristic of a liquid. Two adjoining molecules remain neighbors so short a time (about 10^{-11} s) that their mutual influence is very slight. Thus *molecular motion* is the key to the striking difference between crystals and fluids in respect to the width of the nuclear magnetic resonance.

In many crystals, atoms or molecules occasionally jump from one position to another. Although such events are rare by most standards, they may occur frequently enough to affect the width of the nuclear resonance line. In ice, for instance, the line is distinctly narrower at -10 °C than at a much lower temperature. The narrowing indicates that each hydrogen atom undergoes a displacement within the crystal lattice several thousand times per second. The motion involved here is not the familiar thermal vibration of an atom in a perfectly elastic crystal, but an abrupt shift to a new site. Nuclear resonance studies have disclosed many unsuspected internal motions in crystals, and have helped to reveal the exact nature of motions already suggested by other physical or chemical evidence.[8]

If the magnetic nuclei in a crystal are clustered together in pairs, the action of the nuclear magnets on each other causes a doubling of the magnetic resonance line. Further distortion is caused by more remote neighbors, and the width of the pattern as a whole depends on the orientation of the nuclear pair with respect to the magnetic field. Rather complicated effects are possible, some of which are illustrated in Figure 3. From a complicated effect that is also well understood, one can usually get a good deal of information. These magnetic interactions are now rather well understood. I shall mention only one recent application of the technique to a chemical problem.

Groups of three equidistant protons in randomly oriented crystals give, characteristically, a line with three humps. The methylchloroform line, in Figure 3, is an example. We have a complete quantitative theory of this line structure.[9] Last year Richards and Smith[10] at Oxford, and quite independently Kakiuchi and others[11] in Tokyo, studied the proton resonance in perchloric acid monohydrate ($HClO_4 \cdot H_2O$) and certain related substances. This type of line was found. They were able to prove thereby that in those crystals the 'hydronium' ion, OH_3^+ exists, and to determine its dimensions. It is well known that hydrogen atoms are very hard to locate by X-ray diffraction. Here is an opportunity for nuclear resonance studies to supplement, in special cases, the more general methods of structure analysis.

Many nuclei have, in addition to an intrinsic magnetic dipole moment, an *electric quadrupole moment*. This is a way of saying that the electric charge of the nucleus is not distributed evenly over a sphere. One may think of the nucleus as either an elongated or a flattened ellipsoid. If such a nucleus is put into a nonuniform electric field, it experiences a torque, and precesses. (You will recall that the slow precession of the Earth's axis is a consequence of the ellipticity of the Earth and the nonuniform gravitational fields of the Moon and Sun.) The nuclei in many crystals find themselves in nonuniform electric fields arising from their immediate atomic surroundings. A nuclear electric quadrupole moment then manifests itself in a splitting of the magnetic resonance line. To put it another way, the energy associated with each of the possible orientations of the nuclear spin in a magnetic field is somewhat altered by the electric effect. This is illustrated in Figure 4. The trace in Figure 4 is the nuclear resonance spectrum of ^{23}Na in a crystal

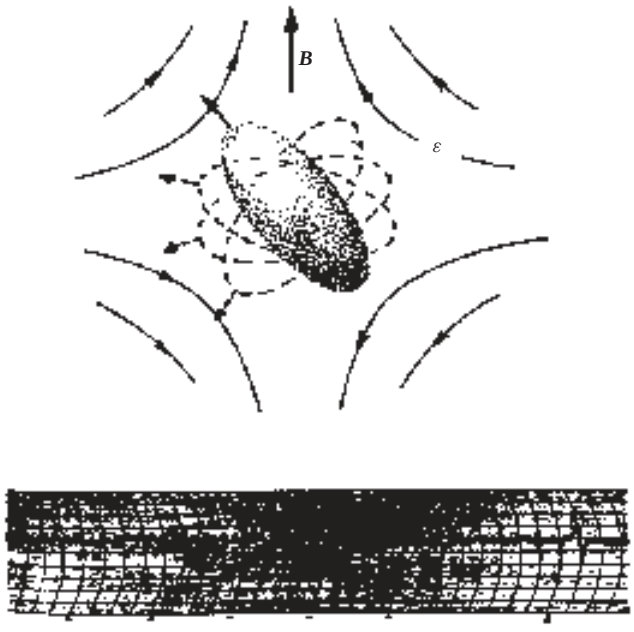

Figure 4 A nucleus with an electric quadrupole moment in a uniform magnetic field (***B***) and a nonuniform electric field (ε). Lower trace: ^{23}Na resonance in a single crystal of $NaNO_3$, showing splitting of magnetic resonance line into a triplet

of sodium nitrate. The line is widely split into a triplet by the quadrupole interaction. The number of components is always twice the nuclear spin I, so we have here a way of determining nuclear spins. This example is due to R. V. Pound who was the first to investigate these effects in crystals.[12]

Another interesting and fruitful branch of nuclear magnetism is the study of nuclear relaxation, by which I shall mean here the attainment of thermal equilibrium between the nuclear spins and their environment. Professor Bloch has already referred to the crucial importance of relaxation in all these experiments. In the first experiment of Torrey, Pound, and myself this question gave us much concern. Our approach was somewhat different from Bloch's and was based on a theoretical paper of fundamental importance by Professor Waller.[13] Waller, in 1932, was dealing with relaxation in electronic paramagnetism, but Torrey was able to adapt his results to our case, with the conclusion that equilibrium should certainly be reached within several hours. We then designed the experiment so that, even if so long a time were required, the resonance could still be detected. As it turned out, the precaution was unnecessary, but that was our introduction to a fascinating problem that has occupied our attention ever since.

I believe we now have a good understanding of nuclear relaxation in many —though not all—physical systems. Experimentally, we find that the time to establish thermal equilibrium ranges widely from hours, in some substances, down to fractions of a millisecond in others. I show only one example, and that mainly to clarify the meaning of the term relaxation. Figure 5 is a plot of the gradual approach to equilibrium magnetization of an originally unmagnetized crystal of ammonium bromide. This can be called, quite properly, a *cooling curve*. The nuclear spins, in order to align themselves with the magnetic field, must give off energy to the crystal lattice. They are coupled so weakly to the lattice that the transfer of energy takes more than several minutes. Actually the approach to equilibrium is exponential, and the corresponding time constant, in this example 32 s, is what one calls the spin–lattice relaxation time.

It may seem astonishing, at first, that so long a time is associated with an atomic process. But in fact, if one looks at the problem more closely, it is hard to understand why the time is not much *longer*. Moreover this crystal, at a somewhat higher temperature, has a relaxation time of only 0.01 s! The explanation of this, and of similar behavior in a wide class of substances, lies in internal molecular motions other than mere vibration. It is closely connected with the cause of line narrowing, mentioned earlier. The particular motion occurring in the ammonium halides is a sudden rotation of the whole tetrahedral ammonium ion inside the cubic unit cell.

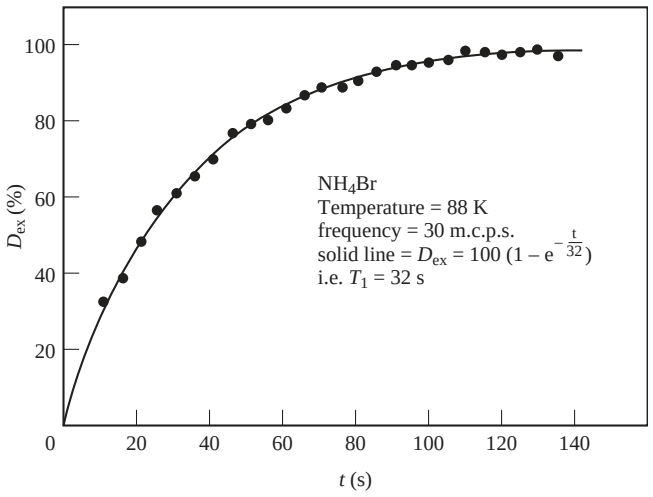

Figure 5 The gradual approach to equilibrium magnetization. The ordinate is proportional to the intensity of nuclear polarization

We have now a fairly general theory of nuclear relaxation,[14] a theory that has proved reliable enough to allow one to draw conclusions about the nature of the internal motion in a substance from the observed nuclear relaxation. My early collaborator, N. Bloembergen, has made essential contributions to this subject. Experimental work at Oxford and at Leiden has added much to our knowledge of other aspects of nuclear relaxation. In many respects this is only a new branch of a somewhat older subject, paramagnetic relaxation, in the study of which the Dutch laboratories and especially Professor Gorter, have long led. The problem of nuclear relaxation has a special attraction for the low-temperature physicist, because, as Professor Simon pointed out many years ago, nuclear magnetization offers a way toward extremely low temperatures, providing the nuclear spins can exchange heat with something else.

There remain several puzzling aspects of nuclear relaxation. In trying to understand them we find ourselves still returning to some of the ideas advanced 20 years ago by Professor Waller. While I speak of theoretical contributions to nuclear magnetism, I must mention also Professor Van Vleck, who has put the theory of linewidth on a rigorous basis, a notable advance.[15]

It is an old story in physics that higher resolving power leads to new effects. We remember that the magnetic moment of the nucleus was itself discovered through the hyperfine structure of lines in the visible spectrum. The nuclear resonance line in a liquid or gas can be remarkably narrow, as you have already seen. As soon as the reason for this was recognized, it became clear that the only practical limit on resolution was the inhomogeneity of the magnetic field applied to the specimen. Efforts were made in many laboratories to improve the magnets, and to use smaller specimens as well. With the improved resolution, it was found that identical nuclei, in the same applied field but in chemically different molecules, do not precess at exactly the same frequency. The explanation is simple: the magnetic field at an atomic nucleus differs slightly from the field externally applied because of the shielding effect of the electron cloud around the nucleus. In different molecules the atom's electron configuration will differ slightly, reflecting differences in the chemical bond. The resulting resonance shifts have been called 'chemical shifts'. They are only a nuisance to the experimenter interested in exact ratios of magnetic moments. But they are interesting to the physical chemist because they reveal something about the electrons that partake in the chemical bond.

No laboratory has more assiduously pursued high resolution than Professor Bloch's, where the striking example shown in Figure 6 was discovered.[16] This is the proton resonance in ethyl alcohol, seen under very high resolution. Each line comes from a chemically equivalent group of protons in the molecule, the intensity being proportional to the number of hydrogen atoms involved, 3 (methyl group), 2 (CH_2 group), and 1 (hydroxyl), respectively.

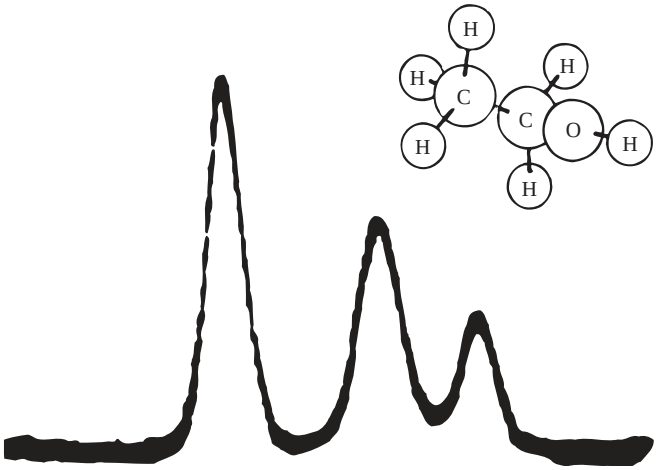

Figure 6 The proton resonance in ethyl alcohol, observed with high resolution. The three lines arise from the CH_3 hydrogens, from the CH_2 hydrogens, and from the OH hydrogen, respectively

I can now return to the splitting observed in the proton and deuteron resonances in Figure 1. This splitting does not arise from any effect on the applied field, but from an indirect coupling of the proton to the deuteron through the medium of the two electrons in the HD molecule. It is as much an intrinsic property of the HD molecule as is the optical spectrum of the molecule.[17] The splitting amounts to $43\,c\ s^{-1}$. I am sure we have only begun to explore the domain of very weak interactions—the 'audio spectrum' of molecules, if I may call it that.

This has been a long story and a complicated one. We are dealing not merely with a new tool but with a new subject, a subject I have called simply nuclear magnetism. If you will think of the history of ordinary magnetism—the electronic kind—you will remember that it has been rich in difficult and provocative problems, and full of surprises. Nuclear magnetism, so far as we have gone, is like that too.

REFERENCES

1. B. Smaller, *Phys. Rev.*, 1951, **83**, 812; F. Bloch, A. C. Graves, M. Packard, and R. W. Spence, *Phys. Rev.*, 1947, **71**, 551; H. L. Anderson, *Phys. Rev.*, 1949, **76**, 1460.
2. A. Bohr and V. F. Weisskopf, *Phys. Rev.*, 1950, **77**, 94.
3. H. A. Thomas, R. L. Driscoll, and J. A. Hipple, *Phys. Rev.*, 1950, **78**, 787.
4. H. Sommer, H. A. Thomas, and J. A. Hipple, *Phys. Rev.*, 1950, **80**, 487.
5. F. Bloch and C. D. Jeffries, *Phys. Rev.*, 1950, **80**, 305.
6. J. H. Gardner and E. M. Purcell, *Phys. Rev.*, 1949, **76**, 1262.
7. S. H. Koenig, A. G. Prodell, and P. Kusch, *Phys. Rev.*, 1952, **88**, 191.
8. H. S. Gutowsky, G. B. Kistiakowsky, G. E. Pake, and E. M. Purcell, *J. Chem. Phys*, 1949, **17**, 972.
9. E. R. Andrew and R. Bersohn, *J. Chem. Phys.*, 1950, **18**, 159.
10. R. E. Richards and J. A. S. Smith, *Trans. Faraday Soc.*, 1951, **47**, 1261.
11. Y. Kakiuchi, H. Shono, H. Komatsu, and K. Kigoshi, *J. Phys. Soc. Jpn.*, 1952, **7**, 102.
12. R. V. Pound, *Phys. Rev.*, 1950, **79**, 685.
13. I. Waller, *Z. Phys.*, 1932, **79**, 370.
14. N. Bloembergen, E. M. Purcell, and R. V. Pound, *Phys. Rev.*, 1948, **73**, 679.
15. J. H. Van Vleck, *Phys. Rev.*, 1948, **74**, 1168.
16. J. T. Arnold, S. S. Dharmatti, and M. E. Packard, *J. Chem. Phys.*, 1951, **19**, 507.
17. N. F. Ramsey and E. M. Purcell, *Phys. Rev.*, 1952, **85**, 143.

Biographical Sketch

Edward M. Purcell. *b* 1912. B.S., 1933, Electrical Engineering, Purdue University, Ph.D., 1938, Physics, Harvard University. Faculty, Harvard University, 1939–present. Radiation Laboratory, MIT, 1940–46. Discovered nuclear magnetic resonance in bulk materials with H. C. Torrey and R. V. Pound in December, 1945. Awarded the Nobel Prize in Physics in 1952.

Radda, George K.: The Development of In Vivo NMR in Oxford

George K. Radda
Oxford University, Oxford, UK

THE BEGINNINGS

Claiming priorities in scientific discovery is fraught with dangers, in that many discoveries are done at about the same time by several groups often working independently. Nevertheless, the paper from Oxford by Hoult et al., in 1974 is regarded by many as the beginning of in vivo NMR spectroscopy.[1] Admittedly, there were other publications before on cells and particularly one by Moon and Richards[2] where they introduced the idea that ^{31}P NMR can be used to measure intracellular pH values.

The Oxford work, like many other firsts, resulted from a set of happy coincidences and some bright ideas by clever young people. The environment was right to make new types of NMR measurements. The Oxford enzyme group had pioneered biological NMR in the 1970s and Rex Richards and his group, who made major contributions to the development of NMR instrumentation, and in particular to the use of superconducting magnets in Oxford, had moved into the Department of Biochemistry. My own group and his had been collaborating for some time in investigating biological membranes by phosphorus NMR and indeed had published several papers on bilayer structures, lipid asymmetry in vesicles, and the presence of chemical shift anisotropy in the phosphorus spectra of lipid bilayers arising out of a set of orientations.

We were more concerned at that time with enzyme regulation and, in particular, we had a long-standing interest in the mechanism by which phosphorylase *a* and *b* were controlled. We had done a series of NMR, spin-label and fluorescent studies, measuring the interactions of many ligands with phosphorylase and came to the conclusion that we were ready to predict how the enzyme should behave in vivo. When we did the appropriate calculations, we found that we were at least an order of magnitude out in our predictions, and this generated a lively discussion in the laboratory concerning what the difference might be between enzyme activities in solutions and those inside the living muscle.

It was during one of these discussions that I believe Steve Busby, one of our graduate students then, suggested that we should try and study the enzyme or at least some metabolic features of the enzyme in vivo in skeletal muscle by NMR. Although there were the usual objections as to why the experiment would not work, Busby, David Hoult, and others went away and obtained a small piece of muscle from the hind leg of a rat and did the first phosphorus NMR study on an intact piece of rat muscle. Immediately we observed high-resolution signals and it was relatively easy to identify these as coming from the major phosphate-containing metabolites: ATP, phosphocreatine and inorganic phosphate. As the muscle became anoxic in the NMR tube, the changes in the spectra observed were what one might have expected, and indeed the shift in the phosphate peak showed that the muscle became acidic (Figure 1).

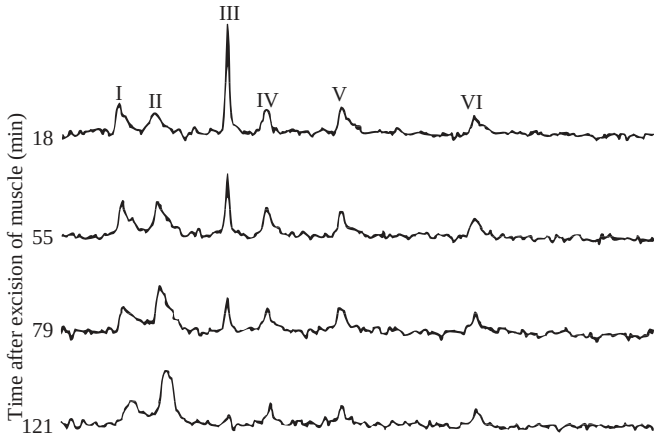

Figure 1 First ^{31}P NMR spectra from tissues. (Reprinted with permission from *Nature*, Ref. 1)

This was a very exciting observation and needed to be done correctly, so we tried to repeat the experiment many times before it worked again, largely because of spectrometer problems. The results were however consolidated and essentially the first set of observations explained why the phosphorylase activity we calculated was higher than that observed in vivo. This arose from the fact that the inorganic phosphate signal measured by NMR was considerably lower than the analytical values obtained previously by freeze extraction. So we had got an answer to the question we set out to investigate, namely, that the K_m value of phosphorylase for phosphate in vivo was much higher than the available phosphate concentration inside the resting muscle cell. We also recognized the general importance of our work for the study of metabolism in muscle and submitted a paper for publication in *Nature*. The manuscript was rejected on the grounds that it described highly specialized experiments, unlikely to be repeated in other laboratories and of no general interest. I think this was the only time in my scientific career that I appealed against an editorial decision. I explained in my letter that we had talked about this work already in a number of places, particularly in the United States, and it created a great deal of excitement. The Editor accepted our argument and published the paper.

FROM MUSCLE TO THE HEART

The results of these first studies were actively pursued by members of the two groups and we investigated perfused adrenal glands, developing frog embryos, and various skeletal muscle preparations in which we studied compartmentation of metabolites, intracellular pH, and the interaction of free ATP with magnesium. After the publication of our first paper and talks given at international meetings, a number of people had approached us with the possibility of some collaborative programs. Of these, in particular, Professor Doug Wilkie and Dr. Joan Dawson, well-known experts on frog muscle

from University College, London, collaborated with David Gadian and solved the physiological problem of keeping muscles oxygenated and contracting by using small muscles and carrying out the experiments at 4 °C. Also in 1976, Britton Chance came over and we carried out the first series of experiments on a small rat heart which could be placed into the 8-mm NMR sample tube that was contained within our existing magnet (Figure 2). This work, published in the *Proceedings of the National Academy of Sciences USA*, formed the background to a joint proposal between Britton Chance and myself to NIH to set up a collaborative program on cardiac bioenergetics.

It was at about this time that Pamela Garlick from the cardiovascular unit of the Hammersmith Hospital, directed by Professor J. P. Shillingford, had joined us as a research assistant, supported by the Science Research Council. Her experience on perfused hearts became important and she managed to perfuse mouse hearts in the 8-mm sample tube, keeping them alive and beating. Although these spectra and these studies were never fully published, they have appeared in several proceedings and book chapters as illustrative of the kinds of phosphorus spectra one could obtain from a live heart.

Again, Chance participated in our first experiments on perfused rat hearts, small enough to be put inside the 8-mm tube. These were done towards the end of 1976, when Chance became aware of similar interests at Baltimore. Indeed the excellent and objective book by Don Hollis under the title 'Abusing Cancer Science' described how they first started phosphorus NMR on perfused hearts with Bill Jacobus following a visit to Baltimore by Bob Shulman who gave a talk about phosphorus NMR in *E. coli*. So these two groups worked on the same problem independently, but they communicated to us the contents of their paper, on perfused rat heart, which they published in *Nature*. We were able to refer to this work prior to publication in our own paper that was published in *Biochem. Biophys. Res. Commun.* the same year, that is in 1977.

The realization that we could do the physiology much better and study adult rat hearts if we were able to put a much larger sample tube into our magnet, led us to a proposal to the British Heart Foundation requesting support for the construction of a new wide bore high-field superconducting magnet, specially designed by Oxford Instruments, for biochemical investigations of the heart. As far as the British Heart Foundation was concerned this project was a bit of a gamble, and they sent down to Oxford two eminent professors of cardiology to investigate what this was all about. After all, no one had asked them before to pay £25 000 for some niobium/titanium wire from which a magnet would be wound. Sir John McMichael, then a retired Professor of Cardiology, previously at the Hammersmith, and Professor Peter Sleight, Professor of Cardiology at Oxford, came to the laboratory and Pamela Garlick managed to show them a perfused mouse heart beating in the spectrometer and the way the spectrum was built up by repeated Fourier transform scanning. We then turned off the oxygen supply and they watched, admittedly with a rather poor time resolution, the disappearance of phosphocreatine and eventually of ATP during the ischaemic period.

Sir John McMichael went back to the British Heart Foundation very excited about the possibilities of looking at the biochemistry of the intact animal heart and recommended support for our venture. With help from Rex Richards and others, and Oxford Instruments, a new magnet was designed and very rapidly constructed. We had the system in the laboratory and working by mid-1977. Our NIH application with Britton Chance was also successful, and we began our joint collaboration using NMR of perfused organs. Our 180 MHz 4.2-T wide bore magnet was used for a whole range of experiments over the next 15 years, when we replaced it with a higher field system.

More work on perfused hearts was followed by a completely new study on transplanted kidneys in the rat, carried out by a surgeon, Peter Bore, who used to come down from Liverpool often after having finished a human renal transplant operation, working in close collaboration with Peter Sehr and John Seeley. Chance, joined by Ian Silver from Bristol, came to try some ^{31}P measurements on excised animal brain, but we couldn't keep them alive long enough. Eventually we studied brain from hibernating hedgehogs as the cooled brain lasted long enough to give good ^{31}P NMR spectra. The results were presented aptly in 1979 at a symposium honoring Mildred Cohn. Much of this early work, including references to results of other groups, can be found in *Annual Reviews of Physiology*.[3]

FROM THE SURFACE COIL TO HUMAN MUSCLE

Two American postdocs joined the program in 1978/9, Jo Ackerman and Tom Grove. Following the kidney transplantation experiments, we decided to try and detect metabolism in vivo inside the animal following surgery. Gordon Wong, a graduate student, together with other members of the group tried to use solenoid coils to look at kidneys in animals but was unable to eliminate signal from adjacent muscle. It was on the basis of this experiment that the suggestion was made that we should just simply squash the solenoid coil into a single loop and try to look at the kidney that way. This was the idea of the surface coil that Jo Ackerman and others immediately used for demonstrating that muscle and brain metabolism in the intact rat can be quantitatively studied in this way.

This exciting experiment was written up for *Nature* and indeed published there, but not until we had sought advice about its potential patentability.[4] The National Research and Development Corporation who was the government organization advising all the research grant holders on these matters, told us that the idea and experiment were not patentable. Looking back and looking at the wide use of surface coils now, both in imaging and spectroscopy, we wonder how sound that advice was in 1979.

The use of surface coils, however, yet again transformed completely the possibilities of in vivo spectroscopy. Chance again visited us and saw the experiments we had done on skeletal muscle. I drove him back to Heathrow airport where we had a long wait for his flight and we discussed what possibilities might arise from the use of such surface coils. It was, I believe, then, at Heathrow airport, that we came to the conclusion that it ought to be possible to investigate human limbs if only we had a horizontal very wide bore, high-field magnet available. Chance suggested that it would be of considerable interest to study patients with peripheral vascular disease and map out where metabolism showed irreversible or reversible damage in the muscle. This measurement could help the surgeon in deciding whether or where to amputate.

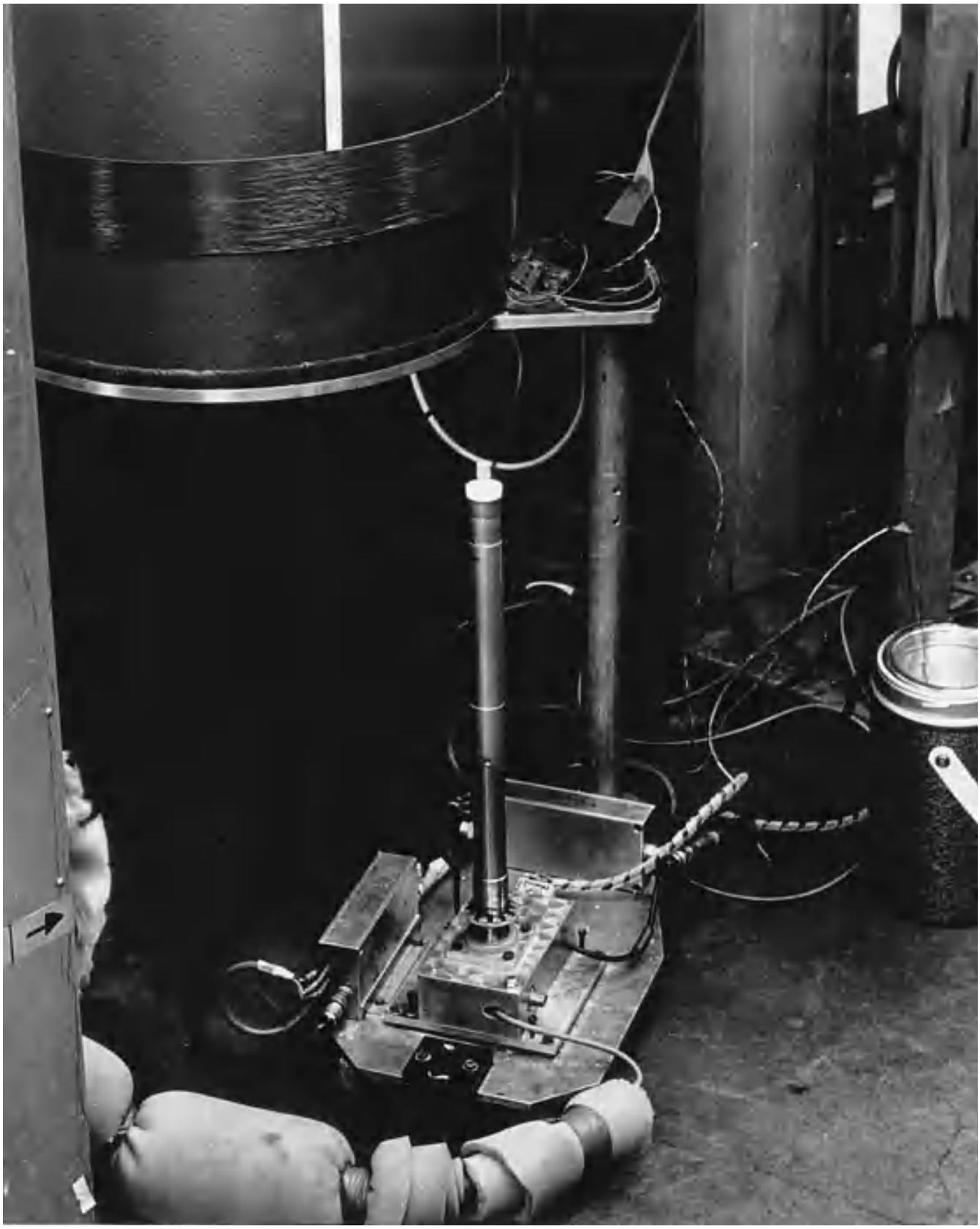

Figure 2 The 8-mm probe and part of the 7.5 T superconducting magnet used for the first and early isolated tissue and organ experiments

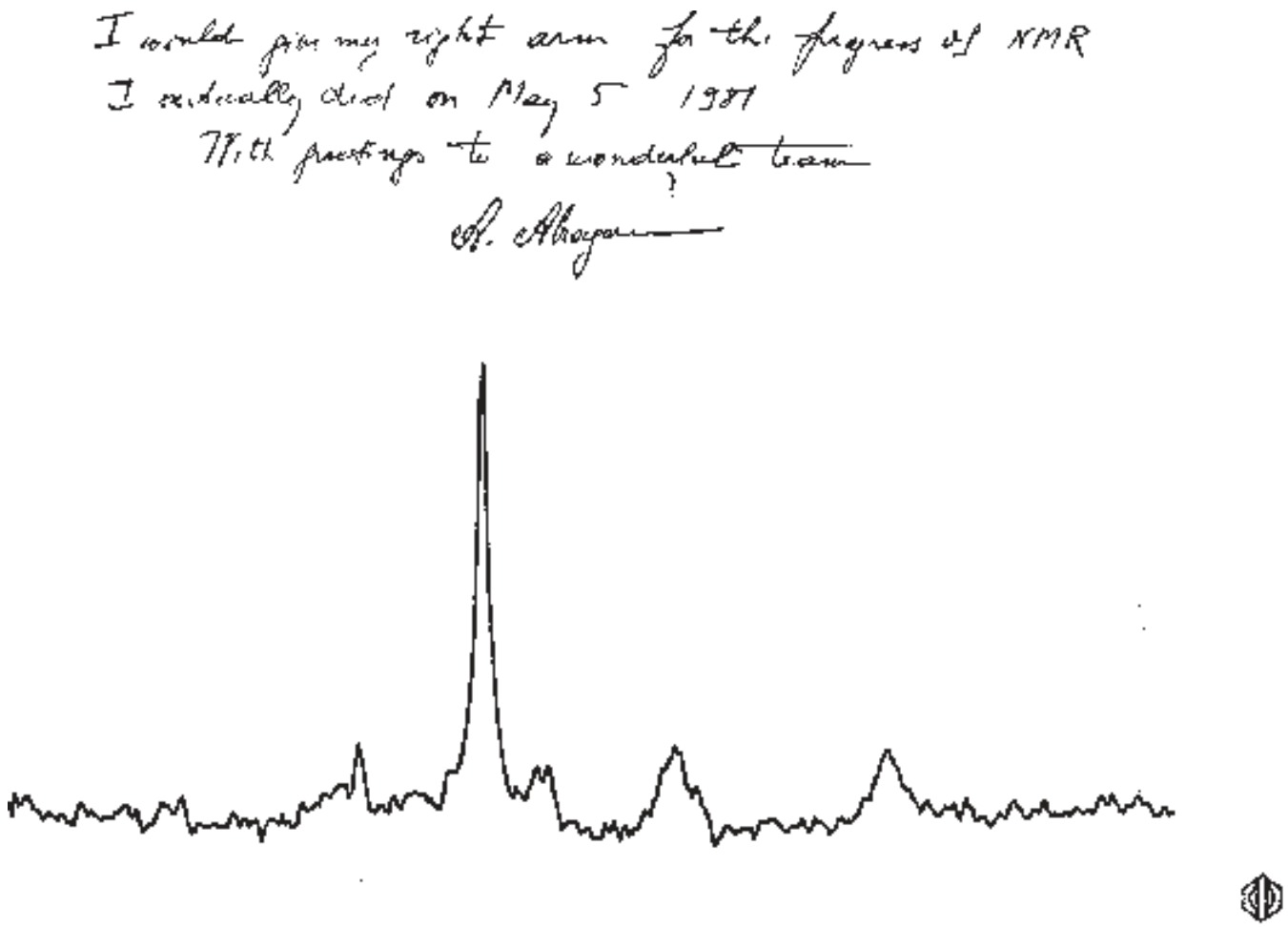

Figure 3 A ^{31}P NMR spectrum of the arm muscle of Anatole Abragam

Both Chance and I approached Oxford Instruments, and with their help a new magnet was designed to operate at 2 T in a horizontal configuration with a clear bore of 30 cm. One of these magnets was delivered to Philadelphia and the other to Oxford, again following support from The British Heart Foundation for this stage of the development. But prior to this, Philadelphia already had a small bore (18 cm) horizontal magnet and Chance managed to put his leg inside it and obtained a ^{31}P'NMR spectrum. The resolution was not very good but Chance's leg in the magnet impressed the *Proceedings of the National Academy of Sciences USA*, where the first spectra were published. The work done in Oxford initially in collaboration with Wilkie and Dawson on arm muscles appeared in the *Journal of the Physiological Society* in 1980.

THE FIRST CLINICAL RESULTS

Having demonstrated the feasibility of obtaining phosphorus spectra on human arms and legs, we decided to embark on a clinical program on muscle diseases. This required that we should build up a team consisting of clinicians as well as biochemists and physicists and move our magnet to a hospital environment. This was achieved following support from The British Heart Foundation and now also the Medical Research Council in early 1981.

In the meantime, we investigated our first patient on 26 January 1981 at 11.45 a.m. (in those days we took very detailed notes), with the magnet still being in the Department of Biochemistry. This was the patient who was shown to have McArdle's Syndrome, i.e. a lack of phosphorylase activity, who showed a clear absence of acidification during exercise. The results of this study, the first clinical study using magnetic resonance spectroscopy, were published in the *New England Journal of Medicine*.[5]

Having moved to the Radcliffe Infirmary in April 1981, we were ready to get down to investigating a whole range of muscle diseases in earnest. We had many interested visitors to see the set-up in the hospital and we took these opportunities to add another control subject to our records. One of these was Anatole Abragam, whose remarks and muscle ^{31}P NMR spectrum are shown in Figure 3.

In order to enhance our interaction with the clinical community, we had a number of open discussions and instituted our Friday morning 8 a.m. clinical meetings. Our first record for these meetings goes back to 5 June 1981 and we have kept up these weekly discussions as well as detailed records of all the patients we have studied since then. In parallel we continued to support the clinical studies with

investigation in the laboratory, on animal muscle, heart, brain, and kidney.

EXPLORING ^{31}P NMR

The period of 1979–82 saw a whole range of new experiments and exciting visitors to the laboratory. Among these, Tom Grove was able to do the first open-heart surgery on an animal and measure metabolic response in the live heart. In vivo kidney experiments brought Bob Balaban and Sheldon Adler to join the group to try and apply some of the methods to renal biochemistry and medicine. Sheldon Adler took a great interest in the clinical developments and contributed much to the early discussions on the design of patient studies. The clinical program owes much to Doris Taylor and Peter Styles, now tenured members of the MRC Unit, and past members, David Gadian, Peter Bore, and Brian Ross.

Professor George du Boulay, the distinguished neuroradiologist from London, came to do some experiments with us and collaborated with Keith Thulborn on measurements of blood flow and metabolism in stroke models in the gerbil and on a monkey. Keith Thulborn's early work with Peter Styles and John Waterton, who is now running the NMR facility at ICI, on flow and oxygenation of the blood formed the basis of the now widely quoted mechanism for susceptibility effects in functional imaging, the work having been published in 1982. In the meantime, soon after the muscle measurements with Doug Wilkie, Truman Brown (then at the Bell Laboratories) came over to help us with the first saturation transfer studies on the creatine kinase reaction in skeletal and heart muscle. The results were reported at Britton Chance's 65th Birthday Symposium in Philadelphia in July 1978.

Of course, others elsewhere, Bottomley and Nunnally in Baltimore, Ingwall in Harvard, were also close on our heels or maybe in parallel doing magnetization transfer experiments. On the perfused heart work, Arnie Schwartz from Cincinnati, Andi Seymour, and Steve Williams have all made major contributions in establishing the technique as a valid physiological and biochemical tool to study the pharmacology as well as basic control features of the heart. Paul Matthews joined the group in this work.

The comparison of control of cardiac and skeletal muscle energetics, as studied by Eric Shoubridge in animals where phosphocreatine was depleted and by Paul Matthews in the heart, was followed by the development of detailed exercise protocols for humans in what we called the Clinical Magnetic Resonance Laboratory at the Radcliffe Infirmary. These protocols were used to study groups of carefully selected patients with, for example, mitochondrial myopathies, muscular dystrophies, and a whole range of other conditions. These early results were already well documented and are still often used by us in comparative analyses of the extensive patient data base which we have now accumulated.

BIOCHEMISTRY OR MEDICINE?

For a biochemist with no knowledge in medicine, the possibility of leading a team investigating clinical problems has been both daunting and exciting. It was a happy coincidence that with a long-standing interest in the control of phosphorylase and glycogen metabolism, the first patient we examined had phosphorylase deficiency. But the decision to take on the commitment of a clinical NMR spectroscopy program was no coincidence and required much preparation and thought.

I personally spent a year (1978–79) talking to various clinicians getting their views, and to my own group involved in the NMR studies, to decide whether we were the right people to set up a clinical research facility if funding was available or whether we should stay with the basic biochemical investigation and pass on to someone else the possible development of a clinical facility. We had no experience in medical matters except for our collaboration with clinicians in our work on heart and kidney. A key meeting took place on 28 November 1979 at Wolfson College, Oxford on the 'Applications of NMR to Medicine'. The purpose of this meeting was to discuss the potential of spectroscopy in clinical research and clinical practice. The participants, by invitation only, included members of my own research group, seven representatives of the English, Scottish, and Welsh Health Departments, officials from the Medical Research Council (MRC), key individuals from Oxford Instruments, who were considering setting up a separate company to develop systems for clinical spectroscopy, and a number of clinicians (largely from Oxford). Talks were given by David Gadian (introduction to NMR), Derek Shaw, Oxford Instruments, now GEC (methods in medical NMR), myself (^{31}P NMR in biochemistry), Peter Hanley, Oxford Instruments (magnets for whole body ^{31}P NMR), Peter Bore (medical applications), and concluding remarks by Rex Richards. There followed an extensive discussion on important clinical problems where spectroscopy might be useful, with significant contributions from John Ledingham (now Associate Clinical Director of my MRC Unit), Bheeshma Rajagopalan (now Senior Clinician in my Unit), and Brian Ross; Roy Gordon from Oxford Instruments (now Bruker) was also present.

The outcome of this meeting was that we decided to try and develop clinical phosphorus spectroscopy, with the 30-cm bore topical magnetic resonance system being an intermediate stage to the final 60-cm whole body magnet. Oxford Instruments set up Oxford Research Systems, the Department of Health agreed to contribute funding and the MRC were going to evaluate a scientific proposal from us. The story of the 2-T small system (we called it Stage 2) has already been given above.

CLINICAL SPECTROSCOPY ON THE WHOLE BODY MAGNET

Once the MRC decided to fund our program, and the cost of the whole body magnet was secured jointly from the Department of Health and the Department of Trade, we could plan for Stage 3. The MRC paid for the cost of a building and the Regional Health Authority, together with the University, agreed to assign a prime site at the John Radcliffe Hospital where our temporary building (temporary in the sense that it was designed for about 10 years) could be put up.

It was at that point that, with MRC support, Bheeshma Rajagopalan joined the team and both he and Peter Styles were appointed by the Medical Research Council to tenured posts.

Thus the core team consisted of a physician, a physicist, and a biochemist (myself). We were also given support to build up a team around these three people. The building operation and the 2-T magnet construction commenced in the middle of 1982. By March 1983, the new Clinical Magnetic Resonance Facility at the John Radcliffe Hospital was completed and the magnet was delivered to the facility in the autumn of that year. The setting up of the system was entirely Peter Styles's responsibility and within a relatively short period we were examining human volunteers by ^{31}P NMR, starting with members of the group and the laboratory. Our records show that the first patient was investigated on the 6 January 1984 in this new clinical building, a patient that had previously been studied in the small magnet with a muscle problem that we later identified as being a deficiency of the sarcoplasmic reticulum Ca^{2+} ATPase.

Styles and C. A. Scott (Rutherford Appleton Laboratory) and later a D.Phil. student, Martin Blackledge, developed rotating frame and depth selection techniques to investigate organs inside the human body in addition to the volume selection technique of topical magnetic resonance that was available at the beginning of the set-up. An early recognition of a cerebral mitochondrial disease was followed by studies on liver diseases and a variety of brain tumors and brain disorders, largely orchestrated by Rolf Oberhaensli who joined the group in 1984. Rotating frame one-dimensional imaging on the liver demonstrated by Styles and Scott was published in 1985, and the method became extensively used to investigate brain and later heart in human volunteers and patients.[6]

Throughout the period the generous support of The British Heart Foundation was available and, indeed, in 1984 with the new building and the new magnet being available, The British Heart Foundation set up a group—The British Heart Foundation Clinical Magnetic Resonance Group—and later established a chair of Molecular Cardiology in the University of Oxford for myself which commenced in 1984. This, together with program grants support from the Medical Research Council and the early success of the method, has established us as a credible research unit within a major clinical medical school with no responsibilities towards diagnosis and patient care. Our clinicians, in particular Bheeshma Rajagopalan, have participated and continue to participate in clinical work in the hospital on a voluntary basis, and this helps enormously with the continuation of the smooth contact between the basic research group and clinicians responsible for patients in the hospital.

THE MEDICAL RESEARCH COUNCIL UNIT

On the 1 April 1988, the MRC set up a new unit for us, the Biochemical and Clinical Magnetic Resonance Unit. We continued to operate on two major sites, in the Department of Biochemistry in the University and at the John Radcliffe Hospital in the Clinical Magnetic Resonance building. The unit works together with the British Heart Foundation Clinical Magnetic Resonance Group. Our primary aim is to investigate the biochemical basis of human disease processes through the development and application of NMR spectroscopy in vivo.[7]

As of now, August 1993, we have detailed records of close to 4000 patient investigations by ^{31}P NMR. The overriding consideration in achieving our aim, however, is the close integration of the basic scientific work with the clinical program. This requires regular discussions, collaborative projects within the unit, and some organizational help. On the last point, since the beginning of our clinical plans in 1980 we instituted an 'annual retreat' for the whole group, where everyone gives a talk and participates in the discussions. The first three of these were held in the oldest inhabited country house in England, Charney Bassett Manor in Oxfordshire, and nowadays they take place in a small Cotswold town. It is there that we evaluate our achievements and weaknesses in the past year and formulate strategy for the next.

With a new MRC Magnetic Resonance Spectroscopy building, and a new 2-T magnet from August 1992, the unit continues to learn new biochemistry using NMR and to investigate control, bioenergetics, and adaptation in health and disease.[8]

REFERENCES

1. D. I. Hoult, S. J. W. Busby, D. G. Gadian, G. K. Radda, R. E. Richards, and P. J. Seeley, *Nature (London)*, 1974, **252**, 285.
2. R. B. Moon and J. H. Richards, *J. Biol. Chem.*, 1973, **248**, 7276.
3. G. K. Radda and P. J. Seeley, *Annu. Rev. Physiol.*, 1979, **41**, 749.
4. J. J. H. Ackerman, T. H. Grove, G. G. Wong, D. G. Gadian, and G. K. Radda, *Nature (London)*, 1980, **283**, 167.
5. B. D. Ross, G. K. Radda, D. G. Gadian, G. Rocker, M. Esiri, and J. Falconer-Smith, *New Engl. J. Med.*, 1981, **304**, 1338.
6. P. Styles, C. A. Scott, and G. K. Radda, *Magn. Reson. Med.*, 1985, **2**, 402.
7. G. K. Radda, *Science*, 1986, **233**, 640.
8. G. K. Radda, *FASEB J.*, 1992, **6**, 3032.

Acknowledgements

Many people have contributed to this development but the list would be longer than the article. Some special contributions were highlighted in the text. Here I wish to acknowledge the support of the late Professor Rodney Porter and also that of many clinical colleagues in Oxford. Only few people have seen the whole of this story, but all that participated at various periods will have benefitted from the willing help and dedication of Sue Bailey. In this unit the philosophy is that everyone contributes to the program, and that without the enthusiasm of the young students and postdoctoral fellows the work would be much less interesting.

The British Heart Foundation, the Medical Research Council, and many other private- and public-funding groups have given us financial support, for which I am most grateful.

Biographical Sketch

George K. Radda. *b* 1936. B.A. 1960, Chemistry, M.A., D.Phil., 1962, University of Oxford UK. (Introduced to NMR by Rex Richards.) Successively junior research fellow, lecturer (Biochemistry) and Professor (Molecular Cardiology) University of Oxford, 1962–present. Approx. 650 publications. Research specialties: in vivo NMR, clinical spectroscopy, control of bioenergetics.

Radeglia, Reiner & Jancke, Harald: The History of the NMR Laboratory in the Former Central Institute for Physical Chemistry of the East German Academy of Sciences in Berlin

Reiner Radeglia & Harald Jancke

In April 1964 a JEOL 60 MHz NMR spectrometer (JNM-3H-60) was delivered to the Berlin-Adlershof NMR Laboratory which at that time belonged to the so-called German Academy of Sciences, Berlin. This spectrometer was designed primarily for liquids, but it also came with a solids accessory. Although this event might be viewed as the birth date of our NMR laboratory, in fact it was not, since solid state, physical NMR research was already well under way in the laboratory of physicists I. Ebert and G. Seifert.

However, before describing further the chronological development of our laboratory, let us first paint a brief picture of the state of research in the natural sciences and the role of the Academy in the former East Germany (Deutsche Demokratische Republik, DDR). In 1964 the Berlin Wall was three years old. Although the bitterness of the East German people over this wrenching event was in sharp contrast to the hopes of the East German government, the people had a cautious optimism for a positive development in the economy and the government had high hopes for research in the natural sciences. The Academy, along with the teaching system, which was based on a Russian model, was comprised of a series of scientific research institutes. It was supposed to play an advanced, central role. In contrast to the universities, the political climate in these institutes was relatively liberal, although it did vary greatly from institute to institute and depended strongly on the personality of the institute director. For the economy in general, and hence also the Academy, there was a severe shortage of hard currency for investment. Modern research instruments could only be imported within certain limits. In addition, the government wished to minimize further embargoes and at the same time wanted to encourage their own manufacture of modern analytical instruments in the DDR.

Already in 1958 an Institute for Instrumentation Manufacture had been founded. In this Institute was located the 'Physical Methods of Analytical Chemistry' Division whose primary task, with the help of instruments imported from Western countries, was the methodical study of instrumentation and the development of applied research in order to keep abreast of state-of-the-art know-how in modern analytical instruments.

In 1961 H. Kriegsmann, a chemist, assumed the leadership of this group. He had broad experience in the characterization of inter- and intramolecular interactions in the area of organosilicon and organotin compounds. He had worked with both infrared and Raman spectroscopy as well as gas chromatography and had used a combination of these tools in the characterization of complex molecular interactions. The chemist, G. Engelhardt, a student of Kriegsmann, and the physicist, W. Storek, who had experience in building NMR instruments, comprised the first laboratory team. Shortly thereafter the physical chemist, R. Radeglia, who had experience in NMR applications, and the chemist, H. Jancke, joined the group. The areas of research for this group included structural studies via normal high-resolution NMR spectroscopy and a wide range of applied experiments, as service work or in direct collaboration with colleagues from other Institutes of the Academy, from the Universities or from industry. The principal research work, which was decided in consultation with other laboratories of Kriegsmann's group, was: (i) the proof and characterization of intramolecular interactions of substituted silanes, especially through the use of one-bond carbon–hydrogen coupling constants [$^1J(^{13}C, ^1H)$] and (ii) proton NMR chemical shift measurements for the quantitative characterization of intermolecular interactions as well as comparison with the results of other spectroscopic and thermodynamic methods (hydrogen bonds in alcohols and silanols, ASIS and LIS effects in merocyanines).

Thus, for example, we wanted to answer the question as to whether silanols were more strongly associated than the corresponding alcohols. In this case we measured the concentration and temperature dependence of the chemical shifts of the hydroxyl protons of $(CH_3)_3SiOH$ and $(CH_3)_3COH$ dissolved in inert solvents. It was found that the silanols were more strongly associated because of the formation of cyclic trimers.[1] In addition, heavy nuclei were also of interest, but only ^{31}P and ^{19}F were accessible experimentally. The isolation brought about politically became progressively more noticeable. Thus, it became much more difficult to invite Western colleagues and the ability to travel to Western countries was sharply limited to a small circle of scientists; anyone with an immediate or closely related family in West Germany was not even considered (in this respect, it was quite surprising that Engelhardt was permitted to collaborate on ^{31}P experiments with Fluck in Heidelberg in 1966). For this reason there was strong collaboration with other colleagues in other parts of the DDR. There was close and friendly contact with the new NMR laboratory of the Organic Institute (E. Gündemann) which carried out analytical structure measurements, and the Inorganic Institute (A.-R. Grimmer, D. Müller) which was especially interested in methods of structure analysis in solids. Various scientific contacts with friendly colleagues in the corresponding institutes of other Eastern block countries were especially fruitful. For example, there were very productive exchanges with J. Schraml (Prague), G. Schneider (Szeged), S. L. Spassov (Sofia), and Z. Kecki (Warsaw). These collaborations were an important source of information for us, since these colleagues, compared with us, could travel virtually 'freely'. The very close contact between Engelhardt and E. Lippmaa (Tallinn, Estonia) was especially important for our laboratory. With this collaboration it was possible for us to carry out experiments on the at-that-time rare nuclei carbon-13 and silicon-29. The first rare nuclei experiments were carried out in Tallinn using a continuous wave spectrometer with a signal averager.

The year 1970 was an interesting one for East Germany for two reasons: with the growing relaxation of the cold war tension, there developed a growing mistrust of all influences from the West. The official policy was called 'isolation'.

At the same time one still hoped for scientific stimulation of the economy. A reform of the Academy was instituted which was supposed to strengthen the political influence of the state (Communist) party in the Institutes and to encourage a change in research emphasis toward more applied problems of importance to the economy. Our research group, which in a roundabout way had long been attached to the Central Institute for Physical Chemistry, and especially Dr. Kriegsmann as its Director, was suspected of giving research results to Western colleagues. He was therefore at least guilty of espionage and of collaborating with 'enemies of the working class'. Although the investigation 'through proper channels' did not uncover any punishable deeds, further contacts with the West were forbidden and Dr. Kriegsmann and all of his co-workers were considered to be 'politically undependable'. That had a number of unpleasant consequences. For example, Radeglia's recommended appointment as Professor of Physical Chemistry at Merseburg and Jena was not permitted. Scientific publications were in general not welcome from the group and were quite forbidden in 'Western' journals.

Fortunately, the close collaboration between Engelhardt and Lippmaa was not disturbed and in 1972, in spite of the problems, we were able to obtain a 100-MHz PFT-100 spectrometer with a Fourier transform accessory (also from JEOL) and a Nicolet NIC 1085 computer. As a consequence, the research program was broadened in a number of directions:

1. ^{13}C characterization of steric interactions (of steroids) and of π-electron systems (e.g. polymethines).
2. Development of FT NMR methods for quantitative analysis.
3. Development of relaxation time methods for the study of molecular dynamics.
4. ^{29}Si NMR for the characterization of substituted silanes, silicons, and silicon resins as well as silicates in aqueous solution.
5. Quantum mechanical theoretical interpretation of NMR parameters.

After the proton spectra of simple polymethines X–$(CH{=}CH)_m$–CH=Y with X = $N(CH_3)_2$ and O^- and Y = $N(CH_3)_2^+$ and O (cyanide, merocyanine, and oxonole) had been studied, one could test whether an analogous relationship for the π-electron structure held for the ^{13}C NMR parameters. After preliminary measurements carried out in Lippmaa's group, it was possible to show with the new spectrometer that there was a corresponding alternation of the π-electron density and the carbon-13 chemical shifts and the coupling constants $^1J(^{13}C, ^1H)$.[2]

Kriegsmann and his group had been interested for a long time in the characterization of organosilicon compounds. Now through the use of ^{1}H NMR spectroscopy it was possible to analyze the complex isomeric structure of cyclosiloxanes. Indeed, the availability of silicon-29 NMR made possible a significant advancement in the description of silanes, siloxanes, and polyoxanes. At this time we were working in a large international 'family' [Harris (UK), Levy (USA), Marsmann (FRG), Schraml (Czechoslovakia) and Pestunovich (USSR)] in the development of liquid phase ^{29}Si NMR.

The silicon chemical shift is, in an especially sensitive way, dependent on the nature of long-range substituents. This observation led to hopes of great progress in the area of the chemistry of inorganic silicon compounds. It was now possible to develop a wide range of ^{29}Si NMR applications in very close collaboration between the Tallinn laboratory and Jancke, Engelhardt, and the newly arrived physicist D. Zeigan.[3] Since a MAS/CP spectrometer was available in Tallinn for high-resolution solid state studies, we developed a wide range of experiments for characterizing solid silicates, especially zeolites, which were of special interest for the Institute as adsorbents and catalysts.

As a result of the oil crisis in 1973, there was a widespread need to develop analytical methods for the detailed structure of oil and coal (the basic methods had already been developed in the 1960s). Because of the great expense of imported crude oil, there was very great interest in East Germany to make chemical use of the resources available from brown coal (a locally abundant, cheap, but high sulfur content, oil). The Academy was given the task of developing the analytical instrumentation for this work. In collaboration with the petrochemical industry, we developed methods for measuring the individual components through the use of a combination of the information available from both proton and carbon-13 spectroscopy.

The theoretical work was concerned with 'sum-over-states' calculations of coupling constants; this work was done in collaboration with Th. Steiger from the theoretical chemistry section of the Institute. The peculiar dependence of the silicon chemical shift on the electronegativity of the substituents in simple silane derivatives $(CH_3)_{4-n}SiX_n$ (with X = OCH_3, F and n = 0–4) was the source of much speculation about the role of $p_\pi - d_\pi$ bonding. Engelhardt wanted to present his new experimental results, including a theoretical interpretation, at the 1973 European Molecular Spectroscopy Conference in Tallinn. That was the stimulation for Radeglia to develop a simple chemical shift model based on theoretical work of Letcher and van Wazer. His new model was able to explain silicon chemical shifts without the need for $p_\pi - d_\pi$ bonding. The physicist, Renate Wolff, developed this work further in her Ph.D. dissertation. Using better basis functions (CNDO/2), she was able to show the correctness of the fundamental importance of the role of the charge on the silicon atoms, the excitation energy, and the possible $p_\pi - d_\pi$ interaction.[4]

The PFT-100 spectrometer did not have a programable pulse sequence capability nor phase-shifting capability; consequently experiments such as APT (attached proton test) and spin echo refocusing experiments were not possible. Inverse gated decoupling experiments could not easily be undertaken because the decoupling rf power could not be turned on during the instrument dead time. In spite of this, one could, by selecting a correspondingly longer dead time, analyze CH_n functional groups (a version for poor people). In collaboration with other laboratories, which in the meantime had obtained more modern spectrometers, we were able to analyze such structural groups properly.

Two very joyful events lifted our hopes for the further development of the scientific life in our laboratory. Firstly, H. J. Osten was able to spend a year working with Cynthia Jameson (University of Illinois Chicago) as a postdoctoral fellow. Since numerous bureaucratic rules and regulations had to be overcome, the trip had to be postponed for a year. This collaboration was also extraordinarily productive in the year after his return and led to further collaborative work on the effects of molecular vibration and rotation on the chemical shift. Secondly, the long-awaited importation of a Bruker MSL 400 spectrometer for the study of both solid and liquid samples was finally realized. At last we had the capability to carry out

CP MAS experiments on zeolites and other solid samples in our own laboratory and to undertake the entire range of 2D NMR experiments.

Due to the relaxation of political tension and the success of the West in improving travel opportunities for East German citizens, Engelhardt had the chance to leave the restrictive regulations in the DDR and to move to West Germany. His book 'High-Resolution Solid-State NMR of Silicates and Zeolites', co-authored with D. Michel (Leipzig), was published from his new address and was a precursor of the reunification of Germany. But no one dared to look that far into the future and the colleagues that he left behind concentrated their work on the new spectrometer. The solid state spectroscopic work on the zeolites was continued by B. Zibrowius and W. Storek. Building on earlier work, the quantitative carbon-13 analysis of hydrocarbon mixtures took on a greater meaning. Dr. Radeglia, who since 1975 had taught at the Technical University of Merseburg (a University devoted primarily to analytical topics including nitrogen-15 NMR and especially photo-CIDNP effects) had to cut back sharply his active participation in the laboratory in March of 1988 due to health reasons; his work in Merseburg was given up entirely.

The political turning point in East Germany began in the fall of 1989. Members of the NMR laboratories of the Academy played an important part in the process of making the Institutes more democratic. The fall of the Berlin Wall brought freedom to travel and one saw that the reunification of Germany might take place. Old and new contacts with colleagues in West Germany and indeed in the entire Western world could now develop unhindered by political directives, letter censorship, and other restrictions. There was a joyful wave of sympathy which expressed itself also in new computers, new programs, and other research needs, speaking invitations and so on.

For several years it had been possible, using various ab initio calculations, to calculate quite accurately the magnetic shielding of a resonant nucleus due to the effects of the electrons in a chemical bond and to predict the chemical shift with good accuracy. Using the IGLO program provided for us by Professor Kutzelnigg and with a grant from the Chemical Industry Foundation, we were able to obtain an IBM R/6000 workstation. With this we could make accurate calculations of the silicon-29 shielding. Of especial interest to us was the theoretical background of the linear relationship between the Si–O bond length and the parallel component of the silicon-29 chemical shift tensor of silicates with C_{3v} symmetry; this relationship had first been observed by Grimmer in the beginning of 1980 and since then many other similar observations have been made. The IGLO methods permitted an exact analysis of the parallel and perpendicular components of the shielding tensor, including the contribution of a single Si–O bond. The change of the Si–O bond length of the symmetry axis causes a change in the electronic structure of the three remaining Si–O bonds, which in turn results in the observed change in the parallel components.

After the fall of the Berlin Wall, our group, which had been formerly headed by Kriegsmann, tried to decouple itself from the little-loved Institute and took the name 'Analytical Centre, Berlin'. The recommendation of the scientific council which had evaluated the East German scientific establishment after reunification, along with the influence of Kriegsmann, thankfully resulted in the establishment of a new department in the Federal Bureau of Materials Research and Testing. Our Division of Analytical Chemistry, although greatly reduced in number, is part of that organization and is responsible for structural and materials analysis. Naturally, a certain redirection of our work into materials research was necessary, but for the future we will be working in such classical fields as (i) characterization of zeolite systems, using, for example, aluminum-27 quadrupole spectroscopy, (ii) silicon-29 NMR characterization of ceramic materials and their precursors, (iii) ab initio (IGLO) theoretical calculations of silicon chemical shifts for improved interpretation of practical measurements, and (iv) methods development work in the area of measurement and analysis.

REFERENCES

1. W. Storek and H. Kriegsmann, *Ber. Bunsenges. Phys. Chem.*, 1968, **72**, 706.
2. R. Radeglia, *J. Prakt. Chem.*, 1973, **315**, 1121.
3. G. Engelhardt, D. Zeigan, H. Jancke, D. Hoebbel, and W. Wieker, *Z. Anorg. Allg. Chem.*, 1975, **418**, 17.
4. R. Wolff and R. Radeglia, *Org. Magn. Reson.*, 1977 **9**, 164.

Biographical Sketches

Reiner Radeglia. Diploma (Chemistry) 1961, Dr. rer. nat. (supervisor Kurt Schwabe) 1963, Technical University of Dresden. Central Institute of Physical Chemistry of the Academy of Sciences, Berlin (East) 1963–91. Dr. habil. Humboldt University, Berlin (East) 1969; Professor of Physical Chemistry 1988. Federal Institute for Materials Research and Testing (BAM), Berlin 1992–present. Approx. 300 publications. Research specialities: NMR parameters and molecular structure.

Harald Jancke *b* 1941. Diploma (Chemistry) 1965, Dr. rer. nat. (supervisor Heinrich Kriegsmann) 1965 at Humbold University Berlin. 1965–92 Central Institute of Physical Chemistry of the Academy of Sciences, Berlin (East). Since 1992 in the Federal Institute for Materials Research and Testing (BAM). 80 publications. Research specialities: NMR analysis in organosilicon and hydrocarbon chemistry.

Ramsey, Norman F.: Origins of Magnetic Resonance

Norman F. Ramsey
Harvard University, Cambridge, MA, USA

INTRODUCTION

I started my Ph.D. research in the summer of 1937 with I. I. Rabi, approximately two months before he invented the molecular beam magnetic resonance method, so I had the good fortune to write the first Ph.D. thesis based on magnetic resonance.[1] As a result I anticipated questions in my oral exam on the origins of the idea of magnetic resonance and looked with interest into the early history.[2]

In this article I recount what I learned from these studies and supplement it with an account of developments in molecular beam magnetic resonance prior to the condensed matter nuclear magnetic resonance experiments of E. M. Purcell, F. Bloch, and their associates.[3,4]

The first work on nuclear magnetic shielding also began in this early era, so I conclude the article with a brief historical account of the development of ideas about magnetic shielding and chemical shifts which underlie the uses of NMR in chemical analysis, biology, and medicine, and about electron-coupled nuclear spin–spin interactions.

EARLIEST SEARCHES FOR A DEPENDENCE OF MAGNETIC SUSCEPTIBILITY ON FREQUENCY

The earliest reported search for a dependence of magnetic susceptibility on frequency was that of Belz[5] in 1922 with different solutions of paramagnetic salts. No frequency dependence was found. Acting on a suggestion of Lenz and Ehrenfest, G. Breit[6] four years later also searched for such a frequency dependence but found none. Perhaps this disappointment contributed to Breit's decision to concentrate on theory, where he had a highly productive career.

SPACE QUANTIZATION WHEN THE DIRECTION OF A MAGNETIC FIELD CHANGES

Theoretical ideas about the magnetic resonance method trace back to early quantum theory speculations and experiments on the changes in space quantization when the direction of a magnetic field is changed. The problem was first posed and partially solved in 1927 by C. G. Darwin[7] and his analysis was subsequently improved by P. Gutinger,[8] E. Majorana,[9] and L. Motz and M. Rose.[10]

In the period 1931–33, O. Stern, T. E. Phipps, and O. Frisch[11,12] in Stern's Hamburg laboratory observed the changes in the space quantization when the direction of the magnetic field was changed, but their observations agreed only partially with theory. I. I. Rabi[13] pointed out that the discrepancy between theory and experiment was due to the neglect of nuclear spins in previous theories. Those theories had neglected nuclear effects because the magnetic moment of the nucleus is about 2000-times smaller than that of the electron. However, the spin angular momenta of nuclei and the electron are comparable in size, so the nucleus produces observable effects when the angular momenta are tightly coupled at low external fields.

Although the techniques of microwave spectroscopy are quite different from those of magnetic resonance, there is sufficient similarity to note that in 1933 Cleeton and Williams[14] using magnetron-generated microwave electric fields observed a single broad spectral line corresponding to the tunneling transition of the NH_3 molecule at a wavelength of 1.1 cm. There were, however, no subsequent microwave spectroscopy experiments for the next decade, until the microwave absorption spectra of O_2 and H_2O were studied for radar purposes near the end of World War II and published[15–17] in 1946.

Another different but related experiment during this period was that of Lasarew and Schubnikow,[18] which showed at low temperature that the nuclear magnetic moments in solid hydrogen contribute significantly to the observed static magnetic susceptibility of solid hydrogen.

FIRST ATTEMPTS TO OBSERVE MAGNETIC RESONANCE IN CONDENSED MATTER

In 1936, using a calorimetric detection technique, C. J. Gorter[19] successfully observed a frequency dependence of the paramagnetic relaxation of a number of alums. He found that the observed effects depend on the frequency, ν, as ν^x where x is a number, usually between 1 and 2; no resonance effects were observed. Utilizing the same calorimetric technique, Gorter[19] attempted to observe a nuclear magnetic resonance for ^{7}Li in LiCl or for ^{1}H in aluminum potassium alum, but found no resonances.

In 1942, subsequent to the success of the molecular beam nuclear magnetic resonance experiments, Gorter and Broer[20] reported unsuccessful attempts to observe nuclear magnetic resonance in powders of LiCl and KF as a frequency pulling of a self-excited oscillator as the applied magnetic field was moved through the resonant value. The reasons for the failures remain a mystery, but they are probably due to detection inefficiencies since Bloembergen many years later was able to obtain a resonance with one of the same crystals used by Gorter. The first published use of the name 'nuclear magnetic resonance' is in Gorter's 1942 paper[20] where he attributes the coining of the phrase to I. I. Rabi.

TRANSITIONS INDUCED BY PASSAGE OF MOLECULES THROUGH DIFFERENTLY ORIENTED MAGNETIC FIELDS

While Gorter was pursuing his unsuccessful experiments, I. I. Rabi[21] and Schwinger[22] were developing theories for

the transitions induced when atoms or molecules in a molecular beam traverse successive regions of space with different directions of magnetic fields. In his brilliant 1937 theoretical paper entitled 'Space Quantization in a Gyrating Magnetic Field', Rabi[21] assumed for simplicity that fields were oscillatory in time even though the application was to molecules moving through fields which varied in space rather than time. Consequently, the formulas in that paper are applicable to resonances with oscillatory fields and the paper, without alteration, provides the fundamental theory for all subsequent magnetic resonance experiments. However, the theoretical transition probability was written in a form which obscured its resonant nature, while the subsequent averaging over molecular velocities eliminated sharp resonances. Thus Rabi did not immediately recognize the advantages of fields oscillating in time rather than space.

MOLECULAR BEAM MAGNETIC RESONANCE METHODS

After writing his paper on the gyrating field, Rabi discussed with some of his colleagues the possibility of using oscillatory rather than space-varying magnetic fields, but his laboratory had a full program of important experiments so no experiments utilizing oscillatory fields were seriously considered during the first five months following the publication of his paper on the gyrating magnetic field. In September 1937, C. J. Gorter visited Rabi's laboratory[23] and described his brilliantly conceived but experimentally unsuccessful efforts[20] to observe nuclear magnetic resonance. Rabi then fully appreciated the advantage of using an oscillatory field and promptly invented the molecular beam magnetic resonance method. Two successful molecular beam magnetic resonance apparatus were soon constructed by Rabi,[24,25] Zacharias,[24,25] Millman,[24] Kusch,[24] Kellogg,[25] and Ramsey.[25] A schematic view[24] of the method is shown in Figure 1. In these experiments the atoms or molecules are first deflected by an inhomogeneous magnetic field and refocused by a second one. When a resonance transition is induced in the region between the two inhomogeneous fields, the final beam intensity is reduced by the failure of refocusing. As a result, when the oscillator angular frequency ω is equal to the Larmor angular frequency

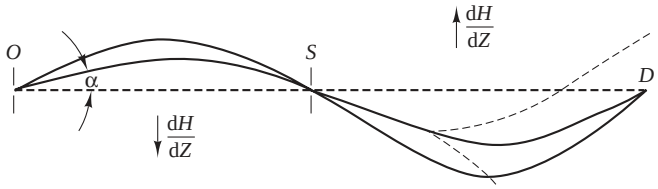

Figure 1 Schematic diagram[24] showing the principle of the first molecular beam magnetic resonance experiments. The two solid curves indicate two paths of molecules having different orientations that are not changed during passage through the apparatus. The two dashed curves in the region of the B magnet indicate two paths of molecules whose orientation has been changed in the C region so the refocusing is lost due to the change in the component along the direction of the magnetic field. (Reproduced by permission of Oxford University Press from N. F. Ramsey, 'Molecular Beams', 1985, p. 159)

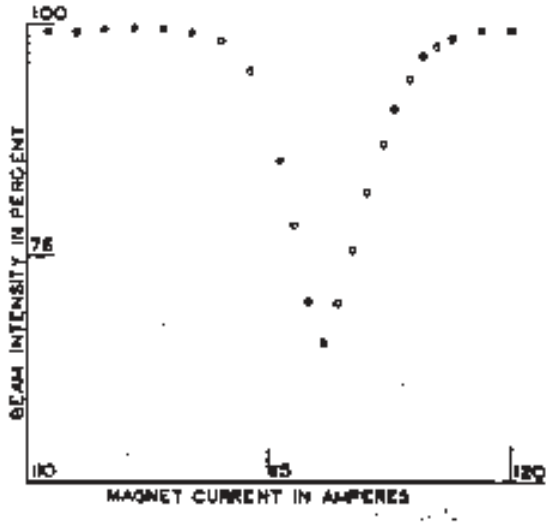

Figure 2 First observed nuclear magnetic resonance.[24] The refocused beam intensity is plotted for various values of the magnetic field; 1 A corresponds to about 1.84×10^{-4} T. The frequency of the oscillating field was held constant at 3.518×10^{6} Hz. (Reproduced by permission of Oxford University Press from N. F. Ramsey, 'Molecular Beams', 1985, p. 161)

ω_0 of a nucleus in magnetic field B_0, a sharp resonance is obtained for

$$\omega = \omega_0 = \gamma_I B_0 \tag{1}$$

where ω_0 is the angular precession frequency of a classical magnetized top with the same ratio γ_I of magnetic moment to angular momentum. Figure 2 shows the first reported nuclear magnetic resonance curve as obtained by Rabi, Millman, and Kusch[24] with a beam of LiCl molecules.

Kellogg, Rabi, Ramsey, and Zacharias[1,25] soon extended the method to the molecules H_2, D_2, and HD. When these experiments were started, it was thought the only measurable interactions would be those of the magnetic moments with the external magnetic field, so that there should be a single resonance for each magnetic moment. Instead the authors made the unexpected discovery of multiple resonances as shown in Figure 3. They soon realized that these arose from internal interactions within the molecule and that the spacings of the resonances measure the molecular spin–spin, spin–rotational and nuclear quadrupole interaction energies. The transitions occur whenever the oscillatory frequency ω is at a Bohr angular frequency ω_0 for an allowed transition where

$$\hbar\omega = \hbar\omega_0 = E_\mathrm{i} - E_\mathrm{f} \tag{2}$$

For the first time, the authors described their results as 'radiofrequency spectroscopy'. The observed spectrum for H_2 is shown in Figure 3. These resonances were the first instances of multiple line spectroscopy with coherent electromagnetic radiation, a characteristic of subsequent radiofrequency, microwave, and laser spectroscopy

The first molecular beam magnetic resonance experiments were with $^1\Sigma$ molecules, but in 1940 Kusch, Millman, and Rabi[26,27] extended the method to paramagnetic atoms

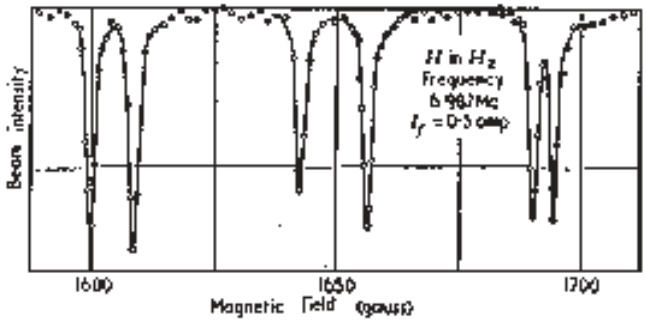

Figure 3 Radiofrequency spectrum of H_2 in the vicinity of the proton resonance frequency.[25] The resonance frequencies are determined primarily by the interaction of the proton magnetic moment with the external magnetic field, but the states of different m_I and m_J are displaced relative to each other by the different values of the nuclear spin–spin and spin–rotational interaction energies. (Reproduced by permission of Oxford University Press from N. F. Ramsey, 'Molecular Beams,' 1985, p. 6)

and in particular to $\Delta F = \pm 1$ transitions of atoms. For such transitions, the relative orientations of the nuclear and electronic magnetic moments are changed, so the resonance frequencies are primarily determined by the internal properties of the atom.

Essentially the same molecular beam magnetic resonance technique was utilized by Alvarez and Bloch[28] to measure the magnetic moment of the neutron with a neutron beam. The first publication on the neutron magnetic resonance came about two years after the first molecular beam magnetic resonance papers, so it is usually considered that the neutron studies of Alvarez and Bloch were merely adaptations of the resonance methods developed by Rabi and his associates. However, Alvarez has stated that Bloch thought of doing the neutron beam resonance experiment before either of them had heard of the earlier molecular beam resonance experiments. It must have been a bitter disappointment to Bloch and Alvarez to learn that their clever idea for magnetic resonance had been anticipated and it is to their credit that they did not let this blight their research careers; instead each went on independently to win Nobel Prizes for other research.

Molecular beam and neutron beam magnetic resonance experiments were interrupted by World War II. In 1944 Rabi and I spent one evening together in Cambridge, MA, planning possible post-war research experiments. Two ideas emerged as leading candidates. One was to test fundamental quantum mechanics by using the molecular beam magnetic resonance method to measure the theoretically predictable hyperfine separation in atomic hydrogen. This experiment was eventually carried out[29] and led to the first indication of an anomalous magnetic moment of the electron[29] and to the development of relativistic quantum electrodynamics (QED).[30] The second idea was to detect the existence of nuclear magnetic resonance transitions by their effects on the oscillator. To our pleasant surprise, the signal-to-noise calculations were favorable and we became enthusiastic about the possibility. Then, we realized we were merely reinventing Gorter's nuclear magnetic resonance experiments[19,20] which had failed for unknown reasons. We, therefore, decided such efforts should be given a lower priority than the atomic beam experiments.

ELECTRON PARAMAGNETIC RESONANCE EXPERIMENTS IN CONDENSED MATTER

Despite his unsuccessful efforts to observe nuclear magnetic resonance, Gorter[19] successfully observed paramagnetic relaxation in condensed matter but his attempts to observe paramagnetic resonances failed. The first successful paramagnetic resonance experiments in condensed matter were those of Zavoisky,[31] who in 1944 observed paramagnetic resonance with $CrCl_3$. Shortly after Zavoisky's pioneering work, other observations of electron paramagnetic resonances were made by Cummerow and Halliday[32] and many others.

NUCLEAR MAGNETIC RESONANCE EXPERIMENTS IN CONDENSED MATTER

Following World War II, two groups independently developed nuclear magnetic resonance experiments with condensed matter and with detection of the resonance by the effect on the electromagnetic radiation. E. M. Purcell, H. C. Torrey, and R. V. Pound[3] at Harvard University observed the nuclear magnetic resonance absorption of the applied electromagnetic radiation while F. Bloch, W. Hansen, and M. E. Packard[4] at Stanford University observed the induced nuclear induction signal. Each group had different reasons for being willing to proceed with these experiments despite the failure of Gorter's earlier experiments.

Purcell, Torrey, and Pound[3] were initially unaware of Gorter's failure. When Rabi learned of their plans and pointed out that Gorter's similar experiment had failed, Purcell was disappointed but felt that their feasibility calculations were favorable including an estimate by Torrey that the nuclear spin relaxation time was about 1 h. Furthermore the work on the new experiment had already gone so far that it should not be stopped. Purcell and his associates devoted special attention to problems of signal size and noise. On December 24, 1945 their letter[3] was received by the *Physical Review* announcing the successful observation of nuclear magnetic resonance absorption of protons in a paraffin-filled 30 MHz resonant cavity whose output was balanced against a portion of the signal generator output. When the magnetic field passed through resonance, an unbalanced signal 20-times the noise was observed.

When Bloch, Hansen, and Packard[4] started their experiments, they were fully aware of Gorter's failed experiments but they thought the failure was due to the relaxation time T_1 being so great that Gorter had not waited long enough. To overcome this difficulty they proposed putting their water sample in a strong magnetic field for several days to allow the nuclear spin system to reach thermal equilibrium. With their apparatus ready for a first test and the water inserted into the high magnetic field, they allowed several days for the system to come to equilibrium, while Bloch went off on a ski trip. When they finally observed the induction signal they learned that the long delay was unnecessary—the relaxation time was

short not long! A letter[4] announcing their successful experiment was received by the *Physical Review* on January 29, 1946. It was soon realized that the two methods were alternatives for obtaining similar information and the general term nuclear magnetic resonance or NMR was applied to both.

CHEMICAL SHIFTS, NUCLEAR MAGNETIC SHIELDING AND ELECTRON-COUPLED NUCLEAR SPIN–SPIN INTERACTIONS

In the early days of molecular beam magnetic resonance experiments, it was recognized that the magnetic field at the nucleus of an atom was not the same as the externally applied magnetic field since the applied field induced a diamagnetic circulation of the electrons in the atom. In 1940, Lamb[33] developed the theory of this magnetic shielding for single atoms and tabulated atomic corrections based on Thomas–Fermi wavefunctions. Later, Dickinson[34] used Hartree–Fock wavefunctions for a better list of atomic corrections. Because of the lack of an alternative theory, these formulas were also applied to molecules. For atoms with many electrons this is a good first approximation since the inner core electrons contribute most to the shielding and the configurations for inner core electrons are similar for atoms and molecules. However, in a paper written in 1949, I noted that for atoms with few electrons this approximation was not valid and, even for many electron atoms, failures of the approximation would lead to different shieldings in different molecules.[35] In a series of papers,[35] I published general formulas for calculating the magnetic shieldings or chemical shifts in different molecules. These publications also pointed out that there could be shielding anisotropies and provided general formulas for calculating the anisotropies.

At about the same time, experimental evidence for shifts began to emerge. Bloembergen,[36] in an abstract published in 1949, noted that in $CuSO_4 \cdot 5H_2O$ the constant magnetic field at the position of each proton in the unit cell is shifted by an amount which depends on the relative positions of the H and Cu atoms and increases with decreasing temperature in the same way as the total static magnetization. Knight[37] discovered that resonance frequencies for some nuclei are several tenths of a per cent higher when in a metallic state than when in the form of either powdered or dissolved salts.

Dickinson,[38] Proctor and Yu,[39] and subsequently many others experimentally found shifts of a few hundredths of a per cent in the NMR frequencies of the same nucleus in different chemical compounds, consistent with my general theory.[35] These shifts are the basis for the widespread use of NMR in chemical analysis, biology, and medicine.

Bloembergen and Dickinson[40] also observed that the NMR resonance frequencies of liquid samples are shifted when paramagnetic atoms are added to the samples to reduce the relaxation times, and that the magnitudes of the shifts are proportional to the ion concentrations.

Normally the magnitudes of the chemical shifts are temperature-independent but occasionally they are not, as first observed by Proctor and Yu[41] and by Packard and Arnold.[42] When the temperature shifts are small compared with the chemical shift, they can be accounted for by my general theory of chemical shifts[35] as due to different thermal excitations of low lying molecular states. On the other hand, that theory did not directly account for Packard and Arnold's[42] observation of a relatively large temperature shift for H in the OH radical of ethyl alcohol. However, Liddel and I[43] found that that experiment could be accounted for by modifying the usual theory of chemical shifts to take into account molecular association in liquid alcohol and its change with temperature.

A different frequency shift in NMR was discovered experimentally by Gutowsky, McCall, Slichter, and McNeil[44] and by Hahn and Maxwell.[45] They found a shift proportional to $I_1 \cdot I_2$ which they could not account for by any previously known interaction. Together with Purcell, I pointed out that this could be attributed to an electron-coupled nuclear spin–spin interaction.[46] Such a newly considered interaction could arise from each nucleus interacting magnetically with the electron spin of its own atom. Since the electrons are tightly coupled together by the exchange coupling that leads to zero resultant electron spin for most molecules, the nuclear spins are effectively coupled together. In a later publication,[47] I developed the theory quantitatively both for the observed scalar interaction as well as showing there could an additional anisotropic electron-coupled spin–spin tensor interaction. Subsequent HD measurements agreed with theory.

From the time of the first NMR experiments and the establishment of the chemical shifts, developments in magnetic resonance advanced at a rapid pace. For this reason, it is appropriate to bring to an end this account of the origins and early history of magnetic resonance.

REFERENCES

1. N. F. Ramsey, *Phys. Rev.*, 1940, **58**, 226.
2. N. F. Ramsey, *Bull. Magn. Reson.*, 1985, **7**, 94; *J. Res. Nat. Bur. Stand.*, 1983, **88**, 301.
3. E. M. Purcell, H. C. Torrey, and R. V. Pound, *Phys. Rev.*, 1946, **69**, 37.
4. F. Bloch, W. W. Hansen, and M. Packard, *Phys. Rev.*, 1946, **69**, 127.
5. M. H. Belz, *Philos. Mag.*, 1922, **44**, 479.
6. G. Breit, *Commun. Kamerlingh Onnes Lab. Univ. Leiden*, **1926**, 168c.
7. C. G. Darwin, *Proc. R. Soc. London*, 1928, **A117**, 258.
8. G. Güttinger, *Z. Phys.*, 1932, **73**, 169.
9. E. Majorana, *Nuovo Cimento*, 1932, **9**, 43.
10. L. Motz and M. E. Rose, *Phys. Rev.*, 1936, **50**, 348.
11. T. E. Phipps and O. Stern, *Z. Phys.*, 1932, **73**, 185.
12. R. Frisch and E. Segre, *Z. Phys.*, 1933, **80**, 610.
13. I. I. Rabi, *Phys. Rev.*, 1936, **49**, 324.
14. C. E. Cleeton and N. H. Williams, *Phys. Rev.*, 1934, **45**, 234.
15. R. Beringer, *Phys. Rev.*, 1946, **70**, 53.
16. G. E. Becker and S. H. Autler, *Phys. Rev.*, 1946, **70**, 300.
17. R. H. Dicke, R. Beringer, R. L. Kyhl, and A. B. Vane, *Phys. Rev.*, 1946, **70**, 340.
18. B. G. Lasarew and L. W. Schubnikow, *Phys. Z. Sowjet Union*, 1937, **11**, 445.
19. C. J. Gorter, *Physica (The Hague)*, 1936, **3**, 503, 995, 1006.
20. C. J. Gorter and I. J. F. Broer, *Physica (The Hague)*, 1942, **9**, 591.
21. I. I. Rabi, *Phys. Rev.*, 1937, **51**, 652.
22. J. Schwinger, *Phys. Rev.*, 1937, **51**, 648.
23. C. J. Gorter, *Phys. Today*, 1967, **20**, 76.
24. I. I. Rabi, J. R. Zacharias, S. Millman, and P. Kusch, *Phys. Rev.*, 1938, **53**, 318; *ibid.*, 1939, **55**, 526.

25. J. M. B. Kellogg, I. I. Rabi, N. F. Ramsey, and J. R. Zacharias, *Phys. Rev.*, 1939, **55**, 595; *ibid.*, 1939, **57**, 728; *ibid.*, 1940, **57**, 677.
26. P. Kusch, S. Millman, and I. I. Rabi, *Phys. Rev.*, 1940, **57**, 765.
27. S. Millman and P. Kusch, *Phys. Rev.*, 1940, **58**, 438.
28. L. Alvarez and F. Bloch, *Phys. Rev.*, 1940, **57**, 111.
29. J. E. Nafe, E. B. Nelson, and I. I. Rabi, *Phys. Rev.*, 1947, **71**, 914; *ibid.*, 1948, **73**, 718.
30. J. Schwinger, *Phys. Rev.*, 1948, **73**, 416; *ibid.*, 1949, **76**, 790.
31. E. K. Zavoisky, *Ph.D. Thesis*, 1944; *J. Phys. USSR*, 1945, **9**, 211, 245; *ibid.*, 1946, **10**, 197.
32. R. L. Cummerow and D. Halliday, *Phys. Rev.*, 1946, **70**, 433.
33. W. E. Lamb, Jr., *Phys. Rev.*, 1941, **60**, 817.
34. W. C. Dickinson, *Phys. Rev.*, 1950, **80**, 563.
35. N. F. Ramsey, *Phys. Rev.*, 1950, **77**, 567; *ibid.*, 1950, **78**, 699; *ibid.*, 1951, **83**, 540; *ibid.*, 1952, **86**, 243.
36. N. Bloembergen, *Phys. Rev.*, 1949, **75**, 1326 (Abs.).
37. W. D. Knight, *Phys. Rev.*, 1949, **76**, 1259.
38. W. C. Dickinson, *Phys. Rev.*, 1950, **77**, 736; *ibid.*, 1950, **78**, 339.
39. W. G. Proctor and F. C. Yu, *Phys. Rev.*, 1950, **77**, 717.
40. N. Bloembergen and W. C. Dickinson, *Phys. Rev.*, 1950, **79**, 179.
41. W. G. Proctor and F. C. Yu, *Phys. Rev.*, 1951, **81**, 20.
42. M. E. Packard and J. T. Arnold, *Phys. Rev.*, 1951, **83**, 210.
43. U. Liddel and N. F. Ramsey, *J. Chem. Phys.*, 1951, **19**, 1608.
44. H. S. Gutowsky, D. W. McCall, C. P. Slichter, and E. B. McNeill, *Phys. Rev.*, 1951, **82**, 748; *ibid.*, 1951, **84**, 589, 1246.
45. E. L. Hahn and D. E. Maxwell, *Phys. Rev.*, 1951, **84**, 1246; *ibid.*, 1952, **88**, 1070.
46. N. F. Ramsey and E. M. Purcell, *Phys. Rev.*, 1952, **85**, 143.
47. N. F. Ramsey, *Phys. Rev.*, 1953, **91**, 303.

Biographical Sketch

Norman F. Ramsey. *b* 1915. B.A., 1935 and 1937, Columbia and Cambridge Universities, Ph.D., 1940, Columbia (supervisor I. I. Rabi), D.Sc., 1957, Cambridge. Higgins Professor of Physics, Harvard University, 1947–86; Emeritus 1986–present. President Universities Research Association, 1966–83. Research ranging from molecular beams to particle physics including first Ph.D. thesis using magnetic resonance, co-discovery of deuteron quadrupole moment, measurement of nuclear magnetic moments including proton, deuteron, and neutron, and first successful theories of the NMR chemical shift and of electron-coupled nuclear spin–spin interactions in molecules. Inventor of method of separated oscillatory fields and co-inventor atomic hydrogen maser. National Medal of Science, 1989 and Nobel Prize in Physics, 1989.

Randall, Edward W.: “Double, Double, Toil and Trouble” (Alias Double Resonance)

Edward W. Randall

University of London, Queen Mary College, London, UK

Although I worked in the room next to Rex Richards’s laboratory at Oxford in the late 1950s, I did not start any magnetic resonance work until I joined Professor Gene Rochow at Harvard in 1959 as a postdoctoral fellow. There I began rebuilding a NUMAR instrument for solid state work which I eventually completed in late 1960. Meanwhile I did some ESR work with Gus Maki before collaborating with a recently arrived instructor, John Baldeschwieler by name, who was starting out on heteronuclear double resonance (d.r.). We collaborated, and my very first NMR paper (and one of John’s) was entitled ‘The Measurement of Chemical Shifts by NMDR’.[1] This ‘indirect’, now usually called ‘inverse’, method using $^{1}H\{^{14}N\}$ d.r. to measure ^{14}N shifts, was later exploited at Queen Mary College (QMC), where I went in 1961, by Duncan Gillies to map out ^{15}N spectra very accurately by $^{1}H\{^{15}N\}$ spin tickling.[2] At first, however, one of the main objectives was merely to sharpen up ^{1}H spectra by $^{1}H\{^{14}N\}$ decoupling so that they could be analyzed more easily. It was a great delight to me more than 30 years later to use exactly the same technique in $^{1}H\{^{14}N\}$ spin echo d.r. to *image* ^{14}N indirectly for the first time,[3] and then to adapt this to spin-$\frac{1}{2}$ nuclei such as ^{15}N.[4]

The early CW double resonance experiments were sometimes truly two-dimensional although all of the 2(frequency)D space was rarely mapped out (except by Ray Freeman and ourselves), but of course it took the introduction of pulsed FT methods in the 1970s to really revolutionize 2D NMR.

John Baldeschwieler and I published a quite influential *Chemical Review* on d.r. in 1963, which among other things popularized the X{Y} nomenclature.[5] The preparation of the review was a pleasure since it put us in touch with other double resonators. Notable was a personal communication from Paul Lauterbur on $^{13}C\{^{1}H\}$ nuclear Overhauser effects. In the UK, I visited that influential NMR group at Teddington headed by John Pople and David Whiffen, which included Keith McLauchlan and Ray Freeman. I was most grateful to that group for allowing my first research student, Tony Bourn, access to their ^{1}H *homo*nuclear d.r. equipment, while my second and third students, Duncan Gillies and Derek Shaw, were building up our own spectrometer around a Mullard permanent magnet (at 0.9 T). Tony Bourn (R.I.P.) with Frank Anet later woke up the chemical NMR community to the benefits of the NOE using the amides we had been working on at QMC. This instrument proved to be the only one in over 30 years of NMR that was exclusively for my group. Thereafter I have always shared instruments with others (a Varian A-60, a Varian HR-100, a Bruker HFX-90, a Bruker WH-400, and now a Bruker AMX2-600 and a Sisco/Varian 200 Imager).

I was lucky on arrival at QMC in 1961 to find it was blessed with an expert NMR group in physics headed by Jack Powles, which included Peter Mansfield and John Strange. I was grateful to Jack for access to one of his instruments which Derek Shaw used for ^{19}F work and gave us the first QMC NMR chemical paper in 1963.[6] In the early 1960s I learned from them the utility of pulse methods and for the first time I came across Fourier transformation: the group took FTs of the CW wiggle beats in field-swept spectra of liquids. I was therefore fully alive to the possibilities for chemical work of the first commercial FT spectrometers. I obtained the first of these in the UK (a Bruker HFX-90) in 1969–70 for work mainly on ^{13}C (organometallics) and ^{15}N (amides and peptides), and we managed the first ^{15}N FT studies at natural abundance[7] as well as the first $^{2}H\{^{1}H\}$ FT work on deuterium.[8] It was a large grant (eventually worth about £90 000) but in return I had to run a national service!

I did not realize either the utility of the ‘solid echo’ which Jack’s group popularized, until much later (in 1992!) when I used it in the stray field imaging technique at Bruker Spectrospin with Klaus Zick[9] for the imaging of liquids in solids.

Since those times I have had a succession of very able colleagues at QMC, notably Paul Pregosin who took us from amides to peptides with FT in the 1970s and with whom I published a review on ^{13}C,[10] and then Geoff Hawkes who had fun with ^{15}N NOEs in peptides,[11] as well as with ^{13}C and ^{17}O in organometallics,[12] Paul Kinchesh and Steve Williams in the 1990s with direct and indirect imaging of ^{14}N and ^{15}N.[3,4,13] There were enjoyable collaborations abroad: Luciano Milone and Silvio Aime at Turin on organometallics,[12] Filippo Conti in Rome on peptides,[14] Rosanna Mondelli and Giovanni Fronza in Milan with heterocycles.[15]

Pieces of work which I enjoy looking back on and not mentioned above are: (i) the structure of pyrrole-^{15}N from ‘liquid crystal spectra’ with Erkki Rahkamma[16] at an accuracy good enough for Jim Emsley to do some vibrational corrections;[17] (ii) similar oriented work on the change of bond angles at nitrogen in 4-substituted anilines produced by the substituent (with the Milan group);[18] (iii) the very beautiful treatment of double resonance spectra by Solveig Paget, which with the aid of Ruth Lynden-Bell and Alex Bain introduced the ‘tilt effect’ on intensities in d.r. spectra;[19] (iv) the work of Derek Shaw on ‘second order paramagnetics’ (paramagnetics with no unpaired electrons);[20] (v) work with Jerry Zuckerman on Si–N systems (in which we introduced the very useful term ‘isotopomers’, which differ only in isotopic composition);[21] (vi) the contributions to the study of lanthanide shift reagents;[22] and (vii) work on NMR studies of ion pairing in solution.[23]

My latest thoughts on the definition of double resonance in the epoch of time domain studies are in a brief review.[24]

I am proud, at the suggestion of Jim Emsley and Kjeld Schaumberg, to have started the *European* Experimental NMR conference at Kent in 1974.[25]

The moral I would offer to a chemist entering NMR is get with the latest instrumentation, your own or someone else’s, find out what the physicists are doing, sniff out (or create) tomorrow’s techniques, and *be lucky*, especially with your collaborators. Lastly, if someone tells you your experiment will not work, remember it is often easier to try it than to argue. I remember (non-NMR) colleagues questioning the utility of trying to measure ^{15}N spectra at natural abundance. Some are now doing the same for ^{15}N imaging! Always press on.

REFERENCES

1. J. D. Baldeschwieler and E. W. Randall, *Proc. Chem. Soc. London*, **1961**, 303.
2. R. J. Chuck, D. G. Gillies, and E. W. Randall, *Mol. Phys.*, 1969, **16**, 121.
3. P. Kinchesh, E. W. Randall, and S. C. R. Williams, *J. Magn. Reson.*, 1992, **100**, 625.
4. P. Kinchesh, E. W. Randall, and S. C. R. Williams, *J. Magn. Reson. Series B*, 1994, **105**, 253.
5. J. D. Baldeschwieler and E. W. Randall, *Chem. Rev.*, 1963 **63**, 81.
6. A. G. Massey, E. W. Randall, and D. Shaw, *Chem. Ind. (London)*, **1963**, 1244.
7. J. M. Briggs, L. F. Farnell, and E. W. Randall, *Chem. Commun.*, **1971**, 680.
8. J. M. Briggs, L. F. Farnell, and E. W. Randall *J. Chem. Soc., Chem. Commun.*, **1973**, 70.
9. P. Kinchesh, E. W. Randall, and K. Zick, *Magn. Reson. Imaging*, 1994, **12**, 305, and references contained therein.
10. P. S. Pregosin and E. W. Randall, ^{13}C Magnetic Resonance, in *Determination of Organic Structures by Physical Methods*, Vol. 4. ed. F. C. Nachod and J. J. Zuckerman, Academic Press, New York, 1971.
11. G. E. Hawkes, E. W. Randall, and C. H. Bradley, *Nature (London)*, 1975, **257**, 767.
12. S. Aime, D. Osella, L. Milone, G. E. Hawkes, and E. W. Randall, *J. Am. Chem. Soc.*, 1981, **103**, 5920, and references contained therein.
13. P. Kinchesh, E. W. Randall, and S. C. R. Williams, *J. Magn. Reson.*, 1993, **A103**, 234.
14. G. E. Hawkes, E. W. Randall, W. E. Hull, D. Gattegno, and F. Conti, *Biochemistry.*, 1978, **17**, 3986, and references contained therein.
15. G. Fronza, R. Mondelli, E. W. Randall, and G. P. Gordini, *J. Chem. Soc., Perkin Trans. 2*, **1977**, 1746.
16. J. M. Briggs, E. J. Rahkamaa, and E. W. Randall, *J. Magn. Reson.*, 1975, **17**, 55.
17. J. W. Emsley and E. W. Randall, *J. Magn. Reson.*, 1976, **23**, 481.
18. G. Fronza, R. Mondelli, F. Lelj, E. W. Randall, and C. A. Veracini, *J. Magn. Reson.*, 1980, **37**, 275.
19. P. S. Albrand, E. W. Randall, and R. M. Lynden-Bell, *J. Magn. Reson.*, 1980, **37**, 61, and references contained therein.
20. E. W. Randall and D. Shaw, *J. Chem. Soc. A*, **1969**, 2867, and references contained therein.
21. E. W. Randall, J. J. Ellner, and J. J. Zuckerman, *J Am. Chem. Soc.*, 1966, **88**, 622.
22. J. M. Briggs, F. A. Hart, G. P. Moss, E. W. Randall, K. D. Sales, and M. L. Staniforth, in *NMR Shift Reagents*, ed. R. E. Sievers, Academic Press, Dallas, TX, 1973, p. 197.
23. J. M. Briggs and E. W. Randall, *Mol. Phys.*, 1973, **26**, 699; E. W. Randall and D. Shaw, *Spectrochim. Acta*, 1967, **23A**, 1235.
24. E. W. Randall, in *Proc. Int. School Phys., Enrico Fermi, Nucl. Magn. Double Reson.*, Varenna, ed. B. Maraviglia, Italian Phys. Soc., Rome, 1992.
25. E. W. Randall, *Chem. Br.*, 1974, **10**, 443.

Biographical Sketch

Edward W. Randall, *b* 1933. B.A., 1956, B. Sc., 1958, D.Phil., 1959, Physical Chemistry, Oxford, UK. Started solid state NMR with Gene Rochow as Postdoctoral Fellow, Harvard, 1959–61, and also collaborated with John Baldeschwieler on double resonance. Faculty in Chemistry at Queen Mary and Westfield College (London University), 1961 to present. Approx. 150 publications. Research specialties: multinuclear MR, especially nitrogen: now imaging, soil science and pulsed EPR.

Raynes, W. T.: Early Work on Gas-Phase Chemical Shifts

W. T. Raynes

University of Sheffield, Sheffield, UK

Although few laboratories at the time had NMR instrumentation, many chemists were aware by 1959 that NMR was the coming thing in chemistry. It was in the same year that the famous monograph of Pople, Schneider, and Bernstein appeared. Theirs was not the first book on NMR but it was the first which made clear that the new technique would have manifold applications in chemistry. Indeed, so rapid were subsequent developments that by the mid-1960s the later chapters of the book were totally out of date.

The National Research Council of Canada had achieved world fame long before 1959, largely because of the research in ultraviolet spectroscopy carried out by G. Herzberg and his associates in the Pure Physics Division in Ottawa. However, from about 1956 the NMR work of H. J. Bernstein and W. G. Schneider in the Pure Chemistry Division had become very well known. In late November 1959, I arrived at the NRC Laboratories on Sussex Drive to take up a postdoctoral fellowship with Bernstein.

He suggested that I continue the work on solvent effects on chemical shifts in liquids that had been started by my predecessor R. J. Abraham who had left some weeks earlier. I first gained some knowledge of chemical shifts from Chapter 4 of Pople, Schneider, and Bernstein's book. It was clear that to measure solvent effects properly it was necessary to obtain the chemical shift of the solute in the gas phase. By February 1960, I had obtained a gas-phase proton signal from HCl at 20 atm pressure. Without realizing the implications, I thought that a result at a lower pressure would be more satisfactory. A 10-atm pressure sample gave a slightly different result. Bernstein immediately saw the importance of this and from then on most of my work involved gaseous samples.

Within a short time I obtained a density dependence of the proton chemical shift of HCl gas with a negative slope. This is now known to be a universal feature of nuclear shielding in the gas phase after correcting for bulk susceptibility. I went on to obtain linear density dependences for the proton resonances of CH_4, H_2S, and C_2H_6. In all these studies samples were at room temperature. At that time 'state-of-the-art' NMR spectrometers operated with field sweep at 60 MHz (or '60 megacycles per second', as one said). There was no lock, and drifting of the field frequently occurred. To allow for this it was the practice to record signals both for increasing and decreasing applied fields in quick succession through resonance. I learnt much about practical NMR from J. Nicholson who was the technician in charge of the Varian V-4300 B instrument with which the work was done.

A. D. Buckingham, who was in Ottawa during the summer of 1960, became very interested in our results. Within a short time he produced a theory of intermolecular effects on nuclear shielding in gases. This was based upon a virial expansion of shielding and incorporated the physical ideas of distinct van der Waals, electric field, and magnetic anisotropy contributions which had been described shortly before.[1]

The theory suggested that it would be profitable to study binary gas mixtures, i.e. the dependence of proton shielding in one gas on the density of a second, perturbing gas. I soon obtained results for a number of gas mixtures and found, with one exception, that they fitted the new theory very well. The exception was the HCl/CO_2 mixture. I suggested to Buckingham that the electric quadrupole moment of CO_2 could be important here. He then produced an extra term to account for this. An excellent fit of all results to the theory was then achieved. I wrote up the work in the summer of 1961 and it was published[2] in 1962. The paper has been cited frequently down the years and is often referred to as 'RBB' or the theory as 'the RBB theory'. It was in this paper that the coefficients A and B, often now used to describe the electric field dependence of shielding, first made their appearance. I left Ottawa in October 1961 and moved to Caltech to work in a different field with G. W. Robinson. During my period in Ottawa other significant NMR work was being done including the first study of substituent effects on carbon-13 shielding[3] and the first measurement of a carbon–carbon spin–spin coupling constant.[4]

In late 1961 Buckingham published a note[5] pointing out that an observed temperature dependence of chemical shifts could be attributed to the stretching of chemical bonds. He wrote the shielding in a diatomic molecule as a power series in the 'reduced' bond length. When I resumed gas-phase studies in the late 1960s, I used this idea with my research student, the late B. P. Chadburn, to determine the bond length dependences of the proton shielding in HCl and HBr from the observed temperature dependence of the proton shielding.[6,7] This was the first use of the NMR technique, I believe, for measuring the dependence of a property on molecular geometry. Shortly after this I turned again to intermolecular effects in gases and, with K. Jackowski, obtained a density dependence of carbon-13 shielding[8] and later with E. Dayan we studied carbon-13 shielding in binary gas mixtures.[9]

The RBB paper was not the first to report density-dependent shielding as Gordon and Dailey[10] published their result for C_2H_4 first. After I left Ottawa, Bernstein continued gas-phase work with L. Petrakis, G. Govil, and S. Mohanty. There was soon a flourishing group in Paris.[11] Important work was also done by Rummens who wrote an early review of the subject.[12] However, since the mid-1970s the field has been dominated by C. J. Jameson. Together with A. K. Jameson and their co-workers, she has made many contributions to the two branches into which the subject is divided—intermolecular and intramolecular. She has also shown that isotope shifts can be accounted for by the same theory which deals with intramolecular effects. She has written the most recent review of the subject.[13]

There is still much work to be done!

REFERENCES

1. A. D. Buckingham, T. Schaefer, and W. G. Schneider, *J. Chem. Phys.*, 1960, **32**, 1227.
2. W. T. Raynes, A. D. Buckingham, and H. J. Bernstein, *J. Chem. Phys.*, 1962, **36**, 3481.
3. H. Spiesecke and W. G. Schneider, *J. Chem. Phys.*, 1961, **35**, 722, 731.

4. K. Frei and H. J. Bernstein, *J. Chem. Phys.*, 1963, **38**, 1216.
5. A. D. Buckingham, *J. Chem. Phys.*, 1962, **36**, 3096.
6. W. T. Raynes and B. P. Chadburn, *Mol. Phys.*, 1972, **24**, 853.
7. W. T. Raynes and B. P. Chadburn, *J. Magn. Reson.*, 1973, **10**, 218.
8. K. Jackowski and W. T. Raynes, *Mol. Phys.*, 1977, **34**, 465.
9. K. Jackowski, E. Dayan, and W. T. Raynes, *Mol. Phys.*, 1977, **34**, 1189.
10. S. Gordon and B. P. Dailey, *J. Chem. Phys.*, 1961, **34**, 1084.
11. G. Widenlocher, E. Dayan, and B. Vodar, *C. R. Acad. Sci.*, 1963, **256**, 2584.
12. F. H. A. Rummens, *NMR Basic Principles and Progress*, 1975, **10**, 1.
13. C. J. Jameson, *Chem. Rev.*, 1991, **91**, 1375.

Biographical Sketch

W. T. Raynes. *b* 1935. B.Sc., 1956, Ph.D., 1959, D.Sc., 1989, University of London, UK. Postdoctoral research fellow, NRC, Ottawa (introduced to NMR by H. J. Bernstein). Postdoctoral fellowships at Caltech and Oxford University. Lecturer, senior Lecturer, and reader in Chemistry, University of Sheffield, UK, 1965–present. Approximately 110 publications. Research interests include the magnetic properties of molecules, especially NMR chemical shifts and coupling constants.

Redfield, Alfred G.: Foundations and Structures

Alfred G. Redfield

Brandeis University, Waltham, MA, USA

The first NMR signal I ever observed was my most interesting one. It was not the result of careful planning, but a true discovery. Despite all kinds of influences, I had not intended to go into NMR until a few months before I found this signal, and I was pursuing relatively routine research at the time.

I come from a scientific tradition, founded by my great great grandfather, William C. Redfield ('C' was his entire middle name which he gave to himself, as he said, 'for Convenience'). He discovered that hurricanes were cyclonic in the 1820s,[1] but never knew what the Coriolis force was, or the rotating frame, or how they explained his discovery. During World War II, I spent winter and summer vacations from school in a research laboratory at Woods Hole, led by E. B. Wilson, where I worked directly with C. P. Slichter. The object of our lab was to record signals from underwater explosions.

In 1946, I entered Harvard where I kept in touch with Slichter, and had Purcell and Pound among my teachers. Slichter recruited me to go to graduate school at Illinois in 1950, and was very helpful to me when I got there, but I did not do my Ph.D. thesis with him because I foolishly thought that it would not be good to work directly for a friend. I worked for the first year at the Illinois betatron, but decided that big science was not for me. (I think times have changed, and NMR is now big science!) However, I took the data for my thesis (on the Hall effect in photoconductors) in Slichter's lab, borrowing the field of an electromagnet built by R. E. Norberg.

For my postdoc, I got an NSF fellowship to work with Harvey Brooks at Harvard. I did not yet realize that I had no talent as a mathematical physicist and it was fortunate that, when I arrived in September 1953, Brooks felt too busy to deal with me and suggested that I work with Nicolaas Bloembergen instead. Bloembergen had just returned from a trip to Japan and suggested I look into some mysterious nonmagnetic resonances observed in a solid by someone there. I had already picked out the vacuum tube to use to repeat these measurements, when I fortunately saw a book about piezoelectricity and recognized that these were piezoresonances.

His next suggestion was to measure T_1 in aluminum and copper, to help verify the prediction by Korringa that T_1 should be inversely proportional to temperature, and be related approximately to the Knight shift. Nico told me to do this using the saturation method with a crossed coil, rather than spin echoes which were then being used by Slichter and his co-workers in alkali metals. Saturation was a better method for aluminum and copper, which did not have the motionally narrowed lines of the alkali metals being studied at Illinois. Furthermore, no one in the lab had experience with the fast recovery pulse methods then being worked out by Slichter, Norberg, Hahn, and Lowe. It was a fortunate accident that Nico had me build a crossed-coil system (it was the first crossed-coil system built on the East Coast) because, not only is it suitable for high CW power, but the noise from vibration is in the absorption mode rather than the dispersion mode of the signal. This was unexpectedly useful because the most obvious anomaly that led to the spin-temperature treatment[2] was in the dispersion mode.

Carson Jeffries kindly sent Nico the design for his spectrometer, which I recognized as the same kind of circuitry familiar to me from my days as an engineer at the Harvard radio station. My version (Figure 1) had six ganged air capacitors driven by a motor and gears to keep the rf stages in tune; I got this idea from my days at Woods Hole where my first job was to wire a master control panel that had several rotary switches ganged together in the same way. Of course, all radio receivers in those days used ganged capacitors. It was the tradition at Harvard to vary the frequency rather than the field, since everyone there tended to use the 'Pound box' marginal oscillator whose frequency could easily be varied. I first set up my system by looking at the sodium resonances in aqueous NaCl. Ted Rowland, who was Nico's first graduate student, working on quadrupolar effects and electron-coupled spin−spin interactions in metals, taught me how to prepare the copper and aluminum samples, and I was ready to go.

Sometime around the end of 1953, I looked at my first true signal in, probably, aluminum. It was easy to find the dispersion signal and I then rephased the system to get the absorption mode. Varying the power, I found that the absorption mode did saturate at fairly low power as predicted by Bloch's equations and Korringa's paper. But the rf level seemed lower than that at which I first saw a dispersion signal, so I rechecked and found that indeed the dispersion signal did not seem to saturate; I later found that the resonance also became narrower and more Lorentzian-looking. Subsequently, I verified this result in copper. Both Bloch's equations and

Figure 1 A. G. Redfield with the equipment used to make the observations that led to the hypothesis of spin temperature in the rotating frame. The original observations were obtained with a permanent magnet having a field of 0.3 T, instead of the Varian magnet shown here. All of the RF components are in the two boxes, mounted at an angle so that the cabling to the probe was short. This was done because there were no matched transmission lines, the tube plate or grid forming part of the tuned circuit. At the bottoms of these boxes is the motor and right-angle drive used to turn the six tuning capacitors in the boxes in synchrony.

an argument based on spin temperature in the fixed frame of reference given in Bloembergen's thesis predicted that absorption and dispersion should saturate together, so my observation was in at least 10-fold disagreement with theory and, therefore, worth thinking about. I did not understand this key phenomenon until around June 1954, six months later, as a result of lots of spare-time reading and thought. In the meantime, I improved the equipment for low temperatures and took more saturation data.

It may seem to the modern reader that my eventual explanation in terms of rotating-frame thermodynamics should have been trivial and obvious. In fact, other physicists observed the same thing at that time without being able to explain it. Finding an explanation required several steps. The rotating frame had been described with clarity by Ramsey and Schwinger, and Van Vleck's truncation of the dipolar interaction was well known to everyone. But it was not immediately obvious to me that the truncated Hamiltonian contained the terms which were rotation-invariant and were the secular terms I would have to keep in any rotating-frame theory. I also had to teach myself about the density matrix. This was not part of the standard training of physics graduate students in those days. The formalism was introduced to NMR by R. K. Wangsness, working with Bloch, but I learned of it in a talk by J. M. Luttinger on the ferromagnetic Hall effect in which he referred to the density matrix as an obscure method, and then I taught myself about it from Tolman's classic book.

Another step that I made on the way to fully understanding my observation was to realize that it could be explained by assuming that relaxation along the effective field was much slower than the normal solid state T_2 of a few microseconds. I named this relaxation time $T_{1\rho}$. However, it was not obvious how to connect this hypothesis to the idea of spin temperature.

Spin temperature was introduced in the 1930s in connection with electron spins at low temperature by Casimir and DuPre, and first mentioned for NMR by Purcell and Pound in their famous paper on negative spin temperature. I learned about it from a 1937 paper by Van Vleck, and I was always of the school that believed in the predictions of thermodynamics (in the fixed frame) for systems of tightly-coupled spins. A second school, whose most eminent member was Abragam, believed that this was not obvious because the nuclear spins were not in contact with a lattice containing many degrees of freedom (I hope I am presenting their view correctly). At about that time, unknown to me, Abragam and Proctor were working on their famous experiments to test the predictions of spin-temperature theory quantitatively. The views of this latter school were encouraged perhaps by the existence of theorists, notably Felix Bloch, who did not believe in spin-temperature predictions at all. The hardest pill for these physicists to swallow was the idea that nuclear spins would remagnetize themselves (for experiments done in a time short compared to T_1) after being adiabatically demagnetized. I recall a meeting around 1956 when Abragam presented his results. That evening I witnessed an animated discussion between him and Bloch which concluded with the friendly advice: 'Well, Anatole, you'd better think about it'. When I presented my plans to study relaxation of demagnetized spins at a meeting in Stanford, Bloch's comment was: 'Well, the spins have to be mighty smart to do that' (i.e. to adiabatically remagnetize themselves).

After months of scribbling pictures of spins flipping each other, and also having them do so in my head, I figured it out. It was not a gradual process: I can remember the exact stretch of road where, during one of my habitual night walks around Woods Hole, the phrase 'canonical distribution in the rotating frame' slipped into my mind. The better description 'spin temperature in the rotating frame' was probably coined by Abragam, some time later. In fact, before I got to this point, I reinvented temperature by asking what would happen to the energy (actually the 'effective energy', as described in the original paper) if a Bloch decay were to occur along the effective field. I provided a very general argument, based on conservation of this energy, that the entropy of the spins would decrease for a complete decay, violating the second law of thermodynamics.

In a few days, I wrote out a summary of the theory and presented it to Bloembergen, who was interested as well as perhaps a little skeptical about my ideas. Three days later, without much discussion, he agreed that my theory was probably correct.

The paper I eventually published in 1955 was too long, and the last section was a disconnected presentation on 'rotary saturation'. This was a CW method for investigating NMR with an audiofrequency field in the rotating frame. Here I found accidentally that the double resonance linewidth was relatively narrow when the effective field was oriented away from the z axis by the magic angle. I gave a correct explanation of this phenomenon, which was kindly mentioned by John Waugh in his papers on development of high-resolution NMR in solids; but I forgot to mention, in my paper that Bloembergen (who graciously declined to co-author my paper) pointed out the explanation of this important phenomenon in terms of an equation I had written but had not looked at carefully, truncating the dipolar interaction in a sort of double Van Vleck method. Later this narrowing was thoroughly investigated by Lee and Goldburg.

Before leaving Harvard, I completed work on a simple low-temperature set-up and measured T_1 of aluminum and copper as requested by Nico, below 4.2 K as well as at room temperature, verifying Korringa's theory (Figure 1). I did this by adiabatic rapid passage thereby demonstrating at least qualitatively a key prediction of my theory, namely adiabatic demagnetization and remagnetization in a spin locked state. This hasty experiment was the first example of intentional spin locking. I say 'intentional' because the original NMR signal seen by Bloch's group in liquids was apparently a similar adiabatic fast passage signal and the 'locking' was against decay due to static field inhomogeneity.

I felt at the time that all this was nice work, and doubted that I would ever do better; this has turned out to be true. I was surprised at how slowly my ideas were accepted and it was not until after Abragam's outstanding book was published that the theory became widely known, if not understood. He gave my paper an excellent treatment, which I appreciated, but I do not agree that my first paper was particularly obscure as seems to be widely believed. I did not have the advantage of three years of other experiments on fixed-frame spin thermodynamics to describe, by way of introduction. My main task was to explain the unexpected observations I had made and these were not easy to connect with the rather simple idea that I eventually proposed. In fact, I suggest that the reader go back and read my 1955 paper.

In 1955, I moved to the IBM Watson Laboratory at Columbia University, and I decided to concentrate on properties of superconductors rather than do more on pure spin theory. I will come back to Harvard and the Watson lab later, and continue with further aspects of spin temperature now.

Within a few years there were tests of the predictions of my theory for spin systems containing only one species of spin by Donald Holcomb and by Walter Goldburg (whose interesting early contributions to this field are not fully recognized). In the meantime, there was widespread investigation of variants of the Overhauser effect, first observed by Carver and Slichter, driven to a considerable degree by interest in the development of polarized targets for particle physics, culminating in the development by Abragam's group, and independently by Jeffries' group, of the solid effect. Hahn continued to perform pulsed double resonance NMR experiments in solids in an obsessive search for ways to observe rare spins using abundant ones as detectors. Possible connections between all these activities were not obvious, at least to me, even though I had almost accidentally included a treatment of what would happen if a second species of spin were present for single resonance in my 1955 paper. I did this because copper has two naturally abundant isotopes.

In 1960, Abragam kindly welcomed me for a sabbatical year's stay at Saclay. When I arrived he asked if I would like to be called 'Al', and then informed me that I could call him 'Anatole', but it would not be a good idea to shorten it to 'An' (non French speakers can consult a dictionary). I spent the year working with André Landesman on a long-shot experiment to polarize helium-3. The experiment did not work, but it was fun trying it. Abragam's book was in press during that year, and it is interesting to reread his treatment of my theory and then to read his sections about two experiments to which it might have been applied, namely the solid effect (which might now be described as Hartmann–Hahn cross polarization, except for minor details), and the first observation of polarization transfer between two nuclear species by Sorokin and Bloembergen. Abragam did not clearly make the connection, and despite the general interest in spin-transfer experiments at the time, engendered by the various nuclear polarization methods, we were not good at extending these ideas to cross polarization.

Among the first papers to describe two-spin-species experiments coherently using spin-temperature theory were those of Landesman and Goldman, discussed elsewhere in this volume by Goldman (see ***Goldman, Maurice: The Time when Spin Temperature was Hot Stuff***), and of Hartmann and Hahn, which appeared as an abstract during my year at Saclay. The famous Hartmann–Hahn cross polarization condition did not come as much of a surprise to us, and I thought the really nice feature of their experiment was their method of draining spin order from the abundant protons by phase reversing the rare spin rf fields. This idea has been nearly forgotten by modern solid state NMR spectroscopists. The second important contribution of Hartmann and Hahn was to use very strong rf fields, several times the dipolar field, for cross polarization. Doing so allows one to neglect various aspects of the spin–spin interaction that are dear to my heart but that most people do not want to know about, and more importantly it leads to efficient polarization transfer. On the other hand, Landesman and Goldman showed that a somewhat greater polarization transfer can be achieved by using a weaker rf field and slightly violating the Hartmann–Hahn condition.

On returning from France, I immediately performed a field cycling pure quadrupole resonance version of the Hartmann–Hahn experiment (borrowing also some ideas from the Landesman–Goldman work), as did several others. I was pleased with this work because it related to the thesis of Ted Rowland who helped me a lot during my stay at Harvard. Magnetic field cycling resonance in zero field has also been used by A. G. Anderson to verify the predictions in the classic papers by Van Vleck on low-field lineshapes, essentially repeating for nuclear spins the 1930s experiments by Gorter on electron spin systems.

A few months later, I received the paper of Landesman and Goldman from the *Physical Review* to referee. On the referee form, typed in red, was the question: 'Is this paper too long?' I read the paper, and said it was too long and should be shortened (almost always good advice). I have forgotten what else I said, but before long I saw the article appear in *Physical Review* with the acknowledgement of the minor help I had given while I was at Saclay [described by Goldman in this volume (see ***Goldman, Maurice: The Time when Spin Temperature was Hot Stuff***)]. The following summer at the Gordon Conference, we heard Slichter describe some experiments related to the rotating frame. Abragam always came to these conferences, sitting in the front row in a leather chair that seemed to be reserved for him, and we awaited his comments on each paper with great interest. This time, after complimenting Slichter on his talk, he said (paraphrasing): 'Two years ago [at the previous Gordon Conference], I described some nice work by Landesman and Goldman ... At that time, I had the impression that no one understood me. Recently we sent it to *Physical Review*, and the referee, I don't know who it was ... [looking about the room for effect] didn't understand it either.' I managed to keep a straight face; of course, there could have been another referee.

To further illustrate some confusion at that time, I will mention some other papers. One was by Goldburg, who ingeniously studied the expected cross saturation of spectral lines which due to quadrupolar splitting could be moved about to overlap or not, by rotating a crystal. The lines did not crossrelax as expected and neither Goldburg, nor I, could explain this, although in my heart I knew that I should be able to. Jean Jeener eventually did so using spin-temperature arguments in a way that seems completely self-evident in retrospect. The same kind of reasoning was later used by Azriel Genack and myself, and by Stengers and Jeener (unpublished), to predict that spin diffusion would be quenched in the presence of large gradients in the static field. Even if one step of cross relaxation or spin diffusion is possible kinetically, because spectral lines may overlap slightly, nevertheless energy is not conserved in the long run by cross relaxation. In the case of spin diffusion in rigid solids (not applicable to proteins!), we deduced a two-component diffusion equation which seems unique in transport theory.

During this period my student, Peter Solomon, investigated cross relaxation between electron spin multiplet lines, and proposed several mechanisms to explain why the peculiar phenomena mentioned above are not seen in these systems. I developed a moment-method expression for spin diffusion in solids and, with William Yu, applied it to estimate the spin diffusion coefficient in solid helium. Herman Bleich and I developed a double resonance method, combining Hartmann–Hahn cross polarization with decoupling, which we

called 'higher resonance NMR in solids' (I did not have the courage to call it high resolution). Bleich and C. S. Yannoni[3] used this method to measure the chemical shift anisotropy in benzene, scooping Pines, Gibby, and Waugh by six months. However, the method was too awkward to compete with their straightforward scheme, and was forgotten. Regretably, the obvious acronym for their method is not approved for this Encyclopedia.

The impact of this work on other fields has not been great, other than its relevance to nuclear polarization and solid state NMR in general. However, R. V. Pound recently pointed out to me that the energetics of trapping of free ions and molecules by rf fields is strongly analogous to phenomena like adiabatic demagnetization of spins in the rotating frame.

I will not say much more about spin-temperature physics, since Goldman has said much about it in this volume including a description of the fascinating ultralow temperature states he and his collaborators have studied (see ***Goldman, Maurice: The Time when Spin Temperature was Hot Stuff***). He says correctly that spin-temperature theory has declined in general interest. I will mention one other reason why the theory is not well known any more. Starting with experiments like those of Hartmann and Hahn, and including the developments by Waugh's group and also the related HOHAHA or TOCSY methods in solution, you do not need this added theory to understand the dominant trick. It is Hartmann–Hahn cross polarization transfer via mutual spin flips that conserves energy or polarization in the rotating frame at high effective field. It is plausible that this process will occur as long as you forget that Bloch would have expected the transverse magnetization to decay in a short time. The fact that it does not was also a problem for electron spin systems at low static fields in the experiments of the 1930s. It is permissible to forget these things for simple processes with good Hartmann–Hahn matching. Only when overall energy is not conserved for a mutual spin flip, as in the Goldburg experiment, will you get unexpected results.

Now I will go back in time, to my postdoc days in Bloembergen's group. In developing the spin-temperature theory, I had to make assumptions about spin–lattice relaxation in order to estimate the steady-state spin temperature. Relaxation of the Zeeman part of the rotating frame energy was straightforward, and I assumed double that rate for the spin–spin part of the energy. My reasoning was that each of two interacting spin partners would relax independently at the single-spin rate. I felt that this could not be exactly true since these spins were close together, at a distance comparable to the electron's wavelength. I think this was why I got interested in relaxation theory on a deeper level. It turns out that the correction implied by what I just described is rather small. Furthermore, Hebel and Slichter later provided an elegant sum-rule to calculate the same correction in their famous papers on relaxation in superconductors. Another stimulus was a lecture I heard by Ionel Solomon, who was then a visitor in Purcell's lab, doing his famous study of two-spin (hydrogen fluoride) interaction and relaxation. He described transverse relaxation somewhat by analogy to longitudinal relaxation in the presence of a small imagined transverse circularly polarized rf field.[4] I thought that he was really using a density matrix in disguise and that I might do better by explicitly using it.

As mentioned above, Wangsness and Bloch had just published their paper on the quantum theory of relaxation of a spin-$\frac{1}{2}$ nucleus, and I also had access to a preprint of Kubo and Tomita's paper but I could not understand either one. So I asked Bloembergen where he got the theory involving spectral densities outlined in his paper ('BPP', with Pound and Purcell) and he referred me to a paper by Pound and Abragam and the review by Wang and Unlenbeck. I had absolutely no other knowledge of correlation functions and noise theory. For quantum theory I just used the notes of the excellent introductory quantum course I had at Illinois, taught by James Snyder, which I audited in my second year there after taking it in my first. I think the first thing I did was to derive T_2 quantum mechanically using the same math as is used to derive 'Fermi's golden rule', relating the transition probability to the density of final states and the square of a connecting matrix element.

At about this point I mentioned to Bloembergen that I had done something like this; at the time I did not think it to be worth much because of the other work on relaxation. He urged me to write a paper, so I began to work harder on it and eventually to solve the problem of spin–lattice relaxation of spin–spin energy that got me started. The developments I just described must have occurred during 1954–55, and I did not complete the article until after I left Harvard.[2] I was persuaded to publish it in the newly founded *IBM Journal of Research and Development*, a poor choice. It would have died there but for the fact that Solomon and Bloembergen used it in their famous papers and that Slichter described it (appropriately coupled with the names of Wangsness and Bloch) in his book.

When I am introduced for talks these days people speak uneasily about 'my' relaxation theory, and mention none of my older work. Actually I feel ambivalent about relaxation theory for a variety of reasons, in addition to the many precursor theories which I already described. I never considered myself a true statistical physicist, and the feeling is no doubt reciprocated by such physicists. Much the same theory was worked out by Bloch and co-workers at the same time, while he was Director of CERN (the joint European high energy physics laboratory). I did not really know what I was doing and certainly did not realize that spin relaxation is in virtual one-to-one correspondence with Brownian motion theory, being the result of Brownian motion in Hilbert space. I also missed the second-order shifts produced by fluctuating perturbations, discussed in another volume of this Encyclopedia by Werbelow (***Dynamic Frequency Shift***). The theory itself is really a straightforward extension to quantum systems of old classical ideas, and the discussions in my paper justifying my methods are nothing more than justifications of perturbation theory. My ambivalence was similar to that of Abragam when he contemplated developing relaxation theory at about the same time, as described in his autobiography. Eventually, of course, he did so in his treatise, emphasizing an operator formalism. Both formalisms are useful for different kinds of problems.

My treatment did have a few unique features. Even though people complain about its complexity, it probably remains the simplest complete paper on the subject for readers who are not specialists in quantum physics. This was mainly a consequence of my amateur status as a quantum physicist. My notation was excruciatingly cumbersome for some problems but was suited for chemical problems; this was a consequence of my interaction with Solomon. It was the first theory to include partially correlated fluctuations. It is perhaps the only paper to explicitly treat relaxation both

classically and quantum mechanically. It contains a section on interaction with the measuring device which no one, to my knowledge, has read. Finally, the paper introduced the idea that transverse relaxation may always exist between off-diagonal density matrix elements, but is ineffective unless they nearly overlap in frequency. I don't think I conceived that such transverse–transverse relaxation could be observed in experiments like CAMELSPIN–ROESY[5] until somewhat later. My only subsequent work in this area was to spend almost the entire summer of 1963 calculating a single correlation function for relaxation in NaCl due to vacancy diffusion, with Maurice Eisenstadt.

Private compliments were paid by Bloch who telephoned me in late 1955 after briefly meeting me and I suppose receiving a preliminary manuscript, to ask me to collaborate; I said, 'no thanks'. Later, probably after I completed the paper and sent it to him, his postdoc Bernard Herzog reported (via my co-worker Richard Blume) that Bloch said to him something like, 'say Bernie, this Redfield . . . he's Jewish, isn't he?' The papers Bloch wrote at that time are probably the first ones on the rf field dependence of $T_{1\rho}$ which I did not treat at all.

During my second year at Harvard, Bloembergen encouraged me to repeat Knight's early experiments on colloidal superconducting mercury. I had a good second-hand feeling for both superconductivity and low-temperature physics from observing my friends at Illinois, and was happy to do so. The only thing that came out of this was the low temperature measurement of T_1 in aluminum and copper that I mentioned earlier; someone tried to make a colloidal mercury sample for me, but was unsuccessful.

This work was cut short in 1955 because Bloembergen recommended me to IBM to take over Erwin Hahn's lab. I visited the IBM Watson Laboratory, meeting Hahn for the first time, and shortly I received and eventually accepted their offer. Meanwhile, I was sharing a lab with a student who was trying to duplicate the Purcell, Pound, and Ramsey experiments to study phenomena at low and zero field by moving a crystal from a high magnetic field to a low one and back. All these things led me to think of measuring T_1 in superconductors in the same way. This was a somewhat risky experiment because it was not clear that the spin polarization would survive the rapid changes in field as the metal went superconducting and back.

Over Christmas in that year I stopped in Illinois on my way to ski in Colorado, and naturally dropped in to Slichter's lab. There I learned in a casual conversation with his students that he had exactly the same idea and that they were working on it. Slichter encouraged me to try it anyway, and told me that we should not discuss our plans further until one of us had some results. However, I didn't have time to start this experiment until I got to my new job at IBM in September 1955. As I expected, I received a letter a few months after arriving there from Charles Hebel, Slichter's student, announcing success and describing the completely unexpected rise in relaxation rate just below T_c in aluminum. Of course I was envious, not because I was scooped but because it must have been truly exciting to make this discovery next to Bardeen, Cooper, and Schrieffer as they finally solved one of the great mysteries of the century. However, had I been in Slichter's shoes I doubt if I would have been smart enough to work out the details of NMR relaxation in the same way that he did. It did not work out so badly for me, because it was of course desirable to check the Hebel–Slichter result and eventually to extend it to a wider temperature range, which was achieved by Arthur Anderson and Yoshika Masuda in my lab.

The IBM Watson Laboratory at Columbia University was my home for the next 15 years. It was a remarkable place and deserves a description for several reasons, including the fact that it housed several distinguished workers in NMR: Hahn, Martin Karplus, Richard Garwin, and Seymour Koenig, as well as others who worked on EPR in biological systems. It was the first more-or-less 'pure', or relatively undirected, research lab in IBM.[6] Most of its senior researchers had adjunct positions in various departments at Columbia University, which was half a block away. It was a small lab, occupying a town house and a nine-storey converted apartment house, and having about 10 research groups. Eight members of the lab eventually became members of the US National Academy of Sciences. One reason Hahn was hired was that it was possible to store information in stimulated spin echoes.[7] By the time he left for Berkeley it became obvious that this idea was not promising; less than 1000 bits of information could be stored in a magnet weighing 100 lb or more, and the pulses came out in time-reverse from the order they were read in.

I was, of course, highly honored and also lucky to succeed Hahn. I inherited a very early Varian magnet and two long-term co-workers: William Kiselewsky, who was still helping Seymour Koenig and Rodney Brown construct NMR relaxivity machines at IBM until shortly before his death in 1993, and Richard Blume, who observed the first electron spin echoes. A student inherited from Hahn, George Whitfield, performed probably the first NMR experiment in a rotating rf field before he became a theorist; his work was extended by Richard Hecht. Another inherited student was Arthur Anderson, who got the superconductivity experiment going, and eventually rose to be Director of Research and then Vice President of IBM. Right next door were Richard Garwin and Haskell Reich, who were doing the earliest experiments on liquid and solid helium-3. It was entertaining to have Garwin as a neighbor; he is probably the smartest individual I know, having been involved in a wide range of government and IBM consulting jobs as well as physics. Early in my stay, I returned from a trip to be informed by Dick Blume that he had with great difficulty prevented Garwin from making off with one of my low-field Helmholz coils. It turned out that this would have been used for the discovery of parity violation in which Garwin participated. Another colleague, L. H. Thomas, almost discovered the fast Fourier transform (FFT) in the 1940s when theorists used mechanical hand calculators, but he did not tell anyone about it.[8]

Masuda and I built a magnetic cooling apparatus and then a helium-3 pumped system and carried the measurement of T_1 in superconductors to 0.2 K. I spent most of the rest of my time at Watson Laboratory applying field cycling NMR[9] to superconductors with the help of Warner Fite, Albert Kung, and Azriel Genack. I showed that the vortex structure in type II superconducting vanadium was triangular, based on the NMR lineshape. I proudly presented this work at the Low Temperature Meeting in Moscow to the many Russians and others who were responsible for so many developments in superconductivity. During that meeting Slichter and I arranged to meet B. N. Provotorov, who kindly invited us to his institute to meet some of his associates. The field cycling circuit that we built was later taken over by Seymour Koenig and Rodney

Brown, who developed it extensively for the study of various problems in protein structure and dynamics, and magnetic resonance imaging.

In the 1960s a biophysics program was started at the Watson Laboratory by R. L. Garwin, who had become Director of the laboratory, and continued by S. H. Koenig, its third Director. Phillip Aisen, a biochemist who used EPR to study metalloproteins, joined the lab. I was encouraged by them, and by a talk I heard by Melvin Klein at a meeting in 1968, to try FT NMR in proteins. The promise of NMR in biochemistry had already been demonstrated by Oleg Jardetsky, Robert Shulman, William Phillips, Mildred Cohn and others, but there were no FT machines available commercially. Ernst's paper had appeared, and two homemade FT machines were under construction by Klein and by Hyam Sternlicht. By the fall of 1968, I had decided to build a proton machine with quadrature detection, soft pulses for water suppression, and a pulse programmer that could control presaturation. I think I thought these things up on my own, possibly influenced by a 1964 paper by W. G. Clark which showed the properties of quadrature detectors feeding 'box-car' integrators. However, I soon learned that Schlom Alexander had already invented the soft pulse in Saul Mieboom's group at Bell Labs, and much later I learned that Richard Ernst had submitted a patent on the quadrature detector in 1968. Jeener told me how to build the timing system based on a single present counter.

I was not sure whether quad detection or soft pulses would work, or what we would study with our instrument except that we would look for saturation transfer in a protein. My main motivation in using quad detection was to reduce the required transmitter power and be able to work on one side of the water resonance with a soft pulse to eliminate the water signal. I knew that the quad detector would improve the signal-to-noise ratio, but I forgot to say so in our first paper. We paid $40 000 for a demonstration 100 MHz JEOL CW spectrometer, and the first thing I did while waiting for it to be delivered was to build the quad detector and filter system. The spectrometer came in the spring and Raj Gupta joined me in furiously building the pulsed modifications and programming a computer.

In the middle of this we learned that the Watson Lab would close soon, but we could not think of anything else to do but to continue. The spectrometer in the basement transmitted data at the end of each run to a computer on the 7th floor, and was controlled in part by a mechanical cam timer and a telephone stepper relay. We would then run up to this computer, which belonged to another project, and would take the 512 punched cards that it produced to a larger computer which could do the FT. Data transmission occasionally dropped a bit and if so Gupta would find the card having the bad bit and manually replace it with one encoding the average of the two adjacent data points. Despite these problems we got our first FT spectrum in the fall. This was the first FT instrument to be used for proton and protein NMR research.

Gupta wisely chose to work on cytochrome-*c*, which had already been studied using CW NMR by Wüthrich and Shulman, and by W. D. Phillips. We soon got acceptable spectra even though we were working at 100 MHz whereas Shulman and Phillips had 220 MHz Varian spectrometers. As suggested by an early paper by Arthur Kowalsky, pointed out to us by Thomas Fabry, we connected assignments of the oxidized and reduced heme methyl resonances using saturation transfer. This permitted an estimate of the electron-transfer rate, and shortly afterwards Gupta found our first NOE. These were the first observations of these effects by FT NMR and in a protein.[10] In the spring of 1970, I reported our machine architecture and spectra at the Experimental NMR Conference, but I did not report the electron exchange results that we obtained a week before since I assumed, erroneously, that others might easily be able to do this experiment. However, I could barely prevent myself from talking about them. These saturation transfer results connected key assignments made separately by Wüthrich, Shulman, and Phillips in the two states of cytochrome-*c*, thereby solidly confirming these results and showing that a methionine was coordinated to the heme in both states. R. E. Dickerson kindly permitted us to visit his lab and view his oxidized-state crystal model. There we learned that his preliminary (never published) reduced-state structure was wrong with respect to the heme coordination, and we told him so. After some delay, he fortunately corrected it before publication.

I spent the following two years in the lab of D. E. Koshland learning biochemistry. Commercial FT instruments appeared around 1971, but they were really inferior to the one we built except for the computers. The engineering level in these instruments remained disappointing until the mid-1980s.

In 1972, I was fortunate to move to Brandeis and we ordered the second Bruker WH-90 to be sold in the US. Meanwhile, I hired Sara Kunz, a recent Brandeis physics major, and we started building a front end for our own system, again starting with the quadrature detector. The WH-90 arrived in the summer of 1973, and as we had planned we used it as a test instrument for our own electronics. Bruker thought they had a good instrument, but we knew better; for one thing it had no quad detector and could not cope with the H_2O solvent problem. Even before final acceptance they were startled to find wires issuing from the back of the instrument leading over to our unprofessional-looking relay rack. This instrument now has a 500 MHz magnet and most of it has been replaced over the years. It probably holds the world's record for length of service.

As I had at IBM, during my decades at Brandeis I tried to maintain a high level of problem-oriented research and spent only a fraction of my time on technical matters. I won't review these years except to note one striking change: the developments in high-resolution NMR which we demonstrated around 1972, namely the use of soft (later composite) pulses to suppress water, and quadrature detection, were not used by anyone else until about five years after I first presented them. I really could not understand why, since they were really easy to implement and obviously useful. The same can be said of 2D FT NMR, invented at the same time. That idea was more complicated to develop, but was much more significant.

In contrast to this period of slow acceptance of new ideas, the pace has increased dramatically over the last 10 years. New methods are seized immediately and developed or used right away. Most likely this is because a lot more smart young people are entering the field or have entered it and are training other talented students; and because NMR has shown itself to be an extremely useful and generally accessible technique in biology.

Although my talent and most important contributions to NMR probably lie in the area of technical development, I am happy that I did all the problem-oriented work that I have hardly described here. It has enabled me to be a

spectator, and in a very minor way a participant, in fields that were developing rapidly and dramatically: superconductivity, biosynthesis of proteins, and the early stage of the part of biological development which is called signal transduction. At the same time, I treasure my contacts with the early giants of magnetic resonance: Gorter, Van Vleck, Purcell, and Bloch, as well as my friendship with the next generation of workers, such as Slichter, Bloembergen, Hahn, and Abragam, continuing all the way to the current group of very talented and dedicated young pulsed NMR jockeys.

REFERENCES

1. W. C. Redfield, *Am. J. Sci.*, 1831, **20**, 17.
2. Most of the topics mentioned are described in papers referenced by: A. G. Redfield, *Science*, 1969, **164**, 1015; M. Goldman, *Spin Temperature and Nuclear Magnetic Resonance in Solids*, Clarendon Press, Oxford, 1970; D. Wolf, *Spin Temperature and Nuclear Spin Relaxation in Matter*, Clarendon Press, Oxford, 1979; L. T. Muus and P. W. Atkins (eds.), *Electron Spin Relaxation in Liquids*, Plenum Press, New York, 1972; and the treatises of Abragam and of Slichter. Works mentioned in the text and not listed below were mostly published in the *Physical Review*.
3. C. S. Yannoni and H. E. Bleich, *J. Chem. Phys.*, 1971, **55**, 5406.
4. I. Solomon, *Phys. Rev.*, 1955, **99**, 559.
5. A. A. Bothner-By, R. L. Stephens, J.-M. Lee, C. D. Warren, and R. J. Jeanloz, *J. Am. Chem. Soc.*, 1984, **106**, 811.
6. J. F. Brennan, *The IBM Watson Laboratory at Columbia University: A History*, International Business Machines Corporation, Armonk, NY, 1971.
7. A. G. Anderson, R. L. Garwin, E. L. Hahn, J. W. Horton, G. L. Tucker, and R. M. Walker, *J. Appl. Phys.*, 1955, **26**, 1324; *ibid.*, 1956, **27**, 196.
8. J. W. Cooley, P. A. Lewis, and P. D. Welch, *Proc. IEEE*, 1967, **55**, 1675.
9. A. Redfield, W. Fite II, and H. E. Bleich, *Rev. Sci. Instrum.*, 1968, **39**, 710.
10. A. G. Redfield and R. K. Gupta, *Cold Spring Harbor Symposia on Quantitative Biology*, 1971, **36**, 405.

Biographical Sketch

Alfred G. Redfield. *b*. 1929. B.A., 1950, Harvard, Ph.D., 1953, University of Illinois at Champaign-Urbana. Postdoctoral research with N. Bloembergen, 1953–55; IBM Watson Laboratory at Columbia University and Adjunct Member, Columbia Physics Department, 1955–72. Professor of Physics and Biochemistry, Brandeis University, 1972–present. Sabbatical visitor in the laboratories of A. Abragam, 1960–61 and D. Koshland, 1970–72. Research primarily in superconductivity, transfer RNA and small G-proteins.

Reeves, Leonard W.: Early Application of NMR to Chemistry at the National Research Council of Canada

Leonard W. Reeves
University of Waterloo, Waterloo, Ontario, Canada

The National Research Council of Canada with laboratories in the capital city of Ottawa was financed directly by the Government of Canada and after World War II came under the directorship of the Canadian scientist E. W. R. Steacie. With much vision and considerable determination, Steacie organized the overall research council into pure science and applied science divisions. Steacie set up a series of competitive postdoctoral fellowships to fill up the funds allocated and provide continuous renewal of ideas. Rapidly after World War II, the laboratories gained international respect in several fields.

W. G. Schneider and H. J. Bernstein were among the permanent scientific staff of the Pure Chemistry Division, and they had combined their capital budgets to purchase an NMR spectrometer from Varian Associates in California. In those early days there were two spectrometers in Canada; the other had been delivered to the University of British Columbia at the request of Cyril (Chris) Reid. I was awarded a postdoctoral fellowship to join the research efforts of W. G. (Bill) Schneider in 1956. When I arrived, the NMR 40 Mc/s spectrometer had been in operation for less than one year. I was offered problems either on ultrasonic relaxation or on the new NMR equipment, and I chose the latter. The original 30 Mc/s equipment of Varian had been upgraded to 40 Mc/s and was only useful for the observation of proton and fluorine magnetic resonance in liquids. While it would be wrong to underestimate the contribution of Varian Associates to the application of the technique to chemistry, there were defects in the equipment as sold at that time. A drawback was the reproducibility of the sawtooth field sweep. The line voltage affected the magnetic field drift, and it was an advantage to work in the evening when the line voltage was more stable. When I arrived in Ottawa, the activities on the spectrometer were suspended while the laboratory awaited the arrival from Varian of the so-called superstabilizer. This device was a sensor of field drift using large search coils set in place on the pole caps of the main magnet. The induced currents from field drift were fed to a galvanometer, and neutralizing currents were fed to buck-out coils in the same assembly, thus stabilizing the magnetic field. If properly used, the superstabilizer almost eliminated the long term drifts. The device was also used to sweep the field slowly, and a slower recorder could be used to approach the slow passage conditions set out by Bloch in his description of resonance.[1]

The philosophy of the laboratory at the time was to try to seek out problems which would illustrate for all time how useful NMR might be in chemistry.

By the summer of 1956, the range of chemical shifts of the proton magnetic resonance in chemical compounds was already known to be about 15 ppm. Those resonances found at lower field were considered to be deshielded with respect to those which appeared at higher magnetic field. The chemical shifts were laboriously measured and calibrated using audio sidebands impressed upon the field sweep coils. The matter of finding a standard chemical shift signal which would serve for referencing all proton signals was discussed at length among members of the group. The signal from cyclohexane was initially used but did not survive because it was not sufficiently separated from other aliphatic-type protons. The cyclohexane peak also suffered line broadening at temperatures below room temperature because of the slowing of the chair-to-chair conversion rate.

Schneider and Bernstein had funds available to invite visiting senior scientists, and we had the pleasure of the addition of John Pople, then with the National Physical Laboratory in England. I was present at many of the afternoon informal seminars though I was myself a student rather than a speaker. The decision to write a book on the subject of high-resolution nuclear magnetic resonance followed.[2] The puzzle of the time was the unusual position of the signal from protons on benzene in the range of chemical shifts of protons. John Pople realized that the large diamagnetic susceptibility anisotropy of the benzene π-electron system was responsible for the anomaly. On one of his trips to Ottawa, he used the time during the trans-Atlantic flight to write a note to the literature showing the correct order of magnitude and direction of the effect.[3] Bill Schneider pursued studies on solvent effects, and there was an immediate application of the large diamagnetic susceptibility of benzene in solvent effects using benzene solutions.[4]

Another subject was the fact that the changes in hydrogen bonding in a solution produced large changes in the chemical shift of the hydrogen-bonded proton. Unfortunately, the lifetime of an individual hydrogen bond is too short to resolve individual peaks of different hydrogen bonded configurations. In benzene solutions there is a weak tendency for hydrogen bonds to form between the π-electron system and a hydrogen-bonding species. In my own experimental work, it became clear that chloroform molecules did form a weak hydrogen bond with benzene, and the large diamagnetic anisotropy of benzene was a special way to illustrate this using proton magnetic resonance.[4]

There was a need for a broad selection of proton resonance spectra in order to present the fundamentals of spectral analysis, where the chemical shifts were not large with respect to the so-called scalar spin–spin coupling between the nuclei to include in the proposed book. After much discussion, the type of nuclear system was classified according to the upper case letters of the alphabet. Two protons which were not chemically shifted became denoted as A_2; those with a small chemical shift and tight coupling were denoted as an 'AB'-type spectrum. As the chemical shift increased in relation to the nuclear spin coupling, the upper case letters were further removed in the alphabetic sequence. This simple notation immediately gives a notion of the complexity of the matrix to be diagonalized in the calculation of theoretical spectra.[5] Pople used the occasion to make full use of symmetry in the choice of nuclear spin functions for the calculations, and this simplifies the overall diagonalization procedure as well as eliminating many spectral transitions.[5] The original notation of Pople has been greatly extended since these early studies,

but the framework of the notation survives up until the present time.

The group at the National Research Council of Canada was approached by R. U. Lemieux, a professor at the University of Ottawa, to look into the problem of conformations of simple sugars and related saturated six-membered rings by NMR methods.[6] A productive and beautiful collaboration followed which laid down the fundamentals of conformational analysis by NMR.[7]

Another classical aspect of organic chemistry, namely the phenomenon of tautomerism, was the object of my own experimental work. At that time the equilibrium between keto and enol forms was studied by crude chemical methods such as rapid saturation of the olefinic bond in the enol form by bromine and a back-titration analysis of unused bromine to determine the proportion in the enol form. Spectroscopic methods had been used by Powling and Bernstein.[8] The earliest NMR study had already been published.[9] NMR proved to be the ideal way to tackle the equilibrium problem by a physical method. The exchange rate between enol and keto forms of the simplest cases such as 2,4-pentanedione proved to be slow enough on the NMR timescale to resolve separately the spectrum of the keto and enol forms. The position of the equilibrium was easily measured using signal intensities, and the effect of different solvents on the equilibrium was studied by NMR for the first time. It is remarkable that the equilibrium measurements of Shoolery et al.[9] and Reeves[10] made at 30 MHz and 40 MHz proton frequency, respectively, have stood the test of repeated measurements with much better equipment. My own work was extensive enough to illustrate that the keto–enol conversion rate could be greatly increased in basic solvents such as amines. The NMR method remains the best manner of studying tautomeric systems. This early investigation provided a model case of chemical exchange between three sites in a molecular system; namely, the keto methylene protons, the –OH proton, and the olefinic proton.

The activity of the Canadian group in pioneering the application of NMR to chemistry touched on many fields which were to be the object of my own future research. The study of chemical exchange by NMR is a case in point. The theoretical basis for such studies was already published.[11] The line broadening from chemical exchange of protons became evident in many of the spectra taken during the period in Ottawa. The exchange of protons among ethyl alcohol molecules modulates the spin–spin coupling of the –OH group protons with the methylene protons. This exchange is catalyzed by hydronium ions which lead in very low concentrations to the collapse of the triplet –OH resonance of ethyl alcohol to a single sharp resonance.[12]

REFERENCES

1. F. Bloch, *Phys. Rev.*, 1956, **102**, 104.
2. J. A. Pople, W. G. Schneider, and H. J. Bernstein, 'High Resolution Nuclear Magnetic Resonance', McGraw-Hill, New York, 1959.
3. J. A. Pople, *J. Chem. Phys.*, 1956, **24**, 1111.
4. L. W. Reeves and W. G. Schneider, *Can. J. Chem.*, 1957, **35**, 251.
5. Ref. 2, Chap. 6, p. 103.
6. R. U. Lemieux, R. K. Kullnig, H. J. Bernstein, and W. G. Schneider, *J. Am. Chem. Soc.*, 1957, **79**, 1005; *ibid.*, 1958, **80**, 6098.
7. Ref. 2, Chap. 14, p. 387.
8. J. Powling and H. J. Bernstein, *J. Am. Chem. Soc.*, 1951, **73**, 4353.
9. H. S. Jarrett, M. S. Sadler, and J. N. Shoolery, *J. Chem. Phys.*, 1953, **21**, 2092.
10. L. W. Reeves, *Can. J. Chem.*, 1957, **35**, 1351.
11. H. S. Gutowsky and C. H. Holm, *J. Chem. Phys.*, 1956, **25**, 1228.
12. Ref. 2, Chap. 15, p. 421, Fig. 15-12.

Biographical Sketch

Leonard W. Reeves. *b* 1930. B.Sc., 1951, Ph.D., 1954, D.Sc., 1965, Bristol University, UK. Postdoctoral research associate of Joel H. Hildebrand, University of California, Berkeley, 1954–56; NRC postdoctoral fellow with W. G. Schneider in Ottawa, Canada, 1956–57; Junior Fellow of Mellon Institute Pittsburgh, 1957–58. Assistant, associate, and full professor, University of British Columbia, Vancouver, Canada, 1958–69; Professor, University of Waterloo, Canada, 1969–present. Introduced to NMR by W. G. Schneider in 1956 and used NMR as a research tool since that date. Approx. 165 publications. Research interests: hydrogen bonding, solvent effects, and tautomerism; detailed studies of chemical exchange using lineshape functions and Carr–Purcell–Meiboom–Gill measurements of dependence of T_2 on pulse repetition rate in an exchanging system; use of NMR as a tool for discovery and investigation of aqueous lyotropic nematic and cholesteric liquid crystals.

Richards, Rex: Development of NMR in Oxford

Rex Richards
Oxford University, Oxford, UK

INTRODUCTION

This is a very personal account of some of the stages which I found particularly exciting in the research in my laboratory at Oxford on magnetic resonance. The considerable body of work could not have been done without the collaboration of the many very able young people who worked there with me, and who due to lack of space I cannot mention individually; but I think many of them shared with me some of the more thrilling moments as well as the inevitable frustrations and periods of exhaustion which so often come in research and especially in instrument development.

My interest over the years has been in attempting to demonstrate new ways in which NMR can usefully be applied to scientific problems and this has often involved the construction of our own spectrometers when commercial instruments were either too expensive for us or too inflexible for our purposes. These homemade instruments did not always have the performance we had hoped for; in those cases we used our ingenuity to find problems to which they *could* be applied. My story starts in 1948, soon after I had been appointed as a Fellow and Tutor of Lincoln College; although this was technically a seven-year appointment, I had sufficient confidence to feel that I could embark on something quite new and need not worry about how speculative it was or whether it was likely to yield immediate publications.

EARLY DAYS

When Bernard Rollin came to visit my laboratory some time in 1949 he remarked 'My word! This really is heat, light, sound, electricity, and magnetism!' That was my first NMR apparatus, built from surplus Royal Air Force electronics and a small 4 in. magnet built by Tickfords to a design from the Clarendon Laboratory. There were some massive, already quite elderly, power supplies giving off a good deal of heat, and, with the loose laminations of their transformers, also emitting a loud hum. The valves (tubes) glowed brightly and the 60 V bank of accumulators drove the magnet to produce a field of about 0.3 T in a gap of about 1.5 in.

The purpose of Bernard Rollin's visit was to see how I was getting on, and give helpful advice. He had made NMR measurements several years before; indeed he published his first observations of NMR in 1946[1] very soon after the original announcements from Harvard and from Stanford. Rollin used the simplest possible system in which a signal generator passed an appropriate radiofrequency through a high impedance to a tuned rf sample coil, which was thus supplied from a constant current source. The voltage on the coil was measured with an rf amplifier and homodyne (phase sensitive) detector; when energy was absorbed in the coil the voltage across it dropped and an NMR signal could be detected. Rollin and Hatton used this simple system to measure proton resonances in liquid and solid hydrogen down to 1 K; they described this work as early as 1949, as well as measurements of deuterium, aluminum, and copper resonances.[2]

Casting around for something quite new to do, I noticed the announcements of the observation of NMR from Harvard and from Stanford Universities and it occurred to me that this new effect might have applications in chemistry. On making enquiries in the Clarendon (Physics) Laboratory, I found that Bernard Rollin had already been making measurements, the publication of which I am afraid that I had overlooked! He was, however, very discouraging; he thought it was all much too difficult for a chemist and could not see much likelihood of its use in chemistry anyway!

However, Linus Pauling was visiting Oxford at about that time and frequently dined in Lincoln College with his old friend N. V. Sidgwick, who was my predecessor as tutor there. One night I told him about the discovery of NMR and his response was 'Well, Rex, the one thing I've learned is to take no notice of the advice of physicists!' So I went back to Bernard Rollin and told him I had decided to have a go anyway, and from then on he could not have been more helpful. That is why he called in to my laboratory to see the first NMR signal I had observed.

By now the big papers from Harvard[3] and from Stanford[4] had appeared and the possibilities of this new technique seemed to me to be very exciting. My first thought was to measure spin–lattice relaxation times in water in the presence of transition metal ions and various ligands. However the only method of measuring T_1 available to me at the time was the progressive saturation method, and I soon realized that, in my hands, it was simply not accurate enough.

DIPOLAR BROADENING IN SOLIDS

So the next thing to turn to was T_2 by measuring linewidths and shapes. The magnet had very limited homogeneity, so only broad lines could be measured and this meant working with solids. By this time I had seen the advantages of using an rf bridge and adopted a twin-T system described by Tuttle. This very much improved the sensitivity of the whole apparatus, the only commercial components of which were the magnet, a few second-hand power supplies, and a radiofrequency signal generator from surplus radar sets. All the rest of the equipment was built in the laboratory from components obtained by carefully unsoldering them from ex-service racks of electronics of mysterious and unknown (to me) function, which we were able to get at virtually zero cost. My research training with H. W. Thompson in infrared spectroscopy had taught me many laboratory arts and crafts and to be ready to improvise and have the confidence to make whatever is needed; an excellent preparation for the early days of NMR!

I studied the important paper by Van Vleck on second moments and dipolar broadening, and the Ph.D. thesis of Bloembergen, but found them pretty heavy going at the time; and it was only the frequent and patient exposition by Ken Stevens, then working with Maurice Pryce in the Clarendon

Laboratory, that helped me to grasp these vital ideas clearly. A paper by Luzzatti in Paris had recently interpreted the X-ray patterns of nitric acid monohydrate crystals in terms of hydrated HNO_3 molecules, and this presented a good opportunity to try out the NMR method. Working with John Smith, my first NMR graduate student, various acid hydrates were frozen and their NMR spectra measured at 90 K (we used liquid oxygen in those days!). Unequivocal results were obtained showing that some crystals contained the H_3O^+ ion, whereas for others the crystals were not ionic; it was also possible to measure the H–H distances.[5] I think this may have been the first occasion on which an unknown chemical structural problem was solved by NMR, though of course the H–H distance in calcite had been measured in classical work by Pake and Purcell; it was certainly very exciting to find that NMR could give such a clear-cut result for a chemical structural problem, even though the problem itself was not of earth-shattering importance!

It proved easy to find simple structures where there was ambiguity about the positions of hydrogen atoms, and my young colleagues and I published a series of papers of this kind over a number of years. Initially we plotted the resonances point-by-point at different fields across the resonances, but we soon changed this to automatic recording by coupling a potentiometer to the chart motor of a recorder, used it to drive a power supply for the field scan, and fed the output of the homodyne amplifier to the recorder. We studied a wide variety of problems, including the determination of the structure of the NH_2^- ion, the structures of perborates, perpyrophosphates, and percarbonates, and showed how the liquid/solid content of fats could be determined, a method now used routinely in industry. Linewidths were often measured from 20 K to 400 K thanks to the ready availability of liquid hydrogen, which was dispensed in the Clarendon Laboratory with warnings to treat it with as much respect as you would gasoline! Changes of linewidth with temperature often showed clearly the type of molecular motion causing the line narrowing, and estimates of the potential barriers to the motion could be obtained; some of the measurements made between 1951 and 1956 were later confirmed, but with greater accuracy, by neutron scattering.

CHEMICAL SHIFTS

The discovery of the chemical shift was of immediate significance to anyone brought up in the early days of infrared spectroscopy, and we set to work to build a better magnet with the very limited funds at our disposal. We constructed an electromagnet with 11 in. pole faces and a gap of 2 in.; it had two sets of coils, one of low impedance driven from a stable power supply, and another of high impedance. The many miles of wire were laid down by hand by me over a period of some weeks! The high impedance coils were driven through series tubes and regulated with a simple NMR feedback loop. In spite of much care and adjustment the performance of the magnet was not good enough for proton shifts, so the obvious answer was to use it to study heavy nuclei, and for this purpose we constructed a simple spectrometer using a 'Pound' marginal oscillator with which we were able to study a very wide range of chemical problems. For example,[6] cobalt chemical shifts were related to the optical spectra of a wide range of complexes and to their respective temperature dependencies; the results were interpreted in terms of the ligand fields and provided an improved value for the absolute magnetic moment of the ^{59}Co nucleus. Measurements were also made on thallium, gallium, indium, and many other elements.

PERMANENT MAGNETS

By this time, more detailed study of magnet design and consideration of the factors affecting homogeneity suggested that a well-designed permanent magnet might give a very cost-effective solution for real high-resolution NMR. I was fortunately able to raise £2000 to build one and to persuade the Mullard company to do it for this sum. Robert Pound spent some leave in Oxford in the early 1950s, and he kindly recommended me for a Research Fellowship at Harvard. I went off to Cambridge, MA from January to July 1955, spending most of the time in the Physics Department. Working in Pound's laboratory, attempting to see the pure quadrupole resonance in D_2O ice, taught me a great deal about electronics and practical NMR. Attending a course on magnetic resonance by E. M. Purcell and then listening to his patient explanations of the physical principles underlying the theory, gave me an insight into some parts of physics which I doubt if I could ever have gained from a study of the literature. I also got to know Ionel Solomon, visiting from Paris, who was doing some very elegant experiments on HF and demonstrating the nuclear Overhauser effect. Whilst in the USA I met Marcel Golay at the Perkin-Elmer Corporation, an inventor of real genius. In the course of conversation over dinner, I told him about my design for a permanent magnet and about the problem of compensating for residual field inhomogeneities arising from imperfections of gap geometry and from the grain structure of the pole pieces.

Some time after I had returned to Oxford, I had a letter from Golay setting out a detailed theory of a design for a set of correcting coils which could, in principle, cancel out any field gradient with a set of orthogonal adjustments. He made the coils initially by embroidering them on calico, and after getting very encouraging results he had some sets of printed circuits made and very kindly sent me one. We installed this on the Mullard permanent magnet and they worked extremely well, though the adjustments were far from orthogonal and required a good deal of patience and skill. This permanent magnet became the basis of a very simple and reliable high-resolution spectrometer; although the field, at 30 MHz for hydrogen, was very modest, the field value and the very good homogeneity were remarkably stable.[7] We used this instrument to explore a wide variety of high-resolution NMR applications many of which would seem commonplace today. At 30 MHz many of the spectra were strongly coupled so that detailed analyses of systems such as A_2B_2X or $ABB'X$ were needed. We studied solvent effects in some detail and some could be interpreted in terms of weak molecular associations. This simple NMR spectrometer was subsequently used as the basis of a series of relatively inexpensive but reliable instruments manufactured by the Perkin-Elmer Co. Ltd. in the UK, and later by other companies.

Meanwhile, the studies of the chemical shifts of heavy nuclei were proving so interesting that I was able to purchase a Varian wideline spectrometer, which we modified in various ways to allow frequency scanning over small ranges and

to improve very much the precision of chemical shift measurements. This instrument was used to study resonances of nitrogen, phosphorus, the halogens, the alkali metals, platinum, and vanadium, in a wide range of materials.

DYNAMIC NUCLEAR POLARIZATION

In the late 1950s, papers appeared describing a range of studies on the the electron nuclear Overhauser effect and ways of producing strong dynamic nuclear polarization. This struck me as worth investigating to see whether there were any chemical applications, to understand the phenomenon more thoroughly, and to see whether this effect could be used in a practical way to enhance the signal-to-noise ratio of the weak nuclear resonances. We mounted a major effort and constructed two spectrometers,[8] one using X-band microwaves (about 3 cm) and another Q-band (about 8 mm); both used permanent magnets with excellent stability and reasonably good resolving power, and were combined with high-resolution spectrometers at the appropriate rf frequencies.

We learnt a good deal about the mechanisms of nuclear relaxation, observed some quite fascinating effects including cases where scalar coupling occurs between an unpaired electron in a dissolved radical and the nucleus of a dissolved molecule,[9] and where nuclear polarization surges from one nuclear species to another during the varying relaxation times of the nuclei,[10] and were able to measure the spectra of some very weak resonances in favorable cases.[11] But it became clear that the use of dynamic polarization to get an order of magnitude improvement of signal-to-noise would not have any general application. It would be limited to substances which do not react with the free radical required, and to solutions in mobile liquids with low viscosities, though this latter difficulty could, in principle, be overcome by carrying out the polarization at low fields and transferring the polarized sample to a high field in a time short compared with T_1.

So after publishing some 22 papers on dynamic nuclear polarization, we dismantled the spectrometers and used the components for other work; nevertheless I believe there is still some fascinating work to be done on these effects. An article published in 1967 summarizes my views at the time about the limitations of using dynamic nuclear polarization for NMR work and particularly in biochemistry.[12] Although the chemical applications of these effects were limited, some of these experiments provided beautiful illustrations of the physics of nuclear relaxation, and a subtle method of studying molecular interactions during collisions in liquids.

SUPERCONDUCTING MAGNETS

The commercial production of Nb/Zr superconductors in the early 1960s brought the possibility of the construction of higher field homogeneous and persistent magnets, and indeed Varian Associates were very quick to take advantage of this and produced their pioneering 220 MHz spectrometer. This instrument was too expensive and too inflexible for our purposes at Oxford, so I resolved to raise funds to develop a magnet ourselves, knowing that Martin Wood (now Sir Martin) had already made a small magnet at the Oxford Instrument Co., and the engineers there were rapidly acquiring the skills required. It was agreed that Oxford Instrument Co. would build two magnets; the first to be a small model to test the design details and the second, a bigger one, to take advantage of lessons learnt from the first. At the same time we thought hard about many details of magnet and spectrometer design and our thoughts at that time were published.[13] This paper was followed a few years later by further reflections containing some novel ideas on spectrometer design in 1975[14] and again in 1976.[15] These papers give a good idea of the care and thought needed for good instrument design, and illustrate how important it is to decide what are the critical parts of the instrument to which particular attention must be given and what are the less important parts. Of course, one sometimes finds that aspects you thought were going to be very difficult (for example superconducting joints) are solved quickly, and others expected to be easy (such as the cryostat) set you back more than expected!

The construction of the first magnet went reasonably smoothly after tiresome problems with thermal oscillations in the cryostat. The Nb/Zr conductor was not very stable and in the early stages we had some rather dramatic quenches of the magnet, but these problems were soon overcome and the magnet performance vindicated the careful designs of the Oxford Instrument engineers. The room temperature gap was only 2.2 cm, yet it produced a truly persistent field of 5 T and the field homogeneity could readily be adjusted to about 1 ppm over 1 cm^3 without spinning. this seemed too good to treat purely as a design exercise, so we designed a spectrometer to use the magnet; although the homogeneity was not good enough for proton high-resolution work, there were plenty of other nuclei to study.

The main problem was the small room-temperature bore, and we solved this by extending an original idea by Redfield and making a crossed-coil probe with an overall diameter of a little less than 2.2 cm which incorporated means for achieving separation of the crossed coils by 100 db, for applying local homogeneity corrections, for temperature control between −100 °C and +100 °C, and to take spherical or cylindrical samples of 8–9 mm; diameter.[16] Chemical shifts could be measured with considerable precision and the instrument was used for a variety of measurements. For example, we studied the resonances for the alkali halides in salt solutions down to quite low concentrations in water and mixed solvents, and interpreted the shifts in terms of ionic collisions using the Debye–Huckel theory; the mechanisms of the shifts were also disentangled.[17] The shifts of cesium resonances between water and D_2O were shown to be due to changes of the water structure rather than to the different weights of the water molecules.[18]

In the meantime Oxford Instruments were building the second magnet using the newly available Nb/Ti conductor which was much more stable than Nb/Zr. This magnet was persistent at about 7.5 T (320 MHz for protons) in a 3 cm room-temperature bore and has been in use more or less continuously since 1969. Its homogeneity could be adjusted for proton high-resolution work, though with some considerable difficulty because there were significant gradients of quite high order, and I guessed that this was because the bore was still rather

small so that the sample coil was rather close to the inner windings.

BIOLOGY

By the late 1960s, I had become convinced that technical developments were going to make it really practicable to use NMR to study biological problems. Of course a good deal of work of this kind had already been done, and indeed we had made some proton relaxation enhancement measurements ourselves, but the complexity of biological molecules was a major problem for NMR at the time. So I decided to aim the new magnet particularly at phosphorus resonances, on the grounds that our new spectrometer would be sensitive enough and the phosphorus spectra would be simpler than the proton ones.

In 1969 I was appointed to be Warden of Merton College and Professor R. R. Porter very generously welcomed me and my colleagues into the Biochemistry Department with all our equipment and engineering. This was a big decision for me (and no doubt for him!), but in the event the next 10 years proved to be among the most thrilling in my life, quite apart from the immense pleasure of being the head of an Oxford College and, together with my wife, getting to know a large number of tremendously able young people in many disciplines.

The obvious success of the 7.5 T magnet made it clear that the Oxford Instruments design was a good one and should be exploited immediately. At the same time, it was clear that a larger bore was required to give more room for the probe and to make homogeneity adjustment easier, and since Oxford Instruments did not feel ready to embark on complete spectrometer design it was decided to invite Bruker Physik to collaborate with us. I remember a meeting in my dining room in Merton College at which representatives of Bruker and of the Oxford Instrument Co. agreed with enthusiasm to work together. It was also decided that the same basic design of magnet was to be used, with the bore increased, and the field reduced to a value corresponding to 270 MHz for protons. This was a field just three-times the field used in the standard Bruker 90 MHz spectrometers at that time. The new 270 MHz magnet was a great success; it had excellent resolution and stability, and is still in use in Oxford some 20 years after its construction. It formed the basis of a long line of high-resolution magnets manufactured by Oxford Instruments, the latest of which is a 750 MHz persistent magnet in use in Oxford for proton resonance work on proteins. The first 270 MHz magnet was exploited energetically by I. D. Campbell, C. M. Dobson, and R. J. P. Williams in very early studies of the NMR spectra of lysozyme and other small proteins.[19]

At the same time, David Hoult and David Gadian developed a new pulsed phosphorus spectrometer for the 7.5 T magnet which was quite sophisticated for the time and had a good performance. A sample size of 8 mm diameter by 1.5 cm height was used and, with spinning, linewidths of less than 1 Hz at 129 MHz were obtained with spinning sidebands less than 1% of the main signal. At that time we did not have an online computer but only a digital memory system into which the output could be dumped. We tried reading out the data on paper tape and then processing it offline on a main frame computer, but this was very slow and frustrating when the paper tape reader or punch made errors. David Hoult therefore designed and built an analog Fourier transformer;[20] it was a very ingenious idea and worked remarkably well. When small computers became available, however, we naturally took advantage of all the power they provided.

The great advantage of having moved into the Department of Biochemistry was that we were surrounded by people who knew what problems were worth tackling and how to handle the complex materials involved. In particular, we were able to start a long and fruitful collaboration with Dr George Radda and his colleagues who were very quick to see the possibilities of NMR techniques and ready to make the effort to understand them.

The 7.5 T instrument was used initially to do a thorough study of the effects on the chemical shifts of phosphorus resonances of typical biological materials of temperature, pH, ionic strength, and the presence of other salts in the solution. The effects on the relaxation times of traces of paramagnetic ions, dissolved oxygen, chemical exchange, and shift anisotropy were also studied, and by then we felt ready to tackle some real problems. One set of experiments was concerned with the phosphorus resonances of the head groups of model and biological membranes; examples are the linewidths and chemical shift anisotropies in oriented DPL/cholesterol membranes[21] and studies of unsonicated phosphatidylcholine liposomes.[22]

Another problem we studied was concerned with substrate binding to phosphoglucomutase,[23] followed by the study of enzyme-bound phosphates in phosphoglumutase, glyceraldehyde-3-phosphate dehydrogenase, and phosphorylase. Because we were members of the Oxford Enzyme Group which was studying the glycolytic pathway in particular, it was also decided to start to look at the phosphorus resonances of muscle extracts. The extracts initially showed only inorganic phosphate, but when a little glucose-1-phosphate was added, the formation of glucose- and fructose-6-phosphate could be seen and their proportions were as expected. Addition of ATP then showed the gradual formation of fructose diphosphate and AMP or IMP.

Many experiments of this kind were done, and it could be shown that glycolysis was fully operational in these extracts with appropriate additions. There was speculation at the time about whether there was any hope of observing these processes in intact muscle, but the expectation was that the relaxation times would be too short. Nevertheless an intact rabbit muscle was placed in the spectrometer and to everyone's surprise five clear resonances were obtained. Initial attempts to repeat the experiment failed, until it was realized how easy it is to allow the glycolysis of an excised muscle to run down before measurements can be made. As a result of this very exciting experiment, attention was transferred to the hind leg of the rat because it was found to be much more easily excised without damage and, of course, had been very extensively studied by classical methods.[24]

Techniques were developed for maintaining perfused organs in the spectrometer. This presented some formidable experimental problems because of the very limited bore of the magnet, but they were solved by a combination of the skills of the physiologists who found ways of keeping the tissue alive inside the magnet bore and our experience in the design of NMR probes of various kinds. Collaboration with D. Wilkie and his colleagues at University College, London, led to a

careful reanalysis of muscle metabolism in working muscle, which largely confirmed earlier work by freeze–clamp methods but with greater accuracy. G. K. Radda and his colleagues extended the measurements to perfused kidneys, liver, and heart.[25] All this work was done on the original 7.5 T magnet and spectrometer in spite of the very limited sample size, and of course it initiated related studies in many laboratories.

As magnet technology developed, larger bores became available and a magnet was installed in Oxford with a 10 cm bore in which whole animals could be studied and even appropriate human limbs. There are, of course, now many instruments being used to study the spectroscopy of phosphorus, and indeed hydrogen, shifts in human patients, and there seems no doubt that this technique will be a very valuable addition to magnetic resonance imaging for medical research and diagnosis.

In 1977 I became Vice-Chancellor of Oxford University and my active participation in day-to-day laboratory work inevitably ceased. Looking back over those years of research, I realize how fortunate I was to have a relatively secure position so early in my career, and wonder whether young people today can afford to take the risks that I felt quite able to take then; I certainly hope that some can. I also realize how important it is not to rely solely on commercial apparatus, but to have the confidence to build equipment oneself when necessary, and not to be put off by the myth, often cultivated by instrument manufacturers, that this is very difficult (though they are often right!).

REFERENCES

1. B. V. Rollin, *Nature (London)*, 1946, **158**, 669.
2. J. Hatton and B. V. Rollin, *Proc. R. Soc. London, Ser. A.*, 1949, **199**, 222.
3. N. Bloembergen, E. M. Purcell, and R. V. Pound, *Phys. Rev.*, 1948, **73**, 679.
4. F. Bloch, W. W. Hansen, and M. Packard, *Phys. Rev.*, 1946, **70**, 474; F. Bloch, *Phys. Rev.*, 1946, **70**, 460.
5. R. E. Richards and J. A. S. Smith, *Trans. Faraday Soc.*, 1951, **47**, 1261.
6. R. Freeman, G. Murray, and R. E. Richards, *Proc. R. Soc. London, Ser. A*, 1957, **242**, 455.
7. J. B. Leane, R. E. Richards, and T. P. Schaefer, *J. Sci. Instrum.*, 1959, **36**, 230.
8. R. E. Richards and J. W. White, *Proc. R. Soc. London, Ser. A*, 1964, **279**, **474**, 481.
9. R. A. Dwek, J. G. Kenworthy, D. F. S. Natusch, R. E. Richards, and D. J. Shields, *Proc. R. Soc. London, Ser. A.*, 1966, **291**, 487; R. A. Dwek, R. E. Richards, D. Taylor, and R. A. Shaw, *J. Chem. Soc. A*, **1970**, 1173.
10. D. F. S. Natusch, R. E. Richards, and D. Taylor, *Mol. Phys.*, 1966, **11**, 421.
11. T. C. Cannon, R. E. Richards, and D. Taylor, *J. Chem. Soc. A.*, **1970**, 1180.
12. R. E. Richards, *Magnetic Resonance in Biological Systems*, Pergamon Press, Oxford, 1967, p. 53.
13. H. D. W. Hill and R. E. Richards, *J. Sci. Instrum.*, 1968, Series 2, **1**, 977.
14. D. I. Hoult and R. E. Richards, *Proc. R. Soc. London, Ser. A.*, 1975, **344**, 311.
15. D. I. Hoult and R. E. Richards, *J. Magn. Reson.*, 1976, **24**, 71.
16. H. D. W. Hill, J. D. Halliday and R. E. Richards, *J. Sci. Instrum.*, 1969, Series 2, **2**, 29.
17. J. D. Halliday, R. E. Richards, and R. R. Sharp, *Proc. R. Soc. London, Ser. A*, 1969, **313**, 45; C. Hall, R. E. Richards, and R. R. Sharp, *Proc. R. Soc. London, Ser. A*, 1974, **337**, 297.
18. J. Halliday, H. D. W. Hill, and R. E. Richards, *Chem. Commun.*, **1969**, 219.
19. I. D. Campbell, C. M. Dobson, and R. J. P. Williams, *Proc. R. Soc. London, Ser. A*, 1975, **345**, 23.
20. D. I. Hoult, *J. Magn. Reson.*, 1973, **9**, 205.
21. A. C. McLaughlin, P. R. Cullis, M. A. Hemmings, D. I. Hoult, G. K. Radda, G. A. Ritchie, P. J. Seeley, and R. E. Richards, *FEBS Lett.*, 1975, **57**, 213.
22. P. R. Cullis, B. de Kruyff, and R. E. Richards, *Biochim. Biophys. Acta*, 1976, **426**, 433.
23. D. G. Gadian, G. K. Radda, and R. E. Richards, *Biochim. Biophys. Acta*, 1974, **358**, 57.
24. D. I. Hoult, S. J. W. Busby, D. G. Gadian, G. K. Radda, R. E. Richards, and P. J. Seeley, *Nature (London)*, 1974, **252**, 285.
25. G. K. Radda, *Science*, 1986, **233**, 640; G. K. Radda, Bheeshma Rajagopalan, and D. J. Taylor, *Magn. Reson. Q*, 1989, **5**, 122; G. K. Radda and P. J. Seeley, *Annu. Rev. Physiol.*, 1979, **41**, 749.

Biographical Sketch

Sir Rex Richards. *b* 1922. D.Sc., 1970, F.R.S.C., F.R.S., 1959, Fellow and Tutor, Lincoln College, Oxford, 1947–64; Dr. Lee's Professor of Chemistry, Oxford, 1964–70; Warden of Merton College, Oxford, 1969–84; Vice-Chancellor, Oxford University, 1977–81; Director of the Leverhulme Trust, 1984–93; Chancellor, Exeter University, UK, 1982–present.

Rigden, John S.: Rabi's Resonance Method

John S. Rigden

American Institute of Physics, College Park, MD, USA

Editor's Note: The following article is taken from 'Rabi: Scientist and Citizen', the definitive biography of I. I. Rabi, published in 1987. This excerpt is used with the permission of the publisher, Basic Books, New York.

The magnetic resonance method was born in the fall of 1937; however, it was in the making for many years. We shall begin in 1931.

How is the feeble glimmer of a star measured against the lustrous brilliance of the Sun? How is the Sun's brightness kept from swamping the faint light of a star? These questions are analogous to the one that faced Rabi early in 1931. He wanted to measure the magnetic moment of a nucleus in the way that Stern had measured the magnetic moment of a silver atom. The problem was that an atom has a magnetic moment about 2000-times larger than that of a nucleus. The question, How can the minute nuclear moment be measured in the face of the swamping effect of the large atomic moment? was answered by the Breit–Rabi theory in 1931.

In the Stern–Gerlach experiment, a strong magnetic field is used to deflect the moving beam particles. This *strong* field acts directly on both atomic and nuclear magnetic moments, and 99.95% of the resulting deflection is due to the large atomic moment. There is virtually no chance of identifying that 0.05% contributed by the nucleus. However, Breit and Rabi showed that if a *weak* magnetic field is used, the tiny nuclear moment is effectively joined with the large atomic moment so as to affect distinctively the pattern of the deflected beam. For example, a strong magnetic field, acting on the large atomic moment, would split a beam of hydrogen atoms into *two* subbeamlets; on the other hand, a weak magnetic field, acting on the atomic moment coupled with the nuclear moment, would split the beam into *four* subbeamlets. Thus, in a weak deflecting field, the nuclear magnetic moment exhibits itself in a definite way. It was on the basis of this theory that Rabi and Cohen began to design and to build a state-of-the-art molecular-beam system in 1931.

The physics department at Columbia was content with Rabi's return to molecular beams. No one hindered him, but neither was there robust support. Financial backing was meager. Anyone, however, interested in physical results rather than splashy equipment, and willing to work at taking data rather than demanding the latest piece of hardware to ease the burden, could do a lot of physics—especially in those days—on a shoestring. As in his high-school days when he built a radio station out of parts scavenged from the streets, alleys, and back lots of Brooklyn, Rabi and Cohen assembled a simple Stern–Gerlach deflection system. This was the first step in the evolution of the magnetic resonance method.

In the simple deflection method, a beam of atoms or molecules passes between the poles of one magnet. These poles are shaped in such a way as to produce a magnetic field stronger at one pole than at the other. This varying, or inhomogeneous, field exerts a force on the magnetic moment of a beam particle as it passes between the pole faces. The beam is long and narrow—a fraction of a millimeter in thickness. The magnetic deflecting force acts at right angles to the beam particle's velocity so as to add to its straight-ahead velocity a small sideways velocity. As a result, the beam particles strike the detector at a position that is slightly shifted, either to one side or the other, from the center position of the undeflected beam.

The principal difficulty with the simple deflection method is that the particles in the beam move with a whole range of velocities. The average velocity of the beam particles depends on the temperature of the source from which they emanate. Most particles have velocities that are near the average velocity; like any quantity of a statistical nature, however, other velocities can be smaller or larger than the average value. Since slow particles are deflected more than fast ones, the deflected beam is not a sharp replica of the undeflected beam, but is smeared out. To interpret the smeared-out deflection pattern, one must make theoretical and experimental assumptions and do extensive analysis—tasks that suited neither Rabi's disposition nor his taste.

A second difficulty with the simple deflection method is that the magnetic-field inhomogeneity must be known: that is, the magnetic-field strength must be calibrated point-by-point. Such calibrations are not only irksome but also impossible to do with great precision. Thus, there is an inherent uncertainty in the strength of the deflecting field, resulting in an inherent uncertainty in any deflection that is measured.

And, most important, the simple deflection method did not allow Rabi to have his answer 'by the end of the day'.

Rabi wondered what combination of forces could be exerted on the beam atoms so that they would reveal their secrets more directly. How could the featureless smear of the deflection pattern be transformed into a pattern with features that conveyed the nuclear spin of sodium just by looking? 'My attitude towards physics ... has always been profound faith and profound skepticism. Profound faith and skepticism. I really felt I wanted to be convinced of nuclear spin. It sounded all right, the theory [of quantum mechanics] explained a whole lot, but I knew enough about the history of physics to know that a good explanation is not necessarily so.'

Rabi relied strongly on his intuition, which allowed him, in a manner of speaking, to put himself into the beam and, along with the other beam particles, experience the sudden jolts and subtle nudges as he streamed through the apparatus. As Polykarp Kusch has said, 'He [Rabi] appears to ride around on the electrons within an atom or asks the question, "If I were an electron, what would I do?" Possibly, through sheer force of character he gets the electron to do precisely that.'[1]

So, Rabi rode the sodium atom, first by clinging to an electron, then by sitting on its nucleus. He could feel the beam split decisively into two beamlets by the force of a strong magnetic field acting directly on the large magnetic moment of the sodium atom's outermost electron. If he could now block out one of these beamlets and thus allow only one to continue on its way into a *weak* and *reversed* magnetic field—weak, so that the field would gently separate the beamlet into still smaller beamlets by acting on the combination of atomic and nuclear magnetic moments, and reversed so that the separated beamlets would be sharpened by collapsing the spread resulting from the difference in deflections between the fast and the slow atoms as they passed through the first

field—then he would need another strong (and also reversed) field to bring the whole pattern of separated and sharpened beamlets back toward the center of the apparatus where the individual beamlets could be detected. If the nuclear spin were I, $(2I + 1)$ beamlets should be detected.

Rabi discussed his ideas with Cohen, and the two men started to work on them. Additional deflection fields were added to the system: the first split the beam into two parts; the second subdivided the beam still further, depending on the value of the nuclear spin; the third shifted the spread-out beamlets back toward the center of the apparatus for detection. Between the first and second deflecting fields, a slit was added which allowed only one beamlet to continue through the apparatus.

Rabi's ideas were sound, but their implementation raised new problems. He and Cohen started with a beam containing a relatively few atoms, half of which were thrown away, and the remaining half further subdivided. How does one detect the rarefied presence of each little beamlet? A new detection system would have to be developed. One by one, solutions to other problems were found.

One morning, Victor Cohen, unable to wait for the elevator to take him to the fifth floor of Pupin Hall, bounded up the steps two or three at a time. Earlier that morning, he had found the nuclear spin of sodium, and now he wanted to show the world. He went straight to the laboratory and threw the switches that brought life to his apparatus. As the source oven slowly heated to its operating temperature, Cohen checked the pressure gauges. The pressure readings were low, indicating a good working vacuum. By this time, a few other laboratory workers had wandered in, and soon Rabi made his appearance. The timing was perfect, and Cohen called them all over. A steady flow of sodium atoms left the hot oven; half of them wended their way through the three deflecting fields. Systematically, Bill Cohen slowly moved the detector wire across the beam: the signal first increased and then decreased—a signal peak—one beamlet. Cohen continued the slow movement of the detector wire. The signal increased again and fell again—a second beamlet. A third time, the detector signal increased and fell—evidence of a third beamlet. Still Cohen moved the detector wire, and a fourth time the signal increased and fell—a fourth beamlet. How long would this go on? Cohen steadily moved the detector wire as Rabi watched the signal monitor. Would there be another beamlet? Rabi watched. The monitor registered nothing—nothing—nothing. Cohen stopped. The drama was over, but the excitement was about to begin. There were four signal peaks, four beamlets, which meant that the nuclear spin of sodium is $\frac{3}{2}$.

To this day, the sodium result obtained with Cohen stands as one of Rabi's most satisfying experiments:

> The world was young and I was young and the experiment was beautiful. It satisfied everything I wanted to see. There was an artistry in it or whatever it is called ... it just charmed me. These atoms in spatially quantized states, analyze them in one field, turn your focus back, and there it is. Count them! It was wonderful. There I really, I really believed in the spin, there are the states, count them! Each one, I suppose, seeks God in his own way.

To manipulate a beam of atoms in such a finely controlled fashion as to bring the atoms in one distinct quantum state onto the detector was the first big step toward the resonance method. The importance of this step was twofold: first, it infused the members of Rabi's team with the confidence that they could control the motion of beam particles in subtle ways; second, this first step, though spectacular, was limited. Counting the peaks gave the size of the nuclear spin, but they wanted to measure other nuclear properties as well, properties such as magnetic moments.

One Saturday afternoon in May 1933, Rabi called into his office Sidney Millman, a graduate student who had just passed the departmental qualifying examination and was therefore about to begin his own dissertation research. Rabi invited Millman to join his molecular-beam group and suggested a thesis topic: the determination of the nuclear spin and the magnetic moment of potassium. Rabi talked to Millman about Cohen's work then in progress and suggested that the 'zero-moment' method that Cohen was going to use for the study of cesium might also be applied to potassium. 'This was all new to me and sounded quite exciting,' Millman recalled later. 'I agreed right there and then to start my research.'[2] He was shown an area in Cohen's laboratory on the fifth floor of Pupin Hall and there began to build his own molecular-beam system.

By the time Millman started his dissertation research, the Rabi laboratory was a pulsating hive of activity. A second laboratory on the 10th floor of Pupin had been started with its own cast of young physicists—mostly postdoctoral fellows. At any time of the day or night, on any day of the week, the lights in the Rabi labs would be aglow and someone would be there working.

The zero-moment method was another experimental technique motivated by Rabi's need for simplicity, his desire for an immediate answer. It had style. The zero-moment method revealed properties of the atomic nucleus with an immediacy whose impressiveness was challenged only by its clarity. The method is based directly on Breit–Rabi theory which shows that, for specific values of the deflecting magnetic field, the *effective* magnetic moment is zero (the *actual* magnetic moment, a property of the nucleus itself, is not zero). This means that, for specific sizes of the deflecting field, all beam particles, regardless of their velocities, will be undeflected (because their effective moment is zero).

Millman could begin an experiment with the deflecting field turned off entirely and line up the detector to receive the full strength of the undeflected beam. The detector signal would, of course, be strong. Then he would turn on the deflecting field and slowly increase its strength. As beam particles were deflected, the detector signal decreased. Then, as the strength of the deflecting field was slowly increased, the detector signal would rise and fall—a peak—indicating that some particles were passing straight through the magnetic field without being deflected. The process was continued until no more peaks appeared. From the number of peaks and from their relative spacing, the nuclear spin could be determined. For his dissertation, Millman studied the alkali metal lithium.

The zero-moment method provided not only nuclear spins but also nuclear magnetic moments. The rendering of these data, however, was neither experimentally nor theoretically straightforward. To begin with, one particular magnetic field strength that allowed particles to pass through undeflected had to be known. In other words, one calibration was necessary (the field inhomogeneity was *not* needed). Even this one calibration, however, proved unnecessary when a new method was developed to generate magnetic fields.

Jerrold Zacharias, a Rabi postdoctoral fellow, doubted that the field between the iron pole faces of a magnet could ever be accurately calibrated. The outcome of his skepticism was a different method for generating a deflecting magnetic field—namely, by electrical currents, which produce magnetic fields. From the geometry of a current, the magnetic field can be calculated directly, and the error-riddled calibration avoided altogether. The trick was to know the geometry accurately.

With Sam Cooey, Rabi's master machinist, the ideas and sketches were translated into hardware. With the smallest of tolerances, a jig was machined to hold two wires in a parallel configuration. The separation of the two wires was known precisely. When these two wires carried an electrical current of known magnitude, the properties of the deflecting field could be calculated directly. Millman, and other 5th floor students, used the two-wire deflecting field and the zero-moment method to determine both the spins and the magnetic moments of several alkali metal nuclei.

The finances of most universities, including Columbia, were strained during the Depression years of the early 1930s, and Rabi got little financial support from the university for his research. When he really needed a piece of equipment, he would go to Dean Pegram and present a carefully reasoned explanation for what he wanted. About this time, however, Harold Urey received a grant of $7600 from the Carnegie Foundation in honor of his discovery of deuterium. (Urey, a faculty colleague of Rabi's from the chemistry department, would win the 1934 Nobel Prize in Chemistry.)

> Well [Rabi later recalled], Urey did one of the most extraordinary things imaginable. He gave me half of it. I had nothing to do with his discovery. What a greatness in Harold Urey—what a tremendous magnanimity to do something like that!
>
> He had a deep faith in me ... He told somebody, referring to me, "That man is going to win the Nobel Prize." I don't know what he saw in me ... but what a tremendous magnanimity! That money set me free. It made me independent of the physics department.[3]

While Rabi could 'see' specific results or 'feel' the outcome of an experiment, to explain in detail to Dean Pegram was very difficult: 'Besides, Pegram was a wonderful guy, extremely intelligent, and he'd have ideas, too. Next thing I knew we were collaborating, and I wasn't interested in collaboration. All I wanted out of him was money, admiration, and encouragement. With Urey's money I was free. I was able to do things on my own.'

And Rabi needed to be free. His laboratory was growing in people, flourishing in ideas, and expanding in experimental methods. A new method, however, did not necessarily render obsolete an older method. A case in point is the refocusing method developed during 1935. The zero-moment method had one major drawback: it could not be applied to atoms whose nuclei had a spin of $\frac{1}{2}$. The refocusing method could be applied to all atoms. There were advantages with both methods, and both methods continued to be used concurrently. As a consequence, it was not possible to cannibalize old equipment and use the parts in the new apparatus. For the refocusing method, new hardware was required, and new hardware required money. With Urey's money Rabi was free to expand his experimental base and to do so on his own.

Whether with sledgehammer techniques or with graceful, teasing subtlety, the experimentalist cannot get something from Nature without a price. The refocusing method allowed the vexing problem of the beam-particle velocity distribution to be artfully sidestepped. The outcome of this method, as with the zero-moment method, did not depend on the speeds of the beam particles. The cost of this independence was that the researcher did need to know the magnetic field inhomogeneity.

In the refocusing method, two deflecting magnets were used. Atoms were deflected once, then once again in the opposite direction, so that in the end they arrived where they would have arrived had there been no deflection at all. Slow beam atoms were deflected more than fast ones by each magnet; but in the end, all were refocused into the detector.

The experimental procedure was beautifully simple. Beam particles went through two deflecting fields in sequence—the first called the A-field which pushed them one way, then the B-field which pulled them the opposite way. With both deflecting fields turned off, the detector's location was adjusted so as to register a strong signal and thereby indicate that it was receiving the undeflected beam. Then the B-field was activated. The B-field split the beam into two major subbeams. One subbeam missed the detector to the right, while the other missed it to the left. The detector signal was essentially zero.

Next, the A-field was activated. Slowly the deflecting field was increased in strength from zero to ever larger values. Atoms in the quantum state identified with the largest effective magnetic moment were the first to be refocused into the detector. The detector signal rose, then fell. Quantum state by quantum state, beamlets of atoms were slowly swept over the detector as the attendant rise and fall of the detector level signaled their passing. From the number of peaks detected and from a knowledge of the magnetic field characteristics, both the nuclear spin and the magnetic moment of an atom could be determined.

Nuclei have intrinsic spins (angular momentum) and magnetic moments. The magnetic moment has both a magnitude and a sign. In 1935, the sign was missing. The sign of a magnetic moment can be either plus or minus: if the spin and the magnetic moment have the same space-quantized direction, the sign of the moment is plus; if these directions are opposed, the sign is minus. The signs of nuclear magnetic moments became important in the mid-1930s as a result of the work on the hydrogens being carried out in the 10th floor laboratory by Rabi, Zacharias, and Jerome (Jerry) M. B. Kellogg, another postdoctoral fellow.

The effect of the signs on their data was subtle—so subtle, in fact, that there was no effect at all. As beamlets of a particular atom were refocused into the detector, the same pattern was observed regardless of whether the sign of the atom's moment was plus or minus. The problem of determining the signs was something like trying to determine whether someone's right hand or left hand is pushing the front-door buzzer.

In 1936, Rabi wrote a theoretical paper (one of the few he ever wrote by himself) in which he analyzed experiments that had been done in Stern's Hamburg laboratory in 1932 and 1933.[4] The purpose of Stern's experiment had been to answer a question that went back to the days of the old quantum theory, the days when the idea of space quantization strained credulity. The question was, can an atom that is 'clinging' to a magnetic field with some particular space-quantized orientation be shaken loose? Can an atom be made to change its orientation?

Putting the question to the potassium atom, Stern and his associates had sent atoms streaming through a magnetic field in which they would take on a specific spatial orientation. Then Stern played a trick: he arranged for the atoms to leave the magnetic field they were in, and suddenly enter another field—a field whose direction changed from the one the atoms were used to, to a new direction. The question could be asked, would the atoms, upon entering the field with the new spatial direction, stubbornly maintain their original orientation, or would they follow the direction of the changing field?

The Stern group determined that, when the direction of the magnetic field is changed quickly enough, the atoms on passing from one field to another will reorient. It was in this reorientation process that Rabi saw the possibility of determining the signs of nuclear magnetic moments. He described this idea in his 1936 paper. The idea was Rabi's; the work to implement it fell to his students.

In their 10th floor laboratory, Kellogg and Zacharias dismantled the molecular-beam apparatus, stretched it out a bit so that a new magnetic field—the 'T-field'—could be inserted between the two deflecting fields. The T-field was a strange one, its configuration giving it a treelike appearance. The direction of the field went up the trunk and then fanned out to right and left like tree limbs. A beam particle entered the T-field moving *against* the field (from the tips of the limbs in toward the trunk of the tree); and, on departure, the particle moved *with* the field (from the trunk out toward the ends of the limbs). As a particle moved rapidly through the T-field, it 'saw' a magnetic field change quickly from one direction to another; it 'saw' a field that appeared to rotate.

Rabi recognized that if this apparent rotation was synchronized with the precession rate of the magnetic moment (the Larmor frequency), the T-field would exert a tipping force on the magnetic moment and make it flop from one orientation to another. These reorientations would open the way for determining the signs of nuclear magnetic moments.

Kellogg and Zacharias made another addition to the apparatus. They added a barrier between the first deflecting field and the T-field. With this barrier, one of the subbeams coming out of the first deflecting field was stopped before it entered the T-field. By observing the changes in the signal level of the detector as *preselected* beamlets were allowed to pass through the T-field, one could infer the signs of the magnetic moments. It all worked: the T-field did its job.

What Kellogg and Zacharias did on the 10th floor, Henry Torrey, another Rabi graduate student, did on the 5th: he built a refocusing system complete with T-field. There he, along with Millman and Zacharias, determined the signs of the nuclear magnetic moments for the alkali metals.

The T-field was the last significant modification made to Rabi's apparatus before the advent of the magnetic resonance method. The refocusing method together with the T-field provided a provocative experimental milieu. With deflecting magnets laid out along the flight paths of the beam atoms, Rabi and his crew learned how to exert a fine sense of control over beams of particles. They learned where and how barriers and gates could be set up to allow only select beamlets to pass on to the second deflection stage and, from there, to the detector. They learned detection techniques and the idiosyncrasies of various deflection systems. They learned how to make atoms flip from one space-quantized orientation to another and to detect a reorientation. The fingers playing over the controls of the apparatus had a feel for beams. Everything was poised for the next step.

Concern with experimental accuracy and precision occupied the thoughts of Rabi and his students during the 1930s. They had started with the simple Stern–Gerlach experiment with uncertainties of at least 10%. The zero-moment method was the best of all and, when it worked, it worked well. The refocusing method produced results with uncertainties of about 5%. The best of their experimental results prior to the resonance method carried uncertainties of about 3%.

The uncertainties associated with these results were not altogether due to the design of either the apparatus or the experiments. Limits were also established by physical theory. Neither the zero-moment method nor the refocusing method yielded the value of the magnetic moment directly; rather, the quantity directly measured is the energy difference between two quantum states. To get from this number to the value for the magnetic moment, one had to use theory—theory that was only approximate. The magnetic resonance method inaugurated a new era of precision: the experimental and theoretical difficulties that limited the precision of earlier results no longer existed.

The idea in Rabi's 1936 paper, the one that led to the determination of the signs of magnetic moments, came to him as he walked up the hill from his home on Riverside Drive toward the campus:

> One day I was walking up the hill on Claremont Avenue and I was thinking about it [the sign of the nuclear magnetic moment] kinesthetically with my body. Now, yes, I was thinking about this as follows: here's the moment and it's wobbling around in the direction of the field and [to find] the sign was to find out in which sense it was wobbling. To do this, I have to add another field which goes with it or against it. This is the idea, just concretely. The whole resonance method goes back to this.

His intuition was sound, and atoms did reorient in such a way that the signs of their magnetic moment could be determined. But Rabi's 1936 paper was essentially qualitative, and later that year he set out to extend his earlier ideas and to develop them into a quantitative theory of atomic reorientations. His theory was published in 1937.

This paper, entitled 'Space Quantization in a Gyrating Magnetic Field,' presented a theory that became the basis for the magnetic resonance method.[5] After World War II, this was the paper cited independently by both the Harvard physicist Edward Purcell and the Stanford physicist Felix Bloch in their papers announcing the discovery of nuclear magnetic resonance (NMR) in bulk matter. Today, more than 50 years later, this paper is cited by laser physicists who use Rabi's 'flopping formula', derived in the 1937 paper, thus showing how a great paper can be applicable far beyond the immediate intentions of its author.

In this paper, Rabi derived an expression that gives the probability that an atom will be reoriented by a magnetic field that changes direction (gyrates). By using the T-field, Kellogg, Millman, Zacharias, and other physicists had been observing these reorientations. Rabi wanted both to know more exactly the conditions conducive for reorientations and also to extend the range of applicability of the general method.

As an atom moves through the T-field, it experiences a changing magnetic field. More specifically, the atom 'sees' a magnetic field—first in one direction, then in another. From the atom's point of view, the magnetic field appears

to rotate. Rabi's 1937 paper showed that the critical factor is the frequency of this apparent rotation.

The frequency of the apparent rotation is significant because of a second frequency. When an atom with a magnetic moment is placed in a magnetic field, its motion is like that of a spinning toy top. The axis of a spinning top precesses (rotates) around the vertical direction. As the spinning top slows, the precessional circles get bigger and bigger until the top topples to the floor. Here the analogy breaks down because the spin of atoms is intrinsic and 'never slows down'. But the spin axis of an atom does precess around the direction defined by the magnetic field. Furthermore, this precession occurs with a specific frequency—the 'Larmor frequency'—that depends on the magnetic moment of the particular atom and on the strength of the magnetic field. Hence, Rabi's result. As an atom goes through the T-field, it 'sees' a rotating field—a field rotating with a specific frequency. If that frequency is equal to the atom's Larmor frequency, then the probability for reorientation is relatively large. On the other hand, if that frequency is either much below or much above the atom's Larmor frequency, the probability for reorientation is small.

Rabi's 1937 paper, completed in February and published in April, is the theoretical basis for the magnetic resonance method. The steps needed to implement the method were simple: the T-field had to be replaced with an oscillating magnetic field embedded in a uniform magnetic field. Zacharias remembers sitting in Rabi's office discussing the fact that 'if you apply a radiofrequency [that is, a magnetic field oscillating with a radio frequency], you can make it flop.' [6] After the basic ideas for this method were in place, however, implementation of the resonance method did not begin for over seven months.

Several factors contributed to the delay. First, there was, in a sense, a backlog of work to finish: namely, determining the signs of the magnetic moments that had been determined earlier; for this task the T-field method was adequate. Second, the T-field method appealed to Rabi: 'It had things in it—splitting the beam, counting peaks, getting the signs of moments.' Third, there was no pressing reason to rush: 'There was this very happy condition that nobody was competing with us. It was such a wonderful period.'

Rabi's happy condition was challenged in September—a challenge answered by the implementation of the resonance method. The Columbia Physics Department and Rabi's laboratory were a natural stopping-off place for European physicists visiting the United States. In September 1937, C. J. Gorter from the University of Groningen in Holland was such a visitor. The previous year, he had unsuccessfully attempted to observe a magnetic resonance effect in a solid sample of lithium fluoride. When visiting Columbia, Gorter, according to Rabi, said, 'Why aren't you doing it this way?' meaning, 'Why aren't you using an oscillating field?' Rabi acknowledges that, 'Gorter's visit was a stimulus. I knew about his work; in fact, he didn't tell us anything we didn't know. But he asked me, "Why aren't you doing it this way?" Well, I liked what we were doing, but I saw that he might go after it and we might get some competition. So I said, "Let's do it." Gorter's visit stimulated me into saying, "It's time to do it the other way."'

Gorter visited on a Saturday. On Monday morning, two days later, the pulsating vacuum pumps connected to Millman's apparatus were shut down, and modifications were started.

The ranks of Rabi's corps of postdoctoral fellows was expanded in September of 1937 by the arrival of Polykarp Kusch and, on that Monday morning, he joined Millman (who by that time had received his Ph.D. degree) and Zacharias in an all-out effort to modify Millman's apparatus so that it could be used for the resonance method. They started with a basic refocusing molecular-beam system. Between the two deflecting magnets that provided the A- and B-deflecting fields, a third magnet was placed. The pole faces of this magnet were flat so that a uniform field, the C-field, was established between them. Embedded in the C-field was a wire loop shaped like a bent hairpin. The loop was connected to a radiofrequency oscillator that sent a radiofrequency current through it. As particles of the beam passed between the sides of the hairpin loop, they were subjected to an oscillating magnetic field—a field that could change the orientation of precessing atoms.

The modifications did not take a long time. With Rabi, Kusch, Zacharias, Kellogg, and other physicists looking on, Sidney Millman made a final adjustment to the collimating slits so that the detector registered the presence of an intense beam. Molecules of lithium chloride were streaming unmolested through the apparatus. Millman turned on the B-field which deflected the beam molecules out of the detector. The detector signal vanished. Millman turned on the A-field and slowly increased its deflecting strength. Everyone watched the detector, waiting for its signal to rise as molecules were refocused back into the mouth of the detector. Molecules left the first deflecting field with a particular spatial orientation. They left the second deflecting field with the *same* spatial orientation and were refocused into the detector. When the detector signal reached full-beam level, everything was ready.

This was the moment. There was no sound except for the pounding vacuum pumps. Millman set the frequency of the oscillator at 3.518×10^6 c/s. His hand moved to the rheostat controlling the current in the electromagnet—the magnet that produced the C-field. Millman steadily turned the rheostat and watched the ammeter that registered the current in the windings of the electromagnet. The current read 110 A. The beam detector was recording a full-beam intensity.

Millman continued to increase the current—111 A—112 A. Rabi's eyes darted back and forth between the ammeter and the beam detector. The full beam was still arriving at the detector: 113 A—full beam. No one spoke. They no longer heard the rhythmic throb of the pumps: 114 A—the level dropped a lot; 116 A—the bottom fell out of the signal level. Much of the beam was no longer being refocused into the detector. There were glints of anticipated excitement in all the eyes fixed on the detector. Millman, with steady hand, continued turning the rheostat: 117 A—the beam was returning to the detector, and the signal level jumped up dramatically; 118 A—jumped up some more; 119 A—back to full-beam strength; 120 A—no change. The watchers stirred restlessly, breaking the tension; 121 A—still no change. The tension broke entirely as cheers filled the lab and reverberated down the corridor.

'Rabi was beside himself,' Kusch said later.[7] Backs were thumped and hands were shaken. For the first time ever, a nuclear magnetic resonance absorption had been recorded. The nucleus was lithium.

What happened as Millman increased the strength of the C-field? Recall that molecules left the first deflecting field with a particular space-quantized orientation. As they moved through the oscillating field, nothing happened until the current reached

115 A. This current produced a C-field in which the Larmor precession frequency of the lithium atoms almost matched the frequency of the oscillating field (3.518×10^6 c/s); thus, some of the lithium atoms flopped to a new orientation and were not refocused into the detector by the second deflecting magnet. At a current of 116 A, the match was almost exact, and many, many lithium atoms flopped from one orientation to another and missed the detector. It was at this point that the bottom fell out of the signal level. At 119 and 120 A, the Larmor frequency was no longer in resonance with the frequency of the oscillating field, and the probability was slight for a reorientation; hence, they were all refocused into the detector, and the signal was once again large.

Helen and Rabi threw a party that night, and graduate students and postdoctoral fellows came to celebrate. Everyone was exuberant, especially Rabi who circulated in high excitement among the members of his team. Rising above the noise of many simultaneous conversations, a frequent sound could be heard: Rabi's high-pitched laugh.

Although even at that time, January 1938, it was likely that the events of the day might be crowned with a Nobel Prize, no one could have foreseen how important the magnetic resonance method would prove to be—for not only physics but also chemistry, biology, medicine, and the whole of science.

REFERENCES

1. 'The Magnetic Dipole Moment of the Electron' (unpublished lecture), Kusch private collection.
2. Sidney Millman, in *A Festschrift for I. I. Rabi, Transactions of the New York Academy of Science*, ed. Lloyd Motz, New York Academy of Science, New York, p. 88.
3. J. Bernstein, *New Yorker*, 13 October 1975, 98.
4. I. I. Rabi, *Physical Review*, 1936, **49**, 324.
5. I. I. Rabi, *Physical Review*, 1937, **51**, 652.
6. J. Zacharias, interview with author, New York, 19 March 1982.
7. P. Kuach, interview with author, University of Texas, Dallas, 12 November 1981.

Biographical Sketch

John S. Rigden. *b* 1934. B.S., 1956, Eastern Nazarene College, Ph.D., 1960, Johns Hopkins University, USA. Postdoctoral research, Harvard University where he published an NMR paper with John D. Baldeschwieler. Faculty member in physics at Eastern Nazarene College, Middlebury College, and the University of Missouri–St. Louis; Director of Physics Programs, American Institute of Physics, 1987–present. Approximately 170 publications. Research specialties: molecular physics, history of physics, physics education.

Roberts, John D.: A Personal NMR Odyssey

John D. Roberts

California Institute of Technology, Pasadena, CA, USA

I was quite improbable material to become an NMR researcher. At the time NMR was liberated from the physicists, I was an organic chemist with substantial experience in synthesis, although I also had great enthusiasm for problems in reaction mechanisms and organic structures. In college, I'd taken courses in mathematics only as far as simple differential equations, I was weak in physics, especially in quantum mechanics and the gamut of electromagnetic phenomena. It could be convincingly argued that I should never be allowed at the controls of the very user-unfriendly early Varian NMR spectrometers. Indeed, in early 1954, when I suggested to Linus Pauling, then Chairman of the Division of Chemistry and Chemical Engineering at the California Institute of Technology, that we absolutely had to have an NMR spectrometer for use by our faculty, he figuratively patted me on the head and opined that it would be much more appropriate to hire a new professorial colleague with expertise in the field so that the required, and expensive, instrumentation (at that time about $26 000) could be used to best advantages. Possibly true, but in the preceding five years, other perhaps comparably complex instruments, such as the Baird and Perkin-Elmer double-beam infrared spectrometers, were being used with great effectiveness by organic chemists and were rapidly becoming indispensable for modern organic research, even for those doing purely synthetic chemistry. I was sure that NMR would soon prove to be very much more useful than infrared and I wanted Caltech to be in the forefront.

Interestingly, Caltech had been very much in the forefront of NMR earlier through the efforts of Professor Don M. Yost, an inorganic chemist of great perspicacity who perceived that NMR could be used to investigate whether the proton in $[F\cdots H\cdots F]^-$ was centered between the fluoride ions or closer to one than the other. Yost built an NMR spectrometer of war-surplus electronic equipment and studied the problem, in the process training and inspiring one of the great NMR researchers of all time, John S. Waugh. About the same time, another Caltech student, James N. Shoolery got his Ph.D. and went to work for Varian, where he made enormous contributions to the practical use of NMR by chemists in both academia and industry. Unfortunately, Don Yost was of a temperament to change research fields often and with great ease. So, shortly after his NMR period, he switched to research on algebra and the very early opportunity that he afforded Caltech to continue in the forefront of NMR was dissipated.

I had heard of NMR when I was on the faculty of the Massachusetts Institute of Technology and, indeed, was exhorted there by Richard Ogg, a professor of chemistry at Stanford, a birthplace of NMR by Felix Bloch and his co-workers, to pay attention to NMR's promise for chemistry. However, I had too little knowledge of magnetism or radiofrequency phenomena to understand what he said about the applications to chemistry. However, Ogg's enthusiasm certainly impressed me.

The catalyst that convinced me that NMR was important enough to become personally involved was William D. Phillips of Du Pont's Central Research Laboratory, who made many important discoveries that are basic to today's NMR. On a consulting visit in 1954 to Du Pont, Phillips, whom I had known previously as a graduate student at MIT, generously educated me about shifts and couplings and showed me how ^{1}H and ^{19}F spectra could be used to establish structures. That was wonderful, but I knew that I had to do NMR myself when he showed me how *N*,*N*-dimethylformamide gave two methyl-group proton signals at room temperature and these coalesced above 120 °C as the result of increased rates of rotation about the C–N amide bond. The prospect of measuring very rapid reaction rates by NMR provided the inspiration for getting an affirmative response from Linus Pauling that 'with NMR, we could investigate the borderline between resonance and tautomerism'. For example, investigating the NMR spectrum of cycloheptatriene with temperature to see if it existed as a rapidly equilibrating mixture of cycloheptatriene and norcaradiene, or was what later would be called a 'monohomobenzene'. The argument was persuasive and we soon ordered a 30-MHz Varian proton and fluorine spectrometer.

The spectrometer arrived in the summer of 1955 already upgraded to 40 MHz, with none other than James N. Shoolery as our Varian installation manager. I had never actually seen an NMR spectrometer before and was blissfully ignorant of how they operated. George Pake's superb articles in the *American Journal of Physics* were my bible for several months.[1] Then, fortunately, Edward Purcell gave some exceptionally clear lectures about NMR in the Caltech Physics Colloquium that were very helpful, as was Felix Bloch's original paper on nuclear induction.[2] Learning to operate the spectrometer was something else again. A slender 'instruction manual' came with the spectrometer, but it was almost useless for actual operations. Your only hope was to learn by watching the installer.

Our Varian spectrometer was impressive for organic chemists, who thought a large instrument was an infrared spectrometer; a massive 6000-lb electromagnet with 12-in. pole faces driven by a very large power supply topped by an enclosure containing an array of eight white-hot 304TL voltage regulator tubes, each about 10-in. high and cooled by a noisy air blast. Operations were controlled by a console studded with dials, meters, and glowing pilot lights.

Jim Shoolery had become one of the early experts on using NMR to determine organic structures and, when he suggested that we supply an illustrative sample, I tried him out with one of our then current synthetic triumphs, 1,3-dimethylenecyclobutane. Jim used the CRT display, which had a long-persistence, bright-yellow trace, to determine the relative number and kind of proton resonances of the sample. He decreed that, along with other resonances, the compound had a methyl group and a single hydrogen on a double bond. This was bad news until we realized that there could have been a rearrangement in the reaction used to introduce the second double bond and the product was 1-methyl-3-methylenecyclobutene. This demonstration of the power of NMR caused me to abandon almost everything else and essentially to live at the spectrometer to determine its capabilities with the kinds of compounds that we were working on at the time.

The spectrometers of this era were quite unsophisticated by present standards. Resolution on the order of 1–2 Hz could usually be achieved, but changes in line voltage, air temperature or cooling-water temperature, movement of magnetic materials in the vicinity, and so on, caused the spectra to be poorly reproducible, even over seconds. So, when we recorded spectra, we used a relatively high-speed Sanborn recorder that wrote with a hot wire on a narrow strip chart. The usual procedure was to run off 10–20 7-s sweeps and then see if two or more spectra could be found that were essentially the same. Of course, these spectra were heavily contaminated with relaxation wiggles whose shape could be useful, as with 2-methylpropene, to determine accurately small couplings that could not be easily measured directly with fast sweeps.

Our first NMR research project was planned to determine the structure of Feist's acid, and we were able to show that it was a methylenecyclopropanecarboxylic acid.[3] About the same time, Jim Shoolery's finding that the NH resonance of pyrrole was broadened at 40 MHz to almost unrecognizability by either ^{14}N quadrupole relaxation or proton exchange attracted my interest. I showed that the broadening was not caused by proton exchange, because when I raised the sample temperature, the triplet expected from the ^{14}N–H splitting appeared. Similar results were obtained with amides and amine salts.[4]

I gave my first lecture on NMR in December of 1955 at the University of Rochester, and although I had been using the instrument for some months, I was still not sure how it worked, but fortunately the night before the lecture an important principle suddenly became clear and my seminar went well.

I had told Pauling that I wanted to look at the spectra of cycloheptatriene as a function of temperature, but there were problems in working at other than room temperature. Varian's early contribution to temperature control was a small Dewar flask with a receiver coil wound around the outside. You had to heat or cool the sample to the desired temperature, put it in the probe, and quickly take a nonspinning spectrum. At best, the temperature was uncertain by several degrees. This situation was so unsatisfactory that I designed a probe insert with which it was possible to maintain a desired temperature and allow sample spinning. The details were worked out with Jim Shoolery and patented by Varian.[5]

My first graduate student to become heavily involved in NMR was A. T. Bottini, who confirmed the structure of *N*-ethyl-2-methyleneaziridine by its proton NMR.[6] We expected the two protons attached to C-3 to be nonequivalent, because the *N*-ethyl group would be on one or the other side of the imine ring and that inversion would be relatively slow, at least on the NMR timescale. However, these protons were equivalent and we decided to see if rapid nitrogen inversion was the cause by lowering the temperature. Despite our primitive temperature controls, we were able to observe a dramatic change in the spectrum at −80 °C.

In connection with our work on cyloadducts from fluorochloroethenes with phenylethyne, we discovered sizable four-bond, cross-ring H,F spin–spin splittings.[7] From this, we embarked on an attempt to understand more-than-three bond couplings and E. I. Snyder set a record in our laboratory of a nine-bond proton–proton coupling in octa-2,4,6-triyne-1-ol.[8] We also worked on through-space couplings, a subject still of substantial interest.

Our research on rotation about single bonds and shift nonequivalences associated with internal molecular asymmetry was undertaken because Drysdale and Phillips had published spectra that I interpreted to mean that appropriately substituted fluorohaloethanes might possibly exist as stable optical enantiomers at room temperature. Although the chances seemed remote, P. M. Nair investigated the ^{19}F spectra of 1,2-dibromo-1,1-difluoro-2,2-dichloroethane that is expected to have three staggered rotational conformations.[9] Two of these conformations are enantiomers that would have nonequivalent fluorines, while the third has a plane of symmetry and would be achiral with equivalent fluorines. The ^{19}F spectra at room temperature showed only a single sharp resonance line and this meant that either rotation about the C–C bond was fast or else that the achiral form dominated. However, below −30 °C, the ^{19}F resonances broadened and, at −80 °C, the spectra showed five ^{19}F peaks as expected for the chiral (with nonequivalent fluorines) and achiral conformations. The ratio of these forms was about 1.4: 1. These spectra seem to represent the first case of the use of NMR to show slow rotation about single C–C bonds. Subsequently, we investigated a variety of compounds showing slow rotation at low temperature. An especially spectacular example was provided by Frank Weigert with 1,1,1,4,4,4-hexafluorotetrachlorobutane.[10] A quite unusual case was of rotation of the phenyls of 1,8-diphenyl-substituted naphthalenes discovered by House. We were able to show that these rotations occurred readily because of large steric interactions in the ground state.[11]

For a brief moment, I thought that nonequivalence of geminal groups might be used as a test for molecular chirality. This notion did not persist and I went through the organic stockroom shelves to find an achiral compound that would also have nonequivalent geminal groupings. Here, I turned up 1,3-dinitro-2-propanol and, indeed, this achiral compound did have nonequivalent $-CH_2-$protons.[9] Kurt Mislow, with a flair and love of nomenclature, aptly christened such geminal groups as 'diastereotopic'.

Later, we measured the rate and activation parameters of nitrogen inversion of benzylmethylhydroxylamine by observing the benzyl $-CH_2-$protons as a function of temperature.[12] An analogous study, one among many applications of this technique to conformational equilibration, led to measuring how fast the double bond of *trans*-cyclodecene turns over against the restraints provided by the methylene groups on the opposite side of the ring.[13] The free energy of activation was found to be about 11 kcal #mol^{-1}, very much smaller than the 35.6 kcal mol^{-1} barrier determined by Cope for *trans*-cyclooctene, a value that allows for isolation of the enantiomers at room temperature. This work was brilliantly carried forward by G. Binsch, later to have a distinguished career at the University of Münich. We also used the diastereotopic protons of diethyl sulfite to show that the ^2J(H,H) geminal couplings had the opposite sign of the ^3J(H,H) vicinal couplings.[14] Further, we investigated how far magnetic nonequivalence could be transmitted down a chain to a diastereotopic group from the site of the dissymmetric structural element before the chemical shift difference can no longer be detected.[15]

The lack of stability of our first NMR spectrometer was both exasperating and time-consuming. The first real sea change in NMR for organic chemists came with the introduction of the Varian superstabilizer in 1956. Now, the 7-s spectra could be abandoned for 1–2-min spectra and these had much reduced

lengths of the relaxation wiggles and so allowed much better resolution. Our order was put in so promptly that we were shipped Serial #1.

The next sea change in NMR for organic chemists came with the development of the Varian A-60 spectrometer in 1961 which finally put NMR on a par for user friendliness with infrared spectroscopy. It was a still a vacuum-tube machine and had fits of temperament requiring tender loving care, but it could be used without a seasoned practitioner hovering in the background. The extension to ^{19}F NMR as the A-56/60 instrument with a temperature-controlled probe was a boon to our research using fluorine NMR for conformational analysis.

When I was invited to speak at a Reaction Mechanisms Conference at Bryn Mawr College in September 1958, it seemed like the right occasion to give a lecture about NMR and its applications to organic chemistry. For this talk I made color drawings and photographed them in Kodachrome. The resulting slides made quite a hit and, even 35 years later, people told me how influential the lecture was for them. The success of this lecture and its many repetitions at universities around the country made it easy to write a short book about NMR basics for organic chemists.[16] Although low-brow compared to Abragam or Pople, Schneider, and Bernstein, the book broke new ground as the first advanced book in chemistry to have four-color illustrations (thanks to the McGraw-Hill's editor, W. A. Benjamin) and the first to use the now widely prevalent spectral problems, where one expects a structure to be derived on the basis of an empirical formula and a spectrum alone.

My second NMR book came about because I was perplexed to understand the quantum mechanics responsible for AA′XX′ spin–spin coupling patterns, especially H. M. McConnell's spectrum of 1,1-difluoroethene. Perhaps it was clear in Pople, Schneider, and Bernstein's excellent book, but it was also sure that the book was not written for the likes of me. Desperate, I corralled my then professional colleague, McConnell, sat him down on a 4th of July afternoon and insisted that he explain. It was a rewarding three hours.

It was a propitious time to write a book, before I knew too much and, in particular, before I lost my missionary spirit. It is unlikely that the major textbook publishers would have been interested in getting out a book on such a level of expertise by someone so new to the game, but it was a propitious time for another reason because W. A. Benjamin had just started his own publishing company and wanted to hit the market with something fast and was willing to go to press without such niceties as peer review.[17] 'An Introduction to Spin–Spin Splitting in High-Resolution Nuclear Magnetic Resonance Spectra', the short book with the long title, is now long out of print, but perhaps it could stand another edition. The portrait (mine) on the back of the dust jacket would also have to be a new edition. Unfortunately, the book was written without the benefit of A. A. Bothner-By's LAOCOON program, which enables one to calculate what spectra would look like for a given set of chemical shifts and coupling constants.[18] Even more, LAOCOON could determine a set of parameters that corresponds to a given spectrum by an iterative process. The program and input data were supplied to the computer on punched cards and it was easy to punch as many new cards as needed to change the data set. The program was rather large then, some 500 lines of source code. In recent years, when I rewrote the FORTRAN code in True BASIC with provisions for revision of the data set in memory and a curve-plotting routine, the program swelled to some 3600 lines of code.

With some knowledge of the analysis of fairly complex splitting patterns, I hoped that we could use proton NMR to solve my UCLA Ph.D. thesis problem carried out with W. G. Young and concerned with the structure of the butenyl Grignard reagent. In a test of proton NMR to study Grignard reagents, J. E. Nordlander found, to our surprise, that 2-propenylmagnesium halides displayed the spectrum of a simple AX_4 system.[19] Furthermore, the spectrum did not change to as low a temperature as we could take proton spectra at that time.

The finding of an AX_4 NMR spectrum for 2-propenylmagnesium bromide was very surprising and could only be understood if there is sufficiently rapid rotation about the C–C bonds to average the expected shift differences for either the classical $CH_2{=}CH{-}CH_2{-}MgBr$ structure or a 2-propenyl anion–Mg^+Br ion pair. For each of these, one would expect enough double-bond character to one or both of the C–C bonds to create a shift difference for the respective *cis* and *trans* protons; if not at room temperature, certainly at $-80\,^{\circ}C$. The simple explanation for the results is that the classical structure is, in fact, correct, but that it undergoes allylic equilibration with the MgBr group moving rapidly from end to end. Such equilibration would make the C–C bonds alternate between single and double bonds, and thus permit facile rotation about both C–C bonds so as to make all of the CH_2 hydrogens magnetically equivalent on the NMR timescale. The rapidity of the allylic equilibration was quite unanticipated and we found that it was still rapid even at $-120\,^{\circ}C$ with di-2-propenylmagnesium, prepared to be free of magnesium halides that might be expected to catalyze equilibration.

In 1944, I had concluded from the study of many reactions of the butenyl Grignard reagent that it almost surely had the primary $CH_3CH{=}CH{-}CH_2{-}MgX$ structure. The proton chemical shifts in the NMR spectrum found by E. Nordlander for this Grignard reagent qualitatively confirmed the $CH_3CH{=}CH{-}CH_2{-}MgX$ structure, but there were clear indications of rapid allylic equilibration, even if the primary isomer predominated to an extent certainly greater than 95%.[20]

These conclusions were confirmed by George M. Whitesides for the 3-methyl-2-butenyl Grignard, $(CH_3)_2C{=}CH{-}CH_2{-}MgX$, that for stereoelectronic reasons is expected to favor the primary isomer much more than the butenyl Grignard reagent itself. At room temperature, the methyl groups of this Grignard are equivalent, but below $0\,^{\circ}C$ they have different chemical shifts and, so in this system, at least, it is possible to slow the rate of equilibration between the allylic isomers.[20]

The problem of determining reaction rates from NMR lineshapes became a priority for our research on the rates of conformational equilibration. Now, a new theoretical barrier arose, that presented by density matrix formalism. Having not really recovered from grappling with spin–spin splitting, I was hesitant to put a toe into these waters. But, as luck would have it, I had a brilliant undergraduate doing research with me, J. L. Beauchamp. This worthy zipped through the theoretical papers of Alexander and Kaplan and produced a working FORTRAN program for calculating lineshapes as a function of reaction rate for the AB system where A and B are exchanging intramolecularly with the equilibrium constant equal to unity. Beauchamp's work was vital to the success

of many of our rate projects and was greatly extended by Whitesides, as a Caltech graduate student, to the problem of the configurational stability of 3,3-dimethylbutyl (neohexyl) Grignard reagents (see ***Organic Chemistry Applications***).[21] A major problem in this work was to obtain lineshapes for the change of an A_2X_2 spin system with $J_{AX} = J_{A'X'}$ to one of the AA′XX′ variety with $J_{AX} \neq J_{A'X'}$.

These changes in lineshape were more complicated than the change of AB to A_2, with which J. L. Beauchamp had dealt. Whitesides was able to show that the lineshapes could be simulated as the sum of the lineshapes of two invariant antisymmetric resonances and the averaging of two different AB spin systems. He worked through the density matrix formalism for relating lineshapes to exchange rates in his thesis, and this provided my own introduction to such matters. Later, I gave a lecture about its use at an Organic Reaction Mechanisms Conference, but it was not received with the same enthusiasm as my earlier talk to the same group about NMR in general. At least, Whitesides was willing to concede afterward that I had achieved a minor acquaintance with the subject.

Conformational equilibria and equilibrations occupied our attention for many years. An important role in investigating rotations around single bonds and conformational equilibrations of cyclic compounds was taken by B. L. Hawkins, who devised computer programs to deal with the more complicated lineshapes involved.[22] The study of rotational barriers about C−C bonds gave information that I hoped would be useful to test a priori calculations of barrier heights along the lines pioneered by Westheimer and Mayer for rates of racemization of optically active biphenyl derivatives. In the best Westheimer manner, I was determined that this not be a semiempirical method, with parameters derived from a best fit to the existing experimental data, but obtained from spectroscopic force constants and gas-phase interaction potentials. The calculations were not easy at that early stage of computer usage and the best test cases seemed to be the various haloethanes for which we and others had obtained barriers. The calculations were largely stymied by difficulties in knowing how to deal with the electrostatic interactions inherent with the electronegative halogen atoms in this class of ethane derivatives. Nonetheless, I was emboldened to make the ethane rotation problem the subject of my Roger Adams Award address at the Organic Chemistry Symposium in 1967. I think it was an artistic triumph, but surely a crashing bore for most of the audience who were dragged through an exposition of principles without much of a take-home lesson of useful knowledge.

Our studies of conformational equilibria and equilibration in cyclic compounds were more successful—because others more talented had analyzed many of the ring systems in which we were interested and there was a large body of speculation that could be subject to experimental test. The problem presented by the complexity of the proton spectra in the slow exchange regime led us to label the various cycles with one or more CF_2 groups. Such labeling takes advantages of the much larger chemical shift differences of fluorine than hydrogen, but suffers from the disadvantage that few organic chemists are willing to accept the notion that the rates of inversion, or of any other processes, occurring with a fluorine-substituted cycle could even qualitatively reflect what happens with the parent hydrocarbon.

We already had our toes in the water of this pond, through J. B. Lambert's study of the changes in ^{19}F chemical shifts with temperature of *gem*-fluoro-substituted cyclobutanes.[23] These results gave some idea of the torsional oscillations and the conformational preferences of cyclobutane rings.

K. Nagarajan found that 1,1-difluorocyclohexane at room temperature gave a simple quintet for its ^{19}F spectrum, as expected for an A_2X_4 system, but this is deceptively simple because each fluorine is not coupled equally to the hydrogens flanking it and the two-bond fluorine−fluorine coupling is large.[24] At −100 °C, an $ABX_2X'_2$ type spectrum was observed, with a 15.7-ppm fluorine chemical-shift difference and a fluorine−fluorine coupling of 237 Hz. The changes of lineshape with temperature gave an E_a value of about 11.5 kcal mol^{-1}, close to the 11.1 kcal mol^{-1} found by Anet for cyclohexane itself, in support of our premise that the *gem*-fluoro compounds could be useful models for studying conformational equilibrations. J. T. Gerig made further progress on cyclohexane systems by a beautiful study of the conformational equilibration of *cis*-decalins.[25]

The larger ring systems of cycloheptane, cyclooctane, and cyclodecane showed dramatically different behaviors, although those for cycloheptane and cyclodecane had been well predicted by Hendrickson and Prelog, respectively. Thus, 1,1-difluorocycloheptane displays no fluorine chemical-shift difference at as low as −170 °C, because the ring assumes a conformation where there is a favored C-2 site for *gem* substituents.[26] Cyclodecane has a favored *gem*-substitution site, but now with nonequivalent fluorines if ring inversion is slow as it is at below about −135 °C.[27]

Cyclooctane is quite conformationally mobile and seems to exist in families of conformations of about equal energy. Interconversions are fast at room temperature and until about −100 °C, where an AB pattern emerges with a small chemical shift difference of 3.9 ppm and a fluorine−fluorine coupling of 245 Hz. Then, below −150 °C, this turns into two overlapping AB spectra with larger chemical-shift differences of 14.3 and 16.7 ppm.[28] Anet was later able to interpret our results by equilibrating chair-like conformations instead of the boat-like structures we had favored.

It is challenging to explain conformational equilibrations for larger rings than cyclohexane in lectures, and for a 1965 Organic Symposium talk at Arizona State University I used molecular models scaled to 1-m bond lengths with 6-in. balls for atoms. These were very unwieldy to handle, but fortunately J. T. Gerig was a most capable assistant in showing how larger rings can undergo equilibration.

To be truly useful, ^{13}C NMR has to be available at the natural-abundance level for at least medium concentrations of organic compounds. However, the signal-to-noise ratio obtainable with natural-abundance ^{13}C using the spectrometers of the 1960s was not favorable. P. C. Lauterbur employed rapid-passage, dispersion-mode procedures to show that natural-abundance ^{13}C had enormous potential for the determination of organic structures, but the technique sacrificed considerable resolution for gains in sensitivity. D. M. Grant and co-workers at Utah then made an important advance through using proton decoupling, but natural-abundance ^{13}C was still by no means routine. An important development in this period was the availability of computers of average transients (CAT) with which electronic signals could be digitized and time-averaged to improve the signal-to-noise ratios. However, the procedure is of limited value unless the spectrometer has good frequency stability, a characteristic missing from NMR spectrometers of

the early 1960s. Fortunately, I got an NIH grant to investigate how to contrive a spectrometer to obtain natural-abundance ^{13}C NMR in a routine fashion.

I was discouraged about knowing where to start, when I saw a Hewlett-Packard advertisement in the *Scientific American* for a digital-frequency synthesizer of extraordinary stability. Further, the synthesizer would change frequency in 0.01 Hz increments with a suitable voltage ramp. Because the frequency range was right for ^{13}C NMR, I put $10 000 (in 1960ish dollars) on the line to get one in the hope that it would solve the stability problem that made long-term signal averaging difficult. I then contacted Varian Associates and suggested that perhaps they could build a ^{13}C spectrometer around the H-P synthesizer. Varian was not optimistic about the success of the project (suggesting that 'phase problems' would sink the ship) and I decided we would have to try to go it on our own.

A short time later, Varian management changed its mind and I put in an order for a digital frequency sweep spectrometer using my H-P synthesizer. The result was a true advance in NMR instrumentation with its excellent resolution for 10-mm diameter samples, frequency synthesizer, digital sweep programmer, field/frequency lock channel, and signal-averaging computer. The stability was superb and spectra could be taken over as long a period as desired. This was a spectrometer wholly dedicated to nuclei other than protons, because proton signals were used for the field/frequency lock at 60 MHz. The spectrometer was installed in late 1966, just in time for it to be taken over by F. J. Weigert, a new graduate student from MIT. An extraordinarily motivated and talented researcher, he cut a broad swath through many aspects of natural-abundance ^{13}C NMR. Weigert completed his Ph.D. thesis in just two years and eight months and produced 16 very substantial papers in the process. His first paper was concerned with the complex proton-coupled ^{13}C spectrum of benzene.[29] Some measure of the sensitivity achieved by the Varian engineers for the DFS spectrometer can be deduced from the fact that Weigert was the first to be able to measure $^{13}C-^{13}C$ couplings at the natural abundance level.[30]

As soon as ^{13}C NMR became relatively routine, there was pressure for the adoption of a reference substance as a frequency standard. Many substances had been proposed and we liked carbon disulfide, because it came near the low-field end of the common range of ^{13}C shifts. The Varian group was strong for tetramethylsilane (TMS) which is a good standard for both ^{13}C and proton NMR, except that, when its resonance is taken as zero, shielding constants become negative instead of positive. G. v. D. Tiers tried to solve this problem for protons with the τ scale and, while initially popular, it had awkward features and rather quickly faded from general use.

Natural-abundance ^{13}C NMR was not really routine until the introduction of broadband noise proton decoupling. Such decoupling removes the proton splittings from the ^{13}C resonances and, in addition, gives a favorable nuclear Overhauser effect (NOE). Thus, a proton-coupled doublet ^{13}C resonance, such as exhibited by trichloromethane, with broadband decoupling produces a singlet peak with a sixfold increase over the intensity of each of the individual doublets. There is hardly a better early example of the utility of broadband proton decoupling for ^{13}C spectra than for cholesterol.[31] Weigert had found it impossible to make sense out of the 15-MHz coupled spectrum of cholesterol, because of the jumble of resonances and the generally poor signal-to-noise ratio, even after hours of signal averaging. In contrast, with broadband proton decoupling, 25 rather well separated resonances were observed. A challenge was thus presented of spectral assignments and was met by H. Reich and M. Jautelat in about six months.[32] An important element in the unraveling of the resonances was D. M. Grant's work on the steric influence of axial methyl groups on ^{13}C shifts in cyclohexane rings (see ***Organic Chemistry Applications***).

With broadband proton decoupling, we were able to analyze the ^{13}C spectra of many natural products. Particularly notable was D. E. Dorman's study of sugars[33] and J. G. Nourse's Herculean effort with erythromycin antibiotics.[34] Another wonderful project was determining the degree of tacticity of the stereoisomers of polypropylene,[35] a subject that became of intense interest in law suits involving possible infringement of the Natta patents on isotactic polypropylene by a gaggle of large US corporations.

About 1970, it was clear that the pulse Fourier technique applied to NMR spectroscopy (FT NMR) by R. Ernst could give superior sensitivity compared with the frequency-sweep procedure we were using with our DFS spectrometer, except when quite narrow ranges of the spectra were to be studied. We were eager to become involved, but Varian was not enthusiastic about upgrading our, by now technically obsolete, DFS spectrometer. The company was enthusiastic about our paying to develop a ^{13}C FT NMR accessory for the 220-MHz instrument obtained for Caltech through the efforts of S. I. Chan, even though the 5-mm sample size available for that spectrometer was too small for reasonable signal-to-noise ratios. Nonetheless, we put in an order and a year later a unit was delivered and found to be of minimal usefulness. Varian said that it would be impossible to move the ^{13}C unit over to the DFS spectrometer, but two highly motivated postdoctoral fellows, B. L. Hawkins and J.-Y. Lallemand, with the help of C. Tanzer of Bruker Magnetics were able to do what needed to be done and, in 1973, we published our first papers using ^{13}C FT-NMR with the DFS unit on tetrahydrocannabinols[36] and Rauwolfia alkaloids.[37] Thus was born the first and only Brukarian pulse Fourier transform spectrometer.

Starting in the late 1940s, I had been deeply involved in the carbocationic rearrangements that so easily interconverted cyclopropylmethyl, cyclobutyl, and 3-butenyl derivatives. While we used NMR in various ways to determine structures and analyze product mixtures in this research, we had little hope of determining the nature of the $C_4H_7^+$ intermediate which was one of the central actors in the prolonged controversy over 'nonclassical' carbocations. Then, in 1965, G. A. Olah developed a procedure for generating stable solutions of carbocations in his 'magic acid' formulations and, furthermore, the proton and ^{13}C NMR spectra could be taken of the carbocations in solution. Applied to $C_4H_7^+$, Olah found the proton spectrum to have only a single-proton high-field CH multiplet and two three-proton doublet resonances.[38] Because $C_4H_7^+$ should have one CH and three CH_2 groups, the carbocation has to possess nonequivalent methylene hydrogens with different couplings to the unique proton and are also not coupled to one another. That the protons on the separate methylene groups have the same chemical shifts must be the result of rapid equilibration of the methylenes, as we had earlier demonstrated by shuffling of carbon atoms in a number of typical carbocationic reactions. In the main, the

NMR spectra are not grossly different from what might be expected from $C_4H_7^+$ as an equilibrating mixture of nonplanar, unsymmetrical bicyclobutonium carbocations, much as we had postulated from chemical evidence earlier on. There is more to the story of NMR in study of the fascinating and unusual $C_4H_7^+$ cation (see ***Organic Chemistry Applications***).

About 1963, we decided to look into ^{15}N NMR spectroscopy. For ^{14}N NMR, there are problems with large linewidths attendant to rapid quadrupole relaxation. On the other hand, while the ^{15}N nucleus has spin $\frac{1}{2}$, its natural abundance is only 0.31% and its magnetic moment only about one-tenth that of protons. At the natural-abundance level, ^{15}N NMR can be expected to have something like a millionth of the signal strength of protons for a substance containing equal numbers of nitrogen and hydrogen atoms. Nonetheless, useful spectra could be obtained from samples isotopically enriched in ^{15}N at 6 MHz with concentrations on the order of 1 M or more. The availability and expense of compounds enriched in ^{15}N made research in this area difficult. We found it expedient to start with a commercial sample, nitrobenzene labeled with ^{15}N, run its spectrum, then convert it to nitrosobenzene, run its spectrum, and so on. Use of this relay technique afforded the ^{15}N shifts of phenylhydroxylamine, azobenzene, azoxybenzene, hydrazobenzene, and aniline. The overall range of chemical shifts found by J. B. Lambert and G. Binsch covered some 900 ppm.[39]

Our next project investigated whether a relationship existed between $^1J(^{13}C, ^{15}N)$ couplings and the 2s characters of the bonding orbitals, as had already been shown for $^1J(^{13}C,H)$ couplings. This required substances doubly-labeled in both ^{13}C and ^{15}N and G. Binsch undertook making 10 such compounds by the relay technique with verve and skill. The resulting $^1J(^{13}C, ^{15}N)$ values gave only a fair parallelism with the expected 2s orbital contributions to the C–N bonds.[40]

Our DFS spectrometer could also be used with ^{15}N and F. Weigert apparently obtained the first natural-abundance ^{15}N spectrum of hydrazine in 1969. R. L. Lichter then developed conditions for taking ^{15}N spectra in a more routine way and, in particular, utilizing the proton decoupling for both simplifying the spectra by removing proton–nitrogen couplings and generating a very favorable, albeit negative, NOE. Under optimum conditions, where all of the ^{15}N relaxation results from dipolar interactions with neighboring protons, the negative signal is about four-times more intense than expected by just removing the proton splitting.

Lichter proved that there was a very close correlation between the ^{13}C shifts of hydrocarbons and primary and secondary amines, where the ^{13}C and ^{15}N are in analogous positions (see ***Organic Chemistry Applications***).[41] These studies were later greatly extended by R. Duthaler.[42]

The sensitivity of the DFS spectrometer for ^{15}N was marginal, especially if the proton NOE was unfavorable. The accumulation times were long and ^{15}N NMR was going to require a single-purpose spectrometer if many ^{15}N spectra were to be taken. A higher field was expected to help greatly with the sensitivity problem. I was able to raise $150 000 from the NIH to purchase a dedicated high-field ^{15}N spectrometer, and a difficult period ensued while the instrument companies blew hot and cold on giving us a quotation within our budget. Varian wanted to use our funds to develop a 300-MHz proton spectrometer with a ^{15}N probe using 10-mm diameter sample tubes for $366 000. Obviously this was out of our price range, and we actually did not want the proton capability, because this would mean that we would surely get requests to use the spectrometer for proton spectra. Bruker's quote was also out of range with a proposal for a 270-MHz proton spectrometer with a ^{15}N probe for $300 000.

As is customary in such cases, we strived to get Varian and Bruker to compete to build the instrument and also limit it to ^{15}N and possibly ^{13}C capability. Finally, we were rescued by D. M. Grant of the University of Utah who proposed that we opt for a lower magnetic field, but larger samples. 'A milk bottle if necessary.' Grant's argument was that a larger sample could gain more sensitivity than a higher field, because a 30-mm sample tube might well contain 10–30-times more sample in the active volume of the coil. Furthermore, he recognized that because the resonance frequency of ^{15}N was smaller by a factor of 10 than that of protons, the requirements for a given level of resolution would be much less stringent than for protons. This concept led to a new competition between Varian and Bruker and now Bruker won with an offer of a 15-MHz ^{15}N spectrometer with 25-mm tubes for $131 500.

Our Bruker order turned out not to have a very high priority within the company and it was not until mid-1974 that Bruker's C. Bradley started with the console of a Bruker WH-90 spectrometer, doubled its frequency to 180 MHz for the proton decoupling channel, and built ^{15}N and ^{13}C probes operating at 18 MHz and 45 MHz, respectively. The electronics embodied quadrature detection, which was new at the time, and the magnet was a superconducting solenoid with a 3-in. bore. The so-called WH-180 worked wonderfully well, with excellent resolution and sufficient stability to allow spectra to be time averaged over as long as 72 h. However, being custom-built, it was bereft of instruction manuals and had minimal documentation of the differences between its electronics and those of its WH-90 predecessor. It seems a fact of life, if you push for a custom-built spectrometer, the builder assumes that because you are smart enough to know what you want, you must be smart enough to get along without a lot, or even any, hand-holding in operations and maintenance.

The sample volumes were on the order of 18 mL and to get useful spectra in just a few hours the concentrations had to be about 1 M in nitrogen. When biochemists would ask us if we could take a ^{15}N spectrum for them, they blanched and quickly departed when they heard how much material we needed to run spectra of enzymes or other high molecular-weight substances at the natural abundance level of ^{15}N. Nonetheless, R. Moon and D. Gust were able to get good natural-abundance ^{15}N spectra of substances such as vitamin B_{12}, lysozyme, trypsin, salmonine, and yeast tRNA.[43] These compounds were not only available in substantial quantities but also, up to a point, the T_1 value of ^{15}N becomes shorter as the molecular weight increases and this allows for improved rates of signal averaging through more rapid pulsing. The success of the WH-180 vindicated Grant's concept of large sample sizes and demonstrated the utility of ^{15}N NMR for medium molecular-weight biochemically interesting compounds.

Much of our research on ^{15}N NMR was aimed at obtaining an understanding of how the spectra are influenced by the chemical surroundings of ^{15}N as exemplified by chemical shifts, coupling constants, and T_1 relaxation rates, as well as rates of chemical exchange. Another focus has been on showing how ^{15}N NMR can be used to examine the active

sites of enzymes, pathways of nitrogen metabolism, and environments within living cells.

A particularly effective use of ^{15}N is where the nitrogens of interest form double or triple bonds and, in addition, possess an unshared electron pair. Pyridine is a good example and its ^{15}N spectrum shows about 85–100 ppm shift to higher magnetic fields on accepting a proton.[44] Even hydrogen bonding to the pyridine nitrogen can cause shifts of up to 35 ppm.[44] We were able to use such changes in shift of nitrogens in C=N**:** groupings to establish the preferred site of protonation of vitamin B_1,[45] as well as of nucleosides and nucleotides.[46]

The most dramatic of our research on enzymes was on the base strength and position of the N–H tautomeric equilibrium for the histidine at the active site triad of serine proteases. It had been postulated by D. Blow from his excellent crystal structure of α-chymotrypsin that the so-called catalytic triad of serine, histidine, and aspartic acid residues acted in concert to assist the hydrolysis of peptide bonds. A small serine protease, α-lytic protease, with a single histidine, had been suggested to favor this hypothesis through an abnormal histidine base strength determined by analysis of ^{13}C chemical-shift changes found to occur with changes in pH.

W. W. Bachovchin undertook a reinvestigation of this enzyme labeled at its histidine with ^{15}N.[47] To do this he generated a myxobacter mutant for which histidine is an essential amino acid and, through extraordinarily careful experimentation, was able to grow the mutant on very expensive ^{15}N-labeled histidine and isolate the desired labeled α-lytic protease. The changes in the chemical shifts of the histidine nitrogens with pH showed that the pK_α value of the histidine was quite normal. We could also infer that there seemed to be significant hydrogen bonding of the protonated histamine, most probably to the aspartate carboxylate. Finally, there was strong evidence that the N–H tautomeric equilibrium was shifted from the usual position with the hydrogen most favorably located on N-1 to predominance for location at N-3, again through probable hydrogen bonding to the aspartate carboxylate. Bachovchin's results supported a very rational formulation of the catalytic triad.

With the help of K. Kanamori, a collaboration was achieved with B. Vallee and Bachovchin, by then a postdoctoral fellow at Harvard Medical School. At issue was the spatial location of a presumed active-site tyrosine of carboxypeptidase. Was it normally complexed with active-site zinc atom in the native enzyme, or did it move up to the zinc only when the enzyme was complexed with a substrate or inhibitor? Kanamori studied the ^{15}N shift changes with pH of the enzyme to which a ^{15}N-labeled azoarsanilic group had been coupled to the tyrosine in question.[48] The ^{15}N NMR results seemed to show that the degree of complexation was pH-dependent, and evidence was obtained of zinc binding at the higher pH values, but not at lower pHs. Substantial effort was required to elucidate the zinc–tyrosine binding, but it was later shown that the particular tyrosine residue was not needed at all for carboxypeptidase to be catalytically active.

N. Becker used ^{15}N NMR to study pyrazole inhibition of the zinc-containing enzyme, liver alcohol dehydrogenase (LAD).[49] This enzyme has a molecular weight of about 80 000 and we found that the ^{15}N resonances of both ^{15}N-labeled pyrazole and ^{15}N-labeled *N*-nicotinamide-adenine dinucleotide, NAD^+, mixed with LAD gave quite sharp resonance lines. The complexed entities were clearly well bonded to the LAD because they were not removed by dialysis. The upshot of Becker's research was to show that pyrazole became complexed to both the zinc and the NAD^+, as well as showing that quite high molecular weight substances could be studied by ^{15}N NMR, provided that they are reasonably conformationally flexible.

About 1980, K. Kanamori started a collaboration with R. Weiss and T. Legerton of UCLA on the pathways of nitrogen metabolism of *Neurospora* molds with ^{15}N NMR.[50] At the outset, this project did not look very hopeful to me from the standpoint of sensitivity and of possible line broadening through complexations or viscosity problems within the cells. Kanamori quickly showed that *Neurospora* fed on ^{15}N-enriched ammonium salts, converted the starting material to glutamate or glutamine, and throughout the resonance lines of the products were sharp, as well as coming from the substances within, not without, the cells. With moderate levels of ^{15}N, spectra could be obtained quickly and the growth and metabolism of *Neurospora* could be studied right within the spectrometer. Kanamori also investigated the ^{15}N NMR shift and relaxation properties of several intracellular amino acids in *Neurospora*.[51] These amino acids appear to become sequestered in vacuoles within the cell and these vacuoles are at different pH values and the amino acids have mobilities less than they have in the cytoplasm.

A fascinating and rewarding ^{15}N project arose in the course an investigation of which of the two natural-abundance ^{15}N resonances of diazocyclopentadiene arises from which nitrogen. For this, we synthesized the compound labeled with ^{15}N at the nitrogen closest to the ring by the reaction of cyclopentadiene anion with ^{15}N-labeled toluenesulfonyl azide ($TsNN^{15}N$). Some rearrangement occurred and part of the diazocyclopentadiene was found from the NMR to be labeled at the terminal nitrogen. This was investigated by C. Casewit who found that the rearrangement in question involved a reaction of $TsNN^{15}N$ and the unlabeled anion of toluenesulfonamide ($TsNH^-$) to yield $Ts^{15}NNN$.[52] Furthermore, at least 10 other resonances of ^{15}N-labeled substances were observed, even though the only labeled starting material was $TsNN^{15}N$. The products identified by NMR were $^{15}NNN^-$ and $N^{15}NN^-$, $Ts^{15}NH^-$, ^{15}NN, $TsN^{15}NN$, $Ts^{15}NNN$, $Ts_2{}^{15}N^-$, $TsN^{15}NNTs^-$, and $Ts^{15}NNNTs^-$. The information of dinitrogen was intriguing, because it seemed best formed from N_6 which would arise from coupling of TsNNN with NNN^- and elimination of Ts^-. Formation of Ts^- was indeed indicated by the presence of $TsNNNTs^-$ formed by Ts^- addition to TsNNN. Did linear N_6 cyclize to hexaazabenzene and then decompose to give $3\,N_2$? Unfortunately, we could not devise an experiment that would prove or disprove that possibility.

About 1984, I decided to look into NMR imaging or MRI as it is now called. An opportunity to undertake such research was available at the Huntington Medical Research Institutes (HMRI) in Pasadena, which had acquired one of the first commercial MR imaging units in the world for the use of W. G. Bradley, a very productive clinical MRI researcher. The contrast scale of MRI is primarily determined by chemistry and it seemed like a natural for study by an organic chemist interested in NMR. We did do imaging experiments on solvent swelling of polymers, but it was a difficult research situation because the imager was heavily scheduled for clinical work and each hour given to our work cost several hundred dollars of clinical revenue. The need for medical emergency scans

sometimes meant that the imaging personnel were shifting from one foot to another waiting for us to finish up our work.

When I 'graduated' to the status of Emeritus Professor in 1988, the then current rules of the California Institute of Technology precluded the operation of a graduate or postdoctoral research program. In principle, all that was allowed was whatever research you could do with your own hands, in whatever space the administration would allow you to function. Wanting to continue NMR research at some level, I decided to test the waters by taking on undergraduate research students. Fortunately, the Institute responded favorably and we have completed several projects. One was concerned with improving ^{15}N signal-to-noise ratios by decreasing T_1 while still maintaining a favorable proton–nitrogen NOE.[53] Another had to do with the T_2 dependence of the water in oxygenated and deoxygenated blood as a function of hematocrit, clotting, and magnetic field.[54] Still another involved determining the rotational barrier about the C–N bonds of urea.[55]

Most of our efforts have, however, been directed to determination of the influence of hydrogen bonding and electrostatic effects on conformational equilibria in ethane and propane derivatives, particularly in water solution (see ***Organic Chemistry Applications***).[56] Along with these research projects, I have written a third textbook, 'Notes on FT-NMR'.

NMR has always been for me the endless frontier—a steady stream of new developments of increasing sophistication and of usefulness. It has been an unending thrill to be able to participate in its growth from near its beginnings.

REFERENCES

1. G. E. Pake, *Am. J. Phys.*, 1950, **18**, 438.
2. F. Bloch, *Phys. Rev.*, 1946, **70**, 460.
3. A. T. Bottini and J. D. Roberts, *J. Org. Chem.*, 1956, **21**, 1169.
4. J. D. Roberts, *J. Am. Chem. Soc.*, 1956, **78**, 4495.
5. J. N. Shoolery and J. D. Roberts, *Rev. Sci. Instrum.*, 1957, **28**, 61.
6. A. T. Bottini and J. D. Roberts, *J. Am. Chem. Soc.*, 1956, **78**, 5126.
7. C. M. Sharts and J. D. Roberts, *J. Am. Chem. Soc.*, 1957, **79**, 1008.
8. E. I. Snyder and J. D. Roberts, *J. Am. Chem. Soc.*, 1962, **84**, 1582.
9. P. M. Nair and J. D. Roberts, *J. Am. Chem. Soc.*, 1957, **79**, 4565.
10. F. J. Weigert and J. D. Roberts, *J. Am. Chem. Soc.*, 1968, **90**, 3577.
11. R. L. Clough and J. D. Roberts, *J. Org. Chem.*, 1978, **43**, 1328.
12. D. L. Griffith and J. D. Roberts, *J. Am. Chem. Soc.*, 1965, **87**, 4089.
13. G. Binsch and J. D. Roberts, *J. Am. Chem. Soc.*, 1965, **87**, 5157.
14. G. M. Whitesides, F. Kaplan, K. Nagarajan, and J. D. Roberts, *Proc. Natl. Acad. Sci. USA*, 1962, **48**, 1112.
15. G. M. Whitesides, D. Holtz, and J. D. Roberts, *J. Am. Chem. Soc.*, 1964, **86**, 2628.
16. J. D. Roberts, *Nuclear Magnetic Resonance. Applications to Organic Chemistry*, McGraw-Hill, New York, 1959.
17. J. D. Roberts, *An Introduction to the Analysis of Spin–Spin Splitting in High-Resolution Nuclear Magnetic Resonance Spectra*, W. A. Benjamin, New York, 1961.
18. A. A. Bothner-By and S. M. Castellano, in *Computer Programs for Chemistry*, ed.; D. F. DeTar, W. A. Benjamin, New York, 1968, Vol. 1, Chap. 3
19. J. E. Nordlander and J. D. Roberts, *J. Am. Chem. Soc.*, 1959, **81**, 1769.
20. G. M. Whitesides, J. E. Nordlander, and J. D. Roberts, *Discuss. Faraday Soc.*, 1962, **34**, 185.
21. G. M. Whitesides, M. Witanowski, and J. D. Roberts, *J. Am. Chem. Soc.*, 1965, **87**, 2854.
22. B. L. Hawkins, W. Bremser, S. Borcic, and J. D. Roberts, *J. Am. Chem. Soc.*, 1971, **93**, 4472.
23. J. B. Lambert and J. D. Roberts, *J. Am. Chem. Soc.*, 1963, **85**, 3710.
24. S. L. Spassov, D. L. Griffith, E. S. Glazer, K. Nagarajan, and J. D. Roberts, *J. Am. Chem. Soc.*, 1967, **89**, 88.
25. J. T. Gerig and J. D. Roberts, *J. Am. Chem. Soc.*, 1966, **88**, 2791.
26. E. S. Glazer, R. Knorr, C. Ganter, and J. D. Roberts, *J. Am. Chem. Soc.*, 1972, **94**, 6026.
27. E. A. Noe and J. D. Roberts, *J. Am. Chem. Soc.*, 1972, **94**, 2020.
28. J. E. Anderson, E. S. Glazer, D. L. Griffith, R. Knorr, and J. D. Roberts, *J. Am. Chem. Soc.*, 1969, **91**, 1386.
29. F. J. Weigert and J. D. Roberts, *J. Am. Chem. Soc.*, 1967, **89**, 2967.
30. F. J. Weigert and J. D. Roberts, *J. Am. Chem. Soc.*, 1967, **89**, 5962.
31. F. J. Weigert, M. Jautelat, and J. D. Roberts, *Proc. Natl. Acad. Sci. USA*, 1968, **60**, 1152.
32. H. J. Reich, M. Jautelat, M. T. Messe, F. J. Weigert, and J. D. Roberts, *J. Am. Chem. Soc.*, 1969, **91**, 7445.
33. D. E. Dorman and J. D. Roberts, *J. Am. Chem. Soc.*, 1970, **92**, 1355.
34. J. G. Nourse and J. D. Roberts, *J. Am. Chem. Soc.*, 1975, **97**, 4584.
35. W. O. Crain, Jr., A. Zambelli, and J. D. Roberts, *Macromolecules*, 1971, **4**, 330.
36. B. L. Hawkins and J. D. Roberts, *Proc. Natl. Acad. Sci. USA*, 1973, **70**, 1027.
37. R. H. Levin, J.-Y. Lallemand, and J. D. Roberts, *J. Org. Chem.*, 1973, **38**, 1983.
38. G. A. Olah, D. P. Kelly, C. L. Jeuel, and R. D. Porter, *J. Am. Chem. Soc.*, 1970, **92**, 2544.
39. J. B. Lambert, G. Binsch, and J. D. Roberts, *Proc. Natl. Acad. Sci USA*, 1964, **51**, 735.
40. G. Binsch, J. B. Lambert, B. W. Roberts, and J. D. Roberts, *J. Am. Chem. Soc.*, 1964, **86**, 5564.
41. R. L. Lichter and J. D. Roberts, *J. Am. Chem. Soc.*, 1972, **94**, 2495.
42. R. O. Duthaler and J. D. Roberts, *J. Am. Chem. Soc.*, 1978, **100**, 3889.
43. G. Gust, R. B. Moon, and J. D. Roberts, *Proc. Natl. Acad. Sci. USA*, 1975, **72**, 4696.
44. R. O. Duthaler and J. D. Roberts, *J. Am. Chem. Soc.*, 1978, **100**, 4969.
45. A. H. Cain, G. R. Sullivan, and J. D. Roberts, *J. Am. Chem. Soc.*, 1977, **99**, 6423.
46. V. Markowski, G. R. Sullivan, and J. D. Roberts, *J. Am. Chem. Soc.*, 1977, **99**, 714.
47. W. W. Bachovchin and J. D. Roberts, *J. Am. Chem. Soc.*, 1978, **100**, 8041.
48. W. W. Bachovchin, K. Kanamori, B. L. Vallee, and J. D. Roberts, *Biochemistry*, 1982, **21**, 2885.
49. N. N. Becker and J. D. Roberts, *Biochemistry*, 1984, **23**, 3336.
50. T. L. Legerton, K. Kanamori, R. L. Weiss, and J. D. Roberts, *Proc. Natl. Acad. Sci. USA*, 1981, **78**, 1495.
51. T. L. Legerton, K. Kanamori, R. L. Weiss, and J. D. Roberts, *Biochemistry*, 1983, **22**, 899.
52. C. Casewit and J. D. Roberts, *J. Am. Chem. Soc.*, 1980, **102**, 2364.
53. A. Wei, *B.S. Thesis*, California Institute of Technology, 1989; M. K. Raymond, *B.S. Thesis*, Reed College, 1991.
54. R. A. Clark, A. T. Watanabe, W. G. Bradley, and J. D. Roberts, *Radiology*, 1990, **175**, 201.

55. Y. Zhao, M. K. Raymond, H. Tsai, and J. D. Roberts, *J. Phys. Chem.*, 1993, **97**, 2910.
56. E. S. Lit, F. K. Mallon, H. Y. Tsai, and J. D. Roberts, *J. Am. Chem. Soc.*, 1993, **115**, 9563.

Biographical Sketch

J. D. Roberts. *b* 1918. B.A., 1941, Ph.D. 1944, UCLA. Introduced to NMR by W. D. Phillips and J. N. Shoolery. Faculty in Chemistry, UCLA, 1944–45; Harvard University, 1945–46; MIT, 1946–53; California Institute of Technology, 1953–present. Approx. 485 publications and 9 books. Research interests include physical organic chemistry and applications of NMR to organic chemistry, particularly the determination of conformational equilibria and conformational equilibration, as well as of ^{15}N NMR to problems in biology and medicine.

Rogers, Emery H.: Remembrance of NMR Things Past

Emery H. Rogers

Formerly, Varian Associates, CA,

Compared with humankind's Stone Age, in which hand-tool invention is obscured in the cobwebs of time, the arrival of nuclear magnetic resonance occurred just yesterday. Thanks to development-time compression, many original NMR cave dwellers are still here to provide reminiscences about how it started and why it engendered such extraordinary dedication and creativity.

It all began for us in California during that period of dynamic rejuvenation at the Stanford University Physics Department following the cessation of World War II, when many government laboratories were yielding experienced professors and degree-seeking students back to academia.

Immediately after my return to Stanford in January 1946 from the Naval Research Laboratory to pursue a physics doctorate, Martin Packard showed me my first proton 'nuclear induction' signal, quite impressive even in a tossing sea of noise. The image then was of *induced* signals from tiny precessing gyromagnets, rather than of stimulated quantum energy state transitions. This approach made it possible to ascertain, beyond admittedly improbable doubt, the absolute signs of the proton and neutron magnetic moments. Professor Hans Staub, a close associate of Professor Felix Bloch, asked me to join him in using nuclear induction along with related polarized neutron cyclotron beam techniques to make these sign determinations experimentally. Although this was quite unpredictable at the time, the ultimate definitive consequences of these obscure events led eventually to my joining the spirited effort to establish a new commercially available analytical method.

Because the creaky cyclotron in the Stanford basement had a frustrating tendency to blow a bulky fuse during the necessarily lengthy neutron runs, a solid copper bar was substituted temporarily for the offending component one memorable day. The electrical power lines to the Physics Department passed under the nearby Law School lecture hall. Several dozen law students, including possibly one or more of today's US Supreme Court justices, never discovered the origin of the rising smoke wisps which briefly sent them scurrying outdoors.

With the signs of the magnetic moments of the proton and neutron safely confirmed in 1949, the time had arrived for pursuing a career. Proving once again that the right person in the right place at the right time can move mountains, Russell Varian became the inspiring answer to our hopes and dreams. He, his brother Sigurd, and several others, had founded Varian Associates in 1948 on a back street in nearby San Carlos. With remarkable clairvoyance, Russ had decided that nuclear induction should be explored and developed within his fledgling klystron company, even though no commercial applications beyond magnetic field measurement then appeared promising. A number of us in the Stanford group, including Packard, Wes Anderson, Jim Arnold, Elliott Levinthal, Warren Proctor, and Harry Weaver, joined Varian during the startup period. The effort to make NMR available somehow to the larger scientific community had begun.

Our first product was a fluxmeter which featured a nuclear induction probe on the end of a flexible cable. Having just emerged from academia, we had to learn how to achieve economies of scale by buying parts and building units in quantity—no mean accomplishment in an enterprise dedicated originally to contract research. We quickly discovered that magnetic field measurement had a rather limited market. Salvation soon arrived, however, in two forms: stand-alone electromagnet systems; and high-resolution NMR spectrometers for *chemists*, a heretofore exotic species to us physicists. The former market arose because of magnetic resonance and ferromagnetism research needs, and the latter arrived dramatically when Arnold, Dharmatti, and Packard saw the majestic three peaks of ethyl alcohol. At this fortuitous instant, Jim Shoolery, a bona fide chemist fresh from his CalTech Ph.D., and eager to lead us across the cultural divide into the promised land of NMR chemical applications, appeared at Varian's front door. Funded mainly by commercial sales of off-the-shelf magnet systems, and galvanized by the unswerving support of Russ Varian, our little team was now on a clear path.

A first major technical challenge was the compelling necessity to achieve much more stable and homogeneous magnetic fields. For several reasons, including flexibility, we chose electromagnets rather than permanent magnets for high-resolution NMR. My early work included shimming many magnets and designing a stable power supply to provide substantial direct currents for the water-cooled magnet coils. A mechanical 'chopper' converted dc error signals to ac for amplification, and then back to dc for correction, while an awesome array of eight glowing Eimac 304TL power transmitter tubes handled the stabilized output current.

Thin metal shims, shaped pole caps and adjustable ring shims helped open up improved volumes of magnetic field homogeneity. Remaining uniformity limitations were then surmounted dramatically by spinning the NMR sample rapidly, an ingenious technique which deceived the observed nuclei into 'seeing' a much more uniform average field. Greatly improved field stability arrived with a clever degenerative feedback coil system, developed for Varian by resident wizard Forrest Nelson.

The continuing story of how NMR was then taken from these developing conditions to standard analytical tool status has been related eloquently elsewhere (see, for example, J. N. Shoolery, *Anal. Chem*., 1993, **65**, 731A). However, two specific personal memories about motivation and nomenclature are perhaps not superfluous here.

One day in 1957, Jim Shoolery and I visited the laboratories of a prominent East Coast chemical company. We took silent note of a wall placard which proudly proclaimed that infrared spectroscopy was the single most definitive analytical technique in existence. On the flight back to California, we were resolutely inspired to generate specifications for what would eventually become the widely successful Varian A-60 high-resolution NMR spectrometer.

Before this watershed time, we had encountered puzzling delays in export licence issuance for our first overseas nuclear magnetic resonance shipments. The mystery vanished when we found that export officials were needlessly alarmed by the

adjective ‘nuclear’, which to them always sounded ominous no matter how harmless the pertinent specific technology. We promptly sat down at a Varian cafeteria table and created the unsophisticated acronym ‘NMR’.

Decades later, the medical profession also concluded that ‘magnetic resonance imaging’—‘MRI’—is more palatable than ‘*Nuclear* magnetic resonance imaging’. If this particular writer is rolled into an MRI machine someday, it will be personally fascinating to observe a nuclear-radiation-free magnet gap up close from the inside rather than from the outside.

Biographical Sketch

Emery H. Rogers. *b* 1921. A.M., 1943, Ph.D., 1951, Physics, Stanford University. General Manager, Analytical Instrument Group, Varian Associates, 1959–1967; General Manager, Analytical Instrument Group, Hewlett-Packard Company, 1967–1979; Executive Director, Hewlett-Packard Company Foundation, 1979–1986.

Saika, A.: Early Applications of NMR in Chemistry and Theoretical Calculations of NMR Parameters Related to the Electronic Structure of Molecules

A. Saika

Kyoto University, Kyoto, Japan

I started working in NMR in 1951 with Professor H. S. Gutowsky at the University of Illinois. At that time NMR was in such an early stage of development that I only needed to read a review article by Pake[1] as a preliminary study of the field. I was fortunate in that I did not need to survey such a formidable bulk of literature as has accumulated up to the present time.

I was first interested in applying Ramsey's theory[2] of nuclear magnetic shielding to interpret the fluorine chemical shift data by Gutowsky and Hoffman.[3] However, the task of evaluating the excitation energies appearing in the perturbation theory by Ramsey seemed time-consuming in those days of desk calculators. So Gutowsky suggested observation of the proton resonances of acid solutions as an alternative. At the time I had no idea at all whether single or double peaks would be observed, but observation revealed only a 'single' peak! This results from fast exchange between the protons of the hydronium ions and water molecules. The effect of chemical exchange on the lineshape was obtained by including the chemical shift between the different chemical species in the Bloch equations[4] for nuclear magnetization. The analysis enabled us to evaluate the apparent degrees of dissociation for various acids and alkalis.[5] This NMR method of lineshape analysis opened up a new means of studying rate processes ranging between 10^{-2} and 10^{-4} s which are not readily accessible by other spectroscopic methods.

Following the work on the dissociation of electrolytes, Lee Meyer and I started to record the proton spectra of simple organic molecules, gathering our samples largely from the organic storeroom and laboratories at the university. During the course of these measurements it became clear that the chemical shifts for each particular proton type ranged over certain distinct bounded shift values. Thus, a graphical presentation[6] of the shift ranges for various proton types serves as a guide map of proton shifts for structural analysis. This map, together with the simple proportionality of the relative absorption intensities to the numbers of nonequivalent protons plus the absorption multiplets due to nuclear spin–spin coupling, has saved considerably the labor in identifying the intermediate and final products obtained in the course of organic syntheses.

Nevertheless, my original plan to account for the much wider range of 10^{-3} of fluorine shift values compared with the proton shift range of 10^{-5} remained to be done. Following the suggestion by Professor C. P. Slichter in the Physics Department that p-electrons must be the cause of such large shifts, I left the diamagnetic term entirely out of my considerations. Furthermore, by neglecting the paramagnetic term arising from other atoms which falls off as $1/r^3$, the problem was reduced to an atomic one. In this model, one p electron is considered to be missing from the closed shell of a covalently bonded fluorine. In order to avoid the difficulties in calculating the above-mentioned excitation energy, I had recourse to a plausible experimental excitation energy. This led to a large paramagnetic shift of -20×10^{-4}, in order-of-magnitude agreement with experiment. On the other hand, the paramagnetic term vanished for a completely ionic F having a filled shell. This paramagnetic shift difference, dependent upon the fraction of unbalanced p electrons on the fluorine atom in question, provided an explanation for its almost linear dependence on the ionic character of the bond.[7] Such considerations may also be generally applicable to molecules with d valence electrons.

After returning to Kyoto University, my main concern turned to the more difficult problem of the theory of nuclear spin–spin coupling. In the early days, Ramsey, followed by many others, resorted to a 'mean excitation energy' approximation in the perturbation expansion. Since the numerator changed sign for each excitation, however, this gave erroneous results. When account of only the lowest excited states was taken, the results appeared to be reasonable. We then extended the procedure to include higher excited states, but no sense of convergence was noted.[8] At this stage, I felt that electron correlation in nuclear spin–spin coupling was particularly important, and so I chose to employ a many-body perturbation theory (MBPT) with the aid of Feynman diagrams as a means of systematically incorporating correlation corrections order-by-order. The Fermi contact contribution up to second order in correlation in the HD molecule was calculated to be 28.1 Hz, as compared to the best estimate of 40 Hz.[9] The result was still far from convergence, suggesting that perturbation of the external field (due to nuclear spins in the present case) is also significant. For this reason, I tried the finite-field (FF) MBPT to examine the validity of this scheme and obtained a value of 37.2 Hz in fair agreement with the best estimate.[10] Thus, this approach, incorporating both electron correlation and field perturbation simultaneously, appears promising and appealing.

Finally, a brief remark should be added on nuclear magnetic shielding. By applying MBPT to shielding, we found that electron correlation is not important in this case, i.e., the coupled Hartree–Fock method affords results in quantitative agreement with experiment,[11] almost 30 years after our previous qualitative model.[7] However, the latter gave a much more transparent insight into nuclear magnetic shielding! This brings back the thought that the noncomputer age still had certain merits.

REFERENCES

1. G. E. Pake, *Am. J. Phys.*, 1950, **18**, 438, 473.
2. N. F. Ramsey, *Phys. Rev.*, 1950, **78**, 699.
3. H. S. Gutowsky and C. J. Hoffman, *J. Chem. Phys.*, 1951, **19**, 1259.
4. F. Bloch, *Phys. Rev.*, 1946, **70**, 460

5. H. S. Gutowsky and A. Saika, *J. Chem. Phys.*, 1953, **21**, 1688.
6. L. H. Meyer, A. Saika, and H. S. Gutowsky, *J. Am. Chem. Soc.*, 1953, **75**, 4567.
7. A. Saika and C. P. Slichter, *J. Chem. Phys.*, 1954, **22**, 26.
8. Y. Kato and A. Saika, *J. Chem. Phys.*, 1967, **46**, 1975.
9. T. Itagaki and A. Saika, *J. Chem. Phys.*, 1979, **71**, 4620.
10. M. Iwai and A. Saika, *Phys. Rev.*, 1983, **A28**, 1924.
11. M. Iwai and A. Saika, *J. Chem. Phys.*, 1982, **77**, 1951.

Biographical Sketch

A. Saika. *b* 1924. B.S., 1947, D.Sc., 1960, Kyoto University. Introduced to NMR by H. S. Gutowsky. Faculty in Chemistry, Kyoto University, 1965–88 (retired). Research interests include study of dynamic processes by high-resolution liquid and solid state NMR; theoretical study of electric and magnetic properties of molecules.

Samoson, Ago: Development of High-Resolution NMR of Quadrupole Nuclei in Solids

Ago Samoson

Estonian Academy of Sciences, Tallinn, Estonia

Our NMR laboratory in Tallinn, established by Prof. E. Lippmaa, has been active in high-resolution solid state NMR since the mid-1970s. Some of the very first CP MAS ^{13}C spectra were run on a homebuilt spectrometer with an original double bearing spinner system. Typical rotation speeds were limited to a few kHz by the strength or expansion of the rotor material. The method was applicable to spin-$\frac{1}{2}$ nuclei and produced important analytical results, for example neat regularities between the structures of silicates and aluminosilicates and ^{29}Si chemical shifts.[1,2] One of our collaborators, Dr. G. Engelhardt from Berlin, insisted on complementing the studies with those of ^{27}Al, as aluminum atoms may occupy various crystallographic positions.

The ^{27}Al nucleus has spin-$\frac{5}{2}$ and is subjected to electric quadrupole interactions, both first and second order. The possibility of averaging the first-order quadrupole interactions was demonstrated for ^{2}H NMR by Ackerman, Eckman, and Pines in Berkeley, using a conical single-bearing spinner.[3] Averaging a first-order quadrupole interaction needs extremely precise spinning angle setting and more stable results were achieved with a double-bearing spinner system by the late M. Alla from our laboratory while working in Berkeley.[4]

Nuclei with half-integral spin $I > 1$ generally exhibit lines from $2I + 1$ transitions with the special property that the central transition is only shifted in second order. Although analysis of the second-order effects employing MAS had not been published, the first ^{27}Al spectra recorded in (East) Germany were encouraging in that they showed two lines, which were assigned to the tetrahedral and octahedral positions of the atoms in the structure.[5,6] We were able to demonstrate, both experimentally and analytically, powder pattern lineshapes of the second-order quadrupole interaction under conditions of fast spinning at 54.7° to the magnetic field.[7,8] Very similar results were reported shortly afterwards by several other NMR groups.[9–11]

While running spectra on various materials we frequently noticed that a 180° pulse was not achieved. A remark by C. Alma-Zeestraten from Amsterdam about difficulties with 270° pulses triggered a suspicion of a more fundamental cause—the process of excitation of a central transition signal is not as straightforward as in the case of a spin-$\frac{1}{2}$ nucleus. Consideration of first-order quadrupole interaction during the rf excitation pulse immediately explained all the anomalies.[12] A systematic extension of the pulse length provides for 2D nutation spectroscopy with a potential of estimating the quadrupole interaction value.[13] This value is needed for a correct interpretation of the field-dependent line shifts in the spectra. Two-dimensional spectroscopy also helped to reveal a missing component in the ^{27}Al spectra of dehydrated zeolites,[14] and to determine the relative orientations of chemical shielding and quadrupole interaction.[15]

Meanwhile, new materials, suitable for rotors, had become available. In 1984, due to our skilful machinist A. Salumäe and crucial design improvements by Dr. M. Alla, we were able to spin samples above 17 kHz. However, the machineable ceramic Macor contained aluminum and for work on aluminosilicates we had to use polymers. The new three-dimensionally cross-linked polymer Vespel allowed speeds of up to 8 kHz, which was a big improvement and facilitated the observation of satellite transitions.[16,17] This method is of benefit for $I = \frac{5}{2}$ and $I = \frac{9}{2}$ nuclei, as one of the transitions features very low residual second-order quadrupolar line broadening. In addition, the narrow line in spin-$\frac{5}{2}$ spectra is very close to the actual chemical shift value and is thus little affected by the ubiquitous dispersion of quadrupole interactions. A combination of fast MAS, nutation, and satellite transition spectroscopy enabled us to measure the chemical shift of ^{27}Al with a precision comparable that of ^{29}Si. Not surprisingly, almost identical shift correlations with the structural features were established for both atoms in aluminosilicates.[18]

The combination of MAS with nutation was somewhat phenomenological and a brief analysis was presented whereby we also proposed a quadrature nutation using a soft pulse after evolution.[19] Although our analytical description was met with some criticism by developers of multipole operators,[20] the fictitious spin formalism used by us offers advantages for one obvious reason: the observable signal is proportional to just one of the operators.

Pines and his students at Berkeley had noticed that spinning at certain angles produces frequency reversed powder patterns. This observation led them to the idea of refocusing the second-order interaction by switching the spinning axis.[21] A systematic increment of evolution time, fractioned to spinning at different angles, produces stick spectra on a parametric axis.

High-resolution spectra in real time require repeated reorientation of the sample at a rate which is fast compared with homogeneous line broadening. Any pertinent reorientation scheme, which would of necessity be more sophisticated than simple rotation about one axis, also had to be feasible mechanically. Conical reorientation instead of a robust tilt of the rotation angle seemed one such possibility and, with a suitable choice of angles and speeds, it was easy to verify that spinning around two axes would create the necessary effect.[22] The same idea was simultaneously forwarded by Llor and Virlet in Saclay.[23] The first attempt at mechanical implementation was derived from the observation that single-bearing conical rotors tended to wobble while spinning. A rotor with a spherical bottom was constructed in the hope that the wobbling would be amplified but the conical motion generated was disappointingly slow and at about 10 Hz the rotors became detached from the stator. Better guidance of the rotor could be achieved using a double bearing and axial support. However, the centripetal or gyroscopic forces would easily exceed the load bearing capacity unless they were opposite and equal. Such forces generally depend on both the shape of the moving body and the trajectory of the motion. The whole project started to look much more feasible after we realized that the dimensions of a cylindrical body performing the required motion are actually quite reasonable: the ratio of the length to the diameter is ca. 3. This triggered the construction of a double rotor system.[24] The outer

rotor of a prototype unit, machined with great patience by C. Gaskins at the Chemistry Department machine shop in Berkeley, spun up to 400 Hz, after few modifications, which was sufficient to demonstrate real-time averaging of the second-order quadrupole interactions.

Further major enhancements to the technique were related to sideband suppression. As opposed to regular MAS, outer rotation objects are characterized by a random interaction strength but not a random orientation. Synchronization of an excitation pulse with the outer rotor phase gives a certain degree of control over the sidebands. The number of sidebands can immediately be reduced twofold[25] and by a factor of four using two inversion pulses.[26] Another peculiar feature of DOR, caused by the orientation of the sample, is the dependence of sideband broadening on the spinning angle of the outer rotor.[27]

The number of applications using DOR is not very great to date. The method requires expensive probes and trained operators. However, with outer rotor speeds above 1000 Hz, and using sideband suppression, DOR has proven useful for the study of glasses, cements, catalysts, and other industrially important materials.[28–31]

Current NMR probe designs, enabling speeds four-times higher than the speed of the DOR prototype, and over 25 kHz MAS, are based on 20 years experience of high-speed rotor development in our laboratory. Although standard machine shop facilities do not guarantee the necessary precision, the prohibitive costs of special equipment have been substituted by the qualifications and devotion of our technicians A. Reinhold and T. Anupõld.

Human curiosity and experience, advances in high-performance materials, and the momentum given by possible analytical applications have generated a new branch of NMR spectroscopy—high-resolution solid state NMR of quadrupole nuclei. This method combines quantum, classical, and machine shop mechanics, at a level which is sophisticated even for each separately. Members of our group have been fortunate to participate in this development and we hope that our contributions will form the basis for further exciting advances.

REFERENCES

1. E. Lippmaa, M. Magi, A. Samoson, G. Engelhardt, and A.-R. Grimmer, *J. Am. Chem. Soc.*, 1980, **102**, 4889.
2. E. Lippmaa, M. Magi, A. Samoson, M. Tarmak, and G. Engelhardt, *J. Am. Chem. Soc.*, 1981, **103**, 4992.
3. J. L. Ackerman, R. Eckman, and A. Pines, *J. Chem. Phys.*, 1979, **42**, 423.
4. R. Eckman, M. Alla, and A. Pines, *J. Magn. Reson.*, 1980, **41**, 440.
5. D. Müller, W. Gessner, H. J. Behrens, and G. Scheler, *Chem. Phys. Lett.*, 1981, **79**, 59.
6. D. Freude and H. J. Behrens, *Cryst. Res. Technol.*, 1981, **16**, 36.
7. A. Samoson and E. Kundla, *Proc. Colloq. AMPERE, Uppsala*, 1981, p. 37.
8. E. Kundla, A. Samoson, and E. Lippmaa, *Chem. Phys. Lett.*, 1981, **83**, 229.
9. D. J. Burton and R. K. Harris, *J. Chem. Soc., Chem. Commun.*, 1982, 256.
10. H.-J. Behrens and B. Schnabel, *Physica B+C*, 1982, **114**, 185.
11. E. Oldfield, S. Schramm, M. D. Meadows, K. A. Smith, R. A. Kinsey, and J. Ackerman, *J. Am. Chem. Soc.*, 1982, **104**, 919.
12. A. Samoson and E. Lippmaa, *Phys. Rev. B.*, 1983, **28**, 6567.
13. A. Samoson and E. Lippmaa, *Chem. Phys. Lett.*, 1983, **100**, 205.
14. A. Samoson, E. Lippmaa, G. Engelhardt, U. Lohse, and H. G. Jerschkewitz, *Chem. Phys. Lett.*, 1987, **134**, 589.
15. A. Samoson, *Exp. Tech. Phys.*, 1988, **36**, 273.
16. A. Samoson, E. Kundla, and E. Lippmaa, *J. Magn. Reson.*, 1982, **49**, 350.
17. A. Samoson, *Chem. Phys. Lett.*, 1985, **119**, 29.
18. E. Lippmaa, A. Samoson, and M. Magi, *J. Am. Chem. Soc.*, 1986, **108**, 1730.
19. A. Samoson and E. Lippmaa, *J. Magn. Reson.*, 1988, **79**, 255.
20. B. C. Sanctuary, *J. Magn. Reson.*, 1989, **85**, 571.
21. B. Chmelka, K. T. Mueller, A. Pines, J. Stebbins, Y. Wu, and J. W. Zwanziger, *Nature (London)*, 1989, **339**, 42.
22. A. Samoson, E. Lippmaa, and A. Pines, *Mol. Phys.*, 1988, **65**, 1013.
23. A. Llor and J. Virlet, *Chem. Phys. Lett.*, 1988, **152**, 248.
24. A. Samoson and A. Pines, *Rev. Sci. Instrum.*, 1989, **60**, 3239.
25. A. Samoson and E. Lippmaa, *J. Magn. Reson.*, 1989, **84**, 410.
26. A. Samoson, *Chem. Phys. Lett.*, 1993, **214**, 456.
27. A. Samoson, *Introduction to DOR NMR*, NATO ASI, Turkey, in press.
28. P. J. Grobet, A. Samoson, H. Geerts, J. A. Martens, and P. A. Jacobs, *J. Phys. Chem.*, 1991, **95**, 9620.
29. G. Engelhardt, H. Koller, P. Sieger, W. Depmeier, and A. Samoson, *Solid State Nucl. Magn. Reson.*, 1992, **1**, 127.
30. A. Samoson, P. Sarv, J. P. van B. Houckgeest, and B. Kraushaar-Czarnetzki, *Appl. Magn. Reson.*, 1993, **4**, 171.
31. G. J. Ray and A. Samoson, *Zeolites*, 1993, **13**, 410.

Biographical Sketch

Ago Samoson. *b* 1955. Ph.D., 1984, Physics, Institute of Physics, Estonia. Scientist at Institute of Chemical Physics and Biophysics, Tallinn, Estonia, 1978–present. About 50 publications. Research interests: solid state NMR—hardware, theory, applications, and software.

Sanders, Jeremy K. M.: Luck, Ignorance, and Daring in Research: NMR Spectroscopy of Nature's Plastics and Spiders' Webs

Jeremy K. M. Sanders

University of Cambridge, Cambridge, UK

Do scientists always set out with a well-defined question and proceed to solve it logically? Some do, but in my experience, accidental discoveries, wrong conclusions, and outrageous experiments are also a good way of undertaking science. One episode in our biological NMR work makes the point—it is described in more detail elsewhere.[1]

In the early 1980s, we began using solution state NMR experiments to study the metabolism of small molecules in live bacteria. By adding ^{13}C- or deuterium-labeled substrates to suspensions of live cells we were able to see the biochemistry that interested us without interference from the hundreds of natural-abundance components present within the cell. These background signals were insignificant in most species. However, in 1986, my student Glenn Barnard found that the spectra of *Methylobacterium* species were dominated by natural abundance signals from within the cell. In particular, one compound with just four signals was present in highly variable amounts; its identity remained a mystery for a few weeks until, browsing in the library, I came across a paper by Jake Schaefer[2] describing the solid state NMR spectrum of polyhydroxybutyrate (PHB). The shifts matched almost perfectly. PHB is a bacterial storage polymer of molecular weight around a million, stored as submicron-sized granules; the isolated polymer is a commercially available biodegradable plastic. Having stumbled across PHB in these cells, we became fascinated: NMR was a new window into the biological and physical chemistry of PHB.

Solids do not usually give high-resolution spectra when solution state techniques are applied; their signals are too broad to be observed by such methods. In 1986, the conventional wisdom was that PHB in granules is a crystalline solid, so the observation of PHB in live cells using solution state NMR was very surprising. Indeed we were successful only because we were ignorant of conventional wisdom. However, the use of solution state NMR techniques, including relaxation experiments, allowed us to show that PHB within the granule is an elastomer, not crystalline as was generally believed.

It had long been recognized that PHB granules have paradoxical properties, many of which were resolved by this insight, but our results raised new problems: how does the cell prevent PHB crystallization in vivo and what triggers crystallization when the granules are isolated? For some years, we and others searched for plasticizers or nucleation inhibitors within the granule, while freeze-drying results suggested that water also plays a role. All this searching was in vain—nobody found any positive evidence. We then realized that the explanation is much simpler: the maximum rate of spontaneous crystal nucleation found for pure isolated PHB is less than 10^2 events $mm^{-3}\,s^{-1}$. The volume of an individual native granule is around $10^{-10}\,mm^3$, so the nucleation rate *per granule* is less than 10^{-8} events s^{-1} and the average lifetime of a native granule before crystallization will exceed 10^8 s, i.e. years. Cells store PHB in a thermodynamically unfavorable state simply because the crystallization kinetics are so slow. If this model is correct, then we should be able to reproduce it in the laboratory, and indeed Daniel Horowitz in my laboratory has done so with great success.[3] It appears that after many twists, turns, and false trails we now have a reasonable working model of the granule interior; fortunately, one of the false trails led us in an unexpected direction—spiders' webs.

Just when we were convinced that water is involved in plasticizing PHB, a paper appeared on the role of water in maintaining elasticity in spiders' webs. The coated capture threads in the web of the common garden spider stretch by up to 400% when absorbing the momentum of a captured flying insect, whereas the structural thread which the spider builds as a rigid scaffolding is barely elastic at all. What is the difference between these threads and how can such elasticity be explained at a molecular level? Either some part of the protein is flexible and acts like a spring, or rigid rods slide past each other as in muscle contraction; in each case water is supposed to act as plasticizer or lubricant. Flexible springs should give high-resolution solution state spectra, while rigid rods would not. Fortunately, Fritz Vollrath agreed to provide suitable web samples. Each web weighs only around 1 mg, and so around 20 capture or structural webs from captive spiders were collected and wound onto a glass capillary, but sensitivity and sample size limited the quality of spectrum: we needed ^{13}C-labeled webs. Captive spiders generally live on fruit flies but Vollrath was able to feed them directly with solutions of ^{13}C-labeled glucose or amino acids. Webs containing only structural threads were collected, and then whole webs containing capture and structural threads were separately collected from the same spiders.

The crucial observation was that, in the presence of water, the capture web has regions which are mobile on the NMR timescale; the spring mechanism was vindicated. Structural threads give no high-resolution signals under the same conditions. They lack molecular mobility or elasticity, even in water, and must have a different arrangement at the molecular level.

Our first breakthrough in understanding PHB granules in 1986 came about accidentally. Nobody who 'knew' that PHB is crystalline in vivo would have attempted our experiment, and nobody could have got a grant to do the work. Our spider work happened because we mistakenly believed that water was a plasticizer for PHB and drew an incorrect analogy.

So how should we do science? One can choose a big problem, lay a plan, obtain funding and people, and solve it; or one can set out to explore a trivial byway while keeping eyes and mind open. The first approach is a vital component of science—the second can be more fun.

REFERENCES

1. J. K. M. Sanders, *Chem. Soc. Rev.*, 1993, **22**, 1.
2. G. S. Jacob, J. R. Garbow, and J. Schaefer, *J. Biol. Chem.*, 1986, **261**, 16 785.
3. D. M. Horowitz and J. K. M. Sanders, *J. Am. Chem. Soc.*, 1994, **116**, 2695.

Biographical Sketch

Jeremy K. M. Sanders. *b* 1948. B.Sc., 1969, Ph.D., 1972, Cambridge University, UK (worked on lanthanide shift reagents with Dudley Williams). Member of staff, University of Cambridge (currently Reader in Chemistry), 1973–present. FRS, 1995. Approximately 150 papers. Research specialties: biological applications of NMR spectroscopy; synthesis of biomimetic systems based on porphyrins.

Saunders, Martin: The First NMR Spectrum of a Protein

Martin Saunders

Yale University, New Haven, CT, USA

When I started teaching at Yale in 1955, there was no NMR spectrometer at the university. In the next year, the Chemistry Department decided to buy one. No one else on our faculty wanted to be associated with it; so, as the most junior member, I was assigned the task of setting it up, operating and maintaining it, and (if possible) finding something to do with it. Our instrument was a 40 MHz Varian spectrometer for protons only, with no field/frequency lock and an electromagnet cooled by city water. The temperature of the water changed with the season, requiring that the magnet be 'shimmed' using an 8 ft. pipe on a wrench on one of the bolts fastening the pole pieces and with all my weight on the end of the pipe.

The Head of the Department, John Kirkwood, was very interested in the physical chemistry of proteins. One day, he asked me what one could learn about proteins with this new instrument. I told him that I did not know but that I would find out. I asked people in the department for a sample of some protein and was given a small amount of ribonuclease. When I looked at an aqueous solution of it, at first I saw nothing but a strong water signal. After shimming the field, increasing the gain, and sweeping more slowly, I eventually saw a tiny peak on the upfield side of the water peak (conceiveably due to the protein). Since the water protons were interfering with the observation of the protein signal, the next step was to dissolve the protein in D_2O instead of water. Now it was clear that a definite signal was produced. However, there was still a very large water peak obscuring part of the spectrum. We decided that this resulted from the water of crystallization and exchangeable protons. At this point Arnold Wishnia, who was a Kirkwood postdoctoral, joined the project. Arnold lyophylized the D_2O solution and dissolved the solid protein in fresh D_2O. When this was repeated several times, the water peak was reduced and the spectrum shown (Figure 1) was obtained.[1] Further work led to spectra of lysozyme and bovine serum albumin.[2]

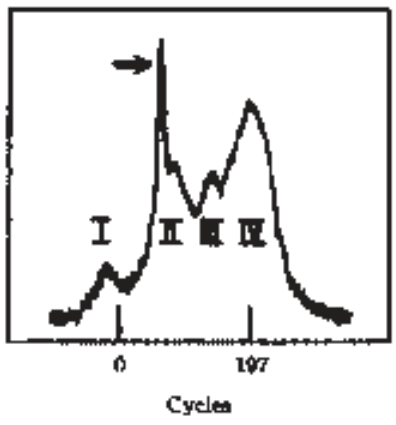

Figure 1 First NMR spectrum of a protein—ribonuclease at 40 MHz

Three per cent polystyrene in CCl_4

Figure 2 First NMR spectrum of a polymer in solution—polystyrene

What did we learn about proteins from this spectrum? The most important thing was that one could obtain a spectrum where aliphatic, aromatic, and NH (as they were exchanged out) were roughly at the chemical shifts expected from those found in smaller compounds and that their peaks were fairly sharp. From diffusion and viscosity data, Kirkwood could estimate the correlation time for rotation of the protein molecules. We concluded that, if the molecules rotated as rigid bodies, there would be much more broadening from dipole–dipole interaction than we saw in the spectrum. The relative sharpness of the peaks seemed to imply that there was internal motion. This conclusion stimulated us to look at the spectrum of polystyrene (mol. wt. 1 500 000) in CCl_4 (Figure 2). Seeing lines about 20 Hz in width confirmed our idea that flexibility leading to local motion could result in sharp lines even in very large molecules. I believe that this is the first spectrum of a high polymer in solution to be published.

The only other work involving proteins which Arnold and I did was on exchange of protons with D_2O. We could see that the exchange rates of various groups spanned a wide range and noted (as others had before us) that the exchange rates were a function of pH value.[3] We did not imagine how it might be possible to improve the resolution so that individual protons could be seen and then to be able to assign these lines. We could not foresee that NMR observations would eventually lead to detailed three-dimensional structural information about the proteins.

REFERENCES

1. M. Saunders, A. Wishnia, and J. G. Kirkwood, *J. Am. Chem. Soc.*, 1957, **79**, 3289.
2. M. Saunders and A. Wishnia, *Ann. NY Acad. Sci.*, 1958, **70**, 870.
3. A. Wishnia and M. Saunders, *J. Am. Chem. Soc.*, 1962, **84**, 4235.

Biographical Sketch

Martin Saunders. *b* 1931. B.S., 1952, City College of New York, Ph.D., 1956, Harvard University. Faculty, Chemistry Department, Yale University, 1955–present.

Schaefer, Jacob: A Brief History of the Combination of Cross Polarization and Magic Angle Spinning

Jacob Schaefer
Washington University, St. Louis, MO, USA

BACKGROUND

My focus in the Monsanto Company in the late 1960s and early 1970s was the development of Fourier transform techniques for the ^{13}C NMR analysis of polymers. After a seminar in the Chemistry Department of Washington University in 1971, I was complaining to Sam Weissman that most of the polymers I was trying to characterize were only partially soluble and that the resolution of spectra of swollen, cross-linked, multiphased systems was inevitably poor. Sam suggested forgetting about solvents and using magic angle spinning on the solid polymers instead. I objected that I didn't want to get involved in an experiment which was both difficult and dangerous. (I recalled a magic angle spinning talk featuring a slide showing the operator at a console separated from the magnet gap by a wall of sandbags!) Sam led me into his office, reached up to a book shelf, and took down a cigar box from behind a pile of journals. Within a few minutes he had assembled a magic angle spinning device consisting of a solid Lowe rotor suspended on two L-shape bronze wires. The short ends of the wires fitted into tiny holes machined into the center of each end of the rotor. The long ends of the wires were held by spacers and Teflon tape to the sides of a glass pipette. The tip of the pipette was aimed at flutes which had been cut around the barrel of the rotor. Sam gave a gentle puff and the rotor whistled into action: magic angle spinning and no sandbags.

Naturally, I was an immediate convert to spinning. I worked with Sam and his graduate student, Stanley Chin, to try ^{13}C NMR experiments on a chunk of truck tire. The tire was fashioned into a rotor by Jim Boyles, the same machinist in the Washington University Physics Department who had made rotors initially for Irving Lowe, and later for Richard Norberg and his students. The pipette was fitted into a cylindrical plastic holder which was the same diameter as a standard 13-mm sample tube, so no changes had to be made to the probe. The holder also had guides for the short ends of the L-shaped wires and these guides fixed the orientation of the spinning axis. The magic angle was set by rotating the entire plastic holder, which altered the spinning axis relative to the static field of the 2.1 T electromagnet. Stanley Chin had taped a cardboard protractor to the top of the plastic holder so that we knew approximately where the magic angle was. We determined how fast we were spinning by the sound. This primitive apparatus worked on the first try. The natural-abundance ^{13}C linewidths of the rubber in the truck tire were narrowed by about a factor of two by the spinning (Figure 1).[1]

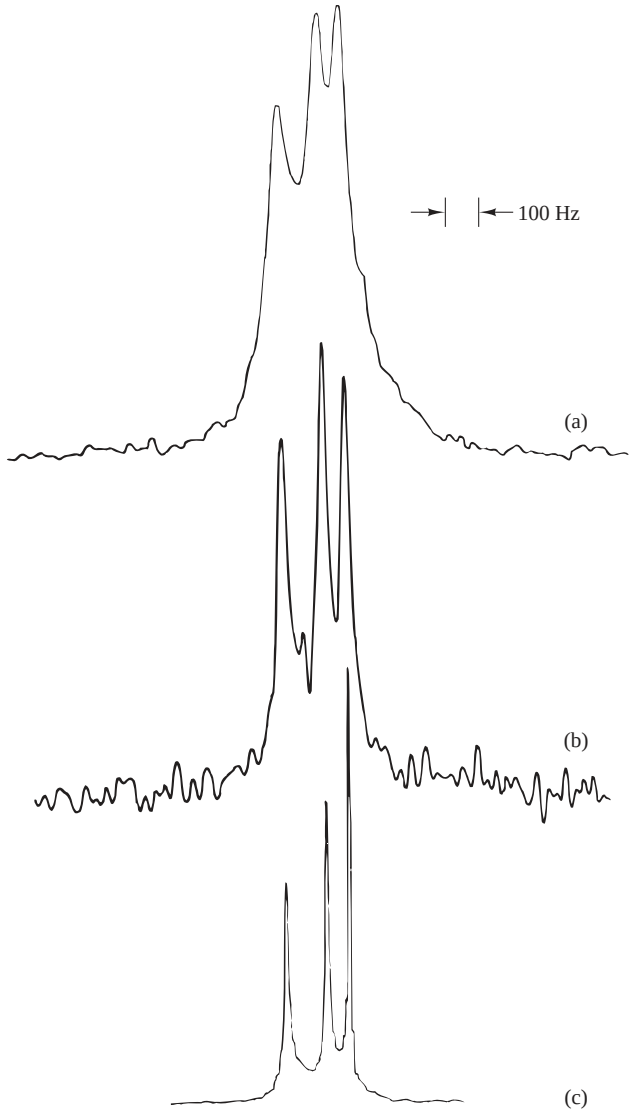

Figure 1 22.6-MHz Fourier transform ^{13}C NMR spectra of the aliphatic region of a carbon-black filled, vulcanized polyisoprene (a) static and (b) spinning at the magic angle at 1 kHz. The nonspinning spectrum of pure polyisoprene is shown in (c). (From Ref. 1)

THE 1972 ASILOMAR EXPERIMENTAL NMR CONFERENCE

I presented these results at the 1972 Experimental NMR Conference, which was the first to be held at the Asilomar conference site on the Monterey peninsula. For most attendees the highlight of the meeting was the dramatic Wednesday evening talk given by Alex Pines, then a graduate student with John Waugh at MIT. Pines showed how natural abundance ^{13}C NMR spectra of crystalline solids could be obtained with high sensitivity using cross polarization transfers from protons. This was the first I had heard of cross polarization for ^{13}C and I was astounded by Pines's spectra: one beautiful slide

after the other made unambiguous correlations of structure, chemical shifts, and dynamics. This presentation convinced me immediately that cross polarization for sensitivity and resonant decoupling of protons for resolution would be important for the ^{13}C NMR of solid polymers. I do not recall thinking at this meeting of trying to combine cross polarization with magic angle spinning.

STEJSKAL'S FIRST ROTORS

Over the next few months I began reading the papers by Hartmann and Hahn, and Slichter and Ailion, to try to gain some insight into the physics of the cross polarization experiment. I was also continuing with magic angle spinning experiments, now in collaboration with Edward O. Stejskal who had joined my research group in the Physical Sciences Center of Monsanto. We became involved with an effort to characterize gases adsorbed on catalytically active molecular sieves, a project motivated by Monsanto's commercial interest in removing pollutants from auto exhaust. The sieves were powders and spinning experiments required a hollow rotor with a payload of about 0.5 cm^3. Jim Boyles was retiring from active service at Washington University, so Ed Stejskal made drawings for a Lowe rotor incorporating Boyles's design features, and we asked a senior Monsanto machinist to give it a try. None of the first few attempts even came close to spinning smoothly. I was becoming worried that while spinning wasn't dangerous, maybe it was a bit too magical for comfort.

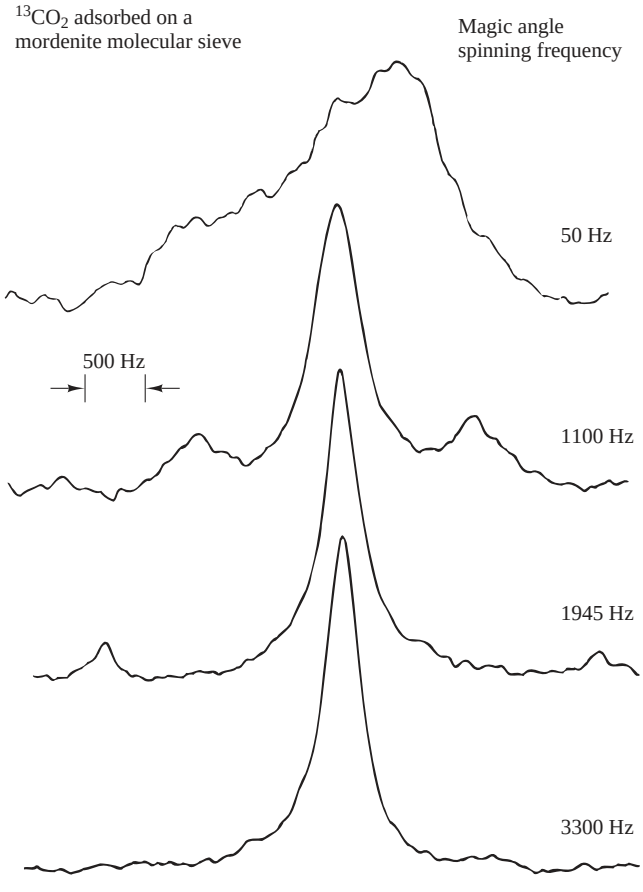

Figure 2 22.6-MHz Fourier transform ^{13}C NMR spectra of $^{13}CO_2$ adsorbed on a mordenite molecular sieve spinning at the magic angle at speeds between 50 and 3300 Hz. (From Ref. 2)

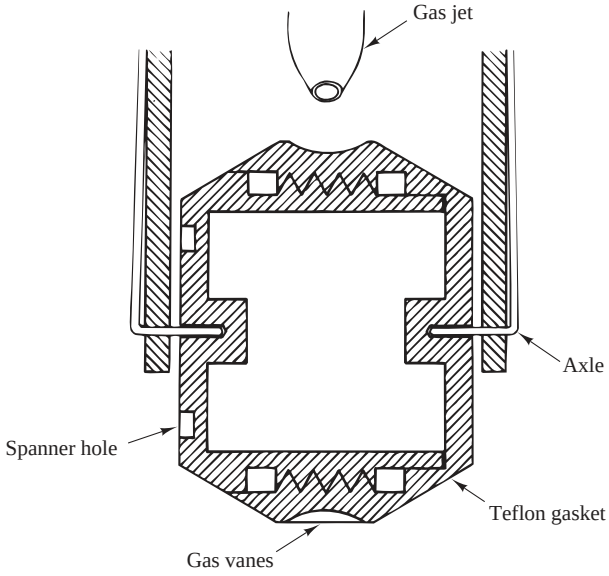

Figure 3 Hollow Lowe rotor used in the mordenite spinning experiment of Figure 2. (From Ref. 2)

Stejskal volunteered to make the rotors. Ed had harbored a life long ambition to be a machinist and I believe he saw this as a golden opportunity. We bought a small, precision lathe and Ed attached several 'plastics and nonferrous metals only' signs (in a suitably official-looking font) to avoid conflicts with the professional machinists in the building. Ed's careful attention to detail, his understanding of what was demanded by the NMR experiment, and his flair for innovation at the lathe made a winning combination. He tried scores of design modifications until he had a rotor that spun easily and reliably. Even though we completely misinterpreted the results of our first experiments on adsorbed gases,[2] the spectra themselves were fine (Figure 2). Moreover, by the end of 1973 we had a sealable, hollow rotor for spinning experiments (Figure 3).

COMBINATION SPINNING EXPERIMENTS

The more I read about cross polarization the more I became convinced that magic angle spinning and cross polarization could not be combined. The latter required static dipolar coupling and the former removed it. A discussion with the most knowledgeable practitioners of cross polarization at the Dallas ACS meeting in April 1973 had reinforced this perspective. In particular, I was afraid that contributions from nonprotonated carbons with only weak couplings would simply disappear from the spectrum, and that the other carbon lines would have distorted, nonrepresentative intensities. Nevertheless, I felt that a *non*spinning, cross polarization spectrum and the associated cross polarization transfer rates might be useful for characterizing molecular dynamics. In addition, I already knew that many of the glassy polymers that we intended to examine had short carbon spin–lattice relaxation times. Thus, I felt that fully relaxed, Fourier transform ^{13}C NMR of polymers would be practical and

informative because the resolution could be dramatically improved by relatively low-speed magic angle spinning to remove broadening due to chemical shift anisotropy, together with strong resonant decoupling of all carbon–proton interactions. Basically, I hoped to get dipolar-decoupled spectra of spinning glassy polymers like those of the rubbery polymers of Figure 1, and then use the resolution to measure T_1 and $T_{1\rho}$ values.

Thus, at the beginning of 1974, Stejskal and I continued to work both on cross polarization and on magic angle spinning, but with no specific intention of combining them. Ed had turned rotor production into a cottage industry. Because we were interested in a variety of engineering plastics, Ed made the rotors directly into analytical samples from melt-pressed molded bars and cylinders. The first rotors were all from Monsanto plastics: polystyrene, polyacrylonitrile, polystyrene/polyacrylonitrile copolymers, and poly(vinyl chloride). A typical result for polystyrene is shown in Figure 4. We were encouraged with the resolution that (almost) allowed our seeing three types of carbons. At the same time, we were collecting nonspinning, cross polarization ^{13}C NMR spectra of a variety of glassy polymers, including poly(methyl methacrylate) (Figure 5). I presented the results of both kinds of experiments at a Chemical Society of London meeting at Bedford, England, in July 1974. I carefully explained the motivation for both experiments and concluded, 'As a practical matter, however, with lines narrowed by magic angle spinning, it may be difficult to establish the Hartmann–Hahn condition and so obtain the sensitivity enhancement of cross polarization'.[3] Because of this outlook, and the preciousness with which we regarded the first few successful plastic rotors, we made no serious attempt at cross polarization combined with magic angle spinning for almost another year.

Actually, the 'practical matter' (see quote above) that really prevented even a casual attempt at cross polarization with magic angle spinning was the limitation of our pulse programmer. We were using crystal-controlled gate and delay

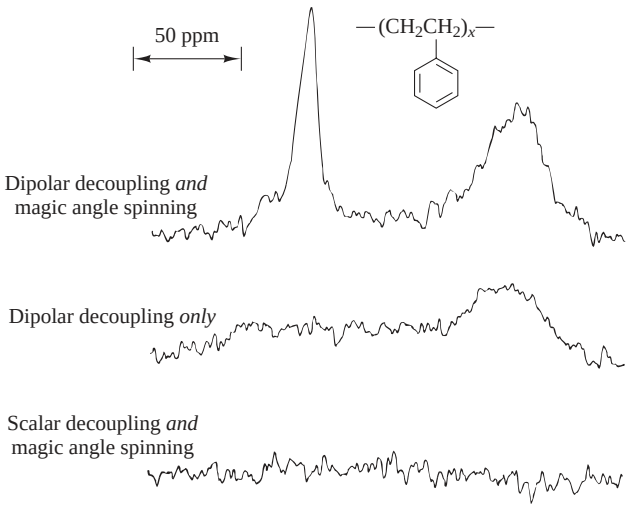

Figure 4 22.6-MHz Fourier transform ^{13}C NMR spectra of a polystyrene Lowe rotor spinning at 2 kHz at the magic angle with no decoupling of the protons (bottom) and with 30 kHz dipolar decoupling (top). The middle spectrum was taken with decoupling but no magic angle spinning. These spectra were obtained on June 27, 1974. (From Ref. 3)

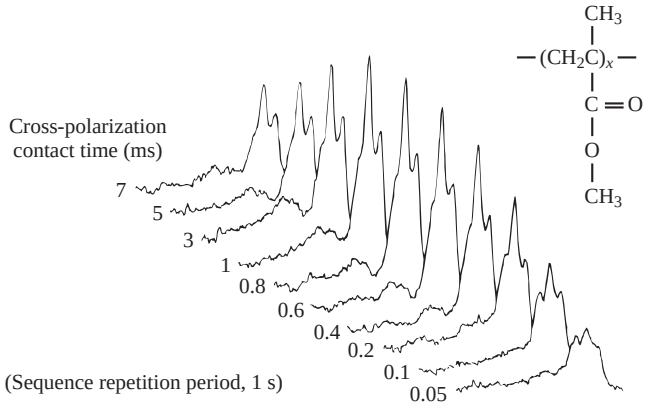

Figure 5 22.6-MHz cross polarization ^{13}C NMR spectra of nonspinning poly(methyl methacrylate) as a function of the Hartmann–Hahn contact time. (From Ref. 3)

generators to make pulses on both carbon and proton rf channels. These units were linked by BNC cabling. The logic of the pulse sequence meant that the cabling had to be physically rearranged depending on whether we were going to do a Fourier transform or a cross polarization experiment. In addition, because the Lowe rotors had lifetimes of only a day or so (the bearing holes wore irregularly on stops and starts), we adopted the practice of not spinning a rotor until the pulse sequence and acquisition were clearly working. Thus, cross polarization and spinning were kept in separate compartments, both in our minds and in the laboratory.

THE FIRST CP MAS EXPERIMENTS

By May 1975 we had acquired additional gate and delay generators so that the logic for both Fourier transform and cross polarization pulse sequences was wired up and switch-selected. Thus, it was inevitable that the combination of cross polarization and magic angle spinning would be tried, and our first CP MAS ^{13}C NMR spectrum of a solid is shown in Figure 6 (middle). We clearly had a strong signal from the low-field, nonprotonated carbonyl carbon of poly(methyl methacrylate). Stejskal and I were astonished. Within 10 days we had finessed the operating conditions so that we knew that the nonprotonated quaternary carbon was also reporting (Figure 6, bottom). The methylene carbon was missing (and we didn't find it until we were able to increase the decoupling to more than 40 kHz about a month later), but otherwise the relative intensities looked representative of the numbers of carbons in the repeat unit.

I excitedly told my superior at Monsanto, Rolf Buchdahl, that Stejskal and I had invented a new analytical technique for polymers. The official name of our group at Monsanto was 'New Analytical Techniques'. Rolf was not amused. Buchdahl suggested that I try the experiment on polycarbonate and I hurried off to look up the exact structure of the polycarbonate repeat unit. I quickly came back to Rolf and complained that there were too many aromatic carbons in polycarbonate that were almost but not quite alike, and that I couldn't promise that the new experiment would work. (As a precaution, I had decided to downscale my description of what we were doing from 'new analytical technique' to 'new experiment'.)

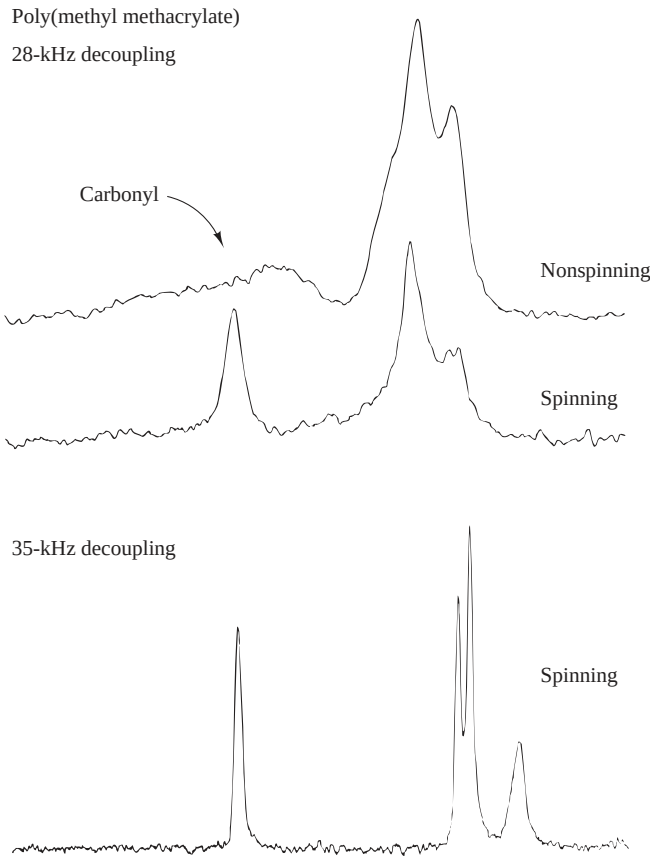

Figure 6 22.6-MHz cross polarization ^{13}C NMR spectra of poly(methyl methacrylate) static (top) and with 3 kHz spinning at the magic angle (middle). These spectra were obtained on June 2, 1975. The proton radiofrequency field amplitude was 28 kHz, both for the 1 ms matched spin lock transfer to carbons and for decoupling. The bottom spectrum, which is displayed using a slightly wider frequency scale, was obtained with 35 kHz decoupling on June 12, 1975

Rolf assured me that the new whatever wouldn't be worth much if it didn't work on polycarbonate. To my relief, the CP MAS spectrum of polycarbonate was well resolved, and even better, carbon spin lock measurements indicated faster $T_{1\rho}$ relaxation for the protonated carbons than for the nonprotonated carbons (Figure 7). We immediately began issuing serious proclamations of the possibility of connecting the microscopic dynamics of polycarbonate with mechanical properties in June 1975, a practice that I have continued on a regular basis to the present.

PUTTING SPIN ON A BILLIARD BALL

Stejskal and I were excitedly trying CP MAS on every polymer we could get our hands on. We tried spinning protein powders in the hollow rotor but had difficulties getting the packing well balanced. We decided to machine a solid rotor out of a piece of bone just as Ed was doing with the plastic samples. At that time, it was legal to buy ivory billiard balls, so I called the A. E. Schmidt Company, a St. Louis supplier of billiards equipment with which my family had dealt for many years. They indeed had ivory balls in stock but they were only rough-cut. This meant that the balls were approximately spherical but had to be trued before they could be used. I explained that I didn't care if they were only rough-cut because I didn't care whether the ball rolled straight or not. Silence on the phone. An ivory billiard ball showed up three days later perfectly trued and polished, and with an elaborate set of instructions on how to break it in before high-impact use. We ignored the instructions and instead used a jeweler's saw under water to cut a center section from the ball. This allowed Stejskal to machine a solid Lowe rotor whose spinning axis was along the eye of the tusk from which the ball had been turned.

CLOSE ENCOUNTERS WITH REVIEWERS

By the fall of 1975 we had generated a sizeable collection of CP MAS spectra of engineering polymers, various woods (including ebony), and the protein in ivory. We submitted a brief communication to the *Journal of the American Chemical Society* describing these results. The manuscript was not accepted based on the negative comments of one of the referees who wrote, 'Basically, there should not be polarization transfer due to a dipolar interaction between nuclei in a sample being spun rapidly at the magic angle.' Stejskal and I were a little at a loss as how to respond to this comment since we both agreed with it completely. We certainly didn't understand how the polarization was being transferred, but there was no doubt that transfers occurred, and to protonated and nonprotonated carbons alike. We knew that the transfers did not depend on some inherent flaw in the experimental set-up (the referee had suggested an error in the setting of the magic angle) because the transfers were just as efficient when the lines were broad as when they were narrow (Figure 6). Reluctantly, I added a paragraph of spin-mumbo to the manuscript, which, on reading today I am sorry to report, has not aged well. Nevertheless, the manuscript was accepted[4] and the spectra that appeared in 1976 are not bad (Figure 8) even by present-day standards.

THE HAND DIAGRAM

Adamantane was one of our favorite samples for cross polarization because it was possible to observe two ^{13}C lines even with modest dipolar decoupling. In January 1976, we decided to see how much additional narrowing could be achieved with combined decoupling and spinning. Following the standard protocol, I established that the cross polarization sequence and the receiver section of the spectrometer were working properly before turning on the spinner. The spinner was gaining speed as the pulsing was going on. I noticed sizeable variations in the shot-to-shot signal-to-noise ratio on the oscilloscope and immediately stopped increasing the flow of the rotor drive gas. The rotor was now spinning at about 1 kHz and I was getting only about 20% of the expected signal intensity, but I couldn't find anything wrong with the spectrometer. I decided that trouble shooting would take considerably longer and that I had better give up on the experiment and turn off the drive gas. As the spinning speed decreased, the lost signal intensity suddenly returned. I stopped changing the gas flow and observed almost full

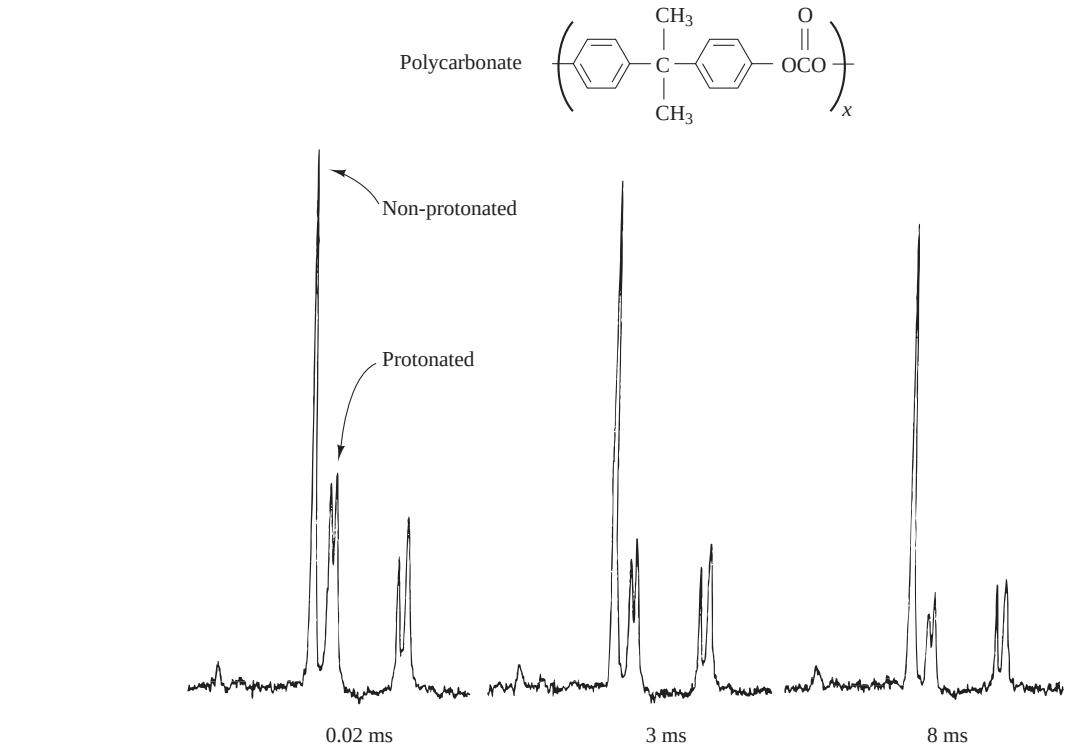

Figure 7 22.6-MHz cross polarization magic angle spinning ^{13}C NMR spectra of polycarbonate as a function of the time held in a 28 kHz spin-lock carbon rf field (with no proton rf field) prior to detection with 35 kHz proton decoupling. The $^{1}H-^{13}C$ cross polarization transfer has discriminated against the protonated carbons. These spectra were obtained on June 12, 1975

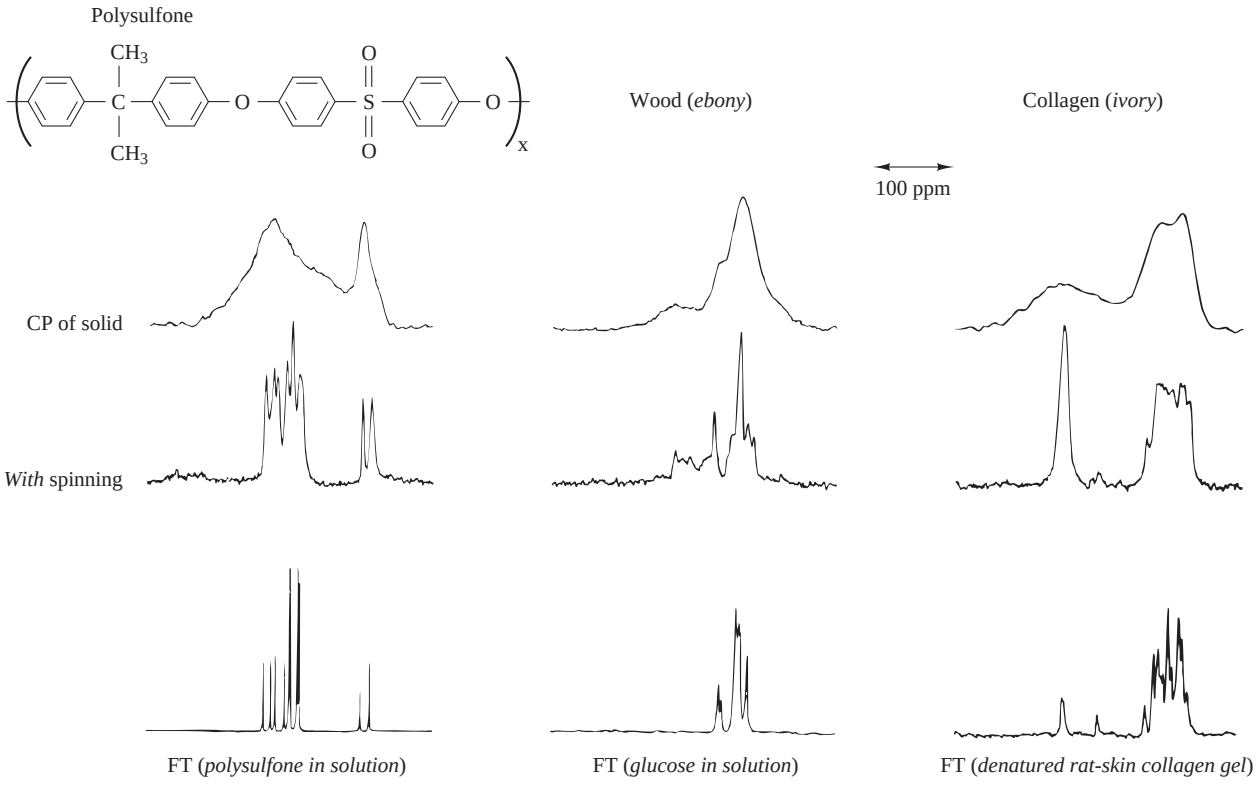

Figure 8 22.6-MHz cross polarization ^{13}C NMR spectra of various solids without spinning (top) and with 3 kHz spinning at the magic angle (middle). Comparative solution state Fourier transform spectra are shown at the bottom of the figure. (From Ref. 4)

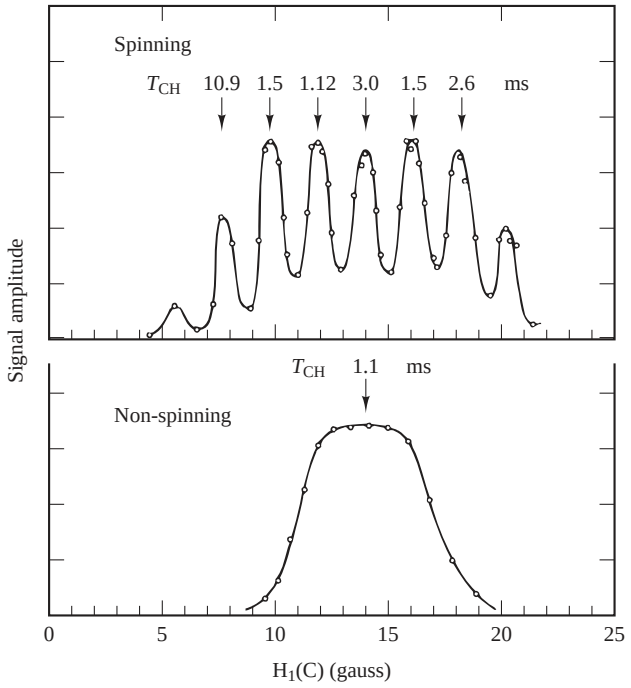

Figure 9 The amplitude of the proton-enhanced ^{13}C NMR signal in adamantane as a function of the Hartmann–Hahn mismatch with 2.2 kHz magic angle spinning (top) and without spinning (bottom). The arrows indicate where the cross polarization time constant was determined by measuring carbon signal intensity as a function of contact time. (From Ref. 5)

intensity. Another 10 minutes or so of this and I convinced myself that I was in control of the signal level. After 10 more minutes, I had convinced Stejskal.

For the next several hours, we made systematic variations in spinning speed and radiofrequency amplitudes resulting in the plot shown in Figure 9. Ed was determining cross polarization transfer rates using graph paper and a hand calculator. He used his 'on-line' plot to suggest new spectrometer settings for me. I recorded the resulting spectra and measured peak heights with a ruler to produce inputs for Ed's plots. We were afraid to stop the experiment because at the time the rotor that was spinning in the magnet was our only functioning hollow rotor, and damage was most likely to occur on stops. Ed ignored increasingly frantic calls from home that dinner guests had arrived long ago. After a while Ed said that the diagram looked like a hand. The hand grew a few more fingers, but we never changed the name. (A less-resolved plot we generated later for another system we refered to as a 'knuckle diagram'. This illustrates how catchy new NMR terms are born.)

WAUGH'S EXPLANATION

I was in the habit of calling John Waugh (he was always in his office around noon, Boston time) and pestering him for help with the mysteries of solids NMR. I told him of our strange CP MAS results on adamantane. Waugh was intrigued and offered to look at the data. A few days later he produced the basic explanation. As with all good theories, his explanation was simple and direct: cross polarization transfers work with no

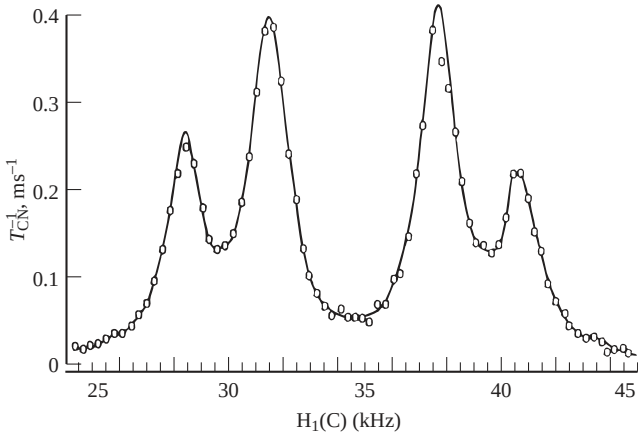

Figure 10 The $^{13}C-^{15}N$ cross polarization time constant as a function of the Hartmann–Hahn mismatch for L-[4-^{13}C, amide-^{15}N]asparagine spinning at the magic angle at 3205 Hz. (From Ref. 6)

complications when the spinning speed is slow compared to the homogeneous proton–proton interactions.[5] This was certainly the case for the polymers and proteins we had examined, but it was not quite true for adamantane which has relatively weak proton–proton interactions. Thus, magic angle spinning does indeed interfere with cross polarization transfers *if* the sample is spun fast relative to *all* dipolar interactions. What I had been forgetting for the last two years was the obvious, well-known fact that 3 kHz spinning had virtually no narrowing effect on a 20 kHz proton linewidth. For adamantane, the 'hand diagram' arose from a combination of frequency and amplitude modulation of homogeneous dipolar coupling, and amplitude modulation of heterogeneous dipolar coupling, all produced by the spinning.[5] For systems with only heterogeneous dipolar interactions,[6] only amplitude modulations are present, and the hand loses a few fingers (Figure 10). In either case, strategies can be worked out so that weak couplings in the presence of fast spinning can still be used for transfers.[6] In other words, magic angle spinning complicates the cross polarization process but doesn't short circuit it.

RETROSPECTIVE

I believe that the combination of cross polarization and magic angle spinning would have been discovered in the late 1970s in the absence of the events described above, or, for that matter, in the absence of Schaefer and Stejskal. However, for us, the experiment was a natural result of our efforts to solve polymer structure problems. It is possible, therefore, that our immediate application of CP MAS to complicated polymer systems helped to convince others of the utility of the technique and thus contributed to its early acceptance and subsequent popularity.

REFERENCES

1. J. Schaefer, S. H. Chin, and S. I. Weissman, *Macromolecules*, 1972, **5**, 798.
2. E. O. Stejskal, J. Schaefer, J. M. S. Henis, and M. K. Tripodi, *J. Chem. Phys.*, 1974, **61**, 2351.

3. J. Schaefer, The Analysis of ^{13}C NMR Relaxation Experiments on Polymers, in *Structural Studies of Macromolecules by Spectroscopic Methods*, ed. K. J. Ivin, Wiley, London, 1976, p. 201.
4. J. Schaefer and E. O. Stejskal, *J. Am. Chem. Soc*., 1976, **98**, 1031.
5. E. O. Stejskal, J. Schaefer, and J. S. Waugh, *J. Magn. Reson.*, 1977, **28**, 105.
6. J. Schaefer, E. O. Stejskal, J. R. Garbow, and R. A. McKay, *J. Magn. Reson.*, 1984, **59**, 150.

Biographical Sketch

Jacob Schaefer. *b* 1938. B.S., 1960, Ph.D., 1964, Physical Chemistry, University of Minnesota, USA. Research scientist at Monsanto Company, St. Louis, 1964–1986; collaborated with E. O. Stejskal in 1976 to combine cross polarization with magic angle spinning. Faculty in Chemistry, Washington University in St. Louis, 1986–present. Approx. 200 publications. Research specialties: development of techniques for the NMR of polymeric and biological solids.

Schaefer, Ted: A Canadian Prairie Youth Discovers the Delights of NMR

Ted Schaefer

University of Manitoba, Winnipeg, Manitoba, Canada

On September 30, 1955, a Canadian youth aged 22 arrived in Oxford, UK, to become a research student of R. E. Richards. (Rex Richards had been a student of H. W. Thompson, a pioneer of infrared spectroscopy. The latter, a student of C. N. Hinshelwood and F. Haber, had once lodged in the home of Max Planck in Berlin.) That youth, myself, hardly appreciated the lucky concatenation of circumstances leading to his presence in the ancient city. I was born in a depression-ridden pioneer village which lacked most physical amenities, even roads. Nevertheless, a good basic education was available, furthered by my multilingual teaching father, and was followed by a sound training in the classical aspects of chemistry at the University of Manitoba; the post-World War II prosperity made university attendance possible although it was still a privilege. Science was glamorous in 1950. Had not the physicists proclaimed that a few grams of nuclear fuel could drive the Queen Elizabeth across the Atlantic?

Another link in the catenary leading to Oxford was the friendship between A. N. Campbell, my supervisor of an M.Sc. thesis on the phase diagram of lead–indium–tin, with W. G. Schneider at the National Research Council in Ottawa. I spent a summer in Bill Schneider's laboratory. Late that summer of 1955 a Varian HR-40 NMR spectrometer arrived. I watched entranced as Bill and H. J. Bernstein 'chased a ^{1}H NMR signal across the oscilloscope screen'—there was no magnetic flux stabilizer, not to speak of a field/frequency 'locking' device. Their signal-chasing culminated in the first comprehensive monograph on chemical NMR (1959), written with J. A. Pople.

The final circumstance was that Bill Schneider facilitated my acceptance by Rex Richards. My first night in Oxford was spent in a bare college room; I read myself to sleep with 'Three Men in a Boat'. Soon, however, I was deep in D. Bohm's book on quantum theory and similar texts. There was a great deal to learn. Unlike today, when a plethora of texts bewilders the novice, there were no NMR texts in 1955. One puzzled over the journals or sought advice. Even C. A. Coulson consented to answer mundane questions about perturbational calculations.

Rex Richards had a homebuilt 12.2-MHz spectrometer whose magnet was energized by lead–acid batteries. He suggested the measurement of the ^{1}H NMR spectra of NH_4NO_3 down to a temperature of 20 K. I carried the required liquid hydrogen from the Clarendon Physics Laboratory over to the Physical Chemistry Laboratory—musing about the neat fact that *para* hydrogen yields no NMR signal—and poured it into the precooled (liquid oxygen!) Dewar containing the NMR probe. The acquisition of the first derivatives of the NMR absorption signals entailed wearisome manipulations.

Rex did not tell me that this instrument had yielded spectra proving the existence of the hydronium ion.[1] This I learned from Ray Freeman, well into his doctoral work on gallium and cobalt NMR; the latter led to an influential paper[2] on the paramagnetic contribution to the chemical shift. Another presence was D. F. Evans, later to do the first relative signs of coupling constants by double resonance.[3] One took the abundant mental stimulation for granted.

In the end I determined some 1200 second moments (Van Vleck) of a variety of ammonium salts. Because the necessary integrations were done with hand-turned mechanical calculators, it helped to memorize the squares and cubes of many integers. The lineshapes and second moments displayed some curious behavior, indicative of subtleties in the motional characteristics of the ammonium ions (in an attempt to understand at least some of the details, I studied the pioneering work by Gutowsky, Pake, and Bersohn[4]). Indeed, such salts have provided challenges to numerous investigators over the years. Our eventual survey paper (less publishing pressure then) is still referenced on occasion, certainly as late as 1993. It is satisfying to have one's work noticed, of course, even when the surname is subjected to amazing spellings.

Rex Richards was also building a simple, high-resolution instrument[5] based on a permanent magnet. He encouraged me to construct the radiofrequency bridge, the NMR probe, and a linear time base for field sweeping. My attempts began with sheets of shiny metal, progressed via bloody fingers and many revisions, ending with workable black boxes. One day, Rex conjured up M. Golay. The 30-MHz spectrometer was thereby endowed with an early set of printed circuits of electrical shims for the adjustment of magnetic field inhomogeneities. Golay also left me with the firm belief that spherical harmonics express the spatial distribution of almost anything and that a baby's rattle can be a scientific device. My eleventh attempt at a probe using everyday materials—yes, a cork will spin—was successful. On a Good Friday we had repeatable ^{1}H NMR spectra with peak widths of about 0.5 Hz for an undegassed sample. Today, careful shimming and digital enhancement will resolve half a dozen peaks in such an envelope, but in 1957 I felt proud of the $10 probe. Furthermore, Rex's machine could be returned from ^{1}H to ^{19}F NMR in a few minutes, a time matched only later on commercial units.

It was a delight to see the many spectral patterns arising from different organic materials. Papers on such patterns appeared between 1955 and 1960, written by pioneers such as H. S. Gutowsky, C. P. Slichter, W. A. Anderson, H. M. McConnell, E. L. Hahn, J. A. Pople, among others. My own small contribution was to puzzle out the appearance of a spectrum from three nuclei, unequally spin–spin coupled to each other but with accidentally equal chemical shifts for two of the nuclei. My 1958 thesis called this an AA′B situation, the first use of the prime notation, later to be used more sensibly by other authors in distinguishing between 'chemical' and 'magnetic' equivalence.

Rex's machine could resolve some long-range coupling interactions, over as many as six formal bonds between the nuclei, as in 4-fluorotoluene. They have tantalized me ever since. In the hands of many experimentalists and theoreticians such interactions turned out to be exquisitely sensitive to the stereochemistry and internal flexibility of a molecule. Sometimes small internal rotational potentials followed for certain molecules in solution, occasionally in cases where other methods appeared to fail.

These facts are twigs on the branches of the elaborate tree into which NMR has grown in 50 years. Yet the satisfaction at having contributed to even one twig is such that I am deeply

grateful to fortune and to my numerous mentors and students for the chance to play in the glorious game called NMR.

REFERENCES

1. R. E. Richards and J. A. S. Smith, *Trans. Faraday Soc.*, 1951, **47**, 1261.
2. R. Freeman, G. R. Murray, and R. E. Richards, *Proc. R. Soc. London*, 1957, **A242**, 455.
3. J. P. Maher and D. F. Evans, *Proc. Chem. Soc. London*, **1961**, 208.
4. H. S. Gutowsky, G. E. Pake, and R. Bersohn, *J. Chem. Phys.*, 1954, **22**, 643.
5. J. B. Leane, R. E. Richards, and T. P. Schaefer, *J. Sci. Instrum.*, 1959, **36**, 230.

Biographical Sketch

Theodore P. Schaefer. *b* 1933. B.Sc., 1954, M.Sc., 1955, Chemistry, University of Manitoba, Canada, D. Phil, 1958, University of Oxford (supervisor, R. E. Richards). Faculty in Chemistry, University of Manitoba, 1958–present. Approx. 300 publications. Research interest: very high resolution NMR yielding precise long-range spin–spin coupling constants and their relationship to conformation and internal motions in highly flexible molecules.

Schneider, William G.: Early Research on High-Resolution Proton Magnetic Resonance

William G. Schneider

The subject of nuclear magnetic resonance has expanded in a remarkable manner since the first experiments on bulk matter in 1945. Early high-resolution work on liquids indicated that magnetic nuclei could detect small changes in chemical environment and promised a number of important applications in various branches of chemistry and chemical physics. In the last few years this promise has been fulfilled and the rapid development of instrumentation has made nuclear magnetic resonance one of the most powerful tools for investigating chemical problems.

—From the preface to the book, 'High Resolution Nuclear Magnetic Resonance', by Pople, Schneider, and Bernstein, McGraw-Hill (1959).

From a 1993 perspective, 34 years after the publication of our book, it is clear our view then of the potential of NMR and its future applications was very much understated. The rapid development of NMR, which was in full swing in 1959, has continued unabated and there are now few scientific disciplines not affected by its impact. These new developments, as was the case before 1959, have been driven by continuing research to understand basic principles and new applications, as well as enormous advances in high-quality magnets, sophisticated instrumentation, and computerization. Before 1959 it was easily possible to know personally most of the active researchers in NMR. The scientific literature in the field was sparse and almost every experiment yielded exciting new results.

The opportunity to enter in on the ground floor of a major new scientific development is not given to many scientists. I consider myself very fortunate to have had such an opportunity although in hindsight I have to admit my entry followed a somewhat circuitous path.

In 1946 I was appointed to the research staff of the Chemistry Division of the National Research Council of Canada in Ottawa. My research was focused on intermolecular forces, intermolecular potentials, and phase transitions. The discovery of proton magnetic resonance in bulk matter in 1945 was an exciting event for any physical chemist. How was it accomplished and what might it lead to? Subsequent research by physicists at Harvard and Stanford Universities led to the discovery of chemical shifts, i.e. a displacement of the nuclear resonance due to different chemical environments of the nucleus being measured. Here was the first indication of an important link to chemistry.

In 1951 I attended one of the national meetings of the American Chemical Society at which I encountered Prof. George Kistiakowsky, Professor of Chemistry at Harvard, with whom I had worked in 1941 and 1942 as a postdoctoral fellow. George talked about his current research interests and specifically about NMR. Some time ago he had attended a colloquium in the Physics Department at Harvard given by Prof. Purcell on NMR. As he listened to explanations of magnetic coupling, of linewidths and lineshapes, it suddenly occurred to him it might be possible to use these properties to investigate hindered internal rotation in crystals, e.g. ammonium salts, methyl groups, etc. He then set out to explore these ideas and mentioned he had some Ph.D. students in his laboratory doing experimental work, notably Herb Gutowsky and Charles Reilly. 'They are getting some very interesting results.' And, he added 'NMR looks like a promising field; you should get into it.'

If further convincing evidence was needed, that same year Arnold, Dharmatti, and Packard observed three separated proton resonance signals in ethanol with intensities in the ratio of $3:2:1$ corresponding to the three chemically distinct hydrogen atoms in the molecule. Additionally, about this time, Gutowsky and co-workers reported on their observations of multiple lines due to J coupling in ^{19}F and ^{31}P resonances in a number of compounds containing these nuclei. There was now little doubt that NMR could have an important future in research in chemistry, and entering the field became a personal goal. However, I had previously applied for and been accepted to take a one-year sabbatical at Cambridge University in England in the Department of Theoretical Chemistry headed by Prof. Sir John Lennard-Jones. In the end the decision was made to delay a possible NMR initiative until after my return.

My sabbatical, from September 1952 to September 1953, was a stimulating experience and scientifically very profitable. Whilst at Cambridge I had many interesting discussions with Dr. John Pople, a very able young researcher who was obviously going to make his mark as a theoretical chemist, and who later was to become a collaborator in our NMR research activities.

On my return to Ottawa I started to review the experimental requirements and options for a research proposal in NMR. The key component for high-resolution work is the magnet which must have a very high degree of field homogeneity over the volume of the sample, as well as a high degree of stability. It soon became apparent that cost would be a major stumbling block, and that such a large investment for my small research group was not likely to be approved. To minimize this risk it was decided to bring on board as a collaborator Dr. Harold Bernstein, head of a small research group in infrared and Raman spectroscopy. Harold had expressed an interest in NMR as a potential new research tool.

By this time we were aware that Varian Associates, a company in Palo Alto, CA, were in the process of developing large electromagnets suitable for high-resolution NMR. The company had also recently taken on staff a very able young physical chemist, Dr. James Shoolery, who together with the company engineers had developed complete instrumentation for high-resolution NMR. The rf signal detection system was of the double-coil type, i.e. with separate and orthogonal transmitter and receiver coils surrounding the sample. The prototype instrument operated at 30 MHz at a field of 0.7059 T for proton resonances. A visit to the company proved to be a rewarding experience. By this time a 40 MHz instrument was being developed with an electromagnet having 12-in. pole faces and fields up to 1.4 T. Jim Shoolery demonstrated the performance of the instrument, which was indeed impressive. The Varian visit quickly resolved for us the 'make or buy' option with respect to equipment acquisition. In fact, Varian's achievement in being able to market a complete NMR spectrometer so early in a new research field was

indeed remarkable. Very fortunately our research proposal was approved by the NRC authorities.

Within our own laboratories, at the time already crowded, there was no suitable area with the necessary reinforced floor to accommodate the weight of the magnet. Eventually the Director of the Chemistry Division, Dr. E. W. R. Steacie, offered us one of his laboratory units. It had been equipped for research in radiation chemistry using a highly radioactive cobalt cell as a source. This had been installed inside a concrete enclosure with walls and ceiling two feet thick to provide necessary shielding, and occupied most of the floor space of the laboratory. It had a fairly wide and heavy sliding door and several observation ports, as well as a solid foundation. 'Could this laboratory satisfy your requirements?' Since no immediate alternatives seemed to be available, we accepted the challenge and the 'concrete hut' became the home for the new NMR spectrometer.

Our early research efforts were directed toward understanding and developing basic principles of proton resonance spectroscopy as a tool for research in chemistry. The most important magnetic parameters measured were chemical shifts, proton spin–spin coupling constants, and proton spin relaxation times. These must then be systematically interpreted so as to yield information useful to the chemist. In order to build up a base of knowledge for this purpose, the proton magnetic resonance spectra of a variety of classes of organic and inorganic compounds of known structure were recorded and analyzed.

After our experimental program was well underway, I had invited John Pople to the National Research Council as a visiting scientist. Having accepted, he was able to arrange extended leaves from Cambridge University during the course of several summers as well as periodic shorter visits in between. John made important contributions to the NMR research program, and our collaboration was both stimulating and productive.

An essential part of high-resolution proton resonances of more complex molecules is that of spectral analysis. When the chemical shifts of nonequivalent protons in the molecule are well separated it is usually a simple matter to assign individual resonances in the spectrum, especially when spin–spin interaction multiplets are also resolved. However when the chemical shift separation (in frequency units) is of the order of magnitude of the proton–proton spin coupling constants, the NMR spectrum consists of a complex pattern of lines and the regularity of individual multiplets is no longer discernible. To interpret a spectrum of this kind requires a quantum mechanical analysis of the energies and relative intensities of transitions among the spin states of the interacting protons in the molecule. A system of nomenclature was devised which distinguishes protons with large chemical shifts from those with small chemical shifts in the same molecule. Starting with two proton systems and building up to larger multiproton systems, it was possible to develop a systematic procedure for spectral analysis.

Another important research focus related to understanding and interpreting the particular atomic and molecular properties which contribute to observed chemical shifts of proton magnetic resonances. It soon developed that this involved both *intramolecular* and *intermolecular* contributions. The major contribution to the chemical shift arises from the induced diamagnetic shielding by electrons surrounding the proton and the nucleus to which it is bonded. The electronegativity of the latter also has a major effect and could be observed in molecules where the proton is several bonds removed. Another important intramolecular contribution, first interpreted by John Pople, is the so-called 'ring current' effect in aromatic molecules. In a magnetic field the delocalized π electrons give rise to a ring current resulting in a magnetic moment perpendicular to the plane of the ring which interacts with the proton spin. The magnitude of this contribution depends on the position of the bonded proton from the center of the ring (and adjacent rings), and the angle of its position with respect to the plane of the ring. Detailed analyses of the spectra of benzene and multiring aromatic hydrocarbons, as well as substituted benzenes containing protons in the substituents, gave satisfactory agreement with the calculated contributions from the ring current effect.

A small intramolecular contribution to the chemical shift of great interest to organic chemists relates to molecular conformation and configuration. Differential contributions to the chemical shift of protons in different molecular isomers are observable unless the thermal interconversion of isomers is sufficiently rapid at the temperature at which observations are made to average out this differential. This can occur where hindered internal rotation becomes possible, as, for example, in substituted cyclohexanes able to interconvert from *chair* to *boat* conformations. Separated chemical shifts for *axial* and *equatorial* protons in carbohydrate molecules provide unique data for establishing their conformations. Isomeric differential proton chemical shifts are due to rather subtle small differences in electron configuration of individual isomers which are not well understood.

In another class of organic compounds, namely, conjugated aromatic molecules, the π-electron densities at individual carbon atoms can be calculated on the basis of molecular orbital theories. By measuring proton chemical shifts (and in some cases ^{13}C chemical shifts) in aromatic compounds and aromatic ions, it was found that to a first approximation the measured shifts correlated well with the calculated electron densities of the carbon atom to which the proton is bonded.[1]

Turning now to *intermolecular* effects, early proton resonance measurements of compounds in solution exhibited some pronounced solvent effects. This was at first a surprising result, since for some solutes the shifts involved were quite large. A systematic study was undertaken to identify and interpret the shifts arising from intermolecular interactions. This included proton resonance measurements of the test compound in the gaseous state at low pressure (where intermolecular effects should be virtually absent) and in various solvents over a wide range of dilution. It was found that the largest shifts occur when the proton being measured is capable of forming hydrogen bonds, either with its own molecules or with solvent molecules. Another fairly large contribution arises when the proton is bonded to a molecule capable of interacting strongly with π electrons in an aromatic solvent, such as benzene, which tends to orient the H–C bond of the solute perpendicular to the aromatic ring. The above-mentioned ring current effect then gives rise to a pronounced resonance shift. Other contributions observed include those arising from the bulk diamagnetic susceptibility of the solvent, its magnetic anisotropy, polar effects of the solvent, and van der Waals interactions with the solvent.[2]

Time-dependent proton resonance measurements provide a powerful tool for studying a variety of chemical processes, a number of which were explored. These include, for example, proton-exchange processes, hindered internal rotation about single bonds, and tautomerism. Since these are thermally activated processes, measurements are required over an appropriate range of temperatures and can yield the respective rate constants and thermal activation energy.

In 1956, we decided to host a research conference on high-resolution NMR at the National Research Council to which then active researchers in this field were invited. It was an outstanding success. The new research initiatives reported on were exciting and demonstrated how rapidly NMR research was expanding. Thereafter an NMR research conference became an annual event, each hosted by a different volunteer research group. Ultimately it spread beyond North America and became an annual international conference.

Meanwhile organic chemists were becoming aware of NMR as a powerful new tool for determining structures of complex molecules and frequently brought samples for proton resonance analyses. It was usually possible to confirm a specific structure or to eliminate proposed alternative structures.

After the Ottawa Conference, we came to the conclusion there was a real need for a book on high-resolution NMR which would cover the basic principles and applications to chemistry. We debated undertaking such a major project with considerable apprehension. None of us was prepared to sacrifice a great deal of time from our on-going research programs. In the end we agreed on a tripartite authorship and to share the workload. The enormity of the task we had taken on became clear after the first draft when an excessive amount of time and energy was needed to produce a coherent and condensed final text. By this time John Pople had accepted a post with the National Physical Laboratory in Teddington and his visits to Ottawa were necessarily less frequent. The book was finally published in 1959.

During the course of our early research activities quite a number of students and postdoctoral fellows were first introduced to NMR research in our laboratory and made many important contributions. It is a pleasure for me to acknowledge my great indebtedness to them. Most of them accepted positions in chemistry departments in universities where they continued their research and set up lecture courses to train the next generation of NMR scientists. With similar developments emanating from other early NMR research laboratories, it transpired that NMR research became institutionalized in a relatively short period of time and set the stage for its subsequent remarkable growth and achievement.

I would like to express my gratitude and appreciation to Dr. John Pople and to the late Dr. Harold Bernstein for their support during the years of our active collaboration.

REFERENCES

1. T. Schaefer and W. G. Schneider *Can. J. Chem.*, 1963, **41**, 966.
2. A. D. Buckingham, T. Schaefer, and W. G. Schneider, *J. Chem. Phys.*, 1960, **32**, 1227.

Biographical Sketch

William G. Schneider. *b* 1915. B.Sc., 1937, Ph.D., 1941 Chemistry, McGill University. Postdoctoral fellowship Harvard University, 1941–42; Woods Hole Oceanographic Institute, Woods Hole, MA under OSRD–NDRC and US Navy contracts, 1943–46; research scientist, 1946–67. President, National Research Council of Canada, Ottawa, 1967–80; President, International Union of Pure and Applied Chemistry, 1983–85. Approx. 130 publications. Research specialties: intermolecular forces, NMR, organic semiconductors and photoconductors.

Scott, A. Ian: ^{13}C NMR Studies of Biosynthesis. A Quarter Century in Retrospect

A. Ian Scott

Texas A&M University, College Station, TX, USA

We began our first experiments 25 years ago on the application of ^{13}C NMR to investigate the biosynthesis of vitamin B_{12}, one of Nature's most complex molecules produced by bacteria. First, in order to determine both the identity of the 'building blocks' and the sequence by which they are assembled in a 20-enzyme cascade in cells of *Propionibacterium shermanii*, we set about the synthesis of ^{13}C-enriched precursors none of which was available commercially. Our primitive NMR equipment was a 1960 vintage Bruker HFX 90 MHz (housed in A. Lipsky's laboratory in the Yale Medical School) which had been converted to FT (with an IBM 1800 computer) by Dr. Robert Cushley. It was by no means certain at the outset that the biosynthetic incorporation of our synthetic precursors into B_{12} using whole cells would give a sufficient signal-to-noise ratio above natural abundance at the sensitivity of the machine. However the appeal of noninvasive analysis overcame all of our misgivings. We were also encouraged by the 1966 experiment by Tanabe at Stanford who observed the ^{1}H satellites of enriched carbons after administering ^{13}C acetate in his classic work on griseofulvin biosynthesis.

After painstakingly isolating 40 mg of enriched B_{12} (about 100 times the amount needed with today's instruments) with C. A. Townsend, M. Kajiwara, and K. Okada, we were able to demonstrate[1,2] that, contrary to previous literature (in which ^{14}C was used as a tracer), seven of the eight methyl groups were derived from methionine and that, most importantly, these methyls were inserted into uro'gen III, the same template which is used for heme and chlorophyll biosynthesis. From that moment we became wedded to carbon-13 as a probe for intermediacy in metabolic pathways and for studying the biosynthetic enzymes with ^{13}C-enriched substrates and inhibitors.[3] The latter work has now matured from the first experiments (with Paul Malthouse in the early 1980s) where we used cryoenzymology (-25°C/DMSO/buffer) to detect covalent complexes of the intermediates in the hydrolysis of peptides catalyzed by serine and thiol proteases,[4] to the more recent discovery (by ^{13}C NMR of labeled enzyme) of the unique dipyrromethane cofactor of the polymerizing enzyme of porphyrin and heme biosynthesis (PBG deaminase)[5] which, in spite of an M_r value of 33 000, reveals only the enriched carbons and the protons attached to them, Figure 1.

The second event which told us that high-field FT NMR would be absolutely necessary for our future experiments came in 1977 when my postdoctoral colleague, Tony Irwin, working with L. Siegel at Duke University on the 670 000 molecular weight six-electron sulfite reductase enzyme from *E. coli*, was able to isolate from a total of 2 g of protein (containing 19 classical and two 'nonclassical' hemes), ca. 200 μg of the isobacteriochlorin, sirohydrochlorin, which is part of the electron transport machinery of the enzyme. The ^{13}C spectrum at natural abundance was obtained for us at Varian by Jim Shoolery at 20 MHz using the first generation of Varian FT-80 instruments. The acquisition of the spectrum from the necessary one million transients took 11 d continuous operation over the Christmas vacation.[6] For the next decade we seldom had more than 50–100 μg of the various B_{12} intermediates, but having quickly adapted to the world of ^{13}C-enrichment ($\geq$90%) we have enjoyed the luxury of the illusion that we were working with 10 mg samples, as far as the signal-to-noise ratio was concerned.

Also in 1977, we began our first in vivo ^{13}C NMR experiments[7] just as R. G. Shulman (then at Bell Laboratories) was starting to follow the fate of ^{13}C-glucose in living cells. An early experiment in Texas involved feeding 2 mg of ^{13}C-U-glucose to the most abundant insect we could find in the lab—the Texas cockroach (*Periplanata americana*). In order to provide the necessary signal lock and to avoid drowning the specimen, we added D_2O carefully to the 10-mm tube up to the 'shoulders' of the cockroach, only to discover later (from our colleagues in entomology) that cockroaches breathe through their sides! Subsequent experiments with *Heliothus spp*. (tobacco budworm) were however much more successful (and rigorous) leading to the identification of several metabolites[8] and to our later work with trypanosomes.[9]

It also seems remarkable to me that when we moved to Texas from Yale in 1977 there were no superconducting magnets in any of the Texas Universities, yet all of our subsequent work has depended on high-field NMR spectroscopy with biosynthetic enzymes and their enriched substrates and inhibitors. More recently (1987) we entered the world of genetic engineering,[10] which has provided us not only with massive amounts of our favorite enzymes but indeed the opportunity to use on-line NMR spectroscopy to follow the mechanisms of more than 30 enzymes necessary to make B_{12}, penicillins, steroids, and antitumor alkaloids. To solve these problems it is now essential to have available in the same laboratory, organic synthesis with stable isotopic enrichment, molecular biology for cloning and overproducing the enzymes and, most importantly, 300–500 MHz NMR, 7 d a week, 24 h a day. We have come a long way from the first experiments of the late 1960s, but it is abundantly clear in retrospect that we could not have solved **any** of our biosynthetic and structural problems without dedicated NMR instrumentation which, to this day, is at the heart of all of our research on natural product biosynthesis, and on the enzymes which control the production of these biologically important molecules.

REFERENCES

1. A. I. Scott, C. A. Townsend, K. Okada, M. Kajiwara, P. J. Whitman, and R. J. Cushley, *J. Am. Chem. Soc.*, 1972, **94**, 8267.
2. A. I. Scott, C. A. Townsend, K. Okada, M. Kajiwara, and R. J. Cushley, *J. Am. Chem. Soc.*, 1972, **94**, 8269.
3. U. Sequin and A. I. Scott, *Science*, 1974, **186**, 101.
4. J. P. G. Malthouse, M. P. Gamcsik, A. S. F. Boyd, N. E. Mackenzie, and A. I. Scott, *J. Am. Chem. Soc.*, 1982, **104**, 6811.
5. A. I. Scott, C. A. Roessner, N. J. Stolowich, P. Karuso, H. J. Williams, S. K. Grant, M. D. Gonzalez, and T. Hoshino, *Biochemistry*, 1988, **27**, 7984.

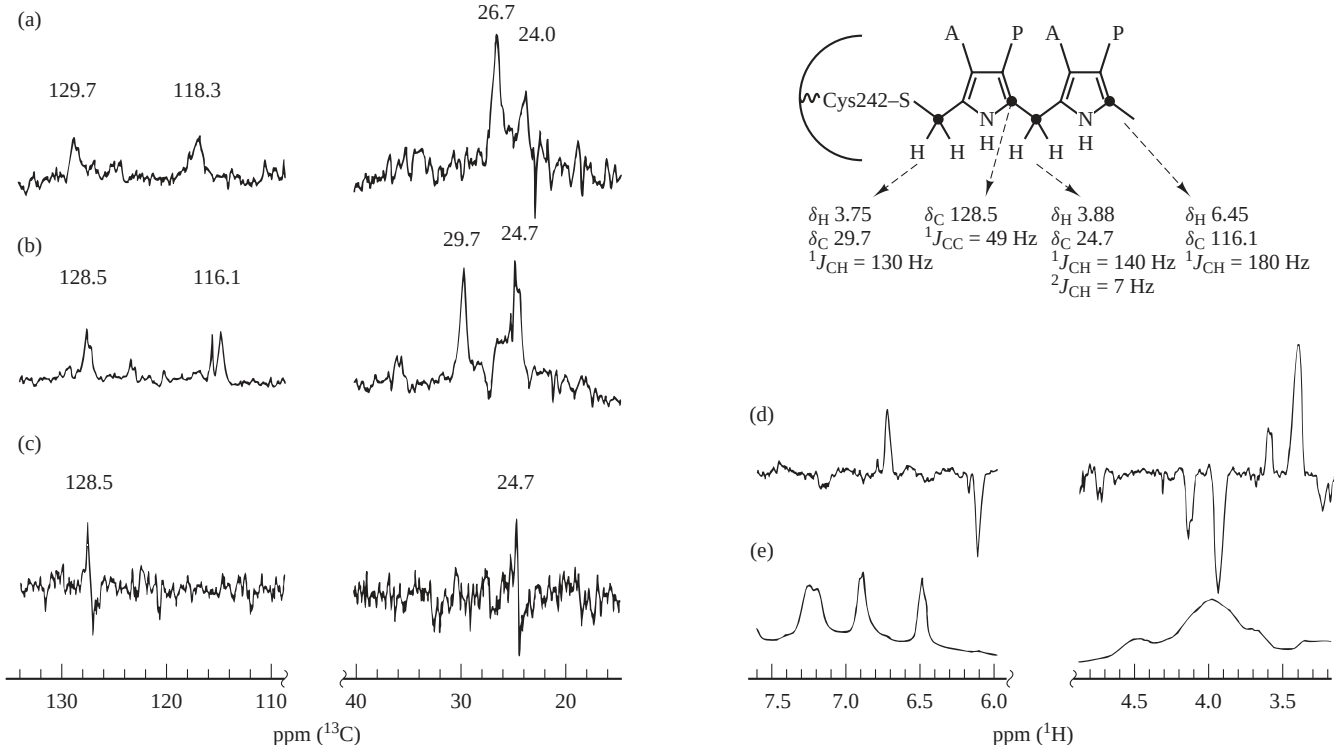

Figure 1 High-field NMR spectra of *E. coli* PBG deaminase (∼1 mM) specifically ^{13}C-enriched in the dipyrromethane cofactor via [5-^{13}C]-ALA. (a) 125 MHz ^{13}C NMR difference spectrum between separate deaminase samples (pH 8) grown in the presence or absence of [5-^{13}C]-ALA demonstrating the four ALA-derived ^{13}C-enriched carbons. (b) Difference spectrum of samples as in (a), recorded at pH 12. Upon alkaline denaturation, the resonance assigned to the thiomethyl carbon has shifted downfield to δ 29.7 ppm, in closer agreement to a model cysteine thiomethylpyrrole conjugate. (c) ^{13}C INADEQUATE spectrum (pH 12) of [5-^{13}C]-ALA-derived deaminase demonstrating the coupling of adjacent carbons, confirming the head-to-tail dipyrromethane structure. (d) Isotope-edited 300 MHz ^{1}H NMR spectrum (pH 12) of biosynthetically enriched deaminase (2 mM) showing the three pairs of signals originating from only those protons directly bound to the ^{13}C carbons derived from [5-^{13}C]-ALA. The observed antiphase splittings are due to the one bond ^{1}H-^{13}C coupling. (e) Normal proton spectrum of same sample illustrating the degree of selection afforded by the pulse sequence for spectrum (d). Insert: structure of the dipyrromethane cofactor and summary of ^{1}H and ^{13}C chemical shifts and coupling constants obtained at pH 12.

6. A. I. Scott, A. J. Irwin, L. M. Siegel, and J. N. Shoolery, *J. Am. Chem. Soc.*, 1978, **100**, 7987.
7. A. I. Scott, G. Burton, and P. E. Fagerness, *J. Chem. Soc., Chem. Commun.*, 1979, 199.
8. G. Burton, R. L. Baxter, J. M. Gunn, P. J. Sidebottom, P. E. Fagerness, K. Shishido, J. Y. Lee, and A. I. Scott, *Can. J. Chem.*, 1980, **58**, 1839.
9. N. E. Mackenzie, J. E. Hall, J. R. Seed, and A. I. Scott, *Eur. J. Biochem.*, 1982, **121**, 657; J. E. Hall, N. E. Mackenzie, J. M. Mansfield, D. E. McCloskey, and A. I. Scott, *Comp. Biochem. Physiol.*, 1988, **89B**, 679.
10. A. I. Scott, *Tetrahedron*, 1992, **48**, 2559.

Biographical Sketch

A. Ian Scott. *b* 1928. B.Sc., 1949, Ph.D., 1952, D.Sc., 1963, M.A.(Hon.), Yale University, 1968. Lecturer, Glasgow University, 1957–62; Professor, University of British Columbia, 1962–65, University of Sussex, 1965–68, and Yale University, 1968–77. Davidson Professor of Science and Distinguished Professor of Chemistry and Biochemistry, Texas A&M University, 1981–present. Director of Center for Biological NMR, 1982–present. Three books, 1 patent, and approx. 320 publications. Research specialties: natural product biosynthesis and NMR spectroscopy.

Seelig, Joachim: NMR and Membrane Structure

Joachim Seelig

University of Basel, Basel, Switzerland

In the late 1960s cooperative transitions in biopolymers were a highly popular theme among biophysicists. The Watson–Crick double helix was firmly established, the genetic code was deciphered, and the first transfer-RNA single crystals were simultaneously obtained in five different laboratories. Biophysicists were particularly interested in the melting behavior of double-stranded DNA since the separation of the helical double strands into a random-coil single strand was the prerequisite for ribosomal translation. In parallel, peptide chemists like P. Doty, E. Blout, and H. A. Scheraga were investigating peptide structure and folding with a large variety of synthetic peptides, with particular emphasis on the helix–coil transition of these synthetic molecules. The elegant modification of the linear Ising model (originally developed for ferromagnetism) by Zimm and Bragg was highly successful in explaining the observed experimental data of helix–coil transitions for both nucleic acids and polypeptides.[1] Modern statistical mechanical textbooks which gave ample space to relevant biological problems, such as that of N. Davidson, contributed to a rapid acceptance of the Zimm–Bragg theory.

As far as biological membranes were concerned, the physical situation was less clear. On the one hand, it was discovered in 1965 that membranes are highly fluid structures. By tagging membrane proteins with a fluorescent probe, it could be demonstrated convincingly that membrane proteins were diffusing in the plane of the biological membrane with a diffusion constant of the order of $D \sim 10^{-9}$–$10^{-10}\,\mathrm{cm^2\,s^{-1}}$, only a factor of 100 smaller than the diffusion of the same molecules in water. Harden McConnell and his co-workers using different types of nitroxide spin probes then demonstrated with EPR techniques that the physical basis for protein movement was a fluid lipid matrix. Lipids were also the only known biological molecules which exhibited polymorphic structures. Depending on the environment, they were organized in bilayer, hexagonal, cubic, or micellar phases, the overall geometries of which were characterized by V. Luzzati in Paris using X-ray diffraction. The Dutch chemist L. van Deenen developed new synthetic methods which made it possible to tailor lipids of well-defined fatty acid composition and D. Chapman showed with infrared and differential scanning calorimetry that lipids with two saturated fatty acyl chains were undergoing a highly cooperative gel-to-liquid crystal phase transition.

Over the period 1966–68, I was a graduate student with M. Eigen working together with G. Schwarz on the kinetics of the helix–coil transition of polypeptides. In the winter of 1967–68, D. Chapman reported his exciting results on the phase transition of lipid membranes obtained by differential scanning calorimetry at a symposium in the Bavarian Alps in honor of M. Eigen's Nobel Prize. Being already biased toward cooperative transitions as a result of my studies on the helix–coil equilibrium, I wondered if a similar approach could also be developed for lipid membranes. However, molecular details were missing. Should membranes be considered as two-dimensional cooperative systems or was their behavior more comparable with three-dimensional crystals? It seemed to me that the only experimental method capable of providing solid experimental results was the nitroxide spin-label EPR method.

In September of 1968 I started my postdoctoral research with Harden McConnell. When I arrived, the first fatty acid spin labels had been synthesized by W. Hubbell and the first description of an anisotropic spin label motion had been formulated. Very soon I succeeded in recording oriented membrane spectra and I could also give a straightforward interpretation of the EPR spin-label spectra in terms of the order parameter formalism which I borrowed from the NMR theory of liquid crystals developed by A. Saupe.[2] Saupe had dissolved small molecules in liquid crystals and was the first to observe ^{1}H NMR high-resolution spectra of molecules with anisotropic motion. He also provided the full theoretical background for the analysis of high-resolution NMR spectra with anisotropic motion. Reading Saupe's papers, it struck me that liquid crystals had many features in common with biological membranes and that it should be possible to take advantage of the residual anisotropic dipolar splittings to elucidate their structure. However, due to the large number of protons attached to a single phospholipid molecule, ^{1}H NMR spectra of membranes gave rise to broad featureless spectra even when recorded with homogeneously aligned membrane systems. The molecular analysis of such spectra was hopeless. However, it was possible to prepare single-walled phospholipid vesicles of small diameter (∼30 nm) by sonification which then yielded high-resolution NMR spectra of good quality, since dipolar interactions were averaged out due to rapid vesicle tumbling. A. F. Horwitz, M. Klein, S. Chan, and co-workers characterized the ^{1}H and ^{31}P NMR relaxation times of these vesicles, and J. Metcalfe was the first to record ^{13}C NMR spectra of such model membranes, the latter providing a much better molecular resolution.

After returning to Basel, Switzerland, in 1970, I first continued with spin label EPR work. However, in 1972, the Biocenter was inaugurated and money was provided for a 90 MHz FT NMR instrument. Since I had no personal experience with NMR, I discussed matters with P. Diehl who had been involved in the NMR of liquid crystals almost since its beginning. Diehl was also the first to publish a high-resolution deuterium NMR spectrum in 1956 and had laid the groundwork for all future deuterium NMR.[3] Whilst discussing the various options for the new instrument, Diehl asked me if I had ever considered ^{2}H NMR since the ^{2}H nucleus had a quadrupole moment. It occurred to me that ^{2}H NMR should indeed have considerable advantages compared with spin-label EPR or ^{1}H NMR: the quadrupole splitting of the deuterium nucleus should provide information on the anisotropy of motion in much the same way as the hyperfine anisotropy of the spin-label group. At the same time, ^{2}H NMR would avoid the perturbing influence of the nitroxide radical since the van der Waals radii of ^{1}H and ^{2}H were rather similar.

Hence we set out in 1973 to synthesize selectively deuterated fatty acids and lipids, and in 1974 my wife and I could indeed publish a first quantitative description of a phospholipid bilayer using exclusively deuterium NMR.[4] A further step in membrane analysis was then the use of ^{31}P NMR. G. Radda and co-workers had one of the first 270 MHz spectrometers and had reported rather unusual

lineshapes for the ^{31}P NMR spectra of membranes which were explained qualitatively by the phosphorus chemical shielding anisotropy. About the same time, M. Klein and S. Kohler at Berkeley and R. G. Griffin at MIT measured the principal components of the ^{31}P chemical shift tensor in crystalline phospholipid model compounds, allowing finally a complete quantitative description of the lipid phosphate moiety. Using this information, W. Niederberger and I then succeeded in measuring the first proton-decoupled ^{31}P NMR spectra of lipid membranes and we could provide a full quantitative description in terms of the order parameter formalism.[5] When I talked to John Waugh (who was *the* authority on solid state NMR) about our proton-decoupled phosphorus NMR spectra, he was disbelieving at first since he thought that 20 W decoupling power would be much too low for membranes. However, when I showed him the experimental results he was convinced and remarked: 'Joe, you and I are the only ones who understand . . . membranes!' Hence, by the end of 1976, the NMR toolbox for membrane studies was wide open and provided the instruments for many biophysical membrane studies to come.

REFERENCES

1. B. H. Zimm and J. K. Bragg, *J. Chem. Phys.*, 1959, **31**, 526.
2. A. Saupe, *Z. Naturforsch.*, 1964, **19a**, 161.
3. P. Diehl and Th. Leipert, *Helv. Chim. Acta*, 1964, **47**, 545.
4. A. Seelig and J. Seelig, *Biochemistry*, 1974, **13**, 4839.
5. W. Niederberger and J. Seelig, *J. Am. Chem. Soc.*, 1976, **98**, 3704.

Biographical Sketch

Joachim Seelig. *b* 1942. M.S., 1966, Physical Chemistry, University of Cologne, Ph.D. (supervisor M. Eigen), 1968, Max-Planck-Institute of Physical Chemistry, Göttingen, Germany. Research associate with H. M. McConnell, Stanford University, 1968–69, working on spin label EPR of membranes. University of Basel, Switzerland, 1970–present. Professor of Structural Biology at the Biocenter of the University of Basel. Approx. 160 publications. Research specialties: deuterium and phosphorus NMR of membranes, in vivo magnetic resonance spectroscopy.

Sergeyev, Nickolai M.: Isotope Effects On Spin–Spin Coupling Constants

Nickolai M. Sergeyev

Moscow State University, Moscow, Russia

In liquids, the energy of the nuclear spin–spin interaction is given by

$$E(\boldsymbol{\mu}_1, \boldsymbol{\mu}_2) = J_{12} h \, \boldsymbol{I}_1 \cdot \boldsymbol{I}_2 \qquad (1)$$

where $\boldsymbol{I}_1$ and $\boldsymbol{I}_2$ are the dimensionless nuclear spin vectors and J_{12} is known as the spin–spin coupling constant. As the nuclear magnetic moments $\boldsymbol{\mu}_1$ and $\boldsymbol{\mu}_2$ are proportional to the magnetogyric ratios, γ_1 and γ_2, it is obvious that the coupling constant J_{12} depends on the product $\gamma_1 \cdot \gamma_2$

In order to be independent of the magnetic properties of interacting nuclei, Pople and Santry[1] suggested using reduced coupling constants defined by

$$K_{12} = (4\pi^2 / h\gamma_1 \cdot \gamma_2) J_{12} \qquad (2)$$

where K_{12} depends only on the electronic (i.e. chemical) structure. The use of K_{12} allows one to replace one interacting magnetic isotope by another and thus to obtain spectral information which is often lost from the NMR spectrum due to the degeneracy of the spin system. Indeed, for a group of magnetically equivalent nuclei (such as, for example, protons in a methyl group), it is impossible to extract information about spin–spin coupling constants between protons. However, if a proton in a methyl group is replaced by an isotope (^{2}H or ^{3}H), the degeneracy is removed and the corresponding splittings become observable. The only question that remains is whether the chemical structure at such replacements changes or not.

The notion of such 'structural effects' was put forward for the first time by Gutowsky et al. in 1962.[2] They were interested in the measurement of geminal H, H spin–spin coupling constants in compounds of the type CH_2XY, but in many cases they met the problem of degeneracy in the ^{1}H NMR spectra. They suggested using compounds of the type CHDXY where one can measure H, D couplings and then use the ratio of magnetogyric ratios to transform to the H,H-scale by using the relationship

$$J^*(\mathrm{D,H}) = (\gamma_\mathrm{H}/\gamma_\mathrm{D}) J(\mathrm{D,H}) \qquad (3)$$

However the question of the 'structural effects' should now be taken into account. Gutowsky et al. suggested that the replacement of H by D may affect angle-bend averaging (as the mean H–C–H angle may be slightly larger than the corresponding angle in the H–C–D case). At that time the dependence of the geminal H,H coupling constants upon the interbond angle was the subject of lively discussion. It had been believed that the angular dependence of the geminal coupling constant in the CH_2 group was nonlinear. This meant that the vibrations should result in a small difference in the values of ^2J(H,H) and ^2J*(D,H). However, this needed experimental support. A test was impossible as the authors could not measure J(H,H). They made an attempt to check this idea by measuring the geminal J(F,H) and J(F,D) coupling constants in compounds of the type CFHXY and CFDXY. However the accuracy was not sufficient to obtain any noticeable difference, so no conclusion was reached. This was perhaps not so unfortunate, because at that time the sign of geminal coupling constants for the CH_2 group was erroneously believed to be positive, so any isotope effect would have been misinterpreted.

In 1962, Ebsworth and Turner[3] studied deuterated silanes and, using the wiggle-beat method in ^{1}H NMR, obtained very accurate values for J(D,H) of 0.427 (±0.003) Hz and 0.412 (±0.004) Hz for SiH_3D and $SiHD_3$, respectively. This was the very first observation of an isotope effect on coupling constants. It is worth noting that the accuracy obtained in 1962 has not been exceeded significantly during the last 30 years in spite of the revolutionary changes in NMR spectroscopy made by introducing the pulse Fourier transform technique. It is also worth noting that in both experiments with SiH_3D and $SiHD_3$ the authors measured J(D,H), so the problem of comparison with any H,H coupling constants in silanes remained unsolved.

Our group at the Department of Chemistry at Moscow University (A. A. Borisenko, Yu. A. Ustynyuk, and the author) encountered the problem of isotope effects on coupling constants at the beginning of the 1970s when we performed investigations on some phosphonates and phosphates containing P–H bonds,[4] for example $(C_6H_5)_2PH$ and $H_2P(O)OH$. To obtain greater concentrations of these compounds, deuterated methanol or heavy water were used as solvents. However, the ^{31}P NMR spectra of these compounds were more complicated than we had expected. For example, with $H_2P(O)OH$ we observed the spectrum reproduced in Figure 1 where at least three groups of signals are seen: a 1:2:1 triplet, a doublet of 1:1:1 triplets, and a quintet of lines with relative intensities 1:2:3:2:1. This proved without doubt that the protons at phosphorus had been partially replaced by deuteriums during sample preparation and what we observed was indeed

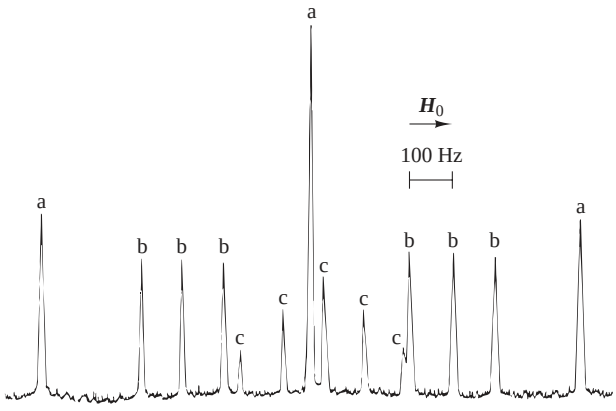

Figure 1 The ^{31}P NMR spectrum at 40.5 MHz of partially deuterated hypophosphorous acid. The lines marked 'a' are the 1:2:1 triplet from H_2POOH, the doublet of 1:1:1 triplets is from HDPOOH (b), and the 1:2:3:2:1 quintet is from D_2POOH (c). Reproduced by permission of Molecular Physics

the spectrum of a mixture of isotopomers containing different numbers of deuteriums at phosphorus, i.e. $(C_6H_5)_2PH_2$ (triplet), $(C_6H_5)_2PHD$ (doublet of triplets), and $(C_6H_5)PD_2$ (quintet). The spectra of different isotopomers were shifted relative to each other revealing the isotope shift on ^{31}P nuclei due to D/H replacement. Even more interesting, however, was the fact that the J(P,H) and J*(P,D) values in $(C_6H_5)_2PHD$ were 199.42 and 201.3 Hz, respectively, compared with J(P,H) in $(C_6H_5)_2PH_2$ which was 199.3 Hz. This allowed us to measure the primary and secondary isotope effects.

In general, we defined the primary effect for X,H coupling in a molecule of type Y−X−H as

$$\Delta J^{p} = (\gamma_H/\gamma_D)J(X, D)(\text{in } Y - X - D) - J(X, H)(\text{in } Y - X - H) \quad (4)$$

and the secondary effect for X,H coupling in a molecule of type XH_2Y as

$$\Delta J^{s} = J(X, H)(\text{in } XHDY) - J(X, H)(\text{in } XH_2Y) \quad (5)$$

We found that for ^{31}P,H coupling constants the primary isotope effects were of the order of 2.0 Hz for three-coordinated phosphorus and about −5 Hz for four-coordinated phosphorus, while the secondary effects were about 0.12 and 0.58 Hz, respectively. As the ^{31}P,H couplings in P(IV) compounds are substantially larger than those in P(III) compounds, we concluded that the primary effects are of the order of 1% and the secondary isotope effects are about 0.1% for both types of phosphorus.

In the same year (1971), another paper was published dealing with isotope effects on $J(^{31}P,H)$.[5] Wojciech Stec from Poland working as a postdoc with Prof. Van Wazer at Vanderbilt University performed a study of the ^{31}P NMR spectra of dialkylphosphonates of the type $(RO)_2P(O)H$ (protonated and deuterated at the O−H bond) and found that the ratio $J(^{31}P,H)/J(^{31}P,D)$ was not invariant but changed from 6.50 to 6.52. Unaware of isotope effects on coupling constants, the authors suggested that the different ratios of coupling constants were due to solvent effects. They believed that phosphonates formed hydrogen bonds with methanol and that P−D···O bonds differed in energy from P−H···O bonds.

Both papers[4,5] were published in November 1971, although the paper by Stec et al. was received by *J. Phys. Chem.* in March whilst our paper was received by *Mol. Phys.* in June. It is interesting to recall a puzzling episode when our paper was submitted.

It was first sent in February, but two months later it became clear that it was lost as the editor, Prof. Buckingham, had not received it. We sent a copy (actually, slightly modified) and after a month the editor informed us that he had unexpectedly received two versions of the same work. The problem for him was which manuscript to choose. He noticed that one of the envelopes had already been opened. He sent us this envelope to confirm that it was the first version. Meanwhile detailed study of the two manuscripts revealed to him which was the later one. In any case Prof. Buckingham kept only one manuscript for further consideration. Probably taking into account the special circumstances in which the manuscript had been received, he suggested not sending it again to Moscow and even proposed helping with checking the proofs. Indeed the paper was published fairly soon after.

The observations of isotope effects on coupling constants were first met with some skepticism, as they referred to systems which might be affected by solvent effects. Shortly after, McFarlane and Rycroft made a careful reinvestigation[6] using several solvents including cyclohexane. Considering cyclohexane as a neutral solvent, they concluded that the situation was more complicated than the previous authors had believed[4,5] because the observed isotope effect was a sum of both intrinsic and thermodynamic effects. However, in any case they confirmed the existence of isotope effects on coupling constants.

Another curious episode with our paper[4] was connected with its translation into English. At that time publication of papers by Soviet authors in western scientific journals was not welcomed by the academic and government authorities in Moscow. In order to publish in the West one needed to obtain special permission from the KGB which had 'otdel' sections at any university and in any office with more than five employees. An anecdote from that time stated that among any five randomly chosen persons at least one would be from the KGB. Most of us defied the law and without obtaining permission submitted manuscripts often with the help of persons going abroad. Such tricks were possible as the system for controlling scientific publications was absurd. But it was still unpredictable and very dangerous. Sometimes you were not allowed to submit the paper abroad, sometimes you might be asked to publish the manuscript in Russian first, sometimes the manuscripts were lost.

Our paper was first written in Russian. Then we waited several months for permission to publish. And only after that did we start translating it. Fortunately Dr. Jim Feeney visited Moscow in early 1971 for a Varian instruments exhibition. We asked him to check our translation. He was very well known in Russia as one of the authors of a two-volume Russian translation of 'High Resolution NMR' and we were sure that half an hour would be enough for him to look over several pages. He did not hesitate to help us but after several minutes we saw that his face became thoughtful and anguished. After an hour we could wait no longer and asked what was the matter. Jim answered that all that time he had been thinking whether it was better to say 'isotope effects' or 'isotopic effects' ... and still could not solve this painful linguistic problem. 'But it is interesting, you know' he said, returning the manuscript to us, I suppose, with relief.

Soon after, many other publications appeared dealing with isotope effects on coupling constants. In 1972, Wojciech Stec was in our laboratory and agreed with our interpretation. In 1973, we met Bill Raynes from the University of Sheffield who made the first theoretical estimates of possible isotope effects for the coupling constants in the six isotopomers of H_2.[7] We agreed to continue these studies together, but for certain reasons (at that time I was not allowed to go abroad) it was delayed for almost 20 years! In 1975, Buckingham and Urland[8] reviewed the theory of isotope effects and reproduced the ^{31}P NMR spectrum from our paper.[4]

Further investigations performed by Cynthia and Keith Jameson,[9,10] Brian Bennett and Bill Raynes,[11] Rod Wasylishen,[12] Harald Günther,[13] Hans Jakobsen,[14] Jeremy Everett,[15] Valerii Tarasov,[16] and others involved many new types of spin−spin coupling constants including $J(^{19}F, ^{1}H)$, $J(^{14}N(^{15}N),^{1}H)$, $J(^{27}Al,^{1}H)$, $J(^{69}Ga$ (and $^{71}Ga),^{1}H)$, and $J(^{77}Se,^{1}H)$. Several attempts were made to explain trends in

isotope effects by using a geometrical approach. The idea was put forward that primary isotope effects may reflect the change in the bond length between interacting nuclei. The X–D bond is usually shorter than the X–H bond (according to many estimates $\Delta R = R(\mathrm{X–H}) - R(\mathrm{X–D}) \simeq 5 \times 10^{-3}$ Å), so it was suggested that the primary isotope effect gives the value of the derivative $\partial J(\mathrm{X,H})/\partial R(\mathrm{X–H})$ as equal approximately to the ratio of ΔJ^{p} to ΔR. This means that in phosphorus compounds with P–H bonds the derivative $\partial J(\mathrm{P,H})/\partial R(\mathrm{P–H})$ is positive for four-coordinated phosphorus and negative for three-coordinated phosphorus.

The most serious difficulties were encountered when the well-known and pratically important ^{13}C,H coupling constants were studied. The first experimental results gave a negative sign for the primary isotope effect and this was even supported by some theoretical calculations made for methane at the FP INDO level. However these results were later questioned and only recently has it been shown exactly that the primary isotope effect on ^{13}C,H coupling constants in methane, although still negative, is exceedingly small (less than 0.1 Hz) and that it is substantially less than the secondary one, i.e. paradoxically the stretching of the bond between the interacting ^{13}C and the proton (in the C–H_1 bond) produces less effect than the stretching of the bond between ^{13}C and a neighboring proton (in a C–H_2 bond). This was then successfully confirmed by ab initio calculations of ^{13}C,H coupling constants in methane by Raynes, Geertsen, and Oddershede.[17] In 1990, I published a review on isotope effects on coupling constants.[18] Currently we are studying halomethanes in order to find out more details about the nature of these isotope effects.

There are several reasons why isotope effects in NMR have been of interest for so many years. One is quite simple and obvious: NMR spectral parameters are at present the most sensitive molecular parameters available. They may therefore be applied to measuring the smallest perturbations of compounds under study and isotopic substitution is only the simplest example of such perturbations. There is also a permanent interest in isotope effects from the viewpoint of the theory of spin–spin coupling constants and chemical shifts. Such interest may be easily understood, as theoretical estimates of isotope effects give the first and often the last check of the theoretical approach. Finally, there is the possibility for an experimentalist in NMR to go into greater detail connected with isotopic variation, e.g., to study ^{13}C satellites, to compare data from ^{1}H, ^{2}H, and ^{3}H NMR, to observe effects due to heavy isotopes such as ^{35}Cl/^{37}Cl or ^{79}Br/^{81}Br, and so on.

REFERENCES

1. J. A. Pople and D. P. Santry, *Mol. Phys.*, 1964, **8**, 1.
2. H. S. Gutowsky, V. D. Mochel, and B. G. Somers, *J. Chem. Phys.*, 1962, **36**, 1153.
3. E. A. V. Ebsworth and J. J. Turner, *J. Chem. Phys.*, 1962, **36**, 2628.
4. A. A. Borisenko, N. M. Sergeyev, and Yu. A. Ustynyuk, *Mol. Phys.*, 1971, **22**, 715.
5. W. J. Stec, N. Goddard, and J. R. Van Wazer, *J. Phys. Chem.*, 1971, **75**, 3547.
6. W. McFarlane and D. S. Rycroft, *Mol. Phys.*, 1972, **24**, 893.
7. W. T. Raynes and J. P. Riley, *Mol. Phys.*, 1974, **27**, 337.
8. A. D. Buckingham and W. Urland, *Chem. Rev.*, 1975, **75**, 113.
9. A. K. Jameson and C. J. Jameson, *J. Magn. Reson.*, 1978, **32**, 455.
10. C. J. Jameson and H. -J. Osten, *J. Am. Chem. Soc.*, 1986, **108**, 2497.
11. B. Bennett, W. T. Raynes, and C. W. Anderson, *Spectrochim. Acta*, 1989, **45A**, 821.
12. R. E. Wasylishen and N. Burford, *Can. J. Chem.*, 1987, **65**, 2707.
13. R. Aydin and H. Günther, *Magn. Reson. Chem.*, 1990, **28**, 448.
14. H. J. Jakobsen, A. J. Zozulin, P. D. Ellis, and J. D. Odom, *J. Magn. Reson.*, 1980, **38**, 219.
15. J. R. Everett, *Org. Magn. Reson.*, 1982, **19**, 169.
16. V. P. Tarasov, V. I. Privalov, Yu. A. Buslaev, and U. Eichhoff, *Z. Naturforsch.*, 1984, **39b**, 1230.
17. W. T. Raynes, J. Geertsen, and J. Oddershede, *Chem. Phys. Lett.*, 1992, **197**, 516.
18. N. M. Sergeyev, in *NMR—Basic Principles and Progress*, 1990, **22**, 31.

Biographical Sketch

Nickolai M. Sergeyev. *b* 1938. B.S., 1961, Moscow Institute of Physics and Technology, Candidate of Physics and Mathematics, 1965, Department of Physics, Kazan University, Doctor of Chemistry, 1981. Professor, Moscow State University since 1993; Research work at the Karpov Institute of Physical Chemistry, 1964–68; NMR Laboratory, Department of Chemistry, Moscow State University, 1968–present. Royal Society Guest Research Fellowship, 1993–94, University of Sheffield, UK. Approx. 200 publications. Research specialties: analysis of high-resolution NMR spectra in liquids, dynamic phenomena and isotope effects, applications of NMR in organic and physical chemistry.

Shapiro, Bernard L.: The NMR Newsletter

Bernard L. Shapiro

Editor/Publisher, 966 Elsinore Court, Palo Alto, CA 94303, USA

The NMR Newsletter is an informal monthly publication that serves as a means of rapid exchange of information among active workers in the field of nuclear magnetic resonance spectroscopy. This field is defined broadly, and includes NMR results, techniques, applications, instrumentation, and theory. Magnetic resonance imaging and medical and biological applications are certainly included. (ESR, NQR, and other related fields are not encompassed except where a direct connection or relevance to NMR spectroscopy is clearly manifest.)

HISTORY

The *Newsletter* began in October 1958 as *MELLONMR* (*Monthly Ecumenical Letters from Laboratories of NMR*) at the Mellon Institute in Pittsburgh, Pennsylvania, before the merger with the Carnegie Institute of Technology to form Carnegie Mellon University. *MELLONMR* was created by Aksel A. Bothner-By and myself to facilitate communication with other laboratories about the problems and opportunities (there often seemed to be more of the former than the latter) in the then smallish NMR world.

At that time, the frontier of chemical NMR was the new 60 Mc (sic) CW spectrometer, Varian's HR-60 model, and Mellon Institute had the first such a marvel east of the Rockies. As difficult as it may be for today's NMR practitioners to imagine, the HR-60 was an unlocked, CW system using a large iron electromagnet. This spectrometer system lacked such amenities as a magnet cooling system, adequate thermal insulation, shim coils, a really reliable strip-chart recorder, etc., etc. The incorporation of computers and other items of digital technology were perhaps only dreamt of by a few visionaries. Multiple resonance, FT methods, and multidimensional NMR were not yet even on the horizon. Getting useful NMR data was a tedious, often frustrating business, and if one got decent numerical data on one small molecule in a day, that was a very good day indeed. Hence the need for mutual therapy with one's colleagues across the country, and hence *MELLONMR*.

In January 1964, the Newsletter went with me to the Illinois Institute of Technology in Chicago. *MELLONMR* became the less pronounceable *IIT NMR Newsletter*, but its nature was not changed. In August 1968, the Newsletter and I moved to College Station, Texas, with the same publication appearing as the *TAMU NMR Newsletter*. Beginning in early 1995, it continues privately as *The NMR Newsletter*. At present, the Newsletter is mailed out to subscribers in 34 states and 20 foreign countries. Three Nobel Prize laureates (so far) have been subscribers to the Newsletter, as have many researchers who have participated in the Newsletter for over 30 years.

From 1958 to 1967, the Newsletter was supported completely by the host institutions, Mellon Institute and the Illinois Institute of Technology. Growth of the Newsletter required a wider financial base, and in 1967, external support was begun on a voluntary basis by over two dozen companies whose generosity enabled the Newsletter to continue without cost to the subscriber/participants. A modest subscription fee was started in 1969, and the further development of the Newsletter resulted in advertizing in the Newsletter beginning with the July 1972 issue. From that date, all Newsletter funding has come from advertizing, sponsorships, and subscription fees. Subscription rates have remained low to the present time because of the generosity and loyalty of the advertizers and sponsors, 10 of whom have supported the Newsletter continuously for over 20 years!

POLICIES

The general policies of the Newsletter have remained unchanged since 1958. *Participation* is the prime requisite for receiving the *The NMR Newsletter*. In order to receive the Newsletter, a subscriber must make at least occasional technical contributions to its contents. Since the subscriber/participant clearly is the best judge of what he or she considers interesting, the Newsletter contents are governed by the principle that 'We print anything'. (This is followed by the reservation, 'that won't land us in jail or bankruptcy court'.) With only a few exceptions, no editorial functions are performed. Technical material must, however, not have been published elsewhere. It is reproduced xerographically and disseminated exactly as submitted. Submissions are usually in the form of an informal letter, but this format is not required.

Another, very important operating policy is that of *nonquotation*: public quotation of Newsletter contents in print or in a formal talk at a meeting, etc., is expressly forbidden (except as follows), and reference to the *The NMR Newsletter* (and predecessors) by name in the scientific literature is never permissible. In order to quote results or use material from the Newsletter, it is necessary, in each individual case, to obtain the prior permission of the author in question and then to refer to the material quoted as a 'Private Communication'.

TECHNICAL CONTENT

The pages of the Newsletter encompass a very wide variety of subject matter, a sampling of which from just six recent issues includes chemical shift data and correlations for many nuclides, relaxation time studies, solid state investigations, instrumentation design and modification, software for analysis and presentation of data, spectrometer control strategies and tactics, new pulse sequences, kinetics of complex formation, pure theory of spin systems, spectroscopy and other studies of biologically interesting systems both in vivo and in vitro, a wide variety of imaging studies, binding to proteins and other biological macromolecules, quantitative analysis, polymer analysis, diffusion studies, multiple quantum spectroscopy, inverse detection schemes and applications, chemical shift calibration, probe design, chemical shift tensors, imaging of human stroke, coupling of HPLC and NMR, isotope effects, several uses of personal computers in the acquisition and processing of NMR data, pulsed gradient spin echo experiments, shaped pulses, etc.

Over the years, many new techniques have been introduced in the pages of the Newsletter. It was used as the first vehicle to show that magnetic resonance imaging was in fact possible. Many new examples of multidimensional NMR were shared in the Newsletter pages. In recent times, techniques and hardware for sensitivity enhancement have received much attention, as chemists strive to obtain useful spectra on smaller and smaller samples in less and less time (Boltzmann is still winning, but by orders of magnitude less than were the case only a few years ago). Two companies made their first results at 750 MHz known in the Newsletter pages. A major value of the Newsletter is the speed with which it communicates results in rapidly changing areas.

In addition to technical results (sometimes extensive and complete, sometimes fragmentary or preliminary), the Newsletter contains meeting notices and programs, book reviews, enquiries, mysteries, 'Positions Available (or Wanted)', 'Equipment Wanted (or Available)' notices, and occasionally, bits of humor, mostly intentional. Informality is encouraged.

Participation in the Newsletter is open to anyone, all around the world, and new subscribers are welcomed.

Biographical Sketch

Bernard L. Shapiro. *b* 1932. B.Sc., 1952, McGill University, Canada, A.M., 1954, Ph.D., 1957 (Chemistry), Harvard Univeristy, USA. Postdoctoral fellow with R. B. Woodward, 1956–58, at Harvard, where he was initiated into NMR spectroscopy by Aksel A. Bothner-By. Fellow Independent Research Program, Mellon Institute, Pittsburgh, Pa, USA, 1958–64; Associate Professor, Illinois Institute of Technology, Chicago, IL, 1964–68. Professor of Chemistry, Texas A&M University, College Station, TX, 1968–87; Professor Emeritus since 1987. Approximately 50 publications. Former research interests: geminal coupling constants, ring current effects, lanthanide-induced shifts. Since 1958, Editor/Publisher, *The NMR Newsletter* and predecessors.

Shaw, Derek: From 5-mm Tubes to Man. The Objects Studied by NMR Continue to Grow

Derek Shaw
GE Medical Systems, Ltd, Slough, UK

'NMR is worked out: move onto something more interesting.' That was the advice I was given by colleagues on finishing my Ph.D. in 1965. This seemed good advice at the time; NMR was giving new insights into molecular structure, but was slow and insensitive with very little potential for improvement. I did not take the advice, instead took a job in Varian's applications laboratory in the UK. Varian was the driving force of NMR at that time, and had an amazing group of people working in Palo Alto, Martin Packard, Warren Proctor, Jim Shoolery, Ray Freeman, Richard Ernst ... , the list goes on.

Then, as often happens, many things came together at the right time. In 1965 following up on suggestions made much earlier by Russell Varian, Wes Anderson and Richard Ernst showed that the concepts developed in 1822 by a former governor of Lower Egypt and friend of Napoleon (Jean Baptist Fourier) could be used to explain how the conduction of heat could speed up NMR! Minicomputers capable of performing the appropriate Fourier transformations in an acceptable period of time became available at a reasonable price, and the face of NMR changed for ever. There was much soul-searching as to whether the spectra obtained by this new method were the same as those that chemists had learned to work with from the traditional CW spectrometers. Fourier theory only works for linear systems, and NMR is not a linear system. There was therefore great concern, for example, as to how factors like chemical exchange manifested themselves with pulse excitation and hence affected the appearance of the final spectrum. Other concerns were the artifacts found in FT NMR, and there were many, particularly when a large dynamic range was involved such as in aqueous solutions; were they acceptable?

A major experimental problem with the current generation of homonuclear spectrometers was maintaining the field/frequency lock with pulse excitation. This issue was partially resolved and crude bolt-on accessories were produced for existing spectrometers such as the HA-100; some new systems, however, like the XL-100 (despite it being the first system to offer a deuterium lock), were not FT-compatible. Then in late 1969 the Bruker WH-90, an *FT-only* system, arrived on the scene and by the 'Pittsburgh Conference' of 1970, after a few months of panic development, there were acceptable FT accessories for the XL-100 and other leading NMR spectrometers. Fourier transform NMR had arrived. The added speed, and hence sensitivity, gave access to new proton applications, especially in the biological area. FT techniques also made other nuclei, especially ^{13}C, accessible; indeed, there was one school of thought that maintained that FT techniques were only useful for ^{13}C, being too artifact prone and unnecessary for proton work. They were wrong, and NMR never looked back.

The next radical development came about five years later when, in 1973, Paul Lauterbur showed that by using field gradients NMR could produce images. At the same period, X-ray computed tomography (CT) was revolutionizing medical imaging. X-ray images were no longer shadow graphs produced from a point source; they were images of axial slices. Radiologists had to rethink their view of anatomy! After a slow start and much pioneering work in the UK, e.g. in Nottingham where many competitive groups existed, and Aberdeen, NMR imaging started to produce recognizable images of human anatomy. Consequently, in the late 1970s, a radically new group of customers (radiologists) and companies (the diagnostic imaging manufacturers EMI, GE, Philips, Picker, Siemens, ...) became interested in NMR. The key factor at this stage was the magnet. Working, as I was at this period, for Oxford Instruments, was in some ways like being in an Alan Aykbourne play. Diverse characters from all the medical imaging companies would come in to discuss their own 'secret ideas' and specify their own unique magnet requirements, resistive/superconducting, 0.15 T/1.5 T, four coil/ six coil ... These requirements were often the same as the company before, leading to the need for considerable 'political sensitivity'.

The early period of MRI, as it was now called (the N had disappeared so as not to frighten the patient, or to resolve a turf battle between radiology and nuclear medicine, depending on your perspective), was dominated by the 'field strength wars'. What was the best field strength for MRI? These battles were essentially commercial, science being used to justify the company competitive position. The resistive magnet soon fell by the wayside due to its inherent instability and low field strength, and the superconducting magnet became supreme.

One pawn in the field strength battle was in vivo spectroscopy. A major benefit of MRI over CT was to be tissue characterization, initially via relaxation time measurements. As it became apparent that there was not going to be sufficient specificity available via T_1 and T_2 determinations, MRS, as in vivo spectroscopy became known, was seen as a potential alternative. In vivo spectroscopy also had the potential to study metabolism; the noninvasive biopsy. MRS needed the highest magnetic field possible in order to achieve the best resolution of small chemical shift differences. This need, along with the higher signal-to-noise ratios achievable at higher field strengths (the truth, or otherwise, of this statement itself was the source of many, often violent, discussions) led, despite their extra costs, to the use of 1.5 T magnets in top-of-the-line systems. Without this push to high field, MRI systems might be quite different today, probably lower down on the cost/performance scale. MRS has made itself felt but has yet to become clinically accepted. There are still signs that this may happen ... soon.

In the space of a relatively short period of time, MRI has become a major medical imaging technique. It has excellent tissue discrimination, though perhaps not as much specificity as was hoped for and, as far as is known, is without significant hazard. It may well be that in the not too distant future MRI and ultrasound will be the dominant medical imaging modalities. NMR has already been recognized by two Nobel Prizes, one in Physics (Bloch/Purcell, 1952), and the other in Chemistry (Ernst, 1991); it would be rewarding to think that MRI would produce a third in medicine.

The development of MRI has dramatically changed the place of nuclear magnetic resonance in society. It is no longer

a remote scientific technique, it is a phenomenon the general public may well become aware of when they visit their local hospital. Indeed, many will be the 'sample' in an NMR system! The next stage will probably be the use of MRI in the operating theatre; minimally and totally noninvasive surgical procedures being planned with the aid of MRI data; and guided and monitored by real-time (EPI) imaging.

Performing surgical operations inside an NMR magnet is a far cry from working hard to build a magnet and probe large enough permit the use of a 5 mm instead of a 4 mm tube. It is a very brave person who will predict where the phenomenon of nuclear magnetic resonance will next impact on our lives. I do not have that courage.

Biographical Sketch

Derek Shaw. *b* 1940. B.Sc., 1962, Ph.D., 1965, Chemistry, University of London. Worked for Varian Associates in NMR applications and marketing, 1968–78. Oxford Instruments Group marketing and product development [in vivo spectrometers (TMR)], 1978–83. GE Medical Systems working in MR imaging, 1983–present. Author of approx. 100 papers in various areas of magnetic resonance and a book on Fourier transform NMR.

Sheppard, Norman: NMR—Some Reminiscences

Norman Sheppard

University of East Anglia, Norwich, UK

My first acquaintance with nuclear magnetic resonance (NMR) was when, in late 1948, I visited the Chemistry Department of Harvard University on my way home after a year spent as a Visiting Assistant Professor at Pennsylvania State College (now State University). A friend of mine at Harvard, Gordon Stone, told me of this new technique which was thought to have promise for chemical structural identification. I was puzzled by this because it seemed to me that most of chemistry is related to the properties of the outer electronic orbitals, and that the role of the nuclei was essentially to act as charged point masses around which the electrons are arranged and move. But I had not anticipated the extremely high resolution of the new technique, soon to reach 0.5 Hz or nearly 10^{-10} cm^{-1}. This compares with 0.1 cm^{-1} which was the best routine resolution in infrared spectroscopy, the then most effective spectroscopic method for molecular structural determination.

Several years later I visited the Texaco Research Laboratory in Beacon, New York State, following a Gordon Research Conference on infrared spectroscopy. I had a mutual interest with Dr. Robert Eischens of Texaco in the infrared spectra of adsorbed molecules. At Beacon I was shown a Varian Associates' brochure which illustrated, I believe, the ^{1}H NMR spectrum of ethanol. From this I learnt of both the effects of differing chemical (electronic) environments on the resonance positions of a particular type of nucleus (the chemical shift), and the way in which spin–spin coupling fine structure in the resonances provides information about the presence of neighboring magnetic nuclei. Shortly after this I accepted the position of Assistant Director of Research in Spectroscopy in the University Chemical Laboratory, Cambridge. My teaching role in the laboratory was primarily to present molecular spectroscopy to the postgraduate chemistry students from the point of view of structure determination. I suggested to Professor A. R. Todd (later Lord Todd), Head of the Laboratory, that NMR would be a valuable addition to the existing UV–visible and infrared spectroscopic facilities. I recall that he obtained a (then 'huge') grant of £18 000 from the Wellcome Foundation in order to purchase our first ^{1}H 40 MHz Varian spectrometer. It was installed by Chris Dersch in 1957. I particularly remember this period because Professor Todd had told ICI of the impending delivery of the spectrometer. They had asked if they could bring a 'few' samples for study by this new technique, and I had agreed to this. However, I had not changed the proposed date of their visit even though the delivery of the spectrometer was delayed by several months. They arrived about a fortnight after the installation by which time Ralph Elsey, a senior technician, and I had only run a few samples of our own and were still mastering the technique of 'dishing' the magnetic field in order to obtain good resolution. The ICI scientists had brought about 50 samples with them and expected the spectra to be interpreted as they came off! In fact it took us several months to run all their samples interspersed into the laboratory's own NMR program that soon became very active.

During the next few years NMR techniques developed rapidly through equipment initiatives taken by Varian Associates. The earlier very tiresome field drift was much reduced by a Super Stabilizer electronic device; resolution became optimized by cranking a handle to change the relative orientations of the magnet pole pieces rather than by 'dishing' the field; then sample spinning was introduced to average-out horizontal field inhomogeneities; and in due course (from Perkin-Elmer) 'Golay coils' enabled inhomogeneities in all three dimensions to be optimized by purely electronic means. Variable temperature operation and double resonance techniques all added to the power of NMR.

Jim Shoolery, in particular, played a vastly important role in acquainting the academic chemists with the use and value of the new techniques developed by the Varian engineers—and, of course, in persuading the chemists to purchase the new spectrometers or accessories! I recall with amusement a sales pitch that he was making at a meeting in Oxford when he pointed out that, although the cost of the latest 60 MHz spectrometer seemed to be very high, it was capable of providing the unprecedented resolving power of 1 in 10^9. For comparison he pointed out that an optical telescope with such a resolving power would be able to resolve the images of two cats sitting side-by-side on the surface of the Moon. A voice with a strong Scottish brogue interrupted from the back of the lecture-hall, 'I don't believe there *are* two cats on the surface of the Moon!'

The impending arrival of the new NMR spectrometer led to strong interest amongst prospective research students who were graduating in Cambridge in 1957. My original NMR research team in that year consisted of Colin Banwell and Jim Turner from Cambridge and David Cohen from Canada. In 1959 they were joined by Robin Harris and Ruth Truscott (Lynden-Bell). It was also very helpful to have John Pople in the Chemical Laboratory as at that time he was interested in the theory of NMR. With Bill Schneider and Harold Bernstein, he later published in 1959 the then-definitive book on chemical applications of NMR.

Colin Banwell immediately got to work on a computer program for calculating NMR spectra from chemical-shift and coupling constant parameters using full symmetry factorization as developed by Harden McConnell.[1] The calculations themselves involved the use of the early EDSAC II computer in Cambridge which was subject to frequent malfunctions because of its dependence on the operation of banks of electron-tube valves. I had to go before the EDSAC Committee to justify our request for computer time. I recall the comment, after my presentation, 'That was very clear.' 'I think that this is probably the first time that I have really understood what a user wants to do!' Colin was very successful with his programing and used it to analyze the 'second-order' ^{1}H spectra of vinyl compounds, with that of the four-spin vinyl fluoride case as a pièce de resistance.[2]

The members of the group became very interested in the stereochemical as well as the electronic factors determining proton–proton coupling constants in hydrocarbon groupings. We helped to establish the planar zigzag interatomic pathway

as a generator of measurable long-range coupling constants across up to five bonds.[3]

Jim Turner's research project originated in an attempt to assess the sensitivity of our Varian spectrometer for detecting ^{1}H spectra. For this purpose, the single expected resonance from chloroform, $CHC1_3$, was studied at high amplification. I then observed an 'extra' weak signal with about 1% of the intensity of the main resonance. I first attributed this to an impurity in the chloroform, until I realized that there was an identical second weak feature at the same distance on the other side. These were not caused by sample-spinning sidebands because they did not move with variations of the spinning frequency. It then occurred to me that this extra widely spaced doublet must arise from the 1% of chloroform molecules that have spin-$\frac{1}{2}$ magnetic ^{13}C nuclei rather than nonmagnetic ^{12}C ones. The separation between the doublet would give the value of the $^{1}J(^{13}C,H)$ coupling constant. In this case, the '^{13}C-satellites' had the same single-maximum shape as that of the 'parent' resonance. However in some other cases the satellites had a much more complex fine structure than did the parent resonance, and similar weak structure could be discerned at the foot of the latter strong single peak.

Second-order spectra are obtained when, as calculated in the same units of Hz, the chemical shift between two adjacent resonances is comparable to their mutual coupling constants. Under these circumstances intensity piles up preferentially in the center of the resulting spectral pattern. In the extreme case, when the chemical shift is zero for reasons of chemical (symmetry-related) equivalence, all the intensity resides in a single combined central peak. For this reason the ^{1}H nuclei of the methyl group of CH_3Cl, for example, give a single combined resonance without features that can be used to derive a value for the magnitude of the proton–proton coupling constant.

However the large separations caused by the $^{1}J(^{13}C,H)$ coupling constant act as an 'effective chemical shift' and lead to the generation of spin–spin fine structure reflecting the presence of otherwise chemically equivalent ^{1}H nuclei attached to an adjacent nonmagnetic ^{12}C nucleus. Hence, the ^{13}C satellites provide accessible coupling constant data which are not available from the spectra of the great majority of molecules with only ^{12}C nuclei.[4] Since it is the important type-molecules, such as acetylene, ethylene, ethane, or benzene, that have all their ^{1}H nuclei chemically equivalent for reasons of symmetry, the extra information available from analysis of the ^{13}C satellites is particularly valuable.

Jim Turner investigated the NMR spectra from a series of substituted ethanes and related cyclic compounds with a view to determining the dependence of the vicinal $^{3}J(H,H)$ coupling constants across the central CC bonds on the azimuthal angle between the CH bonds. The ^{13}C-satellite technique was particularly valuable for determining the coupling constants between chemically equivalent ^{1}H nuclei in XCH_2CH_2X groups as in 1,2-dichloroethane and the cyclic molecule dioxane.[5] The collected results helped to provide the experimental basis of the 'Karplus rules',[6] subsequently used very widely in determining the conformations of large ring-containing organic molecules.

David Cohen found that he could only reproduce some complex second-order spectra from dichloropropenes theoretically if he made the assumption that certain coupling constants were of opposite sign from others.[7] This was an unexpected discovery that received subsequent quantum-mechanical explanation. Another laboratory made this discovery independently at about the same time.[8]

Robin Harris initially followed Jim Turner's conformational interests but using perfluoro compounds.[9] In his Ph.D. thesis, he then studied the temperature dependence of the spectrum of cyclohexane.[10] At room temperature a single observed resonance denotes the chemical equivalence of all the ^{1}H nuclei, brought about by the rapid chair-to-chair inversion of the carbon skeleton on the NMR timescale, i.e. inversion at a rate greater than the chemical shift difference in Hz between axial and equatorial H atoms. Cooling led to the generation of much more complex spectra when the observable chemical shift between these two types of environment in turn led to the manifestation of many $^{3}J(H,H)$ splittings. The parameters determining the inversion process itself were derived from the series of temperature-dependent spectra.

Ruth Truscott synthesized isotopic forms of ethane, ethylene, and acetylene containing one or two ^{13}C nuclei, respectively. Analysis of the NMR spectra gave complete coupling-constant data for these fundamental type-molecules, including the evaluation of $^{1}J(^{13}C,^{13}C)$ coupling constants for the first time.[11] The magnitudes of the $^{1}J(^{13}C,H)$ couplings correlated very well with the s character of the respective carbon orbitals, i.e. contact terms were clearly dominant within the coupling mechanisms. The $^{1}J(^{13}C,^{13}C)$ data were more complex but have probably since been accounted for by ab initio calculations.

The Varian spectrometer was, of course, purchased primarily for use in molecular structure determination, or structural diagnosis as some people refer to it. In fact it soon became very effective in this respect and made important, sometimes decisive, contributions to settling the structures of natural product molecules such as gibberellic acid[12] (a plant hormone that promotes rapid and extensive growth), the alkaloid calycanthine,[13] and the erythroaphins derived from the coloring matters of the aphid group of insects.[14] My role was to advise the chemists concerned on the interpretation of the NMR spectra; the erythroaphin case was instructive in putting the large chemistry effort back on course after a misinterpretation of an earlier chemical step. Over this period NMR brought about a revolution in Cambridge in the effectiveness of structure determination of medium-sized organic molecules, of inorganic coordination compounds with unusual ligands, and particularly of large molecules in the natural product field.

Before I left Cambridge for the then new University of East Anglia in 1964, the systematic teaching of structure determination by spectroscopic methods had moved from the post-graduate to third year undergraduate level. The latter students were presented with UV/visible, infrared, and NMR spectra of the 'unknown' organic compounds given to them for analysis.

The great success of NMR in structural diagnosis led to a consideration of the desirability of recording spectra in a standard format on printed charts. Up to that time, each spectrum had to be calibrated with sidebands because of field drift, etc. The advantages of such a situation were urged on Perkin-Elmer Limited (the UK offshoot of the Perkin-Elmer Corporation of the USA) by a panel of spectroscopic consultants that included Rex Richards, H.

W. (Tommy) Thompson, and myself. It was concluded that a permanent magnet-based spectrometer would be expected to have minimum field drift and also be economical in operational costs. Perkin-Elmer Limited therefore developed such a 40 MHz spectrometer which was installed in Cambridge for my evaluation. Although this was very successful, its development into quantity production was slow, doubtless partly because NMR was a new and unfamiliar technique to the parent corporation. As a result, Varian Associates were the first to realize this aim by marketing the well-known A-60 routine spectrometer. However Perkin-Elmer spectrometers were marketed in due course and later developed up to the feasible permanent magnet limit of 90 MHz for ^{1}H nuclei. For research purposes the Varian HA-100 was the workhorse for many years. Subsequently, as is well known, much higher magnetic fields, now up to the equivalent of 750 MHz for ^{1}H, have been achieved using superconducting magnets, many of them produced by Oxford Instruments Limited following encouragement to move into this field from Rex Richards. The major advances of pulse techniques coupled with Fourier transform analysis, the improved spectral separations and sensitivities from the use of high magnetic fields, and the 2D procedures for spectral analysis developed by Ray Freeman, have together caused NMR to become extremely effective in studying the large molecules of biochemistry, such as enzymes and proteins, in general in solution, again with encouragement from Rex Richards in the UK and from others elsewhere.

Originally the organic chemists, having benefited from the success of ^{1}H NMR, considered that Nature had been most uncooperative in making the abundant isotope of carbon, ^{12}C, nonmagnetic. Clearly, much additional and important structural information could be derived, in principle, from spectra of the magnetic isotope ^{13}C, but unfortunately it is only 1% abundant and gives much weaker signals than ^{1}H on a nucleus-for-nucleus basis. However they had underestimated the capability of technologists for reaching a difficult objective if the need is compelling. In the early 1970s the use of pulse rather than continuous-wave methods produced FT spectrometers which suddenly made the production of ^{13}C spectra routine. These developments were responsible for Richard Ernst's recent Nobel Prize. It then became apparent that, in fact, the organic chemists have the best of both worlds, i.e. readily obtainable spectra which are sufficiently simple that they can be interpreted even from very highly complex molecules. With hindsight, even the ^{1}H spectra that provided the original great stimulus to the development of NMR would have been very much complicated if all the carbon nuclei had been magnetic. In that case, NMR spectroscopy might have stayed as the province of professional spectroscopists capable of analyzing only the spectra from small molecules. Instead NMR has developed into one of the best spectroscopic methods for molecular structure determination—the very best one for organic and biochemistry.

When I moved from Cambridge to the University of East Anglia in Norwich, UK, to help in the foundation of the School of Chemical Sciences, I carried my NMR interests with me and two other of our newly appointed teaching staff, Robin Harris and Kenneth Packer, also had strong interests in this area. I vividly remember our new HA-100 spectrometer being installed by crane in our one-storey temporary building after removal of part of the roof! I continued to carry out a number of NMR studies in a variety of directions of chemical interest, including studies of the solvation shells of metal ions in solution, conformational isomerism, and an evaluation of the potential of ^{17}O spectroscopy. However my principal research interest moved into the direction of the spectroscopy of adsorbed species on catalysts and here NMR had inadequate sensitivity and vibrational spectroscopy was more effective. NMR is still marginal in this respect but is ripe for further progress. However Robin Harris and Ken Packer both made excellent careers in NMR and later, in collaboration, became very well known for their joint development of techniques for obtaining high-resolution NMR spectra in the solid state. In my Cambridge days I had dreamt of overcoming the large linewidths in the spectra of solid samples by spinning powdered samples in spherical plastic ampules with wavy fins driven at high speed within a centrifuge at the sample position! Luckily, spinning very rapidly about a fixed axis at the 'magic angle', as suggested by Raymond Andrew, provided a technologically more feasible route to the same end!

Although I am no longer an 'NMR man', I have remained very highly impressed by the continuing development of versatile experimental and theoretical methods within its field (confines is hardly the right word). To my mind NMR provides a very fine example of the way in which a new idea or experimental technique in science can disseminate itself in many unpredictable but profitable directions. The physicists who did the first successful experiments, Bloch at Stanford and Purcell at Harvard, were interested in the magnetic resonance phenomenon from the point of view of determining the magnetogyric ratios of the nuclei themselves. When high-precision experiments led to slightly different resonance frequencies for the same type of nucleus in different chemical surroundings, the phrase 'chemical shift' was coined, probably as a physicists' swearword! After all, even more precise measurement on bare nuclei were much more difficult to envisage! Applications of this physicist's swearword in due course led to a technique without which the frontiers of chemistry would be much less far-flung than they are today. Even more recently, NMR imaging (with the N for nuclear missed out because of possible misunderstanding by the public) as envisaged by Paul Lauterbur and developed by Peter Mansfield and others, has become a major aid to whole body medical diagnosis.

NMR therefore provides an excellent example of the unity of science and of how the solution of long-standing needs or problems can come from seemingly unrelated directions. But, as in the case of NMR, the applications tend to become apparent only several decades after the original discovery (one and a half decades for NMR in chemistry and four decades in medicine). Unfortunately, it is difficult for politicians and the public to take into account such timescales (for politicians their own timescale is about five years, i.e. the intervals between elections; for financiers interested primarily in next year's profits the timescale is one year). There is therefore a real danger that curiosity-oriented research, which is the mainspring of new science and new technology, will be allowed to wither on the vine for lack of adequate financial support.

I would like to end with a tribute to the Varian brothers, their engineers, and their chemistry front-man, Jim Shoolery, for all they did to develop the techniques of NMR and to draw the attention of the academic chemists to their many fruitful applications.

REFERENCES

1. H. M. McConnell, *J. Chem. Phys.*, 1959, **30**, 126.
2. C. N. Banwell and N. Sheppard, *Proc. R. Soc. London*, 1961, **A263**, 136.
3. C. N. Banwell and N. Sheppard, *Discuss. Faraday Soc.*, 1962, **34**, 115.
4. A. D. Cohen, N. Sheppard, and J. J. Turner, *Proc. Chem. Soc., London*, 1958, 118.
5. N. Sheppard and J. J. Turner, *Proc. R. Soc. London*, 1959, **A252**, 506.
6. M. Karplus, *J. Chem. Phys.*, 1959, **30**, 11.
7. A. D. Cohen and N. Sheppard, *Proc. R. Soc. London*, 1959, **A252**, 488.
8. S. Alexander, *J. Chem. Phys.*, 1958, **28**, 358.
9. R. K. Harris and N. Sheppard, *Trans. Faraday Soc.*, 1963, **59**, 606.
10. R. K. Harris and N. Sheppard, *Proc. Chem. Soc. London*, 1961, 418.
11. R. M. Lynden-Bell and N. Sheppard, *Proc. R. Soc. London*, 1962, **A269**, 385.
12. N. Sheppard, *J. Chem. Soc.*, 1960, 3040.
13. R. B. Woodward, N. C. Young, T. J. Katz, V. M. Clark, J. Harley-Mason, R. F. J. Ingleby, and N. Sheppard, *Proc. Chem. Soc., London*, 1960, 76.
14. D. W. Cameron, R. I. T. Cromartie, Y. K. Hasnied, P. M. Scott, N Sheppard, and Lord Todd, *J. Chem. Soc.*, 1964, 90.

Biographical Sketch

Norman Sheppard. *b* 1921. B.A. (Chemistry), M.A., Ph.D., Cambridge University, UK. Assistant Director of Research in Spectroscopy and Fellow of Trinity College, Cambridge, 1955–64; Professor of Chemical Sciences, University of East Anglia, Norwich, UK, 1964–86, now Emeritus Professor. Approx. 300 publications. Research specialties: vibration spectroscopic and (formerly) NMR studies of molecular structure and dynamics, with particular application to the identification of chemisorbed species on catalyst surfaces.

Shoolery, James N.: High-Resolution NMR: A Dream Come True

James N. Shoolery
Varian Associates, Palo Alto, CA, USA

NMR began in a rather unusual confluence of events, people, and visions. World War II, with its demand for synthetic materials, had focused attention on the limitations of contemporary instrumentation, and by 1946 the first commercial infrared spectrometers were available. In addition, the war also accelerated the development of electronics, including radar, which opened up new possibilities of analytical techniques.

Coincidentally, the klystron tube, which made airborne radar possible, played a role in the early development of NMR. The klystron was invented by Russell and Sigurd Varian, who firmly believed that scientific innovation should find practical applications. While developing the klystron for air navigation and defense, they, together with their friend, Stanford University professor William W. Hansen, began dreaming of having a laboratory of their own.

When the war ended, Hansen returned to Stanford, where he contributed to Felix Bloch's original paper on nuclear magnetic resonance. E. M. Purcell studied the same phenomenon independently at Harvard University and shared the 1953 Nobel Prize for Physics with Felix Bloch for that work. The Harvard group developed a considerable body of theoretical and experimental work but did not participate in the commercial development. Some months later, Russell arrived at Stanford as a Research Associate and quickly saw the potential applications for the new phenomenon. On December 23, 1946, at Russell's urging, Bloch and Hansen signed a patent application and gave an exclusive license to 'Varian Associates', the laboratory the men had envisioned, to develop commercial applications of the nuclear induction device.

In January 1948, Varian Associates actually came into existence. From the beginning, the company was diversified into two products lines: the klystron tube with rapidly growing markets and mature manufacturing techniques, and nuclear magnetic resonance devices with no markets and no manufacturing techniques. The income from the klystron made it possible to nurture the emerging technology during its infancy.

At Stanford, Bloch and his group, working with an improved electromagnet, found that different liquids yielded different values for the proton magnetic moment. The shift in the field at the nucleus, due to screening by orbiting electrons, interfered with accurately measuring nuclear moments. Accordingly, or so the story goes, the physicists christened that irritating obstacle *the chemical shift*.

Varian Associates clearly needed a homogeneous electromagnet for their research into chemical applications. To help pay for building it, the company offered the magnet as a product and issued a data sheet, which, when I came across it, changed the course of my career. I began my university studies in 1941, but in early 1944, the US Navy turned me into a radar technician, a job that gave me a thorough grounding in electronics. The subject of my graduate studies at Caltech was microwave spectroscopy, and in late 1951, as a postdoctoral fellow, I was asked to look at the suitability of Varian klystrons for the microwave spectrometer. At a trade show, I came across Varian's specification sheet for the 12-in. electromagnet and an accompanying stack of reprints of a Letter to the Editor that had appeared in the *Journal of Chemical Physics*.[1]

When I saw the three peaks of ethyl alcohol, I knew what I wanted to do and where I wanted to do it. I wrote to Varian, suggesting that a company far-sighted enough to offer such a technologically advanced product might consider employing a chemist to help develop applications for their instrument. I modestly announced that I would be available. To my delight, Varian Associates offered me the position.

NMR SPECTROSCOPY: IN THE BEGINNING (1952–60)

I reported for work in April 1952, and my badge, number 512, reflected the intimacy of the company. Two members of the Stanford group—Martin Packard and Emery Rogers—were already part of the Varian team; two more, Wes Anderson and Jim Arnold, joined shortly after my arrival; and another two, Warren Proctor and Harry Weaver, somewhat later. (Much later, Ray Freeman, Richard Ernst, and Howard Hill arrived.) Not only was there the excitement of working on the leading edge of a technology, but the Varians had created a unique atmosphere. Russ and Sig, shown in Figure 1, visited the technical projects on almost a daily basis to

Figure 1 Russell Varian (at left) and his brother Sigurd with a klystron tube in the early 1950s

discuss, suggest, and encourage, treating every employee with consideration and respect.

By the time I arrived, a research and development (R&D) group was already working on the first order for a 30 MHz high-resolution instrument with a magnetic field strength of 7050 G, able to resolve the three peaks of ethyl alcohol. Martin Packard, who as a graduate student had built Bloch's original apparatus, headed the team. Emery Rogers was readying the power supply for the magnet. My first job was to design and build the radiofrequency (rf) unit. My second task, in September 1952, was to install the first commercial instrument, the HR-30, in the Humble Oil laboratory in Baytown, Texas.

In January 1953, I happily opened the Varian Applications Laboratory, the Applab as we called it, for business. We had already resolved the fine structure from chemically nonequivalent protons in molecules and even hyperfine structure from spin–spin interactions between nonequivalent nuclei, but there was a very limited theoretical basis for interpreting the new spectra. My next assignment was to establish the empirical relationship between observed spectral features and the molecular structure of the sample. I felt as if I'd died and gone to heaven.

The Applab HR-30 was the state-of-the-art, top-of-the-line nuclear magnetic resonance spectrometer. However, it had a few drawbacks. Its 5400-lb. electromagnet required cooling water and heavy-duty electrical service as well as a very substantial floor. The finer details of the spectrum were apt to vary with the instability of the magnetic field. Sensitivity was so poor that only neat liquids or concentrated solutions would produce signals visible above noise, and at the 7050 G field strength the 10 ppm range of the proton spectral dispersion severely limited the interpretability and usefulness of the spectra.

In addition, it was an operator's nightmare, as can be seen in Figure 2. After locating the signal from a sample of water, the operator had to place the probe (which contained the rf coils and sample) in the homogeneous spot in the magnet. That spot changed its shape, size, and location with changes in temperature and with the effects of hysteresis caused by turning the magnet on and off. When the oscilloscope finally displayed a satisfactory pattern, the sweep width had to be calibrated by generating audiofrequency sidebands of the water signal. Making a permanent record of the data meant taking two Polaroid photographs of the oscilloscope screen, one to establish the reference point of the chemical shift of water, and then, quickly, before the field could drift very far, another of the sample being studied.

Yet, we were excited about presenting the HR-30 to the scientific community. Trying to avoid the ominous word *nuclear* and wanting an acronym, Emery Rogers, the newly appointed marketing manager, and I decided to call the new technique NMR spectroscopy and used that term at every opportunity. As soon as possible, we moved from photographs to high-speed chart recordings. The charts presented the NMR spectrum in a format closer to that of the popular infrared (IR) spectrometers, displaying a magnetic field scan in parts per million (ppm) where IR displayed a wavenumber scale. To differentiate the two techniques, we displayed NMR spectra as peaks with a positive rather than negative deflection. (The choice, we claimed, symbolized the vitality of the new technique.) We referred to the fine structure arising from spin–spin coupling as a *multiplet* rather than an absorption band. (Some years passed before all our ideas were adopted.)

Figure 2 The author and Virginia Royden operating the HR-30 Applab instrument in about 1954

In July, 1953, Emery and I began publishing *Technical Information from the Radio Frequency Laboratories of Varian Associates*, which we sent to the chemistry departments of major universities and the research departments of large chemical companies. The *Technical Information Bulletin*, as it came to be known, appeared, liberally illustrated with spectra, whenever new developments occurred. A few months later, we began a monthly advertisement in *Analytical Chemistry*, titled 'This is NMR at Work', which rigorously described and illustrated a recent example of Applab work.

A year passed before I found an example showing that NMR could solve a significant problem that other more established techniques could not. In mid-1954, E. J. Corey, then working at the University of Illinois, submitted a sample of cycloheptatriene. Neither IR nor UV analysis could unequivocally identify its structure, but our NMR spectrum did so with simplicity and directness.

Daily exposure to the limitations of the HR-30 turned me into a product champion, or as Emery Rogers generously put it, 'a chemist with an antipathy to accepting horizons as they seem to be'. With encouragement from Russ and Sig, the 18 months between mid-1954 and 1956 became an orgy of product development. In rapid succession, the Varian R&D group produced higher field strength, sample spinning, field gradient shimming with electric currents, and magnetic flux stabilization.

Since chemical shift dispersion increases linearly with magnetic field, and sensitivity increases as the $\frac{3}{2}$ power, I welcomed the news in 1954 that the power supply could deliver enough power to the magnet to operate continuously at a field strength of 9400 G, sufficient for operation at 40 MHz. In 1955, Varian introduced the HR-40, which, in addition to its increased power, was equipped with a sample spinner, a device that represented a major breakthrough in the quality of resolution. Work by Arnold and Anderson in Bloch's laboratory at Stanford had shown that spinning the sample with a small air turbine narrowed the NMR lines in liquid samples by averaging the magnetic field over a circular path.[2]

At that time, altering the distribution of field gradients meant loosening the main bolts holding the pole pieces to the yoke and inserting or removing a metal shim. The group at Stanford had experimented with current-carrying coils on the pole faces to modify the distribution of magnetic flux, but the correcting currents were difficult to adjust because they were highly interactive. Varian R&D solved that problem through mathematical analysis. Adjustment of homogeneity with electric shims, while still requiring some expertise, became a systematic procedure.

Before magnetic flux stabilization was developed, obtaining a spectrum was like looking through binoculars at a row of birds on a telephone wire from the back of a truck bouncing over a rutted road. The regulation of the magnet current was, at best, about 1 in 10^7, while we needed a field stable to 1 in 10^8 or better. When we heard that a group at Princeton was using degenerative feedback to attack the problem, we attached a pick-up coil to one of the magnet pole pieces. Any change in the field, even 1 in 10^9, induced a few microvolts across the coil and resulted in a minute current in a galvanometer. The deflection was amplified by a light beam reflected off a mirror attached to the suspension. A split photocell detected the change, and fed back a current to oppose the change.

I remember my first trial of the device in 1956. Closing the switch made it seem that I'd gotten out of the truck and mounted my binoculars on a tripod. I could easily count the birds on the wire and even tell if their feathers were ruffled. In a fit of enthusiasm, we called the device a Super Stabilizer. Offered as an accessory that could be retrofitted to earlier spectrometers, it had the same effect on the acceptance of high-resolution NMR as the double-beam principle had had on IR. Field jitter and slow drift were largely overcome, and NMR spectra became more reproducible.

Having stabilized the electromagnet, it made sense to capitalize on its superior field strength. Operation at 60 MHz (14 096 G) represented a 50% increase in chemical shifts and a doubling of sensitivity. The many metallurgical problems of manufacturing pole caps with predictable high-resolution performance at that field were solved, and a curved profile was developed that produced a much larger homogeneous region in the magnet gap.

The HR-60, announced in 1958, was a commercial success, but more important, it demonstrated what we at Varian so firmly believed: that overcoming the sensitivity and spectral complexity problems would open up unlimited applications of NMR in chemistry and biochemistry. Invitations to make presentations to ACS sections, Gordon Conferences, and analytical chemistry meetings increased, and in October 1957 we held the first annual workshop to introduce the mysterious new technique to chemists. I estimate that by 1960, I had described the principles of NMR to about 20 000 people at home and abroad.

As interest in NMR spectroscopy increased, Emery and I began planning to demonstrate a spectrometer at an instrument exhibit. In 1957, having attended the 9th Pittsburgh Spectroscopy Conference, held on the 11th floor of the William Penn Hotel in Pittsburgh, we decided to take a space for 1958. We were told that the only remaining one big enough for a monster like ours was in the hallway adjacent to the elevators. The location was deemed undesirable because of the traffic there, but the price was right. We booked it and the next year brought an HR-60 to display.

Getting a 5400-lb. magnet to the 11th floor in an elevator was an exciting project. Persuading the hotel to provide cooling water and three-phase 220V power added more challenges. Then, at the moment of truth, our instrument exhibited unexpected instability. Our electronics wizard Forrest Nelson quickly solved the problem by moving the magnet away from the elevators, whose arrival and departure was perturbing the field. The location of our site turned out to be a great asset. Everyone using the elevators passed by, and most stopped to look and talk. Over the next years, the Pittcon booth contributed greatly to an expanded awareness of NMR.

Once the 60 MHz magnet was developed, we set our sights on the highest practical field an electromagnet could reach. Magnetic saturation of the iron set a limit of 100 MHz (23 490 G). The HR-100, introduced in 1959, had resolving power better than 1 part in 10^8. Astronomers with a telescope of equal power would be able to see two cats on the moon sitting 1 ft. apart.

From the outset, NMR spectroscopy enjoyed a fundamental advantage for quantitative work: unlike UV–visible and IR spectroscopy, which must take account of differing absorption coefficients, the NMR signals being compared arise from the same spectroscopic transition. If there were no drift, the total area under the peaks could be compared. Unfortunately, the stability of the dc amplifiers introduced large errors in the integrals. In 1959, we solved the drift problem with an NMR integrator, which sinusoidally modulated the magnetic field and selected the ac signal components, while suppressing the sidebands with a balanced phase sensitive detector. In 1960, I showed that NMR signals from chemically shifted protons could be compared with an accuracy of 1% or better using this approach.[3] Now NMR could match abilities with other analytical instruments.

In 1955, we realized that the long lifetimes of nuclear spin states would allow the chemist to tamper with the energy levels of a coupled system and deduce which nuclei share common energy levels.[4] Those showing coupling must be located in atoms that are close neighbors in the molecular structure. All we needed was a way to irradiate only the protons having a particular chemical shift. In 1961, a minor modification of the NMR integrator and the addition of a variable frequency audiooscillator made selective irradiation a routine matter.

By 1957 the necessary infrastructure was in place for a significant leap forward. With the aid of the R&D group, Emery Rogers and I developed a proposal to build an affordable, reliable, conveniently sized, proton-only spectrometer with high stability and sensitivity. Some of our specifications were so far from realization that meeting them seemed to require a miracle. But we believed in miracles and had faith in ourselves and our co-workers. So did Varian Associates, which funded the four-year project, code-named ASP. (That was not a symbol for a venomous attack on competitors, who were beginning to appear by then, but rather an acronym for the project schedule: As Soon as Possible.) We called the instrument the A-60, A for analytical, 60 for the frequency and our hoped-for year of release.

Our specifications called for a much smaller electromagnet styled to fit into a laboratory environment. An attractive, user-friendly console with logical groupings of controls would have a flat-bed recorder for producing the NMR spectrum, for the first time, on a precalibrated chart. The instrument was to scan the entire proton NMR spectrum and be able to reproduce

Figure 3 The A-60 spectrometer, introduced in 1961

it within the pen width on the chart. Sensitivity had to meet current standards, but the instrument still was to be simple and reliable. And all of this was to cost little more than the better IR instruments then offered.

Precalibration required locking the frequency to the magnetic field, a tough technical challenge that was solved in an ingenious way. A small sample of water in the probe near the analytical sample was irradiated at 60 MHz and modulated by an audiofrequency generated by closing a loop to create a nuclear sideband oscillator, or NSBO as it was called. The circuit would only oscillate at a frequency that placed the sideband exactly at the water resonance line frequency. The rapid response of the device lessened the demands for stability on both the power supply and the flux stabilizer.

The final test of the prototype, introduced at the 1961 Pittsburgh Conference, is a particularly happy memory. I put a sample into the instrument, adjusted the resolution, and ran a spectrum on the precalibrated chart. It was perfect. But could the A-60 reproduce a spectrum with the fingerprint quality of the IR? I moved the pen back and restarted the scan. Momentarily distracted, I looked back and saw only one line on the chart. 'Why didn't the second scan run?' I asked. The answer came back, 'It did'. Amazed, I returned the pen three more times. The five spectra were a single trace on the paper. At that instant, I knew that organic chemistry would never be the same.

We decided that if chemists became familiar with a standard format for the NMR spectrum, they would develop a feel for the interpretation. To that end, we prepared a two-volume catalog containing 700 spectra of a carefully selected variety of chemical compounds, which became the laboratory companion of thousands of organic chemists.[5] Exceptionally reliable and sturdy (see Figure 3), the A-60 became the analytical tool of choice to follow the progress of synthetic work and to analyze the structures of synthetic and natural products. NMR had come of age.

THE 1960S: DECADE OF THE TECHNOLOGICAL BREAKTHROUGHS

With the widespread demand for the A-60, Varian's instrument division grew rapidly. Emery Rogers, the new general manager of the instrument division, persuaded me to take over the marketing, which, for my five-year tenure, consisted mainly of informing chemists of the growing ability of high-resolution NMR to solve their problems.

The market for NMR spectrometers merited the establishment of an European Applab. Set up in 1962, in Zürich, Switzerland, under the direction of Warren Proctor, the new Applab acquired such an enviable reputation that scientists from all over Europe fought for places at its annual NMR workshops. An Eastern Applab was established in Pittsburgh, after Emery and I noticed on one of our trips that space was for rent in the Pittsburgh Airport Terminal Building. The location turned out to be an inspired choice. It became a stop on scientists' annual pilgrimage to the Pittsburgh Conference and, later, to the Experimental NMR Conference (the ENC) at the Mellon Institute.

In 1965, Emery Rogers and I collaborated in our last project. It began after one of the workshops in Zürich, when we were strolling the streets discussing a replacement for the A-60. Although still the best instrument of its kind, the vacuum-tube technology and electromagnet of the A-60 were becoming obsolete. We stopped in a tearoom, roughed out the concept for a permanent magnet replacement, and christened it the T-60, in honor of its origin. The T-60, introduced in 1969, became the workhorse of organic chemists. Its rugged design and reliability resulted in its widespread use in teaching and research. Many of the instruments are still operating after more than 20 years of service.

During most of the 1960s, the instruments in the Applabs changed little in terms of their power, but they did become more stable and easier to use. (In spite of my five-year sojourn in marketing, I managed to publish nearly 60 collaborative papers during the 1960s.) Increasing use was made of quantitative measurements and spin decoupling. Knowledge about spin–spin couplings, chemical shift effects, ring current effects, solvent shifts, second-order spin-coupling effects, dependence of coupling on stereochemistry, effect of chemical exchange, and other phenomena grew rapidly. Varian sponsored NMR workshops and courses in the United States and Europe on a regular basis in order to spread the new knowledge.

There was also a greatly improved product to discuss. During the 1960s, several major developments took shape in research and development. The first arose from the need for better stability in the HR-100. The field/frequency lock system of the A-60, with a separate lock sample located near the observing coil was considered, but there wasn't enough room for it in the HR-100 gap. The solution was to lock the spectrometer (using a feedback loop) on the tetramethylsilane peak, always present in the sample for reference purposes, and to generate a sideband, frequency-swept through the spectrum in a linear fashion. That internal lock was more stable over time than the external lock of the A-60 and was the forerunner of the lock systems in use today. Systems equipped with this accessory were called HA-60 or HA-100.

The second breakthrough was made possible by the commercial availability of superconducting niobium–titanium alloy wire. Varian recognized the opportunity to gain the benefits of increased field strength. Research physicist Harry Weaver designed a high-resolution solenoidal magnet wound from the new wire that, unlike most superconductors, could remain superconducting in a strong magnetic field. The

completed solenoid, based on a mathematical analysis of the flux distribution, achieved resolution comparable to iron magnets. In the persistent mode, with current circulating in the resistance-free solenoid and through a superconducting return path, the stability was exceptional.

We exhibited a spectrometer at the 1962 Pittsburgh Conference with a frequency of 220 MHz. Interest was high, but because of the cost and the difficulties and expense of using liquid helium, buyers were few. The high field gave greater spectral dispersion and more sensitivity, but the improvement was not sufficient for entirely new applications. Nevertheless, research and development went forward on a 300 MHz system based on a multifilament niobium–titanium wire, and the HR-300 was announced in 1967. Although Varian Associates pioneered superconducting magnets for NMR in the early 1960s, the full benefit of those amazing devices was not realized until the 1970s. The breakthrough had been achieved, however, and the days of the electromagnet were numbered.

In 1964, Leland Allen, then at Yale University, brought to our attention a *computer of average transients*, or CAT, being used to study minute electrical transients in biological systems. An initiating stimulus was applied n times, each time sampling the transient response voltage at a high repetition rate, storing the consecutive digitized values in a 400 channel memory, and adding each set of samples to the values already stored. The transient signal increased by the factor n, while random noise increased as the square root of n.

We derived a trigger for the scan from the reference peak in the spectrum and tried out the device in the Applab. The CAT showed the expected improvement in weak signals, and Varian commissioned the Nicolet Company to develop a commercial version, which became the C-1024 accessory. That device was the first application of digital data processing to NMR, a breakthrough that ultimately revolutionized NMR and chemistry.

The most dramatic breakthrough of the 1960s was the demonstration of an apparatus that acquired information simultaneously from all of the nuclei in the sample and obtained the spectrum through digital Fourier transformation of the data. Although Hahn reported pulsed excitation in 1950, and Lowe and Norberg reported the Fourier transform (FT) relationship between the impulse response and the spectrum in 1957, Richard Ernst was the first to combine them in an experiment in 1966. At that time Ernst was working in Wes Anderson's research and development group at Varian. Solving chemical problems in the Applab, I witnessed the milestone efforts going on across the hall. None of us realized then how much FT NMR would change chemistry and instrumentation, nor that Richard Ernst would receive the Nobel Prize in 1991 for that work.

Varian had provided an especially receptive climate for the discovery. Russell Varian planted the seeds in 1958 with a patent application for wideband excitation and Fourier analysis, but no suitable wideband source readily came to mind. Russ urged those of us involved in NMR development to try irradiating the sample with white noise, but we were so set on getting rid of noise that the merits of his idea were lost in our fixation on the more immediate goal. Wes Anderson was already developing a design for multichannel excitation and detection, but the unwieldy approach was crying out for new inspiration. Cross fertilization of ideas occurred when Richard, fresh from his doctoral work in Switzerland, joined Wes's research group. His work led to a practical way to excite a broad band of frequencies by using a pulse of rf power, followed by digitization, time-averaging of multiple pulses, and finally, Fourier transformation.

The experiment worked as predicted, reducing data acquisition time from hours to minutes, and improving sensitivity between 10- and 100-fold. In 1966, the only computers capable of handling Fourier transformation were mainframes that needed punched card or paper-tape input. Varian's accounting and management information systems provided overnight services when computer time was available. A truly useful FT NMR instrument awaited the development of a minicomputer dedicated to the spectrometer.

In 1965, the internal lock system of the HA-60 encouraged us to investigate the ^{13}C nucleus, long of interest in spite of its low abundance (about 1%) and its weak magnetic moment. (Lauterbur's early work using adiabatic rapid passage had not seemed an attractive routine method.) Scanning the ^{13}C spectrum very slowly at low rf power, we could see the multiplet structure of the ^{13}C signals due to C–H coupling in a single scan of a 10 mm sample of neat ethanol. We found that the loss in sensitivity due to further splitting by long-range CH coupling could be recovered by strong irradiation at the proton frequency and observed an Overhauser enhancement of approximately three for the carbon peaks. That work was published as a *Varian Bulletin* but was not followed up by systematic studies.

We had accomplished our objective, however: J.D. Roberts commissioned a custom ^{13}C instrument with a synthesized frequency sweep that could scan more slowly and register successive spectra perfectly for time averaging. With that instrument, he and his students laid the foundations for the widespread adoption of ^{13}C NMR by the organic chemists. Some of the instrumental concepts found their way into the design of the XL-100, a general purpose 100 MHz FT NMR intended to replace the aging HA-100.

Seeking to build on this foundation, Varian incorporated innovative technology in a spectrometer for routine ^{13}C work. We sensed that ^{13}C NMR would become popular with organic chemists only if it became easy. Needing a large sample and as high a field as practical for an instrument whose cost could not exceed the typical analytical laboratory budget, an electromagnet was chosen, operating at 20 MHz around 18.8 kG. A pulsed FT system, using a dedicated minicomputer (the Varian 620-i) and employing an internal lock based on the deuterium nuclei in the deuterated solvent was envisioned as the way to meet the sensitivity and stability requirements. Ease of operation was given a high priority in the design. That development was begun in 1969, and the CFT-20 became a mainstay in Varian's product line during the critical first half of the 1970s. Because of its advanced design, it could compete for some of the research funds in chemistry.

During the 1950s and most of the 1960s, Varian did a considerable amount of custom design to meet specific customer needs. Although high-resolution NMR finds its largest market with the organic chemist, spectrometers for studying ^{19}F, ^{31}P, ^{11}B, ^{15}N, ^{13}C, and others were developed and sold, as well as wideline instruments for studies of solids. The spin and magnetic moment of the unpaired electron led to the development of a commercial electron paramagnetic resonance (EPR) line of spectrometers. Separately sold laboratory magnets broadened the product offerings still more.

Competition had grown as companies sensed the opportunities in a burgeoning NMR market. During this same period, the business climate in the country was changing. Stock prices were influenced by analysts' expectations of earnings, and publicly owned companies like Varian found that a conservative management style was most appreciated. In addition, consolidation and diversification came into vogue in the mid-1960s. The theory being that the same sales force could sell a line of analytical products, Varian acquired in rapid succession Techtron in Australia, Wilkins-Aerograph and Cary Instruments in California, and Atlas-Werke, A.G. in Germany. Our instrument division, already spread thin with diverse NMR and EPR projects, also undertook the development of two mass spectrometers and an ESCA spectrometer.

The effect of those factors led to a shift in the allocation of research and development resources. With the deaths of Russell Varian in 1959 and Sigurd in 1961 the company had lost its two strongest champions of innovation. Thus, as the 1960s wound down, a paradoxical situation was developing. The company that had been responsible for the major breakthroughs of the decade turned its main attention to routine analytical instruments and gave only secondary attention to using its own breakthroughs to create state-of-the-art research spectrometers.

THE 1970S–THE TIME DOMAIN

The 1970s were truly the decade of the ascendancy of Fourier transformation in NMR. By the start of the decade, dedicated minicomputers able to carry out all processing and control functions had become available for use in NMR. Increases in speed and memory accompanied by plunging costs followed soon after and focused attention on the existing possibilities of digital data processing.

Although FT was invented in order to increase sensitivity, it offered other benefits that, within 10 years, made it the method of choice. Apparently incidental to the FT technique is the wideband pulsed excitation of all nuclei. Gradually, however, specialists in NMR research realized that pulsed excitation has value in its own right. After the pulse, the system is found in an excited quantum state. In the absence of external forces, it evolves under the influence of the interactions between the members of the spin system. At a later time, or with appropriate additional excitation, the system will be found in a state from which information about the interactions can be extracted. This general principle can be employed in an almost infinite variety of ways and may well be the greatest benefit of FT NMR.

Beginning with relaxation time measurements at the beginning of the 1970s, special pulse sequences proliferated for a myriad of purposes. Hahn's spin echo experiments from the early 1950s were recognized as a way to refocus chemical shifts and remove their defocusing effects. Coupled spin systems were shown to exhibit predictable redistribution of spin populations in their energy levels, leading to polarization-transfer experiments. Multiple quantum coherence, hard to visualize in vector form but a marvelously selective feature in a variety of experiments, was mathematically analyzed and applied. After Jeener's suggestions in 1971, a wide variety of two-dimensional NMR experiments were developed by Ernst, Freeman, Bax, and many others.

During the 1970s, however, such experiments could be used only by those who had programmable pulse generators, timing circuits, phase shifters, and phase detectors, and the know-how to operate such an array. In other words, time-dependent experiments were not user-friendly, so few chemists used them and the number of complex structure determinations made using the new techniques remained small. Most organic chemists had yet to accept ^{13}C NMR.

A huge task faced the instrument makers to make those powerful new experiments routine and educate the organic chemist in their application. Applying ^{13}C NMR requires a more thorough understanding of the subtleties of FT NMR than proton NMR. Relaxation behavior, spectral width, digital resolution, and quadrature detection were new concepts that had to be mastered. Furthermore, the chemical shifts of ^{13}C nuclei were not yet systematized. Assignments were particularly frustrating, since all the carbon peaks looked alike. But ^{13}C NMR added unique information that, in conjunction with the proton NMR data, could solve chemical structure problems more effectively and more elegantly.

We soon realized that the instrument for the support of organic chemists should be able to switch easily between acquiring proton or ^{13}C NMR spectra. The FT-80 evolved from the CFT-20 to meet this need and was further provided with a broadband synthesizer for multinuclear studies, a homonuclear decoupler, a microprobe accessory, and a second-generation minicomputer. Those improvements prolonged the product lifetime into the 1980s, and familiarized many chemists with the power of FT NMR.

In the Applab, during the first part of the 1970s, I was using an SC-300, a 300 MHz superconducting FT NMR spectrometer that had replaced the HR-220. I soon came to appreciate the value of the spectral dispersion and sensitivity of such a high-field strength. One unit was even pushed up to 360 MHz, providing more evidence of the advantages of higher field strength. But, because of overextended resources, the SC-300 had to be made to order by research and development engineers and technicians, which led to an unacceptable delay in delivery. Despite its excellence, the SC-300 had to be discontinued, and Varian set to work to design and engineer a replacement, the XL-200.

By 1978, when it was introduced, competing instruments were already available at 200, 250, 270, 300, 360, and 400 MHz. As far as leadership in research instruments was concerned, it was a case of too little, too late. But the XL-200 did meet the needs of the average NMR user better than its higher field competitors because of its innovative system for control and data acquisition. Two computers, one for each function, were connected by high speed data busses, and the entire operating program and work space resided on a hard disk. The software, written in PASCAL, made it possible for the operator to address the host computer directly through the keyboard. On command, the host computer would transfer the experiment parameters to a special acquisition computer that ran the experiment, averaged the data, and stored it on the disk. The XL-200, expandable and compatible with standard computer hardware, provided an ideal platform for future high-field instruments. During the late 1970s, Varian accumulated a vast body of software, which was easily transportable to new models with more powerful hardware.

Progress in FT NMR outpaced the ability of chemists to keep up. With new pulse sequences appearing in every issue

of the journals, we realized that many were just variations or specialized forms of standard sequences. The Applab tested promising sequences to define a set of 2D experiments with general applicability. Those were then included in the standard software, along with macro-commands to allow entire experiments from set-up to plotting to be performed by a few keyboard strokes. The results of this work were then communicated to the chemists by bulletins, lectures, workshops, and the chemical literature.

Two decades after the first instrument went to Baytown, Varian's R&D team and Applab represented a fraction of the talent focused on advancing the state of NMR technology. New developments in spin physics were appearing so fast that we could hardly keep up with them. A gradual shift in emphasis in research and development toward system design rather than component design took place, both in hardware and software. At the end of the 1970s, much had been learned about applying FT NMR to problems in chemistry. The time was ripe for a quantum leap in problem-solving power.

THE 1980S: NO PROBLEM IS TOO TOUGH

Even the sophisticated data system of the XL-200 could not overcome the limitations imposed by the slow speeds and small memories of the minicomputers of the 1970s. In the early 1980s, I could see the usefulness of the 2D NMR experiments but, unwilling to devote the time then required, I concentrated on using time-dependent experiments that could be done fairly easily.

To solve the problem that decoupling turned all ^{13}C signals into identical singlets, I used a pulse sequence that I had heard about that delayed acquisition for $1/(2J)$ s with the decoupler off. The precessing magnetization of the carbon is modulated differently for CH, CH_2, and CH_3 groups. With $^1J(C,H)$ = 125 Hz, an 8 ms delay gives positive CH_2 peaks, while CH and CH_3 peaks are negative. The decoupler is then turned on during acquisition. That gave the benefits of decoupling without the loss of information about the protons. We called this experiment APT, an acronym for attached proton test.

An even better experiment for that purpose soon appeared. Double quantum coherence is generated and allowed to evolve, followed by polarization transfer. Complete editing into CH, CH_2, and CH_3 subspectra can be carried out with this DEPT sequence. Spectral assignments and interpretations were greatly facilitated with this pulse sequence.

In the meantime, the XL series of spectrometers had acquired two new members, the XL-300 in 1982 and the XL-400 the following year. The computer was upgraded and disk memory greatly expanded. Now I could apply the whole range of 2D experiments to chemical structure determinations. I was amazed at how consistently we could solve the most formidable problems, even with little beginning knowledge. (By the end of the decade when I retired, I had published a career total of 160 collaborative papers.)

The VXR line of NMR spectrometers, announced in 1985, was offered at 200, 300, 400, and 500 MHz. High-speed dual microprocessors far outperformed the earlier minicomputers, allowing all the 2D experiments to be performed with much larger data arrays which made the new instruments attractive to biochemists.

However, not all chemists had the funding to purchase a research grade instrument The T-60 and FT-80 instruments were no longer cost-effective in comparison with superconducting instruments, so emphasis was given to the development of a powerful, user-friendly 200 MHz superconducting NMR spectrometer, priced to fit the organic chemist's budget. I was again involved in the design of a classic instrument. My assignment was to develop a menu-driven program that would demand no special skills to produce high quality proton and ^{13}C spectra. In August, 1986, the GEMINI-200 was announced, followed in 1987 by the GEMINI-300, and I became the Applab specialist providing on-going support for those products.

In 1987, deliveries from Oxford Instruments finally began for the 600 MHz magnets that had been announced in 1982. The VXR line of research NMR spectrometers was again upgraded in computing power and stability, and renamed UNITY. Varian had again begun to challenge the frontiers of NMR instrumentation technology.

THE 1990S AND BEYOND

The U-600 spectrometers currently in production have achieved 20-times the spectral dispersion of the original HR-30, an increase of 60 000 in sensitivity, several orders of magnitude improvement in stability, and a degree of user-friendliness that was unimaginable in the beginning. Progress in the early 1990s has accelerated although the directions have been changing. Magnetic field strength increased by a small increment (from 600 to 750 MHz) in 1993 but at a disproportionate increase in cost, suggesting that existing superconductors may be approaching a limit. Progress in spin physics has continued and inverse-detected experiments with various dimensionalities offer answers to the most formidable organic and biochemical structure problems. Pulsed field gradient experiments offer superior water suppression and a substitute for unwieldy phase cycling.

Improvement in computers continues unabated. Vastly increased speed and memory, combined with sharply falling costs, will certainly lead to new spectrometers of increased power and cost-effectiveness. Newer computers already incorporated in the spectrometers allow for much more sophisticated data-processing programs, such as linear prediction, multiparameter regression analysis, and molecular structure generation or modeling. Larger data sets can be handled quickly, giving improved resolution. The 1990s may turn out to be the decade of software.

The nature of breakthroughs precludes predicting them. One prediction can be made, however. I will not live to see the last breakthrough in NMR. Through a combination of rare opportunity and some perseverance, I have been privileged to participate in the early stages of a revolution that has succeeded beyond my wildest dreams.

REFERENCES

1. J. T. Arnold, S. S. Dharmati, and M. E. Packard, *J. Chem. Phys.*, 1951, **19**, 507.
2. F. Bloch, *Phys. Rev.*, 1954, **94**, 496.
3. *Varian Technical Information Bulletin No. 3*, 1960, 1.

4. A. L. Bloom and J. N. Shoolery, *Phys. Rev.*, 1955, **97**, 1261.
5. N. S. Bhacca, D. P. Hollis, L. F. Johnson, E. A. Pier, and J. N. Shoolery, *High Resolution NMR Spectra Catalog*, Varian Associates, Palo Alto, CA, 1962/63 (out of print).

Biographical Sketch

James N. Shoolery. *b* 1925. B.S., 1948, University of California, Berkeley, Ph.D., 1952, California Institute of Technology, Physical Chemistry. Joined Varian Associates 1952, founded the NMR Applications Laboratory and served as its Manager until 1960. Marketing Manager for the Instrument Division of Varian, 1960–1965, Applications chemist 1965–retirement, 1990. NMR Consultant 1990–present. Approx. 170 publications. Research specialties: application of NMR to organic structure elucidation, quantitation in high-resolution NMR, microsample techniques.

Shulman, Robert G.: My Years in NMR

Robert G. Shulman

Yale University, New Haven, CT, USA

As a young naval officer at the end of World War II, I was in charge of maintaining radar aboard the USS Saratoga when it served as a troop transport and then as it was readied to be atom-bombed in the Bikini test. Radar had been installed late in the ship's life so that components were distributed throughout, with one particularly troublesome power supply seven decks down from our normal activity. Given certain symptoms, I had been told when taking over the responsibility, one hurriedly descended to that lower deck, dogging and undogging hatches, reached the power supply and kicked it soundly at a particular panel. Since this invariably fixed the radar and since the ship was heading for demolition, we never stopped kicking long enough to solve the recurring problem.

Two years later as a graduate student at Columbia, my advisor Charles Townes came into the laboratory where I was doing microwave spectroscopy using a superheterodyne spectrometer that had been built by Stan Geschwind, a fellow graduate student. It had developed a problem so I was walking around the equipment kicking different panels. Professor Townes walked in and asked what I was doing. 'Fixing it.' I said. He then started a line of questioning reminiscent of my year of training in radar maintenance, but which I had not thought of applying to a research problem. As he enquired about the transmitter output, the crystal detector and the like, I realized that a direction of rational experimentation was being described which could cure the uncertainties that haunted my laboratory hours. However, as my kicking illustrated, heavy duty instrumentation was not my strength. Still the attraction of experimental spectroscopy has remained with me as an understandable reliable methodology that, if working, enabled one to determine the properties of matter. Spectroscopy offered a means to reach the goals set to me as a Columbia College freshman by Professor Charles Beckman in a conversation—'We know the laws that describe the properties of electrons in atoms', he said, 'and we know how materials look, smell and react, but the problem is to describe the properties we can observe from the basic behavior of those particles we can't see.'

Several years later I was at Bell Laboratories in 1954 when John Mays, my friend from graduate school, was building an NMR spectrometer. I was by then engaged in semiconductor research and we thought it might be interesting to study In, Ga, and As in the novel III–V intermetallic semiconductors. We prepared powdered samples, saw the resonances, measured linewidths, calculated second moments, and found that the lines were too broad to be explained by dipole–dipole interactions. We were helped then and many times afterwards by Phil Anderson who had heard of a soon to be published theory by Ruderman and Kittel that calculated the exchange effects between nuclei mediated by conduction electrons. This was analogous to the *J* coupling previously developed for molecular bonds. The calculated exchange coupling from their theory depended upon the band structure of these III–V compounds and we showed that a reasonable band structure agreed well with the NMR observation.[1] This experiment demonstrated how NMR could be useful in understanding electronic properties of semiconductors and by inference of other solids. For the next six years, with numerous young Bell Lab colleagues, I conducted NMR studies of semiconductors, superconductors, and condensed magnetic materials both paramagnetic and antiferromagnetic.

My own collaboration with John Mays continued on semiconductors until his interests turned to more chemical problems (1955). I was quite devoted to NMR investigations of solids by that time and had set up an independent NMR spectrometer with a Varian 12 in. electromagnet. I extended the semiconductor studies to Si, detecting the rather weak ^{29}Si signals and showing that relaxation times depend upon the conduction electron density. In the same issue of *Phys. Rev. Letters* (1956) that my ^{29}Si article appeared,[2] I published with Vince Jaccarino the first report of our NMR studies of magnetic solids starting with MnF_2.[3]

Since I had been able to see a variety of nuclei in semiconductors, I thought that the ^{19}F resonance in MnF_2 was a promising reporter on the paramagnetic state of MnF_2. We mounted a single crystal of MnF_2 and looked at the field satisfying the Larmor conditions without success. It wasn't until later, far downfield from the Larmor condition, that I saw the ^{19}F resonance. For the next five years I studied magnetically shifted resonances. At the time Jaccarino and I started, the literature on the effects of paramagnetic ions on nearby NMR signals was scanty. While Harden McConnell had shown that anisotropic dipolar interactions could produce the so-called 'pseudo-contact shifts', no one had seen shifts and explained them on the basis of hyperfine interactions from spins transferred to the ligand orbitals as we did in our first paper.

I was particularly interested in the chemical bonding information that these measurements could yield, and its consequences for the magnetic ordering. The shifts observed were explained in terms of bonding and antibonding molecular orbitals between Mn^{2+} and F^-. The antibonding orbital, containing the unpaired electron, had a wavefunction of the form $(\psi_{Mn} - \lambda\Psi_F)$. Orbitals of this form could be written for all the 2s and 2p atomic orbitals of six F^- ligands and all five unpaired 3d electrons of Mn^{2+}. The measurements revealed that the unpaired electrons, mainly and nominally Mn^{2+} 3d electrons, were really in antibonding molecular orbitals with a finite probability of being in F^- 2s and 2p orbitals whose coefficients λ were determined from the isotropic and anisotropic components of the ^{19}F shifts. These values were calculated by comparing the measured hyperfine interactions with those expected from a completely unpaired 2s or 2p electron.

In addition to the novel understanding of 'bonding' in previously considered 'ionic' crystals, the measured delocalization of the unpaired electron provided a quantitative basis of the 'superexchange' effect, proposed by Phil Anderson to couple nearby Mn^{2+} spins together in an antiferromagnetic. Put simply, it measured the probability of finding an unpaired spin from an Mn^{2+} neighbor in an F^- orbital. The polarity of this spin would affect the relative energies of up and down spins on a neighboring Mn^{2+} bonded to the same F^- and in this way the orientation of one $Mn^{2+}$was felt by its neighbor.

Amongst the many papers we published on antiferromagnetic solids, I only note that the cubic family of KMF_3, where M was an iron group ion, provided high symmetry sites that made NMR (and subsequent EXAFS measurements) particularly simple to interpret.[4]

Jaccarino and I succeeded in observing the ^{19}F NMR peak at ~170 MHz at 4.2 K in zero external field, in which this Larmor frequency was determined by the local field arising from hyperfine interactions with the antiferromagnetically ordered Mn^{2+} ions.[5] Finally, I measured hyperfine shifts in solution complexes of FeF_6^{3-} and of $H_2{}^{17}O$ bound to Gd^{3+}.[6,7]

Among several other studies of solids by NMR during this time, I had the pleasure of collaborating with Berndt Matthias and Shlomo Alexander on NMR studies of intermetallic superconductors such as Sc_3In and NbMo.[8] These gave Knight shifts in an unusual direction (upfield) which provoked a number of NMR studies of Berndt's exotic superconductors. Berndt was Swiss, a spiritual descendent of Paracelsus, and fascinated us all by his alchemist's power over matter.

I was invited to give a physics seminar at MIT on January 20, 1961 on magnetic materials. Before I visited my former CalTech room mate, Alex Rich, in the Biology Department, I watched John Kennedy's inspiring inaugural address on TV. Then Alex told me that some Russians had reported high concentrations of unpaired electron spins in DNA by electron spin resonance. He gave me some cotton-like threads of DNA which I took back to Bell Labs and persuaded W. M. Walsh to put them into his ESR spectrometer whereupon we saw a strong signal from unpaired electrons.[9] That started a long path of research by ESR, fluorescence, and phosphorescence which I carried on with colleagues for about five years delineating the excited electronic states of DNA, the pathways of excitation transfer and of radiation damage, all of which is another story. The NMR consequence of this interest in biomolecules was that I spoke with Bill Blumberg and Terry Eisinger at Bell Labs who had built a pulsed NMR instrument designed to measure the increased H_2O relaxation they expected to find from free radicals generated during enzymatic reactions. By that time I had shown that the unpaired spins in DNA were from ferromagnetic magnetite inclusions, and I knew that the structure of paramagnetic metal ion binding to DNA was uncertain. If bound outside to the phosphates, the binding efficiency of Mn^{2+} should have been similar to the free ion, while if bound internally, the efficiency should have been reduced from limited H_2O access. We decided to test how the effectiveness of Mn^{2+} as a relaxation agent of the H_2O protons was changed by its binding to DNA. To our surprise, the Mn^{2+} was *more* effective when bound, a phenomenon which we named 'relaxation enhancement'. We explained it on the basis of the altered correlation time between Mn^{2+} and the H_2O protons which was determined by the rotation time of the $Mn(H_2O)_6$ complex—a rotation time that would be slower when the Mn^{2+} was bound to the DNA molecule, making it more effective as a relaxer. We showed that Co^{2+} and Ni^{2+}, with very short electronic T_1 values, did not give this enhancement when bound to DNA, since the rotational time was shunted by the faster electronic relaxation. We published a note in *Nature* in 1961.[10]

That summer, Terry and I went to the Gordon Conference on NMR, where I presented these results. They were enthusiastically greeted by Mildred Cohn, amongst others, and we carefully explained to her the mechanism of relaxation enhancement. It was at that meeting that Mildred Cohn, Oleg Jardetzky, Bill Phillips, Terry Eisinger, and I decided to hold a meeting on magnetic resonance in biology which convened two years later in Boston, and which held its 30th anniversary in the summer of 1994.

I had received a Guggenheim Fellowship to study solid state physics at Oxford, UK, and had received a year's sabbatical, with partial support from Bell Laboratories. However, my interest in the early part of 1962 had shifted to biological problems and Alex Rich had introduced me to Sidney Brenner, so that I received an invitation to work with Brenner and Crick in the academic year 1961–62 in Cambridge. It was my good fortune that both Bell Laboratories and the Guggenheim Foundation welcomed this change of plans and I am grateful to their high minded policies which enabled me to switch my interests to biophysics. In Crick's laboratory, I joined fascinating bacteriophage studies showing that the genetic code was read serially with frame shifts in the triplets following deletions or insertions. My contribution to this exciting project was to demonstrate the existence of chain-terminating triplets. It was published (or buried as Francis said) several years later in a long article in the *Philosophical Transactions of the Royal Society*.[11] I didn't learn very much biochemistry of the sort that would have been helpful during the next 10 years but I did learn, through participation, the excitement of front-line biological research. At the end of my stay I had to decide whether to continue in molecular biology or whether to return to Bell Labs and pursue the magnetic resonance studies of biological molecules I had been doing. I chose to return, in part because Sidney Brenner assured me that the heroic age of molecular biology had passed and in part because physical methods that I understood for studying materials were more advanced and available at Bell Laboratories than anywhere else.

While I was in England, Terry Eisinger and Bill Blumberg extended the relaxation enhancement studies. They had several conversations with Mildred Cohn, keeping her informed of developments which she could apply to her relaxation enhancement studies of Mn^{2+} bound to proteins which she had started at that time. She acknowledged our *Nature* paper and those informative discussions when she and Jack Leigh published their first paper in *Nature* in 1962, but soon afterwards became convinced she had independently discovered relaxation enhancement.

After the 1964 Boston meeting on magnetic resonance in biological systems, my NMR studies concentrated on paramagnetic metal ion binding to biological molecules. Himan Sternlicht came to work with me and with a new Varian XL-100 we looked at the effects of paramagnetic metal ions upon the relaxation times of the ^{31}P and ^{1}H resonances of ATP. We used the r^{-6} dependence of the relaxation rate to determine the structure of the M^{2+}–ATP complexes.[12] This was the first use of dipolar interactions to determine the structure of any compound and we presented these results at the 1964 Boston meeting. We explained the method to Al Mildvan, who subsequently used it to determine distances in numerous metalloenzymes. Once again we had the private satisfaction of seeing our NMR methods applied to enzymology by the group at the University of Pennsylvania. This work occupied our NMR spectrometer until the second meeting of the International Society of Magnetic Resonance in Biology (ISMRB) in Stockholm in 1966. There I was

electrified by the 220 MHz ^{1}H NMR spectra of the small proteins RNase and lysozyme presented by Bill Phillips. Suddenly the spectra showed well-resolved lines, particularly to higher and lower fields than the central resonances, but even in the overlapping region between 1 and 7 ppm sharp resonances could be observed. My previous experience at 100 MHz had led to the conclusion, which was widely if not universally held, that there were very few sharp lines in macromolecules, so that the well-resolved spectra at 220 MHz were very surprising.

I returned to Bell Laboratories and within a week had ordered a 220 MHz spectrometer which, when it arrived in early 1967, was only the second such installation in the world. At that time, Ian Smith was finishing his postdoctoral NMR studies of nucleic acids, particularly tRNA, at 100 MHz. For 220 MHz studies, Tets Yamane purified several milligrams of alanine tRNA, which after being concentrated for the ^{1}H NMR study, unexpectedly formed crystals. We had the crystals examined by the X-ray crystallographer who said they were rather soft crystals of an organic molecule. Since no one had crystals of tRNA at that time, it was a question as to whether I should redissolve the crystals and continue our NMR studies or retain them and become a crystallographer. After some thought, I told Tets to dissolve them. The small improvement in resolution of the ^{1}H NMR spectrum of the purified tRNA[13] was very disappointing at the time and only recently have the NMR studies of nucleic acids rivaled X-ray crystallography as a source of information.

The next chapter in our tRNA studies came several years later, after we had been devoting most of our NMR time to the study of heme proteins. The heme protein study relevant to the tRNA saga came when Brian Sheard, a postdoc from Oxford, wanted to see if he could observe the exchangeable protons in Hb and Mb dissolved in H_2O rather than D_2O as was customary. He identified several histidine N−H protons which helped characterize the quaternary state of Hb.[14] Soon afterwards, in 1969, Dinshaw Patel in my lab continued the studies of Mb and Hb in H_2O and used the exchangeable protons to follow the effects of ligand binding.[15]

In the fall of 1970, David Kearns came to spend about half of his sabbatical year with me to learn NMR with the determination to study tRNA by NMR. David and I had become friendly at meetings on the excited electronic states of biomolecules. I had looked forward to his visit although I warned him that our previous NMR studies of tRNA had not been very informative. When David arrived he continued to ask about tRNA possibilities until one day, thinking of Dinshaw's and Brian Sheard's studies of heme proteins in H_2O and of the observation by Penman and Katz of the hydrogen-bonded protons in the base pairs of Watson−Crick complementary bases when dissolved in aprotic solvents, I suggested that if he dissolved the tRNA in H_2O he would very probably see well-resolved resonances from hydrogen-bonded protons at very low fields. Since Dinshaw was actively studying H-bonded protons (he had by then moved to a permanent position in another department) we asked him to help with the experiment which he readily did. The experiment succeeded very well[16] with unpurified tRNA giving low-field resonances (10−15 ppm) which subsequently were better resolved over the next six years.

Soon after returning to California, David involved his colleague Brian Reid at first because he could supply large amounts of purified tRNA which gave beautiful spectra. However, very soon Brian, like David before him, became excited by NMR acquisitions and both became excellent spectroscopists, soon well instrumented, and pursued their ways separate from me and, soon after, from each other. In these tRNA studies, we used a computer of average transients and swept the field up toward the H_2O resonance which was not suppressed. Baseline correction became a highly developed subject. Resonances were resolved, quantitated, and assigned on the basis of AT pairs intrinsically being at lower fields than GC pairs, while ring current calculations of shifts were made from model structures to aid in assignments. Secondary structures were determined and partially successful efforts were made to identify tertiary structure hydrogen bonds.

One exciting aspect was the work done by Kees Hilbers, a Dutch postdoctoral fellow. In addition to structural studies (we had by then a 300 MHz Varian), he developed the kinetics of hydrogen-bond opening and proton-exchange rates with H_2O protons. In this we had the pleasure of collaborating with Don Crothers.[17] At present, the H-bonded protons are not much better resolved than all the other protons because of powerful multidimensional NMR, and they make only a limited contribution to the structural information being sought. However, because of the unique sensitivity of their shifts to their bond strength and their direct dependence upon bond kinetics, I expect they will become more valuable in the future as NMR provides more functional information.

Although Maurice Gueron had left Bell Labs in 1967, after working with me on excited states of DNA he came several times as a summer visitor and it was on one of those visits in 1974 that his study of ^{31}P in tRNA gave information relating the ^{31}P chemical shifts to their immediate secondary structure, which also continues to be useful.[18]

My interests in the effects of paramagnetic ions upon NMR spectra continued throughout the 1960s. Gil Navon came and substituted Mn^{2+} for Zn^{2+} in carboxypeptidase which from dipole−dipole relaxation gave structural information about the active site. At the same time that we published a short paper on NMR studies of the structure of the active site of carboxypeptidase,[19] Bill Lipscomb and his colleagues published the crystal structure. Their informative structure overwhelmed our limited information and turned me, prematurely (it subsequently developed), against using NMR to determine macromolecular structure. Fifteen years later when multidimensional NMR began to compete favorably with crystallography, I had long since left for in vivo studies.

When the 220 MHz spectrometer arrived in 1967, I had started to study heme proteins with Kurt Wüthrich who was a postdoc. A brief report had been published earlier by Arthur Kowalski about a downfield-shifted proton resonance in cytochrome *c*. I recognized this as a hyperfine shifted resonance and we started to study paramagnetic complexes of Mb, Hb, and cytochrome *c*, a reasonable direction since both Wüthrich and I had backgrounds in NMR paramagnetic shifts.

Our first studies resolved and identified the resonances from protons near the iron, particularly those on and near the heme ring.[20] We measured spin densities around the heme in the paramagnetic state which Martin Karplus, Si Glarum, and I later used to delineate the π-electron wavefunction.[21] Numerous studies followed, including several in which the heme wavefunctions were used to calibrate the energy changes

of the iron–oxygen bond in the high and low affinity states. From this we showed that this bond's energy differed only negligibly in these two states compared with the differences of bonding affinity, so that the affinity differences had to be sought elsewhere in the molecule. We published this in *Science* under the provocative title 'The Absence of Heme–Heme Interactions in Hemoglobin'.[22]

At this point, we were ready to tackle the question of the cooperative oxygenation of hemoglobin. Two theories existed then, as now. One, the Monod–Wyman–Changeux theory (MWC), assigned the increased affinity as more oxygen was bound to a molecular switch to a higher affinity quaternary state. The other theory, most recently presented by Dan Koshland, linked the affinity changes to ligand binding in which the number of ligands already bound (not the quaternary structure) determined the affinity. Because identification of the quaternary state had previously only been made in crystals which cracked during a quaternary state switch, it had not been possible to switch the quaternary state and to measure the affinity while keeping the number of ligands constant. Seiji Ogawa solved that problem (in my laboratory) by separating the four subunits of Hb into α and β chains and recombining them to form the mixed valency hybrids of $(\alpha^{III}CN\ \beta^{II}O_2)_2$ and $(\alpha^{II}O_2\ \beta^{III}CN)_2$. These could be deoxygenated to form the stable half-ligated tetramers. Under these conditions, the two quaternary states were close in energy so that by changing solution conditions it was possible to switch the quaternary state while keeping the number of ligands constant.

We monitored the quaternary state in solution by ^1H NMR since we had previously identified several resonances as quaternary state markers.[23] With the quaternary state identified, we then measured ligand binding kinetics by stopped-flow with Quentin Gibson, and showed that the affinity changed from high to low when the quaternary state was switched while the number of ligands remained constant.[24] This was the experiment that established the MWC model as a true description of hemoglobin cooperativity. John Hopfield, Seiji Ogawa, and I decided that if this model were correct it should be capable of describing the varied experiments on Hb involving kinetics, equilibrium binding, NMR, crystallography, pH dependence, spin-label EPR data, the role of allosteric effectors, etc. Accordingly we reviewed the literature going back 50 years and showed that the same set of three MWC parameters could satisfactorily explain all the data. We published this long review in the *Quarterly Reviews of Biophysics*.[25] When I presented the results in a lecture, I was told by an eminent British kineticist that this would not do because in this field 'Gentlemen do not reinterpret other gentlemen's data'. This comment was, in fact, quite encouraging, showing the need for this study which assumed a consistency in Nature.

Max Perutz came to accept the MWC model at about the same time and has written many descriptions of Hb function from this viewpoint. However, it was my contention at the time (1970) and subsequently that the proof that the affinity was determined by the quaternary structure and not the number of ligands came from Ogawa's hybrid experiments. Furthermore, after our numerous experiments showing that the affinity changes were not localized to the heme, John Hopfield generalized those findings to describe a delocalization of energy as responsible for its dependence on the quaternary state, which once again indicated that the discrete localized changes that could be detected by crystallography were not responsible for the affinity differences. For a quarter of a century most of the scientific world has believed that X-ray crystallography has shown that the quaternary state is responsible for the energetic changes in affinity, but in fact this had been shown by the NMR studies. Furthermore, the NMR studies and Hopfield's theory show that the low resolution of X-ray crystallography cannot localize the bonds responsible for the energy changes.

At this time, I made a second major change in my research directions, turning from the study of macromolecules to metabolism in vivo. Looking back, both of these changes were stimulated by an attraction to the newer field and by a sense of having reached limits in the older field. In 1961, Sugano and I minimized the energy in an LCAO molecular orbital for $KNiF_3$ and obtained excellent agreement with the NMR-determined spin density, the optical, EPR, and magnetic properties of the complex.[26] The minimization done by a numerical calculation used atomic orbitals of Ni^{2+} and F^- because this ionic model obviously was a good first-order description and we were trying to calculate the perturbations from this ionic starting point. Despite the excellent agreement with all the experimental data, Arthur Freeman and Richard Watson made a similar perturbation calculation starting from a linear combination of Ni^{1+} and F^0 atomic orbitals with results that bore no relationship to the data. Since they claimed theirs was the correct perturbation treatment, the field was narrowed not to an understanding of the data but to the formulation of a numerical calculation, i.e. which set of atomic orbitals was the proper basis set—a field which Sugano pursued and resolved, but which did not inspire me to continue in the study of transition element complexes.

Similarly, 10 years later, when we showed that the energy of cooperativity in hemoglobin was diffuse, there seemed to be no way of describing the energies experimentally. The hopes that NMR and spectroscopy could evaluate the small energies of binding cooperativity and of catalysis had excited my Bell Labs group from 1962–72. We were inspired by Albert St. Gyorgi's messianic vision of quantum biology as the biology of the future, but the future was not arriving soon enough. My hopes of establishing a quantum mechanically based biochemistry were frustrated. My intellectual commitments and values were established by my years at Bell Labs studying condensed matter. The structure of solids was easily obtained by X-ray crystallography. It was not the structure but the electronic properties that presented a challenge and which explained the varied functions of solids, e.g. semiconductors, superconductors, and magnetic materials. Furthermore, our understanding of these electronic properties was advancing rapidly in the 1950s and 1960s by combined experimental and theoretical approaches.

The ability to understand the many-body problems posed by the electrons in solids provided a promising starting point for understanding biological complexities. This approach differed sharply from the more popular pathways scientists took into modern biochemistry and molecular biology which were inspired by the advances in macromolecular structure or in organic chemistry. At Bell Labs, in those times, quantum mechanical understanding of function seemed to have an unlimited future—a future that included biological functions as its greatest challenge. At the same time, the macromolecular structural information we had obtained from NMR was very

limited compared with the X-ray structures. Consequently, I welcomed the opportunity to follow metabolism in vivo in order to understand its control, since the control of in vivo fluxes seemed an achievable NMR goal. The control of in vivo fluxes represented an extreme reductionist goal, remote like a quantum explanation of biochemistry, but possibly achievable in a more immediate future. This goal has only recently been reached, as illustrated below in recent studies of glycolysis and gluconeogenesis. State-of-the-art structural determinations by NMR were achieved sooner. In accordance with my evaluation of 1974, quantum biology has progressed negligibly in this era of structural biology.

In 1974, my NMR studies of hemoglobin and tRNA were well established and becoming accepted in the biochemical community. George Robillard's NMR studies of chymotrypsin in my lab were giving information about the electron distribution in the charge relay system at the active sites of serine proteases.[27] In addition, that year I did the first EXAFS experiments on proteins at the Stanford Linear Accelerator with Peter Eisenberger. We started with rubredoxin, the simplest iron–sulfur protein and within a year had done the first studies on other iron–sulfur[28] proteins, several forms of hemoglobin and, with Gil Navon, carbonic anhydrase.[29] All of these studies still flourish 20 years later, and yet in that year, at the age of 50, I discontinued research directions which were finally flourishing after more than a decade of hard work. Why, after looking forward to the future, talking for years with my colleagues about how our work was creating a future molecular biophysics, why did I not continue moving smoothly into that future?

Partly, as I described above, I knew that the victory would be incomplete, that the dream of understanding biochemical function at a quantum mechanical level was still too far in the future. Part was that the challenge of creating a valuable role for NMR in biochemistry was satisfied. Part was that whereas we had been the largest and best equipped laboratory in the world doing NMR and spectroscopy of biochemicals, in 1974 other laboratories were overtaking us in size and equipment, since Bell Labs management, faced with divestiture, began to limit its commitment to NMR equipment. By contrast, the challenging possibility of understanding biochemical pathways in vivo seemed to be a realizable goal with existing equipment that would require a similar marshalling of my energies and intelligence. So that by changing fields I was maintaining the same inner life, where my efforts would strain in order to survive. By contrast I could have continued in NMR studies of biomolecules, although by then, in Sydney Brenner's earlier words it now was a field for 'grown-up boys'.

The early period of my in vivo NMR research started at Bell Labs and extended through my first three years at Yale, i.e. 1974–82. During this period, I used a 360 MHz vertical bore spectrometer to study cellular suspensions and perfused organs. The subsequent period of whole animal studies started in 1982 when Kevin Behar and Jan den Hollander succeeded in obtaining well-resolved ^{1}H NMR spectra from the rat brain at 360 MHz.[30] This was soon followed by the arrival of a 1.9-T 30-cm diameter horizontal magnet which facilitated animal studies and led to human studies in the third period.

These complex studies required expertise in biology, animal preparation, and in NMR physics. Fortunately, I have had a series of brilliant, helpful younger collaborators—Gil Navon, Seiji Ogawa, Kamil Ugurbil, Truman Brown, Jan den Hollander, Hoby Hetherington, Rolf Gruetter, Wei Chen, and particularly Doug Rothman, who have generously shared their knowledge and energies with me.

Several recurring themes motivated the studies during this early period. First, bioenergetics and the Mitchell hypothesis, while gaining acceptance during those years on the basis of a limited number of experiments still lacked direct support. We used ^{31}P NMR to measure the internal pH in tumor cells,[30] mitochondria,[31] yeast,[32] and *E. coli*,[33] and showed, in agreement with the hypothesis, that pH gradients were created when energized. In liver cells we were able to measure mitochondrial pH separately from the $^{31}PO_4$ resonances, cystolic pH from the fructose-6-phosphate shift, and external pH with a pH meter.[34] In mitochondrial suspensions in a divalent metal-free medium, it was possible to separate internal and external ATP peaks as well as those from Pi. These mitochondrial experiments were followed by Seiji Ogawa after I left Bell Labs. My *E. coli* experiments were continued at Yale with Bob Macnab and his student, Anna Castle. We measured all the parameters needed to evaluate the Mitchell hypothesis in its original form as applied to the antiporter coupling between the Na^+ and H^+ free energy gradients across the plasma membrane of *E. coli*. We measured the Na^+ gradient by ^{23}Na NMR and used paramagnetic shift reagents to separate internal and external Na^+ concentrations. At the same time, the pH gradient was measured by ^{31}P NMR and the membrane potential by membrane-soluble ionophores. The results showed that the Na^+–H^+ transporter maintained equilibrium between the ions over most of the range in support of Mitchell's hypothesis.[35] An interesting small electrogenic component was identified by Macnab which represented an extension of the first-order model.

While still at Bell Labs, Truman Brown and Kamil Ugurbil did the first in vivo saturation transfer experiments on the ATP = ADP + Pi reaction in *E. coli*.[36] Truman Brown then brought the saturation transfer method to Oxford to pursue the creatine kinase reaction in George Radda's laboratory, and this reaction has often been studied subsequently.

A second principal direction was the development of ^{13}C NMR and ^{1}H NMR in vivo in order to measure concentrations of metabolites. Our first ^{13}C experiments were done by Navon, Ogawa, den Hollander, Ugurbil, and Brown on suspensions of *E. coli*[37] and yeast[38] using 1-^{13}C glucose as a label. While much of the same information could have been obtained from extracts, we were motivated by two reasons to develop the in vivo method. The first, which to my knowledge has never worked, planned to take advantage of the long T_1 values of ^{13}C resonances so as to facilitate saturation-transfer measurements. The second, which has been very useful, developed label methods of measuring flux in vivo.

Sheila Cohen obtained beautiful spectra of ^{13}C fluxes from labeled alanine, ethanol, and acetate in the perfused liver,[39] as well as in suspensions of hepatocytes.[40] These spectra have been the 'Gold Standard' for me, showing the kinds of informative, resolved spectra that could be obtained in vivo. Technical advances have recently made it possible to obtain spectra of this high quality from the human brain as discussed below.

A third principal direction was the study of the control of fluxes primarily by ^{13}C NMR of labeled compounds. The ^{13}C studies by den Hollander, Brown, Ugurbil, and Sharon Campbell-Burk[41] elucidated the control of glycolysis in yeast

at phospho-fructose-kinase (PFK) which had been identified by numerous classical biochemical studies as 'the controlling enzyme'. From ^{13}C studies summarized elsewhere in these volumes, we concluded that PFK was not controlling the flux changes between different conditions but was being controlled by its substrate.[42] Ten years later we showed that glycogen synthase (GSase), the enzyme reported to control the flux of glycogen synthesis in the muscle, behaved similarly to PFK—being controlled but not controlling.[43] Both of these findings depended upon the novel measurements afforded by in vivo NMR.

Finally, in this period, Jacqueline Barton conducted a series of experiments on yeast spores for which, in the culminating paper with Jan den Hollander and John Hopfield,[44] we showed that during dormancy the ATP level was controlled at a low level (0.2 mM) and maintained there by ATP feedback control of the enzyme trehalase. This change in state came from changes at the somatic level induced by changes in the nutrient supply. In the many papers trying and failing to explain this development by changing gene expression, no attention has been paid to this simple explanation of the change from a growing state to a dormant one.

Since 1986, when we installed horizontal animal and human magnets at the Yale Medical School, I have been concentrating on muscle, liver, and brain research in humans and animals. In the muscle and liver, we have mainly studied glycogen metabolism. This approach started in 1983 when Laurel Sillerud showed that the ^{13}C resonances of glycogen were well resolved and 100% visible despite its high molecular weight.[45] Subsequently, we showed that the ^{13}C glycogen resonances in the muscle[46] and liver[47] in vivo are 100% visible and provide a sensitive, noninvasive means of measuring glycogen concentrations and rates of synthesis. Our human glycogen studies started in collaboration with Ralph De Fronzo, who expected that during a hyperglycemic–hyperinsulinemic clamp simulating postprandial conditions, most of the glucose being stored would be used to synthesize muscle glycogen. By measuring the rate of muscle glycogen synthesis with ^{13}C NMR and comparing it with the rate of glucose consumption, we showed that ~80% of the glucose was converted to muscle glycogen, the small remainder being used for energy and for liver glycogen synthesis. Comparison of the normals with noninsulin-dependent diabetes mellitus (NIDDM) patients showed similar glucose disposal in the patients, but the rate of the muscle glycogen synthesis was reduced ~50%.[48] This reduced rate was responsible for their slow glucose absorption, their major symptom. To locate the defect in the muscle glycogen synthesis pathway, we managed to resolve the ^{31}P resonance of glucose-6-phosphate (G6P) so that its concentration could be measured in vivo. Under identical clamp conditions the G6P was less concentrated in the NIDDMs, showing that the defect was before the G6P in the glucose transport/hexokinase region. The next study was made of prediabetics, children of diabetic parents who had not yet shown the disease. They were studied to test whether the reduced transporter/hexokinase activity noted in the NIDDMs had been induced or 'down regulated' by chronic hyperglycemia. The prediabetics were similar to the NIDDMs, i.e. under the same clamp conditions they had a much slower rate of glycogen synthesis and a lower concentration of G6P than their controls, showing that the transport defect was indigenous.[49]

These NIDDM studies have been complemented by experiments measuring the rate of glycogen synthesis in normals after they have performed intense glycogen-depleting exercise of a muscle.[50] These experiments have shown that immediately after intense exercise there is a rapid glycogen resynthesis and that this rate is insulin independent in contrast to the slower, insulin-dependent rate of glycogen synthesis observed as the glycogen levels approach normal. The insulin-independent rate of glycogen synthesis has clinical consequences for the control of diabetes, suggesting that intense glycogen-depleting exercise would help diabetics. These glycogen experiments illustrate how a definite result of a basic research program, i.e. the visibility of the glycogen ^{13}C NMR, can be developed to the point where in vivo NMR experiments can delineate the control of its synthesis. This allowed us to determine the nature of a serious illness and these studies suggested a means of controlling the disease.

The ^{13}C NMR studies extending over a decade revealed the control of glycolysis in yeast and of glycogen synthesis in muscle. They have finally realized my 1974 hopes that in vivo NMR studies of metabolism can conceptually advance biochemistry. This has been done in the following way. Although the first experiments measuring the flux of glycogen resynthesis after exercise were performed on the human gastrocnemius, the more detailed biochemical understanding has come from subsequent rat studies.[51] In those, Gilles Bloch showed quantitatively that the flux through glycogen synthase (GSase) was controlled by glucose-6-phosphate fed forward from the glucose transporters. The conclusion was that muscle glycogen synthesis during repletion from intense exercise was controlled by glucose transporter activity. GSase activity was regulated so as to accommodate the controlled flux, but it contributed negligibly to the flux control. This noncontrolling role for GSase, the prototypical site of flux control by covalent modifications, has widespread consequences for modern biochemistry and molecular biology where phosphorylation of an enzyme is considered definite proof of control. These studies show that while phosphorylation and flux control play a role during the control process, it is (in GSase) an indication that the flux is being controlled, not a cause of that control.

The study of brain activity has been underway in my laboratory since 1981. Kevin Behar, my first graduate student, said he wanted to do his research on in vivo NMR under my direction. When I asked what he wanted to study he said 'the brain'. From the beginning of the brain studies I have wanted to use in vivo NMR to understand the control of glucose metabolism, as we did in yeast, and to achieve the highly resolved spectra we had seen in our ^{13}C studies of microorganisms and perfused liver. These goals have been steadily approached while we have, as opportunities arose, been able to supplement them with additional goals. The major direction of using ^{13}C as an isotopic label, which we had been doing in the early Bell Labs studies, was extended in the brain to heteronuclear editing in which we followed the ^{13}C label by ^{1}H NMR through the resonances of its J-coupled protons. One of the first experiments I did at Yale compared the ^{1}H spectrum in yeast which had been fed 1-^{13}C glucose, with and without ^{13}C decoupling. This primitive experiment was brilliantly extended by Doug Rothman to the rat brain by a heteronuclear editing method which, with minor improvements, still remains 10 years later the best method for following brain glucose metabolism.[52]

We demonstrated the editing method first on the rat and measured the flow of ^{13}C from 1-^{13}C glucose to C_4 of glutamate.[53] We established a simplified robust model for converting the measured rate of glutamate turnover into the Krebs cycle rate.[54] The measured Krebs cycle flux would determine both the cerebral metabolic rates of oxygen ($CMRO_2$) and glucose (CMR glucose) during normal oxidative glycolysis. PET experiments by Fox and Raichle in 1988 suggested that during visual stimulation the value of CMR glucose increased appreciably in the visual cortex while $CMRO_2$ remained constant. If these rates were truly uncoupled, then our measurement of Krebs cycle activity would reflect $CMRO_2$ but not CMR glucose since glucose was presumably not metabolized past lactate. In response to this need, Wei Chen developed an independent method for measuring changes in CMR glucose during visual stimulation which gave values in agreement with the PET results.[55] That leaves the challenge of measuring changes in $CMRO_2$ by the glutamate turnover method in the visual cortex during photic stimulation—a study which is underway.

In several recent studies we localize the activated region by functional MRI in which, as originally proposed by Seiji Ogawa, one measures the image differences with and without stimulation.[56] He expected that differences in the H_2O resonances forming the image would appear because of changes in the concentration of the paramagnetic deoxygenated hemoglobin—a proposal which clearly goes back to his extensive studies of hemoglobin. The functional MRI method has great sensitivity and resolution in following brain activation both during sensory stimulation[56] and during more complex cognitive tasks.[57,58]

With the great promise of these imaging and spectroscopic studies of the human brain, which bring NMR to the forefront of brain research, I feel that the heroic age of in vivo NMR is reaching its conclusion, just as Sidney Brenner, 30 years ago, advised me that the heroic age of molecular biology had passed. In vivo NMR is now assured of a successful future. As such it may no longer provide the despairing challenge that drove us in the early years.

I have gone from NMR studies of a variety of solids with important electronic properties to biological molecules, to in vivo metabolism, and recently to the localization and energetics of brain function. While I cannot, like the Mongol conquerors, claim never to have slept twice in the same place, I can claim to have steadily broadened the scope of my attempts to explain Nature in atomic terms, and NMR methods have been my sword and shield.

REFERENCES

1. R. G. Shulman, J. M. Mays, and D. W. McCall, *Phys. Rev.*, 1955, **100**, 692.
2. R. G. Shulman and B. J. Wyluda, *Phys. Rev.*, 1956, **103**, 1127.
3. R. G. Shulman and V. Jaccarino, *Phys. Rev.*, 1956, **103**, 1126.
4. R. G. Shulman and K. Knox, *Phys. Rev. Lett.*, 1960, **4**, 603.
5. V. Jaccarino and R. G. Shulman, *Phys. Rev.*, 1957, **107**, 1196.
6. R. G. Shulman, *J. Chem. Phys.*, 1958, **29**, 945.
7. R. G. Shulman and B. J. Wyluda, *J. Chem. Phys.*, 1959, **30**, 335.
8. S. Alexander, E. Corenzwit, B. T. Matthias, R. G. Shulman, and B. J. Wyluda, *Phys. Rev.*, 1963, **129**, 2481.
9. W. M. Walsh, Jr., R. G. Shulman, and R. D. Heidenreich, *Nature (London)*, 1961, **192**, 1041.
10. J. Eisinger, R. G. Shulman, and W. E. Blumberg, *Nature (London)*, 1961, **192**, 963.
11. L. Barnett, S. Brenner, F. H. C. Crick, R. G. Shulman, and R. J. Watts-Tobin, *Philos. Trans. R. Soc. London*, 1967, **B252**, 487.
12. R. G. Shulman, H. Sternlicht, and B. J. Wyluda, *J. Chem. Phys.*, 1965, **43**, 3116.
13. I. C. P. Smith, R. G. Shulman, and T. Yamane, *Science*, 1968, **159**, 1360.
14. B. Sheard, T. Yamane, and R. G. Shulman, *Proc. 1st Inter-American Symp. Caracas, 1969*, eds. T. Arends, G. Bemski, and R. L. Nagel, Karger and Basel, Switzerland, 1971, p. 273.
15. D. J. Patel, L. Kampa, R. G. Shulman, T. Yamane, and M. Fujiwara, *Biochem. Biophys. Res. Commun.*, 1970, **40**, 1224.
16. D. R. Kearns, D. J. Patel, and R. G. Shulman, *Nature (London)*, 1971, **229**, 338.
17. D. M. Crothers, P. E. Cole, C. W. Hilbers, and R. G. Shulman, *J. Mol. Biol.*, 1974, **87**, 63.
18. M. Gueron and R. G. Shulman, *Proc. Natl. Acad. Sci. USA*, 1975, **72**, 3482.
19. G. Navon, R. G. Shulman, B. J. Wyluda, and T. Yamane, *Proc. Natl. Acad. Sci. USA*, 1968, **60**, 86.
20. K. Wüthrich, R. G. Shulman, and J. Peisach, *Proc. Natl. Acad. Sci. USA*, 1968, **60**, 373.
21. R. G. Shulman, S. H. Glarum, and M. Karplus, *J. Mol. Biol.*, 1971, **57**, 93.
22. R. G. Shulman, S. Ogawa, K. Wüthrich, T. Yamane, J. Peisach, and W. E. Blumberg. *Science*, 1969, **165**, 251.
23. S. Ogawa and R. G. Shulman, *J. Mol. Biol.*, 1972, **70**, 315.
24. R. Cassoly, Q. H. Gibson, S. Ogawa, and R. G. Shulman, *Biochem. Biophys. Res. Commun.*, 1971, **44**, 1015.
25. R. G. Shulman, J. J. Hopfield, and S. Ogawa, *Q. Rev. Biophys.*, 1975, **8**, 325.
26. S. Sugano and R. G. Shulman, *Phys. Rev.*, 1963, **130**, 517.
27. G. Robillard and R. G. Shulman, *J. Mol. Biol.*, 1974, **86**, 519.
28. R. G. Shulman, P. Eisenberger, and B. M. Kincaid, *Annu. Rev. Biophys. Bioeng.*, 1978, **7**, 559.
29. G. Navon, S. Ogawa, R. G. Shulman, and T. Yamane, *Proc. Natl. Acad. Sci. USA*, 1977, **74**, 87.
30. K. L. Behar, J. A. den Hollander, M. E. Stromski, T. Ogino, R. G. Shulman, O. A. C. Petroff, and J. W. Prichard, *Proc. Natl. Acad. Sci. USA*, 1983, **80**, 4945.
31. S. Ogawa, H. Rottenberg, T. R. Brown, R. G. Shulman, C. L. Castillo, and P. Glynn, *Proc. Natl. Acad. Sci. USA*, 1978, **75**, 1796.
32. J. M. Salhany, T. Yamane, R. G. Shulman, and S. Ogawa, *Proc. Natl. Acad. Sci. USA*, 1975, **72**, 4966.
33. G. Navon, S. Ogawa, R. G. Shulman, and T. Yamane, *Proc. Natl. Acad. Sci. USA*, 1977, **74**, 888.
34. S. M. Cohen, S. Ogawa, H. Rottenberg, P. Glynn, T. Yamane, T. R. Brown, R. G. Shulman, and J. R. Williamson, *Nature (London)*, 1978, **273**, 554.
35. A. M. Castle, R. M. Macnab, and R. G. Shulman, *J. Biol. Chem.*, 1986, **261**, 7797.
36. T. R. Brown, K. Ugurbil, and R. G. Shulman, *Proc. Natl. Acad. Sci. USA*, 1977, **74**, 5551.
37. K. Ugurbil, T. R. Brown, J. A. den Hollander, P. Glynn, and R. G. Shulman, *Proc. Natl. Acad. Sci. USA*, 1978, **75**, 3742.
38. R. G. Shulman, T. R. Brown, K. Ugurbil, S. Ogawa, S. M. Cohen, and J. A. den Hollander, *Science*, 1979, **205**, 160.
39. S. M. Cohen, R. G. Shulman, and A. C. McLaughlin, *Proc. Natl. Acad. Sci. USA*, 1979, **76**, 4808.
40. S. M. Cohen, S. Ogawa, and R. G. Shulman, *Proc. Natl. Acad. Sci. USA*, 1979, **76**, 1603.
41. S. L. Campbell-Burk and R. G. Shulman, *Annu. Rev. Microbiol.*, 1987, **41**, 595.

42. D. Reibstein, J. A. den Hollander, S. J. Pilkis, and R. G. Shulman, *Biochemistry*, 1986, **25**, 219.
43. G. Bloch, J. R. Chase, D. B. Meyer, M. J. Avison, G. I. Shulman, and R. G. Shulman, *Am. J. Physiol.*, 1994, **266**, E85.
44. J. K. Barton, J. A. den Hollander, J. J. Hopfield, and R. G. Shulman, *J. Bacteriol.*, 1982, **151**, 177.
45. L. O. Sillerud and R. G. Shulman, *Biochemistry*, 1983, **22**, 1087.
46. R. Taylor, T. B. Price, D. L. Rothman, R. G. Shulman, and G. I. Shulman, *Mag. Reson. Med.*, 1992, **27**, 13.
47. I. Magnusson, D. L. Rothman, L. D. Katz, R. G. Shulman, and G. I. Shulman, *J. Clin. Invest.*, 1992, **90**, 1323.
48. G. I. Shulman, D. L. Rothman, T. Jue, P. Stein, R. A. DeFronzo, and R. G. Shulman, *N. Engl. J. Med.*, 1990, **322**, 223.
49. D. L. Rothman, R. G. Shulman, and G. I. Shulman, *J. Clin. Invest.*, 1992, **89**, 1069.
50. T. B. Price, D. L. Rothman, R. Taylor, M. J. Avison, G. I. Shulman, and R. G. Shulman, *J. Appl. Physiol.*, 1994, **76**, 104.
51. G. Bloch, J. R. Chase, M. J. Avison, and R. G. Shulman, *Magn. Reson. Med.*, 1993, **30**, 347.
52. D. L. Rothman, K. L. Behar, H. P. Hetherington, and R. G. Shulman, *Proc. Natl. Acad. Sci. USA*, 1984, **81**, 6330.
53. S. M. Fitzpatrick, H. P. Hetherington, K. L. Behar, and R. G. Shulman, *J. Cereb. Blood Flow Metab.*, 1990, **10**, 170.
54. G. F. Mason, R. Gruetter, D. L. Rothman, K. L. Behar, R. G. Shulman, and E. J. Novotny, *J. Cerebral Blood Flow and Metab.*, 1995, **15**, 12.
55. W. Chen, E. J. Novotny, X.-H. Zhu, D. L. Rothman, and R. G. Shulman, *Proc. Natl. Acad. Sci. USA*, 1993, **90**, 9896.
56. A. M. Blamire, S. Ogawa, K. Ugurbil, D. Rothman, G. McCarthy, J. M. Ellermann, F. Hyder, Z. Rattner, and R. Shulman, *Proc. Natl. Acad. Sci. USA*, 1992, **89**, 11 069.
57. G. McCarthy, A. M. Blamire, A. Puce, A. C. Nobre, G. Bloch, F. Hyde, P. Goldman-Rakic, and R. G. Shulman, *Proc. Natl. Acad. Sci. USA*, 1994, **91**, 8690.
58. G. McCarthy, A. M. Blamire, D. L. Rothman, R. Gruetter, and R. G. Shulman, *Proc. Natl. Acad. Sci. USA*, 1993, **90**, 4952.

Biographical Sketch

Robert G. Shulman *b* 1924. A.B., 1943, Ph.D., 1949, Chemistry, Columbia University, USA. Postdoctoral work at Caltech. Head of biophysics research, Bell Telephone Laboratories, Professor of Molecular Biophysics, Biochemistry, and Chemistry, Yale University, 1979–present. Approx. 400 publications. Current research specialties: in vivo NMR spectroscopy and functional imaging of brain, spectroscopy of liver and muscle.

Slichter, Charles P.: Early Days of Magnetic Resonance Studies of Solids

Charles P. Slichter
University of Illinois, Urbana, IL, USA

In this article, I describe some of the work in which I took part in the early years of magnetic resonance—the time interval 1947–57.

GRADUATE SCHOOL DAYS

My undergraduate study was interrupted by World War II. With the help of my adviser, J. H. Van Vleck, I was hired by the noted Harvard chemist E. Bright Wilson, Jr. at the end of my sophomore year (1943) to work on a war project at the Woods Hole Oceanographic Institution. My duties were to design, build, operate, and repair electronic circuits.

I returned to Harvard in January 1946, and graduated at the end of the summer school. In the fall I began graduate study in physics at Harvard. That winter Professor Van Vleck stopped me in the hallway one day to suggest that I ask Professor Purcell if I could do a thesis with him studying electron spin resonance of paramagnetic salts. I did not know who Professor Purcell was, what electron spin resonance was, nor why paramagnetic salts were of interest. However, I knew Van, as everyone called him, and acted on his advice. His advice was indeed wise, and I will forever be grateful for it because happily for me Purcell agreed to take me on.

At that time Nico Bloembergen, Purcell's first student, was just finishing his thesis research. George Pake (Purcell's second student) was in the midst of his work, and I became Purcell's third student. Bob Pound, a so-called Junior Fellow at Harvard, was working on quadrupole effects in NMR right across the hall from Purcell's laboratories. In my last year, Raymond Andrew came as a Commonwealth Fund Fellow.

I was the only one working on electron spin resonance. Purcell, Pake, and Pound who had all had microwave experience gave me help in designing a microwave cavity and with other aspects of microwaves. I put together a 3-cm microwave spectrometer with a magic tee bridge using surplus microwave parts we got from the Radio Research Laboratory, Harvard's radar countermeasures laboratory. Copying at microwaves the NMR methods, I ran the bridge off-balance but with the cavity tuned to resonance to make the signal proportional to χ''.

My thesis consisted of two parts, measurements of some crystal splittings in some paramagnetic salts using a frequency-stabilized klystron, and the measurement of the electron spin–lattice relaxation time in those salts by studying the saturation of the ESR (using a pulsed magnetron to generate large microwave fields). Although both experiments were pioneering in technique, I foolishly never published the results.

One day, while examining the effect of a magnetic field on the electronic energy levels of an Fe^{3+} ion, I noted that when the electron spin Zeeman energy is about two-thirds of the zero-field crystal splitting, the electron spin $M = -\frac{1}{2}$ and $M = -\frac{3}{2}$ states cross. Reasoning that one should be able to observe the crossing with an NMR rig, which is at a much lower frequency than microwaves, I borrowed George Pake's NMR apparatus to search for this effect. Unfortunately I was unsuccessful, perhaps because the crystal splittings were much smaller than we originally expected. However this failed experiment was very important to me since, as I describe below, it later made me think of doing resonances at nonconventional frequencies and fields, such as electron spin resonances using a nuclear resonance apparatus, searching for the Overhauser effect at static fields of 30 G, measuring conduction electron spin susceptibilities by comparing them to nuclear susceptibilities, and measuring nuclear relaxation times in superconductors by cycling the static magnetic field.

My main interest has always been trying to solve important problems in physics and chemistry by resonance methods, rather than primarily to develop resonance techniques. However, I have wanted to invent new resonance methods when appropriate to solve a given scientific problem.

THE STUDY OF SOLIDS BY MAGNETIC RESONANCE

While I was a graduate student, Pake discovered the famous Pake doublet from water molecules in gypsum. Then, he and Herb Gutowsky (who was doing his Ph.D. thesis with Professor George Kistiakowsky) extended this work to a variety of hydrocarbons containing coupled pairs, triples, and quadruples of protons. They observed static splittings and line narrowing due to molecular motion in the solid state. This work, together with the work of Bloembergen, Purcell, and Pound on relaxation in liquids, led me to believe that magnetic resonance would be a powerful method for studying solids. The recent discovery of the transistor had made everyone aware that solid state physics would be an important area of physics, and the book 'Modern Theory of Solids' by Fred Seitz served to define the existence of such a field. Although I had not taken a course in solid state physics, I knew this book.

I was therefore quite excited when in my final year of graduate work (1949) I was invited to join the Physics Department of the University of Illinois, where Fred Seitz was about to go (from Carnegie Tech) with a small group to start a program in solid state physics. The chance to learn from Seitz and the group he was assembling seemed ideal. I was correct. The interaction with my colleagues at Illinois and also with Herb Gutowsky (and later Harry Drickamer) in chemistry were crucial sources of ideas for what problems to tackle.

When I got to Illinois, there was already a small group working in NMR. Erwin Hahn had just finished his Ph.D. (June 1949), studying the response of proton spins to pulses, and that summer had discovered spin echoes and had developed an explanation of how the echo arose using the Bloch equations. The year we were together prior to his departure for Stanford was truly wonderful for me. Dick Norberg and Ed McNeil were graduate students planning to work in NMR. Hahn, Norberg, and McNeil were all married, but I was 25 years old, single, living in the laboratory morning, noon, and night, and two young theorists, Sid Drell and John Blair, who were also single, became my constant companions and warm friends.

My original idea was to set up an ESR rig and to look for the signal from F-centers. There was no microwave apparatus, but

I intended to order parts to build a microwave superheterodyne. However, I then learned that Beringer and Castle at Yale, using a sensitive bolometer rig, had looked without success for an ESR signal from F-centers, and thus decided instead to start initially with NMR.

In Purcell's group, everyone was doing steady-state experiments. I had not studied Bloch's papers since I was so involved in mastering microwave methods, steady-state magnetic resonance, crystal field theory, and the concept of the famous BPP (Bloembergen, Purcell, Pound) paper. Every calculation we did was quantum mechanical. Erwin taught me the Bloch equations and the beauty and utility of the classical description (especially when considering transient effects). The transformation in my viewpoint (the necessity of understanding both classical and quantum mechanical descriptions) permeates the spirit of the second chapter of the textbook I later wrote.

I made no contribution to understanding why echoes arose. Erwin had already done that. However, when Erwin discovered that diffusion in a magnetic field gradient shortened T_2, I was stimulated to develop a rigorous theory of the effect as Erwin kindly mentions in his article in this Encyclopedia (see ***Hahn, Erwin L.: Pulsed NMR–A Personal History***). The calculation of the effect of diffusion on T_2 is given in a footnote in Erwin's famous spin echo paper. I think neither of us realized that this method would be used for studies of diffusion in liquids. If we had, perhaps we might have written a separate paper on the topic.

Dick Norberg was officially working with Professor Bartlett, but I became his unofficial advisor since Professor Bartlett was not an expert in magnetic resonance. Though Bartlett never worked on magnetic resonance, he was a theorist with enormously broad interests. Aware of Bloch's work on nuclear induction, it was Bartlett who originally suggested the field to Hahn for this thesis. Dick, enrolled in Professor Seitz's course in solid state physics, was excited by the lecture on what happened when hydrogen was adsorbed by Pd. Dick came to me to suggest studying that system by proton NMR. In the course of these studies, Dick used spin echoes to study T_1 and T_2. This was the first use of pulsed NMR to study solids.

Herb Gutowsky, who had joined the Illinois Chemistry Department in 1948 on completion of his Ph.D., had decided that NMR would be a powerful tool in chemistry. Though he had no background in electronics, he assembled a steady-state NMR rig in the Chemistry Department with the help of an electrical engineering undergraduate and embarked on a variety of NMR studies. His decision to undertake this work was an act of great insight as well as courage. Remember, there were no commercial rigs. They only came along after Herb and others proved how important NMR was for chemists.

In one of his studies, Herb observed that in solid Na metal the NMR line began to narrow at about 160 K, continuing the narrowing until 220 K. Above that temperature he could no longer measure the intrinsic linewidth since the linewidth was limited by magnet inhomogeneity. Since the melting point of Na is about 380 K, Gutowsky recognized that the narrowing arose from diffusion in the solid. Realizing that spin echoes eliminated the effects of magnet inhomogeneity on the T_2, Dick and I saw an opportunity for pulse techniques to extend the motional narrowing effects to much higher temperatures. The joint paper we published on our results was my first scientific publication.[1] Dick and my student Don Holcomb then extended these studies to ^{7}Li and ^{6}Li, as well as ^{85}Rb and ^{87}Rb.

Another important first in pulsed NMR took place in our laboratory in spite of me. Myer Bloom, a young Canadian graduate student from McGill University, had joined the group. One day he came to me to propose that it should be possible to produce spin echoes in pure quadrupole resonance. He proceeded to do a long calculation (10 or more pages as I recall) to verify the theory. Meanwhile, I developed a simple symmetry argument which convinced me echoes would not form. He asked me to check his calculations, but I realized that a simple sign error could cause his answer to be nonzero rather than zero. I suggested that he find my error. Dick Norberg (who by then was a postdoc) had built a pulsed rig running at about 30 MHz. Instead of tracking down my error, Myer and Dick (without telling me) set out to observe quadrupole echoes of Cl nuclei. One morning when I arrived at work, I found a scope photo of Myer's quadrupole echo on my desk!

MY INTRODUCTION TO CHEMISTRY

My contact with Herb was natural, since we'd known each other quite well at Harvard. But it was further enhanced by the fact that none of the theorists in the Chemistry Department at Illinois at that time did quantum mechanical calculations. Relative to them, Herb seemed to classify me as a theorist. This attitude led to an interaction which was enormously stimulating, educational, and satisfying to me.

I have already mentioned how our interaction led to my interest in the diffusion in Na. Another conversation with Herb led to the first real effort to understand the relationship of chemical shifts to chemical bonding. It arose from the discovery by Gutowsky and Hoffman[2] of the systematics of F chemical shifts as a function of the electronegativity of the atom bonded to the F. In particular, the most covalent compound, the F_2 molecule, had a paramagnetic shift of 6.3 $\times$ 10^{-4} relative to the most ionic bond in HF. These shifts were enormous compared with the shifts of protons ($\sim 3 \times 10^{-5}$). At that time, Ramsey had developed a general theory of chemical shifts, primarily because of his involvement with molecular beams, and had applied it to the hydrogen molecule. It showed that shifts arose from the orbital motion of electrons. There were two terms, labeled diamagnetic and paramagnetic by Ramsey, but he pointed out that a change in gauge changed the size of the individual terms (though not their sum). Feeling that the most important contributions came from the valence electrons of the atom containing the nucleus under study, I noted that for fluorine these were p electrons. They thus possessed orbital angular momentum which, however, was quenched by the chemical bonds. However, if the applied magnetic field partially unquenched the orbital angular momentum, a large shift should result. This mechanism was not available for s states, hence the large difference in shifts between F and H. One could easily pick out this contribution by proper choice of gauge. I enlisted Herb's student, Apollo Saika, in carrying out the detailed calculations and numerical estimates.[3]

A third interaction with Herb arose when he and his student Dave McCall discovered that both the ^{31}P and ^{19}F resonances in liquid $POCl_2F$, $POClF_2$, and CH_3OPF_3 were split into several narrow lines. By counting lines, one could see that the

splittings arose from coupling of the ^{31}P nuclear spins with the ^{19}F spins (the ^{31}P resonance in $POCl_2F$ consisted of two lines, that in $POClF_2$ consisted of three). Since these were liquids, one expected the direct dipolar coupling to be averaged to zero as in the ^{1}H resonance of water. We discussed some of the proposed explanations (rotational hindrance, second-order dipolar interaction), and found that they could be eliminated. We concluded that the spin–spin coupling must be indirect, going via a polarization of the electron system. The spectra could be understood if the coupling were proportional to $M_{ZA}M_{ZB}$, where M_{ZA} (M_{ZB}) is the component of the nuclear moment A(B) along the static field (z direction). Originally, I thought the mechanism must be via the electron orbital moments, as in chemical shifts, because the splittings in PF_3 were 10-times bigger than those in PH_3. Such a process in a liquid would give a coupling of the form $\boldsymbol{M}_A \cdot \boldsymbol{M}_B$ between nuclei A and B. At that time, Erwin was at Stanford, where he was trying to understand a mysterious modulation of the echo envelope of ^{1}H spectra in various molecules (which he had actually discovered in spectra at Illinois). We called it the 'slow beat'. He also speculated that it arose from a coupling (in this case between chemically nonequivalent ^{1}H atoms in a molecule). Gutowsky suggested that we use echoes to look for a slow beat in BrF_5 in which he and McCall had seen splittings in their steady-state spectra. My student Ed McNeil studied the spin echoes of this material and showed that it had indeed a slow beat, and that the slow beat frequency corresponded to the spin–spin splitting seen by McCall and Gutowsky.[4] Thus we knew that Erwin and we were studying the same phenomenon.

One of the chief mysteries was that in a molecule like BrF_5, in which there are two chemically shifted groups of ^{19}F nuclei, one group containing four atoms, the other a single F, the group of four split the resonance of the single F and it split the resonance of four, but there were no splittings attributable to couplings among the four. Erwin told us that he had done a calculation that showed that for two coupled spins with different chemical shifts, an interaction like $\boldsymbol{M}_A \cdot \boldsymbol{M}_B$ had the desirable feature of giving no splittings when the chemical shift difference vanished. Stimulated by this remark, I succeeded in generalizing the result for larger groups of spins, and for both steady-state and pulse experiments, thereby explaining the absence of splittings arising from couplings within a chemically shifted species.

One of the important facts discovered by McCall and Gutowsky was that we never saw splittings from nuclei whose spins were greater than $\frac{1}{2}$. We decided this must be because they had rapid spin–lattice relaxation times, which flipped their spins so rapidly that they did not maintain their orientation long enough to produce a splitting.

When we were first thinking of some indirect coupling process, I realized it must involve some sort of anisotropic polarizability since the resultant coupling must not average out over the molecular tumbling. I already understood the F chemical shifts including their anisotropy and that influenced me to think that nuclear moment–electron orbital moment coupling, taken to second order, was the most likely candidate. That would explain why the coupling in PF_3 was so much stronger than in PH_3. However, Ramsey and Purcell came up with a mechanism which gave even stronger coupling, based on interaction between the nuclear moments and the electron spin magnetic moments of electrons in bonds. I well remember my feeling of chagrin, when I learned of their mechanism, that I hadn't thought of the electron spins and that I had let Herb and Dave down. In an article on chemical shifts which I had read earlier, Ramsey had pointed out that spins would not contribute to chemical shifts. I had accepted this argument readily since I knew there was no net electron spin in our molecules. But of course, there was no net orbital magnetism either in the absence of an applied field. The question I should have asked was whether or not an applied field could induce a spin polarization. The answer is that a *nonuniform* magnetic field, such as a nucleus produces, can, whereas a uniform field from the magnet cannot.

In a similar way, rapid chemical exchange involving the OH group could explain why in CH_3CH_2OH there were splittings induced between the CH_3 and CH_2 protons, but neither show splittings from the OH. I decided to model this phenomenon by setting up a pair of Bloch equations to describe a nucleus which could precess at either of two frequencies, and that jumped randomly in time between the two frequencies. When I solved the problem, I found that I had a formula to describe how a pair of lines would broaden, turn into three lines, finally collapsing to a single line as the mean time between frequency jumps got progressively shorter. When I showed the result to Herb, he suggested that we include it in the paper we were writing on the multiplets even though we had no experimental confirmation of the equations.[5]

Subsequently, Herb and Apollo Saika and then later others of Herb's students applied the equations (and subsequent generalizations) to study chemical reaction rates in a notable series of papers.

CONDUCTION ELECTRON RESONANCE

In the fall of 1951, Al Overhauser came to the University of Illinois as a postdoc. For his Ph.D. thesis at Berkeley he had calculated the spin–lattice relaxation time, T_1, of conduction electrons in metals. During the course of his calculations, he had discovered that if one saturated the conduction electron spin resonance, the nuclear spin polarization would be increased by the ratio γ_e/γ_n where γ_e and γ_n are the electron spin and nuclear spin gyromagnetic ratios, respectively. He urged us to look for the effect.

At that time, no one had observed the conduction electron spin resonance, but his estimate of the T_1 value was so long (about 1 μs) that the actual electron spin resonance would be only about 0.06 G wide, and thus should be very intense even though only those electrons in the tail of the Fermi distributions would be permitted by the exclusion principle to take part. One might wonder then why the resonance had not already been seen from electrons in the copper walls of the microwave cavities used for studies of paramagnetic salts. Purcell had proposed an explanation when I was a graduate student. He had pointed out to me that the conduction electron ESR line would have been very broad since electrons moving with the Fermi velocity would spend such a short time within the microwave skin depth of the metal surface. At radiofrequencies, however, we were routinely studying NMR in metal powders in which the individual particles of metal were smaller than the skin depth. At this point, I remembered my unsuccessful experiment with George Pake's NMR rig to detect a level crossing on an electron spin system. Why not look for the predicted narrow ESR line with an NMR rig, thereby eliminating skin depth

problems? I wound a solenoid with end-correction windings to produce a very uniform static field, and my student Don Holcomb and I looked with a steady-state NMR apparatus. Though we investigated Cu, Ag, Al, and even a sample of Na, we had no luck. Finally we gave up. Then, one morning in the fall of 1952 a new issue of the *Physical Review* came, containing the famous article by Griswold, Kip, and Kittel reporting observation of the conduction electron resonance in Na. I rushed up to the lab. No one was there (it was lunchtime). I took the sample of Li metal whose NMR Don Holcomb and Dick Norberg were studying, put it into the coil of a transitron NMR circuit which we had built to monitor the static field strength of our magnets, put the coil into the solenoid, connected the solenoid to a Variac to sweep the field of the solenoid, and displayed the output of the transitron on an oscilloscope. Lo and behold, there was the conduction electron spin resonance of lithium metal! The signal was enormous, even at about 30 MHz (20 G), with a width of 5 G, but it was also very much broader than we'd expected.

We quickly checked Na, finding also a broad (10 G width) but strong resonance. Tom Carver and I immediately set to work on the Overhauser effect. Al had suggested several methods of detecting the nuclear polarization effects, but Tom and I felt the best approach would be a direct observation of the population enhancement of the metal nuclei by measuring the increase in intensity of the metal NMR produced by saturating the conduction electron spin resonance (CESR). That is, we proposed to do a double resonance experiment in which we monitored the effect on the NMR intensity of saturating the CESR.

We first proved that the source of the width of the CESR was spin–lattice relaxation by studying the saturation of the CESR in a static field of about 10 G. The broad line breadths meant that we needed a strong rf field (5–10 G) to saturate the CESR.

The most difficult design question was selecting the strength of the static field (H_0) at which to do the double resonance. From the NMR viewpoint, a strong H_0 was important. At 10 G, the ^{7}Li NMR is at a mere 16 kHz. At that frequency, there was no chance of seeing the normal ^{7}Li NMR, but perhaps one could detect the signal if it were enhanced 1000-fold by the Overhauser effect. On the other hand at 3 kG the NMR would be directly observable in a bulk sample, but the CESR would be at the 3 cm microwave band. I knew from my thesis that no power sources available could produce a steady-state saturation of the CESR (a pulsed magnetron would be necessary). Moreover, saturating the CESR would require sample dimensions which kept the electrons within the rf field, i.e. a sample thickness less than the microwave skin depth. Such a thin sample would then lead to a much weaker NMR signal.

We settled on a low static field. We first built an NMR rig to operate at 25 kHz. The bridge element was a brand new design we had not used before. We had no commercial power amplifiers in the 10's of MHz region needed for CESR, so we built a high-power push–pull oscillator following the 'Radio Amateurs Handbook' for the techniques needed for the 100 MHz region. We likewise had no frequency measuring equipment for the CESR oscillator, so we built a parallel wire transmission line arrangement to measure the standing wave pattern to determine the wavelength of the oscillations.

Our first efforts at 25 kHz NMR frequency were unsuccessful, so we tried working at 50 kHz. We still failed to see an NMR signal. We tried to test our apparatus by looking for the proton resonance of glycerin, still with no success. Then we built a 50 kHz preamplifier, followed by a mixer which transformed the signal to 500 kHz which we fed into a communications receiver. With this arrangement we succeeded in seeing the protons in glycerin. Changing the NMR coil (the glycerin sample was much bigger than the Li sample), Tom Carver tuned up the CESR oscillator, then turned it off to balance the NMR bridge. I was across the lab from him when I heard him shout with glee. When he had turned the CESR oscillator back on (thrown the plate voltage switch) a giant NMR line popped up on the scope. There it was—the Overhauser enhancement! Though we could not detect the unenhanced ^{7}Li NMR line at 50 kHz, we quickly checked the enhancement by comparing the enhanced ^{7}Li signal with the glycerin proton signal.[6]

From the time we learned of the success of Griswold, Kip, and Kittel (late November 1952) until our success (July 1953) about nine months had elapsed. We were elated. At the meeting of the American Physical Society, in Washington, DC in April 1953, Overhauser had first described his polarization scheme to the world in a 10 min talk. A large crowd of the most famous people in magnetic resonance were in attendance, drawn by the abstract. They were skeptical of his prediction, feeling that it somehow violated the second law of thermodynamics. Overhauser had announced that Tom and I were trying to test his prediction. Overhauser had to leave quickly after his talk and so the crowd, containing several famous scientists, descended on me to explain further. Erwin Hahn, who was watching, later told me that I got a 'Nobel grilling'! The group, however, soon lost interest in what I was trying to say and began arguing among itself. I finally walked away. The success therefore had an intense personal meaning to Al, Tom, and me.

CONDUCTION ELECTRON SPIN SUSCEPTIBILITY

One of the most important results of the Pauli exclusion principle is its effect on the predictions of the free electron theory of metals. Pauli showed that the spin susceptibility of metals was greatly reduced, as well as becoming independent of temperature rather than obeying Curie's law. One day in the fall of 1953, I encountered Dave Pines in the hallway outside my lab. He had recently come as a postdoc to work with John Bardeen. Dave's interests were many-body physics, especially electrons in solids, dating from his graduate study with David Bohm at Princeton. He was excited because he had just succeeded in calculating the many-body corrections to the Pauli susceptibility. The corrections were significant, though not large. He bemoaned the fact that there was no way of measuring the Pauli susceptibility by itself. Susceptibility measurements gave the sum of the spin and orbital contributions. Since the electron orbital contributions were large and only crudely known theoretically, one could not reliably subtract them from the measured total susceptibility.

When I was a graduate student, I had learned the Kramers–Kronig relationships. In particular, I knew that the static spin susceptibility was proportional to the area under the absorption curve with known constants of proportionality. Purcell had pointed out that relationship to me. I had used

that relationship in a term paper I wrote for the great Dutch physicist Professor C. J. Gorter, who lectured at Harvard in the summer of 1947, to estimate from the known susceptibility the expected ESR signal strength for my Ph.D. thesis. On the spot I told Dave 'I know how to do it. We will measure the area under the conduction electron spin resonance. We will not measure the area in absolute terms. Rather, we will compare the absorption area with that of the host nucleus. We can observe them both at the same frequency, in the same rig, in the same sample by simply changing the strength of the static magnetic field.' The whole experiment just popped into my mind at once—because I had been thinking of doing CESR in an NMR rig at low fields, and because with Dick Norberg and Don Holcomb I had been doing NMR in Li and Na.

I had a new student, Bob Schumacher, in my group. We immediately set to work on the experiment. I actually built a special NMR rig for the experiment, and we operated without a bridge so that we could be sure we measured absorption not dispersion. This concept arose from the method I had employed in my thesis of running a magic tee bridge with a microwave cavity at resonance, but mismatched to the waveguide. Bob completed the results for Li at room temperature. The Na CESR line was too broad at room temperature but much narrower at liquid nitrogen temperature. We did not have a liquid nitrogen dewar. It was typical of Bob that he fashioned a simple one consisting of a glass vial containing the sample which rested on a brass bar which dipped into a liquid-nitrogen-filled cavity scooped from an insulating material called florafoam. With this he measured the Pauli susceptibility of Na.[7]

SUPERCONDUCTIVITY

Shortly after we did the Overhauser effect and spin susceptibility experiments, John Bardeen gave a physics colloquium in which he described a theory of superconductivity. This theory preceded the famous Bardeen, Cooper, Schrieffer (BCS) theory. In his talk he stated that the superconducting transition involved changes which occurred for electrons whose energies were close to the Fermi energy. I did not understand his talk in any detail, but I was instantly struck by the concept of changes near the Fermi energy since I knew from all the work I have just described that these were the electrons which provided the spin–lattice relaxation for nuclei in a metal. Clearly, if electrons at the Fermi surface underwent a change, the nuclear spin–lattice time should change. As I sat there in the audience, excited about a possible experiment, I recalled that a superconductor excludes magnetic fields (this was before Type II superconductors were known). How then could one measure a nuclear relaxation time? By then, I had quit listening and was engrossed with the puzzle. One could make particles smaller than the superconducting penetration depth—but that was technically very hard. Then I thought of field cycling: start with a magnetic field, H_0, sufficiently strong to suppress the superconductivity. Turn off the field, causing the sample to go superconducting, and cooling the nuclear spins (an adiabatic demagnetization). After sitting at zero field for a time, turn the magnet back on. The sample then would become normal and one could quickly inspect the nuclear resonance. If the nuclei warmed while H_0 was zero, they would be hotter when H_0 was turned on than they were before it was turned off and the resonance amplitude would diminish. By measuring resonance amplitude versus the time in zero field, one could deduce the relaxation time in zero field. By the end of John's talk, I had an outline of what to do.

I was fortunate in having a very able new student, Chuck Hebel, who had just joined the group. He was eager to work on the experiment. We realized that we needed a nucleus with a sufficiently slow relaxation time compared with the time it would take to turn on (or off) the magnetic field, H_0. ^{207}Pb or ^{199}Hg had convenient superconducting transition temperatures, but their spin–lattice relaxation times were much too fast compared with the time to turn on or off a magnet. ^{27}Al, however, had a much longer T_1 value (about 1 s at 1 K) and a convenient critical field (98 G at 0 K), so that we could suppress the superconductivity without applying too strong a static field. Its principal difficulty was that its superconducting transition occurred at 1.172 K, a very difficult temperature to reach in those times before the discovery of He dilution refrigerators. No one in my group had ever done an experiment with liquid He before. However, my colleagues, Dillon Mapother and John Wheatley were specialists in low temperatures, so we felt confident of good help.

We chose a magnetic field for resonance of 360 G (putting the ^{27}Al resonance at 400 kHz) to minimize the size of the magnetic field we had to turn off and on. Of course, no one else was doing NMR at such low frequencies, but we felt that with the assistance of the large Boltzmann factor at 1 K, and based on our experience with protons at 50 kHz in our Overhauser effect experiment, we could do the experiment.

We considered building a solenoid for producing H_0, but when we learned that there were some thin iron sheets left over from building the giant Betatron here in Urbana, we instead chose to build a laminated iron magnet.

The field-cycling concept was based on the idea that we were doing an adiabatic demagnetization, a reversible process in the thermodynamic sense. Thus if one turned off the field, the spin temperature would drop, but if we turned the field back on without spin–lattice relaxation having occurred, we would return the spins in high field to their original spin temperature. If one switches the field too fast, this condition is violated. Of course, the big unknown was whether when the sample turned superconducting it would let the nuclear spins act reversibly. There is an extensive discussion of such issues in our *Physical Review* paper.[8]

The most difficult problem we faced was how to cool the sample. There were two alternatives: pumping on the liquid helium bath or building an adiabatic demagnetization refrigerator. The latter approach seemed too formidable given all the other difficult experimental tasks we faced. Mapother and Wheatley explained how we could construct a special pumping scheme to overcome somewhat the limitations involving the Rollin film. Chuck built a three Dewar system: the outer one contained liquid nitrogen, the second Dewar contained liquid He at 4.2 K, as well as the sample coil and leads, and a third Dewar, inside the second one, contained the sample. The system was pumped through two 1-mm constrictions to cut down the flow from Rollin film. We were able to achieve 0.94 K by this method.

Redfield and Anderson independently conceived of the same experiment. They were a bit behind us in time. They built an adiabatic demagnetization apparatus which enabled them to

get to much lower temperatures than we could, and thus were the first to obtain results for temperatures well below T_c.

We built the complete NMR rig from scratch. The full field of the magnet was 450–500 G, but we observed the resonance 'on the fly' as the magnet was turned on at the end of the demagnetization cycle as it passed through the 360 G point corresponding to the 400 kHz ^{27}Al resonant frequency. We also faced a theoretical problem. The conventional theory of spin–lattice relaxation is based on strong field quantization, but we were going to measure relaxation in zero applied field for which the eigenstates were unknown and thus there was no theory. While Chuck was building the rig, I struggled with that problem. Fortunately, I had taken a course taught by Professor C. J. Gorter in the summer of 1947 when he was a visitor at Harvard. He made the class familiar with the beautiful Dutch work on paramagnetic relaxation and how they had used spin temperature to analyze it. I had also studied for my Ph.D. thesis Van Vleck's famous paper on electron relaxation times in Ti and Cr alum in which he showed how by using the concept of spin temperature plus trace methods one could calculate a relaxation time without knowledge of the eigenstates of the system. That proved to be the key to calculate relaxation under the sole influence of a dipolar Hamiltonian. We explored the normal state relaxation time at zero field, and also the field dependence to check our general understanding, then tackled the superconductor (as I recall in the fall of 1956).

Our earliest thinking about how superconductivity would affect the relaxation rate was based on the Gorter–Casimir two-fluid model which led us to expect that only the normal fluid would relax the nuclei, so that the spin–lattice relaxation rate would get progressively longer as we went to lower and lower temperatures. We were therefore amazed when we discovered that the relaxation rate was faster in the superconducting state than in the normal state. At that time, the concept of the energy gap was in the air. In fact, Bardeen had shown in 1955 that if one assumed an energy gap one would probably get the Meissner effect. Chuck and I had seen that paper. We therefore tried just putting a density-of-states function which had a gap, with the missing states piled up at the edge of the gap, in the usual classical expression for the spin–lattice relaxation rate of nuclei in a metal. This approach had all the desired properties: an enhanced relaxation rate just below T_c, a diminished rate far below T_c (a result Reif had found for colloidal Hg).

We showed the calculation to Bardeen, who said the model looked reasonable. With the simple density of states function, however, we did not get as large an enhancement just below T_c as we had found experimentally.

At about this time, Cooper made his famous discovery of Cooper pairs (that was submitted for publication in September 1956). Then one morning in early February 1957, John Bardeen stopped me in the hallway of the Physics building. It was clear that he wanted to talk, but it seemed as though we stood there for minutes before he said 'Well, I think we've solved superconductivity'. Evidently, the previous evening he, Bob Schrieffer, and Leon Cooper had succeeded in calculating the ground-state energy and some other properties. I believe I was the first person apart from them (and perhaps John's family at breakfast) to learn of this breakthrough. John told me succinctly the essence of what they had done. Then in a day or two he gave me a draft of their first submission (received Feb. 18, 1957 at the *Physical Review*). At that time, BCS had not yet developed the equations for $T > 0$, but that work followed quickly.

John showed me their Hamiltonian and wavefunction. It was all in the language of annihilation and creation operators which I had never used. I resolved to try to calculate the spin–lattice relaxation. First, to test what I was doing, I tried to calculate the relaxation time in a normal metal by means of these operators. That was successful. I next tried the calculation with the superconducting wavefunctions. I suggested to Chuck that he do both these calculations too, so we could check each other. To our surprise, we found two terms which connected the initial and final states. We discussed these with Bob Schrieffer, thinking that we must be making a mistake. Meanwhile, he, Bardeen, and Cooper were analyzing a number of other experiments, such as ultrasonic absorption and microwave transmission. They found that all these rate processes had two terms, but they could in some cases add (e.g. NMR) and in others subtract (ultrasound) giving very different temperature dependences below T_c. They explained to us that our experiment when contrasted with the ultrasonic attenuation results of Morse and Bohm, or of Bommel, gave proof of the BCS pairing condition. This was indeed a thrill for Chuck and for me.

PHASE-COHERENT DETECTION AND PULSE SIGNAL AVERAGING

From the first studies by Dick Norberg of ^{1}H in Pd wires, we realized that there was substantial noise present which limited the precision of measurement. This problem was dealt with in steady-state experiments by the use of lock-in amplifiers and field modulation to achieve narrow frequency bandwidths. Pulse systems are necessarily broadband in order to follow the rise and fall of the echo. Clearly we needed to average the results of a number of echoes to improve signal to noise. In our first efforts, we took multiple exposure photographs of scope screens, adjusting the spot intensity so that the 'heavily repeated' values of detection were featured. However, by the time in 1952 and 1953 when Don Holcomb and Dick Norberg were studying diffusion in the alkali metals, we decided we needed an electronic method of recording echo signals on a meter, analogous to the use of lock-in amplifiers with meters or chart recorders used in steady-state resonance. Dick Norberg did some inquiries which led us to the so-called box-car circuit, which was a gated voltmeter which stored the input voltage during the gate interval on a capacitor. By adjusting the charging time constant of the capacitor, one could control the effective number of echo signals which contributed to the signal.

The use of the box-car gave us the ability to average, but it still suffered from two deficiencies. The actual echo signal consisted of a radiofrequency voltage whose envelope rose from zero up to the echo peak and then fell to zero. Superposed was a noise voltage amplified from the input of the radiofrequency amplifier. Thus, the noise consisted of radiofrequency voltages which extended across a band of frequencies determined by the amplifier gain. The noise voltage and the signal voltage were simultaneously present. Their sum was then rectified by a diode in series with a parallel resistor, R, and a capacitor, C. The RC time constant was

adjusted to allow the rectified voltage to follow the rise and fall of the echo envelope.

The first deficiency was that the diode rectification signal at low voltages was not proportional to the amplitude of the input voltage. Thus, even without noise, the output was not a faithful reproduction of the input. This defect led to spin–lattice relaxation curves which were not exponential. Don Holcomb dealt with this defect by a calibration method (output voltage versus input).

The other defect was that when the noise exceeded the signal, the presence of signal could produce either a positive output (if signal and noise were in phase) or a negative output (if signal and noise were 180° out of phase). Thus, averaging N echoes did not give N-times the signal of one echo.

Norberg, Holcomb, and I realized these defects, and that the way to overcome them was to use a phase-coherent system. Such a system was constructed by my student John Spokas for his thesis studying diffusion in Al metal by doing NMR up to 1000 K. The concept was to have a stable oscillator which ran continuously. To generate the rf pulses, we passed that signal through a gated amplifier. At the receiver diode, we inserted a reference signal of adjustable phase in series with the signal. As long as the reference voltage was kept large compared with the signal voltage, the operation was linear and noise signals were equally positive and negative. (Subsequently we went to a balanced mixer to reduce the effect of noise on the reference signal source.) By adjusting the phase of the reference signal, one could pick out NMR signals which had any desired phase with respect to the alternating magnetic field of the pulse. This basic system enabled John Spokas to record with good signal-to-noise echo signals which were only a few per cent of the peak value at temperatures close to 1000 K. John's experiment was the first pulsed NMR experiment in which signal averaging was applied to signals which were much smaller than noise.[9]

Today these systems have been greatly improved by using analog-to-digital conversion of the signals, and by recording simultaneously two channels in which the reference signals differ by 90° phase shift (quadrature detection).

CONCLUSION

Preparing this account has caused me to relive a very exciting time in the history of magnetic resonance. I have enjoyed describing how associations with my colleagues were essential in stimulating the ideas for our experiments. I have again felt the joy of working with a wonderful group of students, each so different from the others, each contributing such unique strengths to our common endeavors. To be launched into orbit by two such teachers as Van and Ed Purcell was a very special privilege. I have tried to transmit their spirit and approach to science to each of my students.

REFERENCES

1. R. E. Norberg and C. P. Slichter, *Phys. Rev.*, 1951, **83**, 1074.
2. H. S. Gutowsky and C. J. Hoffman, *J. Chem. Phys.*, 1951, **19**, 1259.
3. A. Saika and C. P. Slichter, *J. Chem. Phys.*, 1954, **22**, 26.
4. E. B. McNeil, C. P. Slichter, and H. S. Gutowsky, *Phys. Rev.*, 1951, **84**, 1245.
5. H. S. Gutowsky, D. W. McCall, and C. P. Slichter, *J. Chem. Phys.*, 1953, **21**, 279.
6. T. R. Carver and C. P. Slichter, *Phys. Rev.*, 1956, **102**, 975.
7. R. T. Schumacher and C. P. Slichter, *Phys. Rev.*, 1956, **101**, 58.
8. L. C. Hebel and C. P. Slichter, *Phys. Rev.*, 1959, **113**, 1504.
9. J. J. Spokas and C. P. Slichter, *Phys. Rev.*, 1959, **113**, 1462.

Biographical Sketch

C. P. Slichter. *b* 1924. A.B., 1946, Ph.D., Harvard, 1949 (advisor E. M. Purcell). University of Illinois at Urbana-Champaign, Center for Advanced Study, Professor of Physics and Chemistry, 1949–present. Approx. 160 publications. Author of the textbook 'Principles of Magnetic Resonance.' Research interests: Applications of NMR to problems of condensed matter physics, chemistry, and surface science.

Smith, Ian C. P.: Deuterium NMR: Reflections on its Evolution

Ian C. P. Smith

NRC Institute for Biodiagnostics, Winnipeg, Canada

In the early 1970s, when the first multinuclear MR instruments were under development, the perception of the utility of ^{2}H NMR was such that this nucleus was relegated to be the universal nucleus for field/frequency locking. This unfortunate choice in large part excluded the use of ^{2}H NMR by any but those inclined to modify their instruments themselves.

Despite this problem, the 1970s saw significant activity in the direct observation of ^{2}H. In 1976, a group of us at NRC were asked to review all applications to date. We finished the article in 1977,[1] having reviewed some 350 publications. Even so we missed a few where ^{2}H did not figure prominently in the title or key words. This literature survey demonstrated a very useful role for ^{2}H NMR in chemistry and a promising future in biochemistry.

The most dramatic contribution of ^{2}H NMR in biochemistry is undoubtedly in the field of biological membranes. These contain a considerable proportion of fatty compounds such as phospholipids and cholesterol. NMR studies of membranes by the usual ^{1}H or ^{13}C techniques appeared to be impossible due to the diversity of molecular species and the expected very large resonance widths.

Discussions with Dr. Kjeld Schaumburg, University of Copenhagen, led us to attempt the labeling of specific components of membranes with ^{2}H and to tackle the experimental difficulties associated with the expected short T_2 values, long T_1 values, and broad resonances. Our early efforts led to measurable broadline patterns[2] (Figure 1) from which the ordering of lipids within model membranes could be measured, but we knew that we were losing much signal due to our inability to sample early points in the free induction decay. Discussion with Drs. Myer Bloom and Jim Davis at the University of British Columbia led to the modification of our instrument to perform quadrupole echoes. Collaborations with the UBC group led to our incorporating ^{2}H-labeled lipids into a complex biological membrane, that of *Acholeplasma laidlawii*, and the measurement of the ordering for individual positions within the lipids.[3] Finally, by attention to probe characteristics and increased rf power, we were able to observe the 'invisible' lipids—those which gave no spectrum in conventional spectrometers below certain 'melting' temperatures (Figure 2).[4]

Developments in this area were proceeding concurrently in the laboratories of Dr. Joachim Seelig, University of Basel and Dr. Eric Oldfield, University of Illinois. Seelig specialized in both biological applications [5] and theoretical interpretations,[6] whereas Oldfield performed a wide variety of applications.[7] The University of British Columbia group collaborated with a number of laboratories on biological applications.[8,9] A variety of biological applications were ultimately performed by Dr. Anthony Watts, Oxford University.[10] Our laboratory eventually turned its efforts toward the carbohydrate head groups of lipids which are responsible for immunological recognition.[11]

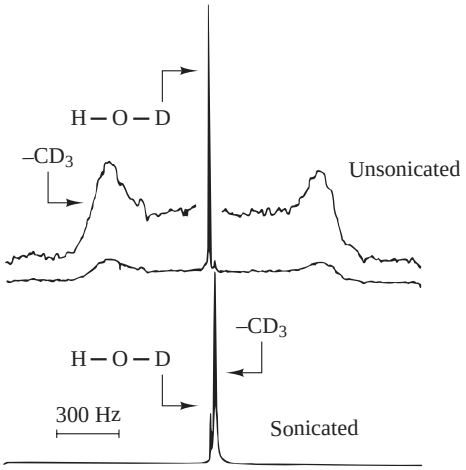

Figure 1 ^{2}H NMR spectra (15 MHz) of *N,N,N*-trimethyl-d_3-phosphatidylcholine, 32 mg ml^{-1} in aqueous dispersion at 31°C. Unsonicated, 11 000 transients; sonicated, 500 transients (reproduced from Ref. 2 with permission)

Deuterium NMR is now a fruitful and mature tool in the fields of chemistry, biochemistry, and biophysics. It has been a pleasure to be part of the group of scientists who contributed to the achievement of this success. In particular, the collaborations with Drs. M. Bloom, H. H. Mantsch, H. Saitô, K. Schaumburg, and J. Seelig are much appreciated.

REFERENCES

1. H. H. Mantsch, H. Saitô, and I. C. P. Smith, *Prog. Nucl. Magn. Reson. Spectrosc.*, 1977, **11**, 211.
2. G. W. Stockton, C. F. Polnaszek, L. C. Leitch, A. P. Tulloch, and I. C. P. Smith, *Biochem. Biophys. Res. Commun.*, 1974, **60**, 844.
3. G. W. Stockton, K. G. Johnson, K. W. Butler, A. P. Tulloch, Y. Boulanger, I. C. P. Smith, J. H. Davis, and M. Bloom, *Nature (London)*, 1977, **269**, 267.
4. I. C. P. Smith, K. W. Butler, A. P. Tulloch, J. H. Davis, and M. Bloom, *FEBS Lett.*, 1979, **100**, 57.
5. F. Borle and J. Seelig, *Biochemistry*, 1983, **22**, 5536.
6. J. Seelig, *Q. Rev. Biophys.*, 1977, **10**, 353.
7. E. Oldfield, in *Membrane and Transport*, ed. A. N. Martonosi, Plenum Press, London, 1982, Vol. 1, Chap. 15
8. M. R. Paddy, F. W. Dahlquist, J. H. Davis, and M. Bloom, *Biochemistry*, 1981, **20**, 3152.
9. A. Bienvenue, M. Bloom, J. H. Davis, and P. F. Devaux, *J. Biol. Chem.*, 1982, **257**, 3032.
10. M. Bitbol, C. Dempsey, A. Watts, and P. F. Devaux, *FEBS Lett.*, 1989, **244**, 217.
11. H. C. Jarrell, A. J. Wand, J. B. Giziewicz, and I. C. P. Smith, *Biochim. Biophys. Acta*, 1987, **897**, 69.

Biographical Sketch

Ian C. P. Smith. *b* 1939. B.Sc., 1961, M.Sc., 1962, Manitoba, Ph.D., 1965, Cambridge, (Research director, Alan Carrington), Fil. Dr. (H.C.)

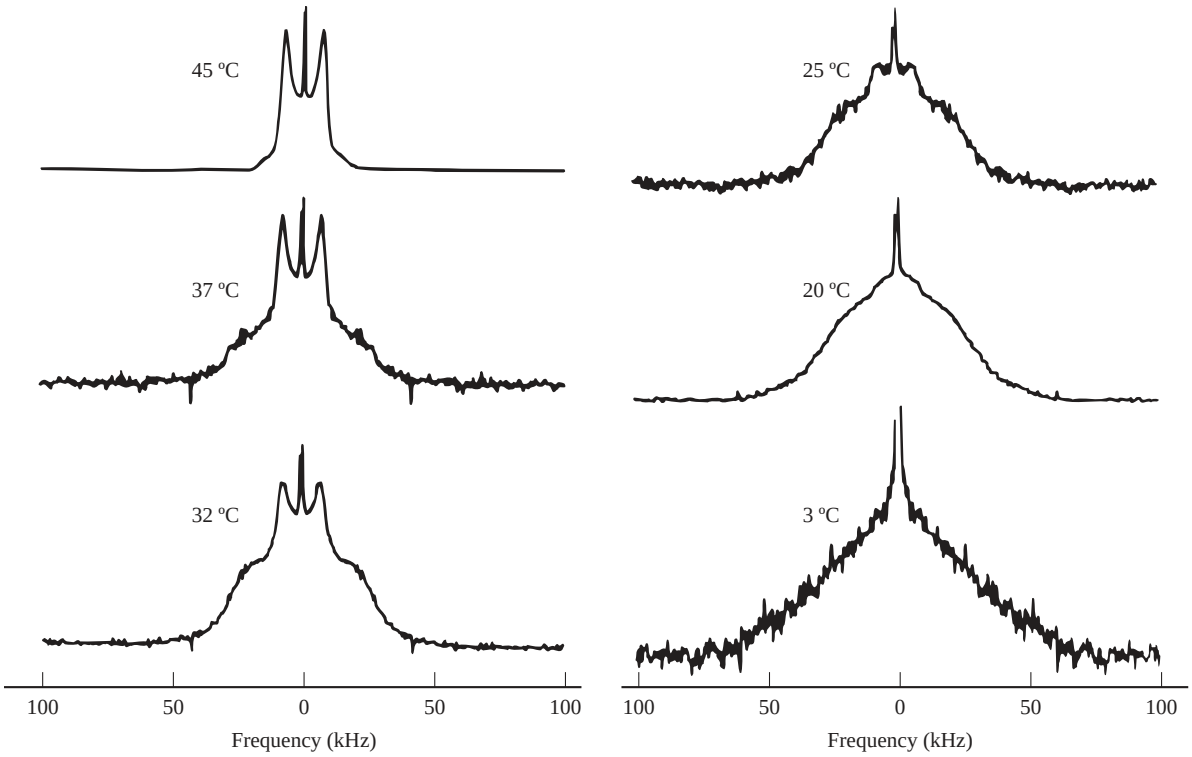

Figure 2 ^{2}H NMR spectra (34 MHz) of the 13,13-d_2-palmitoyl chains of the lipids in membranes of *Acholeplasma laidlawii* at the temperatures indicated, obtained via the quadrupole echo technique ($90^\circ_x - \tau - 90^\circ_y$–echo). The 90° pulse duration was 9 μs and τ was 60 μs. Data were obtained on resonance and the resulting half-spectra were reflected about the center frequency to produce those shown. The recycle time was 0.25 s (reproduced from Ref. 4 with permission)

1986, Stockholm, D.Sc. (H.C.) 1990, Winnipeg. Introduced to NMR by W. G. Schneider, NRC, Ottawa, 1960. Postdoctoral work with H. M. McConnell, Stanford, 1965–66 and R. G. Shulman, Bell Labs, 1966–67. Research officer, Institute for Biological Sciences, NRC, 1967–87; Director-General, 1987–91; Director-General, Institute for Biodiagnostics, NRC, 1992–present. Approximately 380 publications. Research specialty: applications of modern spectroscopic and computational methods in medicine, with emphasis on magnetic resonance spectroscopy.

Spiess, Hans Wolfgang: Multidimensional Solid State NMR of Polymers

Hans Wolfgang Spiess

Max-Planck-Institut für Polymerforschung, Mainz, Germany

INTRODUCTION

NMR of polymers is divided into two major areas. From the *chemist's* point of view, high-resolution NMR provides detailed information about the chain microstructure in solution. This field was pioneered by F. A. Bovey at Bell Labs and quickly developed into an indispensable tool of polymer chemistry. From the *materials science* point of view, many of the macroscopic properties of polymers arise from the organization of macromolecules in the bulk. Therefore, experimental techniques are needed that can characterize the behavior of polymers on a molecular level and on mesoscopic scales in order to relate such behavior to macroscopic properties such as mechanical, electrical, optical, and transport. In particular, NMR by its very nature can provide information about molecular dynamics, molecular order, phase separation, and interfacial effects by exploiting the various anisotropic spin interactions in the solid state.

Hence, besides high-resolution NMR of polymers in solution, wideline NMR of bulk polymers was developed based on the dipole–dipole interaction of protons. However, in contrast to the situation in liquids where the detailed information about chain microstructure available through high-resolution NMR is unique, solid state NMR competes with well-established techniques such as light, X-ray, or neutron scattering, electron microscopy, and dielectric or mechanical relaxation. In order to compete favorably with these techniques, the potential of solid state NMR has to be fully exploited.

The obvious advantage of NMR is its extreme selectivity, since specific chemical, motional, and orientational sites can be investigated. Thus, the advent of high-resolution NMR in solids by the use of multiple pulse irradiation, high power decoupling, and magic angle spinning (MAS) also opened up new possibilities for the NMR of polymers. As far as dynamic processes are concerned, advanced NMR techniques even offered the challenge of unraveling information inaccessible by other methods. This article describes our efforts to develop solid state NMR techniques so as to achieve this goal, and indicates how far we have progressed to date and what we think the prospects are for the future.

PULSED DEUTERON NMR: TIMESCALE OF MOLECULAR MOTIONS

In bulk polymers, *molecular dynamics* are slowed down resulting in correlation times of the order of seconds or even longer. This holds, for example, for vitrifying polymer melts when approaching the glass transition temperature T_g. Moreover, the mechanical properties of solid polymers depend mainly on slow motions with correlation times above 1 ms or so. Consequently, dynamic mechanical testing devices often work with frequencies below 1 kHz. In the early 1970s, such slow motions could not be characterized in any detail via NMR. Apart from ^{1}H NMR wideline techniques, measurements of spin–lattice relaxation in the laboratory or rotating frame were employed to detect motions with rates above 10 kHz. In principle, measurements of T_{1D}, the spin–lattice relaxation of dipolar order among the protons, could have provided a means for studying slower motions, but these lacked the selectivity to enable definite conclusions to be reached.

Why Deuteron NMR?

In the early 1970s, high-resolution ^{13}C as well as ^{1}H NMR in solids were still in their infancies and required investigators with considerable rf expertise. When I joined Hans Sillescu, who had just moved to Mainz as a full professor, we discussed setting up a laboratory for high-resolution NMR in solids using the ^{1}H multiple pulse and ^{13}C NMR techniques I had become acquainted with at the Max-Planck-Institut in Heidelberg, working with Ulrich Haeberlen in the group of Prof. K. H. Hausser. However, it was clear to us that we would not have a chance of competing with other groups, since a suitable spectrometer was not available and funds were limited. However, I was more than willing to take up his interest in deuteron (^{2}H) NMR and agreed to record ^{2}H NMR spectra by Fourier techniques despite the fact that nobody at the time knew how to do this because the Pake pattern for the $I = 1$ spin of ^{2}H is exceedingly broad in rigid solids and covers a width of about 250 kHz.

The reasoning for our decision was very simple. If FT ^{2}H NMR, which had already shown its value in studies of liquid crystals and lipids where the spectra are somewhat narrowed, could be extended to solid polymers, the selectivity needed to study synthetic polymers could be achieved by chemical means, i.e. by selective deuteration, and Hans Sillescu had already developed considerable expertise in this area.

Thus, rather than trying to incorporate methods for studying slow motions directly into sophisticated high-resolution techniques, we set out first to develop such methods independently for ^{2}H NMR. This meant that we could work with a single frequency, rather than double resonance, a few rf pulses rather than multiple pulse trains, and avoid limitations imposed by the mechanical rotation in MAS. Moreover, selected C–H bond directions are monitored in ^{2}H NMR providing well-defined indicators of polymer orientation and dynamics. If this proved successful, the means of obtaining dynamic information through ^{2}H NMR could then be incorporated into ^{13}C and ^{1}H NMR at a later stage. In fact, a similar approach was being pursued by Robert Griffin at the Francis Bitter National Magnet Laboratory (MIT) in Cambridge, MA, while developing solid state NMR methods for biophysics.

Rigid Solid Spectra

The faithful recording of FT ^{2}H NMR spectra covering the full spectral width in solids turned out to be easier

than anticipated. After unsuccessful attempts employing two frequency synthesizers (one for irradiation, the other for detection) we made use of the simple fact that 'the narrower the pulse, the broader the excitation spectrum'. Thus rather than employing a $90^\circ_y-\tau-90^\circ_x$ solid-echo sequence, we reduced the pulse width to $45^\circ_y-\tau-45^\circ_x$ at the expense of the echo signal intensity. As always, we needed a suitable model system to test the idea, namely a rigid solid for which a Pake pattern was anticipated. This turned out to be hexamethylenetetramine (HMT), which we had studied before by wideline techniques. Notably this tetrahedral molecule is an analog of adamantane, the 'drosophila' of ^{13}C NMR in solids and was also used later to test our ideas for studying slow motions.

The first FT ^{2}H NMR spectrum of HMT covering the full spectral width of 250 kHz[1] is reproduced in Figure 1(a). The advantages of Fourier spectroscopy in terms of signal-to-noise ratio were readily exploited by recording the temperature-dependent ^{2}H NMR spectra of semicrystalline polymers such as polyethylene[2] [see Figure 1(b)]. They are superpositions of a broad Pake pattern and partially narrowed lines. Thus, they nicely display the different chain mobilities in the crystalline and amorphous regions. Dietmar Hentschel, the graduate student involved, was extremely pleased that in 1 day he could now record a whole series of such spectra, which before had taken him weeks on a CW wideline spectrometer.

Solid Echoes in the Presence of Motion

The information available from pulsed ^{2}H NMR goes far beyond recording wideline spectra. To any sensible NMR spectroscopist, it is obvious that by recording the FT of the solid echo as a function of the pulse spacing τ, *transverse relaxation* can be studied. However, this did not seem to be particularly interesting, since transverse relaxation was expected to be governed by the weak and rather unspecific dipole–dipole coupling of the deuterons among themselves and with protons.

During a visit I made to his lab, Bob Griffin drew my attention to the fact that the experimental ^{2}H solid echo spectra of lipids in the gel phase deviate considerably from those expected for a rigid solid and, moreover, the lineshape depends on the pulse spacing τ. Although I could not immediately come up with an explanation, the problem of 'echo distortions' was easily solved after I returned home. I suddenly realized that Hans Sillescu had the theory for the dependence of the echo signal as a function of τ worked out already for the motional model of isotropic rotational diffusion. In fact, that problem had already been treated for the time domain in 1969 by D. Woessner et al. However, the chain motion of hydrocarbons, lipids, and polymers alike, was commonly considered as involving kinks and jogs etc., leading to an exchange of C–H bond orientations between only a limited number of sites. Thus at lunch one day I proposed to extend the well-known Anderson–Weiss treatment of spin exchange between two sites to include the formation of an echo. With the limited computational power available in the early 1980s an efficient algorithm for calculating powder lineshapes required an analytical solution. Derivation of this formula turned out to be so easy that I had it worked out the same afternoon and the paper presenting simulated lineshapes for the kink motion (or *trans/gauche* isomerization) was submitted only a week later.[3] Because this simple analytical formula is so much easier to handle numerically than the full treatment of the problem through the stochastic Liouville equation, it has been widely applied in trying to model experimental spectra. In fact, in some cases various authors have proposed simple two-site models of molecular dynamics which seems to indicate their appreciation of a simple computer program rather than a physical insight into the certainly more complex process under study.

First Applications in Polymer Science

However, it has turned out that in synthetic as well as in biopolymers at least one process exists which is often observed and involves a two-site jump when probed by ^{2}H NMR, namely the phenyl flip (rotation about 180°)[4] [Figure 1(c)]. I

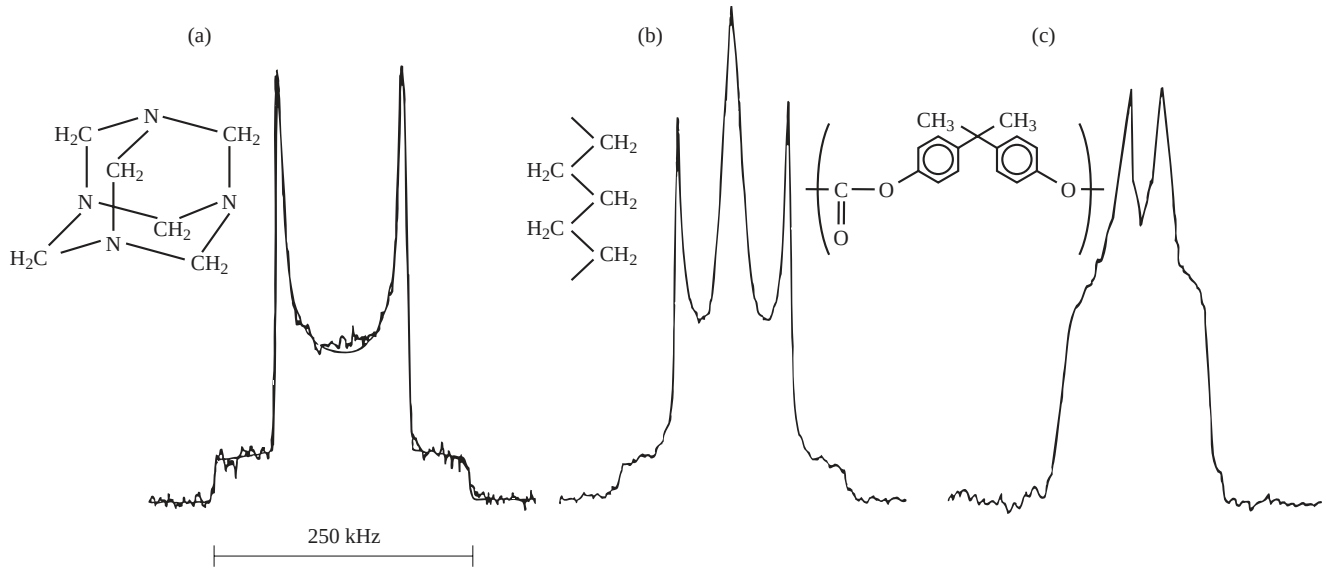

Figure 1 Examples of early FT ^{2}H NMR spectra. (a) Hexamethylenetetramine, (b) polyethylene and (c) polycarbonate

'stumbled' on this process when we started a common project with Prof. E. W. Fischer in Mainz, trying to elucidate the molecular motions responsible for the favorable mechanical properties of glassy polycarbonate, a polymer now known to virtually everyone as the material of compact discs. Fischer was highly skeptical when I first told him that we had found phenyl flips in polycarbonate and readily demonstrated to me how improbable the process would be by the use of a Stuart–Briegleb model of the repeat unit: one person had to hold the bisphenol unit of polycarbonate with two hands while another tried to crank a phenyl ring. Rather than flipping the ring, this procedure would typically break the device that mimics chemical bonds in the model. When that happened, Fischer looked at me and asked 'and you are telling me that you have observed phenyl flips'. This little story demonstrates one of the beauties of solid state NMR, i.e. results are obtained directly, without the need of an a priori knowledge about the probability of a dynamic process. In fact, Prof. Fischer's original skepticism quickly vanished. Not only did he accept our experimental observations, but I feel that this example made him appreciate the potential of solid state NMR and eventually led to the fact that we are now colleagues at the Max-Planck-Institut für Polymerforschung in Mainz, which was founded shortly thereafter.

Until then, phenyl flips had not been considered seriously as an interesting aspect of polymer dynamics. After they had been 'discovered' by ^{2}H NMR and later confirmed by ^{13}C NMR (Alan Jones, Jake Schaefer), they turned out to be ubiquitous and closely related to the mechanical behavior of polymers. In fact, most high strength polymeric materials contain phenyl rings and today the question of whether or not phenyl flips occur in such systems is routinely answered by ^{2}H NMR even in industrial laboratories. Furthermore, pulsed solid state ^{2}H NMR was quickly accepted as a powerful tool for studying chain motions and orientational effects in synthetic polymers, lipids, and even proteins. Thus, within five years or so, it developed into what is sometimes called a 'standard technique'.

Spin Alignment

Despite these successes in polymer science and in biophysics, ^{2}H solid echo spectroscopy only provides information about relatively fast motions on timescales below 1 ms or so. Again, it should have been obvious to experienced NMR spectroscopists how the time range could be extended to include longer times by applying three pulses such as Erwin Hahn's stimulated echo sequence of 90° pulses[5] or the Jeener–Broekaert sequence involving 45° pulses[6] (Figure 2). Again, I have to admit that rather than planning it, I stumbled over this possibility when adjusting the solid echo sequence with 45° pulses. Puzzling behavior was sometimes observed when changing the sequence within a second or so. Knowing how effective 45° pulses are in creating dipolar order, it

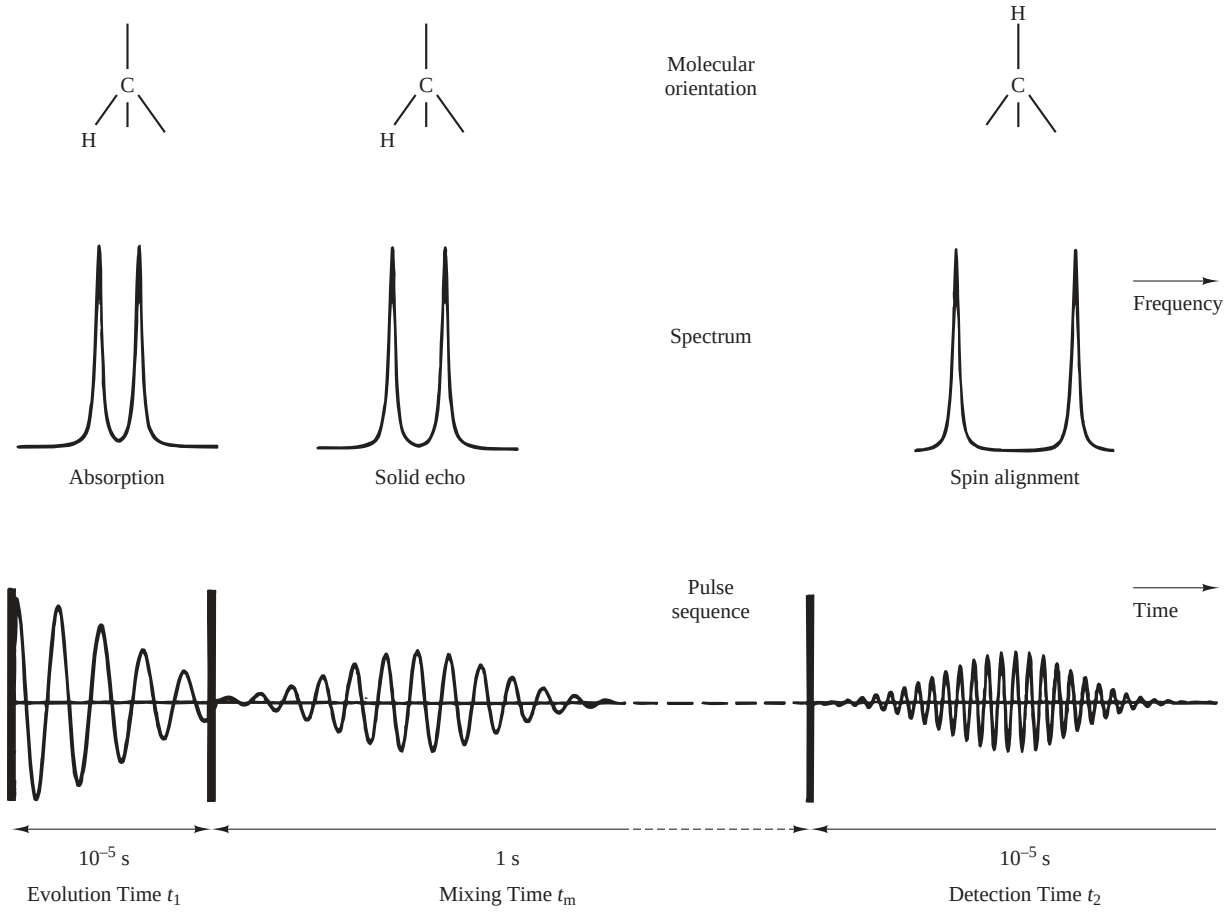

Figure 2 Elucidation of molecular dynamics by pulsed NMR. Relation of molecular orientation, ^{2}H NMR spectra, and pulse sequence

did not take long to work out the mathematics for generating 'quadrupolar order' or *spin alignment* for the spin I = 1 nucleus of ^{2}H.[7] Although in our model system, HMT, we could follow the tetrahedral motion over eight orders of magnitude, including the 'ultraslow' region with only one jump per minute, applications of the spin-alignment technique to polymers were limited because the molecular dynamics there is rather complex.

TWO-DIMENSIONAL EXCHANGE NMR: GEOMETRY OF MOLECULAR MOTIONS

The use of three-pulse sequences (Figure 2) for detecting slow dynamic processes offered the possibility of extending this technique to the *two-dimensional exchange NMR of solids*. However, it was not until I could set up my own research group at the Max-Planck-Institut für Polymerforschung that we actually attempted to record such a 2D spectrum. Again, the choice of a suitable model system was crucial. Figure 3(a) shows the ^{2}H 2D exchange spectrum of dimethyl sulfone (DMS), recorded by Claudia Schmidt as part of her Ph.D. thesis.[8] Here the ^{2}H spectrum is narrowed by the methyl rotation which also leads to a convenient spin–lattice relaxation time at room temperature. The two-fold jump motion of the molecule noted earlier by Dave Grant and co-workers manifests itself in a well-defined elliptical ridge pattern, which directly projects the angle by which the S–C bond has rotated into the 2D spectral plane. There it can be read off with a ruler. That immediately showed that 2D exchange NMR provides unique information about the *geometry* of rotational motions, independent of model assumptions.

Of course, a number of difficulties had to be overcome before a 2D spectrum of this quality was obtained. In fact, when we first recorded a 2D exchange data set of DMS, and processed it to generate a power spectrum by standard software, a pattern full of artifacts, such as t_1 ridges, etc., resulted. However, it also revealed a curved feature and we did not know of any artifact which could be responsible. We realized that a pure absorption mode spectrum was required in order to reveal faithfully the exchange spectrum. However, without knowing what to expect, it proved virtually impossible to achieve the proper phasing of the 2D data set that we subsequently recorded to this end. We thought that a theoretical calculation of the spectrum would be difficult[9] and for this reason we had never attempted to undertake this. As is often the case under such circumstances, a fresh approach was necessary. Thus, shortly after the Christmas break in 1985, I suddenly realized that I had already calculated individual slices of such a 2D exchange spectrum several years previously, when I had analyzed the ^{2}H lineshapes of partially ordered polymers based on conical distributions.[10] Within one day we had identified the curved feature mentioned above as part of the elliptical pattern and within three months Claudia Schmidt had developed the software for data processing.

Besides being highly informative, 2D exchange spectra look pretty and this turned out to be a considerable advantage either when presenting them at scientific meetings or to funding agencies. Within a few years, 2D exchange NMR of deuterons revealed detailed information about the timescale and geometry of chain motion in crystalline and amorphous polymers, both in the solid state and at the glass transition. I had the privilege of supervizing three outstanding graduate students who developed the theory for analyzing such spectra (Stefan Wefing), implementing the technique with MAS NMR (Alfred Hagemeyer), and extending it to ^{13}C NMR (Klaus Schmidt-Rohr).

EXTENSION TO HIGHER DIMENSIONS AND TO OTHER NUCLEI

An example of a 2D ^{13}C NMR spectrum of polyoxymethylene recorded by Klaus Schmidt-Rohr is displayed in Figure 3(b).[11] The exchange pattern results from the helical jump motion of the polymer in its crystalline regions. Thus, although it had taken almost a decade to establish pulsed ^{2}H NMR as a powerful tool for studying molecular dynamics, the development of two-dimensional exchange NMR techniques was not restricted to ^{2}H NMR but was quickly applied to ^{13}C NMR. In his thesis Klaus Schmidt-Rohr also extended exchange NMR to three dimensions [Figure 3(c)]. This allows one clearly to distinguish different *motional mechanisms*, because the orientation of a given unit is probed at *three* subsequent points in time. This unique technique reveals the fundamental differences between the chain motion in crystalline and amorphous polymers. He pushed the technique further to record the reduced 4D exchange NMR spectra which provided previously inaccessible information about the nature of the nonexponential relaxation of polymers above T_g.[12]

Last, but not least, Klaus Schmidt-Rohr designed a simple version of heteronuclear NMR, 2D WISE NMR, allowing separation of the ^{1}H wideline spectra for the protons attached to different carbons in the structure under study.[13] This provides dynamic information with a selectivity equivalent to or sometimes even higher than ^{2}H NMR of selectively deuterated polymers. Moreover, by exploiting spin diffusion we are now able to associate different mobilities with corresponding length scales in heterogenous polymers.

Thus, about 15 years after we started, we have now extended our experience gained in the studies of ^{2}H labeled materials into high-resolution NMR of solids, as originally planned. Since these techniques do not require isotopic labeling, they are widely applicable to academic and industrial research alike.

COMPARISON WITH OTHER METHODS OF POLYMER CHARACTERIZATION

As stated in the Introduction, the solid state NMR of polymers competes with other well-established and highly informative techniques of polymer characterization. In fact, a considerable impetus for the methodological developments described above came from the often expressed expectation that a new insight into polymer dynamics could only be obtained by neutron *scattering*. Again, a comparison of the information available from pulsed NMR with that provided by scattering techniques should have been the obvious course. However, it took a person like Franz Fujara with experience

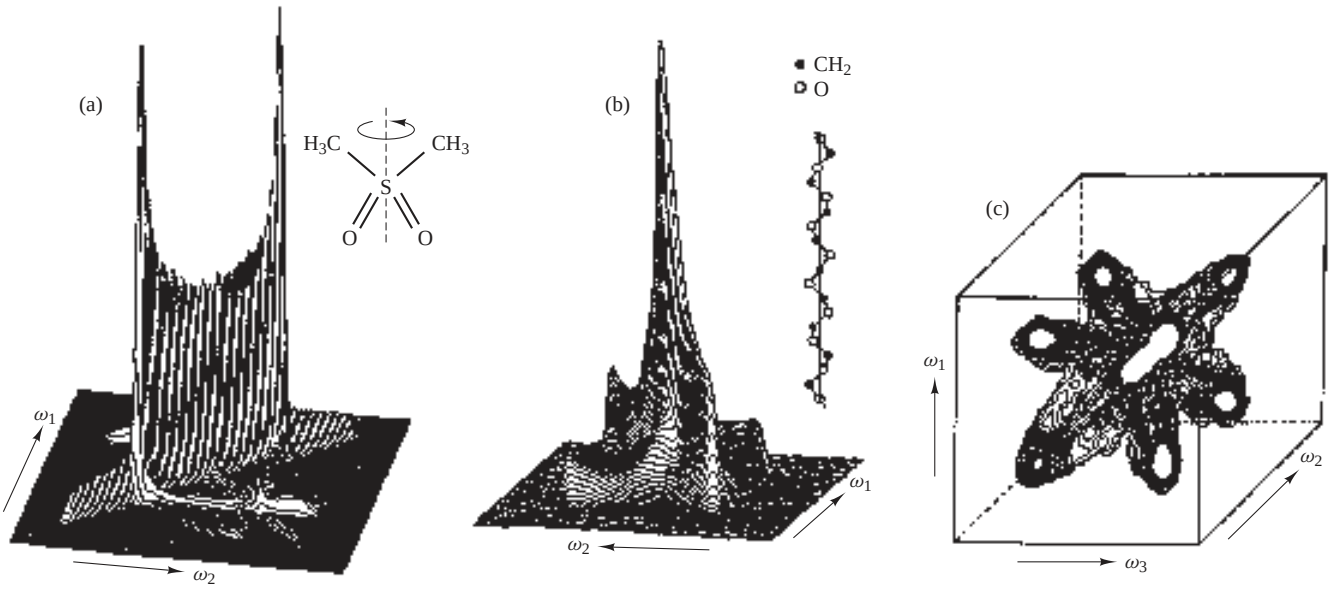

Figure 3 Examples of multidimensional exchange NMR spectra. (a) 2D ^{2}H spectrum of dimethyl sulfone; (b) 2D ^{13}C spectrum of polyoxymethylene; and (c) 3D ^{13}C spectrum of drawn polyoxymethylene

in both fields to realize the subtle analogy between three-pulse (spin alignment) experiments and incoherent neutron scattering.[14]

The analogy between NMR and scattering is far more general than first thought. It is based on the fact that plane waves contain *two* Fourier pairs, viz, time/frequency and position/momentum. Thus two-dimensional NMR exploiting angular-dependent frequencies provides information in orientational space which is completely analogous to that available in reciprocal space through scattering. This has recently been pointed out concerning the determination of orientational distribution functions by 2D NMR relative to the pole-figure analysis in wide-angle X-ray scattering,[15] see Figure 4, and is alluded to in detail in a monograph.[16] While structural determination by scattering is largely restricted to crystalline materials, multidimensional NMR also provides detailed information about chain order in amorphous polymers. Hence, it is applicable to a considerable variety of systems including liquid crystalline polymers from laboratories or from industrial process lines.

As far as electron microscopy is concerned, NMR cannot provide highly resolved images of polymer morphology capable of competing with that technique. Nevertheless, high-resolution NMR in solids now offers a means of monitoring spin diffusion in considerable detail and the accurate determination of domain sizes in heterogeneous polymers.[17] In fact, NMR can provide quantitative information about nanoheterogeneities, due to concentration fluctuations on length scales of a few nm which are difficult to ascertain by X-ray scattering and electron microscopy. In addition, interfacial regions at internal surfaces can be characterized. Most importantly, NMR not only yields information about domain sizes and diameters of interfaces, but also provides detailed information about the motional behavior in the various phases.

The timescale over which NMR provides detailed information about molecular dynamics has been extended by introducing multidimensional techniques to cover about 14 orders of magnitude, from 10^{-12} s to 100 s. Thus molecular processes responsible for dielectric or mechanical *relaxation* phenomena can now be directly identified.

SUMMARY AND OUTLOOK

In order to compete favorably with established techniques of bulk polymer characterization, solid state NMR has to provide unique information inaccessible by other methods. The development of multidimensional solid state NMR has certainly achieved this goal in so far as molecular dynamics are concerned. It yields high order correlation functions which provide stringent tests for theoretical models of dynamic processes in viscous systems. In particular, multidimensional solid state NMR delivers information about molecular dynamics which is direct and free of model assumptions. Thus it is not necessary to wait for theory to

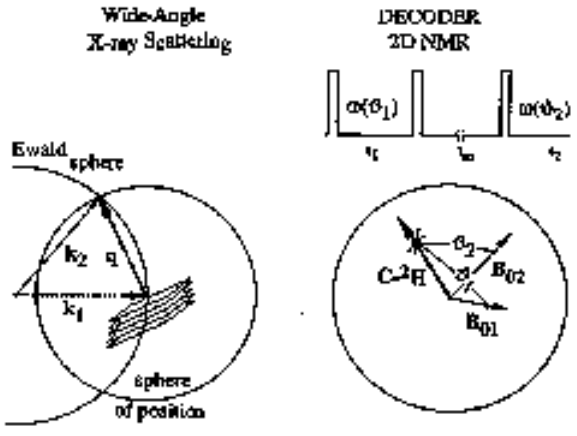

Figure 4 Analogy between wide-angle X-ray scattering and 2D exchange NMR

provide a model that can be tested experimentally, but instead it is possible to provide experimental data that can act as a challenge to theory or molecular modeling by computer simulation.

As far as polymer structure is concerned, multidimensional NMR provides information which supplements that accessible from scattering or microscopic techniques. In fact, after lectures on multidimensional solid state, NMR, I am sometimes asked: 'Are there any problems that cannot be tackled by NMR?' Of course, there are many, but we are working on them. For example, methods are being developed to probe the extent to which rotations of adjacent groups in the solid are *correlated*. Eventually one would like to obtain the information about molecular structure and dynamics accessible by solid state NMR not only for the sample as a whole but *spatially* resolved. One would like to distinguish the molecular parameters in regions close to the surface from those in the bulk. For this reason, together with Bernhard Blümich, we have set out to record spatially resolved solid state NMR spectra of polymers, employing imaging methods. As a first example, a spatially resolved ^{13}C NMR spectrum of a drawn polypropylene sample[18] is shown in Figure 5. It reflects differences in density and chain alignment between skin and core due to the processing and demonstrates that spectroscopic NMR imaging of solids is indeed possible.

Looking back to the 1970s, solid state NMR of polymers has come a long way. A wealth of information about polymer structure and dynamics is now available through advanced multidimensional techniques. Important correlations between macroscopic and molecular behavior are emerging from such studies. Examples are helical jumps or defect diffusion in crystallites, specific local motions in amorphous polymers, and conformational transitions coupled to relaxations of larger chain units in highly viscous polymer melts. Indeed, the results available to date have provided the basis for an extended monograph on the subject.[16] Such information has already been used successfully in the design of polymers with improved properties. Thus it can be anticipated that the importance of multidimensional solid state NMR in materials science and in biophysics will increase substantially in the future.

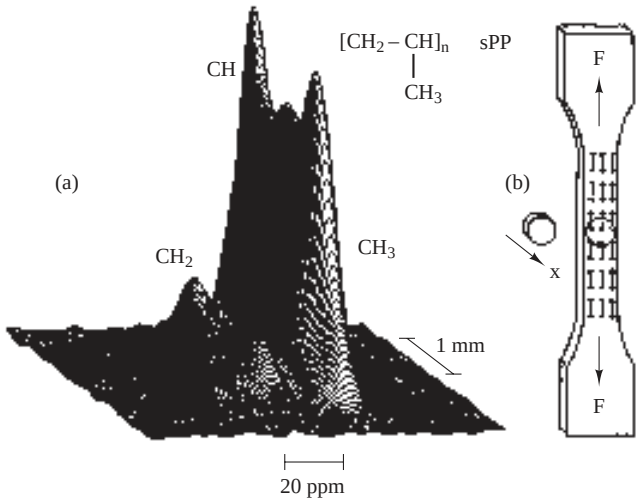

Figure 5 (a) Spatially resolved ^{13}C spectrum of drawn polypropylene; (b) geometry of sample

This article has tried to tell the story of our efforts in the development of multidimensional NMR as a new tool for polymer characterization. It is obvious that a whole research group has been involved and not just a single person. Moreover, other groups have made substantial contributions to the field but are not included here. As far as my own role is concerned, it was that of an active group member in the beginning, where I was actually doing experiments and calculations myself. My role has shifted into supervising my group and sometimes only trying to understand what my coworkers have done. Thus it is my pleasure to thank all my colleagues who have been involved in an endeavor which has sometimes been frustrating but more often stimulating and a lot of fun.

REFERENCES

1. R. Hentschel and H. W. Spiess, *J. Magn. Reson.*, 1979, **35**, 157.
2. D. Hentschel, H. Sillescu, and H. W. Spiess, *Macromolecules*, 1981, **14**, 1605.
3. H. W. Spiess and H. Sillescu, *J. Magn. Reson.*, 1981, **42**, 381.
4. H. W. Spiess, *Colloid Polym. Sci.*, 1983, **261**, 193.
5. E. L. Hahn, *Phys. Rev.*, 1950, **80**, 580.
6. J. Jeener and P. Broekaert, *Phys. Rev.*, 1967, **157**, 232.
7. H. W. Spiess, *J. Chem. Phys.*, 1980, **72**, 6755.
8. C. Schmidt, S. Wefing, B. Blümich, and H. W. Spiess, *Chem. Phys. Lett.*, 1986, **130**, 84.
9. M. Linder, A. Höhener, and R. R. Ernst, *J. Chem. Phys.*, 1980 **73**, 4959.
10. H. W. Spiess, in *Developments in Oriented Polymers-1*, ed. I. M. Ward, Applied Science, London, 1982, Chap. 2
11. A. Hagemeyer, K. Schmidt-Rohr, and H. W. Spiess, *Adv. Magn. Reson.*, 1989, **13**, 85.
12. K. Schmidt-Rohr and H. W. Spiess, *Phys. Rev. Lett.*, 1991, **66**, 3020.
13. K. Schmidt-Rohr, J. Clauss, and H. W. Spiess, *Macromolecules*, 1992, **25**, 3273.
14. F. Fujara, S. Wefing, and H. W. Spiess, *J. Chem. Phys.*, 1986, **84**, 4579.
15. K. Schmidt-Rohr, M. Hehn, D. Schaefer, and H. W. Spiess, *J. Chem. Phys.*, 1992, **97**, 2247.
16. K. Schmidt-Rohr and H. W. Spiess, *Multidimensional Solid-State NMR and Polymers*, Academic Press, London, 1994.
17. J. Clauss, K. Schmidt-Rohr, and H. W. Spiess, *Acta Polym.*, 1993, **44**, 1.
18. E. Günther, B. Blümich, and H. W. Spiess, *Macromolecules*, 1992, **25**, 3315.

Biographical Sketch

Hans Wolfgang Spiess. *b* 1942. Ph.D. 1968, Physical Chemistry, University of Frankfurt, Germany. Research associate, Florida State University, 1968–70; Max-Planck-Institute, Heidelberg with K. H. Hausser, 1970–75; University of Mainz, 1975–78. Professor at University of Mainz, 1978–80, University of Münster, 1981–82, University of Bayreuth, 1983–84. Director, Max-Planck-Institut for Polymer Research, Mainz since 1984. Approx. 250 publications. Current research interests: solid state NMR and its applications in polymer science.

Stejskal, Edward O.: Reminiscences about the Development of Pulsed Field Gradient, Spin-Echo NMR (PFGSE NMR)

Edward O. Stejskal

North Carolina State University, Raleigh, NC, USA

John Tanner joined my research group in the Department of Chemistry at the University of Wisconsin, Madison at the beginning of 1962. Shortly before that time he had been working at a small technology-based company on the outskirts of Madison. He had been working with gelatin–water solutions over a wide range of concentrations. Above a certain concentration, these solutions gel and the viscosity rises rapidly. However, the small water molecules can still pass between the strands of the gel and, therefore, their mobility need not drop off as fast as the viscosity rise would indicate. He proposed to me that he could study the breakdown of the relation between bulk viscosity and water mobility if he could measure the diffusion coefficient of the water directly using spin echo techniques, as had been pioneered by Hahn[1] and Carr and Purcell[2] and much applied by the group of NMR spectroscopists at Bell Labs, especially by Dave McCall.

I encouraged John to try because I had become interested in spin echo diffusion measurements after I read a note by Don Woessner reporting that the diffusion coefficient of benzene in a rubber stopper was dependent upon the parameters of the experiment, particularly on how long it took to make the measurement.[3] His explanation was that for short times, where the diffusion coefficient was larger, the benzene molecules could move more freely than they could for longer diffusion times, where they might meet restrictions among the rubber molecules. The qualitative explanation seemed clear enough but the task of making a quantitative analysis looked like a challenge. Since I was interested in the microscopic details of molecular motion and still fancied myself something of a theoretician, I started trying to understand the problem better. It became clear quickly that while the brute-force analysis of such behavior was probably tractable, it would not be easy, flexible, or insightful. Besides, I was lazy and looking for an easier solution, preferably one that could be presented in closed form rather than as a table of computer output. Remember, in those days, computers were not that fast, did not function interactively, and had poor graphics capabilities. I was too impatient to wait hours or days for the next batch of numbers to come back from the computer lab to decide where I needed to go next. I had had enough of that doing my thesis research on the ILLIAC.

Dave McCall was helpful from the beginning, supplying drawings and photographs of his diffusion apparatus as well as a fistful of reprints describing the work done at Bell Labs, both experimental and theoretical.

John Tanner made good progress implementing the various strategies necessary to measure diffusion by means of a magnetic field gradient. However, it was clear that, no matter how large a gradient one could make and still use, a larger gradient would look like the solution to the problems at hand. Remember, he was trying to measure ever slower diffusion. But, as the gradient increased, the lines got broader (actually the echoes got narrower) and harder to measure. Meanwhile, I kept working with the equations governing restricted diffusion in a steady magnetic field gradient, filling up a file folder with unfruitful attempts to get an easy solution. The problem was that a diffusive jump had a greater or lesser effect on the echo attenuation depending where it occurred during the experiment, never mind about non-Fickian behavior.

Just before midnight on 1st May, 1963, I made a note in the equipment logbook (I didn't have a laboratory notebook, as such): 'Why not vary G in the time between pulses to accentuate the effect of diffusion without unduly narrowing the echoes? . . . ' The sketches of the pulse sequence were quite prophetic and both the rudimentary analysis and the suggested circuit for pulsing the gradient were to prove tolerably accurate. I still have this logbook. I left a note (which also still exists) for John Tanner and went home around 1.00 a.m.

John set about implementing the idea, right away. Since he already had a steady gradient set-up, all he needed to try the first experiment was some way to pulse the gradient current. We both set about trying to analyze the experiment to get the relationship between the gradient pattern and the effects of simple Fickian diffusion. John chose a statistical approach, based on the approach of Carr and Purcell.[2] I chose to obtain a differential equation to solve, based on the analysis of steady gradients and diffusion first developed by Torrey[4] and given in Abragam.[5] I got a useful solution first, which John was then able to check by a totally different approach. It was clear that we had a way to extend the measurement to much smaller values of the diffusion coefficient than had been possible before. It was John, with his much more pictorial, statistical approach, who first noted that the definition of the diffusion time was clear and easily interpretable if the gradient pulses were short compared with the time between them. Thus, suddenly both John's and my problem were solved by the same experiment. As it turned out, John never went back to his original problem. He was too busy working out the details of the pulsed field gradient, spin echo (PFGSE) experiment.[6] He and I worked independently on the theory of restricted diffusion, each preferring his different approach to the diffusive process.[7,8]

The theory I worked out, following and extending Torrey,[4] also predicted that flow would not attenuate the echo but, rather, cause it to shift phase. In common with most pulsed NMR spectrometers of the time, mine was not phase-coherent, so I could not test or apply that aspect of the theory. Later, Ken Packer did.[9] I had a low-resolution magnet and FT NMR had not yet been widely implemented, so the tantalizing possibility of studying diffusion in a multicomponent system had to wait for James and McDonald.[10]

John Tanner received his Ph.D. in 1965 and continued for years developing and improving the PFGSE experiment. He first suggested and implemented the use of the stimulated echo to extend the practical diffusion time. He also proposed a number of ADRF and ARRF experiments to achieve the same thing, but I do not think they were ever tried. By about 1970 I had pretty much lost interest in measuring diffusion since the

Monsanto Company, where I was then working, could not see its practical usefulness and did not encourage me to continue. For the first time since then, I now have a student tooling up to make PFGSE measurements.

What were the real antecedents of the PFGSE measurement? I am not sure. In the course of readying the first manuscript for publication, we were made aware of a recent article by McCall, Douglass, and Anderson,[11] the Bell group, that suggested that varying the gradient (an 'alternating field gradient . . . ' in the language of the paper) could extend the measurement to smaller diffusion coefficients by reducing the power requirements of the pulse transmitter. I had spoken to Dave McCall about a year prior to my first logbook entry about problems of diffusion measurements, in general. Later, having seen the journal statement, I asked Dave whether we had discussed this point earlier. He thought we had, but if so it did not register at the time and I had no conscious memory of it when I made my logbook entry. He is probably right; it would not have been the first good idea he directed my way. It was a reviewer of our first article[6] who pointed out that we were not the first to study spin echoes in the presence of magnetic field gradient pulses. In a 1955 article titled: 'Spin Echo Serial Storage Memory,' Anderson, Garwin, Hahn, Horton, Tucker, and Walker, at IBM-Watson Laboratories, described an expanded use of multiple stimulated echoes in a magnetic field gradient turned on and off during the experiment, as convenient.[12] They were not interested in diffusion, indeed they would have preferred it not to be present, but rather in a computer memory device. I have no excuse for being ignorant of any article of Erwin Hahn's; in those days, however, the American Physical Society recommended crediting multiple-author papers alphabetically, and he was buried in the middle of the list.

With the equipment available at the time, the first PFGSE measurements were extraordinarily difficult to perform with useful precision. I might have continued working with the method at Monsanto if better instrumentation had been available. As it was, a new generation of instrumentation had to come along before the measurements could achieve their full potential. So, the experiment may classify as one just slightly ahead of its time. Not so early that it had to be reinvented, but one that required a period in limbo before it re-emerged as a 'standard method.' When I presented a seminar, on CPMAS, not PFGSE, to a group of Alex Pines' graduate students in 1986, it was reported to me afterward that one of the students, obviously well up on the older NMR literature, asked if 'the guy who did the pulsed field gradient diffusion work in the 1960's' was my father.

The source of these thoughts is John Tanner's notebooks and thesis; my logbook; the various publications cited, especially the dates thereon; a conversation with Dave McCall about 30 years ago; a conversation with John Tanner about two years ago; and, least reliable of the lot, my own recollections.

REFERENCES

1. E. L. Hahn, *Phys. Rev.*, 1950, **80**, 580.
2. H. Y. Carr and E. M. Purcell, *Phys. Rev.*, 1954, **94**, 630.
3. D. E. Woessner, *J. Phys. Chem.*, 1963, **67**, 1365.
4. H. C. Torrey, *Phys. Rev.*, 1956, **104**, 563.
5. A. Abragam, *The Principles of Nuclear Magnetism*, Oxford University Press, London, 1961.
6. E. O. Stejskal and J. E. Tanner, *J. Chem. Phys.*, 1965, **42**, 288.
7. E. O. Stejskal, *J. Chem. Phys.*, 1965, **43**, 3597.
8. J. E. Tanner and E. O. Stejskal, *J. Chem. Phys.*, 1968, **49**, 1768.
9. K. J. Packer, C. Rees, and D. J. Tomlinson, *Adv. Mol. Relaxation Processes*, 1972, **3**, 119.
10. T. L. James and G. G. McDonald, *J. Magn. Reson.*, 1973, **11**, 58.
11. D. W. McCall, D. C. Douglass, and E. W. Anderson, *Ber. Bunsenges. Phys. Chem.*, 1963, **67**, 336.
12. A. G. Anderson, R. L. Garwin, E. L. Hahn, J. W. Horton, G. L. Tucker, and R. M. Walker, *J. Appl. Phys.*, 1955, **26**, 1324.

Biographical Sketch

E. O. Stejskal. *b* 1932. B.S., 1953, Ph.D., 1957, Chemistry, University of Illinois-Urbana (supervisor H.S. Gutowsky). NSF Postdoctoral fellow, Harvard University, 1957–58 (with William Moffitt). Instructor to Assistant Professor, University of Wisconsin-Madison, 1958–64. Research Specialist to Fellow, Monsanto Company, Corporate Research, 1964–86. Currently Professor of Chemistry, North Carolina State University-Raleigh. Approx. 100 publications. Research interests: NMR; molecular motion; spin relaxation; diffusion; high-resolution solid state NMR; NMR probe design; lubrication; polymer motion and morphology.

Sternhell, S.: Development of NMR Spectroscopy as a Structural Tool

S. Sternhell

University of Sydney, Sydney, New South Wales, Australia

The importance of NMR is not principally intrinsic: it is due to its applications. Thus nuclear magnetic resonance spectroscopy is almost certainly the most widely used technique for the elucidation of the structures of organic and organometallic molecules, and is a powerful method for the determination of the composition of mixtures of compounds. In addition, it has direct applications to the study of molecular dynamics and to problems which lie principally in the fields of biology and medicine rather than chemistry, as well as a growing applicability in the analysis of solid state samples. More recently NMR imaging, closely related to NMR spectroscopy, has become established as a powerful clinical technique. NMR spectrometers are ubiquitous in chemical laboratories and represent the greatest single investment in chemical instrumentation, while NMR spectroscopy and its applications form integral parts of chemistry courses at all universities.

Perhaps the most striking feature of the development of NMR spectroscopy has been its speed: the phenomenon of NMR was discovered in 1945, the phenomenon of chemical shift, and hence the first major application, is generally dated[1] to 1950 and any number of active practitioners of chemistry, this author included, vividly remember the dark ages pre-NMR.

The development of NMR took place along a number of parallel but interrelated lines. Thus, one can talk of developments in NMR physics, in NMR instrumentation, in NMR techniques, and in the interpretation of NMR spectra. A constant feature apparent from the beginning of the massive application of NMR to chemistry in the late 1950s to the present has been the gap between sophisticated and unsophisticated users, the latter outnumbering the former by about two orders of magnitude. To my knowledge, this has been a most unusual, if not unique, phenomenon in a major scientific field; in fact, a subcategory of authors has been active over the whole period trying to make the mysteries of NMR accessible to the uninitiated. This brief review of the development of NMR will be written from this perspective, i.e. it will not be concerned with the allocation of priorities but with the appearance of developments which had a major impact on applications of NMR.

NMR PHYSICS

From the point of view of applications, the major developments in NMR physics took place early and were codified by Pople, Schneider, and Bernstein,[2] and Abragam.[3] These two monographs found their way onto the shelves of numerous users of NMR where they were much puzzled over, but rarely understood by most users of the method.

In the early days of NMR the principal problem in interpreting NMR spectra—which were almost entirely what we now term 1D, ^{1}H spectra—was *the analysis of the hyperfine structure*, which to this day is misnamed as 'the analysis of high-resolution NMR spectra'. The underlying principles of the extraction of NMR parameters from spectra are straightforward, were codified early,[2,4] and an excellent text pitched at just the correct level was written by R. J. Abraham[5] in 1971. However, to this day and in spite of relevant advances in instrumentation, computation, and techniques (see below), the analysis of high-resolution NMR spectra baffles most users.

A second physics-related problem concerned the *time dimension* of NMR spectroscopy. While research into dynamic NMR[6] has normally been the preserve of a relatively small number of specialists who had no problems in understanding and applying the relevant concepts, serious physics-related problems for general users emerged with the development of pulsed NMR in the late 1960s. In particular, in spite of the incorporation of such material into standard lecture courses, even the current crop of young researchers in organic and inorganic chemistry often have trouble in understanding the mechanisms of relaxation and the whole concept of spin gymnastics, in spite of the fact that the underlying principles are well established.

NMR INSTRUMENTATION AND TECHNIQUES

The development of NMR *instrumentation* has been dominated by changing magnet technology, microelectronics, and computing, the revolution in the latter fields coinciding with the development of the NMR method. On the one hand, we have seen the unending quest for higher field strengths driven by the requirements of dispersion, sensitivity, and simplification, and on the other the development of the electronics, particularly since the replacement of the CW techniques by pulsed methods. The results have been astonishing, the most routinely used instruments outperforming those which had been the best available about five years before. On several occasions users (myself included) were trapped into declaring the technology 'mature', only to be proven wrong by another quantum leap. Nevertheless, I will predict again that unless a completely new form of superconducting magnet appears, the 400 MHz machine will become the standard nonspecialist's instrument. The firm which will make the cheapest user-friendly version of this instrument should reap considerable benefits.

By NMR *techniques*, I understand the spectroscopic and other experimental methods used to acquire NMR information. For the first few years of commercially available NMR, the commonly usable techniques were simply CW (field sweep or frequency sweep) 1D spectra, but the introduction of spin decoupling made an impact as early as 1962. Interestingly, the signal-averaging techniques, such as Varian's CAT 1024, failed to take hold although they addressed the then principal limitation of NMR spectroscopy, viz. low sensitivity. The two major basic developments in instrumentation and technique became widely known in the late 1960s and early 1970s: I am referring, of course, to the appearance of superconducting magnets and the switch from CW to FT spectroscopy. These developments increased the sensitivity of NMR to a spectacular extent, opened the door to multinuclear MR, and

made ^{13}C NMR (including a little later the edited variety) routinely accessible, thus roughly doubling the utility of the method. At the same time, the interpretability of ^{1}H NMR spectra became easier due to the superior dispersing power of high-field instruments. It is interesting how this development has overshadowed the introduction of shift reagents in 1966[7] which, in principle, helped with this problem as well as giving other useful information at a negligible cost. It is also interesting that the potentially revolutionary nuclear Overhauser effect had to wait for FT spectroscopy for full acceptance.

Two-dimensional NMR, which became routinely accepted during the 1980s,[8] enlarged the utility of NMR by making the determination of connectivity much easier (COSY) and accessing heteronuclear correlations (particularly ^{1}H, ^{13}C) and NOE values. The development of the INADEQUATE technique, which has the potential of defining the complete linkage of the carbon skeleton in a single experiment, has not yet become a part of the routine armory of the chemist, mainly due to the limitations in sensitivity, but there are no inherent reasons why it should not do so. In fact, a problem now faced by the nonspecialist is to decide which of the numerous techniques[8] to apply!

INTERPRETATION OF NMR SPECTRA

Instrumentation and techniques enable us to extract NMR parameters (e.g., chemical shifts, coupling constants, ^{1}H, ^{13}C correlations, etc.) from NMR spectra, but to obtain information about molecular structure it is necessary to correlate such data with structural features. Thus a ^{13}C signal for a quaternary carbon near δ 200 ppm indicates the presence of a ketone or aldehyde, a three proton singlet near δ 4 ppm suggests a methoxyl group, and vicinal ^{3}J(H,H) values obey a well-known (if more complex than is generally realized) Karplus relationship. Unlike the developments in NMR instrumentation and techniques, the appearance of NMR data proceeded incrementally rather than by a series of revolutionary leaps. The first useful compilation accompanying a general text[9] was produced by Jackman in 1959, but not many analogous works have appeared since. The reasons are not difficult to find: the literature contains an astronomical amount of data, but as soon as one attempts to produce useful compilations one finds that all sorts of obvious data are hard to find or even missing, and need to be established experimentally.

The whole exercise is a tedious labour of love because, with the possible exception of ^{13}C chemical shifts, little of the search is simply mechanical. This explains why few useful major compilations and correlations are available and why old favorites[10] are not only found on the shelves of working chemists, but are still much consulted although getting quite elderly.

REFERENCES

1. H. S. Gutowsky and C. J. Hoffman, *J. Chem. Phys.*, 1951, **19**, 1259.
2. J. A. Pople, W. G. Schneider, and H. J. Bernstein, 'High-Resolution Nuclear Magnetic Resonance', McGraw-Hill, New York, 1959.
3. A. Abragam, 'The Principles of Nuclear Magnetism', Oxford University Press, Oxford, 1961.
4. P. L. Corio, 'Structure of High-Resolution NMR Spectra', Academic Press, New York, 1966.
5. R. J. Abraham, 'Analysis of High Resolution NMR Spectra', Elsevier, Amsterdam, 1971.
6. L. M. Jackman and F. A. Cotton (eds.), 'Dynamic Nuclear Magnetic Resonance Spectroscopy', Academic Press, New York, 1975.
7. R. E. Sievers (ed.), 'Nuclear Magnetic Resonance Shift Reagents', Academic Press, New York, 1973; T. J. Wenzel, 'NMR Shift Reagents', CRC Press, Boca Raton, FA, 1987, (this publication lists 1534 references!).
8. M. L. Martin, J. J. Delpuech, and G. J. Martin, 'Practical NMR Spectroscopy', Heyden, London, 1980; A. E. Derome, 'Modern NMR Techniques for Chemistry Research', Pergamon Press, Oxford, 1987.
9. L. M. Jackman, 'Applications of NMR Spectroscopy in Organic Chemistry', Pergamon Press, London, 1959.
10. L. M. Jackman and S. Sternhell, 'Applications of NMR Spectroscopy in Organic Chemistry', 2nd edn., Pergamon Press, Oxford, 1969; H. Gunther, 'NMR Spectroscopy–An Introduction', Wiley, Chichester, 1973; E. Breitmaier and W. Voelter, '^{13}C NMR Spectroscopy', 3rd edn., Verlag Chemie, New York, 1987; E. Pretsch, T. Clerc, J. Seibl, and W. Simon, 'Tables of Spectral Data for Structure Determination of Organic Compounds', Springer-Verlag, Berlin, 1983; W. Brugel, 'Handbook of NMR Spectral Parameters', Heyden, London, 1979; E. Breitmaier, G. Haas, and W. Voelter, 'Atlas of Carbon-13 NMR Data', Heyden, London, 1979.

Biographical Sketch

S. Sternhell. *b* 1930. B.Sc., 1951, M.Sc., 1953, Sydney University, Ph.D., 1961 Imperial College, London (supervisor, D. H. R. Barton), D.Sc., 1966. R&D Monsanto 1953–55, CSIRO 1955–64, University of Sydney since 1964 (Professor of Organic Chemistry since 1977). Author of 185 publications. Current research specialty: molecular engineering.

Strange, John H.: Echoes of the Past

John H. Strange

University of Kent, Canterbury, UK

One of the first papers I read as a new graduate student was the excellent explanation by Pake[1] of the formation of nuclear magnetic resonance spin echoes originally discovered and published by Erwin Hahn in 1950. The fascination of manipulating those minute nuclear magnets to rotate, and then recover lost phase coherence after perhaps more than a million complete rotations under their Larmor precession, fired my early enthusiasm for NMR. I had arrived in London in 1960 to start work on a Ph.D. under the supervision of J. G. Powles, who had recently set up the first pulsed NMR spectrometer in the UK. However, I had to await his 'slow passage return' via the Mediterranean camp sites from an early AMPERE meeting in Pisa and hence I had started some reading on my own. On his return I discovered that he had presented a paper[2] on work with Tony Hartland that described echo amplitude modulation by J coupling interactions in liquids. In those days, pulsed NMR tended to be the domain of the physicist and high-resolution work as a means of chemical analysis was carried out by the chemists using continuous wave methods. Technological development seemed to be aimed at increasing spectral resolution which was usually limited by magnet technology and spectrometer stability. It had occurred to Jack Powles, while sitting in a London traffic jam on his way home from the laboratory, that a (Carr–Purcell) train of echoes should cancel inhomogeneity and also chemical shift and the Fourier transform of the echo amplitudes would reveal J spectra from which J couplings could be determined with great accuracy and data collected rapidly. Following the demonstration of the idea,[2] it became my job to develop and explore this approach.

At this time no commercial pulsed NMR machine was available—we built our own—and the digital computer was in its infancy. My first Fourier transforms were evaluated numerically by using a hand-operated mechanical calculator and it took most of 1 day to transform a set of transient data (obtained in 1 second) to obtain one spectrum. One of our earlier successes was the measurement of the variation of J coupling in acetaldehyde as a function of temperature to an accuracy of 0.01 Hz. We were able to interpret this in terms of internal molecular reorientations, Our work was presented at a Faraday Discussion in Oxford in 1962 and I can still remember John Waugh, who had received a preprint of our results, announcing after our paper had been read, that he had checked our results with his (latest and best) CW Varian spectrometer using the conventional method and (. . . . .pause) confirmed our observations!

Echo amplitude modulation was relatively straightforward to interpret for the first-order spectra of simple molecules but even then we found that the chemical shift could not be ignored. A full theoretical analysis of the echo amplitude modulation became rapidly intractable for more complex molecules although the additional variable parameter—the echo spacing—offered opportunities for the study of dynamical processes such as the rate of chemical exchange.[3] Perhaps it was because we had such poor homogeneity in our magnets that we were rather obsessed with overcoming this, using echoes, and hence overlooked the great advantages to be obtained from the (in retrospect) obvious and simpler approach of Fourier transformation of the free induction decay. This awaited the seminal works of Richard Ernst on Fourier transform NMR (see Ernst's Historical Sketch) which also stimulated commercial manufacture of the pulsed spectrometer, exploited the growing power of the computer, and opened up time-domain experiments, including relaxation work, to scientists in all the disciplines and not just those with DIY (do it yourself) inclinations.

While I was engaged on the echo amplitude modulation work, I shared an old 5 kG (0.5 T) permanent magnet with another graduate student, Peter Mansfield. He was at this time developing a unique high-power pulsed spectrometer designed to allow pulsed NMR to be used for solid materials. I became aware of Peter's observation of unexpected signals obtained while setting up his new spectrometer. We always used a $90^\circ-\tau-90^\circ$ pulse sequence to set up our spectrometers and, of course, when τ is much shorter than T_1 but longer than T_2 and the 90° pulses are set accurately, the signal following the second 90° should be zero. This signal was seen to fluctuate unexpectedly for solids if τ was set to be less than T_2. It should be mentioned that our spectrometer technology of that time usually employed pulsed oscillators so that the radiofrequency pulses were incoherent. The fluctuations, it transpired, were due to the phase fluctuation between the pulses. Peter Mansfield was able to control the phase with remarkable ingenuity using improvised precision time delays from a (very new and expensive) Tektronix oscilloscope timebase. The principle of solid echo formation was established.[4] The echo forms by a partial recovery of phase loss arising from the dipole–dipole interaction between nuclei in a rigid lattice following a $90^\circ-\tau-90^\circ$ sequence where the second pulse is phase-shifted by 90° from the first. Again I became involved in spin echo work, but now in solids. Jack Powles and I were able to demonstrate the general principles of solid echo formation and effectively produce zero time-resolution for observation of free induction decays in solids.[5] This early work on solid echoes laid the foundation for multipulse line-narrowing techniques (MREV8 and WAHUHA for example) for high-resolution spectroscopy of solids developed primarily by Peter Mansfield, John Waugh, and their collaborators in the late 1960s. Fourier transformation of the multiple echo-like signals yielded the otherwise obscured chemical shift and scalar interactions. These methods have continued in their development, requiring sophisticated calculation of spin dynamics. New sequences based on those 'solid echo' developments (see ***Line Narrowing Methods in Solids*** and ***Imaging Techniques for Solids and Quasi-Solids***) as well as multiple-echo methods in liquids (see for example ***Echo-Planar Imaging***) are still appearing today in the techniques applied to magnetic resonance imaging. Spin-echo methods in multidimensional magnetic resonance techniques are now of considerable importance in structural analytical methods of molecules in the liquid state. The work of Jack Powles and his students of the early 1960s in London reechoes still in the contemporary methods of magnetic resonance.

REFERENCES

1. G. E. Pake, *Solid State Phys.*, 1956, **2**, 1.
2. J. G. Powles and A. Hartland, *Proc. 9th Colloque Ampere*, 1960, p. 474.
3. J. G. Powles and J. H. Strange, *Mol. Phys.*, 1964, **8** 169.
4. J. G. Powles and P. Mansfield, *Phys. Lett.*, 1962, **2**, 58.
5. J. G. Powles and J. H. Strange, *Proc. Phys. Soc.*, 1963, **82**, 6.

Biographical Sketch

John H. Strange. *b* 1938. B.Sc., 1960, Ph.D., 1963, London (supervisor Jack Powles). Postdoctoral work with Don Holcomb, Cornell University. Appointed lecturer in Physics, University of Kent, 1964, then senior lecturer, reader, and professor. Director of Laboratory since 1982. Approx 150 publications. Current interests: diffusion and imaging in solids and porous media.

Sutcliffe, Leslie H.: A Career in Magnetic Resonance Spectroscopy

Leslie H. Sutcliffe
University of Surrey, Guildford, UK

My first researches in spectroscopy were in the area of vacuum-ultraviolet spectroscopy with Donald Walsh. At Liverpool University, I used spectroscopic methods to study mechanisms of inorganic oxidation–reduction reactions in solution. There was a lack of a really powerful physical technique for such studies and Charles McDowell suggested that I should consider magnetic resonance methods–which I had never heard of! Being used to constructing our own spectrometers, we set about building an ESR spectrometer. Unfortunately, the sensitivity proved to be far too low for the research projects we had in mind and we got no acceptable results until the arrival of our Varian ESR spectrometer in 1960. While the ESR spectrometer was being built, news came of the availability of a commercial NMR spectrometer. Luckily, Cecil Bawn, the then head of the Donnan Chemistry Laboratories, was anxious to create a first-rate research department, hence he was very keen to acquire such an instrument for my use. The first three Varian HR-40 spectrometers arrived in the UK in 1957, one for Liverpool, one for Cambridge, and one for ICI, Blackley. For me it was the start of parallel researches in NMR and ESR that have given me immense pleasure and satisfaction—and they still continue to do so, but ironically magnetic resonance didn't help much with my reaction kinetics projects! Joe Lee (an optical spectroscopist from Walsh's group) joined me as a postdoctoral fellow to help get the NMR researches underway: our first successes were with the ^{19}F resonance spectroscopy of organic fluorine compounds. This came about from a very fruitful collaboration with the research group at ICI, Widnes, who provided us with a large number of interesting compounds. They had found that IR and mass spectroscopy were not particularly helpful in establishing the structure of such compounds. In one study we were able to prove the structure of the anaesthetic halothane within minutes to Charles Suckling. The power of NMR for solving problems was also demonstrated when Joe Chatt wanted to confirm that he had made the first platinum hydride complex. We were able to prove quickly that the proton NMR spectrum was consistent with his ideas and we also evaluated J(Pt, H) from the ^{195}Pt satellites. Our instrumentation improved continuously as Varian converted our spectrometer first to HR-60 and then to HA-60. This was to be the only new NMR spectrometer to which I have had free access.

In 1959, Jim Feeney became one of my first research students in magnetic resonance—the beginning of a long line of talented co-workers to join my group working in this area. Our researches on fluorine compounds came to the attention of Ken Musgrave at Durham and we started to cooperate with him (Dick Chambers also came on the scene later) on some fascinating fluorinated alicyclics. There must still be many interesting new fluorine compounds synthesized by other fluorine groups that cry out for detailed investigation.

Jim Emsley joined the group as a postdoctoral fellow after gaining NMR experience with John Smith at Leeds on a homebuilt NMR spectrometer; later on, Ken Musgrave recruited him and he moved to Durham. It was clear to me that there was a great need for a book on the chemical aspects of NMR (no Bernstein, Pople, and Schneider as yet!) and so I began to write one. By 1960 it was obvious that the subject was beginning to expand rapidly, hence both Jim Feeney and Jim Emsley were persuaded to become co-authors. When 'High Resolution Nuclear Magnetic Spectroscopy' was published in 1965 by Pergamon Press, after some publisher's delay, it was already out of date. Rather than attempt to revise the book, I suggested that we start the series *Progress in Nuclear Magnetic Resonance Spectroscopy* and the first volume appeared in 1966. As a result of the astounding and continuing expansion of NMR, it continues to flourish.

In the early days of NMR, I was associated with two significant developments. The 'tau' scale for proton chemical shifts was adopted enthusiastically by organic chemists but, apart from the scale being illogical, there were problems as other nuclei began to be studied. The 'delta' scale was more suitable, but people were referring to upfield shifts as being positive but, from our extensive experience on spectral analysis, it was pointed out that these should be negative as frequency (energy) decreases with field increase. When I was chairman of the independent British NMR discussion group, affiliation with the Chemical Society (now the Royal Society of Chemistry) was an attractive proposition but there was no suitable division for the group: after some discussion the Interdisciplinary Division was created to accommodate our group (and other groups later).

Most of my NMR work has been concerned with chemical and structural applications, perhaps the most useful results being (i) the demonstration that F,F 'through-space' coupling can be enormous—I believe that Gordon Tiddy and I hold the world record of 196 Hz; (ii) that the sign of such couplings is always positive; (iii) that these coupling constants can be used to determine F,F distances; and (iv) the provision of rules for assigning fluorine chemical shifts in cyclic compounds. For most of our work, we required a full and precise analysis of spin systems and we encountered many frustrations with early computational methods.

There have been some instrumental developments in my laboratory. After pulse methods had virtually taken over from CW in the 1970s, there still remained the problem of examining a small region of a spectrum at the highest possible resolution. With Peter Craven and Bill McIlwaine, a CW correlation technique was developed that could be controlled by a PC: the system could bring new life to old CW spectrometers. This work is unpublished but it is interesting to note that the method is attracting attention at the present time and that Hitachi market a spectrometer based on an approach similar to ours.

In 1986, I joined forces with Duncan Gillies to enable us to further our interest in molecular dynamics, using mainly ^{13}C T_1 and NOE NMR relaxation measurements and asymmetric line broadening in the ESR spectra of spin probes. Duncan's foresight and great persistence has provided our laboratory with one of the few high-pressure multinuclear MR facilities in the world. We are examining a series of compounds some of which contain normal alkyl chains and others cyclohexyl rings—these are models for low-and high-traction

lubricants, respectively. We have shown that long hydrocarbon chains have the same dynamic behavior whether they are in lubricants, surfactant micelles, or biological membranes. In addition, we are developing radiofrequency ESR spectroscopic and imaging techniques. There is a niche for the latter (EMRI) for areas of research in which NMR imaging is not sufficiently sensitive or is inappropriate. It is pleasing to find that instrumental methods similar to those for CW NMR are directly applicable to ESR radiofrequency spectroscopy.

Biographical Sketch

Leslie H. Sutcliffe. B.Sc., London, Ph.D., Chemistry, Leeds University (supervisors, M. G. Evans and J. H. Baxendale). Postdoctoral work at Leeds with A. D. Walsh. ICI Fellow at Liverpool University, then successively lecturer, senior lecturer, reader, and professor, Royal Holloway College (University of London). Currently Research Professor of Chemistry and Physics at the University of Surrey. Approx. 200 publications. Current research specialties: high-pressure NMR, NMR, and ESR of free radicals, ESR spectroscopy and imaging at radiofrequencies with applications to diffusion in foods, rocks, and plants.

Sykes, Brian D.: When Biochemistry became Chemistry

Brian D. Sykes

University of Alberta, Edmonton, Alberta, Canada

After an introduction to NMR with J. S. Martin at the University of Alberta, and a non-NMR summer (unfortunately) with W. G. Schneider (of the Pople, Schneider, and Bernstein book fame) at the NRC labs in Ottawa, I joined J. D. Baldeschwieler's group at Stanford University in 1965. John's group was very active in several diverse fields including NMR studies using quadrupolar nuclei to follow the rotational dynamics of molecules, halide-ion probe NMR studies of biological macromolecules, and the development of ion cyclotron resonance spectroscopy (ICR); the latter was based in large part on magnetic resonance concepts such as double resonance which John's group had worked on previously. John set me to work on ideas he had for a solution version of the heteronuclear Hartmann–Hahn experiments (after the Ph.D. thesis of F. M. Lurie, University of Illinois, 1963), which was a very good idea and eventually came to light in the experiments of Pines, Gibby, and Waugh, and the HOHAHA correlation experiments which are so popular today. However, I was inexperienced and only barely made the experiment work, mostly due to difficulties in building spectrometer components for the 56 MHz pulsed NMR spectrometer in John's lab at that time. After another false start, I remember John suggesting that I convert to ICR, but I resisted this. I then spent months working through the fascinating paper by Meiboom on NMR studies of exchange in H_2O.[1] This paper, along with the paper by Swift and Connick,[2] set the stage for my involvement with NMR relaxation and chemical exchange processes, and especially with the use of NMR to study the exchange of ligands with biological macromolecules.

I had never intended to work with biological molecules in any way, or to become a biochemist. But biochemistry became chemistry with the determination of the three-dimensional structures of the first protein and enzyme. For me, the 1966 *Scientific American* article on lysozyme[3] had the greatest impact. When I then saw the initial lysozyme NMR papers of Thomas[4] and of Raftery et al.,[5] and the chymotrypsin paper of Richards and co-workers,[6] I recognized that the reported differential broadening of substrate resonances in fast exchange between their free and bound states was not always due to different correlation times, but proportional to the bound chemical shift differences squared and therefore caused by chemical exchange. From that point on I became permanently involved in the field of biological NMR. I developed a sensitive adiabatic half-passage $T_{1\rho}$ method for measuring relaxation times, used this to study the binding of substrates to lysozyme and chymotrypsin, began to label substrates with ^{19}F to study their interactions with biological macromolecules, and got involved, along with Paul Schmidt, with large proteins such as ATCase.

Several memories strike me about that time. Firstly, fields were so unstable that NMR linewidths were different if measured sweeping upfield or downfield. Secondly, in theoretical developments we never considered that nuclei could be outside the extreme narrowing limit. Thirdly, as graduate students we visited Varian in Palo Alto, and I remember Richard Ernst discussing his latest proposals for NMR signal-to-noise enhancement, but I did not listen closely enough to realize that I could have jumped on the FT bandwagon many years earlier than I did.

I then moved to the Chemistry Department at Harvard University in 1969 and was very fortunate to pick up a group of excellent graduate students. We became involved in a wide variety of biological systems, using in turn, a variety of NMR approaches. Amongst other things, we used ^{13}C NMR and ^{1}H NOE methods to determine the structure of retinal analogs, followed J coupling constants to measure distortion of lysozyme substrates, used fluorine-labeled amino acids to probe the structure and dynamics of large proteins such as alkaline phosphatase, developed the theoretical foundations of NOE measurements and relaxation in these systems, used ^{31}P NMR to study the mechanism of alkaline phosphatase, discovered slowly exchanging amide protons and slowly flipping aromatic residues in the bovine pancreatic trypsin inhibitor (BPTI), worked on stopped flow NMR to follow enzyme kinetics, used lanthanides for structural tools, and worked on eliminating the water resonance (like everybody else). We called our method WEFT, since other methods like DEFT had appeared, unfortunately contributing to the relentless drive that is so popular in NMR to add to the acronym alphabet soup. Looking back at how things turned out, I am reminded of the 1974 International Conference on Magnetic Resonance in Biological Systems meeting in Kanterstag, Switzerland, where Grayson Synder and I presented our BPTI results alongside of the very similar results of Wagner and Wüthrich. It was clear this was going to become a very popular protein. Consequently I decided, when I moved to Alberta in 1975, that I would move on to larger and more 'biologically relevant' proteins, while Wüthrich and co-workers began the development along with Ernst of 2D NMR and of the sequential assignment methods that were to eventually turn us all into structural people.

REFERENCES

1. S. Meiboom, *J. Chem. Phys.*, 1961, **34**, 375.
2. T. J. Swift and R. E. Connick, *J. Chem. Phys.*, 1962, **37**, 307.
3. D. C. Phillips, *Sci. Am.*, 1966, **215**, 1055.
4. E. W. Thomas, *Biochem. Biophys. Res. Commun.*, 1967, **29**, 628.
5. M. A. Raftery, F. W. Dahlquist, S. I. Chan, and S. M. Parsons, *J. Biol. Chem.*, 1968, **243**, 4175.
6. T. M. Spotswood, J. M. Evans, and J. H. Richards, *J. Am. Chem. Soc.*, 1967, **89**, 5052.

Biographical Sketch

Brian D. Sykes; *b* 1943. B.Sc., 1965, Ph.D., 1969, Chemistry, Stanford University, USA. Assistant to Associate Professor of Chemistry, Harvard University, 1969–75; Associate to Full Professor of Biochemistry, University of Alberta, 1975–present. Approximately 230 publications. Research specialty: solution structures of biological macromolecules, especially muscle and calcium-binding proteins.

Temussi, Piero Andrea: NMR Studies of Flexible Bioactive Molecules

Piero Andrea Temussi
Università di Napoli Federico II, Napoli, Italy

My relationship with NMR is closely linked to the motivations that led me to study chemistry: I was fascinated by the mystery of the structure–activity relationships of drugs and wanted to find a means of determining them experimentally. The way to do this, in the end, was through NMR but it was a long and winding road.

The prerequisite for anybody who wished to become an NMR spectroscopist was to go to the United States. I was no exception and decided to go to the lab of one of the NMR pioneers, Herbert S. Gutowsky. I learned something about NMR and chemical exchange, enough to export NMR knowledge back to Italy, but was still looking for tools to study bioactive molecules.

Even after real structural work on proteins became a reality, it was very difficult to get the means to study proteins in detail, at least in Naples, in terms of the availability of high-field spectrometers and dedicated computers. I resorted to small peptides that presented little difficulty in their spectra but a big challenge in terms of interpretation. The occasion was furnished by a sweet peptide: aspartame. Its structural study is typical of the difficulties involved in the study of small flexible molecules in solution. It was impossible to detect any diagnostic NOE; all conformational information was derived from coupling constants and energy calculations. Nevertheless, the NMR study of aspartame provided the hint for a complete model of the sweet receptor[1] and encouraged me in the study of more complex bioactive peptides.

The main problem posed by flexibility is that there is not a single well-defined structure in solution. This is what led me to investigate environmental constraints. The first approach was to choose a 'structured' solvent medium. Many peptide hormones interact with active sites of receptors that are hydrophobic pockets of membrane proteins. Normally, peptides are completely insoluble in apolar solvents but, in the case of enkephalin amides, complexation with crown ethers of their N-terminal cationic sites allow their solubilization in organic solvents. Crown ethers act as part of an artificial receptor site[2] and the NMR spectrum resembles that of fully structured cyclic peptides.

A much more general approach is represented by cryoprotective mixtures at low temperature. Initially we were looking for a means of increasing NOEs in small molecules. The obvious answer was to increase the viscosity of the solution. In the case of peptides we wanted solvents that could be considered biocompatible, and in this context, we have experimented with a series of mixed solvent systems, the so-called cryoprotective mixtures. These mixtures, composed of water and an organic solvent in various proportions, had previously been used in crystallographic and biochemical studies on several proteins. Their most distinctive feature is that, at low temperatures, they are isodielectric with water at room temperature. Cryoprotective mixtures are also characterized by a nearly complete biocompatibility, e.g. all enzymes tested in cryoprotective mixtures function normally and, generally, with kinetics identical to that in water. In addition, they have high viscosities whose precise value can be modulated by the proper choice of solvent composition and/or temperature.

Their use for peptides or other flexible molecules was originally proposed as a means of overcoming the technical problem of negligible NOEs exhibited by small molecules, because of the condition $\omega^2\tau_c^2 \approx 1$ generally encountered at high fields. At that time ROESY was just being introduced, but our instrumentation was not compatible with it. That is why we termed our approach with cryomixtures as the 'poor people's ROESY'. Using this system, we succeeded in measuring the first NOEs of enkephalin, a very flexible bioactive peptide.[3]

Subsequently, when ROESY became available to everybody (including us), I realized that the use of cryomixtures had further advantages. High viscosity does not simply increase the size of NOEs by increasing τ_c, as predicted by the theory of microviscosity, but acts as a conformational sieve by limiting the flexibility of small peptides.[4] Thus, conformations detected in cryoprotective mixtures are generally different from those found in pure solvents of low viscosity. This method of studying flexible bioactive molecules is now of general application and may be considered as a first step in structure–activity studies of any peptide hormone.

The most important aspect of the use of highly viscous media in the study of peptide hormones is the simulation of one crucial feature of their biological environment. Neuropeptides exert their biological action at synapses. They are excreted by specialized vesicles of the presynapse and reach membrane receptors located on the postsynaptic membrane by crossing a cleft of 100–500 Å occupied by the intersynaptic fluid. One important physicochemical feature of cytoplasm is viscosity. The typical viscosities of cytoplasm range from 5–30 cP,[5] and it has been postulated[6] that they play an important role in cell communication processes. It is probable that the intersynaptic fluid has a viscosity higher than cytoplasm, because of the ordering effect of membrane heads and of unstirred layer phenomena. It seems reasonable to postulate, therefore, that the viscosity of this fluid also contributes, in addition to the membrane catalysis,[7] in allowing the entropic barrier to the transition state of peptide–receptor interaction to be overcome by selecting ordered conformations prior to receptor interaction.

REFERENCES

1. P. A. Temussi, F. Lelj, and T. Tancredi, *J. Med. Chem.*, 1978, **21**, 1154.
2. P. A. Temussi, T. Tancredi, A. Pastore, and M. A. Castiglione-Morelli, *Biochemistry*, 1987, **26**, 7856.
3. A. Motta, D. Picone, T. Tancredi, and P. A. Temussi, *J. Magn. Reson.*, 1987, **75**, 364.
4. P. Amodeo, A. Motta, D. Picone, G. Saviano, T. Tancredi, and P. A. Temussi, *J. Magn. Reson.*, 1991, **95**, 201.
5. E. C. Pollard, in *The Aqueous Cytoplasm*, ed. A. D. Keith, Marcel Dekker, New York, 1979, p. 1.
6. D. Chapman and W. E. Peel, in *The Aqueous Cytoplasm*, ed. A. D. Keith, Marcel Dekker, New York, 1979, p. 137.
7. R. Schwyzer, in *Peptides 86*, ed. D. Theodoropoulos, Walter de Gruyter, Berlin, New York, 1987, p. 7.

Biographical Sketch

Piero A. Temussi. *b* 1939. Laurea, 1962, Chemistry, University of Naples, Italy. Postdoctoral work at the University of Illinois, 1965–66, where he was introduced to NMR by Herb Gutowsky. Successively lecturer, assistant, and professor, University of Naples, Italy. Approx. 130 publications. Research specialty: structural studies of bioactive peptides in solution.

The Development of NMR

Edwin D. Becker and Cherie L. Fisk
National Institutes of Health, Bethesda, MD, USA

C. L. Khetrapal
Indian Institute of Science, Bangalore, India

THE ORIGINS OF NMR

The history of NMR, like any history, has no real beginning. Every development, every discovery can be traced back to antecedents that provided basic theory or applicable technology ready to be exploited. To the extent that the origin of NMR can be identified, however, it surely must lie in the development of the concept of spin as a quantum mechanical entity. We begin our story of the evolution of NMR with a review of electron spin and nuclear spin and of the experiments that verified these fundamental concepts. We discuss the investigations in which nuclear magnetic resonance was first observed in molecular beams, then describe the discovery of NMR in bulk materials 50 years ago.

As NMR phenomena and theory were better understood, it became apparent that the technique could be applied in many fields, and concurrent developments occurred in physics, chemistry, biology, and other disciplines. New concepts in NMR have continually been discovered, and major improvements in instrumentation and technology have fostered ever-expanding roles for NMR. To present this multifaceted account in a reasonably coherent manner, we have divided our story into 18 sections, each in approximately chronological order internally. We make frequent references to the interplay of the various aspects of NMR development.

This chronology serves only as a summary of the developments that are chronicled in much more detail in the 200 articles that follow. Many of the leading figures in the development of NMR have presented largely autobiographical accounts of many aspects of NMR. In our overall chronology we provide frequent references to these articles.

Electron Spin and Nuclear Spin

Physicists in the 1920s were elated with the success of quantum theory in explaining a number of phenomena that had defied understanding within the framework of classical mechanics. In particular, the existence of discrete lines in the absorption and emission spectra of atoms, and the spacings of those lines, could be understood conceptually and in some instances explained quantitatively. As spectral resolution improved, however, and spectra of additional atomic species were studied, some disturbing observations were made. Closely spaced doublet spectral lines were found that could not be explained by the old (Bohr) quantum theory. In 1925, Uhlenbeck and Goudsmit[1] introduced the concept of a spinning electron, with resultant angular momentum (quantized as $\frac{1}{2}\hbar$) and a magnetic dipole moment arising from the spinning electrical charge.

In 1926, the Schrödinger/Heisenberg formulation of quantum mechanics replaced the old quantum theory and provided a more satisfactory basis for understanding many phenomena, but in its initial form it also failed to account for the doublets. In 1927, Pauli[2] and Darwin[3] developed a theoretical framework for grafting the concept of electron spin onto the new quantum mechanics. The next year, Dirac's formulation of relativistic quantum mechanics showed that a fourth quantum number was required, and this turned out to be the electron spin with its quantum of $\frac{1}{2}\hbar$. While the classical picture of a spinning charged particle is useful, the theory treats the angular momentum and magnetic moment simply as constants of Nature.

Meanwhile, anomalies in the heat capacity of hydrogen led Dennison[4] to propose that the proton has a spin with an angular momentum of $\frac{1}{2}\hbar$. Molecular hydrogen, H_2, would then consist of two proton spins oriented parallel to each other (*ortho*) or antiparallel (*para*). The proton-spin concept completely accounted for the heat capacity results. In fact, in 1924, Pauli had already suggested the possibility of a nuclear spin to account for the hyperfine spectral structure.[5] This proposal came before the idea of electron spin had been formulated and was based on the widespread misconception that the nucleus consists of protons and electrons. (The neutron was not discovered until 1932.) Nevertheless, Pauli is usually regarded as the initial proponent of an intrinsic nuclear spin.

Atomic and Molecular Beams

In 1921, Stern and Gerlach[6,7] had carried out their famous experiment in which a beam of silver atoms was formed in a high vacuum and passed through a magnetic field in an experimental arrangement shown schematically in Figure 1. This was before the development of the idea of an intrinsic spin for either electrons or nuclei, but during the period that the old quantum theory broke with classical mechanics to postulate quantized *orbital* angular momentum for electrons. Thus, the Stern–Gerlach experiment was designed to observe either a continuous range of deflection of the silver atoms in the inhomogeneous magnetic field or a discrete number of atomic beams from the quantized orbital electron motion. The result clearly confirmed the basic tenets of the quantum theory.

With the concept of intrinsic nuclear and electron spin contributing to magnetic moments, Stern and his collaborators made major improvements to the sensitivity of their beam apparatus in order to be able to detect the much smaller

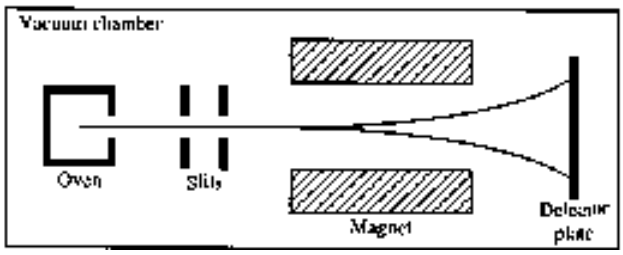

Figure 1 Schematic representation of the experimental arrangement for the Stern–Gerlach experiment

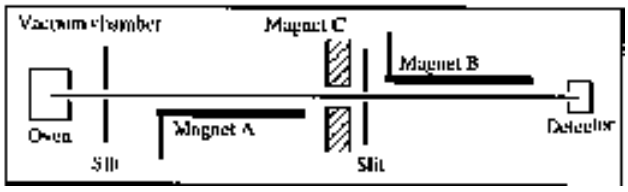

Figure 2 Schematic representation of the apparatus for Rabi's molecular beam experiments. Magnets A and B are electric wires that produce inhomogeneous magnetic fields. The third magnet C, also made of electric wires, was introduced to measure signs of magnetic moments. Later, Magnet C was changed to a homogeneous field for resonance studies

nuclear magnetic moments. In 1933, they were able to measure the effect of nuclear spin by the deflection of a beam of hydrogen molecules, for which there is no contribution to the magnetic moment from electron orbital angular momentum.[8,9] Thus the nuclear magnetic moment of the proton (and in a separate experiment of the deuteron from D_2 molecules) could be determined. However, accuracy was not high, since molecules with different velocities move in somewhat different trajectories, and the detected spots are smeared out.

During the early 1930s, Rabi's laboratory at Columbia University became a major center for atomic and molecular beam studies. Breit and Rabi examined the interactions between nuclear and electron magnetic moments in atomic beams and devised methods to overcome the problem of velocity distribution. For hydrogen, however, it was necessary to modify the apparatus (Figure 2) by introducing a second inhomogeneous magnetic field that would refocus the beam to produce a spot corresponding to the location of an undeflected beam. From the magnitudes of the magnetic field gradients in magnets A and B, together with other parameters, the magnitudes of the ^{1}H and ^{2}H nuclear magnetic moments were determined with greatly improved accuracy. By introducing a third inhomogeneous magnetic field between A and B, they caused nonadiabatic transitions that could reveal the sign of the magnetic moment.[10] In 1936, they found that the signs of both moments were positive and determined the values $\mu_H = 2.85$ ($\pm 5\%$) and $\mu_D = 0.85$ ($\pm 3.5\%$).[11] [These values are to within 1–2% of the current values, $\mu_H = 2.792\ 68$ and $\mu_D = 0.857\ 387$.] However, still greater precision was needed to permit interpretation of the moments in terms of nuclear structure. A breakthrough in the precision of measurement was soon to come with the introduction of *resonance* methods, a subject to which we shall return.

Nuclear Magnetism in Bulk Materials

While molecular beam studies were directed toward precise measurements of nuclear magnetic properties in isolated atoms or molecules, other efforts were underway to measure the effect of nuclear magnetic phenomena in solids. Simple theoretical considerations of the presence of nuclear magnetic moments show that there must be a Boltzmann distribution of the moments among the quantized states and a resultant equilibrium nuclear paramagnetic susceptibility. The problem in detecting this quantity directly is that it is very small relative to the diamagnetic susceptibility from electrons in the sample. However, in 1937, Lasarew and Schubnikow[12] demonstrated the nuclear susceptibility in solid hydrogen at 2 K, where the Boltzmann distribution enhanced its contribution.

Meanwhile, C. J. Gorter, a leading Dutch physicist who had demonstrated paramagnetic relaxation from electrons, attempted in 1936 to observe the effects of nuclear paramagnetism. His approach was to use a *resonance* property of the nuclear spins when they are placed in a magnetic field $\boldsymbol{B}_0$. Gorter knew from the Larmor relation

$$\nu_0 = (\gamma/2\pi)B_0 \tag{1}$$

that at this resonance frequency a magnetic dipole transition should occur if an alternating (radiofrequency) field $\boldsymbol{B}_1$ is applied perpendicular to $\boldsymbol{B}_0$. Gorter used a static field in which $\boldsymbol{B}_0$ could be varied up to 1.4 T, and applied a 20 MHz field with B_1 as large as 1 mT. His plan was to detect the heat produced by resonant absorption in the sample by using a sensitive calorimetric method that he had successfully employed in studies of electron paramagnetic relaxation. He looked for ^{1}H resonance in $KAl(SO_4)_2 \cdot 12H_2O$ and for ^{7}Li in LiF, both pure crystalline materials, at 14–20 K. Gorter expected a temperature rise of 0.3°C min^{-1}, which was about 100 times as large as his limit of detection, *provided* that the Boltzmann equilibrium was established and maintained. Unfortunately, Gorter observed no heat absorption from the resonant process and concluded that a long spin–lattice relaxation time caused the spin system to be partially saturated when radiofrequency (rf) energy was absorbed. In retrospect, it appears that Gorter's choice of samples that he described as 'very pure' prevented relaxation by paramagnetic impurities, and his decision to work at very low temperature exacerbated the problem of long T_1 values. While his experiment was unsuccessful, Gorter did publish the result.[13] His main contribution may have been to focus attention on the potential utility of resonance methods.

Nuclear Magnetic Resonance in a Molecular Beam

Rabi and his colleagues had refined beam methods, and in his 1937 theoretical paper entitled 'Space Quantization in a Gyrating Magnetic Field' Rabi treated a field that was oscillatory in time as a simplification to the actual case of molecules moving through fields which varied in space rather than time.[10] As Norman Ramsey points out in his historical sketch (***Ramsey, Norman F.: Origins of Magnetic Resonance***), this paper provides formulas that were later directly applicable to resonant behavior, but the theoretical transition probability was written in a form that obscured its resonant nature and the subsequent averaging over velocities eliminated sharp resonances. In fact, the word 'resonance' does not appear in the paper. According to Ramsey, Rabi did discuss with colleagues the possibility of using oscillatory magnetic fields, but no experiments were done or even planned for some months.

From more detailed accounts (***van der Waals, J. H.: Gorter's Footprints on the Trail That Led to Magnetic Resonance***, and ***Torrey, Henry C.: Precursive and Early Work on NMR***), it is clear that the stimulus for attempting such resonance studies came from a visit by Gorter to Rabi's laboratory in September 1937. Rabi's apparatus at that time was configured so as to be able to measure the sign of the magnetic moment in one experiment and its magnitude in a

separate experiment. As discussed in Section 1.2, a third inhomogeneous magnet was inserted for the sign determination, as shown in Figure 2, and nonadiabatic transitions between nuclear spin states occurred as the molecules passed through this field. Gorter asked the crucial question why transitions could not be induced more efficiently by resonant absorption of rf energy in a homogeneous magnetic field placed between the A and B magnets of Figure 2. Gorter apparently realized that in Rabi's beam method such rf absorption would cause interchange of the spin orientations in both components of the beam, so the effect of the resonance absorption would be additive in reducing the signal from the focused beam on its target. In his own unsuccessful experiment, on the other hand, only the difference between populations was effective in energy absorption from the rf field.

While Rabi had evidently already recognized the value of a resonance experiment, Gorter's suggestion prompted immediate action. Two days after his visit, modifications to the apparatus had begun to test the resonance approach. John Rigden's historical sketch (***Rigden, John S.: Rabi's Resonance Method***) describes in detail the background of the molecular beam work in Rabi's laboratory and depicts the tension and drama as Rabi and his co-workers steadily increased the magnet current while a fixed 3.5 MHz rf was applied to a coil in the magnet. At a current of 116 A the signal from the detector abruptly dropped, then regained its initial value at higher current. The predicted resonance had been observed! In January 1938, Rabi, Zacharias, Millman, and Kusch submitted to the *Physical Review* a short Letter[14], reproduced in its entirety in Figure 3. The signal from LiCl shown in Figure 3 is really the first reported nuclear magnetic resonance. Rabi et al. correctly noted that 'The method is capable of very high precision and extension to a large number and variety of nuclei'. In 1944, Rabi was awarded the Nobel Prize for his extensive and important work on molecular beams, especially the resonance method.

Rabi's publication in 1938 refers to Gorter's earlier unsuccessful attempt and acknowledges his visit, but does not point out his role in suggesting the experiment. Gorter's reaction to this publication was restrained:[15]

> I cannot deny that I felt some pride, mixed with the feeling that my contribution was somewhat undervalued though my advice was acknowledged in the Letter.

As Torrey says succinctly in his historical sketch (***Torrey, Henry C.: Precursive and Early Work on NMR***):

> No one has ever doubted that Rabi richly deserved the Nobel Prize he was awarded in 1944, but Gorter clearly deserved a noble prize for the good grace and lack of rancor with which he accepted the undervaluation of his contribution to Rabi's success as well as the near misses in his own quest of NMR . . . .

With the new resonance method, Rabi and his colleagues investigated a number of molecules, including paramagnetic species, in which the interaction between nuclear and electron spins had to be considered. They also extended the method to H_2, D_2, and HD, where magnetic dipole, spin–rotation, and nuclear quadrupole interactions are important.[16] In the paper reporting the details of this work, the term *radiofrequency spectroscopy* was introduced. The resonant beam methods provided excellent precision since the lines were sharp and radiofrequencies could be measured quite accurately. However, the determination of the absolute values of the nuclear moments of ^1H and ^2H was limited to about 0.1% because of limitations in the accuracy of the magnetic field measurement.

A method similar in principle to the molecular beam resonance technique was used by Bloch and Alvarez to measure the magnetic moment of the neutron.[17] In this experiment the deflecting and refocusing magnetic fields of Figure 2 were replaced by two magnetized iron plates, which served to polarize and analyze the neutron beam. Between the two sets of plates a homogeneous magnet and rf coil permitted resonance transitions, as in the Rabi method. This method was apparently conceived by Bloch before he had heard of Rabi's successful resonance experiments, but was carried out in 1939. Bloch and Alvarez showed that the moments of the neutron and proton add to give that of the deuteron within 1%, but limitations in the measurement of the magnetic field prevented a more precise comparison. Eventually it was a search for a better method of measuring magnetic fields that led Bloch to try to observe NMR in bulk materials.

The World War II Years

With the outbreak of World War II, most basic research ceased or at least was relegated to secondary status. Rabi moved to Cambridge, MA, where he became Associate Director of the Radiation Laboratory at the Massachusetts Institute of Technology (MIT). He was responsible for the development of microwave sources for use in radar systems. Among the young physicists working in this laboratory was Edward Purcell, later to make his mark on NMR. Bloch worked in the Manhattan Project on studies of the properties of uranium isotopes, then also moved to Cambridge to work at Harvard University's Radar Research Laboratory on radar countermeasures. While the war certainly delayed further research into NMR, the experience of Bloch, Purcell, and many others in radar research or in the practical operation of military radar had an immense positive impact on the speed with which instrumentation for NMR was developed after the war.

Although the war prevented the usual Nobel Prize ceremonies in Stockholm, the Nobel Committee in Physics was not oblivious to the fundamental contributions made by molecular beam research. In 1944, the 1943 Nobel Prize in Physics was awarded to Otto Stern (Figure 4) (who had moved to the United States in 1933)—'for his contribution to the development of the molecular-ray method and his discovery of the magnetic moment of the proton'. At the same time, the 1944 Nobel Prize was awarded to I. I. Rabi (Figure 5) 'for his resonance method for recording the magnetic properties of atomic nuclei'. The awards were presented in New York rather than Stockholm.

Surprisingly, in war-torn Europe, two experiments of note to magnetic resonance were carried out. In the Netherlands, Gorter, encouraged by Rabi's successful resonance experiments, decided to try again to observe NMR in bulk materials. He and his colleague L. J. F. Broer replaced the calorimeter as a means of detection by relying instead on the expected anomalous dispersion of the magnetic susceptibility in the vicinity of a resonance, as indicated in Figure 6. With considerable difficulty, they assembled suitable apparatus and in 1942 carried out the experiment at the Kamerlingh Ohnes Laboratory in Leiden. They used crystalline LiCl and KF samples,

A New Method of Measuring Nuclear Magnetic Moment*

It is the purpose of this note to describe an experiment in which nuclear magnetic moment is measured very directly. The method is capable of very high precision and extension to a large number and variety of nuclei.

Consider a beam of molecules, such as LiCl, traversing a magnetic field which is sufficiently strong to decouple completely the nuclear spins from one another and from the molecular rotation. If a small oscillating magnetic field is applied at right angles to a much larger constant field, a re-orientation of the nuclear spin and magnetic moment with respect to the constant field will occur when the frequency of the oscillating field is close to the Larmor frequency of precession of the particular angular momentum vector in question. This precession frequency is given by

$$\nu = \mu H/hi = g(i)\mu_0 H/h. \qquad (1)$$

To apply these ideas a beam of molecules in a $^1\Sigma$ state (no electronic moment) is spread by an inhomogeneous magnetic field and refocused onto a detector by a subsequent field, somewhat as in the experiment of Kellogg, Rabi and Zacharias.[1] As in that experiment the re-orienting field is placed in the region between the two magnets. The homogeneous field is produced by an electromagnet capable of supplying uniform fields up to 6000 gauss in a gap 6 mm wide and 5 cm long. In the gap is placed a loop of wire in the form of a hairpin (with its axis parallel to the direction of the beam) which is connected to a source of current at radiofrequency to produce the oscillating field at right angles to the steady field. If a re-orientation of a spin occurs in this field, the subsequent conditions in the second deflecting field are no longer correct for refocusing, and the intensity at the detector goes down. The experimental procedure is to vary the homogeneous field for some given value of the frequency of the oscillating field until the resonance is observed by a drop in intensity at the detector and a subsequent recovery when the resonance value is passed.

The re-orientation process is more accurately described as one in which transitions occur between the various magnetic levels given by the quantum number m_i of the particular angular momentum vector in question. An exact solution for the transition probability was given by Rabi[2, 3] for the case where the variable field rotates rather than oscillates. However, it is more convenient experimentally to use an oscillating field, in which case the transition probability is approximately the same for weak oscillating fields near the resonance frequency, except that ϑ is replaced by $\vartheta/2$ in Eq. (13). With this replacement and with passage to the limit of weak oscillating fields, the formula becomes for the case of $i = \frac{1}{2}$

$$P(\tfrac{1}{2}, -\tfrac{1}{2}) = \frac{\vartheta^2}{(1-g)^2+g\vartheta^2} \sin^2 \tfrac{1}{2}\pi t\sqrt{[(1-g)^2+g\vartheta^2]}, \qquad (2)$$

where ϑ is $\frac{1}{2}$ the ratio of the oscillating field to the steady field, g is the ratio of the Larmor frequency of Eq. (1) to the frequency ν of the oscillating field. The denominator of the expression is the familiar resonance denominator. The formula is generalized to any spin i by formula (17).[3]

In the theory of this experiment, t, in Eq. (2), is replaced by L/v, where L is the length of the oscillating region of the field, and v is the molecular velocity. $P(\frac{1}{2}, -\frac{1}{2})$ must then be averaged over the Maxwellian distribution of velocities. However, the first term is not affected by the velocity distribution if t is long enough for many oscillations to take place. The average value of the $\sin^2$ term over the velocity distribution is approximately $\frac{1}{2}$.

To produce deflections of the weakly magnetic molecules sufficient to make the apparatus sensitive to this effect, the beam is made 243 cm long; the first deflecting field is 52 cm in length and the second 100 cm.

We have tried this experiment with LiCl and observed the resonance peaks of Li and Cl. The effects are very striking and the resonances sharp (Fig. 1). A full account of this experiment, together with the values of the nuclear moments, will be published when the homogeneous field is recalibrated.

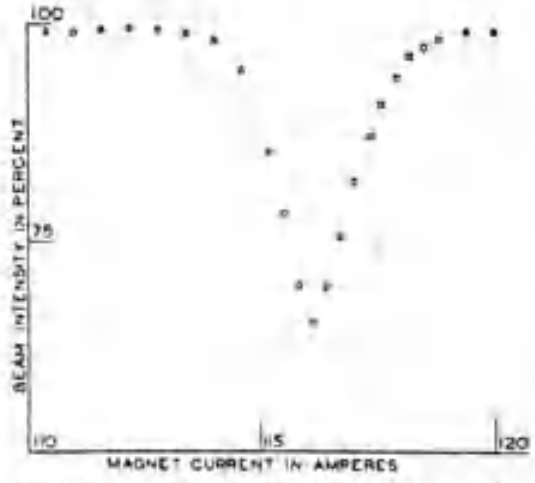

Fig. 1. Curve showing refocused beam intensity at various values of the homogeneous field. One ampere corresponds to about 18.8 gauss. The frequency of the oscillating field was held constant at 3.316×10^6 cycles per second.

I. I. RABI
J. R. ZACHARIAS
S. MILLMAN
P. KUSCH

Hunter College (I. I. R., J. R. Z.), Columbia University, New York, N. Y., January 31, 1938.

*Publication assisted by the Ernest Kempton Adams Fund for Physical Research of Columbia University.

[1] Kellogg, Rabi and Zacharias, Phys. Rev. 50, 472 (1936).
[2] Rabi, Phys. Rev. 51, 652 (1937).
[3] C. J. Gorter, Physica 3, 995 (1936). We are very much indebted to Dr. Gorter who, when visiting our laboratory in September 1937, drew our attention to his stimulating experiments in which he attempted to measure nuclear moments by observing the rise in temperature of solids placed in a constant magnetic field on which an oscillating field was superimposed. Dr. F. Bloch has independently worked out similar ideas but for another purpose (unpublished).

Figure 3 The first demonstration of a nuclear magnetic resonance in a molecular beam. (Reproduced by permission of the American Physical Society.)

Figure 4 Otto Stern. (Reproduced by permission of the Nobel Foundation)

Figure 5 I. I. Rabi. (Reproduced by permission of the Nobel Foundation)

once again choosing molecules that would minimize magnetic dipolar interactions in the hope that this would lead to relatively narrow lines. Again they worked at low temperature (liquid hydrogen and liquid helium) to maximize the magnitude of the static nuclear magnetic susceptibility. However, once again, they observed no effect on passing through the expected resonance.[18] They concluded that T_1 for their samples must have been more than 1000 s (a good estimate, since Bloembergen much later measured T_1 as 600 s at 2.1 K with Gorter's LiCl sample). Unfortunately, they did not (perhaps, under wartime conditions, could not) try other samples at higher temperatures.

The second relevant experiment was the discovery of electron spin resonance by E. K. Zavoisky at Kazan, Russia, in 1944–45. Physicists at the time were aware of the possibility of observing such a resonance, and a substantial body of knowledge existed on electronic interactions and the mechanism of paramagnetic relaxation, whereas detailed mechanisms of nuclear relaxation were unknown. However, according to the account by ***Kochelaev, Boris I.: Discovery of Electron Spin Resonance***, Zavoisky attempted first to detect NMR in 1941. He used a sample of water to which paramagnetic ions were added to shorten the completely unknown relaxation time, and a flowing sample was used in some experiments, presumably to reduce saturation from the rf field. Zavoisky was inspired by Rabi's resonance studies in molecular beams, but he was also aware of Gorter's unsuccessful attempt in 1936 to detect NMR. Kochelaev reports that Zavoisky apparently observed an NMR signal in May or June 1941, but it was not reproducible. Further efforts

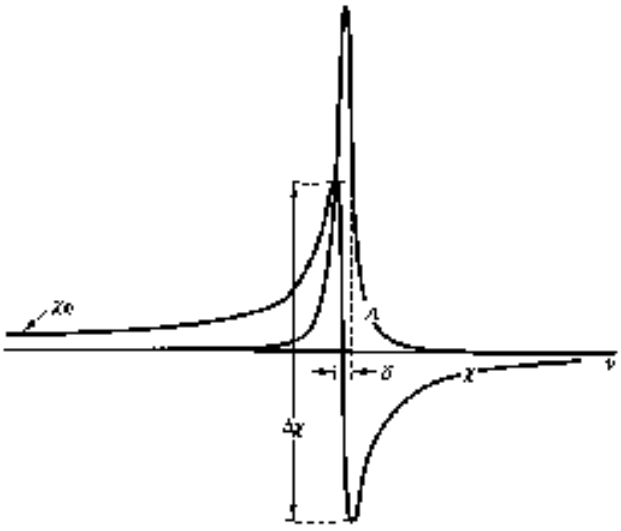

Figure 6 Theoretical absorption and dispersion plots of magnetic susceptibility.[18] (Reproduced by permission of Elsevier Science Publishers)

were cut short by the beginning of hostilities in Russia and the move of several laboratories from Moscow to the more remote Kazan, thereby displacing Zavoisky's laboratory. It is thought that inadequacies in the electronics and poor magnetic field homogeneity prevented any successful experiment.

When Zavoisky was able to resume some research in 1943, he turned his attention to the study of paramagnetic relaxation but retained an interest in NMR. However, he apparently

carried out no successful experiments in NMR. He then moved on to trying to detect electron resonance in both solids and solutions of paramagnetic salts. After he had obtained some dubious results in a solenoid at very low magnetic fields, he built equipment to work in the range of 1 GHz and obtained signals that were reported in his thesis in October 1944. In January 1945, he repeated the measurements at the Institute of Physical Problems in Moscow and published a short paper,[19] which is generally accepted as the first reported observation of ESR.

NMR IN BULK MATERIALS

With the end of World War II in sight, many American scientists began to think of post-war research opportunities. In 1944, Rabi and Norman Ramsey spent an evening together in Cambridge, MA, discussing possible experiments. They considered an effort to look for NMR absorption in bulk materials and were excited by their favorable signal-to-noise calculations. However, they recalled Gorter's failure for unknown reasons and decided to defer such experiments in favor of other research (which ultimately provided important advances in relativistic quantum electrodynamics) (see ***Ramsey, Norman F.: Origins of Magnetic Resonance***). Purcell, who was at that time not aware of Gorter's experiments, also began thinking about such NMR experiments. Meanwhile, Bloch became interested in the possibility of developing an NMR method using bulk materials as a simple means for accurately measuring magnetic fields, so he could make a more precise comparison of the magnetic moments of the neutron, proton, and deuteron in molecular beams. According to J. H. Van Vleck,[20] in whose group Bloch worked at Harvard, Bloch was thinking about possible relaxation processes that would overcome the problems that had defeated Gorter, but without success. Although Purcell and Bloch worked only a few miles from each other during this period, they did not meet (except perhaps at a social function) and did not visit each other's laboratories, partially at least because of security restrictions.

Plans and Preparations at Stanford

Bloch left the Radar Research Laboratory (RRL) at Harvard in 1945 to return to Stanford and re-established a research program. With the experience in rf techniques that he had acquired at the RRL, he believed that the transitions of nuclear magnetic moments in a resonance experiment could be detected in a simpler way than by measuring the deflection of a molecular beam. Bloch reasoned that the macroscopic nuclear magnetization that gives rise to the static nuclear magnetic susceptibility would be tipped away from its equilibrium position along the z axis (Figure 7) by the resonance absorption of energy from an rf field. The resulting magnetization, precessing about the applied magnetic field $\boldsymbol{B}_0$ would induce an electrical signal in a coil placed along the x or y axis. According to Martin Packard's fascinating account of this early work (***Packard, Martin E.: Nuclear Induction at Stanford and the Transition to Varian***) the idea for the method came to Bloch during a concert while he was still at the RRL, and he discussed the feasibility with W. W. Hansen, another Stanford physicist who was at the same laboratory. Back

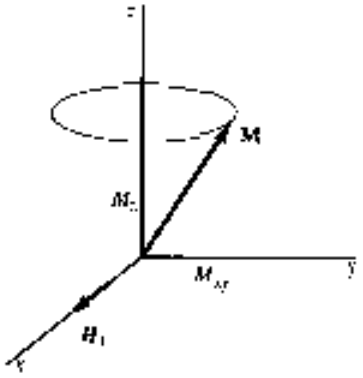

Figure 7 Schematic representation of a macroscopic nuclear magnetization $\boldsymbol{M}$ precessing about the magnetic field along the z axis after being tipped away from its equilibrium position along z by an rf field $\boldsymbol{H}_1$

at Stanford, Bloch formed a collaboration with Hansen, an electronics expert, and recruited Martin Packard as a graduate student. In late September they began to build and assemble apparatus, a process that was to take about three months.

The Discovery at MIT/Harvard

Meanwhile, at the MIT Radiation Laboratory, several staff members had been asked to stay on for up to a year, even though the wartime research effort had ended, to contribute to a series of books that would chronicle the advances made in the classified research. Among them were Edward M. Purcell, leader of a group in fundamental research, Henry C. Torrey, who had led a group on crystal rectifiers, and Robert V. Pound, who had been responsible for crystal mixers. One day in September, 1945, these three met for lunch and Purcell raised the question of detecting the transition between nuclear magnetic energy levels using rf methods. Torrey, who had worked in Rabi's laboratory, recalled that such experiments had been discussed at Columbia but ruled out as not likely to work. However, that evening Torrey calculated the expected magnitude of the signal, provided equilibrium could be attained in the magnetic field, and concluded that the measurement should be feasible. On hearing that result, Purcell proposed trying the experiment.

As described in Bob Pound's lucid account (***Pound, Robert V.: Early Days in NMR***) the project was undertaken as a sideline, since all three were working full time (and that included Saturday mornings) on the Radiation Laboratory books. Purcell looked unsuccessfully for a suitable magnet at MIT but was able to arrange to use a large magnet at Harvard that had previously been employed for cosmic ray research. Thus it came about that the first NMR signals eventually were obtained at Harvard, even though all three authors were employed by MIT, as indicated in their first paper. Purcell designed new pole caps to improve the homogeneity of the magnetic field and had them constructed in the Harvard physics shop, while Pound and Torrey worked at MIT on the design and construction of an electronic bridge circuit. Because they were so engrossed with microwave technology, they elected to build a cavity resonant at 30 MHz rather than use more conventional electronic components. The cavity was enormous

by later NMR standards, about 12 cm in diameter and 8 cm long, and could accommodate an 850 mL sample.

As preparations for the experiment moved ahead, the collaborators' principal concern related to the totally unknown spin–lattice relaxation time. Some estimates based on first-order interactions between nuclear spins and lattice phonons suggested that the relaxation time could be as long as 10^6 years! However, Torrey estimated that second-order processes might reduce the relaxation time at room temperature to as little as one hour. Purcell, Torrey, and Pound were initially unaware of Gorter's somewhat similar unsuccessful experiment. When Rabi learned of Purcell's plans and told him of Gorter's work, Purcell was disappointed but felt that their planned approach was feasible and had progressed to the point that the experiment should be conducted. Rabi also expressed to Torrey his concern that magnetic dipolar interactions in the solid would broaden lines beyond detection.

Preparations were completed for the first attempt on Thursday, December 13. They filled the cavity with about 1 kg of paraffin wax, carefully balanced the bridge circuit, and spent the evening (in fact, until 4 a.m.) looking for an unbalance in the bridge that would indicate passage through resonance. The frequency of their apparatus was fixed at 30 MHz, so scanning took the form of varying the magnetic field in the region where resonance was expected. From molecular beam data, they expected resonance at about 7400 G. With their relatively crude magnetic field measurement capability, they expected resonance to occur at a magnet current of about 73 A. They scanned from about 65 to 80 A to allow for a possible 10% error in calibration, but could see no signal. Finally, they shut down the magnet and decided to try again on the next Saturday afternoon. They suspected that they may not have reached equilibrium, so Purcell agreed to turn on the magnet about 7 a.m. and let the sample equilibrate for several hours.

The frustrations of Thursday night were repeated on Saturday afternoon. The galvanometer remained in its steady-state position as the magnetic field was scanned. They thought about ways of enhancing sensitivity, such as the use of magnetic field modulation and lock-in detection. Before ending their session, however, one of them suggested raising the magnetic field to its maximum value (ca. 100 A current) and reducing the field slowly to zero. At 83 A the meter kicked exactly as they had hoped. There was the resonance! They verified the signal and found the resonance field to be completely reproducible. They removed the sample from the magnet and replaced it. The signal was just as large, demonstrating that the relaxation time was orders of magnitude shorter than expected.

Why did Purcell, Torrey, and Pound almost miss seeing resonance? They had not realized the extent to which the iron in the large gap magnet saturated. Their field measurement actually was within 2% of the correct value and they had allowed what seemed to be a more than adequate ±5% variation in the magnet current, but because of iron saturation it took 15% more current to reach the correct field strength. As Pound says, 'How embarrassing it would have been if we had not accidentally discovered our error.' They did discover the error, however, and for the first time NMR was observed in a bulk material, not only in a molecular beam.

The Letter reporting this discovery (reproduced in Figure 8) was received by the *Physical Review* on December 24, 1945, and published in January, 1946.[21] Later, in his Nobel Prize lecture in 1952 (see ***Purcell, Edward M.: Research in Nuclear Magnetism***), Purcell was to say:

> I remember in the winter of our first experiments, just seven years ago, looking on snow with new eyes. There the snow lay around my doorstep—great heaps of protons quietly precessing in the Earth's magnetic field. To see the world for a moment as something rich and strange is the private reward of many a discovery. But I'm afraid it has little bearing on the sober question we must, as physicists, ask ourselves: what can we learn from all this about the structure of matter?

The answer, 50 years after this initial observation, goes far beyond anything anticipated at that time and forms the basis of this Encyclopedia.

Success at Stanford

During the course of their work, Purcell, Torrey, and Pound had become aware of the similar project at Stanford, and they learned that Rabi described their efforts to Bloch in a visit to Stanford in December. But even without this information the work at Stanford was proceeding, and by early January, 1946, Bloch, Hansen, and Packard were ready to try their experiment. (As mentioned in Packard's historical sketch, ***Packard, Martin E.: Nuclear Induction at Stanford and the Transition to Varian***, the experiment might have been done a week or so earlier if graduate student Packard had not chosen to visit his parents in Oregon over Christmas.) Their apparatus was set up in the cyclotron laboratory at Stanford, a leaky, unheated area in the basement of the original quadrangle. In fact, the magnet that they used, a small lecture demonstration magnet with a 4–5 inch gap, was connected in series with the nearby cyclotron magnet and used that magnet's power supply and regulator. Their electronic setup was considerably different from that used by Purcell, Torrey, and Pound. Rather than looking for a bridge unbalance as energy was absorbed, Bloch, Hansen, and Packard placed the sample in a brass box (called the 'probe') along with two orthogonal electrical coils, one of which was used to excite the sample with rf while the second was used to pick up the nuclear induction signal as the magnetization precessed after the resonant absorption. A novel arrangement of 'paddles' was used to steer magnetic flux between the two coils and permit selection of dispersion or absorption mode. Sensitivity was enhanced by using magnetic field modulation to shift the signal away from dc and avoid low-frequency ($1/f$) noise.

Bloch had assumed that the spin–lattice relaxation time might be very long, perhaps days, while transverse relaxation from magnetic dipole–dipole interactions between nearby protons might occur rapidly and broaden the signal. Because of this concern about a long T_1 value, they allowed their sample of liquid water to come to equilibrium in a fringe field of the cyclotron magnet for 24 h before attempting any measurement. Moreover, the rf field was maintained at a few gauss to minimize saturation of the sample. They adjusted the magnetic field to a value that would provide resonance at their 7.76 MHz excitation frequency. However, the measurement of the field was just as inaccurate as that at Harvard, since the classical methods used were the same.

The experience at Stanford was almost a repeat of that at Harvard. After two hours of fruitless attempts to observe a signal on the oscilloscope screen, the three investigators

Resonance Absorption by Nuclear Magnetic Moments in a Solid

E. M. PURCELL, H. C. TORREY, AND R. V. POUND*
Radiation Laboratory, Massachusetts Institute of Technology, Cambridge, Massachusetts

December 24, 1945

IN the well-known magnetic resonance method for the determination of nuclear magnetic moments by molecular beams,[1] transitions are induced between energy levels which correspond to different orientations of the nuclear spin in a strong, constant, applied magnetic field. We have observed the absorption of radiofrequency energy, due to such transitions, in a *solid* material (paraffin) containing protons. In this case there are two levels, the separation of which corresponds to a frequency, ν, near 30 megacycles/sec., at the magnetic field strength, H, used in our experiment, according to the relation $h\nu = 2\mu H$. Although the difference in population of the two levels is very slight at room temperature ($h\nu/kT \sim 10^{-5}$), the number of nuclei taking part is so large that a measurable effect is to be expected providing thermal equilibrium can be established. If one assumes that the only local fields of importance are caused by the moments of neighboring nuclei, one can show that the imaginary part of the magnetic permeability, at resonance, should be of the order $h\nu/kT$. The absence from this expression of the nuclear moment and the internuclear distance is explained by the fact that the influence of these factors upon absorption cross section per nucleus and density of nuclei is just cancelled by their influence on the width of the observed resonance.

A crucial question concerns the time required for the establishment of thermal equilibrium between spins and lattice. A difference in the populations of the two levels is a prerequisite for the observed absorption, because of the relation between absorption and stimulated emission. Moreover, unless the relaxation time is very short the absorption of energy from the radiofrequency field will equalize the population of the levels, more or less rapidly, depending on the strength of this r-f field. In the expectation of a long relaxation time (several hours), we chose to use so weak an oscillating field that the absorption would persist for hours regardless of the relaxation time, once thermal equilibrium had been established.

A resonant cavity was made in the form of a short section of coaxial line loaded heavily by the capacity of an end plate. It was adjusted to resonate at about 30 mc/sec. Input and output coupling loops were provided. The inductive part of the cavity was filled with 850 cm³ of paraffin, which remained at room temperature throughout the experiment. The resonator was placed in the gap of the large cosmic-ray magnet in the Research Laboratory of Physics, at Harvard. Radiofrequency power was introduced into the cavity at a level of about 10^{-11} watts. The radiofrequency magnetic field in the cavity was everywhere perpendicular to the steady field. The cavity output was balanced in phase and amplitude against another portion of the signal generator output. Any residual signal, after amplification and detection, was indicated by a microammeter.

With the r-f circuit balanced the strong magnetic field was slowly varied. An extremely sharp resonance absorption was observed. At the peak of the absorption the deflection of the output meter was roughly 10 times the magnitude of fluctuations due to noise, frequency, instability, etc. The absorption reduced the cavity output by 0.4 percent, and as the loaded Q of the cavity was 670, the imaginary part of the permeability of paraffin, at resonance, was about $3 \cdot 10^{-4}$, as predicted.

Resonance occurred at a field of 7100 oersteds, and a frequency of 29.8 mc/sec., according to our rather rough calibration. We did not attempt a precise calibration of the field and frequency, and the value of the proton magnetic moment inferred from the above numbers, 2.75 nuclear magnetons, agrees satisfactorily with the accepted value, 2.7896, established by the molecular beam method.

The full width of the resonance, at half value, is about 10 oersteds, which may be caused in part by inhomogeneities in the magnetic field which were known to be of this order. The width due to local fields from neighboring nuclei had been estimated at about 4 oersteds.

The relaxation time was apparently shorter than the time (~ one minute) required to bring the field up to the resonance value. The types of spin-lattice coupling suggested by I. Waller[2] fail by a factor of several hundred to account for a time so short.

The method can be refined in both sensitivity and precision. In particular, it appears feasible to increase the sensitivity by a factor of several hundred through a change in detection technique. The method seems applicable to the precise measurement of magnetic moments (strictly, gyromagnetic ratios) of most moderately abundant nuclei. It provides a way to investigate the interesting question of spin-lattice coupling. Incidentally, as the apparatus required is rather simple, the method should be useful for standardization of magnetic fields. An extension of the method in which the r-f field has a rotating component should make possible the determination of the sign of the moment.

The effect here described was sought previously by Gorter and Broer, whose experiments are described in a paper[3] which came to our attention during the course of this work. Actually, they looked for dispersion, rather than absorption, in LiCl and KF. Their negative result is perhaps to be attributed to one of the following circumstances: (a) the applied oscillating field may have been so strong, and the relaxation time so long, that thermal equilibrium was destroyed before the effect could be observed—(b) at the low temperatures required to make the change in permeability easily detectable by their procedure, the relaxation time may have been so long that thermal equilibrium was never established.

* Harvard University, Society of Fellows (on leave).
[1] Rabi, Zacharias, Millman, and Kusch, Phys. Rev. 53, 318 (1938).
[2] I. Waller, Zeits. f. Physik 79, 370 (1932).
[3] Gorter and Broer, *Physica* 9, 591 (1942).

Figure 8 The first report of a nuclear magnetic resonance in a bulk material.[21] (Reproduced by permission of the American Physical Society)

Nuclear Induction

F. BLOCH, W. W. HANSEN, AND MARTIN PACKARD
Stanford University, Stanford University, California
January 29, 1946

THE nuclear magnetic moments of a substance in a constant magnetic field would be expected to give rise to a small paramagnetic polarization, provided thermal equilibrium be established, or at least approached. By superposing on the constant field (z direction) an oscillating magnetic field in the x direction, the polarization, originally parallel to the constant field, will be forced to precess about that field with a latitude which decreases as the frequency of the oscillating field approaches the Larmor frequency. For frequencies near this magnetic resonance frequency one can, therefore, expect an oscillating induced voltage in a pick-up coil with axis parallel to the y direction. Simple calculation shows that with reasonable apparatus dimensions the signal power from the pick-up coil will be substantially larger than the thermal noise power in a practicable frequency band.

We have established this new effect using water at room temperature and observing the signal induced in a coil by the rotation of the proton moments. In some of the experiments paramagnetic catalysts were used to accelerate the establishment of thermal equilibrium.

By use of conventional radio techniques the induced voltage was observed to produce the expected pattern on an oscillograph screen. Measurements at two frequencies ν showed the effect to occur at values H of the z field such that the ratio H/ν had the same value. Within our experimental error this ratio agreed with the g value for protons, as determined by Kellogg, Rabi, Ramsey, and Zacharias.[1]

We have thought of various investigations in which this effect can be used fruitfully. A detailed account will be published in the near future.

[1] J. M. B. Kellogg, I. I. Rabi, N. F. Ramsey, and J. R. Zacharias, Phys. Rev. 56, 728 (1939).

Figure 9 The first report of nuclear induction.[22] (Reproduced by permission of the American Physical Society)

decided to increase the field well above what was expected to be needed and allow it to drift downward at a rate determined by the time constant of the cyclotron magnet. Packard was watching the screen and saw a weak signal flit across. Nuclear induction was born!

During the next few days, Bloch was able to explain much of what had been observed. He understood in general that the rapid tumbling of the water molecules must be responsible for the much shorter relaxation time, but he did not anticipate the description of 'motional narrowing' later developed by Bloembergen. He did explain the observation of the signal with positive and negative lobes as resulting from the scanning conditions; he named it 'adiabatic rapid passage'. The short Letter describing this work (reproduced in its entirety in Figure 9) was received by the *Physical Review* on January 29, 1946, about a month after the Purcell, Torrey, and Pound submission, and was published in February.[22] Later the Nobel Committee recognized the two discoveries as independent and essentially concurrent. Bloch and Purcell shared the Nobel Prize in Physics in 1952 'for their development of new

Figure 10 Felix Bloch. (Reproduced by permission of the Nobel Foundation)

methods for nuclear magnetic precision measurements and discoveries in connection therewith'. Bloch's Nobel lecture (***Bloch, Felix: The Principle of Nuclear Induction***) includes a concise summary of much of the history of the molecular beam era, as well as a good discussion of the concept of nuclear induction.

One Discovery or Two?

It was not immediately obvious that *nuclear magnetic resonance* and *nuclear induction* measured the same phenomenon. The language in which the initial papers were couched and the theoretical approaches of the two groups somewhat obscured the underlying physics. Moreover, in the initial work the Stanford group reported the dispersion mode, while the MIT group studied absorption. Bloch (Figure 10) has mentioned that, at his first meeting with Purcell (Figure 11), the two had some difficulty communicating in detail because of their different terminology and techniques. However, they, and the broader physics community, soon realized that these two methods probed the same basic phenomena. Purcell's approach was more conventional in terms of treating transitions between quantized energy levels, as was commonly done for molecular beam studies and for all other branches of spectroscopy. Such an approach would prove essential later in understanding many important NMR phenomena. Bloch's treatment of the expectation values of quantum mechanical properties led to a classical picture that was to be the principal method for explaining time-dependent phenomena and for introducing the idea of phase coherence,

Figure 11 Edward Purcell. (Reproduced by permission of the Nobel Foundation)

a concept that is crucial for understanding many aspects of transient NMR experiments.

The experimental methods used in the two laboratories were also quite different. The Stanford group used the novel crossed-coil arrangement mentioned above. In the early days of NMR research, when the magnetic moments of various nuclei were being measured, this geometric arrangement could be adapted to permit the determination of the sign, as well as the magnitude, of the magnetic moment by driving both coils in quadrature. However, in normal operation, with the orthogonal arrangement of the transmitter and receiver coils, ideally there would be no signal appearing in the receiver coil directly from the transmitter, a critical factor in permitting the weak induced voltage to be measured. Since this was long before the advent of phase-sensitive detectors, a phase reference was obtained by deliberately introducing some 'leakage' between the two coils with the flux-steering paddles invented by Hansen. This whole crossed-coil probe arrangement was commercialized and formed the basis of several generations of NMR spectrometers, giving way to a single coil only after the widespread use of pulse methods permitted separation of transmitter and receiver functions in time, rather than space.

As we have pointed out, the MIT apparatus initially used a large cavity reminiscent of microwave methodology. Prior to the first experiment, this cavity with its very large amount of sample was viewed as an advantage in providing a large signal and in being resistant to saturation by the imposed radiofrequency field. When the magnitude of the signal and the shortness of the relaxation times were determined, the MIT workers replaced the cavity with a more conventional single rf coil that enclosed a small sample. Field modulation was added to reduce noise. Detection was still done with a bridge method, a necessity in order to avoid submerging the small absorption signal under the large amplitude from the transmitter. The single-coil arrangement continued for many years to be used in many academic NMR laboratories because of its simple probe design. The rf apparatus was soon improved, particularly by the introduction of the regenerative, or controlled marginally oscillating, detector, commonly called the 'Pound Box', which could be frequency swept.

As often happens in science, the names of the two methods remained in dispute long after there was agreement on the underlying physics. Bloch insisted for some time on using 'nuclear induction', probably with good justification since his experimental technique did measure the induced signal. According to Warren Proctor (***Proctor, Warren G.: When You and I Were Young, Magnet***),

> . . . one day in the basement he [Bloch] called us all together. . . . 'I have had a meeting with Purcell', he explained. 'It is important to be consistent with the nomenclature generally used in physics. It will be known as nuclear magnetic resonance', he concluded.

Early Studies at Stanford

Bloch moved quickly to exploit the new method. Two long papers were submitted to the *Physical Review* in July, 1946, one discussing the theoretical basis of nuclear induction,[23] the other describing the detailed experimental arrangement.[24] These papers seem to have had a major effect in popularizing this new concept in the physics community. Also, at the urging of Russell Varian, then a research associate at Stanford, Bloch and Hansen patented nuclear induction and assigned the patent to 'Varian Associates' a company that was not actually incorporated until several months later. In the fall of 1946, Bloch had discussed with Pound the possibility of a joint patent application, but the MIT group was not interested and it would have been difficult to carry out such a joint effort. The MIT work had been published first, but the Stanford project had commenced earlier and the experimental methods used by the two groups were quite different. The Bloch/Hansen patent application was submitted on December 23, 1946, one day short of a year after the Purcell, Torrey, and Pound paper had been received by the journal, thereby ensuring that the requirements of U.S. patent law would be met. Bloch and Hansen were precluded from applying for patents in many foreign countries, which required that the application be filed before publication. We shall return to the consequences of the patent in a later section.

As we pointed out previously, Bloch's impetus for investigating NMR in bulk materials was to develop an accurate method for measuring magnetic fields. His research interests remained focused on nuclear structure, which he viewed as the then central problem in physics. In 1947, Bloch and his co-workers reported precise values for the magnetic moments of ^{1}H, ^{2}H, and ^{3}H, the last of which was carried out at the Los Alamos National Laboratory.[25,26] In 1948, Bloch, Nicodemus, and Staub reported the quantitative determination of the magnetic moment of the neutron in units of the proton moment,[27] a follow-on to Bloch's work on this subject in the 1930s. Emery Rogers, one of Bloch's graduate students, measured

the signs of the proton and neutron moments with the Stanford cyclotron. Meanwhile, a number of graduate students worked with Bloch in measuring magnetic moments for dozens of nuclides, as detailed in Packard's article.

The consequences of the Bloch equations and their solution under different conditions were also examined during this period. In 1948, Jacobsohn and Wangsness[28] developed an analytical solution to the equations, which accounted for transient effects such as 'wiggles' that followed passage through resonance.

Early Work at Harvard

Purcell and his colleagues were just as eager as Bloch to exploit their discovery, but they were still constrained by completing their writing project, so things initially moved more slowly in Cambridge than at Stanford. However, in February, 1946, Nicolaas Bloembergen came to Harvard from the Netherlands and decided to do graduate work with Purcell, who was slated to return to his faculty position at Harvard in July. Bloembergen had considerable experience in physics and electronics and was able to advance the research while Purcell and Pound were still busy at MIT. The three collaborated, however, on measurements of ^{1}H and ^{19}F NMR in the cavity, and Bloembergen began to make improvements in the apparatus. In July, with the writing task completed, Purcell moved to Harvard, along with Pound, who took up his appointment in the Society of Fellows. Torrey departed for Rutgers, where he later pioneered work in transient NMR methods.

Bloembergen, Purcell, and Pound studied a CaF_2 crystal and found the true linewidth and noted its anisotropic character as it was rotated in the magnetic field. They realized, however, that lines in liquids were much narrower (narrower than could be measured with their existing magnet), and that this narrowing resulted from an averaging of magnetic dipolar interactions as the molecules tumbled. This group also devised an experimental study in hydrogen gas, where molecular collisions would modulate the resonance frequency. With increasing pressure, they found an increase in T_1 (from which an increase in T_2, hence line narrowing, could be inferred) and introduced the term 'pressure narrowing'.[29]

Meanwhile, Bloembergen devoted an intense three months in the fall of 1946 to developing a theory of relaxation in terms of the effects of random motions. He worked out the spectral densities of the interaction terms between two protons and showed that Fourier components at the Larmor frequency ν_0 and at $2\nu_0$ were responsible for longitudinal relaxation, while terms near zero frequency contributed as well to transverse relaxation. The BPP theory (see ***Bloembergen, Nicolaas: My Early Years in NMR, 1946-48***) introduced the idea of 'motional narrowing' and provided the framework for understanding the appearance of NMR spectra. Details of the theory, along with experimental tests in which T_1 was measured as a function of solution viscosity, were published in a preliminary form in *Nature*[30] in 1947 and in the famous BPP paper in the *Physical Review*[31] in 1948. Figure 12 shows the plot that summarized essential features of the theory and provided a guidepost for all future development and understanding of motional effects in NMR.

During this period, Bloembergen also carried out a classic experiment that demonstrated the difference between homogeneous and inhomogeneous broadening. When a truly broad

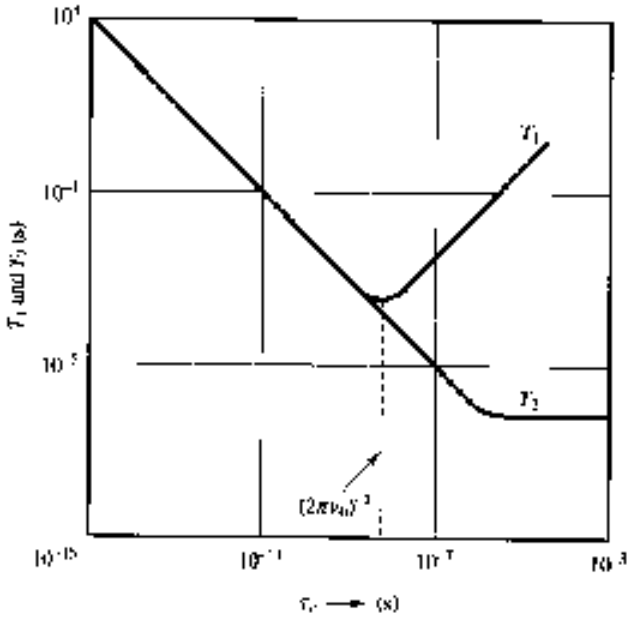

Figure 12 Schematic representation of the variation of relaxation times with correlation time τ_c.[31] (Reproduced by permission of the American Physical Society)

line, such as that of CaF_2, is irradiated with rf power anywhere within the linewidth, the entire line decreases in intensity from saturation. The resonance of water also appeared on an oscilloscope as a broad line, but Bloembergen realized that this broadening arose because nuclei in different parts of the sample had slightly different resonance frequencies in the inhomogeneous magnetic field. He applied rf power at one discrete frequency within the line and observed a decrease in intensity only at that frequency, as saturation 'burned a hole' in the line. This experiment has had considerable application in NMR and, many years later, in optical spectroscopy.

George Pake enrolled in the Harvard physics department in 1946 and became Purcell's second graduate student (perhaps, technically, his first, since Bloembergen was formally enrolled at the University of Leiden). While Bloembergen was busy in the study of nuclear relaxation in liquids, where he observed sharp lines, Pake decided to study solids, where he could observe the natural linewidth of protons in water rigidly bound in a crystal lattice. The essential difference between a liquid and a solid in this context is the lack of molecular motions, resulting in the broadening of the spectral lines in the solid. One of the major factors contributing to such a line broadening arises from the local magnetic fields due to the neighboring magnetic dipoles, which in the liquids are averaged out due to rapid isotropic molecular motions.

For such studies, Pake selected a single crystal of $CaSO_4{\cdot}2H_2O$ (gypsum) for several reasons: (1) it does not contain any paramagnetic ion and is relatively easily available; (2) it has only protons in the water molecule as the major nuclei with nonvanishing spin and consequently with a magnetic moment; (3) large single crystals exist in Nature; and (4) the crystal structure is well known.

The proton resonance in such a simple crystal showed that the linewidth was strongly dependent upon the crystal orientation in the external magnetic field, with pairs of resonance lines (Pake doublets) arising from two alternative

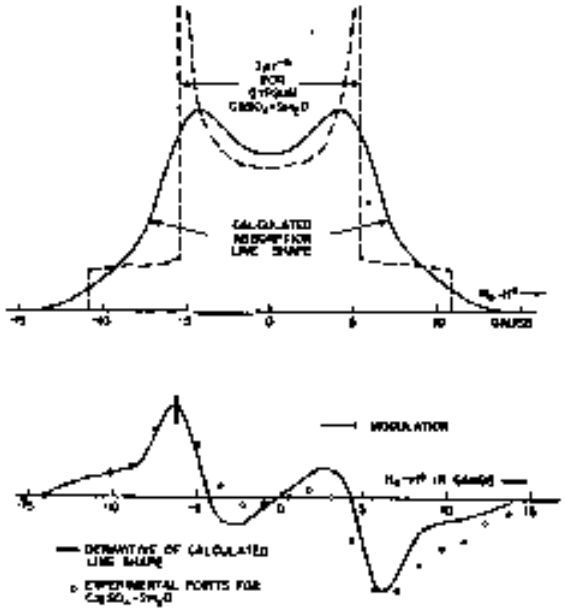

Figure 13 Upper: Calculated distribution of proton resonance frequencies in $CaSO_4 \cdot 2H_2O$ for nearest neighbor interactions (broken line) and for a set of Gaussian lineshapes superimposed onto this distribution function (solid line). Lower: Solid curve above recast as a derivative, with experimental points.[32] (Reproduced by permission of the American Institute of Physics)

orientations (parallel or antiparallel) of the partner protons. It was shown by Pake that, for each proton, the resonance should occur at a field strength $\boldsymbol{H}$ given by:

$$\boldsymbol{H} = \boldsymbol{H}_0 \pm (3/2)(\mu/r^3)(3\cos^2\phi - 1) \qquad (2)$$

where $\boldsymbol{H}_0$ is the applied magnetic field, μ is the proton magnetic moment, r is the pair separation, and ϕ the angle between $\boldsymbol{H}_0$ and the vector connecting the two nuclei.[32]

The theory was extended by Pake to powders, since the spectra for such specimens are the sum of the spectra due to the individual 'single crystals'; the spectral pattern so computed is shown in Figure 13. The figure shows the calculated line-shapes for the proton spectra in polycrystalline gypsum from only the nearest neighbors and from interactions with other neighbors. The experimental results shown in the lower portion of Figure 13 were found to be in general agreement with theory.

From the shape of the line and the separation of the peaks, interproton distances can be computed. NMR thus quickly became a tool for examining *molecular structure*, albeit in rather simple systems. Pake developed a collaboration with Herbert Gutowsky, a graduate student of George Kistiakowsky, in the chemistry department. They developed apparatus to cool samples for NMR study and used their knowledge of magnetic dipolar interactions to interpret linewidth alterations and phase changes in terms of molecular rotations in the solid.[33] Moreover, Pake's work also later became the basis for the use of NMR to study molecules oriented in liquid crystals or by external fields.

Meanwhile, Pound contributed to several projects, especially by utilizing his electronics expertise, but his major interests turned to the effects on NMR spectra of nuclear electric quadrupole interactions in crystals. After studying a number of light nuclei, such as ^{7}Li, ^{23}Na, and ^{27}Al, Pound began to look for 'pure' nuclear quadrupole resonance in the absence of a magnetic field, but before he had succeeded, this phenomenon was discovered in a chlorinated ethylene by Dehmelt and Kruger.[34]

Beginnings of NMR at Other Universities

Although a number of physicists in various parts of the world made forays into NMR very soon after reading the initial papers of the Stanford and Harvard/MIT groups, the early efforts at the University of Illinois were particularly noteworthy and established this institution as one of the early major centers of NMR research. Three separate research efforts came together here within a few years. First, Erwin Hahn entered graduate school in 1946, soon learned about the discoveries of NMR and began work in this field. In 1948, Herbert S. Gutowsky completed his Ph.D. in chemistry at Harvard, where he had done a thesis in infrared spectroscopy but had also studied NMR in solids in collaboration with Pake. He moved to Illinois, where he decided to set up a research program in NMR—one of the first *chemists* to do so. In 1949, Charles P. Slichter arrived in the physics department at Illinois after completing his Ph.D. with Purcell. He had worked primarily in electron resonance rather than NMR, but had gained considerable knowledge of NMR from others in the Harvard laboratory. Each of these three investigators made major contributions to different aspects of NMR, as we shall describe later.

Meanwhile, Pake moved to Washington University and established an NMR laboratory there. He and his students studied quadrupole interactions in ^{6}Li, the spin of ^{9}Be, and ESR in free radicals, much of the last in collaboration with Sam Weissman and Jack Townsend. The most famous publication emerging from these early years was not a research paper but two articles written by Pake for the *American Journal of Physics*, in which he gave lucid explanations of the principles of NMR.[35] There were no NMR textbooks at that time, and these articles provided *the* introduction to this field for hundreds (perhaps thousands) of students in physics and chemistry.

As the initial papers on NMR were read throughout the physics community, several investigators with no ties to the Stanford or MIT groups built apparatus and embarked on NMR experiments. One of the most successful of such early efforts was in England, where Bernard Rollin at Oxford University constructed a simple, but elegant, instrument, obtained NMR signals from ^{1}H and ^{19}F in a variety of solids and liquids, measured their relaxation times, and reported his results in a paper published in November, 1946.[36] Rollin and Hatton[37] used the same apparatus to measure T_1 and T_2 in liquid and solid hydrogen down to 1 K and later to observe ^{2}H, ^{27}Al, and ^{63}Cu resonances.[38] Further details of Rollin's work, as well as an account of the careers of Raymond Andrew and Rex Richards, are given in the historical sketches (***Andrew, E. Raymond: Spinning the Spins: A Lifetime in NMR***, and ***Richards, Rex: Development of NMR in Oxford***).

In 1948–49, E. Raymond Andrew spent a postdoctoral year in Purcell's laboratory, learning about NMR and applying the method to the study of molecular rotations in solid benzenes

and paraffins. On his return to Great Britain (initially at St. Andrews University in Scotland, later at the University of Wales, Bangor), Andrew constructed an NMR spectrometer around a 6000 G permanent magnet and concentrated on the study of NMR in solids. A few years later he discovered magic angle spinning, a subject that we shall cover in detail in a later section. Andrew recognized the need for a book on NMR and in 1954 wrote *Nuclear Magnetic Resonance*.[39] Like Pake's articles, this book became an invaluable source of instruction for the physicists and chemists who were increasingly being drawn into NMR.

In 1948, Rex Richards, fresh from a Ph.D. in infrared spectroscopy, began a faculty appointment at Oxford University and decided that the new technique of NMR might have utility in chemistry. He constructed the necessary apparatus and began investigations of NMR linewidths in solids as a function of temperature for studying molecular motions and for elucidating the structure of simple, usually inorganic, compounds in solids. As in other laboratories at that time, the emphasis was on the study of solids because magnet inhomogeneity determined the width of lines in liquids, and no one as yet had any idea that chemical structure could affect the basic resonance frequencies. Later, Richards would make major contributions in chemistry and biology, as we shall see.

Anatole Abragam began a long and distinguished career in physics just after World War II and started to work in NMR in the early 1950s. He established a magnetic resonance laboratory at Saclay, France, in 1955, somewhat later than the other pioneering laboratories discussed above. Nevertheless, his efforts introduced NMR (and electron spin resonance) to most of the French scientific community, and a number of leading NMR scientists from other countries worked there, as Abragam describes in his autobiography.[40] In Section 4 we discuss some of the innovative work in spin temperature and dynamic nuclear polarization carried out at Saclay. Abragam's historical sketch (***Abragam, Anatole: 'The Bible'***) describes the writing of the widely known monograph *The Principles of Nuclear Magnetism*,[41] published in 1961.

The seeds of NMR research had been planted and were being nourished in an increasing number of laboratories throughout the world. The basic instruments and techniques were still quite primitive, however, and the understanding of NMR theory was still limited. Several additional fundamental discoveries had to be made before NMR began to blossom.

NMR Excitation by Radiofrequency Pulses

Almost all of the early NMR observations were made in the same manner as in the initial experiments at Harvard and Stanford—by sweeping the magnetic field while applying continuous wave (CW) power at a fixed radiofrequency. A few studies (such as those by Pound, mentioned in Section 2.6) used a fixed magnetic field and swept the frequency. But both of these approaches used CW excitation, a means of obtaining NMR spectra that dominated the field for 25 years, as we shall see. Nevertheless, very early in the history of NMR another approach was introduced and developed with very important consequences. This involved the use of short *pulses* of radiofrequency power applied to excite the nuclear spins. Bloch[23] initially suggested this approach in his paper in 1946:

> It is worth while, however, to point out that the observation of nuclear induction should be possible even without any use of the magnetic resonance. Not only a weak rf field, acting at resonance over very many Larmor periods, can produce an appreciable nuclear change of orientation, but also a strong field pulse, acting over only a few periods. Once the nuclear moments have been turned into an angle with the constant field, they will continue to precess around it and likewise cause a nuclear induction to occur at an instant when the driving pulse has already disappeared. . . . it would observe by induction the free nuclear precession while we have studied the forced precession impressed upon the nuclei by the applied rf field.

Surprisingly, there was no effort at Stanford to try this means of excitation. However, at the University of Illinois, Erwin Hahn had built a CW NMR spectrometer, patterned after the one used at Harvard, but he decided to study the dynamics of spin systems after the application of rf pulses and in particular to measure spin–lattice relaxation times. His Ph.D. thesis, completed in 1949, dealt with adiabatic fast passage effects, spin–lattice relaxation times, and the measurement of transient nutational motions of spins after the application of rf pulses. Hahn published on the use of a pulse to invert the magnetization and permit considerable improvement in the precision of measurement of T_1 for water,[42] but he soon learned that he had been scooped by Henry Torrey who had independently discovered and explained transient nutations.

After leaving the MIT Radiation Laboratory in 1946, Torrey had initiated a research program in NMR at Rutgers University. He soon developed the picture of magnetization precessing about the applied magnetic field to include consideration of a frame of reference rotating at the applied radiofrequency. As indicated in Figure 14, in the rotating frame the magnetization $\boldsymbol{M}$ precesses about $\boldsymbol{H}_{\text{eff}}$ as long as the rf $\boldsymbol{H}_1$ is being applied. This picture made it clear that in the laboratory frame the motion of $\boldsymbol{M}$ would be a nutational motion at a frequency $\omega_1 = (1/\gamma)[(\gamma H_1)^2 + (\gamma H_0 - \omega_{\text{rf}})^2]^{\frac{1}{2}}$. Torrey looked for and found the transient signals following the application of an rf pulse, as illustrated in Figure 15.[43] This was the first published application of pulses in NMR. Torrey made it clear that this method of *nutational resonance* was different from the free precession predicted by Bloch. This transient nutation technique was developed largely to measure the transverse relaxation time T_2 in the presence of magnetic field inhomogeneities. The method has had some subsequent uses, but it was rapidly overtaken by events back at Illinois.

After receiving his Ph.D., Hahn remained at Illinois for another year to continue exploring the use of pulses with increased rf power and shorter duration, partially as a means of measuring T_1 in the ms range. Torrey had used pulses of 10 ms or longer in order to record a number of nutations during the pulse, but Hahn's short pulses permitted the magnetization to precess freely between pulses, apparently the first experimental application of Bloch's proposal. His T_1 measurements were made with a 60 Hz modulation of the magnetic field. One day during the summer of 1949, as Hahn describes it (***Hahn, Erwin L.: Pulsed NMR–A Personal History***), 'the weird signal appeared'. He had been experimenting with pairs of high power pulses of, at that time, short duration—of the order of 1 ms. He found a signal at a time that no pulse was applied. After initially dismissing the 'weird signal' as an artifact, Hahn found that it was, in fact, reproducible. He had serendipitously discovered the spin echo! He understood

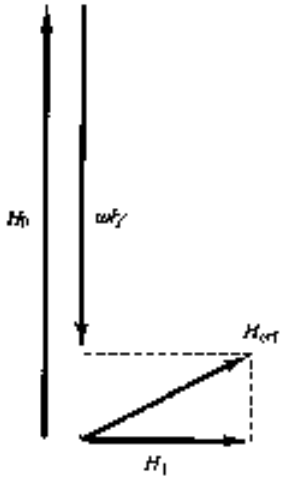

Figure 14 Vector representation of the formation of an 'effective field' from an off-resonance static magnetic field $\boldsymbol{H}_0$ and an rf field $\boldsymbol{H}_1$

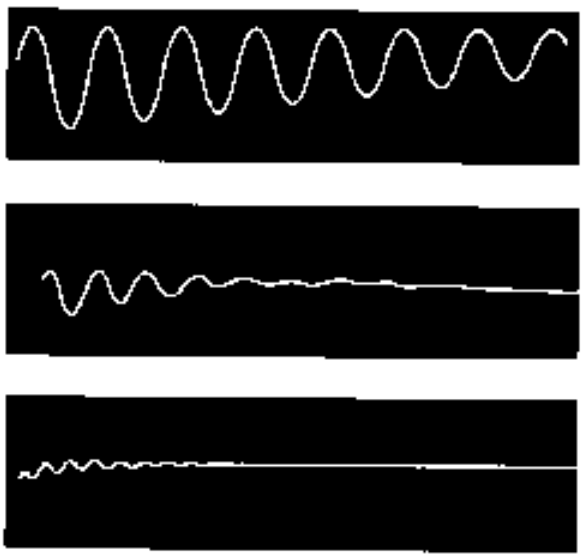

Figure 15 Transient nutations at 9 MHz for glycerine at exact resonance (top), slightly off-resonance (middle), and farther off-resonance (bottom). Sweep time 0.01 s.[43] (Redrawn by permission of the American Physical Society)

that he was observing a free induction decay and eventually deduced from the Bloch equations what caused the 90°, 90° two-pulse echo. Understanding the three-pulse stimulated echo presented even more of a challenge. Hahn gives Purcell credit for first formulating a pictorial representation of a 90°, τ, 90° echo. (Only after several years did Carr and Purcell demonstrate the conceptually much simpler 90°, τ, 180° echo, as we shall discuss in Section 4.) During this period also, Hahn first observed a mysterious beat modulation in the echo envelope of the signal from ethyl alcohol but could not explain it at that time.

The use of short rf pulses and the observation of NMR by free induction decay (FID) signals would ultimately play a vital role in the development of sophisticated modern NMR methods, and we shall return in later Sections to more detailed discussions of advances in pulsed NMR methods. However, about 1950 other discoveries began to change NMR from a technique for studying the properties of the nucleus to a method of examining the electronic environment around the nucleus—largely the province of chemists.

The Chemical Shift

All the early work in NMR was based on the assumption that the resonance frequency of a particular nucleus depends only on the applied magnetic field according to the Larmor relation. If this were strictly so, NMR would have remained an investigative method for physicists enlarging the table of precise nuclear magnetic moments and it would have been of little use in interdisciplinary sciences such as chemistry, biology, and medicine. However, it was fortunately observed as early as 1950 that NMR spectral frequencies of a particular species of nuclei in different chemical environments, whether in the same or different molecules, may be different and that the difference depends upon the molecular structure. This displacement is referred to as the *chemical shift*. As a matter of fact, the idea of the chemical shift is implicit in the earlier work of Knight (in 1949) discussed below.

The first observation of the chemical shift is a classical case of accidental discovery. In order to determine the magnetic moment of ^{14}N more precisely, Proctor and Yu[44] decided to use ammonium nitrate, NH_4NO_3, which was available from the chemistry stockroom of the Stanford University. The main considerations for such a selection were the large solubility of the compound in water and the fact that it possesses two nitrogens per molecule, both factors expected to enhance the NMR signal. A saturated solution in water produced two strong lines instead of one! The observation was attributed to some 'nasty' chemical effect. About the same time, Dickinson[45] observed similar effects for ^{19}F in a variety of fluorine compounds such as $C_2F_3Cl_3$, SbF_3, NaF, KF, HF, BF_3, and BeF_2. He employed two identical magnetic resonance absorption bridges, both fed by the same oscillator. The two sample holders were placed side by side in the magnet so that ^{19}F resonance occurred simultaneously on separate recording milliammeters. In these compounds the maximum separation of the ^{19}F resonances occurred for $C_2F_3Cl_3$ and BeF_2, the former appearing at the lower applied field. The initial experiments were performed at a magnetic field of 0.7 T, and additional studies at 0.25 T demonstrated that the magnitude of the separations was proportional to the field strength.

At nearly the same time, Lindström[46] measured the nuclear magnetic moments of ^2H and ^1H in two different compounds (water and paraffin oil). He observed that the ratios of the magnetic moments for deuterons and protons in the two compounds were slightly different and so was the ratio of the magnetic moments for the protons in paraffin oil and water. Although the observations were published, no explanation of the effect was given. Thomas, on the other hand, in a later issue of the *Physical Review* in the same year[47] explicitly reported the measurement of proton chemical shifts between different compounds such as H_2 gas, water, and mineral oil.

The most dramatic demonstration of the chemical shift, and the real birth of 'high-resolution NMR' was the observation by Arnold, Dharmatti, and Packard[48] of separate lines for chemically nonequivalent protons in the same molecule,

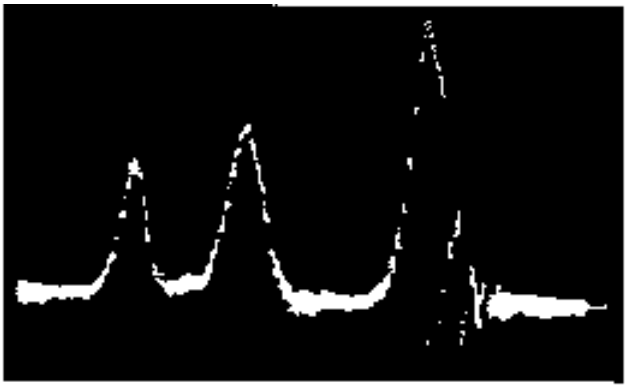

Figure 16 An oscilloscope presentation of the three chemically shifted lines in ethyl alcohol.[48] (Reproduced by permission of the American Institute of Physics)

first acetic acid, then ethanol. Apparently it was Dharmatti, a chemist from India who was working in the physics department at Stanford, who suggested the molecules to be studied (see ***Arnold, James T.: Early Perceptions in Nuclear Magnetic Resonance (NMR)*** and ***Packard, Martin E.: Nuclear Induction at Stanford and the Transition to Varian***). The separation of the chemically shifted lines was found to be field-dependent and only a few parts per million for protons. It was only with very small sample volumes and after substantial empirical searching in the magnet for a homogeneous spot that the separation of the spectral lines could be observed.

For ethyl alcohol, three spectral lines corresponding to the three different chemical groups, CH_3, CH_2, and OH, with relative intensities of 3 : 2 : 1, were observed as shown in Figure 16. This discovery really set the stage for the chemical applications of NMR, since it illustrated the ability of NMR to detect the presence or absence of particular groups of protons in a molecule, and the relative intensities provided a measure of the relative numbers of protons of each type.

This important discovery was possible only because of significant improvements in the instrumentation at Stanford, especially magnet homogeneity. The investigators used an electromagnet with 12-inch diameter pole faces, producing a field of 0.7 T in a 1.5-inch pole gap, designed by Harry E. Weaver, then also one of Bloch's students. This corresponds to the observation of the proton resonance at a frequency of approximately 30 MHz. To improve field homogeneity at the center of the magnet, shims were added to the magnet poles which were basically round with square edges. Enormous effort was required to locate the most homogeneous region in the magnetic field, hence a spherical sample only 1 mm in diameter was employed. Interestingly, however, Packard points out in his historical sketch that with great care further small splittings of the methyl and methylene lines could sometimes be observed, foreshadowing the later discovery of scalar spin–spin coupling. However, the published spectrum of ethanol was deliberately obtained under conditions where such barely resolved features were not evident.

Shortly after publication of the famous Arnold, Dharmatti, and Packard paper, Arnold observed that the separation between the OH and CH_2 peaks was temperature-dependent, whereas the CH_3–CH_2 separation was not. Packard and Arnold reported this unexplained observation in an abstract in the *Physical Review*,[49] and soon thereafter Liddel and Ramsey[50] explained the result as a consequence of hydrogen bonding between ethanol molecules. This observation of a resonance that shifts continuously with temperature (or, as was soon discovered, with dilution of the alcohol in an inert solvent such as CCl_4) implicitly demonstrated the consequence of rapid chemical exchange, a phenomenon that had not yet been explicitly elucidated and explained.

Perhaps the observation of the chemical shift should not have been so unexpected. In 1941, Lamb had developed a theory for magnetic shielding of single atoms,[51] so qualitatively there was an explanation for the field-dependent variation in resonance frequency. However, the Lamb theory is inadequate to account for the magnitudes of the observed chemical shifts, and Ramsey showed in a series of papers in 1950–52 that other terms involving excited electronic states become important for nuclei other than hydrogen.[52,53] The Ramsey theory provided a sound basis for interpreting chemical shifts and still provides the basic framework for all theoretical treatments of chemical shifts.

The discovery and explanation of the chemical shift had a profound influence on the direction that NMR was to take, since chemists began to take notice of its potential. Another related discovery of resonance frequency shifts in metals had a somewhat similar impact in solid state physics.

The Knight Shift

The search for new resonances was in full swing in the late 1940s, and Walter Knight who was doing research at Brookhaven National Laboratory was looking for antimony NMR. However, he observed instead a ^{63}Cu resonance without putting a sample in the probe! In checking the 'background' from the bare probe, Knight found a strong signal near the frequency expected for ^{63}Cu, which could arise from the probe coil, but its frequency was 20 kHz higher than expected from the standard table of nuclear magnetic moments. With a mixture of copper metal and copper(I) chloride, Knight found two well-resolved peaks (as shown in Figure 17), with the resonance of the pure metal appearing approximately 25 kHz above that for the nonmetallic salt, around the average frequency of 10 MHz. The measured relative shift was 0.23% (2300 ppm).

During the next few weeks several other metals such as sodium, aluminum, and liquid gallium were investigated. The effect was found to be common to all the metals. It was also observed that isotope pairs, such as ^{63}Cu and ^{65}Cu, possess equal shifts and the fractional frequency shifts are independent of the resonance field.[56] This fractional shift is at least an order of magnitude larger than the chemical shifts later found in different diamagnetic compounds. It was soon attributed to a hyperfine interaction between the magnetically polarized conduction electrons and the magnetic moments of the nuclei in the metal. This effect was later named the 'Knight Shift' by Bloembergen.[57] The Knight shift provides a sensitive means to probe structural effects and processes in metals, and Knight shifts have been used in many studies including melting of metals, metal–insulator transitions, normal–superconducting transitions, phase transitions, and magnetic couplings in metal alloy systems.

ZEEMAN, LARMOR, AND NMR

Many NMR books and articles refer to 'Zeeman splitting' of nuclear magnetic energy levels and to the 'Zeeman energy' of the nuclear spin system. In addition, NMR is often described in terms of 'Larmor precession' of nuclear magnetic moments and the nuclear resonance frequency is often called the 'Larmor frequency'. Neither Zeeman nor Larmor had anything to do with NMR; their relevant papers were published in 1897.

In a paper published in the *Philosophical Magazine*, P. Zeeman[54] reported 'On the Influence of Magnetism on the Nature of the Light emitted by a Substance'. He found that the well known yellow D lines emitted by sodium vapor when it is heated were broadened when the sodium chloride sample was placed in a magnetic field. Later work showed that the broadening was actually a splitting of the lines, and the term 'Zeeman effect' was applied to this phenomenon in optical spectroscopy. The term was generalized to include the splitting of energy levels through interaction with a magnetic field, regardless of the frequency and energy involved. Thus, the 'Zeeman interaction' of nuclear magnetic moments with an applied magnetic field is generally the dominant energy term in describing the nuclear spin system.

Sir Joseph Larmor followed up on Zeeman's observation and explanation of the optical spectroscopic phenomenon by publishing a theoretical analysis.[55] He treated the motion of charged particles moving in an elliptical orbit and calculated the change in their motion on the introduction of a uniform magnetic field. He showed that the original motion could be restored if the observer is located on a coordinate system rotating at a particular frequency dependent on the charge and mass of the particle. This formalism used to derive the 'Larmor frequency' was later found to describe the motion of other systems, such as magnetic moments interacting with a static magnetic field, and the terminology became standard in phenomenological treatments of NMR.

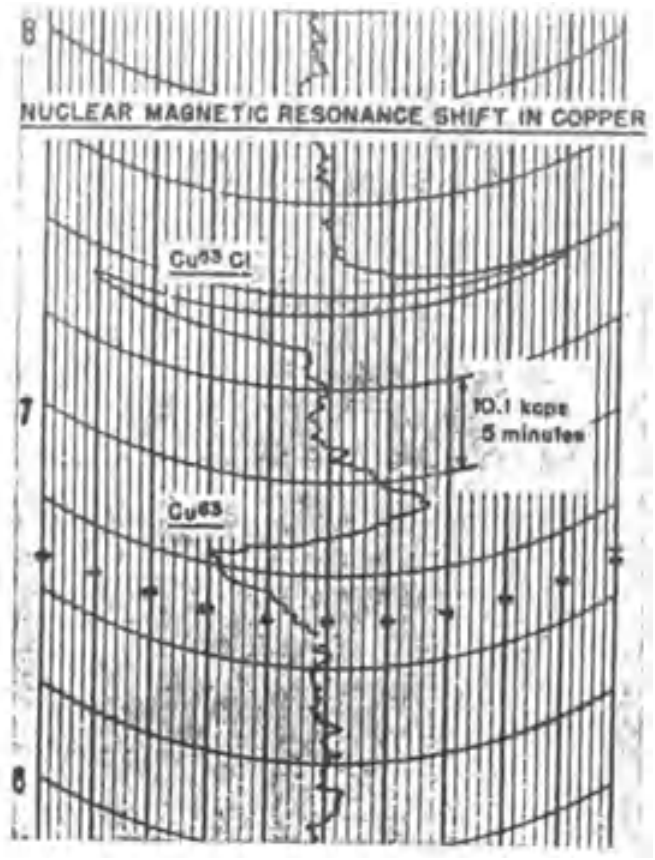

Figure 17 Demonstration of the Knight shift in ^{63}Cu metal relative to the ^{63}Cu signal in CuCl powder.[56] (Reproduced by permission of the American Physical Society)

Indirect Spin–Spin Coupling

The discovery of this important concept is another landmark that led to the application of NMR to the investigation of molecular structure, conformation, and function. As many groups undertook independent investigations of NMR in the early 1950s, discoveries of new effects came so rapidly that it becomes difficult in many cases to identify unequivocally the real 'discoverer' of new phenomena. The discovery of indirect spin–spin couplings is one such example. In fact, independent work by several groups was essential before observations were even recognized as a new phenomenon and unraveled.

On careful examination of the NMR spectra under conditions of high resolution, it was observed that the chemically shifted peaks are themselves composed of several lines since the number of lines observed was more than required by simple consideration of nonequivalent nuclei. The multiplicity was first reported by Proctor and Yu[58] for the ^{121}Sb resonance in $NaSbF_6$. In a carefully purified sample, ensuring that only one form of Sb was present, they observed five lines of different intensities, and Harry Weaver subsequently showed that there were in fact seven lines. They suggested a possible incomplete averaging of the magnetic dipole–dipole interactions between Sb and F by hindered rotation, but this explanation was shown not to account for the results.

Independently, Hoffman and Gutowsky while measuring the ^{19}F resonance in PF_3 observed two close lines of comparable intensity. The effect was also observed for PF_5. It was difficult to explain this result until a systematic study of some fluorochlorophosphorus compounds was undertaken by McCall and Gutowsky.[59] The appearance of a 1 : 1 doublet in $POCl_2F$ and a 1 : 2 : 1 triplet in CH_3OPF_2 for the phosphorus resonance ensured that the observation resulted from a new type of interaction, not (as had initially been thought) the presence of an impurity in the sample. It became clear that the splitting of the fluorine resonance depends upon the number of different phosphorus spin states, while the splitting of the phosphorus resonance depends upon the number of different fluorine spin states.

Meanwhile, Hahn and Maxwell observed the same effect in an entirely different manner, as 'slow beats' in the spin echo envelope for nonequivalent protons.[60] This turned out to be caused by the same interaction as the one in the steady-state multiplets.

Unlike chemical shifts, the magnitude of this splitting was found to be independent of the applied magnetic field,

and hence to represent an interaction not induced by the field. Unlike direct dipole–dipole coupling, the interaction did not average to zero with rapid molecular tumbling of the molecules in the liquid state. Thus this interaction was shown to be of the form of a scalar product, $J_{ij}\boldsymbol{I}_i\boldsymbol{I}_j$, where J_{ij} is a coupling constant related to the molecular structure. Ramsey and Purcell[61,62] developed the theoretical explanation for the interaction as a slight polarization by the nuclear spins of the electron spins which are tightly coupled by exchange interactions in a chemical bond.

With the discovery and explanation of scalar coupling (or indirect spin–spin coupling) to complement the chemical shift, the groundwork had been laid for applications of NMR to chemistry.

NMR—A TOOL FOR CHEMICAL STUDIES

By 1952, when Bloch and Purcell received their Nobel Prizes, the basic principles of NMR had been established. Relaxation processes were generally understood and major parameters influencing the spectra, such as the chemical shift and scalar spin–spin coupling, had been elucidated. The potential of NMR for solving chemical problems had been demonstrated and the time was ripe for innovative chemists to mount a serious exploration of the uses of NMR in a wide range of problems in physical, organic, and inorganic chemistry—an exploration that would lead to an exponential expansion of its use. Although many important developments in the physical principles of NMR and its applications in solid state physics lay ahead, the next two decades were to be largely dominated by the chemical applications of NMR. As Martin Packard, one of the discoverers of NMR put it:

> To borrow a phrase from a writer for Eastman Kodak: 'Chemists got the point very quickly, thanked the physicists, and took over.'[63]

An important factor responsible for the widespread and rapid advances of NMR in chemistry during the 1950s was the commercial availability of a high-resolution spectrometer and, moreover, the rapid progress in the improvement of NMR instrumentation.

The Varian NMR Spectrometer

Soon after the discovery of nuclear induction, Russell Varian sensed the commercial potential of the technique for chemical analysis—a remarkable leap of faith, since the only published spectrum at the time was that of water and the discovery of the chemical shift was still years away. He persuaded Bloch and Hansen to apply for a patent before the end of 1946 and to assign it to the not-yet incorporated Varian Associates. In fact, Russell Varian himself wrote most of the patent application. This patent, which was issued in 1951 but later modified, played a vital role in permitting Varian Associates to invest capital to produce commercial NMR instruments. Further interesting information on the patent is given in two historical sketches (***Anderson, Weston A.: Early NMR Experiences and Experiments*** and ***Packard, Martin E.: Nuclear Induction at Stanford and the Transition to Varian***

At first, Varian's business lay principally in the sale of klystrons and later magnets for physics experiments. The first real commercial NMR instrument was the free precession magnetometer, conceived by Russell Varian in 1948. The idea is simple: polarize the protons in a water sample in a magnetic field oriented perpendicular to the Earth's magnetic field, then turn off the polarizing field and allow the nuclei to precess in the Earth's field. The precession frequency then measures the magnitude of the field, and features such as geological formations or large steel objects (such as submarines), which perturb the field, can be identified. We shall describe some applications of this instrument in a later section.

The first commercial high-resolution NMR instrument, developed in 1952 and purchased by the Humble Oil Company, Baytown, TX, was primitive by today's standards. It was designed for the study of protons at an operating frequency of 30 MHz and a magnetic field of about 0.7 T. The magnet was based on a design by Harry Weaver, then in Bloch's laboratory at Stanford, and became the standard for Varian magnets for many years. It weighed 5400 lb, had 12-inch diameter pole faces separated by less than 2 inches, and required a large power supply containing eight 304-TL vacuum tubes, which produced significant heat. The magnet was water cooled. The pole pieces were made of high quality steel, and pole faces were polished to optical flatness to improve homogeneity. To adjust the pole pieces to be parallel to each other, small pieces of steel ('shims') were placed between them and the steel core of the magnet, and bolts tightened with a 12-ft long wrench. The magnet was specified to be able to resolve the three peaks of ethyl alcohol.

By 1953, the 30 MHz instrument was the state-of-the-art, top-of-the-line NMR spectrometer. It could resolve the fine structure from chemically nonequivalent protons in molecules as well as the hyperfine structure from spin–spin interaction between nonequivalent nuclei. The reproducibility of the spectral parameters was a problem which provided enormous scope for further developments. Sensitivity was such that only neat liquids or concentrated solutions would produce reasonable signal-to-noise ratios.

The operation of the system was not easy. The user had first to locate the signal from a sample of water and move the sample to the most homogeneous region, as judged by the persistence of ringing or 'wiggles' on the oscilloscope trace following a fast scan through resonance. Then the water sample had to be removed and replaced with the sample to be studied. Spectra were thus referenced to water only by noting the relative positions on the scope and hoping that the scan rate and magnetic field strength had remained constant while these measurements were being made. Many repetitions to check reproducibility were required.

Very important improvements in instrumentation were made over the next few years by Varian Associates' staff, including Forrest Nelson, Ralph Kane, and a stream of physicists who came from Stanford—Warren Proctor, Harry Weaver, Weston Anderson, and James Arnold. James N. Shoolery joined Varian in 1952; more about that later. Many of the instrumental advances had their origin at Stanford. The commercialization of these discoveries is an early and markedly successful example of technology transfer from academia to industry, both through sharing of specific information and by Varian's employing a number of highly trained and motivated people from Stanford.

Increasing the strength of the magnetic field while maintaining or improving its homogeneity has long been an objective

for high-resolution NMR, both because chemically shifted resonances can be resolved more easily and because sensitivity increases approximately at the $\frac{3}{2}$-power of the magnetic field strength. By 1955, Varian had found that the 12-inch magnet and power supply could go to about 1.0 T, thus making 40 MHz operation possible for proton NMR. Three years later tapered pole caps and further 'beefing up' of the power supply raised the field to 1.4 T and the ^{1}H NMR frequency to 60 MHz.

Meanwhile, the magnetic field instability required that a spectrum be scanned by sweeping the field rapidly, thus limiting the precision of measurements and obscuring spectral details because of line distortions. A major improvement occurred when Varian introduced the 'super stabilizer', a device that sensed magnetic field variations as a current induced in a pickup coil placed near the magnetic field gap and generated a compensating current via a negative feedback loop. As described by Jim Shoolery (***Shoolery, James N.: High-Resolution NMR: A Dream Come True***):

> Before magnetic flux stabilization was developed, obtaining a spectrum was like looking through binoculars at a row of birds on a telephone wire from the back of a truck bouncing over a rutted road. . . . I remember my first trial of the device in 1956. Closing the switch made it seem that I'd gotten out of the truck and mounted my binoculars on a tripod. I could easily count the birds on the wire and even tell if their feathers were ruffled. In a fit of enthusiasm, we called the device a Super Stabilizer.

As an interesting sidelight, just about this time Russell Varian patented a device that would ultimately displace the super stabilizer and become the standard method for controlling magnetic field strength—the field/frequency lock.[64] However, it would be five years before that principle came into use in the Varian A-60.

Probably no single advance contributed more to improvement of homogeneity than the use of sample spinning, about which an interesting story can be told.

Sample Spinning and Homogeneity Improvement

The limiting factor in high-resolution NMR measurements is often the inhomogeneity of the applied magnetic field and various measures have been taken to obtain the maximum homogeneity. The idea of sample spinning is one of them. Sample spinning in NMR first seems to have been employed in 1951 by Herman Y. Carr[65] in his Ph.D. work at Harvard University (***Carr, Herman Y.: Early Years of Free Precession Revisited***). In studies of spin echoes (about which we will say more in a later section), Carr realized that an echo could be produced by reversing the magnetic field gradient and that one way to do this is to rotate the sample by 180°. He spun samples attached to a motor by a long wooden shaft and, among other applications, observed the chemical shift modulation of the free induction decay in a magnet whose inhomogeneity otherwise obscured the chemical shift effects.

In 1954 Bloch, apparently unaware of Carr's unpublished work, suggested that if one could stir the sample rapidly within the sample tube, the effect of magnetic field variation over the sample could be drastically reduced. The idea for sample stirring occurred to Bloch one day at lunch as he was stirring his tea. He reasoned that stirring the nuclei would cause them to sense the average magnetic field.

Jim Arnold, then a graduate student, immediately fabricated a tiny glass paddle wheel that would fit into the 3-mm diameter sample tube and mounted it on the end of a long glass tube. When the paddle was spun by a tiny air turbine, he found a remarkable improvement in resolution. However, the paddle wheel, which created magnetic susceptibility discontinuities, soon gave way to the technically easier method of simply spinning the entire sample tube. Bloch's proposal for sample spinning[66] and an experimental demonstration by Anderson and Arnold[67] were published consecutively in the *Physical Review*, and Bloch patented the technique.[68] Spinning in excess of 10 rotations per second was shown to reduce the linewidth by a factor of 17, as illustrated in Figure 18. According to Kaplan's later work,[69] periodic rotation is generally more effective than random rotation in producing line narrowing. Williams and Gutowsky[70] and Halbach[71] analyzed spinning in detail under conditions of magnetic field inhomogeneity.

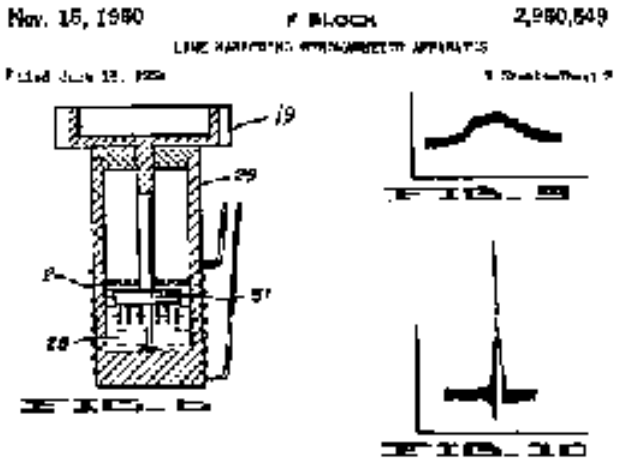

Figure 18 Excerpts from Felix Bloch's patent application for sample spinning.[68] The examples of nonspinning and spinning lineshapes came from the paper by Anderson and Arnold[67]

The method achieves only partial homogeneity improvement since it effects an averaging over the field around coaxial circles in the plane normal to the spinning axis but does not average the field along the axis of spinning. Nevertheless, as sample spinning was introduced into the Varian 40 MHz instrument, 'high-resolution' NMR was finally achieved. Searching for optimum homogeneity was reduced largely to a one-dimensional problem, along the *y* axis, the axis of rotation of the sample in an electromagnet.

One innovation to improve homogeneity along the *y* axis had its origin also at Stanford. The requirement for an extremely high homogeneity magnet was often demonstrated to a visitor by having him push on the strong steel yoke of the 5400 lb magnet, whereupon the NMR signal displayed on an oscilloscope was observed to shift. The effect of such a tiny distortion was turned to advantage when Varian introduced the 'field trimmer', a device mounted on one side of the magnet that used a 1-ft long wrench to distort the magnet yoke and thus permit optimization of homogeneity along the *y* axis.

A final method of homogeneity improvement, developed initially in a crude form by Arnold and Anderson at Stanford, was the use of a number of electrical coils in which the current could be adjusted to generate small, accurately controlled magnetic field gradients that would compensate the unwanted

gradients in the main magnetic field. Since this method would perform the same function (albeit in a very different manner) as metal shims placed behind the pole pieces, the coils were initially called 'shim coils', a term that persists to the present. In 1955, Marcel Golay at the Perkin–Elmer Corporation designed sophisticated shim coils, initially for use by Rex Richards with his 7000 G permanent magnet, and various laboratories experimented with homemade shim coils. While simple in principle, the design of such coils was a challenge and they were not introduced commercially until about 1958.

Chemical Shifts, Chemical Exchange, and Chemical Structure

With the remarkable advances in NMR instrumentation and the availability of commercial NMR instruments, the door was opened for the participation of many more chemists in the NMR revolution. Meanwhile, pioneering chemists with homemade instruments continued to develop new concepts and to correlate NMR data with molecular structure. During the early to mid 1950s a solid foundation for the use of NMR in chemistry was erected.

As stated previously, in 1948 Herbert Gutowsky established an NMR program in the chemistry department at the University of Illinois that became a major center for new developments. Gutowsky and his co-workers initiated efforts to correlate chemical shifts with molecular structure.[72,73] The ^{19}F nucleus was particularly attractive, since it has a spin of $\frac{1}{2}$, almost as high a sensitivity as ^{1}H, generally favorable relaxation times, and a large chemical shift range. In one of the earliest studies, they found that they could distinguish the ^{19}F resonances in a benzene derivative with a CF_3 group and three fluorines in the ring. Gutowsky and Hoffman studied a large number of fluorine compounds and in 1950 reported on the influence of molecular structure on fluorine chemical shifts.[72] The initial observations suggested that in simple covalent compounds the magnetic shielding of an ^{19}F nucleus chemically bound to another element is related to the position of that element in the Periodic Table. For elements in the same period, the shielding was found to decrease with increasing atomic number, while for elements in the same group the shielding increases with increasing atomic number. In complex fluoro compounds, the shielding was found to depend upon the inductive effects of the neighboring chemical bonds. Saika and Slichter[74] developed a quantitative theory of the atomic contributions to the ^{19}F chemical shifts. The experimental observations of Gutowsky and Hoffman[75] reported in 1951 showed a fairly good correlation of the ^{19}F chemical shifts with the electronegativity of the atom to which the fluorine is bonded, a covalently bonded fluorine being less shielded than an ionic one. The ^{19}F and ^{1}H chemical shifts in halomethanes were employed by the same group to derive information on the ionic character of the C–H bonds and the double bond character of C–X bonds, where X is a halogen atom.

In 1953 Gutowsky's group also investigated the proton chemical shifts in a large number of organic compounds. Although proton chemical shifts were discovered only in 1951, Lee Meyer as early as 1952 started a survey of the shifts on a new homemade spectrometer at the University of Illinois.[76] The idea was to see the extent to which they are characteristic of the various functional groups such as CH_3, NH_2, CH_2, OH, etc. This work resulted in the correlation shown in Figure 19. This empirical relationship quickly became valuable for ascertaining the presence or absence of particular functional groups. The results were presented at a meeting of the American Chemical Society in Chicago in the fall of 1953. This correlation chart had an enormous impact on the chemistry community. It was used for a decade and served as the basis of every other proton chemical shift correlation developed with additional data in subsequent years, and was a model for other nuclei such as ^{13}C. It gave organic chemists the same type of feeling for the use of chemical shifts as a measure of molecular structure as the Colthup chart had provided for infrared spectroscopic data a decade earlier. Both types of correlations were undoubtedly oversimplified, but they provided an overall guide to the interpretation of the spectral data.

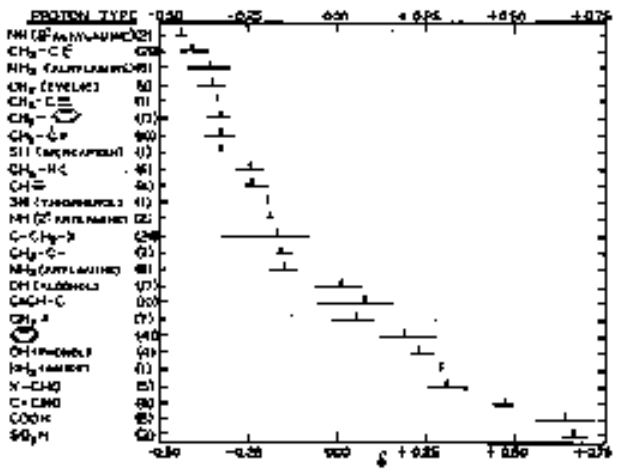

Figure 19 Correlation chart for proton chemical shifts in various organic functional moieties, published by Meyer, Saika, and Gutowsky.[76] (Reproduced by permission of the American Chemical Society)

The ^{31}P nucleus was also studied extensively in early high-resolution NMR, since it has a chemical shift range of about 1000 ppm, possesses reasonable sensitivity, and gives sharp lines. An indication of the existence of phosphorus chemical shifts of about 0.01% among several phosphorus compounds was first given by Knight in 1949 in his seminal paper entitled 'Nuclear Magnetic Resonance Shift in Metals'.[56] Dickinson[77] in 1950, subsequently made a comparison of the differences in the magnetic shieldings for some phosphorus compounds and observed that large shifts occur between phosphorus-(III) and -(V). Soon after this, Gutowsky and McCall[59] made a detailed study of ^{31}P NMR in $POCl_3$, $POCl_2F$, $POClF_2$, and CH_3OPF_2, and observed the chemical shifts and the indirect $^{31}P–^{19}F$ spin–spin couplings wherever present. During the 1950s several hundred phosphorus compounds were subjected to NMR investigations. The ^{31}P chemical shift spread for trivalent phosphorus compounds was found to be much larger than that for pentavalent phosphorus. The effects of solvents, temperatures, substituents, molecular structure, and conformation on the chemical shifts and coupling constants were later studied in detail for a large number of systems, and useful empirical correlations between the NMR and structural parameters derived.

While experimental data were being acquired, many chemists were trying to understand chemical shifts (particularly ^{1}H chemical shifts) in terms of molecular structure. The early correlations by Gutowsky and others made it clear that electron-withdrawing substituents attached to a carbon atom resulted in deshielding of a bonded proton. Spiesecke and Schneider showed such correlations in detail, not only for ^{1}H but also for ^{13}C chemical shifts.[78] It soon became clear that magnetic anisotropy in neighboring functional groups also has a significant effect on chemical shifts. In particular, the presence of 'ring currents' of π-electrons in aromatic rings can cause significant shifts. Meyer, Saika, and Gutowsky[76] observed that the proton signals in benzenes were displaced to lower fields by about 1.4 ppm compared with those in ethylenes. Waugh and Fessenden[79] subsequently measured the shifts in dilute solutions in an inert solvent such as CCl_4 and made theoretical computations. The magnetic dipole model of Pople,[80] and a subsequent refinement by Johnson and Bovey,[81] provided a means of making quantitative estimates of ring-current effects that have been used to the present day.

Another important development, initially largely at Illinois, was the recognition that the rate of chemical exchange could be estimated by its effect on an NMR spectrum. The role of fast exchange in averaging the chemical shifts of several coexisting species was recognized implicitly by Arnold and Packard[82] in their classic study of hydrogen bonding in ethanol (which we shall discuss in Section 3.9). However, in the course of characterizing spin–spin couplings, Gutowsky and co-workers observed that fast exchange can average out splittings as well. They observed a fluorine doublet in aqueous solutions of HPF_6 but not in HF, while for the BF_4^- ion in aqueous HBF_4 no splittings were observed in the ^{19}F spectrum. The absence of splittings was attributed to the chemical exchange of fluorines among the BF_4^- ions. The theoretical treatment of the exchange effect was developed by Gutowsky, McCall, and Slichter[83] using Bloch equations. Subsequently, Gutowsky and Saika[84] examined the concentration dependence of the proton chemical shifts in aqueous strong acids. Because of fast exchange in these systems, the exchange rates could not be determined; only the concentration dependence of the shifts could be examined. However, the lineshapes in the regions intermediate between the fast and the slow exchanges for two equally populated sites were computed. The results indicated that chemical lifetimes in the range 10^{-2} to 10^{-4} s could be measured by such an approach. It was also proposed that the activation energy for the exchange could be evaluated from such studies. The classic example to demonstrate exchange effects was first provided by the study of *N*,*N*-dimethylformamide, where Phillips had found two lines for the nonequivalent methyl groups at room temperature.[85] Gutowsky and Holm[86] investigated the temperature dependence and found that the doublet observed at room temperature alters at higher temperature as internal rotation about the C–C bond leads to exchange. The exchange rate and the activation energies were computed. This opened the field for the study of a large number of exchange processes.

For example, at Caltech, John D. Roberts received one of the early Varian 40 MHz spectrometers and studied nitrogen inversion and various rotational isomerisms (***Roberts, John D.: A Personal NMR Odyssey***), along with many other structural organic problems. W. D. Phillips at DuPont, the purchaser of one of the earliest 30 MHz spectrometers (soon upgraded to 40 MHz), had investigated hindered rotation in amides and other molecules before turning to studies of paramagnetic species and biopolymers (***Ferguson, Raymond C.: William D. Phillips and Nuclear Magnetic Resonance Spectroscopy at DuPont***). At the National Research Council of Canada, which was another early owner of a Varian 40 MHz instrument, William G. Schneider and Harold Bernstein studied a variety of organic and inorganic systems to derive physicochemical information and to develop further correlations of NMR parameters with molecular structure, largely in collaboration with John Pople (See ***Schneider, William G.: Early Research on High-Resolution Proton Magnetic Resonance***). An increasing number of laboratories, both academic and industrial, too numerous to mention here, were drawn into the use of NMR at this still early phase of its use in chemistry.

Shoolery and the Applab

Shortly after receiving his Ph.D. at Caltech in 1952, James N. Shoolery became aware of the existence of Varian Associates and of its plans to offer a commercial NMR instrument designed for chemical studies. As he says in his historical sketch:

> When I saw the three peaks of ethyl alcohol, I knew what I wanted to do and where I wanted to do it. I wrote to Varian, suggesting that a company far-sighted enough to offer such a technologically advanced product might consider employing a chemist to help develop applications for their instrument. I modestly announced that I would be available. To my delight, Varian Associates offered me the position.

Varian management realized that their task was not only to improve instruments but to develop the infrastructure that correlated NMR parameters with chemical structures. By the beginning of 1953 Shoolery had formally opened the Applications Laboratory ('Applab') at Varian Associates. He and his colleagues developed new experimental methods and new ways to interpret NMR spectra, and a number of chemists came to the Applab with problems that NMR might solve. By the middle of 1954, the chemical shifts and coupling constants had been measured for a wide range of compounds with known structures, but no really unknown structure had been elucidated solely by NMR. The first example showing that NMR could solve a significant chemical problem in a straightforward, direct, and simple manner occurred in a sample submitted by E. J. Corey.[87] As illustrated in Figure 20, the problem was to distinguish between the structures of cycloheptatriene (A) or bicycloheptadiene (B). The correct structure (a) was unambiguously established from the relative intensities of the olefinic and aliphatic protons.

Steps were taken to familiarize organic chemists with the potential of NMR for the elucidation of molecular structure. A publicity campaign was initiated by the widespread circulation of reports entitled *Technical Information from the Radio Frequency Spectroscopy Laboratories of Varian Associates*. These bulletins included information on instrumental developments and showed new spectra. Figure 21 shows a portion of the first *Technical Information Bulletin*, dated July 1953, which heralds 'A New Kind of Spectroscopy: High Resolution n·m·r'. The terminology represented a deliberate decision to de-emphasize the word 'nuclear' and emphasize the term 'spectroscopy' in

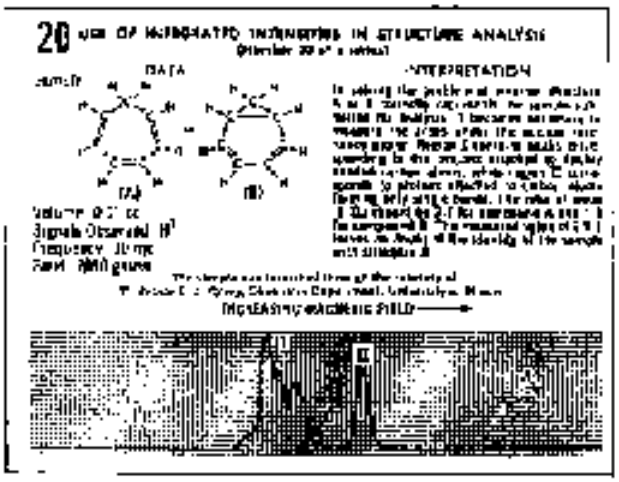

Figure 20 One of the earliest examples of the use of NMR in structure elucidation, as described in J. N. Shoolery's historical sketch, ***Shoolery, James N.: High-Resolution NMR: A Dream Come True***. (Reproduced by permission of Varian Associates)

an effort to capitalize on the popularity of infrared (IR) spectroscopy. However, to carve out some independence from IR, peaks were shown pointed up rather than down as in IR in what was to become a universal format for high-resolution NMR spectra. Figure 22 illustrates some of the 'Typical Proton Signals' shown in this issue as photographs of oscilloscope traces.

By 1955, Volume 1, Number 3 of this bulletin featured an article 'Important New Spinning Sample Technique Improves n·m·r Resolution'. Also included were the first 12 spectra from 'This is NMR at Work', a series of advertisements published each month, first in *Analytical Chemistry*, then in the *Journal of the American Chemical Society*, demonstrating new applications of NMR. The state of the art at that time is illustrated in Figure 23, but the examples became far more sophisticated as the years went by. Chemists and the new breed of NMR spectroscopists awaited these advertisements as eagerly as they anticipated research articles. The rewards for such a methodology were great. Organic chemists soon found that NMR spectroscopy was an ideal technique for elucidating and verifying the structure of moderate-sized molecules. Almost every compound one could lay one's hands on produced new and interesting data.

A classic paper by Shoolery and Rogers[88] in 1958 demonstrated the usefulness of NMR spectroscopy in the study of relatively large molecules such as steroids. Even at 40 MHz, the proton NMR spectra of the 47 steroids studied exhibited informative features. As illustrated in Figure 24, the bulk of the steroid resonances appeared as a broad 'hump' of complex structure that the authors recognized was not interpretable but could serve as a general fingerprint sensitive to structural differences. Nevertheless, a large number of proton chemical shifts were correlated with structural features. These included resonances shifted to low field (from attachment to unsaturated or hydroxyl-substituted carbons), hydroxyl protons, and angular methyl groups. Axial protons in the 3-position were found to be shifted upfield by more than 0.5 ppm relative to equatorial protons. The chemical shifts of angular methyl groups were found to be particularly sensitive to many aspects of structure, and these strong peaks could be observed readily even with small amounts of sample, as shown in Figure 24. This paper had a major impact in demonstrating the utility of NMR in important, practical applications.

In 1959, Goodwin, Shoolery, and Johnson published one of the first examples where the complete proof of the structure of an alkaloid was accomplished by NMR.[89] Illustrative of these early papers, the experimental section noted innovations such as flux stabilization and spinning of the sample tube during the recording of the spectrum. Audiofrequency side bands were used for frequency measurements and two recorders were run simultaneously at different gain settings in order to measure the line intensities of intense and weak signals. This work was begun in the Applab at the then standard proton frequency of 40 MHz, but while the study was in progress, prototype 60 MHz apparatus became available as project SMOFF, 'sixty megacycles or fifty-five', (see ***Anderson, Weston A.: Early NMR Experiences and Experiments***) succeeded in upgrading the magnetic field. The resulting spectra of the alkaloids lunacrine and lunine, with frequencies measured to an accuracy of 0.1 Hz, could be completely interpreted, including an interesting observation of the nonequivalence of the two methyl groups in the isopropyl side chain.

Acquisition and Analysis of Complex Spectra

As chemists began to apply NMR to more complex molecules with instruments operating at 40 MHz or 60 MHz, spin systems were observed more frequently which gave spectra that were not amenable to first-order analysis. Methods had to be developed for analyzing such spectra, but also methods were needed for making accurate measurements of line positions. By the latter part of the 1950s, it was possible to obtain (with considerable effort) adequate homogeneity to produce lines of 0.5 Hz width and, in principle, measurements of line positions could be made to a fraction of this value. However, before the field/frequency lock was implemented, each spectrum had to be calibrated individually, and for precise measurements the experimenter could not rely on a field-sweep scan to be linear over any appreciable range. Two experimental methods were widely used to measure line frequencies. Audiofrequency modulation of the magnetic field (or occasionally of the fixed radiofrequency) generated amplitude modulated sidebands spaced at the audiofrequency, which could be measured independently by a frequency counter to at least 0.1 Hz. Hence, an arbitrarily small portion of a spectrum could be calibrated or a sideband of a reference frequency could be superimposed precisely on a given spectral line to determine its separation from the reference. By using a moderate scan rate that produced ringing or 'wiggles' after the line, exact coincidence of the spectral feature and the audio sideband could be observed on an oscilloscope and the frequency measured quite precisely, often to about 0.1 Hz (about 0.002 ppm at 60 MHz). A second method which made use of the ringing is the *wiggle beat method* for measuring the frequency separation of two closely spaced lines.[90] Again, a moderate rate scan produced wiggles after each line, which then interfered with each other to produce a beat pattern. From the frequency maxima of the beats, the line separations could usually be obtained to about 0.02 Hz,[91] depending on magnetic field homogeneity and T_2, which determine duration of the

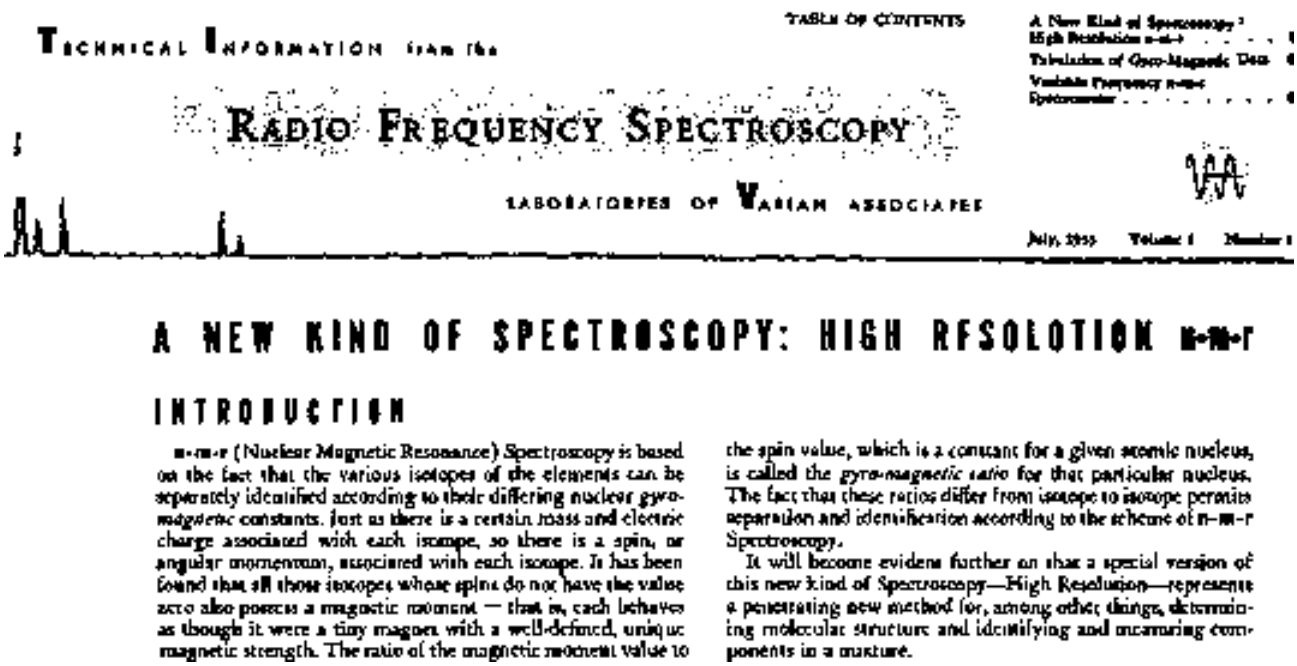

TECHNICAL INFORMATION from the

TABLE OF CONTENTS

RADIO FREQUENCY SPECTROSCOPY

LABORATORIES OF VARIAN ASSOCIATES

July, 1955

A NEW KIND OF SPECTROSCOPY: HIGH RESOLUTION n-m-r

INTRODUCTION

n-m-r (Nuclear Magnetic Resonance) Spectroscopy is based on the fact that the various isotopes of the elements can be separately identified according to their differing nuclear *gyromagnetic* constants. Just as there is a certain mass and electric charge associated with each isotope, so there is a spin, or angular momentum, associated with each isotope. It has been found that all those isotopes whose spins do not have the value zero also possess a magnetic moment — that is, each behaves as though it were a tiny magnet with a well-defined, unique magnetic strength. The ratio of the magnetic moment value to the spin value, which is a constant for a given atomic nucleus, is called the *gyro-magnetic ratio* for that particular nucleus. The fact that these ratios differ from isotope to isotope permits separation and identification according to the scheme of n-m-r Spectroscopy.

It will become evident further on that a special version of this new kind of Spectroscopy—High Resolution—represents a penetrating new method for, among other things, determining molecular structure and identifying and measuring components in a mixture.

Figure 21 Portion of the first issue of the Varian *Technical Information Bulletin*. (Reproduced by permission of Varian Associates)

beat pattern. Measurements were, of course, repeated several times for maximum accuracy and field sweeps obtained in both directions. Viewed in the context of modern Fourier transform instruments with very precise frequency and phase control, it is remarkable how well the measurements made by investigators with the relatively crude instruments of the 1950s agree with current data.

When scalar coupling was first discovered, general rules governing the multiplicity of the NMR spectral lines were developed on the basis of statistical considerations: (i) If a nucleus of spin $\frac{1}{2}$ has n equivalently coupled neighbors of spin $\frac{1}{2}$ each, its resonance splits into $n + 1$ peaks corresponding to $n + 1$ spin states of the neighboring groups of spins. (ii) The peak intensities are determined by simple statistical considerations and are proportional to the coefficients of the binomial expansion. These 'rules' worked very well when applied to the initial systems studied which largely involved nuclei of different species coupled to each other, hence with scalar couplings that are much smaller than the frequency differences caused by chemical shifts. Such spectra are referred to as 'weakly' coupled as compared with those called 'strongly' coupled, where the indirect spin–spin couplings and the chemical shifts are of comparable magnitudes. Even in the early 1950s the distinction was clear to physicists well versed in quantum mechanical principles; for example, at Stanford, Arnold analyzed the splittings in ethanol by means of a second-order perturbation treatment, as illustrated in his historical sketch (***Arnold, James T.: Early Perceptions in Nuclear Magnetic Resonance (NMR)***). However, it was not

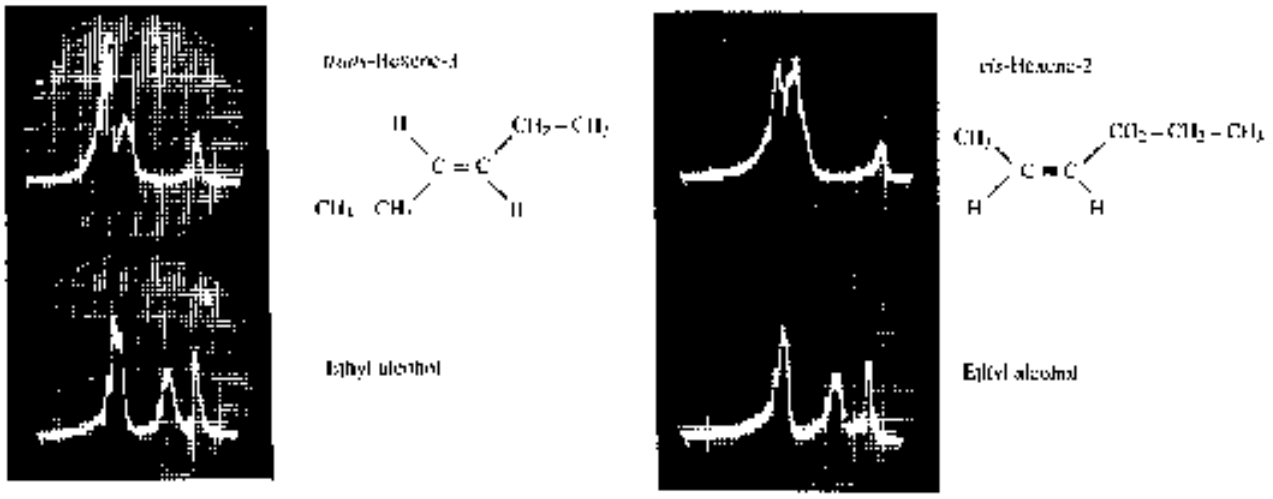

Figure 22 NMR spectra obtained in 1953 as illustrations of the state of the art and published in the Varian *Technical Information Bulletin.* (Reproduced by permission of Varian Associates)

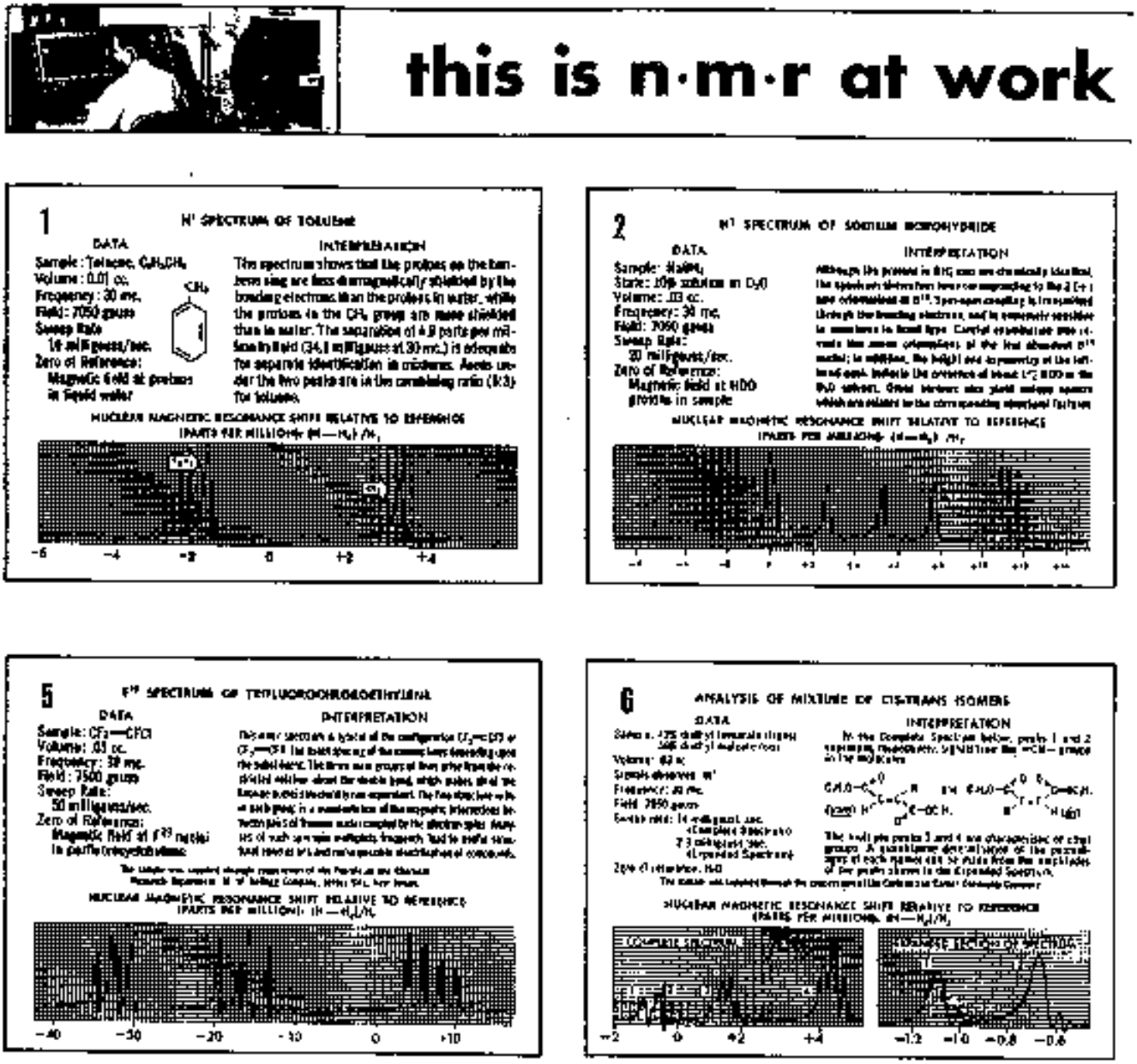

Figure 23 Examples from the series 'This is NMR at Work' published as advertisements in *Analytical Chemistry* (Reproduced by permission of Varian Associates)

Figure 24 The 40 MHz proton NMR spectrum of a steroid, illustrating the general spectral features shown to be characteristic of steroids, as well as the limits of sensitivity. The sample was 1.35 mg of 11-ketoprogesterone as a 0.02 M solution in $CDCl_3$.[88] (Reproduced by permission of the American Chemical Society)

widely appreciated by the early chemists using NMR that, in strongly coupled cases, the derivation of the chemical shifts and coupling constants does not follow the simple rules but must be treated by more rigorous quantum mechanical methods.

The paper by McConnell, McLean, and Reilly[92] in 1955 pointed the way to general methods for dealing with such systems. Soon Pople, Schneider, and Bernstein undertook careful analyses of a variety of spin systems and introduced the now universally used system of classifying spin systems by using letters close to each other in the alphabet (e.g., A, B) to denote strongly coupled systems and those far from each other (e.g., A, M, X) for weakly coupled nuclei. Several papers demonstrated the application of well-known symmetry considerations to NMR spectra, and the concept of 'magnetic equivalence' became more widely appreciated. With this framework, a number of investigators analyzed spin systems that possessed elements of symmetry and/or large chemical shift differences. Under these circumstances the Hamiltonian matrix could be shown to reduce to blocks no larger than 2×2, which were readily subject to algebraic solution. The book by Pople, Schneider, and Bernstein[93] in 1959 provided a comprehensive treatment, but application to specific spin systems was not always straightforward in 1960, as described by Aksel Bothner-By in his historical sketch (***Bothner-By, Aksel A.: Computer Analysis of High-Resolution NMR Spectra***):

> Even with the algebraic solutions in hand, the task of tabulating all the line frequencies and intensities and finding the values of shifts and coupling constants giving a spectrum agreeing with the observed one was tedious, error-prone, and time-consuming. The availability of an IBM 650 through the newly formed Department of Computer Science at the Carnegie Institute of Technology appeared to offer a fast and convenient way to tabulate these spectra, and we set out to write a few programs for specific cases, such as $X_3AA'X'_3$, applicable to the case of the 2,3-dihalobutanes, which we were then studying. From Alan Perlis, the Director, we received a set of instructions in how to prepare a program for the computer in a language called IT. After a couple weeks of puzzling, we produced what we thought would be a working program and brought it to be run. Unfortunately, IT had become obsolete in the interim, and a new language, AT, was now in use. Our second attempt also took about two weeks to write, and, predictably, was also out-of-date when we got it there. Back, to rewrite in GAT. This time we were barely in time, and, amazingly to us, it worked. The computer gave us a list in about two minutes that it would have taken us two days to crank out on a Monroe. We were able to use it for the intended analyses.

Many spin systems, however, could not be treated in this way. Even such simple systems as ABC require the solution of cubic equations and cannot be treated, in general, by algebraic procedures. On the other hand, if estimated numerical values for chemical shifts and coupling constants are introduced, the diagonalization problem becomes purely numerical. Numerical methods for the interactive diagonalization of large symmetric real matrices had long been known and can be conveniently employed with the help of an appropriate computer, but in the late 1950s such computers were in their infancy. Computer programs to read in a set of assumed chemical shift and coupling constant values, evaluate the numerical Hamiltonian, perform the diagonalization, and provide calculated frequencies and intensities for the expected spectra were first developed in 1960. Aksel Bothner-By's FREQINT was one of the first and most popular of these first generation programs.

GORDON RESEARCH CONFERENCES ON MAGNETIC RESONANCE

By the mid-1950s, magnetic resonance (including both nuclear and electron spin resonance) had become sufficiently well established as to warrant the establishment of a Gordon Research Conference in this field. Gordon Conferences had achieved a reputation in a wide variety of topics as a forum in which about 100 active participants in a field could spend a week exploring the frontiers in that area.

The first Gordon Conference on Magnetic Resonance was held in 1958 under the chairmanship of Herbert Gutowsky. Attendees formed a veritable 'who's who' in the rapidly expanding field. Among well-known NMR figures who presented talks or chaired sessions were Harden McConnell, Jim Shoolery, Harold Bernstein, John Zimmerman, John Pople, Saul Meiboom, Nicolaas Bloembergen, Charles Reilly, Dave McCall, Ben Dailey, Martin Karplus, John Waugh, George Pake, Bob Shulman, Ned Baker, and Wes Anderson. Many other then and future eminent figures in the NMR and ESR fields also participated actively. Titles of talks were usually quite broad, e.g., 'Interpretation of High-Resolution NMR Spectra and Current Chemical Applications'; 'Methods of High-Resolution Spectral Analysis'; 'NMR in Magnetic Solids'; and 'Theoretical Interpretation of Electron-Coupled Spin–Spin Interactions'.

The first meeting was so successful that the participants recommended a second meeting in 1959, before going to the biennial schedule that the Conference has followed in subsequent years.

In 1974, in recognition of burgeoning new aspects of NMR applications, a Gordon Research Conference on Magnetic Resonance in Biology and Medicine was established and continues to meet biennially.

One difficulty with the initial programs was that the spectra were computed from the assumed chemical shifts and coupling constants, whereas what was needed was the reverse process, namely the computation of chemical shifts and coupling constants from the spectrum. For quantum mechanical problems of this sort, 'direct' methods of inputting frequencies and deriving the desired parameters are mathematically cumbersome, and have been developed only for the simplest systems (ABC). Consequently, iterative programs providing the 'best' fit values of chemical shifts and coupling constants were subsequently developed. In such programs, either energy levels or spectra are first computed from trial values of the parameters, and the observed and computed spectra are compared. The parameters are then automatically changed such that the sums of the squares of the deviations between the observed and the computed line positions are minimized. Various versions of the programs which have been commonly used were developed by Reilly and Swalen,[94] Hoffman,[95] and Bothner-By et al.[96–98] (see ***Bothner-By, Aksel A.: Computer Analysis of High-Resolution NMR Spectra***). All these programs use the frequencies of the spectral lines for the computations and do not take into account the intensities of the lines. The intensities were subsequently used qualitatively for confirming the

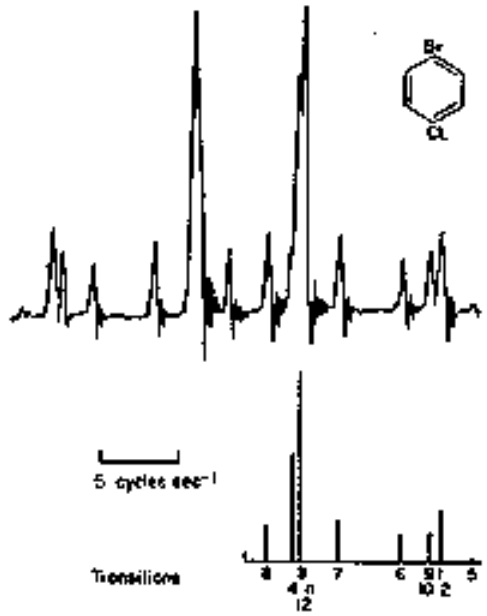

Figure 25 Analysis of an AA′BB′ spectrum.[100] (Reproduced by permission of the American Institute of Physics)

parameters deduced from the iteration, an appropriate procedure in view of the fact that the precision with which the frequencies could be measured was far better than that for the intensities. In 1962, Arata, Shimizu, and Fujiwara[99] proposed a method in which the intensities were also included in the iterative procedures, but this procedure has not been used in any significant investigations. Figure 25 illustrates the result of a typical analysis, this one carried out by a related iterative method developed by Martin and Dailey.[100]

The most widely used program is the one developed by Castellano and Bothner-By, LAOCOON II and its subsequent versions LAOCOON III and LAOCN. These programs were soon modified to improve the efficiency and expand the usage. In 1965, Haigh[101] added the capability of handling groups of magnetically equivalent spins in order to improve the efficiency. Diehl, Khetrapal, and Kellerhals[102] adapted the software to include direct dipolar couplings in the Hamiltonian so that the spectra of molecules oriented in liquid crystals could be analyzed, and named the program as LAOCOONOR. Several other groups have included nuclei with spin $>\frac{1}{2}$ and treated quadrupole couplings. Later analyses focused on the fact that multiple minima are possible in the multiparameter space, hence that different sets of parameters might provide equally acceptable fits of observed spectra.[103] Modern versions of these programs are now commonly available as part of the standard NMR spectrometer software.

Meanwhile, attempts were also made to find simpler analysis procedures as far as possible without the use of a computer, at least in certain special cases. In this connection, Pople and Schaefer[104] and Diehl and Pople[105] in 1960 carefully examined the theoretical expressions for the frequencies and the intensities of spectral lines in cases where two nuclei have a relative chemical shift comparable with their spin–spin coupling constant and all other relative chemical shifts are large, i.e., systems of the type ABR_pX_q and AB_2X_q. They observed that all such systems could be handled within one theoretical scheme and the multiline spectra could be built up as the superposition of the spectra of simpler types and treated by *sub-spectral analysis*.

During the early 1960s the sub-spectral approach became quite popular when computer programs were not yet fully developed and helped to explain the concept of 'virtual coupling'. This procedure has also been utilized for the analysis of complex spectra of certain molecules oriented in nematic liquid crystals. For example, monodeuterobenzene (an AA′BB′CP system, where P is the spin-1 deuterium) was treated as the superposition of three five-spin sub-spectra.[106]

Influence of Molecular Conformation on NMR Spectra

In 1957, Reid[107] demonstrated that chemically similar protons in fused aromatic rings were chemically shifted when their immediate environments were different, and it was found that in saturated six-membered rings equatorial protons normally resonate downfield compared with the chemically equivalent protons in the axial orientation in some substituted cyclohexanes and in symmetrical trioxanes.

The correlation of indirect spin–spin coupling constants with molecular structure was another area in which efforts were concentrated around the same time. By the late 1950s, sufficient data on proton–proton couplings had become available to establish several correlations with molecular structure. For example, it was found that in ethylene derivatives J_{gem}(H,H) was very small, while J_{trans}(H,H) > J_{cis}(H,H). Likewise, in acetylated aldopyranose sugars, Lemieux et al.[108,109,110] showed that the three-bond axial/axial couplings between the protons on neighboring carbon atoms are two to three times as large as those involving equatorial protons. These observations had a very significant impact on the development of carbohydrate chemistry, as described in more detail in Lemieux's historical sketch.

Meanwhile, Martin Karplus developed a theory based on a valence-bond approach for the variation of the three-bond vicinal coupling constant with dihedral angle.[111] This theory was extremely successful in interpreting the salient features of the experimental HH, HF, and FF couplings in aliphatic and ethylenic compounds. The experimental observation that the *trans* coupling is always larger than the *cis* could be explained quantitatively. Karplus concluded that the vicinal coupling (J) for protons on adjacent saturated carbons should depend upon the dihedral angle ϕ according to the relation:

$$\left.\begin{array}{l} J = 8.5\cos^2\phi - 0.28\text{Hz} \quad (\text{for} 0^\circ < \phi < 90^\circ) \\ J = 9.5\cos^2\phi - 0.28\text{ Hz} \quad (\text{for} 90^\circ < \phi < 180^\circ) \end{array}\right\} \quad (3)$$

Unfortunately, as pointed out by Karplus in his historical sketch (***Karplus, Martin: Theory of Vicinal Coupling Constants***), many chemists believed that the relationship was more accurate than the approximations in the theory would allow:

> Most people who use the 'Karplus equation' appear not to have read the original paper and so did not know the limitations of the theory cited there. They assumed that because the equation had been used to estimate vicinal dihedral angles, the theory said that the coupling constant depend *only* on the dihedral angle. By 1963, I had learned that important organic chemists write and read only communications to the *Journal of the*

American Chemical Society and so I decided to publish such a Communication,[112] in which I described various factors, other than the dihedral angle, that are expected to affect the value of the vicinal coupling constant; they include the electronegativity of substituents, the valence angles of the protons (HCC′ and CC′H′), and bond lengths. The main point of the paper was not to provide a more accurate equation, but rather to make clear that caution had to be used in applying the equation to structural problems. My closing sentence, which has often been quoted, was the following: 'Certainly with our present knowledge, the person who attempts to estimate dihedral angles to an accuracy of one or two degrees does so at his own peril'.

Even with these limitations, the Karplus equation has become the cornerstone in the application of NMR to conformational analysis. This relation has proved to be durable over more than 30 years, with subsequent empirical modifications of the parameters to reflect their variation as a function of other aspects of molecular environment. The development of carbohydrate chemistry owes much to this relation and, as we shall see, three-dimensional structure determinations of proteins by NMR make extensive use of the Karplus relation. A previous theoretical treatment of geminal H–H coupling constants in saturated hydrocarbons by Karplus et al.[113] did not fare as well. Initially this calculation appeared to reproduce very well a number of measured coupling constants on the assumption that these values of ^2J are all positive. However, Cynthia Juan (later Jameson), a graduate student in Gutowsky's laboratory, found that the AA′BB′ spectrum from the $-CH_2CH_2-$fragment in metacyclophane could be fitted only by assuming opposite signs for the vicinal and geminal coupling constants. As Jameson describes in her article (***Jameson, Cynthia J.: Early Work on the Ranges of Chemical Shifts and Signs of Coupling Constants***), it was only after considerable effort to disprove this result that the finding was published.[114]

Meanwhile, Lemieux and co-workers had made a similar discovery. During the course of their work on monosubstituted 1,3-dioxolanes, they concluded that the geminal and the vicinal proton–proton couplings were of opposite signs. They submitted this work for publication to the *Journal of Chemical Physics*, but the paper was rejected, presumably because the conclusions were contrary to the published theoretical expectations—an indication of how difficult it is to 'sell' a new product! The paper was finally published in the *Journal of the American Chemical Society*,[115] and Karplus later determined that the erroneous conclusion in the initial theoretical paper resulted from the fact that the calculation relied on a small difference between two large quantities.[116]

^{13}C Satellites

While assessing the sensitivity of their NMR spectrometer in 1958, Cohen, Sheppard, and Turner[117] made a very important discovery when they noticed in the proton NMR spectrum of $CHCl_3$ under high amplification two weak signals placed symmetrically (isotope effects were too small to be observed) about the main central line, with a total intensity of ca. 1% of the intensity of the main central band. They could not be attributed to spinning sidebands since they did not shift with a variation of the spinning frequency, and were eventually explained as 'satellites' arising from the 1.1% of the molecules containing ^{13}C with a frequency separation equal to $J(^{13}C,H)$. The ^{13}C satellites of dioxane showed that J couplings could be extracted even though the main proton spectrum was a singlet. The method proved to be of great importance in permitting the measurement of vicinal coupling constants in symmetric molecules, which was especially important in testing theoretical predictions. Later, satellites due to other nuclei (e.g., ^{29}Si and ^{199}Hg) would be exploited in such studies and in double resonance measurements of chemical shifts.

Direct Observation of Carbon-13 NMR

As the key structural element in organic chemistry, carbon was an early target for NMR investigation, but the combination of only a 1.1% natural abundance for ^{13}C, the only isotope with a nuclear spin, and its relatively low sensitivity made studies difficult with the limitations of instruments in the 1950s. Despite the adverse factors, the first ^{13}C NMR spectrum was reported by two independent workers, Paul Lauterbur[118] and C. H. Holm,[119] who published their results in the same issue of the *Journal of Chemical Physics* in 1957. Most of the compounds that were studied were pure liquids and a signal-to-noise ratio of up to 50 could be achieved. Lauterbur alone studied over 100 compounds, while Holm presented the chemical shift data in the form of a chart (Figure 26) which emphasized the role of substituents. The range of ^{13}C chemical shifts in neutral organic compounds was found to be about 20-times greater than that for protons. Only one-bond couplings of ^{13}C with protons and ^{19}F could be resolved. The directly bonded ^{13}C–H coupling constants were found to vary between about 120 Hz and 210 Hz, depending on the bond hybridization and substituents present. The ^{13}C–^{19}F couplings in some fluorobenzenes were measured as 600 ± 20 Hz.

Despite the poor resolution and sensitivity, a few other intrepid workers, including J. B. Stothers, and Spiesecke and Schneider, joined the efforts to explore ^{13}C chemical shifts and one-bond couplings in a large number of compounds and to develop correlations of the data with molecular structure, substituent properties, solvent, and temperature. For example, a linear relationship was observed by Lauterbur[120] between ^{13}C chemical shifts in methyl halides and the electronegativity of the halide, and similar correlations were found by Spiesecke and Schneider.[78] Stothers, in particular, accumulated a vast amount of information on ^{13}C NMR parameters and eventually published the first book with large compendia of ^{13}C spectral data.[121] In 1961, Gary Maciel began studies of ^{13}C, as he relates in his historical sketch (***Maciel, Gary E.: A Little Polarization Can be Good for You***).

Lauterbur's initial observations of ^{13}C spectra, along with most other early studies, were carried out with 15-mm diameter sample tubes without spinning, which severely limited resolution. In addition, the early work employed rapid passage dispersion mode operation rather than normal absorption mode in order to use high radiofrequency power to detect the weak signal without saturating it. Although this technique resulted in an improvement in the signal-to-noise ratios, the lines were further broadened. In 1962, Shoolery[122] made a significant advance when he employed normal slow sweep absorption mode operation with spinning of a large sample tube to obtain good resolution without sacrificing sensitivity. This improvement was made possible by the

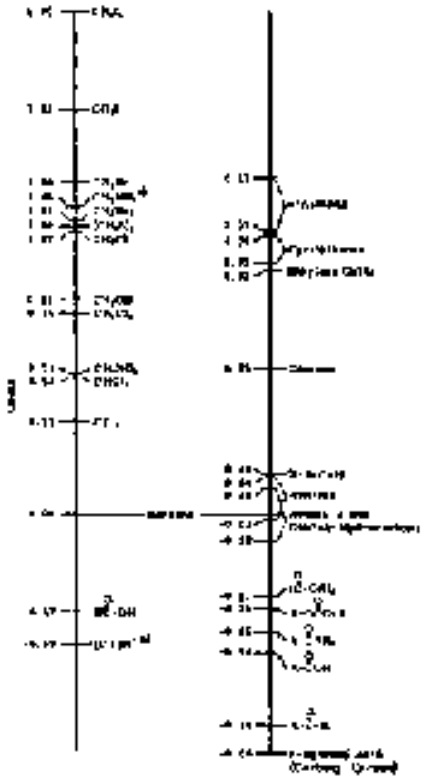

Figure 26 ^{13}C chemical shifts as tabulated by Holm.[119] (Reproduced by permission of the American Institute of Physics)

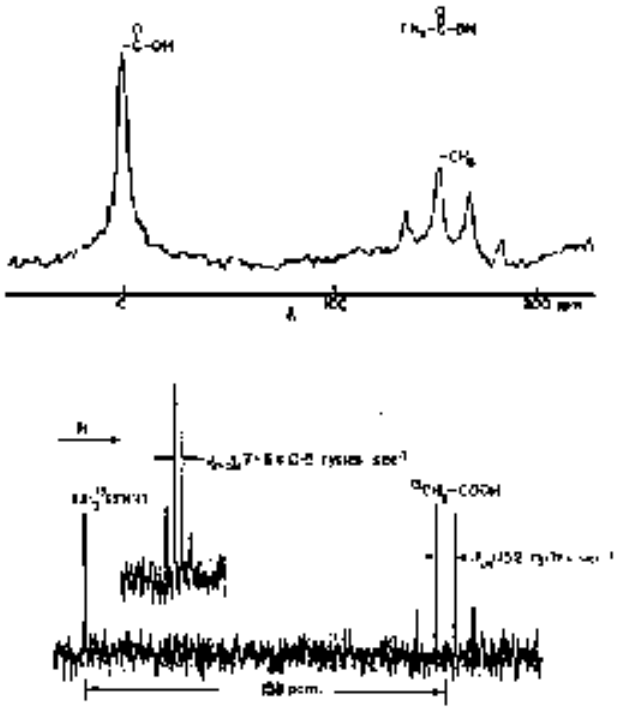

Figure 27 Comparison of the ^{13}C spectra of acetic acid obtained by rapid passage without spinning[120] (top) and slow sweep with spinning[122] (bottom). (Upper portion reproduced by permission of the New York Academy of Sciences)

application of phase-sensitive detection and audio modulation to improve baseline stability. He was able to resolve the two-bond $^{13}C-H$ coupling in acetic acid, as shown in Figure 27, the first observation of such couplings in ^{13}C spectra.

A new era of high-resolution ^{13}C NMR had begun, but further advances would depend also on the use of double resonance, as we shall discuss in Section 6.

Molecular Interactions and Hydrogen Bonding

In 1951, soon after the discovery of the proton chemical shift in ethanol, Packard and Arnold[82] made another landmark discovery by observing that the chemical shift of the OH proton in ethanol exhibited strong temperature dependence, whereas the shifts of the CH_2 and CH_3 protons did not vary with temperature. A few months after this finding was published, Liddel and Ramsey[50] explained the results as probably arising from the effects of hydrogen bonding. They also proposed a test for this interpretation by pointing out that similar results should be observed by diluting ethanol with a nonhydrogen-bonding solvent such as CCl_4. Arnold and Packard did just that and reported their experimental confirmation of the interpretation on the same page with the Liddel–Ramsey paper.[123]

The high-frequency shift on hydrogen bonding became an important factor in interpreting ^1H NMR spectra since the proton chemical shifts of OH, NH, and SH protons were all found to be temperature (and solvent) dependent. In addition, the chemical shift of the hydrogen-bonded proton became valuable for diagnostic purposes in structural elucidations when intramolecular hydrogen bonds were present. Among early work on the study of the hydrogen bonding by NMR was the observation of the shift in the ammonia–water system by Ogg[124] in 1954.

As higher resolution instruments permitted more precise measurements of chemical shifts, the hydrogen-bond effect was exploited by a number of workers to make quantitative measurements of hydrogen-bonding equilibria. For example, in 1955, Huggins, Pimentel, and Shoolery investigated the chloroform–acetone and chloroform–triethylamine systems[125] and the complex equilibria in phenol in CCl_4,[126] while Cohen and Reid,[127] Becker, Liddel, and Shoolery,[128] and Saunders and Hyne[129] reported similar observations on alcohols. The question of the possible correlation of the hydrogen-bond shifts with the strength of the hydrogen bonds was examined by Korinek and Schneider[130] in 1957, and the trend was found to be encouraging.

These observations subsequently provided a valuable new technique not only for the study of well known hydrogen bonds but also for the investigation of other even weaker molecular interactions. For example, the shifts in ethylene and acetylene were interpreted by Schneider, Bernstein, and Pople[131] in terms of 'self-association' in which the hydrogen atoms of one molecule interact with the π-electrons of a neighboring molecule. Reeves and Schneider observed particularly large upfield shifts for $CHCl_3$ bonded to the face of an aromatic ring.[132] Dilution of benzene or other aromatics in nonaromatic solvents was shown to lead to significant shifts which could be understood in terms of the diamagnetic anisotropy of benzene and the ring current

from its π-electrons. In 1960, Buckingham, Schaefer, and Schneider provided an enduring framework for explaining solvent effects in terms of van der Waals interactions, electric field effects, anisotropic interactions, and specific interactions such as hydrogen bonding.[133]

FURTHER DEVELOPMENTS IN THE PHYSICS OF NMR

If the chemists 'took over' NMR in the late 1950s, the physicists were not really aware of it. Although the availability of commercial instruments opened up NMR research and applications to chemical problems, a great deal of important basic physics in NMR was yet to be discovered and developed (by both physicists and physical chemists), and applications to significant problems in solid state physics were just beginning.

Pulse and Spin Echo Methods Mature

Hahn had demonstrated what Bloch predicted, excitation by an rf pulse and acquisition of data in a free induction decay (FID). Hahn's spin echo had introduced a fundamental principle to NMR: reversibility. He showed that some processes that appeared on the surface to be irreversible could, in fact, be reversed. The spin echo from a $90^\circ,\tau,90^\circ$ pulse sequence also gave promise of measuring the real T_2 value for a nuclear spin in a magnetic field that is so inhomogeneous that the decay of the FID is dominated by inhomogeneity. But, in practice, this simple spin echo experiment did not lead to reliable values of T_2, largely because of molecular diffusion.

Carr and Purcell made several significant improvements over Hahn's methods.[134] First, they showed that a $90^\circ,\tau,180^\circ$ pulse sequence is much simpler to understand. Their illustration of the formation of a spin echo (Figure 28) became the basis for countless diagrams in future papers and books. Second, they showed how a $180^\circ,\tau,90^\circ$ pulse sequence could be used to measure T_1. Third, they showed a way to overcome the effects of diffusion in a spin echo experiment by using a series of 180° pulses whose spacing could be made short enough so that any diffusion effects are negligible. The Carr–Purcell method also showed that diffusion effects could, in fact, be measured by a variation of the pulse spacing.

The Carr–Purcell spin echo method, although elegant, nevertheless fell short in making reliable measurements of T_2 because inhomogeneities in the rf field $\boldsymbol{B}_1$ caused cumulative errors as the number of 180° pulses increased. At the instigation of Felix Bloch, the Weizmann Institute of Science in Israel set up an NMR laboratory in 1954 under Saul Meiboom. This group would go on to develop a number of innovations in NMR technology, as described by Zeev Luz in his historical sketch (***Luz, Zeev: The Early Days of NMR in Israel***). In applying the Carr–Purcell method, Meiboom and Gill[135] found that by simply changing the phase of the 180° pulses relative to the initial 90° pulse it was possible to compensate for the $\boldsymbol{B}_1$ inhomogeneity effects. This paper is recognized as the first to emphasize phase relationships among pulses, a factor that would be critical to later developments. Widespread use of this method was delayed for years because the pulse spectrometers of that era rarely incorporated phase-shifting devices or used phase-sensitive detection. Eventually, however, the combination Carr–Purcell–Meiboom–Gill (CPMG) method became the standard, not only for measuring T_2 but also for carrying out many more sophisticated pulse experiments.

Carr's Ph.D. work at Harvard with Purcell is remarkable for the number of innovative experiments that were conducted (***Carr, Herman Y.: Early Years of Free Precession Revisited***). Reference has already been made in Section 3.2 to Carr's work on sample spinning as a means of reversing the effect of magnetic field gradients. Many years later the method of gradient reversal was to assume a major role in NMR imaging, as we shall see later. Likewise, his analysis of the effects of coherent motion on the phase of the NMR signal has had an impact on flow measurement, as in magnetic resonance angiography. Two more aspects of his work are particularly noteworthy.

Long before Fourier transform NMR methods had revolutionized the field (as we shall see in subsequent sections), physicists were aware of the Fourier transform relation between a FID and a slow passage NMR spectrum. Lowe and Norberg, in their study of the NMR spectra of solids (***Lowe, Irving J.: My Life in the Rotating Frame***) derived the relation formally.[136] Much earlier, however, Carr and others had made 'mental' Fourier transforms of FIDs. For two or three lines of equal intensity, it was not too difficult to make the mental transform and picture the CW spectrum. However, for systems with unequal line separations and unequal intensities (e.g., CH_3CH_2OH) the process was more difficult, and to convince others Carr made what in current NMR imaging would be called a 'phantom', three pieces of rubber of volumes 3 : 2 : 1 which were placed in a magnetic field gradient that simulated the chemical shifts in ethanol. The FID obtained from this phantom agreed with that from liquid ethanol itself, thus verifying Carr's interpretation but also providing what may be (inadvertently) the first one-dimensional NMR image ever recorded. It would be 20 years before the idea of deliberately applying a field gradient to obtain spatial images would surface (see Section 13), and with only limited computers and programs available the possibility of using Fourier transforms to improve the acquisition of NMR spectra was given little or no thought.

With the CPMG method it was possible to measure translational diffusion in liquids. Donald Woessner (***Woessner, Donald E.: In a Maze in NMR***) realized that if molecular diffusion is restricted by the presence of small pores in a solid material, the diffusion coefficient D could be measured correctly with small interpulse spacing τ, but at long τ the molecules could not continue random diffusion because of collisions with the solid matrix and the apparent value of D would become smaller. Woessner tested the idea and verified the concept,[137] but it lay to Stejskal and Tanner (***Stejskal, Edward O.: Reminiscences about the Development of Pulsed Field Gradient, Spin-Echo NMR (PFGSE NMR)***) to overcome the technical obstacles in making diffusion measurements by introducing short pulsed gradients separated by a well-defined diffusion time.[138] This method permits easier and more precise measurement of the spin echoes in a homogeneous field. Although the PFGSE technique worked very well, it was difficult to implement with the NMR instruments of the 1960s. Currently, as we shall see later,

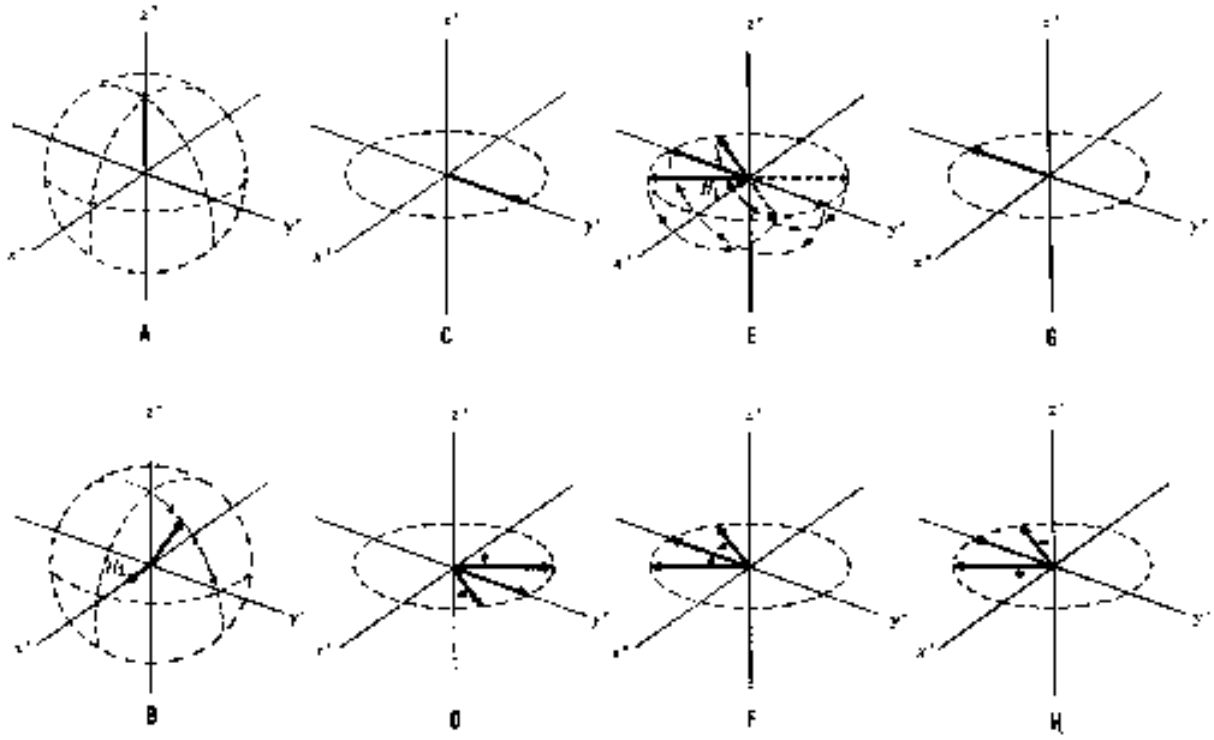

Figure 28 Schematic diagram of the behavior of precessing spins with a 90°,τ,180° pulse sequence to form a spin echo

the PFGSE method is a standard aspect of functional NMR imaging measurements.

Another important advance in spin echoes was the observation in 1954 of an echo in pure nuclear quadrupole resonance (NQR) which involves nuclear magnetic transitions among quadrupole split energy levels in zero magnetic field. Myer Bloom found the echo while he was a graduate student with Charles Slichter at the University of Illinois. According to Slichter (***Slichter, Charles P.: Early Days of Magnetic Resonance Studies of Solids***):

> Myer Bloom ... came to me to propose that it should be possible to produce spin echoes in pure quadrupole resonance. He proceeded to do a long calculation ... to verify the theory. Meanwhile, I developed a simple symmetry argument which convinced me echoes would not form. ... I suggested that he find my error. ... Instead of tracking down my error, Myer and Dick [Norberg] (without telling me) set out to observe quadrupole echoes of Cl nuclei. One morning when I arrived at work, I found a scope photo of Myer's quadrupole echo on my desk!

Meanwhile, at Queen Mary College in London, Peter Mansfield, a graduate student with Jack Powles, was studying relaxation in polymers. During the course of this work, he applied two 90° pulses within about 3–4 μs and occasionally observed 'an effect which looked very much like an NMR spin echo'. In spite of an apparent categorical exclusion of such effects in solids in the accepted theory, he convinced himself that such echoes would form if the pulses had a 90° phase relationship. In the phase-incoherent pulse apparatus, the random phase relationships sometimes permitted formation of such echoes. He and Powles identified the origin of this 'solid echo' in terms of magnetic dipolar interactions.[139] The solid echo would eventually form the basis for the interpretation of the response to a series of 90° pulses, thus laying the groundwork for the theory and experimental implementation of subsequent solid-state line-narrowing methods, as we shall see in Section 8.

AMPERE

The Groupement AMPERE (*A*tomes et *M*olecules *P*ar *E*tudes *R*adio-*E*lectriques) was formed in 1952 to exchange information and organize magnetic resonance meetings. The AMPERE group has played an important role in sponsoring a number of major conferences and in facilitating scientific exchange among scientists, especially in eastern and western Europe, as described by Robert Blinc in his historical sketch (***The AMPERE Society and the Development of Magnetic Resonance in Eastern Europe***)

Spin Temperature and Relaxation in the Rotating Frame

The idea that a nuclear spin system in an applied magnetic field $\boldsymbol{B}_0$ could be described in terms of a spin temperature which is different, under some circumstances, from the temperature of the lattice was understood by physicists working in NMR. Indeed, modeling the behavior of a complex system of spins coupled to one another in terms of the much more tractable thermodynamic picture has been one of the most significant developments for picturing complicated systems, understanding the behavior under pulse sequences, developing new sequences, and extracting information about the connectivity and proximity of spins in solids. In 1951, (***Pound, Robert V.: Early Days in NMR***) demonstrated that

a crystal of LiF with a ^{7}Li T_1 value of 5 min in a 7000 G magnetic field could be removed from the magnet, where it was adiabatically demagnetized to a low spin temperature, and then recovered its magnetization if returned to the high field in a short enough time. (T_1 was found to be about 15 s at zero field.[140]) Purcell and Pound then constructed an apparatus in which they could move the sample to a field of about 100 G, which could be rapidly reversed in direction. By moving the LiF crystal in a few seconds from the high magnetic field to the 100 G field, reversing its polarity, and returning the sample to the high field, they observed an inverted signal, which decayed through zero with a 5-min time constant.[141] They thus introduced to NMR the idea of a spin system at a negative (spin) temperature, a concept that would prove important in other connections.

A few years later, Alfred Redfield, during the course of a postdoctoral fellowship with Bloembergen at Harvard, embarked on a study of T_1 in aluminum and copper. Instead of using rf pulses, he and Bloembergen elected to use a continuous wave saturation method in a crossed-coil probe, a choice that was to have important consequences. Redfield soon discovered that the absorption mode signal saturated as expected with increasing rf power but the dispersion mode was much more difficult to saturate. He confirmed the result with copper. This result was in conflict with the predictions of the Bloch equations and Bloembergen's theory of relaxation. After six months of intense thinking about the problem, as described in his article (***Redfield, Alfred G.: Foundations and Structures***), Redfield developed a theory for spin temperature in the rotating frame. The theory has had a profound effect on the use of NMR in solids. During the course of this work Redfield also realized that relaxation along the effective field in the rotating frame might have a value considerably longer than T_2, and he designated this relaxation time in the rotating frame as, $T_{1\rho}$.

Much of the development of more sophisticated ideas of spin temperature was carried out in France by Anatole Abragam, Maurice Goldman, and their co-workers. Goldman's article (***Goldman, Maurice: The Time when Spin Temperature was Hot Stuff***) provides an excellent account of the evolution of the concepts, the impact of Redfield's ideas, and their rephrasing in Abragam's *Principles of Nuclear Magnetism* (see ***Abragam, Anatole: 'The Bible'***).

Meanwhile, as we have seen, Charles Slichter became one of the pioneers in NMR outside the original Harvard and Stanford laboratories when he established a strong research program in NMR at the University of Illinois. Many of the early successes in developing the concepts of scalar coupling and chemical exchange in Gutowsky's nearby laboratory involved close collaboration with Slichter, especially in providing much of the theoretical underpinning for this work. Most of Slichter's work, however, revolved around studies in solids, especially metals. In Slichter's laboratory at Illinois, experimental work was carried out to verify Redfield's theory from experiments on adiabatic demagnetization in the rotating frame (ADRF).[142] This experiment set the stage for using ADRF to examine relaxation in the rotating frame and thus obtain information on motions too slow to have a measurable impact on T_1. David Ailion, then a graduate student, developed the methods and worked out theory for interpreting the data, as described in his historical sketch (***Ailion, David C.: The First Observations of Ultraslow Motions***). He found that $T_{1\rho}$ in lithium powder was orders of magnitude shorter than T_1 and was able to measure slow motions in solids.[143]

The Overhauser Effect

Another discovery that upset the prevailing theories of thermodynamic equilibrium was the discovery by Albert Overhauser of the effects of polarization of electron spins on NMR signals as described in his historical sketch (***Overhauser, Albert W.: Dynamic Nuclear Polarization***). As Overhauser points out, a scientist's intuition suggests that a small perturbation will probably cause a small effect in a system initially at equilibrium. However, in 1953, he proposed a theory predicting that a small change in the populations of electron spins (~1%) in a metal would lead to a change in nuclear spin polarization by a factor of about 20! Overhauser's presentation of this work at a meeting of the American Physical Society[144] caused an uproar. Abragam[145] assessed the situation in the following words:

> Overhauser's audience at the meeting of the American Physical Society—where he had (in 10 minutes) presented the calculations which had led to his amazing conclusion—was immediately split into two parts, which however overlapped: those who did not understand a single word of his demonstration and those who did not believe a single word of his conclusions. In the first row of the sceptics who did not believe his conclusions shone all the stars of magnetic resonance: Bloch and Purcell, Rabi and Ramsey. Bloembergen was of two minds and so was I.

Nevertheless, Overhauser submitted the article for publication in the *Physical Review* and (as later became apparent) Ramsey was asked to referee it. In letters quoted by Overhauser in his historical sketch, Ramsey describes his initial skepticism, his objective analysis, and his acceptance of the validity of this unexpected result.

Overhauser describes Ramsey's conclusion and the ultimate publication of the work[144,146] as an 'intellectual' verification of the theory, but the real proof lay in experiment. Slichter, along with his student Tom Carver, set out to test the prediction by observing the ^{7}Li signal in metallic lithium when the conduction electron spin resonance (CESR) was saturated. They faced an experimental dilemma: for good NMR sensitivity they should work with a magnetic field of at least a few kilogauss, but then the ESR frequency would be too high to obtain adequate saturating power from the devices available at that time. They decided to work at 30.3 G, where the ^{7}Li resonance is at 50 kHz, with the expectation that a strongly enhanced ^{7}Li signal would be observable even if the normal signal was not. Slichter's historical sketch describes the results:

> With this arrangement we succeeded in seeing the protons in glycerin. Changing the NMR coil (the glycerin sample was much bigger than the Li sample), Tom Carver tuned up the CESR oscillator, then turned it off to balance the NMR bridge. I was across the lab from him when I heard him shout with glee. When he had turned the CESR oscillator back on (thrown the plate voltage switch) a giant NMR line popped up on the scope. There it was—the Overhauser enhancement!

The theory and experimental verification of the Overhauser effect made a major contribution to the understanding of relaxation and thermodynamics in spin systems. It also ushered in a new area of research into 'dynamic nuclear polarization' (DNP). In addition to the substantial signal enhancements

available from DNP, there is also high spatial selectivity since only those nuclear spins reasonably proximate to an electron are affected. DNP was soon found not to be restricted to metals with conduction electrons. In free radicals and paramagnetic ions, magnetic dipolar and/or scalar coupling interactions serve as the mechanism coupling the nuclear and electron spins. Studies were carried out with F centers and solids doped with paramagnetic impurities such as free radicals. In the liquid state also, large DNP effects in solutions containing small amounts of free radicals were observed, for example by Richards et al.[147,148,149] Besides demonstrating signal enhancements of the order of 100, they also showed that it may be possible to obtain internuclear distances between interacting molecules from the NMR signal.

BRITISH RADIO SPECTROSCOPY GROUP (BRSG)

In 1956, E. R. Andrew organized a meeting at the University College of North Wales, Bangor, to discuss the rapid progress being made in various branches of radiofrequency spectroscopy. Out of this meeting grew the informal BRSG, which has subsequently organized a number of meetings (nearly two per year on average), usually at various locations in Britain that constitute centers of relevant research activity. 'Radio Spectroscopy' has been broadly defined to include not only NMR, but EPR, NQR, far-infrared lasers, molecular beams, and related fields. Each meeting, organized independently and on a financially self-sufficient basis normally runs about two days, with invited talks, posters, and laboratory visits. Participants usually come from across Europe as well as from North America. Raymond Andrew's historical sketch (***Spinning the Spins: A lifetime in NMR***) provides additional comments on the BRSG.

In 1955, Ionel Solomon, during a stay at Harvard, developed a general theory for changes in the intensity of NMR lines in a two-spin system when one of the spins is subject to a perturbing rf field. Solomon initially treated the case of purely mutual dipolar relaxation between the spins,[150] and then in collaboration with Bloembergen he extended the treatment to scalar coupling as well.[151] The theory took into account a rotational correlation time τ_c for dipolar relaxation and a correlation time for exchange τ_e that modulates the scalar coupling, and demonstrated that for short τ_c values the *nuclear Overhauser effect*, as the intensity change was called, ranges from $+\frac{1}{2}$ for purely dipolar relaxation to -1 for pure scalar relaxation. Experimental confirmation was obtained in the study of HF, where chemical exchange modulates the scalar coupling and can be controlled to modulate the importance of the two factors.

Application of the nuclear Overhauser effect was neglected for a decade but, as we shall see in Sections 6 and 11, its revival by chemists made it one of the most important tools available for elucidating the detailed molecular structure and conformation of biopolymers.

Some Early Studies of NMR in Solids

As we saw in Section 2, solids provided fertile ground for NMR investigations in the early years when magnet homogeneity was rarely a limitation in studying their broad lines. Gutowsky and Pake had shown in 1948 the narrowing of the proton NMR line in ammonium salts, as increasing temperature permitted the onset of internal rotation. Later Powles and Gutowsky discovered the role of tunneling,[152] an effect that was to be studied in much more detail in later years as described in Stanley Clough's historical sketch (***Clough, Stanley: NMR and Quantum Tunneling Rotation***). NMR was recognized as a very useful tool in investigating such processes as well as other phase changes. Molecules such as benzene and cyclohexane (which are nonpolar) along with nonpolar polymers could not be studied by dielectric loss methods, but NMR clearly demonstrated phase changes and internal motions (see ***Powles, Jack: Reminiscences of the Early Days of NMR***).

These observations invariably showed that the second moment of the line was apparently reduced as the line narrowed, but Van Vleck had shown theoretically that the second moment of an NMR line is invariant even though the shape and width at halfheight might be changed by altering conditions such as the temperature. At the University of Wales, Raymond Andrew speculated that the molecular motion responsible for narrowing the line generated weak, unobservable satellites in the wings of the line. In an attempt to simulate the phenomenon in a way that would make the satellites observable, Andrew decided to rotate the sample to generate a coherent motion at a single frequency. Andrew and his co-workers chose to study the ^{23}Na NMR in a single crystal of sodium chloride, which has cubic symmetry and a modest linewidth (about 833 Hz) arising from weak dipolar interactions. They spun the crystal at speeds up to 800 Hz about an axis perpendicular to the direction of the magnetic field and recorded the ^{23}Na NMR derivative absorption spectrum (as shown in Figure 29) as a function of the spinning speed. Line-narrowing and the appearance of spinning sidebands could be clearly observed at and above spinning speeds of about 500 Hz, and at 800 Hz the central component had narrowed to about half its static width of 833 Hz. This experiment, reported in 1958,[153] demonstrated the motional narrowing effects when the spinning speed is comparable with the static linewidth, confirmed the invariance of the second moment with respect to rotation, and exhibited the appearance of the spinning sidebands separated by multiples of the spinning frequency.

Analysis of the theory showed that sufficiently rapid rotation about an axis inclined at an angle α to the magnetic field should narrow the central component by a factor $-\frac{1}{2}(3\cos^2\alpha - 1)-$. For $\alpha = 90^\circ$, the factor is $\frac{1}{2}$ as had been observed. However, Andrew recognized that for $\alpha = 54^\circ 44'$, $\cos^2\alpha = \frac{1}{3}$, and the dipolar interaction should vanish. Andrew, Bradbury, and Eades[154] extended their study by varying α from 50° to 100° and found the expected narrowing, as illustrated in Figure 30. (The residual 200 Hz width was attributed to quadrupolar interactions because of an imperfect cubic crystal.) Meanwhile, Irving Lowe had developed a similar approach.[155] We shall defer further discussion of sample spinning to Section 8 where we integrate these techniques with others that were introduced later to narrow lines in solids.

The study of hydrogen adsorbed on metals or combined to form metal hydrides became an important area of research. For example, Richard Norberg, both as a student with Slichter and much later as a faculty member at Washington University, studied hydrogen in palladium[156] and various isotopes of

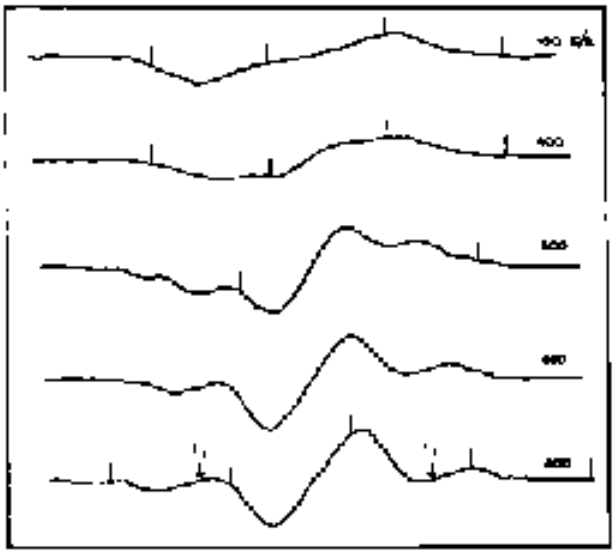

Figure 29 The first published results of solid sample spinning. ^{23}Na NMR (first derivative of the absorption mode) from a single crystal of NaCl rotated about an axis perpendicular to the magnetic field direction.[153] (Reproduced by permission of Macmillan Magazines Ltd)

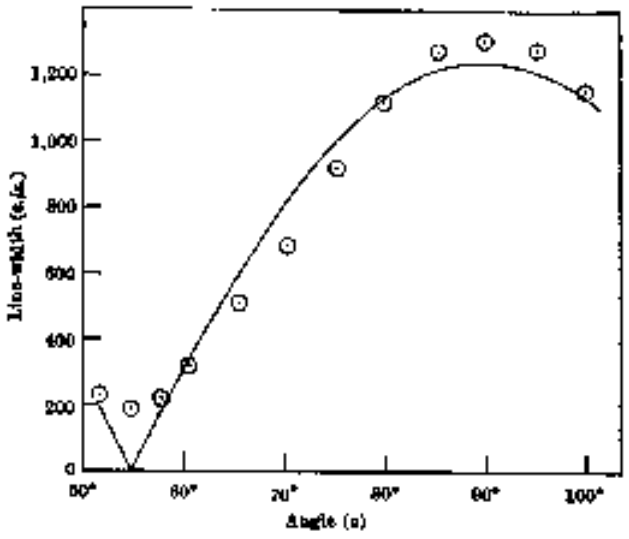

Figure 30 Variation of the linewidth of the ^{23}Na resonance in an NaCl crystal rotated about an axis inclined at an angle α to the magnetic field. The solid line is derived theoretically for a dipolar interaction, while the experimental data points are shown for rotation at 800 revolutions per second.[154] (Reproduced by permission of Macmillan Magazines Ltd)

hydrogen adsorbed on silicon semiconductors.[157] Likewise, Robert Cotts studied the diffusion of hydrogen in niobium hydrides and discovered restricted hydrogen-atom diffusion among the small particles,[158,159] a solid-state analog of Woessner's and Stejskal's work described previously. The historical sketches by Norberg (***Norberg, Richard E.: NMR in Urbana and St. Louis***) and Cotts (***Cotts, Robert M.: Historical Recollections***) provide further details on these and other related investigations.

As described in the previous section, Slichter had used a clever method to measure the Overhauser effect in ^{7}Li. He and Schumacher employed a similar method to measure the Pauli susceptibility of electrons in sodium by measuring the conduction electron spin resonance and the nuclear resonance of ^{23}Na with the same apparatus and frequency but at very different magnetic field strengths.[160] Later, as his colleagues at Illinois, Bardeen, Cooper, and Schrieffer, were developing their famous (BCS) theory of superconductivity, Slichter and Hebel made critical NMR measurements.[161] Their work, in conjunction with ultrasonic measurements, confirmed electron pairing, the basic aspect of the BCS theory.

New Perspectives on Relaxation

The BPP theory had provided the basic framework for understanding the relationship between relaxation rates and molecular motion. In some systems, however, additional factors had to be considered. For example, Lipsicas and Bloom[162] found that an anomalous temperature dependence in T_1 for hydrogen gas resulted from differences in anisotropic effects in collisions between two *ortho*-hydrogen molecules and one *ortho* and one *para* molecule. Meanwhile, Streever and Carr[163] studied spin–lattice relaxation in ^{129}Xe, which has a spin of $\frac{1}{2}$, in both gas and liquid, and found that the measured T_1 values under a variety of conditions were much shorter than would be expected from intermolecular magnetic dipole interaction, presumably as a result of collisional distortions. In this work they recognized the extreme sensitivity of the ^{129}Xe resonance frequency to environmental perturbations, a feature that has recently been exploited in materials science, as mentioned later in Section 15.

In 1962, Donald Woessner (***Woessner, Donald E.: In a Maze in NMR***) extended the BPP theory to situations in which molecules in liquids tumble anisotropically.[164] Less well known is a similar paper by Hiroshi Shimizu at the same time,[165] as discussed in more detail by Yoji Arata in his historical sketch (***Arata, Yoji: Early Days of NMR in Japan***). Later, Woessner used his new formalism to treat the relaxation of molecules such as water that have preferential orientation or undergo anisotropic reorientation on surfaces. This work provided an understanding of the NMR properties of small molecules adsorbed on zeolites and clays, an area that became important in exploration for petroleum and also provided some of the underpinnings for explaining NMR linewidths in anisotropic biological materials, such as cells and tissue.

In 1961, Gutowsky, Lawrenson, and Shimomura[166] observed an unexpectedly short T_1 value for ^{19}F in a Freon gas and recognized the importance of the spin-rotation interaction as a mechanism of relaxation for some nuclei in molecules in the gas phase. In 1963, Hubbard[167] developed the theory of spin-rotation relaxation for liquids in terms of Brownian motion.

Measurement of Static Nuclear Susceptibility

As noted in Section 1.3, it is possible (but only with great difficulty) to measure the small static nuclear susceptibility in the presence of the much larger diamagnetic susceptibility from the electrons in the molecule being studied. Indeed, in

1937, Lasarew and Schubnikow made such a measurement in solid hydrogen at 2 K where the more favorable Boltzmann distribution enhanced the value of the nuclear susceptibility.

In 1955, Evans[168] developed an interesting method for measuring the static nuclear susceptibility at room temperature. Although it has never become important in any practical sense, the idea is worth reviewing here. Evans used an experimental arrangement as sketched in Figure 31, where two thin-walled glass sample tubes about 1 mm in diameter, each containing a sample of solid hexaethylbenzene, are suspended from a 20-μm diameter quartz fiber, which is part of a sensitive torsion balance, in an inhomogeneous magnetic field. With the system at equilibrium, radiofrequency energy is applied over a broad band (obtained by sweeping the oscillator frequency over a range of 5%−10%) in order to saturate the nuclear spin system in the highly inhomogeneous magnetic field and thus reduce the nuclear susceptibility to zero. Although this represents a change of only about 0.05% in the overall susceptibility of the sample, a clear deflection, as shown in Figure 31, is obtained when the radiofrequency is centered at resonance, i.e. 30 MHz. Evans pointed out that the sensitivity of the method was comparable with standard NMR in 1955 (both requiring about 15 mg of sample), but that the susceptibility measurement was unlikely to have practical application since the resolution is extremely low.

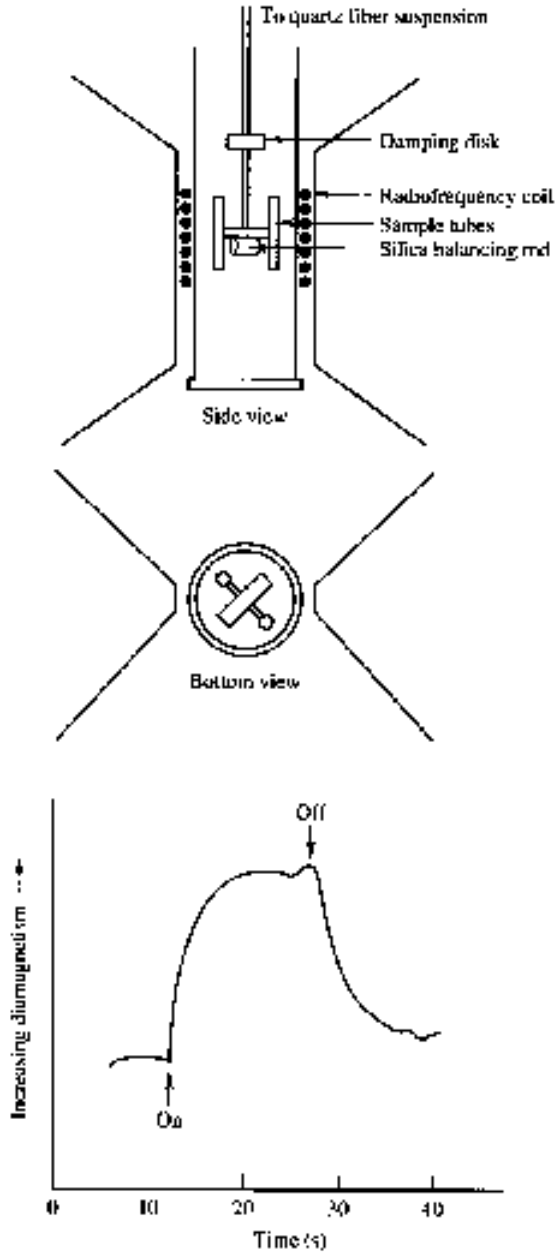

Figure 31 Top: schematic diagram of the apparatus used to observe NMR via change in the bulk magnetic susceptibility of the sample. Bottom: response as a resonant rf field is turned on to saturate the nuclear spin system[168] (Redrawn by permission of Taylor and Francis)

NMR IN CHEMISTRY COMES OF AGE

By 1960 NMR had been established as a valuable method for chemical analysis and for the structure elucidation of organic molecules. It was clear that NMR provided key information that could often be interpreted more readily and unambiguously than other analytical data, such as infrared (IR) spectroscopy. Yet, NMR remained a technique that was carried out only by specialists who could master the idiosyncrasies of the large and complicated instruments needed. Although major improvements had been made in providing commercial spectrometers that were reasonably stable and were capable of adequate resolution for most chemical problems, as discussed in Section 3, the resultant instruments were still large and unwieldy. A ^{1}H resonance frequency of 60 MHz had become the standard, and behind the scenes at Varian, magnet designers were pushing the existing magnet technology as far as possible to create a 100 MHz instrument.

The most significant obstacle to a real widespread acceptance of NMR was the fact that each spectrum had to be individually calibrated and even then was not very reliable, making duplication of most data essential. The basic problem was that frequencies could be generated precisely and reproducibly with crystal-controlled oscillators, but the magnetic field stability (even with a 'super stabilizer') was not very good. Thus an NMR scan covered a range of field strength that was not known precisely.

The A-60: A 'Mass Market' for NMR

In 1956, Russell Varian had advanced the idea of using an NMR line as a control in a feedback circuit to stabilize the field/frequency relationship.[64] Eventually, a number of related schemes were developed independently for achieving field/frequency stability that utilized an NMR line in either the sample being studied (an *internal lock*) or in a different sample (an *external lock*), and these played very important roles in the advance of numerous NMR techniques. Baker and Burd had pioneered the use of a second sample to obtain an external lock,[169] while Primas[170] had implemented the first internal lock based on an error signal from the rf dispersion mode. In this arrangement, as well as in a modification developed by Freeman and Whiffen,[171] an audiofrequency sideband was used to scan the spectrum.

The first commercial use of a field/frequency lock was in the Varian A-60 high-resolution spectrometer for studying proton NMR at 60 MHz. The 'nuclear sideband oscillator', which

provided an external lock via a water sample in the probe, was based on Varian's early idea as implemented by Wes Anderson.[172] With this circuitry, highly reproducible scans became routine. Shoolery describes the initial operation of the A-60 in these words:

> The final test of the prototype, introduced at the 1961 Pittsburgh Conference, is a particularly happy memory. I put a sample into the instrument, adjusted the resolution, and ran a spectrum on the precalibrated chart. It was perfect. But could the A-60 reproduce a spectrum with the fingerprint quality of the IR? I moved the pen back and restarted the scan. Momentarily distracted, I looked back and saw only one line on the chart. 'Why didn't the second scan run?' I asked. The answer came back, 'It did'. Amazed, I returned the pen three more times. The five spectra were a single trace on the paper. At that instant, I knew that organic chemistry would never be the same.

But the A-60 represented more than the introduction of a field/frequency lock. The whole instrument was designed specifically for chemists with the objective of structure elucidation of organic compounds. As illustrated in Figure 32, the 2.5 ton magnet with 12-inch diameter pole pieces was replaced by a much smaller 6-inch magnet, and the magnet power supply and water cooling units were reduced in size and placed in the same case. The large 'console' with its multitude of components became a slim unit with a flatbed recorder for producing the spectra on large precalibrated chart paper. An integrator was provided for measuring areas under the spectral peaks. For the first time, an NMR spectrometer had the look and feel of other then common analytical instruments such as infrared and ultraviolet spectrometers. This development was the culmination of a three-year development effort called Project ASP (for 'as soon as possible'). Emery Rogers (***Rogers, Emery H.: Remembrance of NMR Things Past***) describes the genesis of the project in these words:

> One day in 1957, Jim Shoolery and I visited the laboratories of a prominent East Coast chemical company. We took silent note of a wall placard which proudly proclaimed that Infrared Spectroscopy was the single most definitive analytical technique in existence. On the flight back to California, we were resolutely inspired to generate specifications for what would eventually become the widely successful A-60 High-Resolution NMR Spectrometer.

From its introduction in 1961, the A-60 had a tremendous impact on the development of NMR applications, particularly in organic chemistry. Eventually a model A-56/60 also became available for observation of both ^{19}F and ^{1}H, and various improvements in the circuitry were made. Over 1000 instruments of the A-60 type were sold before it and its modified versions eventually gave way to solid-state, permanent magnet instruments.

With preprinted spectral charts available, chemists were forced to standardize the mode of presentation of NMR data. In the earliest chemical studies, the direction of field sweep and its recording were dependent on the investigator's whim. Largely as a result of practice from the Varian Applab, a low-to-high field sweep from left to right on the chart had become the de facto standard. However, while it was recognized very early on that an internal reference compound dissolved in the sample of interest was necessary for the precise measurement of chemical shifts, the choice of compound was quite variable until George Tiers[173] introduced tetramethylsilane (TMS) as an 'ideal' internal reference compound. The use of TMS caught on rapidly and the A-60 charts were based on TMS as the reference.

Unfortunately, Tiers coupled the introduction of TMS with the proposal for a new scale, the τ scale, in which the TMS reference was designated as exactly 10 ppm rather than 0 ppm, as commonly used for any other reference compound. Students and newcomers to NMR were confused by the two chemical shift scales, as advocates and opponents of 'τ-values' forcefully articulated their positions at NMR conferences. As Shoolery mentions in his historical sketch (***Shoolery, James N.: High-Resolution NMR: A Dream Come True***), he was instrumental in designing the A-60 chart to indicate TMS as 0 ppm and in publishing a large compendium of spectra (the 'Varian Catalog'[174]) in which TMS had a $\delta = 0$ value. Although the τ scale enjoyed considerable popularity for several years and became the basis of tables in several widely read NMR books, it gradually faded from use. For example, Jackman's influential book,[175] published in 1959, used and advocated the τ scale, while the second edition[176] published 10 years later converted entirely to the δ scale. One factor that probably contributed eventually to the demise of the τ scale was the increased study of nuclei other than hydrogen, for each of which a reference scale was developed with a reference compound at $\delta = 0$. Not until the early 1970s was international agreement finally formalized through recommendations by the International Union of Pure and Applied Chemistry to use TMS as a reference at $\delta = 0$.[177,178]

The Varian *High Resolution* NMR *Spectra Catalog* provided a compilation of 368 60 MHz spectra, together with a list of chemical shifts and assignments to individual protons. This catalog (which was expanded in 1963 to comprise a total of 700 spectra) provided simple, diversified, and compelling examples of the application of NMR throughout organic chemistry. A typical page is shown in Figure 33. It became a major resource to the thousands of organic chemists who now found that obtaining and interpreting NMR spectra was within their grasp.

Time Averaging

Although the A-60 brought NMR to almost every chemistry laboratory as a standard analytical method, it did not solve the problem of the low sensitivity of NMR relative to other spectroscopic techniques. The sensitivity specification for the A-60 called for a signal-to-noise ratio of six for the strongest peak of the methylene quartet in a sample of ethylbenzene at a concentration of 1% by volume in a solvent such as CCl_4 or (later) $CDCl_3$. (As is pointed out later, this is about three orders of magnitude lower than modern high field instruments provide.) Although this sensitivity permitted practical use of samples of about 0.1–0.2 M, many organic and especially biochemical applications required lower concentrations. Nuclei with sensitivity much less than that for ^{1}H and/or with low natural abundance could be studied only as neat liquids or in very concentrated solution, and even then the results were usually quite poor.

A method to improve the signal-to-noise ratio became available as NMR spectroscopists realized that the coherent addition of signals from repeated scans could result in substantial enhancement. At least four independent and concurrent efforts resulted in publications in 1963. At Berkeley, Mel Klein adapted a multichannel pulse height analyzer (commonly used in studies of high-energy radiation)

THE EXPERIMENTAL NMR CONFERENCES: THE ENC AND THE EENC

NMR results have been presented at many scientific meetings. Some involve small, select groups, such as the Gordon Conferences on Magnetic Resonance or specialized symposia, while others are part of large national or international conferences of physics or chemistry societies. But the ENC, during its 35 annual meetings, has assumed a special place in which experimental NMR methods (not applications of NMR to specific problems) are emphasized. In a recent article entitled 'ENC, A Motor of Progress in NMR'[178] Nobel Laureate Richard Ernst says:

> Each ENC is a landmark, an hour of truth where success or failure of the previous twelve months of intense research becomes evident. Indeed from 1964 to very recently, I was working and living truly from ENC to ENC, having only one thought in mind: to be properly prepared with a new experiment or a new revealing insight to be presented at the next conference. I think it is important in the unstructured life of a scientist to have these regular caesuras to account for one's achievements.

These conferences evolved from a small, informal, one-day meeting in June 1960 at the Standard Oil Company (Ohio) Research Laboratories near Cleveland, OH. The meeting was organized by Bill Ritchey, SOHIO's resident NMR spectroscopist, who issued invitations to a number of NMR workers drawn primarily from the northeast quadrant of the United States, plus a few westerners from Varian's Palo Alto facility.

Some 42 active NMR practitioners gathered to discuss problems of the still fledgling field of practical, applied NMR spectroscopy, to hear Varian's Wayne Lockhart, Forrest Nelson, and Cappy Joller talk about trouble-shooting, shimming, and magnet cycling. There followed discussions on instrument operation (chaired by George Slomp of the Upjohn Company) and instrument accessories (led by Paul Bender of the University of Wisconsin). There was also a demonstration of Varian's new electric field shim device, the first such accessory commercially available. The meeting was a spectacular success, the few dozen early applied NMR types deriving much benefit from huddling together for comfort against the many vagaries of coaxing 40 and 60 MHz continuous wave spectrometers, with unlocked, temperature-uncontrolled, iron core magnets, into producing useful data on real molecules.

The enthusiasm generated by this meeting engendered an invitation from the Mellon Institute in Pittsburgh, PA, to hold a gathering the following year. The 'Second Conference on Experimental Aspects of NMR Spectroscopy' met in the elegant venue of the Mellon Institute on February 24–25, 1961. The timing was chosen, Pittsburgh winter weather notwithstanding, so that attendees could avail themselves of the large and important Pittsburgh Conference on Analytical Chemistry and Applied Spectroscopy, held in a downtown Pittsburgh hotel the following week.

This conference drew 118 attendees for a two-day immersion in a wide variety of topics and the donut-filling coffee breaks which were to become an integral part of this still small and informal 'group therapy' type of gathering. Scheduled topics included adjustment of field shape and homogeneity, measurement of rf field strength, dispersion mode spectra, quantitative aspects, survey of typical spectrometer performance, spin decoupling, and standards and referencing. In addition to these scheduled presentations and panel discussions, there was a most important development at a banquet concluding the meeting, viz. the unveiling of the brand new Varian Model A-60 NMR spectrometer.

The success of the 1961 meeting led to the continuation of these conferences on an annual basis. The conferences of 1962–70 were also held at the Mellon Institute. Space will not permit a detailed description of each of these conferences, the above descriptions of the first two meetings sufficing to convey the distance the field has come, and perhaps the feeling of community and enthusiasm which prevailed then and which to a remarkable extent remains today.

The fourth conference in 1963 had the impressive title '*O*mmnibus *C*onference on *E*xperimental *A*spects of *N*MR *S*pectroscopy', with the acronym *4th OCEANS*, but the following year the conference became known by the more manageable *ENC*. In 1970, it was recognized that the growth of the field and the demands for attendance had outgrown the cozy, familiar confines of the Mellon Institute, and these conferences moved elsewhere. The 1971 meeting was held in Gainesville, FL, and in 1972, the 13th ENC was held at the Asilomar Conference Center in Pacific Grove (Monterey), CA. This move met with widespread approval and a new pattern for the ENCs was immediately established: from that time onward, the meeting would alternate between sites in the eastern part of the country (very broadly defined) and a western location, Asilomar. Even that rather large venue is now becoming strained, with upwards of 1500 attendees.

While technically an American meeting, the ENC has always had a large number of international attendees and invited speakers. In 1974, following the suggestion by one of those attendees, Ed Randall, the successful format was transplanted to Canterbury, England, where the first European ENC (EENC) was held. A small 'junta', consisting of Ray Freeman, Pierre Servoz-Gavin, and Dieter Ziessow, guided the early development of the EENC with the same informality, ambiance, and emphasis on instrumentation and techniques as its American counterpart. Biennial meetings have been held in 11 countries throughout continental Europe, alternating with the Royal Society of Chemistry's international NMR meetings held in Britain in the intervening years.

to time-average NMR signals. Klein and Barton described the theory of time averaging in some detail, but their article submitted in July 1962 was not published until July 1963.[179]

Meanwhile, at Harvard, Oleg Jardetzky was looking for a method to study biochemical materials at low concentration. He interfaced a commercial time-averaging device produced by the Mnemotron Corporation to a Varian 4300–B 60 MHz spectrometer, primarily for physiological measurements. The Mnemotron Model 400 Computer of Average Transients (CAT) permitted acquisition of 400 channels of data. The paper in *Nature* by Jardetzky, Wade, and Fischer[180] in January 1963 was the first published use of time averaging for NMR. The terminology 'CAT' stuck, even when other time-averaging computers were developed, and is probably the first widely used acronym in NMR—the forerunner of many hundreds of others used to describe a multitude of different techniques.

The field/frequency control of the A-60 lent itself to the use of time averaging. During the summer of 1962, Leland Allen of Princeton University visited the Varian Applab and, as described by Roy Johnson (***Johnson, LeRoy F.: My Early Days in NMR Spectroscopy***), Allen and Johnson interfaced the CAT-400 to the A-60 and achieved sensitivity improvement of as much as a factor of 50 with 2500 repetitions of the spectral scan.[181] Back at Princeton, Allen reported his success and Laszlo and Schleyer quickly duplicated the Allen–Johnson setup and applied the method to the measurement of ^{13}C satellites in order to measure coupling constants in a set of cycloalkenes.[182] Varian developed an improved version of the CAT which had 1024 digital channels and could be triggered by an A-60 scan, and in later years Fabritek and others developed time-averaging computers with up to 4096 channels.

Structure Elucidation by NMR

With the theory of NMR in liquids now quite well understood and sufficient data available from model compounds, chemists (especially the vast number of organic chemists dealing with synthesis and with structure elucidation of natural products) were finally in a position to make routine NMR measurements. The simplicity in interpreting the proton NMR spectrum, as compared with infrared spectra, made NMR very attractive for a generation of chemists and the instrumentation had developed to the state where it was generally reliable and could be used by nonspecialists to obtain readily reproducible data. Applications quickly proliferated. Jackman and Sternhell noted in their book[176] published in 1969 that there were well over 6000 literature references to NMR, compared with about 400 a decade earlier. The vast majority related to the use of NMR in organic structure elucidation.

At 60 MHz, the NMR spectra of many of the protons of alicyclic systems such as steroids were a featureless blur, but the methyl groups were readily recognizable even at 40 MHz, as discussed in Section 3.4. Extensive studies of the effects of small structural variations upon the precise shift of these groups enabled steroid chemists to obtain a remarkable amount of information from the chemical shifts of angular methyl groups in unknown compounds. In 1960, heterocycles did not appear to offer fertile ground for NMR analysis because of the relatively few protons in their rings. However, by the end of the decade, so much useful information had been acquired that a 500 page book entitled *NMR Spectra of Simple Heterocycles* was devoted to the subject.[183]

With a larger collection of NMR data available and more experience in spectral interpretation, chemists were able to draw subtler inferences from observed chemical shifts, coupled with general chemical knowledge. One example of the type of study possible with even a simple spectrometer can be found in the study of an alkaloid, amaryllisine.[184] The A-60 spectrum shown in Figure 34 reveals the presence of three methoxyl groups, an isolated methylene group in an asymmetric environment, and two olefinic protons with one being coupled to a 'carbinol' proton. These features may be fitted readily into one of the structural frameworks known in this class of alkaloid, with the exact substitution of the aromatic system still unresolved. The position of the lone hydrogen on the aromatic ring can be fixed by comparing the chemical shifts of the parent alkaloid and its dihydro derivative, for reduction of the double bond results in an upfield shift of 0.18 ppm of the nearby aromatic proton. Finally, comparison of the aromatic proton shifts of the alkaloid in neutral and basic solutions shows that conversion to the phenolic anion shifts the aromatic proton 0.23 ppm upfield, which is characteristic of a proton *ortho* to the phenol.

This study is illustrative of many which extracted more structural details from the spectra than available at first glance. Comparison of the chemical shifts of the *N*-methyl groups of basic nitrogen in neutral solvents and in trifluoroacetic acid allowed them to be distinguished from those on neutral materials. The problem of assigning the substitution patterns in the methoxy–hydroxy aromatic rings common in natural products was approached by comparing the chemical shifts in neutral and basic solutions. NMR provided key data, but it was the experience of the organic chemist that drove the interpretation of the data. In the 1960s a number of books showed how NMR could be used in structure elucidation, either in its own right or in combination with infrared and mass spectrometry. Emery Rogers' goal (quoted above) of making NMR an analytical method on a par with infrared spectroscopy had been achieved.

NMR of Soluble Polymers

As Frank Bovey points out in his historical sketch (***Bovey, Frank A.: NMR of Polymers***)

> When polymers in solution were first observed by high-resolution NMR some 30 years ago, almost nothing was known about the subject. ... There was in fact somewhat the same feeling about solution spectra as about solid state spectra—namely that they would be too broad and too complicated to be of any interest for the determination of structure. Happily, when the experiment was actually tried this proved not to be the case, and the rest is history.

In the absence of cross-linking, internal flexibility in long polymer chains provided the motional narrowing needed to generate real high-resolution spectra, from which chemical shifts and coupling constants could be derived even at 60 MHz. The principal advantage provided by NMR in polymer analysis was the determination of stereoregularity.

By this time, chemists had begun to understand the role of asymmetric centers in influencing NMR spectra. The paper by Waugh and Cotton[185] and papers by Roberts and others showed that methylene protons can be rendered observably nonequivalent in chemical shift if they are in an asymmetric

Figure 32 Top: the Varian HR-60 spectrometer. Bottom: the Varian A-60 spectrometer

environment. In fact, a range of examples from NMR contributed greatly toward clarifying for most chemists the consequences of molecular symmetry and asymmetry.

In polymers, extensive work by Bovey and others showed that these concepts could be readily applied to groups of two, three, or more repeating functional groups (dyads, triads, etc.). Bovey's historical sketch (***Bovey, Frank A.: NMR of Polymers***) provides a lucid treatment of the reasoning and gives examples of applications to polymers of varying tacticity. Later, such studies were extended to ^{13}C NMR as suitable techniques became available for studying this nucleus, and theoretical treatments provided a better understanding of the origin of chemical shifts in various polymers (see ***Ando, Isao: Structures and Electronic States of Polymers as Studied by High-Resolution NMR Spectroscopy Combined with Quantum Chemistry***).

NMR of Paramagnetic Systems

While the vast majority of NMR studies in the late 1950s and the 1960s were devoted to diamagnetic organic compounds, several physical chemists began the exploration of paramagnetic systems by NMR, a field of study that was eventually to have considerable impact on NMR investigations of organic compounds and biopolymers.

Since the magnetic moment of an unpaired electron is about 10^3 times as large as that of a typical nucleus, the interaction between the paramagnetic center and nuclear magnetic moments in the same molecule (or sometimes in nearby molecules) can give rise to large chemical shifts and/or to a decrease in relaxation times resulting in the broadening of spectral lines.

Observations of the effects on NMR spectra of electrolyte solutions containing paramagnetic species date back to the 1950 studies by Bloembergen and Dickinson.[186] In addition, Phillips et al.[187] in 1957 observed 'anomalous' shifts in the proton spectra of *n*-propanol and *n*-hexanol in the presence of paramagnetic ions such as Mn^{2+} and Co^{2+}.

The first reported NMR spectrum of an intact paramagnetic molecule in solution came in 1957 from McConnell and Holm[188] who observed an 'unusual' proton NMR shift in the paramagnetic sandwich compound nickelocene [dicyclopentadienylnickel, $Ni(C_5H_5)_2$], both as a polycrystalline solid and in toluene solution at room temperature. In toluene, the proton resonance of nickelocene was a line about 300 Hz wide and about 300 ppm more shielded than the toluene resonance. (Only a single broad line for toluene was observed at the

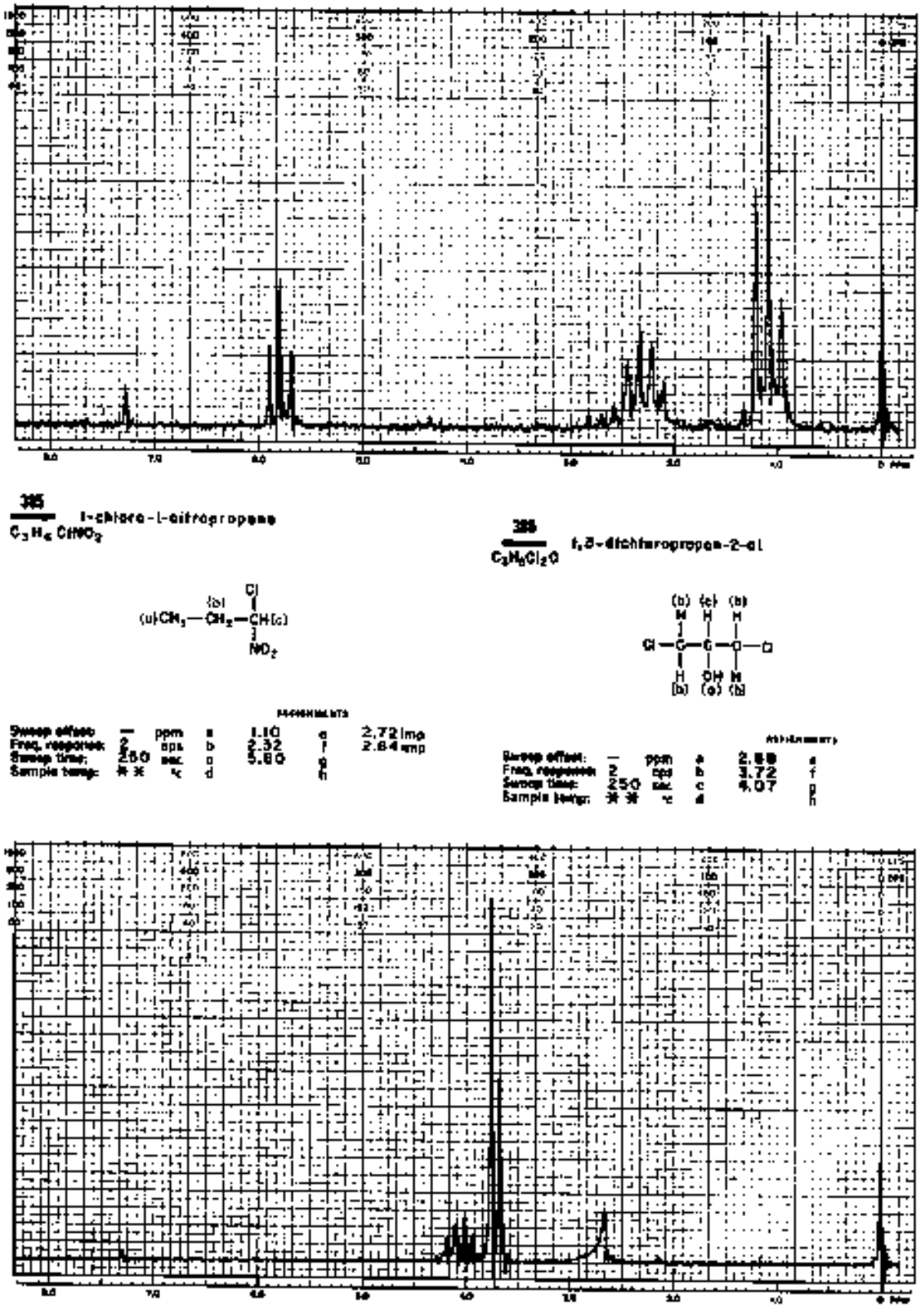

Figure 33 A typical page from the Varian *High Resolution NMR Spectra Catalog*. (Reproduced by permission of Varian Associates)

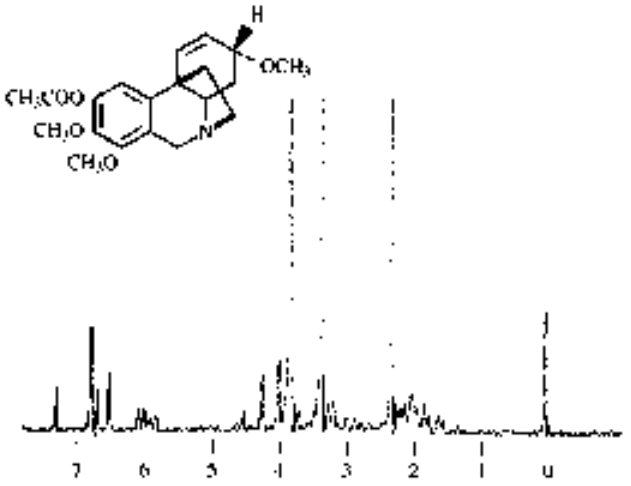

Figure 34 The 60 MHz ^{1}H spectrum of amaryllisine acetate.[184] (Courtesy of R. J. Highet)

operating frequency of 16 MHz). In solid polycrystalline nickelocene, the shift to higher field was over 320 ppm relative to the proton resonance of water containing 0.05 wt% of Mn^{2+}. Similar large shifts, but to lower field, were observed a few months later by McConnell and Holm[189] in $V(C_5H_5)_2$ and $Cr(C_5H_5)_2$ under conditions identical to those for the nickel compound. In 1960, Phillips and Benson[190] observed both high- and low-field shifts in the proton magnetic resonance spectra of solutions of nickel aminotroponeimineates. The proton relaxation times in these compounds are sufficiently long to allow proton spin–spin interactions of about 6–12 Hz to be resolved. The spin–spin couplings, along with the intensities of the spectral lines, permitted unique assignments of the observed proton resonances to various nonequivalent sets of protons of each chelate.

The large differences in the nuclear shieldings observed in such cases were explained quantitatively in 1958 by McConnell and Robertson[191] in terms of an isotropic contact interaction between the nuclei and the unpaired spin density produced in the ligand molecule by the paramagnetic metal atom to which it is bonded.

The large paramagnetic shifts usually generate first-order spectra, which were exploited as an important tool during the 1960s in transition metal chemistry. Contact shifts have thus been reported for the ligand atom nuclei of many transition metals, especially cobalt(II) and nickel(II) which usually display sharp resonances. Studies related to electron distribution, bonding, and structure of metal complexes, including structural and spin equilibria and optical isomerism, have been undertaken extensively. Investigations on ion-pair formation in solution, solvation phenomena, kinetics of chemical exchange processes, electron and proton transfer studies have also been carried out.

Large values of the hyperfine interaction constant are expected to produce line-broadening in the NMR spectra, but species with large values of the hyperfine interaction constant may exhibit sharp lines if the correlation time for the contact interaction is short. This can happen from rapid electron relaxation and/or rapid exchange, as has been demonstrated for the case of electron transfer between diamagnetic and paramagnetic species by DeBoer and MacLean.[192] A typical

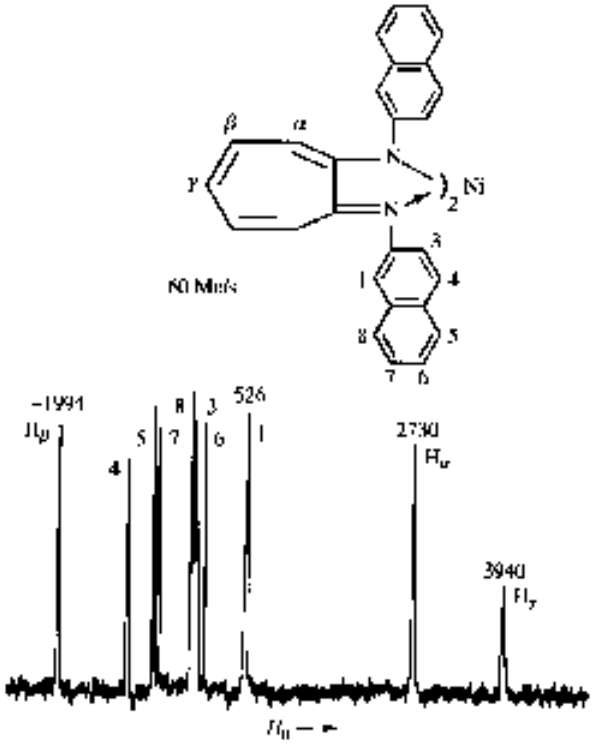

Figure 35 The ^{1}H NMR spectrum of the nickel(II) chelate of 1-(2-naphthylamino)-7-(2-napthylimino)-1,3,5-cycloheptatriene in $CDCl_3$.[193] (Reproduced by permission of the American Chemical Society)

early spectrum,[193] shown in Figure 35, shows 10 sharp proton resonances, four to lower field (negative spin density) and six to higher field (positive spin density). The resonances H_α, H_β, and H_γ were readily assigned to the three nonequivalent sets of protons of the seven-membered ring, and four of the seven resonances attributable to the naphthalene ring exhibited resolvable nuclear spin–spin structure.

The work on paramagnetic species not only provided valuable information in transition metal chemistry but also laid the groundwork for extension of the concepts to NMR investigations of organic structure via shift reagents.

Lanthanide Shift Reagents

During the course of investigations on the binding of cholesterol in solution with complexes of rare earth metals, Hinckley[194] in 1969 made one of the most valuable discoveries in organic NMR. He observed that some paramagnetic lanthanide β-diketones can be employed to induce large shifts in the NMR spectra of molecules to which they complex, thus facilitating spectral analysis by reducing complex spectra to weakly coupled spectra in which chemical nonequivalences can be readily discerned and coupling constants can be easily evaluated. His initial experiment used a dipyridine adduct of tris(dipivalomethanato)europium(III), $Eu(dpm)_3 \cdot 2Py$, with a sample of cholesterol monohydrate in CCl_4. The key to the use of such 'shift reagents' is that they induce substantial paramagnetic shifts without causing relaxation that broadens lines and reduces resolution. With lanthanide shift

reagents (LSR), it became possible to obtain a wealth of useful information for fairly complex systems with even low frequency spectrometers.

In fact, the history of the use of paramagnetic ions as shift reagents can be traced back to 1960 when Lewis, Jackson, Lemons, and Taube[195] observed that the addition of the paramagnetic Co^{2+} ion to aqueous solutions of diamagnetic salts of Be^{2+}, Al^{3+}, and Ga^{3+} resulted in a well-resolved two-line ^{17}O NMR spectrum, one due to the water of hydration of the diamagnetic ion and the other due to solvent water which is in rapid equilibrium with the first hydration sphere of Co^{2+} and hence is shifted. Subsequently, this group observed that the rare earth dysprosium ion may be better suited as a shift reagent since it induces large ^{17}O shifts of water without significant broadening, and large proton shifts were reported for paramagnetic rare-earth acetylacetonates, tropolonates, and acetates by Eaton,[196] Muetterties and Wright,[197] and Reuben and Fiat.[198]

Shifts from LSRs have been found to result from pseudocontact interactions which arise from direct magnetic dipole–dipole interaction between the spins of the unpaired electrons and those of the nuclei. Thus, the magnitude and sign of the LSR-induced shift at each nucleus can be related to the geometry of the molecular complex in terms of both distances and angular factors. Fortunately, many of the lanthanides have sufficiently short electron relaxation times to preclude significant magnetic dipolar relaxation and hence to retain the sharp NMR lines characteristic of most small organic molecules.

UK NMR DISCUSSION GROUP

About the same time that the ENC was formed in the United States, a group of early NMR practitioners in and near London, England, also issued a call for like-minded scientists to assemble for an informal meeting at the Northern Polytechnic, where Eric Mooney had one of the first Perkin-Elmer NMR spectrometers. Ernie Cummins, at Perkin-Elmer, was instrumental in forming the group, modelled somewhat after an infrared spectroscopy discussion group. With the enthusiasm generated by the unexpectedly large attendance (about 150), the attendees formed the UK NMR Discussion Group, which went on to hold semi-annual meetings in various parts of the United Kingdom. In the mid-1960s the Group affiliated with the Chemical Society, and under these auspices sponsored, in 1969, the first of what would become a series of International Meetings on NMR Spectroscopy.

The 26th meeting of the Group, in 1974, under Ed Randall's chairmanship, was devoted entirely to experimental aspects of NMR and included a number of participants from continental Europe. This meeting served as a model for the European ENC, which would eventually be held biennially on the continent, alternating with the International Meetings on NMR Spectroscopy of the Royal Society of Chemistry in the UK.

Many more efficient shift reagents were introduced to study a variety of problems. The use of anhydrous lanthanide complexes of dpm instead of the pyridine adduct was proposed by Sanders and Williams,[199] who employed $Eu(dpm)_3$ for

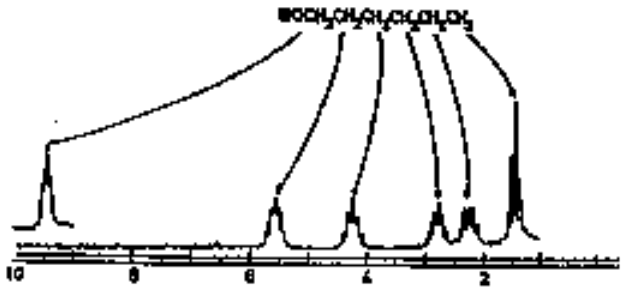

Figure 36 The 100 MHz ^1H NMR spectrum of *n*-hexanol plus $Eu(dpm)_3$ in CCl_4.[199] (Reproduced by permission of the Royal Society of Chemistry)

obtaining a well-resolved first-order spectrum of *n*-hexanol at 100 MHz, as shown in Figure 36. This shift reagent increased selective shifts by a factor of about four in cholesterol under conditions comparable with Hinckley's early experiment. In 1971, Rondeau and Sievers[200] reported that the lanthanide tris-chelates of 6,6,7,7,8,8,8-heptafluoro-2,2-dimethyl-3,5-octanedione [H(fod)] were new 'superior' shift reagents for NMR spectral simplifications. Their effectiveness was especially pronounced for classes of compounds such as ethers that are rather weak donors. The complexes with fod are also considerably more soluble in organic solvents than those with dpm.

In 1970, Whitesides and Lewis[201] reported the first chiral LSR for the study of enantiomers. In this study, lanthanide tris-chelates with the ligand 3-(*t*-butylhydroxymethylene)-*d*-camphor were employed. Subsequently more effective chiral shift reagents were added to the list, and other types of LSRs such as binuclear lanthanide(II)–silver(I) complexes and water-soluble lanthanide complexes were introduced. Effective shift reagents soon became available for most classes of compounds.

The field of shift reagents experienced an explosive growth during the 1970s. As higher field NMR spectrometers became widely available, the general need for LSRs diminished but they continue to be applicable in many instances.

Isotope Effects

As improvements in magnet homogeneity and stability permitted more precise measurements of chemical shifts, NMR spectroscopists began to notice small changes on isotopic substitution. The first report of isotope effects was that of Wimett[202] in 1953 who found differences in the shielding of ^1H and ^2H in molecular hydrogen. However these differences were barely outside experimental error, and isotope effects attracted little attention until Tiers[203] found upfield shifts in ^1H and ^{19}F resonances on substitution of a nearby hydrogen by deuterium. For example, the CF_2D group in *n*-C_3F_7D was shifted by 0.60 ppm to higher field than the corresponding group in *n*-C_3F_7H. Later, Gutowsky Karplus, and Grant (1959) observed an upfield shift of the proton resonance in dicyanomethane by 0.003 ppm as a result of the substitution of one proton by a deuteron,[204] and Gutowsky interpreted these isotope effects as arising from the difference in the vibrational amplitudes of hydrogen and deuterium, in accord with Ramsey's theory of the chemical shift.

Subsequent investigations by a large number of people established the general systematics of the field. The theory has been worked out in great detail, especially by Cynthia Jameson.[205] More recently, long-range effects through as many as 12 chemical bonds in conjugated hydrocarbons have been observed for ^{13}C on deuterium substitution for hydrogen.[206] The isotope shift of about 0.02 ppm arising from the substitution of ^{18}O for ^{16}O bonded to a phosphorus atom has been used to label individual phosphorus atoms and to investigate their fate in biochemical reactions.

Chemically Induced Dynamic Nuclear Polarization

In 1967, Ward and Lawler at Brown University observed unexpected intense ^{1}H NMR signals (both positive and negative) in olefins (alkenes) involved in the rapid reactions of organometallic compounds.[207,208] Since the reaction proceeds by a free-radical mechanism, they reasoned that the intense signals must arise from interactions with the electron spins in a manner analogous to the dynamic nuclear polarization first predicted by Overhauser (see Section 4). Meanwhile Joachim Bargon, a graduate student in Darmstadt, had already observed a strong negative polarization of benzene in a polymerization reaction initiated by benzoyl peroxide.[209,210] He and Hans Fischer coined the name Chemically Induced Dynamic Nuclear Polarization (CIDNP), a name that has persisted despite the fact that later work (principally by Closs[211] and Kaptein[212,213]) established a different mechanism for the phenomenon. Robert Kaptein's historical sketch (***Kaptein, Robert: The Early Days of CIDNP***) points out:

> The first observation of CIDNP dates long before the 1967 publications. In fact, countless discoveries and rediscoveries have been made, often dismissed as artifacts. An example is that from the laboratory of Prof. Th. J. de Boer of the University of Amsterdam. NMR spectra of a cyclopropyl compound in $CDCl_3$ had the chloroform line in emission or absorption depending on the operator who ran the spectrum. It turned out that one operator had the habit of shaking the NMR tube before recording the spectrum, while the other had not! The slight amount of oxygen mixed in the solution oxidized the labile cyclopropyl compound, which resulted in polarized $CHCl_3$ as one of the products of a radical recombination reaction. Since the chloroform proton has a T_1 value of 60 s or so, it is a particularly favorable molecule in which to store nuclear polarization.

Kaptein, who was then a student with Oosterhoff at the University of Leiden, immediately followed up these reports and discovered that products from radical pair combination showed one sign of polarization, while those from radical scavenging reactions had the opposite sign. He developed a quantum mechanical theory based on radical pair interactions that accounted for these results. At the same time, Gerhard Closs at the University of Chicago developed a similar theory based on hyperfine coupling induced by singlet–triplet mixing in the photochemical reactions that he was studying. One of the triumphs of these theories was their ability to explain the observation of sign reversal within a spin-coupled multiplet, as illustrated in Figure 37.[214] CIDNP rapidly became a useful tool in studying organic reaction mechanisms initiated photochemically or by free-radical reactions, and later Kaptein developed a laser photo-CIDNP to obtain information on the sites of binding of ligands to certain proteins.[215,216]

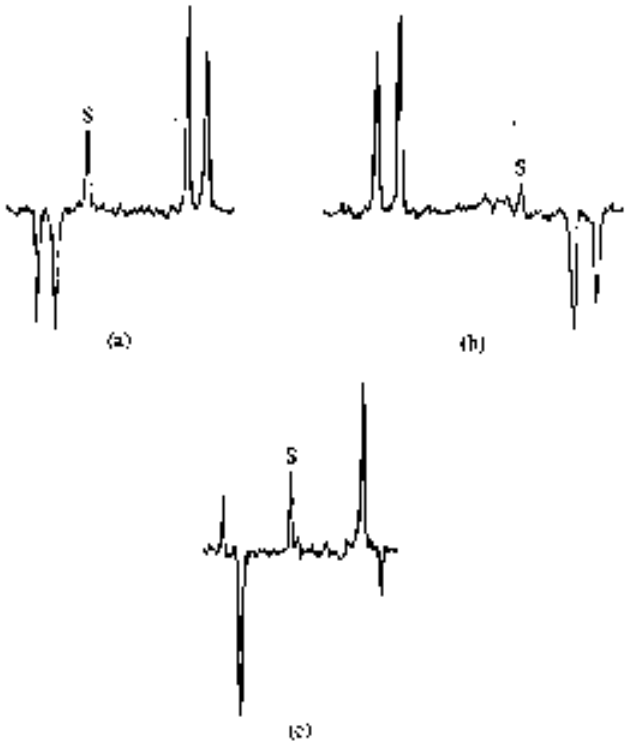

Figure 37 ^{1}H NMR spectra of the CH–CH fragment of 1,2,2-triarylethanol, showing the 'multiplet effect', obtained on irradiation of different starting materials. The line designated S is a ^{13}C satellite of the solvent[214]

High-Pressure NMR

Although temperature has been exploited as a variable in NMR studies since the earliest measurements, pressure was used only sparingly in early work probably because of the complexity of apparatus needed. Nevertheless, David McCall and his colleagues at Bell Laboratories were among the early workers who measured self-diffusion by spin echo methods at pressures up to 700 bar.[217] At Illinois, Jiri Jonas began a long-term program in high-pressure NMR during the late 1960s (see ***Jonas, Jiri: NMR and High Pressure***) in which he successfully made high-resolution NMR measurements, first with conventional continuous wave methods and later with early Fourier-transform techniques. He and his colleagues were able to analyze the effect of changes in viscosity on the rates of reaction without the complicating factors introduced when viscosity is altered by changing solvents. They also examined phase changes in solids and solid polymers and developed insight into the behavior of water at supercritical pressures.

Liquid Crystals

As we saw in Section 2, the earliest NMR studies clearly differentiated between studies in liquids where sharp lines permitted observation of chemical shifts and scalar couplings, and solids where these effects were obscured by broad lines but where additional information could be obtained from anisotropic quadrupolar and magnetic dipolar interactions. During the 1950s some NMR spectroscopists sought methods

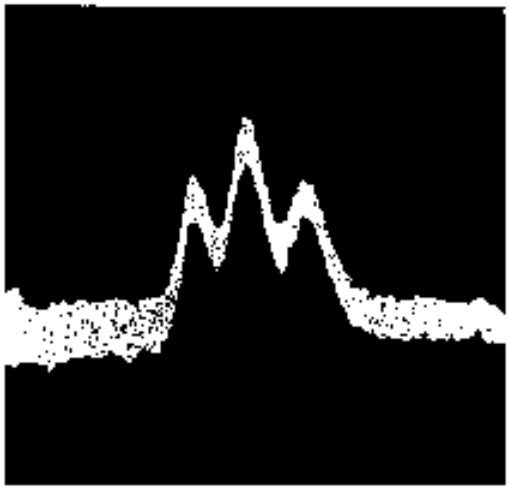

Figure 38 The ^{1}H NMR signal from *para*-azoxyanisole in the liquid crystal phase.[219] (Reproduced by permission of the American Institute of Physics)

whereby such interactions could be observed and measured from line-frequency separations, rather than linewidths, by orienting molecules in the liquid state. Initial attempts to induce molecular orientation included the use of an electric field, the absorption of molecules in polymers with subsequent stretching, and embedding the molecules in zeolite crystal channels. The success achieved in such experiments was insufficient to make them routine techniques for the precise determination of the parameters in question.

A breakthrough was made by Saupe and Englert[218] in 1963 when they proposed the use of liquid crystals as solvents for studying the NMR spectra of small molecules. This gave birth to a new field of NMR spectroscopy of oriented molecules. Since then the field has developed rapidly, particularly for the determination of relative internuclear distances and bond angles, and has provided the only method for the direct measurement of molecular shapes in the liquid state.

The first application of NMR to liquid crystals themselves was made by Spence, Moses, and Jain[219] as early as 1953, when the proton NMR spectrum of *p*,*p*′-dimethoxyazoxybenzene (‘*p*-azoxyanisole’) was observed in a nematic liquid crystalline phase. As shown in Figure 38, three broad lines were observed. The splitting pattern was initially interpreted as arising from very strong hindering of the rotations of the methyl groups or ascribed to the magnetic nonequivalence of the protons in the phenyl rings in the liquid crystal phase. Subsequently, Spence, Gutowsky, and Holm[220] found that at two other magnetic fields the splittings were the same and hence concluded that the spectral features were not attributable to a chemical shift effect but could be interpreted on the basis of dipole–dipole interactions between the protons. The two extreme lines were due to aromatic protons split into the broad doublet by the *ortho* ^{1}H–^{1}H dipolar couplings and the central line arose from the aliphatic protons.

What Saupe and Englert observed were the sharp lines arising from the protons of the small molecules dissolved in the liquid crystalline media superimposed on the broad background arising from the liquid crystal protons. The first spectrum of a molecule (benzene) dissolved in a liquid crystal solvent is shown in Figure 39. Although the linewidth was several Hz (due to temperature gradients and instrumental effects), the lines were sharp enough to be interpreted as arising from intramolecular dipolar couplings, chemical shifts, and indirect spin–spin couplings. Values of the chemical shifts and the indirect spin–spin coupling constants derived from such spectra were shown to contain information on the anisotropic contributions of these parameters. The inverse cube dependence of the direct dipolar couplings provided a method for the precise determination of relative internuclear distances and bond angles. Saupe[221] developed the theory of molecular orientation in terms of the order parameter while Snyder[222] presented an alternative approach, which he also showed to be equivalent to Saupe’s.

The concentration and temperature dependence of the splittings in the spectra of oriented molecules was investigated by Diehl and Khetrapal[223] in 1967. They found that, in general, the order parameter decreases with an increase of temperature and concentration. Any contrary behavior indicates weak molecular interactions; hence the method was employed to study such interactions. Yannoni, Ceasar, and Dailey[224] studied the first metallo-organic compound, the π-complex iron tricarbonyl cyclobutadiene, and showed that the four protons do not lie at the corners of a perfect square. Applications were extended to less symmetric and more complicated molecules, chemical shift anisotropies were determined, and absolute signs of indirect spin–spin couplings could also be determined in many cases.

The spectra of oriented molecules, particularly in thermotropic nematic liquid crystals, were found to be strongly coupled unless heteronuclei were involved, thus resulting in a rapid increase of spectral complexity with increase of the number of interacting nuclei. This has remained the major problem in applying these methods to more complex molecules. Over the years a number of new approaches have been introduced to simplify spectra, including the use of lyotropic liquid crystals,[225] double-resonance techniques,[226] multiple quantum spectroscopy,[227] isotopic substitution with heteronuclear decoupling,[228] the use of near magic angle spinning,[229] the use of two-dimensional NMR,[230] and the use of mixed liquid crystals of opposite diamagnetic anisotropies.[231,232]

The study of ^{2}H NMR in liquid crystal molecules and in small molecules dissolved in liquid crystals has been pursued by a number of workers. Since the deuterium quadrupole coupling constant can often be estimated reliably, spectral splittings provide information on order parameters. For example, Figure 40 shows the ^{2}H NMR spectrum of *p*,*p*′-azoxydi(phenetol-α,α,β,β,β-d_5). The two doublets arise from two types of deuteriums (CD_3 and CD_2) which have different order parameters.[233] In Section 10, we point out the application of such local order parameters to the study of the mobility of fatty acid chains in phospholipids and biomembranes. The values of order parameters determined from the ^{2}H spectra have also been used to aid the analysis of the corresponding proton NMR spectra which, as we have seen, can be quite complex.

MAJOR ADVANCES IN NMR TECHNOLOGY

With NMR firmly established as an indispensable tool for chemistry during the early part of the 1960s, physicists, chemists, and instrument designers began to think about more

Figure 39 The ^{1}H NMR spectrum of benzene dissolved in the nematic solvent *p*,*p*′-dihexyloxyazoxyanisole.[218] (Reproduced by permission of the American Physical Society)

Figure 40 The ^{2}H NMR spectrum of *p*,*p*′-azoxydi(phenetol-α,α,β,β,β-d_5) at 6.5 MHz in the dispersion mode.[233] (Reproduced by permission of the American Institute of Physics)

sophisticated techniques and more powerful instruments. Two principal areas that were developed through most of this decade have had continuing impact on all subsequent NMR applications.

Nuclear magnetic double resonance (NMDR) methods became essential to the analysis of the spectra of complex molecules. Moreover, these methods could be used to follow reaction kinetics and to enhance the sensitivity of NMR spectra. The application of double resonance also provided a major advance in the development of ^{13}C NMR and in studies of other nuclei of low sensitivity.

The continuing attempt to reach higher magnetic fields led to the development of superconducting magnets of the necessary homogeneity and stability for high-resolution NMR. This enormous advance in instrumental capability continues unabated, with no end in sight.

Another factor that played an increasingly important role in the development of NMR was the entry of other instrument companies to challenge the virtual monopoly held by the pioneering Varian Associates.

Double Resonance Methods

The idea of *double* resonance, i.e., perturbing one or more particular transitions while simultaneously monitoring a different transition, has led to many exciting developments in NMR and its applications. The first double resonance experiment was carried out by Pound[234] in his early study of relaxation in ^{23}Na in solid sodium nitrate. He irradiated one line in the spectrum and observed an intensity increase in a second line, thus proving that relaxation occurred by a nuclear quadrupole interaction with the surrounding field gradient, rather than by dipolar relaxation which could be shown to result in no NMDR intensity change. Although it provided only a modest intensity change, this observation really anticipated the Overhauser effect and became the forerunner of other experiments in which intensity changes were observed.

At the other end of the scale of NMDR perturbations, Wes Anderson developed the basic theory of spin decoupling (a suggestion that he attributed to Bloch) while a graduate student at Stanford, but published the results from CERN in 1956 as part of a long paper covering many aspects of spectral analysis.[235] Meanwhile, Virginia Royden, at Varian Associates, reported the first decoupling experiment[236] in 1954, when she irradiated the ^{13}C in 51% enriched $^{13}CH_3I$ to decouple the ^{13}C 'satellite' lines and from the optimum decoupling frequency determined an accurate ratio of the magnetic moments of ^{1}H and ^{13}C, as illustrated in Figure 41. The next year Bloom and Shoolery (also at Varian) partially anticipated Anderson's paper with their theoretical treatment of the effect of a strong perturbing rf field.[237] They showed that for two scalar-coupled spins separated by a large frequency relative to their coupling, the theory could be developed by transforming the problem to a frame rotating at the frequency of the perturbing field—a basic approach followed in almost all subsequent work. They found that with a sufficiently strong rf field the splitting from spin coupling can be almost completely eliminated, but that at somewhat lower field strengths the structure in the spectrum can increase in complexity. Experimental results were presented on ^{19}F and ^{31}P resonances in aqueous solutions of Na_2PO_3F and found to support the theoretical predictions.

The initial double resonance experiments simply employed rf oscillators operating at the nominal frequencies of the two nuclides, with a provision for 'pulling' the perturbing oscillator to obtain the exact frequency desired. Even for the proton–proton decoupling experiments described by Anderson, two separate rf oscillators were used. Considerable simplification of the equipment and superior operation for NMDR and other NMR experiments could be achieved by the use of a lock-in detector to detect an audio modulation sideband.[238,239] Itoh and Sato[240] employed this method to decouple the methyl and aldehyde protons in acetaldehyde. In 1959, Ray Freeman began to study homonuclear double resonance effects by employing audio modulation methods. As he describes in his historical sketch (***Freeman, Ray: Double Resonance Methods***

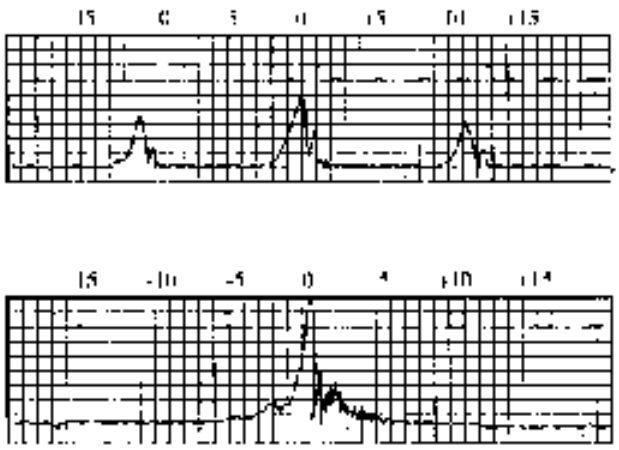

Figure 41 The 30 MHz ^{1}H NMR spectra of CH_3I enriched to 51% in ^{13}C. Top: single resonance spectrum. Bottom: simultaneous irradiation of ^{13}C at 7.5 MHz to decouple the ^{13}C–H doublet. (Reproduced by permission of the American Physical Society)

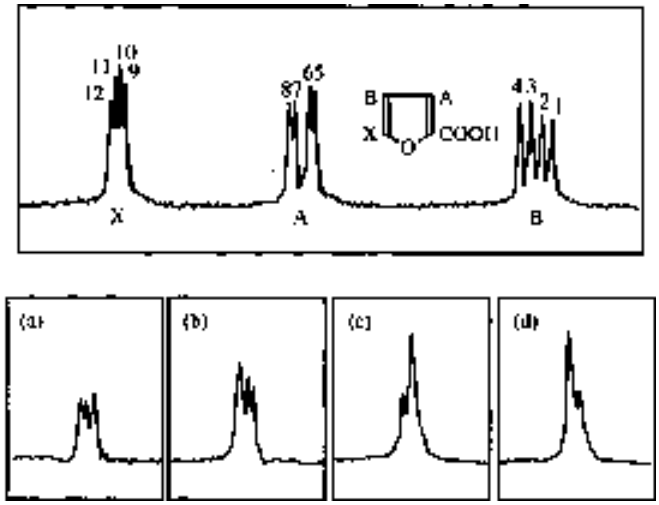

Figure 42 Top: field sweep 60 MHz ^{1}H NMR spectrum of 2-furoic acid, an example of an ABX (nearly AMX) spin system. Bottom: the X portion of the spectrum recorded with simultaneous irradiation of (a) transitions 5 and 6; (b) 7 and 8; (c) 1 and 2; and (d) 3 and 4.[244] (Reproduced by permission of Taylor and Francis Ltd)

in High-Resolution NMR), it was David Whiffen's insight into the difference between a magnetic field sweep and a true frequency sweep of only the observing rf that clarified important elements of the theory. Freeman applied these concepts in field-sweep and frequency-sweep decoupling.[241] Freeman also introduced an internal lock, patterned after the concept developed by Hans Primas and based on an additional modulation sideband. This stable lock permitted precise control over irradiation frequencies and permitted a range of NMDR experiments, since it is essential for slow frequency sweep NMDR.

Meanwhile, at Harvard, John Baldeschwieler was examining the theoretical basis for double resonance under a variety of experimental conditions. The review by Baldeschwieler and Randall[242] in 1963 was influential in pointing out both the complexities and opportunities of NMDR. This review also popularized the A{X} notation, in which the observed nucleus A is listed first and the perturbed nucleus X is given in braces.

The Chemical Applications of Double Resonance

One of the first real applications of decoupling to a chemical problem was made by Evans and Maher[243] in 1961 when they studied the thallium diethyl cation. Two methyl and two methylene group resonances were observed since Tl–H couplings are quite large, but it was not clear which methyl resonance went with which methylene group. A 'selective' decoupling experiment, in which only one of the methyl groups was irradiated, provided the answer. In addition, Evans pointed out that this experiment provided a method for the determination of the relative signs of the coupling constants. This one experiment is remarkable for initiating two completely different sets of applications. First, selective decoupling was developed extensively to identify proton resonances that are coupled and thus to elucidate the structures of a vast number of organic compounds. Second, the NMDR technique rapidly became the standard method for determining the relative signs of coupling constants, a key factor in the analysis of complex spectra and in the development of the theory of scalar coupling. Freeman and Whiffen[244] recognized the generality of Evans's procedure and extended it to the determination of the relative signs of ^{1}H coupling constants in an AMX system. Figure 42 illustrates this work with the spectrum of 2-furoic acid subject to double irradiation.

When Freeman joined Varian Associates in 1961 to work with Anderson, the confluence of these two experts in NMDR was bound to produce further advances in the field. In a series of papers they worked out the optimum conditions for NMDR experiments and investigated the additional splittings sometimes observed at relatively low perturbing rf field strengths. Their systematic treatment of splittings caused by 'spin tickling' showed that unambiguous information could be extracted on energy level diagrams.[245,246] This method became a very useful aid for the assignment of transitions for the computer analysis of strongly coupled spectra, and also picked out sub-spectra that indicated the relative signs of the coupling constants.

The reverse of the tickling experiment, usually termed internuclear double resonance (INDOR),[247] also became quite valuable in locating weak or hidden transitions. In such experiments, the observing field is kept fixed at the peak of a chosen transition and the perturbing field is swept throughout the spectrum in order to search for the connected transition. INDOR soon assumed importance as a method for obtaining the chemical shifts for a nucleus of low sensitivity, such as ^{13}C, by observing the sensitive nucleus (usually ^{1}H) to which it is coupled.

Instrumentation for heteronuclear double resonance steadily improved during the 1960s with the development of more versatile spin decouplers. The 'Gyrocode' decoupler in the XL-100, introduced in 1969, was the beginning of a new, frequency-selectable rf source. Commercially available frequency synthesizers formed the rf centerpiece for multinuclear spectrometers, as we shall see in later sections.

Proton decoupling assumed a vital role in making feasible the direct observation of ^{13}C at natural abundance. Selective

Figure 43 Participants at the Second International Symposium on Magnetic Resonance, Sao Paulo, Brazil, July 1969. This meeting, organized by Leonard Reeves, E. Giesbrecht, and S. Mathias, was a forerunner of the series sponsored by the International Society of Magnetic Resonance. The formation and activities of ISMAR are described in Daniel Fiat's historical sketch (***Fiat, Daniel: The International Society of Magnetic Resonance (ISMAR). Landmarks and Highlights***)

off-resonance decoupling provided a powerful method for the analysis and assignment of individual ^{13}C resonances, but for the greatest sensitivity in simply observing a ^{13}C NMR spectrum, complete decoupling of protons throughout their spectral range provides a threefold advantage: (a) spectral simplification; (b) intensity enhancement resulting from the collapse of the multiplets; and (c) intensity increase due to the nuclear Overhauser effect (as we discuss below). A practical method for such broad-band decoupling was proposed by Ernst[248] in 1966 and became very useful for the decoupling of weakly coupled, primarily heteronuclear, spin systems. This technique, commonly called 'noise decoupling', uses pseudorandom noise to make 180° phase changes in the perturbing rf field and hence irradiate over a broad frequency range. In his historical sketch (***Ernst, Richard R.: The Success Story of Fourier Transformation in NMR***), Ernst describes the initial experiments in these words:

> The first experiments concentrated on a fluorine–proton system. The necessary binary random noise was taken initially from the even/odd character of the last digits in the Palo Alto telephone directory, modulated onto the radiofrequency carrier, and applied to the protons, observing the fluorine resonance at the same time. This led to the initial pseudonym 'phone-book resonance'. Only later was I informed by R. Whitehorn (Varian Associates) that binary noise could be generated in a more convenient and predictable manner by shift register generators that were used from September 1965 onwards.

Noise decoupling was used largely in the form developed by Ernst, with numerous, but only slight improvements, for over 15 years. One investigator is said to have used phonograph recordings of music to generate the random noise; Beatles records were said to work particularly well. Most of the advances, however, involved the tailoring of pseudorandom noise functions to provide a broader and more nearly flat response. In the 1980s fundamental analyses of the decoupling process by Freeman[249] and Waugh[250] gave insight into more efficient procedures using pulse sequences, as outlined in Section 7.

In 1963, Forsén and Hoffman initiated a new application of NMDR when they investigated the transfer of polarization between two exchanging sites.[251] By saturating the nuclei at one site (or, with later technology, using a perturbing rf pulse), the equilibrium population of nuclei at that site can be disturbed, and chemical exchange causes this disturbance to affect a second site. These NMDR methods greatly extended the range that could be studied by NMDR to much slower exchange, the only limitation being the spin–lattice relaxation

times of the exchanging nuclei. With later pulse techniques and especially two-dimensional NMR methods, this type of investigation has assumed increasing importance, as we shall see in later sections.

The NOE Becomes a Useful Technique

In Section 4 we mentioned the initial studies of the nuclear Overhauser effect (NOE), in which one resonance changes intensity when another line is perturbed by an rf field. Although it lay dormant for about 10 years, the NOE rapidly developed into one of the most useful and most widely applicable of all NMDR techniques in chemistry, with three distinctly different uses: (i) estimation of internuclear distances as an aid to the determination of molecular conformation; (ii) enhancement of the NMR intensity of less sensitive nuclei that are close to protons; and (iii) estimation of correlation times to clarify the motions in macromolecules.

The first publication to demonstrate the utility of the NOE in chemical structure determination was that by Anet and Bourn[252] in 1965, who showed that in *N*,*N*-dimethylformamide the assignments of the methyl groups *cis* and *trans* to the formyl proton could be made on the basis of the relative nuclear Overhauser enhancements of their resonances when the formyl proton was irradiated. For two protons in a small molecule tumbling in the fast motion regime, complete saturation of one results in a 50% enhancement of the intensity of the other, provided the two relax each other solely by magnetic dipolar interactions. However, in molecules with other competing relaxation mechanisms, the magnitudes of the NOEs may often provide information on relative internuclear distances. Organic chemists found that the data from the NOE supplied critical information. For example, as Koji Nakanishi points out (***Nakanishi, Koji: First Encounter with NOE in Natural Products--the Ginkgolides***), investigators in his laboratory independently observed a NOE soon after the Anet–Bourn paper was published. Their use of the method in elucidating the structure of the ginkgolides was effective in bringing the potential importance of the NOE to the attention of other natural product chemists.[253,254]

NOE experiments rapidly became a routine technique, so widely used that a book on the subject was soon written by Noggle and Schirmer[255] largely to clarify the complexities involved in multispin systems with various irradiation patterns. The proton *inter*molecular Overhauser effect in a mixture of chloroform, cyclohexane, and tetramethylsilane was first reported by Kaiser,[256] also in 1965.

For nuclei with smaller magnetic moments, such as ^{13}C, the NOE was found to be of great value in intensifying signals according to the ratio of the moments of the perturbed and observed nuclei. For ^{13}C, the additional factor of three in intensity (provided only dipolar relaxation is operative) became a critical factor in the early observations of this nucleus. For nuclei with negative magnetogyric ratios, such as ^{15}N and ^{29}Si, the NOE leads to an enhanced but negative signal for dipolar interactions, but was found sometimes to result in almost complete cancellation of the signal when several relaxation mechanisms are operative.

As larger molecules began to be studied more frequently, the theory of the NOE for slowly tumbling molecules had to be taken into account. In 1972, the observation by Balaram, Bothner-By, and Dadok[257] of a negative intermolecular NOE in a peptide binding to a protein focused attention on another aspect of Solomon's theory of the NOE:[150] in the slow-motion limit, the proton–proton NOE is −1.0 rather than +0.5. This study was the forerunner of an immense amount of work in applying the NOE to biopolymers, both to obtain interproton distance information for the determination of conformation and to examine the dynamics of motion of the polymer. However, further experimental advances in pulse methods and a better understanding of spin diffusion and the transient NOE would be required before quantitative results could be obtained and interpreted. We shall return to this subject in Section 14.

Carbon-13 NMR Develops

Following the initial observations of ^{13}C NMR by Lauterbur and Holm, several laboratories ventured into this difficult field, as discussed in Section 3.8. The early studies used adiabatic rapid passage, but by 1962 the first slow sweep, high-resolution spectra had been obtained.

A breakthrough in studying ^{13}C NMR (which applied in many respects to other nuclei of low sensitivity such as ^{15}N) was the adroit use of proton spin decoupling. At the Third Conference on Experimental Aspects of NMR Spectroscopy held in Pittsburgh in 1962, Lauterbur, Grant, and Shoolery independently announced enhancements of signal-to-noise (S/N) ratios in ^{13}C NMR spectra obtained by double irradiation. Lauterbur and Yajko observed an enhancement of S/N in a proton-decoupling experiment, which exceeded that normally expected from the simple collapse of the proton-coupled multiplets, an early indication of the nuclear Overhauser effect in ^{13}C NMR.

As Dave Grant says (***Grant, David M.: Carbon-13 Magnetic Resonance--An Exquisite NMR Garden of Surprises***), 'the proton decoupler became the crucial component in our first ^{13}C observations'. With the improved sensitivity afforded by the collapse of spin multiplets, together with nuclear Overhauser enhancements, Grant and his co-workers made systematic studies of the relation of ^{13}C parameters to molecular structure. Among the vast amount of information that came from this work was a striking dependence of ^{13}C chemical shifts on molecular conformation.[258,259] By capitalizing on the NOE and the multiplet collapse, it became possible to extend the scope of ^{13}C studies to more dilute solutions. Furthermore, the use of double resonance provided the additional benefit of obtaining more accurate ^{13}C chemical shift data by carefully measuring simultaneously two irradiating frequencies at the instant when the proton-decoupled ^{13}C resonance signal is maximized. Paul and Grant[260] analyzed the effect of the various experimental quantities upon the spectral features and suggested optimum conditions for observing proton-decoupled ^{13}C spectra.

Meanwhile, Jack Roberts, who had been one of the earliest organic chemists to make extensive use of NMR, recognized the potential of ^{13}C NMR now that decoupling methods could be applied. What was missing, however, was a stable, locked, frequency-sweep spectrometer that would permit the use of time averaging to enhance signal-to-noise ratios. As he describes in his historical sketch (***Roberts, John D.: A Personal NMR Odyssey***), Roberts commissioned an instrument from Varian, and in 1966 a 15 MHz digital

frequency-sweep spectrometer, based on an early Hewlett Packard frequency synthesizer, was delivered. With this instrument he and his students were able to observe ^{13}C at natural abundance on a rather routine (but still time consuming) basis, and they were even able to make the first measurements of $^{13}C–^{13}C$ coupling constants at natural abundance.[261] Two additional effects still contributed to the loss of sensitivity and resolution in the ^{13}C spectra: residual splittings due to coupling with irradiated nuclei even when high decoupling power was employed, and the existence of long-range couplings in systems in which all protons are not simultaneously irradiated. When Ernst's noise modulation technique made possible true broadband decoupling. Roberts and his group made spectacular progress in obtaining and interpreting the ^{13}C spectra of a large number of molecules, including steroids,[262] sugars,[263] and antibiotics.[264]

Grant, too, obtained a specially designed frequency-sweep ^{13}C spectrometer, and he and his colleagues broadened their ^{13}C work using decoupling to investigate the quantitative behavior of the NOE[265] and its relation to dipolar relaxation.[266] This work provided the underpinning for interpretation of ^{13}C signal intensities in terms of the number of carbon atoms and furnished additional bases for making spectral assignments. The problem of using proton-decoupled ^{13}C spectra for routine quantitative purposes was tackled by LaMar, who suggested the addition of suitable paramagnetic species to reduce relaxation times and eliminate the NOE, thus enabling quantitative measurements to be made, but with loss of sensitivity.

As locked, frequency-sweep spectrometers (such as the Varian HA-100) became more widely available, the use of ^{13}C NMR spread to a number of laboratories. In Estonia, Endel Lippmaa pursued ^{13}C and double resonance NMR studies, with impressive results obtained under difficult conditions since he and his group had to develop virtually all of their own instruments.

For the assignment of ^{13}C lines, the whole range of double resonance techniques that we have described in previous sections could be brought to bear. Selective, partial, and off-resonance decoupling, as well as spin-tickling and INDOR, were found to be valuable and were employed extensively.

Superconducting Magnets

As we saw in Sections 2 and 3, the quest for ever-higher magnetic field has characterized much of the development of high-resolution NMR from the earliest days. During the 1950s and early 1960s the maximum frequency for ^{1}H NMR had risen from 30 MHz to 40 to 60 and finally to 100 MHz. Every increase in magnetic field was followed by major advances in the quality of data available and in the range of application of NMR in chemistry. Clearly, still higher fields held great promise, but these developments had reached the upper limit of the magnetic field that could be achieved with an electromagnet due to the magnetic saturation of iron at 2.35 T (100 MHz for ^{1}H). Permanent magnets reach saturation at an even lower field, limiting such spectrometers to a 90 MHz proton frequency. The only place to turn was to superconducting magnets.

The superconducting properties of several niobium-based alloys at low temperature were well known, and superconducting magnets had been wound from such wire which was available commercially. The production of a magnet with the stability and homogeneity requirements needed for high-resolution NMR, however, would be no mean task. Varian assigned this job to Harry Weaver, who had designed the first 12-inch high homogeneity electromagnet at Stanford and later brought the design to Varian. Weaver's article (***Weaver, Harry E.: Historical Comments on the Early Years of Superconducting NMR***) provides a vivid description of the inception, progress, and ultimate success of a small program to develop such a superconducting magnet. He and his colleagues had to learn how to obtain and handle the then exotic liquid helium, how to design a Dewar to hold the helium and transfer the liquid, and finally how to design a high homogeneity solenoid that would remain persistently superconductive. Weaver and his team had to work out novel construction methods to ensure good thermal conductivity throughout the solenoid, and they developed homogeneity correction coils (superconducting shim coils) for the ends of the solenoid to cancel first-order field gradients. Finally they had a homogeneous, persistent magnet wound with Nb/Zr wire. As Weaver put it,

> Thus, to our great pleasure and excitement, once the solenoid and its shim coils were placed in the persistent mode and the system of coils removed from the external power supplies, the field and its distribution over the sample appeared to be preserved indefinitely.

The first prototype spectrometer using this magnet operated at 200 MHz and was displayed at the Pittsburgh Conference in 1964 before it was sent to DuPont for further testing. [Varian had ensured financial support for the project by obtaining an order for a superconducting spectrometer (targeted at 300 MHz) from DuPont.] A description of the new superconducting magnet and its potential was published in *Science* in October 1964.[267]

The field was eventually raised to permit operation at 220 MHz, but a higher field was considered too risky for a commercial instrument with the then current technology. The HR-220 spectrometer provided a dramatic improvement for an NMR world that was still largely dependent on 60 MHz instruments, as illustrated in Figure 44 from a review by Ferguson and Phillips.[268] The HR-220 became a standard product and played a particularly important role in NMR studies of biopolymers, as we shall see in Section 10. By 1970, Varian redesigned the magnet to permit operation at 300 MHz, but by that time other technology had appeared and competitive instruments began to hold sway (see Section 6.6).

The efficiency of the Dewar system is an important factor in making a supercon magnet economical. By current standards the Dewar in the HR-220 was awful, since it required refills of liquid helium twice a week when it worked at top efficiency, and more often if anything went wrong. (Currently, spectrometers with superconducting magnets having hold times up to one year are available.) While the operators complained justifiably about refills and other shortcomings of the magnet (see historical sketches by ***Ferguson, Raymond C.: William D. Phillips and Nuclear Magnetic Resonance Spectroscopy at DuPont***, and ***Williams, R. J. P.: The Use of NMR in Biology: Personal Reflections***), this magnet had made a quantum leap in magnetic field. Permanent magnets and electromagnets would still have wide use but all future developments centered around supercons.

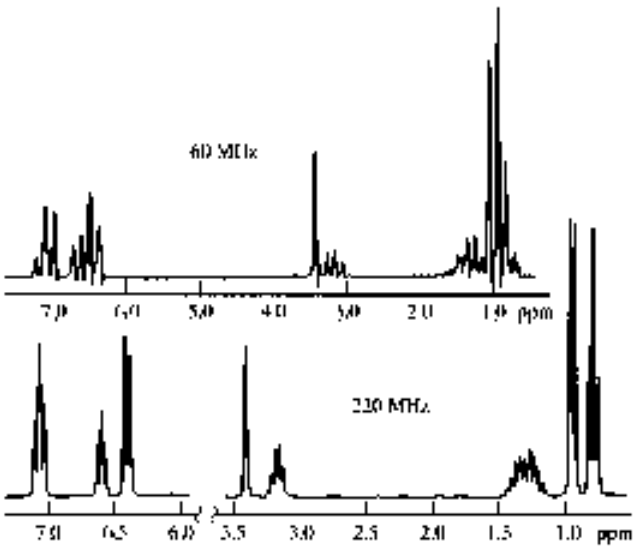

Figure 44 Comparison of 60 MHz and 220 MHz spectra of *N-sec*-butylaniline.[268] (Reproduced by permission of the American Association for the Advancement of Science)

Late in the 1960s the limitations of the HR-220 were becoming apparent. For example, high-order field gradients gave a water line with a very broad baseline 'hump' that severely limited many biochemical investigations, the instrument was designed for protons only, and the double resonance capability was very limited. A field/frequency lock had been deemed unnecessary for a stable supercon magnet, but with increasing need for precise measurement and control of homogeneity, this initially desirable simplification in the electronics became a shortcoming. At Oxford University, Rex Richards worked with the nearby Oxford Instruments Company to design and build a superior magnet (see ***Richards, Rex: Development of NMR in Oxford***). A small prototype functioned well at 5 T and was used for various chemical studies, and in 1969 the final magnet was completed and remained persistent at 7.5 T (320 MHz for ^{1}H). This magnet took advantage of the newer superconductor Nb/Ti, which was much more stable than Nb/Zr. As discussed in the following section, this magnet served as the basis for the first Bruker superconducting system at 270 MHz.

Further development of Nb/Ti technology permitted the construction of spectrometers operating first at 360 MHz and then 400 MHz. Subsequent increases in persistent field strength came only in the late 1970s with the advent of the intermetallic compound Nb_3Sn as the superconductor, which was used in 470 MHz and 500 MHz instruments and eventually in 600 MHz and 750 MHz instruments (the latter at 17.3 T). Substantial technology had to be developed to fabricate a solenoid from the brittle Nb_3Sn and to make joints that remained persistent at these high field strengths.

Figure 45 summarizes the development of commercially available high-resolution NMR spectrometers as a semi-log plot of the operating frequency against the year of introduction.[269] The figure indicates that field intensities increased roughly exponentially with time but only half as fast for superconducting magnets as for iron magnets. The break in the plot between iron and superconducting magnets is clear. Beyond 500 MHz instruments, there is a noticeable change in

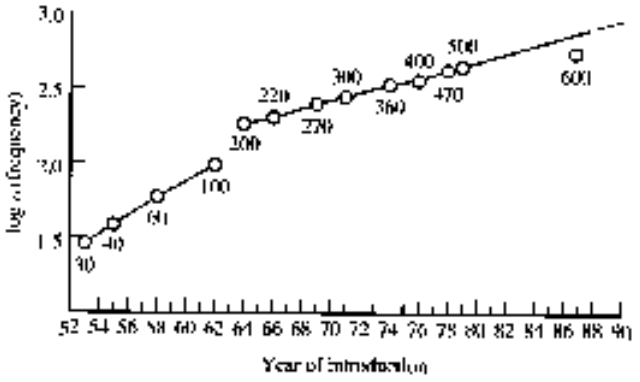

Figure 45 ^{1}H NMR frequency of commercial NMR spectrometers as a function of year of introduction.[269] (Reproduced by permission of Springer Verlag)

the slope as a result of the expense and practical technological problems in developing higher field magnets with immense amounts of stored energy.

Although greatest attention has been given to the development of commercial magnets and spectrometers, developments in several laboratories also played an important role in the race to higher magnetic fields. In 1968, Dadok and Sprecher began work to build a spectrometer for operation at 250 MHz and to adapt a low homogeneity Westinghouse supercon magnet to high-resolution studies. Dadok's historical sketch (***Dadok, Josef: High-Field NMR Instrumentation***) reports that:

> The result was a relatively small persistent magnet for a 250 MHz spectrometer and it was equipped with four superconducting shim coils. After adding 10 mm room-temperature shim coils and an internal field/frequency lock system, we actually ended with a high-resolution spectrometer with resolution better than 0.1 Hz. This was in 1969 and we proudly presented it at the 11th ENC (1970) as the highest operating frequency spectrometer in the world. Only hours later Varian announced their first results at 300 MHz.

This spectrometer, along with others built at UCLA by Frank Anet and his colleagues at 251 and 400 MHz, broadened the base of technology and helped make superconducting magnets a way of life in NMR.

In the 1970s as commercial instruments were operating as high as 360 MHz, Dadok, Bothner-By, and co-workers at Carnegie Mellon University embarked on a project in conjunction with Intermagnetics General Corporation (IGC) to leap to 14.1 T (600 MHz). IGC was able to produce such a field from Nb_3Sn tape wound in a number of pancake coils, each superconducting itself but connected with nonsuperconducting joints. By December 1977 the first ^{1}H NMR spectra had been obtained. The magnet required one liter per hour of liquid helium and the spectrometer had a number of limitations, but it worked well and for almost a decade provided the only high-resolution 600 MHz system.

New Instrument Suppliers

The early history of NMR might have been very different had Varian Associates not been so quick to market commercial instruments suitable for high-resolution studies. The Bloch–Hansen patent that was assigned to Varian in 1946,

as well as a string of later patents including that for sample spinning, proved to be a strong tool in encouraging continuing investment in the improvement of the technology by Varian and in discouraging the entry of other companies into the American market. However, the patent application had been limited to the United States and companies in other countries were free to develop NMR instruments and market them outside the US.

Development of NMR began rather early in Japan where Japan Electron Optics Ltd. (JEOL), which had been formed in 1947 to develop electron microscopes, embarked on NMR instruments in 1955, and by 1956 had offered a 32 MHz instrument with an electromagnet. Subsequently this evolved into the C-60 and by 1966 the C-60-HL, which was marketed worldwide, and in 1970 to the MH-100 (miNiMaR), an early 'table-top' 100 MHz spectrometer. These instruments offered some of the first competition to the Varian A-60 and later the T-60 as 'routine' NMR instruments.

Meanwhile, in England, Associated Electrical Industries (AEI) offered an instrument based on a large electromagnet capable of a field as high as 1.8 T, with a large number of possible rf units. This AEI instrument had a rather short life span. Perkin-Elmer Ltd., however, took a different approach by developing an instrument based on a permanent magnet, the stability of which was good enough to permit the use of preprinted charts even before field/frequency lock had been introduced. Initially introduced in 1961 with lower field, the R-10 was soon upgraded to 1.4 T. Rf units for ^{1}H, ^{19}F, ^{31}P, and ^{11}B were available for the nuclei that were most frequently studied in the early days of NMR. With the introduction of the R-12 with solid-state electronics in 1967, Perkin-Elmer instruments were sold worldwide and competed well in the 'routine' NMR market.

In Switzerland, Hans Primas and Hans Günthard pioneered the construction of a 25 MHz, permanent magnet instrument, which in 1956 was commercialized by the Swiss company Trüb Täuber as the KIS-1. Subsequently, following Primas's development of a 75 MHz instrument, based on an electromagnet with pole caps shaped to improve homogeneity, Trüb Täuber developed the KIS-2 spectrometer equipped with a 5-ton electromagnet with a field of 2.1 T (90 MHz for ^{1}H NMR). Trüb Täuber was dissolved in 1965, but its spectroscopy division served as the heart of Spectrospin AG which became part of Bruker Instruments.

By 1967 Bruker had introduced the first real multinuclear NMR instrument, the HX-90. This spectrometer was marketed in the US in 1968 and with the improved technology that it offered began to challenge the Varian pre-eminence in research-grade NMR instruments. In conjunction with Oxford Instruments, Bruker was able to produce the first 270 MHz instrument by simply tripling all the frequencies from their well-developed and successful 90 MHz instrument, and later the frequencies were quadrupled to produce a 360 MHz instrument when magnet technology permitted.

Joe Dadok's historical sketch (***Dadok, Josef: High-Field NMR Instrumentation***) describes his initial forays into NMR in Brno, Czechoslovakia, where he and his colleagues developed a 30 MHz spectrometer in 1960 and later other instruments operating up to 80 MHz. These designs were commercialized by a company called TESLA BRNO, which for many years was the only supplier of NMR instruments in Eastern Europe.

Later, several other companies were to develop with specific NMR markets in mind. In 1972, Transform Technology was formed to develop and market accessories for Varian spectrometers, but this soon broadened into a full-scale NMR instrument company under the management first of Nicolet Instruments and then of General Electric. IBM entered the NMR field in 1980 and for several years marketed instruments produced by Bruker to IBM specifications. Gary Maciel's historical sketch (***Maciel, Gary E.: A Little Polarization Can be Good for You***) describes the origin of Chemagnetics in 1978, initially to develop probes for NMR studies in solids. This company, too, broadened its scope to produce complete spectrometers for the study of both solids and liquids.

Table 1 provides a summary of the high-resolution spectrometers marketed by the principal NMR instrument companies up to 1994.

For NMR spectroscopists, the sudden onset of competition meant a greater choice of instruments at reasonable cost. For the development of NMR technology, the broadening of the field to an international scope meant that new methods could be invented and commercialized at an ever-faster rate. This existence of a number of NMR instrument companies would have important consequences in the speed of development of the next major advance in NMR—Fourier transform methods.

FOURIER TRANSFORM NMR

The development and widespread use of Fourier transform methods represents a real watershed in the history of NMR. As we have seen, NMR advances were largely driven by applications to chemistry with its requirements for high resolution and high magnetic field. Sensitivity remained low, and nuclei with small magnetic moments or low isotopic abundance (such as ^{13}C) could be investigated only with great difficulty. High-resolution spectra were obtained by slow scan, so that the time-averaging computers were largely limited in applicability to the relatively small number of repetitions that could be obtained in an overnight run. Meanwhile, most of the NMR technology using powerful rf pulses remained largely in the physicist's armamentarium and appeared to be inapplicable to the multiline spectra characteristic of virtually all interesting chemical systems.

Fourier transform methods changed all that. Versatile pulse methods could now be used to study complex molecules. Spectra could be obtained rapidly in order to follow fast reactions or to use time-averaging techniques effectively to improve signal-to-noise ratio (S/N). Developments of NMR in chemistry and physics had proceeded along quite separate paths, but the advent of FT methods brought these two approaches to NMR together.

The name of Richard Ernst, above all others, is associated with FT NMR. Indeed, in 1991 he received the Nobel Prize in Chemistry for his work in developing FT methods, from the first seminal paper with Wes Anderson to his drive to make two-dimensional NMR a reality (as described in a later section). Ernst was not alone, however, in developing FT NMR. In Section 4 we saw that physicists, such as Herman Carr, had done 'mental' Fourier transforms to interpret the results of simple pulse experiments and that Lowe and Norberg had formulated the FT relationship between the FID and the slow passage spectrum in a solid.[136]

Table 1 High-Resolution NMR Spectrometers[a]

Varian Associates, NMR Division (Palo Alto, CA)	
1949	First commercially available NMR instrumentation
1952	First high-resolution NMR spectrometer (30 MHz)
1956	40 MHz spectrometer
1958	HR-60 NMR spectrometer
1961	A-60. Easy to operate, 60 MHz proton only
1964	HR-220. First commercial superconducting NMR spectrometer. Proton NMR only
1965	HA-100. Internal homonuclear field-frequency lock
1966	T-60. First permanent magnet NMR spectrometer for proton observation at 60 MHz
1969	XL-100. Initially CW, later modified for FT. Initially $^{1}H/^{13}C$ observation, later multinuclear capability (Gyrocode observe accessory)
1972	CFT-20. First routine ^{13}C FT NMR (20 MHz) spectrometer for organic chemists
1975	FT-80. Evolved from CFT-20 to provide multinuclear capability. 80 MHz ^{1}H
1975	EM-390. Permanent magnet CW NMR spectrometer for proton observation at 90 MHz; later options for ^{19}F and ^{31}P
1978	XL-200. Superconducting, multinuclear
1982	XL-300. Multinuclear and solids capability
1983	XL-400. Multinuclear and solids capability
1985	VXR series (200/300/400/500). Replacement for XL series with design improvements
1986	Wideline solids accessory for VXR series spectrometers
1986	Gemini-200. Easy-to-use, low-cost superconducting $^{1}H/^{13}C$ spectrometer
1987	VXR series S. Enhanced version of VXR series with UNIX-based SUN workstations
1987	Gemini-300
1988	VXR-600S.
1989	Unity series (200/300/400/500/600). Sun workstations; multinuclear; solids and micro-imaging capability
1989	Broadband Gemini series (200/300).
1989	Ultrashims. Introduction of RRI matrix shim system for improved magnet homogeneity
1991	Gemini-400. Equipped for indirect detection and multinuclear operation.
1992	Unity-plus series (200/300/400/500/600/750). Multiple rf channels; pulsed field gradient accessory; nano-probe
1993	Unity-plus 750. First commercial 750 MHz spectrometer installed
Perkin-Elmer (Beaconsfield, UK)	
1961	R-10. First commercial NMR spectrometer (40 MHz, later 60 MHz) with permanent magnet. Precalibrated strip-chart recorder. First homonuclear spin-decoupling accessory. High-performance variable-temperature probe
1967	R-12. Permanent magnet. First NMR spectrometer (60 MHz) with solid-state electronics. Spin-decoupling or field-locking. (Over 350 R-12s sold worldwide)
1972	R-32. 90 MHz proton only. CW, later FT. First 90 MHz permanent magnet instrument. (Over 150 R-32s sold worldwide)
1976	R-34. 220 MHz superconducting spectrometer. Sold for under $100k. Only seven units sold in the United Kingdom
1979	Perkin-Elmer withdraws from the NMR business having sold over 600 spectrometers worldwide.
Japan Electron Optics Limited (JEOL) (Tokyo, Japan)	
1962	C-60. 60 MHz, electromagnet, high-resolution proton only
1965	C-60H. 60 MHz, high-impedance electromagnet. Variable temperature
1966	C-60HL. Used low-impedance magnet. Other frequency probes available as options
1968	PS-100. Research high-resolution NMR spectrometer for proton observation (CW)
1970	MH-100. Tabletop routine high-resolution spectrometer, proton only. CW
1973	PFT-100. PS-100 with pulsed-FT accessory added
1973	FX-60. Proton (60 MHz)/^{13}C pulse FT. Complete computer control. $^{1}H/^{13}C$ dual switchable probe, noise-decoupling, variable temperature. Light-pen operator interface
1975	FX-100. 100 MHz. Similar to FX-60. Quadrature detection
1976	FX-60Q. Same as FX-60 but with digital phase shifter for quadrature detection
1978	FX-90Q. Proton (90 MHz)/^{13}C, later upgraded to multinuclear operation. Frequency synthesizer-based
1980	FX-200. Broadband, multinuclear. Oxford 4.6 T superconducting magnet
1981	GX series (200/270/400/500). Improved data system and modular design. Broadband
1986	GSX series (200/270/400/500/600). Improvement on GX Series. Addition of GSX-600
1990	CPF series (270/400). Lower cost, automated version of GSX series for routine use
1991	ALPHA series (400/500/600). Pulse-shaping capability, three channels, gradient drivers. VMS data system
1992	CPF/EX series (270/400). Upgraded CPF, with inverse detection and 3D capabilities
1993	Eclipse series (270/400). Improved CPF/EX series. UNIX-based Silicon Graphics workstation.
1994	Flexible, complete computer-tunable broadband probe, ranging from ^{31}P to ^{15}N
Hitachi Instruments (Tokyo, Japan)	
1963	H-60. High-resolution, permanent magnet
1966	R-20. 60 MHz. First permanent-magnet system with proton external lock
1968	R-20A. Same as R-20, expanded to observation of ^{19}F, ^{13}C, ^{31}P, ^{11}B. CAT optional
1969	R-22. First permanent-magnet instrument at 90 MHz
1971	R-24. 60 MHz, proton only. Permanent magnet. Using 4-mm sample tubes

Table 1 *Continued*

1972	R-24A. Same as R-24, but using 5-mm sample tubes and flatbed X–Y recorder
1972	R-22FT. R-22, with FT capability added. First permanent-magnet FT system
1972	R-40. First routine 90 MHz small permanent-magnet system. CW
1975	R-42FT. Replaced R-22FT
1975	R-24B. Replaced R-24A, with improved sensitivity
1978	R-600. First small permanent magnet 60 MHz FT-only spectrometer equipped with ^{2}H internal lock
1978	R-900. First permanent-magnet system for proton (90 MHz)/^{13}C FT-only. $^{1}H/^{13}C$ switchable probe
1980	R-90H. Proton (90 MHz)/carbon pulsed-FT. Computer-controlled multinuclear accessory
1981	R-250H. Pulsed-FT multinuclear superconducting NMR system
1987	R-1500. Replaced R-600. Proton only, 60 MHz, pulsed-FT
1988	R-1100. First 60 MHz computer-controlled multiple scan (CW) spectrometer
1988	R-1200. First commercial spectrometer with rapid scan-correlation method. 60 MHz, proton only. Permanent magnet
1989	R-1900. Replacement for R-90H. $^{1}H/^{13}C$ observation
1989	R-3000. Replacement for R-250H. Proton (300 MHz)/^{13}C. One-year liquid helium hold time. Optional solid state CP MAS
Bruker Instruments (Billerica, MA), Bruker (Karlsruhe, Germany), Spectrospin (Zurich, Switzerland)	
1963	First commercial pulsed NMR spectrometer
1967	First multinuclear NMR spectrometer (HX and HFX series)
1968	HFX and HX series, 60 and 90 MHz spectrometers (CW) introduced in the US
1969	FT accessory for HFX and HX systems
1971	HFX and HX series (180/270/360). Superconducting NMR systems
1972	WH Series (60/90/180/270/360/400). First fully high-resolution FT-only spectrometer using the BNC-12/BNC-28/Aspect 2000 data systems
1972	SXP series. High-power pulse system
1973	WP series (60/80/100/200). High-resolution research and routine NMR spectrometers
1977	WM series (100/200/250/270/300/360/400). High-resolution research spectrometers
1978	CXP series (100/180/200/270/300). For state-of-the-art solids experiments
1979	WM-500. First commercial 500 MHz spectrometer
1981	Automatic sample changer. Allowed truly unattended system operation
1982	AM series (200/250/300/360/400/500). High resolution, broadband
1984	MSL series (90/100/200/300/400). Solids analysis: wideline, CP MAS, CRAMPS
1984	AC series (80/100/200/300/400). Economical routine automated spectrometer
1985	Microimaging. AM and MSL series
1987	AM-600. First commercial 600 MHz spectrometer
1988	MSL-500. First commercial 500 MHz wide-bore spectrometer delivered
1988	AMX series (200/300/360/400/500/600). Liquids, solids, and microimaging experiments. Aspect X-32 data system (UNIX-based)
1991	Gradient spectroscopy. Available for the AMX, MSL, and AC series.
1991	Solids automation. Complete computer control of sample insertion-ejection and spinning
1992	ARX series (200/300/400/500). High-performance, high-resolution spectrometers
1992	ASX series (200/300/400/500). High-power solids spectrometers. CP MAS, CRAMPS, DOR (double-oriented rotation), wideline. High-temperature probes ($>1800^{\circ}C$)
1992	Digital lock in AMX series. Improved field/frequency stability
1992	First NMR spectra at 750 MHz acquired on an AMX-750
1992	Bruker acquires NMR and chemical shift imaging businesses from General Electric Co.
1993	DMX, DRX, DSX series (300–750 MHz). New generation of digital spectrometers with extensive use of distributed processing with fast signal processors
1994	DPX series (200–400 MHz). Two-channel digital spectrometer for routine studies
1994	QXI inverse probe. Faster spin–transfer experiments with four nuclei (^{31}P, ^{15}N, ^{13}C, ^{1}H)
1995	First 800 MHz spectra, DRX-800
GE NMR Instruments (Fremont, CA)	
1972	TT-100 FT accessory. Marketed by Transform Technology Inc. (TTI) for Varian XL-100 and HR-220 spectrometers
1973	TT-7 FT accessory. Introduced by Nicolet Technology Corporation (NTC, formerly TTI) for use on Varian T-60 and Perkin-Elmer Permanent-magnet spectrometers
1973	TT-14 FT console. For use with 1.4 T electromagnet systems
1975	NT-150. $^{1}H/^{13}C$ NMR spectrometer using Nalorac superconducting magnet introduced by Nicolet Magnetics Corporation (NMC, formerly NTC)
1976	NT series (200/300/360/500). Narrow- and wide-bore Oxford magnets
1983	QE (quick and easy)-300. Easy-to-use $^{1}H/^{13}C$ NMR spectrometer
1983	Magnetics Division of Nicolet (NMC) purchased by General Electric Co.
1984	GN series (300/360/500). Replacement for NT series. Multinuclear, multidimensional NMR with solids capability.
1988	OMEGA series (300/360/400/500/600). Design improvement for GN series. UNIX-based SUN 3/160
1992	GE exits the NMR business in August, selling its technology to Bruker.
Chemagnetics (Ft. Collins, CO)	
1978	Company incorporated
1979	CP MAS probes. Double air-bearing design

Table 1 *Continued*

1980	CP MAS accessory. Sold by JEOL with FX-60QS, FX-100, and FX-90Q
1981	High-resolution Nb/Ti superconducting magnets
1983	A-200. First easy-to-operate, 200 MHz FT spectrometer priced under $100k
1984	M-100/M-200. First routine, low-cost ($125k) ^{13}C only, 'solids' spectrometer
1986	CMC-200/-300. Versatile analytical 'solids' spectrometer with broadband 'X' rf channel
1987	CMX Series. Flexible research-grade 'solids' spectrometer
1989	CMX-500. First instrument shipped
1989	Majority holding in Chemagnetics purchased by Otsuka
1990	First overseas CMX shipment made to Japan and Europe.
1991	CMX series (phase II). Major system enhancements. Liquids microimaging, DOR, large volume, high-temperature performance. Choice of computer workstations
IBM *Instruments, Inc. (Danbury, CT, and San Jose, CA)*	
1980	IBM Instruments, Inc., a wholly owned unit of IBM, organized and purchased non-controlling interest in Bruker. Instruments to be manufactured by Bruker to IBM specifications.
1980	NR-80. Electromagnet-based, multinuclear, later fitted with CP MAS capability
1981	SY series (100/270). Superconducting multinuclear liquids NMR spectrometers
1981	Solids accessory for variable-temperature CP MAS capability
1985	AF series (80/100/200/250/300). Multinuclear, single-synthesizer design. Highly automated operation. This was IBM's most successful line of NMR spectrometers.
1985	PCNMR. PC-based off-line processing program for handling routine 1D NMR data sets
1987	The company announced that it would exit the instrumentation business.

The development of FT NMR as a practical method owes much to the availability of on-line computers in the 1970s, however primitive they may seem by current standards. In this section we summarize the unfolding of FT methods (and other related techniques) in the context of the knowledge and technology available at the time.

Ernst and Anderson's Famous Paper

When Richard Ernst joined Varian Associates in 1963 to work with Wes Anderson, the problem of low sensitivity remained central to the further development of NMR methods. As we saw in Section 5, special purpose time-averaging computers had just become available and offered the possibility of a significant improvement in S/N if enough repetitive spectral scans could be co-added. A typical 500–1000 Hz wide ^{1}H NMR spectrum, however, required about 1 second per Hz to scan without spectral distortion. Even if some broadening and distortion could be tolerated at least 100 s would be required for each scan, so a practical limit of about 500 scans could be accommodated in an overnight experiment resulting in an improvement of S/N of only about a factor of 20. For ^{13}C NMR, which was beginning to be of great interest in organic chemistry, the problem was exacerbated: the frequency range was greater (about 3000–5000 Hz), the inherent sensitivity of the nucleus is lower than that of ^{1}H by a factor of 64, and the natural abundance is only 1.1%. Ernst examined the factors important in optimizing scan rates, but any potential improvements seemed marginal. (Only several years later would Dadok and Sprecher show how very rapid scans could be treated mathematically to generate undistorted spectra, as we discuss later.)

What was needed was a method for *simultaneously* exciting nuclei over a range of resonance frequencies and somehow disentangling their nuclear induction signals, rather than *sequentially* bringing them into resonance by a slow field or frequency sweep. Years earlier, Russell Varian had suggested the idea of exciting the nuclei with a wide band of frequencies from a noise generator, recording the signals (heterodyned down to audiofrequencies) on magnetic tape, and playing back the tape at different speeds to extract the individual frequencies. In 1964, Anderson developed a method for carrying out a similar process, as he describes in his historical sketch (***Anderson, Weston A.: Early NMR Experiences and Experiments***), with a comb of evenly spaced frequencies generated by a wheel, later termed the 'wheel of fortune'. Before this device could be worked out in detail, however, Anderson seized on a better idea. His notebook of June 3, 1964 shows the concept of using a train of high power rf pulses to accomplish the excitation and a Fourier transform (FT) of the resulting free induction decay (FID) signal to extract the spectrum.

Ernst spearheaded the implementation of this concept. With support from Varian's electronics staff, he put together a pulse spectrometer in two months and by the end of the summer had obtained the first FT spectra. The whole idea was to speed up data acquisition by exciting the entire spectrum at once, recording the FID in the 400 channels of a CAT in about 1 s, then immediately repeating the process to build up S/N. This part worked well, and in an hour over 3000 repetitions could be co-added. However, the process of analyzing the data, as described in Ernst's historical sketch (***Ernst, Richard R.: The Success Story of Fourier Transformation in NMR***), was time consuming and cumbersome, since no on-line computer yet existed. The cartoon in Figure 46, from a historical article by Ray Freeman,[271] gives a graphic portrayal of the process.

Still, the process did work, and with minicomputers on the horizon the potential for a spectacular advance in NMR technology should have been clear. In fact, the multiplex advantage of using FT methods to obtain a broad frequency range was already well known in infrared spectroscopy (Felgett's advantage), and far-infrared spectra were being obtained routinely by Fourier transformation of the response from a Michelson interferometer. Ernst presented the first FT NMR results at the Experimental NMR Conference in Pittsburgh in February 1965 and drew a mixed response. Some NMR spectroscopists, including those who understood the concept from infrared spectroscopy, appreciated the potential,

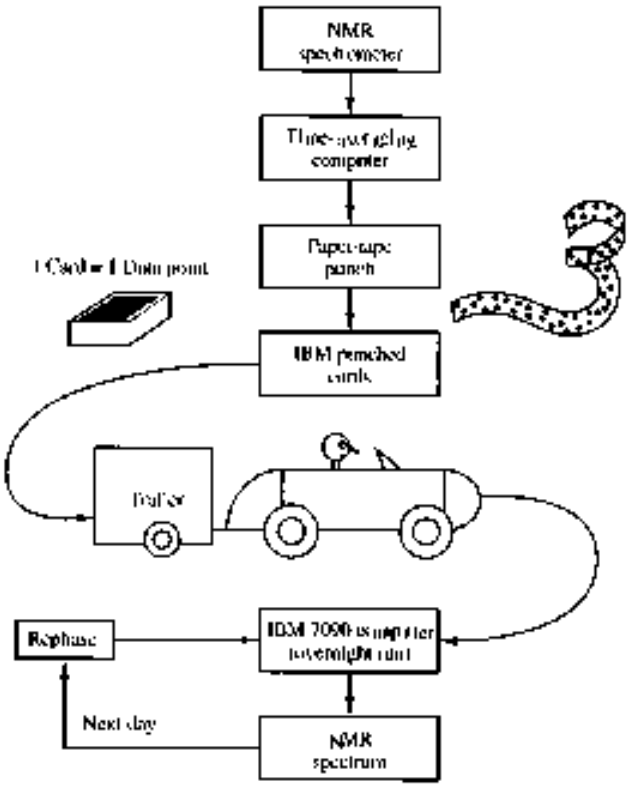

Figure 46 The steps involved in processing Ernst and Anderson's early pulse NMR data to obtain Fourier-transformed spectra.[271] (Reproduced by permission of the American Chemical Society)

while others treated it as an interesting but impractical technique for NMR. Nevertheless, as Ernst says in his article,

> We decided to publish the work in the *Journal of Chemical Physics*. However we had no success, the paper was rejected twice, being considered too technical and not of sufficient originality. We then submitted the paper to *Review of Scientific Instruments* on 9 July 1965 where, after further revision, it was finally accepted on 16 September, 1965.[272]

Varian management, too, failed to appreciate the potential of the new method and the new generation XL-100 spectrometer appeared in 1969 as a continuous wave instrument, configured in such a way that made the eventual addition of FT hardware cumbersome. Meanwhile, the advantage of multiple NMR suppliers became clear when Bruker pioneered in offering an FT accessory to their HX instruments in 1969, and by 1972 had developed a well-designed FT-only spectrometer. During the 1970s Varian began to catch up, and the other major instrument companies also soon got into the FT arena.

The Critical Role of On-Line Computers and Software

Often timing is everything! Without the increasing availability of minicomputers that could be directly interfaced to the spectrometer, FT NMR would have remained an interesting laboratory curiosity. Small laboratory computers that had begun with the development of the LINC at MIT in the early 1960s were available commercially in 1965. However, as Ernst relates,[273] it was not until the fall of 1966 that Varian actually purchased such a computer—the PDP-8 from Digital Equipment Co., a programmable computer with a memory of 4096 12-bit words. Even then, priority was given to its use with an A-60 to carry out homogeneity optimization and various types of data processing. Eventually, however, in several laboratories throughout the world these 'state-of-the-art' computers began to be interfaced to NMR spectrometers. Coincidentally, in 1965, the same year that Ernst and Anderson's work was first displayed, J.W. Cooley and J.W. Tukey at Bell Laboratories had developed a new algorithm for carrying out the Fourier transform in a far more efficient way than had ever been available before.[274] With this advance, a PDP-8 could carry out a Fourier transform of 4096 data points in 'only' 10–20 min. Gradually, the pioneers in FT NMR methods learned how to do phase corrections and how to circumvent the most serious of the artifacts from the experiment and the data processing.

Initially a computer such as a PDP-8 was used to carry out the computations, while data were accumulated in a separate time-averaging computer. The Varian C-1024 was widely used, but gradually gave way in some laboratories to such devices as the Fabritek 1064 which could handle up to 4096 data channels. The first practical computers for on-line FT NMR were the Nicolet 1080, which incorporated the Fabritek technology with a programmable computer, and the Digilab FT NMR accessory, a modification of a Data General computer originally developed for infrared spectroscopy. The dynamic range of the computer was a significant consideration in these early days when computations were limited to fixed point numbers, with Nicolet opting for a 20-bit word while most other manufacturers stayed with the then conventional 16 bits. Each major NMR manufacturer began development of its own special-purpose computer. For example, George Levy, who obtained an early Varian XL-100 that was modified for FT studies, says (***Levy, George C.: Recollections: Computers in the Early Days of 13C NMR and 25 Years of Growth in NMR Computing***):

> The system computer was a Varian 620i with 16 384 16-bit words of core memory and a paper tape punch/reader on its teletype user I/O device. There was no magnetic storage—disk or tape. Every time we had a glitch or (heavens!) software failure, the computer had to be reloaded by hand toggling a starter program and then loading several paper tapes at 110 baud (about 12 characters per second). The very limited computer memory only allowed minimal NMR data acquisition and processing software, and only a single FID of 8k data points could be acquired and stored. In a few months we added an additional 16 kbyte stack of core memory at about $0.70 per 16-bit word, over a million times the cost of much smaller and faster modern memory chips.

The practice of NMR companies of using their own, rather specialized computers with proprietary software continued until relatively recently and probably increased costs and delayed the introduction into NMR of the most advanced general-purpose computers. Nevertheless, the NMR industry and all NMR users eventually benefited from the several revolutions in computer technology over the last 30 years. The complex multiple pulse experiments that we discuss in later sections could not have been developed in a practical way without the infrastructure of the computer age.

FT NMR Becomes a Reality

^{13}C NMR was the big prize. Proton NMR was established and reasonable sensitivity could be obtained for most organic

chemical studies, but the exploitation of ^{13}C NMR really required the order of magnitude improvement in sensitivity furnished by FT methods. Several laboratories pursued this goal. For example, at the National Bureau of Standards in 1969, Tom Farrar and his colleagues used a Fabritek Model 1064 time-averaging computer with 4096 words of memory to record ^{13}C FIDs and go through a tedious procedure in order to process the data and obtain ^{13}C FT spectra. In his historical sketch (***Farrar, Thomas C.: Historical Reminiscences of Some NMR Experiences***), Farrar says:

> FID spectra were output on the punch paper tape and when we had a laundry basket full of tape we would drive 10 miles down the road to NIH to carry out the data reduction. The data reduction at NIH involved several computers since the computer which could read the punched paper tape had no plotter or graphics; it was used to convert the paper tape to punched cards which were then carried to another computer where the Fourier transformation and plotting were done. After a year of this tedious process we convinced Dick Cushing of FabriTek (which later became Nicolet Instruments) to build a very simple computer into the signal averager. My group at NBS purchased model # 1 [Nicolet Model 1080]. It worked beautifully from the first day it was installed and was still working a few years ago.

Meanwhile, also in 1969, at Bruker Instruments, Tony Keller (***Keller, Tony: The Development of the First Multinuclear Fourier NMR Spectrometers***) was able to interface a PDP-8 computer to a Fabritek 1064 and achieve broadband decoupled ^{13}C NMR by pulse excitation followed by on-line processing. Keller reported his results briefly at a meeting of the Society for Applied Spectroscopy at the Disneyland Hotel in Anaheim in late 1969. The difference between the new FT spectra and what had been achieved previously was remarkable. As Keller says in his article,

> When the most famous ^{13}C spectroscopist of the CW era stepped into our hospitality suite, he pondered my decoupled ^{13}C spectra hanging on the wall and asked, 'Do you also have ^{13}C data?' It took me a long time to convince him that, in fact, he had ^{13}C spectra before his incredulous eyes.

The Fourier transform revolution had begun. Organic chemists could see the potential of the new methods and eagerly used the FT accessories offered by the instrument companies. Inorganic chemists, too, began to see the possibilities of studying nuclei of low sensitivity or low natural abundance, and multinuclear instruments became more popular. In later sections we shall explore these advances in more detail.

As computers became more efficient, the productivity of NMR laboratories increased. It became possible to obtain a routine ^{1}H NMR spectrum of a milligram sample of a typical organic compound in a few minutes. FT methods also permitted NMR to be carried out with much smaller amounts of material, thus facilitating the study of samples such as many natural products that were available in only limited amounts. For example, by using microcells containing only about 15 μL of solvent, optimizing instrumental parameters, and carrying out overnight accumulations, it was possible by the mid-1970s to obtain usable ^{1}H spectra of the type shown in Figure 47 from 1 μg of a steroid and ^{13}C spectra with less than 1 mg. Biochemistry, too, benefited enormously from the sensitivity gains of FT techniques, as we shall see in Section 10.

Chemists were eager to exploit the efficiency and versatility of the new methods, but many approached FT NMR with some trepidation. Instead of familiar ideas such as frequency

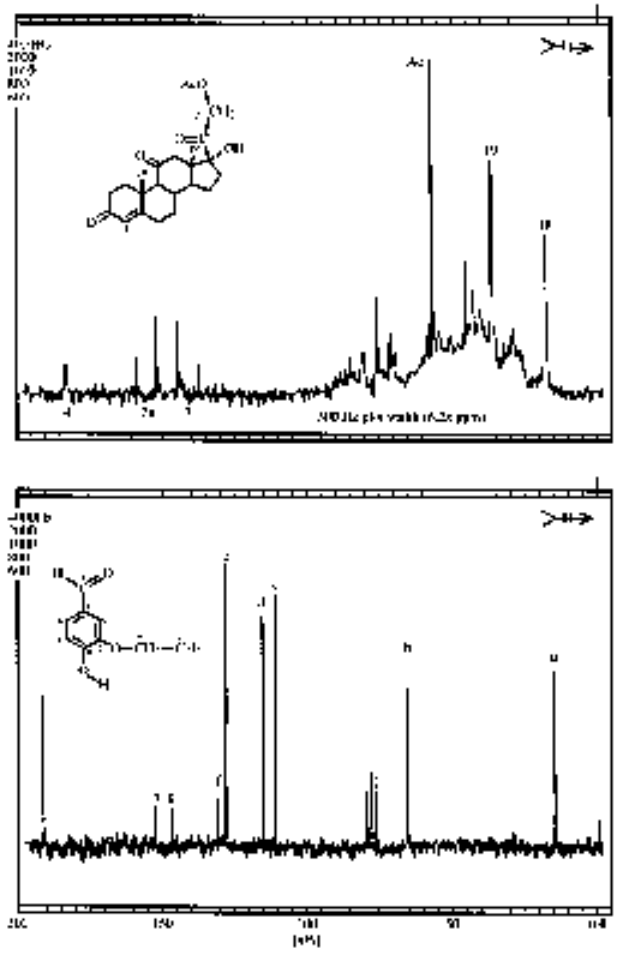

Figure 47 FT NMR spectra obtained in overnight scans with 1.7-mm diameter sample tubes. Top: 80 MHz ^{1}H spectrum of 1.0 μg of cortisone-21-acetate in 15 μL of $CDCl_3$. Bottom: 20 MHz ^{13}C spectrum (proton noise decoupled) of 500 μg ethyl vanillin in 7.5 μL of $CDCl_3$. (Courtesy of J.N. Shoolery)

sweep, scanning speed, and ringing, they encountered a new vocabulary of 'pulse width', 'aliasing', and 'T_2', together with new concepts related to Fourier domains. Help was at hand, however, as new books appeared that were aimed at the chemist. Farrar and Becker's *Pulse and Fourier Transform NMR: Introduction to Theory and Methods*[275] was published in 1971 and helped explain the world of pulses. About five years later Derek Shaw's *Fourier Transform NMR Spectroscopy*[276] and Müllen and Pregosin's *Fourier Transform NMR Techniques: A Practical Approach*[277] gave further welcome guidance. Meanwhile in 1972, Levy and Nelson's *Carbon-13 Nuclear Magnetic Resonance for Organic Chemists*[278] provided examples of the practical value of FT methods, not only in acquiring spectra but in studying dynamic processes.

Time-Dependent Processes with Multiline Spectra

Prior to the onset of FT methods, rf pulses had been used extensively, as we saw in Section 4, to study NMR relaxation, molecular diffusion, and reaction kinetics, but almost entirely in systems with one major NMR line. With FT methods it soon

became possible to adapt many of these pulse sequences to multiline spectra. The short paper by Vold et al.,[279] illustrated in Figure 49, showed the advantages of the FT approach in measuring T_1. Bob Vold (***Vold, Robert L.: Reflections***) describes the origin of this work in an informal evening discussion at a meeting in the summer of 1967:

> We thought for a while that with just two pulses, spin–lattice relaxation AFTER the second pulse would distort the signal beyond recognition. Soon we saw the error in this argument, and realized that if the first pulse were an inversion pulse one could by means of FT measure the T_1 of each line in the spectrum. John Waugh realized the implication of this invention and convinced Melvin Klein (who at Berkeley had one of the few working FT systems) to try the experiment. My main contribution to the resulting paper was the suggestion that a field-gradient pulse, applied between the inversion and detection pulse to destroy unwanted coherence, could also be used in a Fourier transform spin echo sequence to measure diffusion coefficients of individual chemical species.

'Partially relaxed' spectra became common as FT instruments were more widely available. For example, Laurie Hall (***Hall, Laurance D.: NMR Studies of Carbohydrates***) found that T_1 values provided information on the conformation of sugars, since proton relaxation occurred by an intramolecular dipole–dipole mechanism.[280,281] George Levy and co-workers did extensive inversion–recovery studies of ^{13}C to learn about anisotropic tumbling and internal molecular motions,[282,283]

The FOURIER TRANSFORM

Jean Baptiste Joseph Fourier, (Figure 48), born in 1768, had a varied career as a diplomat, administrator under Napoleon, engineer, and research scientist, as described in more detail by Derek Shaw in his book *Fourier Transform NMR Spectroscopy*.[276] Fourier's ideas on using a series of trigonometric functions to represent a general mathematical function arose while he was in Egypt as a diplomat during the end of the 18th century. The concept of the Fourier series and later of the continuous analog, the Fourier transform, were developed in papers in 1807 and 1810, and expanded in 1822 in his book *Théorie Analytique de Chaleur* (Analytical Theory of Heat).

The value of Fourier transformation to extract fundamental frequencies from a function varying in time was well understood by physicists and engineers. However, the calculation of numerical Fourier transforms by 'brute force' summations was difficult and very time-consuming in digital computers until the development of the 'fast Fourier transform' algorithm by Cooley and Tukey in 1965. [274] The new method substituted additions for multiplications and reduced the number of steps for transforming N data points from essentially N^2 to $N \log_2 N$ —a very significant reduction for N in the thousands.

Not surprisingly, similar efforts to develop new computer approaches were underway elsewhere in the same time frame. For example, Yoji Arata in his historical sketch (***Early Days of NMR in Japan***) comments on an FFT algorithm prepared at the University of Tokyo in the mid-1960s. Subsequently, many refinements in FFT programs have been adopted, and more recently alternative techniques to the Fourier transform have been developed for efficient extraction of spectral information from time responses and optimization of signal–to–noise ratios.

Figure 48 Jean Baptiste Fourier, 1768–1830. (Courtesy of Derek Shaw)

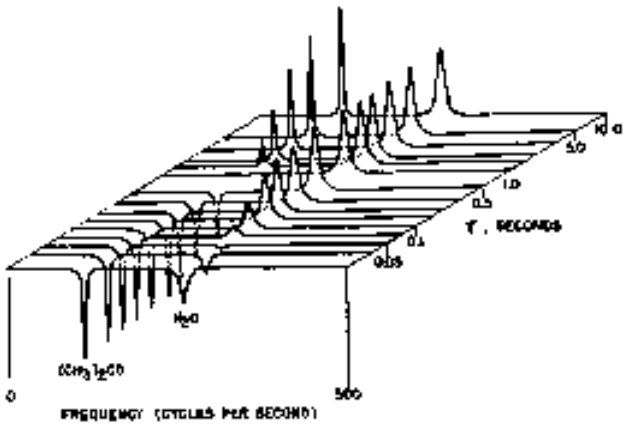

Figure 49 The first application of FT methods in combination with a 180°, τ, 90° pulse sequence to obtain values of T_1 in multiline spectra. Sample: 1:1 mixture of acetone and water, doped with $FeCl_3$ to shorten relaxation times.[279] (Reproduced by permission of the American Institute of Physics)

while Allerhand, Doddrell, and Komoroski found that ^{13}C T_1 values for protonated carbons in moderate size molecules such as steroids were often fractions of a second, rather than the tens of seconds that had been forecast.[284] These fundamental findings provided the data needed for the efficient study of a wide range of organic molecules in order to elucidate structure and conformation.

Forays were made into the use of NMR to measure diffusion, flow, and exchange processes in systems that had been intractable when only single-line spectra could be readily studied. For example, James and McDonald[285] measured self-diffusion coefficients in a solution of dimethyl sulfoxide in water.

Further Advances in FT Methods

Early FT spectrometers relied, as did their continuous wave counterparts, on a single phase-sensitive detector and the exciting pulse had to be set at a frequency that was off to one side of the entire spectrum. It soon became apparent that this procedure wasted half the pulse power (which was always at a premium) and decreased S/N by $\checkmark 2$ from noise folded over into the observed frequency range. One solution is to use two phase-sensitive detectors with their reference signals out of phase by 90°, a quadrature phase detection (QPD), or alternatively, as shown by Redfield and Kunz,[286] to increment the phase of one detector by 90° after each successive pulse. The problem encountered with the implementation of QPD (or the Redfield alternative) was that imperfections in hardware and unavoidable variations in phase caused small, unwanted peaks (quadrature images). Considerable effort went into overcoming this problem, with the most successful method being that developed by David Hoult (***Hoult, D. I., Biomedical NMR Instrumentation–A Personal Viewpoint***) in Rex Richards's laboratory at Oxford. The solution is to permute phases and add or subtract the responses to four successive pulses in a '*CYCL*ically *O*rdered *P*hase *S*equence'. The CYCLOPS method[287] or some variant[288] has been employed on almost all NMR spectrometers since the mid-1970s. Moreover, the concept of phase cycling has become an indispensable part of modern two-dimensional and multiple quantum NMR methods, as we shall see in Section 11.

Most Fourier transform NMR spectra are obtained using short rf excitation pulses, but other broadband methods of excitation have been utilized with varying degrees of success. The use of 'stochastic excitation', in which pseudorandom noise is used to excite all frequencies over a particular range, was conceived by Russell Varian in a little-known patent, but was rediscovered and introduced in concurrent papers by Ernst[289] and Kaiser[290] in 1970. Correlation of the output, which is no longer quite random noise, with the input noise and Fourier transformation produces a spectrum. Tomlinson and Hill[291] carried this process a step further by generating the input 'noise' with a frequency spectrum that is flat except for a 'notch' at the frequency or frequencies that one does *not* wish to excite, such as solvent resonances. These stochastic excitation methods have been improved and are found to be useful in a number of instances, but have never achieved the popularity of the more versatile pulse techniques.

In 1974, Dadok and Sprecher[292] proposed a continuous wave excitation in which the magnetic field or frequency is swept so rapidly that transient effects ('wiggles') dominate the spectrum. They showed that this spectral response can be converted to the ideal slow passage spectrum by a cross correlation with a single line obtained under the same rapid scan condition. With some improvements and limitations suggested in papers by Gupta, Ferretti, and Becker[293] and by Ferretti and Ernst,[294] this rapid scan correlation method served as a useful adjunct to pulse techniques and was exploited in a number of applications, especially those in which a strong solvent signal must be avoided. It has been adopted commercially by Hitachi for routine, low-field spectrometers. While technically not requiring transformation between two Fourier domains, the cross correlation can, in practice, usually be carried out most efficiently by two consecutive Fourier transform steps.

A Pulse Sequence for Almost Every Purpose

While the greatest virtue in pulse FT methods lies in the rapid broadband excitation of an entire spectrum, there has been an increasing need to retain the versatility of pulse methods while restricting the frequency range over which the rf is effective in exciting nuclear spins. Redfield introduced a'long' pulse positioned in such a way as to excite a range of frequencies without exciting one particular frequency (usually that of solvent water)[295] and later improved this with a composite of several pulses applied in succession (the '2-1-4 technique'),[296] which served as the prototype for a large number of further composite sequences.

The converse method using a series of short, high-power pulses to achieve excitation over only essentially a single frequency was developed by Gareth Morris in 1976 while he was an undergraduate doing a research project with Ray Freeman. In his article (***Morris, Gareth A.: The Origins of DANTE***) he describes the thought processes that led to the idea of applying a series of short pulses with intervals in which all nuclei not exactly on resonance dephase are not effectively excited by subsequent pulses. The method worked well. As Morris puts it,

> The most difficult part of the whole exercise was agreeing to a suitably pithy name for the experiment. I had been reading

> the *Divine Comedy* (in translation, after a brief and unequal struggle with Dante's Italian) and had been struck by the parallel between the path taken by Dante and his guide Virgil through Purgatory and the trajectories of nuclear magnetizations during our experiments ... so we settled on the acronym DANTE (*D*elays *A*lternating with *N*utations for *T*ailored *E*xcitation).

A very large number of other specialized pulse sequences have been developed as NMR spectroscopists learned how to tailor excitations to achieve wide-ranging objectives. For example, the idea of using a composite pulse has developed well beyond the original use by Redfield to encompass pulses designed to correct for $\boldsymbol{B}_1$ inhomogeneity and resonance offset effects.[297] Levitt and Freeman (***Levitt, Malcolm H.: A Cyclic Evolution In Spin Space***) went on to combine such composite pulses into cycles and 'supercycles', appropriately named by Freeman MLEV-4, MLEV-16, etc.,[249] that could serve as an effective means of broadband decoupling. Freeman's historical sketch reviews the history of decoupling and shows how this conception of the decoupling process, together with a novel theoretical development by John Waugh (***Waugh, John S.: Alchemy of Nuclear Spins***), completely changed the experimental approach from the idea of noise modulated decoupling, a method that had been in use for 15 years. Subsequently, such pulse sequences as WALTZ (based on a 90°, 180°, 270° sequence of relative lengths 1-2-3) and its successors have dominated all broadband decoupling experiments and are widely implemented in all commercial spectrometers.

An important pulse sequence developed by Morris and Freeman[298] in 1978 and named INEPT (*I*nsensitive *N*uclei *E*nhanced by *P*olarization *T*ransfer) has proved to be a durable method in its own right and later, as we shall see, as a component in several complex multidimensional NMR experiments. The INEPT sequence of 90° and 180° pulses is designed to create a population inversion among the sensitive spins (such as ^{1}H) which then results in polarization being transferred to the less sensitive spins (such as ^{13}C) to enhance their signal by the ratio γ_H/γ_C. In addition to sensitivity enhancement, INEPT and its later modifications discriminate among carbon nuclei bonded to zero, one, two, or three hydrogen atoms, and hence can serve as a means of 'editing' a complex spectrum and aiding in its assignment.

The success and the limitations of INEPT stimulated other sequences such as DEPT (*D*istortionless *E*nhancement of NMR Signals by *P*olarization *T*ransfer), developed by Doddrell, Pegg, and Bendall,[299] as described by Doddrell (***Doddrell, David M.: An Historical Perspective of Research Based Upon Misguided Advice***). DEPT has the same goal as INEPT but is designed for a broader range of applicability and, as its name implies, to avoid the distortions that can occur in INEPT spectra.

An alternative technique, APT (*A*ttached *P*roton *T*est), was introduced by Patt and Shoolery in 1982 specifically for editing ^{13}C spectra.[300] APT is based on the modulation of a spin echo introduced by ^{13}C–H coupling if decoupling is turned off between the initial 90° and 180° pulses and then turned on for the rest of the experiment. APT lacks the polarization enhancement advantage of INEPT and DEPT, but retains the intensity improvement often found from the nuclear Overhauser effect in ^{13}C NMR.

A rather different type of pulse sequence (given the acronym INADEQUATE) was developed in 1980 by the Freeman group[301] to permit the observation of one-bond ^{13}C-^{13}C spin coupling, even though at natural abundance only about one molecule in 10 000 possesses adjacent ^{13}C atoms. To discriminate against unwanted signals from ^{12}C-containing molecules, the phases of the four pulses in the sequence as well as the acquisition are cycled. Together with the CYCLOPS cycling needed for suppression of quadrature artifacts, 128 steps are thus used for INADEQUATE. As Ad Bax says in his historical sketch (***Bax, Ad: NMR of Ethanol and Interferon-γ***) 'Unfortunately, our complex phase cycle led to the idea: "the more phase cycling the better—no questions asked" '.

Dozens of other pulse sequences, many bearing acronyms designed to ensure their place in history, have been developed and contribute immeasurably to the richness and versatility of NMR methods. With the Fourier transform relations to permit the unraveling of the complex time responses from pulse experiments, physicists and chemists were finally given free rein to manipulate nuclear magnetizations and achieve unprecedented results. The era of 'spin gymnastics' had begun. It would bring revolutionary developments to the investigation of NMR in solids, permit nuclei other than hydrogen to be exploited readily, and allow difficult problems in biochemistry and biology to be addressed by NMR.

HIGH-RESOLUTION NMR IN SOLIDS

The history of solid state NMR started with the discovery of NMR itself by Purcell, Torrey, and Pound, who studied solid paraffin in their pioneering experiment. During the early days of NMR, solid state NMR was at least as popular as studies in the liquid state, since the relatively inhomogeneous magnets then available could provide a faithful representation of the inherently broad NMR lines in solids but not the narrow lines known to exist in liquids. The discovery of the chemical shift and the widespread recognition of the importance of this tool for the elucidation of chemical structure put a premium on liquid state studies, since only there were lines sharp enough to reveal this information.

The interaction Hamiltonian in the liquid state corresponds to isotropic chemical shift and scalar spin–spin interactions only, resulting in sharp lines in the spectra and providing the parameters of utmost importance in structural chemistry. In the solid state, on the other hand, anisotropic interactions, such as chemical shift anisotropy, dipole–dipole interactions, and quadrupolar interactions, are all retained in addition to the isotropic chemical shifts and indirect spin–spin couplings. Moreover, the chemical shift anisotropy and the dipolar and quadrupolar interactions usually dominate the spectrum, resulting in broad lines in the solid state. The information carried by the indirect spin–spin couplings and the chemical shifts is consequently 'buried' under the broad and structureless spectral patterns.

As we saw in Sections 2 and 4, many important early applications of NMR had concentrated on the extraction of internuclear distances and orientations from analyses of the usually dominant dipolar interactions. In addition, since the onset of molecular motion by any means could narrow the lines or change the shape of the lines providing a novel method for the study of molecular motions and phase transitions, NMR became a valuable tool for polymer scientists. Spectra of metals and alloys were extensively employed to study Knight

shifts. With the knowledge, however, that spectra in the solid state inherently contain more information than those in the liquid state, many NMR physicists continued to seek methods to obtain spectra with sharp lines, either by eliminating some of the unwanted interactions or by reducing their dominance.

Magic Angle Sample Spinning

As we saw in Section 4, Raymond Andrew first thought about spinning NMR samples in order to resolve the NMR paradox concerning observed line narrowing in the face of a theoretically constant second moment. He and his colleagues developed a method for spinning a solid sample about an axis inclined at an angle of 54°44′ to $\boldsymbol{B}_0$.[154] These results were reported at the AMPERE Meeting in Pisa in 1960. Gorter found the removal of dipolar broadening quite remarkable and referred to it as 'magic' and the technique was henceforth called 'magic angle spinning'.

Meanwhile, at Washington University, Irving Lowe was studying solids by pulse methods. He and Norberg had already demonstrated that a FID following a 90° pulse could be Fourier transformed to obtain the spectrum.[136] Lowe speculated that rotating a sample should produce sharp sidebands at frequencies related to the spinning speed. He recognized from the expression for the dipolar Hamiltonian that at the angle of 54°44′ the leading term vanishes and sidebands should appear at multiples of the spinning speed. After initial unsuccessful attempts to construct a mechanical device to carry out the rotation, Lowe hit on a different method, as he describes in his historical sketch (***Lowe, Irving J.: My Life in the Rotating Frame***):

> About then, I was having some dental work done and saw a new air turbine drill that my dentist used. I decided to try to spin the sample by blowing air past it. A gifted machinist (Jim Boyle) and I made up some NMR samples that were cylinders 7 mm wide, 7 mm in diameter, had nylon bearings and spun on thin phosphor bronze wires as axles. I found that spinning speeds were limited only by the strength of the sample and that speeds up to 7 kHz were easily obtainable. I put the spinner into my NMR probe, found that I could narrow the line of both Teflon and CaF_2 and was so excited that I worked for the next 48 hours taking data, stopping only when I had spun all my prepared samples to destruction.

Lowe's results were published in *Physical Review Letters* in 1959.[155] Data for polycrystalline calcium fluoride are shown in Figure 50 for a spinning axis oriented at α = 0°, 54°44′, and 90° relative to the magnetic field. CaF_2 was a particularly suitable sample for demonstrating the effects since the F-F distance is large enough to reduce dipolar interactions, and the fluorines form a simple cubic lattice so that chemical shift anisotropy is absent.

Subsequently, Andrew and his co-workers demonstrated in 1962 that high-speed rotation about the 'magic' axis removes spectral broadening arising from anisotropy of chemical shifts in polycrystalline or amorphous specimens,[302] and they showed the effectiveness of the high speed magic angle rotation in eliminating spectral broadening arising from anisotropy of symmetric electron-coupled nuclear spin interactions.[303] Examples of chemical shift fine structure resolved in solids by this technique were provided by Andrew and Wynn[304] and by Kessemeier and Norberg,[305] while the first spin multiplets were resolved in the spectra of solids by

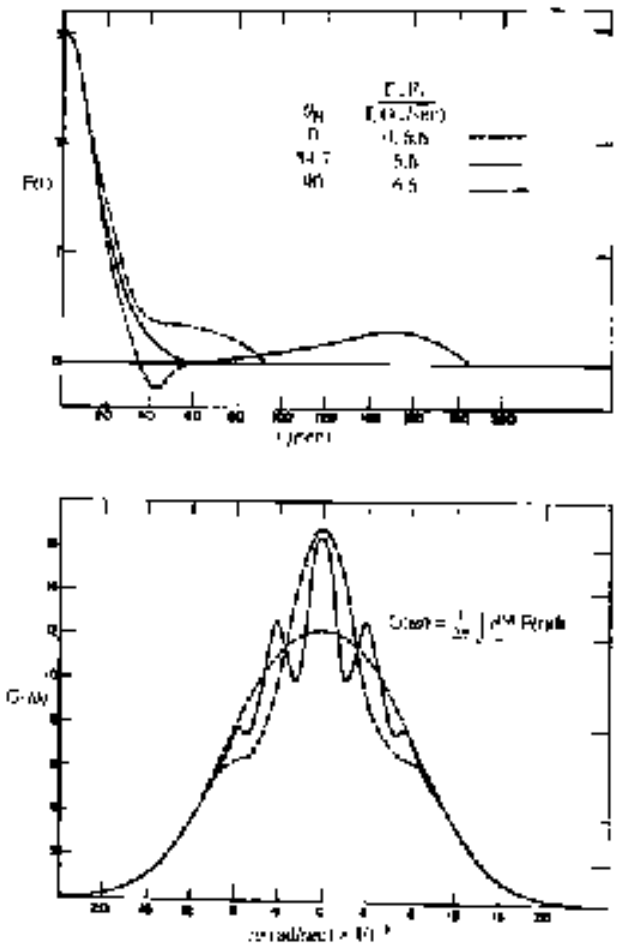

Figure 50 Free induction decays and corresponding FT spectra for polycrystalline CaF_2 as a function of the direction of the spinning axis.[155] (Reproduced by permission of the American Physical Society)

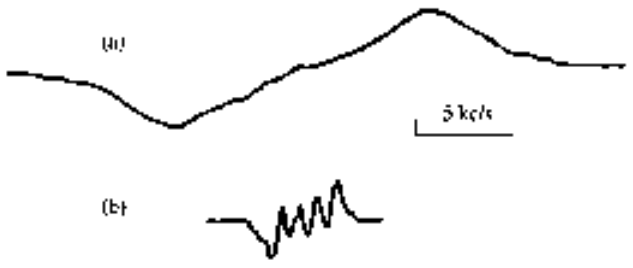

Figure 51 ^{19}F derivative spectra of polycrystalline $KAsF_6$. (a) Nonspinning; (b) magic angle spinning at 5.5 kHz.[306] (Reproduced by permission of the American Physical Society)

Andrew et al.[306] The ^{19}F spectrum of $KAsF_6$, shown in Figure 51, has a width for the nonspinning sample of 13.2 kHz, but the 905 Hz splitting arising from the indirect ^{75}As-^{19}F coupling could be easily resolved in the spectrum of the sample spinning at the magic angle at a rotation frequency of 5.5 kHz.

After this initial burst of activity which established the validity of the method, physicists largely turned to other studies and magic angle spinning was little used and was largely unknown to the chemists who might have applied

the method to interesting problems. By 1970, however, Doskočilová and Schneider in Prague had constructed a magic angle spinner and demonstrated line narrowing in ^{1}H NMR, which they later applied to polyethylene (see ***Doskočilová, Danica & Schneider, Bohdan: Development of Magic Angle Rotation for the Narrowing of Proton NMR Lines in Organic Materials***). Also, their study of ion-exchange resins in 1972 showed that inhomogeneities from magnetic susceptibility variations in a mixed solid/liquid sample could be largely eliminated by MAS.[307]

The widespread revival of MAS began largely with the work of Jacob Schaefer and Edward Stejskal, then at the Monsanto Chemical Company, who were investigating ^{13}C NMR at natural abundance in polymers with the FT methods that had recently become available commercially. As Schaefer points out in his article (***Schaefer, Jacob: A Brief History of the Combination of Cross Polarization and Magic Angle Spinning***), he was frustrated in trying to obtain data in solution from polymers that were only partially soluble. In a visit to nearby Washington University, he recounted these problems to Samuel I. Weissman, a pioneer in the development of electron spin resonance:

> Sam suggested forgetting about solvents and using magic angle spinning on the solid polymers instead. I objected that I didn't want to get involved in an experiment which was both difficult and dangerous. (I recalled a magic angle spinning talk featuring a slide showing the operator at a console separated from the magnet gap by a wall of sandbags!) Sam led me into his office, reached up to a book shelf, and took down a cigar box from behind a pile of journals. Within a few minutes he had assembled a magic angle spinning device consisting of a solid Lowe rotor suspended on two L-shape bronze wires. The short ends of the wires fit into tiny holes machined into the center of each end of the rotor. The long ends of the wires were held by spacers and Teflon tape to the sides of a glass pipette. The tip of the pipette was aimed at flutes which had been cut around the barrel of the rotor. Sam gave a gentle puff and the rotor whistled into action: magic angle spinning and no sandbags.

Schaefer immediately adapted the Lowe spinner to his probe, used a cardboard protractor to adjust the magic angle, set the spinning speed by the pitch of the sound that was emitted, and found that the apparatus worked to narrow the ^{13}C linewidth in a sample of rubber by a factor of two. Schaefer and Stejskal improved the apparatus, learned how to make better rotors by machining solid polymers, and constructed a rotor for enclosing other samples. Their talks and publications stimulated other chemists to try MAS, but the real growth in the use of MAS would come only when commercial probes became available in 1978 and when this technique was combined with other elegant pulse methods, as we describe in following sections.

Two other aspects, namely the setting of the magic angle and the rotor designs, are important for an efficient magic angle spinning experiment. For maximum resolution, the angle between the spinning axis and the magnetic field direction must be as close to the magic angle as possible since imprecise settings produce line broadening. Frey and Maciel[308] developed procedures for measurement of the ^{13}C NMR linewidths in standard samples, such as hexamethylbenzene, or the use of quadrupolar nuclei, such as ^{81}Br in KBr. Bodenhausen et al.[309] suggested the use of a laser beam to align the angle optically. A simple and accurate procedure for setting the magic angle using line separations instead of linewidths in the ^{13}C spectra of molecules such as chloroform oriented in the nematic phase of liquid crystals was proposed and utilized by Khetrapal et al.[310] in 1987.

The rapid growth of magic angle spinning experiments is the result of a variety of modifications in the rotor materials and design. David Doty in his article (***Doty, F. David: A Random Walk Toward High-Speed Sample Spinning***) describes the steps needed to develop MAS probes commercially, and Hans Jakobsen's article (***Jakobsen, Hans J.: A Retrospect on the Development of High-Speed Sample Spinners for Solids since 1980***) recounts some of the improvements in his laboratory and in Gary Maciel's laboratory as they competed to reach supersonic rotation speeds. The rotor materials must be nonconducting and mechanically stable to sustain high rotation speeds. As far as possible, they should not contain the material to be investigated. Boron nitride, Kel-F, Macor, and Delrin have been commonly employed. Before the 1980s, most spinners were based on modifications of Andrew's design employing a conical surface with a single air bearing and drive source. However, cylindrical rotors with separate bearing and drive systems also emerged and the maximum spinning speed generally permitted was 4–5 kHz. There have been gradual improvements in the rotor designs resulting in a considerable increase in spinning speeds. Recently, spinning speeds up to 26 kHz for a 3.5 mm rotor have been achieved.

Magic angle spinning experiments have been widely used to study many solids, polymers, liquid crystals, metals, proteins, biological membranes, and numerous other materials. Not only have the lines been narrowed so as to obtain fine structure due to indirect spin–spin couplings and chemical shifts, but the intensities of spinning sidebands have been employed to derive information which is not otherwise easy to obtain. Lippmaa et al.[311] and Stejskal et al.[312] reported independently that spinning the sample at the magic angle with a rotation speed lower than the frequency spread of the shielding anisotropy profile yields a sharp peak at the isotropic chemical shift value, along with a series of equally sharp sidebands separated by the spinning frequency, and the intensities of the sidebands reflect the profile of the chemical shielding anisotropy. Lippmaa showed that the intensities of the first sidebands could be related to the anisotropy pattern for the axially symmetric shielding tensor. A general procedure to correlate the anisotropy pattern with the intensities of the individual sidebands was described in terms of general integral and series expansions by Herzfeld et al.,[313,314] while Arun Kumar et al.[315] utilized the relative intensities of the spinning sidebands for the determination of the signs of the dipole- and quadrupole-split doublets in the spectra of oriented molecules spinning at the magic angle.

The technique of 'off' magic angle spinning has also been employed instead of 'on' magic angle spinning to derive useful information. In such cases the lineshape of the powder pattern is retained for all angles, while the overall linewidth is governed by the factor $3\cos^2\alpha - 1$, where α is the angle between the spinning axis and the magnetic field. Near magic angle spinning experiments in oriented systems in order to reduce strongly coupled spectra to weakly coupled ones were performed by Courtieu et al.[316] in 1982.

Rotating Magnetic Fields at the Magic Angle

Many of the applications of high-resolution NMR need much higher spinning speeds than are easily available in order to average out anisotropic interactions and produce the desired line narrowing. In order to avoid such problems of very high speed mechanical rotation, Andrew and Eades[302] in 1962 proposed an alternative approach. The idea is simple. It is the motion of the nuclei relative to their magnetic environments that causes the line narrowing and this can be achieved either by motion of nuclei in a static magnetic field or by placing the static sample containing the nuclei in a magnetic field which is rotating. The requirement in such an experiment is a stable and uniform strong magnetic field rotating at a frequency of the order of 50 kHz with the magnetic field vector inclined at an angle of $54^\circ 44'$ to the axis of rotation. This can be achieved by a superposition of fields applied along three mutually orthogonal directions: a steady field along the z direction and two alternating fields along the x and y directions with their phases in quadrature. The feasibility of this technique was demonstrated with the observation of electron paramagnetic resonance in a free radical[317] and of NMR in liquid paraffin,[318] both in very low magnetic fields. However, the difficulty of generating a sufficiently large and uniform rotating magnetic field precluded the development of this intriguing approach into a practical experimental procedure.

Meanwhile, alternative methods based on pulse techniques and phase-sensitive detection were underway at the University of Pittsburgh, where both Lee and Goldburg[319,320] and Barnaal and Lowe[321] independently reported line-narrowing pulse methods in solids in which the rf fields are rotated instead of the samples. They showed that in the rotating frame the effective Hamiltonian has time-independent terms that are the same as the static Hamiltonian but multiplied by a factor $\frac{1}{2}(3\cos^2\alpha - 1)$. For $\alpha = 90^\circ$, the factor becomes $-\frac{1}{2}$ so the FID should evolve half as fast, as shown by Barnaal and Lowe. Lee and Goldburg used the magic angle where the dipolar Hamiltonian vanishes. This method is in many respects equivalent to the observation of a free induction decay in a rotating sample, but the line-broadening associated with anisotropic chemical shifts in polycrystalline materials is not removed in such experiments. Although it did not lead to very high resolution in solids, a lengthened decay corresponding to narrowed NMR lines was observed. In practice, it was difficult to generate a sufficiently uniform strong rf field to ensure that the effective field is directed at the magic angle for all parts of the sample.

Removal of Homonuclear Dipolar Interactions by Multiple Pulse Techniques

The Lee–Goldburg experiment was influential in demonstrating that rf pulse sequences could be used to manipulate nuclear spins into responding to a Hamiltonian that is controlled, at least partially, by the experimenter. To some extent, such investigations had had their origins in Hahn's spin echo and the subsequent Carr–Purcell and Meiboom–Gill techniques. The latter experiment was probably the first to take advantage of not only the timing of pulses, but their relative phases. In 1962, Powles and Mansfield had extended the concept of reversing certain spontaneous effects of the Hamiltonian by showing that the decay of magnetization due to dipolar interactions in a solid can be refocused by applying a second 90° pulse that is 90° out of phase with the initial pulse.

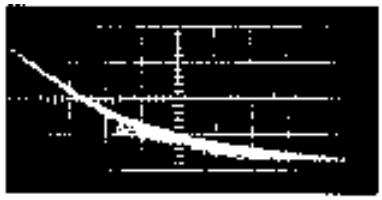

Figure 52 Train of ^{19}F echoes in powdered $Co(NH_3)_6 \cdot (BF_4)_3$, which has a T_2 value of $\sim 45\,\mu$s. The decay shown covers about 10 ms.[322] (Reproduced by permission of the American Physical Society)

All these observations indicated the prospects of observing useful effects as a result of applying more complex pulse sequences. However, in most early pulse spectrometers, pulses were produced by gating electrode voltages on free-running rf oscillators, so that the rf phase of one pulse was unrelated to that of the following or the preceding pulse. In spite of the success of the Meiboom–Gill and Powles–Mansfield techniques, considerable electronic technology had to be developed to permit the incorporation of relatively long and complicated pulse trains coupled with high-power transmitters, all subject to control of phase, with phase-sensitive detection.

A new company formed by the merger of Harvey Wells and Magnion, under the guidance of Edward Ostroff, began to develop a line of pulse NMR spectrometers offering the desired capabilities. John Waugh, who served as a consultant to Magnion, describes some surprising results (***Waugh, John S.: Alchemy of Nuclear Spins***):

> Testing an early machine in the spring of 1965, Ostroff chanced to apply a Carr–Purcell (CPMG) sequence to a solid, and was astonished to see a long train of echoes—up to thousands of them as the pulse spacing τ was decreased. I was equally surprised, but as the consultant I was supposed to explain the effect.

Ostroff and Waugh[322] found that the echoes were optimized for a train of 90° pulses and that solids having T_2 values in the range of tens of microseconds produced echoes lasting as long as 10 ms, as illustrated in Figure 52. Waugh concluded that the known solid-echo[139] could account for the first echo in the train, and developed a rough theory to account for the remaining train, a theory that was later refined and published by Waugh and Wang[323] in 1967.

At Nottingham University in the UK, Peter Mansfield was also exploring the effect of a train of 90° pulses and observed a similar effect as an effective lengthening of the FID in calcium fluoride, and Mansfield and Ware[324] reported the effect in 1966 shortly after the Ostroff–Waugh paper had appeared. Thus began a long competition between these laboratories, which was soon joined by Bob Vaughan and his colleagues at Caltech (See ***Gerstein, B. C.: The Vaughan Days, CRAMPS, and Transient Techniques in NMR*** and ***Dybowski, Cecil: Bob Vaughan and Solid State NMR at Caltech in the 1970s***).

While the theory of multiple pulse studies and several successively improved pulse sequences were developed in all three laboratories, the underlying principles were illuminated primarily by Waugh and his colleagues in terms of Average Hamiltonian Theory. He gradually developed the basic insights

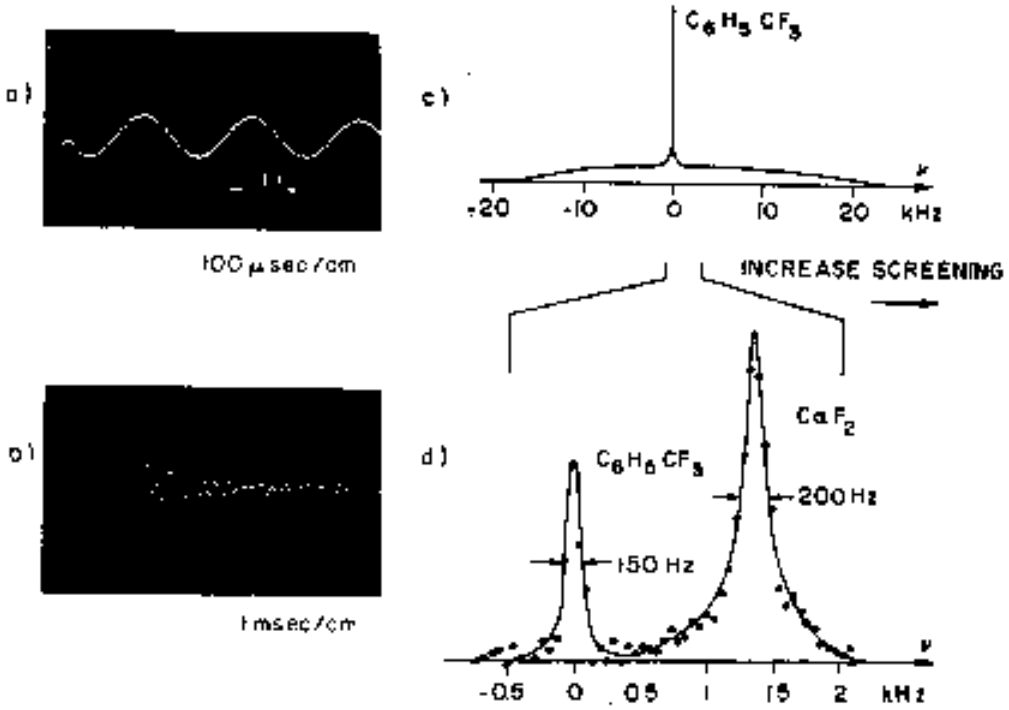

Figure 53 ^{19}F free induction decays for a mixture of solid CaF_2 and liquid $C_6H_5CF_3$, together with their Fourier transforms. Top: 90° pulse. Bottom: application of four-pulse WAHUHA sequence.[326] (Reproduced by permission of the American Physical Society)

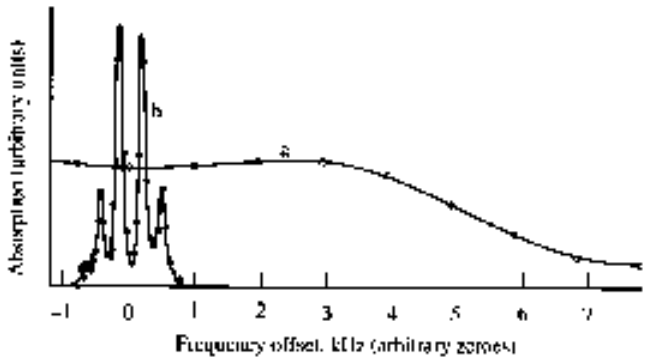

Figure 54 ^{19}F spectra of solid C_6F_{12} obtained by Fourier transformation of (a) the FID following a 90° pulse and (b) the response to a four-pulse WAHUHA sequence.[327] (Reproduced by permission of the American Chemical Society)

into the behavior of a spin system subjected to a cyclic pulse sequence and sampled at particular time intervals. However, as Waugh says,

> The goal remained to design a pulse sequence that would remove dipole–dipole couplings and retain chemical shifts. In hindsight this should have been easy, but in fact I had no idea whether it was even possible. Suddenly one fall morning at breakfast the solution came to me in a rush. Within a few minutes the WAHUHA sequence, ... its scaling factor and timing variants, its relationship to the magic angle and the Lee–Goldburg experiment, etc., were all obvious.

Waugh and his co-workers published the basic ideas of a four-pulse sequence,[325] and with the arrival of Ulrich Haeberlen from Germany the theory was further refined and experimentally tested. He, along with Lee Huber who was already in Waugh's laboratory, modified an old Varian spectrometer for the new sequences. The spectrometer was capable of firing 90° pulses in rapid succession on a timescale of the decay time T_2 of the FID of a solid, i.e. 20–30 μs. Within T_2, four pulses with mutually orthogonal rf phases and spaced by delays $\tau-2\tau-\tau-2\tau$ had to be applied, and the NMR response acquired between the pulses. These were stringent requirements that could be met only with great difficulty.

The first experiment was performed on the ^{19}F resonance of a sample consisting of a small chip of a single crystal of CaF_2 and some liquid $C_6H_5CF_3$.[326] Figure 53 shows the results from the oscilloscope traces. The ordinary FID shows a fast decay of the solid signal, followed by a much longer decay of the liquid signal. Application of the four-pulse sequence $-[-\tau-90°_x-2\tau-90°_{-x}-\tau-90°_y-2\tau-90°_{-y}-]-$, with τ = 6 μs, resulted in a signal for the solid that was comparable in decay time with that of the liquid. The Fourier transforms showed that the sequence was able to resolve chemical shifts (scaled down by a factor of $1\surd3$). The pulse sequence was referred to as WAHUHA after *WA*ugh, *HU*ber, and *HA*eberlen. The net effect of the sequence on the magnetization is easily visualized and can be considered as equivalent to the spin spending equal times (2τ) along the x, y, and z axes, which produces the same average behavior as alignment along the magic angle axis.

Figure 54 shows a true 'high-resolution' ^{19}F spectrum of C_6F_{12} obtained with such a four-pulse WAHUHA sequence (with a cycle time of 21 μs and a 90° pulse width of 1.1 μs) in comparison with an ordinary NMR spectrum in the solid state.[327] The suppression of the dipolar broadening reveals the AB quartet, reflecting the presence of the distinguishable interacting axial and equatorial fluorines. Although this provided a potentially very powerful technique in the solid state, the real exploitation occurred much later

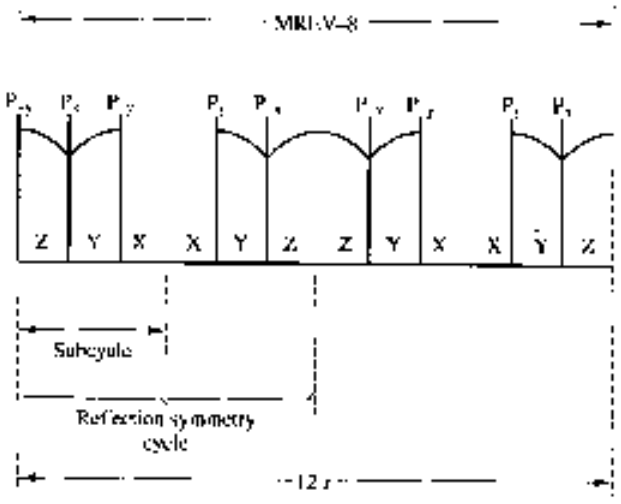

Figure 55 Sketch of the compensated reflection symmetry of the MREV-8 cycle.[335] (Reproduced by permission of the Royal Society)

due to the extreme demands on instrumentation. The historical sketches by Michael Mehring (***Mehring, Michael: Advent and Evolution of High-Resolution NMR in Solids: A Personal View***) and Ulrich Haeberlen (***Haeberlen, Ulrich: The Early Days of Multiple Pulse NMR***) provide additional insights into the course of these developments. As Haeberlen points out,

> The unique *something* which the [multiple pulse] line-narrowing method promised to make amenable to measurement—and eventually did—was the shielding tensor of protons and ^{19}F nuclei. This was clear to us from the very beginning, but it took us almost a full year before at last we could record a [multiple pulse] spectrum from a solid with two separate resonances, and with one of them displaying even a feature which the loving eye could recognize as a chemical shift anisotropy powder pattern.

The first measurement of the chemical shielding tensor for ^{19}F was reported by Mehring et al.[328] in 1970 in fluoranil, and publication of high-resolution ^{1}H spectra[329,330] came in 1973.

The WAHUHA cycle does not correct for rf inhomogeneity effects, and it is this inhomogeneity that limits the resolution of these experiments. Various other more complex pulse schemes using the principles of the four-pulse WAHUHA sequence as the basic building combination were subsequently developed in order to improve performance. One such modification, first shown theoretically by Mansfield[331,332] in 1970–71 and subsequently verified experimentally by Mansfield et al.[333] and also by Rhim, Elleman, and Vaughan[334] in 1973, is an eight-pulse cycle named MREV-8 to reflect its inventors and the number of pulses. The procedure is to follow one reflection symmetry cycle by a second in which the rf carrier phases of, say, the x pulses only are reversed as shown in Figure 55.[335] MREV-8 continues to be used along with various modifications. A 24-pulse sequence BR-24, introduced by Burum and Rhim[336] in 1979, has become one of the standard multiple pulse sequences. Blinc and co-workers[337] developed multiple pulse sequences in combination with gradient pulses to study diffusion in solids. By this method slow diffusion is measurable in solids in a direct fashion.

With the development of improved instruments, including the incorporation of minicomputers in commercial NMR spectrometers, established multiple pulse sequences could better be used for applications to chemical problems, especially in the field of polymers. However, the complexity of the methods and their sensitivity to changes in instrumental parameters delayed their widespread use. As Richard Ernst has pointed out, ' . . . we spend 70% time on solids but get 70% of the publications on liquids . . . '

Work on polymers using multiple pulses provided a wealth of information on their structure and motion, information which otherwise could not be derived easily with reasonable certainty. Teflon was the first polymer investigated by this technique during 1969–71.[338,339] Subsequently, Garroway, Stalker, and Mansfield[340] illustrated that information on orientational ordering and molecular motion in different phases of Teflon can also be obtained from such experiments. Vega and English[341] combined chemical shift information with relaxation data to study the detailed molecular motion in Teflon, while Dybowsky and Vaughan[342] studied anisotropic lattice motions in natural rubber and *cis*-polyisoprene. Rhim and co-workers[343,344] employed multiple pulse NMR in spin-temperature experiments, such as spin-locking and adiabatic demagnetization in the rotating frame. Multiple pulse methods were beginning to have practical application.

The Hartmann–Hahn Concept

In a system containing 'dilute' spins such as ^{13}C or ^{15}N at natural abundance, homonuclear dipolar couplings normally do not show up due to low natural abundance and the heteronuclear dipolar couplings with 'abundant' nuclei such as protons can in principle be eliminated by decoupling experiments, provided adequate continuous wave power is available at the sample. As electronics improved, it became possible to obtain high-resolution spectra in these systems. However, the signals in such cases are rather weak, in general, because of the low natural abundance, small magnetic moment, and long spin–lattice relaxation time of the dilute nucleus. A gain in the sensitivity can be achieved by utilizing the magnetization reservoir of the abundant systems.

A clever means for efficiently transferring polarization from one nuclear species to another, even though their precession frequencies are quite different, was suggested by Sven Hartmann and Erwin Hahn in 1960, and two years later they published a detailed explanation and a demonstration of the effect.[345,346] By drawing heavily on the concept of spin temperature in the rotating frame (see Section 4.2), they showed that two nuclear species of spin I and S with magnetogyric ratios γ_I and γ_S act as though they are strongly coupled when they are acted upon by rotating fields $(\boldsymbol{H}_1)_I$ and $(\boldsymbol{H}_1)_S$ tuned to the respective resonances, provided the amplitudes of these rotating fields obey the relation $\gamma_I(\boldsymbol{H}_1)_I = \gamma_S(\boldsymbol{H}_1)_S$, called the 'Hartmann–Hahn condition'. Even though their precession frequencies in the static field $\boldsymbol{H}_0$ are widely apart, strong coupling occurs via the dipolar interaction between the I and S spins and they can exchange magnetization via mutual spin flips. An application of a nonadiabatic perturbation only to the rare spins may result in a sizeable change in the abundant spin magnetization if the abundant spin relaxation time is long compared with the cross-relaxation time in the rotating frame between the rare and the abundant spins. In this manner, even though the S resonance

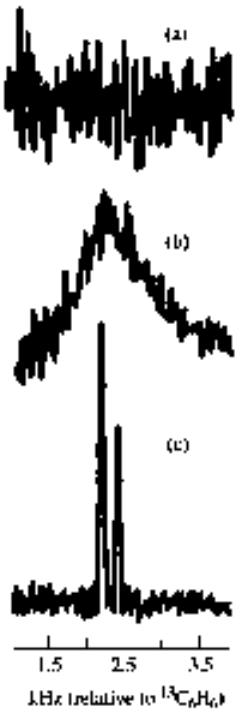

Figure 56 The 24 MHz ^{13}C NMR spectra of polycrystalline adamantane. (a) FT of a FID after a 90° pulse; (b) Cross polarization without decoupling; (c) Cross polarization and decoupling.[351] (Reproduced by permission of the American Institute of Physics)

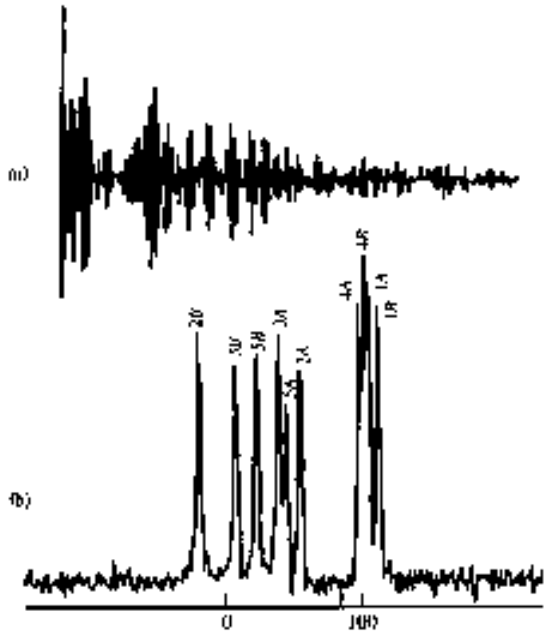

Figure 57 Cross polarization FID and spectrum of ^{13}C in durene, showing lines from the six aromatic and four methyl carbons.[353] (Reproduced by permission of the American Institute of Physics)

may be hard to observe directly, it could be seen indirectly by its effect on the I spins.

A simplification of the experimental technique and the theoretical analysis was subsequently made by Lurie and Slichter[347] in 1963 and published in 1964. In this method, the I spin system is spin-locked at exact resonance while the rare spin is simultaneously irradiated with a train of coherent pulses close to its Larmor frequency. Thermal mixing of the two spin systems occurs via cross relaxation when both these rf fields are on. The combined system approaches thermodynamic equilibrium, characterized by a common spin temperature. The S channel rf field is then turned off for a period greater than $(T_2)_S$. This method differs from the Hartmann and Hahn technique in the manner in which $\boldsymbol{M}_I$ is brought parallel to $(\boldsymbol{H}_1)_I$ and the methodology for inducing changes in the S magnetization. A variation of the Lurie–Slichter method was later developed by Mansfield and Grannell[348] in 1971 for the improved resolution of small resonance shifts of dilute nuclear spin systems. Bleich and Redfield,[349] around the same time, combined the Hartmann–Hahn method with solid state spin decoupling in order to improve resolution of rare spins in solids, and later proposed still another type of Hartmann–Hahn double resonance technique in solids which is particularly suited for the high-resolution spectroscopy of spins with low magnetogyric ratios.[350]

Direct Observation of Dilute Spins by Cross Polarization

The indirect double resonance methods in solids for rare spins are not useful for the study of high-resolution spectra because the spectra observed are, in effect, broadened by the very coupling which makes them possible. Alex Pines, then a graduate student with John Waugh, conceived the idea of dividing the experiment into two parts: first, the rare spins are polarized by the Hartmann–Hahn procedure ('cross polarization'), and second, the rf irradiating the rare spins is turned off and the FID corresponding to the rare spin developing under chemical shifts and decoupled from all the abundant spins is recorded. Pines described this technique at the 1972 ENC, showing beautiful slides of the enhancement of the sensitivity and resolution by the CP experiments with abundant spin (proton) decoupling, and a paper entitled 'Proton Enhanced Nuclear Induction Spectroscopy' soon appeared in the *Journal of Chemical Physics*.[351] The initial ^{13}C spectra of polycrystalline adamantane obtained in natural abundance of ^{13}C, with and without cross polarization, and with and without proton decoupling, are shown in Figure 56. Using this technique, Pines et al. determined the ^{13}C chemical shielding parameters for a number of organic compounds.[352] The utility of such experiments was clear, and its use rapidly became widespread.

The applications of cross polarization are numerous. An early study of the chemical shielding tensors of all the carbons in the single crystals of durene by Pausak, Pines, and Waugh[353] is illustrated in Figure 57, where the expected 10 lines were resolved. The measurement of chemical shielding tensors has provided a versatile tool for the study of the structure and dynamics of molecules. An interesting application of the chemical shielding anisotropy to probe solid state structure was initially proposed by Ripmeester et al.,[354] who examined the ^{129}Xe spectra of the gas intercalated into several solids. The spherically symmetric isolated molecule shows no chemical shielding anisotropy. Any observed anisotropy must consequently arise from the asymmetry in the immediate environment of the atom.

Wind et al.[355] proposed a novel solid state NMR experiment that uses dynamic nuclear polarization for further enhancement of the ^{13}C signals. The experiment was the result of the NMR investigations of coals, which inherently contain free electrons, typically 10^{19} per gram. It was observed that both the proton and ^{13}C signals could be enhanced by significant amounts (one order of magnitude for protons and two orders of magnitude for ^{13}C, the latter also containing a contribution from proton–carbon cross polarization) by irradiating near the electron Larmor frequency. Magic angle spinning can also be performed.[356] Such an experiment provides high spatial selectivity and may serve as an important tool to reduce the measuring time for the ^{13}C spectra for nuclear spins that are near electron spins.

The possibilities of combining various techniques in solid-state NMR appear to be endless! Selective pulse experiments have found applications in the simplification of spectra and in the study of slow dynamic processes such as chemical exchange and spin diffusion. Selective excitation can be achieved either by application of weak rf pulses of appropriate frequency or by a DANTE sequence, which consists of a series of short, intense rf pulses. By adjusting the time between the pulses, one of the pulse sidebands may be centered on the transition corresponding to the selected resonance. The DANTE pulse sequence is appropriate in MAS experiments where the sidebands are separated by the spinning frequency.

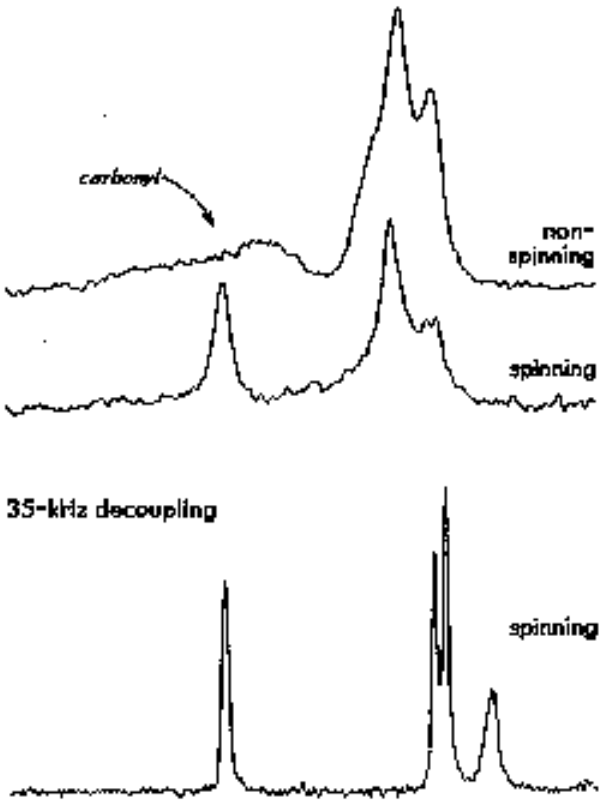

Figure 58 Combined cross polarization and magic angle spinning applied to the ^{13}C spectrum of poly(methyl methacrylate).[357] (Reproduced by permission of the American Chemical Society)

Magic Angle Spinning Returns

The initial attempts to narrow lines in solids by magic angle spinning were of limited success as we have seen, because the dominant dipolar interactions are, in many systems, too large to be eliminated with achievable spinning speeds. The principal methods developed, however, to overcome these interactions—multiple pulse techniques for homonuclear interactions and cross polarization/high-power decoupling for many heteronuclear systems—have their own limitations. These methods specifically eliminate dipolar interactions but, by their nature, do not affect chemical shift anisotropy. It may be an advantage to retain the chemical shift anisotropy information in some experiments, but chemical shift anisotropy can be greater than the total chemical shift range (e.g. of protons) and in that case it severely limits the practical applications for routine analytical purposes. The potential of combining MAS with multiple pulse or CP methods thus became attractive in order to achieve maximum resolution.

Waugh considered combining MAS with the Pines–Gibby–Waugh CP technique, but did not pursue the idea aggressively since he was concerned that the spinning might behave like random molecular motions in removing the very static dipolar coupling required for cross polarization. Schaefer and Stejskal, who had revived MAS for ^{13}C NMR, quickly took up the new CP techniques as well, but in completely different experiments. They did not not try the combined techniques for a year or so, largely because of limitations in their apparatus and concern about wearing out rotors while trying to establish optimum conditions for the new experiment. Nevertheless, the first CP MAS experiment was performed by Schaefer and Stejskal[357] in 1975, the ^{13}C spectrum of poly(methyl methacrylate) as reproduced in Figure 58. A comparison with the 'static' sample spectrum shows the remarkable difference in the two spectra and a strong low field signal due to nonprotonated carbonyl carbon of poly(methyl methacrylate) can be clearly seen. After collecting data on a variety of solids, Schaefer and Stejskal submitted a brief communication to the *Journal of the American Chemical Society*, only to have it rejected initially because of the negative comments of the referees who wrote 'basically there should not be polarization transfer due to a dipolar interaction between nuclei in a sample being spun rapidly at the magic angle.' The skepticism was well founded on theoretical grounds, but the experiments were genuine. With some alterations to the manuscript, the paper was eventually accepted. Actually, as became apparent in later studies, the cross polarization dynamics in CP MAS NMR are not as simple as in plain CP NMR. Schaefer's historical sketch (***Schaefer, Jacob: A Brief History of the Combination of Cross Polarization and Magic Angle Spinning***) describes the unusual effects observed and their explanation in a paper by Stejskal, Schaefer, and Waugh[358] in 1977.

The appearance of liquid-like spectra in solid polymers eventually obtained using CP MAS experiments made this technique a standard tool in polymer research. CP MAS has been extensively employed for the chemical characterization of coal and related materials for differentiating the aromatic and aliphatic contents, but it has not been possible to resolve the aromatics and condensed aromatics in the CP MAS spectra of coals. The shielding anisotropies of such carbons are significantly different, giving better resolved spectra without MAS![359]

In a normal CP MAS experiment, the coherent dipolar decoupling also eliminates the scalar $^{1}H-^{13}C$ coupling in the ^{13}C spectrum. In order to make CP MAS experiments more valuable in structural chemistry, advances have been made by Terao et al.[360–362] and by Zilm and Grant[363] that retain the indirect spin–spin couplings in the high-resolution CP MAS experiments. Also, Opella and Frey[364] developed a technique to assist in the assignment of lines by making use of the large difference in dipolar broadenings of the resonances of carbons with protons attached compared with those without protons.

The possibility of combining multiple pulse experiments such as WAHUHA with MAS was first discussed by Haeberlen and Waugh in 1968, but was not implemented for many years because of both theoretical concerns and practical problems in dealing with two sensitive technologies. The initial combined magic angle multipulse experiments in which both homonuclear dipolar interactions and chemical shift anistropies were sufficiently removed to resolve chemically shifted fluorines in a randomly oriented solid were described by Gerstein et al.[365] and by Schnabel et al.[366] The sample chosen by Gerstein to illustrate the effect was Kel–F (polymerized $FClC{=}CF_2$). The rotation speed was 2.5 kHz and the MREV-8 pulse sequence was used, resulting in a chemical shift scaled by roughly $\frac{1}{3}\surd 2$. The spectrum is shown in Figure 59. The figure shows the spectra obtained with MREV-8, as well as the combined magic angle spinning and multipulse techniques. The natural linewidth of the ^{19}F resonance for a single free induction decay was 10 kHz. The residual linewidth in the combined rotation and multipulse sequence was attributed to the differing stereochemical environments of the fluorine nuclei. The two peaks separated by 23 ppm were identified as fluorines bound to the same carbon and a carbon bound to a chlorine. The method was called CRAMPS for *C*ombined *R*otational *A*nd *M*ultiple *P*ulse *S*pectroscopy. Subsequently, other pulse sequences such as the 24-cycle sequence BR-24 were employed to improve the efficiency.

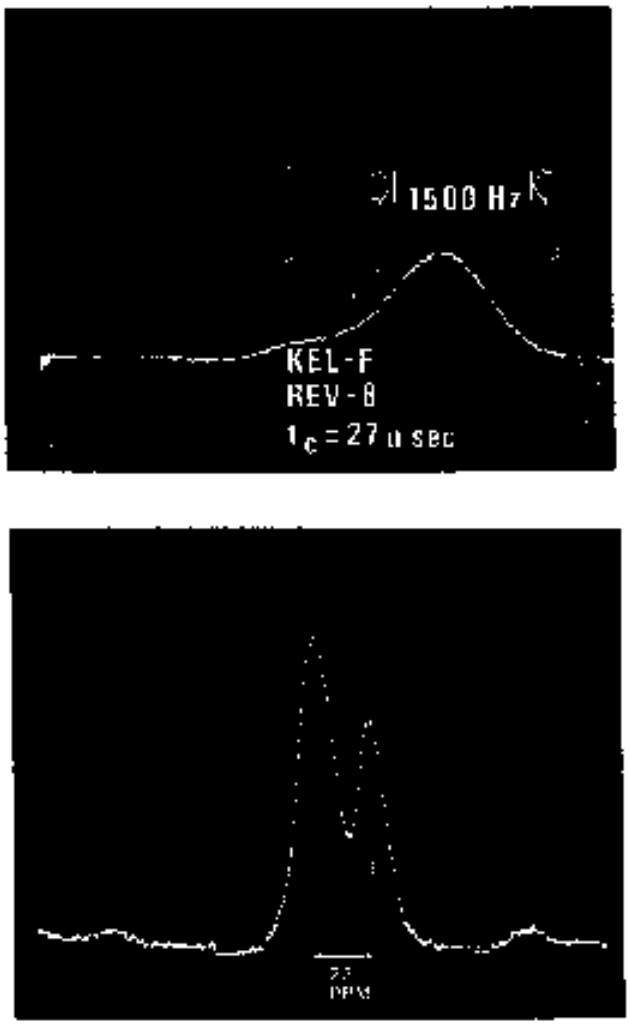

Figure 59 The ^{19}F spectrum of Kel-F obtained with a MREV-8 sequence (top) and MREV-8 combined with magic angle spinning (bottom).[365] (Reproduced by permission of the American Institute of Physics)

Line-Narrowing Techniques for Quadrupolar Nuclei

Line-narrowing techniques for the solid state NMR spectra of quadrupolar nuclei have also been developed. Alex Pines and his group at Berkeley have been particularly prominent in this area. They were able to eliminate the first-order quadrupolar broadening in deuterium by using magic angle spinning along with sampling that was synchronous with rotation frequency.[367] The linewidth could be reduced by three orders of magnitude by the simple MAS experiment, but the stability and the setting of the magic angle was very critical. Further improvements in spinner design permitted the application of MAS to deuterium in solids where the powder static linewidth can be over 255 kHz.

For deuterium, with $I = 1$, Pines utilized the fact that the $1 \leftrightarrow -1$ transition is independent of sample orientation and hence leads to sharp lines. We discuss multiple quantum transitions in Section 11, but it is appropriate to point out here that the Pines group combined double-quantum spectroscopy with magic angle spinning.[368]

Eric Oldfield and his co-workers explored the problem of line narrowing for nonintegral spin quadrupolar nuclei, where the second-order quadrupole interaction dominates the breadth of the $(\frac{1}{2}, -\frac{1}{2})$ spin transitions. At high magnetic field this effect is reduced to the point that many nuclei are amenable to study. For systems with large quadrupole coupling constants (of the order of a few MHz), they observed the optimum line narrowing by rapid sample rotation at angles other than $54°44'$. For ^{23}Na in Na_2MoO_4, an order of magnitude reduction in breadth of the central transition was achieved by rapid rotation at $36°$ or $75°$, over twice that achieved at $54°44'$.[369] The effect originates from the more complex angle dependence of dipolar and chemical shift interactions.

Pines made the most general approach to the problem of averaging second-order quadrupolar interactions. In his historical sketch (***Pines, Alexander: Solid State NMR: Some Personal Recollections***), he says:

> The solution, for which we developed both the theory, with independent work by Llor and Virlet, and demonstrated the initial experiments (with the indispensable support of Berkeley's machine shop), involved motional averaging through sample spinning about two axes. Two techniques emerged—dynamic angle spinning (DAS) and double rotation (DOR)—which brought to quadrupolar nuclei the kind of resolution previously reserved for spins $\frac{1}{2}$. During this period our laboratory often felt

> like a dental clinic, with the whizzing and whining sounds and rich harmonics of dynamic-angle and double rotor probes.

With the development of the techniques described in this Section, along with many others that we have not been able to include, the NMR spectroscopist was largely freed of the constraints imposed by line broadening in solids. Information of value in chemistry, materials science, and biology could now be extracted from solids, as well as liquids.

MULTINUCLEAR MAGNETIC RESONANCE

Although NMR studies of several nuclei have been discussed in previous sections, much of the early history was dominated by ^{1}H NMR. Even now, proton NMR is studied far more than that for any other single nucleus because of its sensitivity, virtually 100% isotopic abundance, and presence in almost all molecules of interest. NMR imaging (which accounts for a significant fraction of all current NMR measurements) is devoted almost exclusively to ^{1}H NMR since this technique focuses primarily on water in the human body. The dominance of ^{1}H NMR has given rise to the practice of referring to non-^{1}H nuclides as 'other nuclei' and to their study as 'heteronuclear NMR', a term that may lack grammatical precision but is correctly understood by all NMR spectroscopists.

Some NMR spectroscopists directed their attention toward a particular nucleus, while others wanted to explore a wide range of nuclei. Otto Lutz's historical sketch (***Lutz, Otto: Heteronuclear Magnetic Resonance***) mentions his observation of more than 50 isotopes, beginning in 1975 with a Bruker high-power pulse spectrometer that was also capable of carrying out high-resolution studies with an internal deuterium lock, along with a number of homemade probes. (The instrument was called MONALISA—a name that contains the symbols for 11 different NMR-active isotopes when read both forward and backward.)

In general, the early NMR spectrometers were not designed to facilitate multinuclear observations, as pointed out by Paul Ellis in his historical sketch (***Ellis, Paul D.: Multinuclear MR Experiments, the Surrogate Probe Strategy, and Other Fun & Games***):

> In the 1960s and early 1970s, it was common for manufacturers of NMR spectrometers to build the spectrometer around specific nuclei rather than being broadbanded. Hence, if you purchased your spectrometer with ^{1}H, ^{13}C, and ^{31}P observe capabilities, you would get three transmitters, three local oscillators, three preamps, and, depending upon the manufacturer, three probes. It was a great marketing tool designed to bring in a gazillion dollars per spectrometer but a poor way to do science. This picture started to change when Dan Traficante learned how to 'fake' a spectrometer into thinking it was performing a ^{13}C experiment when it was really looking at ^{29}Si.

This work led to Varian's 'Gyrocode Observe' option, the first commercially available multinuclear observe accessory, which soon gave way to true frequency synthesizers. Over the last 20 years there has been an increasing awareness of the rich information available in the study of many different nuclei. With FT methods, highly developed double resonance techniques, and spectrometers based on frequency synthesizers with broadband probes, the NMR spectroscopist in the mid-1970s was equipped to make progress with almost any isotope chosen for study in liquids. Moreover, rapid development of multiple pulse methods and magic angle spinning also opened the door to the study of many nuclei in solids.

We have already described many of the early studies of ^{19}F and ^{31}P NMR. These nuclides of spin $\frac{1}{2}$ usually display sharp lines and have much larger chemical shift ranges than ^{1}H, so investigations with magnets of limited homogeneity could often be carried out more readily with these nuclei. We have also told the story of the emergence of ^{13}C studies, as double resonance and Fourier transform methods developed, and have pointed out applications of deuterium NMR. The Periodic Table is large, however, and almost every element has at least one isotope (often several) with nuclear spin, as indicated in Figure 60. In fact, all elements except Tc, Pm, Ar, and Ce in the Periodic Table up to and including lead have one or more suitable stable isotopes accessible to NMR. In 1977, when Harris and Mann completed their comprehensive survey of multinuclear magnetic resonance,[370] only one spin-$\frac{1}{2}$ nucleus (^{103}Rh) and 10 quadrupolar nuclides had not been observed directly. Since then, as mentioned later, at least limited studies have been carried out with four of these nuclei, leaving only ^{91}Zr, ^{105}Pd, ^{177}Hf, ^{179}Hf, ^{191}Ir, ^{193}Ir, and ^{197}Au unobserved directly, but in some instances studied by double resonance methods.

In some ways each isotope is unique, and a historical account perhaps should treat each one separately. We present here a short description of the early NMR history and of some later developments for those nuclides that have engendered the most interest or have demonstrated some particularly important principles. For completeness, the section concludes with a brief summary of early work with several rather infrequently studied nuclides.

General Features of 'Heteronuclear' Magnetic Resonance

The discovery of nuclear induction resulted from Felix Bloch's desire to make more accurate measurements of the magnetic moments of nuclides, and much of the early work in multinuclear MR dates back to the late 1940s when many magnetic moments were determined by Bloch, Proctor, and Yu. In this section, we emphasize the historical developments related to chemical applications and in most instances do not report the initial measurements of magnetic moments.

The problems associated with heteronuclear NMR generally arise from (i) low signal-to-noise ratios due to small magnetic moment and/or low natural abundance, (ii) large linewidths for quadrupolar nuclides, or (iii) long relaxation times. The solubility of compounds in appropriate solvents also presented initial difficulties in many compounds for high-resolution studies. However, the favorable factor, which was well recognized, is the large chemical shift range for many nuclides, which demanded much less effort to resolve spectral lines.

Low natural abundance could sometimes be compensated by artificial isotopic enrichment of the samples, and in some instances (notably ^{13}C) could be advantageous since homonuclear coupling constants are usually not observed, resulting in spectral simplification.

Although quadrupolar nuclides have always been at a disadvantage as compared with those of spin $\frac{1}{2}$, it was found that the problems were often less severe than might be anticipated. Some nuclei (e.g., ^{2}H, ^{6}Li, ^{11}B, and ^{51}V) have

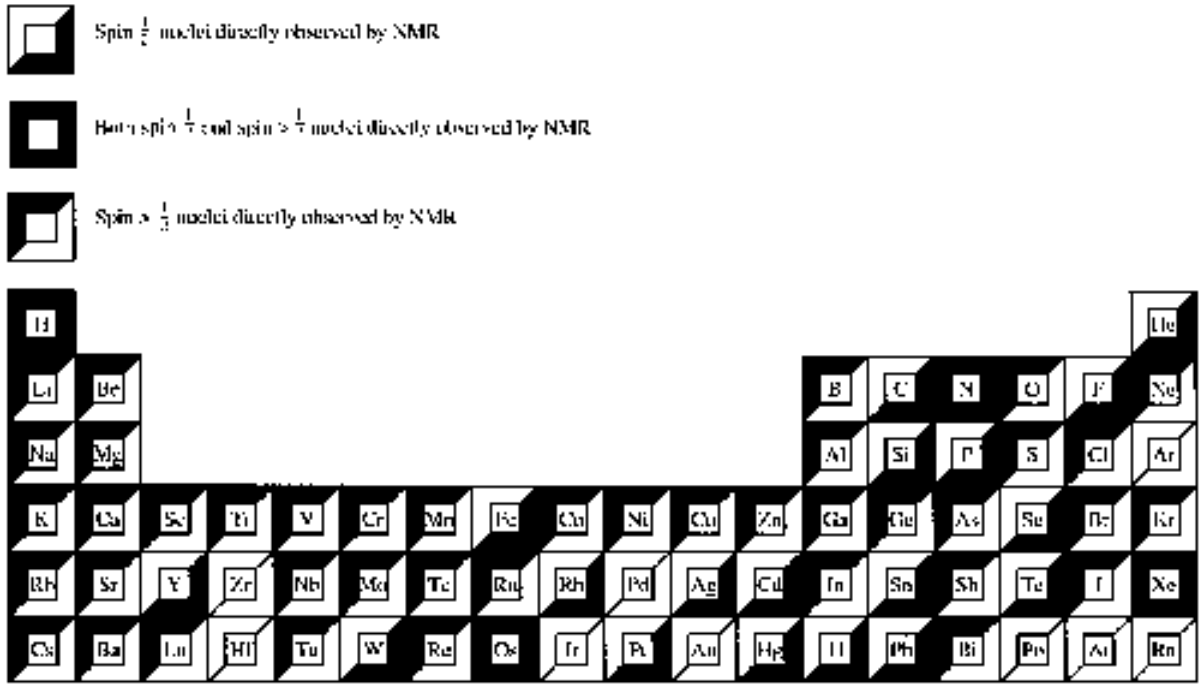

Figure 60 Periodic Table of the Elements, showing nuclides that have been observed directly by NMR. Adapted from Harris and Mann.[370] (Courtesy of R.K. Harris)

relatively small quadrupole moments, and others with large moments can often provide useful information in chemical species in which the electric field gradient is small (e.g., ions).

The development of 'shiftless' relaxation agents, such as chromium acetylacetonate [$Cr(acac)_3$], which shorten relaxation times without significantly altering chemical shifts, provided a valuable means to shorten the relaxation time of such nuclei as ^{15}N, ^{29}Si, and ^{57}Fe, and hence to facilitate their study.

Nitrogen-14 and Nitrogen-15

As pointed out in Section 2, ^{14}N was the nucleus which led to one of the first discoveries of the chemical shift by Proctor and Yu[44] in 1950. During the next few years, chemical shifts in a large number of compounds were determined by Masuda and Kanda[371] and Holder and Klein.[372] They established general correlations with molecular structure and found that nitrogen shifts in nitrates, nitrites, and ammonium ions were concentration- and pH-dependent. In 1957, Ogg and Ray[373] reported that the ^{14}N spectrum of ammonia consisted of a broad signal as compared with that in the NH_4^+ ion, and thus demonstrated the role of charge asymmetry about this quadrupolar nucleus in determining relaxation times.

A range of about 1000 ppm has been observed for ^{14}N chemical shifts, but for a given class of compounds the range is often only 10–50 ppm. Nevertheless, for molecules with relatively narrow lines, useful structural information can be obtained as pointed out by Michal Witanowski in his historical sketch (***Witanowski, Michal: A Short Story about Nitrogen NMR***). Because of the sensitivity of ^{14}N chemical shifts to structural changes, ^{14}N NMR has been extensively employed in organic and inorganic compounds, as well as in metal complexes. ^{14}N NMR parameters are diagnostic of coordination, chelation, protonation, conformation, stereochemistry, and solution equilibria and other dynamic processes such as ligand exchange, intramolecular motions, and tautomerism. The book edited by Webb and Witanowski,[374] as well as review articles,[375] attest to the popularity and value of such studies.

Although ^{14}N lines are often sufficiently narrow for the determination of chemical shifts, there is usually little information on scalar couplings, especially through more than one bond. Moreover, many compounds have lines that are too broad even for the determination of chemical shifts. The ^{15}N nucleus is an ideal complement to ^{14}N, but its low natural abundance (0.365%) and small magnetic moment, together with a long T_1, combined to deter study of this isotope. The first direct observation of ^{15}N NMR at natural abundance occurred as late as 1964 by Ray,[376] but for many years the only useful studies in chemistry were made with enriched materials. Even observing highly enriched ^{15}N NMR was a real feat at 6 MHz with the spectrometers of the period, so indirect detection via INDOR or other double resonance methods often found favor, especially for studying ^{15}N compounds at low concentration as in investigations of hydrogen bonding,[377] since ^{1}H sensitivity is 1000 times that of ^{15}N.

Direct observations were carried out, however. Joe Lambert's historical sketch (***Lambert, Joseph B.: The First Observation of Nitrogen-15 Nuclear Magnetic Resonances***) describes his work in J. D. Roberts's laboratory at Caltech in finding a resonance in 96% enriched nitric acid during the summer of 1963. By sequential synthesis of several labeled molecules, Lambert, Binsch, and Roberts were able to stretch their ^{15}N supply and report the spectra of a number of organic molecules.[378] Further efforts yielded data on one-bond ^{15}N–H coupling constants and their correlation with molecular structure, the first measurement of a ^{15}N-^{15}N coupling constant,[379] and a great deal of other information on the use of ^{15}N in

organic chemistry. Many other studies in a number of laboratories followed, and as FT and double resonance methods were introduced, the more routine study of ^{15}N, even at natural abundance, became feasible. The negative NOE arising from the negative magnetogyric ratio of ^{15}N was not expected by early workers and caused considerable confusion, resulting in the necessity of studying relaxation processes in detail. 'Shiftless' relaxation reagents have been employed to facilitate the observation of ^{15}N NMR. The ^{15}N chemical shifts of up to 1400 compounds and spin–spin couplings (^{15}N-X) for about 1200 structures were reported in 1981 by Martin, Martin, and Gouesnard.[380] During the 1990's, as we shall see in Section 14, many investigations of biopolymers have made use of ^{15}N chemical shifts, but with a return to indirect, rather than direct, detection via two- and three-dimensional NMR methods.

High-resolution ^{15}N NMR spectra in the solid state have become useful in studying biologically important nitrogen linkages, including hydrogen bonding. The full range of NMR methods is increasingly being employed in the study of natural products, usually with biosynthetic ^{15}N enrichment. Stejskal and Schaefer have used double cross polarization, the transfer of proton magnetization to either ^{15}N or ^{13}C, then from one to the other, to study protein turnover in soybean leaves grown with $^{15}NH_4{}^{15}NO_3$ and $^{13}CO_2$[381] and they have used CP MAS to investigate nitrate metabolism.[382] Cross, DiVerdi, and Opella[383] have outlined strategies for biopolymers and applied them to bacterial and viral DNA to show hydrogen bonding and neighbor effects within and between strands. Dilute ^{15}N spin exchange (NOESY) techniques were used by Cross, Frey, and Opella in 1983 to locate ^{15}N sites in α-helical bacteriophage coat proteins.[384] Several applications of ^{15}N NMR in inorganic chemistry have also been made using high-resolution solid state NMR techniques, including studies of nitrogen complexes and adsorption. CP MAS ^{15}N spectra for pyridine and ammonia on γ-alumina and mordenites have been investigated by Ripmeester,[385] Maciel,[386] Ellis[387] and their co-workers.

Silicon-29

Lauterbur and his co-workers[388] observed ^{29}Si resonances at the natural abundance of 4.7% as early as 1956, and in 1962 Baker[247] used INDOR to improve the signal-to-noise ratio in the ^{29}Si spectrum of a 20 mol % solution of tetramethylsilane (Figure 61). However, the generally low receptivity (about twice that of ^{13}C) precluded any significant studies until modern instrumentation became available. Even then, the negative magnetogyric ratio and relatively long T_1 presented experimental problems. The early studies established the overall chemical shift range, demonstrated some ^{29}Si-^{19}F coupling constants of 200–300 Hz, and showed significant line broadening for silicon directly bonded to quadrupolar nuclei such as nitrogen and the halogens.

In the 1970s ^{29}Si studies underwent a renaissance, as a number of groups applied FT techniques in studying a variety of substances. For example, Robin Harris and co-workers found that the wide chemical shift range for ^{29}Si made it invaluable for examining silicones[389] and silicates, but the absence of homonuclear spin coupling at natural abundance of 5% limited interpretation. They decided to use enriched samples and obtained the first such spectra. As Harris says in his historical sketch (***Harris, Robin K.: Chemical Magnetic Resonance goes Multinuclear***):

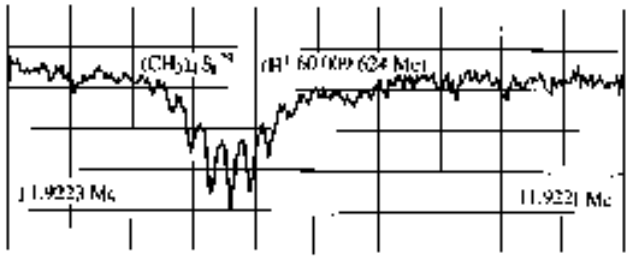

Figure 61 INDOR spectrum of ^{29}Si in tetramethylsilane observed by 60 MHz ^1H NMR.[247] (Reproduced by permission of the American Institute of Physics)

> At one point, I believe we purchased the total supply (at least in the UK) of ^{29}Si-enriched silica—which is one way to stymie any competition! Soon we progressed to the first very high field ^{29}Si spectra (Bruker WM-500 ...). With the ^{29}Si enrichment, coupling became important and, in his Ph.D. with me, Chris Knight used both first-order and second-order spectra to yield the first unequivocal structural determination of many species present in the (potassium silicate) solutions.

Günter Engelhardt's historical sketch (***Engelhardt, Günter: Silicon-29 NMR of Silicates: From Liquids to Solids. An Historical Perspective***) describes other approaches in his laboratory and elsewhere to the study of silicates in solution and the progression to the study of solids as CP MAS methods were developed. Engelhardt collaborated closely in this work with Endel Lippmaa and his colleagues in Tallinn, Estonia where they had developed excellent methods for the study of solid ^{13}C, concurrently with the more widely known work in western countries. In spite of initial difficulties in applying the techniques to ^{29}Si, by 1977 they had successfully measured the first highly resolved ^{29}Si CP MAS spectra of solid silicates and organosilicon compounds.[390] Excited by these results, Jacek Klinowski began a long series of fruitful studies of ^{29}Si (and later ^{27}Al) in zeolites. In ***Klinowski, Jacek: Historical Sketch: Molecular Sieves***, Klinowski points out:

> MAS NMR opened a completely new layer of insight into the structure of molecular sieves, and for several months one could simply take a sample off the shelf to obtain results which were novel, fascinating and important.

Tritium

As we saw in Section 2, tritium was of considerable interest to Felix Bloch in his early efforts to pin down precise values of the magnetic moments of the three isotopes of hydrogen and of the neutron. The magnetic moment of tritium was determined in 1947, independently by Anderson and Novick[391] and Bloch et al.[26,392]

The first high-resolution NMR study of tritium was reported by George Tiers and co-workers[393] in 1964. They studied neat ethylbenzene containing 1 atom % tritium. The experiments were performed on an HR-40 spectrometer. The spectrum consisted of two first-order multiplets corresponding to CH_2T and CHT, from which values of the two- and three-bond ^3H-^1H couplings and the tritium chemical shifts could be

easily determined. In 1971, Elvidge et al.[394] began continuing development of ^{3}H NMR and reported the spectra of several compounds. ^{3}H NMR has been used for the assignment of complex proton spectra, obtained before the advent of high magnetic fields, in such compounds as phenanthridine, pyrrole, benzamides, toluene, and fatty acids. Tritium NMR has also been employed in a number of biomolecular and reaction mechanism studies, and Newmark et al. used ^{3}H NMR to study the pentose pathway in erythrocytes, a living cellular system.[395]

By the standards of radioactive tracers, a very large amount of tritium is required for NMR study, but the weak β-radiation is blocked by the wall of the NMR sample tube. Nevertheless, suitable precautions are required to avoid the fracture of sample tubes or the excessive build-up of pressure from formation of tritium gas from radiolysis. A special Biotechnology Resource for studying tritium NMR under conditions that minimize potential hazards was established by the National Institutes of Health at the State University of New York in Stony Brook in the early 1980s and relocated to the University of California in Berkeley about 1985.

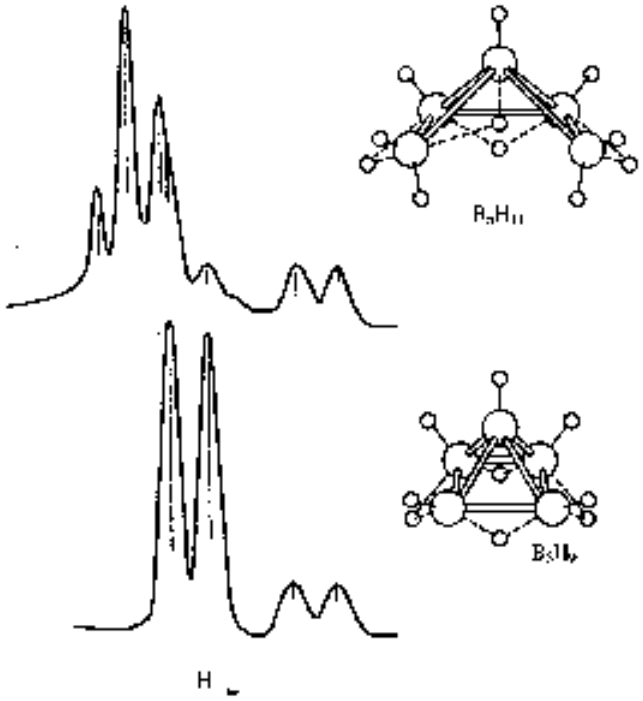

Figure 62 ^{11}B NMR spectra at 12.8 MHz of two pentaboranes.[407] (Reproduced by permission of the American Institute of Physics)

Oxygen-17

Natural abundance ^{17}O was first observed by Alder and Yu[396] as early as 1951, but it took several years until Weaver, Tolbert, and La Force studied a variety of compounds to investigate ^{17}O chemical shifts.[397] With slow passage and dispersion mode, a signal-to-noise ratio of 50 was obtained for H_2O (natural abundance). A chemical shift range of about 700 ppm was observed, with water appearing at the highest field. A few years later, Dharmatti et al.,[398] Christ and co-workers,[399,400] and Figgis et al.[401] showed that useful information on organic and inorganic molecules could be derived from ^{17}O NMR data obtained on wide-line spectrometers with large-bore sample tubes.

With more modern instrumentation, a number of workers have shown that the chemical shift range is over 1200 ppm and have established several correlations of the ^{17}O chemical shifts with structural parameters in molecules. Important among these are correlations with mean excitation energy, π-bond order, and the chemical shifts of nuclei such as carbon and nitrogen. A correlation of the ^{17}O chemical shift with the number of metal atoms coordinated to it has been observed.

^{17}O NMR linewidths have been observed to range from 0.5 Hz to 9000 Hz, with typical values on the order of 100 Hz. Thus it has been possible to measure many spin–spin coupling constants, even with other quadrupolar nuclei. The one-bond H–^{17}O coupling constant is typically 100 Hz and has been measured as 106 Hz in H_3O^+.[402,403]

Many investigators have taken advantage of the significant chemical shift range and linewidth variation to use ^{17}O NMR for structural studies, including estimates of bond polarization, hydrogen bonding, kinetics of oxygen exchange, water orientation in lyotropic phases, and ionic solvation. ^{17}O NMR has also been employed to investigate the structure of biologically relevant medium-sized molecules such as amino acids, small peptides, monosaccharides, polyphosphates, and nucleosides. Eric Oldfield's historical sketch (***Oldfield, Eric: NMR Adventures in Chemistry and Biology***) summarizes his ^{17}O magic angle spinning studies in a variety of solids, including zeolites, heme proteins, and high-temperature superconductors.

Boron-10 and Boron-11

Boron, with two NMR active isotopes, was among the first elements to attract the attention of NMR spectroscopists in the 1950s. Both nuclides have weak quadrupole moments, but ^{11}B is more often studied due to its better sensitivity and greater natural abundance, even though the spectral lines are usually sharper for ^{10}B than for ^{11}B.

The first ^{11}B spectra, obtained by Ogg[404] in 1954, were of $NaBH_4$ (in aqueous solution) and liquid diborane. The spectrum of sodium borohydride showed a five-line pattern with the intensity ratio of 1 : 4 : 6 : 4 : 1 with a ^{11}B-^{1}H coupling of 82 Hz, which established the equivalence of the four protons, while for diborane the spectrum confirmed the bridge structure. At that time the structures of a number of boranes were in question, and the type of bonding in boranes (with nonclassical bridging hydrogens) was a topic of intense interest to both theoreticians and experimentalists. During the next few years, Shoolery et al.,[405,406] Williams et al.,[407] and others established the structures of several boranes using ^{11}B, as well as ^{1}H NMR. For example, Figure 62 shows the ^{11}B spectra at 12.8 MHz of two different pentaboranes, stable B_5H_9 and unstable B_5H_{11}. The success of NMR in elucidating the structures of the boranes provided an early demonstration of the value of the new method in chemistry and helped establish its credibility even before the wave of organic structure elucidations that would soon follow.

Subsequent investigations by a number of research groups have established a chemical shift range for boron of about

220 ppm, with distinctly different ranges for trigonal and tetrahedral boron. Well over 3000 trigonal and tetrahedral boron compounds have now been examined by ^{11}B NMR. One-bond ^{11}B–X coupling constants ranging from 1–5 Hz in BF_4^- up to more than 1 kHz for X = ^{119}Sn or ^{207}Pb have been observed. ^{11}B NMR has been a valuable tool in elucidating the structure and bonding in polyhedral boranes and carboranes.

The Noble Gases

Because of their simplicity and symmetry, the noble gases have found particular use in the development and testing of various theories, and as probes of environmental perturbations. ^{3}He and ^{129}Xe are spin-$\frac{1}{2}$ nuclei, while ^{131}Xe has a quadrupole moment as do ^{21}Ne and ^{83}Kr. Argon has no magnetically active stable isotope.

In Section 4, we mentioned the work by Streever and Carr[163] in measuring T_1 in ^{129}Xe as a function of temperature in the liquid state and as a function of pressure in the gaseous state, and in discovering a strong density-dependent shift in the resonance frequency. Torrey[408] pointed out a connection, given by Ramsey's theory of chemical shifts, between the chemical shift and the spin–rotational coupling constant in ^{129}Xe, a generalization that has been used subsequently in the analysis of other relaxation data. The sensitivity of the chemical shift has been exploited by using ^{129}Xe as a probe of microporous solids. For example, J. Fraissard's historical sketch (***Fraissard, J.: A Look at Solid Catalysts by NMR***) describes the analysis of chemical shift variations to determine the dimensions and form of the internal free volumes of zeolites, to examine structural defects and short-range crystallinity, and to obtain a great deal of useful information on dynamic processes. In Section 15, we shall describe further examples in the study of materials.

In 1963, shortly after the discovery of covalent xenon compounds,[409] Brown, Whipple, and Verdier[410] reported an indirect NMR study of $XeOF_5$, XeF_4, and XeF_2 through ^{19}F observation. The first direct measurement of the ^{129}Xe chemical shift in such compounds was made by Seppelt and Rupp[411,412] in 1974, and new chemical shift data for a wide range of oxidation states of Xe were subsequently obtained by Schrobilgen et al.[413] Chemical shifts range over 7500 ppm and coupling constants, particularly with ^{19}F, have been observed from 100 Hz up to more than 7500 Hz. The parameters are very sensitive to solvent, temperature, and concentration. This has been attributed to the oxidation state of Xe, the ionic character of the Xe–X bond, and solvent interactions.

Helium has played an important role in the development of various theories and concepts in physics because of its unique properties, and ^{3}He has likewise found favor for certain physical studies. ^{3}He has a sensitivity which is 40 % of that of ^{1}H but a natural abundance of only 0.01 %. Much of the work involves the solid and superfluid states. In 1956, Walters and Fairbank[414,415] used ^{3}He NMR to study the phase diagram for ^{3}He-^{4}He solutions at 0.8 K and to examine the pressure-dependence of the density and magnetic susceptibility of ^{3}He below 1 K. Later, Bernier and co-workers[416,417] developed pulse methods to measure the nuclear magnetic susceptibility in solid ^{3}He. More recently, Friedman, Millet, and Richardson[418] discovered that liquid ^{3}He at 10 mK provided efficient relaxation of ^{19}F spins on the surface of Teflon microspheres, and Waugh and co-workers[419] used this phenomenon to explore spin diffusion in single-crystal CaF_2 at very low temperatures.

Recent work by Diehl and co-workers[420] has focused on environmental perturbations in the chemical shift of ^{3}He, dissolved in solids such as Pyrex or Suprasil glasses and in liquid crystals, while Saunders, Anet, and co-workers[421] used ^{3}He to probe the interior of fullerenes. The chemical shift of ^{3}He was interpreted in terms of ring currents in C_{60} and C_{70}.

NMR work on ^{21}Ne and ^{83}Kr has largely been confined to physics problems related to nonspecific intermolecular interactions. Relaxation times and medium shifts have been used to study intermolecular interactions between these atoms from the dilute gas all the way to the pure liquid and solid phases.

Iron-57, Cobalt-59, and Nickel-61

These three elements, which have many chemical similarities, are very different in their NMR properties. The only naturally occurring isotope of cobalt is ^{59}Co. It is less sensitive than protons only by a factor of about three, thus putting it among the top six nuclear species in terms of ease of detection. However, it has a spin of $\frac{7}{2}$ and a large quadrupole moment, and its range of chemical shifts of about 18 000 ppm is among the largest known. Most NMR data come from hexacoordinated Co(III), which is diamagnetic.

The ^{59}Co nucleus occupies a unique position in the history of NMR. In 1951, Proctor and Yu[422] discovered that the resonance frequency of ^{59}Co may vary by as much as 1%, depending upon the compound investigated. Hence, in spite of broad lines (several kHz for asymmetric coordination), it was feasible to acquire a significant amount of chemical shift data for ^{59}Co during the early days of NMR.

The first systematic ^{59}Co chemical shift studies were reported in 1957 by Rex Richards and co-workers,[423] who rationalized the chemical shifts in terms of the paramagnetic term in Ramsey's shielding equation, an important early test of this theory. Cobalt shieldings were found to be relatively insensitive to concentration but to vary up to about 200 ppm in different organic solvents. The shieldings in the solid and solution were found to be the same within the experimental error of about 200 ppm. The ^{59}Co shieldings exhibit a linear dependence on temperature of about 1–3 ppm per degree, a feature that was later exploited by George Levy and co-workers in their estimation of the temperature of NMR samples.[424]

Increasing pressure has been found to cause an increase in cobalt shielding,[425] while shieldings have also been used as a sensitive measure of stereochemistry. Gasser and Richards[426] studied the rate of exchange between ethylenediamine and hexammine cobalt(III) ion in the late 1950s. Subsequently, ^{59}Co NMR has also been employed to study the binding of anions and cations in the second coordination sphere of cobalt(III) complexes. Martin and Fung[427] and Craighead, Jones, and Bryant[428] have examined the rather strong binding of phosphate to cations such as $Co(en)_3^{3+}$.

Although an extensive literature dealing with cobalt chemical shifts in a variety of Co(III) complexes is available, very few instances of spin–spin couplings involving ^{59}Co have been observed, partially because many ^{59}Co lines are

very broad. Linewidths span the range from 175 Hz for $[Co(CN)_6]^{3-}$ to 40 kHz for $HgCo_2(CO)_8$. In $[CO(CN)_6]^{3-}$, a $^{59}Co-^{13}C$ coupling constant of 126 Hz was obtained by Traficante and Simms[429] from the satellite peaks in the ^{59}Co spectrum, while a value of 287 Hz for the $^{59}Co-^{13}C$ coupling constant in $Na[Co(CO)_4]$ was obtained by Lucken et al.[430] Possible relaxation mechanisms contributing to ^{59}Co NMR linewidths have been considered by Yamasaki et al.[431] and Ader and Loewenstein.[432]

In contrast to ^{59}Co, ^{57}Fe (the only NMR-active isotope of iron) has a natural abundance of only 2% and a very small magnetic moment, leading to very low receptivity. With a spin of $\frac{1}{2}$, it has been found to have generally long relaxation times in diamagnetic compounds. These factors combined to prevent any significant application of ^{57}Fe NMR until the advent of more sensitive and versatile instruments.

The first ^{57}Fe NMR signal in a diamagnetic compound, $Fe(CO)_5$, was obtained by Schwenk[433] in 1970 using the pulse technique of Kaufmann and Schwenk.[434] A signal-to-noise ratio of 30 was achieved in a measuring time of 2 h. In order to improve the performance, Schwenk[435] developed a variant of this pulse scheme, *Quadriga Fourier Transform*, using four measurements with different frequencies of the applied rf pulses, and obtained from $Fe(CO)_5$ a ^{57}Fe resonance with a signal-to-noise ratio of 100 by applying over 6 million pulses in 20 h. In a subsequent study, two NMR spectrometers were combined by Sahm and Schwenk,[436] and a special probe assembly was constructed in order to enable simultaneous measurement of signals of ^{2}H and a nucleus such as ^{57}Fe with a small magnetic moment.

Haslinger et al.[437] studied the ^{57}Fe NMR spectra of 20 ferrocene derivatives at natural abundance by conventional FT techniques, and Jenny and von Philipsborn[438] examined the spectra of 35 organo–iron complexes, predominantly of the type $[Fe(CO)_3(diene)]$, and obtained a chemical shift range of 3000 ppm. The ^{57}Fe shieldings were discussed in terms of charge distribution in the complexes. In 1984, Baltzer et al.[439] reported a much larger chemical shift range in porphyrins and some coordination compounds. They also studied the magnetic field dependence of T_1, and concluded that chemical shielding anisotropy provides the principal mechanism for relaxation at superconducting fields.

Mann[440] found that the one-bond coupling constants of ^{57}Fe to ^{13}C and ^{31}P in iron pentacarbonyl and in iron phosphine carbonyls span the range of ca. 23–32 Hz, whereas in ferrocene compounds they are much smaller (2–7 Hz). A value of about 8 Hz for the one-bond $^{57}Fe-^{15}N$ coupling has been obtained by Morishima et al.[441]

In 1985, two groups reported almost simultaneously the first studies of ^{57}Fe NMR in a protein, carbonmonoxymyoglobin. Both Oldfield and co-workers[442] and Baltzer et al.[443] used enriched samples and unusual spectrometer arrangements, in which the sample tube was transverse to the axis of the superconducting solenoid, in order to take advantage of the higher sensitivity of a solenoidal, rather than a saddle-shaped receiver coil. Even then a long scan was required, as illustrated in Figure 63. Both groups reported relaxation times, from which they deduced values of the chemical shielding anisotropy.

The only magnetically active isotope of nickel is ^{61}Ni, with a natural abundance of 1.19%, a sensitivity only 0.4% as great as ^{1}H, and a nuclear spin of $\frac{3}{2}$. These unfavorable

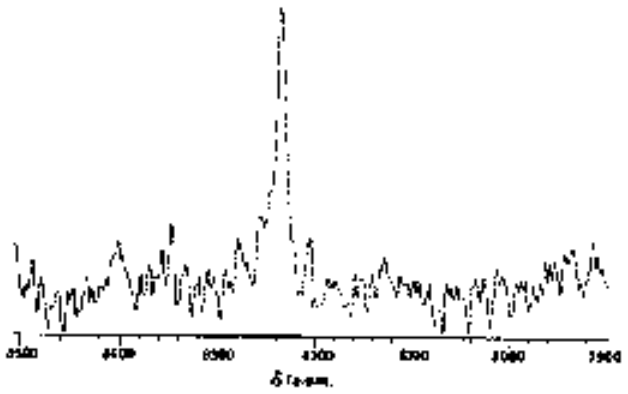

Figure 63 The 16.3 MHz ^{57}Fe NMR spectrum of carbon monoxymyoglobin, enriched to 90% in ^{57}Fe, 1 mL sample, 10 mM. Total experimental time: 10 h[443]

factors are responsible for the fact that ^{61}Ni has received very little attention. After the first report on ^{61}Ni NMR in $Ni(CO)_4$ by Drain[444] in 1964, over 15 years elapsed before Schumann et al.[445] and Hao et al.[446] studied a number of nickel complexes in order to establish the ranges of chemical shifts, coupling constants, relaxation times, and linewidths. In the cases investigated, the chemical shift range was about 1000 ppm, linewidths ranged from 4–90 Hz, one-bond $^{61}Ni-^{31}P$ couplings were found to lie between 398 Hz and 482 Hz, and a two-bond $^{61}Ni-^{19}F$ coupling constant was determined as 28 Hz.

Alkali and Alkaline Earth Nuclei

All these nuclei possess quadrupole moments, but that of ^{6}Li is extremely small, as we discuss later. Except for some compounds of lithium, beryllium, and magnesium, these elements are generally found in ionic form, so quadrupole coupling constants are often sufficiently small to give lines of only moderate width. For ^{7}Li, linewidths of less than 1 Hz (compared with typical linewidths of about 150 Hz for ^{85}Rb and ^{87}Rb) were observed by Hartwell and Allerhand.[447]

The first report on NMR shifts in alkali metal ions was made by Gutowsky and McGarvey[448] in the solid state as early as 1953. This was, in fact, the first publication on shifts in compounds for which the binding is ionic. The shifts of ^{87}Rb and ^{133}Cs in the halides were measured with reference to saturated aqueous solutions of the respective chlorides. The sample and reference were placed in adjacent coils in two separate rf bridge systems. The narrow resonance of the reference was displayed on an oscilloscope, while the broad resonance from the solid halide was detected with a narrow-band amplifier.

In 1956, Wertz and Jardetzky[449] carried out the first investigation of ^{23}Na in aqueous solution. They were unable to observe any change in chemical shift with various anions, but found considerable variation in the linewidths. They attributed the broadening to quadrupolar interactions that reflected departures from the effectively spherical symmetry of charge distribution around the sodium nucleus, such as would occur in ion pair or complex formation. This work established the basic pattern for further observations of alkali

and alkaline earth nuclei in aqueous solution, in which the useful information comes primarily from the linewidth changes that accompany alterations in the quadrupole coupling constant rather than from chemical shift variations. However, the large chemical shift range in cesium (about 120 ppm) has been exploited in many studies.

Aqueous Na^+ interactions with salts of organic acids have been investigated since the 1950s, as have interactions with sugars and with esters of phosphoric acid. ^{7}Li interactions with DNA bases and nucleosides in DMSO have been studied by Plaush and Sharp.[450] Alkali ion NMR has developed into a powerful tool for studies of alkali ion coupling with ionophores. It has been employed extensively in the study of the thermodynamic stability, dynamics, and kinetics of such complexes.

A large number of nonaqueous solutions have also been investigated. The first systematic study on the applicability of alkali ion NMR in nonaqueous environments was conducted in 1966 by Maciel et al.,[451] who determined the ^{7}Li chemical shifts of LiBr and $LiClO_4$ in 11 simple organic solvents and discussed the origin of the chemical shift differences. The work of Bloor and Kidd (1968) on NaI in several organic solvents stimulated keen interest in using ^{23}Na NMR in nonaqueous systems.[452] The ^{39}K chemical shifts of KI in ethylenediamine and of KOH in CH_3OH were studied by Sahm and Schwenk,[453] and later by Shih and Popov,[454] who presented an extensive report on the concentration and counterion dependence. Halliday et al.[455,456] have made extensive studies on ^{133}Cs chemical shifts.

^{6}Li has such a small quadrupole moment that it behaves more like a spin-$\frac{1}{2}$ nucleus, and it should afford narrow lines irrespective of the symmetry of the field gradient at the site of the nucleus. Surprisingly, ^{6}Li high-resolution NMR in solution was first observed as late as 1976 by Felix Wehrli,[457] who describes the experiment in his historical sketch (***Wehrli, Felix W.: From Carbon-13 to Quadrupolar Nuclei NMR and Medical Imaging --Reflections***)

> Upon dialing the frequency of ^{6}Li, to my delight a signal crept across the oscilloscope. However, I was unable to reproduce the finding and aborted the experiment after a while. The elusive signal reappeared in a second attempt several hours later, at which time I became certain that the observation was real. The culprit for the apparent irreproducibility, of course, was the exceedingly long T_1. ... In D_2O, T_1 was found to rise up to 17 min at 80°C!

Organic compounds involving covalent lithium–metal bonding, such as C–Li in alkyllithium compounds, were subjected to investigations beginning in the early 1960s.[458,459] The studies provided valuable information on the structure and dynamic properties of these compounds, primarily through observations of spin–spin coupling. For example, methyllithium was found to be a tetramer based on a tetrahedral arrangement of lithium atoms, with the carbons placed symmetrically above each face of the tetrahedron and bonded to all three adjacent lithium atoms.[460]

From the NMR standpoint, the situation for the alkaline earth nuclei is not as bright as that of the alkali metals. The only nucleus with reasonable sensitivity is ^{9}Be. Barium has two NMR-sensitive isotopes, both with large quadrupole moments and extremely large quadrupole relaxation broadening. The relaxation times of ^{25}Mg and ^{43}Ca ions, as observed by Lindman et al.[461] in 1977, are reasonable (0.15 s for free Mg^{2+} and 1.3 s for Ca^{2+}) but the sensitivities of both nuclei are extremely low. Since these factors put more stringent demands on spectrometer sensitivity, even high-precision measurement of the magnetic moments in these nuclides had to wait until the 1970s when they were made by the Tübingen group of Otto Lutz (^{43}Ca and ^{87}Sr in 1973,[462,463] ^{25}Mg in 1975,[464] and ^{135}Ba and ^{137}Ba in 1977–78[465,466]).

Like the alkali ions, the chemical shift range in the alkaline earth ions increases with atomic number, and the solvent dependence of chemical shifts is also similar to that of the alkalis. Again, linewidth changes on complexation of alkaline earth nuclei have provided the most useful information for metal ion–ligand interactions. Tetrahedral solvates of the beryllium cation with trimethyl phosphate and other ligands have been examined by Delpuech et al.,[467] and the kinetics of the exchange studied from the lineshape analysis of the temperature-dependent ^{9}Be spectra. Bryant[468] derived exchange rates for adenosine triphosphate (ATP) binding to Mg^{2+} from the temperature dependence of the ^{25}Mg linewidth in the presence of excess magnesium chloride. A linear dependence of the ^{43}Ca relaxation time in aqueous Ca^{2+}-ATP solutions has been interpreted in terms of exchange between free and bound calcium ions,[469] the Ca^{2+} binding being with the phosphate portion of the ATP molecule.

Organometallic compounds of beryllium and magnesium have been investigated with the help of ^{9}Be and ^{25}Mg NMR studies. Kovar and Morgan[470] studied a wide range of organoberyllium compounds and reported chemical shifts, linewidths, and spin–spin coupling constants. The beryllium coordination number was found to have a great effect on the chemical shift as well as the linewidth. The chemical shift is higher and the linewidth is much larger (over an order of magnitude) for three-coordinate than for four-coordinate beryllium. Spin–spin couplings of ^{9}Be with ^{19}F and ^{31}P were observed. In the BeF_4^{2-} ion, J_{Be-F} was found to be 34 Hz and in tetrahedral organophosphorus complexes a two-bond Be–P coupling of 4–6 Hz was observed by Delpuech et al.[467] The small values were attributed to the strongly ionic character of the beryllium compounds. Wehrli[471] employed a combined ^{9}Be and ^{13}C relaxation experiment to determine the ^{9}Be quadrupole coupling constant in bis(acetylacetonato)beryllium.

Solid state NMR studies of the alkaline earths are much older than chemical applications. They started as early as 1953 with Knight shift studies[472] in beryllium and are essentially restricted to Knight shifts, relaxation times, and quadrupole coupling constants. ^{87}Sr NMR was used by Weber and Allen[473] in 1963 to study phase transitions in $SrTiO_3$.

The Halogens

Unlike ^{19}F, which has a spin of $\frac{1}{2}$, the other halogens have large quadrupole moments whose presence has virtually precluded high-resolution studies of their resonances in covalent compounds. Most investigations have concentrated on halide anions or other highly symmetric ions such as perchlorate, with information coming primarily from linewidths or T_1 measurements. Sensitivities and natural abundances for several isotopes of chlorine, bromine, and iodine are reasonably satisfactory so as to enable studies in concentration ranges appropriate both to chemical and biological problems.

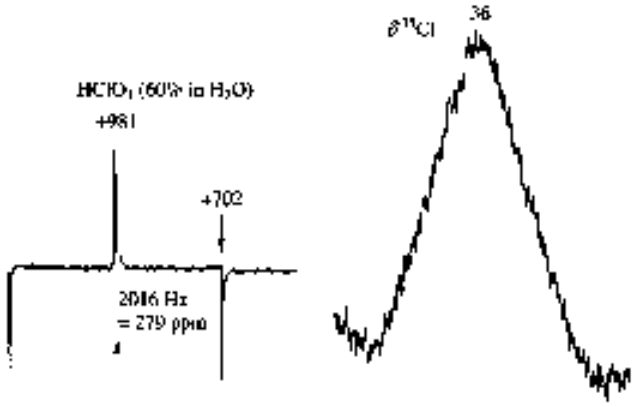

Figure 64 The 7.23 MHz ^{35}Cl spectrum of chlorodimethylsilane in pentane. This continuous wave spectrum used a substitution of a perchloric acid sample during the scan for external referencing, with a 2016 Hz modulation sideband for calibration

^{35}Cl and ^{37}Cl chemical shifts in concentrated hydrochloric acid, barium perchlorate, and perchloric acid were first measured by Proctor and Yu[422] as early as 1951. For both isotopes, they observed that the resonances in perchloric acid were displaced to lower fields by about 900 ppm relative to the resonances in hydrochloric acid. Subsequently, chemical shift measurements of ^{35}Cl, ^{81}Br, and ^{127}I in aqueous solutions of HCl, HBr, and HI were carried out by Masuda and Kanda[474] in 1954. The signals were found to shift to lower fields with increasing concentration due to the presence of undissociated species or some kind of ion pairs.

The use of ^{127}I NMR to investigate the kinetics of the triiodide equilibrium was demonstrated by Myers[475] in 1958. Changes in the linewidth were employed to compute the rate constants of the reaction. Thus, in the 1950s the stage was set for the use of halide ion NMR to obtain a detailed insight into a number of structural and dynamic features of electrolyte solutions, such as solvation, preferential solvation in mixed solvents, and ion–ion distribution in ion pairing. Major contributions to this field of research have been made by H.G. Hertz and co-workers who have performed both experimental and theoretical investigations for over 20 years.

A major application of halogen NMR involves the study of solutions of amphiphiles, proteins, and polyelectrolytes, where quadrupole relaxation is very sensitive to ionic interactions. Halogen quadrupole relaxation has become a standard method for the study of anion binding to proteins.

In covalent compounds, on the other hand, ^{35}Cl linewidths are so great that only low precision can be obtained in the experimental determination of chemical shifts, and the situation is virtually hopeless for bromo and iodo compounds. Bernd Wrackmeyer in his sketch (***Wrackmeyer, Bernd: A Personal Retrospect of Multinuclear Magnetic Resonance in Liquids***) provides an example, reproduced in Figure 64, which contrasts the sharp line from the tetrahedral ClO_4^- ion with that in a less symmetric compound, which has a linewidth of more than 2 kHz. Although improved techniques and much higher magnetic fields have alleviated the problems seen in this early CW study, only few data are available for covalently bound ^{35}Cl. The reported values indicate a range of about 1000 ppm.

Some Heavy Metal Nuclides

^{203}Tl and ^{205}Tl are among the most sensitive NMR nuclides and were investigated quite early. Because of its 70 % isotopic abundance, ^{205}Tl has been commonly selected for study. By 1953, both solid- and liquid-state spectra for thallium had been obtained by Bloembergen and Rowland,[476] and by Gutowsky and McGarvey,[477] respectively. The chemical shift range is about 7000 ppm for Tl(III) and 3400 ppm for Tl(I) compounds, a factor that has made ^{205}Tl NMR useful in many studies, including those in which Tl^+ can be substituted for an alkali cation in studies of ion transport across membranes, and activation and regulation of enzymes. For solid state studies, CP MAS and related techniques have been employed.

^{195}Pt is one of the easiest heavy nuclei to observe by NMR and was initially studied by Proctor and Yu,[422] who measured the magnetic moment with a 1.0 M solution of H_2PtCl_6. However, little work was done until the late 1960s when Pidcock, Richards, and Venanzi[478] and Zelewsky[479] studied several Pt(II) and Pt(IV) complexes, and demonstrated the use of ^{195}Pt NMR for the study of bonding characteristics in platinum complexes. The chemical shift range is about 15 000 ppm. Spectra of chloro–bromo complexes of Pt(IV) were used to estimate the relative stabilities of the complexes, and the applicability in the determination of equilibrium constants of platinum compounds was pointed out.

Although the potential was fully realized from these studies, interest in widespread applications did not pick up until the 1970s when FT methods permitted study of small amounts of expensive platinum compounds. ^{195}Pt coupling constants have been found to be of great interest in structural studies. Values reaching 30 kHz were observed by Ostoja-Starzewski and Pregosin[480] in 1980.

The first high-resolution ^{113}Cd spectrum was obtained by Maciel and Borzo[481] in 1973, and two other trend-setting papers dealing with the general applications of ^{113}Cd NMR were published a few years later by Kostelnik and Bothner-By[482] and by Ellis and co-workers.[483] Spin–lattice relaxation times were typically of the order of a few seconds. The high sensitivity of the chemical shift to structural changes has made ^{113}Cd a promising nucleus for biological applications, especially in metalloproteins as a substitute for zinc or calcium, which are very difficult to study by NMR. Spin–spin coupling to nuclei such as ^{13}C, ^{15}N, and ^{31}P has been found to be quite large and sensitive to the type of binding. Applications of ^{113}Cd NMR both in the solid and the liquid states have been employed in molecular structure and anisotropic motion studies of cadmium-substituted porphyrins by Ellis et al.[484]

^{119}Sn, and to some extent ^{117}Sn, has been studied by several groups. Lauterbur and Burke in 1958 were the first to report chemical shifts in tin compounds at 8.5 MHz.[485,486] Depending upon the spin–lattice relaxation times, the spectra were recorded as rapid or slow passage signals in dispersion or absorption modes. ^{119}Sn has been found to be very useful in the study of redistribution reactions in mixtures of stannic halides and other tin compounds. A good illustration, from the historical sketch by Bernd Wrackmeyer, (***Wrackmeyer, Bernd: A Personal Retrospect of Multinuclear Magnetic Resonance***

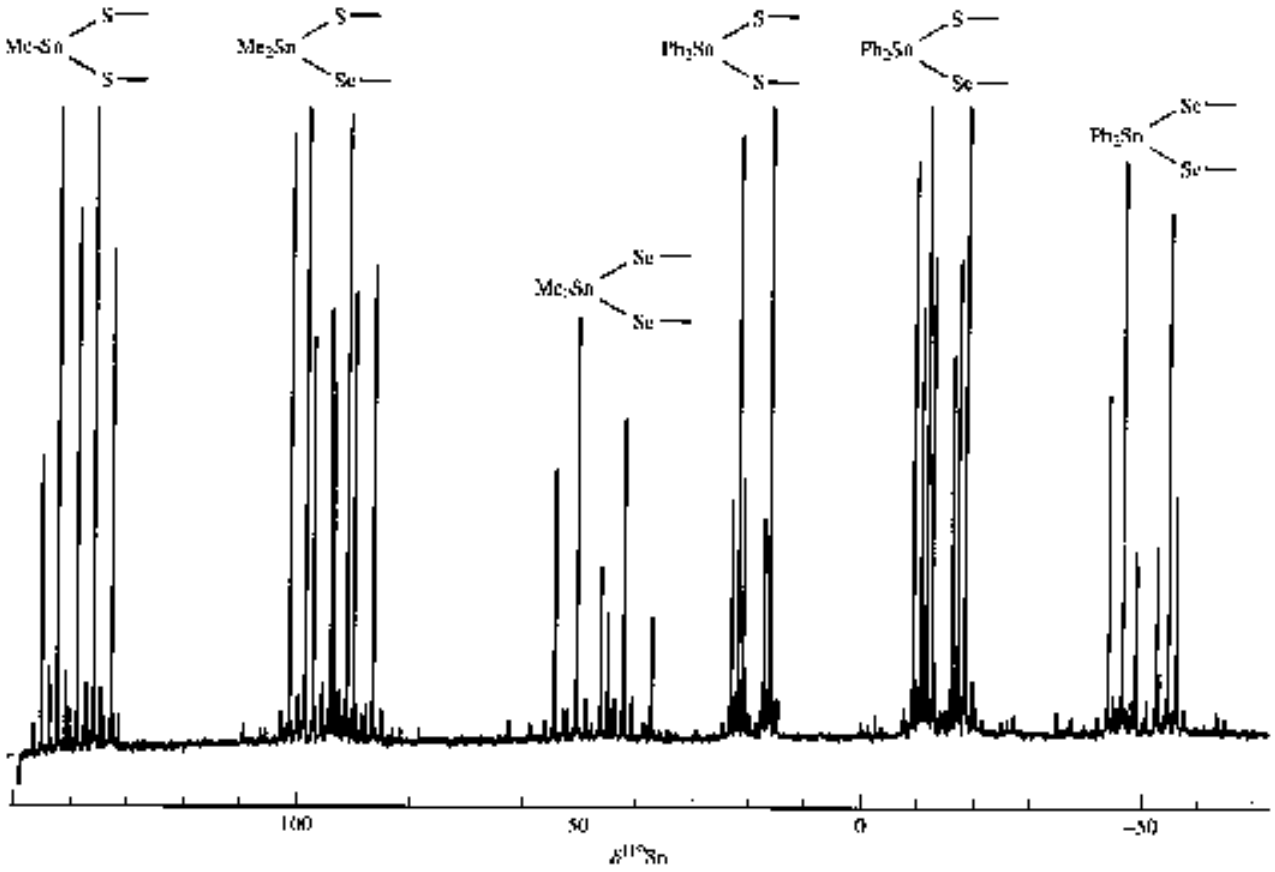

Figure 65 The 74.6 MHz ^{119}Sn spectrum of an equilibrated mixture resulting from the exchange reaction between $(Me_2SnSe)_3$ and $(Ph_2SnS)_3$. In this ^{1}H-decoupled spectrum, a large number of satellite peaks arising from ^{117}Sn and ^{77}Se can be seen

in Liquids) is shown in Figure 65 where 39 out of 40 possible lines are observed.

An overall chemical shift range of about 3000 ppm has been observed in most tin compounds, with a very strong solvent dependence of the shifts due to coordination with the solvents. Solid state ^{119}Sn was pioneered by Lippmaa et al.[390] and has been pursued extensively by Robin Harris and co-workers in investigating insoluble organotin compounds.

The chemical shifts of ^{207}Pb, first measured by Piette and Weaver[487] in 1958, range over 16 000 ppm. In ionic compounds the resonance is shifted to high field, whereas in compounds involving some covalent bonding it is shifted toward lower fields. The one-bond Pb–H coupling constant was found to be about 2400 Hz,[488] and couplings with many other nuclei such as ^{14}N, ^{15}N, ^{13}C, ^{31}P, ^{11}B, and ^{19}F have been measured.

After the first observation of ^{199}Hg NMR in 3.5 M $Hg_2(NO_3)_2$ by Proctor and Yu[489] in 1951, ^{199}Hg chemical shifts in a series of dialkylmercury compounds were measured by Dessy et al.[490] in 1959. The overall chemical shifts of ^{199}Hg were explained by Schneider and Buckingham.[491] ^{199}Hg lines are usually broad because of scalar couplings and exchange.

Although ^{109}Ag is the most favorable NMR isotope of silver, it has low sensitivity, long spin–lattice relaxation times, and a negative NOE. A value of more than 1000 s for the T_1 of ^{109}Ag in $AgNO_3/D_2O$ solution was measured by Kronenbitter, Schweizer, and Schwenk[492] in 1980 using steady-state techniques. Most available ^{109}Ag data refer to labile species, but some results for nonlabile complexes have been reported by van Koten and co-workers.[493]

For a number of years, the direct observation of ^{103}Rh NMR was restricted to rhodium metal and intermetallic compounds.[494] Studies of a few coordination complexes of ^{103}Rh using indirect double resonance techniques were also available[495–497] prior to 1979, when the first direct high-resolution observation of ^{103}Rh NMR was reported by Gansow and co-workers.[498] ^{103}Rh was the only spin-$\frac{1}{2}$ nucleus which had remained unstudied directly by high-resolution NMR in organic systems until that time. The initial spectra were recorded by time-averaging of free induction decays in highly concentrated samples (~2 M) for 10 h with 20 mm sample tubes and using relaxation agents for some samples. In 1980, the efficiency was improved by using the Quadriga FT method to obtain a signal-to-noise ratio of 100: 1 in 2 h without a relaxation agent.[499] Cocivera et al. were subsequently able to obtain a spectrum of a 0.25 M solution of $Rh(acac)(CO)_2$ in 1 min.[500]

Rhodium(III) gives a much larger chemical shift range than Rh(I), about 12 000 ppm. Values of T_1 vary from a fraction of a second to a few tens of seconds. Coupling constants with various nuclei up to about 200 Hz have been observed.

Like rhodium, ^{183}W has been difficult to observe directly because of low sensitivity, and most of the information has been obtained indirectly from double resonance techniques.

The first direct measurement of tungsten was made on solid WO_3 by Narath and Wallace[501] and in liquids (WF_6, WCl_6, and simple WO_4^{2-} ions) by Banck and Schwenk,[502] who used the Quadriga FT technique. The first direct observation of ^{183}W for more complex heteropoly- and isopolytungstates was made by Acerete, Hammer, and Baker[503] in 1979.

^{183}W chemical shifts are very sensitive to structural change, with a difference of about 1200 ppm between the oxidation states W(VI) and W(0). Coupling constants with phosphorus have been most extensively studied, and the values spread over a wide range from about 10–500 Hz for one-bond couplings. Values of T_1 are more difficult to obtain due to low sensitivity, but a typical value of 4.2 s has been observed in WF_6 by Banck and Schwenk.[502]

Other Important Nuclides

^{27}Al chemical shifts and Al–H coupling in $LiAlH_4$ were measured first by O'Reilly[504] as early as 1960. The ^{27}Al–^{1}H coupling was found to be 110 Hz. ^{27}Al has a chemical shift range of nearly 450 ppm. The shifts can be classified according to the ligand symmetry about the aluminum ion, those with octahedral symmetry appearing at the highest field, those with tetrahedral symmetry in an intermediate range, and alkylaluminum compounds and their adducts at the lowest field.

^{27}Al NMR has been used to investigate the physical and chemical properties of aqueous solutions of aluminum salts. For example, Akitt et al.[505] determined the hydration number of the Al^{3+} ion, while both the Akitt and Lutz groups[506–508] studied the hydrolysis, polymerization, and complexation of Al^{3+}. Solvation and complexation in nonaqueous and mixed aquo–organic solvent systems have also been investigated by numerous workers from 1967 onwards.[509–516] The Al^{3+} ion can interact quite strongly with basic solvent molecules and under favorable conditions scalar couplings between ^{27}Al and the nuclei of the solvent molecules have been observed. In some mixed solvents, the ligand exchange rate is slow enough to permit the observation of several solvated species, thus enabling the determination of kinetic and thermodynamic parameters.

Solid state NMR has also been employed for the study of ^{27}Al NMR. Special aluminum-free probes are now commercially available in order to avoid interferences from the signal coming from the probe material. It is possible to distinguish octahedral and tetrahedral aluminum environments, since aluminum in symmetrical sites produces noticeably narrowed lines in MAS experiments. Merryman et al.[517] confirmed the presence of $AlCl_4$ in solid samples prepared from mixtures of $AlCl_3$, ICl, and I_2. Resing et al.[518] used ^{27}Al NMR to study zeolites, while Mueller et al.[519] were able to distinguish between six- and four-coordinate aluminum in a variety of solids.

The ^{33}S nucleus has a small magnetic moment, a spin of $\frac{3}{2}$ and a natural abundance of only 0.76%. The spectral lines are typically several hundred Hz wide except in the most symmetric compounds with tetra-coordinate hexavalent sulfur. In 1972, Retcofsky and Friedel[520] obtained ^{33}S chemical shifts in 13 different compounds and found a chemical shift range of 650 ppm, with linewidths ranging from 61 Hz to 9000 Hz. NMR data on ^{33}S were obtained in the dispersion mode until 1973 when Lutz et al.[521] employed Fourier transform methods to study natural abundance ^{33}S and accurately determine the magnetic moment. The only coupling constant of ^{33}S reported is the one–bond J_{S-F} in SF_6, of 251 Hz.[521] Some natural abundance ^{33}S studies have been applied to chemical problems but generally have been found to be feasible for only a few specific applications.[522]

The ^{51}V nucleus has a quadrupole moment, but in many of its complexes exhibits rather narrow lines. In 1965, Howarth and Richards[523] established ^{51}V NMR as an excellent tool for the characterization of the pH-dependent species existing in aqueous solutions of vanadates. The ^{51}V chemical shifts in various oxidation states have been studied extensively in a host of derivatives—VO^{3+} by Howell and Moss[524] and Rehder,[525] iso- and heteropolyanions of V(V) by Kazanskii and Spitsyn[526] and O'Donnell and Pope,[527] and a series of vandium carbonyl compounds by Rehder et al.[528–530] The chemical shift range is about 2000 ppm, except for $[V(CO)_6]^-$ in MeCN solution for which a value of 5660 ppm was reported.[531] The studies demonstrate the existence of discrete chemical shift ranges for vanadium in different oxidation states. The lowest oxidation state is most highly shielded and ^{51}V becomes progressively deshielded with an increase in the

NMR DISCUSSION GROUPS IN GERMANY,FRANCE, ITALY, AND JAPAN

Several national discussion groups on magnetic resonance are well known.

Fachgruppe Magnetische Rezonanzspektroskopie

A German NMR Discussion Group was formed in 1974 at the initiative of Ernest Lustig, who had recently returned to Germany from the U.S. Others active in the initial organization were Gerhard Binsch, Eberhard Breitmaier, Ludger Ernst, Harald Günther, Horst Kessler, Robert Kosfeld, Dieter Leibfritz and Adalbert Mannschrank. By 1978, at the fifth annual meeting, the group became a division of the German Chemical Society, broadened its scope to ESR as well as NMR, and adopted its current name. The annual meetings generally attract 200–300 participants.

Groupe d'Etude de Résonance Magnetique (GERM)

This French discussion group was founded in 1976 and held its first meeting the next year in Vichy. Subsequently, annual meetings were held until 1985, when a biennial format was adopted for the general meeting, with smaller specialized meetings in the intervening years.

Gruppo di Discussione Delle Risonanze Magnetiche

Founded in 1974 in Milan, the Italian group includes discussions on both NMR and ESR. Initially two meetings per year were held, but there is now an annual meeting of 2–3 days. The group includes chemists, physicists, and biologists.

Research Group of NMR in Japan

The formation and activities of this group and others in Japan are covered in the historical sketch by I. Ando.

oxidation state. Hence ^{51}V chemical shifts are diagnostically useful for the characterization of these compounds.

Coupling constants for ^{51}V with ^{1}H, ^{13}C, ^{31}P, ^{19}F, and ^{119}Sn have all been observed. The values range from about 20 Hz for the couplings to protons to about 900 Hz for $J(^{51}V-^{119}Sn)$. High-resolution ^{51}V NMR spectra of solid vanadium compounds with magic angle or near magic angle spinning were observed by Oldfield et al.[369,532] in 1982.

The ^{93}Nb nucleus is one of the most sensitive and has been studied fairly extensively. The first high-resolution spectrum was reported in 1963 by Packer and Muetterties[533] of the hexafluoroniobate ion, $[NbF_6]^-$. The results indicated the presence of $[NbF_6]^-$ ions in solution rather than $[NbF_7]^{2-}$ ions. Practically all the data on ^{93}Nb deal with compounds in which the ligands are halides or pseudohalides. In these compounds, the shielding decreases with decreasing electronegativity of the halogen. The total chemical shift range observed is about 2400 ppm. Mixtures of $NbCl_5$ and $NbBr_5$ in acetonitrile undergo a slow ligand redistribution reaction to give a mixture of products, each of which gives a characteristic ^{93}Nb spectrum.

Most manganese compounds are paramagnetic and are generally not suitable for high-resolution NMR. In 1974, Lutz and Steinberg[534] not only provided an accurate value of the ^{55}Mn magnetic moment but also reported the concentration dependence of chemical shift in permanganate for a variety of counterions and found an unusually large deuterium-induced isotope shift of 0.76 ppm. ^{55}Mn chemical shifts cover a range of 3000 ppm, with the shielding increasing with oxidation state. Linewidths vary from about 10 Hz in $KMnO_4$ to about 10 kHz in $HMn(CO)(PF_3)_4$, thus offering the prospect of determining electric field gradients from linewidths. Coupling constants of ^{55}Mn with other nuclei have been obtained from the resonances of the other nuclei. Burton and Harris[535] have deduced from MAS experiments a value of 1.60 MHz for the ^{55}Mn quadrupole coupling constant in a polycrystalline $KMnO_4$ sample.

Two isotopes of copper, ^{63}Cu and ^{65}Cu, are readily detected by NMR, but ^{63}Cu is the preferred isotope because of better sensitivity, despite marginally larger linewidths. As mentioned in Section 2, the history of NMR in copper starts even before the discovery of the Knight shift in 1950. In the solution state, McConnell and Weaver[536] analyzed linewidth measurements in concentrated hydrochloric acid solutions containing both copper(I) and copper(II) chloride to determine the bimolecular rate constant for the electron-exchange process. Fujiwara and co-workers[537] also studied an aqueous solution of CuCN and observed marked changes in the ^{63}Cu NMR linewidths with the relative amount of cyanide added, resulting from chemical exchange between the various species $Cu(CN)_4^{3-}$, $Cu(CN)_3^{2-}$, and $Cu(CN)_2^-$. The real problem in the widespread application of ^{63}Cu NMR arises from the fact that Cu(II) is paramagnetic; hence NMR is largely confined to the Cu(I) species, which are less stable and limited in chemistry.

The ^{63}Cu linewidths range between 20–160 kHz. A one–bond $^{63}Cu-^{31}P$ coupling of 1210 Hz has been found[538] in the phosphine complex $Cu[P(OMe)_3]_4^+$. The known chemical shift range for Cu(I) is about 500 ppm.

Solid state NMR methods have been applied to ^{63}Cu. Spin–lattice relaxation times and chemical shifts in copper(I) halides were measured in polycrystalline samples by Günther and Hultsch[539] in 1969 and subsequently by many other workers. The use of high-speed MAS for the determination of precise values of Knight shifts of $^{63}Cu/^{65}Cu$ in metallic copper was made by Andrew et al.[540] in 1971. The ^{63}Cu NMR transitions of divalent copper ions were detected for the first time in copper acetate monohydrate by Kawamori and Soda[541] in 1975, and the quadrupole coupling constant was calculated as 117 MHz.

Some Rarely Studied Nuclides

Each of the NMR-accessible nuclides that we have not yet discussed has provided information important to particular applications, but in general has had only limited study. We mention here only some salient points concerning the initial observation of a particular isotope or unusual features that have been observed.

Of the arsenic, antimony, and bismuth group, only antimony has been studied extensively. The first systematic study of ^{75}As chemical shifts was as late as 1977 by Balimann and Pregosin.[542] Because of quadrupole broadening, the compounds studied were tetra- or hexacoordinated of the pentavalent type. Both ^{121}Sb and ^{123}Sb were among the earliest nuclei to be investigated by NMR. In fact, SbF_6^- was one of the first species for which splittings due to spin–spin coupling constants were observed,[543–545] although not properly understood at that time. Again, the large magnitude of the quadrupole moment is responsible for the fact that observation of less symmetric species has not been possible. The first chemical shift data were provided by Kidd and Matthews for a series of simple antimony compounds.[546] The narrowest line observed (~300 Hz) was for the $SbCl_6^-$ ion. Despite the fact that the ^{209}Bi in aqueous bismuth nitrate was reported[544] as early as 1951, the literature seems to be void as far as the chemical applications of ^{209}Bi NMR are concerned.

The ^{45}Sc nucleus is 100% abundant and has very high NMR sensitivity. The precise magnetic moment and the isotope shift of 6.2 ppm for the ^{45}Sc resonance in aqueous $ScCl_3$ in H_2O and D_2O were measured by Lutz[547] in 1969. Buslaev et al.[548] and Melson et al.[549] have studied ^{45}Sc resonances in a variety of compounds in aqueous and nonaqueous media. However, scandium NMR has not attracted widespread NMR interest thus far.

Both ^{47}Ti and ^{49}Ti have low sensitivity for NMR observation. A unique feature of the two isotopes is the closeness of their resonance frequencies, which differ by just 271 ppm. The only chemically significant data are by Kidd et al.,[550] who investigated the tetrahalides. A typical spectrum of a mixture of the chloride and the bromide (Figure 66) shows spectra from both isotopes.

Both ^{95}Mo and ^{97}Mo have low NMR sensitivity. The earlier work on molybdates was concentrated on relaxation studies, isotope effects, and medium effects. Vold and Vold[551] determined the relaxation times of $[^{95}MoO_4]^{2-}$ and $[^{97}MoO_4]^{2-}$ as 6.5 and 840 ms, respectively. The unusually large difference of the quadrupole moments of the two isotopes has proved to be of some significance in molybdenum NMR studies. The cation, solvent, and pH dependences of the ^{95}Mo shielding in $[MoO_4]^{2-}$ have been studied by Kautt et al.[552] Lutz et al.[553] have obtained chemical shift data for several molybdenum compounds and have even observed $^{34}S/^{32}S$

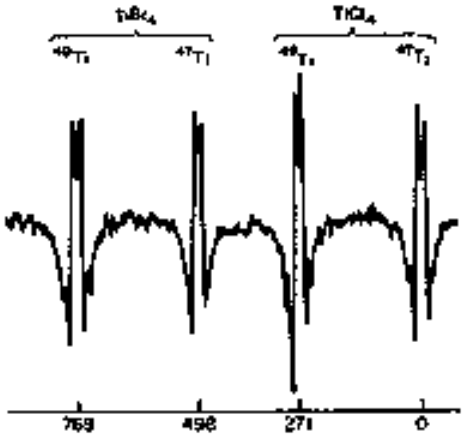

Figure 66 The 3.38 MHz ^{47}Ti and ^{49}Ti NMR spectra recorded as derivative signals from a slow passage dispersion mode sweep. The splitting of each resonance is due to overmodulation at 40 Hz.[550] (Reproduced by permission of the American Chemical Society)

isotope effects on the shielding of the quadrupolar ^{95}Mo in MoS_4^{2-}.

The first measurement of ^{77}Se chemical shifts (for H_2SeO_3 and H_2SeO_4 relative to H_2Se) was made by Walchli[554] in 1953. The initial studies of ^{125}Te NMR concerned Knight shift investigations by Cabane and Froidevaux[555] in 1968 and Warren[556] in 1972. Subsequently, indirect detection of ^{125}Te in several organic compounds was carried out by McFarlane and McFarlane[557] in 1973. The first high-resolution ^{125}Te NMR study in organic compounds was made only in 1976 by Drakenberg et al.[558] The overall chemical shift range exceeds 4000 ppm. The existence of ^{123}Te has made it possible to measure Te–Te couplings in symmetric species.

The first article on the solution NMR of ^{53}Cr at natural abundance was by Egozy and Loewenstein[559] in 1969 and was related to the derivation of the rate constant for the chromate–dichromate equilibrium. Lutz's group reported chemical shift data for the chromate ion as a function of counterion concentration.[560]

Although technetium does not have a stable isotope, radioactive ^{99}Tc, with a half-life of 5×10^5 years, has quite favorable properties for NMR detection—100% natural abundance and a very high sensitivity. In 1981, Kidd[561] observed the ^{99}Tc resonance in $Na[TcO_4]$ and obtained the quadrupole coupling constant.

Both ^{185}Re and ^{187}Re have reasonable sensitivity for NMR detection. The $\frac{5}{2}$ nuclear spin and the large quadrupole moments, however, impose problems in their observation. The first study by Dwek, Luz, and Shporer[562] in 1970 aimed at deriving the quadrupole coupling constant in ReO_4^-. Subsequently, $[ReS_4]^-$ and $[Re(CO)_6]^+$ were investigated.[563,564]

Ruthenium has two NMR active isotopes, namely ^{99}Ru and ^{101}Ru with natural abundances of about 13% and 17% respectively. Both are spin $\frac{5}{2}$ nuclei and have reasonable NMR sensitivities. Only the diamagnetic oxidation states Ru(VIII), Ru(II), and Ru(0) have found interest in NMR. The history of NMR on these nuclei only started in 1981 from work by Brevard and Granger[565] and Dykstra and Harrison.[566]

Weaver[567] observed the resonance of ^{67}Zn in 1953, and the first study of ^{67}Zn shielding by high-resolution pulse NMR was made by Epperlein et al.[568]

After the initial observation of ^{113}In and ^{115}In by Proctor and Yu[569] and several other early papers, the NMR properties of ^{115}In in aqueous and non-aqueous solutions were largely established by the early 1970s.[570–573] Linewidths were found to be sensitive to environmental symmetry around the indium, and exchange between complexed and free ions has been studied.

An accurate value of the magnetic moment of ^{139}La was reported by Lutz et al.[465,574] only in 1977–78. The use of direct NMR observation of other lanthanides has been largely restricted to solid state investigations.

The first resonance of ^{89}Y was studied in $Y(NO_3)_2$ by Brun et al.[575] Subsequently, in the late 1970s, several compounds were studied employing improved methodology. In 1971, Kaufmann et al.[576] were the first to obtain high-resolution ^{73}Ge data on a number of GeR_4 compounds, while a high-precision measurement of the magnetic moment of ^{187}Os was made by Sahm and Schwenk[436] in 1974 in Tubingen.

BIOCHEMICAL APPLICATIONS OF NMR

The initial applications of NMR to biochemistry were generally not different in kind from the chemical studies discussed at length in previous sections. But biochemical systems often provided different sorts of challenges and led to the development of new NMR methods. While the distinction between 'chemical' and 'biochemical' is blurred, especially in the early days of NMR, it is convenient and instructive to trace the developments in the biochemical arena.

The first biochemical NMR applications appeared some 40 years ago in an era when neat or saturated solutions were required, instrumental stability was questionable, and effective resolution was extremely limited compared with modern standards. Since then, the history of this field has been shaped by a succession of major technological advances, including greatly improved sensitivity from advances in electronics and probe design, sufficient field/frequency stability to allow multiscan averaging, the development of pulse Fourier transform methods, the availability of high-field superconducting magnets, significant improvements in data handling facilities, and the development of multidimensional NMR. Many of the advances were realized through the intense developmental efforts of commercial NMR instrument companies. Others were individual endeavors with homebuilt systems and combinations of commercial components to overcome 'the technological problems that present the major barrier between creativity and experimental results,' as aptly put by Ad Bax in his historical sketch (***Bax, Ad: NMR of Ethanol and Interferon-γ***).

In this section we outline major milestones in the development of NMR applications to biochemistry in the period from the earliest experiments through the late 1970s and early 1980s, when the development of two-dimensional NMR methods began to make major impacts on the applicability to biopolymers.

Pioneering CW Work at 40 MHz and Below

During the 1950s, NMR was largely a technique in the hands of the organic chemists. Chemical applications of this new

and powerful tool blossomed into many areas, including the study of organic molecules with biological functions. In the latter half of the decade, more complex compounds began to be investigated, and the potential of the technique for applications in biochemistry became apparent. However, the stability, resolution, and sensitivity of the first commercial instruments restricted the types of quantitative information that could be obtained. Early commercial spectrometers were also often equipped only for the observation of protons—the most sensitive naturally occurring NMR nucleus—creating a special challenge to anyone interested in other nuclei (such as ^{31}P). Spectroscopists were compelled to use highly concentrated solutions, since signal averaging had not yet been introduced into NMR. There was also a problem of standards for chemical shift measurements in aqueous (D_2O) solutions. The residual HOD peak was clearly an unsatisfactory standard because its position varied with pH and temperature. Thus spectroscopists typically inserted a small coaxial tube containing a proton-rich substance such as toluene or TMS. In addition to introducing bulk magnetic susceptibility effects, this reduced the effective sample volume and thus the sensitivity. Despite all of these limitations, however, significant early efforts on many fronts demonstrated the feasibility of NMR as a powerful technique to address complex biochemical problems.

Beginning in 1957, exploratory studies were undertaken at 40 MHz on a number of substances of biochemical interest. For example, chemical shift data for concentrated aqueous solutions of common amino acids and several small peptides at different pH values were first reported by Oleg Jardetzky and co-workers.[577,578] Very shortly thereafter, Bovey and Tiers[579] published a study of all the common amino acids and several glycyl dipeptides in trifluoroacetic acid (TFA), which happened to be an excellent solvent for both those compounds and the chemical shift standard TMS. The resolution was relatively poor in these early studies, and in many cases the coupling constants were estimated from the peak width at half-height. Chemical shift measurements were tabulated and correlated with molecular structure. Among the more interesting observations in TFA, the diastereoisomers d–leucyl–l–tyrosine and l–leucyl–l–tyrosine could be distinguished by an upfield shift in the methylene peaks of the dl isomer.

As we saw in Section 3.6, by 1958 Lemieux and others had found that the magnitude of vicinal proton coupling constants depended on molecular conformation, and a year later Karplus provided a theoretical treatment of the effect. This information became available at the time the first proton NMR studies of nucleic acid bases, nucleosides, and nucleotides were being undertaken at 40 MHz by Oleg and Christine Jardetzky.[580–582] Thus, in addition to documenting the pH-dependence of the chemical shifts in concentrated solutions of these substances, the ribose conformations were estimated from the magnitude of the vicinal couplings between H-1′ and H-2′. These early studies were hampered by poor resolution and the complications of overlapping lines and strongly coupled spin systems. Complete analyses of nucleoside and nucleotide spectra became possible only at higher fields as discussed in a following section. The 1960 studies also noted a large dependence of the chemical shifts of purine protons on concentration, the beginning of what would eventually become a number of quantitative investigations of the vertical stacking of purines and the effect of ring currents on chemical shifts in neighboring molecules.[583]

The first theoretical estimations of the chemical shift effects of ring currents in purines and pyrimidines were made by Giessner-Prettre and Pullman,[584] who extended the calculations of Johnson and Bovey. Their results were later published as isoshielding curves for protons located ± 3.4 Å from the plane of adenine, guanine, cytosine, or uracil.[585] These computations and subsequent refinements by these and other researchers were frequently used in the interpretation of ^1H NMR spectra of di-, oligo-, and polynucleotides.

In 1959, Hopkins and Bernstein published a 40 MHz 'introductory study' of fatty acids, fatty acid esters, and natural glyceride oils in chloroform solution 'at sufficiently high concentration to give signals of moderate intensity', i.e. about 200 mg in 0.5 mL.[586] The authors identified characteristic chemical shifts and were able to estimate the ratios of saturated/monoene/diene fatty acid components in several natural oils (cocoa butter, cottonseed oil, and tung oil).

Explorations at 40 MHz were not limited to small molecules. In 1957, Saunders, Wishnia, and Kirkwood published the first spectrum of a protein, bovine pancreatic ribonuclease.[587] The choice of ribonuclease, a relatively small protein of molecular weight 13 000, was based on practicality: the protein is quite soluble and was available in sufficient quantity for NMR experiments from Saunders' colleagues at Yale. After failing to obtain any spectrum from the protein in H_2O, Wishnia and Saunders repeatedly lyophilized the sample from D_2O and dissolved it in D_2O to obtain the spectrum shown in Figure 67. This spectrum, which is an NMR classic, began an area of research that has now resulted in structural analyses that rival the accuracy of X-ray crystallography, as we shall discuss in Section 14. From the perspective of the 1990s, the spectrum appears bereft of information, with only four broad peaks resolved. However, at the time, it was exciting and revealing, as recounted by Martin Saunders in his historical sketch (***Saunders, Martin: The First NMR Spectrum of a Protein***):

> What did we learn about proteins from this spectrum? The most important thing was that one could obtain a spectrum where aliphatic, aromatic and NH (as they were exchanged out) were roughly at the chemical shifts expected from those found in smaller compounds and that their peaks were fairly sharp. From diffusion and viscosity data, Kirkwood could estimate the correlation time for rotation of the protein molecules. We concluded that, if the molecules rotated as rigid bodies, there would be much more broadening from dipole–dipole interaction than we saw in the spectrum. The relative sharpness of the peaks seemed to imply that there was internal motion.

The Jardetzkys, who had their amino acid data in hand by this time, took the interpretation a step further by demonstrating that the general shape of the observed ribonuclease spectrum could be predicted from the sum of the amino acid constituents.[588]

During the next few years, several additional 40 MHz protein spectra were published, the most revealing of which were those obtained under conditions designed to unfold the native structure.[589,590] Although detailed information on the native structure was not discernible from these spectra, the denaturation experiments demonstrated that the elimination of secondary and tertiary structure significantly sharpened spectral lines, resulting from a decreased chemical shift dispersion and from increased mobility of the polypeptide chain.

The first NMR spectra of a synthetic polypeptide, poly-γ-benzyl-L-glutamate, were published in 1959 at 40 MHz.[590]

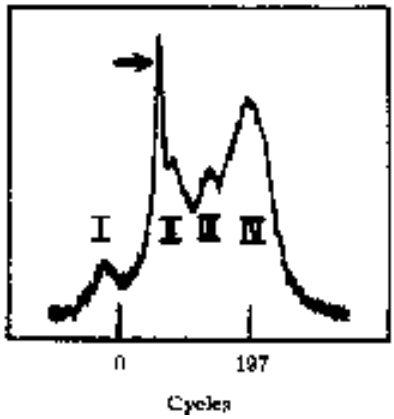

Figure 67 Proton NMR spectrum at 40 MHz of ribonuclease in D_2O.[587] (Reproduced by permission of the American Chemical Society)

This study, and a succession of later papers on this and related systems, focused on the spectral differences observed as the polypeptide converts from the random coil form (exhibited in solvents such as trifluoroacetic acid) to an α-helical form (in inert or weakly hydrogen-bonding solvents such as chloroform or trichloroethylene). The interest in using NMR to study α-helix to random coil transitions really began in earnest in the late 1960s, with so many publications appearing that Frank Bovey would comment in his 1972 book, *High Resolution NMR of Macromolecules*,[591] 'recently the flow of published studies has swelled to near torrential proportions.'

In many of these early examples, as well as in much of the work on steroids, alkaloids, and other classes of compounds discussed in previous sections, the emphasis was on the discovery of chemical shift information and its analysis in terms of structure and configuration/conformation. It took the advent of higher-field instruments and time-averaging techniques, however, to create the experimental environment where complex biochemical molecules could be studied in detail.

Water, Water, All Around

From the very beginning of NMR applications to biochemistry and biology, water played an ambiguous role: both a blessing and a nuisance. At 110 M in protons, this ubiquitous constituent of biological systems produced an intense signal and was thus a natural for observation by NMR, as recounted below. On the other hand, it quickly became clear that if one wanted to observe anything other than water protons in an aqueous solution, it was a distinctly unfriendly solvent for ^1H NMR. Solution in D_2O, usually after repeated lyophilization of the sample from D_2O to remove water of hydration and exchangeable protons, became the norm, but even then the residual HOD peak often dominated the spectrum. Other than optimizing experimental conditions and avoiding scanning through the HOD signal, this problem could not really be solved until pulse-FT became available and water-suppression schemes were developed.

As early as 1950, Shaw and Elsken measured the intensity of the proton NMR signal at 15 MHz in pieces of apple, potato, and maple wood as a function of water content.[592] Subsequent studies attempted to correlate signal area and line broadening with the extent of hydration in a number of substances such as egg albumin, collagen, gelatine, DNA, and solutions of tobacco mosaic virus.[593–596] Although the interpretation of these early experiments was complicated by instrumental artifacts and arbitrary models that could not be tested, 'a beginning had been made', as Oleg Jardetzky put it in his historical sketch (***Jardetzky, Oleg: NMR in Molecular Biology--A History of Basic Ideas***).

In 1957, Davidson and Gold[597] employed the solvent signal for a different purpose. Recognizing from the classic work of Bloembergen, Purcell, and Pound that paramagnetic ions are effective in relaxing solvent protons, they compared the relative efficiencies of $Fe(H_2O)_6^{3+}$, $Fe^{III}(EDTA)^-$, ferriheme, and ferrihemoglobin for relaxing solvent water protons. Although the results obtained from their 40 MHz saturation recovery and line-broadening measurements were not very accurate, the authors could demonstrate that iron in methemoglobin was less effective than in the small molecules in relaxing water protons. They concluded that the heme group in the protein was relatively inaccessible to bulk solvent protons. Their observations, extended in a subsequent paper by Kon and Davidson,[598] were followed by a number of later studies focused on sorting out the relative contributions of the possible relaxation mechanisms in a complex system. One additional outcome of this work, suggested in Davidson and Gold's paper and reported in more detail in a paper by Lumry et al.,[599] was that the diamagnetic protein itself affected the relaxation rates of bulk solvent water, presumably by slowing the rotational motion of the water molecules as they associated with the much larger biopolymer.

In 1961, Eisinger, Shulman, and Blumberg[600] used a spin echo apparatus operating at 50 MHz to measure the longitudinal relaxation times of the solvent water signal in solutions of calf thymus DNA to which paramagnetic ions had been added. Bob Shulman recalls the genesis of the experiment in his historical sketch (***Shulman, Robert G.: My Years in NMR***):

> The NMR consequence of this interest in biomolecules was that I spoke with Bill Blumberg and Terry Eisinger at Bell Labs who had built a pulsed NMR instrument designed to measure the increased H_2O relaxation they expected to find from free radicals generated during enzymatic reactions. By that time I had shown that the unpaired spins in DNA were from ferromagnetic magnetite inclusions, and I knew that the structure of paramagnetic metal ion binding to DNA was uncertain. If bound outside to the phosphates, the binding efficiency of Mn^{2+} should have been similar to the free ion, while if bound internally, the efficiency should have been reduced from limited H_2O access. We decided to test how the effectiveness of Mn^{2+} as a relaxation agent of the H_2O protons was changed by its binding to DNA. To our surprise, the Mn^{2+} was *more* effective when bound, a phenomenon which we named 'relaxation enhancement'. We explained it on the basis of the altered correlation time between Mn^{2+} and the H_2O protons which was determined by the rotation time of the $Mn(H_2O)_6$ complex—a rotation time that would be slower when the Mn^{2+} was bound to the DNA molecule, making it more effective as a relaxer. We showed that Co^{2+} and Ni^{2+}, with very short electronic T_1 values, did not give this enhancement when bound to DNA, since the rotational time was shunted by the faster electronic relaxation.

A note on the work appeared in 1961,[600] and detailed studies were published the following year.[601] Figure 68 shows one illustration of the dramatic effects caused by the

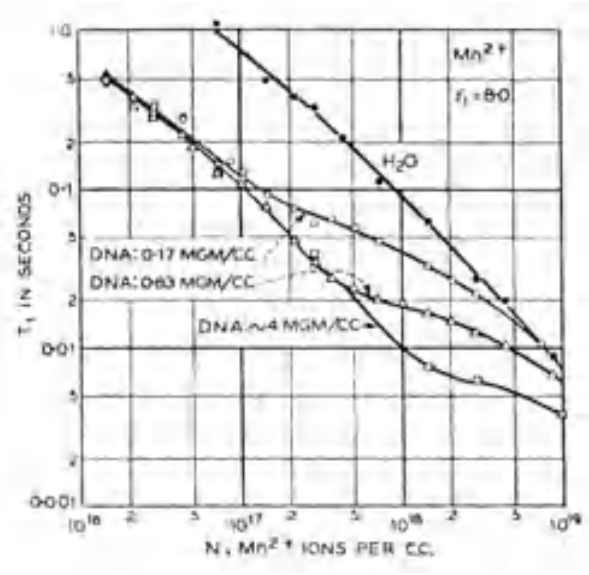

Figure 68 Variation of the proton T_1 value in water as paramagnetic Mn^{2+} ions are added alone or in the presence of varying concentrations of DNA.[600] (Reproduced by permission of Macmillan Magazines Ltd)

combination of macromolecules and paramagnetic ions. The first application of relaxation enhancement as a sensitive probe for the study of enzyme–metal–substrate complexes was also published in 1962 by Cohn and Leigh.[602] Working with Leigh's homebuilt pulse spectrometer, they observed large relaxation enhancements in tertiary complexes of enolase and creatine kinase with Mn(II) and substrate. They found that the metal ion bound directly to enolase but the binding to creatine kinase involved an Mn(II)–substrate–enzyme bridge structure. This work attracted Albert Mildvan to Cohn's laboratory, where he obtained complementary NMR and ESR relaxation enhancement data in Mn(II)–bovine serum albumin solutions in order to establish relaxation enhancement as a quantitative tool for determining association constants and exploring the structure of the binding site. The historical accounts of Cohn (***Cohn, Mildred: Peregrinations of an Enzymologist in NMR***) and Mildvan (***Mildvan, Albert S.: Early Applications to Enzymes of Paramagnetic Effects on Nuclear Relaxation***) summarize their investigations in the 1960s and 1970s, undertaken to explain the physical basis of the enhancement and to use the technique to elucidate enzyme mechanisms. In their hands, and those of many other investigators, relaxation enhancement was used to study the structure and dynamics of a wide variety of metal ion–biopolymer complexes including lanthanide-substituted systems.[603–606] The technique was also extended from the observation of the water proton signal to studies of the substrate itself, using other nuclei such as ^{13}C, ^{19}F, and ^{31}P. A particularly interesting example from the early 1980s, that of the Mn^{2+} derivative of carbonic anhydrase, is provided by J. J. Led (***Led, Jens J.: Aspects of NMR Studies of Paramagnetic Metal Complexes of Biological Relevance. A Historical Sketch***). In this system, sets of complementary magnetization transfer ^{13}C spectra of the substrates CO_2 and HCO_3^- with and without the enzyme allowed the independent determination of relaxation and catalytic exchange rates, and verification of the structure of the metal complex in the catalytic pathway.[607]

During the 1970s and 1980s, attention was placed on quadrupolar nuclei for studies of water in protein solutions, since the interpretation of relaxation measurements using water isotopically enriched with deuterium and/or ^{17}O is simplified by the dominance of the nuclear electric quadrupole interaction. Of the two isotopes, ^{17}O avoided the complication of exchange with ionizable groups and, due to the strong quadrupolar interaction, permitted studies at lower protein concentrations as exemplified by the work of Halle et al.[608]

Full analysis of the relaxation data from both diamagnetic and paramagnetic systems depended on the measurement of relaxation rates as a function of frequency and temperature. This prompted the development of specialized instruments, given the name 'relaxometers' by one of the champions of this approach, Seymour Koenig. The measurement of solvent relaxation has become an extremely important area for research in modern NMR, particularly with the advent of magnetic resonance imaging techniques that contrast different tissues in living systems by sensing the concentration and relaxation of intrinsic H_2O. In the words of Koenig in his historical sketch (***Koenig, Seymour H.: I. I. Rabi, F. Bloch, E. M. Purcell, and the History of NMR and Relaxometry***), 'It remains the best approach for the study of complex macromolecular systems, including tissue.'

Exploitation of True 'High-Resolution' Capability

The introduction of a succession of 60 and 100 MHz instruments in the late 1950s and 1960s resulted in a significant advance in capability, both with respect to increased sensitivity, enhanced field stability and resolution, and the increased spectral dispersion due to the higher field. Improved variable temperature control and multiple resonance techniques became widely available. Although many improvements were focused on ^1H NMR, probes for ^{31}P and ^{13}C observation were available, and other 'nonstandard' nuclei of sufficient sensitivity could be studied by those willing to adjust the field strength to match the frequency of an existing probe and rf unit. In 1962, signal averaging was introduced into NMR (Section 5.2) to increase the sensitivity of the NMR experiment and significantly reduce the amount of material required. Even though these advances in instrumentation only partially solved the problems of sensitivity and resolution, they contributed to a substantial increase in the number of NMR applications in biochemistry during the 1960s. As pointed out by Oleg Jardetzky in his historical sketch (***Jardetzky, Oleg: NMR in Molecular Biology--A History of Basic Ideas***), the classes of problems that NMR could solve were clear as early as 1961: '(a) primary structure, (b) conformation or secondary and tertiary structure, (c) rate processes and molecular motion, and (d) interactions between molecules'. These topics largely determined the program for the research of the 1960s, and 'the agenda has remained the same since'.

During the 1960s, extensive compilations of proton chemical shift and coupling constant data were assembled for many of the basic biochemical building blocks, including amino acids and peptides; nucleic acid bases, nucleosides, nucleotides, and oligonucleotides; and monosaccharides.[609] In addition, as shown by the following examples, groundbreaking work was performed in a number of laboratories to

explore the effects of temperature, pH, neighboring magnetically anisotropic groups, as well as diamagnetic and paramagnetic molecular interactions on chemical shifts and relaxation parameters.

The first study of porphyrins,[610] conducted at 60 MHz in 1959, resulted in the discovery that the NH protons appear as a single resonance, shifted some 13 ppm upfield from a 'normal' position (such as that found in pyrrole), while the bridging methine protons are quite deshielded. The observations, which were explained on the basis of large π-electron ring currents in the macrocyclic rings, foreshadowed interesting later work in heme proteins.

In the early 1960s, several groups investigated hydrogen bonding and base-pairing in nucleosides and nucleotides. Initial studies, using low-temperature experiments on ^{15}N-enriched 1-methylcytosine in nonaqueous solvents, provided unambiguous proof that the predominant tautomer of cytosine is the amino form and that protonation occurs at N-3.[611] Later work on purine and pyrimidine derivatives and nucleosides provided the first NMR confirmation of a Watson–Crick type GC base-pairing.[612,613]

In 1960, Mildred Cohn and Tom Hughes, then at Washington University, published the first ^{31}P spectra of ATP and ADP. Cohn provides a vivid account of these experiments in her historical sketch (***Cohn, Mildred: Peregrinations of an Enzymologist in NMR***), explaining that she had originally thought of NMR in 1955 as a possible means to distinguish the three phosphorus atoms of ATP and thus define the structure of enzyme–metal–ATP complexes. As Washington University's NMR spectrometer was not capable of ^{31}P detection, the actual experiment was delayed until she could arrange to accomplish the work at Varian Associates Applications Laboratory during a 1958 summer break spent in California. She used 'three incredibly viscous solutions, 1 M ATP, 1 M MgATP, and 1 M MnATP, the concentrations necessary to observe ^{31}P in a single scan at 24.3 MHz in a 5-mm tube.' The spectra showed the expected three peaks, which shifted on complexation with Mg^{2+} and broadened with Mn^{2+}.

Cohn extended these original experiments, obtaining higher-resolution spectra (where the P–P coupling could be distinguished as shown in Figure 69), determining the pH dependence of the chemical shifts of ADP and ATP, and studying the effects of metal ions. Early in the metal complex experiments she discovered by accident (as she recounts in her historical sketch) that the effects of Cu^{2+} binding on the ATP spectrum were very different from those of Mn^{2+}:

> In preparation for the metal complex experiments, I removed the sodium from the commercial ATP and substituted the tetramethylammonium ion on an ion-exchange column. Much to my surprise and chagrin, the spectrum of this preparation differed greatly from that of sodium ATP, the β-P and γ-P resonances were very broad and the α-P resonance was sharper and enhanced in height. Disturbed, I consulted my chemist friends, and Dave Lipkin said, 'It looks like a paramagnetic effect'. Whereupon I investigated the history of the resin and found that it had been sized through a brass sieve, the usual procedure at that time. The unlikely supposition that copper had been picked up by the resin during sizing and had been removed by the ATP was indeed confirmed by ashing the ATP sample and analyzing for copper. Because Cu(II) can only form square planar complexes, only the β-P and γ-P resonances were broadened and the narrowing of the α-P represented the collapse of the unresolved α-P doublet due to the greatly increased relaxation rate of the β-P (the poor man's decoupling technique).

Figure 69 ^{31}P NMR spectrum (24 MHz) of adenosine triphosphate (ATP) in water.[614] (Reproduced by permission of the American Society for Biochemistry and Molecular Biology)

This anecdote is interesting historically because it reflects the problems of paramagnetic contamination faced by many early investigators, who sometimes unwittingly drew erroneous conclusions on the significance of line broadenings.

The ATP/ADP results, published in 1960 and 1962,[614,615] set the stage for the development of an enormous body of literature applying ^{31}P NMR to biochemical, biological, and medical problems. In fact, as outlined in Section 12, among the first in vivo NMR experiments were studies of phosphorus-containing metabolites in cells and tissues.

Small linear oligopeptides were initially studied to determine the effect of the peptide bond on amino acid chemical shifts and utilize the information for the analysis of polypeptide spectra. Attempts were also made to see whether chemical shifts could be utilized for primary sequence analysis.[616,617] The effects were small, however, and the true value of NMR for the study of peptides was found in its ability to probe three-dimensional conformation and the dynamics of these molecules in solution.

A large body of work on synthetic and naturally occurring linear and cyclic peptides was conducted in numerous laboratories during the 1960s and 1970s. For example, Vladimir Bystrov and his co-workers[618] were particularly active in using measured vicinal coupling constants together with modified Karplus relations to deduce conformations in peptides, while proton chemical shifts were also found useful for measuring *cis/trans* isomerization in proline peptides.[619,620] A great deal of effort was put into the analysis of hydrogen bonding and solvent accessibility to peptide bonds as measured by the rate of H/D exchange of the peptide N–H protons, a method introduced in 1968 by Stern, Gibbons, and Craig.[621] In noninteracting solvents, linear oligopeptide chains as short as seven residues were found to adopt incipient α–helix conformations.[618,622] NMR studies of both synthetic and naturally occurring cyclic peptides were particularly informative. In 1964, Schwyzer et al. studied the hexapeptide cyclo(GlyProGly)$_2$, which they found to be symmetric since only three sets of resonances were observed.[623] Later, Blout and his colleagues[624] investigated a series of synthetic peptides of the form cyclo(ProGly)$_n$ for n = 3, 4, and 5, and determined the symmetry and conformation of the molecules in relatively noninteracting solvents, such as methylene chloride, and in water. Another example, shown in Figure 70 from work by Kopple et al.,[625] illustrates the temperature-dependent studies used to elucidate internal hydrogen-bonding schemes. Likewise, natural cyclic peptides, such as the antibiotic gramicidin S and the hormone oxytocin, were studied by NMR to ascertain their conformational flexibility.[626,627,628]

During this period, studies of proteins were generally limited either to certain resonances that fortuitously appeared outside the broad unresolved hump that corresponded to the bulk of the protein signals or to 'random coil' resonances that were

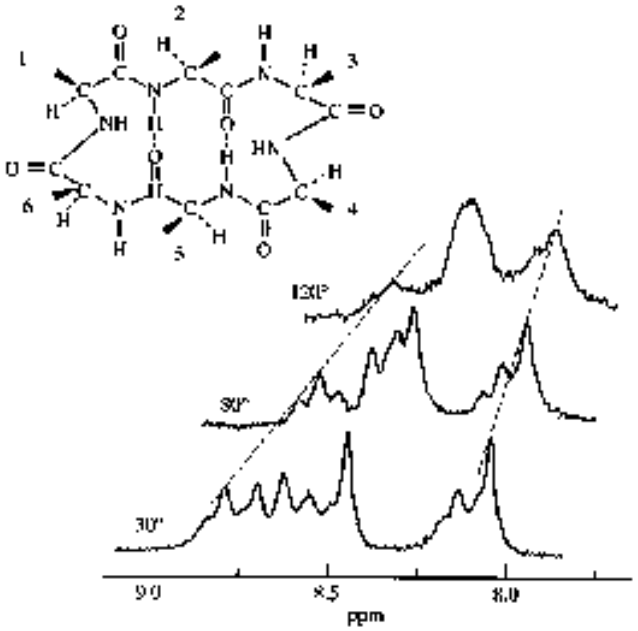

Figure 70 ^{1}H NMR (100 MHz) of the amide region of a partially deuterated cyclic hexapeptide, cyclo(glycyl-d_2–glycyl-d_2-tyrosyl-triglycyl) in a DMSO–water solvent.[625] (Reproduced by permission of the American Chemical Society)

revealed on disruption of the secondary and tertiary structure. Studies focused mainly on chemical shift measurements. Assignment and de novo structural conclusions for native systems were extremely difficult, and thus resolved resonances typically were used as empirical indicators of structural change to follow conformational transitions under widely varying conditions. In a series of papers during the early and mid-1960s discussed below, the existence of resolved resonances in native protein spectra was first revealed and the effects of denaturation on the spectra studied in detail.

In 1962, operating at 60 MHz, Arthur Kowalsky discovered two broad resonances at abnormally high field in the spectra of cytochrome *c* and myoglobin, ascribing them to side chains above and within the circumference of the aromatic porphyrin ring and thus subject to ring current effects.[629] In a subsequent paper[630] he extended these studies and reported the first observation of paramagnetic shifted resonances in ferricytochrome *c*, which appeared well outside the normal chemical shift range and disappeared in spectra of the diamagnetic form. These observations opened the door to a multitude of later publications, reflecting intense research efforts in many laboratories devoted to the study of paramagnetic proteins, including those rendered paramagnetic by the binding of 'unnatural' ions such as lanthanides. The availability of high-field superconducting magnets, discussed in the following section, contributed significantly to the advancement of these studies. Also, as described by Ivano Bertini (***Bertini, Ivano: A Life with Paramagnetic Molecules***), the very large shifts that were subsequently discovered, ranging, for example, between 200–300 ppm in high-spin cobalt(II) proteins, and excessive broadening of many of the shifted resonances, necessitated special techniques to increase the spectral width and handle dynamic range problems in both CW instruments and the later FT spectrometers.

International Conferences on Magnetic Resonance in Biological Systems

As magnetic resonance became a useful method for investigating a number of biological problems, the need for a forum to discuss these emerging techniques became apparent. Informal discussions among Mildred Cohn, Terry Eisinger, Oleg Jardetzky, Bill Phillips, and Bob Shulman soon led to the idea of an international meeting, and ultimately a series of such meetings —the International Conference on Magnetic Resonance in Biological Systems (ICMRBS). From the beginning, these conferences have been characterized by a spirit of enthusiasm and innovation, with an informal structure and a minimum of administrative overhead.

The first ICMRBS was held in Boston in 1964 and was followed by a second meeting two years later in Stockholm. These two meetings established the biennial series as truly international and set the stage for conferences that have largely alternated between western Europe and North America, with a few in more distant locations. The 30 meetings held through 1994 have been in Canada, England, France, Germany, India, Israel, Japan, the Netherlands, Sweden, Switzerland, and the United States.

This series of meetings covers biological applications in the whole range of magnetic resonance, not just NMR. In fact, the programs for the two earliest meetings were dominated by applications of electron spin resonance, which was then more readily applied to biopolymers and to living systems such as photosynthetic bacteria, than was NMR. Of the relatively few NMR talks, about half were devoted to metal–protein interactions. Over the years, as NMR has become more broadly applicable in biology, ESR remained a strong component in the program, but the balance has shifted to emphasize NMR applications to proteins, nucleic acids, and other biopolymers, to in vivo spectroscopy, and to imaging.

During the 1970s and into the 1980s, paramagnetic proteins provided a fertile field for systematic studies of magnetization transfer, relaxation rates, and steady-state and time-dependent NOEs, while the use of paramagnetic ions as probes of biomolecular structure and dynamics evolved into a broad field, utilizing ^{13}C, ^{14}N, ^{15}N, ^{31}P, and other nuclei for studies at nearly every level of biological complexity. In his historical sketch (***La Mar, Gerd N.: NMR of Paramagnetic Proteins***), Gerd LaMar describes the work of his group and others in using isotopic labeling to pin down assignments in heme proteins and thus take advantage of the information available from the large hyperfine shifts. Redfield and Gupta[631] used a saturation-transfer experiment to connect the resonances in oxidized and reduced cytochrome *c*, as Redfield describes in his historical sketch (***Redfield, Alfred G.: Foundations and Structures***):

> This permitted an estimate of the electron-transfer rate, and shortly afterwards Gupta found our first NOE. These were the first observations of these effects by FT NMR and in a protein. In the spring of 1970, I reported our machine architecture and spectra at the Experimental NMR Conference, but I did not report the electron-exchange results that we obtained a week before since I assumed, erroneously, that others might

easily be able to do this experiment. However, I could barely contain myself from talking about them. These saturation-transfer results connected key assignments made separately by Wüthrich, Shulman, and Phillips in the two states of cytochrome *c*, thereby solidly confirming these results and showing that a methionine was coordinated to the heme in both states.

In 1965, Mandel[632] drew attention to the aromatic amino acid resonances (tyrosine, phenylalanine, tryptophan, and histidine) that appeared at the low end of the spectra of proteins, apart from the rest of the complex envelope of signals. Of particular interest was the imidazole C-2 proton resonance of histidine, which not only could be resolved from the rest of the aromatic protons, but whose chemical shift had been shown by earlier studies to vary with the pH of the solution.[633] In Mandel's spectra, obtained at low and high pH, a peak corresponding to the C-2 proton resonances of all four histidine residues of ribonuclease was identified. Shortly thereafter, Bradbury and Scheraga[634] managed to resolve three resonances ascribed to the four histidine residues of ribonuclease at intermediate pH values and plotted their change in chemical shift with the pD of the solution to estimate p*K* values. Subsequently, the histidine C-2 proton resonances of several proteins including ribonuclease were completely resolved in a classic paper by Meadows, Markley, Cohen, and Jardetzky,[635] permitting studies of the effects due to pH changes and the presence of metal ions and inhibitors of enzymatic activity. Spectra from that paper and titration curves derived for each of the four histidine residues are shown in Figure 71. As Jack Cohen says in his historical sketch (***Cohen, Jack S.: Recollections of Early NMR Applications to Proteins and Cells***), these results confirmed the expectation of seeing one signal per histidine residue and demonstrated 'that the p*K* represented not an aggregate p*K* value, but rather reflects the local protein micro-environment'. He applied this concept to HEW and human lysozymes, where significantly different p*K* values for the single histidine resonance implied different local structures.[636]

One of the more interesting and far-reaching observations during this period was that certain resonances of small flexible molecules broadened on binding to biopolymers, while other resonances were relatively unchanged. The earliest studies, which appeared in the mid-1960s, involved the binding of small diamagnetic molecules such as coenzymes, substrates, and drugs to proteins. An example is found in a 1965 study that compared the relative relaxation rates of different peaks in the spectrum of penicillin G as a function of bovine serum albumin concentration, with the conclusion that penicillin binds through the interaction of the benzene ring with the protein rather than the penicillinic acid moiety.[637] Ligand-binding studies were particularly attractive in a period when protein spectroscopy was difficult and relatively unrevealing, and are still in use today to provide quantitative information on binding constants that is unavailable by other techniques.[638]

The problem of poor resolution and overlapping lines in biopolymer spectra resulted in some creative solutions. For example, in 1965, Jardetzky proposed a form of spectral simplification in which selected protonated amino acid residues would be observed on the background of a nearly completely deuterated protein. Meanwhile, Katz and Crespi[639] developed methods for preparing fully deuterated proteins from algae and, in 1968, obtained spectra of a protein that was fully deuterated except for the leucines.[640] In 1970, Markley and

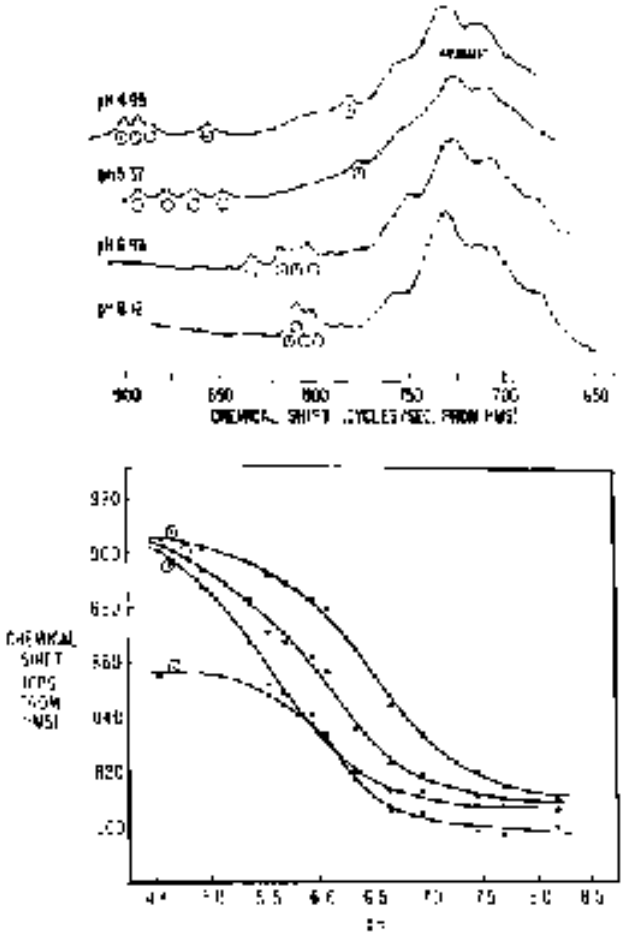

Figure 71 Top: 100 MHz proton NMR spectra of the aromatic region of RNAase A as a function of pH. Bottom: Titration curves of C-2 proton resonances of the histidine peaks shown in the spectra.[635] (Reproduced by permission of the National Academy of Sciences, USA)

Jardetzky obtained greatly simplified spectra of the aromatic region of selectively deuterated analogs of staphylococcal nuclease, which were utilized for detailed NMR studies on enzyme–inhibitor interactions.[641] Isotopic substitution with deuterium was found to be advantageous also in diluting the proton spins, thus reducing the dipolar interaction that leads to line broadening and increasing the resolution in ^{1}H spectra. More recently, random deuteration has been shown to be an important adjunct to multidimensional NMR spectroscopy of proteins, again to reduce proton–dipolar interactions, as discussed in Section 14.

A reverse approach, in which deuterium is introduced at specific sites for assignment purposes, also became useful, particularly with high-field FT instruments where resolved resonances could be studied and/or high-quality difference spectra obtained.[642] In addition, deuterium substitution for the purpose of measuring ^{2}H quadrupolar relaxation times also developed as an important tool during the 1970s for studying molecular dynamics in nucleotides and peptides, and the interaction of small molecules with proteins. This technique has been particularly important in studying oriented or partially oriented systems including model membranes and polycrystalline proteins, as discussed in Section 10.7.

The first spectra of random-coil DNA and synthetic polynucleotides were obtained in 1964.[643–645] In these studies, all conducted at 60 MHz with preparations that were relatively polydisperse with respect to polymer molecular weight, no spectra were detected at ambient temperatures for double-stranded structures such as calf-thymus DNA and poly(A)-poly(U) mixtures. Above the melting temperature, however, the integrated intensity of broad peaks attributable to nonexchangeable base and ribose protons could be used to define a melting curve as the conformational integrity was disrupted. Similarly, in the earliest NMR observations of tRNA,[644,646] several broad peaks corresponding to base and ribose protons appeared as the temperature was increased from 10°C to 90°C. Only spectral regions, rather than specific resonances, could be followed in these early studies, which were also complicated by concentration and salt conditions that contributed to the aggregation of tRNA.[647]

A Major Step Forward: The First High-Field Spectra

The introduction of the Varian HR–220 MHz spectrometer in 1964, operating with the first superconducting magnet, deserves a special place in this history. Although clearly there were limitations to the system as outlined below, the HR–220 made an enormous difference in the ability of many laboratories to make advances in biochemical research. Both sensitivity and resolution were substantially improved, and strongly coupled spin systems could be unraveled by the high field to produce spectra that could be readily analyzed by visual inspection or computer calculation and simulation. For example, it was clear from the earliest studies of nucleosides and nucleotides that ribose conformations could be estimated from application of a Karplus-type relationship to the magnitude of the vicinal couplings. However, those studies had to rely mainly on measurement of $J_{H-1'-H-2'}$ because of the complex spin systems. Complete analyses became possible at 220 MHz, as illustrated in Figure 72 by studies on the molecular conformation of uridine.[648]

At the high end of the molecular weight range, the improvements in the spectra of biopolymers were also very significant. Bob Shulman's historical sketch (***Shulman, Robert G.: My Years in NMR***) describes his experience at the 2nd International Conference on Magnetic Resonance in Biological Systems in Stockholm in 1966:

> There I was electrified by the 220 MHz ^{1}H spectra of the small proteins RNase and lysozyme presented by Bill Phillips. Suddenly the spectra showed well resolved lines, particularly to higher and lower fields than the central resonances but even in the overlapping region between 1 and 7 ppm sharp resonances could be observed. My previous experience at 100 MHz had led to the conclusion, which was widely if not universally held, that there were very few sharp lines in macromolecules, so that the well resolved spectra at 220 MHz were very surprising. I returned to Bell Laboratories and within a week had ordered a 220 MHz spectrometer which, when it arrived in early 1967, was only the second such installation in the world.

In 1967 and 1969, Phillips and McDonald published the first 220 MHz proton spectra of native and denatured (random-coil) proteins and single-stranded DNA.[649,650] They were able to resolve high-field shifted resonances in native lysozyme and cytochrome *c*, explore in more detail the spectral changes induced by denaturation, demonstrate that the spectrum of a random-coil protein can be computed to close approximation using a set of characteristic random-coil amino acid chemical shifts, and estimate purine/pyrimidine ratios for DNA from different species. The work clearly had an impact. In their 1968 review entitled, 'High Resolution Nuclear Magnetic Resonance Studies of Biopolymers',[651] E. M. Bradbury and C. Crane-Robinson began:

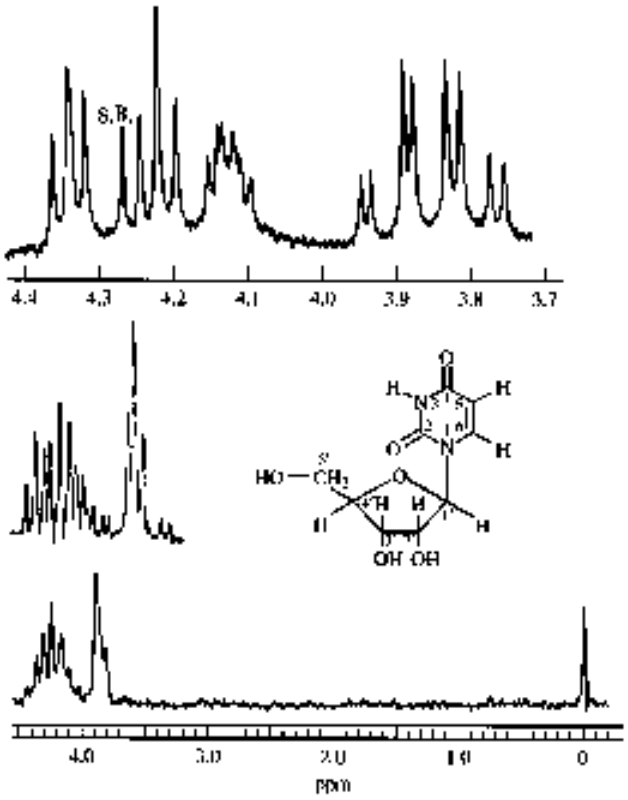

Figure 72 Proton NMR spectra of uridine at 60 MHz (bottom),[174] 100 MHz (middle),[174] and 220 MHz (top).[648] (Reproduced by permission of Varian Associates and the National Research Council of Canada)

> An ex-postdoctoral student of a colleague recently wrote from the United States that everybody in the physical biochemistry field was making nuclear magnetic resonance (NMR) studies of biopolymers. This may be an exaggeration, but it is worthwhile to enquire why there should be this upsurge of interest in a technique which has been available to chemists for the past decade or more ... The pioneers of these applications, Kowalsky, Cohn, and the Jardetzkys, have written extremely lucid and detailed introductions and reviews, while, more recently, details have appeared of the exciting work being carried out by Phillips, McDonald and co-workers at 220 MHz. It is the appearance of their work which has focused attention on the potential of magnetic resonance in the field of molecular biophysics.

High-field spectroscopy also opened a window of opportunity for studies of the hydrogen-bonded protons of polymers. In 1971, Kearns, Patel, and Shulman demonstrated that hydrogen-bonded imino protons in H_2O solutions could be observed in the 11–15 ppm spectral region.[652] The increased sensitivity and resolution of a 220 MHz spectrometer was essential in that study in order to overcome the extreme experimental difficulties of observing peaks corresponding to mM

concentrations in the presence of an enormous solvent water peak. The authors followed the broadening and subsequent disappearance of several semiresolved resonances as the temperature was increased. Further improvements in the resolution and sensitivity of later instruments contributed to extensive research efforts in a number of laboratories to identify the number of resonances contributed by secondary and tertiary structure base–pairs, the role of metal ions in stabilizing tertiary structure, the interaction of tRNA with intercalating drugs, and the kinetics of hydrogen-bond formation and disruption.

In 1967, Bob Shulman and his colleagues, including Kurt Wüthrich and Seji Ogawa, used their new 220 MHz spectrometer to embark on a study of hemoglobin. Shulman describes in his historical sketch (***Shulman, Robert G.: My Years in NMR***) the interpretation of the porphyrin resonances in hemoglobin, and later the preparation and NMR investigation of mixed valency hybrids from the α- and β-polypeptide chains to establish the process involved in the long-studied cooperative oxygen binding.

The Fourier Transform Era Begins

NMR spectrometers utilizing pulse FT methods became commercially available around 1970. The advantages of the pulse FT technique were rapidly exploited by biochemists, and opened a floodgate of applications that until then had been impossible due to the low sensitivity and inherent inflexibility of CW NMR spectroscopy. For example, one could now average in the time domain, typically resulting in as much as a 100-fold increase in sensitivity. This provided an enormous advantage in terms of sample size and length of the experiment. In the case of insensitive nuclei such as ^{15}N, it meant that natural abundance studies finally became feasible, and developments in ^{13}C NMR moved rapidly, as we note in the following section. Fourier transform also enabled the development of special editing and data processing techniques to simplify spectra, enhance resolution, and improve the signal-to-noise ratio. Also, for the first time, pulse sequences to measure relaxation parameters could be used with complex systems rather than single spectral lines.

Initially, the strong water solvent signal was an even greater problem with pulse FT methods than with continuous wave techniques, since its dominance in the FID created severe dynamic range problems. A number of methods were proposed to 'eliminate' the water peak and met with mixed success. Reducing the residual HDO peak in a D_2O solution to a manageable level could usually be achieved, but real mastery over the H_2O solvent peak did not come until much later.

Basically five different approaches were used, one of which—rapid-scan correlation NMR—simply avoided the problem by continuing to use CW rather than pulse methods, albeit with an efficiency comparable with pulse-FT techniques. Dadok and others using his 250 MHz spectrometer[653,654] had considerable success with this approach, but it was not widely used elsewhere. The simplest technique, and one of the most commonly used, involved placing a simple selective presaturation pulse at the frequency of the solvent resonance. Taking up a suggestion advanced by Schaefer[655] in 1972 in connection with ^{13}C studies, Campbell et al.[656] were the first to apply the presaturation pulse to a sample of biochemical interest in 1974. They found that they could reduce the intensity of a 90% H_2O solvent signal by a factor of almost 1000 without significantly affecting peaks more than 0.5 ppm away. The method was successfully employed in many subsequent studies, but at times presaturation complicated the study of exchangeable protons in H_2O because of saturation transfer effects.

In 1972, Patt and Sykes suggested an alternative approach, 'WEFT' (*W*ater *E*liminated *FT*),[657] which employs a nonselective 180°, τ, 90° pulse sequence to null the water signal. Provided the compound of interest has a much shorter relaxation time than water (often the situation for larger biomolecules), data acquisition can be started at time τ and gives, in principle, an undiminished spectrum of the molecule of interest and no water signal. Benz, Feeney, and Roberts[658] soon amplified on the conditions for the use of WEFT, and subsequently a number of modifications were suggested to optimize the method. WEFT was particularly successful in D_2O solutions, where it has been widely applied, but in H_2O a sufficient reduction of the water signal was much more of a challenge, requiring careful optimization of the conditions. Moreover, the technique could not be used if relaxation data were sought or for quantitative studies in certain situations.

Probably the most effective method, in general, is simply not to excite the solvent resonance initially. Redfield and Gupta pioneered the use of a long, selective pulse to observe the remainder of the spectrum without exciting the solvent resonance.[295] Although a number of improvements were made, including Redfield's 2–1–4 pulse sequence introduced in 1975,[296] and other similar composite pulses developed by many other investigators, the technique really became effective for dilute solutions in H_2O only during the late 1980s and early 1990s with improved instrumentation, including pulsed magnetic field gradients. The availability of pulsed field gradients also permitted van Zijl and Moonen[659] to develop a novel approach to water suppression based on a modification of Stejskal and Tanner's technique for measuring diffusion coefficients. Because of the greatly different diffusion rates for water and biopolymers, this method permits excellent water suppression without interfering with the normal pulse excitation schemes.

Another area that benefitted enormously from FT techniques was ^{31}P NMR. In the early experiments by Cohn and Hughes, tricks such as using 12-mm thin-walled tubes (plastic containers of Hughes' Havana cigars) had permitted the observation of ATP spectra with good signal-to-noise ratios for concentrations down to about 0.1 M. Some 10 years later, increased field strength, sample spinning, and time-averaging techniques had improved the situation, but not enough for continuous wave ^{31}P NMR to be useful at mM concentrations. As David Gorenstein points out in his historical sketch (***Gorenstein, David G.: Developments in 31P NMR***), the coupling of a new Nicolet 1080 FT data system with their Bruker HFX–90 pulsed spectrometer made all the difference in studies on the binding of mononucleotides to ribonuclease A. The ability to observe signals at mM concentrations transformed ^{31}P NMR into an extraordinarily useful tool for biochemical, biological, and medical applications. Notable milestones in the realm of biochemistry include the discovery that ^{31}P isotope shifts from the substitution of ^{16}O in phosphate groups by ^{18}O could be used to study enzyme mechanisms,[660] and more recently the coupling of multinuclear MR and new synthetic techniques for the study of self-complementary

oligonucleotides to obtain information on the conformation and dynamics of the phosphodiester backbone.

Carbon-13 in Biochemistry

As we saw in Section 6, even before FT methods were developed, several laboratories were able to carry out studies of ^{13}C in natural abundance (albeit still at molar concentrations) by making use of the combined effect of better homogeneity, improved field stability, frequency-sweep instruments with broadband proton decoupling, and time-averaging techniques. The laboratories of J. D. Roberts and D. M. Grant, both intimately involved in the improvement of ^{13}C NMR techniques, were among the first to profit from the new-found capability by conducting extensive surveys of ^{13}C chemical shift data on steroids, sugars, nucleosides, nucleotides, and other natural products. Recalling this period in his historical sketch (***Roberts, John D.: A Personal NMR Odyssey***) Roberts notes, in particular, the work in his laboratory by H. J. Reich and M. Jautelat to assign the spectrum of cholesterol, D.E. Dorman's study of sugars, and J.G. Nourse's 'Herculean efforts with erythromycin antibiotics'. During the late 1960s and very early 1970s, the amount of ^{13}C data on biologically important substances accumulated in these and other laboratories was impressive, as demonstrated by the contemporary reviews by J. B. Stothers[121] and George Gray.[661]

During this same period, interest was kindled in the use of ^{13}C enrichment as a tracer technique for elucidating biosynthetic pathways, and also as a method for the assignment of ^{13}C resonances in complex biomolecules.[662] Beginning in 1966 with the work of Tanabe and Detre,[663] there were several studies of natural products utilizing ^{13}C satellites in proton spectra, where an increase in the satellite intensity signaled the incorporation of a label at a particular site. In 1970, Tanabe and co-workers[664] fed acetate labeled with ^{13}C at the carbonyl and methyl positions in two separate experiments to cultures of the fungus *Stemphylium radicinum*, and reported the first direct ^{13}C observations of biosynthetically labeled carbon atoms. Their approach not only identified the origin of the carbon skeleton, but allowed for an excellent proton-decoupled CW spectrum to be obtained at 25 MHz. Tanabe's work encouraged other investigators to use ^{13}C to probe metabolic pathways and study biosynthetic enzymes. The challenge for many during this period, however, was formidable: to obtain enough enriched material to give a sufficient signal-to-noise ratio in low-field spectrometers, even those using FT time averaging. Ian Scott's historical sketch (***Scott, A. Ian: 13 C NMR Studies of Biosynthesis. A Quarter Century in Retrospect***) gives a good account of both the difficulties and the triumphs of the early experiments that used both enriched and natural abundance ^{13}C isotopes. Such studies became really practical only with the development of modern high-field spectrometers, with greatly improved electronics and probes, which have cut the amount of required material by some two orders of magnitude.

Biosynthetic random ^{13}C enrichment was utilized in the late 1960s simply as a means of increasing the sensitivity of the NMR experiment sufficiently to obtain chemical shift data. For example, in a series of papers using INDOR, CW, and then FT techniques, Hyman Sternlicht and co-workers used biosynthetic preparations of 15%-enriched amino acids to measure chemical shifts, showing that resonances could be identified and assigned by the use of a set of empirical rules.[665,666] As noted by Jim Feeney in his historical sketch (***Feeney, James: Personal Reminiscences on NMR***), isotopic labeling also permitted detailed investigations of protein–ligand complexes in which multiple conformational states could be characterized and the dynamics of the protein–ligand interaction studied. The use of isotopic labeling continued to be an important adjunct to NMR spectroscopy, both for increasing the intensity of specific resonances so that they could be identified and studied without interference from other signals, and for achieving sufficient sensitivity to study minute amounts (such as in vivo metabolites). Most recently, as discussed in Section 14, advances in genetic engineering have resulted in techniques to produce sizeable quantities of proteins labeled in ^{2}H, ^{13}C, and ^{15}N.

As a final footnote to the pre-FT era, we note the first natural abundance ^{13}C NMR spectrum of a protein (hen egg white lysozyme), published by Lauterbur in 1970.[667] The 25 MHz spectrum was obtained by Roy Johnson in the Varian Applications Laboratory using a 25% aqueous solution of the protein in an 8-mm sample tube containing a 2-mm tube of ^{13}C-enriched CH_2I_2 for a field-frequency lock signal. After over three and a half days of signal averaging, a noisy but tantalizing spectrum was obtained. Lauterbur noted in this paper that only relatively small gains in sensitivity above that observed in this CW experiment were likely and that the future for the routine study of enzymes lay in pulse FT techniques.

^{13}C NMR spectroscopy was a particular beneficiary of pulse FT technology, and the new-found capability resulted in an explosion of applications to biochemical systems. With the introduction of FT techniques, the amount of sample required remained about the same, but after only about 10–12 h (an 'overnight scan') spectra could be obtained with peaks corresponding to as few as three carbons clearly observable. Allerhand, Cochran, and Doddrell[668] were the first to obtain a ^{13}C FT spectrum of a protein, ribonuclease, and commented in their 1970 paper that

> As expected, the ^{13}C spectrum was appreciably richer in detail than the corresponding proton spectrum. Natural abundance ^{13}C Fourier transform NMR appears to be a practical tool for the study of biopolymers in solution.

This new capability was truly noteworthy. In his 1973 review entitled 'Applications of ^{13}C Nuclear Magnetic Resonance in Biochemistry',[661] George Gray noted: 'What until recently was virtually unimaginable is now happening frequently, that is, the observation of ^{13}C NMR spectra of biopolymers such as large polypeptides or enzymes.'

Allerhand and co-workers were keenly interested in pushing the technique a step further to observe resonances corresponding to single carbon sites and thus improve the applicability of NMR for conformational studies. They decided to focus on nonprotonated carbons, showing that they are the least broadened by dipole–dipole interactions and appear in small numbers over a relatively wide chemical shift range. Their solution was to build a probe for 20-mm spinning sample tubes, significantly increasing the sensitivity of the experiment *and* the amount of sample required.[669] As Eric Oldfield remarks in his historical sketch (***Oldfield, Eric: NMR Adventures in Chemistry and Biology***):

> We used to cram 2–3 g of protein into the tube, and wait—but the spectra were extremely nice, although generally restricted

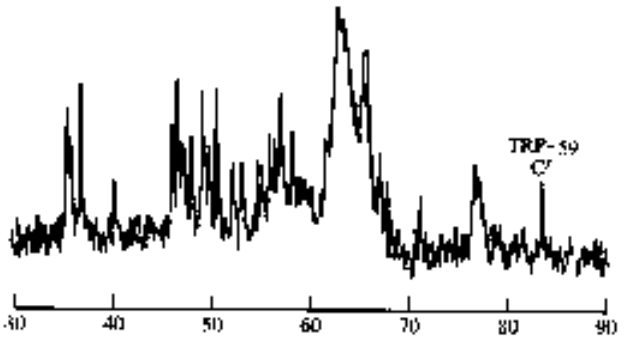

Figure 73 Partial 15 MHz ^{13}C spectrum of reduced cytochrome *c* obtained with a 20-mm diameter sample tube in 11.4 h.[669] (Reproduced by permission of the New York Academy of Sciences)

> to nonprotonated carbons. Of course, these days, such amounts of protein seem absurd—although with labeling the numbers of C-13 spins are about the same!

An example of the success achieved with this approach is given in Figure 73, where the γ-carbon resonance of a single tryptophan can be seen.

As recounted by David Doddrell in his sketch (***Doddrell, David M.: An Historical Perspective of Research Based Upon Misguided Advice***), the availability in 1971 of Allerhand and Clouse's ^{13}C FT spectrometer at the University of Indiana provided the impetus to measure and understand ^{13}C relaxation parameters:

> Our fear was that they may be uselessly long (we guessed tens of seconds for protonated carbons) . . . Of course history proved that we were up to a factor of 100 too long in our guess; the major result of this work was that we had developed a simple method of studying solution molecular dynamics still in use today.

'The Domain of Solid State NMR'

While conventional high-resolution NMR was being employed extensively, other distinctly different approaches were also developed to study the structure and molecular dynamics of biochemical systems. These include the use of solvent water relaxation rates to probe biopolymers in solution (discussed earlier), and methods to study model membranes and solid compounds of biological interest.

During the 1960s, Chapman and co-workers had successfully used wideline ^{1}H NMR to demonstrate the increase in mobility that occurs when phospholipids are heated above the gel-to-liquid crystal phase transition temperature.[670,671] However, analysis of phospholipid bilayer model membranes was limited by their broad and featureless NMR spectra, a result of incompletely averaged anisotropic interactions. Consequently, techniques were developed to prepare small diameter vesicles by ultrasonic irradiation, yielding higher resolution ^{1}H, ^{31}P, and ^{13}C spectra that could be used for chemical shift and relaxation time measurements. For example, Metcalfe et al.[672] measured ^{13}C T_1 values in sonicated lecithin vesicles and related the data to the internal and overall mobility of the molecule.

Developments in the NMR study of liquid crystals also had an impact. In 1967, Lawson and Flautt[225] extended this work from classical thermotropic liquid crystals to a lyotropic mesophase, which can be considered as a model membrane system since it resembles qualitatively the phospholipids of biological membranes. The use of ^{2}H NMR in biomolecular structural studies was further catalyzed by the work of Charvolin et al.[673] in 1973. They studied an oriented lamellar lyotropic liquid crystalline phase of perdeuterated potassium laurate and water, and observed seven distinct quadrupole split doublets when the angle between the normal to the lamellar plane and the applied magnetic field was 90°. This indicated different degrees of order for different C–D bonds, thus providing information on the relative mobilities of the various CD_2 and the terminal CD_3 groups.

Although the use of vesicles had provided a partial solution to the problem of resolution, the sonication technique itself created controversy over the extent to which it altered the physical and chemical properties of the bilayer model or natural membrane structure. In 1971, Metcalfe et al.[672] showed that ^{13}C spectra could be obtained from unsonicated dipalmitoyl lecithin and from erythrocyte membranes, but the lines were quite broad. A breakthrough came in the early 1970s, when it was found that quadrupole splittings from deuterium-labeled lipids could probe the ordering of unsonicated bilayer systems.[674–676] These reports kindled increased interest in applications of ^{2}H NMR to biochemical problems, and from the perspective of the 1990s Ian Smith points out in his historical sketch (***Smith, Ian C. P.: Deuterium NMR: Reflections on its Evolution***) that 'the most dramatic contribution of ^{2}H NMR in biochemistry is undoubtedly in the field of biological membranes.' In 1976, Myer Bloom and associates[677] introduced the quadrupolar echo method, thus solving one of the major experimental problems in ^{2}H spectroscopy at that time: signal loss due to instrumental dead-time in the very early portion of the FID. As pointed out by Bloom in his historical sketch (***Bloom, Myer: Personal Views of NMR History***), this new capability for producing distortion-free ^{2}H spectra, coupled with methods for analyzing the observed Pake doublet splittings, was a crucial step in the ability to study interactions between lipids and other membrane constituents such as proteins, peptides, or cholesterol. Also, by this time, Urbina and Waugh had published the first applications of ^{13}C cross polarization and high-power ^{1}H decoupling to unsonicated phospholipid bilayers, obtaining resolved resonances in both gel and liquid crystalline phases with linewidths determined only by chemical shift anisotropies,[678] while Chapman and Oldfield collaborated with Doskočilová and Schneider to apply ^{1}H magic angle spinning to the study of membranes.[679]

All of these techniques, as well as methods for the analysis of ^{31}P and ^{13}C chemical shift anisotropy, were available in the mid-1970s. As summed up by J. Seelig in his historical sketch (***Seelig, Joachim: NMR and Membrane Structure***), 'by the end of 1976 the NMR toolbox for membrane studies was wide open and provided the instruments for many biophysical membrane studies to come.'

During the 1980s the combination of high-field spectrometers and magic angle sample spinning techniques finally yielded truly high-resolution ^{1}H spectra of lipids,[680] opening a full range of opportunities for the study of natural membranes. NMR studies on the structural and motional properties of vesicles have also continued to this day, driven in part by

an increasing emphasis on potential medical applications such as drug delivery systems.

As a complement to the work on lipids, the 1970s and 1980s saw a growing number of applications of solid state techniques to both small biomolecules and biopolymers. This work was motivated both by the desire to capitalize on information from anisotropic interactions, such as dipolar couplings, and by the fact that standard NMR techniques are unusable when the isotropic reorientation of biomolecules becomes extremely restricted due to large molecular size or association into supramolecular structures such as membranes or virus particles. As Stan Opella remarks in his historical sketch (***Opella, Stanley J.: NMR Spectroscopy and Structural Biology***), 'This is the domain of solid state NMR spectroscopy, even if the samples are actually solutions'.

Two examples are illustrative of both the technical challenges associated with solid state NMR studies and the advances that have been made in the understanding of structure and internal motions of proteins in solid phases. Dennis Torchia describes in his historical sketch (***Torchia, Dennis A.: A Fortuitous Transformation***) his observation that polycrystalline amino acid and peptide model systems demonstrated a surprising amount of rapid molecular motion. This led to the development of equations for anisotropic spin–relaxation and powder lineshapes for a wide variety of models of molecular reorientation. The study of molecular dynamics in crystalline proteins came within reach, however, only when protein expression techniques could be employed to produce sufficient quantities of isotopically labeled protein to achieve the sensitivity and specificity needed for interpretable ^{2}H and ^{13}C/^{15}N solid state spectra. As Torchia says:

> Initially we prepared polycrystalline protein samples containing one type of deuterated amino acid, and obtained clear evidence that the side chain of each type of labeled amino acid was mobile. In order to overcome the problem associated with overlapping powder patterns, we next obtained cross-polarized magic angle spinning spectra of ^{13}C/^{15}N labeled samples. These high-resolution spectra enabled us to observe signals corresponding to individual atomic sites in the protein.

Torchia found that the chemical shifts of the crystalline state almost universally matched those in solution, and thus embarked on heteronuclear NMR studies with his colleague Ad Bax at NIH to assign the solution spectrum (and thus the solid state spectrum) using heteronuclear NMR techniques.

In his historical sketch, Opella discusses the development of solid state spectroscopy to determine the structures of peptides and proteins using oriented samples. He provides an example of the application of these methods in studies of filamentous bacteriophage coat proteins:

> Remarkably, these virus particles orient spontaneously with their filament axis aligned with the direction of the applied magnetic field. All of the structural studies of the filamentous viruses planned when the laboratory was being established at the University of Pennsylvania starting in 1976–79 were designed to take advantage of the fact that these nucleoprotein complexes could be oriented either as fibers, or later as solutions in the magnetic field of the spectrometer. By 1982–83, the implementation of selective ^{15}N labeling of both backbone and side-chain sites and magnetic orientation of virus solutions enabled the high-resolution structural information to be obtained on a protein in a supramolecular structure, the 10^7 dalton virus particles. Subsequently ^{13}C and ^{15}N NMR experiments were used to obtain data from a sufficient number of sites to yield a model of the fd coat protein in the bacteriophage.

In Section 8, we reviewed the development of multiple pulse and magic angle spinning methods that are designed largely to eliminate the line-broadening effects of dipolar interactions in solids. However, with the line narrowing comes the loss of information on interatomic distances that might be derived from dipolar coupling. In the 1980s, Bob Griffin and others, partly motivated by the desire to measure distances in solids of biological interest, developed methods to reintroduce the effect of homonuclear dipolar interactions in a controlled manner—high-resolution dipolar recoupling. The initial method, DIPSHIFT and its derivatives, were successful but were applicable only to molecules with strong dipolar coupling between directly bonded nuclei. What was needed were techniques applicable to weaker interactions from nonbonded ^{13}C, ^{14}N, and ^{31}P. As Griffin says in his historical sketch (***Griffin, Robert G.: Perspectives of Magnetic Resonance***):

> At the time there was a double ^{13}C labeled glycine sample around the laboratory, left over from measurements of double quantum spectra in solids. Dan Raleigh performed a MAS experiment with this sample and happened to observe a pronounced broadening of the ^{13}C resonances at a spinning speed equal to one-third of the isotropic shift difference. We had rediscovered rotational resonance (R^2), a phenomenon initially reported by Raymond Andrew in 1963/65. We described the broadening in glycine in a short paper and pointed out that this was a recoupling effect which could provide internuclear distances. For long distances or weak couplings the lineshapes were too small to be useful, so I proposed a magnetization exchange experiment at R^2 for such cases.

Griffin and co-workers[681,682] obtained the first distance measurements on a protein in 1989, and the method has subsequently been applied to other solids of biological importance.

Meanwhile, Jake Schaefer, who had pioneered the modern renaissance of MAS in ^{13}C studies, developed a related method for studying dipolar interactions between two different rare spins (e.g., ^{13}C and ^{15}N) and hence estimating their internuclear distance. This technique, REDOR (*R*otational *E*cho *DO*uble *R*esonance),[683] involves a cross-polarization/magic angle spinning experiment in which 180° pulses are added in careful synchronization with the rotor speed. A train of rotational echoes is thus created in which intensity alterations result from the dephasing of the magnetization of one spin in the presence of the local dipolar field of the other. By adjusting pulse timing and number of rotor cycles used, the results can be optimized for particular dipolar interactions in a sample containing chemically different carbons and nitrogens.

The Higher the Better: From 220 to 800 MHz ... and Up?

The Varian 220 MHz system in the 1960s and early 1970s had made an enormous difference in the ability of many laboratories to study complex biomolecules. However, there were some significant drawbacks, as described by Kurt Wüthrich (***Wüthrich, Kurt: NMR Structures of Biological Macromolecules***) and R. J. P. Williams (***Williams, R. J. P.: The Use of NMR in Biology: Personal Reflections***). The instrument was largely limited to CW field-sweep, proton-only, operation. The lack of a field-frequency lock and the need for high sample spinning rates led to instability problems during the long accumulations that are a requirement for most

biochemical studies. In addition, double resonance experiments were awkward, requiring homebuilt audiomodulation devices, and perhaps most importantly, data handling was limited to time-averaging computers (with very limited memory sizes) which could be interfaced to the system. In applications to biopolymers, the instrument did not provide sufficient resolution to be able to study the main envelope of signals in proteins. Disappointingly, says Williams, ' ... it proved impossible to get spectra better than those demonstrated by Jardetzky's studies [at 100 MHz] started somewhat earlier. All that could be seen were some histidine residues.'

The next generation of spectrometers, operating at ^{1}H frequencies up to 360 MHz with pulse FT and multinuclear capability, was revolutionary in advancing the state of the art for NMR applications in biochemistry. In the early 1970s, as we saw in Section 6, a joint effort between Oxford University, Oxford Instruments, and Bruker had succeeded in producing the first 270 MHz FT spectrometer. Operating at a field three times that of the then standard Bruker spectrometer, the magnet had excellent resolution and stability and was immediately applied to studies of proteins. Williams describes the excitement of the 270 MHz instrument in his historical account:

> We were able to carry out spin decoupling and NOE experiments for the first time in proteins. In fact it was clear to us all that protein structures could be studied and it became a matter of innovation in pulse sequences and in structure analysis in order for the objective to be reached ... We showed, more importantly, that the dynamics of proteins could be analyzed.

A Bruker 360 MHz instrument followed in 1976. For many investigators who had been largely restricted to 100 MHz instruments, the step from 100 MHz to 360 MHz was revolutionary, and there were major improvements in data-handling capability. Simply repeating some of the experiments from previous years provided a wealth of new results, and opportunities arose for doing experiments beyond measurement of chemical shifts, as we discuss in some detail in Section 14.

These instruments and their successors at 400, 500, 600, 750, and now 800 MHz, created a fertile ground for successful application of NMR to the most complex of biochemical and biological problems. Developments in pulsed NMR methodology were also, however, to become essential, as we shall see in the following section.

TWO-DIMENSIONAL NMR

The early years of the 1970s witnessed two discoveries in NMR that would have far-reaching consequences. Two-dimensional (2D) Fourier transform NMR was proposed in 1971, and a year or two later came the idea of using NMR to obtain macroscopic images. We shall discuss NMR imaging in detail in later sections. The reason for mentioning it here is that 2D NMR and NMR imaging crossed paths very early in their respective developments, as we shall see below. In this section we explore the origins of 2D methods, summarize the variety of techniques that have evolved, and indicate the range of applications that have been developed.

The Origins of 2D NMR

The concept of two-dimensional NMR was first articulated by the Belgian physicist Jean Jeener at an AMPERE Summer School in 1971. The initial idea of 2D NMR grew out of Jeener's studies of spin–lattice relaxation in liquid crystals. As he relates in his article (***Jeener, Jean: Reminiscences about the Early Days of 2D NMR***), Jeener tried to 'cook up a pulse scheme' to examine the relaxation matrix in a kind of stochastic mode. He was concerned about interference from coherent responses from multiple pulses and began investigating such phenomena. This work led to the proposal of a simple sequence of two 90° pulses separated by a time t_1, which would be incremented between experiments just as in numerous other pulse sequences (e.g., that for measurement of T_1 by a 'saturation-recovery' method). The difference was that Jeener proposed to Fourier transform not only the FIDs following the second pulse but also to carry out a second Fourier transform with respect to the time variable t_1. He showed that transfer of coherence as a result of the second 90° pulse would lead to cross peaks in a two-dimensional frequency plot. Jeener and Alewaeters tried to verify the theory experimentally but met with only partial success:

> We tried to observe the effect experimentally on ethylbenzene, spending weekends working with the rather primitive FT spectrometer available in organic chemistry at our university. Due to bad phase stability of this spectrometer, and to our total lack of practice of high-resolution NMR, Gerrit Alewaeters could only observe some of the strongest cross peaks of the 2D spectrum with a signal-to-noise ratio just high enough to confirm that our quantum mechanical predictions were correct (not really a surprise ...), but too low to make the new technique look very usable. Formal publication was deferred until cleaner experimental confirmation would be available, but I kept spreading the idea by personal contacts, lectures (probably for the first time at the AMPERE Summer School in Basko Polje in 1971), and by circulating "unpublished" notes written in November 1971. [*Editor's Note*: Jeener's notes may now be considered 'published' since they were included as a scientific contribution in a book presented in 1994 to Anatole Abragam on the occasion of his 80th birthday.[684]]

Thomas W. Baumann, in Richard Ernst's laboratory in Zürich, attended this Summer School and brought back detailed notes on Jeener's talk, which he discussed with Ernst. In his article (***Ernst, Richard R.: The Success Story of Fourier Transformation in NMR***) Ernst says:

> This was exactly the technique I had been waiting for. I had been thinking for some time about systematic computer-controlled double resonance experiments, but appreciated the complexity of the resulting 2D spectra should they follow the shape of the famous Anderson–Freeman plots. The Jeener two-pulse experiment appeared not to have this disadvantage.

Ernst (Figure 74) and his student Enrico Bartholdi carried out calculations to verify and probe the new idea, but Ernst initially planned no experiments because he considered 2D spectroscopy as 'Jeener's property' and waited for his results to be published. Moreover, Ernst felt that his computer facility was inadequate for 2D data processing and storage. In 1973, Ernst corresponded with Jeener who showed him a rough draft of an unfinished paper (which was never published).

In April 1974, Ernst learned of Paul Lauterbur's use of NMR to create two-dimensional images and realized that Jeener's 2D technique could be adapted to this purpose. Ernst and his co-workers pursued this aspect, as we shall discuss in more detail in Section 13, and thus the first paper using 2D techniques by Kumar, Welti, and Ernst[685] dealt with imaging, not spectroscopy.

Figure 74 Richard Ernst. (Courtesy of R. R. Ernst)

Meanwhile Ernst also undertook 2D spectroscopy experiments, partially in preparation for a talk at the VIth International Conference on Magnetic Resonance in Biological Systems, scheduled for Kandersteg, Switzerland in September 1974. Ernst carried out the initial experiment himself on a modified Varian DA–60 spectrometer and wrote the software for the associated Varian 620i computer with 16 K memory. He presented both the spectroscopy and imaging results and says:

> It was little wonder that my rapidly concocted contribution was rated at the Kandersteg conference as premature! Sometimes, however, even prematurely born children survive and excel. . . . Modern times had started without being noticed at that instant.

The Foundations of 2D NMR Are Established

The first publication on 2D NMR spectroscopy was that of Müller, Kumar and Ernst,[686] which appeared in December 1975. This communication described what would later be termed '2D *J*-resolved NMR', a method we discuss in Section 11.3. This work was soon followed by a long paper by Aue, Bartholdi, and Ernst[687] which was the first formal exposition of the principles of 2D NMR. This publication presented a comprehensive view of the concepts of 2D NMR, together with detailed theoretical and experimental developments of virtually every imaginable aspect of the new technique. The authors dealt with the intensities, phases, and connectivities of transitions; they analyzed the unprecedented and complicated lineshapes that resulted from phase variation

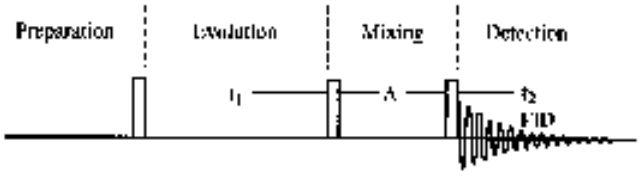

Figure 75 Schematic representation of the four basic periods that characterize a 2D NMR experiment

in two dimensions; they examined the effects of relaxation and magnetic field inhomogeneity, and they considered consequences of strong coupling and limitations imposed by assuming only weak coupling. Moreover, this paper addressed the use of 2D pulse methods to excite and detect multiple quantum coherences.

The basic concept of 2D NMR is simple, and this seminal paper established the framework for treating the many hundreds of innovative variations that were to come. A 2D experiment makes use of four time periods (Figure 75) namely preparation, evolution, mixing, and detection. The preparation period is necessary to bring the system to a known state, often thermal equilibrium, and to place magnetization into the *xy* plane, frequently by application of a 90° pulse. During the evolution period (t_1), the spins are allowed to precess under the influence of the Hamiltonian provided by the molecular system, together with additional perturbations imposed by the experimenter. During this period each spin is, in effect, 'tagged' according to its frequency and at the end of the period has acquired a specific phase relation relative to the rotating frame. The mixing period determines, in large measure, just what the particular 2D experiment achieves. In some examples, this 'period' simply involves turning on or off some external perturbation (such as a decoupler), whereas in other cases a pulse or sequence of pulses may cause the wavefunctions of the spins to interact, or mix, in such a way that information from one is transferred to another. The free induction decay (FID) is then acquired, as in any FT NMR experiment, during the detection period (t_2). By incrementing the period t_1, the phases of the spins at the beginning of the mixing period are systematically altered, with consequences that carry over into the acquisition period. Thus, each successive FID reflects the history of the spin system as a function of t_1. The NMR signal $S(t_1, t_2)$ is thus a function of two time variables and can be double Fourier transformed with respect to both t_1 and t_2, resulting in a two-dimensional frequency spectrum $S(F_1, F_2)$, which correlates the behavior of the spin system during the evolution period with that of the detection period.

Ernst and his group rapidly developed all of the ideas put forth in the 1976 paper, and many more. Ernst refers to 'playing with a new toy', as the ideas and experiments rolled out during the next two to three years. Initially, there was little competition. However, at Oxford University, Ray Freeman immediately appreciated the potential of the new method in providing a much more efficient way to gather large quantities of information that had been available only via the double resonance methods that he had, in part, developed. With only limited instrumentation (initially a Varian CFT-20, which could produce only 20 MHz ^{13}C FT spectra), Freeman and his group quickly conceived some important and novel 2D experiments, of necessity involving ^{13}C NMR. Also, at the University of California in Berkeley, Alex Pines, who was

largely interested in the NMR of solids, recognized the value of multiple quantum effects, thus beginning a line of research that would intersect the more advanced developments in 2D NMR. Meanwhile, at MIT, John Waugh initiated a different set of experiments in which 2D methods were applied to studies of solids.

The power of 2D NMR in studies of liquids, as illustrated by papers coming primarily from the Ernst and Freeman groups in the latter half of the 1970s, inspired an increasing number of NMR spectroscopists to turn to these methods and persuaded NMR instrument companies to develop the necessary hardware and software. High-field spectrometers (up to 400 MHz) were available with generally good sensitivity, and computers had advanced during the last decade to accommodate one-dimensional FT experiments in a reasonably efficient manner. The additional requirements to perform 2D experiments involved mainly software changes, which in the early days were made by individual workers themselves depending upon the experiment desired. Toward the end of the 1970s suitable programs became available along with more versatile pulse programming and phase control. Appropriate software changes for special experiments could be made as and when required. In order to store the large data array S(t_1, t_2) in a 2D experiment, disk storage units became a part of NMR spectrometers but were very limited by later standards.

Plotting the vast amount of data from a 2D experiment was not a trivial problem. Initially, results were presented as a 'stacked plot' of a series of conventional spectra drawn behind each other, as illustrated in Figure 76. 'Whitewash' routines in computer programs were devised to raise the recorder pen whenever a given trace was about to overwrite a peak in the previous trace. The stacked plot is esthetically appealing, but is often difficult to analyze. An alternative display mode, the contour plot (Figure 76), gradually gained favor, even though many old-time spectroscopists had difficulty visualizing the results without the familiar spectral curves.

As in the early days of 1D Fourier transform NMR, improvements in computer capability provided a major impetus. The greatly increased demands for data storage and rapid processing of 2D data could not be met for several years, and it was not until the 1980s that the 2D revolution really began on a broad scale. When it did, however, growth was exponential. Literally hundreds of different experiments or modifications and improvements of previous methods were developed. Almost every one was distinguished by a catchy name or acronym, resulting in a bewildering array of techniques. To provide a flavor of the rich variety of 2D methods, we discuss the development of some of the principal techniques, but with the recognition that many more types of experiments are not included here.

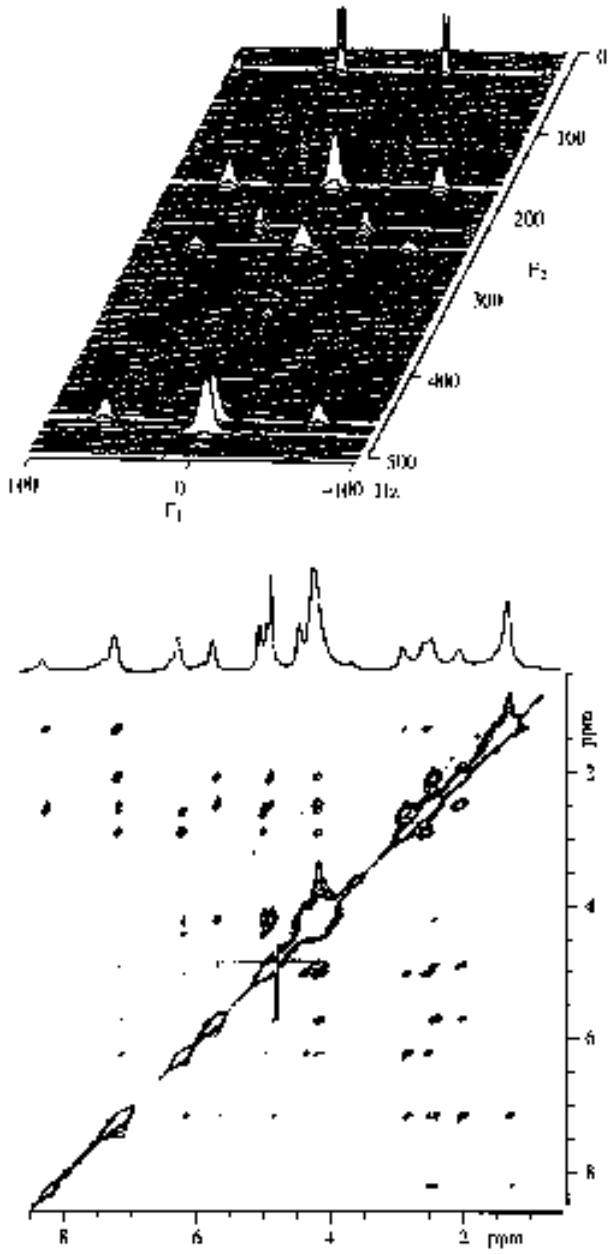

Figure 76 Typical presentation of data from 2D NMR experiments. Top: Stacked plot. Bottom: Contour plot

2D *J*-Resolved NMR

The initial experiment proposed by Jeener involved a pair of 90° pulses and would serve as the foundation of a large series of experiments to be discussed in the following sections. However, much of the early exploitation of 2D NMR capabilities centered on the manipulation of the spin system Hamiltonian by controlling some external perturbation, such as spin decoupling. This freedom to change the experimental conditions is responsible for numerous applications of 2D NMR. If two different NMR parameters operate in the two time intervals t_1 and t_2, these parameters are separated in the two frequency domains F_1 and F_2 after the Fourier transformation. Examples are the separations of multiplet structure from chemical shifts in liquid state NMR and the separation of dipolar couplings from chemical shifts in solid state experiments (which we discuss later). The 2D methodology permits a correlation to be established between the spin systems as they exist in the two states.

One example of such experiments is 2D *J*-resolved NMR, which was first reported by Müller, Kumar, and Ernst.[686] The experiment consisted of allowing ^{13}C magnetization to precess without decoupling during t_1, then observing the signal during t_2 while broadband decoupling is applied. The

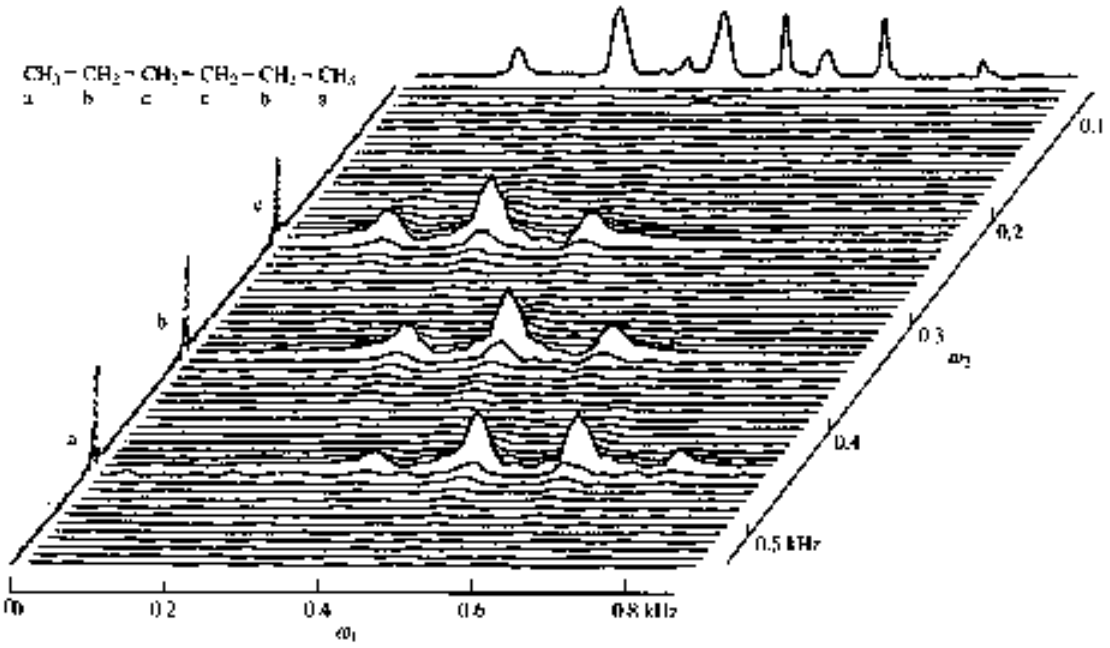

Figure 77 2D *J*-resolved ^{13}C spectrum of *n*-hexane. The ω_1 axis shows the coupled ^{13}C–H multiplets, while the ω_2 axis displays the proton-decoupled ^{13}C spectrum.[686] (Reproduced by Permission of the American Institute of Physics)

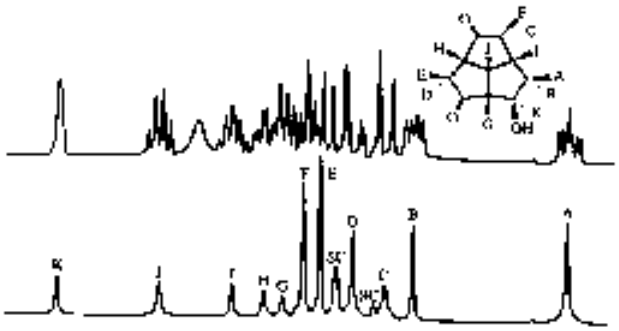

Figure 78 Top: Conventional 200 MHz ^{1}H spectrum of the molecule shown. Bottom: The equivalent of a broadband homonuclear decoupled spectrum from the 45° projection of the 2D *J* spectrum, with pseudo-echoes used in the t_2 domain to suppress dispersion mode contributions. Peaks marked 'SC' are artifacts from the strong coupling.[697] (Reproduced by permission of Academic Press)

spectrum of *n*-hexane shown in Figure 77 clearly demonstrated the power of the method in correlating the coupled and decoupled ^{13}C resonances and showed the potential of 2D methods for facilitating spectral assignments. Freeman and co-workers[688–691] quickly developed improved versions of this method, as did the Ernst group.[692] They provide advantages of additional spectral simplification, resolution, data presentations, or experimental convenience, along with the separation of various multiplets by means of the selective excitation of individual carbon species. Most of the versions utilize homo- or heteronuclear spin echo formation during the evolution period, with or without heteronuclear decoupling, in order to simplify the motion of the system during the evolution period by the elimination of selected terms of the Hamiltonian. In 1982, Bax and Freeman[693] suggested a useful variant of the 2D *J*-resolved experiment which involved the proton flip using a selective 180° pulse. It inverts certain ^{13}C satellites in the proton spectrum in order to measure ^{13}C–^{1}H long-range couplings.

Although complete *homo*nuclear decoupling could be of considerable practical importance as an aid in the analysis of complicated spectra, particularly of large molecules, it is difficult to achieve in the liquid state. Aue, Karhan, and Ernst[694] described an indirect technique to achieve the equivalent of a homonuclear broadband decoupled ^{1}H spectrum. They applied a spin echo sequence during t_1 and started data acquisition at the peak of the echo to generate a 2D *J*-resolved ^{1}H spectrum, and showed that the projection of the 2D data set onto the F_2 axis produced the equivalent of a homonuclear decoupled spectrum. Bax et al.[695] introduced an alternative approach using a 'constant time' method in which the total evolution period remains constant as t_1 is incremented. This method permitted the measurement of the absorption mode rather than the less resolved absolute value, but improvements were also forthcoming for absolute value presentation. Nagayama et al.[696] manipulated the data by 'tilting' the axes and Bax, Freeman, and Morris showed how resolution could be improved by suppressing the dispersion mode contribution.[697] An example of this procedure is shown in Figure 78.

Homonuclear Chemical Shift Correlation via Scalar Coupling

Jeener's initial description of 2D NMR focused on an experiment in which two 90° pulses are used to transfer coherence between two nuclei that interact by scalar coupling. Ernst and his co-workers realized that this concept could be used to establish coupling relationships that often are

diagnostic for the elucidation of molecular structure. Spin decoupling had long been the principal method for obtaining such information, but here was an alternative that could provide data for *all* coupling networks simultaneously, not one at a time as in a typical decoupling experiment. Thus the multiplex advantage that characterized FT NMR and so improved the efficiency of data acquisition had an analog in the initial 2D work.

Techniques for establishing such spin connectivities rapidly became the most popular 2D experiments in both homonuclear and heteronuclear modifications. The correlation between nuclei with different chemical shifts can be displayed as off-diagonal signals, or 'cross peaks' in a two-dimensional plot with the F_1 and F_2 axes representing the frequencies observed after Fourier transforming the two time domains. The homonuclear version of Jeener's original experiment was dubbed COSY (for *CO*rrelated *S*pectroscop*Y*), while the heteronuclear version has had several acronyms. Although the pulse sequence in the COSY experiment is quite simple, the underlying concepts are complex and required a rigorous theoretical development by Ernst and co-workers, employing a density matrix treatment and later the development of the product operator formalism.[698]

In its initial form, COSY had a number of drawbacks, particularly with the limited phase-shifting ability of the spectrometers at the time, coupled with restricted computer capabilities. An early variant of COSY, *S*pin *E*cho *C*orrelated *S*pectroscop*Y* (SECSY), proposed by Nagayama, Wüthrich, and Ernst,[699] proved useful in these early days, but as computers and instruments improved, the reduced spectral dispersion and asymmetric data presentation required by SECSY became overriding disadvantages, and the method was largely displaced by COSY and other, newer techniques. One key advance was the development of phase-sensitive COSY methods by States, Haberkorn, and Ruben[700] and by Marion and Wüthrich,[701] a technique that proved valuable in overcoming limitations in spectral resolution and sensitivity.

Many other improvements in the basic COSY method have been suggested and implemented. For example, DELAYED COSY, a normal COSY sequence modified by inclusion of a fixed delay (Δ) after the evolution period and prior to the acquisition time, was described by Bax and Freeman[702] and applied with considerable success for the derivation of long-range coupling information. Kumar et al.[703] proposed SUPER COSY in which the antiphase character of the cross peaks is transferred to the diagonal peaks, while Cavanagh and Keeler[704] showed that the diagonal peaks in COSY spectra can be suppressed by a difference technique.

Substantial improvements in lineshapes and in the suppression of unwanted peaks have been achieved through various 'filtering' procedures. For example, Oschkinat et al.[705] introduced z-COSY, a technique in which in-phase coherence is converted at one point to z magnetization, while antiphase components can be eliminated by phase cycling, unfortunately with loss in overall sensitivity. Other modifications of COSY use multiple quantum filters as proposed by Piantini, Sørensen, and Ernst,[706] in which undesired components are converted to unobservable multiple quantum coherences while the desired information is recovered from observable magnetization. (A more detailed discussion of the origin and application of multiple quantum effects in general is presented in Section 11.7.)

Double quantum filtered (DQF) COSY is the variant which is most widely employed since it uses only 90° phase shifts, whereas higher quantum filtering requires other than 90° phase shift capabilities. In DQF-COSY, the normal COSY pulse sequence is followed by a minimal duration fixed delay and then a third 90° pulse, whose phase is cycled independently of that of the second. DQF-COSY experiments have been used extensively to simplify 2D spectra. If a system, for example, has a large number of methyl or methoxy groups (which in general provide minimal connectivity information), the methyl/methoxy proton signals dominate and present dynamic range problems in the normal COSY spectra. In the DQF version, such resonances are substantially reduced in intensity. Another important application of multiple quantum filtering is to remove strong signals of solvents such as water, which is most frequently employed in biological systems.

A technique called *E*xclusive *CO*rrelation *S*pectroscop*Y* (ECOSY), where the coherence transfer takes place exclusively between connected transitions as long as the spins are weakly coupled, was proposed and utilized by Griesinger, Sørensen, and Ernst.[707,708] It is based on the fact that the coherence transfers between connected transitions and between nonconnected transitions have different dependences on the rotation angle β of the mixing pulse. A simple alternative to ECOSY called PECOSY (*P*rimitive ECOSY) has been proposed by Müller.[709] Like ECOSY, the technique provides simplified cross-peak patterns by restricting coherence transfer to connected transitions, but it is simple in that it is a regular COSY with the mixing pulse restricted to small flip angle β. Several other 2D experiments involving the properties of multiple quantum coherences such as Bilinear COSY and UNCOSY have been proposed and used by Levitt et al.[710] and by Farmer and Brown,[711] respectively.

COSY experiments normally provide information only on the connectivity between vicinal or geminal protons, which have significant spin coupling constants. Often, however, it is important to establish longer-range connectivities by relaying magnetization beyond a pair of directly connected spins. The idea of relayed coherence transfer was put forth by Eich, Bodenhausen, and Ernst[712] in 1982. In relayed correlation spectroscopy, usually called RELAY, the second pulse of the COSY sequence is replaced by a 90°, τ, 180°, τ, 90° sequence which induces two consecutive coherent transfer processes. Results for crotonaldehyde, an $AMXQ_3$ coupling network, are shown in Figure 79. The aldehyde proton A shows resolvable coupling to M but is not significantly coupled to Q or X. The RELAY spectrum at the bottom provides an unambiguous proof that all the six spins belong to a single coupling network, while the normal COSY spectrum does not reveal connectivities between A and either Q or X (empty circles in the top portion of the figure). More sophisticated sequences can be designed to relay the information over a greater number of couplings, but the use of RELAY is limited by small couplings because of relaxation during the relatively long coherence transfer period.

A technique in which cross peaks are generated between all members of a coupled spin network, leading to the most complete correlation diagram, was developed by Braunschweiler and Ernst[713] and named *T*otal *C*orrelation *S*pectroscop*Y* (TOCSY). It uses a mixing period during which a rapid series of 180° pulses is applied in order to suppress Zeeman

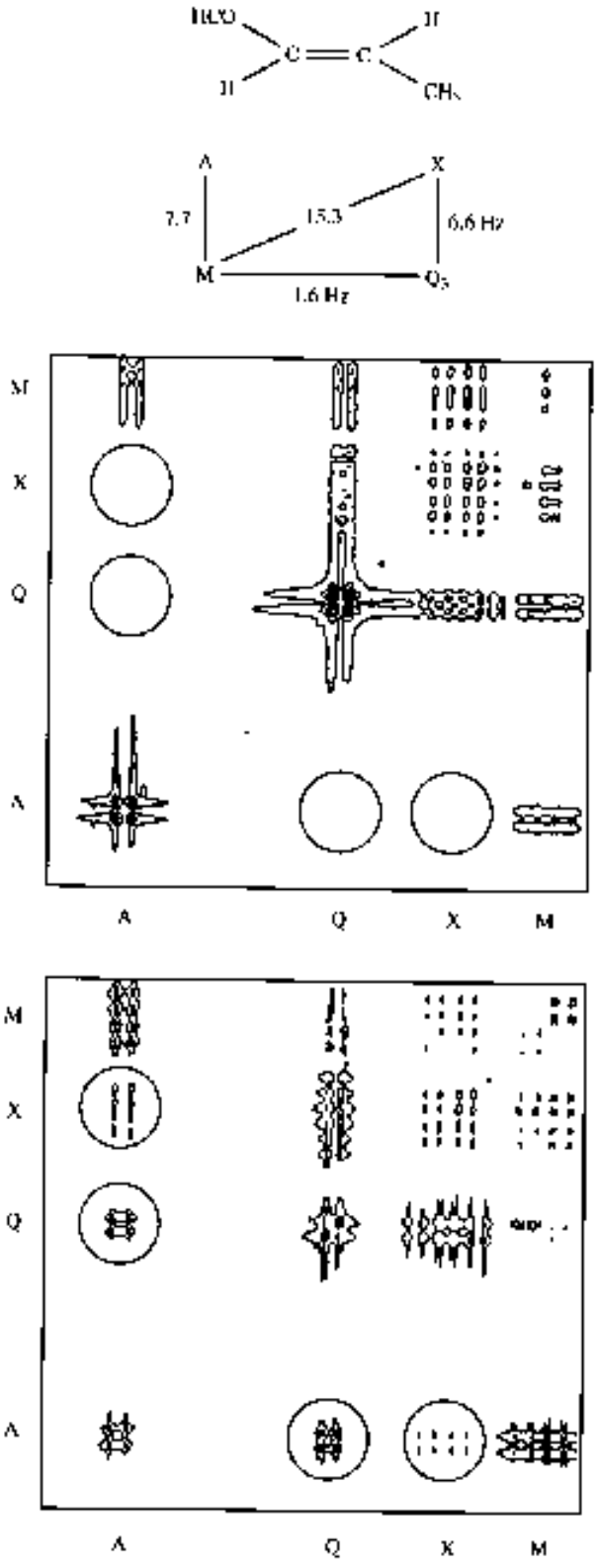

Figure 79 RELAY spectrum of crotonaldehyde (bottom) showing both short-range and long-range couplings. COSY spectrum (top) with the signals from long-range couplings missing.[712] (Reproduced by permission of the American Chemical Society)

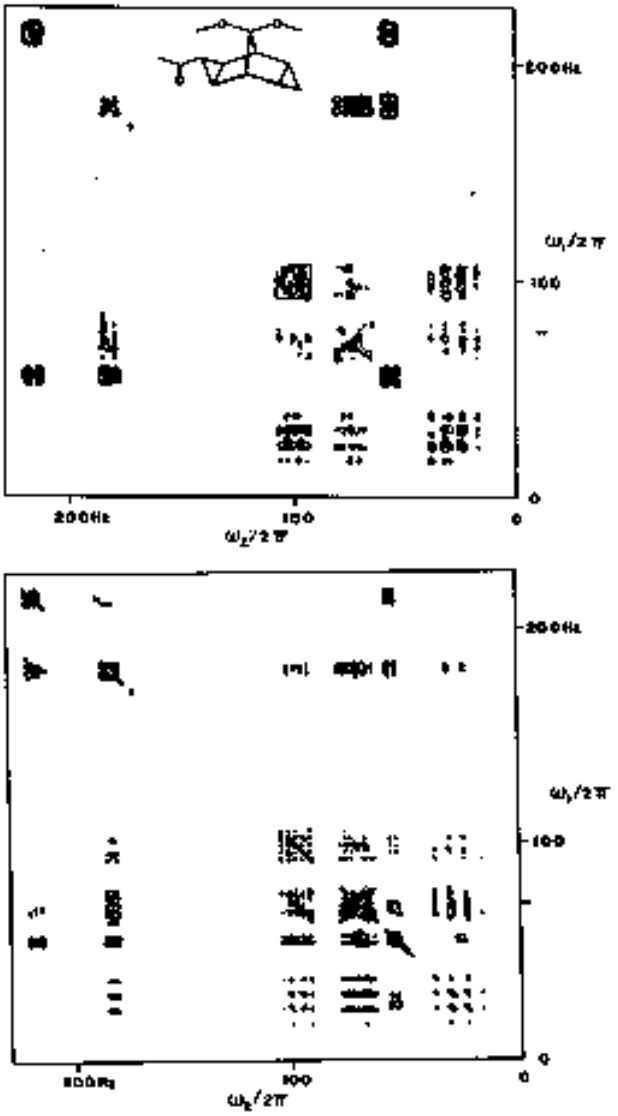

Figure 80 Comparison between a COSY spectrum (top) and a TOCSY spectrum (bottom), showing additional long-range couplings identified by TOCSY.[713] (Reproduced by permission of Academic Press)

interactions and chemical shifts, while retaining all spin couplings. During this 'isotropic mixing' period, coherence can be exchanged among the spins without regard to the magnitude of individual coupling constants. Figure 80 gives an example of a TOCSY spectrum and a comparison with a conventional COSY spectrum. In its initial form, TOCSY was difficult to apply to complex systems because of several experimental problems, but later improvements made the technique very useful.

Meanwhile, Bax and Davis[714] developed a related method of isotropic mixing based on their analysis of cross polarization originally found in solids by Hartmann and Hahn. In his historical sketch (***Bax, Ad: NMR of Ethanol and Interferon-γ***), Ad Bax describes the origin of this work as he and Don Davis looked for the source of artifacts in another experiment:

> It was my solid state NMR experience that tipped us off to the real cause of these anomalous cross peaks: they were due to

> homonuclear Hartmann–Hahn cross polarization. . . . Once we had recognized the origin of the Hartmann–Hahn artifacts, it was relatively straightforward to capitalize on them and use them for obtaining J connectivity. For maximum Hartmann–Hahn transfer, the goal was to make the trajectories of coupled spins as identical as possible. In retrospect therefore not surprising, our improved Hartmann–Hahn cross polarization schemes started to look more and more like heteronuclear decoupling schemes, where the objective is to make ^{1}H spins coupled to ^{13}C in the $|\alpha\rangle$ and $|\beta\rangle$ spin states undergo identical trajectories.

With suitable spin-locking, such a *HO*monuclear *HA*rtmann–*HA*hn (HOHAHA) experiment can provide efficient coherence transfer through a large spin system. Just as in the TOCSY experiment, the duration of the mixing period controls the extent of propagation. Initially Bax and Davis proposed the use of Malcolm Levitt's MLEV-16 sequence,[249] consisting of 16 composite 180° pulses, but subsequently an uncompensated 180° pulse was added to make it MLEV-17 in order to overcome phasing problems. With this improvement, the HOHAHA/TOCSY method has proved to be a durable and widely applicable technique.

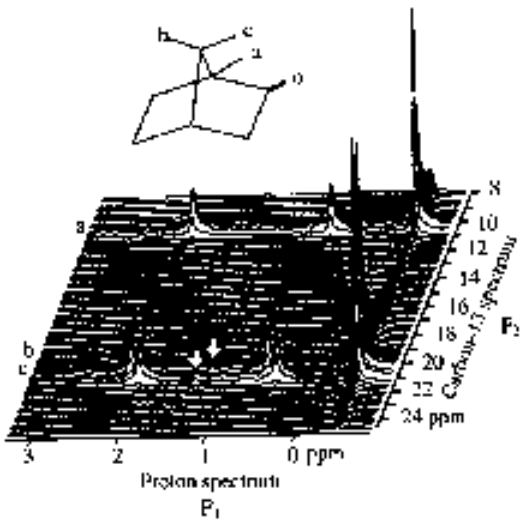

Figure 81 2D ^{1}H/^{13}C spectrum of the methyl-groups in camphor, showing chemical shift correlations for the *gem*–dimethyl groups, b and c. Arrows denote weak responses transmitted through long-range couplings.[717] (Reproduced by permission of the American Chemical Society)

Heteronuclear Correlated Spectroscopy

Correlations between ^{1}H chemical shifts and those of other nuclei, particularly ^{13}C, play an important role in assigning spectra and in elucidating structures in complex molecules. Several 2D techniques have been developed to facilitate this process, again largely supplanting the multiplicity of decoupling or other double resonance experiments that might otherwise be required. These methods provide for the separate or simultaneous evolution of spins of the two species, coherence transfer in one or more steps, and observation of one of the two species. The early 2D experiments generally relied on observation of the less abundant nucleus (e.g., ^{13}C) because such studies could be more readily implemented with the instruments of the 1970s and early 1980s. However, the potential advantages of inverse detection of ^{1}H were recognized and later used extensively, as we discuss in Section 11.8.

2D heteronuclear correlation of ^{13}C and ^{1}H chemical shifts was proposed almost simultaneously by the Ernst and Freeman groups,[715,716] and one of the first demonstrations of its value in chemistry was given by Bodenhausen and Freeman.[717] These experiments involve the application of an initial 90° pulse to protons, an evolution period t_1 to allow free precession of the protons, a second 90° ^{1}H pulse to create nonequilibrium spin populations, and a 90° ^{13}C pulse to effect coherence transfer to ^{13}C, the free induction decay of which is detected. An example of the use of this technique is given in Figure 81, where the 2D spectrum of camphor emphasizes the correlation of the low-field ^{1}H chemical shift with the high-field ^{13}C shift.

As 2D methods were implemented in commercial spectrometers, these correlation techniques became a staple under such names as HETCOR, Hetero-COSY, and Chemical Shift Correlation Map. Heteronuclear shift correlation experiments have been employed for assignment purposes for protons and ^{13}C and protons and ^{15}N for directly bonded nuclei. Correlations of other nuclei, such as protons and deuterium in small molecules, boron–proton, fluorine–proton, and phosphorus–proton, have all been obtained. Extension to long-range coupled nuclei has also been feasible by appropriate selection of the delays during the pulse sequences, or by developing other pulse sequences in order to improve the sensitivity. Kessler et al.[718] introduced and used the sequence COLOC (*CO*rrelation spectroscopy via *LO*ng range *C*oupling), while Freeman and co-workers[693,719] employed different approaches for the same purpose.

Several modifications of the correlation experiments have also been proposed. In most of the heteronuclear shift correlation experiments, the H–H spin multiplets in the F_1 dimension are retained. Although coupling information is often extremely useful, the splittings can result in sensitivity loss or spectral overlap problems. Bax[720] and Garbow et al.[721] independently developed techniques to collapse such multiplets, thus achieving the elusive goal of broadband decoupling of protons attached to ^{12}C from those attached to ^{13}C. This procedure, *BI*linear *R*otation *D*ecoupling (BIRD), has become widely used in other connections as well.

Heteronuclear relayed coherence transfer techniques were developed by Bolton[722] and Bax.[723] They employ the same pulse sequence as the homonuclear case except for additional 180° and 90° observe pulses. In the heteronuclear RELAY experiment, information is passed from remote protons to protons bonded directly to ^{13}C and finally to the ^{13}C itself. Information on ^{1}H–^{1}H couplings is thus transferred to the observed nucleus. A single carbon in the relayed heteronuclear correlation experiment could have more than one peak arising from the directly bonded protons and the protons two bonds away, but the ^1J coupling can be removed through 'low-pass J filtering' described by Kogler et al.[724]

2D Exchange Spectroscopy

The impetus for Jeener's concept of 2D NMR came from his interest in relaxation processes. At the Gordon Conference on Magnetic Resonance in 1978, Jeener suggested to Ernst a pulse sequence that could provide relaxation data, as Jeener

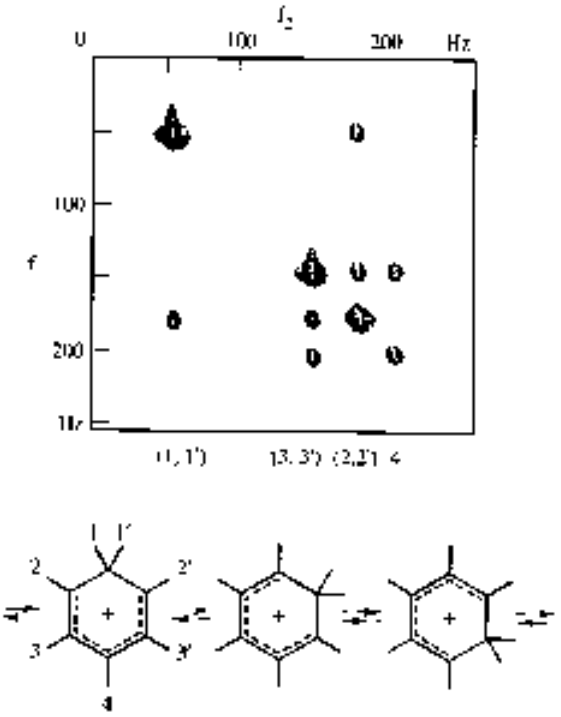

Figure 82 Chemical exchange in the heptamethylbenzonium ion, as measured by 2D NMR.[726] (Reproduced by permission of the American Chemical Society)

put it, 'easily ... much simpler than my original dreams.' This sequence uses three pulses: 90°, t_1, 90°, τ_m, 90°, t_2. If two nuclei, tagged by their precession frequencies during t_1, exchange magnetization during the mixing period τ_m, either by magnetic dipolar relaxation or by chemical exchange, cross peaks will occur in the 2D spectrum.[725] Jeener did not have the instrumentation to develop this technique and readily agreed to a collaboration with Ernst's group. They found it difficult initially to detect cross relaxation effects in the small molecules with which they were working, but they were readily able to observe cross peaks from the chemical exchange of methyl groups in the heptamethylbenzonium ion,[726] as shown in Figure 82. The peaks for the four nonequivalent methyl groups (1,1′; 2,2′; 3,3′; and 4) appear along the main diagonal with the intensity ratio 2 : 2 : 2 : 1, while the off-diagonal peaks immediately establish the exchange network $1 \rightleftharpoons 2 \rightleftharpoons 3 \rightleftharpoons 4$.

The detailed theory underlying 2D studies of cross relaxation and of transient NOEs, a technique called *N*uclear *O*verhauser *E*ffect *S*pectroscop*Y* (NOESY), was developed by Macura and Ernst.[727] The first use of the 2D technique for measurements of intramolecular NOEs was demonstrated by Kumar et al.[728] who obtained data on a small globular protein, basic pancreatic trypsin inhibitor (BPTI). NOESY rapidly became an invaluable tool in biomolecular structure, as discussed in Section 14.

With nuclei of high isotopic abundance, both cross relaxation and exchange usually produce indistinguishable 2D data, but a variation of the experimental parameters, such as temperature or mixing time, can sometimes differentiate between the two phenomena. Alternatively, a method proposed initially by Bothner-By et al.[729] for the measurement of NOEs in the rotating frame under spin-locked conditions distinguishes clearly between NOE and exchange. The experiment was initially named CAMELSPIN (*C*ross relaxation *A*ppropriate for *M*inimolecules *E*mulated by *L*ocked *SPIN*s), but quickly became better known as ROESY[730] (*R*otating frame *O*verhauser *E*ffect *S*pectroscop*Y*) by analogy to NOESY. The value of the NOE in the rotating frame increases monotonically with increasing value of τ_c, the molecular correlation time, so ROESY is particularly valuable in obtaining NOE information for molecules with correlation times of the order of $1/\omega$, where the magnitude of the ordinary laboratory frame NOE goes through zero.

Rotating-frame experiments produce simultaneously coherence transfer through scalar coupling and cross relaxation, which may lead to undesired interference and ambiguities between TOCSY and ROESY effects. Griesinger et al.[731] introduced a technique which provides clean TOCSY spectra and suppresses contributions from cross relaxation based on opposite signs of the longitudinal and transverse cross relaxation rates, while Bax and Davis showed how ROESY effects could be measured without interference from effects transmitted via spin coupling.[730]

Multiple Quantum Coherences

The basic theory of NMR, built on first-order time-dependent perturbations, shows that allowed transitions are limited to those in which quantum number m_I changes only by ± 1. Values for Δm other than unity (including $\Delta m = 0$), which are called 'multiple quantum transitions', were observed in atomic and molecular beams by various workers in the 1950s, and Hughes and Geiger[732] predicted in 1955 that the energy level schemes usually encountered in NMR experiments are particularly suitable for the observation of these nominally forbidden multiple quantum transitions. They were first observed in 1956 by Wes Anderson,[733] who was studying relaxation in 2-bromo-5-thiophene. As he increased the rf power to induce saturation in individual lines, he observed the effects shown in Figure 83. Spectrum (c) showed a line at the center of the spectrum that occurred only at large rf fields, which Anderson attributed to double quantum transitions. He also observed multiple quantum transitions in *p*-chlorobenzoyl chloride. Meanwhile, Kaplan and Meiboom[734] found and explained similar transitions in ethyl alcohol and 1,1,2-trichloroethane, and Yatsiv[735] provided a further theoretical treatment. In 1963, Anderson, Freeman, and Reilly[736] used double quantum transitions as aids for assignments of NMR spectral lines.

After these initial observations, there was little additional research in multiple quantum NMR. With the advent of FT NMR methods, the prospects for studying multiple quantum transitions (MQT) appeared bleak because the FID is recorded in the absence of rf radiation; hence it is not possible to detect such transitions directly. However, with the advent of 2D NMR, Aue, Bartholdi, and Ernst[687] showed that not only double quantum transitions but also zero quantum transitions (preferably termed *coherences*, rather than transitions) could be detected indirectly. They developed the basic theory, suggested several experimental approaches, and demonstrated the effects, as shown in Figure 84. In general, the experimental procedure involves the generation of

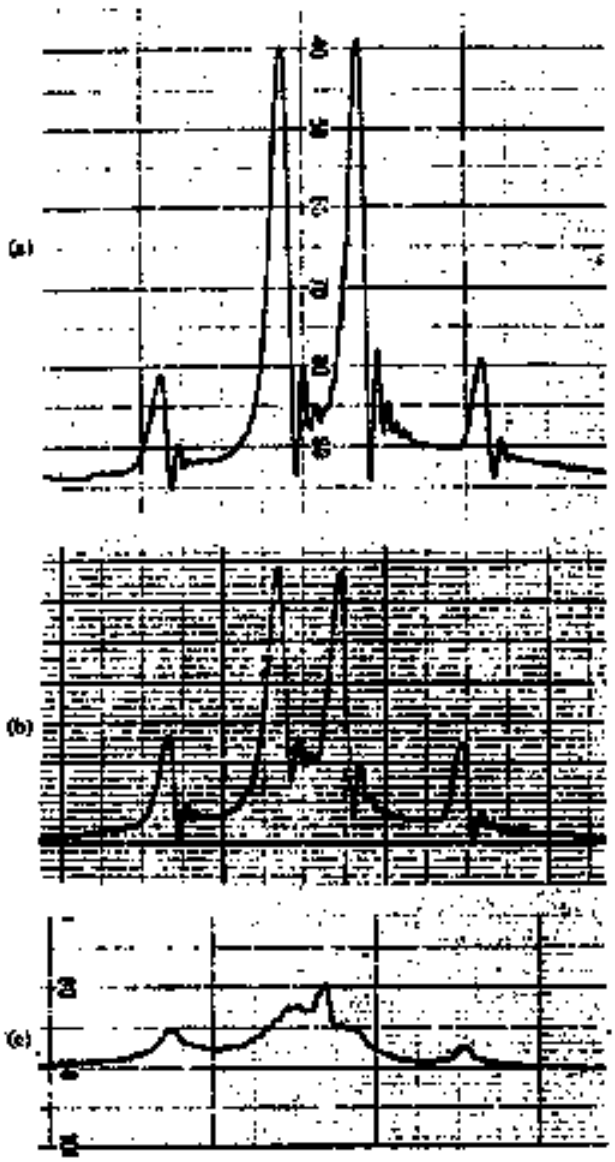

Figure 83 ^{1}H NMR spectrum (30 MHz) of 2-bromo-5-chlorothiophene.[733] (a) Low rf power; (b) rf power increased by a factor of 3.4; (c) rf increased further by a factor of 3.4. Note the double-quantum transition in (c). (Reproduced by permission of the American Physical Society)

multiple quantum coherence through some excitation process, its evolution during t_1, and conversion to observable single quantum coherence during the mixing period.

Wokaun and Ernst[737] followed up this work by discussing methods to detect MQTs and by pointing out three areas in which MQTs could be valuable. (a) They can be utilized for the assignment of spectral lines in complex spectra. Since the number of transitions decreases as Δm increases, the higher quantum spectra are normally easy to interpret. (b) Zero quantum transitions are insensitive to magnetic field inhomogeneities and thus permit the recording of high-resolution spectra in inhomogeneous magnetic fields. (c) They permit the determination of relaxation parameters in a simple manner with high accuracy. The Ernst group continued to

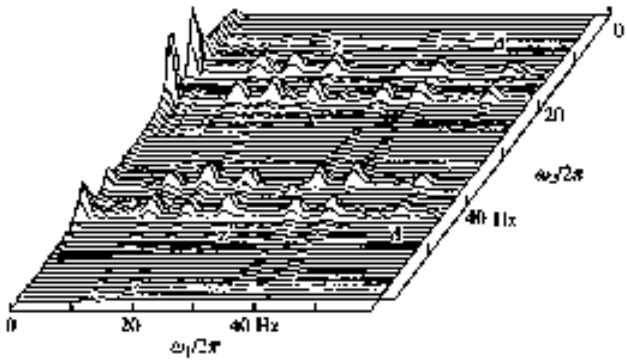

Figure 84 ^{1}H NMR spectrum (60 MHz) of 2,3-dibromothiophene, obtained with a pulse sequence 90°, Δ, 90°, t_1, 90°, t_2, with Δ = 236 ms. The multiple quantum coherence generated by the first two pulses results in lines in the ω_1 dimension from zero quantum (z) and double quantum (d) transitions, as well as the two doublets of the normal single quantum spectrum.[687] (Reproduced by permission of the American Institute of Physics)

improve methods for studying MQTs and to explore various applications.[738,739,740]

Meanwhile, Alex Pines and co-workers, in their study of solids, were led to multiple quantum effects, as Pines describes in his historical sketch (***Pines, Alexander: Solid State NMR: Some Personal Recollections***):

> Our original intention was to study hydrogen NMR in solids, to provide an alternative to homonuclear multiple pulse sequences, this time by diluting protonated samples with deuterium. The idea was reminiscent of the approach taken earlier with carbon, and here again there was a heteronuclear interaction that needed to be decoupled. The hydrogen–deuterium coupling, however, seemed futile to average because the wide, quadrupole broadened deuterium line would require prohibitive radiofrequency power, but it was conceivable that we could exploit double quantum decoupling which had recently been used by Meiboom and co-workers in liquid crystals. Indeed, narrowband irradiation of the (+1, −1) transition of the deuterium with modest power yielded a resolved hydrogen spectrum, and in this way we could observe the chemical shift anisotropy of hydrogen in ice—a notoriously difficult system for homonuclear multiple-pulse techniques. . . . The next question, which emerged from our double quantum decoupling work and our previous experience with indirect detection of invisible microwave coherences, involved the possibility of preparing and observing, in the time domain, the 'forbidden' deuterium double-quantum transition.

The Pines group pursued this objective, and beginning in 1976 they published several papers that described the theory and experimental implementation of double quantum deuterium NMR.[741–744] Concurrently, Hashi et al.[745,746] were pursuing similar types of research.

Shimon Vega, who made major contributions in his work with Pines, describes in his historical sketch (***Veeman, Wiebren S.: Personal Reflections on Solid State NMR in the Early Days***) his previous introduction of a set of fictitious spin-$\frac{1}{2}$ operators to simplify the density matrix description of zero-field NQR of spin-1 nuclei. Such operators played an important role in the detailed theory of double quantum NMR published by Vega and Pines.[742] Pines et al. developed a number of additional aspects of multiple quantum effects, including the n-quantum phase shift, bilinear rotation decoupling (BIRD),

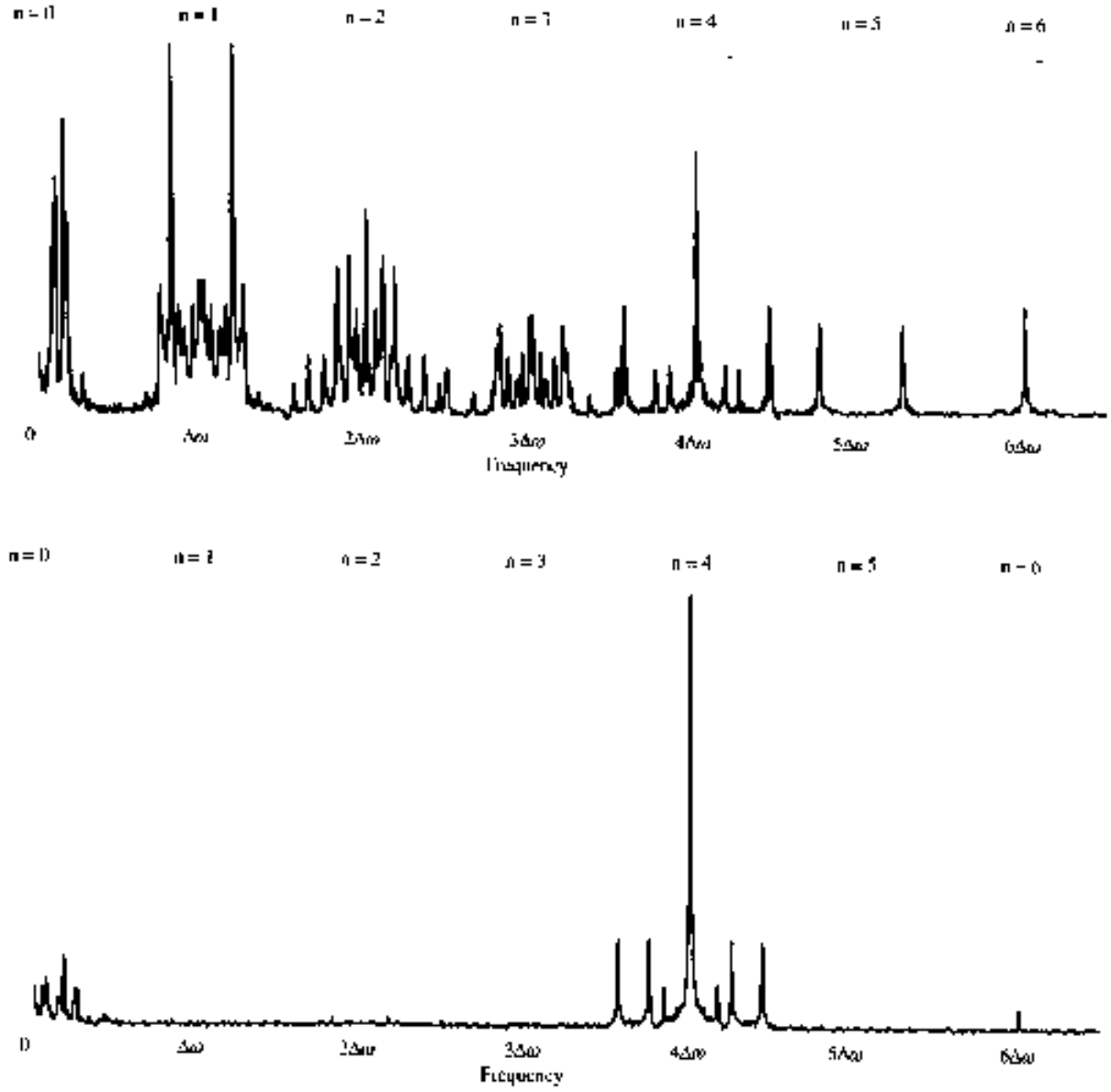

Figure 85 Multiple quantum ^{1}H NMR spectra of benzene oriented in a liquid crystal solvent. Top: Complete multiple quantum spectra. Bottom: Selective excitation of only $n = 0, 4$.[747] (Reproduced by permission of the American Institute of Physics)

multiple quantum filtering, and selective excitation of *n*-quantum spectra. Many of the techniques developed initially for solids were found to be applicable to liquids as well. Selective excitation is illustrated in Figure 85, where *n*-quantum echo spectra and selective excitation of only zero- and four-quantum spectra are shown for benzene oriented in a liquid crystal.[747]

One of the best known and potentially most useful of the many experiments that capitalize on multiple quantum effects is INADEQUATE, a method which suppresses resonances from isolated ^{13}C nuclei while retaining signals from molecules with coupled ^{13}C–^{13}C pairs, as mentioned in Section 7.6. Developed initially by Bax et al.,[748,749] it was modified into a 2D version as well.[750] The pulse sequence (90°, t, 180°, t, 90°, 90°) generates double quantum coherence and reconverts it to observable single quantum magnetization. The signal-to-noise ratio is often a problem with INADEQUATE because it depends on only 0.01% of the molecules, and several improvements have been proposed, including the use of quadrature detection of t_1[751,752] and the application of composite pulses.[753]

Proton-Detected Heteronuclear Shift Correlation

Double resonance methods, especially INDOR, had long been used to observe a more sensitive nucleus in order to obtain information about a less sensitive nucleus to which it is spin coupled. With the advent of 2D NMR it became possible to carry out similar studies, but with the advantage of covering a broad spectral range in a single experiment. The initial 2D heteronuclear chemical shift correlation experiments

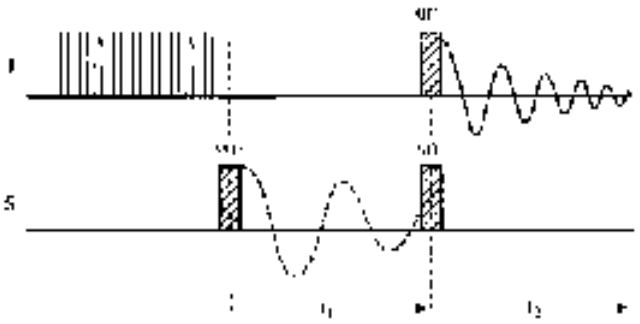

Figure 86 Pulse sequence for indirect detection of S magnetization by observation of I. The initial I pulses saturate the normal I magnetization and provide a nuclear Overhauser enhancement of S.[754] (Reproduced by permission of Elsevier Science)

were proposed by Maudsley and Ernst[754] in 1977. Their pulse sequence (Figure 86) is a generalized version of the homonuclear COSY sequence. Magnetization of S, the less sensitive nucleus, evolves during t_1 and is transferred to I, which is detected, thus providing the correlation between the spins but with the sensitivity of I, in contrast to the other heteronuclear correlation techniques discussed in Section 11.5. If S represents a spin such as ^{13}C at low natural abundance, this apparently simple method encounters difficulty in discriminating against artifacts from the large fraction of I not coupled to S. More sophisticated techniques, together with an improvement in instrumentation, would be needed before indirect detection methods became commonplace.

A distinct advance was made by Bodenhausen and Ruben[755] who used the pulse sequence of the INEPT experiment (Section 7) first to transfer proton mangetization to ^{15}N and, after it had evolved during the period t_1, to transfer it back to ^{1}H, which is detected. The method worked for natural abundance ^{15}N as well as for enriched samples, but a measurement was very time consuming even for concentrated solutions. In addition, the complex pulse scheme did not readily lend itself to solvent suppression. Nevertheless, this procedure, originally termed the 'Overbodenhausen experiment' but later called heteronuclear single quantum correlation (HSQC), has subsequently been modified and incorporated into many more complex pulse sequences, as discussed in Section 16.

In 1979, Luciano Müller[756] introduced a pulse technique, superficially similar to the INEPT sequence but with different phase relationships, that creates heteronuclear zero and double-quantum coherence between the I and S spins, then, after evolution, transfers these coherences to I magnetization which is observed. The method was demonstrated only for an enriched ^{13}C sample and did not attract much attention.

A dramatic improvement in the sensitivity of the indirect measurement of ^{15}N NMR was demonstrated by Bax, Griffey, and Hawkins[757] in 1983, when they formulated a new pulse sequence (called *H*eteronuclear *M*ultiple *Q*uantum *C*orrelation, HMQC) that carries out a transfer process similar to Müller's method but with improved efficiency. The experiment can be carried out with only a single ^{1}H 90° pulse, adjusted to have a null in its excitation profile at the solvent water frequency and thus providing good suppression of the solvent signal. Their application of the method to ^{15}N samples at natural abundance and to a 0.7 mM solution of enriched tRNA provided a clear demonstration of the utility of this approach. As Bax says in his historical sketch (***Bax, Ad: NMR of Ethanol and Interferon-γ***): 'Although the same HMQC pulse schemes, together with a large number of alternative schemes, were proposed independently by the Australian group of Doddrell, Pegg, and Bendall,[758] the application of our experiment to a biological macromolecule and to natural abundance peptides was probably the main reason for the surge in popularity of these HMQC experiments.'

Other improvements in the sensitivity of indirect detection have been advanced. For example, Palmer et al.[759] showed that as much as a factor of $\checkmark 2$ in sensitivity can be gained by refocusing and detecting two orthogonal in-phase proton magnetization components, rather than the conventional single component. In recent years, indirect detection methods have steadily become more popular and easier to implement with commercial spectrometers.

Use of 2D NMR in Structure Elucidation

The structure elucidation of organic molecules continues to be the most widespread application of NMR spectroscopy. Initially, the analysis of NMR spectra relied almost exclusively on correlations of chemical shifts, general ranges of coupling constants, and a great deal of chemical knowledge. In Section 5 we gave one example of this process at work in the structure elucidation of an alkaloid. The availability of double resonance methods, particularly selective spin decoupling to elucidate spin coupling patterns and the nuclear Overhauser effect to estimate spatial proximities (in favorable cases) provided powerful tools to assist in interpretation. But double resonance experiments are tedious and cannot always be readily applied to large or complex molecules.

The development of a very wide variety of 2D methods, some of which we have only touched on briefly here, made a dramatic change to the way in which chemists could approach the problem of structure elucidation. Many 2D techniques can now be applied in an automated manner with commercial software, and their sensitivity is such that it is often almost as easy and as fast to carry out a 2D experiment as to obtain a simple one-dimensional spectrum. In fact, a carefully chosen series of 2D experiments can often provide an unambiguous molecular structure of even a very large organic molecule.

One example, among very many that could be cited, is the elucidation of the structure of desertomycin, an antibiotic of molecular weight 1192,[760] the first molecule of such size to be successfully handled solely by 2D NMR methods augmented only with knowledge of the molecular weight and a general elemental analysis. DQF phase-sensitive COSY and HOHAHA established much of the proton–proton coupling network, while the general carbon framework was deduced from $^{1}H-^{13}C$ correlation experiments, especially *H*eteronuclear *M*ultiple *B*ond *C*orrelation (HMBC) which provides correlations through more than one C–C bond. Without software to aid in the analysis, the process of integrating the vast amount of NMR data to produce the structure shown in Figure 87 was labor intensive but logically straightforward.

Higher Dimensional NMR

The various two-dimensional NMR techniques discussed in this section and the developments of required instrumentation

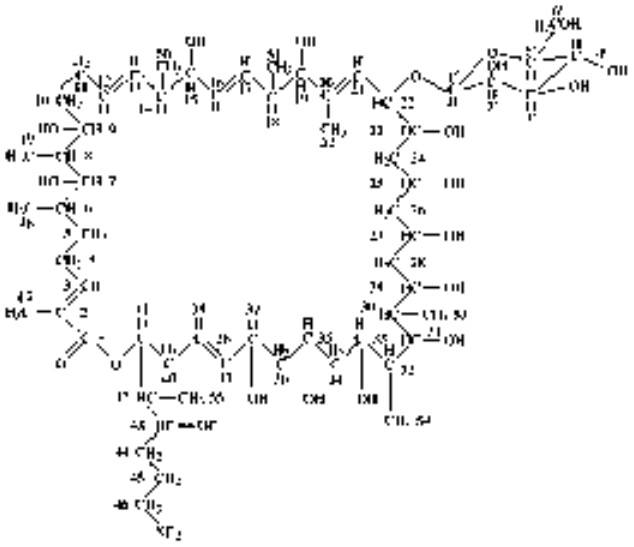

Figure 87 Structure of the antibiotic desertomycin, as deduced from 2D NMR studies.[760] (Courtesy of A. Bax)

have revolutionized the capabilities of NMR for dealing with complex molecules. The information which is restricted to one frequency in a one-dimensional experiment is spread out over the entire (F_1, F_2) plane, a process that results in the enhancement of the resolution and a simplification of the spectral analyses. It was recognized very early in the development of 2D NMR that the general 2D experiment can theoretically be extended to three or more dimensions, which should add further capabilities. However, there were practical difficulties arising from the immense size of the required multidimensional data matrix $\mathbf{S}(t_1, t_2, t_3)$ and problems in devising useful experiments that give good sensitivity and are artifact free. Such methods could be exploited only after improvements in instrumental and computer facilities and additional experience in optimizing the component 2D pulse sequences. Meanwhile, some experiments intermediate between 2D and 3D spectra were developed.

Two-dimensional exchange spectroscopy contains a third time variable, the mixing time τ_m, which is normally maintained at a fixed value for a particular 2D study. However, to map out dynamic processes it is often essential to vary τ_m systematically, in addition to t_1 and t_2. To avoid the time needed to obtain a 2D spectrum for each value of τ_m, Bodenhausen and Ernst[761,762] proposed a novel experiment in which t_1 and τ_m are incremented synchronously: $\tau_m = kt_1$. This 'Accordion' experiment increases the information content of the 2D spectra by incorporating exchange-type information into the 2D peak shape and produces spectra which effectively represent projected 3D spectra.

The next stage of development of 3D NMR spectroscopy was the experiment by Bolton,[763] who obtained ^{13}C spectra in which the signals were modulated by both chemical shift and spin–spin couplings, but it would be about five years before true 3D experiments came into use.

In 1987, Vuister and Boelens[764] reported a homonuclear three-dimensional J-resolved experiment in which the intensities and the phases of the cross peaks of a COSY experiment were modulated by J couplings, permitting the determination of spin multiplets. They applied the method to a single-stranded DNA octamer. During the same year, Griesinger et al.[765] implemented high-resolution correlation spectroscopy in three frequency dimensions. They described a practical approach to 3D NMR, suggested a technique for reduction of data matrices, and mentioned applications where 3D spectra could provide information that would be difficult or impossible to obtain from a series of 2D experiments. Their general formulation of a 3D experiment in terms of two 2D pulse sequences and naming based on the 2D components has been widely used. Initially used combinations, such as COSY–COSY, COSY–NOESY, and NOESY–COSY, have largely given way to NOESY–NOESY, TOCSY–NOESY, or HOHAHA–NOESY as the generally most useful homonuclear 3D methods. In a 3D experiment, the free induction decay is recorded as a function of two independently incremented time periods t_1 and t_2, which leads to a quite large 3D data matrix. Griesinger et al. proposed the use of selective pulses to restrict the 3D volume and thus reduce the number of data points without sacrificing resolution. The results of a soft COSY–COSY experiment applied to a three-spin system (2,3-dibromopropionic acid) are shown in Figure 88, which illustrates various methods of data presentation.

Freeman and co-workers[766,767,768] proposed a distinctly different approach to 3D correlation spectroscopy as a direct extension of pseudo-correlation spectroscopy (ψ-COSY), where a frequency-selective pulse is stepped through the F_1 dimension, perturbing one NMR transition at a time. The ψ-COSY 3D experiment does not involve excessively large data matrices or long three-dimensional Fourier transformations. At nearly the same time, Redfield and co-workers[769] used a 2D multiple quantum coherence experiment to separate signals of a protein in two dimensions, then irradiated selectively to obtain NOE information. They referred to the method as 'saturation transfer 2D forbidden echo'.

Perhaps the greatest need for three- and four-dimensional NMR has been found in studies of proteins, where severe overlap is found in a multitude of resonances. We defer further discussion of multidimensional NMR experiments to Section 14.

Selection of Coherences by Pulsed Field Gradients

Most 2D experiments are subject to artifacts resulting from pulse imperfections and other nonideal factors. A major consideration in the design of any successful 2D technique is a procedure to eliminate or minimize such artifacts, usually by phase cycling. With more sophisticated experiments, especially 3D and 4D techniques, the requirement for sometimes extensive phase cycling on top of a long series of repetitions to cover the evolution time(s) can lead to excessively long experimental times. In many instances, the use of pulsed magnetic field gradients can reduce or eliminate the need for phase cycling.

The dephasing of magnetization in the presence of a magnetic field gradient and its rephasing when the gradient is reversed was first noted by Herman Carr in his 1952 Ph.D. thesis,[65] as mentioned in Section 4. It was clearly recognized in the early 2D work on multiple quantum effects that an n-quantum coherence evolves at n times the rate of a single

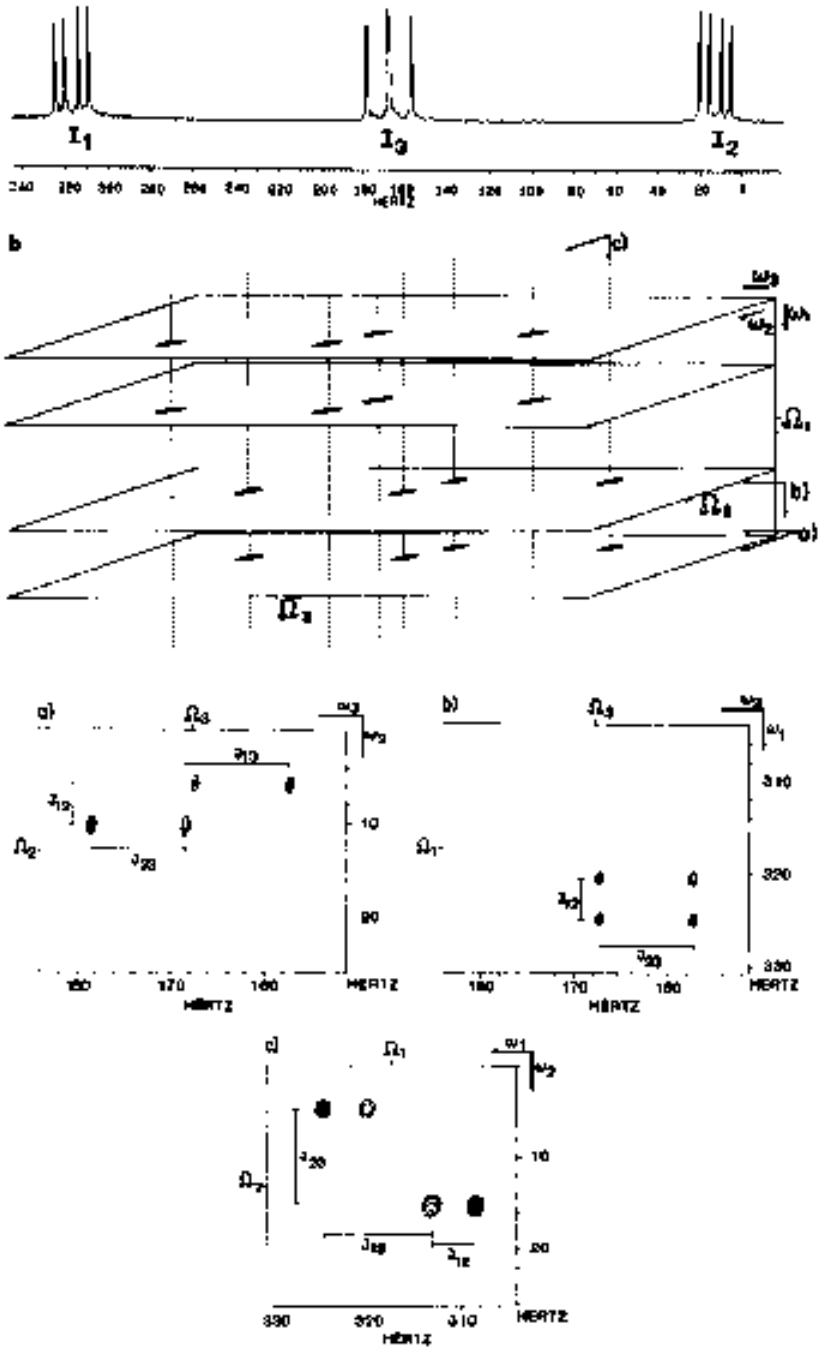

Figure 88 3D ^{1}H NMR study of 2,3-dibromopropionic acid. Top: One-dimensional spectrum. Bottom: Three 2D planes selected, as indicated, from the full 3D data set.[765] (Reproduced by permission of Academic Press)

quantum coherence (magnetization), and Wokaun and Ernst[737] pointed out the effects of magnetic field gradients in dephasing or rephasing such coherences. By manipulating the direction, magnitude, and length of application of gradients, it is feasible to eliminate certain coherence orders while retaining others. Papers by Bax et al.,[770] Barker and Freeman,[771] and the Ernst group[772] showed the potential value of using pulsed field gradients, but practical application was limited because the time needed to stabilize $\boldsymbol{B}_0$ inside the probe after such a strong gradient pulse was very long.

In the late 1980s, with a strong impetus from NMR imaging (as we shall see in Section 13), methods were developed for shielding the probe body and $\boldsymbol{B}_0$ from the effects of the gradient pulse. The adaptation of self-shielded gradient coils to high-resolution NMR, described in Ralph Hurd's historical sketch (***Hurd, Ralph E.: A Brief History of Gradients in NMR***), led to increasingly widespread use of 'gradient enhanced' 2D and 3D pulse methods. For example, John et al.[773] showed that the efficiency of a 3D ^{15}N HMQC–TOCSY study in proteins could be significantly

improved by application of magnetic field gradients, and the Kaptein group[774] exploited the technique for more rapid data acquisition in triple resonance experiments. However, many gradient methods for selecting a particular coherence pathway reject not only unwanted pathways but the 'mirror image' of the desired pathway, thus exacting a price by reducing sensitivity. Bax and Pochapsky[775] showed that gradient pulses can be applied so as to destroy only unwanted magnetization (for example, while the desired magnetization is temporarily aligned along the z axis) without any loss in sensitivity, and demonstrated that protein spectra of uncompromised quality could be recorded in less than two hours.

Suppression of the solvent water resonance has long been critical to the observation of NMR in samples of biological interest, as discussed in some detail in Section 10. Generally, those methods that are most effective in suppressing water also provide nonuniform excitation across the rest of the spectrum. With the use of pulsed field gradients, alternative—and very effective—methods have become available. For example, van Zijl and Moonen[659] showed that the large difference in diffusion coefficients between water and biopolymers can be exploited to reduce the water signal by a factor of about 10^4 to 10^5. The WATERGATE method, introduced by Piotto, Saudek, and Sklenar,[776] excites all resonances equally but includes a 180° refocusing pulse which has a narrow gap in its excitation profile at the H_2O frequency. Pulsed field gradients select only magnetization that experiences the refocusing pulse, thus dephasing and virtually eliminating the water signal. This procedure lends itself to incorporation into complex multidimensional pulse sequences without any significant increase in the overall experiment time.

2D Experiments in Solids

With the wide range of pulse methods and magic angle spinning techniques developed in the late 1960s to obtain high-resolution spectra of solids, as discussed in Section 8, solid state NMR provided fertile ground for the new concepts of 2D NMR in the early 1970s. The initial work by John Waugh and co-workers[777,778] was aimed at measuring dipolar interactions and chemical shifts for ^{13}C in single crystals separately, but in a way that they could be correlated. The pulse sequence for the *S*eparated *L*ocal *F*ield (SLF) experiment, illustrated in Figure 89, served as the prototype of a large number of 2D techniques that would be developed for solids. For example, Linder, Höhener, and Ernst[779] applied the SLF method, combined with off-resonance magic angle proton decoupling during t_1, in order to separate dipolar effects from chemical shielding anisotropy. Meanwhile, Griffin and co-workers developed the SLF method further by adding slow magic angle spinning, along with a WAHUHA pulse sequence during the evolution period.[780] By carefully synchronizing the pulses with the rotational period, they were able to observe rotational echoes and obtain rotational sideband spectra that provided information on both the principal values and the relative orientations of the shielding and dipolar tensors. These techniques were employed to obtain structural data such as $^{13}C-^{1}H$ and $^{15}N-^{1}H$ distances in powder samples. Later, the Griffin group modified the method to improve its efficiency and reduce signal loss by relaxation during the experiment.[781]

Gary Maciel and co-workers introduced two very useful 2D experiments in the early 1980s. Szeverenyi et al.[782] employed

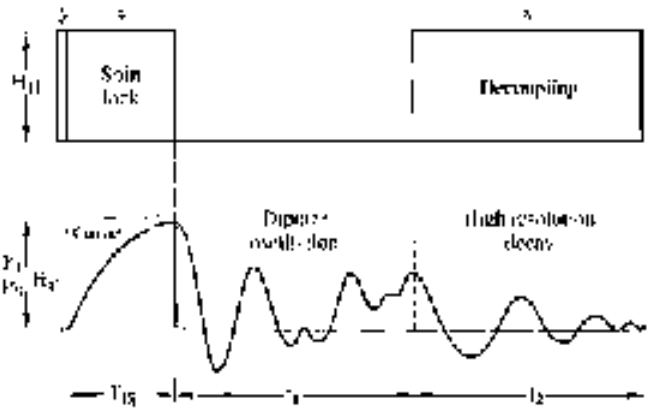

Figure 89 Pulse sequence for the Separated Local Field (SLF) method. After cross polarization, spin S (^{13}C) precesses under the influence of dipolar interactions during t_1, but is decoupled from I (^{1}H) during t_2.[778] (Reproduced by permission of the American Institute of Physics)

a combination of 2D NMR with CP MAS to study chemical exchange and spin diffusion. The pulse sequence is the same as the NOESY sequence originally proposed by Jeener et al.,[725] except that the initial 90° pulse applied to the carbon spins for liquids is replaced by a cross polarization sequence. Subsequently, a large number of investigators studied both exchange and spin diffusion in solids with this method and modifications introduced later. Spiess and co-workers[783] extended the method to deuterium, where exchange can be measured cleanly in the virtual absence of spin diffusion, and applied the technique as described in Spiess's historical sketch (***Spiess, Hans Wolfgang: Multidimensional Solid State NMR of Polymers***). Another interesting adaptation of the basic spin exchange technique was made by Grant and co-workers when they correlated the chemical shifts of ^{13}C lines in a single crystal at two different orientations by flipping the crystal from one orientation to the other during the mixing period.[784]

In 1983, Bax et al.[785] introduced a new 2D technique for providing the isotropic chemical shift of a powder in one dimension and the static chemical shift anisotropy pattern along the other frequency axis. The experiment is performed using discrete 'hops' between evolution segments rather than continuous sample spinning. No spinning sidebands are observed. The experiments showed promise for obtaining powder patterns for individual peaks of complex molecules for which a straightforward nonspinning approach would yield only broad bands of overlapping powder patterns. Subsequently, the Griffin group demonstrated improved performance with an alternative technique, in which slow spinning during t_1 generates data on chemical shielding anisotropy while high-speed spinning during t_2 provides narrow lines.[786] The magnetization is stored along the z axis while the spinning speed is changed. Tycko et al.[787] achieved the same type of presentation by applying 180° pulses synchronized with the sample rotation. Later, Gan[788] developed a slow MAS method in which magnetization evolves during three segments of each rotor period spaced at 120°. Again, the magnetization is stored along the z axis between segments.

A double CP MAS experiment, proposed by Schaefer et al.,[789,790] uses successive cross polarization transfers to permit the selective observation of one type of rare spin which is

directly bonded to another. The cross polarization from ^{1}H to ^{13}C and then from ^{13}C to ^{15}N, for example, with final ^{15}N detection provides a ^{15}N spectrum containing resonances only from the ^{15}N nuclei which are directly bonded to ^{13}C.

THE EVOLUTION OF IN VIVO NMR

NMR began in physics laboratories. However, it was not long before a curiosity developed to stick something that was alive in the spectrometer and see what happened. Thus the co-discoverers of NMR actually conducted the first known in vivo NMR experiments, as described by Raymond Andrew in Volume 3 of this Encyclopedia ***Magnetic Resonance Imaging: A Historical Overview***:

> Soon after the first successful NMR experiments at Stanford University, Bloch obtained a strong proton NMR signal when he inserted his finger in the radiofrequency coil of his spectrometer. In 1948, Purcell and Ramsey in turn inserted their heads into the 2 T field of the Harvard University cyclotron; around their heads was a coil connected to a powerful radiofrequency generator tuned to the proton NMR frequency. The only sensation recorded was that of the EMFs generated in the metal fillings of their teeth as their heads were moved into and out of the magnet and detected by their tongues.

Interest in living systems, however, very quickly went beyond curiosity. As NMR gained importance in biochemical investigations, there were many efforts to apply NMR as a noninvasive tool in biology. Most early attempts were limited by the geometry of the NMR magnets and probes of the time, usually with an NMR sample tube that was typically 5–15 mm in diameter. The same technical problems that limited biochemical applications at the time—sensitivity, resolution, dominance of the water signal in proton spectra, and the relative inflexibility of continuous wave NMR instrumentation—made biological applications difficult. During the 1970s, first the availability of pulse FT techniques and then the introduction of high-field superconducting magnet systems with multinuclear capability resulted in an upsurge of interest as physiological concentrations in the millimolar range became readily observable. By the early 1980s, wide-bore horizontal magnet systems that could accommodate large animals and humans, innovative probe designs such as surface coils, and localization techniques had become available, thus creating a revolution for in vivo NMR research.

This section traces the development of in vivo NMR spectroscopy as it evolved from experiments on isolated cells and excised organs or tissue to studies of intact animals and humans. (We have adopted a broad interpretation of the term in vivo in this article to include preparations of cells, subcellular organelles, and excised organs and tissues, along with intact microorganisms, animals, plants, and humans.) As we shall see, results from in vivo NMR studies provided the impetus for the development of NMR imaging, a subject that forms the basis for Section 13.

Water and Ions in Cells and Excised Tissues

The first efforts to use NMR to step into the realm of living systems focused on the signals observed from abundant small molecules such as water and electrolytes. Shaw and Elsken of the US Department of Agriculture placed 3-mm diameter cylinders of plant tissue (apple, potato, and maple wood) in a radiofrequency coil at 15 MHz to measure the water content in native and dehydrated states.[592] This work, published in 1950, was followed by several additional NMR studies by Shaw and co-workers of water in hygroscopic biological materials.

In 1955, Odeblad and Lindström published the first NMR measurements obtained on living cells and excised animal tissue. In their words, 'In biologic samples, rather complicated phenomena due to the viscosity, presence of paramagnetic enzymes, water adsorption on proteins, etc., predominate. It therefore seemed to be of interest to obtain information concerning certain characteristics of the proton magnetic resonance in biologic objects.'[791] The experiments, conducted at 26.5 MHz, were limited by the inhomogeneity of the magnetic field (typical linewidths were 10 ppm). The area of the water signal was measured by using a planimeter on photographs from the output of the oscilloscope screen, and relaxation times were obtained by a saturation recovery method where the growth of the signal height was recorded on moving film. Although the authors collected data on a broad array of biological samples—rabbit liver, striated muscle, fat tissue, calf cartilage, human Achilles tendon, human blood cells, and living yeast cells—not much could be concluded. The following year, they extended their studies on human red blood cells, using a 16 MHz 'high-resolution' spectrometer with spinning sample tubes and a resolution of less than 1 ppm. They could distinguish narrow and broad spectral components that differed in their exchange rates with D_2O.[792]

Odeblad and co-workers went on in succeeding years to publish the first NMR observations on a number of other biological preparations, including cervical mucus, human milk, tissues and fluids of the eye, vaginal cells, human saliva, and uterine muscle. In 1961, Odeblad published a paper entitled 'A Department for Medical Research with Nuclear Magnetic Resonance',[793] and in 1968 he used T_1 measurements on human cervical mucus to detect ovulation.[794]

In 1964, Bratton, Hopkins, and Weinberg[795] measured relaxation times of water in a living frog skeletal muscle and found that T_2 increased when the muscle contracted isometrically, whereas T_1 was not affected. They speculated on possible restricted rotational freedom of intracellular water and its variation as the muscle contracts.

Meanwhile, other investigators were also thinking about the state of water in biological tissue and began to use NMR as a probe of the mobility of water and ions. During the 1960s and 1970s a very large amount of work was published on relaxation, diffusion, and chemical exchange of water in cells and tissues of all sorts. For the most part, the NMR methods used were standard techniques of the sort we have discussed previously. The unique features were the attempts to interpret this body of NMR data, together with other information, in terms of models of the behavior of water in complex, ordered, anisotropic environments. A very good review by Raj Mathur-de Vré[796] summarizes the work done in a number of major laboratories and gives several general conclusions:

> A considerable effort has been devoted to investigate the relaxation times of water nuclei (^{1}H, ^{2}H, ^{17}O) for a variety of biological samples as a function of temperature and frequency. One common and striking feature observed in nearly all cases studied is that the relaxation times of water nuclei and the diffusion constants of water molecules are much lower than the values observed for free water. Generally, these results can be interpreted in terms of: (1) the restricted and anisotropic

> motion of water molecules and enhanced proton transfer in the hydration layer; and (2) the preferential and dynamic orientations of water molecules in the vicinity of biological macromolecules. ... Two-state and three-state models were proposed to account for the relaxation behaviour of water nuclei. ... There is conclusive evidence showing that water does not serve as an inert medium, but it participates at the molecular level in basic biological interactions and in fundamental biological processes.

Although considerable effort was expended in trying to use NMR data to support a model of the cell put forth by Gilbert Ling,[797] the results, analyses, and interpretations from NMR, while providing valuable parameters, were never able to provide conclusive evidence for or against any particular theory of cellular function.

Sodium-23 NMR was also exploited in studies of cells, largely because of its relatively high NMR sensitivity and cellular concentration. The early observations of ^{23}Na by Jardetzky and Wertz in 1956 had included studies of several physiological samples including whole dog blood, plasma, red blood cell and ghost suspensions in saline, and hemolysate. However, Freeman Cope was the first to investigate ^{23}Na by continuous wave NMR in tissues from muscle, kidney, and brain.[798,799] He found, as did others, that only about 40% of the known sodium could be accounted for by the integrated NMR intensity, and concluded that the remainder of the ^{23}Na signal was 'invisible' because the sodium ions were so immobilized that their resonance is greatly broadened. He interpreted these results in terms of Ling's model for the structure and operation of the cell. However, in erythrocytes, which also constitute a living cellular system, virtually all the sodium could be observed.[800] In 1972, Shporer and Civan[801] showed that the ^{23}Na NMR signal in a liquid crystal was split into one sharp resonance and two very broad resonances with relative intensities 40 : 30 : 30, as expected for quadrupolar relaxation of the spin-$\frac{3}{2}$ ^{23}Na in an anisotropic environment. Soon, Berendsen and Edzes[802] showed that in tissues such as muscle, electric field gradients from a partial ordering of macromolecules over distances of the order of 100 Å could explain the results without requiring that 60% of the sodium ions are immobilized. The ^{23}Na studies were further complicated by the fact that intracellular and interstitial ^{23}Na generally have the same chemical shift. Only in the 1980s could the two components be cleanly separated by a shift reagent, $Dy(P_3O_{10})_2^{3-}$ introduced by Gupta and Gupta,[803] and a more stable dysprosium complex later proposed by Springer and co-workers.[804]

In 1971, Raymond Damadian made an important discovery that would have long-term consequences. With the background of observations of cellular water, Damadian anticipated possible differences in NMR relaxation times for water in normal cells and cancer cells. He measured T_1 and T_2 in pieces of tissue excised from normal rats and from fast-growing tumors that had been implanted into other rats,[805] and found that each of the eight tumor samples had longer relaxation times than any of the normal samples. These results raised questions in two areas: whether NMR could provide fundamental information about cancer and whether relaxation times in excised tissue could be used as an adjunct to the pathologist's microscopic examination to diagnose malignancy. Hollis, Saryan, and Morris[806] soon repeated the measurements with other types of tumors. While they confirmed Damadian's results of long T_1 values with fast-growing tumors, they found some ambiguities with slow-growing tumors. Interestingly, from the NMR standpoint, both Damadian (from Downstate Medical Center in New York) and the Hollis group (from Johns Hopkins University) made their NMR measurements at NMR Specialties, a small company near Pittsburgh, PA, where at that time one of the few reliable pulse instruments was available for making relaxation measurements.

The initial encouraging results gave rise to a number of further studies of excised tissues, primarily from patients where conventional diagnosis by pathology examination was done independently and often in a 'double-blind' experiment. The generally accepted conclusion from the whole body of work was that relaxation times in excised tissues showed such wide variability that relaxation measurements could not be used as a definitive method to distinguish among tissues that are normal, malignant, or pathological but not malignant.[807] Nevertheless, the attention of a large number of NMR investigators had been drawn to the possibility of using this method in medical diagnosis. As we shall see in Section 13, this was one of the factors that eventually led to the development of NMR imaging as a medical diagnostic tool.

High-Resolution Studies

In the early 1970s, with the advent of pulse Fourier transform (FT) techniques and high-field spectrometers of ever increasing sensitivity and resolution, applications of NMR to living systems began in earnest. During the first half of that decade, a number of landmark papers appeared clearly demonstrating the potential of ^{13}C, ^{31}P, ^{1}H and other nuclei as probes for biological processes in vivo.

The first high-resolution spectra obtained on a preparation of isolated living cells were published in 1972 by Nick Matwiyoff and co-workers at the Los Alamos National Laboratory. After first using ^{13}C NMR at 25 MHz to examine whole-blood samples treated with ^{13}CO, $^{13}CO_2$, and $^{13}CN^-$,[808] they obtained spectra of whole cells of the yeast *Candida utilis* which had been randomly enriched to a ^{13}C level of 20% and suspended in D_2O.[809] A number of broad peaks were observed in the yeast suspensions that could be associated with particular types of carbon atoms by comparison with spectra of cell fractions and published spectra of known cellular constituents. The authors demonstrated that the metabolism of a specifically labeled substrate [1-^{13}C]glucose could be observed directly in living yeast cells, and commented:

> This successful demonstration of the use of ^{13}C as a label both for cellular constituents and for monitoring the in vivo metabolism of a substrate illustrates the potential usefulness of this isotope in biochemistry. The labeling of cellular components can have applications analogous to those now being used with *N*-oxyloxazolidine paramagnetic electron spin labels in membrane biochemistry, but with the advantage that the use of the internal ^{13}C nuclear spin does not require external modification of biological material. The specific labeling of substrates can have numerous applications in in vivo metabolic studies.

In 1972, Sunney Chan and co-workers tied an isolated rabbit sciatic nerve at both ends to a capillary with filaments from nylon stockings and placed it in a 5-mm NMR tube containing modified Locke's physiological solution prepared in D_2O.[810] The 220 MHz ^{1}H NMR spectrum contained a water line that

could be resolved into two distinct peaks corresponding to extracellular water and intracellular water by adding Mn^{2+} to the bathing solution. In addition, the high-field region of the spectrum revealed a number of resonances ascribed to mobile phospholipids of the nerve.

Among the NMR-active nuclei, ^{31}P held particular potential for in vivo studies due to its 100% natural abundance and presence in many cellular constituents and metabolites. In 1973, Moon and Richards at the California Institute of Technology were the first to realize this potential, publishing 40.5 MHz pulse FT ^{31}P spectra of whole rabbit blood and hemolysates obtained from sonicated cells.[811] Particularly interested in developing a convenient, nondestructive technique for determining intracellular conditions such as pH, they demonstrated that ^{31}P signals from 2,3-diphosphoglycerate and inorganic phosphate—estimated to be present in physiological concentrations of $\leq$7 mM—could be obtained after several minutes and their relative pH-dependent chemical shift behavior followed in hemolysates. In whole blood, both intracellular and extracellular inorganic phosphate resonances were observable, and the ~0.2 ppm difference could be used along with 2,3-diphosphoglycerate data to estimate the intracellular pH. The following year, Henderson et al.[812] showed that cellular metabolism could be followed directly in intact human erythrocytes by measuring the intracellular levels of 2,3-diphosphoglycerate and inorganic phosphate.

In 1974, a group of investigators in Rex Richards's laboratory at Oxford University decided to take an important step forward: to see if an NMR spectrum of metabolites could be obtained in living excised tissue. They had available the first 7.5 T magnet and a state-of-the-art pulsed-FT spectrometer for observation of ^{31}P at 129 MHz. The instrument could detect phosphorus in 0.5 mM solution, clearly within the range of physiological concentrations. Previous experiments in collaboration with George Radda's group had included investigations of biological membranes and enzyme regulation mechanisms. The interest soon turned to ^{31}P studies of the glycolytic pathway in muscle extracts and thoughts of studying metabolism in vivo. Initial trepidations from members of the research team (about intact muscle possibly spoiling the field homogeneity or whether relaxation times would be too short) were overcome, and an intact muscle freshly excised from the hind leg of a rat was inserted into an NMR tube and immersed in Ringer's solution. Clearly resolved resonances were observed—assignable to ATP, phosphocreatine, inorganic phosphate, and sugar phosphate/phospholipid—and their change with time followed as the muscle tissue became anoxic, as shown in Figure 90.[813] Four members of the Oxford research team conducting these experiments—Hoult, Gadian, Radda, and Richards—provide in this volume personal reminiscences on the genesis of this experiment, and the synergism and excitement of the collaborating team. The results demonstrated that the intracellular pH fell as the muscle became anoxic and that the ATP levels decreased only after the phosphocreatine was depleted. The authors quickly recognized the significance of this work for the study of metabolism in muscle and submitted the paper for publication in *Nature*. In his historical sketch (***Radda, George K.: The Development of In Vivo NMR In Oxford***) Radda recalls:

> The manuscript was rejected on the grounds that it described highly specialized experiments, unlikely to be repeated in other laboratories and of no general interest. I think this was the only time in my scientific career that I appealed against an editorial decision. I explained in my letter that we had talked about this work already in a number of places, particularly in the United States, and it created a great deal of excitement. The Editor accepted our argument and published the paper.

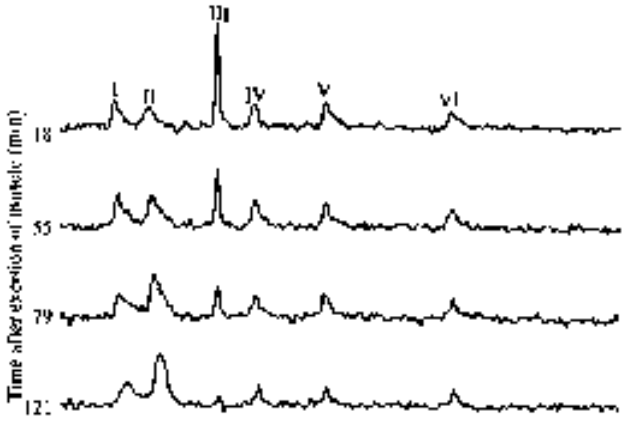

Figure 90 129 MHz ^{31}P NMR spectra of an intact muscle from the hind leg of a rat. Peak assignments: I, sugar phosphate and phospholipid; II, inorganic phosphate; III, creatine phosphate; IV–VI, adenosine triphosphate.[813] (Reproduced by permission of Macmillan Magazines Ltd)

The first observations of living cells by ^{15}N were published in 1975. In these experiments, M. Llinas et al.[814] grew the fungus *Ustilago sphaerogena* on 95% ^{15}N-ammonium acetate and examined a freshly packed cell slurry in a 12-mm NMR tube via proton noise-decoupled ^{15}N NMR spectroscopy at 10.1 MHz. Some 120 000 pulses were required to obtain a spectrum with sufficient signal-to-noise ratio to observe several resolved resonances from compounds within the cell.

Studies on Isolated Cells and Organelles Gain Momentum

The initial studies outlined above were followed over the succeeding years with a veritable explosion of publications exploiting ^{13}C, ^{31}P, and ^{1}H as noninvasive probes of biochemical processes in intact cells and organelles. The study of isolated cellular preparations had a number of attractions, not the least of which was the ability to study in vivo processes with minimal modifications to the conventional NMR equipment available in the 1970s and early 1980s. In addition, the ability to study homogeneous cell cultures and to manipulate extracellular conditions created a fertile environment for basic research in areas such as cellular energetics, metabolic pathways, and membrane permeability and transport.

Many of the early publications emanated from Bell Laboratories and a group of researchers that included R. G. Shulman, G. Navon, S. Ogawa, K. Ugurbil, T. R. Brown, J. A. den Hollander, S. M. Cohen, and others. The work of this group is described by Shulman (***Shulman, Robert G.: My Years in NMR***) and serves as an illustration of the types of experiments conducted during this period on cellular preparations. Shulman and co-workers exploited the high resolution and sensitivity of a Bruker HX-360 spectrometer, which they estimated to provide a six-fold increase in signal-to-noise ratio over that in an XL-100. Their initial experiments[815] used ^{31}P NMR at 146 MHz in suspensions of

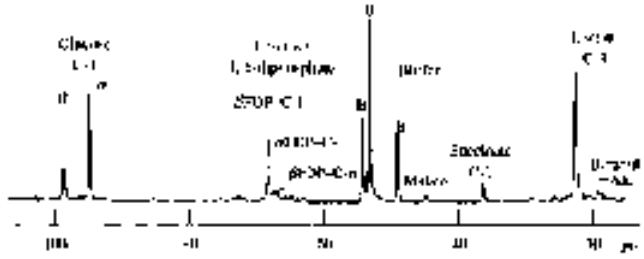

Figure 91 90 MHz ^{13}C NMR spectrum obtained within 1 min from a suspension of *E. coli* at 20°C 5 min after adding glucose enriched with ^{13}C at the C-1 position.[820] (Reproduced by permission of the American Association for the Advancement of Science)

baker's yeast, and were followed by studies of Ehrlich ascites tumor cells, *E. coli*, rat liver mitochondria, and isolated rat liver cells to measure phosphate metabolite concentrations and internal pH, and to demonstrate the important point that pH gradients were created across the membranes when energized. These experiments branched into several research directions. Brown et al.[816] applied the saturation-transfer technique for the first time in vivo to determine exchange rates between inorganic phosphate and the terminal phosphate of ATP in *E. coli*; Ugurbil et al.[817] studied glucose metabolism in *E. coli* using ^{13}C-labeled glucose; Cohen et al.[818] followed the gluconeogenic pathway from ^{13}C-labeled glycerol in suspensions of isolated rat hepatocytes; and Barton et al.[819] used ^{13}C NMR and labeling techniques to study sugar metabolism in dormant and germinating yeast spores. Figure 91 illustrates the detailed information obtainable from the ^{13}C studies.[820]

Concurrent with this work, a number of laboratories began reporting ^{31}P investigations using preparations of cells and subcellular organelles. For example, Daniels et al.,[821] Casey et al.,[822] and Pollard et al.[823] studied the internal structure and pH of bovine adrenal medullae chromaffin granules; Evans and Kaplan[824] conducted a survey of phosphorus compounds present in human cancer (HeLa) cells grown from tissue culture; and Gupta et al.[825] reported a procedure for determining the level of free Mg^{2+} in human red blood cells.

In 1979, the Bell Labs research team published a review of cellular applications, commenting that 'The ^{13}C and ^{31}P nuclei in many ways yield complementary data and, when used on the same system, supply a tremendous amount of simultaneous information about metabolic functions in vivo.'[820] That same year at Oxford University, Styles et al. demonstrated a means of exploiting this potential by publishing details of a spectrometer and probe design that permitted the recording of interleaved ^{31}P and ^{13}C NMR spectra during a single experiment.[826] They presented data on the metabolism of ^{13}C-labeled glucose by erythrocytes to demonstrate the advantages of the technique for simultaneous multinuclear monitoring of metabolic fluxes.

The use of proton NMR to study metabolites initially lagged somewhat because of problems with the intense water line and the multiplicity of resonances, including broad, but strong, background lines from less mobile constituents of the cell (membranes, etc.). In some instances the water could be removed by washing and re-suspension of cellular preparations in D_2O, but for most studies water-suppression methods were needed especially for pulse FT experiments. Selective

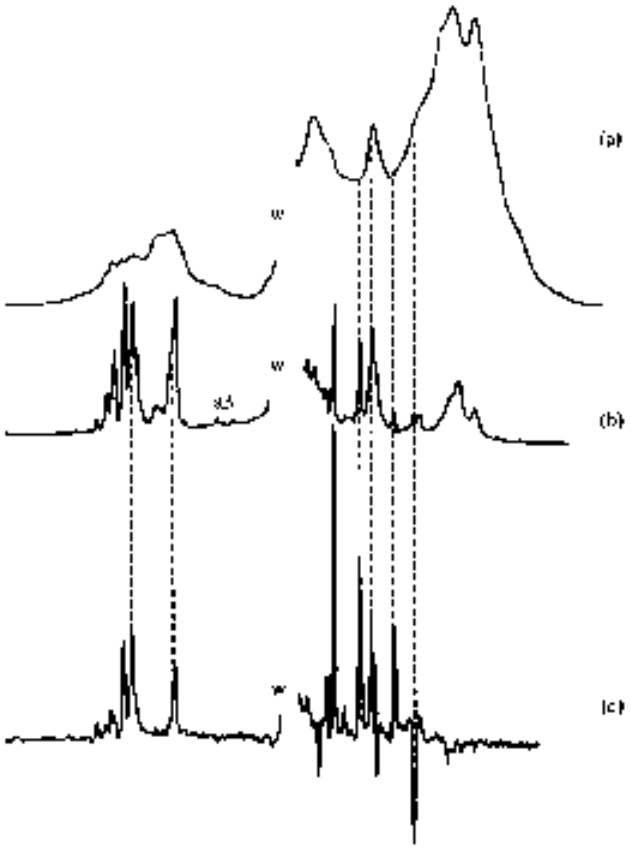

Figure 92 270 MHz ^{1}H spectra of glucose-depleted red cells at 37°C. (a) Normal FT spectrum. (b) Spectrum obtained using a spin echo sequence with τ = 20 ms. (c) Same as (b) but with τ = 60 ms. Differences between (b) and (c) result from J modulation.[828] (Reproduced by permission of Elsevier Science)

presaturation of the water resonance, as discussed in Section 10, was usually the method of choice in early work, but greatly improved methods eventually became available as improved instruments and techniques were developed. Van Zijl and Moonen[827] provide a comprehensive review of methods, and we shall refer to some of these techniques in Section 16.

Methods to edit out broad lines began to appear in the mid-1970s. Brown et al. used a spin echo FT technique to eliminate spectral components with short values of T_2[828] as shown in Figure 92 for human erythrocyte cells suspended in D_2O buffer. The sharp peaks appearing on elimination of the broad, dominant resonance of hemoglobin are assignable to mM concentrations of mobile intracellular species, such as glutathione. Figure 92 also shows the phase modulation of some resonances from homonuclear spin–spin coupling. This proved generally useful as an assignment tool (often in conjunction with spin decoupling) and also for monitoring enzyme-catalyzed deuterium exchange. Other similar editing methods were developed, as described in a 1984 review by Dallas Rabenstein.[829]

Erythrocytes were not the only intact cells studied by ^{1}H NMR. For example, Nicolau et al. studied normal and virus-infected chick embryo fibroblasts,[830] Agris and Campbell reported an investigation of differentiation of Friend leukemia cells,[831] and Mountford and co-workers initiated

detailed investigations of membrane structure in intact nontransformed and malignant cells.[832] The surprising result in many of these studies was the observation of high-resolution spectra characteristic of plasma membrane lipids. This was contrary to the picture that had emerged from the large body of work on model phospholipid bilayers and natural membranes, i.e., that incomplete averaging of dipolar interactions leads to broadline ^{1}H spectra for membrane constituents (Section 10). In 1986, Bloom et. al.[833] published a method for observing the 'complete spectrum' of intact viable rat mammary adenocarcinoma cells by simultaneously determining the high-resolution (nondipolar-broadened) and broadline (dipolar-broadened) components. Their technique (which used Carr–Purcell–Meiboom–Gill and Jeener–Broekaert pulse sequences to separate the spectral components) was capable of identifying the percentage and type of protons associated with the high-resolution and dipolar-broadened spectra.

One aspect of research on isolated cells that attracted (and continues to attract) considerable attention was the exploitation of NMR techniques to discriminate between intracellular and extracellular substances and to study transport processes. In the early ^{31}P studies outlined above, the maintenance of a pH gradient across energized cellular membranes could be demonstrated by the simple observation of both internal and external inorganic phosphate resonances. In many cases it proved possible to dope the exterior medium of cellular preparations with shift reagents or relaxation agents to create the desired discrimination between intracellular and extracellular components.[834] An elegant method introduced by van Zijl et al.[835] made use of the apparent reduction in diffusion coefficient for intracellular molecules that results from restricted motion. They developed a more sophisticated version of the technique used by Stejskal and Tanner[138] to allow excellent discrimination between intracellular and interstitial NMR signals.

The use of cellular suspensions or packed cells, while simple from a procedural standpoint, created experimental difficulties. For example, very viscous solutions had to be used in erythrocyte suspensions (hematocrits >70) or the cells would settle during spectral accumulation.[829] Also, the maintenance of cell viability including adequate oxygenation for aerobic cells, the uniform delivery of substrates or other physiological challenges, and the elimination of waste products were recognized problems with both suspensions or packed cells. A number of innovative techniques were developed to overcome these complications. In their 1977 ^{31}P study of metabolism in aerobic *E. coli* cell suspensions, Navon et al.[836] used oxygen bubbles to oxygenate the cells and maintain them in suspension. To avoid introducing field inhomogeneity, they synchronized the bubbling with rf pulses. An alternative approach, introduced by Balaban et al.,[837] relied upon the space in a 10-cm bore 4.3-T superconducting magnet to set up a 20-mm NMR cell chamber that used a hyperbaric atmosphere of oxygen over a stirred solution to achieve mixing and oxygenation during the NMR experiment.

In 1981, Ugurbil et al.[838] published a technique for the continuous perfusion of intact cells during the NMR experiment, using 'anchorage-dependent' mouse embryo cells that naturally attach and thrive on dextran microcarrier beads. Cancer cells, in particular, were heavily studied in ensuing years with this approach, but not all cells attached well to the microcarrier beads and there was a loss in sensitivity as the beads themselves filled much of the sample space. Jack Cohen, in his historical sketch (***Cohen, Jack S.: Recollections of Early NMR Applications to Proteins and Cells***), describes how he and David Foxall explored alternative approaches:

> After some experimentation, we found that the best means was to make a very fine gel thread by extruding the liquid gel (mixed with cells) through a cooled capillary. This had the advantages that the gel could be packed with cells (thus retaining S/N) and the small diameter of the thread (0.5 mm) allowed effective access to the nutrients, as we showed by extensive diffusion studies. This method has now been applied for ten years and many successful studies of cancer cell metabolism have been published.

Many other perfusion methods were introduced in order to improve the applicability to particular cell types or experimental protocols, increase the NMR sensitivity or magnetic field homogeneity, and promote the long-term physiological stability of the cells during the NMR experiment. Although in vivo techniques for the study of intact animals have advanced dramatically over the last decade (as we discuss in the following sections), the physiological homogeneity of cell populations and the ability to control extracellular parameters in perfusion systems has resulted in the continuing use of these model systems as a means of improving the understanding of fundamental biochemical processes.

Perfused Intact Tissue and Organs

The pioneering 1974 study by Hoult et al. on intact skeletal rat muscle demonstrated the ability of ^{31}P NMR to measure intracellular pH, the complexation of ATP with Mg^{2+}, and to follow changes as the nonperfused tissue dies from anoxia. Reports soon followed of similar ^{31}P NMR studies on a broad range of muscle types, adrenal glands, developing frog embryos, and other tissues. One of the first problems to be tackled was the development of techniques to keep the extracted tissue alive during the several hours length of the NMR experiment. Dawson, Gadian, and Wilkie[839] developed a probe that fitted into the Oxford 7.5 T spectrometer and not only allowed perfusion of small excised muscles with oxygenated Ringer solution, but also permitted electrical stimulation of the muscles and measurement of tension development at the same time as ^{31}P spectra were obtained. Britton Chance joined George Radda and his coworkers at Oxford to measure metabolism in a small rat heart that fitted within the 8-mm sample tube.[840] At that time several other groups were also working on techniques to allow NMR measurements on whole perfused organs from mice or rats, which were suitably small to fit within the confines of available spectrometers. Don Hollis[841] describes the genesis of experiments at Johns Hopkins School of Medicine following a talk by R. G. Shulman, whom Hollis had invited to speak about ^{31}P NMR studies of *E. coli* metabolism:

> After the talk Bill Jacobus, Shulman and I talked informally about our work while standing in the hall waiting for someone to fetch Shulman's coat ... Taking his lead from the Oxford study on frog leg muscle, Jacobus asked, 'Why can't we look at a living, beating animal heart and study its metabolism under various conditions when it is actually working?' I replied, 'I have the largest NMR probe now available commercially and the biggest sample it can take is only 15 mm in diameter. We would have to squeeze the heart and all of your plumbing into that small space.' 'Hell', said Jacobus, I can do that easily'.

> We made a date to try it and the next day Jacobus and several of his co-workers showed up at my laboratory carrying boxes of rats, rolls of polyethylene tubing, bottles of nutrient solutions, tanks of oxygen, surgical tools and sutures. Besides these, they were pushing a cart loaded with an electrocardiograph set-up, a pacemaker, and other electronic gadgets. Within a few hours we had a small beating rat heart in the NMR machine, and we immediately saw what we had hoped for: a beautiful, clear, perfectly resolved spectrum of heart metabolism.[842]

Control of the heart rate in these experiments was achieved by tiny pacemaker leads sewn onto the heart muscle, and the individual heart beats recorded by means of a small water-filled latex balloon sewn into the left ventricle that transmitted the pressure from contraction through a polyethylene tube to a transducer external to the spectrometer.

These initial studies, which demonstrated that ^{31}P NMR could be used not only to monitor metabolism in the normal working heart, but also to investigate the effects of partial and total ischemia, were followed by ^{31}P NMR studies on other organ preparations including, for example, nonperfused hypothermic and blood-perfused rat kidneys as a model system for kidney transplants[843] and ^{13}C NMR studies of gluconeogenesis from labeled alanine in perfused mouse liver.[844] Very shortly thereafter, superconducting wide-bore magnets were developed allowing more room for perfusion apparatus as well as organs from larger animals. The range of reports on perfused whole organs broadened enormously over the following decade. One example, described by Bob Balaban in his historical sketch (***Balaban, Robert S.: Personal Perspective on the History of NMR***), gives a sense of the thrill of discovery that accompanied this research:

> During this time the serendipity of the biological applications of NMR spectroscopy became very clear. In one of our earliest studies we performed a series of studies with ^{14}N NMR attempting to measure the concentration and distribution of urea in the intact kidney (with Mark Knepper). However, our studies revealed a very broad and not very useful urea ^{14}N resonance (exchange broadening), but an extremely sharp and intense resonance in the region of trimethylamines. After a week of library and telephone interviews, it was clear that no one knew what this compound was in the kidney in the 20–80 mM concentration! It turned out to be the oxidation product of choline, betaine, and its discovery started a new area of research in renal studies on the role and regulation of these organic osmolytes in the protection and function of the kidney.

The study of perfused organs continues to find applications today, despite the many technological developments discussed below that now permit NMR studies of intact animals and humans. In part, this is due to the ability to control more easily certain experimental conditions including the administration of labeled compounds.

High-Resolution NMR of Intact Animals

Intact, living animals had been studied by NMR, but only to obtain limited information. In 1968, Jackson and Langham built a shielded solenoid that provided a uniform field of 10 G and obtained the first NMR spectrum of a living animal.[845] The proton NMR spectrum at 40 kHz of a live, anesthetized rat not surprisingly showed only a single broad resonance. In 1972, Weisman et al.[846] conducted an important study in the emerging field of NMR in the study of pathology when they measured T_1 in normal and malignant tissue in a living mouse. They overcame the restrictions of an NMR spectrometer designed for chemical samples by observing the tail of the mouse, which could be fitted into the NMR probe. A tumor implanted in the tail showed a T_1 value that was more than twice as long as that in normal tail tissue. Only crude localization was possible in this apparatus.

The high-resolution NMR spectrometers of the late 1970s were generally narrow-bore (5 cm) systems which were adequate for isolated cells or excised tissue and organs, but could not be considered for studies of intact animals. However, things were changing. By 1977, a 4.2-T 10-cm bore spectrometer had been developed by Oxford University in conjunction with Oxford Instruments, and was being used in Radda's laboratory for perfusion studies in the rat heart and kidney. This magnet had sufficient working space to allow the study of small whole animals, and ^{31}P spectra of a heart in a living, anesthetized rat were obtained with a coil implanted into the animal.[847] However, efforts to obtain similar results from a rat kidney ran into problems with localization, since signals from nearby muscle could not be eliminated. Joe Ackerman, then a postdoctoral fellow in Radda's laboratory, describes in his historical sketch (***Ackerman, Joseph J. H.: Oxford Knights***) the origin of a better method:

> I remember well the repeated unsuccessful attempts to pack gauze pads about the coil in an attempt to push the surrounding tissue out of the antenna coil's transmission/reception range. It was two in the morning, the jokes were getting stale and tempers a bit edgy when I realized the all too simple lesson in front of us: samples don't have to be inside the antenna coil to be detected. I walked out of the spectrometer room and down the hall to our office. This cramped space also served as the coil-design electronics laboratory. The first surface coil was wound. A simple tank circuit frequency-tuned and impedance-matched the surface coil to ^{31}P—80 MHz at 4.2 T. I returned to the spectrometer room to find even more gauze packed about the implanted kidney coil. Tom and Gordon were clearly fed up with the kidney experiment. They agreed to humor me. We put the surface coil on the rat thigh, the largest muscle group. One of us ventured that if we could just get enough ^{1}H tissue water signal to shim the field we might have a chance with the ^{31}P experiment. We were stunned, the ^{1}H FID was enormous. Shimming was remarkably easy. Tom, Gordon, and I quickly switched the spectrometer over to ^{31}P. Within minutes a beautiful muscle spectrum showing inorganic phosphate, phosphocreatine, and the α-, β-, and γ-phosphate resonances of ATP was in hand.

A paper describing the surface coil and its sensitivity was published in *Nature*.[848] Figure 93 shows a ^{31}P spectrum obtained from a rat brain. As indicated, a convolution difference method was used to eliminate the broad ^{31}P resonance, primarily from bone.

In retrospect, surface coils had actually been used by other workers for specific purposes, for example by Jay Singer to measure blood flow[849] as we describe in Section 16. However, their significance and detailed characteristics had not been explored. As shown by Ackerman and co-workers, a surface coil placed adjacent to an object detects signals from a region confined approximately to the coil circumference and to a depth equal to about the radius of the coil. High filling factors resulted in good signal-to-noise ratios. As such, the surface coil provided an extremely sensitive and simple method for observing high-resolution signals from regions localized near the surface of intact animals or in surgically exposed organs. The use of surface coils, according to Radda, 'transformed completely the possibilities of in vivo spectroscopy.' They

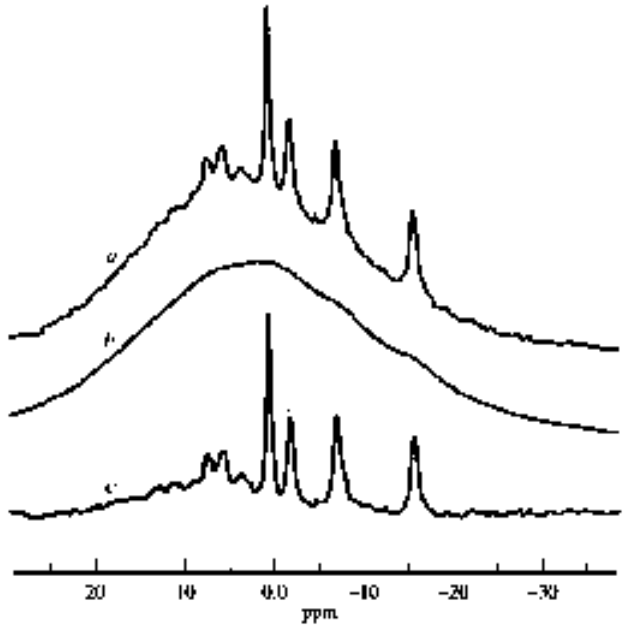

Figure 93 ^{31}P NMR spectra of the brain of an intact rat, obtained with a surface coil. (a) Observed spectrum. (b) Same as (a), with 400 Hz line-broadening applied. (c) Difference spectrum between (a) and (b).[848] (Reproduced by permission of Macmillan Magazines Ltd)

have been utilized very widely since their introduction in 1980. Some 10 years later it was estimated they were being employed in more than 80% of the published in vivo NMR studies.

A surface coil can be used as a receiver only, or as both transmitter and receiver. In 1983, Bendall and Gordon introduced a technique which used to advantage the inherent inhomogeneity of the rf field $\boldsymbol{B}_1$ generated by the surface coil over the roughly hemispherical volume adjacent to the coil. In simple one-pulse experiments, it had been shown that one could set the pulse length so as to obtain a 90° pulse—and thus maximum signal intensity—at a particular depth from the coil. Bendall and Gordon demonstrated that spin echo and inversion–recovery sequences, coupled with phase cycling, can provide markedly increased discrimination against sample regions where pulse angles differ from the ideal values.[850] They coined the name 'depth pulse' to describe this selectivity.

Radiofrequency surface coils and depth pulses continued to provide an important means of spatial discrimination, but variation of the static field $\boldsymbol{B}_0$, rather than $\boldsymbol{B}_1$, across the sample soon furnished the principal means for carrying out localized NMR spectroscopy. Imaging techniques and other means to tailor the homogeneity of $\boldsymbol{B}_0$ provided numerous effective approaches, as we shall discuss later. During the early 1980s, high-field, wide-bore horizontal superconducting magnets became available commercially, ushering in a new era for in vivo NMR. Field strengths of 2–4.7 T, with initially 30 cm and then 40–45 cm diameter bores, could be used to study animals the size of dogs or small sheep. The number of in vivo applications emanating from these animal systems in the succeeding decade has been enormous. Narrower bore systems at even higher fields (e.g., 7 T) also became available commercially.

High-Resolution Studies on Humans

By the time it became technically feasible to perform high-resolution NMR studies on human subjects, a considerable foundation of knowledge had been built from work on perfused cells, tissues, and organs, as well as intact animal models.

The first high-resolution NMR spectra of human subjects were obtained using the same horizontal, wide-bore superconducting magnets developed for animal experiments. Britton Chance managed to get his leg into an 18-cm bore magnet to obtain ^{31}P spectra.[851] According to George Radda, 'the resolution was not very good, but Chance's leg in the magnet impressed *PNAS*, where the first spectra were published.'

The capability for studying muscle metabolism in humans by NMR spectroscopy was quickly put to a clinical test by Radda and his associates in a study of a patient suspected to have a phosphorylase activity disorder termed McArdle's Syndrome. The experimental setting was nonclinical, with the patient placing his forearm into the 30-cm bore of the 2 T magnet that was located in the Biochemistry Department of Oxford University. However, the results published in the *New England Journal of Medicine* in May 1981, were indeed clinically significant.[852] Using a ^{31}P surface coil to follow the intensity and position of the intracellular ATP, phosphocreatine, and inorganic phosphate resonances, the authors were able to demonstrate abnormal responses to ischemic exercise and establish a clinical diagnosis. This work signaled the beginning of an extensive program of medical applications of NMR by Radda's group, which moved clinical studies to a new building at the John Radcliffe Hospital, and obtained a larger bore magnet. His historical sketch (***Radda, George K.: The Development of In Vivo NMR In Oxford***) describes the development of this work, which had involved some 4000 patient investigations by August 1993.

The work of Shulman's group at Yale University is illustrative of research in another important area, ^{13}C NMR studies of glycogen metabolism disorders. Intracellular glycogen is sufficiently flexible that resolved ^{13}C resonances are obtained for this large polymer,[853] and can be used to monitor glycogen concentrations in vivo in normal controls and diabetic patients. Such studies have technical difficulties including the low sensitivity of ^{13}C, rf power deposition during decoupling, and spatial displacement artifacts from the large chemical shift range. Nevertheless, as Shulman recounts in his historical sketch:

> The insulin independent rate of glycogen synthesis has clinical consequences for the control of diabetes, suggesting that intense glycogen depleting exercise would help diabetics. These glycogen experiments illustrate how a definite result of a basic research program, i.e., the visibility of the glycogen ^{13}C NMR, can be developed to the point where in vivo NMR experiments can delineate the control of its synthesis. This allowed us to determine the nature of a serious illness and these studies suggested a means of controlling the disease.

Further advances in in vivo NMR spectroscopy are intertwined with the development of NMR imaging techniques, a subject that we treat in Section 13. We shall return briefly to a summary of some recent examples of in vivo spectroscopy in Section 16.

IMAGES BY NMR

NMR, discovered and initially developed as a technique for obtaining data of importance in physics, had been dominated from the mid-1950s by applications in chemistry, where it had revolutionized the methods used for the structure elucidation of organic molecules and biopolymers. As we have seen in the previous section, living systems, too, were investigated by NMR spectroscopy. But in the early 1970s NMR was to move into totally new areas, as methods were invented for obtaining *spatial* information that had immediate practical value in the fields of biology and medicine.

Zeugmatography

Magnetic field gradients have always been of importance in NMR. Early efforts were directed entirely toward minimizing such gradients in order to produce the largest feasible volume within the magnetic field that had adequate homogeneity for high-resolution NMR. With the development of suitable electric 'shim' coils to generate gradients up to fourth order in various directions, it was possible to compensate for many of the unwanted gradients of a large magnet and to achieve high overall homogeneity. Within this homogeneous field, it then became possible to deliberately apply a gradient (almost always linear) in a particular direction to permit the acquisition of certain information. For example, we saw in Section 4 that Herman Carr had, in 1951, applied a gradient across three pieces of rubber to simulate the effect of local chemical shift fields in ethanol. The Carr–Purcell pulse sequence could also be used to measure diffusion if a known linear field gradient was applied, a process that was improved by using a pulsed gradient, applicable only for a short, fixed period. Gabillard examined the NMR signal in simple glass and liquid objects on which a one-dimensional gradient was imposed,[854] and Walters and Fairbank[414] used a field gradient to detect phase separation between ^{3}He and ^{4}He. In unpublished work at the National Institutes of Health, Kudravcev[855] recognized that field inhomogeneity provided by static or alternating field gradients could be used to localize a volume of interest. All of these applications depended on the spatial variation of the NMR signal, usually along a one-dimensional gradient. Gradients had been used for other purposes, as well, as pointed out by Ralph Hurd in his article (***Hurd, Ralph E.: A Brief History of Gradients in NMR***).

In September 1971, Paul Lauterbur conceived the idea of using magnetic field gradients in a more elegant way—to obtain two- or three-dimensional spatial information about the distribution of magnetic nuclei in a sample placed inside an NMR coil and thus to create a 'picture' of the object by NMR. The Larmor relation $\nu_0 = (\gamma/2\pi)B_n$ ensured that the NMR frequency would precisely monitor the magnetic field B_n at the nucleus, so that if a linear gradient G is applied in the direction x, along with the large static field B_0,

$$\nu = (\gamma/2\pi)B_0(1 + Gx) \tag{4}$$

and the observed frequency can measure the value of x. Lauterbur realized that the homogeneity controls on an ordinary NMR magnet could be adjusted to provide a linear gradient in any one of the three orthogonal directions x, y, or z, and by using combinations of these Cartesian gradients the overall gradient could be set in any chosen direction.

In his historical sketch (***Lauterbur, Paul C.: One Path out of Many--How MRI Actually Began***) Lauterbur describes the inspiration for his idea during a stay at NMR Specialities near Pittsburgh, after he had observed Leon Saryan, a graduate student with Don Hollis, carrying out relaxation measurements with excised tissue from rats (work that was described in Section 12):

> I watched them being done, including the sacrifice of the rats, specimen dissection, and the NMR measurements, and was struck by the consistent differences obtained among various normal and malignant tissues. I knew, however, that biopsies were commonly done and examined by histologists, and I believed that NMR relaxation time measurements on tissue specimens were unlikely to contribute much to the rich variety of information available from optical microscopy. All of this information about the tissues was apparently there, however, within the living organism. Was there any way that one could tell exactly which location an NMR signal was coming from within a complex object? That same evening I realized that inhomogeneous magnetic fields labeled signals according to their spatial coordinates, and made a leap of faith to the conclusion that the information could be recovered in the form of pictures (we would now say that the inverse problem could be solved). I was so sure of this that I immediately went out and bought a notebook and had the idea witnessed.

The first page of that notebook is reproduced in Figure 94. Subsequent pages record further ideas on how to do such experiments. Over the next few months, Lauterbur worked out procedures for disentangling the data obtained from a number of experiments with gradients in different directions and, 'after failing to convince various people and institutions that it was a good enough idea to patent', he carried out a test of the ideas with a standard A–60 spectrometer.

Lauterbur submitted his initial work to *Nature* in October 1972 and eventually it was published, but not without some difficulty in convincing the editor of the potential importance of the work. Although his motivation for inventing this method had been primarily a desire to use NMR methods to image tissue in a living object, his paper emphasized the generality of the physical principle, which at first might seem to contradict the classical laws of diffraction. In general, the resolution obtainable from an electromagnetic wave is no better than its wavelength, so the use of radiofrequencies with wavelengths of meters to image in the range of millimeters might seem absurd to a classical optical microscopist. Lauterbur pointed out that the phenomenon here is quite different, and that it is the combined effect of the static magnetic field and the rf that leads to localization. He coined the term *zeugmatography* (from the Greek $\zeta\epsilon\upsilon\gamma\mu\alpha$, 'that which is used for joining') to describe the technique. After some interesting and amusing correspondence with the editor of *Nature*, as reproduced by Hollis,[857] Lauterbur's paper was accepted and appeared in March 1973.[858]

This paper illustrates the use of gradients in several directions and describes a way of generating two-dimensional images by back-projecting the one-dimensional 'spectra' produced from each gradient. An image of the test sample, two capillaries of water, which would fit within a standard 5-mm diameter NMR tube, was clearly reproduced as illustrated in Figure 95, and the effect of different relaxation times was shown by partial saturation. The relaxation time study was important in the context of using the method to investigate

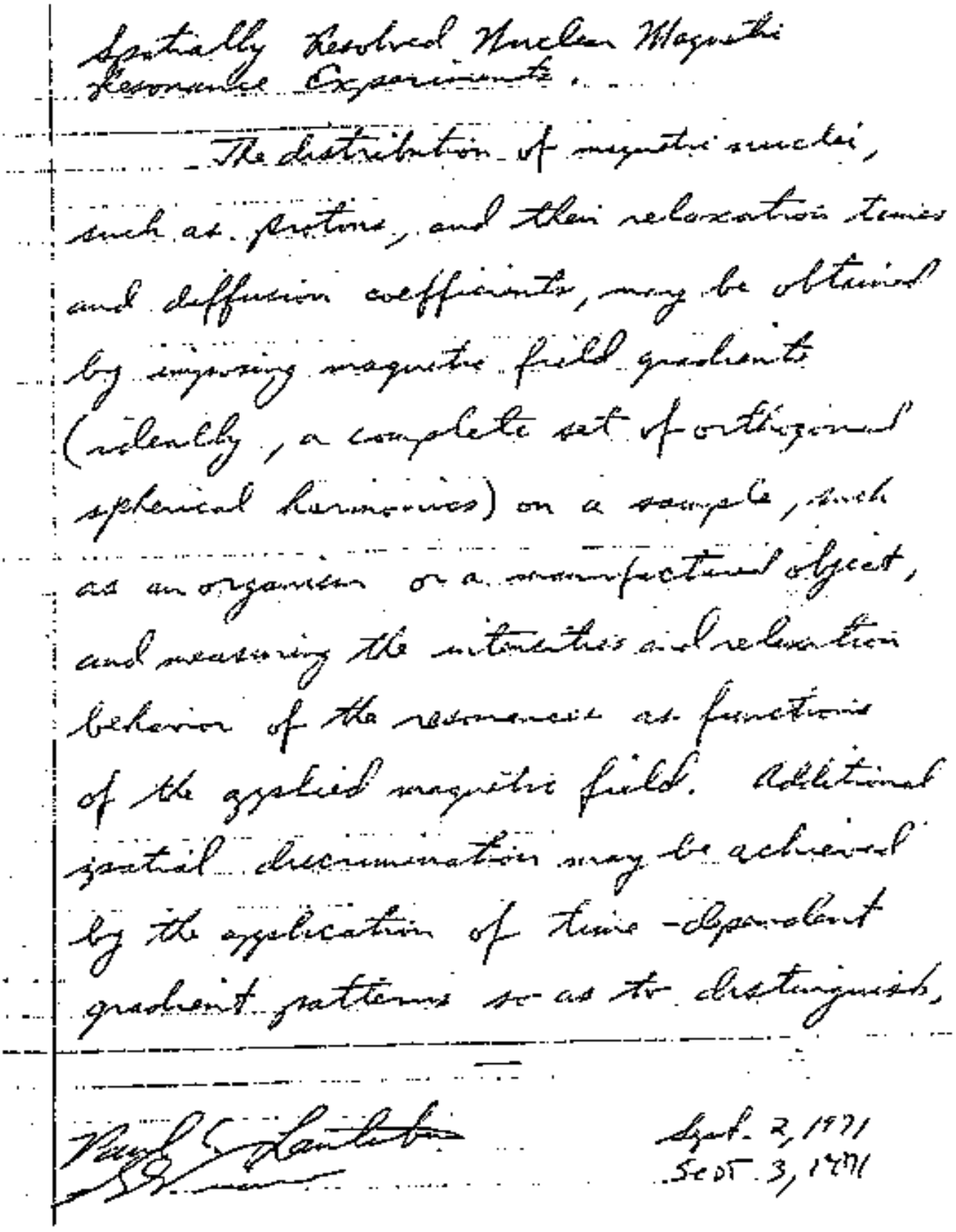
Spatially Resolved Nuclear Magnetic
Resonance Experiments

The distribution of magnetic nuclei,
such as protons, and their relaxation times
and diffusion coefficients, may be obtained
by imposing magnetic field gradients
(ideally, a complete set of orthogonal
spherical harmonics) on a sample, such
as an organism or a manufactured object,
and measuring the intensities and relaxation
behavior of the resonances as functions
of the applied magnetic field. Additional
spatial discrimination may be achieved
by the application of time-dependent
gradient patterns so as to distinguish,

Paul C. Lauterbur

Sept. 2, 1971
Sept. 3, 1971

Figure 94 A page from Paul Lauterbur's notebook in which the basic ideas of NMR imaging are recorded and witnessed (Courtesy of P.C. Lauterbur)

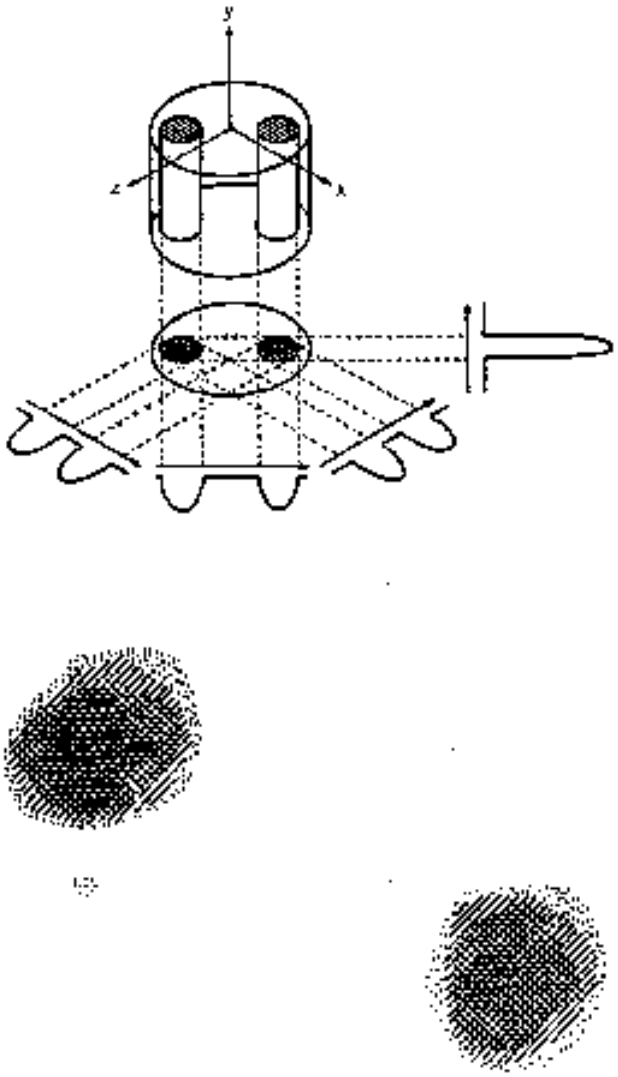

Figure 95 Top: Schematic representation of the use of back-projection to reproduce a two-dimensional image from several one-dimensional projections. Bottom: ^{1}H NMR image of the cross-sections of two tubes of water, obtained by reconstruction from four projections.[858] (Reproduced by permission of Macmillan Magazines Ltd)

living systems, in view of the work described in Section 12 which had shown increased T_1 values in certain tumors, either excised[805,806] or in situ.[846] Lauterbur pointed out the potential for the method in the NMR of solids and liquids, with electron spin resonance, and possibly in other regions of the spectrum. His concluding sentence in the manuscript[858] described the wide utility:

> Zeugmatographic techniques should find many useful applications in studies of the internal structures, states, and compositions of microscopic and macroscopic objects.

In the production process, the words 'and macroscopic' were deleted from the final published article.

With only a standard NMR magnet available, Lauterbur was forced to test the method further with small objects. The first living animal to be imaged was a clam, 4 mm in diameter, which fitted into a standard 5-mm sample tube, and NMR showed the soft structure within the closed shell, the latter not contributing to the proton NMR signal.[859] By 1974, with a modified Varian DA-60 which had a larger magnet gap, he was able to display an image of the thoracic cavity of a living mouse.[860] Two years later, he demonstrated T_1 changes in a tumor implanted in a mouse.

New Twists on Zeugmatographic Methods

Lauterbur's paper, possibly because of its title and general approach, attracted little attention in the NMR community, but his talks at several meetings served to alert NMR spectroscopists to the new method.

The International Society of Magnetic Resonance (ISMAR) held its triennial meeting in Bombay in January 1974. The potential importance of Lauterbur's short submitted paper was recognized by the conference organizers, and his talk was converted to a plenary lecture where it attracted the attention of Raymond Andrew, William Moore, and Waldo Hinshaw, all then at the University of Nottingham. After discussions among themselves, Hinshaw developed a novel approach in which he used time-varying gradients in the x, y, and z directions in which a single small volume experienced only a constant, homogeneous magnetic field.[861,862] An NMR signal could be obtained only from this 'sensitive point' by taking the time integral of the FID, thus canceling out signals from time-varying fields. The sensitive point could be readily moved around the sample by varying dc currents in the three orthogonal directions and a 3D image was thus obtained. The Sensitive Point method was quite simple to implement and required no complex data processing, an advantage at that time, as described in Hinshaw's historical sketch (***Hinshaw, Waldo: Notes on the History of MR Imaging from my Perspective***):

> One constraint we had in developing an imaging method was the lack of a computer. I did have access to Andrew's pulsed NMR spectrometer which had an analog output, and everything in the lab was analog. I spent evenings and weekends assembling clock motors and potentiometers and coils. Bill [Moore] provided constant encouragement. By April of 1974, we had produced the first images. With this work, we were the first group after Lauterbur to produce MR images. Bill and I applied for and were awarded the first patent on MR imaging, or as we called it then, NMR spin-mapping.

This method, however, was inefficient in discarding most of the potential signal and in requiring many repetitions to cover a volume of interest. Although the technique was improved to produce data from a 'line' rather than a 'point', it eventually gave way to more efficient methods.

An alternative method was proposed in 1974 by Garroway, Grannell, and Mansfield,[863] who suggested the use of a selective pulse in the presence of a field gradient to excite only a narrow band of frequencies, hence a thin slice of the sample. Following ideas introduced by Tomlinson and Hill[291] (see Section 7), the exciting pulse was tailored to contain only Fourier components that fitted within the desired slice. A two-dimensional 'column' could be selected by repetition of this process, with the gradient rapidly switched to an orthogonal direction and the resultant signal read out by application of a static gradient in the third orthogonal direction. For the creation of 2D or 3D images, this method was soon supplanted by other, more efficient, techniques. However, as we shall see below, its application to one-dimensional slice selection has been very widespread. David Hoult[864,865] pointed out that this

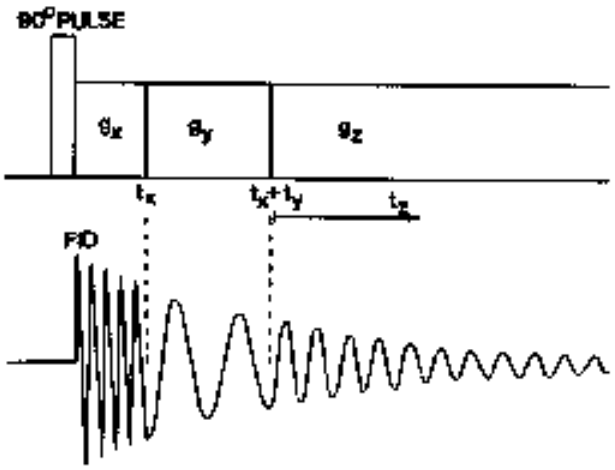

Figure 96 The basic idea of Fourier transform imaging.[685] (Reproduced by permission of Academic Press)

technique as originally proposed suffered from loss of signal from the rapid dephasing of magnetization that occurs during a long selective pulse applied concurrently with a strong field gradient, but the signal can be recovered with the addition of a gradient reversal to rephase the spins and create an echo.

Meanwhile, at the 15th ENC (Experimental NMR Conference) in Raleigh, North Carolina, in April 1974, Lauterbur presented a short talk entitled 'Spatial Resolution of NMR Signals'. Richard Ernst, who was in the audience, had been thinking about Jeener's unpublished work on two-dimensional NMR (see Section 11) and realized that time-domain experiments with switched magnetic field gradients could provide an alternative to the back-projection method in obtaining NMR data across a plane or throughout a three-dimensional volume. This led to the concept of 'NMR Fourier Zeugmatography' published by Kumar, Welti, and Ernst[685] in 1975. The principle of the method is illustrated in Figure 96. Initially, a 90° pulse rotates the magnetization to the *xy* plane, where it precesses in the presence of three orthogonal linear magnetic field gradients, g_x, g_y, and g_z, applied in succession. The FID is sampled in the third time interval as a function of t_z. The experiment is repeated for a full set of equally spaced t_x and t_y values. The three-dimensional Fourier transform of the FID is a measure of the spatial spin density and provides the three-dimensional image of the sample. In the terminology that was later developed, the first two gradients encode the phase of the signal, based on its frequency (hence position along the operative gradient) and the period during which the gradient is imposed.

Ernst moved rapidly to test the idea in a two-dimensional regime, using two tubes of water, a Bruker SPX4-100 spectrometer, a Varian 15-inch magnet, and a Varian 620/L-100 computer with 12k memory. As Anil Kumar relates in his historical sketch (***Kumar, Anil: Development of Two-Dimensional NMR--My Perception***),

> Ernst wrote a few subroutines, Dieter Welti wrote others and I did the experiment. The gradients were applied by switching off the current in the linear shim coils of an electromagnet. A crude 64 × 64 matrix image of two tubes of water was printed on a teletype by digitizing the intensity into blanks, dots, and alphabets. We laughed at the experiment and published it without patenting.

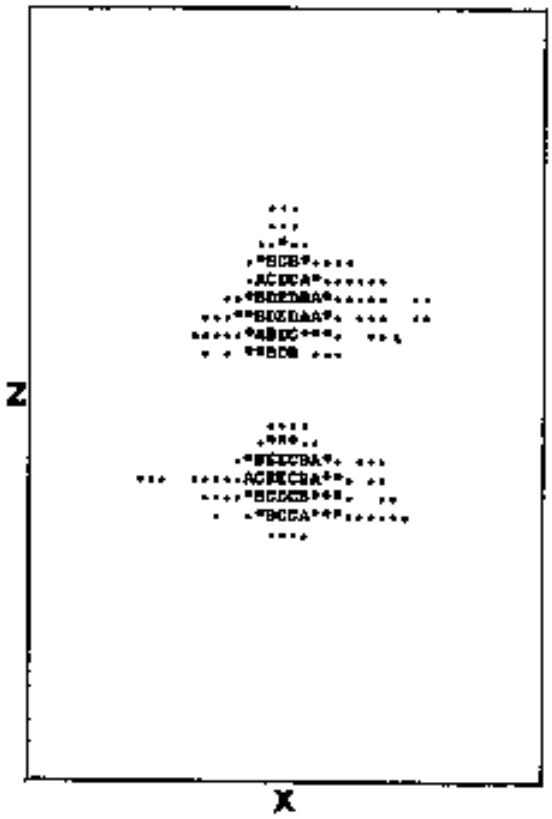

Figure 97 The first two-dimensional Fourier transform NMR image of two tubes of water. The intensity intervals are indicated in increasing order by the symbols (blank), •, *, A, B, C, D, and E.[685] (Reproduced by permission of Academic Press)

[Actually, as Ernst recounts, he later filed a patent (March 1975) and assigned it to Varian Associates for whom he was a consultant.] The two-dimensional Fourier zeugmatogram thus obtained is shown in Figure 97. For this plot, the total intensity range was divided into eight equal intervals and a teletype character was assigned to each interval. As in 2D NMR spectroscopy, the Fourier imaging concept has been extended to the third dimension.

During the 1970s, as various methods were being tried, it became apparent that the 2D/3D FT method of Ernst et al. was an efficient procedure, but the necessity of incrementing the period for applying the phase-encoding gradient (for 2D imaging) or gradients (for 3D) could lead to distortions in the image, since inhomogeneities in the static field cause a phase error that varies as the phase-encoding time changes. At Aberdeen, Edelstein et al.[866] developed a simple variation of the Fourier imaging method to circumvent these problems with the instruments available at that time. Instead of varying the phase-encode time, they maintained a constant time but incremented the magnitude of the phase-encode gradient. Since this process can be pictured as introducing a phase twist to projections along a particular axis, they coined the name 'spin warp' method. The 'constant time' spin warp very quickly replaced the original 2D FT imaging method for practical use.

While the term 'zeugmatography', together with other names, such as 'tomography', have largely given way to the simple and descriptive 'imaging', the method used for most of the commercial development of magnetic resonance imaging

(as we shall see later) has relied on the basic zeugmatographic concept of the application of linear magnetic field gradients. For medical applications, the 2D/3D FT approach, as modified into the spin warp method, has largely been the method of choice. However, a full 3D data set involves many repetitions and usually consumes too long a time for practical use. Moreover, as Hinshaw comments in his historical sketch, 'radiologists preferred the images that could be obtained from a set of separately acquired slices'. The use of several parallel slices became the generally preferred procedure, with slice selection almost invariably carried out by the method of Garroway et al., incorporating Hoult's gradient recalled echo as described above.

Hoult later developed an interesting variant of the imaging method, 'rotating frame zeugmatography', in which one of the static field gradients in the observation plane is replaced by a gradient in the rf field.[867] The method has been used in special circumstances and has been especially valuable for localized spectroscopy, for example in ^{31}P NMR with a surface coil.[868] However, the technique is not widely employed as a general imaging method.

From Diffraction in Solids to Imaging in Liquids

As we saw in Section 8, Peter Mansfield was one of the most active workers in developing multiple pulse techniques for line narrowing in solids during the late 1960s and early 1970s. In 1972, he began to think about the possibility of using NMR to determine atomic structure in a solid in which the dipolar interactions had, in effect, been removed by multiple pulse methods. Allen Garroway's account in his historical sketch (***Garroway, Allen: N., Origins of MRI--A Personal View***) of the first discussion of the idea is informative:

> One day in the early summer of 1972 as Grannell and I were having morning coffee in the Physics tea room, Peter Mansfield pulled up a chair and said, in essence: "I've had this really crazy idea. It seems that one could measure atomic separations in crystalline materials by imposing a magnetic field gradient and observing the resultant NMR diffraction pattern". Grannell rolled his eyes. From my experience in pulsed gradient diffusion, I volunteered that the required magnetic gradients would need to be immense and, further, that the alignment and the perfection of the crystal would need to be of the order of crystal lattice dimensions. . . .

As Mansfield relates in his historical sketch (***Woessner, Donald E.: In a Maze in NMR***), the idea was pursued only sporadically for some time because of other work and his departure for a sabbatical in Heidelberg. Garroway's initial estimates were correct: calculations showed that for diffraction in an atomic lattice a field gradient of ca. 1000 G cm^{-1} would be required, and the multiple pulse methods would have to produce lines two orders of magnitude narrower than were then obtainable. However, Grannell used a multiple pulse sequence to reduce dipolar couplings in an artificial one-dimensional lattice created from layers of camphor crystal separated by layers of cardboard. Mansfield and Grannell were able to obtain a one-dimensional interferogram to a resolution of better than 1 mm, as illustrated in Figure 98.[869] The work was presented at a Colloque AMPERE[870] in Krakow, Poland in September 1973, a meeting which brought together all the major figures in the field of line narrowing in solids (see Section 8). Ulrich Haeberlen, in his historical sketch, (***Haeberlen, Ulrich: The Early Days of Multiple Pulse NMR***)

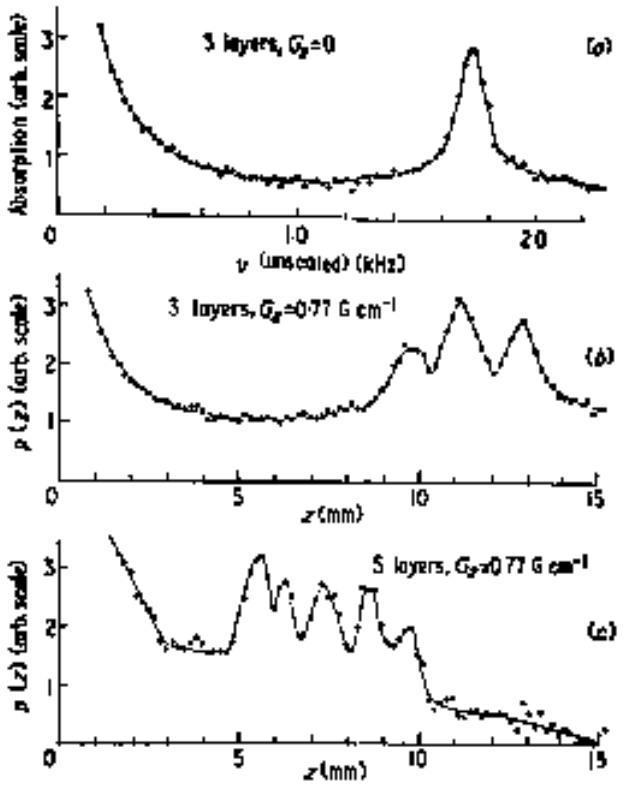

Figure 98 Fourier transform of the transient response to a multiple pulse sequence from layers of camphor. (a) Three layers, no magnetic field gradient. (b) Three layers, gradient of 0.77 G cm^{-1}. (c) Five layers, gradient of 0.77 G cm^{-1}.[869] (Reproduced by permission of the Institute of Physics)

describes the presentations by Waugh, Pines, Vaughan, and many others, and goes on to say:

> And Peter Mansfield what did he talk about? He began with reflection symmetry in [multiple pulse] sequences but soon turned to NMR diffractometry. In retrospect he talked and speculated about spin imaging and actually showed pictures of phantoms! Literally nobody took him seriously. What a mistake.

At the conclusion of Mansfield's talk, John Waugh mentioned Lauterbur's paper on zeugmatography, which Mansfield, Garroway, Hinshaw, and others had not previously noticed. In his historical sketch, Mansfield describes his initial reading of that paper soon after the Krakow meeting and 'the stark contrast between our two approaches to NMR imaging'. Mansfield's emphasis in this early work continued on crystals and other regular structures. He pointed out that 'NMR diffraction could be useful at the macroscopic level for microscopy in biophysical systems with regular, or approximately regular macroscopic structures, e.g. cell membranes and filamentary or fibrous structures'.[870] Mansfield and Grannell pursued the idea of NMR diffraction and microscopy in solids and in less regular samples, including glass spheres in water.[871] They examined the theory and reported one-dimensional responses and 2D images obtained by projection–reconstruction techniques. By 1975, however, Mansfield and his co-workers had broadened the scope and were directing their attention to switched gradient methods with selective-pulse excitation[863] to define a strip within the slice and obtain an image a 'line'

at a time.[872,873] With this method they published, in 1977, a cross-sectional image through a human finger—the first image to reveal anatomical detail in a live human subject.[874] The emphasis was on decreasing scan time so as to be able to study biological samples effectively.

In 1977 Mansfield published a new method, which would eventually be named 'echo-planar imaging' (EPI).[875] This technique utilized his previously developed method for slice selection but then obtained imaging information from an entire slice with one excitation pulse followed by a string of echoes that resulted from a very rapid and repeated switching of field gradients. The idea for this approach, as he points out,[875] could be traced in certain ways to his previous study of periodic structures using Fourier transformation in a continuous time domain, whereas here the complementary situation of a continuous structure was represented by a periodic time function (the echoes).

EPI makes severe requirements for strong and rapidly switched gradients, which were not easily attainable. Nevertheless, within a year Mansfield and Pykett had obtained crude images of a phantom[876] and of anatomical features.[877,878] By 1981, Ordidge et al.[879] had presented the first real-time moving images, which demonstrated the potential for 'freezing' cardiac motions. Mansfield and his group continued to make incremental improvements in the methods, and with the development of actively shielded gradients[880] (as we shall see in Section 16) they were able to overcome many of the practical problems associated with rapidly switched gradients. Meanwhile, former Mansfield students and co-workers advanced EPI techniques in a number of laboratories and companies in several countries. Only in the early 1990s did EPI begin to compete commercially with the more conventional methods based on spin warp FT zeugmatography.[881]

FONAR and Related Methods

As we saw in Section 12, Raymond Damadian's observation of lengthened relaxation times in excised mouse tumors had introduced the hope of a new diagnostic method for malignancy based on NMR data. Although Damadian's early papers in this area were limited to the study of excised tissues, his paper in 1971[805] suggested that 'NMR techniques combine many of the desirable features of an external probe for the detection of internal cancer', and in 1972 he filed a patent application for using NMR to detect pathology (including cancer) on the basis of differences in relaxation times from normal values. In attempting to develop an instrument to carry out such measurements, Damadian initially bypassed the new imaging methods based on the application of linear field gradients but opted instead to design a magnet in which only a small volume would have adequate homogeneity for NMR. The homogeneity would then deteriorate rapidly outside this volume so that little NMR signal would be observed from the remainder of the sample. Damadian referred to the method as field focusing NMR and coined an acronym FONAR.[882,883] Like Hinshaw's initial Sensitive Point method, FONAR had the advantage of simplicity in terms of data processing but the serious disadvantage of measuring only a small volume at a time and thus requiring a long time for a scan through a sample of significant size. Moreover, the homogeneous volume occurred in only one place in the magnet and could not readily be moved by electrical current adjustments, as could the 'sensitive point', hence FONAR required that the sample itself be moved to a different position to obtain data from each volume of interest. As pointed out by Damadian[884] and Hollis,[841] the procedure is reminiscent of early NMR work in which the probe was moved to locate the 'sweet spot' homogeneous volume.

Damadian and his co-workers published the first FONAR image of the thoracic cavity of a live mouse in 1976[885] and also showed an image of a mouse in which a tumor had been implanted in the upper thorax. The resolution was estimated at 3 mm. Meanwhile, in Japan, Abe, Tanaka, and their co-workers[886] proposed a similar method by using pairs of reversed Helmholtz coils to tailor the field homogeneity in a conventional electromagnet. [Chen and Hoult[856] describe and analyze this method and several other early techniques that were intended for imaging.] Crooks et al. used iron shims attached to the pole caps of an electromagnet to generate a locally homogeneous volume and obtained data from a rat by moving the animal and the rf coil through the homogeneous region.[887]

All of these methods were useful in obtaining initial data and in exploring various approaches, but they were dropped as practical imaging methods because of the complexity of moving the sample and the excessive time required to obtain data. The concept survived somewhat longer in obtaining NMR *spectroscopic* data from a localized volume. In fact, in 1980 Oxford Research Instruments introduced a commercial instrument using more sophisticated homogeneity control under the name 'Topical NMR',[888] designed particularly to measure metabolic processes by ^{31}P NMR in a volume of interest inside a living subject. ('Topical' in this context refers to a local place, not a surface, as is sometimes used in medical terminology.) During the mid-1980s, however, further development of imaging methods permitted more effective definition of local volumes for in vivo spectroscopic studies, as we shall see in Section 16.

From Phantoms and Fruits to Human Imaging

Each of the imaging methods began with the study of inanimate objects, often tubes of water ('phantoms' in medical parlance). Much of the early developmental work advanced more rapidly with the use of such well-defined and controllable samples, but the major interest was in studying living animals and humans, and there were many early efforts to do so. As mentioned above, Lauterbur studied the first living animal, a tiny clam. Fruits and vegetables became the object of study in many laboratories since their internal structures were already well known and precise details could be readily verified after completion of the NMR experiment. Images of lemons, onions, peppers, and many other fruits and vegetables were duly recorded and reported in papers and at conferences.

For several years the available magnet sizes precluded the study of large objects, but small animals or portions of animals were frequently examined. In addition to some early measurements mentioned in the preceding sections, other groups examined mice, rats, and a rabbit. These results were important in exploring the various parameters that are under the control of the investigator. In particular, the mobility and relaxation times of water in different tissues could be

exploited to improve image contrast, and pulse sequences were developed to optimize differences in T_1 by using an initial inversion–recovery sequence and T_2 by a spin echo method. The increasingly faithful images of anatomical structure aroused the interest of a medical audience, but human images were clearly needed to demonstrate the potential value of NMR imaging.

The first live human NMR image was published by Mansfield and Maudsley[874] when they used a line scan to examine the internal anatomy of a finger, an appendage small enough to be inserted into a standard NMR magnet. Contrast between bone, bone marrow, nerve, artery, and other tissues was demonstrated. Soon Andrew et al. used the multiple sensitive point method and a larger gap electromagnet to image a hand,[889] while Hinshaw, Bottomley, and Holland examined Bottomley's wrist and discussed potential medical uses.[890]

Serious application to most anatomical studies required a magnet capable of holding a human being. The necessary scale-up from traditional NMR sample sizes was dramatic, but the magnitude of the magnetic field was reduced correspondingly. Most early efforts were directed toward electromagnets with an air core, designed for a field of about 0.1 T (4 MHz for ^{1}H NMR). Damadian and his co-workers constructed a superconducting magnet of 53-inch diameter and used it at 0.05 T (2 MHz) with his FONAR method to obtain the first image of a human chest.[882] With the low-field, point-by-point method, resolution was understandably poor, but major features such as the heart and lungs could be readily identified. Shortly thereafter, Mansfield et al.[891] observed the first image of the human abdomen, and Clow and Young reported the first NMR image of a section through a human head.[892] Features such as the eyeballs and ventricles in the brain were clearly visible. This work was done at EMI, a British electronics company, and represented the beginning of commercial development of NMR imaging, a topic we discuss in the next section.

By 1980 Moore and his colleagues at Nottingham were able to demonstrate one advantage of NMR imaging over X-ray computed tomography (CT) in showing the first sagittal and coronal sections of a human head.[893] In another paper the same year, they showed that NMR images could reveal a wide range of pathology in the head and commented on the 'dramatic ... new advance in neuroradiological capability with its potential impact on clinical management'.[894] Their clinical results provided examples that included tumors, aneurysms, circulatory malformations, and chronic sinus infection. Meanwhile, in 1980 as well, Damadian showed a number of cases of carcinoma in the chest.[895]

A New Tool for Radiology

As we observed in Section 2, once it had been demonstrated (largely by physicists) that NMR could be used to solve real chemical problems, the chemists, as Martin Packard put it, 'took over' in the late 1950s. A similar situation obtained in the early 1980s with NMR imaging. While many questions still had to be answered and much development work had to be done, radiologists and other clinicians became quite interested in the potential of the method, and several companies specializing in equipment for medical diagnosis sensed a possibly lucrative new market and began development projects.

In England, EMI (Electrical and Music Industries, Ltd.), which had pioneered X-ray CT and had a growing business with this modality, began work on NMR imaging in 1974 primarily as a protective measure to explore all possible competitors to CT. The story of this development is recounted in an interesting historical sketch by Ian Young (***Young, Ian R.: EMI's Venture into NMR--An Industrial Saga***), which describes the initial work with a 0.1-T electromagnet and an instrument and computer that provided images by back-projection with 3–6 min of data acquisition. As Young says, 'We began to acquire phantom images with some degree of respectability in late 1977, early 1978, but an attempt to image a volunteer head was quite disastrous, resulting in something like a frayed rabbit with drooping ears.'

In a cooperative project between EMI and the British Department of Health and Social Security, the system was converted to a superconducting magnet as technology was developed by Oxford Instruments to produce such 1-m bore magnets. Derek Shaw's historical sketch (***Shaw, Derek: From 5-mm Tubes to Man. The Objects Studied by NMR Continue to Grow***) provides an amusing perspective from the magnet manufacturer's viewpoint:

> In the late 70s, a radically new group of customers (radiologists) and companies (the diagnostic imaging manufacturers EMI, GE, Philips, Picker, Siemens, ...) became interested in NMR. The key factor at this stage was the magnet. Working, as I was at this period, for Oxford Instruments was in some ways like being in an Alan Aykbourne play. Diverse characters from all the medical imaging companies would come in to discuss their own 'secret ideas' and specify their own unique magnet requirements, resistive/superconducting, 0.15 T/1.5 T, four coil/six coil ... These requirements were often the same as the company before, leading to the need for considerable 'political sensitivity'.

The EMI magnet was designed for 0.3 T but preliminary data at 0.15 T, obtained when the system was set up in Hammersmith Hospital, looked good enough to Graeme Bydder, the radiologist in charge of NMR studies, that he insisted on maintaining that field strength and beginning to examine patients. As Bydder relates (***Bydder, Graeme M.: Magnetic Resonance at Hammersmith Hospital***) from the perspective of a practicing radiologist,

> There were other difficulties. The Department of Radiology was not only installing a new NMR system but also a CT system, and there was no radiologist in the department with any clinical experience with either technique. The new CT system was bought from a rival company (Siemens) and was providing very high quality images of greater spatial resolution than the NMR system. The NMR machine itself was single slice only, and each of these slices took seven minutes to reconstruct (the CT system took only five seconds). It was difficult to see how it would be possible to even complete a single examination of the head (16 slices) with NMR in less than three hours. The patient handling of the NMR system was acutely uncomfortable, the water cooled valve amplifiers were highly unreliable, and the sole copy of the operating manual went missing soon after installation and was never found again.

Nevertheless, progress was made with the cooperation of the radiologists, the engineers from EMI, and the patients, who 'seemed prepared to put up with any amount of discomfort and inconvenience in the interests of research'. The advantages of the inversion–recovery sequence for obtaining T_1-weighted images were demonstrated in time for their presentation at an important meeting at Wake Forest University, Winston-Salem,

NC, where all the leading imaging groups met in October 1981 (see Figure 99).[896] It became apparent that each group had its own problems and discouragements, but substantial progress was being made.

The Hammersmith group continued to advance with the development of a spin echo method to examine pathology in the brain. Meanwhile, at the University of California in San Francisco, Alexander Margulis organized an NMR imaging project with Leon Kaufman and Larry Crooks, together with Jay Singer from nearby Berkeley (where he had pioneered in studying flow by NMR). Margulis (***Margulis, Alexander R.: How NMR Was Started at the University of California, San Francisco (UCSF)***) describes the way in which funding was obtained and progress was made toward a new Radiologic Imaging Laboratory. After developing techniques with animal studies, they started human imaging in 1981 with a 0.35-T magnet that had been purchased by Pfizer, and continued development in collaboration with NMR Diasonics when Pfizer left the imaging business. Crooks's historical sketch (***Crooks, Lawrence E.: Field Strength Selection for MR Imaging***) describes the thought that went into the purchase of the magnet and the decision as to how high a frequency could be employed without encountering problems with rf absorption by the subject. He goes on to say:

> Our contacts at Pfizer Medical Systems were pleased with the superconducting magnet idea. One thought it sounded so sexy that no doctor would pass it up. The usual concern we encountered within our Radiology Department was 'You're going to have cryogens in the hospital!?'. That did not seem to concern Pfizer much and we proceeded to visit Oxford and IGC to review the designs so that Pfizer could assess the companies. Based on business and technical aspects, Pfizer decided to order a magnet from Oxford for placement in our laboratory. Oxford at the same time built a similar magnet for EMI that was placed in Hammersmith Hospital. It worked before ours, but at 0.15 T.

By April 1981, Crooks and colleagues had obtained their first head image by a line scanning method, but they soon converted to 2D FT in order to improve the signal-to-noise ratio and reduce scanning time. They rapidly improved their techniques and learned how to optimize contrast from a knowledge of relaxation times. Their impressive results at 15 MHz[897,898] 'began a race to ever higher field strengths'.

Meanwhile, Waldo Hinshaw, who had invented the Sensitive Point method of imaging and had later worked with Moore and Andrew at Nottingham in further developments of imaging techniques, took up an appointment in 1978 at the Massachusetts General Hospital to set up imaging research in the MGH radiology department. With financial support from the health products firm Johnson and Johnson (J&J), Hinshaw began development of a clinical imaging instrument but soon realized that the development could be better pursued in an industrial environment. In 1979 he moved to Solon, OH and began working with J&J's subsidiary, Technicare, as he relates in his historical sketch (***Hinshaw, Waldo: Notes on the History of MR Imaging from my Perspective***:)

> Technicare was a very aggressive engineering-driven medical imaging company and was the ideal environment for the rapid development of an MRI product. We put together a team of about 14 engineers and, within 9 months, had a small system producing images at 1.5 T. We had the mistaken idea that it would be easier to develop this small system first. We also wanted to explore as early as possible the clinical utility of spectroscopy. This 'small animal' system went to the MGH and enabled the team there to publish several early papers.

Technicare developed and manufactured several imaging systems based on whole body, resistive, water-cooled magnets, then switched to superconducting magnets from Oxford Instruments, first at 0.5 T and then 0.6 T. Hinshaw's sketch describes a number of technical innovations by the Technicare staff before the company was sold to General Electric in 1986.

The General Electric Company's Medical Systems Division (GEMS) had started late in the X-ray CT field but had built a large CT business. Not until 1982 did they become really interested in the NMR imaging market, but meanwhile the GE Corporate Research and Development Center in Schenectady began to explore the fields of imaging and spectroscopy. With the arrival in 1980 of Paul Bottomley and Bill Edelstein, who had had significant experience in Nottingham and Aberdeen, respectively, work began, first on a 0.12-T electromagnet system, and in 1982 on a superconducting magnet that had been targeted at a 2-T field strength but actually barely made 1.5 T. This magnet was intended for spectroscopy, since the prevailing opinion at the time was that imaging would not be effective at so high a field because of problems with rf penetration. Bottomley's historical sketch (***Bottomley, Paul A.: The Development of High-Field NMR Imaging: 0.12 T to 1.5 T***) describes the evolution of the views of the scientists as they found that they could get good images at 1.5 T, and of the GEMS managers as they developed a market strategy based on the better sensitivity and resolution of the high field.

By November 1982, they had obtained images of relatively poor quality but good enough to show at the meeting of the RSNA (Radiological Society of North America) that month. By February 1983, Bottomley and Howard Hart did better. As Bottomley says,

> With the magnet fixed and Howard's head inside the slotted tube resonator, I began obtaining fantastic images with 256 × 256 resolution in 4 mm slices and 100 s scan times. I was ecstatic. My notebook that day is scrawled with expletive next to the polaroid prints. There was no one to show (Howard was magnet-bound). I dragged in the cleaner: 'Isn't this the most incredible picture you've ever seen?' We published in the *Lancet*. We knew the images were better than anything else around the time.

During the next year or so many arguments would ensue on the relative virtues of GE's high field (1.5 T) versus the lower fields (0.3–0.6 T) that were then produced by most other companies. Ultimately systems with a range of field strengths would be sold for various applications, but GE's high-field strategy paid off: in the nine years from the first shipment of 1.5 T systems to the end of 1993 GE sold over 1350, and most other companies adopted 1.5 T as one of their options as well (Figure 100).

Meanwhile in Germany, Siemens, which was a major player in the medical imaging field, started to look seriously at NMR imaging as early as 1977, when the Corporate Research Laboratory considered the construction of large magnets and the generation of magnetic field gradients. A project to develop imaging capability was begun by the Medical Engineering Group in 1978, with Arnulf Oppelt and Andrew Maudsley as the principals, later joined by Wilfried Loeffler. By May 1979 they had constructed a test bed using an Oxford Instruments 0.1-T resistive magnet, and by the end of the year had obtained an image of a green pepper. By March 1980 they had imaged a human head, and later that year began examining patients. Siemens went on to develop a full line of clinical imaging instruments, including one with a 2.0-T magnetic field.

Figure 99 Participants at the Symposium on Nuclear Magnetic Resonance Imaging, Bowman Gray School of Medicine, Wake Forest University, Winston-Salem, NC, October 1–3, 1981. (Courtesy of Waldo S. Hinshaw)

Figure 100 NMR has become best known to the public through its use in medical imaging. A typical whole-body 'scanner' is shown. Courtesy of General Electric Co

Philips Medical Systems Division began work on NMR imaging in 1973 shortly after Lauterbur's initial publication, when Rob Locher started a one-person project with a small-bore magnet. By 1978, work in the Philips Physics Laboratory and advances elsewhere persuaded Philips to undertake a full-scale effort under Andre Luiten, Locher, Cees van Uijen, Jürgen Heinzerling, and Jan den Boef. Their first head scan was carried out in 1980, and by 1983 Philips had tested a 0.15-T system at the University Hospital in Leyden. Philips went on to develop higher field instruments and to become a major manufacturer of NMR imaging equipment.

Some of the major high-resolution NMR manufacturers (as described in Section 6) also made ventures into the imaging field. Starting in the early 1980s, Bruker developed a full range of imaging capability, from microimaging accessories for high-resolution spectrometers to large-bore research instruments for imaging and spectroscopy of animals and humans. Varian started only in the mid-1980s to develop animal systems, initially in cooperation with Technicare and later in a joint venture with Siemens. General Electric Medical Systems purchased the high-resolution NMR business from Nicolet (as noted in Section 6) and with that addition developed animal spectroscopy and imaging systems before selling this phase of its business to Bruker. Later, SMIS (Surrey, England) developed systems for imaging and spectroscopy in animals.

The explosion in commercial NMR imaging activity is reflected in a 1984 review by Battocletti.[899] His comprehensive compilation of organizations using or building NMR imaging systems by 1983 lists some 20 separate groups. Among the industrial enterprises not already discussed above are the Fonar Corporation (Melville, NY), founded by Raymond Damadian, which began with instruments that were based on the FONAR technique and designed specifically to measure T_1 values. Later the Fonar Corporation developed and currently sells clinical instruments using more conventional imaging methods. They have concentrated particularly on permanent magnet systems at low to moderate (0.6 T) field strength. In England, Picker International took over the NMR imaging business from EMI and expanded to a manufacturing facility in Highland Heights, OH. Picker has become a major manufacturer of clinical NMR imaging units. In Finland, early work by Sepponen and Sipponen was based on a 60-cm bore system operating at 0.17 T. These efforts led to a commercial venture, Instrumentarium, which markets an imaging system based on a 0.1-T resistive electromagnet. The

French company, CGR, moved into NMR imaging in the mid-1980s and marketed instruments in Europe before transferring that line of business to GE in a major corporate realignment. In Haifa, Israel, Elscint Ltd. advertized an early superconducting system operating at 0.35 T and subsequently developed a wide range of scanners.

Four Japanese companies entered the NMR imaging business over the course of several years. Shimadzu and Hitachi have concentrated particularly on relatively low-field instruments. Otsuka acquired Chemagnetics (as noted in Section 6) and Phospho-Energetics, a company that had been formed specifically to exploit in vivo NMR spectroscopy. Otsuka developed a compact 1.5 T head-only unit. Toshiba began NMR imaging development in Japan, then acquired Diasonics around 1990 and broadened their research and manufacturing efforts. Advanced NMR Systems was formed in 1988 by Ian Pykett and Richard Rzedzian, both from Peter Mansfield's laboratory in Nottingham, largely to develop and commercialize echo planar methods. In the early 1990s they began offering an EPI accessory to GE's 1.5 T instrument.

Biomedical Magnetic Resonance Meetings

Following the early symposia on NMR imaging at Vanderbilt University in 1980 and at Bowman Gray Medical School, Wake Forest University in 1981, a group of early leaders in the field agreed on the formation of a society to bring together basic scientists and clinicians interested in the new discipline and to hold annual interdisciplinary meetings. Paul Lauterbur, Gerry Pohost, Alex Margulis, Britton Chance, and Tom Budinger served as an Executive Committee to convene a Board of Directors meeting at the 1981 symposium, and the Society of Magnetic Resonance in Medicine (SMRM) was born. Its first scientific meeting, held in Boston in August, 1982, drew a large attendance and served as the prototype of annual meetings in North America and western Europe. With broad representation in membership and among the officers from scientists interested in imaging and in vivo spectroscopy, development of new methods and clinical applications, the Society's meetings grew larger and benefited from interaction with and support by companies that manufactured NMR imaging equipment.

Meanwhile, others had become interested in the potential of NMR imaging, including Sharad Amtey, a medical physicist who had not been involved in research in NMR. He organized a workshop on the subject in Houston in February 1981, and at the Bowman Gray meeting later that year, Amtey and others planned for the Society for Magnetic Resonance Imaging (SMRI), which was formally organized in 1982 and held annual meetings beginning in 1983. The early meetings were poorly attended as compared with those of the SMRM, but gradually attained viability.

Discussions between the SMRM and SMRI resulted in a merger of the two organizations in January, 1994. The first meetings of the combined societies were held in Dallas in April, 1994 and in San Francisco in August of that year. After temporarily using the designation Society of Magnetic Resonance (SMR), the organization decided, in late 1995, to adopt the name International Society for Magnetic Resonance in Medicine (ISMRM).

Other companies have been fashioned to develop specific applications of NMR imaging and/or in vivo spectroscopy, and new enterprises are continually being formed. Our summary here is not exhaustive but illustrates the vitality in the commercial application of NMR imaging.

'MRI' Arrives

In the early 1950s, Jim Shoolery and Emery Rogers introduced the term 'NMR spectroscopy', partly to emulate the then popular IR spectroscopy, but also to avoid the word 'nuclear' which had some poor connotations. In the early 1980s, NMR imaging as a medical technique became increasingly familiar to the general public. Its proponents feared that the ominous 'N' would create storms of controversy as the large magnets were sited. Moreover, 'nuclear' also suggested to hospital personnel that this might be another aspect of Nuclear Medicine Departments. So with general agreement among radiologists and NMR imaging manufacturers (but not without resistance from old-time NMR spectroscopists!), *MRI* became the commonly used term for imaging. *MRS* is often used for spectroscopic applications, and *MR* is the generic abbreviation in medical circles.

By October 1987, sufficient clinical data had been obtained for the National Institutes of Health in the United States to convene a Consensus Conference, in which a 'jury' of radiologists and other clinical experts could assess the state of the art and make recommendations on optimum uses of MRI. The following excerpts from the Conference Statement[900] highlight the prevailing views:

> Even in the short period of its use, it has proved to be unusually rewarding in the detection, localization, and assessment of extent and character of disease in the central nervous, musculoskeletal, and cardiovascular systems. In the brain, for example, it has a proven capacity to define some tumors and the plaques of multiple sclerosis provided by no other technique. It is a competing imaging method in the evaluation of many other organs. Additional prospective studies comparing MRI with other diagnostic methods are essential in those areas where the method has shown promise but where its precise role has not yet been defined. This consensus development conference does not purport to include all of the applications of MRI to the pediatric patient, a subject that will require separate consideration. . . . The full potential of MRI has not been reached, and continuing refinement of equipment, contrast agents, and software may be anticipated. . . .

The final sentence quoted was prophetic. MRI has become widely available and is regarded as an indispensable diagnostic modality. New generations of magnets have been developed at both higher and lower magnetic fields for specific purposes. Faster scanning methods have become available and the quality of images has steadily improved. Moreover, imaging methods have been used to study function as well as anatomy, and imaging principles have been used for localized in vivo NMR spectroscopy. We shall return to an exploration of a few of these more modern developments in Section 16.

PROTEIN STRUCTURES BY NMR

By the early 1980s high-resolution NMR instruments and methods had advanced to the point that very complex

problems in molecular structure could be solved. The vast armamentarium of 2D techniques could be brought to bear on the structure elucidation of organic molecules; inorganic systems could be studied by almost every conceivable magnetic nuclide; and biopolymers, such as proteins, nucleic acids, and complex carbohydrates, could be studied in far greater detail than heretofore. In this short history, it is impossible to discuss even superficially the impact that NMR now has in all these areas.

In this section we focus on one area—protein structure. NMR has contributed in major ways to the study of other important problems involving various types of biopolymers, as well as smaller organic molecules, but the methods used are largely the same kinds of 2D NMR techniques that we have discussed in Section 11. However, for the determination of the three-dimensional structures of folded proteins, the complexity of the problem (previously not amenable to solution by NMR methods) has driven the development of new techniques that have met with spectacular success.

Assignments and Interatomic Distances in Proteins

As we have seen in Section 10, NMR had made significant contributions to our knowledge of the molecular structure and conformation of all types of molecules of biological interest. However, until the development of new approaches during the early 1980s, NMR was not capable of providing a three-dimensional structure of a biopolymer that specified the spatial location of its atoms. Only X-ray crystallography provided that information, and then solely for molecules that formed crystals of suitable quality. Moreover, X-ray crystallography, while clearly still the 'gold standard' for structural determination, often fails to provide important information on dynamic processes that alter conformation in solution.

High-resolution NMR in solution has long furnished in a qualitative way just the sort of information where X-ray crystallography is weak. Its use to determine secondary and tertiary structure in proteins depended, however, as Oleg Jardetzky points out in his article (***Jardetzky, Oleg: NMR in Molecular Biology--A History of Basic Ideas***) on overcoming three obstacles: *Sensitivity*, *Resolution*, and *Rules of Interpretation*. By the late 1970s NMR spectrometers were available with adequate sensitivity to study proteins at reasonable concentrations, and ^{1}H NMR frequencies of 400–500 MHz permitted the resolution of most resonance lines in small proteins where it was clear that chemically identical amino acid residues could be distinguished by differences in chemical shifts caused by secondary and tertiary structure. Interpretation of the spectra, however, depended first on being able to assign each resonance to a specific amino acid residue along the polypeptide chain, the sequence of which was already known from independent data.

Two double resonance techniques had long been used to establish proximity of protons—spin decoupling in some form to identify resonances from nuclei that are spin coupled, and the nuclear Overhauser effect to distinguish protons close in space. In fact, Gibbons et al.[901] had suggested a combination of INDOR and NOE to make sequential assignments of resonances in a peptide, but the method really came into use only during the latter part of the 1970s when Kurt Wüthrich and his co-workers embarked on a major, and ultimately successful, effort to develop and generalize the sequential assignment of proteins.

Gerhard Wagner, in his historical sketch (***Wagner, Gerhard: NMR of Proteins***) provides an insight into the experiments carried out by Andreas Dubs, an undergraduate, on basic pancreatic trypsin inhibitor (BPTI) that initiated development of the sequential assignment technique:

> As the primary work of his thesis, Andreas measured NOEs from the well-resolved slowly exchanging amide protons. When using short irradiation times, there was usually a single H^{α} resonance that showed a much larger NOE than anything else did. Only after a lengthy inspection of the BPTI model did we detect the almost trivial fact that the H^{α} of the preceding residue was generally nearest to an H^{N}, and that other H^{α} protons were a significantly larger distance away. We could show analytically that the initial slope of NOE build-up curves of truncated driven NOEs were directly proportional to r^{-6} and could be related to molecular structure. This identification of the sequential $d_{\alpha N}$ NOE, together with the intraresidue connectivities obtained from spin decoupling, quickly led to sequence specific assignments for 15 β-sheet residues. At the same time, we became aware of different sequential NOEs in helices and established an initial statistic of characteristic distances in β-sheets and helices.

The one-dimensional sequential assignment approach was followed soon thereafter by 2D techniques, as discussed in the following section, that yielded publication in 1982 of the first complete assignment of a protein spectrum, that for BPTI.[902]

Wüthrich's historical sketch (***Wüthrich, Kurt: NMR Structures of Biological Macromolecules***) provides a lucid account of the systematic evolution of his laboratory's work in using NMR methods for protein structure determinations. While the initial work was carried out only with proteins whose structure was already known from X-ray crystallography, it became clear that the approach could be applied to small proteins whose amino acid sequences were known but whose three-dimensional structures had not been established.

An important advance in understanding the intensity build-up in the transient NOE and in avoiding effects of spin diffusion was made by Gordon and Wüthrich[903] in 1978. As additional NOE data accumulated, Wüthrich and his co-workers realized that NOE data could provide the key information needed to estimate proton–proton distances between amino acids that are far apart in the linear sequence but in close proximity because of protein folding. A critical assumption, one that is still a point of contention many years later, is that the folded protein may be treated as a rigid body with a single correlation time for rotation. While clearly an approximation, this assumption served as a working hypothesis, and the ultimate success of NMR structure determinations has provided support for the conjecture. Obtaining the data with the 1D NMR methods that were then in use and interpreting them in a systematic way presented almost insurmountable challenges, but the emergence of 2D NMR provided the critical boost needed for clearing this hurdle. By 1984, the first de novo 3D structure of a small globular protein, BUSI (bull seminal plasma inhibitor), a protein with 57 amino acids and a molecular weight of 6000, had been completed.[904,905]

Critical to the determination of protein structures from NMR data were suitable computational methods for relating interatomic distances to Cartesian coordinates in three dimensions. The development of several such distance geometry methods in a number of laboratories around the world is a story in

itself that is beyond our scope here. Likewise, refinement of structures with techniques of restrained molecular dynamics and simulated annealing, and development of procedures for integrating these with NMR data in efficient computer analyses, constitute an impressive set of accomplishments that have been reviewed in a number of places.[906–908]

The use of NMR for 3D structure determination of proteins was soon taken up and developed further by several other laboratories, including those of Clore and Gronenborn, Wright, Kaptein, and other groups such as those of Jardetzky, Campbell, and Markley, who had long been involved in protein NMR studies. However, many X-ray crystallographers and biochemists were quite skeptical that reliable structures could, in general, be determined in this way. The NMR approach gained widespread credibility as a result of a unique competition, as described by Wüthrich in his historical sketch:

> When I presented the NMR structure of BUSI in some lectures in the spring of 1984, the reaction was one of disbelief and suggestions that our structure must have been modeled after the crystal structure of a homologous protein. In the discussion following a seminar in Munich on May 14 1984, Robert Huber proposed to settle the matter by the independent determination of a new protein structure in his laboratory by X-ray crystallography and in my laboratory by NMR. Each of us received 100 g(!) of pure Tendamistat from Dr. L. Vértesy at Hoechst AG and, as is well documented in the literature, this project was started. Dr. Allen Kline had arrived in Zürich in March 1984 and agreed to join the competition. We obtained complete resonance assignments and the secondary structure determination by the end of the summer 1984. In late 1985, virtually identical three-dimensional structures had been obtained in solution[909] and in crystals.[910] ... The fact that a genuinely novel type of polypeptide fold had been determined in the NMR structure of Tendamistat apparently convinced many of the critics that NMR could actually do the job.

The Role of 2D NMR

In 1976, soon after Ernst's initial publication laying out the field of 2D NMR, he and Wüthrich began collaborative work to apply such methods to protein NMR. As new 2D experiments were designed and computational facilities for handling 2D data were improved, they considered the implications for protein studies, but meanwhile the initial protein structural studies were carried out with conventional 1D methods. It was clear that the 2D approach would be better, with techniques such as COSY substituting for selective decoupling in tracing chemical bonding paths and NOESY providing the critical NOE data throughout the spectrum at one time. Kuniaki Nagayama describes some of the practical problems in implementing these ideas in his article (***Nagayama, Kuniaki: The First Protein Two-Dimensional (2D) NMR***). A 10 mM sample of BPTI (basic pancreatic trypsin inhibitor) served as the sample, run at 60°C at 360 MHz, to obtain well-resolved 2D *J* spectra of 20 methyl groups. A short paper describing this advance was submitted to *FEBS Letters* but was soon rejected 'due to the lack of any biological relevance'. The work was soon accepted by another journal.[911]

2D NMR rapidly became *the* way to carry out NMR studies for protein structure determination. All the three-dimensional structures discussed in the preceding section were obtained primarily with 2D NMR data. In addition to the 'Felgett advantage' of carrying out the equivalent of many decoupling or NOE experiments concurrently, the 2D method permitted more sophisticated approaches. For example, the suppression of solvent water signal could be carried out much more effectively, thus permitting studies in H_2O rather than D_2O, and allowing observation of signals and NOEs from amide protons and bound water.

The total range of 2D methods discussed in Section 11 became available—TOCSY, HOHAHA, NOESY, ROESY, and many modifications of COSY. Along with concurrent (and very important) advances in computational technology, computer speed, and data storage capacity, the 2D approach to protein NMR permitted a number of groups to make rapid progress in determining 3D structures. Old-fashioned 1D concepts were not forgotten, however; use of the Karplus relation to estimate dihedral angles from measured coupling constants played an important role in improving the precision and accuracy of the NMR structures. Figure 101 gives examples of the gradual refinement in the quality of structures over a period of about five years.[912] In general, larger amounts of data from more complex NMR experiments have led to increasing numbers of restraints in the computer-driven process of structure determination, which translate into a more precise structure. In addition, it has been possible to carry out a larger number of independent calculations, each beginning from a random coil form, so that there is greater confidence in the average structure that is determined.

The process worked well for proteins up to 10 kDa or so, but as larger molecules were attacked, problems occurred. There are simply too many NMR lines and, even though spectrometer frequency advanced from 500 MHz to 600 MHz, overlap of 2D resonance contours became a problem. In addition, the larger molecules tumbled more slowly and linewidths increased. An example of the difficulty in interpreting the complex maze of overlapping peaks is given in Figure 102 which shows a NOESY spectrum from *S. nuclease*, a protein of about 17.5 kDa. It looked as though the NMR determination of structures had reached the limit of applicability.

3D and 4D NMR Come to the Rescue

One of the virtues of 2D NMR as compared with 1D NMR is that resonances can spread across a plane instead of being confined to a linear plot. It had long been recognized that 2D concepts could readily be extended to more dimensions but, as discussed in Section 11, two principal problems occurred. The first was to maintain acceptable digitization in the indirectly detected dimensions, as this requires the use of either very narrow spectral windows or a very large number of increments—for 3D, $n_1 \times n_2$, where n_1 and n_2 are the numbers of sampling points in the two indirectly detected dimensions. The second was to devise experiments that provided useful information with good sensitivity. Building on the published 3D studies of a smaller protein, Vuister et al.[913] demonstrated the power of nonselective 3D homonuclear NMR even when the digital resolution was lower than in the corresponding NOESY and HOHAHA–TOCSY 2D NMR spectra. Their NOE–HOHAHA experiment was applied to a relatively large protein, pike parvalbumin, containing 108 residues. The 3D spectrum (illustrated in Figure 103)

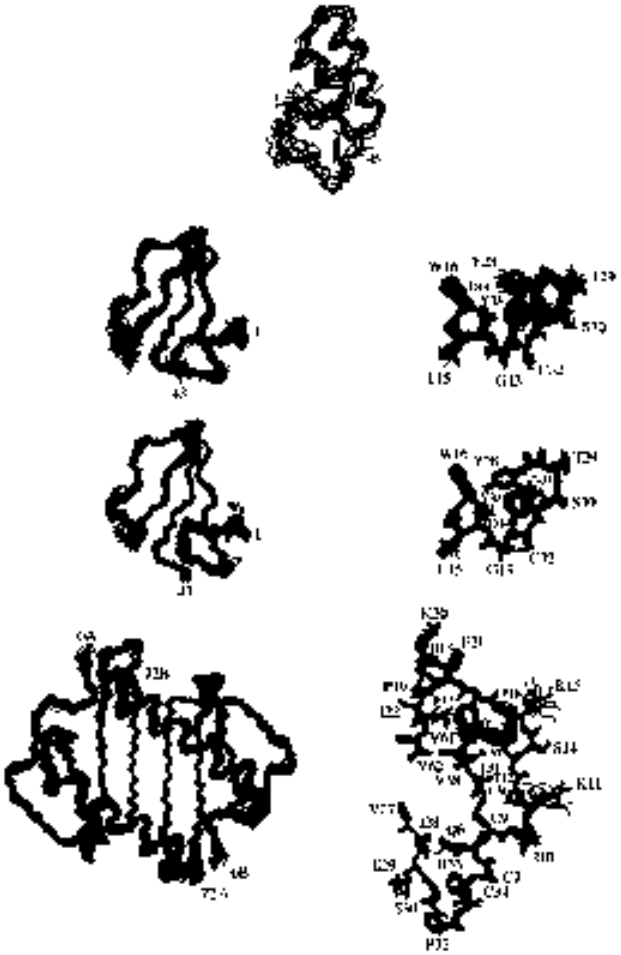

Figure 101 Illustration of the progressive improvement in the precision of NMR structure determinations with increasing number of experimental constraints.[912] (Courtesy of G.M. Clore and A.M. Gronenborn)

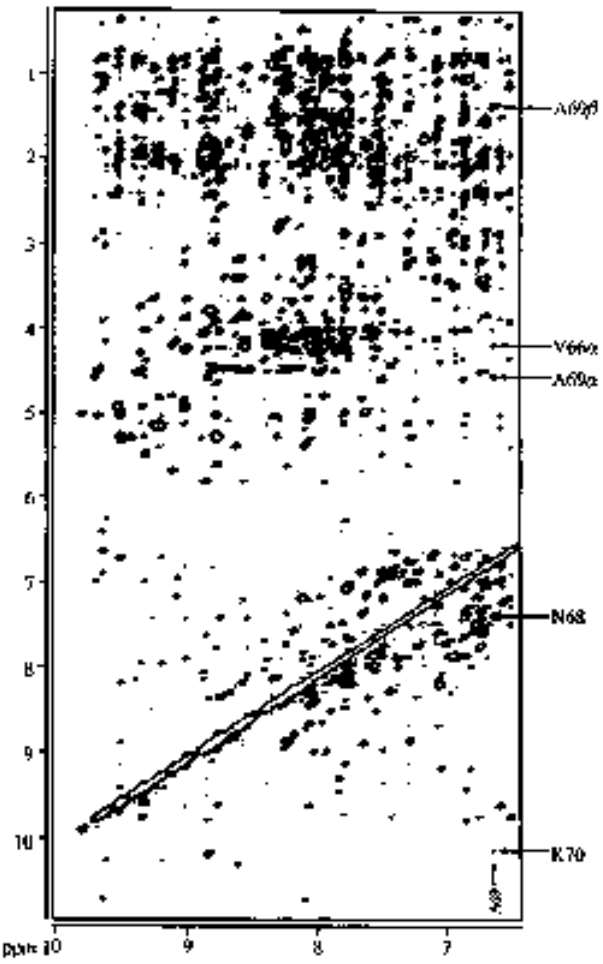

Figure 102 The 500 MHz ^{1}H two-dimensional NOESY spectrum of *S. nuclease*. (Courtesy of D. A. Torchia)

reportedly contains over 50 000 cross peaks and recording the data required about a week of measuring time.

Homonuclear 3D experiments involve two transfers of magnetization, each of which typically is less than 20% efficient, and generate an enormous number of cross peaks as indicated above. These two factors tend to make the 3D experiment considerably less sensitive than its 2D analogs, thus requiring concentrated samples. Groups at Abbott Labs and NIH concentrated on the development of *heteronuclear* 3D, separating the conventional 2D spectrum into a third dimension according to the frequency of ^{15}N or ^{13}C. This type of experiment includes a heteronuclear magnetization transfer step that is nearly 100% efficient and merely resolves the resonance overlap present in the 2D spectrum. This approach requires proteins that are uniformly enriched with ^{15}N and/or ^{13}C. Fortunately, development of recombinant DNA technology during the 1980s made it a fairly routine matter in many instances to over-express a particular protein in a bacterial 'factory' and produce the protein with $^{15}NH_4Cl$ as the only source of nitrogen. Likewise, uniformly ^{13}C-enriched glucose can be used as the source of carbon.

An early example of the use of such methods was in *S. nuclease*, which gave the uninterpretable NOESY spectrum of Figure 102. With the addition of an HMQC step to separate the resonances according to ^{15}N chemical shifts, the NOESY spectrum suddenly became readily interpretable. Figure 104 shows two planes from a 3D spectral plot which show clear discrimination of NOESY peaks.[914]

Further uses of heteronuclear 3D methods, carried out with more modern techniques such as use of pulsed magnetic field gradients, clearly established the utility of 3D spectroscopy. In favorable cases, high-quality 3D spectra on labeled proteins can be recorded in less than 1 h. The urge for the unambiguous interpretations of the spectra of larger proteins prompted the addition of another dimension in the NMR experiments. The first four-dimensional NMR spectrum, published by Kay et al.[915] in 1990, dramatically improved the resolution. The power of the technique was demonstrated by the application of four-dimensional (^{13}C–^{15}N) edited NOE spectroscopy to interleukin 1β, a protein of 153 residues. The NOEs between

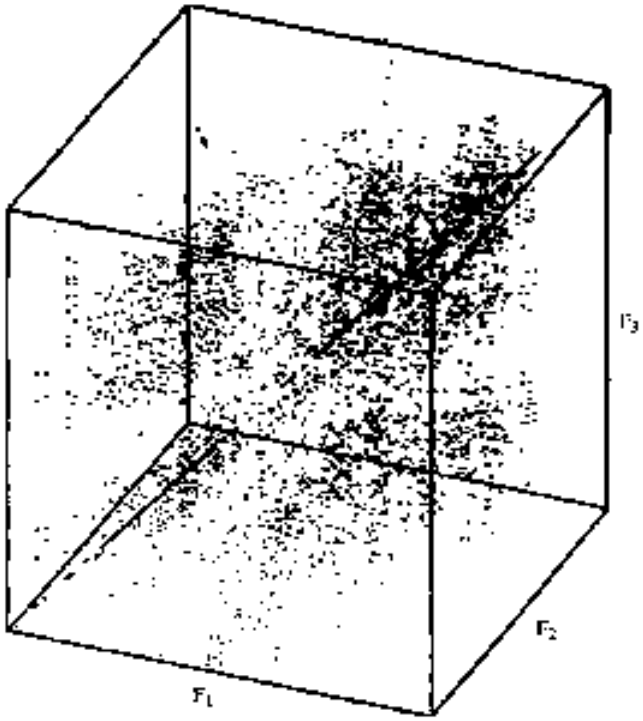

Figure 103 The three-dimensional NOESY–HOHAHA spectrum of the protein parvalbumin.[913] (Reproduced by permission of Academic Press)

NH and the aliphatic protons were first spread out into a third dimension by the ^{15}N chemical shift of the amide ^{15}N atom, and subsequently into a fourth dimension by the ^{13}C chemical shift of the directly bonded ^{13}C atoms.

Other 4D techniques have been successfully employed. For example, the NIH[916] and Abbott groups[917] independently developed 4D $^{13}C/^{13}C$-separated NOESY experiments to resolve ambiguities in NOESY spectra arising from interactions between amino acid side chains. Before pulsed field gradients were available, such spectra tended to be cluttered with artifacts, but by using a very intricate phase cycling scheme, Clore et al.[918] managed to obtain useful spectra. With the use of gradients, it is now clear that if uniformly ^{13}C- and ^{15}N-labeled proteins can be obtained, recording such spectra is practical, and high quality 4D spectra can be obtained on relatively dilute samples (1–2 mM) in about 3 d.

A New Approach to Sequential Assignments

The use of NMR data to derive three-dimensional structural information in proteins rests on the ability to assign each proton resonance to a specific amino acid residue. Limitations in the existing procedure for the sequential assignment of the polypeptide chain became apparent as investigators tackled larger proteins and those that are less receptive to NMR study. For example, the α-helical sections of proteins have relatively poor chemical shift dispersion, and unfavorable dihedral angles often result in small values of $^3J_{H-H}$ between C_α and amide protons, thus inhibiting the coherence transfer essential to establishing sequential assignments. The availability of proteins that are uniformly enriched in both ^{13}C and ^{15}N, together with the ability to record heteronuclear 3D spectra, convinced Ad Bax and co-workers that coherence transfer experiments that operated via the relatively large *one*–bond H–C–N–H couplings would be worthwhile, and they developed a set of such experiments designated by the coupling patterns, as illustrated in Figure 105. In his historical sketch (***Bax, Ad: NMR of Ethanol and Interferon-γ***), Bax describes the genesis of these methods and concludes:

> Primarily due to the creativity and persistence of Lewis Kay, we were finally able to make the triple resonance experiments work, and using the new 3D data, Mitsu Ikura was able to complete his backbone calmodulin assignments shortly thereafter. Of course, we were tremendously impressed by our own accomplishments and were anticipating rave reviews when we submitted our results to the journal *Biochemistry*. To the contrary, the paper was initially rejected. Such 'complicated experiments' requiring the very expensive ^{13}C labeling were deemed to be of no practical interest!

As has happened in many other instances, however, the journal editors reconsidered, the paper was published,[919] and the new triple-resonance procedure became the basis for future resonance assignments in the protein backbone. Similar methods of coherence transfer using one-bond H–C–C–H couplings were developed for assignments in protein side chains by Fesik et al.[920] and Kay et al.[921] Along with these techniques, new methods have been developed for measuring small coupling constants even with the rather broad lines that characterize proteins, and there has been a renaissance of 'Karplus-type' relations to estimate dihedral bond angles. In one interesting paper (the authorship of which reminded some observers of the famous paper on the origin of chemical elements by Alpher, Bethe, and Gamow[922]), Bax, Max, and Zax showed how small two-bond and three-bond C–C couplings could be measured in proteins in the 15–20 kDa range.[923]

NMR in Structural Biology

With NMR techniques capable of handling proteins up to 30 or perhaps 40 kDa, and with spectrometers ranging up to 750 MHz, NMR has become a true rival of X-ray crystallography in providing three-dimensional structures of proteins (and other biopolymers as well). More importantly, however, NMR has become a partner of crystallography in providing complementary information on dynamic processes. For example, NOE measurements have thrown considerable light on the hydration of proteins. Water molecules have been located in the interior of proteins, entirely in accord with results from X-ray crystallography, with residence times of 10^{-2} to 10^{-8} s. In addition, surface hydration has been detected by NMR with residence times below 1 ns.[924]

The mechanism and pathways by which a polypeptide chain of random conformation folds into the compact structure of a globular protein has been probed by hydrogen/deuterium exchange of peptide NHs. By taking advantage of the fact that the rate of such exchange increases by orders of magnitude with an increase in pH but is severely inhibited by hydrogen bonding or solvent inaccessibility in a highly structured region of a protein, Udgaonkar and Baldwin[925] and Roder, Elöve, and Englander[926] pioneered a method for using NMR to study the exchange of specific protons in a protein. These groups and others have determined the kinetics of various steps in

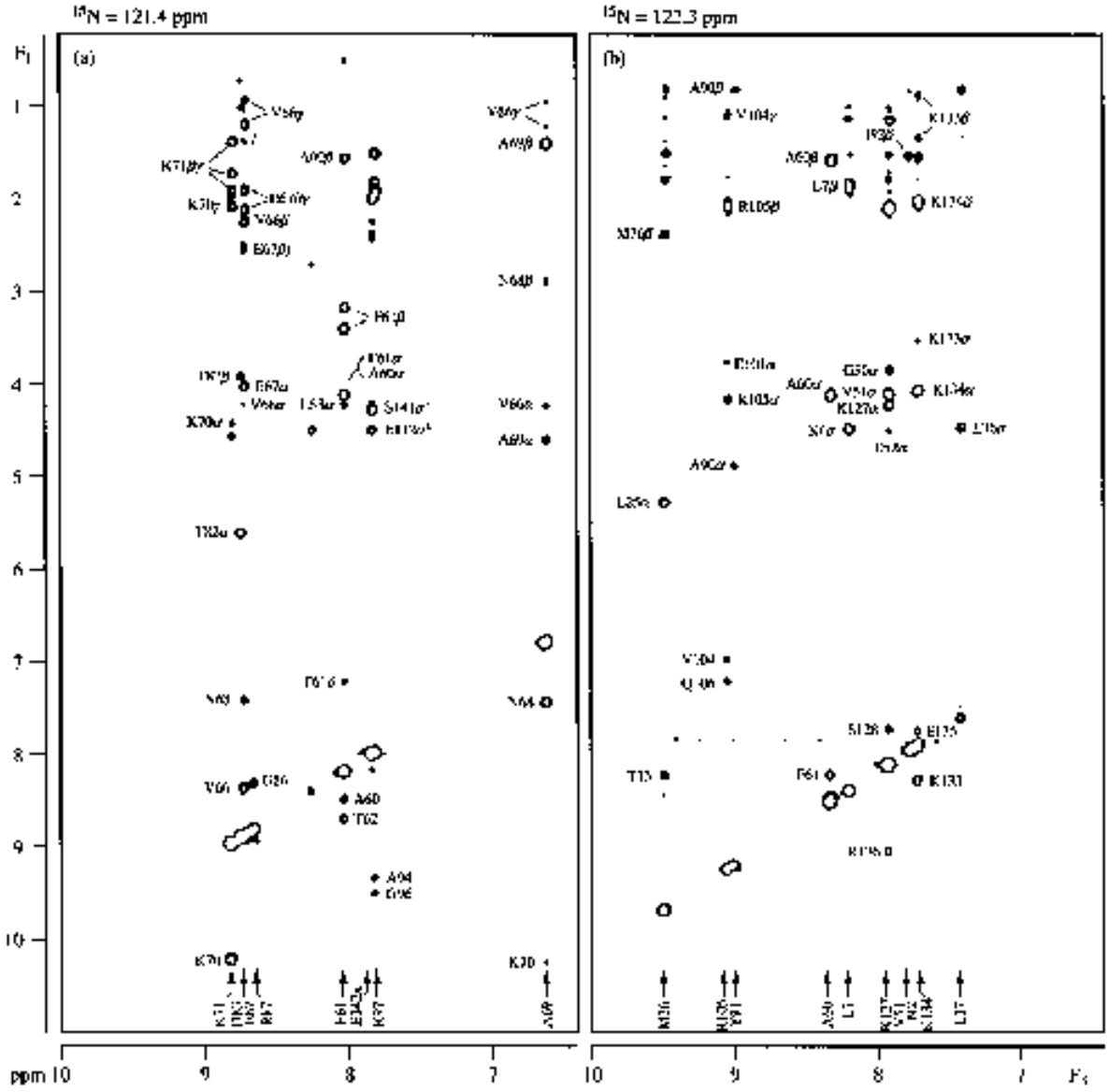

Figure 104 Two adjacent planes from the 3D HMQC–NOESY spectrum of *S. nuclease* uniformly enriched in ^{15}N.[914] (Reproduced by permission of the American Chemical Society)

the folding process and have been able to monitor transient intermediates. The contribution of NMR to the study of protein folding has recently been reviewed.[927]

Other dynamic processes and their impact on protein function have also been investigated. For example, the protein calmodulin binds calcium ions in two globular domains that are connected in the X-ray structure by a long α-helix. Measurements of ^{15}N relaxation times showed that this helical region is highly mobile and serves as a 'hinge' for the somewhat independent motion of the two domains.[928] NMR studies showed that a 26-residue random coil peptide with high affinity for calmodulin adopts an α-helical conformation in the bound form. The complete three-dimensional structure of the complex[929] showed that the two domains of calmodulin, which are far apart in the crystalline structure, clamp around the helical peptide to form an egg-shaped complex. Thus, the flexibility found in the linker region is critical for the ability of calmodulin to bind to its targets.

In the calmodulin complex, the spectrum of the bound peptide could be observed selectively and its NOE interactions identified by means of a spectral filtering technique that discriminated between ^{12}C-attached protons in the peptide and ^{13}C-attached protons in the fully enriched protein.[930] The Wüthrich laboratory, which had previously worked on the development of heteronuclear filtering procedures,[931] used analogous methods to establish the structure of a 68-residue *Antennapedia* homeodomain with a 14 base pair DNA duplex and to locate the recognition site in the DNA major groove.[932] Likewise, Clore, Gronenborn, and co-workers[933] used isotope filtering to determine the structure of a complex between a 16 base pair DNA fragment and the binding domain of the protein GATA 1. In 1994, Oleg Jardetzky and co-workers[934] published the structure of a *trp* repressor–operator DNA complex which

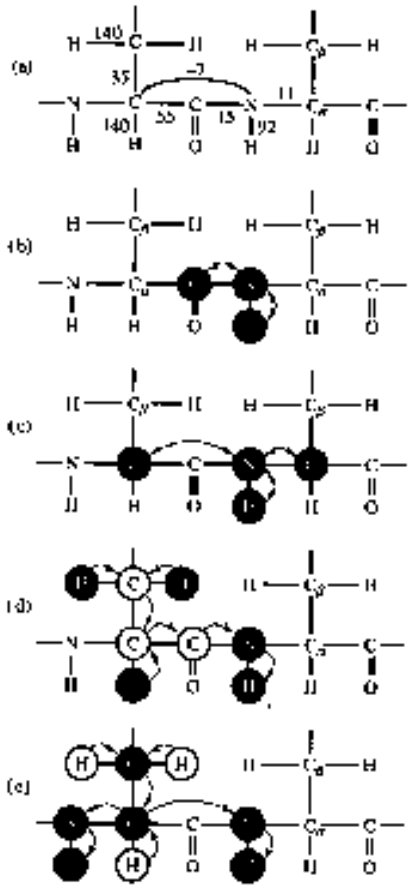

Figure 105 Techniques for sequential assignments in $^{13}C/^{15}N$-enriched proteins. (a) Approximate values of some one-bond and two-bond coupling constants used for coherence transfer. (b)–(e) Schematic diagrams of the nuclei that can be correlated in different experiments. (Courtesy of A. Bax)

represents the largest protein–DNA complex studied thus far by NMR (a 25 kDa protein plus a 20 base pair DNA fragment). They made effective use of selective deuteration and isotope editing to permit separation and assignment of resonances in this large complex.

NMR IN MATERIALS SCIENCE

Over the past 20 years the field of Materials Science has gradually emerged in an effort to integrate physics, chemistry, metallurgy and other disciplines in focusing on the relation of the properties of solid materials to their overall structure, not only their chemical composition. With the development of line narrowing techniques for studying the NMR of solids and the invention of NMR imaging, NMR is making increasingly important contributions to materials science as a useful method for nondestructive evaluation and testing. There is hope that a more detailed understanding of internal microscopic motions as monitored by NMR relaxation times, for example, may be of value in predicting macroscopic properties such as the strength of polymers. In this Section we illustrate a few of the types of studies that have been made and highlight some of the advances in NMR methods that have been required to carry out these investigations.

Molecular Environment and Dynamics

Small molecules can often be studied by normal high-resolution NMR methods in apparently solid materials if, in fact, they retain adequate mobility. For example, water in a gel is known to have a relatively narrow line since it moves rapidly through the matrix formed by the gel. Such small molecules have been added to porous solids to serve as probes of the environment. ^{129}Xe, with a spin of $\frac{1}{2}$, is a particularly attractive probe since it is spherical itself yet has a high polarizability which is reflected in large chemical shifts. Several groups have used ^{129}Xe as a probe to study the formation of zeolites or the symmetry of a cavity in a zeolite or clathrate. For example, Dybowski and co-workers[935] used this technique to follow the removal of template molecules used in the production of zeolites, while Ripmeester et al.[936] studied the nearly spherical cavities in xenon hydrate clathrates and structurally related clathrasils. The sensitivity of the ^{129}Xe probe of a clathrasil structure is illustrated in Figure 106, where the relatively sharp high-field line arises from xenon trapped in the large cavity of cubic symmetry while the low-field line reflects the lower symmetry (threefold) of xenon trapped in the smaller cavity. Fraissard's historical sketch (***Fraissard, J.: A Look at Solid Catalysts by NMR***) describes his use of ^{129}Xe and concludes:

> By means of this technique it is possible to determine the dimensions and the form of the internal free volumes of zeolites without knowing their structures; to reveal structure defects produced, for example, by dealumination, and to determine their characteristics; to calculate the short-range crystallinity, as opposed to that determined by X-rays; to follow the mechanism of the synthesis and crystallization of zeolites during their preparation; to locate cations in the zeolite structure and to follow their migration or change in their environment depending on various factors; to locate any 'encumbering' species, for example, adsorbed molecules, extra-framework species, coke formed during catalytic cracking reactions, etc.; to determine the dispersion of metals (particularly when the particles are too small to be seen by electron microscopy) and the distribution of the molecules adsorbed on the particles (as opposed to the main coverage); to compare the diffusion of species as a function of the size of the zeolite 'windows'. This technique can also be applied to any microporous system (amorphous solid, polymer, clay, etc.). This list of applications is certainly not exhaustive.

The potential applications of ^{129}Xe and the quadrupolar nucleus ^{131}Xe have been broadened by a dramatic improvement in sensitivity resulting from laser optical pumping introduced by Happer et al.[937] The hyperpolarized ^{129}Xe has a magnetization enhanced by about 10^5 as compared with normal thermal equilibrium and can be used as a probe in some of the applications described above, as well as in biological imaging studies of, for example, mouse lungs, blood, and tissue.[938] Hyperpolarized ^{131}Xe, but not ^{129}Xe, shows a splitting of its resonance resulting from collisions with the container wall in a nonspherical container,[939] suggesting that the quadrupolar nucleus might also serve as a useful probe of molecular structure.

Instead of a probe molecule that moves through the solid, the movement of magnetic polarization by spin diffusion can

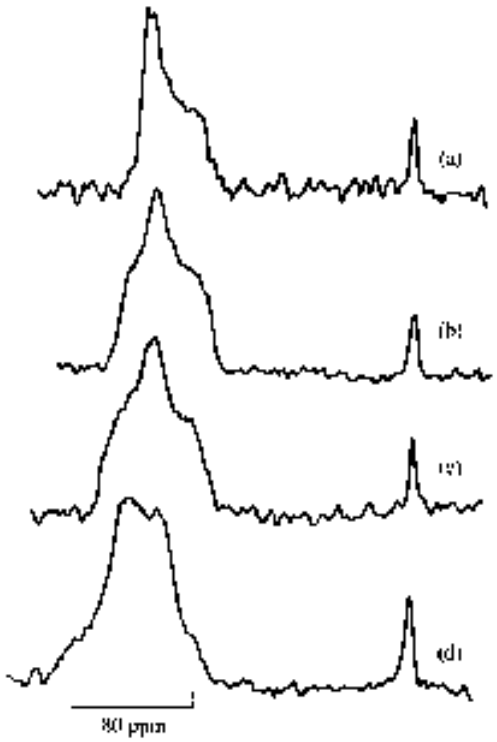

Figure 106 ^{129}Xe spectra of a clathrasil [136 SiO_2·16 $(CH_2)_4O$·8Xe] at (a) 376, (b) 295, (c) 251, and (d) 220 K as the structure changes from tetragonal to cubic. The high-field peak from ^{129}Xe in 0.75 nm cavities is unaffected, whereas the low-field peak from 0.57 nm cavities changes from a shape characteristic of a nonaxial shielding tensor to that of an axial tensor.[936] (Reproduced by permission of the Royal Society of Chemistry)

be monitored. From the rate of spin diffusion, the size and intimacy of the microstructural domains can be monitored in a heterogeneous sample such as a copolymer. For example, Spiess and co-workers[783] examined a polystyrene–polybutadiene blend and observed morphological heterogeneities of 2.5 nm, a size that cannot readily be discerned by other techniques such as electron microscopy. The nature of the morphological structure can often be related to the material's strength and other macroscopic properties.

NMR Imaging *in* Solids

While molecular motions and spin diffusion are suitable for studying small-scale properties, NMR imaging can be used to investigate processes occurring on a larger scale. The diffusion of liquids into polymers or porous solids can be monitored by conventional imaging techniques. One of the very early applications of NMR imaging was carried out by Moore and his co-workers at Nottingham,[940] who used slice-selective imaging to monitor the dynamics of the internal water content distribution in porous inorganic materials such as gypsum and Portland limestone during capillary inflow. Later, Blackband and Mansfield[941] used a similar imaging method to make quantitative measurements of the diffusion of water into solid blocks of nylon, while Weisenberger and Koenig[942] employed the FLASH method[943] to measure the penetration of solvents into poly(methyl methacrylate). Fast imaging methods are needed to cover the diffusion rate of such solvents as methanol and acetone. The NMR method was shown to have distinct advantages over other techniques in permitting an entire measurement to be carried out with one sample in a nondestructive manner and in permitting the observation of inhomogeneous diffusion. Similar imaging methods have been used to follow the reaction as an adhesive sets[944] and to observe changes in local properties of elastomers when they are deformed. Meanwhile, Blümler and Blümich[945] showed that NMR imaging provides a simple method for assessing the aging of elastomers and to observe phase separation, with resolution in favorable cases as small as 30 μm.

In Section 17, we shall see further examples of the imaging of mobile phases in solid materials such as sandstone and soils.

NMR Imaging *of* Solids

Standard imaging methods could be used for studying mobile phases in solids, but imaging of the solid itself presented greater problems since line narrowing techniques must be applied in many instances. For some solids with small magnetic dipolar interactions, such as hydroxyapatite in bone (with all the organic matter extracted), magic angle spinning sufficed to narrow lines. In fact, when dipolar interactions are not too great and the sample can be spun rapidly without distortion, Cory and Veeman found that MAS is generally a better method for imaging than multiple pulse techniques.[946] However, for most samples multiple pulse methods have been employed, sometimes in conjunction with MAS, for ^{1}H imaging while cross polarization/MAS has been the method of choice for imaging ^{13}C and other rare, less-sensitive nuclei.

A key feature to permit imaging in a rotating sample is that the magnetic field gradients required for imaging must rotate synchronously with the sample. The basic idea was patented by Wind and Yannoni in 1981,[947] but implementation was carried out by Cory and Veeman only several years later.[948,949] The rotating gradient technique relies on monitoring the rotor frequency and using this frequency to generate sinusoidal x and y gradients in quadrature.

Work during the 1970s demonstrated one-dimensional profiles in solids, but the first 2D imaging was developed by Chingas, Miller, and Garroway[950] in 1986. They carried out a ^{1}H 2D FT experiment by using the pulse sequence shown in Figure 107. MREV-8 is applied during the evolution period to narrow the lines and a 'storage' period, in which the magnetization is moved to the z axis, facilitates gradient switching. They demonstrated the utility of the method by obtaining an image of a tube of neoprene rubber surrounding a sample of adamantane. By changing the experimental parameters, they were able to discriminate between the two materials on the basis of their relaxation times, as illustrated in Figure 108.

Other techniques have also been used for the ^{1}H imaging of solids, including solid echoes[951] and magic echo phase encoding.[952] The latter uses pure phase encoding for the two-dimensional imaging, hence it can be extended to obtain chemical shift information during the data acquisition period. Cory et al.[953] proposed another method for resolving chemical shifts in solid images obtained by back-projection, which has some advantages over the more commonly used 2D FT method when T_2 values are very short. They tested the

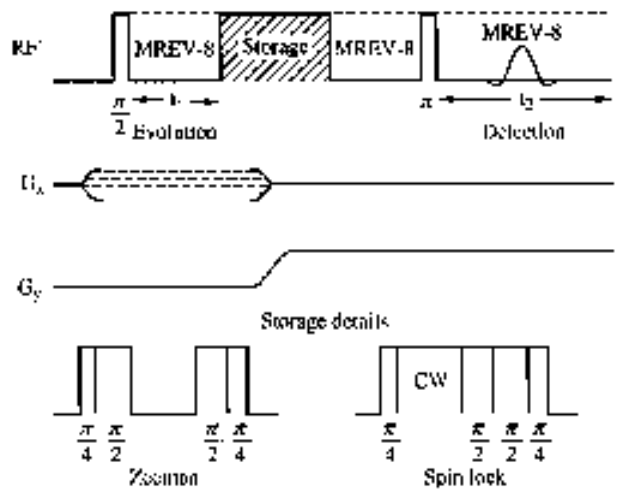

Figure 107 Pulse sequence for ^{1}H solid state imaging.[950] Two different pulse sequences can be used during the storage period as illustrated, in order to provide contrast based on relaxation times. (Reproduced by permission of Academic Press)

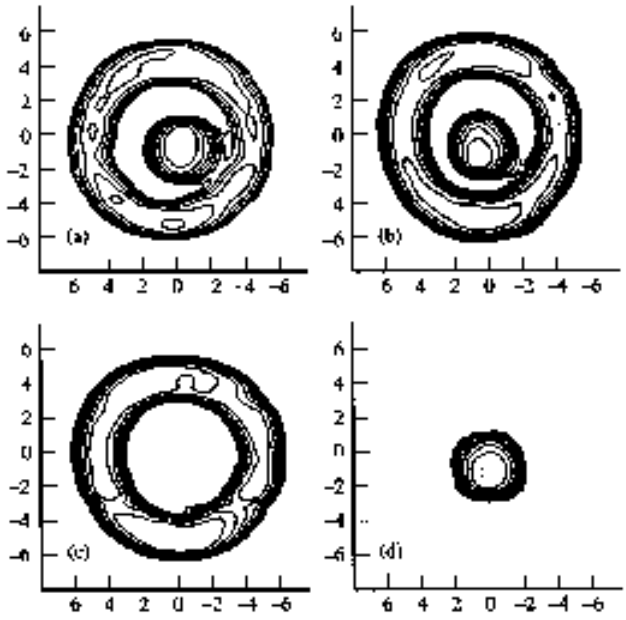

Figure 108 ^{1}H solid state image, using the technique of Figure 107, from a 5-mm diameter tube of adamantane surrounded by a 12-mm o.d. neoprene hose inside a 15-mm diameter glass tube: (a) and (b) illustrate the two storage methods described in Figure 107, while (b), (c), and (d) use spin lock storage with different time periods to discriminate between the components based on T_1 and $T_{1\rho}$.[950] (Reproduced by permission of Academic Press)

ideas with liquid samples but concluded that solids should be amenable to study, and Miller and Garroway used back-projection in their study of one-dimensional ^{13}C imaging of a polyacrylic solid.[954] They developed a method of 'refocused gradient imaging' to remove inhomogeneous broadening and used proton decoupling to remove ^{1}H–^{13}C dipolar broadening.

Maraviglia and co-workers[955] developed a novel imaging method based on *M*agic *A*ngle *R*otating *F*rame (MARF) echoes. They spin-locked the magnetization at the magic angle, then used a 90°, 180° sequence of audiofrequency pulses to carry out a spin echo experiment in a rotating frame that is titled at the magic angle. The MARF method eliminates dipolar and other bilinear interactions and thus permits images of solids to be obtained by the projection-reconstruction method when magnetic field gradients are formed from $\boldsymbol{B}_0$ and $\boldsymbol{B}_1$.

An interesting imaging method that has been applied to solids as well as liquids with broad lines is *STRA*y *F*ield *I*maging (STRAFI), in which the sample is placed outside a superconducting solenoid where it is subject to a large gradient.[956,957] A slice is excited by a sequence of selective pulses and the sample is moved, much as in FONAR and related methods. The method is conceptually simple but the probe needed to reorient the sample to obtain three-dimensional images is quite complex. Nevertheless, STRAFI has been applied to image such materials as Plexiglass and a glass fiber reinforced composite.[958] In addition, the large gradient inherent in this technique has been exploited, for example, by Kinchesh, Randall, and Zick to eliminate the distortions caused by magnetic susceptibility effects in heterogeneous samples.[959]

MODERN BIOMEDICAL APPLICATIONS OF NMR

As we saw in Section 13, NMR imaging methods had developed into a practical medical diagnostic procedure by the mid-1980s, and during the decade since then MRI has truly become the tail that wags the NMR dog. With thousands of units installed in hospitals and clinics worldwide, the resources expended on medical MRI dwarf those for all other NMR applications. MRI has become the modality of choice for diagnosing innumerable types of pathology, as described in detail elsewhere in this Encyclopedia. In this section we describe a few of the recent trends in instrumentation and techniques and discuss development of aspects of NMR imaging and spectroscopy that are not yet in the mainstream of diagnostic radiology.

Faster, Better, Smaller

The principal thrusts in the enhancement of commercial MRI equipment over the past decade have been to increase the speed of scanning, to improve the quality and versatility of images through refinements in both hardware and software, and to provide magnets that confine the magnetic field and weigh less so as to decrease the costs for MRI facilities.

As we pointed out in Section 13, commercial MRI instruments invariably used a selective slice selection, followed by the 2D spin warp method in which the data matrix needed for the image is built up a line at a time as the phase encoding gradient is incremented, a process that can consume several minutes. It was recognized very early that spin–lattice relaxation restricts the minimum time for repetition of the pulse sequence in a given slice, and during this period other slices can be studied to build up a pseudo-3D image. Multi-slice capability soon became part of the standard MRI software packages, thus precluding still further lengthening of scanning time. Nevertheless, the already long imaging times created

severe motion artifacts from cardiac, respiratory, and peristaltic motions, and precluded any sort of dynamic studies.

Jens Frahm in his article (***Frahm, Jens: Toward Rapid NMR Imaging***) describes in some detail projects at the Max Planck Institute for Biophysical Chemistry to enhance the applicability of MRI. Along with several other methods developed there (about which we shall say more later) came FLASH (*F*ast *L*ow *A*ngle *SH*ot), a technique that uses multiple pulses of low angle for excitation rather than the 90° pulse that had conventionally been used in imaging.[943] In a sense, this is a logical extension of the optimum flip angle relation first developed by Ernst and Anderson but, as implemented in MRI, FLASH constituted a major advance. As Frahm puts it:

> The new concept offered an unrestricted and user-dependent choice of spatial and temporal resolution so that speed may be traded off for resolution and image quality (signal-to-noise). . . . The main potential seems to lie in the fast scan domain where cross-sectional images of conventional quality may be acquired within seconds.

Other approaches were also implemented about the same time. Hennig et al.[960,961] utilized principles first demonstrated in the Carr–Purcell–Meiboom–Gill spin echo method to develop a pulse sequence that combined rapid acquisition with contrast due to T_2 in a method known as RARE (*R*apid *A*cquisition with *R*elaxation *E*nhancement). RARE has proved to be a very useful method in clinical studies where pathology, such as multiple sclerosis lesions, can best be detected by T_2 contrast.

What about Peter Mansfield's Echo Planar Imaging (EPI) which was designed to scan an entire plane area of interest in a small fraction of a second? As he says in his Encyclopedia article, EPI was in some ways about 15 years ahead of its time. There were enormous obstacles to overcome, and only around 1990 did former Mansfield collaborators develop EPI commercially at Advanced NMR Systems. One of the major steps along the way was the introduction of shielded gradients, as described in Mansfield's historical sketch:

> Back at Nottingham in the mid 80s we acquired a superconductive 0.5 T whole body magnet. It was clear to me even before we received the magnet that if EPI were to function correctly within the close confines of the magnet something had to be done to decouple the rapidly switched gradient fields from the metal structures comprising the magnet cryostat. Work started on gradient screening in 1984 and culminated in the concept of active magnetic screening during the course of 1985. Active magnetic screening of gradient coils was quickly taken up by GE and other major manufacturers and now forms part of the standard range of features offered on all imaging machines. The solution of gradient decoupling has had other benefits, especially with regard to magnetic resonance spectroscopy.

With the addition of shielded gradients, EPI has come into practical use as described in the article by Stehling et al.,[881] and, as Mansfield indicated, NMR spectroscopy has benefitted enormously. In Section 11, we noted the advances in high-resolution spectroscopy resulting from pulsed field gradients (which became practical only when the gradients were actively shielded), and we shall encounter further applications to in vivo spectroscopy in the following section.

Active shielding of the *static* magnetic field, as well as the magnetic field gradients, was also an important part of this development by Mansfield and Chapman[962,963] and related work at GE by Roemer et al.[964] As 1.5 T magnets became prevalent, siting problems increased since the fringe field can interfere with computers and other equipment, while large, moving steel objects (e.g., automobiles, elevators) can degrade the homogeneity of the magnetic field. Shielding is clearly the answer and it came in two forms. Passive shielding is obtained by surrounding the magnet with tons of steel and became a standard part of commercial magnets. However, active shielding provided an alternative that did not have the deterrent of a large increase in magnet weight.

Also, during the late 1980s several low-field (0.1–0.3 T) permanent magnet systems were introduced to provide lower cost instruments that could be sited more easily. Moreover, in some designs the magnetic field is configured in such a way as to avoid the 'tunnel' effect of a long superconducting solenoid. Although sensitivity (often translated into resolution) suffers at lower field, there is often a compensating improvement in contrast from the generally larger T_1 range of water in different tissues at lower field. At the other end of the magnetic field range, only a few whole body magnets of field higher than 1.5–2.0 T had come into use by the early 1990s, and those (up to 4.1 T) were located at major medical research centers. Magnets with 3 T or 4 T fields designed solely for studies of the head have been developed, primarily for functional imaging studies of the brain (as discussed in a later section).

During the mid-1990s advances in magnet design permitted the construction of magnets that provide better access to the subject. One design, pioneered by General Electric and illustrated in Figure 109, uses a magnet composed of two parts, with a space in the center for interventional studies. In some ways this is a logical extension of the 'inside-out' magnet used by Jackson et al.[965] for other purposes, as we discuss in the following section, but the MRI magnet relies on other innovations as well. For example, very linear x, y and z gradients are generated in the central region where there are no coils, and the 0.5-T superconducting magnet relies on a low-temperature refrigeration system instead of cryogens. Another innovative design introduced by Siemens uses a low-field electromagnet that can be switched on or off rapidly, and provides generous sideways access for physicians and medical technicians. These systems permit MRI to be used as a noninterventional viewing method to guide interventional procedures such as hyperthermia, where NMR can be used to measure localized temperature (by its effect on diffusion, relaxation times, or chemical shifts). Also, the NMR image permits precise localization of catheters and instruments for minimally invasive surgery.

In addition to improved performance from hardware, such as shielded gradients, MRI has benefitted from significant advances in software that permit better data acquisition in gating pulses and in selection of various viewing planes. Moreover, progress in image processing has accorded radiologists and other clinicians enhanced representations of the imaged volume, which is useful in surgical planning especially for neurosurgery. Computer reconstruction of 3D images whose orientation can be manipulated at will and displayed in perspective is beginning to change the conventional use of two-dimensional slices. In addition, advanced concepts such as 'virtual reality' give promise of even better 3D views for an interventional radiologist or surgeon.

Figure 109 Whole body MRI magnet designed to permit access to a patient in the region between the two magnet coils. (Courtesy of General Electric Co)

In Vivo Spectroscopy Advances

As we saw in Section 12, there were many significant accomplishments in in vivo NMR, ranging from metabolic studies in cells to animals and humans. Prior to the invention of NMR imaging, localization of the volume of interest in animal and human studies had been accomplished largely by use of implanted rf coils (in animals) or surface coils, together with carefully designed 'depth' pulses to define the volume that is excited. In addition, topical NMR (as we saw in Section 13) provided a small homogeneous volume in $\boldsymbol{B}_0$ for localization. All of these methods were useful but none provided truly successful localization.

With the development of imaging methods, it became clear that combinations of carefully designed pulse sequences and magnetic field gradients could be used to define a volume of interest and permit chemical shift information to be obtained. In 1975, Lauterbur et al.[966] published a chemical shift imaging (CSI) technique based upon the projection–reconstruction method. Using a composite phantom of tubes containing liquids with different chemical shifts, they demonstrated that one-dimensional spectra corresponding to different spatial regions could be obtained and used to reconstruct two- or three-dimensional distributions of each compound.

However, it was a long way from this early demonstration of CSI in a phantom to the perfection of practical localization methods that can be applied to the study of low concentrations of metabolites in living animals and humans. During the 1980s many approaches were tried with varying degrees of success, and many methods are currently in use. Some techniques utilize a surface coil, either in the presence of a gradient in the static $\boldsymbol{B}_0$ field or based on the $\boldsymbol{B}_1$ gradient inherent in the surface coil design. For example, Bottomley et al.[967] used a static gradient and surface coil to produce a simple method for *D*epth *RE*solved *S*urface *S*pectroscopy (DRESS) that localizes a disc-shaped volume whose depth can be controlled. On the other hand, the concept of rotating frame zeugmatography,[867] which relies on a gradient in the rf field, was exploited with a surface coil to obtain a one-dimensional chemical shift image.[868] Further modifications of this method have been introduced to improve the efficiency with Fourier series windows.[968–970]

A large number of methods have been developed to use one or more gradients in $\boldsymbol{B}_0$, along with suitable pulse sequences, to select a volume of interest (VOI)

without losing chemical shift information. For example, ISIS (*I*mage–*S*elected *I*n Vivo *S*pectroscopy), introduced by Ordidge et al.,[971] makes use of addition and subtraction of the responses to eight selective 180° pulses in the presence of three orthogonal static field gradients to select a VOI. Several methods use a stimulated echo sequence with pulsed field gradients. Frahm et al.[972,973] developed the now widely known STEAM (*ST*imulated *E*cho *A*cquisition *M*ode), while similar approaches were also introduced in VEST (selected *V*olume *E*xcitation using *ST*imulated echoes)[974] and VOSY (*VO*lume *S*elective spectroscop*Y*).[975] Other techniques avoid the disadvantages of an echo and store the magnetization from the VOI along the *z* axis while using pulsed gradients to dephase unwanted signal in the *xy* plane, for example VSE (*V*olume *S*elective *E*xcitation),[976] SPARS (*SPA*tially *R*esolved *S*pectroscopy),[977] and SPACE (*SPA*tial *C*hemical *E*ncoded excitation).[978] A number of other modifications and improvements on each of these techniques together with other novel approaches have appeared over the years. SLIM (*S*pectral *L*ocalization by *IM*aging) uses the anatomical image to improve the efficiency of acquiring spectral information.[979]

The existence of this variety of methods suggests that no 'ideal' technique has appeared. Each method has its advantages and drawbacks for particular types of experiments depending on the nature of the sample and the type of information to be obtained. In general, the availability of good shielded gradients has been one of the major factors in permitting more sophisticated pulse sequences to be applied.

With the availability of useful localization methods, many applications to biomedical problems have appeared. ^{31}P NMR continues to provide noninvasive information on biochemistry, pathology, and pharmacology in humans and experimental animals. The use of localization methods permits studies of the sort illustrated in Figure 110, which show the nonuniform distribution of phosphorus compounds across the human head.[980] ^{19}F NMR is also very useful with appropriately labeled pharmaceuticals, anesthetics, and other compounds. With the relatively high sensitivity of ^{19}F, good localization techniques can provide small NMR localization volumes that often improve NMR resolution over that attainable with ^{18}F positron emission tomography.

As pointed out in Section 12, the clear advantage of in vivo ^{1}H NMR spectroscopy was initially overwhelmed by the dominant signal from water. Although methods discussed in previous sections were helpful in reducing the H_2O signal, real success came from incorporating pulsed gradients and selective excitation developed primarily for imaging with double quantum filtering techniques that originated in 2D NMR.[827] With effective means for the suppression of signals from water (and in some instances from lipids, as well), ^{1}H NMR became an effective means of following biological processes in vivo. For example, chemical shift images of a specific compound could be obtained and displayed, as exemplified in Figure 111 which shows the distribution of several substances in the brain of a patient with a high-grade lymphoma.[981] A number of spectral editing and image processing steps are needed to produce such images. ^{13}C NMR presents special problems because of low sensitivity. Most of the progress has been made with surface coils both for observation and decoupling, or for indirect observation via ^{1}H resonance, in some cases with localization accomplished using ^{1}H NMR

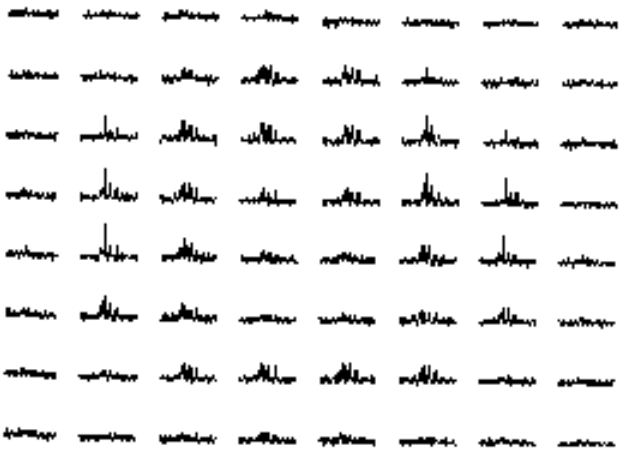

Figure 110 ^{31}P NMR spectra at 1.5 T from localized regions in an axial section of a human head, each covering a cross-sectional area of 9 cm^2. Note decreased signal in the central region corresponding to the ventricles, and a higher creatine phosphate signal near the surface of the head.[980] (Reproduced by permission of the Radiological Society of North America)

followed by polarization transfer to ^{13}C.[982] More sophisticated 2D methods are also being used. For example, heteronuclear multiple quantum coherence (described in Section 11), with pulsed field gradients to select coherence order, has been employed to follow the metabolism of ^{13}C-enriched glucose in the cat brain with ^{1}H sensitivity but ^{13}C spectral dispersion.[983]

Functional Imaging

Medical diagnostic imaging by NMR developed in the wake of X-ray computed tomography as a technique to study anatomical features, and this continues to be the focus in diagnostic radiology. The potential value of localized NMR spectroscopy in providing diagnostic information from analysis of metabolic processes was recognized in the 1980s but has not yet been widely applied beyond research activities. Meanwhile, various sequences of rf pulses and pulsed magnetic field gradients have been developed to probe a number of dynamic processes in the human body that give insight into pathology. We focus here on three aspects of these so-called *functional imaging* studies: blood flow, diffusion in tissues, and capillary perfusion.[984]

Long before imaging techniques were developed, Jay Singer had begun to investigate blood flow by NMR,[849] and work along these lines was continued by Bowman and Kudravcev[985] and by Battocletti and co-workers.[986] The early work built on experience gained in the measurement of flow in industrial fluids (as we mention in Section 17) and used continuous wave or simple pulse techniques to tag a bolus of blood by saturation or an inversion pulse, and subsequently measure the NMR signal 'downstream' from the site of perturbation. With such methods, arterial and venous blood flow could be observed in limbs.[987] The development of imaging opened the door to more general applications, but the initial measurements of blood flow also used a time-of-flight method in which the longitudinal magnetization is perturbed.[988] While simple and relatively free from artifacts, quantification is problematic.

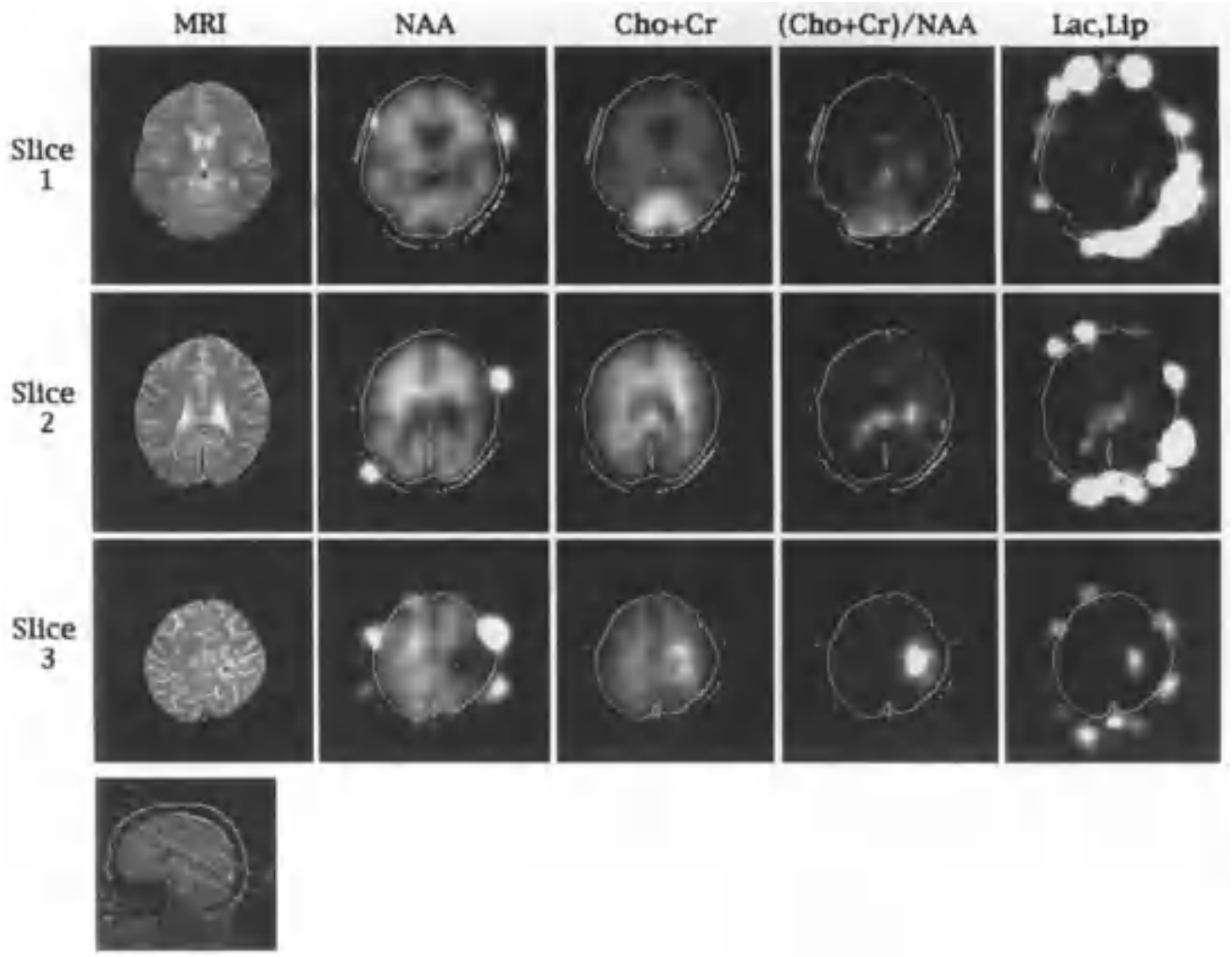

Figure 111 ^{1}H NMR multislice, multispin echo images of the brain of a patient with a high grade lymphoma. Images of three slices are shown, located as shown at the bottom of the figure. MRI: Anatomical images, showing a lesion in the lower right quadrant. NAA: *N*-acetylaspartate image, with lipid artifacts shown as bright spots. Cho+Cr: Image from choline and creatine. (Cho+Cr)/NAA: Ratio image, showing the tumor clearly in lower right quadrant. Lac, Lip: Image from lactate and lipid.[981] (Courtesy of C. T. W. Moonen)

An alternative is the phase contrast method, in which two successive field gradients, identical but of opposite sign, are applied. If no flow (or other change in position) occurs between the pulsed gradients, the phase increment from the first is exactly canceled by the second; otherwise, cancelation is incomplete and a difference measurement provides an NMR signal only of the moving liquid. An example of an NMR angiogram based on this principle is shown in Figure 112. Because blood vessels do not conveniently conform to a plane, gradients in all three Cartesian directions are required, followed by 3D image reconstruction. Development of NMR angiography for routine clinical use, based on both phase contrast and time-of-flight methods, seems promising.

Molecular diffusion has been measured by NMR for many years, beginning with the Carr–Purcell pulse sequence in 1954[134] and becoming more feasible after the introduction of pulsed field gradients by Stejskal and Tanner.[989] The concept is similar to measurement of coherent flow by spin echoes and pulsed gradients, but the theory accounts for diffusion and other *in*coherent motions. In the mid-1980s several groups showed how the method could be combined with imaging techniques to provide a diffusion-weighted image.[990,991,992] The methods have been applied in clinical and experimental situations, for example, to visualize the region of the brain affected by a stroke where the diffusion coefficient is drastically reduced.[993] Diffusion imaging has also found application in distinguishing between tumors and the surrounding region of edema. Rapid echo planar imaging has been found to be of particular value in measuring diffusion without motion artifacts.[994]

The perfusion of blood through the capillary system in tissues contains some elements of coherent blood flow coupled with incoherent motion, since the direction of capillary flow varies in an almost random manner. Analysis of such 'intravoxel incoherent motion' (IVIM) can, in principle, provide measurement of perfusion,[992,995] but quantitation is difficult.[996] An alternative method for visualizing such flow relies on the addition of a paramagnetic contrast agent, usually a gadolinium chelate.[997] The technique consists of injecting a bolus of paramagnetic material, which alters the magnetic susceptibility of the capillary volume as it passes through. The change in susceptibility imposes an additional, local magnetic

Figure 112 Flow imaging of the human head at 1.5 T. Three data sets, each sensitive to flow along one of three mutually orthogonal directions, were combined to produce the image. (Courtesy of C. L. Dumoulin and S. P. Souza, General Electric Co.)

field gradient on the surrounding tissue, and a difference image shows the passage of the bolus even though the ^{1}H signal from the volume of blood in the capillaries constitutes a small fraction of the signal from the total tissue volume being studied. The method has been used successfully to provide data on blood volume and flow,[998] and to produce a functional map of the human visual cortex that reflects changes in regional cerebral blood flow on photic stimulation.[999]

Subsequently, Ogawa et al.[1000] introduced a valuable modification of this imaging method for studying capillary perfusion by employing hemoglobin in the blood as an endogenous contrast agent. Oxyhemoglobin is diamagnetic, but when oxygen is consumed in metabolism the hemoglobin becomes paramagnetic. This fact has been widely exploited in visualizing regions of the brain in which metabolic activity occurs in response to an external stimulus—a technique given the acronym BOLD (*B*lood *O*xygenation *L*evel *D*ependent Contrast).[1001] Since the method depends on local magnetic susceptibility change, which affects T_2* rather than T_2, better contrast can be obtained by basing the image on a gradient recalled echo that has been shifted to a longer time than found normally.[1002]

NMR Microscopy

Lauterbur's first paper on zeugmatography spoke of 'compositions of microscopic objects'. The development of NMR imaging as a microscopic method has received much less attention than the opposite extreme of human whole body imaging, but the techniques have been developed steadily. The two principal problems in this area are sensitivity (since the sample contains relatively few nuclei) and phase errors that result from molecular diffusion (which is important when displacements due to diffusion approach the voxel dimensions). Considerable effort has gone into optimizing parameters so as to produce images with little distortion in the presence of diffusion and of magnetic susceptibility discontinuities in small samples.[1003] Because the sample size for NMR microscopy is comparable with that used for most high-resolution NMR in chemistry, high-field spectrometers can be employed with suitable accessories that are now available for commercial high-resolution NMR spectrometers. The advantage of using magnetic fields (up to 14 T) that are much higher than used for human imaging restores some of the loss in sensitivity resulting from the small sample size.

Microimaging has been applied to studies of various polymers, polymer composites, and elastomers using the techniques described in Section 15, and a number of applications to structures in plants and in wood have been reported. However, the major uses of NMR microscopy thus far have centered around investigations of structure and function in small experimental animals, such as mice and rats, and in developmental biology.[1003] For example, in 1986, Aguayo et al.[1004] used a 400 MHz spectrometer and field gradients of 20 G cm^{-1} to observe images in a single cell. They could distinguish the nucleus and various features in the cytoplasm. The next year, Allan Johnson and co-workers at Duke University showed excellent delineation of anatomical features in a rat brain with a resolution of ca. 100 μm,[1005] and subsequently this group and others have made many further advances. Recently, Mansfield and co-workers have built a sensitive, inductively coupled rf surface coil into a microscopic slide, where it can provide NMR images and also be used for optical microscopy. In a particularly favorable case, they observed a resolution as small as 4.5 μm.[1006]

NMR microscopy is becoming a rival of optical microscopy in histopathological studies of tissue where 'routine' isotropic resolution of less than 10 μm has been reported.[1007] Such results have been obtained with a receiver coil fabricated by Black et al.[1008] from a high-temperature superconductor, $YBa_2Cu_3O_7$, which was used to improve the signal-to-noise ratio by a factor of 50—the first reported use of a high-temperature superconductor for an NMR coil.

OTHER APPLICATIONS OF NMR

In addition to its major uses in chemistry, physics, medicine, and a variety of other sciences, NMR has, since its inception, had application in a number of endeavors of industrial or technological importance. In this section we describe the development of some of these applications, many of which are unfamiliar to the majority of people working with the more common manifestations of NMR.

Searching for Oil, Water, and Submarines

We saw in Section 3 that the first NMR product developed by Varian Associates was the free precession magnetometer, an instrument in which the magnetization from a large sample of water is allowed to precess in the Earth's magnetic field. From the measurement of the resonance frequency (in the range of 2 kHz) and the Larmor equation, a precise value of that field can be measured and variations of the field over some region may provide valuable information. For example, a magnetometer towed on a long rope behind a ship, airplane, or helicopter can sense the presence of a large steel object such as a submerged submarine. Also, variations in geological formations cause small but (with NMR) measurable variations

in the Earth's field, which can give information useful in prospecting for oil or water.

In his historical sketch (***Codrington, Robert S.: Comments on NMR Instrument Development***), Bob Codrington points out that he joined the Physics Department at Rutgers University in 1951 to work for Henry Torrey on a project for the Office of Naval Research to investigate novel methods for submarine detection during the Korean War. Among a number of ideas that were investigated, including the use of ESR and cyclotron resonance of electrons, was the concept of an NMR magnetometer. (Russell Varian was one of the principal members of the guiding committee.) This magnetometer was deployed in the region surrounding the Korean peninsula and apparently worked reasonably well. The NMR magnetometer, in a ruggedized underwater version, was also used in 1963 in an attempt to locate a nuclear submarine (*USS Thresher*) that had sunk in more than a mile of water. Although the NMR magnetometer was regarded as successful in its time, the later development of optical detection methods provided much greater sensitivity and eventually superseded the NMR approach.

The NMR magnetometer was employed in a similar manner in geophysics exploration and provided useful information on possible oil-rich regions. However, even more useful information can be obtained from boreholes. In 1960, Brown and Gamson[1009] developed a 'nuclear magnetic logger' (NML) which was lowered into a borehole and operated by first using a current in a coil to polarize protons in the soil surrounding the instrument, then using the same coil to measure their precession frequency in the Earth's magnetic field, thus functioning as an NMR magnetometer. The NML could measure (i) the strength of the overall ^{1}H signal; (ii) the signal from oil only, obtained by injecting a paramagnetic material to reduce T_2 in the water phase and render it unobservable; or (iii) the T_1 value of the sample.

In 1980, Jasper Jackson and his colleagues published a series of papers with the intriguing title 'Remote (Inside-Out) NMR'.[1010] They used two coaxial coils of opposing polarity to create a magnetic field that has its maximum value and most homogeneous volume outside the coils (see Figure 113). This magnet can be used in a borehole to provide a resonance field at a selected radial distance from the axis of the hole.[965] More recently, Kleinberg et al., at Schlumberger, designed an improved version based on three permanent magnets that produce a homogeneous magnetic field 2 cm or more inside the earth formation, with a ferrite-filled rf antenna to pick up the NMR signal from free precession in the Earth's field.[1011]

With the development of NMR imaging, an additional avenue for obtaining useful information on petroleum became available. For example, Edelstein et al.[1012] used a 2-T NMR system with gradients up to 18 G cm^{-1} to examine cores removed from bore holes in order to measure porosity, permeability, and oil saturation. Figure 114 shows the discrimination that can be obtained between oil-filled and brine-filled core plugs. Other materials that have been pumped into wells to enhance oil recovery can also be identified.[1013] In addition, imaging has been found to be useful to assess the heterogeneity of core plugs before other physical or chemical analyses.[1014]

If NMR can be used to search for oil, it can equally well be used in the search for water. The *hydroscope* is an instrument designed to look for rock strata with a high water content.

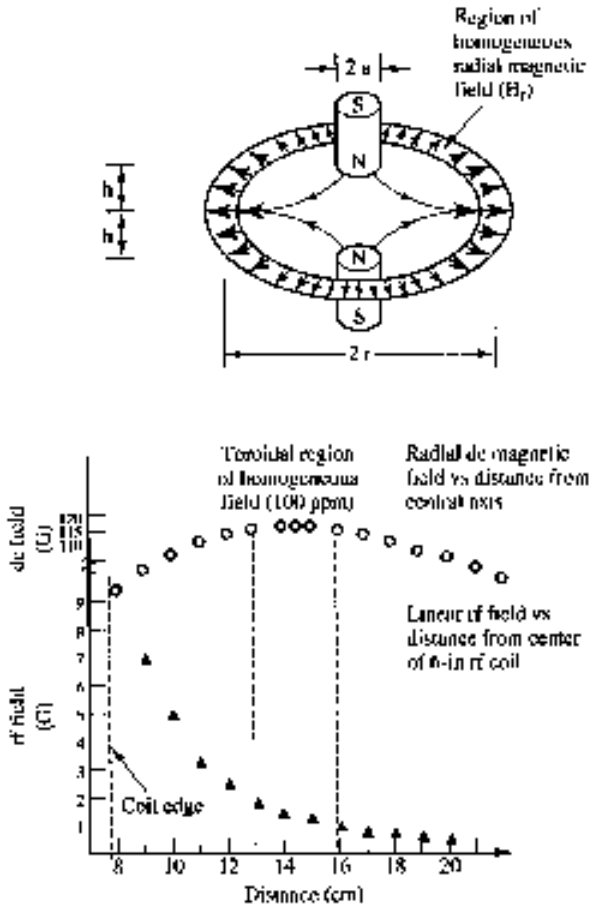

Figure 113 Top: Magnet configuration for the production of a toroidal homogeneous region. Bottom: Plots of the static magnetic field, showing the homogeneous region, and rf field strength.[965] (Reproduced by permission of Academic Press)

The idea of using NMR in this way was suggested initially by Wes Anderson and patented by Varian Associates in 1962,[1015] but was developed into a practical instrument only recently in Russia. Following a patent in 1988 by Semenov et al.,[1016] Legchenko, Shushakov, and co-workers constructed what is probably the world's largest surface coil: a wire some 300 m in length placed in a circle on the surface of the earth in the region to be explored. Pulses at approximately 2.75 kHz provide a response as protons are excited in the Earth's magnetic field. From considerations of the pulse characteristics, it is possible to estimate the depth of the plane from which the principal signal originates. On the assumption that water is likely to lie in strata approximately parallel to the surface, the depth of water-bearing rock and the amount of water present can be determined.[1017,1018]

Measurement of Flow

The first report of NMR in the presence of flowing liquids appeared in 1951 when Suryan, in India, showed that the arrival of a fresh, polarized sample at the rf coil decreased saturation and resulted in a more intense NMR signal.[1019] He was also able to estimate T_1 from the flow rate and the geometric parameters of the system. By 1959, Bowman

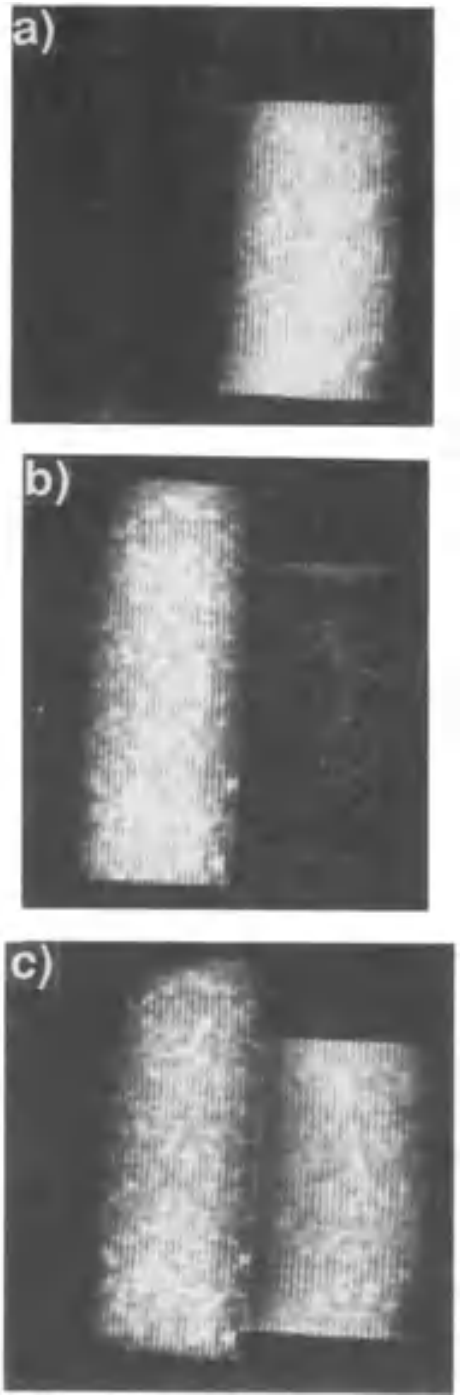

Figure 114 ^{1}H NMR images of dolomite core plugs containing only oil (longer plug on left) or only brine (shorter plug on right). (a) Water-selective image; (b) oil-selective image; (c) nonselective image.[1012] (Courtesy of W. A. Edelstein)

and Kudravcev[985] had begun to explore the use of NMR to measure blood flow. Their experimental studies were limited to the detection of the flow of water or other fluid through a tube surrounded by a detector coil, but their data showed that the NMR signal could be used to measure flow rate. They explored in a preliminary fashion the effects of relaxation and saturation but did not provide any quantitative framework to analyze the flow results. Later, however, they developed techniques for making 'time-of-flight' measurements of blood flow, the forerunner of some of the NMR angiographic methods discussed in Section 16.

Meanwhile, also in 1959, Singer[849] rediscovered the effect of flow on saturation in measurements on a mouse tail. Rather than measure T_1 from flow as Suryan had done, Singer showed that a measurement of both the static T_1 value and the 'apparent' T_1 in the presence of flow permitted an estimate of flow, the principal limitation coming from the fact that the signal was also contributed to by nonmoving tissue. In addition to this procedure, Singer proposed an alternative approach, in which an rf transmitter coil could be used to tag a bolus of blood by saturation or inversion of its magnetization prior to measurement downstream by a second rf coil. This method was demonstrated by Morse and Singer only in 1970[1020] with more sensitive apparatus. Interestingly, they utilized two coils of 6-mm diameter placed over median veins in the forearm of human subjects—certainly one of the first applications of surface coils, well before they were introduced into in vivo spectroscopy as described in Section 12.

Although the measurement of blood flow was intriguing, most of the early applications of NMR in this area were to flow measurements of fluids of industrial importance where it was important to isolate the measuring device from a corrosive or reactive substance. For example, Singer made successful measurements of the flow of jet fuel. The Badger Meter Company developed methods for measuring various fluids,[1021,1022] and by 1970 a commercial NMR flowmeter was being manufactured[1023] with a permanent magnet and a 'tagging' coil preceding the measuring coil. The flowmeter worked well in many applications but was eventually discontinued, primarily because of its relatively high cost.

An interesting use of NMR in flow measurement is a coal flowmeter and analyzer, designed by King et al.[1024] for the on-stream analysis of pneumatically transported powdered coal. From a combination of NMR and electron spin resonance, they could measure not only flow velocity but also moisture, carbon, and ash content.

Moisture Analysis

NMR has long provided a noninvasive method for measuring water in foodstuffs and commercial products, and is being increasingly employed in agricultural and soil sciences. Probably the first such application was reported as early as 1950 by Shaw and Elsken[1025] who studied hydration in foodstuffs. The work was based on the fact that water molecules in many such products are more mobile than the protons in the host products, which are normally crystalline, amorphous, or highly viscous liquids. The proton spectrum, therefore, consists of a relatively sharp signal superimposed on a broad background. During the next few years, Shaw and co-workers examined adsorbed water in meat products and in ingredients such as collagen, gelatin, egg albumin, and glycine. The potential for commercial use was recognized by Bill Rollwitz at the Southwest Research Institute, who discussed design considerations for a practical instrument in 1953[1026] and later described instruments put into service in 1955 that were based on a CW spectrometer and a 1 kG permanent magnet.[1027] The Schlumberger Well Surveying Corporation developed and marketed

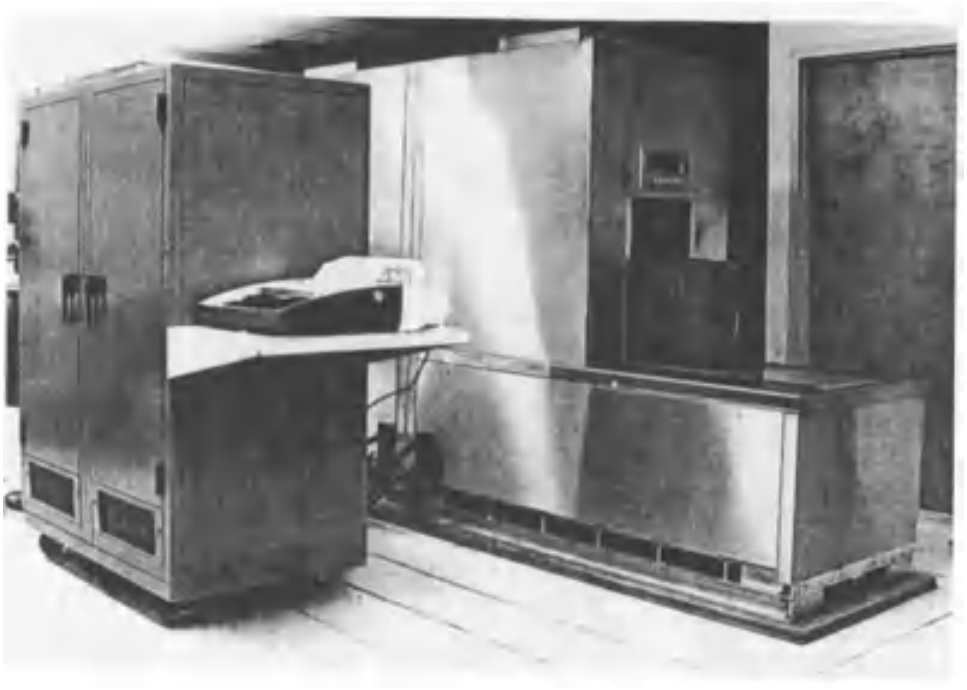

Figure 115 Prototype system for the inspection of baggage by NMR.[1056] (Courtesy of Southwest Research Institute)

the Model 104 Analyzer, a 30 MHz continuous wave instrument of sufficient resolution to distinguish water and oil peaks. A Schlumberger brochure in 1957 boasted 'Accurate moisture tests IN SECONDS . . . not hours'. This product line was sold to Varian in 1961 and a modified version, the Varian PA-7, was used successfully in the grain industry.

Pulsed NMR methods were used also to measure T_1 and/or T_2. The Bruker Minispec, a 10 MHz instrument with provision for a 25 mm or 40 mm diameter sample tube, has been widely used for many years for the analysis of water and other materials where two components are present that differ in T_2. Two measurements at short and long times often serve to measure the total hydrogen and 'mobile' hydrogen. Over 500 of these instruments had been installed by 1979[1028] and the product line in a more advanced form continues to be widely used.

NMR has been employed by numerous workers to study the moisture content in seeds, dairy products, starches, vegetables, and other foodstuffs. For example, the effect of storage on potatoes, garlic, and apples has been investigated, and significant influences of free and bound water on the properties of foods have been reported.[1029] A variation in the T_2 of water in wheat flour with the addition of salt[1030] has been observed, and the moisture content in such diverse foods as margarine, marzipan, chocolate chip cookies, and pulped sugar beets has been studied.[1031] Moisture analysis by NMR has been used successfully in other materials of commercial interest, such as lumber, coal, and concrete,[1032] and in soils as described later.

Oil Content in Intact Seeds

Both wideline and high-resolution NMR have been used for the determination of oil content in individual seeds. In 1963, Bauman, Conway, and Watson[1033] showed that broad-line ^{1}H NMR could be used to measure the total oil content in an individual seed and the results used to select the best seeds for plant breeding. This fast and nondestructive method was able to increase the average oil content of corn 2.25-times faster than was possible with traditional selection methods, resulting in gains over five generations that would otherwise have taken 20–30 generations.[1034] Relatively simple instruments of the type described in the previous section (e.g., the Schlumberger Model 104) were generally used in this work.

The early high-resolution ^{1}H NMR studies were informative as to types of oil and degree of unsaturation, but the limited ^{1}H chemical shift dispersion combined with relatively broad lines in the heterogeneous environment prevented identification of specific fatty acids. Moreover, some of these methods were destructive. However, in 1974 Schaefer and Stejskal[1035] showed that high-resolution ^{13}C NMR can be used for the nondestructive analysis of the major fatty acids in single, viable soybeans. Thus, not only could total fat content be determined, but particularly desirable or undesirable unsaturated fatty acids could be readily determined before the bean is planted. Later, this approach was extended to peanuts, corn, castor beans, and sunflower seeds.[1036,1037] With imaging techniques, Lakshminarayana et al.[1038] studied the distribution of oil and water in sunflower and groundnut seeds.

Other Applications to Food Technology

High-resolution NMR in liquids and in solids (with CP MAS methods) has contributed to analytical methodology in the food industry, as it has in many other commercial enterprises. In most instances the NMR methods are conventional techniques used in chemistry laboratories, even if the samples consist of a wide variety of substances such as cocoa butter,[1039] soybeans,[1040] sugar in beet juice,[1041] rice,[1042] gossypol and

its analog in cotton flower buds,[1043] and butyrate in butter oil.[1044]

An interesting and unusual application is described by Gérard and Maryvonne Martin in their historical sketch (***Martin, Gérard J. & Martin, Maryvonne L.: Ode to Ethanol***). They used deuterium NMR to investigate the adulteration of grape must with added sucrose in order to increase the amount of wine produced—an important economic problem, as they discuss. They go on to say:

> Since, from the chemist's point of view, wine can be reduced somewhat irreverently to mainly water and ethanol, we decided to investigate ethanol with the following questions in mind: Is deuterium statistically distributed on the different molecular sites—and, if not, does the natural deuterium distribution depend on the botanical origin of the sugar precursor? This was the beginning of an exciting research project. NMR revealed that Nature is in fact a fascinating laboratory where isotopomeric molecules are biosynthesized in perfectly reproducible conditions for a given botanical species grown in a given environment. If the deuterium content in the methyl position of ethanol is arbitrarily given the statistical value 3, the methylene site is characterized by a factor which not only deviates strongly from the statistical value 2 but also significantly differs for ethanols derived from grape (~2.55) and beet (~2.75) for instance. A method based on the NMR investigation of 'labeling without enrichment' was born.

This method, called *S*ite-specific *N*atural *I*sotope *F*ractionation (SNIF) NMR, was commercialized in 1987 and used widely in official wine testing laboratories in France.

Proton NMR imaging has made an impact in the study of the composition and structure of various foods and in physiological processes that result in disorders. For example, studies have been reported on ripening and related processes in tomatoes,[1045] apples,[1046] and pears,[1047] water binding in leaf cells,[1048] and chilling injury in citrus fruits.[1049] Processes that occur in the production and cooking of meat are also being investigated by NMR imaging, often using the same methods employed in studies of living subjects, such as techniques to image water and fat separately.[1050]

Plant and Soil Sciences

Since 1960, NMR has been used to study complex mixtures of organic matter extracts from soil where the concentrations of individual components are low. From this work emerged generalizations on the relation between aromatic versus aliphatic components as a function of the age of the soil. Later work in this area has focused primarily on investigations of intact soil samples. Sometimes only the surface water in soil needs to be measured and remote sensing spectrometers have been developed for such applications.[1051] In other instances, CP MAS studies can provide useful information.[1031]

NMR imaging, too, can be valuable in studying plant roots in soil, but magnetic susceptibility discontinuities in heterogeneous soil, especially when iron is present, cause significant distortions. Kinchesh et al.[1052] have made good use of the large magnetic field gradient produced by stray field imaging (as described in Section 15) to overcome susceptibility effects.

The first images of intact plants in soil with a spectral resolution of about 0.5 mm were reported by Bottomley et al.[1053] in 1986. The images demonstrated water transport in roots with light stressed foliage, using water doped with a paramagnetic NMR contrast agent. In addition, the basic root structure and pathology as evidenced by a partial decay of hypogeal cotyledons were indicated. Functional NMR imaging is also being applied to plants in order to define transport pathways in relation to cell water balance.[1054]

Explosives Detection by NMR?

One of the most unusual applications of NMR was to the detection of explosives in packages and in airline baggage. For a number of years, Bill Rollwitz and co-workers at the Southwest Research Institute pursued the development of a practical device to use NMR relaxation times to detect explosives. Much of the work, initially carried out in secret and building on previous military efforts, was presented in only fragmentary form in internal reports and abstracts of talks at meetings. Solid explosives were found to have unusually long T_1 and short T_2 values as compared with other solids and liquids, and techniques were developed to use these parameters as a rapid means of testing for the presence of explosives. The very long T_1 values (around 1 min for some explosives) presented practical problems in carrying out an analysis in a short time, but was overcome by the use of level crossing techniques in which energy is exchanged between ^{1}H NMR energy levels and ^{14}N NQR levels. Pulse sequences were selected to distinguish the characteristic relaxation pattern of solid explosives from the large background ^{1}H NMR signal. A prototype device to detect letter bombs was developed and provided reliable detection of 10–50 g of different types of solid explosives.[1055] In addition, a prototype instrument with a 600 G magnet (Figure 115) was built and used to test thousands of suitcases and other airline luggage and cargo, some of which contained simulated explosives of various sorts. The results were encouraging in that there was a high probability of detection and a low rate of 'false alarms'.[1056] Nevertheless, the NMR method never became operational, primarily because other techniques offering better sensitivity and fewer drawbacks were developed.

RETROSPECTIVE AND PROSPECTIVE

In Section 1 we said that the history of NMR, like all histories, has no real beginning. Some histories have a distinct conclusion, but that of NMR is nowhere in sight. The imminent maturation of NMR techniques and their use in a routine manner has been predicted for at least 25 years. In several of the articles that follow, the authors point out that more senior and presumably wiser scientists had counseled them in the 1960s or 1970s that the 'exciting' period of NMR was over and they should look for greener pastures. Some did, but most continued to bring further innovation to the field. In a review in 1980,[1057] Jonas and Gutowsky pointed out the versatility of NMR and referred to it as 'an evergreen'. The range of articles in this Encyclopedia attests to the continuing richness and practical utility of NMR methods.

The Development of NMR—A Retrospective Look

In this history we have tried to trace the principal threads in the origin and evolution of various aspects of NMR. There are

very many aspects that we have been unable to discuss in detail and others that we have not even mentioned. In the spirit that the history of NMR is a continuing subject, we have focused especially in Sections 14 to 16 on some areas of particularly widespread interest at the time this story was written, but as we examine contemporary developments we clearly lack the perspective that comes only with the passage of time.

This Encyclopedia commemorates the 50th anniversary of the independent discoveries by Purcell, Torrey, and Pound and by Bloch, Hansen, and Packard of methods to observe NMR, as we now know it. Bloch and Purcell did not receive the Nobel Prize for the discovery of NMR, for that had been done by Rabi and his colleagues eight years earlier. Rabi's discovery was an important milestone in physics, but had it not been for the seminal work by the Purcell and Bloch groups, NMR would have remained an important tool for obtaining precise values of nuclear magnetic properties. Period! The observation of NMR in bulk materials, not only in molecular beams, opened new vistas. Physicists and chemists in the 1940s used good judgment in capitalizing on the rich arena opened to them. They worked out the theory in increasingly complex detail and found that NMR could provide unprecedented information about molecular motions in solids and liquids. They learned that chemical environment and bonding had major influences on NMR spectra, and they opened up a whole new industry in analytical chemistry.

Later, it became clear that high-power pulse techniques, which had been used largely by physicists for broadline spectra, and the low-power, sequential scanning that was characteristic of the chemical analysis of multiline spectra could be related in a practical way by Fourier transform methods. The FT revolution ushered in a new era marked by great versatility and by the development of new concepts for studies of solids and ultimately for multidimensional NMR, thus making NMR a far more dynamic and innovative technique. The discovery that NMR could produce three-dimensional spatial images resulted in an even bigger industry in magnetic resonance imaging, which provides not only anatomical, but also spectroscopic and functional information in the biomedical field. Now materials science, too, is benefiting from a combination of all these methods.

Our account of these spectacular developments has been quite limited. In the early days it was largely one-dimensional, as one discovery built on its predecessor. But as the field of NMR underwent exponential growth, it has been impossible for us even to mention many of the valuable contributions by thousands of investigators. In the two most widespread areas in which NMR has been applied over the last 50 years—organic chemistry and medicine—the volume of published work is so overwhelming that we could not even scratch the surface in describing the accomplishments. We have tried to convey some sense of the overall threads of innovation as NMR has developed to its present position. To provide a feeling of continuity in a given specialty, we have divided our account into many sections and subsections. It is clear, however, that the flow of ideas and of technology is not compartmentalized. The concurrent developments in many areas and the interchange of concepts and of new methods continues to be a mark of strength as NMR moves to even greater horizons.

Much more detail and a far greater perception of the excitement in carrying out NMR studies are conveyed in the 200 articles that follow. Had space permitted, many more such interesting stories could have been told. We have introduced a number of these articles within the course of our narrative, but we have not been able to mention others of equal significance.

The Future: 'Plus Ça Change, . . . '

In a field that has repeatedly demonstrated surprising new developments, we would not be so bold as to predict the future. Certainly some aspects can safely be forecast, e.g., a continuing effort to attain higher magnetic fields, the use of high-temperature superconducting materials as they are developed, and increasing reliance on complex computational facilities and image processing procedures; these points are so obvious, however, that they are not worth discussing. In concluding this narrative we highlight three contemporary developments, not because they will necessarily become major new techniques, but because they have particular relevance to our earlier history.

In Section 1, we described the Stern–Gerlach experiment which played a critical role in establishing the principles of quantum mechanics and, in modified form, provided the early measurements of nuclear magnetic moments. These measurements were conducted with a molecular beam, the deflection of which served as a detector of the spin state. All of the developments in NMR that we have discussed depended on the replacement of this form of detection by nuclear resonance and nuclear induction in the bulk material. However, in 1992, John Sidles[1058] proposed an experiment in which a harmonic restoring potential is added to the Stern–Gerlach concept—an approach that he called a 'folded' Stern–Gerlach experiment. In practice such an experiment could be realized by combining the resonance phenomenon and techniques commonly used in atomic force microscopy. He and others calculated that it might be possible with this technique to observe a single nuclear spin, a gain of perhaps 10^{14} over normal NMR sensitivity! Rugar et al.[1059] first demonstrated the feasibility of this approach by using it to measure electron magnetic resonance and, in 1994, this group reported the force detection of NMR.[1060] Their measurement involved 1.6×10^{13} protons in a sample of ammonium nitrate, a far cry from a single proton, but major gains in sensitivity are believed to be attainable. Moreover, with the large magnetic field gradient used in this experiment, the measurement already provided a one-dimensional NMR image with a spatial resolution of about $2.6\,\mu$m, an order of magnitude better than that obtained by conventional NMR imaging of solids.

A second reminder of the earliest aspects of NMR is given in Dan Weitekamp's historical sketch (***Fiat, Daniel: The International Society of Magnetic Resonance (ISMAR). Landmarks and Highlights***). In 1927, Dennison explained anomalies in the heat capacity of hydrogen by pointing out that the existence of nuclear spin would cause this molecule to exist in two very different forms, *ortho*- and *para*-hydrogen, which normally do not interconvert.[4] Weitekamp realized that the perfect spin ordering of *para*-hydrogen might be retained in certain reactions when it is added to other molecules to generate magnetically nonequivalent protons, thereby achieving a very low spin temperature and greatly enhanced NMR signal. The experimental demonstration of this phenomenon at Caltech was published[1061] with the title 'Parahydrogen and Synthesis

Allow Dramatically Enhanced Nuclear Alignment'—leaving it to others to provide the acronym appropriate to the locale of the experiment. The PASADENA experiment as applied to the catalytic hydrogenation of acrylonitrile provided a signal enhancement of 100–200. As Weitekamp points out, this phenomenon was almost certainly observed previously by others in the course of homogeneous hydrogenation, but was either ignored or misinterpreted as arising from chemically induced dynamic nuclear polarization.

Our third example also illustrates a phenomenon that must have been observed but disregarded by many workers over the years. In late 1993, Warren Warren and co-workers published a paper in *Science* with the intriguing title 'Generation of Impossible Cross-Peaks Between Bulk Water and Biomolecules in Solution NMR'.[1062] One of the basic tenets of NMR is that rapid, random tumbling of molecules leads to an averaging out of magnetic dipolar interactions and permits the narrow lines characteristic of high-resolution NMR. A second fundamental assumption in NMR theory is that NMR energy levels lie so close that at room temperature the exponential term in a Boltzmann distribution can be replaced by a linear term—the 'high-temperature approximation'. Warren et al. showed that when a magnetic field gradient is applied, dipolar averaging is incomplete and, together with the limitation of the high-temperature approximation, the usual selection rules do not necessarily apply. In a COSY experiment carried out with a magnetic field gradient, they had found and explained multiple quantum coherences between water and a glycoprotein fragment at low concentration. They called the technique *C*OSY *R*evamped with *A*symmetric *Z*-gradient *E*cho *D*etection (CRAZED) 'because, to an experienced NMR spectroscopist, it *looks* crazed'. The analysis of this phenomenon not only provided guidance on ways to avoid such unwanted cross peaks but also suggested a possible method for measuring molecular interactions at distances of the order of 1 μm or more.

In concluding with these examples of new developments that hark back to some early aspects of NMR, we are surely not asserting that we have come 'full circle'. NMR continues to thrive on innovation and to broaden its scope, apparently without limit. But even in the midst of impressive technology and sophisticated techniques we are sometimes reminded that we are not very far from our roots.

REFERENCES

1. G. E. Uhlenbeck and S. Goudsmit, *Naturwissenschaften*, 1925, **13**, 953.
2. W. Pauli, Jr., *Z. Phys.*, 1927, **43**, 601.
3. C. G. Darwin, *Proc. R. Soc. London*, 1927, **A115**, 1.
4. D. M. Dennison, *Proc. R. Soc. London*, 1927, **A115**, 483.
5. W. Pauli, Jr., *Naturwissenschaften*, 1924, **12**, 741.
6. O. Stern, *Z. Phys.*, 1921, **7**, 249.
7. W. Gerlach and O. Stern, *Z. Phys.*, 1921, **8**, 110.
8. I. Estermann and O. Stern, *Z. Phys.*, 1933, **85**, 17.
9. R. Frisch and O. Stern, *Z. Phys.*, 1933, **85**, 4.
10. I. I. Rabi, *Phys. Rev.*, 1937, **51**, 652.
11. J. M. B. Kellogg, I. I. Rabi, and J. R. Zacharias, *Phys. Rev.*, 1936, **50**, 472.
12. B. G. Lasarew and L. W. Schubnikow, *Sov. Phys.*, 1937, **11**, 445.
13. C. J. Gorter, *Physica (The Hague)*, 1936, **3**, 995.
14. I. I. Rabi, J. R. Zacharias, S. Millman, and P. Kusch, *Phys. Rev.*, 1938, **53**, 318.
15. C. J. Gorter, *Phys. Today*, 1967, **20**, 76.
16. J. M. B. Kellogg, I. I. Rabi, N. F. Ramsey, and J. R. Zacharias, *Phys. Rev.*, 1940, **57**, 677.
17. L. W. Alvarez and F. Bloch, *Phys. Rev.*, 1940, **57**, 111.
18. C. J. Gorter and L. J. F. Broer, *Physica (The Hague)*, 1942, **9**, 591.
19. E. K. Zavoisky, *J. Phys. USSR*, 1945, **9**, 211, 245.
20. J. H. Van Vleck, A Third of a Century of Paramagnetic Relaxation and Resonance, in *Magnetic Resonance*, ed. C. K. Coogan, N. S. Ham, S. N. Stuart, J. R. Pilbrow, and G. V. H. Wilson, Plenum Press, New York, 1970, pp. 1–10.
21. E. M. Purcell, H. C. Torrey, and R. V. Pound, *Phys. Rev.*, 1946, **69**, 37.
22. F. Bloch, W. W. Hansen, and M. Packard, *Phys. Rev.*, 1946, **69**, 127.
23. F. Bloch, *Phys. Rev.*, 1946, **70**, 460.
24. F. Bloch, W. W. Hansen, and M. Packard, *Phys. Rev.*, 1946, **70**, 474.
25. F. Bloch, E.C. Levinthal, and M. E. Packard, *Phys. Rev.*, 1947, **72**, 1125.
26. F. Bloch, A. C. Graves, M. Packard, and R. W. Spence, *Phys. Rev.*, 1947, **71**, 373.
27. F. Bloch, D. Nicodemus, and H. Staub, *Phys. Rev.*, 1948, **74**, 1025.
28. B. A. Jacobsohn and R. K. Wangsness, *Phys. Rev.*, 1948, **73**, 942.
29. E. M. Purcell, R. V. Pound, and N. Bloembergen, *Phys. Rev.*, 1946, **70**, 986.
30. N. Bloembergen, E. M. Purcell, and R. V. Pound, *Nature (London)*, 1947, **160**, 475.
31. N. Bloembergen, E. M. Purcell, and R. V. Pound, *Phys. Rev.*, 1948, **73**, 679.
32. G. E. Pake, *J. Chem. Phys.*, 1948, **16**, 327.
33. H. S. Gutowsky, G. B. Kistiakowsky, G. E. Pake, and E. M. Purcell, *J. Chem. Phys.*, 1949, **17**, 972.
34. H. G. Dehmelt and H. Krüger, *Naturwissenschaften*, 1950, **37**, 111.
35. G. E. Pake, *Am. J. Phys.*, 1950, **18**, 438, 473.
36. B. V. Rollin, *Nature (London)*, 1946, **158**, 669.
37. B. V. Rollin and J. Hatton, *Nature (London)*, 1947, **159**, 201.
38. J. Hatton and B. V. Rollin, *Proc. R. Soc. (London)*, 1949, **A199**, 222.
39. E. R. Andrew, *Nuclear Magnetic Resonance*, Cambridge University Press, Cambridge, 1955.
40. A. Abragam, *Time Reversal*, Oxford University Press, Oxford, 1989.
41. A. Abragam, *The Principles of Nuclear Magnetism*, Oxford University Press, London, 1961.
42. E. L. Hahn, *Phys. Rev.*, 1949, **76**, 145.
43. H. C. Torrey, *Phys. Rev.*, 1949, **76**, 1059.
44. W. G. Proctor and F. C. Yu, *Phys. Rev.*, 1950, **77**, 717.
45. W. C. Dickinson, *Phys. Rev.*, 1950, **77**, 736.
46. G. Lindström, *Phys. Rev.*, 1950, **78**, 817.
47. H. A. Thomas, *Phys. Rev.*, 1950, **80**, 901.
48. J. T. Arnold, S. S. Dharmatti, and M. E. Packard, *J. Chem. Phys.*, 1951, **19**, 507.
49. M. E. Packard and J. T. Arnold, *Phys. Rev.*, 1951, **83**, 210.
50. U. Liddel and N. F. Ramsey, *J. Chem. Phys.*, 1951, **19**, 1608.
51. W. E. Lamb, Jr., *Phys. Rev.*, 1941, **60**, 817.
52. N. F. Ramsey, *Phys. Rev.*, 1950, **77**, 567.
53. N. F. Ramsey, *Phys. Rev.*, 1950, **78**, 699; *Phys. Rev.*, 1951, **83**, 540; *Phys. Rev.*, 1952, **86**, 243.
54. P. Zeeman, *Philos. Mag.*, 1897, **43**, 226.
55. J. Larmor, *Philos. Mag.*, 1897, **44**, 503.
56. W. D. Knight, *Phys. Rev.*, 1949, **76**, 1259.

57. T. J. Rowland, *Progress in Metal Physics*, Pergamon, New York, 1961, Vol. 9.
58. W. G. Proctor and F. C. Yu, *Phys. Rev.*, 1950, **77**, 717.
59. H. S. Gutowsky and D. W. McCall, *Phys. Rev.*, 1951, **82**, 748.
60. E. L. Hahn and D. E. Maxwell, *Phys. Rev.*, 1951, **84**, 1246.
61. N. F. Ramsey and E. M. Purcell, *Phys. Rev.*, 1952, **85**, 143.
62. N. F. Ramsey, *Phys. Rev.*, 1953, **91**, 303.
63. M. Packard, *Varian Associates Brochure*, 1963.
64. R. H. Varian, US Patent 3 109 138 (Filed Aug. 29, 1956, Issued Oct. 29, 1963).
65. H. Y. Carr, *'Free Precession Techniques in Nuclear Magnetic Resonance'*, Ph.D. Thesis, Harvard University, 1952.
66. F. Bloch, *Phys. Rev.*, 1954, **94**, 496.
67. W. A. Anderson and J. T. Arnold, *Phys. Rev.*, 1954, **94**, 497.
68. F. Bloch, US Patent 2 960 649 (Filed June 18, 1954, Issued Nov. 15, 1960).
69. J. I. Kaplan, *J. Chem. Phys.*, 1957, **27**, 1426.
70. G. A. Williams and H. S. Gutowsky, *Phys. Rev.*, 1956, **104**, 278.
71. K. Halbach, *Helv. Phys. Acta*, 1956, **29**, 37.
72. H. S. Gutowsky and C. J. Hoffman, *Phys. Rev.*, 1950, **80**, 110.
73. H. S. Gutowsky and R. E. McClure, *Phys. Rev.*, 1951, **81**, 276.
74. A. Saika and C. P. Slichter, *J. Chem. Phys.*, 1954, **22**, 26.
75. H. S. Gutowsky and C. J. Hoffman, *J. Chem. Phys.*, 1951, **19**, 1259.
76. L. H. Meyer, A. Saika, and H. S. Gutowsky, *J. Am. Chem. Soc.*, 1953, **75**, 4567.
77. W. C. Dickinson, *Phys. Rev.*, 1951, **81**, 717.
78. H. Spiesecke and W. G. Schneider, *J. Chem. Phys.*, 1961, **35**, 722, 731.
79. J. S. Waugh and R. W. Fessenden, *J. Am. Chem. Soc.*, 1957, **79**, 846.
80. J. A. Pople, *J. Chem. Phys.*, 1956, **24**, 1111.
81. C. E. Johnson, Jr. and F. A. Bovey, *J. Chem. Phys.*, 1958, **29**, 1012.
82. J. T. Arnold and M. E. Packard, *J. Chem. Phys.*, 1951, **19**, 1608.
83. H. S. Gutowsky, D. W. McCall, and C. P. Slichter, *J. Chem. Phys.*, 1953, **21**, 279.
84. H. S. Gutowsky and A. Saika, *J. Chem. Phys.*, 1953, **21**, 1688.
85. W. D. Phillips, *J. Chem. Phys.*, 1955, **23**, 1363.
86. H. S. Gutowsky and C. H. Holm, *J. Chem. Phys.*, 1956, **25**, 1228.
87. E. J. Corey, H. J. Burke, and W. A. Remers, *J. Am. Chem. Soc.*, 1955, **77**, 4941.
88. J. N. Shoolery and M. T. Rogers, *J. Am. Chem. Soc.*, 1958, **80**, 5121.
89. S. Goodwin, J. N. Shoolery, and L. F. Johnson, *J. Am. Chem. Soc.*, 1959, **81**, 3065.
90. C. A. Reilly, *J. Chem. Phys.*, 1956, **25**, 604.
91. J. J. Turner, *Mol. Phys.*, 1960, **3**, 417.
92. H. M. McConnell, A. D. McLean, and C. A. Reilly, *J. Chem. Phys.*, 1955, **23**, 1152.
93. J. A. Pople, W. G. Schneider, and H. J. Bernstein, *High Resolution Nuclear Magnetic Resonance*, McGraw-Hill, New York, 1959.
94. C. A. Reilly and J. D. Swalen, *J. Chem. Phys.*, 1960, **32**, 1378.
95. R. A. Hoffman, *J. Chem. Phys.*, 1960, **33**, 1256.
96. A. A. Bothner-By and C. Naar-Colin, *J. Am. Chem. Soc.*, 1961, **83**, 231.
97. A. A. Bothner-By, C. Naar-Colin, and H. Günther, *J. Am. Chem. Soc.*, 1962, **84**, 2748.
98. S. Castellano and A. A. Bothner-By, *J. Chem. Phys.*, 1964, **41**, 3863.
99. Y. Arata, H. Shimizu, and S. Fujiwara, *J. Chem. Phys.*, 1962, **36**, 1951.
100. J. Martin and B. P. Dailey, *J. Chem. Phys.*, 1962, **37**, 2594.
101. C. W. Haigh, *Annu. Rep. NMR Spectrosc.*, 1971, **4**, 311.
102. P. Diehl, C. L. Khetrapal, and H. P. Kellerhals, *Mol. Phys.*, 1968, **15**, 333.
103. P. Diehl, H. P. Kellerhals, and E. Lustig, *NMR Basic Principles Prog.*, 1972, **6**, 1.
104. J. A. Pople and T. Schaefer, *Mol. Phys.*, 1960, **3**, 547.
105. P. Diehl and J. A. Pople, *Mol. Phys.*, 1960, **3**, 557.
106. P. Diehl and C. L. Khetrapal, *Can. J. Chem.*, 1969, **47**, 1411.
107. C. Reid, *J. Mol. Spectrosc.*, 1957, **1**, 18.
108. R. U. Lemieux, R. K. Kullnig, H. J. Bernstein, and W. G. Schneider, *J. Am. Chem. Soc.*, 1957, **79**, 1005.
109. R. U. Lemieux, R. K. Kullnig, H. J. Bernstein, and W. G. Schneider, *J. Am. Chem. Soc.*, 1958, **80**, 6098.
110. R. U. Lemieux, R. K. Kullnig, and R. Y. Moir, *J. Am. Chem. Soc.*, 1958, **80**, 2237.
111. M. Karplus, *J. Chem. Phys.*, 1959, **30**, 11.
112. M. Karplus, *J. Am. Chem. Soc.*, 1963, **85**, 2870.
113. M. Karplus, D. H. Anderson, T. C. Farrar, and H. S. Gutowsky, *J. Chem. Phys.*, 1957, **27**, 597.
114. H. S. Gutowsky and C. Juan, *J. Chem. Phys.*, 1962, **37**, 120.
115. R. R. Fraser, R. U. Lemieux, and J. D. Stevens, *J. Am. Chem. Soc.*, 1961, **83**, 3901.
116. M. Karplus, *J. Am. Chem. Soc.*, 1962, **84**, 2458.
117. A. D. Cohen, N. Sheppard, and J. J. Turner, *Proc. Chem. Soc. (London)*, 1958, 118.
118. P. C. Lauterbur, *J. Chem. Phys.*, 1957, **26**, 217.
119. C. H. Holm, *J. Chem. Phys.*, 1957, **26**, 707.
120. P. C. Lauterbur, *Ann. N.Y. Acad. Sci.*, 1958, **70**, 841.
121. J. B. Stothers, *Carbon-13 NMR Spectroscopy*, Academic Press, New York, 1972.
122. J. N. Shoolery, *Third Experimental NMR Conference*, 1962.
123. J. T. Arnold and M. E. Packard, *J. Chem. Phys.*, 1951, **19**, 1608.
124. R. A. Ogg, Jr., *J. Chem. Phys.*, 1954, **22**, 560.
125. C. M. Huggins, G. C. Pimentel, and J. N. Shoolery, *J. Chem. Phys.*, 1955, **23**, 1244.
126. C. M. Huggins, G. C. Pimentel, and J. N. Shoolery, *J. Phys. Chem.*, 1956, **60**, 1311.
127. A. D. Cohen and C. Reid, *J. Chem. Phys.*, 1956, **25**, 790.
128. E. D. Becker, U. Liddel, and J. N. Shoolery, *J. Mol. Spectrosc.*, 1958, **2**, 1.
129. M. Saunders and J. B. Hyne, *J. Chem. Phys.*, 1958, **29**, 1319.
130. G. J. Korinek and W. G. Schneider, *Can. J. Chem.*, 1957, **35**, 1157.
131. W. G. Schneider, H. J. Bernstein, and J. A. Pople, *J. Chem. Phys.*, 1958, **28**, 601.
132. L. W. Reeves and W. G. Schneider, *Can. J. Chem.*, 1957, **35**, 251.
133. A. D. Buckingham, T. Schaefer, and W. G. Schneider, *J. Chem. Phys.*, 1960, **32**, 1227.
134. H. Y. Carr and E. M. Purcell, *Phys. Rev.*, 1954, **94**, 630.
135. S. Meiboom and D. Gill, *Rev. Sci. Instrum.*, 1958, **29**, 688.
136. I. J. Lowe and R. E. Norberg, *Phys. Rev.*, 1957, **107**, 46.
137. D. E. Woessner, *J. Phys. Chem.*, 1963, **67**, 1365.
138. E. O. Stejskal and J. E. Tanner, *J. Chem. Phys.*, 1965, **42**, 288.
139. J. G. Powles and P. Mansfield, *Phys. Lett.*, 1962, **2A**, 58.
140. R. V. Pound, *Phys. Rev.*, 1951, **81**, 156.
141. E. M. Purcell and R. V. Pound, *Phys. Rev.*, 1951, **81**, 279.
142. C. P. Slichter and W. C. Holton, *Phys. Rev.*, 1961, **122**, 1701.
143. D. C. Ailion and C. P. Slichter, *Phys. Rev.*, 1965, **137**, A235.
144. A. W. Overhauser, *Phys. Rev.*, 1953, **91**, 476.
145. A. Abragam, *Time Reversal*, Oxford University Press, Oxford, 1989, p. 164.
146. A. W. Overhauser, *Phys. Rev.*, 1953, **92**, 411.
147. R. A. Dwek, J. G. Kenworthy, D. F. S. Natusch, R. E. Richards, and D. J. Shields, *Proc. R. Soc. London*, 1966, **A291**, 487.

148. R. A. Dwek, R. E. Richards, D. Taylor, and R. A. Shaw, *J. Chem. Soc. A*, 1970, 1173.
149. T. C. Cannon, R. E. Richards, and D. Taylor, *J. Chem. Soc. A*, 1970, 1180.
150. I. Solomon, *Phys. Rev.*, 1955, **99**, 559.
151. I. Solomon and N. Bloembergen, *J. Chem. Phys.*, 1956, **25**, 261.
152. J. G. Powles and H. S. Gutowsky, *J. Chem. Phys.*, 1955, **23**, 1692.
153. E. R. Andrew, A. Bradbury, and R. G. Eades, *Nature (London)*, 1958, **182**, 1659.
154. E. R. Andrew, A. Bradbury, and R. G. Eades, *Nature (London)*, 1959, **183**, 1802.
155. I. J. Lowe, *Phys. Rev. Lett.*, 1959, **2**, 285.
156. R. E. Norberg, *Phys. Rev.*, 1952, **86**, 745.
157. E. K. Jeong, B. Ouyang, R. E. Norberg, P. A. Fedders, and M. S. Conradi, *Phys. Rev. Lett.*, 1992, **69**, 2983.
158. D. Zamir and R. M. Cotts, *Phys. Rev.*, 1964, **134**, A666.
159. D. Zamir, R. C. Wayne, and R. M. Cotts, *Phys. Rev. Lett.*, 1964, **12**, 327.
160. R. T. Schumacher and C. P. Slichter, *Phys. Rev.*, 1956, **101**, 58.
161. L. C. Hebel and C. P. Slichter, *Phys. Rev.*, 1959, **113**, 1504.
162. M. Lipsicas and M. Bloom, *Can. J. Phys.*, 1961, **39**, 881.
163. R. L. Streever and H. Y. Carr, *Phys. Rev.*, 1961, **121**, 20.
164. D. E. Woessner, *J. Chem. Phys.*, 1962, **37**, 647.
165. H. Shimizu, *J. Chem. Phys.*, 1962, **37**, 765.
166. H. S. Gutowsky, I. J. Lawrenson, and K. Shimomura, *Phys. Rev. Lett.*, 1961, **6**, 349.
167. P. S. Hubbard, *Phys. Rev.*, 1963, **131**, 1155.
168. D. F. Evans, *Philos. Mag.*, 1956, **1**, 370.
169. E. B. Baker and L. W. Burd, *Rev. Sci. Instrum.*, 1957, **28**, 313.
170. H. Primas, *5th Eur. Congr. Mol. Spectrosc.*, Amsterdam, 1961.
171. R. Freeman and D. H. Whiffen, *Proc. Phys. Soc. (London)*, 1962, **79**, 794.
172. W. A. Anderson, *Rev. Sci. Instrum.*, 1962, **33**, 1160.
173. G. V. D. Tiers, *J. Phys. Chem.*, 1958, **62**, 1151.
174. N. S. Bhacca, L. F. Johnson, and J. N. Shoolery, *High Resolution NMR Spectra Catalog*, Varian, Palo Alto, CA, 1962.
175. L. M. Jackman, *Applications of Nuclear Magnetic Resonance Spectroscopy in Organic Chemistry*, Pergamon, New York, 1959.
176. L. M. Jackman and S. Sternhell, *Applications of NMR Spectroscopy in Organic Chemistry*, 2nd edn., Pergamon Press, Oxford, 1969.
177. *Pure Appl. Chem.*, 1972, **29**, 627.
178. R. R. Ernst, *Concep. Magn. Reson.*, 1994, **6**, 201.
179. M. P. Klein and G. W. Barton, *Rev. Sci. Instrum.*, 1963, **34**, 754.
180. O. Jardetzky, N. G. Wade, and J. J. Fischer, *Nature (London)*, 1963, **197**, 183.
181. L. C. Allen and L. F. Johnson, *J. Am. Chem. Soc.*, 1963, **85**, 2668.
182. P. Laszlo and P. von R. Schleyer, *J. Am. Chem. Soc.*, 1963, **85**, 2017.
183. T. J. Batterham, *NMR Spectra of Simple Heterocycles*, Wiley, New York, 1973.
184. A. L. Burlingame, H. M. Fales, and R. J. Highet, *J. Am. Chem. Soc.*, 1964, **86**, 4976.
185. J. S. Waugh and F. A. Cotton, *J. Phys. Chem.*, 1961, **65**, 562.
186. N. Bloembergen and W. C. Dickinson, *Phys. Rev.*, 1950, **79**, 179.
187. W. D. Phillips, C. E. Looney, and C. K. Ikeda, *J. Chem. Phys.*, 1957, **27**, 1435.
188. H. M. McConnell and C. H. Holm, *J. Chem. Phys.*, 1957, **27**, 314.
189. H. M. McConnell and C. H. Holm, *J. Chem. Phys.*, 1958, **28**, 749.
190. W. D. Phillips and R. E. Benson, *J. Chem. Phys.*, 1960, **33**, 607.
191. H. M. McConnell and R. E. Robertson, *J. Chem. Phys.*, 1958, **29**, 1361.
192. E. DeBoer and C. MacLean, *J. Chem. Phys.*, 1966, **44**, 1334.
193. R. E. Benson, D. R. Eaton, A. D. Josey, and W. D. Phillips, *J. Am. Chem. Soc.*, 1961, **83**, 3714.
194. C. C. Hinckley, *J. Am. Chem. Soc.*, 1969, **91**, 5160.
195. W. B. Lewis, J. A. Jackson, J. F. Lemons, and H. Taube, *J. Chem. Phys.*, 1962, **36**, 694; J. A. Jackson, *J. Chem. Ed.*, 1987, **64**, 140.
196. D. R. Eaton, *J. Am. Chem. Soc.*, 1965, **87**, 3097.
197. E. L. Muetterties and C. M. Wright, *J. Am. Chem. Soc.*, 1965, **87**, 4706.
198. J. Reuben and D. Fiat, *Chem. Commun.*, 1967, 729.
199. J. K. M. Sanders and D. H. Williams, *Chem. Commun.*, 1970, 422.
200. R. E. Rondeau and R. E. Sievers, *J. Am. Chem. Soc.*, 1971, **93**, 1522.
201. G. M. Whitesides and D. W. Lewis, *J. Am. Chem. Soc.*, 1970, **92**, 6979.
202. T. F. Wimett, *Phys. Rev.*, 1953, **91**, 476.
203. G. V. D. Tiers, *J. Am. Chem. Soc.*, 1957, **79**, 5585.
204. H. S. Gutowsky, M. Karplus, and D. M. Grant, *J. Chem. Phys.*, 1959, **31**, 1278; H. S. Gutowsky, *J. Chem. Phys.*, 1959, **31**, 1683.
205. C. J. Jameson and H. Jörg Osten, *Annu. Rep. NMR Spectrosc.*, 1986, **17**, 1.
206. S. Berger, *NMR Basic Principles Prog.*, 1990, **22**, 1.
207. H. R. Ward and R. G. Lawler, *J. Am. Chem. Soc.*, 1967, **89**, 5518.
208. R. G. Lawler, *J. Am. Chem. Soc.*, 1967, **89**, 5519.
209. J. Bargon, H. Fischer, and U. Johnsen, *Z. Naturforsch., Teil A*, 1967, **22**, 1551.
210. J. Bargon and H. Fischer, *Z. Naturforsch., Teil A*, 1967, **22**, 1556.
211. G. L. Closs, *J. Am. Chem. Soc.*, 1969, **91**, 4552.
212. R. Kaptein and L. J. Oosterhoff, *Chem. Phys. Lett.*, 1969, **4**, 195.
213. R. Kaptein and L. J. Oosterhoff, *Chem. Phys. Lett.*, 1969, **4**, 214.
214. G. L. Closs, in *Chemically Induced Magnetic Polarization*, ed. A. R. Lepley and G. L. Closs, John Wiley, New York, 1973, p. 118.
215. R. Kaptein, K. Dijkstra, and K. Nicolay, *Nature (London)*, 1978, **274**, 293.
216. R. Kaptein, *Biological Magnetic Resonance*, Plenum Press, New York, 1982, Vol. 4, p. 145.
217. D. W. McCall, D. C. Douglass, and E. W. Anderson, *J. Chem. Phys.*, 1959, **31**, 1555.
218. A. Saupe and G. Englert, *Phys. Rev. Lett.*, 1963, **11**, 462.
219. R. D. Spence, H. A. Moses, and P. L. Jain, *J. Chem. Phys.*, 1953, **21**, 380.
220. R. D. Spence, H. S. Gutowsky, and C. H. Holm, *J. Chem. Phys.*, 1953, **21**, 1891.
221. A. Saupe, *Z. Naturforsch., Teil A*, 1965, **20**, 572.
222. L. C. Snyder, *J. Chem. Phys.*, 1965, **43**, 4041.
223. P. Diehl and C. L. Khetrapal, *Mol. Phys.*, 1967, **14**, 283.
224. C. S. Yannoni, G. P. Ceasar, and B. P. Dailey, *J. Am. Chem. Soc.*, 1967, **89**, 2833.
225. K. D. Lawson and T. J. Flautt, *J. Am. Chem. Soc.*, 1967, **89**, 5489.
226. J. W. Emsley and J. C. Lindon, *NMR Spectroscopy Using Liquid Crystal Solvents*, Pergamon Press, Oxford, 1975.
227. W. S. Warren, S. Sinton, D. P. Weitekamp, and A. Pines, *Phys. Rev. Lett.*, 1979, **43**, 1791.

228. S. Meiboom and L. C. Snyder, *Acc. Chem. Res.*, 1971, **4**, 81.
229. J. Courtieu, D. W. Alderman, and D. M. Grant, *J. Am. Chem. Soc.*, 1981, **103**, 6783.
230. A. Kumar and C. L. Khetrapal, *J. Magn. Reson*., 1978, **30**, 137.
231. C. L. Khetrapal and A. C. Kunwar, *Mol. Cryst. Liq. Cryst.*, 1981, **72**, 13.
232. C. L. Khetrapal and A. C. Kunwar, *Chem. Phys. Lett.*, 1981, **82**, 170.
233. J. C. Rowell, W. D. Phillips, L. R. Melby, and M. Panar, *J. Chem. Phys.*, 1965, **43**, 3442.
234. R. V. Pound, *Phys. Rev*., 1950, **79**, 685.
235. W. A. Anderson, *Phys. Rev*., 1956, **102**, 151.
236. V. Royden, *Phys. Rev.*, 1954, **96**, 543.
237. A. L. Bloom and J. N. Shoolery, *Phys. Rev.*, 1955, **97**, 1261.
238. R. V. Pound, *Rev. Sci. Instrum.*, 1957, **28**, 966.
239. R. Freeman and R. V. Pound, *Rev. Sci. Instrum.*, 1960, **31**, 103.
240. J. Itoh and S. Sato, *J. Phys. Soc. Jpn.*, 1959, **14**, 851.
241. R. Freeman, *Mol. Phys.*, 1960, **3**, 435.
242. J. D. Baldeschwieler and E. W. Randall, *Chem. Rev.*, 1963, **63**, 81.
243. J. P. Maher and D. F. Evans, *Proc. Chem. Soc.*, 1961, 208.
244. R. Freeman and D. H. Whiffen, *Mol. Phys.*, 1961, **4**, 321.
245. W. A. Anderson and R. Freeman, *J. Chem. Phys*., 1962, **37**, 85.
246. R. Freeman and W. A. Anderson, *J. Chem. Phys*., 1962, **37**, 2053.
247. E. B. Baker, *J. Chem. Phys.*, 1962, **37**, 911.
248. R. R. Ernst, *J. Chem. Phys.*, 1966, **45**, 3845.
249. M. H. Levitt and R. Freeman, *J. Magn. Reson.*, 1981, **43**, 502.
250. J. S. Waugh, *J. Magn. Reson.*, 1982, **49**, 517.
251. S. Forsén and R. A. Hoffman, *J. Chem. Phys.*, 1963, **39**, 2892.
252. F. A. L. Anet and A. J. R. Bourn, *J. Am. Chem. Soc.*, 1965, **87**, 5250.
253. K. Nakanishi, *Pure Appl. Chem*., 1967, **14**, 89.
254. M. C. Woods, I. Miura, Y. Nakadaira, A. Terahara, M. Maruyama, and K. Nakanishi, *Tetrahedron Lett.*, 1967, 321.
255. J. H. Noggle and R. E. Schirmer, *The Nuclear Overhauser Effect: Chemical Applications*, Academic Press, New York, 1971.
256. R. Kaiser, *J. Chem. Phys.*, 1965, **42**, 1838.
257. P. Balaram, A. A. Bothner-By, and J. Dadok, *J. Am. Chem. Soc.*, 1972, **94**, 4015.
258. D. M. Grant and E. G. Paul, *J. Am. Chem. Soc.*, 1964, **86**, 2984.
259. D. K. Dalling and D. M. Grant, *J. Am. Chem. Soc.*, 1967, **89**, 6612.
260. E. G. Paul and D. M. Grant, *J. Am. Chem. Soc.*, 1964, **86**, 2977.
261. F. J. Weigert and J. D. Roberts, *J. Am. Chem. Soc.*, 1967, **89**, 5962.
262. H. J. Reich, M. Jautelat, M. T. Messe, F. J. Weigert, and J. D. Roberts, *J. Am. Chem. Soc.*, 1969, **91**, 7445.
263. D. E. Dorman and J. D. Roberts, *J. Am. Chem. Soc.*, 1970, **92**, 1355.
264. J. G. Nourse and J. D. Roberts, *J. Am. Chem. Soc.*, 1975, **97**, 4584.
265. K. F. Kuhlmann and D. M. Grant, *J. Am. Chem. Soc.*, 1968, **90**, 7355.
266. K. F. Kuhlmann, D. M. Grant, and R. K. Harris, *J. Chem. Phys.*, 1970, **52**, 3439.
267. F. A. Nelson and H. E. Weaver, *Science*, 1964, **146**, 223.
268. R. C. Ferguson and W. D. Phillips, *Science*, 1967, **157**, 257.
269. R. Freeman and J. B. Robert, *NMR Basic Principles Prog.*, 1990, **25**, 1.
270. D. C. Lankin, J. R. Ferraro, and R. Jarnutowski, *Spectroscopy*, 1992, **7**, 18.
271. R. Freeman, *Anal. Chem.*, 1993, **65**, 743A.
272. R. R. Ernst and W. A. Anderson, *Rev. Sci. Instrum.*, 1966, **37**, 93.
273. R. R. Ernst, Without Computers—No Modern NMR in *Computational Aspects of the Study of Biological Macromolecules by Nuclear Magnetic Resonance Spectroscopy*, ed. J. C. Hoch et al., Plenum Press, New York, 1991, p. 1.
274. J. W. Cooley and J. W. Tukey, *Math. Comp.*, 1965, **19**, 297.
275. T. C. Farrar and E. D. Becker, *Pulse and Fourier Transform NMR*, Academic Press, New York, 1971.
276. D. Shaw, *Fourier Transform NMR Spectroscopy*, Elsevier, Amsterdam, 1976.
277. K. Müllen and P. S. Pregosin, *Fourier Transform NMR Techniques: A Practical Approach*, Academic Press, New York, 1976.
278. G. C. Levy and G. L. Nelson, *Carbon-13 Nuclear Magnetic Resonance for Organic Chemists*, Wiley-Interscience, New York, 1972.
279. R. L. Vold, J. S. Waugh, M. P. Klein, and D. E. Phelps, *J. Chem. Phys.*, 1968, **48**, 3831.
280. L. D. Hall and C. M. Preston, *Carbohydr. Res.*, 1973, **29**, 522.
281. C. M. Preston and L. D. Hall, *Carbohydr. Res.*, 1974, **37**, 267.
282. G. C. Levy, J. D. Cargioli, and F. A. L. Anet, *J. Am. Chem. Soc.*, 1973, **95**, 1527.
283. G. C. Levy, *Acc. Chem. Res.*, 1973, **6**, 161.
284. A. Allerhand, D. M. Doddrell, and R. Komoroski, *J. Chem. Phys.*, 1971, **55**, 189.
285. T. L. James and G. G. McDonald, *J. Magn. Reson.*, 1973, **11**, 58.
286. A. G. Redfield and S. D. Kunz, *J. Magn. Reson.*, 1975, **19**, 250.
287. D. I. Hoult and R. E. Richards, *Proc. R. Soc. London*, 1975, **A344**, 311.
288. E. O. Stejskal and J. Schaefer, *J. Magn. Reson.*, 1974, **13**, 249.
289. R. R. Ernst, *J. Magn. Reson.*, 1970, **3**, 10.
290. R. Kaiser, *J. Magn. Reson.*, 1970, **3**, 28.
291. B. L. Tomlinson and H. D. W. Hill, *J. Chem. Phys.*, 1973, **59**, 1775.
292. J. Dadok and R. F. Sprecher, *J. Magn. Reson.*, 1974, **13**, 243.
293. R. K. Gupta, J. A. Ferretti, and E. D. Becker, *J. Magn. Reson.*, 1974, **13**, 275.
294. J. A. Ferretti and R. R. Ernst, *J. Chem. Phys.*, 1976, **65**, 4283.
295. A. G. Redfield and R. K. Gupta, *J. Chem. Phys.*, 1971, **54**, 1418.
296. A. G. Redfield, S. D. Kunz, and E. K. Ralph, *J. Magn. Reson.*, 1975, **19**, 114.
297. M. H. Levitt and R. Freeman, *J. Magn. Reson.*, 1979, **33**, 473.
298. G. A. Morris and R. Freeman, *J. Am. Chem. Soc.*, 1979, **101**, 760.
299. D. M. Doddrell, D. T. Pegg, and M. R. Bendall, *J. Magn. Reson.*, 1982, **48**, 323.
300. S. L. Patt and J. N. Shoolery, *J. Magn. Reson.*, 1982, **46**, 535.
301. A. Bax, R. Freeman, and S. P. Kempsell, *J. Am. Chem. Soc.*, 1980, **102**, 4849.
302. E. R. Andrew and R. G. Eades, *Discuss. Faraday Soc.*, 1962, **34**, 38.
303. E. R. Andrew and L. F. Farnell, *Mol. Phys.*, 1968, **15**, 157.
304. E. R. Andrew and V. T. Wynn, *Proc. R. Soc. London*, 1966, **A291**, 257.
305. H. Kessemeier and R. E. Norberg, *Phys. Rev.*, 1967, **155**, 321.
306. E. R. Andrew, L. F. Farnell, and T. Gledhill, *Phys. Rev. Lett.*, 1967, **19**, 6.
307. D. Doskočilová and B. Schneider, *Macromolecules*, 1972, **5**, 125.
308. J. S. Frey and G. E. Maciel, *J. Magn. Reson.*, 1982, **48**, 125.
309. G. Bodenhausen, P. Caravatti, J. Deli, and R. R. Ernst, *J. Magn. Reson.*, 1982, **48**, 143.

310. C. L. Khetrapal, B. S. Arun Kumar, K. V. Ramanathan, and N. Suryaprakash, *J. Magn. Reson.*, 1987, **73**, 516.
311. E. Lippmaa, M. A. Alla, and T. Tuherm, Magnetic Resonance and Related Phenomena, in *Proc. 19th Congr. AMPERE*, ed. H. Brunner, R. Hausser, and D. Schweitzer, Heidelberg/Geneva, 1976.
312. E. O. Stejskal, J. Schaefer, and R. A. McKay, *J. Magn. Reson.*, 1977, **25**, 569.
313. J. Herzfeld and A. E. Berger, *J. Chem. Phys.*, 1980, **73**, 6021.
314. J. Herzfeld, A. Roufosse, R. A. Haberkorn, R. G. Griffin, and M. J. Glimcher, *Philos. Trans. R. Soc. London*, 1980, **B289**, 459.
315. B. S. Arun Kumar, K. V. Ramanathan, C. L. Khetrapal, S. J. Opella, and E. D. Becker, *J. Magn. Reson.*, 1990, **86**, 516.
316. J. Courtieu, D. W. Alderman, D. M. Grant, and J. P. Bayles, *J. Chem. Phys.*, 1982, **77**, 723.
317. E. R. Andrew, Y. Apaydin, and W. S. Moore, *Phys. Lett.*, 1967, **25A**, 44.
318. A. Bradbury, R. G. Eades, and J. G. McCarten, *Phys. Lett.*, 1968, **26A**, 405.
319. W. I. Goldburg and M. Lee, *Phys. Rev. Lett.*, 1963, **11**, 255.
320. M. Lee and W. I. Goldburg, *Phys. Rev.*, 1965, **140**, A1261.
321. D. Barnaal and I. Lowe, *Phys. Rev. Lett.*, 1963, **11**, 258.
322. E. D. Ostroff and J. S. Waugh, *Phys. Rev. Lett.*, 1966, **16**, 1097.
323. J. S. Waugh and C. H. Wang, *Phys. Rev.*, 1967, **162**, 209.
324. P. Mansfield and D. Ware, *Phys. Lett.*, 1966, **22A**, 133.
325. J. S. Waugh, C. H. Wang, L. M. Huber, and R. L. Vold, *J. Chem. Phys.*, 1968, **48**, 662.
326. J. S. Waugh, L. M. Huber, and U. Haeberlen, *Phys. Rev. Lett.*, 1968, **20**, 180.
327. J. D. Ellett, Jr., U. Haeberlen, and J. S. Waugh, *J. Am. Chem. Soc.*, 1970, **92**, 411.
328. M. Mehring, R. G. Griffin, and J. S. Waugh, *J. Am. Chem. Soc.*, 1970, **92**, 7222.
329. U. Haeberlen and U. Köhlschutter, *Chem. Phys.*, 1973, **2**, 76.
330. H. Raber, G. Brünger, and M. Mehring, *Chem. Phys. Lett.*, 1973, **23**, 400.
331. P. Mansfield, *Phys. Lett.*, 1970, **32A**, 485.
332. P. Mansfield, *J. Phys. C*, 1971, **4**, 1444.
333. P. Mansfield, M. J. Orchard, D. C. Stalker, and K. H. B. Richards, *Phys. Rev.*, 1973, **B7**, 90.
334. W.-K. Rhim, D. D. Elleman, and R. W. Vaughan, *J. Chem. Phys.*, 1973, **58**, 1772.
335. P. Mansfield, *Philos. Trans. R. Soc. London*, 1981, **A299**, 479.
336. D. P. Burum and W.−K. Rhim, *J. Chem. Phys.*, 1979, **71**, 944.
337. R. Blinc, J. Pirš, and I. Zupančič, *Phys. Rev. Lett.*, 1973, **30**, 546.
338. D. Ellett, U. Haeberlen, and J. S. Waugh, *J. Polym. Sci., Polym. Lett.*, 1969, **7**, 71.
339. M. Mehring, R. G. Griffin, and J. S. Waugh, *J. Chem. Phys.*, 1971, **55**, 746.
340. A. N. Garroway, D. C. Stalker, and P. Mansfield, *Polymer*, 1975, **16**, 161.
341. A. J. Vega and A. D. English, *Macromolecules*, 1980, **13**, 1635.
342. C. R. Dybowski and R. W. Vaughan, *Proc. 18th Colloque AMPERE*, Nottingham, 1974.
343. W.-K. Rhim, D. P. Burum, and D. D. Elleman, *Phys. Rev. Lett.*, 1976, **37**, 1764.
344. D. P. Burum, D. D. Elleman, and W.-K. Rhim, *J. Chem. Phys.*, 1978, **68**, 1164.
345. S. R. Hartmann and E. L. Hahn, *Bull. Am. Phys. Soc.*, 1960, **5**, 498.
346. S. R. Hartmann and E. L. Hahn, *Phys. Rev.*, 1962, **128**, 2042.
347. F. M. Lurie and C. P. Slichter, *Phys. Rev.*, 1964, **133**, A1108.
348. P. Mansfield and P. K. Grannell, *J. Phys. C*, 1971, **4**, L197.
349. H. E. Bleich and A. G. Redfield, *J. Chem. Phys.*, 1971, **55**, 5405.
350. H. E. Bleich and A. G. Redfield, *J. Chem. Phys.*, 1977, **67**, 5040.
351. A. Pines, M. G. Gibby, and J. S. Waugh, *J. Chem. Phys.*, 1972, **56**, 1776.
352. A. Pines, M. G. Gibby, and J. S. Waugh, *Chem. Phys. Lett.*, 1972, **15**, 373.
353. S. Pausak, A. Pines, and J. S. Waugh, *J. Chem. Phys.*, 1973, **59**, 591.
354. J. A. Ripmeester and D. W. Davidson, *Bull. Magn. Reson.*, 1980, **2**, 139.
355. R. A. Wind, J. Trommel, and J. Smidt, *Fuel*, 1979, **58**, 900.
356. R. A. Wind, F. E. Anthonio, M. J. Duijvestijn, J. Smidt, J. Trommel, and G. M. C. De Vette, *J. Magn. Reson.*, 1983, **52**, 424.
357. J. Schaefer and E. O. Stejskal, *J. Am. Chem. Soc.*, 1976, **98**, 1031.
358. E. O. Stejskal, J. Schaefer, and J. S. Waugh, *J. Magn. Reson.*, 1977, **28**, 105.
359. D. E. Wemmer, A. Pines, and D. D. Whitehurst, *Philos. Trans. R. Soc. London*, 1981, **A300**, 15.
360. T. Terao, H. Miura, and A. Saika, *J. Chem. Phys.*, 1981, **75**, 1573.
361. T. Terao, H. Miura, and A. Saika, *J. Am. Chem. Soc.*, 1982, **104**, 5228.
362. T. Terao, H. Miura, and A. Saika, *J. Magn. Reson.*, 1982, **49**, 365.
363. K. W. Zilm and D. M. Grant, *J. Magn. Reson.*, 1982, **48**, 524.
364. S. J. Opella and M. H. Frey, *J. Am. Chem. Soc.*, 1979, **101**, 5854.
365. B. C. Gerstein, R. G. Pembleton, R. C. Wilson, and L. M. Ryan, *J. Chem. Phys.*, 1977, **66**, 361.
366. B. Schnabel, U. Haubenreisser, G. Scheler, and R. Muller, *19th Congr. AMPERE*, Heidelberg, 1976, p. 441.
367. J. L. Ackerman, R. Eckman, and A. Pines, *Chem. Phys.*, 1979, **42**, 423.
368. R. Eckman, L. Müller, and A. Pines, *Chem. Phys. Lett.*, 1980, **74**, 376.
369. S. Ganapathy, S. Schramm, and E. Oldfield, *J. Chem. Phys.*, 1982, **77**, 4360.
370. R. K. Harris and B. E. Mann, *NMR and the Periodic Table*, Academic Press, New York, 1978.
371. Y. Masuda and T. Kanda, *J. Phys. Soc. Jpn.*, 1953, **8**, 432.
372. B. E. Holder and M. P. Klein, *J. Chem. Phys.*, 1955, **23**, 1956.
373. R. A. Ogg Jr. and J. D. Ray, *J. Chem. Phys.*, 1957, **26**, 1339.
374. M. Witanowski and G. A. Webb, *Nitrogen NMR*, Plenum Press, London, 1973.
375. M. Witanowski, L. Stefaniak, and G. A. Webb, *Annu. Rep. NMR Spectrosc.*, 1993, **25**.
376. J. D. Ray, *J. Chem. Phys.*, 1964, **40**, 3440.
377. L. Paolillo and E. D. Becker, *J. Magn. Reson.*, 1970, **2**, 168.
378. J. B. Lambert, G. Binsch, and J. D. Roberts, *Proc. Natl. Acad. Sci. USA*, 1964, **51**, 735.
379. G. Binsch, J. B. Lambert, B. W. Roberts, and J. D. Roberts, *J. Am. Chem. Soc.*, 1964, **86**, 5564.
380. G. J. Martin, M. L. Martin, and J. P. Gouesnard, *NMR Basic Principles and Progress*, 1981, **18**, 1.
381. E. O. Stejskal, J. Schaefer, and R. A. McKay, *J. Magn. Reson.*, 1984, **57**, 471.
382. G. S. Jacob, J. Schaefer, E. O. Stejskal, and R. A. McKay, *Biochem. Biophys. Res. Commun.*, 1980, **97**, 1176.
383. T. A. Cross, J. A. DiVerdi, and S. J. Opella, *J. Am. Chem. Soc.*, 1982, **104**, 1759.
384. T. A. Cross, M. H. Frey, and S. J. Opella, *J. Am. Chem. Soc.*, 1983, **105**, 7471.
385. J. A. Ripmeester, *J. Am. Chem. Soc.*, 1983, **105**, 2925.

386. G. E. Maciel, J. F. Haw, I.-S. Chuang, B. L. Hawkins, T. A. Early, D. R. McKay, and L. Petrakis, *J. Am. Chem. Soc.*, 1983, **105**, 5529.
387. P. D. Majors and P. D. Ellis, *J. Am. Chem. Soc.*, 1987, **109**, 1648.
388. G. R. Holzman, P. C. Lauterbur, J. H. Anderson, and W. Koth, *J. Chem. Phys.*, 1956, **25**, 172.
389. R. K. Harris and B. J. Kimber, *J. Organomet. Chem.*, 1974, **70**, 43.
390. E. T. Lippmaa, M. A. Alla, T. J. Pehk, and G. Engelhardt, *J. Am. Chem. Soc.*, 1978, **100**, 1929.
391. H. L. Anderson and A. Novick, *Phys. Rev.*, 1947, **71**, 372.
392. F. Bloch, A. C. Graves, M. Packard, and R. W. Spence, *Phys. Rev.*, 1947, **71**, 551.
393. G. V. D. Tiers, C. A. Brown, R. A. Jackson, and T. N. Lahr, *J. Am. Chem. Soc.*, 1964, **86**, 2526.
394. J. A. Elvidge, J. Bloxsidge, J. R. Jones, and E. A. Evans, *Org. Magn. Reson.*, 1971, **3**, 127.
395. R. D. Newmark, S. Un, P. G. Williams, P. J. Carson, H. Morimoto, and M. P. Klein, *Proc. Natl. Acad. Sci. USA*, 1990, **87**, 583.
396. F. Alder and F. C. Yu, *Phys. Rev.*, 1951, **81**, 1067.
397. H. E. Weaver, B. M. Tolbert, and R. C. La Force, *J. Chem. Phys.*, 1955, **23**, 1956.
398. S. S. Dharmatti, K. J. Sundara Rao, and R. Vijayaraghavan, *Nuovo Cimento*, 1959, **11**, 656.
399. H. A. Christ, *Helv. Phys. Acta*, 1960, **33**, 572.
400. H. A. Christ, P. Diehl, H. R. Schneider, and H. Dahn, *Helv. Chim. Acta*, 1961, **44**, 865.
401. B. N. Figgis, R. G. Kidd, and R. S. Nyholm, *Proc. R. Soc. London*, 1962, **A269**, 469.
402. G. D. Mateescu and G. M. Benedikt, *J. Am. Chem. Soc.*, 1979, **101**, 3959.
403. G. A. Olah, A. L. Berrier, and G. K. S. Prakash, *J. Am. Chem. Soc.*, 1982, **104**, 2373.
404. R. A. Ogg, Jr., *J. Chem. Phys*, 1954, **22**, 1933.
405. J. N. Shoolery, *Discuss. Faraday Soc.*, 1955, **19**, 215.
406. R. Schaeffer, J. N. Shoolery, and R. Jones, *J. Am. Chem. Soc.*, 1957, **79**, 4606.
407. R. E. Williams, S. G. Gibbons, and I. Shapiro, *J. Chem. Phys.*, 1959, **30**, 320, 333.
408. H. C. Torrey, *Phys. Rev.*, 1963, **130**, 2306.
409. N. Bartlett, *Proc. Chem. Soc. London*, 1962, 218.
410. T. H. Brown, E. B. Whipple, and P. H. Verdier, *J. Chem. Phys.*, 1963, **38** 3029.
411. Von K. Seppelt and H. H. Rupp, *Z. Anorg. Allg. Chem.*, 1974, **409**, 331.
412. Von K. Seppelt and H. H. Rupp, *Z. Anorg. Allg. Chem.*, 1974, **409**, 338.
413. G. J. Schrobilgen, J. H. Holloway, P. Granger, and C. Brevard, *Inorg. Chem.*, 1978, **17**, 980.
414. G. K. Walters and W. M. Fairbank, *Phys. Rev.*, 1956, **103**, 262.
415. G. K. Walters and W. M. Fairbank, *Phys. Rev.*, 1956, **103**, 263.
416. M. Bernier and J. M. Delrieu, *Phys. Lett.*, 1977, **60A**, 156.
417. G. Deville, M. Bernier, and J. M. Delrieu, *Phys. Rev.*, 1979, **B19**, 5666.
418. L. J. Friedman, P. Millet, and R. C. Richardson, *Phys. Rev. Lett.*, 1981, **47**, 1078.
419. P. L. Kuhns, P. C. Hammel, O. Gonen, and J. S. Waugh, *Phys. Rev.*, 1987, **B35**, 4591.
420. R. K. Mazitov, P. Diehl, and R. Seydoux, *Chem. Phys. Lett.*, 1993, **201**, 543.
421. M. Saunders, H. A. Jiménez–Vázquez, R. J. Cross, S. Mroczkowski, D. I. Freedberg, and F. A. L. Anet, *Nature (London)*, 1994, **367**, 256.
422. W. G. Proctor and F. C. Yu, *Phys. Rev.*, 1951, **81**, 20.
423. R. Freeman, G. R. Murray, and R. E. Richards, *Proc. R. Soc. London*, 1957, **A242**, 455.
424. G. C. Levy, J. T. Bailey, and D. A. Wright, *J. Magn. Reson.*, 1980, **37**, 353.
425. G. B. Benedek, R. Englman, and J. A. Armstrong, *J. Chem. Phys.*, 1963, **39**, 3349.
426. R. P. H. Gasser and R. E. Richards, *Mol. Phys.*, 1960, **3**, 163.
427. T. H. Martin and B. M. Fung, *J. Phys. Chem.*, 1973, **77**, 637.
428. K. L. Craighead, P. Jones, and R. G. Bryant, *J. Phys. Chem.*, 1975, **79**, 1868.
429. D. D. Traficante and J. A. Simms, *Rev. Sci. Instrum.*, 1972, **43**, 1122.
430. E. A. C. Lucken, K. Noack, and D. F. Williams, *J. Chem. Soc. A*, 1967, 148.
431. A. Yamasaki, F. Yajima, and S. Fujiwara, *Inorg. Chim. Acta*, 1968, **2**, 39.
432. R. Ader and A. Loewenstein, *J. Magn. Reson.*, 1971, **5**, 248.
433. A. Schwenk, *Phys. Lett.*, 1970, **31A**, 513.
434. J. Kaufmann and A. Schwenk, *Phys. Lett.*, 1967, **24A**, 115.
435. A. Schwenk, *J. Magn. Reson.*, 1971, **5**, 376.
436. W. Sahm and A. Schwenk, *Z. Naturforsch., Teil A*, 1974, **29**, 1763.
437. E. Haslinger, W. Robien, K. Schlögl, and W. Weissensteiner, *J. Organomet. Chem.*, 1981, **218**, C11.
438. T. Jenny and W. von Philipsborn, *J. Organomet. Chem.*, 1981, **205**, 211.
439. L. Baltzer, E. D. Becker, B. A. Averill, J. M. Hutchinson, and O. A. Gansow, *J. Am. Chem. Soc.*, 1984, **106**, 2444.
440. B. E. Mann, *Chem. Commun.*, 1971, 1173.
441. I. Morishima, T. Inubushi, and M. Sato, *J. Chem. Soc., Chem. Commun.*, 1978, 106.
442. H. C. Lee, J. K. Gard, T. L. Brown, and E. Oldfield, *J. Am. Chem. Soc.*, 1985, **107**, 4087.
443. L. Baltzer, E. D. Becker, R. Tsuchudin, and O. A. Gansow, *J. Chem. Soc., Chem. Commun.*, 1985, 1040.
444. L. E. Drain, *Phys. Lett.*, 1964, **11**, 114.
445. H. Schumann, M. Meissner, and H.-J. Kroth, *Z. Naturforsch., Teil B*, 1980, **35**, 639.
446. N. Hao, J. McGlinchey, B. G. Sayer, and G. J. Schrobilgen, *J. Magn. Reson.*, 1982, **46**, 158.
447. G. E. Hartwell and A. Allerhand, *J. Am. Chem. Soc.*, 1971, **93**, 4415.
448. H. S. Gutowsky and B. R. McGarvey, *J. Chem. Phys.*, 1953, **21**, 1423.
449. J. E. Wertz and O. Jardetzky, *J. Chem. Phys.*, 1956, **25**, 357.
450. A. C. Plaush and R. R. Sharp, *J. Am. Chem. Soc.*, 1976, **98**, 7973.
451. G. E. Maciel, J. K. Hancock, L. F. Lafferty, P. A. Mueller, and W. K. Musker, *Inorg. Chem.*, 1966, **5**, 554.
452. E. G. Bloor and R. G. Kidd, *Can. J. Chem.*, 1968, **46**, 3425.
453. W. Sahm and A. Schwenk, *Z. Naturforsch., Teil A*, 1974, **29**, 1754.
454. J. S. Shih and A. I. Popov, *Inorg. Nucl. Chem. Lett.*, 1977, **13**, 105.
455. J. D. Halliday, R. E. Richards, and R. R. Sharp, *Proc. R. Soc. London*, 1969, **A313**, 45.
456. J. D. Halliday, H. D. W. Hill, and R. E. Richards, *Chem. Commun.*, 1969, 219.
457. F. W. Wehrli, *J. Magn. Reson.*, 1976, **23**, 527.
458. T. L. Brown, D. W. Dickerhoof, and D. A. Bafus, *J. Am. Chem. Soc.*, 1962, **84**, 1371.
459. M. A. Weiner and R. West, *J. Am. Chem. Soc.*, 1963, **85**, 485.
460. L. D. McKeever, R. Waack, M. A. Doran, and E. B. Baker, *J. Am. Chem. Soc.*, 1969, **91**, 1057.
461. B. Lindman, S. Forsén, and H. Lilja, *Chem. Script.*, 1977, **11**, 91.
462. O. Lutz, A. Schwenk, and A. Uhl, *Z. Naturforsch., Teil A*, 1973, **28**, 1534.

463. J. Banck and A. Schwenk, *Z. Phys.*, 1973, **265**, 165.
464. O. Lutz, A. Schwenk, and A. Uhl, *Z. Naturforsch., Teil A*, 1975, **30**, 1122.
465. H. Krüger, O. Lutz, and H. Oehler, *Phys. Lett.*, 1977, **62A**, 131.
466. O. Lutz and H. Oehler, *Z. Phys.*, 1978, **A288**, 11.
467. J. J. Delpuech, A. Peguy, P. Rubini, and J. Steinmetz, *Nouv. J. Chim.*, 1976, **1**, 133.
468. R. G. Bryant, *J. Magn. Reson.*, 1972, **6**, 159.
469. R. G. Bryant, *J. Am. Chem. Soc.*, 1969, **91**, 1870.
470. R. A. Kovar and G. L. Morgan, *J. Am. Chem. Soc.*, 1970, **92** 5067.
471. F. W. Wehrli, *J. Magn. Reson.*, 1978, **30**, 193.
472. W. D. Knight, *Phys. Rev.*, 1953, **92**, 539.
473. M. J. Weber and R. R. Allen, *J. Chem. Phys.*, 1963, **38**, 726.
474. Y. Masuda and T. Kanda, *J. Phys. Soc. Jpn.*, 1954, **9**, 82.
475. O. E. Myers, *J. Chem. Phys.*, 1958, **28**, 1027.
476. N. Bloembergen and T. J. Rowland, *Acta Metal.*, 1953, **1**, 731.
477. H. S. Gutowsky and B. R. McGarvey, *Phys. Rev.*, 1953, **91**, 81.
478. A. Pidcock, R. E. Richards, and L. M. Venanzi, *J. Chem. Soc. A*, 1968, 1970.
479. A. V. Zelewsky, *Helv. Chim. Acta*, 1968, **51** 803.
480. K. H. A. Ostoja-Starzewski and P. S. Pregosin, *Angew, Chem., Int. Ed. Engl.*, 1980, **19**, 316.
481. G. E. Maciel and M. Borzo, *J. Chem. Soc., Chem. Commun.*, 1973, 394.
482. R. J. Kostelnik and A. A. Bothner-By, *J. Magn. Reson.*, 1974, **14**, 141.
483. A. D. Cardin, P. D. Ellis, J. D. Odom, and J. W. Howard, Jr., *J. Am. Chem. Soc.*, 1975, **97**, 1672.
484. P. D. Ellis, R. R. Inners, and H. J. Jakobsen, *J. Phys. Chem.*, 1982, **86**, 1506.
485. P.C. Lauterbur and J. J. Burke, *Abs. Am. Chem. Soc. Meet.*, San Francisco, 1958.
486. J. J. Burke and P. C. Lauterbur, *J. Am. Chem. Soc.*, 1961, **83**, 326.
487. L. H. Piette and H. E. Weaver, *J. Chem. Phys.*, 1958, **28**, 735.
488. N. Flitcroft and H. D. Kaesz, *J. Am. Chem. Soc.*, 1963, **85**, 1377.
489. W. G. Proctor and F. C. Yu, *Phys. Rev.*, 1951, **81**, 20.
490. R. E. Dessy, T. J. Flautt, H. H. Jaffé, and G. F. Reynolds, *J. Chem. Phys.*, 1959, **30**, 1422.
491. W. G. Schneider and A. D. Buckingham, *Discuss. Faraday Soc.*, 1962, **34**, 147.
492. J. Kronenbitter, U. Schweizer, and A. Schwenk, *Z. Naturforsch., Teil A*, 1980, **35**, 319.
493. A. F. M. J. van der Ploeg, Jr., G. van Koten, and C. Brevard, *Inorg. Chem.*, 1982, **21**, 2878.
494. J. A. Seitchik, V. Jaccarino, and J. H. Wernick, *Phys. Rev.*, 1965, **138A**, 148.
495. T. H. Brown and P. J. Green, *J. Am. Chem. Soc.*, 1969, **91**, 3378.
496. T. H. Brown and P. J. Green, *J. Am. Chem. Soc.*, 1970, **92**, 2359.
497. E. M. Hyde, J. D. Kennedy, B. L. Shaw, and W. McFarlane, *J. Chem. Soc., Dalton Trans.*, 1977, 1571.
498. D. S. Gill, O. A. Gansow, F. J. Bennis, and K. C. Ott, *J. Magn. Reson.*, 1979, **35**, 459.
499. K.-D. Grüninger, A. Schwenk, and B. E. Mann, *J. Magn. Reson.*, 1980, **41**, 354.
500. M. Cocivera, G. Ferguson, R. E. Lenkinski, and P. Szczcinski, *J. Magn. Reson.*, 1982, **46**, 168.
501. A. Narath and D. C. Wallace, *Phys. Rev.*, 1962, **127**, 724.
502. J. Banck and A. Schwenk, *Z. Phys.*, 1975, **B20**, 75.
503. R. Acerete, C. F. Hammer, and L. C. W. Baker, *J. Am. Chem. Soc.*, 1979, **101**, 267.
504. D. E. O'Reilly, *J. Chem. Phys.*, 1960, **32**, 1007.
505. J. W. Akitt, N. N. Greenwood, B. L. Khandelwal, and G. D. Lester, *J. Chem. Soc., Dalton Trans.*, 1972, 604.
506. B. W. Epperlein and O. Lutz, *Z. Naturforsch., Teil A*, 1968, **23**, 1413.
507. J. W. Akitt, N. N. Greenwood, and G. D. Lester, *J. Chem. Soc.*, 1969, 803.
508. J. W. Akitt, N. N. Greenwood, and G. D. Lester, *Chem. Commun.*, 1969, 988.
509. W. G. Movius and N. A. Matwiyoff, *Inorg. Chem.*, 1967, **6**, 847.
510. L. D. Supran and N. Sheppard, *Chem. Commun.*, 1967, 832.
511. J. P. Oliver and C. A. Wilkie, *J. Am. Chem. Soc.*, 1967, **89**, 163.
512. J. F. Hon, *Mol. Phys.*, 1968, **15**, 57.
513. R. G. Kidd and D. R. Truax, *J. Am. Chem. Soc.*, 1968, **90**, 6867.
514. E. R. Malinowski, *J. Am. Chem. Soc.*, 1969, **91**, 4701.
515. H. Haraguchi and S. Fujiwara, *J. Phys. Chem.*, 1969, **73**, 3467.
516. R. G. Kidd and D. R. Truax, *Chem. Commun.*, 1969, 160.
517. D. J. Merryman, J. D. Corbett, and P. A. Edwards, *Inorg. Chem.*, 1975, **14**, 428.
518. H. A. Resing and M. Rubinstein, *J. Colloid Interface Sci.*, 1978, **64**, 48.
519. D. Mueller, W. Gessner, and A. R. Grimmer, *Z. Chem.*, 1977, **17**, 453.
520. H. L. Retcofsky and R. A. Friedel, *J. Am. Chem. Soc.*, 1972, **94**, 6579.
521. O. Lutz, A. Nolle, and A. Schwenk, *Z. Naturforsch., Teil A*, 1973, **28**, 1370.
522. P. S. Belton, I. J. Cox, and R. K. Harris, *J. Chem. Soc., Faraday Trans. 2*, 1985, **81**, 63.
523. O. W. Howarth and R. E. Richards, *J. Chem. Soc.*, 1965, 864.
524. J. A. S. Howell and K. C. Moss, *J. Chem. Soc. A*, 1971, 270.
525. D. Rehder, *Z. Naturforsch., Teil B*, 1977, **32**, 771.
526. L. P. Kazanskii and V. I. Spitsyn, *Dokl. Akad. Nauk SSSR*, 1975, **223**, 381.
527. S. E. O'Donnell and M. T. Pope, *J. Chem. Soc., Dalton Trans.*, 1976, 2290.
528. D. Rehder and J. Schmidt, *J. Inorg. Nucl. Chem.*, 1974, **36**, 333.
529. D. Rehder, W. L. Dorn, and J. Schmidt, *Transition Met. Chem.*, 1976, **1**, 74.
530. D. Rehder, *J. Magn. Reson.*, 1977, **25**, 177.
531. D. Rehder, *J. Organomet. Chem.*, 1972, **37**, 303.
532. M. D. Meadows, K. A. Smith, R. A. Kinsey, T. M. Rothgeb, R. P. Skarjune, and E. Oldfield, *Proc. Natl. Acad. Sci. USA*, 1982, **79**, 1351.
533. K. J. Packer and E. L. Muetterties, *J. Am. Chem. Soc.*, 1963, **85**, 3035.
534. O. Lutz and W. Steinkilberg, *Z. Naturforsch, Teil A*, 1974, **29**, 1467.
535. D. J. Burton and R. K. Harris, *J. Chem. Soc., Chem. Commun.*, 1982, 256.
536. H. M. McConnell and H. E. Weaver, *J. Chem. Phys.*, 1956, **25**, 307.
537. T. Yamamoto, H. Haraguchi, and S. Fujiwara, *J. Phys. Chem.*, 1970, **74**, 4369.
538. W. McFarlane and D. S. Rycroft, *J. Magn. Reson.*, 1976, **24**, 95.
539. B. D. Günther and R. P. Hultsch, *J. Magn. Reson.*, 1969, **1**, 609.
540. E. R. Andrew, J. L. Carolan, and P. J. Randall, *Phys. Lett.*, 1971, **35A**, 435.
541. A. Kawamori and G. Soda, *Mol. Phys.*, 1975, **29**, 1085.
542. G. Balimann and P. S. Pregosin, *J. Magn. Reson.*, 1977, **26**, 283.

543. V. W. Cohen, W. D. Knight, T. Wentink, Jr., and W. S. Koski, *Phys. Rev.*, 1950, **79**, 191.
544. W. G. Proctor and F. C. Yu, *Phys. Rev.*, 1951, **81**, 20.
545. S. S. Dharmatti and H. E. Weaver, *Phys. Rev.*, 1952, **87**, 675.
546. R. G. Kidd and R. W. Matthews, *J. Inorg. Nucl. Chem.*, 1975, **37**, 661.
547. O. Lutz, *Phys. Lett.*, 1969, **29A**, 58.
548. Y. A. Buslaev, S. P. Petrosyants, V. P. Tarasov, and V. I. Chagin, *Russ. J. Inorg. Chem.*, 1974, **19**, 975.
549. G. A. Melson, D. J. Olszanski, and E. T. Roach, *J. Chem. Soc., Chem. Commun.*, 1974, 229.
550. R. G. Kidd, R. W. Matthews, and H. G. Spinney, *J. Am. Chem. Soc.*, 1972, **94**, 6686.
551. R. R. Vold and R. L. Vold, *J. Magn. Reson.*, 1975, **19**, 365.
552. W. D. Kautt, H. Krüger, O. Lutz, H. Maier, and A. Nolle, *Z. Naturforsch., Teil A*, 1976, **31**, 351.
553. O. Lutz, A. Nolle, and P. Kroneck, *Z. Naturforsch., Teil A*, 1976, **31**, 454.
554. H. E. Walchli, *Phys. Rev.*, 1953, **90**, 331.
555. B. Cabane and C. Froidevaux, *Phys. Lett.*, 1968, **29A**, 512.
556. W. W. Warren, Jr., *Phys. Rev.*, 1972, **B6**, 2522.
557. H. C. E. McFarlane and W. McFarlane, *J. Chem. Soc., Dalton Trans.*, 1973, 2416.
558. T. Drakenberg, F. Fringuelli, S. Gronowitz, A. B. Hörnfeldt, I. Johnson, and A. Taticchi, *Chem. Script.*, 1976, **10**, 139.
559. Y. Egozy and A. Loewenstein, *J. Magn. Reson.*, 1969, **1**, 494.
560. B. W. Epperlein, H. Krüger, O. Lutz, A. Nolle, and W. Mayr, *Z. Naturforsch, Teil A*, 1975, **30**, 1237.
561. R. G. Kidd, *J. Magn. Reson.*, 1981, **45**, 88.
562. R. E. Dwek, Z. Luz, and M. Shporer, *J. Phys. Chem.*, 1970, **74**, 2232.
563. A. Kececi and D. Rehder, *Z. Naturforsch., Teil B*, 1981, **36**, 20.
564. A. Müller, E. Krickemeyer, H. Bögge, M. Penk, and D. Rehder, *Chimia*, 1986, **40**, 50.
565. C. Brevard and P. Granger, *J. Chem. Phys.*, 1981, **75**, 4175.
566. R. W. Dykstra and A. M. Harrison, *J. Magn. Reson.*, 1981, **45**, 108.
567. H. E. Weaver, *Phys. Rev.*, 1953, **89**, 923.
568. B. W. Epperlein, H. Krüger, O. Lutz, and A. Schwenk, *Z. Naturforsch., Teil A*, 1974, **29**, 1553.
569. W. G. Proctor and F. C. Yu, *Phys. Rev.*, 1951, **81**, 20.
570. Y. A. Buslaev, V. P. Tarasov, M. N. Buslaeva, and S. P. Petrosyants, *Dokl. Akad. Nauk SSSR*, 1973, **209**, 882.
571. H. Haraguchi, K. Fuwa, and S. Fujiwara, *J. Phys. Chem.*, 1973, **77**, 1497.
572. A. Fratiello, D. D. Davis, S. Peak, and R. E. Schuster, *Inorg. Chem.*, 1971, **10**, 1627.
573. T. H. Cannon and R. E. Richards, *Trans. Faraday Soc.*, 1966, **62**, 1378.
574. O. Lutz and H. Oehler, *Z. Phys.*, 1978, **A228**, 11.
575. E. Brun, J. Oeser, H. H. Staub, and C. G. Telschow, *Phys. Rev.*, 1954, **93**, 172.
576. J. Kaufmann, W. Sahm, and A. Schwenk, *Z. Naturforsch., Teil A*, 1971, **26**, 1384.
577. M. Takeda and O. Jardetzky, *J. Chem. Phys.*, 1957, **26**, 1346.
578. O. Jardetzky and C. D. Jardetzky, *J. Biol. Chem.*, 1958, **233**, 383.
579. F. A. Bovey and G. V. D. Tiers, *J. Am. Chem. Soc.*, 1959, **81**, 2870.
580. C. D. Jardetzky and O. Jardetzky, *Fed. Proc.*, 1958, **17**, 380.
581. C. D. Jardetzky and O. Jardetzky, *J. Am. Chem. Soc.*, 1960, **82**, 222.
582. C. D. Jardetzky, *J. Am. Chem. Soc.*, 1960, **82**, 229.
583. S. I. Chan, M. P. Schweizer, P. O. P. T'so, and G. K. Helmkamp, *J. Am. Chem. Soc.*, 1964, **86**, 4182.
584. C. Giessner-Prettre and B. Pullman, *C. R. Acad. Sci. Paris*, 1965, **261**, 2521.
585. C. Giessner-Prettre and B. Pullman, *J. Theor. Biol.*, 1970, **27**, 87.
586. C. Y. Hopkins and H. J. Bernstein, *Can. J. Chem.*, 1959, **37**, 775.
587. M. Saunders, A. Wishnia, and J. G. Kirkwood, *J. Am. Chem. Soc.*, 1957, **79**, 3289.
588. O. Jardetzky and C. D. Jardetzky, *J. Am. Chem. Soc.*, 1957, **79**, 5322.
589. M. Saunders and A. Wishnia, *Ann. N. Y. Acad. Sci.*, 1958, **70**, 870.
590. F. A. Bovey, G. V. D. Tiers, and G. Filipovich, *J. Polym. Sci.*, 1959, **38**, 73.
591. F. A. Bovey, *High Resolution NMR of Macromolecules*, Academic Press, New York, 1972, p. 286.
592. T. M. Shaw and R. H. Elsken, *J. Chem. Phys.*, 1950, **18**, 1113.
593. T. M. Shaw and K. J. Palmer, *Phys. Rev.*, 1951, **83**, 213.
594. T. M. Shaw and R. H. Elsken, *J. Chem. Phys.*, 1953, **21**, 565.
595. B. Jacobson, W. A. Anderson, and J. T. Arnold, *Nature (London)*, 1954, **173**, 772.
596. C. D. Jardetzky and O. Jardetzky, *Biochim. Biophys. Acta*, 1957, **26**, 668.
597. N. Davidson and R. Gold, *Biochim. Biophys. Acta*, 1957, **26**, 370.
598. H. Kon and N. Davidson, *J. Mol. Biol.*, 1959, **1**, 190.
599. R. Lumry, H. Matsumiya, F. A. Bovey, and A. Kowalsky, *J. Phys. Chem.*, 1961, **65**, 837.
600. J. Eisinger, R. G. Shulman, and W. E. Blumberg, *Nature (London)*, 1961, **192**, 963.
601. J. Eisinger, R. G. Shulman, and B. M. Szymanski, *J. Chem. Phys.*, 1962, **36**, 1721.
602. M. Cohn and J. S. Leigh, *Nature (London)*, 1962, **193**, 1037.
603. A. S. Mildvan and M. Cohn, *Adv. Enzymol.*, 1970, **33**, 1.
604. M. Cohn and J. Reuben, *Acc. Chem. Res.*, 1971, **4**, 214.
605. D. R. Burton, S. Forsén, G. Karlstrom, and R. A. Dwek, *Prog. NMR Spectrosc.*, 1979, **13**, 1.
606. M. Cohn and G. H. Reed, *Annu. Rev. Biochem.*, 1982, **51**, 365.
607. J. J. Led, E. Neesgaard, and J. T. Johansen, *FEBS Lett.*, 1982, **147**, 74.
608. B. Halle, T. Andersson, S. Forsén, and B. Lindman, *J. Am. Chem. Soc.*, 1981, **103**, 500.
609. O. Jardetzky and G. C. K. Roberts, *NMR in Molecular Biology*, Academic Press, New York, 1981.
610. E. D. Becker and R. B. Bradley, *J. Chem. Phys.*, 1959, **31**, 1413.
611. H. T. Miles, R. B. Bradley, and E. D. Becker, *Science*, 1963, **142**, 1569.
612. R. R. Shoup, H. T. Miles, and E. D. Becker, *Biochem. Biophys. Res. Commun.*, 1966, **23**, 194.
613. L. Katz and S. Penman, *J. Mol. Biol.*, 1966, **15**, 220.
614. M. Cohn and T. R. Hughes, *J. Biol. Chem.*, 1960, **235**, 3250.
615. M. Cohn and T. R. Hughes, *J. Biol. Chem.*, 1962, **237**, 176.
616. M. Sheinblatt, *J. Am. Chem. Soc.*, 1966, **88**, 2845.
617. A. Nakamura and O. Jardetzky, *Proc. Natl. Acad. Sci. USA*, 1967, **58**, 2212.
618. V. F. Bystrov, V. T. Ivanov, S. L. Portnova, T. A. Balashova, and Y. A. Ovchinnikov, *Tetrahedron*, 1973, **29**, 873.
619. C. M. Deber, F. A. Bovey, J. P. Carver and E. R. Blout, *J. Am. Chem. Soc.*, 1970, **92**, 6191.
620. V. J. Hruby, A. I. Brewster, and J. A. Glasel, *Proc. Natl. Acad. Sci. USA*, 1971, **68**, 450.
621. A. Stern, W. A. Gibbons, and L. C. Craig, *Proc. Natl. Acad. Sci. USA*, 1968, **61**, 734.
622. M. Goodman, A. S. Verdini, C. Toniolo, W. D. Phillips, and F. A. Bovey, *Proc. Natl. Acad. Sci. USA*, 1969, **64**, 444.
623. R. Schwyzer, J. P. Carrion, B. Gorup, H. Nolting, and A. Tun-Kyi, *Helv. Chim. Acta*, 1964, **47**, 441.

624. C. M. Deber, D. A. Torchia, S. C. K. Wong, and E. R. Blout, *Proc. Natl. Acad. Sci. USA*, 1972, **69**, 1825.
625. K. D. Kopple, M. Ohnishi, and A. Go, *J. Am. Chem. Soc.*, 1969, **91**, 4264.
626. T. P. Pitner, J. D. Glickson, R. Rowan, J. Dadok, and A. A. Bothner-By, *J. Am. Chem. Soc.*, 1975, **97**, 5917.
627. D. W. Urry and R. Walter, *Proc. Natl. Acad. Sci. USA*, 1971, **68**, 956.
628. J. Feeney, G. C. K. Roberts, J. H. Rockey, and A. S. V. Burgen, *Nature (London), New Biol.*, 1971, **232**, 108.
629. A. Kowalsky, *J. Biol. Chem.*, 1962, **237**, 1807.
630. A. Kowalsky, *Biochemistry*, 1965, **4**, 2382.
631. A. G. Redfield and R. K. Gupta, *Cold Spring Harbor Symp. Quant. Biol.*, 1971, **36**, 405.
632. M. Mandel, *J. Biol. Chem.*, 1965, **240**, 1586.
633. C. C. McDonald and W. D. Phillips, *J. Am. Chem. Soc.*, 1963, **85**, 3736.
634. J. H. Bradbury and H. A. Scheraga, *J. Am. Chem. Soc.*, 1966, **88**, 4240.
635. D. H. Meadows, J. L. Markley, J. S. Cohen, and O. Jardetzky, *Proc. Natl. Acad. Sci. USA*, 1967, **58**, 1307.
636. J. S. Cohen, *Nature (London)*, 1969, **223**, 43.
637. J. J. Fischer and O. Jardetzky, *J. Am. Chem. Soc.*, 1965, **87**, 3237.
638. Y. Fraenkel, G. Navon, A. Aronheim, and J. M. Gershoni, *Biochemistry*, 1990, **29**, 2617.
639. J. J. Katz and H. L. Crespi, *Science*, 1966, **151**, 1187.
640. H. L. Crespi, R. M. Rosenberg, and J. J. Katz, *Science*, 1968, **161**, 795.
641. J. L. Markley and O. Jardetzky, *J. Mol. Biol.*, 1970, **50**, 223.
642. D. M. LeMaster, *Methods Enzymol.*, 1989, **177**, 23.
643. C. C. McDonald, W. D. Phillips, and S. Penman, *Science*, 1964, **144**, 1234.
644. J. P. McTague, V. Ross, and J. H. Gibbs, *Biopolymers*, 1964, **2**, 163.
645. O. Jardetzky, *Adv. Chem. Phys.*, 1964, **7**, 499.
646. C. C. McDonald, W. D. Phillips, and J. Penswick, *Biopolymers*, 1965, **3**, 609.
647. I. C. P. Smith, T. Yamane, and R. G. Shulman, *Science*, 1968, **159**, 1360.
648. B. J. Blackburn, A. A. Grey, I. C. P. Smith, and F. E. Hruska, *Can. J. Chem.*, 1970, **48**, 2866.
649. C. C. McDonald and W. D. Phillips, *J. Am. Chem. Soc.*, 1967, **89**, 6332.
650. C. C. McDonald and W. D. Phillips, *J. Am. Chem. Soc.*, 1969, **91**, 1513.
651. E. M. Bradbury and C. Crane-Robinson, *Nature (London)*, 1968, **220**, 1079.
652. D. R. Kearns, D. J. Patel, and R. G. Shulman, *Nature (London)*, 1971, **229**, 338.
653. J. D. Glickson, J. Dadok, and G. R. Marshall, *Biochemistry*, 1974, **13**, 11.
654. S. Takahashi, A. K.-L. C. Lin, and C. Ho, *Biophys. J.*, 1982, **39**, 33.
655. J. Schaefer, *J. Magn. Reson.*, 1972, **6**, 670.
656. I. D. Campbell, C. M. Dobson, G. Jeminet, and R. J. P. Williams, *FEBS Lett.*, 1974, **49**, 115.
657. S. L. Patt and B. D. Sykes, *J. Chem. Phys.*, 1972, **56**, 3182.
658. F. W. Benz, J. Feeney, and G. C. K. Roberts, *J. Magn. Reson.*, 1972, **8**, 114.
659. P. C. M. van Zijl and C. T. W. Moonen, *J. Magn. Reson.*, 1990, **87**, 18.
660. M. Cohn, *Acc. Chem. Res.*, 1982, **15**, 326.
661. G. A. Gray, *CRC Crit. Rev. Biochem. Mol. Biol.*, 1973, **1**, 247.
662. U. Sequin and A. I. Scott, *Science*, 1974, **186**, 101.
663. M. Tanabe and G. Detre, *J. Am. Chem. Soc.*, 1966, **88**, 4515.
664. M. Tanabe, H. Seto, and L. R. Johnson, *J. Am. Chem. Soc.*, 1970, **92**, 2157.
665. W. J. Horsley, H. Sternlicht, and J. S. Cohen, *Biochem. Biophys. Res. Commun*, 1969, **37**, 47.
666. W. J. Horsley, H. Sternlicht, and J. S. Cohen, *J. Am. Chem. Soc.*, 1970, **92**, 680.
667. P. C. Lauterbur, *Appl. Spectrosc.*, 1970, **24**, 450.
668. A. Allerhand, D. W. Cochran, and D. Doddrell, *Proc. Natl. Acad. Sci. USA*, 1970, **67**, 1093.
669. A. Allerhand, R. F. Childers, and E. Oldfield, *Ann. N.Y. Acad. Sci.*, 1973, **222**, 764.
670. D. Chapman and N. J. Salsbury, *Trans. Faraday Soc.*, 1966, **62**, 2607.
671. Z. Veksli, N. J. Salsbury, and D. Chapman, *Biochim. Biophys. Acta*, 1969, **183**, 434.
672. J. C. Metcalfe, N. J. M. Birdsall, J. Feeney, A. G. Lee, Y. K. Levine, and P. Partington, *Nature (London)*, 1971, **233**, 199.
673. J. Charvolin, P. Manneville, and B. Deloche, *Chem. Phys. Lett.*, 1973, **23**, 345.
674. E. Oldfield, D. Chapman, and W. Derbyshire, *FEBS Lett.*, 1971, **16**, 102.
675. A. Seelig and J. Seelig, *Biochemistry*, 1974, **13**, 4839.
676. G. W. Stockton, C. F. Polnaszek, L. C. Leitch, A. P. Tulloch, and I. C. P. Smith, *Biochem. Biophys. Res. Commun.*, 1974, **60**, 844.
677. J. H. Davis, K. R. Jeffrey, M. Bloom, M. I. Valic, and T. P. Higgs, *Chem. Phys. Lett.*, 1976, **42**, 390.
678. J. Urbina and J. S. Waugh, *Ann. N. Y. Acad. Sci.*, 1973, **222**, 733.
679. D. Chapman, E. Oldfield, D. Doskočilová, and B. Schneider, *FEBS Lett.*, 1972, **25**, 261.
680. J. Forbes, C. Husted, and E. Oldfield, *J. Am. Chem. Soc.*, 1988, **110**, 1059.
681. C. W. B. Lee, S. K. Das Gupta, J. Mattai, G. G. Shipley, O. H. Abdel-Mageed, A. Makriyannis, and R. G. Griffin, *Biochemistry*, 1989, **28**, 5000.
682. A. E. McDermott, F. Creuzet, R. G. Griffin, L. E. Zawadzke, Q.-Z. Ye, and C. T. Walsh, *Biochemistry*, 1990, **29**, 5767.
683. T. Gullion and J. Schaefer, *J. Magn. Reson.*, 1989, **81**, 196.
684. J. Jeener, Pulse Pair Techniques in High Resolution NMR, in *NMR and More*, ed. M. Goldman and M. Porneuf, Les Editions de Physique, Les Ulis, France, 1994, pp. 265–278.
685. A. Kumar, D. Welti, and R. R. Ernst, *J. Magn. Reson.*, 1975, **18**, 69.
686. L. Müller, A. Kumar, and R. R. Ernst, *J. Chem. Phys.*, 1975, **63**, 5490.
687. W. P. Aue, E. Bartholdi, and R. R. Ernst, *J. Chem. Phys.*, 1976, **64**, 2229.
688. G. Bodenhausen, R. Freeman, and G. A. Morris, *J. Magn. Reson.*, 1976, **23**, 171.
689. G. Bodenhausen, R. Freeman, R. Niedermeyer, and D. L. Turner, *J. Magn. Reson.*, 1976, **24**, 291.
690. G. Bodenhausen, R. Freeman, and D. L. Turner, *J. Chem. Phys.*, 1976, **65**, 839.
691. R. Freeman, S. P. Kempsell, and M. H. Levitt, *J. Magn. Reson.*, 1979, **34**, 663.
692. L. Müller, A. Kumar, and R. R. Ernst, *J. Magn. Reson.*, 1977, **25**, 383.
693. A. Bax and R. Freeman, *J. Am. Chem. Soc.*, 1982, **104**, 1099.
694. W. P. Aue, J. Karhan, and R. R. Ernst, *J. Chem. Phys.*, 1976, **64**, 4226.
695. A. Bax, A. F. Mehlkopf, and J. Smidt, *J. Magn. Reson.*, 1979, **35**, 373.
696. K. Nagayama, P. Bachmann, K. Wüthrich, and R. R. Ernst, *J. Magn. Reson.*, 1978, **31**, 133.
697. A. Bax, R. Freeman, and G. A. Morris, *J. Magn. Reson.*, 1981, **43**, 333.
698. O. W. Sørenson, G. W. Eich, M. H. Levitt, G. Bodenhausen, and R. R. Ernst, *Prog. NMR Spectrosc.*, 1983, **16**, 163.

699. K. Nagayama, K. Wüthrich, and R. R. Ernst, *Biochem. Biophys. Res. Commun.*, 1979, **90**, 305.
700. D. J. States, R. A. Haberkorn, and D. J. Ruben, *J. Magn. Reson.*, 1982, **48**, 286.
701. D. Marion and K. Wüthrich, *Biochem. Biophys. Res. Commun.*, 1983, **113**, 967.
702. A. Bax and R. Freeman, *J. Magn. Reson.*, 1981, **44**, 542.
703. A. Kumar, R. V. Hosur, and K. Chandrasekhar, *J. Magn. Reson.*, 1984, **60**, 143.
704. J. Cavanagh and J. Keeler, *J. Magn. Reson.*, 1987, **71**, 561.
705. H. Oschkinat, A. Pastore, P. Pfändler, and G. Bodenhausen, *J. Magn. Reson.*, 1986, **69**, 559.
706. U. Piantini, O. W. Sørensen, and R. R. Ernst, *J. Am. Chem. Soc.*, 1982, **104**, 6800.
707. C. Griesinger, O. W. Sørensen, and R. R. Ernst, *J. Am. Chem. Soc.*, 1985, **107**, 6394.
708. C. Griesinger, O. W. Sørensen, and R. R. Ernst, *J. Chem. Phys.*, 1986, **85**, 6837.
709. L. Müller, *J. Magn. Reson.*, 1987, **72**, 191.
710. M. H. Levitt, C. Radloff, and R. R. Ernst, *Chem. Phys. Lett.*, 1985, **114**, 435.
711. B. T. Farmer II and L. R. Brown, *J. Magn. Reson.*, 1987, **71**, 365.
712. G. Eich, G. Bodenhausen, and R. R. Ernst, *J. Am. Chem. Soc.*, 1982, **104**, 3731.
713. L. Braunschweiler and R. R. Ernst, *J. Magn. Reson.*, 1983, **53**, 521.
714. A. Bax and D. G. Davis, *J. Magn. Reson.*, 1985, **65**, 355.
715. A. A. Maudsley, L. Müller, and R. R. Ernst, *J. Magn. Reson.*, 1977, **28**, 463.
716. G. Bodenhausen and R. Freeman, *J. Magn. Reson.*, 1977, **28**, 471.
717. G. Bodenhausen and R. Freeman, *J. Am. Chem. Soc.*, 1978, **100**, 320.
718. H. Kessler, C. Griesinger, J. Zarbock, and H. R. Loosli, *J. Magn, Reson.*, 1984, **57**, 331.
719. C. Bauer, R. Freeman, and S. Wimperis, *J. Magn. Reson.*, 1984, **58**, 526.
720. A. Bax, *J. Magn. Reson.*, 1983, **53**, 517.
721. J. R. Garbow, D. P. Weitekamp, and A. Pines, *Chem. Phys. Lett.*, 1982, **93**, 504.
722. P. H. Bolton, *J. Magn. Reson.*, 1982, **48**, 336.
723. A. Bax, *J. Magn. Reson.*, 1983, **53**, 149.
724. H. Kogler, O. W. Sørensen, G. Bodenhausen, and R. R. Ernst, *J. Magn. Reson.*, 1983, **55**, 157.
725. J. Jeener, B. H. Meier, P. Bachmann, and R. R. Ernst, *J. Chem. Phys.*, 1979, **71**, 4546.
726. B. H. Meier and R. R. Ernst, *J. Am. Chem. Soc.*, 1979, **101**, 6441.
727. S. Macura and R. R. Ernst, *Mol. Phys.*, 1980, **41**, 95.
728. A. Kumar, R. R. Ernst, and K. Wüthrich, *Biochem. Biophys. Res. Commun.*, 1980, **95**, 1.
729. A. A. Bothner-By, R. L. Stephens, J. Lee, C. D. Warren, and R. W. Jeanloz, *J. Am. Chem. Soc.*, 1984, **106**, 811.
730. A. Bax and D. G. Davis, *J. Magn. Reson.*, 1985, **63**, 207.
731. C. Griesinger, G. Otting, K. Wüthrich, and R. R. Ernst, *J. Am. Chem. Soc.*, 1988, **110**, 7870.
732. V. W. Hughes and J. S. Geiger, *Phys. Rev.*, 1955, **99**, 1842.
733. W. Anderson, *Phys. Rev.*, 1956, **104**, 850.
734. J. I. Kaplan and S. Meiboom, *Phys. Rev.*, 1957, **106**, 499.
735. S. Yatsiv, *Phys. Rev.*, 1958, **113**, 1522.
736. W. A. Anderson, R. Freeman, and C. A. Reilly, *J. Chem. Phys.*, 1963, **39**, 1518.
737. A. Wokaun and R. R. Ernst, *Chem. Phys. Lett.*, 1977, **52**, 407.
738. A. Wokaun and R. R. Ernst, *Mol. Phys.*, 1978, **36**, 317.
739. A. Wokaun and R. R. Ernst, *Mol. Phys.*, 1979, **38**, 1579.
740. L. Braunschweiler, G. Bodenhausen, and R. R. Ernst, *Mol. Phys.*, 1983, **48**, 535.
741. S. Vega, T. W. Shattuck, and A. Pines, *Phys. Rev. Lett.*, 1976, **37**, 43.
742. S. Vega and A. Pines, *J. Chem. Phys.*, 1977, **66**, 5624.
743. G. Drobny, A. Pines, S. Sinton, D. Weitekamp, and D. Wemmer, *Faraday Symp. Chem. Soc.*, 1979, **13**, 49.
744. S. Vega, T. W. Shattuck, and A. Pines, *Phys. Rev.*, 1980 **A22**, 638.
745. H. Hatanaka, T. Terao, and T. Hashi, *J. Phys. Soc. Jpn.*, 1975, **39**, 835.
746. H. Hatanaka and T. Hashi, *J. Phys. Soc. Jpn.*, 1975, **39**, 1139.
747. W. S. Warren, D. P. Weitekamp, and A. Pines, *J. Chem. Phys.*, 1980, **73**, 2084.
748. A. Bax, R. Freeman, and S. P. Kempsell, *J. Magn. Reson.*, 1980, **41**, 349.
749. A. Bax, R. Freeman, and S. P. Kempsell, *J. Am. Chem. Soc.*, 1980, **102**, 4849.
750. A. Bax, R. Freeman, and T. A. Frenkiel, *J. Am. Chem. Soc.*, 1981, **103**, 2102
751. A. Bax, R. Freeman, T. A. Frenkiel, and M. H. Levitt, *J. Magn. Reson.*, 1981, **43**, 478.
752. T. H. Mareci and R. Freeman, *J. Magn. Reson.*, 1982, **48**, 158.
753. M. H. Levitt and R. R. Ernst, *Mol. Phys.*, 1983, **50**, 1109.
754. A. A. Maudsley and R. R. Ernst, *Chem. Phys. Lett.*, 1977, **50**, 368.
755. G. Bodenhausen and D. J. Ruben, *Chem. Phys. Lett.*, 1980, **69**, 185.
756. L. Müller, *J. Am. Chem. Soc.*, 1979, **101**, 4481.
757. A. Bax, R. H. Griffey, and B. L. Hawkins, *J. Magn. Reson.*, 1983, **55**, 301.
758. M. R. Bendall, D. T. Pegg, and D. M. Doddrell, *J. Magn. Reson.*, 1983, **52**, 81.
759. A. G. Palmer III, J. Cavanagh, P. E. Wright, and M. Rance. *J. Magn. Reson.*, 1991, **93**, 151.
760. A. Bax, A. Aszalos, Z. Dinya, and K. Sudo, *J. Am. Chem. Soc.*, 1986, **108**, 8056.
761. G. Bodenhausen and R. R. Ernst, *J. Magn. Reson.*, 1981, **45**, 367.
762. G. Bodenhausen and R. R. Ernst, *J. Am. Chem. Soc.*, 1982, **104**, 1304.
763. P. H. Bolton, *J. Magn. Reson.*, 1982, **46**, 343.
764. G. W. Vuister and R. Boelens, *J. Magn. Reson.*, 1987, **73**, 328.
765. C. Griesinger, O. W. Sørensen, and R. R. Ernst, *J. Magn. Reson.*, 1987, **73**, 574.
766. S. Davies, J. Friedrich, and R. Freeman, *J. Magn. Reson.*, 1987, **75**, 540.
767. S. Davies, J. Friedrich, and R. Freeman, *J. Magn. Reson.*, 1988, **76**, 555.
768. J. Friedrich, S. Davies, and R. Freeman, *Mol. Phys.*, 1988, **64**, 691.
769. D. F. Lowry, A. G. Redfield, L. P. McIntosh, and F. W. Dahlquist, *J. Am. Chem. Soc.*, 1988, **110**, 6885.
770. A. Bax, P. G. deJong, A. F. Mehlkopf, and J. Smidt, *Chem. Phys. Lett.*, 1980, **69**, 567.
771. P. Barker and R. Freeman, *J. Magn. Reson.*, 1985, **64**, 334.
772. C. J. R. Counsell, M. H. Levitt, and R. R. Ernst, *J. Magn. Reson.*, 1985, **64**, 470.
773. B. K. John, D. Plant, S. L. Heald, and R. E. Hurd, *J. Magn. Reson.*, 1991, **94**, 664.
774. A. L. Davis, R. Boelens, and R. Kaptein, *J. Biomol. NMR*, 1992, **2**, 395.
775. A. Bax and S. S. Pochapsky, *J. Magn. Reson.*, 1992, **99**, 638.
776. M. Piotto, V. Saudek, and V. Sklenar, *J. Biomol. NMR*, 1992, **2**, 661.
777. R. K. Hester, J. L. Ackerman, B. L. Neff, and J. S. Waugh, *Phys. Rev. Lett.*, 1976, **36**, 1081.
778. E. F. Rybaczewski, B. L. Neff, J. S. Waugh, and J. S. Sherfinski, *J. Chem. Phys.*, 1977, **67**, 1231.

779. M. Linder, A. Höhener, and R. R. Ernst, *J. Chem. Phys.*, 1980, **73**, 4959.
780. M. G. Munowitz, R. G. Griffin, G. Bodenhausen, and T. H. Huang, *J. Am. Chem. Soc.*, 1981, **103**, 2529.
781. A. C. Kolbert, M. H. Levitt, and R. G. Griffin, *J. Magn. Reson.*, 1989, **85**, 42.
782. N. M. Szeverenyi, M. J. Sullivan, and G. E. Maciel, *J. Magn. Reson.*, 1982, **47**, 462.
783. C. S. Schmidt, B. Blümich, and H. W. Spiess, *J. Magn. Reson.*, 1988, **79**, 269.
784. C. M. Carter, D. W. Alderman, and D. M. Grant, *J. Magn. Reson.*, 1985, **65**, 183.
785. A. Bax, N. M. Szeverenyi, and G. E. Maciel, *J. Magn. Reson.*, 1983, **52**, 147.
786. A. C. Kolbert, H. J. M. de Groot, and R. G. Griffin, *J. Magn. Reson.*, 1989, **85**, 60.
787. R. Tycko, G. Dabbagh, and P. A. Mireau, *J. Magn. Reson.*, 1989, **85**, 265.
788. Z. Gan, *J. Am. Chem. Soc.*, 1992, **114**, 8307.
789. J. Schaefer, R. A. McKay, and E. O. Stejskal, *J. Magn. Reson.*, 1979, **34**, 443.
790. J. Schaefer, E. O. Stejskal, and R. A. McKay, *ACS Symp. Ser.*, 1982, **191**, 187.
791. E. Odeblad and G. Lindström, *Acta Radiol.*, 1955, **43**, 469.
792. E. Odeblad, B. N. Bhar, and G. Lindström, *Arch. Biochem. Biophys.*, 1956, **63**, 221.
793. E. Odeblad, *Acta Isot.*, 1961, **1**, 37.
794. E. Odeblad, *Acta Obstet. Gynecol. Scand.*, 1968, **47**, Suppl. 8, 39.
795. C. B. Bratton, A. L. Hopkins, and J. W. Weinberg, *Science*, 1965, **147**, 738.
796. R. Mathur-de Vré, *Prog. Biophys. Mol. Biol.*, 1979, **35**, 103.
797. G. N. Ling, *A Physical Theory of the Living State: The Association–Induction Hypothesis*, Blaisdell, New York, 1962.
798. F. W. Cope, *Proc. Natl. Acad. Sci. USA*, 1965, **54**, 225.
799. F. W. Cope, *J. Gen. Physiol.*, 1967, **50**, 1353.
800. H. J. C. Yeh, F. J. Brinley Jr., and E. D. Becker, *Biophys. J.*, 1973, **13**, 56.
801. M. Shporer and M. M. Civan, *Biophys. J.*, 1972, **12**, 114.
802. H. J. C. Berendsen and H. T. Edzes, *Ann. N. Y. Acad. Sci.*, 1973, **204**, 459.
803. R. K. Gupta and P. Gupta, *J. Magn. Reson.*, 1982, **47**, 344.
804. S. C. Chu, M. M. Pike, E. T. Fossel, T. W. Smith, J. A. Balschi, and C. S. Springer, Jr., *J. Magn. Reson.*, 1984, **56**, 33.
805. R. Damadian, *Science*, 1971, **171**, 1151.
806. D. P. Hollis, L. A. Saryan, and H. P. Morris, *Johns Hopkins Med. J.*, 1972, **131**, 441.
807. P. A. Bottomley, C. J. Hardy, R. E. Argersinger, and G. Allen-Moore, *Med. Phys.*, 1987, **14**, 1.
808. N. A. Matwiyoff and T. E. Needham, *Biochem. Biophys. Res. Commun.*, 1972, **49**, 1158.
809. R. T. Eakin, L. O. Morgan, C. T. Gregg, and N. A. Matwiyoff, *FEBS Lett.*, 1972, **28**, 259.
810. P. Dea, S. I. Chan, and F. J. Dea, *Science*, 1972, **175**, 206.
811. R. B. Moon and J. H. Richards, *J. Biol. Chem.*, 1973, **248**, 7276.
812. T. O. Henderson, A. J. R. Costello, and A. Omachi, *Proc. Natl. Acad. Sci. USA*, 1974, **71**, 2487.
813. D. I. Hoult, S. J. W. Busby, D. G. Gadian, G. K. Radda, R. E. Richards, and P. J. Seeley, *Nature (London)*, 1974, **252**, 285.
814. M. Llinas, K. Wüthrich, W. Schwotzer, and W. von Philipsborn, *Nature (London)*, 1975, **257**, 817.
815. J. M. Salhany, T. Yamane, R. G. Shulman, and S. Ogawa, *Proc. Natl. Acad. Sci USA*, 1975, **72**, 4966.
816. T. R. Brown, K. Ugurbil, and R. G. Shulman, *Proc. Natl. Acad. Sci. USA*, 1977, **74**, 5551.
817. K. Ugurbil, T. R. Brown, J. A. den Hollander, P. Glynn, and R. G. Shulman, *Proc. Natl. Acad. Sci. USA*, 1978, **75**, 3742.
818. S. M. Cohen, S. Ogawa, and R. G. Shulman, *Proc. Natl. Acad. Sci. USA*, 1979, **76**, 1603.
819. J. K. Barton, J. A. den Hollander, J. J. Hopfield, and R. G. Shulman, *J. Bacteriol.*, 1982, **151**, 177.
820. R. G. Shulman, T. R. Brown, K. Ugurbil, S. Ogawa, S. M. Cohen, and J. A. den Hollander, *Science*, 1979, **205**, 160.
821. A. Daniels, A. Korda, P. Tanswell. A. Williams, and R. J. P. Williams, *Proc. R. Soc. London*, 1974, **B187**, 353.
822. R. P. Casey, D. Njus, G. K. Radda, and P. A. Sehr, *Biochemistry*, 1977, **16**, 972.
823. H. B. Pollard, H. Shindo, C. E. Creutz, C. J. Pazoles, and J. S. Cohen, *J. Biol. Chem.*, 1979, **254**, 1170.
824. F. E. Evans and N. O. Kaplan, *Proc. Natl. Acad. Sci. USA*, 1977, **74**, 4909.
825. R. K. Gupta, J. L. Benovic, and Z. B. Rose, *J. Biol. Chem.*, 1978, **253**, 6172.
826. P. Styles, C. Grathwohl, and F. F. Brown, *J. Magn. Reson.*, 1979, **35**, 329.
827. P. C. M. van Zijl and C. T. W. Moonen, *NMR Basic Principles Prog.*, 1992, **26**, 67.
828. F. F. Brown, I. D. Campbell, P. W. Kuchel, and D. C. Rabenstein, *FEBS Lett.*, 1977, **82**, 12.
829. D. L. Rabenstein, *J. Biochem. Biophys. Meth.*, 1984, **9**, 277.
830. C. Nicolau, H.-D. Klenk, A. Reimann, K. Hildenbrand, and H. Bauer, *Biochim. Biophys. Acta*, 1978, **511**, 83.
831. P. F. Agris and I. D. Campbell, *Science*, 1982, **216**, 1325.
832. C. E. Mountford, G. Grossman, P. A. Gatenby, and R. M. Fox, *Br. J. Cancer*, 1980, **41**, 1000.
833. M. Bloom, K. T. Holmes, C. E. Mountford, and P. G. Williams, *J. Magn. Reson.*, 1986, **69**, 73.
834. O. Kaplan, P. C. M. van Zijl, and J. S. Cohen, *NMR Basic Principles Prog.*, 1992, **28**, 3.
835. P. C. M. van Zijl, C. T. W. Moonen, P. Faustino, J. Pekar, O. Kaplan, and J. S. Cohen, *Proc. Natl. Acad. Sci. USA*, 1991, **88**, 3228.
836. G. Navon, S. Ogawa, R. G. Shulman, and T. Yamane, *Proc. Natl. Acad. Sci. USA*, 1977, **74**, 888.
837. R. S. Balaban, D. G. Gadian, G. K. Radda, and G. G. Wong, *Anal. Biochem.*, 1981, **116**, 450.
838. K. Ugurbil, D. L. Guernsey, T. R. Brown, P. Glynn, N. Tobkes, and I. S. Edelman, *Proc. Natl. Acad. Sci. USA*, 1981, **78**, 4843.
839. M. J. Dawson, D. G. Gadian, and D. R. Wilkie, *Nature (London)*, 1978, **274**, 861.
840. P. B. Garlick, G. K. Radda, P. J. Seeley, and B. Chance, *Biochem. Biophys. Res. Commun.*, 1977, **74**, 1256.
841. D. P. Hollis, *Abusing Cancer Science*, Strawberry Fields Press, Chehalis, WA, 1987.
842. W. E. Jacobus, G. J. Taylor, IV, D. P. Hollis, and R. L. Nunnally, *Nature (London)*, 1977, **256**, 756.
843. P. A. Sehr, G. K. Radda, P. J. Bore, and R. A. Sells, *Biochem. Biophys. Res. Commun.*, 1977, **77**, 195.
844. S. M. Cohen, R. G. Shulman, and A. C. McLaughlin, *Proc. Natl. Acad. Sci. USA*, 1979, **76**, 4808.
845. J. A. Jackson and W. H. Langham, *Rev. Sci. Instrum.*, 1968, **39**, 510.
846. I. D. Weisman, L. H. Bennett, L. R. Maxwell, M. W. Woods, and D. Burk, *Science*, 1972, **178**, 1288.
847. T. H. Grove, J. J. H. Ackerman, G. K. Radda, and P. J. Bore, *Proc. Natl. Acad. Sci. USA*, 1980, **77**, 299.
848. J. J. H. Ackerman, T. H. Grove, G. G. Wong, D. G. Gadian, and G. K. Radda, *Nature (London)*, 1980, **283**, 167.
849. J. R. Singer, *Science*, 1959, **130**, 1652.
850. M. R. Bendall and R. E. Gordon, *J. Magn. Reson.*, 1983, **53**, 365.
851. B. Chance, Y. Nakase, M. Bond, J. S. Leigh Jr., and G. McDonald, *Proc. Natl. Acad. Sci. USA*, 1978, **75**, 4925.
852. B. D. Ross, G. K. Radda, D. G. Gadian, G. Rocker, M. Esiri, and J. Falconer-Smith, *N. Engl. J. Med.*, 1981, **304**, 1338.

853. L. O. Sillerud and R. G. Shulman, *Biochemistry*, 1983, **22**, 1087.
854. R. Gabillard, *C. R. Acad. Sci. Paris*, 1951 **232**, 1551.
855. V. Kudravcev, *Annual Report, Laboratory of Technical Development, National Heart Institute*, 1960.
856. C.-N. Chen and D. I. Hoult, *Biomedical Magnetic Resonance Technology*, Adam Hilger, Bristol, UK, 1989, pp. 38–40.
857. D. P. Hollis, *Abusing Cancer Science*, Strawberry Fields Press, Chehalis, Washington, 1987, pp. 145–148.
858. P. C. Lauterbur, *Nature (London)*, 1973, **242**, 190.
859. P. C. Lauterbur, In *Proceedings of the First International Conference on Stable Isotopes in Chemistry, Biology and Medicine*, ed. P. D. Klein and S. V. Peterson, Argonne National Laboratory, Argonne, IL, 1973, pp. 255–260.
860. P. C. Lauterbur, *Pure Appl. Chem.*, 1974, **40**, 149.
861. W. S. Hinshaw, *Phys. Lett.*, 1974, **48A**, 87.
862. W. S. Hinshaw, *J. Appl. Phys.*, 1976, **47**, 3709.
863. A. N. Garroway, P. K. Grannell, and P. Mansfield, *J. Phys. C*, 1974, **7**, L457.
864. D. I. Hoult, *J. Magn. Reson.*, 1977, **26**, 165.
865. D. I. Hoult, *J. Magn. Reson.*, 1979, **35**, 69.
866. W. A. Edelstein, J. M. S. Hutchison, G. Johnson, and T. Redpath, *Phys. Med. Biol.*, 1980, **25**, 751.
867. D. I. Hoult, *J. Magn. Reson.*, 1979, **33**, 183.
868. A. Haase, C. Malloy, and G. K. Radda, *J. Magn. Reson.*, 1983, **55**, 164.
869. P. Mansfield and P. K. Grannell, *J. Phys. C*, 1973, **6**, L422.
870. P. Mansfield, P. K. Grannell, A. N. Garroway, and D. C. Stalker, *1st Specialized Colloque AMPERE*, Krakow, 1973, p. 16.
871. P. Mansfield and P. K. Grannell, *Phys. Rev.*, 1975, **B12**, 3618.
872. P. Mansfield, A. A. Maudsley, and T. Baines, *J. Phys. E*, 1976, **9**, 271.
873. P. Mansfield and A. A. Maudsley, *Phys. Med. Biol.*, 1976, **21**, 847.
874. P. Mansfield and A. A. Maudsley, *Br. J. Radiol.*, 1977, **50**, 188.
875. P. Mansfield, *J. Phys. C*, 1977, **10**, L55.
876. P. Mansfield and I. L. Pykett, *J. Magn. Reson.*, 1978, **29**, 355.
877. P. Mansfield and I. L. Pykett, *Abs. 19th Exp. NMR Conf.* Blacksburg, VA, 1978.
878. P. Mansfield, P. G. Morris, R. J. Ordidge, I. L. Pykett, V. Bangert, and R. E. Coupland, *Philos. Trans. R. Soc. London*, 1980, **B289**, 503.
879. R. J. Ordidge, P. Mansfield, M. Doyle, and R. E. Coupland, *Radiology*, 1982, **142**, 244.
880. P. Mansfield and B. Chapman, *J. Phys. E*, 1986, **19**, 541.
881. M. K. Stehling, R. Turner, and P. Mansfield, *Science*, 1991, **254**, 43.
882. R. Damadian, M. Goldsmith, and L. Minkoff, *Physiol. Chem. Phys.*, 1977, **9**, 97.
883. R. Damadian, L. Minkoff, M. Goldsmith, and J. A. Koutcher, *Naturwissenschaften*, 1978, **65**, 250.
884. R. Damadian, M. Goldsmith, and L. Minkoff, in *NMR in Medicine*, ed. R. Damadian, Springer-Verlag, Berlin, 1981, pp. 2–4.
885. R. Damadian, L. Minkoff, M. Goldsmith, M. Stanford, and J. Koutcher, *Science*, 1976, **194**, 1430.
886. K. Tanaka, Y. Yamada, T. Shimizu, F. Sano, and Z. Abe, *Biotelemetry*, 1976, **1**, 337.
887. L. E. Crooks, T. P. Grover, L. Kaufman, and J. R. Singer, *Invest. Radiol.*, 1978, **13**, 63.
888. R. E. Gordon, P. E. Hanley, D. Shaw, D. G. Gadian, G. K. Radda, P. Styles, P. J. Bore, and L. Chan, *Nature (London)*, 1980, **287**, 736.
889. E. R. Andrew, P. A. Bottomley, W. S. Hinshaw, G. N. Holland, W. S. Moore, and C. Simaroj, *Phys. Med. Biol.*, 1977, **22**, 971.
890. W. S. Hinshaw, P. A. Bottomley, and G. N. Holland, *Nature (London)*, 1977, **270**, 722.
891. P. Mansfield, I. L. Pykett, P. G. Morris, and R. E. Coupland, *Br. J. Radiol.*, 1978, **51**, 921.
892. H. Clow and I. R. Young, *New Scientist*, 1978, 588.
893. G. N. Holland, R. C. Hawkes, and W. S. Moore, *J. Comput. Assist. Tomogr.*, 1980, **4**, 429.
894. R. C. Hawkes, G. N. Holland, W. S. Moore, and B. S. Worthington, *J. Comput. Assist. Tomogr.*, 1980, **4**, 577.
895. R. Damadian, *Philos. Trans. R. Soc. London*, 1980, **B289**, 489.
896. *Radiology*, 1982, **142**, 243.
897. L. Crooks, M. Arakawa, J. Hoenninger, J. Watts, R. McRee, L. Kaufman, P. L. Davis, A. R. Margulis, and J. De Groot, *Radiology*, 1982, **143**, 169.
898. L. E. Crooks, D. A. Ortendahl, L. Kaufman, J. C. Hoenninger, M. Arakawa, J. Watts, C. R. Cannon, M. Brant–Zawadski, P. L. Davis, and A. R. Margulis, *Radiology*, 1983, **146**, 123.
899. J. A. Battocletti, *CRC Crit. Rev. Biomed. Eng.*, 1984, **11**, 313.
900. *Magnetic Resonance Imaging: National Institutes of Health Consensus Development Statement*, Office of Medical Applications of Research, NIH, Bethesda, MD, 1987.
901. W. A. Gibbons, D. Crepaux, J. Delayre, J.-J. Dunand, G. Hajdukovic, and H. R. Wyssbrod, *Peptides: Chemistry, Structure and Biology*, Ann Arbor Sci., New York, 1976, p. 127.
902. G. Wagner and K. Wüthrich, *J. Mol. Biol.*, 1982, **155**, 347.
903. S. L. Gordon and K. Wüthrich, *J. Am. Chem. Soc.*, 1978, **100**, 7094.
904. M. P. Williamson, D. Marion, and K. Wüthrich, *J. Mol. Biol.*, 1984, **173**, 341.
905. M. P. Williamson, T. F. Havel, and K. Wüthrich, *J. Mol. Biol.*, 1985, **182**, 295.
906. G. M. Clore and A. M. Gronenborn, *CRC Crit. Rev. Biochem. Mol. Biol.*, 1989, **24**, 479.
907. K. Wüthrich, *Science*, 1989, **243**, 45.
908. W. Braun, *Q. Rev. Biophys.*, 1987, **19**, 115.
909. A. D. Kline, W. Braun, and K. Wüthrich, *J. Mol. Biol.*, 1986, **189**, 377.
910. J. W. Pflugrath, G. Wiegand, R. Huber, and L. Vértesy, *J. Mol. Biol.*, 1986, **189**, 383.
911. K. Nagayama, K. Wüthrich, P. Bachmann, and R. R. Ernst, *Biochem. Biophys. Res. Commun.*, 1977, **78**, 99.
912. G. M. Clore and A. M. Gronenborn, *NMR of Proteins*, MacMillan, London, 1993.
913. G. W. Vuister, R. Boelens, and R. Kaptein, *J. Magn. Reson.*, 1988, **80**, 176.
914. D. Marion, L. E. Kay, S. W. Sparks, D. A. Torchia, and A. Bax, *J. Am. Chem. Soc.*, 1989, **111**, 1515.
915. L. E. Kay, G. M. Clore, A. Bax, and A. M. Gronenborn, *Science*, 1990, **249**, 411.
916. G. M. Clore, L. E. Kay, A. Bax, and A. M. Gronenborn, *Biochemistry*, 1991, **30**, 12.
917. E. R. P. Zuiderweg, A. M. Petros, S. W. Fesik, and E. T. Olejniczak, *J. Am. Chem. Soc.*, 1991, **113**, 370.
918. G. M. Clore, L. E. Kay, A. Bax, and A. M. Gronenborn, *Biochemistry*, 1991, **30**, 12.
919. M. Ikura, L. E. Kay, and A. Bax, *Biochemistry*, 1990, **29**, 4659.
920. S. W. Fesik, H. L. Eaton, E. T. Olejniczak, E. R. P. Zuiderweg, L. P. McIntosh, and F. W. Dahlquist, *J. Am. Chem. Soc.*, 1990, **112**, 886.
921. L. E. Kay, M. Ikura, and A. Bax, *J. Am. Chem. Soc.*, 1990, **112**, 888.
922. R. A. Alpher, H. Bethe, and G. Gamow, *Phys. Rev.*, 1948, **73**, 803.
923. A. Bax, D. Max, and D. Zax, *J. Am. Chem. Soc.*, 1992, **114**, 6923.

924. G. Otting, E. Liepinsh, and K. Wüthrich, *Science*, 1991, **254**, 974.
925. J. B. Udgaonkar and R. L. Baldwin, *Nature (London)*, 1988, **335**, 694.
926. H. Roder, G. A. Elöve, and S. W. Englander, *Nature (London)*, 1988, **335**, 700.
927. C. K. Woodward, *Curr. Opin. Struct. Biol.*, 1994, **4**, 112.
928. G. Barbato, M. Ikura, L. E. Kay, R. W. Pastor, and A. Bax, *Biochemistry*, 1992, **31**, 5269.
929. M. Ikura, G. M. Clore, A. M. Gronenborn, G. Zhu, C. B. Klee, and A. Bax, *Science*, 1992, **256**, 632.
930. M. Ikura and A. Bax, *J. Am. Chem. Soc.*, 1992, **114**, 2433.
931. G. Otting and K. Wüthrich, *Q. Rev. Biophys.*, 1990, **23**, 39.
932. M. Billeter, Y. Q. Qian, G. Otting, M. Müller, W. J. Gehring, and K. Wüthrich, *J. Mol. Biol.*, 1993, **234**, 1084.
933. J. G. Omichinski, G. M. Clore, O. Schaad, G. Felsenfeld, C. Trainor, E. Appella, S. J. Stahl, and A. M. Gronenborn, *Science*, 1993, **261**, 438.
934. H. Zhang, D. Zhao, M. Revington, W. Lee, X. Jia, C. Arrowsmith, and O. Jardetzky, *J. Mol. Biol.*, 1994, **238**, 592.
935. C. Tsiao, C. Dybowski, D. Walker, V. Durante, and D. R. Corbin, *Langmuir*, 1988, **4**, 1219.
936. J. A. Ripmeester, C. I. Ratcliffe, and J. S. Tse, *J. Chem. Soc., Faraday Trans. 1*, 1988, **84**, 3731.
937. W. Happer, E. Miron, S. Schaefer, D. Schreiber, W. A. van Wijngaarden, and X. Zeng, *Phys. Rev.*, 1984, **A29**, 3092.
938. M. S. Albert, G. D. Cates, B. Driehuys, W. Happer, B. Saam, C. S. Springer, Jr., and A. Wishnia, *Nature (London)*, 1994, **370**, 199.
939. Z. Wu, S. Schaefer, G. D. Cates, and W. Happer, *Phys. Rev.*, 1988, **A37**, 1161.
940. R. J. Gummerson, C. Hall, W. D. Hoff, R. Hawkes, G. N. Holland, and W. S. Moore, *Nature (London)*, 1979, **281**, 56.
941. S. Blackband and P. Mansfield, *J. Phys. C*, 1986, **19**, L49.
942. L. A. Weisenberger and J. L. Koenig, *Appl. Spectrosc.*, 1989, **43**, 1117.
943. A. Haase, J. Frahm, D. Matthaei, W. Hanicke, and K.-D. Merboldt, *J. Magn. Reson.*, 1986, **67**, 258.
944. A. O. K. Nieminen and J. L. Koenig, *Appl. Spectrosc.*, 1989, **43**, 1358.
945. P. Blümler and B. Blümich, *Macromolecules*, 1991, **24**, 2183.
946. D. G. Cory and W. S. Veeman, *J. Magn. Reson.*, 1989, **84**, 392.
947. R. A. Wind and C. S. Yannoni, US Patent 4 301 410 (issued November 17, 1981).
948. D. G. Cory, J. W. M. van Os, and W. S. Veeman, *J. Magn. Reson.*, 1988, **76**, 543.
949. D. G. Cory, A. M. Reichwein, J. W. M. van Os, and W. S. Veeman, *Chem. Phys. Lett.*, 1988, **143**, 467.
950. G. C. Chingas, J. B. Miller, and A. N. Garroway, *J. Magn. Reson.*, 1986, **66**, 530.
951. P. J. McDonald, J. J. Attard, and D. G. Taylor, *J. Magn. Reson.*, 1987, **72**, 224.
952. D. E. Demco, S. Hafner, and R. Kimmich, *J. Magn. Reson.*, 1992, **96**, 307.
953. D. G. Cory, J. B. Miller, A. N. Garroway, and W. S. Veeman, *J. Magn. Reson.*, 1989, **85**, 219.
954. J. B. Miller and A. N. Garroway, *J. Magn. Reson.*, 1989, **85**, 255.
955. F. De Luca, B. C. De Simone, N. Lugeri, B. Maraviglia, and C. Nuccetelli, *J. Magn. Reson.*, 1990, **90**, 124.
956. A. A. Samoilenko, D. Yu. Artemov, and L. A. Sibel'dina, *Russ. J. Phys. Chem.*, 1987, **61**, 1623.
957. A. A. Samoilenko and K. Zick, *Bruker Rep.*, 1990, **1**, 41.
958. D. G. Cory, *Annu. Rep. NMR Spectrosc.*, 1992, **24**, 87.
959. P. Kinchesh, E. W. Randall, and K. Zick, *J. Magn. Reson.*, 1992, **100**, 411.
960. J. Hennig, H. Friedburg, and B. Ströbel, *J. Comput. Assist. Tomogr.*, 1986, **10**, 375.
961. J. Hennig, A. Nauerth, and H. Friedburg, *Magn. Reson. Med.*, 1986, **3**, 823.
962. P. Mansfield and B. Chapman, *J. Magn. Reson.*, 1986, **66**, 573.
963. P. Mansfield and B. Chapman, *J. Phys. E*, 1986, **19**, 541.
964. P. B. Roemer, W. A. Edelstein, and J. S. Hickey, *Abstr. Soc. Magn. Reson. Med.*, 1986, 1067.
965. J. A. Jackson, L. J. Burnett, and J. F. Harmon, *J. Magn. Reson.*, 1980, **41**, 411.
966. P. C. Lauterbur, D. M. Kramer, W. V. House, and C.-N. Chen, *J. Am. Chem. Soc.*, 1975, **97**, 6866.
967. P. A. Bottomley, T. B. Foster, and R. D. Darrow, *J. Magn. Reson.*, 1984, **59**, 338.
968. M. Garwood, T. Schleich, B. D. Ross, G. B. Matson, and W. D. Winters, *J. Magn. Reson.*, 1985, **65**, 239.
969. K. R. Metz and R. W. Briggs, *J. Magn. Reson.*, 1985, **64**, 172.
970. M. J. Blackledge, P. Styles, and G. K. Radda, *J. Magn. Reson.*, 1987, **71**, 246.
971. R. J. Ordidge, A. Connelly, and J. A. B. Lohman, *J. Magn. Reson.*, 1986, **66**, 283.
972. J. Frahm, K.-D. Merboldt, W. Hänicke, and A. Haase, *J. Magn. Reson.*, 1985, **64**, 81.
973. J. Frahm, K.-D. Merboldt, and W. Hänicke, *J. Magn. Reson.*, 1987, **72**, 502.
974. J. Granot, *J. Magn. Reson.*, 1986, **70**, 488.
975. R. Kimmich and D. Hoepfel, *J. Magn. Reson.*, 1987, **72**, 379.
976. W. P. Aue, S. Müller, T. A. Cross, and J. Seelig, *J. Magn. Reson.*, 1984, **56**, 350.
977. P. R. Luyten, A. J. H. Marien, B. Sijtsma, and J. A. den Hollander, *J. Magn. Reson.*, 1986, **67**, 148.
978. D. M. Doddrell, W. M. Brooks, J. M. Bulsing, J. Field, M. G. Irving, and H. Baddeley, *J. Magn. Reson.*, 1986, **68**, 367.
979. X. Hu, D. N. Levin, P. C. Lauterbur, and T. Spraggins, *Magn. Reson. Med.*, 1988, **8**, 314.
980. D. B. Vigneron, S. J. Nelson, J. Murphy-Boesch, D. A. C. Kelley, H. B. Kessler, T. R. Brown, and J. S. Taylor, *Radiology*, 1990, **177**, 643.
981. J. H. Duyn, J. A. Frank, and C. T. W. Moonen, *Magn. Reson. Med.*, 1995, **33**, 101.
982. W. P. Aue, S. Müller, and J. Seelig, *J. Magn. Reson.*, 1985, **61**, 392.
983. P. C. M. van Zijl, A. S. Chesnick, D. DesPres, C. T. W. Moonen, J. Ruiz−Cabello, and P. Van Gelderen, *Magn. Reson. Med.*, 1993, **30**, 544.
984. C. T. W. Moonen, P. C. M. van Zijl, J. A. Frank, D. Le Bihan, and E. D. Becker, *Science*, 1990, **250**, 53.
985. R. L. Bowman and V. Kudravcev, *IRE Trans. Med. Electron.*, 1959, **ME−6**, 267.
986. R. E. Halbach, J. H. Battocletti, A. Sances, R. L. Bowman, and V. Kudravcev, *Rev. Sci. Instrum.*, 1979, **50**, 428.
987. J. H. Battocletti, *CRC Crit. Rev. Biomed. Eng.*, 1986, **13**, 311.
988. L. Axel, *Am. J. Roentgenol.*, 1984, **143**, 1157.
989. E. O. Stejskal and J. E. Tanner, *J. Chem. Phys.*, 1965, **42**, 288.
990. D. G. Taylor and M. C. Bushell, *Phys. Med. Biol.*, 1985, **30**, 345.
991. K.-D. Merboldt, W. Hänicke, and J. Frahm, *J. Magn. Reson.*, 1985, **64**, 479.
992. D. Le Bihan, E. Breton, D. Lallemand, P. Grenier, E. Cabanis, and M. Laval-Jeantet, *Radiology*, 1986, **161**, 401.
993. M. E. Moseley, Y. Cohen, J. Mintorovitch, L. Chileuitt, H. Shimizu, J. Kucharczyk, M. F. Wendland, and P. R. Weinstein, *Magn. Reson. Med.*, 1990, **14**, 330.
994. R. Turner and D. Le Bihan, *J. Magn. Reson.*, 1990, **86**, 445.

995. D. Le Bihan, E. Breton, D. Lallemand, M.-L. Aubin, J. Vignaud, and M. Laval-Jeantet, *Radiology*, 1988, **168**, 497.
996. R. M. Henkelman, *Magn. Reson. Med.*, 1990, **16**, 470.
997. A. Villringer, B. R. Rosen, J. W. Belliveau, J. L. Ackerman, R. B. Lauffer, R. B. Buxton, Y.-S. Chao, V. J. Wedeen, and T. J. Brady, *Magn. Reson. Med.*, 1988, **6**, 164.
998. B. R. Rosen, J. W. Belliveau, and D. Chien, *Magn. Reson. Q.*, 1989, **5**, 263.
999. J. W. Belliveau, D. N. Kennedy, R. C. McKinstry, B. R. Buchbinder, R. M. Weisskoff, M. S. Cohen, J. Vevea, T. J. Brady, and B. R. Rosen, *Science*, 1991, **254**, 716.
1000. S. Ogawa, T.-M. Lee, A. S. Nayak, and P. Glynn, *Magn. Reson. Med.*, 1990, **14**, 68.
1001. R. G. Shulman, A. M. Blamire, D. L. Rothman, and G. McCarthy, *Proc. Natl. Acad. Sci. USA*, 1993, **90**, 3127.
1002. C. T. W. Moonen, G. Liu, P. Van Gelderen, and G. Sobering, *Magn. Reson. Med.*, 1992, **26**, 184.
1003. P. T. Callaghan, *Principles of Nuclear Magnetic Resonance Microscopy*, Oxford University Press, Oxford, 1991.
1004. J. B. Aguayo, S. J. Blackband, J. Schoeniger, M. A. Mattingly, and M. Hintermann, *Nature (London)*, 1986, **322**, 190.
1005. G. A. Johnson, M. B. Thompson, and B. P. Drayer, *Magn. Reson, Med.*, 1987, **4**, 351.
1006. P. M. Glover, R. W. Bowtell, G. D. Brown, and P. Mansfield, *Magn. Reson. Med.*, 1994, **31**, 423.
1007. G. A. Johnson, R. D. Black, G. P. Cofer, X. Zhou, and R. R. Maranpot, *Abstr. 2nd Int. Conf. Magn. Reson. Microsc., Heidelberg, Germany, September 1993*.
1008. R. D. Black, T. A. Early, P. B. Roemer, O. M. Mueller, A. Mogro-Campero, L. G. Turner, and G. A. Johnson, *Science*, 1993, **259**, 793.
1009. R. J. S. Brown and B. W. Gamson, *AIME Petrol. Trans.*, 1960, **219**, 199.
1010. R. K. Cooper and J. A. Jackson, *J. Magn. Reson.*, 1980, **41**, 400.
1011. R. L. Kleinberg, A. Sezginer, D. D. Griffin, and M. Fukuhara, *J. Magn. Reson.*, 1992, **97**, 466.
1012. W. A. Edelstein, H. J. Vinegar, P. N. Tutunjian, P. B. Roemer, and O. M. Mueller, *Proc. Soc. Petrol. Eng., 63rd Annu. Conf., Houston, TX, October 1988*.
1013. J. L. A. Williams, G. Maddinelli, and D. G. Taylor, *J. Magn. Reson.*, 1994, **A109**, 124.
1014. J. K. Borchardt, *Today's Chemist at Work*, 1994, **3**, 28.
1015. R. H. Varian, US Patent 3 019 383 (1962).
1016. A. G. Semenov, A. I. Burshtein, A. Yu. Pusep, and M. D. Schirov, USSR Patent 1 079 063 (1988).
1017. M. Schirov, A. Legchenko, and G. Creer, *Explor. Geophys.*, 1991, **22**, 333.
1018. O. A. Shushakov and A. V. Legchenko, *Geol. Geophys.*, 1994, **35**, 130, 161.
1019. G. Suryan, *Proc. Indian Acad. Sci.*, 1951, **A33**, 107.
1020. O. C. Morse and J. R. Singer, *Science*, 1970, **170**, 440.
1021. W. K. Genthe, W. H. Vander Heyden, J. H. Battocletti, W. S. McCormick, and H. M. Snowball, *Instrum. Technol.*, 1968, **15**, 53.
1022. J. H. Battocletti, *Pipe Line Ind.*, 1968, 61.
1023. J. H. Battocletti, *CRC Crit. Rev. Biomed. Eng.*, 1986, **13**, 311.
1024. J. D. King, W. L. Rollwitz, and A. De Los Santos, *Proc. Coal Technol. '82*, Houston TX, December 1982.
1025. T. M. Shaw and R. H. Elsken, *J. Chem. Phys.*, 1950, **18**, 1113.
1026. W. L. Rollwitz, *Proc. Natl. Electron. Conf.*, 1956, **12**, 113.
1027. W. L. Rollwitz, 'A Nuclear Magnetic Resonance Moisture Meter', *Rep. Southwest Research Inst.*, San Antonio, TX, 1956.
1028. *Bruker Rep.*, 1987, **2**, 40.
1029. B. S. Miller, M. S. Lee, J. W. Hughes, and Y. Pomeranz, *Cereal Chem.*, 1980, **57**, 126.
1030. H. K. Leung, J. A. Magnuson, and B. L. Bruinsma, *J. Food Sci.*, 1979, **44**, 1408.
1031. E. W. Randall, Introduction to NMR and Modern Technology, in *NMR in Modern Technology: Proc. NATO Adv. Study Inst., Sarigerme Park (Dalaman), Turkey, September 1992*, ed. G.E. Maciel, Kluwer, Dordrecht, 1995.
1032. C. I. Nicholls and A. De Los Santos, *Drying Technol.*, 1991, **9**, 849.
1033. L. F. Bauman, T. F. Conway, and S. A. Watson, *Science*, 1963, **139**, 498.
1034. T. F. Conway and L. F. Johnson, *Science*, 1969, **164**, 827.
1035. J. Schaefer and E. O. Stejskal, *J. Am. Oil Chem. Soc.*, 1974, **51**, 210.
1036. J. Schaefer and E. O. Stejskal, *J. Am. Oil Chem. Soc.*, 1975, **52**, 366.
1037. V. Rutar, M. Burgar, R. Blinc, and L. Ehrenberg, *J. Magn. Reson.*, 1977, **27**, 83.
1038. M. R. Lakshminarayana, S. S. Joshi, G. A. Nagana Gowda, and C. L. Khetrapal, *J. Bio. Sci.*, 1992, **17**, 87.
1039. E. Brosio, F. Conti, A. di Nola, and S. Sykora, *J. Am. Oil Chem. Soc.*, 1980, **57**, 78.
1040. J. Schaefer, E. O. Stejskal, and R. A. MacKay, *Biochem. Biophys. Res. Commun.*, 1979, **88**, 274.
1041. D. W. Lowman and G. E. Maciel, *Anal. Chem.*, 1979, **51**, 85.
1042. J. H. Bradbury and J. G. Collins, *Cereal Chem.*, 1982, **59**, 159.
1043. A. C. Waiss, Jr., B. G. Chan, M. Benson, and M. J. Lukefahr, *J. Assoc. Off. Anal. Chem.*, 1978, **61**, 146.
1044. P. E. Pfeffer, J. Sampugna, D. P. Schwartz, and J. N. Shoolery, *Lipids*, 1977, **12**, 869.
1045. N. Ishida, T. Kobayashi, M. Koizumi, and H. Kano, *Agric. Biol. Chem.*, 1989, **53**, 2363.
1046. S. Y. Wang, P. C. Wang, and M. Faust, *Sci. Hortic.*, 1988, **35**, 227.
1047. C. Y. Wang and P. C. Wang, *Hortic. Sci.*, 1989, **24**, 106.
1048. L. Walter, A. Balling, U. Zimmermann, A. Haase, and W. Kuhn, *Planta*, 1989, **178**, 524.
1049. B. L. Wild and C. W. Hood, *Hortic. Sci.*, 1989, **24**, 109.
1050. J. M. Tingle, V. Sarafis, P. A. Baumgartner, and J. M. Pope, *Abstr. 2nd Int. Conf. Magn. Reson. Microsc., Heidelberg, Germany, September 1993*.
1051. R. F. Paetzold, G. A. Matzkanin, and A. De Los Santos, *Soil Sci. Soc. Am. J.*, 1985, **49**, 537.
1052. P. Kinchesh, E. W. Randall, and K. Zick, *Magn. Reson. Imaging*, 1994, **12**, 305.
1053. P. A. Bottomley, H. H. Rogers, and T. H. Foster, *Proc. Natl. Acad. Sci. USA*, 1986, **83**, 87.
1054. H. Van As, *Abstr. 2nd Int. Conf. Magn. Reson. Microsc.*, Heidelberg, Germany, September 1993.
1055. J. D. King, W. L. Rollwitz, and A. De Los Santos, Paper presented at *3rd Int. Conf. Security through Sci. Eng., Berlin, Germany, September 1980*.
1056. J. D. King, W. L. Rollwitz, and A. De Los Santos, Paper presented at *ASTM Symp. Explosives Detection for Security Appl., Philadelphia, PA, April 1983*.
1057. J. Jonas and H. S. Gutowsky, *Annu. Rev. Phys. Chem.*, 1980, **31**, 1.
1058. J. A. Sidles, *Phys. Rev. Lett.*, 1992, **68**, 1124.
1059. D. Rugar, C. S. Yannoni, and J. A. Sidles, *Nature (London)*, 1992, **360**, 563.
1060. D. Rugar, O. Züger, S. Hoen, C. S. Yannoni, H.-M. Vieth, and R. D. Kendrick, *Science*, 1994, **264**, 1560.
1061. C. R. Bowers and D. P. Weitekamp, *J. Am. Chem. Soc.*, 1987, **109**, 5541.
1062. W. S. Warren, W. Richter, A. H. Andreotti, and B. T. Farmer II, *Science*, 1993, **262**, 2005.

1063. I. Bertini and C. Luchinat, *NMR of Paramagnetic Molecules in Biological Systems*, Benjamin/Cummings, Menlo Park, CA, 1986.
1064. A. F. Casy, *PMR Spectroscopy in Medicinal and Biological Chemistry*, Academic Press, New York, 1971.
1065. C.-N. Chen and D. I. Hoult, *Biomedical Magnetic Resonance Technology*, Adam Hilger, Bristol, UK, 1989.
1066. J. S. Cohen (ed.), *Magnetic Resonance in Biology*, Wiley, New York, 1983, Vol. 2.
1067. P. L. Corio, *Structure of High-Resolution NMR Spectra*, Academic Press, New York, 1966.
1068. J. W. Emsley, J. Feeney, and L. H. Sutcliffe, *High Resolution Nuclear Magnetic Resonance Spectroscopy*, Pergamon, Oxford, 1965.
1069. D. G. Gadian, *Nuclear Magnetic Resonance and Its Application to Living Systems*, Clarendon Press, Oxford, 1982.
1070. T. L. James, *Nuclear Magnetic Resonance in Biochemistry*, Academic Press, New York, 1975.
1071. A. R. Lepley and G. L. Closs (eds.), *Chemically Induced Magnetic Polarization*, Wiley, New York, 1973.
1072. P. Mansfield and P. G. Morris, *NMR Imaging in Biomedicine*, Academic, New York, 1982, pp. 174, 187–191, 264.
1073. N. F. Ramsey, *Nuclear Moments*, John Wiley, New York, 1953.
1074. R. E. Sievers (ed.), *Nuclear Magnetic Resonance Shift Reagents*, Academic Press, New York, 1973.
1075. E. R. Andrew, *Philos. Trans. R. Soc. London*, 1981, **299A**, 505.
1076. A. Bax, *Annu. Rev. Biochem.*, 1989, **58**, 223.
1077. R. Benn and H. Günther, *Angew. Chem., Int. Ed. Engl.*, 1983, **22**, 350.
1078. P. H. Bolton and D. R. Kearns, *Biol. Magn. Reson.*, 1978, **1**, 91.
1079. D. Chapman, *Q. Rev. Biophys.*, 1975, **8**, 185.
1080. B. F. Chmelka and A. Pines, *Science*, 1989, **246**, 71.
1081. A. D. H. Clague, *Helv. Phys. Acta*, 1985, **58**, 121.
1082. J. S. Cohen; NMR Investigations of the Interactions of Biomolecules, in *Experimental Methods in Biophysical Chemistry*, ed. C. Nicolau, Wiley, London, 1973.
1083. D. G. Cory, *Annu. Rep. NMR Spectrosc.*, 1992, **24**, 87.
1084. P. Diehl, In *Nuclear Magnetic Resonance Spectra of Nuclei Other than Protons*, ed. T. Axenrod and G. A. Webb, Wiley, New York, 1974.
1085. P. Diehl and Th. Leipert, *Helv. Chim. Acta*, 1964, **47**, 545.
1086. D. B. Fenske, *Chem. Phys. Lipids*, 1993, **64**, 143.
1087. R. Freeman, *Proc. R. Soc. London*, 1980, **A373**, 149.
1088. C. A. Fyfe, R. L. Dudley, P. J. Stephenson, Y. Deslandes, G. K. Hamer, and R. H. Marchessault, *Rev. Macromol. Chem. Phys.*, 1983, **C23**, 187.
1089. R. G. Griffin, *Method. Enzymol.*, 1981, **72**, 108.
1090. H. S. Gutowsky, *J. Magn. Reson.*, 1975, **17**, 281.
1091. O. Kaplan, P. C. M. van Zijl, and J. S. Cohen, *NMR Basic Principles Prog.*, 1992, **28**, 3
1092. C. L. Khetrapal and M. R. Lakshminarayana, *Q. Chem. Rev. (India)*, 1984, **1**, 1.
1093. A. Kowalsky and M. Cohn, *Annu. Rev. Biochem.*, 1964, **33**, 481.
1094. P. G. Morris, *Annu. Rep. NMR Spectrosc.*, 1988, **20**, 1.
1095. J. S. Rigden, *Rev. Mod. Phys.*, 1986, **58**, 433.
1096. J. Seelig, *Q. Rev. Biophys.*, 1977, **10**, 353.
1097. J. N. Shoolery, *Anal. Chem.*, 1993, **65**, 731A.
1098. C. P. Slichter, *J. Magn. Reson.*, 1975, **17**, 274.
1099. J. S. Waugh, *Anal. Chem.*, 1993, **65**, 725A.

Acknowledgement

The authors are grateful for help and advice received from many colleagues. First, we thank the authors of the historical sketches that follow. We have learned much about the history of NMR from their articles and have drawn frequently on their words in writing the various sections.

Each of the following has read a draft of one or more sections and provided valuable comments and suggestions for additional items to be included: E. Raymond Andrew, Robert S. Balaban, Ad Bax, James Emsley, James Feeney, Ray Freeman, Allen N. Garroway, Robert J. Highet, and Chrit T. W. Moonen. Their efforts have contributed immensely to the scope and authenticity of this account.

In addition, Eiichi Fukushima, Myra Gordon, Harald Günther, Joel B. Miller, Martin Packard, Edward W. Randall, Bernard L. Shapiro, and Robert G. Shulman have provided very helpful information on a number of historical aspects. Finally, Robin K. Harris and David M. Grant, the Editors-in-Chief of this Encyclopedia have given us constant encouragement and furnished a great deal of assistance in many specific instances.

To enhance the readability of this article, we have provided only limited references, often giving examples rather than attempting a more complete coverage. We hope that the literature cited will furnish a guide to the reader who wishes to obtain further information. In addition to information derived from the specific references given, we have made extensive use of the 200-odd historical sketches that follow, as well as numerous books, monographs, special series on NMR, and review articles that contain material of historical interest. The number is so large that we can provide only a partial list here. In particular, we acknowledge the use of books by Andrew,[39] Bertini and Luchinat,[1063] Casy,[1064] Chen and Hoult,[1065] Cohen,[1066] Corio,[1067] Emsley and Lindon,[226] Emsley, Feeney, and Sutcliffe,[1068] Gadian,[1069] Harris and Mann,[370] Jackman and Sternhell,[176] James,[1070] Jardetzky and Roberts,[609] Lepley and Closs,[1071] Mansfield and Morris,[1072] Pople, Schneider, and Bernstein,[93] Ramsey,[1073] and Sievers.[1074] Also helpful have been the major serial review publications, including *Adv. Magn. Reson.*, *Annu. Rep. NMR Spectrosc.*, *Prog. NMR Spectrosc. NMR Basic Principles Prog.*, and *Nucl. Magn. Reson. Spec. Period. Rep.* In addition, we have drawn material from a number of individual articles, primarily historical or subject reviews, including those by Andrew,[1075] Bax,[1076] Benn and Günther,[1077] Bolton and Kearns,[1078] Chapman,[1079] Chmelka and Pines,[1080] Clague,[1081] Cohen,[1082] Cory,[1083] Diehl,[1084] Diehl and Leipert,[1085] Fenske,[1086] Freeman,[271,1087] Fyfe et al.,[1088] Griffin,[1089] Gutowsky,[1090] Jonas and Gutowsky,[1057] Kaplan et al.,[1091] Khetrapal and Lakshminarayana,[1092] Kowalsky and Cohn,[1093] Morris,[1094] Nelson and Weaver,[267] Pound,[45] Rigden,[1095] Seelig,[1096] Shoolery,[1097] Slichter,[1098] Waugh,[1099] and van Zijl and Moonen.[827]

Our sincere thanks to all those whose written work and oral communications have been helpful in preparing this article.

Biographical Sketch

Edwin D. Becker. *b* 1930. B.S., 1952, University of Rochester, Ph.D., 1955, Chemistry, University of California, Berkeley, USA. National Institutes of Health, 1955–present; Laboratory Chief (1972–80, 1988–); Associate Director for Research Services (1980–88). Concurrent position on Faculty, Georgetown University, 1959–present. Books on NMR. Research interests and publications: hydrogen bonding, molecular structure elucidation, technique development in NMR and other areas of molecular spectroscopy.

Cherie L. Fisk. *b* 1945. A.B., 1967, Biochemistry, Smith College. Ph.D., 1975, chemistry, Georgetown University. Introduced to NMR by C. F. Hammer and E. D. Becker. Postdoctoral NMR research, Laboratory of Chemical Physics, National Institutes of Health. Joined Office of Research Services, National Institutes of Health in 1984. Professional interests: design and management of research facilities.

C. L. Khetrapal. *b* 1937. M.Sc., 1959, Allahabad, Ph.D., 1965, Bombay. Introduced to NMR by S. S. Dharmatti. Worked at Tata Institute of Fundamental Research, Bombay, 1959–73 in various positions, the last one being Reader; Raman Research Institute, Bangalore, 1973–84, as Associate Professor and Indian Institute of Science, Bangalore, 1984–present, as Professor and Head, Sophisticated Instruments Facility. Nearly 200 publications and several reviews, books and monographs. Research interests include NMR of oriented systems with emphasis on molecular structure and function, developments of novel techniques, and applications of NMR imaging and in vivo spectroscopy to problems of agricultural interest.

(l-r) Robert V. Pound, Pierre Seroz-Gavin and Charles P. Slichter at the meeting of the International Society of Magnetic Resonance (ISMAR), Morzine, France, 1989.

(l-r) Maurice Goldman, Endel Lippmaa, Nino Yannoni, Stanley J. Opella, Robert Tycko, Daniel P. Weitekamp, Ditsa Pines and Alex Pines at ISMAR meeting, Rio de Janeiro, 1986.

Noman F. Ramsey

Anatole Abragam

Alfred G. Redfield

John S. Waugh

(l-r) Sven R. Hartmann, Alexander Pines and Erwin L. Hahn at the Hahn symposium, Berkeley, California, 1991.

Torchia Dennis A.: A Fortuitous Transformation

Dennis A. Torchia

National Institutes of Health (NIH), Bethesda, MD, USA

For once, at least, the formidable Professor Breit (my thesis advisor) had to admit that I had a point; theoretical physics would not suffer by my decision to pursue postdoctoral work in biological, as opposed to real, physics. He therefore supported my application to work in Elkan Blout's lab at Harvard Medical School. Although my original intention was to calculate the UV spectra of protein–ligand complexes, I soon found myself doubting that I could calculate anything meaningful, given the complexity of the system, and I therefore decided to do experiments. Fortunately Blout had a talented group who taught me a variety of spectroscopic and wet biochemical techniques. During a luncheon conversation, a colleague suggested that, as a physicist, I should consider using NMR to study biological systems. This struck me as an odd suggestion because, to my knowledge, an NMR spectrometer was a clever device for measuring either γ or $\boldsymbol{B}$. However, further discussion and reading convinced me to give NMR a try. Charlie Deber had joined Blout's lab at about the same time as I had, and he and Blout were enthusiastic about using NMR to characterize the conformations of peptides that Deber had synthesized. Blout had established a collaboration with Frank Bovey at Bell labs for this purpose, and Bovey offered me a postdoctoral position to carry out this work.

At Bell, I found myself in an extraordinarily well equipped lab. Bovey had a 100 MHz instrument as well as a share of the Varian 220 in Bob Shulman's lab. With these instruments we were able to elucidate the structures of several cyclic and linear peptides in solution. My interest in molecular dynamics was first stimulated by our observations that proline residues were typically mixtures of *cis* and *trans* isomers in dynamic equilibrium. In addition, our coupling constant measurements indicated that the proline ring was highly flexible, contrary to conventional wisdom.

At about this time, I attended my first ENC where several talks convinced me that pulsed FT ^{13}C NMR was the way to study the dynamics of macromolecules. Shortly after the ENC, I went to the National Bureau of Standards to fill a position that had been vacated by Tom Farrar. Tom and his colleagues had built one of the first pulsed FT ^{13}C spectrometers, and I was eager to make ^{13}C relaxation measurements on polypeptides. However, having only had experience with commercial spectrometers, it was painful, but ultimately very useful, to learn how to optimize the performance of a homebuilt instrument. With help from Dave VanderHart, I eventually got going and, working with Jim Lyerla, was able to study the segmental mobility of a variety of polymers and polypeptides.

Shortly after arriving at the Bureau, I established a collaboration with Karl Piez of the NIH to study elastin and soluble fragments of collagen. Although elastin is a crosslinked, insoluble protein, it yielded a motionally averaged ^{13}C spectrum consistent with its rubber-like mechanical properties. The work on elastin initiated my interest in solid state NMR, and when I joined Piez's lab in 1974 it was with the intention of studying intact collagen using techniques developed by Pines and Waugh. With the help of Dave VanderHart and Rolf Tschudin, I assembled a solid state NMR spectrometer in Ted Becker's lab at the NIH. Using this instrument and its higher field successors, my group studied the dynamics of collagen in various types of intact tissues.

In order to devise reasonable models for internal motions in the protein, we also studied the dynamics of labeled crystalline amino acids and peptides synthesized by Paul Young. These compounds showed a surprising amount of rapid molecular motion, and I began working on equations for T_1 anisotropy and powder lineshape for simple jump models in order to interpret our results. This work led to a collaboration with Attila Szabo, who had just come to the NIH, that yielded equations for anisotropic spin relaxation and powder lineshapes for a wide variety of models of molecular reorientation.

Instruments and equations, however, were insufficient to provide useful information about the molecular dynamics of collagen and elastin. We also had to incorporate labeled amino acids into the proteins in order to achieve the sensitivity and specificity needed to obtain interpretable spectra. We did this by injecting solutions of labeled amino acids into young rodents for several weeks, and then, after sacrificing the animals, removing the tissues of interest. While this procedure worked, it was distasteful and expensive.

As an outgrowth of our work on crystalline amino acids, I had become interested in studying the internal dynamics of crystalline proteins. A colleague at NIH suggested I contact John Gerlt, at the University of Maryland, who had an efficient system for expressing recombinant staphylococcal nuclease in *E. coli*. By coincidence, John called me to ask for a small amount of ^{13}C labeled proline. I said 'yes', and made a request of my own. John and his postdocs generously provided us with transformed *E. coli* and the advice needed to make and purify nuclease. Initially we prepared polycrystalline protein samples containing one type of deuterated amino acid, and obtained clear evidence that the side chain of each type of labeled amino acid was mobile.

In order to overcome the problem associated with overlapping powder patterns, we next obtained CP MAS spectra of ^{13}C/^{15}N labeled samples. These high-resolution spectra enabled us to observe signals corresponding to individual atomic sites in the protein. Furthermore, we observed in nearly every instance that the ^{13}C and ^{15}N chemical shifts in the crystalline state were the same as in solution. Hence if we could assign the solution spectrum, we would be able to assign the crystalline spectra. At 17 kDa, nuclease was, at the time, considerably larger than any protein that had been assigned; however with the ability to label the protein, it seemed reasonable to suppose that it could be assigned using heteronuclear NMR techniques. This initiated work, in collaboration with Ad Bax, on protein dynamics and structure in solution, which has become the primary focus of my research.

When I reflect upon my decision of 25 years ago to give NMR a try, I was most fortunate to have chosen a technique that has become an essential tool in biophysical research, and I am gratified that I have been able to contribute to its development in this area.

Biographical Sketch

Dennis A. Torchia. *b* 1939. B.A., 1961, Physics, University of California, Riverside, Ph.D., 1967, Physics, Yale University. Postdoctoral fellow, Harvard Medical School, with Elkan Blout, 1967–69, Bell Laboratories, with Frank Bovey, 1969–71. Staff member, National Bureau of Standards, 1971–74; Dental Institute, NIH, 1974–present. Currently, Chief, Protein Biophysics Section, Bone Research Branch. 120 publications. Current research specialty: application of solution state heteronuclear NMR techniques to the study of protein structure and dynamics.

Torrey, Henry C.: Precursive and Early Work on NMR

Henry C. Torrey

Rutgers University, New Brunswick, NJ, USA

Serendipity is defined by Webster as 'the faculty of finding valuable or agreeable things not sought for', and the adjective serendipitous describes those who have this happy faculty and the discoveries they make with it, but perhaps it can also be used to characterize a new field of endeavor replete with valuable, agreeable, and surprising things waiting to be uncovered whether by accident or design. In this sense the field of nuclear magnetic resonance is serendipitous par excellence. The history of this field is full of examples of new, delightful, and surprising developments after one had supposed that its fabulous fecundity must have been finally exhausted. Most of these treasures have been unearthed by informed search or ingenuity, but some by serendipity.

The first observation of NMR by I. I. Rabi and colleagues[1] was anything but serendipitous. They had planned their work carefully and saw what they had expected to see. They interpreted their observations on the basis of a formula for the probability of a spin-$\frac{1}{2}$ flip derived by Rabi[2] a few months before for the case of a gyrating magnetic field. However a curious thing seems to have happened on the way from reference 2 to 1. In the earlier work, the spin flip probability, P, was not displayed with a 'resonance denominator' and the focus was on the asymmetry in its value depending on the direction of rotation of the field, making possible the determination of the sign of the moment; indeed the word *resonance* does not appear anywhere in this paper. In the later work, P was shown with the 'familiar resonance denominator' and the emphasis was on the precise measurement of the moment with an oscillating field. In between times Rabi was visited by the Dutch physicist, C. J. Gorter, who had made an unsuccessful attempt[3] to observe NMR in a solid, but who realized that Rabi's setup was ideal for observing NMR if his spatially rotating field were replaced by an oscillating field transverse to a steady field. He urged[4] Rabi to do that, but felt[4] that he had not succeeded in convincing him.

But actually Rabi **was** convinced. Gorter's visit was on a Saturday; on the following Monday modifications were underway[5] in Rabi's laboratory to prepare for the famous resonance experiment. According to Rabi[6] it wasn't Gorter's advice, 'he didn't tell us anything we didn't know', but the possibility of his competition that provided the stimulus. This remark seems a bit disingenuous. It wasn't like Rabi to be paddling about in backwaters, ' . . . I liked what we were doing . . . nobody was competing with us . . . ', when the tide leading to a Nobel Prize was at the flood. There are other things than competition that can cause the tide to slacken: accidents, ill-health, unexpected and peremptory demands on one's time and attention, etc. It wasn't in Rabi's nature to delay embarkation on a major voyage because he seemed to have all the time in the world. Accepting Rabi's statement that Gorter didn't tell him anything new, it seems likely that the major effect of Gorter's visit was to waken Rabi to the vital significance of the resonance method and to the realization that he had better get on with it before the tide slackened for whatever reason.

Gorter's expressed reaction[4] to the Letter[1] announcing the discovery of NMR was restrained and graceful: 'I cannot deny that I felt some pride, mixed with the feeling that my contribution was somewhat undervalued though my advice was acknowledged in the Letter.' A few years later Gorter and Broer,[7] for reasons still obscure, narrowly missed making the first observation of NMR in bulk matter. No one has ever doubted that Rabi richly deserved the Nobel Prize he was awarded in 1944, but Gorter clearly deserved a noble prize for the good grace and lack of rancor with which he accepted the undervaluation of his contribution to Rabi's success as well as the near misses in his own quest of NMR and his 'bad luck' in other major scientific endeavors.

My own connection with this field began in early 1935 when I was a graduate student in Rabi's molecular beam laboratory at Columbia. At this time Rabi had conceived of a way to determine the sign of a nuclear moment by a new use of the refocusing technique: a deflecting field A, a refocusing field B, and in between a C field to induce nonadiabatic transitions. It was my privilege to be the first to use this technique in Rabi's lab and I set to work with enthusiasm to build my apparatus. My thesis problem was to determine the sign of the nuclear moment of potassium (^{39}K). At the weak fields I was using in A and C, the nuclear spin of $\frac{3}{2}$ was closely coupled to the electron spin, but in the strong B field the three states with total angular momentum $F = 1$ all had nearly the same moment, so no change could be noticed due to transitions among them. On the other hand, the transitions for $F = 2$ of $m = 1$ to $m = 2$ or of $m = -1$ to $m = -2$ would change the sign of the moment in the B field, causing a decrease in the refocused intensity. This difference could easily be exploited to find the sign of the nuclear moment.

Everything went beautifully: the first run I took late in 1935 gave me all the data I needed and I was finished, or so I thought. I had succeeded in inducing detectable changes in the orientation of an atomic moment to which a nuclear moment was coupled, so in a sense I had flipped a nuclear spin and detected it, which no one else had done up to then. Unfortunately, one is not awarded a Ph.D. for demonstrating the calisthenics of atomic and nuclear moments. At least one bit of new information had to be added to the world's knowledge. The sign of the moment of ^{39}K would do and I had that, but soon after my run the highly respected British spectroscopist, D. A. Jackson, published[8] with H. Kuhn their observation of the hyperfine structure of ^{39}K, including the sign of its nuclear moment, and I appeared to be scooped. My thesis was in ruins and I would have to start over again, or so it seemed at first. But fortune smiled again. I had found the moment to be positive and Jackson, near the limit of resolution of the hfs splitting of ^{39}K, had declared it to be negative. I was sure I was right, but to be completely convincing it was felt that I should make a direct comparison with sodium (^{23}Na) which was known, spectroscopically, to have a positive moment.

My apparatus which had behaved impeccably up to this time seemed to resent being asked to accommodate itself to sodium for which it was not designed. It developed hard-to-find leaks and other forms of recalcitrant behavior. Finally, after several months of coercion it produced an acceptable beam, but I then found that my A field was insufficiently long to resolve

the hyperfine magnetic states of sodium to the extent needed to obtain a completely unambiguous result. In the meantime Kellogg, Rabi, and Zacharias[9] had found the sign of the proton moment by a similar method. They had started after I did and had no results when I took my first run, but the delay caused by my work on sodium prevented me from being the first to publish in this field. After all these frustrations I was able to use another apparatus which S. Millman had constructed for a different purpose. This had a sufficiently long *A* field and with the cooperation of Millman and J. R. Zacharias it was modified to my present purpose. With it, I found the signs of ^{39}K and ^{23}Na to be the same and positive, confirming my previous result.[10]

My first post-Ph.D. job was at Penn State, where I arrived about the same time that Gorter made his famous visit to Columbia. I was fascinated by Rabi's stunning development of NMR and wanted to get into the field, but could not hope to compete experimentally. My first foray into magnetic resonance was some theoretical work[11] on radiofrequency spectroscopy with the atomic beam method of Rabi.

One virtue of the Rabi method is its theoretical simplicity. However complicated the atomic or molecular system, you are usually dealing with what may be taken as a two-level system: one level is the refocused state you are observing, the other the state to which you are inducing transitions. I first showed that the Schrödinger equation for a general two-level system perturbed by a sinusoidal potential has, to a close approximation, a solution formally identical to Rabi's solution for a spin-$\frac{1}{2}$ in a gyrating field. The transition probability is a function of the time that must be averaged over the velocity distribution in a molecular beam and this I did. Finally, I derived the matrix elements for the Zeeman components of the hyperfine-split ground states of the alkali atoms in a magnetic field, applying these results to the shapes and intensities of the resonances found[12,13] in Rabi's laboratory.

World War II put a virtual stop to all nonwar-related scientific research. I was called to the Radiation Laboratory at MIT, where I worked on the development of crystal rectifiers which were used in the detection of microwave radar signals. Next door to me at the Rad Lab was Robert V. Pound, head of crystal mixers, who later became my office mate and my collaborator with Edward M. Purcell in the first observation[14] of NMR in bulk matter. Many years later, Purcell and I had a conversation in which we agreed that because of his prodigious memory Pound was best qualified to write the history of this work. The accompanying article by Pound (***Pound, Robert V.: Early Days in NMR***) includes a condensation of this history which he drafted in consultation with Purcell and myself.

Since Pound is the designated 'historiographer' of this work, I will refrain from repeating any of its history here except for a few minor comments on Pound's statements. He gives an account of the lunch where Purcell asked my opinion as to the feasibility of detecting the resonant absorption of radiofrequency power by nuclear spins in bulk matter. I do recall saying something about talk at Columbia being pessimistic on this question, but I now have no memory of such talk and believe that I was perhaps thinking subliminally of Rabi's Letter,[1] announcing his first observation of NMR, in which he refers in a footnote to Gorter's failure[3] to observe NMR in a solid. Incidentally, I seem to recall that there were two other people present at this luncheon, but don't remember now who they were.

Pound mentions my estimate from Waller's work that the nuclear spin relaxation time might be as short as 'several hours'. I have not saved these calculations, but I distinctly recall that my estimate was about an hour, a shaky estimate because Waller's work was for a crystal and did not apply well to paraffin. I was well aware that relaxation through lattice vibrations would only give an upper limit to the relaxation time and hoped that there would be other more efficient processes which turned out to be the case: the actual relaxation time for paraffin is in fact only about 10^{-2} s.

During the course of our work, Rabi called me into his office one day and quizzed me about it. He asked me how we expected to observe a resonance in view of the obscuring effects of local magnetic fields that would be present in a solid. I gave my opinion that any such fields would do no more than broaden the resonance by a few gauss. He was not convinced by my arguments and was very skeptical about our chances for success.

The announcement[15] of the discovery of 'nuclear induction' by Bloch, Hansen, and Packard a month after our report caused some initial confusion. It was clear that the two effects were closely related, but just how was not fully understood at first. A few weeks later Felix Bloch visited MIT, conferred with us and gave a talk on his work with Hansen and Packard, clearing up the remaining confusion on the relationship between our work and 'nuclear induction'. Summaries of his talk were distributed widely and excited considerable interest among some of the physicists still remaining at the Rad Lab, most of whom were engaged in finishing their contributions to the Rad Lab series of books. Before leaving MIT, I had talks with a number of people, including S. A. Goudsmit, who was much taken with the Bloch equations for the components of the nuclear magnetization in the rotating frame. He urged me to make a careful study of them and to examine and test them experimentally. I decided to follow his advice at my postwar job at Rutgers University where I joined the Physics Faculty in June 1946.

Before the war Rutgers had little going in the way of scientific research apart from an active agricultural experiment station. However, Rutgers had been designated the State University of New Jersey and was facing the task of educating hordes of returning war veterans. I was one of six physicists recruited in 1946 from the MIT Radiation Laboratory in a program to build up instruction and research in physics. Included in this program was a substantial grant to acquire research equipment, among which was a large electromagnet, perhaps the first ever to be designed specifically for NMR use. This magnet, built to our specifications by the General Electric Co., had a 3.5 in. adjustable gap separating 18-in. diameter pole faces. It was energized by a motor generator with the output current stabilized electronically by circuits designed and built by H. S. Somers, Jr. and P. R. Weiss of the Rad Lab contingent and was capable of providing more than 1.2 T. It gave excellent service for some 40 years.

Early in the summer of 1946 I gave a seminar at Rutgers on NMR, the notes for which were written up and distributed to the Rutgers staff; copies were sent to other laboratories including Harvard and Columbia. In these talks, I applied (I believe for the first time) to the case of magnetic resonance the well-known kinematic formula for the motion of a vector in a rotating frame in terms of its motion in the original frame. This procedure, soon commonplace, gives a very *anschaulich*

picture of the motion of the magnetization vector if the rotating frame is the one in which the effective rotating component of the magnetic field is fixed. It is seen to be a uniform precession about a fixed vector in the rotating frame with rectangular components: $\gamma \boldsymbol{H}_1$ and $\gamma \boldsymbol{H}_0 - \omega$ at an angular frequency equal to the magnitude of this vector. From the point of view of the laboratory frame, the motion appears as a nodding or nutation of the magnetization vector with the above frequency.

The Bloch equations[16] for the rate of change of the components of the nuclear magnetization in the rotating frame include, besides the magnetic field torque, the interactions of the spins with the lattice and with themselves. These interactions are incorporated simplistically in the equations as linear relaxation terms with different time constants, T_1 for longitudinal decay and T_2 for transverse decay. The steady state is given by putting the time derivatives equal to zero and gives simple Lorentz-shaped resonances with saturation terms in the denominators.[14]

It was clear to me that nutational motions of the nuclear magnetization as predicted above could be observed as transients following the application of pulses of radiofrequency magnetic fields. These transients would be damped by the relaxation terms above and the nutational frequency would also be affected by them. The Bloch equations are simple linear differential equations of the third order and their solutions can be written down in terms of the roots of a cubic algebraic equation. The general result is mathematically messy, but is greatly simplified in three special cases which cover most situations of interest: (a) exact resonance; (b) $T_1 = T_2$; or (c) T_2 long compared with the nutational period. I worked out these solutions and compared them to observations in liquids such as glycerine and distilled water.[17] This was the first application of rf pulses in NMR.

My motivation in using pulses was to observe the nuclear signal during the rf pulse; if I had looked for the free decay of the nuclear signal after a pulse I might also have seen the amazing phenomenon of *spin echoes*, observed soon after my work by E. L. Hahn[18] in the outstanding example of serendipity in the history of this serendipitous subject. Even if I had seen the echoes I might not have divined their nature. Hahn, at the time just a graduate student with no knowledgeable person then at the University of Illinois to advise him, deserves a tremendous amount of credit for finding the right explanation of the phenomenon which he first regarded as a nuisance. It was the excitement generated by spin echoes that was responsible for a surge of interest in pulse techniques in NMR leading to many major developments in the field, many of these the handiwork of Hahn and his collaborators.

My work with pulses continued with an examination of the effects of a long train of pulses, each with the same duration and with equal intervals between pulses. If a pulse starts with the magnetization oriented along the steady field and endures for an integral number of nutational periods, the magnetization will be left with the same orientation and some attenuation due to the relaxation processes, but will grow during the succeeding off-time. After sufficient time a steady state results in which the nuclear signal is large if a pulse duration is short compared with the relaxation times even for fairly closely spaced pulses, but if the condition on the nutational period is not exactly satisfied the magnetization will make increasing angles with the field on succeeding pulses and the signal will be small. This phenomenon, which I called nutational resonance, was used[19] as a means of measuring long T_2 values in the case of motionally narrowed NMR lines. About this time a considerable boost to NMR at Rutgers was made by the addition of H.Y. Carr, whose Harvard thesis under Purcell incorporated many ingenious refinements and extensions of spin echo techniques.

The Bloch equations, in spite of their phenomenological nature, give a surprisingly accurate account of lines sharply narrowed by motion or exchange. Questions have arisen as to their accuracy in weak fields where a distinction might be noticed between relaxation with respect to the steady field or with respect to the instantaneous field. Testing this question in NMR is difficult because of the weakness of signals, but is easy in ESR (electron spin resonance) where the signal is relatively strong. Using free radicals with sharply exchange-narrowed ESR lines, it was found[20] that the ordinary Bloch equations gave results strongly deviating from experiment for the absorption of radiation as a function of magnetic field passing through zero, but these data agreed well with the predictions of Bloch equations modified so that relaxation was assumed to take place with respect to the instantaneous rather than the steady field.

A final modification of the Bloch equations was made[21] to provide for the case of diffusion of magnetization by including diffusion terms. I illustrated the use of these terms by applying the equations to spin echo effects. Just after submitting this article to the *Physical Review*, I read a paper on this subject at a meeting of the American Physical Society in New Haven, CT. In the audience was Lars Onsager, the famous Yale physical chemist, who in the question period pointed out that the equations as I had presented them would not lead in general to thermal equilibrium. I had to agree with him and after the talk I thought of a further modification that would overcome his objection. Seeking him out, I presented this idea to him and he agreed that it would do the trick. I hastily recalled the paper from the *Physical Review* and made the change required. Unfortunately, the footnote in which I acknowledged Onsager's help made it sound as though he had suggested the specific change I made and some people have so interpreted it, giving it a cachet which it doesn't deserve. As I pointed out in the paper, the change, which amounted to a drift current caused by forces on magnetic moments by field inhomogeneity, was not experimentally significant in NMR, although it later turned out to be so in ferromagnetic resonance.

All the modifications of the Bloch equations I have suggested, both for weak fields as well as for diffusion, are incorporated in equation (4) of Ref. 21. Although my researches at Rutgers on NMR extended in other directions, the scope of this article is restricted to my early work on the Bloch equations.

On the evening of December 15, 1945, after our first observation of NMR in a solid, Purcell, Pound, and I were sure that we had started something that would engage the interest and activity of many people, and would have many applications beyond what we could then imagine. But if we had been given a crystal ball to see the state of the art as it is today, we would have been astonished at its extent and variety, and above all its usefulness. A short time ago, Ed Purcell remarked to me that we could be thankful that the uses of NMR were all beneficial. Still imbued with a Cold War mentality, I replied somewhat cynically that some destructive use unknown to us

had probably been found if not for it, then by it. Now I have cast aside such unworthy thoughts and rejoice with Ed and Bob at all the many happy issues of our old enterprise.

REFERENCES

1. I. I. Rabi, J. R. Zacharias, S. Millman, and P. Kusch, *Phys. Rev.*, 1938, **53**, 318.
2. I. I. Rabi, *Phys. Rev.*, 1937, **51**, 652.
3. C. J. Gorter, *Physica (The Hague)*, 1936, **3**, 995.
4. C. J. Gorter, *Phys. Today*, January 1967, **20**, 76.
5. J. S. Rigden, *Rabi: Scientist and Citizen*, Basic Books, New York, 1987, p. 96.
6. As quoted by J. S. Rigden in Ref. 5, p. 96.
7. C. J. Gorter and L. J. F. Broer, *Physica (The Hague)*, 1942, **9**, 591.
8. D. A. Jackson and H. Kuhn, *Nature (London)*, 1936, **137**, 108.
9. J. M. B. Kellogg, I. I. Rabi, and J. R. Zacharias, *Phys. Rev.*, 1936, **50**, 472.
10. H. C. Torrey, *Phys. Rev.*, 1937, **51**, 501.
11. H. C. Torrey, *Phys. Rev.*, 1941, **59**, 293.
12. P. Kusch, S. Millman, and I. I. Rabi, *Phys. Rev.*, 1940, **57**, 765.
13. S. Millman and P. Kusch, *Phys. Rev.*, 1940, **58**, 438.
14. E. M. Purcell, H. C. Torrey, and R. V. Pound, *Phys. Rev.*, 1946, **69**, 37.
15. F. Bloch, W. W. Hansen, and M. Packard, *Phys. Rev.*, 1946, **69**, 127.
16. F. Bloch, *Phys. Rev.*, 1946, **70**, 460.
17. H. C. Torrey, *Phys. Rev.*, 1949, **76**, 1059.
18. E. L. Hahn, *Phys. Rev.*, 1950, **80**, 580.
19. H. C. Torrey, *Phys. Rev.*, 1952, **85**, 365.
20. R. S. Codrington, J. D. Olds, and H. C. Torrey, *Phys. Rev.*, 1954, **95**, 607A.
21. H. C. Torrey, *Phys. Rev.*, 1956, **104**, 563.

Biographical Sketch

Henry C. Torrey. *b* 1911. B.S., 1932, University of Vermont, Ph.D., 1937, Physics, Columbia University, USA. Physics Faculty, Pennsylvania State University, 1937–42. Staff member, Radiation Laboratory, Massachusetts Institute of Technology, 1942–46. Physics Faculty, Rutgers University, 1946–76. Dean of Rutgers Graduate School, 1965–74. Collaborated with E. M. Purcell and R. V. Pound in the first observation of NMR in bulk matter. NMR research in transient effects, Bloch equations, spin relaxation and polarization.

Veeman, Wiebren S.: Personal Reflections on Solid State NMR in the Early Days

Wiebren S. Veeman

Gerhard-Mercator-Universität Duisburg, Duisburg, Germany

After I completed my Ph.D. in Leiden in 1972, I had the opportunity of a postdoctoral stay at the IBM Research Laboratory in San Jose (CA) with Dr. C. S. (Nino) Yannoni. It was from him that I heard for the first time of experiments to obtain 'high'-resolution NMR spectra of solid samples. I learned that, at that time, there were three techniques to obtain high-resolution solid state spectra: a technique invented by Mansfield and Grannell,[1] the now well-known proton-enhanced ^{13}C NMR technique of Pines, Gibby, and Waugh,[2] and a technique from Bleich and Redfield, of which a full account was published much later.[3] Yannoni was working with the latter technique, with which he had been able to obtain the ^{13}C chemical shift anisotropy of solid benzene[4] and the ^{19}F spectrum of 1,1,1-trifluorotrichloroethane in an adamantane host by fluorine–hydrogen intermolecular double resonance.[5]

I was supposed to carry out further work on the development of matrix isolation NMR, whereby the structure of a reactive species in an inert fluorinated matrix could be determined with high-resolution solid state NMR. In contrast to the proton-enhanced method, the Bleich–Redfield technique was basically a continuous wave experiment in which an abundant spin signal was observed. The experiment was switched between a detection period, during which the signal of abundant spins I was observed off-resonance in a time-shared way, and a cross-relaxation period, in which on resonance a Hartmann–Hahn[6] contact was made between spins I and a second spin species S. By selectively irradiating the S spins, the S spin spectrum could be plotted out via the intensity changes of the I spin signal. At that time the experimental difficulty of the Bleich–Redfield technique was tremendous. Three rf irradiation frequencies were needed, adiabatically switched on and off, and the experiment was a constant fight against stability and noise problems. Although we knew, for instance, about the magic angle spinning technique,[7,8] and we talked about the possibility of combining it with the double resonance technique, we did not believe that a combination would be experimentally feasible.

To conclude, I must say that we lost the fight against noise and instability, and after I returned to the Netherlands both of us started to work with the proton-enhanced ^{13}C technique which is much less sensitive to instrumental instabilities. I nevertheless think that I would have learned less of solid state NMR and NMR equipment if the proposed experiment had been successful from the beginning.

REFERENCES

1. P. Mansfield and P. K. Grannell, *J. Phys. C.*, 1971, **4**, L197.
2. A. Pines, M. G. Gibby, and J. S. Waugh, *J. Chem. Phys.*, 1972, **56**, 1776.
3. H. E. Bleich and A. G. Redfield, *J. Chem. Phys.*, 1977, **67**, 5040.
4. C. S. Yannoni and H. E. Bleich, *J. Chem. Phys.*, 1971, **55**, 5406.
5. C. S. Yannoni, *J. Chem. Phys.*, 1973, **58**, 1773.
6. S. R. Hartmann and E. L. Hahn, *Phys. Rev.*, 1962, **128**, 2042.
7. E. R. Andrew, *Arch. Sci. (Geneva)*, 1959, **12**, 103.
8. I. J. Lowe, *Phys. Rev. Lett.*, 1959, **2**, 285.

Biographical Sketch

Wiebren S. Veeman. *b* 1942. M.S., 1967, Technical Physics, University of Delft (supervisor J. Smidt), Ph. D., 1972, University of Leiden (supervisor J. H. van der Waals). Postdoctoral fellow, IBM Research San Jose, CA, 1973–74. Wetenschappelijk medewerker, University of Nijmegen, 1974–86; Professor in Physical Chemistry, University of Nijmegen, 1986–91; Lehrstuhl für Physikalische Chemie, Gerhard-Mercator-Universität, Duisburg, 1991–present. About 120 publications. Research specialty: solid state NMR and its applications to materials.

Vega, Alexander J.: Beginnings, Vaughan, and Solid State NMR

Alexander J. Vega
Dupont, Wilmington, DE, USA

I was born in 1938 in the small town of Ouderkerk in the vicinity of Amsterdam. During the Nazi occupation of the Netherlands, I was hidden by a Christian family in Arnhem and later in the north of the country.

I received my undergraduate degree from the University of Amsterdam with a combined chemistry/physics major. There was a lot of math to catch up on when I decided to continue in physics. Still inspired by my math teacher, S. A. Colthoff from the Amsterdam Jewish High School, I went about this thoroughly. It took me quite a while, as I was a slow student.

I had my first encounter with magnetic resonance when, as part of a required tour of various research labs, I spent two months with John Henning and Cees de Waard who were doing ESR at the Physics Laboratory (the 'Nat Lab') of the University of Amsterdam. I immediately became intrigued by this technique which seemed so fundamental in its physical methods and powerful in its analytical power. I continued my Master's work with John and Cees, who introduced me to NQR and showed me how to build an oscillator. Later the magnetic resonance group was led by Harold de Wijn, a superb inspiring physicist. There I learned to do science and to recognize the essence of physical phenomena without being sidetracked by formalism. At that time I married Ankie Boas who was a math student in Amsterdam.

In the summer of 1967 we made a trip to Israel to look for a place to do my Ph.D. work. I visited the magnetic resonance labs of several academic institutions. At the Weizmann Institute in Rehovot I was received by Daniel Fiat. He showed me Abragam's book and asked if I could read it. Back in Holland we were familiar with Slichter's book while Abragam was considered to be at a more difficult level. Luckily, I had just managed to master a few of its passages, so I could answer 'yes' to the question. A quickly arranged oral exam by Shlomo Alexander got me accepted to the chemistry Ph.D. program before the end of our vacation. At the Weizmann Institute, Danny and his students were enthusiastically investigating the solvation chemistry of paramagnetic ions in aqueous solutions. They educated me in the chemical approach to NMR. However, in view of my earlier transition to physics, which I considered to be superior, I somewhat resented having to practice chemistry myself. Danny did his best to comply with this foolish notion and suggested that I work on crystal water in paramagnetic solids. In all, Fiat has been quite supportive of me. I remember his excitement when he returned from the conference where John Waugh announced the WAHUHA experiment. Danny understood that this technique was going to have a great future. He arranged for me to spend the summer of 1969 at MIT, the year that Ulrich Haeberlen left, Michael Mehring came in, and Alex Pines was a student there. That visit helped me a lot. I was amazed by the innovative thinking in the Waugh group.

Back at the Weizmann Institute, I eventually became deeply involved in solution state NMR. It started with a problem posed to me by Jacques Reuben, Fiat's first doctoral student, who was instrumental in the development of the use of rare-earth shift reagents. The problem had to do with the pseudocontact shift of nuclei in the vicinity of paramagnetic ions in solution and an anomaly that Jacques had identified in the theory developed by McConnell and Robertson. I struggled for a long time to find a suitable formalism to tackle this problem, until I got hold of Jack Freed's first manuscript dealing with the stochastic Liouville equation. Jack just happened to be working on this paper during a sabbatical visit with Zeev Luz at the Weizmann Institute. I now had a way to describe the spin states of molecules with randomly changing orientation.

It finally dawned on me that the pseudocontact shift anomaly arose from an often made but mistaken application of the motional-narrowing concept to the equilibrium state of spins in fast motion: it is wrong to assume that the equilibrium distribution of spin states (in this case those of the unpaired electrons) is averaged by fast molecular motion. I defended this contention in heated discussions with people like Shlomo Alexander at the Hebrew University and Danny Fiat. In fact, the main thrust of my Ph.D. work was a systematic justification of this point. It was amusing to see the debate on motional averaging of the equilibrium spin state, in a slightly different context, resurface in the NMR literature as recently as last year.

My closest associate during my years at Weizmann was Avraham Achlama, a Fiat student who did fundamental work on the contact shift. A particularly enriching experience was the weekly seminar, originally together with Zeev Luz's group, where Abragam's book was thoroughly read and discussed.

In 1974 I was in Nottingham at the AMPERE Congress. There I met Bob Vaughan. I stepped up to him and asked if I could be a postdoc with him. He came to listen to my talk and then said that I could come. I spent two years at Caltech, from 1975 to 1977. The atmosphere there was inspiring. Bob was always talking about new opportunities for innovative developments of NMR, but never as a sterile science. New experiments should be developed with a realistic chemical purpose in mind. This was new to me. At that time I did not know of anyone who was applying modern solid state NMR with that level of dedication to practical problems. I was asked to collaborate with Mike Stoll on the development of the pulse method which is now known as the separate local field technique (SLF). The idea was to use the axis frame of the chemical shift tensor to determine experimentally the directions of internuclear vectors. It was all part of Bob's vision. He vividly pictured molecules sitting on surfaces, undergoing reactions, their structures figured out by NMR.

Working with Mike Stoll and sharing a room with him was a rewarding experience. With him, I marveled at the wonder and beauty of physics and at all things physical and spiritual, for that matter. I was there when Mike stumbled on the pulse sequence *xyxyxy* and calculated that its only effect on the spins was to phase shift their wavefunctions by 180°. He immediately recognized this as a manifestation of the spinor property of half-integer spins and realized that the only way of observing it would be by interference with the wavefunction of a second spin. This led to the 'spinor experiment' which I only began to believe after I worked it out in density matrix

formalism. In that form, it turned out to be nothing more than another example of multiple quantum NMR, the new family of experiments just being initiated by my brother Shimon and by Alex Pines in Berkeley. As a byproduct, we discovered the virtues of multiple quantum relaxation, albeit without calling it such. Soon after completion of his Ph.D., Mike Stoll left spectroscopy to become a radiologist.

Since 1977 I have been at DuPont CR&D, attempting to follow Vaughan's example by trying to perform interesting NMR in the service of the analytical needs of the company. At DuPont, I had the good fortune to collaborate with several outstanding NMR spectroscopists, including Alan English, with whom I worked on ^{19}F multiple pulse NMR of molecular motions in Teflon; Richard Eckman, now at Exxon Chemicals, on deuterium NMR of adsorbed molecules; Zeev Luz, on zeolite characterization and deuterium spin dynamics and relaxation; and Clare Grey, now at Stony Brook, on the TRAPDOR double resonance experiment with quadrupolar nuclei. Over the years, my brother Shimon and I have met on numerous occasions, during family visits or while sharing rooms at conferences. Although we have mutual interests in many aspects of life, our conversations inevitably drift towards magnetic resonance, the topic that evidently continues to intrigue both of us a great deal.

Biographical Sketch

A. J. Vega. *b* 1938. B. S. (kandidaat), 1961, M.S. (doctorandus), 1967, University of Amsterdam, Ph.D., 1974, Weizmann Institute of Science, Israel, (supervisor Daniel Fiat). Postdoctoral work at California Institute of Technology (with Robert W. Vaughan), 1975–77; DuPont CR&D, 1977–present. Approx. 60 publications. Research interests: solid state NMR for applications in materials research.

Vega, Shimon: From Zero Field via Double Quantum to Dressed States

Shimon Vega

Weizmann Institute of Science, Rehovot, Israel

I was born in Ouderkerk, a village about 10 kilometers outside Amsterdam, in 1943, in the middle of World War II. At that time my parents were still at home; my brother and sister, however, were already hiding with good families. When I was six weeks old, the Dutch Underground Movement brought me to a wonderful lady and her daughter, who took good care of me until the end of the war.

Like Lex, I went to high school in Amsterdam and studied physics and mathematics at the Gemeente Universiteit of Amsterdam. For my doctorandus studies, I joined the solid state physics group of Dr. A. R. Miedema who was investigating low-dimensional ferro- and antiferromagnetic materials. Evert Maarschall, a member of this group, was dealing with ^{19}F NMR of K_2NiF_6, and I assisted him in measuring fluorine line-shifts and -widths. Evert loved quantum mechanics and so he taught me the quantum description of NMR with the help of 'The Feynman Lectures on Physics'.

After my wife and I decided to look for a Ph.D. fellowship in Israel, I went there to look for a supervisor who would be ready to take me as a student. During my visit I met Zeev Luz in the hallway of the Physics Department of the Weizmann Institute. He told me that he had just taken charge of the ^{14}N pure NQR spectrometer that belonged to the group of Shlomo Alexander. He invited me to join his group and to start a Ph.D. project on pulsed ^{14}N NQR. I agreed and at the end of 1969 we arrived in Israel. The group of Luz was very active and stimulating. For example, under his leadership his students, together with students of Daniel Fiat, Mordechai Shporer, and David Zamir, held evening seminars, where we read Abragam 'without skipping a word'.

To interpret my experimental results we had to extend some of the basic theoretical descriptions of NQR on $I = 1$ spins. As a result, and with the steady encouragement and guidance of Zeev Luz, I published a paper on second and fourth moments of the spectral lines of $I = 1$ spins and a paper, introducing a set of fictitious spin-$\frac{1}{2}$ operators, that simplified the density matrix description of zero-field NQR on these spins. In these spin systems the three possible transitions are all 'allowed' and all their coherences can be observed.

Toward the end of my Ph.D. studies, Alex Pines visited the Weizmannn Institute and told us about his cross polarization experiments. We were very impressed and I asked if I could become one of his first postdocs. He agreed and in the summer of 1974 I joined his group in Berkeley. He suggested that I work on CIDNP and try to measure the isotope enrichment of molecules that undergo biradical cage recombinations. I was not a very good chemist and not successful. At that time Tom Shattuck was working on ^{2}H NMR experiments and he observed some unexpected experimental results. I joined his efforts to understand his data and tried to help by describing his results in terms of the fictitious spin-$\frac{1}{2}$ operator formalism. After some time we understood the evolution of the coherences of $I = 1$ spins in high fields somewhat better and we started talking about double quantum coherence. I did not have many problems with the 'detection' of the double quantum coherence because I was used to the fact that you could observe *all* transitions of $I = 1$ spins.

At a particular point we came upon the condition for double quantum decoupling of deuterium from protons. Alex looked at the condition on the blackboard and immediately explained to me that in the near future double and multiple quantum spectroscopy was going to become a very important aspect of NMR. I was very impressed. Alex was way ahead of me. Of course, we were aware of the work of Meiboom, Hashi, and Ernst and their co-workers in the field of multiple quantum NMR. I should also mention the frequent visits of Erwin Hahn to Alex's laboratory and our exciting discussions with him about his work with Brewe and our work. Alex, Tom, and I worked hard and developed the various double quantum experiments: cross polarization, decoupling, coherence excitation, and detection.

Alex, together with his students and postdocs, continued to develop the fascinating aspects of multiple quantum NMR. I was offered a position at the Weizmann Institute. In 1976 I returned to Israel, published my paper on fictitious spin-$\frac{1}{2}$ operators at about the same time that Wokaun and Ernst did, and set up my first homebuilt 90 MHz spectrometer with the help of Yuval Zur. Yuval Zur and Ya'akov Naor, my first graduate students, studied double and triple quantum cross polarization and double and triple frequency excitation schemes of spins with $I = 1$ and $I = \frac{3}{2}$.

Ya'akov was the first in our group who tried to describe our multiquantum results in terms of Shirley's Floquet formalism. It took us quite some time before we really understood what the Floquet theory could do for us in NMR. However, eventually, with Yuval and Malcolm Levitt, at that time a postdoc at the Weizmann Institute, we published our first Floquet paper, describing 'N-proton' pulse excitations of single $I = \frac{1}{2}$ spins. Later Eric Krauss continued this work and we became Floquet fans.

I achieved tenure in 1980 and two years later I joined the group of Bob Griffin at the National Magnet Laboratory for one year. Bob taught me all about MAS NMR and I participated in their exciting research of multipulse experiments. We made extensive use of the vector picture, describing the trajectories of the magnetization vectors of rotating $I = \frac{1}{2}$ spins, and again applied the Floquet approach to explain the rotor frequency lines in multiple pulse MAS NMR spectra. Back in Rehovot, the Floquet theory was extended and we started calculating dynamic MAS spectra described the rotational resonance (R^2) phenomena in terms of a degeneracy of Floquet states and searched for selective excitation schemes.

New M.Sc. and Ph.D. students, postdocs, and visiting scientists kept joining the group during the years. We studied three-photon pulses and pulse shaping with Gadi Goelman, David Zax, Ed Sternin, and Dov Abramovitch; magic angle spinning with Asher Schmidt, Lucio Frydman, and Ofer Weintraub; zeolites with Irina Kustanovich, Zeev Luz, and Hans-Martin Vieth; also inclusion compounds with Irina and with Inka Allen and Eduardo Zaborowski; and semiconductors with David Zax, Hans-Martin Vieth, Michal Gavish, Aviva Farag and David Zamir. Of course, the inclusion compound

and zeolite projects were only possible with the help of Herbert Zimmerman.

My interest in MAS NMR continued and in 1990 I went for a sabbatical to St. Louis to join Jake Schaefer. His solid state NMR group was continuing its novel and pioneering work and, as a result of Bob McKay's expertise, they had NMR probes that allowed very unique multispin experiments. Jake's group was applying the REDOR technique for distance measurements between heteronuclear atoms. Working with them made me aware of some limitations of this method and together with Andrew Hing we introduced and developed the TEDOR experiments for heteronuclear spin pairs. Before and during that time I was looking for a pulse method, in addition to the existing DRAMA and R^2 experiments, that would extend the homonuclear distance measurements in rotating samples. The Floquet formalism helped me to realize that a simple set of synchronously applied 180° pulses does the job. Based on this idea, the first results of the SEDRA experiments were published together with Terry Gullion, the RFDR and BDR experiments were introduced by the group of Bob Griffin, and the $\Delta S/S$ SEDRA distance measurements were performed.

Back in Rehovot we generalized the Floquet theory, showing the analogy between the normal spin density matrix and the Floquet density matrix and demonstrating the use of effective Hamiltonians in MAS NMR. Today, in addition to most of the research activities mentioned above, we are still exploiting Floquet theory to describe periodically time-dependent NMR experiments, in particular dynamic MAS ^{2}H NMR and spin lock and CPMAS experiments involving $I = \frac{1}{2}$, $I = 1$, and $I = \frac{3}{2}$ spins with large interactions.

Biographical Sketch

S. Vega. *b* 1943. B.S. (kandidaat), 1965, M.S. (doctorandus), 1969, University of Amsterdam, Ph.D. 1973, Weizmann Institute of Science, Israel, (supervisor Zeev Luz). Postdoctoral work at University of California, Berkeley (with Alex Pines), 1974-76. Senior scientist at Weizmann Institute, 1976–80. Tenure position at Weizmann Institute, 1980–present. Sabbatical at MIT, (with Bob Griffin), 1982–83. Sabbatical at Washington University, St. Louis (with Jacob Schaefer), 1990–91. Approx. 75 publications. Research interest: solid state NMR.

Vold, Robert L.: Reflections

Robert L. Vold

College of William and Mary, Williamsburg, VA, USA

I have been fortunate to observe and participate in the development of nuclear magnetic resonance since the early 1960s. In this article, I will summarize some high points of this continuing journey. These recollections are necessarily personal, and subject to the usual sources of systematic error.

My first exposure to NMR came in 1962, as an undergraduate at the University of California, Berkeley. Professor R. E. Connick was in charge of the advanced inorganic chemistry laboratory, and he gave me and my lab partner some xenon trioxide to characterize as a term project. After I discovered that XeO_3 explodes spontaneously on contact with weighing paper, Prof. Connick informed me that I had used up the world's supply and suggested I find a different project. This involved measuring proton chemical shifts in water/acetone mixtures, with the aim of interpreting the concentration dependence in terms of hydrogen bonding. I was delighted to see, just as described in 'the bible',[1] that at low water concentration the water peak actually appeared at higher field than the methyl protons of acetone. These experiments were done on the latest and snazziest spectrometer, a Varian A-60. This machine was so stable that it wasn't even necessary to calibrate the chemical shifts with an audio sideband generator! I was hooked. I knew I wanted to do graduate work in NMR, and I applied to the University of Illinois because Prof. Gutowsky was there and he had the longest citation list in Pople, Schneider, and Bernstein.

The University of Illinois was a great place for graduate work: there were no scenic distractions for 500 miles in any direction. While standing in registration lines in the fall of 1963, I met Dave VanderHart and Bob Vaughan, who were enrolling in the same courses as I. We became good friends, even though Bob kept telling us that NMR was a dead field and we should all be doing Mössbauer spectroscopy instead! There were about 20 graduate students and postdocs in Prof. Gutowsky's group, working on everything from high-resolution NMR of liquids, to wideline NMR of solids, to ESR. I was struggling to understand the spin density matrix, in order to calculate effects of chemical exchange in multiple pulse Carr–Purcell spin echo experiments on coupled spin systems. About six months into the project, I discovered that a postdoc with a desk just behind me, Ted Wells, was doing exactly the same thing! There was an euphoric time when every few days Prof. Gutowsky would suggest a new potential application, and Ted or I would come into the lab next morning with the appropriate detailed calculation.

The 30 MHz rf transmitter which I was privileged to use at Illinois merits mention. Its rf source was a battery powered World War II vintage oscillator, gated and amplified by a 30-tube circuit which was designed and built by previous generations of students (notably Donald Woessner and Bob McKay). I was warned that the transmitter would work only if it was mounted upside down. I didn't believe this until I had to replace a tube and tried to run the unit mounted right side up. It refused to run at all until I turned it back upside down, and a capacitor (rumored to have been soldered by T. C. Farrar) fell out!

Professor Gutowsky was very generous in providing support for several students to attend the Experimental Nuclear Magnetic Resonance Conference, held annually at the Mellon Institute in Pittsburgh. My first ENC was the 6th, in 1965. Everyone was bemoaning the fact that the meeting had become so large, with over 100 people attending! Richard Ernst announced and demonstrated the first use of Fourier transform NMR at this meeting. I overheard several eminent experts opine that this flashy new technique would never catch on, because phase corrections and other computer-intensive data processing procedures were too complicated, arbitrary, and expensive for the average spectroscopist.

In 1967 I spent a short postdoctoral period in Prof. Waugh's laboratory at MIT. He had just realized the implications of prolonged echo decays in multipulse solid echo experiments, and with Ulrich Haeberlen was developing average Hamiltonian theory. A promising graduate student, Alex Pines, was starting to explore applications to ^{13}C spectroscopy. I became involved with calculations of the chemical shift concertina, a pulse sequence designed to scale the chemical shift interaction in liquids. Since I was to be at MIT only six months before joining the faculty at the University of California, San Diego, I decided not to become involved with any experiments—this was a great mistake, since I missed the chance to learn first hand from Waugh, Pines, and R. G. Griffin how to do multipulse proton experiments on solids and ^{13}C experiments with cross polarization from protons.

Professor Waugh sponsored the attendance of several group members at a small NMR conference held every other year in New Hampshire. At the 1967 meeting, I was sitting at one late night discussion at the bar with Joseph Noggle and Karl Kuhlman, who had recently finished graduate work at Stanford with Prof. Baldeschwieler. The talked turned from density matrices to the newly announced Fourier transform method, and how it worked if the pulses were applied so closely that there wasn't enough time for full recovery of the magnetization. We thought for a while that with just two pulses, spin–lattice relaxation AFTER the second pulse would distort the signal beyond recognition. Soon we saw the error in this argument, and realized that if the first pulse were an inversion pulse, one could by means of FT measure the T_1 of each line in the spectrum. John Waugh realized the implication of this invention and convinced Melvin Klein (who at Berkeley had one of the few working FT systems) to try the experiment. My main contribution to the resulting paper[2] was the suggestion that a field gradient pulse, applied between the inversion and detection pulse to destroy unwanted coherence, could also be used in a Fourier transform spin echo sequence to measure diffusion coefficients of individual chemical species.

It was an enormous shock to leave the established programs of Professors Gutowsky and Waugh, and be faced with the task of developing an NMR program of my own at the University of California, San Diego. Then, as now, startup funds were inadequate: I was given a magnet and an oscilloscope, but had to assemble the rest of the spectrometer from components. And in those days, it was unheard of for any individual to monopolize a whole computer! A few companies, such as Magnion and NMR Specialties, provided complete pulsed spectrometers (at an outrageous price) but it was strictly caveat emptor. It seemed obvious at the time that I was in no position to compete in high-resolution solid state NMR, so while I was learning to build pulsed NMR spectrometers I modified

the departmental machine (a Varian HR-60) to do low power, liquid state Carr–Purcell spin echo experiments. This was my first exposure to the luxury of a phase sensitive detector, but it was disconcerting to see the FID change sign as the field drifted through resonance.

My experiences with chemical exchange at Illinois gave me a lasting interest in relaxation phenomena in coupled spin systems. The natural combination of this with FT methods of measuring T_1 led me to realize the importance of cross-correlation effects in dipolar relaxation of multispin systems. It was exciting to discover that cross-correlation effects in proton spin–lattice relaxation of planar molecules could be analyzed to fix the orientation of a fully anisotropic rotational diffusion tensor—conventional wisdom decreed that this was not possible.

The work on individual spectral densities for proton relaxation in scalar coupled systems set the stage for analogous experiments on systems with dipolar and quadrupolar couplings. I realized that by using deuterons instead of protons or carbon, the number of independent spectral densities to be determined was neatly matched by the number of readily measurable relaxation rates. Moreover, 'everybody knew' that quadrupole relaxation in fluid phases was governed exclusively by rotational motion. So, at first, it seemed that deuteron relaxation of small molecules in liquid crystals was the ideal way to study anisotropic rotational diffusion. However, it soon became clear that the anisotropic fluid was producing unusual effects. In fact, deuteron relaxation measurements of individual spectral densities proved to be as informative about collective processes, such as order director fluctuations, as they were about the effects of an orienting potential on single particle rotation.[3]

The orienting potential felt by a small molecule dissolved in a liquid crystal is just one example of a constrained environment. Much tighter motional constraints are imposed by confining the molecule to a crystal lattice. Channel inclusion compounds represent an interesting intermediate situation, in which motion of the guest provides unique information about the potential energy of host/guest interactions. With recent advances in computer simulation methods, it has become possible to calculate correlation functions of interest in NMR without recourse to simplified models. Equally important, multidimensional techniques for monitoring spin relaxation greatly expand our ability to study motion over a wide range of timescales. Comparing the results of molecular dynamic simulations with experimental NMR data offers a new and powerful method to refine and improve the relevant potential functions. Inclusion compounds are particularly important in this context because the motion is often fast enough to yield pleasantly short relaxation times, and the computer time needed for a simulation scales only linearly with the number of guest molecules.

In my first 35 year involvement with NMR, the increase in its sophistication and scope of applications has been truly incredible. Nobody dreamt in 1962 that it would be possible to determine the fully anisotropic rotational diffusion tensor of a small molecule in a liquid crystal, let alone fully assign the proton spectrum of a small protein, obtain multidimensional high-resolution ^{13}C spectra of solids, or measure the distribution of rotational jump rates in a polymer. One can only guess what the next 50 years will bring.

REFERENCES

1. J. A. Pople, W. G. Schneider, and H. J. Bernstein *High Resolution Nuclear Magnetic Resonance*, McGraw-Hill, New York, 1959.
2. R. L. Vold, J. S. Waugh, M. P. Klein, and D. E. Phelps, *J. Chem. Phys.*, 1968, **48**, 3831.
3. R. R. Vold and R. L. Vold, *Liquid Crystals and Ordered Fluids*, eds. A. C. Griffin and J. F. Johnson, Plenum, New York, 1984, Vol. 4, p. 561.

Biographical Sketch

Robert L. Vold. *b* 1942. B.Sc., 1963, University of California, Berkeley, Ph.D., 1966, (supervisor H. S. Gutowsky), University of Illinois. Postdoctoral work at Massachusetts Institute of Technology, 1966–67 (J. S. Waugh). Assistant, associate, and full professor of Chemistry, University of California, San Diego, 1968–91; Program Officer, National Science Foundation, 1992; National Research Council Fellow, NASA Langley Research Center, 1993; Professor of Applied Science and Physics, College of William and Mary, Virginia, 1994–present. Current research specialty: NMR studies of order and dynamics in solids.

Vold, Regitze R.: Bits and Pieces from My NMR Memoirs

Regitze R. Vold

University of California, San Diego, La Jolla, CA, USA

In Denmark, the era of NMR spectroscopy began in early 1962 with the arrival of the first analytical grade spectrometer—a Varian A-60. I still remember vividly my feeling of excitement on seeing this magic machine and the awe I felt when I was allowed to buy my first small bottle of deuterated chloroform, 25 ml for 500 DKr, ~$70 US, corresponding to roughly half a month's salary for a research assistant at Denmark's Tekniske Højskole in Copenhagen. I had become aware of NMR spectroscopy as a chemical engineering student in the late 1950s, and having decided to do research in organic chemistry, I had started spending a lot of time in the library. It was here that my love affair with NMR began—stimulated mostly by Varian's advertisements for high-resolution 60 MHz spectrometers. (Or were some of them for just 40 MHz?) To me, those spectra with their pretty multiplets and sensible line intensities were clearly destined to become the most valuable probe of chemical structures, and I have since wondered how many other chemists were lured into NMR by those Varian advertisements on the back cover of every issue of the *Journal of the American Chemical Society*.

A special event took place in 1959 that educated many Danish chemists about the beauty of magnetic resonance. Carl Ballhausen had just spent a year or two at Bell Labs in New Jersey, and upon his return to Copenhagen he arranged to have his friend and colleague Bob Shulman give a series of six lectures on magnetic resonance at DTH. Bob started with a thorough explanation of the physical background, and I got quite scared—did I really have to understand that much physics to appreciate the 1:2:3 proton spectrum of ethanol? Much of those lectures was beyond my comprehension, but the resonance phenomenon was so clearly superior to 'ordinary' spectroscopy. And although those two different relaxation times were a complete mystery to me, I was intrigued by the fact that one could actually learn about molecular motion and 'chemical exchange' by measuring T_1 and T_2 values. Through these excellent lectures Bob Shulman showed us that NMR was not just a fantastic analytical tool, but also an exciting field of scientific inquiry.

Another important means of education of chemists in Europe was again due to Varian Associates, who for many years held NMR workshops[1] in Zürich, with lectures given by people like Norman Ramsey, Wes Anderson, and Jim Shoolery, and several other prominent members of the American NMR community. I proudly accepted an invitation to write an article about NMR for a newsletter published by Struers Kemiske Laboratorium in Copenhagen, who in return offered to pay my way to the 1961 NMR Workshop. It was a wonderful opportunity to learn about NMR, and those workshops unquestionably were responsible for getting many chemists started in NMR spectroscopy—as well as bringing Varian many spectrometer sales. I could hardly wait to finish my dissertation, start my position at DTH, and do my own NMR research.

Alas, I had accepted a postdoctoral position at the University of New Mexico and an NMR spectrometer was not available in Albuquerque in 1962. In spite of this, I decided to stay in the US, I got married, and bided my time doing organic synthesis until I had a chance in 1965 to go to work with Ted Becker at NIH. Ted had *two* NMR spectrometers, a Varian A-60 as well as a Varian HR-60 with a lovely 0.2 Hz resolution, diligently maintained by Ted's assistant Bob Bradley, without whom NMR would never have made it at NIH. My first assignment was to work on the structure and chemical exchange in cytosine derivatives, and the most exciting event was our demonstration, together with nucleic acid expert Todd Miles, of Watson–Crick hydrogen bonding between purine and pyrimidine bases.[2] When late one evening in 1966 working on the A-60 in the sub-basement of Building # 2 we observed the 1:2:1 base pairing shift of the NH protons in a DMSO solution of 1-methylcytosine and 9-ethylguanine, we laughed and cried and danced around the spectrometer. NMR was indeed wonderful. To our chagrin we soon found out that a similar study was being conducted at MIT by Katz and Penman,[3] and the two studies were published simultaneously.

A more monumental NMR event took place in 1966, namely the publication of Ernst and Anderson's paper on Fourier transform NMR spectroscopy.[4] At the time I wondered why such an important paper had been relegated to the *Review of Scientific Instruments*, a respectable journal but hardly known for its groundbreaking publications in chemical physics. Many years later, at a dinner in La Jolla, Richard Ernst told me that he and Wes had tried in vain to get it published in the *Journal of Chemical Physics*, but that they had given up after receiving two unfavorable reviews! The promise of higher sensitivity available by using FT methods was not lost on chemists interested in low-abundance nuclei, like Ted Becker who wanted NIH to get involved in doing ^{13}C NMR spectroscopy. Many discussions took place during meetings of the DC area's 'NMR-for-Lunch Bunch' and it soon became clear that the most expedient way to get going was to install a multichannel digitizer/signal averager on Tom Farrar's pulse rig at NBS. The next couple of years were memorable ones. Tom's spectrometer was housed in a shielded room that Tom had built during the days when the National Bureau of Standards was located on Connecticut Avenue in DC, right across the street from the Channel 7 television and radio station. The spectrometer was based on a Varian HR-60 magnet, which normally was run unlocked, and we had to convince solid state chemist Tom Farrar to reinstall the Super Stabilizer and the homogeneity shim coils. But at least he didn't try to convince graduate student Steve Druck and me to polish the pole faces with emery paper, as he had done during his years at Urbana. Tom taught us to find resonance by listening to a loudspeaker—it was a surprise to us how loud ^{13}C enriched methyl iodide would sound as you swept through resonance. Except for the Tektronics 160 series pulsers and waveform generators, everything was homebuilt by Tom and his group at NBS. The probe was based on a design by Woessner, and rf units, power amplifiers, and their power supplies were constructed straight out of the *Radio Amateurs' Handbook*. It was an excellent NMR spectrometer, but it contained so many vacuum tubes that we exceeded the 'von Neumann limit', and we had to replace tubes constantly.

The configuration that finally allowed us to get ^{13}C FT spectra used a General Radio frequency synthesizer as a frequency source, a Fabritek 1074 signal averager with 4 K 18-bit words, and a Tally paper tape punch. The Fabritek signal averager was an excellent piece of equipment, full of sturdy magnetic core memory. But since no one at Fabritek had ever worried about rf sensitive detectors, they were not well shielded. It seemed for several months that Fabritek (soon to become Nicolet) did large amounts of development work for the first 1080 computer in our shielded room, but in return we got the earliest non-OEM 1080 computer to be installed. The paper tape was needed for the transport of free induction decays (three 4 K FIDs per tape) by car to NIH for Fourier transformation and other processing on the PDP-10 computer. The Tally mechanical tape punch worked fine, but the PDP-10 was equipped with a 'high speed' optical reader, and the registration did not always work well. This I/O problem taught Steve and me important aspects of 'data processing', namely the replacement of 'dropped channels' by hand. There were other interesting problems in those early days of FT NMR. Irv Salmeen from Mel Klein's lab at Berkeley had kindly given us his phase correction routine, although he warned us that it was somewhat slow. A classic understatement: when Steve and I executed it for the first time a strange quiet descended on the large computer room in Building #12. After a few minutes, a strange mumbling began to be heard around the room. All work being done by six to 10 people on the PDP-10 had come to a complete halt, and soon everyone, led by the system manager, came over to see what these idiot chemists were doing with their NMR spectra. The phase correction routine worked, but we were told in no uncertain terms that we had better replace that routine with something that didn't bring the whole PDP-10 to its knees for 20 min at a time.

During these years at NIH/NBS, I had become very interested in relaxation theory and measurements. One surprise to all of us involved in the ^{13}C liquids work was that T_2 was always much shorter than T_1. According to most of the textbooks at the time $T_2 = T_1$ in nonviscous liquids, and that was definitely not what I found[5] and the explanation was (of course) that spin–lattice relaxation of coupled protons shortened the ^{13}C T_2 value significantly. In order to understand this phenomenon, I contacted Bob Vold at UCSD. By a strange coincidence, he had just discovered a '$\frac{3}{2}$' effect that made the proton T_2 longer than T_1.[6] We clearly complemented each other—it was love at first sight. During the next nearly 20 years we combined marriage and scientific collaboration, focusing on relaxation in coupled spin systems and developing better methods for characterization of molecular motion in condensed phases.[7] We became particularly interested in combining measurements of rate constants for several relaxation modes[7] in order to determine individual spectral densities of motion. One very useful trick was to use the Jeener– Broekaert pulse sequence[8,9] or to combine selective and nonselective excitation of the deuteron doublet[10] observed in macroscopically ordered phases. This way we could measure the relaxation times for both Zeeman and quadrupolar order, from which the spectral densities of motion $J_1(\omega_0)$ and $J_2(2\omega_0)$ could be determined. Our group was not the only one contributing to this field—several elegant studies of deuterium relaxation measurements were published independently at more or less the same time.[11–14] These methods proved particularly useful in studies of macroscopically ordered phases, because it had been shown[15,16] that only $J_1(\omega_0)$ was sensitive to the small-angle librational motion in liquid crystals aligned along the magnetic field. This allowed us to demonstrate that pseudo-coherent modes of motion, the so-called director fluctuations, contribute significantly to spin–lattice relaxation in the radiofrequency range, and consequently that the cutoff wavelength for these modes had to be no longer than a molecular length.[17] The main lesson of this work however, was that while relaxation measurements are admittedly very tedious, studies of the temperature, frequency, and orientation dependence of relaxation rates can be highly informative about details of molecular dynamics.

REFERENCES

1. E. H. Rogers and M. E. Packard (eds.), *NMR and EPR Spectroscopy*, Pergamon, London, 1960.
2. R. R. Shoup, H. T. Miles, and E. D. Becker, *Biochem. Biophys. Res. Commun.*, 1966, **23**, 194.
3. L. Katz and S. Penman, *J. Mol. Biol.*, 1966, **15**, 220.
4. R. R. Ernst and W. A. Anderson, *Rev. Sci. Instrum.*, 1966, **37**, 93.
5. R. R. Shoup and D. L. VanderHart, *J. Am. Chem. Soc.*, 1971, **93**, 2053.
6. R. L. Vold and S. O. Chan, *J. Chem. Phys.*, 1972, **56**, 28.
7. R. L. Vold and R. R. Vold, *Prog. NMR Spectrosc.*, 1978, **12**, 79.
8. J. Jeener and P. Broekaert, *Phys. Rev.*, 1967, **157**, 232.
9. R. L. Vold, W. H. Dickerson, and R. R. Vold, *J. Magn. Reson.*, 1981, **43**, 213.
10. R. R. Vold and R. L. Vold, *J. Chem. Phys.*, 1977, **66**, 4018.
11. S. B. Ahmad, K. J. Packer, and J. M. Ramsden, *Mol. Phys.*, 1977, **33**, 857.
12. J. P. Jacobsen, H. K. Bildsoe, and K. Schaumburg, *J. Magn. Reson.*, 1976, **23**, 153.
13. J. P. Jacobsen and K. Schaumburg, *J. Magn. Reson.*, 1976, **24**, 173.
14. K. R. Jeffrey, *Bull. Magn. Reson.*, 1981, **3**, 69.
15. P. Pincus, *Solid State Commun.*, 1969, **7**, 415.
16. J. W. Doane and D. L. Johnson, *Chem. Phys. Lett.*, 1970, **6**, 291.
17. R. R. Vold and R. L. Vold, in *The Molecular Dynamics of Liquid Crystals, NATO Advanced Study Institute, Il Ciocco, Italia, 1989*, eds. G. R. Luckhurst and C. A. Veracini, Kluwer Academic, Dordrecht, 1993.

Biographical Sketch

Regitze R. Vold. *b* 1937, M.S. 1960, Chemical Engineering, Ph.D., 1962, Chemistry, Danmarks Tekniske Højskole, Copenhagen, Denmark. Postdoctoral work at the University of New Mexico, 1962–64. Staff fellow at the National Institutes of Health with Edwin D. Becker, 1965–71; research chemist, 1971–82, and Professor of Chemistry, 1982–present, at the University of California, San Diego, USA. Approx. 120 publications. Research specialties: relaxation in multilevel spin systems, especially of ^2H, and molecular motion in liquid crystals, inclusion compounds, proteins, and paramagnetic materials.

van der Waals, J. H.: Gorter's Footprints on the Trail That Led to Magnetic Resonance

J. H. van der Waals
Leiden University, Leiden, The Netherlands

The Dutch physicist Cornelis Jacobus Gorter (1907–80) was the first to demonstrate the phenomenon of paramagnetic relaxation. Understanding its implications, he recognized that—at least in principle—the magnetic dipole transitions between the Zeeman components of a nuclear spin system might be observed as a resonance effect. To his regret, Gorter's attempts at observing such resonances in a solid, made in the years 1936 and 1942, remained fruitless. However, since Zavoisky a few years later reported a successful electron spin resonance experiment (1945), and Bloch, Hansen, and Packard, and Purcell, Torrey, and Pound reported nuclear magnetic resonance experiments (1946), it seems appropriate to give a brief historical sketch of Gorter's seminal efforts in this field (Figure 1).

Gorter studied in Leiden where at the age of 25 years he defended a Ph.D. thesis entitled 'Paramagnetische Eigenschaften von Salzen' (paramagnetic properties of salts). He then began his professional career at the renowned but modest physics laboratory of the Teyler's foundation in Haarlem, moved as reader to the University of Groningen in 1936, and was appointed Professor of Physics at the University of Amsterdam in 1940, to a chair formerly held by Zeeman. While in Groningen he had a very fruitful collaboration with his colleague in theoretical physics, R. de L. Kronig; during the difficult war years in Amsterdam he struggled to keep his research going with the help of bright young students, amongst whom was L. J. F. Broer. Gorter's true allegiance, however, remained with the Kamerlingh Onnes Laboratory in Leiden with, at the time, its almost unique low-temperature facilities. Thus, shortly after the war, Gorter seized the opportunity to move from Amsterdam to Leiden, where in 1948 he became the Director of the Kamerlingh Onnes Laboratory. In retrospect, this promotion must have been a challenge for an ambitious young physicist, but also a mixed blessing to be burdened with the directorship of a famous physics institute in those years just after World War II. While physics in the United States had continued to flourish in places like Harvard or the MIT Radiation Laboratory, the situation in Holland after five years of war was dismal. There is no question that Gorter and some of the leading scientists of his generation in Holland were saddled with tasks that interfered with their creative work.

Figure 1 The Dutch physicist Cornelis Jacobus Gorter (Photograph by E. de Jong)

Gorter might, perhaps, best be characterized as one of the last true, general physicists; a man who frowned on specialization and considered almost the whole of physics as his playground. Together with his Ph.D. students or colleagues in theoretical physics, he made major contributions in subjects as diverse as paramagnetic relaxation, nuclear orientation, and the anisotropy of γ-and β-emissions, superconductivity, superfluidity, and the Senftleben effect. Thus, one may wonder, as did Gorter himself in his acceptance speech when honoured with the Fritz London award in 1967, whether he had perhaps spread his efforts too thinly.[1]

I shall merely consider here Gorter's efforts in relation to magnetic resonance. In his student days, Gorter had already been impressed by Ehrenfest's argument[2] that the validity of the Curie–Langevin formula for the magnetization of a paramagnetic material implied relaxation processes induced by thermal motion. After a preliminary, unsuccessful experiment by Breit and Kamerlingh Onnes, Gorter became the first to demonstrate the reality of such relaxation.[3] Heeding Ehrenfest's suggestion, he measured the heat effects accompanying the (electron–spin lattice) relaxation of Fe^{3+}, Cr^{3+}, V^{3+}, Ti^{3+}, and Gd^{3+} ions in alum crystals placed in an rf magnetic field (ν = 10–21 MHz, B_1 = 0.5–0.8 mT) in a calorimeter cooled by boiling hydrogen or nitrogen.

In parallel with these experiments, Gorter and Kronig worked on the theory of absorption and dispersion in paramagnetic crystals under the influence of an alternating magnetic field.[4] Their work was inspired by Debye's treatment of the dielectric behavior of an assembly of rigid dipoles subject to frictional forces and Brownian motion. Gorter realized that when a system of spins $S = \frac{1}{2}$ (or $I = \frac{1}{2}$) is placed in a constant magnetic field $\boldsymbol{B}_0$ and subjected to a second, alternating magnetic field perpendicular to $\boldsymbol{B}_0$, its response can be described by the real and imaginary parts of the magnetic susceptibility, as sketched in Figure 2. The figure, which is a copy of Gorter and Broer's original drawing,[5] shows the now familiar fact that at the frequency ν_0 where the resonance condition $h\nu_0 \approx \mu B_0$ is fulfilled, a magnetic dipole transition occurs which manifests itself by a maximum in the absorption

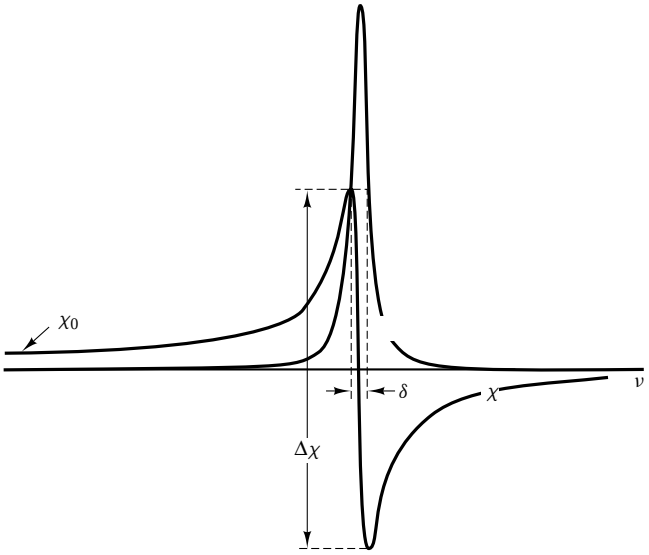

Figure 2 Absorption A and susceptibility χ as a function of frequency ν. The halfwidth δ has been taken equal to $0.05\nu_0$. Reproduced from Gorter and Broer[5] [in current terminology χ denotes the real part (χ') of the susceptibility and A is proportional to its imaginary part (χ'')]. Reproduced by permission of Elsevier Science Publishers

A, accompanied by a 'jump', $\Delta\chi$, in the (real part of the) susceptibility χ. According to Gorter and Broer, this jump, is given by

$$\Delta\chi/\chi_0 = \nu_0/\delta \tag{1}$$

where δ denotes the halfwidth of the spectral transition and χ_0 the static susceptibility due to the spins concerned. If thermal equilibrium obtains, then

$$\chi_0 = N\mu^2/3kT \tag{2}$$

where N is the number of spins per gram and μ is the spin magnetic moment.

Because of the limitation in frequency of the rf equipment at his disposal, Gorter's experiments on the relaxation of paramagnetic salts in strong external fields[6] were restricted to frequencies below those where resonance occurs as depicted in Figure 2. However, Gorter realized that, because of the smallness of the nuclear magnetic moment compared with that of an electron, his equipment should be well suited to investigate *nuclear* paramagnetic relaxation phenomena in the resonance region depicted in Figure 2. Using the calorimetric method that had proved so successful in the demonstration of electron paramagnetic relaxation the same year (1936), Gorter made his first, negative, attempt to detect magnetic resonance transitions of ^{1}H and ^{7}Li nuclei in $K[Al(SO_4)_2] \cdot 12H_2O$ (alum) and LiF crystals, respectively.[7] In these experiments, carried out at liquid hydrogen temperature (14–20 K), the crystals were subjected to a 20 MHz alternating field with a strength B_1 as high as 1 mT and a constant field that could be varied between 0 and 1.4 T. Provided Boltzmann equilibrium was maintained between the $m = \pm\frac{1}{2}$ spin states at the temperature of the lattice, Gorter expected to observe a temperature rise of 0.3 °C min^{-1} in the experiment on protons in alum. However, the actual temperature rise was at most 1% of this estimate and remained hidden in the background due to the heat leakage of the calorimeter. With our present knowledge it is clear that Gorter's explanation . . . .

> The only reasonable explanation of this negative result is that the absorption of energy by the nuclear spin disturbs the Boltzmann distribution over the nuclear energy levels

. . . is the correct one. He further concluded that the 'nuclear temperature' in the experiment must have been in excess of 1400 K and that the spin–lattice relaxation time was longer than 10^{-2} s. Gorter's reasoning, in a sense, anticipated the thermodynamic interpretation of paramagnetic relaxation phenomena by Casimir and du Pré.[8] These authors were the first to formulate clearly that it is reasonable to assume that in the relaxation experiments thermal equilibrium is rapidly established within the lattice and spin systems individually, each at its own temperature, whereas the relaxation reflects the slow heat transfer between the two systems.

A year later, in September 1937, Gorter visited Rabi's laboratory at Columbia University. It proved a fateful visit for both parties and a boost for science. Rabi and his collaborators were pioneers in molecular beam techniques. In their experiments designed to determine the sign of the magnetic moments of the proton and deuteron,[9] changes of the quantum states of hydrogen and deuterium atoms in the incoming beam were effected by passing the beam through a region in which (dc) electric currents in a set of parallel wires generated a highly anisotropic magnetic field pattern. In a coordinate system moving with a given atom, the applied field T then varies in direction and strength as a function of time. If the field pattern relative to the direction of propagation is chosen suitably, nonadiabatic changes in the magnetic quantum number result, from which by a somewhat involved argument the *sign* of the magnetic moment of the nucleus may be derived.[9] The absolute *magnitude* of the nuclear moment, however, must be determined via another beam experiment. Because, as the authors of Ref. 9 stated:

> Since the form of the field T [felt by a particular nucleus] is not known exactly it is not possible to calculate α [an angle specifying the change in quantum state] as a function of the field and of the velocity. There will also be a different value of α for every atomic velocity. We cannot, therefore, begin by setting the field at some particular value and expect to find nonadiabatic transitions.

In other words, in the configuration in which it existed in 1936, with all applied fields of a static nature in the laboratory frame, the beam equipment was not suited for carrying out quantitative magnetic resonance experiments.

In January 1938, a few months after Gorter's visit, the Columbia group heralded the first successful nuclear magnetic resonance experiment. It was carried out on Li and Cl nuclei in a beam of LiCl molecules, and reported in a Letter entitled 'A New Method of Measuring Nuclear Moment'.[10] From Gorter's own account,[1,5] contemporary sources, and the acknowledgement at the end of the Letter, [10] it transpires that Gorter had provided a stimulus which was crucial for this success. Apparently he had asked why, instead of trying to change the Zeeman state of the particles by passing the beam through a highly anisotropic but poorly-defined static field, this was not done by irradiating a magnetic dipole transition between two of the Zeeman states—as in his own recent, unsuccessful calorimetric experiment! This means that between the first, inhomogeneous magnetic field and the refocusing field of the earlier experimental configuration,[9] the beam should be passed through a region with a constant field plus a weak radiofrequency field at right angles to it that could be generated by a simple coil driven at the resonance

frequency. This worked, and six years later Rabi was awarded the Nobel Prize in Physics for his superb beam experiments.

As Gorter saw, Rabi's method had the great advantage that the absorptive ($m \rightarrow m'$) and stimulated emission ($m' \rightarrow m$) transitions have an additive effect on the signal of the beam detector. In contrast, in his own calorimetric experiment they had cancelled one another out. Now, with nuclear magnetic resonance no longer being a figment of the physicist's imagination, Gorter renewed his attempts to detect it in a solid. Or, in his own words:[5]

> The success however obtained by Rabi and his collaborators in 1938 when they combined, on our instigation, the principle of a constant and an oscillating magnetic field perpendicular to each other with their marvellous molecular beam technique, encouraged us to continue the experiments we had undertaken along a somewhat different line. These experiments again related to nuclear magnetic spins in solids, but as the transfer of absorbed energy to the crystal lattice had appeared to be too slow, they aimed at observing the anomalous dispersion which must occur in the neighbourhood of a spectral line. This anomalous dispersion should lead to a rather sharp jump in the susceptibility (compare Figure 2).

In their publication[5] Gorter and Broer then refer to equations (1) and (2) to estimate the magnitude of this jump and somewhat glibly pass over the effect of saturation. If the thermal contact between spins and lattice is insufficient and the spin temperature becomes very high due to saturation, χ_0 tends to zero and so does $\Delta\chi$ according to equation (1) and (2). Yet, they must have realized that with increasing saturation the vertical distance between the two extremes of χ in Figure 2 goes to a finite, asymptotic value, although the absorption A vanishes (for a discussion in modern terminology, cf. Abragam[11]).

The susceptibility experiments by Gorter and Broer were carried out on the ^{7}Li and ^{19}F nuclei in LiCl and KF polycrystalline powders in which the coil of a resonant circuit operating at 3.7 MHz was embedded. These particular substances were chosen in order to minimize the linewidth δ by keeping the local fields due to the neighboring counterions (Cl or K) small. After preliminary experimentation at the boiling point of nitrogen in the Zeeman Laboratory of the University of Amsterdam, the final experiments were carried out at the Kamerlingh Onnes Laboratory at the boiling points of hydrogen (LiCl and KF) and helium (LiCl).

On the basis of a (realistic) estimate of the linewidth due to Kronig and Bouwkamp,[12] a susceptibility change leading to a frequency shift of the oscillator of $\approx$80 Hz was expected on passing with the magnetic field through resonance in the experiment on LiCl in helium, provided the static susceptibility χ_0 was that predicted by the Langevin formula for a temperature of 4.2 K. However, no shift was detected and it must have remained smaller than about 1 Hz. Another experiment, carried out at Casimir's suggestion, in which the sample was cooled down from room temperature to 4.2 K in a strong stationary field of 1 T, was equally unsuccessful. The authors concluded that, as in Gorter's earlier calorimetric experiment, the negative result was most likely due to slow spin–lattice relaxation. They wrote:

> The time characterizing the establishment of equality between the "nuclear spin temperature" and the lattice temperature would have to be considerably larger than 10^3 seconds at the low temperatures.

It is sad that Gorter came so close to making a great discovery and then gave up. Bloembergen later determined the relaxation time T_1 in the LiCl crystals used by Gorter and Broer, and found T_1 = 600 s at 2.1 K. So, if the estimate given in the above quotation was realistic, the authors might have observed a small effect. Although a reasonable knowhow of *electron* paramagnetic relaxation existed, no quantitative information whatsoever was available on *nuclear* relaxation, and no one was aware of the effect paramagnetic impurities might have. On the basis of Waller's[13] theoretical analysis, however, there was every reason to suspect that the Li nuclei in a pure, diamagnetic LiCl crystal would be very slow in coming to thermal equilibrium with the lattice. On considering this dearth of information, the authors might have been well advised to try a few, quite different samples. But hindsight is easy, and the wartime conditions in 1942 were far from conducive to experiments in physics.

Gorter had the advantage of starting his work in the intellectual company of theoretical physicists like Kronig, Casimir, and Kramers, who were all actively interested in problems in magnetism. Together, they had by 1940 arrived at a reasonable understanding of electron paramagnetic relaxation. When, during the later years of World War II further experimentation was out of the question, Gorter gathered his knowledge of the field in a small monograph entitled 'Paramagnetic Relaxation'.[14]

In '***Bloembergen, Nicolaas: My Early Years in NMR, 1946-48***', Bloembergen gives a lucid description of the realization of NMR in condensed phase by the groups at Harvard and Stanford in 1945. This, together with the discovery of electron paramagnetic resonance by Zavoiskii[15] and the formulation of the Bloch equations, opened an entirely new door for looking at the mysteries of relaxation processes in ensembles of spins. Gorter's book, therefore, soon became dated. However, his interest in the field by no means waned, as is apparent from Bloembergen's account. For example, he discovered the phenomenon of exchange narrowing and discussed it with Van Vleck.[16] He was also the first to identify cross relaxation ('third relaxation' in Gorter's terminology),[17] a process for which Bloembergen et al.[18] gave a detailed explanation and which constitutes one of the cornerstones of today's pulsed NMR techniques.

REFERENCES

1. C. J. Gorter, Bad luck in attempts to make scientific discoveries, *Phys. Today*, January 1967, **20**, 76.
2. W. Lenz, *Phys. Z.*, 1920, **21**, 613; P. Ehrenfest, *Leiden Comm. Suppl.*, 1929, **44b**.
3. C. J. Gorter, *Physica (The Hague)*, 1936, **3**, 503.
4. C. J. Gorter and R. de L. Kronig, *Physica (The Hague)*, 1936, **3**, 1009.
5. C. J. Gorter and L. J. F. Broer, *Physica (The Hague)*, 1942, **9**, 591.
6. C. J. Gorter, *Physica (The Hague)*, 1936, **3**, 1006.
7. C. J. Gorter, *Physica (The Hague)*, 1936, **3**, 995.
8. H. B. G. Casimir and F. K. du Pré, *Physica (The Hague)*, 1938, **5**, 507.
9. J. M. B. Kellogg, I. I. Rabi, and J. R. Zacharias, *Phys. Rev.*, 1936, **50**, 472.
10. I. I. Rabi, J. R. Zacharias, S. Millman, and P. Kusch, *Phys. Rev.*, 1938, **53**, 318.
11. A. Abragam, *The Principles of Nuclear Magnetism*, Clarendon Press, Oxford, 1961, p. 47.

12. R. de L. Kronig and C. J. Bouwkamp, *Physica (The Hague)*, 1938, **5**, 521.
13. I. Waller, *Z. Phys.*, 1932, **79**, 370.
14. C. J. Gorter, *Paramagnetic Relaxation*, Elsevier, Amsterdam, 1947.
15. E. K. Zavoiskii, *J. Phys. USSR*, 1945, **9**, **211**, 245; [*Chem. Abstr.*, 1946, **40**, 1072].
16. C. J. Gorter and J. H. Van Vleck, *Phys. Rev.*, 1947, **72**, 1128; J. H. Van Vleck, *Phys. Rev.*, 1948, **74**, 1168.
17. F. W. de Vrijer and C. J. Gorter, *Physica (The Hague)*, 1952, **18**, 549.
18. N. Bloembergen, S. Shapiro, P. S. Pershan, and J. O. Artman, *Phys. Rev.*, 1959, **114**, 445.

Acknowledgements

I wish to thank my colleagues H. B. G. Casimir and R. de Bruyn Ouboter for their help in tracing material related to an intriguing period in the history of science.

Biographical Sketch

J. H. van der Waals. *b* 1920. Ph.D., 1950 University of Groningen. Research physicist and subsequently Associate Director of Research with Shell, 1946–67; Professor of Physics, University of Leiden, 1967–89. Worked as an undergraduate in C. J. Gorter's laboratory (1941); shared an office with Harden McConnell at Shell Development Co., Emeryville, when the Varian #1 NMR spectrometer arrived (1953–54). Current research interest: study of excited states of molecules, frequently by EPR.

Wagner, Gerhard: NMR of Proteins

Gerhard Wagner

Harvard Medical School, Cambridge, MA, USA

While I was working as a physics student on my diploma thesis at the Technical University of Munich on the Mössbauer effect of iron-containing proteins, I first became aware of the field of NMR as a result of my supervisor's (Adalbert Mayer) leaving for a sabbatical to learn NMR in Robert Shulman's group at Bell Labs. After graduation (1973), I joined Kurt Wüthrich's group in Zürich as a Ph.D. student working in the area of biological NMR, essentially against the advice of some of my supervisors who thought that everything had already been done in the field of NMR. I thought so too, but was attracted by biological applications and the phenomena of relaxation, which I didn't understand.

MOBILITY OF AROMATIC SIDE CHAINS IN BPTI

I started working theoretically with molecular orbital calculations of porphyrin systems with the goal of understanding chemical shifts in heme proteins. Kurt Wüthrich convinced me to do some experimental work, and so I took over a project from one of the graduate students, André Masson, who was finishing up. He had been working with the basic pancreatic trypsin inhibitor (BPTI) using the 220 MHz spectrometer at the ETH and had studied NH exchange in D_2O and the thermal unfolding of the protein. When he handed the project over to me, he mentioned that he had essentially understood most of the spectrum, except for an amorphous bump in the base line that could be seen downfield from the aromatic resonances. For some unknown reason it always looked different from one spectrum to another.

This amorphous signal became the main subject of my Ph.D. thesis. Soon I tried to assign the aromatic spectrum of BPTI with spin decoupling in CW experiments on a Bruker 270 MHz spectrometer. Some intensity was missing from the 36 aromatic protons of BPTI. I presented this finding at the 6th International Conference on Magnetic Resonance in Biological Systems in Kandersteg (1974). At the same session Grayson Snyder, a graduate student of Brian Sykes, presented assignments of tyrosine side chains obtained from chemical modifications. He had found that one of the tyrosines, Tyr35, showed four one-proton resonances and appeared to be immobilized. After the conference, Prof. Zeev Luz spent several weeks at the ETH as a guest of Kurt Wüthrich. His knowledge enhanced our understanding and awareness of dynamic processes. As a consequence of discussions with Luz, I did what sounds trivial now but wasn't then—I recorded the spectra of BPTI in D_2O below room temperature. The broad baseline bump disappeared and five one-proton resonances of an immobilized phenylalanine side chain emerged from the noise, accounting for the previously missing intensity,[1,2] and the sidechain could be reversibly mobilized or immobilized by temperature variation. At that time, other NMR groups were also discussing that most aromatic sidechains could be rotating in proteins, despite their rigid appearance in crystal structures.[3,4] The clear transition from slow to rapid rotation was first observed in BPTI. The mobility of the aromatic sidechains in BPTI has subsequently become the subject of numerous experimental and theoretical studies.

SEQUENTIAL ASSIGNMENTS

After the meeting in Kandersteg, Dr. Antonio DeMarco joined Wüthrich's group as a postdoc. He implemented methods of difference decoupling and applied resolution enhancement techniques, such as the convolution difference method developed in the Oxford group, and he introduced the sine-bell multiplication which is still very popular today. These techniques were used for assigning methyl resonances in BPTI. Concurrently, Dr. Regula Keller started measuring NOEs between heme resonances in cytochromes and was able to assign all resonances based on a knowledge of the covalent structure of the heme group,[5] and Sidney Gordon, on sabbatical leave in Wüthrich's group, began applying Solomon's transient NOE experiments to proteins.[6] Also, at that time, Andreas Dubs, an undergraduate student, joined the group to work on his diploma thesis.

Andreas, who had attended a biophysics course I was teaching, had built a labquib model of BPTI as part of his course work. During the ensuing diploma work, he and I spent a large amount of time inspecting the plastic model and exploring the geometry of the molecule. This was a key component in the development of the sequential assignment methods. As the primary work of his thesis Andreas measured NOEs from the well-resolved slowly exchanging amide protons. When using short irradiation times, there was usually a single H^{α} resonance that showed a much larger NOE than anything else. Only after a lengthy inspection of the BPTI model did we detect the almost trivial fact that the H^{α} of the preceding residue was generally nearest to an H^{N}, and that other H^{α} protons were a significantly larger distance away. We could show analytically that the initial slope of the NOE build-up curves of truncated driven NOEs were directly proportional to r^{-6} and could be related directly to molecular structure.[7]

This identification of the sequential $d_{\alpha N}$ NOE, together with the intraresidue connectivities obtained from spin decoupling, quickly led to sequence specific assignments for 15 β-sheet residues.[8] At the same time, we became aware of different sequential NOEs in helices and established an initial statistic of characteristic distances in β-sheets and helices.[8] This was later elaborated by a new graduate student, Martin Billeter.[9] The initial sequential assignment method was limited to D_2O experiments, however, because our spectrometer was not flexible enough to presaturate the water and selectively irradiate a protein resonance to develop NOE. Further progress had to await the development of 2D NMR. This eventually led to the complete assignment of the BPTI spectrum[10] and the development of methods to solve protein solution structures as described by Kurt Wüthrich elsewhere in this Encyclopedia (***Biological Macromolecules: Structure Determination in Solution***).

COUPLING CONSTANTS AND TRIPLE RESONANCE EXPERIMENTS

In 1986 and 1987, when I set up a new NMR lab at the University of Michigan, I had as my top priorities developing

better methods for measuring coupling constants and learning more about relaxation. I had the feeling that a reverse probe that could pulse ^{13}C as well as ^{15}N would be useful for this aspect, so in the fall of 1986, when I ordered my new 500 MHz spectrometer from General Electric, I also ordered a custom built reverse detection $^{1}H-^{15}N-^{13}C$ triple resonance probe. My idea was to measure heteronuclear vicinal coupling constants by some means that would allow us to add and subtract in-phase and antiphase doublets, so that each doublet component could be observed separately.

When the probe was eventually delivered, my postdoc Guy Montelione and I discussed how to use it for such measurements of $^{1}H-^{15}N$ coupling constants. In one of these discussions, in the fall of 1988, we realized that we would not need the triple resonance probe if we ran a 2D experiment that contained cross peaks between amide and β-protons using a ^{15}N-enriched protein. If we did not mix the nitrogen populations between evolution and detection, we could separate the two doublet components by the large $^{1}H-^{15}N$ one-bond coupling constant and measure the vicinal coupling constant without overlap.[11]

After discovering this method, we realized that it utilized the same principle we had ourselves previously used to measure $^{113}Cd-^{1}H$ coupling constants in metallothionein.[12] I presented these results at the UCLA Symposium at Park City (1989). During the conference and on the way home I kept thinking about an extension to measure homonuclear coupling constants. The triple resonance probe could be used for this purpose. But an experiment had to be designed that would achieve cross peaks between the C^{α} carbon and the amide proton without mixing the populations of the H^{α} proton.

My first attempt was to try to achieve this using the long-range coupling between C^{α} and H^{N}-selective proton pulse. Guy Montelione proposed using a relayed transfer via the ^{15}N nucleus and using a TANGO pulse, a 90° pulse selective for the amide proton for the final coherence transfer. This sequence, developed by Guy, showed the desired pattern for the intraresidue $H^{N}-C^{\alpha}$ cross peak.[13] In addition, however, it showed a cross peak between the H^{N} and the C^{α} of the preceding residue, which we discovered was due to the two-bond coupling between the nitrogen and the C^{α} of the preceding residue.[14] This unexpected observation of a sequential triple-resonance cross peak opened a new route to achieving sequence specific assignments in ^{15}N- and ^{13}C-labeled proteins. These results were first presented in the summer of 1989 at an International Conference of the Royal Society of Chemistry in Warwick. Since that time, numerous improvements in this technology have appeared in the literature.

REFERENCES

1. K. Wüthrich and G. Wagner, *FEBS Lett.*, 1975, **50**, 265.
2. G. Wagner, A. DeMarco, and K. Wüthrich, *Biophys. Struct. Mechanism*, 1976, **2**, 139.
3. I. D. Campbell, C. M. Dobson, and R. J. P. Williams, *Proc. R. Soc. London*, 1975, **189B**, 503.
4. G. H. Snyder, R. Rowan, III, S. Karplus, and B. D. Sykes, *Biochemistry*, 1975, **14**, 3765.
5. R. M. Keller and K. Wüthrich, *Biochim. Biophys. Acta*, 1978, **533**, 195.
6. S. L. Gordon and K. Wüthrich, *J. Am. Chem. Soc.*, 1978, **100**, 7094.
7. G. Wagner and K. Wüthrich, *J. Magn. Reson.*, 1979, **33**, 675.
8. A. Dubs, G. Wagner, and K. Wüthrich, *Biophys. Acta*, 1979, **577**, 177.
9. M. Billeter, W. Braun, and K. Wüthrich, *J. Mol. Biol.*, 1982, **155**, 321.
10. G. Wagner and K. Wüthrich, *J. Mol. Biol.*, 1982, **155**, 347.
11. G. T. Montelione, M. E. Winkler, P. Rauenbuehler, and G. Wagner, *J. Magn. Reson.*, 1989, **82**, 198.
12. D. Neuhaus, G. Wagner, M. Vasak, J. H. R. Kägi, and K. Wüthrich, *Eur. J. Biochem.*, 1984, **14**, 659.
13. G. T. Montelione and G. Wagner, *J. Am. Chem. Soc.*, 1989, **111**, 5474.
14. G. T. Montelione and G. Wagner, *J. Magn. Reson.*, 1990, **87**, 183.

Biographical Sketch

G. Wagner. *b* 1945. Diplom., 1972, Physics, Technische Universität München, Germany, Ph.D., 1977, Biophysics, ETH Zürich (supervisor Kurt Wüthrich). Postdoctoral work with John Waugh, 1978–79. Privatdozent ETH Zürich, 1983; Faculty, Biophysics Research Division, University of Michigan, Ann Arbor, 1987–90; Faculty, Department of Biological Chemistry and Molecular Pharmacology, Harvard Medical School, 1990–present. Approximately 180 publications. Research interests include NMR relaxation, protein dynamics and structure, protein interactions.

Warren, Warren S.: The NMR–Optics Connection

Warren S. Warren
Princeton University, Princeton, NJ, USA

Magnetic resonance is an extraordinarily powerful technique, with broad applications in physics, chemistry, and medicine. From a theoretician's perspective, NMR has tremendous advantages: the Hamiltonian is known and simple, quantum mechanical equations of motion can be solved (essentially exactly and often by hand), and the radiofrequency technology exists to create virtually any pulse sequence that can be conjectured.

There are none of these advantages in most other regions of the electromagnetic spectrum, but that has not prevented the daring (or foolish) from trying to extend NMR techniques to other forms of spectroscopy. Nowhere are the contributions more apparent than in laser spectroscopy, which owes much of its utility to the work of magnetic resonance 'émigrés'. The names of Bloembergen, Hahn, and Hartmann are just as recognizable in the laser community as they are in NMR—but not for the same reasons; by the mid-1960s these three men had created most of what we now call coherent optical spectroscopy. By 1980, Michael Fayer, Charles Harris, Douwe Wiersma, and Ahmed Zewail were using optical analogs of simple NMR and ESR sequences (mainly the photon echo and stimulated echo) to characterize relaxation and dynamics in isolated molecules, liquids, and solids. They all acquired their understanding of coherence from work in optically detected magnetic resonance; elegant work from their groups continues today.

The lure of doing something other than NMR was quite strong for me by 1980. If there were a *Guiness Book of Records* entry for the most complicated radiation pulse sequence ever successfully executed, it would belong to the multiple quantum selective excitation sequences I used as a graduate student in Alex Pines's laboratory. Alex's enthusiasm had attracted a truly outstanding group of students (I worked mostly with Dan Weitekamp, Gary Drobny, Steve Sinton, Jim Murdoch, and Jau Tang). There was much creative energy in that group (read that as 'we argued a lot;' we were trying to understand some pretty complex concepts). Even by the standards of the time, we had relatively poor equipment; I remember shimming for days on the group's 180 MHz 'γ machine' and being thrilled ultimately to produce a 25 Hz wideline shape. We did, however, have a spectacular pulse programmer (designed before my time by David Rubin). For a good measure of the level of sophistication of NMR theory and hardware 15 years ago, consider this: we could make the γ give a 4096-pulse selective excitation sequence, with pulse timings and phases predicted precisely by average Hamiltonian theory. If the experimental spectrum did not agree with our predictions, the *spectrometer* had to be tweaked—because the theory had to be right.

Selective excitation experiments eventually worked on a wide variety of samples, but I couldn't imagine what I would want to do next (an 8192-pulse sequence?). At least at first glance, it seemed obvious that if optical analogs of 20- or 30-year-old NMR sequences were useful, analogs of dipolar line narrowing or multiple quantum sequences could be valuable as well. Alex has always been fascinated with optics; he almost took a postdoc with Peter Rentzepis to become a laser spectroscopist. He suggested I consider working with Bloembergen, Fayer, or Zewail. I quickly discovered what had prevented laser spectroscopists from using more recent NMR innovations. Photon echoes and stimulated echoes work because the phases of the pulses do not matter. In fact, most laser spectroscopists had only a vague idea of the *meaning* of the phase of a laser pulse—the vast majority of laser experiments, then and now, really used laser pulses only as intense flashlights. Zewail, Fayer, and Harris understood phase quite well; they just did not know how to control it. Nobody had ever generated a sequence as complex as two nonoverlapping pulses with a controllable phase relationship between the pulses.

There was one partial exception. A few years earlier, Zewail and one of his students (Tom Orlowski) had used an acoustooptic modulator to chop pieces out of a continuous laser beam for three-pulse echo experiments. An acoustooptic modulator uses radiofrequency pulses to diffract light into a different direction. The frequency of the diffracted light is the sum of the input laser frequency (5×10^{14} Hz for red light) and the radiofrequency (500 MHz for common devices). Zewail showed me the commercial rf pulse driver they used, which just gated continuous rf with a mixer, thereby obviously (to an NMR spectroscopist) always giving the same phase of rf pulse. Their three-pulse laser experiment would have failed if the optical phases had been random; they had assumed the pulses were in phase, and this turned out to be correct.

I knew nothing about optics, but I knew that NMR spectrometers often make phase-shifted rf pulses at a low frequency, then mix them up to the final output frequency. I also knew that any device that produced an output at the sum of the frequencies of the two inputs was multiplying the two waves together like a single sideband mixer. To me, this meant that phase-shifting the rf pulses would have to phase-shift the laser pulses. In effect, the transmitter section of an NMR spectrometer could control a laser pulse sequence—phase and all.

Zewail was a bit skeptical, with good reason. After all, I had never turned on a laser. So one afternoon in Berkeley, I sat down for several hours with Charles Harris. Eventually he concluded that the idea had to work. I went to work with Zewail, who steered me in the right directions and within a few months we did the first pulsed experiments with full phase control. We could make rectangular laser pulses with ~10 ns time resolution and peak powers of less than 1 W—good enough for small molecules in the gas phase, but far too slow and weak for most interesting applications. Over the last decade, a variety of groups (including my own) have figured out how to do ps or fs resolution phase-shifting; how to shape laser pulses with better than 30 fs time resolution and peak powers of 10^9 W; and how to use such pulses to create population inversions, enhance signals, or monitor molecular evolution.[1]

I still do both NMR and laser experiments, and I have often found this dual perspective helpful. Some ideas can be transferred directly between NMR and optics. When I started thinking about pulse shaping, the technology did not exist to make complex pulse shapes with lasers, but the MRI community was already using empirically derived shapes

for improved images. So most of our initial applications of shaped pulses were in NMR. For example, the $\mathrm{sech}(\alpha t)^{1+5i}$ pulse shape (equivalently, a hyperbolic secant pulse with a hyperbolic tangent frequency sweep) was first derived in an optics textbook in 1975, first used in an NMR experiment by Hoult and Silver in 1984, and first used in laser experiments by my group in 1986. In addition, radiation damping in NMR was the forerunner of optical superradiance, which has been very extensively explored. That work helped us greatly when we started re-examining radiation damping a few years ago.

The other useful feature of my continued optics connection is a healthy skepticism for theory. The Hamiltonian is essentially never known completely in optics, and many of the assumptions that make NMR spectra easy to interpret do not work. When experiment and theory disagree in laser work, usually the experiment is right. About four years ago, we started doing very simple two-dimensional NMR experiments on samples such as pure water and getting 'theoretically impossible' experimental results. This time we were *not* seeing instrumental artifacts—even though we did not understand what was happening for several years. We found some gaps in the conventional (density matrix) framework of high-resolution NMR in solution, which eventually led to our observation of intermolecular multiple quantum coherences due to long-range dipole–dipole couplings (see ***Concentrated Solution Effects***).

I continue to recommend NMR training as a great background for other kinds of spectroscopy (as well as an important field in its own right). The complexities in optical experiments are severe, and there are quite a few NMR spectroscopists who dabbled with lasers for a few years and later turned back to spins. Nonetheless, many scientists expect substantial accomplishments in molecular reaction control with lasers over the next few years. When this happens, it will be due in no small part to the work of the magnetic resonance émigrés and NMR–laser dual citizens.

REFERENCES

1. For reviews, see W. S. Warren, *Science*, 1993, **262**, 1008; W. S. Warren, H. Rabitz, and M. Dahleh, *Science*, 1993, **259**, 1581; W. S. Warren, *Science*, 1988, **242**, 878.

Biographical Sketch

Warren S. Warren. *b* 1955. A.B., 1977, Harvard, M.S., 1979, Ph.D. 1980, University of California, Berkeley. Professor of Chemistry, Princeton University, 1980–present. Approx. 100 publications. Research specialties: NMR with shaped pulses, multiple quantum NMR, NMR concentrated solution effects, coherent laser spectroscopy.

Waugh, John S.: Alchemy of Nuclear Spins

John S. Waugh

Massachusetts Institute of Technology, Cambridge, MA, USA

INTRODUCTION

In these personal reminiscences I have emphasized a few events and researches which seemed relatively important or were especially interesting to me, most prominently the development of coherent averaging and average Hamiltonians. A number of other subjects are mentioned briefly, most of them with representative literature references, but a great many things have been left out altogether. This selectivity means that many students and colleagues have gone unmentioned; I apologize to them in advance.

EDUCATION: UP TO 1953

I first heard of NMR in 1949 from my research adviser, Don Yost, who had read about it and had an undergraduate thesis student, Floyd Humphrey, building a marginal oscillator. Yost's way of learning about interesting new developments was to inveigle a student into working on it. When Humphrey graduated, I seized the opportunity to become the NMR student. The closest real spectrometer was in Felix Bloch's laboratory at Stanford, and I would have felt it presumptuous, as well as too expensive, to visit there. Subsequently, during vacation trips to the East, I visited the Harvard Labs, and was encouraged by the graduate students, especially Fred Reif and George Benedek. After reading the still rather scarce literature I decided to build a bridge-type spectrometer with field modulation and lock-in detection, in the style of Nico Bloembergen's Harvard thesis. I borrowed an electromagnet from the cosmic ray physicists and had the shop make new pole pieces. The power supply was a set of World War II surplus submarine batteries. A very linear sweep was generated by adding high-resistance windings on the pole pieces driven by a novel circuit using a thyratron: this was the subject of my first scientific publication.[1] This spectrometer was an advance over Bloembergen's in that it recorded its spectra on a strip chart recorder. I loved electronics and had a wonderful time building this machine.

I was greatly stimulated by the atmosphere at Caltech, where a student could mingle informally with the most brilliant and famous scientists. My first exposure to quantum mechanics came in my second year when Richard Feynman arrived from Cornell, an instant celebrity, and took over the standard introductory course in the Physics Department. Most of the faculty and postdocs showed up and spent the term trying to impress Feynman with their smart questions. It was no place for a green chemistry student, but I worked enormously hard and, merely by surviving, convinced myself that I could understand theory. (Feynman did everything with path integrals or, as he called them, 'Broadway' integrals: I taught myself about Schrödinger and Heisenberg later.)

I had to find a subject for a thesis. The chemical shift was obviously going to be important for chemistry, but the homogeneity of my magnet was not good enough for that. I chanced to learn from Richard Newman, a postdoc with Richard Badger, that the very short (2.26 Å) hydrogen bond of the bifluoride ion might mean the proton was in a single potential well. This sounded very promising for a Pake-style study, since we all knew the advantages of protons and ^{19}F for NMR. The spectra were noisy but agreed with my calculations for a symmetric molecule. Of course motional averaging would make both H–F distances the same, as one says nowadays, 'on the NMR timescale'. The value of $\langle r_{\mathrm{HF}}^{-6} \rangle$ measured from the spectra, however, was inconsistent with a structure in which the proton spent very much of its time away from the center.

Herb Gutowsky was organizing a session on NMR for an ACS meeting in Atlantic City for the fall of 1952, and invited Don Yost to contribute. Yost suggested that I go, since I was expecting to defend my thesis just before the meeting and was planning a vacation trip East. This was my first scientific meeting. There were papers by, among others, Ben Dailey, George Pake, Sam Weissman, and Brevis Bleaney. Russell Varian asked a number of questions. At the time no paper could be presented at an ACS meeting unless at least one of the authors was a member of the society. Neither Yost nor I qualified, so we added Floyd Humphrey as a co-author and that is the way the paper was finally published.[2]

I spent the following year as a postdoc with Robert Bacher doing radiocarbon dating, served as the resident associate (housemother) for one of the undergraduate houses, bought a yellow convertible, and generally spent a highly social year. I had several interviews for employment, accepted an offer from MIT, and went East in the summer of 1953. Actually the move was part of an NMR player trade: Jack Roberts (Professor) for Waugh (Instructor) and undisclosed cash.

APPLICATIONS OF NMR AT MIT: 1953–64

In 1953, fledgling academic scientists were not given the kind of dowry that came to be expected later. I had an office but no laboratory and no research grant. I cannot imagine how I would have succeeded without the extraordinary kindness of Francis Bitter, who let me use a laboratory under the lobby of Building 6, and arranged for me to join the Research Laboratory of Electronics. This was the postwar outgrowth of the MIT Radiation Laboratory, where most of the wartime American radar development had occurred. Members had access to their excellent shops and stockrooms, and it was with that support that I built some equipment and continued some researches in NMR of solids.

By about this time Varian Associates had begun selling NMR spectrometers for studying liquids. In 1955 Dick Lord persuaded the rest of the Chemistry Department that this kind of NMR was important, and got them to spend $25 000 on the latest 40 MHz spectrometer. I, being the local expert, was put in charge. This meant that, in addition to working with my own students, I became a consultant on the application of NMR to all manner of chemical problems, leading to a number of rewarding collaborations with colleagues. I was also stimulated by the activity up the river at Harvard. Ed

Purcell, Charlie Slichter, and Anatole Abragam gave lectures, and I had continuing contact with Aksel Bothner-By and, later, John Baldeschwieler.

Mostly, we tried to develop new applications to chemistry and extend old ones, which was relatively easy to do in those days. Chemists knew little of the physics of NMR, and the physicists had no idea of what chemists were interested in. By being somewhere in between, I could see new possibilities. (An advantage of being between fields is that it is easy to fool the specialists in one of them into thinking you know a lot about the other.) Among other things we worked on chemical shifts from aromatic ring currents,[3] rapidly rearranging molecules,[4] methods for analyzing high-resolution spectra,[5] phase transitions in solids,[6] self-diffusion and relaxation in liquids,[7] electric field effects,[8] and relaxation in gases and intermolecular forces.[9] Some of these researches led to forays into other techniques, such as the Mössbauer effect and the Kerr effect in nonideal gases,[10] and we introduced the Avis as the standard unit of angular frequency.

In 1962 I was given a Guggenheim Fellowship which allowed me to take a year's sabbatical leave. I spent the first part in Moscow under the first Interacademy Exchange Agreement. On the way over I visited Ionel Solomon in Paris. He gave me a preprint of his work with Ezratty[11] and awoke my interest in strong rf fields, which I had theretofore avoided because of my difficulty in understanding Redfield's classic paper.[12] I soon had the opportunity to discuss all this with Boris Provotorov, whose approach I found even more impenetrable. (I am grateful to Maurice Goldman[13] for clarifying much of this subject matter later.) On the whole, my stay in Moscow was more a sociological and linguistic than a scientific experience, although it led to a number of friendships and some years later to a lecture tour and a book.[14] The following fall I insinuated myself into Erwin Hahn's lab in Berkeley. The Hartmann–Hahn effect had been published the previous year,[15] Dick Slusher, Russ Walstedt, and Gil Leppelmeier were still there pursuing its corollaries, and I shared an office with Jack Butterworth, who was visiting from Harwell. I learned to become much more at ease with the theory of spin dynamics in solids, and was enormously stimulated by Hahn and by the atmosphere and spirit of his group.

COHERENT AVERAGING: 1965–82

For a few years before and after my stay in Berkeley I was a consultant to Harvey-Wells, Inc., later Magnion Inc., a manufacturer of electromagnets and NMR gaussmeters. Existing commercial NMR spectrometers were of the CW variety, and Ed Ostroff, the Engineering V.P., saw an opportunity to develop a pulsed spectrometer to satisfy increasing interest in that area. His apparatus was the first which could generate long pulse trains, with limited phase control, and at the same time had the high transmitter power and rapid recovery needed for FIDs in solids. Testing an early machine in the spring of 1965, Ostroff chanced to apply a Carr–Purcell (CPMG) sequence to a solid, and was astonished to see a long train of echoes—up to thousands of them as the pulse spacing τ was decreased. I was equally surprised, but as the consultant I was supposed to explain the effect. In further experiments we found that the phase shift of the initial pulse was essential, and that the refocusing pulses had to have a flip angle of less than the canonical 180°; 90° seemed much better.

Under these conditions the first echo had to be Jack Powles's 'solid echo', but the theory of that effect[16] gave no reason to expect long trains such as Ostroff saw. The intensity of the solid echo is given by

$$\langle \hat{I}_x(2\tau)\rangle = \langle \hat{U}(2\tau)\hat{I}_x\hat{U}(2\tau)\rangle \qquad (1)$$

$$\hat{U}(2\tau) = \exp\,(-\mathrm{i}\hat{\mathcal{H}}\tau)\exp\left(-\mathrm{i}\frac{\pi}{2}\hat{I}_x\right)\exp\,(-\mathrm{i}\hat{\mathcal{H}}\tau) \qquad (2)$$

The result can be calculated by writing the dipole–dipole Hamiltonian $\hat{\mathcal{H}}$ in spin operators, expanding the propagator $\exp(-i\hat{\mathcal{H}}\tau)$ in a power series, performing the indicated pulse rotation, collecting terms, and taking the trace. In this way it is found that the decay at time 2τ, which would be of order $M_2\tau^2$ in the FID, is canceled in the echo, the leading term now being of order $M_4'\tau^4$. (Here M_2 is the Van Vleck second moment, and M_4' is a modified fourth moment.) I simply extended the calculation to the second echo at time 4τ and found a cancellation of the τ^4 terms, leaving a decay of order $M_6'\tau^6$ and predicting the second echo to be stronger than the first (as we in fact verified experimentally). The method of calculation did not easily lend itself to extension to later echoes, so I punted by fitting the experimentally observed exponential decay to the rough calculation for the second echo, in the spirit of Boltzmann's molecular chaos assumption. This seemed to give qualitative agreement with experiment and we published a Letter[17] which also contained an alternative interpretation in terms of spin locking. Jim Wang later fleshed out both approaches.[18]

The Fourier transform relationship between FIDs and spectra was well known at that time[19] as was the notion of sampled signals and discrete FTs, and it was natural to think of lengthened decays as somehow corresponding to sharpened spectral lines. From this point of view it was easy to think of the *envelope* of a Carr–Purcell echo train as equivalent to the sampled FID of a system whose inhomogeneous broadening had been artificially suppressed. Extending this logic to Ostroff's pulse sequence (nowadays OW-4 in conventional nomenclature), it seemed that the homogeneous dipole–dipole broadening had been removed. That broadening was generally considered to be a nuisance by chemists, since it concealed the small chemical shifts that they love so well and prevented the widespread use of NMR spectroscopy in solids. Actually the chemical shifts were suppressed, too: an explicit calculation in the style of equations (1) and (2) showed that the inhomogeneous terms refocus on every fourth echo. Nevertheless I wondered whether some other sequence could be found which would remove the dipole–dipole broadening *selectively*.

A somewhat innocent first attempt was based on the obvious fact that the refocusing of inhomogeneous decay could be defeated by alternating the carrier phases of alternate 90° pulses, whereas a pure dipolar decay would not be affected. Lee Huber modified our Magnion spectrometer to try this. When the transmitter was shifted slightly off-resonance the new sequence showed the expected oscillation,[20] but it damped rather quickly. The reason was clear from a calculation including *both* dipole–dipole and shift contributions; cross

terms between them led to damping in about the time it took the shift to exhibit itself, i.e. the dipolar broadening could be reduced only just sufficiently to uncover the largest chemical shift present in the sample.

Lee Huber and I had many conversations trying to see what was wrong and whether our goal could be reached in some other way. We were joined by other members of the group, including David Ellett, Jim Wang, and subsequently Bob Vold. (Bob stimulated the 2D inversion–recovery FT method for measuring T_1s of multiple lines.[21]) In the end I made the most progress while I was away on an extended European trip during the summer of 1967 and thinking intensely about the problem. Several critical insights gradually emerged (though not as neatly as the following would suggest):

- The long decays of OW-4 and WH-2 really resulted not from an annihilation of interactions but rather from a kind of spin locking. To get at the desired result we needed to concentrate on the propagator U [equation (2)], not on particular initial states and observables [equation (1)].
- For *cyclic* sequences the propagator [equation (2)] could be written in a *toggling frame*, in which the pulses disappeared and what was left looked like the result of a time-dependent Hamiltonian $\tilde{\hat{H}}(t)$, periodic *modulo* the cycle time t_c.
- The cycle propagator, being unitary, could be expressed as a function of a Hermitian operator: $\hat{U}(t_c) = \exp(i\hat{A})$, and by writing $\hat{A} = -\bar{\hat{H}}t_c$ one saw that $\hat{H}(t)$ could be replaced by the *time-independent* Hamiltonian $\bar{\hat{H}}$. The signal during the pulse train was identical to the FID which would result from a spin system with Hamiltonian $\bar{\hat{H}}$ if both were sampled at the same interval t_c. I did not see how to construct $\bar{\hat{H}}$ in general, but to lowest order it was just a time average of $\tilde{\hat{H}}(t)$ over the cycle.

The goal remained to design a pulse sequence that would remove dipole–dipole couplings and retain chemical shifts. In hindsight this should have been easy, but in fact I had no idea whether it was even possible. Suddenly one fall morning at breakfast the solution came to me in a rush. Within a few minutes the WAHUHA sequence (now called WHH-4 in East German parlance), its scaling factor and timing variants, its relationship to the magic angle and the Lee–Goldburg experiment,[22] etc. were all obvious. (I am thankful that Walter Goldburg, not being a chemist, never thought about chemical shifts.) I rushed to the lab in great excitement. Wang, Huber, Vold, and I shortly had a series of intense discussions which refined and extended the general ideas and suggested a number of interesting applications. We still did not know how to calculate the higher order corrections to the average Hamiltonian, although we were able to come up with a somewhat tortured discussion of the requirements for validity of the lowest term. We wrote a paper[23] about all this while Lee Huber began modifying an old Varian spectrometer to provide high-powered pulses of the four phases needed for the new sequences. I was once asked whether I had not been guided by some 'arm waving' physical picture, *a la* Hahn, rather than just algebra. I responded that since I was dealing with an essentially many-body problem, I would, like some Hindu deity, need Avagadro's number of arms.

Ulrich Haeberlen arrived from Germany during this time. He knew of the Magnus expansion and showed us how to put the average Hamiltonian on a sounder theoretical basis, to take into account the finite strength of the rf field, etc. He confessed later that he was less sanguine than I about the convergence of the Magnus Hamiltonian under practical experimental conditions. He was also a superb experimenter, and played a major role in the design of that spectrometer and subsequent ones. He remains to this day the ultimate practitioner of multiple pulse NMR, and what is now known about chemical shielding tensors of protons is owed completely to his insight and persistence.

The first experiment was done on the ^{19}F resonance of a sample composed of a small chip of doped CaF_2 and a drop of liquid $C_6H_5CF_3$. All observations were made directly on an oscilloscope. The normal FID showed an initial rapid transient due to the solid, followed by a very long signal from the liquid, which we made oscillatory by setting the magnet a bit off-resonance. When the multiple pulse train was applied, the transmitter pulses drove the scope off-scale, but in the windows between pulses we could see short segments of interleaved free precession signals that showed a complex beating structure. We were sure that this was the expected decay of two narrow resolved signals, one of them from the CaF_2. To make a convincing case for publication, we needed a Fourier transform but we did not have a transient recorder or computer. Lee measured the signals from a scope photograph and calculated the Fourier transform manually.[24]

Armed with Haeberlen's definitive basic theory of the average Hamiltonian and its applications,[25] we demonstrated experimentally some of the ideas we had about the scaling of chemical shifts,[26] and chemical shift anisotropy,[27] and we set about building a more powerful and versatile spectrometer.[28] During this period we bought a signal averager and PDP-8 and PDP-12 computers. Michael Mehring and Bob Griffin joined the group and, with Dave Ellett, provided a major stimulus for further development of multiple pulse ideas and did the first definitive measurements of chemical shielding tensors.[29]

We could have gone on to improve our multiple pulse methods, but it was clear that the general approach of average Hamiltonians had many other possibilities. In principle, the Hamiltonian of a system did not have to be accepted as Nature provided it, but could be transmuted at will into a perhaps more useful form by the experimenter, a sort of alchemist whose philosopher's stone was a pulse sequence. We proceeded to fit known experiments into this unconventional viewpoint and to invent new ones:

- Won-Kyu Rhim and Alex Pines used the new apparatus to explore the idea, originated by Rhim and Kessemeier,[30] of generating a pulse sequence for which the average dipole–dipole Hamiltonian would reverse in sign, thus generating an apparent backward time development of the spin system. This sequence was used to generate an essentially perfect ('magic sandwich') echo in a homogeneously broadened solid after the initial FID had effectively disappeared. This experiment generated a great deal of interest, since it had been a part of the lore of spin physics that the dipolar FID was a thermodynamically irreversible process. In fact our Letter to the Editor[31] was initially rejected by a referee who, despite our derivation, thought that what we claimed was impossible.
- The Hartmann–Hahn experiment was not useful for resolving narrow lines in, for example, ^{13}C spectra, because the spectrum obtained was in effect lifetime-broadened by the very coupling which made it possible. Alex Pines conceived

the notion of dividing the experiment into two stages governed by different average Hamiltonians. In the first, the rare spins were polarized by the Hartmann–Hahn procedure. We called this CP for 'cross polarization', to emphasize that were interested in polarizing the rare (S) spins rather than depolarizing the abundant (I) ones. (This is the Saclay convention: Hahn called them I_b and I_a, possibly for 'bundant' and 'abundant'.) In the second part, the carbon irradiation was turned off and the new average Hamiltonian, whose FID was recorded, corresponded to a ^{13}C system developing under chemical shifts and decoupled from all protons. This very simple proton-enhanced NMR experiment was demonstrated by Pines and Gibby;[32] my principal contribution was in persuading Pines (never an easy task) that he should use CW rather than pulsed rf fields.

- Like Hartmann and Hahn, we had used thermodynamics in the rotating frame[33] to predict the asymptotic magnetizations in the CP process, but it was clear that the transient behavior during approach to quasi equilibrium spoke of the details of the interaction between a rare spin and its neighbors. During a year in our laboratory, Dan Demco had worked out a memory function theory[34] applicable to CaF_2, and had 'explained' the very surprising correlation function observed in CaF_2 by McArthur, Hahn, and Walstedt.[35] I was more interested in the situation in organic solids, where a ^{13}C spin interacted mainly with only one or two proton neighbors. As Ernst's group had shown,[36] its magnetization displayed an oscillatory transient behavior from which internuclear geometries could be calculated. We developed a 2D method which added multiple pulse irradiation of the protons or spin locking at the magic angle. The experiment worked,[37] but was mainly useful in suggesting a simpler scheme which we called separated local field (SLF) spectroscopy.[38]
- It was appealing to think of removing the powder broadening found in multiple-pulse and CP/decoupling spectra by adding magic angle sample spinning, another form of alchemy discovered by Raymond Andrew[39] and Irving Lowe.[40] I borrowed a spinner from Jim Carolan, who had been Andrew's student, and set Stefan Pausak to building one suitable for our use. However I attached a low priority to this task, since I was worried that the spinning, like random molecular motion, would interfere with the narrowing caused by the rf.[41] In this I was too sophisticated for my own good: Soon Ed Stejskal and Jake Schaefer, unafraid of such bugaboos, demonstrated the remarkable power of CP MAS. CRAMPS, the corresponding emendation of multiple-pulse NMR, suffers much more from the interferences that bothered me. Lippmaa's group in Tallinn recognized that the special success of CP MAS depends on the inhomogeneous nature of the chemical shift broadening. Matti Maricq carried out an extensive analysis of the consequences of this fact with many experimental illustrations.[42] Subsequently we explained the interferences between spinning and cross polarization,[43] and showed ways in which interferences could be used to study slow molecular motions.[44]

HETERONUCLEAR DECOUPLING IN LIQUIDS: 1980–82

Chemists began to give increased attention to spin decoupling as magnets became stronger. In ^{13}C spectra, in particular, the power needed to decouple protons throughout their increasing range of chemical shifts became uncomfortably large. Many schemes for broadening the bandwidth by modulating the decoupling transmitter were proposed: the most widely used was Ernst's quasirandom 'noise modulation'.[45] The idea, seductive but entirely wrong, seems to have been that each sideband would somehow decouple whatever spectral line was closest to it. The new schemes all tended to give some modest improvement over CW decoupling, but it seemed that no further dramatic advances were possible or they would have been found by accident. I gave a talk at an ENC conference in which I discussed approaches to the problem from the average Hamiltonian point of view, and was rash enough to 'show' that the limit of possibilities had already been substantially realized. Ray Freeman was in the audience and evidently took this as a challenge. A year or two later he showed experimental results that were enormously better than anyone had previously seen, but wouldn't say how he had done it. I, in turn, took this as a challenge and went back to reexamine the underlying theory—of course with the advantage of knowing that I must have overlooked something important.

After some false starts based on average Hamiltonians, I found a very simple theory which concentrates on what happens to the proton I, not the ^{13}C, during the decoupling sequence. For rf irradiation of phase ϕ, a proton shifted by Δ from the transmitter undergoes a classical precession about a field whose components are:

$$\boldsymbol{B}_{\text{eff}} = \boldsymbol{B}_1(I_x \cos\varphi \boldsymbol{i} + I_y \sin\varphi \Delta \boldsymbol{j}] + \Delta I_z \boldsymbol{k}; \quad \Delta = \delta \pm J/2 \tag{3}$$

As the rf parameters cycle through a series of values, the proton accumulates a net rotation R which is the product of the individual precessions. If R can be made independent of variations in δ, it is as if the proton 'doesn't know about' the term in J. Since coupling is reflexive, the carbon does not know about the proton either. The quality of any decoupling sequence is then analyzed by computing the range of δ over which R does not change locally by more than some agreed upon amount. If one starts with a simple sequence for which R is approximately zero for small δ, it is possible to find iterative schemes for building up longer sequences with better and better properties.[46] I worked out various examples, but Freeman won by constructing some others, e.g. WALTZ, which were superior to the ones I had thought of.

NMR AT LOW TEMPERATURES: 1983–93

A remarkable discovery by Friedman, Millet, and Richardson[47] seemed to me to offer a possible basis for a general method of increasing the sensitivity of NMR by several orders of magnitude. I persuaded the NSF to give me a supplemental grant to buy a dilution refrigerator. I also took on two talented postdocs, Philip Kuhns and Chris Hammel. Hammel brought from the Richardson group at Cornell the knowledge of cryogenics which I lacked. After he went to Los Alamos, Oded Gonen enthusiastically filled the gap he left. We spent more than a year working with Oxford Instruments Ltd. to design a refrigerator with the unusual features needed for 'routine' NMR and an NMR probe to mate with it.[48]

Once the machine was working, we decided to make our first major experiment a measurement of spin diffusion in CaF_2. For various reasons deriving from its slowness ($D \sim 10^{-12}$ cgs), no reliable measurement had been made of this quite fundamental and theoretically interesting transport phenomenon. My notion was to follow the total magnetization (initially saturated) in single crystal plates of CaF_2 immersed in ^{3}He. The low temperature would provide a large source magnetization at the surface, and the absence of bulk relaxation would allow the long runs needed to cross over to the asymptotic $t^{1/2}$ dependence expected for diffusion-limited growth.

The results didn't fit. Ultimately Phil Kuhns persuaded us that in fact we were observing bulk relaxation, at a rate 10^9 faster than anticipated! The next step was to measure T_1 and determine its dependence on the available parameters $\boldsymbol{B}_0$ and T. This required enormous patience, inasmuch as T_1 was sometimes as long as several months. In the end Hammel found that the results accurately obeyed the relation $T_1 \propto \exp\,[c(\boldsymbol{B}_0/T)^{1/4}]$,[49] a dependence which has still not been theoretically understood. Subsequently Charlie Slichter made a suggestion that led to at least a qualitative insight and a joint publication.[50]

I had hoped that well-resolved powder spectra could be routinely obtained, and the resulting chemical shift tensor elements interpreted in terms of electronic structure and chemical bonding. This seemed especially attractive for molecules adsorbed on surfaces, for which the high sensitivity would be extremely important. Unfortunately, it turned out that most such systems displayed a very large amount of inhomogeneous broadening. I believe this must arise from small contaminations with paramagnetic impurities: their local fields average out at higher temperatures through rapid electronic relaxation, but become static much below 1 K because the electronic spins become completely polarized. Thus most of the discoveries we made in millikelvin NMR were interesting academic curiosities rather than foundations of a new technology.[51]

COMPUTER EXPERIMENTS: 1985–94

The failure of our experiment on spin diffusion led me to wonder whether it could be replaced by a computer experiment, in the style of molecular dynamics. At first sight, the flip-flops of neighboring spin-$\frac{1}{2}$ nuclei seemed very quantum mechanical. Because local coherent behavior gives way to apparently dissipative effects only at large distances and times, such a calculation would require diagonalization of matrices of dimension perhaps 10^4 and would be hopeless. However it was clear that the diffusion effect, like most physical processes is not *essentially* quantum in nature, and would exhibit itself in qualitatively the same way for classical gyromagnets. It was even possible to convince oneself, on the basis of the theory of moments,[52] that the correspondence might be semiquantitative. Armed with this encouragement, Changguo Tang undertook a purely classical calculation of diffusion of Zeeman and dipole–dipole energy in crystals. The results were in good agreement with previous approximate theories, and were extended to plausible predictions of effects which have not yet been measured.[53] In a completely independent exercise, my troublesome colleague deBouregas has created and distributed a computer program which is useful for making exact quantum mechanical simulations of a great variety of magnetic resonance experiments, practical and hypothetical.[54]

REFERENCES

1. J. S. Waugh, J. N. Shoolery, and D. M. Yost, *Rev. Sci. Instrum.*, 1952, **23**, 441.
2. J. S. Waugh, F. B. Humphrey, and D. M. Yost, *J. Phys. Chem.*, 1953, **57**, 486.
3. J. S. Waugh and R. W. Fessenden, *J. Am. Chem. Soc.*, 1957, **79**, 846.
4. F. A. Cotton, A. Danti, J. S. Waugh, and R. W. Fessenden, *J. Chem. Phys.*, 1958, **29**, 1427; R. W. Fessenden and J. S. Waugh, *J. Chem. Phys.*, 1962, **37**, 1466.
5. S. Castellano and J. S. Waugh, *J. Chem. Phys.*, 1961, **34**, 295.
6. S. R. Miller, R. Blinc, M. Brenman, and J. S. Waugh, *Phys. Rev.*, 1962, **126**, 528; J. H. Loehlin, P. G. Mennitt, and J. S. Waugh, *J. Chem. Phys.*, 1966, **44**, 3912.
7. J. V. Gaven Jr., J. S. Waugh, and W. H. Stockmayer, *J. Chem. Phys.*, 1963, **38**, 287; C. G. Wade and J. S. Waugh, *J. Chem. Phys.*, 1965, **43**, 3555.
8. J. D. Macomber and J. S. Waugh, *J. Chem. Phys.*, 1966, **45**, 985.
9. C. S. Johnson Jr., and J. S. Waugh, *J. Chem. Phys.*, 1962, **36**, 2266; J. W. Riehl, J. L. Kinsey, J. S. Waugh, and J. H. Rugheimer, *J. Chem. Phys.*, 1968, **49**, 5276.
10. D. W. Schaefer, R. E. J. Sears, and J. S. Waugh, *J. Chem. Phys.*, 1970, **53**, 2127; J. D. Ramshaw, D. W. Schaefer, J. S. Waugh, and J. M. Deutch, *J. Chem. Phys.*, 1971, **54**, 1239.
11. I. Solomon and J. Ezratty, *Phys. Rev.*, 1962, **127**, 78.
12. A. G. Redfield, *Phys. Rev.*, 1955, **98**, 1787.
13. M. Goldman, *Spin Temperature and Nuclear Magnetic Resonance in Solids*, Oxford University Press, Oxford, 1970.
14. J. S. Waugh, *Noviye Metodi Ya. M. R. v. Tverdikh Telakh*, Izdatel'svo MIR, Moscow, 1978.
15. S. R. Hartmann and E. L. Hahn, *Phys. Rev.*, 1962, **128**, 2042.
16. J. G. Powles and J. H. Strange, *Proc. Phys. Soc. (London)*, 1963, **82**, 6.
17. E. D. Ostroff and J. S. Waugh, *Phys. Rev. Lett.*, 1966, **16**, 1097.
18. J. S. Waugh and C. H. Wang, *Phys. Rev.*, 1967, **162**, 209.
19. I. J. Lowe and R. E. Norberg, *Phys. Rev.*, 1957, **107**, 46; R. R. Ernst and W. A. Anderson, *Rev. Sci. Instrum.*, 1966, **37**, 93.
20. J. S. Waugh and L. M. Huber, *J. Chem. Phys.*, 1967, **47**, 1862.
21. R. L. Vold, J. S. Waugh, M. P. Klein, and D. E. Phelps, *J. Chem. Phys.*, 1968, **48**, 3831.
22. M. Lee and W. I. Goldburg, *Phys. Rev. Lett.*, 1963, **11**, 255; *Phys. Rev.*, 1965, **140**, A1261.
23. J. S. Waugh, C. H. Wang, L. M. Huber, and R. L. Vold, *J. Chem. Phys.*, 1968, **48**, 662.
24. J. S. Waugh, L. M. Huber, and U. Haeberlen, *Phys. Rev. Lett.*, 1968, **20**, 180.
25. U. Haeberlen and J. S. Waugh, *Phys. Rev.*, 1968, **175**, 453; 1969, **185**, 420.
26. J. D. Ellett Jr., and J. S. Waugh, *J. Chem. Phys.*, 1969, **51**, 2851.
27. J. D. Ellett Jr., U. Haeberlen, and J. S. Waugh, *Polym. Lett.*, 1969, **7**, 71.
28. J. D. Ellett Jr., M. G. Gibby, U. Haeberlen, L. M. Huber, M. Mehring, A. Pines, and J. S. Waugh, *Adv. Magn. Reson.*, 1971, **5**, 117.
29. M. Mehring, R. G. Griffin, and J. S. Waugh, *J. Chem. Phys.*, 1971, **55**, 746; R. G. Griffin, J. D. Ellett Jr., M. Mehring, J. G. Bullitt, and J. S. Waugh, *J. Chem. Phys.*, 1972, **57**, 2147.
30. W.-K. Rhim, Ph.D. Thesis, University of North Carolina, 1970; H. Kessemeier and W.-K. Rhim, *Phys. Rev.*, 1972, **B5**, 761.
31. W.-K. Rhim, A. Pines, and J. S. Waugh, *Phys. Rev. Lett.*, 1970, **25**, 218.

32. A. Pines, M. G. Gibby, and J. S. Waugh, *J. Chem. Phys.*, 1972, **56**, 1776; 1973, **59**, 569.
33. A. G. Redfield, *Phys. Rev.*, 1955, **98**, 1787.
34. D. E. Demco, J. Tegenfeldt, and J. S. Waugh, *Phys. Rev.*, 1975, **B11**, 4133.
35. D. A. McArthur, E. L. Hahn, and R. E. Walstedt, *Phys. Rev.*, 1969, **188**, 609.
36. L. Mueller, A. Kumar, T. Baumann, and R. R. Ernst, *Phys. Rev. Lett.*, 1974, **32**, 1402.
37. R. K. Hester, J. L. Ackerman, V. R. Cross, and J. S. Waugh, *Phys. Rev. Lett.*, 1975, **34**, 993.
38. R. K. Hester, J. L. Ackerman, B. L. Neff, and J. S. Waugh, *Phys. Rev. Lett.*, 1976, **36**, 1081.
39. E. R. Andrew, A. Bradbury, and R. G. Eades, *Nature (London)*, 1958, **182**, 1659; 1959, **183**, 1802.
40. I. J. Lowe, *Phys. Rev. Lett.*, 1959, **2**, 285.
41. J. S. Waugh, in *NMR and Biochemistry*, eds. S. J. Opella and P. Lu, Marcel Dekker, New York/Basel, 1957, p. 203.
42. M. M. Maricq and J. S. Waugh, *J. Chem. Phys.*, 1979, **70**, 3300.
43. E. O. Stejskal, J. Schaefer, and J. S. Waugh, *J. Magn. Reson.*, 1977, **28**, 105.
44. D. Suwelack, W. P. Rothwell, and J. S. Waugh, *J. Chem. Phys.*, 1980, **73**, 2559; W. P. Rothwell and J. S. Waugh, *J. Chem. Phys.*, 1981, **74**, 2721.
45. R. R. Ernst, *J. Chem. Phys.*, 1966, **45**, 3845.
46. J. S. Waugh, *J. Magn. Reson.*, 1982, **50**, 30; 1982, **49**, 517.
47. L. J. Friedman, P. Millet, and R. C. Richardson, *Phys. Rev. Lett.*, 1981, **47**, 1078.
48. P. L. Kuhns, S. -H. Lee, C. Coretsopoulos, P. C. Hammel, O. Gonen, and J. S. Waugh, *Rev. Sci. Instrum.*, 1991, **62**, 2159.
49. P. L. Kuhns, P. C. Hammel, O. Gonen, and J. S. Waugh, *Phys. Rev.*, 1987, **B35**, 4591.
50. J. S. Waugh and C. P. Slichter, *Phys. Rev.*, 1988, **B37**, 4337; J. S. Waugh and C. P. Slichte, *Phys. Rev.*, 1989, **B40**, 4203.
51. See, for example, J. S. Waugh, O. Gonen, and P. Kuhns, *J. Chem. Phys.*, 1987, **86**, 3816; P. L. Kuhns, O. Gonen, and J. S. Waugh, *J. Magn. Reson.*, 1987, **72**, 548; P. Kuhns and J. S. Waugh, *J. Chem. Phys.*, 1992, **97**, 2166.
52. J. H. Van Vleck, *Phys. Rev.*, 1948, **73**, 1168; S. J. Knak Jensen and E. K. Hansen, *Phys. Rev.*, 1973, **B7**, 2910.
53. Changguo Tang and J. S. Waugh, *Phys. Rev.*, 1992, **B45**, 748.
54. F. S. deBouregas and J. S. Waugh, *J. Magn. Reson.*, 1992, **96**, 280.

Biographical Sketch

John S. Waugh. *b* 1929. A.B., 1949, Dartmouth College, Ph.D., 1953, California Institute of Technology. Faculty of Chemistry, MIT, Instructor–A. A. Noyes Professor, 1953–89; Institute Professor at MIT, 1989–present. Research specialty: NMR, mostly in solids.

Weaver, Harry E.: Historical Comments on the Early Years of Superconducting NMR

Harry E. Weaver
Portola Valley, CA, USA

EARLY 1960S: THE START

On my return to California and the Instrument Division of Varian Associates from a leave of absence of two years as Instructor in the Physics Department of the University of Zürich, Switzerland, the superconducting properties of the alloys of niobium were appearing in the literature. The relatively high transition temperature (relative to 4.3 K), and the tolerance of high magnetic fields (in excess of 70 kG) while maintaining the superconductive state in the alloys, suggested that wires made from these materials might be wound into solenoids to produce fields useful for NMR, especially for high-resolution analytical NMR. If such fields could be made sufficiently homogeneous and stable with time to match or exceed the existing properties routinely available from iron core electromagnets of commercial instruments (operating at 100 MHz for protons), then such an advance would be of great significance and commercial value! At the time, neither of these questions had definitive answers. The high-field properties had been established early on, but the extraordinary requirements of homogeneity over the sample volume and corresponding time stability required measurements by high-resolution NMR **itself** to establish.

A modest program under my direction was started at Varian with the encouragement and support of Dr. Martin Packard, then Director of Research of the Instrument Division at Varian.

SHORT SAMPLE TESTS

Kilometer lengths of the superconducting alloys were not yet easily available at the start of the program, so we began with testing short samples (a few cm) cut from what lengths we could obtain. These samples were mounted in the bore of very small solenoids wound with copper wire which when immersed in liquid helium could be pulsed to a calculated field well in excess of the published critical field (order of 80–100 kG). In this way we could obtain experience measuring these alloys (NbZr and NbTi) as well as with handling liquid helium, for none of us had had any significant experience in obtaining, transporting, storing, or transferring the cryogen from a purchased 25 L storage Dewar to our experimental setup. In fact, helium liquifiers were fairly rare and those present in the immediate area were not easily available to an industrial laboratory. As it turned out, through a personal contact, we could obtain, on a one-time basis, 25 L of liquid from the ADL liquifier at the Naval Post Graduate School in Monterey, CA, providing I supplied the compressed gas necessary to obtain 25 L plus any losses. This liquifier was located some two hours drive from Palo Alto and Varian. Thus, we loaded up a pickup with the necessary number of heavy cylinders, drove to Monterey (no freeways then) with our precooled (with LN_2) helium Dewar and spent the day plumbed to their machine. We kept our fingers crossed that no plugs would form from possible trace impurities in our gas and that the liquefaction rate would be maintained!!

The liquefaction went remarkedly well, but the drive back to Palo Alto with the empty cylinders and Dewar full of cryogens (LHe and LN_2) was an anxious one in our naive state as we had no experience to fall back on as regards what to expect of the effect of jostling from the roadway on the liquid helium and what that action would cost us in terms of evaporation, or whether we were running a significant risk of forming a frozen air plug in the helium Dewar vent tube. (In those days, check valves were homemade and primitive, but ours proved to be effective.) Once we had the liquid available, we could then test our home-constructed vacuum-jacketed transfer line formed from thin-wall stainless-steel tubing and bent in the form of a large U, the ends of which were welded and the concentricity maintained by a number of thin Teflon three-point 'stars' spaced at intervals along the inner tube; any thermal shorts would mean immediate loss of the liquid phase during transfer!! The entire system of evacuated transfer line and nested experimental Dewars containing the material to be tested, leads, and support tubes could not be tested until we had our few liters of helium!! Economy of liquid was uppermost in our minds. It was with this system of nested glass Dewars, immersed pulsed coils, leads, and supports that we were able to verify successfully the short-sample published data of the niobium alloys.

With these data behind us and having eventually solved the liquid helium supply limitation, we were able to push on to the heart of the program, viz. the design, construction, and testing of large-bore solenoids; i.e. large enough for serious high-resolution NMR studies of the solenoidal magnetic fields with the sample at room temperature.

SOLENOIDS, TRAINING EFFECTS AND FLUX TRAPPING IN TYPE II SUPERCONDUCTORS

The first kilometer lengths of niobium alloys were drawn bare without a cladding of copper or insulation, as the techniques for the drawing of clad niobium alloy wire were still in the experimental stages. Hence, our first SC solenoids using bare wire were small bore, but these did provide good vehicles for the design and testing of superconducting/normal state switches. These switches when heated above T_c allowed energizing of the solenoids and, when the heater to the shunting switch was turned off, permitted preliminary studies of the persistent mode. It was with these small solenoids that we first encountered the phenomenon of 'training', viz. successive quenching from the superconducting to the normal state during the energizing to ever higher currents, ultimately 'topping out' at the design current and field. That a solenoid would 'remember' the previous quenches despite the fact that the energy 'dump' was enough to carry the bulk of the wires to a temperature well above T_c was always a puzzle to us.

As the solenoids became larger and larger with corresponding higher L/r, or time constants, it became abundantly clear that the copper-clad wires had to be coated with insulation to avoid the excessively long time constants. Interlayers of copper shim stock were used in an attempt to ensure as good a thermal conductivity to the helium bath as possible at the cost of a smaller fill-factor of the windings. A less efficient (in terms of number of turns of wire) but more stable solenoid operation resulted.

PERSISTENT MODE AND FIELD HOMOGENEITY

Conventional wisdom in those days held that flux trapping and even quenching cycles would frustrate attempts to achieve homogeneous magnetic fields in the region of the sample probe. We proposed using gradient trim-coils wound on forms positioned outside the bulk of the main solenoid. Hence, it would be necessary for the field lines from these coils to penetrate the bulk of the superconductor main coil in a predictable manner. Our experience with the behavior of ferromagnetic domains of iron magnets, and their effect on the field in the gap between pole pieces, suggested that a strong parallel might exist between the behavior of trapped flux domains in Type II superconductors with that of the domains of iron pole pieces. Accordingly, we designed gradient cancelling coils to handle the first-order gradients. These consisted initially of over-wound end sections for the axial gradients and two sets of transverse gradient coils to remove the transverse gradients; each set of coils possessed their individual S/C switches. Thus, with the combined use of these coils, the central field could be 'domed' or 'dished', the transverse gradients cancelled, and the field made uniform to a very high degree as measured by the NMR signal. Any residual nonuniformities introduced by the probe itself could be handled by the conventional room-temperature trim coils mounted on the NMR probe.

With the homogeneity of the central field under control, small time-dependent shifts in the field could then be studied, sometimes upward and sometimes downward, depending upon the precise form of energizing current from the programmed power supplies during energizing of a solenoid for the first time after a cool-down. Magnetic perturbations from outside the Dewar would also cause minor shifts in the central field and its gradients, but these effects could be held at a minimum through proper current programming and choice of environment. **No long-term decay of the persistent current was ever observed.** (It should be noted, however, that a superconducting solenoid is a **flux conserver not a flux density, or field, conserver!**) Thus, to our great pleasure and excitement, once the solenoid and its shim coils were placed in the persistent mode and the system of coils removed from the external power supplies, the field and its distribution over the sample appeared to be preserved indefinitely.

THE FIRST SUPERCONDUCTIVE NMR RESEARCH SPECTROMETER

The first complete prototype NMR spectrometer employing a high-field high-homogeneity superconductive solenoid, with associated Dewar and controls operated at 200 MHz for ^{1}H NMR. It was exhibited to a group of invited analytical chemists at a Pittsburgh Conference in a room at the William Penn Hotel in Pittsburgh (I slept in the same room with the instrument!). It was extremely well received!! This instrument was delivered after the end of the conference to members of the DuPont Experimental Station in Wilmington for field evaluation. Their evaluations formed an important basis for ongoing improvements of the commercial model under construction which was to be subsequently delivered to their laboratory. That first commercial instrument, with subsequent additions to its capability of excitation and detection of proton NMR with the addition of Fourier transform signal-enhancement sections, performed for many years and was retired only a few years ago (along with the technician originally assigned to operate it as a service to the research staff)!! That instrument was indeed a major advance and 'path-finder' for the modern instrument and I don't believe one would find today any analytical chemical laboratory without an NMR spectrometer and associated high-field superconducting solenoid. At many institutions today, multinuclear, Fourier transform instruments are commonplace and are so complex that a trained specialist is needed to operate them. Time on the instruments of today is so tightly scheduled that a student usually only rarely has an opportunity to receive hands-on experience, except possibly during a special well-supervised course on its use!!

Biographical Sketch

Harry E. Weaver. *b* 1923. B.S., 1943, M.S., 1946 (both Case Institute of Technology), Ph.D., 1952, Physics, under Prof. Felix Bloch at Stanford University. Princeton University/Manhattan Project, 1944–46. University of Zürich, Switzerland, 1952–54 and 1959–61. Varian Associates, 1954–69; Hewlett Packard Laboratories, 1969–88 (retirement). SETS, Inc., Mililani, HL 1988–90 (retirement). Developed first commercial EPR and first commercial superconducting high-resolution NMR (1965). Private consultant at present.

Webb, Graham A.: My Developing Interest in NMR Spectroscopy

Graham A. Webb

University of Surrey, Guildford, UK

It all began during the final year of my undergraduate course at Bristol, during the academic year 1959–60. There were lectures on molecular structure determination which included an introduction to the relatively new technique of ^{1}H NMR spectroscopy. The power of the method was very appealing and retained my interest when, in 1960, I went to University College, London to start my Ph.D. research on the measurement and interpretation of variable temperature magnetic susceptibilities of transition metal complexes. In the laboratory next to the one I was working in I saw my first NMR spectrometer. It was being used for ^{13}C, ^{14}N, and ^{17}O NMR measurements by Dick Bramley and Garth Kidd; through them I was introduced to heteronuclear NMR studies and all the problems that studying these nuclei on a 40 MHz CW instrument entailed.

Unfortunately it was not possible to obtain funds to study NMR during my postdoctoral year at UCL (1963–64), so I tried the next best thing, namely ESR of iron(III) complexes. Following this, I was appointed to a lectureship in chemical physics at Surrey University, which found me in charge of a 60 MHz spectrometer and the responsibility of ensuring that the practical chemists had a routine ^{1}H service. Following the ESR work at UCL I was fascinated by the prospect of investigating the NMR spectra of paramagnetic complexes; fortunately my first Ph.D. student, Colin Honeybourne, was well motivated, so together we set out to look at contact and dipolar interactions of paramagnetic systems by means of ^{1}H NMR. At the time, Jim Feeney was working in the nearby Varian laboratory and he very generously helped us by providing access to an HA-100 instrument, which we eventually purchased. The work on paramagnetic systems generated an interest in the theory of chemical shifts on paramagnetic and diamagnetic compounds which was enhanced when, in 1966, I had the opportunity to visit Michal Witanowski and Lech Stefaniak at the Institute of Organic Chemistry of The Polish Academy of Sciences, and to perform some ^{14}N NMR measurements. The large range of chemical shifts which we observed required some theoretical explanations. Fortunately, at Surrey I was able to attract a number of students in the 1970s who had an interest in theoretical chemistry, in particular Kais Ebraheem and Mehdi Jellali-Heravi, and we developed Pople's shielding model to include INDO/S parameterization and nonspecific solute–solvent interactions via the Solvaton model to provide an account of the nitrogen chemical shifts, as well as those of some other first and second row nuclei.

In 1973, Michal Witanowski and I coedited the first book on nitrogen NMR; one of our contributors was Ted Axenrod from City University, New York, who was very interested in ^{15}N–^{15}N spin–spin couplings and persuaded me to become interested in the theory of these, rather unusual, data. Consequently, we developed at Surrey a series of semiempirical MO calculations of spin–spin couplings. The majority of this work was carried out by two Ph.D. students, Tun Khin and Sangwahn Duangthai, and provided an explanation for many of the heteronuclear coupling data appearing in the literature at that time. This work was also extended to include nonspecific solute–solvent interactions by means of the Solvaton model.

My first visit to Japan was in 1978 when I had the great pleasure of meeting Isao Ando at Tokyo Institute of Technology. Like us at Surrey, Isao and his students had a great interest in nuclear shielding calculations including solvent effects. Jointly we developed the Solvaton model further and applied it, with success, to a number of nuclei. In addition to the effects of solvent on chemical shifts and spin–spin couplings, we established an interest in the influence of pressure on NMR parameters and jointly carried out measurements and calculations which helped to explain the observed effects. Our collaboration resulted in the book entitled 'Theory of NMR Parameters' in 1983 which dealt with the current situation regarding calculations of chemical shifts and spin–spin couplings. Our joint interest in the theoretical aspects of chemical shifts has continued and resulted, in 1992 and 1993, in our first papers dealing with ab initio MO calculations of nuclear shieldings using the GIAO procedure. Another aspect of our cooperative research has been in solid state CP MAS measurements of ^{13}C and ^{15}N NMR spectra. A particular area of joint interest has been in the ^{15}N solid state NMR spectra of peptides and polypeptides, and we published a joint review of this work in 1993.

The cooperation with my Polish co-workers is still continuing apace. We have now produced five monographs on nitrogen NMR and another one is in the planning stage. Our joint research activities have tended to concentrate on a study of both specific and nonspecific solute–solvent effects on nitrogen shieldings, treated both experimentally and theoretically, and on multinuclear MR studies of various equilibria and structural properties of molecules both in solution and in the solid state. The importance of making available and reading reviews on current research areas was apparent from my early days as a research student. Consequently, when the opportunity arose in 1975 to take over from Eric Mooney as editor of 'Annual Reports on NMR Spectroscopy', I felt this to be a task which could be of use to the NMR community and I took it on in the hope that I could continue to attract reviews of an acceptable quality. Thanks to the generosity of a number of leading NMR spectroscopists in providing their time and knowledge, my anticipations have not been frustrated. Similar motives lay behind my acceptance, in 1977, of the editorship of 'Specialist Periodical Reports on NMR' which had been successfully launched by Robin Harris and continued by Ray Abraham. Due to the dedication of the contributors, this series has also continued to flourish.

A more recent development is in NMR studies of food constituents. This is involving us in multidimensional NMR measurements on food peptides and ab initio MO calculations of the ^{13}C shieldings of polysaccharides. In 1992 we held the first International Conference on Applications of Magnetic Resonance to Food Science at Surrey, which proved to be sufficiently successful for the second conference to be held in Aveiro, Portugal, in September 1994, and the third to be planned for Nantes, France in September 1996.

Biographical Sketch

G. A. Webb. *b* 1935. B.Sc., Ph.D., D.Sc., 1974, University of London. Successively lecturer, 1964, senior lecturer in chemical physics, 1975, reader, 1985, and professor in chemistry, 1995, at the University of Surrey. Approx. 320 publications and about 50 edited volumes on NMR. Research interests include a study of solute–solvent interactions by nitrogen NMR, solution and solid state NMR studies of molecular structure, theoretical aspects of nuclear shielding and of drug–receptor interactions.

Wehrli, Felix W.: From Carbon-13 to Quadrupolar Nuclei NMR and Medical Imaging—Reflections

Felix W. Wehrli

University of Pennsylvania Medical Center, Philadelphia, PA, USA

CARBON-13: FROM INDIRECT DETECTION TO ROUTINE STRUCTURE ANALYSIS

We owe the continued progress of NMR from a physics curiosity to what promises to become the preeminent medical imaging modality of the 21st Century to the ingenuity and tenacity of the many pioneers whose work is commemorated in the eight volumes of this Encyclopedia. Many of today's capabilities have long been taken for granted by the younger generation of spectroscopists and chemists. A case in point is natural-abundance carbon-13 spectroscopy, part of the development of which I had the good fortune to witness, though much more from the perspective of user than innovator.

My fascination with NMR—undiminished up to the present day—began in earnest in 1965 during a graduate course on instrumental analysis, taught by Professor W. Simon at the Swiss Federal Institute of Technology (ETH). It was the high time of proton NMR, the era of the Varian A-60, the first mass-produced NMR spectrometer which led the diffusion of high-resolution NMR into analytical organic chemistry. In searching for a thesis subject two years later, Simon told me that he thought carbon-13 NMR had, because of its much larger chemical shift range and already proven sensitivity to stereochemistry, even greater potential. I was rapidly convinced after reading David Grant's and Jack Roberts's work in which they showed that separate chemically shifted resonances could be observed for virtually all carbons in molecules as complicated as steroids.

All of this work would, of course, have been impossible without proton noise decoupling, first conceived by Richard Ernst in 1966,[1] enhancing the signal-to-noise ratio at least 10-fold and greatly simplifying the spectra (albeit at a considerable loss in information). I became painfully aware of the critical role of proton noise decoupling during my early attempts to generate natural-abundance ^{13}C NMR spectra on the Bruker-Spectrospin HFX-10 multinuclear spectrometer, purchased by the department specifically for this project. The lack of this capability during the entire period of my dissertation was exacerbated by poor magnetic field homogeneity, which made detection of natural-abundance ^{13}C in large sample tubes virtually impossible, forcing me to resort to 5 mm samples for which the field could be adequately shimmed. Further, pulse Fourier transform techniques, though first described in 1966,[2] were not generally available before about 1970. Hence, I had a two orders of magnitude sensitivity problem!

Unwilling to give up, I thought about ways around this problem. In this effort I came across a paper by Baker in which he succeeded in obtaining a high-resolution spectrum of trifluoroacetic acid by heteronuclear INDOR spectroscopy, achieved by monitoring a carbon-13 satellite in the ^{19}F spectrum while slowly sweeping across the ^{13}C resonance.[3] Since the signal-to-noise ratio (SNR) scales as γ^3, detection of the proton resonance of a nucleus spin-coupled to ^{13}C could be detected with 64-fold increase in sensitivity relative to direct detection. If the proton resonance is saturated, transient nutations are induced and the signal amplitudes can be predicted on the basis of the resultant population redistribution, using the arguments underlying the generalized Overhauser effect. The approach was, of course, limited to those cases where a ^{13}C satellite could be observed, which required sufficiently large coupling constants and fairly high sample concentration. In practice, the method was confined to the detection of methyl carbon resonances. An example is given in Figure 1. Nevertheless, I succeeded in measuring the methyl carbon shifts in a great many compounds and studied substituent effects on ^{13}C shieldings and ^{13}C–^{1}H coupling constants.

As a whole, however, this work had little impact on the subsequent evolution of ^{13}C NMR spectroscopy, and it served merely as a stimulus for future work. In truth, the methodology was, at the time, already outmoded as a result of the anticipated availability of pulse Fourier transform ^{13}C spectroscopy with proton noise and coherent off-resonance decoupling.

The commercialization of multinuclear high-resolution pulse Fourier transform MR in the early 1970s by Varian, Bruker, and JEOL gave ^{13}C MR an unprecedented impetus in that it rapidly turned into a standard analytical tool in the organic chemistry research laboratory, providing a powerful complement to proton spectroscopy. Next to the previously mentioned milestones—pulse FT techniques and broadband proton decoupling—the course of developments was largely spurred by another event, the emergence of the minicomputer as an integral subsystem of the spectrometer rather than just

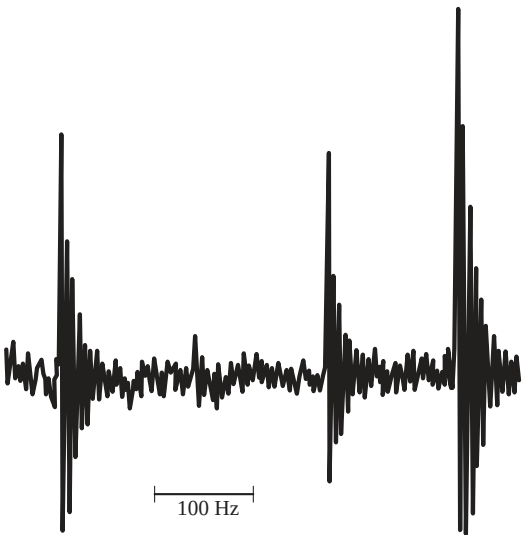

Figure 1 Transient nutations of the high-frequency ^{13}C satellite of the isotopomer $^{13}CH_3$ ^{12}CN at natural abundance, obtained at a ^{13}C sweep rate $d\nu_2/dt$ = 4.8 Hz s^{-1} and $\gamma \boldsymbol{B}_1/2\pi$ = 0.67 Hz for the proton rf field at 90 MHz. (Taken from Ref. 4 with permission)

an add-on. While ^{1}H NMR of organic molecules was conveniently achieved in the continuous-wave (CW) mode, CW carbon NMR, in spite of noise decoupling and signal averaging, was quite impractical for all but the most skillful experimenters and demanded scan times in excess of 1 h on 1 mol solutions. In fact, only a few 'masters of the art' succeeded in acquiring and analyzing ^{13}C spectra of molecules >1000 Da. One of them was Leroy Johnson, then at Varian, who among much unpublished work reported the spectrum and its partial assignment of gramicidin S, using entirely CW methodology.

The period following the introduction of the ^{13}C pulse FT spectrometer represented a phase in the evolution of ^{13}C NMR when it often sufficed to record the spectra of a few off-the-shelf compounds to produce a publication with minimal intellectual effort. However, it soon became clear that, in order to be useful, tools were needed for unambiguous spectral assignment. This problem attracted my interest during the years from about 1971–75 during my early professional career as an application scientist at Varian AG in Switzerland. First, it became obvious that the ^{13}C spectrum could not and should not be analyzed in isolation. In fact, the power of the technique was the synergism of the joint utilization of carbon and proton spectroscopy, for example, by means of ^{1}H–^{13}C double resonance. One of the historic counterparts of the modern carbon–proton heterocorrelated spectrum was off-resonance CW decoupling, presumably first applied by Weigert et al.[5] Though comparably primitive and tedious, it provided for complete cross assignment of proton and carbon resonances from a set of experiments whereby the decoupler frequency was varied incrementally. Wolfgang von Philipsborn at the University of Zürich, with whom I entertained a close working relationship highlighted in annual carbon-13 NMR workshops held throughout most of the 1970s, pointed out early on that most of the structural information resided in the proton-coupled spectrum and thus demanded an analysis of the coupling constants and their angular relationships.[6]

The ability readily to measure T_1 relaxation times by the inversion–recovery experiment, conceived by Vold et al.[7] and Freeman and Hill,[8] added a new dimension to ^{13}C NMR. Inspired by the mechanistic work by David Grant and his co-workers[9] and by Lyerla and Levy,[10] we enthusiastically launched ourselves into applying this marvelous tool for assigning spectral resonances by making use of the structural dependence of dipolar coupling and its modulation by rotational diffusion.[11] A case in point is the inversion–recovery spectrum of cholestane shown in Figure 2 from which backbone methylenes can readily be distinguished from their methine counterparts and carbons belonging to the C-17 side chain, merely on the basis of their differential recovery. Many of these techniques were superseded by the emergence and rapid dissemination of two-dimensional NMR spectroscopy in the mid-1970s by the research groups of Richard R. Ernst and Ray Freeman.[12,13]

By mid-1975 we had accumulated a considerable body of material, much of it too fragmented to warrant separate publication, but as a whole it was probably worthwhile to be shared with fellow chemists and spectroscopists. It is perhaps for this reason that Jim Feeney encouraged me to organize this material into a textbook, a task

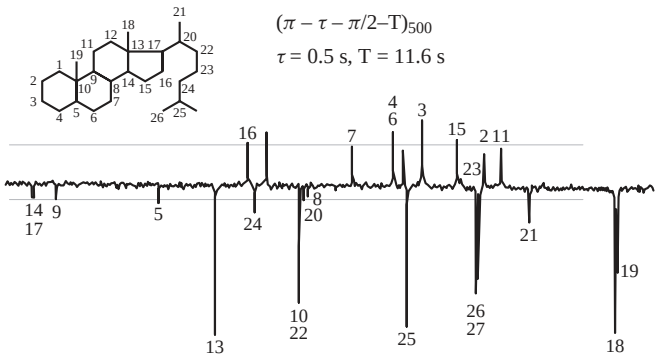

Figure 2 Inversion–recovery ^{13}C NMR spectrum of cholestane. Backbone CH_2 carbons relax fastest (positive signals), followed by CH groups (slightly negative, dotted line), and the side-chain carbons which, by virtue of their longer T_1 values, relax most slowly. (Taken from Ref. 14 with permission)

which I enthusiastically undertook with my co-worker Toni Wirthlin.[14]

EXPLORING THE PERIODIC SYSTEM

Another example how technology can drive applications is multinuclear MR. The technological advance, in this instance, was the frequency synthesizer, the basis of the broadband rf transmitter. The Varian XL-100 spectrometer had a feature called the 'Gyrocode' decoupler, a broadband decoupler which, however, was of limited use until someone had the idea of reversing its function by adding broadband transmitter boxes and preamplifiers.

Following the ^{13}C euphoria, these developments redirected my interests toward heteronuclear NMR. Of course, many of the heteronuclei had already been studied in great detail and applied to organic, inorganic, and bioinorganic chemistry. Among these were virtually all spin-$\frac{1}{2}$ nuclei, which, however, as every NMR spectroscopist knows are a minority within the Periodic Table of the elements. While all elements have at least one magnetically active isotope, the majority of isotopes are of the spin $I > \frac{1}{2}$ type and thus quadrupolar. Many of these were discounted as being useful due to either excessively large quadrupole moments, low isotopic and chemical abundance, poor receptivity, or a combination of these adverse factors. Noteworthy exceptions were the alkali metal ions which, because of their role in biology, had been studied early; sodium by Pierre Laszlo,[15] sodium and other alkali metals by Lindman and Forsén,[16] and deuterium by Ian Smith and his co-workers.[17] However, it was Otto Lutz in Tübingen who, with his early Bruker SXP-100, had explored the NMR properties of many of the more esoteric nuclei. His many contributions to the field are summarized in Ref. 18.

Nevertheless, to my surprise, many of the quadrupolar nuclei had hardly been observed before, and their relaxation properties were largely unknown. Among the ones I had an opportunity to study in some detail were ^{6}Li, ^{9}Be, and ^{133}Cs.[18] In the course of this work, my co-workers and I felt some of the excitement the early pioneers must have experienced when first detecting a resonance signal for the purpose of measuring a nucleus's magnetic moment. An anecdote perhaps

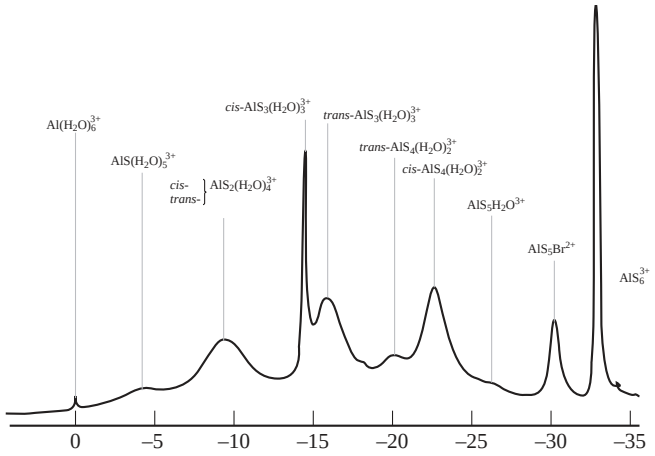

Figure 3 8.4 T ^{27}Al spectra showing the resonances of the mixed complexes $AlS_n(H_2O)_{6-n}^{3+}$ (S = CH_3CN) assigned on the basis of estimated relative quadrupole coupling constants which determine the linewidth. (Taken from Ref. 20)

worth sharing with readers deals with some ^{6}Li experiments I conducted in 1976. Lithium-6 has I = 1, 7.4% natural abundance and resonates at 14.7 MHz at a field of 2.3 T; hence it should be easy to detect. To my surprise, ^{6}Li had, as of 1976, not yet been observed in solution (in contrast to its companion isotope, ^{7}Li, which was widely used in organolithium chemistry). Upon dialing the frequency of ^{6}Li, to my delight a signal crept across the oscilloscope. However, I was unable reproduce the finding and aborted the experiment after a while. The elusive signal reappeared in a second attempt several hours later, at which time I became certain that the observation was real. The culprit for the apparent irreproducibility, of course, was the exceedingly long T_1 value. With its very small quadrupole moment (4.6×10^{-4} b), quadrupole relaxation turned out to be almost negligible and dipolar coupling relatively weak. Nevertheless, a more detailed mechanistic analysis revealed the predominance of dipolar relaxation in aqueous solution with an observed T_1 of 3 min. In D_2O, T_1 was found to rise up to 17 min at 80 °C![18]

Of course these are esoterica, and it was of much more relevance to show that quadrupolar NMR could provide information on solution structure. On a trip to Moscow in 1978 I met Dr. Valerii Tarasov, a co-worker of Professor Buslaev at the Institute of General and Inorganic Chemistry. I was intrigued by a paper in which Tarasov showed that the mixed niobium halides in the ^{93}Nb spectra could be readily assigned on the basis of their symmetries which, of course, govern the quadrupole coupling constants and thus the ^{93}Nb relaxation times. Based on interatomic distances, ligand charges, and symmetry arguments, the electric field gradient tensor invariant can be computed and the relative linewidths predicted, thus permitting assignment of their resonances.[19] My wife, Suzanne, and I applied this method to a number of inorganic solution systems, an example of which is given in Figure 3, showing the ^{27}Al spectra of the mixed solvates of Al^{3+}.[20]

FROM SPECTROSCOPY TO IMAGING

My career as an NMR spectroscopist came to a temporary end upon joining General Electric Medical Systems, where I found a world quite distant from the one I was accustomed to in my earlier career. Whereas spectroscopy, except for the very beginnings, was in its majority the accomplishment of chemists, the medical imaging arena was clearly the realm of physicists. My colleagues at General Electric were very conversant on such subjects as image reconstruction algorithms and the point spread function, concepts which were quite alien to an NMR spectroscopist but which were as much daily bread to them as chemical shifts and correlation times were to me.

We rapidly overcame the mutual knowledge gap and, to my surprise, I soon developed a liking for the intricacies of NMR imaging (or MRI—magnetic resonance imaging, the acronym favored by the American College of Radiology). This kind of cross fertilization occurred in numerous laboratories around the world and certainly greatly enhanced the rate at which MRI evolved. Unlike computed tomography (CT), which was essentially the product of corporate R&D labs, with the details of technical implementation tightly guarded secrets, the accessible knowledge base in NMR was much broader and more of it resided within academia, and was thus readily available in the open literature.

In my responsibility as the manager of magnetic resonance applications, which entailed the development of clinical applications in cooperation with academic institutions, I soon became aware of the enormous need for user education. Unlike the high-resolution NMR user (typically organic or physical chemists), radiologists had, with few exceptions, never been exposed to magnetic resonance. While the acquaintance with CT a few years earlier had been a challenge, it was nevertheless one they could master with relative ease, namely the transition from projection radiography to cross-sectional tomographic imaging. MRI was radically different and much more demanding in that they had to cope with its multiparametric nature and assimilate the property that there was no single gray scale as in X-ray imaging. Image contrast in MRI is, of course, a complete continuum, albeit one that is predictable provided the intrisic parameters, relaxation times, and mobile water concentration (‘proton density’ in MRI jargon) are known. Some of my early work at GE dealt with the quantification of tissue contrast,[21] complementing work by others[22,23] who had recognized that understanding contrast was the key to exploiting the modality’s potential. I was particularly delighted that relaxation times, whose significance in high-resolution NMR clearly trails that of the chemical shift and the spin–spin coupling constant, had a much more significant role in imaging. Like many others, we believed that a precise measurement of relaxation times could add specificity to the diagnosis. It seemed highly unlikely that two different pathologies would be identical in both relaxation times and spin density. Of course, it soon became evident that the problem was more complex and, with few exceptions—a noteworthy one being cerebral hemorrhage[24]—pathology-induced alterations in relaxation times proved to be nonspecific. The problem is further exacerbated by the typically wide distributions of tissue relaxation times, which is not surprising when considering that pathologic tissue is often composed of a multitude of cell types.

MRI has thus remained a largely qualitative technique. Images are ‘read’ by a radiologist and the presence or absence of pathology assessed on the basis of local alterations in gray-scale level, in principle not fundamentally different

from the manner X-ray imaging had been practiced since its inception nearly 100 years ago. This is counter to scientific principles but, of course, clinical medicine does not claim to be an exact science, nor is it obvious to what extent image-based measurements would ultimately benefit the patient. Nevertheless, short of spectroscopic imaging which permits the measurement of metabolite concentrations, it is quite feasible quantitatively to characterize selected properties of biomaterials in vivo entirely on the basis of a bulk proton measurement. A case in point is trabecular (spongy) bone as it occurs in the major load-bearing portions of the skeleton, such as in the vertebrae. In 1989 we postulated that the anomalously short T_2* value of the marrow protons was caused by the dipole fields induced by the bone's diamagnetism. Later we showed the intrinsic magnetic field inhomogeneity to be a function of the density, spacing, and orientation of the trabecular elements[25] after providing evidence that the technique may be able to detect bone loss in osteoporosis.[26] A more detailed account of this work is given elsewhere in this encyclopedia (See ***Imaging of Trabecular Bone***).

REFERENCES

1. R. R. Ernst, *J. Chem. Phys.*, 1966, **45**, 3845.
2. R. R. Ernst and W. A. Anderson, *Rev. Sci. Instrum.*, 1966, **37**, 93.
3. E. B. Baker, *J. Chem. Phys.*, 1962, **37**, 911.
4. F. W. Wehrli and W. Simon, *Helv. Chim. Acta*, 1969, **52**, 1749.
5. F. J. Weigert, M. Jautelat, and J. D. Roberts, *Proc. Natl. Acad. Sci. USA*, 1968, **60**, 1152.
6. W. von Philipsborn, *Pure Appl. Chem.*, 1974, **40**, 159.
7. R. L. Vold, J. S. Waugh, M. P. Klein, and D. E. Phelps, *J. Chem. Phys.*, 1968, **48**, 3831.
8. R. Freeman and H. D. W. Hill, *J. Chem. Phys.*, 1969, **51**, 3140.
9. J. Lyerla and D. Grant, in *M.T.P. International Review of Science—Physical Chemistry Series*, ed. C. McDowell, Medical and Technical Publishing Company, Oxford, 1972, vol. 4, chap. 5
10. J. Lyerla and G. Levy, Carbon-13 Nuclear Spin Relaxation, in *Topics in Carbon-13 NMR*, ed. G. C. Levy, John Wiley, New York, 1974, pp. 81–149.
11. F. W. Wehrli, Organic Structure Assignments Using C-13 Spin–Lattice Relaxation Data, in *Topics in Carbon-13 NMR Spectroscopy*, ed. G. C. Levy, Wiley-Interscience, New York, 1976, pp. 343–389.
12. W. Aue, E. Bartholdi, and R. R. Ernst, *J. Chem. Phys.*, 1976, **64**, 2229.
13. G. Bodenhausen, R. Freeman, and D. L. Turner, *J. Chem. Phys.*, 1976, **65**, 839.
14. F. W. Wehrli and T. Wirthlin, *Interpretation of Carbon-13 NMR Spectra*, Heyden, London, 1976.
15. P. Laszlo, *Angew. Chem.*, 1978, **90**, 271.
16. B. Lindman and S. Forsén, NMR of the Alkaline Earth Metals, in *NMR and the Periodic Table*, eds. R. K. Harris and B. Mann, Academic Press, New York, 1978.
17. H. H. Mantsch, H. Saitô, and I. C. P. Smith, Deuterium Magnetic Resonance: Applications in Chemistry, Physics and Biology, *Progress in NMR Spectroscopy*, 1977, **11**, 211.
18. F. W. Wehrli, NMR of the Less Common Quadrupolar Nuclei, *Ann. Reports NMR Spectroscopy*, 1979, **9**, 126.
19. V. P. Tarasov, V. I. Privalov, and Y. A. Buslaev, *Mol. Phys.*, 1978, **35**, 1047.
20. F. W. Wehrli and S. Wehrli, *J. Magn. Reson.*, 1981, **44**, 197.
21. F. W. Wehrli, J. R. MacFall, G. H. Glover, N. Grigsby, V. Haughton, and J. Johanson, *Magn. Reson. Imaging*, 1984, **2**, 3.
22. L. E. Crooks, C. M. Mills, P. L. Davis, M. N. Brant-Zawadski, J. Hoenninger, M. Arakawa, J. Watts, and L. Kaufman, *Radiology*, 1982, **144**, 843.
23. I. R. Young, *Br. Med. Bull.*, 1984, **40**, 139.
24. K. R. Thulborn and T. J. Brady, Iron in Magnetic Resonance Imaging of Cerebral Hemorrhage, in *Magnetic Resonance Quarterly*, ed. H. Y. Kressel, Raven Press, New York, 1989, pp. 23–38.
25. H. Chung, F. W. Wehrli, J. L. Williams, and S. D. Kugelmass, *Proc. Natl. Acad. Sci. USA*, 1993, **90**, 10250.
26. F. W. Wehrli, J. C. Ford, M. Attie, H. Y. Kressel, and F. S. Kaplan, *Radiology*, 1991, **179**, 615.

Biographical Sketch

Felix W. Wehrli. *b* 1941. M.S., 1967, Ph.D., 1970, Chemistry, Swiss Federal Institute of Technology, Switzerland. NMR application scientist, Varian AG, 1970–79; Executive Vice President, Bruker Instruments, Billerica, 1979–82; NMR Application Manager, General Electric Medical Systems, Milwaukee, 1982–88. Currently Professor of Radiologic Science and Biophysics, University of Pennsylvania Medical School. Approximately 80 publications. Current research specialty: NMR imaging of biomaterials, specifically trabecular bone.

Weitekamp, Daniel P.: Sensitivity Enhancement Through Spin Statistics

Daniel P. Weitekamp

California Institute of Technology, Pasadena, CA, USA

There are two phenomena involving nuclear spin with which every science undergraduate has at least a passing acquaintance. The first, of course, is NMR spectroscopy. The second is nuclear spin statistics, the surprising restrictions on allowed molecular states which, for example, condemn an oxygen molecule ($^{16}O-^{16}O$) to eternal rotation in its ground state. Such restrictions have few consequences for the interpretation of NMR spectra. The well-known exception is that slow interconversion between the *para* (singlet) and *ortho* (triplet) nuclear spin isomers of dihydrogen ($^{1}H-^{1}H$) may allow them to be out of equilibrium with one another over the entire course of the measurement. This disequilibrium can hold even in solution and even though other degrees of freedom, including the spin temperature of the *ortho*-hydrogen, are equilibrated. Thus, *ortho*-hydrogen and *para*-hydrogen are for many purposes distinct chemical species, the latter having only one nuclear spin state and consequently no NMR signal.

My first thoughts concerning a new connection between NMR and nuclear spin statistics[1] occurred during a visit to Caltech in the spring of 1985 that would lead to my faculty appointment there in the fall. I was having a restless night at the faculty club hotel, which I attributed to the lumpiness of the mattress, when my thoughts turned toward what was becoming my principal research interest, increasing the sensitivity of NMR by coupling nuclear spins to other degrees of freedom. The single nuclear spin state of *para*-hydrogen implies that, in a sense, it is cold. A comparable degree of spin ordering is obtainable at equilibrium only at temperatures of a few mK and magnetic fields of several tesla.

However, with no allowed transitions out of this spin state, the order of *para*-hydrogen was spectroscopically useless. It would be necessary to introduce magnetic inequivalence to release this potential signal by connecting the singlet to the triplet states. This would require chemistry, but simple bond cleavage would not suffice. A singlet state of two protons is a relationship of one spin relative to the other and this order would be dissipated if the pair were split and mixed with an ensemble of other such products. Rather, it would be necessary that the pair have a special relationship even after being distinguished by magnetic inequivalence. After moving to Caltech and opening my first inorganic text to learn that such molecular addition reactions were known, the impediment remained that I had no research assistant to try it out. In December C. R. (Russ) Bowers joined my 'group'. We prioritized a number of possible projects. The chemical relevance, simplicity, and absolute novelty of the *para*-hydrogen idea carried the day.

Russ Bowers began learning the experimental side of NMR and *para*-hydrogen production and homogeneous catalysis, while together we worked out the spin-density operator formalism of *para*-hydrogen addition and the spectroscopy of the product molecules. We wrote up our predictions in a *Physical Review Letter* and I appended this work to a talk on another topic I was already scheduled to give at the International Society of Magnetic Resonance meeting in Rio de Janeiro in June 1986. The idea met with interest, but also with considerable skepticism that the spin order would survive the catalytic reaction. The experimental demonstration followed in July, and Russ floated around the lab in bliss, astounded that the spectrum of propionitrile, newly formed from acrylonitrile and *para*-hydrogen, looked exactly like his simulations. We published the early experiments in the *Journal of the American Chemical Society* under the title '*Para*-hydrogen and Synthesis Allow Dramatically Enhanced Nuclear Alignment', but dared not to print the corresponding mnemonic (PASADENA) for fear that an acronym-adverse referee (you know who you are) would spoil our fun.

After our presentation of the first experiments at NMR meetings in 1987, it was pointed out to us that the phenomenon we predicted and demonstrated must also have been responsible for some earlier NMR signal enhancements during homogeneous hydrogenation that had been misinterpreted as the sorting of nuclear spin during the course of free-radical reactions (so-called chemically induced dynamic nuclear polarization or CIDNP), an unrelated way of inducing nonequilibrium spin populations. Although all practitioners have been won over to the Pasadena interpretation and procedure, some have so far resisted the priority (and acronymic splendor) of the PASADENA nomenclature.

The fun was soon shared with an undergraduate, Michael Pravica, who demonstrated the advantage of turning on the magnetic inequivalence adiabatically, and with a graduate student, Paul Carson, who obtained the spectrum of hydrogen chemisorption sites at a catalytic surface. Such reminiscing should not distract from the likely prospect that the chemical significance of this new connection between NMR sensitivity and nuclear spin statistics lies almost wholly in the future; very few systems have been examined. More promising still is the reverse phenomenon in which NMR of a precursor species is detected as a change in the branching ratio to spin isomers of the product hydrogen molecules, for example by optical detection of *para*-hydrogen and *ortho*-hydrogen mole fractions. This has the potential of detecting ensembles that are initially Zeeman-ordered, greatly increasing the range of accessible samples. With single-photon optical sensitivity, such an approach could enable the NMR study of individual catalytic sites.

REFERENCES

1. A review of the method and early work can be found in: C. R. Bowers, D. H. Jones, N. D. Kurur, J. A. Labinger, M. G. Pravica, and D. P. Weitekamp, The Symmetrization Postulate and NMR of Reacting Systems, *Adv Magn. Reson.*, 1990, **14**, 269.

Biographical Sketch

Daniel P. Weitekamp. *b* 1952. B.A., Harvard College, Ph.D., Chemistry (with Alexander Pines), University of California, Berkeley, USA. Postdoctoral work (with Douwe Wiersma) at University of Groningen, The Netherlands. Divisional Fellow, Materials and Molecular Research Division, Lawrence Berkeley Laboratory. Faculty in Chemical Physics, California Institute of Technology, Pasadena, 1985–present. Approx. 60 publications. Research specialties: solid state NMR, sensitivity enhancement by coupling spins to other degrees of freedom.

Whiffen, David H.: Forty-Nine Years Watching NMR

David H. Whiffen

I have followed the advancement of NMR from its earliest days and have heard lectures from most of the senior practitioners and been friendly with many. I have never actually measured an NMR spectrum, which explains the title.

I was introduced to NMR when Charles Townes took me to a lecture by E. M. Purcell in Connecticut in the fall of 1946. There were excellent slides, especially of the 'eating a hole in the curve' effect, and he explained the measurement of nuclear relaxation times: my interest was great as I had measured the rotational relaxation times of molecules in nonpolar solvents.

Returning to Oxford in 1947, I found that a great friend of mine, Rex Richards, was considering what field of research he should follow as he had just become a tenured Fellow at Lincoln College and needed a change of research. He was considering NMR but he feared it would be too difficult and might be dull. Fortunately an Oxford physicist, I think Rollin, had just made the first British experiment and said it was easy. I said the relaxation times would be interesting and so Rex chose NMR; this topic occupied him all his research career.

The advances after 1947 came fast and many new phenomena not envisaged in Purcell's lecture: measurement of interhydrogen distances in solids, the *horrid* chemical shift which meant that the physicists could not agree with each other when measuring really accurate nuclear moments, the spinning of liquid sample tubes, the scalar spin–spin coupling, etc. I followed these closely and explained the science to colleagues and students in Birmingham. I remember a lecture by E. R. Andrew when he had removed the influence of internuclear coupling in solids by rapid spinning of the sample at the magic angle.

Having interesting results concerning the orientation dependence of electron resonance of radicals trapped in a single crystal, I went to a magnetic resonance Gordon Conference in the summer of 1958, as did John Pople. He explained that he had just been appointed by Gordon Sutherland to head a new Basic Physics Division of the National Physical Laboratory and was looking for a senior colleague to guide a section in magnetic resonance. As a consequence, I was appointed to this post from October 1959. John Pople and Ray Freeman were already at work. Ray Abraham, Tom Connor, Tony Hartland, and Keith McLauchlan all had several years in the NMR group. There were shorter terms for Fellows, notably David Cohen and William McFarlane. We also had many foreign visitors for extended periods of six months or more. Most of my own influence was general encouragement rather than specific advice.

My direct involvement followed a chance meeting with an old acquaintance, Dennis Evans, who told me what he had just done, namely used double resonance to show that in thallium triethyl the Tl couplings to the $>CH_2$ and the $-CH_3$ hydrogen nuclei were of opposite signs. The next day I encouraged Freeman to use double resonance to find the relative signs in a molecule with three hydrogens. The experiment was not easy as the couplings were small but he succeeded in showing that the three couplings had the same sign;[1] we invited Evans to join us as an author but he declined as he had thought the experiment was impossible. Freeman and I published a paper showing the merit of a fixed magnetic field with one fixed and one variable frequency. The group provided several other sign determinations with such an arrangement. I suggested to Keith McLauchlan that a related philosophy would apply to double quantum transitions and we published an example; though less elegant, this required only one oscillator frequency with high power. David Cohen had a three-hydrogen case where the J(AB) and J(AC) relative signs were of interest but the usual experiment did not work because J(BC) was virtually zero; I explained this failure and suggested a triple resonance[2] experiment which was successful. There were a few other related experiments on enhancing double resonance signals, on the consequence of using very strong decoupling, on the double resonance with a spin-1 nucleus, etc., but this essentially completed my participation in NMR.

However Ray Cook and I were able to extend work in electron resonance guided by the NMR analogs and using ENDOR. The relative signs of two H couplings to the unpaired electron were determined using a double ENDOR experiment:[3] this relates to the triple NMR experiment as the H–H coupling is weak. For the two H atoms in a CH_2 group in a rigid crystal, the greatest coupling is about -42 kHz when the H $\leftrightarrow$ H direction is parallel to the magnetic flux density. If the ENDOR frequencies can be measured with this accuracy, the relative signs of the ESR hyperfine couplings and the H–H coupling can be determined;[4] this gives absolute hyperfine coupling signs as the H–H sign is certain. Other ENDOR experiments led to quadrupole coupling tensors such as that of the ^{14}N in a Type 1b diamond.

I continued a general interest and saw the early development work leading to the use of NMR in medicine, in particular, the experiments from Nottingham, where Raymond Andrew, Arthur Clough, and especially Peter Mansfield were working. The pictures provided at intervals include the NMR of a lemon, where its pips were counted and checked afterwards by cutting it open, a dead rat, a human finger, and a wrist which demonstrated how NMR was best at a bone cross section in contrast to the X-ray plates.

My interest remains and my diary contains a lecture on the medical uses to be given after this contribution is despatched. These advances and the usefulness of NMR were not remotely apparent when Felix Bloch and Edward Purcell succeeded where C. J. Gorter had, undeservedly, failed.

REFERENCES

1. R. Freeman and D. H. Whiffen, *Mol. Phys.*, 1961, **4**, 321.
2. K. A. McLauchlan and D. H. Whiffen, *Proc. Chem. Soc., London*, 1962, 144.
3. R. J. Cook and D. H. Whiffen, *Proc. Phys. Soc., London*, 1964, **84**, 845.
4. R. J. Cook and D. H. Whiffen, *J. Chem. Phys.*, 1965, **43**, 2908.

Biographical Sketch

David H. Whiffen. *b* 1922. M.A., 1947, D.Phil., 1948, Oxford University (Supervisor, Sir Harold Thompson), D.Sc., 1959, Birmingham

University, UK. Lecturer in Physical Chemistry, Birmingham University, 1949–59; FRS, 1966; National Physical Laboratory (mostly Basic Physics Division), 1959–68; Professor of Physical Chemistry, University of Newcastle upon Tyne, 1968–85; Retired 1985. Principal research interests: infrared spectroscopy, ESR, microwave spectroscopy, molecular force fields.

Williams, R. J. P.: The Use of NMR in Biology: Personal Reflections

R. J. P. Williams
University of Oxford, Oxford, UK

Early in the 1960s I became dissatisfied with my own studies of metal-ion interaction with molecules of biological interest. We had made many interesting observations on thermodynamic properties and UV–visible and ESR spectra but we lacked a tool for more precise structural analysis. Shortly after J. S. Anderson became a Professor of Inorganic Chemistry at Oxford he asked me about future equipment requirements. We decided to go for both NMR and ESR spectrometers. With Dr. H. A. O. Hill we chose to buy both from JEOL in 1964. We realized that our special knowledge of inorganic systems allowed us to use paramagnetic shift and relaxation probes in somewhat novel ways. We therefore applied the NMR method to structure studies of a variety of π complexes between planar metal chelates and planar organic molecules and to vitamin B_{12}. In this way we hoped to understand the interaction of metal porphyrins and chlorins with such molecules as quinones, since such interaction could have been of biological interest. Shortly after this study began (1966) I spent a year in Harvard Medical School studying metal proteins. On my return to Oxford I decided to start the NMR study of these larger molecules in parallel with model studies. The work began using a Varian 220 MHz CW spectrometer located either in a government or an industrial laboratory. The chosen protein was myoglobin since this contained the shift and relaxation probe, haem Fe (III), which could be reduced to a diamagnetic Fe (II) state giving a diamagnetic blank for comparison. In essence the experiments failed, but showed how one might succeed. The resolution was poor and with no computer backup it proved impossible to get spectra better than those demonstrated by Jardetsky's studies started somewhat earlier. All that could be seen were some histidine residues.

No real progress was made until, through a change of policy at research council funding level in Britain, we had the opportunity to bid for funding for expensive equipment opposite a research program which had to involve a large group of people. I drafted a proposal to study enzymes by NMR in parallel with crystal structure studies. Through many consultations with others, the Oxford Enzyme Group was formed and a team went out in search of a suitable company to make an FT high-field spectrometer. The team was led by R. E. Richards, K. McLauchlan, and I. D. Campbell. In fact it was found to be necessary to cobble together two companies—Bruker Spectrospin and Oxford Instruments. After a relatively short time the first FT spectrometer at high field, 270 MHz, was developed to our specification with an appropriate spectrometer suitably connected to a computer. There is no doubt that this was a major technical innovation in NMR, not mine, though stimulated by my drive to study proteins.

The spectrometer was an outstanding success in that it showed clearly that single resonances of all residues in a protein of 15 000 Da molecular weight could be seen and studied. We chose the protein lysozyme because we had agreed to work on a protein with a known crystal structure, and when the Oxford Enzyme Group was set up it had as one leading figure Prof. D. C. Phillips, who had investigated this structure. It was an over-ambitious choice once others started work on smaller proteins! We were able to carry out spin decoupling and NOE experiments for the first time in proteins. In fact, it was clear to us all that protein structures could be studied and it became a matter of innovation in pulse sequences and in structure analysis for the objective to be reached. (See, for example, historical articles in this volume by Ernst, Freeman, and Wüthrich.) We showed, more importantly, that the dynamics of proteins could be analyzed.

The opportunity of using the high-field spectrometer also arose in the investigation of NMR in living organs. We initiated the studies of ^{1}H and ^{31}P NMR of animal chromaffin cells of the adrenal gland (1974), the use of Gd contrast reagents for NMR scanning (1980), and of methods using shift reagents to give field gradients in the analysis of biological space (1987). These developments occurred alongside those of G. R. Radda and R. E. Richards on ^{31}P NMR in muscle.

The work also led almost automatically to a chase to higher field spectrometers by manufacturers, usually with Oxford/Bruker in the lead in colloboration with the Oxford Enzyme Group technical team. Today the 750 MHz spectrometer is a direct consequence of the success of the first one built in 1971.

Of course, my group has been largely concerned with the analysis of paramagnetic molecules or molecules in which paramagnetic ions can be substituted. The finest example is the final study of cytochrome *c* using shift reagent methods. I wish to stress the value of chemical shift analysis. It uses vectors and if the analysis can be made from a single center, as in a haem protein or as in a protein such as lysozyme doped with a lanthanide, then the analysis does not require knowledge of the ***g***-tensor which is left as one of the unknowns. Using a computer search, and assuming a single structure (this is not likely to be true ever, but it is a useful global view as in all NMR studies) it has to be the case that a structure can be determined.[1] There is additional value in 'diamagnetic' shift data since these readily distinguish secondary structure as shown by Clayden. Combination with relaxation scalar probes (paramagnetic or NOE) then leads to very convincing NMR structural data.[2] For example, the studies of cytochromes revealed which proteins changed their H-bond patterns on a change of oxidation state.[3] This is fundamental knowledge since it leads to information concerning redox state changes and proton movements. The method can be greatly extended especially since mobile regions of proteins, difficult to study by NOE, are open to analysis by shift studies. It is worth noting that sections or even whole proteins of low structural content were discovered by us, e.g. chromagranin A, in a cell! Shift analysis should be very valuable in the folding problem, as shown in publications by C. M. Dobson.

The main group of people involved in this work were H. A. O. Hill, B. E. Mann, K. G. Morallee, J. A. Glasel, R. A. Dwek, A. Xavier, I. D. Campbell, C. M. Dobson, P. E. Wright, B. A. Levine, P. J. Sadler, G. R. Moore, R. G. Ratcliffe, C. F. G. C. Geraldes, F. M. Poulsen, F. Inagaki, N. J. Claydon, G. R. Williams, R. E. Klevit,

W. J. Fairbrother, Y. Gao, and H. C. Joao with the technical help of J. Boyd and N. Soffe. All of them now have considerable standing in the NMR field in their own right.

REFERENCES

1. C. D. Barry, A. C. T. North, J. A. Glasel, R. J. P. Williams, and A. V. Xavier, *Nature (London)*, 1971, **232**, 235
2. I. D. Campbell, C. M. Dobson, and R. J. P. Williams, *Proc. R. Soc. London*, 1975, **A345**, 23.
3. Y. Gao, J. Boyd, G. J. Pielak, and R. J. P. Williams, *Biochemistry*, 1991, **7**, 1928.

Biographical Sketch

R. J. P. Williams. *b* 1926. B.A., 1948, Ph.D., 1951, Chemistry, Oxford University. Lecturer and tutor in Chemistry, Oxford University, 1955–65; Fellowship, Harvard University, 1965–66; lecturer, reader, and Napier Royal Society Research Professor, Oxford University, 1967–91. Approx. 500 publications. Research specialties: metal ions and their function in biological systems, use of NMR in biology, in vitro and in vivo studies of biological systems.

Witanowski, Michal: A Short Story about Nitrogen NMR

Michal Witanowski

Polish Academy of Sciences, Warsaw, Poland

A genuine breakthrough in chemical structure investigations was effected by the discovery of the so-called chemical shift in NMR, occurring just at the time when nitrogen NMR was involved since Proctor and Yu had in 1950 detected two ^{14}N resonance signals in ammonium nitrate. They were rather lucky since the chemical shift difference is quite significant in this case (ca. 350 ppm) and the relevant ^{14}N quadrupolar relaxations are slow. However, despite the significance of nitrogen in Nature and chemistry, further progress in the field was hampered by the inherent low sensitivity (low frequencies, about 0.1 and 0.07 for ^{15}N and ^{14}N, respectively, with respect to ^{1}H), a natural abundance of only 0.3% for ^{15}N (spin $\frac{1}{2}$) and its unfavorable relaxation ratio T_1/T_2, and quadrupole relaxation effects in ^{14}N NMR (spin 1, abundance 99.7%) which yield a large range of signal widths in the spectra. It took more than 10 years after Proctor and Yu's work before nitrogen NMR started gaining some momentum.

In the early 1960s, nobody knew too much about the subject and, when we purchased our first NMR machine (a Varian HR-60) in 1962, I had to argue a lot in favor of spending an extra 10% for a nitrogen-14 rf unit and a probe head which could house 15 mm o.d. sample tubes. Fortunately, our group was deeply involved in the chemistry of organic compounds of nitrogen and the arguments were persuasive. We were quite proud of ourselves when we obtained the ^{14}N signal of neat liquid nitromethane (little wonder, in the neat liquid its concentration is 18 M and the signal width is ca. 10 Hz), and even more so when we found that a mixture of nitroalkanes showed discrete signals, spaced at about 10 ppm, which represented nitro groups attached to CH_3, RCH_2, R_2CH, and R_3C moieties, respectively. This was probably the first case when nitrogen chemical shifts provided a useful insight into some fine details of molecular structure, since the first larger collection of ^{14}N data by Herbison-Evans and Richards at Oxford in 1964 had suggested that the distinction of nitrogenous moieties could be achieved only in cases where large differences existed in nitrogen shifts. We encountered severe problems in obtaining ^{14}N spectra which contained overlapping signals of different widths, but we quickly discovered that the newly introduced integrator system with its audio modulation of the resonance frequency could be employed to circumvent this difficulty, by allowing simultaneous measurement of the generated sidebands together with the center-band spectrum and making use of adjustable differences in saturation levels. This gave rise to what we called the differential saturation technique in continuous-wave NMR, implemented with suitable lineshape fitting procedures and spectral accumulation.

All this improved the precision of the measurements of ^{14}N nitrogen shifts to such an extent that it led to a wealth of information about organic chemical structures. In the meantime, during my postdoctoral stay at Caltech in J. D. Roberts's group in 1964–65, I discovered that they also had experimented with nitrogen NMR but by using ^{15}N and labeled samples. They had their problems, too; the long relaxation times of ^{15}N required, in some cases, a wait of a few minutes before starting the next field sweep in order to observe any signal at all. However, until the early 1970s and the advent of the pulsed Fourier transform NMR technique, most nitrogen NMR studies involved ^{14}N. We had a considerable share in this work, in the field of aromatic heterocycles, nitriles, nitro compounds, amines and ammonium ions, and various other nitrogenous moieties.

In 1967, I started a close collaboration with Graham A. Webb (University of Surrey), and in 1973 we edited a collective monograph on all aspects of nitrogen NMR,[1] the first such enterprise in the field. It is my impression that since then the manufacturers of NMR spectrometers have ceased considering nitrogen NMR as being relegated to the not-so-important class of 'other nuclei'. Our further studies have involved both ^{14}N and ^{15}N NMR and applications thereof in chemistry, but we have also made considerable efforts in presenting some more generalized views on nitrogen NMR and the scope of its applicability in solving chemical problems.[2a–d,3] It is not possible to go into detail here, but the following topics are worthy of mention: the general problem of referencing nitrogen chemical shifts and evaluation of the standards, using concentric spherical sample/reference containers in order to get rid of bulk susceptibility effects; the evaluation of nitrogen chemical shift reagents and relaxation reagents; the assessment of nitrogen NMR as a means of localizing protonation sites and for following tautomeric and other chemical equilibria; the identification of isomeric structures; ^{14}N relaxation effects as an aid in nitrogen shift assignments; and nitrogen NMR as a convenient tool for investigations of molecular interactions in liquids.

Today, nitrogen NMR seems to be an important branch of NMR and, from the viewpoint of ^{15}N, its growth is associated with the high magnetic fields available and multiquantum and polarization transfer techniques combined with proton detection of nitrogen transitions, which make possible the study of proteins and nucleotides. High magnetic fields are even more important as far as ^{14}N is concerned, but in my opinion a breakthrough is likely to arrive with the advent of multichannel excitation of the spectra rather than pulse excitation with its inherent phase drifts and baseline distortions.

REFERENCES

1. M. Witanowski and G. A. Webb (eds.), *Nitrogen NMR*, Plenum Press, London, 1973.
2. M. Witanowski, L. Stefaniak, and G. A. Webb, Nitrogen NMR Spectroscopy, in *Annual Reports on NMR Spectroscopy*, ed. G. A. Webb, Academic Press, London: (a) Vol. 7, 1977, pp. 117–244; (b) the whole of Vol. 11B, 1981; (c) the whole of Vol. 18, 1986; (d) the whole of Vol. 25, 1993.
3. G. A. Webb and M. Witanowski, Nitrogen NMR and Molecular Interactions, in *Topics in Molecular Interactions*, eds. H. Ratajczak and W. J. Orville-Thomas, Elsevier, Amsterdam, 1986, pp. 240–290.

Biographical Sketch

Michal Witanowski. *b* 1934. M.Sc., 1956, Ph.D. (supervisor Tadeusz Urbanski), 1962, Sc.D, 1968, Polish Academy of Sciences. Postdoctoral work at California Insititute of Technology, Chemistry Division, Pasadena (with John D. Roberts). Successively research fellow, senior research fellow, assistant, associate, and full professor at Institute of Organic Chemistry, Polish Academy of Sciences in Warsaw, 1956−present. Approx. 160 publications. Current research specialty: NMR of nitrogen nuclei and its applications in chemistry.

Woessner, Donald E.: In a Maze in NMR

Donald E. Woessner

University of Texas Southwestern Medical Center, Dallas, TX, USA

INTRODUCTION

In the autumn of 1952, I entered the University of Illinois Department of Chemistry graduate school to obtain my Ph.D. I chose to major in physical chemistry and minor in physics and mathematics. After a few months, I entered the research group of Herbert Gutowsky. The important factors in choosing Gutowsky as research advisor were the enthusiasm of his graduate students for NMR, the high regard they had for him, and the nature of NMR. Nuclear magnetic resonance was a new field and I had never heard of it before. Research in NMR appealed to me because it involved many interesting fields: chemistry, physics, electronics, and mathematics. I never regretted that decision because the field of NMR has grown continuously over the years.

After appraising my possible role in liquids high-resolution spectroscopy and solids wideline spectroscopy, I decided to work on ^{35}Cl nuclear quadrupole resonance (NQR) of solids. To do this, I constructed a pulse nuclear resonance spectrometer[1] that was designed by John C. Buchta, a graduate student in electrical engineering. This was the first pulse machine in an academic chemistry department in the USA! Besides NQR research on ^{35}Cl in organic solids,[2] I used this equipment to carry out experiments such as ^{1}H and ^{19}F NMR relaxation in liquids,[3] ^{1}H temperature-dependence measurements in natural rubber[4], etc. This research started my interest in the Bloembergen, Purcell, and Pound (BPP) relaxation theory and the deviations from it due to chemical structure. Also, a chance discovery of ^{1}H spin–lattice relaxation via proton–chlorine nuclear spin exchange induced by manual rotation[5] of solid *p*-dichlorobenzene in $\boldsymbol{B}_0$ initiated my interest in chemical exchange.

THE ROLE OF NMR IN INDUSTRIAL PETROLEUM RESEARCH

John R. Zimmerman recruited me in 1958 to carry out research in the petroleum exploration and production research laboratory of Magnolia Petroleum Company in Dallas, TX (now part of Mobil Research and Development Corporation). Magnolia chemists recognized early that NMR could help solve petroleum industry problems involving the analysis of hydrocarbons and the flow and displacement of liquids in oil reservoir rocks. In 1952, at the behest of S. R. Faris, Magnolia made the first industrial purchase from Varian Associates of a wideline spectrometer to study oil/water displacement in rocks. Purchase of a Varian Associates high-resolution NMR spectrometer for hydrocrabon analysis followed a few years later. This equipment started Mobil NMR research that continued in Dallas for 40 years, only to be totally terminated in 1992. Because pulse NMR methods should offer better methods to measure relaxation times and quantify liquid displacement in rocks, Magnolia purchased a pulse NMR spectrometer from Varian. The pulse spectrometer was out of date when I arrived. With the electrical engineering expertise of G. L. Hoehn and then R. A. McKay, I upgraded it to state-of-the-art performance.

The objective of my early work at Mobil was to develop an understanding of the NMR signals from liquids in porous rocks. A promising new oil well logging tool based on NMR in the Earth's magnetic field was under development by an oil well service company. To make use of this tool, Mobil needed to relate the characteristics of the NMR signals to pertinent liquid properties that would allow discrimination between oil and water and the detection of porous permeable rock formations in which these liquids could flow. My early research at Mobil involved the use of NMR relaxation and diffusion experiments to understand the motions of molecules in bulk liquids and of molecules on rock surfaces. The two important surfaces are of silica and clay.

During the years that fundamental research could be carried out at Mobil in Dallas, I enjoyed close collaboration with many capable scientists who provided special insights, knowledge, and expertise. Of my coauthors, J. R. Zimmerman, provided initial encouragement to do fundamental research, E. T. Strom helped in planning much of the research on hydrocarbon liquids, and G. H. Meyer provided invaluable solutions to differential equations. B. S. Snowden provided mathematical analysis and computer programming in much of my work involving clays. In particular, Snowden emphasized the concepts of order and order/disorder transitions in affecting motions in solids, liquids, and heterogeneous systems. These collaborations contributed to much of my research which is not mentioned in this short article.

TRANSLATIONAL DIFFUSION

In a bulk liquid, the diffusion coefficient, which can be found from the attenuation of the $90^\circ-\tau-180^\circ$ spin echo at 2τ due to diffusion in a magnetic field gradient, is independent of 2τ. I had the idea that, in a porous medium, the presence of pore walls would restrict the translational diffusional displacement of the liquid molecules and thus reduce the diffusion coefficient that is obtained from the NMR method. Because only a small fraction of the molecules would encounter a pore wall when 2τ is short, the diffusion coefficient would be almost equal to the bulk liquid value. For large 2τ values, a much larger fraction of the molecules would encounter a pore wall and undergo reduced translational displacement, and the diffusion coefficient could be significantly less than that of bulk liquid. Hence, the diffusion coefficient in a rock should depend on both the 2τ value and the pore size.

To test this idea, I devised a procedure and set up the apparatus[6] to measure the echo amplitude as a function of magnetic field gradient value at selected values of 2τ. The apparent water diffusion coefficients that I measured in a sandstone rock and in suspensions of silica spheres supported this idea. To my knowledge, my paper[7] that described this idea and its experimental verification was the first publication of the use of NMR to study restricted diffusion. This work prompted E. O. Stejskal and his students to develop the pulse magnetic

field gradient method to study restricted diffusion (1965). Although I could not follow up my original experiments, I was pleased that they stimulated much new research.

ANISOTROPIC ROTATIONAL DIFFUSION, INTERNAL MOTION, AND RELAXATION IN LIQUIDS

My research also involved NMR relaxation to study the motions and interactions of hydrocarbon molecules in liquids. Because hydrocarbon molecules are nonspherical, I thought that they did not rotate isotropically and that a proper interpretation of the NMR relaxation in such liquids should take rotational anisotropy into account. Also, many hydrocarbon molecules, toluene and *n*-paraffins, for example, have internal motion such as reorientation of a methyl group about its fixed threefold symmetry axis. All of my magnetic dipolar calculations used pairwise interactions; the relaxing unit was a pair of nuclei that define an internuclear vector. The model in my first derivation[8] was an internuclear vector reorienting about an axis that is fixed to a framework that is undergoing isotropic rotational diffusion. This model should also be a fair approximation for some axially symmetric liquid molecules and for molecules at surfaces. This derivation drew upon previous research. Bloembergen (1956) derived formulas for the relaxation of two magnetically coupled identical spin-$\frac{1}{2}$ nuclei undergoing hindered rotation about a fixed axis; I used his mathematical models of 120° jumps and diffusional rotation. Stejskal and Gutowsky (1958) calculated the proton T_1 of methyl groups, with magnetic dipolar coupling among the three protons, undergoing hindered reorientation within a molecule undergoing random tumbling. I used their mathematical method of treating the two independent motions. My equations show that the relaxation contributions of the types of motion are mutually dependent even if the two types of motion are completely independent. This formulation agreed more closely with the experimental data[9] for the proton T_1 in solid *t*-butyl chloride than previous ones.

I realized from the beginning that this motional model is a special case of molecular anisotropic rotational diffusion. Accordingly, I sought the mathematical formalism for the general case and found two extremely useful papers by Perrin. The first paper[10] contains a comprehensive discussion of the translational and rotational Brownian motions of a completely asymmetric rigid ellipsoid in a continuous viscous medium. In the second paper,[11] Perrin describes exactly what I wanted: an elegant operator method to calculate directly the rates of change of average values of orientation functions for these ellipsoids. I used this method[12] to evaluate the autocorrelation functions of the second-order spherical harmonics in the NMR relaxation interactions. My calculations also included the two models of internal motion just mentioned, applied to an axially symmetric ellipsoid in which the internal rotation axis is parallel to the symmetry axis. The final derivation[13] allowed the internal axis to have any fixed angle with the ellipsoid symmetry axis. In both calculations, the internuclear separations were constant. I removed this constraint[14] for the magnetic dipolar relaxation between protons of two different staggered neighboring methyl groups that undergo 120° jumps about the same axis. This axis is parallel to the symmetry axis of the axially symmetric ellipsoid.

I found that anisotropic motions and internal rotations in all these derivations yield multiple correlation times and have large effects on relaxation times. When a correlation time is much smaller than the others, the predictions of the BPP theory can be much in error. These theoretical results were used by us in the design and interpretation of several pioneering experiments involving anisotropic reorientation and the internal motion of organic liquids.

ANISOTROPIC REORIENTATION AND PREFERENTIAL ORIENTATION OF MOLECULES ON SURFACES

The quartz sand in oil well rock has a low specific surface area. Silica gel has a high surface area, and J. R. Zimmerman and co-workers at Mobil used it to model the rock surface. The high surface area held sufficient amounts of adsorbed water for NMR measurements even at monolayer coverages. Their pioneering NMR research (1956) showed that at room temperature this water exists in two different environmental states with different NMR relaxation times. Exchange theory analysis[15] of relaxation curves showed that protons transfer at kilohertz rates between these states. My initial research extended this work to cover a range of temperatures; this would increase our understanding of the motions and structures of the water molecules interacting with the silica surface. All of this research was concurrent with my diffusion research and my theoretical and experimental work on NMR relaxation in liquids.

In my early efforts to understand the NMR relaxation times of surface water, I delved into the literature on dielectric relaxation of adsorbed water. The isotropic rotational diffusional model predicts that the NMR τ_c is one-third of the dielectric relaxation time τ_{diel}. Odajima (1959) made NMR T_2 studies of water sorbed on fibrous materials and concluded that this relationship is not obeyed for such systems. He suggested that water molecules in the sorbed state do not rotate isotropically. However, Sasaki and co-workers (1960) measured T_1 on the same systems and deduced that the τ_c that determines T_1 is one-third τ_{diel}. Because the water molecule is nonspherical in shape, in intermolecular interactions I believed that physical considerations should lead to preferential orientation and anisotropic rotation. I was hoping to find more direct experimental evidence of anisotropic reorientation than that reported by Sasaki because a distribution of correlation times for different water molecules with chemical exchange could cause the above observations.

My belief was justified and my hope was realized with the publication by Ducros[16] of the proton NMR spectra of water adsorbed in the noncubic cages of zeolite single crystals. Dielectric relaxation measurements made on these crystals showed that the water is in rapid motion, similar to liquid water. Instead of the narrow singlet NMR peak of bulk liquid water, the NMR spectra consisted of a narrow doublet with a splitting that is proportional to $3\cos^2\alpha - 1$, where α is the angle between the optical crystal axis and $\boldsymbol{B}_0$. The nonzero splitting arises from molecular rotation that, although rapid, does not result in a spherically symmetric distribution of the proton–proton direction. As a result, the proton–proton magnetic dipolar coupling is not averaged out by the rapid

motion; this nonzero residual coupling represents a very long correlation time. The nonspherical symmetry is caused by the combined effects of the preferential orientation at the zeolite cage surfaces and the noncubic shape of the cages. Preferential orientation, of course, causes the rotational motions to be anisotropic with respect to the cage wall.

Besides preferential orientation and anisotropic motion, I was concerned about chemical shift effects on the measured relaxation times. Dielectric polarization measurements suggested a decrease of hydrogen bonding for monolayer water molecules (compared with bulk liquid molecules). Because the chemical shift of water is a strong function of hydrogen bonding, the T_2 of exchanging chemically shifted water molecules might be shortened by this effect.

To interpret the proton NMR signals from monolayer water on silica gel, I needed new theoretical tools. First, I derived the equations that describe the free induction signals from spin-$\frac{1}{2}$ nuclei exchanging between two different environmental states with different values of T_1, T_2, number of nuclei, and chemical shift.[17] Next, to include the orientational effects of the surface on the relaxation, I adapted[18] my first anisotropic motion model to comply with the restrictions imposed by stationary surfaces. I used this calculation, with my chemical exchange calculation,[17] to interpret[18,19] my temperature, surface coverage, and NMR frequency dependence measurements of proton T_1 and T_2 of water adsorbed on silica gel. Although the experiments did not involve enough quantifiable parameters to verify the details of the anisotropic motional model, the observations agreed qualitatively with the predicted effects of anisotropic motion. A BPP model with a single isotropic motion in each of the two environmental states disagrees with observations. However, the NMR results only inferred preferential orientation.

I found direct indications of preferential orientation in the proton relaxation measurements of benzene adsorbed on silica gel.[20] The transverse relaxation curves contained a Gaussian decay component that is characteristic of the free induction decay from a powder sample that has a very long τ_c value. Because the T_1 values suggested a short τ_c, this component showed an anisotropic orientation distribution (preferential orientation) of benzene molecules with respect to the silica gel surface.

PREFERENTIAL ORIENTATION, DIFFUSION, AND ORDER IN AQUEOUS HETEROGENEOUS SYSTEMS

The following observations initiated my theoretical and experimental research into the use of quadrupolar and magnetic dipolar splitting from preferential orientation to probe order and structure in aqueous heterogeneous systems.

Because natural smectite clays, such as montmorillonites, contain significant quantities of paramagnetic iron centers, my early research on clay/water interaction used deuteron NMR measurements on D_2O/montmorillonite gels. Such smectites consist of parallel 10 Å thick aluminosilicate sheets stacked like leaves in a book. When the exchangeable cations are Li^+ or Na^+, montmorillonite will absorb large quantities of water and retain a pseudocrystalline structure. To assess the effects of the paramagnetic centers on hydrogen T_1 and T_2, I made a D_2O/clay gel with about 20 wt% clay. Before making the deuteron measurement, I tuned the probe and set the $90^\circ-180^\circ$ pulse sequence with a vial of D_2O. Then I inserted the vial containing the D_2O/clay gel to optimize the probe tuning and pulse widths. I observed a beautiful FID after the 90° pulse; however, the expected spin echo at time 2τ was missing. Thinking that the gel had loaded-down the probe, I retuned the probe and reset the 90° pulse with the gel in the probe. The previous tuning and 90° pulse settings proved to be correct; therefore, the initial 180° pulse setting should be correct! I shortened the second pulse (why, I do not know); a spin echo appeared at time 2τ and its amplitude was a maximum at the setting for the initial 90° pulse. This behavior was completely unexpected and I had no idea of how to explain it.

Serendipitously, a few days later I received a copy of the paper by Powles and Mansfield[21] that described and explained the proton solid echo in gypsum. Their experiments were the same as mine, except that I used the deuteron NMR resonance of the D_2O/clay gel. Because their observations were caused by the proton magnetic dipolar splitting, I thought that my observations might be caused by residual deuteron quadrupolar splitting from preferential orientation of the D_2O molecule at the clay surface. I derived the $90^\circ-\tau-180^\circ$ and $90^\circ-\tau-90^\circ$ pulse NMR signals for spin-1 nuclei with static quadrupole interaction and found the same behavior as reported by Powles and Mansfield. The effect of the 180° pulse refocuses the loss of signal amplitude due to $\boldsymbol{B}_0$ inhomogeneity so that the amplitude at time 2τ is independent of this inhomogeneity. In this calculation, the second 90° pulse refocuses the loss of signal amplitude due to the spread in quadrupole interaction because of the anisotropy for crystallites in a powder sample.

Preferential orientation of liquid molecules at the surfaces of minerals and biomacromolecules provides a unique NMR tool to investigate the ordering of such surfaces in aqueous heterogeneous systems. Of course, preferential orientation means that the relaxation interactions and spectral line splitting depend on the orientation of the surface with respect to $\boldsymbol{B}_0$. Key verifications can be made by making 'oriented' samples and observing whether the relaxation effects obey the $3\cos^2\theta - 1$ dependence on this orientation.

The idea that evolved is based on interfacial molecules that are in rapid motion and are preferentially oriented. This causes NMR *spectral splitting* of these molecules that depends on the orientation of the interface in $\boldsymbol{B}_0$. Rapid *chemical exchange via translational diffusion* between these molecules and the nearby bulk liquid causes all of the molecules to occupy the interfacial location in a time that is short compared with the reciprocal of the interfacial splitting. As a result, all of the molecules exhibit an NMR spectral splitting. This splitting is reduced from that of the interfacial molecules. The reduction factor is the fraction of the molecules that are in the interfacial locations at any instant. Snowden and I verified[22] this by simulation and by NMR experiments on oriented montmorillonite samples that contained interfaces that were essentially parallel. The water in such oriented samples has T_1, T_2, and spectral splitting values that depend on the interface orientation in $\boldsymbol{B}_0$.

Now we introduce ordering. Consider a sample comprising many crystallites arranged in totally random orientations in $\boldsymbol{B}_0$. Molecules undergo *translational diffusion* within and between the crystallites. When the crystallite size is large compared with the diffusion distance in the time in the NMR experiment, the net result is a static 'powder' pattern that is the superposition of the NMR signals. If the diffusion

distance is comparable to or larger than the crystallite size, the former static powder pattern is modified. The shape of the NMR response in various pulse sequences depends on the different splittings and relaxation times that the molecules experience over their diffusional paths. The average lifetime for a molecule to diffuse from a crystallite of a given orientation to one of approximately 1 rad different orientation is the correlation time τ_{cry}. We used two parameters, S and τ_{cry}, to simulate the effects of preferential orientation in several models of migration. These models represent different types of 'order' in the sample.

Our first simulation[23] was an isotropic 'rotational diffusion' model in which the change in orientation θ between successively occupied crystallites is small. We calculated the signal after a 90° pulse as a function of time t. We also calculated the amplitude of the solid echo at time $t = 2\tau$ as a function of τ. Both curves depend on both the splitting constant S and τ_{cry}. Except in the case of very small τ_{cry} values, these curves have different dependencies on t. Therefore, these results enabled us to evaluate both S and τ_{cry} from an analysis of experimental curves. Using these values, we could simulate the deuteron NMR signal amplitudes in the time from $t = 0$ to $t = 5\tau$ in a sequence of three 90° pulses applied at times 0, τ, and 3τ. This simulation reproduced the shape and shift of the first echo that I observed (January 13, 1969). The peak of the first deuteron solid echo in clay gels occurs *before* the expected time 2τ but that of the second echo occurs *at* the expected time 4τ. This shift of the spin echo peak *does not* occur in aqueous paramagnetic ion solutions in an inhomogeneous $\boldsymbol{B}_0$, for example.

We had the idea that small changes in consecutive θ values might not always be realistic. To test this, we undertook the analogous calculation[24] of the pulse NMR signals resulting from random reorientation of the nuclear interaction vector among the four orientations described by the four vectors joining the center and each of the four vertices of a fixed regular tetrahedron. The result was obtained by averaging over all tetrahedron orientations. Both models give approximately the same S values. The main difference lies in the motion that is lumped into τ_{cry}. The translational diffusion path is different for the two models and τ_{cry} is sensitive to this difference. Experimentally, the shape of the signal following two 90° pulses is more sensitive to diffusional path than that following a single 90° pulse. For many clay–water systems, the two-pulse signal more closely approximates the signals generated with the tetrahedral model.

The work just described shows the power of NMR to study dynamics and ordering of water molecules in interfacial systems and of the ordering of the interfaces themselves. This is illustrated by our work[25] on D_2O solutions of the biopolymer Kelzan. We detected and measured partially ordered domains of macromolecules in these solutions. The rate for a molecule to diffuse from a domain is proportional to the diffusion coefficient. We measured the diffusion coefficients at two different temperatures and evaluated the τ_{cry} values with the two models. The tetrahedral model is superior in describing this system. Also, deuteron NMR measurements show that various physical treatments greatly affect the size of the domains. Stirring increases the distance of long-range ordering because of the flow lines and heating decreases it.

Years later, other researchers[26] used an analogous model to explain the transverse NMR relaxation of ^{23}Na in solutions of linear polyelectrolytes. Because macromolecular order occurs in biological tissue, this model should be applicable to the interpretation of NMR relaxation in medical applications of NMR. Actually, anisotropy of the proton T_2 in skeletal muscle and that of the ^{23}Na in hydrated Na^+ ions in tendon is observed. The diffusional paths of water and hydrated ions in tissue should be like wanderings in a maze; the arrival of clinical magnetic resonance imaging emphasizes the importance of understanding it.

REFERENCES

1. J. C. Buchta, H. S. Gutowsky, and D. E. Woessner, *Rev. Sci. Instrum.*, 1958, **29**, 55.
2. D. E. Woessner and H. S. Gutowsky, *J. Chem. Phys.*, 1963, **39**, 440.
3. H. S. Gutowsky and D. E. Woessner, *Phys. Rev.*, 1956, **104**, 843.
4. H. S. Gutowsky, A. Saika, M. Takeda, and D. E. Woessner, *J. Chem. Phys.*, 1957, **27**, 534.
5. D. E. Woessner and H. S. Gutowsky, *J. Chem. Phys.*, 1958, **29**, 804.
6. D. E. Woessner, *Rev. Sci. Instrum.*, 1960, **31**, 1146.
7. D. E. Woessner, *J. Phys. Chem.*, 1963, **67**, 1365.
8. D. E. Woessner, *J. Chem. Phys.*, 1962, **36**, 1.
9. E. O. Stejskal, D. E. Woessner, T. C. Farrar, and H. S. Gutowsky, *J. Chem. Phys.*, 1959, **31**, 55.
10. F. Perrin, *J. Phys. Radium*, 1934, **5**, 497.
11. F. Perrin, *J. Phys. Radium*, 1936, **7**, 1.
12. D. E. Woessner, *J. Chem. Phys.*, 1962, **37**, 647.
13. D. E. Woessner, B. S. Snowden Jr., and G. H. Meyer, *J. Chem. Phys.*, 1969, **50**, 719.
14. D. E. Woessner, *J. Chem. Phys.*, 1965, **42**, 1855.
15. J. R. Zimmerman and W. E. Brittin, *J. Phys. Chem.*, 1957, **61**, 1328.
16. P. Ducros, *Bull. Soc. Fr. Mineral Cristallogr.*, 1960, **83**, 85.
17. D. E. Woessner, *J. Chem. Phys.*, 1961, **35**, 41.
18. D. E. Woessner and J. R. Zimmerman, *J. Phys. Chem.*, 1963, **67**, 1590.
19. D. E. Woessner, *J. Chem. Phys.*, 1963, **39**, 2783.
20. D. E. Woessner, *J. Phys. Chem.*, 1966, **70**, 1217.
21. J. G. Powles and P. Mansfield, *Phys. Lett.*, 1962, **2**, 58.
22. D. E. Woessner and B. S. Snowden Jr., *J. Chem. Phys.*, 1969, **50**, 1516.
23. D. E. Woessner, B. S. Snowden Jr., and G. H. Meyer, *J. Chem. Phys.*, 1969, **51**, 2968.
24. D. E. Woessner, B. S. Snowden Jr., and G. H. Meyer, *J. Colloid Interface Sci.*, 1970, **34**, 43.
25. D. E. Woessner and B. S. Snowden Jr., *Ann. N. Y. Acad. Sci.*, 1973, **204**, 113.
26. B. Halle, H. Wennerström, and L. Piculell, *J. Phys. Chem.*, 1984, **88**, 2482.

Biographical Sketch

Donald E. Woessner. *b* 1930. A.B., 1952, Ph.D. (supervisor Herbert Gutowsky), 1957, Chemistry, University of Illinois, USA. Postdoctoral work at University of Illinois (with Herbert Gutowsky). Successively senior research chemist, research associate, senior research associate, Mobil Research and Development Corporation, Dallas, Texas, USA. Currently Adjunct Assistant Professor of Radiology, The University of Texas Southwestern Medical Center at Dallas, 1992–present. Approx. 70 publications. Research specialties: NMR relaxation and molecular motions in liquids; relationships of NMR relaxation of hydrogen and ionic nuclei to motions, structure and order in aqueous heterogeneous systems and biological tissue.

Wrackmeyer, Bernd: A Personal Retrospect of Multinuclear Magnetic Resonance in Liquids

Bernd Wrackmeyer

Universität Bayreuth, Bayreuth, Germany

A strong relationship between chemistry and NMR had been firmly established since the late 1960s. However, the NMR equipment in most laboratories was not really advanced, in spite of the first cryomagnetic systems on the market and the beginning of pulse Fourier transform (PFT) NMR (R. R. Ernst and W. A. Anderson, 1966). At that time it was widely accepted that all major applications of NMR could be identified with organic chemistry. Of course, research in inorganic and organometallic chemistry already flourished using ^{1}H and ^{19}F NMR, but measurements of other nuclei, even of rather NMR-sensitive nuclei such as ^{11}B or ^{31}P, were far from common. There were no such things as multinuclear probeheads or handy frequency synthesizers with broadband amplifiers. Other techniques for multinuclear MR like INDOR or, generally, heteronuclear double resonance experiments, e.g. ^{1}H{X} or ^{19}F{X}, were used only in a few places.

When I started research work in inorganic chemistry at the University of Munich in 1970, I was very lucky to work in the group of Professor H. Nöth, who began very early on to apply NMR, especially ^{11}B NMR, to inorganic syntheses. My task was to continue with ^{11}B NMR, but also to work with ^{14}N NMR (see Figure 1) and in general to make use of the 'multinuclear' Varian HA-100 spectrometer, equipped for CW (continuous wave) measurements of the ^{1}H, ^{11}B, ^{14}N, ^{19}F, and ^{31}P nuclei.

The appetite for multinuclear MR was growing. Lacking other equipment, we adjusted the magnetic field strength in order to employ the ^{14}N NMR probehead and the transmitter (7.2 MHz) for measuring other NMR-sensitive nuclei such as ^{6,7}Li, ^{9}Be, ^{10}B, ^{23}Na, ^{27}Al, ^{35}Cl (see Figure 2), ^{51}V, or ^{59}Co, to name just a few examples.

In the meantime, PFT NMR began to show its enormous power, the idea of two-dimensional (2D) NMR had been introduced (J. Jeener, 1971), and impressive instrumental developments became apparent, naturally with an emphasis on ^{1}H and particularly on ^{13}C NMR.

For multinuclear MR of less sensitive nuclei (e.g. ^{15}N, ^{29}Si, ^{77}Se, ^{119}Sn, ^{199}Hg, ^{207}Pb, etc.), heteronuclear double or triple resonance experiments, ^{1}H{X}, ^{19}F{X}, or ^{1}H{X,Y}, remained attractive. Again I was lucky; I stayed for one year (1974–75) with the group of Professor W. McFarlane in London and became better acquainted with these techniques and their potential. These were still CW measurements, but at that time it was already clear (even without foreseeing the ever-increasing impact of electronic data handling) that developments in PFT NMR would eventually lead to comparable experiments with much greater scope and sensitivity.

The end of the 1970s marked the first turning point for multinuclear PFT MR. Probeheads or inserts became

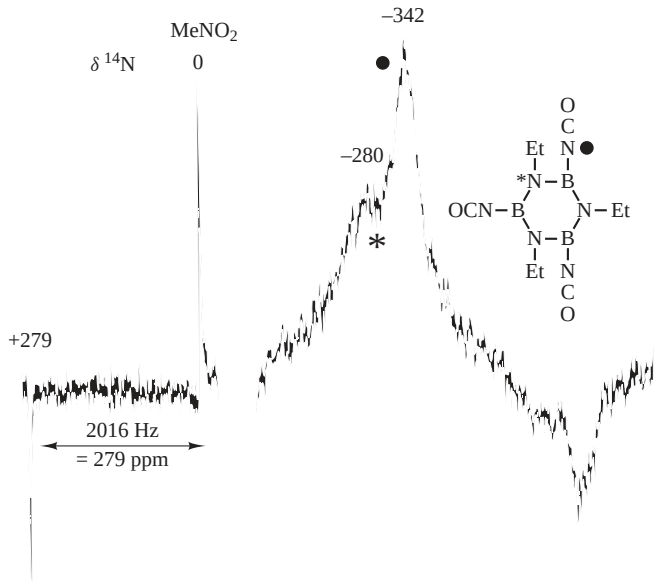

Figure 1 7.23 MHz (2.35 T) ^{14}N NMR spectrum [single scan, CW (continuous wave), Varian HA-100] of a saturated solution of *N*, *N′*, *N″*-triethyltriisocyanatoborazine in CH_2Cl_2. The two different ^{14}N resonances show severe overlap. The calibration was achieved using the 'sideband' method (2016 Hz modulation) with a tube containing neat nitromethane as an external reference (tube exchange during continuous field sweep)

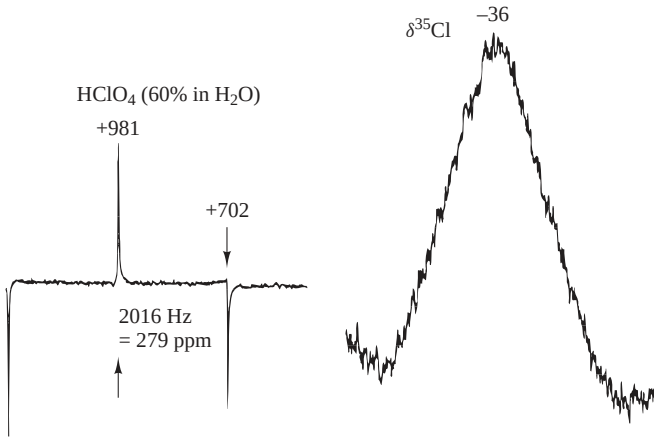

Figure 2 7.23 MHz (1.69 T) ^{35}Cl NMR spectrum [single scan, CW (continuous wave)] of chlorodimethylsilane [$Me_2Si(Cl)H$], 50% solution in pentane. The line is so broad that the centerband and sidebands (2016 Hz; for calibration) are not well separated. The ^{35}Cl NMR signal of $HClO_4$ (60% solution in H_2O) serves as an external reference via sample exchange

commercially available which were tunable over a wide range of frequencies [e.g. including the most common nuclei with frequencies between $\Xi(^{41}K)$ = 2.565 MHz and $\Xi(^{31}P)$ = 40.481 MHz (for $\Xi(^{1}H)$ = 100 000 MHz)] without serious loss of sensitivity as compared with selective probeheads. Together with the steadily advancing computer control of most spectrometer functions (the age of pulse sequences had begun), truly multinuclear MR started to become a powerful tool in many different fields of research. In contrast with conventional ^{1}H or ^{13}C NMR measurements, nondeuterated

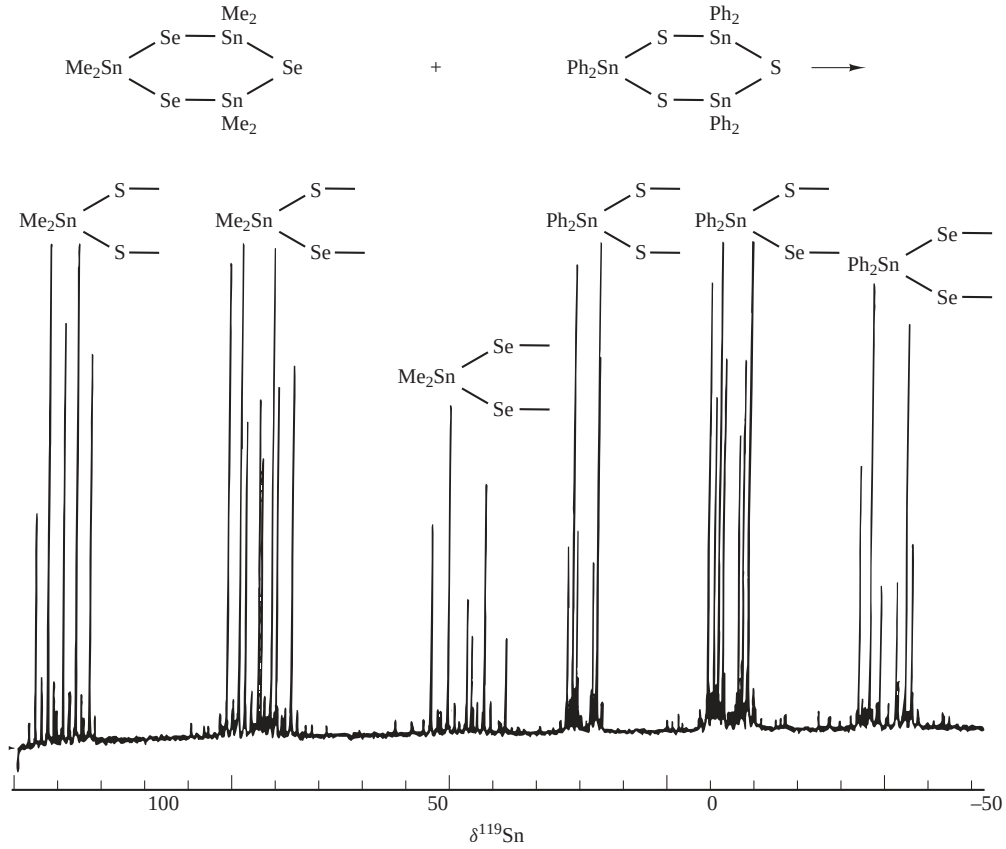

Figure 3 74.6 MHz (4.7 T) ^{119}Sn NMR spectrum (PFT, mode, 5000 transients, ^{1}H broadband decoupled, Bruker WP-200) of an equilibrated mixture resulting from the exchange reaction between $[Me_2SnSe]_3$ and $[Ph_2SnS]_3$ in $CHCl_3$. The mixture contains 20 different six-membered rings which should give rise to 40 separate ^{119}Sn NMR signals of which 39 are resolved. The signals with small intensities are ^{119}Sn, ^{117}Sn, and ^{77}Se satellites corresponding to the coupling constants $^{2}J(^{119}\text{Sn},^{119}\text{Sn})$, $^{2}J(^{119}\text{Sn},^{117}\text{Sn})$, and $^{1}J(^{119}\text{Sn},^{77}\text{Se})$, respectively, which can be used for further assignments

solvents could be used. Hence, reactions could be monitored under realistic conditions, if necessary at variable temperature, observing the NMR signals of relevant nuclei, one after the other, without changing probeheads. In this way it was possible to detect reactive intermediates, to gain information on reaction mechanisms, and to influence the final product distribution by controlling the progress of reactions under carefully designed conditions. The great potential of multinuclear MR as a nondestructive method for the analysis of complex mixtures is shown for ^{119}Sn NMR as an instructive example (see Figure 3).

The theory of NMR parameters was already fairly advanced at the beginning of the 1950s (N. F. Ramsey, 1950–52). However, experimental data for testing theoretical models were often only provided much later by multinuclear MR. A good example is the question as to whether a nonrelativistic treatment is sufficient for explaining NMR data. NMR measurements of heavy nuclei and studies of the influence exerted by heavy nuclei on the NMR parameters of other nuclei showed that relativistic effects have to be taken into account. Extreme bonding situations should be reflected by NMR parameters. In this context, the high nuclear magnetic shielding of the alkali metal anions (Na^-, K^-, Rb^-, Cs^-) with respect to the cations is worthy of mention. In the context of the multifarious chemistry of the transition metals, we can learn from metal NMR many new aspects of the relationship between NMR parameters and structure on a molecular level.

The interplay between chemistry and the availability of suitable analytical tools is well recognized. Thus, from 1975 onwards, my interest in inorganic and organometallic chemistry has focused more strongly on elements which are attractive from the multinuclear MR point of view. Although there are at least one, or often more, magnetically active nuclei for almost any element, the individual magnetic properties are very different. Thus, most spin-$\frac{1}{2}$ nuclei in particular, in addition to ^{1}H and ^{13}C, and many of the numerous quadrupolar nuclei (spin $I > \frac{1}{2}$, are good candidates for multinuclear MR in solution. Here it is important to note that direct structural information obtained by X-ray analysis of crystalline material can now be related to NMR data in solution if solid state NMR data are known. Developments in solid state NMR, starting in the 1970s, have given access to these data. The greater sensitivity of the nuclear magnetic shielding of the heavier nuclei (as compared with ^{13}C) is particularly helpful for demonstrating even small changes in the molecular structure.

The advent of PFT NMR also helped to overcome some major problems in the measurement of both sensitive and many insensitive nuclei. However, the detection of the NMR signals of a number of prominent and important rare spin-$\frac{1}{2}$ nuclei such as ^{15}N [the abundant ^{14}N (99.63%) has a spin $I = 1$] or ^{29}Si remained difficult because of their small magnetic moment and/or unfavorable relaxation properties (e.g. negative NOE of unknown quantity and/or long longitudinal relaxation times

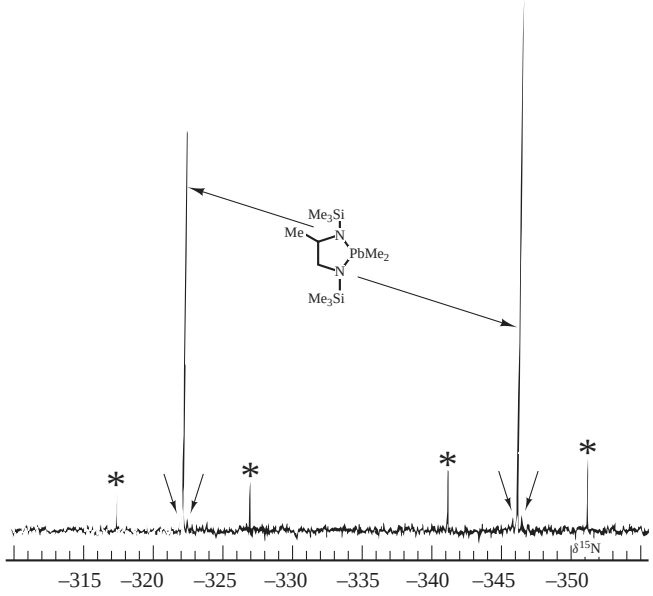

Figure 4 30.4 MHz ^{15}N NMR spectrum of a heterocyclic organolead compound using the refocused INEPT pulse sequence [based on long-range coupling constants $^{3}J(^{15}\mathrm{N,Si,C,}^{1}\mathrm{H}) \approx 1.3$ Hz) with ^{1}H decoupling]. Satellite signals arising from ^{207}Pb–^{15}N and ^{29}Si–^{13}C spin–spin coupling are marked by asterisks and arrows, respectively

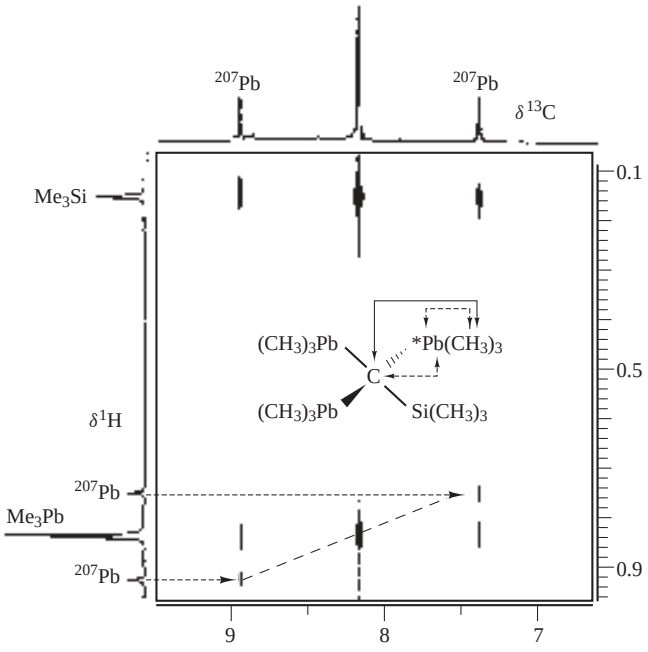

Figure 5 Two-dimensional (2D) ^{13}C/^{1}H heteronuclear shift correlation (HETCOR) of an organolead compound based on a long-range coupling constant $^{3}J(^{13}\mathrm{C,Pb,C,}^{1}\mathrm{H})$ (full line in the formula). The ^{207}Pb nucleus (*) is the passive spin and the signs of the coupling constants $^{1}J(^{207}\mathrm{Pb,}^{13}\mathrm{C})$ and $^{2}J(^{207}\mathrm{Pb,}^{1}\mathrm{H})$ (dashed lines) are compared. The latter is known to have a negative sign. The positive tilt of the cross peaks (dashed line) proves that $^{1}J(^{207}\mathrm{Pb,}^{13}\mathrm{C})$ and $^{2}J(^{207}\mathrm{Pb,}^{1}\mathrm{H})$ have the same sign. Hence $^{1}J(^{207}\mathrm{Pb,}^{13}\mathrm{C})$ must be negative (the first example of a tetraorganolead derivative)

T_1). Polarization transfer from ^{1}H to insensitive X nuclei, based on scalar X–^{1}H spin–spin coupling [$J(\mathrm{X}^{1}\mathrm{H})$] using hard, nonselective pulses (G. A. Morris and R. Freeman, 1979) provided a very useful answer to these problems. Thus, pulse sequences known as INEPT or DEPT (based on a slightly different approach), or modifications of these experiments, allowed sensitivity problems to be circumvented. NMR signals of X are enhanced by a factor of $\gamma(^{1}\mathrm{H})/\gamma(\mathrm{X})$ (for X = ^{15}N, this factor is 9.86) and the recycle time of the experiment no longer depends on long T_1(X) values but on comparatively short $T_1(^{1}\mathrm{H})$ values. Since the approximate magnitude of many coupling constants $^{1}J(\mathrm{X,}^{1}\mathrm{H})$ is known, the widespread application of this method to multinuclear MR became a logical consequence. It turned out that even very small long-range coupling constants $^{n}J(\mathrm{X,}^{1}\mathrm{H})$ (as low as 0.5 Hz) can form the basis for polarization transfer (see Figure 4), although the efficiency is somewhat reduced. Clearly, once again ^{13}C NMR was the center of interest, since 2D ^{13}C/^{1}H heteronuclear shift correlations (HETCOR) based on INEPT or DEPT, taking advantage of one-bond or of long-range coupling constants $J(^{13}\mathrm{C,}^{1}\mathrm{H})$, proved extremely useful in structural elucidation. The value of 2D HETCOR experiments of the general type X/^{1}H has been realized not just for the mutual assignment of ^{1}H and X resonance signals, but also for the determination of relative signs of coupling constants (see Figure 5). A knowledge of the coupling sign is essential for the discussion of this parameter.

An inspection of the literature over the last two decades leaves no doubt about the role of polarization transfer techniques in ^{15}N NMR (at the natural abundance of ^{15}N, i.e. 0.37%) which has emerged from a shadowy existence into an active research area. The same is true for ^{29}Si NMR (see Figure 6) which has become an indispensable tool in organosilicon chemistry. Furthermore, in organometallic chemistry one

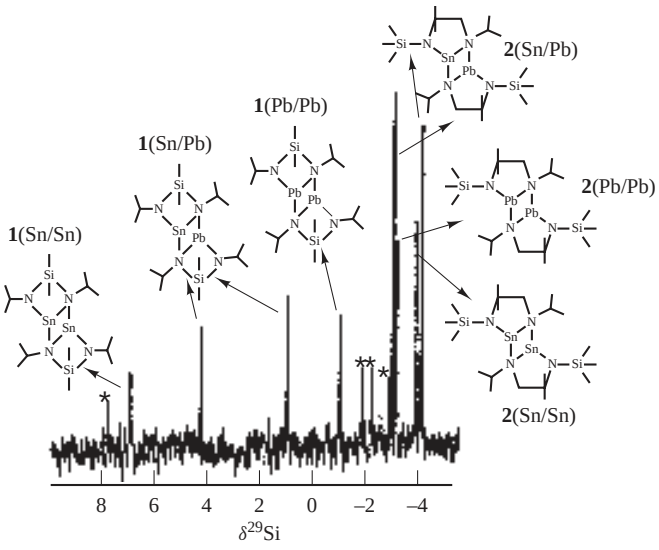

Figure 6 59.6 MHz ^{29}Si NMR spectrum of a mixture (in toluene at −40°C) resulting from the exchange reaction between the dimeric stannylene **1**(Sn/Sn) and the dimeric plumbylene **2**(Pb/Pb) using the refocused INEPT pulse sequence, based on $^{2}J(^{29}\mathrm{Si,C,}^{1}\mathrm{H})$ with ^{1}H decoupling. Consistent with ^{119}Sn and ^{207}Pb NMR spectra, which show four intense resonance signals each, dimers are mainly formed from two four-membered or two five-membered rings (signals marked by an asterisk may arise from a combination of four- and five-membered rings)

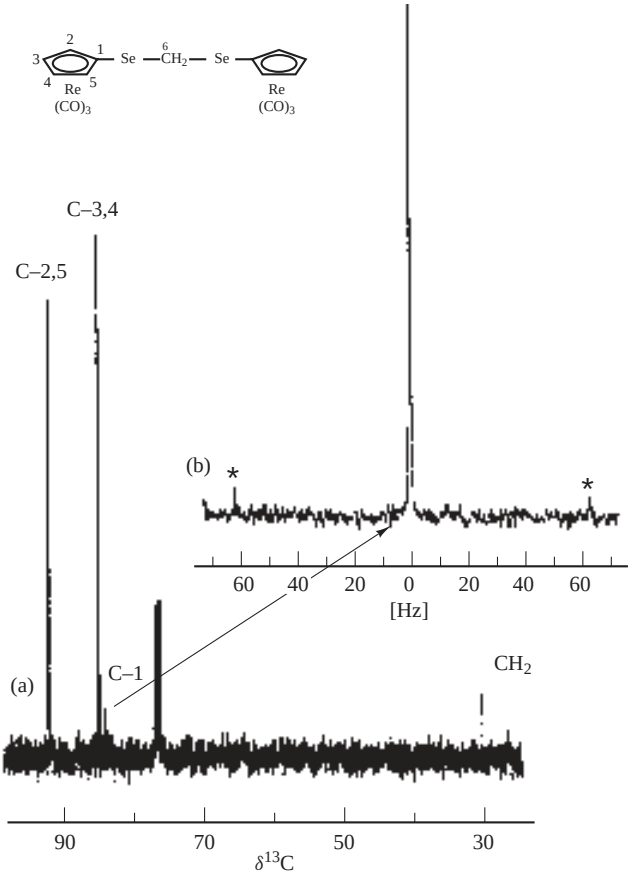

Figure 7 75.5 MHz ^{13}C NMR of a cyclopentadienyl rhenium complex. The detection of the ^{13}C NMR signal of the substituted carbon atom C–1 may be difficult. (a) Normal ^{13}C NMR spectrum, ^{1}H decoupled: the signal of C–1 is just visible; (b) if the spectrum is recorded using the refocused INEPT pulse sequence, based on coupling constants $^{2,3}J(^{13}\mathrm{C},^{1}\mathrm{H}) \approx 7.5$ Hz with ^{1}H decoupling, the signal of C–1 is observed at the same time with a much better signal-to-noise ratio which even allows the detection of the ^{77}Se satellite signals (*) due to $^{1}J(^{77}\mathrm{Se},^{13}\mathrm{C})$

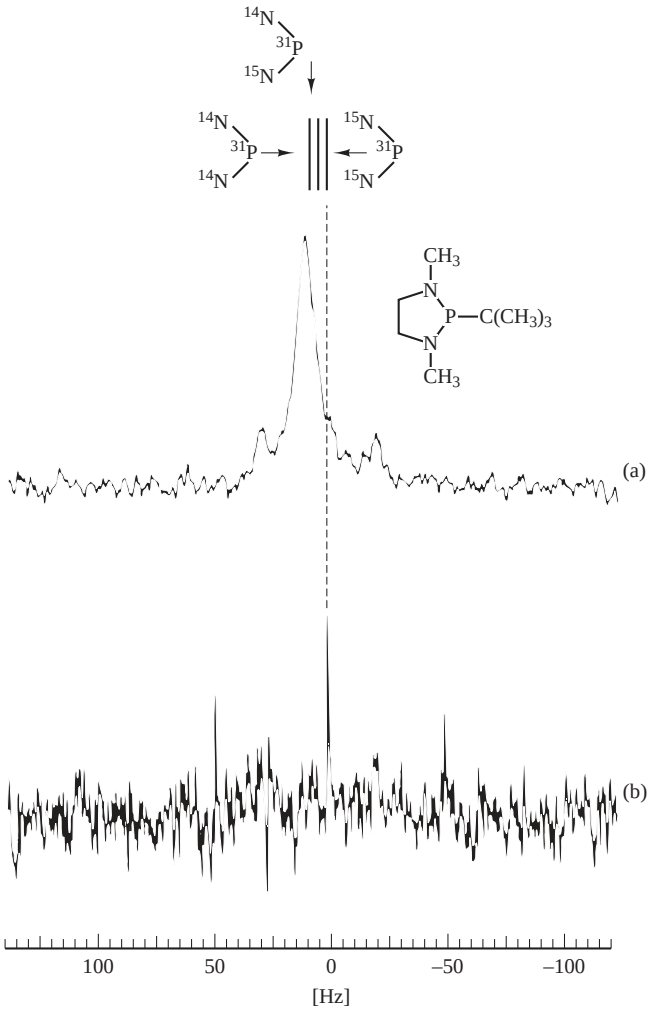

Figure 8 121.5 MHz ^{31}P NMR; application of the HEED-INEPT experiment to 2-*t*-butyl-1,3-dimethyl-1,3,2-diazaphospholidine. Isotope effects are indicated on the top of the diagram. (a) The delay in the Hahn-echo pulse train is selected in order partly to suppress the parent ^{31}P NMR signal of the ^{14}N–P–^{14}N isotopomer and to observe the still broadened doublet of the ^{15}N–^{31}P–^{14}N isotopomer. (b) A longer delay in the Hahn-echo pulse train leads to complete suppression of the ^{31}P NMR signals of ^{14}N–^{31}P–^{14}N and ^{15}N–^{31}P–^{14}N isotopomers, leaving the sharp triplet of the ^{15}N–^{31}P–^{15}N isotopomer. The combined intensity of the triplet is only 1.4×10^{-5} as compared with the parent line (=1)!

frequently encounters 'difficult' ^{13}C nuclei. Again polarization transfer can provide the magic cure for such problems (see Figure 7).

Since NMR is an inherently insensitive method, it follows that in the absence of scalar X–^{1}H coupling polarization transfer cannot work, and other techniques for enhancement, similar to cross polarization in solids, are not straightforward in solution. Thus, even if one nucleus is 100% abundant, such as ^{31}P, it may be difficult to record a ^{15}N NMR spectrum of a phosphorus–nitrogen compound in order to measure the coupling constant $^{1}J(^{31}\mathrm{P},^{15}\mathrm{N})$. In principle, it should instead be possible to record the ^{31}P NMR spectrum with a view to identifying the ^{15}N satellite signals, or in general to record the X NMR spectrum as a means of measuring $^{1}J(\mathrm{X},^{15}\mathrm{N})$ if the NMR sensitivity of X is higher than that of ^{15}N, especially if polarization transfer from ^{1}H to the X nuclei is feasible. However, the intensities of these ^{15}N satellites are very low (0.18%), and hence partial suppression of the parent line due to the X^{14}N isotopomer is necessary. This is readily achieved by *H*ahn-*e*cho *e*xtended (HEED) pulse sequences (E. Kupče and E. Lukevics, 1988; B. Wrackmeyer and E. Kupče, 1991) taking advantage of the faster decay of the transverse X magnetization of the X^{14}N isotopomer. In 1D spectra, coupling constants $^{1}J(\mathrm{X},^{15}\mathrm{N})$ can be measured together with isotope-induced shifts, $^{1}\Delta^{15/14}\mathrm{N(X)}$, at natural abundance (Figure 8). In the past the latter parameter has received little attention in multinuclear MR since its determination is very difficult without ^{15}N labeling. Other important information can be gained in 2D X/^{1}H HEED–HETCOR experiments which is again hardly accessible by conventional techniques, even if ^{15}N labelled compounds are available. In addition to the information on the relative signs of coupling constants $J(\mathrm{X},^{15}\mathrm{N})$ and $J(^{15}\mathrm{N},^{1}\mathrm{H})$, the value of long-range coupling constants $J(^{15}\mathrm{N},^{1}\mathrm{H})$ can be measured accurately (see Figure 9), which is strategically important for obtaining ^{15}N NMR by polarization transfer techniques. All major developments in NMR focus on improve-

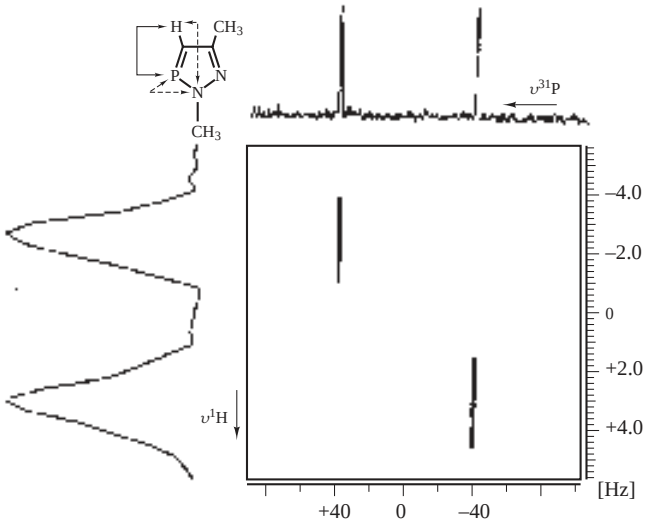

Figure 9 121.5 MHz Two-dimensional (2D) $^{31}P/^{1}H$ Hahn-echo extended heteronuclear shift correlation (HEED–HETCOR) of 2,5-dimethyl-1,2,3-diazaphosphole, based on $^{2}J(^{31}P,^{1}H)$ (connected by the full line). The ^{31}P projection shows the doublet of the $^{31}P-^{15}N$ isotopomer. The magnetization of the parent signal due to the $^{31}P-^{14}N$ isotopomer has decayed completely during the Hahn-echo pulse train (2×40 ms). The doublet in the ^{1}H projection represents the coupling constant $^{3}J(^{15}N,P,C,^{1}H) \approx 6$ Hz (this value can be used for polarization transfer from ^{1}H to ^{15}N in order to obtain ^{15}N NMR spectra). With ^{15}N as the passive spin (connected with the active spins ^{31}P and ^{1}H by dashed lines), the negative tilt of the cross peaks demonstrates that the signs of $^{3}J(^{15}N,P,C,^{1}H)$ and $^{1}J(^{31}P,^{15}N)$ are opposite (from other experiments it is known that $^{1}J(^{31}P,^{15}N) > 0$; therefore it follows that $^{3}J(^{15}N,P,C,^{1}H) < 0$)

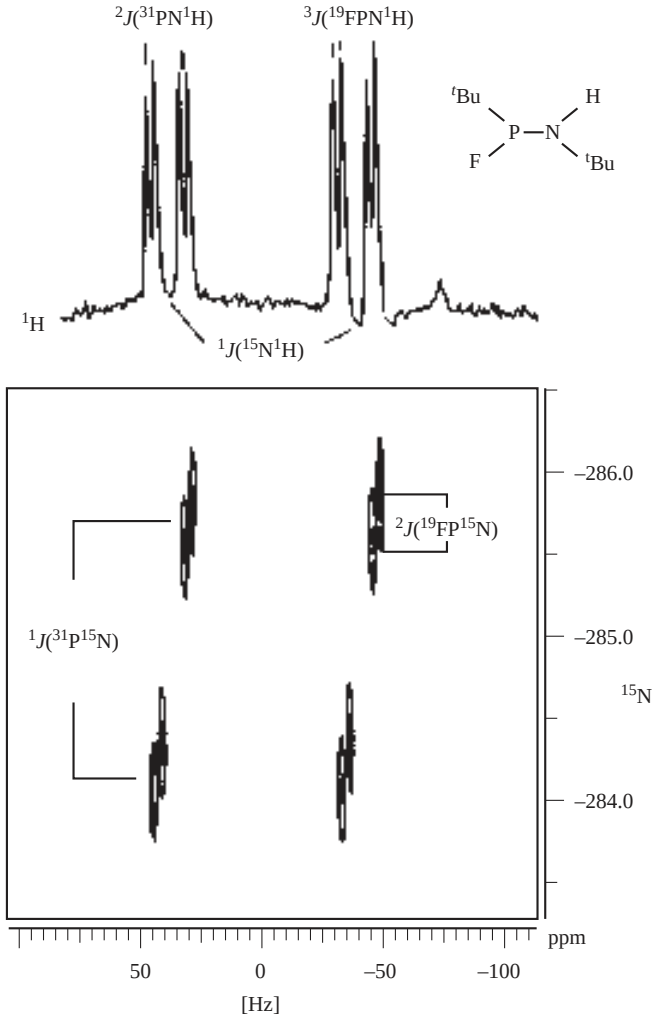

Figure 10 500.13 MHz two-dimensional (2D) inverse $^{1}H/^{15}N$ heteronuclear shift correlation of an aminofluorophosphane. The ^{15}N projection (not shown) of the correlation map gives information on the chemical shift $\delta^{15}N$ and coupling constants $^{1}J(^{31}P,^{15}N)$ and $^{2}J(^{19}F,^{15}N)$. The ^{1}H projection shows the spectrum of the ^{15}N isotopomer in the NH region with the splitting pattern due to spin–spin coupling $^{15}N-^{1}H$, $^{31}P-^{1}H$, and $^{19}F-^{1}H$. The tilt of the cross peaks in the correlation map can be used to compare the signs of coupling constants (see also Figure 5) because either ^{19}F or ^{31}P serve as the so-called passive spin in relation to the active spins ^{1}H and ^{15}N

ments in sensitivity. Interestingly, one of the first 2D heteronuclear shift correlations (A. A. Maudsley, L. Müller, and R. R. Ernst, 1977) was of the type $^{1}H/^{13}C$, using ^{1}H detection (later called inverse or reverse detection) instead of ^{13}C. Clearly, the nucleus with higher NMR sensitivity should be given priority in such experiments. However, with most commercial spectrometers it was only possible to perform 2D X/^{1}H HETCOR experiments until the end of the 1980s, mainly because of the convenience of simpler hardware. For multinuclear MR of low γ spin-$\frac{1}{2}$ nuclei inverse 2D $^{1}H/X$ experiments are very attractive because of the greater sensitivity as compared with the 2D X/^{1}H version. There is also a wealth of information to be gained, as can be seen in Figure 10 in the inverse 2D $^{1}H/^{15}N$ HETCOR spectrum in the case of a phosphorus–nitrogen compound. It should be noted that there are serious problems in detecting the NMR signals of insensitive X nuclei if they are broadened, e.g. by partially relaxed scalar coupling to a neighboring quadrupolar nucleus. This broadening effect is normally negligible for ^{1}H nuclei which have a scalar coupling with X, and 2D $^{1}H/X$ HETCOR experiments are then very efficient (B. Wrackmeyer and E. Kupče, 1992; see Figure 11).

Such inverse 2D $^{1}H/X$ experiments can also be modified for the measurement of coupling constants between rare spin-$\frac{1}{2}$ nuclei (e.g. ^{15}N, ^{13}C; ^{15}N, ^{29}Si; or ^{13}C, ^{29}Si), using ^{1}H sensitivity. For this purpose a preselection of one spin pair (e.g. ^{13}C, ^{1}H) is undertaken in the first part of the experiment in order to eliminate magnetization from the $^{1}H(^{12}C)$ isotopomer. In the second part, the X resonance is detected inversely by 2D $^{1}H/X$ correlation. This experiment may be called a pseudo-triple-resonance experiment (E. Kupče and B. Wrackmeyer, 1992), e.g. $^{1}H\{(^{13}C)X\}$, in which the ^{13}C nucleus acts as a passive spin (see Figure 12). Modern NMR spectrometers are often equipped with several independent frequency channels. Together with suitable probe heads, triple resonance experiments, $^{1}H\{X,Y\}$ or $X\{^{1}H,Y\}$ etc., are feasible, thus further enriching the existing wealth of 2D and 3D NMR experiments.

A major problem in multipulse NMR experiments concerns phase cycling in order to eliminate small errors in pulse length and phases. Thus, more transients are often necessary than are strictly required in relation to the NMR sensitivity of a particular nucleus. This is rather annoying in 2D $^{1}H/X$ measurements where, in many cases, a single transient for each X frequency would be sufficient. Since the resonance frequencies

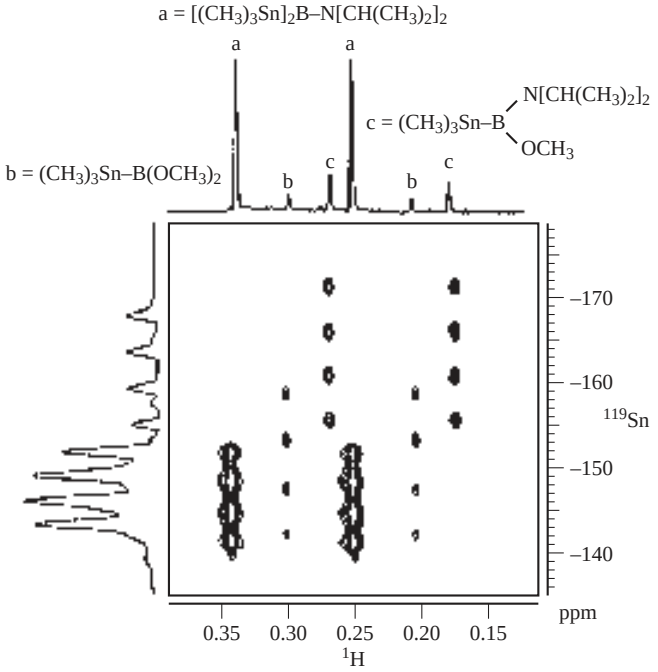

Figure 11 500.13 MHz two-dimensional (2D) inverse $^{1}H/^{119}Sn$ heteronuclear shift correlation of a mixture of boron–tin compounds [exchange reaction between $(Me_3Sn)_2B–N^iPr_2$ and $B(OMe)_3$]. The ^{1}H projection shows the spectrum in the region of the Me_3Sn groups, with the selection of the respective ^{119}Sn isotopomers marked as doublets (a), (b), and (c). The ^{119}Sn projections demonstrate that it would be difficult to record a ^{119}Sn NMR spectrum of a dilute reaction solution within a reasonable time because of the broad ^{119}Sn NMR signals arising from the large coupling constant $^{1}J(^{119}Sn,^{11}B) \approx 1000$ Hz. Furthermore, the detection of the unstable compound $Me_3Sn–B(OMe)_2$ (b) would be extremely difficult in view of the overlap with the intense ^{119}Sn resonances of (a) and (c). In the correlation map, the cross peaks of species (b) are readily resolved

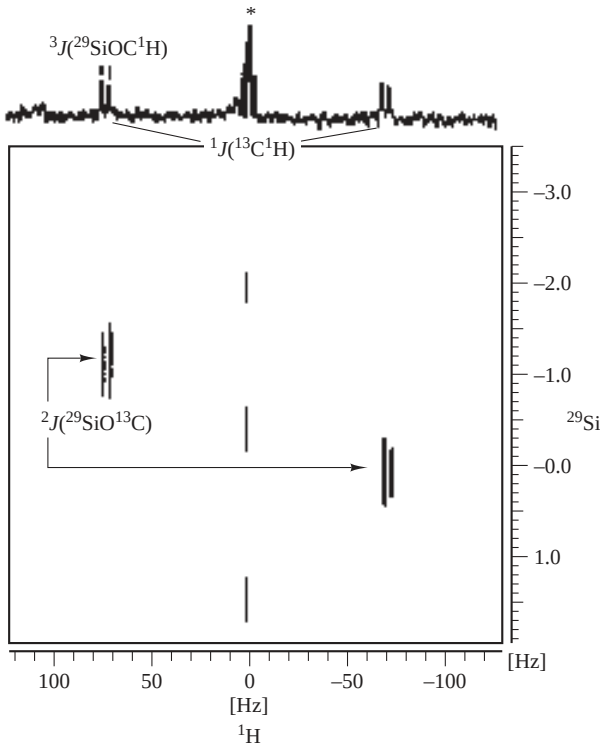

Figure 12 500.13 MHz two-dimensional inverse (^{1}H detected) pseudo-triple-resonance experiment of the type $^{1}H\{(^{13}C)^{29}Si\}$ for tetramethoxysilane $Si(OMe)_4$. This relates the spins ^{1}H, ^{13}C, and ^{29}Si in order to determine the small coupling constant $^{2}J(^{29}Si,O,^{13}C)$ and its sign. In the ^{1}H projection, the small residual signal of the parent line is still detected (*). The other signals correspond to the $^{1}H–^{13}C–^{29}Si$ isotopomer with the spin–spin coupling $^{1}J(^{13}C,^{1}H)$ and $^{3}J(^{29}Si,O,C,^{1}H)$. The cross peaks are separated by $^{2}J(^{29}Si,O,^{13}C) = 1.2$ Hz, and the negative tilt demonstrates that the reduced coupling constants $^{1}K(^{13}C,^{1}H)$ (known to be >0) and $^{2}K(^{29}Si,O,^{13}C)$ [>0; since $\gamma^{29}Si < 0$, it follows that $^{2}J(^{29}Si,O,^{13}C) > 0$] are of opposite sign. It should be pointed out that such small couplings cannot be measured from ^{13}C NMR spectra

of X nuclei may cover a large range (in general much larger than for ^{1}H), many experiments are required in the inverse 2D experiment in order to maintain a reasonable digital resolution in the F_1 domain (X). Together with phase cycling, this uses a great deal of spectrometer time. Pulsed field gradients, in combination with rf pulses (already suggested in 1978 by A. A. Maudsley, A. Wokaun, and R. R. Ernst) circumvent the problem of phase cycling, and as a result the dynamic range problem in multiple quantum experiments is solved, and the t_1 noise in 2D spectra is considerably reduced. This latest development in multidimensional NMR in solution could have a significant influence on multinuclear MR.

The potential of multinuclear MR is now being increasingly exploited by the scientific community. The need for a multinuclear approach is reflected by the commercial availability of very flexible NMR instrumentation. There are still many problems to solve in order to handle better the NMR spectroscopy of insensitive, but important spin-$\frac{1}{2}$ nuclei (e.g. ^{57}Fe, ^{187}Os), or the problem of extremely broad lines in the absence of symmetrical surroundings with quadrupolar nuclei, (e.g. ^{35}Cl, ^{75}As, ^{139}La, ^{181}Ta, etc.), to name just two areas. This means that the fruitful mutual interaction between the development of NMR methods and chemistry will continue to produce exciting results.

Biographical Sketch

Bernd Wrackmeyer. *b* 1947. Diploma, Munich, 1971, Dr. rer.nat, Munich, 1973, Habilitation, Munich, 1979. Introduced to NMR by H. Nöth and W. McFarlane. Institute of Inorganic Chemistry, University of Munich, 1979–1986. Laboratory of Inorganic Chemistry, University of Bayreuth, 1986–present. Approx. 320 publications, and, with H. Nöth the book 'Nuclear Magnetic Resonance Spectroscopy of Boron Compounds'. Research interests include developments of NMR techniques in solution, application of multinuclear MR to problems in inorganic and organometallic chemistry.

Wüthrich, Kurt: NMR Structures of Biological Macromolecules

Kurt Wüthrich

Eidgenössische Technische Hochschule, Zürich, Switzerland

My first job in the field of NMR with biological macromolecules started on October 1, 1967, when I joined the Biophysics Department at Bell Telephone Laboratories in Murray Hill, NJ. The department was headed by Dr. Robert G. Shulman, whose NMR credentials at the time included solid state work on metal compounds, which had attracted my interest because of the implications in the area of crystal field theory, and studies of nucleic acids and proteins in solution using relaxation enhancement techniques. My initial assignment was in line both with my previous work (see below) and with a project pursued at the time by the Bell group: substitution of the Zn^{2+} ion in carboxypeptidase A (CPA) by VO^{2+} to enable ^{17}O relaxation enhancement studies of the active site hydration. During the first few weeks in my new job I assembled an extensive bibliography on CPA and visited the laboratories of Prof. W. N. Lipscomb and Prof. B. L. Vallee at Harvard to obtain first-hand information on CPA. However, before I was ready to start experiments, a Varian HR-220 high-resolution ^1H NMR spectrometer operating at 220 MHz was delivered to our department. I was given responsibility for its maintenance, and in this easy and painless way I was out of relaxation enhancement experiments (see below) and into 'high-resolution NMR'. Fortunately, contacts with Bert Vallee and Bill Lipscomb survived my involvement with CPA, and have continued in most amiable ways over all these years.

HIGH-RESOLUTION NMR WITH BIOLOGICAL MACROMOLECULES IN 1967

A report by Saunders et al.[1] in 1957 which presented a 40 MHz ^1H NMR spectrum of ribonuclease A is the uncontested first paper on high-resolution NMR of a protein, soon to be followed by an interpretation of this spectrum by Jardetzky and Jardetzky.[2] During the following decade, one notes the publication of four papers on the ^1H NMR spectra of amino acids and linear oligopeptides, and 16 papers with ^1H NMR spectra of the proteins ribonuclease A, lysozyme, chymotrypsinogen, and cytochrome *c*. In this context, 'high-resolution NMR' refers exclusively to the fact that the resonance lines of the macromolecule were observed directly; inspection of the spectra makes it clear that there could not be any other implications!

When I entered the field in 1967, these early papers relayed two principal messages. One was simply the information on the approximate ^1H chemical shifts of the common amino acid residues obtained from studies of amino acids and oligopeptides. The second was the notion of the dispersion of the ^1H chemical shifts in folded polypetide chains, which gradually evolved in papers by Kowalsky[3,4] and Mandel,[5] was evident in the data on the histidyl residues in ribonuclease by Bradbury and Scheraga[6] and by O. Jardetzky's group,[7] and was clearly spelled out in an important paper by McDonald and Phillips.[8] The chemical shifts of a limited number of well-separated lines were the only spectral parameters that could be measured reliably at the time, since scalar spin–spin couplings were not resolved even in the ^1H NMR spectra of small proteins. The ideas of 'ring current shifts'[3,8] and 'electron delocalization near paramagnetic centers'[4] giving rise to separated lines in unusual chemical shift positions thus provided an initial rationale for the appearance of protein ^1H NMR spectra.

MY RESEARCH EXPERIENCE UP TO 1967

From the days in the 'Gymnasium' my mind was set on a career in sports and physical education. While recovering from injury occasioned by pursuit of this goal, I nonetheless graduated in physics, mathematics, and chemistry at the University of Bern. Being fit again, I moved to the University of Basel in April 1962 for a formal education in sport as a full-time student for the 'Eidgenössisches Sportlehrerdiplom'. With the kind permission of Prof. Silvio Fallab, I started in October 1962 to spend the evenings doing some research in the Institute of Inorganic Chemistry. Shortly thereafter, Peter Hemmerich, then a young Privatdozent, organized a symposium on biological applications of EPR with the participation of, among others, A. Ehrenberg, H. Beinert, B.G. Malmström, and T. Vanngard. This was my first contact with magnetic resonance. I was fascinated by the fact that one could focus on novel features of metal centers in proteins without interference from the much larger polypeptide chains, and shortly thereafter I found myself in the laboratory of Prof. Peter Diehl in the Physics Institute. He was on sabbatical leave and had left an idle Varian V4501 state-of-the-art EPR spectrometer behind. I received the necessary training in the practice of EPR from Dr. Hans Loeliger, a physicist at Ciba AG who had previously used what was now to be 'my' EPR spectrometer. Some successful experiments with copper complexes that catalyze autoxidation reactions of aromatic amines[9] led to my obtaining a Ph.D. in chemistry and the Sportlehrerdiplom in March 1964.

After spending another year in Basel, teaching high school sports and studying a variety of VO^{2+} complexes with the use of EPR,[10] I joined Prof. Robert E. Connick at the University of California in Berkeley. I continued the studies with VO^{2+} complexes that I had started in Basel, adding ^{17}O, ^1H, and ^2H NMR relaxation enhancement studies to EPR. However much of the time was actually spent solving the problems in M. Tinkham's 'Group Theory and Quantum Mechanics' and recalculating, page for page, large portions of the monographs by A. Abragam and by C. P. Slichter for presentation in the group seminars. It is also worthwhile mentioning that with much help from Dr. Alfred Bauder from the ETH Zürich, who spent a sabbatical in Berkeley, a digital recording device for quantitative analysis of EPR difference spectra was installed. This must have been one of the really early such data handling setups, which contributed significantly to the eventual success of a project on studies of the hydration of VO^{2+} complexes.[11] Overall, while Prof. Fallab and his colleagues in Basel had awakened my interest for oxygen-binding and electron-transferring metalloproteins, Bob Connick and the

Berkeley environment provided me with a thorough basis in the theoretical aspects of both metal complexes per se and the more specialized field of electron and nuclear spin relaxation in metal compounds.

EARLY SURVIVAL WITH PROTEIN NMR

With hindsight, it is clear that there was little to be gained by using NMR for studies of proteins in the late 1960s. The more sophisticated NMR instrumentation at the time operated at ^{1}H frequencies of 60–100 MHz, and the only commercial high-field apparatus, the Varian HR-220, was a field-sweep, protons-only CW spectrometer. There was no field/frequency lock. For paramagnetic compounds the resonances of the center band and two to four sidebands would overlap, since the instrument used a 10 KHz field modulation with the first upfield sideband as the observation frequency.[12] For spin decoupling or other INDOR experiments, we used additional, home-built audio modulation of the observation frequency with the exact difference frequency between the presumed interacting spins, and then performed a field sweep through resonance. For signal averaging we interfaced a Fabritek computer (later to become Nicolet) with the NMR spectrometer, which provided us with rapid accumulation into 4 K of memory. However, for many applications the improved digital resolution (when compared with standard equipment in 1968) was of questionable merit, considering that there was no field/frequency lock. The need for sample spinning at 120–140 rps presented an additional risk for experiments with long accumulation times. Not surprisingly, for a detailed study of bicyclobutane, which is the only NMR at high resolution that I got involved in at the time, we relied mostly on a Varian HA-100 spectrometer.[13]

Other than the above-mentioned study of bicyclobutane,[13] all my projects at Bell Labs had to do with hemoproteins. Due to my background, my interest was focused on metal centers rather than polypeptide chains. Thus, in the seminal paper by McDonald and Phillips[8] I was intrigued by a description of NMR spectral differences between the reduced, diamagnetic state and the oxidized, paramagnetic form of cytochrome *c*; based on my earlier work with Bob Connick, this seemed to present novel perspectives. Fortunately, a collaboration on myoglobin was established with Dr. Jack Peisach, Prof. Emanuel Margoliash kindly supplied me with various cytochromes *c* and for many years with expert advice on this class of proteins, and Dr. Tetsuo Yamane at Bell Labs. prepared hemoglobin KW, using blood sampled from my arm in the first aid station. Within a few months, numerous well-separated resonance lines arising from electron–proton contact and pseudocontact coupling, and from interactions with the porphyrin ring current field were identified in the ^{1}H NMR spectra of all these proteins. This opened new avenues to information on the molecular structure, e.g. in cytochrome *c*,[12] on conformation changes during the oxygenation of myoglobin and hemoglobin,[14] and on the electronic structure of the heme group.[15] Some lucky circumstances ensured rapid acceptance of these results. At the ENC in Pittsburgh in the spring of 1988, Oleg Jardetzky graciously added an unscheduled 5 min presentation of my data to the program of his symposium on biological NMR. Sir Arnold Burgen was in the audience and, as I learned later on, relayed the information on the hemoglobin studies to Dr. M. Perutz. Dr. Perutz immediately called to announce a visit at Bell Labs, to get first-hand information. Clearly, my day was made and support for the continuation of the work ensured. A review of this early work[15] was accepted as the 'Habilitationsschrift' by the ETH Zürich in 1969, and later on became a Citation Classic, reflecting that work in this area has continued during all these years and is still going on.

At the ETH Zürich, where I moved in October 1969, a Varian HR-220 instrument had already been set up. Due to the proximity of the streetcars running with direct current, the absence of an effective field/frequency lock was a disaster for anyone attempting to work at high resolution (see ***Ernst, Richard R.: The Success Story of Fourier Transformation in NMR***), and it did not help that the only data acquisition device available was a Varian CAT with 1 K of memory. However, in hemoproteins the lines of interest were so broad that neither the streetcars nor the low digital resolution presented serious obstacles. Fortunately, I had brought some sample tubes with me that enabled spinning at the required rate of about 120 rps, which apparently had not been achieved previously with the Zürich instrument (only 2–5 out of 100 of the highest-grade tubes then available could be used). As a matter of fact, the unfortunate situation was to my advantage. Although the HR-220 was to be shared equally among five institutes, I was soon encouraged to use most of the measuring time available. Critical measurements had to be made between midnight and 5 a.m., which soon became a routine.

In 1970, we obtained a Varian XL-100 multinuclear MR spectrometer capable of CW and FT operation. Although it was used for some aspects of the hemoprotein projects, e.g. ^{13}C NMR of metalloporphyrin complexes[16] and studies of high-spin ferrous hemoproteins,[17] this instrument primarily enabled us to embark on new projects with synthetic oligo- and polypeptides. In collaboration with Prof. Robert Schwyzer, some encouraging results were obtained with proline-containing cyclopentapeptides, where equilibria between multiple conformations containing *cis* and *trans* Xxx–Pro peptide bonds were characterized.[18] Overall, this and other successful studies at this field strength were mostly achieved with ^{13}C NMR in dimethylsulfoxide and other non-aqueous solvents. To obtain a more reliable basis for such work, 20 peptides TFA–Gly–Gly–Xxx–Ala–OMe_3 where Xxx represents one of the 20 common amino acid residues, were custom made for us by Bachem AG for the collection of ^{13}C reference shifts.[19]

By 1971 I had assembled my first research group. It included Dr. Regula Keller, who had obtained her Ph.D. in solid state physics undertaking EPR spectroscopy with Prof. Werner Känzig at the ETH. Regula's early work on a variety of cytochromes[20] and oxygen-binding proteins,[21] and on the determination of the electronic ***g***-tensor in ferricytochrome b_5 from the ^{1}H hyperfine shifts,[22] started a collaboration that continued for more than a decade. Rudolf Baumann is a chemical engineer who was involved in many of the early research projects[16] and has over all these years been responsible for much of the functioning of the laboratory. The first two graduate students were Jean-Paul Meraldi, who worked with cyclopeptides, and André Masson, whose work will be mentioned below. They were joined in 1972 by Christoph Grathwohl,[19] Jiri Hochmann[17] and Robert Hetzel, who was the first theoretical physicist in the group and initially

worked on ring-closure conditions for cyclic peptides, and in 1973 by Arno Bundi and Gerhard Wagner.

As I felt that we were not in a position to compete with the leading groups abroad, I established a policy of keeping our hands off ribonuclease, staphylococcal nuclease, and lysozyme, a rule which was strictly followed over all these years. We thus had to look around for other polypeptides and proteins that would be suitable for NMR studies. After a long line of inconclusive experiments with polypeptide hormones such as calcitonin and ACTH, Andre Masson's thesis was saved by the discovery of numerous well-resolved resonance lines from slowly exchanging amide protons in the protein BPTI.[23] BPTI subsequently became so central to our research that I was asked to write a special section on this protein for this Encyclopedia (***Pancreatic Trypsin Inhibitor***).

Gerhard Wagner joined us as a graduate student to work on the crystal field theory of hemoproteins, which would have been in line with his diploma thesis in Mössbauer spectroscopy at the TH München, but I convinced him to perform a detailed analysis of the aromatic region of the ^{1}H NMR spectrum of BPTI 'on the side.' We soon became stuck because careful integration yielded the intensity of 30–32 rather than the expected 36 aromatic protons at temperatures from 20–50 °C. After pondering over this for a while, we decided to present this result at the 6th International Conference on Magnetic Resonance in Biological Systems, in Kandersteg in September 1974, where we heard in the discussion that another group had obtained proper integration to 36 protons at the same temperatures (this was never published). One evening I discussed this curiosity over dinner with Prof. Zeev Luz, who spent some time with us following the Kandersteg meeting. He strongly encouraged me to continue the search for dynamic phenomena. Several weeks later we had obtained very direct, quantitative evidence for ring-flipping motions of Phe and Tyr by extending the NMR measurements to a wider temperature range.[24] This result was unexpected because it appeared to contradict the temperature factors measured for the ring carbon atoms in the BPTI crystal structure. However, model calculations that Robert Hetzel performed, in collaboration with Dr. Johannes Deisenhofer during a stay in Prof. Robert Huber's laboratory in Munich, cleared up this apparent discrepancy.[25] The discovery of the ring flips in BPTI in October 1974 probably did more than any other single result to make our existence known to others in structural biology. It came at the end of the first phase of my activity in Zürich during which I had worked quietly with a small group of students, Dr. Regula Keller and Rudolf Baumann, spending much of my time in the laboratory.

1975–76—AN INTERLUDE

The publications from this period show that we obtained more precise data on hemoproteins, oligopeptides, and internal mobility in proteins while further pursuing the projects of the preceding years. Noteworthy are the introduction of the sine-bell for digital filtering[26] and the fact that several papers described nonrandom conformations for linear oligopeptides.[27,28] Most importantly, however, during those two years my research group was more comfortably installed and critical decisions were made for the future.

The technical difficulties mentioned above with the operation of the HR-220 instrument in Richard Ernst's laboratory, and the fact that as a consequence we became the dominant user of the facility, led to the decision to install a Bruker HX-360 multinuclear FT spectrometer in my laboratory. For the first time we could embark on high-field experiments going beyond simple chemical shift measurements. Simply repeating selected experiments of the previous years provided a wealth of new results, since the step from 100 MHz to 360 MHz was really revolutionary, and important improvements had also been made in the data-handling facilities. Although outside users of the 'high-field NMR facility for the ETH and the University of Zürich' were entitled to two days per week of measuring time, it was really 'our' instrument on which we could work continuously on technical improvements. In this way, a most fruitful collaboration with Bruker-Spectrospin AG developed, and has continued over all these years. Attached to the 'high-field NMR facility' was a permanent position for an engineer, which was held first by Alexandra Frey, then for a decade by Albert Eugster, and now by Daniel Braun, all of whom have done a great job in keeping the laboratory up and going. This was a big change, since my entire research group had previously been on soft money. Shortly thereafter, the ETH made a major commitment by allotting permanent positions for additional scientific associates and engineers as well as a secretary, and by increasing our laboratory space severalfold. Another important change came about by the fact that, for the first time, the group was joined by postdoctoral associates with previous NMR experience, i.e. Larry Brown, Antonio DeMarco, Miguel Llinás, and Stephen Perkins, as well as academic guests specialized in biochemistry and other disciplines related to our work, i.e., Joseph Gilboa, Jürgen Lauterwein, Klaus Loth, Lea Stassinopoulou, and Vincenza Viti. This changed the character of the group in dramatic ways, greatly widened the scope of our activities, and helped to open the eyes of local students to the outside world.

For me personally, organizing (jointly with Richard Ernst and Joachim Seelig) the biennial International Conference on Magnetic Resonance in Biological Systems in Kandersteg in 1974, writing a monograph on 'NMR in Biological Research: Peptides and Proteins'[29] in 1975, and experience gained when serving as a member of the then structural biology-oriented council of IUPAB greatly helped to clarify some issues. I realized that we could only attain broader acceptance by the biochemistry community if we worked with a technique capable of de novo determination of molecular structures, other spectroscopic data alone being too difficult to explain or visualize for easy communication. However, a thorough survey of the then available literature of about 500 titles, which was part of the preparation for writing the book, showed that despite some admirable individual efforts there was no existing line of NMR work with polypeptides that could lead to this goal. The literature did not even contain an attempt at determining a previously unknown polypeptide fold on the basis of NMR data. In practice, structural information from X-ray crystallography, and in some instances from a knowledge of the restricted conformational space for cyclic peptides, was typically used as a basis for obtaining resonance assignments and for rationalizing experimental NMR parameters.

This was important groundwork and the field probably had to go through this phase. However, the fact that some unusual ^{1}H chemical shifts could be interpreted on the basis

of protein crystal structures and used for qualitative studies of conformational transitions[29] resulted in the widespread misconception that ^{1}H chemical shifts would eventually provide a basis for de novo structure determination. As a major gain from the effort of working through the available literature, I convinced myself at the time that the local fields which give rise to conformation-dependent shifts, such as ring-current fields, fields near peptide groups, and pseudocontact fields near paramagnetic centers, would, because of their high intrinsic symmetry not be suitable for delineating novel, previously unknown structures. In contrast to the rather disappointing role perceived for NMR in the area of structure determination, the technique had clearly made seminal contributions to the investigation of dynamic features in proteins and to studies of amide proton exchange. However, by 1975, the phenomenon of internal mobility in proteins and the ability to measure exchange kinetics for individual amide protons had been well documented, and further characterization of protein mobility could only be achieved on the basis of additional information on resonance assignments. Similarly, it was clear that further progress with studies of paramagnetic centers in metalloproteins would depend on the additional availability of individual resonance assignments.

Research proposals submitted at the time show that I ended up with three crucial decisions during those two years. Firstly, a research project was submitted that envisaged developing techniques for obtaining resonance assignments in proteins entirely on the basis of spectroscopic data and covalent structure. Secondly, jointly with Richard Ernst, a project to develop 2D NMR techniques for studies of proteins was submitted. Thirdly, I joined a group of colleagues in mathematics and computational sciences to establish the 'Zentrum für Interaktives Rechnen' at the ETH Zürich. From 1977 onward we thus had access to computer graphics facilities for theoretical work with proteins and visualization of our hoped-for results on novel molecular structures.

STUDIES WITH OLIGOPEPTIDES

For some time each newcomer to the group had to start by fully analyzing the 100 MHz ^{1}H NMR spectra of several linear model tetrapeptides, i.e. TFA–Gly–Gly–Xxx–Ala–OMe.[30] With the availability of the 360 MHz spectrometer it soon became apparent that more precise reference chemical shifts were also needed for aqueous solutions. Hence, René Richarz, who joined the group as a graduate student in 1976, and Arno Bundi measured the 'random coil' ^{13}C shifts[31] and ^{1}H shifts[32] of the common amino acid residues Xxx in aqueous solutions of the 20 peptides H–Gly–Gly–Xxx–Ala–OH, which also provided evidence for nonrandom conformational features of these linear oligopeptides. Most notable is the transient formation of amide proton–carboxylate hydrogen bonds,[33] which has also been oberved subsequently on the surface of numerous globular proteins. Overall, in addition to the widely used reference chemical shifts, studies of these peptides provided reference data for conformational studies of flexible regions in proteins based on amide proton titration shifts[33] and the observation of *cis–trans* isomerism of Xxx–Pro peptide bonds.[28] Miguel Llinás and Antonio DeMarco performed a series of beautiful homonuclear and heteronuclear experiments with ^{15}N- and ^{13}C-labeled alumichrome. Although primarily designed for obtaining more detailed insights into the structural and dynamic properties of ferrichromes, these measurements provided important reference data on the calibration of Karplus-type relationships for $^3J_{\alpha\beta}$,[34] $^3J_{\mathrm{HN}\alpha}$,[35] and $^3J_{^{15}N\beta}$.[36]

^{1}H–^{1}H NOEs AND SPIN DIFFUSION

Although heteronuclear NOEs had been used routinely to enhance the signal intensity for the direct observation of ^{13}C or ^{15}N and had also been applied for studies of segmental mobility in proteins, homonuclear ^{1}H–^{1}H NOEs had generated little enthusiasm by 1976. The following quotation from the only monograph on the subject at the time explains some of the reasons for this:[37] 'However, the numerous existing books on NMR written primarily for chemists barely mention the NOE and do not provide the background in nuclear relaxation theory necessary to understand it. Aside from original research papers, only a few references of a highly theoretical nature are extant. The difficulty and rigor of these references has been a source of frequent misunderstandings and has surely limited the growth of the field'. During the period 1970–75 the laboratories of A. G. Redfield, A. A. Bothner-By, and I. D. Campbell had published short reports on the observation of ^{1}H–^{1}H NOEs in proteins, and W. A. Gibbons and his colleagues had used INDOR experiments to observe NOEs in peptides. In 1976, Kalk and Berendsen[38] presented a reevaluation of the classical treatments of spin relaxation in Solomon's 1955 paper and Abragam's book, concluding with a pessimistic outlook regarding selective NOEs in proteins because of the expected dominant effects from spin diffusion. As one of several different approaches to obtaining resonance assignments (see below), we nonetheless decided to investigate the potentialities of our new 360 MHz instrument for NOE studies, with the result that NMR with biological macromolecules was never quite the same again for us.

Hemoproteins once again turned out to be a lucky choice for the initial NOE experiments. The ^{1}H NMR spectrum of diamagnetic ferrocytochrome *c* contains well-separated resonance lines of the axial methionyl ligand of the heme iron at high field between $-$ 4 ppm and $-$ 1 ppm, and at around 10 ppm there are the equally well-separated lines of the four *meso*-protons of the heme group.[12,15] Within a short space of time 1D NOE experiments with irradiation of these well-resolved lines yielded strong, selective negative NOEs. We could thus perform all the studies on the spin physics in the molecular core of a globular protein that would become accessible for other proteins only many years later with the use of 2D NOESY. Regula Keller soon completed a 'sequential NOE walk' around the periphery of the heme group, and the individual resonance assignments thus obtained for reduced cytochrome *c* were extended to the paramagnetic, oxidized protein using magnetization transfer mediated by the electron exchange between the ferrous and ferric states.[39] This was a crucial advance in the characterization of the electronic structure of low-spin ferric hemes, which opened an avenue for investigations of evolutionary changes in heme structure by Regula Keller and a new graduate student, Hans Senn.[40–42] Rene Richarz optimized NOE difference spectroscopy in ways that served us well for several years.[43] In 1977, Prof. Sidney Gordon joined the group to spend a sabbatical year. Combination of his long-standing experience in NOE

spectroscopy with the current state of our work resulted in the 1D transient NOE experiment and the first recordings of NOE build-up curves.[44] Although 1D applications were for technical reasons more limited for transient NOE measurements than for conventional preirradiation techniques,[37] these results had a fundamental impact on our work, not to speak of the fact that the 1D transient NOE experiment contains all the elements of 2D NOESY except for the evolution period (see below). Since transient NOE measurements enabled us to follow the time course of the nonequilibrium magnetization on numerous individually assigned spins in the absence of radiofrequency irradiation, we soon identified the main reason for the success of our 'steady-state' experiments: the preirradiation times had been optimized such that the systems never actually reached the steady state. Gerhard Wagner optimized the use of the preirradiation technique with the 'truncated driven NOE experiment' (TOE),[45] and we checked carefully that coincident information was obtained from TOEs and transient NOEs.[46] The TOE experiment was used extensively until it was replaced by 2D NOESY.

By late 1977 it was clear from the experiments mentioned above that $^1H-^1H$ NOEs would not only help to obtain improved spectral resolution and resonance assignments,[39,43,46,47] but that despite spin diffusion[38] it was a parameter that provided the type of information needed for de novo three-dimensional protein structure determination. Initial success in obtaining novel structural data was achieved for the heme crevice in hemoproteins. Because individual ^1H NMR assignments for the heme groups had been based exclusively on NMR data and the covalent structure of the porphyrin ring,[39] NOE experiments revealed that the previously mentioned evolutionary change of the electronic heme structure in *c*-type cytochromes was related to a change in the chirality of the axially bound methionyl residue.[41,48] The orientation of the heme group relative to the folded polypeptide chain in cytochrome b_5 as described in the crystal structure was revised,[49] and dynamic equilibria between multiple different heme orientations in reconstituted cytochromes b_5 and b_2 were identified and characterized structurally.[47]

SEQUENTIAL RESONANCE ASSIGNMENTS

In 1976–77, we tested a wide range of approaches for obtaining resonance assignments with or without reference to the three-dimensional protein structure. This included ^1H spin system identifications for amino acid side chains using spin decoupling, $^{13}C-^1H$ chemical shift correlation, ^1H chemical shift correlation between the native and denatured forms of the protein, interpretation of NOEs based on the protein crystal structure, and comparison of mutant and chemically modified proteins. Stephen Perkins, a postdoctoral fellow who had joined us from Oxford, applied ring-current calculations and paramagnetic shift reagents with BPTI.[50,51] However, the key experience during those two years was Regula Keller's 'sequential NOE walk' around the periphery of the heme group in hemoproteins[39] (see the preceding section). In March 1978 a young physicist, Andreas Dubs, joined Gerhard Wagner and myself for his diploma thesis, and within a few months had performed a corresponding sequential assignment walk along the strands of the β-sheet in BPTI.[46] The results also included interstrand NOEs, showing that the structure of multistranded β-sheets in proteins could be determined with the techniques used. Although the project started with frequent reference to the BPTI crystal structure, it soon became clear that the method could yield sequence-specific assignments without previous knowledge of the three-dimensional structure, and in the Discussion section of the paper we also proposed the determination of new amino acid sequences using the sequential assignment approach.

After obtaining his ETH diploma, Andreas Dubs left for Australia, and to the best of my knowledge never again touched an NMR spectrometer. For those of us who stayed behind, his contribution gave a clear direction for the further development of assignment techniques, which were from this point on entirely focused on the use of spectroscopic methods for spin system identification and establishing sequential connectivities between the spin systems of individual amino acid residues. The sequential assignment approach using 1D NMR yielded partial assignments in several additional polypeptides and proteins. In 1980, using independently developed 2D NMR experiments (see below), the assignments of Andreas Dubs[46] were extended to molecular areas of BPTI outside of the β-sheet.[52,53] With the use of a newly arrived Bruker WM-500 spectrometer operating at 500 MHz, complete assignments of BPTI were eventually obtained in 1981. Two new graduate students, Martin Billeter and Gerhard Wider, and Dr. Kong-Hung Lee had by that time joined the assignment project. A series of four papers in 1982 presented an outline of the NMR method for protein structure determination in solution,[54] the theoretical basis of the sequential assignment approach,[55] and complete assignments for BPTI[56] and micelle-bound glucagon.[57]

In 1981–82, a group of highly gifted postdoctoral fellows joined the group for work on protein structure determination —Alexandr Arseniev, Françoise Guerlesquin, Ramakrishna Hosur, Dominique Marion, David Neuhaus, Arthur Pardi, Lea Stassinopoulou, Petr Štrop, Michael Williamson, and Eric Zuiderweg. Within two years we obtained sequence-specific assignments for a half-dozen small proteins, which confirmed that the method was generally applicable. Some results were of special interest for the further development of the methodology. Eric Zuiderweg brought the *lac* repressor DNA-binding domain from Robert Kaptein's laboratory to Zürich, and we obtained complete resonance assignments[58] and determined the secondary structure of the *lac* headpiece[59] in my laboratory in Zürich, thus demonstrating the use of the assignment method with an α-protein. With bull seminal proteinase inhibitor (BUSI),[60] a protein brought to Zürich from Prague by Petr Štrop, and rabbit metallothionein,[61] a protein investigated in collaboration with Prof. Jeremias Kägi at the University of Zürich, the sequential NMR assignments led to the identification and correction of numerous errors in the chemically determined amino acid sequences. In 1983, metallothionein was also the first protein where we combined the sequential assignment technique with isotope labeling to achieve the desired result.[62]

Overall, during the period 1982–94, we determined complete sequence-specific assignments for more than 40 proteins and complexes of proteins with DNA and other ligands, using the method based on sequential NOEs. In complex systems this sequential assignment approach was supported by selective or uniform isotope labeling,[63] which also enabled complete assignments for a urea-unfolded protein.[64] In addition, special

labeling techniques were developed for obtaining stereospecific assignments.[65] In recent years much effort has gone into software development for computer support of the resonance assignments, with important contributions by Craig Eccles, a postdoctoral fellow from New Zealand, Martin Billeter and two graduate students, Peter Güntert and Christian Bartels.[66] It has also been a great pleasure to see the assignment field evolve in recent years with alternative sequential approaches developed by others, thus benefitting our own work via these additional techniques.

DETERMINATION OF THREE-DIMENSIONAL NMR STRUCTURES OF PROTEINS

As mentioned previously, we obtained access to modern computer graphics equipment for theoretical studies of proteins in 1977. During the following years up to 1984, two postdoctoral fellows, Werner Braun and Timothy Havel, and a graduate student, Martin Billeter, did a great job using these facilities so that we would be prepared to perform structure determinations once the necessary NMR data became available. We also received valuable outside advice from Prof. Nobuhiro Gō, who spent three months with us as a visiting professor in 1979, and from Prof. Max Engeli of the ETH, an expert in information theory and computer graphics who codirected the Ph.D. thesis of Martin Billeter. Based on what we had learned from NOE build-up measurements, the projects were soon focused on structure determination from qualitative NOE upper distance constraints. These could take account of internal molecular mobility and would be robust relative to possible errors in NOE intensity measurements. Further, it was important to us that the interpretation of the NMR data should be clearly separated from theoretical refinement routines. There was no software available that could be used for our purposes and even basic routines for graphics displays, for example, had to be written. This situation forced us to become heavily involved in software development, which has been an important part of our activities ever since. Three different approaches at different levels of structure determination proved to be of practical use.

Statistical analyses of the small collection of high-resolution protein crystal structures available in 1980 provided not only a basis for the sequential assignments with NOEs,[55] but in addition led to a pattern recognition approach for the identification of regular secondary structures and turns in polypeptides.[67–69] The data collection for resonance assignments based on sequential NOEs supplemented with measurements of amide proton exchange rates thus turned out to be sufficient also for secondary structure identification. In contrast to crystallographic protein structure determination, where the sequence locations of secondary structure elements are one of the last features to evolve, the secondary structures in solution are thus obtained at an early stage of an NMR structure determination. Subsequently, this fact has been used to support crystallographic chain tracings with secondary structures determined by NMR.[70]

As a second approach, Martin Billeter wrote the program CONFOR,[71] which enabled the generation of different conformations of large molecular structures by real-time variation of the torsion angles. A fit to NOE distance constraints was interactively achieved by minimizing constraint violations displayed in the molecular structure on the graphics screen. An early success with the use of CONFOR was the determination of the three-dimensional chain fold of the *lac* repressor DNA-binding domain.[72] The *lac* repressor structure was subsequently refined many times, mainly by Robert Kaptein and his colleagues, but the molecular architecture of 1984[72] has stood the test of additional data collection and more sophisticated computational procedures. Although other programs soon proved more efficient for the determination of complete protein structures, CONFOR served us well for many years, both for interactive local structure refinement and for the visual presentation of the NMR structures.

The third approach was distance geometry in metric matrix space. Initially, Prof. Gordon Crippen kindly provided a software package that was in use in the San Francisco group at the time. Werner Braun then developed a first distance geometry package suitable for structure determination from NMR data, which included complete covalent amino acid structures with proper chirality so that the handedness of the resulting molecular geometries could be unambiguously assessed. Because of the high demands for computing capacity, the application of this program was limited to polypeptides with up to about 10 residues. Using this software and data collected with 1D NMR experiments by Larry Brown and Chris Bösch, a physics graduate student who went on to an M.D. and a successful career in medical NMR, we had gone through all the steps of an NMR structure determination even by 1980, with an application to a 10-residue segment of the polypeptide hormone, glucagon.[73] A complete structure of micelle-bound glucagon based on 2D NMR data collection and structure calculations for overlapping 10-residue segments was obtained in 1983.[74] At this time we also developed a pseudoatom concept for dealing with prochiral centers in the absence of individual assignments for the diastereotopic substituents.[75] Werner Braun left the project in 1982, and Tim Havel took over and wrote the new software package DISGEO.[76] To overcome the limitations imposed by the available computing facilities, DISGEO used an original substructure description of polypeptide chains in the early phases of the calculations. With continuous use of more than 50% of the capacity of the 'Zentrum für interaktives Rechnen' and heroics on Tim's part in making optimal use of the computer facilities, extensive test calculations confirmed that complete globular protein structures could be determined by NMR.[77] Using input data collected by Michael Williamson, the first de novo structure determination of a globular protein, BUSI, was completed in March 1984.[78] The program DISGEO was subsequently widely used worldwide in a large number of NMR structure determinations.

In 1984, Werner Braun rejoined the group after a postdoctoral stay with Professor N. Gō, where he had continued work on a distance geometry approach in torsion angle space that he had originally started in Zürich. From 1985–90 his program DISMAN was used in several important structure determinations, notably Tendamistat[79,80] and metallothionein,[81] and its performance was also compared in detail with that of DISGEO.[82] A big advance then resulted from the work of Peter Güntert, who developed and implemented a wide array of new techniques for all aspects of efficient structure calculation and for dealing with prochiral centers; the most widely used to date are the programs HABAS[83] and DIANA,[84] and

the REDAC strategy.[85] Since 1985, NMR structure calculation has evolved into an exciting, lively field with a variety of different approaches which have also influenced our work, for example, in relaxation matrix refinement of NMR structures,[86] novel strategies for structure calculation of multimolecular complexes with proteins,[87] and in many aspects of structure refinement.[88] Thomas Schaumann, Tai-he Xia, and Berthold Freiherr von Freyberg made important contributions in these areas while getting their Ph.D. degrees in theoretical physics.

ESTABLISHING CREDIBILITY FOR NMR STRUCTURES OF PROTEINS

When I presented the NMR structure of BUSI[78,89] in some lectures in the spring of 1984, the reaction was one of disbelief and suggestions that our structure must have been modeled after the crystal structure of a homologous protein. In the discussion following a seminar in Munich on May 14, 1984, Robert Huber proposed that the matter be settled by the independent determination of a new protein structure in his laboratory by X-ray crystallography and in my laboratory by NMR. Each of us received 100 g (!) of pure Tendamistat from Dr. L. Vértesy at Hoechst AG and, as is well documented in the literature,[79,80,90–93] this project was started. Dr. Allen Kline had arrived in Zürich in March 1984 and agreed to join the competition. We obtained complete resonance assignments and the secondary structure determination by the end of the summer 1984.[90] In late 1985, virtually identical three-dimensional structures had been obtained in solution[79] and in crystals.[91] Some editorials then caused many to believe that Tendamistat, rather than the earlier work by Tim Havel and Michael Williamson with BUSI,[78] was the first complete de novo NMR structure determination of a globular protein. The fact that a genuinely novel type of polypeptide fold had been determined in the NMR structure of Tendamistat[79] apparently convinced many of the critics that NMR could actually do the job.

The Tendamistat experience was comforting when we came out with the structure determination of rabbit metallothionein in the spring of 1985.[94] In response to the first public presentations of this structure at Yale University on June 10 and at the University of Pittsburgh on June 12, I was confronted with a crystal structure of rat metallothionein that was very different from our NMR structure. Early on June 13, I spent several hours on the telephone with Gerhard Wagner to start rechecking our data, a process that was continued for several weeks after my return to Zürich. I am afraid that Gerhard never forgave me for ever harboring doubts about our results at this point and putting him through this painful procedure again (with metallothionein we were at the limits of the techniques available in 1985, and we had previously gone through several tedious rounds of checks on the resonance assignments). Soon thereafter we showed that the NMR structures of three homologous metallothioneins from rabbit, rat, and man are virtually identical, and several years later the crystal structure of rat metallothionein was redetermined and found to coincide actually very closely with our NMR structure.[95]

One consequence of all this was that publication of the initial papers on BUSI,[78] Tendamistat,[90] and metallothionein[94] was delayed by many months in each case, because we faced rejection on a variety of grounds. On a more joyful note, I felt more and more compelled to document our work more carefully in a monograph.[69] To this end I took a sabbatical in the beautiful alpine resort of Wengen, where I eventually spent two winters and made up for the skiing that I had missed during the past two decades. Since 1985, numerous new polypeptide folds have been determined by many different NMR laboratories. During 1992 alone, more than 50 new NMR structures of biological macromolecules were reported,[96] and these are now routinely deposited in data banks jointly with the X-ray crystal structures.

INTRODUCING MULTIDIMENSIONAL NMR TO STRUCTURAL BIOLOGY

In joint projects between Richard Ernst and myself during the period from November 1976 to April 1987, multidimensional NMR techniques were developed to the stage where they could be applied for studies of biological macromolecules. Over these 10 years we had a continuous line of highly gifted postdoctoral fellows working with us. During the initial three-year period, Kuniaki Nagayama was employed full time and Peter Bachmann half-time on the project. Their successors were, in chronological order, Anil Kumar, Slobodan Macura, Mark Rance, Michael Frey, Norbert Müller, and David Redwine. The arrangements were that the postdoctoral associate was stationed in my laboratory on the Hönggerberg campus of the ETH, with the sole exception of Peter Bachmann who was stationed in Richard Ernst's laboratory on the main campus, a distance of about 10 km away. The postdoctoral associates would participate in the research seminars of both groups, all the experimental work was done in my laboratory, and Richard Ernst and I would meet with our research associate at monthly intervals, or more often when required by the course of the work. From 1976–79, the project lived on the solid professionalism of Peter Bachmann in developing software for NMR spectroscopy, the heroics of Kuniaki Nagayama in realizing things on the computer and in the laboratory, and the intense personal involvement of Richard Ernst and myself. Otherwise it was low key and was hardly noticed by other members of my research group, who were mostly working with 1D NOE experiments. This situation changed once Kuniaki Nagayama had demonstrated the practical application of correlation spectroscopy for spin system identification in a protein,[52] and Anil Kumar made the best possible use of two weeks of instrument time allotted to him during the Christmas break of 1979 by recording the first 2D NOESY spectra.[97] At around this time the acronyms SECSY, FOCSY, NOESY, and COSY were coined (I learned only very recently that my old friend George Feher had previously used 'COSY' for 'optical correlation spectroscopy'),[98] and my entire group started to use 2D experiments on a daily basis. Experience from more than a decade of NMR with proteins was thus linked with the new technique, which resulted in further rapid progress. The first major steps were to record homonuclear 2D data sets in aqueous solution[99] and to repeat the NOE buildup studies originally performed with the 1D transient NOE experiment[44] with 2D NOESY.[100] The projects were thereafter largely formulated on the basis of needs arising from our daily work with biological molecules, and since contacts with practical life were ensured, new techniques were often in general use in my group within weeks of the discovery.

We apparently used imaginary threats of imminent competition to impress our collaborators [see ***Nagayama, Kuniaki: The First Protein Two-Dimensional (2D) NMR***]. However, it is actually remarkable (and clearly documented in the literature) that for nearly a full decade after our entry into the field, there was very little outside competition in multidimensional NMR with biological macromolecules. Clearly, our work was hardly considered to have too promising a future, as was also indicated by the fact that the first paper on this project[101] was initially rejected during the refereeing process.

PLAYING THE GAME OF NMR IN STRUCTURAL BIOLOGY

The present account emphasizes method development, but I cannot end without mentioning that at each level of the evolving technologies our research was strongly focused on applications of biological interest. Projects with hemoproteins and oligopeptides have already been mentioned, as have the early results on protein dynamics. Once sequence-specific assignments became available, we mapped the internal mobility of the BPTI molecule on the timescales of chemical shifts as well as relaxation times,[102–105] which also included high-pressure experiments. Gerhard Wagner had pursued this line of research during his Ph.D. thesis, and he also wrote a beautiful Habilitationsschrift on the subject. With regard to the protein-folding problem, the resonance assignments provided the basis for Heiner Roder's development of the now widely used amide proton trap experiment.[106] From 1985 onward, our projects concentrated primarily on structure determinations with proteins relating to a wide spectrum of biological problems, and with the participation of Dr. Arthur Pardi, Dr. Werner Leupin, and a graduate student from China, Mrs. Yan Qiu Qian, we also became involved in work with nucleic acids.[107–118] Complementation of these structures with dynamic information became a focal point again with the introduction of techniques for the observation of hydration water molecules in 1989.[119,120] During these years, NMR method development was pursued mainly when we became stuck with a structure determination. In this way, Gottfried Otting, first as a graduate student and then as an assistant, Gerhard Wider, who rejoined the group in 1987, and Thomas Szypersky, a graduate student and now an assistant in the group, made important contributions to heteronuclear filtering[121] and higher-dimensional NMR.[122,123]

Space does not permit me to give due credit to the achievements of all the postdoctoral fellows and graduate students who joined the group to work on structure determinations. In addition to the new biological insights gained from their work, their interactions with those involved in techniques development have been a vital element in the evolution of the methods used. I can only hope that this fruitful and exciting interplay of biological, biomedical, NMR technical and theoretical interests will also continue in the future.

REFERENCES

1. M. Saunders, A. Wishnia, and J. G. Kirkwood, *J. Am. Chem. Soc.*, 1957, **79**, 3289.
2. O. Jardetzky and C. D. Jardetzky, *J. Am. Chem. Soc.*, 1957, **79**, 5322.
3. A. Kowalsky, *J. Biol. Chem.*, 1962, **237**, 1807.
4. A. Kowalsky, *Biochemistry*, 1965, **4**, 2382.
5. A. Mandel, *Proc. Nat. Acad. Sci. USA*, 1964, **52**, 736.
6. J. H. Bradbury and H. A. Scheraga, *J. Am. Chem. Soc.*, 1966, **88**, 4240.
7. D. H. Meadows, J. L. Markley, J. S. Cohen, and O. Jardetzky, *Proc. Natl. Acad. Sci. USA*, 1967, **58**, 1307.
8. C. C. McDonald and W. D. Phillips, *J. Am. Chem. Soc.*, 1967, **89**, 6332.
9. K. Wüthrich, H. Loeliger, and S. Fallab, *Experientia*, 1964, **20**, 599.
10. K. Wüthrich, *Helv. Chim. Acta*, 1965, **48**, 1012.
11. K. Wüthrich and R. E. Connick, *Inorg. Chem.*, 1968, **7**, 1377.
12. K. Wüthrich, *Proc. Natl. Acad. Sci. USA*, 1969, **63**, 1071.
13. K. Wüthrich, S. Meiboom, and L. C. Snyder, *J. Chem. Phys.*, 1970, **52**, 230.
14. R. G. Shulman, S. Ogawa, K. Wüthrich, T. Yamane, J. Peisach, and W. E. Blumberg, *Science*, 1969, **165**, 251.
15. K. Wüthrich, *Struct. Bonding (Berlin)*, 1970, **8**, 53.
16. K. Wüthrich and R. Baumann, *Helv. Chim. Acta*, 1974, **57**, 336.
17. K. Wüthrich, J. Hochmann, R. M. Keller, G. Wagner, M. Brunori, and C. Giacometti, *J. Magn. Reson.*, 1975, **19**, 111.
18. K. Wüthrich, A. Tun-Kyi, and R. Schwyzer, *FEBS Lett.*, 1972, **25**, 104.
19. C. Grathwohl and K. Wüthrich, *J. Magn. Reson.*, 1974, **13**, 217.
20. R. M. Keller, K. Wüthrich, and P. G. Debrunner, *Proc. Natl. Acad. Sci. USA*, 1972, **69**, 2073.
21. K. Wüthrich, R. M. Keller, M. Brunori, G. Giacometti, R. Huber, and H. Formanek, *FEBS Lett.*, 1972, **21**, 63.
22. R. M. Keller and K. Wüthrich, *Biochim. Biophys. Acta*, 1972, **285**, 326.
23. A. Masson and K. Wüthrich, *FEBS Lett.*, 1973, **31**, 114.
24. K. Wüthrich and G. Wagner, *FEBS Lett.*, 1975, **50**, 265.
25. R. Hetzel, K. Wüthrich, J. Deisenhofer, and R. Huber, *Biophys. Struct. Mech.*, 1976, **2**, 159.
26. A. DeMarco and K. Wüthrich, *J. Magn. Reson.*, 1976, **24**, 201.
27. K. Wüthrich and A. DeMarco, *Helv. Chim. Acta*, 1976, **59**, 2228.
28. C. Grathwohl and K. Wüthrich, *Biopolymers*, 1976, **15**, 2043.
29. K. Wüthrich, *NMR in Biological Research: Peptides and Proteins*, North-Holland, Amsterdam, 1976.
30. A. Bundi, C. Grathwohl, J. Hochmann, R. M. Keller, G. Wagner, and K. Wüthrich, *J. Magn. Reson.*, 1975, **18**, 191.
31. R. Richarz and K. Wüthrich, *Biopolymers*, 1978, **17**, 2133.
32. A. Bundi and K. Wüthrich, *Biopolymers*, 1979, **18**, 285.
33. A. Bundi and K. Wüthrich, *Biopolymers*, 1979, **18**, 299.
34. A. DeMarco, M. Llinás, and K. Wüthrich, *Biopolymers*, 1978, **17**, 617.
35. A. DeMarco, M. Llinás, and K. Wüthrich, *Biopolymers*, 1978, **17**, 637.
36. A. DeMarco, M. Llinás, and K. Wüthrich, *Biopolymers*, 1978, **17**, 2727.
37. J. H. Noggle and R. E. Schirmer, *The Nuclear Overhauser Effect*, Academic Press, New York, 1971, p. IX.
38. A. Kalk and H. J. C. Berendsen, *J. Magn. Reson.*, 1976, **24**, 343.
39. R. M. Keller and K. Wüthrich, *Biochim. Biophys. Acta*, 1978, **533**, 195.
40. R. M. Keller and K. Wüthrich, *Biochem. Biophys. Res. Commun.*, 1978, **83**, 1132.
41. H. Senn, R. M. Keller, and K. Wüthrich, *Biochem. Biophys. Res. Commun.*, 1980, **92**, 1362.
42. H. Senn and K. Wüthrich, *Q. Rev. Biophys.*, 1985, **18**, 111.
43. R. Richarz and K. Wüthrich, *J. Magn. Reson.*, 1978, **30**, 147.
44. S. L. Gordon and K. Wüthrich, *J. Am. Chem. Soc.*, 1978, **100**, 7094.

45. G. Wagner and K. Wüthrich, *J. Magn. Reson.*, 1979, **33**, 675.
46. A. Dubs, G. Wagner, and K. Wüthrich, *Biochim. Biophys. Acta*, 1979, **577**, 177.
47. R. M. Keller and K. Wüthrich, in *Biological Magnetic Resonance*, eds. L. J. Berliner and J. Reuben, Plenum Press, New York, 1981, Vol. 3, pp. 1–52.
48. H. Senn, M. Billeter, and K. Wüthrich, *Eur. Biophys. J.*, 1984, **11**, 3.
49. R. M. Keller and K. Wüthrich, *Biochim. Biophys. Acta*, 1980, **621**, 204.
50. K. Wüthrich, G. Wagner, R. Richarz, and S. J. Perkins, *Biochemistry*, 1978, **17**, 2253.
51. R. Richarz and K. Wüthrich, *Biochemistry*, 1978, **17**, 2263.
52. K. Nagayama and K. Wüthrich, *Eur. J. Biochem.*, 1981, **114**, 365.
53. G. Wagner, Anil Kumar, and K. Wüthrich, *Eur. J. Biochem.*, 1981, **114**, 375.
54. K. Wüthrich, G. Wider, G. Wagner, and W. Braun, *J. Mol. Biol.*, 1982, **155**, 311.
55. M. Billeter, W. Braun, and K. Wüthrich, *J. Mol. Biol.*, 1982, **155**, 321.
56. G. Wagner and K. Wüthrich, *J. Mol. Biol.*, 1982, **155**, 347.
57. G. Wider, K. H. Lee, and K. Wüthrich, *J. Mol. Biol.*, 1982, **155**, 367.
58. E. R. P. Zuiderweg, R. Kaptein, and K. Wüthrich, *Eur. J. Biochem.*, 1983, **137**, 279.
59. E. R. P. Zuiderweg, R. Kaptein, and K. Wüthrich, *Proc. Natl. Acad. Sci. USA*, 1983, **80**, 5837.
60. P. Štrop, G. Wider, and K. Wüthrich, *J. Mol. Biol.*, 1983, **166**, 641.
61. G. Wagner, D. Neuhaus, E. Wörgötter, M. Vašák, J. H. R. Kägi, and K. Wüthrich, *Eur. J. Biochem.*, 1986, **157**, 275.
62. D. Neuhaus, G. Wagner, M. Vašák, J. H. R. Kägi, and K. Wüthrich, *Eur. J. Biochem.*, 1984, **143**, 659.
63. K. Wüthrich, C. Spitzfaden, K. Memmert, H. Widmer, and G. Wider, *FEBS Lett.*, 1991, **285**, 237.
64. D. Neri, G. Wider, and K. Wüthrich, *Proc. Natl. Acad. Sci. USA*, 1992, **89**, 4397.
65. H. Senn, B. Werner, B. A. Messerle, C. Weber, R. Traber, and K. Wüthrich, *FEBS Lett.*, 1989, **249**, 113.
66. C. Eccles, P. Güntert, M. Billeter, and K. Wüthrich, *J. Biomol. NMR*, 1991, **1**, 111.
67. K. Wüthrich, M. Billeter, and W. Braun, *J. Mol. Biol.*, 1984, **180**, 715.
68. A. Pardi, M. Billeter, and K. Wüthrich, *J. Mol. Biol.*, 1984, **180**, 741.
69. K. Wüthrich, *NMR of Proteins and Nucleic Acids*, Wiley, New York, 1986.
70. J. Kallen, C. Spitzfaden, M. G. M. Zurini, G. Wider, H. Widmer, K. Wüthrich, and M. D. Walkinshaw, *Nature (London)*, 1991, **353**, 276.
71. M. Billeter, M. Engeli, and K. Wüthrich, *J. Mol. Graphics*, 1985, **3**, 79; 97.
72. E. R. P. Zuiderweg, M. Billeter, R. Boelens, R. M. Scheek, K. Wüthrich, and R. Kaptein, *FEBS Lett.*, 1984, **174**, 243.
73. W. Braun, C. Bösch, L. R. Brown, N. Gō, and K. Wüthrich, *Biochim. Biophys. Acta*, 1981, **667**, 377.
74. W. Braun, G. Wider, K. H. Lee, and K. Wüthrich, *J. Mol. Biol.*, 1983, **169**, 921.
75. K. Wüthrich, M. Billeter, and W. Braun, *J. Mol. Biol.*, 1983, **169**, 949.
76. T. F. Havel and K. Wüthrich, *Bull. Math. Biol.*, 1984, **46**, 673.
77. T. F. Havel and K. Wüthrich, *J. Mol. Biol.*, 1985, **182**, 281.
78. M. P. Williamson, T. F. Havel, and K. Wüthrich, *J. Mol. Biol.*, 1985, **182**, 295.
79. A. D. Kline, W. Braun, and K. Wüthrich, *J. Mol. Biol.*, 1986, **189**, 377.
80. A. D. Kline, W. Braun, and K. Wüthrich, *J. Mol. Biol.*, 1988, **204**, 675.
81. A. Arseniev, P. Schultze, E. Wörgötter, W. Braun, G. Wagner, M. Vašák, J. H. R. Kägi, and K. Wüthrich, *J. Mol. Biol.*, 1988, **201**, 637.
82. G. Wagner, W. Braun, T. F. Havel, T. Schaumann, N. Gō, and K. Wüthrich, *J. Mol. Biol.*, 1987, **196**, 611.
83. P. Güntert, W. Braun, M. Billeter, and K. Wüthrich, *J. Am. Chem. Soc.*, 1989, **111**, 3997.
84. P. Güntert, W. Braun, and K. Wüthrich, *J. Mol. Biol.*, 1991, **217**, 517.
85. P. Güntert and K. Wüthrich, *J. Biomol. NMR*, 1991, **1**, 447.
86. J. E. Mertz, P. Güntert, K. Wüthrich, and W. Braun, *J. Biomol. NMR*, 1991, **1**, 257.
87. M. Billeter, Y. Q. Qian, G. Otting, M. Müller, W. J. Gehring, and K. Wüthrich, *J. Mol. Biol.*, 1993, **234**, 1084.
88. M. Billeter, T. Schaumann, W. Braun, and K. Wüthrich, *Biopolymers*, 1990, **29**, 695.
89. M. P. Williamson, D. Marion, and K. Wüthrich, *J. Mol. Biol.*, 1984, **173**, 341.
90. A. D. Kline and K. Wüthrich, *J. Mol. Biol.*, 1985, **183**, 503.
91. J. W. Pflugrath, G. Wiegand, R. Huber, and L. Vértesy, *J. Mol. Biol.*, 1986, **189**, 383.
92. M. Billeter, A. D. Kline, W. Braun, R. Huber, and K. Wüthrich, *J. Mol. Biol.*, 1989, **206**, 677.
93. W. Braun, O. Epp, K. Wüthrich, and R. Huber, *J. Mol. Biol.*, 1989, **206**, 669.
94. W. Braun, G. Wagner, E. Wörgötter, M. Vašák, J. H. R. Kägi, and K. Wüthrich, *J. Mol. Biol.*, 1986, **187**, 125.
95. W. Braun, M. Vašák, A. H. Robbins, C. D. Stout, G. Wagner, J. H. R. Kägi, and K. Wüthrich, *Proc. Natl. Acad. Sci. USA*, 1992, **89**, 10 124.
96. W. A. Hendrickson and K. Wüthrich (eds), *Macromolecular Structures 1993*, Current Biology, London, UK, 1993.
97. Anil Kumar, R. R. Ernst, and K. Wüthrich, *Biochem. Biophys. Res. Commun.*, 1980, **95**, 1.
98. G. Feher, *Trends Biochem. Sci.*, 1978, **3**, N111.
99. Anil Kumar, G. Wagner, R. R. Ernst, and K. Wüthrich, *Biochem, Biophys. Res. Commun.*, 1980, **96**, 1156.
100. Anil Kumar, G. Wagner, R. R. Ernst, and K. Wüthrich, *J. Am. Chem. Soc.*, 1981, **103**, 3654.
101. K. Nagayama, K. Wüthrich, P. Bachmann, and R. R. Ernst, *Biochem. Biophys. Res. Commun.*, 1977, **78**, 99.
102. G. Wagner and K. Wüthrich, *J. Mol. Biol.*, 1982, **160**, 343.
103. R. Richarz, K. Nagayama, and K. Wüthrich, *Biochemistry*, 1980, **19**, 5189.
104. K. Wüthrich and G. Wagner, *Trends Biochem. Sci.*, 1984, **9**, 152.
105. H. Roder, G. Wagner, and K. Wüthrich, *Biochemistry*, 1985, **24**, 7396.
106. H. Roder and K. Wüthrich, *Proteins*, 1986, **1**, 34.
107. A. Pardi, R. Walker, H. Rapoport, G. Wider, and K. Wüthrich, *J. Am. Chem. Soc.*, 1983, **105**, 1652.
108. W. Leupin, W. J. Chazin, S. Hyberts, W. A. Denny, and K. Wüthrich, *Biochemistry*, 1986, **25**, 5902.
109. G. T. Montelione, K. Wüthrich, E. C. Nice, A. W. Burgess, and H. A. Scheraga, *Proc. Natl. Acad. Sci. USA*, 1987, **84**, 5226.
110. H. Haruyama and K. Wüthrich, *Biochemistry*, 1989, **28**, 4301.
111. Y. Q. Qian, M. Billeter, G. Otting, M. Müller, W. J. Gehring, and K. Wüthrich, *Cell*, 1989, **59**, 573.
112. C. Weber, G. Wider, B. von Freyberg, R. Traber, W. Braun, H. Widmer, and K. Wüthrich, *Biochemistry*, 1991, **30**, 6563.
113. J. H. Bushweller, M. Billeter, A. Holmgren, and K. Wüthrich, *J. Mol. Biol.*, 1994, **235**, 1585.
114. L. R. Brown, S. Mronga, R. A. Bradshaw, C. Ortenzi, P. Luporini, and K. Wüthrich, *J. Mol. Biol.*, 1993, **231**, 800.

115. M. Billeter, Y. Q. Qian, G. Otting, M. Müller, W. Gehring, and K. Wüthrich, *J. Mol. Biol.*, 1993, **234**, 1084.
116. T. Szyperski, S. Scheek, J. Johansson, G. Assmann, U. Seedorf, and K. Wüthrich, *FEBS Lett.*, 1993, **335**, 18.
117. G. Otting, M. Billeter, K. Wüthrich, H. J. Roth, C. Leumann, and A. Eschenmoser, *Helv. Chim. Acta*, 1993, **76**, 2701.
118. K. Wüthrich, *Current Opinion Struct. Biol.*, 1994, **4**, 93.
119. G. Otting and K. Wüthrich, *J. Am. Chem. Soc.*, 1989, **111**, 1871.
120. G. Otting, E. Liepinsh, and K. Wüthrich, *Science*, 1991, **254**, 974.
121. G. Otting and K. Wüthrich, *Q. Rev. Biophys.*, 1990, **23**, 39.
122. B. A. Messerle, G. Wider, G. Otting, C. Weber, and K. Wüthrich, *J. Magn. Reson.*, 1989, **85**, 608.
123. T. Szyperski, G. Wider, J. H. Bushweller, and K. Wüthrich, *J. Am. Chem. Soc.*, 1993, **115**, 9307.

Acknowledgements

The research projects mentioned in this article were generously supported by the ETH Zürich, the Schweizerischer Nationalfonds, the Kommission zur Förderung der wissenschaftlichen Forschung, and Bruker-Spectrospin AG. I wish to thank Mrs. E Huber and Mr. R. Marani for the careful processing of the manuscript. While writing this article I was a Fairchild Distinguished Scholar at the California Institute of Technology, and I would like to thank the Division of Biology and the Beckman Institute for their gracious hospitality.

Biographical Sketch

Kurt Wüthrich, *b* 1938. Licentiat, 1962, Physics, Mathematics, Chemistry, University of Bern; Eidgenössisches Sportlehrerdiplom, 1964, University of Basel, Ph.D., 1964, Inorganic Chemistry (Prof. S. Fallab) University of Basel. Postdoctoral work, University of Basel (Prof. S. Fallab), University of California, Berkeley (Prof. R. E. Connick), Bell Telephone Laboratories, Murray Hill, NJ (Dr. R.G. Shulman). Since 1969 at ETH Zürich, currently Professor of Biophysics and Chairman of the Department of Biology. Approx. 500 publications. Research specialties: NMR structure determination of biological macromolecules, drug design, and protein engineering.

Yannoni, Costantino S.: A Magnetic Resonance Potpourri

Costantino S. Yannoni
IBM Almaden Research Center, San Jose, CA, USA

PROLOGUE

Although I have devoted much time and energy to NMR, the rewards of working in the field have far exceeded the expectations I had 35 years ago as a graduate student, particularly because I did not expect to make so many good friends or to become part of a magnetic resonance 'family'. So I want to start with an expression of gratitude to my colleagues, too numerous to mention all individually, who have taught me to do science and to grow personally over the years. In these respects, NMR encompasses a special community and I feel privileged to be part of it. And I would like to dedicate this narrative to Raffaela Yannoni for her unstinting love, encouragement, and support over the years.

GRADUATE WORK AT COLUMBIA (1960–66): FAILED AT SOLIDS, BAILED OUT BY LIQUID CRYSTALS

After a brief flirtation with physical organic chemistry, I chose to do my thesis in NMR with Ben Dailey. Rich Bersohn, who had just done calculations of the deuteron quadrupole coupling constant, suggested a measurement in perdeuteronaphthalene and Ben thought this would be a good thesis project. This required labeling the material and building a very low level fixed-frequency marginal oscillator to work with a 1.4 T electromagnet. In the early 1960s, Dailey students were doing high-resolution work without a field/frequency lock, using high-wattage light bulbs immersed in a tank of flowing tap water to control the magnet temperature, while nursing the magnet to high homogeneity over the course of weeks. So when I came along and twirled the fine-current dial to search for resonance over field ranges 100-times larger than they used, all hell would break loose. After building the oscillator and growing single crystals of perdeuteronaphthalene, I would come in first thing in the morning, see two lines separated by about the right splitting, and get nothing for the rest of the day. It turned out T_1 is in the order of hours and since I didn't know much about relaxation, I went to talk to some physicists. Both Sven Hartmann, who had just come to Columbia, and Al Redfield, then at IBM Watson Lab in New York City, suggested that I look in the dispersion mode, which should be less sensitive to saturation.[1] The marginal oscillator could only detect in absorption, so I took advantage of Bob Shulman's generous offer to use his wideline rig at Bell Labs. Despite all this help, by 1962 I had not obtained 'textbook' spectra, and, being somewhat naïve and unwilling to make something of the spectra I did have, gave up the project. Ben, who was very patient with me, rescued me in 1963 when he came back from a meeting with the exciting news that Saupe and Englert had observed high-resolution spectra of benzene oriented in a liquid crystal solvent.[2] We were able to measure order parameters and ^{1}H and ^{19}F shift anisotropies in several symmetrical small molecules.[3] In 1965, I first heard about cyclobutadiene (C_4H_4), a 'square' of C–H bonds and one of the 'holy grails' of reactive chemical intermediates. Roland Pettit at Texas had just succeeded in synthesizing the first stable complex of this fascinating molecule,[4] and he kindly gave us some of the material. We were able to get a spectrum of the oriented iron tricarbonyl complex and determine that, on average, the protons were in a square configuration.[5] Since that time, a theme for much of my research has been the development of methods for studying the structure of reactive intermediates by NMR.

UNION CARBIDE AND 'TICKLING' EXPERIMENTS (1966–67)

In 1966, I went to work for Union Carbide at the Research Institute in Tarrytown, NY, where I had the good fortune to work for Earl Whipple, a whiz at analytical high-resolution NMR, who had the idea of using the spin 'tickling' method[6] to measure the ^{13}C chemical shift anisotropy in methyl iodide.[7] Earl also suggested looking at the proton NMR spectrum of the fluxional molecule, bullvalene, oriented in a liquid crystal solvent.[8] The bullvalene experiment gave me my first taste for the intimate relationship between structure and dynamics that pervades much of physical organic chemistry.

IBM YORKTOWN (1967): TRYING NMR OF REACTIVE INTERMEDIATES—BOOM!!

I was discouraged by the ambivalent attitude toward research at Carbide, so in 1967, I went to work at the IBM T.J. Watson Research Center in Yorktown Heights, NY. The job situation at this time was such that one could move without even changing residence! IBM had bought a Varian HA-60-IL, a workhorse machine that I used to start some methods development, a part of my work which I enjoy to this day. During this time, I was exposed to a lot of photo- and reactive intermediate chemistry by my colleagues at IBM; this motivated me to think more about applying the diagnostic power of NMR to metastable intermediates. The opportunity came when Stephan Boué, a postdoc doing photochemistry, came into my office one day and said he had an idea of how to make tetrahedrane.

Tetrahedrane (another C_4H_4 species) is a tetrahedron of C–H bonds and is a highly strained reactive species of great theoretical interest that has yet to be isolated. I rigged up the HA-60 to do measurements at −150 °C using propane as a solvent. This was very exciting until we blew up Heinrich Hunziker's homebuilt quartz lamp (he was my boss!), poking out every corner of his vacuum line during the low-temperature photolysis of the vinylacetylene precursor—more about that later. During this time, I was introduced to the synergism between chemical reactions and magnetic resonance

by Joachim Bargon, who joined IBM in 1969, shortly after his discovery of the CIDNP phenomenon.[9]

DOUBLE RESONANCE IN THE ROTATING FRAME (1970): THE BLEICH/REDFIELD SCHEME

While trying some liquid crystal work on one of the first FT machines then being built at the IBM Watson Laboratory in New York City by Al Redfield and Raj Gupta,[10] I met Al's student, Herman Bleich, who was working on a technique to do high-resolution NMR of rare spins in solids using indirect detection via the abundant spins.[11] Although I understood little of the spin dynamics underlying the Bleich–Redfield experiment, I did feel that a sensitive, high-resolution solid state NMR technique like this was necessary for doing matrix isolation NMR and continued working on it. Since Bleich was finishing his Ph.D. and wanted to go into the bio area, as did Redfield, I inherited their apparatus and eventually took it to San Jose.

HIGH-RESOLUTION NMR OF RARE SPINS IN SOLIDS (1971): THE FIRST ^{13}C RESULTS

With Bleich's tutoring, and much reading of spin-dynamics papers, I was able to obtain the first high-resolution ^{13}C spectrum of an organic molecule in the solid state, and to measure the chemical shift anisotropy for benzene at 233 K.[12] Shortly after this, the MIT group—Alex Pines, Mike Gibby, and John Waugh—published their elegant cross polarization method, which uses direct detection of the rare-spin FID coupled with time averaging, a mode of operation that is simpler and more familiar to chemists.[13] I could achieve only limited success with the ingenious method that Redfield and Bleich had devised, even though the sensitivity may well be greater than the CP technique for rare spins with a low gyromagnetic ratio or for extremely dilute spins.[14] It was at this time that I got to know the rest of the MIT group, including Michael Mehring and Bob Griffin. I especially enjoyed long walks with Won-Kyu Rhim, who tutored me in the subtleties of spin dynamics. I also met Dave VanderHart, who is one of the 'lone rangers' of solid state NMR and who, with his probing questions, has always forced me to think deeply about spin physics. All have been close friends as well as professional colleagues for many years.

IBM SAN JOSE (1971)

I was transferred by IBM to San Jose in 1971, and within a few months Ray Kendrick, a talented and creative research associate, started to work with me and has remained a friend and indispensable contributor to our research for the last 24 years. Ray has continually generated novel ideas for NMR experiments drawn from his experience as a radio amateur and television transmitter engineer. In 1974, Wiebren Veeman spent the first part of a year stay hunting down sources of noise in the apparatus (including a probe with *plastic* sides) that I was using (against Ray's advice) for the Bleich–Redfield experiment. Subsequently, Wiebren designed and did experiments demonstrating a nifty high-field ^{35}Cl–^{1}H cross polarization technique.[15] In addition to being highly innovative, he showed me that the effect of external fields on the motion of nuclear spins can be calculated as well as measured.

MODULATION-INDUCED DIPOLAR LINE NARROWING (1975)

In 1975, Hans-Martin Vieth spent a year at IBM and showed us how to do our first FT experiments and to signal average using a relatively primitive set-up: a transient digitizer, a computer of average transients ('CAT'), and a spectrum analyzer. We also achieved considerable narrowing of dipolar lines in a rotating frame experiment that used strong modulation fields and Hans-Martin did tour-de-force calculations which explained the rather complex spin dynamics.[16] He has a very strong background in the fundamentals of quantum mechanics and measurement theory, and keeps me honest when I periodically try to violate the laws of physics.

VARIABLE TEMPERATURE MAGIC ANGLE SPINNING (1977)

In 1977, Colin Fyfe visited IBM on a sabbatical and got me and my colleague Jim Lyerla excited about doing low-temperature applications of the famous CPMAS experiment done by Ed Stejskal and Jake Schaefer.[17] The motivation was to obtain low-temperature high-resolution spectra of molecules that undergo exchange processes too rapid to study at the higher temperatures accessible with solution NMR. In collaboration with Horst Mossbrugger, a premier IBM model maker, Colin designed and built a magic angle spinner that worked at low temperatures.[18] This led to many late nights, fraught with frustration at trying 'get the rotor going', but also led to many exciting results.[19] Since he has a strong background in solid state chemistry, Colin showed me the connections between NMR and other methods for characterizing solids, e.g. diffraction, and made the importance of doing applications very clear. In 1983, Hans Limbach visited for a year and initiated a very successful program in hydrogen-bond dynamics using variable temperature ^{15}N MAS spectroscopy,[20] all the while schooling me in the subtleties of dynamic NMR spectroscopy. We had also developed a method for loading and studying frozen liquids using CP MAS spectroscopy, and my colleague Bob Miller and Volker Macho, from Berlin, discovered that the (formal) degeneracy of the Cope rearrangement in semibullvalene is lifted by lattice effects.[21]

FINALLY, MATRIX ISOLATION NMR (1980): ^{13}C SPECTRA OF REACTIVE CARBONIUM IONS IN THE SOLID STATE AND RESOLUTION OF THE NORBORNYL CATION CONTROVERSY

In 1979, I contacted Phil Myhre, a talented physical organic chemist teaching at Harvey Mudd College, who became

interested in my hope motivated by discussions with Colin, to use low-temperature CP MAS to study the structure of carbonium ions. These are molecular ions which are not only thermally unstable, but also rearrange rapidly (on the NMR timescale) so that ^{13}C studies at all but the lowest temperatures yield spectra with average chemical shifts from carbons that occupy more than one molecular site during a measurement. Therefore, in order to obtain unambiguous chemical shift, i.e. structural, data, it is crucial to 'freeze out' these rearrangements by doing experiments at sufficiently low temperatures, often too low for solution NMR work. During a summer visit of only ten weeks, with the help of Carl Rein, a talented model maker, and Alex Kalbin, our glassblower, Phil designed and built a 'poor-man's molecular beam apparatus' to synthesize and load into a magic angle rotor reactive carbocations that would never see a temperature above 100 K.[22] In short order, he started to define the key problems we worked on, and any 'chemical' respectability in our research is due to Phil. We were able to obtain well-resolved ^{13}C spectra and concomitant structural information for the *s*-butyl cation, one of the most elusive carbonium ions.[22] Again, with the help of Volker Macho, we were able to obtain spectra of the norbornyl cation at 5 K[23] using a probe designed and built by Ray Kendrick for triple resonance (decouple both ^{1}H and ^{19}F while observing ^{13}C). It is generally acknowledged that this result gives a very direct solution to the 30 year controversy over the structure of the norbornyl cation.[24] The protocol that was developed for low-temperature MAS of carbonium ions also proved useful in obtaining the low-temperature ^{13}C CP MAS spectrum of methylketene, a reactive molecule produced by low-temperature photolysis of diazopropanone.[25] This experiment, done by Peter Reisenauer showed that it is indeed possible to do matrix isolation NMR spectroscopy of photolytically generated reactive species. Peter also explained that the explosion we had during our abortive tetrahedrane 'synthesis' was the result of a radical chain reaction; he knew this because the same thing had happened in his lab.

ACCURATE MEASUREMENT OF BOND LENGTHS BY NMR (1981): NUTATION NMR SPECTROSCOPY

After reading Redfield's famous paper on spin temperature in the rotating frame and rotary saturation,[1] I understood that a strong resonant field would selectively eliminate chemical shift effects while preserving dipolar coupling, which is inversely proportional to the third power of the internuclear distance. Therefore, I thought it might be possible to use this method to determine the geometry of reactive intermediates by accurately measuring bond lengths. Such an approach would be more general than diffraction techniques since reactive species are usually generated and isolated in a highly disordered matrix. Although I had initial success using rotary saturation,[1] a CW rotating frame experiment, Veeman suggested[26] that it might be possible to use transient nutations.[27] Since I felt that it was important to have a 'simple' method, I decided to use a train of single-phase rf pulses to produce a transient nutation. Fourier transform of the nutation signal would yield a 'nutation NMR' spectrum consisting of a Pake doublet[28] which would then yield the desired dipolar splitting and corresponding bond length. Although an approach like this is conceptually simple since there are no phase shifts, the instrumental price is high and was paid largely through the efforts of Don Horne, a physicist at IBM who does beyond-state-of-the-art electronics and continues to be the final word for us on our most challenging electronics projects. In 1981 we made our first successful measurement of a carbon–carbon bond length[29] and eventually increased the accuracy of the measurement to 1%.[30] At that time, much research was being done at IBM San Jose on organic conductors. Polyacetylene was one of the most interesting of these since it had been predicted that the ground state of the all-*trans* isomer involved soliton excitations.[31] The notion of alternating bond lengths was a consequence of this hypothesis and it seemed like a 'natural' to test this idea using nutation NMR. My colleague Tom Clarke made the appropriate doubly-^{13}C labeled material and we observed two Pake doublets, the first direct proof for bond alternation in *trans*-polyacetylene.[32] In collaboration with Tom Katz at Columbia, we used dipolar spectra like this to probe the mechanism by which acetylene is polymerized.[33] Our goal for developing nutation NMR to measure reactive-molecule geometry was also reached with a measurement of the carbon–carbon bond lengths in the *t*-butyl cation.[34] So, solid state NMR methods had been used to solve key problems in fields as disparate as solid state physics and physical organic chemistry. In 1988, Mario Engelsberg, a Brazilian physicist with a very strong resonance background, spent a sabbatical and calculated and confirmed experimentally that scaling of the dipolar splitting in a Carr–Purcell sequence depends linearly on the rf duty factor.[35] This result made it possible to distinguish between bonds that are much closer in length than is possible by nutation NMR since the latter scales dipolar splittings by one-half while scaling in the Carr–Purcell sequence can be minimized by reducing the rf duty factor. Shortly thereafter, this result proved to be critical since it enabled us to make the first measurement of the molecular geometry of C_{60}.[36]

DYNAMIC NUCLEAR POLARIZATION (1984)

In 1979, I met Robert Wind, then at Delft, who spent two summers in my laboratory, during which he came up with a number of highly innovative ideas, one of which was to apply modulation-induced line narrowing[16] to do one of the first solids imaging experiments.[37] He also had the idea of a nuclear solid effect which we demonstrated during one of his stays.[38] I was motivated by Robert's success with DNP to use it selectively to obtain NMR spectra of molecules at the surface of metal particles. Unfortunately, DNP did not fare well in my hands; however, in the process of setting up a program, I had the opportunity to interact with a number of first-rate electron spin resonators like David Singel and Günter Maresch. David designed our DNP probe/spectrometer[39] and suggested measuring the chemical shift in a conductor by suppressing the Knight shift via saturation of the ESR, an experiment done for ^{13}C in an organic conductor by Waldemar Stöcklein, a postdoc from Bayreuth.[40] A similar experiment was done independently by Robert Wind, in collaboration with Michael Mehring.[41] Günter not only developed our low-temperature

DNP capability but also did experiments on interfaces[42] and DNP spin dynamics.[43]

MAGIC ANGLE SPINNING AT LIQUID HELIUM TEMPERATURES (1986)

In 1986, Harald Seidel, who came from Stuttgart with a strong background in ESR and microwave instrumentation, and Walt Baier, a highly-skilled model maker, were designing and building a low-temperature DNP–MAS probe. In order to minimize interference with the microwaves, I had decided to use a spinner design[44] in which only the glass tube and sample would be in the coil/cavity region. While bench-testing the low-temperature spinning for this probe, we noticed that it should be possible to lower the sample temperature without limit since, unlike a probe we had previously used (with difficulty) for spinning at temperatures below 77 K,[45] the cooling and spinning gas functions were separated. This idea had already been used by Kurt Zilm at temperatures close to 77 K.[46] However, since we were interested in magic angle spinning at temperatures considerably below 77 K, it was necessary to use helium as a spinning/bearing gas. It is well known that high-power decoupling in a helium atmosphere causes gas discharge, preventing detection of the NMR signal.[47] We solved this ubiquitous age-old problem by using a remotely tuned probe designed by Ray Kendrick, and careful construction practice.[48] Our low-temperature MAS probe has worked well at temperatures down to 5 K[48] and has been used to determine the elusive structure of some carbonium ions.[49]

COHERENT RAMAN BEATS IN MAGNETIC RESONANCE (1986)

While collaborating with my colleagues Bob Shelby and Roger Macfarlane to do rf–optical double resonance experiments,[50] I became aware that Dick Brewer at our lab had observed some optical coherence phenomena that he and Erwin Hahn had analyzed and called coherent Raman beats.[51] It seemed that it might be possible to borrow this idea from optics and in 1985, in collaboration with Po Wang, then at IBM, I used coherent Raman beat detection to do a multiple quantum NMR experiment in which the evolution, mixing, and detection periods were combined, with potentially large savings in time.[52] I was also trying to use the same approach to detect electron spin echo envelope modulation (ESEEM),[53] but was not successful until I teamed up with Mike Bowman, then at Argonne National Laboratory, who carried out some beautiful experiments.[54] He and Mel Klein have since refined this method to the degree that it seems to hold promise as a sensitive method for detecting highly resolved nuclear sublevel coherences in paramagnetic systems.[55]

BUCKMINSTERFULLERENE (1990): A DREAM FOR NMR SPECTROSCOPISTS

An all-carbon molecule that is 'round' captured the imagination of the scientific (and even layman's) world so that in 1990, when Don Bethune at our lab started a program to study C_{60}, I was intrigued by the possibility of using solid state NMR to probe the dynamics of C_{60}, which I thought would be very 'slippery' in the solid state. As a result of that interest, and an exciting collaboration over a period of only a little more than a year, Don, Bob Johnson, Jesse Salem, Mattanjah deVries, and I did the first solid state magnetic resonance experiments on fullerenes and metallofullerenes,[56] including freezing out the reorientation of C_{60}.[57] We also made the first measurement of C_{60} geometry using the resolving power of the Carr–Purcell method to observe two Pake doublets from bonds of nearly equal (1.40 Å and 1.45 Å) length.[36] Patrick Bernier, from CNRS in Montpelier, who visited IBM in late 1990, collaborated on the C_{60} bond-length measurements,[36] while Harry Dorn from Virginia Polytechnic Institute was also bitten by the fullerene 'bug' during a sabbatical stay in 1991, and broke significant ground in fullerene separation technology.[58] Both have since developed strong programs in fullerene research.

NEW GROWTH ON THE EVERGREEN (1991): FORCE DETECTION OF MAGNETIC RESONANCE—WILL IT BE POSSIBLE TO DETECT ONE SPIN AT A TIME?

The field of magnetic resonance continues to bring me the excitement of good science and the personal satisfaction of meeting and working with new colleagues. In late 1991, my colleague Dan Rugar, a premier force microscopist, told me that John Sidles, who is a medical physicist from the University of Washington, had the idea of detecting magnetic resonance using force, with the incredible potential for *imaging a single nuclear spin*!![59] Although I got very excited, I was too involved in fullerene work to be of much help, but did suggest doing ESR, so Dan went off and did the first force detection of magnetic resonance.[60] We have recently collaborated on an experiment that demonstrates the remarkable potential of force detection of NMR, observing 1.6×10^{13} spins in a single shot at room temperature in a field of 2.4 T.[61] This result, which corroborated Dan's theoretical expectations for the performance of the microscope, has encouraged us to continue a program to develop a magnetic resonance force microscope capable of imaging one nucleus at a time. A workable method with this capability could become an extraordinarily powerful tool for the determination of molecular structure.

EPILOGUE

I hope it is clear that many of the ideas for experiments that I have done have come from co-workers with backgrounds ranging from synthetic and physical organic chemistry to solid state physics. As a result, part of the magic of NMR for me is that it encompasses such a broad range of disciplines. As one who has said (if I don't admit it, many colleagues will remind me) on many occasions that 'NMR is dead', I now have also to admit that I marvel at this perrenial of science and am optimistic that there will continue to be lots of 'boomlets' and perhaps a few more big 'booms' in new ideas and activity in the years to come.

REFERENCES

1. A. G. Redfield, *Phys. Rev.*, 1955, **98**, 1787.
2. A. Saupe and G. Englert, *Phys. Rev. Lett.*, 1963, **11**, 462.
3. References in C. S. Yannoni, *'Anisotropic Nuclear Magnetic Resonance Interactions in Liquid Crystal Solution'*, Ph.D. Thesis, Columbia University, 1967
4. G. F. Emerson, L. Watts, and R. Pettit, *J. Am. Chem. Soc.*, 1965, **87**, 131.
5. C. S. Yannoni, G. P. Ceasar, and B. P. Dailey, *J. Am. Chem. Soc.*, 1967, **89**, 2833.
6. R. Freeman and W. A. Anderson, *J. Chem. Phys.*, 1962, **37**, 2053.
7. C. S. Yannoni and E. B. Whipple, *J. Chem. Phys.*, 1967, **47**, 2508.
8. C. S. Yannoni, *J. Am. Chem. Soc.*, 1970, **92**, 5237.
9. J. Bargon, H. Fischer, and U. Johnsen, *Z. Naturforsch.*, 1967, **22a**, 1551.
10. A. G. Redfield and R. K. Gupta, *Adv. Magn. Reson.*, 1971, **5**, 82.
11. H. E. Bleich and A. G. Redfield, *J. Chem. Phys.*, 1971, **55**, 5405.
12. C. S. Yannoni and H. E. Bleich, *J. Chem. Phys.*, 1971, **55**, 5406.
13. A. Pines, M. G. Gibby, and J. S. Waugh, *J. Chem. Phys.*, 1972, **56**, 1776.
14. H. E. Bleich and A. G. Redfield, *J. Chem. Phys.*, 1977, **67**, 5040; A. Pines, M. G. Gibby, and J. S. Waugh, *J. Chem. Phys.*, 1973, **59**, 569.
15. W. S. Veeman and C. S. Yannoni, *Chem. Phys. Lett.*, 1975, **32**, 499.
16. C. S. Yannoni and H.-M. Vieth, *Phys. Rev. Lett.*, 1976, **37**, 1230.
17. J. Schaefer and E. O. Stejskal, *J. Am. Chem. Soc.*, 1976, **98**, 1031.
18. C. A. Fyfe, H. Mossbruger, and C. S. Yannoni, *J. Magn. Reson.*, 1979, **36**, 61.
19. J. R. Lyerla, C. S. Yannoni, and C. A. Fyfe, *Acc. Chem. Res.*, 1982, **15**, 208.
20. H. H. Limbach, J. Hennig, R. Kendrick, and C. S. Yannoni, *J. Am. Chem. Soc.*, 1984, **106**, 4059.
21. V. Macho, R. D. Miller, and C. S. Yannoni, *J. Am. Chem. Soc.*, 1983, **105**, 3735.
22. P. C. Myhre and C. S. Yannoni, *J. Am. Chem. Soc.*, 1981, **103**, 230.
23. C. S. Yannoni, V. Macho, and P. C. Myhre, *J. Am. Chem. Soc.*, 1982, **104**, 7380.
24. G. A. Olah, G. K. Surya Prakash, and M. Saunders, *Acc. Chem. Res.*, 1983, **16**, 440; C. Walling, *Acc. Chem. Res.*, 1983, **16**, 448.
25. C. S. Yannoni, H. P. Reisenauer, and G. Maier, *J. Am. Chem. Soc.*, 1983, **105**, 6181.
26. W. S. Veeman, Private communication.
27. H. C. Torrey, *Phys. Rev.*, 1949, **76**, 1059.
28. G. E. Pake, *J. Chem. Phys.*, 1948, **16**, 327.
29. C. S. Yannoni and R. D. Kendrick, *J. Chem. Phys.*, 1981, **74**, 747.
30. D. Horne, R. D. Kendrick, and C. S. Yannoni, *J. Magn. Reson.*, 1983, **52**, 299.
31. W. P. Su, J. R. Schrieffer, and A. J. Heeger, *Phys. Rev. Lett.*, 1979, **42**, 1698.
32. C. S. Yannoni and T. C. Clarke, *Phys. Rev. Lett.*, 1983, **51**, 1191.
33. T. C. Clarke, C. S. Yannoni, and T. J. Katz, *J. Am. Chem. Soc.*, 1983, **105**, 7787; T. J. Katz, S. M. Hacker, R. D. Kendrick, and C. S. Yannoni, *J. Am. Chem. Soc.*, 1985, **107**, 2182.
34. C. S. Yannoni, R. D. Kendrick, P. C. Myhre, D. C. Bebout, and B. L. Petersen, *J. Am. Chem. Soc.*, 1989, **111**, 6440.
35. M. Engelsberg and C. S. Yannoni, *J. Magn. Reson.*, 1990, **88**, 393.
36. C. S. Yannoni, P. P. Bernier, D. S. Bethune, G. Meijer, and J. R. Salem, *J. Am. Chem. Soc.*, 1991, **113**, 3190.
37. R. A. Wind and C. S. Yannoni, *J. Magn. Reson.*, 1979, **36**, 269.
38. R. A. Wind and C. S. Yannoni, *J. Magn. Reson.*, 1986, **72**, 373; 1987, **72**, 108.
39. D. J. Singel, H. Seidel, R. D. Kendrick, and C. S. Yannoni, *J. Magn. Reson.*, 1989, **81**, 145.
40. W. Stöcklein, H. Seidel, D. Singel, R. D. Kendrick, and C. S. Yannoni, *Chem. Phys. Lett.*, 1987, **141**, 277.
41. R. A. Wind, H. Lock, and M. Mehring, *Chem. Phys. Lett.*, 1987, **141**, 283.
42. G. G. Maresch, R. D. Kendrick, C. S. Yannoni, and M. E. Galvin, *Macromolecules*, 1988, **21**, 3523.
43. G. G. Maresch, R. D. Kendrick, and C. S. Yannoni, *J. Magn. Reson.*, 1989, **82**, 41.
44. I. D. Gay, *J. Magn. Reson.*, 1984, **58**, 413.
45. V. Macho, R. Kendrick, and C. S. Yannoni, *J. Magn. Reson.*, 1983, **52**, 450.
46. K. W. Zilm, R. A. Merrill, M. M. Greenberg, and J. A. Berson, *J. Am. Chem. Soc.*, 1987, **109**, 1567.
47. M. Linder, A. Höhener, and R. R. Ernst, *J. Magn. Reson.*, 1979, **35**, 379.
48. A. Hackmann, H. Seidel, R. D. Kendrick, P. C. Myhre, and C. S. Yannoni, *J. Magn. Reson.*, 1988, **79**, 148.
49. P. C. Myhre, G. G. Webb, and C. S. Yannoni, *J. Am. Chem. Soc.*, 1990, **112**, **8991**, 8992.
50. R. M. Shelby, C. S. Yannoni, and R. M. Macfarlane, *Phys. Rev. Lett.*, 1978, **41**, 1739; R. M. Macfarlane, C. S. Yannoni, and R. M. Shelby, *Opt. Commun.*, 1980, **32**, 101.
51. R. G. Brewer and E. L. Hahn, *Phys. Rev.*, 1973, **A8**, 464.
52. C. S. Yannoni, R. D. Kendrick, and P.-K. Wang, *Phys. Rev. Lett.*, 1987, **58**, 345.
53. L. G. Rowan, E. L. Hahn, and W. B. Mims, *Phys. Rev.*, 1965, **A61**, 61.
54. M. K. Bowman, R. J. Massoth, and C. S. Yannoni, *Pulsed Magnetic Resonance: NMR, ESR, and Optics—A Recognition of E. L. Hahn*, ed. D. M. S. Bagguley, Clarendon Press, Oxford, 1992, Chap. 19
55. M. K. Bowman, *Isr. J. Chem.*, 1992, **32**, 339; O. Burghaus and M. P. Klein, *Chem. Phys. Lett.*, accepted for publication.
56. R. D. Johnson, M. S. de Vries, J. Salem, D. S. Bethune, and C. S. Yannoni, *Nature (London)*, 1992, **355**, 239; R. D. Johnson, D. S. Bethune, and C. S. Yannoni, *Acc. Chem. Res.*, 1992, **25**, 169.
57. C. S. Yannoni, R. D. Johnson, G. Meijer, D. S. Bethune, and J. R. Salem, *J. Phys. Chem.*, 1991, **95**, 9.
58. C. S. Yannoni, H. R. Wendt, M. S. de Vries, R. L. Siemens, J. R. Salem, J. Lyerla, R. D. Johnson, M. Hoinkis, M. S. Crowder, C. A. Brown, D. S. Bethune, L. Taylor, D. Nguyen, P. Jedrzejewski, and H. C. Dorn, *Synth. Metals*, 1993, **59**, 279.
59. J. A. Sidles, *Appl. Phys. Lett.*, 1991, **58**, 2854.
60. D. Rugar, C. S. Yannoni, and J. A. Sidles, *Nature (London)*, 1992, **360**, 563.
61. D. Rugar, O. Züger, C. S. Yannoni, S. Hoen, H.-M. Vieth, and R. D. Kendrick, *Science*, 1994, **264**, 1560.

Biographical Sketch

Costantino S. Yannoni. *b* 1935. B.A., 1957, Harvard College, M.A., 1960, Ph.D., 1966, Chemistry, Columbia University, USA. Staff member, Union Carbide Research Institute, Tarrytown, NY; research staff member, IBM Research Division, T.J. Watson Research Center, Yorktown Heights, NY 1967–71; Almaden Research Center, San Jose, CA, 1971–present. Approx. 100 publications. Research specialties/interests: development and application of solid state NMR methods for solving problems involving structure and dynamics in materials, especially organic reactive intermediates; magnetic resonance analogs of coherent optical phenomena; current interest is force detection of magnetic resonance for ultra high-resolution imaging.

Young, Ian R.: EMI's Venture into NMR—An Industrial Saga

Ian R. Young

Hammersmith Hospital, London, UK

EMI began work on magnetic resonance imaging in 1974, simply because the company wanted to be involved in any, and all, modalities with any potential to rival its then burgeoning CT X-ray business. It sought scientists to work on magnetic resonance imaging from amongst its employees on the basis that if someone had some experience in magnetics of any kind, he (or she) must know sufficient about nuclear magnetic resonance. Thus Hugh Clow and W. S. Percival, who were those first involved, had extensive backgrounds in magnetic tape research. Peter Walters was recruited to do the necessary computer simulations while I was originally employed to develop methods of handling and using a unique magnetic tape on which a permanent coding had been impressed which could be detected by special means, but which was transparent to other, conventional, recording and reading. I soon discovered that that project was much less significant in EMI's eyes than the development of new magnetic deflection systems for scanning X-ray systems, and the development of nuclear magnetic resonance imaging (as it then was—according to folklore, the 'nuclear' was dropped in 1983, after an emotional misinterpretation at the site of a new scanner complex in Cleveland, OH).

The original EMI plan was to build a scanner based on a 0.1 T resistive magnet (the prototype of which was bought from Walker Magnetics, Danbury, CT) with a single driven equilibrium Fourier transform (DEFT) method of data acquisition. The gradients were planned to be outside the magnet structure, driven by thyristor-switched resonant discharge circuits, and image formation would be by back projection (entirely predictably in the light of EMI's CT experience).

All the gradients (including slice selection and during signal acquisition) would be sinusoidal so that, in order to meet the Nyquist criterion and cover k-space uniformly, the data were to be sampled at nonuniform time intervals. (This method was fully investigated, though only published in a pair of patents.)[1,2]

Colin Harrison, with a background at CERN and in precision power engineering, made extraordinary efforts to make the concept work during 1977, but by the end of that year we had decided to start again, and Colin built a set of more conventional gradient coils and I designed a new electronics unit to operate these. Mike Burl, who had recently joined us, developed the rf system for the machine. We continued to use one of the resonant discharge units for the slice selection (Z axis) coils but X and Y were driven by amplifiers originally intended for driving an electronically swept CT X-ray tube. The slice-selection gradient pulse was sinusoidal (as was the rephasing one) and a $\sin^5$-shaped rf profile was used for the rf transmitter pulses. This was generated using an analog network, but the amplitudes and shapes of the scanning gradients were formed digitally, though the logic was all hard wired. The nonlinear sampling circuitry was built the same way with the time intervals between the nonlinearly spaced sampling pulses blown into programmable read-only memories (PROMs) by hand. The values used were obtained by sampling the signal from a small phantom linearly, averaging multiple FIDs until we had reduced the signal uncertainty to manageable proportions, then calculating (using a pocket calculator) the varying time increments needed to meet the Nyquist criterion, and achieve constant phase increments.

The machine's computer was a small 16-bit Data General Eclipse, similar to that being used on the company's CT scanners, with the back-projection algorithm loaded into the writeable control store (the feature which had led EMI to choose the computer in the first place). Essentially we could, initially, acquire a $90^\circ - \tau - 90^\circ$ image with a back-projection scan incremented in 1° steps, and reconstruct and display the data as a 128×128 image interpolated to a 256×256 matrix, using a 10 mm slice. Image acquisition took 3 min (with one average, or 6 min with two, which was the extent of the options we originally had).

We began to acquire phantom images with some degree of respectability in late 1977 early 1978, but an attempt to image a volunteer head was quite disastrous, resulting in something like a frayed rabbit with drooping ears. The attempt produced a crisis in that Peter Walters felt we had violated the machine's virginity in the process—because Colin, Mike, and I had got fed up with waiting for him and Hugh Clow to appear and made the attempt ourselves.

We decided we simply had not got adequate stability and accuracy in the electronics, and homogeneity in the magnet and tore the machine apart, replacing the magnet adjustments supplied by the manufacturers with our own, and giving up the YIG EPR probes which we had been using for field monitoring in favor of homebuilt NMR ones.

The failure was multiply embarrassing in that the company, coming under severe pressure in its CT business and anxious to share the financial risk of this new development, wanted to collaborate with the Department of Health and Social Security (DHSS) as it had done with the original CT scanner. It also knew that the vast British GEC Company (which had recently employed Waldo Hinshaw who had shortly before left Nottingham) was preparing a rival proposal.

Our initial interaction with DHSS, represented by John Williams, was not encouraging. John was very familiar with Peter Mansfield's work and his recent publication of the first description of echo planar imaging (EPI).[3] We knew of Peter's paper, and had Raymond Andrew and Bill Moore as consultants, but could not reconcile what we knew of the method, and its claimed performance, with our own theoretical and practical results. Colin, Mike, and I concluded we would have to go to a higher operating field, and the proposal which was finally submitted to DHSS involved a field cycling resistive whole body magnet, normally operating at 0.1 T, but switched to 0.3 T to image.

In retrospect the concept was insane, certainly at that time and with the specification we wrote for it. Nevertheless, after a presentation to the DHSS scientific branch (headed at the time, as during the original CT work, by Gordon Higson, a man with a quite extraordinary record for backing winners, and a genius for very clear assessment of both failure and success,

as he later described),[4] it was agreed that EMI and DHSS would jointly develop a prototype NMR imaging machine to be installed in a hospital in London to be selected in the next few months. The program would begin on 1 July, 1978.

After the event, in July, Colin and I spent long hours contemplating the horror of what we had done, faced with the need actually to design and build this new magnet system (bearing in mind that we were still struggling to get our first vaguely adequate image of a human head—something we did not actually achieve until early September, and which was published in *New Scientist* shortly after,[5] see Figure 1). Quite fortuitously there was a cryogenics conference, with an associated trade exhibition, in London in August, and Colin went to that to see if any manufacturer would even talk to us about a whole body magnet. He came back with the names of Oxford Instruments and Thor Cryogenics and we gave both of them our magnet specification and asked for quotations.

Both responded, Thor with what I considered was the better specification but with an insistence on a refrigerator system. We were dubious both about the reliability of this item and the substantially increased cost of the Thor magnet. The latter was enough to ensure that Bill Ingham (the then Director of EMI Central Research Laboratories) made it plain that it would be preferable if we were to choose Oxford, and a contract was signed to a value of £70 600 for the design and purchase of a magnet to operate at 0.3 T with a clear bore of 1050 mm to be delivered to EMI CRL at Hayes, Middlesex, in late 1979. A proportion (£10 000) of the cost was to pay for the design. (Though EMI never did anything about the matter, it could be argued that EMI actually owned the design of the Oxford whole body magnet!) Ingham (who had spent most of his working career in EMI military electronics) insisted that Oxford sign endless confidentiality agreements. As Raymond Andrew pointed out to us, these held for about three weeks before Oxford set out to see who else might be interested—long enough to print descriptive leaflets and make some contacts.

Figure 1 First vaguely successful NMR image of the human head taken in September 1978 using a Walker 0.1 T resistive magnet. The method was filtered back projection, using a half-Fourier data acquisition (including non-linear sampling) with 180 angular increments of 2° each. Slice thickness was 10 mm. Repetition time was 1 s, and the time between selective rf pulse centre and the start of data acquisition was 5 ms

We chose the Data General Eclipse 250 computer—a 16-bit top of the range unit that was manufactured for about six months before being superseded by the 32-bit VX4000 series. This was a mistake in retrospect, but a worse one was our inability to obtain approval to buy an array processor. EMI CRL were more than happy that we should use the one they were developing for a new CT scanner. We saw that as largely underdeveloped and underfunded. It looked to us that the CRL management saw our role as funding the software needed for this array processor. We wanted to buy the Data General product compatible with our computer—and in the end nothing was fitted.

In the spring of 1979 sadly, Colin Harrison left us (going to work for IBM in San Jose) and Alasdair Hall joined us as his replacement. Alasdair thereafter carried the load of developing the facilities and techniques needed to cope with the new cryomagnet.

In planning the new machine, we decided we had to achieve real flexibility of technique, and that the hard-wired approach of the resistive prototype was impracticable. In fact, after a steady improvement in head image quality in the early months of 1979, using volunteers since neither animals nor patients were really feasible in the laboratory environment, we did not seem to be making significant further progress. We began to redevelop the prototype to give it some measure of sequence variety.

During this time we were seeking a suitable hospital site. My first choice was the hospital at which the original CT head scanner had been placed. In spite of the assistance of my immediate boss Alan Blay, Dr. James Ambrose, the neuroradiologist at that hospital, declined the offer saying that either the machine would fail, in which case he would waste two years of his time, or it would succeed in which case he would be flooded out with visitors, as he had been with the CT scanner (of which he had had the first clinical unit), and that would waste his time also.

We next offered the machine to the Hammersmith (partly because my brother had done his Ph.D. there), and Professor Robert Steiner agreed to install the machine in a building to be funded by the DHSS with some support from the University of London, since the new facility would provide better accommodation for the Medical School Department of Anaesthetics. Professor Steiner asked Professor Frank Doyle to be the direct link with, and supervisor of, the new project. In the fall of 1979, he and Jackie Pennock began to bring rabbits out to Hayes in circumstances of great secrecy, and started a series of experiments which included the use of paramagnetic contrast agents.

EMI, in the meanwhile, was under severe financial pressure because of the heavy losses both in its medical and music businesses. In the fall of 1979, another large electrical company, mainly involved in domestic electrical and electronic

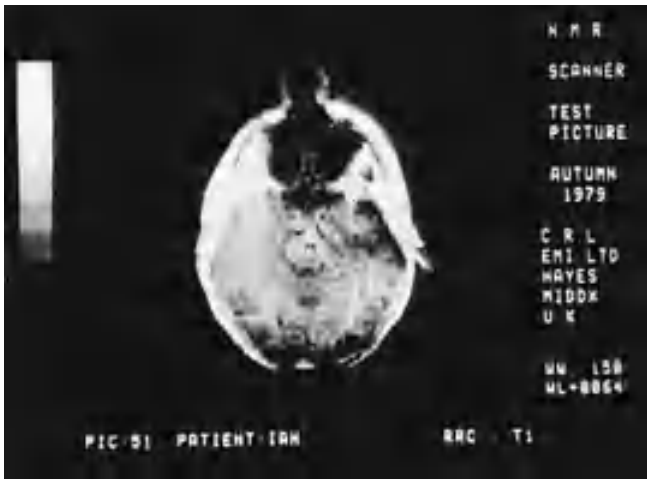

Figure 2 Very early (late 1979) inversion recovery images of the brain of a volunteer, showing the dramatic contrast between gray and white matter that would become the method's hallmark. (Acquired as described for Figure 1, except that the 360 angular increments had a 1° interval, and there was an inverting, nonselective, 180° pulse 300 ms ahead of the 90° one)

equipment and lighting, made an offer to take the company over. On the day the new management was installed we finally achieved the beginnings of satisfactory high contrast inversion recovery images (Figure 2), and within the next three weeks spin echo images, including a pulsed gradient spin echo experiment to measure flow (based on the Stejskal and Tanner diffusion experiment[6] and using the same process that we published finally in 1984).[7] The latter two experiments produced results, but with the sequence parameters we had chosen, retrospective wisdom reveals they were not destined to be exciting from a contrast point of view. We were simply lucky in that we reworked the spin echo two years later with patients, and were able to publish the huge efficacy of spin echo sequences in time to avoid someone else getting there first.[8]

Bill Ingham's concern about security, which ultimately led to the cryomagnet being installed in a room at CRL in which the windows had been painted out, extended to publications. The one exception was patenting—which he encouraged feverishly. On Friday nights we used to retire to a pub and draw up ideas to patent next week, always attributing part of the invention to the brewer. The idea was to get this past the management, since one of our party was our patent engineer who could always delete the reference at the last moment. One irony was that the patent department recommended we did not apply for a patent on the flow encoding technique, as the prior art was too substantial. Hindsight shows this was too pessimistic a view!

During late 1979 and 1980, collaborating with a general practitioner from Portsmouth and a neurologist from Hammersmith, we worked-up the old resistive machine, including one day when we scanned 10 volunteers in 8 h, and recommended to DHSS and EMI (by then Thorn-EMI) that, regardless of the success of the cryo machine, we should launch a product based on the 0.1 T resistive magnet. The new management, who were much more concerned to get out of the medical business altogether, were uninterested.

The cryomagnet was delivered in early May 1980, with the field initially set at 0.26 T, and the system assembled by July. Because of a lack of software on the Eclipse 250, we reconstructed data on the computer belonging to the 0.1 T machine.

We had, we considered, good images by October, and began to discuss the transfer of the machine to Hammersmith and the new building. John Williams of DHSS decided that the acceptance test for the machine was that it should produce the same highly contrasted T_1-weighted inversion recovery images that we were getting off the 0.1 T machine. I decided I was going to warm the magnet up over Christmas 1980, and ship it on 4 January, 1981. We simply could not get matching images (because we did not understand the field dependencies of tissue relaxation behavior—there were so few relevant results around) and, in the end, with the magnet running out of helium, we cut the field to 0.1 T on 22 December, caused a partial quench in the process with subsequent accelerated boil-off, and finally got an acceptable image on 23 December, just before the magnet finally quenched.

The magnet was shipped as planned and installed at Hammersmith very quickly. We then found a major problem. For reasons which again look bizarre in hindsight, we had used huge valve amplifiers to run the X and Y gradients, with rail voltages of 6 kV and demineralized water cooling. The atmosphere at Hammersmith was more humid than at Hayes and we suffered continuous corona from the gradient windings. In the end we had to strip the system down and reinsulate the gradients in situ. This meant that we were not able to begin scanning until March, and the machine sat there forlornly with its rf screen raised, looking for all the world what the hospital called it—'a white elephant'. Professor Steiner and his colleagues spent some time trying to decide what to do with the space when the machine was removed (something that was expected imminently).

Professor Steiner had recruited Graeme Bydder as the radiologist responsible for supervising the machine and its research in mid-1980. Though Graeme attended one or two meetings prior to that, he did not join until January 1981. When the machine was finally ready to begin operation we decided that we needed to understand the behavior of tissue signals as we changed field. We felt we knew about 0.1 T and that we should increase to our real operating field in 0.05 T steps. We set the field at 0.15 T and began volunteer studies. Then, in March, Graeme began to put patients through the machine and, thereafter, no further changes were permitted (even if Mike Burl and I did do experiments on odd days thereafter at higher fields). Post-September 1981 the field did not change again, and so this machine was probably the only one in NMR history of which the field was reduced.

The first (*Lancet*) papers[9,10] were prepared in June and July, very sadly in the absence of Frank Doyle who had suffered a severe stroke in May. True to his beliefs, Bill Ingham found it desperately difficult to agree to their publication. He made the mistake of going on vacation, though phoning from any public callbox he passed in the remotest part of the Scottish Highlands, to raise further objections to the papers' submission. Graeme and Robert sent them off anyway.

In their efforts to get out of medical equipment, Thorn-EMI wanted to do a deal with General Electric (GE), and a party from GE, which included Bill Edelstein, visited CRL in early fall 1980. Technicare (including Waldo Hinshaw by

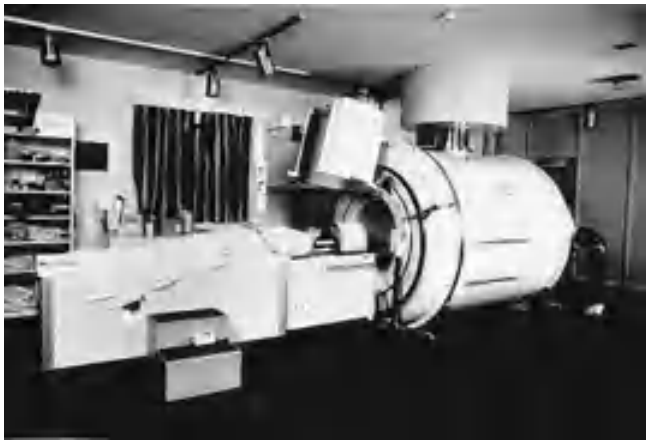

Figure 3 First cryogenic magnet shown installed in its site at Hammersmith Hospital, with its trunk raised in characteristic pose. There were many who thought at the time that the photograph was taken that its continued presence was more likely to be measured in weeks than years

then) also came and, I believe, Philips also wanted to acquire the NMR work. Thorn-EMI were, I think, only interested in the GE proposal, and a contract was drawn up between the two companies which was due to be finalized on 31 January, 1981. The contract required a third signature however (that of the DHSS, as part-owner of the project), but the British GEC, using all its influence, succeeded in preventing this being appended, and the deal collapsed. GEC (in April) acquired Picker, but it was not until the end of the following September that they actually bought the Hammersmith project from Thorn-EMI, leaving us in a curious limbo for eight months. We found out what it was like to be unwanted! GEC had to wrestle with the fact that, by then, they had their own program, which was being heavily influenced by Bill Moore and Neil Holland who were using the SSFP ideas they had pioneered with Waldo Hinshaw, whilst we had turned against steady-state methods. It was not an easy situation and I think it is fair to say that this dual parentage of ideas was a problem that Picker subsequently found very troublesome to resolve.

The sale of Thorn-EMI to GEC was completed just before the Winston-Salem Conference in September/October 1981 at which magnetic resonance imaging came of age. The machine (which is shown in Figure 3 in its favorite ‘white elephant’ pose) survived, and will ultimately wend its way to the Science Museum in London. Sadly, largely because the magnet gaskets are leaking, it was taken out of service in mid-1993. On the whole it did not have a bad run.

REFERENCES

1. H. Clow, W. S. Percival, and P. E. Walters, 1978, US Pat. 4254778.
2. H. Clow and W. S. Percival, 1978, US Pat. 4315216.
3. P. Mansfield, *J. Phys. C*, 1977, **10**, L55.
4. G. R. Higson, *Br. J. Radiol.*, 1987, **60**, 1049.
5. H. Clow and I. R. Young, *New Scientist*, 1978, **80**, 588.
6. E. O. Stejskal and J. E. Tanner, *J. Chem. Phys.*, 1965, **42**, 288.
7. D. J. Bryant, J. A. Payne, D. N. Firmin, and D. B. Longmore, *J. Comput. Assist. Tomogr.*, 1984, **8**, 588.
8. G. M. Bydder, R. E. Steiner, I. R. Young, A. S. Hall, D. J. Thomas, J. Marshall, C. A. Pallis, and N. J. Legg, *Am. J. Roentg.*, 1982, **139**, 215.
9. F. H. Doyle, J. C. Gore, J. M. Pennock, G. M. Bydder, J. S. Orr, R. E. Steiner, I. R. Young, M. Burl, H. Clow, D. J. Gilderdale, D. R. Bailes, and P. E. Walters *Lancet ii*, **1981**, 53.
10. I. R. Young, A. S. Hall, C. A. Pallis, N. J. Legg, G. M. Bydder, and R. E. Steiner, *Lancet ii*, **1982**, 1063.

Biographical Sketch

Ian R. Young. *b* 1932. B.S.c., 1954, Ph.D., 1988, Aberdeen. No involvement with NMR until joining EMI in 1976, where charged with leading the engineering group developing first a resistive, then a cryogenic machine. This was installed at Hammersmith Hospital in 1980–1. Approx. 150 papers and 30 patents in whole body NMR and related aspects. Research interests are in obtaining better images and spectra in vivo.

Birdcage Resonators: Highly Homogeneous Radiofrequency Coils for Magnetic Resonance

Cecil E. Hayes

University of Washington, Seattle, WA, USA

1 INTRODUCTION

Whole body MR imaging (MRI) at the commonly used field strengths makes demands on rf coil design that cannot be met by a conventional multiple-turn solenoid nor by a microwave cavity. The dimensions of the sample volume are neither a small nor a large fraction of a wavelength at the Larmor frequency. Whole body MRI employs a new rf coil technology which combines lumped and distributed elements. Such a structure is better characterized by the term 'resonator'. The term 'coil' implies a lumped-element multiple-turn solenoid tuned by a discrete capacitor, with a clear spatial separation between the inductor that stores energy in its magnetic field and the capacitor that stores energy in its electric field. On the other hand, a cavity stores both electric and magnetic energy somewhat diffusely; each extends over a significant fraction of the enclosed volume. The MRI whole body resonator creates a homogeneous $\boldsymbol{B}_1$ field within the patient by distributing the current over a large portion of its surface area, as in the case of the cavity resonator. By confining most of the electric field energy to multiple, discrete capacitors distributed over a large portion of the surface area, the MRI body resonator minimizes the electric fields within the patient and reduces dielectric losses.

Most whole body MR scanners use a large-bore superconducting solenoidal magnet to supply $\boldsymbol{B}_0$. The rf resonator must produce a homogeneous, transverse rf field and provide unimpeded axial access for the patient to the center of the magnet. To generate a rapidly oscillating $\boldsymbol{B}_1$ of about 2.5×10^{-5} T in an area of about $1\,\mathrm{m}^2$, the resonator must sustain voltages on the order of 10 kV.

The birdcage resonators[1] in Figure 1 were developed to accommodate whole body MRI. The basic birdcage resonator includes two circular conductive loops, referred to as endrings, connected by a number of conductive straight segments, evenly spaced on the surface of the cylinder. The conductive framework constitutes the inductive element of the resonator. A multitude of capacitors inserted along the conductive paths provide distributed storage of electric field energy. The novel feature of a birdcage resonator is that one of its natural resonant modes produces a homogeneous, transverse rf magnetic field within its volume. Furthermore, the ideal current distribution can be achieved by using the same value of capacitor in all the capacitor locations.

This article treats the design and construction of volume resonators with particular focus on the birdcage resonator. The first section covers general principles applicable to large resonators. The next section discusses the birdcage resonator extensively to give an intuitive understanding of how an ideal birdcage works. In spite of the seemingly straightforward structure shown in Figure 1, an actual birdcage embodies numerous imperfections which can alter the operation of the birdcage. Without a full understanding of all the issues, attempts to rectify one problem may create new difficulties. Sections on design and construction aid a researcher to build a birdcage suitable for a particular research project. The final section reviews alternative treatments of the birdcage and other volume coils or resonators.

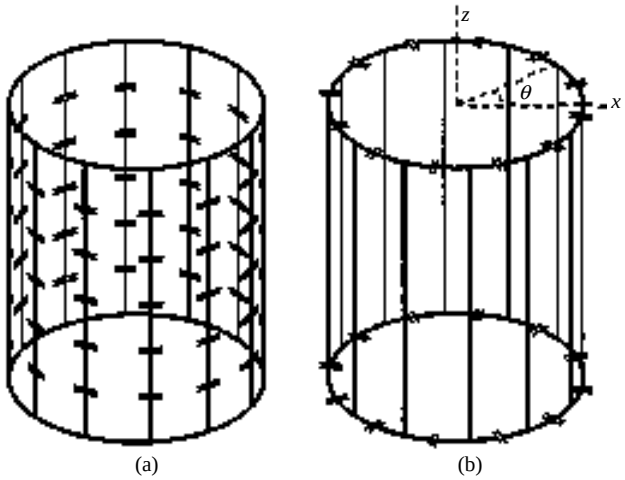

Figure 1 (a) Lowpass birdcage resonator with multiple capacitors on each straight segment. (b) Highpass birdcage resonator with polar coordinates

2 GENERAL PRINCIPLES FOR LARGE-VOLUME RESONATORS

It is assumed that the reader is familiar with the basic concepts of conventional rf coil design such as the coil sensitivity factor B_1/I, the coil quality factor Q, coil losses and tissue losses, the coil filling factor, quadrature excitation and reception, tuning and matching, etc. (see ***Sensitivity of Whole Body MRI Experiments***; ***Radiofrequency Systems and Coils for MRI and MRS***). Some of these topics are also covered by Hayes et al.[2]

The body coil primarily excites the spins with a homogeneous $\boldsymbol{B}_1$. Field homogeneity is particularly important for pulse sequences employing multiple spin echoes, where errors in flip angle compound. The body coil can also be used for signal reception, but this function is often better satisfied by surface coils or phased arrays specialized for specific body parts. (see ***Surface and Other Local Coils for In Vivo Studies***; ***Whole Body Machines: NMR Phased Array Coil Systems***). Whole body MRI exposes a large volume of tissue to the high-frequency magnetic field. Eddy currents induced by the rf field usually become the dominant power loss mechanism compared with coil losses. When this condition occurs, increasing the filling factor or reducing coil losses will produce only marginal improvements in the signal-to-noise ratio. In traditional NMR

with small sample losses, a solenoid wound on a cylindrical sample is inherently more sensitive than a structure that produces transverse rf fields in the cylinder. The long solenoid has a better filling factor because much of its magnetic energy is channeled through the sample volume by the conductive cylindrical walls. The transverse field stores more magnetic energy outside the sample because the flux must exit through the cylindrical walls. When sample losses dominate, the differences in filling factors for the two configurations no longer matter.

The use of a high-field superconducting solenoidal magnet imposes constraints on the design of the whole body rf resonator. Axial access for the patient requires the resonator to have open ends, which are a major source of rf field inhomogeneity. Rf field homogeneity can be improved by lengthening the resonator, but this has the disadvantage of increasing the power deposition during excitation and reducing the signal-to-noise ratio during reception. The magnet geometry imparts cylindrical symmetry to the available sample volume and strongly suggests the resonator uses the same symmetry. Such symmetry implies that a circularly polarized rf field is naturally preferred over linear polarization, because there is no preferred x- or y-direction in a superconducting magnet. Circular polarization decreases power deposition during quadrature excitation and increases the signal-to-noise ratio during quadrature reception. This is an added advantage that a transverse resonator has over the solenoid, whose geometry favors a linearly polarized $\boldsymbol{B}_1$.

A long solenoid approximates a constant circumferential surface current density that produces a homogeneous field in the axial direction. To produce a homogeneous transverse magnetic field in a long cylinder, the surface current density must be parallel to the long axis and proportional to $\sin\theta$ or $\cos\theta$, where θ is the polar coordinate azimuthal angle measured from the x axis. The $\sin\theta$ current distribution creates a linear polarized field along the x direction. For a particular instant, the positive values of $\sin\theta$ imply current is flowing in the positive z direction on the top half of the cylinder, and the negative values of $\sin\theta$ correspond to current on the bottom half of the cylinder flowing in the negative z direction.

In an rf solenoid, the conducting surface can be opaque to rf fields because the desired field is parallel to the cylindrical surface. For a transverse field resonator, the cylindrical surface must be both conductive and transparent to the emerging rf field. Such a surface can be approximated by a large number of evenly spaced copper wires or foil strips. The field homogeneity is disrupted in the sample volume for a distance comparable to the spacing of the conducting wires. If conductor width is small compared with the spacing, high current densities generate large local field concentrations near the conductors. High current densities also correspond to higher ohmic losses. If the conductors are too wide, the field is concentrated in the narrow slots between the conductors. A 50% coverage by the conductor is an arbitrary but useful compromise between the two extremes.

Because of the large voltages induced by rf fields in the cross-sectional area of the sample volume, only a single-turn inductor or multiple turns connected in parallel are desirable. Extraneous inductance, that is, any magnetic field that does not intersect the sample, should be minimized. For example, the lead inductances of the capacitors are eliminated by placing the capacitors directly on the conducting surface of the resonator. Likewise, high concentrations of current density also increase inductance because the locally enhanced magnetic field stores excess magnetic energy.

Distributing a large number of capacitors in series around the surface of the resonator has numerous advantages. First, the large voltages are broken up into series of small voltage steps, creating a number of virtual ground planes intersecting the resonator. Hence, voltage on no single component is elevated so far above ground that a coronal discharge occurs. The many small voltage steps create weaker, alternating stray electric fields that average to zero at shorter ranges than would a large dipole electric field from a single capacitor. This reduces the effective stray capacitance of the resonator to ground and thus raises its self-resonant frequency. Dielectric losses occur in the sample when stray electric fields from the coil's capacitors distort the electric fields induced in the sample by the rapidly changing rf magnetic field. The even distribution of capacitors effectively substitutes for a Faraday shield between the sample and the coil. Multiple capacitive breaks in conducting paths of the resonator also reduce eddy currents generated by the switched gradient fields during the imaging process. Many relatively inexpensive, discrete capacitors substitute for the more bulky and expensive vacuum capacitors commonly used in high-voltage rf circuits.

3 FUNDAMENTALS OF BIRDCAGE RESONATORS

3.1 The Basic Lowpass Birdcage

The chief advantage of the birdcage resonator is its ability to approximate the ideal sinusoidally weighted surface current on a cylinder with a large number of discrete conductors. To understand the origin of the sinusoidal distribution, consider the resonant properties of a finite length L of transmission line. If both ends are open circuits, the transmission line supports standing wave resonances for all frequencies for which the length is an integer number of half wavelengths long. If the two ends of the transmission line are joined to form a closed loop, the new boundary condition gives resonances when the length equals an integer number m of full wavelengths, that is, $m\lambda = L$. Now consider a twin-lead transmission line formed from two closed loops of wire around the circumference of the cylindrical sample volume. For the standing wave with one wavelength, the magnetic field between the wires enters the sample volume on one side and exits it on the other side. For an air dielectric between the wires, the desired resonance at $m = 1$ occurs at too high a frequency compared with the Larmor frequency. The capacitance per unit length of the transmission line determines its phase velocity. Lowering the phase velocity lowers the resonant frequency of the line. The transmission line can be made to resonate at the Larmor frequency either by filling the volume surrounding it with a high-dielectric material or by shunting the gap between parallel wires with evenly spaced discrete capacitors. The two wire loops can be separated widely to form the endrings of the birdcage because the capacitance per unit length of the transmission line no longer depends on the spacing of these wires. The current in the capacitor leads approximates the

sinusoidally weighted current density on the surface of the cylinder. That is, the sum of the fields generated by the lead inductances of the discrete capacitors create the homogeneous $\boldsymbol{B}_1$ field in the enclosed volume. The resulting configuration is a lumped element delay line with N repeat elements, and can support resonant modes for $m = 1, 2, \ldots, N/2$ (if N is even).

The resonant current in the straight segments can be proportional to $\sin m\theta$ or $\cos m\theta$, where values of θ are incremented by $2\pi/N$. The discrete wires correspond to a digital sampling of a continuous current distribution. The highest frequency resonance, $m = N/2$, corresponds to the Nyquist condition, where successive straight segments have currents with opposite phase. Each mode except $m = N/2$ is doubly degenerate because there are two current distributions with the same frequency. The cylindrical symmetry of the birdcage implies that $\sin(m\theta + \alpha)$ and $\cos(m\theta + \alpha)$ with an arbitrary α are also equally good choices for the two modes. For the ideal birdcage, there is no preferred azimuthal direction to call the x axis. The homogeneous mode ($m = 1$) occurs at the lowest frequency. The higher-order modes ($m = 2, 3, \ldots, N/2$) produce rf magnetic fields that decrease to zero on the central axis of the cylinder. The highest mode has the shortest range of penetration into the central volume of the cylinder. The cut off frequency occurs because the lumped element configuration resembles an N stage lowpass filter. This form of resonator is, therefore, referred to as a lowpass birdcage resonator [Figure 1(a)].

The two degenerate modes, $\sin\theta$ and $\cos\theta$, are orthogonal modes, both in the sense that the two functions are mathematically orthonormal and in the sense that their respective fields are perpendicular to one another. The two modes can be excited simultaneously and independently of one another. Equal simultaneous excitation of both modes with the same phase would create a linearly polarized field in the $\theta = \pi/4$ direction. Equal simultaneous excitation of both modes with a $\pi/2$ phase difference creates the circularly polarized field needed for quadrature excitation.

For simplicity, most of the following discussion will consider the birdcage operating with a linear polarized field along the x direction. It is also instructive to take a global viewpoint toward resonators in terms of how they store energy. Consider the composite lowpass birdcage structure as a resonator which alternatingly stores energy in electric fields and magnetic fields. All the energy is stored as magnetic field energy in the space in and around the resonator at the instant that all capacitors are completely discharged and the elemental currents are at their maximum values. Likewise, all the energy is converted into electric field energy at the instant when the elemental currents cease flowing and the capacitors are charged to their maximum values.

For the $\sin\theta$ mode, the birdcage resonator can be thought of as a single current loop encircling the x axis but branching and recombining in multiple short parallel paths. The current goes up one side of the cylinder, around the two halves of an endring, down the other side and across the other endring to the starting point. The total current is the sum of all the currents going the same direction on one-half of the cylindrical surface. One half of the endring current enters the endring from straight segments between $\theta = 0$ and $\theta = \pi/2$, has its maximum at the point $\theta = 0$, and then exits the endring into the straight segments between $\theta = 0$ and $\theta = -\pi/2$. Hence, the endring current is a discrete sum that is approximately proportional to $\cos\theta$, which is the integral of the surface current. The net effective inductance of the birdcage corresponds to all of the magnetic energy storage arising from the total current. As the number of straight segments is increased, the net inductance decreases toward a lower limit. For a fixed field strength at the center of the birdcage, adding straight segments reduces the current required in each segment and decreases the field inhomogeneity in the proximity of each segment. Lowering the fluctuations in field strength near the straight segments reduces the stored magnetic energy density. The lowest inductance corresponds to a homogeneous field with an infinite number of straight segments. Because of their high current density, endrings may be the dominant source of inductance in the resonator.

All of the capacitors on one-half of the cylindrical surface are effectively wired in parallel, but they are not weighted equally because they carry differing amounts of current and hence store different amounts of the electric field energy. The collective net capacitance of one half surface is wired in series with the net capacitance of the other half surface. As the number of straight segments is increased, the capacitance required for each straight segment decreases, since the total net capacitance asymptotically approaches a limit for an infinite number of straight segments.

For a practical lowpass birdcage operating at a high frequency and/or large volume, the single capacitor of value C in each segment is replaced by a number M of capacitors of value MC spaced evenly along the whole length of the straight segment. The net capacitance per strip is retained. This reduces electric field concentrations that create excess dielectric losses in the sample and eliminates the possibility of coronal breakdown. At high frequencies, the length of the straight segment may be a non-negligible fraction of the wavelength. In that case, the inclusion of multiple evenly spaced capacitors effectively increases the phase velocity of the straight segment. The wavelength is increased in that direction so the current is essentially constant along the whole length of the straight segment.

3.2 Generalized Forms of the Birdcage Resonator

The lumped element delay line may be thought of as a chain of repeating elements. Each element is a lowpass LC filter which generates a frequency dependent phase shift. The resonant condition corresponds to each repeat element adding a phase shift equal to $2\pi m/N$. For the lowpass birdcage, the phase shift per repeat unit increases with increasing frequency. Hence as a generalization, any chain of phase shifters or coupled resonant circuits can develop the desired sinusoidal current distribution. The highpass birdcage [Figure 1(b)] is so named because each repeat element forms a highpass LC filter. For a highpass birdcage, the phase shift per repeat unit decreases as the frequency increases. Hence, in the highpass birdcage, the frequency of each $\sin m\theta$ mode decreases as m increases. In addition to the transverse modes, the highpass birdcage has axial modes. These modes correspond to resonance currents in the endrings with no current along the straight segments. There can be a corotating mode and counter-rotating mode wherein the current circulating in one endring is either in

phase or out of phase with the current in the other endring. The axial modes usually occur at higher frequencies than the desired homogeneous modes.

For the homogeneous $\sin\theta$ mode of the highpass resonator, the endring capacitors on one side of the ring are essentially connected in series. But the net capacitive impedance is not a simple sum of the individual impedances because each capacitor has a different current and different electrostatic energy storage. The advantages of distributing the large induced voltage across multiple capacitors are intrinsically incorporated in the highpass design. As the number of straight segments is increased to improve field homogeneity, the number of capacitors must be increased proportionally. But the capacitive value of each capacitor must also be increased disproportionately. The net effective capacitance of the series-connected capacitors must also be increased to accommodate the decrease in inductance with an increasing number of straight segments. Hence, there is a practical limitation to the number of straight segments that can be utilized in a highpass birdcage.

3.3 Differences Between Highpass and Lowpass Birdcages

The fundamental difference between the highpass and lowpass birdcages arises from the wave nature of time-varying electromagnetic fields. Although it is possible, in principle, to make a uniform static magnetic field, it is not possible to make a uniform time-varying magnetic field. The wave equation requires a spatial variation due to the vector wavenumber $\boldsymbol{k}$, or inverse wavelength, which is determined by the dielectric constant and magnetic susceptibility of the medium. The highpass and lowpass resonators have different directions for $\boldsymbol{k}$ in the volume. Consider the case of a very long birdcage structure where the field contributions of the endrings can be ignored. Operating in the $\sin\theta$ mode, the long highpass resonator resembles a set of twin-lead parallel-wire transmission lines along the z direction. Each wire carrying current of the top half of the cylinder is paired with a wire on the bottom half carrying current in the opposite direction. Because the endring network terminates both ends of this long composite transmission line symmetrically, it supports a standing wave along the z direction. The surface current is proportional to $\sin\theta \cos k_z z \sin\omega t$, where k_z corresponds to wavelength at frequency ω and is determined by the average dielectric constant in and around the birdcage. For a birdcage whose diameter is small compared with the wavelength, the transverse field is approximately proportional to $\cos k_z z \sin\omega t$ in the x direction. Applying Faraday's law gives a transverse electric field in the y direction proportional to $\sin k_z z$.

The long lowpass resonator must have many capacitors evenly spaced along each wire to tune out the inductive impedance between each capacitor. The resulting composite transmission line generates no phase shift along the z direction at the resonant frequency. The current is uniform along z, therefore k_z is zero. However, k_y is not zero. Hence, the transverse rf field is still in the x direction but is proportional to $\cos k_y y \sin\omega t$. The time-dependent $\boldsymbol{B}$-field generates a longitudinal electric field along the z direction proportional to $\sin k_y y$. For both highpass and lowpass resonators, the electric fields are directed parallel to the distribution of capacitors. The electric field is large near the capacitors and diminished to zero at the center of the coil and reverses direction and becomes large at the other side or end of the coil. There is a nearly linear gradient in the electric field strength for coils of modest size compared with the wavelength. The different directions for the electric field in the highpass and lowpass resonators can determine which is more suitable for a given application.

3.4 Imperfect Birdcage Resonators

The preceding treatment was for ideal birdcages with full N-fold rotational symmetry. Difficulties arise when the symmetry is broken. Typically, the geometric layout of the conductive runs can be controlled sufficiently accurately to maintain the required symmetry. But the capacitors will usually have a distribution of values around the nominal value. Random fluctuations in the value of capacitance applied around the birdcage destroys its symmetry and perturbs its operation. Tropp provides a mathematical treatment of the perturbed coil performance[3]. The following treatment gives a simplified discussion of small, accidental perturbations as well as an example of a deliberate major perturbation. For small perturbations, the current distributions are assumed to remain sinusoidal but the resonant frequencies and directions of the two homogeneous modes may be shifted. Even small perturbations are therefore detrimental to quadrature operation of the resonator. Large perturbations such as cutting the endrings will drastically alter the current distribution.

Consider a lowpass birdcage with all capacitors having equal values except that the one capacitor located at $\theta = \beta$ is incremented by δC. For this situation the two natural modes have current distributions proportional to $\sin(\theta - \beta)$ and $\cos(\theta - \beta)$. The frequency for the $\sin(\theta - \beta)$ mode is unchanged because none of its current flows through the perturbed capacitor. The perturbation is invisible to this mode. In contrast, the $\cos(\theta - \beta)$ mode is affected by the change in capacitance because that mode has its current maximum in that capacitor. This mode stores electrostatic energy in the perturbed capacitor. The frequency of the $\cos(\theta - \beta)$ mode shifts up or down for a negative or positive value of ΔC, respectively, because the total effective capacitance of this resonant mode is altered. The two homogeneous modes no longer have the same frequency. This is called a splitting of the degenerate modes. The two modes still produce fields that are orthogonal in direction to one another, but the orientation of the two modes is no longer arbitrary. The position of the perturbation determined a preferred orientation for the coordinate system.

For the more general case, where there is a few percent random scatter among all the capacitor values, the $\sin(\theta - \alpha)$ and $\cos(\theta - \alpha)$ modes become oriented so the lower-frequency mode experiences a maximum effective net capacitance and the higher-frequency mode activates a minimum effective net capacitance. In general, there is a continuous range of possible values for the orientation α even though the straight segments are located at only a discrete set of angles. If the frequency splitting is large compared with the linewidth of the two resonances, operation of the coil in quadrature will be very difficult because only one or neither mode will be driven at its resonant frequency. Even if the two drive points are aligned along the natural orientations, α and $\alpha + \pi/2$, of the two perturbed modes, the induced currents will usually have different magnitudes and erroneous phases.

As an example of a major perturbation, consider a birdcage knee coil that is constructed so the top half is removable for easy positioning on the patient. Each endring is cut at $\theta = 0$ and π, and is not reconnected electrically when the top half is repositioned. The $\cos\theta$ mode has no current in the endring at these points normally. The cuts are invisible to this mode, which therefore can produce a homogeneous linear field along the y axis at the original unperturbed frequency. However, the former $\sin\theta$ mode is destroyed because it would require a current maximum where the endring conductors are removed. A new mode appears with current proportional to $\cos\theta$ on the top half and proportional to $-\cos\theta$ on the bottom half. This mode requires no current in the endring at the cuts, and, in fact, creates a discontinuous voltage step across the cuts. The resulting counter-rotating currents in the two halves of the birdcage resonate at a frequency about 10% higher than the remaining homogeneous mode. Such a disjoint coil cannot be operated in quadrature.

3.5 Rf Shields

The rf body coil is placed inside the magnet bore in close proximity to three or more gradient coils. Gradient coils are audiofrequency devices with multiple turns in overlapping layers. Such constructions can contain many spurious resonances which will absorb rf power and detune an enclosed rf resonator. Generally, an rf shield is placed between the rf coils and gradient coil to isolate the rf coil from the gradient coils and the rest of the outside world. The shield must be opaque to rf fields but transparent to the switched gradient fields. The shield generates rf surface currents that deflect any perpendicular component of the impinging rf magnetic field. The shield currents tend to flow in the opposite direction to the primary currents in the coil. Therefore, the shield cancels part of the field in the sample volume but strengthens the field in the space between the coil and shield. The shield reduces the inductance of the birdcage and raises its frequency significantly. The flux that exits one side of the coil is squeezed into a confined area as it returns to the opposite side of the coil. The energy density in the sample volume is reduced and the energy density outside the sample volume is increased. Hence, the shield will drastically reduce the filling factor as its diameter approaches that of the coil. For a shield 10% larger in diameter than the birdcage, more than 80% of the rf magnetic field energy is outside of the sample volume. Because whole body tissue losses are high at 1.5 T, the poor filling factor does not greatly reduce the signal-to-noise ratio at this frequency. At lower frequencies or smaller sample volumes, the shield can adversely affect the signal-to-noise ratio. Because gradient amplifier power requirements increase as the fifth power of gradient coil radius, there is an inherent disincentive to enlarge the space between the rf coil and the gradient coil.

The shield can simply be a cylindrical shell of copper foil no more than four or five rf skin depths thick. To prevent degradation of gradient field rise time, the shield should be divided up with slits into long narrow segments that run essentially parallel to the induced rf currents. Rf bypass capacitors interconnect shield segments wherever rf current must cross a slit.

4 BIRDCAGE DESIGN CONSIDERATIONS

The underlying assumption of the following sections is that a researcher can build a birdcage for a particular application faster by making a series of experimental prototypes than by starting with an extensive theoretical or computational analysis.

The initial required design decisions include determining the overall size, number of repeat elements, width of conductive elements, mode of coupling to the transmitter/receiver, need for a shield, choice between highpass or lowpass, and choice between quadrature or linear operation. The diameter chosen should be no bigger than needed to accommodate the desired sample or subject without touching the side walls. Excessively large diameters would decrease the filling factor and add coil losses. If the tissue losses are much bigger than the coil losses, then the filling factor is good enough. The length of the birdcage controls the major source of field inhomogeneity. Measured along the central axis of the cylinder, the rf field strength begins to decrease significantly within a distance of one coil radius from the open ends. At the plane of the endring, the rf field on the axis has fallen to about one-half the strength at the center of the coil. The choice of length for the birdcage is an engineering trade off between improved field homogeneity and increased noise from portions of the sample not being imaged. Obviously the rf field need not be homogeneous in a volume bigger than the homogeneous region of the static magnetic field $\boldsymbol{B}_0$.

The size and shape of the conductive paths determine the effective coil inductance. Copper foil is a good choice for conductors in a birdcage where there is limited clearance between coil radius and shield. The width of the straight segments is limited by the need for the surface to be transparent to the exiting transverse field. Equal widths of copper foil and air space have worked well enough. The width of the endring has a major effect on the total inductance of the birdcage because of larger current carried on the endring compared with the individual straight segments. The endrings should be several times wider than the individual straight segments. Low inductance means lower voltage and less detuning by stray capacitance.

In choosing between the highpass or lowpass configuration, the principal factor is how the shape of the subject effects stray capacitance between the subject and the coil. Shunting electric fields through tissue or a conductive sample detunes and loads the coil. For example, placing the patient's arms close to the capacitors in the straight segments of a lowpass body resonator will disproportionally load and detune the vertical mode and degrade the quadrature operation of the coil. The patient's shoulders being close to the endring of a head or body birdcage will affect the highpass but not the lowpass birdcage. Practical limitations on the values of capacitance available may dictate the selection of highpass or lowpass. For example, at low frequencies the endring capacitors in a highpass resonator might become unacceptably large. In contrast, the capacitors on a lowpass resonator are inherently smaller, especially when the number of repeat elements is increased. The choice of the number of repeat elements is a trade off between the short-range inhomogeneity generated and the number of components required. The regions of inhomogeneity extend radially inward for a distance comparable to the distance between segments. Sixteen repeat elements is a reasonable compromise.

The most direct way to determine whether an rf shield is required is to observe what happens to lineshape and frequency as a prototype coil is inserted in the magnet bore. Line broadening or position-dependent frequency shifts indicate a shield is needed. A shield will probably be required unless the new coil is much smaller than the bore diameter. Because it shifts the resonant frequency, the shield must be considered as an integral component of the overall coil design and construction. Without a shield, the tuning of the two modes for quadrature operation may not track as the coil is positioned in different places within the magnet bore.

The chief advantage of linear operation is greater simplicity of construction, tuning, matching, and operation. Initially a resonator can be operated linearly to determine the feasibility of an experiment. It can be converted to quadrature if the advantages justify the increased complexity. The advantages include a reduction in rf power amplifier capacity, lower power deposition, increased signal-to-noise ratio or shorter data acquisition time, improved field homogeneity by averaging the nonuniform currents in the endrings, and removal of the azimuthal angle dependence of rf penetration effects in the patient.

The resonator can be connected to the transmitter/receiver by capacitive or inductive coupling techniques (see ***Radiofrequency Systems and Coils for MRI and MRS***). Capacitive coupling requires applying a voltage across one or more of the birdcage's capacitors. Directly connecting cables to the birdcage tends to break the symmetry of the birdcage and detune the two quadrature modes. Isolating the cables' grounds with baluns is only partially effective. Inductive coupling through an air gap avoids some of the ground isolation issues. The inductive loops can be linked directly to the transverse flux entering at the cylindrical wall. If an inductive loop is tuned to self-resonance when isolated, moving it close to a birdcage will vary the matching without significantly detuning the birdcage. Alternatively, the inductive drive can intersect the return flux where it is concentrated between the coil and the shield. Inductive coupling is usually more convenient.

5 CONSTRUCTION TECHNIQUES

To construct a birdcage requires equipment for observing its frequency spectrum such as a network analyzer, a spectrum analyzer with tracking generator, or a variable-frequency signal generator plus an oscilloscope. A small inductive loop connected by cable to the signal source is placed close to the edge of one endring of the birdcage. As the frequency is swept, the resonator is excited for all modes that carry current in the endring near the driven inductive loop. A second small inductive loop connected to the receiving device can be used to observe the strength and orientation of the generated field.

Initial construction starts with laying out the foil conductive strips on an appropriately sized nonconducting substrate. A hot glue gun is convenient for attaching the copper foil. A narrow cut is made in each straight segment for a lowpass, or each repeat segment of both endrings for a highpass. A relatively large-valued capacitor is soldered across each gap. These test capacitors should be premeasured to ensure they are all nominally equal in value. The frequency spectrum of the birdcage is observed for several positions of the drive loop with the shield in place, if used. All transverse modes except the two desired homogeneous modes should be zero near the central axis. To confirm that the number of repeat elements and the length are large enough to give the desired region of homogeneous $\boldsymbol{B}_1$, the homogeneous modes should then be further probed.

Generally the two homogeneous modes will differ in frequency by a few percent or less but both will be well separated from the other modes. Presumably, the average homogeneous frequency measured is low enough so there are no significant stray capacitance or wavelength effects. To change the resonant frequency to the Larmor frequency, calculate the new capacitor value as the old capacitor value times the old frequency squared divided by the new frequency squared. No dimensional changes to the foil layout that alter its inductance should be made hereafter. Replace each of the capacitors with the new calculated value. Trying to pull the frequency by a large amount by changing only one capacitor will degrade the homogeneity. If a lowpass resonator is being constructed, additional cuts can be spaced along each straight segment; proportionally larger-valued capacitors are applied to each cut to generate a net series capacitance equal to the calculated value.

Fine tuning is needed to align both desired modes to the same frequency. In principle, only two capacitors need be changed to eliminate the frequency splitting[3]. Alternatively, four variable-trim capacitors can be added at 45° intervals on one side or endring. By deducing from the orientation of the split modes which capacitors carry the largest currents, the variable capacitor nearest each current maximum can be appropriately adjusted. Iteration is required, but the inductive pickup loops must be repositioned frequently because the modes shift orientation as the splitting decreases. Four variable capacitors rather than one for each repeat element should be sufficient to reduce the splitting to a small fraction of the loaded linewidth. If linear operation is acceptable, a major perturbation will lock the remaining linear mode in a well-defined position where it can be more easily tuned.

6 ADDITIONAL INFORMATION

Because birdcage resonators were initially developed commercially, the original patents provide extensive discussions of the properties, homogeneity, fabrication, and rf shielding of birdcage resonators.[4–6] Another patent describes the use of conductive endcaps to reduce the roll off of rf field strength at the ends of a birdcage.[7] Joseph and Lu discuss tuning the two homogeneous modes of a highpass resonator to two different frequencies for imaging both protons and fluorine.[8]

Mathematical and empirical treatments of the spectrum of the birdcage have been given by several authors.[9–11] The periodic structure of the birdcage resonator has analogies in other branches of science and engineering. For example, if a lowpass resonator is made with large capacitors in the even-numbered straight segments and small capacitors in the odd-numbered ones, the spectrum has a low-frequency branch and a high-frequency branch corresponding to the acoustical and optical vibrational lattice modes of an ionic crystal. Such a resonator could in principle give quadrature excitation at two frequencies. Other forms of the dual-tuned quadrature birdcage utilize dual tuning of each repeat element[12] or combine more than one birdcage on the same cylinder (see ***Multifrequency Coils for***

Whole Body Studies). A spherical volume of uniform rf field can also be generated using principles similar to the birdcage.[13]

7 RELATED ARTICLES

Multifrequency Coils for Whole Body Studies; Radiofrequency Systems and Coils for MRI and MRS; Sensitivity of the NMR Experiment; Sensitivity of Whole Body MRI Experiments.

8 REFERENCES

1. C. E. Hayes, W. A. Edelstein, J. F. Schenck, O. M. Mueller, and M. Eash, *J. Magn. Reson.*, 1985, **63**, 622.
2. C. E. Hayes, W. A. Edelstein, and J. F. Schenck, in 'NMR in Medicine: Instrumentation and Clinical Applications', ed. S. R. Thomas and R. L. Dixon, AAPM, New York, 1986, p. 142.
3. J. Tropp, *J. Magn. Reson.*, 1991, **95**, 235.
4. C. E. Hayes, US Patent 4 694 255, 1987.
5. W. A. Edelstein, J. F. Schenck, O. M. Mueller, and C. E. Hayes, U S Patent 4 680 548, 1987.
6. C. E. Hayes and M. G. Eash, U S Patent 4 642 569, 1987.
7. C. E. Hayes, US Patent 4 692 705, 1987.
8. P. M. Joseph and D. Lu, *IEEE Trans. Med. Imaging*, 1989, **8**, 286.
9. J. Tropp, *J. Magn. Reson.*, 1989, **82**, 51.
10. M. D. Harpen, *Med. Phys.*, 1990, **17**, 686.
11. M. D. Harpen, *Magn. Reson. Med.*, 1993, **29**, 263.
12. A. R. Rath, *J. Magn. Reson.*, 1990, **86**, 488.
13. M. D. Harpen, *J. Magn. Reson.*, 1991, **94**, 550.

Biographical Sketch

Cecil E. Hayes, *b* 1941. B.Eng.Phys., 1964, Ph.D. (supervisor Robert V. Pound), 1973, Physics, Harvard University, USA. Postdoctoral work at Rutgers University, USA (with Herman Y. Carr), and at University of Utah, USA (with David C. Ailion). Senior Physicist, GE Medical Systems 1982–91. Presently Professor of Radiology, University of Washington, USA. Approx. 45 publications, 12 patents. Current research specialty: rf coils for MRI.

Coils for Insertion into the Human Body

Gregory C. Hurst

MetroHealth Medical Center and Case Western Reserve University, Cleveland, OH, USA

and

George J. Misic

Medrad, Inc., MRI Products, Indianola, PA, USA

1 INTRODUCTION

Internal coil placement may allow smaller coil size and/or closer positioning than is possible for a conventional externally located coil. Although it is conceivable that any magnetic field needing generation or detection could be served by internally placed coil(s), this article considers only coils used for detection of the NMR signal. Such internally placed receiver coils have been the subject of substantial attention by several research groups during the past dozen years. This attention is driven by two potentially substantial advantages associated with reduced coil size and/or distance from subject: (1) increased signal to noise ratio (SNR), and (2) reduced aliasing. The SNR is a fundamental limiting factor in the quality of many clinical studies, and increasing the probe SNR performance may allow better resolution and/or shorter acquisition time. Aliasing may compromise the ability to obtain images of a small target within a larger object, which may in turn also have consequences affecting resolution and/or acquisition time.

The performance advantages of internal coils are conceptually identical to those associated with tailoring the size and location of the receiver coil to the target region by using a 'surface coil' or other external specialty coil (see Related Articles).[1] 'Surface coils' are now routinely used in clinical whole body NMR imaging, whereas internal coils, although conceived relatively soon after the birth of the surface coil, have not yet been established in similarly widespread use (see Table 1, and Related Articles). Currently, disposable internal coils designed for three different target anatomic areas are available for operation at 1.5 T and 1.0 T on a number of different MRI system platforms. Coils optimized for prostate, cervical, and colorectal studies are available; all are designed for endorectal insertion. Repeated use coils have been offered

Table 1 The Evolution of Internal Coils, with Surface Coil Milestones Provided for Reference

Year	Nonhuman subjects	Human subjects
1980	*Surface coil* Spectroscopy of rat brain[2] *Inside annular phantom* Spectroscopy of oil well model[3]	
1983	*Surgically implanted* Spectroscopy of rat kidney, heart, liver[4]	
1984	*Intravascular* Spectroscopy of dog heart[5] *Endorectal* Imaging of dog prostate[7] *Esophageal* Imaging of dog esophagus[6]	*Surface coil* Imaging of orbit, neck, chest wall, lumbar spine[6]
1985	*Surgically implanted–wireless coupling* Spectroscopy of rat brain[8]	
1986	*Intraoral* Imaging of dog maxillofacial region[9] *Surgically implanted–wireless coupling* NMR and MRI of rat and cat, kidney and liver[11]	*Endorectal* Imaging of prostate[10]
1988	*Inside annular phantom* Imaging of arterial model[12]	*Intraoral* Imaging of mouth[13]
1989	*Surgically implanted–wireless coupling* Imaging of rabbit femoral artery[14]	
1992	*Intravascular* Imaging of dog iliofemoral artery[15] Imaging of pig jugular vein[16]	*Intravaginal* Imaging of cervix[17]
1993	*Surgically implanted–wireless coupling* Imaging of cat lumbar spine[18]	

by two MRI system manufacturers for use on their own systems. In light of the standard arsenal of five to ten surface coils at a typical clinical MRI site, the relatively slow rate of development and adoption of internal coils may be attributed to a reluctance to make MRI an 'invasive' procedure. Another barrier is that currently dominant clinical uses for MRI (imaging of the brain, spine, and musculoskeletal system) are not obvious candidates for improvement by use of internal coils, so that the burden of proving new applications is carried simultaneously with probe development efforts.

The current status of the proposed uses of internal coils, as listed in Table 1, is somewhere between proof of feasibility and reasonably informed judgment of the relative costs and benefits. Accurate assessment of potential benefit requires knowledge of ideally achievable performance, which is still an open question. Estimating potential performance, as well as answers for some unique challenges associated with obtaining that performance in practice, involves a body of engineering problems. These problems, together with some current solutions, are presented in the remainder of this article.

2 SPECIAL CONSIDERATIONS IN THE DESIGN OF INTERNAL COILS

Although a particular application may have its own unique design constraints, there are a few general considerations which characterize internal coils as a class, based on differences with current conventional external magnetic resonance (MR) probes.

2.1 Size

The limited space which is available for locating and/or inserting coils imposes size constraints. For endorectal imaging, mechanisms have been designed to expand the coil after insertion by inflation with air from an external source. Several methods have been devised, including direct inflation of a balloon containing the coil, and inflation of an inner balloon with the coil itself affixed to an external balloon of an optimal shape and size.

In addition to size constraints on the coil windings and substrate, the limited 'real estate' may impose a size limitation on the number and size of capacitors, cables, insulating layers, sterility barriers, and other probe components. Because of the inherently close coupling to the sample and other tissue material, capacitive and inductive sample 'loading' can be expected to dominate noise considerations down to relatively small conductor sizes (at currently popular high operating frequencies, e.g. 64 MHz); however, at some point of miniaturization and/or lower operating frequencies, these losses may become significant. Resistive losses in connecting cables will show a similar trend (increasing losses with smaller size); note that these losses will generally increase with higher operating frequencies, and for connection schemes that do not implement the connecting cable as a nonresonant transmission line operating at its characteristic impedance.

At moderate sizes, such as endorectal applications, capacitor size is not a dominant issue; standard series of high Q capacitors are available in capacitance of up to 100 pF at sizes of the order $2 \times 2 \times 2$ mm. At much smaller probe sizes, such as for intravascular application, this size is too big; unfortunately, achieving the same capacitance at smaller size requires a compromise in breakdown voltage (related to plate spacing) and/or loss of circuit and coil Q due to increased losses in the dielectric material between the capacitor plates. This issue is compounded by the reduced inductance of smaller coils, which require larger capacitance to achieve resonance.

2.2 Shape

Conventional external probe design locates the coil in a region of approximately free space (typically, the air around the patient), with the target region either inside or adjacent to this free space; because it does not contribute either signal or noise, the probe designer may essentially ignore the free space, and use all available degrees of freedom to construct a desired response in the target region. In contrast, the internal probe is immersed in material which contributes both signal and noise. Any unnecessary noise contribution is, of course, never desirable; the unnecessary MR signal may be harmless, or may be a detriment due to aliasing, depending on the desired field-of-view.

For some applications, such as imaging of the prostate from inside the rectal cavity, the coil is adjacent to the target region, and the probe sensitivity design problem is similar to that of a 'surface coil'; this situation is well served by some version of a loop coil of linear design; quadrature and array coils are difficult to implement in an effective manner in the confined space, and with the variable shape. Inflatable balloon endorectal coils have been customized for specific targets. To optimize coil operation in the prostate area, the coil balloon can include a saddle-shaped surface to surround the bulge containing the gland. This enhances probe operation in two ways. First, the coil itself is more readily placed in the immediate region of the gland; second, the probe is retained in correct alignment following inflation due to the conformal nature of the balloon structure. Probe coils for imaging the cervix from an endorectal location can include a flatter, wider balloon shape, and a means for remotely steering the probe assembly into the proper position relative to the target anatomy. For colon imaging, the coil is generally centered in the balloon structure to provide a uniform degree of sensitivity around the probe structure.

For other applications, such as intravascular arterial imaging, the target region partially or completely surrounds the coil, giving a novel perspective to probe sensitivity patterns. This has led to consideration of several novel coil winding patterns. An opposed solenoid configuration, as shown in Figure 1, has proven useful in imaging an annular target region around the coil, with remarkable homogeneity in axial planes between the two solenoids.

2.3 Getting the Signal Out

For external coils, the standard way of transferring the NMR signal from the probe to the rest of the receiver is via a coaxial cable or other transmission line structure. This is not necessarily appropriate for internal coils, due to the size of such cable, and is further complicated by the cable running through lossy and NMR-signal-generating media on its way out of the body. Several coupling schemes which attempt to deal with these considerations are shown in Figure 2.

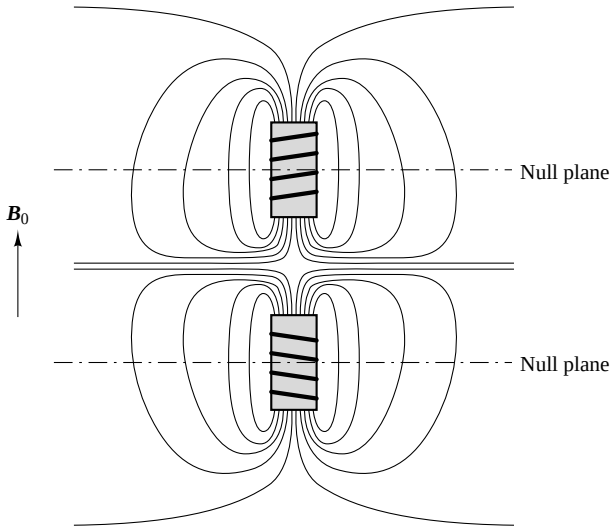

Figure 1 Magnetic field pattern for a pair of opposed solenoids. Note that with the probe aligned along $\boldsymbol{B}_0$ as shown, there is a region of relatively high sensitivity and homogeneity, in a plane between the two solenoids. Note also the pair of approximate null planes (— · —) where the opposed solenoid field is essentially parallel to $\boldsymbol{B}_0$, with negligible $\boldsymbol{B}_{xy}$

The scheme shown in Figure 2(a) utilizes a balanced transmission line, ideally operating at or near its characteristic impedance. This will minimize the VSWR (voltage standing wave ratio) on the transmission line, and thus minimize associated losses. However, due to the electric field of the balanced transmission line, proximity to surrounding tissue may cause significant losses. A similar approach, shown in Figure 2(b), uses an unbalanced coaxial transmission line rather than twisted pair, which reduces such losses, assuming the circuit achieves negligible signal currents on the outside of the cable shield conductor.

Figure 2(c) illustrates a wireless inductive coupling similar in concept to that sometimes seen with external probes. In an internal application, lossy tissue in the space between the primary and secondary coils can make this a suboptimal solution. Inductive coupling with both coils internal to the probe assembly is typically precluded by space considerations.

Figure 2(d) illustrates a means to employ a locally mounted preamplifier. With sufficient signal gain from this amplification, the losses in the transmission line become negligible; the coupling scheme SNR performance is then essentially determined by the noise figure of the amplifier active device as implemented.

Figure 2(e) describes a method to locate a high impedance field effect transistor (FET) preamplifier at a substantial distance from the coil, while retaining many of the advantages of 'local' placement. The coil itself acts as a series resonant circuit, with impedance transformation accomplished by a one-quarter wavelength output cable. Due to the high VSWR on the cable, the losses are greater than those for a direct connection to a parallel resonant coil; however, this scheme offers several practical advantages, as discussed in the following section.

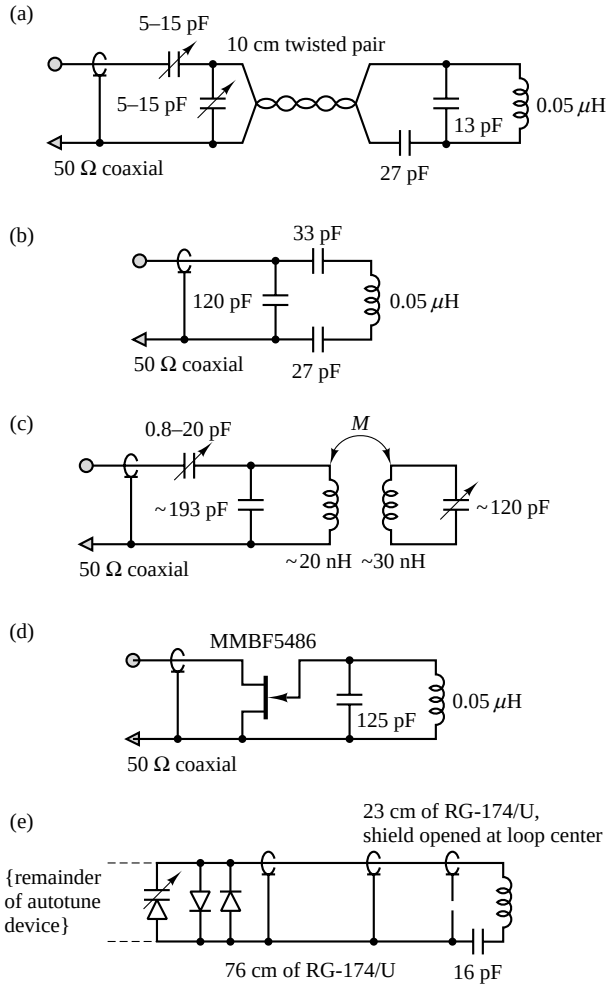

Figure 2 Several different tuning/matching/coupling schemes which have been used for internal coils: (a) parallel resonant probe coil, with balanced capacitive coupling to a balanced transmission line; (b) parallel resonant probe coil, with capacitive balun match to unbalanced transmission line; (c) parallel resonant probe coil, with wireless inductive coupling; (d) parallel resonant probe coil, with coupling via a field effect transistor active device; (e) series resonant 'transmission line' coil, with quarter-wave line coupling and diode switch. The component values given are for different operating frequencies: (a) 97.3 MHz; (b) 97.3 MHz; (c) 81 MHz; (d) 64 MHz; (e) 64 MHz

3 COMMERCIALLY PRODUCED ENDORECTAL COILS

Internal coils for prostate, cervical, and colorectal imaging at 1.5 and 1.0 T have been commercially available since 1991 [Medrad; Indianola, PA, USA]. These endorectal coils are disposable and designed for single-use applications to avoid the problems associated with re-use. The coils have similar internal electronics, but component and mechanical variations depending upon application. Interface devices are available for use with a variety of host MRI systems and also to allow the endorectal coils to be used in combination with external phased array coils to improve coverage and utility.

To reduce the product cost to a level compatible with a single-use, disposable probe, some design decisions were made concerning the configuration of the endorectal coil and the associated interface device. The disposable endorectal coils themselves are designed for a specific target anatomy and operating field strength only. Differences in various commercial MRI systems, operating frequencies, and the hardware needed to manage utilization with existing external phased array coils are accommodated in a separate re-usable interface device; it contains the majority of the electrical components. Figure 2(e) shows the decoupling diodes and tuning diode that are part of the interface device connected to the endorectal coil.

3.1 Coil Design

The coil itself is constructed from approximately 23 cm of coaxial cable, retained in an appropriate shape by the outer balloon of the probe assembly. The coaxial shield conductor is opened halfway around the loop. In this 'transmission line' design, the coaxial shield may be conceived as a Faraday shield, which provides some balancing effect on the coil, and reduces the level of rf currents flowing on the outside of the output coaxial cable. The coil is series resonated to the approximate operating frequency by a single series capacitor; this capacitor, and the coil conductor, are the only electrical components on the disposable probe itself.

3.2 Coupling and T/R Decoupling

Signal is extracted via a one-quarter wavelength coaxial cable, as shown in Figure 2(e). This simple arrangement serves two needs: (1) the series resonance of the probe coil is transformed to a parallel resonance at the end of the cable, thus providing an appropriate source impedance to drive a low-noise FET preamplifier; and (2) it affords transmit/receive decoupling by placing an rf short at the output end of the $\lambda/4$ cable, with the short inverted by the cable to a high impedance at the coil end, thus effectively opening the loop of the coil during transmit excitation. The rf short is accomplished by using either crossed rf switching diodes, or a selectively-biased p-i-n diode within the interface device.

3.3 Interface to the Scanner Surface Coil Input

Because the endorectal coil is a volume-produced disposable device and is usually inflated after insertion into the patient, the tuning of the coil may benefit from optimization on a per-coil and per-patient basis. Some interface devices include an electronic circuit to accomplish this automatically; the tuning is done by applying an optimized DC potential to the varactor diode shown in Figure 2(e). With the advent of low-noise preamplifiers having very low input impedance in most MRI systems, the need to perform the per-use tuning can be negated by proper interface circuit design. To accomplish this, a network is employed that tunes the nominal endorectal coil under average loading conditions to appear as a 50 ohm resistive source. The electrical length from the signal output end of the one-quarter wavelength (76 cm) cable, which is part of the endorectal coil, to the input of the low impedance preamplifier is an integer multiple of one-half wavelength; this allows the endorectal coil to provide the proper source impedance to the low-noise preamplifier; it also allows the low impedance of the preamplifier both to isolate and to broaden the tuning of the endorectal coil. This is especially beneficial when using the endorectal coil as one coil of a phased array set of coils.

3.4 Coil Array Combinations

More recent developments enable the family of endorectal coils to be used with pelvic or torso array coils. New versions of the interface device provide a network to combine the signals from the two posterior coil elements in the four element torso or pelvic array coil (Signa, GE Medical Systems, Milwaukee, WI; MR Innervu, Medrad, Indianola, PA), thus creating an available phased array input port for the endorectal coil signal. The results include a substantial improvement in image SNR (see Table 2) relative to the body coil, torso array, or pelvic array alone, along with substantially greater image uniformity relative to the endorectal coil alone.

3.5 Ongoing Developments

Presently, several development programs are underway to expand the utility, functionality, performance, and capabilities of commercially available endorectal and intracavity coils. Projects in process include spectroscopic applications, quadrature and array probe coils, re-usable probes and coils, and additional field strengths.

4 COMPARISON OF SNR FOR INTERNAL AND EXTERNAL COILS

To decide if it makes sense to use an internal coil rather than an external coil in a particular application, it would be helpful to have a measure of relative performance. Two common performance indices for conventional receiver probes are SNR and homogeneity. For 'surrounding' coils like solenoids or saddles, the homogeneity in the region of interest is relatively high; this means that SNR is well represented by an average value over a region of interest (or even a single measurement at the center of that region), and homogeneity can be represented by a single number expressing the range of intensities (normalized by the average value). Due to extreme proximity of sample and coil, the homogeneity of internal coils is typically much less than surface coils (which are themselves much less homogeneous than surrounding coils); with decreasing homogeneity, accurate and meaningful measurement of the SNR or homogeneity is not so straightforward. Furthermore, selecting an appropriate external coil used for reference is problematic, for two reasons: (1) defining an 'optimum' single external coil requires exact definition of many variables, including proximity to surface and size of target region; and (2) an array coil configuration, such as are currently entering routine clinical use, may supersede a single surface coil as an 'optimum' external reference standard.

Bearing in mind these caveats, it is instructive to survey reported SNR improvements obtained using internal coils. As shown in Table 2, this improvement in SNR can be as small as two-fold (applied to imaging the lumbar spine of a cat), and as

Table 2 Comparison of SNR for Internal and External Probes[a]

Internal coil	Subject	External coil	Relative SNR (int./ext.)
Circular loop, d = 2.5 cm; inductive coupling; around subject	Phantom	Spherical, d = 25 cm	4.2
Solenoid, $d = l$ = 1.5 cm; inductive coupling; immersed/implanted	Phantom Rat kidney	Birdcage, d = 6 cm	~ 10
Opposed solenoids, $l \approx 4d$ = 20 mm; FET or capacitive coupling; immersed	Phantom	Loop, $d \approx$ 10 cm	~10
Elliptical loop, 8.5 × 4.5 cm; capacitive coupling; phantom adjacent to loop; inflatable, endorectal	Phantom	Body coil (quadrature), $d \approx l \approx$ 50 cm	2
Rectangular loop, 3 × 8 cm; capacitive coupling; inflatable, endorectal, commercial	Phantom	Body coil (quadrature; commercial)	5
Above, plus pelvic array	Phantom	Pelvic array (commercial)	3.5
Rectangular loop, 5 × 4 cm; capacitive coupling; inflatable, endorectal	Human prostate	Body coil, $d \approx l \approx$ 50 cm	13
Half-saddle loop, 3 × 2 × 1.2 cm; inductive coupling; surgically implanted	Cat, L1–L3	Loops, 4 × 6 cm; quadrature (surface coil)	1.32

[a]d, Diameter; l, length.

large as 10-fold (as found for intravascular phantoms). For human endorectal imaging, the observed gains in image SNR at the target anatomy range from three to eight times the performance of alternative coils such as the body or torso array coils.

5 RELATED ARTICLES

Birdcage Resonators: Highly Homogeneous Radiofrequency Coils for Magnetic Resonance; Radiofrequency Systems and Coils for MRI and MRS; Sensitivity of Whole Body MRI Experiments; Surface and Other Local Coils for In Vivo Studies; Whole Body Machines: NMR Phased Array Coil Systems; Whole Body MRI: Local and Inserted Gradient Coils.

6 REFERENCES

1. G. J. Misic, E. J. Rhinehart, T. C. Claiborne, H. Y. Kressel, R. E. Lenkinski, and M. D. Schnall, *Proc. VIIIth Annu. Mtg. Soc. Magn. Reson. Med.*, Amsterdam, 1989, p. 179.
2. J. J. H. Ackerman, T. H. Grove, G. G. Wong, D. G. Gadian, and G. K. Radda, *Nature*, 1980, **283**, 167.
3. J. A. Jackson, L. J. Burnett, and J.F. Harmon, *J. Magn. Reson.*, 1980, **41**, 411.
4. J. Murphy-Boesch and A. P. Koretsky, *J. Magn. Reson.*, 1983, **54**, 526.
5. H. L. Kantor, R. W. Briggs, and R. S. Balaban, *Circ. Res.*, 1984, **55**, 261.
6. L. Axel, *J. Comput. Assist. Tomogr.*, 1984, **8**, 381.
7. W. G. Holcomb and J. C. Gore, *Proc. IIIrd Annu. Mtg. Soc. Magn. Reson. Med.*, New York, 1984, p. 333.
8. A.L. Benabid, M. Decorps, C. Remy, J.P. Albrand, H. Reutenauer, and P. Blondet, *Proc. IVth Annu. Mtg. Soc. Magn. Reson. Med.*, London, 1985, p. 441.
9. M. D. Schnall, H. Y. Kressel, H. M. Pollack, and R. E. Lenkinski, *Proc. Vth Annu. Mtg. Soc. Magn. Reson. Med.*, Montreal, 1986, p. 197.
10. J. F. Martin, P. C. Hajek, L. L. Baker, V. Gylys-Morin, and R. R. Mattrey, *Radiology*, 1986, **161**(Suppl. P), 318.
11. M. D. Schnall, C. Barlow, V. H. Subramanian, and J. S. Leigh, Jr., *J. Magn. Reson.*, 1986, **68**, 161.
12. G. C. Hurst, J. L. Patrick, J. L. Duerk, P. Diaz, R. Malaya, A. M. Cohen, and E. M. Bellon, *Proc. VIIth Annu. Mtg. Soc. Magn. Reson. Med.*, San Francisco, 1988, p. 155.
13. R. R. Harman, P. C. Butson, A. S. Hall, I. R. Young, and G. M. Bydder, *Magn. Reson. Med.*, 1988, **6**, 49.
14. J. C. Ford, R. F. LeVeen, M. D. Schnall, and P. M. Joseph, *Proc. 37th Annu. Mtg. Assoc. Uni. Radiologists*, Seattle, 1989, Abstract 14–4.
15. G. C. Hurst, J. Hua, J. L. Duerk, and A. M. Cohen, *Magn. Reson. Med.*, 1992, **24**, 343.
16. A. J. Martin, D. B. Plewes, and R. M. Henkelman, *JMRI*, 1992, **2**, 421.
17. C. J. Baudouin, W. P. Soutter, D. J. Gilderdale, and G. A. Coutis, *Magn. Reson. Med.*, 1992, **24**, 196.
18. E. D. Wirth III, T. H. Mareci, B. L. Beck, J. R. Fitzsimmons, and P. J. Reier, *Magn. Reson. Med.*, 1993, **30**, 626.

Biographical Sketches

Gregory C. Hurst. *b* 1957. B.S. (Chemistry), University of Illinois, 1979 (research with R.L. Belford on EPR of copper in polycrystalline metal complexes); Ph.D. (Chemistry), University of Rochester, 1983 (research with R.W. Kreilick on proton/copper ENDOR of polycrystalline metal complexes). Picker Intl. NMR Advanced Development, developing first-generation commercial whole body superconducting MRI systems, 1984–86; Picker NMR Marketing, selling second generation whole body MRI systems, 1986–87. Currently, imaging scientist, Department of Radiology, Cleveland MetroHealth Medical Center, and Assistant Professor of Radiology and Chemistry, Case Western Reserve University. Approx. 75 manuscripts, abstracts, and patents. Research interests in techniques and applications for human NMR imaging.

George J. Misic. *b* 1949. B.S.E.E., Case Institute of Technology, 1971. HAM license received 1963. Chief Engineer, Dentron Radio, designing commercial, military, and amateur radio products for hf, vhf, and uhf, including satellite downlink hardware, 1981–83. Picker Intl. NMR Advanced Development and Engineering, lead design engineer for rf systems and components in first and second generation whole body clinical MRI systems, including basic spectrometer architecture, preamplifiers, power amplifiers, T/R switches, head, body and surface coils, 1983–88. Currently Director of MR Technology, Medrad, Inc., MRI products. Nineteen patents and approx. 25 presentations at scientific meetings.

Cryogenic Magnets for Whole Body Magnetic Resonance Systems

David L. Rayner, Peter J. Feenan, and Rory J. Warner
Magnex Scientific Ltd, Abingdon, Oxon, UK

1 INTRODUCTION

One of the most critical parts of the instrumentation in a magnetic resonance (MR) system is the magnet, which tends to be an expensive high technology item. Cryogenic (superconducting) magnets were first used in MR systems in the early 1980s,[1] and have since become the preferred type of magnet system for most users. This is largely because they possess the advantage of being able to operate at high field strengths (potentially up to 10 T in some configurations), with excellent time dependent field stability.

The main features of a superconducting magnet for MR applications are the superconducting coils, the cryogenic container (cryostat), the method of field homogeneity control (field shimming), and, where necessary, the method used to confine the magnet's fringing field. All these features are discussed in detail in this article, together with information on special high field superconducting magnet systems and systems designed for mobile MR applications.

The design of MR magnet systems has advanced considerably since the earliest 0.35 T versions were introduced. Today's systems are normally designed to be operated at a fixed field strength of either 0.5, 1.0, 1.5, or 2.0 T, and to have a clear room-temperature bore (before the introduction of gradient coils) of 80–100 cm. Most systems of this type are screened to reduce the fringing fields and today have relatively short 1.5–1.7 m) bore length. After introduction of the gradient coils and rf body coil, the patient access is reduced to 55–65 cm (see ***Gradient Coil Systems*** and ***Radiofrequency Systems and Coils for MRI and MRS***). A typical 2.0 T whole body superconducting MR magnet system is shown in Figure 1.

Higher-field magnets have been introduced in the late 1990s that operate at field strengths of 3.0 T, 4.0 T, and even as high as 8.0 T (with an 80 cm bore). In addition, the last few years have seen the increasing popularity of open-aspect, low-field (0.2–0.35 T), magnets. These magnets, which depart from the cylindrical format, give greater access to the patient through gaps in the structure. Most open-aspect magnet systems utilize permanent magnetic materials and operate in the field strength range 0.2–0.25 T; however, systems operating at 0.35 T have also been introduced that utilize superconducting driver coils. Higher field strength (greater than 0.5 T) open-access magnet systems are already in an advanced stage of development and are expected to be commercially available within a few years.

The 1990s have also seen an increase in the demand for MRI magnet systems for interventional or minimally invasive surgical studies. One of the magnet design solutions chosen to address this application is the split pair or 'double doughnut' superconducting magnet system. These systems are of standard cylindrical geometry but the magnet and cryostat are split into two halves and are separated such that the clinician or surgeon can gain access to the patient through the split. Field strengths for these types of system are generally limited to 0.5 T.

2 MAGNET DESIGN

Cryogenic (superconducting) magnet systems rely on the physical phenomenon of superconductivity,[2] whereby certain materials behave as if they have no measurable dc electrical resistivity when they are cooled below what is defined as their 'critical temperature'. The wire used in the construction of such magnets is normally niobium-titanium (NbTi) which has a critical temperature of approximately 10 K and consists of a number of filaments of NbTi embedded in a copper stabilizing matrix. Most whole body superconducting MR magnets are wound from NbTi and are designed to operate in a reservoir of liquid helium boiling at a temperature of 4.2 K.

The magnet consists of a group of coaxial coils, the positions and number of turns of which are carefully chosen to produce a homogeneous field region at its center.[3] The coils are electrically connected together in series, and a complete circuit is formed with a superconducting switch. The switch consists of a short length of superconducting wire which is in close contact with a heating element. When the heater is on, the switch is warmed above its critical temperature and there is no longer a continuous superconducting circuit. Under these conditions the switch is said to be 'open', and current can be run into the magnet windings using a dc power supply. When the current flowing through the magnet is such that the central field is at the required value, the switch heater can be turned off. The switch quickly cools, becomes superconducting and so forms a continuous superconducting circuit. The switch is now referred to as being 'closed', and the power supply can be removed, leaving the current flowing in the magnet. The magnet is now operating in the persistent mode and will have a field stability of typically better than 0.1 ppm h^{-1}. A simple superconducting magnet circuit is shown schematically in Figure 2.

Figure 1 A 2.0 T whole body superconducting MR magnet system

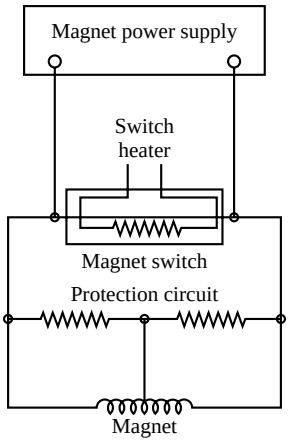

Figure 2 Schematic drawing of a superconducting magnet circuit

In the event of an emergency it may be necessary to de-energize the magnet within a few seconds. Special heaters placed in good thermal contact with the magnet windings are generally provided for this purpose. The heaters are driven by a device known as an emergency run-down unit (ERDU). When the ERDU is operated, the heaters warm part of the magnet windings above their critical temperature and thus out of the superconducting state. Once part of the magnet windings are resistive they are further warmed by ohmic heating and the current quickly decays. The heat generated by the magnet causes the liquid helium surrounding it to evaporate and the evaporated gas is quickly expelled from the cryostat. This process is referred to as a 'quench'.

In order to avoid damage to the magnet windings occurring during a quench, a protection circuit is normally employed.[4] This circuit, which typically consists of resistors or diodes, is connected in parallel across the magnet or individual sections of the magnet windings, and prevents excessive heat generation within the windings from occurring. The protection circuit is also used to prevent potentially harmful high voltages being generated within the windings.

3 CRYOSTAT DESIGN

The liquid helium vessel containing the magnet needs to be thermally isolated from room temperature, and therefore the three principal mechanisms of heat transfer (convection, conduction, and radiation) need to be minimized.

Heat transfer via convection is almost completely eliminated by evacuating the cryostat. The external structure of the cryostat which contains the vacuum is normally referred to as the 'outer vacuum container' (OVC). Heat conduction from the OVC to the helium vessel is minimized by ensuring that the internal mechanical supports for the helium reservoir are long, of small cross-section, and made from materials of low thermal conductivity. Stainless steel, titanium and glass-reinforced plastic (GRP) are commonly used materials for the internal suspension of the cryostat. Radiation from the OVC to the liquid helium vessel is intercepted with radiation shields. Normally there are two shields which completely surround the helium reservoir. These shields can be cooled by one of two methods. Some cryostats utilize two-stage cryorefrigerators,[5] with each stage being thermally linked to one of the radiation shields. The cryorefrigeration system is based on the Gifford–McMahon principle using a closed helium gas cycle. The system comprises an expansion chamber, often referred to as a 'cold head', connected via high pressure gas lines to a compressor. The cycle works by allowing the helium gas to expand and cool in the expansion chamber. The helium gas is circulated to a compressor and the heat is removed from the system as the gas is recompressed. By this method typical inner and outer radiation shield temperatures of 20 and 80 K, respectively, are achieved.

Alternatively, some cryostats are designed with an integral liquid nitrogen reservoir which is used to serve as the outermost radiation shield and is maintained at the boiling point of liquid nitrogen (77 K). The inner radiation shield is thermally linked to part of the neck portion of the helium reservoir, and is cooled by the evaporated gas leaving the helium reservoir.

Radiation effects are further minimized by the use of multilayers of thin aluminized Mylar (called 'superinsulation') which is wrapped over the shields. Typically up to 50 layers of superinsulation are wrapped over the radiation shields. Figure 3 shows a typical cross-section of a cryostat with an integral liquid nitrogen reservoir.

The cryostat cannot completely thermally isolate the helium vessel, and so it is inevitable that small amounts of liquid helium will evaporate. The helium reservoir normally contains enough liquid helium to keep the magnet at least partially immersed in liquid for typically up to a year. Eventually this evaporated helium will need to be replenished. Liquid helium

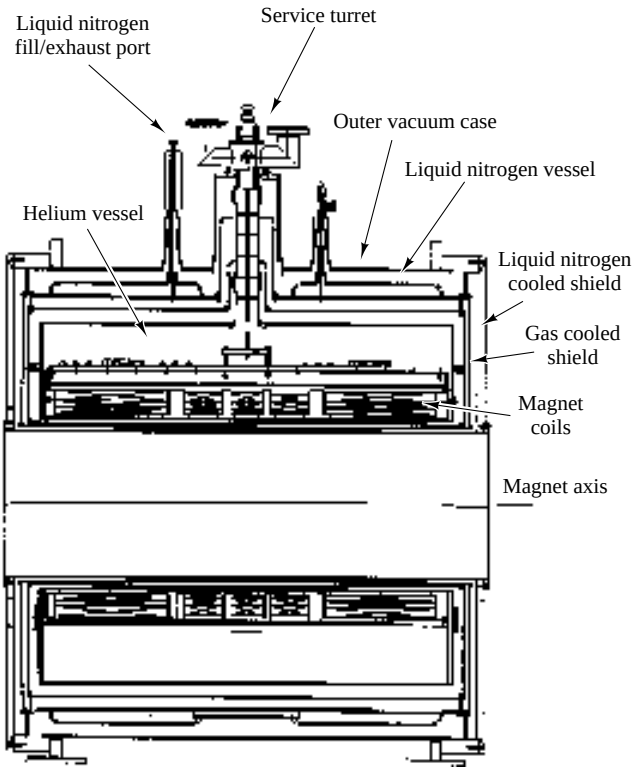

Figure 3 Cross section of a cryostat with an integral liquid nitrogen reservoir

for refilling is normally supplied in transport Dewars and is transferred to the cryostat using a vacuum-insulated transfer siphon which minimizes the heat load on the helium as it passes through.

Recent developments in cryocooler technology include two-stage refrigerators that achieve temperatures below 4.2 K at the second stage. This allows the possibility of completely stopping the helium boil-off or eliminating the need for liquid helium and relying on conduction cooling of the superconducting windings. These devices rely on special rare-earth compounds in their internal heat-exchanger elements to achieve the low base temperature. Since they do not rely on the expansion of gas through a Joule–Thompson valve, with the consequent danger of blockage by contamination, they promise much improved reliability. Many MRI system manufacturers are now beginning to offer instruments with zero boil-off capability.

In the event of a quench a large volume of gas will be expelled from the cryostat in a short period of time, giving rise to a potential asphyxiation hazard for patients and for personnel operating the system. Unless the magnet is sited in an extremely spacious room it will be necessary to provide exhaust ducting from the cryostat to the outside environment. Gas flow rates during a quench can be very high, and therefore the actual size, length and route of the pipework should be carefully chosen to avoid excessive pressure build up due to flow impedance.

4 FIELD SHIMMING

Although the magnet coils are designed to produce a homogeneous field in the central region of the magnet bore, manufacturing tolerances and effects from external magnetic sources will disturb the homogeneity. Small magnetic fields can be generated to cancel these effects, and this process is called 'field shimming'.[6–8] The field is normally shimmed using either small pieces of iron (passive shims), small coils (shim coils), or a combination of both.[9] Shim coils can be wound from superconducting wire and placed inside the helium vessel. They then operate in a similar way to the magnet. The current in each superconducting shim is set during initial operation, after which the shim power supply can be removed leaving the shim permanently energized at the appropriate current. Alternatively, shim coils can be wound from conventional conductor and operated at room temperature in the warm bore of the magnet. In this configuration the shim coils need to be continuously driven from a suitable high stability power supply.

The variation of the central field of the magnet is usually expressed as a sum of Legendre polynomials and associated Legendre polynomials in a coordinate system in which the origin is at the magnet center. The following equation shows the expansion expressed in spherical coordinates:

$$\hat{H}(r,\theta,\phi) = \sum_{n=0}^{\infty}\sum_{m=0}^{m=n} r^n P_n^m(\cos\theta)[A_n^m\cos(m\phi) + B_n^m\sin(m\phi)] \qquad (1)$$

where the functions $P_n^m(\cos\theta)$ are known as associated Legendre polynomials; A_n^m and B_n^m are constants which define the field variation; r, θ, and ϕ are the polar coordinates; and m and n are the polynomial order and degree, respectively.

This is a convenient method of specifying the field variation, as reasonably good approximations to Legendre polynomials can be produced easily with a series of circular arcs. The arcs can then be connected together to form a set of shim coils. A magnet may be supplied with several shim channels, each shim channel being identified by the particular shape of field it produces (defined in the Cartesian coordinate system with the magnet axis defined as the z axis). Table 1 lists the Cartesian representation of the most commonly used shim channels.

Table 1 Cartesian Representation of the Most Commonly Used Shim Channels

Shim	Order, n	Degree, m	Function[a]
z^1	1	0	z
z^2	2	0	$z^2 - 0.5p^2$
z^3	3	0	$z^3 - 1.5p^2z$
z^4	4	0	$z^4 - 3p^2z^2 + 0.375p^4$
x	1	1	x
y	1	1	y
zx	2	1	$3zx$
zy	2	1	$3zy$
$x^2 - y^2$	2	2	$3(x^2 - y^2)$
xy	2	2	$3(2xy)$
z^2x	3	1	$6(z^2 - 0.25p^2)x$
z^2y	3	1	$6(z^2 - 0.25p^2)y$
$z(x^2 - y^2)$	3	2	$15z(x^2 - y^2)$
zxy	3	2	$15z(2xy)$
x^3	3	3	$15(x^3 - 3xy^2)$
y^3	3	3	$15(y^3 - 3yx^2)$

[a] $p^2 = x^2 + y^2$

During initial installation of a magnet system the variation in the central field is normally mapped by measuring the field strength at selected points in the central field region. The field map can then be analyzed and the required current in each shim channel or the required passive shim distribution calculated.

5 SITING ISSUES AND MAGNETIC SHIELDING

The stray field from an unshielded whole body superconducting magnet will extend far beyond the confines of the room temperature bore. For example, the 0.5 mT contour from a 1.5 T, 1000 mm room temperature bore magnet will typically extend to 11 m on the axis from the magnet center (the earth's magnetic field is approximately 0.05 mT). Most health and safety guidelines[10] require that people with cardiac pacemakers or other mechanically active implants be excluded from areas in which the magnetic field exceeds 0.5 mT. In regions closer to the magnet where the field exceeds 5 mT ferromagnetic objects start to experience a magnetic force comparable with their weight. In these regions such objects can become extremely dangerous projectiles. In addition to the dangers posed to individuals, certain equipment can be particularly sensitive to magnetic fields. Table 2 gives a guide to the maximum field levels to which various types of equipment should be exposed.

Table 2 Guidelines for the Maximum Field Levels to which Various Equipment should be Exposed

Equipment[a]	Maximum Exposure (mT)
PET scanners	0.1
Nuclear medicine instruments	0.1
CT scanners	0.1
Ultrasound instruments	0.1
Linear accelerators	0.1
Lithotriptors	0.1
Image intensifiers	0.1
Televisions and video monitors	0.1
Computer screens and terminals	0.1
Electron microscopes	0.1
High precision measuring scales	0.1
Cyclotrons	0.1
Cardiac pacemakers	0.5
Neurostimulators	0.5
Biostimulators	0.5
Magnetic media (floppy disks, etc.)	1.0
Video recorders	1.0
X-ray tubes	1.0
Radiography equipment	1.0
Analog watches and clocks	1.0

[a]CT, computed tomography.

The fringe field of a magnet system can be reduced either by passive shielding or by active shielding. Passive shielding normally involves the use of mild steel. The steel can be placed within, on, or in close proximity to the cryostat, such that it provides a 'return path' for the magnetic field outside the windings and thereby reduces the overall fringe field. The greater the weight of steel used the greater the shielding effect. Care must be taken to balance the potentially high forces between the magnet and the shield and to ensure that the shield does not disturb the central field homogeneity. Therefore shields placed close to the magnet generally have a high degree of geometric symmetry. Steel placed more distant from the magnet has less effect on the overall fringe field, but can still provide effective local shielding.

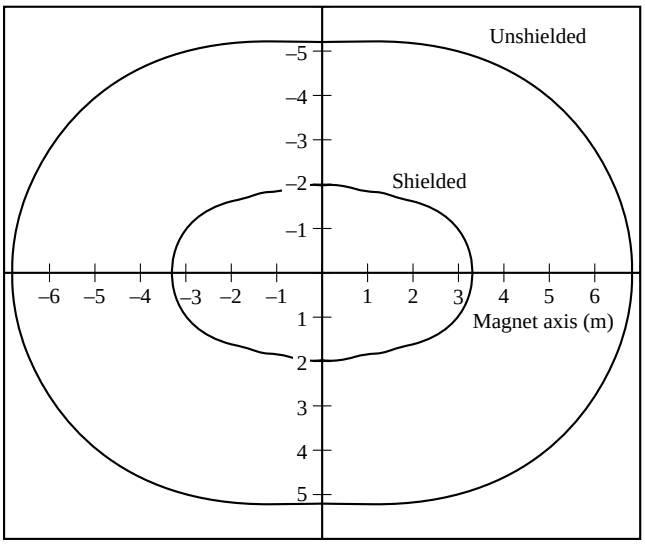

Figure 4 Comparison of the stray fields from an actively shielded and an unshielded 0.5 T, 900 mm bore magnet

Actively shielded magnets have additional superconducting coils located outside the main coil windings. These extra coils are connected in series with the main coil windings and have their current flow direction reversed. The coil positions and the number of turns are selected to ensure a resultant homogeneous central field region whilst reducing the magnet's fringe field. The advantage of using superconducting coils compared with steel is mainly that the system weight is minimized. Typically 500 kg of superconductor provides the same amount of shielding as 10 000 kg of mild steel. Except for magnets of ultrahigh field strength (greater than 4.0 T), where the technical difficulties are severe, active shielding is usually the preferred method. Figure 4 compares the fringe fields (0.5 mT) from a 0.5 T, 900 mm room temperature bore magnet system in nonshielded and actively shielded configurations.

6 HIGH FIELD SUPERCONDUCTING MAGNET SYSTEMS

Most whole body superconducting magnet systems used for routine clinical MRI operate at field strengths between 0.5 and 2.0 T. However, recent research in areas such as MR spectroscopy, spectroscopic imaging and functional imaging benefit from the improved signal-to-noise ratio and spectral resolution gained from operating at high field strengths (above 2.0 T). Currently, 3.0 and 4.0 T is proving to be a popular field strength for such applications. These systems are now being offered with active screening, which significantly reduces siting problems.

Application-specific 3.0 T systems, with reduced bore size, have recently been introduced, primarily for neuroscanning applications. These systems provide an ultracompact alternative to the whole-body systems. Using NbTi superconductor, whole-body sized magnets with a field strength of up to 10.0 T are theoretically possible. Two ultrahigh field magnets have already been delivered and installed, an 8.0 T, 80 cm bore magnet is being used at Ohio State University and a 7.0 T, 90 cm bore magnet is in use at the University of Minnesota. Magnets at higher fields than these are already in the planning stage.

Ultrahigh field strength magnets have extremely large fringe fields, and therefore siting and shielding issues become very important considerations with such systems. Active screening is technically difficult and iron screens are extremely heavy. Therefore these systems often need to be sited in new buildings where a large area can be reserved for the magnet.

Magnets designed to operate above 10.0 T require part of the coil windings to be constructed from materials other than NbTi. This is because the critical current of NbTi starts to fall very rapidly once the background magnetic field on the superconductor exceeds 10.0 T. Therefore, the innermost windings of the magnet are wound from a material with a higher critical current at these high background field levels. The superconducting material normally chosen is niobium-tin (Nb_3Sn) which has a critical temperature of approximately 18 K. Unfortunately, Nb_3Sn tends to be a very brittle material

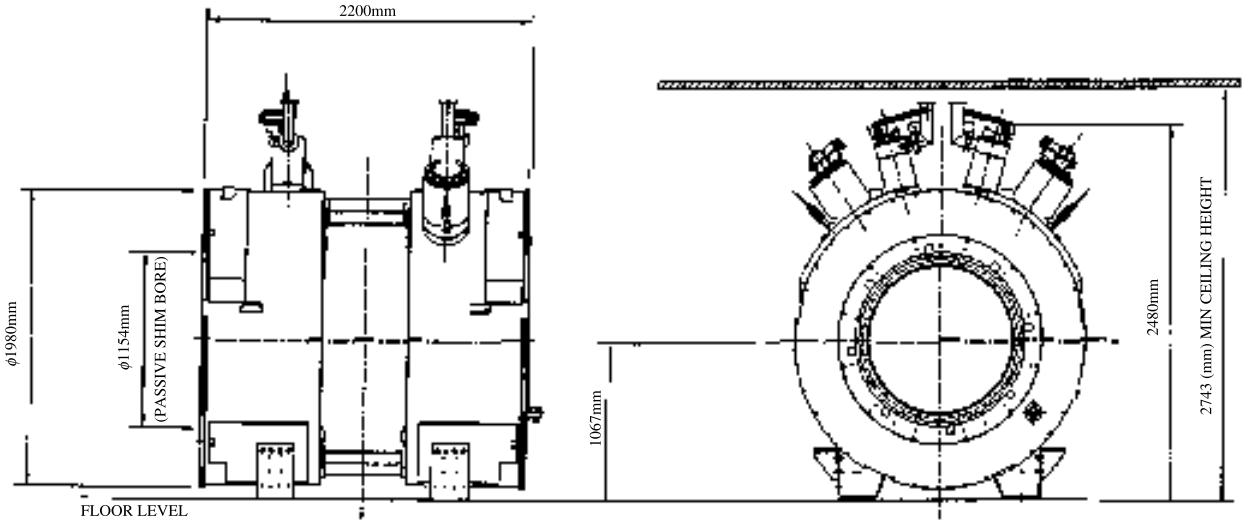

Figure 5 An open aspect MR magnet in the Helmholtz pair arrangement

and, as such, is very difficult to handle during manufacture. It is also very expensive compared with NbTi, and therefore magnets which incorporate Nb_3Sn windings tend generally to be limited to small bore analytical NMR magnets.

7 MOBILE SUPERCONDUCTING MAGNET SYSTEMS

A complete imaging facility including a whole body superconducting magnet may be built on a trailer or bus and taken to sites where normally such facilities would not be available. These systems have tended to serve a number of sites within a region. Normally the magnet is energized when the mobile unit arrives on site and is then de-energized before moving to a new location. The magnets used in mobile applications generally have the ability to be ramped rapidly to field and then shimmed automatically. It is typical for the magnet to be ready for MR use within 1 hour of arriving at a site.

8 NOVEL MAGNET GEOMETRIES

Even today's relatively short-bore cylindrical geometry magnets can present problems of claustrophobia for some patients. It is also desirable for the clinician to have good access to the patient, both to reassure them and to be able to perform simple clinical procedures such as insertion of catheters during imaging. These requirements have led to the development of MR magnets with 'open access'.

One example of an open-aspect MR magnet is the Helmholtz pair arrangement (shown in figure 5) whereby two cryostats are positioned opposite each other with an intervening gap. The intervening gap allows an attendant or even a surgeon to have access to the patient during the imaging process. There needs to be connection between the two cryostats in which to feed magnet wires and to allow cooling to be shared between the halves. A particular design challenge for this type of magnet is to contain the relatively high attractive forces between the halves with a minimally obtrusive structure. Some versions of this format are actively screened; currently 0.5 T is the highest field strength offered.

Another example of an open-access cryogenic magnet is the 'super-C'. This consists of a pair of superconducting driver coils with an iron structure forming pole pieces and a return flux path. A variety of formats have become available using superconducting drivers with iron structures to produce a homogeneous field region. Some have pole gaps in the horizontal direction, others in the vertical direction.

9 RELATED ARTICLES

Gradient Coil Systems; Radiofrequency Systems and Coils for MRI and MRS; Resistive and Permanent Magnets for Whole Body MRI.

10 REFERENCES

1. P. Hanley, *Br. Med. Bull.*, 1984, **40**, 125.
2. R. G. Scurlock, 'Low Temperature Behaviour of Solids', Routledge Kegan Paul, London, 1966.
3. D. B. Montgomery, 'Solenoid Magnet Design', Wiley-Interscience, New York, 1969.
4. M. N. Wilson, 'Superconducting Magnets', Clarendon, Oxford, 1983.
5. R. A. Ackerman, 'Proceedings of the Sixth Cryocoolers Conference', 1991, p. 3.
6. R. C. Longsworth, 'Advances in Cryogenic Engineering', Plenum, New York, 1986, Vol. 31, p. 517.
7. G. N. Chmurny & D. I. Hoult 'Concepts in Magnetic Resonance' 1990, 2, 131.
8. F. Romeo and D. I. Hoult, *Magn. Reson. Med.*, 1984, **1**, 44.
9. E. N. Chen and D. I. Hoult 'Biomedical Magnetic Resonance Technology', Adam Hilger/American Institute of Physics, Bristol/New York, 1989.
10. J. Schaefer, in 'Biomedical Magnetic Resonance Imaging', VCH, Weinheim, 1988, Chap. 13.

Biographical Sketches

David L. Rayner. *b* 1947. B.Sc. (physics), London University, 1969; Ph.D. (low temperature physics), University of Southampton, UK, 1976. Introduced to superconducting magnet systems whilst working at Thor Cryogenics Ltd, UK 1979–82. Founded Magnex Scientific Ltd in 1982; currently Managing Director.

Peter J. Feenan. *b* 1951. B.Sc. (physics), Ph.D. (low temperature physics), 1976, Leeds University, UK. After several years of postdoctoral research in low temperature physics, joined Oxford Instruments plc where gained experience in magnet design for NMR. Joined Magnex in 1983; currently Technical Director.

Rory J. Warner. *b* 1962. B.Sc. (physics), Birmingham University, UK, 1984. Worked at Oxford Research Systems Ltd, Abingdon, UK, for 3 years as an NMR systems engineer before joining Magnex Scientific in 1987 where is currently employed as a Product Manager.

Design and Use of Internal Receiver Coils for MRI

Nandita M. deSouza
Imperial College School of Medicine, London, UK

David J. Gilderdale
Engineering Consultant, UK

and

Glyn A. Coutts
Marconi Medical Systems, UK

1 INTRODUCTION

The motivation for investigating the use of internal coils in MRI and MRS is based on the fact that the closer an MR signal detector is placed to its target the better the signal-to-noise ratio (SNR) of the resultant data. Abragam described the significance of the 'filling factor' of an object in a coil[1] and Hoult and Richards developed the theory of the SNR of the MR experiment round this concept.[2] SNR is maximized if the coil size is matched to that of the region of interest; coils located very close to the target to be studied can achieve dramatic improvements in SNR relative to conventional external enveloping coils. Internal access for such small local coils may be gained via natural orifices or using other minimally invasive techniques.

In the first part of this article the design and construction of the current range of internal coils used for human MRI is reviewed. Discussion of types that are in development and which may become of clinical relevance in the next few years follows, including descriptions of their clinical use where relevant. The second section describes the main clinical applications to date. Development has been gathering pace during the 1990s, and it is expected that within the next few years the variety of devices will increase substantially.

1.1 Historical Note

The first implanted or inserted coils to be described were intended for spectroscopic investigations.[3,4] These were followed by initial studies of devices for MRI.[5,6] The first clinical studies using an inflatable rectal probe (Medrad Inc., Pittsburgh, USA) were published in 1989.[7] Various studies were undertaken with this probe (e.g., that of Schnall *et al.*[8]), but it was not until 1992 that other designs began to appear. The first of these was a coil designed for the imaging of the cervix;[9] this was followed by probes for the anus[10,11] and an alternative design for the rectum.[12] Other coils were used in conjunction with endoscopes, principally for gastroscopy,[13,14] and smaller versions were designed for such applications as imaging the inner ear[15], and the female urethra.[16]

All these devices are designed for insertion through natural orifices to acquire imaging (or in some instances, spectroscopic) data from adjacent regions of interest. Another class of detector acts as markers. An early design used a small coil to mark the tip of a catheter.[17] Later versions of this concept were designed to generate signals along significant lengths of conductor, mimicking a guidewire. These included stub aerials[18,19] and extended coil windings.[20] Of these, the aerial version gives a wider field of view and may eventually prove useful for local imaging.[19] We have used the same approach to mark the location of a naso-gastric tube (unpublished data), and it is likely that other clinical applications will develop over the next few years. A specialist application is in the development of marker (fiducial) technology, which provides a spatial reference point. Fiducials can be passive (as developed primarily for frameless stereotaxy[21]) or active, in which rf circuitry is used to enhance or characterize signals. The latter typically use tiny vials of an MR-visible material enclosed within the windings of a very small coil.[22] Fiducial markers may also be integrated into internal coils or biopsy devices in order to track their trajectories.[23]

2 DESIGN CONSIDERATIONS

2.1 General Features

Insertable coils may be designed for use in one of three ways: (i) as an enveloping coil with the principal target for study being tissue within the coil (the cervical coil described here uses this strategy); (ii) as an 'inside-out' coil in which a winding design normally used in MRI to produce images from the volume enclosed within it is used to obtain data from outside it (e.g., the endoanal coil); (iii) as a coil used in a manner analogous to that of a conventional surface coil (e.g., the endorectal coil).

Insertable coils can be used as receivers only (either single or in arrays) or as combined transmit/receivers. In general, the coils are directly coupled to the input receiver via a cable. However, in certain specific applications (e.g., endoscopic) the coil may be inductively coupled to the external receiver.

Coil size is limited by the size of the orifice through which it is inserted and by other structures en route to its intended location. The useful field-of-view of the coil is a function of its dimensions. Typically, for a saddle coil in which the winding width is a quarter of its length, sensitivity drops to about one third of that at the coil surface at a distance equal to the diameter of the former on which it is wound. While it is arguable as to what is acceptable from a SNR point of view, a rule of thumb is that the useful field-of-view of a coil is approximately equal to twice the winding width.

Patient safety is a key requirement. In most instances, electrical connections have to be made to the outside world and there are potential risks from conductors behaving as aerials, or from the formation of conducting loops. Insulation of conductors and biocompatibility of constructional materials are, therefore, important. A further complication is the sterilization of devices. Unless the devices are cheap enough to be discarded, consideration of the requirements for cleaning and sterilization for re-use is necessary. In order to avoid motion artefact degrading imaging quality, the coil also needs to be

immobilized relative to both the machine measurement frame and the tissue surrounding it during data acquisition.

2.2 Transmit/Receive Operation

In typical MRI studies where spatial encoding is used with the coil in receive mode, voxels are smaller than the coil dimensions and coherence of signal phase is preserved within each voxel. The SNR is much lower in spectroscopic data acquisitions than in imaging studies, and the voxel size is correspondingly larger. The filling factor gains in SNR associated with MRI do not then apply. This is because the rapid changes in flux direction relative to the small coil result in partial signal cancellation if the whole volume round the coil is excited uniformly by an external transmitter (Figure 1) and there is a subsequent reduction in the net SNR in the large voxel studied. A transmit/receive coil avoids this signal loss because the phase and magnitude of the transmit field mirrors the flux pattern in the receive mode.

Internal transmit/receive coils may also be used for imaging in cases where the volume of excitation must be restricted. This has proved useful in the case of the twisted pair guidewire tracking device and in the cervical coil where rf irradiation to a pregnant uterus may be undesirable.

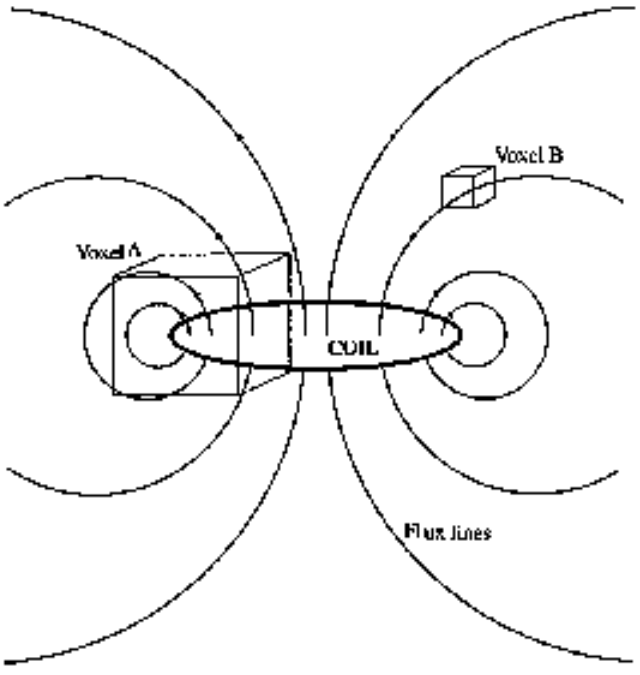

Figure 1 The effect on signal of the voxel size relative to coil size. In a voxel large enough to envelop flux in opposing directions (A), spins in regions of opposing flux cancel each other and reduce the net signal. In a small voxel (B), the flux is unidirectional and all the spins contribute to the net signal. If, however, the coil is used to transmit as well as receive, the flux reversal applies in both transmit and receive modes even in a large voxel and all the spins contribute to the net signal

2.3 Tuning, Matching, and Decoupling

Solenoidal magnets commonly operate between proton resonant frequencies of 21 and 65 MHz, while magnets with transaxial fields currently have proton resonant frequencies in the range of 8.1–25 MHz. Since the windings are constrained to be similar at all fields for any one class of coil, and are of low inductance, all rely on substantial tuning capacitors mounted close to the imaging field-of-view for good performance. The requirement for small components with minimal ferromagnetic content is an important consideration particularly for capacitators.

Figure 2 shows the tuning, matching, and decoupling circuitry for the endorectal array described by Gilderdale *et al*.[24] This circuitry is designed for receive-only operation and includes the components needed for active decoupling of rf transmitter pulses. The component values, and circuit detail, are those for operation at 0.5 T (21.3 MHz) in a solenoidal magnet. Active decoupling is used to ensure that the coupling between the receiver coil and the transmit field is eliminated and is independent of the time-dependent rf $\boldsymbol{B}_1$ fields, levels, though it does require that suitable control lines are available from the machine being used.

2.4 Direct or Inductive Coupling

The elimination of cable connections to internal coils is very attractive in some circumstances; for example, if there is reason to implant a detector (in the same way as a pacemaker) and leave it in position while the patient continues with other activities between repetitive scans. The approach is also potentially valuable in circumstances where there may be technical difficulties in making connections, where there are safety issues if direct coupling is used, and where cabling becomes an embarrassment (either because of the number or the extent of the cables).[4,22,25]

Normally the external and internal coils are loosely coupled, since the latter are typically at a distance from the former. The external coils are several times larger in dimension than the internal coils; reciprocity means that the system is generally applicable to reception of signals as well as transmission. Figure 3 is an illustration of the technique used with a small fiducial coil, used either as a position marker or to track motion. The small coil can act as a flux amplifier which enables a 90° flip angle to be achieved within the marker sample while the magnetization of the surrounding tissue experiences negligible disturbance. This allows motion tracking to be interleaved with image data acquisition without the latter being compromised.

2.5 Orientation of Coils Relative to the Main Field

Certain coil designs (e.g., enveloping solenoid used for imaging the uterine cervix) give near optimal performance because anatomic features allow them to be orientated perpendicularly to the fixed magnetic flux density field $\boldsymbol{B}_0$. However, in situations where the orientation is not fixed (e.g., in endoscopic applications) significant improvements in SNR of internal coils and implanted devices can be achieved with a quadrature design. At least one of the two quadrature windings must be orthogonal to the main field and so capable of detecting excited

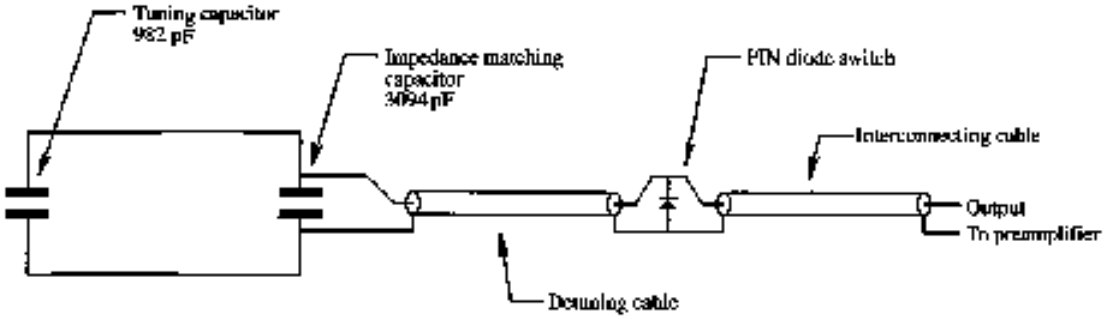

Figure 2 Circuitry associated with the endorectal array

signals. Three orthogonal windings, though increasingly hard to implement in a small unit, ensure signal detection at all times.

Because of anatomic considerations for coil insertion, the formers are often cylindrical. This implies that windings are either short solenoids or saddles. Variants of these designs were the basis of most external receiver coils employed in early MRI systems using cryogenic magnets.[26]

2.6 Artefacts

The sensitivity profile of a small internal coil results in very high signal adjacent to the coil surface and obscures image detail in this region. In general, a correction algorithm needs to be applied to the images to optimize their interpretation. In some applications it is possible to use the known sensitivity profile of the receiver coil to generate the correction.

As with conventional external coils, loss of signal occurs wherever the flux lines are parallel to the $\boldsymbol{B}_0$ field. If this happens within the imaging region of interest it can cause 'blind spot' artefacts. This is of particular relevance in endoscopic applications and can be counteracted by the use of quadrature designs (cf. Section 2.5).

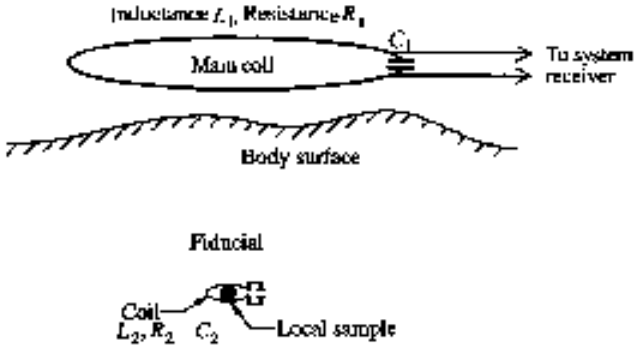

Figure 3 Coupling of a small inserted or implanted coil and a large external one. The shaded volume is a small vial of an appropriate NMR signal-generating material around which is wound a small tuned coil of inductance L_2 and resistance R_2, which is tuned to the system resonance frequency by a capacity C_2. The large coil, which is connected to the scanner, has respective tuning parameters L_1, R_1, and C_1. Its quality factor (Q, reflecting the efficiency of the system), is given by $\omega L_1/R_1$, where ω is frequency

The most pernicious artefact encountered with internal coils is caused by motion, in which the coils move relative to the tissues of interest. Even when the coil is apparently firmly situated within the body, any patient motion can re-orientate the coil relative to the target source of signals. In endoscopic applications where the coil is located at, or ahead of, the tip of a flexible endoscope, the coil is liable to uncontrollable small movements. Reduction of motion artefact can be accomplished using fast imaging techniques; however, these not only suffer from a lack of robustness but also the small fields-of-view and thin slices used with internal coils make enormous demands on the machine gradients. Other well-established methods for motion artefact control use navigator echoes and phase-encode reordering, but again with the restricted field-of-view from the internal receiver, anatomic landmarks are difficult to identify clearly. Currently we are investigating the use of fiducial markers attached to the imaging coil former to generate reference signals that permit correction of the incoming data.[27]

Motion artefact can also be controlled by providing a firm anchor in the form of a clamp for the coils wherever possible. The unit shown in Figure 4 is suitable for clamping coils for use in the pelvis. The whole assembly is made from Delrin, with the baseplate being underneath the patient's thighs and so being held in position by their weight. The double bosshead arrangement allows sufficient flexibility in orientation for a range of coils, and the whole unit is simple to clean.

3 IMAGING TECHNIQUE

Imaging techniques at 0.5 T (Asset) or at 1.0 T (HPQ Vista, Picker International, Highland Heights, OH) include T_1-weighted spin echo [repetition time (*TR*) range 720–820 ms; echo time (*TE*) 20 ms], T_2-weighted spin echo (*TR* 2500 ms; *TE* 80 ms), and fast spin echo (*TR* 4500 ms; *TE* 96 ms) sequences. Transverse and sagittal 3.5 mm contiguous slices obtained with a 192×256 matrix, two to four signal averages, and a 10–12 cm field-of-view, provide optimal resolution while maintaining the SNR. In addition, a short inversion time (107 ms at 0.5 T) inversion recovery sequence (STIR) (*TR* 2500 ms; *TE* 30 ms) provides robust fat suppression and enables delineation of lesions with long T_2 times, for example fluid collections and tumors.

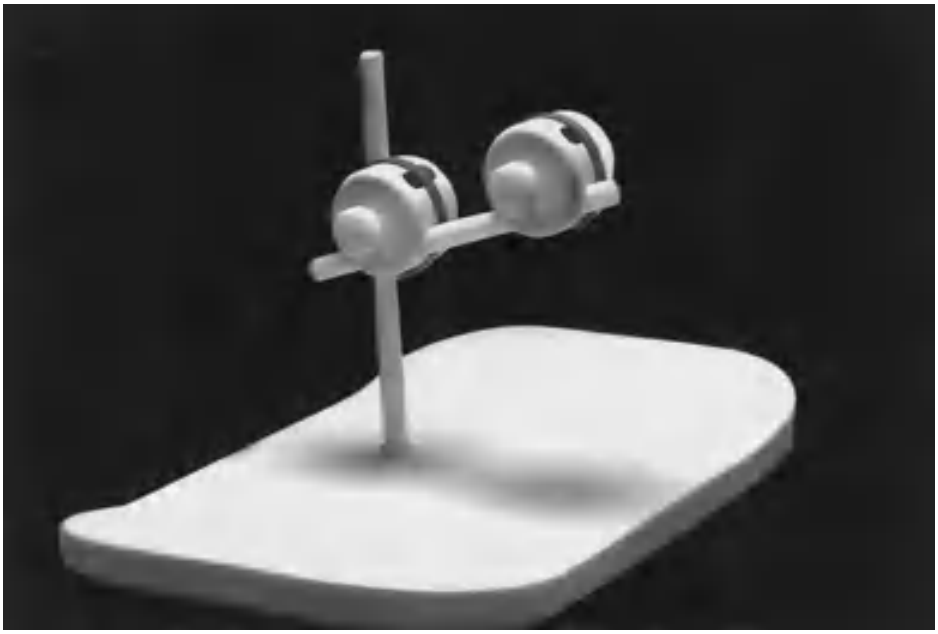

Figure 4 A clamp used to immobilize coils. For pelvic applications, the baseplate is placed under the patient's thighs. The double bosshead provides sufficient adjustment to cope with variations for the different coils and for individual patient requirements

4 CONSTRUCTION AND APPLICATION OF TYPICAL COILS

Coil formers are made of an acetyl homopolymer (Delrin), as this is mechanically easy to handle and machine, has good rf properties, and is a nontoxic, biocompatible material that meets sterilization requirements. Delrin is water resistant and retains its shape despite repeated soaking in noxious sterilization fluids. The coils are wound from solid copper wire and are coated with an epoxy resin that is water resistant, biocompatible, and provides a seal for the electronics. In our experience, a typical coil has lasted for several hundred patient examinations without requiring renewal. The following sections describe the range of coils that we have developed and indicate what may be possible as capabilities expand.

4.1 Cervical Coils

Intravaginal enveloping cervical coils have been designed for use at 0.5, 1.0, and 1.5 T to operate in receive mode. A range of coil diameters has been investigated, 37 mm being a good compromise between accommodation of the cervix and ease of insertion. The coil is mounted on a cylindrical Delrin former attached to a 20 cm long Delrin handle (Figure 5a).

The anatomy of the uterine cervix provides a rare opportunity to exploit the superior SNR performance of a solenoid coil in a conventional MR scanner where $\boldsymbol{B}_0$ is parallel to the long axis of the patient. Although the use of a coil in the vagina to image the cervix has been described by others,[28] the coils used had a simple loop geometry. The use of an enveloping cervical ring provides the best resolution of the cervix and the adjacent parametrium; with good positioning, such a coil provides a uniform signal from the structure it encircles. The coil is easy to position following digital examination, particularly in the anteverted uterus. However, even in retroverted uteri, a speculum examination is unnecessary. Although artefacts may obscure a few millimetres of the surrounding vaginal vault because of the proximity of the coil, these artefacts cause no problems in diagnostic accuracy. Also, the coil assists with interpretation by distending the vaginal vault and separating the vaginal wall and cervix.

4.1.1 Normal Anatomy

Both T_1- and T_2-weighted images show the normal cervix to consist of two distinct stromal zones and the mucosa surrounding the central canal.[29] The mucosa has a relatively high signal on both T_1- and T_2-weighted images. Mucosal detail can be appreciated with this technique (pixel size 0.6 mm) (Figure 6). It shows a smooth and regular outline in the nulliparous cervix and a more irregular and indented outline in the parous cervix. In addition, dilated glands filled with secretions are sometimes seen in the latter.

On administration of 0.1 mmol kg^{-1} body weight gadopentate dimeglumine, brisk mucosal enhancement begins at 30 s after injection and peaks at 120 s. The fibromuscular stroma enhances more slowly, with the outer ring showing more prominent enhancement, making zonal differentiation maximum at 90 s.

4.1.2 Cervical Cancer

There is good agreement between the high-resolution MRI findings obtained with an endovaginal coil and the pathological findings in patients with clinical evidence of stage I cervical cancer.[30] With standard body coil images, it is often difficult to assess the integrity of the stromal ring (Figure 7). The cervical coil makes such assessments easier, which has been confirmed by comparison with histology.[30]

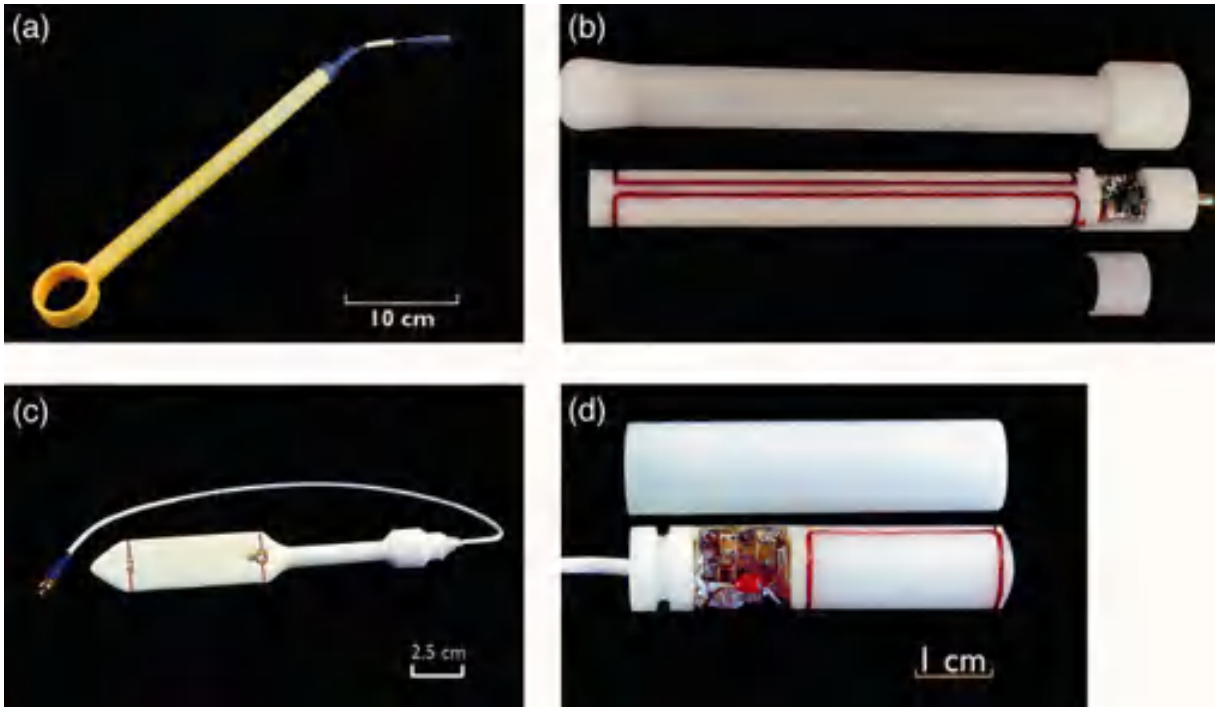

Figure 5 Coils for internal use. (a) Cervical coil; (b) cylindrical anal coil; (c) solid endorectal coil; (d) coil for use with a gastroscope or colonoscope

Parametrial invasion may be recognized when there is loss of the low-signal-intensity stripe of normal stroma of the cervix together with diffuse or localized abnormal signal intensity within the parametrial region. Parametrial tumor spread may be overestimated because of peritumoral inflammatory tissue, which is well known as a cause of tumor overstaging.[30] With carcinoma of the cervix, intravenous contrast agents are of limited value,[31] although dynamic contrast enhancement has been

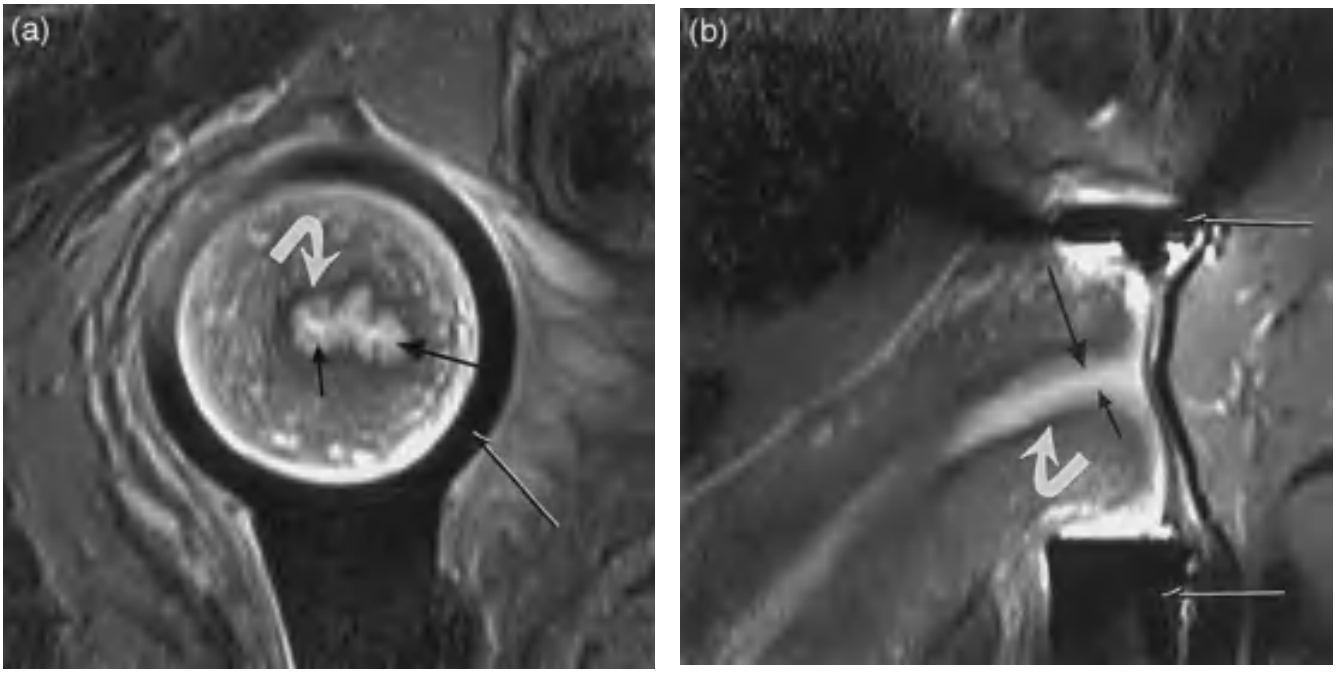

Figure 6 Images of the normal cervix using T_2-weighted spin echo (repetition time 2500 ms; echo time 80 ms) images through the cervix in (a) transverse and (b) sagittal planes. The coil is seen as an outer ring of signal void (black and white arrows). The mucosal layer is irregular (small straight arrow). There is an inner zone of low signal intensity (curved arrow) that corresponds to a highly cellular layer and an outer intermediate signal intensity zone (large arrow) that is less cellular

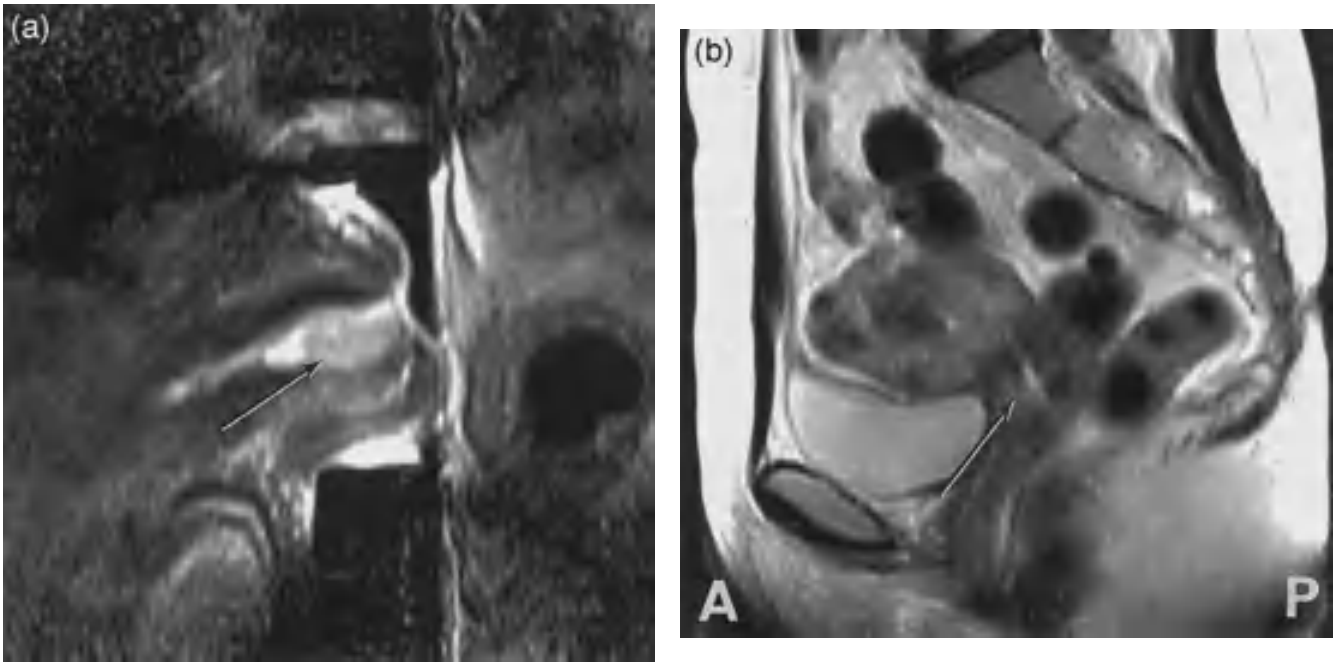

Figure 7 Images of Stage Ib squamous carcinoma of the cervix. Sagittal T_2-weighted spin echo (repetition time 2500 ms; echo time 80 ms) images through the cervix using (a) a cervical coil and (b) a phased array coil. The small tumor with intermediate signal intensity (arrows) is seen in both instances. However the margins are clearly defined in (a) and are difficult to differentiate in (b). There is no extension to parametrium or vagina. This was confirmed on the histology of the radical hysterectomy specimen. A, anterior; P, posterior

reported to be valuable in the accurate assessment of cervical invasion by tumor.[32] We used dynamic contrast-enhanced imaging in three slice positions over a 5 min period, though in no case did these images provide information not available on T_2-weighted images.

High-resolution images of the cervix are particularly important in defining tumors that are less than 1 cm^3 in volume because the definition of their extent has a significant impact on clinical decision making.[33] High-resolution images also may guide the approach to the histologic dissection of the resected tumor and thus not only optimize the surgical approach but also facilitate longer-term management.

4.2 Anal and Urethral Coils

Anal and urethral coils are simple saddle windings when implemented for solenoidal magnets. A variety of coil sizes have been developed for use at different field strengths and for different applications. Cylindrical endoanal coils have diameters ranging from 9 to 12 mm, and lengths of 75–100 mm: the largest version is shown in Figure 5b. Variants of the basic design include arrays and the integration of a pair of fiducial coils.

A wide variety of pathology in adults and children has been imaged using these coils, including infection, trauma, tumors and congenital malformations of the anal sphincter. [33–38] The superior image resolution allows identification of small fistulae-in-ano, assesses muscle defects, and defines the extent of tumors.

4.2.1 Normal Anatomy

From medial to lateral, several layers are recognized. A layer of mucosa with high signal is surrounded by a region of submucosa and subepithelial muscle (musculus submucosae ani) with low signal. The abundance of collagen and elastic tissue probably accounts for the short T_2 time of this region (Figure 8). The internal sphincter is distinguished by its high signal intensity on all sequences and often appears crescentic, being thicker anteriorly. The characteristic high signal appearance of the internal sphincter is not merely a result of its closeness to the coil; persistence of this high signal pattern on correction with a signal intensity profile from phantom data suggests that it is intrinsic to the smooth muscle of the internal sphincter. Its presence in vitro also suggests that it is not a consequence of the normal resting tone of the internal sphincter.[38] The intersphincteric region has a high signal on T_1- and T_2-weighted spin echo images: this is nulled on the STIR images, which is consistent with the presence of fat. The conjoined longitudinal muscle and external sphincter have a low signal intensity (Figure 8). The oblique coronal plane is particularly useful in demonstrating the three components of the external sphincter (subcutaneous, superficial, and deep) (Figure 8) and their relation to the levator ani.

Like the model described by Oh and Kark,[39] the female anal sphincter is shorter anteriorly than posteriorly. Inferiorly, the anterior margin of the superficial and deep external sphincter are continuous with and inseparable from the perineal body (Figure 8b). The transverse perineal muscle bridges the inferior part of the external sphincter anteriorly (Figure 8c). Superiorly,

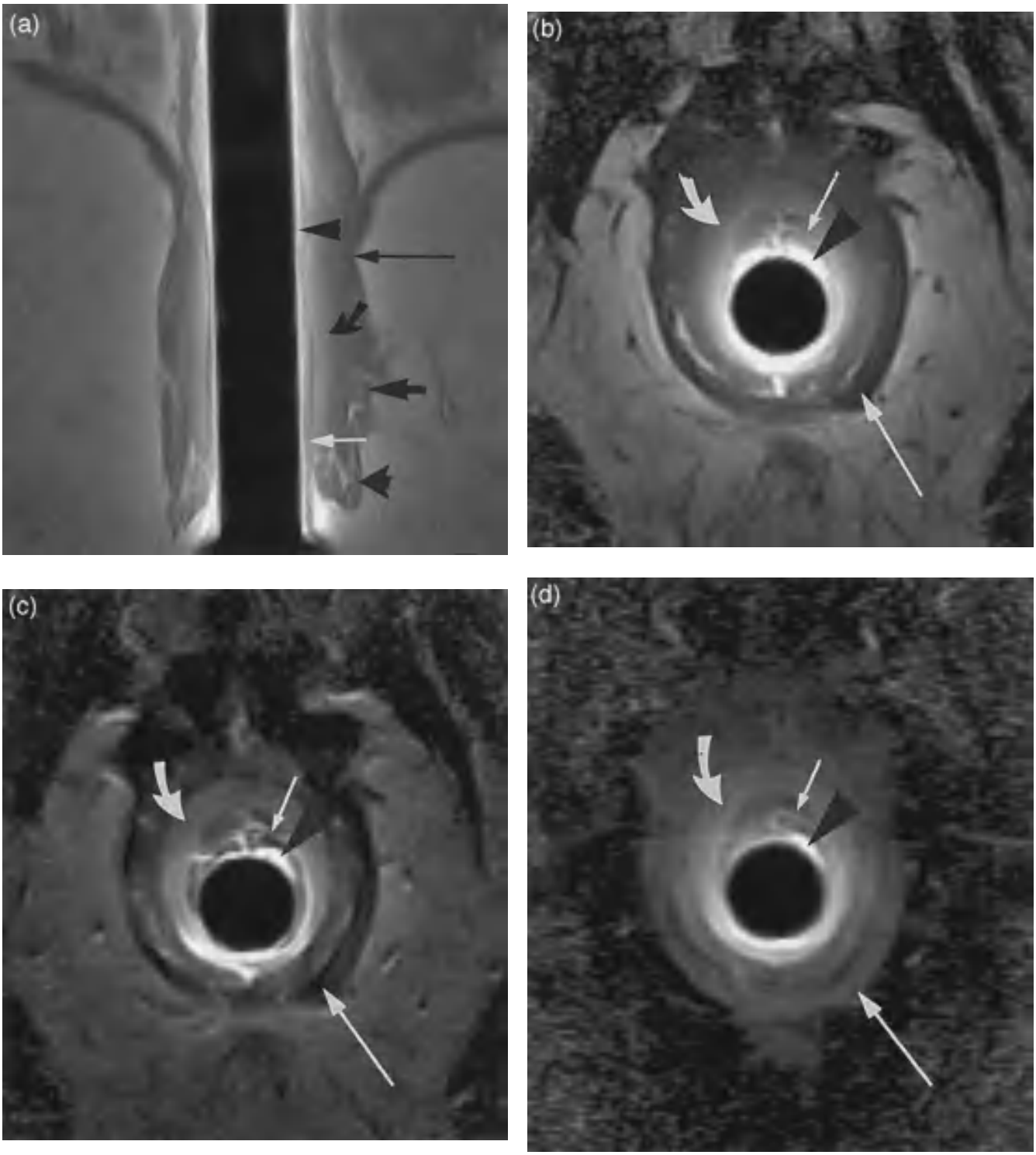

Figure 8 Normal anal anatomy in a 44-year-old female. Spin echo T_1-weighted [repetition time (*TR*) 720 ms; echo time (*TE*) 20 ms] images in (a) coronal and (b) transverse planes; (c) spin echo transverse T_2-weighted image (*TR* 2500 ms; *TE* 80 ms); (d) STIR (short inversion time inversion recovery; inversion time 107 ms; *TR* 2500 ms; *TE* 30 ms) images at a mid-sphincteric level in two planes. The coil is seen as a central signal void. The mucosa (black and white head) gives a very high signal on all sequences. The submucosa (small white arrow) is low signal. The internal sphincter is a homogeneous band (curved arrow) and has a particularly high signal in (c) and (d). The external sphincter is relatively low signal on all sequences. In (a) it is seen in its three components, subcutaneous (lower broad arrowhead), superficial (short black arrows), and deep (long black arrow)

perineal glands directly abut the internal sphincter anteriorly and laterally, separating it from the muscle of the vaginal wall.

4.2.2 *Perianal Sepsis*

The change in T_1 and T_2 times associated with infection produces high soft tissue contrast and enables abscesses and fistulous tracks to be demonstrated. Although previous studies using a conventional body coil have detailed the efficacy of MRI in demonstrating fistulae[40] and changes in Crohn's disease,[41] the excellent image quality provided by an internal coil results in further improvement. With more traditional anal endosonographic techniques,[42] tissue contrast is less good, the technique is more operator dependent, and it is no more accurate than digital examination under general anesthesia.[43] With endoanal imaging, in simple as well as in complex fistulae, it is relatively easy to identify a collection and define its extent (Figure 9b) as well as to follow the primary tracks in multiple planes to find the site of the internal fistula opening.

The position and course of the track in relation to the anal verge and the levator ani can be documented from the coronal and sagittal images. The resolution of the technique (pixel size 0.6 mm×0.6 mm) ensures that even small collections of the order of a few millimeters can be identified. Surgical management critically depends on the detection of these small collections, the site of the primary track, and the position of the internal opening.

4.2.3 *Fecal Incontinence from Surgical Trauma*

Perineal surgery may inadvertently cause a breach of the external or internal sphincter. The external sphincter is particularly at risk during procedures such as hemorrhoidectomy, vulvectomy, and colposuspension. The internal sphincter is particularly vulnerable in lateral sphincterotomies for chronic anal fissure when complete division of the internal sphincter may result in fecal leakage.

4.2.4 *Fecal Incontinence from Obstetric Trauma*

Early-onset fecal incontinence Fecal soiling immediately following childbirth is a dramatic symptom and, because intact sphincter musculature is essential to maintain continence, this suggests that part of the external sphincter has been ruptured. Defects in both internal and/or external sphincter are usually strikingly apparent on endoanal MRI. Tears involving the internal sphincter are immediately recognized because of the profound loss of the high signal intensity normally seen in this homogeneous muscle ring. In patients with rectovaginal fistulae, long T_2 tracks are seen to course anteriorly between anus and vagina.

Although endoanal sonography can provide anatomic information, particularly of internal sphincter damage in obstetric trauma,[44] it poorly defines the echogenic external sphincter against the echogenic perianal fat. Endoanal MRI not only

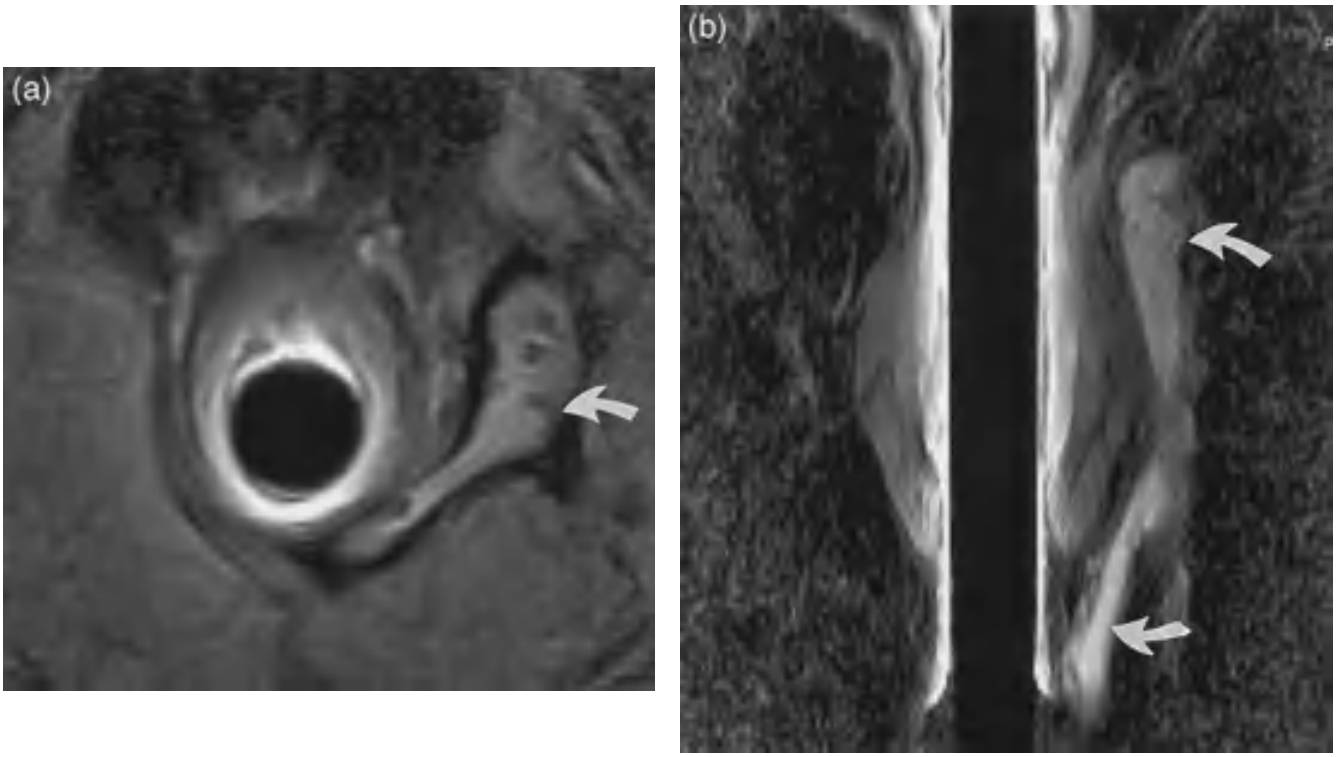

Figure 9 Images of the anal sphincter in anal sepsis using a 12 mm, endoanal coil; (a) transverse T_2-weighted spin echo [repetition time (*TR*) 2500 ms; echo time (*TE*) 80 ms]; (b) coronal short inversion time inversion recovery (STIR) (inversion time 107 ms; *TR* 2500 ms; *TE* 30 ms). The endoanal coil appears as a central signal void. An extrasphincteric collection is seen at 3 o'clock in (a) (arrow); however, there is no extension above the levators in (b) (arrows)

shows internal sphincter damage but also accurately delineates how much of the external sphincter has been disrupted.

Late-onset fecal incontinence In patients presenting with fecal incontinence starting several years after childbirth, a different pattern of sphincter abnormality is seen. The internal sphincter is relatively normal in thickness, but marked atrophy of the superficial and deep components of the external sphincter is evident (Figure 10). The subepithelial muscle is thicker in the fecally incontinent group compared with that in age-matched normal controls,[38] probably because of compensatory hypertrophy.

4.2.5 *Fecal Incontinence in Systemic Conditions*

Patients with scleroderma and fecal incontinence show a striking abnormality of the anterior sphincter musculature. There is buckling forward of the anterior rectal wall and anal sphincter musculature, with descent of rectal air and feces below the levators into the upper half of the anal canal.[45] There is also a significant reduction in internal anal sphincter bulk compared with age-matched fecally incontinent subjects who do not have scleroderma.[45] Patients with scleroderma but without fecal incontinence sometimes show these features.

4.2.6 *Tumor*

In patients with low carcinoma of the rectum, the extent of tumor invasion of the sphincter can be delineated with endoanal MRI.[36] Irregular lobulated masses of high signal intensity may be seen (Figure 11) on T_2-weighted sequences, which allow visualization of tumor invasion and breakthrough of the muscular coat of the anorectum. If lack of anal invasion is confirmed on endoanal MRI patients may be offered an anterior resection.

The multiplanar facility of MRI allows clear delineation of tumor extent and invasion particularly in relation to the levator floor. The exact distance from each of the components of the external sphincter and the extent of internal sphincter involvement can be accurately asserted prior to surgical planning.

4.2.7 *Congenital Anorectal Anomalies*

Smaller diameter (7 and 9 mm) coils are used for defining sphincter abnormalities in children with anorectal anomalies. The sensitive region of the various diameters of coil is chosen to suit the dimensions of the anal sphincter in the various age groups. The technique delineates the thickness and position of the muscle components as well as the presence of fistulae with neighboring structures (Figure 12).

The use of an anal coil causes minor discomfort but is acceptable and well tolerated in unsedated children of more than 8 years of age and appears to be better tolerated than digital examination. Children aged less than 8 years normally require sedation for an MRI scan even with an external coil.

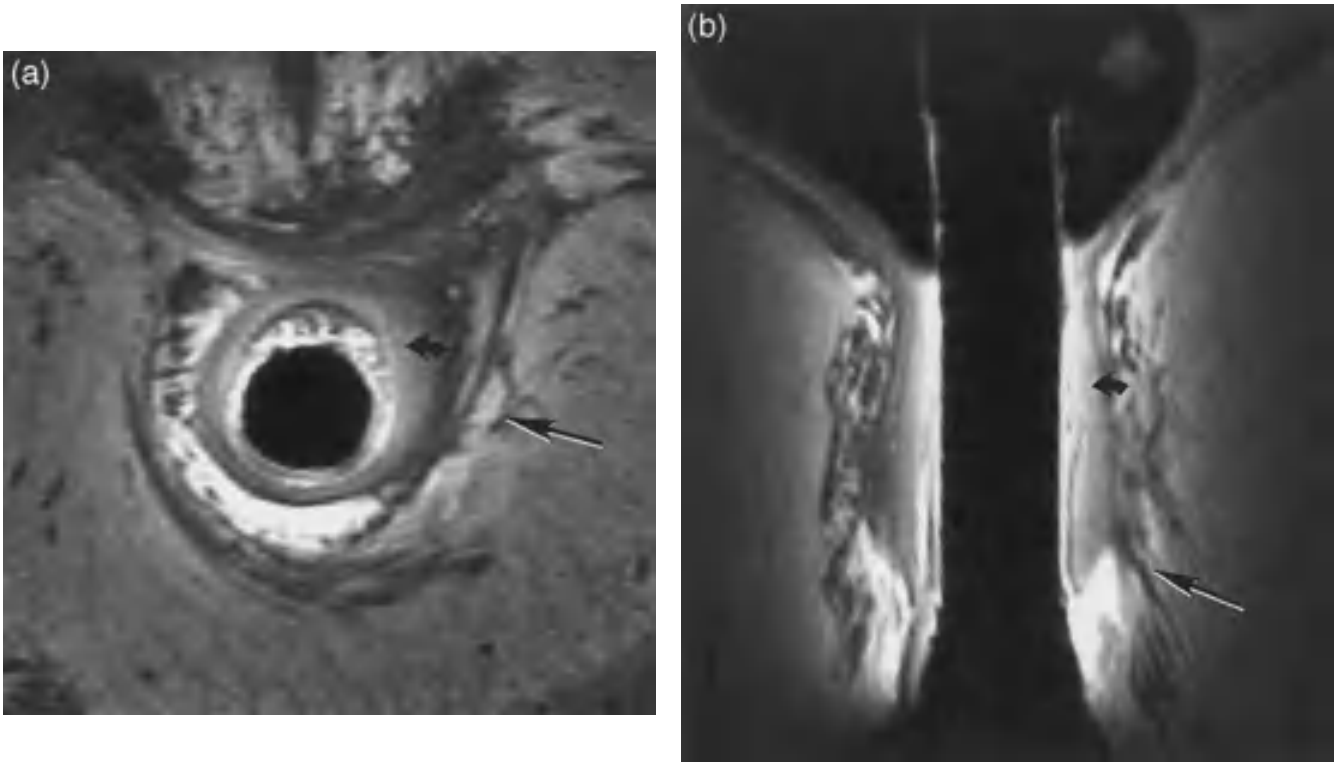

Figure 10 Sphincter atrophy in a patient with long-standing fecal incontinence following childbirth. Spin echo images (repetition time 720 ms; echo time 20 ms) T_1-weighted in (a) transverse and (b) coronal planes. Following traumatic childbirth several years earlier, there is focal atrophy of the internal sphincter (small arrow) in this patient and more global atrophy of the external sphincter (large arrow)

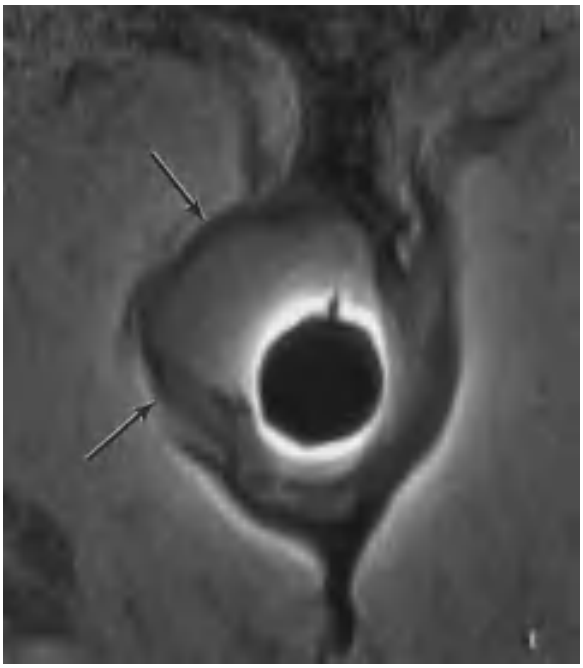

Figure 11 Squamous cell carcinoma of the anus. Transverse T_1-weighted spin echo image (repetition time 660 ms; echo time 20 ms) showing an intermediate signal lump (arrows) in the right anterior quadrant between 9 and 12 o'clock involving the subcutaneous external sphincter

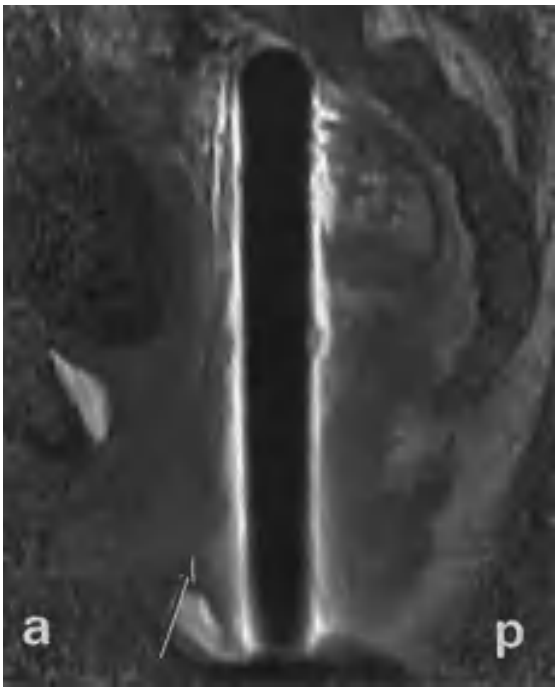

Figure 12 Perineal fistula in an 18-month-old girl. Sagittal T_1-weighted spin echo image (repetition time 720 ms; echo time 20 ms) through the mid-sphincter (a, anterior, p, posterior). The 7 mm coil is seen as a central signal void. There is generally good sphincter bulk. A high signal track is seen to extend anteriorly (arrow). It communicates with an opening in the posterior vaginal fourchette that was seen to discharge feces

4.3 Endorectal Coils

The balloon type of endorectal coil was the first internal coil to be developed.[5] We developed a similar version of our own to operate at 0.5 T as coils for that field strength were not available commercially. Subsequently, a smaller rigid device was developed which both operators and patients preferred,[12] and this device is described here.

This coil (Figure 5c) is essentially a surface coil designed to be placed in the rectum posterior to the prostate gland, and consists of an 8.5 cm × 2.5 cm semicylindrical former. The flat upper surface is used as the base for the 6.5 cm × 2.5 cm winding. This solid, one-piece surface coil is placed in the rectum. The tip of the coil is tapered and it is easy to insert and position following standard digital rectal examination in the lateral decubitus position.[12] Our solid one-piece endorectal coil is easy to handle and set-up, is re-usable, and does not require external tuning and matching. Also, unlike the commercially available coil, there are no artefacts from susceptibility effects of the air in the balloon, which degrade the prostatic images. The solid design also allows incorporation of a needle guide, and with further refinements will enable MR-guided transrectal biopsy.

4.3.1 Normal Anatomy

The zonal anatomy of the prostate may be identified clearly on the high-resolution T_2-weighted images obtained using the endorectal coil. The outer homogeneous zone of high signal intensity (peripheral zone) forms the bulk of the gland in young males. The inner zone (central zone), which histologically comprises the 'transitional' lobe of the prostate, increases in size with age and displaces the peripheral zone laterally.

4.3.2 Benign Prostatic Hypertrophy

In benign prostatic hypertrophy, the enlarged central zone of the prostate forms a nodular, inhomogeneous adenoma that often includes cystic nodules and calcification. With increase in size it commonly causes compression of the prostatic urethra and leads to bladder outflow obstruction. This normally requires intervention with conventional surgery or minimally invasive thermal ablative techniques. In the latter instances, intraoperative image guidance is becoming increasingly popular. We have demonstrated that intraoperative changes seen on endorectal imaging may be used to predict more long-term outcome;[46] the development of a periurethral band of low signal at the time of surgery correlated with a significant reduction in symptoms at 3-month follow-up (Figure 13).

4.3.3 Prostate Cancer

Endorectal imaging is routinely used in the detection of prostate cancer (Figure 14). Malignant nodules are usually recognized as low-signal foci within the peripheral lobes: however, they are sometimes iso- or even hyperintense compared with background and, therefore, are difficult to detect. Also the multifocal nature of this disease means that small malignant foci may go unrecognized. Recently, dynamic contrast-enhanced techniques have been used to map out the full site and extent of malignant foci,[47] and this approach may be adopted to monitor the response to medical therapy.

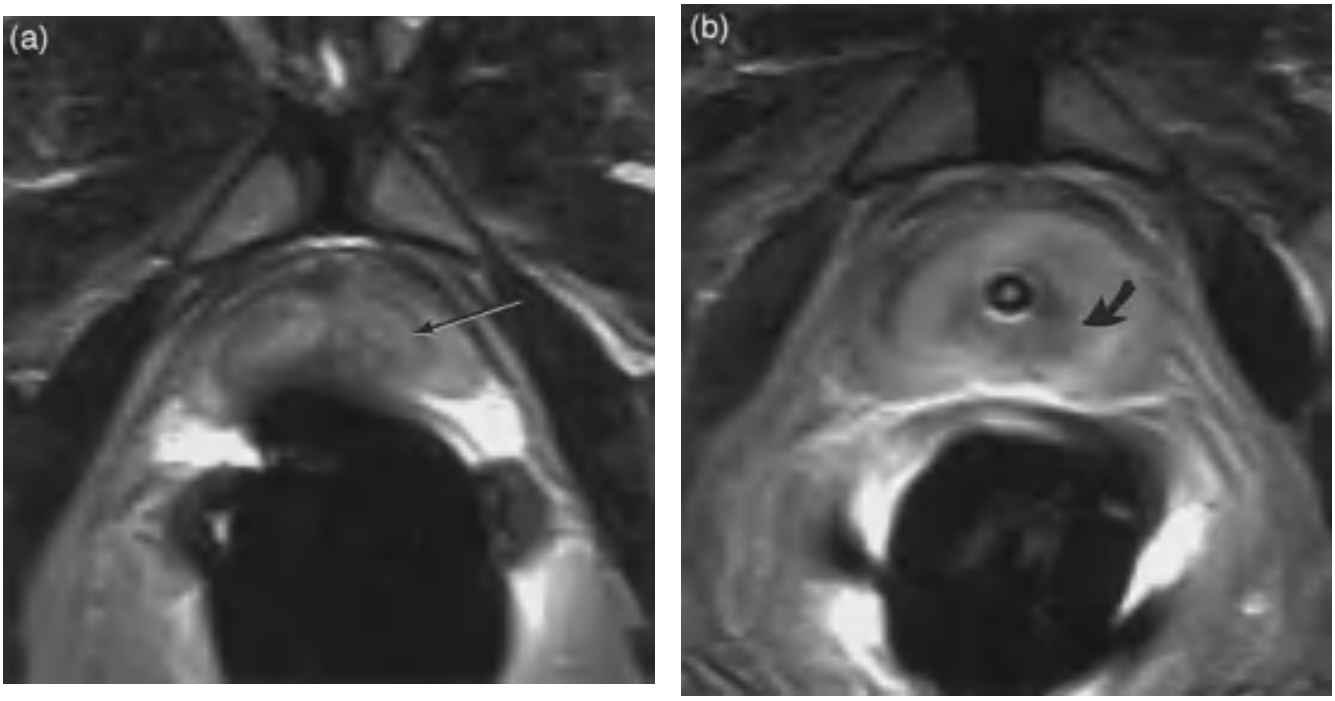

Figure 13 Appearances after endoscopic laser prostatectomy for benign hypertrophy. Transverse T_2-weighted spin echo images (repetition time 2500 ms; echo time 80 ms) before (a) and immediate after (b) a four-quadrant ablation of the prostate using a noncontact laser. (a) The small central adenoma (arrow) was causing significant symptoms. (b) There is overall swelling of the gland with loss of the normal zonal differentiation. A periurethral ring of low signal is seen (curved arrow) that is likely to represent coagulative necrosis

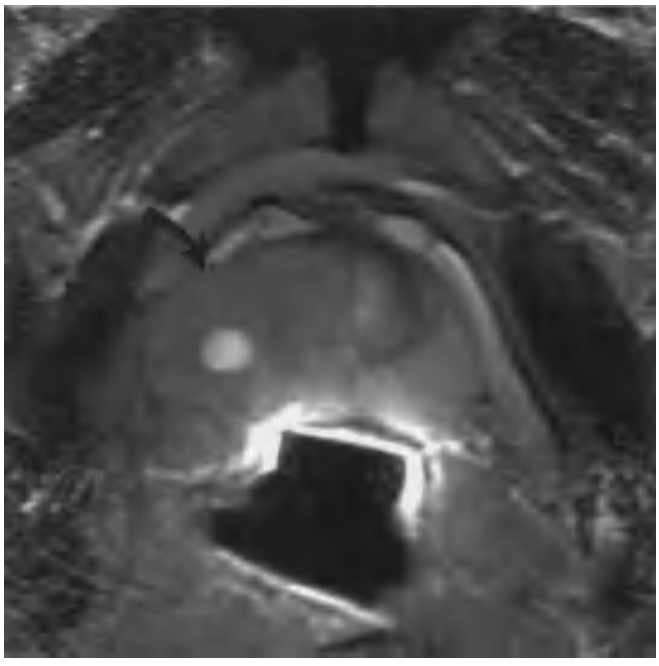

Figure 14 Prostate carcinoma with extracapsular extension. Transverse T_2-weighted spin echo image (repetition time 2500 ms; echo time 80 ms) through the mid-prostate. A large mass is seen on the right that extends into the periprostatic tissues (curved arrows)

4.4 Endoscopic Coils

A gastroscope and colonoscope coil design is shown in Figure 5d for comparison (see ***Gastroscopy and Colonoscopy***). This uses a Delrin former with a saddle winding and connecting cable. The coil unit is located ahead of an MR-compatible gastroscope or colonoscope and the cable is passed through the 3 mm channel usually allocated for biopsy devices.

4.5 Miscellaneous Coils

Use of small coils in the external auditory meatus, within blood vessels, and for dental applications have been investigated. The problems with such coils include achieving a useful field-of-view from something with a diameter small enough to be located around or within the structure being studied.

5 CONCLUDING REMARKS

The use of internal coils allows high-resolution images of the part under study. Improved performance is achieved by superior coupling to the tissue of interest while minimizing coupling to irrelevant regions. A solid design with external immobilization results in re-usable coils without susceptibility artefacts.

6 RELATED ARTICLES

Coils for Insertion into the Human Body; Gastroscopy and Colonoscopy; Male Pelvis Studies Using MRI; MRI of the Female Pelvis.

7 REFERENCES

1. A. Abragam, 'The Principles of Nuclear Magnetism', Clarendon Press, Oxford, 1961, p. 71
2. D. I. Hoult, and R. E. Richards, *J. Magn. Reson.*, 1976, **24**, 71.
3. H. L. Kantor, R. W. Briggs, and R. S. Balaban, *Circ. Res.*, 1984, **55**, 261.
4. A. L. Benabid, M. Decorps, C. Remy, J. P. Albrand, M. Retenauer, and P. Blondet, *Proc. IVth Annu. Mtg. Soc. Magn. Reson. Med.*, London, 1985, p. 441.
5. M. D. Schnall, C. Barlow, V. H. Subramanian, and J. S. Leigh Jr, *J. Magn. Reson.*, 1986, **68**, 161.
6. R. R. Harman, P. C. Butsen, A. S. Hall, I. R. Young, and G. M. Bydder, *Magn. Reson. Med.*, 1988, **6**, 49.
7. M. D. Schnall, R. E. Lenkinsi, H. M. Pollack, Y. Inai, and H. Y. Kressel, *Radiology*, 1989, **172**, 570.
8. M. D. Schnall, T. Connick, C. E. Hayes, R. E. Lenkinski, and H. Y. Kressel, *JMRI*, 1992, **2**, 229.
9. C. J. Baudouin, W. P. Soutter, D. J. Gilderdale, and G. A. Coutts, *Magn. Reson. Med.*, 1992, **24**, 196.
10. N. M. deSouza, W. A. Kmiot, R. Puni, A. S. Hall, C. I. Bartram, and G. M. Bydder, *Gut*, 1995, **37**, 284.
11. S. M. Hussain, J. Stoker, J. W. Kuiper, W. R. Schouten, J. C. den Hollander, and J. C. Lameris,, *Radiology*, 1995, **197**, 671.
12. N. M. deSouza, D. J. Gilderdale, R. Puni, G. A. Coutts, and I. R. Young, *JMRI*, 1996, **6**, 801.
13. N. M. deSouza, A. H. Gibbons, G. A. Coutts, A. S. Hall, R. Puni, J. Calam, and I. R. Young, *Minim. Invas. Ther.*, 1996, **4**, 23.
14. A. D. Williams, G. A. Coutts, A. S. Hall, W. A. Kmiot, D. J. Gilderdale, M. Dinneen, I. R. Young, and N. M. deSouza, *Proc. VIth Annu. Mtg. (Int.) Soc. Magn. Reson. Med.*, Sydney, 1998, p. 472.
15. D. J. Gilderdale, D. J. Bryant, G. M. Bydder, and I. R. Young, *JMRI*, 1992, **2**(P), 153.
16. D. J. Gilderdale, N. M. deSouza, G. A. Coutts, and I. R. Young, *Proc. IVth Annu. Mtg. (Int.) Soc. Magn. Reson. Med.*, New York, 1996, p. 1437.
17. C. L. Dumoulin, S. P. Souza and R. D. Darrow, *Magn. Reson. Med.*, 1993, **29**, 411.
18. G. C. McKinnon, J. F. Debatin, D. A. Leung, S. Wildermuth, D. J. Holtz, and G. K. von Schulthess, *Proc. IInd Annu. Mtg. Soc. Magn. Reson. Med.*, San Francisco, 1994, p. 429.
19. O. Ocali, and E. Atalar, *Magn. Reson. Med.*, 1997, **31**, 112.
20. M. Burl, G. A. Coutts, D. J. Herlihy, R. Hill-Cottingham, J. F. Eastham, J. V. Hajnal, and I. R. Young, *Magn. Reson. Med.*, 1999, **41**, 636.
21. G. H. Barnett, D. W. Kormos, W. P. Steiner, and J. Weisenberger, *J. Neurosurg.*, 1992, **78**, 510.
22. M. Burl, G. A. Coutts, and I. R. Young, *Magn. Reson. Med.*, 1996, **36**, 491.
23. G. A. Coutts, D. J. Gilderdale, K. M. Chui, L. Kasuboski, and N. M. deSouza, *Magn. Reson. Med.*, 1998, **40**, 908.
24. D. J. Gilderdale, G. A. Coutts, and N. M. deSouza, *Proc. Vth Sci. Mtg. (Int.) Soc. Magn. Reson. Med.*, Vancouver, 1997, p. 1509.
25. R. R. Harman, I. R. Young, G. M. Bydder, P. C. Butsen, and D. Spencer, *Proc. Vth Annu. Mtg. Soc. Magn. Reson. Med.*, Montreal, 1986, p. 57.
26. D. I. Hoult, and P. C. Lauterbur, *J. Magn. Reson.*, 1976, **24**, 71.
27. G. A. Coutts, D. J. Gilderdale, A. D. Williams, and N. M. deSouza, *Proc. VIth Annu. Mtg. (Int.) Soc. Magn. Reson. Med.*, Sydney, 1998, p. 724.
28. B. N. Milestone, M. D. Schnall, R. E. Lenkinski, and H. Y. Kressel, *Radiology*, 1991, **180**, 91.
29. N. M. deSouza, I. C. Hawley, J. E. Schwieso, D. J. Gilderdale, and W. P. Soutter, *Am. J. Roentgenol.*, 1994, **163**, 607.
30. N. M. deSouza, D. J. Scoones, T. Krausz, D. J. Gilderdale, and W. P. Soutter, *Am. J. Roentgenol.*, 1996, **166**, 553.
31. S. Thurner, *Am. J. Roentgenol.*, 1992, **159**, 1243.
32. Y. Yamashita, M. Takahashi, T. Sawada, K. Miyazaki, and H. Okamura, *Radiology*, 1992, **182**, 643.
33. N. M. deSouza, G. A. J. McIndoe, C. Hughes, W. P. Mason, M. K. Chui, T. Krausz, and W. P. Soutter, *Br. J. Obstet. Gynaecol.*, 1998, **105**, 500.
34. N. M. deSouza, W. A. Kmiot, R. Puni, A. S. Hall, C. I. Bartram, and G. M. Bydder, *Gut*, 1995, **37**, 284.
35. N. M. deSouza, R. Puni, D. J. Gilderdale, and G. M. Bydder, *Magn. Reson. Q.*, 1995, **11**, 45.
36. N. M. deSouza, A. S. Hall, R. Puni, D. J. Gilderdale, I. R. Young, and W. A. Kmiot, *Dis. Colon Rectum*, 1996, **39**, 926.
37. N. M. deSouza, D. J. Gilderdale, D. K. MacIver, and H. C. Ward, *Am. J. Roetgenol.*, 1997, **169**, 201.
38. N. M. deSouza, R. Puni, A. Zbar, D. J. Gilderdale, G. A. Coutts, and T. Krausz, *Am. J. Roentgenol.*, 1996, **167**, 1465.
39. C. Oh, and A. E. Kark, *Br. J. Surg.*, 1972, **50**, 717.
40. P. H. Luniss, P. G. Barker, A. H. N. Sultan, *et al.*, *Dis. Colon Rectum*, 1994, **37**, 708.
41. J. J. Tjandra, and G. R. J. Sissons, *Aust. N. Z. J. Surg.*, 1994, **64**, 470.
42. P. J. Law, R. W. Talbot, C. I. Bartram, and J. M. A. Northover, *Br. J. Surg.*, 1989, **76**, 752.
43. S. Choen, S. Burnett, C. I. Bartram, and R. J. Nicholls, *Br. J. Surg.*, 1991, **78**, 445.
44. S. J. D. Burnett, C. Spence-Jones, C. T. M. Speakman, M. A. Kamm, C. N. Hudson, and C. I. Bartram, *Br. J. Radiol.*, 1991, **64**, 225.
45. N. M. deSouza, A. D. Williams, H. J. Wilson, D. J. Gilderdale, G. A. Coutts, and C. M. Black, *Radiology*, 1998, **208**, 529.
46. N. M. deSouza, R. Flynn, A. G. Coutts, D. J. Gilderdale, A. S. Hall, R. Puni, M. Chui, D. N. F. Harris, and E. A. Kiely, *Am. J. Roentgenol.*, 1995, **164**, 1429.
47. A. R. Padhani, J. E. Husband, and G. J. M. Parker, *Diagn. Imag. Eur.*, 1996, **June**, 20.

Acknowledgements

We should like to acknowledge the support of Picker International in the development of the probes, of the Wellcome Trust who provided the 0.5 T machine resource on which much of the work was done, and of the Medical Research Council who supported the work during the earlier part of the program. We would like to thank our clinical collaborators Mr E. Kiely, Dr J. Waxman, Mr W. Kmiot, Mr G. A. McIndoe, and Mr W. P. Soutter. We are also grateful to Mrs M. C. Crisp for her secretarial assistance.

Biographical Sketches

Nandita M. de Souza. *b* 1957. B.S.c. Hons (Physiology) 1978, MBBS, 1983, University of Newcastle upon Tyne, UK, M.R.C.P. 1986, F.R.C.P. 1991, M.D. 1996. House Surgeon and Physician and Senior House Physician, Newcastle upon Tyne 1983–85. Registrar in internal medicine 1986–87. Registrar and Senior Registrar in Diagnostic Radiology, Guy's Hospital, London, 1987–92. Senior Research Fellow in MR Imaging, Royal Postgraduate Medical School, Hammersmith Hos-

pital, 1993–97. Senior Lecturer 1997–present. Research Interests: internal receiver coils, interventional MRI.

David J. Gilderdale. *b* 1947. B.S.c. telecommunications, Ph.D. computer simulation as an aid to lighting design. Research Assistant, Plymouth Polytechnic, 1974–78. Electronic Engineer, Central Research Laboratories, Thorn-EMI Ltd, 1978–81. Senior Scientist, GEC Hirst Research Centre, 1981–84. Senior Lecturer, Department of Electrical Engineering, Plymouth Polytechnic, UK, 1981–88. Engineering Consultant, 1988–present.

Glyn A. Coutts. *b* 1959. B.A. (Physics) University of Oxford, UK, 1980, D.Phil. University of Oxford 1985. Senior Research Associate at Picker Research UK, 1987–99. Marconi Medical Systems, UK, 1999–present. Approx. 30 publications in the field of MRI and MRS. Current interest: interventional MRI.

Eddy Currents and Their Control

Michael Burl and Ian R. Young

The Robert Steiner MRI Unit, Hammersmith Hospital, London, UK

1 INTRODUCTION

Even in very early imaging systems it became apparent that the pulsed gradient waveforms were being distorted by eddy currents induced in parts of the magnets and other structures. The first machines were resistive, and the coil formers were the main source of trouble. These could be split, which helped to some degree, but the problems were even more severe in the cryogenic magnets introduced later.[1] The use of composition cylinders, instead of aluminum, for their warm bores minimized some problems but, in the end, meant that the structures where the eddy currents circulated were at low temperature with much increased conductivity so that the currents induced persisted for long periods. This article discusses the principal manifestations of eddy currents, and describes the main strategies which are used to combat them.

2 FORMS OF EDDY CURRENT DISTURBANCE AND ANALYSIS

Eddy currents are induced in conducting structures exposed to changing magnetic fields. These currents distribute themselves so as to expel the external field. In superconductors the magnet fields are excluded completely from the material by surface currents. In normal conductors the induced currents give rise to an electric field within the conductor which allows the magnetic field to propagate through the conductor. The finite conductivity of normal conductors results in Joule heating from the induced eddy currents. These effects have been well described by Skilling[2] and later by Lammerauer and Slapfl.[3] In the context of magnetic resonance the eddy currents distort the time domain gradient waveform shape. Furthermore, the distortion may have a spatial dependency.

2.1 Time Domain Analysis

An analytic treatment of the effects of eddy currents is given by Lammerauer and Slapfl[3] for the transmission line problem. Although this is a transient solution, giving an answer directly in the time domain, the mathematics needed are apt to be very untidy. A more general and practical solution is to use the finite-difference time domain (FD TD) solution to Maxwell's equations.[4] This finite element method allows the computer solution of complex metal/dielectric structures, but is expensive in terms of computer resources. Since the frequency components in the gradient waveform are essentially low (>1 MHz) the dielectric effects can be safely ignored and a reduced set of Maxwell's equations may be used.[5,6]

Table 1 Skin depths (δ in mm) for Various Frequencies and Materials

Frequency (Hz)	Cu $\sigma = 5.8 \times 10^7$	Al $\sigma = 3.54 \times 10^7$	Tissue $\sigma = 0.5$
50	9.44	12.3	112×10^3
1000	2.11	2.75	25×10^3
10 000	0.677	0.87	8×10^3
42×10^6	0.01	0.013	123[a]

[a]At frequencies above 50 MHz the high dielectric constant of water has a strong effect on the electromagnetic field.

2.2 Frequency Domain Analysis

The normal analytic treatment[7] considers the solution of Maxwell's equations for a sinusoidal excitation field. This gives rise to the notion of 'skin depth' δ, which is given, for nonferromagnetic materials by

$$\delta = \sqrt{\frac{2}{\mu_0 \sigma \omega}} \tag{1}$$

The skin depths for different frequencies and materials are given in Table 1.

The current distribution as a function of depth in a thick plate is shown in Figure 1. Although the current distribution follows the solid line the effective resistance is given by the conductivity and the skin depth. The resulting gradient field will be the superposition of the free space gradient field and the various fields resulting from the eddy currents.[8] The gradient waveform may well have frequency components from a fraction of a hertz up to 10 kHz. The resulting waveform will be the Fourier synthesis of each component modified by the frequency dependent nature of the eddy current.

Some structures in the machine, the rf screen for example, are thin compared with δ and a simple coupled circuit analysis gives a useful insight into and estimate of field distortion and power deposition. Considering Figure 2, we find

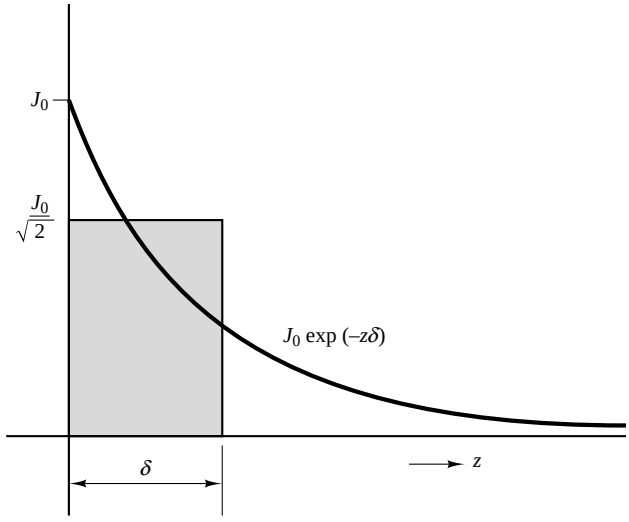

Figure 1 Current flow versus depth due to skin effects

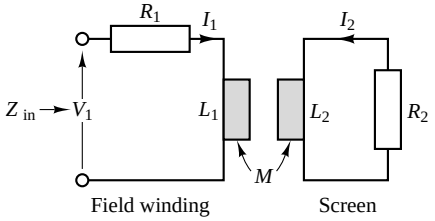

Figure 2 Equivalent circuit for eddy current induction into the rf screen (or other identified component)

$$V_1(s) = sL_1 i_1(s) + R_1 i_1(s) + sMi_2(s) \tag{2}$$

$$0 = sMi_1(s) + R_2 i_2(s) + sL_2 i_2(s) \tag{3}$$

Rearranging equation (3) gives

$$i_2(s) = -i_1(s)\frac{sM}{R_2 + sL_2} \tag{4}$$

and then substituting back in equation (2) and dividing by i_1 gives

$$Z_{in}(s) = \frac{V_1(s)}{i_1(s)} = sL_1 + R_1 + \frac{s^2M^2}{sL_2 + R_2} \tag{5}$$

Putting $s = i\omega$ and rearranging

$$Z_{in} = R_1 + \frac{R_2\omega^2 m^2}{R_2^2 + \omega^2 L_2^2} + i\omega\left[L_1 - \frac{L_2\omega^2 m^2}{R_2^2 + \omega^2 L_2^2}\right] \tag{6}$$

This analysis was tested on a model gradient coil, first without rf screen material and then with three types of screen material. The results for copper foil, mesh and plate are summarized in Table 2. The current in the screen is given in equation (4). The resulting field at some point in space will be

$$\begin{aligned} B &= S_1 I_1 + S_2 I_2 \\ &= L_1\left\{S_1 - S_2\frac{sM}{R_2 + sL_2}\right\} \end{aligned} \tag{7}$$

where S_1 is the sensitivity of the field winding and S_2 is the effective sensitivity of the shield. It may be helpful to regard $S_1 - S_2$ as the sensitivity of the field winding in the presence of a superconducting shield and L_2/R_2 as the time constant of the shield. The cutoff frequency for a 35 μm copper screen is about 1–2 kHz although the skin depth δ only becomes equal to the thickness at 4 MHz.

This simple model works over a wide frequency range but can fail when the screen material is thicker than δ. However, good agreement between calculated and measured power deposition is found when the screen resistance takes into account the skin depth. The time response for a thick screen will be different from that of a simple CR or LR circuit due to the frequency dependent nature of skin resistance. For this reason several stages of feedforward compensation would need to be employed to get an accurate approximation.

Some, at least, of the eddy current components induced in very cold structures in superconducting magnets can have a very long time constant indeed (a 'field soaking' effect), so much so that they appear to cause a dc offset, detuning the resonance a little. An additional, quite different, problem arises with magnets where the pole pieces are made wholly or partly of iron. In these, the gradient fields spreading into the poles drive the iron locally round different hysteresis loops. Apart from the energy that is dissipated this results in a local nonlinear distortion of the field.

3 CORRECTION STRATEGIES

Correction strategies can be divided into two main types: those which depend on eliminating the fields, or current circulation paths, which are responsible for the induction of, or for supporting, the unwanted currents; and those which try to modify machine operation to compensate for the undesirable effects.

3.1 Correction by Coil Design and Modification

The best known, and most effective, means of restraining fields are the actively shielded gradient coil systems first described in 1986.[8,9] These are fully described elsewhere (see ***Gradient Coil Systems***). An outer set of gradient windings is used to prevent field spreading outside them. Actively shielded gradients typically still allow a leakage of 1% of the flux, so it is usually still necessary to apply other measures to eliminate residual effects.

Though this form of shielding is effective outside the gradient coil assembly it has to be designed to have minimal effects inside the volume of the coil. In this, fabrications such as rf coils and screens must be designed so as to avoid circulating, low-frequency currents. Large areas of conductor should be slit and large value capacitors may be used to bridge gaps in rf circuits introduced to stop low-frequency currents circulating. Both simple coils, such as surface coils (see ***Surface and Other Local Coils for In Vivo Studies***), and sophisticated designs, such as birdcages (see ***Birdcage Resonators: Highly Homogeneous Radiofrequency Coils for Magnetic Resonance***), can include such paths unwittingly. Prevention is illustrated in Figure 3. As shown in Table 2, the design of good rf screens is not a trivial matter.

3.2 Correction by Adjustment of Drive Currents

All the other forms of correction depend on modifying the currents supplied to the gradient coils. As a result they can only be used effectively if the structures in which the eddy currents are induced are concentric with the original coils. This limited their effectiveness in many earlier machines before all the problems associated with the relative eccentricities of parts of magnet structures were appreciated.

Several methods have been used to modify the current profile in the coils. These are described in the next section. One other technique depends on adjusting the data sampling rate to accommodate errors in the gradient field.[10] In this method an NMR probe (see Section 4) is sited at a convenient distance from the center of the machine and its output signal is sampled at a constant rate during the period in which signal is to be recovered while the relevant gradient waveform is applied. If

Table 2 Comparison of Measurement and Calculation of rf Screen ac Resistance for Different Thicknesses and Forms of Copper

$$R_{\text{in}} = R_1 + R_2 \frac{\omega^2 M^2}{(R_2^2 + \omega^2 L_2^2)}$$

Frequency (Hz)	$\omega^2 M^2 \times 10^{-6}$	$\omega^2 L_2{}^2 \times 10^{-6}$	$R_2{}^2 + \omega^2 L_2{}^2 \times 10^{-3}$	R_1 (mΩ)	R_{in} (mΩ)	Measurement
(a) Copper screen (35 μm thick) R_1 = 2.55 mΩ at 100 Hz R_2 = 10.5 mΩ $R_2{}^2 = 110 \times 10^{-6}$		L_1 = 5 μH L_2 = 0.5 μH M = 1.5 μH				
100	0.9	0.1	110	2.55	2.75	2.76
300	8	0.9	111	2.8	2.88	
500	22	2.4	112	2.94	5.0	5.06
700	43	4.8	115	3.1	6.73	
1 000	90	10	120	3.35	11.22	11.48
1 500	199	22	132	3.6	19.43	
10 000	900	1000	1100	6.7	92.6	77.8
(b) Copper mesh R_1 = 2.5 mΩ at 100 Hz R_2 = 10.5 mΩ $R_2{}^2 = 110 \times 10^{-6}$		L_1 = 5 μH L_2 = 0.5 μH M = 1.5 μH				
500	22	2.5	1.76	2.94	3.46	3.47
1 000	90	10	1.76	3.55	5.5	5.48
2 000	360	40	1.8	3.95	12.35	11.95
3 000	810	90	1.85	4.5	22.9	
10 000	9000	1000	2.76	6.7	143	121
(c) Copper plate R_1 = 2.5 mΩ at 100 Hz R_2 = 0.3 mΩ $R_2{}^2 = 0.09 \times 10^{-6}$		L_1 = 5 μH L_2 = 0.5 μH M = 1.5 μH				
50	0.22	0.025	0.115	2.56	3.13	3.38
100	0.9	0.1	0.19	2.67	4.09	4.06
200	3.6	0.4	0.49	2.68	4.88	4.83
500	22	2.5	2.59	2.94	5.49	5.5
1 000	90	10	10	3.35	6.05	5.79
2 000	360	40	40	3.92	6.6	6.13
5 000	2.2×10^{-3}	0.25×10^{-3}	0.25×10^{-3}	5.11	7.8	7.39
10 000	9×10^{-3}	1×10^{-3}	1×10^{-3} (0.42)[a]	6.7	9.4 (10.5)[a]	9.6
20 000	36×10^{-3}	4×10^{-3}	4×10^{-3} (0.6)[a]	9.38	12.0 (14.7)[a]	13.7
50 000	220×10^{-3}	25×10^{-3}	25×10^{-3} (0.94)[a]	15	17.7 (23)[a]	22.3
100 000	900×10^{-3}	100×10^{-3}	100×10^{-3} (1.34)[a]	17.5	20.2 (29.5)[a]	31

[a]Values in parentheses are values of R_2 (mΩ) adjusted for the skin effect.

any gradients were constant during this period, the sampled signals would be acquired at fixed phase intervals.

Then, after demodulation,

$$S(n) = S_0 \exp\left(-\frac{n\Delta t}{T_2} - in\gamma r G_r \Delta t\right) \tag{8}$$

at a distance r from the center along a field gradient G_r, and where Δt is the incremental time interval and $S(n)$ is the value for the nth sample. S_0 is the signal at the start of the sampling window. If the sample size is small enough, the output waveform is a decaying sinusoid of fixed frequency, as long as G is constant. In the presence of a varying gradient the phase increment from one sample to the next varies. As long as the gradient instability is invariant, however, and the signal is sufficiently oversampled, i.e. $n > N$ where N is the number of samples actually needed, then the values of time increment needed [Δt_r for ($1 \leqslant r \leqslant N$)] to permit a constant phase increment between each sample can be calculated. This defines a sampling table which will both comply with the Nyquist criterion, and produce consistent data for Fourier reconstruction. This method was used by one group in particular in early experiments,[10] and is particularly useful for early acquisition of data after excitation to form a half-Fourier data set, but fell into disuse until it was necessary to try and extend the periods of data acquisition in echo planar data acquisition[11] in particular. Modern practice is to oversample the data as far as possible and then process them, with interpolation, to establish what signals would have been obtained if the data had been sampled correctly though at nonuniform intervals.

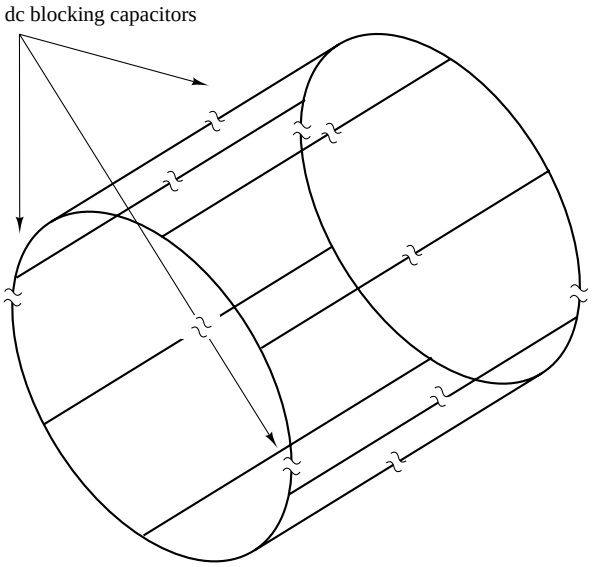

Figure 3 Drawing of an enveloping coil showing the large capacitors across the low-frequency blocks in the coil

By far the most common method (apart from the use of shielded gradients—and frequently used in conjunction with these as well) is the use of pre-emphasis (G. N. Holland, private communication, 1984), possibly better known as feed-forward. The circuit configuration typically used to correct for four eddy current terms is sketched in Figure 4. The theoretical relationship for one section of the circuit is

$$H(s) = \frac{A_1 sC}{1 + sC} = \frac{A_1 s}{s + (1/CR)} \tag{9}$$

(continuing to use the notation $s = i\omega$). After some rearrangement, this may be compared with equation (4):

$$I_2(s) = I_1(s)\frac{s(M/L_2)}{s(R_2/L_2)} \tag{10}$$

The transfer function for the whole circuit is:

$$H(s) = \frac{1}{5}\left\{1 + \frac{A_a s}{s + \dfrac{I}{C_a R_a}} + \frac{A_b s}{s + \dfrac{1}{C_b R_b}} + \cdots\right\} \tag{11}$$

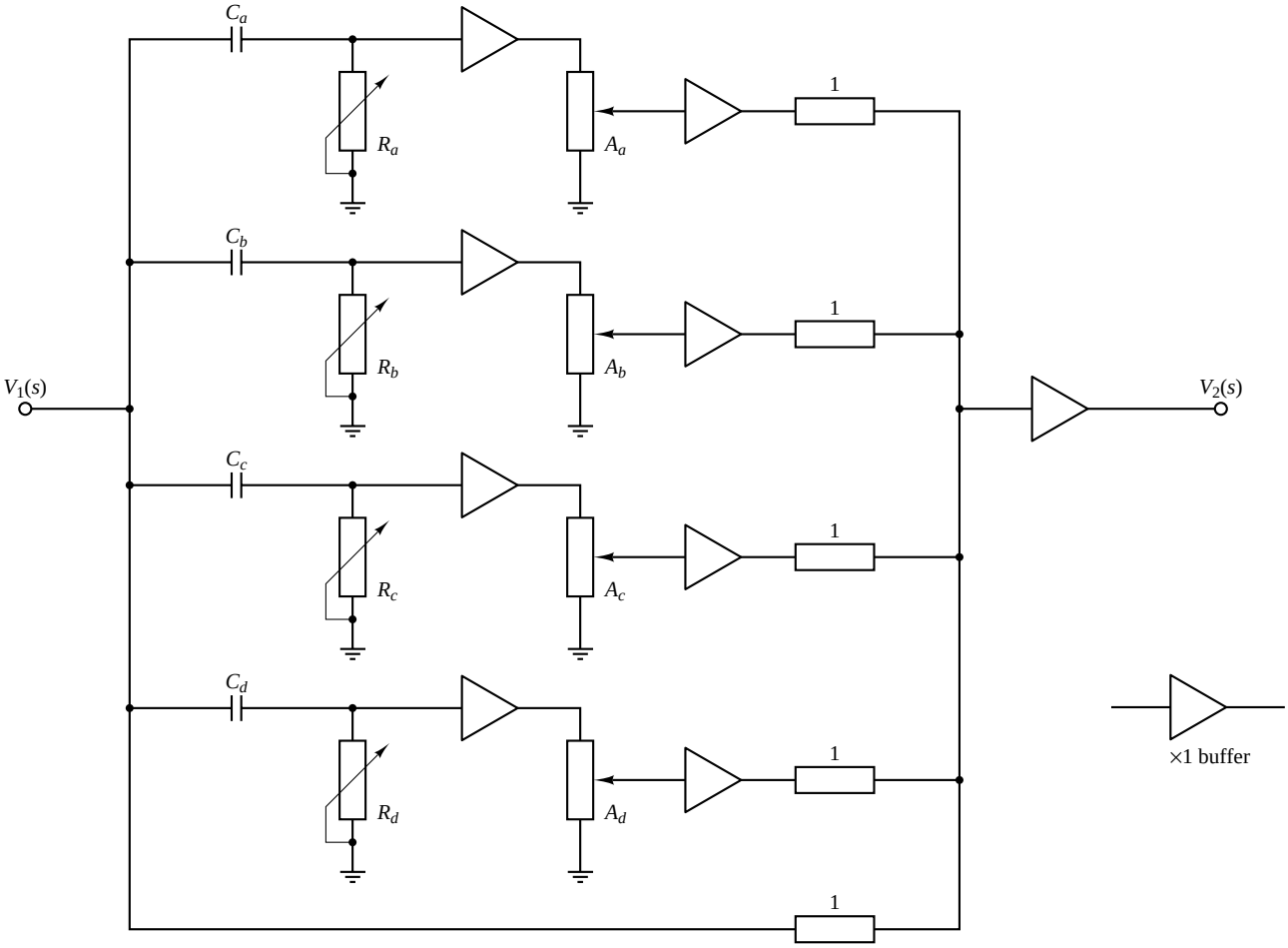

Figure 4 Schematic circuit design of a four-term pre-emphasis eddy current correcting circuit

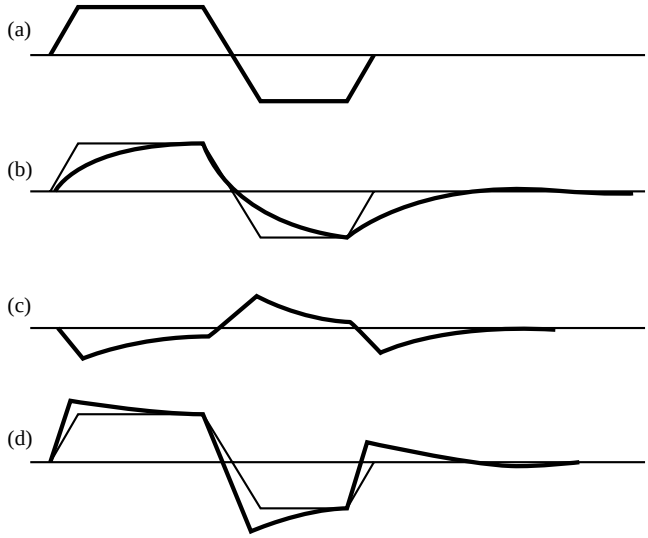

Figure 5 Design showing the introduction of a profile correction into a current demand waveform: (a) desired waveform; (b) actual waveform as monitored by probe (before any correction); (c) difference between measured and desired waveform; (d) predistorted gradient drive waveform

Equation (11) may be compared with equation (7). The resistances R_a to R_d are adjusted for each section time constant, and A_a to A_d are adjusted for each section gain factor. The gain factor of $\frac{1}{5}$ is adjusted by further amplification.

Pre-emphasis is a much used and convenient strategy because, if properly implemented, it means sequence designers can ignore the consequences of the pulse patterns they create, and, in principle, any sequence can be run on any machine. The other strategies which depend on the modification of the current pattern to the coils do not have this advantage, but have to be set up sequence by sequence, machine by machine. In these systems the actual gradient profiles are modified so that the demands fed to the amplifiers include correction components for adjusting the current so that it includes a component offsetting the effects of the eddy currents. This technique avoids the problem with the pre-emphasis system of having to decompose all the eddy current components to allow their relatively simple adjustment.

The process can be automated as shown in Figure 5 (D. J. Bryant and G. A. Coutts, private communication 1994). In this approach the iteration starts with the basic desired gradient (a) and the field generated is monitored by a probe (b). The difference between the desired and measured gradient waveform (c) is an indication of the distortion caused by eddy currents. For the period following a slice select or phase encode gradient this should be zero. This difference can be inverted and added to the original demand waveform as a first correction (d). The first correction will not be perfect due to second-order effects, and the correction process can be repeated as required.

An iterative approach is also used for the adjustment of pre-emphasis circuits. In this case a test gradient waveform is followed by field detection after some delay time T_d (Figure 6). Initially, T_d is set of the order of 1 s and the long time constant

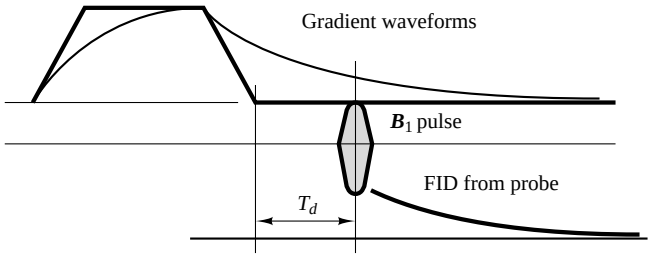

Figure 6 Magnetic resonance probe measurement of eddy current effects

effects are compensated for by adjusting the corresponding parameters in the pre-emphasis circuit. The time delay is progressively reduced and the correspondingly shorter time constant parameters are then adjusted.

4 MEASUREMENT TECHNIQUES

Two prime measuring methods are used to observe the eddy current fields in order to correct them: search coils and NMR probes (see Figure 7). The former [Figure 7(a)] are simple induction loops connected to precision integrators. They work most effectively at middle frequencies (components from 5 to 500 Hz typically) and several coils may be used to measure different ranges of time constants. The NMR probe [Figure 7(b)] is a theoretically better solution, but it may require very substantial signal averaging to give adequate signal-to-noise

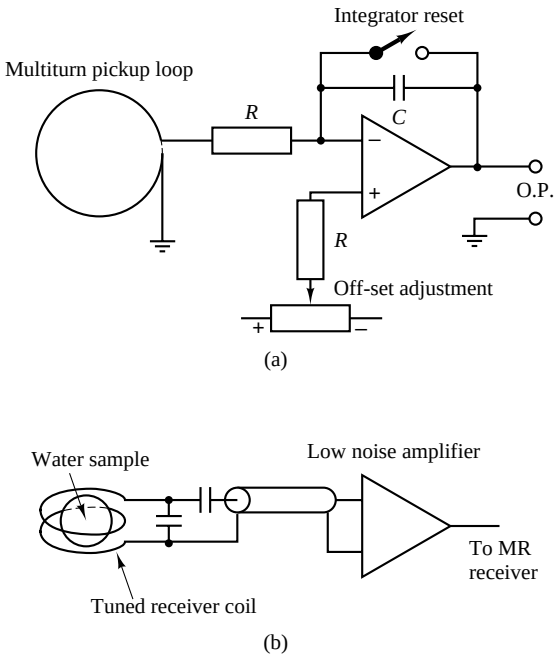

Figure 7 (a) Schematic representation of the induction loop and integration approach to waveform monitoring. (b) Schematic representation of the NMR probe approach to eddy current monitoring

ratio. Probes are a well known means of setting and checking the fields of the main magnets, and are usually small spheres filled with doped water. When used for calibrating gradient fields, the dimension of the probe in the direction of the gradient should be less than one voxel. This means that the volume of signal source in the probe may be very limited; hence the need to average. Typical probe dimensions for this application are around $1 \times 1 \times 15$ mm (giving a volume of 15 μL).

5 CONCLUSIONS

Eddy currents were initially little mentioned, and then treated by those who had worked out how to control them as something to be kept secret, not just for commercial reasons, but also by scientific groups who knew it gave their research a competitive advantage. As a result it is hard to give credit to those who really did develop useful methods of overcoming the problems eddy currents create. However, the problems they represent in whole body spatially localized magnetic resonance cannot be underestimated.

6 RELATED ARTICLES

Birdcage Resonators: Highly Homogeneous Radiofrequency Coils for Magnetic Resonance; Cryogenic Magnets for Whole Body Magnetic Resonance Systems; Gradient Coil Systems; Image Formation Methods; Resistive and Permanent Magnets for Whole Body MRI; Surface and Other Local Coils for In Vivo Studies.

7 REFERENCES

1. I. R. Young, D. R. Bailes, M. Burl, A. G. Collins, D. T. Smith, M. McDonnell, J. S. Orr, L. M. Banks, G. M. Bydder, R. H. Greenspan, and R. E. Steiner, *J. Comput. Assist. Tomogr.*, 1982, **6**, 1.
2. H. F. Skilling, 'Fundamentals of Electric-Waves', 2nd edn, Wiley, Chichester, 1948, p. 141.
3. J. Lammerauer and M. Slapfl, 'Eddy Currents', Iliffe Books, London, 1964, pp. 42, 76.
4. A. Taflone and K. Umashankar, 'Users Code for the Finite-Difference Time Domain Method', Report RADC-TR-82-16, Rome Air Development Center, Air Force Systems Command.
5. D. Rodger and J. F. Eastham, *IEEE Trans. Mag.*, 1993, **19**, 2443.
6. P. J. Leonard, D. Rodger, and R. J. Hill-Cottingham, *IEEE Trans. Mag.*, 1990, **26**, 490.
7. I. S. Grant and W. R. Phillips, 'Electromagnetics', 2nd edn, Wiley, Chichester, 1990, p. 390.
8. P. Mansfield and B. Chapman, *J. Magn. Reson.*, 1986, **66**, 573.
9. P. B. Roemer, W. A. Edelstein, and J. S. Hickey, *Proc. Vth Ann Mtg. Soc. Magn. Reson. Med.*, Montreal, 1986, p. 1067.
10. H. Clow and W. S. Percival. US Patent 4 315 216, British Patent 1 584 948, 1978.
11. P. Mansfield, *J. Phys. C, Solid State Phys.*, 1977, **110**, L55.

Biographical Sketches

Michael Burl. *b* 1946. B.Sc., 1972, Ph.D., 1976, Westminster (formerly PCL). First involved in NMR on joining EMI in 1977 where he was responsible for the first rf systems for the resistive and then a cryogenic imaging machine. Approx. 10 papers and 6 patents related to whole body NMR. Research interests: obtaining better images and spectra in vivo.

Ian R. Young. *b* 1932. B.Sc., 1954, Ph.D., 1958, Aberdeen. First involved with NMR on joining EMI in 1976, where he was charged with leading the engineering group developing first a resistive, then a cryogenic machine (installed at Hammersmith Hospital, 1980–81). Approx. 150 papers and 30 patents in whole body NMR and related aspects. Research interests: obtaining better images and spectra in vivo.

ESR Probes as Field Detectors in MRI

Gösta Ehnholm
Picker Nordstar Inc., Helsinki, Finland

1 INTRODUCTION

ESR methods are potentially attractive for monitoring field levels in NMR in general, and MRI in particular, because of their unique combination of great sensitivity, fast response and high signal-to-noise ratio even with very small samples. Resonance lines of many of the possible candidates for use are very narrow, and so the quality of the signals obtained is also high. Some moieties have multiple lines and can resonate in a mode different from that intended; however, those described here do not suffer from that problem and are consequently easy and reliable to use.

There are two major purposes for which such ESR probes are being developed in MRI. These are to monitor and control the main field ($\boldsymbol{B}_0$) in, particularly, electromagnets, and to act as markers for the positioning of devices and components used in interventional MRI. The former is an extension of methods that have been in use in NMR for many years, but the latter is something quite new and, as yet, there has been a limited description of it[1] in the scientific literature. After some years in which virtually all attention in MRI was focused on superconducting magnets, the recent increase in low-field open magnets has revived the need for field-control systems. These had become largely anachronistic as superconducting units contain flux-locking loops that are used to protect the region where the good field is located against ambient field disturbances.

ESR techniques and methods are being applied in a variety of ways in MRI, but all suffer from the problem that the resonant frequencies at which they operate are very high (gigahertz in typical MRI fields); consequently, direct use of ESR phenomena is very difficult in whole body systems because of rf deposition. This may not seem directly relevant to the topic under discussion, but it arises because it means that communicating with remote probes (which would be very convenient in many circumstances) using the operating frequency of the device itself becomes difficult.

2 ESR SYSTEMS USED

One advantage of the applications discussed here is that the signal power level needed is low and as a result, solid-state devices can generally be used as linewidth requirements are not excessive. There are a number of materials available that are suitable as the basis of the resonance. The units needed for the two applications noted above need not be similar. Good spatial resolution is needed for the localizer but is largely irrelevant for the field monitor. Additional constraints would be added if it were desired to mount the unit outside the homogeneous volume or it was to be located in a region where the field was changing very rapidly.

It is useful here to consider the spatial resolution that is needed for a localizer. If its performance is to be such that it does not contribute significantly to system errors, then it is desirable that it should have a resolution of 100 μm, bearing in mind that several localizers may be used in a single configuration. Factors determining the spatial sensitivity of a localizer are the size of the volume of resonant material, its linewidth, and the magnitude of the gradient fields used to provide a scale with which to detect its location. Field gradients (G) of around 15 m T m^{-1} are typical with lower field machines of the kind normally used for interventional MRI. This implies a field variation of 15 μT mm^{-1} (0.15 G mm^{-1}), which happens to be close to the linewidth of the materials used. For a sample size that is a fraction of a millimeter, this gradient does not widen the resonance line appreciably, which would decrease the signal-to-noise ratio. For the field-tracking system the field sensitivity $\Delta\boldsymbol{B}$ can be expressed as the product of noise density S (in units of T $Hz^{-1/2}$) and the square root of the measuring bandwidth $\Delta f^{1/2}$. Spatial resolution (ΔR) is then given by:

$$\Delta R = \Delta B/G = S\Delta f^{1/2}/G$$

where G is the gradient strength (T m^{-1}). The value of S is proportional to sample volume and that of $\Delta f^{1/2}$ to the inverse of the square root of the measuring time. As the localizer may be used to monitor the positions of thin objects such as needles and catheters, it is very desirable that the volume should be very small.

In principle, there are no size limitations for the field lock, apart from the mechanical convenience of finding a suitable location for a small unit rather than a large one. However, it is usually convenient to mount the unit in a poorer part of the field and thereby avoid obstructing the volume where the patient is located; consequently, small sensor size is an advantage. Sample size should be small enough so that the field gradients in the location used do not broaden the resonance line.

One potential problem, however, is the very high operating frequencies needed for use in magnets with fields of 1.5 T or even higher (typically around 41 GHz and upward). At this time, all the work relevant to this article has been performed at low field (0.23 T), with resonance frequencies of around 6.5 GHz.

3 FIELD LOCK SYSTEM

3.1 Description

The system used so far for field lock applications has been a dielectric resonator (Figure 1a) in the configuration shown in Figure 1b. The resonator is normally located in the lower pole of the iron-yoked 'C-core' magnet, towards its center.

3.2 Use of the Field Lock

Figure 1 illustrates the construction and mode of operation of the dielectric resonator used for field locking. The field modulation, as it sweeps the system through the ESR reson-

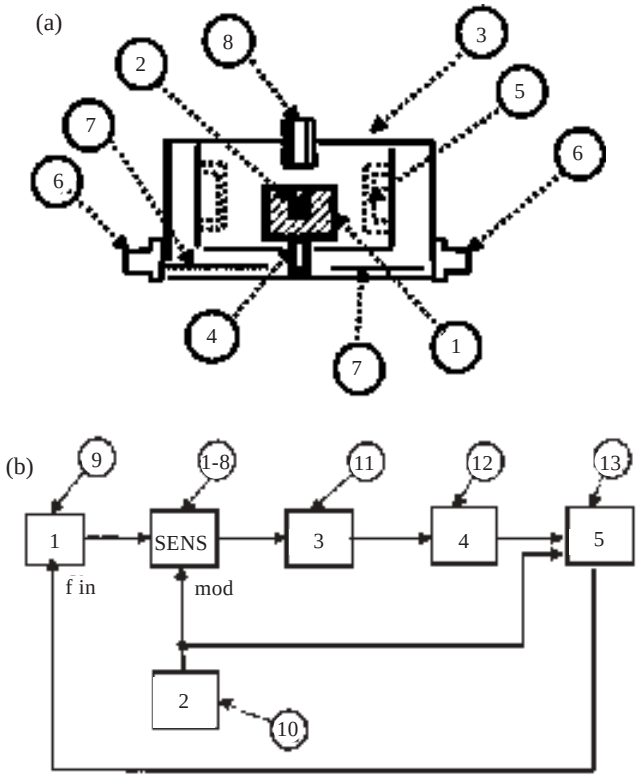

Figure 1 (a) The dielectric ESR resonator. 1. Dielectric resonator; 2. ESR sample; 3. probe cover; 4. resonator support; 5. field modulation coil; 6. input and output ESR signal plugs; 7. stripline coupling to dielectric resonator; 8. tuning screw for dielectric resonator resonance frequency. (b) Circuit configuration used with the resonator. The box designated SENS contains the probe depicted in (a) 9. Voltage-controlled oscillator; 10. audio oscillator for field-modulation signal (mod) to field modulation coil and reference to phase-sensitive detector; 11. diode detector for detecting amplitude modulation of ESR signal; 12. band pass filter, centered around audio oscillator frequency; 13. phase-sensitive detector, which forms a signal proportional to the offset of the voltage-controlled oscillator frequency from the ESR resonance frequency. The latter is used to control the former and lock it by means of feedback to 'f in'.

ance frequency, in effect results in an output signal that is the derivative of the resonance line. This goes through zero at resonance so that the gain of the signal chain (which is difficult to control) becomes unimportant when the feedback is applied with sufficient gain.

The output of the system to the scanner is obtained from the voltage-controlled oscillator. This signal has to be mixed down to obtain a difference frequency having a low enough value to be readily tracked by a frequency counter. The noise density (S) of the system has been measured inside a MRI magnet with gradients quiescent to find the noise of the unperturbed probe. The measurement was made during a few hundred seconds and the noise spectrum calculated. The white noise floor is typically 0.1 nT $Hz^{-1/2}$. In addition to this, a component below approximately 1 Hz was noted. This had a $1/f$ dependence and was believed to be caused by influences from external disturbing fields. The electronics used could only measure the frequency of the voltage-controlled oscillator by counting integral periods. If the measurement time was shorter than about 0.1 s this would have produced another source of noise, which would increase inversely with measurement time or, in other terms, proportionally with bandwidth. This contribution was equal to 0.04 nT Hz^{-1}.

4 FIDUCIAL SYSTEM

4.1 Description

There are a number of materials that could be used as the sample in an ESR resonator for use as the fiducial. These have been evaluated principally for use at zero field by Duret et al., who published data that led directly to the choice of the quiniolinium-*bis*-tetracyanoquinodimethane radical anion (QTCNQ) as the preferred material.[2] This is a polycrystalline solid that is relatively easily handled and is chemically stable. In a typical application—a probe to locate the tip of a biopsy needle[3]—a small lump, about 0.5 mm in diameter, of the material is placed inside a loop or cavity (Figure 2). The signals to and from the loop are connected through a thin semi-rigid coaxial cable to a coupling circuit, which contains a varactor for tuning cable and loop together to the ESR frequency, and means for capacitively coupling the probe to an interconnecting cable. This is connected at the other end to a directional element, such as a circulator, to separate the incoming signal from the outgoing one. The circulator matches the cable so that standing waves are avoided; this makes the system insensitive to the length of the cable which can be several meters long. The probe is used with the same electronics as shown in Figure 1b, though it lacks the coils for modulating the $\boldsymbol{B}_0$ field. This is taken care of by using a separate coil that is made large enough to surround the whole arrangement and so is not in the way.

There is concern, particularly when higher frequencies are used, that probes located inside patients with connecting cables

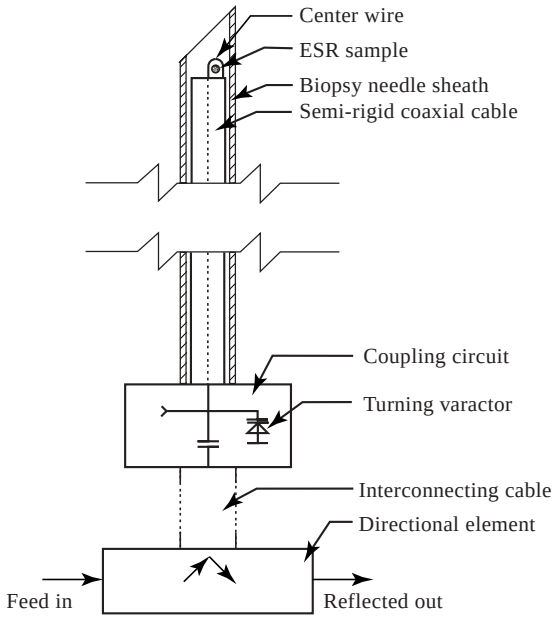

Figure 2 The type of configuration used with the QTCNQ ESR probe in applications such as the location of the tip of a biopsy needle (QTCNQ, quiniolinium-*bis*-tetracyanoquinodimethane).

that are taken out of the machine could act as aerials for the $\boldsymbol{B}_1$ field exciting the NMR resonance. These could result in very high localized current flows, capable of significant regional heating of tissue, particularly near the tip of the probe. It is necessary that insulation round the fiducial system is adequate to ensure that this does not happen in any likely set of circumstances. Because of the high frequency of the ESR excitation, this is easy to accomplish: a cable connection at the probe can be designed that has the needed dielectric insulation for lower frequencies, both at the center and at the outer conductor.

4.2 Use of the Fiducial System

In typical applications of the fiducial system, it is necessary to define the position of the probe in three dimensions. The technique used is analogous to that used by Dumoulin et al. to determine the location of a small coil intended for catheter positioning.[4] Gradients are applied consecutively in the x, y and z directions. In the study of Ehnholm and Vahala, the gradient pulses were approximately 10 ms in duration.[3] The position of the probe can then be automatically computed, knowing the values of the applied gradients and the measured field. From the measurements obtained, the noise level could also be found, which was determined in this study to be about 50 nT RMS. Comparing this to the values that might be expected from the field probe, it is about one order of magnitude bigger than expected. This is probably because of a combination of field disturbances caused by the gradient and/or the field-modulating coils and the fact that the feedback loop has to work very hard in tracking the ESR frequency, which makes it more susceptible to noise. Even so, the value is quite small; consequently, the applied gradients can be very modest and good precision for the localization is still obtained.

5 CONCLUSION

ESR probes have been useful for field monitoring, where they have a combination of speed and precision that cannot easily be obtained with proton NMR-based detectors. At the same time, they can be used in less homogeneous fields, thanks to the small dimensions of the sample.

For positional probes, the same properties make it possible to achieve a very small design that can be fitted inside objects as small as a biopsy needle. A further advantage is the chemical and physical stability of the material used as the sample in the ESR resonator.

6 RELATED ARTICLES

MR-Guided Biopsy, Aspiration, and Cyst Drainage; Neurosurgical Procedures Monitored by Intraoperative MRI.

7 REFERENCES

1. G. J. Ehnholm, E. T. Vahala, J. Kinnunen, J. E. Niemenen, C. Standertskjold-Nordenstam, and M. A. Uusitalo, *JMRI*, 1999, **10**, 216.
2. D. Duret, M. Beranger, M. Moussavi, P. Turek, and J. J. Andre, *Rev. Sci. Instrum.*, 1991, **62**, 685.
3. G. J. Ehnholm and E. Vahala, *J. Magn. Res.*, 2000, in press.
4. C. L. Dumoulin, S. P. Souza, and R. D. Darrow, *Magn. Reson. Med.*, 1993, **29**, 411.

Biographical Sketch

Gösta J. Ehnholm. *b* 1943. M.Sc., 1968, D.Tech., 1972 Helsinki University of Technology. Assistant in Physics Helsinki University of Technology 1966–71; Senior Scientist Finnish Academy and Finnish National Commission of Natural Science 1972–78; Deputy Head of Helsinki University of Technology Low Temperature Laboratory 1977; Senior Research Associate Cornell University 1979; R&D Manager Istrumentarium OY Finland 1980–92; Chief Scientific Officer Picker Nordstar, Inc. Finland 1993–present; Acting Project Manager Superconducting MRI Magnet Project 1983–86; SQUID Magnetoencephalogram Project 1987; Overhauser MRI Project 1988–97; Interventional MRI Project 1998–present.

Gradient Coil Systems

Robert Turner
Institute of Neurology, London, UK

1 INTRODUCTION

The effect of static magnetic field gradients on the nuclear magnetic resonance signal has been a subject of research interest since the pioneering work of Gabillard.[1] Many practical uses of NMR require the presence of coils in the bore of the magnet which can generate additional fields of specified spatial variation. These are called 'gradient coils', and improvements in gradient coil design have frequently led the way to major technical developments in NMR spectroscopy and MRI. This article will describe the basic issues relating to gradient coil design, fabrication, and activation with electric current. Fuller descriptions of the NMR techniques to which reference is made will be found elsewhere in the Encyclopedia.

Typically, the magnetic field variations desired consist of linear variations in space of the prevailing, and otherwise homogeneous, static magnetic field $\boldsymbol{B}_0$, which is commonly taken to define the z direction of the coordinate system used in coil design. Thus three independently driven coils are required which generate fields with constant $G_x = \mathrm{d}B_z/\mathrm{d}x$, $G_y = \mathrm{d}B_z/\mathrm{d}y$, and $G_z = \mathrm{d}B_z/\mathrm{d}z$ respectively, over a usefully large volume of space within the larger magnet supplying $\boldsymbol{B}_0$. This enables the complete MRI repertoire of slice selection and formation of images of slices of arbitrary orientation. The quantities G_x and G_y are referred to as transverse gradients, and G_z is the longitudinal gradient. Most often $\boldsymbol{B}_0$ is produced by a solenoid with a cylindrical bore, in which case the gradient coils are generally wound on coaxial cylindrical formers within the bore. Other arrangements are sometimes found, such as the 'transverse geometry' configuration,[2–4] in which the axis of the coil formers is perpendicular to $\boldsymbol{B}_0$. Normally, windings for G_y are obtained by rotating the pattern for G_x by 90°.

2 USES, DESIRED CHARACTERISTICS, AND LIMITATIONS OF GRADIENT COILS

The use of gradient coils has the greatest practical importance in MRI (magnetic resonance imaging), and arises from consideration of the Larmor equation (q.v.), $\omega = \gamma B$. Here ω is the resonant frequency, γ is the magnetogyric ratio, and B is the magnitude of the magnetic field. If a linear field gradient is applied to an object containing NMR-sensitive nuclear spins, their Larmor frequencies become spatially dependent. Different planes in space are thus labeled with different frequencies, so that frequency analysis of the NMR signal can reveal the relative quantities of nuclear spins along the direction of the field gradient. It was this insight, first perceived by Gabillard,[1] which was put into practical use by Lauterbur[5] and Mansfield[6] in their implementation of MRI in the early 1970s. Other important uses of field gradients include their role in the selective NMR excitation of subvolumes of objects[7] (such as slices which can subsequently be imaged), labeling of moving spins (allowing magnetic resonance angiography,[8] quantitation of flow,[9] and molecular mobility[10]), and defining of coherence pathways in multiquantum[11] or multinuclear[12] NMR spectra.

Given the crucial role of magnetic field gradients in NMR, a surprisingly small number of workers have made major contributions to their development. Well-established recipes, giving coils with reasonable efficiency but with gradients of poor linearity, were the norm until the mid-1980s.[13,14] There were few attempts to optimize designs, and little debate in the literature. This came about partly because at that time an MR image took many minutes to acquire, and so gradients did not have to be very large or rapidly switched. Furthermore, MR spectroscopy did not then use gradients at all; localized spectroscopy and spectroscopic imaging were mostly developed after 1985, partly in response to improved hardware.

When it became clear that there was a serious need for better quality gradient coils, a number of improvements were made, the details of which are often unfortunately buried in patents and other less-easily accessible reports. They include (a) the use of distributed-winding coils, (b) the introduction of the stream function for current density, (c) the use of the cylindrical harmonic expansion of the magnetic field variation, (d) minimization methods for power dissipation and inductance, (e) improved fabrication methods, such as printed circuit techniques, and (f) high-current gradient drivers.

These innovations allow greater control over a set of gradient coil performance goals, which includes high current efficiency (defined as the ratio of gradient generated to current drawn), rapid switching time (i.e. low inductance), gradient linearity over a large volume, low power consumption, and minimal eddy-current producing interaction with any other equipment. Some of these requirements are obviously in conflict: for instance, to increase the volume over which the gradient is uniform increases the stored magnetic energy, and hence the inductance, as we shall see.

The inductance and power dissipation of a discrete-wire coil cannot easily be written down in a closed form amenable to analytic optimization procedures. It is much simpler to start with an expression for a continuous current density flowing on the surface of a coil former, which is optimized and then approximated with great accuracy by a distribution of wires. However, many gradient coils are still built using a discrete current path approach from the outset. Such coils often have the advantage of simplicity, though their performance may be poor in other respects. There are clearly established limitations to gradient coil performance. These arise from two sources: the laws of electromagnetism, and the physiological effects on nerves of rapidly switched large magnetic fields.

The smoothness of the variation of the magnetic field, which obeys the Laplace equation, away from current sources, means that any coil wound on a cylindrical former gives fields which are nonzero at greater axial distances than the region over which the linear gradient is desired to be established. Physically, a field gradient established in a given volume has a finite stored energy. Any coil which generates this gradient has a larger stored energy E, since for most coil geometries and all methods of coil winding the magnetic field extends beyond the region over which the field is specified as a linear gradient.

Now E is related to the coil inductance L and the supply current I by the equation

$$E = LI^2/2 \tag{1}$$

and thus a gradient coil has a clearly definable minimum inductance consistent with its specified field performance. For a given gradient current amplifier, with maximum voltage and current outputs V_{max} and I_{max}, the rise time to maximum current (assuming negligible resistance and capacitance) is simply

$$\tau = LI_{max}/V_{max} \tag{2}$$

The inductance is thus normally the major determinant of how fast a coil may be ramped with a given power supply, and hence, for a given specified gradient and power supply, the rise time has a well-defined minimum.

However, because of physiological effects, this minimum may not be attainable. For fast enough risetimes and large enough field strengths, the voltage induced in tissue by a rapidly changing field may stimulate the firing of peripheral nerves to a painful degree.[15] The magnetic field threshold for nerve stimulation in most parts of the human body is on the order of 10 mT if the field is switched in 100 μs or less. To produce cardiac arrhythmias, rapidly switched fields of two to three orders of magnitude higher are necessary.[16]

3 CURRENT AMPLIFIERS FOR GRADIENT COILS

The current efficiency of a gradient coil, as defined earlier, increases linearly with the number of coil turns. However, the inductance increases as the square of the number of coil turns. Thus, since the voltage (required to switch the current rapidly) available in a current amplifier has an inevitable upper limit, there is a major incentive to reduce the number of coil turns as much as possible (short of sacrificing the purity of the gradients produced) and to compensate for the reduced efficiency by using amplifiers capable of generating very large currents. Several amplifier design strategies were introduced between 1985 and 1990. The first was simply to use more Class A linear audio amplifiers, connected in series and/or in parallel to achieve the desired combination of voltage and current output. Typically these amplifiers are rated at 160 V, 100 A. Their chief advantage is the ease of generation of any desired current waveform, though this is offset by the very poor energy efficiency, complexity, and bulk of such systems. Usually they are driven in a 'current-controlled' mode, in which a large voltage (sometimes called 'preemphasis') is available to counteract the back-emf generated in the gradient coil during switching, and hence to obtain the fastest possible slew rate [see equation (2)].

Another solution is to supply a large (typically 350 A), well-regulated dc current, and to control it by chopping it at a high frequency (80 kHz or higher). The mean amplitude of the chopped output can be controlled by altering the mark/space ratio of the chopping. The output is then passed though a low-pass filter to remove ripple. Switching times of 150 μs for currents of hundreds of amperes can be achieved by this means. Many such current drivers can be arranged in parallel to increase the output further. The advantages are low complexity, compactness, and large current output. However, eradicating all traces of the chopping frequency is not easy.

Perhaps the preferred solution[17] is to use recently developed high power silicon switches (SCRs and MOSFETs), which can handle currents of several hundred amperes and voltages up to 1000 V, in so-called 'stored-energy' devices. Here the required high voltage needed to overcome the back-emf created by the coil inductance is provided by a small ancillary high voltage power supply, charging up a large capacitor which can be switched into the gradient coil circuit when necessary. The large steady current needed between gradient current switches is provided by a simple, well-regulated dc current supply.

4 MEASURES OF GRADIENT COIL PERFORMANCE

A satisfactory measure of coil performance includes coil efficiency, inductance, and gradient homogeneity. If the coil efficiency (gradient/current or field/current, depending on the application) is denoted as η, the inductance as L, and the desired field and the achieved field as B_D and B, respectively, over a volume of interest V, the figure of merit β is given by[18]

$$\beta = \frac{\eta^2/L}{\{V^{-1}\int_V d^3r\,[B(r,\phi,z)/B_D(r,\phi,z) - 1]^2\}^{1/2}} \tag{3}$$

This combines a dimensionless measure of inhomogeneity with a term which is independent of the number of turns of the coil, depending only on the winding configuration and coil radius. For purposes of comparison this radius is set at 1.0 m.

It is worth noting that for constant efficiency and winding configuration, by dimensional arguments, the inductance of a cylindrical gradient coil varies as the fifth power of its radius. This underlies the importance of keeping coils as compact as possible.

5 COILS WITH DISCRETE WINDINGS

The most fundamental equation used in gradient coil design is the Biot–Savart law (1820), which relates the magnetic field $d\boldsymbol{B}$ at a point in space (Figure 1) to the current element I flowing in a line element $d\boldsymbol{l}$ at a distance $\boldsymbol{r}$ from the point in question:

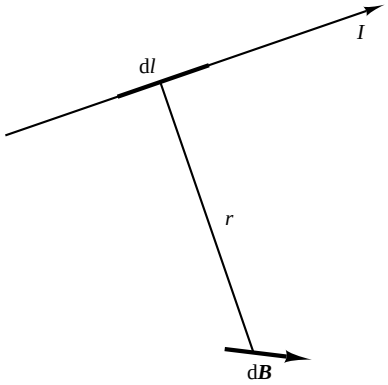

Figure 1 Diagram showing definition of variables for the Biot–Savart law

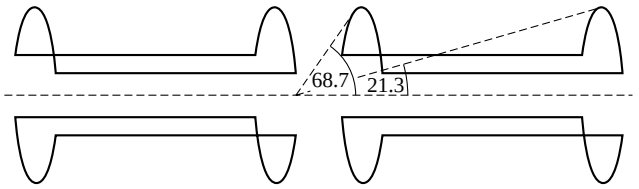

Figure 2 Double-saddle transverse gradient coil with coil spacing for optimal gradient uniformity

$$d\boldsymbol{B} = \frac{\mu_0 I\, d\boldsymbol{i} \times \boldsymbol{r}}{4\pi r^3} \tag{4}$$

This equation is used to calculate fields produced by discrete-wire coils, whether designed by approximating to an optimized continuous current sensity, or directly as discussed below. Where conductors of large cross section are used it is inappropriate unless the current distribution within the conductor is known or can be estimated.

The archetypal discrete coil is the well-known Helmholtz pair, which consists of two equal coaxial circular coils spaced by their radius. This particular coil spacing removes the quadratic term from the Taylor expansion of the field as a function of the axial coordinate z, so by symmetry the lowest order term beyond a constant field is z^4. A field uniform to 5% is obtained within a sphere of roughly half the coil diameter. This trick, removing terms of specific order in the Taylor expansion, is widely employed in the design of coils with discrete paths. It can be performed in a systematic way by using the spherical harmonic expansion.[19]

In practice, it is difficult to make a discrete arc coil with sufficient accuracy. Any deviation from the prescribed positions will create lower order terms, since a detailed cancellation is implicit in the design technique. Frequently a single turn at each position is insufficient, and when turns are piled up it is difficult to maintain accuracy of positioning. Furthermore, the performance of the coil off-axis is not guaranteed by this design method.

However, the simplest z gradient designed in this way, the so-called Maxwell pair, consisting of two circular arcs spaced by $\frac{1}{2}a\sqrt{3}$, where a is their radius, with antiparallel currents, has proved so simple to construct and of such high current efficiency that it has remained popular even when z gradient coil designs with better field characteristics have become available. This coil, corrected to fifth order, gives a gradient uniform to 5% within a sphere of radius $0.5a$. The gradient uniformity rapidly worsens beyond this radius. At the origin, the gradient efficiency is

$$\eta = \frac{8.058 \times 10^{-7}}{a^2} \qquad (\mathrm{T\ m^{-1} A^{-1}}) \tag{5}$$

For transverse gradients, the so-called 'Golay'[20–22] or double saddle arrangement of eight 120° circular arcs arranged on a cylinder (Figure 2) has been used extensively. For maximum efficiency the return path, distal, arcs should be placed at positions $2.57a$ from the central plane,[20] resulting in a coil which is unwieldy in its length and also of large inductance. For this coil the efficiency is

$$\eta = \frac{9.18 \times 10^{-7}}{a^2} \qquad (\mathrm{T\ m^{-1} A^{-1}}) \tag{6}$$

Compromise positions, with reduced efficiency, have been derived by many workers.[22,23] Adding further arcs, of different angular widths and at different axial positions,[24] allows more design flexibility, culminating in the designs of Siebold.[25] However, the poor off-axis performance of this type of gradient coil (uniform to 5% only within a sphere of radius of $0.6a$) does not permit such coils to benefit from the great improvement in efficiency and risetime to be obtained by using a smaller former.

Other types of discrete element gradient coils rely on straight wires arranged on planes. Simple but effective configurations can be derived by considering the expression[26]

$$B_z(y,z) = \frac{\mu_0 I}{2\pi} \mathrm{Re} \sum_{n=0}^{\infty} (\xi/r)^n \, \mathrm{e}^{-\mathrm{i}(n+1)\phi} \tag{7}$$

where $r\mathrm{e}^{\mathrm{i}\phi} = a + \mathrm{i}b$, a and b are the (z, y) coordinates of an infinite wire carrying a current I in the x direction, and $\xi = z + \mathrm{i}y$. This series expansion rapidly converges and allows calculation of combinations of wires for which specific higher order terms cancel, as we have seen earlier for the spherical harmonic case.

One useful arrangement[27] places four wires carrying current in the same direction symmetrically about the origin. If $\phi = 22.5°$, the 'trapezoidal' design of Bangert and Mansfield shown in Figure 3 is obtained, when return paths are included. This design is compact, of low inductance, has low fringe fields, and offers good access. However, its efficiency is low ($2.62 \times 10^{-7}/a^2$ T m^{-1} A^{-1}) and the volume of uniform gradient is restricted to within a sphere of radius $0.4a$.

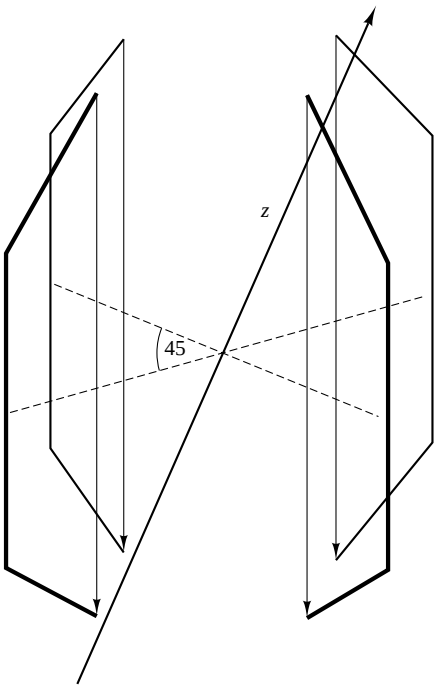

Figure 3 'Trapezoidal' transverse gradient coil

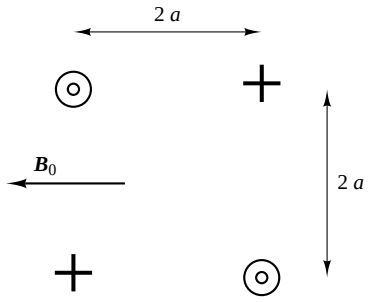

Figure 4 'Anderson' longitudinal gradient coil. The z direction is taken to be the same as $\boldsymbol{B}_0$

A further class of coils formed from straight wires was originated by Anderson.[28] These are suited to a transverse geometry, being mountable on the pole faces of an electromagnet in which configuration they offer excellent access. A typical example, the counterpart of the Maxwell pair, is an arrangement of four infinite wires at the corners of a square, with currents alternating in direction around the square (Figure 4). This coil, corrected up to fifth order, gives a linear G_z out to about half of the wire separation. It has an efficiency of $\eta = 10^{-7}/a^2$ T m^{-1} A^{-1}, noticeably poorer than that of the Maxwell pair. There are two reasons for this; firstly, the wire spacing in the z direction is somewhat greater, and secondly, the straight wire paths are generally further from the volume of interest at the origin. This instructive comparison demonstrates the importance of keeping gradient coils compact.

Anderson coils have been used extensively[29] where simplicity of design and construction have outweighed efficiency and risetime in importance.

6 COILS WITH DISTRIBUTED WINDINGS

As early as 1951, Garrett[19] mentioned the 'well-known precision of a cylindrical winding' by comparison with a discrete Helmholtz pair. Coils wound to approximate a continuously varying current density on formers of simple symmetry, such as cylindrical shells or planes, generate much smaller undesired, rapidly varying, high-order fields in conjunction with the desired slowly varying terms. This means that more compact coils can be used to give gradients uniform over a given volume, so that much higher efficiency is possible. Furthermore, the inductance of such coils is in general lower, because the current density is less concentrated, and hence there is less of a field build-up in the space around the conductors.

A number of approaches to the problem of finding optimal positions for the multiple windings of such coils have been pursued. These include matrix inversion techniques, 'stream function' methods, and the 'target field' approach developed by Turner and followers. Usually such methods initially derive, by some optimization technique, a continuous current density on a coil former, such as a cylinder. A simple approximation is then used to convert this into a pattern of discrete current paths, so that a real coil may be constructed.

6.1 Matrix Inversion Methods

These methods are related to finite element methods, in that they can cope with any shape of coil former, are relatively slow in computation time, and give little physical insight regarding the dependence of field on coil configuration. Much has been written about the use of finite element methods in calculations of magnetic field distributions, and it is not appropriate to review this literature here. A few examples relevant to gradient coils will be discussed.

Hoult suggested in 1977[30] that a solenoid could be optimized to give a very uniform field by writing

$$B_z(z_m) = \sum_{n=1}^{N} A_{m,n} I_n \tag{8}$$

where

$$A_{m,n} = \frac{\mu_0 a^2}{2[(z_m - z_n)^2 + a^2]^{3/2}} \tag{9}$$

is a matrix relating the axial field $H_z(z_m)$ at a point z_m on the axis to the current I_n flowing in the nth circular loop at a position z_n of the solenoid of radius a. If N such points are chosen the matrix may be invertible, giving a set of currents at N positions which may be approximated by piling up appropriate numbers of turns at these positions. It should be noted that it is possible to specify the field in such a way that the matrix becomes singular, corresponding to an unphysical coil configuration. In practice, coils designed in this way may require large variations in current from one turn to the next, even current reversals.

At a time when the highest level of sophistication for transverse gradient coils was the use of a double saddle arrangement, Compton[31] developed a distributed-arc coil design giving gradients departing from the desired characteristics by a predetermined error. This involved dividing the surface of a cylindrical coil former into 2048 equally sized elementary areas, and calculating the current densities which should flow in each of these areas in order to give the least-squared departure from a chosen field within a spherical volume at the center of the coil. A set of n simultaneous equations was derived, which was solved by matrix inversion or Gaussian elimination to give the surface current elements. Current paths were deduced by integrating over the elements of surface area until the current required by the coil designer to flow in a discrete wire is accumulated, at which point a conductive path is laid on the cylinder.

This approach led to high-quality transverse and longitudinal gradient coil designs,[31] which are optimal in the sense that they give the most uniform field over the volume of interest possible for a coil of a prescribed extent (length in the case of a cylindrical coil). The computation is very slow, however, since a 2048 $\times$ 2048 matrix must be inverted. Furthermore, neither inductance nor power dissipation is constrained, so that optimal trade-offs cannot be explicitly obtained.

Further improvements in this approach were made by Schweikert et al.[32] and Wong et al.[33] Schweikert used a Lagrange multiplier formalism to allow the field specified at N selected points in space to be used as constraints in an explicit minimization of the power dissipated by a coil (in the case

described, a solenoid). This method was used to produce an excellent low power dissipation solenoid, capable of switching 1.2 T in 400 μs, and of high homogeneity, and can be applied to gradient coil design.

Wong et al.[33] took another approach, closely related to that of Compton. Instead of calculating optimized currents at specific surface elements, they kept the current and the number of turns fixed, while the current element *position* was allowed to vary. The error function was then minimized using the method of conjugate gradient descent, about 20–200 iterations being required. The product of the error function and the inductance could also be minimized, giving coils which are compact as well as giving gradients accurate over a large volume. For a longitudinal gradient coil, where the number of wire positions is small (10–50) the calculation takes only a few minutes on a small computer.

The chief advantage claimed for this method is that there is no stage of approximation between a calculated continuous current density and the practical realization of discrete current paths (see below). Thus the fields predicted by the calculation should be identical to those produced by the actual coil. This advantage is not significant, however, in coils with as few as 20 turns, because the field from an array of wires approximating a current sheet converges very rapidly to that of the current sheet as the number of wires increases.

For coils of very few turns to be constructed using wire rather than etched copper sheet, it is clear that the Wong technique is optimal in that it will give the best coil possible for that number of turns, and also takes a relatively short time to perform the calculation. However, computation time increases rapidly with the number of turns, unlike the continuous current density techniques to be described below which use the symmetry of the coil former radically to simplify the calculation of the fields. Furthermore, the technique does not lend itself to the design of coils consisting of copper sheet with etched or machined tracks between successive turns, which generally dissipate less power than wire coils.

6.2 Stream Function Methods

The stream function $I(z,\phi)$ on a cylinder is that function which, if differentiated with respect to z or ϕ, gives the current density in the azimuthal or axial direction, respectively. Stated otherwise, $I(z,\phi)$ is the integral of the current density. If a continuous current density distribution is to be approximated by discrete wires, the obvious place to locate them is at equally spaced contours of the stream function. Analogous definitions can be given for stream functions on surfaces of other geometries.

A number of successful distributed-arc coil designs have been obtained by considering the most simple stream functions capable of generating gradient fields of the desired symmetry. Take, for instance, the function (Figure 5)

$$I(z,\phi) = \begin{cases} \left(\dfrac{I_0 z}{d}\right)\cos\phi & (|z| < d) \\ \left[\dfrac{I_0(c-z)}{(c-d)}\right]\cos\phi & (d < |z| < c) \\ 0 & \text{elsewhere} \end{cases} \tag{10}$$

This has the correct symmetry to generate a transverse gradient and if d and c are sufficiently large the field generated is a linear G_x gradient over a large volume. This arrangement is the transverse gradient coil equivalent of a uniform solenoid, with no end corrections to compensate for its finite length.

To determine the arc positions, we have only to find the equally spaced contours of this function. For instance, for $|z| < d$, dividing the total current I_0 into N turns, the locus (z, ϕ) of the nth contour is given by

$$\left(n+\frac{1}{2}\right)\frac{I_0}{N} = \left(\frac{I_0 z}{d}\right)\cos\phi \tag{11}$$

i.e.

$$\phi = \cos^{-1}\left\{\frac{\left(n+\frac{1}{2}\right)d}{Nz}\right\} \tag{12}$$

The factor $(n + \frac{1}{2})$ is used rather than n when the coil is to be formed from wire, since this ensures that the wire is positioned at the center of the equivalent strip of current density for which it is an approximation.

Alternatively, a coil may be constructed by cutting tracks of constant width in a continuous conducting sheet, which then separates the conductor into turns of varying width. In this case the factor to be used in equation (12) is simply n. This approach has formed the basis of coil designs by Edelstein et al.[34] and Sutherland.[35] Adjustment of the parameters d and c allows some degree of optimization. The method gives rise to coils of good efficiency when sufficiently short, but the gradient homogeneity tends to be poor under these circumstances, good to 5% only within a volume of radius $0.4a$ because there is no end correction. In MRI applications the resultant image distortion is corrected in software, using a look-up table describing the known gradient field inhomogeneities, a strategy which has limitations when gradients are used for other purposes besides imaging, such as the measurement of water diffusion.[10]

6.3 Target Field Methods

A powerful method of designing coils, in which Ampere's law is inverted in order to calculate the currents required directly from the specification of the desired fields, has been termed the target field approach.[36] It relies, like the inversion of many integral equations, on the Fourier transform, and thus

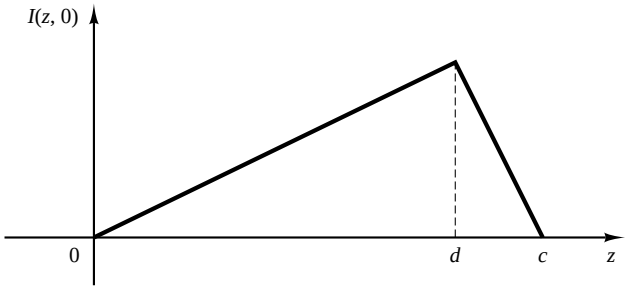

Figure 5 Stream function $I(z,\phi)$, for $\phi = 0$, for Edelstein-type transverse gradient coil

can take full advantage of the speed and ease of implementation of the Cooley–Tukey finite Fourier transform (FFT) algorithm.[37]

The starting point is to assume that the source of the magnetic field is a current density, $\boldsymbol{J}$, on a shell of simple geometry, such as a cylinder of circular or elliptical cross-section, a plane, or a sphere. The shell may have finite thickness, as long as the current distribution across the thickness is specifiable. The next step is to consider the Fourier transform of $\boldsymbol{J}$, denoted $\boldsymbol{j}$. For currents lying in a thin cylindrical shell, this is written

$$j_z^m(k) = \frac{1}{2\pi}\int_{-\pi}^{\pi} \mathrm{d}\phi\, \mathrm{e}^{-\mathrm{i}m\phi} \int_{-\infty}^{\infty} \mathrm{d}k\, \mathrm{e}^{-\mathrm{i}kz} J_z(\phi, z) \tag{13}$$

$$j_\phi^m(k) = \frac{1}{2\pi}\int_{-\pi}^{\pi} \mathrm{d}\phi\, \mathrm{e}^{-\mathrm{i}m\phi} \int_{-\infty}^{\infty} \mathrm{d}k\, \mathrm{e}^{-\mathrm{i}kz} J_\phi(\phi, z) \tag{14}$$

where J_z and J_ϕ are the orthogonal components of the current in the surface, related by the equation of continuity $\nabla\cdot\boldsymbol{J} = 0$. This implies that

$$j_\phi^m(k) = -\frac{ka}{m} j_z^m(k) \tag{15}$$

where a is the radius of the former. Expanding the field variation in cylindrical harmonics, the following result is obtained:[36,38,40]

$$B_z(r,\phi,z) = -\frac{\mu_0 a}{2\pi} \sum_{m=-\infty}^{\infty} \int_{-\infty}^{\infty} \mathrm{d}k\, \mathrm{e}^{\mathrm{i}m\phi}\, \mathrm{e}^{\mathrm{i}kz} |k|\, j_\phi^m(k) \times K_m'(|k|a)\, I_m(|k|r) \tag{16}$$

where $I_m(x)$ and $K_m(x)$ are the modified Bessel functions.[39] These functions are easy to calculate and monotonic. Writing

$$B_z^m(r,k) = \frac{1}{2\pi}\int_{-\pi}^{\pi} \mathrm{d}\phi\, \mathrm{e}^{-\mathrm{i}m\phi} \int_{-\infty}^{\infty} \mathrm{d}k\, \mathrm{e}^{-\mathrm{i}kz} B_z(r,\phi,z) \tag{17}$$

we can invert equation (16) for a specified $r = c$:

$$j_\phi^m(k) = -\frac{B_z^m(c,k)}{\mu_0 a|k| K_m'(|k|a) I_m(|k|c)} \tag{18}$$

Thus if the axial field B is specified everywhere on a cylinder of radius c which allows the Fourier transform $B_z^m(c,k)$ to be evaluated, the current density required to generate this field can be immediately deduced from a Fourier transformation of $j_\phi^m(k)$. Once this is calculated, the stream function can be evaluated, and the positions of wires or tracks to be removed from a continuous conducting sheet can be easily determined. This is illustrated in Figure 6, showing the integrated current density required to produce a good quality z gradient field. Many useful coil designs have been generated by these means.[36,41]

In a similar way[42–44] target field equations may be derived in Cartesian coordinates, relating the current densities on planes to the field produced. This results in flat transverse gradient coil designs giving more uniform gradients than those produced by simply flattening out a cylindrical coil design.[45]

These equations, which may be generalized for arbitrary frequency, provide useful tools for gradient coil design. For instance, the power dissipation P in a coil consisting of a current density flowing in a cylindrical conductor of thickness t and resistivity ρ may be written in the form

$$P = \frac{\rho a}{t} \sum_{m=-\infty}^{\infty} \int_{-\infty}^{\infty} \mathrm{d}k\, |j_\phi^m(k)|^2 \left(1 + \frac{m^2}{k^2 a^2}\right) \tag{19}$$

and the energy $E = LI^2/2$ stored in the field may be written[18,46] as

$$E = -\frac{\mu_0 a^2}{2} \sum_{m=-\infty}^{\infty} \int_{-\infty}^{\infty} \mathrm{d}k\, |j_\phi^m(k)|^2 I_m'(|k|a) K_m'(|k|a) \tag{20}$$

Such quadratic expressions lend themselves to constrained minimization, similar to the approach of Schweikert mentioned earlier. Either P or E, or a suitably weighted sum of the two, can be minimized whilst the coil efficiency is held fixed at a desired selection of points in space, introduced using Lagrange multipliers. A matrix equation results, which can be solved by Gaussian elimination, matrix inversion, or singular value decomposition. The important point to note is that the matrix has dimensions $N \times N$, where N is the number of points at which the field is constrained. To obtain coils which are entirely adequate for MRI and MRS, a small number of target points is sufficient, perhaps eight. Once the Lagrange multipliers are known, the current density j can be easily derived and winding positions determined as before.

This technique, as described, places no direct restriction on the overall length of the coil, which may cause problems where space is restricted. However, a further set of Lagrange multipliers, representing length constraints, may easily be added.[48] This allows straightforward truncation of coils, still with the guarantee of minimum inductance or power consistent with the constraints applied.

Similar expressions may be derived for currents flowing on planes. Minimum inductance planar designs have been developed by Martens et al.[44] and minimum power designs by Bowtell and Mansfield.[42]

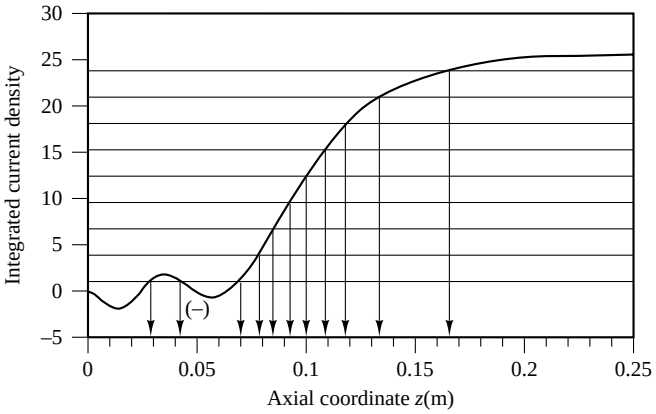

Figure 6 Integrated current density on the surface of a cylinder radius a required to produce a uniform longitudinal gradient over a volume of interest radius $0.7a$, length $1.0a$. Arrows indicate positions, at equal increments of integrated current, where wires would be placed to approximate this current density in a practical implementation. Note single reverse turn (−) (Reproduced by permission of *Magnetic Resonance Imaging*)

These methods of coil design can be implemented on a relatively small computer, and if the fast Fourier transform is used to calculate the matrix elements, as well as to evaluate the current densities, a computation time of a few minutes is all that is needed, even if a large array of points (say 2048) is used. The winding pattern and the field distribution can be computed at thousands of points in space in a few seconds, using equations (17) and (18). It is recommended to use extended precision to ensure stable results.

A similar approach using spherical harmonics has recently been devised.[47]

6.4 Apodization

With minimum inductance and power dissipation designs, it is often desirable[18] to remove the most rapidly varying current components by 'apodization'. This involves multiplication of the calculated $j(k)$ by a Gaussian function before it is Fourier-transformed back into real space to give the current distribution. The effect, for apodization lengths of about one-tenth of the coil radius, is to smooth out the field variation at a negligible cost in conformity to specifications while reducing the inductance slightly, and removing the undesirable current density oscillations.

6.5 Comparison of Minimum Inductance and Minimum Power Designs

Minimum power designs are less compact than minimum inductance coils and their inductance is about 10% higher, but they have a smoother variation of current density and a lower power dissipation[48] (Figure 7). If minimizing coil risetime is the primary objective the minimum inductance approach is best, but if the space available for coil windings is limited radially the minimum power approach is preferable.

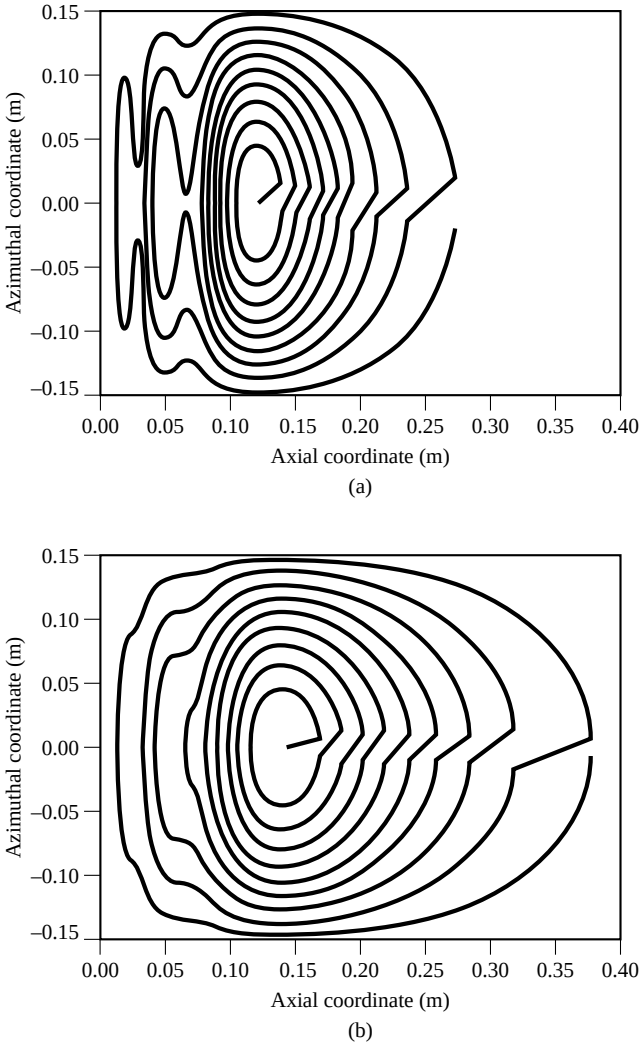

Figure 7 Primary coil turn layouts for (a) minimum inductance transverse gradient coil (inductance 61 μH, power dissipation 23 mW A^{-2}) and (b) minimum power dissipation transverse gradient coil (inductance 73 μH, power dissipation 15 mW A^{-2}). For both designs: primary coil radius, 0.1 m; shield radius, 0.5 m; coil efficiency, 0.5 mT $m^{-1}A^{-1}$; target cylinder radii, 0.01 m, 0.06 m; axial spacing of target points, 2.5 mm; number of target points per cylinder, 5; copper thickness, 1 mm

7 PASSIVE AND ACTIVE SHIELDING

One of the major problems in the use of switched magnetic field gradients in MRI and MRS has been the interaction of the rapidly switched fields with other conducting structures in the magnet assembly. Such structures may include heat shields in the Dewar holding the superconducting magnet, supports for these heat shields, and also radiofrequency coils and local rf shielding. Eddy currents are induced in these structures, which produce fields opposing that of the switched gradient. The behavior of the gradient fields at the center of the magnet is degraded, both temporally and spatially. The rise time of a switched gradient is increased and transient currents which are slow to decay may cause a long settling time.

A somewhat crude solution to this problem is to adjust the gradient waveform which is fed to the gradient amplifiers so as to compensate for the effect of induced eddy currents.[49,50] This is often performed by adding a feedback circuit to each gradient amplifier, containing a set of appropriate resistance and capacitance values to provide up to four time constants which can be separately adjusted. Apparently clean and fast switching may thus be obtained for the gradient current. This implies increasing the voltage available for current switching and thus adding to the cost of the gradient drivers. But a more serious problem remains. The eddy currents induced by switching do not disappear simply because compensation has been applied. They may persist for many milliseconds after the gradient current has stabilized at a new level, producing time-varying distortions in the gradients experienced at the sample as we have mentioned. These fields can produce major distortions in NMR spectra, prevent the use of short echo times in fast imaging, and render diffusion imaging, which uses large precisely-matched gradient pulses, completely impossible.

The best way to solve this problem, as pointed out by Chapman and Mansfield[51,52] and Roemer and Hickey,[53] is to avoid the occurrence of eddy currents altogether, by using gradient coils which do not have fringe fields and rf coils which

will not support persistent eddy currents. Such gradient coils consist of an inner 'primary' coil, which supplies most of the gradient, surrounded by a 'screen' or 'shield' coil, which is designed to cancel exactly any field from the primary coil outside the screen.

The mathematics for the calculation of screen coils in a cylindrical geometry[38,51] relies on the expansion of the magnetic field in cylindrical harmonics [equation (16)]. If a second coil of radius b is added, the total field outside the coil becomes:

$$B_z(r,\phi,z) = -\frac{\mu_0 a}{2\pi}\sum_{m=-\infty}^{\infty}\int_{-\infty}^{\infty} \mathrm{d}k\, \mathrm{e}^{\mathrm{i}m\phi}\mathrm{e}^{\mathrm{i}kz}|k|\, j_\phi^m(k) I'_m(|k|a)K_m(|k|r)$$

$$+\frac{\mu_0 b}{2\pi}\sum_{m=-\infty}^{\infty}\int_{-\infty}^{\infty} \mathrm{d}k\, \mathrm{e}^{\mathrm{i}m\phi}\mathrm{e}^{\mathrm{i}kz}|k|\, J_\phi^m(k) I'_m(|k|b)K_m(|k|r) \quad (21)$$

where $J_\phi^m(k)$ is the Fourier transform of the current in the screen $J(\phi, z)$. For the field outside the screen to be zero, a necessary and sufficient condition is that

$$J_\phi^m(k) = -\frac{aI'_m(|k|a)}{bI'_m(|k|b)} j_\phi^m(k) \quad (22)$$

Thus, given a particular primary coil current, the continous current needed for screening may easily be calculated using two Fourier transforms. Finite element calculations[54] give substantially the same results as expected, but with much longer computation times.

Generally speaking, the field produced by the screen coil perturbs that of the primary, so that the net field diverges from what is desired. The primary coil may either be redesigned in a somewhat ad hoc way,[38] or another approach, the 'integrated design', may be adopted.

This method is an extension of the target field method. The field is now specified on two target surfaces and the current densities $J(\phi, z)$ and $j(\phi, z)$ on two coil formers are taken as unknowns. As an illustration, consider a primary cylindrical coil of radius a and a screen coil of radius b. Taking the first target surface as an inner cylinder of radius c at which the desired gradient is specified, and the second target surface at the radius of the screen where the field is set to be zero everywhere, we obtain two simultaneous equations for the Fourier transforms of the current densities which are easily solved, giving[55–57]

$$j_\phi^m(k) = \frac{-B_z^m(kc)}{\mu_0 bkI_m(|k|c)\left[K'_m(kb) - \{I'_m(|k|b)/I'_m(|k|a)\}K'_m(ka)\right]} \quad (23)$$

$$J_\phi^m(k) = -\frac{aI'_m(|k|a)}{bI'_m(|k|b)}\, j_\phi^m(k) \quad (24)$$

Here $B_z^m(kc)$ is the Fourier transform of the desired target field at the radius c of the target cylinder.

These results provide complete specifications for a coil with prescribed field variation in a defined region within the primary coil, and zero fringe field outside the screen. The mathematical formalism will of course support many other configurations, for instance a prescribed field outside the screen and zero field inside the primary. Furthermore, the operation can be carried out for other coil geometries, such as coils formed on parallel planes[57] or cylinders of elliptical cross section.[58]

Preferably, the active gradient shield should be made from a continuous conducting sheet, with a narrow slot formed in it constraining the current to follow the appropriate path. In this way a closer approximation to the continuous current density really required can be obtained than by using discrete wire. However, such a configuration gives a degree of shielding which varies with frequency, owing to changes of the current distribution within the width of the conducting paths. Even at the highest frequencies, when this problem is most severe, the shielding from a slotted continuous shield is better than with discrete wires. A further recommendation is to arrange the wiring of the shield in series with the primary coil, to ensure that the current changes in each are in phase. There are further engineering details outside the scope of this article. It has generally been found that active shields are not 100% effective in practice, reducing the fringe fields to at best 1% of the unshielded values. Eddy current compensation circuits continue to be advisable, although the current and voltage requirements of these devices are drastically reduced. Using a combination of active shielding and eddy current compensation, gradient settling times can be reduced to a few hundred microseconds.

8 COIL PERFORMANCE

Using the minimum inductance algorithm, it is possible to create plots defining optimal gradient performance as a function of primary and active shield coil radius, and coil length.

Figure 8 shows the dependence of inductance on primary coil radius for fixed coil efficiency at target points, spaced proportionately to the primary coil radius, and fixed shield radius,

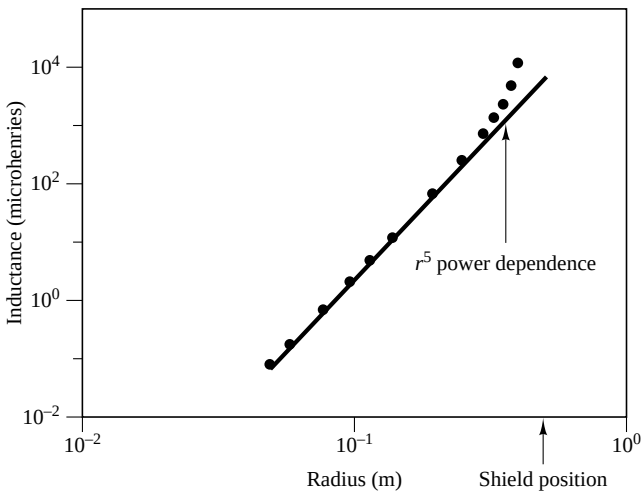

Figure 8 Calculated effect of increasing primary coil radius on the inductance of a transverse gradient coil while keeping shield coil radius and coil efficiency fixed. The spacing of the target points chosen was kept proportional to the primary coil radius. Without shielding this would give geometrically similar designs with inductance proportional to the fifth power of the radius, shown by the asymptotic straight line fit on this log–log plot

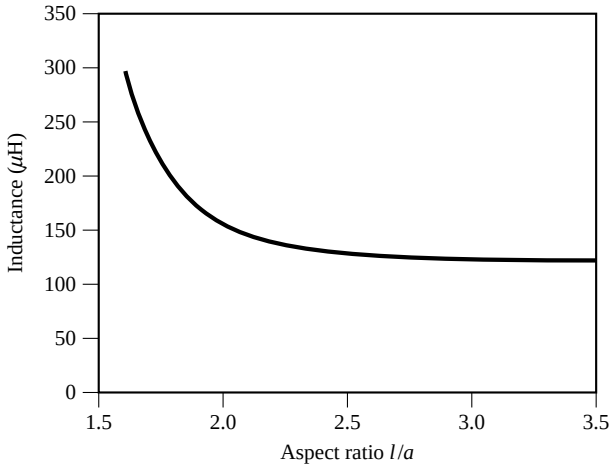

Figure 9 Calculated effect of coil length on inductance for a truncated minimum inductance transverse gradient coil. The target points, efficiency, primary coil radius, and shield radius are all kept fixed

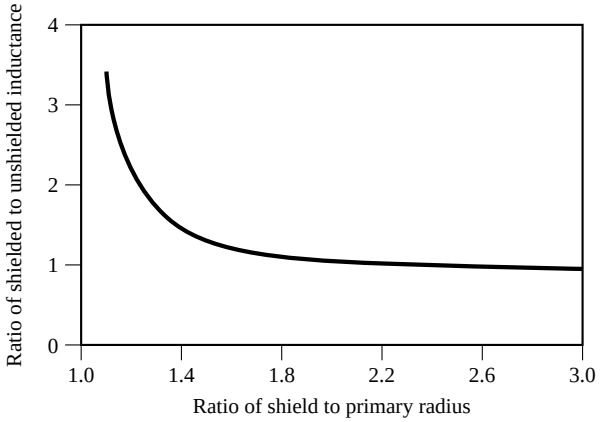

Figure 10 Calculated effect of change of shield radius for a minimum inductance transverse gradient coil for fixed primary coil radius, target points, and efficiency

for a minimum inductance transverse gradient coil. The straight line represents the fifth power dependence expected without shielding. The divergence of the inductance as the primary radius approaches that of the shield is evident, and represents a serious limitation inherent in active shielding. More and more magnetic energy comes to be stored between the primary and shield radii as they approach each other, and the number of turns of conductor on each also diverges causing major problems in fitting conductors of adequate cross-section into the available space.

Figure 9 shows the effect of coil length on inductance in a truncated minimum inductance transverse gradient coil design, in which the length of the coil is used as a further constraint in the constrained inductance minimization algorithm. Here the efficiency is kept fixed and fixed target points are used. As the coil is shortened the inductance diverges, corresponding to the increasing proximity of the windings generating the desired gradient and the return paths, which tend to cancel this gradient. For fixed efficiency, the total number of turns needed thus increases rapidly as the coil is shortened, thereby increasing the inductance. If very short transverse gradient coils are required, the only practical recourse is to put the return paths at an increased radius, as described in the next section.

Finally, Figure 10 shows the effect on the coil inductance of changing the shield radius keeping the primary coil radius, the target points, and the efficiency fixed. The divergence of the inductance as the shield approaches the primary is clearly seen. It is interesting to note, nevertheless, that the effect of the shield is actually to reduce the inductance of the coil about which it is placed.

9 UNORTHODOX DESIGNS

Having outlined the various mathematical techniques which have been used to design good gradient coils, we will now consider the constraints of patient access and mechanical design. Patient access is an issue because of the a^5 power law problem; it pays to make coils as small as possible. Hence special coils fitting snugly round the head have been developed.[59] These allow echo planar imaging (EPI), and also enable ultrathin slices and short echo times to be achieved.

The longitudinal gradient is easy; a Maxwell pair (see above) or a modification[59,60] with better linearity is short enough to provide good gradient fields in the brain and brain stem while resting on the shoulders. However, transverse gradient coils of conventional design cause serious access problems. Several solutions have been proposed. The first is to use a target field design, truncated as far as possible without decreasing the efficiency intolerably, and then to distort the current return paths to provide shoulder slots. Another, more radical approach, was proposed by Turner and implemented by Myers and Roemer[61] and others. This consists of taking only one-half of a conventional transverse gradient coil design, the positive z-axis section say, to give an asymmetric coil with a region of interest with approximately linear gradient close to one end.[62] The unbalanced torques in such an arrangement, which may cause serious mechanical stability problems, can be avoided by providing additional counterbalancing current paths at the expense of increased coil inductance.[63] A related effective stratagem is to design a symmetrical coil, using the target field method which provides uniform gradients at both ends, only one of which is used for imaging. Again, this gives a higher inductance.

Yet another solution is provided by designing a very short, heavily truncated, conventional double saddle 'fingerprint' transverse gradient coil.[64] The difficulty with this approach is that the gradient uniformity is inevitably rather poor in the axial direction, and the coil efficiency is also low because the current return paths are close to the active sections. The best solution is to arrange the return paths on a former of larger radius, so that they partially screen the active turns. A first step in this direction has already been made, by Bangert and Mansfield, as described earlier,[27] though the volume of uniform gradient in this coil is rather small and its efficiency is low. Very recently Wong and Hyde[65] have used the conjugate gra-

dient descent method to develop such a design on a pair of concentric cylinders, and Brey et al.[66] have developed an elegant coaxial design made from identical modular elements.

If easy access to the interior of the gradient coils is not required, the approach of Lowe[67] has some merit. Here the idea is to approximate by wires the continuous current density on the surface of a sphere required to generate the single spherical harmonic terms which represent each of the three orthogonal linear gradients needed. Such coils give excellent gradient fields everywhere inside the spherical former and are also maximally efficient.

For body imaging, flat gradient coils, either alone[45] or paired,[42–44] offer better access and efficiency than cylindrical coils of circular section, because they can be placed closer to the body. The ideal configuration is probably coils wound on a cylindrical former of elliptical cross-section.[58]

10 COIL FABRICATION METHODS

Several methods have been used to translate curvilinear coil designs which are sometimes quite complicated into practical pieces of equipment. Coils built from discrete wire often utilize a guide slot machined into a nonconductive (e.g. glass-reinforced plastic) cylindrical former. The complex curve is generated using a computer-driven lathe or milling machine. The wire is then laid in this slot and bound in place with a further layer of resin-soaked glass fiber. Sometimes very heavy gauge rectangular-section copper wire is used, typically for 'Golay' type double-saddle coil arrangements in which the coil is almost self-supporting. For coils formed from slotted continuous copper sheet, various methods are used for forming the slot. The simplest is to use a machine fretsaw, although this carries the risk of coil distortion as the sheet of copper becomes progressively more delicate. A computer-driven milling machine or high-speed punching machine can also be employed, allowing thicknesses of copper of more than 1 mm to be utilized. The quickest method is undoubtedly to use a printed-circuit board technique,[34] in which a layer of photoresist is deposited on the copper sheet and the slot is formed by etching out the track photographically marked in the photoresist. This method is feasible only for a limited thickness of copper.

A full discussion of manufacturing tolerances is out of place in this review which focuses primarily on mathematical methods. However, it needs to be stated that for distributed winding designs, random positional errors of 0.5% of the former radius cause no significant errors in the gradient homogeneity obtained.

11 SUMMARY AND CONCLUSIONS

Gradient coil design has reached a level of some maturity. The limitations imposed by the Laplace equation and material parameters such as conductor resistivity have become clearly definable. Coil design algorithms have been implemented which optimize a variety of coil features, such as stored energy, dissipated power, and combinations of the two. Coils may be constrained to produce fields precisely specified at points, on surfaces, and within volumes as the integrated least-square departure from a desired configuration. Coil formers may be flat, cylindrical, ellipsoidal, or even more irregular, though for most rapid computation and evaluation Cartesian or cylindrical geometries are preferred, enabling the power and speed of the fast Fourier transform to be utilized. The new generation of gradient coil designs has opened the way to new and powerful magnetic resonance techniques, such as echo planar imaging (EPI, q.v.), diffusion imaging, and gradient editing of multinuclear spectra.

12 RELATED ARTICLES

Echo-Planar Imaging; Health and Safety Aspects of Human MR Studies; Image Formation Methods; Whole Body MRI: Local and Inserted Gradient Coils.

13 REFERENCES

1. R. Gabillard, *Rev. Sci. Paris*, 1952, **90**, 307.
2. R. J. Sutherland, J. M. Hutchinson, W. A. Edelstein, and J. R. Mallard, *US Pat. 4 310 799* (October 15th, 1979).
3. K. Halbach, *Int. Pat. G01R33/12* (11th February, 1985).
4. R. Bowtell and P. Mansfield, *Meas. Sci. Technol.*, 1990, **1**, 431.
5. P. C. Lauterbur, *Nature (London)*, 1973, **242**, 190.
6. P. Mansfield and P. K. Grannell, *J. Phys. C*, 1973, **6**, L422.
7. A. N. Garroway, P. K. Grannell, and P. Mansfield, *J. Phys. C*, 1974, **7**, L457.
8. J. L. Duerk and R. E. Wendt, in 'Magnetic Resonance Angiography', eds. E. J. Potchen, E. M. Haacke, J. E. Siebert, and A. Gottschalk, Mosby, St Louis, MO, 1993, pp. 80–133.
9. P. R. Moran, *Magn. Reson. Imag.*, 1983, **1**, 197.
10. D. Le Bihan, E. Breton, D. Lallemand, P. Grenier, E. Cabanis, and M. Laval-Jeantet, *Radiology*, 1986, **161**, 401.
11. C. H. Sotak, D. M. Freeman, and R. E. Hurd, *J. Magn. Reson.*, 1988, **78**, 355.
12. A. Bax, P. G. De Jong, A. F. Mehlkopf, and J. Smidt, *Chem. Phys. Lett.* 1980, **69**, 567.
13. F. Romeo and D. I. Hoult, *Magn. Reson. Med.*, 1984, **1**, 44.
14. B. H. Suits and D. E. Wilken, *J. Phys. E.*, 1989, **23**, 565.
15. T. F. Budinger, H. Fischer, D. Hentschel, H. E. Reinfelder, and F. Schmitt, *J. Comput. Assist. Tomogr.*, 1991, **15**, 909.
16. G. A. Mouchawar, J. D. Bourland, J. A. Nyenhuis, L. A. Geddes, K. S. Foster, J. T. Jones, and G. P. Graber, *Med. Biol. Eng. Comput.*, 1992, **30**, 162.
17. O. M. Mueller, P. B. Roemer, J. N. Park, and S. P. Souza, *Proc. 10th Ann Mtg. (Int) Soc. Magn. Reson. Med., San Francisco*, 1991, p. 130.
18. R. Turner, *J. Phys. E.*, 1988, **21**, 948.
19. M. W. Garrett, *J. Appl. Phys.*, 1951, **22**, 1091.
20. M. J. E. Golay, *US Pat. 3 515 979* (4th November, 1957).
21. P. A. Bottomley, in 'NMR Imaging: Proceedings of an International Symposium on Nuclear Magnetic Resonance Imaging, The Bowman Grey School of Medicine, Winston–Salem, NC, 1982,' eds. R. L. Witcofski, N. Karstaedt, and C. L. Partain, pp. 25–31; P. A. Bottomley, *J. Phys. E*, 1981, **14**, 1081.
22. S. R. Thomas, L. J. Busse, and J. F. Schenck, in 'Magnetic Resonance Imaging', eds. C. L. Partain, R. R. Price, J. A. Patton, M. V. Kulkarni, and A. E. James, W. B. Saunders Co., Philadelphia, PA, 1988, Vol. II, pp. 1162–1182.

23. J. V. Hajnal, M. Doran, A. S. Hall, D. Bryant, G. M. Bydder, and I. Young, *J. Comput. Assist. Tomogr.*, 1991, **15**, 1.
24. C. Prevot, B. Rigeade, and J. Miscopein, *Eur. Pat. Appl. 86 402 294.2* (18th October, 1985).
25. H. Siebold, *IEEE Trans. Magn.*, 1990, **26**, 841, 897.
26. I. Zupancic and J. Pirs, *J. Phys. E*, 1976, **9**, 79.
27. V. Bangert and P. Mansfield, *J. Phys. E*, 1982, **15**, 235.
28. W. A. Anderson, *Rev. Sci. Instrum.*, 1961, **32**, 241.
29. H. E. Simon, *SPIE J.*, 1981, **273**, 41.
30. D. I. Hoult, *D.Phil. Thesis*, Oxford University, UK, 1977.
31. R. C. Compton, *US Pat. 4 456 881* (18th January, 1982).
32. K. H. Schweikert, R. Krieg, and F. Noack, *J. Magn. Reson.*, 1988, **78**, 77.
33. E. Wong, A. Jesmanowicz and J. S. Hyde, *Magn. Reson. Med.*, 1991, **21**, 39.
34. J. F. Schenck, M. A. Hussein, and W. A. Edelstein, *US Pat. 4 646 024* (November 2nd, 1983); W. A. Edelstein and J. F. Schenck, *US Pat. 4 840 700* (July 13th, 1987).
35. R. J. Sutherland, *Ph.D. Thesis*, University of Aberdeen, UK, 1980.
36. R. Turner, *J. Phys. D*, 1986, **19**, L147.
37. R. N. Bracewell, 'The Fourier Transform and its Applications', McGraw-Hill, New York, 1986.
38. R. Turner and R. M. Bowley, *J. Phys. E*, 1986, **19**, 876.
39. M. Abramowitz and I. A. Stegun, 'Handbook of Mathematical Functions', Dover, New York, 1965.
40. Q. Liu, *M.Sc. Thesis*, University of Alberta, Canada, 1991.
41. M. Engelsberg, R. E. De Souza, and C. M. Diaz Pazos, *J. Phys. D*, 1988, **21**, 1062.
42. R. Bowtell and P. Mansfield, *Proc. 8th Ann. Mtg. Soc. Magn. Reson. Med.*, *Amsterdam*, 1989, p. 977.
43. K. Yoda, *J. Appl. Phys.*, 1990, **67**, 4349.
44. M. A. Martens, L. S. Petropoulos, R. W. Brown, J. H. Andrews, M. A. Morich, and J. L. Patrick, *Rev. Sci. Instrum.*, 1991, **44**, 2639.
45. P. B. Roemer, *US Pat. 4 926 125* (August 22nd, 1988).
46. J. W. Carlson, K. A. Derby, K. C. Hawryszko, and M. Weideman, *Magn. Reson. Med.*, 1992, **26**, 191.
47. D. I. Hoult and R. Deslauriers, *Proc. 10th Ann. Mtg. Soc. Magn. Reson. Med., San Francisco*, 1991, p. 732.
48. R. Turner, *Magn. Reson. Imag.*, 1993, **11**, 90.
49. M. A. Morich, D. A. Lampman, W. R. Dannels, and F. T. Goldie, *IEEE Trans. Med. Imag.*, 1988, **7**, 247.
50. J. J. Van Vaals and A. H. Bergman, *J. Magn. Reson.*, 1990, **90**, 52.
51. P. Mansfield, R. Turner, B. L. W. Chapman, and R. M. Bowley, *US Pat. 4 978 920* (September 20th, 1985).
52. P. Mansfield and B. L. W. Chapman, *J. Magn. Reson.*, 1986, **66**, 573.
53. P. B. Roemer and J. S. Hickey, *Eur. Pat. Appl. 87 101 98* (February 7th, 1986).
54. R. D. Pillsbury and F. B. Punchard, *IEEE Trans. Magn.*, 1986, **21**, 2273.
55. R. Turner, P. Mansfield, and B. L. W. Chapman, *UK Pat. GB 2 193 322B* (June 28th, 1986).
56. P. Mansfield and B. Chapman, *J. Magn. Reson.*, 1987, **72**, 211.
57. R. Bowtell and P. Mansfield, *Magn. Reson. Med.*, 1991, **17**, 15.
58. L. S. Petropoulos, M. A. Martens, R. W. Brown, M. A. Morich, and J. L. Patrick, *Proc. 10th Ann. Mtg. Soc. Magn. Reson. Med., San Francisco*, 1991, p. 708.
59. R. Turner, D. Le Bihan, and A. S. Chesnick, *Magn. Reson. Med.*, 1991, **19**, 247; T. G. McFarland, C. C. Myers, D. J. Schaefer, R. Turner, and R. M. Vavrek, *US Pat. 5 185 576* (August 12th, 1991).
60. J. F. Schenck, *US Pat. 4 617 516* (September 6th, 1983).
61. C. C. Myers and P. B. Roemer, *Proc. 10th Ann. Mtg. Soc. Magn. Reson. Med., San Francisco*, 1991, p. 711.
62. L. S. Petropoulos, M. A. Morich, J. L. Patrick, D. A. Lampman, H. Liu, and R. W. Brown. *Proc. 11th Ann. Mtg. Soc. Magn. Reson. Med., Berlin*, 1992, p. 4032.
63. J. V. Hajnal, A. S. Hall, I. R. Young, and G. M. Bydder, *J. Magn. Reson. Imag.*, 1991, **1**, 209.
64. P. B. Roemer, *US Pat. 5 177 442* (July 1st, 1991).
65. E. C. Wong and J. S. Hyde, *Proc. 11th Ann. Mtg. Soc. Magn. Reson. Med., Berlin*, 1992, p. 583.
66. W. W. Brey, J. L. Dougherty, and T. H. Mareci, *Proc. 12th Ann. Mtg. Soc. Magn. Reson. Med., New York*, 1993, p. 1308.
67. I. J. Lowe, personal communication with author.

Biographical Sketch

Robert Turner. *b* 1946. B.A., 1968, Cornell University, Ph.D., 1972, Simon Fraser University, B.C., Canada. Postdoctoral work in NMR of liquid crystals, University of Cambridge, UK, 1973–75; lecturer in physics, University of Nottingham, UK (working with Peter Mansfield on MRI hardware and software), 1975–88; visiting scientist, NIH, Bethesda, MD, 1988–93; Institute of Neurology, London, UK, 1993–present. Approx. 70 publications. Current research interests include gradient coil design, applications of echo planar MRI, and functional imaging of human brain.

Multifrequency Coils for Whole Body Studies

Joseph Murphy-Boesch
USA Instruments Inc., Aurora, OH, USA

1 INTRODUCTION

In whole body MRI, the dominant hydrogen resonances of water and fat provide a wealth of information which may be used to diagnose conditions associated with bone and soft tissues. Important biochemical and physiological information, however, may be derived from the resonances of other naturally occurring nuclei, such as phosphorus (^{31}P), carbon (^{13}C), sodium (^{23}Na), and deuterium (^{2}H), exogenous nuclei, such as fluorine (^{19}F), and the weaker resonances of hydrogen (^{1}H) or protons. These resonances can be used to identify important metabolites, measure metabolite concentrations, tissue pH, and metabolite rate constants, and provide information on molecular structure and binding. Because the sensitivity of these low-γ-emitting nuclei is low (with the exception of fluorine), coils must be positioned and tuned close to the tissue being observed. Because human spectroscopic data are generally acquired in the context of an integrated imaging/spectroscopy examination, multifrequency coils offer distinct advantages over single-frequency coils. For example, MR images are used early in the examination to identify a tissue region for localization and later during processing for registration of spectroscopic data with anatomy. Localization techniques are employed to enhance signals from a specific region of tissue and attenuate signals from outside (see ***Spatial Localization Techniques for Human MRS***).

Before acquiring spectra from phosphorus and other 'low-γ' nuclei, it is generally necessary to adjust static magnetic field homogeneity on a strong and pervasive resonance such as that of water. For simple protocols involving more than one nucleus, it may be sufficient to switch coils or retune the coil during the examination. This, however, usually involves movement and repositioning of the subject, and to expedite the examination, it is generally preferable to position the subject and tune the NMR probe once at the beginning. When acquiring ^{31}P or other nuclei that are coupled to protons, it may be desirable to transmit at the proton frequency simultaneous with acquisition of the ^{31}P signal to decouple the proton resonance. To implement this double resonance sequence requires a dual-frequency coil that conforms to anatomy together with filtering and other specialized receiver circuitry to remove interactions between the two active radiofrequency (rf) channels.

2 GENERAL DESIGN CONSIDERATIONS

According to Hoult and Richards, who first recognized the principle of reciprocity for NMR, the sensitivity of a coil at a selected location can be gauged by the strength of the $\boldsymbol{B}_1$ field produced by a unit of current I in the coil.[1] Thus, the signal induced in a coil by a small volume of sample is proportional to the product of the volume and the normalized field, $b_1=B_1/I$. To carry this one step further, coil sensitivity is reflected in the rate, $\omega_1=\gamma B_1$, by which nuclei are nutated about the $\boldsymbol{B}_1$ field in the rotating frame, i.e. the efficiency of the transmitter in producing a 90° pulse. They further showed that sensitivity could be related to the ratio $B_1/\sqrt{R}$, where R is a series resistance which incorporates all coil and sample related losses. Coil sensitivity can thus be 'mapped', either theoretically with a computed $\boldsymbol{B}_1$ profile, or empirically with measurement of 90° pulses at each location. Much analysis of sensitivity and transmitter efficiency for single and multiply tuned high-resolution and solid state probes has been published[1–5] (see ***Sensitivity of the NMR Experiment***). This analysis is relevant for the large volume coils of high-field, whole body instruments, and has been extended to include the strong conductive and dielectric loading associated with tissue.[6] While conductive losses from eddy currents induced in tissue are unavoidable, losses associated with electric field couplings may be reduced by careful attention to coil geometry and circuit design[7] and use of distributed capacitance.[8] A review of basic principles of probe design, circuit techniques and performance measurement can be found in the monograph by Chen and Hoult[9] (see ***Sensitivity of Whole Body MRI Experiments***).

Another design consideration has to do with the physics of nuclear induction. Nuclei nutate, or 'flip', their orientations with respect to the static field as a result of a *circularly polarized* component of the $\boldsymbol{B}_1$ field. In the rotating frame this is a field of slowly changing amplitude which rotates with the same sense as the precessing nuclei. A single, 'linearly polarized' coil can be used to excite and detect nuclei, because it produces both left and right circularly polarized fields simultaneously, one component of which has the correct sense of rotation. In a frame with a z oriented static, or $\boldsymbol{B}_0$, field, two or more such 'linear mode' coils can be oriented to produce linearly polarized fields which are transverse to one another, as indicated in Figure 1(a,b). Sample geometry often makes it possible to construct such 'crossed-coil' arrangements, in which two coils have little magnetic coupling, providing electrical isolation of their tuned circuits. These circuits may be tuned either to different frequencies, permitting excitation and detection of different nuclei, or to the same frequency, to provide quadrature excitation and reception. Upon transmission in quadrature phase, the latter will produce minimally an elliptically polarized field and, ideally, a circularly polarized $\boldsymbol{B}_1$ field in the tissue region of interest.

In another configuration, two coils can be aligned with one another as they are for the concentric coils shown in Figure 1(c). These coils have have strong inductive coupling and, by Faraday induction, the smaller, inner coil will oppose the field of the larger coil and shield its interior. This shielding may be eliminated by passive or active circuits which increase the impedance of the smaller coil. For coils tuned to widely separated frequencies, $\boldsymbol{B}_1$ flux from the outer coil can circumvent the inner coil and excite the region below it. For loops tuned to approximately the same frequency, strong coupling or 'overcoupling' of the two resonant loops will produce new resonant modes. Alternatively, these modes may be exploited to produce a multiresonant rf coil, as discussed below.

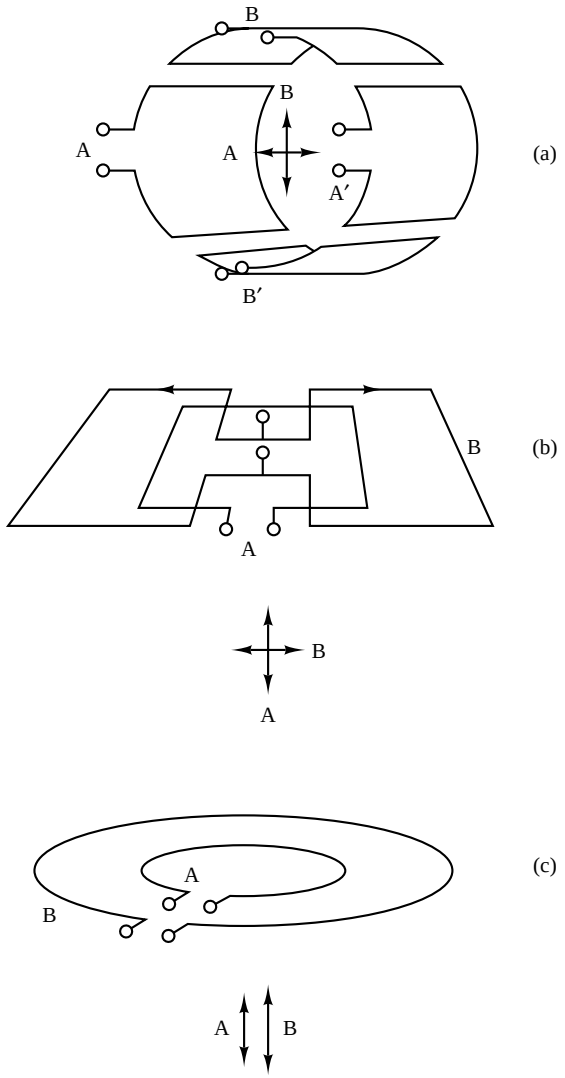

Figure 1 (a) A volume crossed coil with coil pairs A–A′ and B–B′ oriented to produce transverse linearly polarized $\boldsymbol{B}_1$ fields at two frequencies, (b) a planar crossed-coil configuration to produce transverse fields below the coil, and (c) two concentric coils which produce colinear fields along the central axis

Many design possibilities exist for multiply tuned probes. They can employ a single sample coil which is part of multiply resonant circuit or multiple resonant coils, each of which produces $\boldsymbol{B}_1$ flux in the sample. Connection to the coil can be made in the form of single or multiple ports and coupling to the resonant modes can be either inductive or capacitive. The operational modes of individual coils within a probe can be transmit only, receive only, or both. Finally, while a single coil provides only a linearly polarized field, the availability of additional coils or modes within a complex resonator can provide quadrature or circulary polarized operation. With sensitivity being a primary design consideration, the constraints which limit design possibilities will often be the shape of the body and the limited space within the magnet. There is also an interplay between the particular sequence of rf pulses, gradients, and acquisition intervals and the design of the probe. For example, the limited $\boldsymbol{B}_1$ profile of a surface coil can provide a measure of localization in two dimensions, with localization in the third dimension provided by slice selection which uses the $\boldsymbol{B}_1$ gradient of the coil (see ***Rotating Frame Methods for Spectroscopic Localization***).

3 MULTIPLE TUNING TECHNIQUES

3.1 Multiple Tuning Using a Single Sample Coil

An economical way of performing multiple frequency NMR is simply to switch or retune the elements of a single sample coil. There are various ways of accomplishing this. With the coil mounted at the end of a flexible, low-loss transmission line, tuning elements can be placed well away from the subject.[10] The coil is then easily positioned on the subject, and tuning may be switched remotely, although some loss in sensitivity can be expected from cable resistance. Alternatively, a box containing tuning and matching circuitry can be inserted at the end of a length of cable connected to a probe pretuned for a single frequency,[11] although this generally results in loss of sensitivity for the second nucleus. All these methods, of course, permit only sequential use of the probe for each nucleus and may require movement and repositioning of the subject, lengthening examination time.

More commonly, a single sample coil provides an adequate field-of-view and adequate sensitivity for the detection of two or more nuclei and may be multiply tuned to observe them. Methods for multiple tuning high-resolution and solid-state probes using resonant sections of transmission lines[12] and parallel and series resonant L–C 'trap' circuits[4,13] are well developed. These are multiple port designs which use one port for each nucleus, and are readily adapted for use with a surface coil. With the motivation of reducing the number of reactive components in a multiple tuned probe, Schnall et al.[14] proposed using simpler, impedance modifying networks which substitute for the capacitor of a simple resonant L–C circuit, as indicated in Figure 2(a). The composite element shown in Figure 2(a) presents a negative (capacitive) impedance to the sample inductor at two frequencies resulting in two resonances. Circuits of this type have been recognized as 'Foster networks', after R. M. Foster[15] who demonstrated that any purely reactive network must necessarily have a driving point impedance which alternates between zero and infinity. Multiple tuning of a sample coil for $N+1$ frequencies can be achieved using a composite circuit of N traps, as indicated in Figure 2(b). The sensitivity of this circuit is reduced by resistive losses of the additional trap circuits. Since these losses tend to be concentrated in the series resistances of the trap inductors and since the majority of current for the low-frequency mode flows through these inductors, the low-frequency mode tends to suffer the greatest loss in sensitivity compared with the single resonant circuit. In general, there are many more configurations for multiple tuning a sample coil than indicated in Figure 2(b), and the possibilities grow rapidly with the number of NMR frequencies resonances to be observed (see also Schnall et al.,[14] Figures 7 and 8, and Foster,[15] Figures 1 and 2). Methods for multifrequency coupling to these probes are not well described. It is apparent, however, that a single matching capacitor can be replaced with the composite network shown

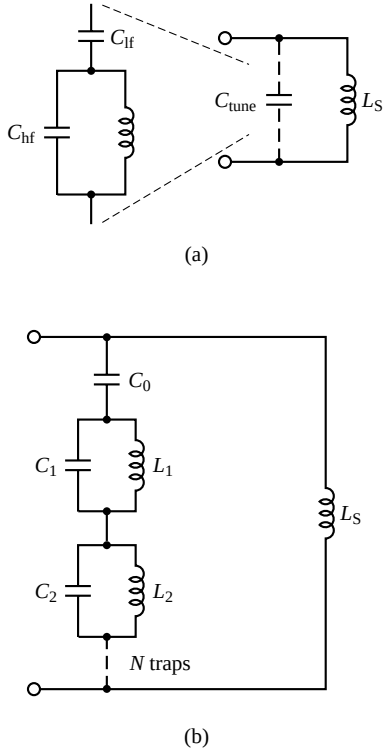

Figure 2 (a) Double tuning of a simple resonant circuit by replacement of the tuning capacitor with a composite circuit element. Capacitors C_{lf} and C_{hf} are used to tune the low frequency and high frequency, respectively. (b) Use of a Foster network to multiple tune a single coil for $N + 1$ frequencies

in Figure 2(a) for single port matching at two frequencies: a more complex composite network would be used for three or more frequencies. This type of matching is efficient, since any losses in coupling in the coupling network are typically in series with a 50 Ω source impedance of the rf system.

If an additional 'odd' impedance element is added to the four circuit elements in Figure 2(a), one obtains a circuit of different characteristics. For example, the odd element can be the coupling element between two resonant L–C or 'tank' circuits of approximately the same frequency, as indicated in Figure 3. This coupling can be capacitive or inductive or take the form of the mutual inductance between the resonant inductors. If the coupling is strong, the modes of the two resonant circuits tuned to the same frequency will split into two new distinct modes. This effect is referred to as overcoupling, and Schnall et al. have shown that overcoupled tank circuits can be applied to the acquisition of two and even three nuclei.[16] The motivation for using the overcoupled circuit was to tune resonant modes for nuclei with closely spaced frequencies, such as ^{1}H and ^{19}F or low-γ nuclei such as ^{13}C and ^{31}P. Another characteristic of an overcoupled circuit using inductive coupling is that little current tends to flow through the coupling inductor in the low-frequency mode. Thus, the situation with regard to sensitivity is reversed compared with the double tuned circuit shown in Figure 2(a), with the lower frequency mode suffering less of a loss in sensitivity compared with the higher frequency mode. Grist et al.[17] have reported an overcoupled resonator assembled with two identical resonant loops coupled primarily by their mutual inductance. The modes of the coil can be resolved into corotating and counterrotating modes, according to the sense of circulation of the currents, and these modes can be tuned separately for the ^{31}P and ^{1}H frequencies, respectively (see ***Surface and Other Local Coils for In Vivo Studies***). The lower loop residing close to the tissue surface produces most of the $\boldsymbol{B}_1$ flux within the tissue. Because of its greater distance from the tissue, the upper loop has less of an effect upon the $\boldsymbol{B}_1$ field of the coil, providing a small positive contribution at the ^{31}P frequency and a small negative contribution at the ^{1}H frequency. With the greater tissue loading encountered at the ^{1}H frequency, little loss in sensitivity is generally experienced at either frequency compared with single resonant coils of the same size.

3.2 Multiple Tuning using Multiple Sample Coils

A straightforward method of implementing multiple frequency spectroscopy on a clinical instrument is to use the body coil for ^{1}H imaging and a surface coil for spectroscopy at a second frequency. If the body coil operates in linear mode, the surface coil can be oriented transverse to it in crossed-coil configuration. When the body coil is circularly polarized, coupling between the coils is strong, and other measures must be used to decouple them. With a surface coil tuned to a much lower frequency, it is possible to image through it if the distortion to the $\boldsymbol{B}_1$ field is acceptable. Another coil configuration which provides good image quality is one in which the body coil is used for uniform transmission and a surface coil is tuned for ^{1}H reception. Care must be exercised, however, to avoid excess power deposition from power absorbed by the surface coil and transmitted to the tissue.[18] To prevent this, passive diode or active PIN junction diode switching must be used to detune the coil, or otherwise render it high impedance. Another method to prevent coupling to the body coil is to use the symmetric mode of a 'counterrotating' coil for imaging,[19] since the antisymmetric mode of the coil does not couple with a uniform external field.

Multiple sample coils are often employed in whole body spectroscopy because they offer distinct advantages over single coils for integrated imaging/spectroscopy examinations. The requirements of imaging, shimming, and proton-decoupling

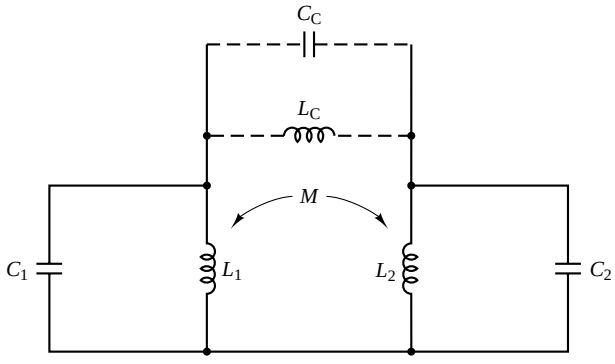

Figure 3 An overcoupled 'tank' circuit illustrating three types of electrical coupling: capacitive via C_C, inductive via L_C, and mutual inductive via M

generally dictate using a larger field-of-view for the ^{1}H coil. Multiple coils can be crossed-coil designs such as surface coil 'butterfly' coil combinations[20,21] or concentric coils that use a larger coil for ^{1}H imaging.[22] Single or multiple ports can be used to connect to multiple coils. Two-port coils take advantage of the natural isolation of crossed-coils to maintain isolation between frequencies. Single-port coils require more complicated filtering and crossover networks for double resonance experiments, since transmission at one frequency must be simultaneous with transmission and/or reception at the second frequency. Recent progress has been made in the use of multiple receiver coils, or 'phased arrays',[23] which improve sensitivity at intermediate tissue depths (see ***Whole Body Machines: NMR Phased Array Coil Systems***). Application of coil arrays for spectroscopy has so far been implemented in 'receive only' mode, with larger coils being used for homogeneous excitation.[24]

4 VOLUME AND QUADRATURE COILS

Volume coils are distinguished from surface coils by the way in which they surround the sample. Accordingly, they are used for the head, extremities, or the entire body. They offer more possibilities for quadrature operation because the coil has more ability to produce two transverse $\boldsymbol{B}_1$ fields in the sample. While methods of multiple tuning volume coils bear similarities with methods of tuning high-resolution probes, it is difficult simply to scale upwards the dimensions of a small high-resolution coil, since the inductances become too large to resonate efficiently at fields of 1.5–3.0 T. It has generally been necessary to use wide conductors with low inductance and add distributed capacitance, such as for the Alderman–Grant coil,[25] to achieve coil dimensions suitable for studies of the head.[26] A dual frequency probe for 1.9 T has been reported which uses two linear mode, Alderman–Grant coils in the crossed-coil configuration.[27]

An alternative to the saddle, solenoid or other high-resolution coil geometries is the birdcage resonator,[28] which is cylindrically symmetric and exhibits two isolated linear modes (see ***Birdcage Resonators: Highly Homogeneous Radiofrequency Coils for Magnetic Resonance***). These modes are ordinarily tuned for quadrature operation at a single frequency. Joseph and Lu[29] have demonstrated that these modes can be tuned independently to the ^{1}H and ^{19}F resonances without significant loss in $\boldsymbol{B}_1$ homogeneity by using differential capacitive loading. Since this method uses the birdcage in linear mode at each frequency, it cannot provide the efficiencies of quadrature operation. To obtain quadrature operation at the phosphorus frequency, Bottomley et al.[30] used a phosphorus birdcage for the head and a body coil for imaging through the phosphorus coil, thereby accepting a nominal loss in the signal-to-noise ratio at the ^{1}H frequency from shielding by the phosphorus bird cage. This method must be implemented with great care, since it is possible to couple considerable power from the body coil to a higher order mode of the birdcage. This caveat applies, of course, to any multimodal coil contained within the body coil. More recently, Dürr and Rauch[31] have reported a dual tuned body coil for 4 T. The primary purpose of the phosphorus mode is to obtain homogeneous rf transmission, permitting reception by a more sensitive surface coil or phased array.

In early reports of quadrature, dual tuned volume coils, composite double-tuning elements were inserted into the legs or end rings of a standard birdcage.[32] In another approach, the repeating elements of the birdcage were viewed as analogs of the repeating elements of a rf filter,[33] and these were used by Rath[34] to produce bandpass and bandstop configurations which could be dual tuned. These designs have not yet found routine use in clinical spectroscopy, possibly because of difficulties in tuning and mode alignment.

More recently, a four-ring birdcage design has been reported that produces homogeneous quadrature modes at two frequencies.[35] As shown in Figure 4, the coil contains an inner birdcage structure which shares inner rings with two outer structures of identical design. The outer structures can assume either a low-pass configuration with capacitors in the outer legs, as indicated in the figure, or a single-sided, high-pass configuration with capacitors placed only in the outer rings. The inner birdcage structure operates substantially independently of the two outer structures to produce quadrature modes for a low-frequency nucleus, such as phosphorus. The two outer structures couple strongly through the inner legs of the coil, producing corotating and counter-rotating mode pairs in the manner of overcoupled resonators. Of these mode pairs, the corotating fundamental mode produces a highly homogeneous $\boldsymbol{B}_1$ field in the coil and can be used to obtain high-quality MR images. Sensitivity comparisons at 1.5 T with standard birdcage coils show no loss of sensitivity at the phosphorus frequency and 85–90% sensitivity at the ^{1}H frequency. Finally, four-ring birdcage coils tuned for ^{1}H and ^{31}P have been used routinely to obtain high-quality proton-decoupled phosphorus spectra from the head and leg, demonstrating that the coil can be operated simultaneously in transmit and receive modes at two frequencies.

Implementation of volume coils for very high magnetic fields (3.0–8.0 T) require new schemes. Even with distributed capacitance, coil dimensions at these field strengths become comparable to the wavelength of propagation and the coils become efficient radiating antennae. Coupling to the inner bore of the magnet and connecting cables becomes strong, and it is

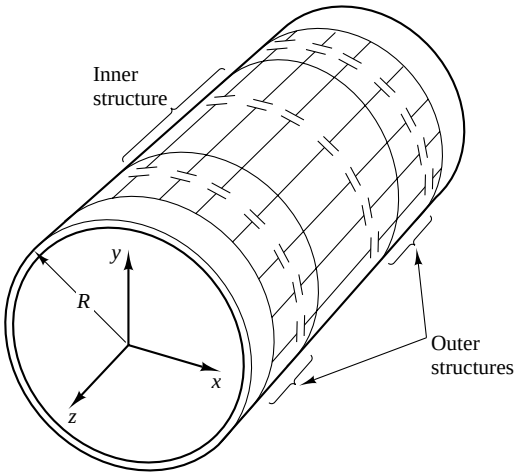

Figure 4 The low-pass, low-pass configuration of the four-ring birdcage

necessary to confine the electric and magnetic fields of the coil inside a conductive shield. While shielded birdcage designs have been found to work well at up to 3.0 T, higher frequency operation requires the use of the shield as an element of a cavity resonator. A coil that performs well in this capacity is the TEM resonator reported by Vaughan and co-workers.[36] This coil is a 're-entrant' configuration, with transmission line elements that connect directly to the shield. It takes advantage of the natural modes of a cylindrical cavity resonator to produce a homogeneous $\boldsymbol{B}_1$ field over the head. This configuration can be dual tuned by alternating the tuning of the transmission line elements, and both head and body coil configurations of the coil have been implemented above 4.0 T.

5 APPLICATIONS

An early motivation for using dual and triple tuned coils was simply to acquire spectra sequentially from more than one nucleus at a time. Surface coils provided a degree of spatial localization, but this localization was found to be inadequate for proper interpretation of spectra. As newer and more precise methods of localization were developed, spectroscopy was integrated with imaging examinations, so that spectroscopic data could be registered and correlated with anatomy (see ***Whole Body Studies: Impact of MRS***). For this application, the spectroscopy coil required good sensitivity, and the ^{1}H imaging coil required both good sensitivity and a somewhat larger volume of excitation. For ^{31}P and ^{13}C human studies, improved spectral quality could be obtained with proton decoupling,[20,21] and improved sensitivity could be obtained from NOE enhancement.[21,37] To implement proton decoupling, greater isolation is required between the proton decoupling transmitter and the phosphorus preamplifier, either via the probe or through the use of additional filtering, to prevent noise at the phosphorus frequency from being injected into the preamplifier. This isolation is also required to prevent the preamplifier from being saturated by the ^{1}H signal. Transmission at the ^{1}H frequency can then be simultaneous with acquisition of the phosphorus signal. The reverse of these requirements would, of course, apply for the inverse experiment, that is, excitation at the low frequency and detection at the ^{1}H frequency. In clinical studies, especially for those which monitor treatment, it is often important to quantify metabolites in a localized volume. Tissue concentrations are usually determined by calibrating the instrument with a known standard, which is generally one of two types: an external standard or an internal standard, with water in tissue being a convenient choice for the latter.[38] To use water as a standard, a single, double-tuned sample coil is generally employed to eliminate the need for complicated field corrections at two frequencies.

In summary, a great many multifrequency coil designs are available for providing multinuclear capability with optimum coil efficiency at each frequency. Unlike single tuned designs, there are few generic designs which can fulfill the many requirements of spectroscopy studies. Except perhaps for the head coil and the basic crossed-coil, dual-frequency surface coil, sensitivity and the demands of integrated spectroscopy/imaging examinations often require coils that are specialized for each application.

6 RELATED ARTICLES

Birdcage Resonators: Highly Homogeneous Radiofrequency Coils for Magnetic Resonance; Coils for Insertion into the Human Body; Proton Decoupling During In Vivo Whole Body Phosphorus MRS; Proton Decoupling in Whole Body Carbon-13 MRS; Radiofrequency Systems and Coils for MRI and MRS; Rotating Frame Methods for Spectroscopic Localization; Surface and Other Local Coils for In Vivo Studies; Whole Body Machines: NMR Phased Array Coil Systems; Whole Body Studies: Impact of MRS.

7 REFERENCES

1. D. I. Hoult and R. E. Richards, *J. Magn. Reson.*, 1976, **24**, 71.
2. H. D. W. Hill and R. E. Richards, *J. Sci. Instrum., Ser. 2*, 1968, **1**, 977.
3. D. I. Hoult, *Prog. NMR Spectrosc.*, 1978, **12**, 41.
4. F. D. Doty, R. R. Inners, and P. D. Ellis, *J. Magn. Reson.*, 1981, **43**, 399.
5. F. D. Doty, T. J. Connick, X. Z. Ni, and M. N. Clingan, *J. Magn. Reson.*, 1988, **77**, 536.
6. D. I. Hoult and P. C. Lauterbur, *J. Magn. Reson.*, 1979, **34**, 425.
7. J. Murphy-Boesch, in 'Biomedical Magnetic Resonance', ed. T. L. James and A. R. Margulis, Radiology Research and Education Foundation, San Francisco, 1984, p. 47.
8. B. Cook and I. J. Lowe, *J. Magn. Reson.*, 1982, **49**, 346.
9. C.-N. Chen and D. I. Hoult, 'Biomedical Magnetic Resonance Technology', Adam Hilger, New York, 1989.
10. H.-J. Zabel, R. Bader, J. Gehrig, and W. J. Lorenz, *Radiology*, 1987, **165**, 857.
11. R. E. Gordon and W. E. Timms, *J. Magn. Reson.*, 1982, **46**, 322.
12. V. R. Cross, R. K. Hester, and J. S. Waugh, *Rev. Sci. Instrum.*, 1976, **47**, 1486.
13. S. Kan, M. Fan and J. Courtieu, *Rev. Sci. Instrum.*, 1980, **51**, 887.
14. M. D. Schnall, V. H. Subramanian, J. S. Leigh, Jr, and B. Chance, *J. Magn. Reson.*, 1985, **65**, 122.
15. R. M. Foster, *Bell System Tech. J.*, 1924, **3**, 259.
16. M. D. Schnall, V. H. Subramanian, and J. S. Leigh, Jr, *J. Magn. Reson.*, 1986, **67**, 129.
17. T. M. Grist, A. Jesmanowicz, J. B. Kneeland, W. Froncisz, and J. S. Hyde, *Magn. Reson. Med.*, 1988, **6**, 253.
18. P. Boesiger, R. Buchli, M. Saner, and D. Meier, *Ann. NY Acad. Sci.*, 1992, **649**, 160.
19. W. Froncisz, A. Jesmanowicz, J. B. Kneeland, and J. S. Hyde, *Magn. Reson. Med.*, 1986, **3**, 590.
20. P. R. Luyten, G. Bruntink, F. M. Sloff, J. W. A. H. Vermeulen, J. I. van der Heijden, J. A. den Hollander, and A. Heerschap, *NMR Biomed.*, 1989, **1**, 177.
21. P. A. Bottomley, C. J. Hardy, P. B. Roemer, and O. M. Mueller, *Magn. Reson. Med.*, 1989, **12**, 348.
22. N. V. Reo, C. S. Ewy, B. A. Siegfried, and J. J. H. Ackerman, *J. Magn. Reson.*, 1984, **58**, 76.
23. P. B. Roemer, W. A. Edelstein, C. E. Hayes, S. P. Souza, and O. M. Mueller, *Magn. Reson. Med.*, 1990, **16**, 192.
24. C. J. Hardy, P. A. Bottomley, K. W. Rohling, and P. B. Roemer, *Magn. Reson. Med.*, 1992, **28**, 54.
25. D. W. Alderman and D. M. Grant, *J. Magn. Reson.*, 1979, **36**, 447.
26. V. J. Sank, C.-N. Chen, and D. I. Hoult, *J. Magn. Reson.*, 1986, **69**, 236.
27. T. A. Cross, S. Mueller, and W. P. Aue, *J. Magn. Reson.*, 1985, **62**, 87.
28. C. E. Hayes, W. A. Edelstein, J. F. Schenck, O. M. Mueller, and M. Eash, *J. Magn. Reson.*, 1985, **63**, 622.

29. P. M. Joseph and D. Lu, *IEEE Trans. Med. Imaging*, 1989, **8**, 286.
30. P. A. Bottomley, H. C. Charles, P. B. Roemer, D. Flamig, H. Engeseth, W. A. Edelstein, and O. M. Mueller, *Magn. Reson. Med.*, 1988, **7**, 319.
31. W. Dürr and S. Rauch, *Magn. Reson. Med.*, 1991, **19**, 446.
32. G. Isaac, M. D. Schnall, R. E. Lenkinski, and K. Vogele, *J. Magn. Reson.*, 1990, **89**, 41.
33. J. C. Watkins and E. Fukushima, *Rev. Sci. Instrum.*, 1988, **59**, 926.
34. A. R. Rath, *J. Magn. Reson.*, 1990, **86**, 488.
35. J. Murphy-Boesch, R. Srinivasan, L. Carvajal, and T. R. Brown, *J. Magn. Reson., Ser. B*, 1994, **103**, 103.
36. J. T. Vaughan, H. P. Hetherington, J. O. Out, J. W. Pan and G. M. Pohost, *Magn. Reson. Med.*, 1994, **32**, 206.
37. J. Murphy-Boesch, R. Stoyanova, R. Srinivasan, T. Willard, D. Vigneron, S. Nelson, J. S. Taylor, and T. R. Brown, *NMR Biomed.*, 1993, **6**, 173.
38. K. R. Thulborn and J. J. H. Ackerman, *J. Magn. Reson.*, 1983, **55**, 357.

Biographical Sketch

Joseph Murphy-Boesch. *b* 1947. S.B. (Physics, EE) MIT, 1971; Ph.D. (EECS), University of California, Berkeley, 1978. Introduced to NQR and NMR by Dr Stephen Senturia, MIT, and to in vivo NMR (blood flow) by Dr Jerome R. Singer, University of California, Berkeley and Michael Weiner, University of California, San Francisco. Postdoctoral work, University of California, San Francisco (Dr T. L. James). Adjunct Professor, University of California, San Francisco, 1984–87; staff scientist, Fox Chase Cancer Center, Philadelphia, PA, 1987–99; Vice-President of Engineering, USA Instruments, Aurora, Ohio, 1999–present. Approx. 40 publications and 4 patents. Research specialties: NMR instrumentation and coil design, proton-decoupled ^{31}P and ^{19}F whole body spectroscopy.

Radiofrequency Systems and Coils for MRI and MRS

William A. Edelstein

General Electric Corporate Research and Development, Schenectady, NY, USA

1 INTRODUCTION

The MR rf (radiofrequency) system includes a waveforming and transmitting portion that applies rf magnetic field pulses to targeted nuclear spins via an rf coil. The applied field, $\boldsymbol{B}_1$, causes the spins to nutate (or tip) relative to the direction of the static magnetic field, $\boldsymbol{B}_0$. The nutated spins collectively form a transverse precessing magnetization which is picked up by the transmitting rf coil or a separate rf receiving coil. The resulting signal is amplified, mixed down to an audiofrequency, digitized, and processed by a computer which turns the signal into an image or spectrum.

Rf coils come in many shapes and sizes but can be generally characterized as *volume coils* or *surface coils*. Volume coils (e.g. a solenoidal winding) contain the sample of interest; surface coils (e.g. a simple loop) are placed on the surface of the sample. Volume coils usually produce a homogeneous rf magnetic field and have a large FOV (field-of-view), a fairly uniform sensitivity, and a moderate S/N (signal-to-noise ratio). Surface coils produce a rapidly varying rf magnetic field (strongest in their vicinity), and consequently a high S/N for a small volume of the sample near their location, and thus, effectively, a small FOV.

The NMR *phased array* is an assembly of overlapping surface coils which cover a large surface area and can have the sensitivity and S/N of a surface coil combined with the FOV of a volume coil. They require, however, considerable complexity in the rf receiving system and system image processing capabilities.

The MR requirements for large rf coils, which operate efficiently at high frequencies, have produced a number of interesting technical advances such as the use of distributed capacitances, the *birdcage* rf coil (see ***Birdcage Resonators: Highly Homogeneous Radiofrequency Coils for Magnetic Resonance***) and the NMR phased array (see ***Whole Body Machines: NMR Phased Array Coil Systems***).

2 RF SYSTEM

Shown in Figure 1 are block diagrams of two typical rf systems. In general, the rf system can be divided into two parts: transmit and receive. The transmit portion sends out high-power rf pulses (milliwatts to kilowatts) which are applied to the spin system through the transmit rf coil. The NMR signal is then picked up by the transmit rf coil or by a separate receive rf coil. Figure 1(a) uses a single rf coil which both transmits (applies the rf excitation pulse) and receives (the NMR signal). Figure 1(b) uses separate transmit and receive coils.

The system computer (or a pulse programmer, which is an attached microprocessor) generates pulse waveforms which are used to modulate an rf carrier (an rf signal at constant phase and amplitude). The resulting waveform contains a high-frequency signal at the NMR frequency (typically tens of MHz) whose amplitude and phase are varied by the modulation.

Following the pulse programmer is a low-level rf transmitter (capable of power output up to tens of watts) followed by an rf power amplifier, which produces watts to kilowatts. The high-level rf signal proceeds through the T/R (transmit/receive) switch[1,2] to the rf coil. The T/R switch is designed to let the high-level rf through during transmit but close off the rf transmit channel during receive. This is because the rf transmit channel may have appreciable noise.

The rf signal then produces currents in the rf coil and a consequent rf magnetic field, generally called $\boldsymbol{B}_1$ (in contrast to the

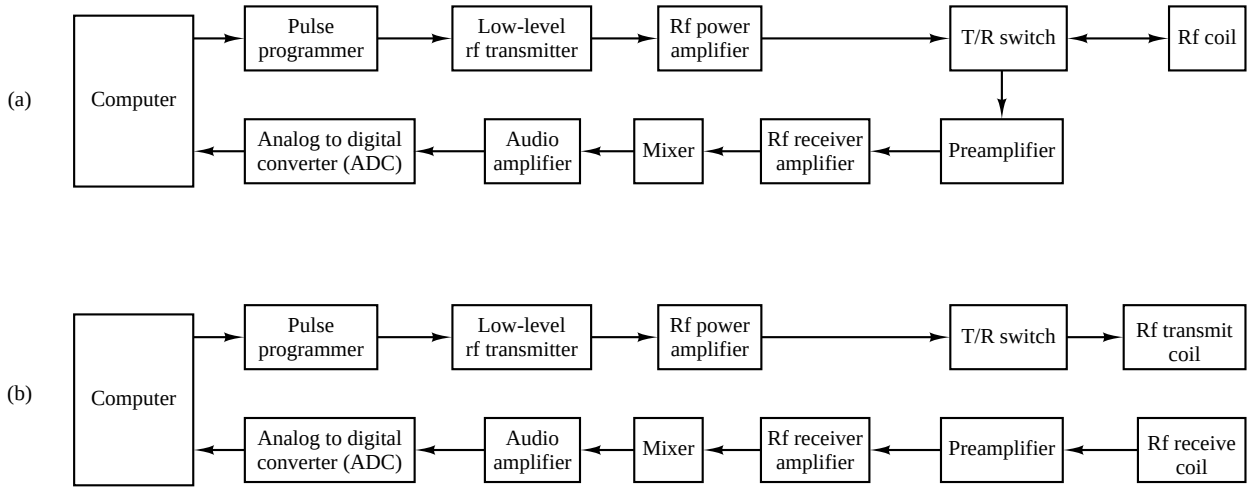

Figure 1 Rf systems: (a) with single rf coil used for both transmission and reception, (b) with separate transmit and receive coils

static magnetic field, usually called $\boldsymbol{B}_0$). The rf magnetic field, in the presence of field gradients (see ***Magnetic Resonance Imaging: A Historical Overview***) manipulates the sample magnetization and nutates (turns) particular portions (i.e. all magnetization in a selected slice or volume) away from the direction of $\boldsymbol{B}_0$. Inhomogeneous $\boldsymbol{B}_1$ can cause undesirable nonuniform nutation in different parts of the sample.

The simplest modulated rf signal is a 'square' pulse, that is, on at a fixed level for some period of time and then off. More complex pulse shaping is often used in MRI to excite the magnetization in selected slices or volumes of the sample. One common example is the 'sinc' function, $\sin(x)/x$, used for slice selection. More sophisticated magnetization can be accomplished by a series of complex pulses.

After the magnetization is prepared in the desired way by one or more rf pulses, the transmission is shut off (usually by the transmitter and the T/R switch) and the receive chain listens for the NMR signal from the precessing nuclei. In the system shown in Figure 1(a) a voltage and current are induced in the single rf coil by precessing nuclei and are first picked up by a *preamplifier* or 'preamp'. The preamp must have a low noise figure, that is, it should add very little noise to the signal coming from the rf coil. The amplified signal from the preamp proceeds through an rf receive amplifier, which further increases the signal strength to a high level. The signal is then fed to a *mixer* which 'mixes' the NMR signal with a local rf frequency oscillator. An 'audio' signal is produced whose frequency is the difference between the local oscillator and NMR frequencies. Audio signal frequencies typically lie in the range 0–100 000 Hz.

The system shown in Figure 1(b) is similar to that in Figure 1(a) except that there are separate transmit and receive rf coils. The rf magnetic field $\boldsymbol{B}_1$ which causes the spins to nutate is produced by the transmit coil, and the receive coil senses the returning signal from the precessing nuclear magnetization. Examples of this arrangement might be to transmit with a volume coil (i.e. a body coil) and receive with a surface coil.

The audio signal is finally digitized (i.e. turned into numbers representing amplitude as a function of time) and fed into the system computer where it is processed to form an image or spectrum.

3 RF COILS

Two general classes of rf coils are *volume coils* and *surface coils*. Volume coils are constructed to enclose a substantial portion of the body such as the torso, the head, or an extremity. A typical surface coil is a small, simple metal loop which is placed up against the portion of the body to be examined. Generally speaking, volume coils have a large field-of-view but modest S/N, while surface coils have a small (shallow) field of view but better S/N. The *phased array* is an assembly of overlapping surface coils which can have the field-of-view of a volume coil but the S/N of a surface coil.

3.1 Signal and Noise in Rf Coils: S/N

One of the most critical parameters for imaging or spectroscopy is the S/N. The signal comes from precessing nuclear spins and is picked up by the rf coil. Electrical noise generally takes the form of random excursions of the electrical signal and is associated with thermal fluctuations in electrical resistances of the rf receiving system.

We can examine the sources and characteristics of signal and noise from the schematic model of the NMR receiving electrical circuit shown in Figure 2. The rf coil has an inductance (L_C) and is resonated by capacitors C_1 and C_2 in series. The capacitive divider C_1/C_2 is arranged so that the input/output impedance of the rf coil is approximately 50 Ω. (C_1 and C_2 may be the equivalent of the series or parallel resultant of many capacitors in a real rf coil.)

The electrical losses represented by resistors R_C and R_S correspond to electrical losses in the coil and sample, respectively. Electrical noise in the circuit comes from the resistors. The coil and sample noise voltages corresponding to the resistors are given by the Johnson noise formulas $V_{nC}^2 = 4R_C kT\,df$ and $V_{nS}^2 = 4R_S kT\,df$ respectively, where k = Boltzmann's constant, T = temperature in Kelvin and df is the observed bandwidth in Hz. V_{NMR} is the NMR signal voltage.

The NMR voltage, then, is competing with the noise voltages produced by losses in the coil and losses in the sample, so minimizing the losses will minimize the noise.

Another measurement of losses is the 'Q' of a resonant circuit which can be applied to Figure 2 by the equation $Q = \omega L_C/R$, where R = total resistance. Thus, the higher the Q, the smaller the losses.

The losses in the coil itself can be decreased by making it with a metal conductor with low resistance or, as has been tried recently, high-temperature superconductors.[3] However, the sample losses are a function of the relative geometry of the rf coil and sample (or parts of the body, in this case). So a body coil, which wraps around a person, will have a maximum S/N for a voxel of a certain size which can be approached (but never quite reached) by ensuring that $R_C << R_S$. This can be defined as the 'intrinsic S/N' for that geometry.[4]

Physically, a voxel of a certain size produces a precessing magnetization which is picked up by the rf coil. The sample (i.e. the human body) has thermally generated circulating currents which are also received by the coil. So the S/N is basically a competition between the NMR signal and the noise produced by the circulating currents.

The sensitivity of an rf coil to a voxel of precessing magnetization is proportional to the rf $\boldsymbol{B}_1$ magnetic field created at the position of the voxel by unit current flowing in the coil.[1,5] Whole body and head coils have fairly uniform sensitivities throughout their volumes. They are, however, somewhat distant from voxels of interest, and are therefore relatively insensitive.

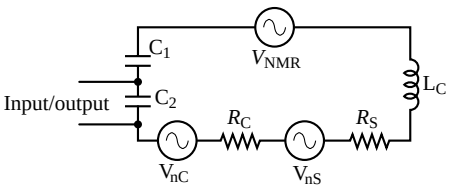

Figure 2 Equivalent electrical circuit for rf coil showing inductance of the coil, resonating and matching capacitors C_1 and C_2, equivalent loss resistors R_C and R_S for losses in the coil and sample, respectively, and noise sources V_{nC} and V_{nS} corresponding to the loss resistors R_C and R_S. Also shown is V_{NMR}, the NMR signal voltage

Since they also contain large portions of the body, the noise picked up from the thermally generated noise currents measured above is relatively large. Surface coils are comparatively close to volumes of interest and see smaller regions of the body, which gives them less noise. As would seem reasonable, therefore, S/Ns in general increase as one goes from body to head to surface coil.

For a voxel at a particular depth inside the body, the best possible S/N can be closely approached by using a circular loop surface coil whose diameter is approximately equal to the depth of the target voxel.[1,6] (The actual relationship is optimum coil diam. = 0.89 × voxel depth).

Finally, for a given coil and sample geometry, the intrinsic S/N is proportional[4] to the magnitude of the static magnetic field, B_0. As the field increases, a larger magnetization is produced proportional to B_0 and the signal for a given magnetization is proportional to the precession frequency which is in turn proportional to B_0. Thus the net signal is proportional to the product of these factors, or $S \propto B_0^2$. Higher frequencies cause the losses in the thermally generated circulating currents in the body to increase and the noise $N \propto B_0$. The net effect is that the intrinsic S/N $\propto B_0$.

There are two other factors that affect S/N for practical MRI and MRS systems. First, T_1 relaxation times increase slowly as a function of field strength,[7] which works against the advantage of increasing field for MRI repetitive pulse sequences; this effect is not large, however.

Second, as the field decreases, it becomes more difficult to make rf coils which approach the geometric intrinsic S/N limit, that is, rf coils whose electrical losses are small compared with the losses of rf-induced currents in the body. Generally speaking, systems at B_0 = 1.5 T can easily achieve negligible noise contributions from the rf coils, whereas systems with B_0 less than 0.1–0.2 T have substantial noise contributions from rf coils. Superconducting rf coils[3] may reduce noise contributions from coils and help low-field systems approach the intrinsic S/N limit. However, at best, such coils can only get to S/N $\propto B_0$, so a 0.1 T system will, in the most favorable case, have an S/N approximately 15 times worse than the S/N for a 1.5 T system.

3.2 High-Frequency Rf Coil Considerations: Distributed Capacitances

There are two important challenges to making large-volume high-frequency rf coils suitable for MRI and MRS of human subjects. The first is to obviate adverse effects of stray capacitance between wires comprising the coil and external conductors or between various parts of the coil itself. The second is to make volume coils having uniform magnetic fields that will therefore provide uniform excitation and reception of magnetization.

We illustrate the stray capacitance problem by considering how to make a large loop work at high frequencies. The problem is that there is capacitive coupling between the loop and its surrounding and between different parts of the loop. Electric fields around the loop tend to divert current through the stray capacitances instead of keeping the currents in the loop, which spoils the coil's operation. In principle, there are two possible ways to mitigate this effect: decrease or control the stray capacitance, or decrease the electric field.

The Faraday screen[2] is an attempt to control stray capacitance. It is a structure consisting of a collection of wires, usually in a plane, having a common connection but no closed loops. It is supposed to offer a low impedance path for electric fields. It is generally placed between the coil and other conducting structures (i.e. the body) in the hope of preventing coil electric fields from interacting with external objects. Thus stray electric fields tend to return through the Faraday screen and therefore do not produce currents from the coil to external conducting objects.

The Faraday screen is helpful in decreasing the interaction between the rf coil and nearby conducting structures such as gradient windings. However, it does little to solve the problem of currents through coil-to-coil stray capacitance. Second, the wires which comprise the Faraday screen have substantial inductance and therefore do not offer a much lower impedance path than the stray capacitances. So currents through Faraday screens do introduce some electrical loss that can have an observable effect on coil Q, where only extremely low losses can be tolerated.

Using multiple distributed capacitances in the rf coil decreases the electric fields generated by the coil and thereby reduces currents through stray paths. This idea was known to some electrical engineers for specialized antennas,[2,8] but was not really utilized in the NMR community before the advent of MRI. The problem and solution are illustrated in Figures 3 and 4. Figure 3 shows the application of distributed capacitances to a loop coil (often used as a surface coil). Figure 3(a) uses a single capacitance C to resonate the loop inductance at the desired frequency. The capacitance C is divided in order to provide an impedance match to 50 Ω. Figure 3(b) is the same size loop, also resonated with net capacitance C. However, this time the capacitance value C is achieved by putting eight capacitors, each with capacitance 8×C, in series. (The input capacitance is again divided in order to achieve an impedance match).

Distributing capacitances actually decreases the electric fields. Figure 4 is a sketch of radial electric fields around a

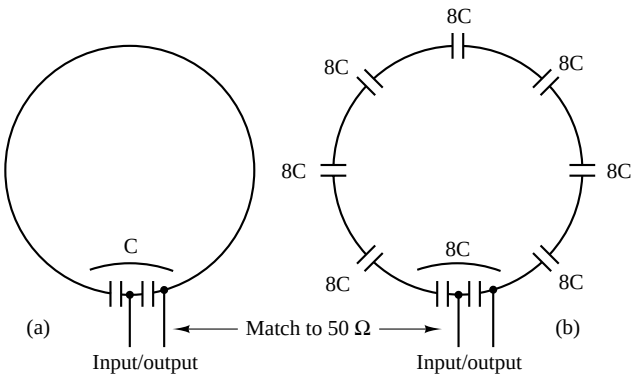

Figure 3 Distributing capacitances in an rf coil decrease electric fields and allow operation at high frequencies. (a) Single-loop rf coil whose inductance L is resonated with capacitance C in one location. The capacitance is divided in order to provide an impedance match to 50 Ω. (b) Single-loop rf coil with inductance L, also resonated with net capacitance C. However, this time capacitance value C is obtained by putting eight capacitors of value 8×C in series, physically distributed around the loop

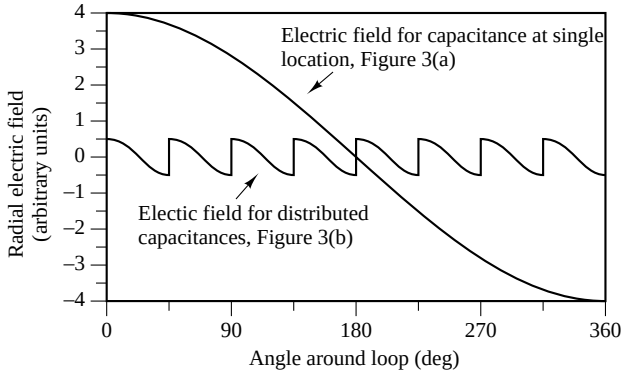

Figure 4 Sketch of radial electric fields around a simple loop surface coil using a single capacitance or multiple capacitances as shown in Figure 3(a) and (b) respectively

simple loop surface coil using a single capacitance or multiple capacitances as shown in Figures 3(a) and (b) respectively. With capacitance concentrated in one part of the loop, the radial electric field for a given current changes around the loop as shown by the single large curve, and varies from −4 to +4 in arbitrary units. With distributed capacitances, the electric field change of each section of the conductor (which has inductance) is approximately canceled by the opposite electric field change across the adjacent capacitor. Thus, putting in eight capacitors instead of one in the loop reduces the electric fields available to drive currents through stray paths by about a factor of 8.

3.3 Solenoid, Saddle, and Birdcage Rf Coils

The three most commonly used volume rf coils (Figure 5) are the *solenoid* coil, the *saddle* coil and the *birdcage* coil. The solenoid coil is simply a helical winding on a cylinder which produces a field down its cylindrical axis. It is used when the symmetry axis of the static field is perpendicular to the direction of insertion of the sample, i.e. the patient, because the rf field $\boldsymbol{B}_1$ has to be perpendicular to the static field $\boldsymbol{B}_0$.

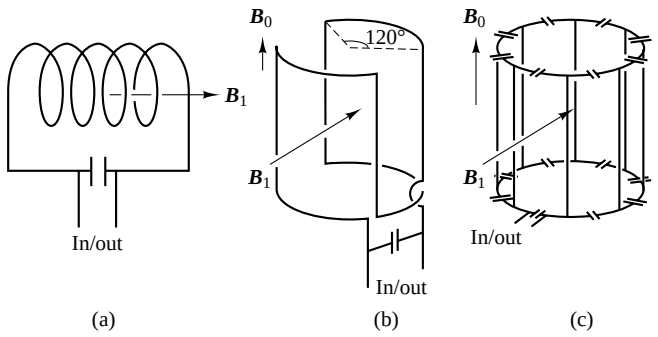

Figure 5 Rf coils: (a) solenoid; (b) saddle; (c) birdcage. In MRI, cylindrical symmetry is often important. The solenoid coil produces an rf field down its symmetry axis which must be perpendicular to the static field ($\boldsymbol{B}_0$) axis. The saddle coil and birdcage coils produce their $\boldsymbol{B}_1$ field perpendicular to their cylindrical symmetry axis which is aligned with $\boldsymbol{B}_0$

The saddle coil and the birdcage coil[9] (see ***Birdcage Resonators: Highly Homogeneous Radiofrequency Coils for Magnetic Resonance***) both produce rf $\boldsymbol{B}_1$ fields perpendicular to their cylindrical axis. The birdcage coil is a more sophisticated design and has a higher degree of azimuthal symmetry. A birdcage coil can easily be adapted for quadrature excitation and quadrature reception. Two perpendicular saddle coils would be necessary for quadrature, whereas a solenoid coil would need to be used with a saddle coil in order to get quadrature.

At high frequencies, where most of the electrical losses (and therefore electrical noise) comes from the sample, i.e. the patient, solenoid, saddle, and linearly excited birdcage coils will give about the same S/N. At low fields (and hence low NMR frequencies), electrical loss in the coil can be significant or even dominant compared with electrical loss in the patient. The solenoid coil has less resistance per unit field generated than the saddle or birdcage coils.[5] So at low frequencies the solenoid coil can offer some S/N advantage over a linearly excited saddle or birdcage coil. Quadrature operation of a birdcage (or double saddle coils) gains back S/N. The exact comparison depends on the particular system and its parameters.

3.4 Homogeneity of the Applied Rf Field and Receive Sensitivity

It is important that the rf magnetic field $\boldsymbol{B}_1$ applied to the spin sample be uniform in order to get the nutated magnetization consistent over the target volume. Homogeneous excitation is particularly important for complex pulse sequences. These sequences may contain multiple pulses, and relatively small errors can accumulate to produce large magnetization errors at the end of the pulse train. Thus volume coils, which have fairly uniform $\boldsymbol{B}_1$, are often used for sample excitation.

Surface coils may be used for the transmit pulse when the homogeneity of excitation is not critical, for example, in spectroscopy, when a single excitation is applied. Pulse sequences containing refocusing (i.e. 180° pulses) usually require more precision and are generally applied with a volume coil.

The $\boldsymbol{B}_1$ produced at a point in space by a unit current in an rf coil is proportional to the sensitivity of the coil to the NMR signal coming from that point in space.[1,5] Because volume coils produce a uniform $\boldsymbol{B}_1$, they also have fairly uniform sensitivity. The sensitivity of surface coils is strongest near the coil and falls off with distance away from the coil. Surface coil S/N near the sample surface is generally substantially greater than S/N for volume coils. The enhanced surface coil S/N is frequently more important than its nonuniform sensitivity. A common strategy is to use a volume (or other large) coil to produce a uniform excitation and a surface coil for high S/N reception. With this arrangement, however, it is generally necessary to use some sort of electronic *decoupling* of volume and surface coil in order to avoid having the transmitted pulse create currents in the receive coil, which will distort the applied rf $\boldsymbol{B}_1$ field. One such decoupling scheme uses resonant blocking circuits in the receive coil to block current flow.[1,2,10]

The only real problem with the surface coil is its limited FOV. The NMR phased array[11] is a collection of overlapping surface coils which has the sensitivity of a surface coil and the FOV of a volume coil (see ***Whole Body Machines: NMR Phased Array Coil Systems***). Each surface coil requires its

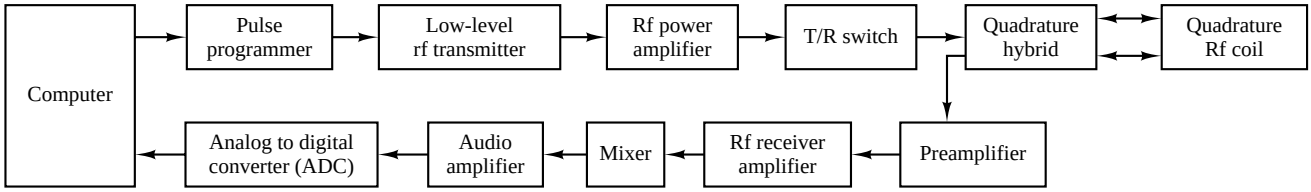

Figure 6 Example of quadrature rf system. During transmit, the quadrature hybrid splits the incident rf power into two equal parts which are 90° out of phase. These outputs are fed to two quadrature ports of the rf coil and produce a circularly polarized rf excitation pulse. During receive, the circularly polarized NMR signal creates signal at the two quadrature ports which are 90° out of phase. These are fed back through the quadrature hybrid which causes them to combine in phase and produce an output at the fourth quad hybrid port. The resulting signal is then sent through the receive chain and processed in the usual way

own receiver chain and the processing is complex. The phased array has so far been used for applications using a few surface coils in the array, such as arrays to study spines, knees, neck, or shoulder. In principle, one- and two-dimensional phased arrays (some of them large) could be used to carry out all imaging and spectroscopy optimally. However, universal application of this technology would require considerable hardware and software development.

3.5 Quadrature

Once the magnetization in a spin system has been nutated away from the static field direction, it precesses around the static field with a circular polarization; that is, the spins precess either clockwise or counterclockwise when viewed along the static field direction. It has long been known[1,5] that applying a circularly polarized rf excitation could save a factor of 2 in rf energy, and, receiving in a way that is only sensitive to the correct circular polarization, would gain a factor of approximately $\sqrt{2}$ in S/N.

The general idea for quadrature transmit is to apply two linear $\boldsymbol{B}_1$ excitations at right angles in a plane perpendicular to the static field, $\boldsymbol{B}_0$. If the excitations are 90° out of phase, a circularly polarized $\boldsymbol{B}_1$ results. The angular direction of the circular polarization is determined by the relative phase of the excitations, that is, whether the second excitation is 90° ahead or behind the first. In the language of electrical engineering, we will call the quadrature connections to the coil the quadrature ports.

Quadrature reception is achieved by taking the outputs of the quadrature ports and combining them with the correct 90° phase delay so the signals from the circularly polarized NMR magnetization reinforce.

The birdcage rf coil[9] (see ***Birdcage Resonators: Highly Homogeneous Radiofrequency Coils for Magnetic Resonance***) is naturally suited to quadrature excitation and can easily be connected in a quadrature configuration. Other possible quadrature configurations with volume coils are two saddle coils at right angles and a solenoidal coil plus saddle coil. This arrangement requires two coils, one on top of the other, which is inconvenient.

Figure 6 shows an example of a quadrature rf system. The key new element (not found in our earlier system diagrams, Figure 1) is a *quadrature hybrid.*[1] A quadrature hybrid is a symmetrical four-port device with a pair of equivalent ports at the input end and a corresponding pair at the output end. A signal sent into a port at the input is split into two equal parts at the output; the output signals are 90° out of phase. Such splitting is ideal for quadrature coil operation. During transmit, the rf power excitation pulse is connected to one of the hybrid inputs. The hybrid outputs are fed to the two quadrature ports of the rf coil and produce a circularly polarized rf excitation pulse. During receive, the circularly polarized NMR signal feeds back through the hybrid output ports, which causes them to combine in phase and produce an output at the second input hybrid port. The resulting signal is then sent through the receive chain and processed in the usual way.

A phased array can also make some gain in S/N by combining perpendicular elements of the magnetization signal using weighting that takes the S/N of each component and the circular phase properly into account.[1] However, this enhancement is generally less than the $\sqrt{2}$ improvement in S/N that can be realized in a volume rf coil.

4 RELATED ARTICLES

Birdcage Resonators: Highly Homogeneous Radiofrequency Coils for Magnetic Resonance; Sensitivity of Whole Body MRI Experiments; Surface and Other Local Coils for In Vivo Studies; Whole Body Machines: NMR Phased Array Coil Systems; Whole Body Magnetic Resonance Spectrometers: All-Digital Transmit/Receive Systems.

5 REFERENCES

1. C.-N. Chen and D. I. Hoult, 'Biomedical Magnetic Resonance Technology', Adam Hilger, Bristol, 1989, p. 210ff.
2. J. F. Schenck, in 'The Physics of MRI', 1992 AAPM Summer School Proceedings, eds. M. J. Bronskill and P. Sprawls, American Institute of Physics, Woodbury, NY, 1993, p. 124.
3. R. D. Black, T. A. Early, P. B. Roemer, O. M. Mueller, A. Mogro-Campero, L. G. Turner, and G. A. Johnson, *Science*, 1993, **259**, 793; R. D. Black, P. B. Roemer, A. Mogro-Campero, L. G. Turner, and K. W. Rohling, *Appl. Phys. Lett.*, 1993, **62**, 771; S. J. Penn, N. M. Alford, A. S. Hall, T. W. Button, R. Johnstone, S. J. Zammattio, and I. R. Young, *Appl. Supercond.*, 1993, **1**, 1855.
4. W. A. Edelstein, G. H. Glover, C. J. Hardy, and R. W. Redington, *Magn. Reson. Med.*, 1986, **3**, 604; C. N. Chen, V. J. Sank, S. M. Cohen, and D. I. Hoult, *Magn. Reson. Med.*, 1986, **3**, 722.
5. D. I. Hoult and P. C. Lauterbur, *J. Magn. Reson.*, 1979, **34**, 425.
6. W. A. Edelstein, T. H. Foster, and J. F. Schenck, *Proc. IVth Ann Mtg. Soc. Magn. Reson. Med.*, London, 1985, p. 964; P. B. Roemer, and W. A. Edelstein, *Proc. VIth Ann Mtg. Soc. Magn. Reson. Med.*, New York, 1987, p. 410.

7. P. A. Bottomley, T. H. Foster, R. E. Argersinger, and L. M. Pfeifer, *Med. Phys.*, 1984, **11**, 425.
8. A. Alford, A. G. Kandoian, *Trans. Am. Inst. Electr. Eng.*, 1940, **59**, 843; C. E. Ermatinger, *IEEE Trans. Antennas Propag.*, 1968, **16**, 488.
9. C. E. Hayes, W. A. Edelstein, J. F. Schenck, O. M. Mueller, and M. Eash, *J. Magn. Reson.*, 1985, **63**, 622.
10. W. A. Edelstein, C. J. Hardy, and O. M. Mueller, *Proc. IVth Ann Mtg. Soc. Magn. Reson. Med.*, London, 1985, p. 1084; W. A. Edelstein, C. J. Hardy, and O. M. Mueller, *Magn. Reson. Med.*, 1986, **67**, 156; L. K. Hedges, and D. I. Hoult, *Proc. IVth Ann Mtg. Soc. Magn. Reson. Med.*, London, 1985, p. 1096.
11. P. B. Roemer, W. A. Edelstein, C. E. Hayes, S. P. Souza, and O. M. Mueller, *Magn. Reson. Med.*, 1990, **16**, 192.

Biographical Sketch

William A. Edelstein. B.S., 1965, physics, University of Illinois, Urbana; A.M., 1967, physics, Ph.D., 1974, physics, Harvard University, Cambridge, MA. Research fellow, Glasgow University, 1974–77, gravitational waves; research fellow, Aberdeen University, 1977–1980, NMR imaging; physicist, GE Corporate Research and Development, Schenectady, NY, 1980–present, Research specialties; MR imaging, thermal remediation of environmental contamination.

Refrigerated and Superconducting Receiver Coils for Whole Body Magnetic Resonance

Michael Burl and Ian R. Young

The Robert Steiner MRI Unit, Hammersmith Hospital, London, UK

1 INTRODUCTION

Though the potential gains in signal-to-noise ratio for the NMR experiment of refrigerating the detector coils was pointed out some time ago,[1] they have been rarely applied[2] and then without a sufficiently large gain in performance to persuade machine-users that they should be widely adopted. The use of very cold coils for experiments involving human studies imposes additional constraints. Clearly, the degree of thermal protection needed is much greater and the design of the cryostat to be used is influenced by factors such as the need for it to be tailored to the shape of the body, or be comfortable if the patient has to lie on it.

Whole body experiments differ from most high-resolution experiments in that, at most fields, the dominant noise in the system is derived from the subject's body rather than the detector coils. Where body noise is the major contributor, even reducing coil noise to nothing may not result in significant improvements in signal-to-noise ratio, and the additional technical difficulties added by the necessary cryogenic system seem quite unjustified. It has been considered that cooling is only useful in low-field systems where it can be difficult to reduce coil noise to a level where it is a small fraction of that due to the body.

However, there are circumstances in which it can be predicted that cooling may be useful in machines operating at fields which are quite comfortably in the range normally used for whole body studies, and, with the increasing interest of researchers in the application of MR to interventional investigations and the monitoring of therapy, which are likely to be conducted at lower fields rather than higher for reasons associated with the other facilities needed to perform such procedures, there is the prospect of increasing interest in the investigation of cooled detector coils in whole body studies.

First experiments with whole body systems were conducted using copper coils cooled to liquid nitrogen temperature.[3] Subsequently there was little interest in the topic until the development of coils based on high-temperature superconductors (HTSC) such as YBCO ($YBa_2Cu_3O_{7-x}$).[4]

2 BASIC CONCEPTS

Hoult and Richards[1] derived the relationship for the signal-to-noise ratio of the NMR experiment as:

$$\mathrm{S/N} = K_\mathrm{A}\omega_0^{7/4}T^{-1/2}\rho^{-1/2} \tag{1}$$

where ω_0 is the frequency of the resonance, T is the absolute temperature and ρ is the resistivity of the material of which the detector coil is made. K_A is a constant embracing all the other terms in the relationship. (In this article, only those terms in S/N, and other formulations which are directly relevant to the argument will be identified. All other terms will be included in a series of constants, of which K_A is the first, to be followed by K_B, etc.)

As Hoult and Richards pointed out, equation (1) implied a potential gain of about 2.8 times in signal-to-noise ratio as a copper coil was cooled from ambient to liquid nitrogen temperature. (The direct gain in S/N from the reduction in temperature is augmented by a parallel, though smaller, decrease in resistance of the copper coil.)

The whole body experiment, in which body loading can represent the dominant noise contribution, presents a more complex picture. Hoult and Lauterbur[5] derived the S/N for a head in this case as having the form:

$$\mathrm{S/N} = \frac{K_\mathrm{B}\omega_0^2}{\left(K_\mathrm{C}\omega_0^2 T_\mathrm{B} + K_\mathrm{D}\rho_\mathrm{C}\omega_0^{1/2}T_\mathrm{C}\right)^{1/2}} \tag{2}$$

where T_B is the body temperature and T_C that of the coil. ρ_C is the resistivity of the coil. As ω_0 increases, the first term in the denominator grows so large relative to the second that the latter can be ignored.

Refrigerated coils can therefore only be expected to be of significant utility in whole body experiments in three circumstances:

1. At very low fields, where significant body loading of coils is difficult.
2. For very small coils, for studying very localized regions, where coil and preamplifier input noise can again be predominant.
3. For whole body situations where, for clinical reasons, coil loading may be very light. [An example of this might be in pediatric (neonatal) studies in which the coil was designed to surround the incubator containing the very small baby, rather than moving the child from its normal incubator into a special container with a more closely coupled probe with the consequent need to ensure transfer of all the monitoring and life support connections.]

The use of refrigerated coils in high-resolution systems seems to have been very limited[2] until the advent of HTSC (high-temperature superconductor coils) which has provoked substantial further interest,[6,7] particularly for microscopy applications.[8,9] These have been operated at fields of 9–11 T at liquid helium temperature and for small samples.

3 REFRIGERATED CONVENTIONAL METAL COILS

The behavior of refrigerated metal coils is much more predictable than that of HTSC ones (see the next section). The principal metals from which coils might be made (Cu, Al, and Ag) all show falling resistivity as their temperature is reduced, though their rf resistance falls more slowly than does ρ, since the skin depth (δ) is given by,

$$\delta = \sqrt{\frac{2\rho}{\mu_0 \omega}} \tag{3}$$

However, the skin depth is still likely to be much less than the mechanical thickness of the metal used in the range of frequencies of interest, even at 4 K. In any form of refrigeration which is likely, it is reasonable to expect that the coolant can most conveniently be handled by making the coil conductor of a tube through which it is passed. Wall thicknesses of 1–2 mm are then reasonable, though more difficult to use in very small coils. This was the method used in the first whole body studies, as shown in Figure 1.

The performance reported in Hall et al.[3] using this coil at liquid nitrogen temperature showed a gain of S/N of around 28% in in vivo experiments relative to its operation at room temperature. (The experiments were conducted at 0.15 T). Reducing the temperature toward liquid helium temperature (as in Styles et al.[2]) can be predicted to show further gains, though these have not yet been demonstrated in vivo, and the reduction in noise obtained in the experiments in Styles et al.[2] was largely offset by a reduction in filling factor in the high-resolution system used.

The use of refrigerated conventional metals, as against superconductors, does have the advantage of avoiding the impact of the Meissner effect, which can produce local perturbations in $\boldsymbol{B}_0$. Since imaging requires a data acquisition bandwidth that is generally quite substantial compared with that of high-resolution studies an excessively high coil Q value has to be reduced as noiselessly as possible. In this context, in any case, it should be remembered that the main benefit for S/N comes from the reduction in T, rather than R [in the noise voltage expression of $(4kTR)^{1/2}$]. In practice, the maximum usable Q value in most experiments can be achieved by refrigerated metal, and, while there are methods of reducing Q without introducing more than small amounts of noise, the gain in performance of superconducting coils may be very small. Note, too, that reducing the source temperature seen by the preamplifier may actually cause the noise figure of that unit to be degraded. The limited extent of the potential gains are well illustrated by Figure 2. This shows results obtained by computer modeling for the S/N at various depths for two different coil designs, of one turn and three turns. The performance of the former coil was modeled at room and liquid helium temperatures. Simulation assumed an operating frequency of 21 MHz. The gains obtained are useful, but not startling, as was confirmed by the practical work in Hall et al.[3]

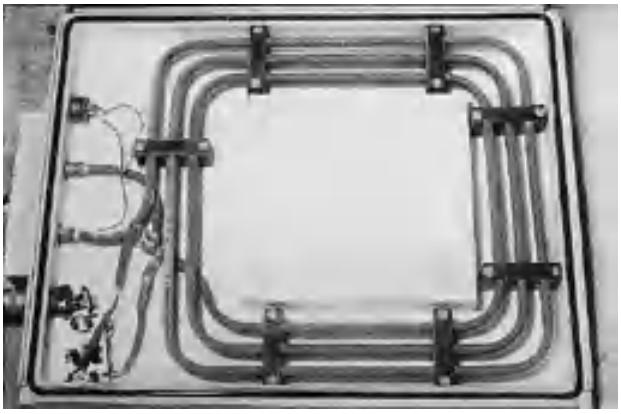

Figure 1 Copper conductor-based surface coil designed to be cooled by liquid nitrogen passed through thin copper tube used to form the probe. (Reproduced by permission of Academic Press from Hall et al.[3])

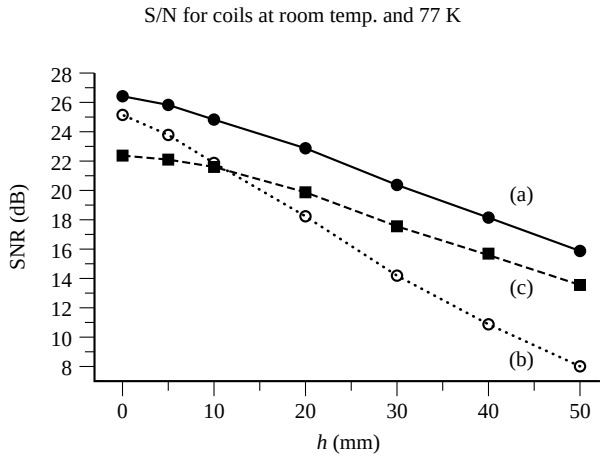

Figure 2 Results of computer modeling of coil behavior, assuming surface coils of one turn (a) and (b), and three turns (c), at an operating frequency of 21 MHz with a body resistivity of 0.85 Ω m loading them. The single-turn coil had a diameter of 30 mm, and the three-turn one a mean diameter of 70 mm. Curves (b) and (c) were obtained by modeling at 293 K and curve (a) at 77 K. (Reproduced by permission of Pergamon Press from Penn et al.[10])

4 SUPERCONDUCTING DETECTORS

Were it possible to make a noiseless probe system, the filling factor of the sample in it would become irrelevant. In the case of a small sample, the coil would collect signal and sample noise with equal efficiency regardless of its size. In a large sample, with spatial localization, this observation is no longer generally true. As the coil size is increased relative to the object, it detects noise in more of the body while signal collection efficiency is reduced.

Three forms of coil, all using YBCO, have been evaluated as rf probes. Hall et al.[4] used bulk ceramic rod wound into a helix (Figure 3) and designed to be self-supporting inside its cryostat of thick-walled expanded polyethylene. Black et al.[8] (for microscopy), and Withers et al.[7] for whole body imaging, used vacuum-deposited thin films. Hall and his colleagues[6,10] later went to a thick-film form (Figure 4). This last coil is formed on a Zirconia plate. As was suggested in Hall et al.,[6] the thick-film coil was less affected by the presence of the magnetic field than the bulk ceramic.

YBCO is a type 2 superconductor with a relatively high critical temperature (T_C) but with a range of transition behavior between its normal conductivity and a complete superconducting state which is a function of its processing and formation. There is an extensive literature on this, but Hojaji et al.'s work[11] is typical, showing the variation of properties of one particular YBCO form at varying temperatures. T_C is typically

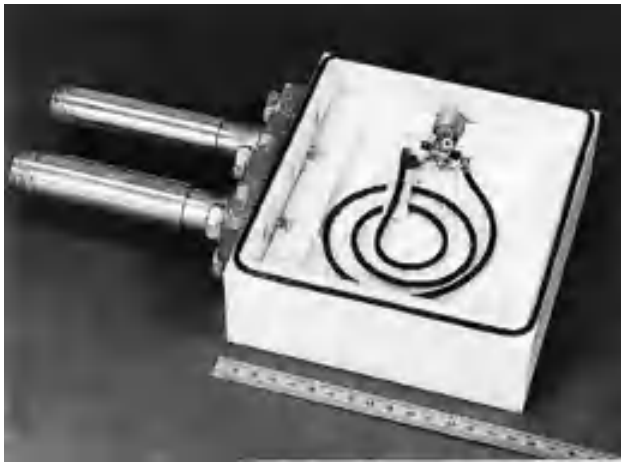

Figure 3 HTSC YBCO coil fabricated from rod and formed into a spiral. The coil is shown mounted inside its expanded polyethylene cryostat. (Reproduced by permission of Academic Press from Hall et al.[4])

around 90 K, but the transition in properties is by no means necessarily complete at 77 K (the temperature defined by the boiling point of liquid nitrogen). The material used by Hall et al. in these various studies shows considerable further improvement in its superconducting properties as the temperature is reduced by a further 7–8 K[12] below that of liquid nitrogen. Cooling below 77 K is therefore a potential source of benefit, but substantially less convenient. The consequences are however important as Black et al.[8] suggest in comparison with Hall et al.[6] The former reported quality factors (Q) at relatively high field (7 T) of 24 000 at 10 K, while the latter struggled with significant Q variation from a thick-film coil with increasing field in the range 0–0.15 T at 77 K, beginning at 650 and falling to 500. Cooling substantially below 77 K, however, raises the issue as to whether it is desirable to persist with the use of current HTSC, or to use classic metal superconductors, with the temperature reduced to the order of 4 K. Two-stage refrigerator systems can conveniently reach 20 K or so, avoiding the need for liquid helium, but are quite expensive. Thin-film coils are generally of much better quality than thick-film ones as Withers et al.[7] report Q values of up to 14 000 at liquid nitrogen temperature at 6.6 MHz. However these coils have to be deposited onto single crystal sapphire or $LaAlO_3$ wafers. These limit the size of coils to perhaps 5–6 cm in diameter, and are expensive, meaning that large area coverage of the body can be very costly.

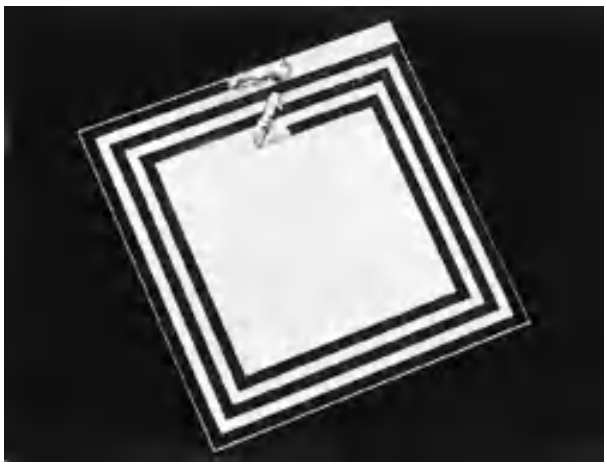

Figure 4 Thick-film HTSC coil on Zirconia. The Zirconia plate was 100 mm square. The HTSC is approximately 100 μm thick, and is made by forming a film of slurry, fixing it, then machining in the pattern

The thin-film coils can incorporate their own tuning capacitors as part of the artwork,[7] and so avoid many of the problems that Hall and his colleagues found with making connections to their thick-film and solid ceramics, and the limitations imposed by the limited Q values of available conventional tuning capacitors of appropriate size and form.

The ultimate limitations on superconducting coil performance are set by an ω^2-dependent edge noise, and radiation resistance.[13] The former is significant in materials such as a machined thick-film layer, though small in vacuum-deposited, masked and etched layers. The radiation resistance is essentially a far-field concept, so that it is relevant only to small coils in large systems at higher frequencies. It can be derived using the argument in Hall et al.,[13] where

$$L = \frac{\mu_0 \pi a^2 N^2}{(8a + 11b)} \tag{4}$$

for an N turn spiral of average radius a and where b is the difference between the inner and outer radius of the coil (b>0.2a). The radiation resistance is given by

$$R_r = \frac{\pi}{b}\sqrt{\frac{\mu_0}{\epsilon_0}} N^2 \left(\omega \frac{a}{c}\right)^4 \tag{5}$$

where c is the velocity of light, and the radiation-limited value of Q by

$$\frac{1}{Q} = 1/6(8a + 11b)\frac{\omega^3 a^2}{c^3} \tag{6}$$

Figure 5 illustrates the approach of cooled conventional and HTSC coils toward this limit. The results suggested that factors such as the dielectric loss angle of the coil substrates are not going to determine ultimate performance. The limiting parameter is likely to be the noise temperature of the preamplifier in practical systems.

5 REFRIGERATION

A key problem in the development of cryogenic coils, regardless of the materials used, is that the gap between subject and detector should not be allowed to grow excessively. In theory, as noted earlier (Section 4), if the detector systems were to be perfectly superconducting filling factors would be irrelevant. With extended objects, far exceeding the region from which useful signal is expected, this is not so. It is important therefore to reduce the gap between the detector and the skin of the subject as far as is practicable.

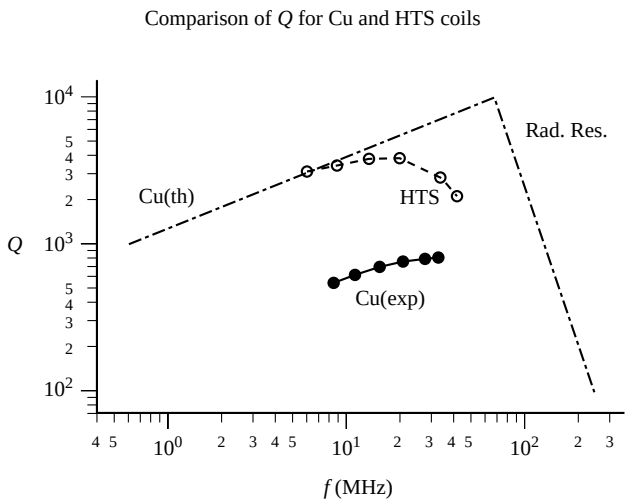

Figure 5 Approach of cooled copper (77 K) and HTSC coils to the limits set by radiation resistance. Both coils were of three turns and

The problems are, in fact, little different between nitrogen and helium temperatures from the subject's point of view. There should not be physiologically noticeable cooling of the region of the patient due to the coil in, at least, 1 h. Since coils could be used at intervals throughout the day, this means in practice that the insulation must be good enough to last for very long periods without substantial change in the outer temperature of the vessel. In practice only vacuum insulation is good enough to achieve this, while keeping an acceptably small distance between the cool coil and the outside of the cryostat. In this context most coils can be useful in tubular form to provide the passage for the refrigerant, with thermal radiation being the main source of loss. This can be reduced by making surfaces highly reflecting, and the use of layers of Mylar film vacuum-coated with aluminum.

Coils can conveniently be cooled by passing cold gases, rather than cold liquid, through them, so that a reservoir containing boiling liquid can be employed, or some other kind of refrigerator. All transfer lines to and from the coil have obviously to be insulated to the same extent as the coil chamber itself.

Since a cold environment is available preamplifiers (or the first stages of preamplifiers) can also usefully be placed in it. If a metal coil is in use, this can be used as a cold source for the preamplifier (as, for example, in Figure 1), though even just the input stage of the amplifier represents a significant heat load.

6 CONCLUSION

The use of detectors at cryogenic temperatures is of much greater interest in low-field whole body systems than in higher, as body noise is dominant in all except the lowest fields. It seems likely that the main early applications of refrigerated coils will be for microscopy and other systems involving very small samples.

7 RELATED ARTICLES

Radiofrequency Systems and Coils for MRI and MRS; Sensitivity of Whole Body MRI Experiments; Surface and Other Local Coils for In Vivo Studies.

8 REFERENCES

1. D. I. Hoult and R. E. Richards, *J. Magn. Reson.*, 1973, **24**, 71.
2. P. Styles, N. F. Soffe, C. A. Scott, D. A. Cragg, F. Row, and P. C. J. White, *J. Magn. Reson.*, 1984, **60**, 397.
3. A. S. Hall, B. Barnard, P. McArthur, D. J. Gilderdale, I. R. Young, and G. M. Bydder, *Magn. Reson. Med.*, 1988, **7**, 230.
4. A. S. Hall, N. McN. Alford, T. W. Button, D. J. Gilderdale, K. A. Gehring, and I. R. Young, *Magn. Reson. Med.*, 1991, **20**, 340
5. D. I. Hoult and P. C. Lauterbur, *J. Magn. Reson.*, 1979, **34**, 425
6. A. S. Hall, N. McN. Alford, T. W. Button, and D. J. Gilderdale, *Proc. Xth Ann Mtg. Soc. Magn. Reson. Med.*, San Francisco, 1991, p. 725.
7. R. S. Withers, G.-C. Liang, B. F. Cole, and M. Johanson, *IEEE Trans. Appl. Supercond.*, 1993, **3**, 2450
8. R. D. Black, P. B. Roemer, W. A. Edelstein, S. P. Souza, A. Mogro Campero, and L. G. Turner, *Proc. Xth Ann Mtg. Soc. Magn. Reson. Med.*, San Francisco, 1991, p. 1250.
9. W. A. Brey, Verbal Contribution to the 4th World Congress on Superconductivity, Orlando, FL, 28 June 1994.
10. S. J. Penn, N. McN. Alford, A. S. Hall, T. W. Button, R. Johnston, S. J. Zamottio, and I. R. Young, *Appl. Supercond.*, 1993, **1**, 1855.
11. H. Hojaji, S. Hu, A. Barkett, D. D. Davis, and A. N. Thorpe, *Physica C*, 1992, **195**, 135.
12. D. A. Cardwell, Cambridge University, personal communication, 1994.
13. A. S. Hall, R. Johnston, D. Gilderdale, W. A. Phillips, S. Zammattio, and I. R. Young, *Proc. XIth Ann Mtg. Soc. Magn. Reson. Med.*, Berlin, 1992, p. 4016.

Biographical Sketches

Michael Burl. *b* 1946. B.Sc., 1972, Ph.D., Westminster University (formerly PCL), 1976. First involved in NMR on joining EMI in 1977 where responsible for the first radiofrequency systems for the resistive and then a cryogenic imaging machine. Approx. 10 papers and 6 patents related to whole body NMR. Research interests: obtaining better images and spectra in vivo.

Ian R. Young. *b* 1932. B.Sc., 1954, Ph.D., Aberdeen, 1958. No involvement with NMR until joining EMI in 1976, where charged with leading the engineering group developing first a resistive, then a cryogenic machine, installed at Hammersmith Hospital in 1980–1. Approx. 150 papers and 30 patents in whole body NMR and related aspects. Research interests: obtaining better images and spectra in vivo.

Resistive and Permanent Magnets for Whole Body MRI

Frank Davies
Oxford Magnet Technology Ltd, Witney, Oxfordshire, UK

1 INTRODUCTION: ADVANTAGES OF MAGNET TYPES

Permanent magnets are the simplest source of static magnetic field, at least from the perspective of the user. Once magnetized, they require no further expenditure of energy to sustain a stable magnetic field indefinitely. Yet in many applications the limitations of the materials mean that the preferred choice is some form of electromagnet, either resistive or superconducting. MRI is an application where all three types of magnet have found a role, with each having advantages in different areas.

Superconducting magnets rely on conductors that can support current densities of several hundred amperes per square millimeter but need an expensive cryogenic system to support them and are, therefore, used for high-field applications.[1] The reason for considering resistive or permanent magnets is to avoid the cost and restrictions of magnet geometry that the cryogenic requirements of superconductivity bring. When a low field strength is acceptable, permanent magnets offer extreme reliability, while resistive magnets can achieve large working volumes more cost-effectively for the same field strength, up to about 0.2 T.

From an engineering point of view, magnets that provide fields of sufficient quality (field strength and homogeneity) for NMR experiments require more accurate design and build standards than are generally needed for electromagnetic machines. Unique design and manufacturing methodologies have been evolved in the periods since 1960 for NMR spectroscopy and since 1975 for MRI. However, the methodologies are based on conventional analysis of the physics of magnetic fields as developed in the 19th century.

2 FIELD CREATION

The flux density B in the SI system is measured in tesla (i.e., webers per square meter, $\mathrm{Wb\,m^{-2}}$, the weber being a unit of flux). The flux density in a material is related to the magnetic field intensity H by a constant characteristic of the material considered, namely, the permeability μ (in Henries per meter, $\mathrm{H\,m^{-1}}$): $B = \mu H$. Values of measured permeability μ are available for different materials: $\mu = \mu_r \mu_0$, where $\mu_0 = 4\pi \times 10^{-7}$ H m^{-1} is the permeability of a vacuum and μ_r is the relative permeability of the material. For air, μ_r is almost one, so a loose convention is to talk of the magnetic field in the working volume of a magnet in tesla.

2.1 Importance of Current Density

The magnetic field intensity generated by a current I flowing in a circular loop of wire with cross-sectional area A at a position z along the centerline of the loop of radius a [see Figure 1(a)] is given by:

$$H_z = \frac{I}{2}\frac{a^2}{(a^2+z^2)^{3/2}} = \frac{JA}{2}\frac{a^2}{(a^2+z^2)^{3/2}} \tag{1}$$

where $J = I/A$ is the current density. If the loop of conductor has resistivity ρ, power will be expended to maintain the current I, where the dissipation of power W is given by:

$$W = 2\pi\rho a J^2 A. \tag{2}$$

For electrical machines in general, the power dissipated in the winding must be removed by appropriate cooling arrangements so that the machine may operate in a stable manner at a constant temperature (with inadequate cooling arrangements,

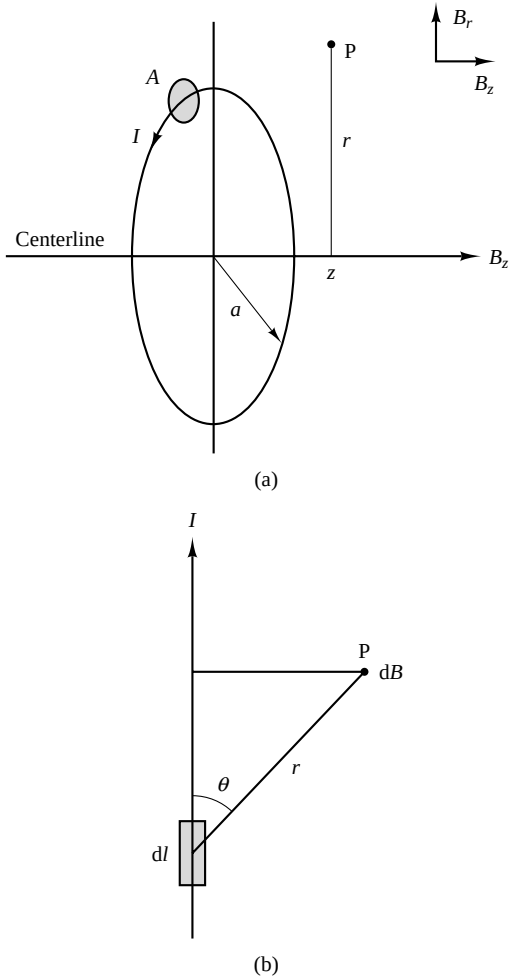

Figure 1 (a) Field of an elemental loop of current for consideration of B_z along the centerline and at point P in terms of a, z, and r. (b) Magnetic field at point P due to a current element $I\,dl$

rising temperature causes an increase in resistivity, which, at constant current density, increases power dissipation, and thermal runaway follows).

There are various possible arrangements for cooling, which usually involve deploying air or forced water circulation, that can be applied to magnets. These have been discussed by Montgomery[2] in terms of optimizing the design of resistive solenoids. Practical considerations of cooling windings limit continuous (dc) current density magnets to some 2–10 A mm^{-2} of conductor cross-section, which, in a winding large enough for whole body MRI, sets practical upper field values of 0.2–0.3 T. (Pulse magnets and Bitter magnets can reach much higher current densities, to produce very high fields up to 70 T and 20 T, respectively, but the structural characteristics of these magnets are not suitable for the production of uniform fields.)

2.2 Materials

Ferromagnetic materials, of which permanent magnets are a special class, exhibit very high permeability as a result of the ordering of atomic magnetic moments.[3] These arise from the flow of current represented by the spins of the valency electrons in the crystals comprising the material. A ferromagnetic material can be viewed for engineering purposes as an array of microscopic current loops that have a 'fictitious' equivalent current around the surface of the material. However the nonlinear relationship between this current and the applied magnetic field makes accurate design a difficult process.

A ferromagnetic material exhibits a characteristic hysteresis curve of magnetization against applied field, examples of which are shown in Figure 2. The materials are classified into 'soft' and 'hard' magnetic materials, determined by the shape of the hysteresis curve. In particular, they are distinguished by the level of reverse field intensity needed to demagnetize the material, known as the coercivity, indicated by the extreme value of H where the curve crosses the $B = 0$ axis. Soft materials, such as low-carbon steel, have coercivities below 1 kA m^{-1}, while hard materials can have values as high as 1 MA m^{-1}. These latter materials retain substantial magnetization even in the presence of strong demagnetizing fields and are consequently more commonly described as permanent magnets.

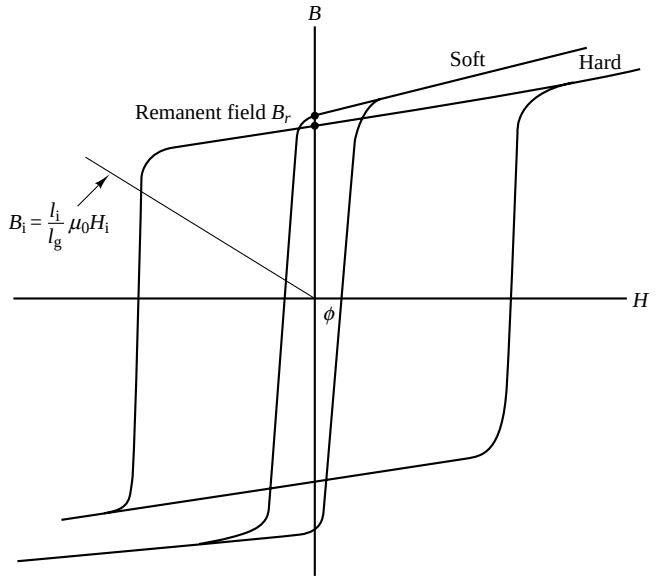

Figure 2 Hysteresis curve of magnetization versus applied field for a permanent (or hard) material, and a soft (nonpermanent but high-permeability) material, (e.g., iron). The shearing line for a simple magnetic circuit is also shown

Soft magnetic materials are of great benefit to the magnet designer in reducing the current, or the amount of permanent magnet material, required to achieve a given field intensity in a defined volume by providing a low reluctance flux return path.

3 MAGNET DESIGN

The dominant issue with magnet design is to achieve uniformity of magnetic field throughout the working volume, which for MRI has been defined by Morris[4] to be ideally better than the natural proton linewidth, i.e. 20–50 Hz or 1–2.5 ppm at an operating frequency of 21 MHz corresponding to 0.5 T. In reality, some relaxation of this requirement is possible, and commercial MRI systems look to provide homogeneity of field at 10–100 ppm of the central field over the working volume.

The exact physical position of conductors or permanent magnets is important in the magnet structure for achieving field uniformity. Inevitably, engineering tolerances for the construction plays a part in deciding the merits of particular features of a design. However, almost all magnets contain secondary arrays of coils, iron or permanent magnets whose contribution to the iron can be adjusted for fine-tuning.

3.1 Analytical Approach to Magnet Design

Any magnet design involves calculating the field created at points of interest by current sources, whether these are current paths or fictitious equivalent currents of permanent magnets, the latter being taken as magnetic moments. Computer-aided simulations are possible that calculate the field from any arrangement of sources although it is usually desirable to simplify this modeling process by such steps as using two-dimensional rotational symmetry.[1,5] Hand-calculation of all but the very simplest geometries is extremely laborious and not practical for real designs.

With reference to Figure 1(b), the Biot–Savart relation can be used to define the flux density dB for a current I flowing in an element of conductor at a point P:

$$\mathrm{d}B = \frac{\mu I \mathrm{d}l \sin\theta}{4\pi r^2} \tag{3}$$

For any continuous path, the contribution of all the elements dl can be summed to derive the total field B at any point.

Considering circular coils means that solenoidal MRI magnets can be modeled accurately, particularly when they are air-cored magnets and the current uniquely specifies the strength of each source. Simple addition of loops by straightforward computing techniques builds up the overall cross-section of each coil. In this approach, it is possible to define a desired field profile and compute the required current for each loop in the array, subsequently applying engineering criteria to limit computed currents to practical values.

Noncircular sources can be modeled using arrays of current loops to define the equivalent surface current (Figure 3a). When permanent magnets are considered, there is no particular merit in a circular source geometry, and in any case, whatever layout of magnet is envisaged, it must be built from brick size and shape permanent magnetic materials. This latter point arises because of the high temperatures and pressures used in the manufacture of permanent materials necessary to achieve high levels of magnetization. The most important problem in dealing with permanent magnets is in defining the value of the magnetization in each element of the array.

3.2 Magnetic Circuit

The difficulty of allowing the magnetization of each element to be a function of field as this affects the design process can be illustrated by considering a simple magnetic circuit (Figure 3b).[6] The flux density B_i in the material is related to the field intensity in the material H_i by the ratio of the lengths of the magnetic circuit to the air gap (l_i and l_g, respectively):

$$B_i = -\frac{l_i}{l_g}\mu_0 H_i \tag{4}$$

This demonstrates that as the gap increases relative to the magnetic circuit the available flux will decrease. The behavior of the circuit can be related to the magnetic properties of the material under consideration by plotting the demagnetization or shearing line on the (B,H) curve of the material (Figure 2). For the simple magnetic circuit, the volume of magnetic material needed for a given gap flux density B_g is given by

$$V_i = B_g^2 l_g A_g \frac{1}{\mu_0(-B_i H_i)} \tag{5}$$

This provides the useful rule of thumb that the optimum permanent magnet design is one where the maximum value of B_iH_i is obtained on the demagnetization sector of the (B,H) hysteresis curve. This maximum value is an important characteristic of a permanent magnet material and is expressed as an energy density, commonly in nonstandard units of gauss oersted (1 MGOe = 7.96 kJ m^{-3}). Complex magnetic circuits are treated by Abele.[7]

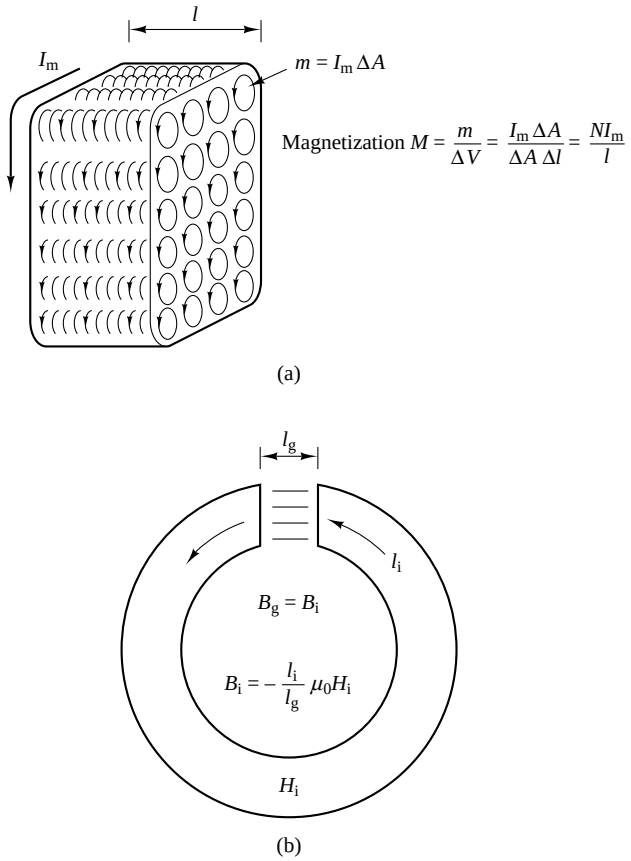

Figure 3 (a) Array of coils, to define an equivalent current surface. (b) Simple magnetic circuit

4 COMPUTER-AIDED DESIGN (MORE GENERAL DESIGN METHODS)

4.1 Finite Element Methods

Analytical expressions relating field and magnetic sources have been successful in enabling the design of NMR/MRI magnets. However, since the 1980s, the availability of low-cost computers with large processor and memory capabilities has made possible the more general approach of solving field equations using numerical methods, without recourse to analytical description of the source geometry. This approach has been summarized by Trowbridge.[8]

Considering fields that do not vary with time, the field equations used are (in vector form)

$$\nabla \times \boldsymbol{E} = -\frac{\partial \boldsymbol{B}}{\partial t} \qquad \text{(Faraday's law)} \tag{6}$$

$$\nabla \times \boldsymbol{H} = \boldsymbol{J} \qquad \text{(Ampere's law)} \tag{7}$$

where $\boldsymbol{E}$ is the electric field intensity. The material constituent properties are accounted for, as before, by $\boldsymbol{B} = \mu\boldsymbol{H}$, $\boldsymbol{J} = \rho^{-1}\boldsymbol{E}$. The expressions we shall use are in terms of potentials, since these avoid difficulties of handling discontinuities in the fields at physical boundaries. Employing the magnetic vector potential, with $\boldsymbol{B} = \nabla \times \boldsymbol{A}$, the field equation can be written as

$$\frac{\partial}{\partial x}\left[\frac{1}{\mu}\frac{\partial A_z}{\partial x}\right] + \frac{\partial}{\partial y}\left[\frac{1}{\mu}\frac{\partial A_z}{\partial y}\right] = -J_z \tag{8}$$

This equation is solved numerically by dividing the region in which the field is required into many triangular or rectangular units (for a two-dimensional case) or tetrahedrons or cuboids (for a three-dimensional case). In each unit, or element (see Figure 4), the solution of the equation is assumed to be of the form

$$A_z = \alpha_1 + \alpha_2 x + \alpha_3 y \tag{9}$$

which describes a linear variation of potential between the nodes of the triangular region.

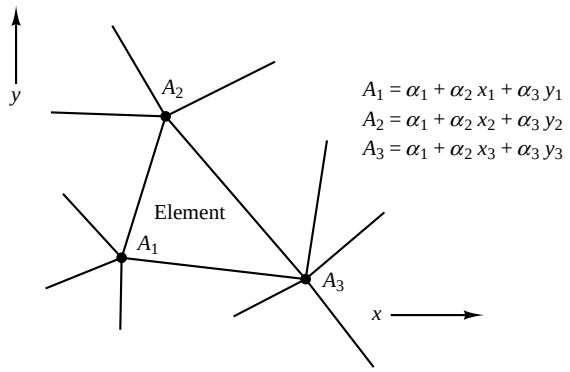

Figure 4 Field modeling by subdivision of space into finite elements

The field within each element may be defined by the value of the potential at the vertices of the triangular elements. A numerical solution is obtained by solving the equations for the elements simultaneously, which involves setting targets for the matrix of simultaneous equations. One way of doing this is to minimize the energy of the array by using variational methods and trial elemental functions. This is a powerful method for handling the nonlinear material properties because it is relatively straightforward to iterate the solution, with each successive approximation using the previous value of the field as a basis for a new estimate of the level of magnetization.

Although the finite element approach is a systematic way of replacing algebraic equations for field mapping, there are still difficulties of accuracy. These are predominantly associated with designing the mesh of elements, but boundary modeling and representing material properties are associated difficulties.

Commercial software packages are available from a number of suppliers,[5] with extensive features involving time-dependent solutions (eddy currents) and automatic mesh generation. Other numerical approaches are possible, involving integration over active boundaries that have been divided into a mesh in terms of the magnetic scalar potential.

4.2 Shimming (Focus on Accurate, Special Solutions)

The procedure for obtaining fine control of the field profile is to build weak arrays of magnets that can be controlled in strength independently of the main magnet. Small adjustments to errors in the main field of the magnet can be achieved—either by changing the current strength of elements in the shim array or by changing the position of permanent magnets. In this latter context, ferromagnetic materials that are magnetized in the main field of the magnet are practically useful, and develop high levels of magnetization.

The process of calculating how much shimming material to add, and in which locations, involves sampling the magnetic field at a large number of points in the working volume and then solving the equation $\boldsymbol{Ax} = -\boldsymbol{B}$, where $\boldsymbol{B}$ is the array of field errors at the measurement points, $\boldsymbol{x}$ is the unknown array defining the amount of shim material needed at each possible location, and $\boldsymbol{A}$ is a sensitivity matrix relating the two. In practice the values of $\boldsymbol{x}$ are constrained to a limited number of discrete values, so a complex optimization algorithm is required to achieve a satisfactory solution.

5 EXAMPLES OF MRI MAGNETS

The low-field limitation of permanent and resistive magnets has traditionally led to them being viewed as low-cost systems of modest performance, which resulted in their playing a minor role in the development and spread of MRI. However the dominance of high-performance superconducting systems has been challenged in the late 1990s by a number of designs that provide a dramatic improvement in the openness and accessibility of the field.

5.1 Resistive Magnets

The major concern with any resistive magnet is the stability of the field. This is directly linked to the stability of the current control system in the power supply but is also dependent on the cooling system, since any change in temperature will result in a sufficiently large change of dimension, through thermal expansion, to disturb the central field.

5.1.1 Air-Cored Solenoids

The very first whole body system used for MRI was an air-cored solenoid and a number of examples were built during the early years. A typical configuration is a four-coil assembly operating at 0.15 T as shown in Figure 5. The exposed structure did not create a very friendly appearance, but at least the open space between the coils was some compensation for the small bore size. Despite this limitation on size, the power dissipation was extremely high, and the systems suffered from relatively poor stability and homogeneity. They were rapidly overtaken by the development of superconducting magnets, and production of these early magnets ceased in 1984.

A small number of air-cored solenoids continue to be manufactured. With better mechanical stability and improvements in power supply technology, they offer a cheap alternative at very low fields.

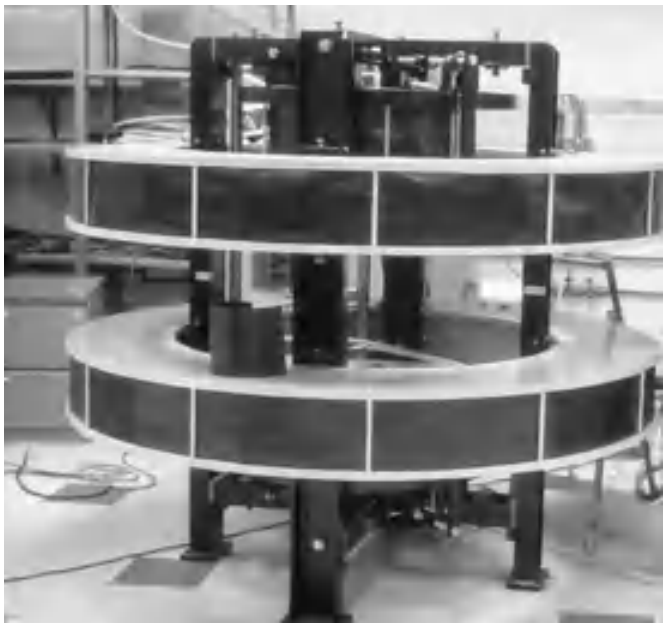

Figure 5 Air-cored, four-coil resistive magnet

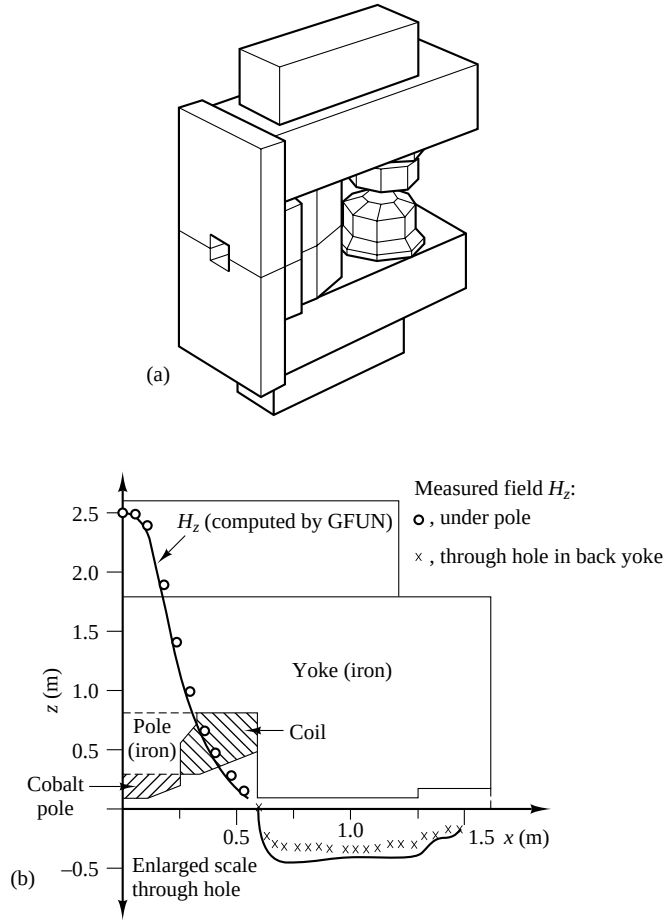

Figure 6 CAD design of a C magnet (a), with field profile predicted by finite element methods compared with measured results (b). (From Binns et al.,[5] with permission)

5.1.2 Resistive Iron Magnets

The combination of resistive coils and iron yoke has been used for generating and shaping magnetic fields since the magnetic effect of electric currents was first discovered.

An early version of the resistive/iron C magnet was used for particle physics experiments, and the design process using CAD techniques was refined by comparing predicted and measured performance (Figure 6). However, it has only recently been developed to provide a practical MRI system with the advantage of a much greater freedom of choice of system geometry.

The advantages of this system derive from the use of cheap materials and simple processes, with simple coils to generate the field, and iron to guide the magnetic flux and control the shape and homogeneity of the imaging region. The iron yoke makes the magnetic circuit design efficient, unlike the air-cored solenoid, and a large patient gap can be provided with only modest power dissipation and low stray field. The use of iron does, however, result in a relatively heavy system—comparable with permanent magnet designs. Nevertheless, the possibility of extremely open designs, such as the 'C' shape, make this combination attractive.

An MRI system based around a resistive C magnet is shown in Figure 7. A pair of water-cooled coils wound from aluminum strip is fitted to the yoke, one around each leg to maintain symmetry. Together they dissipate around 17 kW to generate a central field of 0.2 T. The total weight is around 11 tonnes.

The use of resistive coils rather than permanent magnet material for generating fields has significant advantages during construction and installation, since these can be performed without the hazards presented by a strong magnetic field. They allow the magnet to be shut off rapidly in an emergency, a feature that is not possible in a permanent magnet.

The stability of the magnet is of course controlled by the power supply, which in this case uses a state-of-the-art current sensor to maintain the current stable to 1 part in 10^7. The sensor employs a fluxgate magnetometer to sense the magnetic field generated by the current flowing in a supply lead. Thermal stability (and hence dimensional stability) is assured by precise temperature control of the coil cooling system.

The pole faces defining the patient space are specially shaped to provide adequate homogeneity of the magnetic field while maximizing the gap and minimizing the pole diameter. The conductivity of iron in these pole regions can result in interactions with pulsed gradient coil fields, and measures have to be taken to reduce the resulting field disturbances. The shimming system is also mounted on the pole faces and uses small permanent magnet tokens to correct for local field errors, though additional resistive coils could also be used.

5.2 Permanent Magnets

Permanent magnets are constructed by preparing blocks of the magnetic material that are magnetized in the appropriate

Figure 7 OPEN VIVA: MRI resistive C magnet. (Photograph courtesy of Siemens AG)

direction before being forced into position in the assembly and glued in place. Although the field stability is good, the materials do exhibit marked sensitivity to temperature; consequently, all practical MRI magnets involve considerable attention to ensuring constant temperature operation.

5.2.1 Ferrite

Early examples of permanent magnets for whole body MRI were based on ferrite building blocks. The most notable examples were supplied by Fonar Corporation but suffered from the disadvantage of being extremely heavy. This was a direct consequence of the low energy density, and the need for an efficient yoke to complete the magnetic circuit. Figure 8 shows some of the designs of permanent magnet in schematic cross-section.

More recent samples have used the so-called 'magic ring' design, usually implemented in octagonal form. This has the advantage of being very efficient magnetically but suffers from the disadvantage of a long fully confined tube for the patient, so having all the disadvantages of a superconducting solenoid with none of its performance advantages. Magnets of this type have been produced by Field Effects and Asahi. Typical performance figures show ±20 ppm homogeneity on a 36 cm sphere at 0.2 T from a magnet weighing less than 9 tonnes. The latest variants of this design feature an elliptical cross-section to accommodate the patient more efficiently.

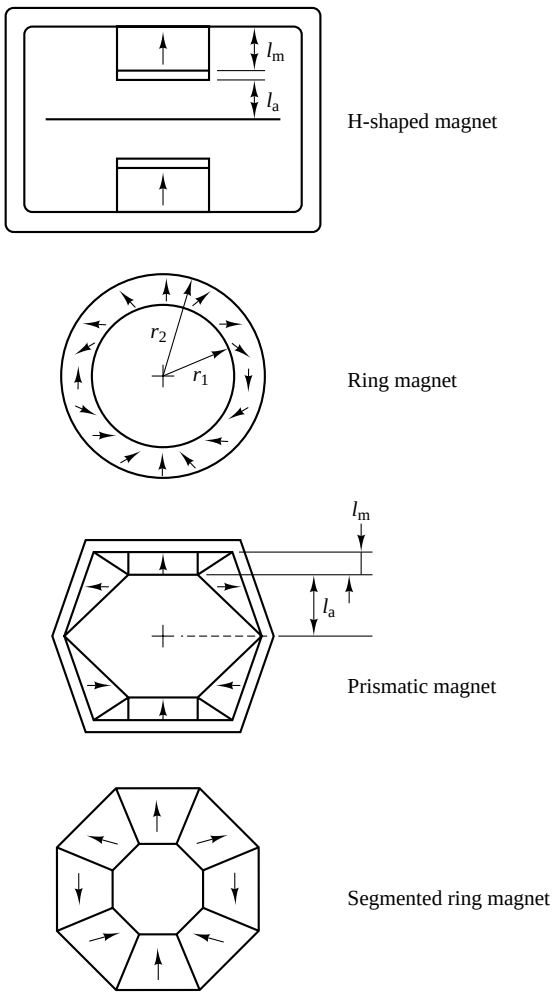

Figure 8 Schematic cross-sections of permanent magnet structures

As with all magnetically efficient designs, the stray field external to the magnet is very small, but the stability of the central magnetic field is very sensitive to temperature. A temperature-control system is frequently necessary, though good thermal insulation may be adequate if the room itself has a reasonable temperature control. Ferrite is an attractive material because of its sintered form, which results in inherently low conductivity. This minimizes problems that can arise from eddy currents induced by rapidly switched gradients.

Shimming of these magnets to yield the optimum homogeneity is relatively straightforward. It can be accomplished by a set of specially shaped low-power resistive coils surrounding the patient aperture, each with its own independently adjustable power supply. An alternative shimming method is adjustment of the permanent magnet material itself, either by mechanical adjustment of the main field-generating blocks or by the addition of small magnetized tokens to reduce the local distortions of the field. Generally, a combination of methods will be employed for maximum performance.

5.2.2 Neodymium–Iron–Boron

The development of this high-energy material, first produced in 1982, has allowed a fresh look at permanent magnets. Although it is relatively much more expensive than ferrite, the fact that it can provide more than 10 times higher energy density means that much less material is needed, allowing magnets of 0.3 T to be built at reasonable cost and weight. Unlike ferrite magnets, where the bulk of the magnetic circuit is built out of the permanent magnet material, the Nd–Fe–B is usually contained in a simple structure, such as thin disks, mounted to a soft iron frame. The usual configuration is an 'H' or 'four-poster' design with two large disks of permanent magnet material mounted just behind the pole-faces.

The most widely used magnet of this type is manufactured by Sumitomo Special Metals (who developed the material) for use in the Hitachi Airis system shown in Figure 9. An unusual feature of this design is that the return path through the iron yoke takes the form of two compact columns that are displaced backwards from the centerline. This provides a more open access for the patient, very similar to the 'C' design, but without sacrificing all of the improvement in mechanical stability that comes from using the 'H' design.

A central field of 0.3 T can be achieved with around 2 tonnes of Nd–Fe–B alloy out of a total weight of about 12 tonnes, depending on the size of the patient gap.

With the permanent magnet material occupying a relatively small part of the structure, the properties of the iron used for the remainder have a significant effect on the system characteristics. Interactions between the pulsed gradient coil fields and the iron in terms of both hysteresis and eddy current effects can become significant, and the usual practices of sintering or laminating the material in the regions of changing fields become important.

The properties of Nd–Fe–B would allow its use in magnets of even higher field, but this is precluded by its relatively high cost. This is partly owing to the cost of the rare-earth raw material and partly owing to the complex processing involved, requiring the alloy to be ground into a powder, pressed to shape in the presence of a magnetic field and then sintered, all

Figure 9 AIRIS II: high-performance premium open MR system. (Photograph courtesy of Hitachi Medical Systems America, Inc.)

in an inert atmosphere. These high costs allow superconducting magnets to be competitive, despite the cost of the cryogenic system. Furthermore, as cryogenic technology develops, especially closed-loop refrigerators that allow magnets to operate without cryogenic liquids, the boundaries of competition between the different technologies are becoming blurred.

6 RELATED ARTICLES

Cryogenic Magnets for Whole Body Magnetic Resonance Systems; Low-Field Whole Body Systems.

7 REFERENCES

1. J. Evetts, ed., 'Concise Encyclopaedia of Magnetic and Superconducting Materials', Pergamon Press, Oxford, 1992.
2. D. B. Montgomery, 'Solenoid Magnet Design', Wiley-Interscience, New York 1969.
3. D. Jiles, 'Introduction to Magnetism and Magnetic Materials', Chapman & Hall, London, 1991.
4. P. G. Morris, 'Nuclear Magnetic Resonance Imaging in Medicine and Biology', Clarendon Press, Oxford, 1986.
5. K. Binns, P. Lawrenson, and C. W. Trowbridge, 'The Analytical and Numerical Solution of Electric and Magnetic Fields', Wiley, New York, 1992.
6. M. A. Plonus, 'Applied Electromagnetics', McGraw-Hill, New York, 1978.
7. M. G. Abele, 'Structure of Permanent Magnets', Wiley, New York, 1993.
8. C. W. Trowbridge, in 'Concise Encyclopaedia of Magnetic and Superconducting Materials', ed. J. Evetts, Pergamon Press, Oxford, 1992, p. 114.

Biographical Sketch

F. Davies. *b* 1949. M.A. 1974, Oxford. Joined Oxford Magnet Technology in 1983 after working in unrelated industries on the development of design tools and production processes. Director of Research leading team designing superconducting and resistive magnets 1992–present.

Surface and Other Local Coils for In Vivo Studies

James S. Hyde
Medical College of Wisconsin, Milwaukee, WI, USA

1 INTRODUCTION

Radiofrequency (rf) coils for MRI and magnetic resonance spectroscopy (MRS) can be classified as (1) transmit–receive, (2) transmit only, and (3) receive only. Transmit–receive coils are almost always either of the birdcage type,[1] with the axis of the coil parallel to the static magnetic field, or solenoidal,[2] with the axis transverse to the static field. A transmit–receive switch connects the coil during excitation to an rf power amplifier and during reception to a low noise preamplifier. Transmit–receive coils can be optimized for particular anatomic structures, i.e. whole body, head, knee, fingers, etc. Transmit-only coils are nearly always of the same type as transmit–receive coils, but are seldom optimized to a specific anatomic structure. Typically, they are whole body. Receive-only coils detect the signal produced by a transmit-only coil. Because receive-only and transmit-only coils are tuned to the same frequency, special provision must be made to decouple the receive coil from the transmit coil during excitation. It is also desirable to decouple the transmit coil during reception. This article is concerned with transmit–receive coils for specific applications (i.e. fingers) and with receive-only coils. The presentation is in the context of MRI.

The central principle of local coils is the reciprocity theorem.[3] If unit rf current is introduced into a matched local coil that is placed on or around an object of interest, an rf magnetic field is produced in the object. The magnitude of those components of the field that are perpendicular to $\boldsymbol{B}_0$ at a point in space is a complete and sufficient measurement of the relative sensitivity of that coil when used as a receiver. One speaks of the 'vector reception field' in implicit recognition of the reciprocity theorem, when discussing the spatial variation of the sensitivity of a local coil. Figure 1 shows a surface coil placed on a test tank containing 0.1 M saline. A small probe is placed in the tank, as illustrated. Relative performance of a series of coils can be tested on the bench by successively introducing unit current into each matched coil and moving the pickup coil around in space and orientation in order to plot the field. The region of sensitivity (ROS) of each coil can be determined by plotting iso-contours of constant magnitude of the components of the vector reception field that are perpendicular to $\boldsymbol{B}_0$. Alternatively, and fully equivalent, current can be introduced into the pickup coil, which then becomes the transmitter. If this coil is rotated to give maximum signal at each point in space, the vector reception field can also be determined, i.e. the magnitude of the induced signal in the surface coil under test as a function of the position and orientation of the small transmit or pickup coil.

Local coils are usually close to match, and noise is generated in an ideal system that is the same as that of a 50 Ω resistor. This noise is called thermal, Brownian, or Joulean—all synonyms. The noise contributed by the preamplifiers is usually included in the thermal noise.

In an ideal scanner, thermal noise would dominate. In our laboratory, we use the term 'system noise' to refer to noise from static phantoms that is in excess of thermal noise. There are many causes of system noise. Thermal noise has a normal or Gaussian distribution, whereas system noise does not. In living systems, additional noise is generated by pulsatile motion of blood, displacement of tissues because of pulsatile blood flow, respiratory motion, involuntary tissue pulsations, and, possibly, gross subject motion. This noise has recently been discussed in the context of functional MRI using echo planar imaging (EPI).[4–6] It is physiological in origin and has been called 'physiological fluctuations'. It is, in fact, signal rather than noise, since it is spatially encoded in EPI sequences. If physiological noise dominates and is spatially uniform, one would expect the ratio of anatomic signal to physiological noise to be independent of voxel dimensions. There ought to exist a crossover at sufficiently small voxel size where thermal noise dominates, but no experiments have yet been published at this level of detail. In the remainder of this article, it is assumed that thermal noise dominates system and physiological noise, but the reader is cautioned that this may not be true in the real world.

The fundamental equation for the signal-to-noise ratio (S/N) as given by Abragam[7] is valid for local coils:

$$\psi = \frac{\pi}{f}\left[\frac{1}{2}\eta\left(\frac{\nu}{\Delta\nu}\right)Q\chi_0\left(\frac{\chi_0 H_0^2 V_s}{kT}\right)\right]^{\frac{1}{2}} \qquad (1)$$

where f is a factor that takes into account all additional noise of the apparatus, ν is the rf, $\Delta\nu$ is the receiver bandwidth, Q is the quality factor of the receiver coil, χ_0 is the static susceptibility, H_0 is the static field strength, and V_s is the volume of the sample. The filling factor η is given by the expression:

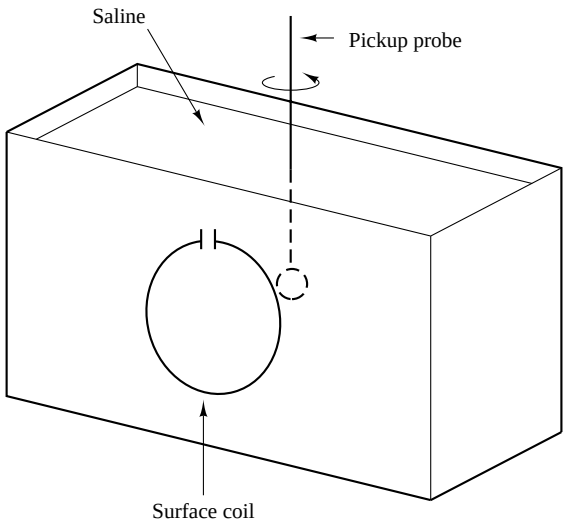

Figure 1 Bench setup for testing local coil performance

$$\eta = \frac{\int_{\text{sample}} B_1^2 \sin^2 \phi \, dV}{\int_{\text{all space}} B_1^2 \, dV} \quad (2)$$

where $\boldsymbol{B}_1$ is the rf field produced by unit current in the rf coil, and ϕ is the angle between the static field and the vector reception field. Inclusion of the $\sin^2 \phi$ term is a special feature for surface coils because of the highly curvilinear nature of the vector reception field; ϕ is normally set to 90° in discussions of high-resolution NMR probes.

The extensions of equation (1) by Hoult and Richards are helpful.[3] However, these fundamental papers were concerned with high-resolution NMR. The thermal noise generally arises from resistive losses in the rf coil in NMR of organic compounds in solution. In MRI, thermal noise arises from eddy currents associated with ionic conductors in the body. Furthermore, the sample size cannot be conveniently changed in MRI in order to alter the ratio of contributions to thermal noise from the body and the coil. The treatments given by Hoult and Richards[3] and Abragram[7] remain rigorously correct, but not necessarily convenient in considering issues of S/N in an MRI context. For a further discussion of these aspects, see Froncisz et al.[8]

2 SURFACE COIL FUNDAMENTALS

2.1 Dominant Loading

Equation (1) shows a dependence of the S/N on $Q^{\frac{1}{2}}$. The quality factor Q can be defined as:

$$Q = 2\pi\nu \frac{P_0}{K} \quad (3)$$

where P_0 is the incident power, and K is the energy loss per cycle. We can divide the energy loss per cycle into loss in the body because of eddy currents K_{body}, and energy loss in the coil because of coil resistance K_{coil}, and define

$$Q_{\text{body}} = 2\frac{P_0}{K_{\text{body}}} \quad (4a)$$

$$Q_{\text{coil}} = 2\frac{P_0}{K_{\text{coil}}} \quad (4b)$$

It follows that

$$\frac{1}{Q} = \frac{1}{Q_{\text{body}}} + \frac{1}{Q_{\text{coil}}} \quad (5)$$

Here Q_{coil} is the quality factor that would be experimentally measured with the coil in free space, Q is experimentally measured with the coil on the body, and Q_{body} is a theoretical quantity to be calculated using equation (5). (Sometimes Q is called Q_{L}, the loaded Q, because the coil is loaded by the body. This is technically incorrect. In the engineering literature, Q_0 is the Q value in the absence of any coupling to a transmission line and Q_{L} is the Q value when the coil is matched. For details, see Ginston.[9] The MRI literature is not consistent on this point.)

For a given coil geometry, Q_{body} is fixed. Since signal goes as $Q^{\frac{1}{2}}$, Q_{coil} should be made as high as possible by careful attention to construction details if $Q_{\text{body}} >> Q_{\text{coil}}$. Conversely, if $Q_{\text{body}} << Q_{\text{coil}}$ it does not much matter how the coil is built. A general rule of thumb is to strive in coil construction to satisfy the condition that $Q_{\text{body}} < \frac{1}{4}Q_{\text{coil}}$, which would result in a less than 10% loss in S/N relative to a perfect (i.e. superconducting) coil. The general principle is to arrive at dominant loading by the body. Dominant loading becomes easier to achieve as the rf increases and more difficult to achieve as the coil dimensions decrease.

The frequency dependence of Q_{body} is a difficult subject that has not been investigated extensively. The ion mobility is frequency and tissue dependent, as is the complex dielectric constant. It seems unlikely that Maxwell's equations could be solved in any realistic computation for the human body, even if these quantities were known. Actual experimental measurements for every coil geometry at the field strength of interest are required.

Loading by the body also causes shifts in resonant frequency. There are two effects: shifts down in frequency because of radiofrequency electric fields in the body from voltage potentials in the coil, and shifts up in frequency because of inductive properties of the body. Downward shifts can be minimized by use of distributed capacitors, and adjustment of the number of capacitors to cancel frequency shifts is possible.

2.2 Crossovers

Figure 2 shows sensitivity data[10] obtained using the test setup shown in Figure 1. Figure 2(a) shows on-axis sensitivity in free space and Figure 2(b) shows the sensitivity in a 0.1 M saline solution for a series of circular coils of various diameters. Small coils are always better than large coils close to the surface. Quantitatively, one would expect large coils to be better than small coils at great depth, and this is clearly seen in Figure 2(a) for free space. For any pair of coils of different diameter, a crossover exists where the coils have the same sensitivity. This point occurs at the 'crossover' depth. In saline, crossovers are much less pronounced [Figure 2(b)]. A conclusion is that for any imaging problem using a surface coil, one should use the smallest possible coil, noting that fields off-axis fall off more rapidly with small than with large surface coils. We are led to the principal theorem of surface coil usage. One should match the ROS of the coil to the anatomic region of interest (ROI). This theorem is patently valid close to the surface, but seems also, from Figure 2(b), to be true at great depth.

A second class of crossovers exists: the depth at which the surface coil sensitivity equals the sensitivity of a whole volume coil. Estimates of head and whole body sensitivities at 1.5 T are indicated in Figure 2. As a rough guide, surface coils are better than quadrature birdcage coils at depths closer to the surface than 6 cm with a head coil and 8 cm with a body coil.

2.3 Decoupling

Surface coils and transmit coils are resonant circuits tuned to the same frequency and in close proximity. Decoupling of a surface coil from the transmit coil is essential. Electrical breakdown can occur, and skin burns are possible if decoupling is inadequate.

The simplest type of decoupling, conceptually, is called 'geometric'. In early MRI scanners, transmit fields were line-

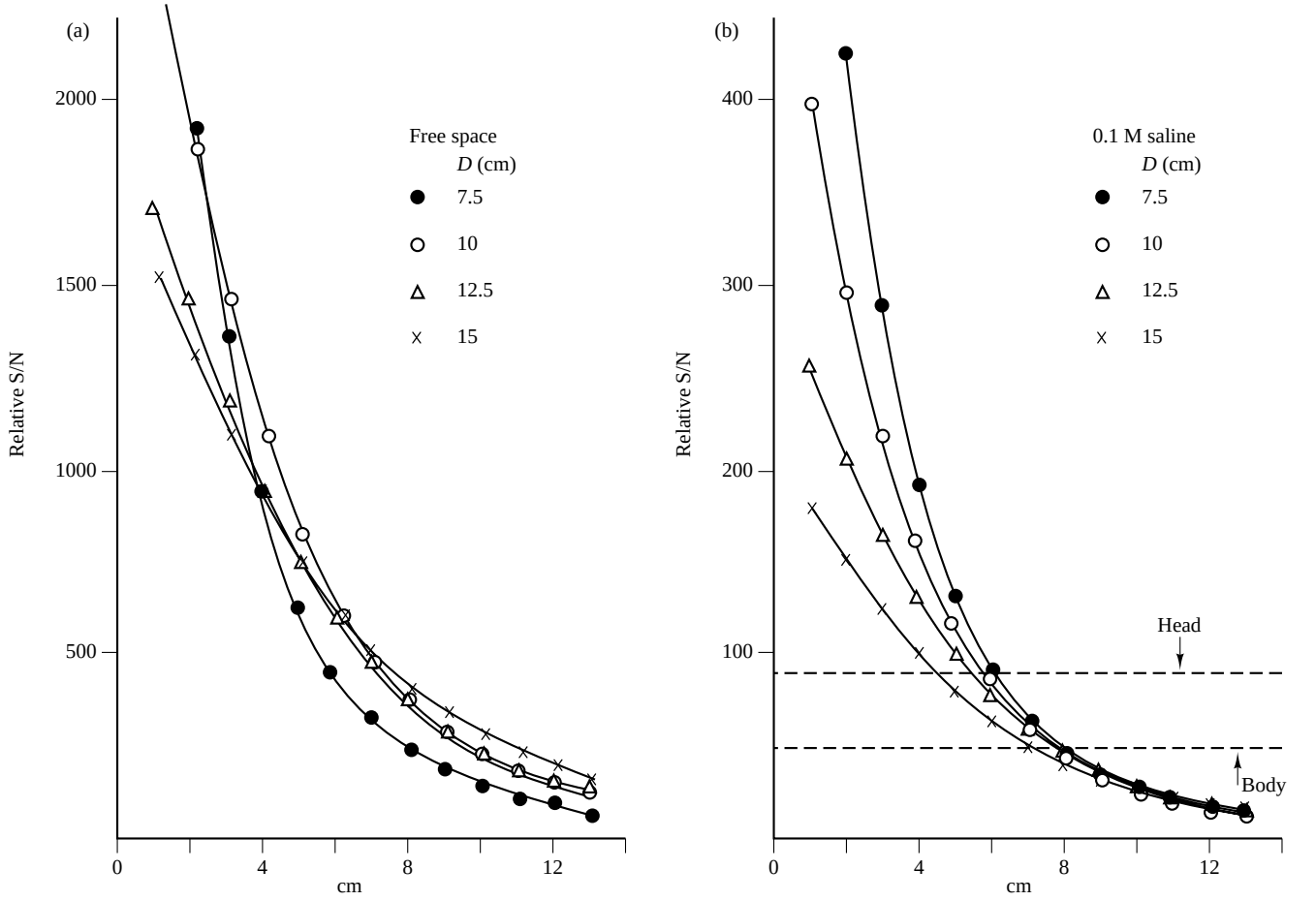

Figure 2 On-axis sensitivity of one-turn circular coils of various diameters (a) in free space, and (b) using the bench setup shown in Figure 1. Head and body coil sensitivities in (b) are estimates

arly polarized. The first surface coils were planar and oriented such that the lines of magnetic flux from the transmit coil were parallel to the coil surface. That is, with z along the bore, x horizontal, and y vertical, if the transmit field is along x, a geometrically decoupled surface coil must lie in the xz plane.

There remains a possibility for geometric decoupling even with quadrature excitation: planar coils can be placed in the xy plane. However, components of the vector reception field that are parallel to the static field will be MRI inactive. Geometric decoupling is never used alone in modern setups because of risk to the patient. It may, nevertheless, be useful in some circumstances in concert with other decoupling strategies.

Edelstein describes active decoupling circuits and passive decoupling circuits.[11] The general idea is to use diodes to detune the receive coil during transmit. The diodes are switched with a voltage pulse from the scanner in active decoupling, and by the rf pulse itself in passive decoupling. Several strategies are possible, but decoupling by pole insertion is the method of choice (see Figure 3). An infinite impedance resonant pole is switched into the receiver coil circuit when the diodes fire, and no current flows in spite of the substantial electromotive force (emf) that occurs because of the transmit field. Active decoupling circuits are favored in most commercial surface coils. Passive decoupling can be more convenient for academic researchers. For more details on passive decoupling, see Hyde et al.[12] It is noted that with small tip angle sequences, active decoupling is favored over passive.

Decoupling can also be achieved by the use of surface coils that are intrinsically isolated by symmetry from any transmit coil which has a uniform field. Intrinsic isolation involves the

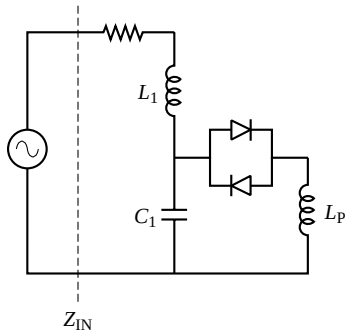

Figure 3 Passive decoupling circuit. During receive, the back-to-back diodes are open and resonance occurs at $\omega^2 L_1 C_1 = 1$. During excitation, the emf in the loop causes the diodes to close. If $L_p = L_1$, an impedance pole occurs at ω, and current no longer flows

use of pairs of surface coil loops organized such that the emf induced in one loop during transmit is equal and opposite to the emf in the other loop, and no current flows.[8,10] One can say that the mutual inductance between the transmit coil and the intrinsically isolated surface coil is zero. There are a number of symmetries where this condition is satisfied. Intrinsic decoupling was pioneered in the author's laboratory, but is now seldom used except in concert with active or passive decoupling. Research continues into properties of surface coils that have different symmetries, but passive or active decoupling is usually preferred even when using a coil that, in principle, possesses the intrinsic isolation property.

2.4 Coupling

The surface coil must be coupled to a transmission line, and two methods are possible: capacitive and inductive. In either case, the coupler serves to transform the impedance of the coil to that of the transmission line, thereby achieving the 'impedance match' condition.

Capacitive coupling provides a convenient means to introduce a voltage to switch a diode in order to decouple a coil, and is therefore preferred in commercial surface coils when active decoupling is employed.

Inductive coupling[13] is accomplished by flux linkage between the surface coil and a loop that terminates the transmission line. Since there is no dc pathway to the resonator, either passive decoupling is required or additional wires must be brought to the coil. A particular advantage of inductive coupling is that the surface coil is free floating with respect to the grounds of the scanner and is, therefore, said to be electrically 'balanced' with respect to the patient.

Safety hazards exist because of rf standing waves in the cable connecting the surface coil. Burns have been reported. This cable should be positioned carefully and should never be looped. Use of a balun can reduce this class of problems.

2.5 Tuning and Matching

Whether to tune-and-match or plug-and-go was a hotly debated question in the early days of MRI. It seemed self-evident that the resonant frequency of the coil should correspond precisely with the Larmor frequency, and the impedance match condition should be satisfied in order to achieve best performance. But, this required valuable scanner and technologist time, and it was suggested that use of a surface coil with fixed tune-and-match (i.e. plug-and-go) might be a practical compromise.

This question was addressed experimentally by Hyde et al.,[14] who made provision for remote tuning and matching in order to measure the S/N carefully without touching the coil setup. The conclusion is that the S/N is not very sensitive to match, and is somewhat sensitive to tuning. In fact, we were surprised: plug-and-go coils are an acceptable solution. The improvement in S/N by tuning and matching is modest. Nevertheless, in the author's laboratory, we always tune and match. Requirements for tune-and-match are greater with high Q than low Q coils. For example, a spine coil is very heavily loaded with a Q less than 50; a finger coil may be lightly loaded with a Q of 200. The latter probably should always be tuned and matched.

2.6 Summary of Fundamentals

1. Match the ROI to the ROS. Additionally, one should match the scanner field-of-view (FOV) to the ROI in order to avoid aliasing:

$$\mathrm{FOV} \simeq \mathrm{ROI} \simeq \mathrm{ROS} \tag{6}$$

2. Strive to satisfy the dominant loading condition:

$$Q_{\mathrm{body}} \ll Q_{\mathrm{coil}} \tag{7}$$

3. The crossovers determine coil selection.
4. Tune-and-match when $Q_{\mathrm{body}} > 100$. Check tuning of plug-and-go coils periodically.
5. Consider coupling and decoupling methods carefully, with patient safety in mind.

3 LOCAL COIL CLASSES

A classification system of local coils, namely surface, partial volume, whole volume, intracavity, and coil arrays, was introduced by Kneeland and Hyde,[15] and is adopted here.

3.1 Surface Coils

Simple loops can be either single turn or multiple turn. If the dominant loading condition is satisfied, single-turn loops are preferred because of the more convenient use of distributed capacitors. For surface coils smaller than 2 or 3 cm, the use of multiple-turn coils may be desirable simply to increase the inductance in order to bring capacitive values into the 100 pF range.

The license-plate geometry (Figure 4) is a rectangular configuration used for spine imaging. This figure permits introduction of the concept of the vector reception field of a current segment. Consider first the current segments in the coil shown in Figure 4 that are parallel to the static field $\boldsymbol{B}_0$. The lines of flux lie in xy planes and, therefore, are always perpendicular to the static field. On the other hand, the current segments at the ends of the coil are perpendicular to $\boldsymbol{B}_0$, and the lines of flux are in yz planes. Positions exist in space where they are parallel to z, and 'black holes' in the image occur at these points. The locus of black holes is seen readily in a sagittal midline slice. They begin at the surface near the wires at each end and curve upward and outward. Black holes restrict the useful ROS of the coil. A current segment parallel to $\boldsymbol{B}_0$ is more useful than a current segment perpendicular to $\boldsymbol{B}_0$. This is because currents in both parallel and perpendicular segments make the same deleterious contribution to Q_{body}, but the z com-

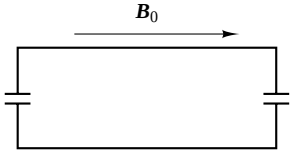

Figure 4 License-plate geometry used for spine imaging

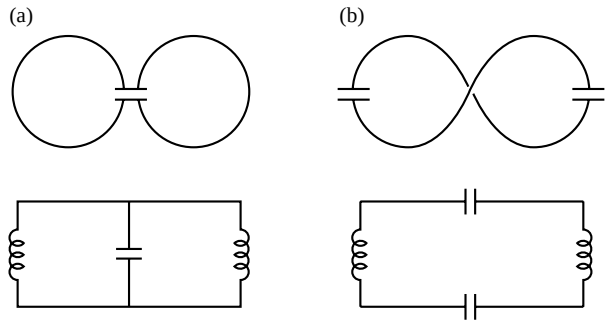

Figure 5 (a) Planar pair and (b) figure-of-eight, with equivalent circuits

ponent of the field associated with a perpendicular element gives no signal.

A surface coil can be placed 'on-edge'. We imagine a square loop with one edge against the body and parallel to $\boldsymbol{B}_0$. We have called this configuration 'remote current return' (RCR). It is difficult to achieve the dominant loading condition at 1.5 T, but at very high fields (3–4 T) such configurations may be useful.

The planar pair[10] and figure-of-eight coils (Figure 5) have the same vector reception fields. The equivalent circuits show that the planar pair and figure-of-eight have two loops in parallel and in series, respectively. A map of the vector reception fields is shown in Figure 6. We have found this class of surface coils to be useful in many different imaging problems, including, in particular, as one member of a quadrature surface coil (see below).

The so-called counter rotating current (CRC) coil (Figure 7) introduces a new surface coil concept: that of resonant modes.[8] As can be seen in Figure 7, the two coaxial loops exhibit a strong mutual inductance that splits the resonant frequency of the mode where both current directions are the same from that of the mode where they are antiparallel. Both modes can be used simultaneously, for example, for ^{1}H and for ^{31}P spectroscopy, adjusting the separation of the loops and capacitor values as required.

At high fields, the CRC coil works about as well as a surface coil of the same dimensions. The filling factor [equation (2)] is very poor—most of the stored energy is remote from the body. One might think, from equation (1), that the sensitivity would suffer. However, Q_{body} is correspondingly higher and the ηQ product is unchanged [see equation (1)]. The concept of the filling factor is not very useful in MRI surface coil design, so long as the condition of dominant loading is satisfied. CRC coils require dominant loading; they work well at 1.5 T and above, but are less satisfactory at 0.5 T.

3.2 Partial Volume Coils

In this class of coils, the coil geometry is no longer planar, but has a curved surface that conforms more closely to the contours of the body. The fundamental debate in the design of coils of this type is whether to make mechanically rigid coils

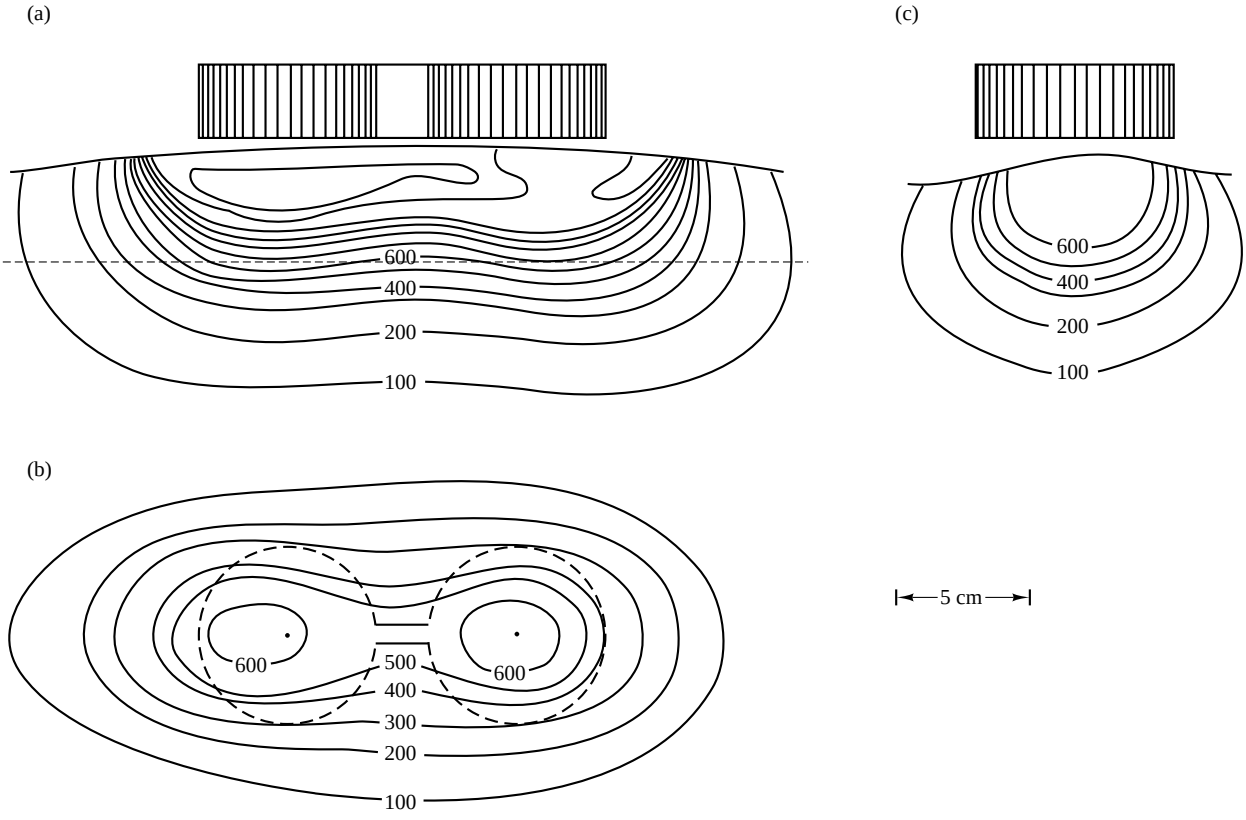

Figure 6 Map of vector reception fields of a planar pair coil using the test setup shown in Figure 1. The planes for plots (a) and (c) pass through the midline of the resonator. The plane of plot (b) is 4.5 cm from the surface of the coil [dotted line in (a)] and orthogonal to the midline

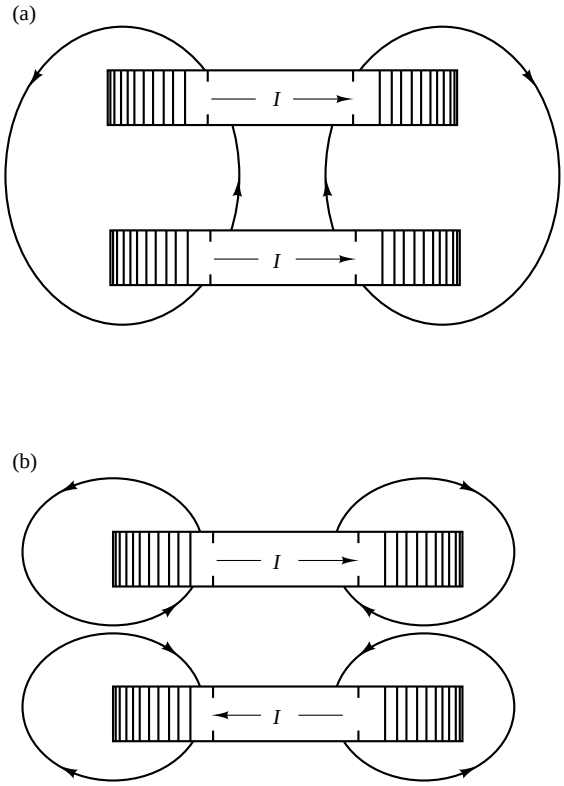

Figure 7 Counter rotating current coil, exhibiting two modes: (a) fundamental or low-frequency mode; (b) high-frequency mode. Arrows indicate the relative directions of current flow at some arbitrary moment in time

that conform, for example, to the anatomy of interest of some substantial fraction of the population, or to make flexible coils that conform to essentially everyone. Rigid coils are more rugged and the rf properties do not change; flexible coils have more variable rf properties and tend to experience mechanical failures. Images obtained with flexible coils can be both better and worse than images obtained with a similar rigid coil. To the author's knowledge, no information exists, beyond these rather qualitative comments, which can be used to compare rigid nonplanar coils and flexible coils.

The butterfly coil (Figure 8) has been adapted for cervical spine as well as lumbar and thoracic spine imaging. This coil has a number of free parameters, including individual loop geometry, angle of loops, and separation of loops. These free parameters permit optimization to the anatomy of interest. A cervical spine coil of this type was in commercial production for a time, but it is no longer available. Radiologists in our institution continue to favor it when very high quality images are required in well-defined regions of the cervical spine.

3.3 Whole Volume Coils

The classic whole volume coil is the birdcage (see ***Birdcage Resonators: Highly Homogeneous Radiofrequency Coils for Magnetic Resonance***). Consider a continuum of current elements parallel to the axis on the surface of a cylinder. If the currents in these elements vary sinusoidally with one full cycle,

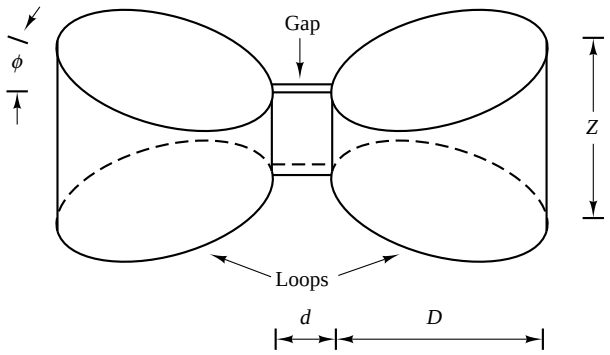

Figure 8 Butterfly coil. Parameters ϕ, d, and D can be adjusted to shape the vector reception field. This coil exhibits the property of geometric isolation for the component of the excitation field that is along the x direction, and intrinsic resolution for the y component. The vector reception field is very similar to that of a planar pair with the same value of d and D that is folded by angle ϕ, although the parameter Z does permit some shaping of the field

it has been known for many years that a uniform transverse field will be produced. The breakthrough in Hayes's work was to arrive at a practical way to accomplish this objective at radiofrequencies.[1]

A few comments concerning birdcage geometries may serve to supplement the detailed article by Hayes. A Helmholtz pair [Figure 9(a)] consists of two circular loops on an axis with a separation equal to the radius. Theoretically, the rf field is uniform along the axis of the loops. If, instead of circular loops, the loops are rectangular with the long elements parallel to $\boldsymbol{B}_0$, a saddle coil is obtained [Figure 9(b)]. Figure 9(c) shows a six-element birdcage coil. No current flows in two of the elements in the linear mode, and the vector reception fields of the coils shown in Figures 9(b) and 9(c) are identical. This progression is illustrated in Figure 9. It is felt that this conceptual similarity of three well-known coil types (Helmholtz pair, saddle, and birdcage) may be instructive. Modern whole volume coils usually are of the birdcage type, because, as the number of current element increases, the uniformity of the field increases.

A possible exception is the one-turn solenoid.[2] The solenoid must be used with the axis transverse to the static field, which in the usual solenoidal geometry of superconducting magnets limits its use in human imaging to the foot, and, in the awkward arm-above-the-head position, to the hand and wrist. But, for these applications, we have always achieved better image quality using the solenoid than with any quadrature birdcage coil that we have tested. It is noted that the solenoid geometry gives exceptionally uniform rf field distribution.

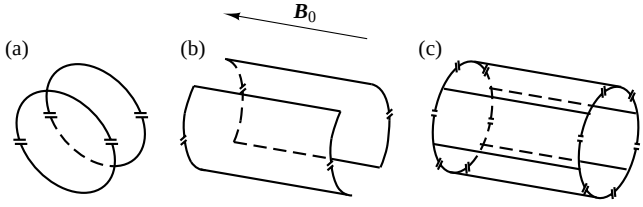

Figure 9 (a) Helmholtz pair; (b) saddle coil, and (d) six-element birdcage coils

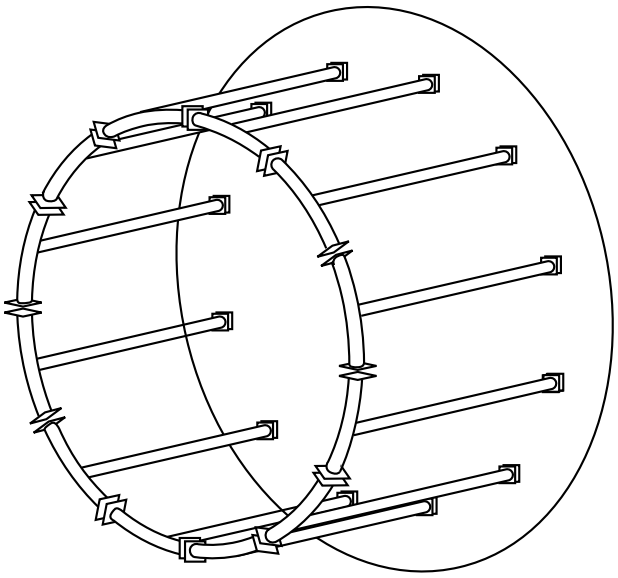

Figure 10 Quadrature endcap transmit–receive birdcage coil used at 3 T. The bandpass design permitted use of more capacitors, which proved helpful at the high field strength

Figure 10 illustrates a type of birdcage coil that has been used in the author's laboratory for functional MRI (FMRI) of the human brain. It is a quadrature, bandpass, endcap transmit–receive coil, and can serve to illustrate a number of the principles presented in this article:

1. The endcap feature increases the filling factor by a factor of 2, assuming that the object of interest is the human brain. This would make no difference in image quality if the condition of dominant loading (see Section 2.1) is satisfied. Its effect is to increase the degree to which this condition is satisfied. Versions have been built at 0.5, 1.5, and 3 T. It is of particular benefit at 0.5 T, of modest benefit at 1.5 T, and probably of negligible benefit at 3 T.
2. By matching the ROI (i.e. the brain) to the ROS, an improvement of sensitivity relative to a conventional quadrature head coil of about $2^{\frac{1}{2}}$ can be achieved.[16] This is because the Q_{body} is increased due to the fact that there is no coupling to the tissues of the lower part of the head and of the neck and shoulders.
3. If the head is progressively removed from the coil, the S/N increases in the portion of the brain that continues to lie within the coil. The improvement in S/N can be as great as a full factor of 2 relative to that achieved with a conventional head coil. The whole volume coil is in the process of becoming a partial volume coil. In the limit, as the head is withdrawn, it seems almost like a surface coil. The distinctions between these three types of local coil is blurred.
4. The crossover in sensitivity between this head coil and any surface coil will lie closer to the surface because of the improved S/N. It is estimated to occur at about 4 cm depth.
5. The coil has been used in the plug-and-go mode, with tune-and-match checkups every few weeks.

3.4 Intracavity Coils

Coils of this type, while building on the principles of local coils, have a number of unique aspects that are discussed in more detail elsewhere (see Related Articles at the end of this article).

3.5 Coil Arrays

It is self-evident that the sample, namely the human body, is quite large and that it should be possible to perform a number of separate experiments simultaneously. All that is required is a number of separate signal channels for rf amplification, detection, and image formation. The feasibility of experiments of this type was suggested by the present author and his colleagues[17] and was first demonstrated by Roemer et al.[18] (see Related Articles at the end of this article).

Opportunities presented by the availability of four parallel channels for signal acquisition, as in the GE Signa scanners, go well beyond the ideas of the earliest papers. Some of these are discussed here.

3.5.1 Quadrature Surface Coils

If a planar pair or figure-of-eight coil is centered over a single-turn loop, the coils exhibit zero mutual inductance, and the vector reception fields are orthogonal on-axis. Dimensions can be adjusted so that these orthogonal fields are also equal in magnitude. This provides the opportunity for quadrature reception, increasing the S/N by $2^{\frac{1}{2}}$ or, alternatively, halving the acquisition time for equivalent S/N.[19] In one study,[19] signals were combined using a hybrid combiner, and a single channel was used. Nearly ideal performance on-axis was achieved, but phases and amplitudes no longer matched off-axis, and use of a hybrid combiner was less than ideal. Independent signal formation and appropriate summation using two channels should overcome this problem. It is noted that quadrature surface coils of the type described here are in commercial production and are widely available.

3.5.2 Multimode Coils

One and the same surface coil can exhibit a number of independent modes that can be tuned to the same frequency (Figure 11).[20] In this coil geometry, there are four independent modes, all resonant at the same frequency. Signals were acquired simultaneously and independently from these four modes and combined, after image formation, for optimum S/N. As the number of spokes increases, the number of modes increases, although the depth sensitivity decreases as the order of the modes increases. There is a similarity, conceptually, between the higher order modes of a birdcage coil and those of this multielement planar coil.

3.5.3 Simultaneous Signal Acquisition from a Surface Coil and a Whole Volume Coil

During reception, mutual inductance between a whole volume transmit-only coil and a receive-only surface coil can couple noise from the transmit coil to the receive channel. For this reason, transmit-only coils should be automatically detuned during reception. However, if the transmit coil and the rf coil have zero mutual inductance because of geometric or intrinsic

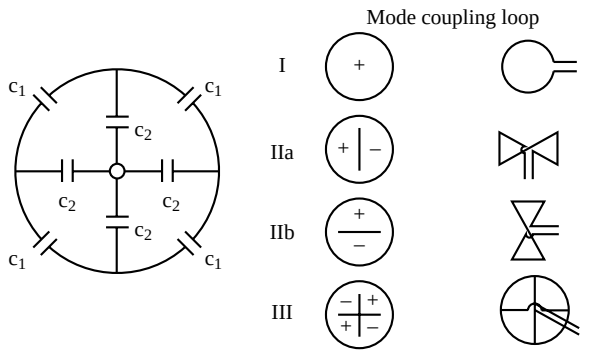

Figure 11 Multimode surface coil. Inductive coupling is used. Each coupling loop has the same symmetry as that of the corresponding mode

isolation, detuning is not required. We have seen that geometric and intrinsic decoupling methods are not very satisfactory for isolating the coils during transmit because more than 40 dB of isolation is required. For reception, however, 10–20 dB of isolation is sufficient and this is readily obtainable. Thus, we have the possibility of simultaneously receiving and processing a signal from the transmit coil and from an intrinsically isolated surface coil. This idea was suggested several years ago,[21,22] and recently demonstrated.[23] An improvement in the S/N of $2^{\frac{1}{2}}$ is expected at the crossover. Closer to the surface, the head coil signal modestly improves the S/N in the combined image; at depths greater than the crossover, the reverse is true, and it is the surface coil signal that modestly improves the S/N in the combined image. At all points in space, using the method of weighted sums,[18,24] image quality is improved.

Parallel acquisition using the head coil and three modes of the multimode surface coil shown in Figure 10 has been reported in a context of MRS. Use of parallel acquisition improves the S/N in in vivo MRS.

3.5.4 Resolution Enhancement

Ra and Rim[25] and Carlson[26] have independently suggested that the spatial variation of the overlapping vector reception fields from members of a coil array constitutes information that can be used to improve the spatial resolution by suitable post-processing. This is another intriguing opportunity for the use of parallel acquisition technology.

3.5.5 Summary of Coil Arrays

There are two broad classes of applications of coil arrays using parallel acquisition: (1) to achieve a large field-of-view with a low coil sensitivity in order to break the FOV $\approx$ ROS constraint; and (2) to target a number of coils or modes at the same area in order to improve the S/N or spatial resolution. It has been shown that there can be no correlation of thermal noise in the signals from these modes so long as all mutual inductances are sufficiently small.[27] However, system noise and physiological noise may cause an apparent noise correlation. These matters are a subject of current investigation.

4 FUTURE TRENDS

In electrical engineering, the lumped-circuit limit of inductance and capacitance changes progressively to the distributed circuit limit of magnetic and electrical field distributions as the rf increases or the characteristic dimensions of the apparatus decrease. Radiofrequency coils in MRI at high field strengths fall between these limits, and lumped- and distributed-circuit vocabularies are used interchangeably, as in this article. Surface coils can be thought of as near-field antenna—a regime where this type of mixed vocabulary has always been appropriate. This intermediate regime has historically received rather little engineering development, which presents opportunities for continued research.

Local coils have, for the most part, been designed in the past in a highly intuitive manner. This is changing in several ways:

1. Network analyzers are now routinely used for detailed characterization of the rf properties of the coil.
2. Efforts to simulate rf field distributions by using Maxwell's equations are underway in several laboratories. Wardenier's earlier paper on the local intensity shift artifact[28] is particularly relevant to surface coils. Finite element methods using powerful computers greatly extend the range of possibilities.
3. Use of optimum control theory approaches for numerical optimization of the coil design, which was introduced by Wong et al.,[29] seems certain to increase in usage. These authors employed the method of conjugate gradient descent for the design of both gradient and rf coils.

The trade-off between exquisite small FOV images using surface coils and lower quality images using whole volume coils is a difficult one. Pathology can be missed using either approach. Systematically investigating an extended region with surface coils uses valuable scanner time in an inefficient manner. Parallel acquisition strategies offer a number of opportunities for ameliorating this difficult trade-off situation, but substantial coil development efforts are required to take advantage of this opportunity.

5 RELATED ARTICLES

Birdcage Resonators: Highly Homogeneous Radiofrequency Coils for Magnetic Resonance; Coils for Insertion into the Human Body; Multifrequency Coils for Whole Body Studies; Radiofrequency Systems and Coils for MRI and MRS; Whole Body Machines: NMR Phased Array Coil Systems.

6 REFERENCES

1. C. E. Hayes, W. A. Edelstein, J. F. Schenck, O. M. Mueller, and M. Eash. *J. Magn. Reson.*, 1985, **63**, 622.
2. S. J. Erickson, P. B. Canal, G. F. Cartera, J. E. Johnson, M. J. Shereff, J. S. Gold, J. S. Hyde, and A. Jesmanowicz, *Radiology*, 1991, **181**, 833.
3. D. I. Hoult and R. E. Richards, *J. Magn. Reson.*, 1976, **24**, 71.
4. R. M. Weisskoff, J. Baker, J. Belliveau, T. L. Davis, K. K. Kwong, M. S. Cohen, B. R. Rosen, in *Proc. XIIth Ann Mtg. Soc. Magn. Reson. Med.*, New York, 1993, p. 7.

5. P. Jezzard, D. LeBihan, C. Cuenod, L. Pannier, A. Prinster, and R. Turner, in *Proc. XIIth Ann Mtg. Soc. Magn. Reson. Med.*, New York, 1993 p. 1392.
6. B. Biswal, P. A. Bandettini, A. Jesmanowicz, and J. S. Hyde, in *Proc. XIIth Ann Mtg. Soc. Magn. Reson. Med.*, New York, 1993, p. 722.
7. A. Abragram, in 'The Principles of Nuclear Magnetism', Oxford Press, London, 1961, p. 83.
8. W. Froncisz, A. Jesmanowicz, J. B. Kneeland, and J. S. Hyde, *Magn. Reson. Med.*, 1986, **3**, 590.
9. E. L. Ginston, in 'Microwave Measurements', McGraw-Hill, New York, 1957, Chap. 9.
10. J. S. Hyde, W. Froncisz, A. Jesmanowicz, and J. B. Kneeland, *Med. Phys.*, 1986, **13**, 1.
11. W. A. Edelstein, C. J. Hardy, and O. M. Mueller, *J. Magn. Reson.* 1986, **67**, 156.
12. J. S. Hyde, R. J. Rilling, and A. Jesmanowicz, *J. Magn. Reson.*, 1990, **89**, 485.
13. W. Froncisz, A. Jesmanowicz, and J. S. Hyde, *J. Magn. Reson.*, 1986, **66**, 135
14. J. S. Hyde, R. J. Rilling, A. Jesmanowicz, and J. B. Kneeland, *Magn. Reson. Med.*, 1989, **12**, 50.
15. J. B. Kneeland, and J. S. Hyde, *Radiology*, 1989, **171**, 1.
16. E. C. Wong, E. Boskamp, and J. S. Hyde, in *Proc. XIth Ann Mtg. Soc. Magn. Reson. Med.*, Berlin, 1992, p. 4015.
17. J. S. Hyde, A. Jesmanowicz, W. Froncisz, J. B. Kneeland, T. M. Grist, and N. F. Campagna, *J. Magn. Reson.* 1986, **70**, 512.
18. P. B. Roemer, W. A. Edelstein, C. E. Hayes, S. P. Souza, and O. M. Mueller, *Magn. Reson. Med.*, 1990, **16**, 192.
19. J. S. Hyde, A. Jesmanowicz, T. M. Grist, W. Froncisz, and J. B. Kneeland, *Magn. Reson. Med.*, 1987, **4**, 179.
20. W. Song, A. Jesmanowicz, and J. S. Hyde, in *Proc. XIIth Ann Mtg. Soc. Magn. Reson. Med.*, New York, 1993, p. 1334.
21. J. S. Hyde, W. Froncisz, A. Jesmanowicz, and J. B. Kneeland, *Magn. Reson. Med.*, 1988, **6**, 235.
22. J. B. Kneeland, A. Jesmanowicz, W. Froncisz, and J. S. Hyde, *Radiology*, 1988, **169**, 255.
23. J. S. Hyde and A. Jesmanowicz, in *Proc. XIth Ann Mtg. Soc. Magn. Reson. Med.*, Berlin, 1992, p. 4024.
24. A. Jesmanowicz, J. S. Hyde, and J. B. Kneeland, in *Proc. VIIIth Ann Mtg. Soc. Magn. Reson. Med.*, Amsterdam, 1989, p. 923.
25. J. B. Ra and C. Y. Rim, *Magn. Reson. Med.*, 1993, **30**, 142.
26. J. W. Carlson and T. Minemura, *Magn. Reson. Med.*, 1993, **29**, 681.
27. A. Jesmanowicz, J. S. Hyde, W. Froncisz, and J. B. Kneeland, *Magn. Reson. Med.*, 1991, **20**, 36; A. Jesmanowicz and J. S. Hyde, *Magn. Reson. Med.*, 1992, **25**, 408.
28. P. H. Wardenier, in *Proc. VIIIth Ann Mtg. Soc. Magn. Reson. Med.*, Amsterdam, 1989, p. 1175.
29. E. C. Wong, A. Jesmanowicz, and J. S. Hyde, *Magn. Reson. Med.*, 1991, **21**, 39.

Biographical Sketch

James S. Hyde. *b* 1932. B.S., 1954, Ph.D. (physics), 1959, MIT. Member of the scientific staff, Varian Associates (working under the direction of W. A. Anderson and M. E. Packard), 1959–75. Professor of Biophysics, Medical College of Wisconsin, 1975–present. Approx. 320 publications, 27 patents. Research specialties: ESR spectroscopy, ENDOR, musculoskeletal MRI, surface coils, functional MRI, electron- and nuclear-spin physics, and magnetic resonance instrumentation.

Surface Coil NMR: Detection with Inhomogeneous Radiofrequency Field Antennas

Coleen S. Bosch and Joseph J. H. Ackerman
Washington University, St Louis, MO, USA

1 INTRODUCTION

Magnetic resonance antennas characterized by inhomogeneous rf fields ($\boldsymbol{B}_1$) have been used in a wide variety of biological and medical NMR applications as noninvasive probes of local cellular and molecular environments in intact tissues. Perhaps the simplest inhomogeneous $\boldsymbol{B}_1$ antenna is the original circular surface coil.[1] This antenna consists of a loop(s) of wire tuned to resonance at the desired NMR frequency and positioned adjacent to the sample of interest. The principal coil axis is aligned perpendicular to the static magnetic field ($\boldsymbol{B}_0$). In this orientation, NMR signal excitation and/or detection is accomplished over a spatial region local to the coil.

The region of sensitivity of the coil can be fundamentally thought of as determined by the magnetic field lines produced by an idealized unit current flowing in the coil.[2] The magnetic field lines parallel to the coil axis have the greatest flux density in the plane of the coil. They diverge and become less dense with increasing distance from the coil. This highly inhomogeneous (in both magnitude and phase) rf field defines both the excitation and reception profiles of the coil. The transverse component of the antenna's magnetic field, $(\boldsymbol{B}_1)_{xy}$, the component orthogonal to $\boldsymbol{B}_0$, contributes to NMR signal excitation and detection.[2] The spatial distribution of $(\boldsymbol{B}_1)_{xy}$ for a circular surface coil lying in the *yz* plane is illustrated for both the *xy* and *xz* planes in Figure 1. When the surface coil is used in the single-coil mode as both the transmit and receive coil, the volume over which signal is acquired experiences a dual dependency on $(\boldsymbol{B}_1)_{xy}$, further restricting the localized volume, as shown in Figure 2. From Figures 1 and 2 it is apparent why the shape of the sensitive volume of a circular surface coil is often regarded as a hemisphere, with the majority of the signal originating within a depth of approximately one coil radius. While this is a convenient approximation, a more rigorous description of the volume interrogated by the surface coil requires consideration of experimental conditions such as the pulse width, pulse repetition rate, and resonance offset.[2–4]

The sensitivity of a receiver coil is quantified in terms of the signal-to-noise ratio achieved for a sample volume element, and is related to the $(\boldsymbol{B}_1)_{xy}$ experienced at the location of the volume element. Surface coils (or, alternatively, local coils) typically achieve a high signal-to-noise ratio over the interrogated volume of the coil. This results from the ability to position the sample region of interest directly within the region of intense $(\boldsymbol{B}_1)_{xy}$ and, at the same time, to minimize noise contributions from other parts of the sample. Additionally, because of their small size, surface coils generally have much higher $(\boldsymbol{B}_1)_{xy}$ than do large volume coils.

In spite of the high signal-to-noise ratio and localized signal detection advantages associated with surface coils, the inhomogeneous $(\boldsymbol{B}_1)_{xy}$ can pose severe technical limitations for in vivo NMR applications. The inhomogeneous $(\boldsymbol{B}_1)_{xy}$ of surface coils produces excitation and detection signal volumes that do not have well defined boundaries. Additionally, when the surface coil is used for excitation, the wide variation in $(\boldsymbol{B}_1)_{xy}$ produces a wide distribution of flip angles within the sample. This makes applications requiring constant flip angle spatial distribution more challenging with a surface coil. The intense $(\boldsymbol{B}_1)_{xy}$ near the coil and curved iso-$(\boldsymbol{B}_1)_{xy}$ lines can also result in significant signal contamination from unwanted superficial tissues. The use of specialized pulse sequences, static field gradients, and separate transmitter and receiver coils have been applied to surface coil spectroscopy to improve local signal detection and surmount these deleterious effects of the inhomogeneous rf field.

Surface coils have found considerable use in human and animal NMR investigations in vivo, including studies of phosphorus energetics, carbohydrate metabolism, blood flow, and diagnostic clinical imaging. Surface coils have been employed as single- or multi-frequency transmitter and receiver antennas, as well as in conjunction with other coils to optimize signal detection and localization (see ***Surface and Other Local Coils for In Vivo Studies***).

2 SHAPING THE INTERROGATED VOLUME OF SURFACE COILS

A variety of techniques and pulse sequences have been developed to define and shape better the localized signal volume achieved with surface coils.[5] Numerous spectral localization techniques utilize linear $\boldsymbol{B}_0$ gradients in conjunction with surface coil excitation and detection, or detection alone in the presence of homogeneous excitation, to achieve a high-resolution spectrum over a well localized signal volume. Examples include volume selective excitation (VSE), image selected in vivo spectroscopy (ISIS), depth resolved surface coil spectroscopy (DRESS), stimulated echo acquisition mode (STEAM), and related techniques. These localization methods acquire data from a specific, well defined region within the sensitive volume of the coil by either dephasing unwanted signal contributions from other regions, avoiding direct excitation of unwanted regions, or subsequently subtracting out the unwanted signal in a postacquisition data manipulation. Techniques such as topical magnetic resonance (TMR) and surface spoiling[6] employ nonlinear $\boldsymbol{B}_0$ gradients to discriminate against signal contributions from unwanted regions. These techniques eliminate signal contamination by rapidly dephasing the unwanted signal in the presence of highly inhomogeneous local $\boldsymbol{B}_0$ gradients.

Other techniques have been developed that exploit the natural $(\boldsymbol{B}_1)_{xy}$ gradients of surface coils to improve signal localization capabilities. Rotating frame imaging and related

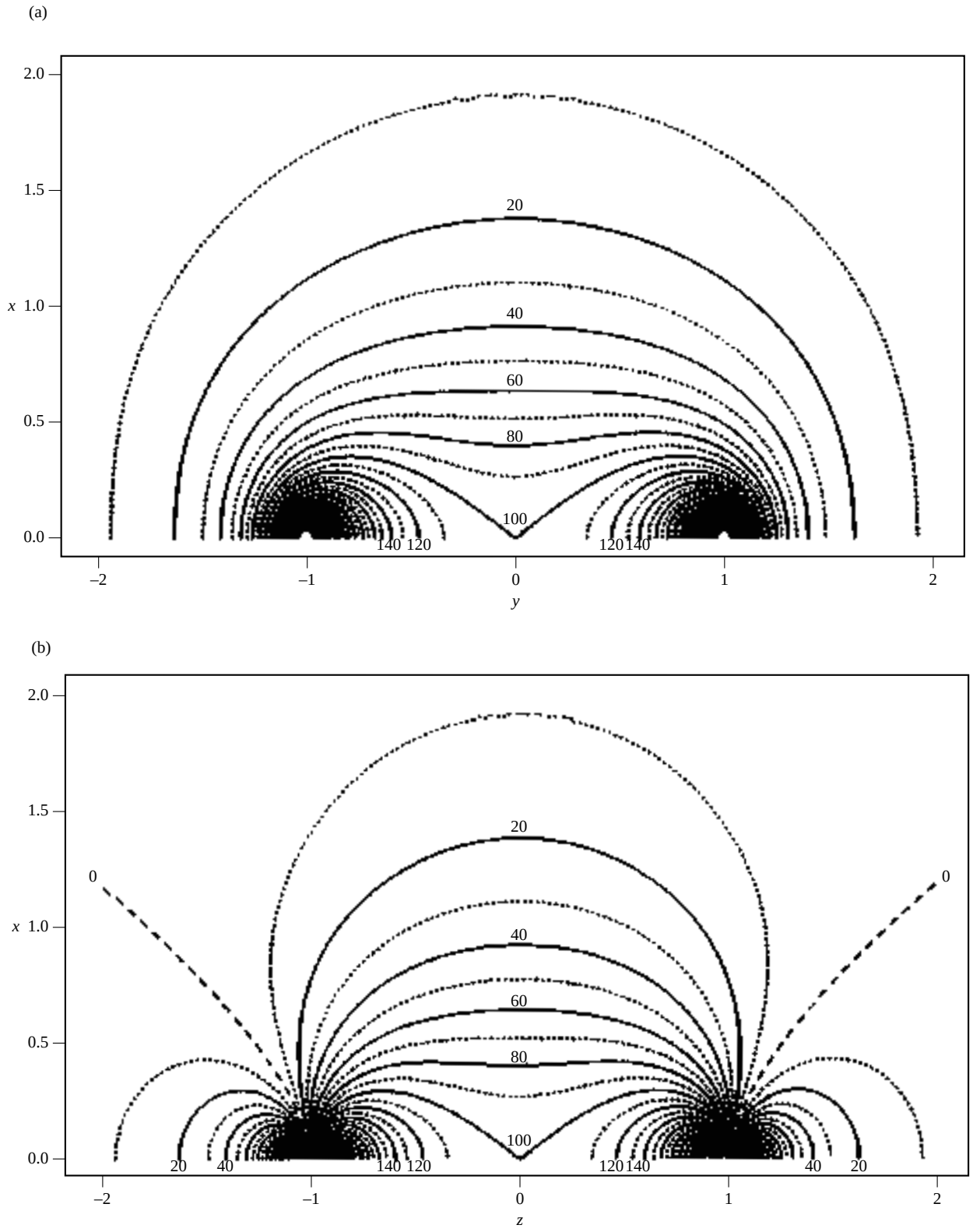

Figure 1 Magnitude of calculated $(\boldsymbol{B}_1)_{xy}$ as a function of spatial coordinates for a one-turn circular surface coil lying in the *yz* plane. The axes are given in units of coil radii. The *x* axis represents the depth into the sample. The $(\boldsymbol{B}_1)_{xy}$ intensity is normalized relative to a value of 100 at the coil center. Iso-field contours are plotted for (a) the *xy* plane at $z = 0$, and (b) the *xz* plane at $y = 0$. (Reproduced by permission of Springer-Verlag from C. S. Bosch and J. J. H. Ackerman, in 'NMR Basic Principles and Progress', ed. P. Diehl, E. Fluck, H. Günther, R. Kosfeld, and J. Seelig, Berlin, 1992, Vol. 27, p. 3)

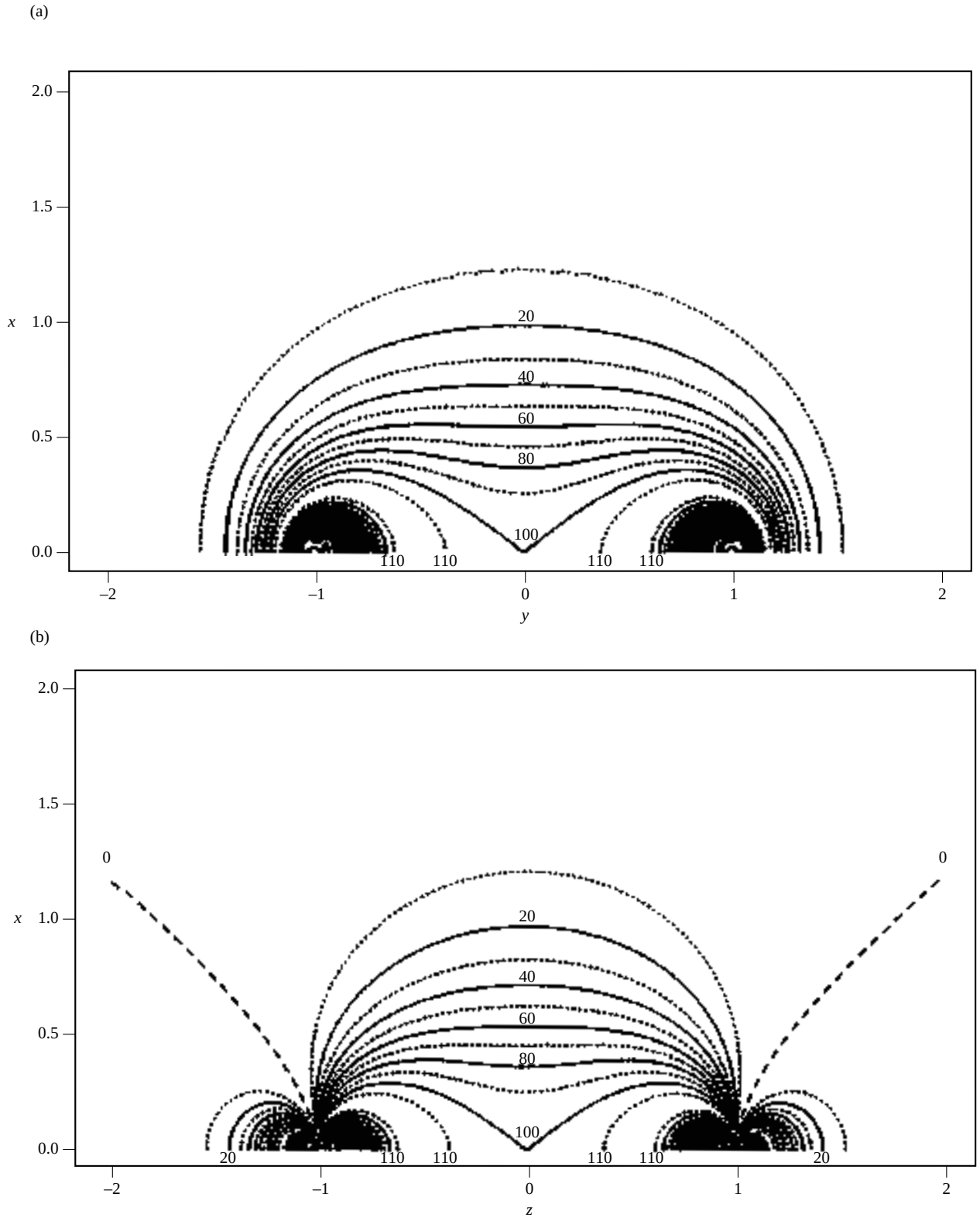

Figure 2 Calculated signal-amplitude distribution maps for a single pulse from a one-turn circular surface coil (used as both transmit and receive coil) lying in the *yz* plane. The axes are given in units of coil radii. The *x* axis represents the depth into the sample. Signal amplitudes are normalized relative to an amplitude of 100 for a 90° flip angle at the coil center. Iso-amplitude contours are plotted for (a) the *xy* plane at $z = 0$, and (b) the *xz* plane at $y = 0$. (Reproduced by permission of Springer-Verlag from C. S. Bosch and J. J. H. Ackerman, in 'NMR Basic Principles and Progress', ed. P. Diehl, E. Fluck, H. Günther, R. Kosfeld, and J. Seelig, Berlin, 1992, Vol. 27, p. 3)

methods such as Fourier series windowing (FSW) spatially map the distribution of chemical moieties within the tissue along iso-$(\boldsymbol{B}_1)_{xy}$ contours. Special composite pulses have been used with surface coils that are designed to increase the sensitivity of the NMR response to the inhomogeneities of the rf field.[7] A family of pulse sequences, called 'depth' pulses, made up of phase-cycled simple or composite pulses, achieve spatial signal discrimination through enhanced sensitivity to regions corresponding to very specific flip angles.[8] Combining multiple composite pulses or 'depth' pulses accentuates this flip angle selective spatial property. The effect of such pulses can be further enhanced by using separate transmit and receive coils with overlapping sensitive volumes.

In contrast to the above techniques that attempt to sharpen further the localization, other schemes have been proposed to compensate for the inhomogeneous $(\boldsymbol{B}_1)_{xy}$ of surface coils. Phase-cycled composite pulses and amplitude- and frequency/phase-modulated adiabatic pulses have been developed which are insensitive to wide ranges of $(\boldsymbol{B}_1)_{xy}$.[9,10] Such pulses have been successfully applied with surface coil spectroscopy to provide a more homogeneous excitation profile, thereby increasing sensitivity, improving signal inversion and refocusing capabilities, and enhancing efficiency of water suppression and spectral editing techniques.

The use of a homogeneous $(\boldsymbol{B}_1)_{xy}$ antenna for excitation in the presence of surface coil detection not only produces a single flip angle across the sample (thereby allowing use of pulse sequences demanding homogeneous excitation), but can also allow signal reception from regions deeper within the sample.[11] When used as a receiver coil only, the inhomogeneous $(\boldsymbol{B}_1)_{xy}$ of the surface coil defines only the reception profile (Figure 1). This is in contrast to the case of surface-coil transmission and detection in which the interrogated volume is determined by both the excitation and reception profiles (Figure 2). An important application of homogeneous excitation with surface-coil reception has been found in MRI in which optimum signal excitation is combined with the high reception sensitivity and localized detection (field of view) of the surface coil.

3 ENDOGENOUS PROTON SIGNAL DETECTION

The homogeneity of the static magnetic field can be optimized on biological samples most readily through monitoring the ^{1}H signal arising from tissue water.[12] The $\boldsymbol{B}_0$ homogeneity shim gradient controls are adjusted to optimize the tissue water ^{1}H FID profile. In many instances, NMR antennas (including surface coils) that are frequency tuned and impedance matched for a resonance other than that of ^{1}H can still adequately detect the water signal. This is a consequence of the large ^{1}H concentration in tissue water (i.e. pure water is 110 M in equivalent ^{1}H), its ubiquitous distribution in tissue (i.e. most tissues are about 70% water), and the very high NMR sensitivity of the ^{1}H nuclide (i.e. signal proportional to γ^2). If necessary, sensitivity to the ^{1}H tissue water signal can be significantly enhanced by remotely tuning and matching the coil circuitry to the ^{1}H frequency.[13] Assuming that tissue magnetic susceptibility gradients dominate spectral resolution, the linewidth (in ppm) obtained for the ^{1}H tissue water signal will reflect the linewidth (in ppm) that will be obtained for the nuclide of interest.

The ^{1}H tissue water signal can also be used as both an internal chemical shift reference and an amplitude (i.e. concentration) reference. This is especially useful when there is no suitable internal (endogenous) reference for the nuclide of interest.

In spite of the utility of the endogenous ^{1}H tissue water signal for the purposes mentioned above, the intense water signal (and, to a lesser degree, the endogenous fat signal) can pose a severe dynamic range problem when attempting to observe ^{1}H signals from metabolites occurring in low concentrations such as lactate and amino acids. In such situations, water suppression and spectral editing techniques applicable to surface coils are required (see ***Water Suppression in Proton MRS of Humans and Animals***).[14]

4 MEASUREMENT OF RELAXATION TIMES

Accurate T_1 relaxation times can be determined using surface coils in spite of their inhomogeneous $\boldsymbol{B}_1$ fields.[15] Both saturation–recovery and inversion–recovery type pulse sequences are applicable as long as three conditions are met. First, the number of spins interrogated should remain invariant over the course of the experiment. This can be a problem if metabolite concentrations are changing with time. Second, each spin or each arbitrarily small voxel of the sample must be consistently prepared in the same initial nonequilibrium state prior to relaxing toward the equilibrium state during variable recovery delay periods. Third, each spin or arbitrarily small voxel of the sample must be consistently interrogated at the end of each relaxation delay period. It is not necessary that all spins or voxels experience the same preparation or interrogation conditions. Spin–lattice relaxation will still result in exponential signal recovery characterized by the true T_1 exponential time constant. Phase cycling of the sampling pulse and receiver can be used to reduce errors caused by unwanted transverse magnetization generated by the imperfect pulses.[16] Pulsed field gradients can also be employed to the same effect. Artifactual transverse magnetization is not generally a problem unless rapid pulse repetition conditions (overall recycle periods less than $3T_2$) are employed. Assuming the T_1 recovery is a first-order rate process, a three-parameter single exponential fit of the recovery curve will provide an accurate estimate of the T_1 relaxation time.

Composite or adiabatic pulses used in place of simple square pulses in surface coil T_1 pulse sequences can achieve a more homogeneous sampling response. While not essential for an accurate estimate of the T_1 time, these pulses do result in improved dynamic range and signal-to-noise ratio. Phase-cycled 'depth' pulses can also been used in place of simple square pulses to enhance signal localization to regions receiving flip angles near 180° and 90° that are ideal (maximized dynamic range) for the inversion–recovery experiment.[17]

One important, but often unappreciated, consequence of the inhomogeneous field of surface coils and the resultant distribution of flip angles produced within the sample is a spatially dependent partial saturation of signal intensity when data are collected under rapid (relative to the T_1 of the sample) pulse repetition conditions. Regions near the coil, where the flip

angle is typically greatest, will experience greater magnetization saturation, while regions further from the coil will experience less magnetization saturation, and hence may contribute proportionately more to the total signal.

Accurate T_2 relaxation times are more difficult to obtain with surface coils in the single coil mode since the inhomogeneous rf field precludes spatially consistent repetitious refocusing of the spins using simple square pulses. Spin echo pulse sequences can be employed using surface coils although care must be taken to phase cycle refocusing pulses properly to remove artifacts introduced by imperfect refocusing of the transverse magnetization.[18] A further difficulty relevant to the measurement of T_2, however, is that the phase cycling enhances signal detection from regions receiving close to the ideal 90° and 180° flip angles.[17] In this respect, the spin echo sequence performs as a type of 'depth' pulse sequence. Multiple refocusing pulses (as in a Carr–Purcell–Meiboom–Gill sequence) increase the discrimination against signals not receiving perfect 180° flip angles, changing the interrogated volume as a function of echo number. The use of plane-rotation adiabatic or other $(B_1)_{xy}$-insensitive pulses provides a more spatially uniform interrogation which significantly improves the refocusing capabilities of the surface coil.

5 CONCENTRATION DETERMINATION

The ability simultaneously and continuously to observe multiple chemical moieties noninvasively in near-real-time makes NMR spectroscopy highly applicable to studies of evolving metabolism in vivo. Since the NMR frequency domain integrated resonance area (signal amplitude) is directly proportional to the number of spins detected, metabolite levels can be quantified in relative or absolute terms.[19]

Certain experimental factors must be considered in any quantitative determination of metabolite levels from NMR data. These include knowledge of the interrogated volume and the flip angle distribution over the volume, calculation of magnetization saturation factors if the spins are not sampled under equilibrium conditions, determination of nuclear Overhauser enhancement in decoupling experiments, and assessment of instrumental stability and rf filter response over multiline spectra. Additionally, if metabolite resonance areas are calibrated against a signal from a different sample, or from a different nuclide, differences in antenna loading, as reflected by changes in the quality factor Q of the coil, for the two comparative measurements must be made. Finally, data analysis techniques such as baseline correction, integration methods, and deconvolution of overlapping resonances can also introduce uncertainty in quantitative measurements.

The use of inhomogeneous $(\boldsymbol{B}_1)_{xy}$ coils for signal excitation and/or detection further complicates quantitative metabolite concentration determination since exact knowledge of the interrogated tissue volume obtained and the signal sensitivity distribution achieved over that volume is difficult to determine. Furthermore, the metabolites being measured are generally characterized by different T_1 relaxation times. When signal collection is obtained under rapid pulse repetition conditions, the spatially and T_1 dependent partial magnetization saturation results in each species with a different T_1 having a different effective interrogated volume (see above).

Relative changes in a given metabolite concentration can be obtained in a straightforward manner using surface coils even under rapid pulse repetition conditions by comparing ratios of peak areas. This assumes the metabolite's T_1 does not change during the experiment. If different metabolites are equivalently or uniformly distributed over the same tissue volume, their relative concentrations can be obtained directly from the ratio of their peak areas if the data are acquired quantitatively. Corrections must be made for differential saturation when T_1 values are different and rapid pulse repetition conditions are used. Determining relative concentrations in this manner avoids the problem of the ill-defined interrogated volume characteristic of surface coils.

Determination of absolute (e.g. molar) metabolite concentrations requires calibration of the integrated resonance area against a signal of known concentration or spin count (moles). If an internal concentration standard exists for the nucleotide of interest, absolute concentrations can easily be determined by comparing the peak areas, again assuming equivalent distribution of species over the interrogated tissue volume and either quantitative acquisition conditions or correction for partial saturation.

In the absence of a suitable internal homonuclear reference species, resonance areas can be referenced to the endogenous tissue water ^{1}H resonance (or, equivalently, that of the natural abundance deuterium signal).[20,21] This assumes that the tissue water ^{1}H signal is invariant over the physiological response(s) being investigated and that the tissue water and the metabolites of interest are equivalently or uniformly distributed over the interrogated volumes. Since the ^{1}H concentration in tissue water is known, the absolute concentrations of metabolites can be referenced relative to tissue water volume, or relative to tissue mass after determination of tissue water content. Referencing a non-^{1}H nucleotide to the ^{1}H tissue water signal typically requires use of a dual-tuned receiver coil [ensuring equivalent $(\boldsymbol{B}_1)_{xy}$ distributions], correcting for differences in antenna loading for all measurements, and calibration of relative signal amplitudes using standards of known composition at the two frequencies.[21] An external reference (point sample) fixed relative to the coil such that it consistently experiences the same $(\boldsymbol{B}_1)_{xy}$ field provides a convenient signal to correct for sample loading and to achieve the same flip angle distribution for each measurement.

Metabolite concentrations can also be determined by referencing directly to a fixed external reference signal of known content, the signal response of which has been calibrated relative to a standard solution whose characteristics mimic that of the tissue of interest. This assumes that the signal sensitivity and volume of detection of the coil over the reference and standard sample are equivalent (or correctable) to that over the reference and tissue of interest. Volume localized spectroscopic techniques have utilized fixed external references for absolute quantification of metabolite concentrations from well-delineated sample volumes.

6 APPLICATIONS

Since the early applications of surface coils, many studies have focused on detection of the so called 'high-energy phosphates' via ^{31}P NMR.[22] The in vivo phosphorus spectrum is

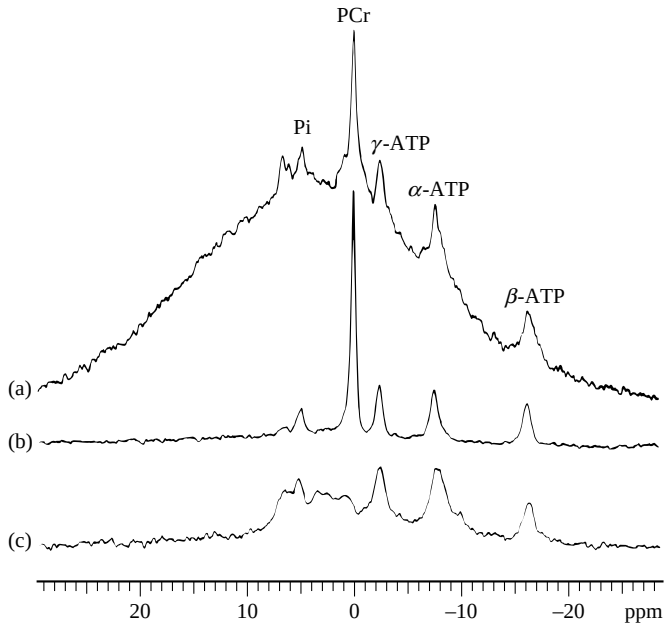

Figure 3 ^{31}P surface coil spectra of rat (a) brain, (b) leg muscle, and (c) liver obtained in vivo at 80.98 MHz (4.7 T) with a 10 s recycle time and 256 averaged transients. (Data courtesy of S.-K. Song)

composed of rather well resolved resonances, as shown in Figure 3. These resonances consist of α-, β-, and γ-phosphates of adenosine triphosphate (ATP), phosphocreatine (PCr), and inorganic phosphate (Pi). These compounds are important in the regulation of cellular energy metabolism.

The pH of the tissue can be determined from the ^{31}P chemical shift of Pi, a quantity readily measured by surface coil NMR. Under physiologic conditions, the Pi resonance represents the rapid chemical exchange averaged shifts of the mole fraction weighted sum of the acid ($H_2PO_4^-$) and base (HPO_4^{2-}) phosphate species. The observed chemical shift of Pi (δ_{obs}) and the chemical shifts of the acid and base phosphate forms, combined with the Henderson–Hasselbach representation of the acid–base equilibrium, yields an expression for the chemical shift of Pi as a function of pH:[22]

$$\mathrm{pH} = \mathrm{p}K_a + \log_{10}\left(\frac{\delta_{obs} - \delta_{acid}}{\delta_{base} - \delta_{obs}}\right) \quad (1)$$

Since in most tissues the NMR visible Pi signal originates primarily from intracellular spaces, this provides a powerful means of measuring intracellular pH.

The PCr ^{31}P resonance is insensitive to pH changes in the physiologic range (i.e. pH $\geqslant$ 6.2), and thus is widely used as the ^{31}P chemical shift reference. However, not all tissues possess high levels of PCr [see, for example, Figure 3(c)]. In its absence the α-ATP resonance can be employed as a chemical shift reference as it also is pH invariant in the physiologic range.

The chemical shifts of the phosphate resonances of ATP are dependent upon the degree of magnesium binding to ATP. The intracellular free Mg^{2+} concentration can be determined from the chemical shifts of ATP and consideration of the appropriate chemical equilibria in a manner similar in concept to the measurement of pH from the Pi shift.[22]

Resonances coupled via chemical exchange provide a unique window for probing chemical kinetics under equilibrium or steady-state conditions.[23] Considerable ^{31}P surface coil work has been reported in this area. For example, the PCr and γ-phosphate of ATP resonances are chemical exchange coupled through the creatine kinase (CK) catalyzed equilibrium reaction:

$$\mathrm{PCr} + \mathrm{MgADP} + \mathrm{H}^+ \rightarrow \mathrm{Cr} + \mathrm{MgATP} \quad (2)$$

By perturbing the ^{31}P magnetization state of one member of this exchange-coupled pair the state of the other is affected in a time-dependent manner related to the kinetic flux. The rate constant for the reaction can be derived from the magnetization transfer process (see ***Magnetization Transfer and Cross Relaxation in Tissue***).

A rather unusual use of magnetization transfer with surface coils has been the suppression of the so called 'bone hump' from brain ^{31}P spectra.[24] When a surface coil is placed on the head of a subject to examine brain phosphorus metabolites, a very intense broad resonance is detected (primarily) from bone adjacent to the coil (see Figure 3(a)). This resonance can be conveniently suppressed by applying a weak saturating irradiation at one edge of the hump. Efficient communication within the broad resonance envelope allows the saturation to spread rapidly throughout the bandwidth of the hump and effectively suppress this unwanted signal.

The high sensitivity of surface coils has made them useful for following exogenously administered NMR active substrates. Of particular significance to in vivo applications has been the use of ^{13}C- and ^{19}F-labeled substrates.[25,26] The use of fluorinated compounds offers the advantages of negligible endogenous background signal and a ^{19}F sensitivity almost that of ^{1}H. Many pharmaceuticals obtain their unusual reactivity by incorporating fluorine near their active sites. These compounds are excellent targets for observation by ^{19}F surface coil NMR. Observation of both ^{13}C and ^{19}F nuclides is often complicated by ^{1}H coupling. Thus, proton decoupling is often required to simplify spectra and improve the signal-to-noise ratio. Figure 4 shows one application of proton decoupled ^{13}C surface coil NMR used to follow the metabolism of administered ^{13}C-labeled glucose and alanine in rat liver in vivo. A time resolution of 5 min was achieved. Because of the high level of metabolic activity and dependence on glucose and other carbohydrates as energy sources, brain and liver tissue have been the focus of many such surface coil studies.

A rather novel use of surface coils has been in the measurement of tissue perfusion (blood flow) via ^{2}H NMR in concert with ^2H_2O employed as a freely diffusible tracer of aqueous space.[27] The surface coil is used to track quantitatively the wash-in or wash-out of ^2H_2O administered in a known controlled fashion. Standard compartmental modeling, developed for use with freely diffusible radioactive tracers, can be readily applied to ^{2}H NMR kinetic data, yielding tissue perfusion in units of mL-blood/(g-tissue·min). This approach can be combined with concurrent surface coil measurements of tissue metabolism to give blood flow and metabolic assessment from the same tissue site in near-real-time.

Finally, note should be made of the use of surface coils in ^{1}H imaging. Surface coils provide two important attributes in imaging. The first is high signal-to-noise ratio for tissues near

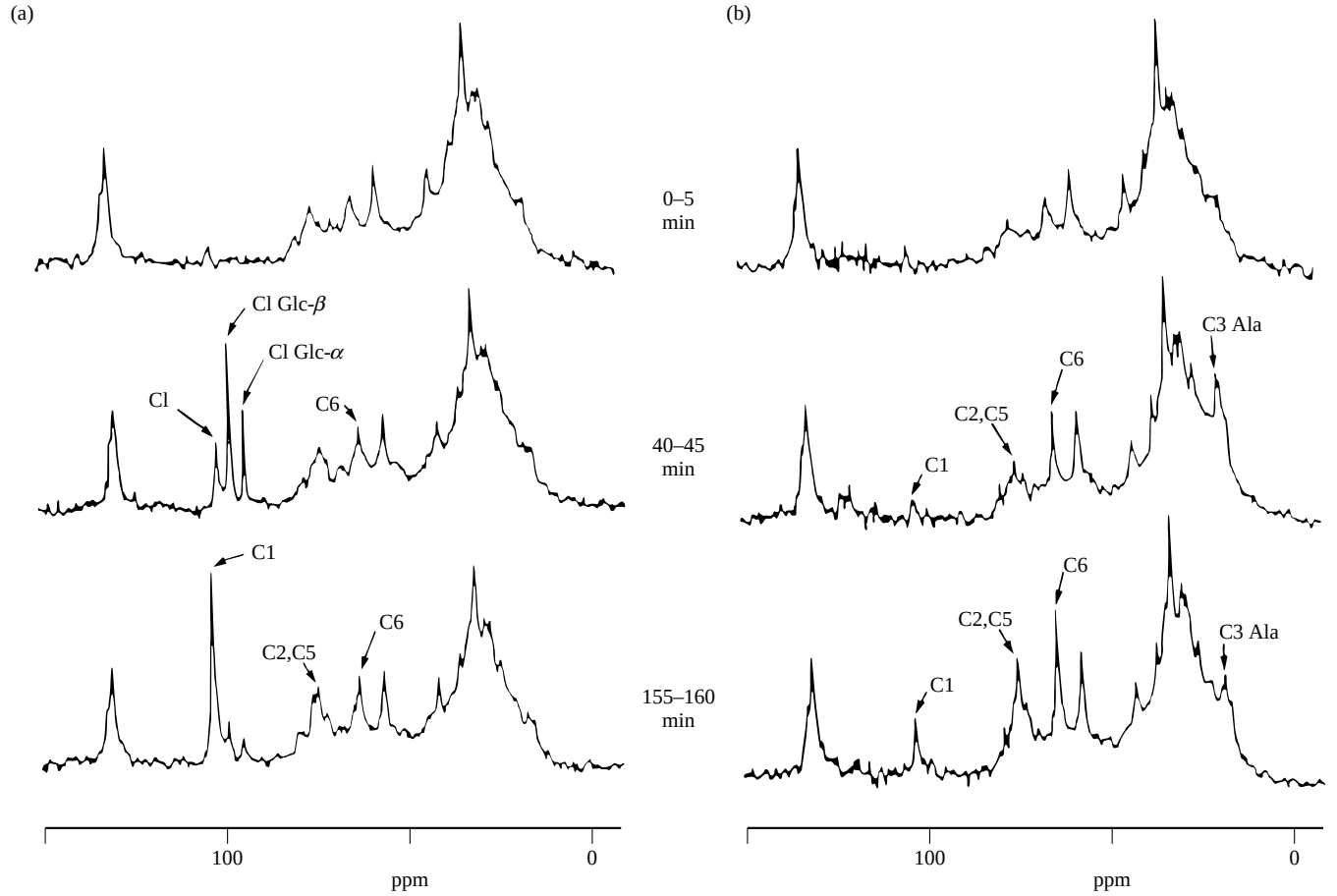

Figure 4 Proton decoupled ^{13}C spectra of surgically exposed rat liver in vivo representing the time course of hepatic metabolism of (a) [1-^{13}C]glucose and (b) [3-^{13}C]alanine. Data were obtained at 90.52 MHz (8.45 T) with 5 min time resolution and 1083 averaged transients. The first spectrum (0–5 min) in each case represents background signal contribution before duodenal injection of 0.67 mmol/100 g body weight glucose plus 0.67 mmol/100 g body weight alanine at 20 min. In (a) half of the glucose administered was [1–^{13}C]glucose; in (b) the alanine was [3-^{13}C]alanine. C1 Glc-β, the β anomer of C-1 glucose; C1 Glc-α, the α anomer of C-1 glucose; C1, C-1 glycogen; C2,C5, combined C-2 and C-5 glucose and glycogen; C6, C-6 glucose and glycogen; C3 Ala, C-3 alanine. (Reproduced by permission of The American Society for Biochemistry and Molecular Biology from R. A. Shalwitz, N. V. Reo, N. N. Becker, A. C. Hill, C. S. Ewy, and J. J. H. Ackerman, *J. Biol. Chem.*, 1989, **264**, 3930)

the coil. Thus, organs and structures near the surface, such as the spine and eye, can be imaged with substantially higher sensitivity than provided by larger homogeneous $\boldsymbol{B}_1$ volume coils. The second attribute is a limited or localized field of view. This serves to eliminate aliased signals from structures outside the surface coil's field of view. Artifacts from motion outside the surface coil's field of view are also reduced. These two attributes provide the opportunity to use strong gradient encoding for fine image resolution of near surface structures.

7 SUMMARY

Surface or local coils serve as NMR transmit and/or receive antennas with very high sensitivity for tissues adjacent to the coil structure. This signal sensitivity is generally much higher than that afforded by larger, homogeneous $\boldsymbol{B}_1$ volume coils. Additionally, because of their small size, surface coils have low inductance relative to larger volume coils. Thus, they are generally more routine to tune and match using traditional tank circuit approaches. The high sensitivity and robust design characteristics have made surface coils the antenna of choice for a wide range of NMR and MRI applications. The inhomogeneous $\boldsymbol{B}_1$ characteristics of many surface coil designs limit some applications. However, many strategies (hardware, pulse sequence, and data analysis) have been developed that allow quantitative tissue monitoring with surface coils. These antennas continue to play an important role in basic and clinical magnetic resonance.

8 RELATED ARTICLES

Magnetization Transfer and Cross Relaxation in Tissue; Quantitation in In Vivo MRS; Surface and Other Local Coils for In Vivo Studies; Water Suppression in Proton MRS of Humans and Animals.

9 REFERENCES

1. J. J. H. Ackerman, T. H. Grove, G. G. Wong, D. G. Gadian, and G. K. Radda, *Nature*, 1980, **283**, 167.
2. J. J. H. Ackerman, *Concepts Magn. Reson.*, 1990, **2**, 33.
3. C. S. Bosch and J. J. H. Ackerman, in 'NMR Basic Principles and Progress', ed. P. Diehl, E. Fluck, H. Günther, R. Kosfeld, and J. Seelig, Springer, Berlin, 1992, Vol. 27, p. 3.
4. J. L. Evelhoch, M. G. Crowley, and J. J. H. Ackerman, *J. Magn. Reson.*, 1984, **56**, 110.
5. W. P Aue, *Rev. Magn. Reson. Med.*, 1986, **1**, 21.
6. W. Chen and J. J. H. Ackerman, *NMR Biomed.*, 1990, **3**, 147, 158.
7. R. Tycko and A. Pines, *J. Magn. Reson.*, 1984, **60**, 156.
8. M. R. Bendall, *Bull. Magn. Reson.*, 1986, **8**, 17.
9. R. Freeman, S. P. Kempsell, and M. H. Levitt, *J. Magn. Reson.*, 1980, **38**, 453.
10. M. Garwood and K. Uğurbil, in 'NMR Basic Principles and Progress', ed. P. Diehl, E. Fluck, H. Günther, R. Kosfeld, and J. Seelig, Springer, Berlin, 1992, Vol. 26, p. 109.
11. M. G. Crowley, J. L. Evelhoch, and J. J. H. Ackerman, *J. Magn. Reson.*, 1985, **64**, 20.
12. J. J. H. Ackerman, D. G. Gadian, G. K. Radda, and G. G. Wong, *J. Magn. Reson.*, 1981, **42**, 498.
13. R. E. Gordon and W. E. Timms, *J. Magn. Reson.*, 1982, **46**, 322.
14. P. C. M. van Zijl and C. T. W. Moonen, in 'NMR Basic Principles and Progress', ed. P. Diehl, E. Fluck, H. Günther, R. Kosfeld, and J. Seelig, Springer, Berlin, 1992, Vol. 26, p. 67.
15. J. L. Evelhoch and J. J. H. Ackerman, *J. Magn. Reson.*, 1983, **53**, 52.
16. D. E. Demco, P. Van Hecke, and J. S. Waugh, *J. Magn. Reson.*, 1974, **16**, 467.
17. M. R. Bendall and R. E. Gordon, *J. Magn. Reson.*, 1983, **53**, 365.
18. G. Bodenhausen, R. Freeman, and D. L. Turner, *J. Magn. Reson.*, 1977, **27**, 511.
19. E. B. Cady, in 'NMR Basic Principles and Progress', ed. P. Diehl, E. Fluck, H. Günther, R. Kosfeld, and J. Seelig, Springer, Berlin, 1992, Vol. 26, p. 249.
20. K. R. Thulborn and J. J. H. Ackerman, *J. Magn. Reson.*, 1983, **55**, 357.
21. S.-K. Song, R. S. Hotchkiss, and J. J. H. Ackerman, *Magn. Reson. Med.*, 1992, **25**, 45.
22. M. Rudin and A. Sauter, in 'NMR Basic Principles and Progress', ed. P. Diehl, E. Fluck, H. Günther, R. Kosfeld, and J. Seelig, Springer, Berlin, 1992, Vol. 28, p. 161.
23. M. Rudin and A. Sauter, in 'NMR Basic Principles and Progress', ed. P. Diehl, E. Fluck, H. Günther, R. Kosfeld, and J. Seelig, Springer, Berlin, 1992, Vol. 27, p. 257.
24. J. J. H. Ackerman, J. L. Evelhoch, B. A. Berkowitz, G. M. Kichura, R. K. Deuel, and L. S. Lown, *J. Magn. Reson.*, 1984, **56**, 318.
25. N. N. Becker and J. J. H. Ackerman, in 'NMR Applications in Biopolymers' (Basic Life Sciences, Vol. 56), ed. J. W. Finley, S. J. Schmidt, and A. S. Serianni, Plenum, New York, 1990, p. 317.
26. M. J. W. Prior, R. J. Maxwell, and J. R. Griffiths, in 'NMR Basic Principles and Progress', ed. P. Diehl, E. Fluck, H. Günther, R. Kosfeld, and J. Seelig, Springer, Berlin, 1992, Vol. 28, p. 101.
27. J. J. Neil, *Concepts Magn. Reson.*, 1991, **3**, 1.

Biographical Sketches

Coleen S. Bosch. *b* 1960. B.S., 1982, John Brown University; Ph.D. (chemistry), 1988, Washington University (with Professor J. J. H. Ackerman), St Louis, MO, USA. Postdoctoral work at Washington University (with Professor Ackerman). Approx. 13 publications. Current research interests: raising a family.

Joseph J. H. Ackerman. *b* 1949. B.A., 1972, Boston University; Ph.D. (chemistry), 1978, Colorado State University (with Prof. Gary Maciel), Fort Collins, CO, USA. Postdoctoral work at Colorado State University (with Prof. Maciel) and University of Oxford (with Sir Rex Richards and George Radda). Faculty at Washington University, MO, 1979–present. Currently, William Greenleaf Eliot Professor and Chair, Department of Chemistry, School of Arts and Sciences; Research Professor of Chemistry in Medicine, Department of Medicine, and Professor, Department of Radiology, Washington University School of Medicine. Approx. 100 publications. Research specialties: multinuclear NMR spectroscopy and imaging of living systems.

Whole Body Machines: NMR Phased Array Coil Systems

Peter B. Roemer
Advanced NMR, Wilmington, MA, USA

William A. Edelstein
General Electric Corporate Research and Development, Schenectady, NY, USA

and

Cecil E. Hayes
University of Washington, Seattle, WA, USA

1 INTRODUCTION

A small surface coil gives a good MRI (magnetic resonance imaging) or MRS (magnetic resonance spectroscopy) signal-to-noise ratio (S/N) close to the coil for a region whose dimensions are comparable to the size of the coil. A small coil has the drawback, however, that its field-of-view (FOV) is therefore limited. A volume coil, which surrounds a substantial portion of the body such as the torso or head, has a large field-of-view but poorer S/N. The *NMR phased array* collects data simultaneously from a distribution of surface coils (one- or two-dimensional) to achieve the S/N of a surface coil with the FOV of a volume coil.

The present discussion generally focuses on MRI. However, the NMR phased array is equally applicable to providing good S/N over a large FOV for spatially resolved MRS, which is accomplished using imaging techniques.

There are a number of technical difficulties that must be overcome in order to use closely spaced surface coils. There is an electrical interaction, which can be eliminated for adjacent coils by overlapping just the right amount to produce zero mutual inductance. Next-nearest neighbors and more distantly positioned coils can be decoupled by attaching a low-input-impedance preamplifier to one of the resonating capacitors for each surface coil.

The simplest realization of the NMR phased array acquires and processes separate images for each surface coil in the array, and produces a final image that is the optimized weighted sum of the images from all the coils. A further advance convolves a few Fourier coefficients from the Fourier transform of the coil sensitivity profiles with the NMR signal in the time domain, and yields a single, small data set that can be processed into images by straightforward Fourier transformation. While this latter procedure has been proven by computer modeling, a true implementation of the convolution scheme will require the development of sophisticated hardware using dedicated high-speed signal processing electronics.

2 OPTIMUM S/N FOR SURFACE COILS: APERTURE SYNTHESIS

The best S/N for a circular-loop surface coil is obtained when the loop diameter is approximately equal to the voxel depth.[1,2] (The actual relationship is optimum coil diameter = 0.89 × voxel depth.) This relationship is derived by considering the signal from the target voxel versus the electrical noise from the body as the loop size is varied.

Roemer et al.[3] calculated the S/N for arbitrary, abstract current distributions on the body surface, and concluded that the best possible S/N consistent with the laws of electromagnetism (the 'ultimate' S/N) would be achieved by a current distribution that approximates the current in a circular loop. A real circular loop has an S/N over 90% of the ultimate S/N.[3] Thus a simple circular loop is a useful building block in trying to maximize the S/N quality of MRI and MRS.

With an array of small coils, it is possible to synthesize a larger coil and achieve the optimum S/N for that larger coil. Roughly speaking, if one wishes to look at a voxel at a depth large compared to one of the coils in the array, the optimum SNR is obtained by adding the signals from a collection of circular loops whose total diameter is approximately equal to the depth of the voxel in question.

3 NMR PHASED ARRAY TECHNIQUES: OVERLAPPING COILS AND LOW-INPUT-IMPEDANCE PREAMPLIFIERS

Figure 1 shows a schematic diagram of a four-element phased array for imaging of the spine that illustrates some technical aspects of the phased array assembly.[4] The basic difficulty of using an assembly of surface coils is their interactions. If two resonant circuits (i.e., surface coils) tuned to the same frequency are brought close together and have significant mutual inductance, the pair develops two new resonances: one above and one below the desired frequency. There are two steps that can correct this problem. First, as the coils actually overlap and the degree of overlap varies, the sign of the mutual inductance changes. There is an overlap for which the mutual inductance is exactly zero, and both coils can be tuned independently to the same frequency. Thus, in Figure 1, coil 1 and coil 2 are overlapped to have zero mutual inductance, as are the coil pairs 2 and 3, and 3 and 4.

The interaction between next-nearest neighbors, for example, coils 1 and 3, and 2 and 4, in Figure 1, can be alleviated by the electrical circuitry of the preamplifier attached to each coil in the array. If one of the several capacitors that tune each coil (see coil 4 in Figure 1) is shorted out, that coil is no longer resonant at its original frequency and no longer disturbs the operation of other nearby coils at the target frequency. Alternatively, if one of the capacitors were resonated with an inductor then current would be prevented from flowing in the coil, and again that coil would not interfere with its neighbors.

In the phased array of Roemer et al., preamplifiers with low input impedance (a few ohms or less) are connected, in series with an inductor, across one of the capacitors in each coil to receive the NMR signal. The inductance plus series low impedance of the preamplifier resonates the coupling capacitor and

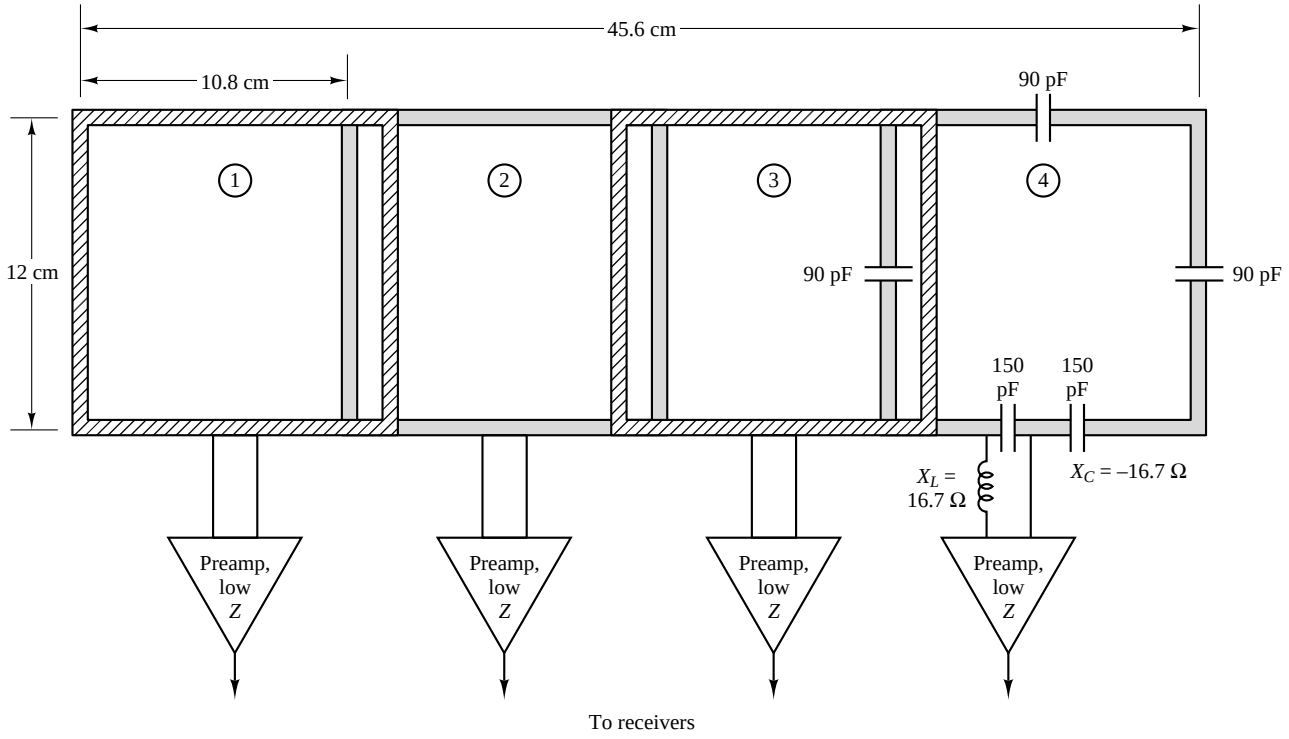

Figure 1 Four-element linear phased array coil for spine imaging. Nearest-neighbor interactions are eliminated by overlap. Next-nearest-neighbor and more distant coil interactions are reduced to negligible levels by connection to low-input-impedance preamplifiers, which, with a series inductor, act as a blocking network

forms a blocking network that decreases currents in the surface coil at the NMR frequency, thereby destroying interactions with other coils in the array. The preamplifier–surface coil combination still works as an efficient, low-noise receiver at the NMR frequency, although a complete explanation of this point is beyond the scope of this article.

4 CONVENTIONAL NMR PHASED ARRAY SYSTEM ARCHITECTURE

Figure 2 shows a conventional system architecture for the NMR phased array that is present commercial practice. Each separate surface coil making up the array has its own receiver chain, consisting of preamplifier, mixers, analog-to-digital converter (A/D), and computer buffer. The signals from each coil are digitized and individually converted into images by a two- or three-dimensional FFT (fast Fourier transform). The individual coil images are then combined to form the final image (see Section 5). The drawback of this arrangement is the large amount of data and consequent data manipulation required if there are more than a few coils in the phased array. Present commercial implementation is limited to simultaneous imaging from four coils.

A more advanced concept, time domain processing of phased array data, which makes coil arrays with many individual coils practical, will be discussed below; realization of that scheme requires a very different system architecture.

5 PHASED ARRAY IMAGE RECONSTRUCTION

The present method of image reconstruction takes images from individual surface coils in the NMR phased array and combines them into a final image using weights that maximize the S/N of the result. In a radar phased array, signals in the antennas composing the array have the same amplitude but differ in phase. An image is produced by adjusting each signal

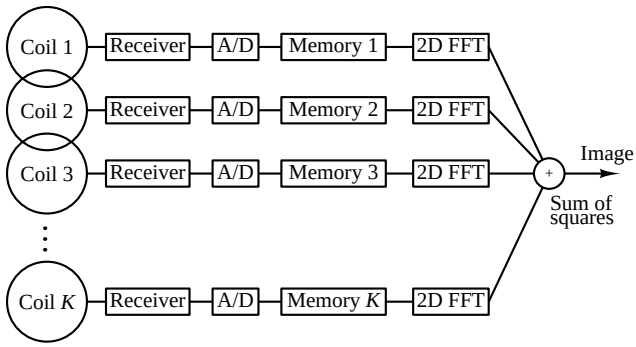

Figure 2 NMR phased array system architecture for sum-of-squares reconstruction. Each coil in the array has its own receiver chain. The signal from each coil is digitized and FFT-processed. The result is combined to give the final image by adding the sums of squares of the individual signals. All receivers operate from the same local oscillator, and the data on all channels are sampled simultaneously

phase to a common value and then adding the signals constructively. For the NMR phased array, each voxel induces a signal in each coil that varies in both phase and amplitude, depending on the relative location of coil and voxel. Individual coil signals produced by a particular voxel are not of equal quality, so a simple summing of the signals is not adequate.

Intuitively, it is evident from Figure 1 that a voxel above, for example, coil 1, will, in the final image, be mostly composed of the image signal for that voxel from coil 1. Similarly, a voxel above coil 2 will, in the end, be mostly composed of the image signal for that voxel from coil 2. A voxel midway between coil 1 and coil 2 will consist of about half of the image signal from coil 1 and half the image signal from coil 2, with a small amount of additional information from other coils. The image intensity of the ith pixel would, in general, be given by[4,5]

$$I(i) = \sum_j w(i,j)S(i,j) \tag{1}$$

where $S(i,j)$ includes the phase and magnitude of the signal in coil j due to pixel i, and $w(i,j)$ is the weighting factor needed to compensate for the phase and magnitude differences between coils.

If all coils in the array are exactly the same, and have the same gain in their receiver chains and the same amount of noise from the body, the signal magnitude $S(i,j)$ is a good measure of signal quality and can be used as the weighting factor $w(i,j)$. Hence, to a good approximation, the best S/N for the final image is obtained if the image intensity $I(i)$ at pixel i is given by[4,5]

$$I(i) = \left[\sum_j S(i,j)^2\right]^{1/2} \tag{2}$$

where the square root is taken in order to restore the appropriate image contrast. This method of combining the images is called 'sum of squares', and is shown at the combining '+' in Figure 2. For arrays with different coil sizes and receiver chain gains, the inverse of the noise variance for each coil must be included in $w(i,j)$ in order to give the correct statistical weighting. Equation (2) becomes

$$I(i) = K\left[\sum_j \frac{S(i,j)^2}{\langle N(j)^2\rangle}\right]^{1/2} \tag{3}$$

where $\langle N(j)^2\rangle$ is a time average of the square of the noise at the output of the receiver chain for coil j, and K adjusts the dynamic range of the displayed image. The technique using equation (3) is known as the 'sum-of-squares' method, and is presently used in commercial phased arrays because it requires no prior knowledge of coil location or sensitivity and hence is easy to use. A drawback is that image artifacts (e.g., wraparound signal) may give false weights.

The above equations produce an image that retains the strong intensity variations characteristic of surface coil imaging: the image intensity decreases for objects farther from the coils.

The weighting can also be determined using the 'reciprocity principle'.[6] The signal $S(i,j)$ in each coil is proportional to a coil sensitivity factor times the nuclear magnetization $M(i)$, which contains the clinically relevant information. According to reciprocity, the sensitivity of coil j to the magnetization contained in a given voxel i is proportional to the magnitude of the magnetic field $B_1(i,j)$ that would be produced at voxel i by unit current in coil j. Since the spins are only sensitive to rf fields perpendicular to the static field, the component of the calculated $\boldsymbol{B}_1(i,j)$ perpendicular to the static magnetic field must be used.

A combined image without the surface coil variations in intensity can be constructed from a weighted average of each coil's estimate of $M(i)$, which is proportional to $S(i,j)/B_1(i,j)$ The appropriate weighting factor for each $M(i)$ is the inverse noise variance scaled by the relative signal strength, which is proportional to $B(i,j)$. After cancellation of some of the factors of $B_1(i,j)$, the intensity corrected image is calculated as

$$I(i) = \frac{\sum_j S(i,j)B_1(i,j)/\langle N(j)^2\rangle}{\sum_j B_1(i,j)^2/\langle N(j)^2\rangle} \tag{4}$$

where the sum in the denominator normalizes the total weighting to unity. Figure 3 shows a system architecture for B_1 field-map weighting phased array image reconstruction.

The B_1 weighting in equation (4) requires detailed knowledge of the location of the rf coils and a stored array of calculated weights $B_1(i,j)$, and is harder to implement than the sum-of-squares method. Unlike the sum-of-squares method, B_1 weighting is not subject to wraparound artifacts.

The sum-of-squares method [equation (2) and (3)] does not achieve the highest possible S/N for a given reconstruction because the use of signal magnitudes does not produce the optimum combination of signals when the S/N is low or noise is correlated between coils. An additional refinement using the correct phase relationships makes the final expressions somewhat more complicated.[4,5] To take correlated noise fully into account, the optimum reconstruction would combine signals with a phase angle dependent on the amount of noise correlated in-phase and 90° out of phase with the NMR signal. In practice, the small gain in S/N, typically less[4] than 10%, is not worth the added complexity in keeping track of the coil positions.

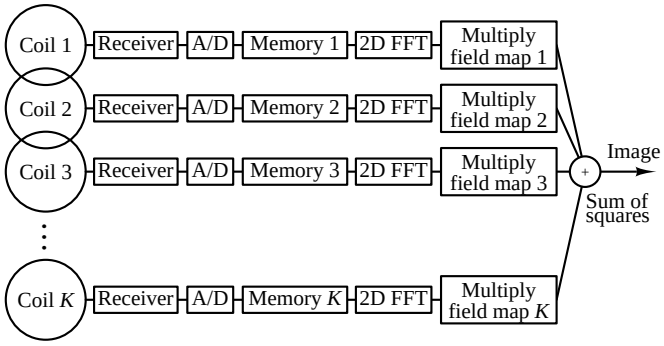

Figure 3 NMR phased array system architecture for field-map weighting reconstruction. Each coil in the array has its own receiver chain. The signal from each coil is digitized and FFT-processed. The result is combined to give the final image by dividing the image strength for a given voxel from a particular coil by the sensitivity of that coil to the voxel position. The sensitivity is proportional to the field strength at the voxel position caused by a unit current in the coil

Figure 4 Four sagittal images taken with a four-element linear phased array coil shown schematically in Figure 1. The four coils receive data simultaneously. The FOV is 48 cm, with a 512 × 512 pixel resolution, NEX = 2, 5 mm slice, TR = 400 ms, TE = 20 ms, imaging time = 6 min 50 s, and B = 1.5 T. Phase encoding is vertical. Only the central 256 points in the horizontal direction are shown. Artifacts at the top and bottom of the images are caused by wraparound

Figures 4 and 5 show the initial images from a four-element spine phased array combined into a final image. In this case, the final image (Figure 5) has also been corrected for nonuniform sensitivity of the surface coils. Areas with low signal (and poor S/N) have been boosted so that all regions have approximately the same signal level. The noise levels in these regions are also increased, so areas that started with weak signals still have the same (poor) S/N.

Figure 5 Image obtained by combining the images shown in Figure 4. Regions with weak signals have had their image intensity boosted so that the signal levels are approximately constant over the image. Areas with very poor S/N have been suppressed. The S/N gets worse away from the spine

6 NOISE CORRELATIONS AMONG SURFACE COILS IN THE NMR PHASED ARRAY

The NMR phased array receives both NMR signals and electrical noise from the imaging subject. The latter is the result of thermally generated noise currents in the subject that produce fluctuating rf magnetic fields picked up by the array. Thermally generated noise in the electrical components of the phased array system also contributes to noise in the final signal and resultant image or spectrum.

Noise generated by the subject can be received simultaneously by several coils in the array, which may produce noise correlations among the coils. The relative amount of correlated noise in two coils depends on the proximity of the coils—the closer the coils, the greater the correlation.

Although noise is one of the most difficult and fascinating theoretical aspects of the NMR phased array system, the practical effects of noise correlation are minor. The amount of correlated noise is sufficiently small that it cannot be used to reduce noise significantly in the reconstructed image or spectrum. Roemer et al.[4] show that, for a typical case such as adjacent overlapped coils in a spine array, the correlated noise power is calculated to be a maximum of 41%, assuming a dissipative, infinite half-space. The measured correlated noise power was 23%, because the body is finite.[4] After accounting for the uncorrelated noise in a preamplifier and receiver components and performing the optimum reconstruction, less than a 10% improvement in S/N could be realized by using knowledge of these correlations.

7 CLINICAL APPLICATIONS

A variety of phased array coil geometries have been used for clinical applications. The improved S/N obtained with the phased array has enabled established diagnostic procedures to be performed faster and/or with higher spatial resolution, and has made possible new procedures that were not practical with conventional coils.

Clinical phased arrays can be classified by configuration into surface coil arrays and volume arrays. The surface coil array is usually a linear chain of coils, and is best suited to observe a superficial structure whose length is greater than its depth. The coils of a volume array attempt to examine all the internal structures of the body part they circumscribe.

The spinal phased array is a prime example of a surface coil array used to improve an established MRI application. Spine imaging with conventional surface coils has been a time-consuming endeavor, because conventional coils have to be repositioned and the scan repeated for several locations along the spine.[7] The spinal phased array allows the acquisition of a 40–45 cm linear field-of-view in a single imaging period. Using 512 × 256 pixel resolution on a rectangular field-of-view can yield high-resolution sagittal images. One commercial spinal phased array design is made up of six coils spaced 12 cm apart along the spine. Three choices of four contiguous coils can be activated to image the cervical, thoracic, or lumbar spines. Phased array techniques reduce total examination time for spinal studies by a factor of two or more, and lead to greater patient acceptance and scanning efficiency.[7]

Volume phased arrays were first applied to pelvic imaging[8] because it was assumed that improved resolution was only meaningful where respiratory motion was minimal. As an alternative to the more traditional volume imaging coils such as the birdcage resonator (see ***Birdcage Resonators: Highly Homogeneous Radiofrequency Coils for Magnetic Resonance***), the volume phased array offers several advantages. First, the individual coils of the array can be tailored to fit the anatomy with fewer constraints than are needed for a standard volume coil. Therefore the array can provide a tighter coupling to the signal from the region of interest and can exclude noise from more distant tissue. Second, the array that circumscribes the volume of interest incorporates the benefits of quadrature reception without needing to satisfy the usual requirements of field orthogonality and mode isolation for a traditional quadrature coil.[5] Finally, superficial regions yield the high S/N of an individual surface coil, whereas the central region has the S/N resulting from averaging signals of the four coils forming the array. The S/N at the center is no better than that of a small quadrature volume coil that has the same overall dimensions as the array. Motion of subcutaneous fat can produce disproportionally larger motion artifacts from the surface array because of tight coupling to the array.

A four-coil pelvic array comprises two coils placed anteriorly and two posteriorly. The S/N for the pelvic array is approximately three times higher than the S/N for a full-sized body coil imaging the same region.[9] Such an S/N increase permits pelvic imaging with smaller fields-of-view (16 cm), thinner slices (3 mm), and/or higher resolution (512 × 512).

Phased arrays also facilitate the use of FSE (fast spin echo) techniques to obtain T_2-weighted images. Long effective echo times provide good contrast in pelvic structures, but at reduced signal strength. The enhanced S/N of the phased array permits good images to be acquired in a practical scan time using FSE.[10]

High-speed imaging sequences using low-flip-angle excitation and gradient-recalled echoes can produce images in about 1 s. Such images taken with a body coil have marginally useful S/N. With the volume phased array, low-flip-angle, gradient-recalled echo sequences can produce clinically useful, motion-free images of the liver[11] and pulmonary vasculature[12] during a single breath-hold.

High-resolution images of brain structures can be acquired by applying a volume phased array to the head.[13] The head array consists of two pairs of coils that cover about 16 cm of the circumference on each side of the head. When studying temporal lobe epilepsy, the coils are placed over both hippocampi, which lie about 5–6 cm from the lateral scalp surfaces in adults. At this depth, the S/N is about 1.67 times better than that of the standard quadrature head coil. Figure 6 is an example of a T_2-weighted fast spin echo image acquired for a 512 × 512 matrix on a 3 mm thick slice. The 0.3 mm × 0.3 mm in-plane resolution is degraded by pulsatile motion of the brain tissue unless flow compensation and cardiac gating are used with the pulse sequence.

MR neurography is an example of a new MR diagnostic technique whose development depends on the S/N advantages of phased arrays. MR neurography[14] employs pulse sequences tailored to highlight peripheral nerves and suppress signals from surrounding tissue such as fat, vessels, and muscle. Inflamed nerves appear hyperintensive compared with normal nerves. Because the resulting signals are weak, a high S/N performance is required from the coil array in order to distinguish the nerve structures from the surrounding tissue.

A linear surface coil array has been built to track the brachial plexus, which runs from the neck to the axilla. The brachial plexus is a complex network of four cervical and one thoracic nerves that fuse, mix, and split into nerves supplying the arm, shoulder, and chest. The brachial plexus array has six

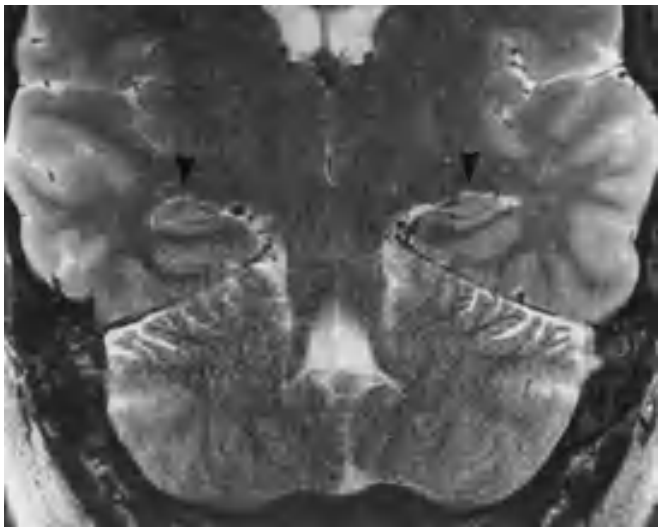

Figure 6 Portion of a high-resolution oblique coronal brain image, showing the internal architecture of the hippocampi (the almond-shaped structures indicated by the arrowheads)

coils contoured fit with one coil anterior to each axilla and each clavicle, and a lateral pair covering the volume of the lower neck. The three coils on one side plus the opposite neck coil are activated for a unilateral study. Selecting the middle four coils can give a bilateral study of the central region. The tight coupling of the array to the region of interest produces S/N not possible with conventional coils.

8 REAL-TIME PROCESSING

Real-time data processing techniques, similar to those used for radar and ultrasound, have been developed for NMR signals from the multiple receivers in the NMR phased array.[15] This approach has not been implemented on commercial imagers, since they have relatively few receive channels and since there is not presently a great demand for real-time imaging. As methods of building phased arrays with larger numbers of coils develop and the applications of fast imaging expand, the increased amount of data may make real-time processing attractive.

To see how a real-time processing method is implemented, we need only look at equation (4) and construct a mathematically equivalent expression in the time domain. According to equation (4), the reconstructed image from each coil is multiplied pixel-by-pixel with the associated field map from the rf coil. The results from each channel are then added together. The multiplication function in the image domain corresponds to convolution in the time domain. Hence the NMR signal from each receiver can be convolved with an appropriately designed filter, the results of which are added to form a composite time domain signal.

Figure 7 is a schematic diagram of a real-time processing system. The information from each coil is processed by its associated filter, and the results from all coils are combined into an array in memory as shown. The contents of the memory are then processed by a single FFT. This arrangement differs from that shown in Figure 2 where the data from each coil must be FFT-processed. The point is that the FFT is generally done in an array processor, which is relatively expensive. For a coil assembly consisting of a few surface coils, the FFTs of the coils can be done sequentially. For a coil assembly containing many coils, sequential FFTs would impose a significant time penalty. So the present scheme allows the processing of data from many coils in a short time.

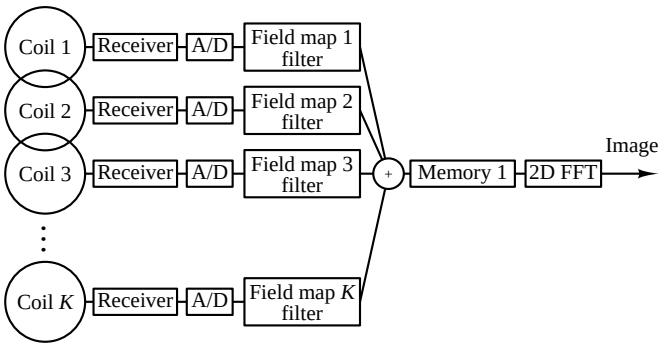

Figure 7 NMR phased array system architecture for time domain filtered reconstruction. Each coil in the array has its own receiver chain. The signal from each coil is digitized, multiplied by a filter kernel, and combined in a data array with signals from other array coils. The data array is FFTd to give the final image. So only one FFT needs to be done in this case, no matter how many individual coils in the array, in contrast with one FFT per coil in the conventional system (Figures 2 and 3)

The remaining difficulty is the filters, which, at least conceptually, are straightforward. They represent the Fourier transform of the field map generated by each coil. A substantial practical simplification results when one realizes that the coil field map is slowly varying in the image space and needs relatively few terms to describe it properly in the time domain. With this simplification, a practical implementation of the time domain processing uses a filter kernel derived by Fourier transforming the field map and truncating the result. It would be implemented by the application of programmed high-speed signal processing integrated circuits, which would multiply the incoming signal by the appropriate filter function and then combine into an array in memory. These methods are discussed in detail by Roemer.[15]

9 RELATED ARTICLES

Birdcage Resonators: Highly Homogeneous Radiofrequency Coils for Magnetic Resonance; Surface and Other Local Coils for In Vivo Studies; Whole Body Magnetic Resonance Spectrometers: All-Digital Transmit/Receive Systems; Whole Body MRI: Local and Inserted Gradient Coils.

10 REFERENCES

1. W. A. Edelstein, T. H. Foster, and J. F. Schenck, *Proc. IVth Ann Mtg. Soc. Magn. Reson. Med.*, London, 1985, p. 964.
2. C.-N. Chen and D. I. Hoult, 'Biomedical Magnetic Resonance Technology', Adam Hilger, Bristol, 1989.
3. P. B. Roemer and W. A. Edelstein, *Proc. VIth Ann Mtg. Soc. Magn. Reson. Med.*, New York, 1987, p. 410.
4. P. B. Roemer, W. A. Edelstein, C. E. Hayes, S. P. Souza, and O. M. Mueller, *Magn. Reson. Med.*, 1990, **16**, 192.
5. C. E. Hayes and P. B. Roemer, *Magn. Reson. Med.*, 1990, **16**, 181.
6. D. I. Hoult and R. E. Richards, *J. Magn. Reson.*, 1976, **24**, 71.
7. D. M. Yousem and M. D. Schnall, *J. Comput. Assist. Tomogr.*, 1991, **15**, 598.
8. C. E. Hayes, N. Hattes, and P. B. Roemer, *Magn. Reson. Med.*, 1991, **18**, 309.
9. C. E. Hayes, M. J. Dietz, B. F. King, and R. L. Ehman, *J. Magn. Reson. Imaging*, 1992, **2**, 321.
10. R. C. Smith, C. Reinhold, T. R. McCauley, R. C. Lange, R. T. Constable, R. Kier, and S. McCarthy, *Radiology*, 1992, **184**, 671.
11. A. E. Holsinger-Bampton, S. J. Riederer, N. G. Campeau, R. L. Ehman, and C. D. Johnson, *Radiology*, 1991, **181**, 25.
12. T. K. Foo, J. R. MacFall, C. E. Hayes, H. D. Sostman, and B. E. Slayman, *Radiology*, 1992, **183**, 473.
13. C. E. Hayes, J. S. Tsuruda, and C. M. Mathis, *Radiology*, 1993, **189**, 918.
14. A. G. Filler, F. A. Howe, C. E. Hayes, M. Kliot, H. R. Winn, B. A. Bell, J. R. Griffiths, and J. S. Tsuruda, *Lancet*, 1993, **341**, 659.
15. P B. Roemer, US Patent 5 086 275 (1989).

Biographical Sketches

Peter B. Roemer. 1978, Ph.D., 1983, M.I.T., Cambridge, MA. Electrical engineer, GE Corporate Research and Development, 1983–1990; Manager, MRI, GE Corporate Research and Development, 1990–1994; Engineering Manager, Advanced NMR Systems, June 1994–present. Research specialities: MRI imaging systems, MRI gradient and RF coils.

William A. Edelstein. 1965, U. Illinois, Urbana, IL; A.M., 1967; Ph.D., 1974, Harvard University, Cambridge, MA. Research fellow, Glasgow University, 1974–77; Research Fellow, Aberdeen University, 1977–1980; physicist, GE Corporate Research and Development, Schenectady, NY, 1980–present. Research specialties: MR imaging, thermal remediation of environmental contamination.

Cecil E. Hayes. *b* 1941. B.Eng.Phys., 1964, Cornell University, Ithaca, NY; Ph.D., 1973, (supervisor Robert V. Pound), Harvard University, Cambridge, MA. Postdoctoral work at Rutgers University (with Herman Y. Carr) and at University of Utah (with David C. Ailion), 1973–1982. Senior physicist, GE Medical Systems 1982–91. Associate Professor of Radiology, University of Washington, 1991–present. Approximately 25 publications. Current research specialty: rf coils for MRI.

Whole Body Magnetic Resonance Spectrometers: All-Digital Transmit/Receive Systems

G. Neil Holland

Erbtec Engineering, Boulder, CO, USA

1 INTRODUCTION

In a magnetic resonance (MR) imaging system, the spectrometer acts as the transmitter of radiofrequency (rf) waveforms and the receiver of the MR signal. Although MR was traditionally implemented by analog circuits,[1] advances in digital circuits have enabled rf transceivers in MR systems to be designed with digital devices for performing those functions previously implemented with analog circuitry.[2] As with the compact disk player and digital cellular telephone, when used in a spectrometer for MR imaging, digital technology can provide improvements in clarity and fidelity, since digital circuits are not subject to the imprecision and temporal drift inherent in analog equipment.

Implementation of spectrometer functions using digital electronics can provide benefits in the speed and precision of performing frequency shifts for multislice excitation and presaturation pulses, can give improved fidelity and linearity of the transmitted signal waveform resulting in improved slice profiles, can provide precise splitting of the received signal into real and imaginary parts, thus avoiding 'quadrature ghosts', and can give improved filtering for the prevention of aliasing or 'wraparound' artifacts. In addition, the digital spectrometer lends itself to being configured as a multichannel system, and thus is particularly important for implementation of phased array multiple receive coil technology.

2 MR TRANSMITTER AND RECEIVER

2.1 Transmitter

The transmitter forms the rf pulses required for imaging sequences. These rf pulses are fed to an rf power amplifier and ultimately the rf transmitter coil to excite the spin system and to generate a resonance signal. Slice-section techniques use spectrally tailored rf pulses for selective excitation, which is achieved by amplitude modulation of the transmitted rf pulse. The phase of the rf pulses is computer-controlled, and is used in artifact rejection schemes or advanced excitation schemes. To excite multiple slices, the transmitted rf pulse must vary in frequency for each excitation. Consequently, four forms of modulation of the rf carrier are used in MR imaging sequences: pulse, frequency, amplitude, and phase.

In a conventional transmitter, the rf frequencies are generated from a frequency synthesizer controlled by the system computer. Generally, two or more frequencies are mixed, whether in single or multiple stages, by devices known as double balanced mixers to form the final output frequency. Amplitude and phase modulation may also be accomplished with double balanced mixers. For amplitude modulation, the audiofrequency modulation envelope (or pulse shape) is fed as an analog waveform to one input of the mixer and fixed rf level (the 'carrier') to the other input. The modulation envelope is derived from a computerized waveform through a digital-to-analog converter (DAC).

On the transmitter side, several important performance parameters can affect image quality. The first of these, known as 'carrier feedthrough', is in the amplitude modulation section. All mixers have some signal leakage (carrier feedthrough) from input to output, which means that when an amplitude of zero is programmed, the modulator output is not truly zero. This small residual signal affects the quality of the rf pulses, particularly at lower modulation levels (such as for low-flip-angle sequences), and can affect slice profile. In addition, most imaging pulse sequences use a scheme in which the phase of successive rf pulses is alternated. Phase alternation works in conjunction with the data acquisition process to remove artifacts. This requires an exact balance between the 0° and 180° rf phases. Carrier feedthrough can contribute to phase imbalance, as can amplitude imbalance due to dc offset on the DAC that provides the audiofrequency modulation envelope. The exact manifestation of artifacts caused by carrier feedthrough and the complexity of design required to avoid them depend on the detailed implementation of the transmitter mixing scheme. However, the principal advantage of the digital implementation is that modulation artifacts of this form are eliminated entirely.

2.1.1 Digital Transmitter Implementation

A description of a typical digital transmitter is given below, and is illustrated in Figure 1. The major digital building block for this device is known as a numerically controlled oscillator (NCO), or as a direct digital synthesizer (DDS). This device is essentially a single chip frequency synthesizer, which can be interfaced to and controlled by the pulse programmer or host computer, and is set to produce an intermediate frequency (IF) (e.g., 3.5 MHz) via a DAC, which is mixed with a fixed frequency (e.g., 60 MHz) to generate the final output frequency (e.g., 63.5 MHz). The NCO architecture digitally divides the phase of a highly accurate clock by a digital tuning word (typically 32 bits) and uses a look-up table to convert the phase information to the desired frequency and sine wave output format. Structurally, the output of the NCO feeds a digital multiplier, which is used to perform amplitude modulation of the rf pulse. This is achieved by feeding one port of the multiplier with the digital modulation envelope while the frequency data stream from the NCO feeds the other port of the multiplier. Note that with higher levels of digital integration now being achieved, the modulation may be internal to the NCO chip. In addition, the NCO has a phase port that allows coherent control of the phase of the output frequency. Consequently, all four forms of modulation referred to above can be accomplished with a single large-scale integrated (LSI) circuit. Not only does this significantly reduce parts count, and

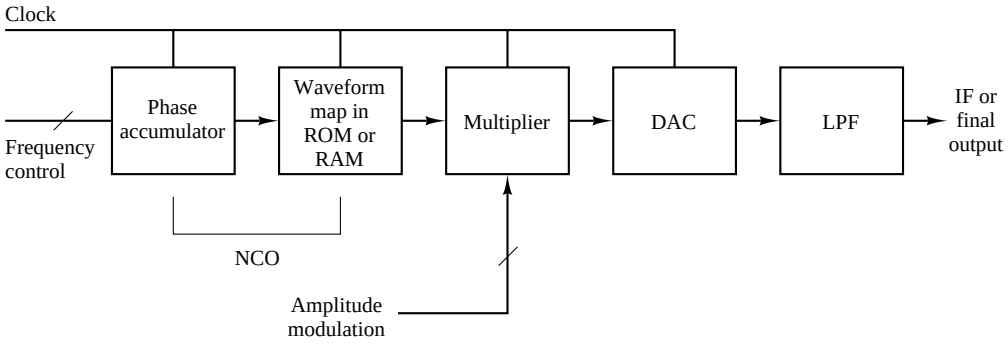

Figure 1 Digital transmitter representation showing the direct digital synthesis of the output frequency and digital modulation of the rf waveform. Depending on the final required Larmor frequency, an additional mixing step may or may not be required

hence increase reliability, but the implementation also overcomes limitations of the analog design described earlier—basically, by avoiding the generation of the Larmor frequency during the time a zero profile is selected. In both the digital and analog implementations of the transmitter, the final output frequency is generated by mixing the modulated IF to the final output frequency. Although it is possible to get NCO devices that operate at frequencies as high as those used with MRI systems—thus, at least in principle, meaning that an MRI transmitter can be constructed from a single digital device—the output DAC cannot be greater than 8 bits owing to speed requirements, which places limitations on modulation accuracy and hence the quality of the resultant slice profile. The effect of DAC accuracy or number of bits on slice profile has been studied.[3] Evaluating the transverse magnetization profile following a small-tip-angle pulse shows that beyond 6 bits, the magnitude of unwanted signal is less than 1%. However, the DAC is also used to set the amplitude of the rf pulse for rf calibration, and must handle the range of tip angles from 180° to as low as approximately 10° for pulse sequences. This means about 5 bits of 'headroom' are required, thus meaning that an 11-bit converter would be recommended. The limiting factor in modulation accuracy is not, in fact, the word depth or number of bits used but rather the 'glitch' energy of the output DAC. Typically, this results in the loss of another bit of resolution, meaning that in practice a 12-bit DAC is required for rf pulse modulation.

2.2 Receiver

The receiver in an NMR spectrometer or MR imaging system takes the incoming NMR signal from the preamplifier and presents it to the computer system for data processing by FFT. The signal is preprocessed in the receiver to remove the rf carrier in a process known as demodulation or phase-sensitive detection, and split into phase quadrature. This is accomplished by splitting the incoming signal into two identical channels. The signals feed the rf ports of identical double balanced mixers. The mixer local oscillator (LO) ports are fed with reference frequencies at the same center frequency as the input signals, but the phase of the two reference signals differs by 90°. In a conventional receiver, programmable audiofrequency low-pass filters (usually Butterworth) operate on the quadrature signals to remove unwanted upper sidebands and to improve the signal-to-noise ratio (S/N) by matching the bandwidth of the filters to the known bandwidth of the NMR signal. After the filters, the quadrature NMR signals are digitized by a pair of analog-to-digital converters (ADCs). The conversion rate of the ADCs is determined by the bandwidth of the NMR signal. Typically, twofold oversampling is used. For example, for a 256^2 matrix image, 512 sampled points at 8 μs per point would result in a 62.5 kHz bandwidth. This operation is illustrated in Figure 2. This 'classical' implementation has a number of drawbacks. First, after the signal is split, the two channels must be exactly matched in both amplitude and phase. This is difficult to accomplish over a wide bandwidth. Second, the demodulation process places dc at the center of the signal bandwidth, with the result that any low-frequency noise causes a center frequency artifact (usually seen as a faint central line in an image). Last, quantization noise in the ADCs limits the overall S/N performance of the system.

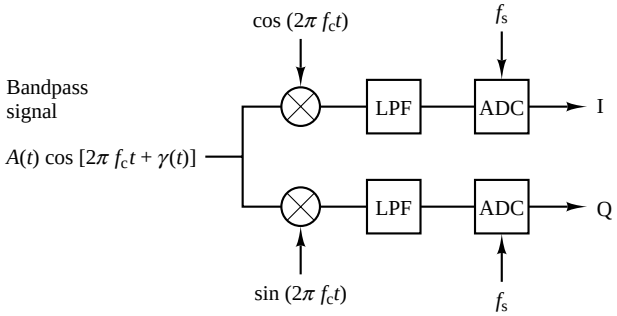

Figure 2 Classical receiver representation demonstrating the demodulation of incoming signal θ into in-phase and quadrature components by the use of parallel mixers to remove the rf carrier. After the mixers are low-pass filters (LPF), followed by analog-to-digital converters (ADCs)

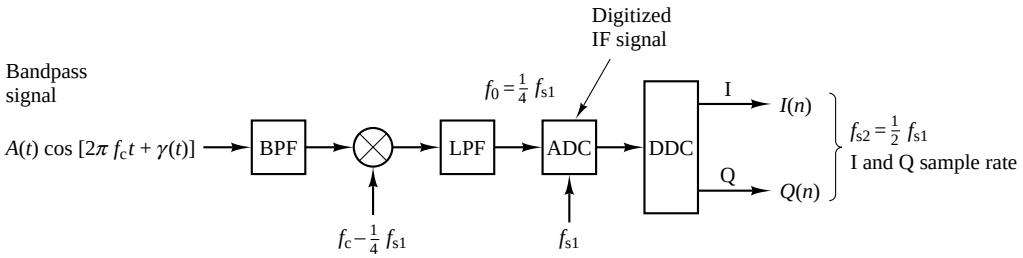

Figure 3 Digital receiver representation demonstrating the same operational steps as shown in Figure 2. The initial signal is filtered and mixed to an intermediate frequency which is one-fourth of the ADC sample frequency. A digital down-converter (DDC) performs final demodulation and low-pass filtering

2.2.1 Digital Receiver Implementation

Turning now to a digital receiver (Figure 3), the basic difference in design is that the NMR signal is mixed down to some intermediate frequency and digitized by a single ADC, so that final demodulation, separation into I and Q channels and low-pass filtering is performed in the digital domain.[4] The ADC is set to a fixed sampling frequency, operating at $N \times$ IF where IF is the intermediate frequency. Generally, $N = 4$, i.e., fourfold oversampling, is used. The choice of IF is determined by the maximum sampling rate of the ADC, but, in general, should be as high as possible, for two reasons. First, it dictates the minimum sampling interval, which then impacts the total sampling period, which then in turn can place a limitation on minimum echo time (*TE*). Second, to maximize S/N, the ratio between final subsampled baseband sampling rate and the IF should be as great as possible. This minimizes the ADC quantization noise per unit bandwidth.[5] There is another trade-off to be made when selecting the intermediate frequency, namely, the word depth of the ADC, i.e., the number of bits. As the number of bits decreases, conversion speed increases. For example, 8-bit converters can operate at speeds up to 100 MHz, whereas 16-bit converters only up to 1 MHz are readily commercially available. Quantization noise magnitude is determined by the voltage step size of the converter, and S/N is therefore proportional to $2^N/\sqrt{}$(conversion rate), where N is the number of bits in the converter. In other words, from a quantization noise perspective, a 14-bit converter operating at 4 MHz is equivalent to a 16-bit converter operating at 0.5 MHz.

To achieve the equivalent function of quadrature phase-sensitive detection for fourfold oversampled data, the input data stream is multiplied by the cosine and sine of the IF, which simplifies to multiplication by +1, 0, −1, 0, ... for one channel and 0, +1, 0, −1, ... for the other. This process generates an exact 90° phase difference between channels, and centers the signals around dc. Low-frequency analog noise that in an analog receiver manifests self as a 'dc' artifact in the scheme just described is placed outside the imaging bandwidth so that the need for dc correction is eliminated. A second stage of digital filtering is implemented in each demodulated channel to provide the variable sampling required by the MR sequences. Finite-impulse-response (FIR) filters[6] perform this operation. These are multistage, linear phase filters, which are ideally suited to an implementation in silicon because of their repetitive pipelined operation. The selectable output sampling rate required by the NMR pulse sequence is achieved by choice of the decimation factor, which is the difference between input and output rates from the filters. FIR filter characteristics are more variable than their analog counterparts. Whereas the roll-off of an analog filter is determined by the number of poles (or filter stages), so that, for example, a six-pole filter attenuates at 36 dB per octave, the FIR filter design process allows tailoring of roll-off by trading final attenuation value (stopband attenuation) with rate of attenuation and ripple within the passband. FIR filters are defined in terms of the number of 'taps' they contain, where each tap represents a multiply–accumulate operation. With increasing decimation factor, a larger number of taps are needed to implement a filter with effective attenuation (> 80 dB at twice the corner frequency). Therefore, narrowband filters, such as would be used in spectroscopy sequences, require a greater number of taps, potentially up to 256, whereas for an imaging sequence with a decimation factor of say 32 only about 32 taps may be needed. While cut-off frequencies can be extremely sharp, with filters designed with many taps, actual implementation may require a large number of devices. In early digital receiver systems, each of the functions described above were implemented with individual digital devices. Today, the key building block for a current state of the art digital receiver is known as a digital down-converter (DDC). This is a single chip synthesizer, quadrature mixer, and lowpass filter, whose input is a sampled data stream taken directly from the ADC. Devices are available that can handle data up to 16-bits wide at a 52 MSPS (mega-samples-per-second) rate. The complex result of the demodulation process is lowpass-filtered with identical filters in the in-phase (I) and quadrature (Q) processing chains. Lowpass filtering is accomplished via a high decimation filter (HDF), followed by a fixed finite-impulse-response (FIR) filter. The devices provide automatically optimized matched bandwidth in that the lowpass filter inherently tracks the output (decimated) sampling rate. FIR filter coefficients are generated internally to the chip, so no preprogramming of filter parameters is required. Another advantage of the DDC is that automatic quadrature spectral reversal can be performed. In techniques such as EPI where echoes are taken alternately from read gradients of opposite sign, the frequency of each readout is therefore reversed and must be reordered. This is accomplished in the DDC by translating the lower sideband of the input to baseband rather than the upper sideband.

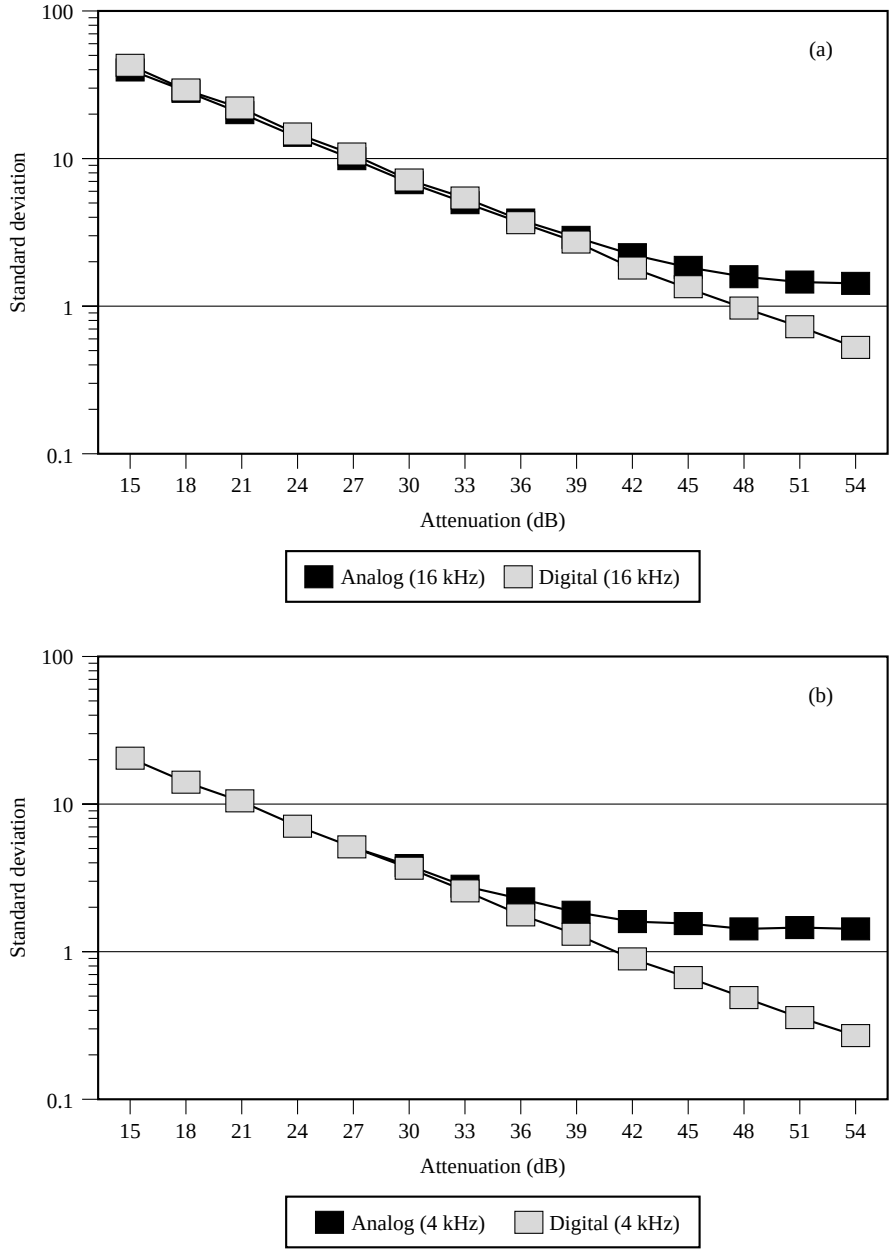

Figure 4 (a) A plot of image noise versus receiver attenuation for both analog and digital receivers operating at a 16 kHz bandwidth. Note the improved linearity at high attenuation factors (corresponding to high signal strength). (b) Data plotted for the same conditions as in (a), except with a 4 kHz bandwidth. The linearity and dynamic range of the digital system are unchanged, whereas the quantization noise per unit bandwidth of the analog system has increased fourfold

2.3 Experimental Validation of Digital Spectrometer S/N Improvements

An experimental validation of the relative performance between analog and digital receivers has been conducted (S. Mitchell, personal communication). The focus was to demonstrate that the reduced quantization noise of the digital receiver was reflected in actual image S/N improvement. An MR imaging system with identical 'front end' configuration (coils and preamplifiers), but different 'back end' equipment (spectrometer, data acquisition, and processing and display computers) was used. Images using identical scan parameters were taken first with the analog spectrometer and then with the digital spectrometer. Since the gains of the two spectrometers were different, the image pixel values and spectrometer input attenuator values were used to compute the gain difference between the two units. Then, a series of 'air scans' were taken at different receiver gain settings for the two spectrometers, with the standard deviation of the image noise being measured at each gain setting.

The results are shown in Figures 4(a) and (b). With increasing attenuation (i.e., as signal magnitude increases), the

image noise as evidenced by standard deviation measurement exhibits progressively nonlinear behavior. In Figure 4(a), the response for digital and analog receivers is plotted for effective sampling at 16 μs per point. This shows that the digital receiver exhibits about another 12 dB of dynamic range over its analog counterpart. The situation is demonstrated even more clearly for narrow bandwidth sequences. As shown in Figure 4(b), where data for a sampling rate of 64 μs per point are plotted, the analog receiver performs even more poorly relative to the digital design. The linearity of response for the digital system is unchanged by switching bandwidth whereas the analog system S/N drops by 6 dB. This because the quantization noise per unit bandwidth for the digital system is fixed, but the quantization noise generated by the ADCs in the analog implementation is now spread over a fourfold-narrower bandwidth, thus increasing the noise per unit bandwidth. The practical effect of this is to cause the signal magnitude at which reduced image S/N is visualized to be reduced.

2.4 Implementation of Multichannel Systems

Digital rf architecture is readily amenable to configuration in multichannel systems for both transmitter and receiver. In MRI, the most common use is in multichannel receive systems used with phased array rf coils. In such schemes, individual rf receive coil elements are formed into an array to cover the anatomical region of interest.[7] Each array element is connected to a separate receiver, and the resultant receive signals, either before or after Fourier transformation to the image domain, are combined to form a single image. The digital receiver implementation where the demodulator is connected to a digital signal processor (DSP) is particularly suited to the processing of phased array data. The DSP can be used for preprocessing of data to give weighted summation and correction for amplitude and/or phase variation between channels. The compact nature of a digital receiver design allows multiple receive channels to be configured on a single PC board, thus reducing the cost and complexity of multichannel systems and allowing the S/N advantages of phased array designs to be achieved without significant increase in system equipment. The use of a local NCO for receiver offset frequency allows each receiver in a multichannel array to have a unique demodulation frequency. This can be used to advantage for avoidance of aliasing and in the implementation of arrays where final composite images are not required, such as when used for imaging bilateral structures (e.g., TMJ). In addition, a multichannel system can be used advantageously with conventional quadrature coils by feeding each of the coil quadrature pair outputs to a separate receiver. This can improve performance by allowing for amplitude and phase balance as discussed above, but also can improve S/N by eliminating losses in analog hybrid combiner circuits, since these circuit components are not required.

3 CONCLUSIONS

Digital rf technology has now been widely adopted for use in MR imaging spectrometers, and is the technology of choice for new designs. Since initially demonstrated in the mid to late 1980s, advances in the speed and degree of integration of the digital devices required to implement spectrometer functions on both the transmitter and receiver side have increased dramatically. Other than the D/A converter (DAC) on the transmit side and the A/D converter (ADC) for the receiver, it is now possible to construct a spectrometer for a low- to mid-field system with only two devices—a single digital device for transmitter and a second for the receiver. With this degree of integration and forecasted improvements in speed of operation, the majority of whole body MR systems are expected to utilize direct-conversion digital spectrometers. In addition, because of the high degree of integration of digital spectrometers, it is anticipated that multichannel systems will become the operating standard in the near future. The inherent programmability and built-in self test features of the digital systems are also beneficial to reducing set-up and calibration time. The digital designs offer improvements in terms of accuracy and precision, and on the receive side can demonstrate improved dynamic range, which can be translated into improved S/N for high signal scans.

4 RELATED ARTICLES

Birdcage Resonators: Highly Homogeneous Radiofrequency Coils for Magnetic Resonance; Coils for Insertion into the Human Body; Echo-Planar Imaging; Radiofrequency Systems and Coils for MRI and MRS; Sensitivity of Whole Body MRI Experiments; Surface and Other Local Coils for In Vivo Studies; Whole Body Machines: NMR Phased Array Coil Systems.

5 REFERENCES

1. D. I. Hoult, in 'Progress in Nuclear Magnetic Resonance Spectroscopy', eds. J. W. Emsley, J. Feeney, and L. H. Sutcliffe, Pergamon Press, Oxford, 1978, Vol. 12, p. 41.
2. G. N. Holland and J. R. McFall, *J. Magn. Reson. Imaging*, 1992, **2**, 241.
3. J. Slotboom, J. H. N. Creyghton, D. Korbee, A. F. Mehlkopf, and W. M. M. J. Bovee, *Magn. Res. Med.*, 1993, **30**, 732.
4. L. E. Pellon, *IEEE Trans. Sig. Process.*, 1992, **40**, 1670.
5. A. V. Oppenheim and R. W. Schafer, 'Discrete Time Signal Processing', Prentice-Hall, Englewood Cliffs, NJ, 1989, Chap. 3. Section 3.7.3
6. A. V. Oppenheim and R. W. Schafer, 'Digital Signal Processing', Prentice-Hall, Englewood Cliffs, NJ, 1975, Chap. 5.
7. P. B. Roemer, W. A. Edelstein, C. E. Hayes, S. P. Souza, and O. M. Mueller, *Magn. Res. Med.*, 1990, **16**, 192.

Biographical Sketch

G. Neil Holland. *b* 1952. M.Phil., 1979, University of Nottingham UK. Research fellow in Physics, Nottingham University, 1979–81. Picker International, Cleveland, Ohio, 1981–92; Otsuka Electronics 1992–present. Approximately 35 publications. Current interests include digital rf technology applied to MRI and MRI systems design.

Whole Body MRI: Local and Inserted Gradient Coils

Eric C. Wong
Medical College of Wisconsin, Milwaukee, WI, USA

1 INTRODUCTION

The gradient subsystem of the MRI scanner is responsible for all forms of spatial encoding, including image formation, encoding of flow information, encoding of diffusion information, and spatial modulation of magnetization for tissue tagging and selection of desired coherences (see also ***Gradient Coil Systems***). In many applications, the quality of the data obtained is limited by hardware-imposed limitations on the gradient amplitude or the gradient slew rate. Two examples are echo planar imaging (EPI),[1] which is typically limited in its spatial resolution by gradient amplitude and slew rate, and diffusion imaging,[2] which is limited primarily by gradient amplitude to very long echo times on conventional whole body systems.

Local gradient coils (LGCs) are gradient coils that are smaller than the whole body gradient coils built into clinical imaging systems, and are designed for specific purposes or areas of anatomy. Their smaller size gives them two advantages over whole body gradients.

The first advantage is that LGCs can produce stronger gradients per unit current, and higher gradient slew rates per unit voltage than whole body coils. For many clinical imaging systems, the use of local gradient coils makes more imaging techniques feasible (such as EPI), and improves the performance of many other techniques (i.e., higher resolution, shorter *TE*, etc.). This advantage is a technical and practical one. It brings higher performance gradients to clinical systems in a convenient and inexpensive way because local gradient coils are relatively simple add-on components, much like local rf coils, which are very widely used. However, there is active research at several institutions in the development of more powerful electronics to generate the current and voltage necessary to create strong, rapidly switched gradients using whole body gradient coils, and several commercial units are already available.

The second advantage is that LGCs can create higher gradient slew rates for a given limit on field slew rate. Because time-varying magnetic fields can induce electric currents and neuronal stimulation, there are limits on maximal field slew rates allowed in humans. In the United States, the FDA currently sets this limit at $20\,\mathrm{T\,s^{-1}}$. This field slew rate can be achieved not only using local gradient coils, but also by some of the higher performance whole body gradient systems available today. However, a local gradient coil will in general create a lower field slew rate for a given gradient slew rate, because the physical extent of the fields generated by a local gradient coil is smaller. For example, if a whole body Z gradient coil is used to image the head, the peak field will be in the area of the mid-chest, while the peak field of a local head gradient coil will be in the neck, and will be two to three times lower for a given gradient. This advantage is a more fundamental one in that local gradient coils can achieve stronger and faster switching gradients than whole body gradient systems, regardless of advances in whole body gradient system technology.

The primary disadvantage of using local gradient coils is that they add some complexity to the subject set-up procedure. The added time and effort are similar to that of using specialized rf coils, and, as local gradient coils become more common, commercialized, and integrated into gradient/rf coil units, the additional set-up time should be minimal. In some cases, patient comfort is decreased by the presence of local gradient coils owing to decreased visibility, restriction of patient movement, or acoustic noise. For a given imaging technique, LGCs are generally quieter in operation than whole body gradients. However, because LGCs allow the use of stronger and more rapidly switched gradients, acoustic noise at higher frequencies can be generated, and can attain high wound pressure levels (SPL). The SPL during EPI scanning in a local head gradient coil is approximately 100 dB, but is easily attenuated to tolerable levels using standard (30 dB) foam earplugs.

2 SAFETY

Two potential safety hazards accompany the use of LGCs: mechanical injury from forces and torques on the coil, and injury from electrical currents and voltages.

LCGs are usually designed so that there is no net force of torque on the coil when the coil is in place for imaging. However, if the coil is moved to an inhomogeneous area of the static field, or a portion of the coil fails without opening the circuit, then net forces and torques can result. If 100 A is applied to a coil in a 1.5 T field, torques on the order of 100 N m can be generated in a head gradient coil. If the coil is in an inhomogeneous portion of the field then forces on the order of 1000 N can result. Therefore, the system should be safeguarded so that current cannot be applied when the coil is not in place for imaging. The coil structure and support system should be strong enough to withstand the internal forces encountered during normal operation, and to prevent injury in case of an internal short.

The maximum voltage that drives most LGCs is on the order of 300 V. Although this is enough to cause injury, voltages of this magnitude are easily insulated from patients with only minimal measures such as plastic insulation. However, care must be taken, especially during installation and removal of the coil, that high voltage does not appear at any accessible terminals.

3 DESIGN CONSIDERATIONS

Many factors must be taken into account in the design of local gradient coils, including coil geometry, size, anatomy of interest, desired gradient strength, efficiency, inductance, desired switching rate, eddy currents, gradient uniformity, forces and torques, heat dissipation, and bioeffects. A large

number of trade-offs exist between these factors, and only basic principles are discussed here.

The geometry of LGCs, like that of local rf coils, can be divided into three categories:

1. whole volume coils, which completely surround the anatomical structure of interest;
2. partial volume coils, which partially surround the structure;
3. surface gradient coils, which are placed against one side of the structure.

The primary deciding factor in the choice of coil geometry is the structure of the anatomical region of interest (ROI). If a whole volume coil can be placed around the ROI, as is usually the case for the head and the upper and lower extremities, this is generally preferable from the point of view of coil efficiency (gradient per unit current) and gradient field uniformity. The main drawbacks of whole volume coils are that they limit access to the patient, and they interfere more strongly with the rf fields. For large structures such as the chest and abdomen, a whole volume coil would be essentially a whole body coil. In order to obtain the advantages of smaller coils in these structures, partial volume or surface coils must be used. These will, in general, have smaller regions of usable gradient field uniformity, but can be useful for imaging of relatively small or superficial anatomical structures such as the heart.

The advantages gained by the use of a LGC have a strong dependence on the size of the coil. Two of the desirable properties of gradient coils are high efficiency and low inductance. For a coil of a given design, with a fixed number of turns,

$$\text{Efficiency} \propto \frac{1}{\text{size}^2} \tag{1}$$

$$\text{Inductance} \propto \text{size} \tag{2}$$

These factors indicate that the size of the coil should be as small as possible. The lower limit on the size of the coil is set by three other factors:

1. the coil must have a region of usable gradient field uniformity (the coil ROI) that encompasses the anatomical ROI;
2. the coil itself must be large enough to accommodate the anatomy of interest;
3. sufficient room must be left for the rf structure and return flux to allow dominant loading of the rf coil by the subject.

The largest of these three lower limits should, in general, determine the optimum size of the coil.

Once the desired gradient strength has been determined, the gradient coil should be designed to generate the required gradient and not more. If the available gradient strength is unnecessarily large then the inductance is higher and the maximum switching rate slower than they could otherwise have been. An exception to this principle can occur for the case of small coils in which the number of turns of wire required to produce the desired gradient is small, and may not be sufficient to produce the desired gradient field uniformity.

The inductance of a coil limits its maximum switching rate. A gradient coil can be thought of as a series resistance/inductance circuit. For a step voltage V_0 applied to the terminals of this circuit, the current will have the form

$$I = \frac{V_0}{R}(1 - \mathrm{e}^{-Rt/L}) \tag{3}$$

where L and R are the inductance and resistance of the circuit, respectively. Thus the current decays towards the final current with a time constant L/R. From this, it appears that either decreasing the inductance or increasing the resistance will decrease the switching time, but this is usually not the case. In practice, if an abrupt change in the current is desired, the voltage is not simply stepped to its new equilibrium value, but is given a 'pre-emphasis' pulse, which is a large overshoot of the voltage in order to increase the current slew rate. As the desired current is approached, the voltage is decreased to its equilibrium value. The current slew rate is limited by the maximum voltage output of the gradient amplifier ($V_{\max}$), which is usually much higher than the voltage required to sustain the maximum current at steady state. The maximum current slew rate is calculated by differentiating the above equation with respect to time, replacing V_0 with $V_{\max}$:

$$\left(\frac{\partial I}{\partial t}\right)_{\max} = \frac{V_{\max}}{L}\,\mathrm{e}^{-Rt/L} \tag{4}$$

For ramps that are short compared with L/R, as is usually the case, the current slew rate is simply $V_{\max}/L$. Therefore, if fast switching is important to an application, the inductance of the gradient coil used should be minimized.

The importance of fast switching rates varies greatly, depending upon the imaging technique. For diffusion imaging using pulsed field gradients in a conventional spin echo sequence, the diffusion weighting gradient must have a large amplitude to minimize *TE*, but the switching rate of the gradient is, in general, not critical. For such an application, a gradient coil with many turns, a high efficiency, and a relatively high inductance would be practical. For fast imaging techniques such as echo planar, fast gradient switching speed is critical to the performance of the technique, and a coil with a minimum acceptable efficiency and low inductance should be used.

Eddy currents are currents induced in conducting structures due to time-varying magnetic fields. Eddy currents generate fields that oppose the field variations that induced the currents. Gradient eddy currents effectively limit the field slew rate by creating transient fields that usually oppose the desired gradient fields. Structures in an MRI scanner that may support eddy currents include the cryostat, the rf coil, and the rf shield. For whole body gradient coils, eddy currents generated in the cryostat are usually of the greatest concern, because the cryostat is physically close to the gradient coil and has very low resistance. In general, LGCs are much smaller than whole body gradient coils, and couple much less strongly to the cryostat. However, if rf coils or shields that have low-resistance closed current paths are used in close proximity to the gradient coil then these can support eddy currents and degrade the gradient field waveforms. Close attention to this problem must be paid in the design of rf coils and shields for use with local gradient coils.

Because the gradient fields directly map the spatial coordinates of physical space to the coordinates of the image, perfect gradient field uniformity is desired. However, if the gradient fields are not perfectly linear but are known then spatial transformations can be applied to the images to determine the

location in space from which the signal in each pixel came. This can partially alleviate the problems associated with using nonlinear gradients, but several problems remain. In 2D imaging—the most common type—if the slice select gradient is nonuniform then information is obtained from tissue outside of the desired slice and the slice cannot be correctly reconstructed. If 3D data are collected, or if the slices are contiguous, then 3D spatial transformations can be used. Spatial transformations to correct for nonlinear gradients are straightforward, but increase image reconstruction time. Because nonlinearities in the gradients cause variations in the voxel sizes, the signal intensity, signal-to-noise ratio (S/N), and spatial resolution will be modulated by these variations, potentially adding to the difficulty of image interpretation. An interesting possibility is also raised by the availability of nonuniform voxel sizes. If gradient and rf coils with matched field nonuniformity are used then images with uniform S/N could be obtained using rf coils with high sensitivity but very nonuniform sensitivity profiles, such as surface rf coils.

If gradient pulses are used for functions other than spatial encoding then these functions will be affected by gradient nonlinearities as well. Nonlinear diffusion weighting or flow-encoding gradients will cause spatial variations in the diffusion or flow weighting. Gradient pulses that are used to dephase transverse magnetization will have an effectiveness that has spatial variations if the gradients are nonlinear.

The currents carried by a gradient coil interact with both the static field and self-generated fields. Because the static field is much stronger than the gradient fields for high- and mid-field scanners, interaction with the static field is of greater concern, and large forces on the current-carrying elements can result. In a uniform static field, a closed current loop cannot experience net forces, but can experience net torques. If these torques are not internally balanced then the coil must be mounted in a very strong and rigid mechanical structure that is tied to the structure of the main magnet in order to prevent large-amplitude vibration of the coil. Torques on an unbalanced head coil in a 1.5 T field are on the order of 100 N m. Internal balancing of the torque in a coil can be achieved by symmetry or by explicit nulling of the torque moment in an asymmetrical design.

4 DESIGN TECHNIQUES

Numerous mathematical techniques have been used to design gradient coils, many of which are described in a review article by Turner.[3] Most designs to date describe current patterns on the surface of one or two cylinders, since this is the most natural geometry for whole body patient access, and for LGCs a natural geometry for the head and extremities. Early designs consisted of simple counter-rotating pairs of loops for longitudinal gradients, and saddle coils for transverse gradients. Romeo and Hoult[4] used a spherical harmonic expansion of the fields to produce simple coils that approximate the lower order harmonics. These were then combined to approximate the desired fields. These designs give linear gradient fields in only a relatively small fraction of their enclosed volume, but are simple, easy to construct designs that can be useful if gradient uniformity is not critical.

Compton[5] introduced direct inversion of the field equations to derive a distribution of current density that would produce a desired field pattern. He defined an error function to describe the uniformity of the gradient fields over a region of interest, and used a least-squares approach to minimize this function. This approach can directly derive a current distribution that creates the desired fields for any coil geometry and any shape region of interest. The derived current density is approximated by a set of wires or etched current paths to arrive at a final coil design.

Turner[6] introduced an elegant approach to explicitly minimize inductance while creating the desired fields within the region of interest. Inductance is a quantity that is difficult to minimize using other techniques, because every element of the coil contributes not only self-inductance, but also mutual inductance with all other elements of the coil. For a given coil geometry, an appropriate transform applied to the current density linearizes the inductance so that each element of the design has zero mutual inductance with all other elements. For planar and cylindrical geometries, simple 2D Fourier transformation serves this purpose. In the transformed space, the inductance is a linear function of the transform components, and a Lagrange multiplier technique can be used to satisfy the desired field constraints while minimizing inductance. After deriving a current density pattern in transform space, a reverse transform is applied to produce a current density pattern in physical space, and again approximation by discrete current paths gives a final design. Several variations of the minimum inductance technique have been introduced to apply the technique to different geometries, and to use the same principles to minimize power dissipation instead of inductance.

Another class of design techniques uses numerical methods to optimize combinations of gradient uniformity, inductance, and coil efficiency. Using either a parameterized or a point-by-point description of the current path, mathematical techniques such as gradient descent, simulated annealing, Monte Carlo, and simplex can be used to minimize the chosen cost function. The author has used gradient descent techniques to design some of the coils that are shown in the examples below.[7] Numerical methods are, in general, more computationally intensive than analytical techniques, but they allow incorporation of arbitrary physical constraints in a simple manner, and they directly produce final designs, avoiding errors that may be introduced by the approximation of continuous current densities by discrete wires.

5 EXAMPLE COIL DESIGNS

Examples of whole volume, partial volume, and surface gradient coils are shown here.

The head coil shown in Figure 1 is an example of a whole volume local gradient coil. It is a three-axis design, torque-balanced by symmetry, and designed using gradient descent for gradient linearity. It was designed for EPI of the human brain, taking into account the specifications of the system in which it was to be used. The scanner it was designed for has a maximum sampling rate of 125 kHz and gradient amplifiers with a nominal current output of 85 A. The coil was designed to produce 20 mT m^{-1} gradients at 85 A, giving a minimum field of view of 16 cm at 125 kHz bandwidth, which was the smallest

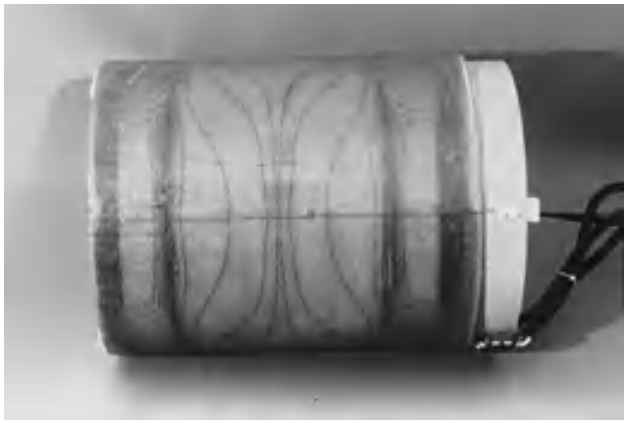

Figure 1 Three-axis local head gradient coil

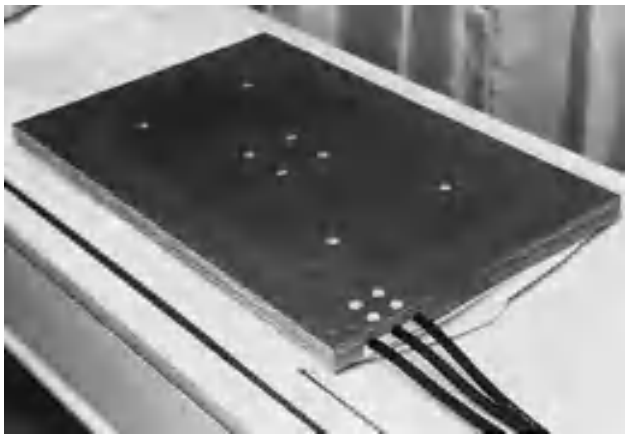

Figure 3 Three-axis surface cardiac gradient coil

anticipated useful field-of-view in the human brain. Because the minimum coil efficiency for the application was specified, the number of turns of wire was kept to a minimum, and very low inductance was achieved. Inductances of 0.08–0.17 mH for the three axes allow switching times below 100 μs.

Figure 2 shows a biplanar cardiac gradient coil—an example of a partial volume coil. Although the coil structure encloses the chest for mechanical stability, the current-carrying elements occupy only two 30 cm $\times$ 40 cm rectangular regions, one above and one below the patient, making it in principle a partial volume coil. This coil produces only a single axis gradient in the vertical direction, and therefore requires the use of the whole body axial and horizontal gradient for imaging. It was also designed by gradient descent, and is used for EPI of the human heart. Because it only generates a vertical gradient field, only axial and saggittal EPI imaging, as well as oblique imaging intermediate to these, is possible.

Figure 3 shows a surface cardiac gradient coil. This coil is a three-axis design, upon which the patient lies prone, and generates nonlinear gradient fields that fall off by a factor of approximately two from the anterior surface to the posterior surface of the heart. The surface coil design in this case was chosen primarily for patient comfort, since the chest is not enclosed in the coil structure. This coil is used in conjunction with a surface rf coil, giving nearly uniform S/N across non-uniform voxel sizes, as described above.

Figure 2 Single axis biplanar cardiac gradient coil

6 APPLICATIONS

The most straightforward applications of LGCs are in high-resolution and short-*TE* conventional imaging techniques, which are usually severely limited by available gradient strength in whole body systems. In principle, high resolution can be obtained using lower gradient strengths and longer pulse durations, but, in practice, the resolution will be limited by the T_2^* of the tissue. It is therefore often necessary to obtain high-resolution images with short *TE* and data acquisition times. An example is the image of the proximal interphalangeal joint of the human finger shown in Figure 4.[8] This image was acquired using a cylindrical LGC of 10 cm diameter and a small

Figure 4 Axial image through the proximal interphalangeal joint of the middle finger. Acquisition parameters: gradient echo, FOV 3 cm $\times$ 1 mm, *TE* = 12 ms, matrix 256 $\times$ 256, *TR* = 500 ms, flip angle 90°, two excitations

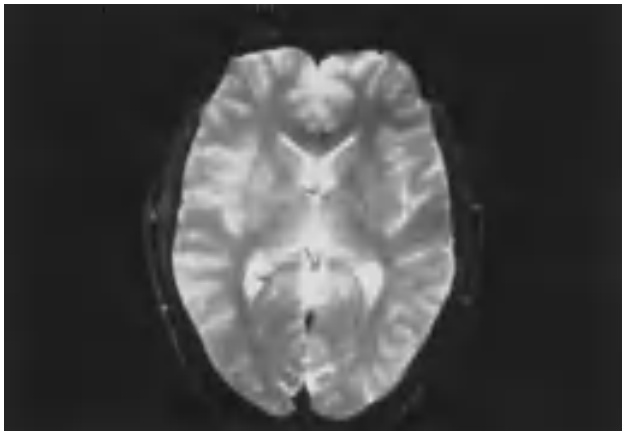

Figure 5 Single shot axial EPI image of the head. Acquisition parameters: single shot spin echo EPI, matrix 128 × 128 partial *k*-space, TE = 20 ms

transmit–receive rf coil. The gradient strengths used were 60 mT m^{-1} in the slice select direction, and 27 mT m^{-1} in the in-plane direction.

An example of ultrafast imaging using a LGC is shown in Figure 5. This is a single shot EPI image of the human head acquired in 80 ms (see ***Echo-Planar Imaging***). For this image, the head gradient coil of Figure 1 was used, and no correction for gradient nonuniformity was employed. Only 15 mT m^{-1} gradients were used, but the coil was switched in just 112 μs using standard gradient amplifiers.

An extension of the EPI technique is functional neuroimaging using either BOLD contrast or flow-dependent contrast.[9–11] An example using BOLD contrast is shown in Figure 6. In this example, gradient-recalled EPI images through the motor cortex were collected repetitively while the subject alternately performed right and left finger tapping tasks. The figure shows a difference image between images acquired during right finger tapping and images acquired during left finger tapping, clearly demonstrating synchronous modulation of signal from the motor cortices with opposite phase.

Diffusion imaging is an example of the use of strong gradients for encoding of desired contrast, rather than for image formation (see ***Methods and Applications of Diffusion MRI***). Figure 7 shows a calculated diffusion image of the eye of an anesthetized rabbit. This image was collected using the same 10 cm diameter LGC as that used to acquire Figure 4, inserted into the same clinical scanner. Diffusion weighting was achieved using pulsed gradients of 80 mT m^{-1} and 12 ms duration, resulting in a b factor of approximately 400 s mm^{-2}. With these gradients, the minimum TE for a conventional spin echo imaging sequence was 30 ms, similar to the average T_2 of the lens, which was the object of interest. If similar diffusion weighting is to be achieved using typical whole body gradients (10 mT m^{-1}), the minimum TE would be approximately 200 ms, which is many times longer than the T_2 of the tissue, and very little signal would be collected.

There are many other applications of LGCs for which examples are not shown. In angiography, stronger and faster gradients allow for shorter flow-compensating gradients and hence shorter TE. This decreases flow-related dephasing and increases the detected signal. In magnetic tissue tagging, such as myocardial tagging to observe cardiac wall motion, stronger gradients can improve tag profiles and decrease tagging time, thus generating sharper tagged grids in the final images. For imaging of very short T_2^* species, it is necessary to employ

Figure 6 Calculated axial image of functional activation in the motor cortices during alternating right and left finger tapping. Acquisition parameters: single shot gradient-recalled EPI, 100 repetitions at 1 s intervals with five alternating periods of right and left finger tapping, matrix 64 × 64, TE = 40 ms. The displayed image is a subtraction of images collected during left finger tapping minus images collected during right finger tapping

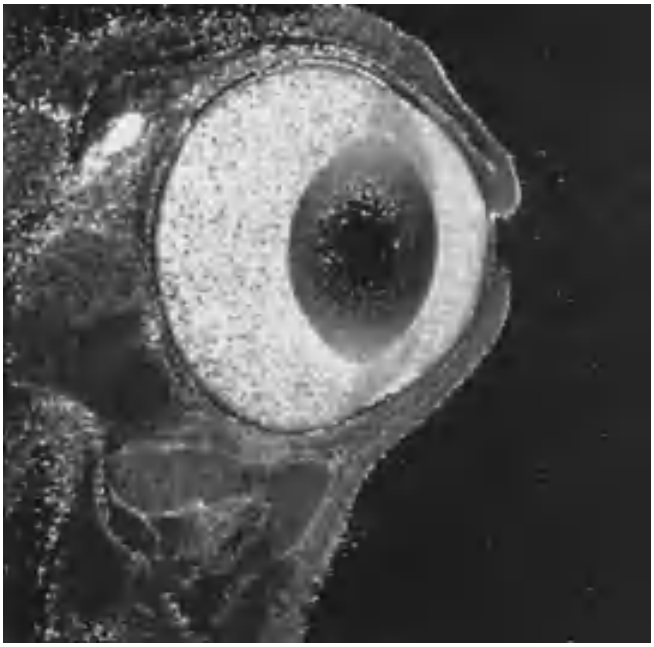

Figure 7 Calculated diffusion coefficient image of the normal rabbit lens. Acquisition parameters: spin echo with pulsed field gradients on either side of the refocusing pulse, b factor 400 s mm^{-2}, direction of diffusion sensitivity left/right on image, FOV 3 cm × 1 mm, TE = 30 ms, matrix 256 × 256, TR = 500 ms, two excitations

strong gradients in order to assure that the imaging gradients dominate the static field inhomogeneities. Short T_2^* occurs primarily in areas with strong susceptibility gradients, such as lung tissue. In localized spectroscopy, spectral resolution can be severely compromised by the presence of gradient eddy currents. For this reason, gradient switching rates are in general very conservative, resulting in relatively long minimum echo times. For shorter-T_2 species, LGCs can be used to improve switching rates with minimal eddy currents, and thereby decrease echo times.

7 SUMMARY

Many applications in MRI are either dependent upon or improved by the availability of stronger and more rapidly switched gradients than are typically found in whole body clinical systems. The use of local gradient coils is a simple and inexpensive means of obtaining high-performance gradients, and has the advantage of higher permissible gradient switching rate than whole body coils for a given limit on field switching rate.

8 RELATED ARTICLES

Echo-Planar Imaging; Eddy Currents and Their Control; Gradient Coil Systems; Methods and Applications of Diffusion MRI.

9 REFERENCES

1. P. Mansfield, *J. Phys. C*, 1977, **10**, L55.
2. D. Le Bihan, E. Breton, D. Lallemand, P. Grenier, E. Cabonis, and M. Laval-Jeantet, *Radiology*, 1986, **161**, 401.
3. R. Turner, *Magn. Reson. Imag.*, 1993, **11**, 903.
4. F. Romeo and D. I. Hoult, *Magn. Reson. Med.*, 1984, **1**, 44.
5. R. A. Compton, US Patent 4 456 881 (1984).
6. R. Turner, *J. Phys. E: Sci. Instrum.*, 1988, **21**, 948.
7. E. C. Wong, A. Jesmanowicz, and J. S. Hyde, *Magn. Reson. Med.*, 1991, **21**, 39.
8. E. C. Wong, A. J. Jesmanowicz, and J. S. Hyde, *Radiology*, 1991, **181**, 393.
9. P. A. Bandettini, E. C. Wong, R. S. Hinks, R. S. Tikofsky, and J. S. Hyde, *Magn. Reson. Med.*, 1992, **25**, 390.
10. K. K. Kwong, J. W. Belliveau, D. A. Chesler, I. E. Goldberg, R. M. Weisshoff, B. P. Poncelet, D. N. Kennedy, B. E. Koppel, M. S. Cohen, and R. Turner, *Proc. Natl. Acad. Sci. U.S.A.*, 1992, **89**, 5675.
11. S. Ogawa, D. W. Tank, R. Menon, J. M. Ellerman, S. G. Kim, H. Merkle, and K. Ugurbil, *Proc. Natl. Acad. Sci. U.S.A.*, 1992, **89**, 5951.

Biographical Sketch

Eric C. Wong, *b* 1964. B.A., 1985, biophysics, University of California, San Diego. Ph.D., 1991, biophysics, M.D., 1994, Assistant Professor of Biophysics, 1992–present, Medical College of Wisconsin. Approx. 12 publications. Research specialties: design and applications of local gradient coils for MRI, pulse sequences for ultrafast MRI, contrast mechanisms in functional MRI.

Image Processing of Functional MRI Data

Karl J. Friston

The Wellcome Department of Cognitive Neurology, London, UK

1 INTRODUCTION

This chapter reviews the issues that arise when using functional MRI (fMRI) to make inferences about functional brain architectures. These include issues common to all functional neuroimaging and some considerations that are special to fMRI. The general issues pertain to the relationship between neurobiological hypotheses and models of what one expects to see and how they are realized in terms of the statistical models used to analyze fMRI time series. Because fMRI encompasses areas of interest to many specialities, this chapter initially defines some technical terms that are commonly encountered. It continues with a review of the distinction between functional specialization and integration and how these principles serve as the motivation for most analyses of fMRI data.

1.1 Glossary of Terms

AR(n) Autoregression model of order n for a time series that obtains by taking a linear compound of the previous n values and an independent component (usually referred to as an innovation). For every AR(n) model, there is an equivalent representation in terms of a moving average of the innovation.
Contrast A linear compound (i.e., weighted linear combination) of the parameter estimates from a general linear model. The compound is specified by series of contrast weights.
CVA (*Canonical variates analysis*) The identification of patterns of activity in terms of the generalized eigen-vectors of the covariance matrices of the fitted effects and residuals of a multivariate time series.
EC (*Euler characteristic*) A topological measure that is applied to some excursion set of a Gaussian field. The excursion set comprises all components that exceed a threshold (the EC is roughly equivalent to the number of blobs minus the number of holes).
Efficiency The inverse of the variance of the estimated parameters of a model.
Effective connectivity The influence that one neuronal system exerts over another in terms of measurable changes in activity.
Functional connectivity The temporal correlations between measurable changes in activity in two brain areas.
FIR (*finite impulse response*) Response of a system to an impulse expressed over a finite series of discrete times.
Gaussian field theory The mathematical framework describing spatially extended multidimensional stationary stochastic fields. SPMs (qv) are assumed to be good lattice approximations to realizations of Gaussian fields.
General linear model The mathematical basis of most parametric statistics; it expresses a response variable in terms of a linear combination of explanatory variables and a multinormal error term with known correlations.
HRF (*hemodynamic response function*) Regionally specific FIR (qv) to some underlying neuronal impulse, expressed in terms of fMRI signal changes.
ICA (*independent component analysis*) The identification of patterns of activity that render the associated time-variates independent.
LTI (*linear time-invariant*) Used to describe systems with stationary and linear input–output characteristics.
PCA (*principal component analysis*) The identification of patterns of activity in terms of the eigen-vectors of the covariance matrix of a multivariate time series.
Resel (*resolution element*) The volume of an elementary image component defined by its intrinsic smoothness.
Sensitivity The probability of getting a true positive (i.e., β where β is the probability that some statistic reaches criterion given the alternative hypothesis is true).
Specificity The probability of getting a true negative (i.e., $1-\alpha$ where α is the probability that some statistic reaches criterion given the null hypothesis is true). Specificity is sometimes expressed directly in terms of α (the probability of a false positive).
SOA (*stimulus onset asynchrony*) The time intervals between successive onsets of stimuli.
SPM (*statistical parametric map*) An image process of statistical values with a known multivariate distribution under the null hypothesis (usually images of Student's T or F statistic).
SVD (*singular value decomposition*) Orthogonal decomposition of a matrix commonly employed in PCA (qv).
Volterra series A functional Taylor expansion of a functional of a [vector] function of time. This expansion is commonly construed as a polynomial expansion with 'memory' or a nonlinear convolution of the [vector] function (input) to give the functional (output) of a nonlinear system.

1.2 Overview

Statistical parametric mapping (SPM) is generally used to identify functionally specialized brain regions and is the most prevalent approach to characterizing functional anatomy. The alternative perspective, namely that provided by functional integration, requires a different set of (multivariate) approaches that examine the relationship between changes in activity in one area and another. SPM is a voxel-based approach, employing standard inferential statistics to make some comment about regionally specific responses to experimental factors. In order to assign an observed response to a particular brain structure or cortical area, the data must conform to a known anatomical space. Before considering statistical modeling, this chapter deals with how a time series of images are realigned and mapped into some standard anatomical space (e.g., stereotactic space). The general ideas behind SPM are then described and illustrated with attention to the different sorts of inference that can be made with different experimental designs. fMRI is special in the sense that the data lend themselves to a signal processing perspective that can be exploited to ensure that both the design and analysis are as efficient as possible. Linear time

invariant (LTI) models provide the bridge between inferential models employed by statistical mapping and simple signal processing approaches. Temporal autocorrelation in noise processes represents another important issue, specific to fMRI, and approaches to maximizing efficiency in the context of serially correlated error terms will be discussed. Nonlinear models (Volterra series) will be considered because they provide constraints on when the assumptions behind linear models are likely to hold. fMRI can capture data very fast (in relation to other imaging techniques) allowing event-related responses to be measured. The distinction between event- and epoch-related designs will be discussed from the point of view of efficiency and the constraints provided by nonlinear characterizations. Before considering multivariate analysis and effective connectivity in the final section we will close the discussion of inferences about regionally specific effects by looking at the distinction between fixed and random effect analyses and how this relates to inferences about the subject studied or the population from which these subjects came.

2 FUNCTIONAL SPECIALIZATION AND INTEGRATION

The brain appears to have two fundamental principles of functional organization, *functional integration* and *functional specialization*, where the integration within and among specialized areas is mediated by effective connectivity. The distinction between these principles relates to that between localizationism and disconnectionism, which dominated thinking about cortical function in the nineteenth century. Since the early anatomic theories of Gall, the indentification of a particular brain region with a specific function has become a central theme in neuroscience. However, functional localization per se was not easy to demonstrate. For example, a meeting that took place on 4 August 1881 addressed the difficulties of attributing function to a cortical area given the dependence of cerebral activity on underlying connections.[1] This meeting was entitled 'Localisation of function in the cortex cerebri'. Goltz accepted the results of electrical stimulation in dog and monkey cortex but considered this excitation method was inconclusive in that movements elicited might have originated in related pathways, or current could have spread to distant centers.[2] In short, the excitation method could not be used to infer functional localization because localizationism discounted interactions, or functional integration, among different brain areas. It was proposed that lesion studies could supplement excitation experiments; ironically, it was observations on patients with brain lesions[3] some years later that led to the concept of disconnection syndromes and the refutation of localizationism as a complete or sufficient explanation of cortical organization. Functional localization implies that a function can be localized in a cortical area, whereas specialization suggests that a cortical area is specialized for some aspects of perceptual or motor processing, and that this specialization is anatomically segregated within the cortex. The cortical infrastructure supporting a single function may then involve many specialized areas linked by functional integration. In this view, functional specialization is only meaningful in the context of functional integration and vice versa.

2.1 Functional Specialization and Segregation

The functional role played by any component (e.g., cortical area, subarea, or neuronal population) of the brain is largely defined by its connections. Certain patterns of cortical projections are so common that they could amount to rules of cortical connectivity: 'These rules revolve around one, apparently, overriding strategy that the cerebral cortex uses—that of functional segregation.[4]' Functional segregation demands that cells with common functions are grouped together. This architectural constraint in turn necessitates both convergence and divergence of cortical connections. Extrinsic connections between cortical regions are not continuous but occur in patches or clusters. This patchiness has, in some instances, a clear relationship to functional segregation. For example, cortical region V2 has a distinctive cytochrome oxidase architecture, consisting of thick stripes, thin stripes, and inter-stripes. When recordings are made in V2, directionally selective (but not wavelength- or color-selective) cells are found exclusively in the thick stripes. Retrograde (i.e., backwards) labeling of cells in region V5 is limited to these thick stripes. All the available physiological evidence suggests that V5 is a functionally homogeneous area that is specialized for visual motion. Evidence of this nature supports the notion that patchy connectivity is the anatomical infrastructure that mediates functional segregation and specialization. If it is the case that neurons in a given cortical area share a common responsiveness (by virtue of their extrinsic connectivity) to some sensorimotor or cognitive attribute, then this functional segregation is also an anatomical one. Challenging a subject with the appropriate sensorimotor attribute or cognitive process should lead to activity changes in, and only in, the area of interest. This is the model upon which the search for regionally specific effects is based.

The analysis of fMRI data involves many steps that can be broadly divided into spatial preprocessing, estimation of the parameters of a statistical model, and making inferences about modeled effects using the parameter estimates and their associated statistics (Figure 1). We will deal first with spatial transformations: the relationship between regionally specific effects and homologous responses in other subjects or nonhuman primates has to be established in order to understand functional anatomy. This necessitates some form of anatomical designation for regional responses that is facilitated by analyzing the data in relation to some standard anatomical space.

3 SPATIAL REALIGNMENT AND ANATOMICAL NORMALIZATION

The analysis of fMRI studies starts with a series of spatial transformations to reduce artifactual variance components in the voxel time series. The first step is to realign the data in order to 'undo' the effects of subject movement during the scanning session. After realignment, the data are then transformed using linear or nonlinear mappings into a standard anatomical space. The data are usually spatially smoothed before being entered into the analysis proper.

3.1 Realignment

Changes in signal intensity from any one voxel can arise from head motion and this represents one of the most serious

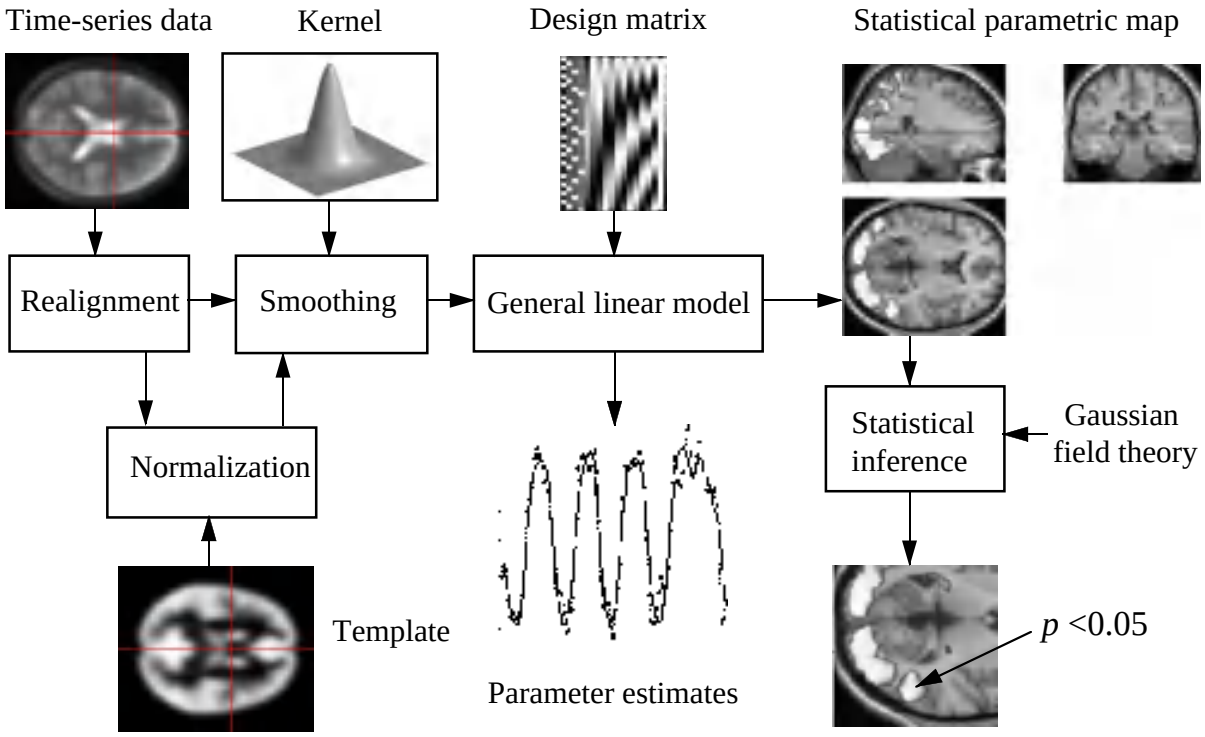

Figure 1 Schematic depicting the transformations that start with the fMRI time series and end with a statistical parametric map (SPM). SPMs can be thought of as 'X-rays' of the significance of an effect. Voxel-based analyses require the data to be in the same anatomical space: This is effected by realigning the data (and removing movement-related signal components that persist after realignment). After realignment the images are subject to non-linear warping so that they match a template that already conforms to a standard anatomical space. After smoothing, the general linear model is employed to estimate the parameters of the model and to derive the appropriate univariate test statistic at each and every voxel (see Figure 2). The test statistics that ensue (usually T or F statistics) constitute the SPM. The final stage is to make statistical inferences on the basis of the SPM (see Figure 3) and characterize the responses observed using the fitted responses or parameter estimates

confounds in fMRI studies. Despite restraints on head movement, even cooperative subjects still show displacements of up to a millimeter or so. Realignment involves estimating the six parameters of an affine 'rigid-body' transformation that minimizes the (sum of squared) differences between each successive scan and the first and applying the transformation by resampling the data using trilinear or sinc interpolation. Estimation of the affine transformation is usually effected with a first-order approximation of the Taylor expansion of the effect of movement on signal intensity using the spatial derivatives of the images. This allows for a simple iterative least squares solution (that corresponds to a Gauss–Newton search).[5] However, even after perfect realignment, movement-related signals can still persist. This calls for a final step in which the data are adjusted for residual movement-related effects.

3.2 Adjusting for Movement-related Effects

In extreme cases, as much as 90% of the variance in an fMRI time series can be accounted for by the effects of movement *after* realignment.[6] These movement-related components are the result of subject movement between slice acquisitions, interpolation artifacts, nonlinear distortion through magnetic field inhomogeneity, and spin-excitation history effects.[6] The last can be pronounced if the repetition time (*TR*) approaches T_1, making the current signal a function of movement history. These multiple effects render the movement-related signal (y) a nonlinear function of displacement (x) in the nth and previous scans $y=f(x_n, x_{n-1}, \ldots)$. By assuming a sensible form for this function, its parameters can be estimated using the observed time series and the estimated movement parameters x from the realignment procedure. The estimated movement-related signal is then simply subtracted from the original data. The form for $f(x)$ proposed in Friston et al. was an autoregression 1 [AR(1)] model that was motivated by spin-excitation history effects.[6] Generally, for *TR* values of several seconds, interpolation artifacts supersede and an expansion of $f(x_n)$ in terms of periodic basis functions of the current displacement appears to be sufficient.

Movement-related effects require a spatial realignment. In addition, temporal realignment may be required in multislice acquisition to ensure that the data from any given volume were sampled at the same time. This is usually performed using sinc interpolation over time and only when the temporal dynamics of evoked responses are important.

3.3 Spatial Normalization

After realigning the data, a mean image of the time series or some other co-registered (e.g., a T_1-weighted) image is used to estimate the warping parameters that map it onto some template that already conforms to a standard anatomical space.[7]

This estimation can use a variety of models for the mapping, including: a 12-parameter affine transformation where the parameters constitute a spatial transformation matrix, low-frequency-basis spatial functions (usually a discrete cosine set or polynomials) where the parameters are the coefficients of the basis functions employed, and a vector field specifying the mapping for each control point (e.g., voxel center). In the last the parameters are vast in number and constitute a tensor that is bigger than the image itself. Estimation of the parameters of all these models can be accommodated in a simple Bayesian framework to find the deformation β that has the maximum posterior probability $p(\beta|\boldsymbol{Y})$ given the data $\boldsymbol{Y}$, where $p(\beta|\boldsymbol{Y}) \propto p(\boldsymbol{Y}|\beta)p(\beta)$. This reduces to minimizing the likelihood and prior potentials $H(\boldsymbol{Y}|\beta)$ and $H(\beta)$, respectively, where $p(\boldsymbol{Y}|\beta)=\exp\{-H(\boldsymbol{Y}|\beta)\}$ and $p(\beta)=\exp\{-H(\beta)\}$. The likelihood potential is generally taken to be the sum of squared differences between the template and deformed image and reflects the probability of actually getting that image if the transformation is correct. The prior potential can be used in the context of weighted least squares to incorporate prior information about the likelihood of a given transformation. Prior potentials can be determined empirically[8] or motivated by constraints on the mapping[9] and play a more essential role as the number of parameters specifying the mapping increases.

In practice, an affine or spatial basis function model is usually used with iterative least squares to minimize the likelihood potential. As with realignment, this involves linearizing with Taylor expansions. A nice extension of this approach is that the difference between the template and index image can be minimized by using a (linear) combination of templates (e.g., depicting gray matter, white matter, cerebrospinal fluid, and skull tissue partitions). This models intensity differences that are unrelated to registration differences and allows different modalities to be co-registered.[5]

3.4 Co-registration of Functional and Anatomical Data

It is useful to be able to co-register functional and anatomical images. However, with echo planar imaging, geometric distortions of T_2^* images, relative to anatomical T_1-weighted data, are a particularly serious problem because of the very low frequency per point in the phase-encoding direction. Typically, for echo planar fMRI, magnetic field inhomogeneity sufficient to cause dephasing of 2π through the slice corresponds to a 1 voxel distortion in the plane. 'Unwarping' schemes have been proposed to correct for the distortion effects.[10] Note that this is not an issue if the functional data are normalized spatially.

3.5 Spatial Smoothing

The motivations for smoothing the data are fourfold: (i) By the matched filter theorem, the optimum smoothing kernel corresponds to the size of the effect anticipated. The spatial scale of hemodynamic responses is, according to high-resolution optical imaging experiments, about 2–5 mm. Despite the potentially high resolution afforded by fMRI, an equivalent smoothing is suggested for most applications. (ii) By the central limit theorem, smoothing the data will render them more parametric in their distribution and ensure the validity of inferences based on parametric tests. (iii) When making inferences about regional effects using Gaussian field theory (see below), one of the assumptions is that the data are a reasonable lattice representation of an underlying and smooth Gaussian field. This necessitates smoothness to be substantially greater than voxel size. If the voxels are large then they can be reduced by sub-sampling the data and then smoothing (with the original point spread function) with little loss of intrinsic resolution. (iv) In the context of intersubject averaging, it is often necessary to smooth more (e.g., 6 mm) to project the data onto a spatial scale where homologies in functional anatomy are expressed among subjects.

4 STATISTICAL PARAMETRIC MAPPING AND FUNCTIONAL SPECIALIZATION

Functional mapping studies are usually analyzed with some form of SPM where spatially extended statistical processes are constructed to test hypotheses about regionally specific effects.[11] SPMs are image processes with voxel values that are, under the null hypothesis, distributed according to a known probability density function (usually Student's T or F distributions). The success of SPM largely stems from the simplicity of the idea. Namely, each and every voxel is analyzed using any standard (univariate) statistical test. The resulting statistical parameters are assembled into an image: the SPM. SPMs are interpreted as spatially extended statistical processes by referring to the probabilistic behavior of stationary Gaussian fields.[12–15] Stationary fields model both the univariate probabilistic characteristics of an SPM and any stationary spatial covariance structure (stationary means not a function of position). 'Unlikely' excursions of the SPM are interpreted as regionally specific effects, attributable to the sensorimotor or cognitive process that has been manipulated experimentally.

4.1 Different Approaches?

Statistical analysis corresponds to modeling the data in order to partition observed neurophysiological responses into components of interest, confounds, and error. A brief review of the literature may give the impression that there are numerous ways to analyze fMRI time series with a diversity of statistical and conceptual approaches. This is not the case. With only a few exceptions, every analysis presented is a variant of the general linear model. This includes: (i) simple T tests on scans assigned to one condition or another, (ii) correlation coefficients between observed responses and box-car stimulus functions, (iii) inferences made using multiple linear regression, (iv) evoked responses estimated using LTI models, and (v) selective averaging to estimate event-related responses. Mathematically they are all identical. The use of the correlation coefficient[16] deserves special mention because of its popularity in fMRI. The significance of a correlation is identical to the significance of the equivalent T value testing for a regression of the data on some stimulus waveform. The correlation coefficient approach is useful but the inference is effectively based on a limiting case of multiple linear regression that obtains when there is only one regressor. In fMRI, many regressors usually enter into a statistical model. For this reason, the T statistic provides a much more flexible and general way of assessing the significance of regional effects and is preferred over the correlation coefficient.

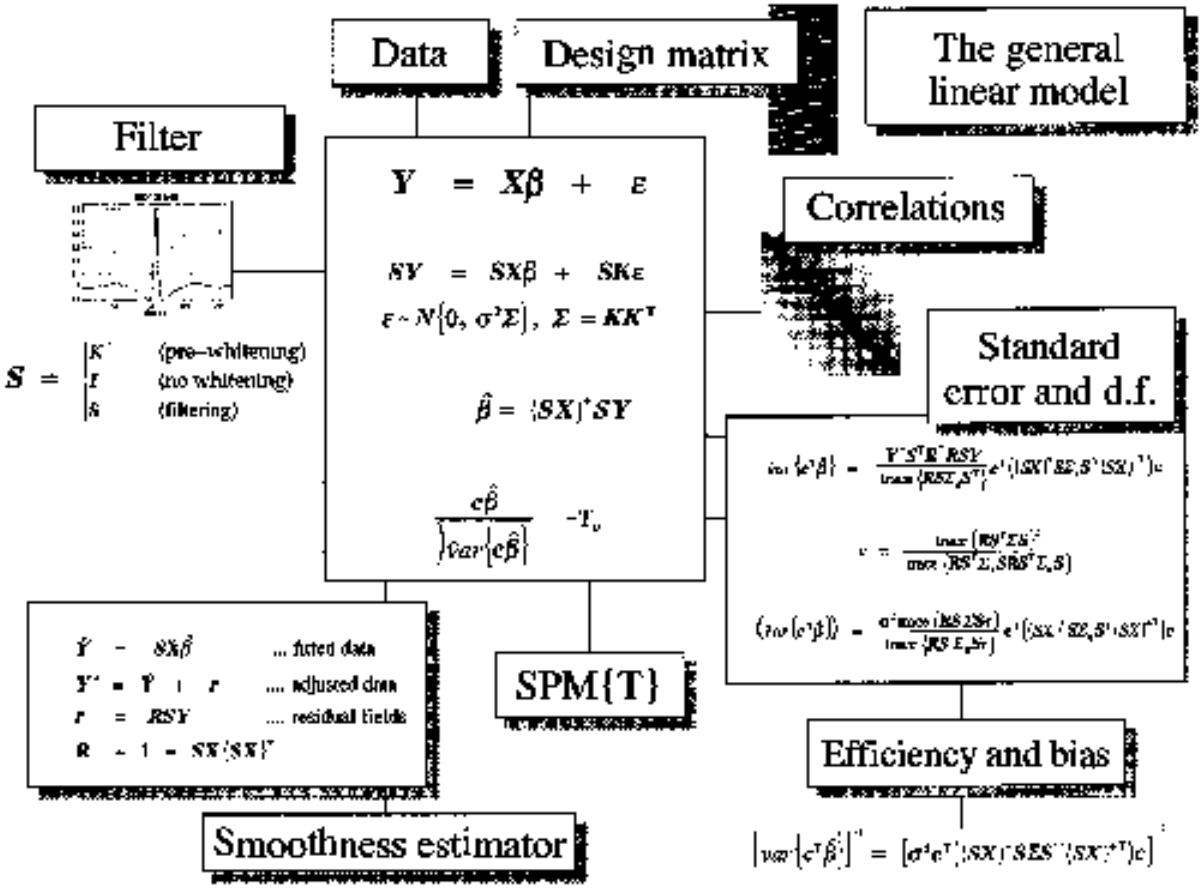

Figure 2 The general linear model. The general linear model is an equation expressing the response variable $\boldsymbol{Y}$ in terms of a linear combination of explanatory variables in a design matrix $\boldsymbol{X}$ and an error term with assumed or known autocorrelation $\boldsymbol{\Sigma}$. In fMRI, the data can be filtered with a convolution matrix $\boldsymbol{S}$, leading to an augmented general linear model that includes (intrinsic) serial correlations and applied (extrinsic) filtering. Different choices of $\boldsymbol{S}$ correspond to different (de)convolution schema, as indicated on the upper left. The parameter estimates obtain in a least squares sense using the pseudoinverse (denoted by +) of the filtered design matrix. Generally an effect of interest is specified by a vector of contrast weights $\boldsymbol{c}$ that give a weighted sum or compound of parameter estimates $\boldsymbol{c}\hat{\beta}$, referred to as a contrast. The T statistic is simply this contrast divided by the estimated standard error (i.e., square root of the estimated variance). The ensuing T statistic is distributed with ν degrees of freedom. The equations for the estimated variance of the contrast and the degrees of freedom associated with the error variance are provided in the right-hand panel. Efficiency is simply the inverse of the variance of the contrast estimate. Discrepancies between the actual and assumed intrinsic correlations ($\boldsymbol{\Sigma}$ and $\boldsymbol{\Sigma}_a$, respectively) can result in systematic bias in the actual and estimated variance of the contrast. These expressions are useful when assessing the relative efficiency and robustness of a model. The parameter estimates can either be examined directly or used to compute the fitted responses (see lower left panel). Adjusted data refers to data from which estimated confounds have been removed. The residuals $\boldsymbol{r}$ obtain from applying the residual forming matrix $\boldsymbol{R}$ to the data. These residual fields are used to estimate the smoothness of the component fields of the SPM used in Gaussian field theory (see Figure 3).

Some researchers construct statistical maps based on non-parametric tests that eschew distributional assumptions about the data.[17] These approaches may, in some instances, be useful but are generally less powerful (i.e., sensitive) than parametric approaches. This approach was based on the (specious) assumption that the residuals in fMRI data are not normally distributed.

4.2 The General Linear Model

The general linear model is an equation $\boldsymbol{Y}=\boldsymbol{X}\beta+\epsilon$ that expresses the observed response variable $\boldsymbol{Y}$ in terms of a linear combination of explanatory variables $\boldsymbol{X}$ plus a well-behaved error term (see Figure 2). The general linear model is variously known as 'analysis of covariance' or 'multiple regression analysis' and subsumes simpler variants, like the 'T test' for a difference in means, to more elaborate linear convolution models such as finite impulse response (FIR) models. The matrix $\boldsymbol{X}$ that contains the explanatory variables (e.g., designed effects or confounds) is called the 'design matrix'. Each column of the design matrix corresponds to some effect one has built into the experiment or that may confound the results. These are variously referred to as explanatory variables, covariates, regressors, or, in fMRI, stimulus functions. The example in Figure 1 relates to an fMRI study of visual stimulation under four conditions. The effects on the response variable are modeled in terms of functions of the presence of these conditions (i.e., box-cars smoothed with a hemodynamic response func-

tion) and constitute the first four columns of the design matrix. There then follows a series of terms that are designed to remove or model low-frequency variations in signal caused by artifacts such as aliased biorhythms. The final column is whole brain activity. The relative contribution of each of these columns is assessed using standard least squares and inferences about these contributions are made using T or F statistics, depending upon whether a particular linear combination of these contributions is examined or all of them together. The operational equations are shown in Figure 2. In this scheme the general linear model has been extended[18] to incorporate intrinsic autocorrelations or serial correlation among the error terms and to allow for some specified filtering or smoothing of the data.

These equations can be used to implement a vast range of statistical analyses. The issue is, therefore, not so much the mathematics but the formulation of a design matrix $\boldsymbol{X}$ appropriate to the study design and inferences that are sought. The design matrix can contain both covariates and indicator variables. Each column of $\boldsymbol{X}$ has an associated unknown parameter. Some of these parameters will be of interest (e.g., the effect of particular sensorimotor or cognitive condition or the regression coefficient of hemodynamic responses on reaction time). The remaining parameters will be of no interest and pertain to confounding effects (e.g., the effect of being a particular subject or the regression slope of voxel activity on global activity). Inferences about the parameter estimates are made using their estimated variance. This allows one to test the null hypothesis that all the estimates are zero using the F statistic to give an SPM{F} or that some particular linear combination (e.g., a subtraction) of the estimates is zero using a SPM{T}. The T statistic obtains by dividing a contrast or compound (specified by contrast weights) of the ensuing parameter estimates by the standard error of that compound. The latter is estimated using the variance of the residuals about the least squares fit. An example of contrast weights would be [−1 1 0 0 ...] to compare the differential responses evoked by two conditions, as modeled by the first two condition-specific regressors in the design matrix. If several parameter estimates are potentially interesting (e.g., using polynomial expansions[19] or basis functions of some parameter of interest), then the SPM{F} is usually employed.

An important example, from the perspective of fMRI, of the general linear model is the LTI model.

4.2.1 *The General Linear Model, Linear Time Invariant Systems, and Finite Impulse Response Models*

In Friston et al. the form of the hemodynamic impulse response function (HRF) was estimated using a least squares deconvolution and a FIR LTI model, where evoked neuronal responses are convolved with the HRF to give the measured hemodynamic response[20] (see also Boynton et al.[21]). The estimated HRF resembled a Poisson or Gamma function peaking at about 5 s. This simple linear framework is the cornerstone for making statistical inferences about activations in fMRI with the general linear model. The notion of using temporal basis functions to model evoked responses in fMRI was subsequently introduced[22] and applied to event-related responses[23] (see also Lang and Zeger[24]).

4.2.2 *Temporal Basis Functions*

Temporal basis functions are important because they provide a graceful transition between conventional multilinear regression models with one stimulus function per condition and FIR models with a parameter for each time point following the onset of a condition or trial type. Temporal basis functions offer useful constraints on the form of the estimated response that retain the flexibility of FIR models and the efficiency of single regressor models. In practice, the implementation of these constrained FIR models involves setting up stimulus functions that model expected neuronal changes (e.g., box-cars of epoch-related responses or spikes (delta functions) at the onset of specific events or trials). These regressors are then convolved with a set of basis functions that model the HRF, in some linear combination, and are assembled into the design matrix. The basis functions can be as simple as a single canonical HRF through to a series of delayed delta functions. The latter case corresponds to a FIR model proper and the coefficients are the impulse response function for the event or epoch in question. Selective averaging in event-related fMRI is mathematically identical to this limiting case.[25]

The advantage of using temporal basis functions (as opposed to an assumed form for the HRF) is that one can model voxel-specific forms for hemodynamic responses[24] and formal differences (e.g., onset latencies) among responses to different sorts of events. The advantages of using basis functions over FIR models are that the parameters are estimated more efficiently and stimuli can be presented at any point in the interstimulus interval. The latter is very important because time-locking stimulus presentation and data acquisition gives biased sampling over peristimulus time and can lead to differential sensitivities, in multislice acquisition, over the brain.

4.3 Statistical Inference and the Theory of Gaussian Fields

Inferences using SPMs can be of two sorts depending on whether the area involved is known in advance. With an anatomically constrained hypothesis, about effects in a particular brain region, the uncorrected p value associated with the height or extent of that region in the SPM can be used to test the hypothesis. With an anatomically open hypothesis (i.e., a null hypothesis that there is no effect anywhere in the brain) a correction for multiple dependent comparisons is necessary. The theory of Gaussian fields provides a way of computing this corrected p value that takes into account the fact that neighboring voxels are not independent by virtue of smoothness in the original data. Provided the data are sufficiently smooth, the correction based on Gaussian field theory is less severe (i.e., is more sensitive) than a Bonferroni correction for the number of voxels.

The only assumptions underlying the use of Gaussian field theory are that: (i) the residual fields (but not necessarily the data) are a reasonable lattice approximation to an underlying Gaussian field; (ii) the fields have a twice differentiable autocorrelation function (a common misconception is that the autocorrelation function has to be Gaussian; it does not) and (iii) their multinormal correlation structure is wide sense stationary. The only way in which these assumptions can be violated is if the data are not smoothed (with or without subsampling of the data to preserve resolution) or the statistical

model is mis-specified and spatially coherent signals (e.g., global effects) end up in the residuals.

4.3.1 *Anatomically Closed Hypotheses*

When making inferences about regional effects (e.g., activations) in statistical maps, there is often some idea about where the activation should be. In this instance, a correction for the entire search volume is inappropriate. However, a problem remains in the sense that activations that are 'near' the predicted location should be considered even if they are not exactly coincident. There are two approaches to this: prespecify a small search volume and make the appropriate correction[15] or use the uncorrected p value based on the spatial extent of the nearest cluster.[26] This probability is based on obtaining the observed number of voxels, or more, in a given cluster (conditional on that cluster existing) and can be calculated using distributional approximations from the theory of Gaussian fields.

4.3.2 *Anatomically Open Hypotheses and Levels of Inference*

To correct for the volume of brain analyzed, the SPM is subject to thresholding, using some height and spatial extent thresholds, and p values are derived that pertain to: (i) the number of activated regions (i.e., number of clusters above the height and volume threshold), known as *set-level inferences*; (ii) the number of activated voxels (i.e., volume) comprising a particular region, known as *cluster-level inferences*; and (iii) the p value for each voxel within that cluster, known as *voxel-level inferences*. These p values are corrected for the multiple dependent comparisons and are based on the probability of obtaining c, or more, clusters with k, or more, voxels, above a threshold u in an SPM of known or estimated smoothness.[27] This probability has a reasonably simple form and is derived using distributional approximations from the theory of Gaussian fields (see Figure 3 for details).

Set-level inference refers to the inference that the number of clusters comprising an observed activation profile is highly unlikely to have occurred by chance and pertains to the activation profile as characterized by its constituent regions. Cluster-level inferences are a special case of set-level inferences that obtain when the number of clusters is 1. Similarly, voxel-level inferences are special cases of cluster-level inferences that result when the cluster can be small (i.e., k=0). Using a theoretical power analysis[27] of distributed activations, it can be shown that set-level inferences are generally more powerful than cluster-level inferences and that cluster-level inferences are generally more powerful than voxel-level inferences. The price paid for this increased sensitivity is reduced localizing power: Voxel-level tests permit individual voxels to be identified as significant, whereas cluster and set-level inferences only allows clusters or sets of clusters to be so identified.

4.4 Experimental Design and Analysis

4.4.1 *Cognitive Subtractions and Conjunctions*

The tenet of cognitive subtraction and conjunction is that the difference between two tasks can be formulated as a separable cognitive or sensorimotor component and that the regionally specific differences in hemodynamic responses identify the corresponding functionally specialized area. Early applications of subtraction range from the functional anatomy of word processing[28] to functional specialization in extrastriate cortex.[29] The latter studies involved presenting visual stimuli with and without some sensory attribute (e.g., color, motion, etc.). The areas highlighted by subtraction were identified with homologous areas in monkeys that showed selective electrophysiological responses to equivalent visual stimuli.

Cognitive conjunctions[30] can be thought of as an extension of the subtraction technique, in the sense that they combine a series of subtractions. In subtraction, a hypothesis pertaining to the activation in one task relative to another is tested. In conjunction analyses, several hypotheses are tested, asking whether all the activations, in a series of task pairs, are jointly significant. Consider the problem of identifying regionally specific activations caused by a particular cognitive component (e.g., object recognition). If a series of task pairs can be identified with differences that have only that component in common, then the region which activates in all the corresponding subtractions can be associated with the component in question. Conjunction analyses demonstrate this context-insensitive nature of regional responses. One important application of conjunction analyses is in multisubject fMRI studies where generic effects are identified as those that are conjointly significant in all the subjects studied (see below).

4.4.2 *Parametric Designs*

The premise behind parametric designs is that regional physiology will vary systematically with the degree of cognitive or sensorimotor processing. Examples of this approach include the positron emission tomographic (PET) experiments of Grafton et al., who demonstrated significant correlations between hemodynamic responses and the performance of a visually guided motor tracking task.[31] On the sensory side, Price et al. demonstrated a remarkable linear relationship between perfusion in peri-auditory regions and frequency of aural word presentation.[32] This correlation was not observed in Wernicke's area, where perfusion appeared to correlate not with the discriminative attributes of the stimulus but with the presence or absence of semantic content. These relationships or 'neurometric functions' may be linear or nonlinear. Using polynomial regression, in the context of the general linear model, nonlinear relationships between stimulus parameters (e.g., stimulus duration or presentation rate) and evoked responses can be identified; this is usually achieved using a SPM{F}.[19]

The example provided in Figure 4 illustrates subtraction, conjunction, and parametric approaches to design and analysis. These data were obtained from a fMRI study of visual motion processing using radially moving dots. The stimuli were presented over a range of speeds using isoluminant and isochromatic stimuli. To identify areas involved in visual motion, a stationary dots condition was subtracted from the moving dots conditions (see contrast weights on the upper right). To ensure significant motion-sensitive responses, using both color and luminance cues, a conjunction of the equivalent subtractions was assessed under both viewing contexts. Areas V5 and V3a are seen in the ensuing SPM{T}. The responses in left V5 speak to a very compelling inverted 'U' relationship between speed and evoked response that peaks at around 8° s^{-1}. It is this sort of relationship that parametric designs try to characterize. Interestingly, the form of these speed-dependent

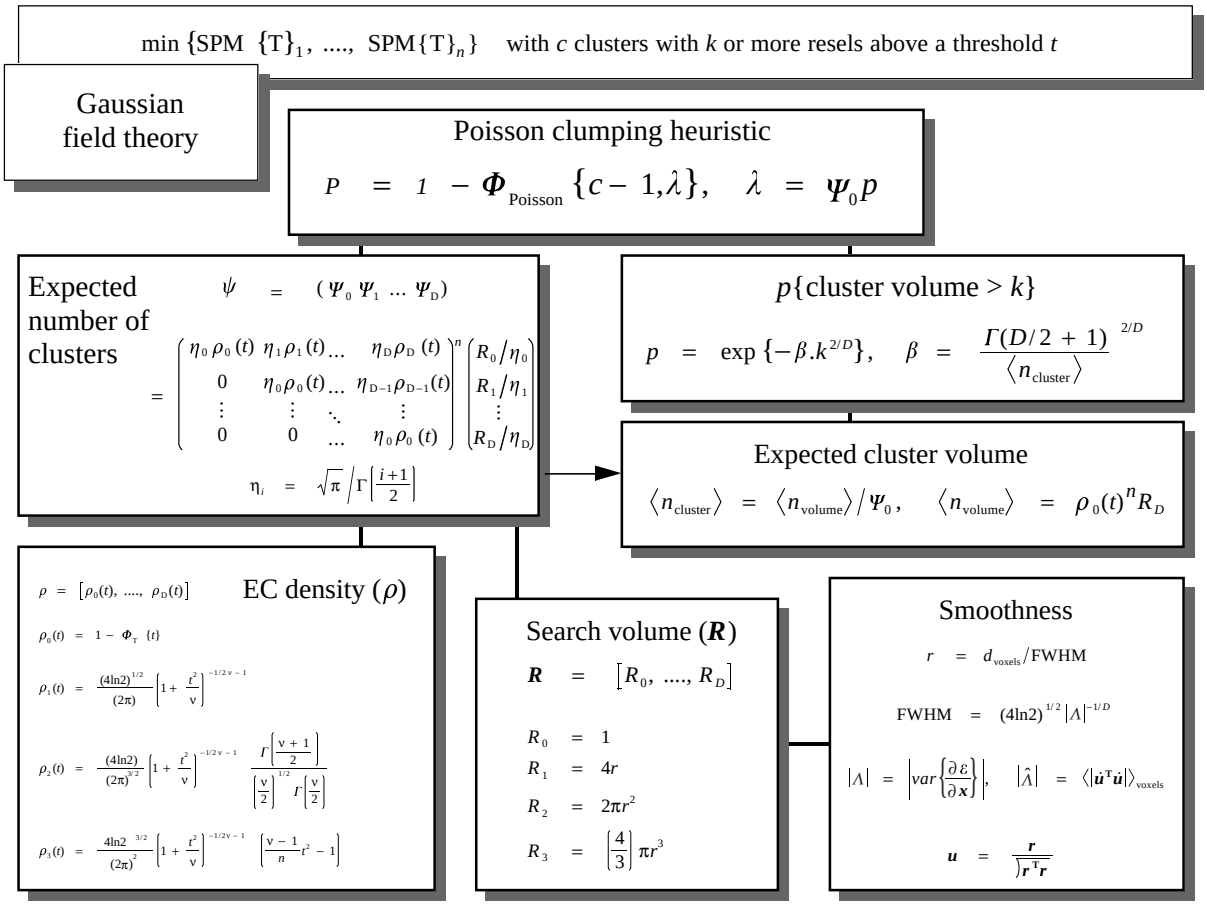

Figure 3 The theory of Gaussian fields. If an anatomical location is already suspected, inference can be based on the value of the statistic at the specified location in the SPM without correction. If, however, there was no anatomical constraint, then a correction for multiple dependent comparisons has to be made. These corrections are usually made using distributional approximations from the theory of Gaussian fields. This schematic deals with the most general case of n SPM{T} where the voxels all survive a common threshold t (i.e., a conjunction). The central probability, upon which all voxel-, cluster- or set-level inferences rest is the probability P of getting c or more clusters with k or more resels (resolution elements) above this threshold. By assuming that clusters behave like a multidimensional Poisson point process (i.e., the Poisson clumping heuristic) P is simply determined given that the distribution of c is Poisson with an expectation λ. The term λ is the product of the expected number of clusters of any size and the probability that any cluster will be bigger than k resels. The latter probability is shown using a form for a single Z-variate field constrained by the expected number of resels per cluster (<.> denotes expectation or average). The expected number of resels per cluster is simply the expected number of resels in total divided by the expected number of clusters. The expected number of clusters is estimated with the Euler characteristic (EC) (effectively the number of blobs minus the number of holes). This estimate is, in turn, a function of the EC density for the statistic in question (with ν degrees of freedom) and the resel counts. The EC density is the expected EC per unit of D-dimensional volume of the SPM where the D-dimensional volume of the search space is given by the corresponding element in the vector of resel counts. Resel counts can be thought of as a volume metric that has been normalized by the smoothness of the SPM component fields expressed in terms of the full width at half maximum (FWHM). This is estimated from the determinant of the variance–covariance matrix of the first spatial derivatives $\boldsymbol{u}$ of the normalized residual fields $\boldsymbol{r}$. In this example, equations for a sphere of radius r are given. The term Φ denotes the cumulative distribution function for the subscripted statistic in question.

responses was similar using both stimulus types although luminance cues are seen to elicit a greater response. From the point of view of a factorial design, there is a main effect of cue (isoluminant versus isochromatic), a main (nonlinear) effect of speed, but no speed by cue interaction.

4.4.3 Factorial Designs

At its simplest, an interaction represents a change in a change. Interactions are associated with factorial designs where two or more factors are combined in the same experiment. The effect of one factor on the effect of the other is assessed by the interaction term. Factorial designs have a wide range of applications. An early application in neuroimaging examined physiological adaptation and plasticity during motor performance by assessing time by condition interactions.[33] Psychopharmacological activation studies are examples of factorial designs.[34] In these studies, cognitively evoked responses are assessed before and after a drug is taken. The interaction term reflects the modulatory drug effect on the task-dependent activation. Factorial designs have an important role in the context of cognitive subtraction and additive factors logic by virtue of being able to test for interactions, or 'context-sensitive activations' (i.e., to demonstrate the fallacy of 'pure insertion').[35] These interaction effects can sometimes be interpreted as the integration of the two or more (cognitive) processes or

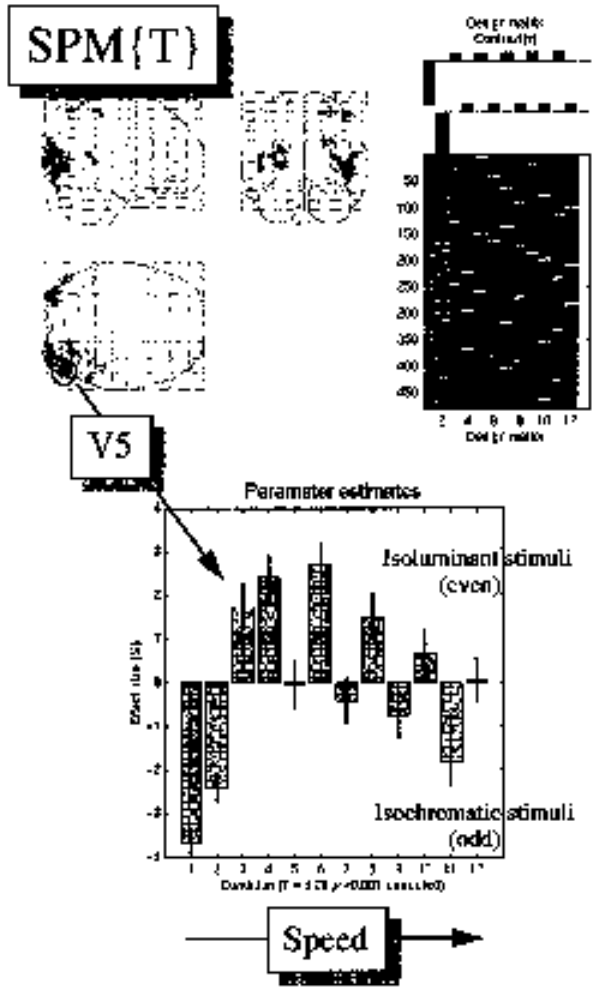

Figure 4 The design matrix is shown as an image representation where contrasts are the vectors of contrast weights defining the linear compounds of parameters tested. The contrasts are displayed over the column of the design matrix that corresponds to the effects in question. The design matrix here includes condition-specific effects (box-cars convolved with a hemodynamic response function). Odd columns correspond to stimuli shown under isochromatic conditions and even columns model responses to isoluminant stimuli. The first two columns are for stationary stimuli and the remaining columns are for conditions of increasing speed. The final column is a constant term. The SPM{T} is a maximum intensity projection of the SPM{T} conforming to the standard anatomical space of Talairach and Tournoux.[7] The T values here are the minimum T values from both contrasts, thresholded at p=0.001 uncorrected. The most significant conjunction is seen in the left V5. A plot of the condition-specific parameter estimates for this voxel is shown. The T value was 9.25 ($p<0.001$ corrected; see Figure 3)

as the modulation of one (perceptual) process by another being manipulated (see Figure 5).

5 A SIGNAL PROCESSING PERSPECTIVE

In this section we consider fMRI time series from a signal processing perspective with particular reference to frequency domain representations.

5.1 Temporal (serial) Autocorrelations and Efficiency

fMRI time series can be viewed as a linear admixture of signal and noise (Figure 6). Signal corresponds to neuronally mediated hemodynamic changes that can be modeled as a (non)linear convolution of some underlying neuronal process responding to changes in experimental factors. Noise has many contributions that render it rather complicated in relation to other neurophysiological measurements. These include neuronal and non-neuronal sources. Neuronal noise refers to neurogenic signal not modeled by the explanatory variables and with the same frequency structure as the signal itself. Non-neuronal components have both white (e.g., rf (Johnson) noise) and colored components (e.g., pulsatile motion of the brain caused by cardiac cycles and local modulation of the static magnetic field ($\boldsymbol{B}_0$) by respiratory movement). These effects are typically low frequency or wide band (e.g., aliased cardiac-locked pulsatile motion). The superposition of all these components creates temporal correlations among the error terms in the statistical model (denoted by Σ in Figure 2) that can have a severe effect on sensitivity to experimental effects. Sensitivity depends upon the relative amounts of signal and noise and the efficiency of the experimental design. Efficiency is simply a measure of how reliable the parameter estimates are and can be defined as the inverse of the variance of a contrast of parameter estimates (see Figure 2). There are two important considerations arising from this perspective of fMRI time series: the first pertains to optimal experimental design and the second to optimum (de)convolution of the time series to obtain the most efficient parameter estimates.

5.1.1 The Hemodynamic Response Function and Optimum Design

As noted above, an LTI model of neuronally mediated signals in fMRI suggests that, whatever the frequency structure of experimental variables, only those that survive convolution with the HRF can be estimated with any efficiency. By convolution theorem, the experimental variance should, therefore, be designed to match the transfer function of the HRF. The corresponding frequency profile of this transfer function is shown in Figure 7 (solid line in the upper left panel). It is clear that frequencies around 0.03 Hz are optimal, corresponding to periodic designs with 32-s periods (e.g., 16-s epochs). Generally the first objective of experimental design is to comply with the natural constraints imposed by the HRF and to ensure that experimental variance occupies these intermediate frequencies.

5.1.2 The Noise Spectrum: Efficiency and Bias

The noise spectrum is a complicated but important area. Conventional signal processing approaches dictate that whitening the data engenders the most efficient parameter estimation. This corresponds to filtering with a convolution matrix $\boldsymbol{S}$ (see Figure 2) that is the inverse of the intrinsic convolution matrix $\boldsymbol{K}$ ($\boldsymbol{K}\boldsymbol{K}^T = \Sigma$). There are, however, two fundamental problems with this: one generally does not know the intrinsic correlations Σ and even if they were known for any given time series, adopting the same assumptions for all voxels will lead to bias and loss of efficiency because each voxel has a different temporal autocorrelation structure (e.g., brainstem voxels will be subject to pulsatile effects; ventricular voxels will be subject to cerebrospinal fluid flow artifacts; white matter voxels will not

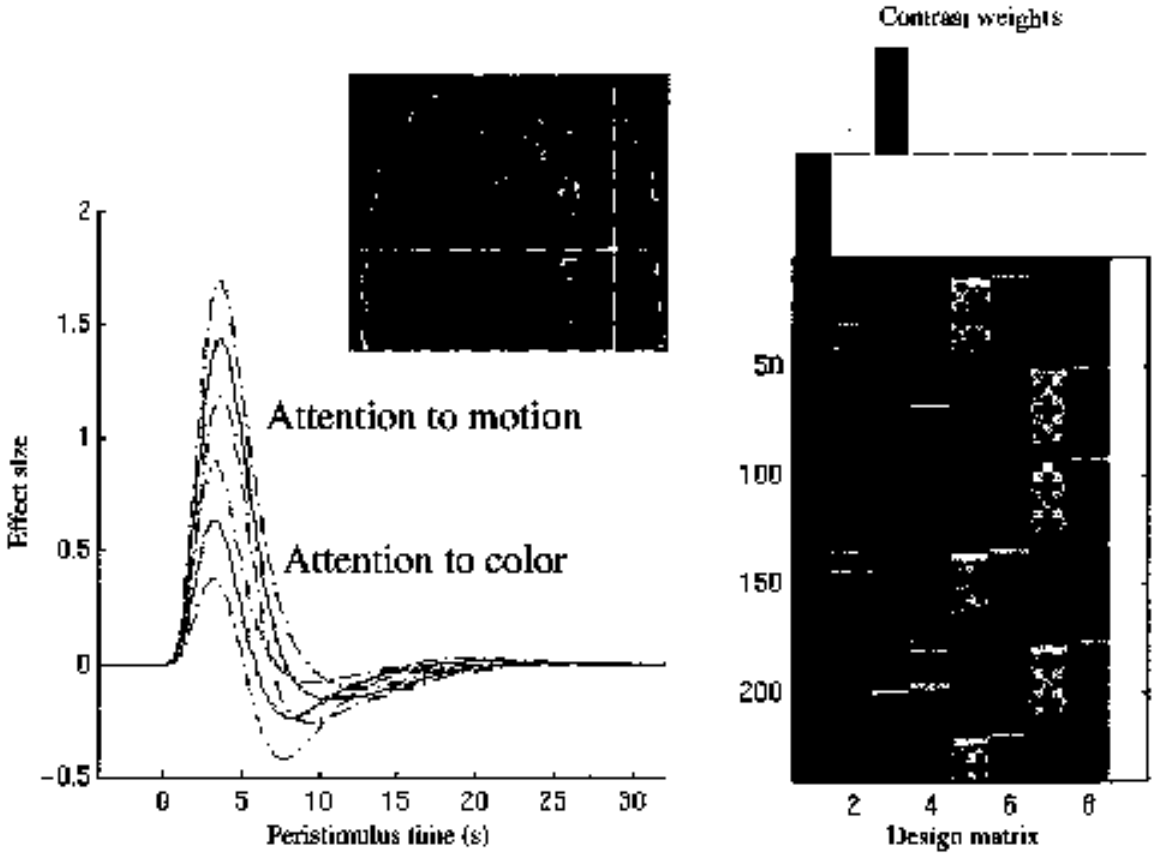

Figure 5 Assessing an interaction using an event-related design: attentional modulation of V5 responses. Subjects viewed stationary monochromatic stimuli that occasionally changed color and moved at the same time. These compound events were presented under two levels of attentional set (attention to color and attention to motion), The event-related responses are modeled, in an attention-specific fashion, by the first four regressors (delta functions convolved with a hemodynamic response function and its derivative) in the design matrix on the right. The simple main effects of attention are modeled as similarly convolved box-cars. The interaction between attentional set and visually evoked responses is simply the difference in evoked responses under both levels of attention and is tested for with the appropriate contrast (upper right). Only the first 256 rows of the design matrix are shown. The most significant modulation of evoked responses under attention to motion was seen in left V5 (insert). The fitted responses and their standard errors are shown on the left as functions of peristimulus time

be subject to neurogenic noise). The first problem is highlighted in Figure 6. Here the residuals from a long (1000 scan, *TR*=1.7 s) time series were used to estimate the spectral density and associated autocorrelation functions (where one is proportional to the Fourier transform of the other) using the Yule–Walker method with an autoregression order of 32. Estimates using a commonly assumed AR(1) model[36] and a modified 1/*f* model[37] are also shown. The AR(1) is inadequate and fails to model long-range correlations (i.e., low frequencies). The 1/*f* model shown here is an extremely good approximation (even more so since the parameters of this model were not estimated using the data but taken from the literature). However, the 1/*f* model fails to model the short-term correlation structure as well as it could. The discrepancy between the assumed and actual form of temporal correlations means that, when the data are whitened in accord with the assumed models, the standard error of the parameter estimates (i.e., their variance) is over-[AR(1)] or under-(1/*f*) estimated. This leads directly to bias in the ensuing statistics (the T statistic is simply the quotient of the contrast and its estimated standard error; see Figure 2). The effect is not trivial and can easily reach 50% for common experimental epoch- and event-related designs. Expected bias is computed using the intrinsic and assumed autocorrelations and the expression for the expected estimate of parameter estimate variance in Figure 2.

5.2 Temporal Filtering and the Bias Problem

One solution to the 'bias problem' involves 'regularizing' the temporal autocorrelation structure by filtering.[18] This effectively imposes a structure on the temporal autocorrelations that renders the difference between the assumed and actual correlations less severe. Although less efficient, the ensuing inferences are less biased and more robust. The loss of efficiency can be minimized by appropriate experimental design and choosing a suitable filter *S*. The example in Figure 7 combines the HRF and high-pass filtering at 1/64 Hz, which, when applied to the time series, markedly reduces the differences among the various models assumed for the autocorrelations (compare Figure 6b with Figure 7b).

Not only does appropriate temporal filtering reduce bias engendered by mis-specification of the intrinsic correlations but it also addresses the nonstationary nature of serial correlations over voxels. Figure 7c,d shows bias over 512 voxels using a voxel-specific estimate for the intrinsic correlations and the

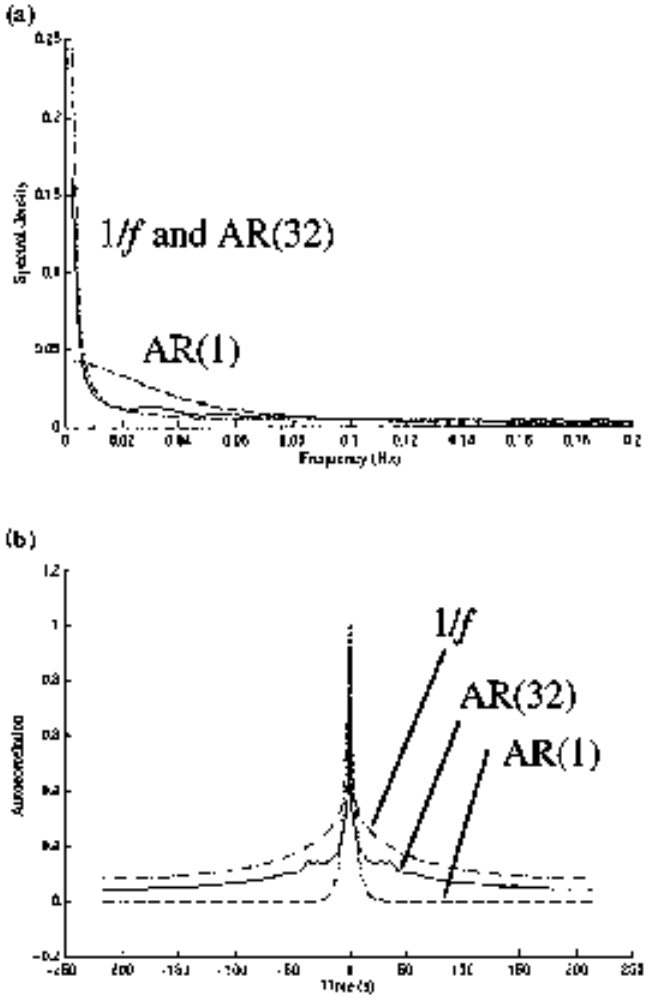

Figure 6 Spectral densities (a) and corresponding autocorrelation functions (b) for the residual terms of a fMRI time series for an AR(32) model estimated using the Yule–Walker method (this is taken to be the closest to an 'empirical' estimate), an AR(1) model estimate using the same method, and a model of the form $(q/f+1)$ where f is frequency in hertz and q=0.0178 (line 1/*f*)

average over all voxels for the assumed structure. Without filtering, the biases (solid bars) range from 80 to 150%. With filtering (open bars) they are reduced substantially. The effect on efficiency is shown in Figure 7d. It is interesting to note that temporal autocorrelations render the efficiency very variable over voxels (by nearly an order of magnitude). This is important because it means that fMRI is not homogeneous in its sensitivity to evoked responses from voxel to voxel.

5.3 Spatially Coherent Confounds and Global Normalization

Implicit in the use of high-pass filtering is the removal of low-frequency components that can be regarded as confounds. Other important confounds are signal components that are artifactual or have no regional specificity. These are referred to as global confounds and can have physiological causes (e.g., global perfusion changes mediated by changes in partial pressure of CO_2) and nonphysiological causes (e.g., transmitter power calibration, $\boldsymbol{B}_1$ coil profile and receiver gain). The latter will generally scale the signal before the MRI sampling process. Other nonphysiological effects may have a nonscaling effect (e.g., Nyquist ghosting or movement-related effects). Instrumentation effects that scale the data are treated by a global normalization by proportional scaling using the whole brain mean. Spatially coherent confounds will, however, still persist, and a more sensitive statistical model obtains when these can be identified and modeled.

5.4 Nonlinear System Identification Approaches

So far we have only considered LTI models and first-order HRFs. Another signal-processing perspective is provided by nonlinear system identification.[38] This section considers nonlinear models as a prelude to the next section on event-related fMRI where nonlinear interactions among evoked responses impose constraints on experimental design and analysis.

We have described an approach to characterizing evoked hemodynamic responses in fMRI based on nonlinear system identification, in particular the use of Volterra series.[39] The approach employed enables *Volterra kernels* to be estimated that describe the relationship between stimulus presentation and the hemodynamic responses that ensue. Volterra series are essentially high-order extensions of linear convolution or FIR models. These kernels, therefore, represent a nonlinear characterization of the HRF that can model the responses to stimuli in different contexts and interactions among stimuli. In the context of fMRI, the kernel coefficients can be estimated by using a second-order approximation to the Volterra series to reformulate the problem in terms of a general linear model and by expanding the kernels in terms of temporal basis functions. This allows the use of the standard techniques described above to estimate the kernels (Figure 8) and to make inferences about their significance on a voxel-specific basis using SPMs.

One important manifestation of the nonlinear effects, captured by the second-order kernels, is a modulation of stimulus-specific responses by preceding stimuli that are proximate in time. This means that responses at high-stimulus presentation rates saturate and, in some instances, show an inverted U behavior (see Figure 9a). This behavior appears to be specific to BOLD (blood oxygenation level-dependent) effects (as distinct from evoked changes in cerebral blood flow) and may represent a hemodynamic 'refractoriness'. This effect has important implications for event-related fMRI.

6 EPOCH- AND EVENT-RELATED fMRI

A crucial distinction in fMRI is that between epoch- and event-related designs. An important issue in event-related fMRI is the choice of interstimulus interval, more precisely termed stimulus onset asynchrony (SOA). The SOA, or the distribution of SOA values, is a critical factor in experimental design and is chosen, subject to some constraints, to maximize the efficiency of response estimation. The constraints on the SOA clearly depend upon the nature of the experiment but are generally satisfied when the SOA is small and derives from a random distribution. Rapid presentation rates allow for the maintenance of a particular cognitive or attentional set, decrease the latitude that the subject has for engaging alternative strategies (incidental processing), and allows the

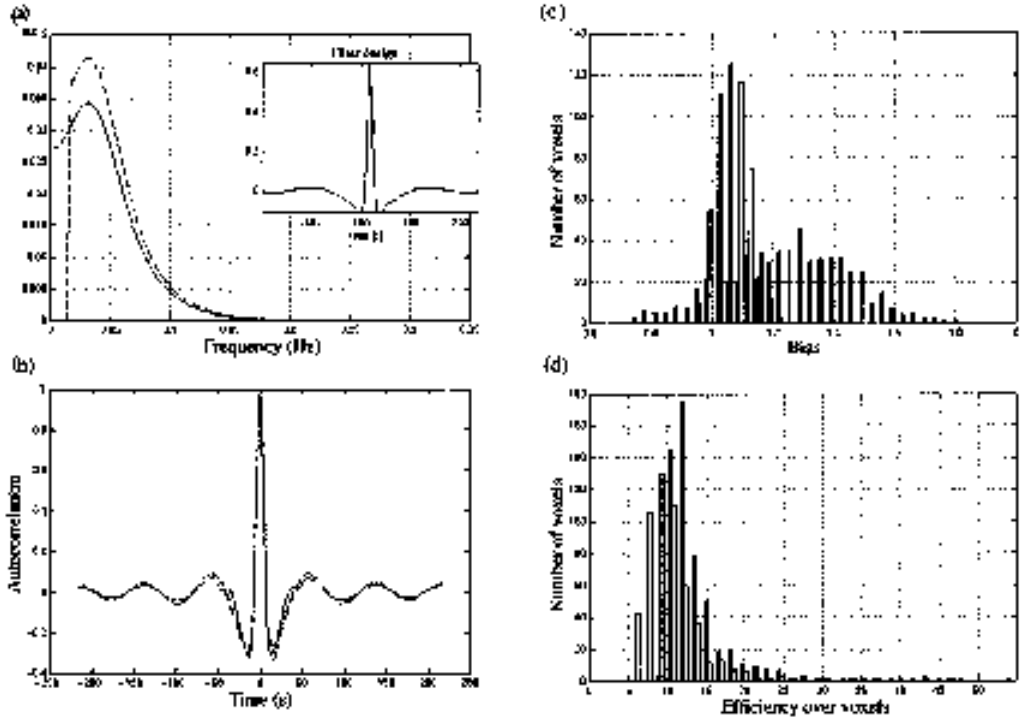

Figure 7 Bias and filtering: the effect of smoothing on bias when estimating the variance of contrasts. (a) The spectral density of the hemodynamic response function (a mixture of two gamma functions) (solid line) and after high-pass filtering at 1/64 Hz (broken line). The corresponding filter in time is shown in the insert. (b) The autocorrelation functions predicted on the basis of the three models shown in Figure 6 after filtering with the kernel in the insert. Compare these autocorrelation functions with those in Figure 6. The differences are now ameliorated. (c,d) The distribution of bias (c) and efficiency (d) over voxels using an AR(8) model to estimate serial correlations at each voxel and assuming a stationary autocorrelation structure over voxels. Distributions are shown with (white bars) and without (filled bars) filtering. Note how filters reduce bias (at the expense of reduced efficiency). Bias is expressed as the ratio of estimated to actual contrast estimate variance and should, ideally, be unity. Efficiency is the inverse of the actual contrast estimate variance

integration of event-related paradigms using fMRI and electrophysiology. Random SOAs ensure that preparatory or anticipatory factors do not confound event-related responses and ensure a uniform context in which events are presented. These constraints indicate the well-documented advantages of event-related fMRI over conventional blocked designs.[23,40–42]

In general, the explanatory variables are created by convolving a set of delta functions, indicating the presence of a particular event, with a small set of basis functions that model the hemodynamic response to those events.[23] A special case of this general approach obtains when the basis functions are delta functions placed at a discrete set of peristimulus times. This special case corresponds to selective averaging[25] and requires stimulus presentation and data acquisition to be synchronized (which in general is not a good idea). We find the most useful basis set to be a canonical HRF and its derivatives with respect to its parameters (e.g., latency and dispersion). The nice thing about this approach is that it partitions differences among evoked responses into differences in magnitude, latency, or dispersion that can be tested for using specific contrasts and the SPM{T} (see Friston et al.[43] for details).

6.1 Stochastic and Deterministic fMRI Designs

fMRI designs can vary over a large number of parameters. In order to compare the efficiency of different designs it is useful to have some common framework that accommodates them all. The efficiency can then be examined in relation to the parameters of the design. Any design can be 'stochastic' or 'deterministic'. In stochastic designs, the probabilities of an event occurring must be specified at all times those events could occur.[44] In deterministic designs, the occurrence probability is unity and the design is completely specified by the times of stimulus presentation or trials. The distinction between stochastic and deterministic designs pertains to how a particular realization or stimulus sequence is created. The efficiency afforded by a particular event sequence is a function of the event sequence itself, and not of the process generating the sequence (i.e., deterministic or stochastic). With a stochastic design, the design matrix $\boldsymbol{X}$, and associated efficiency, are random variables. However, for finite length sequences, the expected efficiency over an infinite number of realizations of $\boldsymbol{X}$ is easily computed, as now described. In the framework considered here the probability $\boldsymbol{p}$ of any event occurring is specified at each time it could occur (i.e., every SOA_{min}). This gives the vector $\boldsymbol{p}$ with an element for every SOA_{min}. This formulation shows the distinction between 'stationary' stochastic designs, where the occurrence probabilities are constant, and nonstationary or 'dynamic' stochastic designs, where they change over time. For deterministic designs, the elements of $\boldsymbol{p}$ are 0 or 1, the presence of a 1 denoting the occurrence of an event. An example of $\boldsymbol{p}$ might be the box-cars used in conven-

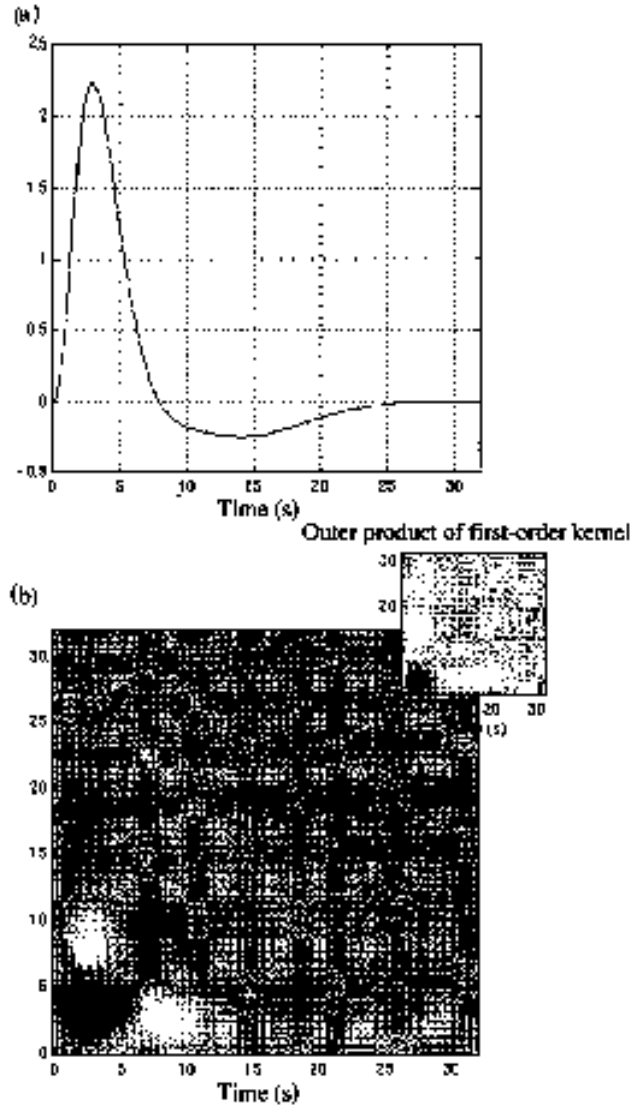

Figure 8 Volterra kernels $\boldsymbol{h_1}$ and $\boldsymbol{h_2}$ based on parameter estimates from a voxel in the left superior temporal gyrus at −56, −28, and 12 mm. These kernel estimates were based on a study in a single subject of aural word presentation at different rates (from 0 to 90 words per minute) using a second-order approximation to a Volterra series expansion modeling the observed hemodynamic response to stimulus input (a delta function for each word). These kernels can be thought of as a characterization of the second-order hemodynamic response function. (a) The first-order kernel ($\boldsymbol{h_1}$) represents the (first-order) component usually presented in linear analyses. (b) The second-order kernel ($\boldsymbol{h_2}$) is presented in image format. The color scale is arbitrary; white is positive and black is negative. The insert represents $[-\boldsymbol{h_1}.\boldsymbol{h_1}^T]$, the second-order kernel that would be predicted by a simple model that involved convolution with $\boldsymbol{h_1}$ followed by some nonlinear scalar function

tional block designs. Stochastic designs of the sort proposed by Dale and Buckner correspond to a vector of identical values and are therefore stationary in nature.[25] Stochastic designs with temporal modulation of occurrence probability correspond to probability vectors with time-dependent probabilities varying between 0 and 1. With these probabilities, the expected design matrices and expected efficiencies can be computed. The nice thing about this formulation is that by setting the mean of the probabilities to a constant, different deterministic and stochastic designs can be compared given the same number of events (or equivalently same mean SOA). Some common examples are given in Figure 9b for an SOA_{min} of 1 s and 32 expected events or trials over a 64-s period (except the fixed-SOA deterministic example with four events). It can be seen that the least efficient is a fixed-interval deterministic design (despite the fact that the SOA is roughly optimal for this class), whereas the most efficient is a block design. A slow modulation of occurrence probabilities gives high efficiency while retaining the advantages of stochastic designs and may represent a very useful compromise between the high efficiency of block designs and the psychological benefits and latitude afforded by stochastic designs.

6.2 What is the Minimum Stimulus Onset Asynchrony?

The minimum SOA can be found using Volterra series (see section 5.4) and the results of a typical analysis are given in Figure 9a. This represents the average response, integrated over a 32-s train of stimuli as a function of SOA within that train. These responses were based on kernel estimates using data from a voxel in the left posterior temporal region of a subject obtained during the presentation of a single word at a variety of rates. The solid line represents the estimated response and shows a clear maximum at just less than 1 s. The points represent estimates based on empirical data from the same experiment. The broken line shows the expected response in the absence of nonlinear effects (i.e., those predicted by setting the second-order kernels to zero). It is clear that nonlinearities become important at around 2 s leading to an actual diminution of the integrated response at SOA values less than a second. The implications of these data are that SOAs should not really fall much below 1 s and at short SOA values the assumptions of linearity are violated. It should be noted that these data pertain to single-word processing in the auditory association cortex. More 'linear' behaviors may be expressed in primary sensory cortex,[25] where the feasibility of using SOA_{min} values as low as 500 ms has been demonstrated even when sampling at a lower rate (e.g., TR=1 s).[45]

6.3 Stationary Stochastic Designs and Efficiency

In this section we consider why, in some instances, a very short average SOA is best whereas in others a longer SOA is more appropriate. Here we deal explicitly with multiple trial types[43] and define the trial onset asynchrony (TOA) as the interval between onsets of a particular trial type. The best TOA depends upon the nature of the characterization of evoked responses that is required. For any given event type, the associated $\boldsymbol{p}$ value determines the average or expected TOA for that event type. This is simply $SOA_{min}/\langle \boldsymbol{p} \rangle$, where $\langle \boldsymbol{p} \rangle$ is the mean probability for the each trial type. By varying $\boldsymbol{p}$ and SOA_{min} the most efficient design can be identified for examining evoked responses themselves or differences among evoked responses. These two situations are depicted in Figure 9c. It is immediately obvious that for both sorts of effect very small SOA values are optimum. However, the optimum occurrence

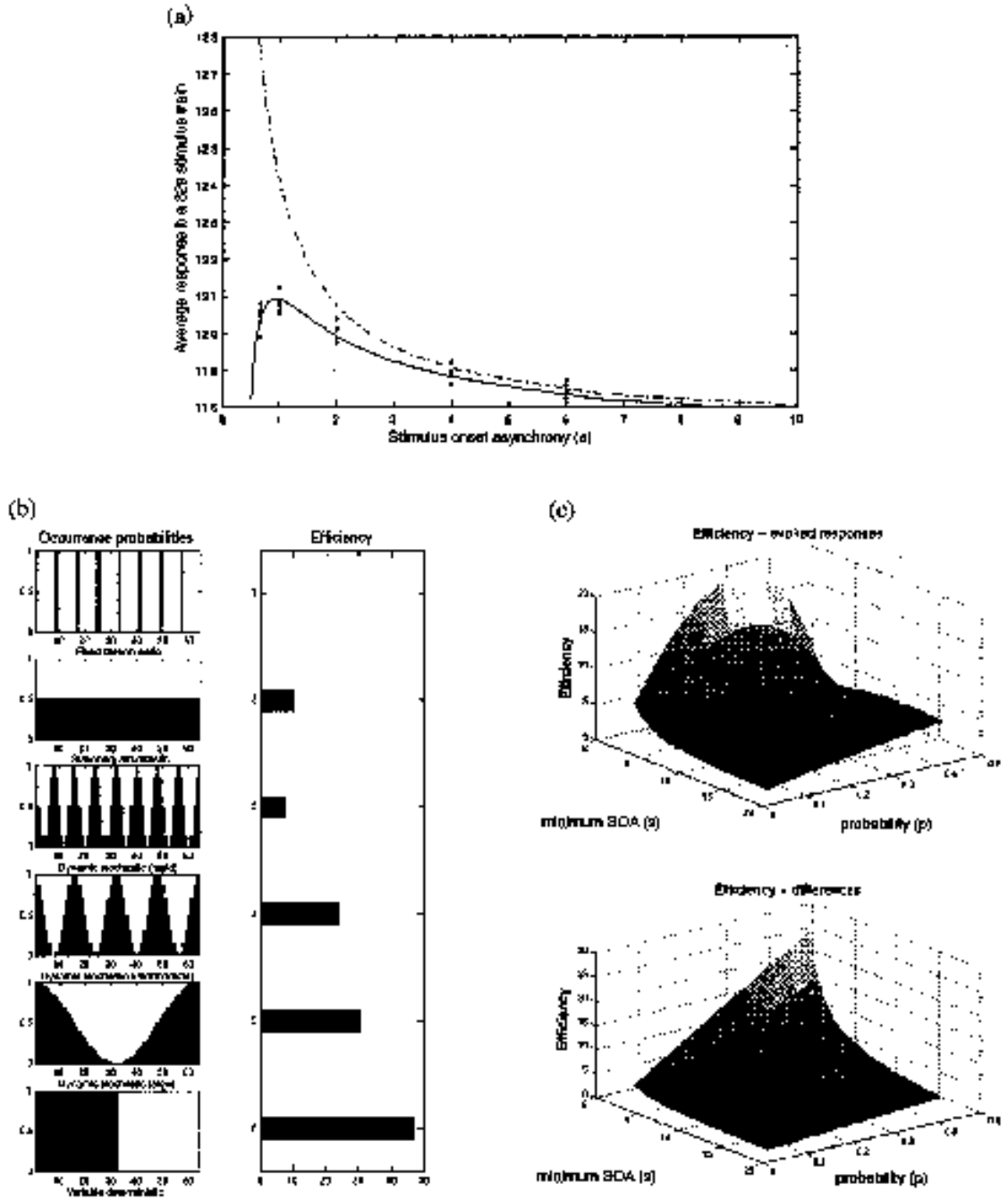

Figure 9 (a) Plot of integrated responses over a 32-s stimulus train as a function of stimulus onset asynchrony (SOA): estimates based on a nonlinear convolution model (see Figure 8) (—); averages of empirical data from the presentation of actual stimulus trains (●); responses expected in the absence of second-order effects (– – –). (b) A comparison of some common (and some untried) stationary and nonstationary stochastic designs. The left-hand column is a graphical representation of the occurrence probabilities p expressed as a function of time (seconds). The efficiency of each design is shown along the ordinate assuming an SOA_{min} of 1 s and a time series of 64 s for a single trial-type design. The expected number of events (i.e., the mean value of $\boldsymbol{p}$) was 0.5 in all but the first, corresponding to an expected trial onset asynchrony of 2 s or 32 events. (c) Efficiency in a stationary stochastic design with two event types each presented with probability $\boldsymbol{p}$ every SOA_{min}. The upper graph is for a contrast testing for the response evoked by a particular trial type and the lower graph is for a contrast testing for differential responses

probabilities are not the same. More infrequent events (corresponding to a smaller $\boldsymbol{p}$) are required to estimate efficiently the responses themselves. This is equivalent to treating the baseline or control condition as any other condition (i.e., by including null events, with equal probability, as further event types). Therefore, by making the probability of null events and all other events equal to $1/(n+1)$, where n is the number of event types, we get a mean TOA of $(n+1)SOA_{min}$. Such designs result in optimal and equivalent efficiency for all comparisons (within stationary stochastic designs).

7 INFERENCES ABOUT SUBJECTS AND POPULATIONS

For a given group of subjects, there is a fundamental distinction between saying that the average response is significant in relation to the variability *of* the subjects' responses and saying that there is a significant response in relation to the variability *about* those subject-specific responses. This distinction relates directly to the difference between 'fixed' and 'random' effect analyses. The following example tries to make this clear. Consider what would happen if we scanned six subjects during the performance of a single task, relative to a baseline. We then constructed a statistical model where task-specific effects were modeled separately for each subject. Unknown to us, only one of the subjects activated a particular brain region. When we examine the contrast of parameter estimates assessing the mean activation over all the subjects, we see that it is greater than zero by virtue of this subject's activation. Furthermore, because that model fits the data extremely well (modeling no activation in five subjects and a substantial activation in the sixth) the error variance, on a scan-to-scan basis, is small and the T statistic is very significant. Can we then say that the group shows an activation? We can say, quite properly, that the mean group response embodies an activation but clearly this does not constitute an inference that the group's response is significant (i.e., that this sample of subjects shows a consistent activation). The problem here is that we are using the scan-to-scan error variance and this is not necessarily appropriate for an inference about group responses. In order to make the inference that the group showed a significant activation, the variability in activation effects must be assessed from subject to subject (using the contrast of parameter estimates for each subject). This variability now constitutes the proper error variance. In this instance, the variance of these six measurements would be large relative to their mean, and the corresponding T statistic would not be significant.

The distinction between the two approaches above relates to how the appropriate error variance is calculated. The first represents a fixed-effect analysis and the second a random-effect analysis. In the former, the error variance is estimated on a scan-to-scan basis, assuming that each scan represents an independent observation (ignoring serial correlations). Here the degrees of freedom are essentially the number of scans (minus the rank of the design matrix). Conversely, in random-effect analyses, the appropriate error variance is based on the activation from subject to subject where the effect per se constitutes an independent observation and the degrees of freedom fall dramatically to the number of subjects. The term random-effect indicates that we have accommodated the randomness of differential responses by comparing the mean activation to the variability in activation from subject to subject. Both analyses are perfectly valid but only in relation to the inferences that are being made.

7.1 Random Effects Analyses

The implementation of random effect analyses in SPM is fairly straightforward and involves taking the contrasts of parameters estimated from a first-level (fixed-effect) analysis and entering them into a second-level (random-effect) analysis. This ensures that there is only one observation (i.e., contrast) per subject in the second-level analysis and that the error variance is computed using the subject-to-subject variability. The nature of the inference made is determined by the contrasts entered into the second level (Figure 10). The second-level design matrix simply tests the null hypothesis that the contrasts are zero (and is usually a column of ones implementing a single sample T test).

7.2 Conjunction Analyses and Population Inferences

There is an alternative approach based on fixed-effect analyses that allows qualitative inferences about population effects. This approach uses conjunctions (as described in Section 4.4.1). Conjunction analyses in the context of multisubject fMRI studies allows an inference to be made at the level of the fixed-effect analysis based on the null hypotheses of no activation in any of the subjects studied, and allows an inference to be made at a second level about the population in terms of the proportion of the population that is likely to show the regionally specific effect. If, for any given contrast, a conjunction of effects over n subjects can be established using a test with a specificity of α and sensitivity β, the probability, under the null hypotheses, of this occurring by chance can be expressed as a function of γ, the proportion of the population (from which the subjects were sampled) with the effect (see the equation in Figure 10). Now this probability has an upper bound (α_c), corresponding to a critical proportion (γ_c), which is realized when the (generally unknown) sensitivity is one. In other words, under the null hypothesis (at the second level) the proportion of the population evidencing this effect is less than or equal to γ_c and the probability of getting a conjunction over n subjects is equal to, or less than, α_c (where $\alpha_c > \alpha$). In short, a conjunction allows one to say, with a specificity of α_c, that more than γ_c of the population show the effect in question. Formally, we can view this analysis as a conservative $100(1-\alpha_c)\%$ confidence region for the unknown parameter γ. Specifically, the confidence region is $\gamma \geqslant \gamma_c$ if the conjunction occurs, and all values of γ if it does not. This approach retains the sensitivity of fixed-effect analyses yet still provides qualitative inferences about the population. These inferences can be construed as statements about how typical the effect is without saying that it is necessarily present in every subject.

In practice, a conjunction analysis of a multisubject/session fMRI study comprises the following steps: (i) A design matrix is constructed where the explanatory variables pertaining to each experimental condition are replicated for each session. This subject-separable design matrix implicitly models session by condition interactions (i.e., different condition-specific responses among sessions). (ii) Contrasts are then specified that test for the effect of interest in each session to obtain a set of SPM{T}. (iii) These SPM{T} are thresholded at u (corresponding to some uncorrected specificity α) and combined to give a SPM of the conjunction. The ensuing SPM has two equivalent interpretations: first it represents the intersection of the excursion sets, defined by u, of the subject-specific SPM{T}; second, it is an SPM of the minimum value of the T values at u. (iv) The corrected (for search volume) and uncorrected p values associated with each voxel are now computed as described in Figure 2. These p values provide for inferences about the particular subjects studied. However, because we have demonstrated regionally specific conjunctions, we can

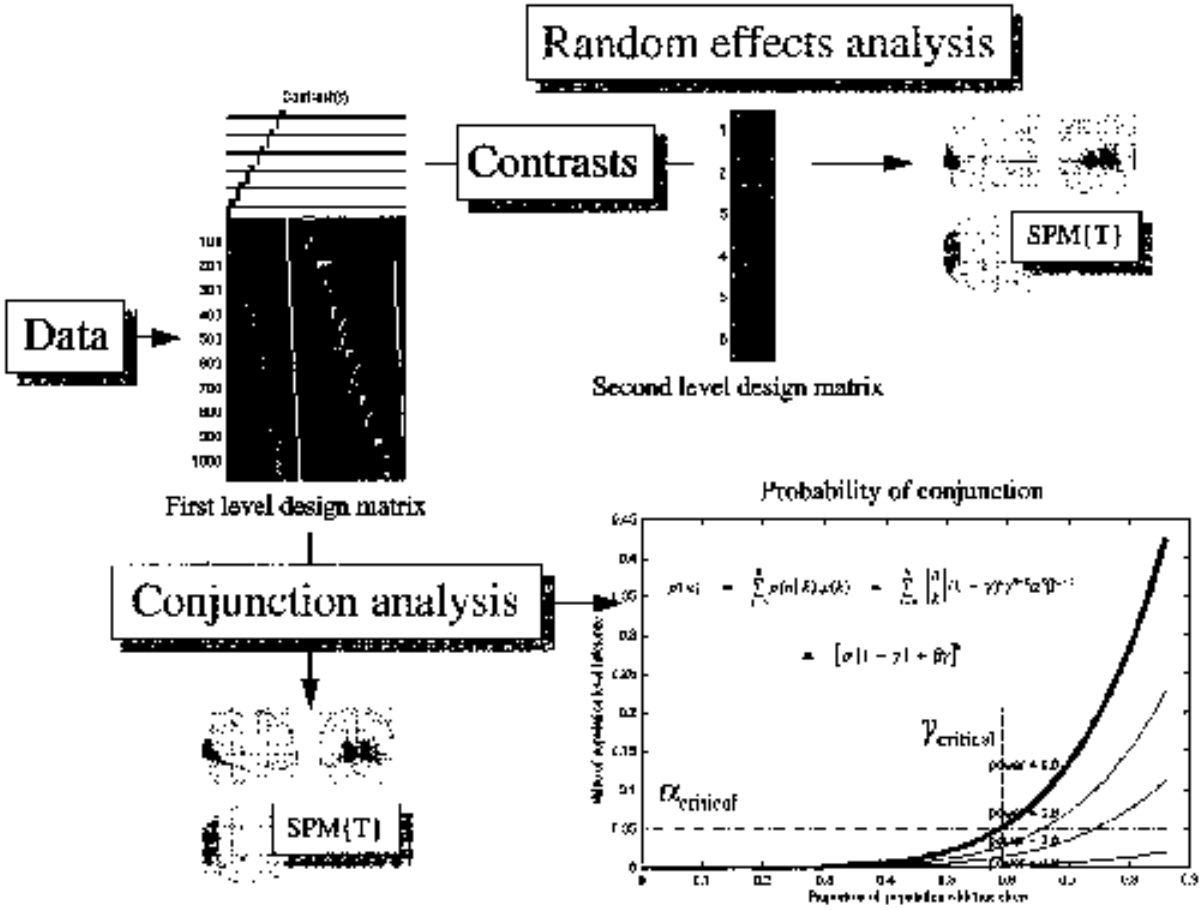

Figure 10 Schematic illustrating the implementation of random-effect and conjunction analyses for population inference. The lower right graph shows the probability of obtaining a conjunction, conditional on a certain proportion γ of the population expressing the effect in question, for a test with specificity of α=0.05, (corresponding to a Z-variate threshold of 1.64) at several sensitivities (β=1, 0.9, 0.8, and 0.6). The critical specificity for population inferences α_{critical} and the associated proportion of the population γ_{critical} are denoted by the thin lines. This probability $p(n)$ is given by the function of α, β, and γ

now proceed to make an inference (at a second level) about the population from which these subjects came using the confidence region approach described above.

8 EFFECTIVE CONNECTIVITY AND FUNCTIONAL INTEGRATION

There is a necessary relationship between approaches to characterizing functional integration and multivariate analyses because the latter are necessary to model interactions among brain regions. Multivariate approaches can be divided into those that are inferential in nature and those that are data led or exploratory. Most are based on the singular value or eigen decomposition of the between-voxel covariances in a fMRI time series.

8.1 Eigen-image Analysis and Related Approaches

Voxel-based PCA of neuroimaging time series can be used to characterize distributed brain systems implicated in sensorimotor, perceptual, or cognitive processes.[46] These distributed systems are identified with principal components or eigenimages that correspond to spatial modes of coherent brain activity. This approach represents one of the simplest multivariate characterizations of functional neuroimaging time series and falls into the class of exploratory analyses. PCA or eigen-image analysis generally uses SVD to identify a set of orthogonal spatial modes that captures the greatest amount of variance, expressed over time. As such, the ensuing modes embody the most prominent aspects of the variance–covariance structure of a given time series. Noting that the covariances among brain regions is equivalent to functional connectivity renders eigenimage analysis particularly interesting because it was one of the first ways of addressing functional integration (i.e., connectivity) in the human brain. Subsequently, eigen-image analysis has been elaborated in a number of ways including CVA[47] and multidimensional scaling.[48] CVA was introduced in the context of ManCova (multiple analysis of covariance) and uses the generalized eigen-vector solution to maximize the variance that can be explained by some explanatory variables relative to error. CVA can be thought of as an extension of eigen-image analysis that refers explicitly to some explanatory variables and allows for statistical inference.

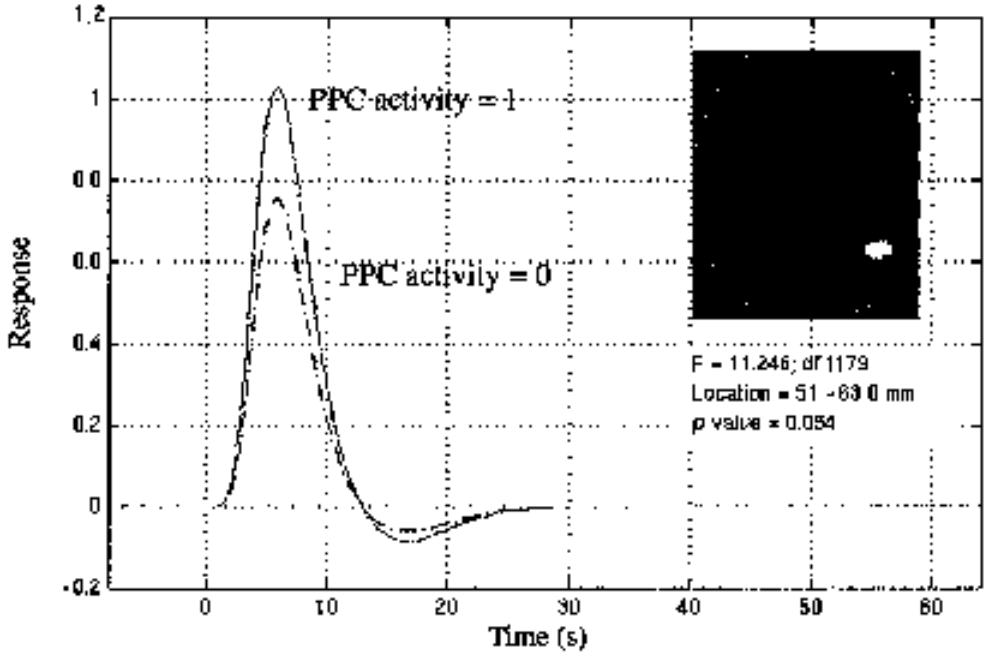

Figure 11 Characterization of effects of V2 inputs on V5 and the modulation of these effects by posterior parietal cortex (PPC) using simulated inputs at different levels of PPC activity. The broken lines represent estimates of V5 responses when PPC activity is 0, according to a second-order Volterra model with inputs based on the activity in V2, PPC, and the pulvinar (all normalized to zero mean and unit standard deviation). The simulated input, from V2, corresponded to a square wave of 500 ms duration convolved with a hemodynamic response function. The solid curves represent the same response when PPC activity is one. It is evident that V2 has an activating effect on V5 and that PPC increases the responsiveness of V5 to these inputs. The insert shows all the voxels in V5 that evidenced a modulatory effect ($p < 0.05$ uncorrected). These voxels were identified by thresholding SPMs of the F statistic testing for the contribution of second-order kernels involving V2 and PPC while treating all other components as confounds. Results for three subjects are shown. Subjects were studied with fMRI under identical stimulus conditions (visual motion subtended by radially moving dots while manipulating the attentional component of the task (detection of velocity changes)

In relation to fMRI data[49] eigen-image analysis is generally used as an exploratory device to characterize coherent brain activity. These variance components may, or may not, be related to experimental design, and endogenous coherent dynamics have been observed in the motor system.[50] Despite its exploratory power, eigen-image analysis is fundamentally limited for two reasons. First, it offers only a linear decomposition of any set of neurophysiological measurements and, second, the particular set of eigen-images or spatial modes obtained are uniquely determined by constraints that are biologically implausible. These aspects of PCA represent inherent limitations on the interpretability and usefulness of eigen-image analysis of biological time series. These observations have motivated the exploration of nonlinear PCA and neural network approaches to imaging time series.[51]

Two other important approaches deserve mention. The first is ICA, which uses entropy maximization to find, using iterative schemes, spatial modes or their dynamics that are approximately independent. This is a stronger requirement than orthogonality in PCA and involves removing high-order correlations among the modes (or dynamics). It was initially introduced as spatial ICA in which the independence constraint was applied to the modes (with no constraints on their temporal expression).[52] More recent approaches use, by analogy with magneto and electrophysiological time series analysis, temporal ICA where the dynamics are enforced to be independent. In fMRI, this requires an initial dimension reduction (usually using conventional eigen-image analysis). Finally, there has been a considerable interest in cluster analysis. Conceptually, this can be related to eigen-image analysis through multidimensional scaling and PCA. In cluster analysis, voxels in a multidimensional scaling space are assigned belonging probabilities to a small number of clusters, thereby characterizing the temporal dynamics (in terms of the cluster centroids) and spatial modes (defined by the belonging probability for each cluster). These approaches eschew many of the unnatural constraints imposed by eigen-image analysis and can be a very useful exploratory device.

8.2 Functional and Effective Connectivity

Imaging neuroscience has firmly established functional specialization as a principle of brain organization in humans; however, the functional integration of specialized areas has proven more difficult to assess. Functional integration is usually inferred on the basis of correlations among measurements of neuronal activity.[53] Functional connectivity has been defined as correlations between remote neurophysiological events.[46] However, correlations can arise in a variety of ways. For example, in multiunit electrode recordings they can result from stimulus-locked transients evoked by a common input or reflect stimulus-induced oscillations mediated by synaptic connections.[54] Integration within a distributed system is usually better understood in terms of effective connectivity; this refers explicitly to the influence that one neural system exerts over another, either at a synaptic (i.e., synaptic efficacy) or population level. It has been proposed that 'the [electro-

physiological] notion of effective connectivity should be understood as the experiment- and time-dependent, simplest possible circuit diagram that would replicate the observed timing relationships between the recorded neurons'.[55] This indicates two important points: effective connectivity is dynamic (i.e., activity and time dependent), and it depends upon a model of the interactions. The models employed in functional neuroimaging can be grouped as those based on regression models[56] or those based on structural equation modeling (i.e., path analysis).[57]

8.3 Characterizing Nonlinear Coupling among Brain Areas

Linear models of effective connectivity assume that the multiple inputs to a region are linearly separable. This assumption precludes activity-dependent connections that are expressed in one sensorimotor or cognitive context and not in another. The resolution of this problem lies in adopting nonlinear models that include interactions among inputs. These interactions can be construed as a context- or activity-dependent modulation of the influence that one region exerts over another, where that context is instantiated by activity in further brain regions exerting modulatory effects. These nonlinearities can be introduced into structural equation modeling using so-called 'moderator' variables that represent the interaction between two regions in causing activity in a third.[58] From the point of view of regression models, modulatory effects can be modeled with nonlinear input–output models and, in particular, with the Volterra formulation described above. In this instance, the inputs are not stimuli but activities from other regions. Because the kernels are high order they embody interactions over time and among inputs. The influence of one region j on another i can therefore be divided into two components: the direct influence of j on i irrespective of the activities elsewhere, and an activity-dependent component that represents an interaction with inputs from the remaining regions. The example provided in Figure 11 addresses the modulation of visual cortical responses by attentional mechanisms and the mediating role of activity- or context-sensitive changes in effective connectivity.[59] Figure 11 shows a characterization of this modulatory effect in terms of the increase in V5(MT) responses to a simulated V2 input when posterior parietal activity is zero (broken line) and when it is high (solid lines). This sort of result suggests that parietal activity may be a sufficient explanation for attentional modulation of visually evoked extrastriate responses.[60]

9 RELATED ARTICLES

Functional MRI at High Fields: Practice and Utility; Hemodynamic Changes owing to Sensory Activation of the Brain Monitored by Echo-Planar Imaging.

10 REFERENCES

1. C. G. Philips, S. Zeki, and H. B. Barlow, *Brain*, 1984, **107**, 327.
2. F. Goltz, in 'Transactions of the 7th International Medical Congress', Vol. I, ed. W. MacCormac, Kolkmann, London, 1881, p. 218.
3. J. R. Absher and D. F. Benson, *Neurology*, 1993, **43**, 862.
4. S. Zeki in 'Vision: Coding and Efficiency', ed. C. Blakemore, Cambridge University Press, Cambridge, 1990, p. 321.
5. K. J. Friston, J. Ashburner, C. D. Frith, J.-B. Poline, J. D. Heather, and R. S. J. Frackowiak, *Hum. Brain Mapping*, 1995, **2**, 165.
6. K. J. Friston, S. Williams, R. Howard, R. S. J. Frackowiak, and R. Turner, *Magn. Res. Med.*, 1996, **35**, 346.
7. P. Talairach and J. Tournoux, 'A Stereotactic Coplanar Atlas of the Human Brain', Thieme, Stuttgart, 1988.
8. J. Ashburner, P. Neelin, D. L. Collins, A. Evans, and K. Friston, *Neuroimage*, 1997, **6**, 344.
9. M. I. Miller, G. E. Christensen, Y. Amit, and U. Grenander, *Proc. Natl. Acad. Sci., USA*, 1993, **90**, 11944.
10. P. Jezzard and R. S Balaban, *Magn. Res. Med.*, 1995, **34**, 65.
11. K. J. Friston, C. D. Frith, P. F. Liddle, and R. S. J. Frackowiak, *J. Cereb. Blood Flow Metab.*, 1991, **11**, 690.
12. R. J. Adler, in 'The Geometry of Random Fields', Wiley, New York, 1981.
13. K. J. Worsley, A. C. Evans, S. Marrett, and P. Neelin, *J. Cereb. Blood Flow Metab.*, 1992, **12**, 900.
14. K. J. Friston, K. J. Worsley, R. S. J. Frackowiak, J. C. Mazziotta, and A. C. Evans, *Hum. Brain Mapping*, 1994, **1**, 214.
15. K. J. Worsley, S. Marrett, P. Neelin, A. C. Vandal, K. J. Friston, and A. C. Evans, *Hum. Brain Mapping*, 1996, **4**, 58.
16. P. A. Bandettini, A. Jesmanowicz, E. C. Wong, and J. S. Hyde, *Magn. Res. Med.*, 1993, **30**, 161.
17. G. K. Aguirre, E. Zarahn, and M. D'Esposito, *Magn. Res. Med.*, 1998, **39**, 500.
18. K. J. Worsley and K. J. Friston, *Neuroimage*, 1995, **2**, 173.
19. C. Buchel, R. J. S. Wise, C. J. Mummery, J.-B., Poline, and K. J. Friston, *Neuroimage*, 1996, **4**, 60.
20. K. J. Friston, P. J. Jezzard, and R. Turner, *Hum. Brain Mapping*, 1994, **1**, 153.
21. G. M. Boynton, S. A. Engel, G. H. Glover, and D. J. Heeger, *J. Neurosci.*, 1996, **16**, 4207.
22. K. J. Friston, C. D. Frith, R. Turner, and R. S. J. Frackowiak, *Neuroimage*, 1995, **2**, 157.
23. O. Josephs, R. Turner, and K. J. Friston, *Hum. Brain Mapping*, 1997, **5**, 243.
24. N. Lange and S. L. Zeger, *J. R. Stat. Soc. Ser. C*, 1997, **46**, 1.
25. A. Dale and R. Bucker, *Hum. Brain Mapping*, 1997, **5**, 329.
26. K. J. Friston, *Hum. Brain Mapping*, 1997, **5**, 133.
27. K. J. Friston, A. Holmes, J.-B. Poline, C. J. Price, and C. D. Frith, *Neuroimage*, 1996, **4**, 223.
28. S. E. Petersen, P. T. Fox, M. I. Posner, M. Mintun, and M. E. Raichle, *J. Cog. Neurosci.*, 1989, **1**, 153.
29. C. J. Lueck, S. Zeki, K. J. Friston, N. O. Deiber, P. Cope, V. J. Cunningham, A. A. Lammertsma, C. Kennard, and R. S. J. Frackowiak, *Nature*, 1989, **340**, 386.
30. C. J. Price and K. J. Friston, *Neuroimage*, 1997, **5**, 261.
31. S. Grafton, J. Mazziotta, S. Presty, K. J. Friston, R. S. J. Frackowiak, and M. Phelps, *J. Neurosci.*, 1992, **12**, 2542.
32. C. Price, R. J. S. Wise, S. Ramsay, K. J. Friston, D. Howard, K. Patterson, and R. S. J. Frackowiak, *Neurosci. Lett.*, 1992, **146**, 179.
33. K. J. Friston, C. Frith, R. E. Pasingham, P. F. Liddle, and R. S. J. Frackowiak, *Proc. R. Soc. Lond. Ser. B*, 1992, **248**, 223.
34. K. J. Friston, P. Grasby, C. Bench, C. Frith, P. Cowen, P. Little, R. S. J. Frackowiak, and R. Dolan, *Neurosci. Lett.*, 1992, **141**, 106.
35. K. J. Friston, C. J. Price, P. Fletcher, C. Moore, R. S. J. Frackowiak, and R. J. Dolan, *Neuroimage*, 1996, **4**, 97.
36. E. T. Bullmore, M. J. Brammer, S. C. R. Williams, S. Rabe-Hesketh, N. Janot, A. David, J. Mellers, R. Howard, and P. Sham, *Magn. Res. Med.*, 1996, **35**, 261.
37. E. Zarahn, G. K. Aguirre, and M. D'Esposito, *Neuroimage*, 1997, **5**, 179.
38. A. L. Vazquez and C. D. Noll, *Neuroimage*, 1998, **7**, 108.

39. K. J. Friston, O, Josephs, G. Rees, and R. Turner, *Magn. Res. Med.*, 1998, **39**, 41.
40. R. Buckner, P. Bandettini, K. O'Craven, R. Savoy, S. Petersen, M. Raichle, and B. Rosen, *Proc. Natl. Acad. Sci., USA*, 1996, **93**, 14878.
41. V. P. Clark, J. M. Maisog, and J. V. Haxby, *J. Neurophysiol.*, 1998, **76**, 3257.
42. E. Zarahn, G. K. Aguirre, and M. D'Esposito, *Neuroimage*, 1997, **5**, 179.
43. K. J. Friston, P. Fletcher, O. Josephs, A. Holmes, M. D. Rugg, and R. Turner, *Neuroimage*, 1998, **7**, 30.
44. O. Heid, F. Gönner, and G. Schroth, *Neuroimage*, 1997, **5**, S476.
45. M. A. Burock, R. L. Buckner, M. G. Woldorff, B. R. Rosen, and A. M. Dale, *Neuroreport*, 1998, **9**, 3735.
46. K. J. Friston, C. Frith, P. Liddle, and R. S. J. Frackowiak, *J. Cereb. Blood Flow Metab.*, 1993, **13**, 5.
47. K. J. Friston, J.-B. Poline, A. P. Holmes, C. D. Frith, and R. S. J. Frackowiak, *Hum. Brain Mapping*, 1996, **4**, 140.
48. K. J. Friston, C. D. Frith, P. Fletcher, P. F. Liddle, and R. S. J. Frackowiak, *Cerebr. Cortex*, 1996, **6**, 156.
49. J. J. Sychra, P. A. Bandettini, N. Bhattacharya, and Q. Lin, *Med. Phys.*, 1994, **21**, 193.
50. B. Biswal, F. Z. Yetkin, V. M. Haughton, and J. S. Hyde, *Magn. Res. Med.*, 1995, **34**, 537.
51. N. Mørch, U. Kjems, L. K. Hansen, C. Svarer, I. Law, B. Lautrup, and S. C. Strother, 'IEEE International Conference on Neural Networks', Perth Australia, 1995, p. 2085.
52. M. McKeown, T.-P. Jung, S. Makeig, G. Brown, S. Kinderman, T.-W. Lee, and T. Sejnowski, *Proc. Natl. Acad. Sci., USA*, 1998, **95**, 803.
53. R. Baumgartner, G. Scarth, C. Teichtmeister, R. Somorjai, and E. Moser, *JMRI*, 1997, **7**, 1094.
54. G. L. Gerstein and D. H. Perkel, *Science*, 1969, **164**, 828.
55. A. Aertsen and H. Preil, in 'Non Linear Dynamics and Neuronal Networks', ed. H. G. Schuster, VCH, New York, 1991, p. 281.
56. K. J. Friston, L. G. Ungerleider, P. Jezzard, and R. Turner, *Hum. Brain Mapping*, 1995, **2**, 211.
57. A. R. McIntosh and F. Gonzalez-Lima, *Hum. Brain Mapping*, 1994, **2**, 2.
58. C. Buchel and K. J. Friston, *Cerebr. Cortex*, 1997, **7**, 768.
59. S. Treue and H. R. Maunsell, *Nature*, 1996, **382**, 539.
60. D. LaBerge, 'Attentional Processing', Harvard University Press, Cambridge.

Acknowledgements

I would like to thank all my colleagues in the Department of Cognitive Neurology and others, especially Keith Worsley, Anders Dale, Ed Bullmore and Eric Zarahn, for useful discussions. This work was funded by the Wellcome Trust.

Biographical Sketch

Karl J. Friston. *b* 1959. B.A. (Camb.) 1980, M.B.B.S. 1983 London University, M.A. (Camb.) 1985, M.R.C. Psych. 1988. Wellcome Trust Research Fellow, MRC Clinical Neuropharmacology Unit, Oxford, UK 1987–88, Honorary Senior Registrar, Department of Psychiatry, Charing Cross and Westminster Medical School and Wellcome Trust Research Fellow, Hammersmith Hospital, London 1988–91, Honorary Lecturer and Senior Registrar, Royal Post Graduate Medical School, London 1991–94, W.M. Keck Foundation Fellow in Theoretical Neurobiology, The Neurosciences Institute, La Jolla, CA, USA 1992–94, Senior Lecturer, Wellcome Department of Cognitive Neurology, Institute of Neurology, UK, Honorary Senior Lecturer, University Department of Psychiatry, Royal Free Hospital School of Medicine, 1994–97, Wellcome Senior Fellow in Clinical Science and UK Honorary Consultant, The National Hospital for Neurology and Neurosurgery, London, UK 1994–present, Reader, Institute of Neurology, University College London, UK 1997–present. Wiley Young Investigator Award in Human Brain Mapping (1996). Approx. 150 publications. Current research interests: theoretical neurobiology, acquisition and characterization of brain data, functional brain mapping (statistical parametric mapping), functional MRI, biomathematics of functional integration in the brain.

Image Quality and Perception

Brian S. Worthington
University of Nottingham, Nottingham, UK

Image quality is an elusive concept; a perfect image would reflect its underlying physical counterpart in all respects. In practice all clinical images fall short of this and provide less than complete information about their underlying substrate. They have physical limitations, which can be expressed in terms of such measures as signal-to-noise ratio, spatial resolution and contrast, and these depend on the performance of the imager, the display system and choice of imaging protocol; they are contaminated by noise and artifacts and furthermore the information they contain has to be abstracted and interpreted by a human observer.

Vision is central to radiology yet our perception of images because it occurs unconsciously, without effort, is all too often taken for granted. In reality human observers have significant physiological and cognitive limitations to their performance, and this has important implications in reporting errors and our efforts to reduce them.

1 INTRODUCTION

The totality of MRI scans which can be derived from any part of the human body represents the set of mappings of the spatial distribution of one or more of its properties. The great diversity of structures and pathological changes which are of relevance in radiological diagnosis imposes widely differing requirements for such images. In the detection of a microadenoma of the pituitary, for example, high spatial resolution is a prerequisite whilst, in the detection of intracranial hemorrhage, sensitivity to small tissue contrast differences is required. Any practical definition of magnetic resonance image utility must take account of the purpose for which the images are to be used; furthermore, in comparing the performance of different MRI scanners, any assessment must take account of the effectiveness with which the images generated can be used for their intended task. The design and construction of the scanner and especially the performance characteristics of such basic components as the magnet and gradient assembly set limits to the fundamental quality of data which are collected during imaging. It cannot always be assumed, however, that the quality of the final displayed image will faithfully reflect the quality of these collected data; appropriate choice of the level and width of the gray scale is necessary, for example, to ensure conspicuity of all clinically relevant features.

When radiologists speak of interpreting a set of MRI scans they dismiss in a phrase an act of enormous complexity which is being carried out by less than perfect observers. It is a matter of concern to all of them, that no matter how conscientiously they carry out their task errors occur and differences are found between the opinion of experienced radiologists as to the presence or otherwise of ostensibly relevant features in a given set of images. If one assumes adequate image quality and optimum viewing conditions then one must look elsewhere for an explanation of these apparent lapses and variations; consideration has to be given to the possibility that these arise from differences in the performance of observers in analyzing the complexity embodied in the image structure.

2 THE RADIOLOGICAL REPORTING TASK

The radiological reporting task contains several parts; detection, classification, and additional observations of clinical relevance. Detection involves identification of relevant features in a particular image set which then allows it to be classified, that is, assigned to one of a number of categories, the simplest being the binary decision of whether it is normal or abnormal. The radiologist makes an involuntary selection of features in an image, rejecting others as insignificant; unrelated contours are disregarded whilst other image elements are associated in a meaningful way. This process of abstraction from the overall background of an image, so rich in information, is perhaps the least understood and yet most important part of the diagnostic process; it occurs spontaneously on the part of the observer, its successful performance is unquestionably related to training and experience, and it is, in all probability, the single most important source of error.

The identification of the disease process underlying any abnormality is what constitutes the process of making a diagnosis, and whilst this is necessary for management, it may not be sufficient in itself to ensure that this is entirely appropriate. In the case of a malignant tumor, for example, one also needs to know the extent of spread in order to plan treatment. MRI like other techniques is applied after a history has been taken from a patient and a physical examination carried out. Its purpose is to reduce diagnostic uncertainty which may relate to the presence, type or extent of a disease process. In striving to achieve a diagnosis with MRI, it may be that we can only at best indicate that some abnormality is present without being able to characterize it. More frequently, taking into account the clinical picture, we can place an abnormality within a generic category of diagnosis, as with the identification of a tumor in the cerebellopontine angle cistern. Further features may permit tissue characterization to a degree where it is possible to make a specific diagnosis. Over and above its diagnostic capabilities MRI has proved invaluable in providing information which facilitates the planning of surgical operations.

In order to provide the maximum information from which an accurate diagnosis can be made so as to guide patient management, an appropriate set of images must have been generated.

3 THE ACQUISITION OF APPROPRIATE IMAGE SETS

The outstanding attribute of MRI is its ability to provide a substantially greater tissue contrast than has hitherto been available. This reflects the multiplicity of intrinsic tissue parameters which determine the MRI signal and their dynamic range. The complex user-controllable interdependence of these parameters

has profound effects on the signal-to-noise ratio, spatial resolution, image contrast and total examination time. Before selecting a protocol for a given examination, careful thought must be given to the possible prospective diagnosis so that appropriate choice of pulse sequence, field-of-view, matrix size, and number and thickness of slices is made to best accomplish demonstration of the suspected pathology in an acceptable time frame.[1] It has to be recognized that there is typically no single optimal set of parameters to achieve this objective and that the repertoire of possibilities is constantly being refined and extended as the knowledge base of clinical MRI expands.

Once the data have been acquired they are stored in a numerical matrix which represents relative signal intensities. The dynamic range of this data is far greater than can be encompassed in a tonal range of gray scale levels distinguishable by a human observer. In order, therefore, to facilitate interrogation of the whole data set, it is viewed at different gray scale window widths around a central level. Even when an appropriate protocol is chosen for a given pathology its presence may not be recognized; furthermore, early pathological changes may incorrectly be suspected in images which are in fact normal. There are several factors which contribute to such incorrect categorization of images. Noise, which occurs in the process of data acquisition, may mask the presence of relevant signal. Artifacts due to the inadequacy of data underlying image formation may simulate a lesion. Inappropriate display characteristics may lead to a lesion being overlooked and, finally, one has to consider the limitations of the human observer carrying out the task.

4 THE PERFORMANCE CHARACTERISTICS OF THE HUMAN VISUAL SYSTEM: IMPLICATIONS FOR IMAGE APPRAISAL

In order to analyze adequately the complexity embedded in the image structure, information which is transmitted through the display medium, be it film or a monitor, must match so far as possible the performance characteristics of the human visual system.

There is now convincing evidence that two separate stages are involved in the examination of visual displays, referred to as the preattentive and attentive phases by Julesz.[2] A display is examined holistically during the first glimpse, and this leads to the detection of features within the stimulus which allow a distinction to be made between 'figure and ground'. This has been shown to depend critically on simple local patterns of texture, the individual elements of which are referred to as textons. The methodology to investigate this phase of vision has been the use of tachistoscopic displays which have revealed the surprising level of information which can be assimilated in an exposure time as short as 100 milliseconds. Another approach has been to examine the statistical properties of artificial textural patterns which can and cannot be immediately segregated on visual inspection.

The second, or attentive phase of vision is where the display is serially examined using eye movements. During the individual fixations information is processed not just from the foveal area but a larger area around the fovea subtending approximately 6° of arc which Mackworth[3] has called the useful field-of-view. Of relevance to analysis of images is the demonstration that the density of irrelevant items in the display influences the size of this area and also that as the foveal load increases, the size of this area shrinks, although this effect can be mitigated to some extent with experience.

The spatial frequency model of vision due to Campbell and Robson[4] provides us with a clear appreciation of the physiological constraints to vision and provides the rationale for the use of a number of strategies to improve our assimilation of relevant information contained in MRI scans. Using as a test object a grating of light and dark bars whose intensity varies sinusoidally across the stimulus, the contrast sensitivity of the human visual system has been measured at different spatial frequencies and reveals that the highest sensitivity to low contrast is at 3 cycles per degree with a response up to 50 cycles per degree but only at very high contrast. There is electrophysiological evidence to support the hypothesis that the visual system contains several independent channels each tuned to a narrow band of spatial frequencies. The modulation transfer function of the human visual system can be likened to a bandpass filter such that the attenuation of low frequencies results in edge enhancement and the higher-frequency limitation introduces a degree of smoothing. In the filter model proposed by Ginsburg,[5] visual stimuli are decomposed into a hierarchy of filtered images from low to high bandpass, which together provide spatial information of form, detail and contrast.

The rationale of using a magnifying glass when examining images is well understood; this shifts the modulation sensitivity curve of the visual system in the spatial frequency domain by the amount of the magnification. The use of altered viewing distance or a minifying lens can also facilitate appreciation of relevant information by ensuring the best match in the spatial frequency domain between low contrast detail of a given size and the performance characteristics of the visual system. High-frequency noise present in the pixel margins can mask important information, and this can be attenuated by the technique of spatial filtration or by linear interpolation of the data on to a larger matrix.

During the past 10 years, several computational models of visual performance have been proposed depending essentially on a serial hierarchy of feature-based stages.[6] Unfortunately, such models have not so far provided significant insight into human visual performance which has available more powerful parallel processing capabilities.

Many techniques for image processing and restoration are now available, and several of these are applied on a purely empirical basis. One cardinal principle which should be observed in applying any such technique is that it should provide better segmentation of the image consistent with the underlying anatomical, physiological or pathological substrate so that abnormalities can be better appreciated, as, for example, the subtraction technique which underlies the creation of phase contrast MRI angiograms. Adding color to MRI scans by equating shades of gray to spectral colours is, on the other hand, totally valueless because this would introduce artificial boundaries into the image which have no anatomical reality.

Modern imaging systems provide increasingly greater amounts of data which can be displayed in a wide variety of formats including 'pseudo-3D' projections and cine presenta-

tions, which allow currently under-utilized information channels in the observer to be used. The rapid cinematic presentation of contiguous transverse axial MRI body scans can allow information across several sections to be integrated more readily than on inspection of the individual hard copy images. In cine presentations, which are now a familiar mode of display in cardiac studies, image noise may be integrated by the observer, effectively increasing the signal-to-noise ratio and the perceptibility of relevant information.

5 COGNITIVE ASPECTS OF IMAGE INTERPRETATION

The principal cognitive factors which set a limit to an observer's capacity to apprehend the correct significance of information derived from an image set include our limited memory capacity, our selectivity in data abstraction, our inability to integrate a great deal of information simultaneously and that our simplification of judgment tasks introduces bias into our decision making.[7] We know also of the human tendency to seek confirmatory rather than disconfirmatory evidence during problem solving.

To overcome the first two of these limitations the possibility of using computer-assisted diagnosis based on discriminant function analysis applied to specific radiological features has been suggested, for example, to assist in distinguishing multiple sclerosis from other diseases in MRI brain scans.[8] If this method is to be used by several different radiologists, then it is necessary to ensure that an unambiguous and consistent method of codifying image descriptors is applied. This problem has recently been addressed in a study assessing high-signal foci on T_2-weighted brain images.[9] In this type of research a consensus agreement must be reached on image criteria in advance by participants so that inevitable interobserver variation is minimized.

6 ASSESSMENT OF THE DIAGNOSTIC EFFICACY OF IMAGE SETS

At the simplest level, asking observers to declare the relative fidelity with which some feature or features are displayed (e.g. on images derived from different MRI systems or produced with different pulse sequences) is open to several sources of bias which include a preference for the esthetically pleasing and inconsistencies between different observers in the use of any rating scale.

One method of reporting the diagnostic value of particular image sets is to assess the diagnostic accuracy or percentage of correct diagnoses achieved in a group of positive and negative cases for the particular pathology under consideration. This index has severe limitations, however, because it fails to take into account the prevalence of true-positive cases in the study population and also it does not reveal the balance of false-positive and false-negative errors and their clinical consequences. The latter deficiency is overcome by reporting the performance of an image set in terms of the sensitivity (or the fraction of patients having the pathology actually declared positive) and the specificity (the fraction of patients without the disease declared negative).[10]

This is best achieved by determining all the different combinations of sensitivity and specificity that an imaging procedure provides in a particular detection task, for example the detection of focal liver lesions on MRI scans, as the observer's internal criterion for making the diagnosis is varied over all possible settings. The sensitivity (true-positive rate) is then plotted against (1 − specificity), the false-positive rate, to produce a receiver operating characteristic (ROC) curve.[11] In practice the observer is asked to select one of several levels of confidence [e.g. (1) definitely positive, (2) probably positive, (3) indeterminate, (4) probably negative, (5) definitely negative] or ratings to report their impression of whether an abnormality is present or not. The areas under the ROC curves of different observers for a given task provide an assessment of their inherent performance in carrying out the required discrimination. ROC analysis, although time-consuming, can be used to compare the detectability of specified abnormalities in image sets generated using different imaging systems or different protocols.

7 CONCLUSION

There are two principal ways in which diagnostic accuracy in the interpretation of MRI scans can be improved. Firstly, one can improve the quality of the image set which is generated so that relevant abnormalities are more readily appreciated. Secondly, one can address limitations of human observer performance and its inherent variability which has set us a new set of problems to solve in a era when the range of image formats and our ability to manipulate and transform them has never been greater.

8 RELATED ARTICLES

High-Field Whole Body Systems; Low-Field Whole Body Systems; MRI at Midfield Strength; Outcome and Efficacy–Analysis of Healthcare Models.

9 REFERENCES

1. E. Kanal and F. W. Wehrli, in 'Biomedical Magnetic Resonance Imaging', ed. F. W. Wehrli, D. Shaw, and J. B. Kneeland. VCH, New York, 1988, Chap. 2, p. 47.
2. B. Julesz, in 'Dynamic Aspects of Neocortical Function', ed. G. M. Edelman, W. E. Gall, and W. M. Cowan. Wiley, New York, 1984, p. 160.
3. N. H. Mackworth, in 'Eye Movements and Psychological Processes', ed. R. A. Monty and J. W. Senders, Wiley, New York, 1976, p. 307.
4. F. W. Campbell and J. G. Robson, *J. Physiol. (London)*, 1968, **197**, 551.
5. A. P. Ginsburg and W. R. Hendee, in 'Quantification of Visual Capability', ed. W. R. Hendee and P. N. T. Wells, Springer-Verlag, 1993, Chap. 3.

6. D. Marr, 'Vision', Freeman, San Francisco, 1982, p. 103.
7. 'Judgment Under Uncertainty; Heuristics and Biases', ed. D. Kahneman, P. Slovic, and A. Teversky, Cambridge University Press, Cambridge, 1982.
8. G. Du Boulay, B. H. Teather, W. P. Jeffrey, M. H. Higgott, and D. Pleumona, *Rev. Neuroradiol.*, 1994, **7**, 37.
9. F. Z. Yelkin, V. M. Haughton, M. E. Fischer, R. A. Rapke, D. L. Daniels, L. P. Mark, L. E. Hendrix, R. J. Asleson, and J. Johansen, *Am. J. Roentgenol.*, 1992, **159**, 185.
10. L. B. Lusted, *Semin. Nucl. Med.*, 1978, **8**, 299.
11. C. E. Metz, *Invest. Radiol.*, 1986, **21**, 720.

Biographical Sketch

Brian S. Worthington. *b* 1938. B.Sc., Physiology, 1963, M.B.B.S., London, 1963. F.R.C.R. (Rohan Williams Medal), 1969. FRS 1998. Successively consultant, reader and Professor of Radiology, University of Nottingham. Gold Medal of Society of Magnetic Resonance in Medicine, 1990. Approx. 300 publications. Research interests: cognitive aspects of observer performance and clinical applications of echo planar imaging.

Image Segmentation, Texture Analysis, Data Extraction, and Measurement

Stephen J. Riederer
Mayo Clinic, Rochester, MN, USA

1 INTRODUCTION

Very early in its development MRI was recognized as a modality in which the final image depended upon a variety of tissue-specific as well as operator-dependent parameters.[1] Considerable initial work was devoted to the determination of these dependences as well as the 'optimization' of scanning parameters for given tissue-specific quantities. However, several other questions were raised from a more fundamental standpoint.

One question was whether all relevant information for a section could be provided in an image of a fundamental parameter itself. An example would be the presentation of an image of the T_2 relaxation time for every pixel in the section of interest. This could possibly be used more effectively than the images actually acquired at one or more fixed echo times. We loosely call this the 'simplification' question.

A second broad, fundamental question was whether the specificity of MRI could be improved if tissues were somehow characterized by their multiple tissue-specific properties. For example, although actively malignant tissue and edema might both be distinguished from surrounding normal tissue because of a prolonged observed T_2 relaxation time, they are often not distinguished from each other on this basis alone. However, upon further consideration of other properties, such as the T_1 relaxation time, this could be possible. This use of multiple parameters—either independent measurements or derived parameters such as relaxation times—to attempt to distinguish various materials we loosely call the 'characterization' problem. When taken to an extreme one could even speculate that different types of cancer (e.g. different grades of malignancy) could be distinguished on the basis of where they lay in a plot of T_1 against T_2 space.

It is arguable to what degree these questions have been addressed in the decade since they were initially posed. With respect to the first of these, the 'simplification' question, very rarely are computed T_1 or T_2 images used in actual diagnosis made from MRI scans. Thus, one might conclude that the answer to this question is a resounding 'No'. On the other hand, with many clinical MRI protocols, images are acquired at a 'long' repetition time (*TR*) of say, 2000 ms or more, at two different echo times, for example 30 and 80 ms. The long *TR* time effectively reduces or removes the dependence of the observed signal on the T_1 relaxation time. The radiologist may then attempt to detect relatively bright objects on the late echo time (*TE*) image, indicative of a prolonged T_2 relaxation time, and then determine from the image acquired at the early echo time how the signal intensity of the object of interest compares with some standard, such as the cerebrospinal fluid (CSF) in known anatomic locations. In this way the radiologist is qualitatively performing an estimation of T_2 relaxation, or effectively placing the observed relaxation time of the object of interest into one of three coarse T_2 bins: (i) normal; (ii) modestly prolonged, indicative of many pathologies; or (iii) substantially prolonged, indicative of CSF or certain specific pathologies such as cavernous hemangioma in imaging of the liver.

Likewise, the degree of success with which the second question of 'characterization' has been addressed is also arguable. It is true that MRI cannot now be used noninvasively to determine the grade of malignancy or the primary site from which metastatic cancers originate. On the other hand, much of the art of clinical MRI interpretation involves the assessment of how the signal from a material behaves in one type versus another type of acquired image. For example a 'T_1-weighted' image, formed with a *TR* time comparable to the T_1 relaxation times of the materials under study and an echo time as short as possible, will often be acquired to get a good morphological picture and to assess any areas with abnormally long T_1 times. Additionally, 'T_2-weighted' images will generally also be acquired, and it is this combination of images which is initially considered in making any diagnosis. If necessary, additional sequences will be performed to improve specificity. For example, these might be sensitized to flow, chemical shift, or differences in susceptibility.

Since the time these two general questions were initially posed a decade ago, additional questions have been raised, in many cases much more specific. For example, is it possible automatically to determine the number and volume of multiple sclerosis lesions in the brain? If so, might it then be possible automatically to assess the effectiveness of any therapy by monitoring the total lesion volume over time? Similarly, is it possible automatically to monitor the volume of a primary brain tumor and determine the tumor location with respect to major blood vessels. Although in principle these processes can be done by the human observer, just as for the coarse binning of T_2 relaxation times for image interpretation, the complexity and volume of the data suggest that automation is the preferred approach.

The purpose of this article is to describe how data extracted from a set of magnetic resonance images acquired from some volume under study can be used to provide diagnostic information. This is a very broad area, ranging from straightforward image interpretation to elaborate, automated image segmentation techniques. In the next section an overview of data extraction techniques is provided, and then specific methods are discussed.

2 OVERVIEW OF DATA EXTRACTION METHODS

Image processing techniques such as image segmentation, texture analysis, and data extraction are most appropriately motivated by specific tasks or goals. The purpose of this section is to describe a hierarchy of such tasks or goals and show how a hierarchy of data extraction techniques follow. These goals and techniques are arranged in order, according to the relative

Table 1 Hierarchy of Data Extraction Techniques[a]

Technique	Purpose	Input Images	Automated Processing	Example
No additional processing				
Image interpretation	Detection and characterization	T_1-weighted, T_2-weighted, and other (?) images	None, simple visual interpretation	Interpretation of 'standard' brain MRI scan
Point Processing				
Calculated relaxation times	Improved characterization	Set of T_1 or T_2 dependent images	Fitting procedure	Computation of T_2 times in basal ganglia[2]
Calculation of other physical quantities	Quantification of physical phenomenon	Set of images acquired with different sensitivities to phenomenon	Fitting procedure coefficient	Estimation of diffusion[3]
Synthetic images	Improved characterization and sensitivity	T_1 and T_2 dependent images	Fitting procedure and synthesis	Simulation of arbitrary pulse sequences[4–6]
Generalized image combination	Improved conspicuity and sensitivity	Arbitrary set of images	Appropriate image combination	Eigenfiltering[7]
Regional processing				
Image segmentation	Identification of specific structures	High contrast images of volume of interest	Seed planting; thresholding	Rendering of brain[8]
Quantitative image processing	Volumetry; lesion counting	High contrast images of contiguous sections, multiple contrasts	Segmentation thresholding volume algorithm	Volume determination of hippocampus[9]

[a]The simplest tasks (those requiring the least amount of automated image processing) are listed first. Tasks become more computationally intensive as one moves down the table.

amount of automated image processing required beyond standard image reconstruction. The least computationally intensive is presented first; the complexity of the data extraction technique increases subsequently. This hierarchy is shown in Table 1

The first task shown in Table 1 is one in which no additional automated processing is required. The data extraction technique is one of interpretation of MRI scans by the radiologist. The next tasks shown are ones involving 'point processing'. That is, pixel values from the same location from each of several images are used to determine some quantity, such as the estimate of a relaxation time. This is usually performed with some kind of automated technique, such as a regression. Also included in this general category are estimation of other physical parameters as well as methods for combining or synthesizing magnetic resonance images. The final entries to the table are those involving 'regional processing'. The mathematical algorithm used typically must consider groups of pixels in an image, such as by the use of thresholding or boundary detection. These algorithms are generally the most computationally intensive. Next, individual data extraction techniques are considered.

3 IMAGE INTERPRETATION

Image interpretation, defined as the radiological interpretation of the set of reconstructed images making up a clinical MRI examination, is presented as the lowest level data extraction technique. Despite this low level, this data extraction technique has proven to be the most useful by far during the 10 and more years in which MRI has been used clinically.

Clearly, an MRI examination can be indicated for many different reasons. However, a common purpose is the detection of any pathology, and, if any is detected, the characterization of the pathology. The data extraction method used by the radiologist, and that for which he or she has been trained, can be defined as magnetic resonance image interpretation.

Image interpretation is performed in many ways, and, indeed, can be regarded as a skill or art gained after many years of experience. As with any data extraction method, the success of the extraction is dictated to a great degree by the quality of the acquired images. The types of images acquired for an MRI examination depend significantly on the anatomy under study, the patient's clinical signs or symptoms, and the preferences of the radiologist. Thus, with the understanding

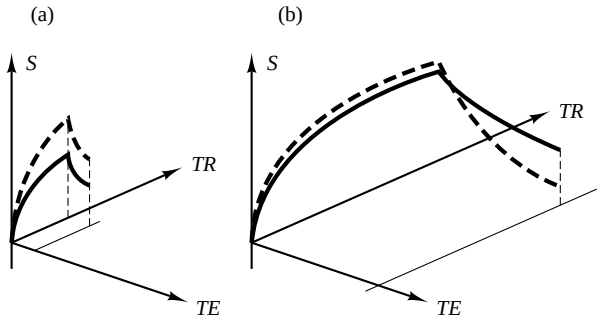

Figure 1 Schematic diagrams of the T_1- and T_2-weighted spin echo image signal as a function of the *TR* and *TE* times used in the pulse sequence. Normal tissue is designated by the broken curve, typical pathological tissue (with slightly increased T_1 and T_2 relaxation times relative to normal tissue) in bold. (a) For T_1-weighted imaging the *TR* is chosen so that the difference in signal due to differential recovery is maximized. The echo time *TE* is chosen to be as short as possible. (b) For T_2-weighted imaging the *TR* is chosen to be several T_1 time constants long (e.g. >2000 ms for many biological materials at typical field strengths for whole body MRI) in order to densensitize the signal to T_1 differences between materials. The echo time *TE* is then chosen to provide high signal difference between materials on the basis of their T_2 relaxation times

that many protocols can be effective, the following suggested protocol is simply provided as a specific example. Once the patient has been properly positioned in the bore of the MRI scanner, typically some combination of 'T_1-weighted' and 'T_2-weighted' images are acquired of the volume under study. These are both commonly multislice rf refocused spin echo sequences. The *TR* times used cover a range, but typically one group of images is acquired using a *TR* time which is comparable to or less than the T_1 relaxation times of the materials in the volume. Such a *TR* provides signal differentiation on the basis of differences in T_1, and such images are often called 'T_1-weighted'. A specific *TR*/*TE* combination could be 500/15 ms. For the long *TR* set, images are commonly formed at two or more echo times, a late echo for 'T_2'-weighting, and an early echo for 'pseudodensity' weighting. This combination of three images per section can be very effective in the detection and subsequent characterization of pathology. A specific example is $TR/TE_1/TE_2$ of 2500/30/100 ms.

These basic sequences are illustrated schematically in Figures 1(a) and (b). Figure 1(a) is a plot of the signal strength for two hypothetical materials as a function of the repetition (*TR*) and echo (*TE*) time used in the spin echo pulse sequence. The broken curve is designated as the signal for 'normal' tissue, with the solid curve corresponding to a material having slightly increased T_1 and T_2 relaxation times, common of many pathologies. For the T_1-weighted sequence the *TR* is chosen to match approximately the T_1 times expected in the volume under study, causing separation of the relative signals. The echo time is chosen to be as short as possible to minimize any T_2 related effects.

Figure 1(b) shows a similar plot but for T_2-weighted imaging. Here the *TR* time is chosen to be several T_1 time constants long so that the magnetization of most materials has substantially recovered to equilibrium. Next, several echo times might be used for the acquisition of data, the latter echo being that which provides large separation between signals as based on T_2 differences. Although these sequences have been available for 10 years, even today they remain the workhorses of clinical MRI.

One may question why simple image interpretation is the most effective data extraction technique used today, and yet the one which requires virtually no image processing after the reconstruction operation. In the author's opinion this is due to several things. First, the degree of data extraction required for routine image interpretation in MRI does not require computation. The radiologist can estimate relative degrees of relaxation by comparing signals from questionable materials with those of standards in the same image, such as CSF or fat. Second, the quality of contemporary magnetic resonance images is so high that except for very specific applications little additional sensitivity is to be gained from more elaborate means beyond image interpretation. Third, there is considerable overlap in relaxation times and densities of normal, neoplastic, ischemic, inflammatory, and malignant tissues, thereby suggesting that the extra effort spent in performing data extraction procedures may not in the long run be worth the effort in improving characterization or specificity. These first three reasons are fundamental. Finally, from a more practical standpoint, clinical reality requires that image interpretation be performed shortly after the MRI examination has been completed. There is no time for time consuming image processing algorithms. Nonetheless, despite the success of image interpretation as the most useful means for routinely extracting data from magnetic resonance images, the further development of data extraction methods is a worthwhile undertaking.

4 CALCULATED RELAXATION TIMES AND OTHER PHYSICAL PARAMETERS

Relaxation times are fundamental tissue-specific quantities in magnetic resonance. They characterize the state of the tissue under study. An early hypothesis in the developmental stages of MRI was that relaxation times could be used to characterize disease. Elevation of T_1 relaxation time was noted early by Damadian,[10] while Herfkens et al.[11] undertook a study in which both T_1 and T_2 relaxation times were measured from normal tissues and tumors in mice. Although normal tissues could be distinguished to some extent on the two-dimensional plot, the points corresponding to tumor covered a broad range. This was very foreboding as it suggested that malignant tissue could not be well characterized by the use of relaxation times, and this has proven to be the case.

Additional articles in the Encyclopedia cover the estimation of and use of relaxation times (see ***Relaxation Measurements in Imaging Studies***, ***Relaxation Measurements in Whole Body MRI: Clinical Utility***, and ***Relaxometry of Tissue***). Although relaxation times are not routinely calculated as part of the every day MRI examination of a patient, estimation of relaxation time is very important in other ways.

In Section 3 the emphasis was on the success with which directly acquired magnetic resonance images can be interpreted. This success is largely because the images themselves are acquired at *TR* and *TE* times which are optimally 'tuned' to the relaxation times of the materials under study. Without knowledge of such relaxation times it would be difficult to tune the

Table 2 Summary of Estimated T_1 Relaxation Times in Humans in Liver and Spleen (Milliseconds at 1.5 T)

Volunteer	Liver T_1	Spleen T_1
1	329	797
2	364	866
3	398	745
4	398	866
5	415	848
6	415	779
7	415	797
8	433	918
9	450	832
10	468	814
11	468	883
12	468	883
13	485	883
14	589	900
Mean ± SD	435 ± 62	844 ± 51

sequences. The following example may show how mean relaxation times can be used for such sequence 'tuning' as well as illustrate the significant interindividual variability in relaxation times.

Consider the specific task of selecting the proper inversion time (*TI*) of an inversion recovery pulse sequence which is to be used to detect pathology in the liver. Such pathology is often metastatic cancer, the relaxation times of which are known to mimic those of normal spleen.[12] This task was addressed by first measuring the T_1 relaxation times for both liver and spleen in a set of 14 volunteers. In this case the T_1 was estimated by using a breath-hold magnetization prepared pulse sequence[13] in which the *TI* was varied from one image to the next until the signal from the targeted organ was nulled out as well as possible. The T_1 was then estimated as $TI'/\ln(2)$, where TI' was that inversion time providing the best nulling. The results are shown in Table 2.

The mean T_1 values, 435 and 844 ms for liver and spleen, respectively, were subsequently used in the selection of a *TI* of 550 ms as being a reliable value and nearly optimum for the ranges of T_1 values encountered. This value has been used effectively in many subsequent clinical studies. This example shows the importance of determining relaxation times and using these values in tuning a pulse sequence. Another incidental point to note in this study is the extent of the variation of T_1 values encountered. The standard deviation of liver T_1 exceeded 10% of the mean value, while that for spleen exceeded 5%. With variations this large in the patient population alone, it is easy to see why the use of absolute relaxation times can have considerable intrinsic imprecision.

The relative lack of specificity of relaxation time analysis has tempered enthusiasm about this technique. Another plausible limiting factor is the potentially long acquisition time required to obtain an adequate set of images to be input to the fitting algorithm used for the relaxation estimation. This can be especially problematic in imaging of the body, where respiratory motion induced artifacts can degrade image quality if the acquisition time is longer than a breath-hold. However, recent developments in fast scan techniques may facilitate the determination of relaxation times for abdominal and cardiac structures. An example of this is shown in Figure 2, which is a comparison of images all acquired of the same section of the abdomen. Note the large lesion positioned anteriorly [arrowed in Figure 2(a)]. Figures 2(a) and (b) were acquired using standard, several minute long, rf-refocused spin echo techniques: Figure 2(a) *TR*/*TE* 250/14 ms, 134 s acquisition time; Figure 2(b) *TR*/*TE* 2500/60 ms, 1015 s acquisition time. Figures 2(c) and (d) were both acquired with breath-hold acquisition techniques, magnetization-prepared gradient echo[13] and interleaved echo planar techniques[14] respectively: Figure 2(c) *TI*/*TR*/*TE* 550/9/4.5 ms, 8 s acquisition time; Figure 2(d) *TR*/*TE* 2000/66 ms, 18 s acquisition time. Note the visually comparable liver lesion contrast-to-noise ratio (CNR) in Figure 2(c) versus Figure 2(a) and in Figure 2(d) versus Figure 2(b). Conceivably the sequences used in Figures 2(c) and (d) could be modified to provide images at alternative *TI* and *TE* times, respectively, so as to provide suitable data for the estimation of T_1 and T_2 relaxation times uncorrupted by motion artifacts.

A specific example of the use of relaxation times in the explanation of an observed phenomenon in magnetic resonance images is the work of Darwin et al.,[2] in which the T_2 relaxation time of structures in the basal ganglia correlated with the distribution of iron in the normal brain. This is due to the gradual accumulation of ferritin in these structures with age.

The use of several measurements at a specific location to estimate the value of a physical parameter at that location needs not be limited to relaxation times. Other techniques which can technically be considered 'data extraction' methods include the estimation of diffusion coefficients,[3,15] or of inhomogeneity-induced signal decay, sometimes referred to as T_2*, or maps of exchange coefficients related to magnetization transfer.[16] In all cases several images with different relative sensitivities to the phenomenon under study are acquired, and the relationship between observed signal intensity and the phenomenon is inverted to enable determination of an actual numerical value for the relevant quantity.

5 SYNTHETIC IMAGES AND IMAGE COMBINATION

The next entries in Table 1 also correspond to point processing. The first, image synthesis,[4–6] can be regarded as an extension of the computation of relaxation times. The concept of synthetic imaging is first to acquire images for several sets of pulse sequence parameters and then mathematically to simulate or 'synthesize' images at alternative parameter values. This process was motivated by the hypothesis that sensitivity or specificity could be improved if one could observe images of an anatomic section at *TR* and *TE* times different from those used in the actual acquisition. In fact, the synthesis step can be performed in 'real time'; i.e. the observer can interactively adjust a sequence parameter such as *TE* and immediately see the effect on the image.

Once the original images are acquired, an intermediate step is generally one in which images of the relaxation times are formed for each section of interest. That is, T_1, T_2, and M_0 are determined for each pixel in the image. In the final step of synthesis these relaxation time images are mathematically

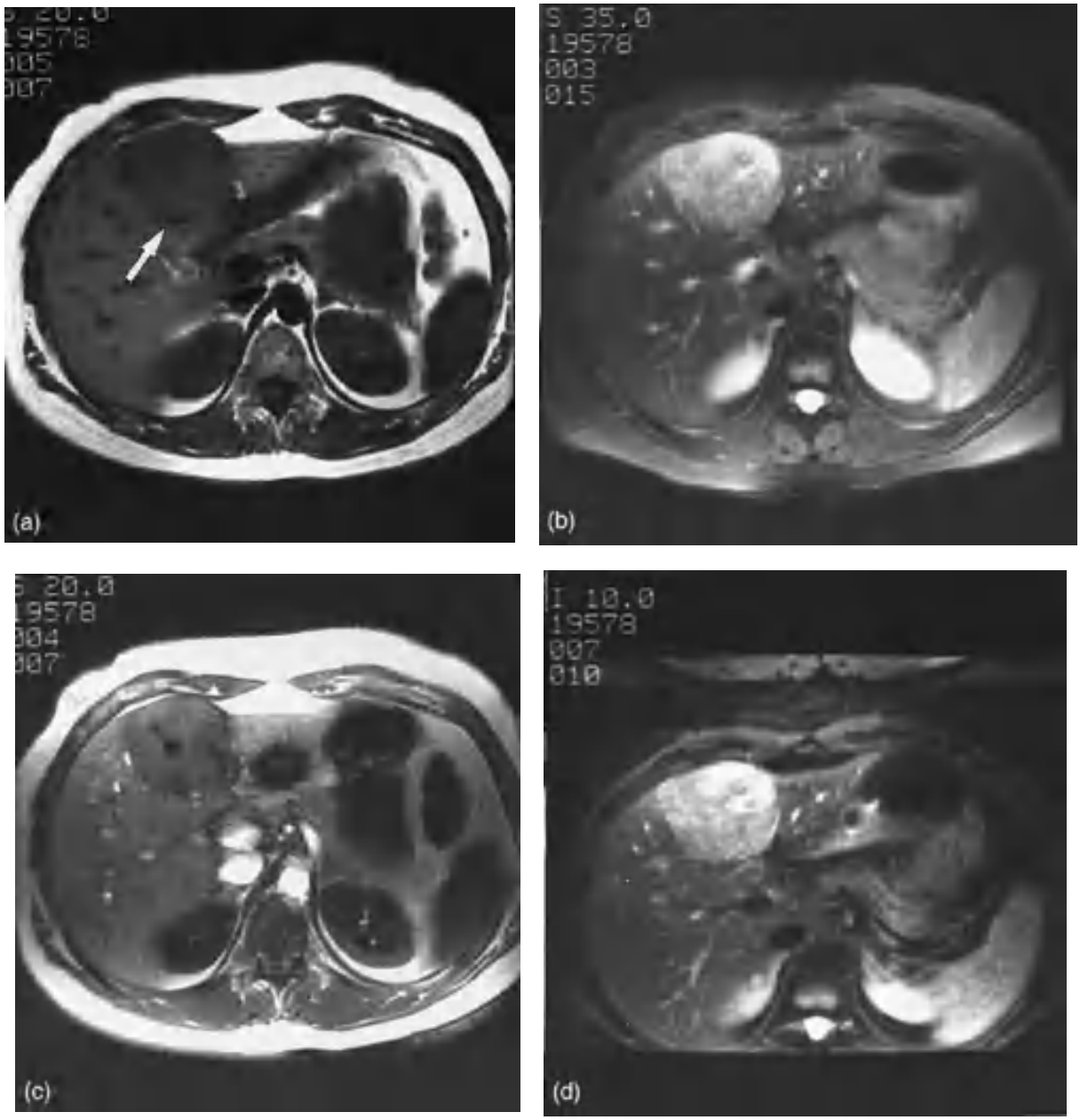

Figure 2 Comparison of conventional non-breath-hold (a) T_1 and (b) T_2 weighted images of the liver with (c) breath-hold T_1 and (d) T_2-weighted images of the same anatomic section. A large lesion is seen [arrowed in (a)] in all four images. The overall quality of the breath-hold images approximately matches that of the non-breath-hold results

combined. For example, if the signal S of a spin echo pulse sequence were to be synthesized at sequence parameters TR and TE, the density and relaxation time images would be combined mathematically:

$$S(x,y) = M_0(x,y)\{1 - \exp[-TR/T_1(x,y)]\} \exp[-TE/T_2(x,y)] \quad (1)$$

where the fact that S, M_0, T_1, and T_2 are images is explicitly noted by the (x,y) dependence. At this point it should be clear that the equation used for the synthesis need not correspond to the signal behavior for the pulse sequence used in the acquisition. That is, the original images could have been acquired with a spin echo pulse sequence but used to synthesize inversion–recovery images. In fact, such an example is shown in Figure 3 which shows a comparison of a synthetic inversion–recovery image (right) generated from images acquired using a standard spin echo pulse sequence. Also shown is an inversion–recovery image acquired directly (left) using the same parameters as those used for the synthesis. Note the close visual correspondence.

Image synthesis is limited by several factors. First, the signal-to-noise ratio (S/N) in the original images ultimately limits the S/N which can be attained in the synthesis step.[17,18] For example, it is not possible without significant S/N penalty to acquire images at, say, TR values of 100 and 200 ms and then synthesize at TR 2500 ms. Second, the process is also poten-

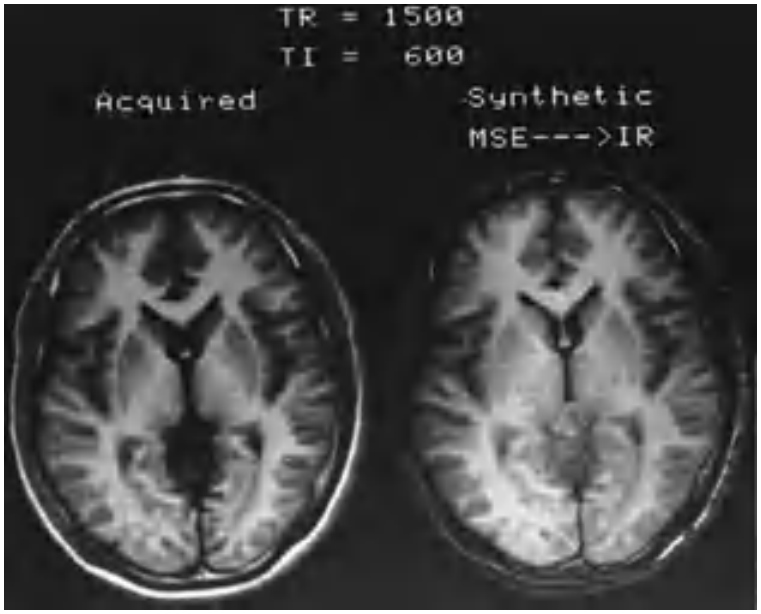

Figure 3 Comparison of synthetic inversion–recovery image (right) formed from spin echo images and a directly acquired inversion–recovery image (left)

tially limited in the accuracy with which it can portray the actual performance of pulse sequences. Effects of $\boldsymbol{B}_1$ inhomogeneity, flow or motion, misregistration of the acquired images, or a breakdown of the monoexponential behavior of relaxation can all cause inaccuracies. Finally, for routine interpretation of MRI examinations the added diagnostic capability provided by image synthesis has not proven to be significant. That is, the acquired images themselves often provide adequate sensitivity and specificity.

Despite these limitations, when used in a real time or interactive mode, image synthesis can be an effective teaching tool which illustrates visually and rapidly the effect of different pulse sequence parameters on the appearance of MR images.

It was noted in the above discussion that the signal which is synthesized need not correspond to the pulse sequence used for the actual acquisition of the original images. In fact, this concept can be further generalized in that the mathematical combination used need not correspond to any pulse sequence. From an electrical engineering standpoint one has a set of measurements $\{S_i\}$, and from these one wishes to combine them in some optimum fashion according to a relevant criterion. For example, one such criterion is to form that image combination which provides the highest net CNR between two targeted structures. For the case in which the measurements are to be linearly combined, the ith image weighted by the coefficient k_i, it is straightforward to show that the optimum k_i value is proportional to the CNR in the ith image. This is sometimes referred to as a 'matched filter'. If one knew beforehand the two targeted structures to be distinguished, then rather than acquire a set of images each with a different pulse sequence, a superior procedure would be to spend all of the allotted acquisition time in performing that single pulse sequence which provided the highest CNR, performing signal averaging if time allowed.

Image combination methods can potentially be useful for cases in which the criterion to be considered in the optimization is more involved than CNR maximization alone. For example, one may wish to optimize the contrast between materials A and B, subject to minimizing the contrast between materials A and C. This problem has been approached in several ways, but an elegant theory for addressing this uses 'eigenimages'.[7] In the same way that diagonalization of a matrix problem can be performed using eigenvectors in linear algebra, a set of coefficients $\{k_i\}$ can be derived from the observed signal intensities which performs the desired task.

Although the theory of linear image combination is well-posed, and the results are straightforward to implement, in practice, linear image combination has not proven to be a widely accepted method in clinical MRI. The reasons are much the same as those for the relative lack of use of relaxation times and of synthetic images. The original acquired images often have excellent sensitivity to pathology in the first place. If the radiologist detects pathology but cannot characterize it using the images already in hand, then it is straightforward to order another pulse sequence which addresses a specific differential question. This process thus circumvents the image combination route. Another advantage is that, unlike image combination, this approach has no requirement that the images from all sequences be spatially registered to a very high degree of accuracy.

6 IMAGE SEGMENTATION

The last entries in the hierarchy of Table 1 pertain to processes which are more ambitious in terms of what the processing is to provide. A general goal of these techniques is the automated determination of some structure of interest. This process of decomposing an image set consisting of hundreds of thousands of voxels into a much smaller number of identifiable structures can be called 'image segmentation'.

The technique of image segmentation is not limited to the practice of MRI. In fact, a good reference on basic techniques for image segmentation is found in the work by Udupa and Herman.[19] Once structures in an image are segmented, additional processes can be performed such as integration or rendering.[8] Segmentation techniques can be broadly categorized as those based on the determination of boundaries or those based on the identification of specific regions.

Boundary-based algorithms are those which perform mathematical tests on the reconstructed pixel values in an image, which are designed to be sensitive to large changes in value in adjoining or nearly adjoining pixels. Typically a gradient operator is used. If the calculated gradient between two pixels is adequately large, then an 'edge' is designated as occurring between the two pixels. Next, the neighboring pixels are considered and the gradient operator is again applied in various directions. In this way the edge or boundary between the materials can be tracked across the image. For small objects this process will generally result in the boundary eventually finding its way back to its origin, resulting in a closed curve and a segmented object. For the typical case in which a set of images is acquired corresponding to parallel sections, the process is repeated for each image for that region containing the structure to be segmented. In this way an object which extends across several sections can be segmented in its entirety.

Clearly, an alternative to automated boundary detection algorithms is manual tracing. With this approach the operator traces with a cursor the suspected edge between various materials until the structure of interest is circumscribed. Just as for the automated case described above, this can be repeated if necessary for multiple images which span the volume containing the structure.

Region identification algorithms make use of the reconstructed signal intensities within the image. One approach is to use thresholding of the signal as a means for segmenting a specific structure. That is, those pixels whose reconstructed signal values fall between S_1 and S_2 are assumed to consist of material X, etc.

Simple thresholding can have limited success in MRI because many materials can have an overlap in their magnetic resonance signal, such distinctions being further compromised by inadequate S/N in the images. One way to address this is to apply the equivalent of thresholding to more than one image of the same anatomic section. If the reconstructed signal falls between S_1 and S_2 in image I_1, and between S_3 and S_4 in image I_2, then such pixels are assumed to consist of material X. This process is shown schematically in Figure 4. One axis corresponds to the reconstructed signal value in one specific image, for example the early echo in a dual-echo sequence at a long *TR* time. The second axis corresponds to the signal in the late echo. Each pixel in the image is mapped to a specific point in this feature plot, the coordinates of that point determined by the signals in the early and late echo images for that pixel. Clusters of points in such feature space plots are assumed to correspond to specific tissue types, such as gray matter or white matter in brain imaging. Such techniques have been used with some success in designating structures in magnetic resonance images of the brain and body.[20]

Clearly, the success of segmentation depends critically on the quality of the acquired images. Ideally the acquisition parameters are chosen with the type of segmentation already in mind. For example, if liver cancer is to be segmented from normal liver parenchyma in inversion–recovery images, then the same considerations discussed in Section 4 with respect to contrast optimization would also be relevant here. In fact, inversion–recovery or other heavily T_1-weighted sequences can be effective in providing large contrasts between different materials.

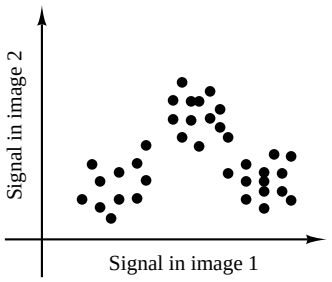

Figure 4 Schematic diagram of feature space analysis. Each pixel in an anatomic section of interest is assigned a point in this space on the basis of the signal at that pixel in two images. In principle, segmentation can be performed on the basis of clustering in such a feature space plot of pixels of similar make-up. In this example, three different materials are suggested

An example of the application of segmentation techniques in MRI is the work by Jack et al.[9] in which the side of origin, right or left, of temporal lobe seizure patients was studied by volume measurements of the hippocampal formation. Obliqued coronal contiguous 4 mm-thick T_1-weighted images were acquired of the brain. An image oriented similarly to those used in the study is shown in Figure 5. The hippocampal formation was manually segmented from the images and the volumes determined. Compared with other MRI-based tests, such as increased signal intensity on the suspect side in T_2-weighted images, the volumetric approach had significantly increased usefulness.

7 SUMMARY

Data extraction encompasses a broad range of techniques in MRI. An excellent, relatively recent review of data extraction

Figure 5 Example of identification of the right hippocampal structure (arrow) in an obliqued coronal section of the brain of a normal subject. In this example the segmentation was performed by manual tracing. Such segmented regions can be pooled from contiguous sections and integrated to form an estimate of the hippocampal volume

methods in MRI is the book edited by Higer and Bielke.[20] Data extraction techniques also vary in their computational complexity. The least computationally intensive method of data extraction is also that which has been proven to be most useful in clinical MRI, namely radiological image interpretation. Techniques such as the determination of relaxation times have not in general added significantly to sensitivity or specificity in everyday MRI, but such methods are absolutely essential in assisting in establishing proper pulse sequence parameters. The use of automated methods is expected to grow in specific instances in which the complexity of the processing, the volume of data to be considered, and the sensitivity of the test preclude simple human interpretation. Examples include the volumetric measurements and the automated determination of the lesion load, such as in multiple sclerosis. Further improvements in the quality of the acquired images themselves, such as improved S/N due to topical coil arrays or reduced artifacts resulting from breath-hold acquisition times, will also enable improved performance of automated data extraction techniques.

8 RELATED ARTICLES

Image Formation Methods; Inversion–Recovery Pulse Sequence in MRI; Relaxation Measurements in Imaging Studies; Relaxation Measurements in Whole Body MRI: Clinical Utility; Relaxometry of Tissue.

9 REFERENCES

1. F. W. Wehrli, J. R. MacFall, and T. H. Newton, 'Modern Neuroradiology: Advanced Imaging Techniques', Clavadel Press, San Anselmo, CA, 1983, p. 81.
2. R. H. Darwin, B. P. Drayer, S. J. Riederer, H. Z. Wang, and J. R. MacFall, *Radiology*, 1986, **160**, 375.
3. D. LeBihan and R. Turner, *Magn. Reson. Med.*, 1991, **19**, 221.
4. D. A. Ortendahl, N. Hyton, L. Kaufman, J. C. Watts, L. E. Crooks, C. M. Mills, and D. D. Stark, *Radiology*, 1984, **153**, 479.
5. S. A. Bobman, S. J. Riederer, J. N. Lee, S. A. Suddarth, H. Z. Wang, and J. R. MacFall, *Radiology*, 1985, **155**, 731.
6. G. Bielke, M. Meves, S. Meindl, A. Brückner, W. Y. Seelen, P. Rinck, and P. Pfannenstiel, in 'Technology of Nuclear Magnetic Resonance', ed. P. D. Esser and R. E. Johnston, Society of Nuclear Medicine, New York, 1984, p. 109.
7. J. P. Windham, M. A. Abd-Allah, D. A. Reimann, J. W. Froelich, and A. M. Haggar, *J. Comput. Assist. Tomogr.*, 1988, **12**, 1.
8. D. N. Levin, X. Hu, K. K. Tan, and S. Galhotra, *Radiology*, 1989, **171**, 277.
9. C. R. Jack, F. W. Sharbrough, C. K. Twomey, G. D. Cascino, K. A. Hirschorn, W. R. Marsh, A. R. Zinsmeister, and B. Scheithauer, *Radiology*, 1990, **175**, 423.
10. R. A. Damadian, *Science*, 1971, **171**, 1151.
11. R. J. Herfkens, P. Davis, L. Crooks, L. Kaufman, D. Price, T. Miller, A. R. Margulis, J. Watts, J. Hoenninger, M. Arakawa, and R. McRee, *Radiology*, 1981, **141**, 211.
12. D. D. Stark, *Radiology*, 1988, **168**, 323.
13. A. E. Holsinger-Bampton, S. J. Riederer, N. G. Campeau, R. L. Ehman, and C. D. Johnson, *Radiology*, 1991, **181**, 25.
14. K. Butts, S. J. Riederer, R. L. Ehman, J. P. Felmlee, and R. C. Grimm, *Radiology*, 1993, **189**, 259.
15. E. O. Stejskal and J. E. Tanner, *J. Chem. Phys.*, 1965, **42**, 288.
16. S. D. Wolff and R. S. Balaban, *Magn. Reson. Med.*, 1989, **10**, 135.
17. D. A. Ortendahl, N. M. Hylton, L. Kaufman, and L. E. Crooks, *Magn. Reson. Med.*, 1984, **1**, 316.
18. J. R. MacFall, S. J. Riederer, and H. Z. Wang, *Med. Phys.*1986, **13**, 285.
19. J. K. Udupa and G. T. Herman, '3D Imaging in Medicine', CRC Press, Boca Raton, FL, 1991.
20. H. P. Higer and G. Bielke, 'Tissue Characterization in MR Imaging', Springer-Verlag, Heidelberg, 1990.

Biographical Sketch

Stephen J. Riederer. *b* 1951. B.A., University of Wisconsin. S.M., Massachusetts Institute of Technology; Ph.D., University of Wisconsin. Actively performing research in technical aspects of diagnostic medical imaging 1974–present. Introduced to NMR in 1983. Approx. 100 journal articles. Principal interests are fast scan techniques in MRI, abdominal imaging, high speed cardiovascular imaging, and real time interactive MRI techniques including MR fluoroscopy.

Outcome and Efficacy–Analysis of Healthcare Models

Martin J. Lipton, Charles E. Metz, and Larry A. Ranahan

The University of Chicago, IL, USA

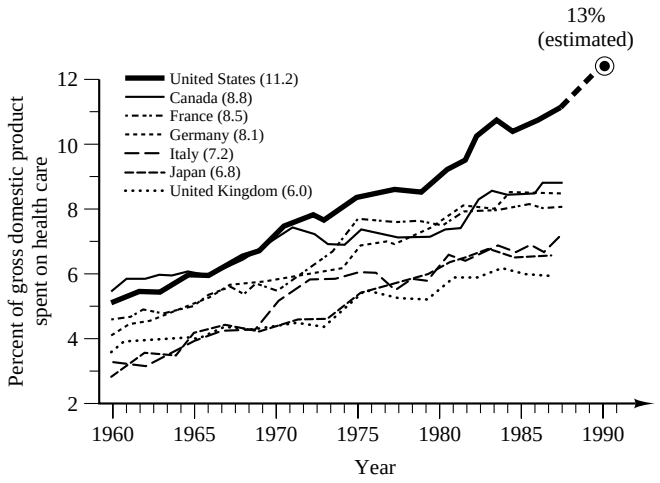

Figure 1 Health care spending per person in various countries as a percentage of GDP, by year. (Reproduced by permission of the Economist Newspaper Group, Inc., © 1991, from J. Peet, *The Economist*, 6 July 1991 (Insert), **320**, 1)

1 INTRODUCTION

Public and private attention in the USA has focused sharply on health care reform during the early 1990s. Health care costs seem to be out of control, and enormous pressure to reduce these costs has emerged. Health care is a colossal business—perhaps the world's largest. Most wealthy nations spend a substantial percentage of their gross domestic product (GDP) on health care, with the USA heading the pack (Figure 1) and with the UK's National Health Service (NHS) once boasting that it took over from the Red Army as Europe's biggest employer.[1] However, people working in health care often deny that they are in 'business' at all. Many physicians believe that their long, demanding training places them at the head of the professions, not down among service providers. Moreover, physicians often resent attempts to constrain their professional activities and demands for objective evidence concerning the outcomes of those activities. This attitude is now being challenged, but it remains widespread.

Government intervention in medicine has a long history, perhaps because people often have doubted that public-market forces can stimulate and control health care like other goods and services. Hammurabi, King of Babylon, enacted laws in 2200 BC that limited doctor's fees and provided punishments for those who injured their patients. Mandarins in ancient China paid doctors only if their patients became well.[1] Hence, it is clear that many current trends in health care—capitation payments, prospective budgets, and health maintenance organizations (HMOs), etc.—are not new concepts. Today, the financing and delivery of health care differ greatly in different countries, but the financial crises and turmoil associated with health care in these countries are strikingly similar. A common theme emerges: the need for governments to ensure universal access to health care at reasonable cost, particularly as populations age, and the need to limit the utilization of increasingly sophisticated (and expensive) technology. However, most governments appear to be dealing with health-care reform in isolation. Few nations have tried to understand and learn from the mistakes of others, perhaps in part because none has found a satisfactory solution, and perhaps in part because each country believes that at least some aspects of its own system are inherently best.

All systems of health care are imperfect and expensive. Governments have jumped into the marketplace in two principal ways. One involves regulating both insurers and doctors. This regulation may be broad, or it may narrowly control prices, volumes and even methods of treatment. The alternative is subsidy of health care costs.

Health care systems can be classified according to three general models, though most nations' systems include aspects of more than one:

1. The US model is based upon private health insurance, which usually is purchased by individuals or families through their employer. Health care is delivered largely by private hospitals and physicians.
2. In the Beveridge model, named after the founder of the UK's NHS, health care is funded by government and paid from general taxes. Care is delivered by publicly owned hospitals and salaried physicians. Sweden and Italy have similar systems.
3. The Bismarck system, named after the founder of Germany's compulsory social insurance, represents a mixed form in which health care is publicly financed, usually by payroll taxes, but is provided primarily by private physicians and hospitals. Japan, Canada, Holland, and France employ variations of this hybrid model.

Figure 2 shows annual percentage increases in health care spending per person by decade for the past 30 years. The continuing rise in the costs of the Canadian and American system is evident. Employers who bear the cost of health insurance in the USA are struggling to pay the escalating premiums, which are being driven more and more aggressively by for-profit insurers. Many large employers are underwriting the medical bills of their employees directly, in order to escape state regulation. This 'self-insurance', usually through an intermediary, is now allowed by Federal law. Medicare, the government insurer in the USA, spends more than US $110 billion annually, which is roughly twice the cost of the UK's NHS.[1] Fee-for-service payments, which can influence patient management and therefore costs, are seen by many as a key aspect of the US healthcare system's current difficulties.

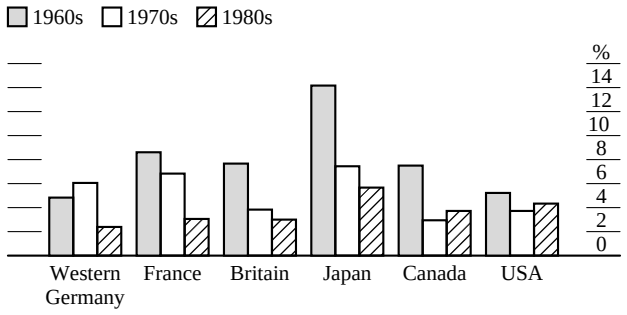

Figure 2 Annual percentage increases in real (based on GDP deflators) health care spending per person in various countries, by decade. (Reproduced by permission of the Economist Newspaper Group, Inc., J. Peet, *The Economist*, 6 July 1991 (Insert), **320**, 1)

Increasing health care costs have led, naturally enough, to increasing demands from insurers for objective, quantitative evidence concerning the effectiveness of diagnostic and therapeutic techniques. However, health care evaluation of this kind is difficult, in part due to the complexity of the technical and ethical issues that are involved, but perhaps also in part because physicians and hospitals traditionally have managed patients with little regard or knowledge of costs or outcomes. Little information is available concerning real costs—which may be quite different from what doctors charge. Systematic accounting of outcomes is also rare, though Florence Nightingale called for detailed records of what happens to patients and why more than a century ago:[1] there is little concrete evidence regarding which procedures work and for which patients. Such information is becoming crucial in the new climate of managed care.

2 LEVELS AT WHICH EFFICACY AND EFFECTIVENESS CAN BE ADDRESSED

A diagnostic test has value—and therefore is justifiable—only if it is effective in some sense. Strictly, 'efficacy' indicates the value of a test when it is performed and utilized under ideal conditions, whereas 'effectiveness' indicates the test's value under typical or routine conditions. The distinction between these terms is not one of mere technical jargon; *Webster's New Collegiate Dictionary*,[2] for example, defines 'effective' as '*producing* a decided, decisive, or desired result' but 'efficacy' as 'the *power* to produce an effect' (emphasis added). Many of the same issues arise in considerations of both efficacy and effectiveness, however, so in the following we use 'efficacy' broadly to indicate both, emphasizing the distinction only where necessary.

'Value' can be conceived and defined in many ways, of course, so every meaningful analysis of diagnostic efficacy must include a clear indication of the sense in which value is to be measured. A conceptually useful model that unites the various ways in which efficacy can be defined and measured was formulated in the early 1980s by Scientific Committee No. 69 of the National Council on Radiation Protection and Measurements.[3] This model considers the efficacy of a diagnostic test in terms of hierarchical levels that range from the test's technical behavior to its overall impact on society. An important attribute of the model is that efficacy at lower levels is necessary, but not sufficient, for efficacy at higher levels. Efficacy at the model's higher levels usually is of greater direct interest, but lower level efficacy is almost always easier to measure reliably. Fortunately, efficacy at the higher levels sometimes can be estimated from measurements at lower levels by use of collateral data and (hopefully) appropriate assumptions.

The model's six tiers are:

1. *Technical efficacy*. At this lowest level, a diagnostic test is considered efficacious if its result is accurate and precise in a physical sense—for example, if the test measures the physical attribute that it purports to measure and if its results are reproducible. Aspects of technical efficacy in medical imaging include spatial and/or temporal resolution, noise magnitude and texture, and contrast sensitivity. Standard protocols for the measurement of technical efficacy have been formulated in radiography,[4–7] for example. Protocols for such measurements are less well established in MRI, in part due to the very broad range of conditions under which images can be acquired in that modality, but some guidelines are available.[8]
2. *Diagnostic-accuracy efficacy*. This level concerns the extent to which the results of a diagnostic test agree, in some statistical sense, with patients' actual states of health or disease. Virtually all practical measures of diagnostic-accuracy efficacy that have been proposed to date quantify the ability of a test to distinguish between two (usually composite) states of truth, such as 'normal' versus 'abnormal', or 'positive' versus 'negative' with respect to a specified disease. Examples of diagnostic-accuracy measures include per cent correct, sensitivity and specificity, and receiver operating characteristic (ROC) curves. Of these, an ROC curve is the most comprehensive in that it displays all the combinations of sensitivity and specificity which a diagnostic test is able to provide as the test's 'decision criterion' is varied. The advantages of ROC analysis over more traditional measures of diagnostic accuracy have been discussed by Metz.[9,10]
3. *Diagnostic-thinking efficacy*. If a diagnostic test's sensitivity and specificity (level 2 efficacy) are known, one can compute the factor by which the objective odds of disease change after the test is performed, but the question of whether the test affects physicians' subjective estimates of disease likelihood must be answered empirically.[3] This intermediate level of efficacy is difficult to quantify, but it provides an important conceptual link between the more clearly specified levels above and below.[11] Measurement of diagnostic-thinking efficacy is complicated by the difficulty of interpreting subjective probability estimates,[12] but appropriately designed studies can identify situations in which the impact of a test on diagnostic thinking is clearly great or small. Large-scale studies of diagnostic-thinking efficacy have been reported by Lusted et al.[13] and by the US Food and Drug Administration,[14] for example.
4. *Therapeutic efficacy*. This is the lowest level at which the effects of a diagnostic test on patient management are assessed directly. The basic question here is how and by how much a particular diagnostic test changes the way in which a patient is treated—i.e. how does therapy differ when it is chosen with and without the diagnostic test? It is

important to notice that carefully controlled studies of a diagnostic test at this level require either that patients' therapy be thoroughly planned without the test's result and then replanned after the test's result is provided, or that a randomly selected control group of patients be treated without all the diagnostic information that might otherwise be obtained. Despite the difficulties raised by these practical and ethical issues, therapeutic efficacy has been studied in preoperative chest radiography of children[15,16] and in computed body tomography,[17,18] for example.

5. *Patient-outcome efficacy*. Here the goal of diagnostic medicine is confronted directly: a diagnostic test is considered efficacious (or effective) at this level only if patient health (as measured in 'quality-adjusted life years', for example) is demonstrably improved by use of the test. This is the kind of efficacy which is of greatest interest to most patients and physicians, and it is an indispensable component of any meaningful cost–benefit or cost–effectiveness analysis. However, definitive assessments of patient-outcome efficacy require prospective randomized and controlled clinical trials in which practical, statistical, and ethical problems can be formidable.[3] Therefore, patient-outcome efficacy often is inferred by using decision analysis to combine measurements of diagnostic accuracy (i.e. level-2 efficacy) with epidemiological and other collateral data. Relationships between ROC analysis, in particular, and cost–benefit or cost–effectiveness analysis have been described by Metz and co-workers,[9,19] Phelps and Mushlin,[20] and Sainfort.[21]
6. *Societal efficacy*. Any cost–benefit or cost–effectiveness analysis of a diagnostic test at the patient-outcome level focuses on the benefits and effectiveness that accrue to the patients who are candidates for the test. However, one must ask 'Cost to whom?'. The inescapable answer that medical costs are borne increasingly by society as a whole implies that social utilities should somehow be taken into account when benefits and effectiveness are evaluated. This is the domain of 'societal efficacy', which in principle merges technical, economic, and political considerations to assess diagnostic tests within the context of the social endeavor. Consideration of societal efficacy leads inevitably to philosophical and political questions of how society's resources should be allocated—not only within a 'health care budget' but also more broadly. Rigorously scientific measurements and wholly rational analyses of efficacy at this level are impossible, of course, but 'the challenge is to bring policy and practice into line with knowledge'[22] and to increase knowledge that will inform policy and practice.

Studies that attempt to assess diagnostic tests must differ in many ways across the six levels of efficacy, but several practical issues arise in virtually all efficacy studies. Perhaps the most fundamental issue is the need to avoid effects of sampling bias, which may arise in a variety of subtle ways and can lead to misleading estimates or conclusions.[23,24] Another common issue is the decision as to whether the efficacy of each diagnostic test of interest must be quantified in strictly defined units on some meaningful scale or, alternatively, needs only to be ranked relative to other tests. Absolute measurements of efficacy are desirable in principle, but appropriately designed 'ranking' studies often are more practical because their results may be much less sensitive to sampling bias.[25] Similarly, the relative merits of prospective and retrospective studies should be considered carefully in each situation; carefully controlled prospective studies are preferable in principle, but appropriately designed retrospective studies are often more practical. Yet another issue in most efficacy studies is the question of whether a diagnostic test should be assessed in isolation or in the context of its use within a particular diagnostic strategy. Trade-offs between rigor and practicality are inevitable in any assessment of efficacy; the key needs are to consider those trade-offs rationally and to report them clearly.

3 LEVELS AT WHICH COSTS CAN BE ADDRESSED

Government and industry are demanding objective evidence and criteria upon which to make health care purchasing decisions. This information will be based upon the aggregate outcomes of health system activity.[26–30] An important driving force behind efficacy and effectiveness research is cost or, more broadly, health care economics. Most recent cost-containment efforts in the USA have focused on the reduction of administrative and production costs, as is evident from numerous media announcements of corporate and hospital mergers, consolidations, restructurings, reductions in staff, and hard bargaining with labor unions and producers of equipment and supplies. Outcomes analysis shifts the focus of cost containment from the cost of each unit of production, or episode of care, to maintaining the health of each patient from cradle to grave. The demand for cost-effective health care ultimately will require difficult choices concerning the allocation of financial resources. To the greatest degree possible, such decisions should be based upon comprehensive, scientifically derived knowledge of the efficacy and effectiveness of competing diagnostic and therapeutic methods and technologies.

US industry views employee health care as a commodity—a component of the cost of production—and health care providers as suppliers. Quality control is taken for granted in business, and perhaps is illustrated best by the Japanese concept of *kaizen*—the philosophy of overall system improvement.[31] Therefore, health care quality must be defined, measured and controlled, and the costs of these services must be reduced and guaranteed prospectively. Outcome analysis has become important because it measures that which is being supplied. Quality assessment and outcome analysis are not new, of course, but until now they have been applied rarely to medicine, which traditionally has been seen as a 'noble' profession in which performance could not—or should not—be measured. Outcome analysis is here to stay, however, and it requires that the performance of radiologists, as well as other physicians, be evaluated as part of the overall health care system.

Outcome analysis is motivated in large part today by the need to determine cost effectiveness, in which competing technologies are compared in terms of their costs and results. This process requires both the identification of costs and the measurement of benefits derived.[32] The cost of any technology can be measured in terms of three components: direct, indirect, and intangible. Direct costs include capital and operating expenses for acquisition, personnel, materials and supplies, maintenance and support, etc. Indirect costs include elements such as administration, overheads, utilities, support personnel, and others. Intangible costs are far more complex and often

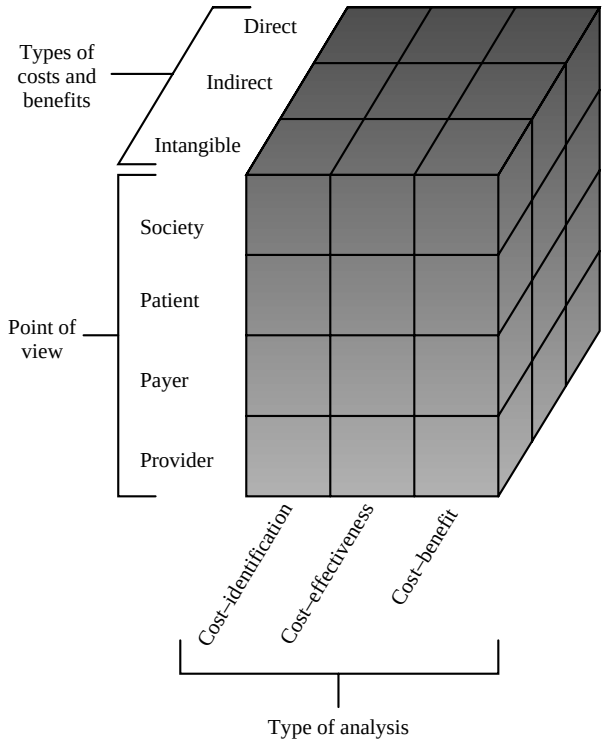

Figure 3 The dimensions of economic analyses. (Reproduced with permission from C. Bombardier and J. Eisenberg, *J. Rheumatol.*, 1985, **12**, 201)

become the critical issue in outcome analysis. These latter costs can be represented by a trade-off in investments in competing technologies, as measured at the highest levels in the six-tier model.

In any cost–benefit analysis, perspective, or point of view, is the third dimension of the process. These perspectives include those of the provider, payer, patient, and society.[33] Each point of view must be considered in order to establish a complete understanding of the economic decision that is required in determining the most efficacious technologies. MRI technology is particularly vulnerable due to its high acquisition and support costs, and often competes against lower cost technologies. It is critically important for future outcome analysis research to focus on these factors in order to provide an objective basis for decisions concerning the appropriate use of medical technology.

In economic terms, the three-dimensional model of types of analysis, types of costs and benefits, and point of view (Figure 3) takes on additional meanings. Direct costs include nonmedical costs related to a specific illness that are often borne by the patient, such as transportation or lost income, which can be measured in objective terms. Measurements of indirect costs must attempt to include the cost due to a loss of livelihood or life. These can be quantified in terms of a human capital approach,[34] loss of earning potential for individuals, or lost productivity for employers. Intangible costs are frequently framed in terms of pain and suffering, which are beginning to be assessed in terms of quality-adjusted life years (QALYs). This outcome-based analytical framework is intended to provide a rational foundation for decisions concerning resource allocation.

4 OUTCOMES AND EFFICACY RESEARCH IN RADIOLOGY

Traditionally, the outcome of diagnostic radiology is thought of as images—usually recorded on X-ray film—and typed reports of their interpretation. However, individual reports are no more than isolated pieces of data, and the task of integrating these data into a diagnosis often is left to the referring clinician. As Drucker has pointed out, data become useful information only when they are endowed with relevance and purpose.[35] Radiologists are in an especially good position to access, collate, and distribute this information, because their practice now includes an increasing variety of sophisticated computerized methods for displaying, managing, transferring, and interpreting image data. In particular, radiologists currently enjoy a unique opportunity to study the value of the vast array of new imaging technology in the context of specific diagnostic tasks and patient populations. MRI, the most recently developed medical imaging technology, is especially well suited to this task. Moreover, objective demonstration of the benefits of MRI is crucial, because high-technology imaging costs in medicine are widely blamed for the current rise in health care costs, despite the fact that only 3.5% of expenditures for health care is spent on radiology.[36] However, a variety of difficulties must be faced in attempting to assess the extent to which a diagnostic study influences patient outcomes. A survey of the literature since 1985, soon after MRI was introduced, illustrates many of the fundamental problems of outcomes research in radiology. These problems are sketched briefly here, with examples.

In their day-to-day work, referring physicians and radiologists usually are unable to take into account objective information concerning patient-outcome (level 5) efficacy. Most referring physicians and radiologists are interested in and sensitive to their patient's outcomes, but objective and systematically collected level-5 information usually is either unavailable—because the necessary large randomized controlled trials have not been performed—or unknown—because a trial's results were published in an obscure journal or described in abstruse methodological jargon. Some radiological procedures, notably mammography for diagnosis of breast cancer, have been studied at level 5. However, virtually all assessment studies of MRI have been restricted to levels 1–3.

A physician may order a diagnostic imaging examination for many reasons: to make a diagnosis; to guide therapy; to assess prognosis; to avoid successful malpractice litigation; to increase income; to accede to the referring physician or patient's demands in the case of the radiologist; or to reassure the patient (and/or the physician). Ultimately, however, the efficacy of diagnostic imaging must be viewed as one part of the entire process of medical care, which exists to improve patients' well-being. This end-point lies in the domain of level-5 efficacy, as described above.

An awareness of potential sources of bias in evaluation studies is basic to any understanding of outcome efficacy. For example, a new imaging technology such as MRI evolves through several phases. The first is a discovery phase that

involves using the modality in patients to determine if disease, often severe, can be distinguished from healthy, normal volunteers.[37] This has been the foundation of early clinical trials since the discovery of X-rays by Roentgen in 1895, and it provides a basis for estimating rates of false-positive results. However, diagnostic accuracy (i.e. level-2 efficacy or effectiveness) often is found to fall as the technology is applied to a broader spectrum of patients.[23] This has been called the 'diffusion' phase. Moreover, many—often the vast majority of—evaluation studies are performed in tertiary academic centers, where referral bias is inherent.

Ideally, each diagnostic technique would be evaluated in each diagnostic setting by means of a large-scale, carefully controlled study that is designed and carried out by investigators who are expert in evaluation methodology. In practice, however, assessments of efficacy are often based upon published research that varies greatly in rigor and quality. For example, Cooper and colleagues analyzed 54 articles concerning the evaluation of MRI that were published between 1980 and 1984, early after the introduction of the technique, by using ten commonly accepted criteria for adequate research methodology.[38] They found that five fundamental indices of efficacy—sensitivity, specificity, false-positive or false-negative results, accuracy, and predictive value—were used infrequently, and that fewer than 20% of the publications employed three of these terms appropriately. Only 22% compared the MRI results with an independent 'gold standard' such as surgery or autopsy. In 63% of studies another imaging procedure was employed as the reference standard, and only one study was prospective. None of the studies used appropriate statistical methodology such as randomization or measurement of observer error. Cooper et al. concluded that those paying for such expensive new diagnostic technology should demand better research in diagnostic efficacy. A later study by Taylor and colleagues in 1993 examined a sample of 146 publications from two radiology journals;[39] three physician reviewers categorized the articles according to phase, modality, and design. Research in MRI comprised 45% of the publications and was oriented to phase 1 (32%) rather than phase 5 (0%) studies. Only 27% of 48 diagnostic-efficacy studies were externally funded. Taylor et al. concluded that analysis of research trends requires a standard taxonomy, which adopts a modality-based, phased approach. Assessment of the clinical efficacy of diagnostic imaging technologies frequently involves reviews of published research. Reports may be classified in three dimensions: by disease, by type of assessment, and by the quality of the research methods employed. The disease dimension describes the condition or conditions shown by an imaging technique. The assessment dimension spans five levels: technical capacity, diagnostic accuracy, diagnostic impact, therapeutic impact, and patient-outcome impact. The methods-quality dimension can be expressed as four levels: excellent, good, fair, or poor. An important interaction exists, in that the level of efficacy addressed by a research project dictates which methodological procedures are important. For example, randomization is important only when a research report addresses the levels of therapeutic and patient outcome impacts. Taylor et al. suggest that classification of studies according to the three proposed dimensions maps the breadth (across diseases), depth (across levels of clinical efficacy), and quality of the assessment of complex imaging technologies. Such a map should help participants in technology assessment define the progress they have made. The authors illustrated their classification strategy by applying it to assess the clinical efficacy of MRI in diagnosis of neurological disease.

Another major question concerns the likelihood that objective assessments of patient-outcome (level 5) efficacy will substantially influence physician behavior in the utilization of diagnostic tests, at least without strict oversight by the insurers of health care costs. Although reliable diagnostic information may improve patient outcomes, it is clear that physicians engage in many activities that appear to have little effect on outcome, especially in dealing with chronic diseases and malignancies. For example, it is difficult to show that outcomes are improved by routinely searching for the unknown primary tumor in patients with known metastatic cancer.[40] Nonetheless, many physicians do just that. Rigidly controlled scientific studies are required to substantiate or refute suspicions of this kind. However, such clinical trials must meet appropriate standards of medical ethics and will require a delicate balance in their design and interpretation.

For the immediate future, there is an increasing need for scientific studies that measure and compare the efficacies of diagnostic imaging examinations in appropriate clinical settings.[41] These studies will require more and higher quality data in all of the phases through which diagnostic technology evolves and for all of the levels at which diagnostic efficacy can be evaluated.

5 OVERVIEW

Radiologists, like all physicians, have resisted accountability assessment. Historically, new imaging technologies have not been evaluated adequately before they have been used widely. Radiologists are not trained to conduct rigorous efficacy analyses, and reimbursement and other political issues may have been underestimated. However, lessons learned from the past should help in developing improved plans for the careful research that is now sorely needed in the field.

Rigorous, yet practical, methodology must be developed, investigators must be trained, and standard protocols must be designed. Moreover, successful completion of efficacy studies requires the establishment of experienced *teams* of investigators. Radiologists should be deeply involved in the process of outcomes research, and they must cultivate the capacity to build a multidisciplinary team which has the skills and perspective necessary for success. In addition to radiologists, these teams should include referring physicians, medical physicists, biostatisticians, epidemiologists, full-time research assistants, and perhaps individuals with expertise in other areas such as computer science and health care economics. Advice of external consultants with expertise in efficacy research should be sought periodically, particularly during the early stages of each team's development. The targeting of areas for study is equally critical; usually it should focus on technologies and settings where the greatest clinical impact is most likely and, at least initially, where objective demonstration of value will be relatively easy.

The task of technology assessment is complex and expensive, but current trends in health care funding require that it be done—and done well.

6 RELATED ARTICLE

Image Quality and Perception.

7 REFERENCES

1. J. Peet, *The Economist*, (Insert), 1991, **320**, 1.
2. 'Webster's New Collegiate Dictionary', G. & C. Merriam, Springfield, MA, 1975, p. 362.
3. D. G. Fryback and J. R. Thornbury, *Med. Decis. Making*, 1991, **11**, 88.
4. American National Standards Institute, 'Method for the Sensitometry of Medical X-Ray Screen-Film Processing Systems', ANSI Publication PH.2.43-1982, American National Standards Institute, New York, 1982.
5. K. Doi, G. Holje, L.-N. Loo, H.-P. Chan, J. M. Sandrik, R. J. Jennings, and R. F. Wagner, 'MTFs and Wiener Spectra of Radiographic Screen-Film Systems', HHS Publication FDA 82-8187, US Government Printing Office, Washington, DC, 1982.
6. J. M. Sandrik, R. F. Wagner, and K. M. Hanson, *Appl. Opt.*, 1982, **21**, 3597.
7. International Commission on Radiation Units and Measurements, 'Modulation Transfer Function of Screen-Film Systems', ICRU Report 41, International Commission on Radiation Units and Measurements, Bethesda, MD, 1986.
8. M. C. Steckner, D. J. Drost, and F. S. Prato, *Med. Phys.*, 1994, **21**, 483.
9. C. E. Metz, *Sem. Nucl. Med.*, 1978, **8**, 283.
10. C. E. Metz, *Invest. Radiol.*, 1986, **21**, 720.
11. J. R. Thornbury, D. G. Fryback, and W. Edwards, *Radiology*, 1975, **114**, 561.
12. R. M. Poses, R. D. Cebul, and R. M. Centor, *Med. Decis. Making*, 1988, **8**, 233.
13. L. B. Lusted, H. V. Roberts, W. Edwards, D. L. Wallace, M. Lahiff, J. W. Loop, R. S. Bell, J. R. Thornbury, D. L. Seale, J. P. Steele, and D. G. Fryback, 'Efficacy of Diagnostic X-ray Procedures', American College of Radiology, Reston, VA, 1980.
14. Food and Drug Administration, 'Assessment and Modification of Clinical Utility in Radiology: The Oral Cholecystogram and the Upper Gastrointestinal Examinations', HHS Publication FDA 85-8250, US Government Printing Office, Washington, DC, 1985.
15. S. M. Sane, R. A. Worsing, C. W. Wiens, and R. K. Sharma, *Pediatrics*, 1977, **60**, 669.
16. P. B. Farnsworth, E. Steiner, R. M. Klein, and J. T. San Filippo, *J. Am. Med. Assoc.*, 1980, **244**, 582.
17. J. Wittenberg, H. V. Fineberg, E. B. Black, R. H. Kirkpatrick, D. L. Schaffer, M. K. Ikeda, and J. T. Ferrucci, *Am. J. Roentgenol.*, 1978, **131**, 5.
18. J. Wittenberg, H. V. Fineberg, J. T. Ferrucci, F. J. Simone, P. R. Mueller, E. van Sonnenburg, and R. N. Kirkpatrick, *Am. J. Roentgenol.*, 1980, **134**, 1111.
19. C. E. Metz, S. J. Starr, L. B. Lusted, and K. Rossmann, in 'Information Processing in Scintigraphy', ed. C. Raynaud and A. E. Todd-Pokropek, Commissariat à l'Energie Atomique, Département de Biologie, Service Hospitalier Frédéric Joliot, Orsay, France, 1975, pp. 420–439.
20. C. E. Phelps and A. I. Mushlin, *Med. Decis. Making*, 1988, **8**, 279.
21. F. Sainfort, *Med. Decis. Making*, 1991, **11**, 208.
22. H. V. Fineberg, *Am. J. Roentgenol.*, 1978, **131**, 1.
23. D. F. Ransohoff and A. R. Feinstein, *N. Engl. J. Med.*, 1978, **299**, 926.
24. C. B. Begg and B. J. McNeil, *Radiology*, 1988, **167**, 565.
25. C. E. Metz, *Invest. Radiol.*, 1989, **24**, 234.
26. J. E. Wennberg, *JAMA*, 1987, **258**, 2568.
27. E. F. Lawlor, *Public Policy Aging Rep. (Chicago)*, 1992, **4**, 1.
28. R. L. Kravitz, S. Greenfield, W. Rogers, W. G. Manning, M. Zubkoff, E. C. Nelson, A. R. Tarlov, and J. E. Ware, *J. Am. Med. Assoc.*, 1992, **267**, 1617.
29. W. H. Straub, *Radiology*, 1993, **188**, 51A.
30. D. R. Enzmann, *Diagnostic Imaging*, 1993, Nov., 71.
31. I. M. Kaizen, 'The Key to Japan's Competitive Success', Random House Business, New York, 1986.
32. J. M. Eisenberg, *J. Am. Med. Assoc.*, 1989, **262**, 2879.
33. C. Bombardier and J. M. Eisenberg, *J. Rheumatol.*, 1985, **12**, 201.
34. A. L. Hillman, *Wharton Hlth Care*, 1993, **1**, 15.
35. P. F. Drucker, *Harvard Business Rev.*, 1988, **66** (Jan./Feb.), 45.
36. A. R. Margulis, J. Kucharczyk, S. W. Hetts, and A. M. Werne, *Eur. Radiol.*, 1994, **4**, 1.
37. H. C. Sox, Jr., M. A. Blatt, M. C. Higgins, and K. I. Marton, 'Medical Decision Making', Butterworths, Boston, 1988, pp. 117–119.
38. L. S. Cooper, T. C. Chalmers, M. McCally, J. Berrier, and H. S. Sacks, *J. Am. Med. Assoc.*, 1988, **259**, 3277.
39. C. R. Taylor, J. G. Elmore, K. Sun, and S. K. Inouye, *Invest. Radiol.*, 1993, **28**, 155.
40. R. J. Steckel and A. T. Kagan, *Radiology*, 1980, **134**, 367.
41. J. R. Thornbury, D. K. Kido, A. I. Mushlin, C. E. Phelps, C. Mooney, and D. G. Fryback, *Invest. Radiol.*, 1991, **26**, 829.

Biographical Sketches

Martin J. Lipton. *b* 1936. M.D., 1960, University of Liverpool Medical School, UK. Residency in internal medicine and radiology, Hammersmith Hospital, Royal Postgraduate School of London. Training in cardiovascular radiology, St. George's Hospital and National Heart Hospital, London. Successively, instructor and assistant professor, Department of Radiology, Stanford University, USA, 1969–77. Visiting research scientist, Cardiovascular Research Institute, University of California at San Francisco, 1976. Successively, associate professor and Professor, Department of Radiology, University of California at San Francisco, 1977–88. Chairman of Radiology and Professor of Radiology and Medicine, University of Chicago, 1988–present. Over 300 publications. Research specialties: cardiovascular radiology, CT, MRI, and nuclear medicine.

Charles E. Metz. *b* 1942. A.B. *cum laude* (Physics), 1964, Bowdoin College, USA; M.S., 1966, Ph.D. (radiological physics), 1969, University of Pennsylvania. Successively, instructor, assistant professor, associate professor, and Professor, Department of Radiology, University of Chicago, 1969–present. Approx. 180 publications. Research specialties: receiver operating characteristic methodology, image reconstruction from projections, and mathematical analysis of medical imaging systems.

Larry A. Ranahan. *b* 1955. B.G.S., 1986, M.B.A., 1988, Oakland University, USA. Executive Director, Department of Radiology, University of Pennsylvania, 1991–93. Director, Department of Radiology, University of Chicago, 1993–94. Research specialties: health care economics, management information systems, and operational work engineering and design.

Quality Control and Quantification in Whole Body MRI and MRS

Franca Podo
Istituto Superiore di Sanità, Rome, Italy

Wim M. M. J. Bovée
Delft University of Technology, Delft, The Netherlands

and

J. Stewart Orr
Hammersmith Hospital, London, UK

1 INTRODUCTION

A whole body system is one used for clinical investigations and studies of living human subjects. The studies may be of any part of the body. A whole body system includes the machine itself plus associated equipment and the mode of use. A whole body system may be used for magnetic resonance imaging (MRI), magnetic resonance spectroscopy (MRS), or both.

Quality control means

1. ensuring that an individual system performs in a way that consistently gives reproducible results that render good clinical value and provide a basis for improving techniques;
2. ensuring that any system gives results conveying the same clinical interpretation as other systems for the same mode of use, so that comparisons of diagnoses and clinical opinion can be made, trained staff can apply their skill generally, new techniques can be propagated, and the body of useful knowledge increased.

1.1 Necessity for Quality Control and its Evolution

Quality control is needed because whole body systems do not automatically perform to give the desirable results referred to above. Nor does any one system automatically convey the same interpretation as others.

Examples of poor results from checks on systems and comparisons between them are shown in Figure 1. Progress occurs through improvements in equipment and techniques, combined with local quality control, and the analysis of clinical results that are reproducible and made comparable by controlled calibration.

For NMR characteristics such as relaxation times, spin density, and chemical shift, pressures have grown for the development of methods for quality control. The pressures come from users (both clinical and scientific), from suppliers, and from government agencies. Users want quality control for improving performance and clinical usefulness, and so do suppliers, together with the public demonstration of high quality. Government agencies want quality control to ensure safety and value for money.

The evolution of quality control is an iterative process, because all the details of a method cannot be clear when work begins, and because practical advantages and disadvantages cannot all be foreseen. There have been several lines for developments in quality control of whole body systems.

Government agencies in individual countries were faced with responsibilities for approving the purchase of the new systems and judging performance. Progress was made in many countries, and in the United States the suppliers' organization (NEMA) produced standard methods for selected parameters.[1–4] Manufacturers needed methods for checking performance during development, before despatch, and on site. Such methods were the basis of the NEMA standards. The international standards body, IEC, is adopting some of the methods as tests of compliance with health and safety requirements.[5]

In the European Community, NMR Concerted Actions, mainly of users, ran from 1984 to 1996.[6–8] These Actions, which had useful interactions with individual manufacturers and with NEMA, went through the repeated iteration of steps for defining the parameters to be measured, creating test objects and substances, specifying protocols, and assessment in practical trials.[9–21] The methods were then tested in quantitative studies of selected organs.[22–24] The EC Concerted Action standard methods and test objects have been available and used in Europe and elsewhere.

1.2 Physical Basis and Practical Requirements for Quality Control

Whole body systems can use NMR features to define the position of tissues and also to establish their characteristics. The link between characteristics and positions is the NMR signal. These signals are dependent on basic parameters and functions, and the measurement of these is part of quality control. However, it has been found that tests using simulations of actual use are necessary.

The purpose of the test objects and methods is to define absolutely and separately the characteristic and the position. Quality control with test objects then assesses performance in stimulation and detection of the signal. However, the complexities of whole body systems makes clear separation difficult, and interpretation of tests is not straightforward.

A general practical requirement in quality control is that the results can be obtained in an acceptably short period of time, by using the normal clinical operating modes of the system. The methods may, however, require the use of additional computer software.

Quality control is of value only if the finding of any deficiency is followed up by effective action. The control tests, the recommended actions, and the outcomes should be systematically recorded.

2 MRI: TEST PARAMETERS AND PROTOCOLS

Most of the MRI test parameters need different features in the relevant test objects. The use of a standardized set of test

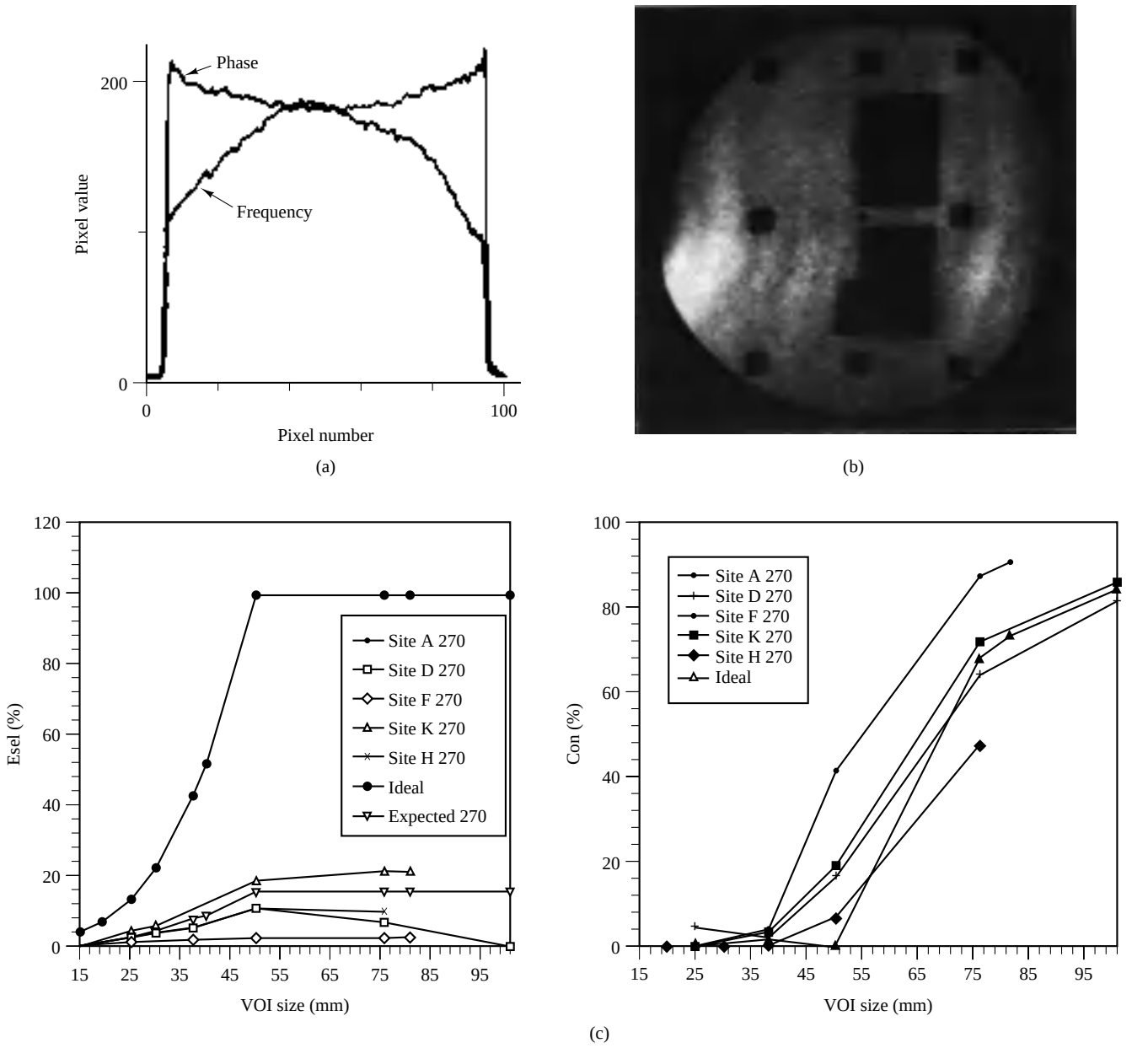

Figure 1 (a) Low-quality uniformity profiles and (b) gross geometric distortion in MRI. (c) Measurements of selection efficiency (Esel) and contamination (Con) in volume-selected proton MRS, using STEAM with TE = 270 ms. ((a) and (b) reprinted with permission of Pergamon Press, Oxford, from R. A. Lerski et al., *Magn. Reson. Imaging*, 1988, **6**, 203, 205. (c) reprinted with permission of Elsevier Science Ltd., New York, from S. F. Keevil et al., *Magn. Reson. Imaging*, 1995, **13**, 148)

objects[9,11] in combination with the test procedures offers some clear advantages to the users of MRI equipment, especially when these methods have been validated in multicenter trials performed on different MRI systems.[10,12] Some protocols (NEMA) provide only recommendations on the essential requirements for test objects. These requirements[1–4] are expressed primarily as the geometry and NMR characteristics of the signal-producing volume, together with definitions for the specification volume and area and the measurement region of interest (ROI).

Key parameters for assessing performance in quality control are signal uniformity, geometric distortion, signal-to noise ratio, slice thickness, and profile. Additional important parameters are spatial resolution, signal linearity, uniformity of image signal-to-noise ratio, slice position and warp, and image contrast-to-noise ratio. Of particular importance for quantitation and diagnosis of malfunction are T_1, T_2, and spin density precision and accuracy.[9,11] Deviations of these parameters from their expected values indicate malfunction or erroneous calibration of instrument components.

Key parameters are described below, together with their value for assessing performance and the basics of measurement. It is worth noting that there are three aspects of variation

of signal across the image of a uniform test object: uniformity, artifacts, and signal-to-noise ratio.

Uniformity of image signal refers to the ability of the equipment to produce an image with identical signal response over one plane from a test object with uniform NMR characteristics. This parameter, which characterizes the low-spatial-frequency nonuniformities (i.e., non-noise) typical of MRI, may be affected by main field and rf inhomogeneities, rf penetration and coil geometry, gradient field nonlinearities, inadequacies in gradient pulse calibration or eddy current corrections, irregular response of the rf receiver, and signal processing.[2,11]

Uniformity is given by pixel variations within the full ROI occupied during clinical use. The parameter can be quantified as the deviation in the image signal intensity relative to the midrange pixel value in the profiles derived from scans in both the phase-encoding and frequency-encoding directions.

Geometric distortion is the deviation between measured distances in an image and the actual corresponding dimensions in the object (allowance being made for magnification).

This parameter (produced by factors such as field inhomogeneity, gradient defects, or signal sampling imperfections[3,11]) is derived by measuring the distances between fixed points in the image of the test object and determining their deviations from the respective expected values. These deviations are measured in the three orthogonal planes centered at the isocenter.

Image *signal-to-noise ratio* (S/N) represents the mean of the pixel values over the ROI divided by their standard deviation. This noise is the random variations in pixel intensity. It affects the clarity of MR images and is also an index of hardware performance.[1,9–11] Changes in image S/N values may occur as a consequence of variations in system calibration, gain, coil tuning, rf shielding, etc.

To simulate image noise in a typical clinical situation, the rf receiver coil must be electrically loaded. Loading may be accomplished by the test objects themselves or with accessories, or by the use of inductive damping loops that can be adjusted for the loaded Q of individual machines.[1,11] The use of nonstandard test objects that provide some loading for a system may provide a convenient tool for routinely checking the S/N of equipment. Results acquired on different types of system may not, however, be comparable unless standardized test objects and loading procedures are applied.[11] The problems of loading are very important and difficult to solve with complete satisfaction.

Slice thickness is the width at half-maximum of the *slice profile*, which itself is the variation in contribution to the image signal as a function of position orthogonal to the plane. It expresses the variation in effectiveness of the selective excitation process through the slice. The slice thickness depends on the rf pulse shape and sequencing, rf field homogeneity, the selection gradient and other parameters. Although slice selection attempts to achieve reception of signal solely from a slab of rectangular profile, the selected slice may have a profile quite different from the ideal. The slice profile can be assessed either by direct measurement with a thin inclined slab of signal-producing material, or by numerical differentiation of the measured edge response function from an inclined surface of an inert wedge immersed in a signal-producing material.[4,9–11]

Spatial resolution is usually pixel-limited, but several features may lead to a loss of resolution. It is, for instance, degraded by filtering the raw data through a function used for reducing the image S/N. Eddy currents produced by rapid gradient switching will lead to uneven resolution loss throughout the imaging field. In 2D FT MRI, the frequency-encoding and phase-encoding resolutions will differ, since the sampling and filtering in these directions are independent. Spatial resolution can be measured by determining the minimum bar separation detectable in the image of a bar pattern of varying spacing.[9,11] The image profile available on most systems may be used to measure the modulation across a particular set of bars. Spatial resolution can also be assessed from an edge-containing test object, by calculating the modulation transfer function (MTF) associated with the obtained edge spread function.[11]

In addition to the above parameters, *signal linearity* represents the linearity of the relationship between image signal and the concentration of the excitation-sensitive material. This can be measured with the use of a test object including a series of tubes containing substances with different spin densities.

Uniformity of image signal-to-noise ratio measures the variation of image S/N over one imaging plane, obtained from the same test object utilized for S/N, while *slice position* and *slice flatness* or *warp* jointly describe defects in the selection and expression of planar slices. They can be measured with the same test object.[9,11]

T_1, T_2, *and spin density precision and accuracy* are the basis of the contrast in MRI images, without which they have no clinical value. Their long- and short-term precision is therefore worth study and control.

Many centers are also interested in the accuracy of T_1, T_2, and spin density, for both clinical and scientific reasons. The accuracy of measurements with the whole body system is the closeness with which parameter values correspond to the known values of standards that have been separately calibrated.[9,11]

2.1 MRI Test Objects

As mentioned above, NEMA gives recommendation on some of the features needed for suitable test objects. These recommendations are similar to the detailed final designs worked out and tested by the EC Concerted Action (Figure 2).

2.2 Levels of Quality Control in MRI

There are several levels of quality control appropriate for different circumstances. When receiving a new machine, complete acceptance tests should be done, preferably in the presence of the manufacturer or the supplier.

Periodic maintenance requires tests less detailed than acceptance tests, but more extensive than those for routine application by users. The latter need to be acceptably rapid and to provide control, particularly of signal quality and geometry.

One of the most critical performance indicators is S/N. It is necessary to measure this frequently, because it is easy to lose signal or gain noise. The quality of image is also critically dependent on optimal adjustment of rf pulses and sequence timings, and it is important that these should be checked on a regular basis. For all tests, it is necessary to have a series of techniques with standard protocols, so that each performance feature may be measured and compared with least effort and time.

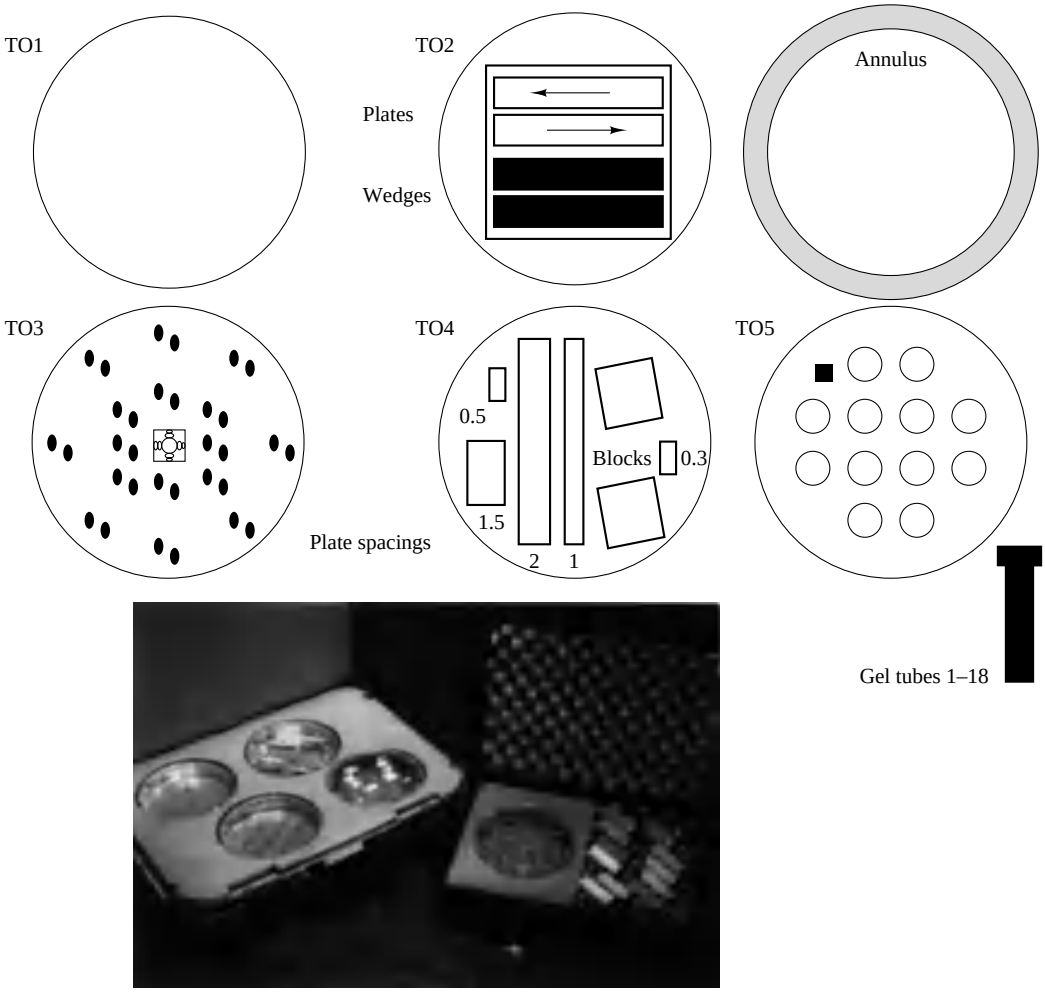

Figure 2 MRI test objects designed and constructed by the EC Concerted Action for quality control in whole body clinical systems:[9–12] TO1 [uniformity of image signal; image S/N; uniformity of image S/N; artifacts (ghosting)]; TO2 (geometric distortion; slice profile; slice thickness); TO3 (slice position; slice warp); TO4 (spatial resolution; modulation transfer function); TO5 (T_1, T_2, and spin density accuracy and precision; signal linearity; image contrast-to-noise ratio). The annulus represents one approach to providing appropriate loading for measuring S/N. (Schemes of test objects are reproduced with permission of Pergamon Press, Oxford, from R. A. Lerski et al., *Magn. Reson. Imaging*, 1993, **11**, 837. Photograph of test objects courtesy of R. A. Lerski)

3 MRS: TEST PARAMETERS, TEST OBJECTS, AND PROTOCOLS

While the same basic procedures in principle might be used (with appropriate adaptations) for MRI and *magnetic resonance spectroscopic imaging* (MRSI),[21] for single volume spectroscopy, where only one volume of tissue is under study, additional and different tests are needed.[13]

For single volume spectroscopy, the localization performance is the important factor for many of the parameters. *Localization* is the process of maximizing signal from the single volume that is the object of study and of restricting signals from outside. There are many useful techniques used for localization but none are ideal.

A simple approach that does not put much demand on the MRS equipment and software is to employ a test object having two compartments (an inner and outer one) for the localization testing,[13,15–18] and to use standard bottles and spheres for some other tests. The inner and outer compartments may each contain a substance with a single NMR line, but with different chemical shifts. The relative intensities of the two lines in the spectrum then vary as the size and position of the localized volume of study varies with respect to size and position of the two compartments.

It should be noted that some of the parameters below are also relevant to techniques that do not employ localization.

3.1 Test Parameters

Linearity is the linearity of the relations between signal strength and concentration, and signal strength and volume.

Spectral resolution is the full linewidths at one-half and at one-tenth of the maximum peak height for the spectral peaks from the inner and outer compartments. To assess the effect of the measuring sequence, this test can be performed with and without localization.

The *signal-to-noise ratio* (S/N) is measured per unit concentration in a fixed volume.

The *selection efficiency* is the ratio of the signal strengths from the inner compartment with and without localization. This parameter indicates signal loss due to the applied localization sequence. Ideally, its value equals one if the selected volume is isocentric with and equals or exceeds that of the inner container. In practice, this signal loss will depend on the ratio of the selected volume and the inner compartment volume, and should therefore be determined for various ratios.

The *extra volume suppression factor* is the ratio of the signal strengths from the outer compartment without and with localization. This parameter quantifies unwanted signal leakage from outside into the selected *volume of interest* (VOI). Ideally, its value is unity if the selected volume is centered in and smaller than or equals the volume of the inner container. Owing to imperfect slice profiles, it will depend on the ratio of the selected and the inner compartment volumes. It should therefore also be measured for various ratios.

Contamination is the ratio of the unwanted signal from outside the VOI and the total signal in the spectrum. This is a less fundamental localization performance property than the suppression factor and selection efficiency. It depends on the relative volumes of and the concentrations in the two compartments, and it directly expresses the percentage of unwanted signal in the spectrum, using the actual pulse sequence and VOI.

The *VOI profile* characterizes the slice profile in one, two, or three dimensions. Ideally, the profile should be plotted and specified, for instance by the full width at 20, 50, and 80% of the maximum signal height. The profile can be determined using imaging methods.

The *accuracy of the VOI position* is the deviation between the position of the center of the VOI, as determined with a test object and procedure, and the true position. An imaging method can be used, after performing the imaging quality control tests.[9] The VOI center is estimated from the slice profile.

Selective suppression of signals in the spectrum is the ratio of the signal strength without and with suppression, obtained from two localized experiments, with and without suppression of the signal of the inner compartment. This parameter can be used to test the effectiveness of suppression methods (e.g., for water and fat), and with spectral editing.

For assessing the *stability* of localization, an experiment is repeated several times. The average value of the strengths of the signals from the two compartments and their standard deviations are determined. This test can be used to assess the short- and long-term stability of the equipment.

Precise descriptions of the implementation of the tests to determine the parameters indicated above, and more detailed information about the parameters themselves and other quantities involved, can be found in the literature.[13–18]

3.2 Test Objects and Substances

Substances are needed for constructing and filling test objects. For single volume spectroscopy, the two-compartment object is very useful (Figure 3). The inner compartment is usually a rectangular volume, since most methods localize this shape. For shimming reasons, a sphere as outer compartment is advisable for proton MRS, and a material with a favorable diamagnetic susceptibility should be chosen from which to construct the test objects. Plexiglass is therefore to be preferred to glass. Moreover, it is less fragile—but it is not inert, and therefore imposes restrictions on the choice of the substances for filling the compartments.

Figure 3 Test object designed and constructed by the EC Concerted Action for quality control of volume selection in whole body MRS systems.[13,15] (Courtesy of Dr. S. F. Keevil)

The substances used to fill the two compartments should, as far as possible, meet requirements that are sometimes conflicting.

1. The NMR spectrum of a substance should be a single line.
2. The chemical shift difference between the compounds in the two compartments should be sufficient to minimize line overlap in the spectrum, but also small enough to minimize localization artifacts when selecting slices or volumes by means of frequency-selective pulses and gradients.
3. The relaxation times T_1 of the two lines should be equal, as should be the T_2 values; both should be in the range of in vivo values. Doping with paramagnetic substances can sometimes give the desired relaxation values. If suitable values cannot be obtained, equal T_1 values are to be preferred for assessing the quality of localization obtained by using ISIS sequences in ^{31}P MRS. For ^{1}H MRS, equal T_2 values are preferable, because, in general, echo techniques are employed for localization.
4. If possible, the compounds should be easily available, not poisonous, not flammable, stable, and have relaxation times with a weak temperature dependence and chemical shift values with none.

Details are given by Keevil et al.[17]

The field of MRS is still in development, and new techniques evolve. Therefore quality control needs continued adaptation to extend its application to innovative techniques, including spectroscopic imaging.[21] Quality control, which should be used to check and calibrate apparatus and techniques regularly, represents an essential requirement for absolute metabolic measurements by *in vivo* MRS.[24]

3.3 Data Analysis

In vivo MRS data do not have a high signal-to-noise ratio, and considerable line overlap occurs. As a consequence, data

analysis methods have to be chosen very carefully. Several quantification methods exist, which may lead to widely varying results, owing to systematic and operator-dependent errors. Model function fitting is the best way to quantify the data and minimize these errors. The effect of the pulse sequence and the data analysis method can be checked using test objects and standard solutions. The results can be incorporated as prior information in the data analysis method, which significantly decreases the systematic errors and the standard deviation.[13,19,25,26]

4 RELATED ARTICLES

Quantitation in In Vivo MRS; Relaxation Measurements in Imaging Studies; Surface Coil NMR: Detection with Inhomogeneous Radiofrequency Field Antennas.

5 REFERENCES

1. NEMA Standards Publication No. MS 1, 'Determination of Signal-to-Noise Ratio (SNR) in Diagnostic Magnetic Resonance Images', National Electrical Manufacturers Association, Washington, DC, 1988.
2. NEMA Standards Publication No. MS 3, 'Determination of Image Uniformity in Diagnostic Magnetic Resonance Images', National Electrical Manufacturers Association, Washington, DC, 1989.
3. NEMA Standards Publication/No. MS2, 'Determination of Two-dimensional Geometric Distortion in Diagnostic Magnetic Resonance Imaging', National Electrical Manufacturers Association, Washington, DC, 1990.
4. NEMA Standards Publication/No. MS5, 'Determination of Slice Thickness in Diagnostic Magnetic Resonance Imaging', National Electrical Manufacturers Association, Washington, DC, 1992.
5. IEC/TC 62 B Medical Electrical Equipment. Part 2: Particular Requirements for the Safety of Magnetic Resonance Equipment for Medical Diagnosis. SC62B, EN 60601-2-33: 1995-11, 1995.
6. F. Podo, J. S. Orr, K. H. Schmidt, and W. M. M. J. Bovée, *Magn. Reson. Imaging*, 1988, **6**, 175.
7. F. Podo, J. S. Orr, W. M. M. J. Bovée, J. D. de Certaines, and D. Leibfritz, *Magn. Reson. Imaging*, 1993, **11**, 809.
8. F. Podo, O. Henriksen, W. M. M. J. Bovée, M. O. Leach, D. Leibfritz, and J. D. de Certaines, *Magn. Reson. Imaging*, 1998, **16**, 1085.
9. EEC Concerted Research Project, *Magn. Reson. Imaging*, 1988, **6**, 195.
10. R. A. Lerski, D. W. McRobbie, K. Straughan, P. M. Walker, J. D. de Certaines, and A. M. Bernard, *Magn. Reson. Imaging*, 1988, **6**, 201.
11. R. A. Lerski and J. D. de Certaines, *Magn. Reson. Imaging*, 1993, **11**, 817.
12. R. A. Lerski, *Magn. Reson. Imaging*, 1993, **11**, 835.
13. W. M. M. J. Bovée, in 'Magnetic Resonance Spectroscopy in Biology and Medicine', eds. J. D. de Certaines, W. M. M. J. Bovée, and F. Podo, Pergamon Press, Oxford, 1992, Chap. 12.
14. F. Podo, W. M. M. J. Bovée, J. de Certaines, D. Leibfritz, and J. S. Orr, *Magn. Reson. Imaging*, 1995, **13**, 117.
15. EEC Concerted Action Project, *Magn. Reson. Imaging*, 1995, **13**, 123.
16. M. O. Leach, D. J. Collins, S. Keevil, I. Rowland, M. A. Smith, O. Henriksen, W. M. M. J. Bovée, and F. Podo, *Magn. Reson. Imaging*, 1995, **13**, 131.
17. S. F. Keevil, B. Barbiroli, D. J. Collins, E. R. Danielsen, J. Hennig, O. Henriksen, M. O. Leach, R. Longo, M. Lowry, C. Moore, E. Moser, C. Segebarth, W. M. M. J. Bovée, and F. Podo, *Magn. Reson. Imaging*, 1995, **13**, 139.
18. F. Howe, R. Canese, F. Podo, B. Vikhoff, J. Slootboom, J. R. Griffiths, O. Henriksen, and W. M. M. J. Bovée, *Magn. Reson. Imaging*, 1995, **13**, 159.
19. R. de Beer, P. Bachert-Baumann, W. M. M. J. Bovée, E. Cady, J. Chambron, R. Dommisse, C. J. A. van Echteld, R. Mathur-De Vré, and S. R. Williams, *Magn. Reson. Imaging*, 1995, **13**, 169.
20. F. Podo, *Adv. Biomed. Eng.*, 1993, **7**, 304.
21. W. Bovée, R. Canese, M. Decorps, E. Forssell-Aronsson, Y. Le Fur, F. Howe, O. Karlsen, A. Knijn, G. Kontaxis, H. Kügel, M. McLean, F. Podo, J. Slotboom, B. Vikhoff, and A. Ziegler, *Magn. Reson. Imaging*, 1998, **16**, 1113.
22. J. D. de Certaines, O. Henriksen, A. Spisni, M. Cortsen, and P. B. Ring, *Magn. Reson. Imaging*, 1993, **11**, 841.
23. O. Henriksen, J. D. de Certaines, A. Spisni, M. Cortsen, R. N. Müller, and P. B. Ring, *Magn. Reson. Imaging*, 1993, **11**, 851.
24. S. F. Keevil, B. Barlinoli, J. C. W. Brooks, *et al.*, *Magn. Reson. Imaging*, 1998, **16**, 1093.
25. R. de Beer, B. Barbiroli, G. Gobbi, A. Knijn, H. Kügel, K. W. Langenberger, I. Tkác, and S. Topp, *Magn. Reson. Imaging*, 1998, **16**, 1107.
26. R. de Beer, A. van den Boogant, E. Cady, D. Graveron-Dennilly, A. Knijn, K. W. Langenberger, J. C. Lindon, A. Ohlhoff, H. Serraï, and M. Wylezinska-Arridge, *Magn. Reson. Imaging*, 1998, **16**, 1127.

Acknowledgements

The authors are grateful to the Commission of European Communities, DG XII, for support to the Concerted Actions on MRI and MRS COMAC-BME II.1.3 and BIOMED 1 PL 920432. FP also acknowledges support by PF CNR ACRO.

Biographical Sketches

F. Podo. *b* 1944. Laurea Physics, 1967, University of Rome. Research associate, Rockfeller University, New York, 1971–1972 (Prof. G. Némethy) and University of Pennsylvania, 1972 (Professor B. Chance). Staff member, Istituto Superiore di Sanità, Rome, 1969–1980; Research Director 1980–present; Director of Physical Biochemistry, 1982–present. Introduced to NMR by Professor M. Ageno (1968). Over 100 publications. Research specialty: physical chemistry, biochemistry, cell biology and oncology.

W. M. M. J. Bovée. *b* 1938. M.Sc., chemistry, 1969, Ph.D., physics, 1975, Delft University. Billiton Research Laboratories, 1969. Delft University, 1970–present. Approx. 140 publications. Research specialty: in vivo NMR.

J. S. Orr. *b* 1930. B.Sc., physics, 1952, D.Sc., physics, 1972, University of Glasgow. FRSE, 1974. Introduced to MRI by Professor Robert Steiner, 1979; involved with early EMI imaging. Head of Radiotherapy Physics, Glasgow, 1962–1977. Professor of Medical Physics, Royal Postgraduate Medical School, Hammersmith Hospital, 1977–1986. Experience as Chairman of MRC Committee on MRI Technological Performance, and Member, Project Management Group of two Concerted Actions of the European Communities. Over 100 publications.

Inversion–Recovery Pulse Sequence in MRI

Graeme M. Bydder
University of London, London, UK

1 INTRODUCTION

The inversion–recovery (IR) pulse sequence has been used to provide heavily T_1-weighted images since the earliest days of clinical MRI. They were used in the first studies which showed an advantage of MRI over ultrasound[1] and computed tomography (CT).[2] The sequence produced high contrast between normal tissues and pathological tissues which had a prolonged T_1, and was the single most effective imaging technique available from 1980 to early 1982.

The introduction of the heavily T_2-weighted spin echo sequence into clinical practice in 1982[3–5] provided a very useful approach to disease detection based on differences in T_2, and has since become the mainstay of clinical diagnosis in many regions of the body. T_1-weighted spin echo sequences also provide a method for obtaining T_1-weighted images which are lower in contrast than inversion–recovery, but are quicker.

MRI studies in 1980 to early 1982 involved only a single slice and were performed at low fields (0.04–0.15 T). After this time there was a general tendency to increase operating field strength, which increases tissue T_1 and prolongs the time required for the IR sequence for equivalent image contrast. Multiple slice techniques were also developed at this time, and these required slice selective 180° pulses. While slice selective 90° pulses were easy to implement, it took some time to achieve this with 180° pulses. Also, the IR sequence with its relatively long interval between the initial 180° pulse and the subsequent 90° was more difficult to interleave into a multislice format than conventional spin echo sequences.

For these reasons, the conventional IR pulse sequence was displaced as the principal pulse sequence used for diagnostic purposes, but it continued to have many applications when high T_1-weighted contrast was desired, such as in detecting contrast enhancement[6,7] or in demonstrating early myelination in infants.[8,9]

A particular variant of the IR sequence in which the timing of the initial inversion pulse was set to null the signal from fat (which has a very short T_1) and TE was chosen to provide very high contrast images proved to be very useful in body and orthopedic applications.[10,11] This short inversion time IR (STIR) sequence combined fat suppression with high lesion contrast and did not require careful shimming as with frequency selective techniques. At a time when some orthopedic, bone marrow and oncological applications were difficult, it proved a valuable addition to MRI and remains in active use at the present time. It is particularly suited to mid- and low-field applications where chemical shift techniques for fat suppression are difficult.

The capacity of the IR sequence to null fluids has also been exploited in the form of the fluid attenuated inversion–recovery (FLAIR) sequence where cerebrospinal fluid (CSF) is suppressed and heavy T_2-weighting (long TE) is used to detect lesions in brain and spinal cord.[12]

Both fluid suppression and fat (or white matter) suppression can be combined in the form of the doubly attenuated inversion recovery (DAIR) sequence, which can be used, for example, to isolate the cerebral cortex or to demonstrate liver pathology.[10] Inversion pulses have also been used to label inflowing blood outside of the slice of interest as a measure of tissue perfusion.[13]

With the development of faster imaging techniques for clinical use, such as the rapid acquisition with relaxation enhancement (RARE) sequence,[14] the rapid gradient echo,[15,16] and echo planar imaging,[17] there has been renewed interest in the use of the IR sequence. With these sequences the time penalty associated with the sequence is no longer felt so acutely. Many of the faster sequences have unfavorable contrast properties which can be modified to make them useful by application of an appropriately timed inversion pulse prior to the data collection. The clinical uses of these sequences parallel those previously developed with slower versions of the IR sequence, but have the advantage that they can be performed much more rapidly.

In the following section the basic form of the IR sequence will be described, followed by outlines of the STIR, FLAIR, other forms of the IR sequence, and fast variants.

2 THE BASIC FORM OF THE IR SEQUENCE

The dependence of signal intensity seen with the IR sequence on proton density, T_1 and T_2 can be described in mathematical terms using the Bloch equations, but a qualitative description of the IR sequence will be used in this section. The proton magnetization induced in the patient by the static magnetic field can be represented by a vector $\boldsymbol{M}$. The component of the magnetization in the transverse plane at any given time is then represented by M_{xy}, and that in the longitudinal direction at the same time by M_z. The effect of a 90° pulse is to rotate M_z into the transverse plane to become M_{xy}.

Following a 90° pulse, M_z increases exponentially from zero with time constant T_1 [Figure 1(a)], and M_{xy} decays exponentially with time constant T_2 [Figure 1(b)]. At the following 180° pulse M_z is inverted to become $-M_z$ and recovers with a time constant T_1, but at twice the rate for the earlier longitudinal recovery after the 90° pulse. At the next 90°, pulse M_z is rotated to become M_{xy}. M_{xy} then decays exponentially with time constant T_2. Using a gradient echo or spin echo data collection, the signal is collected at a mean time TE after the 90° pulse, and the cycle is repeated.

A composite diagram following firstly M_z then M_{xy} after the second 90° pulse can be used to represent the 'potential signal intensity' at various stages in the sequence [Figure 1(c)]. The size of the received signal and, ultimately, the signal intensity or pixel value in the image is proportional to M_{xy} at the time of the data collection (DC). M_{xy} is also proportional to tissue proton density.

The times TI and TE are shown in Figure 1(c). TI is the inversion time between the inverting 180° pulse and the fol-

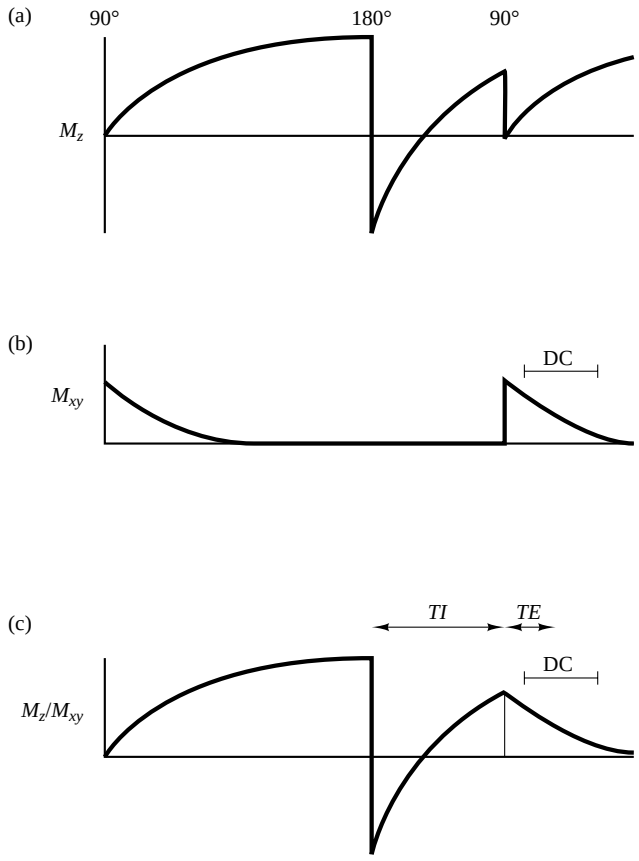

Figure 1 Changes in M_z (a) and M_{xy} (b) with time in the IR sequence (medium *TI*) using a field echo data collection (DC). Figure 1(c) shows M_z initially then M_{xy} in the last segment

lowing 90° pulse, and *TE* is the time from the last 90° pulse to the following echo. Repetition time (*TR*) is the duration of each cycle of the sequence.

Using Figure 1(c) as a model of the IR sequence, we can next compare the signal intensities of white matter (a tissue with a relatively short T_1), gray matter (a tissue with a longer T_1), and CSF (which has a very long T_1), as in Figure 2. The signal intensity observed is proportional to the height of M_{xy} at the time of the DC, and it can be seen that the shorter T_1 of white matter results in a higher signal intensity than for gray matter. The very long T_1 of CSF results in a low signal intensity, which may be negative as in Figure 2. The last segment of the decay converges towards zero for both gray and white matter with their positive signal intensities, as well as for CSF with its negative signal intensity. Display of the resultant image after phase corrected processing (see later) gives white signal intensity for white matter, light gray for gray matter, and black for CSF. The signal for gray matter is slightly greater than that for white matter at the time of the 180° pulse because of its greater proton density.

The general rule is that a *TR* of at least $3T_1$ should be allowed for recovery of the longitudinal magnetization between the final 90° pulse of one cycle and the initial 180° pulse of the next pulse cycle to allow a high level of recovery of M_z, though, in practice, it may be possible to use times less than this. Reducing *TR* produces a reduction in signal intensity for tissues with a long T_1, though there is little effect on tissues with a short T_1 where *TR* is still greater than $3T_1$. Reducing *TR* is therefore used to reduce the relative signal intensity of tissues or fluids such as CSF which have a very long T_1.

There are two types of image reconstruction available: (1) phase corrected, where positive values of signal intensity are shown positive and negative values appear negative; and (2) magnitude reconstruction, where the magnitude of the signal is used irrespective of its sign. In the above sequences the CSF appears dark with phase corrected processing but may show a 'rebound' with a lighter central area with magnitude processing. The signal intensities follow directly from considering Figure 2.

The 90° pulse in the IR imaging sequence is always slice selective, though for single scans the 180° pulse(s) need not be. However, when the inversion–recovery sequence is used to obtain an interleaved set of slices, the 180° pulse(s) must be slice selective. When the 180° pulse is slice selective, it is possible for flowing blood to experience only part of the IR sequence, depending on where it is at the time of the inversion pulses. For example, blood flowing into a slice may only experience a 90° pulse and behave as though it is being imaged with a partial saturation sequence, producing a high signal intensity rather than the usual low signal intensity.

It is useful to consider three main variants of the IR sequence according to their values of *TI*:

1. the medium *TI* inversion recovery sequence;
2. the short *TI* sequence; and
3. the long *TI* sequence

These will be dealt with in the next sections.

3 THE MEDIUM *TI* IR SEQUENCE

The working rule to obtain an image with good contrast between two tissues of different T_1 values is to choose a value of *TI* intermediate between the two tissues of interest (neglecting the effects of proton density and T_2). Thus, satisfactory contrast between white matter (T_1 = 350 ms) and gray matter (T_1 = 450 ms) is achieved with a *TI* of about 400 ms at a field of 0.15 T. Note that the signal intensity is not maximal at this point, so the image appears noisier than that obtained with, for example, *TI* = 500 ms where the signal is higher (although the

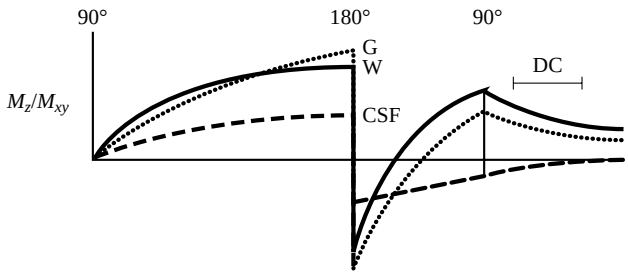

Figure 2 Changes in M_z/M_{xy} with time in the IR sequence (medium *TI*) for white matter (W), gray matter (G), and CSF using a field echo data collection (DC). The signal intensity on the image is proportional to the height of M_{xy} at the middle of DC. White matter is highest, followed by gray matter, then CSF

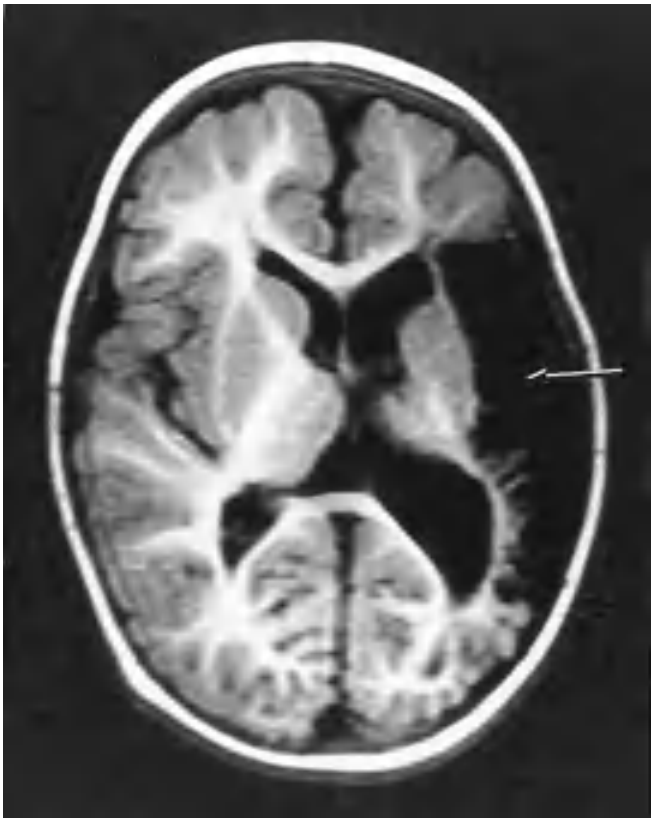

Figure 3 Cerebral infarction in an infant aged 9 months: Transverse IR3400/30/800 (IR *TR/TE/TI*) scan. The white matter (partially myelinated) is white, the gray matter is gray, and the infarction (arrow) is black

gray–white matter contrast is less). In theory, maximum contrast is obtained when *TI* is about 0.6 times the average of the T_1 for the two tissues, but the signal levels in this case are close to zero, so maximizing the appearance of the noise of the image. Note that the *TI* for optimum contrast between gray matter and a tumor or an infarct (which have an increased T_1) is greater than that for gray and white matter. These features are illustrated in Figure 3, which shows a cerebral infarct in an infant aged 9 months. White matter is white, gray matter is gray, and the infarction is dark, using phase corrected processing.

There are two additional modifying factors. The increased mobile proton density of gray matter relative to white matter results in slightly less tissue contrast. More important is the fact that the T_2 dependent period following the 90° pulse and prior to data collection may produce a reduction in tissue contrast. This is particularly so for lesions which follow the common pattern and have an increase in both T_1 and T_2. Thus, the T_2 dependent decay, in the last component of the sequence, reduces the T_1 contrast developed earlier in the sequence.

The method of image reconstruction and the type of data collection affect *TE*. *TE* can generally be shorter with projection reconstruction than with 2D Fourier transformation since a single vector encoding gradient is used, without the need for a previous phase-encoding gradient as with 2D Fourier transformation. A gradient echo data collection can be completed earlier than a spin echo collection with the same bandwidth, although the former is more vulnerable to $\boldsymbol{B}_0$ field inhomogeneities.

With the brain (T_2 about 100 ms) the T_2 dependence of the IR sequence is not such a big problem as it is in the body, where values of T_2 are typically half of those in the brain (45–60 ms), making the same IR sequence much more T_2 dependent than when it is used in the brain. The use of short values of *TE* to control this problem then becomes important. Figure 4 shows a transverse CT image of the liver in which a metastasis is shown in the quadrate lobe (large arrow) but an additional lesion with a long T_1 value is seen in the liver with the IR sequence (small arrow).

4 THE SHORT *TI* IR (STIR) SEQUENCE

Values of *TI* under discussion here are about 0–250 ms. In the limit where *TI* equals zero (or, from a practical point of view, about 1 ms) the 90° and 180° pulses add, to give a 270°

Figure 4 Metastases in the liver: (a) transverse contrast enhanced CT and (b) IR1400/10/400 scans. One metastasis is seen with both scans (large arrow), but another (small arrow) is only seen with the IR scan (b)

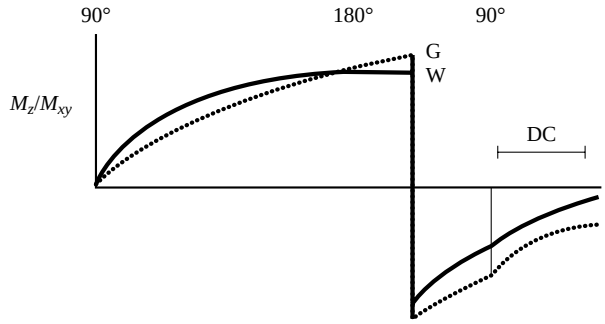

Figure 5 Changes in M_z/M_{xy} with time for the STIR sequence. The size of the signal from gray matter (G) is greater than that for white matter (W). When magnitude processing is used, it has a higher signal

pulse which is equivalent to a $-90°$ pulse. This is equivalent to a 90° pulse, and the sequence becomes 90° data collection, or the partial saturation (PS) sequence. Thus the PS sequence can be regarded as a limiting case of the IR sequence with $TI = 0$. The same reasoning applies when a spin echo data collection is used and the IR sequence (with $TI = 0$) becomes equivalent to a spin echo sequence. Using magnitude reconstruction with *TI* in the range of 0 to about 250 ms, an IR image of the brain appears like a spin echo one, although with greater gray–white matter contrast. The magnetization curves can be represented as shown in Figure 5.

Note that following the final 90° pulse the T_1 contrast and the T_2 contrast are additive, i.e. increasing the T_1 of a tissue increases the tissue's relative signal intensity and so does increasing its T_2. (This is not the case in Figure 2, which illustrates medium values of *TI*.) The short *TI* IR (STIR) sequence is sensitive to changes in T_1 and T_2, and can be used as a screening sequence in the brain in a similar way to the spin echo sequences with long *TE* and long *TR* such as SE1500/80.

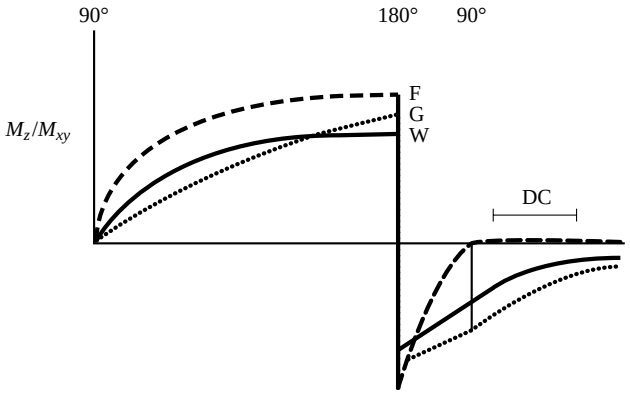

Figure 6 Changes in M_z/M_{xy} with time for fat (F), white matter (W), and gray matter (G) using a fat suppressed STIR sequence. The signal from gray matter is greater than that from white matter. Fat gives no signal

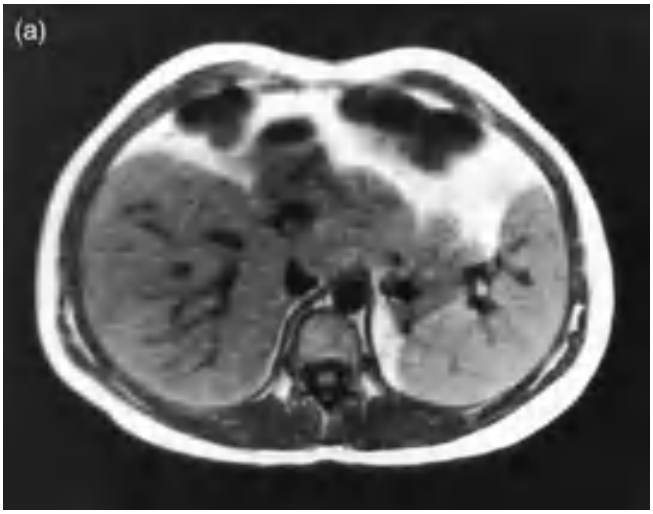

Figure 7 Recurrent liver metastases and para-aortic tumor: (a) transverse SE544/44 and (b) IR1500/44/100 images. The liver and para-aortic lesions show low contrast in (a) but are highlighted in (b) (arrows). Fat gives no signal in (b)

To reduce the signal intensity of CSF to less than that of white matter, *TR* can be shortened to 1000 ms with a sequence such as IR1000/44/100 (at 0.15 T).

Since many pathological lesions produce an increase in both T_1 and T_2, the addition of these two types of contrast with the STIR sequence produces a high net tissue contrast. This type of sequence also enables some T_1 dependent decay to be substituted for the T_2 dependent decay in the equivalent spin echo sequence. This is of particular value where the T_1 and T_2 decays of the tissues differ and explains why the gray–white matter contrast of this sequence is greater than that of the equivalent spin echo sequence.

It is also possible to choose particular values of *TI* so that the signal intensity of a particular tissue is zero at the time of the 90° pulse. (This occurs at a value of *TI* typically between 0.56 and 0.69 T_1 for $TR > 3T_1$.) Values of about 100 ms are suitable to eliminate the fat signal, while 255 ms is adequate for white matter (Figure 6). In this situation the tissue signal is said to be 'suppressed'. Suppression or partial suppression of

Figure 8 Bilateral avascular necrosis of the hips: coronal IR2500/30/140 scan (at 1 T). The pathological regions in the heads of both femurs and the adjacent acetabulum and muscle on the left are highlighted (arrows)

the fat signal is of particular value in imaging of the orbit, body (Figure 7) and musculoskeletal system (Figure 8), and this is the most common use of the STIR sequence.

5 LONG *TI* OR FLUID ATTENUATED INVERSION–RECOVERY (FLAIR) SEQUENCE

If the *TI* is increased to 2000–2500 ms, then the signal from CSF can be reduced to zero while the magnetization from brain very largely recovers (Figure 9). With the signal from CSF very greatly reduced, it is then possible to use the echo times of 120–200 ms and develop very heavily T_2-weighted contrast without problems from CSF artifacts.

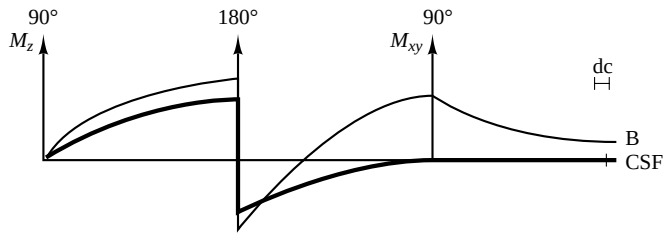

Figure 9 M_z followed by M_{xy} for brain (B) and CSF during the FLAIR sequence. Following the first 90° pulse, the brain recovers more quickly than the CSF. After the 180° pulse brain largely recovers, but CSF with its long T_1 only reaches zero magnetization when the second 90° pulse is applied. Brain then decays with time constant T_2 while the CSF signal remains zero

The resultant FLAIR sequence has been used to image the brain in multiple sclerosis (Figure 10), hippocampal sclerosis (Figure 11), and many other conditions.

It is particularly useful in regions of the brain where partial volume effects from CSF cause difficulty. Its reduced gray–white contrast (as a result of incomplete recovery of the brain magnetization) provides a bland background against which lesions are readily seen. The same principles apply to the spinal cord, where lesions with a long T_2 are readily seen (Figure 12).

6 OTHER FORMS OF THE IR SEQUENCE

The DAIR sequence combines features of the FLAIR and STIR sequences (Figure 13). It can be used to null the signal from CSF as well as from fat, white matter, or gray matter (Figure 14).

The same principle can be applied to null the signal from bile (very long T_1) and fat in the abdomen (Figure 15).

It is also possible to apply an inversion pulse outside of the imaging plane and detect the change in magnetization within the slice as the inverted magnetization is carried into the slice by flowing blood to provide a measure of perfusion. The effect depends on the T_1 of the blood, the position of the slice, the field strength, and other factors.

7 FASTER FORMS OF THE IR SEQUENCE

The RARE sequence, in which more than one phase-encoding step is used after each excitation,[14] enables the imaging time to be reduced. It can be combined with each form of the IR sequence and can result in a substantial reduction in imaging time. Results with turbo-STIR and turbo-FLAIR sequences of this type have now been published.

The rapid gradient echo sequences can be used to acquire data in 1 or 2 seconds. When these are preceded by a 180° pulse they also provide the basic options available with the IR sequence. The term ‘magnetization preparation’ has been applied to the use of not just inversion pulses but pulsed gradients, magnetization transfer, and chemical shift sensitive pulses in this context. The magnetization prepared rapid acquisition gradient echo (MP-RAGE) sequence has proved useful with a medium *TI* in producing highly T_1-weighted volume images of the brain.[15,16]

The echo planar sequence can[17] be used similarly to exploit the range of *TI* values described above.

These forms of the IR sequence are now receiving greater emphasis and are likely to be the forms in which it is used in the future.

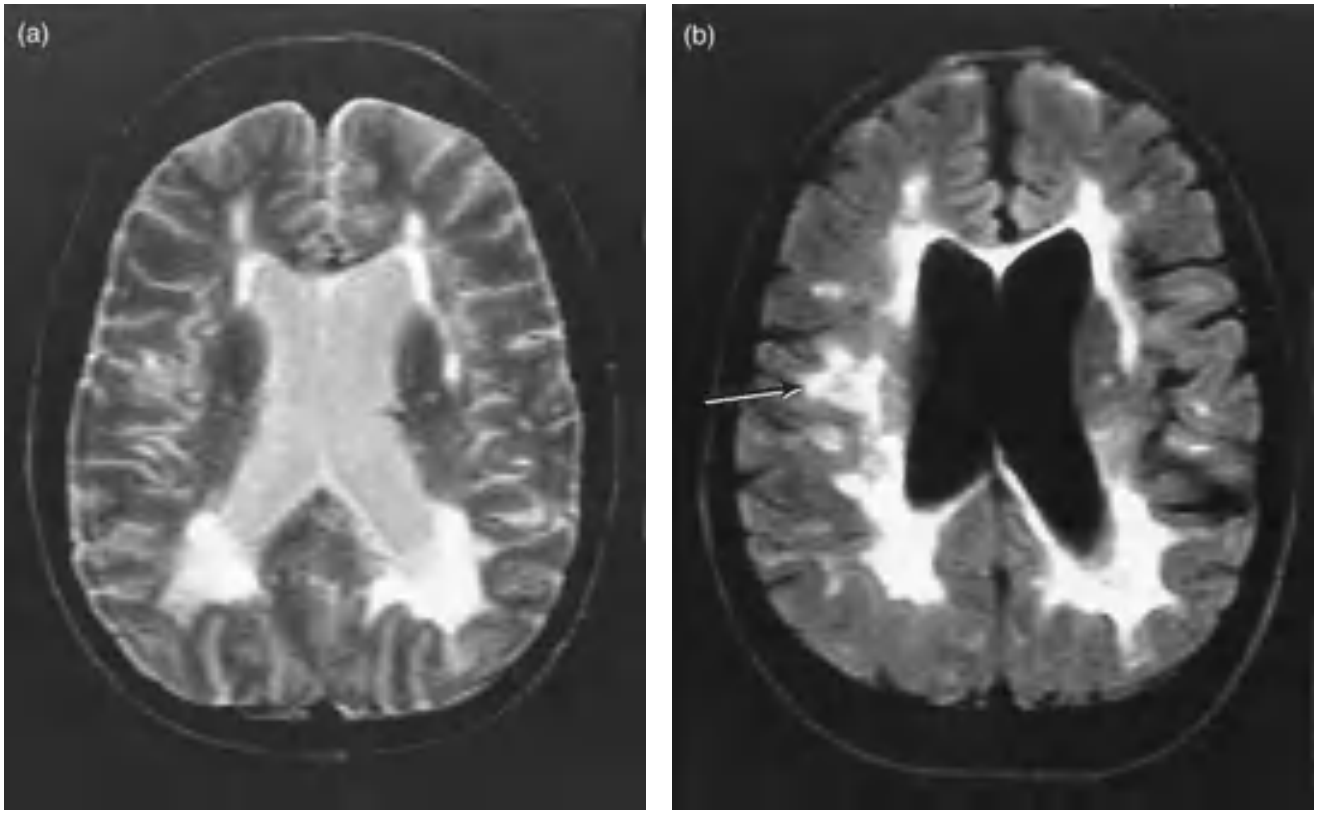

Figure 10 Multiple sclerosis: (a) transverse SE2500/80 and (b) IR6000/160/2100 scans. Many lesions are readily seen in both (a) and (b), but some lesions are only seen in (b) (arrow)

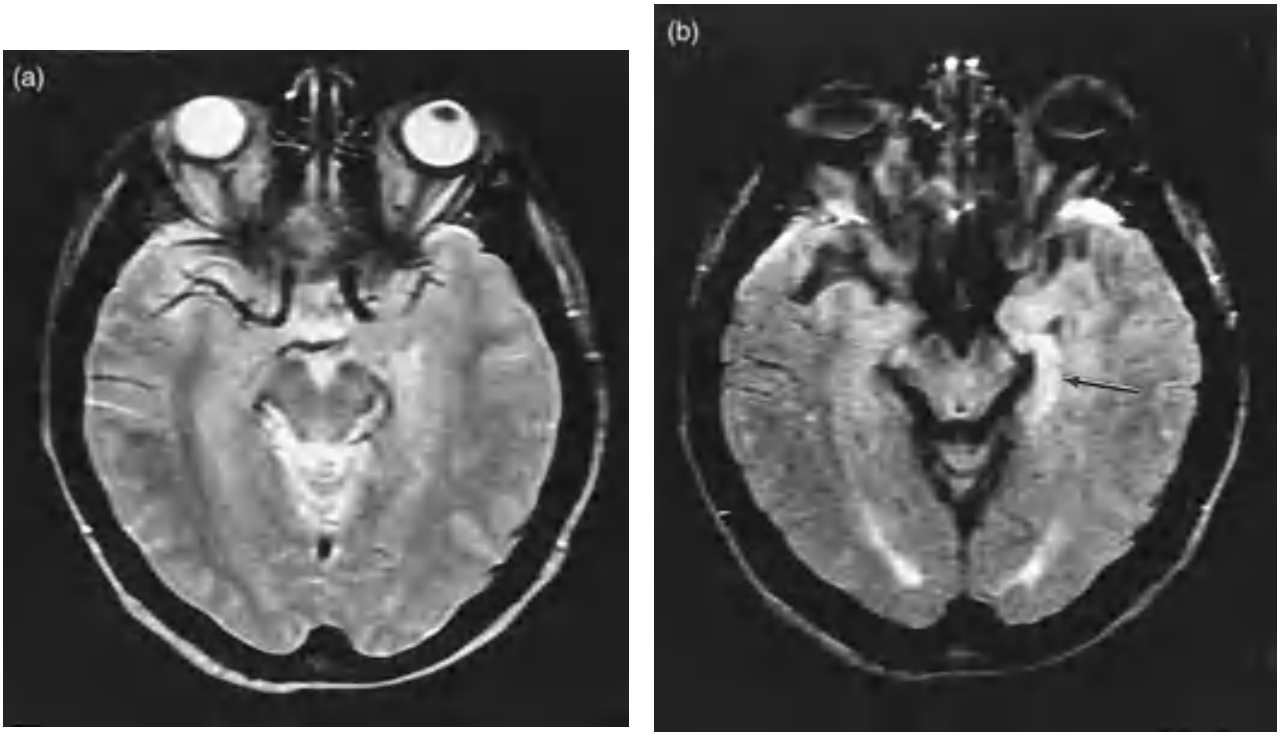

Figure 11 Hippocampal sclerosis: (a) transverse SE2500/80 and (b) IR6000/160/2100 scans. No abnormality is seen in the left hippocampus in (a) but it is highlighted in (b) (arrow)

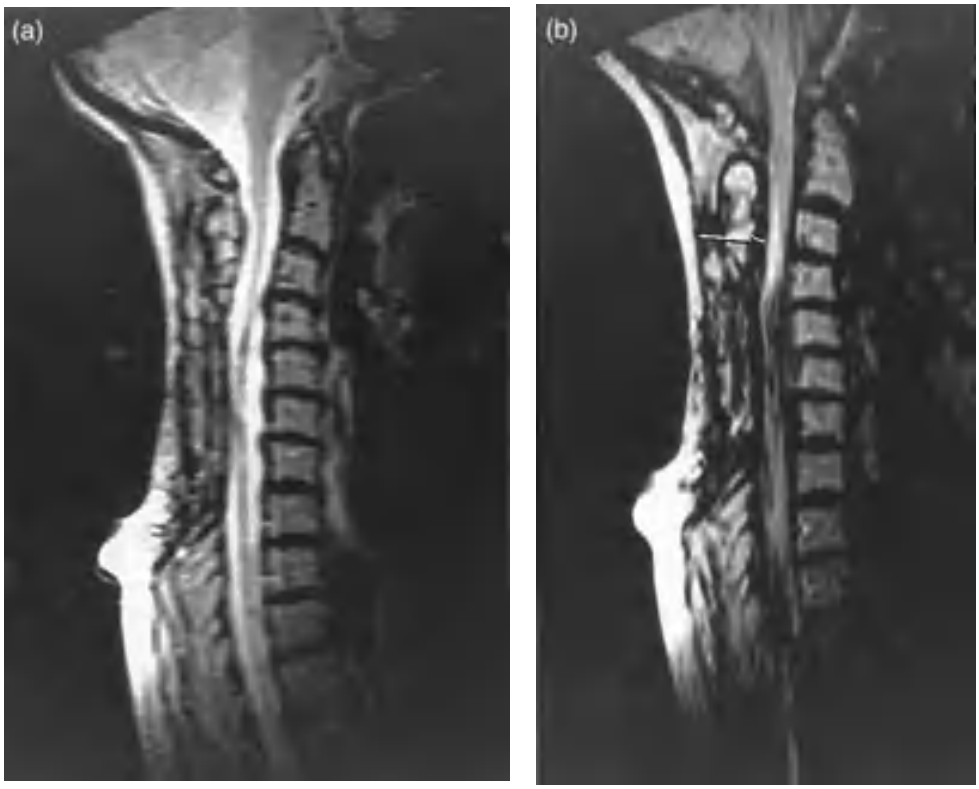

Figure 12 Ependymoma following surgery: (a) sagittal SE2500/80 and (b) IR6000/160/2100 scans. Following surgery the atrophic cord is well seen in (b). There is also a high signal area, which may be residual tumor, edema, or recurrence (arrow)

8 CONCLUSION

Different aspects of each of the given pulse sequences have been described, and simplified approaches to understanding the contrast developed by each of them have been outlined. Considerable effort has been expended in evaluating pulse sequences and adopting them for a particular purpose, but in some ways the most surprising thing has been the ease with which the results can be predicted from these simple models.

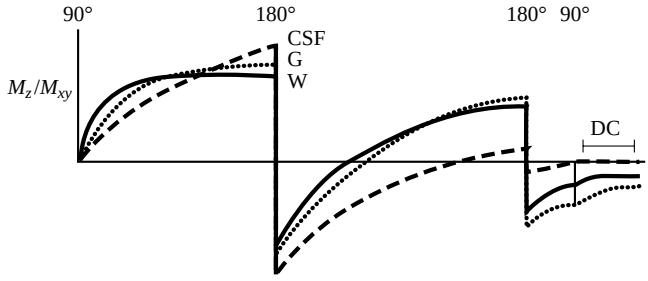

Figure 13 The DAIR sequence: M_z followed by M_{xy}. This sequence combines the FLAIR and STIR sequences. Note that after the first 180° pulse the CSF is allowed to recover beyond the null point before being inverted a second time and nulled at the time of the second 90° pulse

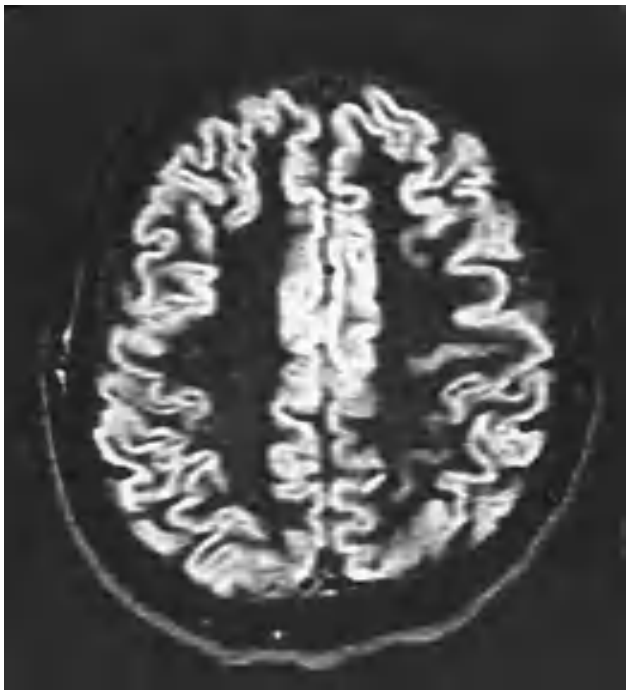

Figure 14 Transverse head scan: DAIR sequence IR3000/20/2300/245. The gray matter has been isolated and gives a high signal. The complex folding of the cortex is readily seen

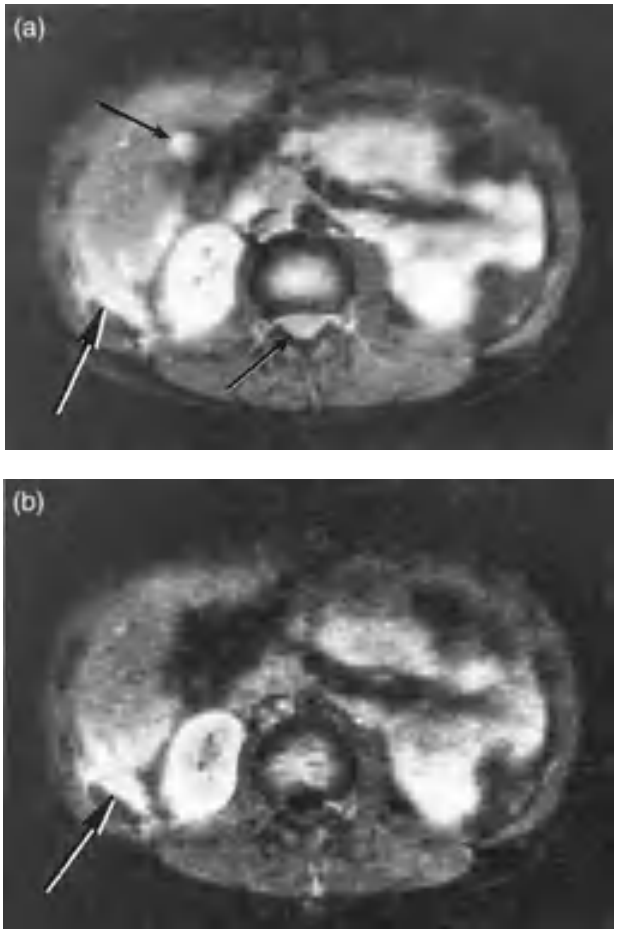

Figure 15 Liver abscess: (a) transverse IR1000/44/100 and (b) IR3000/44/1200/100 sequences. The high signal in the posterior aspect of the liver is shown with both sequences (large arrow). The gall bladder and CSF are shown in (a) (small arrows) but suppressed in (b)

9 RELATED ARTICLES

Echo-Planar Imaging; Multi Echo Acquisition Techniques Using Inverting Radiofrequency Pulses in MRI; Projection–Reconstruction in MRI; Tissue Water and Lipids: Chemical Shift Imaging and Other Methods; Whole Body Magnetic Resonance: Fast Low-Angle Acquisition Methods.

10 REFERENCES

1. F. W. Smith, J. R. Mallard, A. Reid, and J. M. S. Hutchison, *Lancet*, 1981, **i**, 963.
2. I. R. Young, A. S. Hall, C. A. Pallis, N. J. Legg, G. M. Bydder, and R. E. Steiner, *Lancet*, 1981, **ii**, 577.
3. L. E. Crooks, M. Arakawa, J. Hoenninger, J. Watts, R. McRee, L. Kaufman, P. L. Davis, A. R. Margulis, and J. De Groot, *Radiology*, 1982, **143**, 169.
4. D. R. Bailes, I. R. Young, D. J. Thomas, K. Straughan, G. M. Bydder, and R. E. Steiner, *Clin. Rad.*, 1982, **33**, 395.
5. G. M. Bydder, R. E. Steiner, I. R. Young, A. S. Hall, D. J. Thomas, J. Marshall, C. A. Pallis, and N. J. Legg, *Am. J. Roentgenol.*, 1982, **139**, 215.
6. D. H. Carr, J. Brown, G. M. Bydder, H.-J. Weinmann, U. Speck, D. J. Thomas, and I. R. Young, *Lancet*, 1984, **i**, 484.
7. M. Graif, G. M. Bydder, R. E. Steiner, H. P. Niendorf, D. G. T. Thomas, and I. R. Young, *Am. J. Neuroradiol.*, 1985, **6**, 855.
8. M. I. Levene, A. Whitelaw, V. Dubowitz, G. M. Bydder, R. E. Steiner, C. P. Randell, and I. R. Young, *Br. Med. J.*, 1982, **285**, 774.
9. M. A. Johnson, J. M. Pennock, G. M. Bydder, R. E. Steiner, D. J. Thomas, R. Hayward, D. J. Bryant, J. A. Payne, M. I. Levene, A. Whitelaw, L. M. S. Dubowitz, and V. Dubowitz, *Am. J. Roentgenol.*, 1983, **141**, 1005.
10. G. M. Bydder and I. R. Young, *J. Comput. Assist. Tomogr.*, 1985, **9**, 659.
11. B. A. Porter, A. F. Shields, and D. O. Olson, *Radiol. Clin. North. Am.*, 1986, **24**, 269.
12. B. De Coene, J. V. Hajnal, P. Gatehouse, D. B. Longmore, S. J. White, A. Oatridge, J. M. Pennock, I. R. Young, and G. M. Bydder, *Am. J. Neuroradiol.*, 1992, **13**, 1555.
13. J. A. Detre, J. S. Leigh, D. S. Williams, and A. P. Koretsky, *Magn. Reson. Med.*, 1992, **23**, 37.
14. J. Hennig, A. Nauerth, and H. Friedburg, *Magn. Reson. Med.*, 1986, **3**, 823.
15. J. P. Mugler, and J. R. Brookeman, *Magn. Reson. Med.*, 1990, **15**, 152.
16. M. Brant-Zawadski, G. D. Gilan, and W. R. Mitz, *Radiology*, 1992, **182**, 769.
17. P. Mansfield, *J. Phys. C: Solid State Phys.*, 1977, **10**, L55.

Biographical Sketch

Graeme M. Bydder. *b* 1944. M.B., Ch.B., 1969, Medicine, University of Otago, New Zealand (NZ). House surgeon and physician, NZ, 1970–71. Registrar, Otago Medical School NZ, 1972–78. Nuffield Fellow in X-ray computed tomography and research fellow, Clinical Research Centre, Northwick Park Hospital, 1978–80. Research fellow and senior lecturer, 1981–89 and Professor of Diagnostic Radiology, Royal Postgraduate Medical School, Hammersmith Hospital, 1989–present. Approx. 300 publications. Research interests: clinical applications of imaging and spectroscopy.

Susceptibility Effects in Whole Body Experiments

Jerrold L. Boxerman, Robert M. Weisskoff and Bruce R. Rosen

Massachusetts General Hospital, Charlestown, MA, USA

1 INTRODUCTION

This chapter summarizes susceptibility-based NMR image contrast. Susceptibility phenomena can affect MR images on both a *macroscopic* level, which leads to typical image artifacts associated with poor shimming, metallic implants, and susceptibility differences at air–tissue interfaces, and on a *microscopic* level, which has been exploited by dynamic imaging with and without contrast agents in order to quantify tissue hemodynamics and to measure a variety of physiological parameters. In this chapter, we will review our current understanding of the susceptibility contrast physics that underlies these artifacts and applications.

2 THE FUNDAMENTALS OF MAGNETIC SUSCEPTIBILITY

The response of the internal magnetization of a material to an applied external magnetic field is referred to as its *magnetic susceptibility*. Both orbital and spin angular momentum of electrons generate a magnetic field, $\boldsymbol{B}$. Because magnetic moment is inversely proportional to mass, the nucleus contributes much less to the magnetic properties of the atom than do the electrons, despite having both charge and spin angular momentum. Therefore, whereas nuclear magnetization is responsible for MR signal, electron magnetization determines the bulk magnetic properties of tissue.

2.1 Diamagnetism

Diamagnetic materials include most organic and many inorganic compounds containing low molecular weight elements (C, H) with paired electrons. These materials reduce the magnitude of the external field by induction of an opposing Lenz field. No magnetic field arises from the spin angular momentum of electrons paired according to the Pauli exclusion principle. Paired electrons do have orbital angular momentum, however, and according to Lenz's law, will diminish $\boldsymbol{B}$ at the center of the orbital by generating a magnetic field that opposes the external magnetic field. Because magnetic moments arising from electron orbital motion are much smaller than those resulting from electron spin, these diamagnetic effects are dominant only in the absence of unpaired electrons which would otherwise overwhelm the effect. Diamagnetism accounts for air–tissue artifacts in the brain and lungs (since the susceptibility of air is near zero), and diamagnetic materials primarily affect MR signals by displacing normal contents such as water, fat, perfluorocarbons, or CO_2 in the bowel.

2.2 Paramagnetism

Within transition metal ions, like ferrous and ferric oxidation states of iron, gadolinium, and dysprosium, some orbital electrons are unpaired and therefore possess both net spin and orbital angular momentum. When randomly oriented, zero total magnetic field is generated. However, much like the weaker nuclear magnetic dipoles, electron magnetic dipoles respond to an external magnetic field by aligning parallel or antiparallel to the applied field thus producing a net magnetization. Because more dipoles align parallel to the field, the ambient field is enhanced, and this effect dominates the weaker diamagnetic properties when there are sufficient unpaired spins. Materials that enhance the magnitude of the external field in this manner are said to be *paramagnetic*.

For both dia- and paramagnetic materials, the induced magnetic field is proportional to the strength of the applied magnetic field, $\boldsymbol{B}_0$:

$$\boldsymbol{M} = \chi \boldsymbol{B}_0 \tag{1}$$

where $\boldsymbol{M}$ is the induced magnetization. The constant of proportionality, χ, is positive for paramagnetic materials and negative for diamagnetic materials.

2.3 Superparamagnetism and Ferromagnetism

In *superparamagnetic* materials (such as the contrast agent AMI-227, Advanced Magnetics Inc., Cambridge, MA), whole domains of unpaired spins act together as if they were one large paramagnetic, single domain particle that can reorient its net dipole in an applied field in a time frame that is short compared with the observation time (see ***Contrast Agents in MRI: Superparamagnetic Iron Oxide***). In response to an applied field, each domain aligns parallel or antiparallel to the field, analogous to paramagnetic materials, but the resultant magnetic moment for the domain of interacting unpaired electrons is much greater than that for the paramagnetic case. As with normal paramagnetic materials, the induced fields for superparamagnetic materials increase linearly with applied field strength at low fields, but saturate at high fields and return to zero without hysteresis upon removal of the applied field.

Ferromagnetic materials have unpaired electrons aligned in Weiss domains, each with a net magnetic field. The magnetic dipoles of the unpaired electrons of adjacent atoms interact to form magnetically stable configurations, and these adjacent domains interact via their fields to minimize the applied external field. Each domain responds to both the applied and the neighboring domain fields. Orientation of the magnetic dipoles of each domain is along a crystal axis, and the sum of the dipoles for all domains is nonzero. The material therefore has a net dipole even in the absence of an applied field, which renders these materials suitable for use in magnetic recording devices. However, ferromagnetic materials rarely have a useful purpose in MRI, though they can be a source of hazard and artifact.

2.4 Magnetic Susceptibility and MR Images

Depending on the properties of the material, $\boldsymbol{M}$, induced by $\boldsymbol{B}_0$, will yield an effective magnetic field $\boldsymbol{B}_{\text{eff}}$, with an order of magnitude χB_0, that is either greater than (paramagnetic, ferromagnetic; $\chi > 0$) or less than (diamagnetic; $\chi < 0$) the applied field. The actual magnetic field will depend strongly upon the geometry of the magnetic material. Nuclear spins precess about the axis of the applied $\boldsymbol{B}_0$ with an angular frequency ω_0, defined by the Larmor equation:

$$\omega_0 = \gamma B_0 \tag{2}$$

where γ is the gyromagnetic ratio. An applied field will therefore induce a perturbing field in susceptible materials, which in turn will cause protons to precess at angular frequencies other than ω_0. This can have profound macroscopic and microscopic effects on MR images.

3 MACROSCOPIC EFFECTS: FREQUENCY AND PHASE SHIFT

Similar to the effects of chemical shift and main magnetic field inhomogeneity, magnetic susceptibility geometrically distorts the MR image and perturbs image intensities. It is instructive to illustrate this from a theoretical perspective[1,2] by considering a typical two-dimensional Fourier transform imaging experiment, with the main magnetic field and slice selection oriented along z, frequency encode along x, and phase encode along y.

3.1 Geometrical Distortion in the Image Plane

MR signal can be expressed in a $\boldsymbol{k}$-space formalism as:

$$S(k_x, k_y) = \iint \rho(x, y) \mathrm{e}^{-\mathrm{i}(k_x x + k_y y)} \, \mathrm{d}x \, \mathrm{d}y \tag{3}$$

where $\rho(x, y)$ is the two-dimensional spin density for a selected slice, $k_x = \gamma G_x t_x$ and $k_y = \gamma G_y T_y$ are defined for frequency and phase-encoding gradients G_x and G_y, respectively, t_x is the time at which a k_x sample is obtained (defined relative to echo time TE) and T_y is the duration of the phase encode gradient. Along a row of $\boldsymbol{k}$-space in the frequency-encode direction, each sample is acquired at a distinct point in 'real' time, and k_x is varied by sampling the signal for each phase-encode step at incremental times t_x. Along a column of $\boldsymbol{k}$-space in the phase-encode direction, 'pseudo' time evolves as a function of $G_y T_y$, the product of gradient amplitude and duration. k_y is typically varied by incrementing G_y at each phase-encoding step for a fixed T_y.

The manifestation of susceptibility differences in MR images is apparent when considering how magnetic field inhomogeneities propagate through the imaging equation. The phase that has evolved by each sample in the k_x direction has both a component due to the frequency-encode gradient G_x, and a component due to magnetic field inhomogeneities:

$$\phi = \omega t = k_x x + \gamma \Delta B (TE + t_x) \tag{4}$$

where $\Delta B(x, y)$ is the total field inhomogeneity at spatial location (x, y) and has contributions from static field (ΔB_0), chemical shift-dependent (ΔB_c) and susceptibility-dependent (ΔB_s) inhomogeneities:

$$\Delta B(x, y) = \Delta B_0(x, y) + \Delta B_\mathrm{c}(x, y) + \Delta B_\mathrm{s}(x, y) \tag{5}$$

The contribution to ϕ from ΔB evolves from the $\pi/2$ pulse to the sample acquisition for a total time of $TE + t_x$, and is therefore a function of t_x. The phase that has evolved by each sample in the k_y direction is also a function of the magnetic field inhomogeneities (included in the $\gamma \Delta B \; TE$ term above). But because each line of $\boldsymbol{k}$-space represents a distinct acquisition, phase errors do not accumulate through multiple phase-encode steps, and hence the ϕ that evolves due to ΔB is not a function of 'pseudo' time.

The expression for NMR signal $S(k_x, k_y)$ in the presence of ΔB is therefore given by:

$$\begin{aligned} S(k_x, k_y) &= \iint \rho(x, y) \mathrm{e}^{-\mathrm{i}(k_x x + \gamma \Delta B(x,y)(TE + t_x) + k_y y)} \, \mathrm{d}x \, \mathrm{d}y \\ &= \iint \rho(x, y) \mathrm{e}^{-\mathrm{i}\gamma \Delta(x,y) TE} \\ &\quad \times \mathrm{e}^{-\mathrm{i}\{k_x [x + \Delta B(x,y)/G_x] + k_y y\}} \, \mathrm{d}x \, \mathrm{d}y \end{aligned} \tag{6}$$

Field inhomogeneity effects are therefore primarily reflected along the frequency-encode direction and spatially transform x to $x + \Delta B(x, y)/G_x$. Consequently, a pixel at position (x, y) will be displayed after Fourier reconstruction at a new position (x', y), where

$$x' = x + \frac{\Delta B(x, y)}{G_x} = x + \Delta x \tag{7}$$

Spatial displacement is reduced with stronger frequency-encode gradients (larger bandwidth); however larger gradients decrease S/N and increase aliasing artifacts. Techniques using the phase difference between two scans have been described that correct for susceptibility-based geometrical distortions.[3]

In gradient echo (GE) acquisitions, the $\mathrm{e}^{-\mathrm{i}\gamma \Delta B(x,y) TE}$ term results in a phase shift throughout the image that reflects the field inhomogeneities and can actually be used to map field inhomogeneities[4,5] In spin echo (SE) acquisitions, this term vanishes, since the π pulse corrects for static inhomogeneities. In echo planar imaging[6] (see ***Echo-Planar Imaging***), phase errors accumulate in the phase-encode direction because of the continuous readout, and in fact are much more significant than phase errors in the frequency-encode direction because the total acquisition time (~50 ms) is much greater than the read period for any individual line of $\boldsymbol{k}$-space (~0.5 ms). Phase-encode distortion is thus far more significant than frequency-encode distortion on echo planar imaging.

3.2 Intensity Distortion

If $\Delta B(x, y)$ varies with x, then the signal intensity for the shifted pixel will be attenuated. This is appreciated by considering that a constant amount of signal, originally contained in a pixel with area xy, is now being spread over a transformed pixel with new area $x'y$. The areas are related by:

$$dx'\,dy = |J|\,dx\,dy \tag{8}$$

where J is the Jacobian of the transformation:

$$|J| = \begin{vmatrix} \partial x'/\partial x & \partial x'/\partial y \\ \partial y/\partial x' & \partial y/\partial y \end{vmatrix} = 1 + \frac{1}{G_x}\frac{\partial \Delta B(x,y)}{\partial x} \tag{9}$$

Therefore, the reconstructed spin density ρ' will be related to the original spin density by:

$$\rho'(x',y) = \frac{\rho(x,y)}{1 + \dfrac{1}{G_x}\dfrac{\partial \Delta B(x,y)}{\partial x}} \tag{10}$$

If $\partial \Delta B(x,y)/\partial x = 0$, then a spatial shift occurs with no concomitant signal attenuation, assuming that shifted pixels do not overlap with other portions of the image.

3.3 Slice-Selection Error

In the absence of magnetic field inhomogeneities, a frequency

$$2\pi f = \gamma(B_0 + zG_z) \tag{11}$$

is used with an rf excitation to select a slice centered at position z, where G_z is the slice-select gradient. The slice actually selected in the presence of magnetic field inhomogeneities $\Delta B(x,y,z)$ is defined by

$$z'(x,y,z) = z + \frac{\Delta B(x,y,z)}{G_z} = z + \Delta z \tag{12}$$

For a slice-selection rf bandwidth of 1.25 kHz and G_z = 1 G cm^{-1}, a slice thickness of 3 mm is obtained at 1.5 T. Therefore, magnetic field inhomogeneities on the order of 20 ppm yield a slice-select displacement equivalent to one slice thickness.

3.4 Clinical Examples

Figure 1 demonstrates the geometrical and intensity distortion associated with fast SE (*TR* = 4000 ms, *TE* = 16 ms) metal artifact in the right parietoccipital cortex from prior surgery. Note the geometry artifact predominant in the frequency-encode direction, and the bright rim due to pixel displacement and overlap.

Figure 2 demonstrates the (a) GE and (b) SE (*TR* = 2000 ms, *TE* = 120 ms) artifacts due to a ferromagnetic surgical clip at 0.6 T. The artifact on the GE image is far more severe.

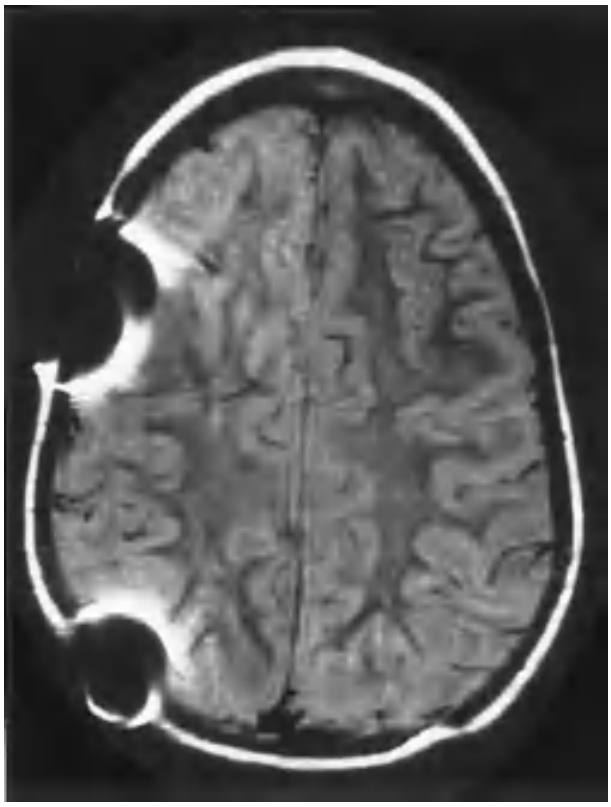

Figure 1 Geometrical and intensity distortion associated with fast spin echo (*TR* = 4000 ms, *TE* = 16 ms) metal artifact in the right parietoccipital cortex from prior surgery. Note the geometry artifact predominant in the frequency-encode direction, and the bright rim due to pixel displacement and overlap

4 MICROSCOPIC EFFECTS: LINE BROADENING

Heterogenous distributions of magnetic susceptibility *within* a voxel will cause microscopic perturbations of local proton resonance frequencies by modifying the magnetic field sensed by local spins and can profoundly affect MR signal in three ways:

1. The magnetic field variations can displace intravoxel resonance frequency, resulting in phase shifts for phase-sensitive acquisitions (phase mapping or 'zebra' techniques[7]).
2. Intravoxel resonance linewidth can be increased by virtue of the diversity of magnetic fields, which decreases MR signal from pulse sequences that do not completely correct for static inhomogeneities (GE and asymmetric SE acquisitions).
3. Diffusion of spins through magnetic field variations introduces nonstatic inhomogeneities and leads to MR signal loss, even for pulse sequences that completely correct for static inhomogeneities (SE acquisitions).

These mechanisms are responsible for the MR signal loss associated with intravascular (IV) paramagnetic chelates (such as Gd-DTPA and Dy-DTPA) that alter dynamically the magnetic susceptibility of tissue during passage through the compartmentalized intravascular space (i.e. in the brain), and for many of the signal changes associated with the extravasation of blood in hemorrhage[8] (see ***Hemorrhage in the Brain and Neck Observed by MRI***) and with iron sequestering diseases. Compartmentalization of agent in these cases induces long range magnetic field perturbations that act at a distance of many micrometers to shorten transiently the T_2 and T_2* of tissue protons. These perturbations occur in addition to short-range, T_1 enhancement by agents such as Gd-DTPA that occurs when protons diffuse within the coordination sphere of the molecule (see ***Contrast Agents in Magnetic Resonance: Operating Mechanisms***).

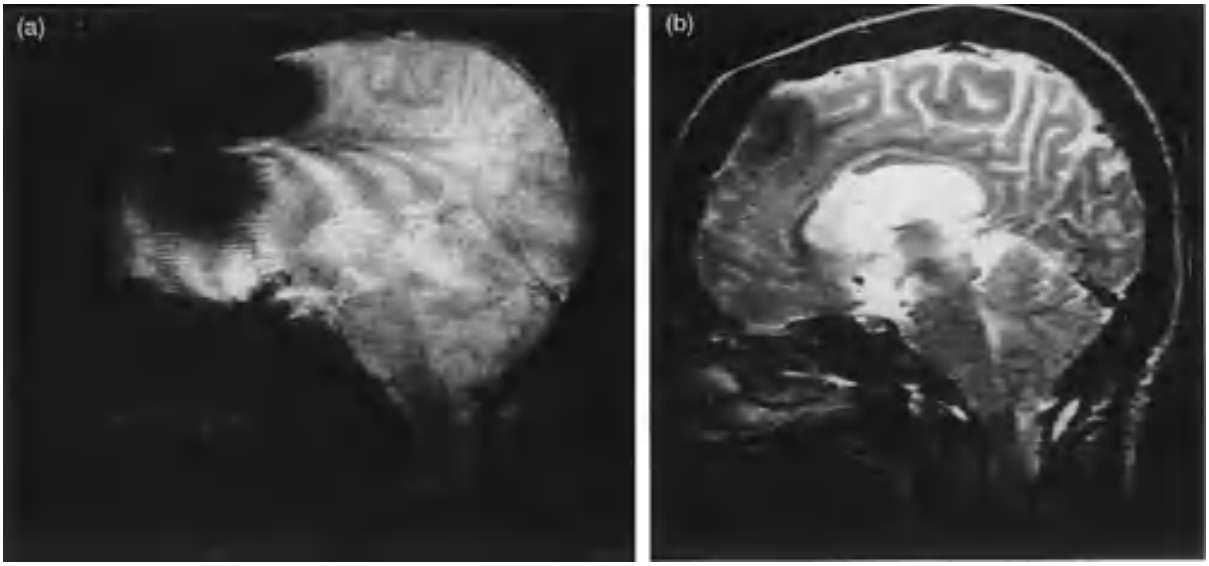

Figure 2 (a) GE and (b) SE (*TR* = 2000 ms, *TE* = 120 ms) artifacts due to a ferromagnetic surgical clip at 0.6 T. The artifact on the GE image is far more severe

4.1 Susceptibility Contrast Signal Loss

Protons lose transverse coherence as they diffuse through the inhomogeneous magnetic field established by compartmentalized contrast agent, and the transverse relaxation time of the diffusing spins is shortened:

$$\Delta R_2 = \frac{1}{T_{2\text{post}}} - \frac{1}{T_{2\text{pre}}} \approx -\frac{\ln(\text{SA})}{TE} \tag{13}$$

SA is the signal attenuation due to phase dispersion and can be expressed as an expectation of proton phases:

$$\text{SA}(t) = \langle e^{i\phi(t)} \rangle = \frac{1}{V}\int_V d\bar{x} \int d\phi \cdot P(\phi, t; \bar{x}) e^{i\phi(t)} \tag{14}$$

taken over all paths through the medium for each initial proton position, where $P(\phi, t; \boldsymbol{x})$ is the probability that a proton starting at position $\boldsymbol{x}$ acquires phase ϕ by time t. SA(t) depends upon the size of the confining vessels (r), the vascular volume fraction (f_v), the susceptibility difference between agent and surrounding tissue ($\Delta\chi$), and specific pulse sequence parameters. This complex relationship is often inaccessible with analytic techniques and has best been elucidated with numerical methods, such as Monte Carlo techniques that estimate SA(t) by accumulating the phase from the stochastic walk of many protons through a simulated environment that generates the appropriately distributed set of phases, $P(\phi, t; \boldsymbol{x})$, in equation (14).[9–11]

Despite small vascular volume fractions (<5% in cerebral cortex), substantial signal attenuation (up to 50%) reflecting extravascular susceptibility changes are typically realized due to the intravascular compartmentalization of the agent. A clinical example is provided in Figure 3, which depicts the dynamic cerebral passage of a paramagnetic contrast material

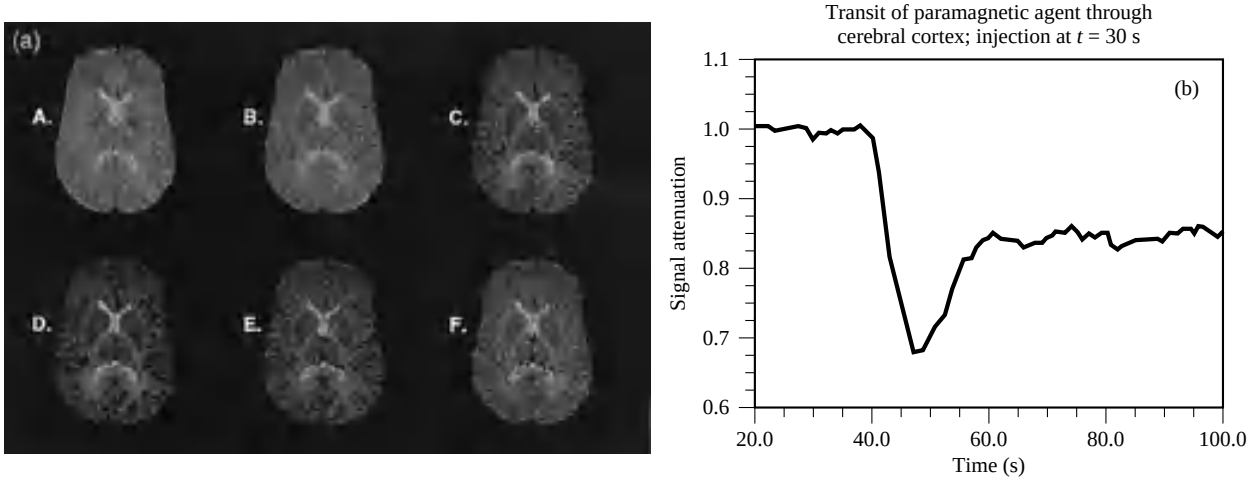

Figure 3 Dynamic cerebral passage of a paramagnetic contrast material with high magnetic susceptibility. (a) Six SE echo planar images (*TR* = 1 s, *TE* = 100 ms) from the series (11, 14, 17, 20, 25 and 31 s postinjection) reflect the parenchymal signal attenuation during transit of agent. (b) Complete time course from a cortical region of interest. (Courtesy of A. Gregory Sorensen, and Sarah F. Kulke)

with high magnetic susceptibility. Six SE echo planar images (TR = 1 s, TE = 100 ms) from the series (11, 14, 17, 20, 25 and 31 s post-injection) are shown in Figure 3(a), and reflect the parenchymal signal attenuation during transit of agent. Figure 3(b) shows the complete time course from a cortical region of interest.

4.2 Applications

Dynamic first-pass contrast agent studies using Gd-DTPA[12] and Dy-DTPA have produced relative cerebral blood volume (CBV) maps. From tracer kinetic theory,[13] the area under the tissue concentration–time curve for a purely intravascular tracer is proportional to local blood volume. In the presence of an intact blood–brain barrier, Gd-DTPA and Dy-DTPA remain intravascular during cerebral passage, and the associated relaxivity–time curve for each pixel can be numerically integrated to yield a map proportional to CBV.[14] Such maps have been used for understanding fundamental questions of neuroscience, assessing cerebrovascular accident, and also for improving diagnostic sensitivity and specificity in various neuropathologies, as they appear closely correlated to tumor grade, match PET ^{18}FDG maps in a majority of cases studied, and may differentiate recurrent tumor from radiation necrosis.[12,15] Exogenous susceptibility-contrast studies have also been proven to be sensitive to local changes in CBV concomitant with increased neuronal activity, and have been used to map the visual cortex.[16] Endogenous susceptibility contrast, sensitive to neuronal activity-induced changes in both CBV and hemoglobin oxygenation, is currently being used at several sites to map changes in cerebral neuronal activity associated with task activation.[17–21]

Measurement of hemodynamic parameters with dynamic susceptibility-contrast MRI[22] necessitates understanding the mechanisms of susceptibility-induced contrast, and knowledge of the relationships between relaxivity change and compartment size, agent concentration, and vascular volume fraction.

4.3 Size Dependence

Phantom studies with polystyrene microspheres suspended in contrast agent have demonstrated convergence between Monte Carlo models and experiment for spherical magnetic field perturbers.[9] Figure 4 plots ΔR_2 versus sphere size with 3.2 and 9.6 mM Dy-DTPA for both empirical (solid symbols) and Monte Carlo (open symbols) measurements. These results demonstrate the strong compartment size dependence for SE images.

Cylindrical Monte Carlo models more accurately represent contrast agent within the vasculature[11] and have elucidated features of in vivo contrast. Figure 5 depicts the GE (TE = 60 ms) and SE (TE = 100 ms) vessel size-dependence of relaxivity change for f_v = 2% and $\Delta\chi = 1 \times 10^{-7}$ (cgs units; equivalent to $\approx$3.6 mM Gd-DTPA,[23] a typical first-pass concentration for a 0.1 mmol kg^{-1} injection). Whereas SE relaxivity peaks for microvessels, GE relaxivity exceeds SE relaxivity at all radii and reaches a plateau for macrovessels.

This selective sensitivity to microvessels for SE contrast comes from the balance between two competing effects. For large enough compartments, protons diffuse a short distance compared with the compartment radius and can be considered

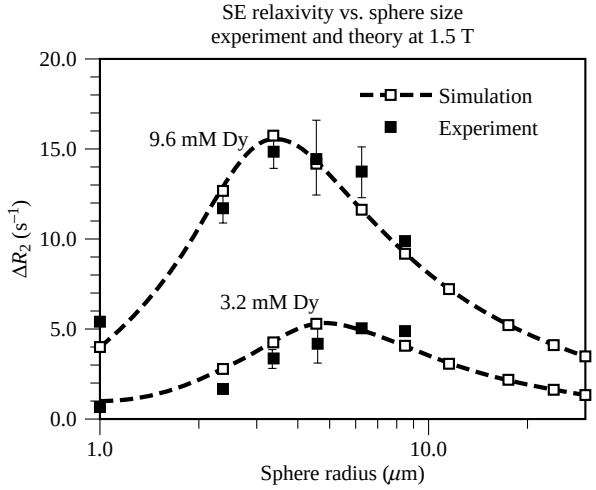

Figure 4 Size dependence of susceptibility-induced relaxation for two values of $\Delta\chi$. For both concentrations, SE relaxivity peaks between R = 2 and 5 μm. To the left of this peak, motional averaging reduces ΔR_2; to the right of this peak, the size of the gradient decreases with increasing particle size. Increasing concentration (increasing $\Delta\chi$) shifts the curves up and to the left. By tripling the concentration, we approximately triple the peak relaxation, and shift the curve over by approximately $\sqrt{3}$ in radius. The filled symbols are experimental data points, the open symbols are Monte Carlo data points. The error bars for the Monte Carlo simulations are smaller than the plot symbols. (Experimental data courtesy of Chun S. Zuo)

to diffuse in a constant, though spatially varying, gradient that is inversely proportional to the compartment size. Because relaxation is a function of the square of the gradient, relaxivity diminishes dramatically with increasing compartment size. For small compartments, each proton accumulates little phase as it diffuses by a compartment, since phase accumulation is proportional to the time required to diffuse past a perturber, τ ~

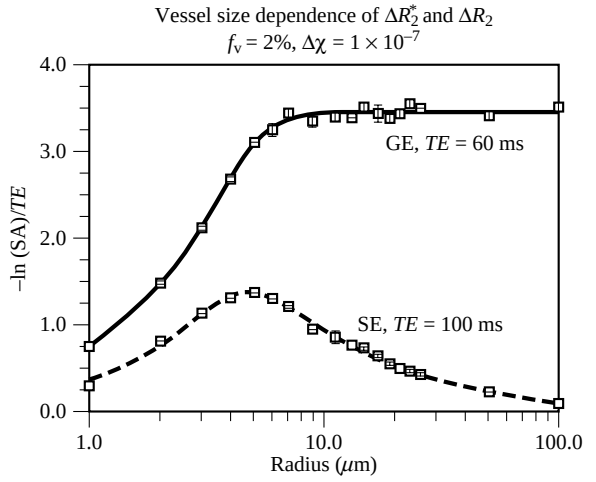

Figure 5 Size dependence of GE (TE = 60 ms) and SE (TE = 100 ms) relaxivity change for f_v = 2% and $\Delta\chi = 1 \times 10^{-7}$. At this $\Delta\chi$, SE relaxivity peaks for microvessels. GE relaxivity exceeds SE relaxivity at all radii, reaches a plateau for macrovessels, and is actually greater for macrovessels than for microvessels

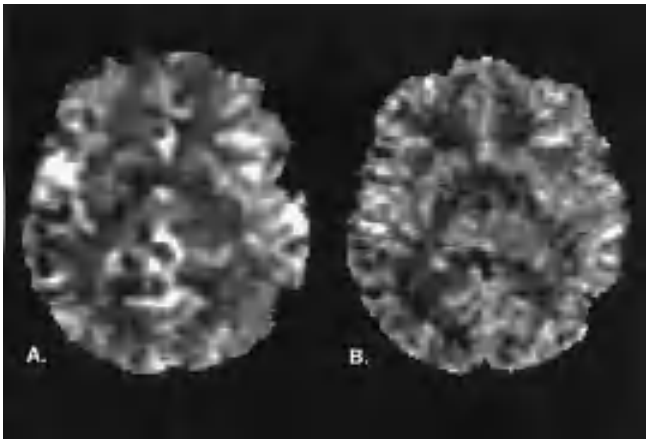

Figure 6 Relative CBV maps obtained with dynamic susceptibility-contrast bolus tracking. (A) GE acquisition, with TE = 60 ms, TR = 1500 ms, and dose = 0.1 mmol kg^{-1}. (B) SE acquisition, with TE = 100 ms, TR = 1500 ms, and dose = 0.2 mmol kg^{-1}. The TE and dose were chosen to produce approximately equal signal drops. The GE map is dominated by large vascular structures: note the macrovascular prevalence along the convexity and falx. By comparison, the SE map exhibits superior gray–white tissue discrimination and definition of central structures due in part to superior tissue-level microvascular sensitivity. (Images acquired by Hannu Aronen)

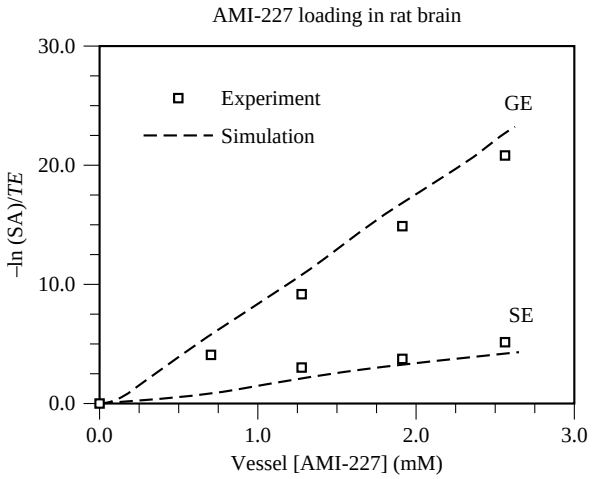

Figure 7 Comparison of GE and SE (TE = 20 ms) Monte Carlo (f_v = 1.5% composed of 0.75% r = 3 μm vessels and 0.75% r = 25 μm vessels) and experimental (f_v = 1.54 ± 0.78%, n = 5 rats) relaxivity change for one rat as a function of vascular concentration of AMI-227 at 4.7 T. (Experimental data courtesy of Leena M. Hamberg)

r^2/D. The diffusion of each proton averages the effect of many perturbers, effectively narrowing the broad distribution of frequencies and reducing relaxivity.

Spin echo acquisitions are therefore selectively sensitive to microvascular contrast and are capable of reflecting true tissue level blood volume, whereas GE acquisitions reflect total vascular blood volume because all vessels contribute approximately equally to GE contrast. However, because SE acquisitions have significantly less signal attenuation than GE acquisitions, a tradeoff exists between overall sensitivity and microvascular specificity. The ability of MR to be selectively sensitive to microvascular contrast is unique among tomographic modalities, and constitutes the appeal of MR for assessing true blood volume at the microvascular level. Radionuclide contrast, by comparison, is directly proportional to the amount of tracer in vessels of all sizes, and can therefore only reflect total blood volume.

The clinical implications of the size-dependence relationships are exemplified in Figure 6, which depicts a GE [Figure 6(A); TE = 60 ms, dose = 0.1 mmol kg^{-1}] and an SE [Figure 6(B); TE = 100 ms, dose = 0.2 mmol kg^{-1}] relative CBV map from dynamic bolus tracking of Gd-DTPA with TR = 1500 ms. The TE and dose were chosen to produce approximately equal peak signal drops. The GE map is dominated by large vascular structures, including macrovascular prevalence along the convexity and falx. By comparison, the SE map exhibits superior gray–white tissue discrimination and definition of central structures due to superior tissue level microvascular sensitivity.

4.4 Concentration Dependence

The concentration dependence of relaxivity change has been determined through simulation and experiment to be generally linear for typical first-pass concentrations of contrast agent. Figure 7 demonstrates relatively linear behavior between cumulative doses of AMI-227 [with a long intravascular halflife and a measured $\Delta\chi$ in blood of 3.4 $\times$ 10^{-7} mM^{-1} (cgs) at 1.5 T[22]] and measured GE and SE relaxation in Wistar rat brain at 4.7 T. Contrast agent concentration in the blood was determined by assuming total retention of contrast agent during the experiment and complete, uniform mixing of agent in a total blood volume of 6 mL per 100 g of total body weight.[24] Also shown in Figure 7 is the Monte Carlo concentration dependence for f_v = 1.5% (the average whole-brain CBV for n = 5 rats determined by a radiolabeled albumin technique) equally distributed between capillaries (R = 3 μm) and venules (R = 25 μm). The model also predicts a linear concentration dependence and agrees well with experiment for this volume fraction.

4.5 Volume Fraction Dependence

The application of tracer kinetic theory to relaxivity–time data requires that relaxivity be proportional to f_v.[25] This dependence is difficult to assess in vivo, but can be predicted with numerical techniques. In Figure 8, the Monte Carlo model was used to plot the ratio of GE [Figure 8(a); TE = 60 ms] and SE [Figure 8(b); TE = 100 ms] relaxivity change for f_v = 2–6% to that for f_v = 1% at $\Delta\chi$ = 1 $\times$ 10^{-7}. The results demonstrate that for all vessel sizes, relaxivity scales proportionally with volume fraction. A linear relationship over a physiologically relevant range of vascular volume fraction is therefore predicted for a vasculature composed of any combination of vessel sizes.

5 SUMMARY

This article summarizes the susceptibility-contrast physics that underlies the artifacts and applications of susceptibility-based NMR image contrast. Macroscopic susceptibility effects create artifacts associated with poor shimming, metallic implants, and susceptibility differences at air–tissue interfaces.

Microscopic effects can be exploited by dynamic imaging with and without contrast agents to impact profoundly the quantification of important physiological parameters like blood flow, volume, and oxygenation under a wide range of physiologic and pathophysiologic conditions.

6 RELATED ARTICLES

Assessment of Regional Blood Flow and Volume by Kinetic Analysis of Contrast-Dilution Curves; Chemical Shift Imaging; Contrast Agents in Magnetic Resonance: Operating Mechanisms; Contrast Agents in MRI: Superparamagnetic Iron Oxide; Contrast Agents in Whole Body Magnetic Resonance: An Overview; Echo-Planar Imaging; Functional MRI at High Fields: Practice and Utility; Gadolinium Chelate Contrast Agents in MRI: Clinical Applications; Hemorrhage in the Brain and Neck Observed by MRI; Imaging of Trabecular Bone.

7 REFERENCES

1. K. M. Ludeke, P. Roschmann, and R. Tischler, *Magn. Reson. Imaging*, 1985 **3**, 329.
2. H. W. Park, Y. M. Ro, and Z. H. Cho, *Phys. Med. Biol.*, 1988, **33**, 339.
3. T. Sumanaweera, G. Glover, T. Binford and J. Adler, *IEEE Trans. Med. Imaging*, 1993, **12**, 251.
4. M. Prammer, J. Hasselgrove, M. Shinnar, and J. Leigh, *J. Magn. Reson.*, 1988, **77**, 40.
5. E. Schneider, and G. Glover, *Magn. Reson. Med.*, 1991, **18**, 335.
6. M. S. Cohen, and R. M. Weisskoff, *Magn. Reson. Imaging*, 1991, **9**, 1.
7. I. R. Young, G. M. Bydder, and J. A. Payne, *Magn. Reson. Med.*, 1986, **3**, 175.
8. K. Thulborn, and T. Brady, *Magn. Reson. Q*, 1989, **5**, 23.
9. R. Weisskoff, C. Zuo, J. Boxerman, and B. Rosen, *Magn. Reson. Med.*, 1994, **31**, 601.
10. R. P. Kennan, J. Zong, and J. C. Gore, *Magn. Reson. Med.*, 1994, **31**, 9.
11. J. L. Boxerman, L. M. Hamberg, B. R. Rosen, and R. M. Weisskoff, *Magn. Reson. Med.*, 1995, **34**, 555.
12. B. R. Rosen, J. W. Belliveau, H. J. Aronen, D. Kennedy, B. R. Buchbinder, A. Fischman, M. Gruber, J. Glas, R. M. Weisskoff, M. S. Cohen, F. H. Hochberg, and T. J. Brady, *Magn. Reson. Med.*, 1991, **22**, 293.
13. N. A. Lassen, and W. Perl, 'Tracer Kinetic Methods in Medical Physiology', Raven Press, New York, 1979.
14. J. L. Boxerman, B. R. Rosen, and R. M. Weisskoff, *Magn. Reson. Imaging*, 1997, **7**, 528.
15. H. J. Aronen, I. E. Gazit, D. N. Louis, B. R. Buchbinder, F. S. Pardo, R. M. Weisskoff, G. R. Harsh, G. R. Cosgrove, E. F. Halpern, F. H. Hochberg, and B. R. Rosen, *Radiology*, 1994, **191**, 41.
16. J. W. Belliveau, D. N. Kennedy, Jr., R. C. McKinstry, B. R. Buchbinder, R. M. Weisskoff, M. S. Cohen, J. M. Vevea, T. J. Brady, and B. R. Rosen, *Science*, 1991, **254**, 716.
17. K. K. Kwong, J. W. Belliveau, D. A. Chesler, I. E. Goldberg, R. M. Weisskoff, B. P. Poncelet, D. N. Kennedy, B. E. Hoppel, M. S. Cohen, R. Turner, H. Cheng, T. J. Brady, and B. R. Rosen, *Proc. Natl. Acad. Sci. U.S.A.*, 1992, **89**, 5675.
18. P. A. Bandettini, E. C. Wong, R. S. Hinks, R. S. Tikofsky, and J. S. Hyde, *Magn. Reson. Med.*, 1992, **25**, 390.
19. S. Ogawa, D. W. Tank, R. Menon, J. M. Ellermann, S.-G. Kim, H. Merkel, and K. Ugurbil, *Proc. Natl. Acad. Sci. U.S.A.*, 1992, **89**, 5951.
20. J. Frahm, H. Bruhn, K. D. Merboldt, and W. Hanicke, *J. Magn. Reson. Imaging*, 1992, **2**, 501.
21. A. M. Blamire, S. Ogawa, K. Ugurbil, D. Rothman, G. McCarthy, J. M. Ellermann, F. Hyder, Z. Rattner, and R. G. Shulman, *Proc. Natl. Acad. Sci. U.S.A.*, 1992, **89**, 11 069.
22. R. Weisskoff, J. Belliveau, K. Kwong, and B. Rosen, in 'Magnetic Resonance Angiography: Concepts and Applications', eds. E. Potchen, E. Haacke, J. Siebert, and A. Gottschalk, Mosby, St. Louis, MO, 1992, p. 473.
23. R. M. Weisskoff, and S. Kiihne, *Magn. Reson. Med.*, 1992, **24**, 375.
24. H. B. Lee, and M. D. Blaufox, *J. Nucl. Med.*, 1985, **26**, 72.
25. R. M. Weisskoff, D. A. Chesler, J. L. Boxerman, and B. R. Rosen, *Magn. Reson. Med.*, 1993, **29**, 553.

Acknowledgements

The authors wish to acknowledge the contributions of Leena M. Hamberg, A. Gregory Sorensen, Sarah F. Kulke, and Hannu Aronen, to this article.

Biographical Sketches

Jerrold L. Boxerman. *b* 1966. S.B. and S.M. (electrical engineering), 1989, Ph.D. (medical engineering), 1994, MIT, M.D., 1996, Harvard. Currently completing a residency in Diagnostic Radiology at Johns Hopkins Hospital, Baltimore, MD. Research specialties include MR susceptibility contrast in physiological systems.

Robert M. Weisskoff. *b* 1962. A.B., 1983, Harvard, Ph.D., 1988, physics, MIT. Senior physicist, Advanced NMR, Inc., 1988–90. Assistant Professor of Radiology, Harvard Medical School 1990–96, Associate Professor of Radiology 1996–present. Research specialties include ultra-high-speed imaging, functional MRI, breast MRI, effects of motion in MRI, and cardiac MRI.

Bruce R. Rosen. *b* 1955. A.B., 1977, Harvard, M.S., 1980, physics, MIT; M.D., 1982, Hahnemann; Ph.D. (Medical Physics), 1984, MIT. Clinical research fellow, Department of Radiology, Massachusetts General Hospital and Harvard Medical School, 1984–87; instructor in radiology, Harvard Medical School, 1987–88; Assistant Professor of Radiology, Harvard Medical School, 1988–91. Currently Associate Professor in Radiology, Harvard Medical School, and Director, NMR Center, Massachusetts General Hospital, USA. Research specialties include functional MRI and chemical shift imaging.

Tissue Water and Lipids: Chemical Shift Imaging and Other Methods

W. Thomas Dixon
Emory University, Atlanta, GA, USA

1 INTRODUCTION

Most signal contributing to images in vivo comes from water and from lipid methylene protons which resonate at a frequency about 3.4 ppm lower. Other spins are so much rarer they are not seen without special effort. Spectroscopic imaging sensitive to these additional, minor lines as well is discussed in ***Chemical Shift Imaging***. Because more measurements are required to determine more unknowns, imaging methods that can determine pixel intensities at the chemical shifts of many rarer resonances are slower or provide coarser spatial resolution than those dealing with only a two-line spectrum. Methods described in this article typically produce images with the same spatial resolution as standard, chemical shift blind imaging methods. Because images are made from echoes, only water and lipid lines with reasonable T_2 values contribute. Lipid droplets are readily seen but membrane lipids are not. The contribution of intracellular water to most images has been questioned.[1] This article explains why and how this basic, two-line spectrum is manipulated in imaging. The subject has been reviewed more thoroughly before.[2,3]

2 MANIPULATION TYPES AND USES

What water and lipid manipulations are desired and why? When lipids are a nuisance in images, fat suppression is needed; when lipid is to be studied, water suppression may be useful; when fat/water interfaces, displacement of water by fat or of fat by water are to be detected, an image of water signal minus lipid signal is very sensitive.

2.1 Lipid Suppressed Images

Lipids signals are often a nuisance. Because lipid is abundant, has high proton density, and repolarizes before the water in most tissues, it is the dominant source of signal in many images. A small fraction of the lipid signal in the wrong place often degrades images of less intense but medically important, watery regions. Optic nerves are surrounded by fat and provide an example of the benefit of suppressing fat. Signal increases in the spinal chord, brain, optic nerves, and retinas following injection of Gd–DTPA are a sign of pathology. Ordinarily, a barrier around blood vessels in these organs prevents Gd–DTPA and many other substances from escaping into the surrounding tissue. However, when this barrier is damaged, Gd in the tissue enhances longitudinal relaxation and therefore increases signal intensity. The patient shown in Figure 1 has autoimmune optic neuritis affecting the right side with an apparently normal left side. The increased intensity of the right optic nerve, relative to the left side or to the brain, is easily seen when fat is suppressed, but not when the nerve is surrounded by high intensity fat.

Fat signal gets out of control in several ways. The most important are probably spreading of the lipid signal in the phase-encoding direction when fat moves (heart beat, breathing, wiggling), Gibbs's ringing, and the 'chemical shift artifact'. This artifact is an offset in apparent position of lipid in the slice selection and read gradient directions caused by the water–lipid chemical shift difference. Gibbs's ringing and the chemical shift artifact obscure small structures near a large amount of fat. Cartilage in joints and the optic nerve are examples. Moving fat produces long-range phase-encoding artifacts which are a serious problem in the abdomen and thorax. These can, for example, interfere with the detection of low contrast masses in the liver. Side lobes or other slice selection problems, quadrature errors, lack of dynamic range in signal detection, instrument instability, and coil tuning variations caused by

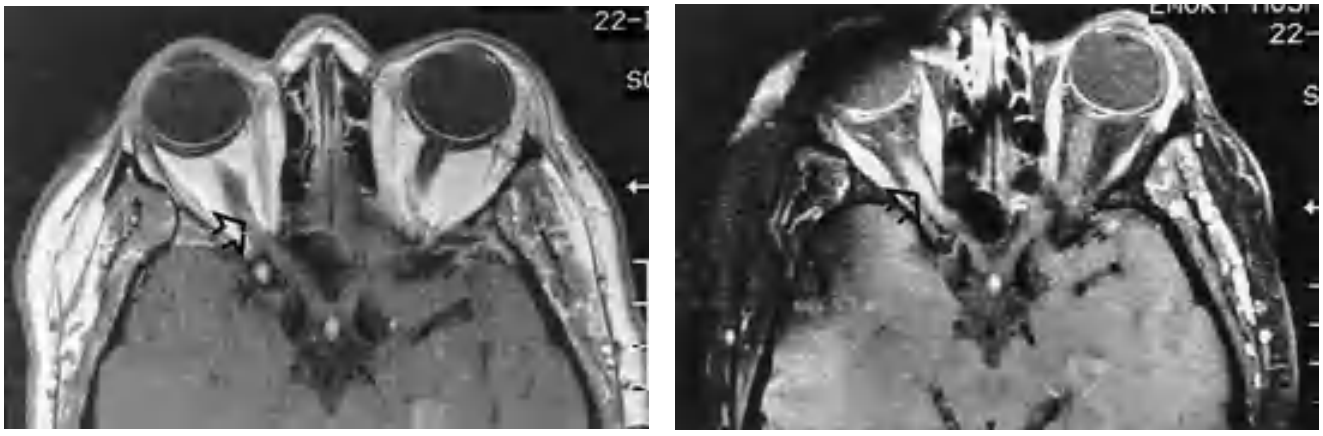

Figure 1 T_1-Weighted images of the optic nerves. The right optic nerve (arrow, left side of image), but not the left optic nerve, is enhanced in intensity by Gd–DTPA. Saturation of the surrounding fat by a selective pulse made this easier to detect in the image at right. (Courtesy of Dr. Susan B. Peterman)

breathing can also spread lipid signal to lipid-free regions of an image.

Fat suppression methods are not perfect. Generally, partial water suppression is a more serious image flaw than is incomplete or nonuniform fat suppression; however, both flaws may be serious in quantitative imaging. Examples of quantitative studies in organs which accumulate lipid are measuring the fat content of the heart[4] or the water relaxation rates of the liver.[5] Water relaxation measurements may be distorted by partial water suppression and will be by any lipid signal, whether it originates within the region of study or elsewhere.

2.2 Water Suppressed Images

Most methods suitable for fat suppression can suppress water instead, and some easily produce an image pair, one of fat, the other of water. Replacement of cancer by fat is a favorable prognostic indicator. Lipid signal from heart muscle may indicate myocardial ischemia or infarction.[4] For some nutritional studies, quantitation of adipose tissue is needed. Water suppression is useful here.

2.3 Opposed Images

Lipid images by themselves can be hard to interpret because interesting organs and landmarks for finding them are lipid-free and invisible. However, the presence of fat can be a useful source of contrast or mark the distinction between muscles or other organs. Images in which the phase of the fat signal is opposite to that of the water, 'opposed images', have the chemical shift information of a lipid image but show all anatomic structures. These images can be made on purpose, and in gradient echo imaging occur incidentally when certain echo times are chosen. Usually images are presented as absolute values. At fat/water interfaces in absolute value opposed images, a line of dark pixels occurs where the water and fat signals within the pixels cancel. A dark outline can make it easy to see a lymph node or an adrenal gland surrounded by fat of similar intensity. Of course, if the absolute value is not taken, or rather the effort is made to preserve the sign, all organs are easily distinguished from fat.

Liver can be diffusely infiltrated by fat. Opposed images are more sensitive to infiltration than water-suppressed or fat-suppressed images because they show both the increase in fat signal and decrease in water signal caused by displacement. Decreasing liver intensity this way can aid detection of metastases in liver[6] because the intensity of the metastases is not affected.

Some applications simply require any manipulation that identifies lipids. For example, in leukemia, fatty bone marrow in the spine is replaced by water but reappears after successful treatment.[7]

3 METHODS

The following outline orders some of the many published fat–water manipulation methods by principle of operation. Many pulse sequences combining different methods of operation have been demonstrated also.

Longitudinal relaxation (Section 3.1):
- Single inversion (STIR)
- Double inversion

J Coupling (Section 3.2):
- Classical multiple quantum sequences
- Multiple echo fast imaging sequences

Chemical shift (Section 3.3):
- Selective rf pulses
  - rf pulses without gradients (selective excitation; selective suppression
  - rf pulses with gradients
- Phase methods
  - Hahn and gradient–echoes
  - gradient–echoes only

3.1 T_1 Based Fat Suppression

The T_1-based, short inversion time inversion–recovery, STIR,[8] is a very simple fat suppression method. An inversion–recovery image is made with *TI* chosen to null signal from undesired fat. With a long *TR*, this is (ln 2)T_1. With proper interleaving of pulses, multislice IR imaging can be quite time efficient.

Because this method is not sensitive to shimming and is hardly sensitive to flip angle variations, it can give uniform suppression over a large region. Adipose tissue contains some water and varies regionally in composition. Temperature and relaxation rates also vary, especially in the skin; therefore, suppression is not completely uniform. Either the lipid signal or the combined lipid and water signal from adipose tissue can be nulled with the proper *TI*; the difference is slight.

Objections to STIR for fat suppression are that it partially suppresses water, by a different amount in different tissues, and it fixes *TI* so that T_1-weighting cannot be effectively adjusted. Figure 2 illustrates this for a typical STIR sequence. Assuming relaxation rates for fat and most other tissues are around 4 s^{-1} and 1 s^{-1}, respectively, this sequence gives

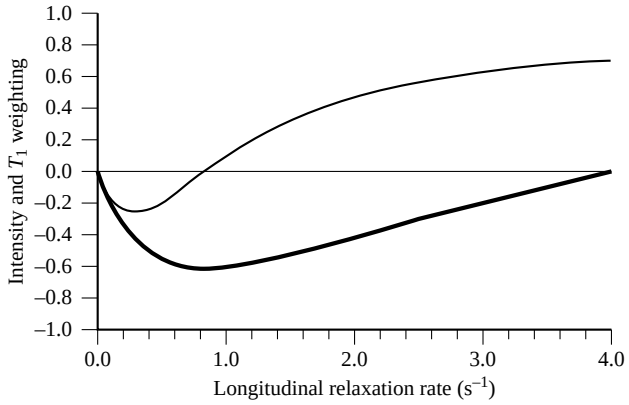

Figure 2 Intensity and T_1-weighting in STIR images. Signal intensity (bold line) and T_1-weighting (fine line) versus longitudinal relaxation rate. Weighting is defined here as 100-times the intensity change caused by a 1% rate change. Weighting and intensity are measured in units of equilibrium magnetization. (Pulse sequence *TR*/*TI*/*TE* = 2500/175/negligible ms)

essentially no T_1-weighting for most tissues and most tissue magnetizations are just over one-half their equilibrium values.

Following a second inversion pulse, tissues with two different T_1 values can recover to zero magnetization simultaneously. Two inversion times must be adjusted to align the two zero crossings. In angiograms, pictures of flowing blood, this has been done[9] to eliminate both fat and one other tissue (muscle or brain) from images.

3.2 *J* Coupling

Lipids have *J*-coupled spins while water does not. Classic multiple quantum pulse sequences have been combined with imaging to produce lipid images.[10] More recently, *J* coupling has been proposed as an important reason that fat is more intense in certain fast images than in conventional images having the same nominal *TE*. These fast images (RARE) collect several lines of *k*-space in closely spaced Hahn echoes following each excitation [***Multi Echo Acquisition Techniques Using Inverting Radiofrequency Pulses in MRI***]. *J* coupling reduces the intensity of coupled spins less when more 180° pulses are used to produce an echo at a given time. This has led to the production of lipid images by subtracting fast images made with the same echo time but different numbers of refocusing pulses.[11] Water intensity is much less dependent on the number of refocusing pulses used. A threshold can be set to identify voxels containing fat, and postprocessing then used to produce either water or lipid images.[11]

J coupling methods are immune to shimming problems and are temperature-independent. They require that two images be made to obtain any chemical shift information. This takes additional time and increases sensitivity to motion, even if acquisitions of the two images are interleaved. Water images will necessarily be T_2-weighted and lipid images will have an intensity which may depend in a complicated way on lipid chemistry.

3.3 Chemical Shift Based Methods

For most of our concerns, the spectrum of tissues can be approximated as two δ functions 3.4 ppm apart. An approximation that cannot be made is that the water Larmor frequency is everywhere the same. Shimming is by far the most serious problem with chemical shift based lipid manipulation schemes. Even if the magnet is perfectly shimmed when empty, the susceptibility of the subject distorts the field by an amount comparable to the 3.4 ppm separation between fat and water resonances. To aid shimming, the subject can be surrounded by a material with a susceptibility near that of water, but near cavities such as sinuses, airways, lungs, or bowel gas, this does not help.

3.3.1 Chemically Selective rf Pulses without Gradients

A simple approach to chemical shift imaging is to saturate either the water or the fat magnetization before a standard imaging sequence.[12] This can be done with a soft, frequency selective pulse of about 90° in the absence of a gradient, followed by a spoiling gradient, then the rest of the imaging sequence. As an alternative to the extra chemical shift selective pulse, one of the pulses in a multipulse imaging sequence can be made chemically rather than spatially selective. A chemical shift selective saturation pulse can be applied during an inversion–recovery sequence at the time of the zero crossing of fat. This combined method has been compared with some other chemically selective pulse methods.[13] Of these shift selective pulse methods, those with pulses selective for the desired signal are harder to incorporate in multislice methods than those selectively exciting the unwanted species.

In the presence of shimming errors, an rf pulse intended to suppress fat may suppress water instead in regions with a lower field and suppress nothing at all in higher field regions. Such pulses can give good results in relatively small regions that are not near odd-shaped air spaces and which can be placed at the magnet isocenter, for example the knee. A suppression pulse combined with surface coil reception is useful in examining the spine. The surface coil's lack of sensitivity to moving fat in the front of the body prevents phase-encoding artifacts, so the suppression pulse need only be effective near the spine. Magnet shimming is in general much better now than when selective pulse methods were put forward. Originally only of academic interest, selective pulses are now included in commercial, clinical software for fat saturation.

3.3.2 rf Pulses with Gradients

Angiograms, or images of flowing blood, can be made from a stack of thin, highly T_1-weighted images. Most tissues are dark because there is little time for recovery between acquisitions. Blood flows into the slice fully polarized if it moves more than a slice thickness in *TR*. Fat limits the smallest vessels that can be seen because it recovers magnetization rapidly and has an intensity comparable to the blood in small vessels. Veins present another problem in images of arteries. Veins usually run along arteries but are less often of interest. Both problems can be solved simultaneously by saturating a thick slab on one side of the slice being imaged.[14] This is done using a soft pulse with a weak gradient. The slab is positioned to saturate venous blood upstream of the slice but arterial blood downstream, thus removing veins but not arteries from the angiogram. The region of fat saturated by the extra pulse is not exactly the same as the region of water saturated because of the Larmor frequency difference. The gradient direction and magnitude for saturating the slab are chosen so that fat in the region to be imaged is saturated, but upstream blood is not. The shimming effect on this fat suppression method depends on the gradient strength. Excited slices are not perfectly flat but are warped like potato chips. Consecutive slices will nest perfectly if made with the same gradient and the same rf pulse (except for a frequency shift) but otherwise will overlap or leave gaps where none are intended.

3.3.3 Phase Based Methods

These methods are based on the difference between a gradient echo and Hahn's original spin echo, better called a Hahn, rf recalled, or rf echo to avoid confusion (Figure 3). Pixel phase in the image is the spin phase at the time of the gradient echo. At a Hahn echo, spin phase is independent of chemical shift and shimming. Therefore, when these echoes coincide, water and fat have the same phase in the reconstructed image.

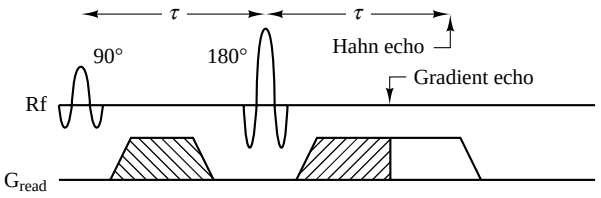

Figure 3 Hahn and gradient echoes in a spin echo imaging sequence

When they do not, phase accumulates at the Larmor frequency from the Hahn echo until the gradient echo. (For simplicity, the model uses a frame rotating at the instrument frequency.) Because the water–fat Larmor frequency difference is known, images with any desired phase difference between lipid and water can be produced by choosing the two echo times carefully.

Availability of starting images with known water–lipid phase shifts creates an urge to Fourier transform them for presentation. Transforms with one,[15] two,[16,17] three,[18] four,[19] and more[20] starting images have been used. Using more starting images allows the solution of more equations (by FT) for more unknowns. Formally, the output of a one-point FT is the same as its input. This is appropriate for opposed images as discussed before. The output of a two-point FT is the sum and the difference of the input points. Given images with water and lipid in phase and 180° opposed, a two-point FT produces separate, quantifiable images of lipid and of water. Additional unknowns of interest that can be imaged by phase-based methods include regional B_0 variation and the lipid linewidth.

Phase-based manipulations are most straightforward when refocusing pulses produce Hahn echoes. This allows images with different phase relations to be made with the same gradient echo time. In these, regions differ because of chemical shift differences but not because of T_2 differences. Nevertheless, phase-based fat suppression has been done with gradient echoes alone in the absence of refocusing pulses.[21]

The sign of a signal is often a question in IR imaging, especially when contrast agents are employed. In images produced by phase-based fat–water manipulations, the sign is always a question and occasionally a problem. If the phases and the signs of signals were ideal, separation of fat (F) from water (W) images given in phase (Si) and opposed (So) images would be unambiguous.

$$\left.\begin{array}{l} \mathrm{Si} = \mathrm{W} + \mathrm{F} \\ \mathrm{So} = \mathrm{W} - \mathrm{F} \end{array}\right. \quad \rightarrow \quad \left.\begin{array}{r} 2\mathrm{W} = \mathrm{Si} + \mathrm{So} \\ 2\mathrm{F} = \mathrm{Si} - \mathrm{So} \end{array}\right\} \tag{1}$$

However, if only absolute value images are available,

$$\left.\begin{array}{l} 2\mathrm{W} = |\mathrm{Si}| + |\mathrm{So}| \\ 2\mathrm{F} = |\mathrm{Si}| - |\mathrm{So}| \end{array}\right. \quad \text{or} \quad \left.\begin{array}{r} 2\mathrm{F} = |\mathrm{Si}| + |\mathrm{So}| \\ 2\mathrm{W} = |\mathrm{Si}| - |\mathrm{So}| \end{array}\right\} \tag{2}$$

The second solution applies where F > W. Simple-minded addition of images to produce a water image and subtraction to produce lipid images incorrectly reports a 60:40 mixture of lipid and water signal as 40:60 and so forth. The impact of this twofold ambiguity varies. Adipose tissue appears in the water instead of in the lipid image. Quantitative studies of fatty livers are affected while searches for liver metastases are not. Wherever the absolute value reverses the sign of the opposed image, misclassification occurs.

In principle, use of the original, complex images rather than absolute value images prevents the twofold ambiguity in fat signal fractions. In practice, images made with gradient and Hahn echoes which do not coincide have complicated phases depending on things other than chemical shift, shimming being the most important. The sign problem has been solved by noting that chemical shift often changes suddenly from one voxel to the next but $\boldsymbol{B}_0$ always changes gradually. In a phase map, fat/water boundaries can produce buttes or mesas superimposed on slowly rolling hills produced by shimming or other instrumental errors. A global view allows identification of region boundaries and therefore correction of signs in absolute value and absolute value-derived images. This phase unwrapping shows that one region is primarily lipid and another primarily water, but another method, usually inspection, is needed to show which is which.

When the phase of a particular pixel corresponds to a frequency 3.4 ppm off reference, that could indicate its signal comes from lipid rather than water. Alternatively B_0 could be 3.4 ppm low at that location. No local method using information from that voxel alone can distinguish chemical shift differences from B_0 differences, regardless of what pulse sequence is used or how many basis images are available. Even though the fat signal fraction ambiguity can only be solved by improved reconstruction methods, not by improved pulse sequences, desire to solve this ambiguity has led to new pulse sequences. Pulse sequence changes can make phase unwrapping easier. For example, increasing the phase difference between water and lipid from 180° to 360° removes the chemical shift induced cliffs from the opposed image phase map while doubling the height of the pattern of rolling hills caused by shimming and other variables.[19,22] The resulting $\boldsymbol{B}_0$ map helps unwrap the opposed image and can be used to adjust the instrument. Using comparison images of a phantom with uniform chemical shift also helps solve the sign problem.[23]

A less elaborate solution has been used to determine fat fractions in large regions of interest in vertebral bone marrow of leukemia patients.[7] Examination of the real opposed image determines whether signals from the marrow and from the intervertebral disks have the same or opposite signs. The disks contain no fat and have a positive signal. Knowing the sign of the opposed image signal removes the twofold ambiguity in fat signal fraction.

4 OTHER USES

Manipulations described here can be used for substances other than fat. T_1-Based fat suppression has been combined with frequency selective water suppression pulses[24,25] to image silicone prostheses. Silicone images have also been produced using opposed images in which delays were chosen to produce water/lipid, methylene/silicone, methyl proton phases of 0°, 0°, 180°.[26] Fluorinated blood substitutes are difficult to image because multiple resonances with large shift differences frustrate position determination in both slice selection and read directions. Pulse sequence[27] and reconstruction changes[28,29] can help. Imaging the sugar distribution in grapes[30–32] is a challenging application because glucose and fructose spectral lines lie closer to water than do lipid lines.

5 RELATED ARTICLES

Breast MRI; Chemical Shift Imaging; Inversion–Recovery Pulse Sequence in MRI; Motion Artifacts: Mechanism and Control; Multi Echo Acquisition Techniques Using Inverting Radiofrequency Pulses in MRI; Selective Excitation Methods: Artifacts; Water Suppression in Proton MRS of Humans and Animals; Whole Body Magnetic Resonance Artifacts.

6 REFERENCES

1. M. Neeman, K. A. Jarrett, L. O. Sillerud, and J. P. Freyer, *Cancer Res.*, 1991, **51**, 4072.
2. J. H. Simon and J. Szumowski, *Invest. Radiol.*, 1992, **27**, 865.
3. L. Brateman, *Am. J. Roentgenol.*, 1986, **146**, 971.
4. A. Bouchard, M. Doyle, P. E. Wolkowicz, R. Wilson, W. T. Evanochko, and G. M. Pohost, *Magn. Reson. Med.*, 1991, **17**, 379.
5. C. S. Poon, J. Szumowski, D. B. Plewes, P. Ashby, and R. M. Henkelman, *Magn. Reson. Imag.*, 1989, **7**, 369.
6. D. D. Stark, J. Wittenberg, M. S. Middleton, and J. T. Ferrucci, *Radiology*, 1986, **158**, 327.
7. E. L. Gerard, J. A. Ferry, P. C. Amrein, D. C. Harmon, R. C. McKinstry, B. E. Hoppel, and B. R. Rosen, *Radiology*, 1992, **183**, 39.
8. G. M. Bydder and I. R. Young, *J. Comput. Assist. Tomogr.*, 1985, **9**, 659.
9. W. T. Dixon, M. Sardashti, M. Castillo, and G. P. Stomp, *Magn. Reson. Med.*, 1991, **18**, 257.
10. C. L. Dumoulin and D. Vatis, *Magn. Reson. Med.*, 1986, **3**, 282.
11. R. T. Constable, R. C. Smith, and J. C. Gore, *JMRI*, 1993, **3**, 547.
12. P. A. Bottomley, T. H. Foster, and W. M. Leue, *Proc. Natl. Acad. Sci. USA*, 1984, **81**, 6856.
13. E. Kaldoudi, S. C. R. Williams, G. J. Barker, and P. S. Tofts, *Magn. Reson. Imag.*, 1993, **11**, 341.
14. M. Doyle, T. Matsuda, and G. M. Pohost, *Magn. Reson. Med.*, 1991, **21**, 71.
15. J. K. T. Lee, J. P. Heiken, and W. T. Dixon, *Radiology*, 1985, **156**, 429.
16. W. T. Dixon, *Radiology*, 1984, **153**, 189.
17. D. D. Blatter, A. H. Morris, D. C. Ailion, A. G. Cutillo, and T. A. Case, *Invest. Radiol.*, 1985, **20**, 845.
18. G. H. Glover and E. Schneider, *Magn. Reson. Med.*, 1991, **18**, 371.
19. G. H. Glover, *JMRI*, 1991, **1**, 521.
20. R.E. Sepponen, J. T. Sipponen, and J. L. Tanttu, *J. Comput. Assist. Tomogr.*, 1984, **8**, 585.
21. J. Szumowski and D. B. Plewes, *Magn. Reson. Med.*, 1988, **8**, 345.
22. H. N. Yeung and D. W. Kormos, *Radiology*, 1986, **159**, 783.
23. J. A. Borrello, T. L. Chenevert, C. R. Meyer, A. M. Aisen, and G. M. Glazer, *Radiology*, 1987, **164**, 531.
24. B. Pfleiderer, J. L. Ackerman, and L. Garrido, *Magn. Reson. Med.*, 1993, **29**, 656.
25. S. Mukundan, Jr., W. T. Dixon, B. D. Kruse, D. L. Monticciolo, and R. C. Nelson, *JMRI*, 1993, **3**, 713.
26. E. Schneider and T. S. Chan, *Radiology*, 1993, **187**, 89.
27. H. K. Lee, O. Nalcioglu, and R. B. Buxton, *Magn. Reson. Med.*, 1991, **21**, 21.
28. L. J. Busse, R. G. Pratt, and S. R. Thomas, *J. Comput. Assist. Tomogr.*, 1988, **12**, 824.
29. H. K. Lee and O. Nalcioglu, *JMRI*, 1992, **2**, 53.
30. J. M. Pope, H. Rumpel, W. Kuhn, R. Walker, D. Leach, and V. Sarafis, *Magn. Reson. Imaging*, 1991, **9**, 357.
31. J. M. Pope, R. R. Walker, and T. Kron, *Magn. Reson. Imag.*, 1992, **10**, 695.
32. B. A. Goodman, B. Williamson, and J. A. Chudek, *Magn. Reson. Imag.*, 1993, **11**, 1039.

Biographical Sketch

W. Thomas Dixon. *b* 1945. B. Mech. Engr., 1967 Ph.D., 1980, physics, (with O. Lumpkin), University of California, San Diego. Postdoctoral work at Washington University/Monsanto with J. Schaefer. Approx. 40 publications. Research areas: cross polarization, magic angle spinning, proton imaging.

Whole Body Studies Involving Spin–Lattice Relaxation in the Rotating Frame

Raimo E. Sepponen

Helsinki University of Technology, Helsinki, Finland

1 INTRODUCTION

The dependence of the longitudinal relaxation time T_1 of biological tissue on the strength of the polarizing magnetic field $\boldsymbol{B}_0$, i.e., on the NMR frequency ν_0 is often called T_1 dispersion.[1] The efficiency and the number of relaxation mechanisms related to water–macromolecule interaction increase with decreasing ν_0, and tissue T_1s get shorter. Longitudinal relaxation observed at low field strengths may therefore discriminate better between normal and pathological tissues than that observed at high field strengths. The spin lock (SL) technique allows studies of relaxation at very low field strengths with a high signal-to-noise ratio.

In an SL experiment, nuclear spins are locked with a radiofrequency (rf) field. The locked nuclear magnetization relaxes along the magnetic component of the locking rf field, $\boldsymbol{B}_{1L}^{\nu_1}$, which rotates at an angular velocity ω_1. If the frequency ν_1 of the rf field is equal to ν_0, the relaxation is characterized by the relaxation time $T_{1\rho}$, which is approximately T_1 at B_{1L}. If ν_1 differs from ν_0 then the relaxation time is called $T_{1\rho}^{\text{off}}$, which approaches T_1 as the frequency offset increases; generally $T_2 < T_{1\rho} < T_{1\rho}^{\text{off}} < T_1$.[2] At very low strengths of $\boldsymbol{B}_{1L}^{\nu_1}$, $T_{1\rho}$, $T_{1\rho}^{\text{off}} \approx T_2$. The strength of $\boldsymbol{B}_{1L}^{\nu_1}$ may be varied by variation of the strength and/or frequency of the rf field. Hence, the SL technique allows studies of dispersion of relaxation in the rotating frame, i.e., $T_{1\rho}$ dispersion.

The relative efficiencies of different relaxation mechanisms under the locking conditions are still to be evaluated. It has been assumed that thermal motion of macromolecules and slow motions of water molecules such as chemical exchange are important sources of relaxation. However, it has been suggested that relaxation under the locking conditions is mainly a manifestation of magnetization transfer (MT) between mobile water protons and solid state broadened protein proton levels.[3–5]

The potential to provide unique relaxation information and tissue contrast has motivated the development of clinically feasible SL imaging techniques.[6,7]

2 SPIN LOCK IMAGING TECHNIQUES

In an SL experiment, the longitudinal nuclear magnetization M_z is tilted from the direction of the polarizing magnetic field $\boldsymbol{B}_0$ by an rf pulse or an adiabatic sweep. This is followed by a locking pulse, $\boldsymbol{B}_{1L}^{\nu_1}$, which is applied during the locking time *TL*. This is illustrated in Figure 1, which shows the basic SL imaging sequence.[8] The phase of $\boldsymbol{B}_{1L}^{\nu_1}$ is adjusted so that the

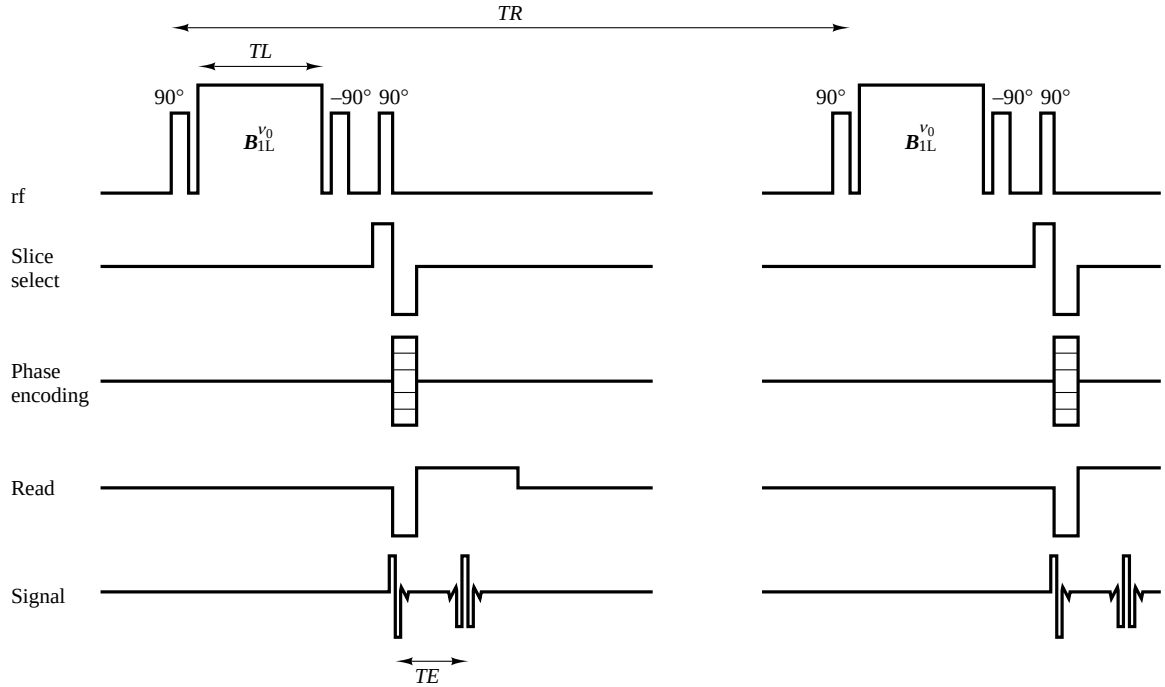

Figure 1 The basic pulse sequence for $T_{1\rho}$ imaging. *TR* is the repetition time, $\boldsymbol{B}_{1L}^{\nu_0}$ is the locking radio frequency pulse applied at ν_0, *TL* is the length of the locking pulse, and *TE* is the time to echo: 'rf' indicates radiofrequency operations; 'Slice select' indicates slice-selection gradient operations, 'Phase encoding' indicates phase-encoding gradient operations; 'Read' indicates read gradient operations, and 'Signal' indicates NMR signals

magnetic component of the effective field is aligned with the tilted $\boldsymbol{M}$. The locked magnetization relaxes along $\boldsymbol{B}_{1L}^{\nu_1}$ with a characteristic relaxation time $T_{1\rho}$ or $T_{1\rho}^{\text{off}}$.

In imaging applications of the SL technique, $\boldsymbol{B}_{1L}^{\nu_1}$ is followed by an excitation, gradient encoding, and signal collecting sequence (Figure 1).

The intensity S of the signal is given approximately by

$$S \propto M_0(1 - e^{-TR/T_1})\, e^{-TE/T_2}\, e^{-TL/T_{1\rho}} \tag{1}$$

Generally, tissues with a long T_2 also have a long $T_{1\rho}$, so the inevitable T_2 weighting of the final image does not decrease the contrast. This allows optimization of the signal-to-noise ratio by selecting *TE*. *TR* should be relatively long in order to minimize the antagonistic T_1 weighting.

If the strength of $\boldsymbol{B}_{1L}^{\nu_1}$ is low, the contrast properties of $T_{1\rho}$-weighted images are similar to those of T_2-weighted images.[9] An increase in the strength of $\boldsymbol{B}_{1L}^{\nu_1}$ makes the $T_{1\rho}$ of tissues longer and alters the contrast.[8]

$T_{1\rho}$ dispersion may be quantified by collecting two or more SL images with different $\boldsymbol{B}_{1L}^{\nu_1}$ strengths. This unique information about relaxation processes may prove useful in tissue characterization.

For calculated $T_{1\rho}$ images, at least two images with different *TL* values need to be collected. The calculation is similar to the calculation of a T_2 image.

A multiple slice SL imaging technique has been recently introduced.[10] The multiple slice SL imaging sequence is presented in Figure 2. Nonselective, short locking pulses are used for the generation of the $T_{1\rho}$ contrast in the whole imaging volume. After each locking pulse, the magnetization is returned to the direction of $\boldsymbol{B}_0$. In this way, the generated contrast is 'stored' in the longitudinal magnetization. The images are obtained with the multiple slice technique.

The intensity S of the signal is given by

$$S \propto M_0 \sin\theta \frac{E_2[1 - (E_D E_L)^N](1 - E_D)E_L}{[1 - (E_D E_L)^N \cos\theta](1 - E_D E_L)} \tag{2}$$

where

$$E_2 = e^{-TE/T_2}, \quad E_D = e^{-TD/T_1}, \quad E_L = e^{-TL/T_{1\rho}} \tag{3}$$

The contrast also depends on the number N of slices and the time delay *TD* between successive locking pulses. A small θ generally has a synergistic effect on the contrast by reducing the antagonistic T_1 weighting.

With this sequence, high-contrast images may be obtained by using a short *TE*. This minimizes motion artifacts and allows a large number of slices to be accommodated within a given *TR*. This makes the sequence feasible for abdominal imaging, for example. *TL* may be short, because of the cumulative effect of the locking pulses. *TD* should be short compared with T_1s of tissues.

3 RESULTS WITH T_1 AND $T_{1\rho}$ DISPERSION IMAGING

$T_{1\rho}$ imaging may prove to have a good capability for tissue differentiation. For example, $T_{1\rho}$ measured at B_{1L} = 0.23 mT discriminated tumor from normal fat and fibrous breast tissues. Conventional T_2 and T_1 measurements at B_0 = 0.15 T failed to demonstrate this difference.[11]

$T_{1\rho}$ dispersion imaging has been used to evaluate brain and muscle diseases. Fresh brain infarctions and plaques of multiple sclerosis have a long $T_{1\rho}$ and a slightly smaller $T_{1\rho}$ dispersion than normal brain tissue in the B_{1L} range 0.05–0.46 mT.[7]

A difference in $T_{1\rho}$ dispersion has been found between normal and diseased muscle tissue. The B_{1L} range used was 0.025–0.25 mT. The method seems to provide better identification of affected muscles than T_1- and T_2-weighted imaging.[12]

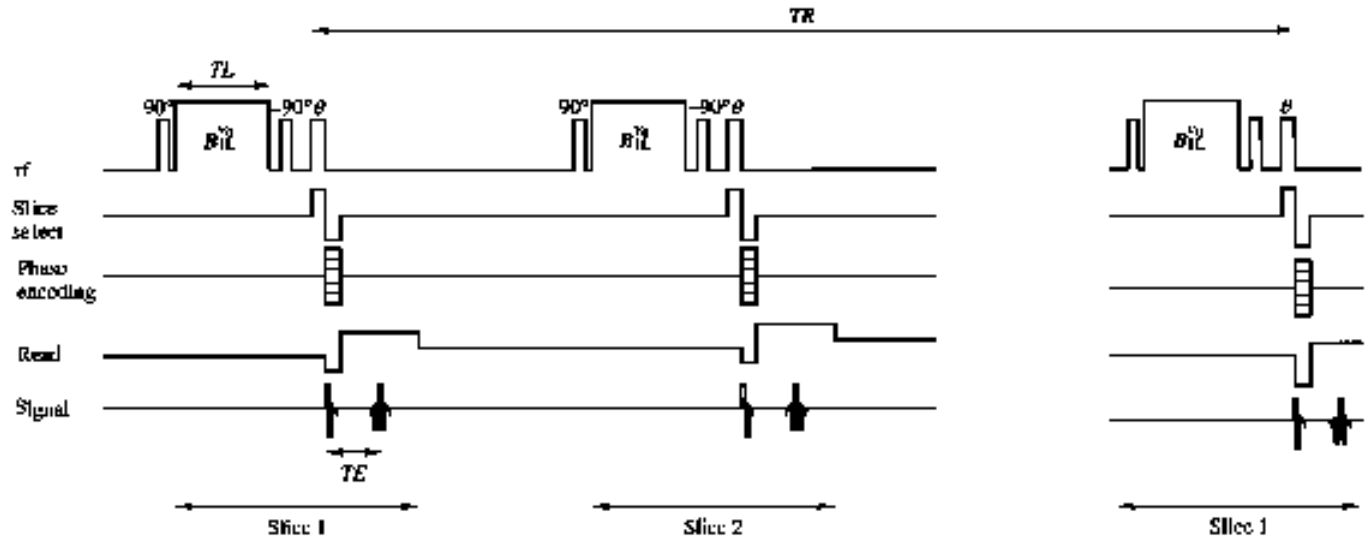

Figure 2 The multiple slice SL sequence. The notation is the same as in Figure 1; θ indicates a θ° excitation pulse

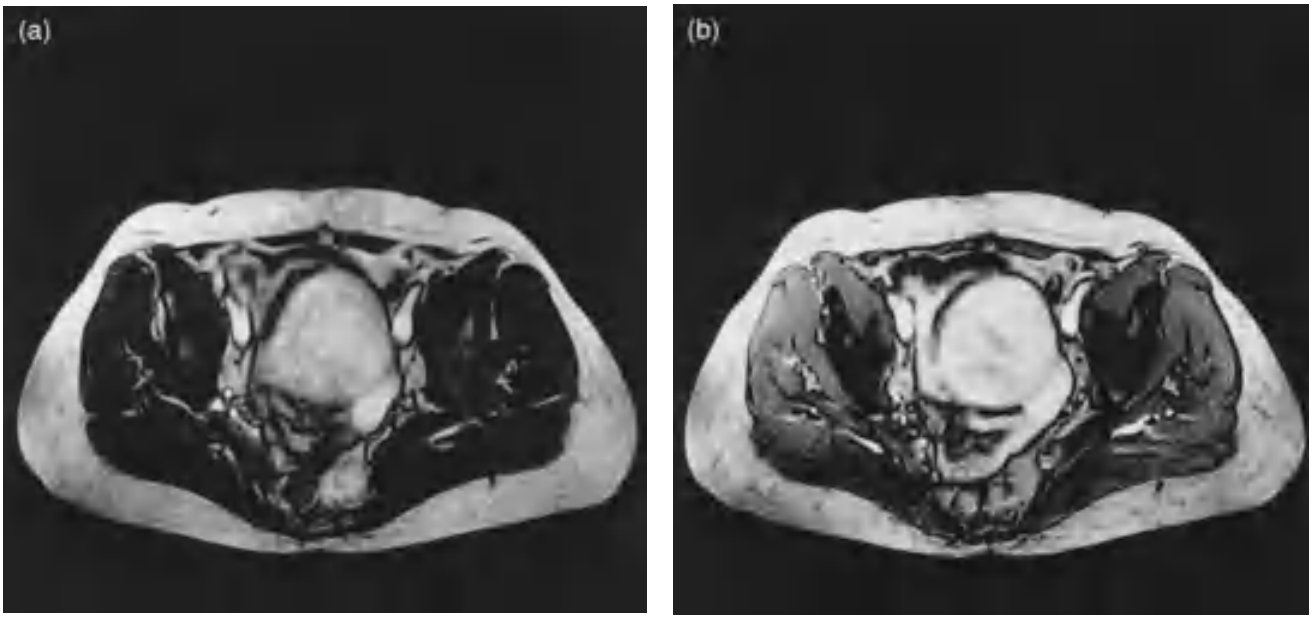

Figure 3 (a) A multiple slice SL image of a female pelvis. The imaging parameters are TR = 1500 ms, TE = 40 ms, B_{1L} = 60 μT, TL = 10 ms, θ = 60°, and B_0 = 0.1 T. The gradient echo technique has been used. A cyst is visible adjacent to the urinary bladder, with a high signal intensity. The wall between the urinary bladder and the cyst is also visible. (b) A gradient echo (GE) image of the same slice as in (a). The imaging parameters are TR = 1500 ms, TE = 40 ms, θ = 60°, and B_0 = 0.1 T. Note that the intensity of the adjacent intestine is as high as that of the cyst. The contrast between muscle and fat tissues is better in the SL image than in the GE image

$T_{1\rho}$ dispersion imaging has been shown to be highly sensitive to the presence of paramagnetic substances. This has been demonstrated in a mouse tumor. $T_{1\rho}$ dispersion imaging seems to be superior to conventional T_1-weighted imaging in detecting the presence of a paramagnetic contrast agent.[13]

The SL technique may be used with the inversion–recovery method to improve the conspicuity of blood vessels in angiography. The length of the locking pulse and the inversion time may be adjusted in order simultaneously to suppress, for example, fat and muscle signals.[14] SL contrast between blood and cardiac muscle has been exploited in cardiac imaging at 1.5 T.[15]

The SL technique seems to provide a sensitive method to detect fluid collections, such as edema and cysts in different body areas. This is demonstrated in Figures 3 and 4. In Figure 3, a cyst adjacent to the urinary bladder is differentiated better in the SL 1500/30 (B_{1L} = 60 μT, TL = 10 ms, θ = 60°, N = 15, B_0 = 0.1 T) image (a) from intestines than in a gradient echo GE 1500/30 image (b). Note that the contrast between subcutaneous fat and muscle tissue is better in the SL image than in the conventional GE image.

In Figure 4, fluid collections in an injured knee are better discriminated in the SL 1500/40 (B_{1L} = 50 μT, TL = 8 ms, θ = 60°, N = 12, B_0 = 0.1 T) image (a) than in the GE 1500/40 image (b). Note the high contrast between fluid and cartilage tissue in the SL image.

As already mentioned, the SL technique may provide complementary information for tissue characterization to the conventional imaging methods. In Figure 5, the visualization of a multiple sclerosis plaque is demonstrated with the multiple slice SL technique (a) and with the conventional T_2-weighted spin echo (SE) technique (b). In the SL 1500/45 (B_{1L} = 60 μT, TL = 10 ms, θ = 60°, N = 12, B_0 = 0.1 T) image, the center of the lesion has a relatively low intensity. This feature is difficult to appreciate in the SE 2100/120 image. $T_{1\rho}$ imaging has been successfully used for perfusion imaging of brain. An introduction of ^{17}O enriched water in blood increases $T_{1\rho}$ dispersion of perfused tissue.[16]

Because the contrast in SL images is closely related to the contrast obtained with the MT technique, the potential of SL imaging has been studied in areas of the body where MT contrast has been explored. It has been demonstrated that SL imaging provides an effective method for detection of pathologies in the head and neck area.[17] Detection and differentiation of liver tumors is one application for SL imaging.[18]

SL contrast is generated when the spins are locked and, therefore, short TE may be employed. Hence, SL technique may be used in areas such as lungs where susceptibility artifacts are significant and the use of conventional spin echo technique with long TE is not feasible.

4 INSTRUMENTATION AND SAFETY

The instrumentation required for spin lock experiments is usually available in a standard MRI unit. However, the rf power amplifier for supplying the long, high-amplitude $\boldsymbol{B}_{1L}^{\nu_1}$ pulse may be limited to ensure rf safety. The excitation and $\boldsymbol{B}_{1L}^{\nu_1}$ pulses are emitted by the same coil system, which should be able to withstand the required rf power.

The rf absorption of biological tissues is described by the specific absorption rate (SAR). This is proportional to the product $(\boldsymbol{B}_{1L}^{\nu_1})^2 B_0^2\, TL/TR$. The duty cycle TL/TR and amplitude of $\boldsymbol{B}_{1L}^{\nu_1}$ at B_0 are limited by the maximum allowed SAR.[7]

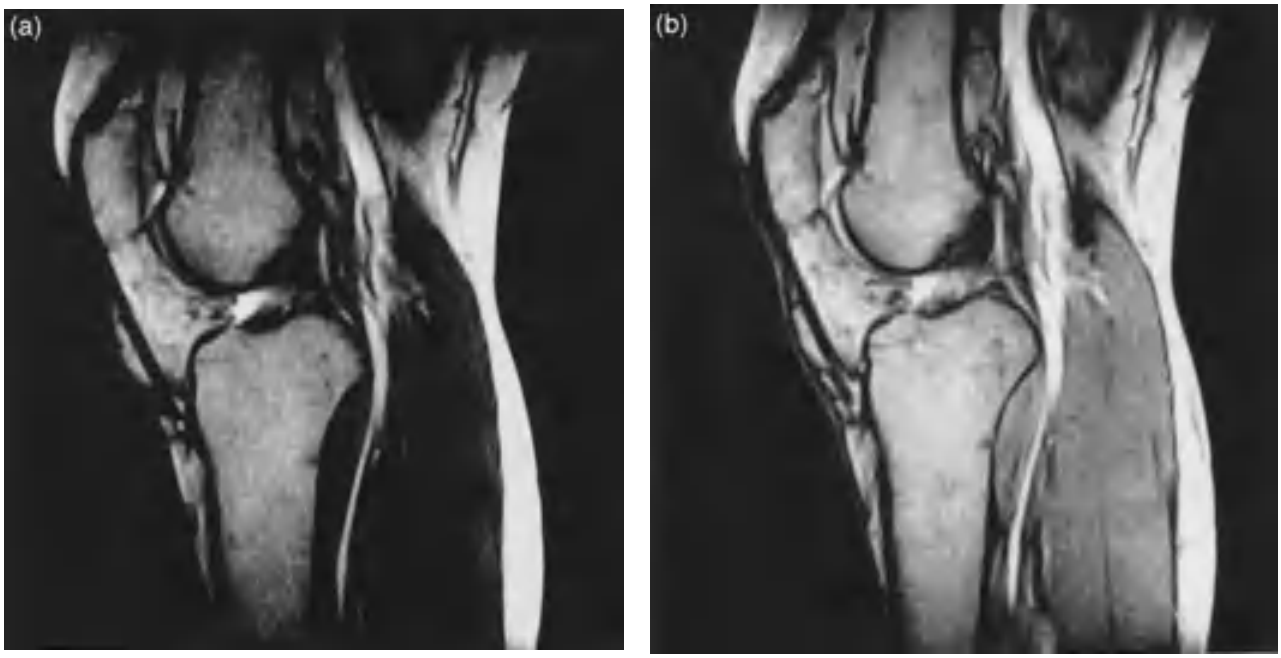

Figure 4 (a) A multiple slice SL image of an injured knee. The imaging parameters are $TR = 1500\,\text{ms}$, $TE = 40\,\text{ms}$, $B_{1L} = 50\,\mu\text{T}$, $TL = 8\,\text{ms}$, $\theta = 60^\circ$, and $B_0 = 0.1\,\text{T}$. The gradient echo technique has been used. A small fluid collection adjacent to the patellar cartilage is clearly visible, with a high signal intensity. Muscle tissue shows a very low signal intensity. (b) A gradient echo (GE) image of the same slice as in (a). The imaging parameters are $TR = 1500\,\text{ms}$, $TE = 40\,\text{ms}$, $\theta = 60^\circ$, and $B_0 = 0.1\,\text{T}$. Note that the contrast between the fluid collection and the patellar cartilage is low. Muscle tissue has a markedly higher signal intensity than in the SL image

The SL technique can be applied at medium and high fields by locking the magnetization with an off-resonance rf pulse B_{1L}^{off} and by using the multiple slice SL technique. The SAR in the multiple slice SL images presented earlier is less than $0.12\,\text{W}\,\text{kg}^{-1}$. This indicates that the technique may be safely used at any field strengths currently in clinical use.

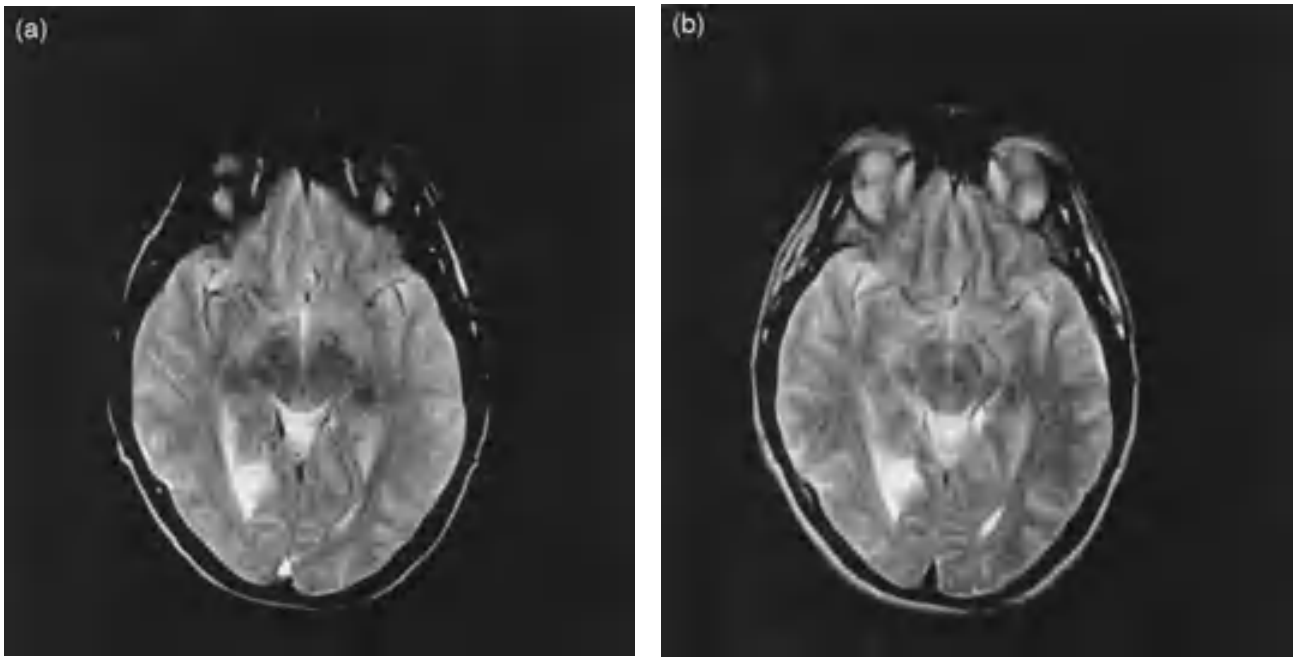

Figure 5 (a) A multiple slice SL image of a patient suffering from multiple sclerosis. A multiple sclerosis plaque is visible, with a high signal intensity. The center of the lesion has a slightly lower intensity. The imaging parameters are $TR = 1500\,\text{ms}$, $TE = 45\,\text{ms}$, $B_{1L} = 60\,\mu\text{T}$, $TL = 10\,\text{ms}$, $\theta = 60^\circ$, and $B_0 = 0.1\,\text{T}$. (b) A T_2-weighted SE 2100/120 image of the same slice as in (a). The lesion has a high signal intensity. The imaging parameters are $TR = 2100\,\text{ms}$, $TE = 120\,\text{ms}$, $\theta = 90^\circ$, and $B_0 = 0.1\,\text{T}$

5 CONCLUSIONS

The spin lock technique provides an effective method to generate MR images with a high tissue contrast. Magnetization transfer between protons of macromolecules and those of water molecules seems to be an important source of relaxation in the rotating frame. Slow motions of large molecules and paramagnetic substances also play an important role.

The technique may be used even at high field strengths via the utilization of the multiple slice technique or off-resonance locking pulses. The clinical potential of SL imaging is still to be evaluated. It may be assumed that it will find applications, especially in tissue characterization, abdominal imaging, and concurrent use with contrast agents and angiography.

6 RELATED ARTICLES

Magnetization Transfer and Cross Relaxation in Tissue; Magnetization Transfer between Water and Macromolecules in Proton MRI; Magnetization Transfer Contrast: Clinical Applications; Relaxometry of Tissue.

7 REFERENCES

1. S. H. Koenig, R. D. Brown III, D. Adams, D. Emerson, and C. G. Harrison, *Invest. Radiol.*, 1984, **19**, 76.
2. G. P. Jones, *Phys. Rev.*, 1966, **148**, 332.
3. G. H. Caines, T. Schleich, and J. M. Rydzewski, *J. Magn. Reson.*, 1991, **95**, 558.
4. J. H. Zhong, J. C. Gore, and I. M. Armitage, *Magn. Reson. Med.*, 1989, **11**, 295.
5. R. D. Brown III and S. H. Koenig, *Magn. Reson. Med.*, 1992, **28**, 145.
6. E. Rommel and R. Kimmich, *Magn. Reson. Med.*, 1989, **12**, 390.
7. R. E. Sepponen, in 'Magnetic Resonance Imaging', eds. D. D. Stark and W. G. Bradley, 2nd edn., Mosby-Year Book, St. Louis, 1992, Vol. 1, Chap. 8.
8. R. E. Sepponen, J. A. Pohjonen, J. T. Sipponen, and J. I. Tanttu, *J. Comput. Assist. Tomogr.*, 1985, **9**, 1007.
9. R. V. Mulkern, S. Patz, M. Brooks, P. C. Metcalf, and F. A. Jolesz, *Magn. Reson. Imaging*, 1989, **7**, 437.
10. R. E. Sepponen and J. I. Tanttu, *Radiology*, 1993, **189** (P), 320.
11. G. E. Santyr, R. M. Henkelman, and M. J. Bronskill, *Magn. Reson. Med.*, 1989, **12**, 25.
12. A. E. Lamminen, J. I. Tanttu, R. E. Sepponen, H. Pihko, and O. A. Korhola, *Br. J. Radiol.*, 1993, **66**, 783.
13. E. Rommel, R. Kimmich, H. Körperich, C. Kunze, and K. Gersonde, *Magn. Reson. Med.*, 1992, **24**, 149.
14. J. I. Tanttu and R. E. Sepponen, *Radiology*, 1993, **189** (P), 187.
15. W. T. Dixon, J. N. Oshinski, J. D. Trudeau, B. C. Arnold, and R. I. Pettigrew, *Magn. Reson. Med.*, 1996, **36**, 90.
16. S. R. Charagundla, A. H. Stolpen, J. S. Leigh, and R. Reddy, *Magn. Reson. Med.*, 1998, **39**, 588.
17. A. T. Markkola, H. J. Aronen, T. Paavonen, E. Hopsu, L. M. Sipilä, J. I. Tanttu, and R. E. Sepponen, *Radiology*, 1996, **200**, 369.
18. J. T. Halavaara, R. E. Sepponen, A. E. Lamminen, T. Vehmas, and S. Bondestam, *Magn. Reson. Imaging*, 1998, **16**, 359.

Biographical Sketch

Raimo E. Sepponen. *b* 1950. M.S., 1974, D.Sc., 1986, Helsinki University of Technology. Instrumentarium Inc., Manager of Research & Development (MRI) 1978–1988, Manager of Clinical Applications 1988–1992. Picker Nordstar Inc., Consultant, 1993–1994. Helsinki University of Technology, Senior Lecturer, 1976–1994, Professor (applied electronics), 1994–present. 42 Publications. Research interests; tissue characterization with NMR and imaging techniques.

Imaging of Wide-Band Systems by Line-Narrowing Methods

Bruno Maraviglia, Francesco De Luca, Bruna C. De Simone, and Nicola Lugeri
Università di Roma 'La Sapienza', Rome, Italy

1 INTRODUCTION

The overwhelming majority of NMR imaging procedures and applications are based on the observation of a system of very mobile spins, whose intrinsic linewidth, $\Delta\nu$, hardly exceeds a few tens of hertz. It is well known that a number of authors have reached microscopic resolution in their images, by applying very intense gradients on small objects, owing to the 'imaging condition'[1] that relates the resolution in the image, Δr, to the gradient G and the linewidth of the system:

$$\gamma G \Delta r \geq \Delta\nu \tag{1}$$

Quite a different situation is faced when the nuclei to be imaged are constrained in a more or less rigid matrix with a correspondingly wider (of several orders of magnitude) NMR line, as is clear from equation (1): the wider the line, the greater the intensity of the gradient required for a given resolution (or, with fixed G, the poorer the resolution). In contrast, a large number of very interesting biological systems fall into this category, from rigid, crystalline solids, to polymers, ceramics, pastes, biological macromolecules, bones, and so on. Moreover, such systems show a number of very interesting phenomena related to molecular motion that can be investigated using well-known NMR relaxation parameters. Although in several systems, by means of a moderate increase in gradient intensity, one can apply standard imaging schemes, alternative approaches to equation (1) have been proposed to perform imaging also in systems whose linewidth would require exceedingly intense gradients.[2]

In this contribution we focus our attention on the various techniques of solid state imaging (SSI) based on the introduction of external perturbations (in excess of the 'traditional' ones, required for MRI) to the spin system, in order effectively to reduce its linewidth down to a value which makes equation (1) more easily obtainable.

2 BROADENING AND NARROWING

Why do solids give rise to NMR lines much broader than do liquids? Such a difference in behavior is due to the difference in rapidity of molecular reorientation in such systems, which allows an averaging effect on the interaction Hamiltonian to take place much more efficiently in liquids than in solids.[3] It can be shown that for solid-like systems the whole of the interaction Hamiltonian affects their NMR spectrum and, in particular, the anisotropic contribution.[4]

Line-narrowing techniques, then, tend to simulate what occurs naturally in narrow band systems: they make the spin move, following certain 'rhythms' and directions, such that the anisotropy of the Hamiltonian is drastically reduced.

Two main families can be defined among spin manipulation line-narrowing techniques, the difference relying on the space which is chosen to induce the motion of the spins. The first one, the older, is related to motion in real space, i.e. the spatial coordinates of the spins and the orientations of their vector radii (for spin–spin couplings) are made to vary in time by fast rotation of the whole solid sample around a 'magic' direction in space, for which every spin interaction tensor loses its anisotropic contribution. This technique is called magic angle spinning (MAS).

A complementary approach is followed by the second family of methods, where the motion on the system is imposed on their spin coordinates (in spin space) by means of a common precession induced by rf (pulsed or continuous; on- or off-resonance) excitation. Multipulse (MP), magic echo, and magic angle in the rotating frame (MARF) techniques are the most widely used methods in this family.

3 BASIC THEORY OF MANIPULATION IN SPIN SPACE

It is well known in quantum mechanics that whenever the Hamiltonian of a system can be decomposed into a main, time-independent part and a much weaker (interaction) contribution, the most convenient approach to the study of the system is that of the interaction representation.[5] In NMR such an approach is, let us say, physiological, as it is translated to the geometrical view called the rotating frame (RCF). In the RCF the part of the Hamiltonian which introduces the common precession of the spins, $\hat{\mathcal{H}}_0 = -\gamma B_0 \hat{I}_z$, is effectively removed (except for an eventual resonance offset ΔB_0), and the shape of the spectrum around zero frequency (or around $\gamma\,\Delta B_0$) is determined by the interaction Hamiltonian.

It is also well known that until the rf field $\boldsymbol{B}_1 = B_1 \cos\omega t\, \boldsymbol{i}_L$ is 'on', a precession at a frequency $\omega_e = \gamma B_e$ occurs around a static $\boldsymbol{B}_e$ field in the xz plane of the RCF, as illustrated in Figure 1 where $\boldsymbol{B}_e = B_1 \boldsymbol{i} + (\omega - \omega_0)/\gamma \cdot \boldsymbol{k}$. (Here $\boldsymbol{i}_L$ is the unit vector in the X direction of the laboratory frame (LCF); $\boldsymbol{i}$ and $\boldsymbol{k}$ are those in the x and z directions of the RCF, respectively.

Provided that the 'new' Zeeman Hamiltonian $\hat{\mathcal{H}}_e = -\gamma \boldsymbol{B}_e \cdot \boldsymbol{I}$ is much stronger than the interaction ones ($\omega_e >> 2\pi\,\Delta\nu$), quantization of the spin system along $\boldsymbol{B}_e$ can be defined. Consequently one can introduce a tilted RCF with the z' axis along $\boldsymbol{B}_e$ by a rotation of $\theta = \tan^{-1}(B_1/\Delta B_0)$ around y in the RCF[6] (primed axes and unit vectors pertain to the TRCF). A further interaction representation—a double RCF—can then be introduced, in order to remove the contribution $\boldsymbol{B}_e = B_e \boldsymbol{k}'$ of the static field effectively and look at the interactions in this new frame. Of course, the interaction Hamiltonian undergoes several transformations, each one describable by a rotation. In order to see the consequences of these transformations, one has to define the rotation operators[7] corresponding to the external perturbations leading to the DRCF:

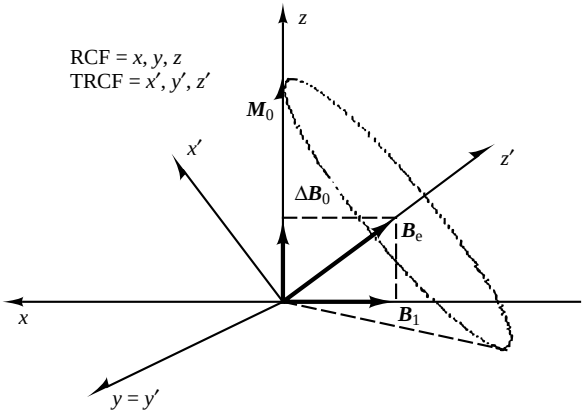

Figure 1 Definition of the fields and of the frames used in the text. Precession of the magnetization vector around the effective field in the RCF is also displayed

$$\begin{aligned} \text{LCF} \rightarrow \text{RCF} \qquad & \hat{R}_{\text{R}} = \exp(\text{i}\omega t \hat{I}_z) \\ \text{RCF} \rightarrow \text{TRCF} \qquad & \hat{R}_{\text{T}} = \exp(\text{i}\theta \hat{I}_y) \\ \text{TRCF} \rightarrow \text{DRCF} \qquad & \hat{R}_{\text{D}} = \exp(\text{i}\omega_{\text{e}} t \hat{I}_{z'}) \end{aligned} \tag{2}$$

In terms of Euler angles, the spin dependent interaction tensor $\boldsymbol{A}_q$ relative to the interaction q then transforms as

$$\begin{aligned} A_q^{lm} &\rightarrow \hat{R}^{-1}(\omega t, \theta, \omega_{\text{e}} t) A_q^{lm} \hat{R}(\omega t, \theta, \omega_{\text{e}} t) \\ &= \sum_{m'} D^l_{mm'}(\omega t, \theta, \omega_{\text{e}} t) A_q^{lm'} \end{aligned} \tag{3}$$

where $D^l_{mm'}$ are the elements of the lth rank Wigner rotation matrix and $\hat{R} = \hat{R}_{\text{D}}\hat{R}_{\text{T}}\hat{R}_{\text{R}}$. It can be shown that the transformed internal Hamiltonian in the doubly rotating frame is scaled to first order by $D^1_{00} = \cos\theta$ or $D^2_{00} = \frac{1}{2}(3\cos^2\theta - 1)$ according to the rank of the interaction, as considered in the subspace where the transformation takes place (the resonant spin subspace).

Equations (2) and (3) contain the basis for all of the known line-narrowing methods. However, they differ in the procedures followed to take advantage of these transformation properties and on the detection of the signal representative of the spin system under narrowing conditions. MP techniques introduce a cyclic succession of 'infinitely' short on-resonance pulses, which define a corresponding succession of differently tilted RCFs; the so-called toggling frame. In this frame, selective averaging can be obtained and observed by means of stroboscopic detection (sampling time = cycle time).

Magic echo also works on-resonance ($\theta = 90°$), but with long pulses, during which the scaling of dipolar coupling by the factor $-\frac{1}{2}$ is exploited to refocus the dipolar dephasing which is usually considered irreversible.[8]

Finally, in MARF experiments one observes the evolution of the magnetization in the tilted RCF under a $\boldsymbol{B}_{\text{e}}$ which makes the magic angle with $\boldsymbol{B}_0$. If one considers bilinear interactions, the value is the same as in MAS experiments, $\theta_{\text{M}}^{(2)} = 54°44'$, while it becomes $\theta_{\text{M}}^{(1)} = 90°$ (on-resonance field) if one wants to eliminate linear couplings. The signal can be observed only through its z' components, since it is the only axis which has no time dependence with respect to the laboratory frame. Detection can be performed directly, by means of a coil along z tuned to ω_{e},[9,10] or by the indirect Lee–Goldburg[11] method.

4 IMAGING OF SOLIDS BY SPIN MANIPULATION

Each one of the above described line-narrowing techniques has been exploited, in conjunction with some spatial encoding scheme, to obtain imaging in broadband systems. The modality of introducing spatial discrimination to the system is usually very different from traditional imaging, and peculiar to the narrowing method, since the perturbing gradients should not influence the narrowing power and, more important, they have to 'work' in the reference frame where averaging occurs, and where the signal is detected.

4.1 MAS Imaging

The frame to be considered is the one fixed with the sample spinning at ω_{R}. A transverse linear field gradient, static in such a frame, can be generated by a field rotating at ω_{R} with respect to the LCF. Such a situation is implemented by means of two gradient coils, wound around the static surface of the rotor with their gradient directions at right angles between them and the rotation axis. Once fed by quadrature currents oscillating at the same rotor angular frequency, the composition of the resulting oscillating fields gives the desired linear rotating gradient. Since the geometry of the coils is dictated by that of the rotor, the gradient coils give rise to a field gradient tensor, the effect of which is a distortion of the projections, unless attention is paid, to both the geometrical arrangement of the coil axes and the intensity and phase of the current flowing in them.[12]

Projection reconstruction (PR) and two-dimensional Fourier transform (2D FT) imaging procedures may be used with this method. In each case there is a need for an accurate control of the phase φ and $\varphi + 90°$ between each component of the gradient and the reference frequency extracted from the rotor spinning velocity by an optical detector.

If φ is incremented in small steps, PR can be straightforwardly implemented; 2D FT requires a phase change ($\Delta\varphi = 90°$) in each component of the current in order to switch the gradient direction from encoding to read-out, following the incremented time imaging scheme of Figure 2.[13] Since MAS narrowing power is limited by the spinning frequency (up to about 10 kHz), which has to be greater than the bandwidth of the sample, this method can be usefully applied to solid systems with small or intermediate bandwidths, although several interesting developments toward a larger variety of samples have recently been proposed, including combination with MP techniques and spectroscopic investigations on ^{13}C with sideband suppression.[14] Interesting methods of contrast and resolution enhancement have also been proposed.[15]

4.2 Imaging by Multipulse Narrowing

In MP techniques one has to follow (and detect) the evolution of the spin system in the toggling frame, as defined by the sequence chosen. Several techniques have been proposed; in general, every MP sequence can be combined with gradient schemes to obtain SSI, mainly differing in how and when the gradients are applied within the whole imaging scheme, in order to match as well as possible the requirements of narrow-

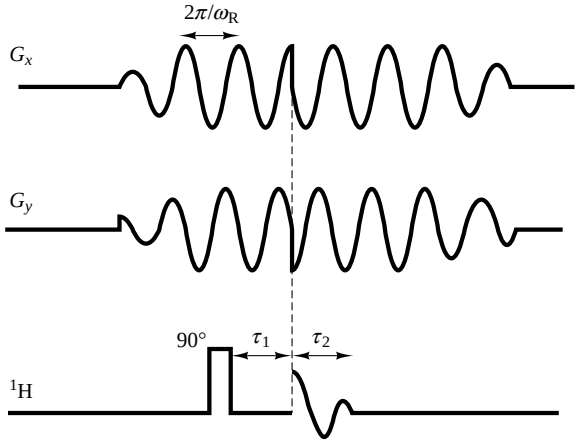

Figure 2 2D FT MAS imaging scheme by means of rotating gradients. Incremented evolution time phase encoding is performed. (Reproduced by permission of Academic Press from Cory et al.[12])

ing efficiency, spatial resolution, and sequence flexibility. In Figure 3(a) the sequence used to obtain the first MP image of a solid is shown:[16] MREV-8 is the MP narrowing sequence in the presence of a static gradient.

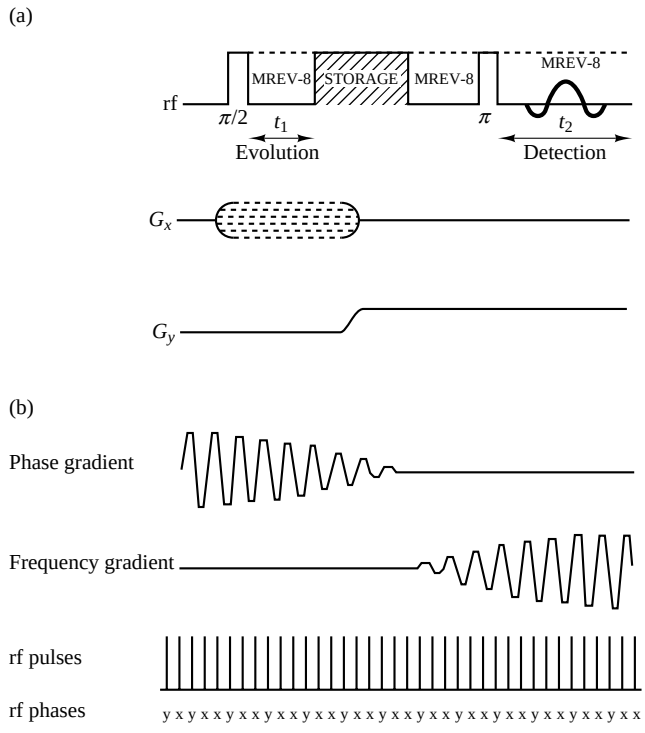

Figure 3 (a) Timing diagram for 2D FT MP imaging of solids. The MP line narrowing and the magnetization storage sequences are schematically indicated. Constant evolution time phase encoding is employed. (Reproduced by permission of Academic Press from Chingas et al.[16]) (b) MP SSI by oscillating gradients. A six-90° pulse sequence is employed; the number of cycles in an actual imaging sequence is much larger than shown here. Each shot is acquired under the amplitude modulated read gradient, after constant time evolution in the phase encoding one. Amplitude modulation of the latter is ranged in the various shots according to the typical 2D FT scheme. (Reproduced by permission of North-Holland from McDonald et al.[18])

Magnetization storage sequences are also introduced in order to provide the time interval necessary for gradient switching without loss of signal. Such storage periods also make it possible to obtain T_1, T_2, and $T_{1\rho}$ contrast in heterogeneous systems.[17] A further possible scheme is indicated schematically in Figure 3(b). It describes the use of MP imaging by oscillating gradients:[18] the decrease of the narrowing power due to resonance offsets (such as those introduced by the field gradients) is avoided by matching frequency and phase of the oscillating gradient with the timing of the sequence in such a way that the ideal δ pulses occur only at zero gradient (zero offset). Moreover, high gradient intensities can be reached by tuning of the gradient coils. Resolution is typically well below 1 mm; nevertheless, MP SSI suffers from the presence of artifacts and distortions because of its sensitivity to even small maladjusments of the experimental set-up; these can be minimized by several expedients.[19] This usually requires a very careful adjustment of all the intensities and timing of the sequence, which keeps it from becoming a routinely practised technique.

4.3 Magic Echo Imaging

This is the most recent among the line narrowing SSI methods. It is based on the refocusing effect which occurs in bilinear interactions, in particular in the dipolar Hamiltonian $\hat{\mathcal{H}}_D$, under the so called 'magic sandwich' sequence of Pines and co-workers.[8] Referring to the sequence of Figure 4, the system totally evolves for a time 2τ under no $\boldsymbol{B}_1$ field ($\theta = 0$ between RCF and TRCF) and for 4τ under an on-resonance $\boldsymbol{B}_1$. Refocusing occurs at $t = 6\tau$ because the system has evolved under $-\frac{1}{2}\hat{\mathcal{H}}_D$ twice as long as under $\hat{\mathcal{H}}_D$. The rf intensity during the long pulses should match the condition of a nominal 'flip' angle, α, which is a multiple of 360°.

By stroboscopic sampling every 6τ one obtains a signal influenced only by the linear interactions. Moreover, by combination with a CPMG sequence, linear interactions are also nulled, leading to an extreme narrowing.[20] This sequence leads to a double advantage where imaging is concerned: the first is directly linked to the narrowing which is generated, so that low intensity gradients can be inserted for spatial encoding; the second is that signals are recovered very far from the start of the experiment, providing a very long time interval for phase encoding of the spatial information with strong gradients using the constant time imaging approach.[21,22] Gradients can be

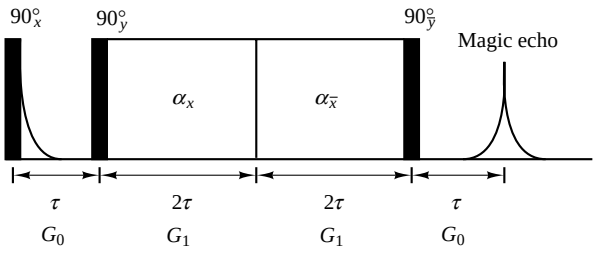

Figure 4 Magic sandwich echo sequence for application to imaging of solids. Phase inversion of the long rf pulse is introduced in order to recover from field inhomogeneity and chemical shift induced limitations. (Reproduced by permission of Springer Verlag from Blümler et al.[2])

applied in the windows indicated in Figure 4, either in the free evolution period (static gradient, G_0) or during the rf excitation (rf gradient, G_1). The method can also be made sensitive to several contrast parameters, leading in some cases to images of the NMR parameter distribution in the samples.[2,23]

4.4 MARF Imaging

The last technique which is going to be described is the one we have been developing since its presentation in 1986 as a means of obtaining spin mapping of narrowed band solids.[24] The line-narrowing MARF technique has been known since 1963, when Lee and Goldburg[11] proposed a method to reconstruct, starting from ordinary FIDs of solids, the evolution of a system in the TRCF under magic angle conditions. There are a large number of experiments where the evolution of the spins in the rotating frame is studied, especially involving relaxation in solids, and each one can be considered as a 'consequence' of the historical work of Redfield on the saturation in solids.[5] The approach to imaging by the MARF method, like the preceding ones, relies on the combination of the narrowing sequence with well defined field gradients.

Here one has to observe what happens in the doubly rotating frame, as defined by equation (2), since in that frame the interaction Hamiltonians are scaled by $D^2_{00}(\theta)$ or $D^1_{00}(\theta)$. Spatial encoding must then be introduced in the signal coming out from this frame, i.e. $\boldsymbol{B}_e$ should become space dependent. Concerning ourselves with bilinear interactions only, it is then clear that a static linear field gradient would not be sufficient because it would degrade the narrowing efficiency, as a consequence of the spread in tilt angles over the sample. $\boldsymbol{B}_e$ intensity variation and a tilt angle uniformity is instead obtained by an effective field gradient $\boldsymbol{G}_e = \boldsymbol{G}_1 + \boldsymbol{G}_0$, given by the composition of an rf ($G_1 = \partial B_1/\partial r$) and a static gradient ($G_0 = \partial B_0/\partial r$), whose intensities match a further 'magic' condition ($G_1/G_0 = \tan\theta_M = \sqrt{2}$).

Two detection methods have been mentioned. In the direct one, a very sensitive coil with its magnetic axis along z is tuned to ω_e and used both to induce transitions between the RCF Zeeman levels and to detect the precession of the perturbed system around $\boldsymbol{B}_e$ in the return to equilibrium. Excitation is performed by the so called 'audio pulses' $\boldsymbol{B}_2(t) = 2B_2(t)\cos\omega_e t\,\boldsymbol{k}$, which provide the transverse component in the TRCF $\boldsymbol{B}_{2\perp}(t) = B_2 \sin\theta_M \cos(\omega_e t + \gamma)\,\boldsymbol{i}'$ necessary to generate the observable $\boldsymbol{M}_{x'y'}$. Every NMR pulse sequence among the 'traditional' ones can, in principle, be reproduced in the TRCF. The MARF spin echo sequence which we implemented to perform imaging on crystalline adamantane is sketched in Figure 5(a).[25] The first 'spin lock' pulse is used to tilt $\boldsymbol{M}_0$ with z to z' (a θ_M pulse about 63° out of phase from the long $\boldsymbol{B}_e$ pulse) so that the initial conditions for TRCF experiments are the same as in traditional NMR ($M_{z'} = M_0$, $M_{x'} = M_{y'} = 0$). The collected signal can also be demodulated by means of the audio-frequency (af) reference ω_e in order to visualize the behavior of the system in the DRCF. In Figure 5(b) the results of a PR procedure performed on two adamantane phantoms by the MARF echo direct detection method are shown. Due to the possibility of the sample having to withstand long measurement times, and in order to avoid excessive probe complexity, PR by sample rotation along a direction perpendicular to the single gradient direction has been chosen, although 2D FT schemes are under test.

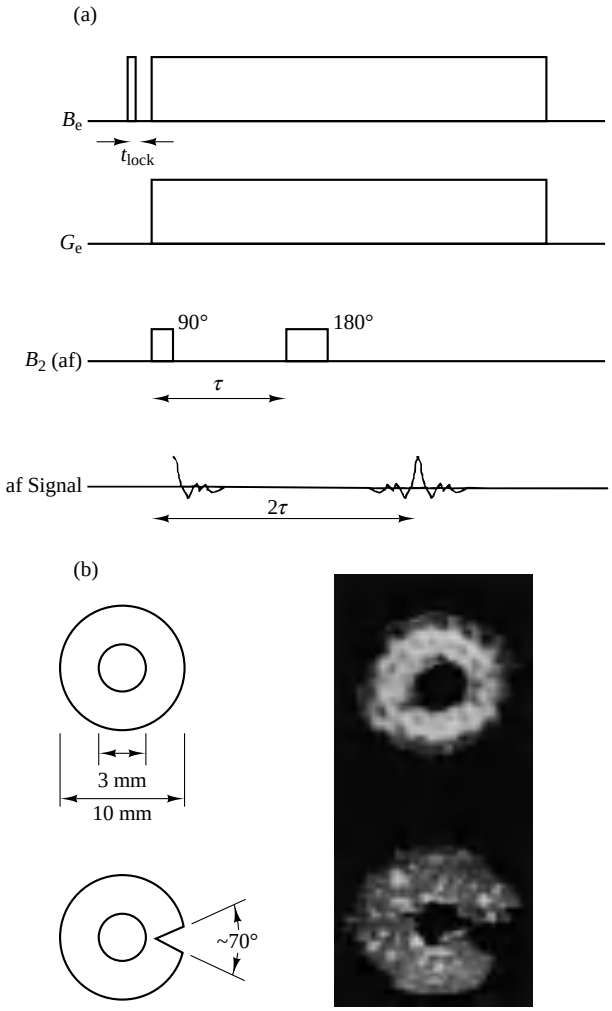

Figure 5 (a) Sequence for MARF spin echo imaging. Direct detection in the RCF provides the echo signal of the 'narrowed' solid. Its FT gives the projection along G_e. (Reproduced by permission of Società Italiana di Fisica from Lugeri et al., *Proc. Int. Summer School ''E. Fermi'', Course CXXIII, Varenna*, 1993). (b) Proton images of two adamantane samples ($\Delta\nu \approx 18$ kHz) obtained by reconstruction of 16 projections. The effective field intensity was approximately 17 mT m^{-1}, for a resolution of about 1 mm. (Reproduced by permission of Academic Press from De Luca et al.[25])

The second method is potentially very promising among the various SSI techniques. It differs from the previous one only in the way of looking at the spin system in the TRCF. As Lee and Goldburg proposed, the TRCF FID can be reconstructed by means of several experiments where the spins are made to precess around $\boldsymbol{B}_e$ for incremented time intervals $n\Delta t$ ($n = 0, \ldots, N$). $M_z(n\Delta t)$ can be read indirectly by a 90° pulse applied far enough from $n\Delta t$ to let any residual transverse magnetization be destroyed. The $(N + 1)$ M_z values so obtained represent the TRCF FID sampled with frequency $1/\Delta t$, and the spectrum is obtained by direct FT. If the evolution in the TRCF occurs under the presence of the above described $\boldsymbol{G}_e$,

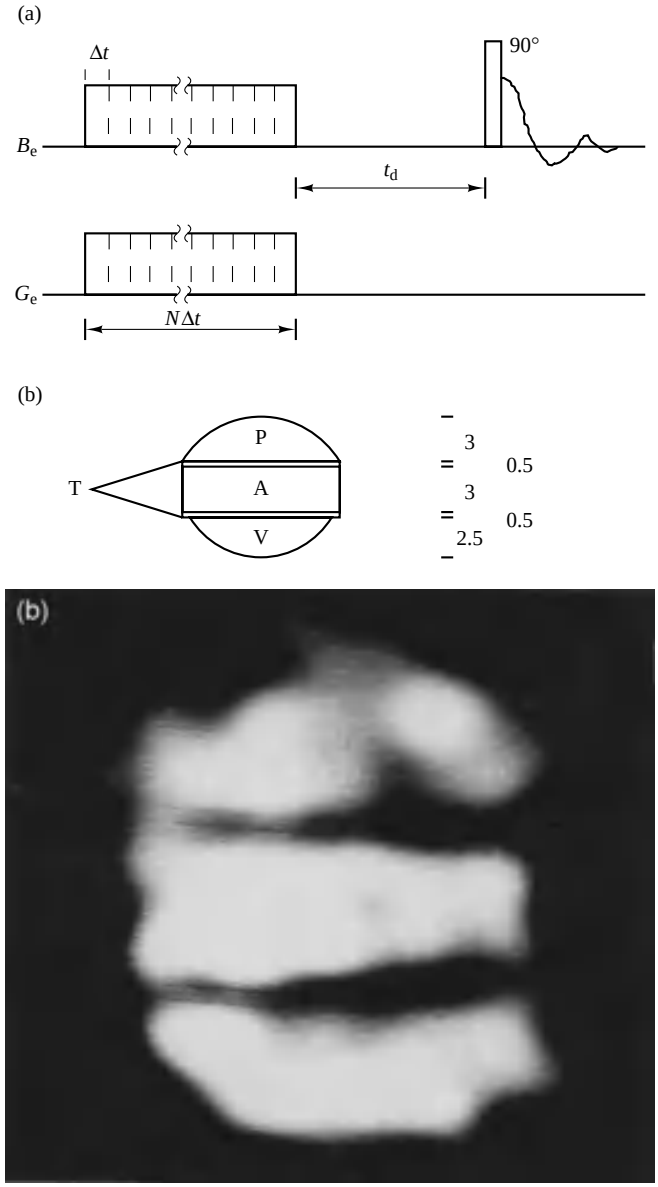

Figure 6 (a) Timing diagram of Lee–Goldburg MARF imaging. Each projection is obtained by N shots with a regularly increasing rf excitation in the magic angle condition. (Reproduced by permission of Società Italiana di Fisica from Lugeri et al., *Proc. Int. Summer School ''E. Fermi'', Course CXXIII, Varenna*, 1993). (b) PR proton image of a composite sample of polyethylene (P, length = 35 mm), adamantane (A, length = 25 mm), and Vulkollan (V, length = 15 mm) layers separated by Teflon spacers (T). Polyethylene is a rigid polymer ($\Delta\nu \approx 40$ kHz); while Vulkollan is a relatively narrow-band elastomer ($\Delta\nu \approx 1.5$ kHz). Eighteen projections were taken under a G_e of about 25 mT m^{-1}. The corresponding resolution was estimated to be about 200 μm

one can obtain spatial discrimination of the spectrum. The Lee–Goldburg imaging sequence is illustrated in Figure 6(a). Again PR is the easiest imaging method to use in such conditions, and by this procedure we obtained the well resolved image ($\Delta r \approx 200\,\mu$m) of Figure 6(b).

It should be noted that, apart from a slight complexity in the probe arrangement, the technique is very easy to implement, since it is based on repeated LCF experiments, with a consequent relatively high signal-to-noise ratio. A home-made computer-assisted apparatus ensures stability, reliability and rapidity of the whole sequence;[27] it also allows a wide variety of preparation and reading pulse sequences to be built instead of the basic method of Figure 6(a). These sequences are used to introduce sensitivity to different relaxation parameters. In particular, T_1-, T_2- and $T_{1\rho}$-weighted images of rigid polymers and crystalline solids have been obtained, leading to interesting data on the slowest molecular motions in such systems.[28,29]

5 RELATED ARTICLE

Polymer MRI.

6 REFERENCES

1. P. T. Callaghan, 'Principles of Nuclear Magnetic Resonance Microscopy', Clarendon Press, Oxford, 1991, Chap. 3.
2. P. Blümler and B. Blümich, *NMR Basic Principles Progr.*, 1993, **30 I**, 209.
3. A. Abragram, 'Principles of Nuclear Magnetism', Clarendon Press, Oxford, 1961, Chaps 3, 5.
4. M. Mehring, 'Principles of High Resolution NMR in Solids', 2nd edn., Springer-Verlag, Berlin, 1983; U. Haeberlen, *Adv. Magn. Reson. (Suppl.* 1), 1976.
5. C. P. Slichter, 'Principles of Magnetic Resonance', 2nd edn. Springer-Verlag, Berlin, 1990, p. 163.
6. A. G. Redfield, *Phys. Rev.*, 1955, **98**, 1787.
7. M. E. Rose, 'Elementary Theory of Angular Momentum', Wiley, New York, 1957.
8. A. Pines, W. K. Rhim, and J. S. Waugh, *J. Magn. Reson.*, 1972, **6**, 457.
9. A. E. Mefed and V. A. Atsarkin, *Sov. Phys. JEPT, 1978*, **47**, 378.
10. F. De Luca, B. C. De Simone, B. Maraviglia, and C. Nuccetelli, *Solid State Commun.*, 1989, **70**, 797.
11. M. Lee and W. I. Goldburg, *Phys. Rev.*, 1965, **140**, 1261.
12. D. G. Cory, J. W. M. Van Os, and W. S. Veeman, *J. Magn. Reson.*, 1988, **76**, 543.
13. G. Schauss, B. Blümich, and H. W. Spiess, *J. Magn. Reson.*, 1991, **95**, 437.
14. U. Scheler, B. Blümich, and H. W. Spiess, *Solid State Nucl. Magn. Reson.*, 1993, **2**, 105.
15. U. Scheler, G. Schauß, B. Blümich, and H. W. Spieß, *Solid State Nucl. Magn. Reson.*, 1996, **6**, 105.
16. G. C. Chingas, J. B. Miller, and A. N. Garroway, *J. Magn. Reson.*, 1986, **66**, 530.
17. M. A. Hepp and J. B. Miller, *Solid State Nucl. Magn. Reson.*, 1996, **6**, 375.
18. P. J. McDonald and A. R. Lonergan, *Physica B*, 1992, **176**, 173.
19. D. G. Cory, *Solid State Nucl. Magn. Reson.*, 1996, **6**, 347.
20. S. Matsui, *Chem. Phys. Lett.*, 1991, **179**, 187.
21. D. E. Demco, S. Hafner, and R. Kimmich, *J. Magn. Reson.*, 1992, **96**, 307.
22. S. Hafner, D. E. Demco, and R. Kimmich, *Solid State Nucl. Magn. Reson.*, 1996, **6**, 275.
23. F. Weigand, D. E. Demco, B. Blümich, and H. W. Spieß, *Solid State Nucl. Magn. Reson.*, 1996, **6**, 357.

24. F. De Luca and B. Maraviglia, *J. Magn. Reson.*, 1986, **67**, 169.
25. F. De Luca, B. C. De Simone, N. Lugeri, B. Maraviglia, and C. Nuccetelli, *J. Magn. Reson.*, 1990, **90**, 124.
26. F. De Luca, B. C. De Simone, N. Lugeri, and B. Maraviglia, *J. Magn. Reson. A*, 1993, **102**, 287.
27. F. De Luca, N. Lugeri, S. Motta, G. Cammisa, and B. Maraviglia, *J. Magn. Reson. A*, 1995, **115**, 1.
28. F. De Luca, G. H. Raza, A. Gargaro, and B. Maraviglia, *J. Magn. Reson.*, 1997, **126**, 159.
29. F. De Luca, A. Gargaro, B. Maraviglia, G. H. Raza, and C. Casieri, *Magn. Reson. Imaging*, 1998, **6**, 435.

Biographical Sketches

B. Maraviglia. *b* 1938. M.Sc., Ph.D. University of Florence. Assistant Professor, Duke University, 1968–69; Associate Professor, Rome, 1970; Full Professor, University of Rome, 1980–present. Head of the NMR Spectroscopy and Imaging Group of the University of Rome 'La Sapienza' 1994–present. President of the Groupement AMPERE 1994–present. Approx. 200 publications. Research interests: low-temperature physics, quantum solids, NMR imaging in biomedicine and solids, ultraslow motions, double resonance rare nuclei imaging.

Francesco De Luca. *b* 1950. Degree, 1974, University of Rome. Assistant Professor, 1975, Associate Professor, 1986–present, University of Rome. Approx. 120 publications. Research interests: NMR imaging of solids and of living systems, molecular solids, dielectric spectroscopy on membranes, ultraslow motions, double resonance, low-γ nuclei imaging, electrical impedence tomography.

Bruna C. De Simone. *b* 1955. Degree, 1979, University of Rome. Researcher, Department of Physics University of Rome, 1984; researcher, University of Calabria, 1992–present. Approx. 60 publications. Main research interests: computer-assisted tomography, maximum entropy, solid state imaging, bioimaging, liquid crystals, electrical impedence tomography.

Nicola Lugeri. *b* 1963. Degree, 1988, University of Rome. Specialist in Health Physics, 1994. Remote sensing staff manager at the Dept for National Technical Surveys, 1996–present. Approx. 25 publications. Research interests: solid state NMR imaging, ultraslow motions, probe and coils design.

Imaging Techniques for Solids and Quasi-Solids

John H. Strange and Morley R. Halse
University of Kent, Canterbury, Kent, UK

1 INTRODUCTION

Liquids, and materials of biological interest such as water and fat, typically have T_2 values in the region of 100 ms or longer and the success of medical MRI has amply demonstrated our ability to image such materials. As the target material becomes more solid-like, however, the problems of imaging become more severe. As well as an immediate problem of lower resolution, there is also a general deterioration in signal-to-noise ratio. It is an unfortunate fact that short T_2 materials do not have a correspondingly short T_1. Since the signal-to-noise ratio in the final image depends critically on the fraction of time that signal is available, it is actually the generally unfavorable ratio of T_2:T_1 in solids as much as the inherently short T_2 itself that is the root cause of the problem of broadline imaging.

The standard technique of reducing the T_1 of pure water by doping with paramagnetic relaxation centers is a common example in which the T_1 of the material can be artificially reduced, but such treatment is not generally available for most applications. All attempts so far have therefore been directed at increasing T_2 by adapting the standard line-narrowing techniques of solid state NMR (e.g. MREV, WAHUHA and their many variants, as well as magic angle spinning) to imaging.

These techniques are technically very demanding. A second 'direct' approach has been simply to accept the broadline and adjust the imaging parameters such as echo time, and in particular, gradient strength, so as to generate an image within a timescale of the order of T_2. This 'direct' approach has proved itself particularly suited to the more nonmedical materials science applications where short imaging times are not a restriction. One sophisticated variation uses the large enhancement in effective field gradients that result in multiple quantum NMR.

As well as the brief descriptions offered in this short article, the reader is referred to the various reviews on the subject by Blümler and Blümich,[1] Miller et al.,[2] and Strange,[3] the articles on solid state imaging by Veeman et al. in the book 'Magnetic Resonance Microscopy' by Blümich and Kuhn,[4] and to Callaghan's book.[5]

At present, no one method has emerged with a clear advantage and the story of solids imaging is one of parallel progress being made steadily on a number of fronts. In practice, the choice of technique is likely to be determined by consideration of the severity of the broadline problem, the necessity to preserve spectral information such as chemical shift, the physical nature of the specimen, or the need to apply slice selection.

2 MRI IN SOLIDS: THE PROBLEM STATED

We first give a basic analysis of the imaging resolution expected in MRI. Consider two groups of protons separated by a distance dz in a gradient $G_z = \mathrm{d}B_z/\mathrm{d}z$ applied in the z direction as shown in Figure 1(a). The difference between the Larmor frequencies of the two groups of protons will be $\gamma \mathrm{d}z G_z$. After a 90° pulse, we therefore have the situation shown in Figure 1(b) in which the received signal will be a beat pattern within a decaying envelope of time constant T_2. The FT of this FID will give two peaks as shown in Figure 1(c). The decay of the envelope will broaden each line by an amount $1/\pi T_2$ Hz. The shorter T_2 is, the greater is the broadening. The limit of resolution will occur roughly when the width of each line is comparable to or greater than their frequency separation, i.e.

$$1/\pi T_2 \sim \gamma \mathrm{d}z G_z \tag{1}$$

For a typical medical MRI scanner, the image echo time TE is designed to fall well within T_2 so that signal is not lost. Under these circumstances, the broadening of the line due to each group of protons in Figure 1(a) is due to the finite data capture window (~TE) rather than the T_2 decay itself. Thus

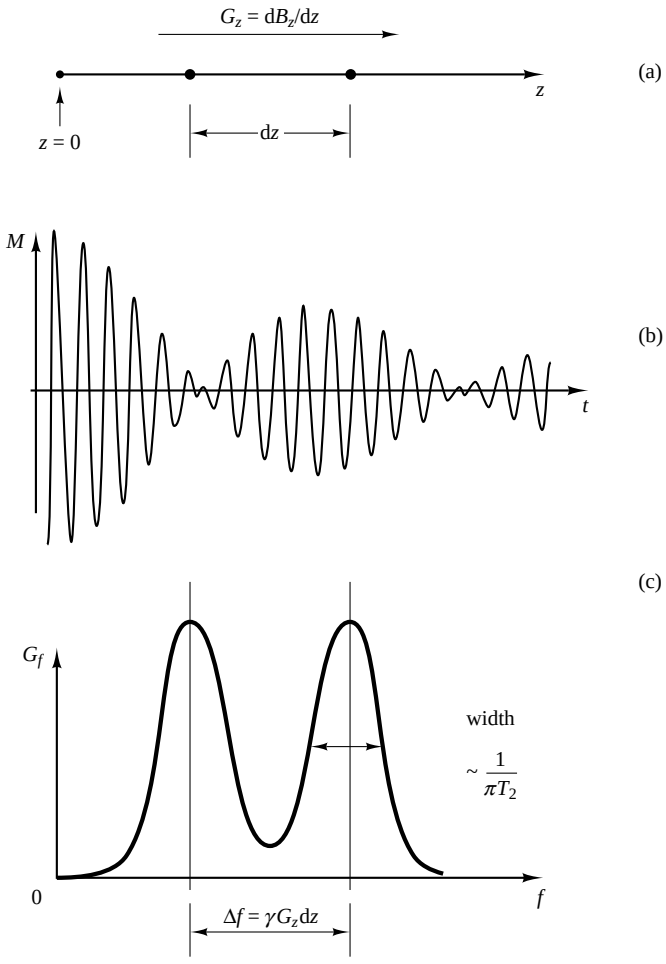

Figure 1 Illustration of linewidth limited resolution in NMR imaging (see text)

$$dz \sim 1/\gamma G_z \pi TE \quad (2)$$

With TE = 20 ms and G_z = 10 mT m^{-1} we find that $dz \sim 60$ μm.

Now consider the situation in a solid where T_2 may be 100 μs or less. Even if we relax the signal-to-noise consideration and take $TE = T_2$, equation (2) predicts a resolution (with G_z = 10 mT m^{-1}) of little better than 10 mm.

The resolution can obviously be improved by increasing the gradient. But increasing G_z will increase the spread of Larmor frequencies generated by the extremities of the sample. If the field-of-view is to be maintained, the receiver bandwidth will have to be increased and the receiver signal-to-noise ratio will suffer. The inevitable conclusion is that the direct approach leads to a reduced signal-to-noise. Longer imaging times are therefore required if signal-to-noise ratios are to be restored by signal averaging.

The various schemes put forward to circumvent this basic truth are now discussed.

3 IMAGING METHODS

3.1 Multipulse Line Narrowing

The earliest multipulse sequences designed to average out the dipole–dipole interaction and preserve chemical spectroscopic information in solids were those of Waugh and Mansfield and their collaborators.[6] These sequences artificially provide the essential time dependence required to average out the magnetic interaction between neighboring dipoles. Many variants have been designed which not only cancel the dipole–dipole interaction, but also successfully cancel other broadening interactions such as anisotropic chemical shift. Sequences are usually designed to suppress the effects of magnetic field inhomogeneity broadening as well.

But therein lies the crux of the problem with the 'standard' line-narrowing approach. Sequences which cancel the effects of field inhomogeneity are clearly of no use in imaging unless they can allow a separation of magnetic inhomogeneity and applied field gradient effects. What is required is a pulse sequence that is tolerant to field offset: i.e. one which produces line narrowing in the presence of a field gradient, yet essentially preserves the gradient interaction. The solutions which have been proposed require an advanced understanding of quantum mechanics and are tricky to implement in practice. However, one of the underlying principles of all of these methods is simply stated: make sure that the imaging gradient is zero during the rf pulses. Two approaches have been suggested.

The first is due to McDonald and Tokarczuk who proposed a 6-pulse (ZIG-ZAG) sequence[7] in which the pulses are timed to coincide with the zero crossing of an oscillatory imaging field gradient. Remembering that multipulse sequences attain their full efficiency only when the pulse separation is much less than T_2, typical interpulse times are of order 20 μs. Thus a high frequency oscillatory imaging gradient (~25 kHz) is required. Several imaging schemes have been demonstrated and an example of an image of two 5 mm cubes of the organic crystal adamantane[8] is shown in Figure 2. The image was formed from a two-dimensional FT using a modulated gradient technique. Adamantane has a linewidth of 20 kHz at room temperature. The normal T_2 has been extended to several milliseconds by the ZIG-ZAG sequence.

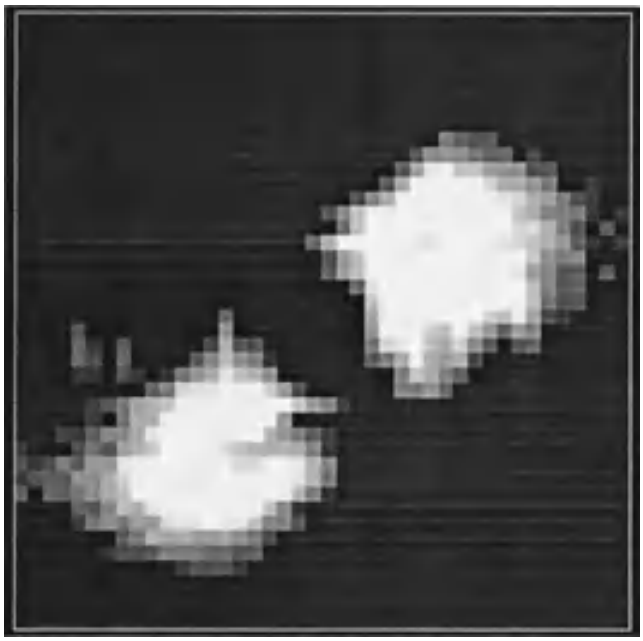

Figure 2 Two-dimensional FT image of two 5 mm cubes of adamantane obtained using the ZIG-ZAG multipulse line-narrowing technique. (Reproduced by permission of Elsevier Science B.V. from P. J. McDonald and A. R. Lonergan[8])

The second approach, and currently regarded as the most successful of all the solids imaging schemes proposed to date, has been that of Cory et al.[9] They circumvent the problem of the simultaneous application of rf and imaging gradients by applying the gradients only in very short bursts between the rf pulses. Their second-averaging method can produce astonishing results, as the high-resolution multipulse images of sections through a polyacetal (Delrin) phantom[1] shown in Figure 3 testify. Although this method shows that, in principle, the problem of solids imaging has been solved, very powerful rf and gradient amplifiers are required together with very low inductance imaging gradient coils. The equipment is expensive and well beyond the resources of most laboratories. One would therefore have to say of these line-narrowing techniques, that while their efficiency is impressive, they are difficult to set up and their use is not yet routine.

3.2 Magic Angle Spinning (MAS) Imaging

Magic angle spinning is a mechanical line-narrowing technique first proposed by Andrew and Eades[10] in which the sample is rotated at high speed at an angle of 54.7° to the $\boldsymbol{B}_0$ field. At this angle, the dipole–dipole interaction can be reduced and eventually averaged to zero provided the speed of rotation is comparable to or larger than the NMR linewidth. Although MAS spinners are now a standard facility on most spectrometers, the proposal that MAS might be modified to allow simultaneous imaging has only recently been explored because of the technical demands. The aim is to generate a rotating imaging gradient field matched in frequency and phase

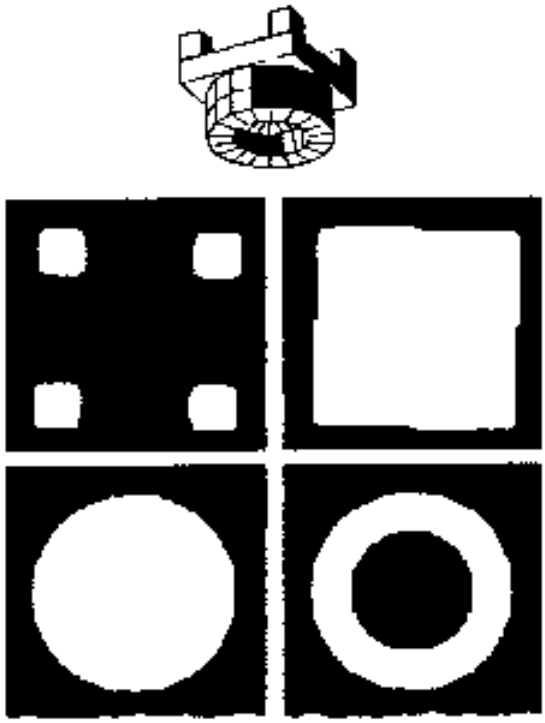

Figure 3 Multipulse image using second-averaging of a Delrin (polyacetal) phantom formed from 64 × 64 × 16 voxels obtained at 400 MHz. Voxel size is 92 μm × 92 μm × 625 μm. Four sections through the sample (given schematically above) are shown. (Reproduced by permission of D. G. Cory)

to that of the MAS rotor. Under such circumstances, the gradient field will appear stationary with respect to the sample and imaging becomes relatively simple. Clearly such a scheme imposes severe restrictions on sample size and strength and its use is therefore always likely to be limited. An example of two such MAS images taken from the work of Cory et al.[11] is shown in Figures 4(a) and (b). The experiment is tolerant of small errors in setting up and effects due to spinning sidebands can be eliminated. Available rotation rates will not, however, narrow the broadest lines. To overcome this problem, it has been necessary to combine MAS with multipulse line-narrowing sequences such as MREV-8. This has been successfully demonstrated for polyethylene particles of about 2 mm in size by Conradi et al.[12] The application of this technique to plastically deformable solids is clearly a problem as a spinning rate of 5 kHz can produce centrifugal acceleration of 10^5 g!

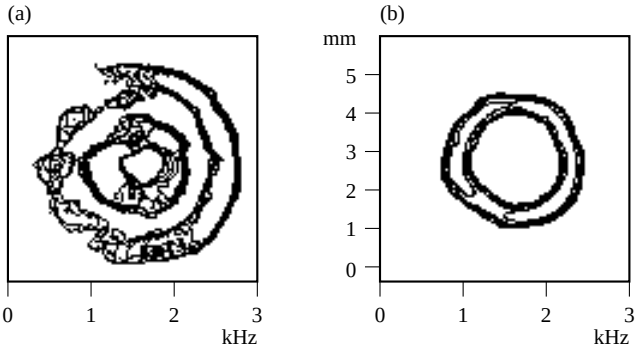

Figure 4 Ring of polybutadiene imaged by MAS showing (a) distortion due to chemical shift, (b) improvement by deconvolution. (Reproduced by permission of Academic Press from D. G. Cory et al.[11])

Synchronous rotation of sample and gradient allows either radial scanning of k-space to produce an image by filtered back projection reconstruction or two-dimensional Fourier transform imaging. It is also possible to scan k-space by rotating the gradient at a different frequency to that of the sample rotation. For more detail and variations of the MAS method, readers can consult the reviews by Blümler and Blümich[1] and by Veeman et al. in Blümich and Kuhn.[4]

Although MAS methods are less successful in line narrowing, an attraction of this method for broadline MRI is that spectroscopic information such as the chemical shift is preserved and ^{13}C spectroscopic imaging is attractive.

3.3 Rotating Frame Imaging

This technique is another example of the extension of a solid state line-narrowing method to imaging. The idea is to take the main $\boldsymbol{B}_0$ field off-resonance and apply rf of suitable amplitude so as to generate an effective field $\boldsymbol{B}_{\text{eff}}$ at the magic angle in the rotating frame (MARF). The net result is that the magnetization is spin locked about the effective field at the magic angle and line narrowing is achieved.[13] For imaging, a gradient in the resonance offset is established across the sample while at the same time ensuring that the effective field remains everywhere at the magic angle. This is done by suitable modulation of both the $\boldsymbol{B}_0$ and $\boldsymbol{B}_1$ fields. Compared with the MAS method, corresponding rotation rates are higher and therefore line narrowing is more efficient. Another advantage over MAS is of course that the sample itself remains static. Sensitivity is however low, corresponding to the low (audio) frequency of resonance in the effective field, and is directly related to $\boldsymbol{B}_1$.

A variation of this experiment, whereby signal is only observed after the pulsed rf and gradient encoding and is acquired slowly point-by-point, requires varying the length of the spin lock and gradient pulses. The signal is observed at radiofrequencies with the corresponding advantages of high signal-to-noise. Technically, the equipment is demanding, as specially matched gradient coils are required. An example of a rotating frame image of compressed adamantane taken from de Luca et al.[14] is shown in Figure 5.

Note finally that if θ denotes the angle between $\boldsymbol{B}_{\text{eff}}$ and the main $\boldsymbol{B}_0$ field, the isotropic chemical shift and gradient interactions scale as $\cos\theta$, whereas the anisotropic interactions scale as $(3\cos^2\theta - 1)$. Thus MARF can retain some aspects of the isotropic chemical shift, while averaging the anisotropic parts to zero.

Another example of rotating frame imaging is that proposed by Barrall et al.[15] and by Woelk et al.[16] and is a beautiful example of lateral thinking. The method exploits the $1/r$ dependence of the magnetic field surrounding a straight wire carrying a current to provide a gradient of the rf field. The wire forms part of a resonant rf cavity, and the sample to be imaged is placed near to the wire or may be deposited or painted onto the wire. When an rf pulse is applied to the wire, the resulting magnetization rotation angle in the sample will be inversely proportional to radial distance. By applying an rf

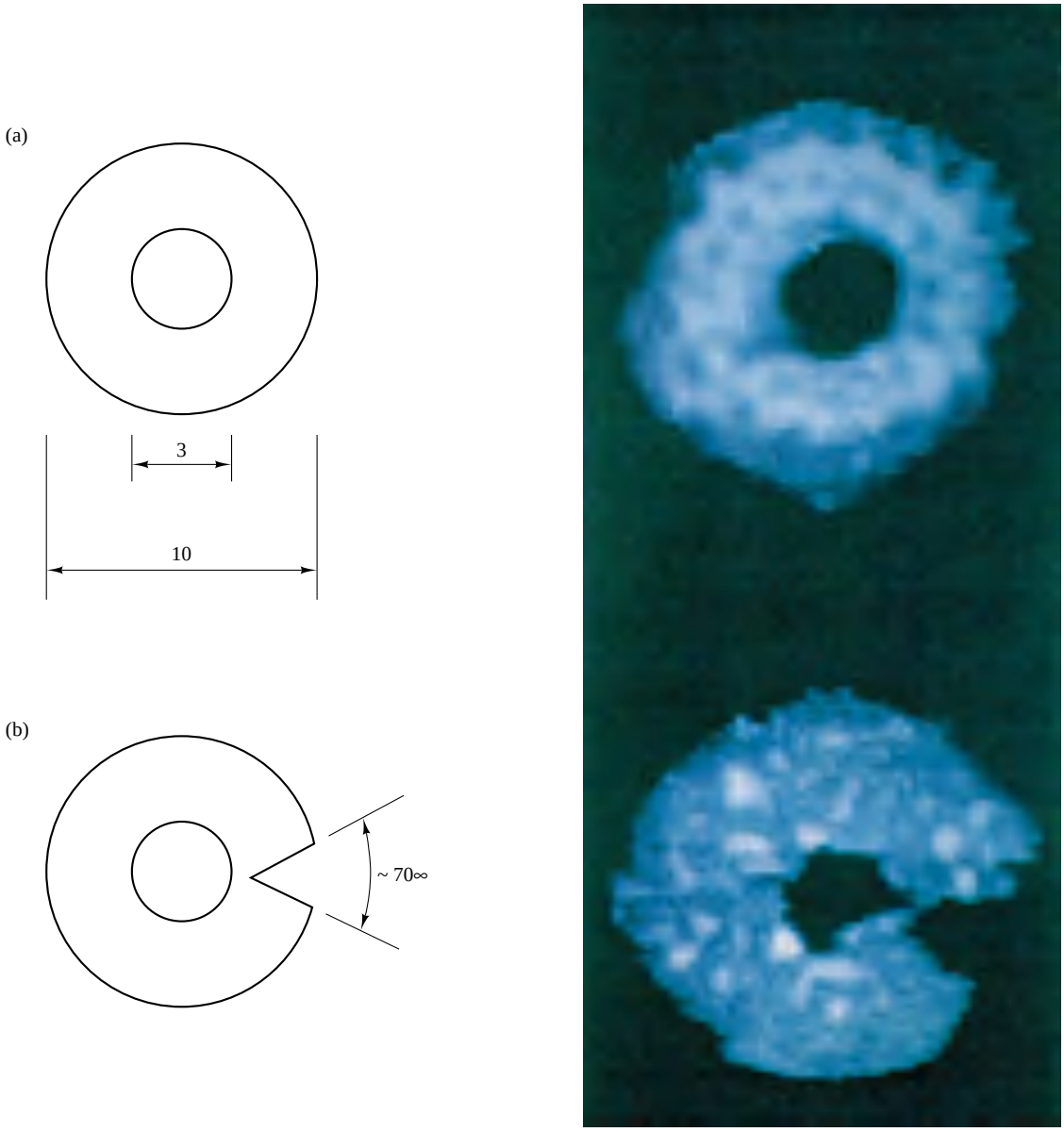

Figure 5 Phantom of organic crystalline material formed from compressed adamantane imaged using MARF. (Reproduced by permission of Academic Press from F. de Luca et al.[14])

nutation sequence consisting of rf pulses interleaved with data acquisition points, the total signal $S(t)$ will be given by[15]

$$S(t) = \int \omega(r)\rho(r)\sin[\omega(r)t]\,\mathrm{d}r \qquad (3)$$

The radial spin density distribution $\rho(r)$ can be readily calculated from $S(t)$. The method is essentially the same as MARF, except that the nutation is about y' in the rotating frame rather than the magic angle and so there is no consequent benefit from line narrowing. However the rf gradients can be made very large near the wire and the quoted resolution is of the order of 20 μm for a Teflon sample.

3.4 Magic Sandwich Echo Imaging

This technique has been discussed by Matsui et al.[17] and by Demco et al.[18] The basic sequence 90_x–τ–90_y–2τ–90_x–2τ–90_{-x}–τ–90_{-y}–τ–echo, first described by Rhim et al.,[19] produces a 'magic echo' after a time 6τ. By repeating the sequence, a train of magic echoes can be generated decaying with a much extended FID. The application of imaging gradients and data acquisition are undertaken in the appropriate windows of a 24τ sequence. The scheme appears to be much more robust to experimental imperfections in timing and phase errors than the other multipulse sequences and is considered to be one of the most promising broadline imaging schemes suggested to date. An example of a three-dimensional magic

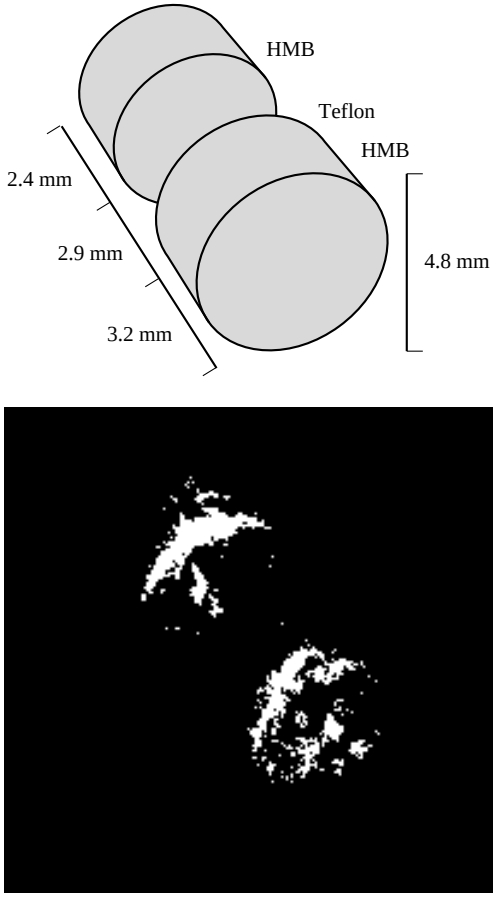

Figure 6 A three-dimensional magic echo phase-encoded image of a hexamethylbenzene (HMB) phantom. Voxel resolution is 300 μm. A drawing of the sample is shown at the top. (Reproduced by permission of Academic Press from S. Hafner et al.[20])

echo phase-encoded image of a hexamethylbenzene phantom taken by Hafner et al.[20] is shown in Figures 6(a) and (b).

3.5 Stray Field Imaging (STRAFI)

This technique, pioneered by Samoilenko et al.,[21] is a successful example of the 'direct' approach and bears some similarity to the sensitive plane method developed many years ago by Hinshaw. It exploits the fact that a very large field gradient is naturally available in the fringing field of a superconducting magnet. In a region displaced well away from the magnet center and in some cases physically outside the magnet altogether the gradient can approach 40 T m^{-1} for a 4.7 T magnet. The gradient is of course static, so the sample has to be moved through the gradient by means of stepper motors and the image reconstructed by back projection. The width of the sensitive plane dz is given by

$$\gamma G_z \mathrm{d}z = 1/T_{90} \tag{4}$$

i.e.

$$\mathrm{d}z = 1/\gamma G_z T_{90} \tag{5}$$

Thus dz is simply the spectral width of the rf pulse in Hz divided by the gradient in Hz m^{-1}. With a 90° pulse of 20 μs and a gradient of 25 T m^{-1}, equation (5) predicts a resolution of 50 μm. With such a huge gradient, the FID is extremely short, so 90_y pulses are used to hold up the magnetization by generating a train of solid echoes.[22] The signal from the slice is simply proportional to the integrated sum from all of the echoes.

The method has two interesting additional features. The first is that because the sample is moved through the sensitive slice during imaging, T_1 saturation effects can be avoided and the pulse sequence repetition rate can be much faster than dictated by the normal $5T_1$ rule. Signal averaging can be carried out by ramping the sample through the sensitive slice many times.

The second advantage is that STRAFI suppresses susceptibility artifacts. These occur in any sample at the boundaries between regions of differing magnetic susceptibilities. At such boundaries, small changes in the internal $\boldsymbol{B}$ field are generated proportional to $\boldsymbol{B}_o(\chi_1 - \chi_2)$. Since the distance over which this change in internal field is generated can be measured in μm, even if the differences between the susceptibilities is only 10^{-5}, the internal gradients generated can be enough to distort the image. With STRAFI, however, the very large imaging gradient ensures that these internal gradients are rendered negligible. It is therefore capable of imaging materials containing paramagnetic impurities such as soil or rock (see, for example, Kinchesh et al.[23]).

The method has progressed from early one-dimensional profiles across a group of human hairs showing the μm resolution capability of the method, to full high resolution three-dimensional images of small, solid, manufactured components.

Clearly STRAFI has a promising future as a materials science tool but because of the time penalty, it is most likely, in our opinion, to find its greatest use in the generation of one-dimensional profiles. An example from Perry et al.[24] showing the ingress of acetone vapour into poly(vinyl chloride) (PVC) is shown in Figure 7. The profile is due to a combination of mobile, absorbed acetone (T_2 ~ 25 ms), swollen PVC (T_2 ~ 2 ms), and rigid PVC (T_2 ~ 90 μs)

3.6 Oscillating Field Gradients

This method is the second example of the direct approach and has been developed over the years by the authors and others since an early paper by Cottrell et al.[25] The method has found most application in the semi-solid regime covering T_2 values in the millisecond region. A large oscillating gradient with a period T, whose magnitude defines the attainable image resolution, is established in a gradient coil. After any initial transients have decayed, a 90° rf pulse is applied at the moment of zero crossing of the gradient field. Provided the rf pulse is very short, the gradient will be sensibly zero throughout the pulse and all spins in the sample will receive a 90° rotation. After one cycle of the gradient field, a gradient echo forms. Due to the restriction of the T_2 decay, the period T of the gradient field must be of the order of T_2. As a consequence of the varying gradient, sampling of the echo in the data capture window from $T/2$ to $3T/2$ at a uniform rate results in a nonlinear coverage of k-space. Fortunately compensation for this effect can be achieved in software, and a one-dimensional

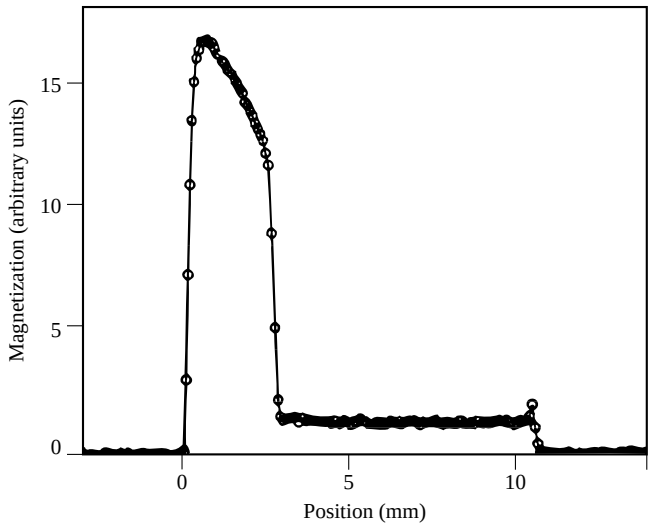

Figure 7 Acetone vapor diffusing into PVC. The image, obtained by STRAFI, shows the acetone concentration variation from 0 to 3 mm penetration superimposed on the rigid PVC signal from 0 to 11 mm. (Reproduced by permission of Butterworth Heinemann Ltd © 1994 from K. L. Perry et al.[24])

profile can then be obtained from an FT in the usual way. Two-dimensional images can be obtained by back projection.

The method has the merit of great simplicity, but it also has its disadvantages and its traps for the unwary. The main disadvantage is that the large gradients necessitate the use of a large receiver bandwidth. As outlined in Section 2, this inevitably leads to a degradation in signal-to-noise ratio. An example of a back projection image taken of a rubber sample with a T_2 of approximately 700 μs is shown in Figure 8.

The method can also suffer from the presence of a very small dc bias in the gradient current which can severely attenuate the amplitude of the echo if the *k*-space trajectory fails to return to the origin. All dc coupled amplifiers suffer to a greater or lesser extent from varying dc offsets and these offsets can have disastrous effects on the image. To prevent this happening, and at the same time to eliminate many of the effects due to the inductance of the gradient coils, a capacitor is used to series resonate the gradient current.

One further disadvantage of the method is that since it uses a *gradient* echo, the images can be degraded by an intensity modulation effect due to phase shifts caused by inhomogeneities in the main $\boldsymbol{B}_0$ field. Unlike a spin echo, there is no automatic compensation for $\boldsymbol{B}_0$ inhomogeneity. A further consequence is that in its simplest form, the method is limited to the study of materials with a T_2 of less than the T_2* of the magnet.

Despite these disadvantages, oscillating gradient imaging has proved to be of considerable practical utility. Several variants of the basic method have been proposed. In one scheme by Mat Daud and Halse,[26] imaging is carried out with two oscillating gradients, one having twice the period of the other. The second gradient is used for phase encoding. Working out the two-dimensional (2D) *k*-space trajectories for this data set is even more complicated, but the final step involves a 2D FT and leads directly to an image in the normal way. An example of a ^{19}F image of a 'C' shaped piece of Teflon is shown in Figure 9. The T_2 here is approximately 60 μs. The peak gradient was 1 T m^{-1} and the imaging time was 20 min.

The solid echo (90_x–τ–90_y) arising from a refocusing of the dipole-dipole interaction can of course be used to extend the signal in oscillating gradient imaging as well as in STRAFI. An example of an extended train of echoes from rubber[3] for which T_2 ~ 500 μs is shown in Figure 10. The 90_y pulses are applied at the zero crossing of every odd gradient cycle (thus unfortunately destroying the odd-numbered gradient echoes) but leaving the even-numbered echoes unaffected.

Note that in Figure 10, although the train of solid echoes extends to ~$10T_2$, in this example, the decay was in fact limited by the inhomogeneity of the magnet. In practice, therefore, for semi-solids such as rubber, it is found that a series of 180_y pulses is more beneficial for extending the decay envelope. Compensating for the inhomogeneity of the $\boldsymbol{B}_0$ field in this way does not extend T_2. However, when the 180_y pulses are closely spaced, they can be regarded as generating a form of average spin locking field in the y' direction in the rotating frame. The decay of the magnetization therefore tends to $T_{1\rho}$.

Unfortunately, extending the decay by generating multiple echoes in this way cannot be exploited to increase the image

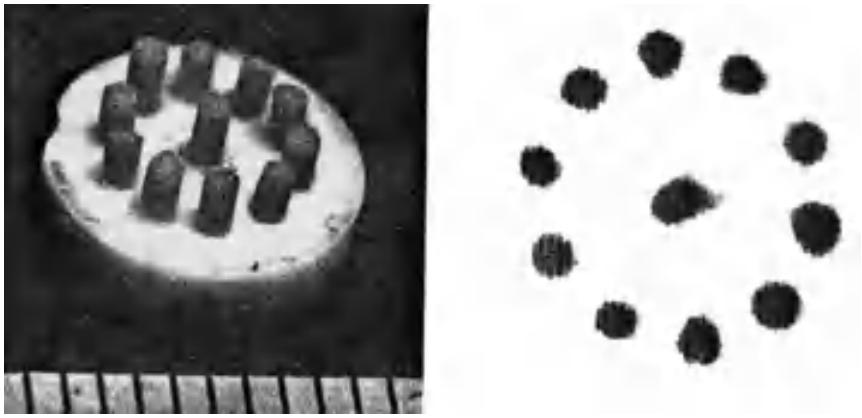

Figure 8 Image of 11 pieces of 1 mm diameter rubber in a Teflon holder obtained from echoes formed by the direct application of large oscillating field gradients. (Reproduced by permission of The Royal Society, London from J. H. Strange[3])

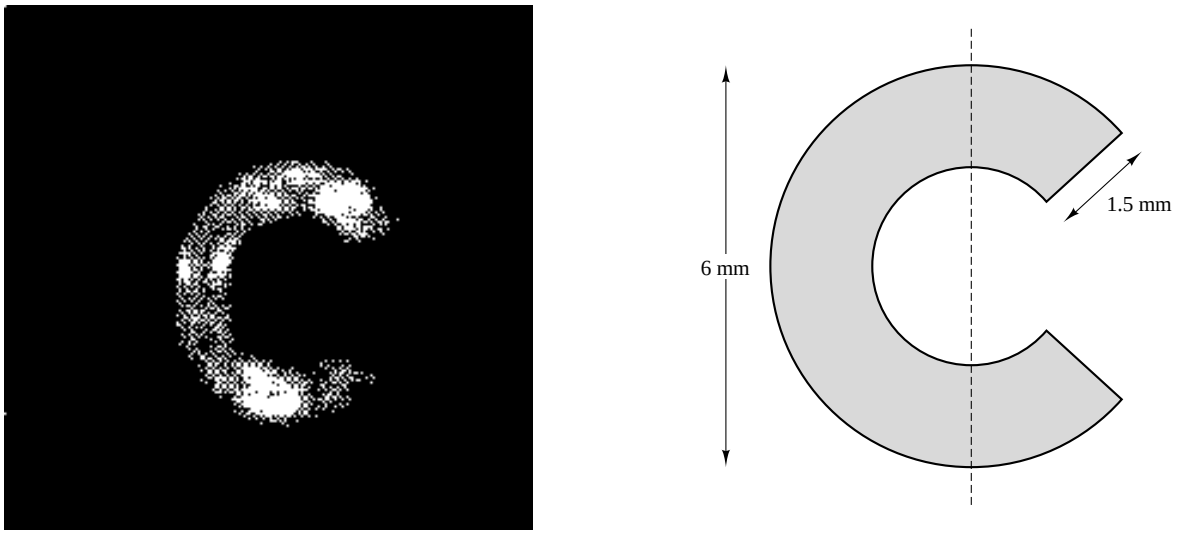

Figure 9 Two-dimensional FT ^{19}F image of a poly(tetrafluoroethylene) phantom obtained by the use of two large oscillating field gradients. The phantom is 6 mm in diameter and 4 mm thick. (Reproduced by permission of Elsevier Science B.V. from Mat Daud and Halse[26])

resolution for a given gradient field strength and the apparent line narrowing is illusory. The reason for this is that the time-scale of each individual data capture window and the shape of each individual echo is unaltered (see Figure 10). However, the method does have the advantage that the signal-to-noise ratio can be improved by averaging all the echoes together.

The 'direct' imaging approach using large oscillating gradients has also been used to study the ingress of water vapor into compacted zeolite powders[27] in which the T_2 of the adsorbed water is again of order 1 ms. The 'direct' approach with large imaging field gradients has also been used for ^{23}Na imaging in sodium chloride crystals. By taking advantage of the signal 'wipe-out' arising from large electric quadrupole interactions in the vicinity of a defect, the crystal defect density can be mapped.[28]

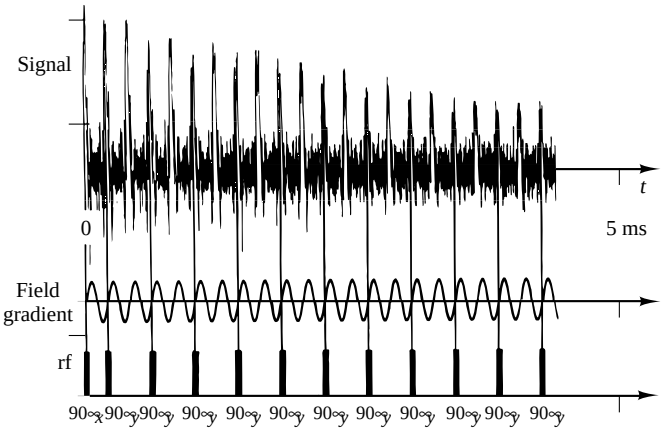

Figure 10 Timing diagram of an oscillating field gradient pulse sequence combining gradient and multiple solid echoes for imaging of semi-solids. (Reproduced by permission of The Royal Society, London from J. H. Strange[3])

3.7 Phase Encoding or Constant Time Imaging

In the scheme as first proposed by Emid and Creyghton,[29] it was supposed that the effects of a short T_2 could be eliminated by taking measurements *at a single point in time* on a series of FIDs in which a field gradient is systematically varied. The method is essentially equivalent to normal phase encoding, but as such it does have two significant advantages. The first is that phase encoding is immune to $\boldsymbol{B}_0$ field inhomogeneities and to susceptibility artifacts (cf. STRAFI). The reason for this is very easily understood by considering the phase evolution of a group of spins contributing to a particular pixel in the final image. Although from the time of rf excitation to the formation of the imaging echo, field inhomogeneities will have caused unknown phase shifts, *these phase shifts remain constant for that particular group of spins*, whereas the phase shift encoded by the imaging gradient varies in a systematic way. When the modulus of the image is computed, these unknown phase shifts are eliminated.

The second advantage of phase encoding is that, as mentioned above, the data can be gathered at a single, constant point in time and that this time can be arranged to be after the phase-encoding gradient has been switched off. With no gradient present at the moment of data acquisition, the bandwidth of the receiver can be much reduced, thus significantly improving the signal-to-noise ratio. The disadvantage of all pure phase-encoding methods is, of course, a much increased imaging time.

It must not be forgotten that the rise time of the large gradient pulses needed for phase encoding in a time of the order of T_2 or less can become significant. A novel scheme was proposed by Rommel et al.[30] to overcome the gradient rise-time problem. They used a SLISE (*s*pin *l*ock-*i*nduced *s*lice *e*xcitation) pulse for slice selection followed by a Jeener–Broekhart 90_x–45_y–$45_{y,x}$, echo sequence repeated with two-dimensional phase encoding. The gradients were applied and allowed to stabilize before the 90_x rf pulse was applied and removed only after the magnetization had been stored with the 45_y pulse.

3.8 Deconvolution

An image of any object is of course simply that of the original object convolved with an imaging point spread function. If the image could be correspondingly deconvolved, the original image can be recovered. One of the earliest attempts at this approach was that of Suits and White[31] who ingeniously incorporated the deconvolution procedure into the back projection algorithm itself. Their measurements demonstrated the feasibility of solid state diffusion studies. Deconvolution can also be used to unscramble the effects of chemical shift. Butadiene, for example, contains two chemically distinct protons. Figure 4(a) shows a MAS image of a sample of butadiene in which the two resulting images are misplaced. In Figure 4(b) the image has been deconvolved.[11] Another approach, closely allied to deconvolution, is maximum entropy (ME). Here, the fitting is done by the forward convolution of an arbitrary starting function (e.g. a completely uniform gray image) followed by comparison with the observed blurred data. Iteration takes place until a satisfactory fit is obtained consistent with the signal-to-noise, but no better. Of all such possible fits, the ME method chooses the image with the least detail. The technique is now well established as a useful tool for the deconvolution of high-resolution spectra. The problem with solids imaging however is that not only is the point spread function proportional to $1/T_2$ and therefore very large, but, more importantly, solids imaging inevitably gives a poor signal-to-noise ratio. Under these circumstances, deconvolution methods can be unstable and prone to failure. It nevertheless remains a technique that can be applied to sharpen up any image and may yet have a future place in solids imaging.

4 OTHER CONSIDERATIONS

4.1 Slice Selection

In Section 3, brief references have been made to the feasibility or otherwise of incorporating slice selection into the various imaging schemes. In this short section, we briefly review the general principles behind broadline slice selection.

The standard methods of slice selection in MRI require the application of a sinc-shaped rf pulse in the presence of a magnetic field gradient to excite nuclei within the slice. The gradient is then removed and orthogonal gradients applied for spatial encoding. Since this process must occur on a timescale of much less than T_2, it creates very serious problems for short T_2 materials. Several approaches have been developed to overcome the problem and some are considered by Cottrell et al.[32] and also by Rommel et al.[30] The basic idea is to spin lock the magnetization in the presence of a slice selection gradient. A comprehensive discussion of slice selection in solids can be found in the reviews by Blümler and Blümich[1] and by Kimmich et al. in Blümich and Kuhn.[4]

An alternative solution is to vary the encoding gradient over all directions in 3D space and use back projection or Fourier reconstruction to obtain a 3D image from which any slice, or indeed any voxel, can be computed. The method is very time consuming, but for inanimate matter the advantage of simplicity may be paramount.

Another relatively simple approach is to saturate all but the selected slice using shaped rf pulses with appropriate gradients. The unperturbed slice is then subjected to a 'solids' imaging sequence. Wideline samples require wideband irradiation and high power rf pulses are essential. The long T_1 values that are often associated with such samples are an advantage here as there is then time to change the large field gradients from slice select to encode mode.

Another approach, similar in effect to selective saturation, is 'spin lock-induced slice selection' (SLISE) which employs a hard 90° pulse followed by a spin lock pulse in the presence of a gradient. A selected slice only is spin locked and this decays with a time constant $T_{1\rho}$ which is typically much longer than the non spin-locked magnetization decay time ($\sim T_2$). SLISE is valuable for localized spectroscopy.

Finally, it should be noted that broadline imaging by MAS has yet to employ satisfactory slice selection, whereas, by its very nature, STRAFI incorporates slice selection automatically.

4.2 Contrast and Relaxation Filters

For solids and liquids alike, the basic imaging method portrays a map of nuclear spin density. Relaxation time mapping, i.e. the visualization of the spatial variation in a particular relaxation time, can be very valuable in distinguishing the differing character of parts of a sample. Relaxation times, particularly T_2 and $T_{1\rho}$, often have a much wider variation in solid-like samples than in mobile liquids. Their temperature and pressure dependence is also visually much greater. Relaxation time mapping, and the use of these parameters as filters,[33] has been clearly demonstrated for broadline materials, particularly polymeric materials, and exploitation of such techniques is to be expected in the future. When used to characterize materials, contrast ratios are often more important than signal-to-noise ratios. An example of a $T_{1\rho}$-weighted image of oxidatively aged rubber can be found in the article by Kuhn in Blümich and Kuhn.[4]

The multiple echo method version of large oscillating gradient imaging can also be put to good use in 'T_2 mapping'. Referring to Figure 10, one can see that at least seven echoes are available from which seven images can be obtained with imaging times ranging from 0.4 to 3 ms. By comparing the decay in signal intensity from the same pixel in each of the seven images, a true T_2 map can be produced. This technique has been used by Halse et al.[34] in a study of the ingress of decane into rubber. T_2 maps were generated showing the increase in T_2 of the rubber as it softened.

5 CONCLUSION

At this time it appears that a specialized multipulse sequence will produce the sharpest image in a small, solid object. The much simpler magic echo appears more robust, but carries a time penalty as the effective T_2 is not so efficiently increased. Of the 'direct' methods, STRAFI is capable of excellent results in small, static, easily manipulated objects. Although there is a time penalty involved in being restricted to the use of only one fixed gradient, the selective nature of the rf excitation means that the usual '$5T_1$' rule can be circumvented. For moderately broad lines, the 'direct' methods employing

oscillating gradients combined with a sustaining pulse sequence are very promising and can be adapted for larger samples and in vivo measurements. Applications of broadline sample imaging have been directed at polymeric materials in which cross-link density, fluid ingress and chemical reaction effects have been studied. Other examples include the study of diffusion in the solid state and defect density in crystalline solids.

6 RELATED ARTICLES

Chemical Shift Imaging; Imaging of Wide-Band Systems by Line-Narrowing Methods; NMR Microscopy: Resolution; Polymer MRI; Rotating Frame Methods for Spectroscopic Localization.

7 REFERENCES

1. P. Blümler and B. Blümich, in '*NMR Basic Principles and Progress*', eds. P. Diehl, E. Fluck, and R. Kosfeld, Springer, Berlin, 1994, Vol. 30, p. 209.
2. J. B. Miller, D. G. Cory, and A. N. Garroway, *Philos. Trans. R. Soc. London Ser. A*, 1990, **333**, 413.
3. J. H. Strange, *Philos. Trans. R. Soc. London, Ser. A.*, 1990, **333**, 427.
4. B. Blümich and W. Kuhn (eds.), 'Magnetic Resonance Microscopy', VCH, Weinheim, 1992.
5. P. T. Callaghan, 'Principles of Nuclear Magnetic Resonance Microscopy', Clarendon, Oxford, 1991.
6. B. C. Gernstein and C. R. Dybowski, 'Transient Techniques in NMR of Solids', Academic Press, London, 1985.
7. P. J. McDonald and P. F. Tokarczuk, *J. Phys. E.*, 1989, **22**, 948.
8. P. J. McDonald and A. R. Lonergan, *Physica B*, 1992, **176**, 173.
9. D. G. Cory, J. B. Miller, R. Turner, and A. N. Garroway, *Mol. Phys.*, 1990, **70**, 331.
10. E. R. Andrew and R. G. Eades, *Proc. R. Soc. London, Ser. A*, 1953, **216**, 398.
11. D. G. Cory, A. M. Reichwein, and W. S. Veeman, *J. Magn. Reson.*, 1988, **80**, 259.
12. M. S. Conradi, A. N. Garroway, D. G. Cory, and J. B. Miller, *J. Magn. Reson.*, 1991, **94**, 370.
13. M. Lee and W. I. Goldburg, *Phys. Rev.*, 1965, **140**, 1261.
14. F. de Luca, B. C. de Simone, N. Lugeri, B. Maraviglia, and C. Nuccetelli, *J. Magn. Reson.*, 1990, **90**, 124.
15. G. A. Barrall, Y. K. Lee, and G. C. Chingas, *J. Magn. Reson., A*, 1994, **106**, 132.
16. K. Woelk, J. W. Rathke, and R. J. Klingler, *J. Magn. Reson., A*, 1993, **105**, 113.
17. S. Matsui, Y. Ogasawara, and T. Inouye, *J. Magn. Reson., A*, 1993, **105**, 215.
18. D. E. Demco, S. Hafner, and R. Kimmich, *J. Magn. Reson.*, 1992, **96**, 307.
19. W. K. Rhim, A. Pines, and J. S. Waugh, *Phys. Rev. Lett.*, 1970, **25**, 218.
20. S. Hafner, P. Barth, and W. Kuhn, *J. Magn. Reson. A*, 1994, **108**, 21.
21. A. A. Samoilenko, D. Yu Artemov, and L. A. Sibel'dina, *JETP Lett.*, 1988, **47**, 417.
22. J. G. Powles and J. H. Strange, *Proc. Phys. Soc.*, 1963, **82**, 6.
23. P. Kinchesh, E. W. Randall, and K. Zick, *J. Magn. Reson.*, 1992, **100**, 411.
24. K. L. Perry, P. J. McDonald, E. W. Randall, and K. Zick, *Polymer*, 1994, **35**, 2744.
25. S. P. Cottrell, M. R. Halse, and J. H. Strange, *Meas. Sci. Technol.*, 1990, **1**, 624.
26. Y. Mat Daud and M. R. Halse, *Physica B*, 1992, **176**, 167.
27. B. Leone, M. R. Halse, J. H. Strange, A. R. Lonergan, P. J. McDonald, and E. Smith, *Magn. Reson. Imag.*, 1994, **12**, 247.
28. B. H. Suits and J. L. Lutz, *J. Appl. Phys.*, 1989, **65**, 3728.
29. S. Emid and J. H. Creyghton, *Physica B*, 1985, **128**, 81.
30. E. Rommel, S. Hafner, and R. Kimmich, *J. Magn. Reson.*, 1990, **86**, 264.
31. B. H. Suits and D. White, *Solid State Commun.*, 1984, **50**, 291.
32. S. P. Cottrell, M. R. Halse, D. A. Ibbett, B. L. Boda-Novy, and J. H. Strange, *Meas. Sci. Technol.*, 1991, **2**, 860.
33. P. Blümler and B. Blümich, *Macromolecules*, 1991, **24**, 2183.
34. M. R. Halse, H. Rahman, and J. H. Strange, *Physica B*, 1994, **33**, 267.

Biographical Sketches

John H. Strange. *b* 1938. B.Sc. 1960, Ph.D. 1963, London (supervisor Jack Powles). Postdoctoral work with Don Holcomb, Cornell. Appointed lecturer in Physics, University of Kent, 1964, then senior lecturer, reader and Professor. Director of the Laboratory since 1982. Approx. 150 publications. Current interests: diffusion and imaging in solids and porous media.

Morley R. Halse. *b* 1942. B.A. 1964, Ph.D. 1967, Mond Laboratory, Cambridge (supervisor David Shoenberg, FRS). English Electric Nelson Research Labs, Stafford, England, 1967–69; lecturer in physics, University of Kent 1969–present. Came to NMR from low temperature physics via acoustic imaging. Approx. 30 publications. Current interests: diffusion and imaging in semisolids.

NMR Microscopy: Resolution

Z. H. Cho

University of California, Irvine, CA, USA

and

S. C. Lee and M. H. Cho

Korea Advanced Institute of Science, Cheongyangni, Seoul, Korea

1 INTRODUCTION

NMR microscopy is one of the newly emerging tools for the high-resolution three-dimensional imaging of live animals and plants for biological as well as medical research. More recent developments include application of the technique to such things as porous materials and microflow, the study of which is essential for oil research. One of the main attractions of NMR microscopy is that it is a truly noninvasive three-dimensional high-resolution imaging tool with which micrometer resolution can be achieved. However, NMR imaging, especially NMR microscopy, has a number of formidable drawbacks, namely: a small signal-to-noise ratio due to the inherently small object size; diffusion and bandwidth limitations; and other inhomogeneity effects such as chemical shifts and susceptibility effects.[1–10] Some potentially feasible solutions to the above problems have been addressed by a number of researchers.[1,9,11]

Among other problems, that of diffusion due to the random Brownian motion of (water) molecules appears to be one of the fundamental physical limitations to NMR imaging, especially in high-resolution microscopy where these molecular diffusion distances are close to the resolution limits.[1,7] Although the diffusion effect in NMR has been studied extensively,[12–17] the effect on NMR microscopy has not yet been observed experimentally due to the current limitations of NMR microscopes. Theory, however, suggests substantial resolution broadening in NMR microscopy if molecular self-diffusion prevails, especially when dealing with molecules that have large diffusion coefficients.[1,7,11] This article describes the details of the resolution limits, especially those due to diffusion effects, in NMR microscopy. The discussion given covers: (1) the effects of phase variation due to molecular self-diffusion during data acquisition; (2) the effects of signal attenuation and related line broadening; and (3) some diffusion effects of molecules which, when confined within boundaries or walls, exhibit anomalies in resolution in NMR microscopy. The first two effects are based on free water molecules while the third is based on the model of water molecules confined by boundaries, which have significant physical consequences. Before discussing the effects of diffusion on the resolution of microscopic imaging, the other resolution limits are discussed briefly, namely the resolution limit due to the phase factor, which is related to the finite bandwidth of the imaging instrumentation; that is, the available gradient strength and acquisition time, both of which are intimately related to the diffusion effect.

2 RESOLUTION LIMITS DUE TO FINITE SYSTEM BANDWIDTH

Let us first assume that the signal-to-noise ratio is sufficiently high and the detection system is ideal, i.e. there is no uncertainty in the measurement. Since NMR imaging is a phase-encoding technique, it is natural to consider the minimum detectable phase difference to be a function of the signal separation between two points (resolution), the gradient strength G, and the data acquisition time T_{acq}. The two encoded phases during the acquisition time, or period (T_{acq}), for a pair of objects located at positions r_1 and r_2 are given by

$$\phi(r_1) = \gamma r_1 \int_0^{T_{\text{acq}}} G(t')\mathrm{d}t' \tag{1}$$

and

$$\phi(r_2) = \gamma r_2 \int_0^{T_{\text{acq}}} G(t')\mathrm{d}t' \tag{2}$$

respectively, where γ is the gyromagnetic ratio. From these two equations, the well-known bandwidth limited resolution can be defined using the phase difference between two points:

$$\Delta\phi_r = \phi(r_1) - \phi(r_2) = \gamma(r_1 - r_2)\int_0^{T_{\text{acq}}} G(t')\,\mathrm{d}t' = \gamma \Delta r G T_{\text{acq}} \tag{3}$$

where γ is the gyromagnetic ratio, and Δr is the spatial difference between two points r_1 and r_2. In equation (3), a constant amplitude gradient G is assumed. From equation (3) the bandwidth limited resolution can now be defined as

$$(\Delta r)_{\text{B}} = \Delta\phi_r^{\min}/(\gamma G T_{\text{acq}}) \tag{4}$$

where $\Delta\phi_r^{\min}$ is the minimum detectable phase.

Equation (4) is a fundamental relationship representing the intrinsic resolution as a function of the minimum detectable phase and the gradient–time product. The minimum detectable phase $\Delta\phi_r^{\min}$ is dependent on the reconstruction algorithm. For example, $\Delta\phi_r^{\min} = \pi$ if Fourier imaging is used with a half-echo data set. For a given minimum detectable phase, the resolution can be improved by increasing the gradient–time product. As implied in equation (4), relatively large gradients (0.1–1 mT m^{-1}) will be needed for microscopic resolution imaging. Since $(\Delta r)_{\text{B}}\gamma G$ corresponds to the bandwidth of the microscopic imaging system, resolution related to this limitation is often called 'bandwidth limited resolution', and we will use this term henceforth. Examples of the bandwidth limited resolution discussed above [e.g. equation (4)] are given in Figure 1, where the relationship between the gradient strength G and data acquisition time T_{acq} are given for 1 μm and 10 μm resolution.

3 RESOLUTION LIMITS DUE TO DIFFUSION EFFECTS

Let us first consider two resolution limits due to the diffusion effect, namely the minimum detectable phase related to

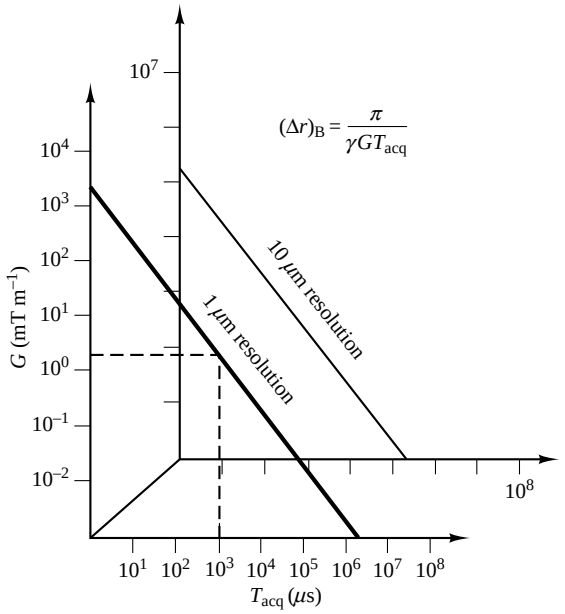

Figure 1 Bandwidth limited resolution $(\Delta r)_B$ in relation to the applied gradient G and data acquisition time T_{acq}. To obtain a high-resolution image in the order of 1–10 μm, it is necessary to have either a large gradient or long data acquisition times. Since excessively long data acquisition time is not advantageous due to the expected increase of the diffusion limited resolution, a large gradient strength is usually necessary. For this reason, NMR microscopy usually requires much larger gradient strengths than those employed in conventional whole body imaging

the random phase fluctuation and the phase dispersion related to the signal attenuation. In each case, our experimental model assumes free water molecules physically unbounded by impenetrable boundaries or walls. Following these two limits, a Monte Carlo (MC) simulation study of water molecules confined within boundaries or walls will be discussed as an alternative model for diffusion related resolution on the microscopic scale.

3.1 Resolution Limit as a Minimum Detectable Phase Difference due to Random Brownian Motion

According to the random walk model of the diffusion process developed by Carr and Purcell,[12] one-dimensional movement of the spin from an initial position x_0 due to the diffusion process is expressed as

$$\begin{aligned} x_i &= x_{i-1} + \alpha_1\zeta \\ &= x_{i-2} + \alpha_{i-1}\zeta + \alpha_1\zeta \\ &\vdots \\ &= x_0 + \zeta\sum_{j=1}^{i}\alpha_j \end{aligned} \tag{5}$$

where x_i is the position after a movement with reference to the previous position x_{i-1} with a discrete distance ζ, and α_i is a random variable which is either +1 or −1 with equal probability. In the case of imaging using a time varying gradient field $G(t)$ along the x direction, the total accumulated phase ϕ_N after a given time ($t = N\epsilon$) can be expressed as

$$\begin{aligned} \phi_N &= \gamma\epsilon\sum_{k=1}^{N}(G_k x_k) \\ &= \gamma\epsilon\zeta\sum_{k=1}^{N}\left[G_k\left(\sum_{j=1}^{N}\alpha_j\right)\right] \\ &= \gamma\epsilon\zeta\sum_{k=1}^{N}\left[\alpha_k\left(\sum_{j=K}^{N}G_j\right)\right] \end{aligned} \tag{6}$$

where ϵ is a time interval for each movement, and G_k is the gradient field at $t = N\epsilon$, i.e. $G(t = N\epsilon)$.

If the initial time is set at the beginning of the imaging gradient, the initial-position-dependent phase $\phi = \gamma G x_0 t$ is deterministic, and can be retrieved by the FT. It is, therefore, excluded in equation (6) where only the random-phase terms are considered. From equation (6), assuming that the mean phase is zero, the variance of the phase fluctuation at $t = N\epsilon$ is given by

$$\sigma_\phi^2(t = N\epsilon) = E[\phi_N^2] = \gamma^2\epsilon^2\zeta^2 E\left\{\left[\sum_{k=1}^{N}\alpha_k\left(\sum_{j=k}^{N}G_j\right)\right]^2\right\} \tag{7}$$

where $E[\cdot]$ denotes the statistical expectation. Considering the fact that the α_k terms are the only stochastic terms, and α_m and α_n are mutually independent, i.e. $E(\alpha_m,\alpha_n) = 0$ for $m \neq n$, and $E(\alpha_m^2) = 1$ for all $m = 1, 2, \ldots, N$, equation (7) can be rewritten as

$$\sigma_\phi^2(t = N\epsilon) = \gamma^2\epsilon^2\zeta^2\sum_{k=1}^{N}\left(\sum_{j=k}^{N}G_j\right)^2 \tag{8a}$$

For a sufficiently small time interval ϵ, equation (8a) can be expressed in integral form as

$$\sigma_\phi^2(t = N\epsilon) = 2\gamma^2 D\int_0^t\left[\int_{t'}^{t}G(t'')\,\mathrm{d}t''\right]^2\mathrm{d}t' \tag{8b}$$

where the quantity $\zeta^2/2\epsilon$ is replaced by the diffusion coefficient D and ϵ by $\mathrm{d}t'$ and $\mathrm{d}t''$. Equation (8b) describes the diffusion related phase variance as a function of continuous time rather than at a specific time, such as the time relative to an echo forming point, etc. In order to apply equation (8b) to NMR microscopy, a basic pulse sequence is considered, i.e. the data acquisition is started immediately after the 90° rf pulse. In this case, i.e. $t' = 0$ and $t = T$ in equation (8b), the variance is given by

$$\sigma_\phi^2(t) = 2\gamma^2 D G^2 T^3/3 \tag{8c}$$

Using equation (3) and equation (8c), one obtains the diffusion limited resolution $(\Delta r)_D$ as

$$(\Delta r)_D = \sqrt{\tfrac{2}{3}DT_{acq}} \tag{9}$$

For example, in water with $D = 10^{-5}$ cm^2 s^{-1}, if an acquisition time of $T_{acq} = 1.5$ ms is used, then the diffusion related resolution limit is

$$(\Delta r)_{\mathrm{D}} = \sqrt{\tfrac{2}{3}(10^{-5}\,\mathrm{cm^2\,s^{-1}})(1.5\times 10^{-3}\,\mathrm{s})} = 1.0\,\mu\mathrm{m} \qquad (10)$$

Figure 2 shows the diffusion dependent resolution limit as a function of diffusion coefficient D for several data acquisition periods ranging from 200 μs to 5.0 ms. As shown, with a given data acquisition time of T_{acq} = 1.5 ms, the diffusion limited resolution is only 1 μm. Therefore, it appears that the diffusion limited resolution does not have a significant effect on the overall resolution of NMR microscopy. With a large diffusion coefficient (about 10^{-4} cm^2 s^{-1}) and a long data acquisition time (about 5 ms), however, diffusion limited resolution, based purely on the minimum detectable phase criterion alone, could reach a resolution up to the order of 10 μm, a significant value in micrometer resolution NMR microscopy.

3.2 Resolution Limit as a Line-spread due to the Diffusion Dependent Signal Attenuation

As shown in the previous section, molecular diffusion results in a spin phase dispersion which eventually leads to signal attenuation. With a Gaussian distribution, the signal intensity can be expressed as

$$A(t) = A(0)\int_{-\infty}^{\infty}\frac{1}{\sqrt{2\pi\sigma_\phi^2}}\exp\left[-\frac{\phi^2(t)}{2\sigma_\phi^2}\right]\cos\phi\,\mathrm{d}\phi \qquad (11)$$

where ϕ denotes the phase, $A(0)$ is the initial amplitude, and σ_ϕ is the standard deviation given in equation (8b). Equation (11) can be further simplified to

$$A(t) = A(0)\exp[-\sigma_\phi^2(t)/2] \qquad (12)$$

If we substitute the variance given in equation (8b) into equation (12), we obtain

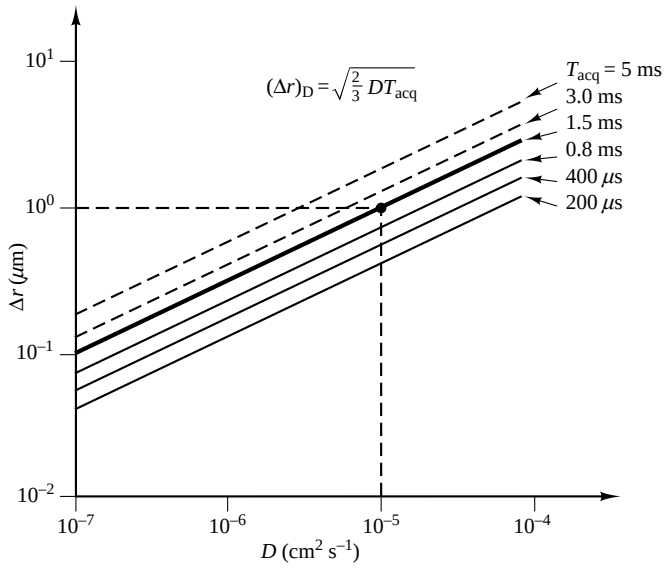

Figure 2 Diffusion limited resolution $(\Delta r)_{\mathrm{D}}$ based on the minimum detectable phase difference as a function of the diffusion coefficient D, with the data acquisition time T_{acq} as a parameter. It can be seen that the resolution degradation due purely to the minimum detectable phase difference is relatively small in water-like molecules

$$A(t) = A(0)\exp\left\{-\gamma^2 D\int_0^t\left[\int_{t'}^{t}G(t'')\,\mathrm{d}t''\right]^2\mathrm{d}t'\right\} \qquad (13)$$

Alternatively, equation (13) can also be written as

$$\ln[A(t)/A(0)] = -\gamma^2 D\int_0^t\left[\int_{t'}^{t}G(t'')\,\mathrm{d}t''\right]^2\mathrm{d}t' \qquad (14)$$

It is worth noting that, for the special case of echo formation, equation (13) becomes identical to the formula derived previously.[17] For example, if an echo is formed at time $t = TE$, $\int_0^{TE} G(t')\mathrm{d}t' = 0$. The term in brackets in equation (14) can then be written as

$$\begin{aligned}\int_{t'}^{TE}G(t'')\,\mathrm{d}t'' &= \int_{t'}^{0}G(t'')\,\mathrm{d}t'' + \int_0^{TE}G(t'')\,\mathrm{d}t'' \\ &= -\int_0^{t'}G(t'')\,\mathrm{d}t''\end{aligned} \qquad (15)$$

Equation (15) is identical to the equation given by Karlicek and Lowe.[17]

We also find that the echo signal amplitude derived by Stejskal and Tanner[16] in the pulsed gradient experiment is consistent with equation (13), as it should be. The time dependent signal attenuation will then lead to image degradation as a part of the diffusion phenomena, since signal amplitude attenuation during the data acquisition period will lead to line broadening, similar to the Lorentzian broadening due to T_2 decay.

By numerical FT of the diffusion affected signal given in equation (13), the line spread function $P(x)$ can be derived:

$$P(x) = [1/A(0)]\int_{-\infty}^{\infty}A(t)\exp(-\mathrm{i}2\pi xt)\,\mathrm{d}t \qquad (16)$$

In order to examine the line broadening effect due to the time varying signal attenuation during the data acquisition period, the full width at half maximum (fwhm) of the line spread functions for FIDs with several different diffusion coefficients were calculated; the results are given in Table 1. Although the resolution given by equation (16) is not an intrinsic resolution compared with the diffusion-limited resolution based on the minimum detectable phase, it is nevertheless an important practical measure of the resolution in NMR microscopic imaging.

3.3 Monte Carlo Simulations of Diffusion Effects and Resolution Anomalies in the Case of Water Molecules Confined by Boundaries or Walls

In the two previous sections, the basic principles and effects of diffusion in free space on the NMR signal were discussed. However, in many practical cases, such as biological samples, the nuclei in a sample during NMR imaging experiments do not diffuse freely in a finite and limited space; this generates substantial anomalies in resolution and image formation. In general, the purpose of NMR imaging is to distinguish the domains where imaging parameters, such as spin density (ρ) and physical or chemical properties (T_1, T_2, χ) of the nuclei, are different, provided that the nuclei belonging to one domain barely move to neighboring domains, at least during the data acquisition time. That is, there are impenetrable boundaries between the domains within an image or object. Therefore, the

Table 1 The fwhm (μm) of the line spread functions as a function of the diffusion coefficient for three different gradient field strengths in NMR microscopy[a]

G (mT m^{-1})	D (cm^2 s^{-1}) 0	10^{-6}	10^{-5}	10^{-4}
0.4	4.8	4.9	5.1	7.5
0.2	4.8	4.9	5.3	10.1
0.1	4.8	4.9	5.8	14.0

[a]The resolution given by the reciprocal of the bandwidth was set at 4 μm. The line spread functions are given in fwhm (μm) and were obtained by FT of the FID data.

general analysis based on free diffusion may not be a suitable model for NMR microscopy of small objects or regions confined by boundaries, since in this case diffusion is no longer free diffusion. However, in principle, resolution is only important near the boundary, because inside a homogeneous domain far from boundaries it is not necessary to distinguish two neighboring pixels and resolution does not matter.

Lauterbur et al.[18] and Pütz et al.[19] have reported how these impenetrable boundaries or walls can distort or even enhance images at the microscopic scale in MRI. Image intensity is enhanced near the boundaries when the diffusion coefficient is modest, and increases or focuses around the center of the domain when the diffusion coefficient becomes large.[19] Pütz derived an expression of the lineshape function for the case of diffusion in a bounded case by solving the diffusion Bloch equation[19] numerically. The same result can be obtained by means of a Monte Carlo simulation based on the random walk molecular diffusion process. The Monte Carlo simulation could possibly provide better insight into the problem, since it can simulate the random walk problem more closely than can the analytical approach. In the following, Monte Carlo approaches to the problem are described. We have assumed that the molecular self-diffusion stems from microscopic scattering between molecules. The direction and speed of molecules after each scattering are assumed to be random, as are the intervals and distances between movements and scatterings (Figure 3). In this simulation study, however, this random process was simulated by the random walk model, where each direction of the scattered molecules is determined randomly while the interval and distance are fixed at their average values. In the following Monte Carlo simulation, based on this random walk model, both unrestricted free molecular motion and molecular motion that is restricted in one dimension are described. It is also assumed that the direction of each Monte Carlo step is chosen as either left or right, and the phase of each spin in a linear magnetic gradient field is traced as a function of time. The FID signal is then obtained at the end by vectorially summing the phases. The FID obtained in this way is Fourier transformed and the lineshape function is obtained. The phase of a spin in a linear gradient field at time $N\Delta t$ is calculated as

$$\phi(N\Delta t) = \sum_{i=1}^{N} \gamma G x_i \Delta t \tag{17}$$

where G is the gradient, Δt is the time interval between each Monte Carlo step, and x_i is the particle position at time $i\Delta t$.

The position or spatial distribution of the spins by the random walk follows the binomial distribution and approaches the normal distribution in the limit when the number of trials is large. The approximation is good if the number of trials is greater than 10, when the probabilities of two events are the same.[20] Since the diffusion equation predicts a normal distribution when the initial density distribution has the form of a delta function, the number of the random walk steps was chosen always to be greater than 10 in order to match the macroscopic prediction. Data acquisition was started immediately after the magnetic gradient field was applied, i.e. the FID was detected and the phase value was updated at every ΔT interval. Note that here ΔT is assumed to be $10\,\Delta t$.

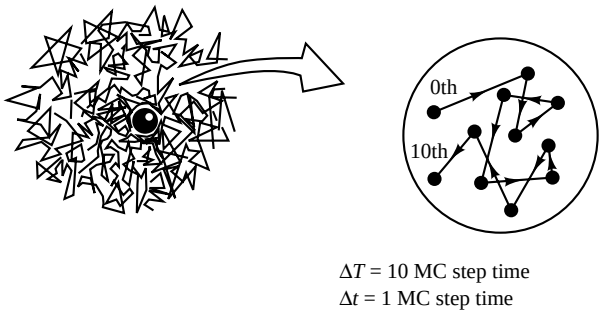

Figure 3 Illustration of the random Brownian motion and Monte Carlo (MC) steps assumed in the simulation study. The data sampling or updating time ΔT is assumed to be 10 times the individual spin movement time Δt. The drawing on the right is an example of the expanded details of a local Brownian motion shown on the left

Figures 4(a) and Figure 4(b) show the spatial distributions of the spins for the cases where molecules are unbounded (molecular diffusions in free space) and bounded by a wall to the right, respectively, after 400 Monte Carlo steps. In Figure 4(b), the spins were distributed over an infinitesimally thin slab at position $x = 0$ at $t = 0$. Spins are randomly moved one step to the left or right with equal probability at every Monte Carlo step, except for those near the wall in the case of bounded diffusion. As can be seen, the profile of the spatial distribution of the spins which diffuse freely in an infinite space are very close to the normal Gaussian distribution. In the case of bounded diffusion, however, those spins that reached the wall moved one step back with a probability of -1. The spin density near the wall, therefore, increased as shown in Figure 4(b). In other words, the spatial or position distribution in the presence of the wall is expected to have a form which has a similar distribution function to that for the free diffusion on the left side of the wall ($x < 0$), but on the right side of the wall ($x > 0$) the distribution function is of an asymmetrical form, as shown in Figure 4(b). This is because those spins supposed to be outside the wall are now symmetrically folded over to the inside.

The important factor for imaging, however, is not the position but the phase distribution of these spins, since the spin phase distribution, not the spin position, determines the image. It is also important to note that the linear gradient is added in MRI, which is space variant, and therefore gives a different amount of phase variation along the x direction, i.e. the phase value increases proportionally as the position moves to either the right or the left. Figure 5 shows the position and phase distributions for comparison. The phase distribution profile in free diffusion is Gaussian, as for the case of the position distribution. However, in the case of bounded diffusion it is

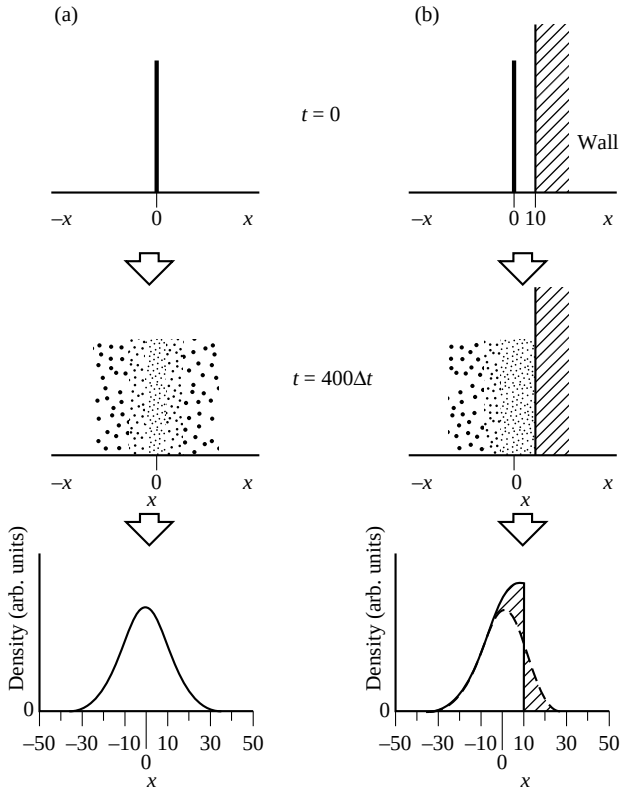

Figure 4 Spreads of the unbounded (free) and bounded spins located at $x = 0$ (with $t = 0$) at $t > 0$. At $t = 400\Delta t$, the typical spin position spread follows a Gaussian distribution in the free diffusion case (a), but in the bounded or restricted case (b) an asymmetrical Gaussian distribution is seen

different [Figure 5(b)] and requires further explanation. In MRI, the differences between the position distribution and phase distribution in the case of bounded spins are due to the fact that it is not the spin positions but the phases that are recorded, and thereby the phase increases as time goes on. The final distribution of the phase, therefore, becomes distorted, as shown in Figure 5(b).

To observe the bounded spin effect in an imaging situation, both the spatial and phase distributions are measured for spins that are distributed uniformly in a box. First, the spatial distributions should be uniform and time invariant. The phase distributions, however, would be different. To observe this effect near the boundary of an image, a Monte Carlo simulation was performed using equation (17). Then the phase distribution of the nuclear spins distributed uniformly in a one-dimensional box was recorded. The size of the box was 20 μm divided into 200 pixels with a linearly changing magnetic field which becomes zero at the center of the box (Figure 6). Similarly to the case of the delta function distribution shown in Figure 5(b), the resulting phase distribution, approaching the walls or boundaries, is different from the position distribution. At the boundaries, the number of spins that should be at $\phi = \phi_{max}$ decreases substantially, and instead are recorded at values larger than and smaller than ϕ_{max} [see Figure 5(b)]. This means that the spin phase distribution in the reverse direction, that is towards the center of the wall, would increase and show a peak, which would then again decrease to a normal value approaching the center. On the outside of the walls, i.e. $\phi \geqslant \phi_{max}$, there could be a small leakage, as shown in Figure 5(b). Except near the boundaries, the phase distribution does not change even in the presence of diffusion, because the number of spins of a given phase, other than those near the boundaries, does not change, as discussed previously, although the spin positions change during a data acquisition period. Therefore, the central part of the image is not distorted and the resolution is not affected for the spins well inside the boundaries.

Based on the phase distributions obtained, image reconstruction was performed by FT, the results of which are shown in Figure 7. The figure shows only the right-hand halves of the final reconstructed images obtained by FT of the FID signal. The dashed line is the image with no diffusion. These images were obtained from 256 FID data points and each FID is obtained by summing the phases of all the spins (10^6) at every 10 Monte Carlo steps up to 2560 steps. Since the average collision time of water molecules interacting with biological macroscopic molecules is about 10^{-6} s,[21] we set one Monte

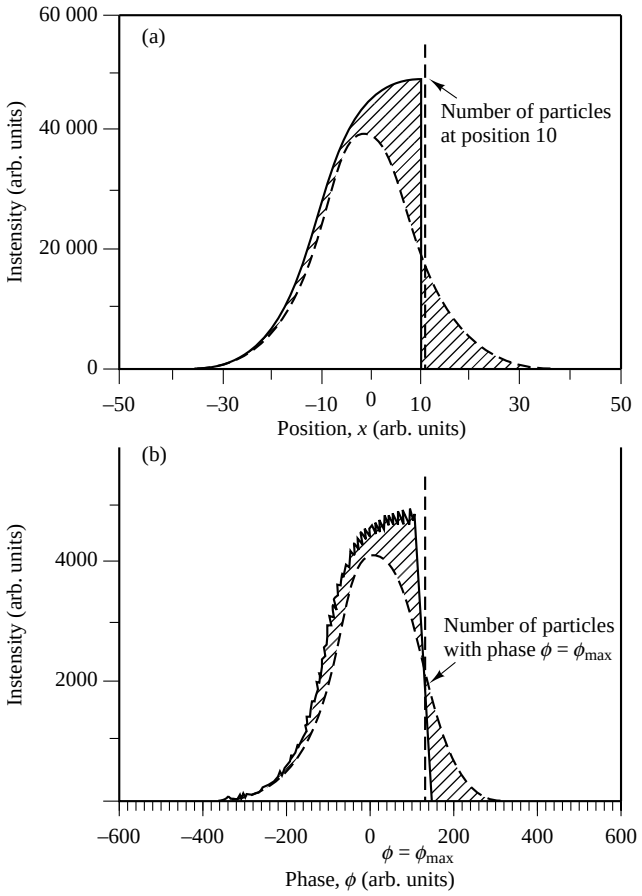

Figure 5 (a) The spin position distribution, and (b) the phase distribution of the free (- - - -) and bounded (——) spins originated from $x = 0$ (at $t = 0$) observed at time $t = 400\Delta t$. (a) The position spread of the bounded spins is limited at the wall, while the unbounded spins follow a normal Gaussian distribution. (b) Although the position distribution and phase distribution look similar, there is a difference. In the case of the phase distribution, at $\phi = \phi_{max}$, the maximum phase of the bounded spins is normalized by the phase value at the boundary where the gradient field is strongest. The number of spins having the maximum phase is less than half the peak value, suggesting that there will be less intensity in the reconstructed image based on the phase values

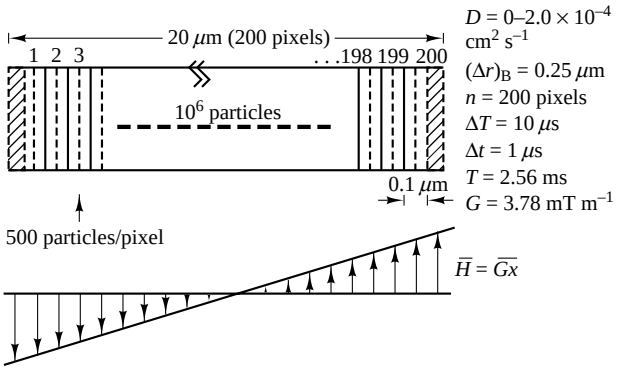

Figure 6 Modeling of the Monte Carlo simulation study of the diffusion process in a one-dimensional box. Uniformly distributed water molecules in a box restricted over a 20 μm (in the x direction) length was assumed. Each pixel is then assumed to be 0.1 μm long in the x direction, with 5000 spins (or particles) in each pixel. The applied gradient G, total data acquisition time T, data sampling time interval ΔT, each Monte Carlo step Δt, range of values of the diffusion coefficient D, bandwidth limited resolution $(\Delta r)_B$, and number of pixels in the box n are indicated on the figure. The total number of spins or particles used for the simulation was 10^6

Carlo step (Δt) as 1 μs in order to simulate the imaging of a biological cell, and the sampling or data updating interval (ΔT) was set at 10 μs. The total data acquisition time is then 2.56 ms for 256 sampled data. Given this step time (Δt), the assignment of 0.1 μm for the distance moved during each step gives a diffusion coefficient close to those of the biological samples described below. The simulated length of the object, and therefore the image, was assumed to be 20 μm, with the size of each pixel being 0.1 μm. The right-hand half of the image (10 μm) is shown in Figure 7. Since the variation in position in the binomial distribution σ^2 is $N\Delta x^2/4$, where N is the total number of trials and the variation in position at time t is given by $(2Dt)^{\frac{1}{2}}$ in a diffusion process, one obtains the relationship $D = N\Delta x^2/8T$ when the total number of trials N is defined as the total number of Monte Carlo steps (N = 2560) and the time T is the total data acquisition time (T = 2.56 ms). From these data, one obtains a diffusion coefficient of $D = 1.25 \times 10^{-5}$ cm^2 s^{-1}. The third curve shown in Figure 7 corresponds to the case of this diffusion coefficient, which is close to the diffusion coefficient of free water. In the same figure, the first curve from the right has a diffusion coefficient 16 times smaller than that of the third curve. The rest of the curves have diffusion coefficients that are 4 times larger than the one to the left. The magnetic gradient field was set to make the phase at the right end increase by 1 rad at every sampling or updating interval ΔT. This condition corresponds to a gradient field of 3.78 mT m^{-1} and a bandwidth limited resolution of 0.25 μm. The overall simulation conditions are depicted in Figure 6.

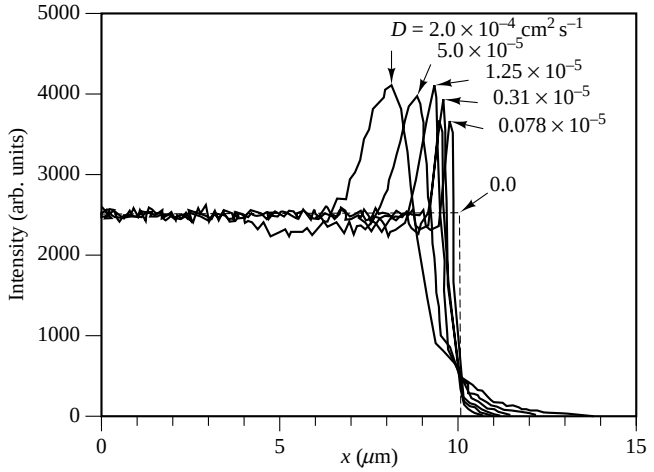

Figure 7 Reconstructed image patterns based on the phase distributions obtained by Monte Carlo simulation for various values of diffusion coefficient D. Some edge enhancement and image deformation are evident, but the edge enhancement effect is visible only within a few micrometers, even with a diffusion coefficient as large as $D = 2.0 \times 10^{-4}$ cm^2 s^{-1}. For normal water molecules (e.g. $D = 1.25 \times 10^{-5}$ cm^2 s^{-1}), therefore, deformation or contraction of the image size and enhancement effect may not be readily visible at the resolution of NMR microscopes currently available

Although small signal penetration or leakage exists in the immediate vicinity of the boundary, the values seen are small and of no significant consequence. Inside the domain or box the signal intensities show peaks or overshoots in the immediate vicinity of the boundary, as discussed earlier. In addition, each curve settles to the normal value as it approaches the center. Overall, those overshoots or anomalies in the signal intensity of the reconstructed image at the boundary appear as an image resolution enhancement near the boundaries. These kinds of resolution anomalies are the unexpected result of the conventional idea that the image would be blurred by diffusion effects, regardless of the presence of boundaries or other barriers. At the same time, this boundary enhancement effect will appear as a signal void (or a dark region) between the two neighboring domains if these are adjacent to each other, thereby making a clearer boundary. An undesirable part of the effect, however, is the image distortion, e.g. a domain or an image contracts with increasing diffusion coefficient and the distances of the peaks from the boundary also tend to increase as the diffusion coefficient increases (see Figure 7). Although these peakings and image contractions appear significant in this example, the effect may not be readily observable in current in vivo NMR microscopy of biological samples, where the resolution is at best, in the range 4–10 μm, with diffusion coefficients in the range 1–2 $\times$ 10^{-5} cm^2 s^{-1}.[1,5]

4 RELATED ARTICLES

Anisotropically Restricted Diffusion in MRI; Susceptibility and Diffusion Effects in NMR Microscopy.

5 REFERENCES

1. Z. H. Cho, C. B. Ahn, S. C. Juh, H. K. Lee, R. E. Jacobs, S. Lee, J. H. Yi, and J. M. Jo, *Med. Phys.*, 1988, **15**, 815.
2. W. V. House, *IEEE Trans. Nucl. Sci.*, 1984, **31**, 570.
3. P. C. Lauterbur, *IEEE Trans. Nucl. Sci.*, 1984, **31**, 1010.
4. J. B. Aguayo, S. J. Blackband, J. Schoeniger, M. A. Mattingly, and M. Hinterman, *Nature*, 1986, **322**, 190.
5. G. A. Johnson, M. B. Thompson, S. L. Gewalt, and C. E. Hayes, *J. Magn. Reson.*, 1986, **68**, 129.
6. C. D. Eccles and P. T. Callaghan, *J. Magn. Reson.*, 1986, **68**, 393.

7. P. T. Callaghan and C. D. Eccles, *J. Magn. Reson.*, 1988, **78**, 1.
8. Z. H. Cho, C. B. Ahn, S. C. Juh, J. M. Jo, R. M. Friendenberg, S. E. Fraser, and R. E. Jacobs, *Philos. Trans. R. Soc. London, Ser. A*, 1990, 333.
9. Z. H. Cho, D. J. Kim, and Y. K. Kim, *Med. Phys.*, 1988, **15**, 7.
10. P. T. Callaghan, *J. Magn. Reson.*, 1990, **87**, 304.
11. C. B. Ahn and Z. H. Cho, *Med. Phys.*, 1989, **16**, 22.
12. H. Y. Carr and E. M. Purcell, *Phys. Rev.*, 1954, **94**, 630.
13. E. L. Hahn, *Phys. Rev.*, 1950, **80**, 580.
14. H. C. Torrey, *Phys. Rev.*, 1953, **92**, 962.
15. G. E. Wesbey, M. E. Moseley, and R. L. Ehman, *Invest. Radiol.*, 1984, **19**, 491.
16. E. O. Stejskal and J. E. Tanner, *J. Chem. Phys.*, 1965, **42**, 288.
17. R. F. Karlicek and I. J. Lowe, *J. Magn. Reson.*, 1980, **37**, 75.
18. P. C. Lauterbur, W. B. Hyslop, and H. D. Morris, XIth Conference of the International Society of Magnetic Resonance, Vancouver, BC, Canada, 19–24 July 1992, Abstract O-79.
19. B. Pütz, D. Barsky, and K. Schulter, *J. Magn. Reson.*, 1992, **97**, 27.
20. See, for example, M. R. Spiegel, 'Statistics, Schaum's Outline Series in Mathematics', 2nd edn, McGraw Hill, New York, 1990; A. Papoulis, 'Probability, Random Variables and Stochastic Process', 3rd edn, McGraw Hill, New York, 1991.
21. T. R. Nelson and S. M. Tung, *Magn. Reson. Imaging*, 1987, **5**, 189.

Biographical Sketches

Z. H. Cho. *b* 1936. B.S., M.Sc., Seoul National University, 1960–62; Ph.D., Uppsala University, 1966. Faculty, Stockholm University, 1972–75; University of California, Los Angeles, 1972–77, University of California, San Diego, 1977–78; Korea Advanced Institute of Science, 1978–95; Columbia University, 1979–85; University of California, Irvine, 1985–present. Approx. 180 publications. Research interests: NMR imaging and microscopy, image reconstruction algorithms, NMR imaging methods and instruments, functional MRI and nuclear medical imaging, and X-ray and positron computed tomography.

S. C. Lee. *b* 1957. B.S., Seoul National University, 1980; M.Sc., 1983; Ph.D., 1987, Northwestern University. Faculty of Korea Advanced Institute of Science, 1987–present. Research interests: NMR in solids, NMR microscopy.

M. H. Cho. *b* 1960. B.S., Seoul National University, 1983; M.Sc., Korea Advanced Institute of Science, 1985; Ph.D., Korea Advanced Institute of Science, 1990. Faculty of Suwon University, 1992–present. Research interests: NMR imaging, image processing, computer architecture.

Contrast Agents in Magnetic Resonance: Operating Mechanisms

Robert N. Muller
University of Mons Hainaut, Mons, Belgium

1 THE MR IMAGE AND ITS CONTRAST

For the creation of a clinical magnetic resonance image, the electromagnetic signal emitted by each volume element (*voxel*) of the body is spatially identified by the application of magnetic field gradients. It is subsequently registered at its proper location in the two- or three-dimensional array of the digital picture. The brightness of any of the picture elements (*pixels*) is directly related to the intensity of the NMR signal broadcasted by the corresponding voxel (see ***Image Formation Methods***). Consequently, intensity differences between adjacent voxels determine the image contrast.[1] At this point, it is worth remembering that MRI differs fundamentally from X-ray computerized tomography since it maps a signal emitted by each voxel while the latter imaging modality reflects an attenuation of the beam of ionizing radiation passing through the body of a patient.

Inherent contrast of a magnetic resonance image can be manipulated to a much larger extent than in any other technique. This *natural* contrast enhancement is achieved by modifying the instrumental or *extrinsic* factors of the imaging procedure such as the type and the timing parameters of the pulse sequence. This strategy can highlight the influence of certain *intrinsic* parameters such as the local concentration of nuclei (also called ρ, the spin density), their relaxation parameters (T_1, T_2, T_2*, $T_{1\rho}$), the relative bulk magnetic susceptibility, bulk flow of cerebrospinal fluid (CSF) or blood, or the molecular self-diffusion coefficient.

In common imaging sequences, signal intensity is proportional to ρ and spin–spin relaxation (T_2 as well as T_2*) and inversely related to the spin–lattice relaxation, T_1. In other words, main contrast influencing factors in MRI are proton density and the two relaxation times T_1 and T_2.

Despite the outstanding contrast flexibility of MRI, some diagnostic questions have prompted the need for exogenous contrast material. These pharmaceuticals aim at enhancing the contrast between normal and diseased tissues or at providing functional information regarding the state of an organ by dynamically modifying the intrinsic parameters of the tissues. This can be done by either increasing signal intensity (positive agents) or by decreasing signal intensity (negative agents). The straightforward target in the development of such MR contrast agents is alteration of proton density and of relaxation times.

2 MODIFICATION OF PROTON DENSITY

Possible contrast agents which can modify the water content of tissues are diuretics, hormones, and alcohol. Because of their limited contrast changes and their manifold side-effects, these drugs are not used for clinical applications. A more feasible approach is to displace water in the region of interest.

Among the compounds applied for this purpose is perfluorooctyl bromide (PFOB) which is used as a negative oral contrast agent.[2] By replacing the watery content of the intestines, PFOB darkens the bowels. For the same purpose, barium sulfate and clays have been proposed; they partly replace water in the gastrointestinal tract and also modify its nuclear relaxation kinetics by offering large adsorption surfaces. Relaxation parameters may indeed be influenced by an alteration of molecular dynamics but are more efficiently modified by intensifying dipole–dipole magnetic interactions.

3 MODIFICATION OF NUCLEAR RELAXATION RATES

Theory predicts that an excited proton isolated in the vacuum and submitted to a static magnetic field of 1.5 T would require more than 10^{16} years to return spontaneously to its stable Zeeman state. On the other hand, if another magnetic center, such as a proton, is fluctuating nearby, the relaxation process takes place in a timescale of a second. This is the situation encountered in pure liquid water or in tissues where the longitudinal relaxation times T_1 are around 4 s or fractions of a second, respectively. If an electron, which is 658 times more magnetic than a proton, were to be located in the close vicinity of the hydrogen nucleus, the dipole–dipole (electron–nucleus) interaction, which increases by the square of the magnetic moments, would lead to a relaxation process taking place in a few microseconds.

Assuming a concentration of 1 mM of electrons for a hypothetical aqueous solution, its global relaxation time would be around 0.5 s. MR relaxation agents should thus be chemical structures rich in unpaired electrons, i.e. be *paramagnetic*. Potential candidates are organic stable free radicals, molecular oxygen, ions, and complexes of transition metals (Fe^{2+}, Fe^{3+}, Mn^{2+}, Mn^{3+}, etc.) or of lanthanides (Gd^{3+}, Ho^{3+}, Dy^{3+}, etc.). Nanocrystals of ferrites which are known to exhibit extremely high magnetic moments at high magnetic fields are also drawing interest. These latter compounds belong to the family of *superparamagnetic* materials.

Such contrast agents catalyzing the relaxation processes are sometimes called *magnetopharmaceuticals*. Here again, a clear distinction between X-ray and MRI has to be made. In the former technique, the contrast media are themselves visualized since they scatter or block the incident beam, while in MRI the contrast enhancing material is indirectly observed through its action on the proton relaxation of water in tissue. For this reason, these materials should be called *contrast agents* rather than *contrast media*, the latter term being reserved for directly visible substances.

4 RELAXIVITY

The efficiency of relaxation agents with respect to the longitudinal (T_1) or transverse (T_2) relaxation processes is usually quantified in terms of their *relaxivity* r_i (i = 1 or 2), the increment brought to the solvent (water) protons' relaxation rate by 1 mmol L^{-1} of the paramagnetic center:

$$R_{i(\text{obs})} = \frac{1}{T_{i(\text{obs})}} = \frac{1}{T_{i(\text{diam})}} + r_i C; \quad i = 1 \text{ or } 2 \tag{1}$$

where $R_{i(\text{obs})}$ and $1/T_{i(\text{obs})}$ are the global relaxation rate of the aqueous system (s^{-1}); $T_{i(\text{diam})}$ is the relaxation time of the system before addition of the contrast agent (s); C is the concentration of the paramagnetic center (mmol L^{-1}); and r_i is the relaxivity (s^{-1} $mmol^{-1}$ L).

5 RELAXATION MECHANISMS

5.1 Paramagnetic Relaxation

Quantitative models describing dipolar interaction have been developed to express mathematically the relaxivity of the paramagnetic centers. The complete picture is given by a juxtaposition of the two mechanisms depicted in Figures 1 and 2, which are called the 'innersphere' and the 'outersphere' mechanisms, respectively.[3]

5.1.1 Innersphere Mechanism

A paramagnetic moiety, characterized by an electronic spin S (7/2 for Gd^{3+}, 5/2 for Mn^{2+}, etc.) is surrounded by n water molecules lying at a distance r in its first coordination sphere (Figure 1). From a dynamical point of view, it has to be taken into account that the magnetic interaction fluctuates, because:

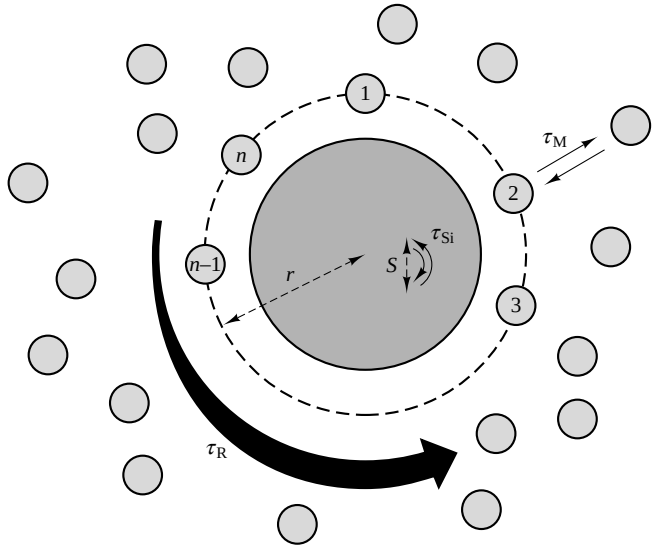

Figure 1 Schematic representation of the innersphere relaxation mechanism induced by a paramagnetic center on temporarily coordinated water molecules

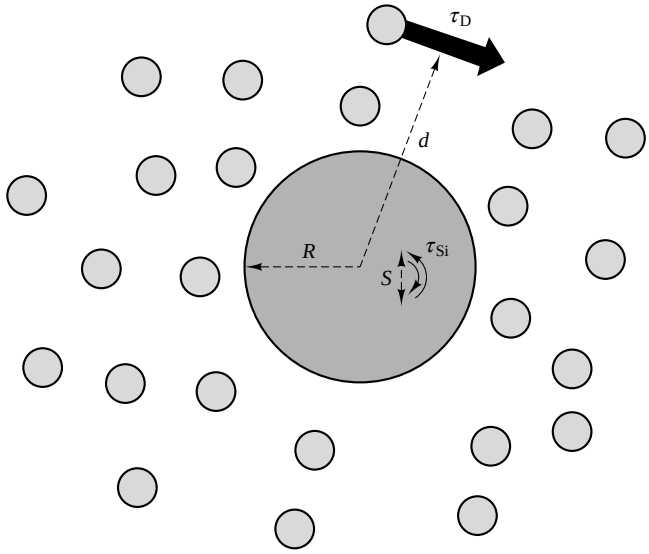

Figure 2 Schematic representation of the outersphere relaxation mechanism originating from the interaction between a paramagnetic center and water molecules diffusing at close vicinity

1. The temporarily coordinated molecules are exchanging with the bulk water (residence time τ_M).
2. The whole complex is experiencing Brownian motion (rotational correlation time τ_R).
3. The electrons are subject to their own relaxation processes, i.e. flip-flop exchange between their Zeeman levels (electronic relaxation times τ_{S1} and τ_{S2}).

The efficiency of the energy transfer between the excited nuclei and the lattice depends critically on the timescale of this modulation.

The relaxation times of the water protons located in the first coordination sphere of the metal are T_{1M} and T_{2M}. Assuming a propagation of the effect due to the exchange with the bulk (τ_M) the net contribution of this 'diluted' innersphere mechanism to the global relaxation rate will be:

$$R_{1,2\ \text{inner}} = \frac{1}{T_{1,2\ \text{inner}}} = \frac{P_M n}{T_{1,2M} + \tau_M} \tag{2}$$

with $P_M << 1$, where P_M is the mole fraction of the paramagnetic center; n is the number of water molecules bound in the first coordination sphere of the metal, and τ_M is the residence time of the water bound to the paramagnetic center.

This equation, which is always correct for R_1, is more complex for R_2 if τ_M becomes longer than 1 μs. On the other hand, an exchange time of water (τ_M) of the order of or longer than T_{1M}, the relaxation time in the first coordination sphere, will drastically reduce the relaxivity.

Calculation of T_{1M} or of $(1/T_{1M})$ is based on a model which includes the amplitude of the magnetic interaction, its temporal modulation (τ_R, τ_M, τ_{Si}) and the effect of the intensity of the external static magnetic field $\boldsymbol{B}_0$.

The complete set of simplified equations for $1/T_{1M}$ [equation (3a)] and $1/T_{2M}$ [equation (3b)] are known as the Solomon–Bloembergen–Morgan relations:

$$\frac{1}{T_{1M}} = \frac{B}{r^6}\left[\frac{7\tau_{c2}}{1+(\omega_S\tau_{c2})^2} + \frac{3\tau_{c1}}{1+(\omega_I\tau_{c1})^2}\right] + \frac{2A^2S(S+1)}{3\hbar^2}\left[\frac{\tau'_{c2}}{1+(\omega_S\tau'_{c2})^2}\right] \quad (3a)$$

$$\frac{1}{T_{2M}} = \frac{B}{r^6}\left[\frac{6.5\tau_{c2}}{1+(\omega_S\tau_{c2})^2} + \frac{1.5\tau_{c1}}{1+(\omega_I\tau_{c1})^2} + 2\tau_{c1}\right] + \frac{A^2S(S+1)}{3\hbar^2}\left[\frac{\tau'_{c2}}{1+(\omega_S\tau'_{c2})^2} + \tau'_{c1}\right] \quad (3b)$$

where: $B = 2\gamma_I{}^2\gamma_S{}^2\hbar^2S(S+1)/15$; $A/\hbar$ is a constant characterizing the scalar interaction (v.i.); and

$$\frac{1}{\tau_{ci}} = \frac{1}{\tau_R} + \frac{1}{\tau_M} + \frac{1}{\tau_{Si}} \quad (3c)$$

$$\frac{1}{\tau'_{ci}} = \frac{1}{\tau_M} + \frac{1}{\tau_{Si}} \quad (3d)$$

Equations (3a) and (3b) show a clear field dependence of the relaxivities through the Larmor frequencies of the electron (ω_S) and the proton (ω_I), respectively. The additional field dependence of τ_{Si}, is less obvious, but also influences the relaxivities.

Except for aquo ions of some transition metals, like manganese, which delocalize their electronic orbitals on the water protons, the second term of these equations (representing the so-called *scalar term*) has to be neglected. This is also the case for lanthanide complexes relaxing water protons.

At low field or for fast molecular motion conditions ($\omega_S\tau_{ci}$, $\omega_I\tau_{ci} << 1$), $1/T_{1M} = 1/T_{2M}$. Unless a scalar interaction exists, this relationship is maintained as long as the condition $\omega_I\tau_{ci} << 1$ is fulfilled. When the product $\omega_I\tau_{ci}$ becomes larger than 1, $1/T_{1M}$ drops progressively to 0, while $1/T_{2M}$ maintains a significant value, usually referred to as the *secular term*. This divergent behavior leads to the large r_2/r_1 observed for macromolecular paramagnetic systems.

5.1.2 Outersphere Mechanism

Water molecules moving freely in the vicinity of the paramagnetic center can also interact with the electronic spin. This phenomenon, which does not require any binding between the two species, is governed by the relative motion of the molecules and their distance of closest approach (Figure 2). The time modulation of the magnetic interaction is characterized by a diffusion correlation time τ_D:

$$\tau_D = d^2/(D_I + D_S) \quad (4)$$

where d is the distance of closest approach, and D_I and D_S are the molecular self-diffusion coefficients of water and the magnetic center, respectively.

The equations describing the outersphere relaxation mechanism have some similarities with those of the innersphere relaxation, i.e. a strong field dependence, equal r_1 and r_2 at low field, and an increasing r_2/r_1 ratio when $\omega_I\tau_D$ becomes larger than 1. Here again, high field conditions and long correlation times (τ_D), such as those encountered with large magnetic bodies like magnetic particles, may induce such a situation where the transverse relaxivity is faster than the longitudinal one (see Sections 5.1.1 and 5.2).

From the foregoing, the global relaxation rate of a paramagnetic aqueous solution has to be written as:

$$R_{1,2\ obs} = \frac{1}{T_{1,2\ obs}} = \frac{1}{T_{1,2\ diam}} + \frac{1}{T_{1,2\ inner}} + \frac{1}{T_{1,2\ outer}} \quad (5)$$

5.1.3 Nuclear Magnetic Relaxation Dispersion Profiles and Field Cycling Relaxometry

The influence of each parameter contained in the rather complex equations expressing the relaxivities is better visualized when r_1 and r_2 are represented as functions of the static magnetic field (or of the proton Larmor frequency). These curves are called nuclear magnetic relaxation dispersion (NMRD) profiles. Figure 3 shows, for instance, the effect of the rotational correlation time τ_R on the r_1 innersphere for a system which could be made of a gadolinium(III) ion complexed by organic chelates of increasing molecular size.

In addition, the experimental NMRD profiles are of paramount importance, if not mandatory, to understand, improve, and quantify the relaxation phenomena. They are conveniently recorded over a wide range of fields, typically from a few tens of a millitesla up to 1 T and more, on a special instrument, the field-cycling relaxometer developed from the original idea of Redfield.[4,5] Data are subsequently fitted with the relevant theoretical models mentioned above.

Complementary information can be obtained by alternative techniques like luminescence (number of coordinated water molecules, n), oxygen-17 nuclear relaxation (water residence time in the first coordination sphere τ_M), carbon-13 nuclear relaxation (rotational correlation time τ_R), and crystallography (distance between water protons and the metal, r).

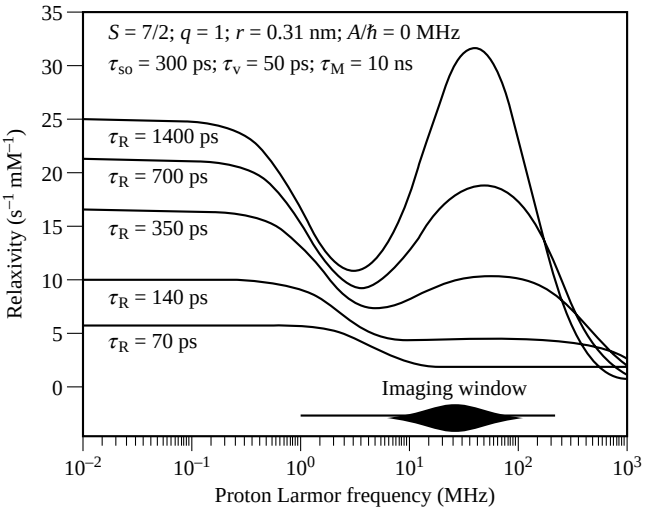

Figure 3 Simulated longitudinal innersphere relaxivity (r_1) profiles of gadolinium chelates of increasing molecular size. The peculiar evolution in the high field range is due to the involvement of the electronic relaxation in the global modulation time τ_c for larger molecular weight [see equation (3c)]

5.2 Superparamagnetic Relaxation

Small crystals (<20 nm) of magnetite (Fe_3O_4) and of other ferrites are known to exhibit extremely high magnetic moments due to a cooperative alignment of the electronic spins of the individual paramagnetic ions they contain.[6,7] These nanoparticulate materials do not retain any remanent bulk magnetization after having been exposed to a strong magnetic field. Although they are always fully magnetized, these particles have their magnetic moment flipping rapidly and randomly between some preferred directions of the crystal. This means that at very low external magnetic field the net bulk magnetization of these particulate materials tends to null, while the mean squared modulus of their individual magnetization vector measured along the direction of the external field is one-third of the value measured at high field where all the moments are locked, yielding the saturation magnetization. In addition to the external field, the magnetic moment of the particle experiences another constraint caused by the crystal anisotropy. This effect, which presents some analogies with the zero-field splitting well known in paramagnetic systems, causes an attenuation of a low-field dispersion that can totally disappear, as in Figure 4 (for a complete description of the relaxation induced by superparamagnetic particles see, for instance Roch et al.[8]).

Relaxation induced by such systems is obviously of the outersphere type. Considering the size of these grains ($R \approx 10$ nm in Figure 2), the time during which the traveling water protons 'feel' the magnetic heterogeneity is relatively long. In this situation one can predict that the effect on the proton transverse relaxation will be by far more important than on the longitudinal one (see Section 5.1.2). These contrast agents are referred to as *T_2 relaxers*. However, it should not be overlooked that they can nevertheless present impressive r_1 relaxivities.

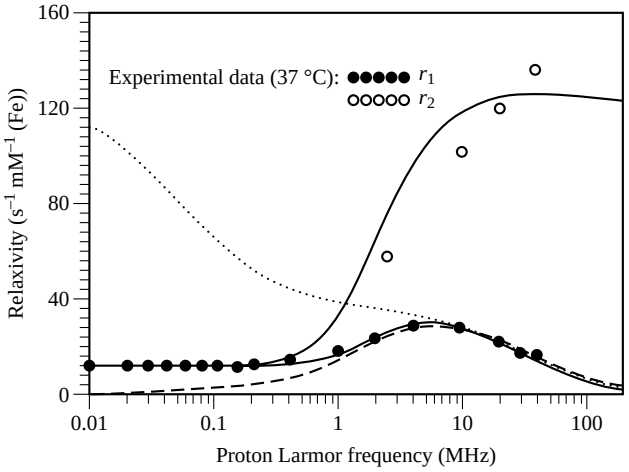

Figure 4 The r_1 and r_2 NMRD profiles of an aqueous colloidal suspension of superparamagnetic iron oxide (Fe_3O_4, crystal diameter 10.8 nm, particle diameter ca. 120 nm, specific magnetization 49 emu g^{-1}). Best fits of the experimental data according to the model described by Roch and Muller[8] (parameters of the best fit: diameter 12.8 nm, specific magnetization 41 emu g^{-1}, ca. 30 crystals per particle). Neither the classical outersphere theory (·····) nor its variation assuming no bulk magnetization of the particles suspension at zero field[9] (– – – –) give satisfactory fits. Note that, as expected for such large magnetic centers, the transverse relaxivity r_2 (○) is much higher than r_1 (●) in the usual imaging field range

Classical outersphere theory is not applicable to these systems which, as mentioned above, are characterized by unusual sizes and magnetic properties. In recent studies,[9,10] a new model has been proposed (Figure 4) which adequately fits the NMRD experimental data of longitudinal relaxivity and allows predictions regarding the influence of various parameters (size, saturation magnetization, etc.).

Transverse relaxivity can be analytically predicted for ideally dispersed crystals of rather small size (ca. 20 nm for magnetite). The influence of larger grains or clusters on T_2 and T_2*, however, has to be estimated by computer simulations which evaluate the dephasing of spins diffusing in a three-dimensional space containing the randomly distributed magnetic centers.[11,12]

5.3 Susceptibility-Induced Relaxation

The mechanisms presented so far involve the acceleration of the relaxation processes due to short range interactions between the water protons and the individual magnetic centers. The processes thus influence the water molecules that are permanently or temporarily located in their compartment. Another type of relaxation enhancement which is strictly limited to the transverse evolution of the nuclear magnetization can be induced by microscopic magnetic field gradients created by susceptibility differences between compartments (see ***Susceptibility and Diffusion Effects in NMR Microscopy*** and ***Susceptibility Effects in Whole Body Experiments***). The bulk magnetic susceptibility of the intravascular space is for instance increased by a high concentration of paramagnetic or superparamagnetic compounds.

Because of the molecular diffusion of water through the transcompartmental magnetic field heterogeneities, the apparent transverse relaxation time T_2* will be shortened. This phenomenon will be maximal in gradient echo imaging sequences which do not contain spin refocusing rf pulses able to minimize this irreversible loss of phase coherence. Pure susceptibility effects are only achievable with magnetic materials exhibiting negligible r_1. Otherwise antagonistic influences will develop between the inner and the outer compartments. In the former a signal increase could be expected, while in the latter the T_2* would lead to a loss of intensity.

Among such susceptibility-only agents are those paramagnetic ions and complexes which have a very short electronic relaxation time τ_s, e.g. dysprosium.

6 CLINICAL CONTRAST AGENTS

6.1 Relaxation Agents

6.1.1 Paramagnetic Complexes

Mn^{2+} was proposed very early on by Lauterbur et al.[13] as the first in vivo relaxation agent. However, this ion, as with the other potentially efficient paramagnetic aquo ions (Gd^{3+}, Mn^{3+}, etc.) is rather toxic and cannot be used as such. Coordination chemistry offers elegant ways to prepare compounds made of paramagnetic ions locked in organic molecules, which are far less toxic than the free ion or even the free organic ligand.

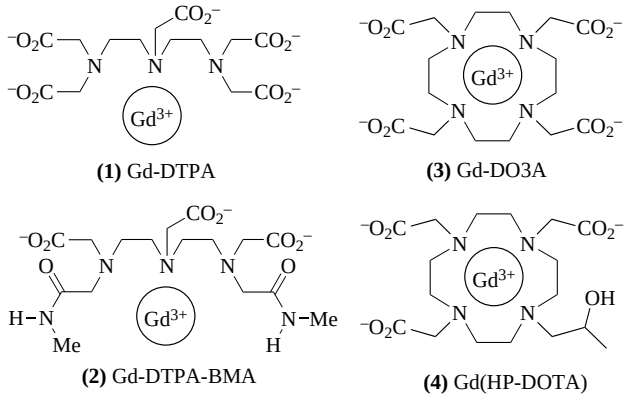

Figure 5 Molecular structures of some open chain (**1**, **2**) and macrocyclic (**3**, **4**) chelates of the Gd^{3+}

Indeed, when the ion and ligand are bound together in a supramolecular complex, neither is able to react in vivo and thus the ion does not replace important physiological ions such as calcium, and the ligand does not trap some other ion such as zinc.

The gadolinium ion (Gd^{3+}) has been chosen as the active center for the first generation of commercial complexes (Figure 5) because of its favorable physicochemical properties: seven unpaired electrons (S = 7/2), long electronic relaxation time (τ_{S1}, τ_{S2}), and nine coordination sites. From the point of view of relaxivity, structures which accept only one water molecule at a close distance to the gadolinium are obviously less efficient than the bare aquo ion. In spite of this, and due to their large size and an efficient outersphere relaxation mechanism, all of these compounds show relaxivities of around 4 s^{-1} $mmol^{-1}$ L at 0.5 T.

As for these small complexes, $\omega_I \tau_{ci}$ much smaller than 1 (see Sections 5.1.1 and 5.1.2), the relaxivities r_1 and r_2 are almost equal. In other words, these contrast agents bring the same *absolute* rate increment to both R_1 and R_2 relaxation rates of tissues. However, since the transverse relaxation rates of tissues are larger than their R_1 the *relative* contribution these compounds add to the latter mechanism (at least for moderate concentrations) is predominant (see ***Relaxometry of Tissue***, ***Relaxation Measurements in Imaging Studies***, and ***Relaxation Measurements in Whole Body MRI: Clinical Utility***). These magnetopharmaceuticals act as positive agents and are called *T_1 agents*. At present, the typical clinical dose is 0.1 mmol kg^{-1} body weight. For an adult, this corresponds to an injected volume of around 15 mL, considering that the concentration of the usual formulation is 0.5 mol L^{-1}.

The chemical stability of these compounds is very high as their dissociation constants in water at 37 °C and pH 7 are lower than 10^{-16}. In other words, less than one molecule of the complex of around 100 million is dissociated.

As mentioned above, the active center of the paramagnetic complexes is an ion which is electrically charged. Sequestration of the triple-positive charge of the gadolinium ion is achieved in part by electrostatic interactions with the negatively charged carboxylate groups (O=C–O$^-$). As shown in Figure 5, the diethylenetriaminepentaacetic acid (DTPA) chelate offers more groups than necessary, since five negative charges are open to compensate for the positive charge carried by gadolinium. Gd-DTPA thus has two negative charges in excess, Gd-DOTA has one, and Gd(HPDOTA) and Gd-DTPA-bis(methyl)amide (Gd-DTPA-BMA) are neutral. The last two compounds are thus called *nonionic* with respect to the former ones which belong to the class of *ionic* contrast agents.

Any negative charge in excess has to be neutralized by a counterion. The ammonium group (NH_3^+) of meglumine (methylglucamine), an organic molecule, has been chosen for this task. Gd-DTPA has thus to be considered as being composed of three molecules (i.e. the complex and two meglumine molecules), Gd-DOTA of two, while Gd-HPDO3A and Gd-DTPA-BMA are composed of only one molecule, the complex itself. For the same 0.5 mol L^{-1} concentration of gadolinium, the osmolarity of the latter compounds will be 0.65 osmol L^{-1} which is half the osmolarity of Gd-DOTA and one third that of Gd-DTPA.

All these contrast agents are nonspecific and, owing to their low molecular weight and hydrophilicity, freely diffuse after intravenous injection from the intravascular into the extravascular and extracellular space. In the brain, while they do not cross the intact blood–brain barrier, they do enhance lesions with blood–brain barrier disruption or absent blood–brain barrier. The enhancement is also dependent on vascularization of damaged regions as well as on the tissue content of lesions.

The design of blood pool agents, potentially useful for MR angiography, is based on the synthesis of systems with a long life in the blood stream, while the development of hepatobiliary and tumor-seeking compounds requires appropriate knowledge of the mechanisms of internalization and of interactions with receptors. Among those specific agents, it is worth mentioning Gd(EOB-DTPA)[14] (**5**) a very promising hepatobiliary contrast media and MS-325[15] (**6**), which strongly interacts with albumin through noncovalent binding and appears as an efficient blood pool agent for angiography (Figure 6).

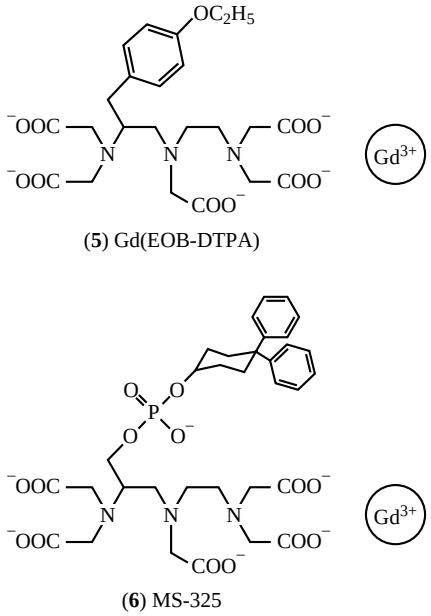

Figure 6 Structure of the hepatobiliary contrast agent Gd(EOB-DTPA) (**5**) and the albumin-binding agent MS-325 (**6**)

6.1.2 Superparamagnetic Particles

Superparamagnetic particles have been used as the active core of several preparations: large beads of polystyrene (micrometer size) coated with magnetite crystals and used as oral contrast agents, and colloidal systems made of superparamagnetic grains embedded in polysaccharide or other polymeric matrices have been applied. These particles can be targeted, according to their coating and their size, to the liver or to lymph nodes, the vascular compartment, or to antigen receptors.[16] The preparation of well-characterized formulations of these materials is rather complex since not only the chemistry and the physical properties of the crystals but also their coating and final particle size have to be carefully adjusted and controlled. Although small superparamagnetic particles can be used as positive (R_1) agents (see Section 5.2) it is mainly their effect on T_2 and T_2* which has been exploited so far (see ***Contrast Agents in MRI: Superparamagnetic Iron Oxide***).

Finally it has to be stressed that the effect of these materials on the transverse relaxation of water protons critically depends on their level of aggregation and on the type of imaging procedure used. For instance, superparamagnetic particles internalized and packed in the macrophages of the liver induce a strongly multiexponential regime related to the type and timing of the echo sequence.[17,18]

Theoretical models and computer simulations can explain these observations, which are related to the evolution of the microscopic dimensions of the system. Considering the high relaxivities and magnetic properties of these agents, the clinical doses required will be low (0.02 mmol Fe kg^{-1} body weight).

6.2 Susceptibility Agents

As mentioned previously, susceptibility agents are aimed at inducing magnetic field gradients around the boundaries of contiguous compartments.

Dy-DTPA-BMA, a compound of the same family as the relaxation agent Gd-DTPA-BMA, has been proposed to be of use in evaluating cerebral and myocardial perfusion. Perfused zones which are made of distinct compartments will show signal decrease due to the diffusion of water through magnetic field inhomogeneities, while the signal of less or nonperfused tissues will remain unchanged due to an absence of the contrast agent or, in the case of blood–brain barrier disruption, due to its homogeneous distribution. The remaining question regarding the distinction between these last two situations can be solved by the subsequent or simultaneous administration of a relaxation agent which will modify the signal of the damaged area.

Contrary to relaxation agents which are usually injected as perfusions (unless the kinetics of uptake and clearance is studied), susceptibility agents demand higher local concentrations and thus must be administered by bolus injection and, consequently, fast imaging sequences are required. In this respect, the osmolarity of the formulation might be of concern (see Section 6.1.1).

Owing to their very high magnetization, superparamagnetic particles could also be used if their effect on T_1 is minimized by proper choice of the imaging conditions.

7 CONCLUSIONS

The first step in the development of MRI agents has led to molecular and particulate systems that influence the relaxation processes. The first generation compounds proved to be very safe and rather efficient in spite of their lack of specificity. However, it can be predicted that in the near future new compounds exhibiting better organ and disease specificity will appear.

Efforts to increase the relaxivity of MRI contrast agents require a good knowledge of the underlying physical mechanisms, and skill in various domains like coordination, colloidal, and supramolecular chemistry. Furthermore, the characterization of these agents has prompted the need for the development of dedicated instrumental and theoretical tools.

From the point of view of the doses of contrast material required by the modality, MRI is far less demanding than radiography, but more so than nuclear medicine.

Finally, some other interesting directions in contrast agent research should be mentioned, i.e. those concerning pH, pO_2 temperature-sensitive molecules, and those based on NMR signal enhancement by electron or proton magnetization transfer (see ***Overhauser Effect Imaging of Free Radicals*** and ***Magnetization Transfer and Cross Relaxation in Tissue***).

8 RELATED ARTICLES

Contrast Agents in MRI: Superparamagnetic Iron Oxide; Image Formation Methods; Magnetization Transfer and Cross Relaxation in Tissue; Overhauser Effect Imaging of Free Radicals; Relaxation Measurements in Imaging Studies; Relaxation Measurements in Whole Body MRI: Clinical Utility; Relaxometry of Tissue; Susceptibility and Diffusion Effects in NMR Microscopy; Susceptibility Effects in Whole Body Experiments.

9 REFERENCES

1. P. A. Rinck (ed.), 'Magnetic Resonance in Medicine', 3rd edn, Blackwell, Oxford 1993.
2. R. F. Mattrey, P. Hajek, V. M. Gylys-Morin, L. L. Baker, J. Martin, and D. C. Long, *Am. J. Roentol.*, 1987, **148**, 1259.
3. See for example: R. B. Lauffer, *Chem. Rev.*, 1987, **87**, 901; I. Bertini and C. Lucinat, 'NMR of Paramagnetic Molecules in Biological Systems', Benjamin/Cummings, Menlo Park, 1986.
4. F. Noack, in 'Progress in NMR Spectroscopy', eds. J. W. Emsley, J. Feeney, and L. H. Sutcliffe, Pergamon, Oxford, 1986, Vol. 18, p. 171.
5. S. H. Koenig and R. D. Brown, in 'NMR Spectroscopy of Cells and Organisms', ed. R. K. Gupta, CRC, Boca Raton, FL, 1987, Vol. 2, Chap. 11.
6. J. L. Dormann, *Rev. Phys. Appl.*, 1981, **16**, 275.
7. R. E. Rosensweig, 'Ferrohydrodynamics', Cambridge University Press, Cambridge, 1985.
8. A. Roch et al., *J. Chem. Phys.*, 1999, in press.
9. A. Roch and R. N. Muller, in *Proc. XIth Ann Mtg. Soc. Magn. Reson. Med.*, Berlin, 1992, p. 1447.
10. A. Roch, P. Gillis, and R. N. Muller, in *Proc. IIIrd Ann Mtg. Int. Soc. Magn. Reson. Med.*, Nice, 1995, p. 1095.

11. S. H. Koenig, *Prog. NMR Spectrosc.*, 1992, **22**, 487.
12. F. Moiny, P. Gillis, A. Roch, and R. N. Muller, in *Proc. XIth Ann Mtg. Soc. Magn. Reson. Med.*, Berlin, 1992, p. 1431.
13. P. C. Lauterbur, M.-H. Mendonça-Dias, and A. M. Rudin, in 'Frontiers of Biological Energetics', eds. P. L. Dutton, J. S. Leigh, and S. Scarpa, Academic, New York, 1978.
14. L. Vander Elst, F. Maton, S. Laurent, F. Seghi, F. Chapelle, and R. N. Muller, *Magn. Reson. Med.*, 1997, **38**, 604.
15. R. B. Lauffer, D. J. Parmelee, S. U. Dunham, H. S. Ouellet, R. P. Dolan, S. Witte, T. J. McMurry, and R. C. Walovitch, *Radiology*, 1998, **207**, 529.
16. R. Weissleder and M. Papisov, *Rev. Magn. Reson. Med.*, 1992, **4**, 1.
17. R. N. Muller, P. Gillis, F. Moiny, and A. Roch, *Magn. Reson. Med.*, 1991, **22**, 178.
18. A. Roch, T. Bach-Gansmo, and R. N. Muller, *MAGMA*, 1993, **1**, 83.

Biographical Sketch

Robert N. Muller. *b* 1948. Lic.Sci., 1969, Ph.D., 1974, University of Mons-Hainaut, Belgium. Successively, assistant, lecturer, and professor, University of Mons-Hainaut, 1969–present. Sabattical at Paul C. Lauterbur's research group at the State University of New York at Stony Brook 1981–82. Cofounder of the European Workshop on Nuclear Magnetic Resonance in Medicine; Vice-Chairman of the European Magnetic Resonance Forum Foundation, 1991–present; President of the European Society for Magnetic Resonance in Medicine and Biology, 1987–88. Approx. 80 publications and 5 books. Research in recent years mainly in relaxometry and development and applications of MRI contrast agents.

Contrast Agents in MRI: Superparamagnetic Iron Oxide

Liliane A. Harika and Ralph Weissleder

Massachusetts General Hospital and Harvard Medical School, Boston, MA, USA

1 HISTORY

Dextran coated iron oxide preparations were first used for in vitro magnetic resonance (MR) experiments by Ohgushi in 1978.[1] MR images of animals injected with iron oxide solutions were acquired as early as 1983. The first iron oxide enhanced MR image was published in 1985.[2] Within the next years, several investigators reported on the use of superparamagnetic iron oxide as an MR contrast agent.[3,4] In 1988, results from the first clinical trials became available.[5] Later, the use of ultrasmall iron oxides,[6,7] monocrystalline iron oxides, and iron oxides with surface bound ligands were reported.[8] Ligand derived iron oxides have been used for receptor imaging,[9,10] antibody imaging and neuronal transport imaging. Currently, preclinical and clinical trials of some of these newer agents are underway.

2 SYNTHESIS

The synthesis of *non-pharmaceutical* colloidal iron oxide solutions ('ferrofluids') used for recording technology, as paint ingredients and for electromechanical devices, and the synthesis of *pharmaceutical* colloidal iron oxide solutions vary considerably. Pharmaceutical iron oxides must be water based, biocompatible, and nontoxic.

Typically, pharmaceutical grade iron oxides are synthesized by alkaline magnetite precipitation from iron(II) and iron(III) salt solutions in the presence of a carbohydrate such as dextran, dextran derivatives, or starch. The synthesis from which many iron oxides can be derived was originally described by Molday and Ohgushi.[1,11,12] The end-products of such syntheses vary considerably, even if minor changes [temperature, pH, starting concentrations, amount of dextran/iron, iron(II)/iron(III) ratio] occur during the synthesis. Because of this variability during synthesis, pharmaceutical iron oxides are best characterized by their chemical, magnetic, and biological properties (Table 1).

Pharmaceutical superparamagnetic iron oxide preparations can be divided into four groups according to the size, blood halflife and the mechanism by which they are transported to different end organs:

- *Large Superparamagnetic Iron Oxide (SPIO).* Typically these preparations have a large variation in particle size and are usually polycrystalline. If administered intravenously, SPIO are usually characterized by a short blood halflife (<15 min) and a predominant uptake by phagocytic cells of the reticuloendothelial system in liver and spleen. SPIO have also been used as the active ingredient for MR contrast agent of the gastrointestinal tract.
- *Ultrasmall Iron Oxide Preparations (USPIO) and Monocrystalline Iron Oxide (MION) Preparations.* These are chemically similar to agents described above, but have a smaller size (usually <30 nm as determined by laser light scattering). Because of their smaller size and often higher dextran/iron ratio, agents of this class are capable of slowly leaving the vascular system, and are commonly taken up by macrophages of lymph nodes, spleen, and bone marrow.
- *Receptor-Directed Iron Oxides.* These consist of iron cores to which are bound carbohydrates with receptor specificity (e.g. arabinogalactan), or of dextran iron oxides the surfaces of which have been modified with receptor-specific ligands. Preparations with affinity to asialoglycoprotein (ASG) receptors on hepatocytes and to cholecystokinin receptors on pancreatic cells, have been reported.
- *Antibody-Labeled Iron Oxides.* These usually consist of small iron oxides (e.g. MION) derivatives, to which have been covalently bound antibodies or antibody fragments.[8]

Table 1 Characterization of pharmaceutical iron oxides

Physical chemistry
Size of the core (electron microscopy)
Chemical structure (analytical methods)
Particle size, size distribution and structure (electron microscopy, light scattering, column chromatography, sedimentation, etc.)
Crystallographic structure (X-ray diffraction)
Magnetic characteristics
Relaxivity in aqueous solution (relaxation time measurement)
Relaxivity in tissues (relaxation time measurement)
Bulk magnetization measurements
Relaxation behavior of spins (Mössbauer spectroscopy)
Pharmacological behavior
Blood halflife and biodistribution
Organ, tissue, target capture coefficients
Degradation and elimination
Toxicity

3 MAGNETIC PROPERTIES

The magnetic properties of iron oxide solutions are governed by the chemical structure, packing of the iron oxide core (Table 2) and the presence or absence of aggregation of individual crystals into larger clusters, in solution or inside cells. Pharmaceutical iron oxides usually exhibit superparamagnetic behavior (no remnant magnetization at zero field strength; induced magnetization is not linear with increasing magnetic field).

Iron oxides decrease proton relaxation times (T_2*, T_2, T_1) of tissues in which they accumulate or to which they are distributed. The effect on T_2* relaxation times usually predominate; however, effects on tissue T_1 relaxation times become more prominent as the diameter of the iron oxide cores become

Table 2 Characteristics of different iron oxide compounds

Parameter	Magnetite	Maghematite	Hematite	Oxyhydroxide
Formula	Fe_3O_4	γ-Fe_2O_3	α-Fe_2O_3	FeOOH
Magnetic strength[a]	4	4	0–0.01	1–2
Crystallography	Inverse spinel	Inverse spinel	HCP[b]	CCP[c]

[a]Bohr magneton/unit formula. [b]HCP, hexagonal closed packed. [c]CCP, cubic closed packed.

smaller.[13] Because of these effects, MR imaging in patients who have received iron oxides is usually done with T_2-type pulse sequences, proton density sequences, and gradient echo pulse sequences.

4 CLINICAL APPLICATIONS

4.1 Liver Imaging

A variety of agents have been or are currently being tested for liver imaging by the following pharmaceutical companies: Advanced Magnetics, Schering, Nycomed, Bristol-Myer-Squibb, Mallinkrodt, and Guerbet. After intravenous administration of most agents (usual intravenous dose 10–20 μmol Fe per kg), liver signal intensity decreases, whereas that of liver metastases remains unchanged or is only minimally changed. Because of this differential enhancement pattern, hepatic tumors become more conspicuous. Usually, liver signal intensity returns to precontrast values within several days as iron oxide particles are degraded within phagolysosomes of macrophages (Figure 1).[14] As a general rule, mildly T_2-sensitive spin echo or T_2*-dependent gradient echo sequences show the greatest decrease in liver signal intensity.

Early clinical reports on the efficacy of iron oxides are equivocal. Whereas some authors have found an increase in lesion conspicuity and an improved contrast-to-noise (C/R) ratio with the use of iron oxides, other authors have concluded that these agents do not substantially improve diagnosis in a clinical setting. The latter have claimed that the decrease in liver signal-to-noise (S/N) ratio makes visualization of normal anatomic structures difficult. Another often cited disadvantage of iron oxide enhanced MR imaging, is the low S/N ratio of pulse sequences required to exploit the T_2* and/or T_2 effect of iron oxides.

Other studies have evaluated the use of iron oxide in cirrhosis, hepatitis, and acute hepatic failure.[15] These studies have shown that the uptake is inhomogeneously altered in cirrhosis, and homogeneously decreased in hepatitis. On the basis of these and other experimental studies, it has been concluded that superparamagnetic iron oxides can be used as an imaging marker of reticuloendothelial function.[15]

4.2 Spleen

The rationale for using iron oxides for imaging of the spleen is similar to that of liver imaging. Iron oxide particles are phagocytosed by splenic macrophages, but not (or to a much lesser degree) by splenic metastases. Metastases thus become more conspicuous because of their relative lack of such macrophages.

Clinical trials have confirmed that splenic mass lesions can be more reliably detected with iron oxide enhanced MRI than by other conventional imaging methods (contrast enhanced computed tomography).[16] Iron oxide has also been used for the differentiation of normal spleens and spleens diffusely infiltrated by lymphoma.[17] Phagocytosis of superparamagnetic iron oxide in lymphomatous spleens is reduced because of diffuse displacement of splenic macrophages by lymphomatous cells and/or by immunologic suppression of macrophage activity. Since phagocytosis is not significantly reduced in reactive splenomegaly, splenic signal intensity decreases after administration of iron oxide to a similar extent as in normal spleens, enabling the differentiation of some causes of splenomegaly, on the basis of signal intensity.

4.3 Lymph Nodes

Experimentally, several contrast agents have been used for MR lymphography, and different administration routes have been studied: subcutaneous,[18] intralymphatic,[19] intravenous, and intraarterial. Of these techniques, the intravenous mode appears to be the preferred one, because it is capable of delivering the contrast agent to all 600–800 human lymph nodes following a single administration.

In order for iron oxides to accumulate in lymph nodes, certain prerequisites must be met. Firstly, iron oxides must have a small hydrodynamic radius size, in order to gain access to the interstitium via capillary pores.[20] Secondly, lymphotropic iron oxides must have a long blood halflife in order to minimize rapid extraction by liver and spleen. Ultimately, iron oxides have to express surface characteristics that enable them to be recognized by phagocytic cells within lymph nodes.

At the time of writing, only one clinical study has evaluated the use of an ultrasmall iron oxide preparation for imaging of cervical lymph nodes in human volunteers. The dose employed was higher (>1.7 mg Fe per kg) than that for liver–spleen imaging because of lower nodal accumulation efficiency.[21] To determine whether iron oxide based lymphotropic agents will ultimately be clinically useful for cancer staging, controlled clinical trials are required.

4.4 Gastrointestinal Tract

Different iron oxide preparations (OMP, AMI-121), have been used as 'negative' (i.e. darkening of luminal contents) gastrointestinal contrast agents.[22,23] Enhanced images usually show improved delineation of the head of the pancreas, paraaortic regions and anterior margins of the kidneys. There is currently no consensus in the radiologic community whether

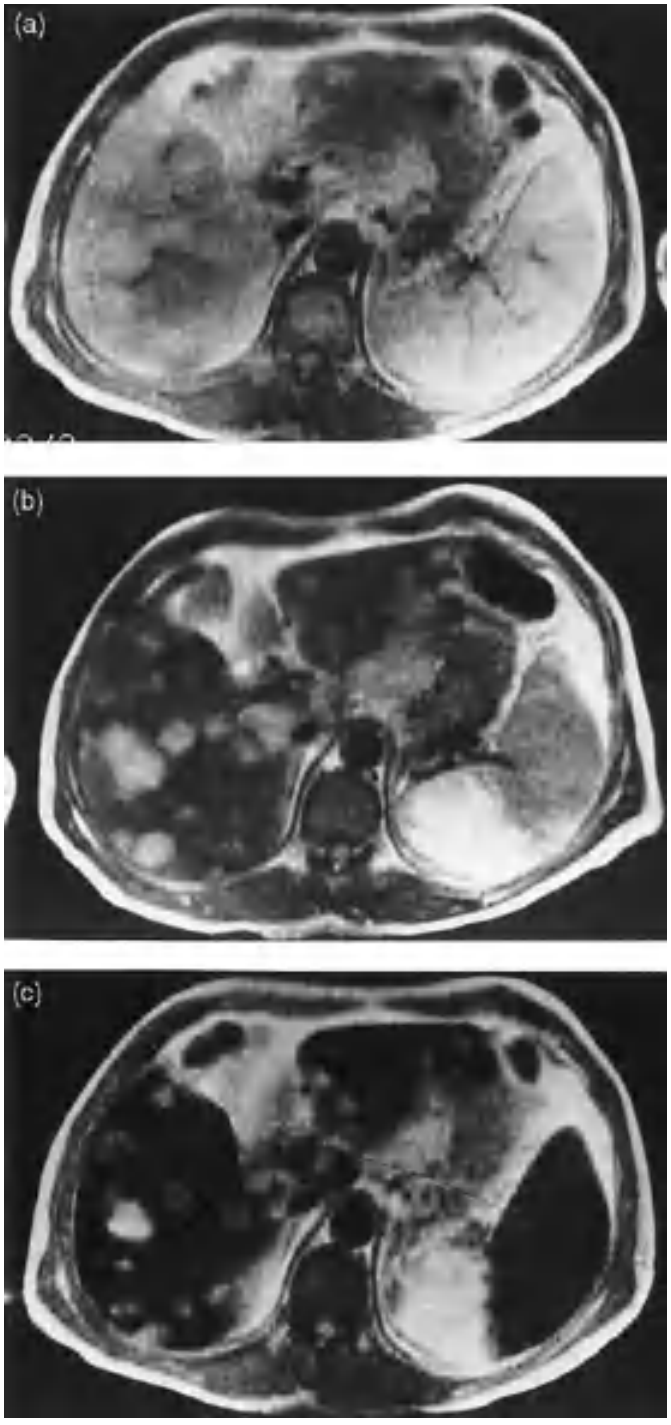

Figure 1 Detection of hepatic and splenic metastases using a superparamagnetic iron oxide preparation. (a) Nonenhanced spin echo (SE) 1500/42 MR image. Multiple hepatic metastases appear slightly hyperintense. The splenic tumor is undetectable. (b) SE 1500/42 MR image obtained 1 h after intravenous administration of a superparamagnetic iron oxide (AMI-25; 30 μmol kg^{-1}). Multiple hepatic metastases are now easily detected in both liver lobes, and one-half of the spleen is replaced by a solid tumor. This image demonstrates the efficacy of superparamagnetic iron oxides for enhancing tumor–liver/spleen contrast. (c) Three days after administration, the contrast between tumor and surrounding liver and spleen has decreased because of biodegradation of the iron oxide particles. (Reprinted with permission from *Radiology*)

the routine use of such agents will ultimately improve the detection of intraabdominal pathology.[22] Because of the high osmotic load, a significant amount of patients experience diarrhoea, nausea, and vomiting.

5 EXPERIMENTAL USE

5.1 Bone Marrow

Different iron oxides have been used as contrast agents for bone marrow imaging.[7] In vivo MR imaging of rabbits and rats has confirmed that certain small iron oxides decrease the signal intensity of red and yellow marrow. The decrease in signal intensity is usually most marked with gradient echo pulse sequences. Iron oxides can potentially be used to differentiate between normal and abnormal red marrow and between tumor deposits and hyperplastic red marrow, as shown in animal studies.

5.2 Blood Pool Imaging

It has been shown that a single intravenous administration of small iron oxide preparations (e.g. MION) has a significant R_1 effect and that this effect can be exploited to decrease the T_1 of blood over prolonged periods of time (blood halflife in rodents 3 h). Animal experiments have shown that 15–50 μmol Fe per kg (0.8–2.8 mg Fe per kg) of MION resulted in a three- to four-fold increase in aortic S/N ratio, and in an improvement in the image quality of pulmonary, abdominal, and extremity vasculature by MR angiography.[24]

Iron oxide preparations have also been used experimentally to assess myocardial perfusion (conventional iron oxides).[8,25] For example, myocardium supplied by an occluded coronary artery does not decrease in signal intensity following injection of the iron oxide, whereas normally perfused myocardium decreases homogeneously in signal intensity.

5.3 Receptor Agents

Certain galactose-containing iron oxide preparations can be delivered to ASG receptors on hepatocytes. MR imaging with such receptor agents, has demonstrated that a significant decrease in liver S/N ratio can be obtained at lower doses of iron oxide than with conventional iron oxides. This is presumably due to the effective cell adhesion, internalization, high receptor density or different spatial distribution, as compared to reticuloendothelial-system-specific iron oxides.

The main impetus for developing receptor specific liver agents is to enable functional MR imaging. For example, primary malignant hepatic tumors lose the expression of the ASG cell surface receptor during malignant degeneration, and, therefore, are not expected to take up ASG-receptor agent. Furthermore, ASG-receptor agents potentially allow differentiation of ASG(−) (i.e. malignant tumors such as hepatocellular carcinoma and ASG(+) (i.e. benign tumors such as focal nodular hyperplasia (FNH) or adenoma). Direct targeting of hepatocytes, rather than hepatic phagocytic cells, also allows direct assessment of hepatic function as shown in animal models of diffuse liver disease.

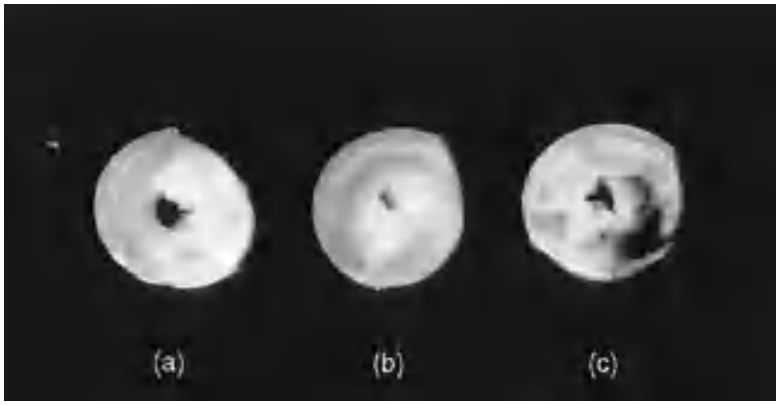

Figure 2 Detection of myocardial infarction with MION-antimyosin. MR microscopic T_2-weighted images of an infarcted rat heart with: (a) no contrast, (b) MION (control), or (c) MION-antimyosin. Only in (c) is there a significant decrease in signal intensity of damaged myocardium (arrow). (Reprinted with permission from *Radiology*)

5.4 Antibody Imaging

To assess myocardial viability by MR imaging, MION has been coupled to an antimyosin.[8] One hour after intravenous administration of MION-antimyosin to rats or rabbits, a marked decrease in the signal intensity of infarcted myocardium was observed, whereas the signal intensity of normal myocardium was essentially unaltered (Figure 2). This and other agents, may have future applications for in vivo tissue typing, tumor diagnosis, and differential diagnosis.

5.5 Other Uses

A variety of different experimental iron oxide preparations have been used for MR experiments. 'Ferrosomes', lipid vesicles loaded with superparamagnetic iron oxide crystal aggregates, have been used for MR imaging. Attachment of tumor-specific monoclonal antibodies to iron oxide aggregates has been described, as well as introduction of the iron oxide particles into the fetal neural tissue. Axonal transport has also been studied using wheat germ agglutinin labeled iron oxide.

6 RELATED ARTICLES

Contrast Agents in Magnetic Resonance: Operating Mechanisms; Contrast Agents in Whole Body Magnetic Resonance: An Overview; Gadolinium Chelate Contrast Agents in MRI: Clinical Applications; Gadolinium Chelates: Chemistry, Safety, and Behavior; Relaxometry of Tissue.

7 REFERENCES

1. M. Ohgushi, K. Nagayama, and A. Wada, *J. Magn. Reson.*, 1978, **29**, 599.
2. G. Wolf, K. Burnett, E. Goldstein, and P. Joseph, *Magn. Reson. Ann.*, 1985, 231.
3. H. Mendoca-Dias and P. Lauterbur, *Magn. Reson. Med.*, 1986, **3**, 328.
4. S. Saini, D. Stark, P. Hahn, J. Wittenberg, T. Brady, and J. Ferrucci, *Radiology*, 1987, **162**, 211.
5. D. Stark, R. Weissleder, G. Elizondo, P. Hahn, S. Saini, L. Todd, J. Wittenberg, and J. Ferrucci, *Radiology*, 1988, **168**, 297.
6. R. Weissleder, G. Elizondo, J. Wittenberg, A. Lee, L. Josephson, and T. Brady, *Radiology*, 1990, **175**, 494.
7. E. Seneterre, R. Weissleder, D. Jaramillo, P. Reimer, A. Lee, T. Brady, and J. Wittenberg, *Radiology*, 1991, **179**, 529.
8. R. Weissleder, A. Lee, B. Khaw, T. Shen, and T. Brady, *Radiology*, 1992, **182**, 381.
9. R. Weissleder, P. Reimer, A. Lee, J. Wittenberg, and T. Brady, *Am. J. Roentgenol.*, 1990, **155**, 1161.
10. L. Josephson, E. Groman, E. Menz, J. Luis, and H. Bengele, *Magn. Reson. Imaging*, 1990, **8**, 637.
11. R. Molday and L. Molday, *FEBS Lett.*, 1984, **170**, 232.
12. R. Molday and D. Mackenzie, *J. Immunol. Methods*, 1982, **52**, 353.
13. L. Josephson, J. Lewis, P. Jacobs, P. Hahn, and D. Stark, *Magn. Reson. Imaging*, 1988, **6**, 647.
14. R. Weissleder, D. Stark, B. Engelstad, B. Bacon, C. Compton, D. White, P. Jacobs, and J. Lewis, *Am. J. Roentgenol.*, 1989, **152**, 167.
15. G. Elizondo, R. Weissleder, D. Stark, J. Guerra, J. Garza, C. Fretz, L. Todd, and J. Ferrucci, *Radiology*, 1990, **174**, 797.
16. R. Weissleder, P. Hahn, D. Stark, G. Elizondo, S. Saini, L. Todd, J. Wittenberg, and J. Ferrucci, *Radiology*, 1988, **169**, 399.
17. R. Weissleder, G. Elizondo, D. Stark, P. Hahn, J. Marfil, J. Gonzalez, S. Saini, L. Todd, and J. Ferrucci, *Am. J. Roentgenol.*, 1989, **152**, 175.
18. R. Weissleder, G. Elizondo, L. Josephson, C. Compton, C. Fretz, D. Stark, and J. Ferrucci, *Radiology*, 1989, **171**, 835.
19. B. Hamm, M. Taupitz, P. Hussmann, S. Wagner, and K. Wolf, *Radiology*, 1989, **173(P)**, 274.
20. N. Simionescu and G. Palade, *J. Cell Biol.*, 1971, **50**, 616.
21. S. McLachlan, M. Morris, M. Lucas, and B. Scheetz, in *Proc. XIIth Ann Mtg. Soc. Magn. Reson. Med.*, New York, 1993, p. 495.
22. P. Rinck, O. Smevik, G. Nilsen, O. Klepp, M. Onsmed, A. Oksenckl, and A. Borseth, *Radiology*, 1991, **178**, 775.
23. P. Hahn, D. Stark, J. Lewis, S. Saini, G. Elizondo, R. Weissleder, C. Fretz, and J. Ferrucci, *Radiology*, 1990, **175**, 695.
24. H. Frank, R. Weissleder, and T. Brady, *Am. J. Roentgenol.*, 1994.
25. P. Reimer, R. Weissleder, A. Lee, J. Wittenberg, and T. Brady, *Radiology*, 1990, **177**, 729.

Acknowledgements

From the Department of Radiology, Massachusetts General Hospital and Harvard Medical School. This work was supported by NIH Grant RO1 CA 59649-01.

Biographical Sketches

Liliane A. Harika. *b* 1965. M.D., Lebanon, 1992. Currently resident in the Department of Radiology, Lakey Clinic, Boston, MA, USA. Research interests include evaluation of novel MR contrast agents.

Ralph Weissleder. *b* 1958. M.D., Ph.D., Germany, 1985. Currently Associate Professor of Radiology in the Department of Radiology, Massachusetts General Hospital and Harvard Medical School, Boston, MA, USA and director of the Center for Molecular Imaging Research at Massachusetts General Hospital. Author of three radiology textbooks, and over 100 original publications. Major research interests include the development of diagnostic pharmaceuticals, iron oxides, new MRI techniques and cell and molecular biology.

Contrast Agents in Whole Body Magnetic Resonance: An Overview

Thomas J. Brady

Massachusetts General Hospital and Harvard Medical School, Charlestown, MA, USA

and

Peter Reimer

Institute for Clinical Radiology, Munster, Germany

1 INTRODUCTION

During the first decade since its introduction into clinical medicine, magnetic resonance (MR) has developed into a highly sensitive imaging modality with great flexibility. While many intrinsic and extrinsic parameters can alter MR image appearance, differences in tissue proton relaxation times, (T_1 and T_2) provide the dominant source of image contrast between normal and disease states. Because of this excellent tissue contrast, it was originally felt that MR, unlike other techniques, would not require the administration of exogenous contrast agents. However, it soon became apparent that relaxation times of normal and abnormal tissue, such as meningomas and small metastases, can overlap with normal tissue, resulting in decreased diagnostic sensitivity and specificity.[1] The introduction of paramagnetic contrast agents has overcome many of these problems. In addition, 'magnetopharmaceuticals' can also be used to assess physiologic processes (e.g. tissue perfusion), and newer agents have the potential for target specific (receptor and antibody) imaging. Thus, MR contrast agent imaging combines the advantages of high spatial resolution with the functionality of nuclear medicine imaging. This offers both a challenge and an opportunity to the radiology community. This article provides an overview of the principles of MR contrast agents and reviews new agents for enhancement of the liver, lymph nodes, and vessels.

2 PRINCIPLES

A paramagnetic substance is one that contains one or more unpaired electrons which enhance the relaxation rates ($1/T_1$ and $1/T_2$), i.e. shorten T_1 and T_2 relaxation times, of water protons. The pharmaceutical manipulation of tissue signal intensity arises from the interaction of the magnetic moments of protons with the magnetic moments of these materials. Unlike iodinated radiographic and radionuclide agents, paramagnetic agents have an indirect effect on image intensity. The alteration in the observed MR image intensity is the result of decrease in the proton relaxation times: the agent per se is not 'imaged'. In addition, the effect on MR signal intensity is not straightforward but depends on several factors including:[2]

- Magnetic moment.
- Concentration.
- Dipole–dipole distance ($1/r^6$).
- Magnetic field strength.
- Water exchange.
- Rotational motion.

It is the magnitude of the magnetic moment that is principally responsible for enhanced proton relaxation and alteration of image signal intensity. Gadolinium (Gd), a lanthanide series element, is the most potent paramagnetic element, possessing seven unpaired electrons. Thus, Gd has received considerable attention, although other paramagnetic metal ions such as manganese and iron, both of which possess five unpaired electrons, are currently being investigated. In the design of a clinically useful magnetopharmaceutical one must not only consider the relaxation efficiency but also pay close attention to potential in vivo toxicity. While metal ions are very efficient relaxation agents, they are quite toxic. Chelation of the ion with a suitable organic ligand [e.g. diamine tetracarboxic pentaacetic (DTPA)] dramatically reduces toxicity, but also leads to diminished relaxivity since the ligand prevents close interaction between water protons and the paramagnetic ion. The attachment of various carrier molecules will also affect the tissue distribution and determine the clinical use of the agent.

2.1 T_1 Agents

In practice, the radiologist has little control over many of these factors. In general, it is the biodistribution and resulting tissue concentration of an MR contrast agent that determines the change in MR signal intensity. T_1 shortening enhances tissue signal, while T_2 shortening decreases tissue signal intensity. Although paramagnetic species equally enhance both T_1 and T_2 relaxation rates, at clinically recommended doses, T_1 effects dominate the alteration in image signal intensity. Therefore, paramagnetic metal substances are known as 'T_1 agents'.

2.2 T_2 Agents

Superparamagnetic iron oxide particles (IOPs) are a new class of MR contrast agents that predominantly effect T_2 relaxation. These particles, which have very large magnetic moments (2–3 orders of magnitude greater than those of paramagnetic metal ions) and associated magnetic field gradients, are referred to as 'homogeneity spoilers'.[3] When water molecules diffuse through these induced field gradients, protons experience spin dephasing (T_2* relaxation) which leads to decrease in MR signal intensity. The initial IOP preparations with a relatively large size (>50 nm) are rapidly taken up by reticuloendothelial cells of the liver and spleen and produce 'negative' contrast. New ultrasmall iron oxide particles (USIOPs) with a size of <10 nm pass through capillaries and reach the macrophages in lymph nodes. These preparations are discussed in ***Contrast Agents in MRI: Superparamagnetic Iron Oxide***.

3 CLINICALLY APPROVED AGENTS

In 1988, gadolinium DTPA (Gd-DTPA, Magnevist®, Schering AG, Berlin) became the first MR contrast agent to be

approved for clinical use. Administered intravenously, Gd-DTPA has an extracellular distribution (analogous to the iodinated radiographic agents) and undergoes rapid renal excretion by glomerular filtration.[4] In humans Gd-DTPA has a plasma halflife of <15 min and >90% can be recovered in the urine within 3 h following intravenous administration. Enhancement of the MR image signal is obtained at doses of 0.1–0.2 mmol kg^{-1} with a median lethal dose (LD_{50}) of approximately 10 mmol kg^{-1}. This results in a safety factor of approximately 50–100, which is superior to that of iodinated compounds.

Recently, three additional gadolinium chelates have been approved for clinical use: Gd-DTPA-bis(methyl)anoide (Gd-DTPA-BMA, Omniscan®, Nycomed), Gd-HP-DO3A (Gadoteridol, ProHance®, Squibb Diagnostics), and Gd-DOTA (DOTAREM® Guerbet). All three agents possess an electrically neutral charge and lower osmolarity, potentially offering greater safety for high-dose studies and rapid bolus injections. A more complete description of gadolinium chelates can be found in ***Gadolinium Chelates: Chemistry, Safety, and Behavior***.

3.1 Clinical Applications of Gadolinium Chelates

Gadolinium chelates are frequently used in central nervous system (CNS) imaging, while their role in body MR imaging is still evolving. In addition to dosage, appropriate selection of MR pulse sequences and acquisition time following injection are critical for certain applications. Due to their extracellular distribution, gadolinium chelates highlight breakdown of the blood–brain barrier and detect small lesions missed on conventional T_1-weighted imaging (Figure 1). In the brain and spine, gadolinium chelates have a high sensitivity in detecting pathologic conditions[5] including:

- Primary and secondary malignancies.
- Infectious processes.
- Activity of multiple sclerosis plaques.
- Extraaxial lesions, especially small neuromas and meningiomas.
- Differentiating scar from recurrent disk.

The role of these interstitial agents in CNS disease, as well as their application in the cardiovascular and musculoskeletal systems, is addressed in greater detail in other articles in this volume.

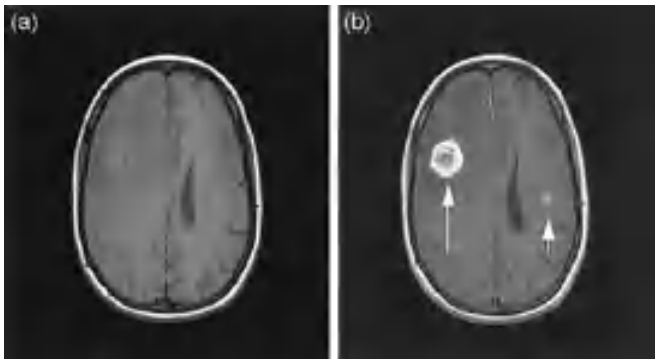

Figure 1 T_1-weighted MR brain images in a patient with metastatic cancer before (a) and after (b) Gd-DTPA. While an abnormality with mass effect is visible in (a), Gd-DTPA provides enhancement of the metastatic focus [long arrow in (b)], and a second, unsuspected lesion [small arrow in (b)] is detected on the opposite side

4 NONAPPROVED AGENTS

While interstitial T_1 agents have demonstrated clinical utility, these agents have been less successful in identifying pathology in the liver and lymph nodes and for enhancement of vessels in MR angiography. Thus a significant effort has been made to develop MR agents that are tissue specific.

4.1 Oral Contrast Agents

A major limitation of MR imaging in the abdomen has been the lack of a bowel contrast agent. These are required in order to differentiate bowel loops from normal and pathological anatomy. In general, oral contrast media may be catagorized as positive-enhancing T_1 agents or negative-enhancing T_2 agents.[6] Positive enhancers include Gd-DTPA and ferric ammonium citrate. Gd-DTPA dimeglumine dissolved in mannitol (Magnevist enteral®, Schering) has been developed as an oral agent with positive bowel lumen enhancement. In a multicenter clinical trial, gastrointestinal enhancement improved the definition of abdominal mass lesions in 62% of cases. Ferric ammonium citrate, known as a supplemental source of iron in geritol (Beecham, Bristol) has been shown to improve the delination of gastric margins, pancreas, and colon in normal volunteers.

Different iron oxide preparations have been used as negative gastrointestinal negative contrast agents.[7] Images obtained before and after ingestion of the contrast material at doses of 22.5–225 mg Fe in a volume of 600–900 mL demonstrated delivery of contrast material into the distal small bowel. The enhanced images showed improved delineation of the head of the pancreas, para-aortic regions, and anterior margins of the kidneys. The contrast agent did not generate MR artifacts.

4.1.1 MR Agents in Liver Imaging

The detection and differentiation of hepatic tumors have important diagnostic and therapeutic implications in cancer patients.[8] However, conventional MR imaging of the liver is limited by motion artifacts and intrinsic contrast between lesions and normal liver tissue. The combination of nonspecific interstitial agents with conventional MR imaging can result in lower lesion to liver contrast.[6] Because of the transient effects with these agents, fast MR imaging is required to detect lesions. However, there are several approaches to enhancing liver tissue that can be used with conventional MR imaging, including targeting of agents to hepatocytes. (Use of IOPs for targeting the reticoloendothelial system is discussed in great detail in ***Contrast Agents in MRI: Superparamagnetic Iron Oxide***).

4.2 Hepatobiliary Agents

The design of MR contrast agents for the hepatobiliary system is based on the chelation of paramagnetic ions to ligands with high affinity for hepatocytes. Subsequent to the initial demonstration in animals that Fe-EHPG is taken up by hepatocytes and excreted into the bile,[9] three new hepatobiliary agents

have been developed including manganese(II) *N*,*N*′-dipyridoxal-ethylenediamine-*N*,*N*′-diacetate-5,5′-bis(phosphate) (Mn-DPDP; Salutar, Nycomed), Gd-BOPTA (Bracco) and Gd-EOB(ethoxy-benzyl)-DTPA (Schering). Initial clinical findings show encouraging results.

4.2.1 Mn-DPDP

Mn-DPDP is a manganese chelate of pyridoxal-5′-phosphate, a catalytically active form of vitamin B_6, and is therefore recognized by the cell-membrane transport system.[10] Since uptake of Mn-DPDP is thought to be related to liver cell function only those parts of liver tissue with preserved hepatocellular function show enhancement after injection of Mn-DPDP.[11] Because of relatively slow excretion of the agent, liver enhancement is visible 10–23 h postinjection. This extended 'imaging window' provides adequate time for patient preparation and multiple MR imaging techniques.

In Phase I and II trials, patients with liver metastases demonstrated significant increase in tumor–liver contrast-to-noise (C/N) ratio after the injection of 10 and 5 μmol kg^{-1} Mn-DPDP on T_1-weighted images (Figure 2). The highest increase in C/N ratio was achieved with the fast and heavily T_1-weighted gradient recalled echo (GRE) imaging techniques.[12] The confidence level of lesions detected increased after the injection of Mn-DPDP and the number of small lesions ($\leqslant$1.0 cm diameter) detected was considerably higher as compared with unenhanced MR images.

In patients with primary hepatocellular carcinoma (HCC), uptake of Mn-DPDP was found to vary. In patients with well differentiated HCC, marginal or inhomogeneous uptake of the contrast agent was noticed; however, in patients with dedifferentiated HCC no uptake of Mn-DPDP was found. In these patients nodules obscured on unenhanced T_1- and T_2-weighted images due to peritumoral edema were clearly visible after administration of Mn-DPDP. Tumor enhancement in HCC has also been investigated experimentally, demonstrating that tumoral uptake depends on tumor differentiation with peripheral rim enhancement in highly malignant tumors and late central enhancement in differentiated tumors.[13] These findings were confirmed more recently in the US Phase II trial when primary tumors of the liver like fibronodular hyperplasia (FNH), adenoma, regenerative nodule, HCC, and fatty infiltration also demonstrated enhancement.[14]

Extrahepatic enhancement after the injection of Mn-DPDP was found to varying degrees in pancreatic tissue, cortical zones of the kidneys, and stomach wall. This is most likely due to instability of the complex resulting in dissociation to some degree with uptake of free manganese in the tissues listed. Pancreatic enhancement has been exploited for contrast-enhanced MRI of the pancreas, improving visualization of pancreatic disease. Despite the concerns of free manganese, preclinical animal studies have shown that the safety factor (ratio of the acute toxicity to dose used for imaging) of Mn-DPDP is similar to that of Gd-DTPA.[15] None of the patients studied showed signs of severe allergic reactions, but minor side-effects were found in 28/141 patients (19.5%). Neither significant electrocardiogram (ECG) changes nor significant changes in vital signs were seen after the injection of Mn-DPDP.

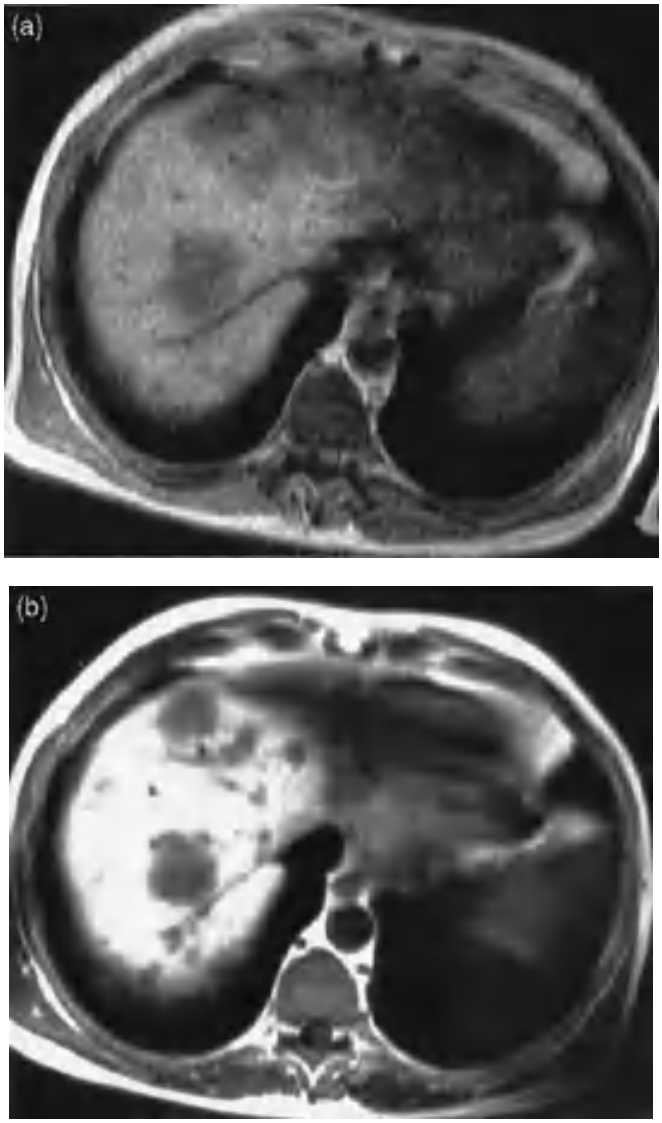

Figure 2 (a) T_1-weighted SE 500/15 image shows metastases hypointense relative to uninvolved liver. (b) T_1-weighted SE 500/15 image after administration of 10 μmol kg^{-1} Mn-DPDP shows metastases hypointense relative to enhanced, uninvolved liver tissue. Note the improved lesion–liver contrast and detectability of small hepatic metastases as compared with unenhanced MR images

4.2.2 Gd-BOPTA/Dimeg

Gd-BOPTA (Gadobenate Dimeglumine) is a hepatobiliary agent that is similar to Gd-DTPA, differing only in the substitution of a CH_3 group by a benzyloxymethyl side chain. The molecule is recognized by the transmembrane carrier protein within the hepatocyte cell membrane, and thus represents a liver specific drug.[16] Intravenous administration of Gd-BOPTA shortens T_1 values of liver parenchyma for a prolonged period of time, thus increasing liver signal intensity on T_1-weighted images. Since most malignant liver tumors are devoid of the transmembrane carrier protein, tumor–liver contrast increases for more than 2 h.[17] Contrast is especially high on late images (>45 min postinjection).

Phase I studies demonstrated enhancement almost independent of biliary elimination kinetics. Peak liver enhancement

occurred 40–45 min following intravenous administration of 0.1 mmol kg^{-1} body weight, with a slow decrease over several hours. The European Phase II trial of Gd-BOPTA has demonstrated convincing tolerance and safety data, with mild or moderate side effects in less than 2% of 359 patients. Figure 3 demonstrates the clinical utility of Gd-BOPTA.[18] Nonspecific enhancement in tumor tissue during or immediately after administration of Gd-BOPTA was also observed during the Phase II trial. An additional application is the detection and characterization of myocardial ischemia.[18]

4.2.3 Gd-EOB-DTPA

Gd-EOB-DTPA is a derivative of Magnevist®, modified by substitution of a side chain altering pharmacokinetics and biodistribution in vivo.[19] The agent is a hepatocyte-directed contrast agent that is preferentially cleared by the hepatocellular organic anion system and subsequently excreted into bile. Previous studies in rats have shown that 63–80% of Gd-EOB-DTPA is excreted in bile;[20] 20–37% of the injected dose is eliminated through the kidneys by means of glomerular filtration. The plasma halflife of Gd-EOB-DTPA in rats is approximately 10 min.[19]

Gd-EOB-DTPA has a T_1 relaxivity of 16.6 L $mmol^{-1}$ in liver tissue of rats. With a median lethal dose of 10 mmol kg^{-1} in mice and rats after intravenous injection, Gd-EOB-DTPA seems to have a fairly high margin of safety. The safety factor in rats of 400 is higher than any other factor for a clinically approved contrast agent in radiology.[21] Up to 75% of this agent is excreted by the hepatobiliary system, and more than 200% liver enhancement is achieved at a dose of 0.1 mmol kg^{-1}. As demonstrated recently, this agent may also be used to perform MR cholangiography.

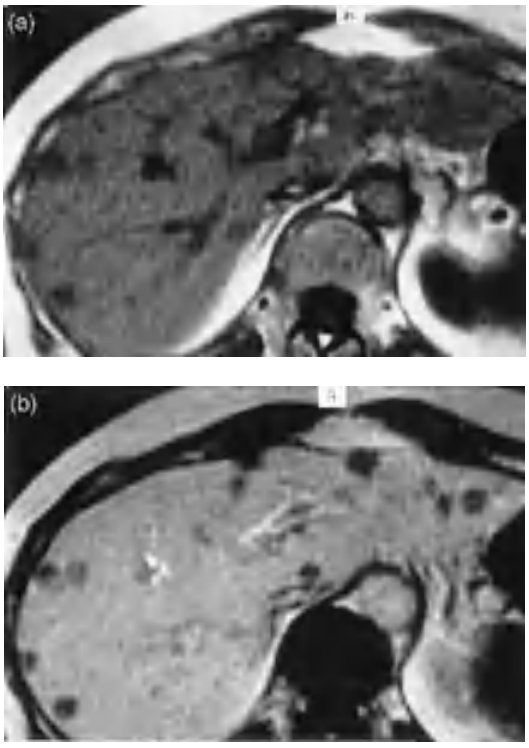

Figure 3 Axial T_1-weighted images at 1.5 T in a patient with colon carcinoma before (a) and 120 min following (b) intravenous administration of 0.1 mmol kg^{-1} body weight Gd-BOPTA (Dimeg). Tumor–liver contrast is increased on the postcontrast image, improving detection of metastases, i.e. more lesions are visualized. (Reproduced by permission of F. Cavangna, Ph.D., Bracco AG, Italy)

Tumor–liver contrast is improved since malignant lesions demonstrate only nonspecific enhancement via the extracellular space.[22] Contrast is achieved 3–5 min following the administration of 30 μmol kg^{-1}, and remains high for more than 30–60 min.[23] Potential clinical applications besides liver imaging are imaging of the biliary tract and the upper small bowel.

4.3 Vascular Agents

A number of different angiographic MR techniques have been described for various applications. Previous reports have clearly demonstrated that vessel-to-background ratios, and thus image quality, can be significantly improved by decreasing blood T_1 with paramagnetic contrast agents and optimizing pulse sequences. Whereas Gd-DTPA decreases blood T_1 in cerebral vessels without significantly increasing the signal intensity of the CNS, short blood halflife and rapid extravasation into the extravascular space limits the usefulness of low molecular weight paramagnetic MR contrast agents in the remainder of the body. Despite some interesting results with slow infusion of Gd-DTPA, several macromolecular agents with a longer intravascular distribution have been developed.

Ideal macromolecular MR angiographic contrast agents should have a distribution limited to the intravascular space, a sufficiently long blood halflife, and no immunogenicity. In addition, the agent together with chelated metal ion should be excreted in toto. To achieve this, chelating groups have been attached to a variety of natural or synthetic macromolecules [e.g. proteins, polysaccharides, poly(L-lysine), polyethyleneimine].[24] Chemical attachment (conjugation) of DTPA to bovine serum albumin (BSA) results in a macromolecular label with a longer blood halflife than that of Gd-DTPA. Unfortunately, large doses of labeled BSA have to be administered to achieve sufficiently high concentrations of the paramagnetic label in blood. In addition, BSA-Gd-DTPA has been found to be immunogenic and thus potentially anaphylactic.[25] Synthetic polypeptides, such as poly(L-lysine), offer an alternative to natural macromolecular carriers. Poly(L-lysine) modified with DTPA has been shown to be an effective carrier molecule for paramagnetic or radioactive cations.[26] The toxicity and immunogenicity profile of poly(L-lysine)-Gd-DTPA is better than that of albumin-Gd-DTPA. Despite these significant advantages over protein-based macromolecular agents, poly(L-lysine)-Gd-DTPA (molecular weight 48.7 kDa) is rapidly removed from blood.[27] Larger poly(L-lysine) molecules have been reported to exhibit a longer residence in the blood pool.

Bogdanov et al.[28] reported a new macromolecular agent consisting of monomethoxy ether of poly(ethylene glycol) 5000 (MPEG5) covalently attached to a poly(amino acid), wherein the poly(amino acid) serves as the carrier of Gd-DTPA. Experiments in animals have demonstrated two major features: (1) absence of immune response against Gd-DTPA and the carrier molecule following intravenous administration; and (2) minimal accumulation of the agent in the reticuloendothelial system. Biokinetic studies revealed that the blood halflife of the agent is 14 h. The new agent [MPEG-poly(L-lysine)-Gd-DTPA], has a high R_1/Gd relaxivity of 18.0 $(mM\ s)^{-1}$ compared with Gd-DTPA

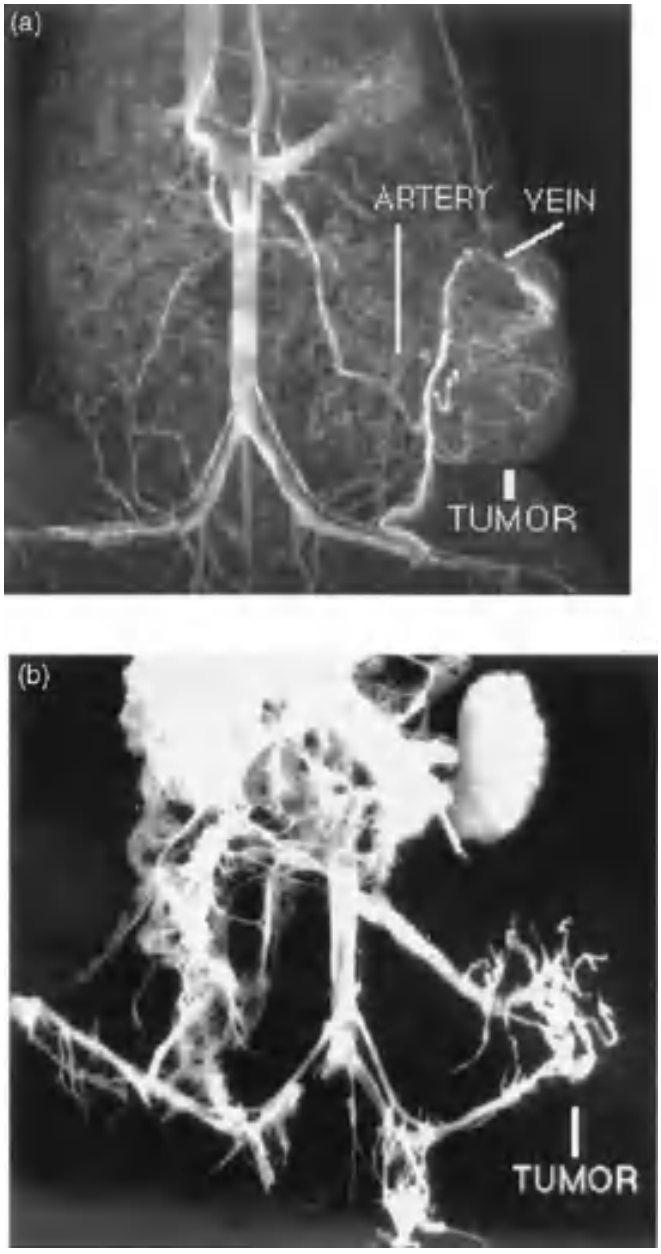

Figure 4 Tumor neovasculature in a rat with R3230 adenocarcinoma implanted in a left flank. (a) MR angiography (3D-TOF, TE = 8 ms, TR = 60 ms, 60°); (b) polymer cast. The MR imaging results and the polymer replica of the vasculature were obtained from the same animal. Note iliac and epigastric venous in-growth in the tumor

[3.7 (mM s)$^{-1}$] and poly(L-lysine)-Gd-DTPA [13.1 (mM s)$^{-1}$]. Dose–response studies demonstrate that doses of 20 μmol Gd kg^{-1} are sufficient to increase the vessel/muscle ratio four- to five-fold using three-dimensional 'time-of-flight' (3D-TOF) MR angiographic pulse sequences. Contrast is significantly improved and remains unchanged for at least 2 h after intravenous administration allowing good visualization of small and peripheral vessels (Figure 4).

4.4 Lymph Node Agents

Detection of lymph node metastases is a critical part of cancer staging.[29] Conventional MR imaging offers the advantages of high spatial resolution and inherent soft tissue contrast to distinguish nodes from adjacent fat, muscle, and vessels.[30] Unfortunately, because in vitro measurements of human T_1 and T_2 relaxation times of normal, metastatic, lymphomatous, and hyperplastic lymph nodes demonstrate considerable overlap, these parameters by themselves are of limited clinical utility.[31] Thus, MR detection of lymph node metastases (i.e. size criteria) has the same limitations as X-ray computed tomography.

A method of MR lymphography which delivers contrast agent to all 600–800 human lymph nodes with a single intravenous administration would be an ideal clinical tool. Currently, research efforts are concentrated in maximizing the delivery of iron oxide (see ***Contrast Agents in MRI: Superparamagnetic Iron Oxide***) and specific T_1 agents to lymph nodes. Initial attempts to perform MR imaging with Gd-DTPA labeled target-specific carrier molecules has failed because of the necessity to deliver large amounts of paramagnetic labels to the target tissue (10^{-4} M), considerably higher amounts than necessary for scintigraphy (10^{-11} M) Recently, Papisov et al.[32] reported a targeted T_1-label, polyglucosylated macrocomplex (PGM), which accumulates in lymph nodes to a high degree after intravenous administration. This agent consists of a poly(L-lysine) backbone to which Gd-DTPA molecules are attached. To prevent uptake by the reticuloendothelial system cells, a peripheral dextran coating is also attached which sterically protects the inner T_1 macromolecular labels [e.g. Gd-DTPA-poly(L-lysine)] from recognition. Intravenous administration of 10 mg kg^{-1} of a double labeled (^{111}In, Gd) preparation in rats resulted in significant uptake at 24 h in central lymph nodes (35–45% dose g^{-1}), spleen (15–30% dose g^{-1}), while only 1–2% accumulated in liver. The uptake in lymph nodes reflected their activity, with significantly increased accumulation in the lymph nodes draining sites of inflammation (100% dose g^{-1} or more). Fat saturated T_1-weighted MR images clearly demonstrate lymph node enhancement (Figure 5). As other molecules can be incorporated into the PGM complex, e.g. chemotherapeutic agents, this class of agent may also play a role in drug delivery to lymph nodes.

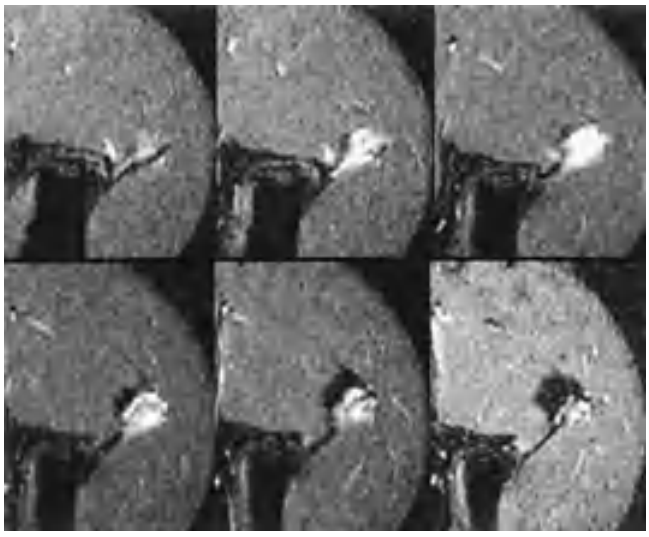

Figure 5 Fat suppressed T_1-weighted MR images (700 μm slices) of the popliteal fossa in a rat, demonstrating enhancement of lymph nodes, 3 h after intravenous injection of 10 μm kg^{-1} of PGM

5 SUMMARY

MR contrast agents, both paramagnetic and superparamagnetic susceptibility agents, enhance proton relaxation rates and provide improved lesion detection with MR imaging. Interstitially distributed gadolinium chelates have a demonstrated utility in CNS disease. However, it is likely that tissue specific agents will be required for MR imaging of the liver, vessels, or lymph nodes. Agents are now available at various stages of development in these three areas. Further developments in MR contrast media, in combination with improved imaging techniques may lead to expansion and novel applications of diagnostic MR imaging.

6 RELATED ARTICLES

Contrast Agents in Magnetic Resonance: Operating Mechanisms; Contrast Agents in MRI: Superparamagnetic Iron Oxide; Gadolinium Chelate Contrast Agents in MRI: Clinical Applications; Gadolinium Chelates: Chemistry, Safety, and Behavior.

7 REFERENCES

1. T. Brady and B. Rosen, 'National Conference on Biologic Imaging. II. Clinical Aspects', National Academy Press, Washington, 1984.
2. R. Lauffer, *Chem. Rev.*, 1987, **87**, 901.
3. R. Weissleder, and M. Papisov, *Magn. Reson. Rev.*, 1992, **4**, 1.
4. H. Weinmann, R. C. Brasch, W. R. Press, and G. E. Wesbey, *Am. J. Roentgenol.*, 1984, **142**, 619.
5. M. Brant-Zawadzki and D. Norman, 'Magnetic Resonance Imaging of the Central Nervous System', Raven, New York, 1987.
6. R. Brasch, *Radiology*, 1992, **183**, 1.
7. P. A. Rinck, O. Smevik, G. Nilsen, O. Klepp, M. Onsrud, A. Oksendahl, and A.-N. Borseth, *Radiology*, 1991, **178**, 775.
8. M. A. Adson, *Am. J. Roentgenol.*, 1983, **140**, 695.
9. R. B. Lauffer, W. L. Greif, D. D. Stark, A. C. Vincent, S. Saini, V. J. Wedeen, and T. J. Brady, *J. Comput. Assist. Tomogr.*, 1985, **9**, 431.
10. S. M. Rocklage, W. P. Cacheris, S. C. Quay, F. E. Hahn, and K. N. Raymond, *Inorg. Chem.*, 1989, **28**, 477.
11. M. E. Bernardino, S. W. Young, J. K. Lee, and J. C. Weinreb, *Radiology*, 1992, **183**, 53.
12. E. J. Rummeny, C. Ehrenheim, and H. B. Gehl, *Invest. Radiol.*, 1992, **26**, 879.
13. Y. Ni, G. Marchal, J. Yu, E. J. Rummeny, X. Zhang, K. P. Lodemann, and A. L. Baert, *Radiology*, 1993, **188**, 45.
14. N. M. Rofsky, J. C. Weinreb, M. E. Bernardino, S. W. Young, J. K. T. Lee, and M. E. Noz, *Radiology*, 1993, **188**, 53.
15. K. O. Lim, D. D. Stark, P. T. Leese, A. Pfefferbaum, S. M. Rocklage, and S. C. Quay, *Radiology*, 1991, **178**, 79.
16. G. Vittadini, E. Felder, P. Tirone, and V. Lorusso, *Invest. Radiol.*, 1988, **23 (Suppl 1)**, S246.
17. F. Cavagna, P. Tirone, E. Felder, and C. de Haën, 'Developments in Contrast Agent Research', Eur. Magn. Reson. Forum, Blonay, Switzerland, 1991.
18. K. K. Yu, M. Saeed, M. F. Wendland, N. Derugin, F. M. Cavagna, and C. B. Higgins, *Invest. Radiol.*, 1992, **27**, 927.
19. H. J. Weinmann, G. Schuhmann-Giampieri, H. Schmitt-Willich, H. Vogler, T. Frenzel, and H. Gries, *Magn. Reson. Med.*, 1992, **22**, 233.
20. O. Clement, A. Mühler, V. Vexler, Y. Berthezene, and R. C. Brasch, *Invest. Radiol.*, 1992, **27**, 612.
21. G. Schuhmann-Giampieri, H. Schmitt-Willich, W. R. Press, C. Negishi, H. J. Weinmann, and U. Speck, *Radiology*, 1992, **183**, 59.
22. A. Mühler, O. Clement, V. Vexler, Y. Berthezene, W. Rosenau, and R. C. Brasch, *Radiology*, 1992, **184**, 207.
23. O. Clement, A. Mühler, V. Vexler, R. Kuwatsuru, Y. Berthezene, and W. Rosenau, *JMRI*, 1993, **3**, 1.
24. R. Lauffer, T. J. Brady, R. D. Brown, C. Baglin, S. H. Koenig, *Magn. Reson. Med.*, 1986, **3**, 541.
25. P. van Hecke, G. Y. Marchal, H. Bosmans, K. Johannik, Y. Jiang, H. Vogler, C. van Ongeval, A. L. Baert, and U. Speck, *Magn. Reson. Imag.*, 1991, **9**, 313.
26. V. P. Torchilin, A. L. Klibanov, N. D. Nossiff, M. A. Slinkin, H. W. Strauss, E. Haber, V. N. Smirnov, and B. A. Khaw, *Hybridoma*, 1987, **6**, 229.
27. G. Schuhmann-Giampieri, H. Schmitt-Willich, T. Frenzel, W. R. Press, and H. J. Weinmann, *Invest. Radiol.*, 1991, **26**, 969.
28. A. Bogdanov, R. Weissleder, H. W. Frank, A. V. Bogdanova, N. Nossiff, B. K. Schaffer, E. Tsai, M. Papisov, and T. J. Brady, *Radiology*, 1993, **187**, 701.
29. J. Berek, N. F. Hacker, Y. S. Fu, T. R. Sokale, R. C. Leuchter, and L. D. Lagasse, *Obstet. Gynecol.*, 1985, **65**, 46.
30. G. M. Glazer, *Radiology*, 1988, **166**, 303.
31. G. C. Dooms, H. Hricak, M. E. Moseley, K. Bottlos, M. Fisher, and C. B. Higgins, *Radiology*, 1985, **155**, 691.
32. M. I. Papisov, A. A. Bogdanov, B. K. Schaffer, N. Nossiff, T. Shen, R. Weissleder, and T. J. Brady, *J. Magnetism Magn. Mater.*, 1993, **122**, 383.

Biographical Sketches

Thomas J. Brady. *b* 1946. B.S., King's College, 1968; M.D., Loyola, 1972. Currently Director, MGH-NMR Center, Department of Radiology, Massachusetts General Hospital and Harvard Medical School, Charlestown, MA, USA. Approx. 160 publications. Research interests include evaluation of novel MR contrast agents.

Peter Reimer. *b* 1959. M.D., FRG, 1985. Currently Head of MR at the Institute of Clinical Radiology, Westfalische-Wilhelms University, Munster. Major research interests include clinical application of cell specific MR contrast agents and ultrafast MR imaging techniques.

Gadolinium Chelate Contrast Agents in MRI: Clinical Applications

Val M. Runge
University of Kentucky, Lexington, KY, USA

1 INTRODUCTION

Intravenous contrast administration, utilizing water soluble gadolinium chelates, has assumed an increasingly important role in clinical magnetic resonance imaging (MRI)[1] during the last 5 years. The positive impact of this new class of contrast media on overall health care is clear from the high level of use.[2,3] For example, in the USA more than half of all head examinations and more than a quarter of all spine examinations are currently performed with intravenous contrast injection. Current utilization is less in anatomical regions outside the head and spine, although definite indications exist in body MRI. Worldwide, four chelates are in use in humans—gadopentetate dimeglumine [NMG_2(Gd DTPA)], gadoterate meglumine [NMG(Gd DOTA)], gadodiamide (Gd DTPA-BMA), and gadoteridol (Gd HP-DO3A). (NMG^+ is the *N*-methylglucammonium ion.) The relaxivities, and thus the contrast effects, are comparable for these agents when given at standard dose (0.1 mmol kg^{-1}). Increased efficacy has been demonstrated at high dose (0.3 mmol kg^{-1}) in certain disease states, in particular for the detection of intracranial metastatic disease. In these applications, the more stable ring chelates, gadoterate meglumine and gadoteridol, offer a higher theoretical safety margin. (Further information on the structure of these chelates is given in ***Gadolinium Chelates: Chemistry, Safety, and Behavior***.)

In head imaging, contrast administration provides improved lesion recognition and characterization. Disease states for which contrast enhancement is indicated include neoplasia, infarction, infection, and other inflammatory conditions. In spine imaging, contrast administration primarily improves diagnostic specificity, although in certain instances improved lesion detectability is also provided. Foremost in spine applications is the use of contrast to differentiate scar from disk material in the postoperative patient, with the identification of recurrent or residual disk herniation an indication for surgery in the appropriate clinical setting. In body imaging, the primary indication at present for contrast use is in the liver for improved lesion characterization. Early postcontrast scans can also be used to improve liver lesion detection. Elsewhere in the body, applications exist principally with regard to improved lesion characterization.

2 CLINICAL APPLICATIONS IN THE HEAD

Diseases of the head and its contents can be subdivided by type into four categories: neoplasia, infarction/vascular disorders, infection/inflammatory disease, and congenital lesions. Clinical referrals for MRI come principally from the first three categories. Contrast administration provides such critical information in these patients as to be mandated.[4] The fourth category, congenital disease, is smaller, and for purely structural lesions in this group use of contrast is not indicated. However, in many instances these patients also manifest related neoplastic, vascular, or inflammatory conditions for which contrast administration is indicated. Several prospective clinical trials have been conducted examining the question of efficacy for contrast administration in all patients referred for head MRI. In one such study, contrast administration was judged to change scan interpretation significantly in 25% of cases, with both the failure to identify lesions (5%) and misdiagnosis (20%) contributing to the lower efficacy of precontrast scans.[5] In addition to demonstrating the value of abnormal contrast enhancement, these trials revealed that the absence of abnormal contrast enhancement can provide important diagnostic information.[6]

With intra-axial primary brain tumors, contrast enhancement principally provides information with regard to lesion characterization (Figure 1). Low-grade astrocytomas in general do not enhance, while higher grade lesions (anaplastic astrocytomas and glioblastomas) demonstrate substantial disruption of the normal blood–brain barrier and thus abnormal contrast enhancement. In the differentiation of these tumors, the identification of an irregular thick rim of enhancement with central necrosis points to the diagnosis of a glioblastoma multiforme. It is important, however, to note that in glial cell tumors abnormal contrast enhancement does not correlate precisely with lesion extent. The presence of tumor cells beyond the area of blood–brain barrier disruption noted on scans has been demonstrated in histologic studies. Contrast enhancement in glial cell tumors can also be used to direct surgical biopsy, as enhancing portions of a lesion tend to be of higher grade. Enhancement is also important for clinical follow-up, with recurrence or progression most easily recognized in higher grade lesions on the basis of abnormal contrast enhancement.

With intra-axial metastatic disease, contrast administration is crucial for lesion identification. Many small metastatic lesions are isointense to surrounding brain on precontrast scans, mandating contrast administration for recognition (Figure 2). Enhanced MRI is now recognized as the modality of choice for detection of intracranial metastases, with markedly improved sensitivity relative to X-ray computerized tomography (CT). In one study of 23 patients suspected of having cerebral metastases, enhanced MRI revealed 67 lesions, as compared with 40 lesions on precontrast T_2-weighted MRI and 37 lesions on double dose delayed CT.[7] Recent experience with MRI has shown the further advantage of high dose gadolinium chelate contrast administration in the detection of intracranial metastatic disease.[8] In one such study, which compared 0.1 and 0.3 mmol kg^{-1} doses, the higher dose resulted in the detection of 46 new lesions in 19 of 27 patients.[9]

With extra-axial brain lesions, contrast administration is often crucial for lesion identification. Small meningiomas and nerve tumors, in particular acoustic neuromas, are often isointense with brain on precontrast studies, and can thus be difficult to detect or clearly marginate on precontrast MRI alone (Figure 3). That these tumors are often small, with little

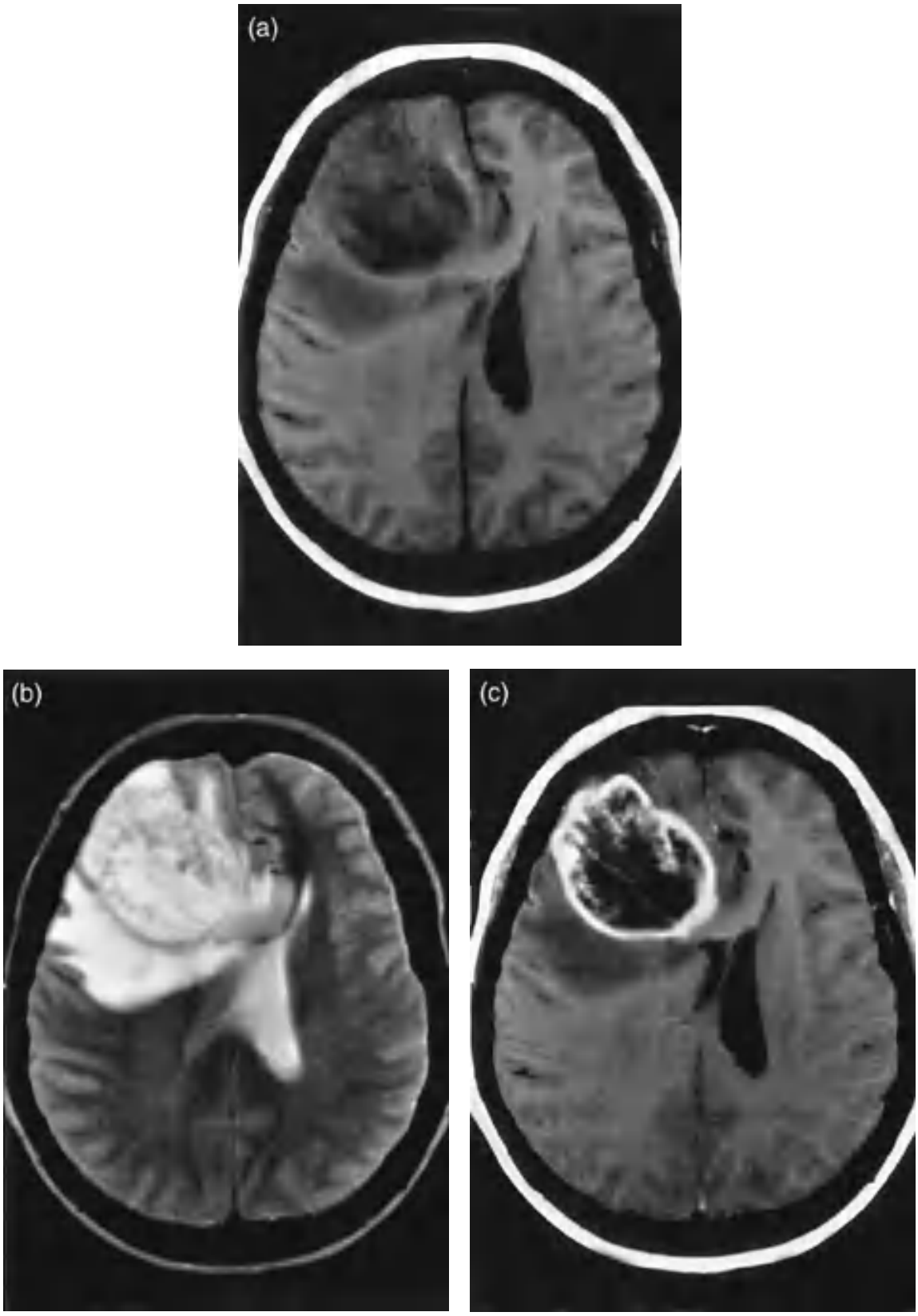

Figure 1 Glioblastoma multiforme. The contrast medium delineates the extent of blood–brain barrier disruption associated with primary intra-axial neoplasms of the central nervous system and assists in characterizing these lesions. The pattern of enhancement is often useful in narrowing the differential diagnosis. This middle-aged female presented with persistent headaches. (a) The precontrast T_1-weighted axial scan reveals a large low signal intensity lesion in the right frontal lobe with significant mass effect. (b) Surrounding edema is best demonstrated on the T_2-weighted image. (c) Postcontrast, the mass exhibits a thick irregular ring of enhancement with central necrosis. This constellation of findings suggests the diagnosis of a high-grade glial cell tumor

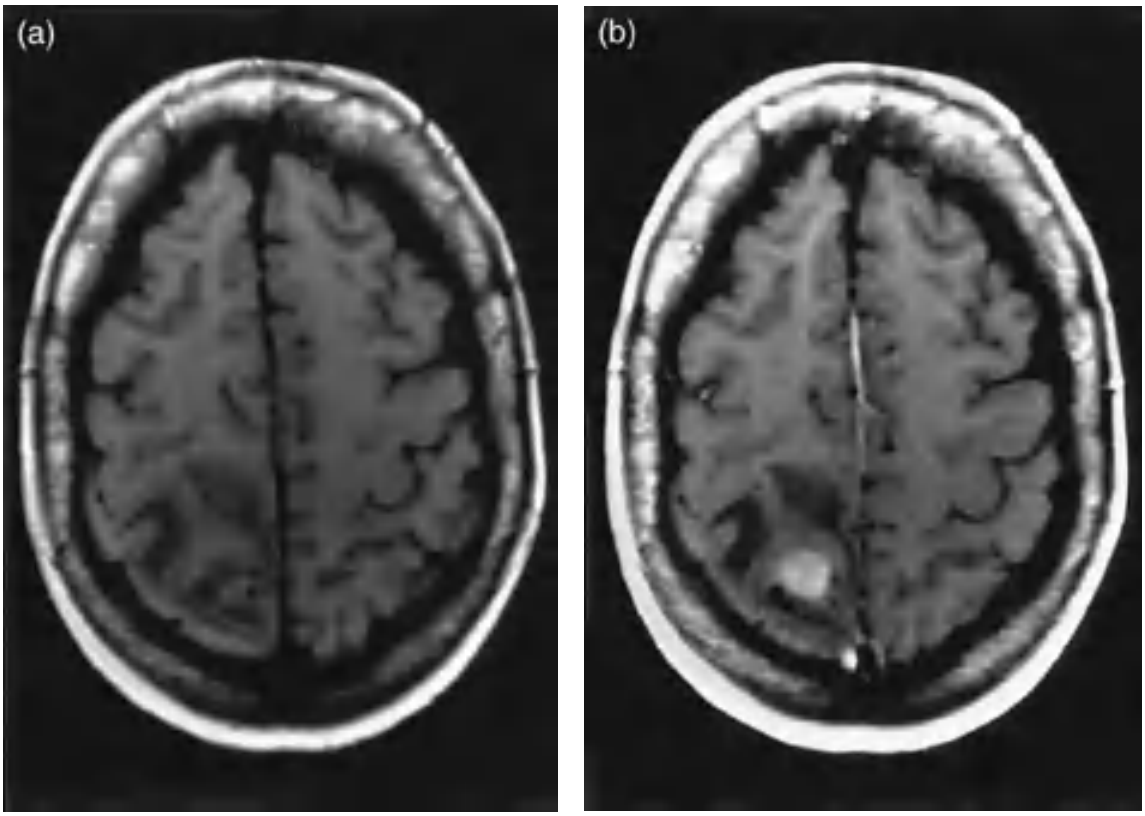

Figure 2 Metastatic breast carcinoma. The contrast medium aids in identification of metastatic lesions which may be masked by edema or are too small to be visualized on a noncontrast examination. This middle-aged female with a primary breast malignancy presented with sudden onset of left-sided weakness. (a) The precontrast T_1-weighted axial image demonstrates edema in the white matter surrounding an ill-defined mass. The (b) postcontrast image confirms the presence of a mass, with enhancement seen on the basis of blood–brain barrier disruption

mass effect, compounds the problem of their identification on precontrast scans. With extra-axial lesions, contrast enhancement is dependent upon intrinsic vascularity. This is unlike the situation with intra-axial lesions, where lesion enhancement depends principally upon disruption of the normal blood–brain barrier.

In cerebral ischemia, intravenous gadolinium chelate administration routinely provides information with regard to dating of the lesion (Figure 4). Also provided are important data relative to lesion characterization, improving differential diagnosis. In a minority of cases, principally certain subacute infarcts, lesions may not be visualized without contrast administration. The pattern of abnormal contrast enhancement in cerebral infarction is dependent upon the time of imaging relative to ictus. In early infarction, days 1–3, abnormal intravascular enhancement can be noted secondary to slow flow or vascular engorgement. From days 2 to 6, meningeal enhancement adjacent to the area of cortical infarction can be noted, although this finding is less common than intravascular enhancement. Seven to fourteen days following ictus, parenchymal enhancement can be noted secondary to blood–brain barrier disruption. This finding may persist as long as 6–8 weeks after clinical presentation. In other vascular diseases, contrast administration can also provide important ancillary information. Enhancement is routinely observed postcontrast in regions of slow flow, improving the depiction of giant aneurysms, the venous component of arteriovenous malformations, and venous angiomas.

In cerebral ischemia, and other disease states which affect brain perfusion, a new application of gadolinium chelates has recently emerged. Unlike conventional magnetic resonance contrast studies which rely principally upon detection of differences in structure, perfusion studies provide functional information. To obtain these data, the contrast agent is given as a bolus, with higher doses being more efficacious, and the first pass of the gadolinium chelate observed through the brain with rapid dynamic imaging.[10] In this manner, either qualitative or quantitative information regarding cerebral blood volume can be obtained.

With infection and other inflammatory disorders, intravenous gadolinium chelate administration improves lesion characterization and makes possible the assessment of lesion activity (Figure 5). Rarely, a lesion will not be identifiable other than following contrast administration. Contrast enhancement is particularly important for the identification of inflammatory disease of the meninges. In this application, contrast enhanced MRI is markedly superior to contrast enhanced CT. In the demyelinating diseases, and in particular multiple sclerosis, contrast administration is employed when the assessment of disease activity is important. Active or acute lesions demonstrate disruption of the blood–brain barrier, and thus positive contrast enhancement on T_1-weighted MR images (Figure 6).

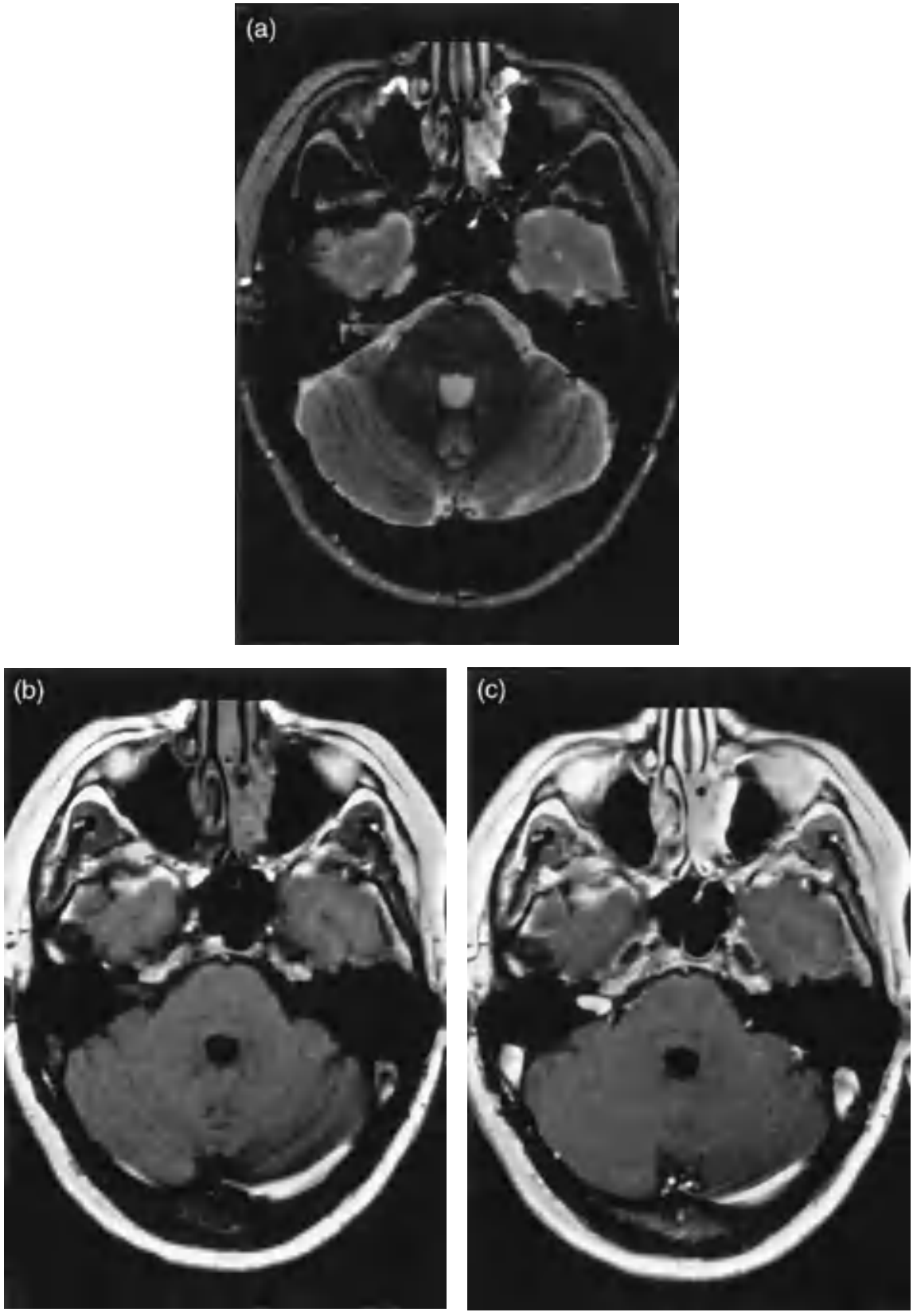

Figure 3 Right intracanalicular acoustic neuroma. This patient presented with a 5-month history of vertigo and tinnitus. Inspection of axial (a) T_2-weighted, together with (b) pre- and (c) postcontrast T_1-weighted, scans illustrates the value of contrast administration in the visualization of small extra-axial tumors. If it were not for the subtle expansion of the internal auditory canal on the precontrast images, this lesion could be easily overlooked. The postcontrast image reveals intense homogeneous enhancement of the right seventh and eighth nerve complex, making possible the diagnosis of an acoustic neuroma

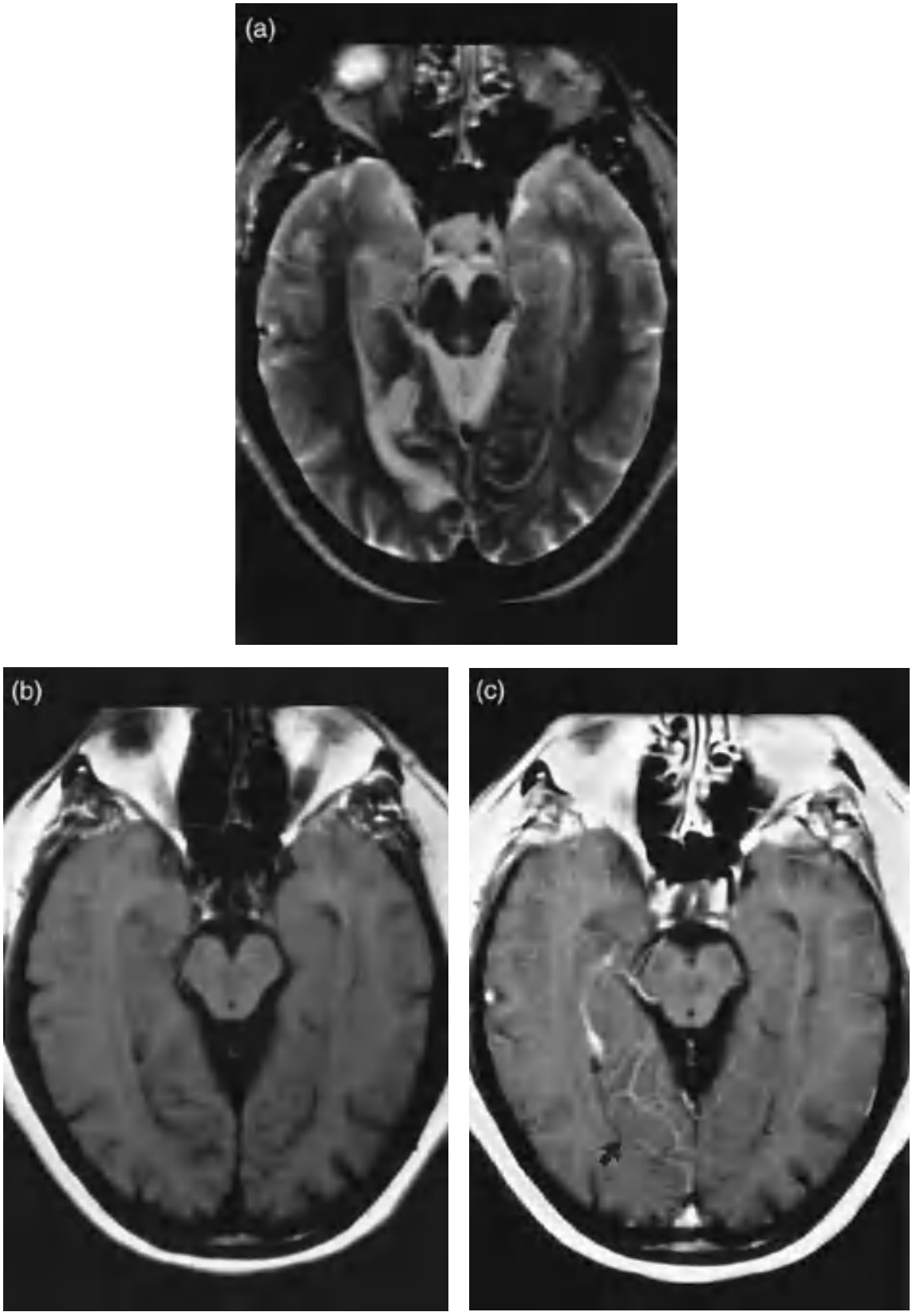

Figure 4 Acute right posterior cerebral artery infarction. Contrast administration in brain infarction improves lesion characterization, providing information that points to the diagnosis of an infarct. It also permits dating of the event, and at times enables recognition of a lesion which would otherwise go undetected. This patient presented with sudden onset of left visual problems of 2 days' duration. Illustrated are the (a) T_2-weighted, (b) precontrast T_1-weighted and (c) postcontrast T_1-weighted axial images. There is subtle effacement of sulci in the right posterior cerebral artery (PCA) territory on the precontrast T_1-weighted image with corresponding abnormal high signal intensity on the T_2-weighted image. Postcontrast, intravascular enhancement (arrow) is noted in the PCA distribution, consistent with the diagnosis of an acute cortical infarct

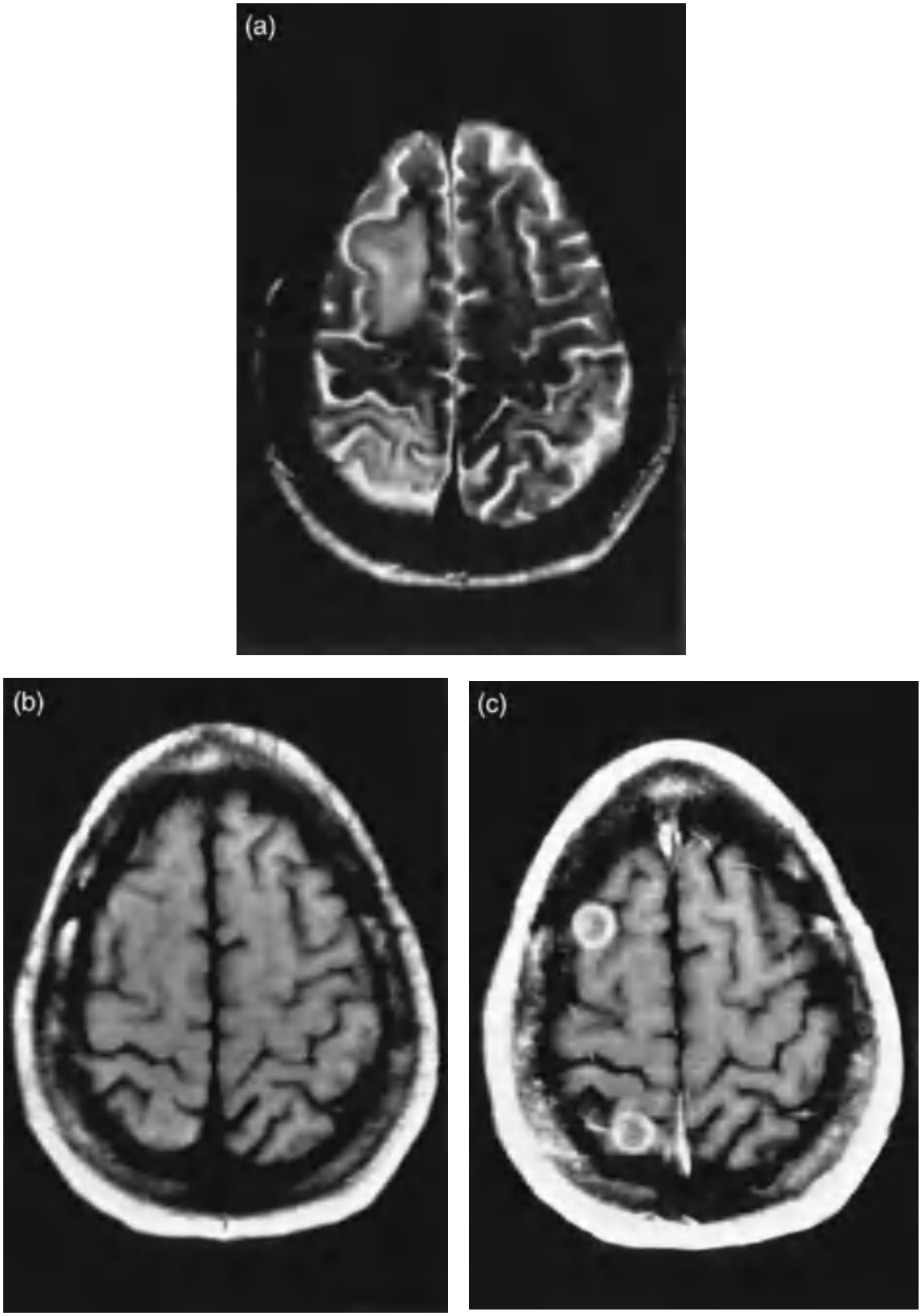

Figure 5 Infection. (a) T_2-weighted, (b) precontrast T_1-weighted, and (c) postcontrast T_1-weighted axial images are shown from the MRI exam of an HIV-positive young adult male presenting with mental status changes. Gadolinium chelate administration improves detection of the two ring-enhancing lesions in the right frontal lobe, which are obscured by edema on the precontrast images. Although the findings are nonspecific, the diagnosis of toxoplasmosis should be considered in this clinical setting. In this case, the use of contrast allowed the identification of a treatable cause of the patient's symptoms

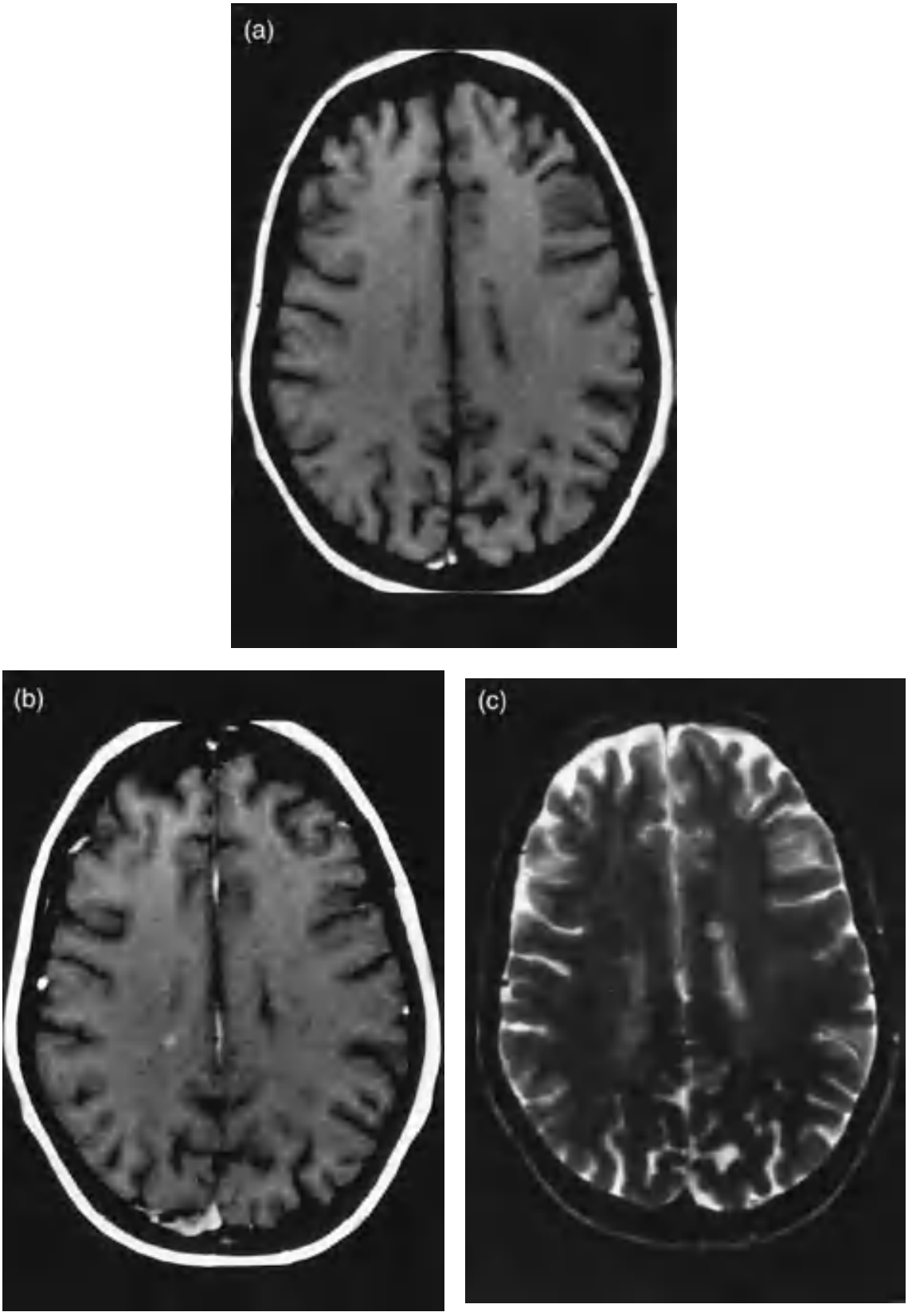

Figure 6 Multiple sclerosis (MS). The (a) precontrast T_1-weighted, (b) postcontrast T_1-weighted, and (c) precontrast T_2-weighted axial images, from a young adult female (with a 6-day history of double vision), demonstrate several points about the usefulness of contrast in imaging patients with suspected MS. The precontrast T_1-weighted image is essentially normal. After administration of a gadolinium chelate, a single focus of enhancement is identified in the periventricular white matter on the right. The T_2-weighted image shows a corresponding focus of high signal intensity, as well as several other high signal intensity foci which did not enhance. Active MS plaques enhance after contrast administration, while older inactive plaques do not. Both will appear as high signal intensity abnormalities on T_2-weighted images. Contrast administration in this case aids not only in establishing the diagnosis, but also in determining which lesions are active and which are not

3 CLINICAL APPLICATIONS IN THE SPINE

Although MRI became accepted as a major clinical tool for examination of the brain in the early 1980s, it was not until later in that decade that technical developments permitted routine diagnostic quality spine examinations. Limited by these technical constraints, the first use of contrast agents in spine imaging also postdated that in the brain by several years. This sequence of events continues to have impact today, with the clinical knowledge base relative to contrast use in the spine still lagging behind that in the brain. Thus contrast use is limited in the spine in many clinical practices to a small subset of patients, despite the existence of studies demonstrating broader clinical application.

To date, in spine MRI, contrast media play their greatest role in the postoperative back, infection, and intradural neoplastic disease. Recurrent back pain following lumbar diskectomy is a major clinical problem, with many different etiologies. With the appropriate findings on physical examination, the identification of a recurrent disk herniation or the presence of residual disk material is an indication for reoperation. However, on precontrast MRI, scar tissue and disk material can be difficult to differentiate. In the first 10–20 min following intravenous gadolinium chelate administration, differentiation between these two entities is permitted (Figure 7). Postoperative epidural scar is a relatively vascular tissue, with enhancement seen postcontrast due to diffusion of the agent into the extravascular space via leaky junctions and endothelial discontinuity. Disk material per se is avascular, and will not demonstrate enhancement. It is important to recognize that the degree of enhancement seen in scar tissue is moderate, being substantially less than that seen in most intracranial disease processes. Furthermore, the timing of postcontrast examinations is critical, with delayed scans allowing for diffusion of the contrast agent into disk material and rendering impossible the distinction between scar and disk.

In infection involving the spine, gadolinium chelate administration provides information principally relative to the extent of involvement of soft tissue and the disease activity (Figure 8). Although characteristic changes on T_2-weighted examinations have been described specifically in disk space infection, the ability to diagnose infection is, without question, markedly improved by contrast administration. A prospective clinical study in the early 1990s concluded that gadolinium chelate enhanced MRI provides excellent anatomical delineation of disease involvement, gives increased diagnostic confidence, enables localization of portions of a mass most likely to provide diagnostic biopsy, and identifies active infection that has not responded to antibiotic infection.[11]

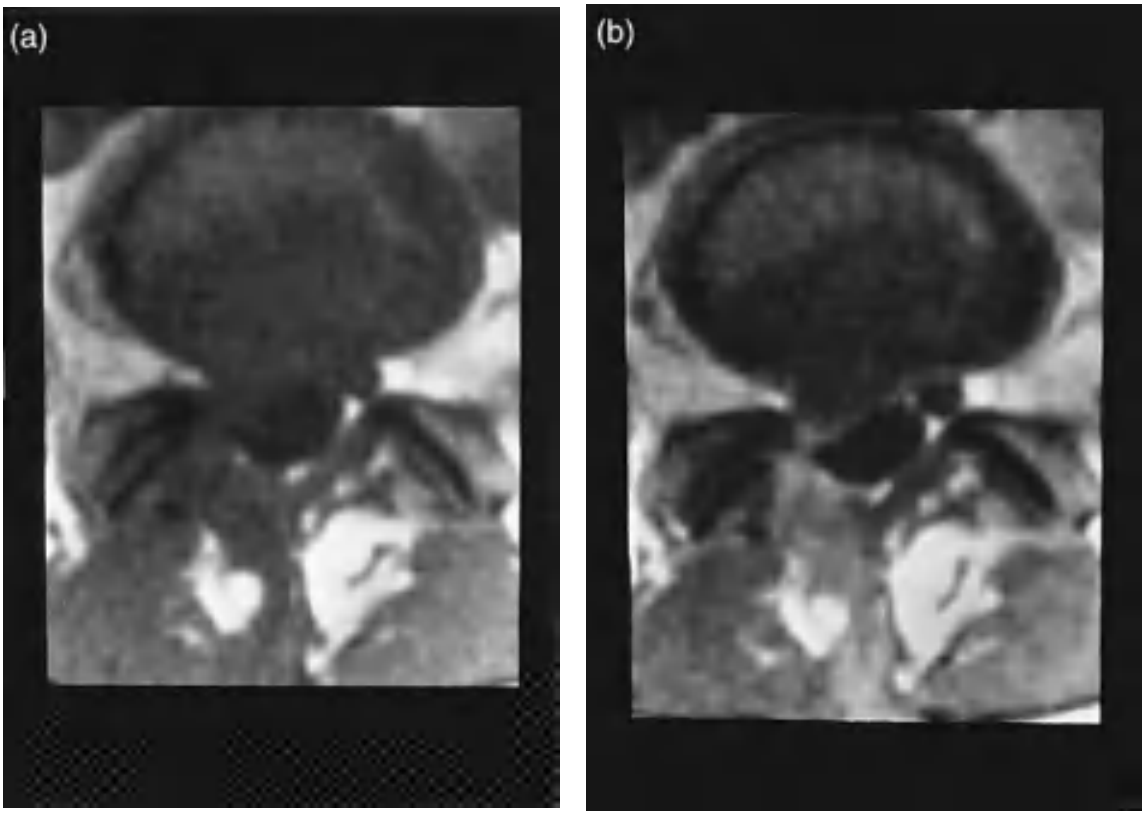

Figure 7 Recurrent disk herniation. Persistent pain after back surgery may be due to postoperative scar or recurrent disk herniation. These two entities are radiographically indistinguishable without the benefit of contrast enhancement. The distinction is crucial in that surgery can be successful in alleviating pain in patients with a recurrent disk herniation, while surgery is not recommended in the presence of scar alone. The patient had persistent low back pain radiating to the right lower extremity following surgery for a herniated disk. (a) The precontrast T_1-weighted axial image at the L5–S1 intervertebral disk level reveals a right paracentral mass displacing the dural sac posteriorly and medially. (b) Following contrast administration, enhancement is limited to the rim of the mass, making possible the diagnosis of a recurrent disk herniation. Postoperative scar would have demonstrated uniform enhancement

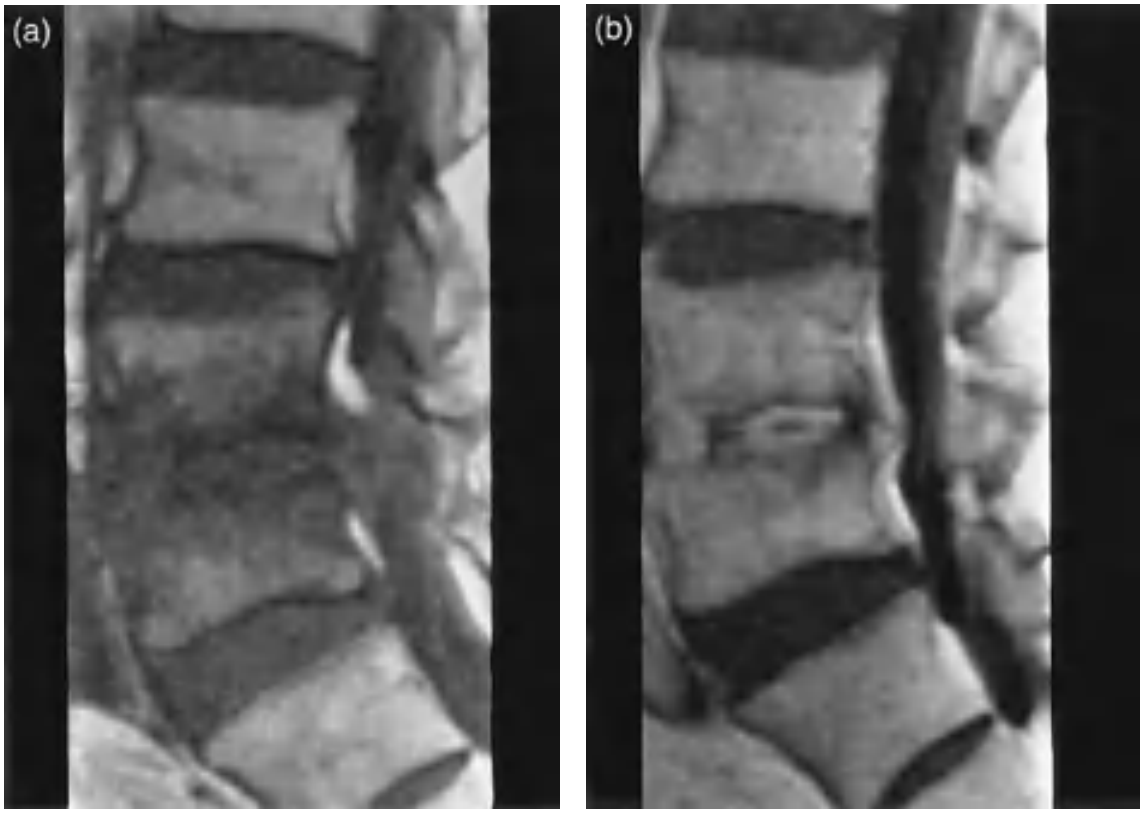

Figure 8 Diskitis. MRI is the modality of choice in the diagnosis of diskitis. Degenerative changes of the spine may have a similar appearance to infection on noncontrast examination. This patient had recent back surgery and complained of increasing pain. (a) The precontrast T_1-weighted sagittal examination reveals decreased signal intensity of the vertebral body endplates adjacent to the intervertebral disk at one level. (b) Following contrast administration, both the disk and endplates enhance. Enhancement also improves recognition of abnormal paravertebral soft tissue. Both findings point to the diagnosis of infection

Although most neoplastic disease, regardless of its location (intramedullary, intradural, or extradural), demonstrates enhancement following gadolinium chelate administration, it is particularly in the intradural compartment that contrast finds its greatest application.[12] Differentiation between neoplastic and non-neoplastic syrinxes is markedly improved.[13] In addition, the sensitivity to small intradural extramedullary tumors, in particular leptomeningeal disease, is greatly increased.[14]

4 CLINICAL APPLICATIONS IN THE BODY

Abnormal accumulation of gadolinium chelates following intravenous administration can be demonstrated on MRI in early myocardial infarction. This finding has been used to improve the depiction of acute and subacute infarction.[15] However, initial results with gadolinium chelates were disappointing in the liver. At a dose of 0.1 mmol kg^{-1} with conventional 5–10 min duration scans, many lesions became isointense following contrast administration, thus decreasing their detectability. This situation has been reversed by the implementation of dynamic imaging and bolus contrast administration.[16] Imaging with this approach provides both improved lesion detectability and lesion characterization (Figure 9). The clinical introduction of gadolinium chelates to assess both renal and hepatobiliary excretion provides an additional dimension to postcontrast liver examinations. The first agent in this class to receive clinical approval was gadobenate dimeglumine. With such an agent, dynamic postcontrast scans are initially acquired. These are, in essence, identical to that using an agent with pure extracellular distribution. Delayed scans, reflecting the hepatobiliary uptake of the agent, are obtained 1–2 h following injection. Delayed scans can be used to advantage for improved detection of small metastatic lesions, as well as for characterization of tissue according to the presence or absence of functioning hepatocytes.[17]

In general body imaging, there is excellent tissue differentiation provided by T_1- and T_2-weighted images without contrast administration. Despite this intrinsic tissue contrast, gadolinium chelate administration has proven valuable in specific clinical problems.[18] These include the identification of recurrent tumor, differentiation between benign and malignant tumors, and identification of necrotic tissue.[19] Initial studies in the abdomen, pelvis, and extremities have focused on improved tumor detection and differential diagnosis.

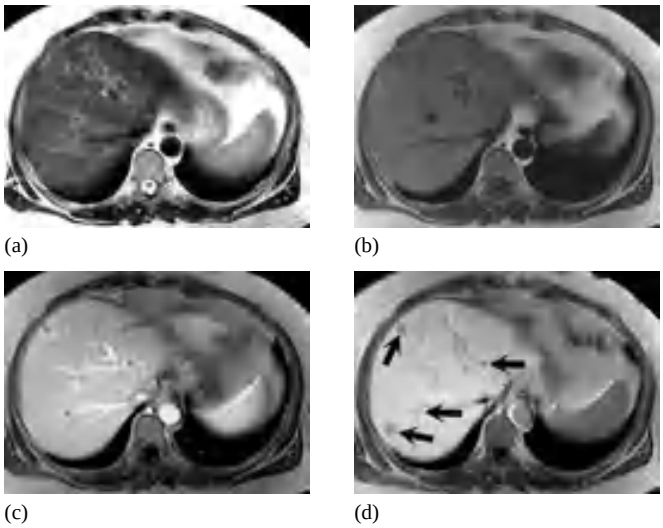

Figure 9 Metastatic liver disease from colon cancer. (a) T_2-weighted fast spin echo scan. Breathhold T_1-weighted gradient echo scans prior to (b), 1 min after (c) and 80 min after (d) intravenous injection of gadobenate dimeglumine (Gd BOPTA). This chelate has both renal and hepatobiliary excretion. Initial postcontrast scans depict the extracellular distribution of the agent, with delayed scans reflecting hepatobiliary uptake. The precontrast T_2-weighted scan is normal, with the precontrast T_1-weighted scan raising the question of several lesions. At least four metastatic lesions (arrows) are well seen on both the dynamic (c) and delayed (d) postcontrast scans. The signal intensity difference between the lesions and normal surrounding liver, and thus lesion conspicuity, is markedly improved postcontrast. Both dyanmic and delayed scans are typically acquired following injection of gadobenate dimeglumine, with dyanmic scans useful for lesion detection and characterization and delayed scans important for improved detection of small lesions. (Reproduced by permission of CRC Press from V. M. Runge, *Crit. Rev. Diagnostic Imaging*, 1997, **38**, 207)

5 FUTURE DIRECTIONS

In recent years, several new chelates have been introduced in competition to the single agent initially available, gadopentetate dimeglumine, which defined this class of contrast media. Clinical use now includes four compounds, gadopentetate dimeglumine [NMG_2(Gd DTPA)], gadoterate meglumine [NMG(Gd DOTA)], gadodiamide (Gd DTPA-BMA), and gadoteridol (Gd HP-DO3A). At the same dose, these agents show little difference with regard to enhancement characteristics. However, they can be differentiated on the basis of stability, osmolality, and viscosity (Table 1). Future development of extracellular agents is likely to be confined to the ring-shaped chelates, which demonstrate greater in vitro and in vivo stability.

Initial clinical trials with gadopentetate dimeglumine were principally confined to a single dose (0.1 mmol kg^{-1}), due to concerns about safety at higher doses. With the introduction of gadoteridol, a more kinetically inert agent, and continued experience with other compounds, interest has been renewed in the subject of contrast dose. This interest has led to several clinical trials with high dose, using 0.2–0.3 mmol kg^{-1}. As noted in the section on head applications, it has been shown that higher doses, and in particular 0.3 mmol kg^{-1}, provide improved detectability of brain metastases. Preliminary work in brain infarction and infection suggest broader clinical applicability for high doses.

Although work to date has focused on gadolinium chelates with extracellular distribution and renal excretion, it is also possible to synthesize agents with some tissue selectivity. How far this work will go is unknown, although promising initial results have been obtained with agents (such as gadobenate dimeglumine) which demonstrate partial hepatobiliary excretion.[20] Chemical synthetic work is also in progress in an attempt to increase the relaxivity of compounds per gadolinium ion, opening possible other doors relative to clinical applications.

6 CONCLUSIONS

As with MRI itself, the clinical importance of contrast media has far exceeded initial expectations. Gadolinium chelates today play a dominant role in clinical MRI, with applications which encompass nearly every major examination type. Improved lesion identification, differential diagnosis, and definition of lesion extent are direct results of this development.

7 RELATED ARTICLES

Contrast Agents in Magnetic Resonance: Operating Mechanisms; Contrast Agents in MRI: Superparamagnetic Iron Oxide; Contrast Agents in Whole Body Magnetic Resonance: An Overview; Gadolinium Chelates: Chemistry, Safety, and Behavior.

Table 1 The Physicochemical Properties[a] of Gadolinium Chelates in Clinical Use[b]

	Relaxivity	log K_{eq}	$k_{obs'}$ (s^{-1})	Osmolality	Viscosity
NMG_2(Gd DTPA)	3.8	22.1	1.2×10^{-3}	1.96	2.9
NMG(Gd DOTA)	3.5	25.8	2.1×10^{-5}	1.35	2.0
Gd DTPA-BMA	3.8	16.9	$>2 \times 10^{-2}$	0.65	1.4
Gd HP-DO3A	3.7	23.8	6.3×10^{-5}	0.63	1.3

[a]Macrocycles are more kinetically inert to dissociation of gadolinium and leave less residual free gadolinium in vivo. Nonionic chelates have lower osmolality and viscosity, and may be delivered faster and at higher doses.
[b]These chelates are equivalent with respect to relaxivity.

8 REFERENCES

1. V. M. Runge, 'Contrast Media in Magnetic Resonance Imaging', J. B. Lippincott, Philadelphia, 1992.
2. V. M. Runge, *Curr. Opinion Radiol.*, 1992, **4**, 3.
3. S. W. Atlas, *J. Comput. Assist. Tomogr.*, 1993, **17S**, 1.
4. V. M. Runge and D. Y. Gelblum, *Magn. Reson. Q.*, 1990, **6**, 85.
5. B. R. Carollo, V. M. Runge, A. C. Price, K. L. Nelson, C. R. Wolf, and M. I. Pacetti, *Magn. Reson. Imag.*, 1990, **8**, 381.
6. A. D. Elster, D. M. Moody, M. R. Ball, and D. W. Laster, *Radiology*, 1989, **173**, 231.
7. P. C. Davis, P. A. Hudgins, S. B. Peterman, and J. C. Hoffman, Jr, *Am. J. Neuroradiol.*, 1991, **12**, 293.
8. V. M. Runge, J. E. Kirsch, V. J. Burke, A. C. Price, K. L. Nelson, O. S. Thomas, B. L. Dean, and C. Lee, *JMRI*, 1992, **2**, 9.
9. W. T. Yuh, J. D. Engelken, M. G. Muhonen, N. A. Mayr, D. J. Fisher, and C. J. Ehrhardt, *Am. J. Neuroradiol.*, 1992, **13**, 335.
10. V. M. Runge, J. E. Kirsch, J. W. Wells, and C. E. Woolfolk, *Am. J. Roentgenol.*, 1993, **160**, 593.
11. M. J. Post, G. Sze, R. M. Quencer, F. J. Eisment, B. A. Green, and H. Gahbauer, *J. Comput. Assist. Tomogr.*, 1990, **14**, 721.
12. G. K. Sze, *J. Comput. Assist. Tomogr.*, 1993, **17S**, 8.
13. T. Kahn, N. Roosen, G. Furst, E. Lins, W. J. Bock, H. G. Lenard, and U. Modder, *ROFO Fortschr Geb Rontgenstr Nuclearmed*, 1989, **151**, 602.
14. B. Schuknecht, P. Huber, B. Buller, and M. Nadjmi, *Eur. Neurol.*, 1992, **32**, 11.
15. P. R. van-Dijkman, E. E. vanderWall, A. deRoos, N. A. Matheijsson, A. C. van Rossum, J. Doornbos, A. van der Laarse, A. E. van Voorthursen, and A. V. Bruschke, *Radiology*, 1991, **180**, 147.
16. R. R. Edelman, J. B. Siegel, A. Singer, K. Dufuis, and H. E. Longmaid, *Am. J. Roentgenol.*, 1989, **153**, 1213.
17. R. Caudana, G. Morana, G. P. Pirovano, N. Nicoli, A. Portuese, A. Spinazzi, R. Di Rito, G. F. Pistolesi, *Radiology*, 1996, **199**, 513..
18. B. Hamm, M. Laniado, and S. Saini, *Magn. Reson. Q.*, 1990, **6**, 108.
19. G. M. Bydder, *Topics Magn. Reson. Imaging*, 1991, **3**, 74.
20. T. J. Vogl, W. Pegios, C. McMahon, J. Balzer, J. Haitzinger, G. Pirovano, and J. Lissner, *Am. J. Roentgenol.*, 1992, **158**, 887.

Biographical Sketch

Val M. Runge. *b* 1956. B.S. (chemistry), 1978, M.D., 1982, Stanford University, USA. Diagnostic Radiology Residency, Vanderbilt University, 1982–85. Chief of Service, Magnetic Resonance, New England Medical Center Hospitals (Tufts University), 1986–89. Rosenbaum Professor of Radiology, University of Kentucky, 1990–present. Approx. 200 publications. Research interests: magnetic resonance contrast media.

Gadolinium Chelates: Chemistry, Safety, and Behavior

Hanns-Joachim Weinmann, Andreas Mühler and Bernd Radüchel

Research Laboratories Schering AG, Berlin, Germany

1 INTRODUCTION

Since the relaxation times of the nuclei of interest—the hydrogen protons of the water molecules—determine the MRI signal intensity exponentially, even a slight modification of the relaxation times exhibits a significant change in the signal strength. Substances characterized by at least one unpaired electron are known to enhance the relaxation process very effectively. Hydrophilic compounds from the nitroxyl class were found to be interesting candidates because of their good tolerance.[1] However, the paramagnetic effect of these cyclic organic molecules is relatively weak inasmuch as it derives from just one unpaired electron. Elements from the series of transition metals offer a more realistic approach for developing substances to be used as contrast agents for MRI.

The first publications on the use of paramagnetic metals as contrast agents appeared at the beginning of the 1980s.[2,3] In particular, manganese chloride with its five unpaired electrons was discussed as the prototype of a paramagnetic contrast-giving compound. The free ions of the transitional elements (e.g. Mn^{2+}, Cu^{2+}, Fe^{3+}, and Cr^{3+}) exert a stronger paramagnetic effect, but are unsuitable for clinical use because of their interaction (toxicity) with the body and their poor solubility at pH 7.

Due to its seven unpaired electrons, the gadolinium ion exhibits the strongest effect of all elements on T_1 relaxation times. The element gadolinium belongs to the lanthanides; the term 'rare earths' also used for these compounds is somewhat misleading because the concentration of lanthanides in the Earth's crust is about 100 times higher than that of iodine. Tons of lanthanides are used in industry as antiknock agents, in TV screens, in lasers, glasses and ceramics, to name just some applications. Use of the gadolinium ion in the form of its chloride, sulfate or acetate is prohibited by its poor tolerance by the body. Like many other metallic salts, these compounds form acid solutions in water, and insoluble hydroxides or phosphates arise in the neutral pH range which quickly accumulate in the reticuloendothelial system after intravenous administration. These compounds are therefore unable to provide optimum contrast-giving properties.

The purpose of this article is to summarize the different possibilities of using stable and biologically inert gadolinium chelates as contrast agents for diagnostic imaging. Their safety profile and their pharmacodynamics will be discussed in detail with special attention to the first and most widely used contrast agent: Magnevist®. Future developments of tissue specific agents will expand the potential of this new class of pharmaceuticals based on the paramagnetic atom gadolinium.

2 CHEMISTRY OF GADOLINIUM-BASED CONTRAST AGENTS

The gadolinium ion is that paramagnetic species which most efficiently enhances the signal in magnetic resonance imaging. It has seven unpaired electrons distributed isotropically in its 4f shell. Since tolerance of the ion in laboratory animals is not sufficient to allow clinical studies, it was necessary to detoxify the gadolinium ion without eliminating the paramagnetic effect or, to be more precise, without affecting the enhancing properties too much. This goal was achieved by chelation of the ion with various ligands. The basis for the chelation of metal ions by coordination with suitable ligands is described in several excellent monographs and reviews.[4,5]

The effective chelation of an ion affords an array of atoms that are capable of interacting with the ion. Chelation can be achieved by electron donation of an electronegative atom to the ion. This process can be regarded as the interaction of an acid with a base. The metal ion functions as the acid and the donating atom as the base. The force of interaction can be described by the principle of hard and soft acids and bases.[6] Pearson[7] came up with this concept by which reactivities and stabilities may be predicted. Chemical entities including atoms, ions and radicals are classified as 'hard' and 'soft' Lewis acids or bases. The 'hard' species have a small atomic radius, high charge and low polarizability, whereas 'soft' species possess the opposite characteristics. The principle states that acids show greater affinity for bases of the same class, and vice versa. Thus, hard acids (acceptors) tend to form strong bonds with hard bases (donors), but bind reluctantly or weakly to soft bases.

With respect to the principle, Gd^{3+} is regarded as a hard acid. Hard bases are neutral or negatively charged oxygen species, nitrogen is also regarded as a hard base, but to a lesser extent than oxygen. On the other hand, sulfur and phosphorus are soft bases. According to this classification the gadolinium ion is most effectively coordinated by oxygen and nitrogen, and all gadolinium chelates which are used clinically take advantage of this relationship. The backbone of most chelation agents is derived from polyazapolycarboxylic acids. As can be seen from Figure 1 both open chain and macrocyclic gadolinium chelates are used.

Although the nature of the coordinating atoms (oxygen and nitrogen) are the same, there are differences concerning the stability of the chelates. One has to look at both the thermodynamic and the kinetic stabilities, as these potentially influence the pharmacology of the agents (see Table 1). Since macrocyclic chelates exhibit high kinetic stabilities[8] they are not likely to undergo transchelation with metals that occur in vivo. On the other hand, the open chain chelates can equilibrate rapidly with endogenous metals.[9]

The characteristic coordination number of Gd^{3+} is, in many cases, 9. Gadolinium has neither the restricted coordination number nor the restricted geometry of transition metal complexes which are imposed on the latter by the requirement for orbital overlap in bonding. In aqueous solution Gd^{3+} is coordinated by nine water (and/or hydroxyl groups) molecules. In the chelates shown in Figure 1 the ligands deliver eight co-

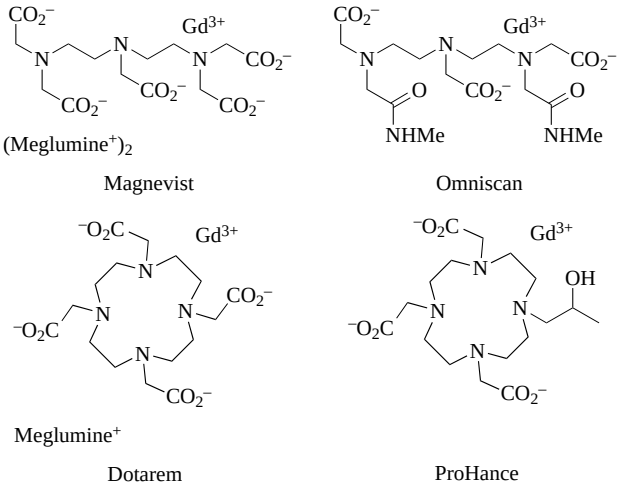

Figure 1 Chemical structure of gadolinium chelates used as contrast agents in MRI

ordination sites (oxygen and nitrogen atoms); the ninth position is occupied by a water molecule and it is this water molecule in the first coordination sphere of the ion that contributes most to the signal enhancing properties of the chelate. X-ray crystallographic structure determinations have been performed on all four chelates mentioned. The coordination geometries of all these chelates are remarkably similar and the typical structure is best described as a distorted tricapped trigonal prism.[10]

Gadolinium chelates are formed by the direct reaction between stoichiometric amounts of a polyazapolycarboxylic acid and gadolinium oxide. The synthesis of the clinical compounds is well described. The starting material for gadopentetate dimeglumine[11] and gadodiamide[12] is pentetic acid [diethylenetriaminepentaacetic acid, (DTPA)]. The macrocyclic products gadoterate meglumine[11] and gadoteridol[13] are synthesized starting with 1,4,7,10-tetraazacyclododecane.

Chelation of the metal ions leads to a dramatic change in their pharmacological and toxicological properties.[14] One of the most important alterations is the dramatic improvement in their solubility in water at neutral pH. Gd-DTPA and other comparable metal chelates are extremely hydrophilic substances with a partition coefficient between butanol and water of sometimes less than 0.001. The positive charge of the central paramagnetic metal ion such as Gd^{3+} is compensated by the negative charge of the ligand. If necessary, any excess negative charge of the ligand can be compensated by counter cations such as $(meglumine)^+$ or Na^+. A highly concentrated and stable aqueous solution (0.5 mol L^{-1}) is a special prerequisite for a diagnostic agent administered intravenously in small volumes.

Table 1 Thermodynamic Stability Constants for Clinically used Gadolinium Chelates

Chelate	$\log(K_{Therm})$
Gadopentetate dimeglumine	22.5
Gadodiamide	16.9
Gadoterate meglumine	24.7
Gadoteridol	23.8

The ligand can modulate the paramagnetic properties of the free metal ion. Lauffer has described this subject in greater detail in a recently published review.[15] A closer examination of the multifactorial term, the correlation time τ_c, which describes the interaction between the paramagnetic ion and the atomic nucleus that is to be affected, reveals that relaxivity can be optimized depending on field strength. At a field strength of 1 T the optimum values are obtained with a correlation time of approximately 10^{-8} s. The correlation time τ_c is made up of at least three variable factors:

$$\tau_c^{-1} = \tau_s^{-1} + \tau_m^{-1} + \tau_r^{-1} \quad (1)$$

where τ_s is the longitudinal electronic relaxation time of the paramagnetic ion, τ_m is the lifetime of the proton in the complex, and τ_r represents the rotational relaxation time due to Brownian rotational motion.

The rotational correlation time τ_r of low molecular weight compounds is so short that it is usually the determining factor for the overall correlation time. Taking 1 T, for example, a correlation time of approximately 10^{-8} s would be desirable in order to achieve optimum relaxivity. For low molecular weight gadolinium complexes such as Gd-DTPA, τ_r is in the order of 10^{-10} s and thus too short to elicit perfect relaxation. Consequently, a longer rotational correlation time has to be attained by raising the viscosity of the medium or by increasing the size of the paramagnetic molecule. Using larger molecules the rotation rates decline to such an extent that they are no longer the determining factor in the correlation time τ_c. High molecular weight gadolinium chelates exhibit an improvement in the T_1 relaxivity which levels off at about 15 L $mmol^{-1}$ s^{-1}. In these compounds it is the electronic relaxation time and the intramolecular motion that determine the influence on the relaxation time of the nuclei to be affected.

In addition to the optimization of τ_c, there is another way in which relaxivity can be increased. Relaxivity is determined more or less linearly by the number of water molecules that interact directly with the paramagnetic ion. In the case of gadolinium there are, in principle, nine available coordination sites where water binding can take place. Depending on the pH value of the aqueous solution, some of those coordination sites may be occupied by anions (e.g. Cl^- or OH^-) or water molecules. The complexation of the gadolinium ion diminishes its interaction with OH^- and the pH dependency of the relaxivity. The ligand occupies several coordination sites of the metal ion. However, even in the least favorable case [gadolinium triethylenetetraminehexaacetic acid (GdTTHA)], when all the coordination sites are occupied, the central ion can decrease the relaxation times of the bulk water molecules, and a T_1 relaxivity of about 2 L $mmol^{-1}$ s^{-1} at 0.47 T was measured. This may correspond to outer sphere relaxation. If too many coordination sites are unoccupied, the possibilities for unwanted interaction (transchelation) between the central atom and endogenous substances of the organism increase.

The goal is to find compounds with correlation times of about 10^{-8} s. Such substances, probably of oligomeric or polymeric nature, could elicit relaxivities of up to 50 L $mmol^{-1}$ s^{-1} per metal ion. Certain chelates (polymeric substances) are very useful for enhancing the paramagnetic effect. In this particular situation the strength of the magnetic field is of special

importance. Polymeric chelates display their optimum relaxivities in the range between about 0.5 and 1.0 T.

3 TOLERANCE AND PHARMACOLOGY OF GADOLINIUM CHELATES

The major concern about the use of metal chelates was the potential release of the metal ion from the chelate. PbEDTA which was investigated as a potential contrast agent for X-ray studies in man in the mid-1950s was not useful because of severe side-effects, probably due to intoxication by the released toxic metal ion.

All transition metals exhibit intolerable toxicity. However, gadolinium does not belong to the class of metals such as cadmium or lead with high toxicity. After intravenous administration in the rat, the gadolinium salt displayed an LD_{50} of about 0.5 mmol kg^{-1}. The tolerance of the chelator DTPA was even lower. The chelation of the lanthanide drastically changes not only its water solubility but also the tolerance profile and pharmacological behavior. Most of the basic pharmacological properties were investigated when the dimeglumine salt of the gadolinium complex of DTPA (generic name gadopentetate dimeglumine, for short Gd-DTPA) was commercially developed as the first contrast agent for MRI in the early 1980s.[14]

It has been shown in animal experiments that toxic effects of Gd-DTPA occur only at very high dosages. For instance, an intravenous LD_{50} in the range of 10 mmol kg^{-1} was found for rats, mice, rabbits and dogs. The gadolinium complex is also highly stable under physiological conditions. The ions occurring in plasma do not displace the gadolinium atom from its complex bond. Autoradiographic trials and tissue distribution studies with the ^{153}Gd and double-labeled ($^{153}Gd/^{14}C$) compound demonstrate the excellent in vivo stability of the substance. Excretion and tissue distribution studies revealed complete elimination with no body retention of the agent.

In subchronic toxicity studies in rats and dogs the compound was administered over a period of 4 weeks in a daily dose of up to 5 mmol kg^{-1}. Vacuolization of the proximal tubuli (osmotic nephrosis) was the most obvious sign of toxicity. Cardiovascular tolerance tests in dogs proved that the compound is safe when administered intravenously. None of the toxicological tests elicited a specifically metal ion induced intolerance profile.

Magnevist®, the aqueous formulation of Gd-DTPA containing 0.5 mol L^{-1}, was the first contrast medium approved for clinical use in cranial and spinal MRI in Germany, the USA, Japan, Switzerland and The People's Republic of China in 1988. These approvals were extended to whole body MRI with a total dose of up to 0.2 mmol kg^{-1} bodyweight in patients older than 2 years of age. Up to 1993, more than 7 million patients have been diagnosed using Magnevist® contrast enhanced MRI. The pharmacokinetic properties of the compound are very much the same as those of well known radiographic contrast agents.

After intravenous injection, Gd-DTPA is distributed in the extracellular water space of the body. Gd-DTPA leaves the organism in unaltered form by renal excretion with a halflife of about 1–2 h. The extrarenal elimination is negligible. Gd-DTPA does not diffuse through plasma membranes, and is therefore unable to pass the intact blood–brain barrier; it is thus an excellent tool for investigating accurately any disturbances of the barrier. The detection of lesions such as metastases improves after a dose of 0.1 mmol kg^{-1} corresponding to 0.2 mL kg^{-1} or 10–20 mL of Magnevist® per patient.

The first clinical trials were conducted at the end of 1983 in the Department of Radiology of the Free University of Berlin (Professor R. Felix[16]) and the Hammersmith Hospital, London (Professor R. Steiner).[17] The tolerance of Magnevist® is excellent. Results from standardized protocoled European clinical trials in more than 13 000 patients demonstrate that the incidence of adverse drug reactions (ADRs) was even lower than that of non-ionic X-ray contrast agents.[18] A value of 1.46% ADRs including local warmth was recorded. Almost the same value was found in a US study.[19] It was shown that there are no hemodynamic alterations in patients following bolus injection of doses up to 0.3 mmol kg^{-1}.[20]

The favorable safety profile was also confirmed by results of postmarketing surveillance reports.[18] Severe adverse reactions can occur, but the incidence of life threatening reactions is very rare. Out of more than 5 million applications conducted up to December 31, 1992, 60 severe drug reactions (convulsion, edema of the glottis, anaphylactoid shock, and death) were reported. In some cases a causal relationship between the ADR and the drug injection was not clear. In patients with impaired renal function, the halflife in the plasma and the urine is delayed.[21] However, the compound can be eliminated from the plasma by dialysis.[22]

The tolerance of a biologically inert substance is determined by its physicochemical properties. Although the osmotic load produced by the intravenous injection of 0.1 mmol kg^{-1} bodyweight of Magnevist® is extremely low, a much higher dosage might be necessary in special circumstances. This consideration led to the synthesis of gadolinium complexes with reduced osmotic activity (see Figure 1 and Table 2).

By converting two of the carboxyl groups of the DTPA molecule into amides, neutral gadolinium complexes (e.g. gadodiamide) with reduced osmolality (0.5 M = 0.78 osmol kg^{-1}) and improved acute intravenous tolerance (LD_{50} in rats >25 mmol kg^{-1}) were obtained.[9] In addition to the open chain metal complexes, macrocyclic gadolinium complexes were developed. One of the first of these compounds was gadoterate meglumine (GdDOTA, Dotarem®, Laboratoire Guerbet, France). Dotarem® is a cyclic compound with four carboxyl groups and is characterized by excellent tolerance.[23] By 1993, Dotarem® was available in a limited number of European and South American countries. Unlike gadoterate meglumine, gadoteridol is an electrically neutral macrocycle. Gadodiamide (Omniscan®) and gadoteridol (ProHance®) were introduced on to the US market at the beginning of 1993 (marketed by Nycomed and Bracco, respectively).[24,25]

All clinically used extracellular gadolinium chelates exhibit virtually identical contrast enhancing and pharmacological properties. It is too early to confirm significant differences in the safety profile between the new agents and Magnevist®, although some publications highlight a somewhat higher incidence of ADRs in patients investigated with ProHance®.[26] Obviously, large clinical trials are needed to explore any differences between the tolerance profile of Magnevist® and that of the new agents.

Table 2 Gadolinium Chelates used in Clinical Practice[a]

Generic name	Trade name	Company	Year of first marketing approval	Type of chelator	Osmolality[b] (osmol kg^{-1})
Gadopentetate dimeglumine	Magnevist	Schering AG, Germany	1988	Open chain	1.96
Gadoterate meglumine	Dotarem	Guerbet, France	1989	Macrocyclic	1.35
Gadodiamide	Omniscan	Nycomed Imaging AS, Norway	1992	Open chain	0.78
Gadoteridol	ProHance	Bracco SpA, Italy	1992	Macrocyclic	0.63

[a]Marketing authorization by the health authorities is different in the various countries with respect to the mentioned gadolinium complexes and their application.
[b]The values for the 0.5 M formulations are taken from the package inserts of the commercially available agents.

4 PRINCIPLES OF CONTRAST ENHANCED MRI

The mechanism of action of a paramagnetic contrast agent in MRI is very complex. Although the phenomenon of relaxation was described by Bloembergen and co-workers as early as the mid-1950s, the enhancement effect cannot simply be transferred from spectroscopy to the imaging technique. The situation in a living organism is very complicated. Physical factors like motion, temperature, viscosity, binding to biomolecules and compartmentalization influence the relaxation rates of the bulk water and the relaxivity of paramagnetic materials.

Even the phenomenon of contrast enhancement in pure water is confusing at first glance. In a classical imaging sequence such as a T_1-weighted spin echo experiment, the signal intensity increases nonlinearly with the concentration of the contrast agent, reaches a maximum, and then decreases nonlinearly as the concentration continues to increase (Figure 2). The decrease of the intensity at higher concentrations is due to the T_2 effect of the paramagnetic substance.

The contrast effect depends to a great extent on the MRI sequence applied. Generally, the best enhancement is achieved using T_1-weighted techniques such as a spin echo sequence with a *TR* of <0.6 s and a short echo delay time *TE* of <0.04 s. Optimal are those techniques with very short *TR* and *TE* times. Gradient echo techniques are also useful, provided an adequate pulse angle is applied (e.g. Ernst angle). However, in clinical practice some contrast enhancement is also visible on the application of proton density or even T_2-weighted imaging sequences, since the applied repetition rates of 1.5–2.0 s are not sufficient for full relaxation of most of the protons.

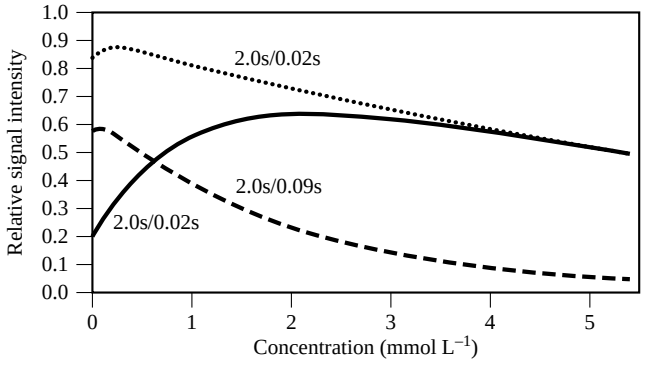

Figure 2 Contrast enhancement of a hypothetical tissue using different concentrations of a homogeneously distributed paramagnetic gadolinium chelate (Gd-DTPA). The calculations using the exponential equation of a spin echo sequence taking into account the various *TR*, *TE*, T_1, and T_2 values were performed with intrinsic T_1 and T_2 times of 0.8 and 0.2 s and relaxivity values of R_1 = 4.5 L $mmol^{-1}$ s^{-1} and R_2 = 5.5 L $mmol^{-1}$ s^{-1}

The strength of the magnetic field modulates the contrast effect in two ways. First, the relaxivity is field dependent. The relaxivity of low molecular weight substances decreases with increasing field strength, but the differences are relatively weak in the field range of diagnostic imaging units (0.04–2 T). Second, the intrinsic relaxation times of the nuclei in the organism are also field dependent. At low field strength (<0.1 T) the tissue already has very low relaxation times and a further decrease of the relaxation time does not lead to a significant increase in the signal intensity. A very good effect of the contrast agents is seen at high field strength because of the longer intrinsic relaxation times of the tissue protons.

At least three factors regulate the contrast-enhancing ability of the tissue:

1. distribution volume of the contrast material;
2. concentration and relaxivity of the contrast material;
3. intrinsic relaxation times of the tissue without the contrast material.

Only tissues with a large distribution volume of the paramagnetic contrast material and a long intrinsic relaxation time exhibit a significant change in their relaxation times. In consequence, marked contrast enhancement is visible only in those areas (lesions) with increased extracellular space or distribution volume. Contrast is seen, therefore, in lesions (inflammation, tumor, edema) or large accumulations of fluids (urine). No significant increase in intensity is seen in tissues (e.g. normal brain, liver, muscle) with small distribution volumes and/or short intrinsic relaxation times. An already short intrinsic T_2 relaxation time allows almost no increase in signal intensity using a paramagnetic contrast agent, but may respond to a T_2-sensitive relaxation agent (e.g. ferrites) which decreases the signal intensity.

Relatively low concentrations of a paramagnetic species are needed to reduce the T_1 relaxation time significantly. A gadolinium concentration as low as 10 μg mL^{-1} is sufficient to elicit a strong effect on the signal intensity. The strong paramagnetism of gadolinium ions, even when chelated, facilitates the relaxation of nearby water protons causing both T_1 and T_2 relaxation times to decrease. Although both T_1 and T_2 times are affected, the T_1 shortening effect predominates for MRI at

low concentrations. However, at very high concentrations (>5 mmol L^{-1}, depending on the sequence parameter) the T_2 or susceptibility effect of gadolinium dominates even in T_1-weighted imaging, and signal reduction occurs. Using current clinical doses of 0.1 mmol kg^{-1}, such a T_2 effect can only be observed in the urinary bladder. Contrast enhancement is almost undetectable in the normal brain parenchyma because the cerebral blood volume is very small (about 2–3% of total volume) and extracellular gadolinium chelates are unable to pass cellular membranes such as the intact blood–brain barrier.

In combination with its conventional T_1-based signal enhancement properties, the T_2* effect of gadolinium chelates is of interest in those imaging studies[27] where quantification of the blood supply is of clinical relevance. Ideal conditions for gadolinium complexes such as susceptibility agents can be found in the brain where only slow water diffusion due to the blood–brain barrier occurs, and the distribution volume of the contrast agent is limited. Even bolus injection of 0.1 mmol kg^{-1} of Gd-DTPA (Magnevist®) in conjunction with T_2*-weighted gradient echo imaging was sufficient to generate maps of cerebral blood volume in patients.[28] Since the T_2* effect is directly proportional to the magnetic moment, the efficacy of gadolinium as a T_2* agent is about 30% less than for the same complex based on dysprosium.

5 TISSUE-SPECIFIC GADOLINIUM COMPLEXES

One of the disadvantages of currently available contrast agents for MRI is their relatively unspecific distribution in the organism. The compound reaches all tissues in a more or less homogeneous concentration. Exceptions are the excretory organs, the vascular space (shortly after administration only) and certain organs such as the brain. An improvement in the diagnostic potential may be attainable by directing the paramagnetic molecule to targets of interest, thus achieving higher local concentrations, and this may allow for a reduction in the dose and should lead to an improvement in the differentiation between target and surrounding tissue.

Extracellular compounds such as Gd-DTPA are highly tissue specific with respect to their accumulation in the kidneys. When compared with other tissues, much higher concentrations are reached because of renal elimination. This effect is the basis of contrast-enhanced urography by means of heavily T_1-weighted imaging sequences.[29] One of the most important tissues, the vascular system, can be targeted by injecting substances which are not subject to fast extravasation through the epithelial pores.

Higher molecular weight compounds exhibit a prolonged correlation time and, hence, increased relaxivity. In addition, larger molecules display a unique distribution characteristic: they do not diffuse into the extravascular space and thus are fundamentally useful as blood-pool contrast agents which demonstrate the perfusion characteristics of the area of interest. Using a suitable high molecular weight backbone such as albumin or polylysine, 50–100 gadolinium atoms can be incorporated in one molecule. Compounds with a relative gadolinium content of 20% (w/w) can be synthesized.

Several macromolecular, polymeric gadolinium chelates have been studied in animals including Gd-DTPA–albumin, Gd-DTPA–dextran, Gd-DTPA–polylysine and a Gd-DTPA–polylysine substituted with methoxypolyethyleneglycol succinates.[30–33] Such molecules with very high molecular weight, and consequently, larger size, are not subject to glomerular filtration and may stay in the blood or organism for a very long period of time. This disadvantage may be overcome by using biodegradable substances or molecules with matched molecular diameters which stay in the blood at high concentration sufficiently long to allow the diagnosis of tissue perfusion. After imaging, which may take place in the first minutes after injection, the compound may be renally excreted at a somewhat reduced filtration rate.

Gd-DTPA–polylysine is such a contrast agent with a tailored molecular size.[33] A Gd-DTPA–polylysine derivative with a molecular weight of approximately 40 000 results in a plasma relaxivity of about 14 $L\,mmol^{-1}\,s^{-1}$ at 0.47 T, which is three to four times higher than that of Gd-DTPA.[21] The resulting compound is highly stable and is soluble in water even at high gadolinium concentrations. Solutions of >0.1 mol L^{-1} do not exhibit a major increase in the viscosity. Macromolecular structures may have a significant impact for the diagnosis of tissue perfusion and capillary integrity.

On intravenous injection, such a compound demonstrates a prolonged halflife in plasma. After distribution in the vascular system the agent is eliminated by renal filtration. By carefully selecting the size of the molecule, their molecular structure, and their chelating residues, it is possible to develop substances which undergo complete renal elimination without accumulation in the body and/or transchelation of the gadolinium ion. Determination of the tissue concentration of gadolinium showed that the polymer is distributed proportionally to the fractional blood volume and, therefore, reflects the differing degrees in the perfusion of different tissues.

Adverse reactions have been reported with the cationic polymer polylysine. When substituted with a Gd-DTPA derivative, however, the molecule loses the positive charge and displays an excellent tolerance profile. An LD_{50} in mice of 17 mmol kg^{-1} has been reported, a value significantly higher than that of Magnevist® (6–7 mmol kg^{-1}). Taking together both the increased relaxivity and the excellent tolerance of the substance, this contrast agent has a margin of safety superior even to that of low molecular weight compounds.

The blood-pool agent Gd-DTPA–polylysine is fundamentally suitable as an angiographic contrast agent. It allows the demonstration even of tiny structures of less than 1 mm diameter without the need for complicated subtraction procedures and scanning techniques, which are sometimes flow sensitive (Figure 3). This compound offers advantages not only in the differential diagnosis of tumors, but also, and in particular, in perfusion studies of the myocardium and pulmonary MRI. Recently, researchers from Boston reported selective accumulation of a Gd-DTPA–polylysine derivative in the lymphatic system.[34]

Because of the high sensitivity of the contrast enhancing mechanism, only minor amounts of exobiotic substances are necessary to achieve a significant change in the signal intensity. Thus the selective targeting of receptors becomes possible using relatively small amounts of contrast agents. Channeling substances to the bulk excretory transporters located in the hepatocellular plasma membrane is a very efficient possibility to create highly liver-specific substances. Thus, higher local concentrations can be achieved by the use of derivatives of the Gd-

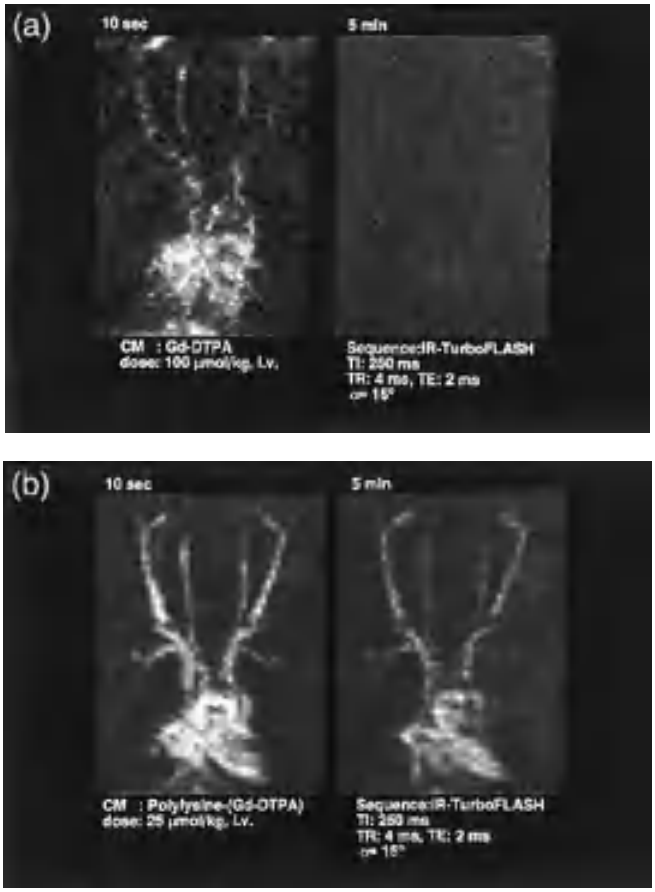

Figure 3 Contrast-enhanced MRI (2 T SISCO experimental MR imager) of a rat after intravenous injection of 100 μmol kg^{-1} Magnevist® (top) or 25 μmol kg^{-1} Gd-DTPA–polylysine (bottom). The IR-Turbo-FLASH sequence only demonstrates areas of very short T_1 relaxation times, thus producing a much longer vascular enhancement using the polymeric gadolinium chelate

DTPA complex such as GdBOPTA (gadobenate, Bracco, Italy) or Gd-EOB-DTPA (gadolinium-ethoxybenzyl DTPA) or the Gd complex of the disodium salt of (4*S*)-4-(4-ethoxybenzyl)-3,6,9-tris(carboxylatomethyl)-3,6,9-triazaundecanedioic acid (Schering AG, Germany)[35–37] (Figure 4).

Gd-EOB-DTPA is a gadolinium complex with a lipophilic side chain attached to the DTPA backbone. The molecule, still ionic and extremely hydrophilic and water soluble, diffuses in

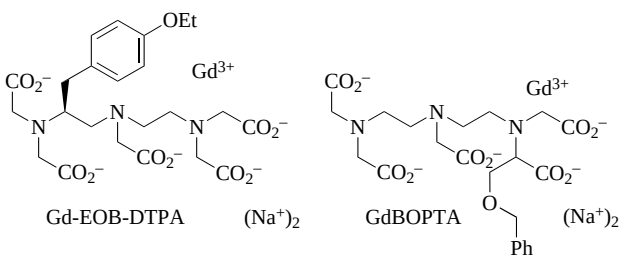

Figure 4 Chemical structure of gadolinium chelates used as liver-specific contrast agents in MRI

the extracellular space and is, at the same time, eliminated from the body both by glomerular filtration and hepatocellular transport mechanisms.[36,37] Specific carriers of the hepatocytes ensure that this water soluble substance is transported into the hepatocytes and is, therefore, able to reach the intracellular water compartments and to shorten their relaxation times. As a result of this additional excretory mechanism such compounds become tissue specific, i.e. they demonstrate the healthy liver parenchyma selectively. On intravenous injection, a dose of less than 25 μmol kg^{-1} bodyweight is sufficient to achieve selective enhancement of the liver parenchyma. Implanted tumors or metastases do not take up this contrast agent, but appear as low-signal structures and can be visualized better because of the increased contrast between the healthy liver parenchyma and the pathological area. Studies in rats demonstrated some uptake into hepatocellular carcinomas, depending upon the differentiation of the neoplasm. Gd-EOB-DTPA displays some transient protein binding either in plasma or in the cytoplasma of the hepatocytes. The protein binding ensures that the correlation time of the low molecular weight contrast agent is optimized. Such compounds do, in fact, have much greater relaxivity in plasma than in water. As a result, an increase in efficacy by a factor of 2 is possible.

Gd-EOB-DTPA exhibits favorable characteristics. In addition to its good diagnostic potential, the compound displays high solubility in water, high stability, rapid and quantitative elimination and, most important, a tolerance as good as Magnevist®. Clinical Phase I trials just recently conducted in Berlin by Schering AG (Dr. Th. Staks et al.) and the Radiological Department of the Free University of Berlin, Steglitz (Professor K. J. Wolf, and Professor B. Hamm) have demonstrated the excellent tolerance and imaging properties of Gd-EOB-DTPA (Figure 5). Doses as low as 10 or 25 μmol kg^{-1} enhance the healthy liver parenchyma during a comfortable imaging window up to 2 h after bolus injection. The convenient complex is eliminated from the body in an unaltered form and in equal amounts renally and with the feces.

One of the ultimate goals of contrast agent research is to identify a tumor-seeking material. The high sensitivity and

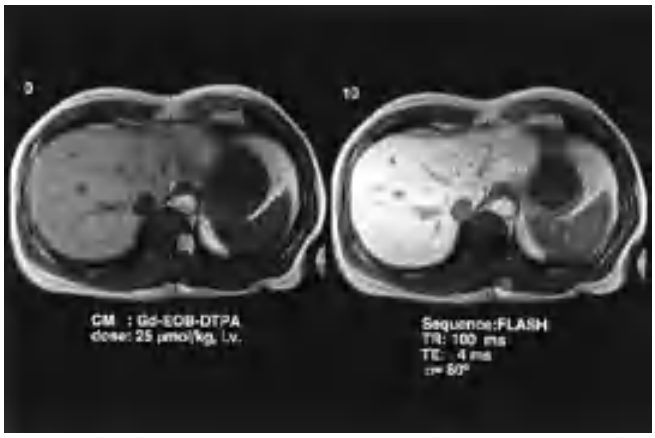

Figure 5 Contrast enhancement of the human liver after intravenous injection of 25 μmol kg^{-1} Gd-EOB-DTPA. The images (T_1-weighted FLASH sequence, 1.5 T Magnetom, Siemens, Germany) for the Phase I study were obtained by Professor B. Hamm at the University Clinics of Berlin-Steglitz

excellent spatial resolution of MRI in combination with highly effective contrast agents may make the dream come true. Thanks to advanced biotechnology, the synthesis of tumor-specific monoclonal antibodies has become possible. Gadolinium labeled antibodies have produced tumor-specific enhancement in laboratory animals.[38] The feasibility of this approach to tumor-specific imaging has been demonstrated in a mouse study in which an implanted colorectal carcinoma was significantly enhanced at 24 and 48 h after administration of 2–3 mg gadolinium labeled tumor-specific monoclonal antibody.

Since most of the contrast agents administered do not accumulate in the tumor, the dose necessary to produce an adequate enhancement is still too high. Up to 10 g of a monoclonal antibody, each molecule labeled with dozens of paramagnetic ions, will be required to achieve diagnostically useful enhancement in man. Being tissue-specific, the contrast agents have to interact with biological structures and so lose their inertness. Special attention has to be focused on the tolerance to those materials in order to ensure that the diagnostic benefits are not obtained at the cost of a higher incidence of adverse reactions. However, it is very likely that clinical diagnostic imaging will be further improved by well-tolerated tissue-specific MRI contrast agents.

6 RELATED ARTICLES

Contrast Agents in Magnetic Resonance: Operating Mechanisms; Contrast Agents in MRI: Superparamagnetic Iron Oxide; Contrast Agents in Whole Body Magnetic Resonance: An Overview; Gadolinium Chelate Contrast Agents in MRI: Clinical Applications; Liver, Pancreas, Spleen, and Kidney MRI; Relaxometry of Tissue.

7 REFERENCES

1. R. C. Brasch, *Radiology*, 1983, **147**, 781.
2. M. H. Mendonca-Dias, E. Gaggelli, and P. C. Lauterbur, *Semin. Nucl. Med.*, 1983, **13**, 364.
3. V. M. Runge, J. A. Clanton, C. M. Lukehart, C. L. Partain, and A. E. James, Jr, *Am. J. Roentgenol.*, 1983, **141**, 1209.
4. A. E. Martell and M. Calvin, 'Chemistry of the Metal Chelate Compounds', Prentice Hall, New York, 1952.
5. G. Schwarzenbach, *Angew. Chem.*, 1958, **70**, 451.
6. Tse-Lok Ho, *Chem. Rev.*, 1975, **75**, 1.
7. R. G. Pearson, *J. Chem. Educ.*, 1968, **45**, 581.
8. J. F. Desreux and P. P. Barthelemy, *Int. J. Rad. Appl. Instrum. B*, 1988, **15**, 9.
9. W. P. Cacheris, S. C. Quay, and S. M. Rocklage, *Magn. Reson. Imag.*, 1990, **8**, 467.
10. H. Gries and H. Miklautz, *Physiol. Chem. Phys. Med. NMR*, 1984, **16**, 105.
11. H. Gries, D. Rosenberg, and H.-J. Weinmann, German Patent Appl. DE-OS 3 401 052, Schering AG, 1981.
12. S. C. Quay, US Patent 4 687 659, 1987.
13. D. D. Dischino, E. J. Delaney, J. E. Emswiler, G. T. Gaughan, J. S. Prasad, S. K. Srivastava, and M. F. Tweedle, *Inorg. Chem.*, 1991, **30**, 1265.
14. H.-J. Weinmann, R. C. Brasch, W.-R. Press, and G. E. Wesbey, *Am. J. Roentgenol.*, 1984, **142**, 619.
15. R. Lauffer, *Chem. Rev.*, 1988, **87**, 901.
16. W. Schörner, R. Felix, M. Laniado, L. Lange, H.-J. Weinmann, C. Claussen, W. Fiegler, U. Speck, and E. Kazner, *ROFO Fortschr Geb Rontgenstr Nuklearmed*, 1984, **140**, 493.
17. D. H. Carr, J. Brown, G. M. Bydder, H.-J. Weinmann, U. Speck, D. J. Thomas, and I. R. Young, *Lancet*, 1984, **3**, 484.
18. H. P. Niendorf, J. C. Dinger, J. Haustein, I. Cornelius, A. Alhassan, and W. Clauss, *Eur. J. Radiol.*, 1991, **13**, 15.
19. E. Kanal, G. R. Applegate, and C. P. Gillen, *Radiology*, 1990, **177** (P), 159.
20. H. P. Niendorf, J. Haustein, T. Louton, W. Beck, and M. Laniado, *Invest. Radiol.*, 1991, **26**, S221.
21. G. Schuhmann-Giampieri and G. Krestin, *Invest. Radiol.*, 1991, **26**, 975.
22. K. Lackner, Th. Krahe, R. Götz, and J. Haustein, 'International Workshop Berlin', ed. G. Bydder, R. Felix, E. Bücheler, B. P. Drayer, H. P. Niendorf, M. Takahashi, and K.-J. Wolf, Medicom Europe BV, Bussum, 1990, p. 321.
23. P. M. Parizel, H. R. Degryse, J. Gheuens, J. J. Martin, M. Van Vyve, C. De La Porte, P. Selosse, P. Van de Heyning, and A. M. De Schepper, *J. Comput. Assist. Tomogr.*, 1989, **13**, 378.
24. G. Sze, M. Brant-Zawadzki, V. M. Haughton, K. R. Maravilla, M. T. McNamara, A. J. Kumar, A. M. Aisen, J. N. Dreisbach, W. G. Bradley, Jr, J. C. Weinreb, B. P. Drayer, J. S. Tsuruda, J. R. Hesselink, C. E. Johnson, R. D. Zimmerman, and G. R. Weingast, *Radiology*, 1991, **181**, 693.
25. M. F. Tweedle and V. M. Runge, *Drugs Fut.*, 1992, **17**, 187.
26. F. G. Shellock, H. P. Hahn, J. H. Mink, and E. Itskovich, *Radiology*, 1993, **189**, 151.
27. J. Kucharczyk, H. Asgari, J. Mintorovitch, Z. Vexler, S. Rocklage, A. Watson, and M. Moseley, *Am. J. Roentgenol.*, 1993, **14**, 289.
28. J. C. Böck, B. Sander, J. Hierholzer, J. Haustein, M. Scholz, K. H. Radke, W. Schörner, W. Lanksch, and R. Felix, *ROFO Fortschr Geb Rontgenstr Nuklearmed*, 1992, **157**, 378.
29. L. R. Schad, W. Semmler, M. V. Knopp, M. Deimling, H.-J. Weinmann, and W. J. Lorenz, *Magn. Reson. Imag.*, 1993, **11**, 319.
30. U. Schmiedl, R. E. Sievers, R. C. Brasch, C. L. Wolfe, W. M. Chew, M. D. Ogan, H. Engeseth, M. J. Lipton, and M. E. Moseley, *Radiology*, 1989, **170**, 351.
31. S. C. Wang, M. G. Wikstrom, D. L. White, J. Klaveness, E. Holtz, P. Rongved, M. E. Moseley, and R. C. Brasch, *Radiology*, 1990, **175**, 483.
32. A. A. Bogdanov, Jr, R. Weissleder, H. W. Frank, A. V. Bogdanova, N. Nossif, B. K. Schaffer, E. Tsai, M. I. Papisov, and T. J. Brady, *Radiology*, 1993, **187**, 701.
33. G. Schuhmann-Giampieri, H. Schmitt-Willich, T. Frenzel, W. R. Press, and H.-J. Weinmann, *Invest. Radiol.*, 1991, **26**, 969.
34. L. Harika, R. Weissleder, K. Ross, C. Zimmer, M. I. Papisov, and T. J. Brady, *Magn. Reson. Med.*, 1995, **33**, 88.
35. A. Davies and C. De-Haen, *Drugs Fut.*, 1991, **16**, 1001.
36. H.-J. Weinmann, G. Schuhmann-Giampieri, H. Schmitt-Willich, H. Vogler, T. Frenzel, and H. Gries, *Magn. Reson. Med.*, 1991, **22**, 233.
37. G. Schuhmann-Giampieri, H. Schmitt-Willich, W. R. Press, C. Negishi, H.-J. Weinmann, and U. Speck, *Radiology*, 1992, **183**, 59.
38. S. Göhr-Rosenthal, H. Schmitt-Willich, W. Ebert, H. Gries, H. Vogler, H.-J. Weinmann, and J. Conrad in *Proc. Xth Ann Mtg. Soc. Magn. Reson. Med.*, San Francisco, 1991, p. 356.

Biographical Sketches

Hanns-Joachim Weinmann. *b* 1949. B.S., 1976, Ph.D., 1980, Biology, Free University of Berlin, Germany. Research scientist, Institute of Contrast Media Research, Schering AG (supervisor Professor Ulrich Speck), 1979–84. Intercompany liaison imaging, Berlex Laboratories,

Wayne, NJ, USA, 1984–85. Director, Contrast Media Research Department for MRI, Schering AG, Berlin, 1985–present. Approx. 40 publications. Research interests: pharmaceutical development of contrast media and their application in diagnostic imaging (MRI), tissue-specific contrast agents, and general physiology.

Andreas Mühler. *b* 1963. M.D. 1989, Medicine, Humboldt-University of Berlin, Germany. Resident in Radiology, Institute for Diagnostic Radiology of the Charitè Hospital, Berlin, Germany (supervisor Professor Meinhard Lüning), 1989–90. Research fellow, Contrast Media Laboratory (supervisor Professor Robert C. Brasch), Department of Radiology, University of California, San Francisco, CA, USA, 1990–92. Currently, head of a research group, Contrast Media Research Department for MRI, Schering AG, Berlin, Germany. Approx. 35 publications. Research interests: pharmacology and application of MRI contrast media, design of tissue-specific contrast agents, and MRI.

B. Radüchel. *b* 1941. B.S., 1968, Ph.D., 1971, Chemistry, Technical University of Berlin, Germany. Research scientist, Institute of Pharmaceutical Chemistry, Schering AG, Berlin, 1971–present. Director, MRI Contrast Media Chemistry Department, Schering AG, Berlin, 1992–present. Approx. 80 publications. Research interests: synthesis of paramagnetic and radioactively labeled metal chelates and iodinated compounds.

Relaxation Measurements in Imaging Studies

Margaret A. Foster

University of Aberdeen, Aberdeen, UK

and

Axel Haase

Physikalisches Institut, Universität Würzburg, Würzburg, Germany

1 INTRODUCTION

T_1 and T_2 relaxation times of water or lipid protons vary between different tissues and pathologies, making them major properties in determining contrast within the NMR image. This has led to interest in the actual relaxation time values, in addition to their effects in 'weighting' images. Indeed, a number of investigators have looked for diagnostic or characteristic information from the diversity of relaxation values of normal and pathological tissues. In general, however, such numerical values have proved of more interest in research studies than as clinical tools. This is due to a combination of reasons including the variety of data collection techniques, the lack of true specificity of T_1 and T_2 for individual tissues and the wide and overlapping value ranges when pathologies are examined, see e.g. reviews by Bottomley et al.[1,2] In addition, many of the techniques available on commercial imaging systems do not fully take into account the many technical difficulties in T_1 and T_2 measurement, resulting in poor relaxation time evaluation. This has been shown in several studies in which calibrated test objects have been imaged on several systems operating at the same frequency but have yielded results up to 100% different for a given value (see Section 4). Another important problem for clinical use of relaxation time values is the inherent difficulty in obtaining reliable tissue T_1 and T_2 values when applying MRI techniques to living subjects.

To obtain a T_1 or T_2 value from a small sample in vitro, the signal collection conditions can be optimized to remove many of the extrinsic factors which can affect the result. The sample is placed in a homogeneous $\boldsymbol{B}_0$ field and is provided with one or more short, shaped rf pulses, The most commonly used pulse sequences for such measurements are, for T_1, the Inversion–Recovery (IR) sequence (180°rf–τ_i–90°rf–collect FID) repeated with variable τ_i (equivalent to *TI* in imaging) and for T_2 the Carr–Purcell–Meiboom–Gill (CPMG) sequence (90°rf(x)–τ–180°rf(y)–τ–collect spin echo–τ–180°rf(y)–τ–etc.). In this latter sequence all the required data points can be collected after a single excitation, but for IR only one data point is collected per repetition of the IR sequence so adequate time must be allowed between sequences (*TR*) to allow complete relaxation to occur (normally >5 times the tissue T_1 value). In both cases a long train of signal size values can be collected to give sufficient data for a good quality analysis of signal size versus duration from the initial excitation. With such optimized methods and careful sample preparation, reliable, repeatable tissue T_1 and T_2 values can be collected (see e.g. EEC Concerted Research Project, In Vitro Protocol[3]), with the major remaining questions relating to the nature of the information that is provided by these values. In NMR imaging, however, it is much more difficult to obtain high quality values.

2 IMAGING METHODS FOR T_1 AND T_2 DETERMINATION

During the early 1980s, attention was given to parametric mapping since it was felt that, in addition to the clinical value of pathology demonstration in parameter-weighted images, fundamental information about disease processes and useful classification of diseases might be obtained by quantitation of the parameters that yielded contrast in the weighted images. Attempts were made to obtain this information either by pixel-by-pixel calculated parameter maps or by calculations within regions of interest in images.

Most of the early attempts at T_1 and T_2 mapping used adaptations of the pulse sequences normally employed for in vitro studies, e.g. IR for T_1 mapping and CPMG, or repeated single spin echo sequences for T_2. It was frequently felt that several points on the relaxation curve should be obtained, to improve the calculation (even when the calculation method assumed a single exponential relaxation process) and for both IR and single echo T_2 collections this implied long imaging times with the consequent problems of patient discomfort, movement, and misregistration artifacts. An increasing interest, therefore, developed in more rapid pulse sequences for this purpose. For T_1 this led to the use of Saturation–Recovery (SR) sequences with shorter *TR* intervals: results were obtained in a few minutes and so signal averaging could be employed to reduce noise leading to the suggestion of the greater 'efficiency' of SR over IR for T_1 mapping during an equal signal collection period.[4,5]

Unfortunately reduction of *TR* has its own problems, especially relating to the slice profile (see later) which may degrade the accuracy of the results. Another approach to shortening the required time for T_1 and T_2 mapping was the development of multiple image collection strategies producing a short series of images of varying nature from which both T_1 and T_2 could be calculated (and often proton density as well),[6] hence reducing the overall time of the patient in the imager (compared with the collection of separate image series for T_1 and T_2 calculation) and presumably also reducing misregistration artifacts. Such strategies may have improved the efficiency of parameter acquisition but did not necessarily improve the absolute accuracy, particularly if either the transverse or the longitudinal relaxation processes were not monoexponential, or if a short *TR* was used.

As the fast imaging sequences became readily available, possibilities for using these to provide T_1 and T_2 information were investigated. These studies still continue but often the results show little improvement in the overall ability to produce consistent and accurate T_1 and T_2 values, especially from living tissues, which offer a much greater challenge than does the simplicity of a paramagnetic metal ion-doped solution.

For both SR, in which a series of identical rf pulses are used to excite the system, and the IR sequence, in which the spin population is inverted along z by means of an 180° rf pulse prior to the rf pulse (which puts the spins onto the xy plane for measurement), the 'standard' form of the equation

showing expected signal size makes certain assumptions about the experimental procedures. For example it is assumed that the slice profile is a perfect rectangle, i.e. that all the spins throughout the slice are able to respond in the same way. As we will see, particularly in short *TR* sequences, this may not be a valid assumption. It is also assumed that all the spins are on resonance, but field inhomogeneities and local distortions due, for example, to susceptibility effects, may invalidate this assumption, hence affecting the calculated T_1 values. Also, in both cases, the signal may be obtained as a gradient (field) echo by reversal of at least one of the field gradients in order to rephase the spins, or by insertion of a 180° rf pulse after the main sequence, to produce a spin echo.

2.1 Saturation–Recovery

In its most basic form this sequence is: α_{rf}–*TR*–α_{rf}–*TR*–etc. where α_{rf} is the rf pulse required to produce a flip angle of α and *TR* is the interval between the centers of two adjacent 90° pulses. Such a sequence rapidly achieves the steady state situation and at this stage the signal size (M_S) of a gradient echo can be designated as

$$M_S = \frac{M_0[1 - \exp(-TR/T_1)]\sin\alpha}{1 - \exp(-TR/T_1)\cos\alpha} \quad (1)$$

if the following assumptions are made:

1. that the rf pulse is too short for significant T_1 relaxation to occur during it
2. that the flip angle is applied each time along the same axis with alternate phases
3. that the interval between α_{rf} and collection of the gradient echo is very short
4. that *TR* is considerably longer than T_2^* so that all transverse magnetization has dephased before each rf pulse.

Assuming that an accurate M_0 value can be obtained (e.g. by using this sequence with a *TR* much greater than the longest T_1 in the slice), a T_1 value can be calculated by rearrangement of equation (1). It has, however, been pointed out[7] that a progressive inaccuracy will occur in such calculations if any residual transverse magnetization remains before the rf pulses. In cases where *TR* is less than or similar to T_2^* it is necessary to include additional terms involving $\exp(-TE/T_2^*)$ to take this into consideration or to make use of 'spoiler' gradients to dispose of any residual transverse magnetization before the next rf pulse. In addition, if the interval between the rf pulse and gradient echo is a significant proportion of T_2, a term $\exp(-TE/T_2)$ must be included in the numerator to account for transverse relaxation during this delay. The equation for the SR signal with spoiler gradients then becomes (where *TE* is the interval between the rf pulse and the gradient echo)

$$M_S = \frac{M_0[1 - \exp(-TR/T_1)]\sin\alpha\,\exp(-TE/T_2)}{1 - \exp(-TR/T_1)\cos\alpha} \quad (2)$$

In proton imaging the use of a spin echo for signal collection is more frequent than that of a gradient echo. To attain this a 180° rf pulse is inserted after α_{rf} and a term similar to that used for T_2 effects in gradient echo collection in equation (2) is inserted to allow for T_2 relaxation that has occurred during *TE* (in this case the interval between the center of the α_{rf} pulse and the center of the spin echo). Additional terms are required when *TE* is a significant proportion of T_1 to allow for the shift in origin of the T_1 recovery.

2.2 Inversion–Recovery

This sequence basically consists of: 180°rf–*TI*–90°rf–(echo)–//–180°rf–*TI*–90°rf–(echo)–etc., where the dominant time intervals are the repetition time, *TR*, and inversion interval, *TI*. Both of these can be manipulated to put T_1 information into a signal. In the most basic form, the signal size is expressed by

$$M_S = M_0\,[1 - 2\exp(-TI/T_1) \quad + \quad \exp(-TR/T_1)] \quad (3)$$
$$\text{(inversion effects)} \qquad \text{(saturation effects)}$$

Once again this is multiplied by $\exp(-TE/T_2)$ for a spin echo collection. This sequence has been used in experiments where strong T_1 contrast is required and in particular with short *TI* intervals for rapid imaging, e.g. the short tau IR (STIR) sequence.[8] For calculating T_1 values the sequence would normally be used with a long *TR* and repeated with varying *TI* intervals. A plot of signal size against *TI* yields the T_1 value of the tissue in a voxel. However, obtaining adequate numbers of images for an accurate T_1 plot can take an hour or more and the tendency has been, therefore, to reduce the procedure to a two-point determination, i.e. to extrapolate a T_1 value from two points on the relaxation curve. A similar approach[9] has been to interleave the IR sequence with a long *TR* SR sequence to provide an M_0 value and calculate the T_1, assuming a single exponential relaxation, from M_0 and one point affected by T_1 relaxation. The accuracy of such an approach, as for all versions of the SR and IR sequences, is dependent on the use of perfect 180° and 90° pulses[10,11] (the 180° pulse is replaced by an adiabatic fast passage inversion by Edelstein et al.[9] which may bring in complications, e.g. arising from magnetization transfer effects), and a truly monoexponential relaxation for the T_1 process. Some allowance can, however, be made for imperfect rf pulses if a sufficient number of images are collected to allow a three-parameter fitting procedure to be applied to the data. The fit is of the form[12]

$$S(TI) = A + B\exp(-TI/T_1) \quad (4)$$

where A and B can take into account imperfections in the rf pulses. Unfortunately collection of sufficient data takes a considerable amount of time.

Since the duration of the collection time is a major problem for both SR and IR sequences, when used for T_1 mapping, attempts have been made to reduce the necessary time by obtaining the relaxation time data from limited regions within the slice, rather than over the full slice area. For example, Morrone and co-workers[13,14] have proposed a method for obtaining T_1 data from a strip through the image. The method, which employs a selective 180° rf pulse to distinguish the strip, results in a slightly reduced signal-to-noise ratio but this can be improved by signal averaging without losing all of the collection time improvement.

2.3 Variable Flip Angles

One method that has been tried for shortening the time required to obtain a full T_1 map using the SR sequence is the use of variable flip angles.[15] From equation (2) it can be seen that the signal for the SR sequence (with gradient echo collection: spin echo cannot be used here because of the transverse rephasing due to the 180° rf pulse) can be modified by varying either *TR* or the flip angle α. If *TR* is kept constant, and a series of images collected with different α, T_1 (on a pixel basis) can be calculated as a linear regression of $I\alpha/\sin\alpha$ vs. $I\alpha/\tan\alpha$, where $I\alpha$ is the signal intensity from the collection using flip angle α. This relationship is directly derived from equation (2) and is a straight line with slope $\exp(-TR/T_1)$. Since the slope depends only on *TR* and T_1, T_1 can be calculated without needing a value for the equilibrium magnetization (M_0), hence saving considerably in collection time. In addition, *TR* can be kept short, thus adding to the time saving. Unfortunately the technique is particularly sensitive to artifacts due to magnetic field inhomogeneities, inflow, and changes of the slice profile when short *TR* is used.[16] It is also very sensitive to errors in the flip angle used.[17]

2.4 Spin Echo Sequences

Discussion of the above sequences has mainly been directed toward T_1 measurement. In fact, T_2 is also available from SR and IR images collected with a spin echo, by manipulation of the *TE* intervals whilst maintaining *TR* and *TI* constant. In such cases the influence for variation between the images will be the T_2 decay given by the term $\exp(-TE/T_2)$ shown in equation (2). T_2 can be calculated from two or more images in the same way and with the same assumptions and restrictions as shown for T_1. Such methods are the basis for the integrated T_1/T_2/proton density collection strategies mentioned earlier and are discussed in detail, along with the necessary data analysis technique, by Bakker and de Graaf.[18] Where a T_2 value is calculated from two separate echoes, however, the result may be heavily affected by diffusion processes.

When T_2 is required alone, or in greater detail, a multiecho sequence such as the CPMG is normally chosen. An image of different T_2-weighting can be produced from each, or from selected echoes of the train and T_2 can be calculated from these on a pixel-by-pixel basis. In some cases, multiecho sequences have been extended over a considerable period, allowing accumulation of sufficient points on the relaxation curve for bi- or even multiexponential analysis, separating the T_2 values of several relaxation components represented within the overall curve. Such techniques have been the basis for studies in which different components are assigned to different tissue elements within the overall organ.[19] Problems may, however, arise in such signal collections from pulse imperfections and incorrect rephasing of the signal.

2.5 Stimulated Echoes

The T_1 techniques discussed so far have required the collection of at least two independent full or partial images (although these may be from a combined image collection procedure). Methods do exist, however, to collect information from several points on the T_1 relaxation curve after a single excitation, hence considerably reducing collection time. One method for achieving this involves the use of stimulated echoes in which an image is created by the application of three 90° rf pulses.[20] This can be shown as

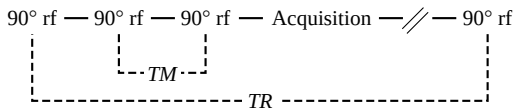

in which the initial 90° rf pulses are used to store a part of the magnetization longitudinally. This decays according to T_1 and the decay is sampled, after time *TM*, by the third pulse. The signal intensity of the echo is given by

$$M_S = M_0[\exp(-TE/T_2)\ \exp(-TM/T_1)] \tag{5}$$

Hence by varying *TM*, a series of signal values can be obtained with different T_1 weightings. If, however, a chain of rf pulses of variable flip angle is inserted in place of the third 90° pulse, the technique becomes a single-shot method which yields the T_1 information directly.[21] The sequence is now

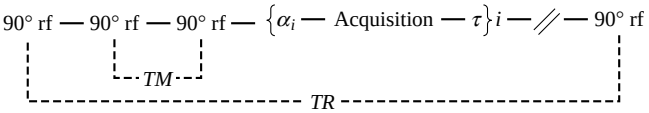

where i is the number of repeats in the train of limited flip angle rf pulses, each of which is followed by an echo acquisition. Each limited flip angle rf pulse samples the decay of the longitudinal magnetization by tipping out a small transverse component of it (*TM* increases for each sampling). The complete i set of rf pulses, with the final one being 90°, gives a series of values along the T_1 relaxation curve.

The method has the advantage of speed and it also provides a large database for the T_1 calculation, since i can be a substantial number. The method does, however, suffer from the major disadvantage that a stimulated echo gives only 50% of the maximum available signal strength, hence reducing the efficiency of the technique.[22]

2.6 Look–Locker Sequences and TOMROP

The NMR and ESR spectroscopy sequence proposed by Look and Locker[23] also uses a series of limited flip angle pulses to sample the T_1 relaxation curve after a single excitation. A 180° inverting pulse is followed by a train of closely spaced, equal amplitude, limited flip angle rf pulses which forces the magnetization to evolve toward a new equilibrium state. The signals acquired from this represent points along the T_1 relaxation curve which, for this sequence, has the appearance of a normal inversion curve ($-M_0$, through zero to $+M_0$) but with a set of 'saw-teeth' superimposed upon it due to the low flip angle pulses. There can be a substantial number of these pulses (e.g. more than 32 even in imaging) and each one provides information about the relaxation at a different time after inversion. Hence a 32 (or more) point T_1 relaxation curve can be produced in the time normally required for the collection of a single *TI* point with the normal IR procedure. The concept has been developed into an imaging technique[24] and has given rise to the TOMROP (T One by Multiple Read Out

Pulses) method.[25] The signals are collected as gradient echoes, and the dynamic range of this procedure is much greater than that of the one-shot stimulated echo method.[22] The technique, however, does suffer from the disadvantage of a low signal-to-noise ratio due to the low flip angle of the pulses used for signal collection. Despite this, it still represents a reliable and fast method for in vivo T_1 mapping.

2.7 Echo Planar Imaging Methods

Echo planar imaging (EPI)[26] allows extremely fast image acquisition. An early attempt at obtaining T_1 from echo planar images involved varying the delay time between image collections. The longitudinal signal component decays during this delay period, so collecting signals after varying delay times inserts T_1 information into the images.[27] A two-point T_1 map can be produced rapidly from a sequence of three EP images. The authors point out, however, that there are problems with the method which lead to systematic errors in the calculated T_1 values. A later technique by the same group[28] involved the insertion of a 180° inverting rf pulse immediately before the collection of the EP image. One image is collected after each inversion and this image has the T_1 contrast related to the inversion-recovery time before its collection. A series of such images can, therefore, yield the T_1 relaxation curve. This technique has the advantage of very high speed acquisition of the T_1 information but suffers from problems related to the spatial resolution of EPI and to low signal-to-noise ratio. It is also very sensitive to magnetic field inhomogeneities.

2.8 Snapshot FLASH Method

This technique employs the FLASH (Fast Low Angle SHot) technique[29] in which a train of low flip angle rf pulses are employed with a very short *TR* between them. The signal is collected as a gradient echo with a very short echo delay time. Recent developments of the FLASH technique (to snapshot-FLASH) have brought the image acquisition time down to 200 ms for a 64 × 128 pixel image.[29] The technique has been developed as a quantitative T_1 imaging method in which, by use of *TR* values of less than 10 ms, the total imaging time is less than an average tissue T_1 value. T_1 information is provided in the same way as in IR-EPI, by the insertion of an inverting 180° rf pulse before the snapshot-FLASH imaging sequence. During the inversion–recovery of the longitudinal magnetization, several IR-weighted images can be obtained which show dynamic changes of contrast relating to the time since the spin inversion. T_1 values can be calculated on a pixel basis using a three-parameter fit. This technique is the fastest T_1 imaging technique proposed to date and gives accurate T_1 values compared with known standards.[30] Certain problems still need to be addressed, however. For example spatial distortions may occur in the images due to effects on the point spread function arising from the 'inversion–recovery' during the imaging period[29] (the pixel is broadened by more than one-pixel diameter if the measuring time is equal to the T_1 value). Also of importance may be the T_1 relaxation which occurs during the acquisition of each of the snapshot-FLASH sequences following the spin inversion. The FLASH acquisition requires approximately 200 ms for the full image. This, however, can be a significant proportion of the T_1 relaxation time of certain tissues, particularly if the method is used at lower magnetic field strengths. The effects of this on the T_1 weighting of the image need to be assessed (the same problem is true for IR-EPI).

Snapshot-FLASH can also be used to obtain T_2 information by preceding the FLASH sequence by a spin echo preparation (e.g. of the DEFT type) rather than by an IR pulse. Limited tests have shown that such a sequence can produce acceptable values.

3 PROBLEMS IN OBTAINING T_1 AND T_2 VALUES IN IMAGING

As will have been seen from comments whilst discussing the various methods for T_1 and T_2 estimation, there are a wide variety of problems to be overcome before any imager-derived value can be regarded as acceptable. Only a few of these can be highlighted here, with the majority of the discussion relating to the longer collection sequences which have been more fully examined and tested.

Some of the major problems encountered when measuring relaxation times in vivo are:

1. magnetic field inhomogeneity effects, including those due to the field gradients,
2. slice profile effects, related to pulse sequence timing etc.,
3. problems relating to rf pulses and signal phase,
4. errors when multislice collection procedures are used,
5. misregistration problems when T_1 and T_2 are calculated from several image data sets,
6. partial volume effects due to tissue inhomogeneity,
7. assumptions made in the T_1 and T_2 calculation, e.g. regarding relaxation monoexponentiality,
8. a wide variety of effects arising from the living tissue/body itself, such as flow, diffusion, magnetic susceptibility, etc. which can all either affect the relaxation time value directly or alter the apparent place from which the information is coming.

The extent to which any of these problems will distort calculated T_1 and/or T_2 values is dependent on interactions between the properties of the tissues in the slice, the imaging technique being used, and the precise nature and timings of the pulse sequence being applied.

3.1 Magnetic Field Inhomogeneities

An automatic assumption in all signal size or relaxation time calculations is that all the spins in the sample (i.e. one voxel, or all the voxels to be averaged together in a single region of interest) have the same resonance frequency and hence are able to respond in exactly the same way to each rf or gradient field manipulation. If the applied magnetic field is inhomogeneous for any reason, the proton Larmor frequencies will be different in different regions of the sample. Modern magnet technology has helped reduce the scale of this problem as it relates to the applied static (main) field but in all MR imaging, the spatial information is obtained by the application of one or more magnetic field gradients. This automatically implies that the sample will experience a spread of B values and hence of Larmor frequencies. Although carefully shaped rf pulses of

appropriate bandwidth can reduce the effect, there will inevitably be some reduction in the precision of relaxation time measurements due to the statistical spread of the values.

3.2 Slice Profile Effects

In some ways this problem is a continuation of the above, in that the effect arises from the lack of ability of the entire spin population to respond equally to the manipulation. In this case, however, inaccuracies originate from saturation effects developing during the selective excitation that defines the image slice.[16]

An increasing need to obtain the NMR image rapidly has led to the almost universal use of *TR* times that are short in relation to the time necessary for full longitudinal relaxation. In such a case, if there is any deviation (which is always the case) from a 'perfect', i.e. completely rectangular, slice profile, saturation effects will demonstrate themselves as variations in the flip angle through the width of the image slice. To demonstrate this let us take a 'worst case' situation in which a Gaussian rf pulse is applied, yielding a Gaussian-shaped slice profile. On first application of the slice selective rf pulse, the spins in the center of the slice thickness receive, say, a 90° flip, but those toward the edges will be flipped by progressively less than this. With a sufficiently long *TR* all the spins will completely relax and the overall effect will be that the spins on the outer edges of the slice width contribute less to the signal from the voxel than do those in the center. In itself this is a source of error but is less significant than that arising when *TR* is short. In this case, relaxation is incomplete so at the next excitation the spins at the edges, which have had less relaxing to do, will have returned fully to the preexcitation state and further excitations will induce a contribution to the signal which is the same as that at the first excitation. The spins in the center of the slice, however, have further to relax and will not have completed their relaxation during *TR*, so the next excitation, which returns these central spins to the *xy* plane, will operate on a partially saturated population. These spins, therefore, will make a smaller contribution to the overall voxel signal. With *TR* values that are substantially shorter than the T_1 of the material in the voxel, this can lead to a slice profile that has a considerable dip in the middle and 'horns' at either side. Two types of error arise in this situation. Firstly the information is not coming evenly from where it is expected. Secondly, and most important, the effect causes inaccuracy in the actual calculation of the relaxation time, to an extent dependent on the nature of the pulse sequence and calculation method.[31]

3.3 Rf Pulses and Signal Phase

Problems that may arise due to imperfect rf pulses (i.e. inappropriate flip angles being produced) have been highlighted during the discussions of the pulse sequence types. The extent of sensitivity to such effects is very closely related to the nature of the particular pulse sequence. In addition, some pulse sequences may be very sensitive to phase errors which accumulate as the sequence is repeated during the image acquisition procedure. The dependence of the calculated T_1 value on the accuracy of the 180° pulse has been calculated for an interleaved SR/IR sequence.[31] In a case where the slice selection rf pulse is assumed to be an accurate 90° and the slice profile to be a perfect rectangle, it was shown that varying the angle of the inverting rf pulse from 180° to 150° produced a systematic error in the measured T_1 value. For actual T_1 values comparable to the *TI* of the simulated sequence, the 150° 'inversion' produced T_1 values that were 5% lower than expected, but the difference rapidly increased for longer T_1 values, producing e.g. a value of 750 ms when the true value was 1 s and *TI* was 200 ms. Inaccuracies in the 180° and 90° pulses may arise from instrumental factors but can also be due to rf power absorption in the body,[32] and hence may vary from patient to patient or even between tissues of the same individual.

3.4 Multislice Collection

Increased pressure for more rapid MR image acquisition has led to the almost universal introduction of multislice techniques. This can, however, lead to extensive problems if specific parameters such as T_1 and T_2 are being calculated. Several workers have emphasized the potential inaccuracy of T_1 values when these are calculated from slices other than the first one in a multislice acquisition.[33,34] They have particularly highlighted the fact that the measured 'T_1' value depends on the width of the gap between the slices. Such findings are consistent with the suggestion by Dixon et al.[35] that the frequency selection rf pulse, in the presence of the field gradient used to select a particular slice, acts as an off-resonance pulse in neighboring slices in which the protons are experiencing different levels of the field gradient and, therefore, have different Larmor frequencies. Such effects are, of course, observable only in tissues or gels and are not seen in the paramagnetic metal ion solutions that are usually used to calibrate relaxation time measurements.[36] In addition, since different tissues show different amounts of magnetization transfer (which is the basis for the use of MTC to enhance image contrast) the T_1 values will be distorted to different extents. From this it is obvious that T_1 measurement must be a single-slice experiment.

Accurate T_2 estimation is also problematic during multislice collects.[22] If the slices are contiguous, unwanted echoes can be produced at the slice edges, distorting calculated parameter values.

3.5 Misregistration

This problem arises when T_1 and T_2 values are calculated from several image data sets. The relaxation time value(s) are calculated either on a pixel-by-pixel basis to form a parameter map or from a group of pixels forming a region of interest. Since the individual images represent points on the relaxation curve, it is obviously essential that they come from the same sample of tissue (or test object). If, however, the patient moves or the imager slightly changes its performance during the serial image collection, then any specified pixel may contain different material before and after the move. Any relaxation time values calculated from the signal intensity of the two pixels would, therefore, be completely misleading. When homogeneous test objects are studied, this effect will only be of importance close to the edges of the objects, but if an organ of complex geometry is studied, e.g. white and gray brain tissue, then any slight movement, in any direction, could result in erroneous values.

This problem is difficult to overcome if several images are required to be collected sequentially, each with a substantial

TR. For two-point longer *TR* sequences the most successful approach has been that of interleaving the signal collection. For example, one sequence for producing a T_1 map[37] employs one SR and one IR image. These are collected together using a compound SR/IR sequence. In this way any movement or imager changes occur equally, and simultaneously, to both image collections, and misregistration between pixels of the two images is prevented.

3.6 Partial Volume Effects

This is a problem met in all forms of imaging. In a large, homogeneous test object, regions for T_1 and T_2 estimation are available in which the entire voxel is filled with the same material. This is almost never the case in the living body. Obvious examples of this can be seen in the brain, where the gray brain tissue is a thin layer over the white matter, in intimate contact with it (and also with cerebrospinal fluid; CSF). In such a case, a high proportion of voxels in the general gray matter regions will also contain, in variable amounts, white matter and/or CSF. Attempts have been made to sort out the tissues in such cases, often by multiexponential analysis of the relaxation curve. Success is usually limited, however. Often the 'partial voluming' is more subtle than this, with the mix being at the cellular level. For example, liver tissue, occurring in large lobes in the abdomen, gives the impression of being an ideal subject for relaxation time measurement because of its apparent homogeneity but this appearance is deceptive. In the general regions of the lobes (i.e. away from the attachment areas), the liver comprises two major cell types: about 80% hepatocytes and 10% Kupfer cells (the latter are part of the reticuloendothelial system). The rest is a mixture of cell types forming blood and bile vessels, etc. It may be assumed that all these cell types have different T_1 and T_2 values which average together to produce the 'normal' figure. In different parts of the liver, however, the cellular proportions can vary considerably, giving subtle differences that are, nonetheless, directly equivalent to partial volume effects between two adjacent tissues.

3.7 Calculation Method

Only under exceptional information collection conditions are sufficient data points available along the relaxation curve to allow bi- or multiexponential analysis. In the great majority of imaging T_1 and T_2 experiments, the data are more sparse and have to be analyzed as a single exponential. The crudest methods for this are when only two data points are available: for T_1 these are normally the M_0 value obtained after a single 90° pulse and one point along the relaxation curve. Under perfect conditions, if the relaxation really is a monoexponential relaxation, the value can be calculated accurately from these points. However, as pointed out with the list of problems above, many factors can distort the measured data points. Fundamentally a 2-point method has to 'use' all the information of those two points, so any form of inaccuracy in either point (e.g. delay in sampling so that relaxation has started before the M_0 measurement is made or noise affecting either point) will have a direct and fundamental effect on the calculated result. If, however, a third point (i.e. another image with a different T_1 weighting) can be added, then the total reliance on each point is reduced, and adding further points progressively helps; this, of course, is only true if the adverse effect results in random effects on the signal. Where it is systematic, no improvement in the number of points will necessarily help to improve the accuracy of the calculated value. The effects of noise on these signals have been analyzed by Kurland.[38] One of the major advantages of the rapid, single-shot techniques is that they can produce a large number of data points along a single relaxation curve, hence improving the accuracy of the T_1 and T_2 calculations.

Not all tissues exhibit monoexponential relaxation behavior. For most tissues, T_1 relaxation, within the limits detectable by most imaging methods, is generally considered to approximate to a single exponential process unless there are proton populations which are not in fast exchange (e.g. the lipid and water protons in adipose tissue). In these cases multiexponential T_1 behavior can be observed. T_2 is a more complex phenomenon and, depending on the way the experiment is performed, a high proportion of body tissues show multiexponential relaxation.

Biexponential fitting procedures, to be reliable and repeatable, require a considerable number of data points in the curve: the more points (spread over a substantial part of the total curve) the better the chance of obtaining a good separation of the two exponentials. The precise ability of any separation algorithm will depend upon:

1. the number of data points and their spread
2. the amount of noise on the signals
3. the separation between the two T_1 and T_2 values: it is easier to separate two values that are very different (i.e. 100% or more) than similar ones
4. the amount of each spin population that is present: if the population contributing one T_2 value accounts for only 10% of the total signal, it will be more difficult to separate out than if the two populations are more similar in their contribution (i.e. magnitude).

All the above points govern the chances of success of any biexponential fitting procedure, whether this is the relatively crude method of 'curve stripping' in which the long T_1 or T_2 component is isolated and then deducted from the overall curve to leave the short relaxing component (a method which is extremely sensitive to noise), or whether a more elaborate, iterative, 5-parameter fitting technique is used. All the requirements become even more demanding if attempts are made to separate more than two exponentials, and the problem becomes computationally very demanding.

3.8 Biological Effects

There are a wide range of biological parameters and tissue interactions that can influence the measured relaxation times. For example distorted T_1 and T_2 values can arise due to flow and perfusion effects, diffusion, especially where this is anisotropic, e.g. in oriented tissues such as muscle or nerve tracts, magnetic susceptibility differences between tissues, etc. A full discussion of these effects is outside the scope of this article but most of the biological factors can be seen as changes in the local magnetic field so that the spins in a voxel can no longer be regarded as a homogeneous population, or due to movement of part or all of the spin population during the data collection period so that the signal from the same pixel in different images no longer arises from the same spin population. A very good example of the effects of life processes on measured tissue relaxation time is

provided by Katz et al.,[39] who looked at T_2 measurement from myocardium. They demonstrated differences between in vivo and ex vivo T_2 values in this tissue and also showed the variability of the in vivo measurements and their relationship to factors such as the velocity of movement of the cardiac wall.

4 THE VALUE OF CALIBRATION

We have emphasized the methods for, and problems in, direct measurement of T_1 and T_2 when using imaging techniques. The problems are indeed so great that, for longer *TR* methods at least, the use of 'dead reckoning' techniques (i.e. direct signal acquisition and calculation of the relaxation times from the basic equations), except over limited ranges on certain specifically designed MR imaging systems, can produce very misleading results. Even the use of manufacturer's recommended methods, which often include the use of 'look-up' tables rather than full calculation, can produce erroneous results. This has been demonstrated, for example, by the EEC Concerted Research Program[40] in which a set of carefully prepared test objects were imaged on a number of MR imagers sited throughout Europe. The test object for T_1 and T_2 testing consisted of a set of gadolinium (Gd)-doped agarose gels of known relaxation time values and with known frequency-dependence characteristics. The Gd/agarose mixtures were chosen to cover a wide range of T_1 and T_2 values and ratios between these parameters, so that a close match to tissue properties was obtained. The various imagers were tested using their own procedures for acquisition and calculation and enormous variability was found in the ability to produce accurate results. The responses ranged from acceptable accuracy over at least part of the relaxation value range, to systems which gave a virtually flat response, i.e. produced the same parameter value whatever the actual value of the gel being tested. Such studies show that reliance on manufacturer's built-in procedures can lead to inaccuracies as great as those produced by 'dead-reckoning'.

Perhaps the best method to improve the accuracy of imager T_1 and T_2 values is by appropriate calibration. If a reasonable range of doped gels or solutions is examined by detailed relaxometry at the appropriate frequency and temperature, and these 'real' values are compared with the T_1 and T_2 values obtained for the same samples on the MR imager, a calibration curve for each relaxation time can be produced, against which the tissue values can be corrected. This will help to remove systematic errors in T_1 and T_2 measurement, as seen in the study of MacFall et al.[41] Even this, however, will not remove all the difficulties met when living subjects are examined. As already mentioned, the flip angle produced by the rf pulse will vary in different individuals and for different tissues in the same individual. In such cases, calibration will not be of help in improving accuracy.

5 CONCLUSION

Measurement of T_1 and T_2 values, using MRI methods and equipment, and especially when attempted on living subjects rather than small, static test objects, is not easy and can be very inaccurate. Variations in the measured or calculated values may be induced by a wide range of machine and sample variables and even careful calibration can only partially help in reducing the inaccuracies. These difficulties and potential inaccuracies have led to considerably reduced clinical interest in obtaining this quantitative information. It is still possible, however, that studies of relaxation behavior could provide information leading to better tissue characterization and even to an improved understanding of some aspects of disease processes. With this in mind, therefore, we can hope that future developments and validation of the very fast, single-shot techniques for relaxation time measurement will restore confidence and interest in this quantitative aspect of MRI.

6 RELATED ARTICLES

Echo-Planar Imaging; Quality Control and Quantification in Whole Body MRI and MRS; Relaxation Measurements in Whole Body MRI: Clinical Utility; Selective Excitation Methods: Artifacts; Whole Body Magnetic Resonance: Fast Low-Angle Acquisition Methods.

7 REFERENCES

1. P. A. Bottomley, T. H. Foster, R. E. Argersinger, and C. M. Pfeifer, *Med. Phys.*, 1984, **11**, 425.
2. P. A. Bottomley, C. J. Hardy, R. E. Argersinger, and G. Allen-Moore, *Med. Phys.*, 1987, **14**, 1.
3. EEC Concerted Research Project, *Magn. Reson. Imaging*, 1988, **6**, 179.
4. W. A. Edelstein, P. A. Bottomley, H. R. Hart, and L. S. Smith, *J. Comput. Assist. Tomogr.*, 1983, **7**, 391.
5. P. R. Moran, *Magn. Reson. Imaging*, 1984, **2**, 17.
6. G. Johnson, I. E. C. Ormerod, D. Barnes, P. S. Tofts, and D. MacManus, *Br. J. Radiol.*, 1987, **60**, 143.
7. I. R. Young, I. J. Cox, G. A. Coutts, and G. M. Bydder, *NMR Biomed.*, 1989, **2**, 329.
8. G. M. Bydder and I. R. Young, *J. Comput. Assist. Tomogr.*, 1985, **9**, 659.
9. W. A. Edelstein, J. M. S. Hutchison, G. Johnson, and T. Redpath, *Phys. Med. Biol.*, 1980, **25**, 751.
10. G. H. Weiss, R. J. Gupta, J. A. Ferretti, and E. D. Becker, *J. Magn. Reson.*, 1980, **37**, 369.
11. E. D. Becker, J. A. Ferretti, R. K. Gupta, and G. H. Weiss, *J. Magn. Reson.*, 1980, **37**, 381.
12. J. L. Evelhoch and J. J. H. Ackermann, *J. Magn. Reson.*, 1983, **53**, 52.
13. T. Morrone, *Magn. Reson. Med.*, 1987, **5**, 434.
14. T. Morrone, J. Benevento, R. DiMassimo, A. Martino, E. Orbach, and M. Weiss, *Am. J. Physiol. Imaging*, 1987, **2**, 17.
15. E. K. Fram, R. J. Herfkens, G. A. Johnson, G. H. Glover, J. P. Karis, A. Shimakawa, T. G. Perkins, and N. J. Pelc, *Magn. Reson. Imaging*, 1987, **5**, 201.
16. I. R. Young, D. J. Bryant, and J. A. Payne, *Magn. Reson. Med.*, 1985, **2**, 355.
17. H. Z. Wang, S. J. Reiderer, and J. N. Lee, *Magn. Reson. Med.*, 1987, **5**, 399.
18. C. J. G. Bakker and C. N. de Graaf, *Magn. Reson. Imaging*, 1988, **6**, 3
19. M. Jungke, W. von Seelen, G. Bielke, S. Meindl, G. Krone, M. Grigat, P. Hilger, and P. Pfannenstiel, *Magn. Reson. Imaging*, 1988, **6**, 683.
20. J. Frahm, K. D. Merboldt, W. Hanicke, and A. Haase, *J. Magn. Reson.*, 1985, **64**, 81.
21. A. Haase and J. Frahm, *J. Magn. Reson.*, 1985, **65**, 481.

22. A. P. Crawley and R. M. Henkelman, *Magn. Reson. Med.*, 1988, **7**, 23.
23. D. C. Look and D. R. Locker, *Rev. Sci. Instrum.*, 1970, **41**, 250.
24. W. H. Hinson and W. T. Sobol, *Med. Phys.*, 1988, **15**, 551.
25. G. Brix, L. R. Schad, M. Deimling, and W. J. Lorenz, *Magn. Reson. Imaging*, 1990, **8**, 351.
26. P. Mansfield and I. Pykett, *J. Magn. Reson.*, 1978, **29**, 355.
27. P. Mansfield, D. N. Guilfoyle, R. J. Ordidge, and R. E. Coupland, *Phys. Med. Biol.*, 1986, **31**, 113.
28. M. K. Stehling, R. J. Ordidge, R. Coxon, and P. Mansfield, *Magn. Reson. Med.*, 1990, **13**, 514.
29. A. Haase, *Magn. Reson. Med.*, 1990, **13**, 77.
30. R. Deichmann and A. Haase, *J. Magn. Reson.*, 1992, **96**, 608.
31. J. M. S. Hutchison in 'Physics of NMR Spectroscopy in Biology and Medicine', ed. C. Corso, Italian Physics Soc., 1988, p. 370.
32. P. A. Bottomley and E. R. Andrew, *Phys. Med. Biol.*, 1978, **23**, 630.
33. M. Just, H. P. Higer, and P. Pfannensteil, *Magn. Reson. Imaging*, 1988, **6**, 53.
34. S. Majumdar, H. D. Sostman, and J. R. MacFall, *Invest. Radiol.*, 1989, **24**, 119.
35. W. T. Dixon, H. Engels, M. Castillo, and M. Sardashti, *Magn. Reson. Imaging*, 1990, **8**, 417.
36. S. D. Wolff and R. S. Balaban, *Magn. Reson. Med.*, 1989, **10**, 135.
37. J. M. S. Hutchison, W. A. Edelstein, and G. Johnson, *J. Phys. E*, 1980, **13**, 947.
38. R. J. Kurland, *Magn. Reson. Med.*, 1985, **2**, 136.
39. J. Katz, L. M. Boxt, R. R. Sciacca, and P. J. Cannon, *Magn. Reson. Imaging*, 1990, **8**, 449.
40. R. A. Lerski, D. W. McRobbie, K. Straughan, P. M. Walker, and J. D. de Certaines, A. M. Bernard, *Magn. Reson. Imaging*, 1988, **6**, 201.
41. J. R. MacFall, F. W. Wehrli, R. K. Breger, and G. A. Johnson, *Magn. Reson. Imaging*, 1987, **5**, 209.

Biographical Sketches

Margaret A. Foster. *b* 1940. B.Sc., 1962, M.Sc., 1968, Ph.D., 1978, Medical Physics, University of Aberdeen, UK. Successively research fellow, lecturer, senior lecturer, and reader, University of Aberdeen, 1978–present. President of European Society for Magnetic Resonance in Medicine and Biology, 1991–92. Approx. 150 publications. Present research specialties; ESR spectroscopy, NMR relaxometry, MRI in excised tissues and animal models.

Axel Haase. *b* 1952. Diploma, 1977, physics, University of Giessen, Germany; Ph.D., 1980, working at Max-Planck-Institute, Göttingen, submitted to University of Giessen. Postdoctoral position, 1982 University of Oxford, UK, with Professor G. K. Radda. Research position at Max-Planck-Institut, Göttingen, 1983–1988. Chair of Biophysics, University of Würzburg, Germany, 1989–present. Approx. 150 publications on NMR imaging, fast NMR imaging, and in vivo NMR applications. Present research interests: quantitative fast NMR imaging and NMR microscopy and NMR applications to cardiology and plant physiology.

Relaxation Measurements in Whole Body MRI: Clinical Utility

Peter A. Rinck

University of Mons-Hainaut Medical Faculty, NMR Laboratory, Mons, Belgium

1 INTRODUCTION

The use of relaxation times for medical applications was first proposed, attempted, and patented in 1974 by Damadian and collaborators.[1,2] Originally, Damadian did not intend to use the relaxation times for imaging but for tissue characterization. The method was aimed at screening humans for cancer cells. This idea has since occupied the minds of many researchers, as the ultimate goal of diagnostic medicine is noninvasive tissue characterization and the external identification of malignant cells within the human body without touching the body. Damadian's claim that relaxation time changes highlight cancer cells seemed to be the pivotal step in medical progress. Thus, it is understandable that relaxation has been described as the Holy Grail of magnetic resonance. Damadian's assertion that NMR can detect cancer has proven partly true, but in a different way: MRI with images based on relaxation times has become one of the main medical technologies applied in cancer diagnosis and follow up. In clinical routine, relaxation time measurements are not used for this purpose.

2 METHODS

2.1 In Vitro Determination of T_1 and T_2

High-resolution magnetic resonance spectroscopists have measured T_1 and T_2 values for more than four decades. The in vitro measurement is done on a small sample, approximately 0.1–1.0 ml or larger in volume, in an extremely homogeneous magnetic field. Usually, the measurements are performed at relatively high magnetic field strengths compared with those used for clinical MRI.

A variety of methods has been developed to obtain maximal precision with minimal time consumption. Typically, 15–30 magnetization measurements are performed on the sample for different time delays (*TI* and/or *TR*) using inversion recovery (IR) or saturation recovery (SR) pulse sequences. Based on these results, an observed T_1 value is calculated. Usually the error limits are better than 5%.

T_2 can be calculated with a single multiecho sequence. The more echoes one uses the more accurate the measurement will be.

2.2 In Vivo Determination: Localized Measurement

For magnet systems with larger bores, it is possible to examine whole organisms. One of the major problems of in vivo relaxation time measurements is the localization of the volume to be observed. Details of such localization techniques are given elsewhere in this book. The actual accuracy of in vivo measurements depends on the number of points acquired and the quality of localization.

2.3 In Vivo T_1 and T_2 Images

The current method used to obtain a T_1 image, i.e. an image whose picture elements represent pure T_1 values, relies on a mathematical manipulation of separately obtained images with different T_1 influence. In clinical surroundings, typically two to four images are used. Bearing in mind that in vivo relaxation can be multiexponential, it is somewhat inadequate to perform the analysis by such a limited fit to an exponential curve. T_2 images are calculated from the images of a multiecho series. Both methods can be combined into mixed sequences such as the one described in Figure 1.[3]

All methods relying on slices through the examined object will have as additional error sources, among others, partial volume effects from the edges of the slices and inaccuracies created by the slice profile. The only method that avoids this slice problem is the true three-dimensional (3D) volume imaging method. Still, in vivo relaxation time values can only be considered as estimated values.

Recently, progress has been made in using rapid imaging sequences to measure T_1; such techniques may prove useful e.g. for estimating the concentration of paramagnetic contrast agents in an organ.

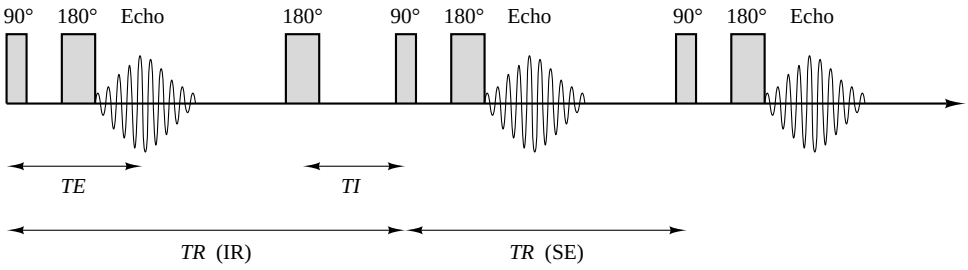

Figure 1 Timing of a mixed sequence for the in vivo determination of T_1, T_2, and ρ values in a whole body MR machine

2.4 T_1 (T_2) Images and T_1- (T_2-)-Weighted Images

In clinical routine, people often talk about T_1, T_2 or proton density images. The correct terms should be *T_1-weighted*, *T_2-weighted*, and *proton density-weighted* (or better: *intermediately-weighted*) images, because these images have only a certain T_1, T_2, or proton density dependence. However, they are not calculated pure relaxation time or proton density images.

3 PROBLEMS

The original idea of replacing hospital pathology departments by MRI equipment did not materialize. In vivo relaxation time measurements based on MRI have been tried over the years by a large number of researchers who used relaxation time values for tissue characterization in the brain, body, muscles, and bones. The task proved to be in vain because all efforts to characterize or even to type tissues largely failed. The reasons are manifold and include systematic measurement errors, inaccuracy of two-point plotting methods of relaxation curves, inherent variability of tissue composition, partial volume effects, and interobserver variability. Researchers realized that it is futile to measure a point or a region of interest within a tumor because too many different components, such as tumor and necrotic cells, small vessels, calcifications, and other structures, can be found within a volume of interest (see Figure 2).

In addition, T_1 and T_2 values overlap with those of other pathologies and sometimes of normal tissue, and T_1 and T_2 values of normal tissue change with age and hormonal cycles, breast tissue being a good example.

In 1985 Rinck et al. demonstrated that even carefully performed in vivo T_2 measurements are nondiagnostic in cancer detection, characterization, or typing.[4] After absolute T_1 and T_2 values had been used unsuccessfully by researchers, combinations of T_1 and T_2, histogram techniques, and more sophisticated 3D display techniques of factor representations were used.[5] However, the heterogeneity of normal tissues, as well as that of pathological benign and malignant tissues, did not allow the pathologist's view through the microscope to be replaced with MRI techniques. Thus, for tissue characterization new techniques have been proposed which are not based upon relaxation time measurements.[6]

Damadian also claimed that T_1 values of tumorous tissue are always higher than those of normal tissue. His dream of MRI becoming the perfect screening method for cancer tissue in the human body was finally shattered when this claim was refuted. T_1 values depend on the magnetic field strength, i.e., they increase with the magnetic field. Some tumor values can be lower than the values of normal tissue at certain fields; some are even the same at certain fields so that they cannot be distinguished.[7]

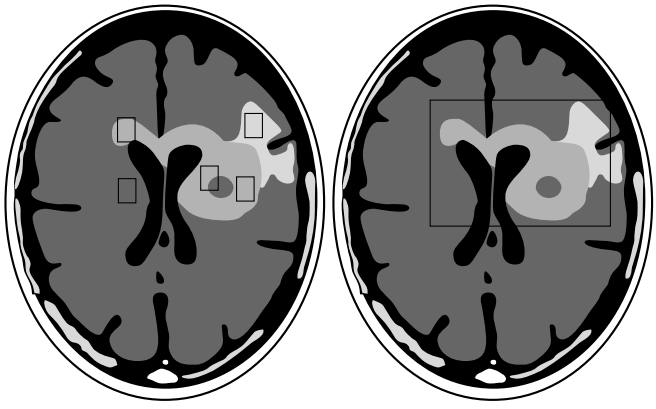

Figure 2 Malignant brain tumor. Relaxation time measurements in vivo can be performed pixel-by-pixel and by regions of interest of different size (left: small regions of interest covering edema, tumor, necrosis, etc.; right: large regions covering the entire tumor). Partial volume effects and other factors influence the measurements and contribute to inaccurate values. (Reproduced by permission of Blackwell Scientific, Oxford, from Rinck[16])

4 APPLICATIONS

Every year, the literature announces new attempts to exploit relaxation time measurements in vivo. There are some positive reports about the successful use of relaxation time measurements in vivo. These all concern follow up of therapy with patients being their own reference. Publications include, for instance, the report that relaxation times from leukemic bone marrow can be used for the differential diagnosis of this disease.[8] Similar results in high-grade gliomas were published by another research group.[9]

Another quite interesting relaxation time study is the measurement of normal-appearing white brain matter in multiple sclerosis (MS) patients. Not only MS plaques but also the inconspicuous-looking white matter are changed by the disease. Relaxation time measurements revealed generally longer T_1 and T_2 values than in normal subjects. Pixel-by-pixel mapping suggests that there might be minute invisible changes in the white matter which might explain brain function deficits not explainable by the size and location of visible MS plaques.[10,11]

When magnetic resonance began to be used for medical purposes, it was thought that relaxation times could help to distinguish between tumors and normal tissue since most T_1 (and in a similar way, T_2) values of pathologic tissue can differ markedly from the T_1 of similar normal tissue.[4] But the ability to discriminate, type, or even grade tumors using relaxation time values has remained a dream despite the sophisticated multipoint fits introduced over the years.

Figure 3 shows that there are differences between T_2 values of normal and diseased tissues. Although T_2 values are more accurate than those of T_1 because more points are used for their calculation, there are no significant differences between the T_2 values of e.g. tumors and demyelinating disease or infarction.

This overlapping is due to variations within the same lesion related to vascularity, necrosis, and cell behavior. Similar lesions may have more than a single exponential relaxation rate, e.g. brain tumors and MS plaques. This is not unexpected, considering the heterogeneous nature of tumors. Furthermore, matrix size and slice thickness, i.e. partial volume effects, are limiting factors in relaxation time measurements in vivo because of the many different biological structures within one volume element. Standard deviation in fitting, artifacts, and

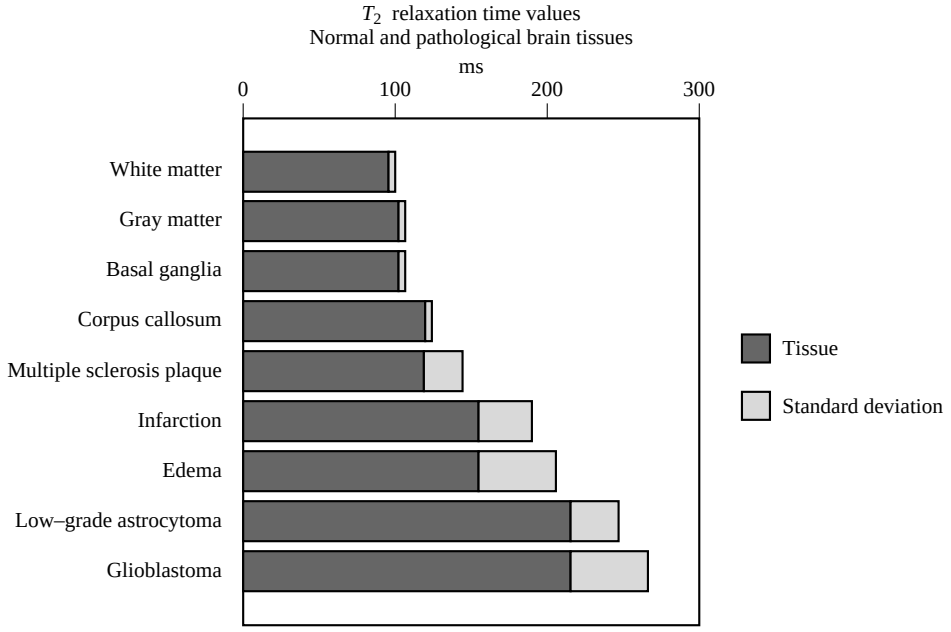

Figure 3 T_2 values of different normal and pathological brain structures. (Reproduced by permission from Rinck et al.[4])

variations in the selection of volume elements by the operator are all possible sources of error. System changes over time add to the uncertainty. Therefore, the follow up of treatment based upon relaxation time values is difficult and in most instances dubious (Figure 4).

The availability of databases of in vivo relaxation time measurements is very limited. The largest collection of data was published by Bottomley et al.[12,13] A comparison between in vivo and in vitro relaxation measurements is quite difficult because many T_1 relaxation time values change rapidly after excision. Only brain tissues reveal a relatively stable relaxation behavior after they have been removed from the body.[14] As with T_1, pure T_2 images or techniques such as T_2 profiles through parts of the body do not increase the specificity of clinical diagnoses.

5 FIELD CYCLING RELAXOMETRY

An area of relaxometry which developed specific medical applications in the second half of the 1980s is field cycling relaxometry. This technique requires a special NMR machine, the field cycling relaxometer. With this machine, ex vivo or in vitro measurements of the relaxation behavior of tissue samples or contrast-enhancing compounds can be performed at any field strength.

The advantages of this method are obvious: (a) identical samples can be examined under identical conditions; (b) there is no interference by motion, diffusion, perfusion, flow, imaging artifacts, partial volume effects, or interindividual variations in region-of-interest/volume-of-interest delineation; (c) exact multiple-point fits are possible; (d) the entire field range used for MRI can be covered; and (e) the standard error is less than 3%. Field cycling relaxometry showed that T_1 increases nonuniformly with field, leading to specific fingerprints of T_1 increase for different tissues.

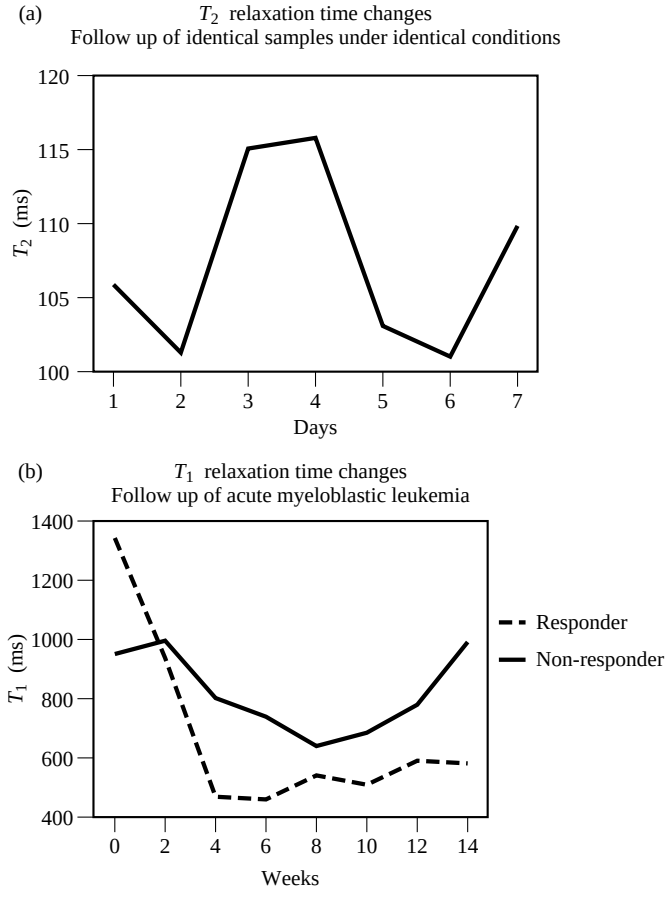

Figure 4 (a) T_2 relaxation time measurements of identical samples under identical measurement conditions which can reveal large standard deviations as shown in this example.[17] (b) Relying on in vivo measurements to evaluate the outcome of treatment is dubious. Only in some instances do massive changes allow a positive assessment (Reproduced by permission from Rinck[17] and Jensen et al.[8])

It also showed that T_1 contrast for brain tissues is best at low/medium field.[7,14] The pivotal benefit of such relaxation time or relaxation rate ($R_1 = 1/T_1$ and $R_2 = 1/T_2$) measurements is to allow the prediction of image contrast and the development of more specific contrast agents.[15,16]

6 CONCLUSIONS

From a physician's point of view, in vivo relaxometry, at its present stage, is suited neither to characterize nor to type or grade diseases in the human body; it is possibly useful in the follow up of therapy, but other methods seem more feasible in clinical surroundings. From a scientist's point of view, relaxometry is a challenging area of research: (a) in vivo, to try monitoring therapy; (b) ex vivo or in vitro, to try to characterize tissues and to understand contrast behavior. The optimum method for the latter is field cycling relaxometry.

7 RELATED ARTICLES

Gadolinium Chelates: Chemistry, Safety, and Behavior; Quantitation in In Vivo MRS; Relaxation Measurements in Imaging Studies; Relaxometry of Tissue.

8 REFERENCES

1. R. Damadian, *Science*, 1971, **171**, 1151.
2. R. Damadian, K. Zaner, D. Hor, and T. Dimaio, *Physiol. Chem. Phys.*, 1973, **5**, 381.
3. J. J. E. In den Kleef and J. J. M. Cuppen, *Magn. Reson. Med.*, 1987, **5**, 513.
4. P. A. Rinck, S. Meindl, H. P. Higer, E. U. Bieler and P. Pfannenstiel, *Radiology*, 1985, **157**, 103.
5. M. Skalej, H. P. Higer, M. Meves, A. Brückner, G. Bielke, S. Meindl, P. Rinck, and P. Pfannenstiel, *Digitale Bilddiagn*, 1985, **5**, 112.
6. A. Alaux and P. A. Rinck, in 'Tissue Characterization in MR Imaging', eds. H. P. Higer and G. Bielke, Springer, Berlin, 1990, p. 165.
7. P. A. Rinck, H. W. Fischer, L. Vander Elst, Y. Van Haverbeke, and R. N. Muller, *Radiology*, 1988, **168**, 843.
8. K. E. Jensen, P. G. Sørensen, C. Thomsen, P. Christoffersen, O. Henriksen, and H. Karle, *Acta Radiol.*, 1990, **31**, 445.
9. P. Boesiger, R. Greiner, R. E. Schoepflin, R. Kann, and U. Kuenzi, *Magn. Reson. Imaging*, 1990, **8**, 491.
10. D. Lacomis, M. Osbakken, and G. Gross, *Magn. Reson. Med.*, 1986, **3**, 194.
11. S. Barbosa, L. D. Blumhardt, N. Roberts, T. Lock, and R. H. T. Edwards, *Magn. Reson. Imaging*, 1994, **12**, 33.
12. P. A. Bottomley, T. H. Foster, R. A. Argersinger, and L. M. Pfeifer, *Med. Phys.*, 1984, **11**, 425.
13. P. A. Bottomley, C. J. Hardy, R. A. Argersinger, and G. Allan-Moore, *Med. Phys.*, 1987, **14**, 1.
14. H. W. Fischer, P. A. Rinck, Y. Van Haverbeke, and R. N. Muller, *Magn. Reson. Med.*, 1990, **16**, 317.
15. R. N. Muller, L. Vander Elst, P. A. Rinck, P. Vallet, F. Maton, H. W. Fischer, A. Roch, and Y. Van Haverbeke, *Invest. Radiol.*, 1988, **23**, S229.
16. P. A. Rinck and R. N. Muller, *Eur. Radiol.*, 1998, in press.
17. P. A. Rinck (ed.), 'Magnetic Resonance in Medicine', 3rd edn., Blackwell Scientific, Oxford, 1993.

Biographical Sketch

Peter A. Rinck. *b* 1953. M.D., 1979, Ph.D., 1980, Free University of Berlin. Resident in radiology, Free University of Berlin, 1979–1981. Introduced to NMR by Paul C. Lauterbur at State University of New York at Stony Brook, 1982/83. Physician-in-charge, NMR Research Group, Deutsche Klinik für Diagnostik, Wiesbaden (Germany) 1983–1984. Resident in Radiology, Wiesbaden General Hospital 1984–85. Senior lecturer, University of Mons (Belgium), Medical Faculty 1986–present. Professor of radiology and magnetic resonance and Head of MR-Center, Medical Section, University of Trondheim (Norway) 1987–1995. Visiting Professor of Radiology, University of Mons, 1995–present. Approx. 100 publications. Research in recent years mainly in basics and applications of MRI contrast agents and appropriate clinical utilization of MRI.

Relaxometry of Tissue

Seymour H. Koenig
Relaxometry, Inc., Mahopac, NY, USA

and

Rodney D. Brown III
Field Cycling Systems, Inc., River Edge, NY, USA

1 INTRODUCTION

1.1 Proton $1/T_1$ and $1/T_2$ Nuclear Magnetic Relaxation Dispersion Profiles of Mobile Water of Tissue

The clinical utility of magnetic resonance imaging (MRI) derives directly from the fact that $1/T_1$ and $1/T_2$ of the protons of (mobile) tissue water vary from one tissue to another.[1] This is true despite the important physiological fact that (with the notable exceptions of brain[2] and adipose tissue[3]) all soft tissues, and blood as well, contain close to 80% water; the remainder is predominantly protein. Gray matter of adult brain has a somewhat greater water content. Furthermore, as indicated by the linewidths and integrated intensities of the proton water signals, most, if not all, tissue water is highly mobile and not highly compartmentalized on an MRI timescale,[4,5] the latter indicated by the observed rate of self-diffusion of tissue water, generally found to be within a factor 2 of that of pure water. This means that, in an image in which relative brightness is derived solely from the intrinsic magnitude of the proton signal, in turn proportional to the mean local *density* of tissue water (the protein proton lines are too broad to contribute to the signal), there will be little contrast between adjacent tissues, and MRI would be of limited clinical utility. Indeed, such a water-density map of the adult head would show gray matter brighter than white (contrary to what is often seen in clinical practice, in which many brain images are heavily T_1-weighted) since the latter has ~10% of its water displaced by lipid-rich myelin, with protons that also have too broad a linewidth to contribute measurably to signal intensity; hence the importance of relaxation rates.

We first examine the phenomenology of water–proton relaxation in tissue and its models (solutions of immobilized protein), concentrating mainly on $1/T_1$ (rather than on $1/T_2$, which is much more difficult to measure) as a function of static magnetic field B_0, for which most data are extant.[6] Such a data set is termed a nuclear magnetic relaxation dispersion (NMRD) profile.[7] The rather remarkable finding is that NMRD profiles of almost all tissues (excluding white matter and fat) have very nearly the same functional form,[6] with a magnitude that varies little with temperature (less rapidly, for example, than does water viscosity). It is this magnitude, which increases with decreasing temperature, that is tissue-dependent but, unfortunately, not tissue-specific, due to the spread and overlap of amplitudes for different types of tissue. A noteworthy fact, only recently realized,[8,9] is that the form of the NMRD profiles of tissue is indistinguishable from that of protein–water systems in which the rotational mobility of the macromolecules is highly restricted. Examples are polymeric protein, including adult sickle deoxyhemoglobin[10] and the fibers of collagen;[11] globular proteins cross-linked either by thermal denaturation[5] or chemical linking;[8,9,12,13] protein restricted by close packing;[14–16] and highly hydrated protein powders.[17] This correlation between the profiles of immobile protein and tissue is intriguing, particularly when it is realized that, to a first approximation, the tissues of concern are indeed mainly protein and water. An immediate inference is that the protein of tissue is itself rotationally immobile (unlike, for example, similar concentrations of hemoglobin in red cells).[10] Accordingly, we speculate (at the end of the paper) how this may relate to both cell function and cell dysfunction since, in the last analysis, it is the molecular basis of relaxation that relates directly to the success of MRI in diagnostic medicine.

The mechanistic relation of the rates of solvent nuclear relaxation to the degree of immobilization of solute protein has only recently been clarified,[8] and a quantitative molecular theory developed.[9] Accordingly, after presenting the phenomenology of NMRD profiles of tissue and its protein models, and the implications of this phenomenology, we summarize the theory, first its qualitative aspects and then its quantitative molecular details. An important finding is that the dominant contributions to $1/T_1$ and $1/T_2$ of protein and tissue (which include the mechanisms that transfer magnetization between the solvent and solute Zeeman reservoirs) involve protein–water interfacial sites that cover but a small fraction of the traditional hydration monolayer,[8,9] a point that was argued for solutions of mobile protein as early as 1969.[7] For these all-important sites (accounting for only $\sim 4 \times 10^{-4}$ of the life history of a water molecular of tissue, and related to multiple hydrogen bonding[8,9]), the interfacial interaction lifetime τ_M is ~1 μs; the remainder of the time water molecules are essentially as free and mobile as in pure water. For immobile protein, this relatively long τ_M becomes the correlation time for the relaxation processes that dominate all water relaxation in tissue. In addition, the relaxation mechanisms for the protein protons become characteristic of the solid state. This, together with these special interfacial sites, is the basis for the NMRD profiles of tissue and immobile protein. In addition, it is at these few sites that, to first order, *all* proton relaxation in tissue, water and protein, occurs.[9]

1.2 Relaxometry and Relaxometers

The fact that tissue water is essentially liquid means that motional narrowing mechanisms determine $1/T_1$ and $1/T_2$ of tissue water.[18,19] It follows that relaxation rates depend on the applied field B_0 for nuclear Larmor frequencies $\geqslant 1/2\pi\tau_M$ which, for tissue and its model systems, means $\geqslant 0.1$ MHz. A concomitant is that $1/T_1$ and $1/T_2$ should become equal (except in certain unusual cases) at lower values of B_0. At typical imaging fields, which are higher ($\geqslant 20$ MHz proton Larmor frequency, or $\geqslant 0.5$ T), both $1/T_1$ and $1/T_2$ have decreased substantially, with $1/T_1$ having the greater field dependence. Typically, $1/T_2 \approx 10/T_1$ for tissue water protons over much of the imaging range. Measurement of the dependence of relaxation rates on B_0 is one aspect of a broad research field (named 'Relaxometry' about a decade ago; by SHK) which also includes augmentation and application of theory and development of

instrumentation. In order to gain insight into mechanisms, relaxation rates must be measured over a wide range of B_0 that includes the major dispersive regimes of the NMRD profiles and, preferably, the temperature dependence of the profile itself. For the present purposes, this means measurements to fields as low as 0.01 MHz and as high into the imaging range as possible (the latter data are also useful for predicting MRI intensities, often convenient in their own right), and from 5 to 35 °C.

Measurements of NMRD profiles require specialized instrumentation not available commercially. Ours, called a 'field cycling[20] relaxometer' (FCR), has been refined and optimized for measurements of $1/T_1$ of both protons and deuterons of 'liquid' samples. (As a result, for example, contributions from broad solid state lines are not seen, nor can the fast component of biexponential decays readily be studied. Designs for solid state applications exist;[21] the major trade-off is a much increased power requirement.) In the present applications, only mobile water contributes to the signal, typically ~90 M protons, quite unlike the mM protein–proton concentrations common in high-resolution NMR. Nonetheless, by the nature of field cycling, signal sensitivity varies as B_0^2, and special procedures are needed to obtain good data at low fields. In addition, because the field must be switched, the signal is incoherent and signal averaging is not readily done; rather, adequate signal amplitude at lower fields is obtained by initially polarizing the proton spins in a high field (50 MHz presently), then switching the field rapidly [(at a rate of ~1 MHz (ms^{-1})] to the value at which $1/T_1$ data are desired. Then the magnetization is allowed to decay toward its equilibrium value for a 'measure time,' and the resonant field is switched to 7.5 MHz in the present system, where a 90 °–180 °-echo sequence is used to measure the remaining magnetization. This cycling sequence is repeated for a number of measurement times within the interval $1.5T_1$, and several times at $7T_1$, to obtain the equilibrium magnetization at the measure field. These raw data are then fit to a single exponential to obtain $1/T_1$. For measurements of $1/T_1$ at fields above 25 MHz (greater than one-half the polarizing field), the increase in magnetization from zero polarization is monitored. In either case, the resonant frequency remains fixed, so that measurements at any field require but one radiofrequency (rf); no retuning is necessary over the entire range of B_0, and the system can be readily automated. With appropriate rf coils, $1/T_1$ of protons can be measured within ±1% for sample volumes between 20 and 600 μL. To measure deuteron profiles, the resonant *field* is increased to produce a deuteron resonance at 7.5 MHz (~48 MHz for protons), and the rf pulse lengths adjusted appropriately.

Clones of our FCR, with improved circuitry based on the early ideas of Redfield et al.[20] and highly automated, both for data collection and analysis,[22] have been installed in a small number of university laboratories in the US and Europe. However, the present article, essentially a monograph, is based on data taken by us in association with many visiting collaborators.

2 PROTON $1/T_1$ NMRD PROFILES OF TISSUE AND MODEL SYSTEMS

2.1 Tissue

Figure 1 shows profiles of three tissues from an adult male (accident victim):[6] skeletal muscle, spleen, and lung. Data for a resected astrocytoma (a common, highly variable, often aggressive brain tumor) are also shown. For a given normal adult tissue, there is little variation of $1/T_1$ profiles among individuals, whereas, for different tissues, the range of relaxation rates at a given B_0 is about a factor of 3 between the lowest magnitude profiles (gray matter) and the highest (liver and muscle). In contrast to normal tissue, astrocytomas have a comparably large range of $1/T_1$ for *fixed* protein content, and a comparably large (and uncorrelated) range of protein content as well.[23] How, and to what extent, this variability relates to neoplastic (cancerous) transformation of the native tissue that produces the astrocytoma is an open question at this writing.

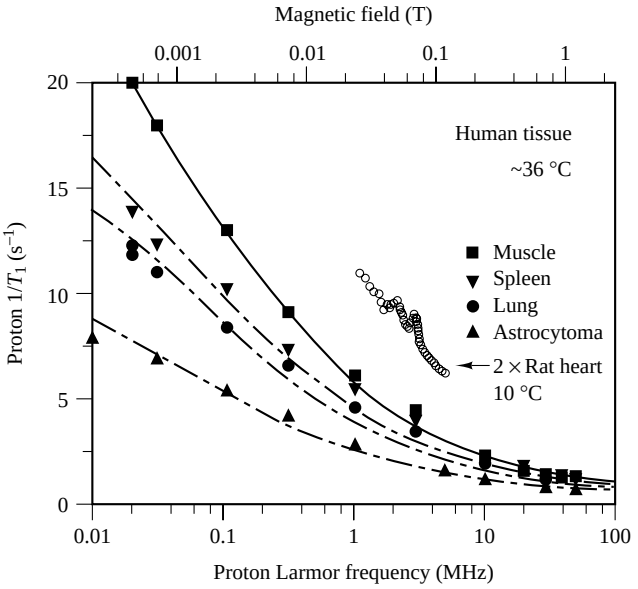

Figure 1 Proton $1/T_1$ NMRD profiles[6] of three normal human tissues, skeletal muscle (■), spleen (▼), and lung (●), and that of an astrocytoma (brain tumor, ▲), all near 36 °C. Also shown are expanded data, in the 1–4 MHz range, for rat heart (○), at 10 °C, the latter to illustrate spectral structure generally found in profiles of tissue (see text). The solid curve through the human muscle data is a smooth curve generated to match these data.[22] The broken curves derive from the solid curve by scaling it vertically by a constant factor (with a small correction for the water background), indicating that all the profiles have the same functional form

Figure 1 also includes a limited portion[24] of the profile of rat heart (which is mostly muscle), on an expanded vertical scale, to illustrate peaks in $1/T_1$ that are seen in the 2–4 MHz region in most tissues, and are always present in immobilized protein model systems, but never in mobile systems. Taking sufficient data to characterize these peaks is very time-consuming so that there are few published studies of these spectral features.[12,13,24–26]

The solid line, Figure 1, derives from a least-squares comparison of the muscle data with a nonintegral inverse power of B_0, often a good representation of tissue-like NMRD profiles.[22] The broken curves all derive from the solid curve by scaling it down by a different constant factor (first subtracting and then adding back the small water background rate of 0.3 s^{-1}). These impressive fits, to four tissues of widely different type and function, demonstrate the similarity of the NMRD profiles of

most tissues. This means that, at a given temperature, a single number characterizes the relative relaxation rates of any two given tissues, for all B_0. A further implication is that tissue-specific details of either morphology or anatomical structure do not enter into the gross aspects of the NMRD profiles, perhaps not surprisingly since it has been previously noted that, on an MRI timescale, tissue water molecules diffuse sufficiently far so as to sample both the intra- and intercellular tissue environments; their protons thus report a grand average of the relaxation mechanisms present throughout the tissue.

It may well be that the structure and magnitude of the peaks is more tissue-dependent than the form of the underlying monotonic behavior of the typical tissue profile; this remains to be determined. At present, it is known that the origin of these peaks relates to the amino (NH) groups of the protein as sources and sinks of magnetization. The ^{14}N nuclei, with S = 1, differ in energy because of the interaction of their electric quadrupole moments with local electric field gradients, giving two excited levels about 2.2 and 2.8 MHz (proton Larmor frequency) above their ground states. There is rapid transfer of magnetic energy between these ^{14}N nuclei (which also have a small magnetic moment) and their NH protons (which are very close) when the proton Zeeman splitting matches possible transitions among the quadrupolar levels. These protons then become sinks for proton magnetization that diffuses by. Although the theory is difficult to quantify (since insufficient data exist regarding the ^{14}N relaxation parameters), the existence of such peaks in the $1/T_1$ profiles of mobile water indicates that there is extensive coupling of the water Zeeman reservoir with NH groups throughout the protein molecules. In support of the foregoing ideas, these peaks are replaced by the deuteron quadrupole splitting when the protein amino groups are deuterated.[13]

Figure 2 shows $1/T_1$ NMRD profiles of human gray and white matter from adult and neonatal brains.[2,27] Here one sees a specific contribution from myelin, the water–cytoplasm–phospholipid 'jelly-roll' which surrounds the neuronal axons of adult, but not neonatal, white matter. This phospholipid is ~50% cholesterol. Again, the three broken curves have the same functional form, that of the curves in Figure 1. The relative magnitudes of the adult and neonatal gray matter can be accounted for by the known differences in water content.[2] The contribution of myelin (the difference between the white and gray matter profiles) has been ascribed to water molecules that hydrogen bond to the cholesterol molecules,[27] imbedded in myelin, at their hydrophilic hydroxyls; these cover much of the myelin surface. This binding, with residence times $\tau_M \sim 10^{-10}$ s, allows the protons of the bonded water molecules to interact with cholesterol protons in the lipid bilayer, itself rigidified by the cholesterol, thereby producing conditions not dissimilar to those of immobilized protein. Two major differences from protein–water interfaces are the much shorter value of τ_M for myelin lipid and its much larger density of surface sites for hydrogen bonding.

Adult white matter is one of the very few tissues for which the $1/T_1$ NMRD profile cannot be fit by the standard 'immobile' form. [Interestingly, adipose tissue (fat) has an NMRD profile very similar to the myelin contribution in adult white matter, Figure 2, but with a threefold greater magnitude.[3,4,6]] That this profile includes a specific myelin contribution has also been argued from the temperature dependence of this profile, which is anomalous.[2] In myelinated white matter, the water in direct interaction with cholesterol is ~15% of the total water and it must mix with the majority axonal water within a relaxation time to communicate its relaxation rate, which reflects the state of the myelin lipid, to the signal. This requires diffusive permeation by water of many layers of lipid and one might indeed think that the mixing rate would be too slow for the foregoing mechanism to account for the white–gray difference in adult matter, Figure 2. In fact, in humans, the mixing rate is adequately rapid at physiological temperature, but not at 5 °C; the putative myelin contribution, Figure 2, has been shown to disappear progressively as the temperature is lowered.[2] No such temperature anomaly is seen in the profiles of neonatal (unmyelinated) white matter.

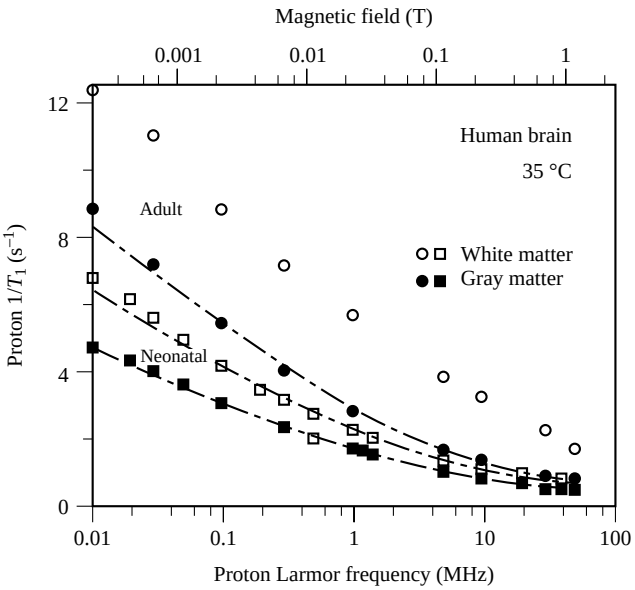

Figure 2 Proton $1/T_1$ profiles of four samples of human brain,[2] adult white (○) and gray (●) matter, and neonatal white (□) and gray (■) matter, at 35 °C. The broken curves are scaled from the solid curve, Figure 1. The difference between these lower three profiles has been attributed to differences in water content.[2] The difference in functional form of adult white and gray matter has been attributed to cholesterol, a component of myelin lipid.[2,27] Neonatal white matter is unmyelinated

Myelin is a complex lipid, containing phospholipids (such as sphingomyelin and galactocerebroside) with OH groups to which myelin water can hydrogen bond. Certainly, the $1/T_1$ component of white matter attributable to myelin is associated to a large degree with the presence of cholesterol which, as noted, rigidifies the lipid structure. This not only augments the contribution of hydrogen bonding to relaxation at cholesterol sites, but can also enhance the role these other lipids may play. Little, if any, of this has been sorted out at present, something that will have to be addressed if applications of quantitative MRI are to be made, for example, to the many diseases associated with breakdown of myelin (including multiple sclerosis).

2.2 Irreversible Immobilization of Albumins

The upper profiles of Figure 3(a) are the $1/T_1$ NMRD profiles of two *irreversible* albumin models for tissue: egg-white

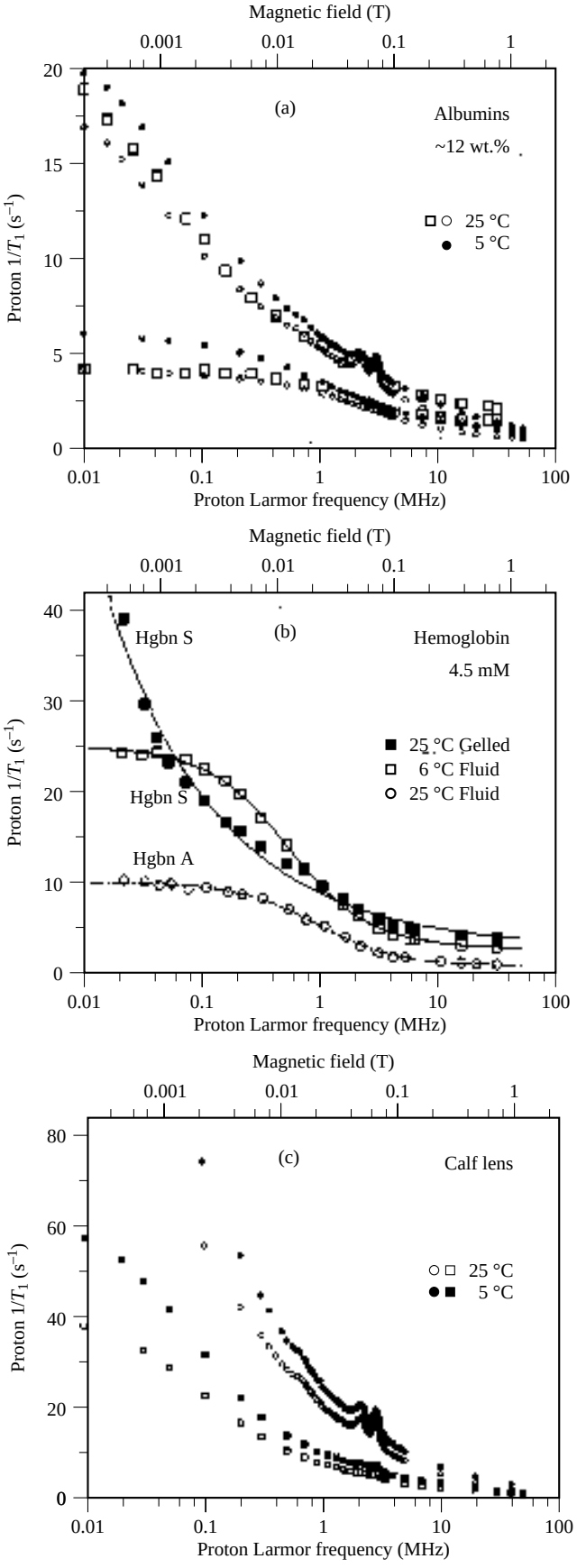

immobilized by thermal denaturation,[14] at 5 and 25 °C, and serum albumin immobilized by chemical[12] cross-linking. The lower profiles are those of the native albumins, before immobilization. The inflection frequencies of the latter, in the 1–2 MHz range, are known to relate to the rate of protein rotational Brownian motion.[28] This relationship has been apparent for almost 25 years,[7] and has since been confirmed for globular proteins over a 1000-fold range of molecular weight.[6] The upper three profiles show the changes brought on by immobilization, which alters the profiles in three major ways visible in Figure 3(a): the functional form changes; the dependence on temperature decreases; and structure appears in the 2–3 MHz range, as also seen in Figure 1 for heart muscle. Another change, not shown, is that the high-field $1/T_2$ increases dramatically. For mobile protein, the high-field value approaches 0.3 of the low-field value (consistent with the predictions of motional narrowing theory[19]) whereas, after cross-linking, the high-field $1/T_2$ becomes about equal to the 0.01 MHz value of $1/T_1$. This is also the case for tissue. And finally, a point that will be returned to, the rate of interchange of Zeeman energy between protein and water protons is enhanced at least 20-fold.[29,30]

2.3 The Reversible First-Order Transition of Sickle Hemoglobin

Figure 3(b) shows a sharp but *reversible* change in form of the NMRD profile from mobile to immobile,[10] here due to the entropy-driven first-order phase transition of sickle deoxyhemoglobin from monomeric (or slightly oligomeric) protein at 6 °C to a polymeric gel at 25 °C. (The hemoglobin concentration was chosen to bring the transition temperature into a convenient range.) The profiles of sickle hemoglobin (□) and adult normal hemoglobin at 6 °C (the latter not shown) are essentially the same. Were the fluid–gel transition not to occur, the near-Lorentzian sickle hemoglobin profile (□) would change form, because of the variation of solvent viscosity, to that of the 25 °C profile of normal hemoglobin (○), shown here as a control. Instead, the form of the profile (■) becomes indistinguishable from that of tissue, Figure 1. Thus, with sickle hemoglobin (because the transition is sharp, reversible,

Figure 3 (a) A comparison of the proton $1/T_1$ NMRD profiles of native (mobile, lower profiles) and irreversibly immobilized albumins (upper profiles), ~12 wt.% protein, at 5 (●) and 25 (□ ○) °C. One sample was bovine serum albumin (□),[12] chemically cross-linked using glutaraldehyde, and the other hen egg-white,[14] native and cross-linked by thermal denaturation (○ ●). It is clear that immobilization alters the functional form of the profiles, reduces their temperature dependence, and introduces structure akin to that shown in Figure 1 for heart muscle. (b) The mobile–immobile distinction, here illustrated for the reversible first-order transition found in sickle hemoglobin[10] (Hgbn S). The profile of sickle hemoglobin at 6 °C (□) is that of mobile protein, as in (a), and is the same as that of normal adult hemoglobin (not shown) at that temperature. Were the reversible polymerization associated with sickle hemoglobin not to occur, its profile would become that of normal adult hemoglobin (Hgbn A, ○) at 25 °C, the change being that of the viscosity of water. Instead, the profile becomes like those of the immobile albumins (a) and tissue, Figure 1. (c) The reversible mobile–immobile transition in a homogenate of calf eye-lens,[14] here brought on by dilution of the homogenate (○ ●) 1:1 with buffer (□ ■). Data[14] are shown for 5 (● ■) and 25 (○ □) °C

and both oxygen and concentration dependent) one can study the mobile–immobile change in profile by a slight alteration of temperature for a wide range of specimen conditions.

2.4 The Continuous Reversible Transition with Concentration of Eye-Lens Protein

Figure 3(c) shows another *reversible* mobile–immobile comparison,[14] here a striking change that varies continuously with protein concentration (i.e., not abruptly with either temperature or concentration as for the first-order transition of sickle hemoglobin.) The initial sample (upper profiles) was from calf eye-lens homogenate at 5 °C (●) and 25 °C (○), which was then diluted 1:1 with buffer to obtain the lower profiles (■ □). The concentration-dependent transition is known to be dominated by the protein α-crystallin,[14] the largest of three classes of crystallins; profiles of the purified protein behave similarly.[15] α-Crystallin is a roughly spherical protein which, for reasons relating to lens transparency, is somewhat akin to a sponge: each molecule contains close to its own volume of water, making it twice the volume of most soluble proteins of comparable protein mass. As a result, and unlike most globular proteins, above ~15% solute by volume, intermolecular protein interactions significantly slow rotational motion. As an aside, similar effects are seen in many crystallins, mammalian and nonmammalian, and relate to the need to reduce the density fluctuations in lens, and thus in refractive index, so as to lower scattering and increase lens transparency. That this packing does enhance protein–protein interactions, important for NMRD profiles, is readily confirmed by the large colloidal osmotic virial coefficients for crystallins.[31,32]

Nitrogen-14 peaks, at 2.2 and 2.8 MHz, are particularly clear in the upper two profiles, as is the small difference peak near 0.6 MHz, which is barely apparent in Figure 3(a). (The apparent greater width of the 0.6 MHz peak is an artifact of the logarithmic horizontal scale.) They are essentially gone at the 50% lower protein concentration, which emphasizes the highly nonlinear behavior of the mobile–immobile transition.

2.5 Summary and Implications of Phenomenology from Proton NMRD Profiles

The data so far demonstrate the universality of the form of the proton $1/T_1$ NMRD profiles found for tissue and systems of immobile protein. It is fair to say that, over four decades of B_0, for a fixed protein content, the profiles are essentially indistinguishable. Indeed, from measurements of any relaxation parameter, $1/T_1$, $1/T_2$, $1/T_{1\rho}$, and cross relaxation, at any temperature and field, whether using a relaxometer or an imager, it is not possible to distinguish tissue from one of its immobile protein model systems. This is remarkable.

We have assumed throughout that water of tissue is highly mobile, and that its bulk properties are little influenced by most macromolecular structures, including membranes, a view supported by a large body of data. The rapid self-diffusion of water in most tissue means that, within a typical relaxation time (~0.1 s), a water molecule diffuses about 35 μm, i.e., about five or more cell radii. That water is not impeded significantly in averaging the intra- and extracellular environments in tissue within a relaxation time means that considering tissue water as free is an excellent starting point for going beyond phenomenology to a molecular theory of relaxation in tissue. To the extent that some tissue-sensitive effects can be observed, which arise from a breakdown of these simplified views, for example at the boundary of two tissues, or that they can be magnified by experimental design, means that NMRD methods can be used to study the impediments to the motion of water that in reality do exist in tissue. This was already discussed here for myelin of white matter.[2] A second example is $1/T_1$ of blood. Here, the intracellular hemoglobin and the extracellular plasma proteins are mobile, and the $1/T_1$ profiles of blood are essentially the sum of these independent contributions, even though about one-third of the water is intracellular at physiological temperature; this confirms the rapid exchange rate of water across the red cell membranes.[33] However, at lower temperatures, particularly with a sufficient concentration of paramagnetic ions added to the plasma, the assumption of rapid averaging by the water molecules of the accessible environments becomes invalid; water exchange rates from cells have been measured by NMRD methods. Calculations for tissues, using these rates, reinforces the validity of assuming the high mobility and extensive diffusive range of water in tissue.

From the foregoing phenomenology, we can speak of tissue and solutions of immobilized protein interchangeably, and consider water in each as highly mobile. It is particularly convenient to do this, since rewarding studies can be carried out either on more dilute macromolecular systems or with partially deuterated solvent, something difficult (but not impossible[12]) to accomplish with tissue.

The arguments that water molecules of tissue diffuse as if in neat water, essentially that there is no long-range structure to tissue water, can be extended to estimate the time for permeation of membranes by water molecules from the 'dissolve-and-diffuse' model.[34] In this view, membranes (typically ~150 Å thick) are regarded as lipid solutions in which water molecules have very low solubilities but maintain their usual high mobility. Those few water molecules that penetrate the lipid diffuse across the membrane in a time determined by the diffusion constant of water in the neat bulk lipid, close to that for self-diffusion of water. The concept is that, except for minor effects of hydrogen bonding, diffusion of water through an array of (mostly) CH_2 moieties cannot be much different, mechanistically, from diffusion through an array of H_2O molecules; it is the low probability of a water molecule being in a hydrophobic lipid environment that dominates permeation. Using measured bulk solubilities of water in lipid accounts for the observed permeabilities quite well, considering the wide range of their values. One can then estimate this permeation time to be ~0.1 μs, sufficiently rapid to support the basic approach used here.

3 PROTON AND DEUTERON NMRD PROFILES IN MODEL SYSTEMS WITH DEUTERATED SOLVENT

3.1 Cross Relaxation, Magnetization Transfer, and Immobilization

In protein solution and in tissue, a given water proton can be relaxed by the proton on the same water molecule (both in

solution and when hydrating protein) and by protein protons. The first contribution is proportional to the probability that its neighbor is a proton; deuteration of solvent reduces this contribution proportionately. Its effect on relaxation rates arises from the influence of binding of water to protein on the overall molecular dynamics of solute waters, and is often called the 'hydrodynamic' contribution. The magnitude of this contribution can, in principle, be obtained by measuring solvent deuteron $1/T_1$ profiles, since intramolecular electric quadrupolar interactions dominate deuteron relaxation in water molecules; magnetic dipolar interactions with either solvent or solute protons are usually negligible. In practice, however, decreased signal intensity and an altered Larmor frequency range (associated with the sixfold lower g value of deuterons) makes measurements of deuteron NMRD profiles less informative. In addition, the ~30% contribution of proton–proton interactions between different water molecules in solution (a contribution that is not known precisely for protons and does not exist for deuterons) reduces the accuracy of the comparison of proton and deuteron results in the presence of protein, and hence the accuracy with which the proton hydrodynamic contribution can be obtained. Nonetheless, such comparisons have been invaluable in clarifying the nature of the proton $1/T_1$ NMRD profiles of immobilized protein.

The second contribution, from protein–water intermolecular proton interactions, is properly called[35] 'cross relaxation'. It is the totality of those interactions that determines the relaxation rates of water protons, which can be attributed to the presence of protons in solute protein (not simply because of the presence of solute). It includes 'magnetization transfer', the exchange of Zeeman energy between solute and solvent reservoirs without alteration of the *total* Zeeman energy; i.e., without exchange of energy with the lattice. This magnetization transfer arises from zero quantum spin flips when water molecules are bound at interfacial sites. It also includes the single and double quantum transitions that cause exchange of Zeeman energy between either (or both) Zeeman reservoir(s) with the thermal energy of the lattice. It is only these dissipative cross-relaxation transitions that determine, ultimately, the rate of interconversion of magnetic and thermal energy in the system. In reality, however, the observed $1/T_1$ is the slower of the biexponenial decay; it *appears* to be influenced by magnetization transfer, as clarified below. Cross-relaxation effects, and their resolution into magnetization transfer and dissipative components, have recently been clarified by measurements of proton profiles in systems with partially deuterated solvent.[9] Deuteration reduces the hydrodynamic contribution for protons, as well as the size of the solvent Zeeman reservoir, hence enhancing the importance of cross relaxation in two ways, as seen below.

3.2 Deuteron NMRD Profiles in Albumin Solutions

Figure 4 is the deuteron analog of Figure 3(a); it shows deuteron $1/T_1$ NMRD profles of native and chemically cross-linked bovine serum albumin (BSA).[8] The near-Lorentzian profile of the native protein is similar in form to the lower proton profile, Figure 3(a) (○), with comparable inflection frequency. Its magnitude is greater because the quadrupolar relaxation mechanism of deuterons leads to relaxation rates that are intrinsically about eightfold greater than analogous rates for protons, as judged from their comparative values of $1/T_1$ in pure water (light and heavy) at 35 °C. What is grossly different is the deuteron profile of the cross-linked protein, here seen to be also near-Lorentzian, rather than tissue-like. Cross-linking has lowered the major inflection, which is now centered near 0.1 MHz. In addition, there is a second, smaller, contribution to $1/T_1$ at higher fields (under the tail of the major dispersion), with an inflection in the 2–4 MHz region. Its presence is emphasized by the expanded profile (●); there is a clear contribution to $1/T_1$ here that cannot be attributed to the tail of a Lorentzian dispersion centered near 0.1 MHz. (The immobile deuteron profile can be fit, within experimental error, by the sum of two Lorentzians,[9] one centered at 0.1 MHz, the other at 4 MHz.) The major question, however, is what motion the 0.1 MHz inflection represents, since cross-linking inhibits protein rotation. The answer, discussed at length earlier,[8,9] is that it is the lifetime of a class of water molecule bound at the protein–water interfaces; these dominate the hydrodynamic contribution to relaxation in immobile protein systems. It corresponds to $\tau_M \approx 1.0\ \mu s$, which becomes the correlation time for the water–protein interaction. [The relation of inflection frequency[6,7] ν to τ_M is $\tau_M \approx 1/(2\pi\sqrt{3}\nu) \approx 1/(11\nu)$.] From the magnitude of the profile, one readily computes the number of these sites, which is ~2 per protein molecule; this is out of about 700 water molecules that occupy the traditional first hydration layer of albumin. Refining things somewhat, one finds that there is a second class of water molecules, with $\tau_M \approx 23$ ns, and a density of ~16 per protein molecule. The greater number of shorter-lived sites is offset by their much shorter τ_M, so that the net contribution to the low-field $1/T_1$ is about 25% of the total.

When the protein is mobile, the correlation time for the longer-lived sites becomes the rotational relaxation time of the protein, ~50 ns; the amplitude of the profile is reduced accordingly and the inflection shifted upward. For the 23 ns sites, their correlation time is shortened somewhat, but is still dominated by the faster exchange rate. The net result is a broadened dispersion, centered near 2 MHz, that is in reality the sum of two Lorentzians and which, in the past, was not appreciated; rather, a single, broader, Cole–Cole expression was used to catalog the data.[5,28]

Historically, the deuteron data, Figure 4, are the more recent, whereas major insights into understanding the mobile–immobile transition in the NMRD profiles of protons came somewhat earlier.[6] However, didactically, the data (Figure 4) present the clearest arguments for the global views being developed here to explain proton $1/T_1$ NMRD profiles of tissue and, by extension, contrast in MRI. So far, four parameters are sufficient to describe the *deuteron* $1/T_1$ NMRD profiles of both mobile and immobile protein systems: the surface densities of two classes of water binding sites (about 2 and 16 for the area of an albumin molecule) and the lifetimes (τ_M values) of water molecules in these sites (1 μs and 23 ns respectively). The mobile–immobile transition of Figure 4, as noted, is then explained by a lengthening of the correlation time for relaxation of a deuteron upon immobilization, mainly at the 1 μs site (for albumin).

3.3 Proton NMRD Profiles in Albumin Solutions

Figure 5 shows proton $1/T_1$ profiles for 9 wt.% cross-linked BSA[9] in undeuterated (▲) and 90% deuterated (▼) solvent, at

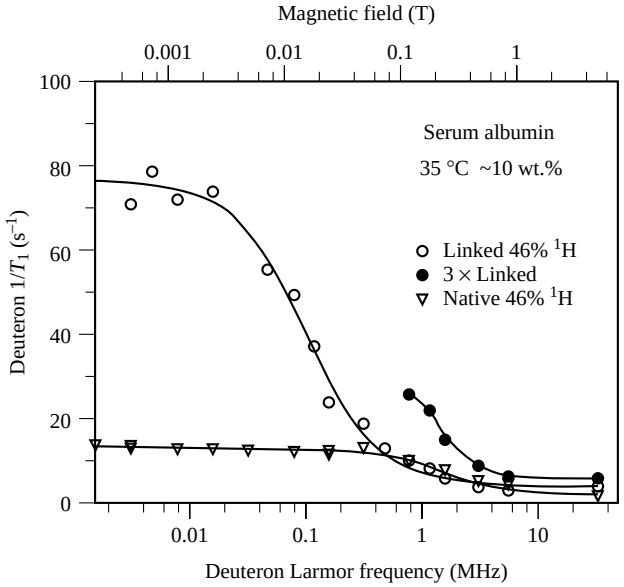

Figure 4 Deuteron $1/T_1$ NMRD profiles for mobile (▽) and glutaraldehyde cross-linked bovine serum albumin[8] (○), ~10 wt.%, at 35 °C. The solvent water is 46% protonated. (Deuteron profiles do not change with solvent isotopic composition.[35]) The solid curves derive from a fit to the Cole–Cole expression. The major dispersion in the profile for the immobile protein is clear; another, smaller, contribution to $1/T_1$, with a dispersion in the 2–4 MHz region is readily seen when the data are expanded vertically threefold (●)

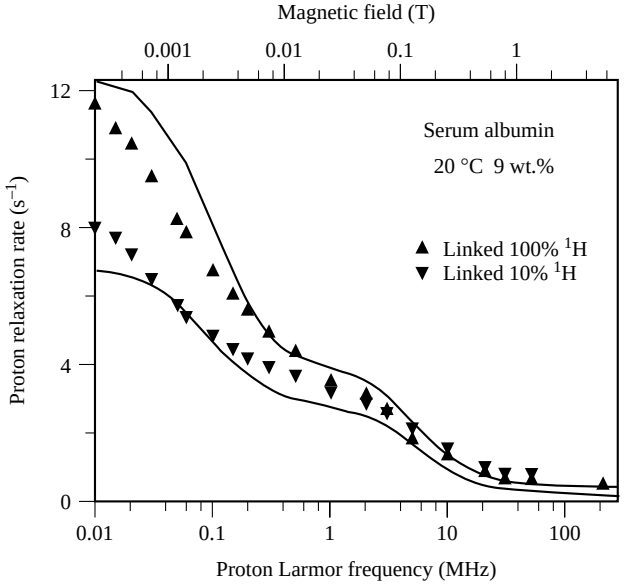

Figure 5 Proton $1/T_1$ profiles of cross-linked bovine serum albumin,[9] 9 wt.%, in 100% (▲) and 10% (▼) protonated water solution, at 20 °C. The two solid curves derive from the theory of two interacting Zeeman reservoirs, as outlined here, with two classes of solute–solvent interfacial water binding sites. One class has two sites per macromolecule with a lifetime τ_M = 1 μs, and a protein proton–water proton interaction equal to the intraproton interaction in water; the second class has 16 water molecules per macromolecule, τ_M = 23 ns, and a solute–solvent intertaction four times greater. The two values of τ_M are associated with the dispersions near 0.1 and 4 MHz. The field dependence of the profiles below ~0.03 MHz is related to a mechanism[36] not considered here at all

20 °C. Despite the monotonic, tissue-like, dispersion of the data for the undeuterated sample (upper curve), it is clear from the profile for the sample with deuterated solvent (in which the role of cross relaxation is enhanced) that the situation is more complex: two distinct dispersive regions are clearly seen. This, and the fact that the amplitude of the profile for the sample with deuterated solvent is not 10% of that of the upper profile (as it would be if hydrodynamic interactions dominated relaxation), can only be explained in terms of cross relaxation. Moreover, if a global view of relaxation in these systems is to be had, it can involve no more than two additional parameters to explain the proton data in terms of the deuteron results (Figure 4): the cross relaxation rates at each of the two classes of sites. The two solid curves derive from a recent theory that does just this.

4 THEORY

4.1 A Qualitative Picture

The following is a sketch of a theory of interfacial relaxation that readily accounts for, *quantitatively*, all the data in the Figures, and more. We assert that the mobile–immobile transition relates to a transition from liquid to solid state relaxation for protein protons.[9] The main criterion for such a transition is that the precession rate of these protons in the local field generated by their neighbors becomes comparable to the rate of Brownian rotation of the protein (sometimes called the Redfield criterion). The division is at a molecular weight of ~50 000 kDa. For slower rotation, protein protons relax as in a solid; to first order, nondissipative spin diffusion is rapid, with jump times (T_2) ~ 13 μs, so that magnetization spreads rapidly and without loss since, again to first order, there are no dissipative (T_1) processes except at specialized sites. The latter include the protons of all the protein NH groups, which cross relax rapidly with ^{14}N nuclei when electric quadrupole splittings match proton Zeeman transitions, and the particular 1 μs interfacial sites being discussed. (The contribution of rotationally mobile protein methyl groups, often discussed for high-resolution NMR at high fields, is minor at the fields considered here.[9])

For albumins (as illustrated here), and for lysozyme,[13] myoglobin (unpublished), carbonic anhydrase,[8] hemoglobin,[10] α-crystallin[15] and, by inference, most of the proteins of tissue, there are sites at the protein–water interface for which the water lifetime τ_M is close to 1 μs. The density of these sites is low, covering $\leqslant$1% of the surface area, corresponding to only 2 (on average) for albumins (64 kDa), and, despite the fluctuations in number that might be expected, the surface density is found to be relatively constant among the proteins measured. (For cross-linked lysozyme, the profile is that of tissue, with a magnitude in keeping with that of other proteins. However, for crystalline lysozyme,[37] with water content comparable to that of cross-linked material, the profiles are quite different; a satisfactory explanation is that the ostensible, single, 1 μs site of lysozyme is at the point of intermolecular contact in the crystallin form studied. However, for the still smaller trypsin inhibitor studied by multidimensional NMR at 600 MHz,[38] and for which the correlation time for coupling of protein and water protons is not longer than ~100 ps, it would appear that there are no long-lived interfacial sites of the sort important in larger

proteins and in tissue.) Fluctuations in the average number density of these sites, however, could be large enough to account for the range of relaxation among different tissues, a point not yet established.

It was conjectured,[9,29] and argued from water molecules found in neutron scattering studies of myoglobin crystals,[39] that such long-lived water molecules are each bound by four hydrogen bonds. The view was that each proton of a bound water molecule is held symmetrically between two hydrogen acceptors as, for example, the two oxygen atoms of a surface carboxylate, both deprotoned at physiological pH values. For myoglobin, one long-lived water proton was found shared between the nitrogen atoms of two surface histidines (B. P. Schoenborn, personal communication), in accord with the conjecture. For immobilized protein, τ_M becomes the correlation time for interfacial proton–proton interactions. For mobile proteins, this time is sufficiently long for the bound waters to sense the Brownian rotation of proteins lighter than ~3000 kDa.

For the 23 ns sites, corresponding to the higher field dispersion centered near 4 MHz, Figure 4, it was suggested that the waters are held by three hydrogen bonds.[9] Their surface density, about 10 times that of the 1 μs sites, as already noted, is not enough to make up for the shorter lifetime, so that their contribution to the NMRD profiles of immobile samples is relatively small.

It is implicit in the foregoing that the NMRD profiles derive from exchange of interfacial water molecules and not individual protons. This point was addressed very early on;[7] the major qualitative arguments against proton exchange being important in the systems considered here are the insensitivity of NMRD profiles (a) to pH over the range 4–8 and (b) to buffer concentration.[9] Quantitative arguments[7] show that τ_M values for proton exchange near neutral pH, in unbuffered solutions, are longer than ~100 μs, too long to be important here. The quantitative theory, based on water exchange, follows.

4.2 A Quantitative Molecular Formulation

Here we present an outline of the interaction of two Zeeman reservoirs in contact at a common interface, in terms of specific sites for their interaction.[9] It is assumed that each reservoir can be characterized by a spatially uniform, time-dependent magnetization. Solvent uniformity is established rapidly by chemical self-diffusion, whereas solute uniformity depends on 'spin-diffusion' which, when effective (as it is in immobile protein), is not a true diffusion but a lossless quantum mechanical spreading of a wave packet of magnetization. For mobile protein, in which spin diffusion is of limited range (~5 Å), the net effect is to reduce the apparent size of the protein Zeeman reservoir as seen by solvent protons; the theory is then applicable to both mobile and immobile systems. We consider only longitudinal relaxation; the analogous theory for transverse relaxation has been given.[9]

Let δS and δP be the fractional deviations from thermal equilibrium of the magnetizations (or total magnetic moments) of the solvent and solute Zeeman reservoirs respectively, and let m (generally >1) be the ratio of solvent to solute total equilibrium Zeeman energy. (m is *not* the ratio of two magnetizations, each of which is a volume density of magnetic moment and similar for solvent and solute protons.) As an aside, if the Zeeman reservoirs are both of the same spin species, such as protons, then m is the ratio of the total number of protons in each. On the other hand, if the two reservoirs are of different species, e.g., electrons and protons, then m is the ratio of total number multiplied by the ratio of g values, including sign. This has implications for magnetization transfer by the Overhauser effect,[40] not considered here, except to note that the difference in sign of the electron and proton g values makes m negative and can make the signal *larger* when the 'protein reservoir', now the electron system, is saturated.

δS and δP span the range ±1, with -1 corresponding to infinite temperature, i.e., saturation. The solvent NMR signal is relatively narrow (typical of a liquid) whereas that of the macromolecular solute (whether mobile or immobile) is broad; thus the signals in NMRD and MRI of tissue and model systems can be taken to be those of solvent. Conveniently, the width of the solute levels allows one to manipulate the magnetization of the solute spins, independently of solvent, by rf irradiation off-resonance from the solvent line but within the solute proton linewidth.

The most general description of the time dependences of δS and δP is given by two linear, coupled, differential equations,

$$\begin{aligned} \mathrm{d}(\delta S)/\mathrm{d}t &= -\lambda_S(\delta S) - \sigma_S(\delta P) \\ \mathrm{d}(\delta P)/\mathrm{d}t &= -m\sigma_S(\delta S) - \lambda_P(\delta P) \end{aligned} \tag{1}$$

where the major assumption is that the influence of one reservoir on the other is linearly proportional to the difference in their spin temperatures. (The factor m in the second equation is dictated by the principle of detailed balance.) As a result of linearity, the effect can be expressed, as in equation (1), in terms of the individual deviations of each reservoir from its own equilibrium magnetization. We note, even before defining the coefficients λ_S, σ_S, and λ_P in equation (1), that a consequence is to introduce the interactions that couple protein and solvent into both the diagonal and off-diagonal coefficients, equation (1) (see below).

The most general solution of the two equations is that both δS and δP vary in time as the sums of (the same) two exponential decays of the form $\exp(-\lambda t)$, with the two eigenvalues for λ satisfying the quadratic equation

$$\lambda_\pm = ((\lambda_P + \lambda_S) \pm \{[(\lambda_P - \lambda_S)^2 + 4m\sigma_S^2]^{1/2}\})/2 \tag{2}$$

It is readily shown that both roots are positive, so that magnetization always approaches an equilibrium or steady state limit; it may decay or grow in time, but it never diverges exponentially. In most experiments, it is λ_-, the slower rate, that is actually measured and reported as $1/T_1$ (by us and others, in relaxometry and MRI).

Before relating the coefficients in the differential equations to molecular mechanisms (which is the major problem to solve, and which has only recently been accomplished[9]), we consider cross relaxation and magnetization transfer. From the first expression of equation (1), if δP can be maintained constant in time, by whatever means, then the time course of δS becomes a single exponential with rate constant λ_S. This is the situation in the many current reports of MRI-related experiments, loosely referred to as 'magnetization-transfer contrast' (MTC).[41–43] Off-resonance irradiation is used to saturate the

solute magnetization, i.e., force $\delta P = -1$. (This is not as straightforward as it may seem, since the solvent line, though narrow, is near-Lorentzian, and thus has long tails, whereas the solute line is Gaussian; it can be difficult to achieve $\delta P = -1$ by off-resonance irradiation without putting unwanted energy into the solvent line.[44])

In a typical MRI–MTC experiment, in which only the signal intensity due to δS is measured, its magnitude is unity without irradiation (since $\delta S \rightarrow 0$ at long times), whereas it approaches σ_S/λ_S for saturating irradiation [from the first of equation (1), provided that m is positive], thus reducing the range of signal swing when σ_S is negative, as it is at imaging fields [as seen in equation (3) below]. Since the time constant at saturation gives λ_S, one can obtain the off-diagonal 'transfer' term from the change in signal amplitude when the off-resonance rf field is applied.

As already noted, for a proton of a water molecule bound to protein, its magnetic dipolar interaction with a neighboring proton, either on the same water molecule or within the protein, can be described completely in terms of three transition probabilities, w_0, w_1, and w_2, respectively the zero, single, and double quantum transition rates. The first is a mutual spin flip, with both spins always aligned antiparallel, and involving no energy exchange with the lattice; the second is a single flip with Zeeman–lattice exchange; and the third a double flip of parallel spins, again with energy exchange with the lattice. In terms of microscopic interactions, we can define

$$\begin{aligned} \rho_S &= f_S(w_0 + 2w_1 + w_2) \\ \sigma_S &= f_S(w_2 - w_0) \end{aligned} \tag{3}$$

where

$$\begin{aligned} w_0 &= 0.1R_{\mathrm{T}}\tau_{\mathrm{c}} \\ w_1 &= 0.15R_{\mathrm{T}}\tau_{\mathrm{c}}/[1 + (\omega\tau_{\mathrm{c}})^2] \\ w_2 &= 0.6R_{\mathrm{T}}\tau_{\mathrm{c}}/[1 + (2\omega\tau_{\mathrm{c}})^2] \end{aligned} \tag{4}$$

Here ω is the proton angular Larmor frequency and R_{T} is a constant that characterizes the magnitude of the proton–proton magnetic dipolar interaction; for protons of water, $R_{\mathrm{T}} \approx 7 \times 10^{10}$ s^{-2}. f_S (<<1) is the fraction of the solvent molecules bound at a particular class of site. Then, as we have shown,[9]

$$\lambda_S = R_S + \rho_S, \qquad \lambda_P = R_P + m\rho_S \tag{5}$$

R_S includes the background rate of buffer (which may contain paramagnetic contrast-enhancing agents). R_P is $1/T_1$ of the protein protons in the absence of interactions with solvent. R_{SH}, the hydrodynamic contribution from interfacial interactions, is given by

$$R_{SH} = 2f_S(w_1 + w_2) \tag{6}$$

for undeuterated solvent, with R_{T}, equation (4), that of water. It is implicitly to be understood that there is a different f_S, R_T, and τ_{c} for each class of interfacial site; that the intramolecular transition rates must be reduced appropriately as solvent is deuterated; and that the w_0, w_1, and w_2 values that enter equation (3) are sums over all classes of sites. For immobile systems, τ_{c} is equal to the τ_{M} of any particular site.

The w_0 value, the only transition rate that is not a function of B_0, is the measure of the rate of those mutual spin-flip transitions that transfer magnetization between Zeeman levels without exchange of energy with the lattice. The w_1 transitions catalyze solvent relaxation by inducing exchange of one quantum of Larmor energy between the Zeeman reservoir and lattice, giving cross relaxation but no magnetization transfer. Finally, w_2 causes double spin flips of parallel spins, with a net interchange of two Larmor quanta between Zeeman reservoirs and lattice, again producing cross relaxation with no magnetization transfer. As has been discussed above, for systems of immobilized protein and, by extension, tissue, w_1 and w_2 at the 1 μs sites are the major mechanisms for relaxation of solute and solvent protons at all fields below ~2 T. At particular level-crossing fields, the totality of NH groups gives a $1/T_1$ contribution comparable to these few interfacial sites. At high fields, to ~5 T, relaxation by mobile methyls dominates proton $1/T_1$, for *all* the protons present, until, at higher fields, this too disperses.[9]

For immobile systems, at high fields, defined such that $\omega\tau_{\mathrm{M}} >> 1$, $-\sigma_S = \rho_S = K$ as used in considerations of magnetization transfer contrast. It is interesting to note, from equation (3), that there can be a value of field at which σ_S goes through zero and changes sign. The sign is not important since σ_S enters quadratically in equation (2). However, when $\sigma_S = 0$, δS is uncoupled from δP [equation (1)], magnetization transfer contrast effects vanish, the hydrodynamic and cross-relaxation contributions to $1/T_1$ (at that field) become additive, and both can be obtained by comparing $1/T_1$ for protons and deuterons, or for protons as a function of solvent composition.

5 DATA AND THEORY

5.1 Proton NMRD Profiles of Immobilized Albumin in Deuterated Solvent

The solid curves in Figure 5 depend on six parameters:[9] the surface densities of two classes of long-lived interfacial water binding sites, the respective water lifetimes, and the extent of cross relaxation at each class of site. The first four parameters were derived from, and therefore account for, the two deuteron profiles, (Figure 4). One need only shorten the correlation times for the hydrodynamic interactions, equation (2), to take account of the rotation of the native material, to go from the upper profile to the lower. In addition, by changing the value of R_{T}, equation (4), from that of deuterons to that of protons, still ignoring cross relaxation, one can account for the native proton profiles, Figure 3(a)[9] (since, as already noted, the effective size of the solute Zeeman reservoir is much reduced for mobile protein). Two more parameters, the extent of cross relaxation of protons at each class of site for immobilized protein, give the two solid curves in Figure 5. The appropriate values of m are also required, here computed from the amino acid composition of the protein and the isotopic composition of the solvent. Three major features of the data are immediately accounted for: the dispersions near 0.1 and 4 MHz, and the comparable amplitudes of the two profiles (recall that one should be tenfold greater than the other in the absence of cross relaxation).

We submit that the essential nature of the proton $1/T_1$ NMRD profiles are explained quite well by the foregoing theory, par-

ticularly in view of the following two approximations. First, as B_0 is decreased below 0.03 MHz, the two Zeeman levels of the protein protons, which are quite broad in the solid state (essentially the width found for the excitation of MTC effects in MRI), begin to overlap. The result is a loss of quantization along the field direction in ~13 μs, essentially introducing a very effective T_1 mechanism into the protein where none existed before.[36] In the present work, this effect has not been considered, either for the protein protons or those of the bound waters. Thus, the comparison of data and theory below 0.03 MHz is expected to be poor. Second, all the data (for protons and deuterons in mobile and immobilized systems) are fit with six parameters associated with less than 3% of the traditional hydration layer: two classes of sites, with all the waters within each class taken as identical. These are rather gross simplifications.

5.2 Predictions of Theory

5.2.1 $1/T_{1\rho}$

There are several experimental findings that may not obviously relate to the ideas outlined here, but that are readily explained by the foregoing, and difficult to explain otherwise. One example is $1/T_{1\rho}$, in which $1/T_2$ of tissue (at relatively high values of B_0) is measured as a function of the amplitude of the rf resonance field B_1. A dependence of $1/T_2$ on B_1 (by definition, $1/T_{1\rho}$) is found.[36,45] Traditionally, such a dependence is attributed to the correlation time of fluctuations that induce relaxation. However, the reality is that, at large B_0, when the Zeeman levels in the immobile material are well separated, the levels in the transverse plane, parallel and orthogonal to B_1 in the rotating frame, overlap unless B_1 is sufficiently large to remove this degeneracy. The dependence of $1/T_2$ on B_1 at high B_0, then, should mimic the dependence of $1/T_1$ at low B_0. The prediction has been verified;[36] both dispersions reflect the solid state linewidth of the protein proton Zeeman levels, and not a correlation time.

5.2.2 MTC Experiments in Solutions of Mobile Protein

If there is essentially no propagation of Zeeman energy from a protein–water interface to deep within the protein (essentially, because magnetization relaxes as it diffuses[6]) unless the protein is immobile, the net effect is to make the protein Zeeman reservoir very small from the viewpoint of a solvent proton. The major prediction is that magnetization transfer effects will be small in mobile systems. This has been shown for irreversibly immobilized albumin,[29] for the reversible 'crowding' transition for α-crystallin,[30] and even for whole blood,[43] for which the $1/T_1$ profiles are like those of mobile protein, and unlike those of tissue.

A particularly striking example of the linking of two relatively disparate physical observations is shown in Figure 6. Here, the magnitude of the magnetization transfer coefficient K, the high-field limit of $-\sigma_S$, measured in α-crystallin at 200 MHz in an MRI environment,[30] and the height of the 2.8 MHz peak [Figure 3(c)], obtained using a relaxometer,[15] are plotted against crystallin concentration. The vertical scales were adjusted so that the data overlap, and the solid curve is chosen empirically to emphasize the similarity of the concentration dependences of these two variables. Recall that K is a measure of the rate of (dissipationless) magnetization transfer across the protein–water interface, obtained by driving the protein proton spin temperature to infinity by saturation with off-resonance irradiation. These spins are tightly coupled to the radiation, and their relaxation rate within the protein is irrelevant. On the other hand, the ^{14}N peaks are obtained at low fields, and are a measure of the dissipation of solvent Zeeman energy caused by magnetization transfer across the interface, coupled with spin diffusion to NH moieties deep within the protein. The rather remarkable correlation between the two phenomena, both of which are easily linked only by the theoretical ideas elaborated here, is perhaps the best demonstration of their intrinsic validity.

5.2.3 The Equivalence of MTC and T_2-Weighted Images

Most MRI protocols tend to rely on images constructed in the main from T_2 values of tissue since, as noted earlier, $T_2 \sim 0.1T_1$ in the MRI range, and a clinically useful image can be obtained in a shorter time than one that is T_1-weighted. A second reason is that, as MRI moves to progressively higher fields, the observed $1/T_1$ values tend to disperse toward the water background rate, and distinctions among different tissues tend to disappear, whereas (as already noted) $1/T_2$ at high fields is comparable to $1/T_1$ at ~0.01 MHz. Thus the two types of weighting provide very different image contrast. (It is mainly for brain that T_1-weighting is used, since this shows the gray–white matter distinction far better than does T_2-weighting.[2])

From the arguments that water of tissue is highly mobile, the ideas of motional narrowing apply, and $1/T_1$ and $1/T_2$ become equal in the limit of low B_0, and are nearly so at 0.01 MHz. Since it has now been established that cross relaxation dominates $1/T_1$ at low fields, then it must dominate $1/T_2$ at both low and high fields. The contribution of cross relaxation to $1/T_2$ of tissue has not as yet been demonstrated directly, since MTC protocols are all modifications of pulse sequences for measuring $1/T_1$. Nonetheless, it is the general observation in the MTC–MRI community that MTC images are very much

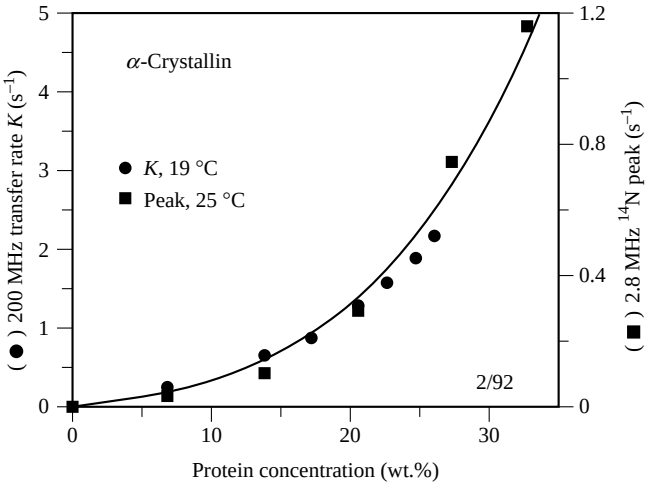

Figure 6 Variation with protein concentration of K[28] at 200 MHz and 19 °C (●) and of the magnitude of the 2.8 MHz peak[15] at 25 °C (■), measured for α-crystallin. The vertical scales have been adjusted so that the data overlap and the smooth, solid curve (linear plus cubic terms) is drawn to indicate the similarity in the dependences of both parameters on protein concentration

like the analogous T_2-weighted ones. From the argument above, following from the validity of motional narrowing, this is expected: $1/T_2$ at high fields is like $1/T_1$ at low fields, as regards cross relaxation. Thus, an MTC image, which by definition is an image of the spatial dependence of cross relaxation (which at high fields is dominated by magnetization transfer), should look like a T_2-weighted image. It only remains to point out why magnetization transfer does not contribute significantly to $1/T_1$ of tissue at imaging fields, which requires a description of the biexponental decay modes of the two Zeeman reservoirs, protein and water, at imaging fields.

The two eigenvalues of equation (2) are associated with two decay modes which, because the transition probabilities w_1 and w_2 are field dependent, change character with field. At imaging fields, $w_0 >> w_1, w_2$, which means that in the regime where cross relaxation is essentially all magnetization transfer, the eigenmodes become particularly simple: one is the very rapid mixing of the two Zeeman reservoirs, with $\lambda_+ = mK$, and the other an overall relaxation of the two coupled systems, at a rate determined by whatever relaxation mechanisms remain nondispersed. In this limit of rapid equilibrium between the two reservoirs, the actual rate of mixing (i.e., K) does not influence the slower $1/T_1$; both reservoirs relax toward ambient temperature together, slowly. However, if off-resonance irradiation is used to bring the protein Zeeman reservoir to infinite spin temperature, then the net relaxation rate is a balance between the rate K at which magnetization crosses the interface and the intrinsic $1/T_1$ in the absence of this irradiation; clearly the resulting $1/T_1$ is a function of K. Interestingly, the range of K among various tissues is about a factor 5, which is greater than the threefold range of $1/T_1$ or $1/T_2$ values, a reason that MTC contrast is, at present, being investigated rather intensively in many quarters. Nonetheless, few clear clinical applications have appeared as yet.

5.2.4 The Other 97% of the Hydration Layer

Extending the idea that one fewer hydrogen bond holding an interfacial water means an approximately 45-fold decrease in τ_M, corresponding to a correlation frequency of ~200 MHz for binding by two bonds, were all the waters this well bound, their $1/T_1$ would be ~350-fold greater because of the density of sites, and (45^2)-fold less because of the shortened τ_M, for a net value of 0.15 of the low-field contribution to $1/T_1$ of the 1 μs sites. For the data of Figure 1, this means high field rates (after solvent correction) threefold greater than observed. This is consistent with conclusions from earlier thinking that, although some dispersion in the 200 MHz region is observed[7] (for mobile protein, for which the same arguments hold at high fields), no more than about one-third of the water molecules could have this two-bond lifetime of $\sim 4 \times 10^{-10}$ s^{-1}, which are those ostensibly associated with polar surface groups.[46] The remainder, the majority, must be even shorter lived.

6 CYTOPLASMIC ORDERING AND CYTOPLASMIC CHAOS

The major question posed by the foregoing is: why is a solution of immobilized protein such a good model for the magnetic relaxation of the water protons of tissue? As already stressed, whether studied by relaxometry or by MRI, a sample of tissue cannot be distinguished by any measurement from a sample of immobile protein, a remarkable fact that indicates that the majority of protein in normal tissue is immobile, i.e., rotationally restricted. This is the more remarkable since there is not nearly sufficient lipid in tissue to form membranes that interact with all tissue protein molecules independently, a point not often realized. Yet there is significant cross relaxation observed only in tissue and immobilized protein, not in mobile protein solutions[29] nor in blood,[43] with its red cells that have no nuclei and little function other than to transport hemoglobin, and in which the hemoglobin is known to be mobile.[10]

We may conjecture that protein in normally functioning cells is organized into separate functional groups; e.g., those enzymes and structural proteins needed for a sequence of successive reactions that relate to a single complex biochemical function (such as electron transport) are held together, in specific relative spatial relationships, by interprotein and lipid–protein interactions that have developed over time in response to evolutionary pressures. These groups of protein may well be pinned to lipid at several points, but the general result, from geometric arguments, must be three-dimensional in its spatial organization, with a net inhibition of rotational mobility such that motion is slower than that of a mobile protein of 50 000 kDa. Another method of organization may involve controlled unfolding of protein, with the backbone threading through a membrane, conceivably more than once. Heat shock proteins and chaperonins may be examples. Whatever the mechanism, from NMRD observations, a majority of the protein of most tissue must be so organized to account for the magnitudes of the many profiles measured.

In addition, to account for recent results on abnormal cells,[23] an argument can be made that, again for reasons of cellular efficiency, the overall organization is such that groups of protein associated with disparate functions might well be arranged to interact minimally with each other so as not to impede their different functionalities.

Two points follow from this picture of functional organization of cytoplasmic protein, both of clinical relevance. The first is a conjecture regarding the effect of neoplastic (cancerous) transformation, in which normal cell functions become progressively more disrupted the more aggressive the tumor-type. One could imagine that, as an initial change, the delicate balance of protein interactions (those that cause proteins related to a particular function to group and those that keep separate groups apart) would be compromised. The net result would be 'cytoplasmic chaos', in which disparate groups of proteins begin to crowd each other with a net *loss* of the rotational mobility that remains. (Recall that, at the concentrations of protein in tissue, rotational mobility is a sensitive function of interprotein interactions.[46]) This disorder, introduced by dysfunction, should increase cross relaxation, relative to some carefully normalized value related to the cell's macromolecular content. However, many changes are occurring in these circumstances so that it is difficult to do this normalization accurately. Nonetheless, recent studies[23] of astrocytomas (brain tumors arising from transformed astrocytes, which can range from relatively benign to very aggressive) indicate that these ideas of cytoplasmic chaos may be realistic: as the tumor cells become more primitive, the cell protein appears more immobile in NMRD profiles.

A second inference from the ideas of cytoplasmic organization and cytoplasmic chaos relates to tissues more complex than those considered here, such as joints. These structures are composites of a range of macromolecules, including collagen-containing cartilage. Here, the integrity of the collagen polymer is essential for normal functioning of joints. There is no question that magnetization transfer in collagen solutions is sensitive to structure, and there is the possibility that preclinical disease, e.g., arthritis, may manifest itself by changes in magnetization transfer arising from subtle alterations in the spatial organization of polymeric proteins in joints and their interaction with other cellular macromolecules, as evidenced in both the monotonic and structured regions of the proton $1/T_1$ NMRD profiles of resected tissue, of model systems, and, ultimately, in MRI.

7 PERSPECTIVES

Much progress has been made in understanding the relaxometry of tissue, motivated by the desire to understand, at the molecular level, the basis of contrast between tissues in MRI. It is fair to remark that the essence of longitudinal and transverse relaxation of water protons in tissue can now be accounted for: it is the protein of tissue, immobilized by interactions and structures yet to be further explored, which gives the NMRD profiles their characteristic form. Magnetization transfer and $1/T_{1\rho}$ are also accounted for. This should not only impact diagnostic clinical imaging, but also be of use in prognosis and monitoring therapy. Much remains to be explored: examples of diamagnetic systems are adipose tissue (important in breast cancer[3,6]) and brain tumors that contain calcified deposits (which behave anomalously in MRI and relaxometry[23]). In addition, there are open problems, not discussed here at all, that involve the natural paramagnetism associated with iron in the body: examples here are the iron storage protein ferritin and the evolving biochemical events following hemorrhage. Finally, there are questions that relate to potential pharmaceuticals which could compete with water at the relatively small total number of water binding sites in the body that make MRI useful in clinical medicine, thereby dramatically altering MRI contrast. Little of this was envisioned 50 years age, at the genesis of NMR in the solid and liquid states.

8 RELATED ARTICLES

Anisotropically Restricted Diffusion in MRI; Heart: Clinical Applications of MRI; Magnetization Transfer and Cross Relaxation in Tissue; Magnetization Transfer between Water and Macromolecules in Proton MRI; Magnetization Transfer Contrast: Clinical Applications.

9 REFERENCES

1. S. H. Koenig and R. D. Brown III, in 'NMR in Physiology and Biomedicine', ed. R. J. Gillies, Academic Press, San Diego, FL, 1994, pp. 57–73.
2. S. S. Kasoff, M. Spiller, M. P. Valsamis, T. A. Lansen, K. R. Duffy, S. H. Koenig, and M. S. Tenner, *Invest. Radiol.*, 1995, **30**, 49.
3. S. H. Koenig and R. D. Brown III, in 'Encyclopedia of Nuclear Magnetic Resonance', eds. D. M. Grant and R. K. Harris, Wiley, Chichester, UK, 1996, pp. 4108–4120.
4. S. H. Koenig, in 'Encyclopedia of Nuclear Magnetic Resonance', eds. D. M. Grant and R. K. Harris, Wiley, Chichester, UK, 1996, pp. 1819–1830.
5. S. H. Koenig, I. I. Rabi, F. Bloch, and E. M. Purcell, in 'Encyclopedia of Nuclear Magnetic Resonance', eds. D. M. Grant and R. K. Harris, Wiley, Chichester, UK, 1996, pp. 437–439.
6. S. H. Koenig, *Biophysic. J.*, 1995, **69**, 593.
7. M. S. Tenner, M. Spiller, S. H. Koenig, M. P. Valsamis, S. Childress, R. D. Brown III, and S. S. Kasoff, *Invest. Radiol.*, 1995, **30**, 345.
8. S. H. Koenig, *Academ. Radiol.*, 1996, **3**, 597.
9. M. Spiller, S. M. Childress, S. H. Koenig, K. R. Dufy, M. P. Valsamis, M. S. Tenner, and S. S. Kasoff, *Invest. Radiol.*, 1997, **32**, 320.
10. T. D. Lindstrom, S. H. Koenig, T. Boussios, and J. M. Bertles, *Biophys. J.*, 1976, **16**, 679.
11. S. Peto, P. Gillis, and V. P. Henri, *Biophys. J.*, 1990, **57**, 71.
12. R. G. Bryant, D. A. Mendelson, and C. C. Lester, *Magn. Reson. Med.*, 1991, **21**, 117.
13. C. C. Lester and R. G. Bryant, *Magn. Reson. Med.*, 1991, **22**, 143.
14. C. F. Beaulieu, R. D. Brown III, J. I. Clark, M. Spiller, and S. H. Koenig, *Magn. Reson. Med.*, 1989, **10**, 362
15. S. H. Koenig, R. D. Brown III, M. Spiller, B. Chakrabarti, and A. Pande, *Biophys. J.*, 1992, **61**, 776.
16. S. H. Koenig, R. D. Brown III, A. K. Kenworthy, A. D. Magid, and R. Ugolini, *Biophys. J.*, 1993, **64**, 1178.
17. G. Schauer, R. Kimmich, and W. Nusser, *Biophys. J.*, 1988, **53**, 397.
18. N. Bloembergen, E. M. Purcell, and R. V. Pound, *Phys. Rev.*, 1948, **73**, 679.
19. I. Solomon, *Phys. Rev.*, 1955, **99**, 559.
20. A. G. Redfield, W. Fite, and H. E. Bleich, *Rev. Sci. Instrum.*, 1968, **39**, 710.
21. F. Noack, *Prog. NMR Spectrosc.*, 1986, **18**, 171.
22. S. H. Koenig and R. D. Brown III, in 'NMR Spectroscopy of Cells and Organisms', ed. R. K. Gupta, CRC Press, Boca Raton, FL, 1987, Vol. 2.
23. M. Spiller, S. S. Kassof, T. A. Lansen, S. Rifkinson-Mann, M. P. Valsamis, S. H. Koenig, and M. S. Tenner, *J. Neuro-Oncol.*, 1994, **21**, 113.
24. S. H. Koenig, *Biophys. J.*, 1990, **53**, 91.
25. F. Winter and R. Kimmich, *Mol. Phys.*, 1982, **45**, 33.
26. F. Winter and R. Kimmich, *Biochim. Biophys. Acta*, 1982, **719**, 292.
27. S. H. Koenig, *Magn. Reson. Med.*, 1991, **20**, 285.
28. K. Hallenga and S. H. Koenig, *Biochemistry*, 1976, **15**, 4255.
29. S. H. Koenig, R. D. Brown III, and R. Ugolini, *Magn. Reson. Med.*, 1993, **29**, 311.
30. S. H. Koenig, R. D. Brown III, A. Pande, and R. Ugolini, *J. Magn. Reson., Ser. B*, 1993, **101**, 172.
31. F. Vérétout and A. Tardieu, *J. Mol. Biol.*, 1989, **205**, 713.
32. A. D. Magid, A. K. Kenworthy, and T. J. McIntosh, *Exp. Eye Res.*, 1992, **55**, 615.
33. S. H. Koenig, M. Spiller, R. D. Brown III, and G. L. Wolf, *Magn. Reson. Med.*, 1986, **3**, 791.
34. A. Finkelstein, 'Water Movement through Lipid Bilayers, Pores, and Plasma Membranes: Theory and Reality', Wiley-Interscience, New York, 1987.
35. S. H. Koenig, R. G. Bryant, K. Hallenga, and G. S. Jacob, *Biochemistry*, 1978, **17**, 4348.

36. R. D. Brown III and S. H. Koenig, *Magn. Reson. Med.*, 1992, **28**, 145.
37. R. G. Bryant, R. D. Brown III, and S. H. Koenig, *Biophys. Chem.*, 1982, **16**, 133.
38. G. Otting, E. Liepinsh, and K. Wüthrich, *Science*, 1991, **254**, 974.
39. X. Cheng and B. P. Schoenborn, *Acta Crystallogr., Sect. B*, 1990, **46**, 195.
40. D. J. Lurie, D. M. Bussell, L. H. Bell, and J. R. Mallard, *J. Magn. Reson.*, 1988, **76**, 366.
41. S. D. Wolff and R. S. Balaban, *Magn. Reson. Med.*, 1989, **10**, 135.
42. J. V. Hajnal, C. J. Baudouin, A. Oatridge, I. R. Young, and G. M. Bydder, *J. Comput. Assist. Tomogr.*, 1992, **16**, 7.
43. J. I. Tanttu, R. E. Sepponen, M. J. Lipton, and T. Kuusela, *J. Comput. Assist. Tomogr.*, 1992, **16**, 19.
44. R. M. Henkelman, X. Huang, Q.-S. Xiang, G. J. Stanisz, S. D. Swanson, and M. J. Bronskill, *Magn. Reson. Med.*, 1993, **29**, 759.
45. J. I. Tanttu, R. E. Sepponen, J. T. Sipponen, and J. Heiskanen, *Proc. Vth Ann Mtg. Soc. Magn. Reson. Med.*, Montreal, 1986, p. 1137.
46. S. H. Koenig, *ACS Symp. Ser.*, 1980, **127**, 23.

Biographical Sketches

Seymour H. Koenig. *b* 1927. B.S., 1949, M.A., 1951, Ph.D., 1952, physics, Columbia University, USA. IBM Research, 1952–1993. Presently, Research Professor, Department of Medical Information Sciences, University of Illinois, Urbana, IL, USA and President, Relaxometry, Inc., Mahopac, NY. Approx. 200 publications. Research specialties: atomic beams, solid state electrical transport, phonon and neutron scattering, laser-light scattering, and relaxometry, including protein structure and function, water–proton relaxation in protein solutions and in tissue, and magnetic contrast-enhancing agents for MRI.

Rodney D. Brown III. *b* 1931. B.S., 1954, University of Scranton; M.A., 1960, Columbia University; Ph.D., 1969, physics, New York University. IBM Research, 1954–1993. Presently, Adjunct Professor of Radiology, New York Medical College, Valhalla, NY, and President, Field Cycling Systems, Inc., River Edge, NJ, USA. Approx. 120 publications. Research specialties: low-temperature solid state physics; applications of relaxometry techniques to the study of the structure and function of diamagnetic and paramagnetic proteins in solution and to the study of relaxation effects in tissues; field cycling instrumentation for relaxometry.

Bioeffects and Safety of Radiofrequency Electromagnetic Fields

Frank G. Shellock

American Health Services Corporation, Newport Beach, CA, USA;
Future Diagnostics, Inc., Los Angeles, CA, USA;
UCLA School of Medicine, Los Angeles, CA, USA

1	Introduction	1
2	Characteristics of rf Radiation-Induced Heating During MR Procedures	2
3	MR Procedures and the Specific Absorption Rate (SAR) of rf Radiation	2
4	Assessment of Thermal and Other Physiological Responses to rf Radiation-Induced Heating During an MR Procedure	2
5	Thermal and Other Physiological Responses to rf Radiation-Induced Heating during an MR Examination	3
6	MR Procedures and Temperature-Sensitive Organs: The Testis and Eye	4
7	MR Procedures and 'Hot Spots'	4
8	Future Studies of rf Radiation-Induced Heating During MRI	5
9	Related Articles	5
10	References	5

1 INTRODUCTION

Radiofrequency (rf) radiation is defined as nonionizing electromagnetic radiation in the frequency range of 0–3000 GHz, as distinguished from the very high photon energies and frequencies associated with ionizing electromagnetic radiation (e.g., γ and X-rays).[1–4]; The rf spectrum includes radar, UHF and VHF television, AM and FM radio, and microwave communication frequencies.

Various research studies conducted over the past 30 years have reported that exposure to rf radiation may produce a variety of physiological effects including alterations in visual, auditory, endocrine, neural, cardiovascular, immune, reproductive, and developmental function.[1–4] These biological changes were generally felt to occur due to rf radiation-induced heating of tissues.[1–10]

Exposure to rf radiation may also cause athermal, field-specific alterations in biological systems that are produced without a significant elevation in temperature.[1,4,5,11] The athermal bioeffects of radiation are somewhat controversial due to assertions concerning the role of electromagnetic fields in causing cancer as well as developmental abnormalities, along with the concomitant ramifications of such effects.[1,4,5,8,11] A report from the United States Environmental Protection Agency indicated that the existing evidence on this issue is sufficient to demonstrate a relationship between chronic exposures to low level, electromagnetic fields and cancer.[8] However, the mechanism(s) responsible for such effects have yet to be defined. Therefore, there is an on-going effort to determine if there is any association between exposure to athermal levels of rf radiation and the abnormalities described above.

To date, no research has been performed to investigate the potential athermal bioeffects of rf radiation associated specifically with MR procedures. Those interested in thorough discussions of this topic are referred to the extensive review articles written by Adey[5] and Beers.[11]

During MR procedures, the majority of the rf power transmitted for imaging or spectroscopy is transformed into heat within the patient's tissue as a result of resistive losses.[12–22] Not surprisingly, the primary bioeffects associated with the rf radiation used for MR procedures are directly related to the thermogenic qualities of this electromagnetic field.[12–22] Therefore, this article will specifically discuss this aspect of rf radiation and its implications for individuals undergoing MR imaging or spectroscopy.

Prior to 1985, there were no published reports concerning the thermal and other physiological responses of human subjects exposed to rf radiation during MR procedures. In fact, there has been a general lack of quantitative data on thermal responses of human subjects exposed to rf radiation from any source. The previous investigations performed on this topic examined therapeutic applications of diathermy or thermal sensations related to exposure to rf radiation.[1,3,4,23,24] These studies typically involved exposures to rf energy that were localized to small regions of the body.

Although there have been many investigations performed using laboratory animals to determine thermoregulatory reactions to tissue heating associated with exposure to rf radiation, these experiments do not directly apply to the conditions that occur during MR procedures for various reasons. For example, the pattern of rf absorption or the coupling of radiation to biological tissues is highly dependent on the organism's size, anatomic factors, the duration of exposure, the sensitivity of the involved tissues, and a myriad of other variables.[1,3,4,17,25] Of further note is that there is no laboratory animal that sufficiently 'mimics' the thermoregulatory responses of a human subject to heating in regards to the activation of heat dissipation mechanisms (i.e., the alterations in regional circulations and sweating that occur in response to a heat load). Therefore, experimental results obtained in laboratory animals cannot be simply 'scaled' or extrapolated to predict thermoregulatory or other physiological changes in human subjects exposed to rf radiation-induced heating during MR procedures.[17,18,25]

Elaborate mathematical models have been devised to predict 'worst-case' scenarios of how human subjects may respond to the rf energy that is absorbed during MR procedures.[26–28] However, a recognized major limitation of mathematical modeling is that it is difficult to account for the numerous critical variables (i.e., circulatory abnormalities, amount of subcutaneous, 'insulative' fat, etc.) that can affect the thermoregulatory responses of human subjects, particularly patients.

Many individuals that are exposed to rf radiation during MR procedures have some health condition or are taking medication that can alter or impair their ability to dissipate a heat load. More importantly, none of the mathematical models developed to predict thermal responses to rf radiation

have been validated. Nevertheless, mathematical models that presume a 'worse case scenario' may approximate a given situation during an MR procedure that may be of some use. More precise characterization of thermal responses to rf radiation-induced heating requires experiments performed in human subjects. Several investigations have been conducted in recent years that have yielded extremely beneficial and important data about the human thermoregulatory system and other physiological reactions to the tissue heating produced by rf radiation during MR procedures.

2 CHARACTERISTICS OF RF RADIATION-INDUCED HEATING DURING MR PROCEDURES

The physical dimensions and configuration of the tissue in relation to the incident wavelength of rf radiation are important factors that determine the relative amount and pattern of energy that is absorbed by the organism.[1–4] If the tissue size is large in relation to the incident wavelength, energy is predominantly absorbed on the surface.[1–4] If it is small relative to the wavelength, there is little absorption of rf power.[1–4]

The most efficient absorption of rf energy occurs when the tissue is approximately 50% the size of the incident wavelength and this frequency of maximum absorption is known as the 'resonant frequency'. Exposure to a resonant frequency of rf power is considered to be the most hazardous because of deep and, often times, uneven absorption patterns.[1–4] In consideration of this, rf radiation is believed to be a unique source of tissue heating due to its ability to penetrate superficial tissues and directly heat internal sites of the body at certain incident wavelengths.[2,3]

Tissue heating that results from the rf radiation used for MR procedures is primarily caused by magnetic induction with a negligible contribution from the electric fields.[12–21] Therefore, ohmic heating of tissue during MR procedures occurs the most at the surface or periphery and is minimal at the center of the body. Predictive calculations and measurements obtained in phantoms and in human subjects exposed to MR imaging support this pattern of temperature distribution.[12–21]

The actual increase in tissue temperature caused by exposure to rf radiation is dependent on a variety of factors associated with the thermoregulatory system of the individual and the surrounding environment.[2,3,15–19] When subjected to a thermal challenge, the human body loses heat by means of convection, conduction, radiation, and evaporation. Each of these mechanisms is responsible to a varying degree for heat dissipation as the body attempts to maintain thermal homeostasis.[2,3] If the thermoregulatory effectors are unable to dissipate the heat load, then storage of heat occurs and there is an increase in local and/or overall tissue temperatures.[2,3]

There are various health conditions that may affect an individual's ability to tolerate a thermal challenge. These conditions include: cardiovascular disease, hypertension, circulatory abnormalities, diabetes, fever, old age, obesity, and others.[29–35] Various types of medications (diuretics, beta blockers, calcium blockers, amphetamines, muscle relaxers, sedatives, vasodilators, vasoconstrictors, inotropes, etc.) can also alter the thermoregulatory responses to a heat load, especially if the medications produce alterations in peripheral circulations. Additionally, certain medications are known to augment the heating that is caused by exposure to rf radiation.[36,37]

The environmental conditions that exist in and around the MR system will also affect the tissue temperature changes of the individual that occur during rf radiation-induced heating. During an MR procedure, the amount of tissue heating that occurs and concomitant exposure to rf radiation that is tolerable are dependent upon environmental factors that include the ambient temperature, relative humidity, and the presence and amount of air flow.

3 MR PROCEDURES AND THE SPECIFIC ABSORPTION RATE (SAR) OF RF RADIATION

The thermoregulatory and other physiological changes that a human subject displays in response to exposure to rf radiation are dependent on the amount of energy that is absorbed. Specific absorption rate or SAR is the term that is used to describe the absorption of rf radiation.[1–4] The SAR is the mass normalized rate at which rf power is coupled to biological tissue and is typically indicated in units of watts per kilogram (W kg^{-1}).[1–4] The relative amount of rf radiation that an individual encounters during an MR procedure is usually characterized for safety reasons with respect to the whole body averaged level and peak SAR levels (i.e., the SAR averaged in 1 g of tissue) of the exposure.

Of note is that measurements or estimates of SAR are not trivial, particularly in human subjects, and there are several methods of determining this parameter for the purpose of dosimetry of rf energy associated with MR imaging or spectroscopy.[12–22] The SAR that is produced during an MR procedure is a complex function of numerous variables including the frequency (which, in turn, is determined by the static magnetic field strength of the MR system), the type of rf pulse used (i.e., 90° or 180°), the repetition time, the pulse width, the type of rf coil used (i.e., transmit/receive body coil or send/receive surface coil), the volume of tissue contained within the coil, the resistivity of the tissue, the shape of the anatomical region exposed, the orientation of the body to the field vectors, as well as other factors.[12–22]

4 ASSESSMENT OF THERMAL AND OTHER PHYSIOLOGICAL RESPONSES TO RF RADIATION-INDUCED HEATING DURING AN MR PROCEDURE

Obtaining thermal and other physiological measurements in human subjects within the harsh electromagnetic environment associated with the MR system is not a simple task. The high-field strength static magnetic field of the MR system can create missiles out of monitors because these devices usually contain ferromagnetic components.[39–42] In addition, the static, gradient, and rf electromagnetic fields may adversely interfere with the proper operation of the monitoring equipment.[39–42] In turn, the monitors themselves may produce subtle or significant imaging artifacts during operation by generating 'rf noise' that can significantly distort the quality of the MR images.[39–42]

In consideration of the above, monitors must be specially modified and then rigorously tested prior to use in the MR environment. Otherwise, the data pertaining to thermal and other physiological responses may be erroneous.

Currently, there are a variety of MR-compatible monitors, as well as other patient support devices that are commercially available.[39–42] Every physiological parameter that may be obtained in the critical care unit or operating room may be recorded during an MR procedure, including heart rate, oxygen saturation, end-tidal carbon dioxide, respiratory rate, blood pressure, cutaneous blood flow and, most importantly, body and skin temperatures.[39–42]

For the assessment of thermal responses during an MR procedure, volunteer subjects or patients have been continuously or semicontinuously monitored throughout the experimental procedures using several different types of devices. Sublingual pocket or tympanic membrane temperature (note that there is a good relationship between temperatures measured in the sublingual pocket or tympanic membrane and esophageal temperatures) are typically obtained immediately before and after MR procedures using sensitive electronic thermometry or infrared devices.[43–53] Skin temperatures may also be measured immediately before and after MR procedures using highly accurate, infrared thermometry or thermographic equipment.[43–53] Body and skin temperatures measured at multiple sites can be recorded before, during, and after MR procedures using a fluoroptic thermometry system that is unperturbed by electromagnetic radiation.[42] Heart rate, oxygen saturation, blood pressure, respiratory rate, and cutaneous blood flow, which are important physiological variables that change in response to a thermal load, are typically monitored before, during, and after MR procedures to assess the reaction of the thermoregulatory system of human subjects exposed to rf radiation-induced heating. All of these parameters are recorded with MR-compatible devices that have been extensively tested and demonstrated to provide sensitive and accurate data.[43–53]

5 THERMAL AND OTHER PHYSIOLOGICAL RESPONSES TO RF RADIATION-INDUCED HEATING DURING AN MR EXAMINATION

As previously mentioned, the increase in tissue temperature caused by exposure to rf energy during an MR procedure depends on multiple physiological, physical, and environmental factors including the status of the patient's thermoregulatory system, underlying health conditions, duration of exposure, the rate at which energy is deposited, the ambient temperature, humidity, and airflow over and around the patient within the MR system. Although the primary cause of tissue heating during MR procedures is attributed solely to rf radiation, it should be noted that various reports have suggested that exposure to static magnetic fields used for MR procedures may also cause temperature changes.[55,56]

The mechanism(s) responsible for such an effect resulting from exposure to the static magnetic field remains unclear, but the results of these studies have warranted investigations in human subjects to determine if there is any contribution of the static magnetic field to the temperature changes that may be observed during an MR procedure. Therefore, studies have been conducted in human subjects exposed to a 1.5 T static magnetic field in order to determine if there was any effect on body and/or skin temperatures.[57,58] The data from these investigations revealed that there were no statistically significant alterations observed in any of the recorded temperature or other physiological parameters.[57,58] Tenforde[59] examined this phenomenon, as well, in laboratory animals exposed to static magnetic fields of as high as 7.55 T and also reported no effect. As far as the potential for production of heat by gradient magnetic fields is concerned, this is not believed to occur as a result of the conventional pulse sequences used for present-day clinical MR procedures.[16]

The first study of human thermal responses to rf radiation-induced heating during an MR procedure was conducted by Schaefer et al.[60] Temperature changes and other physiological alterations were assessed in volunteer subjects exposed to relatively high whole body averaged SARs (i.e., approximately 4.0 W kg^{-1}). The data indicated that there were no excessive temperature elevations or other deleterious physiological consequences related to this exposure to rf radiation.[60]

Several studies were subsequently conducted involving volunteer subjects and patients undergoing clinical MR procedures with the intent of obtaining information that would be applicable to the patient population typically encountered in the MR setting.[43–45,47,50,52,54,60–62] The whole body averaged SARs ranged from approximately 0.05 W kg^{-1} (i.e., for MR procedures involving imaging with a transmit/receive head coil) to 4.0 W kg^{-1} (i.e., for MR procedures involving the imaging of the spine or abdomen with a transmit/receive body coil).[43–52] These studies demonstrated that changes in body temperatures were relatively minor (i.e., less than 0.6 °C). There tended to be statistically significant increases in skin temperatures that were also of no serious physiological consequence. Furthermore, there were no associated deleterious alterations in any of the hemodynamic parameters that were assessed during these investigations (i.e., heart rate, blood pressure, and cutaneous blood flow).

Of further note is that there was a poor correlation between body or skin temperature changes versus whole body averaged SARs during clinical MR imaging. This is not unusual considering all of the variables that may alter thermal responses in a patient population. Therefore, the thermal reactions to a given SAR may be quite variable depending on the individual's own thermoregulatory system and the presence of one or more underlying condition(s) that may alter or impair the ability to dissipate heat.

An extensive thermophysiological investigation using multiple fluoroptic thermometry probes that are unperturbed by electromagnetic fields demonstrated that human subjects with normal thermoregulatory systems exposed to MR imaging at whole body averaged SAR levels up to 4.0 W kg^{-1} had no statistically significant increases in body temperatures, and have statistically significant elevations in skin temperatures that were not excessive.[50] The results of this study indicated that the SAR recommendations issued by some of the regulatory agencies (i.e., United States Food and Drug Administration and United Kingdom's National Radiological Protection Board) for exposure to rf radiation for patients with normal thermoregulatory function may be too conservative.[50]

Research has been performed in volunteers exposed to MR imaging performed at a whole body averaged SAR of 6.0 W kg^{-1} in cool (22 °C) and warm (33 °C) environments in order to characterize thermal and other physiological

responses to this high exposure to rf energy, since some of the newly developed pulse sequences have very high SARs associated with their use.[53] Tympanic membrane temperature, six different skin temperatures, heart rate, blood pressure, oxygen saturation, and skin blood flow were monitored before, during, and after exposure to the rf energy. In the cool environment, there were statistically significant increases in tympanic membrane, abdomen, upper arm, hand, and thigh temperatures as well as heart rate and skin blood flow. In the warm environment, there were statistically significant increases in tympanic membrane, hand, and chest temperatures as well as systolic blood pressure and heart rate. These data indicate that MR imaging performed at 6.0 W kg^{-1} can be physiologically tolerated by individuals with a normal thermoregulatory function.[53]

Of additional note is that the subjective perception of tissue heating was greater when the subjects underwent MR imaging at an SAR of 6.0 W kg^{-1} in the cool environment compared with their experience in the warm environment. This indicates that it would not be useful to precool subjects that will subsequently undergo high SAR procedures in order to help them better tolerate these procedures, as has been suggested by some researchers and manufacturers of MR systems.

6 MR PROCEDURES AND TEMPERATURE-SENSITIVE ORGANS: THE TESTIS AND EYE

Certain human organs that have reduced capabilities for heat dissipation, such as the testis and eye, are particularly sensitive to elevated temperatures. Therefore, these are primary sites of potentially harmful effects if rf radiation exposures during MR procedures are excessive.[12–19,22]

Laboratory investigations have demonstrated detrimental effects on testicular function (i.e., a reduction or cessation of spermatogenesis, impaired sperm motility, degeneration of seminiferous tubules, etc.) caused by rf radiation-induced heating from exposures sufficient enough to raise scrotal and/or testicular tissue temperatures between 38–42 °C.[7] Scrotal skin temperatures (which are an index of intratesticular temperatures because a high correlation has been demonstrated between intratesticular and scrotal skin temperatures)[63] were measured in volunteer subjects undergoing MR imaging at a whole body averaged SAR of 1.1 W kg^{-1}.[48] The largest change in scrotal skin temperature was 2.1 °C and the highest scrotal skin temperature recorded was 34.2 °C.[48] These temperature changes were below the threshold known to impair testicular function.[7,48] However, inordinately heating the scrotum during MR imaging could exacerbate certain pre-existing disorders associated with increased scrotal/testicular temperatures (e.g., acute febrile illnesses, varicocele, etc.) in patients who are already oligospermic, and could lead to temporary or permanent sterility. Therefore, additional studies designed to investigate these issues are needed, particularly if patients are subjected to MR-procedure SARs that are higher than those previously evaluated (which is entirely possible, since there is a trend to use some of the newly developed pulse sequences that have associated high SARs to image the scrotum).

Dissipation of heat from the eye is a slow and inefficient process due to its relative lack of vascularization.[6] Acute near-field exposures of rf radiation to the eyes or heads of laboratory animals have been demonstrated to be cataractogenic as a result of the thermal disruption of ocular tissues if the exposure is of a sufficient intensity and duration.[6] An investigation conducted by Sacks et al.[64] revealed that there were no discernible effects on the eyes of rats produced by MR procedures at exposures that far exceeded typical levels used in the clinical setting. However, as previously indicated, it may not be acceptable to extrapolate these data to human subjects considering the coupling of rf radiation to the anatomy and the tissue volume of laboratory rat eyes compared with those of human subjects.

Corneal temperatures (corneal temperature is a representative site of the average temperature of the human eye)[65] have been measured in patients undergoing MR imaging of the brain using a transmit/receive head coil at peak SARs up to 3.1 W kg^{-1}.[46] The largest corneal temperature change was 1.8 °C and the highest temperature measured was 34.4 °C. A more recent study[49] examined corneal temperatures in patients with suspected ocular pathology who underwent MR imaging using a special eye coil. Again, there were no excessive corneal temperature elevations. Because the temperature threshold for radiation-induced cataractogenesis in animal models has been demonstrated to be between 41–55 °C for acute near-field exposures,[6] it does not appear that clinical MR imaging using a head coil or an eye coil has the potential to cause thermal damage to ocular tissue. The effect of MR procedures performed using higher SARs on ocular tissue remains to be determined.

7 MR PROCEDURES AND 'HOT SPOTS'

Theoretically, rf radiation 'hot spots' caused by an uneven distribution of rf power may arise whenever current concentrations are produced in association with restrictive conductive patterns.[13–22] There has been the suggestion that rf radiation 'hot spots' may occur during an MR procedure and generate thermal 'hot spots' under certain conditions. Because rf radiation is mainly absorbed by peripheral tissues, thermography has been used to study the heating pattern associated with MR procedures performed at high whole body averaged SARs.[44,54] This research demonstrated that there was no evidence of surface thermal 'hot spots' related to performing MR imaging in human subjects. The thermoregulatory system apparently responds to the thermal load induced by rf radiation by distributing the heat, producing a 'smearing' effect of the surface temperatures.[44,54] However, there is a possibility that internal thermal 'hot spots' may develop during an MR procedure. This issue is currently undergoing investigation in human subjects.

Shuman et al.[66] reported that significant temperature rises occur in the internal organs of laboratory dogs produced during MR imaging performed with high SARs. Of further note is that this study was conducted on anesthetized animals and is unlikely to be pertinent to conscious adult human subjects because of the previously discussed factors related to the physical dimensions of the animals, the fact that an anesthetic agent was used which may affect thermoregulation, as well as due to the dissimilar thermoregulatory systems of these two species. However, the data obtained by Shuman

et al.[66] may have important implications for the use of MR procedures in pediatric patients because this patient population is typically sedated or anesthetized for MR examinations and the physical dimensions of the dog are comparable with those of the pediatric population. Obviously, research is required to examine this issue more closely.

8 FUTURE STUDIES OF RF RADIATION-INDUCED HEATING DURING MRI

Several new pulse sequences have been developed and are currently undergoing clinical trials that use high levels of rf energy for their implementation.[67,68] For example, the latest versions of the 'fast spin echo' (FSE) and magnetization transfer contrast (MTC) pulse sequences may use SARs that easily exceed whole body averaged SARs ranging between $4-8\,\mathrm{W\,kg^{-1}}$.

The FSE pulse sequences are hybrids of RARE (rapid acquisition relaxation enhanced) pulse sequences and have increased rf power depositions compared with conventional spin echoes.[69] This is due to the high density of 180° refocusing pulses used for these pulse sequences.[69] MTC pulse sequences involve the use of selective and continuous saturation of macromolecular protons utilizing an off-resonance rf pulse during the implementation of the technique, so that the rf power deposition is of considerable concern.[68] This is particularly a potential problem in MR imaging examinations that involve large body parts that require rf transmission using the body coil.

Both the FSE and MTC pulse sequences offer several important clinical advantages over conventional pulse sequences. However, before FSE and MTC pulse sequences are routinely used for all clinical applications, investigations must be performed to assess and characterize thermal and other physiological responses to the rf radiation-induced heating related to these new pulse sequences. Therefore, studies are currently examining the human thermoregulatory responses to SARs that are even higher than those that have been studied in recent years. Preliminary results of these investigations are encouraging with respect to the ability of individuals with normal thermoregulatory function to tolerate MR examinations that require high SARs.[53]

Other MR procedures where rf radiation-induced heating may cause appreciable increases in tissue include ^{1}H decoupling, Overhauser enhancement, and burst sequences used in MR spectroscopy. Therefore, these MR procedures will need to be evaluated in the future in order to determine the relative safety of performing these applications in patient populations.

In addition, there are now several 4.0 and one 5.0 T whole body MR systems that are being used for a combination of imaging and spectroscopy in human subjects. These devices use approximately 7–10-times as much rf energy as 1.5 T MR scanners during MR procedures.[70,71] Investigations evaluating thermal responses in human subjects will also need to be performed to assess the safety of these powerful devices.

Additional studies are presently needed in order to assess the thermal responses of patients with conditions or medications that may impair their ability to dissipate heat before subjecting them to MR procedures that require high SARs. There is currently an ongoing effort to characterize the thermal and other physiological responses of these various patient groups to rf radiation-induced heating during MR examinations using high SARs.

Elevated body temperature is teratogenic in various animals, including primates.[7,9,10] Research studies have shown that excessive heat may cause birth defects and prenatal mortality when the body temperature of the pregnant mother reaches 40–44 °C.[7,9,10] Lower, but still elevated, body temperatures may significantly increase the incidence of reduced body weight, cause physiological changes, or behavioral alterations.[7,9,10] Increased temperatures that specifically result from exposure to rf radiation have been reported to affect adversely the developing embryo.[7,9,10] To date there have been no studies designed to examine the thermal effects of rf radiation-induced heating during MR procedures performed in pregnant patients. Therefore, experiments will be needed to assess the potential adverse effects of rf radiation with respect to pregnant patients undergoing MR procedures.

9 RELATED ARTICLES

Health and Safety Aspects of Human MR Studies; Overhauser Effect Imaging of Free Radicals; Magnetization Transfer Contrast: Clinical Applications; Magnetization Transfer between Water and Macromolecules in Proton MRI; Multi Echo Acquisition Techniques Using Inverting Radiofrequency Pulses in MRI; Proton Decoupling During In Vivo Whole Body Phosphorus MRS; Proton Decoupling in Whole Body Carbon-13 MRS

10 REFERENCES

1. NCRP, Biological effects and exposure criteria for radiofrequency electromagnetic fields, Report No. 86, National Council on Radiation Protection and Measurements, Bethesda, MD, 1986.
2. C. J. Gordon, Biological Effects of Radiofrequency Radiation, EPA600/8-83-026A, 4-1, 1984.
3. C. J. Gordon, *ISI Atlas Sci. Plants Anim.*, 1988, **1**, 245.
4. S. M. Michaelson and J. C. Lin, *Biological Effects and Health Implications of Radiofrequency Radiation*, Plenum, New York, 1987.
5. W. R. Adey, *Physiol. Rev.*, 1981, **61**, 435.
6. J. A. Elder, Biological Effects of Radiofrequency Radiation, EPA600/8-83-026A, 5-64, 1984.
7. E. Berman, Biological Effects of Radiofrequency Radiation, EPA600/8-83-026A, 5-29, 1984.
8. US Environmental Protection Agency, Office of Health and Environmental Assessment, EPA-600/6-90-005A, US Environmental Protection Agency, June 28, 1990.
9. M. E. O'Conner, *IEEE*, 1980, **68**, 56.
10. J. M. Lary and D. L. Conover, *IEEE*, 1987, **44**, 42.
11. J. Beers, *Magn. Reson. Imag.*, 1989, **7**, 309.
12. R. R. Edelman, F. G. Shellock, and J. Ahladis, *Clinical Magnetic Resonance*, ed. R. R. Edelman and J. Hesselink, Saunders, Philadelphia, PA, 1990.
13. B. R. R. Persson and F. Stahlberg, *Health and Safety of Clinical NMR Examinations*, CRC Press, Boca Raton, FL, 1989.
14. F. G. Shellock and J. V. Crues, *MRI Decisions*, 1988, **2**, 25.
15. F. G. Shellock, *Magn. Reson. Q.*, 1989, **5**, 243.

16. E. Kanal, F. G. Shellock, and L. Talagala, *Radiology*, 1990, **176**, 593.
17. F. G. Shellock and J. V. Crues, *Magnetic Resonance Imaging Syllabus*, American College of Radiology, Reston, VA, 1991.
18. F. G. Shellock, *Magnetic Resonance Imaging of the Brain and Spine*, ed. S. Atlas, Raven Press, New York, 1990.
19. F. G. Shellock, *N.Y. Acad. Sci. Symp., Biological Effects and Safety Aspects of Nuclear Magnetic Resonance Imaging and Spectroscopy, Proc. Meet.,*. 1992
20. P. A. Bottomley, R. W. Redington, W. A. Edelstein, et al., *Magn. Reson. Med.*, 1985, **2**, 336.
21. P. A. Bottomley and W. A. Edelstein, *Med. Phys.*, 1981, **8**, 510.
22. F. G. Shellock, C. Litwer, and E. Kanal, *Rev. Magn. Reson. Imag.*, 1992, **4**, 21.
23. S. Coulter and S. L. Osbourne, *Arch. Phys. Ther. Chicago*, 1936, **17**, 679.
24. J. W. Gersten, K. G. Wakim, J. F. Herrick, and F. H. Krusen, *Arch. Phys. Med.*, 1949, **30**, 7.
25. C. J. Gordon, *Bioelectromagnetics*, 1987, **8**, 111.
26. T. W. Athey, *Magn. Reson. Med.*, 1989, **9**, 177.
27. E. R. Adair and L. G. Berglund, *Magn. Reson. Imag.*, 1986, **4**, 321.
28. E. R. Adair and L. G. Berglund, *Magn. Reson. Imag.*, 1989, **7**, 25.
29. G. E. Burch and N. P. DePasquale, *Hot Climates, Man and his Heart*, Thomas, Springfield, IL, 1954.
30. L. B. Rowell, *Circ. Res.*, 1983, **52**, 367.
31. B. L. Drinkwater and S. M. Horvath, *Med. Sci. Sport Exer.* 1979, **11**, 49.
32. W. H. Fennel and R. E. Moore, *Am. J. Physiol*, 1969, **67**, 118.
33. W. L. Kenny, *Sports Med.*, 1985, **2**, 279.
34. F. R. Barany, *Acta Med. Scand. Suppl.*, 1955, **304**, 556.
35. E. F. Buskirk, H. Lundergren, and L. Magnussen, *Ann. N.Y. Acad. Sci.*, 1965, **131**, 637.
36. J. R. Jauchem, *J. Gen. Pharmacol.*, 1985, **16**, 307.
37. F. G. Shellock, J. K. Drury, S. Meerbaum, and E. Corday, *Clin. Res.*, 1983, **31**, 64A.
38. Food and Drug Administration, *Fed. Regist.*, 1988, **53**, 7575.
39. F. G. Shellock, *Med. Electron.*, 1986, Sept, 93.
40. B. Holshouser, D. B. Hinshaw, and F. G. Shellock, *J. Magn. Reson. Imag.*, 1993, **3**, 553.
41. E. Kanal and F. G. Shellock, *Radiology*, 1992, **85**, 623.
42. K. A. Wickersheim and M. H. Sun, *Med. Electron.*, 1987, February, 84.
43. F. G. Shellock and J. V. Crues, *Radiology*, 1987, **163**, 259.
44. F. G. Shellock, D. J. Schaefer, W. Grundfest, and J. V. Crues, *Acta Radiol. Suppl.*, 1986, **369**, 514.
45. F. G. Shellock, C. J. Gordon, and D. J. Schaefer, *Acta Radiol. Suppl.*, 1986, **369**, 512.
46. F. G. Shellock and J. V. Crues, *Radiology*, 1988, **167**, 809.
47. F. G. Shellock and J. V. Crues, *Am. J. Neuroradiol.*, 1988, **9**, 287.
48. F. G. Shellock, B. J. Rothman, and D. Sarti, *Am. J. Roentgenol.*, 1990, **154**, 1229.
49. F. G. Shellock and C. J. Schatz, *Radiology*, 1992, **185**, 697.
50. F. G. Shellock, D. J. Schaefer, and J. V. Crues, *Br. J. Radiol.*, 1989, **62**, 904.
51. F. G. Shellock, S. A. Rubin, and C. E. Everest, *Med. Electron.*, 1986, **86**, 81.
52. F. G. Shellock, D. J. Schaefer, and J. V. Crues, *Magn. Reson. Imag.*, 1989, **7**(Suppl 1), 335.
53. F. G. Shellock, D. J. Schaefer, and E. Kanal, *Radiology*, 1994, in press.
54. D. J. Schaefer, F. G. Shellock, J. V. Crues, and C. J. Gordon, *Proc. Bioelectromagnetics Soc., 8th Annu. Meet.*, 1986, p. 68.
55. D. Sperber, R. Oldenbourg, and K. Dransfeld, *Naturwissenschaften*, 1984, **71**, 100.
56. H. Gremmel, H. Wendhausen, and F. Wunsch, *Biologische Effeckte Statischer Magnetfelder bei NMR-Tomographic Am Menshen*, Wiss. Mitt. Univ. Radiol. Klinik, Kiel, 1983.
57. F. G. Shellock, D. J. Schaefer, and C. J. Gordon, *Magn. Reson. Med.*, 1986, **3**, 644.
58. F. G. Shellock, D. J. Schaefer, and J. V. Crues, *Magn. Reson. Med.*, 1989, **10**, 371.
59. T. S. Tenforde, *Bioelectromagnetics*, 1986, **7**, 341.
60. D. J. Schaefer, B. J. Barber, C. J. Gordon, J. Zhelonka, and J. Hecker, *Abs. Soc. Magn. Reson. Med.*, London, 1985, Vol. **2**, p. 925.
61. T. Vogl, K. Krimmel, A. Fuchs, and J. Lissner, *Med. Phys.*, 1988, **15**, 562.
62. D. K. Kido, T. W. Morris, J. L. Erickson, D. B. Plewes, and J. H. Simon, *Am. J. Neuroradiol.*, 1987, **8**, 263.
63. K. R. Kurz and M. Goldstein, *J. Urol.*, 1986, **135**, 290.
64. E. Sacks, B. V. Worgul, G. R. Merriam, and S. Hilal, *Arch. Ophthalmol.*, 1986, **104**, 890.
65. R. Mapstone, *Exp. Eye Res.*, 1968, **7**, 233.
66. W. P. Shuman, D. R. Haynor, A. W. Guy, G. E. Wesby, D. J. Schaefer, and A. A. Moss, *Radiology*, 1988, **167**, 551.
67. J. Hennig, A. Nauerth and H. Friedburg, *Magn. Reson. Med.*, 1986, **3**, 823.
68. R. S. Balaban and T. L. Ceckler, *Magn. Reson. Q.*, 1992, **8**, 116.
69. P. S. Melki, R. V. Mulkern, L. P. Panych, and F. A. Jolesz, *JMRI*, 1991, **1**, 319.
70. R. W. Redington, C. L. Dumoulin, J. F. Schenck, P. B. Roemer, S. P. Souza, G. M. Muehler, D. R. Eisner, and W. A. Edelstein, *Abs. Soc. Magn. Reson. Imag.*, Boston, 1988, Vol. **1**, p. 20.
71. D. A. Ortendahl, *Radiology*, 1988, **169**, 864.

Biographical Sketches

Frank G. Shellock. *b* 1954. B.S., 1976, Loyola-Marymount University, Los Angeles, CA, M.S., Biology, 1980, California State University, Ph.D., 1982, Physiology, Columbia Pacific University, San Rafael, CA. Over 300 publications. Research specialties: bioeffects of MR procedures; bioeffects of electromagnetic fields; MR imaging of skeletal muscle, cartilage, and other musculoskeletal applications; kinematic MR imaging; dynamic MR imaging of the upper airway; MR mammography.

Health and Safety Aspects of Human MR Studies

Thomas F. Budinger

University of California, Berkeley, CA, USA

1 HISTORICAL DEVELOPMENT

The study of the biological and human health effects of static and oscillating magnetic fields started over 100 years ago and currently there are well over 700 published reports on biological effects. The earliest well-known measurement of magnetic field effects in human beings is the induction of visual phenomenon (phosphenes) by $\boldsymbol{E}$ fields induced by switched magnetic fields near the human eye in experiments by d'Arsonval in 1896.[1] The best-known effect of static field was the observation of torque on biological assemblages such as retinal rods, chloroplasts, and sickle cells in magnetic fields below 1 T reported in the early 1970s.[2–4] A third phenomenon observed at that time was electrocardiograph (ECG) abnormalities in monkeys placed in magnetic fields; however, this effect was shown to be the superimposition of electric potentials induced by flow of blood, which is a conductor, across the field flux lines.[5,6] Examination of safety and human physiology experiments in MR commenced at the end of the 1970s[7] with research continuing to the present.[8–16] Safety issues continue to evolve because of initiatives to carry out studies in humans at higher static fields and with more rapidly switching gradients than currently employed. The use of MR in subjects with prostheses and the contemporary application of MR in therapy present safety problems in all fields.

Some effects scale with the square of the field increase and some thresholds for physiological effects are not well defined. However, the fundamental physics underlying evaluations of the safety and health effects of static and oscillating magnetic fields is not complex; nor is the validated interaction of magnetic static and oscillating fields with tissues and human organ systems as mysterious as is sometimes implied.[17,18] The controversial issues of the biological effects of power-line $\boldsymbol{E}$ fields and power frequency time-varying magnetic fields (0.1 μT s^{-1}) are discussed elsewhere.[10,19]

2 STATIC MAGNETIC FIELDS

2.1 Physical Effects

Four physical effects that have a potential for the interaction of magnetic fields with tissues are (i) the translational force, which is important in assessing the effect of ferromagnetic projectiles; (ii) the twisting force or torque on molecules, assemblages of molecules, or ferromagnetic objects implanted in tissues; (iii) the force on ions or charged objects moving in a magnetic field; and (iv) the magnet's hydrodynamic retarding force.

The translational or projectile force ($\boldsymbol{F}$) on a ferromagnetic object is given by:

$$\boldsymbol{F} = \boldsymbol{H}\chi V \,\mathrm{d}\,\boldsymbol{H}/\mathrm{d}\,x \tag{1}$$

where $\boldsymbol{H}$ is the external field, χ is the susceptibility, and V is the volume. The magnetic flux density ($\boldsymbol{B}$) in an object is the result of the magnetizing field ($\boldsymbol{H}$) to which the object is exposed. Omitting the permitivity of free space and recognizing that the susceptibility of tissues is very small (e.g., -10^{-6}), $\boldsymbol{H}$ and $\boldsymbol{B}$ are used interchangeably. This equation shows that the magnitude of the force depends on the susceptibility of the object, the field strength, and the gradient of the field strength. Because the magnetization of human tissues is so small, there is an insignificant force on the body. For example, the force on 1 g water is -1.4×10^{-4} N in a gradient of 0.15 T m^{-1} and a field of 1.5 T but the force on 1 g iron is 2.8 N (20 000 times greater in the opposite direction), about the force of gravity on a 0.6 lb (270 g) mass. This force scales as mass; consequently, a 0.5 lb (225 g) tool would become a force equivalent to a 134 lb (61 kg) weight accelerated by gravity.

The maximum magnetic force around a magnet is related to $\boldsymbol{B}$ by d$\boldsymbol{B}$/dt and is 8.8 T^2 m^{-1} for a 4 T magnet. This results in a force on red blood cells relative to plasma that is less than 3% of the gravitational force, and can therefore have no significant effect on living organisms.[15] There will be no force on an object inside the bore of a magnet where d$\boldsymbol{H}$/dx is 0 no matter what the susceptibility is unless there is a variation of susceptibility across the object, in which case the inbalance in magnetization will result in a *torque*.

The magnetization energy or interaction energy of a field $\boldsymbol{H}$ with biological molecules of diamagnetic susceptibility is given as

$$W = -\frac{1}{2}\int_v \boldsymbol{H}\bar{\chi}\boldsymbol{H}\,\mathrm{d}v \tag{2}$$

where $\bar{\chi}$ is the magnetic susceptibility tensor and the integration is carried out over the volume of the biologic structure (v). Normally the energy is similar in magnitude to the thermal energy (4×10^{-21} J) but if cell structures or molecular assemblages have structures that result in different susceptibilities in different axes, as with sickle cells,[20] retinal rods,[3] and chloroblasts,[2] then in vitro a torque will cause the structures to orient along the magnetic field lines in accord with

$$W = -\frac{v}{2}(\chi_r + \mid \chi_e - \chi_r \mid \cos^2\theta \mid \boldsymbol{H}^2 \mid) \tag{3}$$

where v is the volume of the structure, χ_r and χ_e are the susceptibilities for the short and long axes of the biological molecule or assemblage, respectively, and θ is the angle between the field $\boldsymbol{H}$ and the long axis.

Macromolecular assemblies such as lipid bilayers can have relatively large magnetic moments. It has been hypothesized that changes in the orientation of ordered structures in the membrane bilayer caused by magnetic fields may lead to permeability changes, and changes in Ca^{2+} transport in lymphocytes in vitro have been reported at 7.5 T.[21] However, there are no reported physiological effects in animals exposed

at 9 T (M. Garwood, University of Minnesota, personal communication, 1998) and humans exposed at up to 8 T (A. Kangarlu, Ohio State University, personal communication, 1998).

The third force associated with conductors moving in a magnetic field is given by the Lorentz force equation in the absence of electric fields:

$$\boldsymbol{F} = q(\boldsymbol{v} \times \boldsymbol{B}) = q(|\ \boldsymbol{v}\ | \cdot |\ \boldsymbol{B}\ |\ \sin\theta) \tag{4}$$

where q is a unit positive charge, $\boldsymbol{v}$ is the velocity and θ is the angle between the velocity vector and the induced field $\boldsymbol{B}$.

Negative ions will move in opposite directions, resulting in a separation of charges or an electric potential (emf),

$$\text{emf} = |\ \boldsymbol{v}\ | \cdot |\ \boldsymbol{B}\ | (\sin\theta)d \tag{5}$$

where d is the distance or width of the flow. For blood flowing at 0.4 m s^{-1}, in a 0.016 m (16 mm diameter) aorta at right angles (i.e., sin θ=1.0) to a field in the tissues of 1 T, the electric potential will be 6.4 mV. When measured on the human torso, this will appear as a signal of a few millivolts superposed on the ECG (Figure 1). This phenomenon was first observed in 1967[6] with detailed studies since.[22] It presents a safety problem because the artefact interferes with monitoring of patient heart stress by ECG during MRI examinations to evaluate heart function (Figure 1). The $\boldsymbol{E}$ field for an aorta of 1.6 cm is 0.4 V m^{-1}. A potential of approximately 64 mV across the aorta is predicted in a 10 T field; however, there is no suggestion that this could be a hazard: the $\boldsymbol{E}$ field is 4 V m^{-1}, which is below that causing cardiac stimulation and orders of magnitude below the local $\boldsymbol{E}$ field (10^8 V m^{-1}) across membranes of sub-micrometer thickness. The effective DC electric field acting in a person traveling across the USA in an airplane at 500 mph (223.5 m s^{-1}) is about 10 mV m^{-1}.

Currents associated with nerve firing could be distorted by large magnetic fields. This would be reflected in the nerve conduction velocity, and decreases of 10% at 18 T have been predicted.[23] Studies at up to 7.5 T have shown no changes.[22] Earlier reports of detected changes have been shown to be the result of inadequate temperature control as conduction velocity changes by 1% for a temperature change of 0.1–0.2°C.

Magnetohydrodynamic effects can result in some retardation of flow in blood, a conductor. The effect is greatest in large vessels. Blood flowing in a magnetic field creates an electric field; however, ions in this $\boldsymbol{E}$ field moving perpendicular to the magnetic field will experience a force in a direction that is opposite to the direction of blood flow. This comes from the relationship

$$\boldsymbol{F} \propto \boldsymbol{E} \times \boldsymbol{B} \tag{6}$$

Substitution of Equation (4) gives:

$$\boldsymbol{F} \propto q(\boldsymbol{v} \times \boldsymbol{B}) \times \boldsymbol{B}$$

The force direction is opposite to the vector direction of the flowing blood. The retardation of flow will not be significant in a 10 T field, based on our previous studies at 4.7 T. Analyses prior to 1990 which suggested a strong effect were found to be in error and no significant effect will be observed even at 10 T.[24]

Other forces, the NMR effect, the cyclotron resonance effect, and ion paramagnetic resonance effect are not significantly relative to thermal forces and tissue viscosity to warrant concern regarding safety.[10]

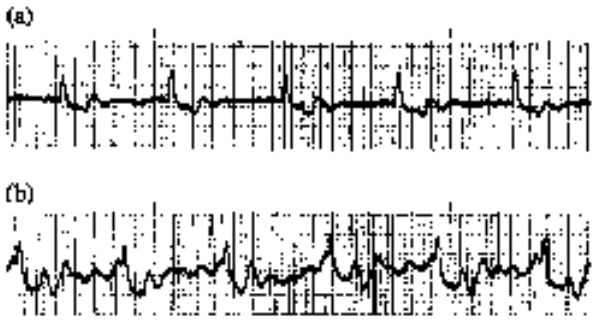

Figure 1 Static field effects on human electrocardiograph signals. (a) Normal trace from outside the magnetic field. (b) Trace is the resultant electric potential from both the normal signal and the induced potential of blood flowing in a magnetic field (1.5 T) [see Equation (8)]

2.2 Health Effects

Though measureable effects of static magnetic fields have been observed in animals and humans, there are no known or expected harmful physical or physiological effects of fields as high as 10 T. The naturally occurring magnetic field of the Earth can influence the swimming direction of a bacterium containing magnetite particles.[25] The Earth's magnetic field can also influence the migratory pattern of birds by a mechanism believed to be associated with magnetite.[26] Sharks, skates, and rays contain internal organs that use the induced currents generated by the animal swimming through the Earth's magnetic field as a navigational compass.[4,27]

Though not considered to be harmful, dizziness and stimulation of nerves in the palate associated with head movement in the field have been reported at 4 T. Dizziness or nausea could be caused by motion of the endolymph in the semicircular canals[14] or by a magnetomechanical mechanism[28] and subject motion within the magnetic field. Subject evaluation after exposure to 4 T fields has not revealed any lasting effects.[14,29] Additionally, as noted earlier, the ECG changes at 1.5 T and above[30] can be explained as insignificant effects associated with the static fields or magnetic environment.

Epidemiological studies have followed workers in aluminum plants who are exposed to fields up to 29 mT,[31–34] radiation workers near accelerators and bubble chambers,[28] and technicians in the MR environment.[35] Though Milham in 1985 reported increased disease incidence in one aluminum plant survey,[36] other studies have not shown a deleterious effect.

3 TIME-VARYING MAGNETIC FIELDS

3.1 Physical Effects

In NMR, rapidly oscillating magnetic fields known as rf pulses are used to stimulate the NMR signal and less rapidly

oscillating or time-varying magnetic fields are used to provide the gradients for imaging. The typical effect from the oscillating fields is the induction of $\boldsymbol{E}$ fields, which generate heat at high frequencies and neural or neuromuscular stimulation at low frequencies. Heat or pain thresholds limit the extent of the MR procedure. Though $\boldsymbol{E}$ fields are produced by high- or low-frequency oscillations, it is convenient to consider the main effect of low-frequency oscillations as an electrical effect and the effects of high-frequency or rf fields as a heating phenomenon.

Gradient fields of up to 10 mT m^{-1} are used in contemporary MRI instruments, with some recent installations at 20 mT m^{-1}. Functional MRI applications use rise times such that the value of $d\boldsymbol{B}/dt$ approaches 50 T s^{-1}. If 8–10 T fields are to be used to improve the spatial resolution of ^{1}H imaging, the gradient strength must increase. Both safety and engineering considerations may limit the maximum useful gradient field, but plausible design goals lie in the range 20–50 mT m^{-1}. The force on ferromagnetic objects, including components of the magnet and coils, is proportional to the gradients. But the rate at which these gradients are achieved is a critical factor for human studies. For example, if the gradient is switched from 0 to 10 mT m^{-1} in 200 μs, $d\boldsymbol{B}/dt$ is 50 T s^{-1} at the end of a 1 m long gradient coil and the $\boldsymbol{E}$ field around a 0.4 m diameter abdomen is 5 V m^{-1}. This is near the threshold for neuromuscular stimulation of 6 V m^{-1}.

The generation of a voltage from oscillating fields is derived from Faraday's Law

$$\text{emf} = \frac{d\boldsymbol{B}}{dt}\pi r^2 \tag{7}$$

where $\boldsymbol{B}$ is the magnetic field in the tissue and πr^2 is the area exposed to the time-varying field. Since the electric field is the voltage per distance around the loop $2\pi r$, Equation (7) becomes

$$\boldsymbol{E} = \frac{-r}{2}\frac{dB}{dt} \tag{8}$$

For a switched field of 10 T s^{-1} and a body radius of 0.2 m, the $\boldsymbol{E}$ field will be 1 V m^{-1} at the surface of the body.

For a sinusoidal oscillation

$$\boldsymbol{B}(t) = B_{\max}\sin 2\pi f t \tag{9}$$

where f is the frequency and $B_{\max}$ is the amplitude of the sinusoidal oscillating magnetic fields; therefore,

$$d\boldsymbol{B}/dt = 2\pi f B_{\max} \tag{10}$$

and Equation (8) becomes

$$\boldsymbol{E} = -r\pi f\boldsymbol{B} \tag{11}$$

The current density is the $\boldsymbol{E}$ field multiplied by the tissue conductivity (σ); consequently the relationship between the tissue current density and the time-varying magnetic field is

$$J = -r\frac{\sigma}{2}\frac{d\boldsymbol{B}}{dt} \tag{12}$$

For a loop radius of 10 cm, a conductivity of 0.2 s m^{-1} and a $d\boldsymbol{B}/dt$ of 1 T s^{-1}, an $\boldsymbol{E}$ field of 0.05 V m^{-1} and a current density of 0.01 A m^{-2} or 1 μA cm^{-2} would be expected. These fields and associated current densities can be compared with the naturally occurring fields in the body: 1 V m^{-1} in the brain and 1 mV m^{-1} at the scalp. Fields at the surface of the heart are 1–10 V m^{-1} and at the surface of the chest are 10–50 mV m^{-1}. Near power lines, where fields of 10 kV m^{-1} occur, the body $\boldsymbol{E}$ field is 10 mV m^{-1}; for 60 Hz and a $B_{\max}$ of 0.5 G, the induced body $\boldsymbol{E}$ fields are 2 mV m^{-1}

Time-varying fields of the amplitudes used in MRI are not capable of interfering with cardiac rhythm, but these rapidly changing gradients can induce electrical peripheral neuromuscular stimulation.

3.2 Health Effects

Since a time-varying field induces currents in the body proportional to $d\boldsymbol{B}/dt$, exposure standards are generally listed in Tesla/second, the rate of field change, or milliampere per square meter, the induced current density in the tissue. For complex waveforms, a root-mean square measure is used, or the rate of field change is scaled by a function of the pulse duration.

The threshold for neuromuscular stimulation of the torso by sinusoidal fields is 60 T s^{-1} at 1 kHz.[37,38] This threshold is the rate of change at which the sensation of a mild electric shock is reported by the subject. The $\boldsymbol{E}$ field for this stimulation is 6 V m^{-1}, or a current density of about 1.2 A m^{-2} for a path loop of 40 cm diameter. For the head, the effective loop radius for the z axis is less than that for the torso and the threshold is higher; however, the transverse field is such that even for a head coil, the threshold for slight pain is 50–60 T s^{-1}. The coil type, coil size, and geometry, as well as the rise time and gradient, are all important factors in the calculation of the $\boldsymbol{E}$ field that will be induced. The primary hazard associated with currents in the body is interference with neuromuscular function; however, before this occurs, the pain of an electric shock will be felt. Current densities greater than 20 A m^{-2} when induced by direct electrical contact can cause irreversible cardiac fibrillation; alternating electrical current densities of 5 A m^{-2} can cause cardiac ectopic events. It is erroneous to extrapolate the 1.2 A m^{-2} current density for a body coil operating at 60 T s^{-1} to that expected at the heart because the conductive loop is only 10 cm. Consequently, the current density is likely to be 0.3 A m^{-2} or 30 times larger than endogenous current densities of 10 mA m^{-2}.

The effect on nerves of time-varying fields is frequency dependent, being most sensitive near 60 Hz for mammalian nerve cells. Applied currents as small as 10 mA m^{-2} at 60 Hz have been observed to cause reversible changes in the nerve firing rate in in vitro preparations of nerves in petri dishes. This threshold is dependent on the frequency and the relative orientation of the current and the nerve, and a threshold in the body may be substantially higher.

Visual effects (magnetophosphenes) are reported at 2 T s^{-1} for 30 Hz. As the flicker fusion threshold for visualizing phosphenes is about 40 Hz, one would not expect to observe phosphenes at switched field rates greater than 500 Hz, which are those normally encountered in MRI exposures.

4 THE RADIOFREQUENCY HEATING THEORY

Heating by rf waves during MR occurs via magnetic induction [Equation (11)] with negligible ohmic contributions. The power absorbed by the tissue is given as power divided by mass m, or specific absorbed power, SAR (watts kg^{-1}):

$$\mathrm{SAR} = \frac{\sigma \boldsymbol{E}^2}{2\rho} \tag{13}$$

where ρ is the tissue density (usually 1 kg l^{-1}). However, the induced $\boldsymbol{E}$ fields vary over the body dependent on the loop diameter [i.e., the value of r in Equation (11)]. Heating will occur predominantly at the surface of the body with relatively little deep body heating. For a homogeneous sphere of radius R, the average SAR will be

$$\mathrm{SAR}_{\mathrm{sphere}} = \frac{\sigma D \boldsymbol{E}^2 R^2}{20\rho} \tag{14}$$

where D is the duty cycle. The rf power ratio between the outer radius, R, and a smaller radius, r, is:[13]

$$1 - \frac{r^5}{R^5} \tag{15}$$

The peak power is 2.5 times the average power. The mean temperature (T) elevation can be determined from

$$\Delta T(^\circ C) = \frac{\mathrm{SAR} \times \mathrm{time\ (s)}}{\mathrm{specific\ heat}} \tag{16}$$

For a specific absorbed power of 4 W kg^{-1} for 10 min, the maximum temperature rise is equal to 0.7°C using the soft tissue specific heat of 3.5 kJ kg^{-1} $°C^{-1}$ (0.83 kcal kg^{-1} $°C^{-1}$). The expected increase in signal to noise with field or frequency increases is shown in Figure 2.

Heating by rf waves at the higher fields (i.e., 4–10 T) and the corresponding higher frequencies for protons (i.e. 170–430 MHz) can be a serious limitation. Theoretical and experimental phantom studies[39,40] on a homogeneous sphere simulating the human head show the increase in absorbed power with frequency (Figure 3). Studies using a realistic layered model show that the SAR increases quadratically with f below 200 MHz, and linearly above 250 MHz.[41,42] Even at 10 T, a 30°, 2 ms sinc pulse with 10 zero-crossings can be applied as fast as once every 13 ms for ^{1}H and once every 26 ms for ^{31}P and ^{23}Na without any local heating. Theory also shows that fast imaging of the head with soft rf pulses can be performed at field strengths as high as 10 T. Localized spectroscopic studies of ^{1}H, ^{31}P, ^{23}Na, and ^{13}C with surface coils are feasible up to 10 T, although localized heating can reach a harmful level.

4.1 Radiofrequency Heating in Humans

Temperature elevation from the absorbed energy associated with the rf power is the major measurable physiological effect of present and future MR imaging and human spectroscopy studies. The thermoregulatory and other physiological changes that a human subject displays in response to exposure to rf radiation are dependent on the amount of energy that is absorbed and the rate at which this energy is distributed in the body and released to the environment.

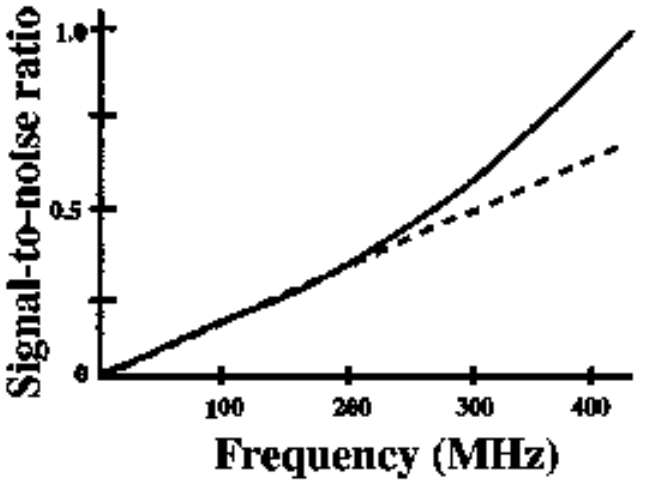

Figure 2 The signal-to-noise ratio increases with frequency linearly up to about 80 MHz (about 2 T). Theoretical predictions show that, for the human head, there will be quadratic dependence between the signal-to-noise ratio and frequency above 80 MHz

Several studies of volunteer subjects and patients undergoing clinical MR procedures have derived information that would be applicable to the patient population typically encountered in the MR setting.[43–45] The whole-body-averaged SAR values ranged from approximately 0.05 W kg^{-1} (for MR procedures involving imaging with a transmit/receive head coil) to 4.0 W kg^{-1} (for MR procedures involving the imaging of the spine or abdomen with a transmit/receive body coil). These studies demonstrated that changes in body temperatures were relatively minor (less than 0.6°C). Skin temperatures increased by as much as 4°C, but this increase reached an asymptote after 30 min as the body lost heat through Joule–Thompson cooling. There were no associated deleterious alterations in any of the hemodynamic parameters that were assessed during these investigations (heart rate, blood pressure, and cutaneous blood flow).[46]

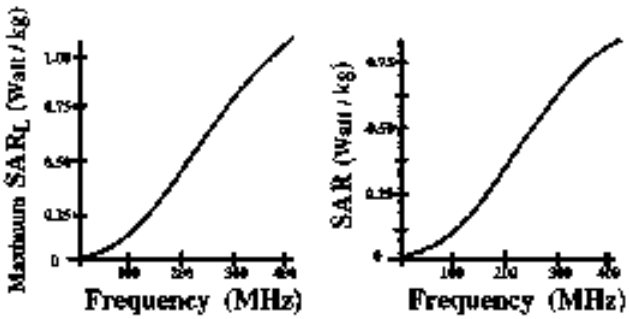

Figure 3 The maximum locus specific absorption rate (SAR_L) and the SAR are plotted versus frequency for a 20 cm diameter sphere with appropriate frequency-dependent conductivity and dielectric properties. The data are for a 12 cm diameter coil displaced 2 cm from the sphere. The rf for these studies was a 75 μm pulse with a repetition every 400 ms and with an amplitude to give a 35° tip in a volume element 5 cm into a sphere

As the operating frequency is increased, tissue conductivity increases, resulting in a higher ionic current and consequently a higher SAR. Higher tissue conductivity also means weaker $\boldsymbol{B}_1$ field penetration, and higher rf power is needed to achieve the same $\boldsymbol{B}_1$ field strength (the same flip angle) at a given spatial location as obtained at a lower frequency. For imaging and spectroscopy at fields as high as 10 T, power deposition calculations must incorporate not only the influence of intervening tissue (skin and skull in the head, fat in the body)[42] but also standing-wave effects; the wavelength inside brain matter is approximately 10 cm at 430 MHz.

5 CONTRAST AGENTS

The major contrast agent for MRI studies is a gadolinium chelate (gadopentatate dimeglumine), which is injected at a dose of 0.1 mmol kg^{-1} body weight. The largest study of adverse reactions completed in 1995 included 15 496 patients.[47] Adverse reactions occurred in 2.4% of patients. Only two patients had serious, but not fatal, adverse reactions and these were thought to be caused by interaction of the underlying disease with the contrast agent. Contrast studies have been done in all age groups and it does not appear that the use of contrast agents represents a hazard even to children younger than 2 years of age. Other contrast agents include 0.1 μm magnetite particles in various adjuvants, magnesium in chelate forms, and gadolinium attached to proteins such as albumin. The last has also been found to be a safe imaging agent for the vascular system.

6 IMPLANTS

MRI procedures might be performed on patients with temporary or permanent ferromagnetic objects in the body. There are five types of permanent implant (metallic foreign bodies, metal plates, prostheses, surgical clips, and cardiac valves), a number of different semi-permanent devices (pacemakers, hearing aids, cerebrospinal fluid shunts), and temporary devices (e.g., therapeutic instruments, esophageal pacers, stereotaxic surgery frames, cervical fixation devices). The hazards of metallic foreign bodies, particularly those associated with the eye, surgical clips, and pacemakers, have been extensively studied.[48]

Three potential hazards are associated with pacemakers.[49] One or more of the interactions of the physical components of the MR exposure (static magnetic fields, time-varying magnetic fields, and rf exposure) may cause an effect. Synchronous pacemakers have a special sensing circuit that analyzes incoming electrical activity and initiates a pulse to pace the heart only if the actual heart rate slows. Modern pacemakers are programmable and output voltage, current, pulse width, and rate can be determined and altered noninvasively.

When a patient with a demand pacemaker is examined, a hand-held magnet (approx. 0.1 T) is used to close a reed switch, thereby bypassing the pacemaker sensing system and converting the pacemaker to asynchronous operation. Demand pacemakers entering the magnetic field of a MRI unit will revert to asynchronous operation as a result of the reed switch being closed. If a demand pacemaker does not have a functioning reed switch, electromagnetic interference can fool the circuitry into thinking appropriate electrical activity is present. These false signals are generated because the pacemaker lead is an antenna that is susceptible to electromagnetic environments. The numerous ferromagnetic components within a cardiac pacemaker will exhibit a force of attraction and torque in a magnetic field. A torque will be experienced as the pacemaker attempts to align itself properly along the magnetic lines of the field. Most of the actual tests done with patients having pacemakers were at 0.35 and 0.5 T. These tests have not reported disturbances when systems are tested in the asynchronous mode.

The induced current for a cardiac pace catheter are below the cardiac stimulation threshold, which is 5 A m^{-2}. However, tissues surrounding wires that act as antennae can be heated through $\boldsymbol{E}$ field induction from the local magnetic field associated with the currents in the conductor.

The dangers associated with implanted surgical clips result from translational forces, or torque, between the magnetic material in the clip and external magnetic field. The earliest quantitative studies of forces on surgical clips were in 1983.[50] Some clips, while not considered ferromagnetic by the manufacturer, can have magnetism induced in the manufacturing processes. Criteria for testing clips have been established wherein displacement and rotation thresholds are set at 0.15 T m^{-1} and 0.15 T, respectively, and an extensive catalog of test results has been compiled.[51–54] For example type 316L stainless steel is nonmagnetic but type 301 or 17-7 (P)M stainless steel is magnetic. The potential of twisting or displacement is dependent on how well the clip is imbedded in the surrounding tissue. Dental stainless steel (type 316) for orthodontics is magnetic and causes artefacts, but the hazard of dislodgment is minimal.

Cardiac valves in patients do not preclude MRI examinations. Field distortions associated with some ferromagnetism might preclude imaging but in general these valves will not be twisted or rendered nonfunctional at 1.5 T.[55]

Cerebrospinal fluid shunts are frequently used in patients with brain disorders who require MRI studies (e.g., with hydrocephalus). These metallic devices cause less artefacts in MRI than in computed tomography. The deflection forces at 1.5 T can be as much as 0.02 N.[56] Cervical fixation devices and stereotaxis frames have also been studied; if these are made of nonferromagnetic material they are compatible with MRI.[57]

7 CONCLUSIONS AND GUIDELINES

In 1997, the American Food and Drug Administration revised the guidelines from 1982 regarding the assessment of risk in proposed clinical studies of investigational MR devices.[58] These guidelines are: (i) the limit of the static magnetic field is 4 T (but the Institutional Review Board can approve studies beyond 4 T); (ii) SAR is limited to 4 W kg^{-1} averaged over the whole body for any period of 15 min, 3 W kg^{-1} averaged over the head for any period of 10 min, and 8 W kg^{-1} in any gram of tissue in the head or torso or 12 W kg^{-1} in any gram of tissue in the extremities for any period of 5 min; (iii) $d\boldsymbol{B}/dt$ is limited to levels that will avoid 'severe discomfort or painful nerve stimulation'; and (iv) peak unweighted sound pressure level limit is 140 dB or an A-weighted root-mean-square sound pressure level greater than 99 dBA with hearing protection in place.

The static fields now considered safe are 8 T and beyond. The switched fields used at many installations today are 50 T s^{-1}. The whole body SAR of 4 W kg^{-1} or more is needed if the core temperature elevation of 1°C is the criterion, though earlier work with rf did show operant behavior changes in subhuman primates at 4 W kg^{-1}. The 0.4 W kg^{-1} as a whole body guideline for rf remains a prudent guideline from the IEEE (Institute of Electrical and Electronics Engineers) Standards Board. The partial body guideline of 8 W kg^{-1} will not result in a 1°C temperature change for organs with blood flow of 1 ml min^{-1} 100 g^{-1}. Records of MRI operations have been without serious incident other than the avoidable incidents of burns from external wires near the patient, projectiles entering the magnet space, or ferromagnetic foreign objects imbedded near vital organs. As the magnet designs of the near future are changing and MRI is being used for new applications such as minimally invasive surgery, continuing surveillance of the potential hazards is needed.

8 RELATED ARTICLES

Echo-Planar Imaging; Gradient Coil Systems; High-Field Whole Body Systems; Radiofrequency Fields: Interactions, Biological Effects, and Safety Issues.

9 REFERENCES

1. M. A. d'Arsonval, *C. R. Hebd. Séances Mémoires Soc. Biol.*, 1986, **3**, 450.
2. N. E. Geacintov, *Biochim. Biophys. Acta*, 1972, **276**, 65.
3. F. T. Hong, D. Mauzerall, and A. Mauro, *Proc. Natl. Acad. Sci., USA*, 1971, **68**, 1283.
4. A. J. Kalmijn, *Prog. Clin. Biol. Res.*, 1988, **257**, 23.
5. T. S. Tenforde, C. T. Gaffey, F. R. Moyer, and T. F. Budinger, *Bioelectromagnetics*, 1983, **4**, 1.
6. T. Togawa, O. Okai, and M. Oshima, *Med. Biol. Eng.*, 1967, **5**, 169.
7. T. F. Budinger, *IEEE Trans. Nucl. Sci.*, 1979, **26**, 2821.
8. T. F. Budinger, *J. Comput. Assist. Tomogr.*, 1981, **5**, 800.
9. T. F. Budinger, *Ann. N. Y. Acad. Sci.*, 1992, **649**, 1.
10. T. F. Budinger, *Magn. Res. Imag. Clin. North Am.*, 1998, **6**, 701.
11. E. Kanal, F. G. Shellock, and L. Talagala, *Radiology*, 1990, **176**, 593.
12. B. R. R. Perrson and F. Stahlberg, 'Health and Safety of Clinical NMR Examinations', CRC Press, Boca Raton, FL, 1989.
13. D. J. Schaefer, *MRI Clin. North Am.*, 1998, **6**, 775.
14. J. F. Schenck, *Ann. N. Y. Acad. Sci.*, 1992, **649**, 285.
15. J. F. Schenck, *MRI Clin. North Am.*, 1998, **6**, 715.
16. T. S. Tenforde and T. F. Budinger, 'NMR in Medicine: Instrumentation and Clinical Applications', ed. S. R. Thomas, and R. L. Dixon, American Association of Physicists in Medicine, New York, 1986, p. 493.
17. E. L. Carstensen, 'Biological Effects of Transmission Line Fields', Elsevier, New York, 1987.
18. M. Grandolfo, S. M. Michaelson, and A. Rindi, 'Biological Effects and Dosimetry of Static and ELF Electromagnetic Fields', Plenum Press, New York, 1985.
19. W. R. Bennett Jr, 'Health and Low-Frequency Electromagnetic Fields', Yale University Press, New Haven, CT, 1994.
20. M. Murayama, *Nature*, 1965, **206**, 420.
21. R. P. Liburdy, *Ann. N. Y. Acad. Sci.*, 1992, **649**, 74.
22. C. T. Gaffey and T. S. Tenforde, *Radiat. Environ. Biophys.*, 1983, **22**, 61.
23. J. P. J. Wikswo and J. P. Barach, *IEEE Trans. Biomed. Eng.*, 1980, **BME-27**, 722.
24. J. R. Keltner, M. S. Roos, P. R. Brakeman, and T. F. Budinger, *Magn. Reson. Med.*, 1990, **16**, 139.
25. R. B. Frankel and R. P. Blakemore, *Bioelectromagnetics*, 1989, **10**, 223.
26. J. L. Kirschvink, D. S. Jones, and B. J. MacFadden, 'Magnetite Biomineralization and Magnetoreception in Organisms: A New Biomagnetism', Plenum Press, New York, 1985.
27. A. J. Kalmijn, *J. Exp. Biol.*, 1971, **55**, 371.
28. T. F. Budinger, K. S. Bristol, C.-K. Yen, and P. Wong, *Proc. IIIrd Annu. Mtg. Soc. Magn. Reson. Med.*, New York, 1984.
29. H. Barfuss, H. Fischer, D. Hentschel, R. Ladebeck, A. Oppelt, R. Wittig, W. Duerr, and R. Oppelt, *NMR Biomed.*, 1990, **3**, 31.
30. P. Jehenson, D. Duboc, T. Lavergne, L. Guize, F. Guerin, M. Degeorges, and A. Syrota, *Radiology*, 1988, **166**, 227.
31. R. L. Davis and S. Milham, *Am. J. Ind. Med.*, 1990, **18**, 79.
32. G. W. Gibbs, *J. Occup. Med.*, 1985, **27**, 761.
33. J. J. Spinelli, P. R. Band, L. M. Svirchev, and R. P. Gallagher, *J. Occup. Med.*, 1991, **33**, 1150.
34. G. P. Theriault, C. G. Tremblay, and B. G. Armstrong, *Am. J. Indust. Med.*, 1988, **13**, 659.
35. J. A. Evans, D. A. Savitz, E. Kanal, and J. Gillen, *J. Occup. Med.*, 1993, **35**, 1191.
36. S. J. Milham, *Environ. Health Perspect.*, 1985, **62**, 297.
37. T. F. Budinger, H. Fischer, D. Hentschel, H. E. Reinfelder, and F. Schmitt, *J. Comput. Assist. Tomogr.*, 1991, **15**, 909.
38. M. S. Cohen, R. M. Weisskoff, R. R. Rzedzian, and H. L. Kantor, *Magn. Reson. Med.*, 1990, **14**, 409.
39. J. R. Keltner, J. W. Carlson, M. S. Roos, S. T. Wong, T. L. Wong, and T. F. Budinger, *Magn. Res. Med.*, 1991, **22**, 467.
40. R. W. Singerman, T. J. Denison, H. Wen, and R. S. Balaban, *J. Magn. Reson.*, 1997, **125**, 72.
41. O. Ocali and E. Atalar, *Magn. Reson. Med.*, 1998, **39**, 462.
42. S. T. S. Wong, J. R. Keltner, and M. S. Roos, *Proc. Xth Annu. Mtg. Soc. Magn. Reson. Med.*, San Francisco, 1991, 971.
43. D. K. Kido, T. W. Morris, J. L. Erickson, D. B. Plewes, and J. H. Simon, *Am. J. Roentgenol.*, 1987, **148**, 1215.
44. F. G. Shellock, D. J. Schaefer, and J. V. Crues, *Magn. Reson. Med.*, 1989, **11**, 371.
45. T. Vogl, K. Krimmel, A. Fuchs, and J. Lissner, *Med. Phys.*, 1988, **15**, 562.
46. F. G. Shellock, 'Encyclopedia of Nuclear Magnetic Resonance', ed. D. M. Grant, and R. K. Harris, John Wiley, Chichester, 1996, p. 2268.
47. K. L. Nelson, L. M. Gifford, C. Lauber-Huber, C. A. Gross, and T. A. Lasser, *Radiology*, 1995, **196**, 439.
48. F. G. Shellock, and V. J. Shellock, *Magn. Reson. Imag.*, 1998, **8**, 1338.
49. G. Lauck, A. von Smekal, S. Wolke, K. C. Seelos, W. Jung, M. Manz, and B. Luderitz, *Pacing Clin. Electrophysiol.*, 1995, **18**, 1549.
50. P. F. New, B. R. Rosen, T. J. Brady, F. S. Buonanno, J. P. Kistler, C. T. Burt, W. S. Hinshaw, J. H. Newhouse, G. M. Pohost, and J. M. Taveras, *Radiology*, 1983, **147**, 139.
51. M. Dujovny, M. S. Alp, N. Dujovny, Y. J. Zhao, N. R. Gundamraj, M. Misra, and G. Dobben, *J. Neurosurg.*, 1997, **87**, 788.
52. E. Kanal, F. G. Shellock, and J. S. Lewin, *Radiology*, 1996, **200**, 576.
53. F. G. Shellock, and J. V. Crues, *Radiology*, 1998, **208**, 407.
54. F. G. Shellock, and E. Kanal, *Magn. Res. Imag.*, 1994, **4**, 749.
55. R. L. Soulen, T. F. Budinger, and C. B. Higgins, *Radiology*, 1985, **154**, 705.
56. M. Ortler, H. Kostron, and S. Felber, *Neurosurgery*, 1997, **40**, 1050.

57. F. G. Shellock, *Magn. Reson. Med.*, 1996, **14**, 1093.
58. Food and Drug Administration, *http://www.fda.gov/cdrh/ode/magdev.html*, 1997.

Biographical Sketch

Thomas F. Budinger. *b* 1932. B.S., 1954, M.S., 1957, M.D., 1964, Ph.D., 1971, Medical Physics. Faculty Senior Scientist, Lawrence Berkeley Laboratory, Professor of Bioinstrumentation, Electrical Engineering and Computer Sciences, UCB and Henry Miller Professor of Medical Research, Donner Laboratory and Lawrence Berkeley Laboratory, 1976–present. Professor, Department of Radiology, University of California, San Francisco, 1984–present. Head, Center for Functional Imaging, Lawrence Berkeley Laboratory, and Director, PET UCSF, 1992–present. Director, Magnetic Resonance Science Center, UCSF, 1993–present. Approx. 400 publications. Research specialities: biomedical research and development of positron emission tomography, single-photon emission computed tomography and MRI and spectroscopy.

Patient Life Support and Monitoring Facilities for Whole Body MRI

Chris Boesch
University of Bern, Switzerland

1 INTRODUCTION

'Patient life support and monitoring' is a subject that arises with MRI examinations within whole body magnets of patients experiencing unstable vital functions. It includes any type of method, device or activity employed to survey or to maintain the vital functions of a patient undergoing an MRI examination.

1.1 Overview

Patient monitoring and care during magnetic resonance (MR) examinations is a subject that combines principles from very diverse fields of applied engineering, electronics, and MR physics, with medical considerations of patient care and intervention.[1–19] The MR system environment is, in general, incompatible with standard hospital life support and monitoring devices due to strong electromagnetic interactions between the equipment and the MR system, affecting both. An estimate of the magnitude of the interactions involved is dramatically illustrated by the following example: while the MR system generates rf pulses of several kilowatts power and of a few milliseconds duration within the whole body coil, patient electrocardiogram (ECG) monitoring requires the registration of electrical signals from the patient's heart with a magnitude of several millivolts. This incompatibility problem is compounded by the fact that the patient is hidden from view during the relatively long time period of the MR examination.

1.2 Historical Perspective

In the past, many high-risk patients (i.e. those with unstable vital functions) have either been excluded from vital MRI studies, or have been examined with insufficient monitoring and care, since MR-compatible monitors and life support devices were unavailable. In the early years of widespread MR use, MR sites had individually to seek monitoring solutions for select patients and for certain affected instruments.[1–17] Many designs for monitoring solutions appeared in the literature; however, some were not generally applicable or were impractical for routine MR examinations (e.g. locating an anesthesia ventilator 10 m from the patient). Because of the lack of commercial MR-compatible devices and the lack of technical understanding of the many concepts involved, government regulations and device approvals in many countries have lagged behind the diagnostic success of MRI.

2 MEDICAL CONCEPTS: BACKGROUND

Medical management of a patient confined within the restrictive magnet bore differs considerably from that of a surgical patient or one monitored in the ward where there is complete accessibility. Patient monitoring should also not be confused with the detection of the patient's heart rate for MR pulse sequence triggering purposes only. Monitoring and life support during MRI examinations requires adapting some basic concepts to the medical needs specific to a patient group. For example, a healthy but sedated child requires much less monitoring and treatment compared to an unstable patient from the intensive care unit (ICU).

2.1 Relevant Patient Categories

The diagnostic power of MRI has led to an increasingly larger number of examinations involving high-risk patients, who necessarily may require treatment and monitoring during an MRI scan. These include, for example: anxious[20] or uncooperative patients (e.g. children, and patients in a confused state) who need to be examined under sedation[21–24] or anesthesia because of their illness or lack of cooperation; critically ill patients from the ICU (e.g. patients with acute craniocerebral trauma,[14] spinal cord injury,[25,26] or myocardial infarction[15]), especially those who are intubated and artificially ventilated, require optimal life support; and premature infants,[5,12] who need a controlled atmosphere within an incubator[12,27–30] and require dedicated equipment due to smaller volumes.[16]

Even MRI examinations of completely stable patients or outpatients may require monitoring.[22] In particular, sedated patients being examined in the supine position can vomit, leading to potentially life-threatening situations (aspiration and airway obstruction). MR guided medical interventions will increase the number of patients who absolutely require continuous vital function monitoring.

2.2 Monitoring Functions

In addition to verbal contact with the patient (if possible), three general categories of physiological functions of the human body are monitored:[2–4,11–13,18,19] cardiovascular parameters, respiratory parameters, and body temperature. Table 1 summarizes these and the vital functions which they indicate.

ECG records electrical potentials at the body surface generated by the activity of the heart. An ECG gives an immediate measure of heart activity, unlike observation of the pulse in the periphery which is delayed by the finite speed of the pulse wave. In addition, the ECG contains slowly varying components which are a consequence of body impedance changes during respiration. These components can be used to evaluate respiration rate by 'impedance plethysmography'. The cardiovascular system can be assessed by pulse oximetry, skin blood flow, and noninvasive or invasive blood pressure (NIBP and IBP). Pulse oximetry exploits the effect that binding of oxygen to hemoglobin in erythrocytes changes the absorption spectrum. Absorption of light at two different wavelengths, red and infrared, by the tissue (e.g. finger, toe, or neonate foot) allows the determination of both the oxygen saturation of the blood and

Table 1 List of Vital Physiological Parameters

Physiological parameter	Observed vital function
Electrocardiogram (ECG)	Electrical heart action
Pulse oximetry (SaO_2)	Cardiovascular (peripheral pulse)
	Oxygenation (blood saturation)
Temperature	Body or skin temperature
Noninvasive blood pressure (NIBP)	Cardiovascular (blood pressure)
Invasive blood pressure (IBP)	Cardiovascular (blood pressure)
Capnography	Respiration frequency
	End-tidal CO_2/NO_2
Inspired O_2, anesthesia gases	Mixture of breathing air
Transcutaneous pO_2, pCO_2 (neonates)	Partial pressure of O_2 and CO_2
Impedance plethysmography	Respiration rate
Skin blood flow	Perpheral perfusion

the pulse rate. In infants, transcutaneous estimation of oxygen and carbon dioxide partial pressure is possible, but is not widely used during MR examinations. Cutaneous blood flow can be assessed by the Doppler effect of light which is reflected by moving blood cells. The NIBP determination measures systemic blood pressure by the inflation of a cuff around an extremity; the blood flow in the extremity is compared with the pressure applied by the cuff. In the IBP determination the pressure from within the vascular system is transmitted by an inserted tube to a pressure transducer outside of the magnet bore. Capnography analyzes the absorption of infrared light by the expired air in a chamber located outside of the magnet bore. In an intubated patient with a closed ventilation circuit, capnography determines respiratory rate, absolute concentrations of end-expiratory CO_2 and of some anesthetic gases. In a nonintubated patient, absolute concentrations cannot be measured by capnography, but the respiratory rate can be measured by using a sampling tube in the airflow (e.g. in the nose). During mechanical ventilation, anesthetic gas and O_2 concentrations in the inspired air flowing through the ventilator can be analyzed.

2.3 MR Scanning Room and Monitor Setup

Figure 1 shows a typical MRI suite with monitoring and life support devices. At most sites, the MR scanning room has a wall-integrated Faraday shield, and the door (as part of the shield) must be closed during scanning. Environmental rf noise is attenuated by 100 dB, typically, by the Faraday-shielding, leaving the magnet room almost rf noise free. Residual rf noise would be additionally attenuated by the inherent Faraday shielding effect of the magnet bore. Potential sources of rf noise inside the magnet room, including patient monitoring devices, must be shielded carefully.

2.4 Patient Accessibility and Visibility in the Magnet

During an MR examination in a classically designed cylindrical bore whole body magnet, the patient lies in a tube that is 2 to 3 m long and approximately 60–70 cm in diameter, which is relatively narrow for an average adult. The patient is only partially visible and accessible by the medical staff. In patient surveillance on the ward, direct staff contact with the patient and inspection of his or her respiration, skin color, heart action, and body temperature are important monitoring factors. During an MRI examination (typically 20–60 min long) this contact is severely restricted. Even use of a stethoscope is limited by the loud noise of the switched magnetic field gradients. Therefore, technical monitoring devices are needed to provide the necessary patient physiological information.

The inaccessible patient cannot be treated without special preparations. Arrest of bleeding or emergency treatment are not generally possible while the patient is in the magnet bore. Infusions and intubation must be prepared outside the magnet bore, prior to the MRI examination, with tubing of appropriate longer length. Replacement of misplaced or detached sensors is usually not possible without interruption of the MRI examination. Fortunately, MR examinations have the feature that they typically can be interrupted, unlike a surgical intervention which must be finished regardless of unexpected events. New advanced MR methods introduce elements of classical surgery into MRI, and interventions under MR control thus need to be continued without interruption or delay.

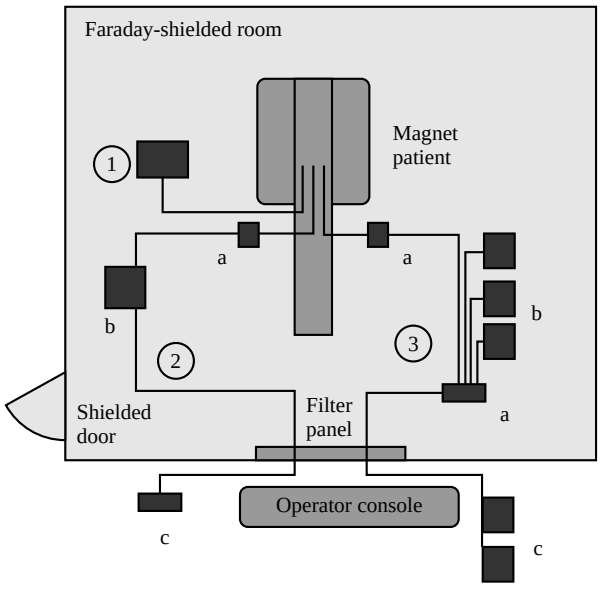

Figure 1 Schematic arrangement of an MRI site with monitoring devices. The magnet with the patient is located inside a Faraday-shielded room which is completed with a shielded door, that must remain closed during scanning. The inner part of the Faraday-shielded room is intended to be free from any rf noise. Thus, all additional devices inside the room have to be carefully rf shielded and all connections between the inside and the outside have to go through a filter panel. Three different monitoring and life support systems are indicated: (1) single components such as ventilators or single-parameter devices; (2) a complete integrated monitoring system; (3) a complete modular monitoring system. (2) and (3) both have (simplified) connection boxes (a), one or more monitors (b), and satellite devices at the console (c)

2.5 Monitoring Scenarios and Staff

During most MR examinations the Faraday shielded magnet room door must be closed, and thus the monitoring staff cannot enter or exit freely. This barrier distinguishes two different approaches to monitoring: surveillance by one responsible staff member located adjacent to the patient inside the magnet room, and complete remote monitoring from outside the magnet room. As either approach could be appropriate for a specific patient, control and display devices of the monitoring system should be available at different locations inside and outside the magnet room.

Stable outpatients are often monitored by use of displays outside the MR room, in some cases by the MR technicians, who are simultaneously operating the MR system. Notably, with mild patient sedation there is a chance of vomiting, requiring immediate action to prevent aspiration. This response can be delayed by a technician who is also responsible for the MR image acquisition.

Any instability of the patient's vital functions, including administration of common doses of sedatives, requires that one medical staff member be responsible for monitoring and intervention[22] and remains in the magnet room with the patient. This staff member must have available a display of all monitoring parameters, and be able to modify the sensing and display of the measured parameters (e.g. ECG derivation and amplification). Depending on the specific patient, this staff member can either be an anesthesiologist, a pediatrician or another specialist.

2.6 Triggering vs Monitoring

The terms 'triggering' and 'monitoring' are often confused. Most MR manufacturers provide an ECG recording sensor for triggering, i.e. the temporal coordination of MR pulse sequences with the heart action. These sensors can also be used for patient monitoring between MR scans. However, for monitoring purposes during MR examinations, the ECG needs to be recorded and displayed continuously without any degradation, and without any treatment which could suppress physiologically important features of the ECG. Supplied ECG sensors for triggering are often neither continuous nor undistorted. Severe distortion of the ECG, blanking of preamplifiers governed by the acquisition sequence, strict filtering, or post-processing of the ECG signal can suppress signals from the heart which would indicate a malfunction, or mimic heart function failure.

3 PHYSICAL PRINCIPLES OF INTERACTIONS: BACKGROUND

During a MRI examination, various electromagnetic fields are generated by the MR system and monitoring and life support devices. Each of these fields can be the basis of mutual interactions between the different devices and/or the patient.[31] For a description of an MRI acquisition, see also ***Image Formation Methods***; ***Gradient Coil Systems***. For effects of the various fields on the patient, see also ***Radiofrequency Systems and Coils for MRI and MRS*** and ***Health and Safety Aspects of Human MR Studies***.

3.1 Applied Physical Principles

The interactions that can occur between the MR system and monitoring devices can be described in terms of several physical principles:

1. Mechanical forces and a distortion of the magnetic field occur when ferromagnetic material is within a static magnetic field.
2. Faraday's law describing electromagnetic induction states that a temporal change in the magnetic flux (defined as the product of a magnetic field and the penetrated area) induces an electrical voltage in a conductor surrounding the penetrated area. Thus both a changing magnetic field (switched gradients, rf) and variations in the area (moving body, wires) generate induced voltages.
3. The 'Lorentz force' is experienced by electrical particles [e.g. electrons in a cathode ray tube (CRT), or ions in blood] moving in a magnetic field, with this force being perpendicular to both the path of the particle and to the magnetic field direction.[31]

These different physical principles are applied below to explain a number of interactions (Figure 2).

3.2 Static Magnetic Field

The static magnetic field (typically 0.2–2 T for whole body MR systems) is always present, having a very homogeneous region inside the magnet bore and decaying within several meters outside the magnet bore (i.e. the fringe field). The most well-known characteristics of a static magnetic field are the attractive force and torque it exerts on ferromagnetic objects, the effects of which depend on the size and shape of the

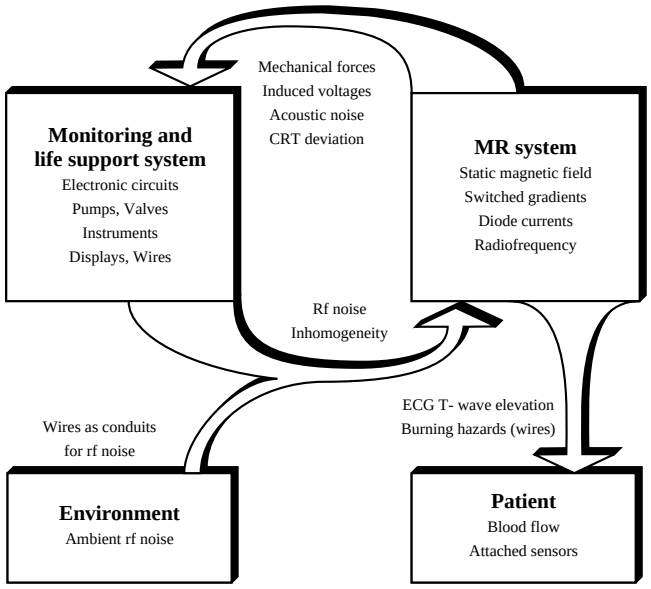

Figure 2 Synopsis of possible interactions between an MR system, monitoring devices and life support systems, the patient, and the environment. CRT, cathode ray tube

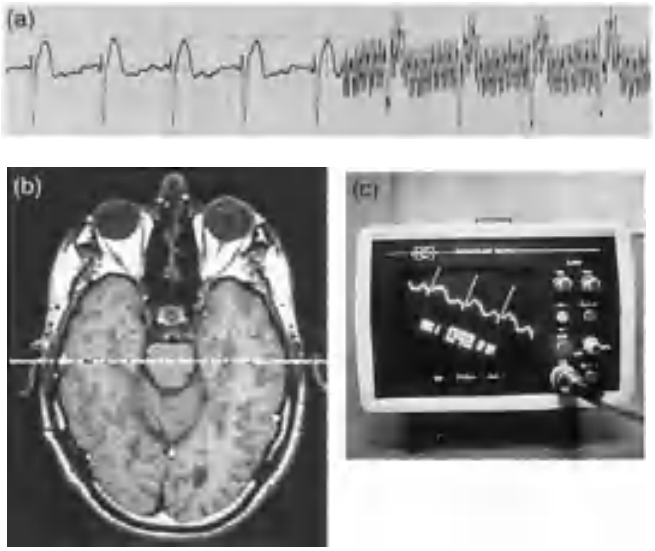

Figure 3 Examples of interactions between an MR system and monitoring devices. (a) ECG recording before and during an MRI sequence. The sharp spike is called the QRS complex; it is followed by the smooth T-wave, which is elevated by the static magnetic field.[32] (b) A rf emission from an unshielded monitor causes artifacts in an MR image (horizontal stripes). (c) A tilted trace on the CRT screen of an ECG monitor located several meters away from the magnet

object. The largest attraction is experienced in a highly inhomogeneous static field, which in the case of MRI is at the opening of the magnet. Valves, relays, etc., can be influenced by the static field, and CRT displays are distorted even at a distance of several meters from the magnet (Figure 3). Ions in blood flowing in the static magnetic field experience the Lorentz force, which generates voltages that distort ECG registration.[32] This effect elevates the T-wave of an ECG reversibly (Figure 3) such that its diagnostic value is limited to an observation of cardiac rate and rhythm; it cannot be used to determine an ischemic heart attack, for example.

Based on the Faraday law, any motion of a part of the body in the magnetic field induces electrical potentials. These electrical potentials seem to be harmless, but nevertheless can interfere with electrical physiological measurements such as an ECG recording. Depending on the size and location of ferromagnetic objects relative to the magnet, the static magnetic field can be distorted by the induced magnetic field. The resulting inhomogeneity in the region of interest can, in particular, impair MR spectroscopy, although the forces experienced by the ferromagnetic object are usually the more pronounced problem.

3.3 Switched Gradients and Diode Currents

Time and spatially varying gradients (typically around 10 mT m^{-1}) are switched in fractions of milliseconds on MR systems. (New equipment has maximum slew rates of approximately 250 mT m^{-1} ms^{-1}.) Diode currents are switched in fractions of a millisecond and are used to change detection and excitation coils from the resonant to a nonresonant mode.

Switched gradients are a source of audio noise and induced potentials in conducting objects, as explained by the Faraday law. The audio noise is a direct consequence of the mechanical force experienced by the gradient coils when the current producing the gradient fields is flowing in the main field (Lorentz' law). Voltages induced by the gradients are picked up in loops formed by wires in the magnet such as the ECG electrodes.

3.4 Radiofrequency Fields

Strong rf fields at the resonance frequency of the MR system (usually between 10 and 100 MHz for whole body systems) are generated for the excitation of the spins in specially tuned and shaped coils, driven by transmitters of up to 20 kW. These strong rf fields are the basis for very complicated, rarely reproducible, yet important interactions. Radiofrequency induced voltages in other devices cause distortion of electrical measurements, saturation of preamplifiers, or even the destruction of electronic circuits. Even with high-resistance carbon ECG electrodes, moderate warming of the skin has been observed under test conditions.

An additional and important effect of rf interference has been observed in situations lacking any direct galvanic contact between a patient's skin and the conducting wires. Each conducting wire represents an inductance and can—in connection with the capacitance-like structure which exists in every loop of a cable—form a resonant circuit. This can be excited by the electromagnetic field and subsequently focus considerably high electromagnetic field strength within small distances (less than 5 mm) around the wire. Thus, hazards of burning (up to third degree, requiring surgical skin grafting) have been reported in connection with pulse oximeters.[33,34] These interactions are not limited to direct (galvanic) contact with the patient or to cases of destroyed sensors, but can occur with any conducting structure of low resistance. Since the wiring arrangement affects the resonance behavior, these effects are rarely reproducible.

Modern patient monitors may contain a large amount of digital electronics having rf emissions of frequencies up to several megahertz; these typically cause image artifacts (Figure 3).

The intrinsic Faraday-shielding property of a magnet bore can be reduced by the presence of electrically conducting structures entering the magnet, e.g. an ECG cable. This effect can lead to puzzling observations. A wireless non-rf-shielded device (e.g. a NIBP monitoring device with plastic tubes) can work successfully without causing MR image degradation. However, when other devices such as an ECG are introduced alongside, image artifacts can appear, leading to the incorrect assumption that the additional device (i.e. the ECG) is the source of rf noise. Actually, the wires of the additional device were used as a guide for the rf noise from the electronics of the first device outside the magnet bore to circumvent the rf shielding effect of the magnet tube. Similarly, rf from the environment, if not attenuated by the wall-integrated Faraday-shield of the MR suite, can use monitoring wires to bypass the Faraday-shielding effect of the magnet bore.

3.5 MR Sequence Timing and Differentiation of Interactions

During an MRI sequence, different physical forces act simultaneously (Figure 4). Motion in the static magnetic field,

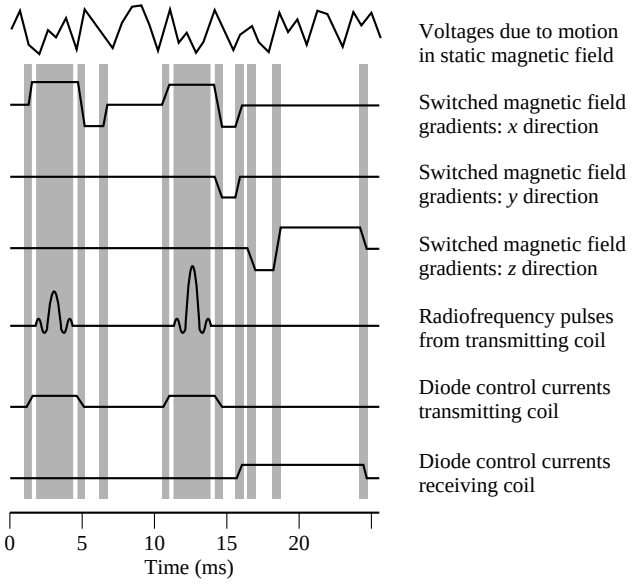

Figure 4 Schematic representation of a simplified MRI sequence (one phase step of a conventional spin echo sequence with a typical timescale) with different physical effects acting as possible sources of interactions with patient monitoring. Shaded lines indicate the generation of voltages in conducting structures by changing electromagnetic fields

switched gradients, diode currents, and rf pulses generate voltages in electrically conducting structures such as wires and the patient's body. These electromagnetic fields are switched (i.e. pulsed) several times within a few milliseconds and are indistinguishable to a human observer. Only interactions with the static field which are not synchronous with the acquisition are identified easily. To determine unambiguously the source of a particular electromagnetic interaction it is necessary to program the MR system such that only one of the electromagnetic fields (rf, gradients, diode currents) is generated at a time.

4 REDUCTION OF INTERACTIONS

Interactions between the MR system and monitoring and life support devices can be reduced by several different means depending on the physical nature of the interaction.[10–13,16–19,26–30,35–44] In general, a reduction of an undesirable interaction is preferable to postcorrection of the effects. For example, a reduced pick-up of voltages in the registration of the ECG is superior to filtering the distorted signal.

4.1 Monitoring vs Life Support Devices

Experience has shown that it is much more difficult, in general, to modify patient monitoring devices for MR compatibility than it is to modify life support equipment, especially mechanical ventilation units.[4,7,8,11,13,16–19] For hygiene reasons, most life support devices are constructed from inert, anticorrosive material such as stainless steel. This material is, conveniently, mostly nonmagnetic. Monitoring devices, on the other hand, usually contain many more electronic components, especially digital circuits, which interfere with the MR system.

4.2 Static Magnetic Field Effects and Use of Nonmagnetic Material

If possible, all ferromagnetic parts (valves, batteries, screws, boxes) of monitoring devices should be replaced with nonmagnetic components. The inevitable remaining ferromagnetic parts of equipment (e.g. the motors of the blood pressure cuff, transformers) should be located as far as possible from the magnet in order to reduce attraction and malfunction. CRT screens or oscilloscopes used near the magnet can be replaced by liquid crystal or plasma displays. Magnetic shielding and rotation of the CRT display deflection unit is only successful at a certain distance from the magnet. MR examinations using magnetic field strengths below 0.3 T are less problematic[14,25] than high-field MR systems because of the weaker fringe field and the large bore size of the magnets.

4.3 Radiofrequency Effects and Shielding

Radiofrequency interference can arise both from rf emissions originating from the monitor and interfering with the MR system, and from the strong rf pulses of the MR system rf coil and detected by the monitoring equipment sensors. Faraday shields surrounding electronic devices and high grade low pass filters can stop the emission and detection of rf. Some sensors (e.g. in pulse oximetry), however, require well-defined signals at higher frequencies (for the definition of the edges of signals), thus limiting the use of low pass filters. Reduction of rf interference from the environment is generally achieved by a wall-integrated Faraday shield (Figure 1), thus keeping the magnet room free from ambient rf noise. One manufacturer has utilized the inherent Faraday shielding effect of the magnet bore in its system design, by the use of an additional cylindrical tube which represents an elongation of the magnet bore.[17] This scheme requires different monitoring approaches and is not considered here.

MRI should be considered as a very sensitive experiment done over an extremely narrow frequency bandwidth. Even military-grade rf test sites are less sensitive than is necessary for MR system interference testing. Rf interactions and interference depend largely on the actual resonance frequency (i.e. field strength) of the MR system, the arrangement of the emitter, wires, the patient, the rf coils, and the imaging sequence. Therefore, the rf interactions that affect equipment are rarely reproducible. Only very careful design of filters, a large number and variety of tests, and use of nonelectrical measurements (see below) guarantees successful prevention of electromagnetic interactions.

In order to reduce the risk of burns caused by wires forming a resonant structure, MR manufacturers usually request that no loops and no direct contacts between the patient and any electrically conducting material are made.[18,19] ECG recording, however, inherently requires a galvanic (i.e. direct electrical current) contact with the patient. Burn hazards associated with ECG electrodes are reduced by using carbon electrodes with an increased specific electrical resistance.[35]

4.4 Magnetic Field Gradient Effects

According to the Faraday law, reducing the area surrounded by conducting wires has the effect of decreasing induced po-

Figure 5 Two examples of MR compatible monitoring systems, both with a complete set of observable vital parameters (e.g. ECG, pulse oximetry, NIBP, end-tidal CO_2 and O_2, impedance plethysmography, temperature, IBP). Both systems have an additional data display on a slave monitor in the MR console operator room. [Reproduced by permission of In Vivo Research (bottom) and ODAM-Bruker (top)]

tentials. This principle should be utilized whenever possible. For example, an appropriate positioning of ECG electrodes and twisting of the cables can considerably reduce artifacts on the ECG recording.[10,12,36]

Low pass filters,[37] blanking of the preamplifier, postprocessing or other methods can efficiently eliminate spikes from an ECG trace due to pulsed MR magnetic field gradients. However, since monitoring needs a continuous, clean ECG, some of these methods are limited to triggering purposes, as mentioned above.

4.5 Location of Monitoring Equipment

In the past, many MR sites used MR-incompatible monitors located outside the magnet room. This separation of monitors and MR system (including the patient) in two different rooms can solve the strong interaction problems, but it also introduces new problems. First, it requires wires and tubes that are too long. Also, two members of the medical team are necessary, one observing the monitors and describing his or her impressions to the other who is examining and, if necessary, treating the patient. This can cause misunderstandings and delays between the first observation of irregularities and an intervention.

4.6 Use of Optical, Mechanical, and Pneumatic Devices

Whenever possible, optical or mechanical means instead of electrical recording should be used for monitoring devices in order to avoid electromagnetic interferences.[38–44] In recent MR compatible pulse oximeters, the light source and detector are located outside the magnet and coupled to a fiber optic cable leading to the patient.[19,42] Temperature can be measured by means of optical sensors.[43] An ECG monitor, which amplifies and transforms the electrical signal to an optical light directly on the patient,[44] avoids interference by using a miniature preamplifier box and only optical fibers. NIBP measurement is inherently mechanical; here, pressure variations in an overly long tube can cause problems with accurate detection. Long sampling tubes can also affect detection by causing a delay in the remote analysis of breathing gases (capnography). Also, mixing of gases flowing through a long tube averages the gas content readings. For IBP measurement, the pressure transducer can be located outside the magnet bore, connected to the patient with a long plastic tube (e.g. two infusion sets in series).

5 STATE OF THE ART

The present state of patient monitoring during MRI examinations includes a heterogenous mix of commercially available, home built, and MR incompatible systems. Several complete systems (Figure 5) and various single purpose instruments[19] are commercially available.

5.1 Medical Needs of Different Patient Categories

Table 2 summarizes the frequently used combinations of parameters and life support for patients with different levels of medical needs. It can be seen that very different levels of

Table 2 Use of Vital Parameters for Determining the Status of Different Patients[a]

Patient condition	Examples of observed parameters and life support
Stable cooperative patient	ECG (for triggering)
Sedated stable patient	ECG, pulse oximetry
Premature baby	ECG, pulse oximetry, capnography (respiration frequency), temperature, incubator
Intubated, ventilated patient	ECG, pulse oximetry, capnography, temperature, NIBP/IBP, ventilator, inspired O_2, anesthesia gases, infusion sets, intubation, emergency equipment

[a]This table represents typical cases and is meant to be an illustration. In practice every case has to be considered individually by the staff responsible, taking into account the medical history of the patient and the guidelines of the corresponding professional association.

monitoring equipment are required for different patient categories. Each patient must be considered individually by the staff responsible. It is important that an MR site is equipped such that all patient categories examined at that site can be monitored safely. For example, a private hospital which exclusively examines outpatients with stable vital functions can be equipped appropriately with only an MR compatible pulse oximeter. The MR department of a large hospital with ICU patients and/or premature infants requires a complete set of MR compatible monitoring and life support devices, a set of MR compatible medical instruments, and, most importantly, well trained staff following strict regulations.

5.2 Monitoring Systems

Approximately a dozen MR compatible single components used mainly for monitoring heart rate, oxygen saturation, peripheral pulse, and respiratory rate are available that can provide surveillance of stable patients in the manner in which they are commonly examined in nonhospital MR sites.[18,19] For hospital needs, however, where some patients require a higher level of surveillance, only a few complete monitoring systems are commercially available (see e.g. Figure 5). When using an assortment of single devices to provide comprehensive monitoring, the interactions between the different equipments and their mutual compatibility (including user interface, location of the equipment, length of tubes and cables, power connections) need to be considered prior to purchase.

5.3 Ventilators

Various MR compatible ventilators are manufactured and available commercially.[18,19] However, since anesthesia equipment is heavily regulated by local authorities (following often very traditional local rules), not all commercial systems are approved in all countries.

5.4 Incubators

MR compatible incubators need to satisfy the spatial restrictions within the magnet, and to prevent interactions between the accompanying heater/ventilator apparatus and the MR system. Some incubators used for research studies have apparently solved these technical problems,[12,27–30] but governmental regulations and the limited market seems to inhibit the approval of these as commercial products.

5.5 Medical Instruments

MR compatible nonmagnetic medical instruments (infusion sets, laryngoscope, intubation material, lamps, scissors, stethoscope, clamps) are commercially available.[13] The supply of MR compatible medical instruments is only one aspect of their usage in the MR environment. Since these devices sometimes look identical to their MR incompatible magnetic counterparts, it is very important to separate MR compatible from ferromagnetic instruments by strict rules. In some cases, only invisible inserts make the difference, for example a nonmagnetic laryngoscope can contain highly ferromagnetic batteries.[6] As a rule, all devices and instruments in an MR site should be MR compatible, including those which are used only in the preparation room. Emergency carts are specially prone to causing accidents, since they are used in hectic situations with reduced attention to the hazards of the strong magnetic field of the MR system.

5.6 Patient Positioning Aids

While most MR system manufacturers provide MR compatible positioning aids, such as coil holders for the different organs of an adult patient, only a few offer special devices for certain patients such as infants. Different approaches have been suggested and, inevitably, every MR site invents its own equipment. One commercially available solution is a vacuum mattress for the positioning and immobilization of patients, especially infants. This mattress contains small plastic spheres in an airtight bag which retains its shape after evacuation.

5.7 Accident Prevention and Training

Many MR sites still have limited experience with the MR examination of high risk patients and, generally, anesthesiologists and pediatricians are not very familiar with MR technology. Since the interactions that exist in this environment are unfamiliar, invisible, and nonintuitive, the education of radiologists, anesthetists, pediatricians, and technicians must include some background information on the relevant electromagnetic forces.

Technical devices have a very limited capacity to correct human errors in an MRI room. Metal detectors are available in many sites, but typically are ineffective since they detect electrical conductance and not ferromagnetism—an MR compatible stainless steel device is detected in the same way as a 20 kg iron oxygen bottle.

6 OUTLOOK

Future developments will influence patient monitoring and life support considerably. Future MR technology (e.g. magnets, sequences), new MR diagnostic procedures, the increasing number of MR sites, and governmental regulations will change many aspects.

6.1 Governmental Regulations

Due to the lack of generally accepted devices and strategies in the past, many individual solutions, some inappropriate, were arrived at and reluctantly accepted.[22] Since MR-compatible monitoring devices are now available, governmental rules and guidelines of the corresponding professional association[21,22,24] will increasingly regulate patient monitoring in different countries.

6.2 High Risk Patients and Interventional MRI

The increasing number of MR systems in use increases the possibility that MR sites will scan more high risk patients. Subsequently, new experience gained from high risk patients will increase the potential of MRI and expand its possible applications (e.g. hemorrhage, trauma). Interventional MRI will

introduce the monitoring needs typical for conventional surgery into the concerns for patient monitoring during MRI.

6.3 Magnet Technology

Magnets with efficient passive or active shielding of the fringe field are already commercially available. Mainly designed for easier placement of the magnet in a building, this innovation also helps to reduce the effect of the fringe field on monitoring systems. Recently introduced 'open magnets', e.g. as used in interventional MRI will give more access to the patient and make monitoring easier. However, the inherent rf shielding effect of long cylindrical magnets is lost in open magnets.

6.4 New MRI Sequences

Very rapid MR sequences (see e.g. ***Echo-Planar Imaging***) will reduce the total time needed for an MR scan session, as well as the time taken for a single scan. This will open up a new field of applications (e.g. breath-hold images, images of the abdomen, images of arrhythmic hearts) and will allow the examination of noncooperative patients and children in a shorter period without the need for lengthy immobilization. This will increase the number of problematic patients receiving MR examinations, yet reduce monitoring problems due to the shortening of the examination time. Since electromagnetic fields are switched more quickly during examinations using these sequences, interactions with other technical devices such as monitors will increase.

6.5 Developments in Patient Monitoring

Patient monitoring itself will develop such that most parameters will be measured by optical or hydraulic/pneumatic means. Electrical measurements will be avoided whenever possible.[38–44] Inherent electrical measurements, such as an ECG, will be altered so that the electrical component will be miniaturized.[44]

6.6 Summary

Patient monitoring will have an increased importance in the future because of the increasing number of high risk patients examined and interventional MRI applications. Monitoring will be less problematic due to new technical developments in the engineering of monitoring systems and of the advancement of MR technology, including magnet design and very rapid image acquisition.

7 RELATED ARTICLES

Echo-Planar Imaging; Gradient Coil Systems; Health and Safety Aspects of Human MR Studies; Image Formation Methods; Radiofrequency Systems and Coils for MRI and MRS.

8 REFERENCES

1. R. S. Geiger and H. F. Cascorbi, *Anaesth. Analg.*, 1984, **63**, 622.
2. J. L. Roth, M. Nugent, J. E. Gray, P. R. Julsrud, T. H. Berquist, J. C. Sill, and D. B. Kispert, *Anesthesiology*, 1985, **62**, 80.
3. G. Weston, L. Strunin, and G. M. Amundson, *Can. Anaesth. Soc. J.*, 1985, **32**, 552.
4. V. Dunn, C. E. Coffman, J. E. McGowan, and J. C. Ehrhardt, *Magn. Reson. Imaging*, 1985, **3**, 169.
5. C. B. McArdle, D. A. Nicholas, C. J. Richardson, and E. G. Amparo, *Radiology*, 1986, **159**, 223.
6. C. Nixon, N. P. Hirsch, I. E. C. Ormerod, and G. Johnson, *Anaesthesia*, 1986, **41**, 131.
7. L. W. Hedlund, J. Deitz, R. Nassar, R. Herfkens, P. Vock, J. Dahlke, R. Kubek, E. L. Effman, and C. E. Putman, *Invest. Radiol.*, 1986, **21**, 18.
8. D. S. Smith, P. Askey, M. L. Young, and H. Y. Kressel, *Anesthesiology*, 1986, **65**, 710.
9. A. Boutros and W. Pavlicek, *Anesth. Analg.*, 1987, **66**, 367.
10. R. N. Dimick, L. W. Hedlund, R. J. Herfkens, E. K. Fram, and J. Utz, *Invest. Radiol.*, 1987, **22**, 17.
11. G. H. Barnett, A. H. Ropper, and K. A. Johnson, *J. Neurosurg.*, 1988, **68**, 246.
12. C. Boesch and E. Martin, *Radiology*, 1988, **168**, 481.
13. S. J. Karlik, T. Heatherley, F. Pavan, J. Stein, F. Lebron, B. Rutt, L. Carey, R. Wexler, and A. Gelb, *Magn. Reson. Med.*, 1988, **7**, 210.
14. D. M. Hadley, G. M. Teasdale, A. Jenkins, B. Condon, P. MacPherson, J. Patterson, and J. O. Rowan, *Clin. Radiol.*, 1988, **39**, 131.
15. D. L. Johnston, S. L. Mulvagh, R. W. Cashion, P. G. O'Neill, R. Roberts, and R. Rokey, *Am. J. Cardiol.*, 1989, **64**, 172.
16. J. E. McGowan and A. Erenberg, *Magn. Reson. Imaging*, 1989, **7**, 145.
17. V. S. Rejger, B. F. Cohn, G. J. Vielvoye, and F. B. de Raadt, *Eur. J. Anaesthesiol.*, 1989, **6**, 373.
18. E. Kanal and F. G. Shellock, *Radiology*, 1992, **185**, 623.
19. F. G. Shellock, C. A. Liwer, and E. Kanal, *Rev. Magn. Reson. Med.*, 1992, **4**, 21.
20. M. E. Quirk, A. J. Letendre, R. A. Ciottone, and J. F. Lingley, *Radiology*, 1989, **170**, 463.
21. American Academy of Pediatrics. Committee on Drugs, *Pediatrics*, 1992, **89**, 1110.
22. D. M. Fisher, *Radiology*, 1990, **175**, 613.
23. A. M. Hubbard, R. I. Markowitz, B. Kimmel, M. Kroger, and M. B. Bartko, *J. Comput. Assist. Tomogr.*, 1992, **16**, 3.
24. E. Kanal, F. G. Shellock, and SMRI Safety Committee, *JMRI*, 1992, **2**, 247.
25. E. M. Larsson, S. Holtas, and S. Cronqvist, *Acta Radiol.*, 1988, **29**, 69.
26. C. B. McArdle, J. W. Wright, W. J. Prevost, D. J. Dornfest, and E. G. Amparo, *Radiology*, 1986, **159**, 273.
27. C. Boesch, K. Luescher, P. Brunner, P. Kaelin, M. Zuerrer, P. Dangel, and E. Martin, *Radiology*, 1988, **169** (P), 384.
28. R. J. T. Corbett, A. R. Laptook, and R. L. Nunnally, *Neurology*, 1987, **37**, 1771.
29. P. L. Hope and E. O. R. Reynolds, *Clin. Perinatol.*, 1985, **12**, 261.
30. D. P. Younkin, M. Delivoria-Papadopoulos, J. C. Leonard, V. H. Subramanian, S. Eleff, J. S. Leigh, and B. Chance, *Ann. Neurol.*, 1984, **16**, 581.
31. T. F. Budinger, in 'Medical Magnetic Resonance. A Primer—1988', ed. T. F. Budinger and A. Margulis, Society of Magnetic Resonance in Medicine, Berkeley, CA, 1988, p. 327.
32. T. S. Tenforde, C. T. Gaffey, B. R. Moyer, and T. F. Budinger, *Bioelectromagnetics*, 1983, **4**, 1.

33. F. G. Shellock and G. L. Slimp, *Am. J. Roentgenol.*, 1989, **153**, 1105.
34. G. Bashein and G. Syrovy, *Anesthesiology*, 1991, **75**, 382.
35. H. R. van Genderingen, M. Sprenger, J. W. de Ridder, and A. C. van Rossum. *Radiology*, 1989, **171**, 872.
36. R. E. Wendt, R. Rokey, G. W. Vick, and D. L. Johnston, *Magn. Reson. Imaging*, 1988, **6**, 89.
37. R. Rokey, R. E. Wendt, and D. L. Johnston, *Magn. Reson. Med.*, 1988, **6**, 240.
38. G. Martens, T. Helzel, and J. Kordts, *Proc. SPIE Int. Soc. Opt. Eng.*, 1985, **586**, 250.
39. C. F. Roos and F. E. Carroll, *Radiology*, 1985, **156**, 548.
40. Y. Shah, R. A. Valsler, and A. W. Palmer, *J. Biomed. Eng.*, 1985, **7**, 326.
41. J. P. Legendre, R. Misner, G. V. Forester, and Y. Geoffrion, *Magn. Reson. Med.*, 1986, **3**, 953.
42. F. G. Shellock, S. M. Myers, and K. J. Kimble, *Am. J. Roentgenol.*, 1992, **158**, 663.
43. K. H. Taber and L. A. Hayman, *J. Magn. Reson. Imaging*, 1992, **2**, 99.
44. J. Felblinger, C. Lehmann, and C. Boesch, *Magn. Reson. Med.*, 1994, **32**, 523.

Biographical Sketch

Chris Boesch. *b* 1951. Ph.D. (physics), 1979, ETH (Swiss Federal Institute of Technology), Zürich, Switzerland, (high-resolution NMR studies of polypeptide conformation); M.D., 1986, University Zürich. University Children's Hospital Zürich, 1985–90 (installation of a clinical 2.35T/40cm MR system, patient monitoring systems for pediatric and neonatal patients, MRI and MRS studies of brain development); Professor and Director of MRS and methodology, University of Bern, Switzerland, 1991–present. Current research specialties: in vivo spectroscopy (^{1}H, ^{31}P, and ^{13}C) of various organs, methodology of in vivo NMR, patient monitoring.

Radiofrequency Fields: Interactions, Biological Effects, and Safety Issues

Jeffrey W. Hand
Hammersmith Hospital, London, UK

1 INTRODUCTION

The term radiofrequency (rf) is often used in the biological effects and occupational health literature to cover the frequency range from 300 kHz to 300 GHz. Sometimes there is additional discrimination within this range in that use of the term rf is restricted to frequencies up to 300 MHz while the higher frequencies are referred to as microwaves. Radiofrequency fields and radiation differ from ionizing radiation in that the photon energy, given by the product of the frequency and Planck's constant, is much smaller than the 12.4 eV required for ionization. In MR applications, the frequency of the $\boldsymbol{B}_1$ field usually matches the Larmor precession frequency ν, which is related to the static magnetic field $\boldsymbol{B}_0$ as in Equation (1)

$$\gamma B_0 = \nu \tag{1}$$

where γ is gyromagnetic ratio. The value of γ is 42.57 MHz T^{-1} for the hydrogen atom and so the $\boldsymbol{B}_1$ field frequency for typical clinical MR systems (with $\boldsymbol{B}_0$ of 0.2–2 T) lies in the range 8.5–85.14 MHz. Higher frequencies, up to about 400 MHz, are encountered in high $\boldsymbol{B}_0$ MR systems used for research. Typically, rf energy is applied as a series of pulses with duration ranging from 10 s of microsecond pulses to 10 s of millisecond pulses depending upon the MR application.

Traditionally, the consensus of scientific opinion is that interactions between rf fields and the human body are considered to be thermal, although there have been claims for other mechanisms of interaction. The energy absorbed is directly related to the rf fields inside the body and not those incident upon the body. The internal and incident rf fields can be quite different, depending on the size and shape of the body, its electrical properties, its orientation with respect to the incident rf field, and the frequency of the incident field. However, since direct measurement of the incident field is easier and more practical than measurement of the internal fields, especially in people, dosimetry is used to relate the internal fields to the incident field.

Much effort has been applied to understanding the interaction of rf fields with biological tissues and the associated dosimetry since the 1960s, resulting in effective procedures that minimize rf field exposure of the general public and as an occupational consequence.[1–3] However, there are also therapeutic applications of rf fields such as diathermy and hyperthermia in which the patient is purposely exposed to high-level fields with the intention of raising tissue temperature, and a considerable body of knowledge regarding thermal responses in patients has been accrued.[4] The evidence for harmful biological effects associated with exposure to rf radiation at field intensities lower than those that produce significant and measurable heating is less clear.[3]

Several studies have investigated the thermal responses of humans undergoing MR examinations[5] and safety guidelines associated with rf fields in MR have been produced. However, the dissemination of advanced MR techniques such as sequences that enable data to be acquired rapidly, the use of coils with close coupled designs and local transmit systems, the increasing availability of high $\boldsymbol{B}_0$ field systems, and the development of interventional techniques is making realistic assessment of rf power deposition and its consequences increasingly important.

2 INTERACTIONS BETWEEN rf FIELDS AND TISSUES

2.1 Dielectric Properties

For essentially nonmagnetic media such as tissues, interaction with an rf field is predominantly through the electric ($\boldsymbol{E}$) field, or the $\boldsymbol{E}$ field, induced in the tissue by the $\boldsymbol{B}_1$ field and involves polarization of charges, orientation of molecules such as water and proteins that possess permanent electric dipoles, and a drift of conduction charges. In MR applications, the interaction is primarily caused by magnetic induction, with a negligible contribution directly from the incident $\boldsymbol{E}$ field. Exceptions are when tissue is placed close to feed points of transmit coils or other regions with locally high $\boldsymbol{E}$ fields, when capacitive coupling may occur.

Conduction and polarization effects are both taken into account in the quantity ϵ, known as the complex permittivity of the material and defined as:

$$\epsilon = \epsilon_0(\epsilon' - i\epsilon'') \tag{2}$$

where ϵ_0 is the permittivity of free space (8.854×10^{-12} F m^{-1}) and $(\epsilon'-i\epsilon'')$ is the relative permittivity. The dielectric constant, ϵ', accounts for the additional polarization charge and ϵ'', the loss factor, is a measure of how much power is absorbed from the rf field. Equation (3) shows the relationship between ϵ'', conductivity σ, and angular frequency of the field ω.

$$\epsilon'' = \frac{\sigma}{\omega\epsilon_0} \tag{3}$$

The term σ takes account of not only the conductivity arising predominantly from mobile charges but also a frequency-dependent part arising from dielectric polarization. Both ϵ' and ϵ'' depend upon the frequency of the applied field. Radiofrequencies encountered in MR fall within the so-called β (extending from about 10 kHz to 100 MHz) and δ (extending from around 300 MHz to 1 GHz) regions of dispersion exhibited by ϵ' and ϵ'' of tissues.[6] The β dispersion results from inhomogeneous structures including the cell membrane and intra- and extracellular fluids. At the higher frequencies within the β dispersion, and in the δ dispersion, there are contributions from the rotation of permanent dipoles (small amino acids, charged functional groups in polypeptide chains, and protein-bound water). The variation of tissue dielectric properties with frequencies may be predicted[7] and Figures 1 and 2 show typical values for several tissues.

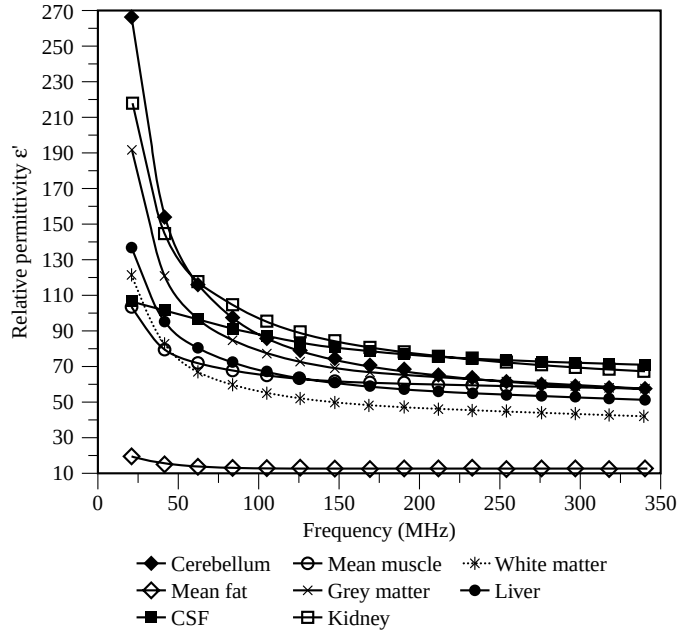

Figure 1 Frequency dependence of relative permittivity ϵ' for several tissues; CSF, cerebrospinal fluid

The permeability of tissues may be taken to be that of free space, $\mu_0 = 4\pi \times 10^{-7}$ H m^{-1}. The velocity of propagation is given by $1/\sqrt{(\mu\epsilon)}$ and so (see Figure 1) the wavelength associated with $\boldsymbol{B}_1$ field in tissues of high water content is reduced by about an order of magnitude compared with that of free space at rf frequencies used in MR.

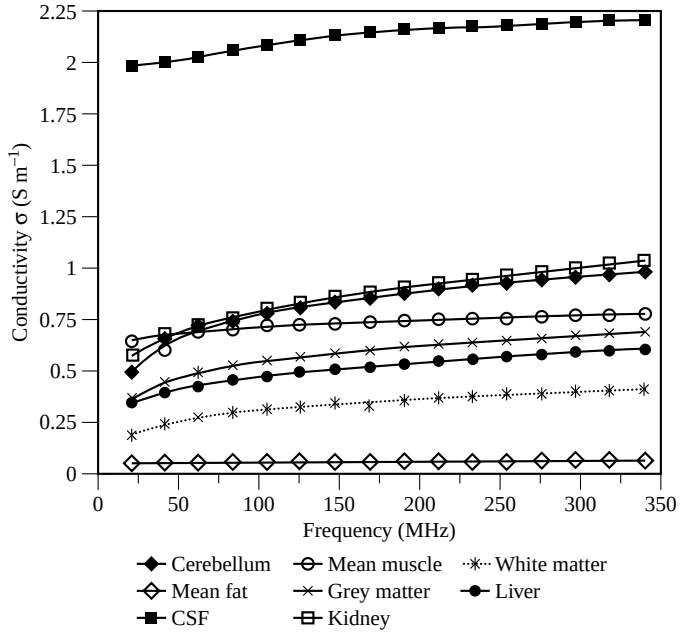

Figure 2 Frequency dependence of conductivity σ for several tissues; CSF, cerebrospinal fluid

2.2 Specific Absorption Rate

The transfer of energy from rf fields to tissue is described by the specific absorption rate (SAR), defined as the time derivative of the incremental energy (dW) absorbed by an incremental mass (dm) contained within a volume element (dV) of a density ρ:[8]

$$\mathrm{SAR} = \frac{\mathrm{d}}{\mathrm{d}t}\left(\frac{\mathrm{d}W}{\mathrm{d}m}\right) = \frac{\mathrm{d}}{\mathrm{d}t}\left(\frac{\mathrm{d}W}{\rho\,\mathrm{d}V}\right) \tag{4}$$

This is the local SAR and it is related to the local internal $\boldsymbol{E}$ field through Equation (5)

$$\mathrm{SAR} = \frac{\sigma\,|\,E\,|^2}{2\rho} = \omega\epsilon_0\epsilon''\frac{|\,E\,|^2}{2\rho} \tag{5}$$

where $|E|$ is the magnitude of the $\boldsymbol{E}$ field vector. In addition to the local SAR, spatially averaged values are also used. These are determined by dividing the time rate of change of the total energy transferred to the absorber by the appropriate mass (e.g., the total mass of the body, 1 g, 1 kg, etc.).

The importance of SAR in dosimetry arises from the fact that the absorbed energy is directly related to the internal $\boldsymbol{E}$ and $\boldsymbol{B}$ fields. These fields can be quite different from the external ones and depend on the size and shape of the body, its electrical properties, its orientation with respect to the incident fields, and the frequency of the incident fields. SAR provides measures of both the energy absorption that leads to tissue heating and the internal fields. The ability to determine the values of SAR in irradiated subjects for given exposure conditions permits meaningful extrapolation of biological effects observed in laboratory experiments to similar effects that might occur in irradiated people.

A simple estimate of the penetration of the rf field (f; MHz) into a planar dielectrically uniform tissue is the plane wave penetration depth (skin depth) d:

$$d = \frac{1}{\sqrt{2}\pi f\sqrt{\mu_0\epsilon_0}\sqrt{\sqrt{\epsilon'^2 + \epsilon''^2} - \epsilon'}} = \frac{67.48}{f\sqrt{\sqrt{\epsilon'^2 + \epsilon''^2} - \epsilon'}} \quad (\text{in meters}) \tag{6}$$

and over which the SAR is reduced to 13.5% of its original value. This attenuation leads to nonuniform rf excitation over the imaging volume. However, Equation (5) provides only qualitative understanding of realistic problems since exposure is in the near field of the transmitter coil and the body is neither planar nor dielectrically uniform. In particular, the frequency dependence of SAR exhibits resonant behavior and peak absorption occurs in an irradiated object when typical dimensions are approximately equal to half the wavelength. The value of SAR varies approximately as f^2 below resonance and as $1/f$ just beyond resonance. For appropriate polarizations, resonance occurs at around 70 MHz for the average adult whole body, above 100 MHz for a child or a neonate, and around 200 MHz for the adult head and neck.

2.3 Measurement of SAR

Two recommended methods for determining SAR in relation to rf safety of MR systems are outlined in international and national standards.[9,10] In the 'pulse energy method', the peak power absorbed in a test object that simulates coil loading resulting from the patient, corrected for the power absorbed by the unloaded coil, is determined. The average power absorbed during the rf pulse sequence under investigation is found and the SAR is given by Equation (7).

$$\mathrm{SAR} = \frac{1}{M}\sum_i \frac{P_{\mathrm{object}} \int \frac{B_1(t)^2}{B_{1\mathrm{peak}}^2}\,\mathrm{d}t}{S} \qquad (7)$$

where M is the mass of the test object, P_{object} is the peak power absorbed by the test object, $B_1(t)/B_{1\,\mathrm{peak}}$ is the rf pulse waveform normalized to its peak value for each pulse (e.g., 90° pulses, 180° pulses) in the pulse sequence, and S is the total scan time. The 'calorimetric method' (for whole-body averaged SAR only) involves use of an annular test object containing NaCl solution that simulates the coil loading observed with 50–90 kg patients. The test object is subjected to rf pulses for a period sufficient to create a temperature increase at least 20 times the uncertainty associated with the thermometry system used.

Local SAR values greater than a few watts per kilogram may be measured within tissue-like phantoms or in vivo by determining the local change of temperature (ΔT) following a brief exposure ($\Delta t = 5$–30 s) to the fields using the relationship $\mathrm{SAR} = c(\Delta T/\Delta t)$ where c is the specific heat (J kg^{-1}) of the medium. A nonperturbing thermometer with a resolution of 0.01–0.1°C is required. Measurements are difficult to make in regions of high SAR or when several SAR hot-spots are present (because of thermal conduction effects) and in the presence of high SAR gradients.

SAR may also be determined by measuring the internal $\boldsymbol{E}$ field with a calibrated minimally perturbing probe[11] and using Equation (5). The technique may be used for 10–120 MHz but can be extended to higher frequencies (hundreds of megahertz) if a suitable probe is available.

3 BIOLOGICAL EFFECTS OF rf FIELDS

The major effect of absorption of energy at frequencies above 10 MHz is heating. Increases in body temperature of more than 1–2°C may have adverse effects such as heat exhaustion and heat stroke. Exposure of resting humans to SAR in the range 1–4 W kg^{-1} for periods of about 30 min causes a change in body temperature of less than 1°C. However, the use of drugs or alcohol while a person is under thermal stress may compromise the body's thermoregulatory system. The induction of a high frequency current of about 100 mA in a limb leads to a sensation of warmth but is unlikely to result in a temperature increase of more than 1°C. Exposure of laboratory animals to E-M (electromagnetic) fields that result in SAR above 4 W kg^{-1} has been shown to result in increases in blood volume, heart rate, and blood pressure. Levels of exposure that result in changes in body temperature of more than 1–2°C may lead to changes in neural and neuromuscular functions, increase in blood–brain barrier permeability, lens opacities and corneal abnormalities, changes in the immune system, hematological changes, reduced sperm production and motility, and teratogenicity.[12,13]

Areas of the body that are poorly perfused (e.g., the eyes and the testes) are particularly susceptible because of their inability to dissipate an abnormal thermal load. For example, short-term exposure to rf radiation at 100–200 mW cm^{-2} can cause cataracts in experimental animals[14,15] while temporary sterility, caused by changes in sperm count and in sperm motility, is possible after exposure of the testes to high-level rf radiation.[16]

Thermal sensations experienced by humans following exposure to E-M fields may persist after cessation of the irradiation. This effect is probably a consequence of several factors including a long latency to detection, a persistent effective temperature gradient across subcutaneous tissues and their thermal inertia, and the volume of subcutaneous tissue heated. Although changes in skin and muscle blood flow occur as a result of the increase in tissue temperature, quantitative information regarding this redistribution of thermal energy is sparse.

Indirect effects of rf fields on humans include shock and burn caused by contact with metallic objects in the field. For frequencies in the range 100 kHz to 110 MHz, the threshold for perception is 25–40 mA while that for pain is about 30–55 mA. Contact currents above 50 mA may be associated with severe burns.

The 'microwave auditory effect' can arise when the heads of humans and animals are exposed to pulse-modulated rf fields with frequencies in the range 200 MHz to 6.5 GHz, peak incident power densities of the order of 300 mW cm^{-2}, time-averaged power densities as low as 0.1 mW cm^{-2} and pulse widths varying from 1 to 100 μs. The effect is perceived as a buzzing, clicking, hissing, or popping noise depending upon modulation characteristics. The perception threshold for pulses shorter than 30 μs depends upon the energy density per pulse; the specific energy absorption threshold is around 20 mJ kg^{-1}. The most widely accepted explanation is that absorption of energy from the rf field leads to a thermoelastic interaction in the auditory cortex of the brain.[13,17]

Investigations on the effects of occupational rf exposure on pregnancy outcome have produced both negative and positive results. Epidemiological studies of physiotherapists indicated that there were no statistically significant effects on abortion or fetal malformation[18] but other studies of similar populations of female workers showed an increased risk of miscarriage and birth defects.[19,20] Hyperthermia is teratogenic to several mammalian species including primates and has been implicated in defects of the central nervous system and facial defects in children whose mothers suffered prolonged exposure to temperatures above 39°C during the first trimester of pregnancy. Until further epidemiological data on exposed individuals and more precise quantitative assessment of the exposures involved are available, it is difficult to draw firm conclusions on reproductive risk associated with rf fields.

The few studies that address the risk of cancer following exposure to rf fields generally lack quantitative assessment of the exposures involved. Studies of populations living near rf transmitters have suggested a local increase in the incidence of leukemia but the results are inconclusive. Overall, the few pub-

lished epidemiological studies provide only limited information on rf fields and the risk of cancer.[21–23]

The numerous studies of the effects of amplitude-modulated E-M fields, mostly involving low levels of exposure, have yielded both positive and negative results. These effects are highly dependent upon exposure parameters, the types of cell and tissue involved, and the end-points considered; they are small and difficult to relate to potential health effects.[3] There is no convincing evidence of frequency and power windows in the responses to these low-level amplitude-modulated E-M fields.

The International Commission on Non-Ionizing Radiation Protection (ICNIRP), in summarizing biological effects and epidemiological studies involving frequencies from 100 kHz to 300 GHz, concluded:[3] 'Epidemiological studies on exposed workers and the general public have shown no major health associated with typical exposure environments. Although there are deficiencies in the epidemiological work, such as poor exposure assessment, the studies have yielded no convincing evidence that typical exposure levels lead to adverse reproductive outcomes or an increased cancer risk in exposed individuals. ... In general, the effects of exposure of biological systems to athermal levels of amplitude-modulated electromagnetic fields are small and are very difficult to relate to potential health effects.' Other official bodies have come to similar conclusions.[24,25]

4 MR PROCEDURES AND rf CONCERNS

The consequences of a lack of thermoregulation during exposure to rf fields from 1.5 T MR imagers are highlighted by studies carried out on anesthetized animals. In dogs, SAR values of 5.9–10.5 W kg^{-1} led to site-specific (including deep tissues) mean temperature increases of up to 4.6°C.[26] In sheep, whole body SAR values of 1.5–4 W kg^{-1} led to temperature increases in subcutaneous and deep tissues that were insufficient to produce adverse thermal effects,[27] although it was postulated that such effects might be produced at SAR levels around 8 W kg^{-1}. The dependence of rf dosimetry on subject size, and the thermal consequences of an impaired thermoregulatory system, must be taken into account when extrapolating these results to nonanesthetized adult humans. However, the experimental conditions may be more representative of exposure of sedated pediatric patients.

Statistically significant temperature increases of 7.5, 3.9, and 2.9°C were recorded on the upper arm, forearm, and chest, respectively, in healthy volunteers exposed to whole-body-averaged SAR values of 2.7–4 W kg^{-1} during a 30 min procedure in a 1.5 T scanner.[28] The greatest increase in core temperature was 0.2°C. Fifty patients undergoing imaging of the trunk at whole-body-averaged SAR values ranging from 0.42 to 1.2 W kg^{-1} showed a statistically significant increase in core temperature.[29] Increases in body temperature were greater than those in healthy volunteers, probably because these patients had impaired thermoregulation. In other investigations,[30–32] local temperatures in patients were monitored prior to and following MRI of various anatomical sites involving averaged SAR values >0.4 W kg^{-1}. A poor correlation was found between changes in tissue temperature and whole-body-averaged SAR values.[5] This highlights the complexity of the thermoregulatory system and suggests the importance of assessing safety in terms of tissue temperature as well as averaged SAR. Shellock et al. studied volunteers undergoing imaging performed at whole-body-averaged SAR values of 6.0 W kg^{-1} in cool and warm environments.[33] Although there were statistically significant increases in temperatures monitored in several body regions as well as increases in heart rate, skin blood flow, and systolic blood pressure, this level of SAR was physiologically tolerated by these individuals with normal thermoregulation. The subjective perception of heating was greater during those experiments carried out in the cool environment than in the warm environment.

Auditory perception of pulsed rf energy absorption in the human head associated with head coils was studied in six volunteers.[34] Frequencies in the range 2.4–170 MHz and pulse widths in the ranges 3–100 μs were considered and the threshold pulse energy was found to be around 16 mJ. Local rf exposure with optimized surface coils positioned flush with the ear reduced the threshold to approximately 3 mJ. Radiofrequency-induced auditory noise is usually masked by noise associated with switched gradient fields.

Certain MR pulse sequences are more rf intensive than others. Fast spin echo uses rapid high-power rf pulses and leads to greater energy absorption. Magnetization transfer sequences and the less common T_1 in the rotating frame sequences also increase power to the patient, as do spectroscopic procedures involving, particularly, homo- or heteronuclear decoupling. Radiofrequency energy absorption is dependent upon the type of coil used. Small or local coils deposit less energy than large ones and circularly polarized coils require less power than linearly polarized ones. Shorter rf pulses require higher power to attain the same flip angle as achieved with longer pulses.

If the frequency dependence of the tissue dielectric properties is neglected, then the transmitted rf power required to achieve a given flip angle increases as the square of the resonance frequency ν. In reality, the power requirement will increase more rapidly since tissue conductivity increases with increasing frequency (Figure 1).

5 DOSIMETRY AND MODELING

5.1 Dosimetry and Modeling of E-M Fields

Early predictions of rf fields and power absorption associated with coils used in MR were based on geometrically simple homogenous models[35–37] or inhomogenous phantoms.[38] While such studies provide valuable insight into the problem and reasonable estimates of the average rf power absorption during MR procedures, they cannot predict reliably local peak SAR levels in dielectrically heterogeneous bodies.[39]

Beginning in the late 1980s, more realistic electromagnetic models were developed. Power absorption in the body from an idealized $\boldsymbol{B}_1$ field (the phase was assumed to be constant across the body) associated with whole body imaging at 1.5 T was calculated using a quasistatic method.[40,41] In quasistatic models, the inherent coupling between time-varying $\boldsymbol{E}$ and $\boldsymbol{B}$ fields is neglected and the spatial distribution of the $\boldsymbol{B}_1$ field is taken to be that of the static field from the coil, with a superposition of the time variation, simplifying the calculation of the

field since propagation effects are ignored. Quasistatic methods are considered suitable for frequencies up to 40–60 MHz, that is when the wavelength is large compared with the dimensions of the coil and body or body region considered. At high frequencies, conduction and displacement currents lead to changes in the rf field within the subject, quasistatic approximations are inadequate, and a solution of the time-dependent Maxwell's equations is necessary. The assumption that the rf field is not perturbed by the body, inherent in the quasistatic approach, leads to an overestimation of SAR at higher frequencies.[42]

Several techniques are available to solve time-dependent E-M field problems (method of moments, finite elements, finite differences, boundary integrals, etc.). A method apparently well-suited to the computation of rf fields in MR applications is the finite difference time domain method[43] in which the propagation of the rf field from its source through the dielectrically heterogeneous tissues is simulated in a time-stepped manner until the solution converges to the steady state. Such numerical methods are useful in predicting detailed structure of the rf field distribution and provide insight into the relationship between peak SAR and spatially averaged SAR values.

Tissue inhomogeneities can lead to localized peaks of induced current density and so to 'hot spots'. The patient or volunteer undergoing a MR examination is subjected to the near field of the rf transmit coil and this may also lead to localized heating close to the coil. Recent analyses of fields and SAR produced by coils for anatomically realistic cases include those in the head[44–47] and other body parts.[48–50]

5.2 Thermal Modeling

Thermal sequelae of rf power deposition associated with MR procedures have been studied using compartmental models that describe human thermoregulation.[51] However, this approach uses SAR values averaged over the volume of the compartment and so details of local temperature fields cannot be predicted. Models that describe the detailed local heat transfer within tissues are more suited to predicting local temperature fields.

Seminal work in the development of models describing heat transfer within tissues was that of Pennes,[52] who analyzed the quantitative relationship between arterial blood and tissue temperatures. The cooling effect of perfusion (Q_{BF}) was determined using:

$$Q_{BF} = w_b c_b K(T - T_{art}) \quad (8)$$

where w_b is the volumetric perfusion rate (kg m^{-3} s^{-1}), c_b is the specific heat of blood, T_{art} is the local arterial temperature (taken to be equal to body core temperature), T is the local tissue temperature, and K is a constant ($0 \leq K \leq 1$) related to thermal equilibrium between capillary blood and local tissue. Pennes' data, when considered over a length scale of a few centimeters or more, are in very good qualitative agreement and reasonable (to within about 0.5°C) quantitative agreement with measurements. The shortcomings of this approach include the assumption that blood enters the local tissue volume at arterial temperature and leaves at local tissue temperature. In addition, heat transport related to the mass transport of blood, the actual temperature of the blood entering the local tissue volume, individual cooling or heating by large vessels, and the effects of the complete venous vessel network are all neglected.

Considering the underlying assumptions, this approach has been successful in simulating experimentally determined elevated temperature distribution.[50,53,54] Other studies[55] have highlighted the importance of large vessels and a high density of vessels on local heat transfer within tissues. Arkin et al. summarized several alternative thermal models and findings from experimental verifications and recommended vessel structures for which the practical implementation of the models is appropriate.[56] Thermal models that include discrete vessels and vascular trees have also been developed.[57,58]

6 INTERNATIONAL AND NATIONAL rf SAFETY GUIDELINES

Since the main adverse effects that are likely to result from acute exposure to rf magnetic fields are those associated with responses to an increased thermal load and the effects of elevated body or local tissue temperatures, the degree of local heating must be considered in assessing safety of MR imaging and spectroscopy examinations. Burns may be caused by touching conducting objects. Several factors may contribute to an individual's decreased ability to adapt to an increased thermal load. These include old age, obesity, hypertension, and use of drugs such as diuretics, tranquillizers, sedatives, and vasodilators. Thermoregulation in infants is not well developed and heat loss from the embryo and fetus may be less than that from well-perfused tissues.

MR rf safety guidelines are based on more general safety guidelines that limit exposure to known adverse health effects.[3,24,59,60] Some guidelines[3,24] include basic restrictions (based directly on established health effects and reference levels derived from measurements and/or computed predictions) that provide practical exposure assessment. Federal Communications Commission (FCC) guidelines[60] on procedures for evaluating environmental effects of rf emissions incorporate limits of maximum permissible exposure (MPE) in terms of electric and magnetic field strength. Most guidelines (with the exception of the National Radiological Protection board (NRPB)[24,61]) propose different limitations on occupational and general public exposures. Basic restrictions[3,24] are summarized in Table 1. MPE values,[60] together with ICNIRP[3] reference levels and NRPB[24] investigation levels, are summarized in Table 2.

For pulsed fields, conditions that invoke the microwave auditory effect in people with normal hearing should be avoided. NRPB recommends that the peak specific energy absorption in the head should be less than 10 mJ kg^{-1} over any 30 μs period.[24] The assessment of compliance for situations such as magnetic fields with high harmonic content, pulsed and transient magnetic fields, and exposure to the inductive near-field of rf sources is discussed by Chadwick.[62]

NRPB MR safety guidelines[63,64] for exposure to rf fields are intended to avoid a rise of more than 0.5°C in core temperature of patients and volunteers, including those who have an impaired thermoregulatory ability. The 'uncontrolled level' limits on time-averaged (15 min) whole-body SAR assume a specified environment (relative humidity <50% and ambient temperature <22°C) and are 1 W kg^{-1} (for >30 min), 30 W

Table 1 Basic restrictions on exposure to rf fields

Frequency	RMS current density (mA m^{-2})		Whole-body-average SAR (W kg^{-1})	Localized SAR (W kg^{-1})			
	Head and neck	Head, neck and trunk		Head and trunk	Neck and trunk	Head and fetus	Limbs
International Commission on Non-ionizing Radiaton Protection[a]							
100 kHz to 10 MHz	$f/100$[b]		0.4[c]	10[d]			20[d]
10 MHz to 10 GHz			0.4[c]	10[d]			20[d]
National Radiological Protection Board[24]							
0.1–10 MHz		$f/100$	0.4[e]		10[f]	10[g]	20[h]
10 MHz to 10 GHz			0.4[e]		10[f]	10[g]	20[h]

f, frequency (in Hz); RMS, root mean square; SAR, specific absorption rate.
For pulses of duration τ_p the equivalent frequency is determined by $1/(2\tau_p)$. For pulsed exposures in the frequency range 0.3–10 GHz and for localized exposure of the head, the specific absorption should not exceed 10 mJ kg^{-1}, averaged over 10 g tissue.
Sources: ICNIRP[3] and NRPB.[24]
[a] ICNIRP values are for occupational exposure; values relating to exposure of the general public are lower by a factor of 5.
[b] Current density is averaged over a cross-section of 1 cm^2 perpendicular to the current direction.
[c] SAR time-averaged over any 6 min.
[d] SAR averaged over 10 g tissue and time-averaged over any 6 min period.
[e] SAR time-averaged over any 15 min period.
[f] SAR in the neck and trunk averaged over 100 g tissue and time-averaged over any 6 min period.
[g] SAR in the head and fetus averaged over 10 g tissue and time-averaged over any 6 min period.
[h] SAR in the limbs averaged over 100 g tissue and time-averaged over any 6 min period.

min kg^{-1} (for 15–30 min), or 2 W kg^{-1} (for <15 min). If core temperature, blood pressure, and heart rate are monitored, then these limits are relaxed by an additional factor of two to 'upper level' limits. For exposure of body parts, the local SAR limit should prevent local temperature exceeding 38°C in the head and fetus, 39°C in the trunk, and 40°C in the limbs. The local SAR (averaged over any 1 kg tissue and period of 6 min) limits (for >30 min) are 2, 4, and 6 W kg^{-1} for the head and fetus, trunk, and limbs, respectively. For shorter periods, the corresponding limits are 60, 120, and 180 W min kg^{-1} (for 15–30 min) or 2, 4, and 6 W kg^{-1} (for <15 min) The Medical Devices Directorate (MDD) guidelines, based on the NRPB's two-level approach to limits, include a normal mode of operation (when exposure is less than the uncontrolled level), a

Table 2 Reference levels, investigation levels, and maximal permissible exposures (MPE) to rf fields

Frequency	Magnetic field strength (A m^{-1})	Magnetic flux density (μT)	Electric field strength (V m^{-1})	Equivalent plane-wave power density (W m^{-2})
International Commission on Non-ionizing Radiation Protection reference levels[a]				
1–10 MHz	$1.6/f$[b,c]	$2.0/f$[b,c]	$610/f$[b,c]	–
10–400 MHz	0.16[b]	0.2[b]	61[b]	10[b]
National Radiological Protection Board investigation levels[d]				
12–200 MHz	0.13	0.16	50	6.6
200–400 MHz	$0.66f$[e]	$0.70f$[e]	$250f$[e]	$(165f^2)$[e]
Levels when there is no possibility of small children being exposed				
10–60 MHz			60	10
60–137 MHz			$1000f$[e]	$(2700f^2)$[e]
0.137–1.1 GHz			137	50
Federal Communications Commission MPE[f]				
3.0–30	$4.89/f$[b,c]		$1842/f$[b,c]	$(9000/f^2)$[b,c]
30–300	0.163[b]		61.4[b]	10[b]
300–1500	–		–	$f/30$[b,c]

[a] Reference levels for occupational exposure to rf fields.[3]
[b] Time-averaged over any 6 min period.
[c] *f*, frequency in MHz.
[d] Investigation levels for exposure to rf fields.[24]
[e] *f*, frequency in GHz.
[f] Limits for 'controlled' exposure to rf fields.[60]

Table 3 The International Electrotechnical Committee limits on specific absorption rates (SAR)[10]

	Normal operating mode	First level controlled operating mode	Second level controlled operating mode
Whole-body SAR[a]	≤ 1.5 W kg^{-1} averaged over 15 min	≤ 4 W kg^{-1} averaged over 15 min	>4 W kg^{-1} averaged over 15 min
Head SAR[a]	≤ 3 W kg^{-1} averaged over 10 min	Not applicable	>3 W kg^{-1} averaged over 10 min
Local tissue SAR[b]		Not applicable	
Head and torso	≤ 8 W kg^{-1} averaged over 5 min		>8 W kg^{-1} averaged over 5 min
Extremities	≤ 12 W kg^{-1} averaged over 5 min		>12 W kg^{-1} averaged over 5 min

It is assumed that the SAR averaged over any 10 s period does not exceed five times the stated time-averaged SAR limit.
[a] Values of SAR averaged over the whole body or over the head.
[b] Local tissue SAR is the value of SAR averaged over any 1 g tissue.

controlled mode (when exposure is between the uncontrolled and upper levels), and a mode that is not recommended (for exposures above the upper level).[65]

The International Electrotechnical Committee (IEC) also defines SAR limits for three differing modes of operation (Table 3).[10] All persons, regardless of health status, should be able to tolerate the normal operating mode. The first-level controlled operating mode should be tolerated by people with unimpaired thermoregulatory and cardiovascular systems; however, since individual tolerance to hyperthermia is variable, medical supervision is required. Second-level controlled operating mode exposures require a protocol that is approved by a local ethics committee or investigational review board. Like earlier recommendations,[64] these guidelines also assume moderate environmental conditions (temperature <24°C and relative humidity <60%). Under the first-level controlled operating mode, whole-body SAR limits should be decreased by 0.25 W kg^{-1} for each 1°C above 24°C, and by 0.1 W kg^{-1} for each 10% increase in relative humidity. For the normal operating mode, the reductions in SAR limits should be reduced by a factor of two.

The Food and Drug Administration considers that MR investigations in which SAR is greater than 4 W kg^{-1} whole body for 15 min, 3 W kg^{-1} averaged over the head for 10 min, 8 W kg^{-1} in any 1 g tissue in the head or torso for 15 min, 12 W kg^{-1} in any 1 g tissue in the extremities for 15 min are 'significant risk'.[66] This is a relaxation of earlier guidance that had stated a level of concern related to whole body rf heating of 0.4 W kg^{-1} or that resulting in an increase in core temperature of 1°C. The new level is in accord with the first-level controlled mode in IEC[10] and operation resulting in SAR values above this level requires an approved human studies protocol.

7 FUTURE DEVELOPMENTS IN rf SAFETY

Widely used multi-echo sequences are time efficient but can greatly increase rf exposure compared with conventional methods. Even in routine examinations, it is not uncommon for operators to have to modify sequence parameters in order to remain within the limits imposed by manufacturers to ensure that scanners operate within safety regulations. These practical limits are generally based on relatively simple, spatially averaged models. By being conservative, safety is assured but the restrictions imposed increasingly impact on routine practice. There has also been a proliferation in the routine use of specialist coils with a trend towards close-coupled designs and use of local transmit systems, particularly for spectroscopy. Such trends create a pressing need for assessment of localized SAR and temperature changes in a realistic manner.

8 RELATED ARTICLES

Birdcage Resonators: Highly Homogeneous Radiofrequency Coils for Magnetic Resonance; Coils for Insertion into the Human Body; Complex Radiofrequency Pulses; Health and Safety Aspects of Human MR Studies; High-Field Whole Body Systems; Radiofrequency Systems and Coils for MRI and MRS; Temperature Measurement Using In Vivo NMR.

9 REFERENCES

1. C. H. Durney, H. Massoudi, and M. F. Iskander, 'Radiofrequency Radiation Dosimetry Handbook', 4th edn., USAFSAM-TR-85-73. USAF School of Aerospace Medicine, Brooks Air Force Base, Texas, 1986
2. NCRP (National Council on Radiation Protection and Measurements), 'A Practical Guide to the Determination of Human Exposure to Radiofrequency Fields. NCRP Report No 119', NCRP, Bethesda, MD, 1993.
3. ICNIRP (International Commission on Non-ionizing Protection), *Health Phys.*, 1998, **74**, 494.
4. P. Fessenden and J. W. Hand, in 'Radiation Therapy Physics', ed. A. R. Smith, Springer, Heidelberg, 1995, p. 315.
5. F. G. Shellock and E. Kanal, 'Magnetic Resonance: Bioeffects, Safety and Patient Management', 2nd edn., Lippincott-Raven, Philadelphia, 1996.
6. H. P. Schwan, *Adv. Biol. Med. Phys.*, 1975, **5**, 147.
6. S. Gabriel, R. W. Lau, and C. Gabriel, *Phys. Med. Biol.*, 1996, **41**, 2271.
8. NCRP (National Council on Radiation Protection and Measurements), 'Radiofrequency Electromagnetic Fields: Properties, Quantities and Units, Biophysical Interaction and Measurements. NCRP Report No 67', NCRP, Bethesda, MD, 1981.
9. NEMA (National Electrical Manufacturers Association) 'Characterization of the Specific Absorption Rate for Magnetic Resonance Imaging Systems MS 8-1993', NEMA, Rosslyn, VA, 1993.
10. IEC (International Electrotechnical Committee), 'Medical Electrical Equipment–Part 2: Particular requirements for the safety of magnetic resonance equipment for medical diagnosis'. IEC 601-2-33: 1995 IEC Geneva, 1995.
11. H. C. Taylor, M. Burl, and J. W. Hand, *Phys. Med. Biol.*, 1997, **42**, 1387.

12. S. M. Michaelson and E. C. Elson, in 'Biological Effects of Electromagnetic Fields', eds. C. Polk and E. Postow, CRC, Boca Raton, FL, 1996, p. 337.
13. NCRP (National Council on Radiation Protection and Measurements), 'Biological Effects and Exposure Criteria for Radiofrequency Electromagnetic Fields, NCRP Report No 86', NCRP, Bethesda, MD, 1986.
14. A. Cutz, *Lens Eye Toxic Res.*, 1989, **6**, 379.
15. P. Kramar, C. Harris, and A. W. Guy, *Bioelectromagnetics*, 1987, **8**, 397.
16. R. M. Lebovitz, L. Johnson, and W. K. Samson, *J. Appl. Physiol.*, 1987, **62**, 245.
17. J. C. Lin, in 'Electromagnetic Interaction with Biological Systems', ed. J. C. Lin, Plenum, New York, 1989, p. 165.
18. B. Kallen, G. Malmquist, and U. Moritz, *Arch. Environ. Health*, 1982, **37**, 81.
19. A. I. Larsen, J. Olsen, and O. Svane, *Scand. J. Work Environ. Health*, 1991, **17**, 324.
20. R. Oullet-Hellstrom and W. F. Stewart, *Am. J. Epidemiol.*, 1993, **138**, 775.
21. H. Dolk, H. Shaddick, P. Walls, C. Grundy, B. Thakrar, I. Kleinschmidt, and P. Elliot, *Am. J. Epidemiol.*, 1997, **145**, 1.
22. H. Dolk, P. Elliot, G. Shaddick, P. Walls, and B. Thakrar, *Am. J. Epidemiol.*, 1997, **145**, 10.
23. B. Hocking, I. R. Gordon, M. L. Grain, and G. E. Hatfield, *Med. J. Aust.*, 1996, **165**, 601.
24. NRPB (National Radiological Protection Board), 'Documents of the NRPB, Vol. 4, Part 5: Board Statement on Restrictions on Human Exposure to Static and Time-varying Electromagnetic Fields and Radiation', NRPB, Chilton, UK, 1993.
25. HCN (Health Council of the Netherlands: Radiofrequency Radiation Committee), *Health Phys.*, 1998, **75**, 51.
26. W. P. Shuman, D. R. Haynor, A. W. Guy, G. E. Wesbey, D. J. Schaefer, and A. A. Moss, *Radiology*, 1988, **167**, 551.
27. B. J. Barber, D. J. Schaefer, C. J. Gordon, D. C. Zawieja, and J. Hecker, *Am. J. Roentgenol.*, 1990, **155**, 1105.
28. F. G. Shellock, D. J. Schaefer, and J. V. Crues, *Br. J. Radiol.*, 1989, **62**, 904.
29. F. G. Shellock and J. V. Crues, *Radiology*, 1987, **163**, 259.
30. F. G. Shellock and J. V. Crues, *Radiology*, 1988, **167**, 809.
31. F. G. Shellock, D. J. Schaefer, W. Grundfest, and J. V. Crues, *Acta Radiol.*, 1986, Suppl. **369**, 514.
32. F. G. Shellock, B. Rothman, and D. Sarti, *Am. J. Roentgenol.*, 1990, **154**, 1229.
33. F. G. Shellock, D. J. Schaefer, and E. Kanal, *Radiology*, 1994, **192**, 865.
34. P. Röschmann, *Magn. Reson. Med.*, 1991, **21**, 197.
35. P. A. Bottomley and E. R. Andrew, *Phys. Med. Biol.*, 1978, **23**, 630.
36. P. A. Bottomley and W. A. Edelstein, *Med. Phys.*, 1987, **8**, 510.
37. P. A. Bottomley, R. W. Redington, W. A. Edelstein, and J. F. Schenck, *Magn. Reson. Med.*, 1985, **2**, 336.
38. P. Röschmann, *Med. Phys.*, 1987, **14**, 922.
39. P. A. Bottomley and P. B. Roemer, *Ann. N. Y. Acad. Sci.*, 1992, **649**, 144.
40. N. Orcutt and O. P. Gandhi, *IEEE Trans. Biomed. Eng.*, 1988, **35**, 577.
41. M. Grandolfo, P. Vecchia, and O. P. Gandhi, *Bioelectromagnetics*, 1990, **11**, 117.
42. M. Grandolfo, A. Polichetti, P. Vecchia, and O. P. Gandhi, *Ann. N. Y. Acad. Sci.*, 1992, **649**, 176.
43. A. Taflove, 'Computational Electrodynamics: The Finite Difference Time-Domain Method', Artech, Boston, 1995.
44. J.-M. Jin, J. Chen, W. C. Chew, H. Gan, R. L. Magin, and P. J. Dimbylow, *Phys. Med. Biol.*, 1996, **41**, 2719.
45. D. Simunic, P. Wach, W. Renhart, and R. Stollberger, *IEEE Trans. Biomed. Eng.*, 1996, **43**, 88.
46. J. Chen, Z. Feng, and J.-M. Jin, *IEEE Trans. Biomed. Eng.*, 1998, **45**, 650.
47. C. M. Collins, S. Li, and M. B. Smith, *Magn. Reson. Med.*, 1998, **40**, 847.
48. W. Renhart, A. A. Magele, and N. Modl, *IEEE Trans. Magn.*, 1994, **30**, 3092.
49. A. J. van den Bergh, H. J. van den Boogert, and A. Heerschap, A. *Magn. Reson. Med.*, 1998, **39**, 642.
50. J. W. Hand, R. W. Lau, J. J. W. Lagendijk, J. Ling, M. Burl, and I. R. Young, *Magn. Reson. Med.*, 1999, **42**, 183.
51. E. R. Adair and L. G. Berglund, *Ann. N. Y. Acad. Sci.*, 1992, **649**, 188.
52. H. H. Pennes, *J. Appl. Physiol.*, 1948, **1**, 93.
53. K. M. Sekins and A. Emery, in 'Therapeutic Heat and Cold', ed. J. Lehmann, Williams & Wilkins, Baltimore, 1982, p. 70.
54. K. Schreier, M. Budhina, H. Lesnicar, L. Handl-Zeller, J. W. Hand, M. V. Prior, S. T. Clegg, and I. A. Brezovich, *Int. J. Hypertherm.*, 1990, **6**, 431.
55. J. J. W. Lagendijk, H. Crezee, and J. W. Hand, *Int. J. Hypertherm.*, 1994, **10**, 775.
56. H. Arkin, L. X. Xu, and K. R. Holmes, *IEEE Trans. Biomed. Eng.*, 1994, **41**, 97.
57. J. W. Baish, *ASME J Biomech. Eng.*, 1994, **116**, 521.
58. A. N. T. J. Kotte, G. M. J. van Leeuwen, and J. J. W. Lagendijk, *Phys. Med. Biol.*, 1999, **44**, 57.
59. IEEE (Institute of Electrical and Electronics Engineers), 'IEEE C95.1-1991 Standard Safety Levels with Respect to Human Exposure to Radio Frequency Electromagnetic Fields, 3 KHz to 300 GHz', IEE, New York, 1992.
60. FCC (Federal Communications Commission), 'Guidelines for Evaluating the Environmental Effects of Radiofrequency Radiation. Report and Order, ET Docket 93-62', FCC 96-326, 61 Federal Register 41006. FCC, Washington DC, 1996.
61. NRPB (National Radiation Protection Board), 'Radiological Protection Bulletin No. 204', NRPB, Chilton, UK, 1998, p. 26.
62. P. J. Chadwick, 'Occupational Exposure to Electromagnetic Fields: Practical Application of NRPB guidance, NRPB-R301', NRPB, Chilton, UK, 1998.
63. NRPB (National Radiological Protection Board), 'Documents of the NRPB, Vol. 2, Part 1: Principles for the Protection of Patients and Volunteers during Clinical Magnetic Resonance Diagnostic Procedures', NRPB, Chilton, UK, 1991, p. 1.
64. NRPB (National Radiological Protection Board) 'Documents of the NRPB, Vol. 2 Part 1: Limits on Patient and Volunteer Exposure during Clinical Magnetic Resonance Diagnostic Procedures', NRPB, Chilton, UK, p. 5.
65. MDD (Medical Devices Directorate), 'Guidelines for Magnetic Resonance Diagnostic Equipment in Clinical Use with Particular Reference to Safety', MDD, Department of Health, HMSO, London, 1993.
66. FDA (Food and Drug Administration), 'Guidance for the Submission of Premarket Notifications for Magnetic Resonance Diagnostic Devices', Center for Devices and Radiological Health, Rockville MD, 1998.

Biographical Sketch

Jeffrey W. Hand. *b* 1946. B.Sc. 1964, Ph.D. 1972, D.Sc. 1995, Newcastle-upon-Tyne. First involved with medical applications of microwave and radiofrequency fields in 1976. Currently Head of Radiological Sciences, Hammersmith Hospitals NHS Trust and Reader in Imaging Physics at Imperial College School of Medicine. Approx. 110 papers and book chapters; co-editor of two books on medical applications of microwave and radiofrequency fields and related topics. Current research interests: safety aspects of nonionizing radiations, microwave radiometry.

Elastography

Alexia J. Lawrence, Raja Muthupillai, and Richard L. Ehman
Mayo Clinic, Rochester, MN, USA

1 INTRODUCTION

Advances in medical imaging over the last several decades have provided important new diagnostic capabilities. Yet, it is generally agreed that there is still considerable scope for further development. Medical imaging technologies such as computed tomography (CT), ultrasonography, and MRI can be regarded as methods for obtaining maps depicting various tissue properties such as X-ray attenuation, echogenicity, and magnetic properties, respectively. What other tissue properties might be useful to probe by imaging?

The time-tested value of palpation as a diagnostic tool used by physicians provides motivation for seeking methods to image the mechanical properties of tissue. In some series, for example, 30% of breast cancers are detected only by palpation and not by mammography.[1] It is also not uncommon during abdominal operations for surgeons to discover tumors by palpation that were previously undetected by CT, MRI, or ultrasound.

The value of palpation stems from the fact that many disease processes such as neoplasia can dramatically alter the mechanical properties of tissue.[2] There is some evidence that changes in tissue elastic properties may accompany early stages of carcinogenesis, and that such changes might even have some degree of predictive value for certain types of cancer.[3–5] Tissue mechanical properties are not directly assessed by any of the available conventional imaging techniques, such as CT, ultrasound, or MRI: they are distributed over a much larger range than the physical properties assessed by conventional imaging modalities (Figure 1).

These considerations provide a rationale for seeking practical methods for 'palpation by imaging'. The potential value of such technology might be used to assess regions of the body that are not accessible to the physician's hand, to reveal lesions that are too small to detect by touch, and to provide new parameters for tissue characterization.

2 THEORY OF MEASURING TISSUE ELASTICITY

A straightforward approach for measuring the mechanical properties of an object is to apply a known stress to the object and then to measure the resulting strain response in some way. The response of an object following some external stress is either rigid body motion or deformation. Deformation, unlike rigid body motion, depends entirely on the material properties of that object, which can be reversible (elastic), irreversible (viscous, plastic, or flow) or a combination of the two. Soft tissues, for the most part, are a combination, known as viscoelastic.

Given that the measure of applied load (stress tensor) and the measure of deformation (strain tensor) are linearly related for an infinitesimally small elastic deformation, this simple equation follows.[6]

$$\sigma_{ij} = \boldsymbol{C}_{ijkl}\gamma_{kl} \tag{1}$$

where σ_{ij} is the stress tensor, γ_{kl} is the strain tensor, and $\boldsymbol{C}_{ijkl}$ is the elastic modulus tensor. A full description of the elastic modulus tensor of a material requires as many as 81 independent constants. Soft tissues, however, given a few simplifying assumptions, can be described by as few as two constants.

There are four most commonly used elastic constants for characterizing materials: bulk elastic modulus (K), shear elastic modulus (μ), Young's modulus (E), and Poisson's ratio (σ). For an isotropic, Hookean solid, the shear and bulk elastic moduli are related to Young's modulus and Poisson's ratio by the following relationships:[6]

$$\mu = \frac{E}{2(1+\sigma)} \tag{2}$$

$$K = \frac{E}{3(1-2\sigma)} \tag{3}$$

Soft tissues, however, are generally neither isotropic nor Hookean. Additionally, the elastic moduli can depend on the scale of deformation and temporal behavior of applied stress. Nevertheless, these parameters are adequate for approximating the mechanical properties of soft tissues.[2,3,7]

Poisson's ratio, which describes the ratio of lateral contraction to longitudinal elongation, ranges from 0.490 to 0.499 for most soft tissues. This very small dynamic range limits its value as a contrast parameter for soft tissue elasticity imaging. According to Equation (2) and with this ratio being very nearly 0.5 (the reason soft tissues are described as incompressible),

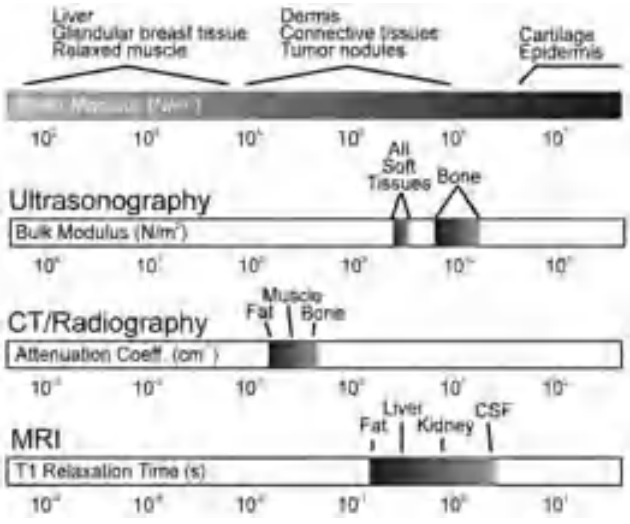

Figure 1 Spectrum of physical parameters that may be used to evaluate biological tissues. The shear modulus of soft tissues ranges over five orders of magnitude. Available soft tissue contrast is much less for conventional ultrasonography, X-ray-based imaging modalities, and MRI. CSF, cerebrospinal fluid

Young's modulus is simply related to shear modulus by a factor of three: $E=3\mu$.

The bulk modulus describes the response of a material to a change in its volume. The relationship between longitudinal mechanical wave speed (ν_l) and the bulk elastic modulus is:

$$K \approx \nu_l^2 \rho \tag{4}$$

where ρ is the density of the medium. The bulk modulus variations in soft tissues are less than a few per cent, and bulk modulus variations with respect to mechanical wave frequency are also within a few per cent. Bulk modulus then, like Poisson's ratio, offers little contrast as an elasticity parameter.

By comparison, shear elastic modulus describes the changes of a material in response to changes in its shape. The relationship between shear wave speed (ν_t) and shear elastic modulus is given by:[8]

$$\mu \approx \nu_t^2 \rho \tag{5}$$

Equations (4) and (5) are similar, but unlike the bulk elastic modulus the shear elastic modulus varies greatly within soft tissues. In addition, the value of the latter is highly dispersive over a broad range of frequencies, unlike the bulk modulus, which is basically nondispersive in soft tissues.[9,10]

Investigators have attempted to use a variety of forms of mechanical stress for the purpose of assessing mechanical properties, including both endogenous and exogenous sources. Endogenous sources of stress, such as respiration and cardiac pulsations, essentially allow for only a qualitative estimate of tissue elasticity because the stress distribution is unknown.

Exogenous stress sources can be static or quasi-static as well as time-varying periodic mechanical waves. In a quantitative sense, the main disadvantage of static and quasi-static compressions is that it is difficult to know the boundary conditions with sufficient accuracy to characterize the input stress distribution appropriately.

Time-varying periodic sources of stress, such as mechanical waves, can be longitudinal or transverse. Longitudinal waves are not ideal sources of stress because their behavior is governed by the bulk modulus which varies by only a few per cent within soft tissues. Transverse mechanical waves could be used as a source of stress, but frequencies greater than 500 Hz attenuate greatly in soft tissues, thereby limiting their use. Therefore, very-low-frequency transverse acoustic mechanical waves remain as a source of stress for quantitative elasticity imaging.

Existing techniques to measure the strain response within tissues noninvasively are based on conventional echo ultrasound and various MRI methods.[2,3,7,11–36] Ultrasound-based methods are, to some extent, limited by the fact that they are only capable of measuring the component of motion that occurs along the axis of the beam. They are also limited by the necessity of finding an acoustic window into the body. MRI, in principle, is capable of measuring 3D displacements of soft tissues within the body with moderate spatial resolution.

More recently, an MRI-based technique has been described that is capable of providing quantitative images depicting tissue elasticity.[37,38] This technique, called magnetic resonance elastography (MRE), uses low-frequency transverse mechanical waves as the source of stress (for reasons described above) and uses MR-based methods to measure the small displacements caused by the low-frequency oscillating stress. MRE is capable of quantifying shear elastic modulus in biological tissues, both ex vivo and in vivo.[10,36–41] The technique is reviewed in the following sections.

3 THEORY OF MAGNETIC RESONANCE ELASTOGRAPHY

It is well known that MR experiments can be designed with exquisite sensitivity to measure spin motion, from bulk motion to microscopic diffusion.[42–49] Conventional MRI encodes the spatial position of spins with appropriate magnetic field gradients.[50,51] If the position of the spin varies in the presence of a gradient, it can induce a phase shift in the received signal.[45] This is the basis of phase contrast-based MRI sequences, which provide a versatile means of measuring spin motion.[44,45,48] With special modifications, such sequences can be designed to measure the cyclic motion of fluid in the cochlea resulting from applied sound,[52] and cyclic motion of tissue caused by applied propagating shear waves.[37,38]

Based on the discussions in the previous section, MRE uses externally applied low-frequency transverse mechanical waves to probe the object. This requires that small cyclic displacements caused by the propagating mechanical waves be detected using appropriate motion-encoding gradients. In MRE, the motion-sensitizing gradients are cyclic and the frequency of the gradient waveform is the same as that of the mechanical excitation. Such cyclic motion-sensitizing gradient waveforms can act as 'filters' to detect only the shift caused by spin motion occurring at the desired frequency. Very small cyclic motion (of the order of nanometers) can be detected using cyclic magnetic field gradients that are phase-locked with the spin motion. (A detailed description of the formalism behind the principles of acoustic wave imaging is presented by Muthupillai et al.[37])

The phase shift (φ) induced in the received NMR signal by cyclic motion caused by a mechanical wave propagating within a medium at a given frequency ($1/T$), in the presence of a cyclic motion-encoding gradient, is given by the following expression:

$$\varphi(\vec{r}, \alpha) = \frac{\gamma N T(\vec{\boldsymbol{G}} \cdot \vec{\xi})}{2} \cos(\vec{\boldsymbol{k}} \cdot \vec{\boldsymbol{r}} + \alpha) \tag{6}$$

The above equation indicates that the accumulated phase shift is proportional to the scalar product of the gradient vector $\vec{\boldsymbol{G}}$ and the displacement vector $\vec{\xi}$, the number of gradient cycles (N), and the period of the gradient waveform (T). The quantity γ is the gyromagnetic ratio, α is the phase relationship between the motion-encoding gradient and the externally applied mechanical excitation, and $\vec{\boldsymbol{r}}$ is the nuclear spin position vector. The scalar product relationship indicates that wave motion occurring along any direction can be measured. Equation (6) indicates that the sensitivity of the method to spin motion can be enhanced by increasing the number of gradient cycles (within the limitations of the spin–spin relaxation time) or by increasing the amplitude of the encoding gradient (within the hard-

ware limitations of the imager) or by both. The measured quantities, the spin displacement $\vec{\xi}$ and the wave vector $\vec{k}$, can yield information about the mechanical properties of the material (which will be discussed in detail in the next section).

Similar to other phase contrast-based techniques, two measurements are acquired by alternating the polarity of the motion-encoding gradients between the measurements. This process not only increases the sensitivity of the technique but also reduces any systematic errors. The phase images (generated from each acquisition) are then subtracted to yield a phase difference image that reflects the phase shift caused by the propagating mechanical wave.

The experimental method to obtain such 'wave' images is shown in Figure 2. Note that the motion-sensitizing gradients act synchronously with the applied mechanical motion. By varying the time, θ, between the onset of the mechanical motion and the beginning of the motion-sensitizing gradients, the propagating waves can be 'captured' at various points throughout their cycle. This makes it possible to study the temporal behavior of propagating waves.

By superimposing gradients along any desired direction, the component of spin motion in that direction can be measured. Thus, by acquiring volumetric data with motion encoding along all three directions, the 3D wave vector can easily by computed for a volumetric object. The ability to measure the 3D wave vector makes it possible for MRE to estimate elasticity measurements robustly.

4 ESTIMATING SHEAR ELASTIC MODULUS

From the acquired displacement maps, wavelength and displacement amplitude of the propagating waves are the two parameters that can be directly measured. The mechanical properties of wave speed, strain, attenuation, and shear elastic modulus can then be derived from this information. In a simple homogeneous material, ν_t is easily calculated from the wavelength (λ) of the shear wave and the frequency of the externally applied mechanical excitation (f):

$$\nu_t = f\lambda \tag{7}$$

The simple definition of the shear modulus given in Equation (5) is only true for purely elastic materials. In viscoelastic tissues, true wave speed depends on the viscous properties of the material as well. This relationship is given by:[53]

$$\nu_t = \sqrt{\frac{2(\mu_1^2 + f^2\mu_2^2)}{\rho(\mu_1 + \sqrt{\mu_1^2 + f^2\mu_2^2}}} \tag{8}$$

where μ_1 is the coefficient of shear elasticity, μ_2 is the coefficient of shear viscosity, ρ is density, and f is the frequency of the mechanical wave. When μ_2=0, as in a purely elastic material, or $f\mu_2 << \mu_1$, Equation (8) can be reduced to Equation (5). The frequency-dependent viscous properties of soft tissues

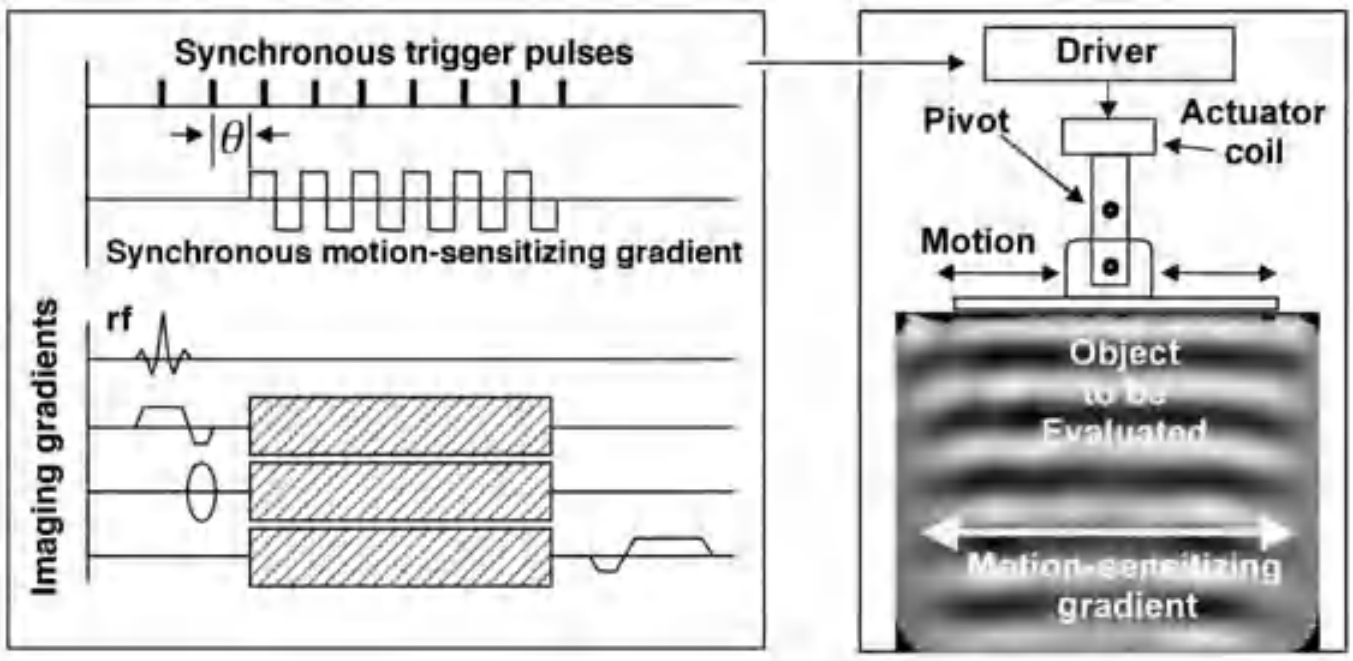

Figure 2 Schematic diagram of a magnetic resonance elastography experiment. The conventional gradient echo pulse sequence for spatial encoding is shown at the bottom left. Superimposed onto each axis are the cyclic motion-sensitizing gradients (shaded areas). As shown at the top left, these gradients oscillate with the motion driver that applies acoustic shear waves to the object. The phase offset (θ) between the onset of the gradients and the triggering of the driver can be varied to allow multiple time offsets for the propagating waves to be captured at various points throughout their cycle

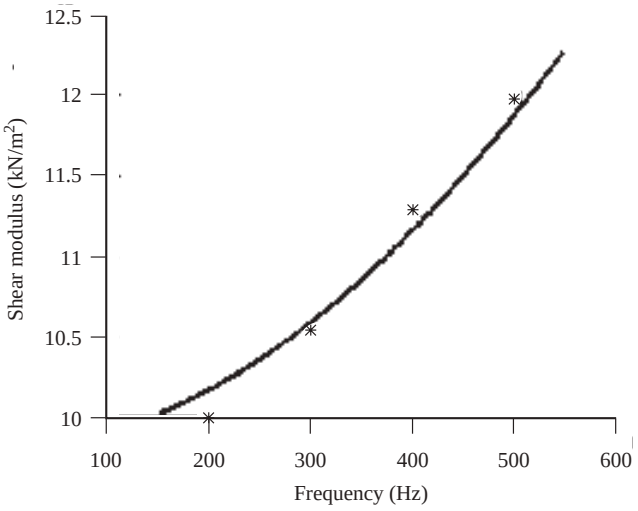

Figure 3 A frequency dispersion curve of a tissue-simulating phantom (18% bovine gel) illustrating the viscous properties of soft tissues. Apparent shear modulus increases with increasing acoustic wave frequency

may be an important contrast parameter that could be further explored for better tissue characterization. In fact, our experiments have shown that tissues and tissue-simulating materials show frequency dispersion; that is, the shear modulus increases with increasing frequency (Figure 3).[10] However, the simplified estimation of shear modulus in Equation (5) is a reasonable approximation for most soft tissues.

The wavelength from the acquired wave images in a homogeneous material is sufficiently estimated by fitting the acquired displacement amplitude profile to a damped sinusoidal function. For heterogeneous material, however, it is necessary to estimate the wavelength of the propagating waves in local regions of the image so that an estimate of the local shear modulus throughout the material can be made.

Several techniques have been presented to estimate the local wavelength, and others are currently being investigated. For heterogeneous materials, a local frequency estimator (LFE) algorithm can be applied to the wave images to estimate the wavelength at each point in the image.[54–58] This algorithm estimates the local spatial frequencies (or wavelengths) by constructing lognormal quadrature wavelets (acting as filters) and combining the local estimates of instantaneous spatial frequency obtained from these filters. We have shown that this algorithm is isotropic and can estimate the wavelength accurately, even on either side of a transition between two regions of different stiffnesses.[54,55] We have made some modifications to the basic algorithm so that it functions well in the presence of noise.

Additionally, by obtaining a series of 'snapshots' of the acoustic wave propagating within the material, it is possible to perform a Fourier transformation along the time axis to extract the desired component of motion. The LFE can be applied to these time-filtered wave images to help to reduce the noise and other systematic errors that may be present in the data. It has been shown that the resolution at which this technique can correctly calculate local wavelength and, therefore, quantify shear modulus, is about one quarter to one half of a wavelength.[54] Simulations have shown, however, that smaller than one eighth of a wavelength may be adequate for a simple qualitative assessment of tissue elasticity. That is, a very small stiffer inclusion can be resolved from the softer surrounding material, but the actual wavelength the algorithm calculates within that small inclusion may not be accurate.[59]

5 EXPERIMENTAL RESULTS AND PROOF OF CONCEPT

In all the experiments shown, the source of propagating shear waves is an electromechanical driver triggered synchronously with the motion-encoding gradients. An alternating current is pulsed through the driver, which is simply a small resistive coil, creating an associated alternating magnetic field. When the coil axis is not aligned with the main magnetic field, the resulting torque between the two fields can be used to create cyclic motions. This kind of driver is capable of delivering frequencies of vibration in the desired acoustic range of 10–1000 Hz.

Tissue-simulating phantoms were first used as a medium to show that propagating acoustic shear waves can be visualized using MRE and that shear modulus measurements can be estimated. Imaging was done in a conventional 1.5 T imager. Figure 2 graphically illustrates a typical experiment with a gel phantom, the electromechanical driver, and the motion-encoding pulse sequence. The resulting displacements caused by the planar wavefront in the gel are visualized.

The pulse sequence for these experiments is a standard gradient echo sequence. For all experiments shown here, the added motion-encoding gradients $\vec{G}(t)$ were applied collinear with the applied direction of motion $\vec{r}(t)$ and perpendicular to the direction of wave propagation. Typical imaging parameters are *TR* 50–300 ms, *TE* 15–60 ms, number of views 128–256, acquisition time 20–120 ms, flip angle 10–60°. Mechanical excitations ranged from 100 to 1100 Hz, and the number of gradient pulses ranged from 2 to 30 cycles. After acquiring two acquisitions, each with the motion-sensitizing gradients opposite in polarity, the phase images are subtracted. This phase-difference image is referred to as a 'shear wave' image. A group of 6 to 16 wave images were acquired, each with a slightly different time offset between the onset of the mechanical stimulation and the onset of the motion-sensitizing gradients. This offset enables multiple 'snapshots' of the waves at various points throughout their cycles to be acquired (see Figures 6 and 7, below).

Once the multiple time offset wave images have been acquired, the data are processed to calculate shear modulus. Figures 4 and 5 show wave images in gel phantoms at 250 Hz and the resulting quantitative shear modulus maps calculated using the local wavelength estimator. Figure 4a is a wave image of a gel phantom with two cylindrical inclusions of different stiffnesses. One inclusion is softer than the surrounding gel, and the other is stiffer. The changes in wavelength (increased wave speed in the stiffer gel and the decreased wave speed in the softer gel) are apparent within each inclusion in the wave image. The computed elastogram is shown in Figure 4b and quantifies the calculated shear modulus.

Figure 5 shows a gel phantom comprising an oblique slab of soft gel bounded by stiffer gel on the top and bottom. Figure 5a shows a single wave image of the propagating shear waves.

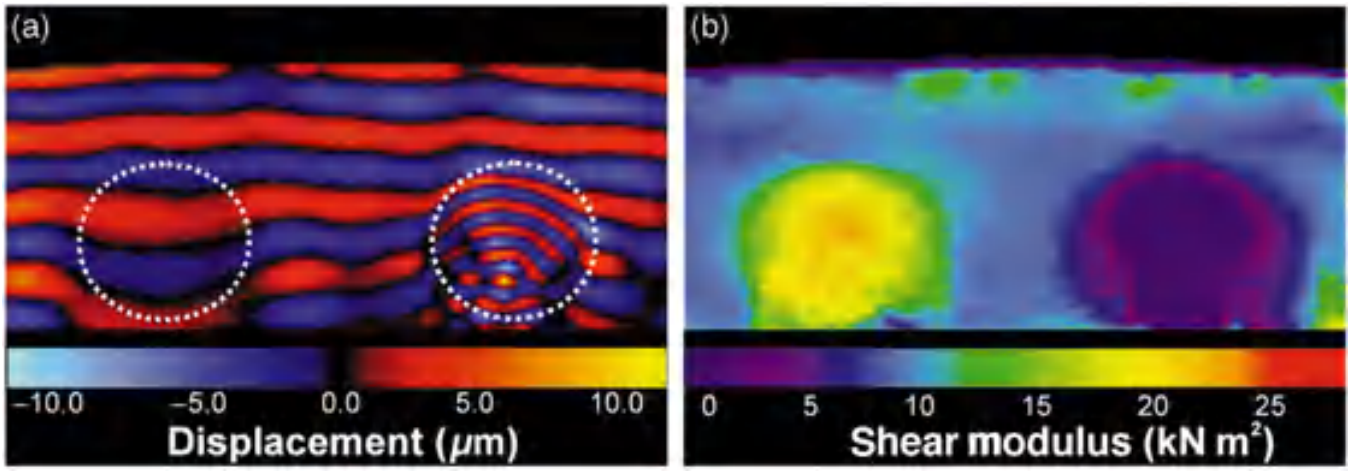

Figure 4 Magnetic resonance elastography of an agarose gel phantom with two inclusions, the outlines of which are shown by dotted circles. The inclusion on the left is stiffer than the surrounding gel and the inclusion on the right is softer. Shear motion at 250 Hz was applied to the top surface of the gel and is along the right–left direction. (a) The shear wave image in which the resulting displacements are shown in color and quantified at the bottom of the figure. The changes in wavelength within the inclusions are apparent, as well as a refraction phenomenon in the softer inclusion causing a focusing effect. (b) Quantitative map of shear modulus produced by calculating the local wavelength at each pixel from the shear wave images. It shows that the stiffer inclusion is about 22 kN/m^2 and the softer one is about 6 kN/m^2. Reprinted with permission from Muthupillai et al.[37] Copyright 1995 American Association for the Advancement of Science

The change in the direction of the wavefront as it reaches the interface between the stiff and the soft gel compartments is evident. The decrease in wavelength as the waves travel from the upper stiffer gel to the middle softer gel can also be clearly seen again. The wavelengths lengthen again as they traverse the stiff layer at the very bottom. The elastogram shown in Figure 5b correctly depicts the stiffer upper, softer middle, and stiffer lower layers.

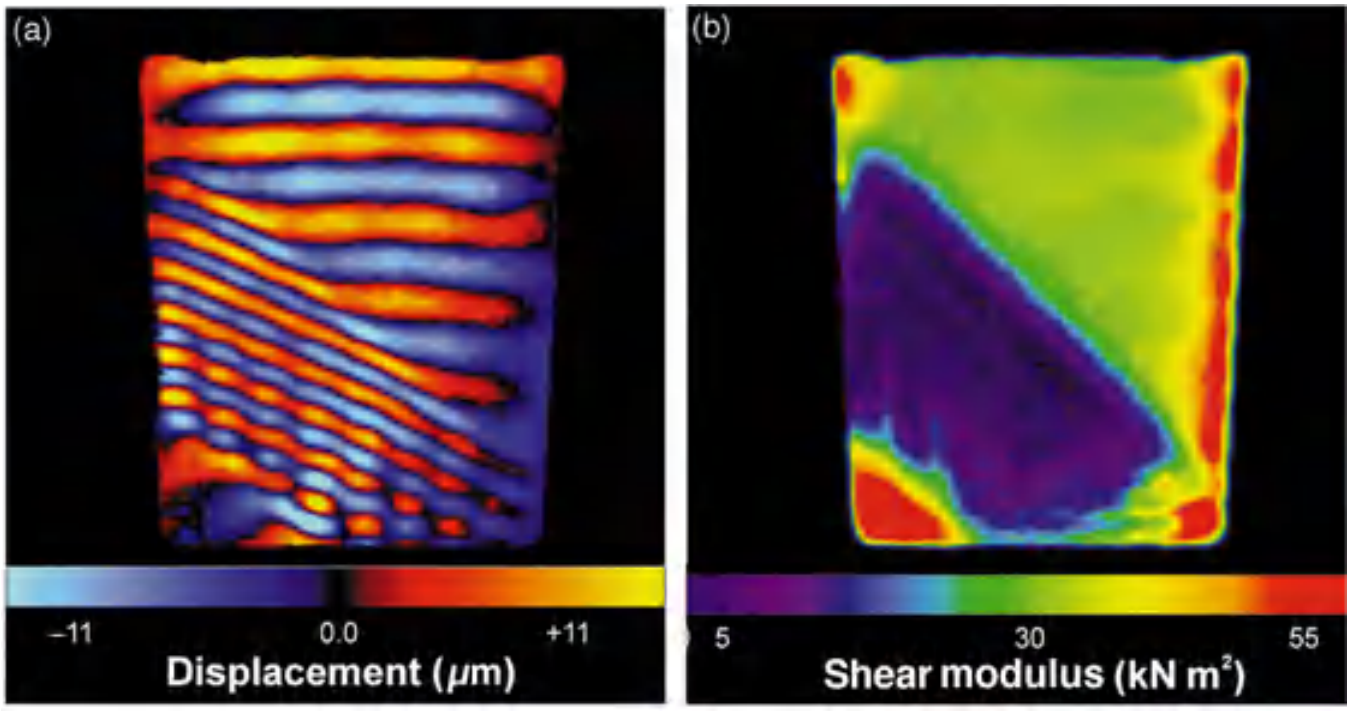

Figure 5 Magnetic resonance elastography of a phantom comprised of three oblique slabs of agarose gel. The upper and lower layers are stiffer than the softer middle layer. Shear motion at 250 Hz was applied to the top surface of the phantom. The measured displacements are between +5 and −5 μm. (a) Shear wave image showing the deflection of the waves and change in wavelength as they traverse the different interfaces. Images of multiple phases are processed to calculate the local wavelength at each pixel with the local frequency estimator algorithm. (b) Quantitative elastogram generated by processing the wave images is color coded to show the shear modulus values. Reproduced with permission from *Nature Medicine* **2**, 601–603, 1996

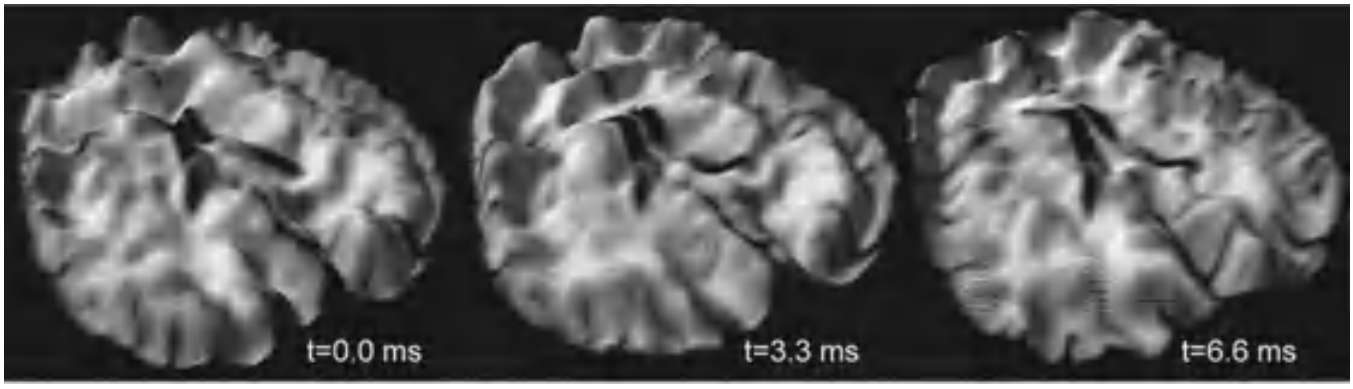

Figure 6 Propagating acoustic waves at 100 Hz in the human brain, observed with magnetic resonance elastography (MRE) in vivo. Low-amplitude intracranial acoustic waves were generated via inertial interactions using an electromechanical driver coupled to the head of normal volunteers. MRE wave images were used to warp a transverse T_1-weighted anatomic image using a 3D rendering program to create this visualization. The apparent amplitudes of the waves are magnified approximately 10 000 times from the actual amplitude of brain motion. The pattern of shear wave displacement reflects the applied 'nodding' motion, with shear waves arising 180° out of phase at the anterior and posterior dural surfaces. Prominent shear waves are also generated in the posterior region of the falx

6 IN VIVO AND EX VIVO EXPERIMENTS

We have demonstrated that MRE is feasible in tissue-simulating materials. We have also shown that shear waves can be generated and imaged in biological tissues, both in vivo and ex vivo. Ex vivo biological tissues that are currently under investigation using MRE include human prostate specimens and porcine liver, kidney, and muscle specimens. Shear waves have also been successfully generated and imaged in vivo in brain, skeletal muscle, and breast of human volunteers (Figures 6–8).

Shear waves in the brain are shown in Figure 6. The source of wave motion was a bite-bar moving at 100 Hz that was grasped by the teeth of a volunteer. The resulting inertial effects caused the shear waves to propagate through the brain with very small displacement amplitudes. The 3D rendition in Figure 6 magnifies the actual displacements by about 10 000 times.

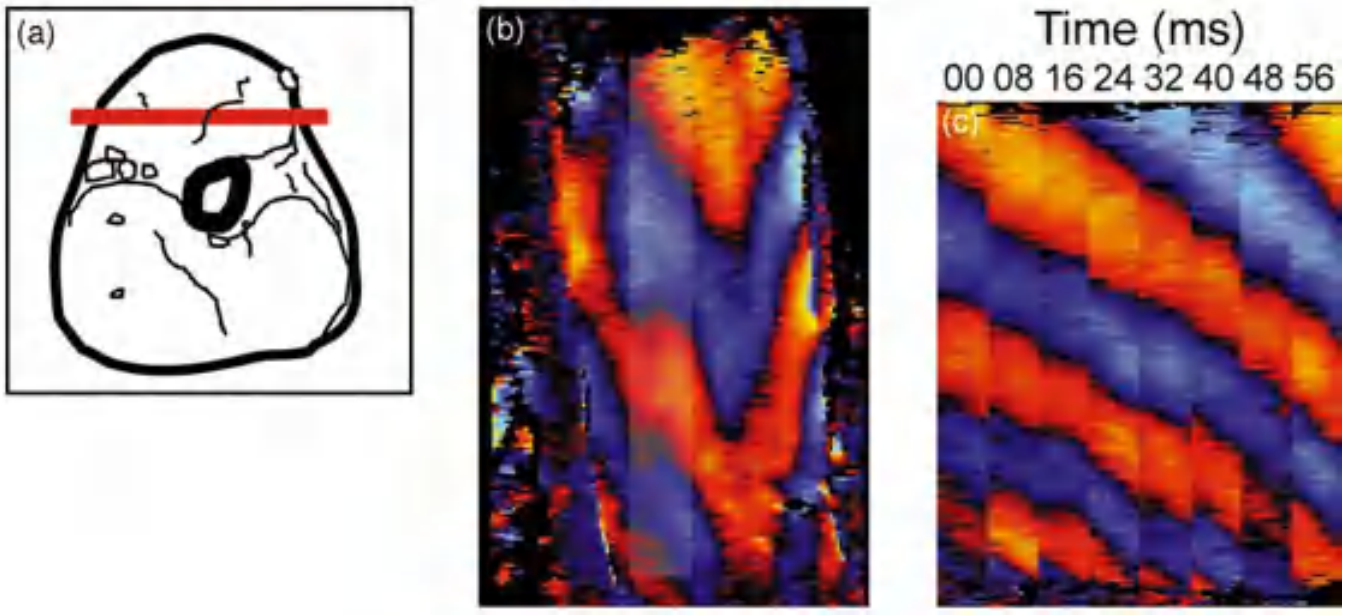

Figure 7 Propagating acoustic waves in human skeletal muscle in vivo shown by magnetic resonance elastography (MRE). An electromechanical driver was used to apply 150 Hz shear waves with about 100 μm amplitude to the distal musculotendinous junction of the biceps brachii muscle. (a) A sketch of an axial section of the arm showing the location of the coronal plane that was imaged using MRE. (b) Imaging of this coronal slice with the MRE sequence depicts propagating acoustic waves. The field of view in this figure is 20 cm and the flexion loading on the arm was 12 lb (26.4 kg). By varying the time offset between the applied mechanical waves and the cyclic motion-encoding gradients (θ in Figure 2), the temporal pattern of wave propagation can be observed. (c) A vertical strip from the wave image (indicated by the highlighted section in (b)) is shown at various phase offsets in the wave cycle. The steepness of the diagonal pattern (wave velocity) was observed to depend on muscle loading

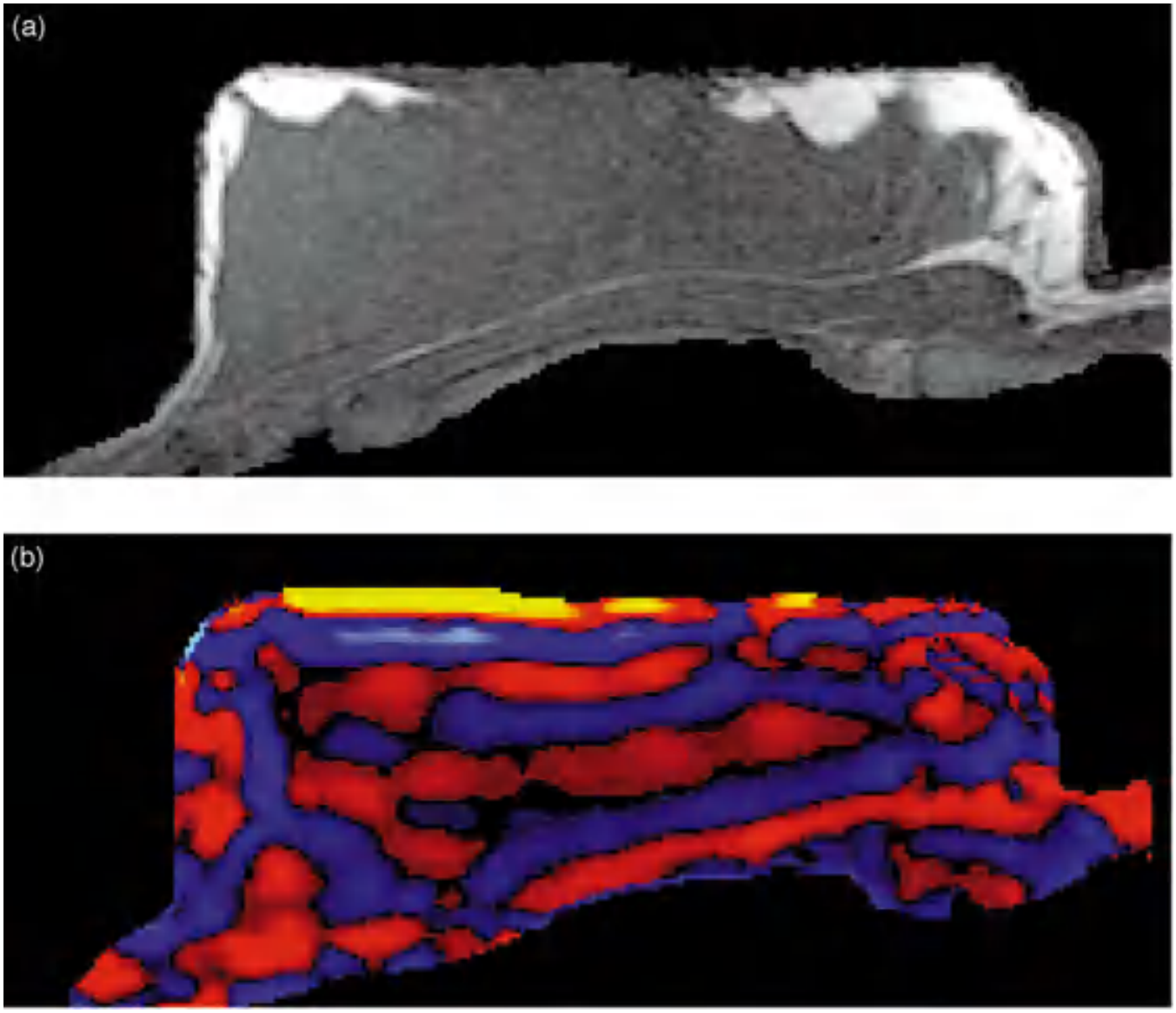

Figure 8 An example of in vivo propagating acoustic waves in the breast of a volunteer. (a) An axial T_1-weighted spin-echo image of the breast showing the section of tissue evaluated in (b). (b) A color representation of the propagating acoustic shear waves. This is a single snapshot of the propagating waves in time at a mechanical frequency of 100 Hz. The mechanical motion is through-plane, so tissue displacement into the plane is represented as shades of blue, and displacement out of the plane is represented as shades of red. The waves are propagating toward the chest wall

Shear waves were visualized in the human biceps brachii by tapping the distal musculotendinous junction of the muscle at a frequency of 150 Hz. The amplitude of the applied motion was about 100 μm. During the experiment the muscle was slightly flexed and under a small amount of load. The wave image shown in Figure 7b is from a coronal slice of the muscle. The motion-encoding direction was along the slice-select direction, and the component of the displacement caused by the propagating wave in the slice-select direction is shown. The imaging plane was chosen so that the orientation of the muscle fibers was in the imaging section. Eight different snapshots of the wave propagating within one section of the muscle are shown in Figure 7c.

An example of the ability to visualize wave propagation in human breast tissue in vivo is shown in Figure 8. The volunteer is in the prone position with an electromechanical driver coupled to the anterior part of the breast. Mechanical motion is in the superior–inferior direction and the resulting shear waves propagate toward the chest wall. Adequate penetration is usually achieved with mechanical frequencies in the range 75–200 Hz.

The wave propagation in a 3D heterogeneous object such as soft tissues in vivo is very complex. We are continuing to refine both our acquisition techniques as well as the post-processing methods, to allow a robust characterization of the elasticity of soft tissues in vivo. We are also continuing to

evaluate the elasticity of various normal and cancerous tissues in vivo and ex vivo.

7 SUMMARY

MRE is a new imaging technique that shows promise for noninvasive evaluation of the mechanical properties of tissues and tissue-like materials. By choosing an appropriate motion-sensitizing gradient waveform, it is possible to visualize and measure externally applied propagating mechanical waves within phantoms and tissues. From these measurements, it is possible to estimate the mechanical properties of the material under investigation quantitatively.

Preliminary experiments have shown that it is possible to visualize shear waves propagating within materials in vivo, specifically in the brain, skeletal muscle, and breast of volunteers. Future work will involve more extensive tissue characterization experiments using MRE for evaluating the mechanical properties of normal and pathological tissues. These tissue characterization experiments will provide the necessary information to further optimize experimental methods to visualize shear waves in vivo. Further efforts are attempting to refine both acquisition methodology (to include rapid 3D acquisitions with motion encoding along all three cardinal axes) and image-processing techniques to analyze the complex wave propagation observed in vivo.

The development of an elasticity imaging modality that can accurately assess the mechanical properties of soft tissues could aid in the detection and characterization of pathological tissues. The large scale of contrast available by imaging the mechanical properties of tissues may lead to an elasticity imaging modality that is more sensitive in the early detection and characterization of certain diseases compared with standard imaging modalities.

8 RELATED ARTICLES

Brain Parenchyma Motion Observed by MRI; Marker Grids for Observing Motion in MRI.

9 REFERENCES

1. L. Chapuis and C. Hessler, *Helv. Chir. Acta*, 1989, **55**, 895.
2. A. Sarvazyan, D. Goukassian, E. Maevsky, A. R. Skovoroda, S. Emelianov, A. Klishko, G. Mironova, V. Sholokhov, and V. Ermilova, *Proc. Int. Workshop Interaction of Ultrasound with Biol. Media*, Valenciennes, France, 1994, p.69.
3. A. P. Sarvazyan, A. R. Skovoroda, S. Y. Emelianov, J. B. Fowlkes, J. G. Pipe, R. S. Adler, R. B. Buxton, and P. L. Carson, 'Acoustical Imaging', ed. J. P. Jones, New York, Plenum Press, 1995.
4. E. A. Modjanova and A. G. Malenkov, *Exp. Cell Res.*, 1973, **76**, 305.
5. A. Malenkov and K. V. Asoian, *Biofizika*, 1983, **28**, 326.
6. W. C. Elmore and M. A. Heald, 'Physics of Waves', Dover Publications, York, 1985.
7. A. Sarvazyan, *Proc. 125th Mtg Acoustical Soc. Am. J. Acoust. Soc. Am.*, 1993, 2329.
8. H. L. Ostreicher, *J. Acoust. Soc. Am.*, 1951, **23**, 707.
9. E. L. Madsen, H. J. Sathoff, and J. A. Zagzebski, *J. Acoust. Soc. Am.*, 1983, 74.
10. J. A. Smith, R. Muthupillai, J. F. Greenleaf, P. J. Rossman, T. C. Hulshizer, and R. L. Ehman, *Radiology*, 1996, **20**, P194.
11. I. Céspedes, J. Ophir, H. Ponnekanti, and N. Maklad, *Ultrason. Imaging*, 1993, **15**, 73.
12. L. Gao, K. J. Parker, S. K. Alam, and R. M. Lerner, *J. Acoust. Soc. Am.*, 1995, **97**, 3875.
13. B. S. Garra, E. I. Céspedes, J. Ophir, S. R. Spratt, R. A. Zuurbier, C. M. Magnant, and M. F. Pennanen, *Radiology*, 1997, **202**, 79.
14. F. Kallel, J. Ophir, K. Magee, and T. Krouskop, *Ultrasound Med. Biol.*, 1998, **24**, 409.
15. F. J. Lee, J. P. Bronson, R. M. Lerner, K. J. Parker, S. R. Huang, and D. J. Roach, *Radiology*, 1991, **181**, 237.
16. R. M. Lerner, S. R. Huang, and K. J. Parker, *Ultrasound Med. Biol.*, 1990, **16**, 231.
17. S. F. Levinson, M. Shinagawa, and T. Sato, *J. Biomech.*, 1995, **28**, 1145.
18. K. J. Parker, S. R. Huang, R. A. Musulin, and R. M. Lerner, *Ultrasound Med. Biol.*, 1990, **16**, 241.
19. D. B. Plewes, I. Betty, S. N. Urchuk, and I. Soutar, *JMRI*, 1995, **5**, 733.
20. D. J. Rubens, M. A. Hadley, S. K. Alam, L. Gao, R. D. Mayer, and K. J. Parker, *Radiology*, 1995, **195**, 379.
21. C. J. Lewa, *Spectrosc. Lett.*, 1991, **24**, 55.
22. J. Ophir, I. Céspedes, H. Ponnekanti, Y. Yazdi, and X. Li., *Ultrason. Imaging*, 1991, **13**, 111.
23. C. J. Lewa, *Acustica*, 1992, **77**, 43.
24. K. J. Parker and R. M. Lerner, *J. Ultrasound Med.*, 1992, **11**, 387.
25. H. Ponnekanti, J. Ophir, and I. Céspedes, *Ultrasound Med. Biol.*, 1994, **20**, 27.
26. C. J. Lewa and J. D. de Certaines, *JMRI*, 1995, **5**, 242.
27. E. J. Chen, R. S. Adler, P. L. Carson, W. K. Jenkins, and W. D. Obrien, *Ultrasound Med. Biol.*, 1995, **21**, 1153.
28. J. B. Fowlkes, S. Y. Emelianov, J. G. Pipe, A. R. Skovoroda, P. L. Carson, R. S. Adler, and A. P. Sarvazyan, *Med. Phys.*, 1995, **22**, 1771.
29. S. Y. Emelianov, M. A. Lubinski, W. F. Weitzel, R. C. Wiggins, A. R. Skovoroda, and M. O'Donnell, *Ultrasound Med. Biol.*, 1995, **21**, 871.
30. L. Gao, K. J. Parker, R. M. Lerner, and S. F. Levinson, *Ultrasound Med. Biol.*, 1996, **22**, 959.
31. E. Konofagou and J. Ophir, *Ultrasound Med. Biol.*, 1998, **24**, 1183.
32. K. J. Parker, D. S. Fu, S. M. Graceswki, F. Yeung, and S. F. Levinson, *Ultrasound Med. Biol.*, 1998, **24**, 1437.
33. T. L. Chenevert, A. R. Skovoroda, M. O'Donnell, and S. Y. Emelianov, *Magn. Reson. Med.*, 1998, **39**, 482.
34. C. L. de Korte, A. F. van der Steen, E. I. Céspedes, and G. Pasterkamp, *Ultrasound Med. Biol.*, 1998, **24**, 401.
35. C. L. Walker, F. S. Foster, and D. B. Plewes, *Ultrasound Med. Biol.*, 1998, **24**, 137.
36. J. Bishop, G. Poole, M. Leitch, and D. B. Plewes, *JMRI*, 1998, **8**, 1257.
37. R. Muthupillai, D. J. Lomas, P. J. Rossman, J. F. Greenleaf, A. Manduca, and R. L. Ehman, *Science*, 1995, **269**, 1854.
38. R. Muthupillai, P. J. Rossman, D. J. Lomas, J. F. Greenleaf, S. J. Riederer, and R. L. Ehman, *Magn. Reson. Med.*, 1996, **36**, 266.
39. G. H. Rose, M. A. Dresner, P. J. Rossman, J. P. Felmlee, R. Muthupillai, and R. L. Ehman, *Radiology*, 1998, **209**, P425.
40. A. Lawrence, G. Rose, P. Rossman, A. Manduca, L. Hartmann, and R. Ehman, *Proc. VIth Sci. Mtg (Int.) Soc. Magn. Reson. Med.*, Sydney, 1998, p.233.
41. M. A. Dresner, G. H. Rose, P. J. Rossman, R. Muthupillai, and R. L. Ehman, *Radiology*, 1998, **209**, P181.
42. W. G. Bradley Jr and V. Waluch, *Radiology*, 1985, **154**, 443.
43. D. J. Bryant, J. A. Payne, D. N. Firmin, and D. B. Longmore, *J. Comput. Assist. Tomogr.*, 1984, **8**, 588.
44. P. van Dijk, *J. Comput. Assist. Tomogr.*, 1984, **8**, 429.
45. P. R. Moran, *Magn. Reson. Imaging*, 1982, **1**, 197.

46. E. O. Stejskal, *J. Chem. Phys.*, 1965, **13**, 3597.
47. M. O'Donnell, *Med. Phys.*, 1985, **12**, 59.
48. V. J. Wedeen, R. A. Meuli, R. R. Edelman, S. C. Geller, L. R. Frank, T. J. Brady, and B. R. Rosen, *Science*, 1985, **230**, 946.
49. C. L. Dumoulin, H. E. Cline, S. P. Souza, W. A. Wagle, and M. F. Walker, *Magn. Reson. Med.*, 1989, **11**, 35.
50. R. R. Ernst and W. A. Anderson, *Rev. Sci. Instruments*, 1966, **37**, 93.
51. A. Kumar, D. Welti, and R. R. Ernst, *J. Magn. Reson.*, 1975, **18**, 69.
52. W. Denk, R. M. Keolian, S. Ogawa, and L. W. Jelinski, *Proc. Natl. Acad. Sci., USA*, 1993, **90**, 1595.
53. Y. Yamakoshi, J. Sato, and T. Sato, *IEEE Trans. Ultrasonics, Ferroelectrics Frequency Control*, 1990, **37**, 45.
54. A. Manduca, R. Muthupillai, P. J. Rossman, J. F. Greenleaf, and R. L. Ehman, 'SPIE's International Symposium Medical Imaging 1996', ed. M. H. Loew, K. M. Hanson, The International Society for Optical Engineering, Newport Beach, CA, 1996, p. 616.
55. A. Manduca, R. Muthupillai, P. J. Rossman, J. F. Greenleaf, R. L. Ehman, *Proc. IEEE Int. Conf. Image Processing*, 1996, p. 527.
56. A. Manduca, R. Muthupillai, P. J. Rossman, J. F. Greenleaf, and R. L. Ehman, *Proc. 18th Annu. Int. Conf. IEEE EMB Soc.*, Amsterdam, IEEE, 1996.
57. A. Manduca, J. A. Smith, R. Muthupillai, P. J. Rossman, J. F. Greenleaf, and R. L. Ehman, *Proc. Vth Annu. Mtg (Int.) Soc. Magn. Reson. Med.*, Vancouver, 1997, p. 1903.
58. H. Knutsson, C. J. Westin, G. Granlund, *Proc. IEEE Int. Conf. Image Proc.*, 1994, **1**, 36.
59. R. Muthupillai, V. Dutt, A. Manduca, J. A. Smith, J. F. Greenleaf, and R. L. Ehman, *Proc. 83rd Sci. Assembly Annu. Mtg RSNA*, 1997, **20**, P469.

Biographical Sketches

Alexia J. Lawrence. *b.* 1971. B.A., Chemistry, 1993, D.V.M., 1997. Work with magnetic resonance elastography began in 1997 during research fellowship in the magnetic resonance research laboratory at Mayo Foundation, Rochester, MN. Research interests: medical and veterinary MRI.

Raja Muthupillai. *b*. 1968. B.E., 1989, University of Madras, Ph.D. 1997 The Mayo Clinic (developing techniques to measure the elastic properties of biological tissues using MRI). Staff scientist at Philips Medical Systems 1998–present. Research interests: elasticity imaging, measuring physiological function with MRI.

Richard L. Ehman. *b*. 1952. B.Sc. (Physics), 1974, M.D., 1983. Diagnostic Radiologist, involved in clinical and technical development of MRI since 1983. Recipient of ISMRM Gold Medal in 1995. Approx. 150 scientific publications and 12 patents. Research interests: elucidation of motion artifacts in MRI and development of correction methods, vascular MRI, fast imaging, and development of MRI methods for assessing viscoelastic properties of materials.

Hyperpolarized Gas Imaging

James R. MacFall
Duke University Medical Center, Durham, NC, USA

and

Bastiaan Driehuys
Magnetic Imaging Technologies, Inc., Durham, NC, USA

1 INTRODUCTION

Hyperpolarized gas imaging has been enabled by fundamental research in atomic physics[1–3] and in techniques for producing spin polarized targets to study elementary particle physics.[4–8] The polarization of a spin-1/2 substance is defined as the difference in the percentage of nuclear spins that are in the mz = +1/2 state versus the mz = −1/2 state.[9] Even with the most powerful magnets, it is difficult to attain a polarization that is greater than a few parts per million. This is the reason that nuclear magnetic resonance (NMR) is often referred to as being a low-sensitivity technique. For the protons on a water molecule, the small polarization is compensated for, somewhat, by the high concentration of nuclei. Consequently, MRI of protons in the water and lipids in living subjects can be performed with adequate signal-to-noise ratios (SNR) in modern MRI systems.

Recent extension of the research on spin polarization has made it possible to polarize in liter quantities the spins of certain noble gases, such as ^{3}He and ^{129}Xe, to levels near 100%. While gases do have much lower density than water at room temperature, the huge increase in polarization, of the order of a factor of 10^5, more than compensates for this loss.

In human and animal subjects, water proton MRI provides adequate images for most of the body. There are regions of the body that are not available to conventional MRI because of low proton spin concentration, such as the lung air spaces, the cranial sinus cavities, the bowel, and the nasopharynx. Since both ^{3}He and ^{129}Xe are gases that are biocompatible, these regions are obvious candidates for application of hyperpolarized gas MRI. The first application of this technique in vivo was accomplished in guinea pig lungs in 1994 using ^{3}He.[10]

Other possible applications of this new source of MRI signal have been suggested. It appears possible to suspend bubbles of these gases in liquids that can be injected into a living subject for improved blood flow or perfusion images.[11] Also, since ^{129}Xe is transported to the blood from the lungs, this may provide a noninjected blood perfusion measure for the brain, heart, or other organs.[12,13] Finally, there may be applications in nonliving systems for nondestructive testing, such as evaluation of tiny cracks in materials or studying the movement of gas through porous media.

The first section of this chapter describes the properties of ^{3}He and ^{129}Xe, the two gases that have been used successfully in hyperpolarized gas imaging, and the polarization methods that have been developed for their use. The following section describes the most common imaging methods that have been used in animals and humans, and some of the results obtained.

2 THE GAS POLARIZATION PROCESS

2.1 Magnetization and Polarization Concepts

The signal strength in a given image voxel is proportional to the amount of magnetization present in that voxel. The magnetization M of a substance is given by $M = \mu n P$, where μ is the nuclear magnetic moment, n is the density of nuclei, and P is the degree of polarization of these nuclei. Polarization is defined as the difference in the fraction of nuclear moments which are aligned ($N_\uparrow$) with the magnetic field versus antialigned ($N_\downarrow$):

$$P = \frac{N_\uparrow - N_\downarrow}{N_\uparrow + N_\downarrow} \tag{1}$$

In conventional proton MRI, this polarization is determined by thermodynamic equilibrium and amounts to only about 5 ppm in a 1.5 T magnetic field. However, because the proton density n is so high in most substances ($n = 7\times10^{22}$ protons cm^{-3} in H_2O) very strong signals can be achieved. By contrast, a gas at standard temperature and pressure has a density of only about 2.6×10^{19} nuclei cm^{-3}, which corresponds to a decrease in signal relative to liquids of about 2700. For these reasons, gases have not been seriously considered as good imaging agents for MRI. Recently matured technologies now enable an artificial increase of the nuclear spin polarization of certain noble gases by as much as five orders of magnitude above thermal equilibrium. This polarization increase more than overcomes the spin density sacrifice of gases relative to liquids.

2.2 Methods of Gas Polarization

There are effectively only two gases, ^{3}He and ^{129}Xe that exhibit sufficiently long relaxation time to be amenable to hyperpolarization. Diatomic molecular gases are poor candidates because the coupling of the nuclear spin to rotational angular momentum of the molecule results in rapid relaxation. This leaves only noble gases as potential candidates for hyperpolarization. The only noble gas isotopes that are both stable and have a spin of 1/2 are ^{3}He and ^{129}Xe. Isotopes with higher spin values possess a quadrupole moment that couples to electric field gradients to cause rapid relaxation. While noble gases with higher nuclear spin have been polarized to some extent, the polarization levels are generally low, and the lifetime of the polarization is short.[14]

There are several methods for inducing hyperpolarization. Perhaps the most intuitive are the thermodynamic equilibrium polarization methods. In principle, by cooling the gas to low temperatures and using extremely high magnetic fields, nuclear spin polarizations of nearly 100% could be attained. Such methods are just now being explored and are technically quite challenging. Calculations indicate that with a magnetic field strength of 15 T and a temperature of 5 mK, ^{3}He polarizations of 96% could be achieved.[15] However, no practical implementations of such schemes have been realized to date.

The two more mature techniques for inducing hyperpolarization in noble gases involve the indirect transfer of angular momentum from photons to atomic electrons and then to nuclear spins. One technique called metastable optical pumping was originally developed by Colegrove, Schearer, and Walters[16] and is suitable only for polarizing ^{3}He. The other hyperpolarization method, which is capable of polarizing either ^{3}He or ^{129}Xe, is called optical pumping and spin exchange (OPSE).

2.2.1 *Polarization of ^{3}He*

The present state-of-the-art method, the metastability exchange ^{3}He hyperpolarization system, was developed by a group at Johannes Gutenberg-Universitat Mainz.[17] In this technique, low pressure (~1–3 mbar) ^{3}He gas is held in an rf discharge, promoting a small fraction of the atoms to an excited metastable $1s2s^3S_1$ state. From this state, the ^{3}He gas is able to absorb circularly polarized light at a wavelength of 1083 nm. Absorption of this net angular momentum from the photons induces a high degree of electron spin polarization in the gas that is then transferred through the hyperfine interaction to the ^{3}He nuclei. The Mainz system incorporates four 1 m long optical cells to absorb roughly 4–11 W of laser power from an $La_{0.83}Nd_{0.15}MgAl_{11}O_{12}$ laser. The gas in the optical cells is polarized with a time constant of about 25 s. However, because the gas is at very low pressures, it must then be compressed to atmospheric pressure to become useful for imaging. This compression is achieved through a specialized titanium piston that does not induce significant depolarization. The present stated performance of this polarizer is a polarization level of 50% achieved at a production rate of 0.5 l h^{-1} and further improvements are being forecast. The only drawbacks of this elegant approach are that the system can be quite large and costly and is limited to polarizing ^{3}He.

The other hyperpolarization method, which is capable of polarizing either ^{3}He or ^{129}Xe, is OPSE (Figure 1). In this technique, an alkali metal such as Rb is used to absorb circularly polarized laser light (795 nm for Rb). This absorption of net angular momentum from the laser beam preferentially depopulates only one of the valence electron spin states of the alkali metal. Eventually all of the electrons are 'optically pumped' into the other spin state, causing a large electron spin polarization. This electronic polarization is then transferred via collisions to the noble gas nucleus of interest. During a Rb–^{3}He collision, the valence electron of the Rb atom overlaps briefly with the nucleus of the ^{3}He atom. This hyperfine contact interaction can cause a simultaneous spin flip of the ^{3}He nuclear spin and the Rb valence electron spin or 'spin exchange'. After such a collision, the Rb atom becomes repolarized through absorption of another photon and the process continues. The polarization of the noble gas builds up exponentially, akin to the charging of a capacitor. Time constants for this process can range from many hours to just a few seconds depending on laser power, gas composition, and other factors.

Polarization of ^{3}He through spin exchange with optically pumped Rb has been studied since 1960.[18] However, it is only recently that advances in high-power laser technology have made production of liter quantities of polarized ^{3}He practical. Several university research groups have built systems for gas polarization using this approach. A commercially manufactured unit even exists (Magnetic Imaging Technologies (MITI), Durham, NC, USA), as pictured in Figure 2, illustrating the compactness of such a system, which can fit in a hospital hall-

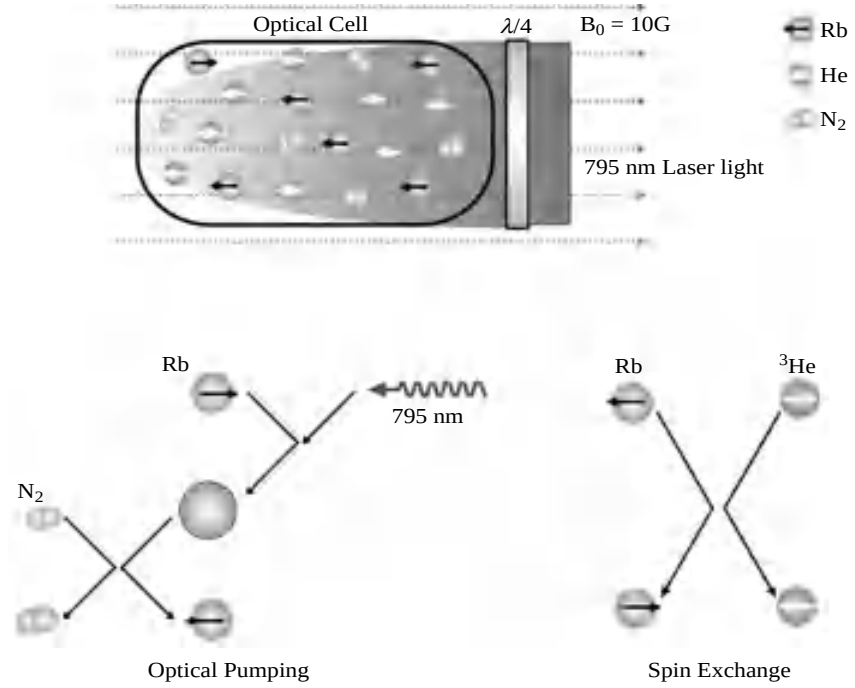

Figure 1 The optical pumping and spin exchange method of producing hyperpolarized gas. The dotted lines (top) indicate the small magnetic field in the chamber that provides an alignment axis for the optical pumping and polarization. The $\lambda/4$ plate circularly polarizes the laser light. The optical pumping (bottom left) preferentially populates one Rb electronic state that then exchanges with the He nucleus (bottom right)

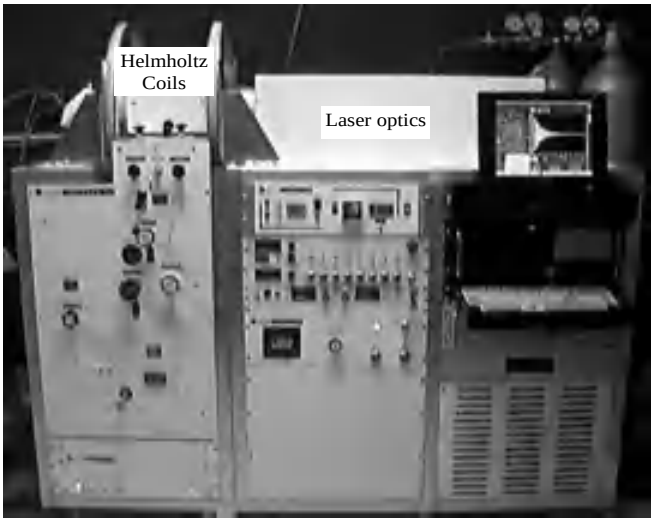

Figure 2 A commercially manufactured optical pumping and spin exchange system showing the Helmholtz coils, the laser optics, and control computer and illustrating that hyperpolarization equipment can be compact enough to fit in laboratory or hospital environments

way or research laboratory. Such systems are presently based on a 120 W AlGaAs diode laser. An optical chamber roughly 220 cm^3 in volume contains about 8–10 atm ^{3}He gas and a few milligrams of Rb metal. The chamber is heated to around 200 °C to increase the Rb vapor density to about 1×10^{15} atoms cm^{-3} (~1 ppm of the ^{3}He concentration). Optical pumping under these conditions results in a time constant for polarization build-up of about 4 h and a saturation polarization level of about 45%. Thus, 2 l of highly polarized ^{3}He gas can be produced in about 4 h.

2.2.2 *Polarization of ^{129}Xe*

Polarization of ^{129}Xe through the OPSE technique has been studied since the first demonstration by Grover in 1978.[19] However, unlike polarized ^{3}He, where its utility as a nuclear target has stimulated substantial efforts towards its production in large quantities, high-volume production of polarized ^{129}Xe was not pursued until its potential importance in MRI was realized.[13] Predicted polarization levels and production rates for ^{129}Xe are not too different from those achievable with ^{3}He. Both gases should be able to be polarized to near 100% with production rates of the order of liters per hour, depending on available laser power. However, practical implementations for polarizing ^{129}Xe are somewhat more complex.

One approach has been to polarize ^{129}Xe in batch mode, as described for the ^{3}He process.[20] With this technique, polarizations of 7.5% have been realized for batches of 157 cm^3. Unfortunately, batch techniques, while simpler to implement, are limited in the ultimate achievable polarization and production rate. An alternative scheme is to polarize a dilute mixture of ^{129}Xe in a ^{4}He carrier gas in a continuous flow method with subsequent cryogenic extraction and storage of hyperpolarized solid ^{129}Xe.[21] This technique is being explored by several research teams and for the commercial system mentioned previously. Polarization levels as high as 45% have been observed in the flowing gas stream. However, after cryogenic accumulation and thawing, the highest observed polarization level has been 20% for a 250 cm^3 batch.[22] Undoubtedly, with continued development efforts, ^{129}Xe polarization techniques will soon reach the level of robustness that has been achieved with ^{3}He systems.

2.2.3 *Polarized Gas Storage, Transport and Supply*

To date, most MRI studies using hyperpolarized ^{3}He or ^{129}Xe have been performed with the polarizer in close proximity to the MR magnet. One notable exception has been the early imaging work performed at Heidelberg with polarized ^{3}He produced at Mainz and subsequently transported roughly 100 km to the imaging site.[23] Such demonstrations emphasize the unique properties of polarized gases, which could allow polarized ^{3}He and ^{129}Xe to be produced in centralized locations and then transported to hospitals or imaging facilities on an as-needed basis, similar to what now occurs with radioisotopes.

Polarized ^{3}He relaxation times in excess of 100 h have been observed in specially coated vessels.[24] The longest reported observed relaxation time was 171 h in a specially prepared, sealed aluminosilicate cell containing 4 atm ^{3}He.[25] This same study showed that the theoretical limit to the ^{3}He relaxation time imposed by ^{3}He–^{3}He collisions is 750 h at 1 atm. Such polarization lifetimes are more than sufficient to give serious consideration to centralized distribution of polarized ^{3}He. However, considerable development effort is still required to achieve such long relaxation times routinely.

Long gas phase relaxation times are more difficult to achieve for ^{129}Xe. The ^{129}Xe–^{129}Xe relaxation mechanism is quite efficient, limiting the gas phase relaxation time to 56 h at 1 atm.[26] However, more problematic is that the much stronger adsorption energy for Xe on surfaces makes relaxation resulting from interactions with the container walls much more effective. Typical gas-phase relaxation times of ^{129}Xe are 20–60 min. Relaxation times as long as 4 h have been observed in specialized high-purity vessels, but this has not been reproducible. It will require a committed research effort to realize gas-phase relaxation times of even tens of hours in the foreseeable future. Fortunately, it has been shown that ^{129}Xe can be frozen and thawed without substantial loss of polarization.[27] The relaxation time of solid ^{129}Xe at 77 K (liquid N_2) is a modest 2–3 h; however when ^{129}Xe is cooled to 4.2 K (liquid He), relaxation times as long as 12–20 days have been observed.[28] While significant engineering challenges still lie ahead in distributing polarized gases, early results are promising.

The world supply of these gases is of tremendous importance to the future viability of this technology. For example, ^{3}He is not naturally abundant in substantial quantities. Its primary source is through the decay of tritium in nuclear weapons. The total available supply is classified but is not substantially larger than a few tens of thousands of liters per year. Therefore, the true commercial success of imaging with hyperpolarized ^{3}He will require both a small dose of ^{3}He to be used for each imaging scan (~100 cm^3) and potentially some recycling of the exhaled gas. Recycling of ^{3}He should be feasible with high efficiency, allowing as much as 95% of each administered dose to be recovered. The supply of Xe gas is essentially infinite, which makes Xe a good long-term prospect. However, the ^{129}Xe isotope is only 26% naturally abundant, and enrichment may be desired to increase image SNR. However, while natural abundance Xe costs only about US $10 per liter, present prices (1999) of 80% enriched ^{129}Xe are much

more expensive and are unlikely to be reduced in cost based on present technology.

3 IMAGING OF POLARIZED GAS

3.1 System Requirements

3.1.1 Magnetic Field Strength

Hyperpolarized gas imaging can be accomplished on nearly any MRI system that meets the requirement of being able to operate at a resonant frequency that is very different from the proton Larmor frequency for the field strength of the system. Such systems are often called 'broadband' systems. Alternatively, for a fixed frequency (narrowband) system, it may be possible to change the magnetic field strength so that the fixed frequency is the resonant frequency of the gas. This is not likely to be the case for most MR systems since the resonant frequency of ^{3}He and ^{129}Xe (48 MHz and 17 MHz, respectively, at 1.5 T) are well below that of hydrogen (64 MHz at 1.5 T). Therefore, the magnetic field would have to be increased when most systems are usually operating at the maximum field for which they were designed.

A variant of the broadband system is the 'multinuclear' design, for which certain, fixed frequency bands are allowed in addition to the hydrogen band. A 1.5 T system might have frequencies available for ^{19}F (60 MHz), ^{31}P (26 MHz), ^{13}C (16 MHz), and ^{2}H (10 MHz) as well as the ^{1}H frequency.[29] For this type of system, it may be possible to lower the main field to have the gas resonate at one of these lower frequencies.

The choice of field strength is usually guided by the fact that the SNR of conventional MRI increases nearly linearly with the magnetic field for constant bandwidth and full relaxation.[30] For hyperpolarized gas, the magnetization does not depend on the magnet and, therefore, the considerations in the choice of field strength are altered. The origin of the linear magnetic field dependence for conventional SNR is the increase in the polarization as field increases. The transverse magnetization created by rf pulses is that much larger, leading to larger induced voltages in the rf coil. The increased frequency also contributes to the increased voltage, but its effect is canceled by the increased noise voltage at higher frequency. The conclusion from these considerations is that the SNR for hyperpolarized gas imaging should be independent of the main magnetic field strength.[10]

This result could be very advantageous for imaging tissues such as the lung or bowel since tissue–air interfaces distort the local magnetic field through the magnetic susceptibility difference at the interface. The magnetic field distortion causes rapid dephasing of the MR signal, leading to poor SNR for conventional imaging in the lungs.[31] The susceptibility-related dephasing is more rapid at high magnetic fields. Therefore, the use of hyperpolarized gas for lung imaging may be better at lower magnetic fields. While most commercial MRI systems use a magnetic field of 1.0–1.5 T, there are many systems in the 0.1–0.5 T range. Unfortunately, these lower field systems usually operate at a fixed (hydrogen) frequency.

3.1.2 Radiofrequency System and Coils

For broadband MR systems, the main considerations for the equipment are a suitable rf coil and associated preamplifier. For truly broadband systems, the preamplifier may not require modification, but multinuclear systems often have tuned preamplifiers that do not operate at other frequencies. Usually, for research groups, it is not too difficult to construct rf coils and obtain preamplifiers that are compatible with an MR system. These rf coils can often be constructed out of readily available materials to existing designs,[30] although certain expensive equipment, such as a network analyzer, must be available for tuning and troubleshooting. However, until manufacturers of commercial MR systems offer ^{3}He and ^{129}Xe capability, hyperpolarized gas imaging will remain a research tool.

For convenience, it is useful to consider a dual-tuned coil that can image at the desired gas frequency and at the hydrogen frequency so that conventional images can be obtained for comparison and reference. On MR systems that have a built-in body-sized rf coil, it is often possible to obtain conventional images with this coil and have a single tuned, smaller coil for gas imaging that is 'blocked' or detuned so as not to interfere with the conventional imaging. Such arrangements avoid possible subject movement during coil changes. Coil performance is often compromised when it has two resonant frequencies; therefore, the best choice may be a single tuned coil that is proton blocked. Another advantage of single tuning is that a circularly polarized or 'quadrature' design can be used.[32] This is hard to achieve for dual-tuned coils and gives nearly the same performance as a so-called 'phased array' coil.[33,34]

3.2 Helium MRI

3.2.1 Gas Diffusion Solubility, and Lifetime Considerations

Table 1 gives some of the physical characteristics of ^{3}He and ^{129}Xe. Helium-3 has very low solubility in blood or tissue and, therefore, is considered mainly suitable for air space imaging such as in the lung, bowel, nasopharynx, or sinuses. While ^{3}He is inert and mixtures of ^{4}He and oxygen have been breathed in diving mixtures for many years, there are still medical regulatory issues with both ^{129}Xe and helium since, at

Table 1 Physical data for ^{3}He, ^{129}Xe and O_2

Gas	Density (g l^{-1} at STP)	Gyromagnetic ratio (MHz T^{-1})	Solubility			T_1 (s, in lung)
			Blood	Brain	Fat	
^{3}He	0.133	32.4	0.01	–	0.02	28.8
^{129}Xe	5.75	11.8	0.15	0.17	1.9	31.3
O_2	1.43	0	0.026	–	0.13	–

Solubility: Oswald solubility at 37 °C (ml gas per ml fluid).[35] Value for T_1 from Moller et al.[36]

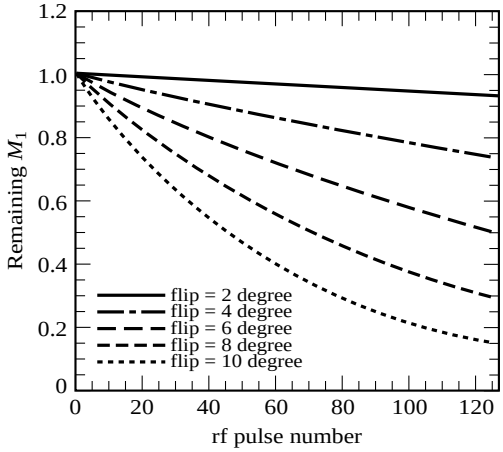

Figure 3 The decline in longitudinal magnetization for a hyperpolarized gas as a function of the rf pulse number for different flip angles (α). As the flip angle increases, the polarization is used up more quickly since gas polarization does not recover toward the initial value but rather to an extremely small equilibrium value

least in the USA, they fall under the FDA authority, which regulates medical gases as drugs.

Helium-3 diffuses rapidly but appears, from imaging experiments to date, to be reasonably well confined by biological membranes. Its lifetime is shortened considerably when mixed with oxygen.[37] As an example, the lifetime (T_1) of ^{3}He when mixed with 21% oxygen is only about 11 s while it is of the order of 1 h in its prepared state. Therefore, the primary considerations in imaging hyperpolarized gas are the need to perform the imaging as rapidly as possible and the fact that the magnetization does not recover to any useful degree toward the large initial magnetization. This leads to a 'use it or lose it' approach to MR pulse sequence design. There are two types of pulse sequence that have been used for ^{3}He imaging: gradient-echo, Fourier phase-encoded imaging (GRE)[38] and projection-encoded imaging (PE).[39] Both methods require a number of encoding steps, each step preceded by a rf pulse. After every rf pulse of flip angle α, the magnetization is reduced by a factor of cos α. The reduction of magnetization is illustrated in Figure 3 for 128 consecutive rf pulses (a typical number for an MR scan sequence) for flip angles ranging from 1 to 10°. For such constant flip angle scans, it is easy to calculate the flip angle that will reduce the magnetization to zero by the end of the scan. The graph shows that the magnetization is largest at the beginning of the scan and decreases monotonically.

It has been shown that the acquired signals that correspond to the low spatial frequencies of the image are responsible for most of the image intensity value and, thus, the image SNR.[40] This leads to the idea of the use of 'centric' phase encoding for GRE methods such that the low spatial frequency values are acquired at the beginning of the imaging to obtain the highest SNR value. The gradual lowering of the signal can lead to a loss of resolution in the final image with the centric scheme since the high spatial frequencies of the image have a reduced amplitude. Consequently, another method has been suggested in which the flip angle is varied: using a smaller flip angle at the beginning and leading to a larger flip angle at the end.[41]

The PE methods usually require a larger number of encodings for an image than an equivalent GRE approach because they oversample the low spatial frequencies. The larger number of encodings lead to the use of smaller flip angle, which can reduce SNR. However, the oversampling of the low frequencies allows the use of normalization strategies to compensate for signal changes during the scan. Also, PE methods can achieve a shorter *TE* than GRE and show fewer motion artifacts.

3.2.2 Animal Lung Imaging of ^{3}He

Early ex vivo ^{3}He images in guinea pigs were made with the GRE pulse sequence after inflating the lungs with the polarized ^{3}He.[42] Subsequent in vivo studies have concentrated on the PE method.[36,43–45] An advantage of this method is that the first points of each signal after an rf pulse sample the average lung intensity, thus allowing high-time resolution studies of gas dynamics. In addition, for small animals, the imaging gradients in GRE sequences can cause large diffusive signal loss; consequently the PE method is more easily employed for diffusion evaluation.

The great advantage of animal studies is that control can be exerted over the flow of gas and the mixture of gas to the lung as well as the consumption of smaller amounts of gas. This allows the study of how the flow of gas and rf flip angle interact to emphasize different parts of the lung. As the gas flows into the trachea, it experiences several rf pulses on its way to the lung periphery. Large rf flip angles use up the magnetization before the gas reaches the periphery, small angles allow the gas to still give signal at the periphery, as shown in Figure 4.

Animal studies have also shown that the gas has a very short T_2* in the lungs, emphasizing the need for very short *TE* values, as illustrated in the figure. While T_1 has been estimated in human and animal lungs to be 30 s, the T_2* is only about 10 ms.[46] As illustrated in Figure 5, the rapid decay of magneti-

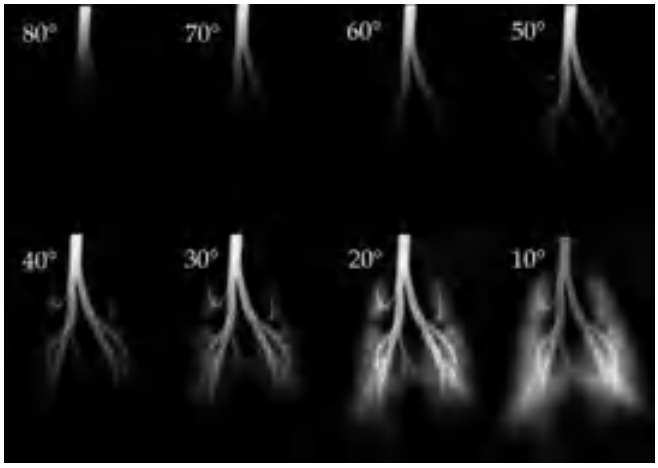

Figure 4 Images of hyperpolarized ^{3}He in a guinea pig's lungs for different flip angles. The gas polarization level was 7%. Images were acquired with a projection-encoded pulse sequence with *TR* 5 ms, FOV 48 mm, 800 projections, in-plane resolution 188 μm; the slice thickness contains the entire lung. Small flip angles emphasize the lung periphery while large flip angles emphasize the airways. (Reproduced by permission of Williams & Wilkins Press from Chen et al.[44])

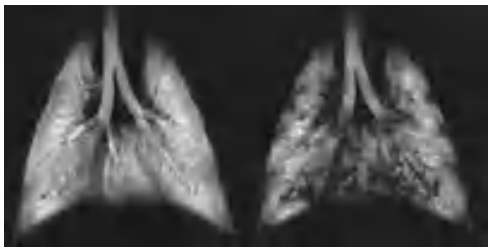

Figure 5 Images of hyperpolarized ^{3}He in a guinea pig's lungs for two different *TE* values. The gas polarization level was 20%. Images were acquired with a projection-encoded pulse sequence with *TR* 5 ms, FOV 48 mm, 800 projections, in-plane resolution 188 μm, and 5 mm slice thickness. The left image has an acquisition delay or *TE* of 1 ms, while the right image has a value of 5 ms. Even modest *TE* values (greater than 1 to 2 ms) can show undesirable signal loss that may be mistaken for lung abnormalities (Images courtesy of X. J. Chen and G. A. Johnson, Center for In Vivo Microscopy, Duke University Medical Center)

zation can make ventilated regions appear not to be receiving gas.

Imaging of gases also must take into account their much larger diffusion coefficients compared with liquids. Measurement of ^{3}He gas in a sealed container[47] gives values of 1.8 cm^2 s^{-1} while that of water is 2.1×10^{-5} cm^2 s^{-1}. As a result, a gas atom will move several millimeters in 10 ms (several pixels in the image), while a water molecule moves only a fraction of that distance. The gas is likely to exhibit restricted diffusion in lungs, thus opening up the potential for use of diffusion changes to indicate progressive deterioration of lung structure.[48]

The basic conclusions that have been drawn from animal studies are that the image intensity is proportional to the amount of gas inhaled and the level of polarization: T_1 is of the order of 30 s, T_2* is of the order of 10–20 ms at 2.0 T, and the gas diffusion is likely to be affected by lung structure.

3.2.3 Human ^{3}He Lung Imaging

Imaging human lungs is reasonably straightforward compared with animal imaging because the human subject can cooperate with the procedure. This removes much of the difficulty of preparing and supporting animal subjects. While animal imaging can produce images over the course of several breath-holds, the human images must usually be accomplished in a single breath-hold. As a practical matter, most polarization systems produce a limited supply of gas. While 1 l of hyperpolarized ^{3}He is sufficient for several animal studies or many breaths for a guinea pig, it is just enough for one or two human breath-holds. Smaller quantities can be used as technology improves the level of polarization of the ^{3}He. Presently, studies have been performed with gas that has up to a 45% polarization and a volume of 200–600 ml,[23,49,50] although good studies can also be achieved with 10% polarization and a larger gas quantity.[51] Most of the human studies to date have been performed with the GRE method since it is readily available on most human MRI systems, while PE methods require pulse sequences and image reconstruction methods that are not usually commercially available.

A set of images of the lungs of a human volunteer are shown in Figure 6. The dark lines in the images indicate blood vessels in the lung. Such images are encouraging since they show good ventilation in this healthy volunteer. Images of the lungs of a subject with cystic fibrosis are shown in Figure 7. Another subject, who has received a lung transplant and is experiencing early rejection symptoms, is shown in Figure 8.

Early human imaging with ^{3}He shows clearly altered lung ventilation patterns in disease states compared with that in healthy subjects. However, it is yet unproven to what degree this may be useful in following disease progress. Studies of healthy volunteers have shown that even relatively benign processes such as allergy or colds can show transient ventilation differences with ^{3}He imaging, leading to concerns that the method may be 'too sensitive'. As with any new medical technique, it requires controlled clinical trials to establish the eventual medical utility of this new capability.

3.3 MRI and MRS with ^{129}Xe

Xenon-129 potentially has even greater promise than ^{3}He since it has higher solubility (about 15%) in blood and tissue (Table 1). Early spectroscopic measurements have shown that the ^{129}Xe that has moved from the lung air space to the blood has nearly a 200 ppm chemical shift, as shown in Figure 9.[52,53] There appear to be four distinguishable chemical shifts, owing to (a) the gas phase in the lungs (0 ppm), (b) the alveolar tissue phase (200 ppm), (c) the plasma phase (192 ppm), and (d) the red blood cell phase (213 ppm). There is some controversy as to the interpretation of the peak at 200 ppm, with some investigators suggesting that it results from the effect of lung tissue-induced $\boldsymbol{B}_0$ inhomogeneity on the other nearby peaks. In any case, this rich chemical shift structure should afford many possibilities for study of lung structure and function.

While ^{129}Xe diffuses more slowly than ^{3}He and, therefore, may imitate the flow of air more closely, it has two major difficulties for use as an imaging agent. It has a much lower gyromagnetic ratio than helium, which leads to the requirement for more rf power during excitation (for equal pulse time) than for helium and to lower SNR for equal spin density. Also, ^{129}Xe acts as an anesthetic above concentrations of 70%, with noticeable effects (light-headedness, slowed reaction) at concentrations above 30% in humans.[54,55] Therefore, while natural abundance, nonpolarized xenon has been used for short periods in computed tomography brain blood flow imaging[56] at a concentration of 39%, its use in humans must take into account such effects. It is interesting to note that because of its prior medical use, natural abundance xenon may have a simpler regulatory environment than the more inert ^{3}He.

In addition to lung imaging, ^{129}Xe has also been proposed as a brain or cardiac perfusion agent because of blood solubility. Investigators have shown ^{129}Xe signals from the brains of human subjects who breathe hyperpolarized ^{129}Xe.[12] Calculations have been published which indicate that a signal can be obtained from blood perfusion that is approximately 2–4% of the proton brain signal.[57,58] This is comparable with noninvasive arterial spin labeling approaches for perfusion measurement[59] and should have the advantage of having no 'background' signal to subtract. However, for repeated

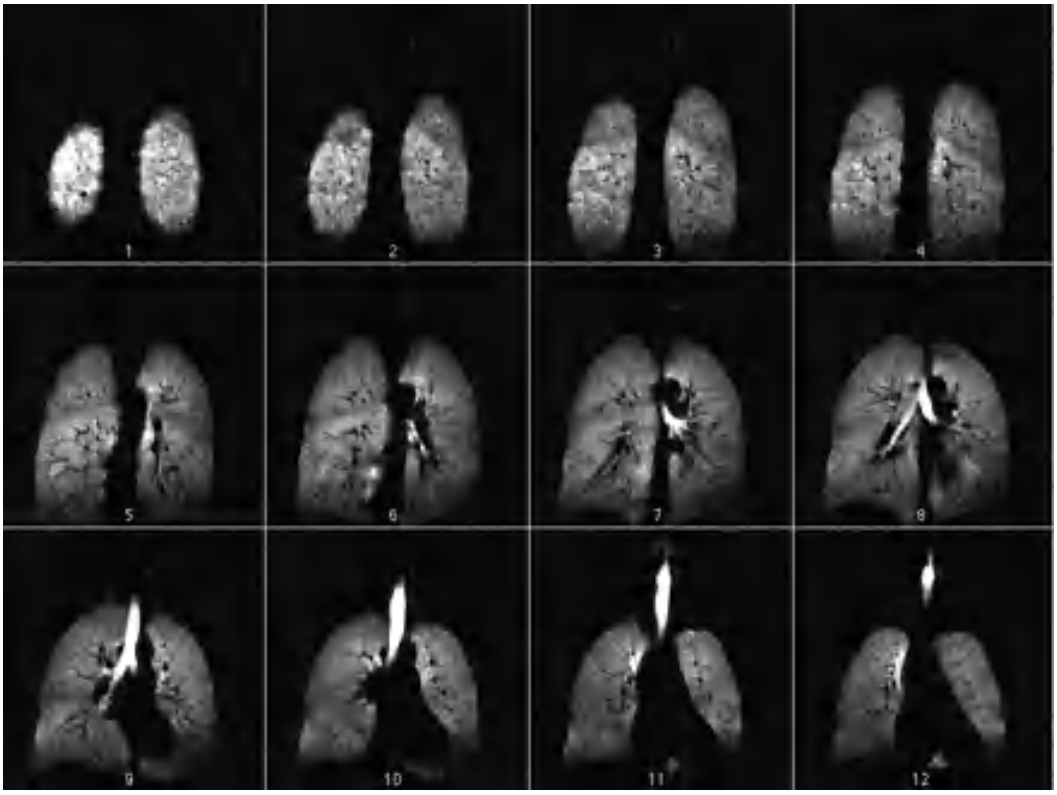

Figure 6 Images of hyperpolarized ^{3}He in the lungs of a healthy human volunteer. The gas polarization level was 10% and the quantity was 1.5 l. Images were acquired with a gradient-echo pulse sequence with *TR* 11 ms, *TE* 2 ms, FOV 36 cm, flip angle 6°, slice thickness 1 cm, 128 phase encodings, and in-plane resolution 1.7 mm. Healthy lung parenchyma shows a uniform intensity with dark lines along the course of blood vessels

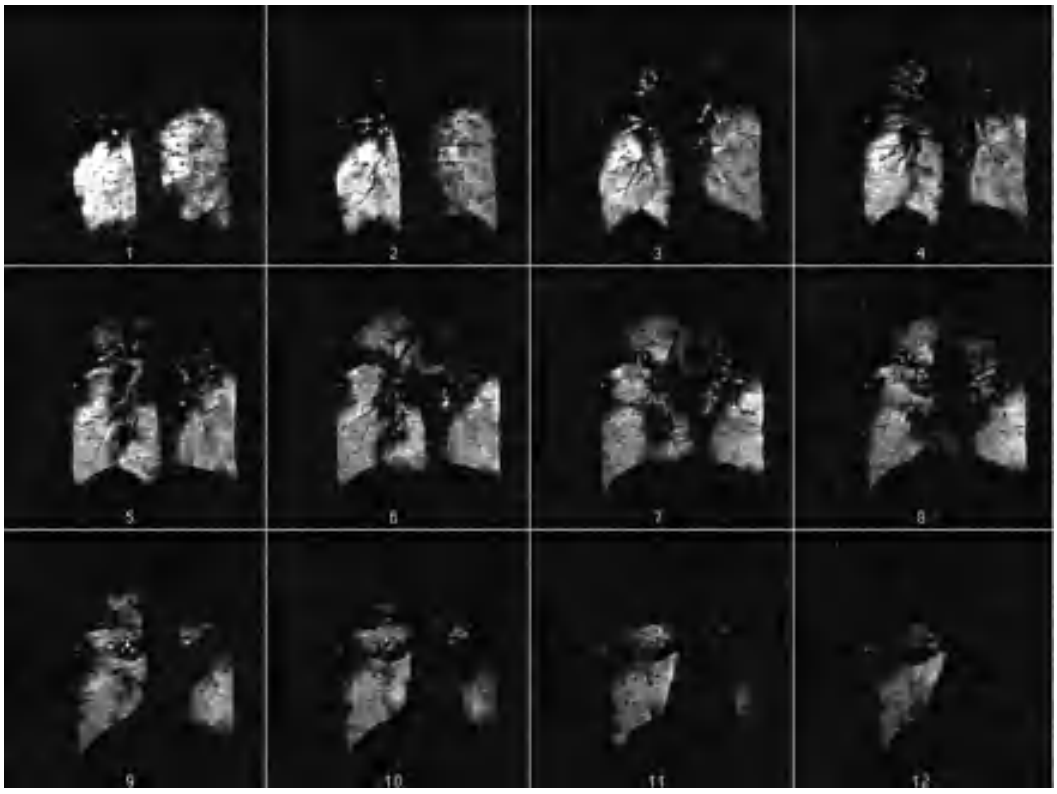

Figure 7 Images of hyperpolarized ^{3}He in the lungs of a subject with cystic fibrosis. The gas polarization level was 15% and about 0.75 liter was inhaled. Images were acquired with a gradient-echo pulse sequence with *TR* 11 ms, *TE* 2 ms, FOV 36 cm, flip angle 6°, slice thickness 1 cm, 128 phase encodings, and in-plane resolution 1.7 mm. The lung shows a patchy appearance

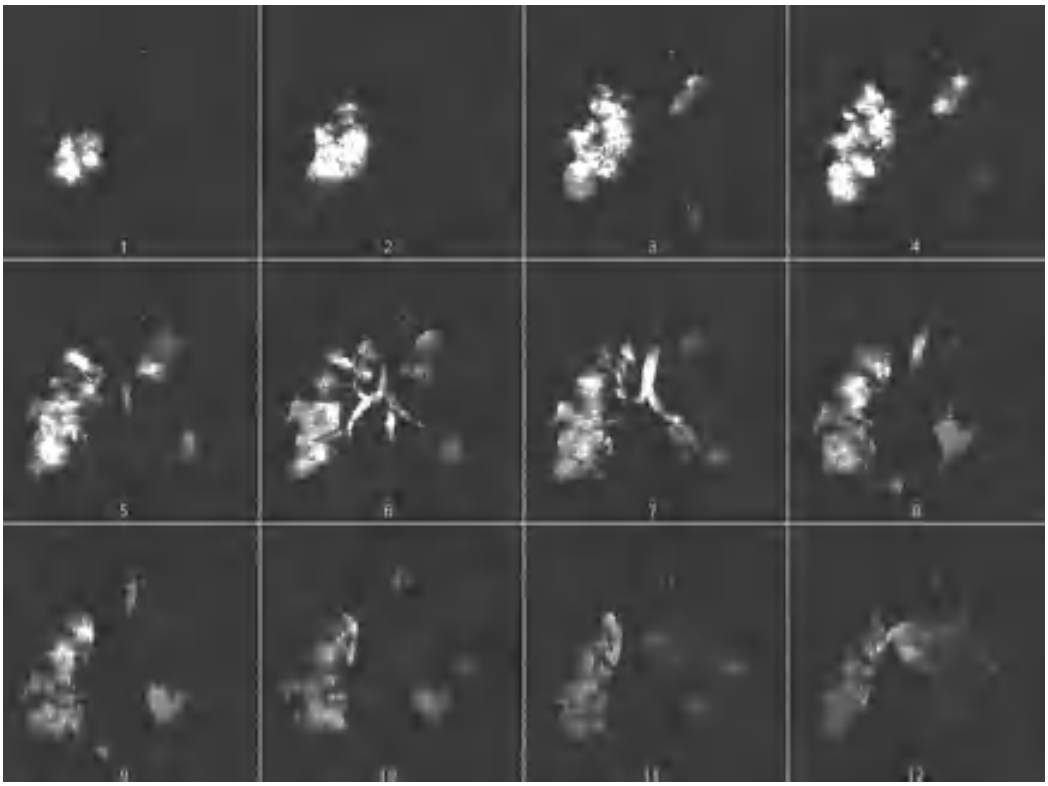

Figure 8 Images of hyperpolarized ^{3}He in the lungs of a subject after a single-side lung transplant. The gas polarization level was 15% and about 0.75 liter was inhaled. Images were acquired with a gradient-echo pulse sequence with *TR* 11 ms, *TE* 2 ms, FOV 36 cm, flip angle 6°, slice thickness 1 cm, 128 phase encodings, and in-plane resolution 1.7 mm. The left side of the image is the transplanted lung, showing more ventilation than the right-side (native) lung

measures, the noninvasive nature of arterial spin labeling approach may prevail over repeated breathing of ^{129}Xe.

In addition to providing chemical shift data, the animal studies have shown that the T_1 of ^{129}Xe in the lung is approximately 30 s.[36,53] Therefore, single breath-hold studies should be able to be accomplished in a manner similar to ^{3}He studies by using GRE pulse sequences with short echo times.

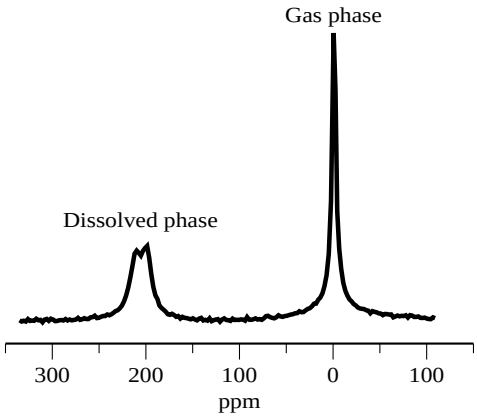

Figure 9 Spectrum of ^{129}Xe in the chest of a dog acquired using enriched (80%) ^{129}Xe, showing the gas phase and the dissolved phase peaks. (Spectrum courtesy of K. D. Hagspeil, and J. Mugler, University of Virginia)

Because of the lower gyromagnetic ratio and lower practical polarizations (up to 20%) reached to date, images made this way show lower resolution and SNR. However, as the images in Figure 10 show, it is still possible to make very good images of the lung with the lower costing, natural abundance hyperpolarized ^{129}Xe.

4 CONCLUSIONS

Hyperpolarized gas imaging provides a tremendous new opportunity to visualize the airways and air spaces in the lungs

Figure 10 Images of natural abundance (26% ^{129}Xe) hyperpolarized ^{129}Xe in the lungs of an anesthetized beagle. The gas polarization level was 10% and the quantity was 160 ml. Images were acquired with a gradient-echo pulse sequence with *TR* 300 ms, *TE* 6 ms, FOV 50 cm, flip angle 8°, slice thickness 3 cm, 128 phase encodings, and in-plane resolution 0.4 cm

as well as in body cavities such as the bowel or nasopharynx. Possibilities also beckon for use in measuring brain perfusion or as vascular contrast agents. The work to date in animals and humans has shown that the technique is easily performed given the proper equipment. Some commercially available MRI systems can provide the necessary ability to tune to the ^{3}He or ^{129}Xe resonant frequency. Coil development is straightforward for small animal systems and well within the typical research laboratory capability. Coil design for human systems may be best done by commercial coil companies or the MRI manufacturers since they should be created under strict safety standards and must interface properly with manufacturers' safety equipment. Development of custom equipment for gas polarization can be done in research laboratories with equipment that can be purchased commercially.

Early results show that the techniques are sensitive to lung pathology and that gas signals can be obtained from the brain and blood, but much work is yet to be done in controlled trials to demonstrate sensitivity, specificity, and cost-effectiveness.

5 RELATED ARTICLE

Contrast Agents in Whole Body Magnetic Resonance: An Overview.

6 REFERENCES

1. R. L. Gamblin and T. R. Carver, *Phys. Rev.*, 1965, **138**, A946.
2. W. Happer, *Rev. Mod. Phys.*, 1972, **44**, 169.
3. T. G. Walker and W. Happer, *Rev. Mod. Phys.*, 1997, **69**, 629.
4. P. L. Anthony, R. G. Arnold, H. R. Band, et al. *Phys. Rev. D*, 1996, **54**, 6620.
5. T. E., Chupp, R. J. Holt, and R. G. Milner, *Annu. Rev. Nucl. Particle Sci.*, 1994, **44**, 373.
6. M. E. Wagshul and T. E. Chupp, *Phys. Rev. A*, 1994, **49**, 3854.
7. G. Eckert, W. Heil, M. Meyerhoff, E. W. Otten, R. Surkau, M. Werner, M. Leduc, P. J. Nacher, and L. D. Schearer, *Nucl. Inst. Meth. Phys. Res. A*, 1992, **320**, 53.
8. R. Sukau, J. Becker, M. Ebert, T. Grossman, W. Heil, D. Hofmann, H. Humblot, M. Leduc, E. W. Otten, D. Rohe, K. Siemensmeyer, M. Steiner, F. Tasset, and N. Trautmann, *Nucl. Instr. Meth. Phys. Res. A,*1997, **384**, 444.
9. J. W. Hennel and J. Klinowski, 'Fundamentals of Nuclear Magnetic Resonance', Wiley and Longman Scientific & Technical, New York, 1993, p. 288.
10. R. D. Black, H. L. Middleton, G. D. Cates, G. P. Cofer, B. Driehuys, W. Happer, L. W. Hedlund, G. A. Johnson, M. D. Shattuck, and J. C. Swartz, *Radiology*, 1996, **199**, 867.
11. M. S. Chawla, X. J. Chen, H. E. Moller, G. P. Cofer, C. T. Wheeler, L. W. Hedlund, and G. A. Johnson, *Proc. Natl. Acad. Sci. USA*, 1998, **95**, 10832.
12. J. R. Brookeman, J. P. Mugler, B. Driehuys, C. D. Phillips, G. D. Cates, and W. Happer, *Radiology*, 1997, **202**, KH03.
13. M. S. Albert, G. D. Cates, B. Driehuys, W. Happer, B. Saam, C. S. Springer Jr., and A. Wishnia, *Nature*, 1994, **370**, 199.
14. T. G. Walker, *Phys. Rev. A*, 1989, **40**, 4959.
15. G. Frossati, *Nucl. Instr. Meth. Phys. Res. A*, 1998, **402**, 479.
16. F. D. Colegrove, L. D. Schearer, and G. K. Walters, *Phys. Rev.*, 1963, **132**, 2561.
17. J. Becker, W. Heil, B. Krug, M. Leduc, M. Meyerhoff, P. J. Nacher, E. W. Otten, T. Prokscha, L. D. Schearer, and R. Surkau, *Nucl. Inst. Meth. Phys. Res. A*, 1994, **346**, 45.
18. M. A. Bouchiat, T. R. Carver, and C. M. Varnum, *Phys. Rev. Lett.*, 1960, **5**, 373.
19. B. C. Grover, *Phys. Rev. Lett.*, 1978, **40**, 391.
20. M. S. Rosen, T. E. Chupp, K. P. Coulter, S. D. Swanson, and R. C. Welsh, *Rev. Sci. Instr.*, 1999, **70**, 1546.
21. B. Driehuys, G. D. Cates, E. Miron, K. Sauer, and D. K. Walter, *Appl. Phys. Lett.*, 1996, **69**, 1668.
22. J. P. Mugler, University of Virginia, personal communication.
23. P. Bachert, L. R. Schad, M. Bock, M. V. Knoop, M. Ebert, T. Groszman, W. Heil, D. Hofmann, R. Surkau, and E. W. Otten, *Magn. Reson. Med.*, 1996, **36**, 192.
24. W. Heil, H. Humbolt, E. Otten, M. Schafer, R. Sarkau, and M. Leduc, *Phys. Lett. A*, 1995, **201**, 337.
25. N. R. Newbury, A. S. Barton, G. D. Cates, W. Happer, and H. Middleton, *Phys. Rev. A*, 1993, **48**, 4411.
26. E. R. Hunt, and H. Y. Carr, *Phys. Rev.*, 1963, **130**, 2302.
27. G. D. Cates, D. R. Benton, M. Gatzke, W. Happer, K. C. Hasson, and N. R. Newbury, *Phys. Rev. Lett.*, 1990, **65**, 2591.
28. M. Gatzke, G. D. Cates, B. Driehuys, D. Fox, W. Happer, and B. Saam, *Phys. Rev. Lett.*, 1993, **70**, 690.
29. N. Salibi and M. A. Brown, 'Clinical MR Spectroscopy, First Principles', Wiley, New York, 1998, p. 220.
30. C. E. Hayes, W. A. Edelstein, and J. F. Schenck, 'NMR in Medicine: The Instrumentation and Clinical Applications', ed. S. R. Thomas and R. L. Dixon, American Institute of Physics, New York, 1986, p. 142.
31. C. J. Bergin, G. H. Glover, and J. M. Pauly, *Radiology*, 1991, **180**, 845.
32. A. Sotgiu, G. Gualtieri, and R. Passariello, *Magn. Reson. Imag.*, 1988, **6**, 249.
33. C. E. Hayes, N. Hattes, and P. B. Roemer, *Magn. Reson. Med.*, 1991, **18**, 309.
34. P. B. Roemer, W. A. Edelstein, C. E. Hayes, S. P. Souza, and O. Mueller, *Magn. Reson. Med.*, 1990, **16**, 192.
35. P. K. Weathersby and L. D. Homer, *Undersea Biomed. Res.*, 1980, **7**, 277.
36. H. E. Moller, X. J. Chen, M. S. Chawla, B. Driehuys, L. W. Hedlund, and G. A. Johnson, *J. Magn. Reson.*, 1998, **135**, 133.
37. B. Saam, W. Happer, and H. Middleton, *Phys. Rev. A*, 1995, **52**, 862.
38. A. Haase, J. Frahm, D. Matthaei, W. Haenicke, and K. D. Merboldt, *J. Magn. Reson.*, 1986, **67**, 217.
39. S. L. Gewalt, G. H. Glover, L. W. Hedlund, G. P. Cofer, J. R. MacFall, and G. Johnson, *Magn. Reson. Med.*, 1993, **29**, 99.
40. A. E. Holsinger and S. J. Riederer, *Magn. Reson. Med.*, 1990, **16**, 481.
41. L. R. Zhao, C.-H. Tseng, D. Williamson, S. Patz, R. Kraft, R. L. Walsworth, F. Jolesz, and M. S. Albert, *J. Magn. Reson. B*, 1996, **113**, 179.
42. H. Middleton, R. D. Black, B. Saam, et al. *Magn. Reson. Med.*, 1995, **33**, 271.
43. G. A. Johnson, G. Cates, X. J. Chen, G. P. Cofer, B. Driehuys, W. Happer, L. W. Hedlund, B. Saam, M. D. Shattuck, and J. Swartz, *Magn. Reson. Med.*, 1997, **38**, 66.
44. X. J. Chen, M. S. Chawla, L. W. Hedlund, H. E. Moller, J. R. MacFall, and G. A. Johnson, *Magn. Reson. Med.*, 1998, **39**, 79.
45. X. J. Chen, M. S. Chawla, G. P. Cofer, L. W. Hedlund, H. E. Moller, and G. A. Johnson, *Magn. Reson. Med.*, 1998, **40**, 61.
46. X. Chen, H. Moller, M. Chawla, G. Cofer, B. Driehuys, L. Hedlund, and G. Johnson, *Magn. Reson. Med.*, 1999, **42**, 721.
47. M. Bock, *Magn. Reson. Med.*, 1997, **38**, 890.
48. X. Chen, H. Moller, M. Chawla, G. Cofer, B. Driehuys, L. Hedlund, J. MacFall, and G. Johnson, *G. Magn. Reson. Med.*, 1999, **42**, 729.
49. H. U. Kauczor, D. Hofmann, K. F. Kreitner, H. Nilgens, R. Surkau, W. Heil, A. Potthast, M. V. Knopp, E. W. Otten, and M. Thelen, *Radiology*, 1996, **201**, 564.

50. H. U. Kauczor, M. Ebert, K. F. Kreitner, H. Nilgens, R. Surkau, W. Heil, D. Hofmann, E. W. Otten, and M. Thelen, *JMRI*, 1997, **7**, 538.
51. J. R. MacFall, H. C. Charles, R. D. Black, H. Middleton, J. C. Swartz, B. Saam, B. Driehuys, C. Erickson, W. Happer, G. D. Cates, G. A. Johnson, and C. E. Ravin, *Radiology*, 1996, **200**, 553.
52. M. E. Wagshul, T. M. Button, H. F. Li, Z. Liang, C. S. Springer, K. Zhong, and A. Wishnia, *Magn. Reson. Med.*, 1996, **36**, 183.
53. K. Sakai, A. M. Bilek, E. Oteiza, R. L. Walsworth, D. Balamore, F. A. Jolesz, and M. S. Albert, *J. Magn. Reson. B*, 1996, **111**, 300.
54. S. L. Whitehurst, E. M. Nemoto, L. Yao, and H. Yonas, *J. Neurosurg. Anesthesiol.*, 1994, **6**, 275.
55. H. Yonas, B. Grundy, D. Gur, L. Shabason, S. K. Wolfson Jr., and E. E. Cook, *J. Comput. Assist. Tomogr.*, 1981, **5**, 591.
56. D. Gur, H. Yonas, and W. F. Good, *Cerebrovasc. Brain Metab. Rev.*, 1989, **1**, 68.
57. C. C. Martin, R. F. Williams, J. H. Gao, L. D. Nickerson, J. Xiong, and P. T. Fox, *JMRI*, 1997, **7**, 848.
58. S. Peled, F. A. Jolesz, C. H. Tseng, L. Nascimben, M. S. Albert, and R. L. Walsworth, *Magn. Reson. Med.*, 1996, **36**, 340.
59. E. C. Wong, R. B. Buxton, and L. R. Frank, *NMR Biomed.*, 1997, **10**, 237.

Biographical Sketch

James R. MacFall. *b* 1945. B.A., 1967, Northwestern University, M.S., 1971, Ph.D., 1976, University of Maryland. Pfizer Medical Systems, Inc. designing X-ray systems for computed tomography systems 1976–82. GE Medical Systems developing applications for magnetic resonance imaging systems 1982–88. Duke University Medical Center 1988–present. Current research interests: medical imaging physics with emphasis on MR imaging. Approx. 75 papers and 6 patents in MR imaging.

Bastiaan Driehuys. *b* 1968. B.A., 1990, Franklin & Marshall College, M.S., 1992, Ph.D., 1995, Princeton University. Postdoctoral fellow with William Happer, Princeton University 1995–96. Joined Magnetic Imaging Technologies in 1996 as a founding research physicist. Responsible for development of a commercial Xe hyperpolarizer. Director of R&D at Magnetic Imaging Technologies, 1998 President of Magnetic Imaging Technologies, 1999.

Lung and Mediastinum: A Discussion of the Relevant NMR Physics

David C. Ailion
University of Utah, Salt Lake City, UT, USA

1 INTRODUCTION

Of all organs in the human body, lung is one of the most difficult to image. This difficulty has three primary causes: (1) lung has a relatively low water density (about 20%) compared to that of other organs; (2) the NMR lineshape in lung is inhomogeneously broadened by susceptibility effects[1] (see ***Susceptibility and Diffusion Effects in NMR Microscopy*** and ***Susceptibility Effects in Whole Body Experiments***) arising from the existence of air–water interfaces associated with the alveoli; and (3) its NMR image is subject to motional artifacts[2] arising from the asynchronous motions of the heart and chest wall. In spite of these difficulties, considerable progress has been made in recent years in developing imaging techniques that minimize errors due to the susceptibility and motional effects. Furthermore, significant advances have been made in measuring the parameters[3] (e.g. linewidth, relaxation times, diffusion constants) that characterize the NMR behavior of lung and in understanding their underlying physical mechanisms. The techniques used in these studies are also currently being used in medical applications[3] to determine the state of normal and injured lungs (see ***Lung and Mediastinum MRI***). The current status of NMR methods for studying lung tissue (including medical applications) have been reviewed.[4] Techniques for imaging the gas-filled regions are described briefly at the end of this article (see also ***Hyperpolarized Gas Imaging***).

An explanation of the physical origin of the inhomogeneous broadening in lung is given and is followed by a discussion of the present state of our understanding of the mechanisms responsible for the various NMR parameters: lineshape, spin–spin relaxation time (T_2), spin–lattice relaxation time (T_1), and diffusion constant (D). Finally, techniques that are currently used to investigate and image lungs are presented.

2 INTERNAL INHOMOGENEOUS LINE BROADENING IN LUNG

2.1 Free Induction Decay in Lung

Most biological tissues are characterized by a free induction decay (FID) of a duration of the order of several hundred milliseconds. In contrast, lung has a much shorter FID (broader NMR line), the value of which (about 2–4 ms)[5] depends on $\boldsymbol{B}_0$ and the state of inflation of the lung. Since this very short FID is much less than the inhomogeneity in $\boldsymbol{B}_0$ in most magnets, it must arise from a mechanism internal to lung. The signal loss due to this mechanism has been shown to be reversible (corresponding to an inhomogeneous broadening), since the application of either a 90–180° pulse sequence or a Carr–Purcell sequence[6] recovers the signal in an echo. The fact that the FID is shorter in inflated lungs than in normal or degassed (airless) lungs[5] suggests that the line broadening is associated with the presence of air–tissue interfaces at the boundaries of the alveoli of lung. Similar measurements[5] performed on an alumina/water (Al_2O_3/H_2O) slurry consisting of 5 μm diameter alumina particles in water also showed a short FID that can be recovered in an echo (see Figure 1). Since alumina has a bulk diamagnetism that is approximately twice that of water, these results suggest that the broadening arises from the presence of interfaces between materials having different magnetic susceptibilities (air–tissue in lung, and alumina–water in the slurry). The decay time of the FID owing to internal inhomogeneous broadening mechanisms, such as these susceptibility effects, is called T_2'.

2.2 Theoretical Models for Calculating NMR Lineshapes in Lung

2.2.1 Spherical Shell Model

The confirmation that susceptibility effects at the water–tissue interfaces are indeed responsible for the inhomogeneous line broadening and corresponding shortening of the FID in lung came from a combination of model calculations and phantom experiments.[1] In all these calculations, lung tissue is treated as pure water, having some predetermined geometrical shape. For instance, consider the well-known behavior of a diamagnetic sphere (of, for example, water) in an otherwise uniform applied magnetic field $\boldsymbol{B}_0$. Calculations[1] of the magnetic induction $\boldsymbol{B}$ using Maxwell's equations[7] predict a shift in the value of the magnetic induction but not a spread in its values. This can be seen from Figure 2(a), in which the lines of force within the sphere are parallel, but have a slightly different density from those outside the sphere and far from it. The magnetic induction shift caused by a uniform sphere of

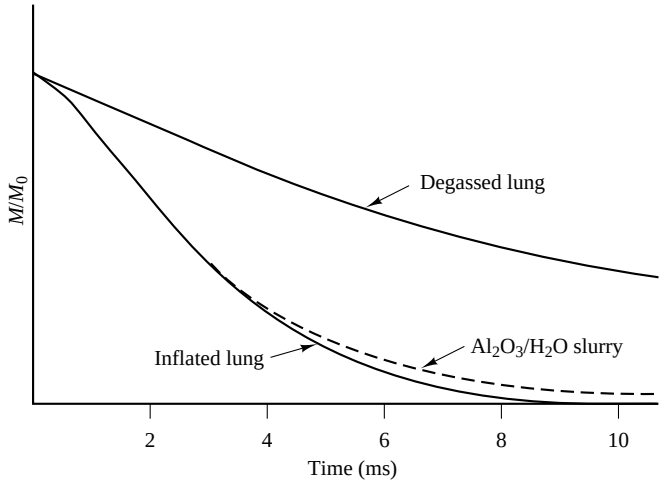

Figure 1 FIDs of inflated lung, degassed lung, and an alumina/water slurry

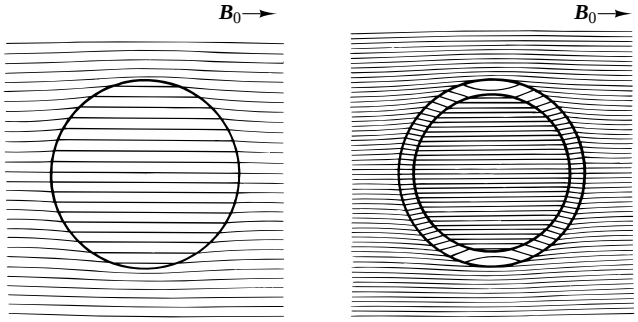

(a) Water sphere (b) Water shell

Figure 2 (a) Lines of force for sphere of water in an otherwise uniform magnetic field; (b) lines of force for spherical shell of water in an otherwise uniform magnetic field. (Reproduced by permission of Pergamon Press from D. C. Ailion, *Magn. Reson. Imaging*, 1992, **10**, 799)

radius a and relative permeability μ (= 1 − $\Delta\mu$) is given to first order by[1]

$$\Delta \boldsymbol{B} = -2\Delta\mu \boldsymbol{B}_0/3 \qquad \text{if } r < a \tag{1}$$

and

$$\Delta \boldsymbol{B} = \Delta\mu \boldsymbol{B}_0 a^3(r^2 - 3z^2)/3r^5 \qquad \text{if } r > a \tag{2}$$

where $\Delta\mu$ represents the difference in relative permeability of the diamagnetic sphere and air (about 9 ppm for water), and r is the distance of the field point from the center of the sphere. The field shifts can also be calculated for a diamagnetic spherical shell by simply superimposing the results for two concentric spheres of different radii and different permeabilities.[1] In this case, there will be a spread in the values of $\boldsymbol{B}$, since the lines of force are no longer precisely parallel [see Figure 2(b)]. In fact, the flux density $\boldsymbol{B}$ will be reduced for those portions of the shell (top and bottom) that are approximately parallel to the field, but will be unaltered for those regions (middle) that are perpendicular to it.

This spread in $\boldsymbol{B}$ will result in a broadening of the NMR linewidth. The existence of this broadening has been observed experimentally in a spherical shell phantom consisting of two concentric glass spheres with water filling the space between them.[1] Excellent agreement was obtained between the measured and theoretical lineshapes for this phantom.

2.2.2 *Spherical Foam Model*

A better model [Figure 3(a)] for the alveolar region than that of a single spherical shell consists of a lattice containing spheres of air with water in between, with each sphere of air (representing an alveolus) centered on a different lattice point. Calculations using this model[1] showed that the linewidth increases (though not precisely linearly) with the air percentage of the total volume. Furthermore, by calculating the inverse Fourier transform of the lineshape, the FID time constant T_2' was determined to be 3.4 ms for 70% air at 40 MHz, which is in excellent agreement with our measurements on lung.

2.2.3 *Wigner–Seitz Model*

A disadvantage of the spherical foam model is that it can not be used for large air/water ratios, since the spheres will touch and the model will break down when the percentage of air reaches 74%. A better model has been employed in which the spherical air spaces are replaced by space-filling Wigner–Seitz polyhedra[8] [Figure 3(b)], with the water occupying the interfaces between the polyhedra. This model can be improved [Figure 3(c)] by rounding the corners of the polyhedra, so that the shape corresponds more to that of actual alveoli, and by thickening their walls, in order to accommodate any desired air/water ratio from 0 to 100%. This model gives a slightly asymmetric lineshape, which has been observed experimentally in isolated rat lung.[9] Figure 4 shows a comparison between a

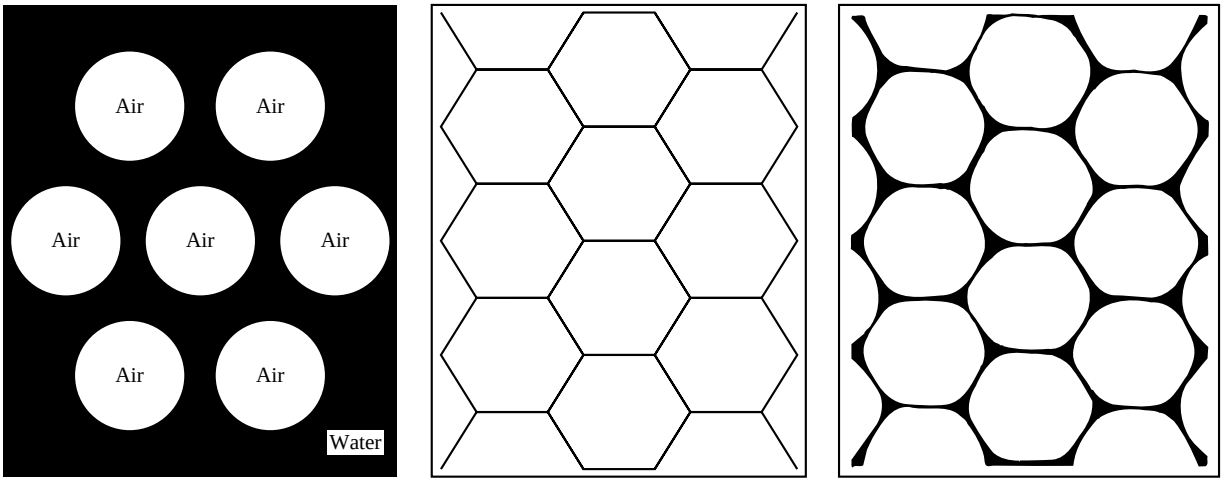

(a) (b) (c)

Figure 3 Two-dimensional cross-section of various models of the alveolar region: (a) spherical foam; (b) Wigner–Seitz foam; (c) modified Wigner–Seitz foam with thickened boundaries and rounded corners. In the Wigner–Seitz models, the air is in the polyhedral spaces, and the water (representing alveolar wall tissue) is in the boundaries

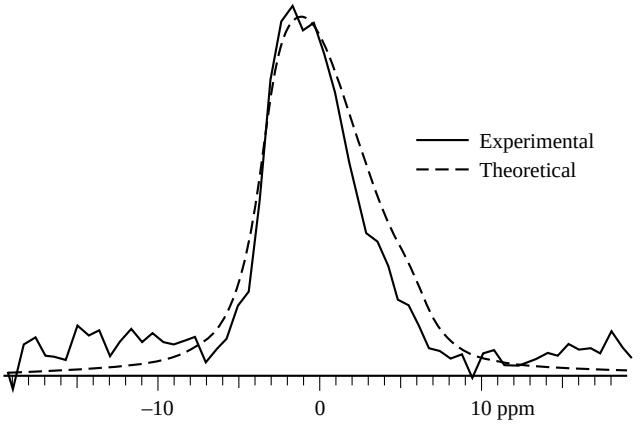

Figure 4 NMR lineshape from the outer, or alveolar, region of excised rat lung, showing a comparison of the measured and calculated lineshapes based on the modified Wigner–Seitz model. (Reproduced, with modifications, by permission of Pergamon Press from D. C. Ailion, *Magn. Reson. Imaging*, 1992, **10**, 799)

calculated Wigner–Seitz lineshape (for 90% air volume) and one measured from a voxel in the outer (alveolar or parenchymal) region of an excised isolated rat lung.

2.2.4 Long Cylinder Model

A very different model (cylindrical)[9] is needed for the central (mainly nonparenchymal) region of the lung, which contains bronchi and large blood vessels. This model predicts a symmetric, but shifted, NMR line the shift of which depends on the orientation of the cylinder relative to the magnetic field. The shift is largest for the cylinder's long axis parallel to $\boldsymbol{B}_0$ and smallest for the long axis perpendicular to $\boldsymbol{B}_0$. In a similar comparison[9] between calculated and experimentally measured NMR lineshapes from the central region of an isolated excised rat lung, the experimental shape can be fit as a superposition of parenchymal (Wigner–Seitz) and nonparenchymal (cylinder) lines, suggesting the presence of both kinds of structure in the central region. These results suggest that regional lineshape measurements can distinguish different types of geometry in rat lung.

2.2.5 Other Geometries (Slabs, Cubes, Cubical Shells)

Because of the obvious sensitivity of the NMR lineshape to water geometry, theoretical investigations have been extended to other types of water geometry[10,11] (slabs, cubes, cubical shells). A comparison of experimental measurements with theoretical lineshapes is shown for various geometrical phantoms in Figure 5.

For the slabs, as with the cylinders, the field shift depends on the orientation of the slab relative to the magnetic field direction, being maximum (about -9 ppm) for $\boldsymbol{B}_0$ parallel to the face of the slab and minimum (close to zero) for $\boldsymbol{B}_0$ perpendicular to it. For cubes, the field shift is intermediate (about -6 ppm) between these extremes and is comparable to that for a solid sphere. However, unlike the sphere, the field inside a cube is not uniform, so that the cube produces some line broadening. The cubical shell for which $\boldsymbol{B}_0$ is perpendicular to one face has four faces which are parallel to the field and two that are perpendicular to it. These features appear in the figure. In summary, it appears that the NMR properties of water can be categorized on the basis of the aspect ratio of the water containing region in terms of 'thick' water (resulting in a narrow linewidth) and 'thin' water (resulting in a broad linewidth whose field at the peak depends on the orientation of the thin water relative to the magnetic field).

3 RELAXATION TIMES IN LUNG

Knowledge of the transverse (T_2) and longitudinal (T_1) relaxation times are important not only in optimizing an NMR image but also in determining the underlying structure and dynamics (see ***Relaxation Measurements in Imaging Studies*** and ***Relaxometry of Tissue***).

3.1 T_2 Behavior

3.1.1 Hahn Echo

A common way to measure the spin–spin relaxation time in a liquid is to apply a 90° pulse, followed a variable time τ later by a 180° pulse, thereby producing an echo (the so-called 'Hahn echo') at 2τ, whose amplitude decreases (in principle, exponentially) with a time constant T_2. However, if the spins can diffuse without restriction in a magnetic field gradient (either internal or external) then the decay will not be exponential, but will be given by[6]

$$M(2\tau)/M(0) = \exp(-2\tau/T_2)\exp[-2(\gamma g)^2 D\tau^3/3] \qquad (3)$$

where γ is the gyromagnetic ratio, g is the magnetic field gradient, and D is the diffusion constant. For sufficiently rapid diffusion in large gradients, a measurement of the Hahn echo time constant will provide information about the nature of the diffusion, but will not reflect the underlying T_2.

3.1.2 The Carr–Purcell–Meiboom–Gill Technique

Carr and Purcell developed a one-shot technique[6] for eliminating the τ^3 term from the decay. This technique, later modified by Meiboom and Gill to minimize errors due to inaccurate pulse widths, consists of following the initial echo by a series of equally spaced echo-producing 180° pulses. By making the time between these pulses sufficiently short, the τ^3 term can be virtually eliminated, thereby providing a measurement of the underlying T_2.

3.1.3 Diffusion Measurements in Lung

A comparison of the Hahn decay with the Carr–Purcell–Meiboom–Gill (CPMG) decay measured in excised rat lung (Figure 6) reveals that the Hahn decay is much shorter than the CPMG, indicating the presence of significant diffusion in internal gradients, probably arising from the alveolar air–tissue interfaces.

The Hahn decay time provides a measure of the product Dg^2, but not of either parameter alone. However, by applying large known pulsed gradients g_a; D can be determined from a plot of log $[M(2\tau)/M(0)]$ versus g_a^2. Because of the presence of large internal magnetic field gradients, special techniques[12,13] should be employed to separate the effects of the internal and

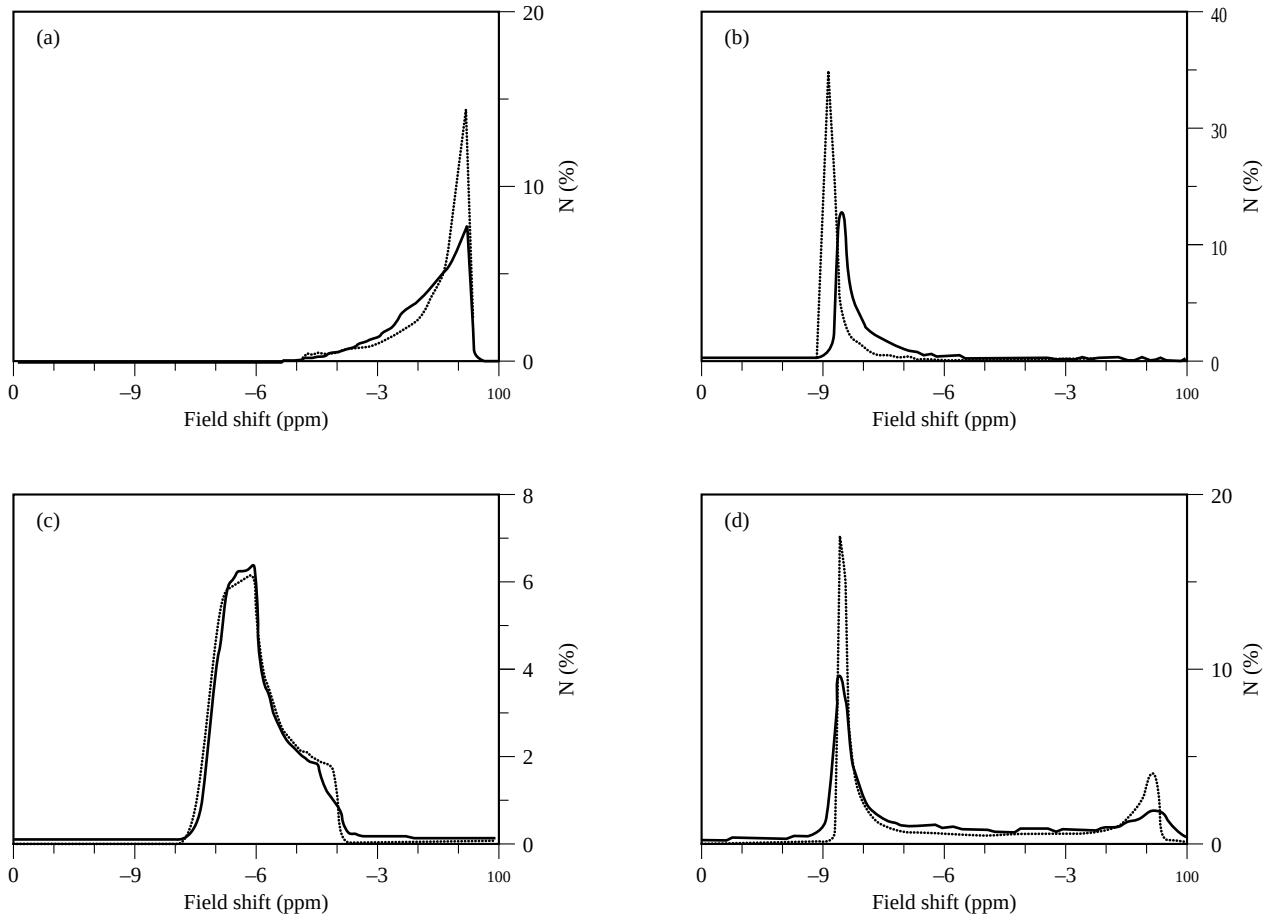

Figure 5 Comparison of theoretical (....) and experimental (——) NMR lineshapes for various water geometries. (a) Water slab (thickness 0.10 in. (2.5 mm)) perpendicular to $\boldsymbol{B}_0$. (b) Water slab parallel to $\boldsymbol{B}_0$ (thickness 0.10 in. (2.5 mm)). (c) Water cube with face perpendicular to $\boldsymbol{B}_0$ (thickness 1.0 in. (2.5 mm)). (d) Cubical water shell (thickness 0.125 in. (3.2 mm)) with face perpendicular to $\boldsymbol{B}_0$. (Reproduced, with modification, by permission of Pergamon Press from D. C. Ailion, *Magn. Reson. Imaging*, 1992, **10**, 799)

external gradients. One of the approaches[12] uses pulsed field gradients (PFG) arranged (e.g., in a 13-interval sequence[14]) to eliminate the effects of the internal gradients on the magnetization decay. The other approach[13] uses extremely large (~0.2–1 T/cm) static magnetic field gradients (SFG) obtained either from the fringe field of superconducting magnets or from specially wound anti-Helmholtz magnets.[15] Since the applied gradient g_a cannot be conveniently varied with this technique, a stimulated echo sequence[13,15] is used in which the magnetization decay is monitored (and D is determined) by varying the time τ between the first two 90° pulses. Because of the extremely large size of the external gradient, dephasing through the internal gradients and T_2 can safely be neglected. By varying the time between the second and third pulses of the stimulated echo sequence, the time dependence of D can be measured. Even for restricted diffusion, the molecules will appear to be diffusing freely over times short compared with the mean time for a molecule to reach the restricting boundaries; however, for much longer diffusion times, the molecules' spatial displacements may be restricted, resulting in a change in the time dependence of D. The mean distance separating the barriers restricting the diffusion can be estimated from measurements of the time at which this crossover from 'free' to 'restricted' diffusion occurs.[13]

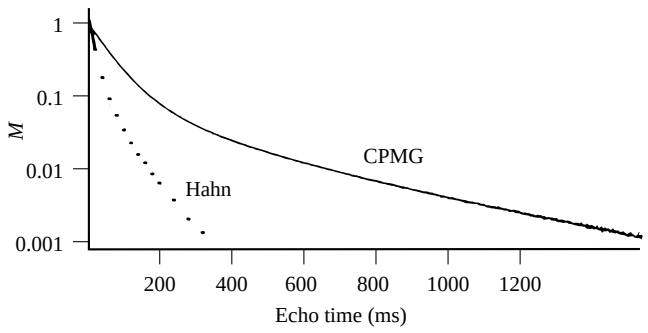

Figure 6 Normalized spin echo amplitude versus echo time for passively collapsed lung at 1.9 T. (Reproduced by permission of the Society of Magnetic Resonance in Medicine from H. Kolem, C. Goodrich, K. Ganesan, D. C. Ailion, A. G. Cutillo, S. Chen, A. H. Morris, S. Shioya, and S. Watanabe, in *Proc. VIIIth Ann Mtg. Soc. Magn. Reson. Med.*, New York, 1989, p. 685)

Measurements of D in excised rat lungs[12,13] by both these techniques indicate the presence of at least two diffusion coeffi-

cients. Imaging measurements of D using the 13-interval sequence were performed[12] in the central (mainly nonparenchymal) and outer (parenchymal) regions in excised intact rat lungs and compared with the results of separate nonimaging measurements on lung fragments taken from the central and outer regions. These experiments indicate that both diffusion components are present in each lung region, but perhaps in differing propostions, with the more rapid component being more significant in the central lung region and the slower component being relatively large in the alveolar region.[12] Similar measurements on edematous rat lung indicate an increase in the magnetization associated with the more rapid decay even in the alveolar region, suggesting that edema is characterized by an increase in the more rapidly moving (presumably freer) water. Since the relative size of the larger D is still an order of magnitude smaller than that of free water, it can be concluded that even the diffusion in the central portion of the lung is restricted. Measurement of the time dependence of D in fragments from the alveolar region of excised rat lungs using the large SFG approach indicates a crossover from 'free' to 'restricted' diffusion corresponding to several micrometers.[14] A careful analysis of the data indicates that the shape of the crossover may be explained by a distribution of restriction sizes extending up to 18 μm but with a mean value of 3.7 μm. This value corresponds quite well to the known thickness of epithelial cells in the alveolar walls, which is typically approximately 3 μm, suggesting this to be the primary origin of restricted diffusion in the alveolar portion of the lung.

3.1.4 CPMG T_2 Measurements in Lung

CPMG T_2 measurements[16] in rat lung reveal a multiexponential decay with a time constant increasing gradually from a few to several hundred milliseconds. This decay can be fitted by four time constants. Time course measurements of these components on a lung which is gradually drying out reveal that the longest T_2 component disappears completely before the next starts to decrease, and the second longest disappears competely before the next decreases, and so on. These results suggest that the longer T_2 components are associated with less tightly bound water and the short T_2 components with more tightly bound water. Pulsed gradient measurements of the diffusion constant associated with each T_2 component show a strong correlation between T_2 and D, with the longer T_2 components corresponding to the more rapidly diffusing (larger D) molecules.

3.2 T_1 Behavior

As with T_2, the spin–lattice relaxation time T_1 can provide useful information about the microscopic environment of a spin. In contrast to T_2, which is multiexponential, T_1 is monoexponential in lung. Imaging measurements[17] have shown that T_1 varies regionally in lung.

3.2.1 Frequency Dependence of T_1 in Lung

In general, the Larmor frequency dependence of T_1 is sensitive to the microscopic relaxation mechanism. Accordingly, measurements of T_1 as a function of frequency can often be used to eliminate and/or confirm possible spin–lattice relaxation mechanisms. Rorschach and Hazlewood[18] developed a model for water molecules in contact with a macromolecule (or biopolymer) that are relaxed by segmental motions of the polymer and, in turn, cross relax to the solvent water molecules. This model, valid at high Larmor frequencies, predicts that

$$1/T_1 = A + B\omega_L^{-1/2} \tag{4}$$

where ω_L is the Larmor frequency and A and B are constants. This frequency dependence has been observed[19,20] in whole excised rat lung over the range 6.7–80.5 MHz. The theory has recently been extended[19,20] to very low Larmor frequencies and to rotating frame relaxation times ($T_{1\rho}$), and has shown excellent agreement with the results of measurements in rat lung.

3.2.2 Inflation Dependence of T_1 in Lung

Measurements of the Larmor frequency dependence of $1/T_1$ for various intact excised rat lungs, degassed as well as inflated with various gases[21] (air, O_2, and N_2), all agree with equation (4), but with different values for A and B. Furthermore, at any given frequency, measurements of $1/T_1$ versus inflation pressure show a linear dependence, the slope of which increases with oxygen content. Together, these results indicate that paramagnetic oxygen also plays a significant role in spin–lattice relaxation in inflated lung.[21]

4 IMAGING TECHNIQUES FOR LUNG

This section deals only with those techniques used in lung imaging. For a more general treatment of imaging techniques, see ***Hyperpolarized Gas Imaging***; ***Image Formation Methods***; ***Spin Warp Data Acquisition***; ***Echo-Planar Imaging***, and ***Projection–Reconstruction in MRI***.

4.1 Asymmetric Imaging

Over the last 10 years, techniques have been developed for imaging tissues that exhibit internal inhomogeneous broadening. These techniques involve pulse sequences that are temporally symmetric or asymmetric with respect to the time interval τ between the 90° and 180° pulses and the time interval τ' between the 180° pulse and the echo (see Figure 7). With these techniques the regions in an image that are inhomogeneously broadened can easily be separated from those that are not.

Typically, a frequency-encoding magnetic field gradient G_x is applied between the 90° and 180° pulses and a rephasing gradient follows the 180° pulse. For an internally broadened sample, there will be two sources of dephasing: (1) the dephasing due to the sample-induced inhomogeneous broadening which will refocus at 2τ; and (2) the dephasing owing to the external field gradient G_x, which will refocus at a time $(\tau + \tau')$ when the area under the gradient following the 180° pulse equals the area under the gradient that precedes it. The combined effect of these two sources of dephasing determines the amplitude of the spin echo. In a symmetric sequence ($\tau = \tau'$), these two dephasings will refocus at the same time (2τ), resulting in maximum echo height. In the asymmetric sequence ($\tau \neq \tau'$), the refocusing of the dephasing due to internal field gradients will still occur at 2τ but will no longer be coincident with the refocusing of the dephasing due to the external field

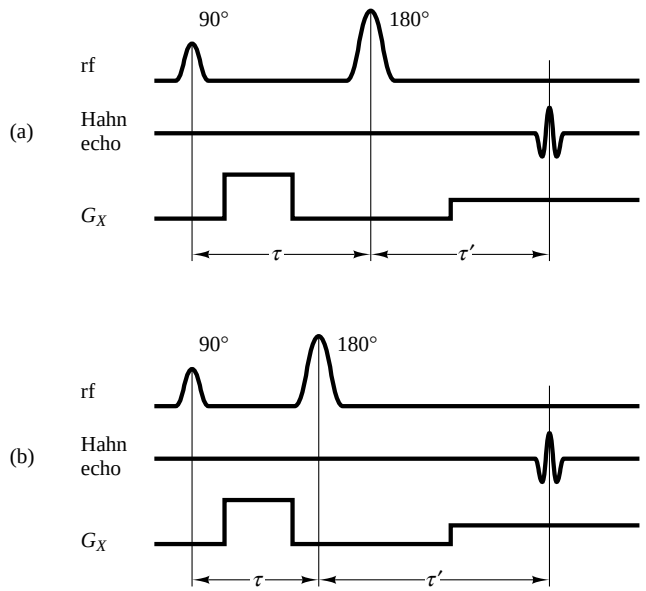

Figure 7 Pulse sequences used in NMR imaging of lung: (a) symmetric ($\tau = \tau'$); (b) asymmetric ($\tau \neq \tau'$). (Reproduced by permission of Pergamon Press from D. C. Ailion, *Magn. Reson. Imaging*, 1992, **10**, 799)

gradient G_x, which will occur at $\tau + \tau'$. Since these signals refocus at different times, the echo height obtained with the asymmetric sequence will be reduced compared with that obtained with the symmetric sequence. For normal tissue, such as liver, which shows no internal inhomogeneous broadening, the signals obtained with the symmetric and the asymmetric sequences will be equal. In contrast, the asymmetric signal in inflated lung, which shows considerable internal inhomogeneous broadening due to the air–water interfaces, will be considerably reduced compared with the symmetric signal. Thus, by subtracting voxel by voxel the asymmetric from the symmetric image, a difference image representing only those regions exhibiting internal inhomogeneous broadening can be formed.[5]

4.2 Techniques for Minimizing Motional Artifacts in Lung

A problem in in vivo lung MRI is that lung is a relatively low water density organ, adjacent to higher density regions, the heart and the chest wall, that move asynchronously due to the heartbeat and respiration, respectively. These motions cause nonlocal artifacts in two-dimensional Fourier transform (FT) images[2] (see ***Motion Artifacts: Mechanism and Control***). Since each phase-encoded echo used to construct the image arises from the entire object, any motion of the object between successive spin echoes in the same scan will result in a widespread motional artifact. Since this artifact can result in the occurrence of wispy white regions throughout the lung, it would be difficult to distinguish these from regions of local edema. Even though these artifacts may be tolerated in some qualitative applications, they are clearly unacceptable in quantitative studies.

4.2.1 Line Scan Techniques

4.2.1.1 Conventional line scan. The nonlocal artifacts described above can be largely avoided by the use of the line scan technique,[22] in which a planar region is selectively excited (see ***Selective Excitation in MRI and MR Spectroscopy***) with a 90° pulse after which a perpendicular plane is excited by a 180° pulse, so that only nuclei on the line of intersection of the two planes contribute to the echo. By applying a readout gradient along this selective line, an almost instantaneous one-dimensional image of the nuclei along this line is obtained. By shifting the rf frequency slightly and repeating this process, an adjacent line can be excited. In this way a two-dimensional image can be formed from a sequence of one-dimensional lines. A major advantage of this technique is that motions will result in localized, rather than widespread, artifacts involving only the particular selective lines that include the moving nuclei. A major disadvantage of this technique compared with the two-dimensional FT and other techniques is its slowness, since a time of the order of T_1 must elapse between each successive line scan. A second disadvantage is that the spatial resolution is usually poorer than with two-dimensional FT, because of the difficulty in selectively exciting spatially adjacent regions without overlap. The signal-to-noise (S/N) ratio is considerably poorer than with two-dimensional FT, in which data are obtained from an entire plane rather than from a single line. The first disadvantage (slowness) can be circumvented by the use of the rapid line scan (RLS) (see below). The second disadvantage (poor spatial resolution) can be reduced by interleaving the excitation order, using the interleaved line scan (ILS) technique (see below).

4.2.1.2 Rapid line scan. The slowness of the conventional line scan, due to the need to wait a time of order T_1 between successive scans, can be overcome by selectively exciting lines along a diagonal plane, rather than along either the 90° or 180° planes. In this case, the NMR signals from each line come from previously unexcited nuclei, so that successive lines can be excited in rapid succession, without requiring a delay of the order of T_1. The implementation of this sequence is similar to that of conventional line scan, except that the rf frequencies of both the 90° and 180° pulses are shifted before the next line scan.

One potential problem with this simple scheme is that spurious echoes can arise from the nuclei from previously excited planes. However, by simply applying spoiler gradients after each echo, the spurious echoes can be eliminated.[2]

Using the above technique an entire planar image can be excited within a single T_1. This RLS technique gives a S/N ratio similar to that of two-dimensional FT, but without the motional artifacts. Furthermore, it can produce a fully resolved planar image in the time required for the simple two-dimensional FT technique to obtain only one phase encode.

4.2.1.3 Interleaved line scan. A disadvantage of the RLS technique is that its spatial resolution in lung studies is usually much poorer than that of other techniques. Because of the relatively short T_2 of lung tissue, long highly selective rf pulses cannot be used. Because of the resulting imperfect slice selection, spins near the boundaries of the 90° and 180° planes are only partially excited, resulting in signal loss when the successive lines are closely spaced. This signal loss can be minimized by spacing the lines sufficiently far apart, resulting in limited spatial resolution. The signal loss can be reduced

and/or the spatial resolution improved by waiting a time of the order of T_1 between successive line scans. By interleaving the excitation order, adjacent line scans are separated temporally but without losing information from regions between the lines. Thus the ILS is a compromise between the higher speed RLS and the higher resolution conventional line scan technique. In imaging longer T_2 systems, more highly selective rf pulses can be used, so that improved resolution can be obtained with RLS in a relatively short time.

4.2.2 Rapid Projection–Reconstruction (PR) Technique

Another technique[23] which produces motional artifact-free images consists of using a slice-selection self-refocusing rf pulse followed immediately by two orthogonal frequency encoding gradients (see ***Projection–Reconstruction in MRI***). By using a self-refocusing pulse, the time needed for the refocusing gradient lobe is eliminated, so that a FID can be obtained immediately after the rf pulse. By varying the relative strengths of the orthogonal gradients, different projections can be obtained. Since the NMR signal is acquired immediately after the slice-selective excitation, essentially all biological motional artifacts are eliminated. Another feature of PR imaging is that the low-frequency data are oversampled, which is analogous to averaging the gross features of the object being imaged. Motional artifacts appear as streaks, largely outside the region of interest. This technique can obviously be applied to short T_2 systems, and has been successfully used in lung imaging.[24] Even though this technique clearly gets rid of the ghost-like artifacts of the two-dimensional FT techniques, it is not entirely free from motional errors. The time between the rf pulse and the data acquisition can be very short, but the time between successive projections would be of the order of T_1, with the result that motions within this time interval can result in noisy or distorted images. It is not necessary to wait a time of the order of T_1 between successive projections if small flip angles are used; however, the S/N ratio will be reduced considerably with this procedure. Another disadvantage of this technique is that the projection–reconstruction procedure requires a relatively long time to form a complete two-dimensional picture, since many projections are required. Nevertheless, under favorable conditions projection–reconstruction techniques have been able to obtain finely detailed microscopic pictures of rat lung.

4.3 Gas Imaging

A desirable complement to the tissue imaging described earlier in this article would be to image inhaled gases directly in the airways and alveoli. It is essentially impossible to image the air directly because of the very low density of paramagnetic nuclei and the corresponding small signal. However, two different approaches have been introduced in recent years that allow the direct imaging of the inhaled gases. One uses inhaled fluorinated gases in which the ^{19}F is imaged directly and the other uses inhaled hyperpolarized inert gases (either ^{3}He or ^{129}Xe) (see ***Hyperpolarized Gas Imaging***). The advantages of gas imaging using nuclei other than protons are (1) significant reduction in susceptibility distortion (because the alveoli are, to a first approximation, spherical), (2) elimination of artifacts arising from the motions of nearby high-density tissue (heart, chest wall), since these tissues will not contain the nuclei being imaged (i.e., the inhaled fluorocarbons or hyperpolarized ^{3}He); (3) enhanced signal-to-noise, particularly for the hypoerpolarized gases, and (4) the ability to observe directly the gas exchanging regions (alveoli, bronchi) whose properties can be inferred only indirectly from proton tissue imaging.

4.3.1 Fluorinated Gas Imaging

These imaging techniques typically involve inhaling fluorinated gases (e.g., hexafluoroethane or sulfur hexafluoride) mixed with approximately 20% oxygen. Because of the short ^{19}F T_1 (about 5.9 ms in hexafluoroethane),[25] the relatively low density of the ^{19}F in the gas can be partially compensated for by the higher efficiency of the signal averaging. Nevertheless, the signal is still somewhat reduced, and considerable time is required to obtain good images. In spite of this drawback, impressive images of the lungs of live rats[25] have been obtained in about 4 h. This technique has recently been applied to the detection of obstructed ventilation in the airways of lung, which results in an increased fluorocarbon concentration.[26,27] The main advantages of this technique over the use of hyperpolarized gases, to be described below, are its lower cost and experimental simplicity as well as its reduced sensitivity to oxygen relaxation. Its main disadvantage is that it is limited to imaging steady-state gas concentrations because of its lower sensitivity and the corresponding longer time required to obtain an image.

4.3.2 Hyperpolarized Gas (^{3}He or ^{129}Xe) Imaging

Hyperpolarized gas imaging is also called spin exchange[28] and is based on using laser light to prepolarize alkali nuclei (typically Rb) via the electrons and then to transfer this polarization to the nuclei that are to be imaged (^{3}He or ^{129}Xe). A variant of this technique (called metastability-exchange optical pumping)[29] involves direct optical pumping of the ^{3}He and does not involve Rb metal. The pumping efficiencies are comparable to those of spin exchange, but the metastability technique can be used only for ^{3}He and not for ^{129}Xe. These techniques can increase the signal strength of the polarized nucleus by four or five orders of magnitude, resulting in a signal strength that is even an order of magnitude larger than that of protons in a comparable volume of tissue.[30] Because of this enormous signal strength, signal averaging is not really necessary and images can be obtained within a signal breathing cycle. Comparing the advantages and disadvantages of ^{3}He and ^{129}Xe, the ^{3}He spin polarization has a much longer lifetime than that of ^{129}Xe. Furthermore, ^{3}He does not penetrate tissue, in contrast to ^{129}Xe, which readily dissolves in blood and tissue. As a result, ^{3}He is probably preferable for imaging the voids in the lung, whereas ^{129}Xe may be more useful for imaging tissue or gas–tissue mixtures (as in the alveolar regions of the lung). Both nuclei have been used to obtain high-quality images in humans.[31,32] Recently, ^{3}He has been reported to have been able to detect emphysema in humans.[33] The emphysema causes decreased elasticity in the alveolar walls, resulting in a decreased ability of the alveoli to expand upon inhalation. This results in a lower gas concentration in the emphysematic regions, resulting in a reduced signal intensity compared with that of the normal regions. Also, regional differences in apparent D values of the ^{3}He owing to the breakdown of alveolar

walls have been observed in emphysemic patients.[34] These patients also exhibit abnormal ventilation patterns in rapid 'real-time' echo-planar lung imaging.

5 RELATED ARTICLES

Anisotropically Restricted Diffusion in MRI; Diffusion: Clinical Utility of MRI Studies; Echo-Planar Imaging; Hyperpolarized Gas Imaging; Image Formation Methods; Lung and Mediastinum MRI; Motion Artifacts: Mechanism and Control; Projection–Reconstruction in MRI; Relaxation Measurements in Imaging Studies; Relaxometry of Tissue; Selective Excitation in MRI and MR Spectroscopy; Spin Warp Data Acquisition; Susceptibility and Diffusion Effects in NMR Microscopy; Susceptibility Effects in Whole Body Experiments.

6 REFERENCES

1. T. A. Case, C. H. Durney, D. C. Ailion, A. G. Cutillo, and A. H. Morris, *J. Magn. Reson.*, 1987, **73**, 304.
2. D. C. Ailion, K. Ganesan, T. A. Case, and R. Christman, *Magn. Reson. Imaging*, 1992, **10**, 747.
3. A. G. Cutillo, A. H. Morris, D. C. Ailion, and C. H. Durney, *Chest*, 1989, **96**, 643.
4. A. G. Cutillo (ed.), 'Application of Magnetic Resonance to the Study of Lung', Futura, New York, 1996.
5. D. C. Ailion, T. A. Case, D. D. Blatter, A. H. Morris, A. G. Cutillo, C. H. Durney, and S. A. Johnson, *Bull. Magn. Reson.*, 1984, **6**, 130.
6. C. P. Slichter, 'Principles of Magnetic Resonance', 3rd edn, Springer, Berlin, 1990.
7. J. D. Jackson, 'Classical Electrodynamics', Wiley, New York, 1962.
8. N. W. Ashcroft and N. D. Mermin, 'Solid State Physics', Holt, Rhinehart & Winston, New York, 1976.
9. D. C. Ailion, *Magn. Reson. Imag.*, 1992, **10**, 799.
10. C. H. Durney, J. A. Bertolina, D. C. Ailion, R. A. Christman, A. G. Cutillo, A. H. Morris, and S. Hashemi, *J. Magn. Reson.*, 1989, **85**, 554.
11. J. A. Bertolina, C. H. Durney, D. C. Ailion, A. G. Cutillo, A. H. Morris, and K. C. Goodrich, *J. Magn. Reson.*, 1992, **99**, 161.
12. G. Laicher, D. C. Ailion, and A. G. Cutillo, *J. Magn. Reson. B*, 1996, **111**, 243.
13. B. Geil, D. C. Ailion, G. Laicher, and A. G. Cutillo, in 'Spatially Resolved Magnetic Resonance', eds. P. Blümler, B. Blümich, R. Botto, and E. Fukushima, Wiley-VCH, Weinheim, 1998, p. 323.
14. R. M. Cotts, M. J. R. Hoch, T. Sun, and J. Markert, *J. Magn. Reson.*, 1989, **83**, 252.
15. I. Chang, F. Fujara, B. Geil, G. Hinze, H. Sillescu, and A Tölle, *J. Non-Cryst. Solids*, 1994, **172–174**, 674.
16. K. C. Goodrich, D. C. Ailion, A. G. Cutillo, K. Ganesan, C. H. Durney, T. L. Simpson, and A. H. Morris, in *Proc. IXth Ann Mtg. Soc. Magn. Reson. Med.*, New York, 1990, p. 129.
17. A. G. Cutillo, A. H. Morris, D. C. Ailion, K. Ganesan, T. A. Case, C. H. Durney, and F. Watanabe, *Magn. Reson. Med.*, 1989, **12**, 137.
18. H. E. Rorschach and C. F. Hazlewood, *J. Magn. Reson.*, 1986, **70**, 79.
19. A. Hackmann, D. C. Ailion, K. Ganesan, G. Laicher, K. C. Goodrich, and A. G. Cutillo, *J. Magn. Reson. B*, 1996, **110**, 132.
20. A Hackmann, D. C. Ailion, K. Ganesan, K. C. Goodrich, S. Chen, G. Laicher, and A. G. Cutillo, *J. Magn. Reson. B*, 1996, **110**, 136.
21. K. C. Goodrich, A. Hackmann, K. Ganesan, D. C. Ailion, and A. G. Cutillo, in *Proc. XIth Ann Mtg. Soc. Magn. Reson. Med.*, Berlin, 1992, p. 1307.
22. P. Mansfield and A. A. Maudsley, *Phys. Med. Biol.*, 1976, **21**, 847.
23. G. H. Glover and J. M. Pauly, *Magn. Reson. Med.*, 1992, **28**, 275.
24. C. J. Bergin, J. M. Pauly, and A. Macovski, *Radiology*, 1991, **179**, 777.
25. D. O. Kuethe, A. Caprihan, E. Fukushima, and R. A. Waggoner, *Magn. Reson. Med.*, 1998, **39**, 85.
26. D. O. Kuethe, A. Caprihan, E. Fukushima, H. M. Gach, and I. J. Lowe, in 'Book of Abstracts, 39th Experimental Nuclear Magnetic Resonance conference', 1998.
27. D. O. Kuethe, A. Caprihan, E. Fukushima, H. M. Gach, and I. J. Lowe, in 'Book of Abstracts, 4th International Conference on Magnetic Resonance Microscopy and Macroscopy', 1997, p. 47.
28. T. G. Walker and W. Happer, *Rev. Mod. Phys.*, 1997, **69**, 629.
29. F. D. Colegrove, L. D. Shearer, and G. K. Walters, *Phys. Rev.*, 1963, **132**, 2561.
30. H. Middleton, R. D. Black, B. Saam, G. D. Cates, G. P. Cofer, P. Guenther, W. Happer, L. W. Hedlund, G. A. Johnson, K. Juvan, J. Swartz, *Magn. Reson. Med.*, 1995, **33**, 271.
31. P. Bachert, L. R. Schad, M. Bock, M. V. Knopp, M. Ebert, T. Grossmann, W. Heil, D. Hoffmann, R. Surkau, and E. W. Otten, *Magn. Reson. Med.*, 1996, **36**, 192.
32. J. P. Mugler III, B. Driehuys, J. R. Brookeman, G. D. Cates, S. S. Berr, R. G. Bryant, T. M. Daniel, E. E. de Lange, J. H. Downs III, C. J. Erickson, W. Happer, D. P. Hinton, N. R. Kassel, T. Maier, C. D. Philips, B. T. Saam, K. L. Sauer, and M. E. Wagshul, *Magn. Reson. Med.*, 1997, **37**, 809.
33. H.-U. Kauczor, M. Ebert, K.-F. Kreitner, H. Nilgens, R. Surkau, W. Heil, D. Hofmann, E. W. Otten, and M. Thelen, *JMRI*, 1996, **7**, 538.
34. B. Saam, D. A. Yablonskiy, D. S. Gierada, M. S. Conradi and J. D. Cooper (private correspondence).

Biographical Sketch

David C. Ailion. *b* 1937. A.B., 1956, M.S., 1958, Ph.D., 1964, Physics, University of Illinois, under supervision of C. P. Slichter. Faculty member (currently Professor of Physics) University of Utah, 1964–present. Fellow of American Physical Society, Humboldt Senior Research Award (1994–5), University of Utah Distinguished Research Award (1995), NIH Special Fellow (1971–2), Guest Member of the AMPERE Committee. Approx. 170 publications. Current research specialties: magnetic resonance imaging of lungs, NMR of partially disordered systems (incommensurate insulators and glasses).

Magnetization Transfer between Water and Macromolecules in Proton MRI

Robert S. Balaban

National Heart, Lung and Blood Institute, Bethesda, MD, USA

1 INTRODUCTION

Biological macromolecules enhance water spin–lattice relaxation.[1–5] The potential mechanisms for this phenomenon have been appreciated since the early 1970s and are presented in Figure 1 which was adapted from Noack.[6]

These early theoretical evaluations established that several kinetic and geometric factors are important in determining the extent of the relaxation enhancement. These include the correlation time of the water proton/macromolecular complex (i.e. as restricted water or proton chemical exchange sites), chemical and diffusion exchange rates, as well as the proximity of the water and macromolecular protons. More recent studies have suggested that the through-space dipolar coupling pathway between the restricted motion protons of the macromolecules and a small pool of water protons is the major relaxation pathway.[1,7–9] This interaction apparently involves a small portion of the hydration water protons with a net correlation time in excess of 10^{-8} s, caused by either the titration of a proton-accepting site or the restriction of water itself. This dipolar coupling between the macromolecule protons and water results in a magnetization transfer pathway between these spin baths which results in the coupled cross relaxation between water and macromolecule protons.

The most notable approaches in the past to studying macromolecule/water interactions have used selective inversion transfer[5,10] and field dependence techniques[11] which have established many of the limiting parameters for these interactions in tissues and model macromolecule systems. Several mathematical approximations for this process have been presented in the literature;[1,12–14] however, the actual nature of the water and macromolecule proton magnetization transfer pathway is still not understood with regard to the chemical nature of the interaction sites and the specific rate-limiting steps.

Interest in this topic was increased recently by the demonstration that saturation transfer between macromolecule and water protons can be used to assay the extent of magnetization transfer in vitro and in vivo.[15] This simple approach combined with conventional MRI techniques also permitted the determination of the topology of this interaction in biological tissues.[15]

The use of saturation transfer techniques in monitoring the water/macromolecule magnetization transfer process is dependent on the relaxation differences between water and macromolecule protons resulting in distinctly different NMR lineshapes. A schematic diagram outlining the use of saturation transfer to monitor magnetization transfer is presented in Figure 2.

The restricted motion of the macromolecule protons results in a very short spin–spin relaxation rate (T_2) with an intermediate T_1. This results in a very broad NMR lineshape extending many kHz off-resonance. In contrast, the water protons have a very short correlation time, ~10^{-11} s, resulting in relatively long relaxation times and narrow linewidths on the order of 10–20 Hz, in vivo. Thus, by applying an irradiation energy sufficiently off-resonance as shown in Figure 2, the molecular protons can be preferentially saturated. Any chemical exchange or magnetization transfer between the water and macromolecular protons will result in a decrease in the water proton signal or saturation transfer as originally described by Forsén and Hoffman for simple chemical and dipolar interactions.[16] Using

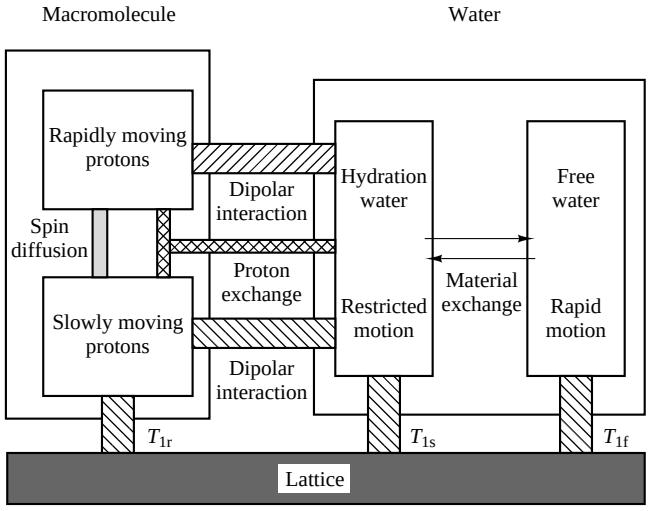

Figure 1 Schematic diagram of water/macromolecule magnetic interactions highlighting the pathways and relevant pools. Adapted from Noack[6]

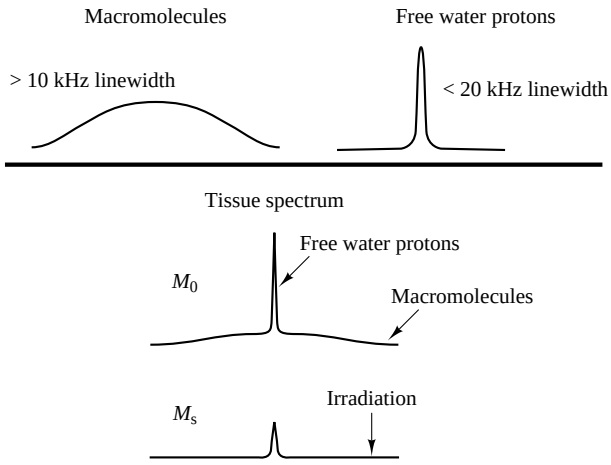

Figure 2 Schematic diagram of water and macromolecule proton linewidths (top), and the use of an off-resonance irradiation to detect magnetization transfer in tissue where both lines overlap (bottom)

this scheme, tissues with strong macromolecule/water proton magnetization exchange will have a lower water proton NMR signal in the presence of the off-resonance irradiation.

The contrast generated in these images has been termed magnetization transfer contrast (MTC). Using this approach, Wolff and Balaban[15] showed that the magnetization transfer pathway between water and macromolecules could be detected in biological tissues in vivo using an off-resonance irradiation scheme, and that the topology of the interaction could be determined by combining MRI techniques with the off-resonance irradiation. This is accomplished by simply applying the off-resonance irradiation in an appropriate power and duty cycle anytime when the gradients will not interfere with the frequency selectivity or the irradiation will interfere with the data acquisition.[15,17]

2 CONTROLLING PARAMETERS IN SATURATION TRANSFER

There are several key parameters in the off-resonance saturation transfer technique which can alter the quantitative and qualitative aspects of the experiment as well as provide unique information on the macromolecule dynamics. The effect of the irradiation will have a frequency, power, and time or duty cycle dependence.[17] All of these parameters can affect the magnitude of the negative NOE observed with off-resonance irradiation, as well as the source of this phenomenon which might not involve magnetization transfer alone as will be discussed below.

2.1 Frequency/Power of Irradiation, The Magnetization Transfer Spectrum

The frequency dependence of the interaction is intimately linked to the power applied.[17,18] An example of the frequency dependence of the water proton signal as a function of off-resonance frequency at fixed power is presented in Figure 3 for sphingomyelin at two different temperatures, in vitro. Also presented are the calculated effects of the irradiation on water alone based on its measured T_1 and T_2 relaxation times. The large difference between the predicted and observed effect of the off-resonance irradiation is due to the magnetization transfer effect resulting in a decrease in water proton signal with irradiation far off-resonance.

These spectra have been called magnetization transfer spectra (MT spectra) or Z spectra.[9] At 25 °C, below the phase transition temperature for sphingomyelin, the MT spectrum is ~30 kHz with a distinctive Gaussian characteristic consistent with the rigid lipid structure below its phase transition. At 65 °C, above the phase transition, the linewidth collapses to <10 kHz with a more Lorentzian lineshape consistent with the increase in lipid mobility above the phase transition. From the characteristics of the MT spectrum, the spectral density and associated dynamics of the macromolecules involved in the interaction can be determined as demonstrated in this simple lipid model.

The changes in the macromolecule MT spectrum with temperature illustrate the importance of calibrating the off-resonance irradiation scheme used for the macromolecular system. Models of even simple macromolecular systems demonstrate that predicting the optimal irradiation frequency/power is extremely difficult due to the complex nature of the macromolecular structure and the interaction. Indeed, it is clear that the MT spectrum represents a complex sum of all of the coupled spins in the macromolecule. This was recently demonstrated using site-specific deuterium labeling in lipid systems[19] which reveals the different motional domains interacting with water in this simple system, resulting in the net spectrum presented in Figure 3. These results demonstrated that the magnetization transfer spectrum will only reflect the average motions of all of the coupled spins within the macromolecule and not the interaction site alone. This may have major consequences in the use of magnetization transfer spectra for in vivo tissue characterization.

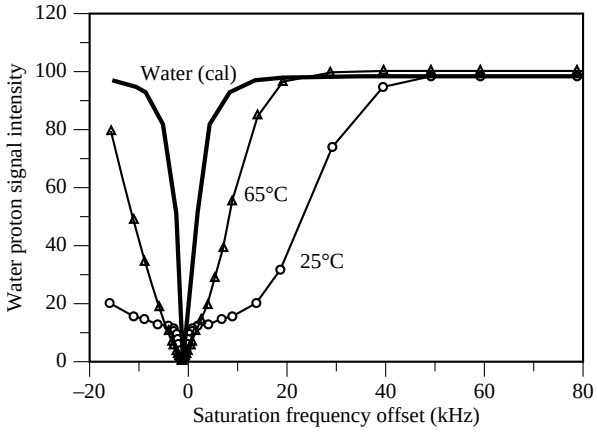

Figure 3 Effect of off-resonance irradiation frequency on sphingomyelin bilayer water signal. Experiments were conducted at 4.7 T with a 50/50 wt.% sphingomyelin preparation. Irradiation power was 1×10^{-6} T. The amplitude of the water signal is normalized to 100. Data for 25 °C (below the lipid phase transition) and 65 °C (above the phase transition) are presented. The solid line is the calculated effect of the off-resonance irradiation based on the measured relaxation times of the water protons[17]

An example of an off-resonance irradiation frequency study on the human brain is presented in Figure 4 where a fixed power is applied at different off-resonance frequencies. The marked change in tissue contrast is clearly observed and the magnetization transfer spectrum of each tissue type can be extracted. An optimum in gray matter/cerebrospinal fluid contrast was obtained at ~1000 Hz off-resonance with 6 W continuous wave in this 4 T study as shown in Figure 5. It is also important to note that the magnetization transfer effect could even be optimized at 4 T below the SAR guidelines of the US Food and Drugs Administration. Thus, MTC can be generated well below the rf levels of concern at lower fields.

Though magnetization transfer contrast has proven to be extremely useful in numerous MRI examinations as discussed below, little attention has been applied to the use of the MT spectrum in vivo. Due to the complex nature of the MT spectrum, the only way to assure that a specific and optimal MT effect is being observed is to perform an MT spectrum study on the tissues of interest.[17] Numerous values are now available in the head for accepted parameters (references follow in appli-

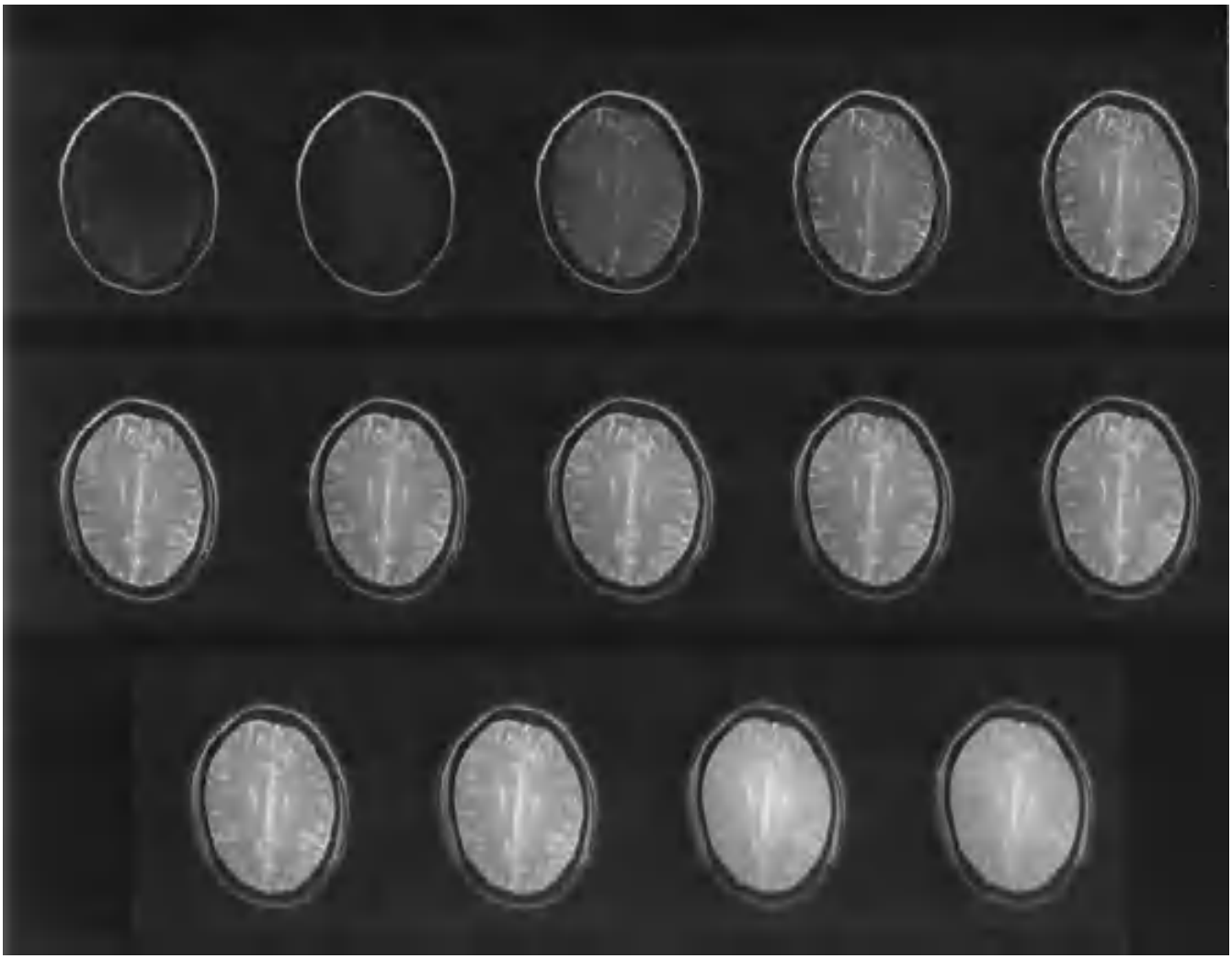

Figure 4 Effect of off-resonance irradiation frequency on MTC of the human head at 4 T. Data were collected with varying off-resonance irradiation frequency in gradient recalled echo images (*TE* = 6.5 ms, *TR* = 500 ms). The irradiation was 6 W applied CW for 450 ms just before the slice selection. A gradient spoiling pulse was applied immediately after the irradiation to cancel any remaining transverse magnetization induced by the off-resonance irradiation. The off-resonance irradiation frequency was stepped-up 200 Hz/image from on-resonance in the first 10 images reading right to left from the top. The last images are at 3000, 4000, 5000, and 7500 Hz off-resonance

cations section); however, other tissues will require more studies to develop the most appropriate irradiation frequency and power for a given contrast requirement. This is not unlike what has already been done to determine the optimal *TE*, *TR* and flip angle values to detect pathology using conventional MRI.

2.2 Macromolecule Irradiation Schemes

There have been numerous methods published in the literature to apply off-resonance irradiation in an MRI study. These methods include continuous wave (CW) irradiation which is highly accurate and effective only when adequate time is available during the *TR* period,[15,17] or shaped pulses which provide a method of presenting a well-defined frequency irradiation in a short period of time, much the same way as fat suppression or slice selection is performed in conventional MRI.[20–22] Another method involves the use of an on-resonance jump and return method[23] which is very power efficient but critically dependent on $\boldsymbol{B}_0$ homogeneity. Yeung and Aisen[24] have provided a good theoretical analysis of the pulsed methods along with several studies comparing CW and pulse methods[25] as well as duty cycle and power issues.[21,26,27] In summary, due to the homogeneity limitations of the on-resonance jump and return methods, shaped frequency-defined off-resonance pulses seem to be the most appropriate time efficient excitation method for MRI studies. Naturally, any approach will still require the frequency/power calibration discussed above.

2.3 Nonmagnetization Transfer Effects of Off-Resonance Irradiation

It is also important to note that the effects of off-resonance irradiation is not limited to the magnetization exchange processes discussed above. Due to the nature of the Lorentzian line of water, the off-resonance irradiation if not properly con-

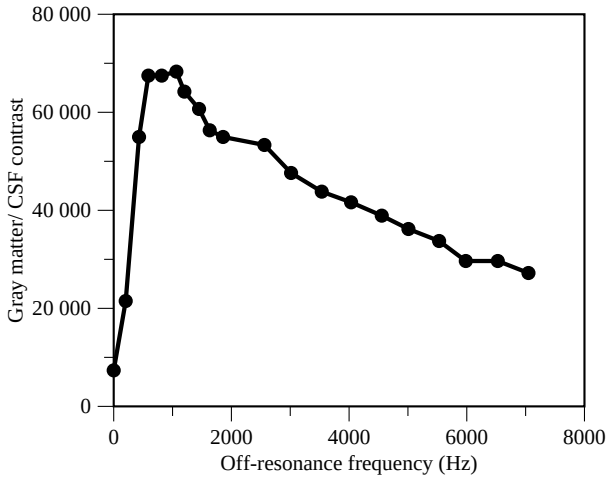

Figure 5 Contrast data from the images presented in Figure 4. The gray matter/cerebrospinal fluid (CSF) contrast (i.e. difference) is plotted as a function of irradiation frequency. An optimal contrast is obtained at ~1000 Hz off-resonance

trolled can also result in several interesting direct effects on the water line which are not directly related to macromolecule/water magnetization transfer. The most notable of these are the direct saturation effects[17] which will reduce net water magnetization based on its T_1 and T_2[28] or T_1 values in the rotating frame.[29] Both these effects occur if the irradiation power is sufficiently high to affect the water protons directly, independently from the magnetization transfer interaction with the macromolecules. In a properly calibrated magnetization transfer experiment these effects should be minimized, but will always influence the MT spectrum at high power or close to on-resonance conditions.[17,30] An excellent comparison of magnetization transfer and the spin locking phenomenon has been provided recently by Kuwata et al.[30]

2.4 Time-Dependence

The time-dependence of the irradiation is rather more straightforward. Since the rate of magnetization transfer is on the order of 1 s^{-1}, it takes seconds for the two spin populations to reach steady-state magnetization levels.[15,18] This has very important consequences with regard to the quantitation of magnetization transfer rates, as well as the optimization of magnetization transfer contrast. For quantitative studies, either the time-dependence has to be determined or long preirradiation times must be used to assure steady state. In imaging experiments, the duty cycle of the irradiation must be adequate to maintain the macromolecular saturation in conventional phase-encoding schemes or the magnetization preparation period must be on the order of seconds in fast imaging techniques.[31]

3 QUANTIFICATION

As far as the absolute quantification of the magnetization transfer rate is concerned, the powerful simplification provided by the Forsén–Hoffman approach requires that complete saturation of the macromolecular pool be obtained. This condition has been apparently reached in some in vivo systems[15,18] but clearly not in some in vitro model systems.[13] Indeed, due to the rapid magnetization exchange between the macromolecular system and the very large water proton pool, reaching saturation by irradiating the macromolecules alone may prove difficult in many systems. Without this key simplification, the quantification of the magnetization transfer rate becomes dependent on complex models with numerous unknowns[13] even if the aforementioned compartmentation of the macromolecules is not taken into account. These data suggest that the absolute quantification of magnetization transfer rates in vivo may be extremely difficult if the Forsén–Hoffman approximation cannot be used. However, to date it is not clear whether the actual magnetization transfer rate, MTC, or MT spectrum will be the most useful in evaluating pathology. In any event, the proper quantification of the effect will greatly aid our understanding of the molecular mechanisms involved in the process.

4 APPLICATIONS

Magnetization transfer contrast is most useful in two basic areas: improving image contrast and tissue characterization. It can generate contrast with minimal *TE* values, reducing motion, susceptibility, and flow artifacts.[17] Improvements in image contrast have been reported in the musculoskeletal system,[27,32] brain,[33–35] liver,[36–38] eye,[39] and heart.[40–43] MTC has also proven to be extremely useful in the reduction of the 'background' signal in MRA and contrast agent studies. Since there is very little water/macromolecule magnetization transfer in blood, and the macromolecules that are there are difficult to saturate due to flow, the blood signal is only slightly decreased in MTC while the surrounding tissue is decreased. This additional background suppression by MTC results in the resolution of smaller vessels in MRA.[44,45] Since contrast agents are usually trapped in regions with low macromolecule/water magnetization transfer, the signal enhancement by T_1 contrast agents usually complements the MTC effect. This additive effect has been shown to reduce the dose requirements in MR contrast agent studies.[46–48]

Much less work has been done with regard to tissue characterization with magnetization transfer. Studies have revealed that the effect is very specific to particular macromolecules in rather complex tissues. Collagen seems to be the most effective macromolecule in cartilage[49] and meningiomas,[50] while surface −OH groups seem to be critical in lipid systems.[7,51,52] Studies on a large number of macromolecules reveal that surface −OH groups may be the most effective site in most macromolecules,[7] but whether this is due to the titration of the site or coordination of water[53] is yet to be definitively demonstrated. The importance of water content has also been demonstrated in the heart.[40] More complete studies and hypotheses must be generated to evaluate whether the magnetization transfer effect can be used to improve the specificity of MRI examination. Potentially the use of the magnetization transfer spectrum will aid in this effort.

5 SUMMARY

In summary, the use of water/magnetization transfer has proven to be a useful tool in the evaluation of water/macromolecule interactions as well as providing another contrast tool in MRI examinations. As our understanding of the molecular processes involved in this interaction improves, the specificity and utility of MTC in clinical MRI will also benefit.

6 RELATED ARTICLES

Magnetization Transfer Contrast: Clinical Applications; Magnetization Transfer and Cross Relaxation in Tissue; Relaxometry of Tissue.

7 REFERENCES

1. S. H. Koenig, R. G. Bryant, K. Hallenga, and G. S. Jacob, *Biochemistry*, 1978, **17**, 4348.
2. R. Mathur-DeVre, *Br. J. Radiol.*, 1984, **57**, 955.
3. B. M. Fung, *Methods Enzymol.*, 1986, **127**, 151.
4. R. Mathur-DeVre, *Prog. Biophys. Mol. Biol.*, 1979, **35**, 103.
5. H. T. Edzes and E. T. Samulski, *Nature (London)*, 1977, **265**, 521.
6. F. Noack, *NMR Basic Principles Prog.*, 1971, **3**, 83.
7. T. L. Ceckler, S. D. Wolff, V. Yip, S. A. Simon, and R. S. Balaban, *J. Magn. Reson.*, 1992, **98**, 637.
8. T. L. Ceckler and R. S. Balaban, *J. Magn. Reson.*, 1991, **93**, 572.
9. J. Grad and R. G. Bryant, *J. Magn. Reson.*, 1990, **90**, 1.
10. H. T. Edzes and E. T. Samulski, *J. Magn. Reson.*, 1978, **31**, 207.
11. S. H. Koenig and R. D. Brown, 'NMR Spectroscopy of Cells and Organisms', ed. R. K. Gupta, CRC Press, Boca Raton, FL, 1987, Vol. 2, p. 75.
12. R. Kimmich, W. Nusser, and T. Gneiting, *Colloids Surf.*, 1990, **45**, 283.
13. R. M. Henkelman, X. Huang, Q. S. Xiang, G. J. Stanisz, S. D. Swanson, and M. J. Bronskill, *Magn. Reson. Med.*, 1993, **29**, 759.
14. S. H. Koenig, R. D. Brown, and R. Ugolini, *Magn. Reson. Med.*, 1993, **29**, 77.
15. S. D. Wolff and R. S. Balaban, *Magn. Reson. Med.*, 1989, **10**, 135.
16. R. A. Hoffman and S. Forsén, *J. Chem. Phys.*, 1966, **45**, 2049.
17. R. S. Balaban and T. L. Ceckler, *Magn. Reson. Q.*, 1992, **8**, 116.
18. J. Eng, T. L. Ceckler, and R. S. Balaban, *J. Magn. Reson.*, 1991, **17**, 304.
19. T. L. Ceckler and R. S. Balaban, *Proc. 1st Ann Mtg. Int Soc. Magn. Reson. Med.*, Dallas, 1994, **1**, 394.
20. D. P. Flamig, W. B. Pierce, S. E. Harms, and R. H. Griffey, *Magn. Reson. Med.*, 1992, **26**, 122.
21. J. C. McGowan, III, M. D. Schnall, and J. S. Leigh, *J. Magn. Reson. Imag.*, 1994, **4**, 79.
22. J. V. Hajnal, C. J. Baudouin, A. Oatridge, I. R. Young, and G. M. Bydder, *J. Comput. Assist. Tomogr.*, 1992, **16**, 7.
23. B. S. Hu, S. M. Conolly, G. A. Wright, D. G. Nishimura, and A. Macovski, *Magn. Reson. Med.*, 1992, **26**, 231.
24. H. N. Yeung and A. M. Aisen, *Radiology*, 1992, **183**, 209.
25. E. Schneider, R. W. Prost, and G. H. Glover, *J. Magn. Reson. Imag.*, 1993, **3**, 417.
26. S. D. Wolff, J. Eng, and R. S. Balaban, *Radiology*, 1991, **179**, 133.
27. S. D. Wolff, S. Chesnick, J. A. Frank, K. O. Lim, and R. S. Balaban, *Radiology*, 1991, **179**, 623.
28. A. D. Bain, W. P. Y. Ho, and J. S. Martin, *J. Magn. Reson.*, 1981, **43**, 328.
29. T. L. James, G. B. Matson, I. D. Kuntz, R. W. Fisher, and D. H. Buttaire, *J. Magn. Reson.*, 1977, **28**, 417.
30. K. Kuwata, D. Brooks, H. Yang, and T. Schleich, *J. Magn. Reson., Ser. B*, 1994, **104**, 11.
31. R. A. Jones and T. E. Southon, *Magn. Reson. Med.*, 1991, **19**, 483.
32. X. P. Zhu, S. Zhao, and I. Isherwood, *Br. J. Radiol.*, 1992, **65**, 39.
33. A. Gass, G. J. Barker, D. Kidd, J. W. Thorpe, D. MacManus, A. Brennan, P. S. Tofts, A. J. Thompson, W. I. McDonald, and D. H. Miller, *Ann. Neurol.*, 1994, **36**, 62.
34. V. Dousset, R. I. Grossman, K. N. Ramer, M. D. Schnall, L. H. Young, F. Gonzalez-Scarano, E. Lavi, and J. A. Cohen, *Radiology*, 1992, **182**, 483.
35. J. M. Boorstein, K. T. Wong, R. I. Grossman, L. Bolinger, and J. C. McGowan, III, *Radiology*, 1994, **191**, 799.
36. K. C. Li, R. B. Jeffrey, Jr., S. C. Ning, A. Kandil, G. M. Hahn, B. Pike, G. Glover, and J. Kosek, *Invest. Radiol.*, 1993, **28**, 896.
37. A. M. Aisen, K. Doi, and S. D. Swanson, *Magn. Reson. Med.*, 1994, **31**, 551.
38. E. Outwater, M. D. Schnall, L. E. Braitman, B. J. Dinsmore, and H. Y. Kressel, *Radiology*, 1992, **182**, 535.
39. T. L. Ceckler, K. Karino, P. F. Kador, and R. S. Balaban, *Invest. Ophthalmol. Vis. Sci.*, 1991, **32**, 3109.
40. T. D. Scholz, T. L. Ceckler, and R. S. Balaban, *Magn. Reson. Med.*, 1993, **29**, 352.
41. P. V. Prasad, D. Burstein, and R. R. Edelman, *Magn. Reson. Med.*, 1993, **30**, 267.
42. R. A. Jones, O. Haraldseth, J. Schjott, H. Brurok, P. Jynge, A. N. Oksendal, and P. A. Rinck, *J. Magn. Reson. Imag.*, 1993, **3**, 31.
43. R. S. Balaban, S. Chesnick, K. Hedges, F. Samaha, and F. W. Heineman, *Radiology*, 1991, **180**, 671.
44. R. R. Edelman, S. Ahn, D. Chien, W. Li, A. Goldmann, M. Mantello, J. Kramer, and J. Kleefield, *Radiology*, 1992, **184**, 395.
45. G. B. Pike, B. S. Hu, G. H. Glover, and D. R. Enzmann, *Magn. Reson. Med.*, 1992, **25**, 372.
46. J. I. Tanttu, R. E. Sepponen, M. J. Lipton, and T. Kuusela, *J. Comput. Assist. Tomogr.*, 1992, **16**, 19.
47. A. D. Elster, V. P. Mathews, J. C. King, and C. A. Hamilton, *Neuroimag. Clin. N. Am.*, 1994, **4**, 185.
48. D. A. Finelli. G. C. Hurst, R. P. Gullapali, and E. M. Bellon, *Radiology*, 1994, **190**, 553.
49. D. K. Kim, T. L. Ceckler, V. C. Hascall, A. Calabro, and R. S. Balaban, *Magn. Reson. Med.*, 1993, **29**, 211.
50. N. Lundbom, *Am. J. Roentgenol.*, 1992, **159**, 1279.
51. T. A. Fralix, T. L. Ceckler, S. D. Wolff, S. A. Simon, and R. S. Balaban, *Magn. Reson. Med.*, 1991, **18**, 214.
52. W. Kucharczyk, P. M. Macdonald, G. J. Stanisz, and R. M. Henkelman, *Radiology*, 1994, **192**, 521.
53. G. Otting, E. Liepinsh, and K. Wuthrich, *Science*, 1991, **254**, 974.

Biographical Sketch

Robert S. Balaban. *b* 1953. B.S., 1975, Ph.D., 1980, Physiology and Pharmacology, Duke University, USA. First experience in NMR during Postdoctoral Fellowship with G. Radda at University of Oxford (1981). National Heart Lung and Blood Institute, NIH, 1982–present. Currently Chief, Laboratory of Cardiac Energetics. Approx. 200 publications. Research specialties: macromolecule/water magnetization transfer, in vivo NMR applications, coil development, tissue energetics, mitochondrial respiratory control.

Magnetization Transfer Contrast: Clinical Applications

Christine J. Baudouin
Freeman Hospital, Newcastle upon Tyne, UK

1 INTRODUCTION

The signal obtained in clinical magnetic resonance imaging comes from mobile protons. These are largely present in free water with a smaller contribution from lipid. There are, in addition, a large number of protons in tissues contained in macromolecules or in water bound to these macromolecules. No signal is normally detected from these protons by standard clinical imaging techniques because they have a very short T_2 value (of the order of 1 ms or less) and any transverse magnetization is rapidly dephased before data collection is possible.

There is, however, a constant exchange of magnetization between the protons in these two pools, the free pool and the bound pool, which occurs by through-space dipole–dipole interactions or probably less importantly direct chemical exchange. By means of this interchange, the bound pool influences the signal obtained from the free pool even though the bound pool cannot be directly visualized.

In magnetization transfer (MT) imaging, the normal equilibrium between free and bound pools is perturbed and the resulting contrast, magnetization transfer contrast, is an indication of the exchange processes with the bound pool in that particular tissue. Greater detail on the theory and tissue interactions involved will be found in the related articles on magnetization transfer. The techniques described in this article are those concerned with clinical imaging.

2 MAGNETIZATION TRANSFER TECHNIQUES IN CLINICAL IMAGING

Magnetization transfer or saturation transfer techniques have been used in magnetic resonance spectroscopy for many years.[1,2] Despite an early report of the use of off-resonance saturating irradiation in 3D imaging of the limbs in 1983,[3] interest in possible clinical applications was not stimulated until Wolff and Balaban published their initial findings in 1989.[4] These authors perturbed the normal equilibrium between free and bound pools by selectively saturating the bound pool. The signal obtained from the free pool decreased, and the degree of signal reduction varied between tissues. Adipose tissue showed little reduction in signal; kidney and muscle showed greater magnetization transfer effects.

2.1 The Saturating Pulse

The bound pool has a broad linewidth reflecting its short T_2, while protons in the free pool have a narrow linewidth reflecting their longer T_2 values. A saturating pulse placed off-resonance can saturate the bound pool while having minimal direct effect on the free pool. Any reduction in signal in the free pool caused by the saturating pulse then represents magnetization transfer effects. A similar effect can be obtained by using a composite pulse, such as a binomial pulse.[5] The latter approach gives lower radiofrequency absorption rates (SARs) than off-resonance irradiation but is more technically demanding.

As the duration or amplitude of an off-resonance pulse of a given frequency is increased, the signal obtained from a tissue which shows magnetization transfer effects, such as muscle, decreases to a plateau.[6,7] As the frequency offset of the saturating pulse is reduced towards zero, signal from tissue falls due to magnetization transfer effects until at small offsets direct saturation of the free pool occurs. Ideally the saturating pulse should give maximal saturation of the bound pool with no direct saturation of the free pool, but often a compromise is necessary in clinical imaging.

The saturating pulse is thus characterized by offset frequency, duration, and amplitude. In addition, it may be applied continuously or as pulses of various configurations. All of these characteristics alter the degree of saturation obtained and must be known before quantitative comparisons can be made between different clinical studies.

2.2 Effect of Saturating Pulses on Normal Tissue

Tissues which demonstrate magnetization transfer show two changes in the presence of saturating pulses:

1. A reduction in available longitudinal magnetization.
2. A reduction in T_1, the new value being termed T_{1sat}.

It is possible to measure both of these values and calculate the rate constant for magnetization transfer (k_f). Values are available for animal tissue,[4,8,9] normal human muscle, and gray and white matter.[6,7]

It is time-consuming to obtain the measurements necessary to derive these values and few figures are available for human pathological tissue in vivo.[10] Instead a simple measurement of the reduction in signal intensity of a tissue when a saturating pulse is applied is usually quoted in clinical studies.

Confusingly, this may be given either in the form M_s/M_0 or $1 - M_s/M_0$ where M_s is the signal intensity of a region of interest (ROI) on a scan obtained in the presence of a saturating pulse and M_0 is the signal of the same ROI on a scan obtained with no saturating pulse. Such values allow comparison of magnetization transfer effects in different normal and abnormal tissues within one MR unit but are highly dependent on the base sequence used, characteristics of the saturating pulse, and field strength and, therefore, the results from different institutions cannot be readily compared. Numerical values may be given, or the information displayed as a difference image. When numerical values are given in this article the notation M_s/M_0 will be used.

Simple fluids, e.g. cerebrospinal fluid (CSF), bile, and urine, show little magnetization transfer, presumably due to the small

number of macromolecules present. Fat also shows little change in signal as the protons in fat do not exchange with the bound pool.[4] Skeletal muscle shows the largest magnetization transfer effect with a reduction in signal to approximately one-third of the normal value (M_s/M_0 of the order of 0.3),[6,7] with articular cartilage also showing a large effect.[11] Spleen, liver,[12,13] kidney,[4] and brain tissue[6,14] show intermediate effects. Within organs, different components show different degrees of MT, e.g. renal cortex more than medulla,[4,8] and white matter more than gray matter.[6,14]

Stationary blood has a relatively small MT effect[4,12] and flowing blood is not subjected to the same degree of saturation as stationary tissues. Both of these features contribute to the improvement of time-of-flight angiography in the presence of MT pulses.

2.3 The Use of Saturating Pulses with Imaging Sequences

Initial magnetization transfer studies in vivo generally combined a saturating pulse with a spin echo or gradient echo sequence of long repetition time (*TR*) and short echo time (*TE*), or shorter *TR* and a low flip angle.[12–15] Such sequences have little T_1 or T_2 weighting and are of low intrinsic contrast; the addition of an off-resonance pulse increases contrast between tissues showing magnetization transfer effects (e.g. muscle) and those that do not (e.g. adipose tissue). This is the approach usually employed when a quantitative measure of magnetization transfer is required.[12–14] In this instance, the reduction in signal observed is largely due to the reduction in available magnetization, the alteration in T_1 under saturating conditions playing little or no part. As already mentioned, quantitation allows comparison of results only when all imaging parameters are kept constant.

An alternative strategy to quantitation in clinical magnetization transfer imaging is to use the technique to develop clinically useful contrast and improve lesion conspicuity. It may then be useful to use sequences which exploit T_1 alterations in addition to the reduction in available magnetization such as short *TR*, short *TE* T_1-weighted spin echo sequences, and inversion–recovery sequences.[6] Saturating pulses can (and often have) been applied to virtually any imaging sequence including volume imaging[3,11] and ultrafast sequences where the saturating pulse can be used as the preparation pulse for single shot techniques.[16]

2.4 Safety Issues in Clinical Imaging

Initial magnetization transfer experiments required hardware modifications to provide the necessary saturating pulses and resulted in the deposition in tissues of relatively large amounts of power. The problem of power deposition is most worrying at high field strength and much of the early human work was performed at low field strength (0.1 or 0.15 T). A number of methods for overcoming these problems have been developed.

1. Balaban and Ceckler[17] showed that the power of an off-resonance saturating pulse can be reduced and the same degree of signal reduction maintained if the frequency offset is also reduced. As offset frequency is reduced, care must be taken to avoid direct saturation effects.
2. The use of pulsed radiofrequency which may be off-resonance or binomial.[5] Binomial pulses result in lower SARs but appear to be technically more demanding in clinical imaging.
3. Off-resonance radiofrequency can be used as the preparation pulse for a fast imaging sequence.[16]

Using these modifications, MT can now be routinely implemented on clinical imaging systems (i.e. up to 1.5 T) without major hardware modifications and with power absorption within present guidelines.

3 CENTRAL NERVOUS SYSTEM

CSF shows little magnetization transfer, while normal brain tissue shows moderate signal loss.[6,14] Normal white matter has a slightly greater reduction in signal than normal gray matter. There are also regional variations in the exact degree of MT effect within gray and white matter, with occipital white matter showing less magnetization transfer than other white matter regions.[18]

Although the signal from CSF does not alter with the application of saturating pulses, it may become of higher signal intensity than normal brain. Rescaling of the images results in CSF appearing bright, as illustrated in Figure 1.

3.1 Multiple Sclerosis

The most thorough investigation of magnetization transfer in a single disease process has been made in multiple sclerosis. Dousset et al.[14] using a 3D gradient echo sequence studied 15 patients, and reported a wide variation in the reduction of signal, from 2–36% reduction (M_s/M_0 = 0.98–0.64) in individual plaques with a mean of 26.3% (M_s/M_0 = 0.73) compared with a 40% reduction (M_s/M_0 = 0.60) from normal white matter in volunteers. The authors suggest this variation between lesions may represent differences between acute plaques with edema and inflammatory response and chronic plaques with more marked demyelination and gliosis (which may show smaller magnetization transfer effects). Such differentiation of the age of plaques would be useful not only for diagnosis but for implementing and monitoring the effects of appropriate treatment. This group also found a decrease in magnetization transfer in the normal appearing white matter of their patients, particularly those with chronic and/or progressive multiple sclerosis compared with normal volunteers which could be important in determining prognosis in individual cases.

Gass et al.[18] also found a variation in the degree of magnetization transfer in plaques of demyelination and found that this correlated with the severity of disability, the lesions in patients with more severe disability showing less magnetization transfer, i.e. a higher M_s/M_0 value.

Further work has confirmed and expanded these findings.[19–21]

Magnetization transfer techniques may reflect histological changes in multiple sclerosis and help to predict long-term outcome.

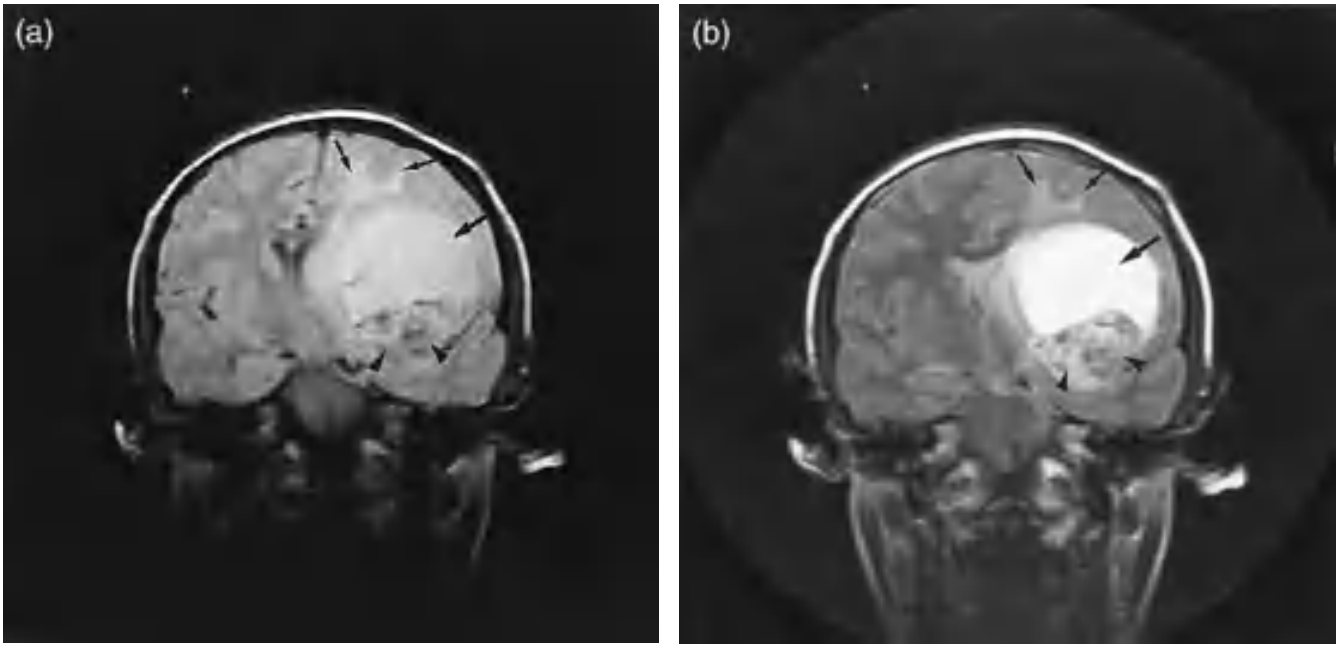

Figure 1 Mildly T_2-weighted spin echo scan (TR = 2500 ms, TE = 20 ms) (a) without and (b) with off-resonance irradiation of a patient with an astrocytoma. The signal from normal gray and white matter is markedly reduced in (b), while there is no change in the signal from CSF. Rescaling of the image results in CSF appearing bright. The cystic component of the tumor (large arrow) shows little magnetization transfer while the solid component (arrowheads) and edema (small arrows) show intermediate loss of signal

3.2 Cerebral Infarcts

In general, as in multiple sclerosis, pathological tissue shows less magnetization transfer than the corresponding normal tissue. Such an effect has been seen in infarcts both in rats[22] and humans.[6,23] Magnetization transfer measurements may help to distinguish demyelinating plaques from ischemic lesions.[24]

3.3 Neoplasms

There have been a number of reports of quantitative magnetization transfer in various brain tumors.[10,23,25,26] These results and our own work show a very variable degree of magnetization transfer between different tumors and between different components of the same tumor in one patient. Overall pathological tissues show less magnetization transfer than normal white matter, although isolated cases of meningioma, pituitary adenoma, acoustic neuroma, and one metastasis show similar levels. In the largest study, Kurki et al.[26] studied 28 patients with intracranial tumors at 0.1 T using a T_1-weighted gradient echo sequence (TR = 200 ms, TE = 20 ms). The mean M_s/M_0 value for the tumors was 0.77, compared with a mean value in normal appearing white matter in the patients of 0.69. Astrocytomas tended to show less magnetization transfer than hemangioblastomas, meningiomas, and pituitary adenomas.

Within a single lesion, cystic components show little or no magnetization transfer, with different solid components showing greater signal loss, as illustrated in Figure 1. We have found cystic components to have an M_s/M_0 value of 0.84–0.98, while the range in solid components in one patient was as great as 0.61–0.84. Small magnetization transfer effects are often seen in hemorrhage[23] while edema shows intermediate magnetization transfer. The degree of cellularity and nature of the tissue correlate to some extent with magnetization transfer[25] but as yet do not allow histological differentiation of tumors on imaging. The variability of measurements within individual lesions and within types of lesions is likely to limit the role of simple quantitative measurements. More exhaustive measurements, for example exchange rate constants, may be more tissue-specific.[10]

The discussion so far has concentrated on quantitative measurements. An alternative approach is to combine saturating pulses with other sequences, with more inherent contrast and sequences which also exploit T_1 effects such as the STIR sequence[6] or short TR, short TE T_1-weighted sequences. The signal from normal gray and white matter can be markedly reduced using a magnetization transfer STIR (MT-STIR) sequence leaving lesions seen with high contrast.[6] In fact, this may be one instance in which using maximal saturation is not ideal, as the signal from normal tissues may be reduced so much that normal anatomy is obscured and overall image quality is reduced. Backing off on amplitude, duration, or offset of the saturating pulses may result in a more useful image.

Magnetization transfer short TR/short TE T_1-weighted scans may show dramatic signal changes in both normal and pathological tissues. In Figure 2, central gray matter is of lower signal intensity than normal white matter on the standard T_1-weighted scan, but the relative signal intensities are reversed on the scan with saturating pulses as gray matter shows less signal loss than white matter. A similar reversal of contrast is seen in edema in this image. Lesions with a short T_1 due, for example, to hemorrhage or calcification, may be highlighted using this technique.[27] These sequences are also used when

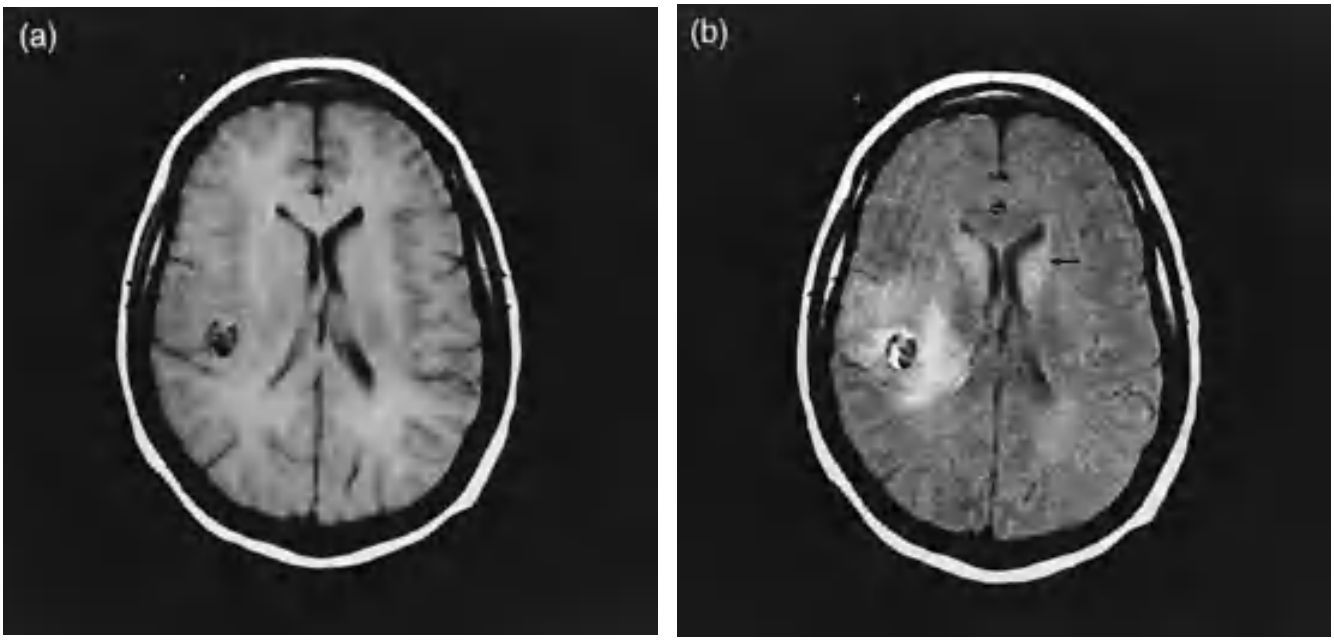

Figure 2 T_1-Weighted spin echo scans (TR = 760 ms, TE = 20 ms) (a) without and (b) with off-resonance irradiation showing a vascular malformation with surrounding edema. Edema shows less magnetization transfer than normal brain tissue and is of higher signal intensity than surrounding normal gray and white matter on scan (b). Normal caudate (arrow) shows less magnetization transfer than normal white matter. Regional variation in degree of signal loss is seen within white matter with less signal loss in the occipital region

magnetization transfer is combined with the administration of exogenous contrast agents.

3.4 Contrast Agents

Many intracranial tumors are enhanced by intravenous contrast agents[28] such as gadolinium diethylenetriamine pentaacetic acid (DTPA) and these tumors often show less magnetization transfer than normal tissue. Combining the two techniques might therefore improve visualization of contrast enhancement. Tanttu et al.[29] showed this to be true in vitro and in vivo, and in a larger clinical study Kurki et al.[26] reported improved contrast to noise for lesions post-gadolinium in the presence of an MT pulse compared with no MT pulse in 25 out of 28 patients with intracranial tumors. On standard T_1-weighted scans, lesions are frequently hypointense to normal white matter. Application of saturating pulses, with greater signal loss in normal tissue, may result in lesions becoming hyperintense as in Figure 2, but could also cause lesions to become isointense or less hypointense than on the standard image. MT T_1-weighted scans pre-gadolinium may result in lesions being less well seen than on standard T_1-weighted images. However, such scans are important to obtain in order to distinguish magnetization transfer effects from exogenous contrast enhancement on post-gadolinium MT T_1-weighted scans.[30] Figure 3 demonstrates the use of magnetization transfer with gadolinium in a patient with multiple meningiomas. Phantom studies suggest that in the presence of saturating pulses, gadolinium not only reduces T_1 but also alters available magnetization giving a synergistic effect in short TR scans.[31]

Initial studies suggest that although lesion-to-background ratios may not be quite as high for standard dose gadolinium studies combined with MT as high dose gadolinium without MT, standard dose gadolinium MT studies detect as many, if not more, lesions than triple dose gadolinium.[32,33] Unfortunately it does not seem that half-standard gadolinium with magnetization transfer can replace standard dose imaging.[34]

4 THE HEART

Images of the heart are degraded by severe motion artifact on T_2-weighted sequences with long echo times. Fast T_1-weighted scans are less motion artifacted and show good contrast between blood in the ventricular cavity and the ventricular wall, but do not demonstrate intrinsic abnormality of cardiac muscle well. Magnetization transfer techniques markedly reduce the signal from normal skeletal and cardiac muscle while blood is virtually unaffected, due to its macromolecular constitution and inflow effects. Using a surface transmit/receive coil, Balaban and colleagues[35] showed improved contrast between ventricular cavity and wall when MT was combined with gradient echo sequences with short TE values. Magnetization transfer may be useful for volumetric studies, and the authors also postulated that the technique may be useful for tissue characterization in abnormal myocardium.

5 THE BREAST

At present, intravenous paramagnetic contrast agents are recommended in MR mammography. Magnetization transfer reduces the signal from normal fibroglandular breast tissue

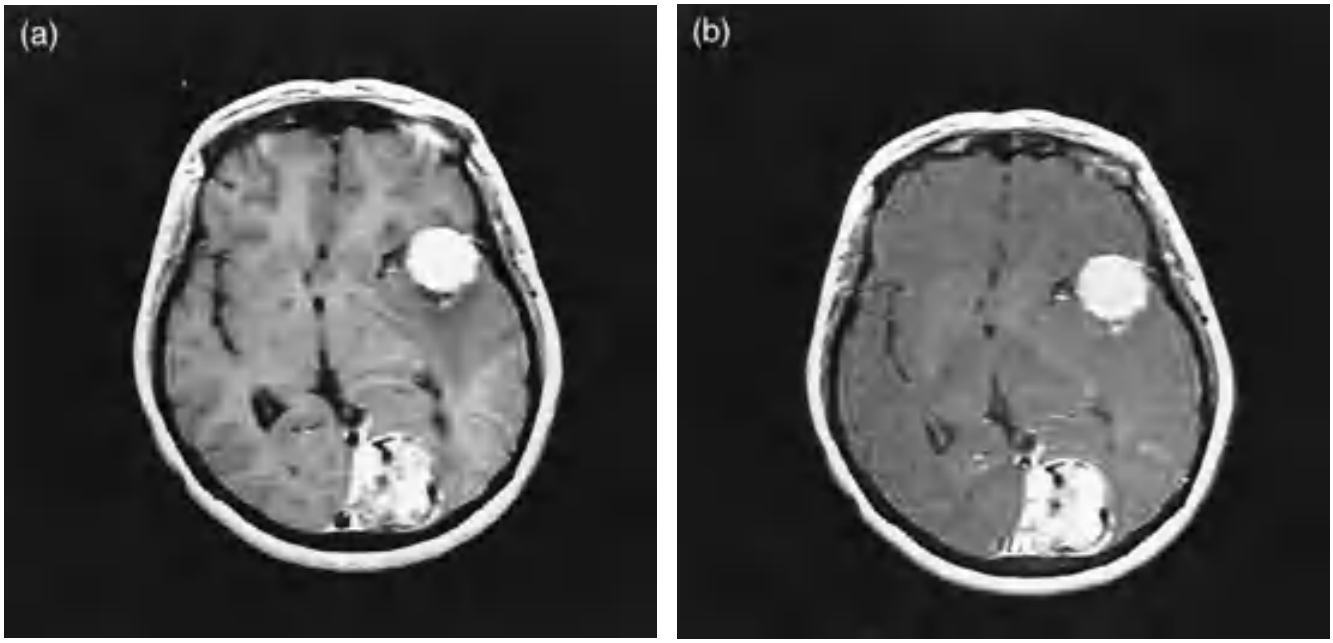

Figure 3 T_1-Weighted spin echo scans (TR = 580 ms, TE = 20 ms) post-gadolinium (a) without and (b) with off-resonance irradiation in a patient with multiple meningiomas. Signal from normal gray and white matter is reduced in (b) compared to the two enhancing lesions

while potentiating contrast enhancement in abnormal areas. The abundant adipose tissue in the breast shows no MT effects and high signal fat may obscure subtle enhancement by gadolinium. Pierce et al.[36] implemented a three-dimensional fat-suppressed steady-state sequence with magnetization transfer and demonstrated good contrast enhancement in carcinomas, an adenoma, and fibrocystic change, but not in fat necrosis or postoperative scar.

Schreiber et al.[37] found gadolinium enhancement combined with magnetization transfer useful in detecting enhancing breast lesions.

6 THE ABDOMEN

Two reports of magnetization transfer imaging of hepatic lesions at very different field strengths have shown variable results. Kahn et al.[13] working at 0.1 T studied 18 patients with primary or secondary neoplasms using a single-slice gradient echo sequence (TR = 1000 ms, TE = 30 ms) with saturating pulses 8 kHz off-resonance. Normal liver showed moderate magnetization transfer with an M_s/M_0 value of 0.67, with spleen showing less marked effects (M_s/M_0 = 0.76). Liver lesions gave similar values to normal spleen (M_s/M_0 = 0.77). Lesion-to-liver contrast was therefore improved on the scan with off-resonance radiofrequency compared with the standard gradient echo image. The authors point out that the magnetization transfer sequence may result in less lesion-to-liver contrast than standard heavily T_1- or T_2-weighted images, but may have improved signal-to-noise ratios and less motion artifact.

Outwater et al.[12] reported rather different results at the higher field strength of 1.5 T. In this study, a multislice gradient echo sequence (TR = 400–600 ms, TE = 5 ms, flip angle = 20°) with saturating pulses 1.5 kHz off-resonance was used to study 26 patients with benign or malignant liver lesions. Using this protocol, liver and spleen showed similar magnetization transfer [M_s/M_0 (liver) = 0.64, M_s/M_0 (spleen) = 0.66]. Malignant lesions had an average value of 0.62, not significantly different from normal liver, with no resultant increase in lesion-to-liver contrast on magnetization transfer images. Primary hepatocellular carcinoma tended to give lower values (0.57) than metastases (0.64). In contrast, benign cysts and hemangiomas showed less magnetization transfer than normal liver, with improved lesion-to-liver contrast on the sequence with saturating radiofrequency pulses. Simple cysts demonstrated less signal loss than hemangiomas, presumably because the magnetization transfer effects in blood, although small, are greater than in simple fluids, and the presence of stromal tissue in hemangiomas. Measurements of the magnetization transfer effects allowed a separation between metastases and hemangiomas comparable to standard long TR, long TE (160 ms) T_2-weighted spin echo sequences.

These two studies highlight the problems of comparing magnetization transfer results when different sequences, different saturating pulses, and different field strengths are used. Although quantitative measurements provide some tissue-specific information, at present magnetization transfer techniques are unlikely to replace standard imaging sequences in the liver. These studies are important, however, in that they will help in understanding tissue contrast generated by standard sequences in which magnetization transfer has been shown to play a role, for instance the fast T_2-weighted spin echo sequences. These effects will be discussed in a later section. Despite further work in the abdomen[38–41] results remain variable, and magnetization transfer does not yet have a major role in liver imaging. Although Wolff and Balaban's paper in 1989[4] showed different magnetization transfer values in the renal cortex and medulla of the rabbit, there has been little work on

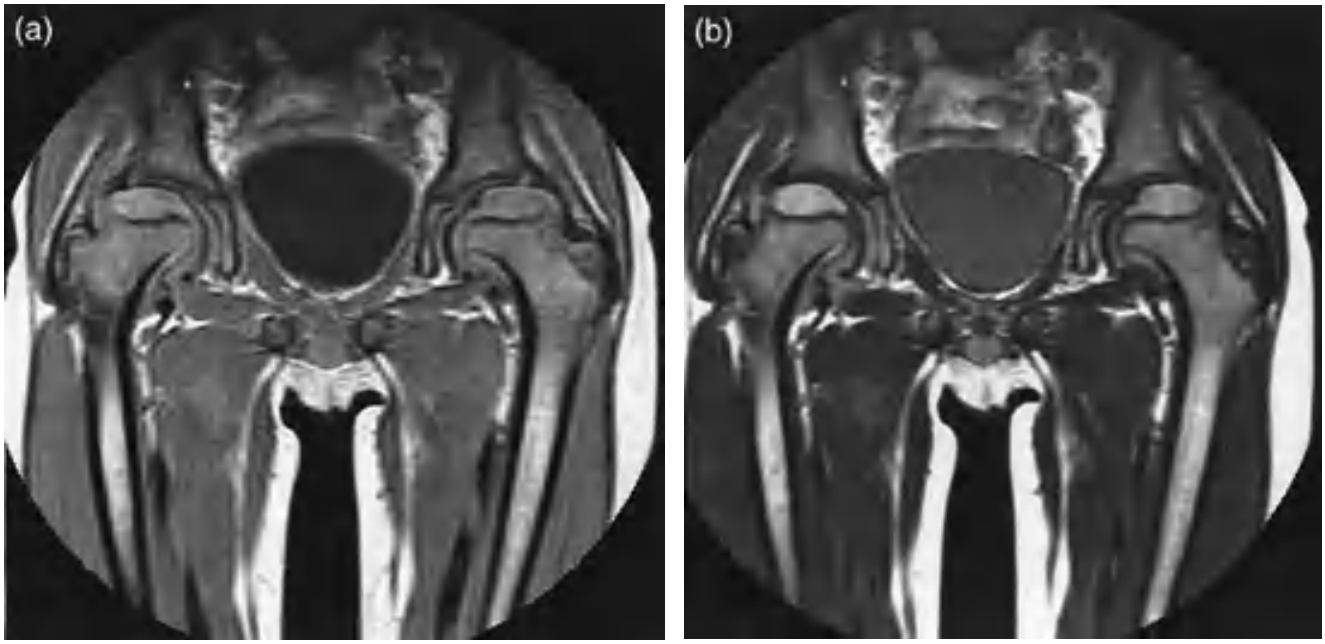

Figure 4 Twelve year old male with juvenile chronic arthritis. Coronal mildly T_2-weighted spin–echo images (TR = 2000 ms, TE = 16 ms) (a) without and (b) with off-resonance irradiation. Signal from muscle is reduced and the synovium and joint fluid are more clearly visualized in (b). (Reprinted with permission from *Clinical MRI*)

abdominal organs other than the liver, or on the pelvis in humans.

7 MUSCULO-SKELETAL SYSTEM

The musculo-skeletal system seems to be ideally designed for magnetization transfer techniques. Muscle shows large magnetization transfer effects, fat virtually none. Cartilage shows large magnetization transfer effects, synovial fluid virtually none. Magnetization transfer can thus be used to increase the contrast between muscle and fat, and between cartilage and joint fluid (Figure 4).

Wolff et al.,[11] imaging the knees of normal volunteers at 1.5 T, showed that magnetization transfer improved the contrast between these pairs of tissues on a single-slice gradient echo sequence at all repetition and echo times and all but the lowest flip angle tested. The contrast was improved over standard T_2-weighted spin echo sequences in a much shorter imaging time. Three-dimensional gradient echo sequences with high spatial resolution are ideal for studying the musculo-skeletal system, but often suffer from poor contrast. The same authors combined magnetization transfer with a 3D gradient echo sequence, again with excellent muscle/fat and cartilage/fluid contrast.

The strong magnetization transfer effect in articular hyaline cartilage appears to be due to collagen with little or no contribution from proteoglycans.[42] It has been suggested that magnetization transfer may help identify early alterations in degenerating cartilage which displays focal fluid loss and increased collagen concentration. At 1.5 T using a 3D MT GRASS sequence, articular cartilage defects were shown more clearly than on routine sequences.[43] A second study at 0.5 T using a T_1-weighted spin echo MT sequence found no improvement over standard T_2-weighted spin echo sequences.[44] Lenz et al. using a 3D FISP sequence at 0.2 T found that although saturating pulses improved cartilage/fluid contrast-to-noise ratios, meniscal tears were less well seen due to low signal-to-noise from cartilage.[45]

Magnetization transfer has been used to study physiological and pathological effects in muscle. Magnetization transfer improves the contrast between active and inactive muscle after leg exercise on a gradient echo sequence at 0.26 T.[46] This effect may be due to the increase in extracellular water which is thought to occur with exercise.

The different effects on muscle and fat may allow an estimation of the fat content of muscles. Lamminen et al.[47] reported that magnetization transfer studies could give similar information to chemical shift imaging in the assessment of fatty infiltration of muscle in dystrophia myotonica.

Pathological tissue, both neoplastic and inflammatory, generally shows less magnetization transfer than normal muscle and may be seen with increased conspicuity on magnetization transfer sequences.[48–50] In the study of muscles a magnetization transfer STIR sequence may be advantageous. Standard STIR sequences combining fat suppression with additive T_1 and T_2 contrast are sensitive to musculo-skeletal pathology. Fat suppression is advantageous in magnetization transfer imaging, as fat shows little magnetization transfer and retains a high signal. In addition, saturating pulses reduce the T_1 value of tissues demonstrating magnetization transfer such as skeletal muscle. In the MT-STIR sequence, the shortening of T_1 reduces the signal from normal muscle still further. At 0.15 T, the T_1 value of normal muscle becomes similar to that of fat and both tissues are nulled in an MT-STIR sequence. This can be used to obtain an angiogram of peripheral vessels.[6] In imaging mus-

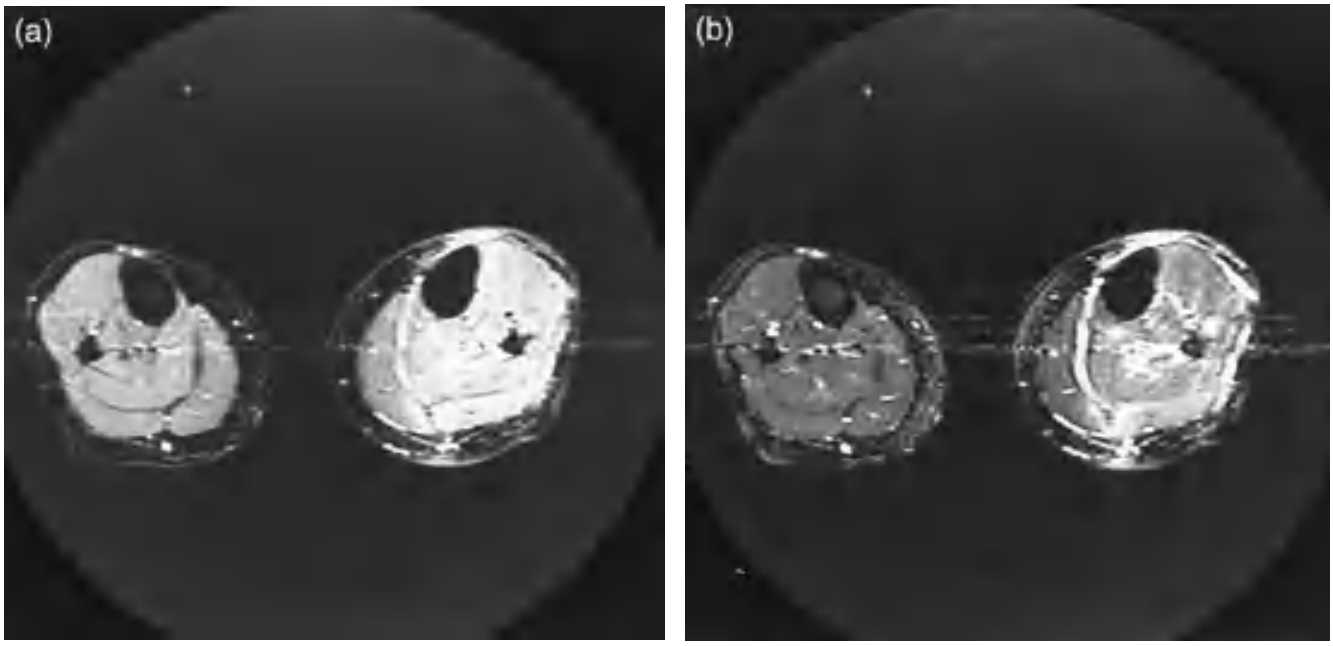

Figure 5 Thirty-eight year old male who received postoperative radiotherapy for a liposarcoma. Axial STIR (*TR* = 2500 ms, *TE* = 30 ms, *TI* = 130 ms) images of the calf (a) without and (b) with off-resonance irradiation. The signal from subcutaneous and marrow fat is nulled in both examinations. The signal from muscle is reduced in (b), highlighting the abnormal thickening and high signal of the stroma between the muscle compartments

culo-skeletal pathology, it may be preferable not to saturate normal muscle maximally but, as in the brain, to back off on the intensity of the saturating pulse to allow some signal to remain to improve overall signal-to-noise ratios and allow visualization of normal anatomy. Figure 5 illustrates the use of a MT-STIR sequence in a patient with inflammatory changes secondary to radiotherapy.

8 MAGNETIZATION TRANSFER EFFECTS IN CONVENTIONAL CLINICAL IMAGING

The discussion so far has concerned sequences in which saturating pulses are deliberately added to imaging sequences. Dixon et al.[51] pointed out in 1990 that in multislice imaging radiofrequency pulses which are on-resonance for one slice will be off-resonance for adjacent slices and will result in incidental magnetization transfer effects. These were of the order of 10–20% for brain and muscle compared with fat and aqueous solutions. The effects are more pronounced in sequences with multiple refocusing pulses, such as rapid acquisition relaxation enhanced (RARE) or fast spin echo sequences[52,53] and can result in alterations in tissue contrast; for instance, gray/white matter contrast-to-noise ratio increases with increasing slice number in proton density-weighted fast spin echo images as a result of magnetization transfer effects.[52] Other pulses including fat saturation and presaturation pulses will have similar effects. In many instances these incidental magnetization transfer effects may be beneficial in lesion detection, as most pathological tissue shows less magnetization transfer than normal tissue, but the end result will depend on relative magnetization transfer effects and the starting signals of tissue. As discussed earlier, hepatic neoplasms may not follow the general rule with similar magnetization transfer to normal liver. This is important when fast spin echo imaging is used in the abdomen.

9 CONCLUSIONS

Magnetization transfer studies have now been shown to be feasible in patients in a variety of body regions at a range of field strengths and have already had an impact on clinical imaging. Many imaging systems now routinely use magnetization transfer to improve the visualization of cerebral vessels in cranial magnetic resonance angiography. It is clear that magnetization transfer improves the appreciation of tissue enhancement by intravenous contrast agents and T_1-weighted magnetization transfer sequences are being used in conjunction with gadolinium at a number of centers for brain and breast imaging. In other body areas, interesting effects have been observed, but the usefulness of magnetization transfer in clinical imaging remains largely unevaluated.

Quantitative measurements of magnetization transfer effects seem to be bearing fruit in the study of multiple sclerosis, but quantitation has been disappointing in other areas due to the overlap between different pathological tissues. More precise evaluation, for instance of rate constants, may provide more tissue-specific information.

We now recognise that incidental magnetization transfer plays a role in almost every imaging sequence. Knowledge of magnetization transfer will enable us to predict the effects, particularly in such sequences as fast spin echo and use them to our advantage.

10 RELATED ARTICLES

Brain Neoplasms Studied by MRI; Magnetic Resonance Imaging of White Matter Disease; Magnetization Transfer and Cross Relaxation in Tissue; Magnetization Transfer between Water and Macromolecules in Proton MRI; Time-of-Flight Method of MRA.

11 REFERENCES

1. S. Forsen and R. A. Hoffman, *J. Chem. Phys.*, 1963, **39**, 2892.
2. H. T. Edzes and E. T. Samulski, *JMRI*, 1978, **31**, 207.
3. R. N. Muller, M. J. Marsh, M. L. Bernardo, and P. C. Lauterbur, *Eur. J. Radiol.*, 1983, **3**, 286.
4. S. D. Wolff and R. S. Balaban, *Magn. Reson. Med.*, 1989, **10**, 135.
5. B. S. Hu, S. M. Conolly, G. A. Wright, D. G. Nishimura, and A. Mackovski, *Magn. Reson. Med.*, 1992, **26**, 231.
6. J. V. Hajnal, C. J. Baudouin, A. Oatridge, I. R. Young, and G. M. Bydder, *J. Comput. Assist. Tomogr.*, 1992, **16**, 7.
7. M. Komu, *Magn. Reson. Imag.*, 1992, **10**, 35.
8. J. Eng, T. L. Ceckler, and R. S. Balaban, *Magn. Reson. Med.*, 1991, **17**, 304.
9. P. T. Niemi, M. E. S. Komu, and S. K. Koskinen, *JMRI*, 1992, **2**, 197.
10. T. Kurki, N. Lundbom, M. Komu, and H. Kormano, *JMRI*, 1996, **6**, 573.
11. S. D. Wolff, S. Chesnick, J. A. Frank, K. O. Lim, and R. S. Balaban, *Radiology*, 1991, **179**, 623.
12. E. Outwater, M. D. Schnall, L. E. Braitman, B. J. Dinsmore, and H. Y. Kressel, *Radiology*, 1992, **182**, 535.
13. C. E. Kahn, S. D. Perera, R. E. Sepponen, J. I. Tanttu, E. K. Tierala, and M. J. Lipton, *Magn. Reson. Imag.*, 1993, **11**, 67.
14. V. Dousset, R. I. Grossman, K. N. Ramer, M. D. Schnall, L. H. Young, F. Gonzalez-Scarano, E. Lavi, and J. A. Cohen, *Radiology*, 1992, **182**, 483.
15. S. D. Wolff, J. Eng, and R. S. Balaban, *Radiology*, 1991, **179**, 133.
16. R. A. Jones and T. E. Southon, *Magn. Reson. Med.*, 1991, **19**, 483.
17. R. S. Balaban and T. L. Ceckler, *Magn. Reson. Q.*, 1992, **8**, 116, containing an excellent review of the theory, techniques, and applications of magnetization transfer.
18. A. Gass, G. Barker, D. Kidd, J. W. Thorpe, C. Davie, G. Newcombe, D. MacManus, A. Brennan, W. I. McDonald, and D. H. Miller, *Proc. XIIth Ann Mtg. Soc. Magn. Reson. Med.*, New York, 1993, p. 327.
19. L. A. Loevner, R. I. Grossman, J. A. Cohen, F. J. Lexa, D. Kessler, and D. L. Kolson, *Radiology*, 1995, **196**, 511.
20. M. Fillippi, A. Campi, V. Dousset, C. Baratti, V. Martinelli, N. Canal, G. Scotti, and G. Comi, *Neurology*, **45**, 478.
21. J. R. Petrella, R. I. Grossman, J. C. McGowan, G. Campbell, and J. A. Cohen, *Am. J. Neuroradiol*, 1996, **17**, 1041.
22. R. J. Ordidge, J. A. Helpern, R. A. Knight, Z. X. Qing, and K. M. A. Welch, *Magn. Reson. Imag.*, 1991, **9**, 895.
23. J. M. Prager, J. D. Rosenblum, R. E. Halbach, S. Verma, R. Mojtahedi, and R. G. Ramsey, *Proc. Xth Ann Mtg. Soc. Magn. Reson. Med.*, San Francisco, 1991, p. 1002.
24. R. C. Mehta, G. B. Pike, and D. R. Enzmann, *Am. J. Neuroradiol.*, 1996, **17**, 1051.
25. N. Lundbom, P. Niemi, T. Kurki, and M. Kormano, *Proc. Xth Ann Mtg. Soc. Magn. Reson. Med.*, San Francisco, 1991, p. 177.
26. T. J. I. Kurki, P. T. Niemi, and N. Lundbom, *JMIR*, 1992, **2**, 401.
27. N. M. deSouza, J. V. Hajnal, and C. J. Baudouin, *Neuroradiology*, 1995, **37**, 278.
28. V. P. Matthews, A. D. Elster, J. C. King, J. L. Ulmer, C. A. Hamilton, and J. M. Strottman, *Am. J. Roentgenol.*, 1995, **164**, 169.
29. J. I. Tanttu, R. E. Sepponen, M. J. Lipton, and T. Kuusela, *J. Comput. Assist. Tomogr.*, 1992, **16**, 19.
30. J. R. Meyer, R. W. Androux, N. Salamon, B. Rabin, C. Callahan, T. B. Parish, J. Prager and E. J. Russell, *Am. J. Neuroradiol*, 1997, **18**, 1515.
31. J. V. Hajnal and I. R. Young, *Proc. XIth Ann Mtg. Soc. Magn. Reson. Med.*, Berlin, 1992, p. 1411.
32. D. J. Fisher, W. T. C. Yuh, H. D. Nguyen, and N. A. Mayr, *Proc. XIIth Ann Mtg. Soc. Magn. Reson. Med.*, New York, 1993, p. 183.
33. M. Knauth, M. Forsting, M. Hartmann, S. Heiland, T. Balzer, and K. Sartor, *Am. J. Neuroradiol.*, 1996, **17**, 1853.
34. D. Han, K. H. Chang, M. H. Han, J. Y. Cho, S. W. Han, H. D. Kim, and S. O. Seong, *Am. J. Roentgenol.*, 1998, **170**, 189.
35. R. S. Balaban, S. Chesnick, K. Hedges, F. Samaha, and F. W. Heineman, *Radiology*, 1991, **180**, 671.
36. W. B. Pierce, S. E. Harms, D. P. Flamig, R. H. Griffey, W. P. Evans, and J. E. Hagans, *Radiology*, 1991, **181**, 757.
37. W. G. Schreiber, G. Brix, M. V. Knopp, T. Hess, and W. J. Lorenz, *Magn. Res. Med.*, 1996, **35**, 861.
38. H. Onaya, H. Yoshioka, Y. Itai, M. Niitsu, I. Anno, and T. Okumura, *JMRI*, 1995, **5**, 273.
39. A. C. Loesberg, M. Kormano, and M. J. Lipton, *Invest. Radiol.*, 1993, **28**, 726.
40. M. D. Hollett, A. M. Aisen, H. N. Yeung, I. R. Francis, and R. L. Bree, *Magn. Res. Imag.*, 1994, **12**, 1.
41. F. Schick, W. Stern, J. Forster, M. Laniado, O. Lutz, and C. D. Claussen, *JMRI*, 1997, **7**, 280.
42. D. K. Kim, T. L. Ceckler, V. C. Hascall, A. Calabro, and R. S. Balaban, *Magn. Reson. Med.*, 1993, **29**, 211.
43. S. M. Brown, E. Schneider, M. A. Nissenbaum, S. Song, and W. G. Bradley, *Radiology*, 1992, **185(P)**, 148.
44. M. Vahlensieck, C. Leutner, F. Dombrowsky, J. Vogel, F. Traber, R. deBoer, and M. Reiser, *Proc. XIIth Ann Mtg. Soc. Magn. Reson. Med.*, New York, 1993, p. 881.
45. G. W. Lenz, A. R. Goldmann, M. Deimling, and U. Boettcher, *Proc. XIIth Ann Mtg. Soc. Magn. Reson. Med.*, New York, 1993, p. 181.
46. X. P. Zhu, S. Zhao, and I. Isherwood, *Br. J. Radiol.*, 1992, **65**, 39.
47. A. E. Lamminen, J. I. Tanttu, R. E. Sepponen, and H. Somer, *Proc. Xth Ann Mtg. Soc. Magn. Reson. Med.*, San Francisco, 1991, p. 309.
48. C. J. Baudouin, J. V. Hajnal, and I. R. Young, *Proc. XIIth Ann Mtg. Soc. Magn. Reson. Med.*, New York, 1993, p. 862.
49. M. Haliloglu and M. D. Cohen, *Pediat. Radiol.*, 1996, **26**, 894.
50. K. C. Li, K. L. Hopkins, S. G. Moore, N. N. Loh, G. Bergman, G. B. Pike, and G. H. Glover, *Skel. Radiol.*, 1995, **24**, 21.
51. W. T. Dixon, H. Engels, M. Castillo, and M. Sardashti, *Magn. Reson. Imaging*, 1990, **8**, 417.
52. P. S. Melki and R. V. Mulkern, *Magn. Reson. Med.*, 1992, **24**, 189.
53. G. E. Santyr, *Magn. Reson. Imag.*, 1993, **11**, 521.

Acknowledgements

The author wishes to acknowledge the contribution of Dr. I. Young, Dr. J. Hajnal, Prof. G. Bydder, Ms. A. Oatridge, and others at the Robert Steiner Magnetic Resonance Unit and thank Angela Oatridge for the preparation of the illustrations.

Biographical Sketch

Christine J. Baudouin. *b* 1957. B.A., 1978, Natural Sciences (Biochemistry) University of Cambridge, B.M., B.Ch., 1981, University of Oxford. Trained as a radiologist in London and Sheffield, 1984–89.

Senior Research Fellow at the Robert Steiner Magnetic Resonance Unit, Hammersmith Hospital, London (with Prof. Graeme Bydder and Dr. Ian Young), 1989–93, working on in vivo magnetization transfer, and the use of internal coils. Consultant in Radiology, St James's University Hospital, Leeds, 1993–94. Consultant in charge of MRI, Freeman Hospital, Newcastle upon Tyne, 1994–present. Previous and present interests include application of magnetization transfer techniques in a clinical setting, internal coils and abdominal imaging.

Overhauser Effect Imaging of Free Radicals

David J. Lurie
University of Aberdeen, Aberdeen, UK

1 INTRODUCTION

Since its prediction by Overhauser and experimental verification by Carver and Slichter in 1953, the electronic Overhauser effect has had many and varied applications. This article will describe the combination of the electronic Overhauser effect with MRI in order to image the distribution of free radicals in phantoms, biological samples, animals and, potentially, humans.

Free radicals are defined as molecules with one or more unpaired electrons in their outer orbitals. Various free radicals are involved in normal metabolism, and changes in their concentration in the body have been associated with many diseases and pathological conditions. Furthermore, there exist free radicals which are stable in aqueous solution, and have the potential for use as contrast agents or tracers in biological and clinical MRI. Thus, a technique to image free radicals in vivo would have profound implications for biological and medical research as well as for clinical practice.

The electronic Overhauser effect is based on a combination of NMR and ESR on the same sample at the same time. It is also known as dynamic nuclear polarization (DNP). Applied to liquid samples, DNP involves the observation of the solvent's NMR signal while simultaneously irradiating one or more ESR resonances of a free radical solute. Under favorable conditions, the ESR irradiation can give rise to a large enhancement (increase in intensity) of the NMR signal, the amount of enhancement depending on a number of factors including the type and concentration of free radical and the strength of the ESR irradiation.

In the imaging experiment, the ESR irradiation is applied to the sample during the acquisition of an MRI image. The NMR signal is enhanced in parts of the sample containing free radical, and these regions exhibit greater intensity in the final image, revealing the distribution of the free radical. This combined imaging technique was first demonstrated in 1987, and was given the name proton electron double resonance imaging (PEDRI).[1] (The same technique has also been dubbed Overhauser MRI and DNP imaging by other workers in the field, but the acronym PEDRI will be used from now on.)

2 PERTINENT RESULTS FROM THE THEORY OF THE ELECTRONIC OVERHAUSER EFFECT

The theory of the electronic Overhauser effect and of DNP is well developed, and is covered elsewhere[2] and in excellent review articles on the subject.[3,4]

The enhancement factor E in an electronic Overhauser effect experiment can be written:

$$E = 1 - \rho f s \frac{|\gamma_S|}{\gamma_I} \tag{1}$$

E can be defined as the ratio A_z/A_0, where A_z and A_0 are respectively the NMR signal amplitudes obtained with and without ESR irradiation. γ_S and γ_I are the electronic and nuclear gyromagnetic ratios. ρ is the coupling factor, and depends on the nature of the interactions between the unpaired electrons and the NMR nuclei: $\rho = -1$ if the interactions are purely scalar, while $\rho = +\frac{1}{2}$ if dipolar interactions dominate (this is usually the case for small free radical molecules in solution).

The leakage factor, f, is an indication of the fraction of nuclear spin–lattice relaxation arising from the presence of the free radical in solution. It can be written as:

$$f = 1 - \frac{T_1}{T_1^0} \tag{2}$$

where T_1 is the spin–lattice relaxation time of the free radical solution, while $T_1{}^0$ is the spin–lattice relaxation time of the solution without free radical.

The saturation factor, s in equation (1), depends on the strength of the ESR irradiation and on the ESR relaxation times. It can be written as follows:

$$s = \frac{1}{n}\left(\frac{\gamma_S^2 B_2^2 \tau_1 \tau_2}{1 + \gamma_S^2 B_2^2 \tau_1 \tau_2}\right) \tag{3}$$

where B_2 is the rf magnetic field strength of the ESR irradiation, τ_1 and τ_2 are the electronic longitudinal and transverse relaxation times, and n is the number of lines in the free radical's ESR spectrum.

Assuming $\rho = \frac{1}{2}$, and considering proton NMR (so that $|\gamma_S/\gamma_P| = 658$), we can combine and rearrange equations (1)–(3) into the form:

$$\frac{1}{1-E} = \frac{n}{329}\left(1 + \frac{1}{\alpha P}\right)\left(1 + \frac{1}{kcT_1^0}\right) \tag{4}$$

where P is the power of the ESR irradiation and α is a constant, k is the longitudinal NMR relaxivity of the free radical of interest and c is its concentration. The terms in parentheses are respectively the reciprocals of the saturation and the leakage factors.[5]

If we assume that $n = 3$ (as is the case with nitroxide free radicals), then we can predict the maximum enhancement factor $E^{\max} = -109$, obtained with infinite ESR irradiation power (causing total saturation of the ESR resonance) and with a highly concentrated solution, giving a leakage factor of unity. (A negative value of E means that the phase of the NMR signal obtained while irradiating the ESR resonance is altered by π radians compared with the normal NMR signal, while the ratio of the signal intensities is $|E|$.) Enhancements as large as $E^{\max}$ are not observed in practice, but it is nevertheless possible to observe enhancement factors of -50 or -60 depending on the system under study. In general, the type of free radical has a strong influence on the achievable enhancement factor: a free radical with few ESR lines (n), each of which is narrow (long τ_2), and which exhibits high NMR relaxivity (k) will, accord-

ing to equations (1), (3), and (4), result in a large enhancement factor at a given level of ESR irradiation.

3 PEDRI TECHNIQUES

3.1 Magnetic Field Strength

Most clinical MRI is carried out at field strengths of 0.5 T or above. Unfortunately, the ESR frequency even at 0.5 T is greater than 14 GHz, much too high to penetrate into ionic samples due to dielectric losses. In order to achieve sufficient penetration of the ESR irradiation into small animals or human limbs, its frequency must be less than 300 MHz or so, corresponding to magnetic field strengths of 10 mT and below: this is the range of magnetic fields which must be used in biological PEDRI experiments. Furthermore, it can be shown that the ESR irradiation power required to achieve a given enhancement is proportional to the volume of the sample and to the square of the ESR frequency used; it is therefore necessary to use frequencies below 300 MHz in order not to overheat the sample under study.

3.2 PEDRI Pulse Sequences

Apart from the necessity of using static magnetic fields of 10 mT or less, and the addition of hardware to irradiate the ESR resonance (described in Section 4.2 below), PEDRI uses standard MRI hardware and virtually standard software. Any MRI pulse sequence can be converted to a PEDRI pulse sequence by the addition of one or more periods of ESR irradiation. Figure 1 shows an example of a simple PEDRI pulse sequence based on a gradient echo MRI sequence. Here, the basic spin warp pulse sequence is preceded by a period of ESR irradiation of length T_{ESR}. Since the nuclear magnetization builds exponentially toward its enhanced equilibrium value upon switching on the ESR irradiation, with a time constant equal to T_1, it is not necessary to apply the ESR irradiation continuously. However, if it is desired to maximize the enhancement, one must ensure that T_{ESR} is longer than about three times the longest T_1 in the sample. Similarly, the enhanced magnetization decays at a rate governed by T_1 after the ESR irradiation is removed, so the time between the end of ESR irradiation and the NMR detection pulse should be short.

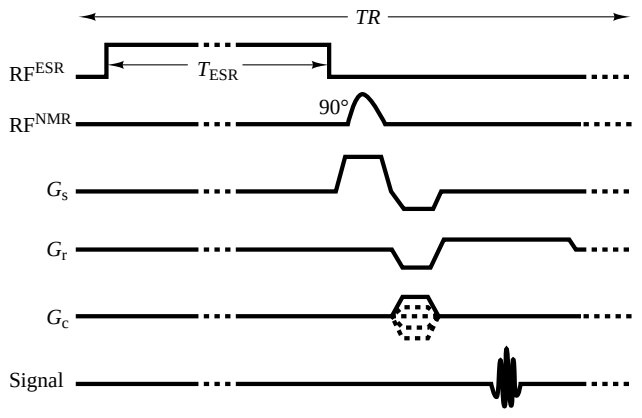

Figure 1 The basic PEDRI pulse sequence. A period of ESR irradiation, shown as RF^{ESR}, duration T_{ESR}, precedes the normal MRI sequence (shown here as a gradient echo, spinwarp sequence). The sequence repetition time is *TR*. G_s, G_r, and G_c are the orthogonal selection, readout and phase-encoding gradient waveforms, respectively

While the intensity in a PEDRI image depends on the local concentration of free radicals, unless the enhancement factors are very high it is not easy to differentiate free radical-containing regions from those which would normally exhibit high intensity in the MRI image. Thus, it is useful to collect two images of the same slice in the object under study: one with, and one without, ESR irradiation. Subtraction of the two image data sets then yields a 'difference' image in which nonzero image intensity indicates the presence of a free radical. The complex data sets (rather than the image intensities) should be subtracted in order to account correctly for negative values of the enhancement factor. It is convenient to use an interleaved pulse sequence, each alternate NMR excitation being preceded by ESR irradiation, with two signals being recorded at each phase-encoding view, contributing separately to 'with ESR' and 'without ESR' images.[5]

With low concentrations of free radical (such that $kc << 1/T_1^0$), the image intensity in a 'difference' image is proportional to the free radical concentration, but the constant of proportionality will differ between samples (or tissues) with different T_1^0 values (e.g. liver and kidney) by virtue of equation (4). In samples with short T_1^0, the inherent relaxation pathways are stronger in comparison with the free radical related dipolar interactions than in samples with long T_1^0, and result in lower enhancement factors for any given free radical concentration.

3.3 Field Cycled PEDRI

The quadratic dependence of the ESR irradiation power on the ESR frequency means that one would ideally perform PEDRI experiments at magnetic fields well below 10 mT. Very low magnetic fields are required also for PEDRI experiments on large animals or the human abdomen, since the penetration depth of electromagnetic radiation at 250–300 MHz is not sufficient to provide uniform excitation in these cases. While it is certainly possible to reduce the ESR irradiation frequency to 100 MHz (say) by lowering the magnetic field B_0 to 2.5 mT, such a reduction in B_0 would have a catastrophic effect on the signal-to-noise ratio (S/N) of the MRI experiment, with a consequent reduction in sensitivity and image quality. The combination of PEDRI with magnetic field cycling enables the rf power requirement to be reduced (while maintaining enhancement) without reducing the S/N.[6]

In a field cycled NMR pulse sequence, the applied magnetic field $\boldsymbol{B}_0$ is not constant, but is switched between a number of levels (usually three), each of which has its effect on the spin system.[7] The field cycled PEDRI (FC-PEDRI) pulse sequence (Figure 2) commences with the polarization period at field strength $\boldsymbol{B}_0^P$, during which the nuclear magnetization reaches thermal equilibrium. The magnetic field is then reduced rapidly to $\boldsymbol{B}_0^E$ where it is held for the duration of the evolution period, when the ESR irradiation is applied at the appropriate frequency and power. The Overhauser enhancement occurs during this period. Finally, the magnetic field is increased again before

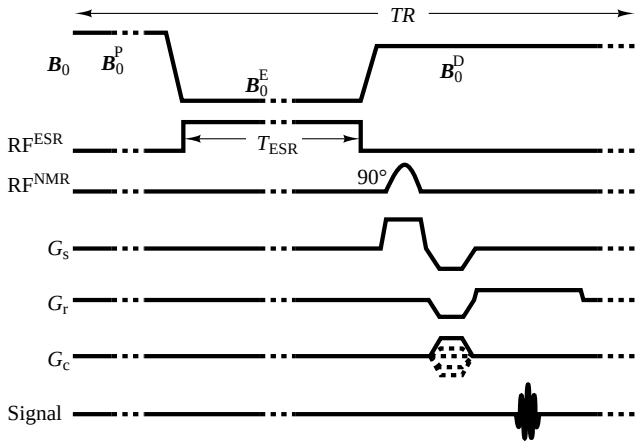

Figure 2 Field cycled PEDRI pulse sequence, showing the polarization period at magnetic field $\boldsymbol{B}_0{}^{P}$, the evolution period at $\boldsymbol{B}_0{}^{E}$ and the detection period at $\boldsymbol{B}_0{}^{D}$. The ESR irradiation is applied during the evolution period, at a frequency and power appropriate to $\boldsymbol{B}_0{}^{E}$. The S/N is largely determined by the magnetic field applied during the detection period

the start of the detection period at $\boldsymbol{B}_0{}^{D}$, during which the NMR detection pulse(s) and imaging magnetic field gradients are applied as usual. The time to switch between $\boldsymbol{B}_0{}^{E}$ and $\boldsymbol{B}_0{}^{D}$ must be as short as possible to minimize the decay of the enhanced magnetization following the end of the ESR irradiation. The S/N depends on the relative timing of the three periods, and on the magnetic fields, but especially on the value of $\boldsymbol{B}_0{}^{D}$. By judicious selection of the sequence parameters it is possible to reduce the specific applied rf power while maintaining the enhancement, without sacrificing the S/N of the experiment.

4 HARDWARE REQUIREMENTS

As PEDRI makes use of virtually standard MRI techniques, most of the hardware required is identical, and will not be discussed here (see ***Low-Field Whole Body Systems***). The two areas where differences arise between standard MRI and PEDRI are the magnet and the rf coil assemblies.

4.1 The Magnet

PEDRI does not place any more demand than conventional MRI on the specification of the magnet. It has already been mentioned that PEDRI requires the use of fields of 10 mT or less; while there is no reason why one could not use a superconducting magnet to generate the static field, it is likely to be more convenient (and cheaper) to use resistive (or permanent) magnets.

Not surprisingly, FC-PEDRI does require the use of specialized magnet and power supply hardware. The magnetic field applied during the detection period must be as homogeneous and as stable as required by conventional MRI. Because of the broad nature of ESR resonances (say 0.2 mT at a field strength of 10 mT for a typical nitroxide free radical), the stability and homogeneity can be relaxed considerably during the evolution period, as indeed they can during the polarization part of the pulse sequence since small local differences in the initial magnetization have negligible effect on the image. The final requirement is the necessity to switch magnetic fields between levels in a time considerably less than the T_1 of the sample under study. In biological studies, one would not wish to switch between the evolution and detection magnetic fields in more than 50 ms, to avoid losing valuable enhanced magnetization.

There are two basic methods of field cycling.[6] In the first, direct method, a single resistive magnet and power supply is used, the current through the magnet windings being altered in order to change the magnetic field at the sample. The electrical characteristics of the magnet and power supply must be such that the current can be changed sufficiently rapidly, and the magnetic field must be accurately and repeatably held constant during the detection period.

The second method, called 'field compensation', makes use in its simplest incarnation of two coaxial magnet coils, with separate power supplies. The large primary magnet is supplied with a constant current to generate $\boldsymbol{B}_0{}^{D}$, with good homogeneity and stability. The smaller secondary coil, which surrounds the sample under study, generates a field parallel or antiparallel to the primary coil's, and the current is altered during the pulse sequence in order to achieve field cycling.[5–7]

Field compensation is probably to be preferred over direct field cycling, because only the stable, homogeneous primary magnet is energized during the critical detection period: the current in the secondary coil is 'clamped' to zero during this part of the pulse sequence, and this is inherently simpler and more reliable than trying to reproduce precisely the same nonzero current each cycle. This advantage is at the expense of some complexity, however, since two magnets and two power supplies are required, and there is inevitably some degree of mutual inductance between the two coils which may destabilize the detection magnetic field. Replacing the primary coil by a suitable permanent magnet offers the possibility of a simpler design, but care must be taken to avoid eddy currents in the magnet structure which might scupper attempts to cycle rapidly. Whichever method is chosen, field cycling on a whole body scale is a considerable technical challenge, since the magnetic field energy (which must be removed and replaced every half cycle of the pulse sequence) increases in proportion to the magnet volume. Nevertheless, the offer of high enhancements and good S/N, without high rf power is extremely appealing, and is probably the only means of detecting micromolar concentrations of free radicals. Lurie et al. have recently constructed a large-scale FC-PEDRI imager, based on a whole-body 59 mT permanent magnet with a co-axial resistive magnet for field-compensation.[8]

4.2 ESR Irradiation Hardware

Perhaps the most significant difference between MRI and PEDRI hardware is the need to deliver a continuous or pulsed ESR irradiation in the latter technique. The apparatus used to generate the ESR irradiation consists basically of a signal generator, power amplifier and tuned coil or resonator.

The first two items will normally be off-the-shelf commercial units, the specification of which is largely determined by the

magnetic field strength being used (ESR frequency) and the size of the sample (irradiation power). As ESR resonances are rather broad (see Section 4.1 above) the signal generator need not be especially stable. However, the ease of adjustment of frequency and amplitude offered by synthesized frequency generators make these instruments particularly suitable.

The most specialized item of hardware is undoubtedly the coil or resonator used to apply the ESR irradiation to the sample under study. The design of the ESR resonator is complicated by the fact that it is also necessary in PEDRI to excite the NMR resonance of the sample and to detect NMR signals, and the NMR coil and ESR resonator should be designed together as an integrated structure. Ideally, the quality- and filling-factors of both the NMR coil and the ESR resonator should be optimized. In practice, the design is inevitably a compromise, and optimization of the NMR coil should take precedence over the characteristics of the ESR resonator. (Loss of S/N caused by reduced filling factor or quality factor of the NMR coil can only be recovered by signal averaging, while a compromise based on reducing the ESR resonator's filling factor will only result in a greater power requirement from the ESR irradiation power amplifier.) One design of NMR/ESR coil assembly for use with vertical-field magnets uses a solenoidal NMR coil with a coaxial, external ESR resonator based on the design of Alderman and Grant.[9]

5 APPLICATIONS AND POTENTIAL OF PEDRI

PEDRI is a relatively young technique, with (at the time of writing) only a small number of sites contributing to its development. The potential applications of the technique are, however, quite considerable, particularly if the technology can be developed to apply the technique on a whole body scale. Applications can be divided into two groups: those involving the detection of exogenous (i.e. externally introduced) free radicals and those which aim to image the distribution of endogenous free radicals. The latter is by far the most challenging (and potentially rewarding).

There are many endogenous free radicals which have been implicated in the disease process. Two of the most important are hydroxyl (·OH) and nitric oxide (NO·); however, neither is amenable to direct detection in the body by magnetic resonance, because of their short lifetimes and unsuitable ESR characteristics. Nevertheless, it may be possible to detect and image these and other endogenous radicals by combining PEDRI with a chemical stabilization technique called spin trapping.[10] In this method, a spin trap molecule (not itself a free radical) is first dissolved in the system under study. If short-lived free radicals are subsequently formed near a spin trap molecule, they may be 'trapped', forming a longer-lived free radical called a spin

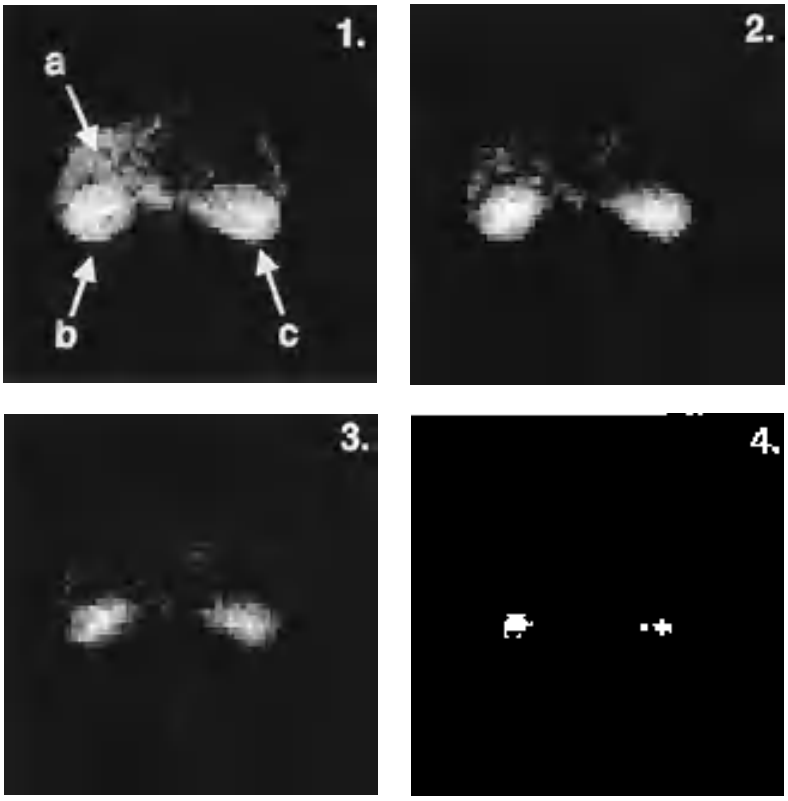

Figure 3 A set of PEDRI 'difference' images through the abdomen of a supine, 350 g, anesthetized Sprague–Dawley rat, following the administration of a 300 mM solution of bicarbonate-buffered PCA nitroxide free radical at a dose of 0.8 mmol per kg of body weight. Image matrix size: 64 × 64; field-of-view 10 × 10 cm; slice thickness 2 cm; field strength 10 mT; ESR irradiation frequency 238.7 MHz. An interleaved pulse sequence was used, with an overall sequence repetition time (*TR*) of 2000 ms, and T_{ESR} = 300 ms. Image 1 was collected 1 min after administration of PCA, and the remaining images were collected at 6, 11 and 16 min postinjection respectively. The labels are: (a) liver; (b) right kidney; (c) left kidney

adduct which can then be detected. The imaging by PEDRI of spin trapped hydroxyl free radicals formed in a chemical model system has already been demonstrated,[11] and work is underway at the time of writing to detect free radicals generated in a variety of biological systems.

The imaging of exogenous free radicals in vivo also offers the possibility of interesting applications. Here, stable free radicals are injected and used as 'contrast agents', PEDRI images being collected to follow the progress of the free radical through the body. (There is a class of compounds known as nitroxide free radicals which are virtually stable in aqueous solution, and whose chemical properties make them potential candidates for PEDRI studies.)

The first in vivo PEDRI studies were carried out in 1990. Grucker administered an intraperitoneal injection of nitroso disulfonate (Fremy's salt) to an anesthetized rat, and imaged the distribution of the free radical solution in the animal's peritoneal cavity, thus demonstrating the feasibility of in vivo PEDRI experiments.[12] Unfortunately, although Fremy's salt has very narrow ESR lines, resulting in large enhancement factors, it is too unstable and toxic for intravenous injection. Lurie et al. injected anesthetized rats intravenously with a solution of a nitroxide free radical (3-carboxy-2,2,5,5-tetramethylpyrrolidine-1-oxyl or PCA), and were able to observe by PEDRI the clearance of the free radical through the animal's liver and kidneys.[13] Subsequent analysis of images collected over the course of 30 min postinjection allowed pharmacokinetic data to be obtained.[4] Figure 3 shows a set of images from the author's laboratory demonstrating the clearance of PCA through the kidneys of a rat; this type of study gives information on the functionality of the kidneys.[14] Recent studies of normal and diseased rats have provided useful information in a model of analgesic nephropathy.[15] Nitroxide free radicals are extremely versatile compounds, and can be 'labeled' onto larger molecules, offering the possibility of 'tracer' studies by targeting contrast agents to specific tissues. A contrast agent with a single narrow ESR line is being developed by industry for use with PEDRI; it has already been used to produce very-high-resolution images of rats.[16]

Another potential application of PEDRI using exogenous free radicals is localized in vivo oximetry.[1,17] It is well known that oxygen in solution broadens the ESR lines of nitroxide free radicals. Broad ESR resonances are more difficult to saturate, resulting in lower enhancement factors in the PEDRI experiment. The main difficulty is to differentiate between low enhancement caused by high oxygen concentration and low enhancement caused by low free radical concentration. Research is currently underway to address this problem.

PEDRI is developing into a useful technique for the study of free radicals in vivo. Good results have been obtained in studies of exogenous free radicals in small animals, and these experiments are starting to give useful results on organ function. PEDRI is easier to implement than ESR imaging and produces images with better spatial resolution (see ***EPR and In Vivo EPR: Roles for Experimental and Clinical NMR Studies***; also ***In Vivo ESR Imaging of Animals***).[18] At the time of writing, the sensitivity of PEDRI is such that it ought to be able to detect spin-trapped endogenous free radicals in model systems (free radicals at concentrations of 5–10 μM can be detected), offering a novel research tool in biology and medicine. Current research aims to improve the sensitivity, for example by field cycling to higher magnetic fields.

The technology to apply PEDRI to human-sized samples is currently being developed; its actual use in human subjects depends to a large extent on the development of suitable contrast agents (and perhaps spin traps) by the pharmaceutical industry.

6 RELATED ARTICLES

Birdcage Resonators: Highly Homogeneous Radiofrequency Coils for Magnetic Resonance; EPR and In Vivo EPR: Roles for Experimental and Clinical NMR Studies; In Vivo ESR Imaging of Animals; Low-Field Whole Body Systems.

7 REFERENCES

1. D. J. Lurie, D. M. Bussell, L. H. Bell, and J. R. Mallard, *J. Magn. Reson.*, 1988, **76**, 366.
2. D. M. Grant and R. K. Harris, 'Encyclopedia of Nuclear Magnetic Resonance', John Wiley & Sons, Chichester, UK, 1996.
3. R. A. Dwek, R. E. Richards, and D. Taylor, *Annu. Rev. NMR Spectrosc.*, 1969, **2**, 293.
4. W. Muller-Warmuth and K. Meise-Gresch, *Adv. Magn. Reson.*, 1983, **11**, 1.
5. D. J. Lurie and I. Nicholson, 'Proton-Electron Double-Resonance Imaging of Exogenous and Endogenous Free Radicals In-Vivo', in *Proc. Int. School of Physics Enrico Fermi*, Course CXIII, 'Nuclear Magnetic Double Resonance', ed. B. Maraviglia, Italian Physical Society, distributed by North-Holland, Amsterdam, 1994.
6. D. J. Lurie, J. M. S. Hutchison, L. H. Bell, I. Nicholson, D. M. Bussell, and J. R. Mallard, *J. Magn. Reson.*, 1989, **84**, 431.
7. F. Noack, *Prog. NMR Spectrosc.*, 1986, **18**, 171.
8. D. J. Lurie, M. A. Foster, D. Yeung, and J. M. S. Hutchison, *Phys. Med. Biol.*, 1998, **43**, 1887.
9. D. W. Alderman and D. M. Grant, *J. Magn. Reson.*, 1979, **36**, 447.
10. G. R. Buettner, in 'Superoxide Dismutase' ed. L. W. Oberley, CRC Press, Boca Raton, FL, 1982, Vol. 2, Chap. 4.
11. D. J. Lurie, J. McLay, I. Nicholson, and J. R. Mallard, *J. Magn. Reson.*, 1991, **95**, 191.
12. D. Grucker, *Magn. Reson. Med.*, 1990, **14**, 140.
13. D. J. Lurie, I. Nicholson, M. A. Foster, and J. R. Mallard, *Philos. Trans. R. Soc. London, Ser. A*, 1990, **333**, 453.
14. I. Seimenis, M. A. Foster, D. J. Lurie, J. M. S. Hutchison, P. H. Whiting, and S. Payne, *Magn. Reson. Med.*, 1997, **37**, 552.
15. I. Seimenis, M. A. Foster, D. J. Lurie, J. M. S. Hutchison, P. H. Whiting, and S. Payne, *Magn. Reson. Med.*, 1998, **40**, 280.
16. K. Golman, I. Leunbach, J. H. Ardenkjær-Larsen, G. J. Enholm, L.-G. Wistrand, J. S. Petersson, A. Järvi, and S. Vahasalo, *Acta Radiol.*, 1998, **39**, 10.
17. D. Grucker and J. Chambron, *Magn. Reson. Imaging*, 1993, **11**, 691.
18. S. Colacicchi, M. Ferrari, and A. Sotgiu, *Int. J. Biochem.*, 1992, **24**, 205.

Biographical Sketch

David J. Lurie. *b* 1956. B.Sc., Aberdeen University, 1979; M.Sc., 1980, Ph.D., 1984, London University. Postdoctoral work at University of Aberdeen 1983–85 (with J. M. S. Hutchison). Lecturer, 1985; senior lecturer, 1992–present, University of Aberdeen. Approx. 40 publications in refereed journals, 100 conference abstracts. Research specialties: double resonance NMR/ESR techniques for imaging free radicals; low-field ESR; field-cycled NMR imaging.

Susceptibility and Diffusion Effects in NMR Microscopy

Paul T. Callaghan

Massey University, Palmerston North, New Zealand

1 INTRODUCTION

NMR microscopy concerns the imaging[1,2] of small-scale samples at high spatial resolution.[3–7] Resolution in NMR imaging is limited by the reduction in intrinsic signal-to-noise ratio as the voxel (volume element) size is decreased.[7,8] In NMR microscopy these elements will typically have at least two dimensions (the 'pixel' or image picture element) smaller than 100 μm. Most microscopy experiments are carried out using vertical bore magnets with fields in excess of 5 T. These fields, coupled with the inevitable heterogeneity of the sample, lead to significant susceptibility-related line broadening and consequent image artifacts. Furthermore, at such high spatial resolution the effects of molecular self-diffusion become significant[9] leading to profound effects in the image when the distance moved by the molecules over the image acquisition time is comparable to the voxel dimensions. In this article we examine some of the influences arising from susceptibility and diffusion and show how they may be used to profitable effect.

The disturbance to the local magnetic field near a boundary between two regions of differing diamagnetic susceptibility, is well-known in large-scale MRI.[10] The parameter of significance in the associated image distortion is scale-independent, and given by $\gamma B_0 \Delta\chi / 2\pi\Delta f$, where Δf is the acquisition bandwidth, $\Delta\chi$ is the local susceptibility change and $\boldsymbol{B}_0$ is the polarizing field. Susceptibility effects in imaging have recently featured prominently in clinical MRI studies of the human brain, where it has been shown that capillary blood flow associated with neural activity can be directly observed.[11–16] The contrast in this so-called 'functional' MRI is believed to derive from changes in paramagnetic susceptibility associated with transitions in the oxygenation state of hemoglobin. While noting their importance, we shall not deal directly with such effects in this article. One reason that susceptibility inhomogeneity effects are especially important in NMR microscopy is that the desire to optimize signal-to-noise ratios leads, customarily, to use of large $\boldsymbol{B}_0$ and, in some cases, small Δf.

By contrast with susceptibility effects, resolution and sensitivity limitation due to molecular self-diffusion is significant only in microscopy. While the effects of self-diffusion can be subtle, as a 'rule of thumb', the parameter of significance is $\Delta x_{\text{diff}} / \Delta x_{\text{pixel}}$, where Δx_{diff} is the rms displacement of the spins over the signal acquisition period and Δx_{pixel} is the pixel dimension. Given that acquisition periods are usually on the order of several milliseconds, Δx_{diff} is on the order of 10 μm.

A clue to the presence of local field variations is given by comparing images obtained using gradient and spin echoes. Examples of these respective pulse sequences are shown in Figure 1. In the spin echo sequence, any dephasing of spin magnetization caused by inhomogeneity in the magnetic field is refocused at the center of the signal acquisition while for the gradient echo such dephasing is allowed to evolve relentlessly, leading to severe image attenuation in regions where the local field variation is strong. It is important to note that such an influence arises from the static field distribution and is associated with the inhomogeneous broadening of the NMR line. However molecular motion leads to fluctuations in this field in a manner which leads to irreversible decay of magnetization, a relaxation effect which contributes to homogeneous broadening. Both influences are generally present in NMR microscopy and are dealt with in turn in the following sections of this article.

2 STATIC SUSCEPTIBILITY EFFECTS

2.1 Gradient and Spin Echoes

When a heterogeneous sample is placed in a uniform magnetic field, local field distortions are most apparent near susceptibility boundaries. By applying Maxwell's equations under the usual boundary conditions it is possible to compute $\Delta B_0(\boldsymbol{r})$, the difference in magnitude between the local field and the average magnetic field over the sample. The influence of the local field variations can be seen by adding the local precession frequency offset, $\gamma \Delta B_0(\boldsymbol{r})$, to that which arises from the magnetic field gradient.[7,17] Thus the signal acquired under the influence of a steady gradient $\boldsymbol{G}$ applied for a time t is given by

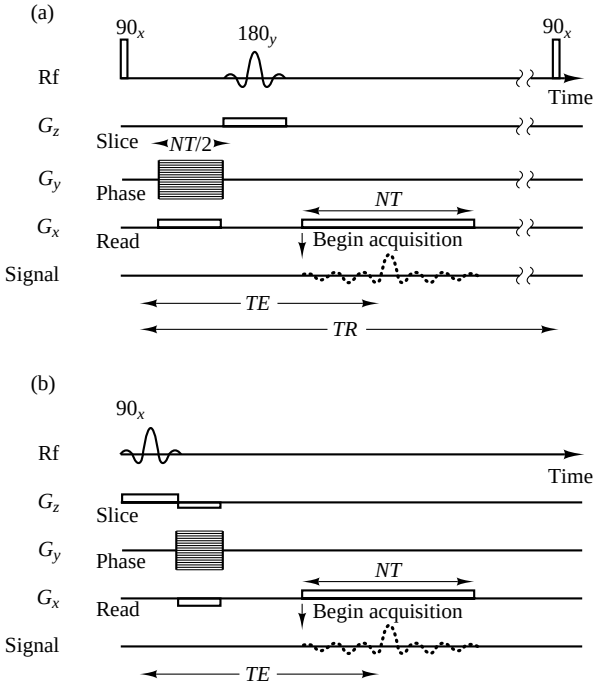

Figure 1 Imaging pulse sequences showing the timing of gradient and rf pulses in the spin warp scheme for (a) spin echo and (b) gradient echo refocusing respectively. Note that the delay in echo formation following excitation is given by *TE*

$$S(t) = \iiint \rho(\boldsymbol{r}) \exp\{\mathrm{i}\gamma[\boldsymbol{G}\cdot\boldsymbol{r} + \Delta B_0(\boldsymbol{r})]t\}\, \mathrm{d}^3 r \tag{1}$$

a result which leads to a Fourier pair

$$S(\boldsymbol{k}) = \iiint \rho(\boldsymbol{r}) \exp[\mathrm{i}\gamma \Delta B_0(\boldsymbol{r})t] \exp(\mathrm{i}2\pi \boldsymbol{k}\cdot\boldsymbol{r})\, \mathrm{d}^3 r \tag{2}$$

$$\rho_{\mathrm{I}}(\boldsymbol{r}) = \iiint S(\boldsymbol{k}) \exp(-\mathrm{i}2\pi \boldsymbol{k}\cdot\boldsymbol{r})\, \mathrm{d}^3 k \tag{3}$$

where $\boldsymbol{k}$ is the usual product $(2\pi)^{-1}\gamma \boldsymbol{G}t$. Inverse Fourier transformation of $S(\boldsymbol{k})$ is used to reconstruct the apparent spin density function, $\rho_{\mathrm{I}}(\boldsymbol{r})$, and it is clear from equations (2) and (3) that the presence of the term involving $\Delta B_0(\boldsymbol{r})$ will cause ($\rho_{\mathrm{I}}(\boldsymbol{r})$ to deviate from the ideal result, $\rho(\boldsymbol{r})$. The distorting influence of this local field depends specifically on the pulse sequence used to obtain the image.

Consider the gradient echo and spin echo sequences of Figure 1. The center of '$\boldsymbol{k}$-space', which determines the overall image intensity, occurs at the center of the echo half-way through the read gradient. For the spin echo, the dephasing effect of the spread in $\Delta B_0(\boldsymbol{r})$ over each pixel is refocused to zero at $\boldsymbol{k} = 0$, whereas it remains to produce attenuation in the gradient echo, thus providing a nice 'signature' for local field effects. An example of how this sensitivity of the gradient echo to local fields can be used to good advantage is shown in Figure 2 where a spin echo and gradient echo image from the same plant stem (*Stachys sylvatica*) are compared.[18] In the gradient echo image, dephasing of water proton magnetization at the boundaries of cells in the parenchyma tissue causes each cell to be highlighted in sharp relief.

2.2 Image Distortion

Despite the fact that static susceptibility attenuation effects are removed at the centre of $\boldsymbol{k}$-space in spin echo imaging, perturbations to the local magnetic field will still produce a residual distortion of the image. In considering this effect we will concentrate on the commonly used spin warp[19,20] variant of Fourier imaging in which a fixed duration phase gradient (G_y) is applied for a time t_y. For such a raster equation (1) may be rewritten,[7,17]

$$S(k_x, k_y) = \iint \rho(x,y) \exp\{\mathrm{i}2\pi k_x[x + \Delta B_0(x,y)/G_x]\} \times \exp(\mathrm{i}2\pi k_y y) \exp[\mathrm{i}\gamma \Delta B_0(x,y)t_y]\, \mathrm{d}x\, \mathrm{d}y \tag{4}$$

The effect of the field offset in equation (4) is to cause each element of the original object at (x, y) to contribute to a single element in the final image displaced from the original position to $[x + \Delta B_0(x,y)/G_x, y]$ and to acquire a local phase shift given by $\exp[\mathrm{i}\gamma \Delta B_0(x,y)t_y]$. Generally this phase shift, which develops during the phase-encoding period, is removed by calculating a final modulus image and, with few exceptions,[21] its effect can generally be ignored. The read gradient element displacement, $\Delta B_0(x,y)/G_x$, is common to all pulse sequences (for example spin warp and projection–reconstruction) which utilize frequency encoding. Pure phase-encoding sequences are therefore useful in avoiding susceptibility distortions but, while intrinsically as efficient as other methods, they incur a severe penalty in image acquisition time.[19]

The condition for avoiding image distortion in pulse sequences using frequency encoding is $\Delta B_0(x,y)/G_x << \Delta x$ or $(\Delta x)^{-1}\, \Delta B_0(x,y) << G_x$. This states that the local field offset should be less than the variation in applied (gradient) field

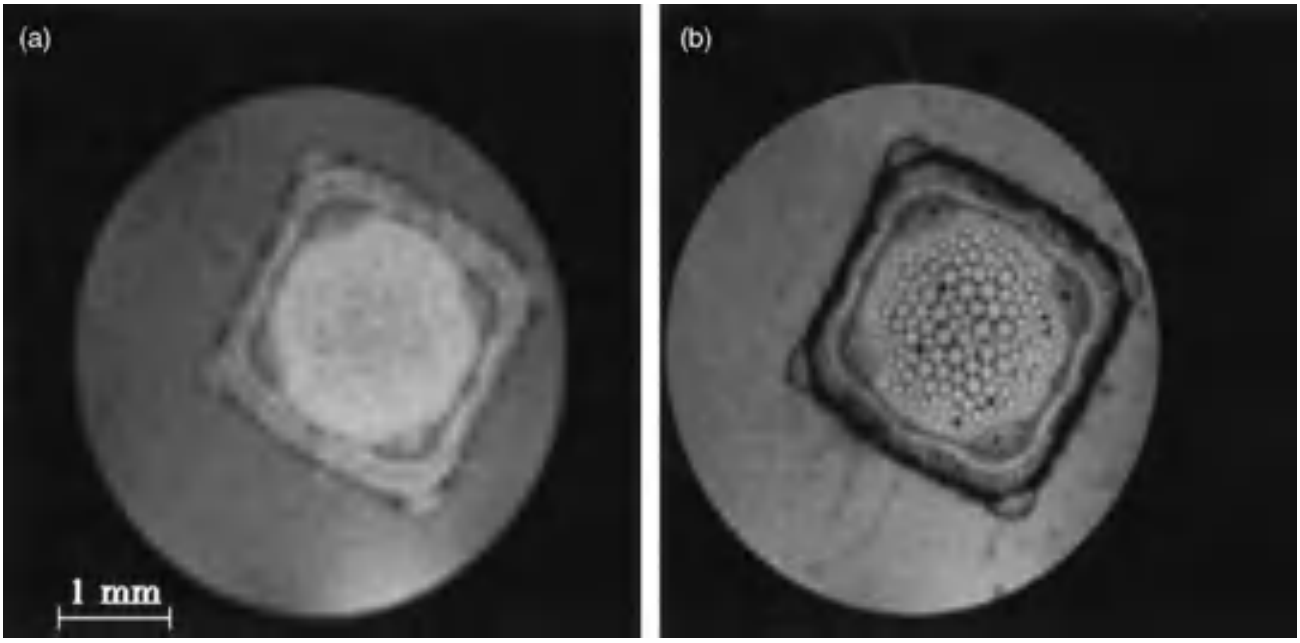

Figure 2 Gradient and spin echo ^{1}H NMR images obtained from the stem of *Stachys sylvatica*, in which the slice thickness was 1 mm and the imaging bandwidth was 40 kHz in each case.[15] In the 256 × 256 pixel gradient echo image (TE = 7.8 ms) dephasing of magnetization occurs due to local fields near the cell boundaries

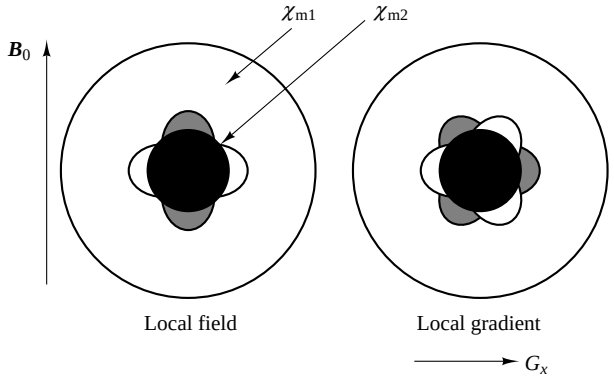

Figure 3 Schematic diagram of the local field $\Delta \boldsymbol{B}_0(x, y)$ and associated gradient $G_x(x, y)$ for the glass rod system pertaining to Figure 4. The black and white lobes correspond to oppositely signed regions of field and gradient

across a single pixel, a condition which points to the desirability of large magnetic field gradients. An example of susceptibility-induced image distortion is shown in Figures 3 and 4, in which aqueous solutions surrounding a small glass rod are imaged at two different read gradient strengths. The applied transverse polarizing field induces a local offset field around the central glass rod which varies as[17,22]

$$\Delta B_0(x, y) \approx \frac{\chi_{m1} - \chi_{m2}}{2} \frac{a^2}{r^2} \left(\frac{2y^2}{r^2} - 1 \right) B_0 \qquad (5)$$

where y is taken to be the direction of the polarizing field, $\boldsymbol{B}_0$, and $r = (x^2 + y^2)^{\frac{1}{2}}$. χ_{m2} and χ_{m1} are the diamagnetic susceptibilities of the glass rod and the medium outside the glass rod respectively. $\Delta B_0(x, y)$ has both positive and negative 'lobes' around the glass rod as shown schematically in Figure 3. Consequently spins are shifted either 'upfield' or 'downfield' in the subsequent reconstruction, leading to the classic arrowhead distortion. Note that in Figures 4(a) and (b), the polymer proton signal in a polyethylene oxide solution is observed by means of a chemical shift selective rf excitation pulse. For such a large molecule diffusive effects are insignificant. By contrast, in Figures 4(c) and (d) the corresponding water images are shown. Here molecular diffusion plays a major role.

3 READ GRADIENTS AND DIFFUSION

3.1 Diffusive Relaxation

The translational diffusion of molecules in the presence of a spatially dependent magnetic field induces phase shifts in the spin transverse magnetization which cause signal attenuation. In imaging experiments such attenuation arises from both the imaging gradients and the local field variations caused by susceptibility inhomogeneity, and both effects can be highly significant in NMR microscopy.[21,23]

For a steady uniform gradient G applied for a time duration t, diffusive attenuation is described by the factor $\exp(-\frac{1}{3}\gamma^2 G^2 D t^3)$ whilst the attenuation for an echo under two closely spaced gradient pulses of duration $\frac{1}{2}t$ and separation $t' \approx \frac{1}{2}t$, is given by $\exp(-\frac{1}{12}\gamma^2 G^2 D t^3)$. In the spin echo variant of spin warp imaging shown in Figure 1(a), the echo amplitude, as measured at $k_x = 0$, suffers a diffusive attenuation at the center of $\boldsymbol{k}$-space because of the two read gradient pulses. Ignoring the somewhat subtler effects of phase gradient diffusive attenuation,[21] and assuming a minimum possible echo time, we can write the attenuation factor as $\exp(-\frac{4}{3}\pi^2 k_x^{\max 2} DNT)$, where $k_x^{\max}$ is the maximum value in the k_x raster, $(2\pi)^{-1} G_x(\frac{1}{2}NT)$, and NT is the echo signal acquisition time, T being the reciprocal of the bandwidth, Δf. Clearly the effect of diffusive relaxation increases as the sampling bandwidth decreases or the number of pixels increases.

One important point to note is that in NMR microscopy experiments, a simple spin echo experiment, of the type shown in Figure 1(a), cannot be used to measure T_2 by simply varying TE, since such a measurement would be strongly affected by diffusive attenuation in the read gradient.[24] In consequence, it is essential to use a precursor spin echo or Carr–Purcell–Meiboom–Gill[25,26] (CPMG) pulse sequence to allow T_2 relaxation contrast before the read gradient is applied if the influence of diffusive attenuation in the read gradient is to be avoided. Such a pulse sequence is shown in Figure 5.

3.2 Special Contrasts: Edge Enhancement and Read Gradient Null Points

Figure 6 shows how the intensity of an image obtained at microscopic resolution can reduce dramatically because of diffusive relaxation when the numbers of pixels are increased from Figures 6(a) to 6(b). While such relaxation clearly limits the available resolution, it can also be deployed to useful effect, as apparent in the higher resolution image where attenuation effects are particularly severe. Near the walls, where the molecular diffusion is impeded, the attenuation is less severe and bright edges appear.[24,27] A similar effect is apparent in Figure 6(c) where an image of a cylindrical capillary of water is shown. Here crescent-shaped edges appear where molecular diffusion is impeded in the direction of the read gradient. These 'edge-enhancement' effects indicate the usefulness of diffusive relaxation as a means of indicating restrictions to Brownian motion.

The bright edge features apparent in Figure 6 arise because of modulation in the local self-diffusive coefficient under imaging conditions where strong diffusive relaxation is expected because of the applied read gradient. Another form of bright feature can occur when susceptibility-related fields modulate the net local gradient. As a result of such gradient superposition, the total gradient at any point may be either larger or smaller than the applied read gradient thus leading to attenuation enhancement or reduction. In particular, at well-defined sites, gradient null points can occur, provided that the read and local gradients are comparable in magnitude and opposite in direction. This cancellation should result in sharp, point-like, bright spots in an image where the read gradient otherwise causes signal attenuation. By contrast the regions where the read and local gradients add constructively will be somewhat larger, leading to diffuse features where additional attenuation is observed. These effects are apparent in Figure 4(d). It is interesting to note that whereas the local field ΔB_0 has two-fold symmetry, the symmetry of the x- and y-components of the gradient in the local field is three-fold, leading to the bright spots being arranged in a triangular array.[21]

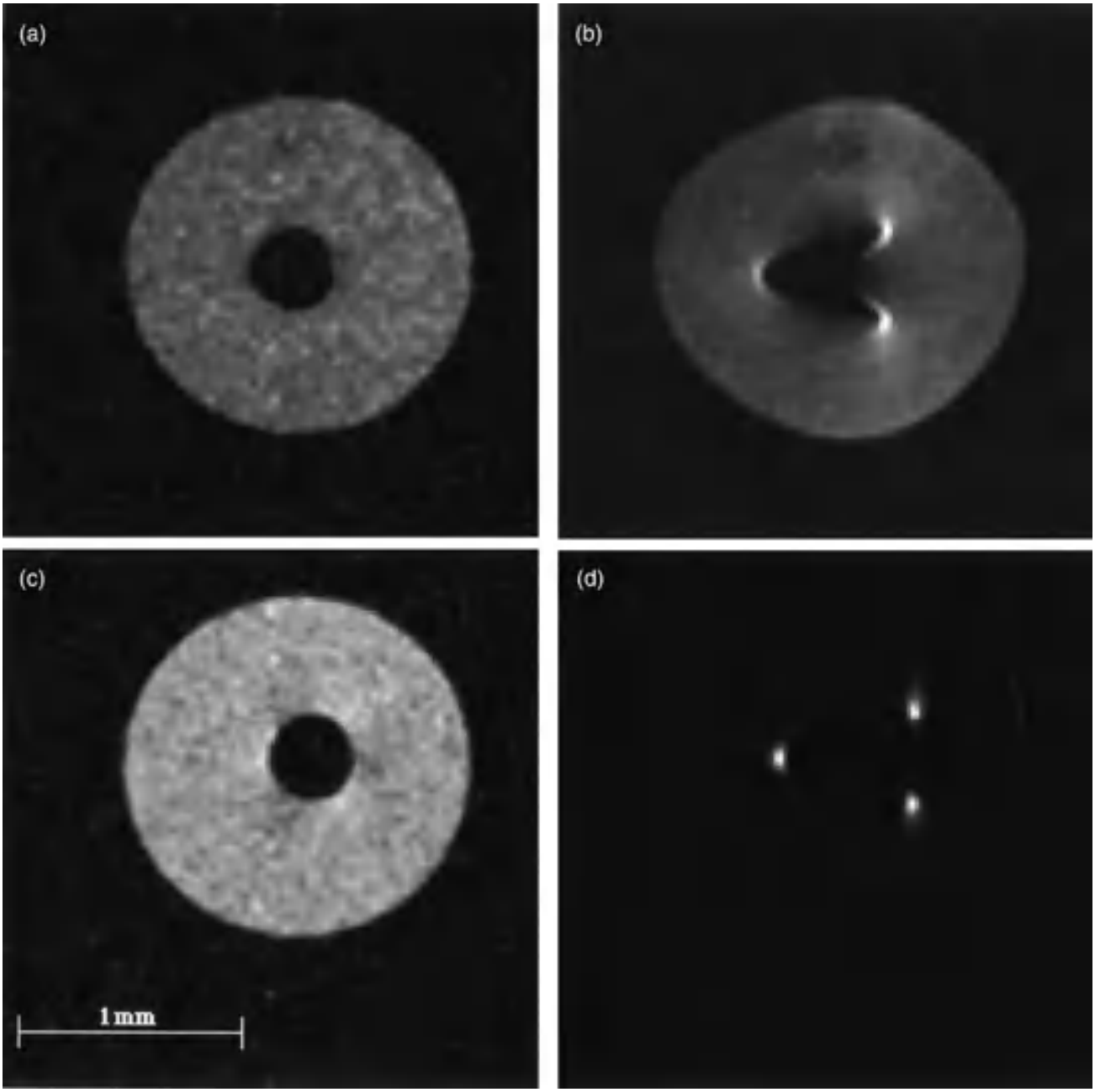

Figure 4 Proton NMR images from the aqueous solution surrounding a glass rod (diameter 370 μm) inserted inside a cylindrical capillary (i.d. 1600 μm). The susceptibility difference is 0.7 ppm and the polarizing field $\boldsymbol{B}_0$ is transverse to the capillary. (a) and (b) show images obtained from the polymer proton signal in the sample for which diffusive effects are absent, at 20 kHz and 1 kHz bandwidth respectively. The arrowhead shape in (b) is symptomatic of the local field distortion produced by the glass rod through the center of the sample. (c) and (d) are the corresponding images for a pure water sample. In (d) bright spots appear where the gradient in the local field, $\Delta\boldsymbol{B}_0$, precisely cancels the read gradient (G_x). (Reproduced by permission from Callaghan et al.[21])

The usefulness of gradient null points is suggested in Figure 6(c), where we observe bright spots in the water. These disappear when microfiltered water is used, suggesting that the bright regions are associated with local dust particles, too fine to be observed directly.[21] The local field thus provides a means of indirect detection via a local modulation of diffusive attenuation. By this means NMR microscopy can be made sensitive to more delicate structural features than might be expected from the usual sensitivity limits to pixel resolution.

4 DIFFUSION IN LOCAL GRADIENTS

4.1 Fast and Slow Exchange

The read gradient and acquisition bandwidth conditions which lead to strong diffusive attenuation are a somewhat pathological case in which nonetheless intriguing and useful contrast can arise. Most NMR microscopy experiments will

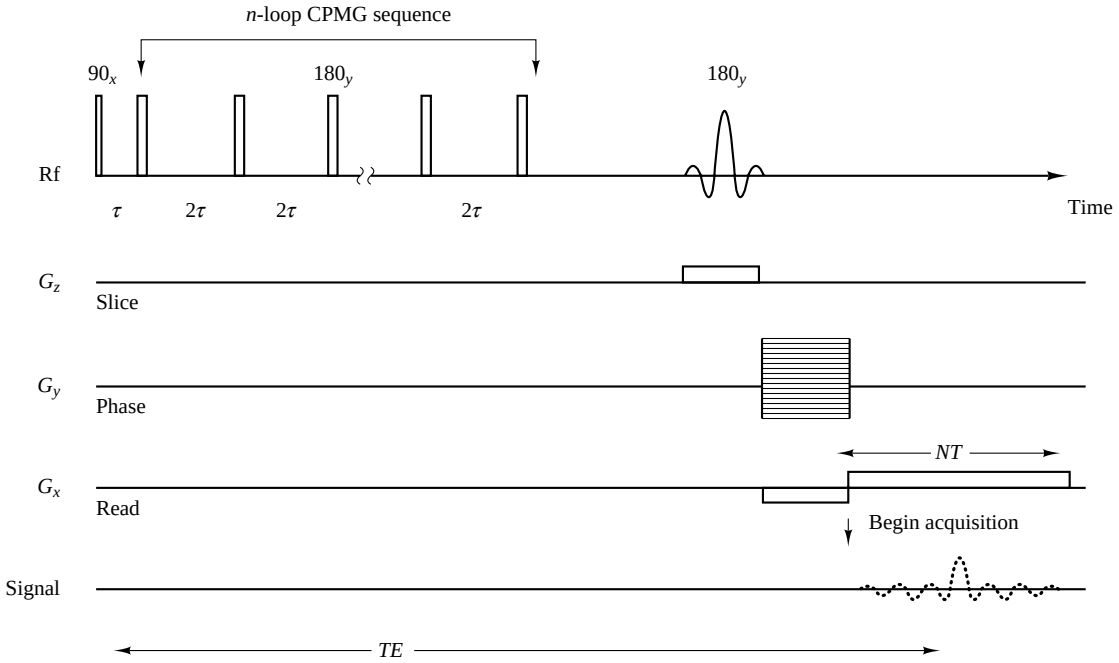

Figure 5 Imaging pulse sequence for which the spatial encoding is preceded by an *n*-loop CPMG rf pulse train, thus imparting T_2 contrast to the image. This sequence avoids diffusive attenuation artifacts in T_2 (due to the read gradient) as *TE* is increased, in contrast with the standard echo sequence of Figure 1. This sequence can also be used to distinguish local (susceptibility-related) gradient contributions to T_2

however be performed using values of the factor $\exp(-\frac{4}{3}\pi^2 k_x^{\max 2} DNT)$ close to unity. Under these conditions, we need only consider the diffusive relaxation effects arising from the local gradients, $\nabla\,[\Delta B_0(r)]$, due to susceptibility inhomogeneity. In a wide class of examples this heterogeneity results in a fluctuation of the local Larmor frequency [with rms frequency range $(\overline{\Delta\omega_0^2})^{\frac{1}{2}}$] as the molecules diffuse. Associated with this effect will be an average fluctuation correlation time, τ_c, corresponding to the time taken for a spin to diffuse over the distance associated with the local field variation. Given these parameters, two regimes, fast exchange and slow exchange, may be defined according to $\overline{\Delta\omega_0^2}\tau_c^2 << 1$ or $\overline{\Delta\omega_0^2}\tau_c^2 >> 1$.

In slow exchange the spin echo attenuation at time $2t$ will be given by[7,28,29] $\exp(-\frac{2}{3}\overline{\Delta\omega_0^2}\tau_c^{-1}t^3)$. Slow exchange also corresponds to inhomogeneous broadening in the spectrum, an effect which is immediately apparent in the different behaviors of spin and gradient echoes. In fast exchange, where hom-

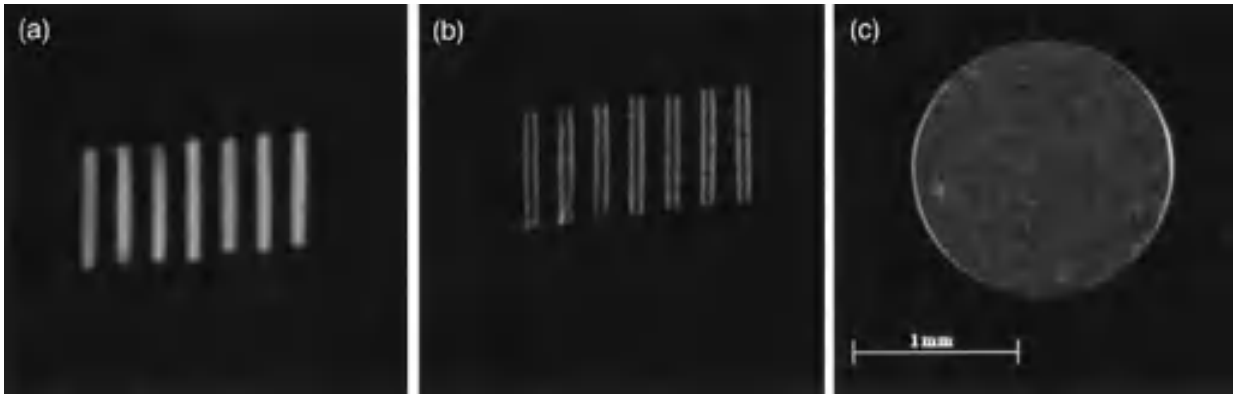

Figure 6 (a) ^{1}H NMR image of a stack of seven pentane-filled microcapillaries obtained with an acqusition bandwidth of 20 kHz. In (a) 128 × 128 pixels are used while in (b) a 256 × 256 array is used. Note the severe diffusive attenuation consequent on resolution increase and the bright edges due to inhibition of Brownian motion near the walls. In (c) a similar effect is apparent in a 256 × 256 image of a 1.6 mm i.d. capillary of water under the conditions $\Delta x_{\text{diff}} = 1.4\Delta x_{\text{pixel}}$. Bright crescent features are apparent near the walls where diffusion along the direction of the read gradient is impeded. Note the appearance of bright features in the water which we ascribe to the influence of dust particles in which local gradients arising from susceptibility inhomogeneity cancel the read gradient, leading to reduced diffusive attenuation. (Reproduced by permission from Callaghan et al.[24])

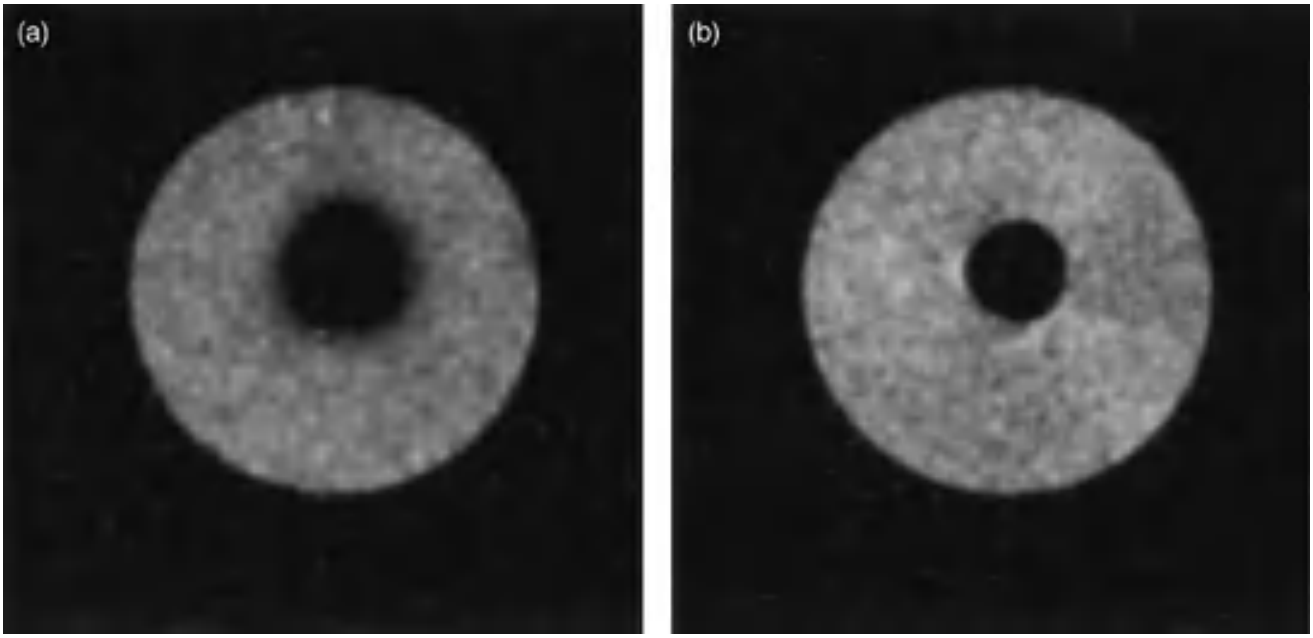

Figure 7 Images of the same water sample used to obtain the images shown in Figure 4 but using a preceding CPMG pulse sequence to maintain transverse magnetization before position-encoding the image. In (a) t = 113 ms and n = 1 whilst in (b) t = 113 ms and n = 10. Note the strong diffusive relaxation in the vicinity of the local susceptibility gradient surrounding the rod in (a) and its removal on reducing the CPMG pulse spacing in (b). (Reproduced by permission from Forde[18])

ogenous broadening applies, the relaxation is given by $\exp(-\overline{\Delta\omega_0^2}\tau_c t)$.

In NMR microscopy, where intrinsic sensitivity limits resolution to the micrometer scale, slow exchange conditions are of predominant interest. Given some correlation length ξ in the local field variation, τ_c is of order ξ^2/D. Typical susceptibility inhomogeneities of a few parts per million lead to spectral fluctuations of a few kilohertz at most, while fluctuations of less than a few hertz will be irrelevant because of the intrinsic NMR linewidth associated with background field inhomogeneity or T_2 relaxation. With this likely range of $(\overline{\Delta\omega_0^2})^{\frac{1}{2}}$, fast exchange conditions will only apply for correlation times below 10 ms, corresponding to correlation lengths below a few micrometers in the case of freely diffusing water molecules. This means that heterogeneity on a scale larger than the pixel dimension will generally be associated with the slow exchange criterion. For example, when susceptibility variations arise from bonding surfaces with radii of curvature much larger than a few micrometers, the broadening is inhomogeneous and slow exchange applies.

The t^3 dependence of the relaxation exponent provides a clear signature for slow exchange. Another indication is provided by the pulse spacing dependence of echo attenuation in a CPMG pulse train (see Figure 5) in which the time t is separated into n periods each of time (t/n) by the 180° rf pulses. By this means t^3 is reduced to $n(t/n)^3$, thus drastically reducing the attenuation. Figure 7 shows the attenuation caused by molecular self-diffusion of water molecules in the vicinity of the glass rod, using the same sample depicted in the images of Figure 4, but with a pulse sequence employing a CPMG pulse train which precedes the imaging gradients. In Figure 7(a) a single spin echo loop is used (n = 1) and strong diffusive attenuation is apparent around the entire perimeter of the rod, while in Figure 7(b), where n = 10, the attenuation is absent. Taking a ratio of these images can provide a nice measure of the local field gradient intensity, $|\boldsymbol{G}|^2$.

5 OVERCOMING SUSCEPTIBILITY AND DIFFUSION

Where susceptibility and diffusive phenomena produce undesirable effects in NMR microscopy, these can be overcome, provided that sufficiently large gradients are available. For example, the use of sufficiently large read gradients in spin warp imaging can remove the distortion caused by local fields. The signal-to-noise loss which results from the need to correspondingly increase the acquisition bandwidth can be avoided[17] by coadding recycled magnetization using a multiple pulse (CPMG) train. Another alternative is to use pure phase encoding since the signal may then be acquired in the absence of a read gradient under optimal bandwidth conditions.[7,21] A further advantage of phase-encoding gradients concerns their avoidance of diffusive attenuation. The signal loss factor[21] for a phase gradient pulse of duration t is given by $\exp(-\frac{4}{3}\pi^2 k^2 Dt)$. While the smoothing effect of such $\boldsymbol{k}$-dependent attenuation leads to blurring of sharp features in the image, the average image amplitude is determined by the height of the signal at $\boldsymbol{k}$ = 0 where no diffusive attenuation occurs, and hence the average image amplitude remains unattenuated. Furthermore the blurring effect may be arbitrarily reduced by using a shorter phase encode time, t. This requires a proportionate increase in phase encoding gradient amplitude, $\boldsymbol{G}$. For resolution close to the sensitivity limit of around 10 μm pixels, and allowing for

the diffusion coefficient of water molecules, a gradient amplitude of at least 1500 mT m^{-1} (150 G cm^{-1}) is implied.

6 CONCLUSION

It is clear that both diamagnetic susceptibility and molecular self-diffusion phenomena are particularly important in NMR microscopy. Furthermore the interplay between these effects, and the applied gradients used to encode for spatial position of the spins, can lead to subtle and intriguing artifacts in the image. While these artifacts can be a nuisance, and can strongly limit the resolution available with a given imaging pulse sequence, they may be avoided altogether if sufficiently large gradients are available, without any consequent loss in image signal-to-noise ratio. It is equally clear that the effects of susceptibility and diffusion are also potentially useful in providing a signature for structure on a distance scale smaller than the pixel size. In particular susceptibility and diffusive phenomena are strongly related to the presence of heterogeneity and interfacial surfaces in the imaged sample, since both induced local fields and the inhibition of diffusive attenuation effects due to collision with surfaces arise from the presence of boundaries.

7 RELATED ARTICLES

Chemical Shift Imaging; Echo-Planar Imaging; Spin Warp Data Acquisition.

8 REFERENCES

1. P. C. Lauterbur, *Nature (London)*, 1973, **242**, 190.
2. P. Mansfield and P. G. Morris, 'NMR Imaging in Biomedicine', Academic Press, New York, 1982.
3. J. B. Aguayo, S. J. Blackband, J. Shoeniger, M. A. Mattingley, and M. Hinterman, *Nature (London)*, 1986, **322**, 190.
4. C. D. Eccles and P. T. Callaghan, *J. Magn. Reson.*, 1986, **68**, 393.
5. P. C. Lauterbur, in 'NMR in Biology and Medicine', eds. S. Chien and C. Ho, Raven Press, New York, 1986.
6. H. Kamei and Y. Katayama, IEEE/Eighth Annual of the Conference Engineering in Medicine and Biology Society, Abstracts, 1986, p. 1159.
7. P. T. Callaghan, 'Principles of NMR Microscopy', Oxford University Press, Oxford, 1991.
8. P. T. Callaghan and C. D. Eccles, *J. Magn. Reson.*, 1987, **71**, 426.
9. P. T. Callaghan and C. D. Eccles, *J. Magn. Reson.*, 1988, **78**, 1.
10. K. M. Ludeke, P. Roschmann, and R. Tischler, *Magn. Reson. Imaging*, 1985, **3**, 329.
11. S. Ogawa, D. W. Tank, R. Menon, J. E. Ellermann, S. G. Kim, H. Merkle, and K. Ugurbil, *Proc. Natl. Acad. Sci. U.S.A.*, 1992, **89**, 5951.
12. J. Frahm, H. Bruhn, K. D. Merboldt, and W. Hänicke, *Magn. Reson. Imaging*, 1992, **2**, 501.
13. J. Frahm, K. D. Merboldt, and W. Hänicke, *Magn. Reson. Med.*, 1993, **29**, 139.
14. R. S. Menon, S. Ogawa, D. W. Tank, and K. Ugurbil, *Magn. Reson. Med.*, 1993, **30**, 380.
15. S. Ogawa, R. S. Menon, D. W. Tank, S.-G. Kim, H. Merkle, J. M. Ellermann, and K. Ugurbil, *Biophys. J.*, 1993, **64**, 803.
16. K. Ugurbil, M. Garwood, J. M. Ellermann, K. Hendrich, R. Hinke, X. Hu, S.-G. Kim, R. S. Menon, H. Merkle, S. Ogawa, and R. Salmi, *Magn. Reson. Q.*, 1993, **9**, 259.
17. P. T. Callaghan, *J. Magn. Reson.*, 1990, **87**, 304.
18. L. C. Forde, M.Sc. thesis, Massey University, New Zealand, 1994.
19. W. A. Edelstein, J. M. S. Hutchison, G. Johnson, and T. W. Redpath, *Phys. Med. Biol.*, 1980, **25**, 751.
20. G. Johnson, J. M. S. Hutchison, T. W. Redpath, and L. M. Eastwood, *J. Magn. Reson.*, 1983, **54**, 374.
21. P. T. Callaghan, L. C. Forde, and C. J. Rofe, *J. Magn. Reson., Ser. B*, 1994, **104**, 34.
22. J. B. Miller and A. N. Garroway, *J. Magn. Reson.*, 1986, **67**, 575.
23. S. Posse and W. P. Aue, *J. Magn. Reson.*, 1990, **88**, 473.
24. P. T. Callaghan, A. Coy, L. C. Forde, and C. J. Rofe, *J. Magn. Reson., Ser. A*, 1993, **101**, 347.
25. H. Y. Carr and E. M. Purcell, *Phys. Rev.*, 1954, **94**, 630.
26. S. Meiboom and D. Gill, *Rev. Sci. Instrum.*, 1959, **29**, 688.
27. D. Barsky, B. Pütz, K. Schulten, J. Schoeniger, E. W. Hsu, and S. Blackband, *Chem. Phys. Lett.*, 1992, **200**, 88.
28. A. Abragam, 'Principles of Nuclear Magnetism', Oxford University Press, London, 1963.
29. P. W. Anderson and P. R. Weiss, *Rev. Mod. Phys.*, 1953, **25**, 269.

Biographical Sketch

Paul T. Callaghan. *b* 1947. B.Sc., 1970, Physics, Victoria University of Wellington, New Zealand, D.Phil., 1974 (radiative detection of NMR in oriented nuclei at milliKelvin temperatures), University of Oxford, UK, D.Sc., 1995, University of Oxford, UK. Lecturer. Senior Lecturer in Physics, 1975–1983, Professor of Physics, 1984–present, Massey University, New Zealand. Approx. 150 publications. Author of book 'Principles of Nuclear Magnetic Resonance Microscopy', published by Oxford University Press, 1991. Research specialties: pulsed gradient spin echo NMR and NMR microscopy, molecular translational dynamics in porous media, in polymers and in other complex fluids.

Complex Radiofrequency Pulses

Peter G. Morris
Nottingham University, UK

1 INTRODUCTION

Selective pulses were first described by Garroway, Grannell and Mansfield in 1974.[1] Their principal application is in MRI and localized MRS, where they are used in conjunction with an applied linear magnetic field gradient to isolate a slice of controlled thickness and orientation.[2–5] They are also used, in the absence of any field gradients, as frequency, rather than spatially selective pulses, typically for suppressing signals from unwanted chemical species, for example, the lipid resonances in a high-field ^{1}H MRI study. Selective pulses are also gaining in importance in conventional high-resolution spectroscopy, where potential applications include solvent suppression without distortion of the frequency response (a highly undesirable feature of the binomial pulse sequences normally used for this purpose), magnetization transfer and reduction of bandwidth in two- and three-dimensional high-resolution experiments.[6] A review dedicated to high-resolution applications is available.[7]

The basic principles of selective pulses and their design are described in the article by Maudsley (see ***Selective Excitation in MRI and MR Spectroscopy***). For reasons that will shortly become apparent, selective pulses are rarely perfect and some of the consequences of their inherent imperfections are discussed in a further article by Hutchison (see ***Spin Warp Method: Artifacts***). This article concentrates on the more advanced design techniques that have led to a series of sophisticated selective pulses, with properties such as self-refocusing, prefocusing or multidimensional excitation.[8]

The guiding principle for the design of selective pulses has been Fourier transform theory. On this basis, in order to achieve a slice with a square profile, the rf carrier should be modulated by the Fourier transform of a square, namely a sinc function. However, the spin system does not respond to rf pulses in a linear way, and the simple Fourier transform approach only yields acceptable results in the case of small flip angles, for which the spin system is approximately linear. How can we do better than this? Ideally, we would like to be able to define the response we need and calculate the rf envelope required to achieve it. For noninteracting spins, this amounts to being able to invert the Bloch equations. Particular solutions and a general theoretical approach to this problem based on inverse scattering theory (IST) are discussed in Section 3 of this article. However, there seems to be no completely general method for their inversion and most improvements in the performance of selective pulses have resulted from numerical optimization schemes. For example, optimal control theory has been applied by Conolly and Macovski[9] and Lent and Kritzer[10] to generate selective inversion pulses. Such gradient descent methods are prone to terminate prematurely in a local minimum. Two optimization schemes, simulated annealing and a method based on a transformation to a switched reference frame known as SPINCALC, neatly avoid this problem of local minima and have enjoyed considerable success in the generation of novel pulses. These schemes, together with two novel approaches that were inspired by the natural processes of genetic evolution and the synaptic model of brain function are described in Section 4. Particular novel pulse designs are described in Sections 5–7.

2 *k*-SPACE ANALYSIS

The description of an MRI experiment in terms of its trajectory through $\boldsymbol{k}$ space has proven to be an excellent basis for comparing different MRI techniques.[11] A similar $\boldsymbol{k}$-space analysis has also been applied by Pauly and colleagues[12] to rf pulse design. M_z is approximated by the equilibrium magnetization M_0, and the solution to the Bloch equations for noninteracting spins, with the magnetization initially in the state $(0,0,M_0)$ is then:

$$M_{xy}(\boldsymbol{r}) = \mathrm{i}\gamma M_0 \int_0^T B_1(t) \exp\left[-\mathrm{i}\gamma \boldsymbol{r} \cdot \int_t^T \boldsymbol{G}(s)\ \mathrm{d}s \right] \mathrm{d}t \qquad (1)$$

where $B_1(t)$ and $\boldsymbol{G}(s)$ are the rf and gradient amplitudes, respectively. This can be rewritten as:

$$M_{xy} = \mathrm{i}\gamma M_0 \int_K p(\boldsymbol{k}) \exp(\mathrm{i}\boldsymbol{r} \cdot \boldsymbol{k})\ \mathrm{d}\boldsymbol{k} \qquad (2)$$

where

$$\boldsymbol{k}(t) = -\gamma \int_t^T \boldsymbol{G}(s)\ \mathrm{d}s \qquad (3)$$

It is clear from this that the transverse magnetization is just the Fourier transform of the weighted $\boldsymbol{k}$-space trajectory. Theoretically, this $\boldsymbol{k}$-space approach to selective pulse design is only valid in the small tip-angle limit, but in practice it works rather well even for π pulses. It also indicates very clearly the need to cover fully the appropriate region of $\boldsymbol{k}$ space. For two-dimensional pulses this leads to the introduction of spiral rather than the inappropriate circular paths for the gradient vector trajectories (see Section 7). Although by no means perfect, this approach at least provides a useful starting approximation for numerical optimization methods.

3 ANALYTICAL SOLUTIONS

Until recently, few analytical solutions to the Bloch equations were known, the only familiar example being the hyperbolic secant pulse,[13,14] which is widely used where accurate selective inversion is required. Interest has grown in methods for obtaining exact general solutions. The Shinnar–Le Roux (SLR) algorithm, originally developed for generating specific m_z responses, without regard for the effects on the transverse magnetization m_{xy},[15] has been developed to produce selective pulses of controlled phase, including self-refocusing pulses.[16] It can be shown that the SLR algorithm is actually a special case of the inverse scattering algorithm.[17] This method,

based on the inverse scattering transform (IST) described by Zakharov and Shabat,[18] was originally developed to determine the potential giving rise to the measured scattering coefficients of a one-dimensional wave function. Several workers have shown that the problem of the inversion of the Bloch equations can be recast in this form.[19–23] The potential is then replaced by the rf pulse envelope and the scattering matrix is simply related to the desired magnetization profile. Rourke and Morris[22] have shown how to obtain general solutions, provided the desired magnetization profile is described by a rational function. They have also developed a 'soliton lattice algorithm', that allows the inversion problem for rational reflection coefficients to be reduced to one for zero reflection coefficient.[23] The solutions to the zero reflection coefficient problem are 'solitons'—pulses that leave the spin system undisturbed. At first sight this does not appear to be particularly helpful. However, whereas a soliton pulse achieves nothing, it turns out that half-solitons are almost perfect refocusing pulses (both $\pi/2$ and π pulses). Furthermore, the algorithm is extremely efficient: the computation time is proportional to the number of time points defining the pulse, and for a typical pulse would usually be much less than 1 central processing unit (CPU) minute. A more general algorithm, using a conventional stereographic projection method, has been described[24] which does not require the magnetization response to be defined as a rational function. Although it is much less efficient than the soliton lattice algorithm, it is conceptually simple and easy to implement.

4 OPTIMIZATION METHODS

4.1 Simulated Annealing

Conventional computer optimization schemes are based on gradient descent methods in which a single error function (usually the mean square difference between the trial and target response) is minimized. They are prone to entrapment, and the multidimensional parameter space in which the pulse response is normally optimized does appear to be riddled with local minima. Clearly, this is one reason for the diversity of optimized pulse shapes in the literature. Simulated annealing[25,26] is a widely applicable optimization technique that is effective in reaching the 'global minimum'. Its use was first reported in the optimization of integrated circuit layouts, but its name comes from the analogy with the annealing of a metal. For annealing to be effective, the cooling must be suitably slow—if molten silicon dioxide is cooled slowly, it forms a crystalline structure, whereas, if it is cooled rapidly, it forms glass (a disordered ordered state of higher energy).

In simulated annealing, the error or cost function E is analogous to the energy of the system. The optimization proceeds by varying a degree of freedom by a small, random amount and recalculating the cost. A change resulting in a reduced cost is always accepted (as it is in conventional optimization methods). However, some changes resulting in increased cost are also accepted, with a probability that is determined by $\exp(-\Delta E/kT)$, where the parameter T can be thought of as the temperature of the system. Its choice is crucial to the success of the method. (Acceptance of a small detrimental change to the cost function is analogous to the thermal energy which permits a structure to 'jump out' of a local energy minimum.) The cycle of random changes to each degree of freedom is repeated a number of times at each temperature step. As the system cools, the range of fluctuations becomes progressively more restricted. A typical simulated annealing procedure is illustrated in Figure 1, in which 20 changes are made to each degree of freedom at each temperature, and the full simulated annealing cycle is repeated three times. The cost function decreases monotonically in the first two cycles of optimization, but a small increase, representing escape from a local minimum, can be discerned near the start of the third cycle.

Although simulated annealing is conceptually simple and straightforward to implement, it can be costly in computation time, taking several hours or days to run, even on a mainframe computer. Also, its 'random' nature means that the same optimization, run a second time, is not guaranteed to yield the same result—unless a true global minimum is found.[27] Simulated annealing has proved successful in the ab initio design of a wide range of selective pulses. In particular, Ray Freeman's group in Cambridge have generated a family of self-refocusing or BURP (band-selective uniform response prephase) pulses.[28–30] Prefocused pulses, obtained using simulated annealing in both time[31] and Fourier domains,[6] have also been

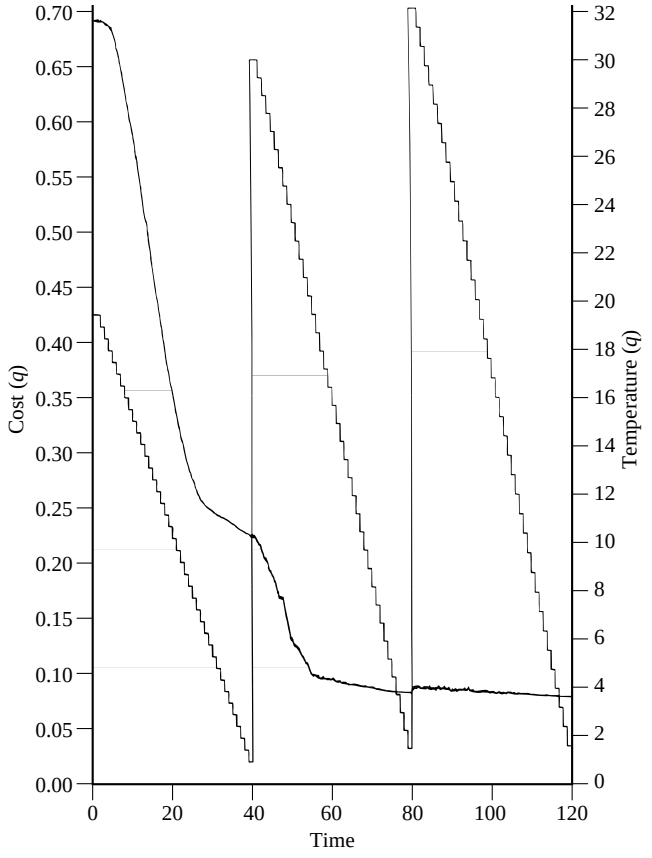

Figure 1 The cost function and temperature during three cycles of optimization by simulated annealing of a prefocused $\pi/2$ selective pulse. (Reproduced by permission of Wiley from P. G. Morris, D. J. O. McIntyre, D. E. Rourke, and J. T. Nago, *NMR Biomed.*, 1989, **2**, 257)

described. Simulated annealing is also useful in refining selective pulses derived by other means. An example of this is their use in the refinement of early two-dimensional selective pulses, such as the sombrero, egg carton and stalagmite pulses of Bottomley and Hardy.[32,33] Although virtually unusable as designed, the performance of these pulses was greatly improved by optimizing rf and gradient waveforms using simulated annealing.[27,34] As for the prefocused pulse, optimization of the Fourier coefficients of the rf and gradient waveforms resulted in smoother and more practical pulses.

4.2 Neural Networks

Neural networks are becoming increasingly important in a wide range of pattern recognition applications. In high-resolution NMR, they have been shown to be effective in analysing spectra from complex mixtures and, to a lesser degree, in classifying spectra from tissue or blood samples, for the purpose of medical diagnosis. Spectroscopists in the cancer field are most active in this area, and multicenter trials are being set up at the time of writing.

The idea of a neural network is to mimic the human brain.[35] The net is constructed in several layers (typically three for selective pulse design). Input, in the form of a desired excitation profile, is presented at the first layer, and the output, in the form of selective pulse amplitudes or Fourier coefficients, is taken from the last layer. The intermediate layers receive signals from the 'neurons' in the preceding layer, sum them with appropriate synaptic weighting, and pass the resultant signal on to the next layer. Before the neural net can be used for pulse design, it must first be trained. During the training process, excitation profiles (calculated from the Bloch equations) are presented to the net, and the synaptic weights are adjusted so that the output pulse parameters match those of the input pulse. A wide range of different types of pulse is needed if the network is to be adequately trained. This process is very time consuming, but once complete, new pulse shapes can be very rapidly determined, on presentation of the desired excitation profile at the input. Neural networks are thus attractive in situations where it is necessary to calculate selective pulses online. The practicality of the method has been demonstrated through the design of a pulse to excite antiphase magnetization ($2I_xS_x$) over a range of J values.[36]

4.3 Genetic Methods

In genetic methods of selective pulse design,[37] the parameters defining the selective pulse are considered as genes. Random changes or mutations in these genes lead to a series of trial solutions, one of which is selected by the spectroscopist on the basis of some perceived desirable characteristic to be the parent of the next generation of pulses. The design does not proceed as a smooth passage through parameter space, but rather as a series of branches in 'evolution space'. Although not widely applied to selective pulse design, genetic methods have been used to design a prefocused selective pulse[38] and a broadband excitation pulse with extremely uniform amplitude and phase characteristics.[39] Clearly one would normally set out with a particular objective in mind. However, the random nature of the mutations can throw up unforeseen novel possibilities; the broadband excitation pulse is a case in point.

4.4 SPINCALC

SPINCALC, a numerical optimization scheme introduced by Ngo and Morris[40–42] in 1986, uses a switched rotating frame of reference to linearize effectively the Bloch equations and hence permit their inversion. In the absence of relaxation, the Bloch equation describing the magnetization $\boldsymbol{M}(t,q)$ of a single isochromat, labelled q, can be written as:

$$\frac{\mathrm{d}}{\mathrm{d}t}\boldsymbol{M}(t,q) = \boldsymbol{\omega}(t,q) \times \boldsymbol{M}(t,q) \tag{4}$$

where the instantaneous angular velocity $\boldsymbol{\omega}(t,q)$ is given by $-\gamma\boldsymbol{B}(t,q)$. Equation (4) can be cast in matrix form:

$$\boldsymbol{M}(t+\delta t,q) = \boldsymbol{R}[\boldsymbol{\omega}(t,q)\,\delta t]\boldsymbol{M}(t,q) \tag{5}$$

which can be 'integrated' to give:

$$\boldsymbol{M}(T,q) = \prod_0^T \boldsymbol{R}[\boldsymbol{\omega}(t,q)\,\delta t]\boldsymbol{M}(0,q) = \boldsymbol{R}_{\mathrm{tot}}(q)\boldsymbol{M}(0,q) \tag{6}$$

where the total rotation matrix $\boldsymbol{R}_{\mathrm{tot}}(q)$ is given by the product $\boldsymbol{R}_n(q)\cdots\boldsymbol{R}_2(q)\boldsymbol{R}_1(q)$, corresponding to the n discrete intervals of the pulse. The optimization proceeds by finding, for each q, a new rotation matrix that better approximates the target response:

$$\boldsymbol{R}_{\mathrm{tot,new}}(q) = \delta\boldsymbol{R}_n(q)\boldsymbol{R}_n(q)\cdots\delta\boldsymbol{R}_1(q)\boldsymbol{R}_1(q) \tag{7}$$

The problem with equation (4) is a familiar one in NMR theory—the rotation matrices do not, in general, commute. The solution is similar to that adopted in the theoretical description of multipulse line-narrowing experiments, namely a transformation to a switched frame of reference:

$$\delta\boldsymbol{R}'_m(q) = \boldsymbol{U}_m(q)\delta\boldsymbol{R}_m(q)\boldsymbol{U}_m(q)^{-1} \tag{8}$$

where $\boldsymbol{U}_m(q) = \boldsymbol{R}_n(q)\ \boldsymbol{R}_{n-1}(q)\cdots\boldsymbol{R}_{m+1}(q)$ for $m = n-1$, $n-2,\ldots,0$, and $\boldsymbol{U}_m(q) = 1$ for $m = n$.

In this representation

$$\boldsymbol{R}_{\mathrm{tot,new}}(q) = \delta\boldsymbol{R}_{\mathrm{tot}}(q)\boldsymbol{R}_{\mathrm{tot}}(q) \tag{9}$$

where $\delta\boldsymbol{R}_{\mathrm{tot}}(q) = \delta\boldsymbol{R}_n'(q)\cdots\delta\boldsymbol{R}_1'(q)$. For small changes, the product of these matrices can be replaced with a sum of small vectors:

$$\delta\boldsymbol{R}_{\mathrm{tot}}(q) = \sum_m \delta\boldsymbol{R}'_m(q) \tag{10}$$

Values of $\delta\boldsymbol{R}_m'(q)$ are determined for each degree of freedom (e.g. rf amplitude and phase) and a least-squares fitting procedure is used to approximate the target response. The optimization does not usually proceed directly to the final response in a single step; the corrections must be consistent with the linearity requirements and so a few intermediate targets are usually set up.

SPINCALC is extremely versatile; it can be used to design virtually any type of selective pulse, if necessary in the presence of known imperfections in, for example, the magnetic field homogeneity. Additional constraints can also be imposed at the level of the least-squares fitting, to minimise peak or mean rf power, for example.

5 ADIABATIC SELECTIVE PULSES

The hyperbolic secant is a near-perfect inversion pulse.[13,14] It is also an adiabatic pulse; that is, it is insensitive to variations in $\boldsymbol{B}_1$ amplitude, a feature which has been crucial to the success of the ISIS[43] technique for volume selection in MRS. It is not a refocusing ('pancake flip') pulse and so does not solve the problem of providing a good π pulse for multislice spin–echo imaging experiments. Refocusing does occur after each pair of hyperbolic secant pulses. However, in a multiple echo train, significant error accumulates. This arises because the hyperbolic secant is an analytic function of infinite extent. In practice it must be curtailed, and the magnetization, instead of being perfectly spin locked, precesses around the B_1 direction.

The SPINCALC technique has been used to generate a complex adiabatic pulse of finite duration that does not give rise to cumulative errors in a multiple echo sequence[44] such as might be used for imaging in a highly inhomogeneous static field. The rf magnitudes of the optimized and the hyperbolic secant pulse are compared in Figure 2(a), and the complex

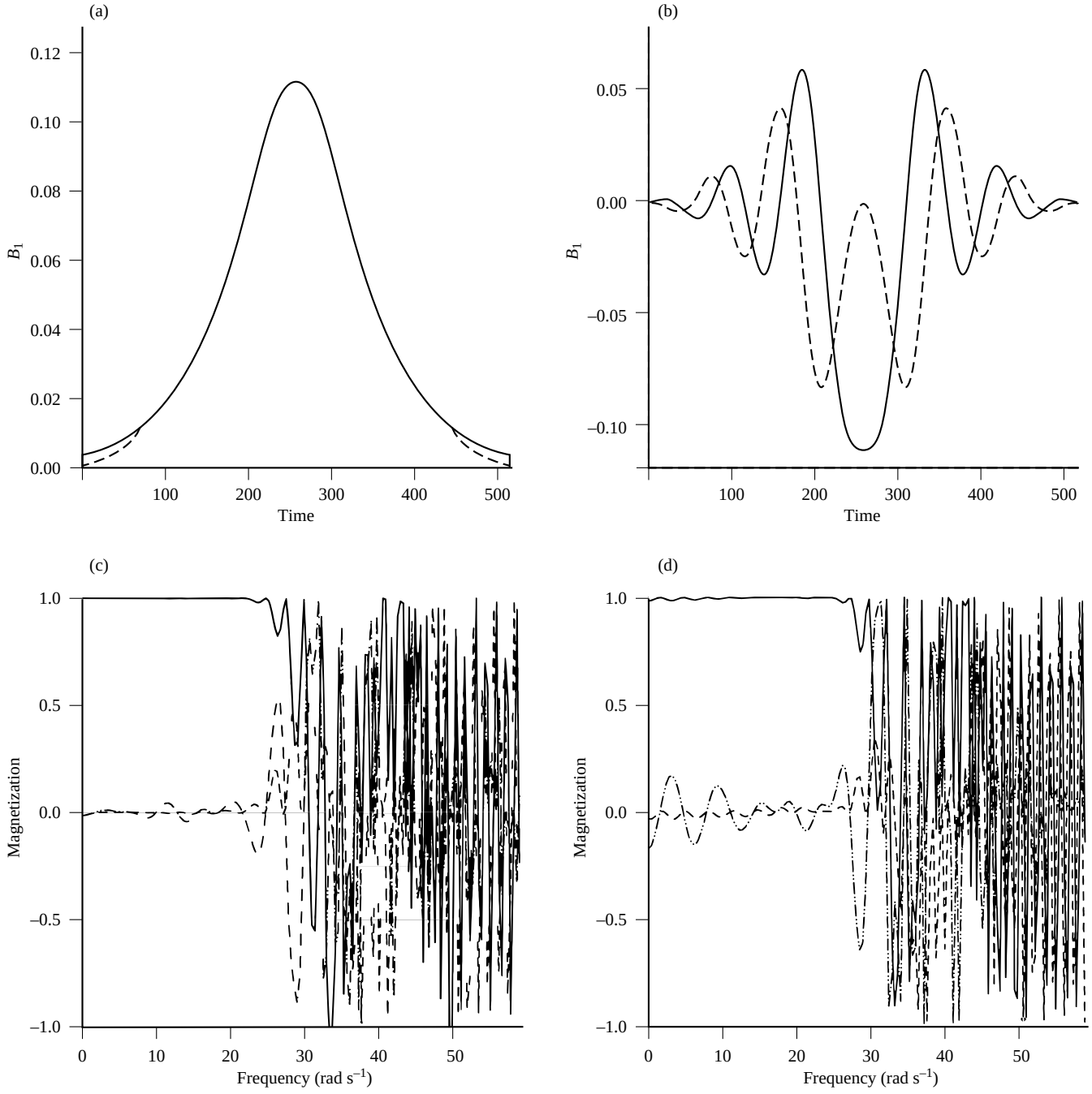

Figure 2 Adiabatic refocusing π pulse. (a) Magnitudes of optimized and hyperbolic secant (——) pulses. (b) Complex amplitudes of optimized pulse: (——) $B_{1,x}$; (– – –) $B_{1,y}$. Comparison between the responses to optimized (c) and hyperbolic secant (d) pulses after a train of four phase-cycled (*xyxy*) π pulses, with the magnetization originally along the x direction: (——) M_x; (– – –) M_y; (– · · –) M_z

amplitudes (B_{1x}, B_{1y}) of the optimized pulse are shown in Figure 2(b). The responses after four consecutive refocusing pulses are compared for optimized and hyperbolic secant pulses in Figures 2(c) and (d), respectively.

6 SELF-REFOCUSING PULSES

Slice-selective $\pi/2$ pulses, such as a truncated sinc pulse, require a negative gradient lobe to refocus the linear phase shift introduced during the course of the rf pulse. This process is time-consuming and can be a limitation when very short echo times are required—for example, in the imaging of lung tissues, or for chemical shift imaging of short T_2 species, such as the phosphate groups of adenosine triphosphate (ATP). The SPINCALC optimization procedure has been used to generate a number of phase-compensated pulses (self-refocused or prefocused). Some of these used a selective $\pi/2$ selective π pair as an initial guess, and the optimized solution retains many of the features of its progenitor,[41] whereas others were derived ab initio.[42] As discussed in Section 3, the soliton lattice algorithm[43] is particularly efficient at producing refocusing pulses. An example, with an essentially perfect response, is illustrated in Figure 3.

7 MULTIDIMENSIONAL PULSES

Multidimensional pulses that localize in more than one dimension have many potential applications in MRI and MRS. For example, two-dimensional pulses can be used to limit the lateral spread of excitation from a surface coil, and a three-dimensional pulse would have obvious attractions for volume-selective spectroscopy.

k-space analysis indicates quite clearly that a uniform coverage of (multidimensional) ***k*** space is required. If the pulse is also to be inherently phase compensated then the traversal of ***k*** space must terminate at the origin. In two dimensions, the gradient trajectory that most readily meets these requirements is a (decreasing) spiral. Many choices are possible for the rf envelope. Pauly et al.[12] chose a circularly symmetric Gaussian excitation, whereas Hardy and Cline[45] have developed a variety of two-dimensional pulses which give radially symmetric excitation.

Multidimensional pulses designed on the basis of ***k***-space analysis represent a great improvement over previous designs. However, they still display a variety of undesirable artifacts. Hardy et al.[46] have extended ***k***-space analysis to eliminate effects due to nonuniform coverage of ***k*** space, but effects arising from the low tip angle approximation inherent in the analysis remain. These can be eliminated by numerical optimization methods, as illustrated in Figure 4, where SPINCALC has been used to optimize a radially symmetric two-dimensional π pulse.[47]

There are practical limitations to the use of multidimensional pulses on standard whole body imaging systems. In particular, such systems impose severe constraints on gradient amplitudes and slew rates.[48] One way around this difficulty is to split the coverage of *k*-space over many pulses. In one implementation, the normal spiral gradient trajectory is replaced by spiral arms resembling a pinwheel. Although potentially

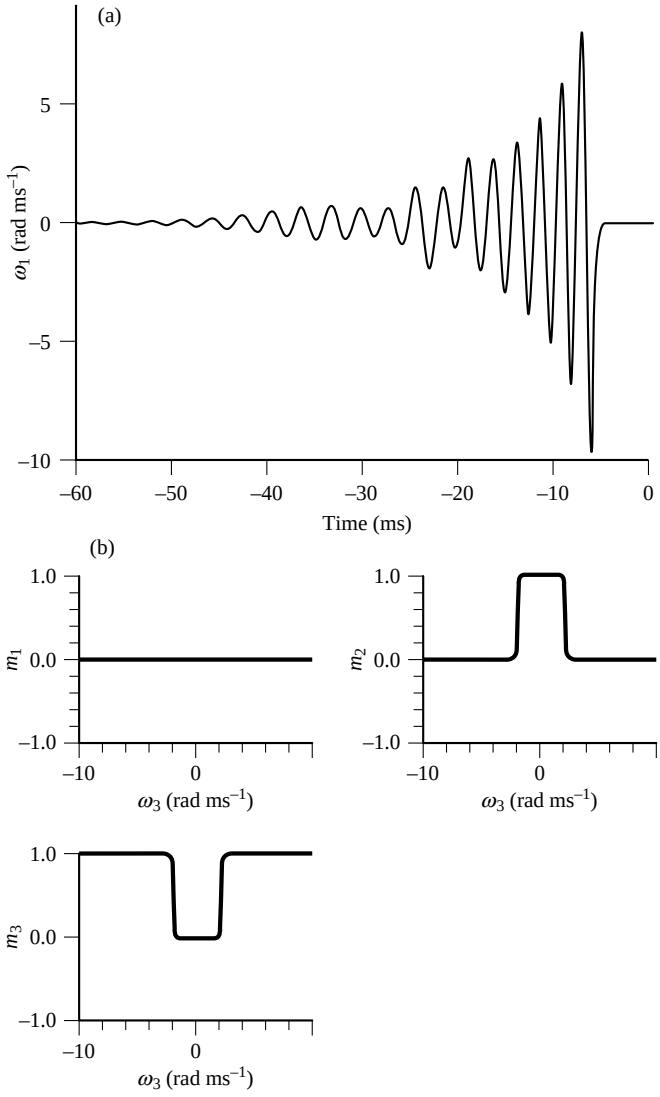

Figure 3 (a) A half-soliton real self-refocusing $\pi/2$ pulse. (b) Magnetization responses to the pulse shown in (a). (Reproduced by permission of the American Physical Society from D.E. Rourke and P.G. Morris, *Phys. Rev. A*, 1992, **46**, 3631)

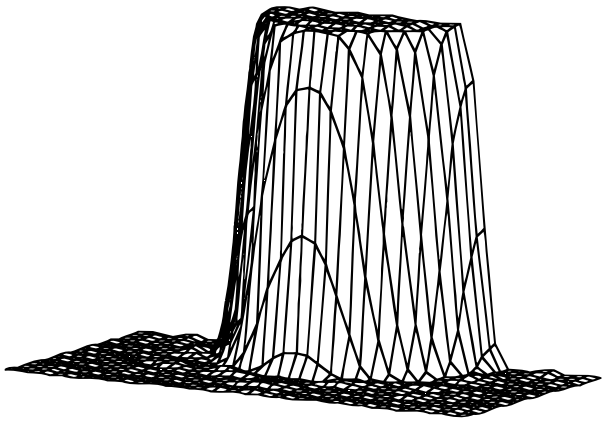

Figure 4 The M_z response (shown inverted) to a two-dimensional π pulse optimized using SPINCALC

prone to motional artifacts, such pinwheel pulses have been used successfully to record localized ^{31}P spectra from different depths within the cardiac wall.[49]

8 RELATED ARTICLES

Selective Excitation in MRI and MR Spectroscopy; Selective Excitation Methods: Artifacts.

9 REFERENCES

1. A. N. Garroway, P. K. Grannell, and P. Mansfield, *J. Phys. C*, 1974, **7**, L457.
2. P. Mansfield and P. G. Morris, 'NMR Imaging in Biomedicine', Academic, New York, 1982.
3. P. G. Morris, 'NMR Imaging in Medicine and Biology', Oxford University Press, Oxford, 1986.
4. W. P. Aue, *Rev. Magn. Reson. Med.*, 1986, **1**, 21.
5. P. G. Morris, *Ann. Rep. NMR Spectrosc.*, 1988, **20**, 1.
6. P. G. Morris, D. J. O. McIntyre, D. E. Rourke, and J. T. Ngo, *NMR Biomed.*, 1989, **2**, 257.
7. R. Freeman, *Chem. Rev.*, 1991, **91**, 1397.
8. P. G. Morris, in 'In-Vivo Magnetic Resonance Spectroscopy. I: Probeheads and Radiofrequency Pulses, Spectrum Analysis', Springer, Berlin, 1992, pp. 149–170.
9. S. Conolly and A. Macovski, *Proc. 4th Ann. Mtg. Soc. Magn. Reson. Med., London*, 1985, p. 958.
10. A. H. Lent and M. R. Kritzer, *Proc. 4th Ann. Mtg. Soc. Magn. Reson. Med., London*, 1985, p. 1015.
11. S. Ljunggren, *J. Magn. Reson.*, 1983, **54**, 338.
12. J. Pauly, D. Nishimura, and A. Macovski, *J. Magn. Reson.*, 1989, **81**, 43.
13. J. Baum, R. Tycko, and A. Pines, *J. Chem. Phys.*, 1983, **79**, 46.
14. M. S. Silver, R. I. Joseph, C.-N. Chen, V. J. Sank, and D. I. Hoult, *Nature*, 1984, **310**, 681.
15. M. Shinnar, S. M. Eleff, V. H. Subramanian, and J. S. Leigh, *Magn. Reson. Med.*, 1989, **12**, 74.
16. J. Pauly, P. Le Roux, D. Nishimura, and A. Macovski, *IEEE Trans. Med. Imag.*, 1991, **10**, 53.
17. M. H. Buonocore, *Magn. Reson. Med.*, 1993, **29**, 470.
18. V. E. Zakharov and A. B. Shabat, *Sov. Phys. JETP*, 1972, **34**, 62.
19. A. Hasenfeld, *J. Magn. Reson.*, 1987, **72**, 509.
20. W. S. Price and P. W. Ruchel, *J. Magn. Reson.*, 1991, **94**, 133.
21. J. W. Carlson, *J. Magn. Reson.*, 1992, **97**, 65.
22. D. E. Rourke and P. G. Morris, *J. Magn. Reson.*, 1992, **99**, 118.
23. D. E. Rourke and P. G. Morris, *Phys. Rev. A*, 1992, **46**, 3631.
24. D. E. Rourke, M. J. W. Prior, P. G. Morris, and J. A. B. Lohman, *J. Magn. Reson. A*, 1994, **107**, 203.
25. S. Kirkpatrick, C. D. Gelatt, and M. P. Vecchi, *Science*, 1983, **220**, 671.
26. N. Metropolis, A. W. Rosenbluth, M. N. Rosenbluth, A. H. Teller, and E. Teller, *J. Chem. Phys.*, 1953, **21**, 1087.
27. C. J. Hardy, P. A. Bottomley, M. O'Donnell, and P. Roemer, *J. Magn. Reson.*, 1988, **77**, 233.
28. H. Geen and R. Freeman, *J. Magn. Reson.*, 1991, **93**, 93.
29. H. Geen, S. Wimperis, and R. Freeman, *J. Magn. Reson.*, 1989, **85**, 620.
30. H. Geen and R. Freeman, *J. Magn. Reson.*, 1990, **87**, 415.
31. D. E. Rourke, D. J. O. McIntyre, and P. G. Morris, *Proc. 8th Ann. Mtg. Soc. Magn. Reson. Med., Amsterdam*, 1989, p. 863.
32. P. A. Bottomley and C. J. Hardy, *J. Magn. Reson.*, 1987, **74**, 550.
33. P. A. Bottomley and C. J. Hardy, *J. Appl. Phys.*, 1987, **62**, 4284.
34. C. J. Hardy, P. A. Bottomley, and P. Roemer, *J. Appl. Phys.*, 1988, **63**, 4741.
35. F. Rosenblatt, in 'Principles of Neurodynamics: Perceptrons and the Theory of Brain Mechanisms', Spartan, Washington, DC, 1961.
36. J. D. Gezelter and R. Freeman, *J. Magn. Reson.*, 1990, **90**, 397.
37. F. Loaiza, K. T. Lim, W. S. Warren, M. Silver, H. Egloff, B. Keifer, and G. Laub, *Health Care Instrum.*, 1986, **1**, 188.
38. X. Wu, P. Xu, and R. Freeman, *Magn. Reson. Med.*, 1991, **20**, 165.
39. R. Freeman and X. Wu, *J. Magn. Reson.*, 1987, **75**, 184.
40. J. T. Ngo and P. G. Morris, *Biochem. Soc. Trans.*, 1986, **14**, 1271.
41. J. T. Ngo and P. G. Morris, *Magn. Reson. Med.*, 1987, **5**, 217.
42. J. T. Ngo and P. G. Morris, *TAMU Newsl.*, 1986, **337**, 38.
43. R. J. Ordidge, A. Connelly, and J. A. B. Lohman, *J. Magn. Reson.*, 1986, **66**, 283.
44. D. J. O. McIntyre, personal communication, December 1993.
45. C. J Hardy and H. E. Cline, *J. Magn. Reson.*, 1989, **82**, 647.
46. C. J. Hardy, H. E. Cline, and P. A. Bottomley, *J. Magn. Reson.*, 1990, **87**, 639.
47. P. G. Morris, D. J. O. McIntyre, D. E. Rourke, and J. T. Ngo, *Magn. Reson. Med.*, 1989, **11**, 167.
48. C. J. Hardy and H. E. Cline, *J. Appl. Phys.*, 1989, **66**, 1513.
49. C. J. Hardy and P. A. Bottomley, *Magn. Reson. Med.*, 1991, **17**, 315.

Biographical Sketch

P. G. Morris. *b* 1953. B.A., 1974, M.A., 1978, Cambridge; Ph.D., 1978, Nottingham. Introduced to NMR by Sir Peter Mansfield. Scientific staff, MRC Biomedical NMR Centre, London, 1980–85; Lecturer in Biochemistry, Cambridge, 1985–90; Chair of Physics, Nottingham, 1990–present. Over 150 publications in NMR, including, 'NMR Imaging in Medicine and Biology' (Oxford University Press, 1986), and, with P. Mansfield, 'NMR Imaging in Biomedicine' (Academic Press, 1982). Research interests include the development of techniques for MRI/MRS and their application to biological systems, especially the brain.

Echo-Planar Imaging

Peter Mansfield
University of Nottingham, UK

1 INTRODUCTION

Echo-planar imaging (EPI) is an extremely rapid snap-shot technique which can capture the complete data set necessary to form an image in times ranging from 20 to 150 ms. The technique was originally proposed in 1977 in a paper 'Multiplanar Image Formation using NMR Spin Echoes'.[1] In fact the multiplanar part of the technique as originally proposed has never been properly exploited, although there is now a related technique called 'echo volumar imaging' (EVI) which can, in principle, capture a volume data set in a similar time range as that indicated above.[2] The name EPI has evolved from the first publication and is really a shortened version of 'spin echo planar imaging.' These days, of course, people make the distinction between spin echoes and gradient echoes, but in the original version of EPI the possibility of using gradient reversals to form spin echoes and the use of 180° rf pulses to form spin echoes were both mentioned. Of course the use of rf pulses, especially at high frequencies, is a problem in medical imaging applications where rf deposition in the patient has to be limited for safety reasons.

The object of EPI then, quoting from the original paper,[1] 'is to produce, at high speed, cross-sectional NMR images corresponding to the mobile spin density variations throughout a living biological specimen. This speed is imperative if NMR is to be successfully used in medical imaging'.

2 EPI TECHNIQUE

The EPI technique is a Fourier imaging method that arose out of earlier work by Mansfield and Grannell in 1973 which was concerned with the imaging of discretely distributed systems.[3] In that work NMR imaging was regarded as a special case of plane wave scattering of a pseudowave giving rise to a diffraction pattern in k-space. It was realized very early on that because of the properties of FTs, discreteness in real space and discreteness in k-space were effectively equivalent, and therefore imposing a temporal discreteness on the spin system effectively converted a continuous distribution in real space into a discontinuous distribution. Thus by exploiting these properties of k-space it was possible to encode a complete imaging plane, or indeed a whole volume of material, in an extremely short time by creating a set of suitably phase-encoded spin echoes.

3 BARRIERS TO PROGRESS—AN HISTORICAL NOTE

In the 1970s, the barriers to progress in EPI were considered to be the sheer size of gradient requirements, the speed at which they were modulated, rapid digitization in data acquisition, and the physiological effect of fast rapidly switched gradients on the patient. Any one of these points was sufficient at that time to deter other researchers from entering the field. The combination of all the points was lethal and effectively killed the idea at birth. It was really only the determined effort of the Nottingham group to implement the technique, steadily demonstrating its applicability from initial applications in small objects and small image array sizes through to applications in pediatric imaging, again with small image array sizes, through to adult imaging that showed the way for others to try out the ideas for themselves.

4 SPECTROSCOPIC EXPLANATION OF EPI

Although we were fully aware of the k-space description of imaging[3] (introducing the concept into NMR imaging in 1973), because of our concern that our ideas should be completely clear to our co-workers we chose to describe EPI in spectroscopic language so that the NMR community at large were immediately able to understand the concepts. Thus in 1984, for example,[4] an essentially spectroscopic explanation of EPI went as follows: In EPI, the nuclear signal following slice selection with a tailored rf pulse in the field gradient G_z is encoded in frequency space by applying a trapezoidally modulated gradient G_y with period $4\tau_y$, together with a steady read gradient G_x. The timing diagram for an early EPI experiment is shown in Figure 1. The act of periodically reversing the gradient G_y is to form a series of spin echoes. That is to say, the signal response is turned into a periodic function of time with spin echos formed in both positive and negative gradient excursions. Sampling of two echo sequences with appropriate starting phases of G_y yields, after editing and splicing, a new periodic echo function with period $2\tau_y$ for echoes formed in either a wholly positive or wholly negative gradient. This generated function is Fourier-transformed to yield a discrete, periodic function of frequency (or space through the linear dependence of displacement and frequency shift caused by the gradient). The stick spectrum produced represents an enfilade view of the spin magnetization contained in the selected slice of material (Figure 2). Although the slice has a continuous spin distribution, the stick spectrum obtained makes the slice appear like a physically discrete structure. Spin magnetization is bunched into the sticks thus creating apparent gaps in the spin projection.

In order to turn the view from enfilade to oblique, the disk must be rotated slightly, so as not to cause overlap, thereby obscuring the end of each row. This is achieved in effect by applying the steady gradient G_x (see Figure 1). The sticks in the spectrum broaden to yield the oblique view (as in Figure 2). Each broadened stick represents one line in the image. The data are correctly ordered and presented to an image display device. The signal amplitude is represented as image intensity on a linear gray scale. Low signals are dark and high signals bright. The data sampling time is 32 ms. Further data manipulations and display screen update take an additional 200 ms and restrict the repetition rate to about 4 frames per second in the immediate viewing mode. Without immediate viewing, the repetition rate may be increased to 10 frames per second. Sub-

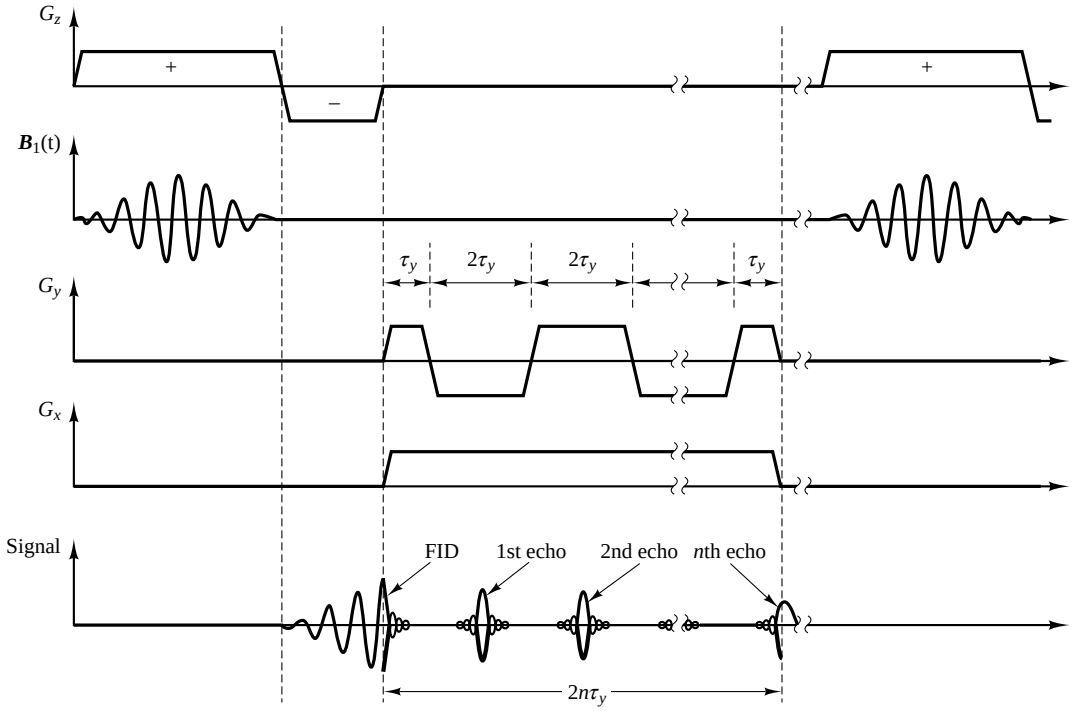

Figure 1 Pulse sequence timing diagram for EPI. Initial slice selection is performed using a tailored rf pulse $\boldsymbol{B}_1$ (T) in a magnetic field gradient $+G_z$. For better slice definition, focused selection is used in which B_z is reversed to form the signal growth. At the signal maximum, G_z is switched off and G_x and $\pm G_y$ are switched on to create a series of spin echoes following the initial FID. The experiment is repeated with the opposite starting phase of G_y after a short delay. (Reproduced by permission of Churchill Livingstone from Mansfield[4])

sequent viewing may be performed in a visual playback mode directly following a recorded sequence of shots.

At that time the EPI probe access was 22 cm with an object field of 19.2 cm. The imaging field was represented by a relatively crude 32 × 32 pixel array and the in-plane resolution was 6 mm with a selective slice thickness of 8 mm.

5 *K*-SPACE DESCRIPTION OF EPI

As time has passed, a number of minor variants of the EPI technique have been introduced to overcome magnet inhomogeneity effects. In the modern language of *k*-space scanning, the original EPI technique was essentially a half Fourier method. The modulus blipped EPI sequence[5] is a full *k*-plane imaging method and, because it is a modulus technique, removes all orders of phase error in the image which may arise from local inhomogeneity effects in the specimen. In the modern vernacular[6] EPI is described as follows. 'In EPI a different *k*-space sampling strategy is used. After a single spin excitation, the whole of *k*-space is sampled most efficiently in a single, continuous trajectory (Figure 3) by generating all the echoes as required, up to 256 in a single FID $S(t)$ (see Figure 4). Since the decay of $S(t)$ is governed by the transverse relaxation time T_2 ($T_{2,\text{brain}}$ = 80 ms and $T_{2,\text{muscle}}$ = 50 ms) and field inhomogeneity (in the case of gradient echoes), data acquisition needs to be completed within 50–100 ms. When this can be achieved, more complete use is made of the available spin magnetization than with conventional MRI, and the signal-to-noise (S/N) ratio per unit time is consequently much greater,[7] although the image is more vulnerable to distortion due to field inhomogeneity'

The echoes can either be formed as gradient echoes, as in true EPI sequences (MBEST,[8,9] BEST,[10] FLEET,[11] InstaScan,[12] spiral and square spiral EPI[13]) or as spin echoes (RARE[14]). The EPI pulse sequence timing diagram (Figure 4) illustrates the typical, rapidly switched, frequency-encoding gradient G_x that generates the gradient echo train $S(t)$. The rise and fall times of the gradient are of the order of 100 μs, rendering the gradient waveforms trapezoidal. The fast rise and fall times of such waveforms require low-inductance coils—100 μH in one system we have built—with low efficiency (0.04 mT m^{-1} A^{-1}), and thus put severe demands on the gradient drivers, which in that system supply up to 1000 A at 320 V. Alternatively, the waveform may be sinusoidal,[12] which requires more complicated data sampling or image processing, but allows the gradient coils to be driven as part of a resonant LC tank circuit, with considerably reduced power requirements. Phase encoding, in which the *k*-lines are spaced out along k_y (Figure 3), is established by pulses or 'blips' of the phase-encoding gradient G_y while the read gradient is being switched. Where high spatial resolutions are required, which are beyond the scope of the available gradients in the time available before the signal-to-noise ratio decays too far, or where images cannot be obtained which are of the desired quality, interleaved acquisitions are sometimes used. In these only sub-sets of *k*-space are recovered at each data acquisition, with the complete data set being assembled after several are completed. The off-setting of data in *k*-space which is needed

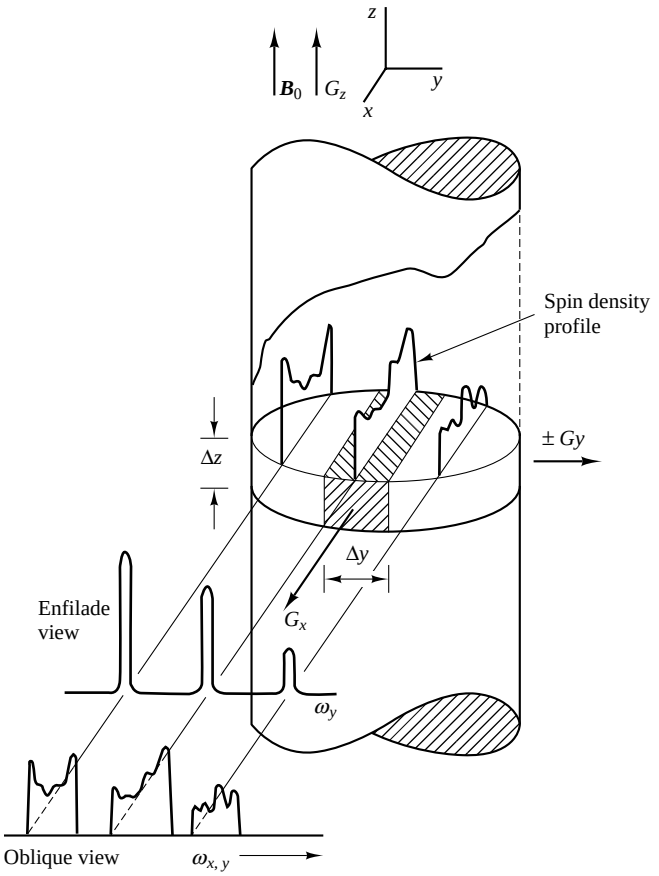

Figure 2 A sketch summarizing the main features of the EPI method. The initial selected slice of thickness Δz is produced with G_z along the direction of the static magnetic field $\boldsymbol{B}_0$, which also coincides with the patient axis. Modulation of G_y produces a discrete spin density profile, or stick spectrum, which corresponds to the enfilade view. Each stick comprises the signal from the shaded strip of width Δy and thickness Δz. Application of G_x broadens the sticks to give an oblique view of the spin density profile as seen between rows. (Reproduced by permission of Churchill Livingstone from Mansfield[4])

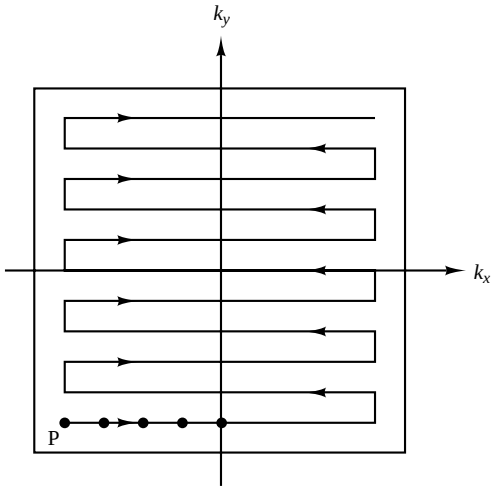

Figure 3 In EPI, *k*-space is sampled in a single, continuous *k*-space trajectory within a fraction of a second. The diagram shows the starting point P. The black dots on the trajectory represent the first few points of a regular sampling pattern

is ensured by the use of different amplitude pre-pulses of the 'blip' gradient, and by making the 'blip' pulses such that they step the individual scans by enough lines of the final form of *k*-space for the interleaved scans to fill in the gaps in an ordered manner. Three-dimensional data acquisition with EPI is possible in various ways.[15]

The typical modular structure of EPI sequences is also shown in Figure 4. A spin-preparation module, which can be used to encode a variety of magnetic resonance (MR) parameters such as T_1, T_2, diffusion, and flow, and incorporates a fat–water separation module, is followed by the EPI image formation, or read-out module.[16] The relative independence of the spin-preparation and imaging modules in EPI allows fast and interactive optimization of imaging parameters, such as contrast without any fundamental changes of the sequence.

Proton density, T_1, and T_2 are the most important MR parameters for differentiation between the various organs and between normal and pathological tissue. In diseased tissue both relaxation times are often increased, but they can have opposite effects on image contrast. In the worst case, this effect can lead to a cancellation such that pathological tissue appears normal.[17] A careful separation between T_1 and T_2 contrast effects is thus necessary. This separation has not been easy in fast MRI methods such as turboFLASH, although good progress has recently been made by incorporation of a spin-preparation module.[18]

EPI has an inherently modular sequence structure which allows real-time changes in contrast to be introduced into images by virtue of the intrinsic NMR relaxation parameters. Comprehensive mapping of one of these NMR parameters has been demonstrated.[19]

In tissue, two species of proton give rise to the principal NMR signal, those in alkenic hydrocarbon chains of a fat and those of free water. Their resonance frequencies differ by 147 Hz T^{-1} because of the slightly different electronic orbital states that surround these protons, an effect known as the chemical shift. In a 100 ms echo planar image, the bandwidth separation between pixels in the blipped gradient direction is only 10 Hz (total bandwidth 160 Hz, 128 × 128 pixels) and thus a misregistration of 15 pixels per tesla between images of the two species occurs. Selective eradication of the signal of either proton species in the fat–water separation module avoids this artifact and provides pure water or fat images that facilitate organ delineation'.

6 FUTURE PROSPECTS

Although EPI was conceived to tackle imaging of the body where involuntary motion is present, such as the heart and gut, with few exceptions very little work has been done in either of these areas so far. In the very recent past, more attention has been paid to the cardiac imaging, and dedicated machines for this purpose are now being supplied. These have EPI capability as a central feature in the light of the accumulating evidence

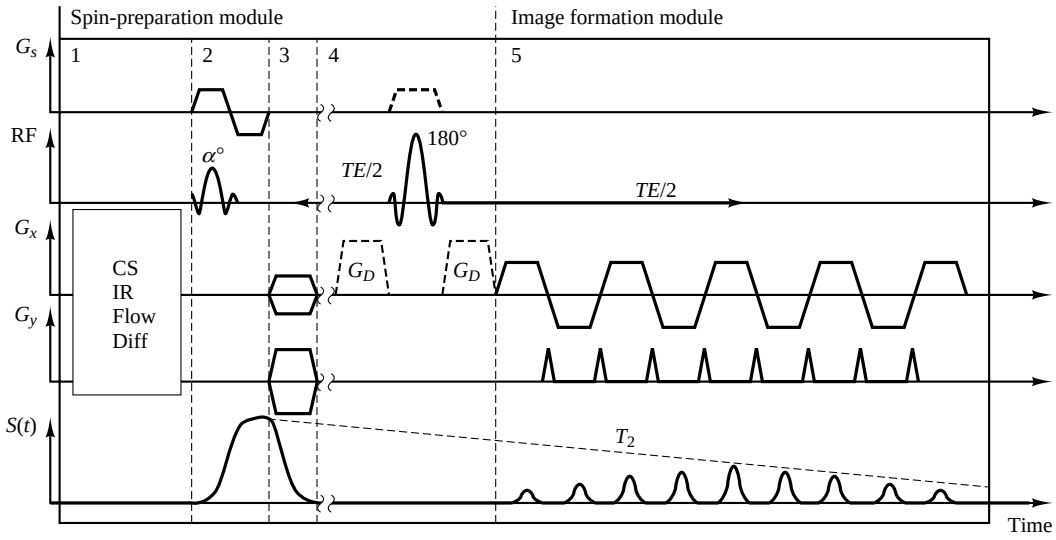

Figure 4 Diagram of a typical EPI sequence, showing the time dependence of the three orthogonal gradients G_s, G_x, and G_y, the rf pulses, and the gradient echo train $S(t)$ thus produced. The choice of axes s, x, and y is made by the operator, which allows any oblique slice to be selected if the imaging system has adequate gradient equipment. Box 1 contains optional pulses for fat or water suppression, chemical shift data, T_1-weighting with inversion recovery, or flow encoding. Box 2 is for selective excitation. Boxes 3 and 4 show the required pulses for gradient-recalled echo (full lines) and spin echo (broken lines) EPI. The largest echo is formed at a time TE after the initial rf pulse. Optional diffusion sensitization gradients are shown in gray. The dashed line T_2 in $S(t)$ indicates the inevitable signal decay that occurs during EPI sequences; this limits the duration of the acquisition window. (Reproduced by permission from Stehling et al.[6] Copyright 1991 American Association for the Advancement of Science)

that it is very effective in this application.[20] Other areas of the body attracting increasing interest include imaging of the fetus during pregnancy. The advent of numbers of commercial machines with EPI capability will result in many more such applications being developed. In the meantime, a niche area for EPI applications which is creating worldwide interest is neurofunctional imaging of the brain. This effect manifests itself more readily at high magnetic field strengths and has been observed over the field range 1.5–4.0 T. Susceptibility changes of blood in oxy- and deoxy-hemoglobin manifest themselves as an increase in EPI image intensity of the venous blood in the oxyhemoglobin rich, as against the deoxyhemoglobin rich, state.[21] These effects show up in localized cortical regions of the brain in response to sensory, motor, or other inputs to the brain that cause signal changes in the relevant cortical regions. This topic is rapidly expanding at the present time and seems assured of a regular position in the range of EPI applications for the study of brain neurophysiology in normal and abnormal states, and also in the study of cognitive processes in psychology and psychiatry. Another important developing role is the use of EPI for the acquisition of diffusion weighted images, particularly where it is intended to acquire the data needed to measure the diffusion tensor.[22] This requires typically between six and twelve images each with different diffusion sensitization. Patient motion has been found to be a major problem in this work and EPI is a preferred data recovery method. Clinically this is of rapidly growing importance in the assessment of stroke patients for their suitability for thrombolytic therapy on admission to hospital as an emergency.[23]

In all the above described applications of neurofunctional imaging considerable progress has already been made using PET. EPI, and possibly echo-volumar imaging (EVI),[24,25] although intrinsically less sensitive than PET, will have a role to play by virtue of the speed by which functional MR images can be obtained. At this stage, at least, MRI and PET should properly be regarded as complementary rather than competitive techniques.

The quest for higher quality EPI images combined with the greater magnetic field strengths (currently 3.0 T at Nottingham) have created a new and potentially serious problem associated with acoustic noise that is emitted during the gradient modulation process. Without suitable precautions, perceived sound levels can transcend the pain threshold and could result in permanent hearing impairment. Of course when scanning human fetuses in utero and also in veterinary applications it is not possible to use ear defenders, for example, to attenuate the noise level.

With this in mind we have recently introduced the concept of active acoustic screening in the design of high power gradient coils.[26,27] In this approach we address the cause of the acoustic noise problem rather than treat its symptoms by balancing all Lorentz forces within the coil structure. Active acoustic screening by this means significantly attenuates the emitted noise level from the coil structure itself, thereby reducing the danger to patients of high level exposure to noise during medical MRI scans. Active acoustic screening can of course be combined with active magnetic screening, an idea introduced by Mansfield and Chapman[28] to combat the problem of induced currents in the structure of the static superconductive magnet when high powered gradient coils are switched within the close confines of the magnet. Reduction of sound levels will not only remove a potential danger to both operators and patients, but will also make for a more relaxed and comfortable scanning procedure.

7 CONCLUSIONS

The road to clinical EPI has been a long one lasting 20 years from its original inception. It may be argued that it was a technique ahead of its time in view of the inadequacies of magnet technology and general computing ability. However, it now seems positioned to enter its true role as the fastest method of acquisition of NMR images yet discovered with potentially very wide applications.

8 RELATED ARTICLES

Multi Echo Acquisition Techniques Using Inverting Radiofrequency Pulses in MRI; Whole Body MRI: Strategies for Improving Imaging Efficiency.

9 REFERENCES

1. P. Mansfield, *J. Phys. C.*, 1977, **10**, 55.
2. P. Mansfield, A. M. Howseman, and R. J. Ordidge, *J. Phys. E.*, 1989, **22**, 324.
3. P. Mansfield and P. K. Grannell, *J. Phys. C.*, 1973, **6**, 422.
4. P. Mansfield, *Br. Med. Bull.*, 1984, **40**, 187.
5. A. M. Howseman, M. K. Stehling, B. Chapman, R. Coxon, R. Turner, R. J. Ordidge, M. G. Cawley, P. Glover, P. Mansfield, and R. E. Coupland, *Br. J. Radiol.*, 1988, **61**, 822.
6. M. K. Stehling, R. Turner, and P. Mansfield, *Science*, 1991, **254**, 43.
7. P. Mansfield and P. G. Morris, 'NMR Imaging in Biomedicine', Academic, New York, 1982.
8. M. K. Stehling, A. M. Howseman, R. J. Ordidge, B. Chapman, R. Turner, R. Coxon, P. Glover, P. Mansfield, and R. E. Coupland, *Radiology*, 1989, **170**, 257.
9. G. Johnson and J. M. S. Hutchison, *J. Magn. Reson.*, 1985, **63**, 14.
10. M. Doyle, R. Turner, M. Cawley, P. Glover, G. K. Morris, B. Chapman, R. J. Ordidge, R. Coxon, R. E. Coupland, B. S. Worthington, and P. Mansfield, *Lancet*, 1986, **ii**, 682.
11. B. Chapman, R. Turner, R. J. Ordidge, M. Doyle, M. Cawley, R. Coxon, P. Glover, and P. Mansfield, *Magn. Reson. Med.*, 1987, **5**, 246.
12. R. R. Rzedzian and I. L. Pykett, *Am. J. Roentgenol.*, 1987, **149**, 245.
13. J. H. Kim, in 'Abstracts, Fifth Annual Meeting of the Society of Magnetic Resonance in Medicine, Montreal, 12–14 August 1986', Society of Magnetic Resonance in Medicine, Berkeley, CA., p. 659.
14. J. Hennig, A. Nauerth, and H. Friedburg, *Magn. Reson. Med.*, 1986, **3**, 823.
15. M. K. Stehling, J. L. Firth, B. S. Worthington, R. J. Ordidge, and P. Mansfield, *Magn. Reson. Imaging*, 1990, **8** (Suppl. 1), 17.
16. M. K. Stehling, P. Mansfield, R. J. Ordidge, R. Coxon, B. Chapman, A. M. Blamire, P. Gibbs, I. R. Johnson, E. M. Symonds, B. S. Worthington, and R. E. Coupland, *Magn. Reson. Med.*, 1990, **13**, 314.
17. I. R. Young, D. R. Bailes, M. Burl, A. G. Collins, D. T. Smith, M. J. McDonnell, J. S. Orr, L. M. Banks, G. M. Bydder, R. H. Greenspan, and R. E. Steiner, *J. Comput. Assisted Tomogr.*, 1982, **6**, 1.
18. D. Chien, D. J. Atkinson, and R. R. Edelman, *J. Magn. Reson. Imaging*, 1991, **1**, 63.
19. R. J. Ordidge, P. Gibbs, B. Chapman, M. K. Stehling, and P. Mansfield, *Magn. Reson. Med.*, 1990, **16**, 238.
20. D. N. Firmin, R. H. Klipstein, G. L. Hounsfield, M. P. Paley, and D. B. Longmore, *Magn. Reson. Med.*, 1989, **12**, 316.
21. S. Ogawa, R. S. Menon, D. W. Tank, S.-G. Kim, J. M. Ellerman, and K. Urgubil, *Biophysical J.*, 1993, **64**, 803.
22. P. van Gelderen, M. M. de Vleeschouwer, D. DesPres, J. Pekar, P. C. M. van Zijl, and C. T. W. Moonen, *Magn. Reson. Med.*, 1994, **31**, 154.
23. S. Warach, D. Chien, W. Li, M. Ronthal, and R. R. Edelman, *Neurology*, 1992, **42**, 1717.
24. P. Mansfield, A. M. Howseman, and R. J. Ordidge, *J. Phys. E*, 1989, **21**, 275.
25. P. Mansfield, R. Coxon, and J. Hykin, *J. Comput. Assist. Tomogr.*, 1995, **19**, 847.
26. P. Mansfield, B. Chapman, P. Glover and R. Bowtell. UK Patent Application, Priority No. 9 311 321.5, 2 June 1993.
27. P. Mansfield, P. Glover, and R. Bowtell, *Meas. Sci. Technol.*, 1994, **5**, 1.
28. P. Mansfield and B. Chapman, *J. Magn. Reson.*, 1986, **66**, 573.

Biographical Sketch

Sir Peter Mansfield, FRS. *b* 1933. B.Sc., 1959, Ph.D., 1962 (Supervisor Jack Powles), University of London. Research Associate, Urbana, Illinois, under Charlie Slichter, 1962–64. Knighted, January 1993. Currently Emeritus Professor of Physics, Magnetic Resonance Centre, University of Nottingham. Approx. 240 publications. Current research specialty: magnetic resonance imaging and its applications in medicine, biology and porous media.

Image Formation Methods

Lawrence E. Crooks
Toshiba America MRI, South San Francisco, CA, USA

1 INTRODUCTION

MRI has moved from the conceptual stage in the 1970s to a multibillion dollar industry in the 1990s. Its main use today is medical diagnosis. Although this review of MRI methods centers on medical applications, MRI has potential applications in many other areas. Imaging solids is an open area that requires techniques beyond those covered here. My hope is that interested readers will use this review as a starting point for further work.

2 CONCEPTS FOR SPATIAL LOCALIZATION

Magnetic resonance images distinguish signals from distinct volume elements in an object. The basic concept underlying all techniques to achieve spatial resolution is that the resonant frequency of the nuclei is proportional to magnetic field strength. This is explicitly stated by the Larmor relationship

$$f_{\mathrm{L}} = \gamma B \tag{1}$$

where γ is the magnetogyric ratio of the nuclear species and B is the magnetic field strength. So, by making the magnetic field in an object vary with position, one makes the resonant frequency of the nuclei vary with position. By knowing the position dependence of the magnetic field, the position of resonating nuclei is defined by their resonant frequency. We shall describe later the many varied ways of tailoring magnetic fields and magnetic resonance sequences to create the desired image, but will start here with an example that illustrates the concept.

Consider an object in a magnetic field that is made to vary by using what is known as a linear field gradient. In this case, the field is

$$B = B_0 + Gr \tag{2}$$

where B is the field at position r along some axis of the object, B_0 is the main field value, and G is the strength of the gradient that defines the field variation along the axis. The resonant frequency of the nuclei as a function of position along r is

$$f = \gamma B_0 + \gamma G r \tag{3}$$

and B_0, γ, and G are all known constants (γ is 42.58 MHz T^{-1} for hydrogen), so position as a function of resonant frequency is

$$r = \frac{(f/\gamma) - B_0}{G} \tag{4}$$

For imaging, resonant frequency is made to correspond to position. Resonant frequency is either measured during reception or defined by the spectrum of a rf pulse excitation. During reception, frequency is measured by recording the magnetic resonance signal as a function of time and then using the frequency spectrum of the signal. Usually, a Fourier transformation analyzes the shape of the time-dependent signal and finds the strength of each of the component frequencies of the signal. The result is the relation of signal strength to frequency. Equation (4) allows the magnetic resonance frequency versus signal strength spectrum to be translated to a relationship of intensity to position.

The above equations contain a term due to the main field B_0. By subtracting γB_0 from f one gets a new frequency centered at

$$f_0 = \gamma B_0 \tag{5}$$

This new frequency simplifies the equations and is directly available in the imager electronics. We will use this frequency in all further discussion. The simplified versions of equations (3) and (4) are

$$f = \gamma G r \tag{6}$$

and

$$r = \frac{f}{\gamma G} \tag{7}$$

Again, these provide direct relationships between the frequency and position of the nuclei. We will next consider ways to exploit this concept for spatial localization.

2.1 Selective Irradiation

One fundamental process used in imaging and localized spectroscopy is selective irradiation. Selective irradiation uses a narrow rf range to excite only a restricted volume by matching field strength and frequency. In this case the frequency content of the rf excitation is the determining factor.

Selective irradiation for imaging[1] restricts a volume by the following sequence. First, a field gradient is applied across the object. A particular frequency now corresponds to a plane of constant frequency perpendicular to the direction of the gradient. While this gradient is present, a low-level rf pulse of relatively long duration (e.g. 10 ms) is applied to the object. The rf pulse is chosen so that its spectrum is a narrow block of frequencies (e.g. a range of 1 kHz). The region in the object whose nuclei resonate at the frequencies contained in the rf pulse will be excited, but the rest of the object is not. In this way, a planar slice through the object can be activated (Figure 1). The slice thickness and position depend on the rf pulse and on the strength of the gradient. The position of the plane can be moved by simply changing the frequency of the pulse, thereby activating nuclei at another field strength.

Consider the following example of a transaxial slice acquisition. Slice selection is performed by turning on a magnetic field gradient in the slice direction, shown along the z axis in Figure 1. A linear gradient G_z is used such that the field in the z direction has the form

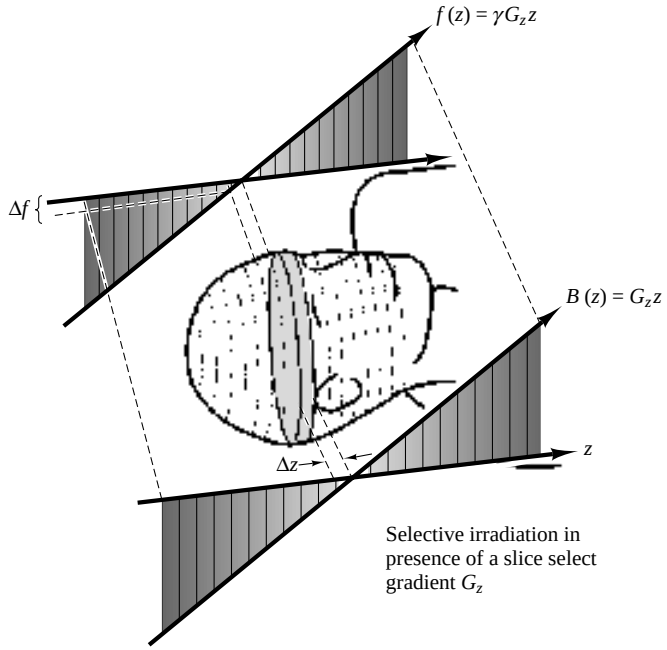

Figure 1 In this example of a transaxial image acquisition, a selected plane of tissue is excited by using rf excitation that contains a narrow bandwidth of frequencies, Δf, corresponding to a section Δz along the z direction in the presence of the gradient G_z

$$B(z) = G_z z \tag{8}$$

With the z gradient on, every position along z has a different field value. So, every position has its own frequency

$$f(z) = \gamma G_z z \tag{9}$$

The rf pulse used for excitation is tailored to contain frequencies corresponding only to the Larmor frequencies of spins contained within the slice z:

$$z = \frac{f(z)}{\gamma G_z} \tag{10}$$

Only these spins will be affected and experience rotation of their magnetization vectors. These spins now have a transverse component to their magnetization and can generate signal.

The above description is accurate for small excitations, but nonlinearities in the response of the nuclei complicate the process.[2–4] A number of papers provide effective solutions to the nonlinear excitation problem.[5–7]

2.2 Spectral Resolution

The next fundamental imaging process is localization of the received signal. Two approaches are available, frequency and phase encoding. Frequency encoding for projection imaging was first proposed by Lauterbur.[8]

2.2.1 Frequency Encoding

Frequency encoding uses a gradient during reception to define the readout direction, shown as x in Figure 2. The readout gradient remains on while a signal is being recorded. The readout gradient is given by

$$B(x) = G_x x \tag{11}$$

Spins at different positions along x generate signals at different frequencies. A Fourier transform decomposes the signal into its individual frequency components. Each frequency corresponds to an x position:

$$x = \frac{f(x)}{\gamma G_x} \tag{12}$$

The strength of each frequency is related to the 'density' of spins in the object. This 'density' includes all the relaxation and other effects mentioned in the next section. We shall call this 'density' $\rho(\boldsymbol{R})$ where $\boldsymbol{R}$ is a three-dimensional position vector. The signal from an entire object is the sum of the signals from all the nuclei (Figure 2). Each signal includes a complex frequency and phase term for every location:

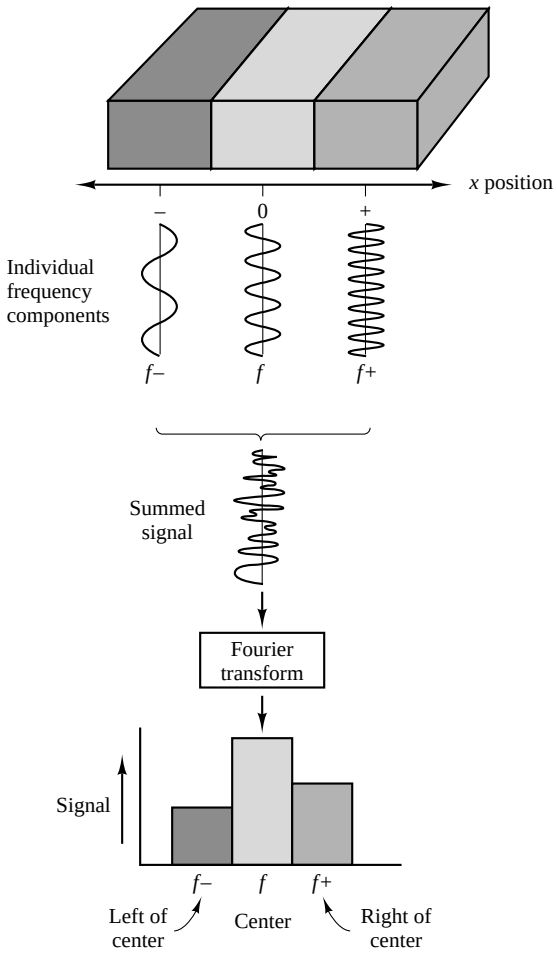

Figure 2 With frequency encoding, the collective signal from spins with different Larmor frequencies is measured and processed by a Fourier transformation to separate the individual frequency components of the input signal. By using magnetic field gradients to vary the main field spatially, frequency can be interpreted to give the location of the signal

$$\rho(\boldsymbol{R})\exp(\mathrm{i}2\pi f(\boldsymbol{R})t) \tag{13}$$

The total signal is thus

$$S(t) \propto \int_{-\infty}^{\infty} \rho(\boldsymbol{R})\exp(\mathrm{i}\gamma \boldsymbol{G_R}\cdot\boldsymbol{R}t)\,\mathrm{d}^3R \tag{14}$$

For a two-dimensional object, a single gradient G_x projects the density of the object onto a line (Figure 3). In this case the signal is

$$S(t) \propto \int_{-\infty}^{\infty} \rho(x)\exp(\mathrm{i}\gamma G_x x t)\,\mathrm{d}x \tag{15}$$

For this signal, the above integral has a Fourier transform twin that lets us calculate the spin density projection from the recorded signal:

$$\rho(x) \propto \int_{-\infty}^{\infty} S(t)\exp(-\mathrm{i}\gamma G_x x t)\,\mathrm{d}t \tag{16}$$

These equations have infinite signal duration and possible object size. Real imaging has limited observation time and limited object size. The time limit restricts image resolution. If the signal is recorded for T seconds the Fourier integral becomes

$$\rho(x) = \int_{-T/2}^{T/2} S(t)\exp(-\mathrm{i}\gamma G_x x t)\,\mathrm{d}t \tag{17}$$

The frequency resolution is limited to $1/T$ Hz. γG_x is the frequency spread in hertz per meter, so resolution is $1/(T\gamma G_x)$ m. With discrete sampling recording a value every Δ second the maximum frequency (Nyquist) represented is $1/2\Delta$ Hz. The maximum object width is $1/(\Delta\gamma G_x)$ for complex samples. Excessively high frequencies must be rejected by filtering. These frequencies would otherwise alias and appear on top of the lower frequency parts of the image.

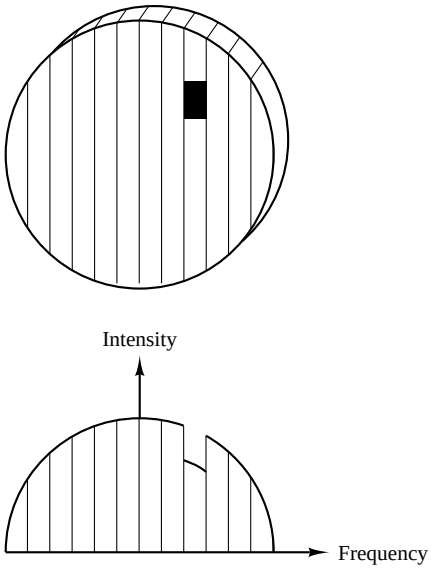

Figure 3 Projection of nuclei in a plane onto a line. In the presence of a field gradient, all the nuclei along each column in the plane have the same frequency, so each frequency in the spectrum corresponds to a projection of a line of nuclei onto a single point

If two gradients are applied at the same time, their effect is like a single gradient at an intermediate angle. For example, equal x and y gradients are like a $\sqrt{2}$ stronger gradient applied at 45° between the x and y axes. This allows electronic rotation of the projection direction. This is also true for selective irradiation since it is a frequency based technique.

2.2.2 *Phase Encoding*

Next we consider phase encoding, which was first proposed by Kumar.[9] In this process, gradients are used between the excitation and reception. The process is repeated with different gradient durations or strengths[10] over many excitation/reception measurements. While a gradient during reception has a direct effect on the frequency of the signal, the gradient before reception affects the phase of the signal. Consider an example phase encoding gradient turned on such that the field in the y direction has a linear dependence of the form

$$B(y) = G_y y \tag{18}$$

The phase-encoding gradient is turned on for a short period of time, τ, and then removed. During this time the frequencies of the nuclei are

$$f(y) = \gamma G_y y \tag{19}$$

The phase of the nuclei at position y and time t during the gradient pulse is the integral of the frequency:

$$\phi(t) = \gamma \int_0^t G_y y\,\mathrm{d}t = \gamma G_y y t \tag{20}$$

After the pulse the frequencies drop back to normal, but the accumulated phase remains constant:

$$\phi(\tau) = \gamma G_y \tau y \tag{21}$$

The repeated measurements cover a range of values of $G_y\tau$. The signal after the gradient pulse is the sum of densities with phases shifted by $\phi(\tau)$. If an infinite number of values were measured, this sum would again be an integral:

$$S(G_y\tau) \propto \int_{-\infty}^{\infty} \rho(y)\exp(\mathrm{i}\gamma G_y \tau y)\,\mathrm{d}y \tag{22}$$

For this collection of signals, the above integral has a Fourier transform twin that lets us calculate the spin density:

$$\rho(y) \propto \int_{-\infty}^{\infty} S(G_y\tau)\exp(-\mathrm{i}\gamma G_y \tau y)\,\mathrm{d}(G_y\tau) \tag{23}$$

Again, these equations have an infinite $\gamma G_y\tau$ range and possible object size. The limited number of repeated observations restricts image resolution. Object size must also be limited. For phase encoding, image resolution is determined by the range of $\gamma G_y\tau$ covered. If $\gamma G_y\tau$ ranges from $-\Gamma\pi$ through 0 to $+\Gamma\pi$, the resolution is $1/(2\Gamma\pi)$. The repeated measurements enforce discrete sampling. If N values of $\gamma G_y\tau$ are measured, the maximum object width is $N/(2\Gamma)$. For phase encoding there is no equivalent of filtering to reject signal from outside this

size range. Any signal producing object outside this range will alias and appear on top of the inner part of the image. Prevention of aliasing requires that the outer areas do not produce signal. Selective irradiations are often used to limit the signal production to the desired region only.

Unlike frequency encoding, two phase-encoding gradients applied at the same time add their effects together as if they were applied independently. This allows overlapping of different direction phase-encoding pulses, saving time in the imaging sequence.

3 IMAGE INTENSITY DEPENDENCE ON IMAGING PARAMETERS

Before further considering spatial localization, we need to determine the strength of the signal from various tissues. This is because the signal strength determines the brightness of the tissue in an image. The stronger signals give brighter tissues. Strong signals also improve the image signal-to-noise ratio (S/N). Electronic noise is included in every magnetic resonance signal, giving the final image a grainy appearance. This limits one's ability to detect image features. Thus, an improved S/N is a goal in most MRI.

The main determinants of signal strength are: nuclei density [N(H) for hydrogen], the relaxation times T_1 and T_2, and motion (cf. blood flow). Various excitation and reception parameters interact with these tissue characteristics to vary the signal intensity between tissues or between images with different parameters. Tissue motion and imaging technique response to motion is variable and will only be generally considered here. This leaves the density and relaxation times.

3.1 Relaxation Time Dependences

Three parameters that interact with the relaxation times are the pulse repetition interval *TR*, the echo delay time *TE*, and the flip angle Θ. *TR* is the time between successive rf excitations of a given location. The intrinsic T_1 value of the tissue determines the rate at which longitudinal magnetization recovers. By choosing *TR* appropriately, one can control whether a portion, or all, of that magnetization is allowed to recover. A long *TR* means a higher signal level but also lengthens the total imaging time. Since in most cases a heterogeneous group of tissues with a range of T_1 values will be imaged simultaneously, *TR* must be chosen judiciously to portray best all the tissues of interest.[11]

TE is the time delay between the rf excitation and the measurement of the signal. Transverse magnetization created by an rf pulse begins to dephase immediately after the pulse due to T_2 and other effects such as field inhomogeneity. A 180° refocusing pulse at time *TE*/2 creates a spin echo at time *TE* that is corrected for field inhomogeneity effects. Without the 180° or similar refocusing pulse, the rate of signal decay will be faster, as characterized by T_2*. A short *TE* will measure maximal signal early in the decay while a long *TE* will measure less signal later in the decay.

The flip angle is the angle through which the magnetization is rotated away from the longitudinal direction by the rf pulse. A 90° pulse will maximize the transverse component but will also require a long recovery time before the next excitation to restore longitudinal magnetization fully. Since the recovery rate varies for different tissues depending on T_1, a single choice of flip angle will have a different effect on each tissue. Choice of *TR*, *TE*, and flip angle will determine the image contrast and S/N as well as the total imaging time and the ability to obtain multiple sections in a single experiment.[12]

The excitation and reception schemes we consider are: (1) repeated spin echo, (2) inversion–recovery, (3) repeated limited flip angle with gradient echo, and (4) steady-state free precession. The following analysis considers that $T_2 << T_1$ and transverse magnetization decays completely during the repetition times of techniques (1)–(3).

In technique (1) the signal intensity of the repeated spin echo is strongly dependent on T_1 and T_2. For single time constant relaxation and no flow, the dependence is

$$I = N(\mathrm{H})[1 - \exp(-TR/T_1)]\exp(-TE/T_2) \tag{24}$$

T_1 recovery limits signal strength, with long T_1 tissues being darker than short T_1 tissues.

Other excitation sequences can have a different dependence on T_1. Technique (2), an inversion–recovery, further enhances T_1 dependence:

$$I = N(\mathrm{H})[1 - 2\exp(-TI/T_1)]\exp(-TE/T_2) \tag{25}$$

assuming $TR >> T_1$.

Here, *TI* is the interval between an inverting rf pulse and the 90° observing rf pulse. This technique has the highest sensitivity to T_1. For $TI/T_1 = \ln(2)$ the signal is zero. This allows 'nulling' of the signal from one value of tissue T_1 in an image. All other T_1 valued tissues will still appear.

If the repeated excitation has a limited flip angle θ, one has technique (3). The intensity dependence using a gradient echo experiment is then

$$I = N(\mathrm{H})\frac{1 - \exp(-TR/T_1)}{1 - \cos\theta\exp(-TR/T_1)}\sin\theta\exp(-TE/T_2) \tag{26}$$

This allows fast imaging with a short *TR*. The small flip angle reduces dependence on T_1.

If the transverse magnetization lasts longer than *TR*, equation (26) is no longer valid. One moves into a mode where each rf pulse creates a free induction decay (FID) and refocuses a spin echo. These two signals overlap, providing the steady-state free precession (SSFP) of technique (4). The signal dependence on relaxation times and motion is complex,[13] but reaches a limit where

$$I = N(\mathrm{H})\frac{T_2}{T_1} \tag{27}$$

The brightest tissues in these images have $T_2 \approx T_1$.

4 IMAGE INTENSITY DEPENDENCE ON SIGNAL

The magnetic resonance signal is a complex valued signal. Ordinarily, it is the display of the magnitude of the signal that shows us the soft tissue anatomy. Alternatively, the phase of

the signal or the real or imaginary components of the signal can be displayed. Under ideal conditions for tissues with the same magnetic susceptibility values, the phase angle at every position in the image will be the same, and displaying phase values will be uninformative. However, field inhomogeneity, an improperly tuned imaging sequence, or disturbances such as flow can result in variations in the phase. Another cause of phase disturbance is differences in the magnetic susceptibilities of different tissues. This is seen particularly at boundaries between air and tissue or between tissue and blood. The phase image is frequently used to detect these occurrences. If desired, just the real or imaginary portion of the signal can be examined.

In most MRI data acquisitions, Fourier transformation is an essential step of digital image processing before a recognizable image is obtained. Additional levels of digital signal processing are often used such as smoothing and edge enhancement to improve the appearance of the image. The image data can be manipulated to present a different form of the data; for example, an image composed of the T_1 or T_2 values at every pixel.

5 IMAGING TECHNIQUES

Throughout the development of MRI techniques there have been many methods used for data acquisition and image reconstruction, including the sensitive point and line methods, reconstruction from projections, and Fourier imaging. A number of texts provide details about the development and historical significance of each of these.[14–16]

MRI techniques can be classified into four types, depending on the volume that produces the received signal used to make an image: a single point, a line, a plane, or an entire three-dimensional object. Images are made of individual, resolved points, but there is a variation in when these points are defined in the imaging sequence. Single-point methods determine the points in the image most directly, by measuring points one at a time; on the other hand, three-dimensional reconstruction repeatedly measures all points simultaneously from many viewing directions or with many phase encodings and then calculates the signal contributed by each point in the object. The line and plane techniques fall between these extremes.

The basic magnetic resonance experiment starts with a sample in a magnetic field. A transmitting coil excites the spin system with an rf pulse, or pulses, causing the net magnetization vector to rotate into the transverse plane. When each pulse ceases, the spin system begins to return to equilibrium. The receiver coil is turned on, and the system acquires a FID, spin echo, gradient echo, or SSFP signal. One way to create an image would be to repeat this process for every location within the object. Such point-by-point mapping produced some of the earliest magnetic resonance images. Some point measurement techniques are also used for localized spectroscopy.[17–19]

5.1 Single-Point Techniques

Several methods of defining sensitive points have been developed. The oldest single-point technique shapes the main magnetic field, so that the nuclei in a star-shaped region are at the resonant frequency and the nuclei outside this region are not at the resonant frequency.[20] The center of the star is the sensitive point; the points of the star taper rapidly and contribute a minor amount of signal. The star shape is the point-spread function of the imager (i.e. the shape of the volume from which the signal is being received). An image is scanned by moving the object through the sensitive point. This is a very direct way to produce an image and does not require a computer for image generation. This method produced images from small animals[20,21] and was used for human imaging by Damadian.[22]

Another sensitive-point method was developed by Hinshaw.[13] It uses alternating currents applied to three gradient coils to superimpose alternating gradients on the main field. An alternating current applied to a set of gradient coils produces an alternating magnetic field everywhere, except at the plane at the center between the coils where the field is unchanged. By applying three alternating currents of unrelated frequencies to the three perpendicular gradient coils, three mutually perpendicular planes intersect, so that only the point of intersection has an unchanging field. Areas of the object outside the point of intersection are exposed to the varying magnetic field, and the resonance signals from nuclei outside the sensitive point are frequency modulated by the variations in field. The received signal is thus a combination of the on-resonance signal from the point of intersection and the frequency modulated signals from the rest of the object. Electronic filtering removes the modulated part of the signal, leaving the signal from the point of intersection.

This intersection point can be moved by varying the currents in the gradient coils, allowing electronic scanning of the object. The point-spread function of this method is a cube with rounded edges. The signal observation technique used with the alternating gradient is the SSFP pulse sequence.[13]

Since resonance is localized to a point, most of the techniques developed for chemical NMR on isolated samples can be applied directly. Measurements of T_1 and T_2, and $N(\mathrm{H})$, as well as localized chemical analysis, can be made at the selected point. Making chemical measurements at all the image points takes prohibitively long imaging times; therefore, this localized chemistry capability has usually been applied to points of interest selected from an image. In addition, if the point is positioned at a blood vessel, it is possible to acquire the signal versus time plot for pulsatile blood flow. Using gated observation, one can stop motion at a point, although nongated techniques, by averaging over the motion, usually blur movement to an average value. The single-point imaging volume limits motion artifacts to blurring because motion modifies only the intensity of the point through which something moves.

The main problem with single-point techniques is that they are slow. In the time that it takes to observe one point, all the points along a line could be observed with the same S/N. Speed would increase by the number of points in the line.

5.2 Line Techniques

Imaging speed improves considerably when all the points along a line are observed simultaneously by frequency encoding with a field gradient along the line. A Fourier transformation separates the points along the line by correlat-

ing resonant frequency with position along the line. The presence of the gradient during reception mixes chemical and spatial information. Images are made more rapidly, but they require computer processing for the Fourier transformation. Line scanning requires more complex signal excitation hardware and software than the simplest point scanners. However, they are less demanding of magnetic field and field gradient uniformity than are the reconstruction techniques to be described later.[8] Frequency encoding collects all the points at once but requires that the signal originates only from a line volume in the object. Many different line scan techniques[23–29] have been developed to limit the signal to a line. The techniques grew from two basic sources, Hinshaw's sensitive point, which we have just described, and Garroway's selective irradiation.[1]

5.2.1 *Selective Lines*

When selective irradiations are used to define a line volume, a sequence of at least two irradiations with different selected directions are used. The type, order, and timing of the irradiations and signal observations determine how the line is defined and the T_1 and T_2 dependence of the signal intensity. The selective irradiation sequence we used in our work[27,28] consisted of a 90° selective irradiation that defines a plane perpendicular to the z axis (Figure 4). Then a 180° selective irradiation inverts the nuclei in a plane perpendicular to the y axis. At a later time, a spin echo signal will arise only from the nuclei that have experienced both the 90° and 180° irradiations, that is, the line volume along the x axis that is the intersection of the two perpendicular planes (Figure 4). The line can be scanned through an object by methodically changing the frequency of either of the selective irradiations, thus exciting planes at different magnetic field strengths. The effect of motion is to blur or displace individual lines. Equation (24) gives the dependence of signal intensity on N(H), T_1, and T_2.

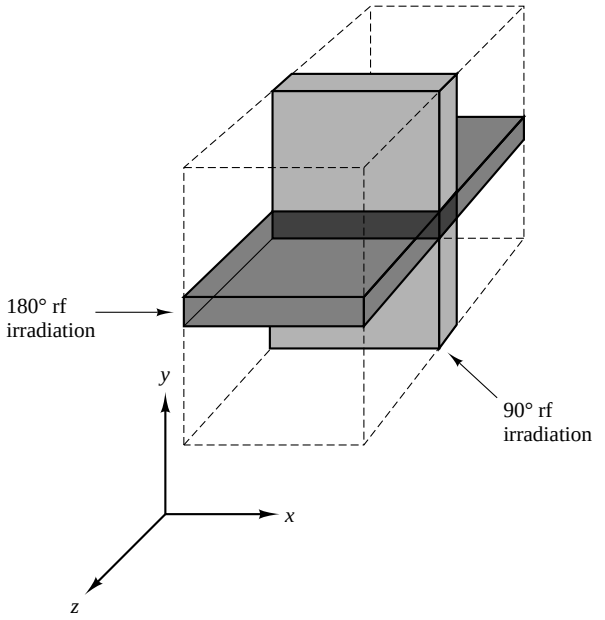

Figure 4 The line of intersection of two selectively irradiated planes defines the line that produces the spin echo signal

Other selective irradiation sequences have different dependences on T_1. For example, Hutchison's line scan sequence[29] used the inversion–recovery described by equation (25). To define a line, this sequence requires the subtraction of two planar signals. The technique has a strong dependence on motion. This characteristic can be seen in a human chest image,[29] where the motion of the heart produced intense areas in the image outside the subject's body. One of the selective irradiation sequences developed by Mansfield[26] produced human images with no obvious motion artifacts.

5.2.2 *Sensitive Lines*

In Hinshaw's sensitive line technique,[23,30,31] an extension of the sensitive-point technique, two alternating electric currents of the same frequency but different phases are applied to two of the gradient coils. These two varying gradient fields combine to form a rotating field gradient. Only along the axis of rotation, a linear volume, is the magnetic field constantly on resonance, so this axis is the only region of the object that is observed once all the time-dependent signal has been filtered out. Applying a constant gradient along the line allows frequency-encoded observation of the individual points along the line. The line can be scanned through an object to produce a planar image by varying the currents in the gradient coils. Because the signal is again observed as an SSFP, its intensity is given by equation (27). This technique has produced images of animals[23,30–32] and a human head.[24] The effect of motion in these images is to blur or displace individual lines.

The sensitive-line techniques are more efficient than single-point techniques and are usually resistant to motion artifacts. Gating can be used to stop motion, as it can in single-point techniques. Most techniques are sensitive to blood flow.[28,33] With selective rf pulses, blood moving within a slice has a reduced intensity. Blood moving through a slice can have increased or decreased intensity.[34] T_1 and T_2 can be investigated by varying timing parameters in the irradiation sequences. The presence of the gradient during the signal observation complicates the derivation of chemical information, a restriction that applies as well to planar and whole-volume techniques.

5.3 Planar Volumes

Two techniques produce images based on signals arising simultaneously from all points in a plane: projection reconstruction or zeugmatography, developed by Lauterbur,[8] and Fourier imaging, proposed by Kumar.[9] Zeugmatography, like X-ray computerized tomography, reconstructs a two-dimensional image from projections of a plane onto a line. Each projection is obtained by exciting all the nuclei in a plane, then frequency encoding in the presence of a linear gradient. Frequency encoding projects all the points in the plane onto a line (Figure 3). This process is repeated many times, each time with a different gradient direction, until a collection of projections is accumulated from which a computer can reconstruct a two-dimensional image of the plane (Figure 5). This process is called projection reconstruction.

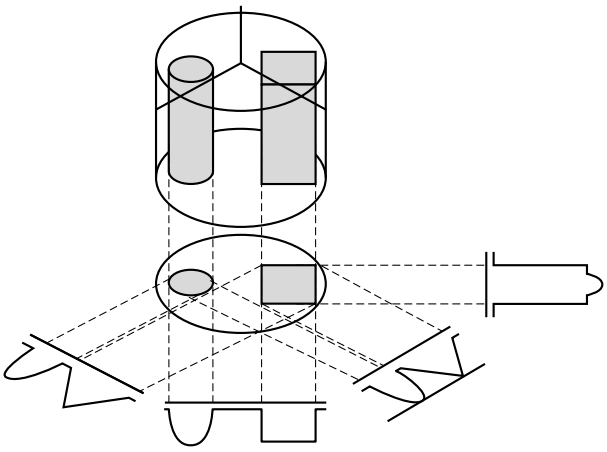

Figure 5 By acquiring projections of an object using many different gradient directions, a two-dimensional image of a plane can be reconstructed

5.3.1 *Projection Reconstruction Imaging*

To reconstruct an image with $N \times N$ pixels requires at least $\pi/2N$ projections of $\sqrt{2}N$ points. The advantage of this technique over sensitive lines is that the signal that arises from the entire plane is a mixture of N single lines, and the electronic noise in each of the N projections is independent. The reconstruction unscrambles the N projections into N separate lines. The effect on the noise is like averaging N measurements. Thus, the final S/N of the reconstructed image is $\sqrt{\pi N/2}$ better than the S/N of a sensitive-line image.[35] This improvement is counteracted somewhat by 'reconstruction algorithm noise'.[36] Another important effect on image quality is motion artifacts. While line scans limit artifacts to individual lines, projection reconstruction distributes artifacts throughout the image.[37]

Several human images have been generated by projection reconstruction. Lauterbur produced projection images of phantoms[8] and, with House, of a rat by this method.[38] Head images have been produced by Hawkes[39,40] using a plane through the head defined by a single alternating gradient used in the same way that the two or three alternating gradients were used by Hinshaw to define a line or a point.

5.3.2 *Fourier Imaging*

Like projection reconstruction techniques, two-dimensional Fourier transformation (2D FT) imaging uses frequency encoding to project the entire plane onto a line. Instead of progressively changing the direction of the line (i.e. changing the direction of the gradient across the plane), the duration or strength of a phase-encoding gradient perpendicular to the line of projection is varied to phase-encode position along the perpendicular dimension[9,10] (Figure 6). As the strength of the perpendicular gradient increases, phase-encoding progressively increases, so that the phase encoding can be decoded using the Fourier transformation of equation (23).

Now we consider the 2D FT method that has become the standard of commercial systems today. In a typical data acquisition, position along the x direction is encoded into the frequency, and position along the y direction into the phase.

Three steps are used to localize points spatially along the three axes in space. In a two-dimensional data acquisition, the first of these is the slice selection. This is done using selective irradiations. For gradient echo imaging a z gradient is applied along with a ϕ selective rf pulse. This excites an x–y planar slice. For spin echo imaging, spatially overlapping selective 90° and 180° rf pulses are used. Additional 180° rf pulses are added if more echo images with increasing T_2 dependence are needed.[28,41] Once a slice has been selected, phase encoding is used to provide differentiation along the y direction. Frequency encoding of the gradient echo or spin echo is used along the x direction.

Slice excitation and signal readout are repeated for N_{pe} different values of the phase-encoding gradient. Along each column, the combined signal will be increasingly distorted with each increasing phase-encoding step. As we saw in equations (22) and (23), the effect on the signal of a changing gradient over N_{pe} steps is the same as the effect of frequency encoding the signal. Figure 6 shows the effect of three increasing values of the phase-encoding gradient on the signal. Fourier transformation along the y direction gives the frequency components along y, and thus position. The two dimensions of Fourier transformation done in x and y are identical.

The acquired data are in the form of rows of sampled signals with increasing phase-encoding gradient values. Because of the unique relationship between position and precession frequency established by the field gradients, the acquired data represent the spatial frequency contributions of the image, and are called k-space data, where k is the wavenumber or value of the spatial frequency. In most human and animal images, the largest contributions to the image are made by the low spatial frequencies with decreasing contributions at higher k values. The highest k values contribute details such as edges and features of small dimension.

The three gradients of the magnet can be used interchangeably to perform slice selection, phase encoding, or signal readout. This allows images of any orientation (transaxial, sagittal, coronal, or oblique) to be defined. There are often benefits to choosing one orientation over another. It is generally desirable to orient the readout direction along the long axis of the object (for example the right–left axis through the chest in a transaxial image plane) and the phase-encoding direction along the short axis (anterior–posterior). The reason for this is that there is a time penalty incurred for increasing the number of phase-encoding cycles, but none for increasing the number of samples taken along the readout direction. Another consideration when deciding the phase-encoding direction is to align it in the direction of least motion, as it shows the greatest motion sensitivity.

In this case, to produce an image of $N \times N$ pixels, N projections of N points must be acquired. Gradients in either the main magnetic field or in the rf magnetic field used to excite the nuclei are capable of producing the phase encoding. An rf gradient is created by reversing the current direction in one half of an rf coil pair. Hoult produced a phantom object image using the rf field gradient.[42]

Edelstein produced human images using a frequency-encoded gradient echo and a gradient of the main field for phase encoding.[10] This 2D FT technique used a selective irradiation to select the plane to be imaged. We produced spin echo 2D FT images with the same type of encoding.[41]

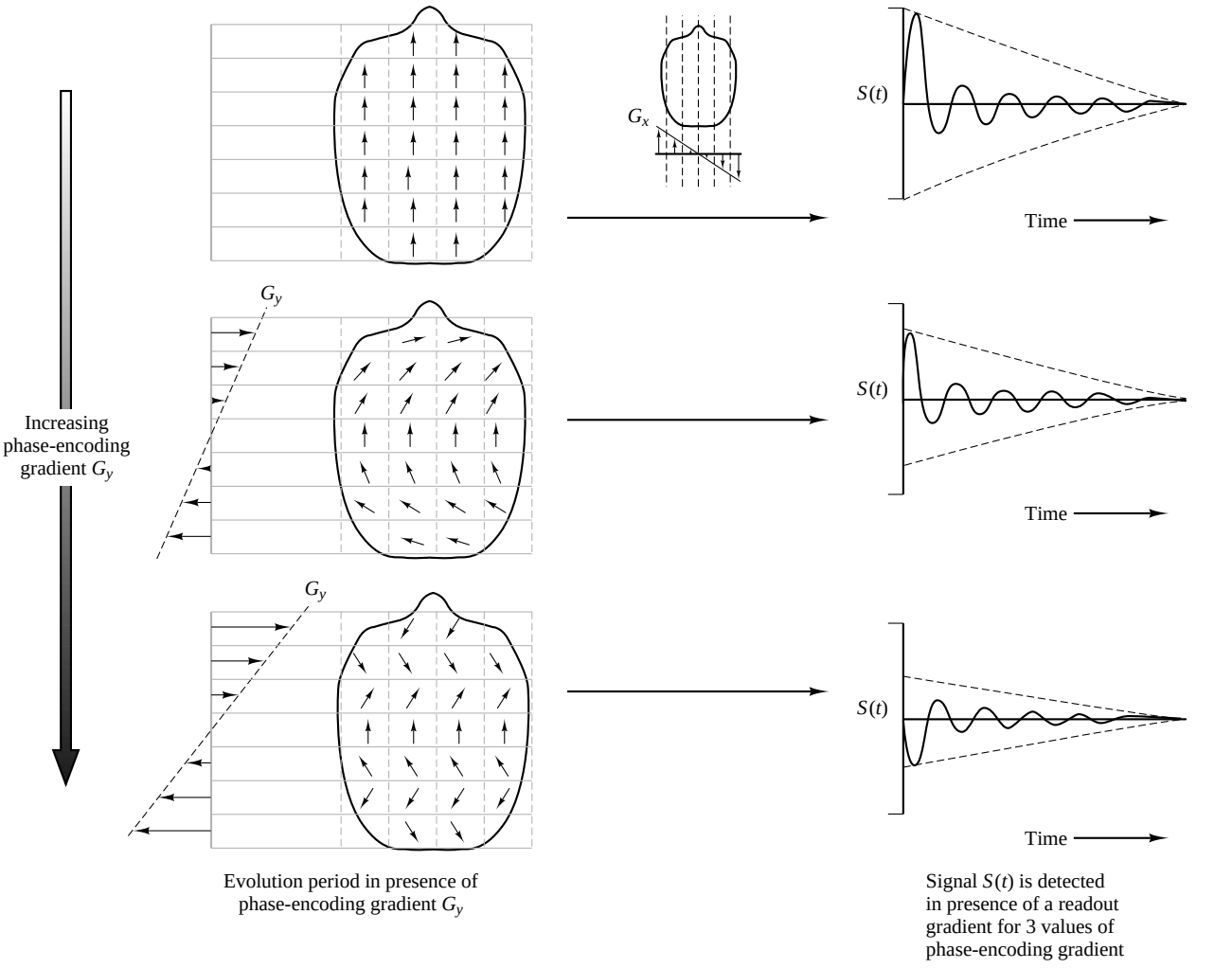

Figure 6 Increasing values of the *y* phase-encoding gradient cause increasing distortions of the signal that is read out in the presence of an *x* gradient

The S/N is $\sqrt{N}$ better than the S/N of a line scan image. Its response to motion is to produce ghost-like versions of the image displaced in the phase-encoding direction.

In summary, the two planar imaging techniques just described require a computer to perform the reconstruction. The algorithms for projection reconstruction are more complex because the fast Fourier transformation, which is a standard computer algorithm, is used for 2D FT imaging. The magnetic field and field gradients have to be very uniform to produce good projections in this technique. Some distortions can be corrected by additional data processing. 2D FT images are insensitive to field variations in the phase-encoding direction. Gradient nonuniformities produce geometric distortion. Because the planar signal is measured many times, they have an S/N advantage over sensitive-point or line techniques. The larger signals associated with this advantage place greater demands on the imager because a greater dynamic range is required of the receiver. The reconstructions require signals from all points in the object, so that the value of each point depends on all the signals of the other points. Reconstructed images require a preset number of projections; therefore, the number of picture elements cannot be varied during imaging, unlike the situation with single-point and line techniques, in which an image itself can be restricted to a specific area of interest. As in the sensitive-line techniques, the presence of a gradient complicates the determination of chemical information. Using two dimensions of phase encoding and no gradient during reception, chemical images can be made.[43–45] These take *N* times longer to acquire and require three-dimensional Fourier transform processing. Gating can be applied in the same way as for selective lines.

5.3.3 Multiple Slice Imaging

So far, only single slice images have been considered. An *N* line image takes $N \times TR$ seconds. If one wants many slices, acquiring them one at a time is very slow. Since tissue T_2 is much less than T_1, only a small part of *TR* has sufficient signal for recording. This leaves a large amount of dead time in the sequence. If the plane is defined by a selective irradiation we can use the dead time to image other slices. These multislice techniques allow the sequential selective irradiation of many planes, the signal from one plane being observed while the

other planes are returning to equilibrium.[41] This is a significant increase in efficiency for clinical imaging.

For example, for a double spin echo sequence with *TE* values of 30 and 60 ms and a *TR* value of 2000 ms, allowing 100 ms to complete data readout, an interval of 1900 ms is available before the next excitation occurs. In this time 19 additional slices can be acquired by moving the slice selection to a new location that is parallel and usually contiguous to the previous slices. In this way, multislicing improves the duty cycle of the acquisition without increasing the total imaging time.

5.4 Whole-Object Imaging Techniques

It is possible to extend the simultaneous observation of the signal to all the points in an object, not just to the points in a plane. This results in the reconstruction of an entire three-dimensional object and can be done by projection reconstruction (zeugmatography), three-dimensional Fourier transformation (3D FT), or combinations of both. As far as signal acquisition is concerned, all are extensions of the two-dimensional procedures.

An alternative when using selective irradiations is to excite a thick slab rather than individual slices and use an extra dimension of phase-encoding to localize planes spatially within the slab. There is an increase in imaging time proportional to the number of phase-encoding steps used in the slice dimension. This increase is less than that associated with reconstructing the whole object.

In either case, using projection reconstruction the entire signal producing object is projected onto a line, and the direction of the line is rotated in three dimensions, so that N^3 pixels can be determined from N point projections taken over N^2 unique directions. For the 3D FT, the object is projected onto a line, and phase encoded in the two directions perpendicular to the line of projection by systematically varying the gradients in these two directions, so that N^2 projections, each with a unique phase encoding, of N points can be reconstructed into N^3 pixels. This technique is popular in low field imagers[46–49] especially with faster limited flip angle techniques.

Because the signal arises from the entire object and is measured N^2 times, it is stronger than the signal from a single plane, and these techniques have an S/N advantage of $\sqrt{N}$ over planar imaging techniques. Of course, they take N times longer. The larger signal is even more demanding of dynamic range than planar imaging. For producing multiplanar images, they compete with two-dimensional multislice techniques. An advantage of whole-object techniques is that all pixels can have the same size, giving image slices with the same thickness as resolution. Because most other techniques are slice oriented, they have a slice thickness larger than the resolution within the plane. In projection reconstruction, when the angles of projection are all equal, the pixels are cubed elements. The computer can be used to select any view of the three-dimensional collection of pixels. 3D FT imaging easily allows different resolutions in each direction by changing gradient strengths. The image field-of-view ($N \times$ resolution) in each direction must be larger than the signal producing region or the object will alias onto itself.

The whole-object imaging techniques have increased technical requirements and enhanced performance characteristics that are direct extensions of their planar versions. The problem of storing and reconstructing N^3 pixels requires substantial computer resources. Effective approaches to the reconstructions have been developed.[50,51] Artifacts in 3D FT imaging are extensions of the ghosts of 2D FT. Lauterbur has used three-dimensional zeugmatography to produce images of human brain[51] and heart.[52]

6 IMAGE CONTRAST

Magnetic resonance image intensity dependence on imaging parameters gives MRI a powerful control of image contrast. Contrast is defined by the expression

$$C = \frac{(I_A + I_B)}{I_B} \tag{28}$$

where I_A is the feature signal and I_B is the background signal. As we saw, the magnetic resonance image intensity depends on the density distribution and the relaxation characteristics of the nuclei.

Since the water content in human soft tissue varies only by about 20%, hydrogen density $N(H)$ accounts for only a small portion of the contrast seen with MRI. Certain pathological conditions, such as edema or fluid-containing cysts, will have an increased water content and may be detectable on that basis alone.

6.1 Relaxation Time Based Contrast

Equations (24)–(27) give the image intensity dependence of tissues with various relaxation times for several imaging techniques. Figure 7 illustrates the behavior of the signal difference as a function of choice of *TR* and *TE* for tissues with different T_1 and T_2 values for technique (1) [equation

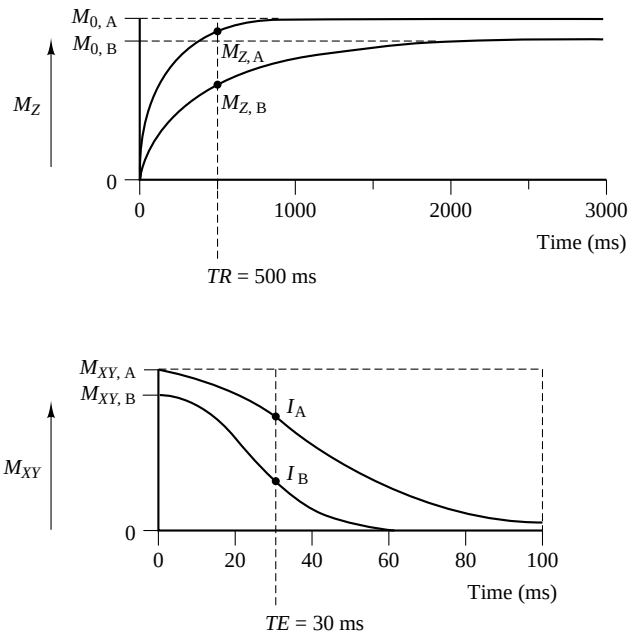

Figure 7 The effect of choice of *TR* and *TE* on the relative signal intensities I_A and I_B of tissues A and B with hydrogen density, T_1, and T_2 values $M_{0,A}$, $T_{1,A}$, and $T_{2,A}$ for tissue A and $M_{0,B}$, $T_{1,B}$, and $T_{2,B}$ for tissue B

(24)]. Two tissues A and B have relative hydrogen density values reflected by $M_{0,A}$ and $M_{0,B}$. After a 90° rf excitation, T_1 relaxation occurs at different rates, $T_{1,A}$ and $T_{1,B}$ for the two tissues. The choice of the repetition time *TR* determines the relative amounts of magnetization $M_{xy,A}$ and $M_{xy,B}$ that become transverse magnetization. $M_{xy,A}$ and $M_{xy,B}$ decay with relaxation rates $T_{2,A}$ and $T_{2,B}$, respectively. The choice of the echo delay time *TE* will determine the relative signal intensities I_A and I_B at the time of readout. It is clear from this example that the final intensity difference is affected by both *TR* and *TE* as well as the hydrogen density, T_1, and T_2 values of the tissues.

6.2 Vascular Contrast

All imaging sequences are sensitive to motion. Such sensitivities can be tailored to visualize blood vessels and blood flow. The contrast between vessels, blood, and surrounding tissue is based on combinations of motion, relaxation times, and spin phase. All three effects may be present in any image, but usually only two are used at a time for flow studies.

6.2.1 Relaxation and Motion Contrast

The imaging of blood often relies on the inflow of spins, which have received no previous rf excitation, into a volume of stationary tissue that is darkened by frequent rf excitation (short *TR* value). Inflowing blood carries full longitudinal magnetization. This gives it a bright signal compared with the suppressed background signal,[34,53] an effect known as flow-related enhancement. In these techniques, *TR* and flip angle must be selected to give sufficient background suppression while allowing enough time for fresh spins to enter the volume.

These are also called time-of-flight effects. Using this mechanism, vascular contrast is generated by creating large differences in longitudinal magnetization between stationary tissue and flowing blood.

It has recently been shown that the magnetization transfer effect[54] can help to improve vascular contrast in magnetic resonance angiography.[55] Using this method, the stationary tissue signal is affected by using an off-resonance rf excitation to reduce the longitudinal magnetization of immobile protons contained in macromolecular structures of the stationary tissue. Through chemical exchange of these immobile protons with the mobile water based protons the reduced magnetization is transferred to the mobile protons. This reduces the detectable signal since signal comes mainly from mobile protons. The result is a further suppression of the stationary tissue signal without a similar suppression of the signal from flowing blood. This gives greater vascular contrast.

6.2.2 Phase Dependent Contrast

The other mechanism commonly used to generate vascular contrast exploits differences in the phase of flowing and stationary spins. This is done by using magnetic field gradients to introduce velocity-dependent phase changes. Stationary spins (zero velocity) acquire no phase angle. Moving spins acquire a phase angle that is proportional to their velocity.

When a nucleus moves through a field gradient, its frequency changes. For nuclei moving with constant velocity v along the gradient direction, their frequency is

$$f_v = \gamma G(t) v t \tag{29}$$

where $G(t)$ is the gradient as a function of time and t is time. If the gradient is on for some time Γ, the phase accumulated is the area of this function. Thus the phase Φ is

$$\phi = \gamma \int_0^{\Gamma} G(t) v \, dt \tag{30}$$

Consider a bipolar gradient waveform $G(t)$ similar to ones used for gradient echo readout. $G(t)$ is a constant pulse of $-G$ for a time τ and then reverses to $+G$ for time τ. The phase accumulated by spins moving at a constant velocity v during this gradient waveform is

$$\phi = \gamma G v \tau^2 \tag{31}$$

For stationary spins $v = 0$, and there is no phase accumulation. All other velocities add phase to their nuclei.

When flow changes phase, if all of a sample moves at one velocity (like a plug pushed through a tube) all the nuclei have some phase change Φ. Thus, the total signal would still be strong, but will have a phase offset from zero. However, if there are many different velocities in the sample, as in laminar or turbulent flow, then each velocity will have a different phase. This distribution of phases reduces the signal and provides phase based contrast.

The distribution of phases will be centered around the phase proportional to average velocity. This allows velocity measurement. Hahn first realized that one could find the average velocity of sea water by measuring the phase of a spin echo.[56] This experiment had no spatial resolution. In MRI, the velocity dependent distribution of phase is another form of phase encoding. Here, velocity along the gradient direction is encoded rather than position. By repeating the measurement with many different values of gradient one can recover the velocity distribution.[57–59] On the other hand, if the voxel is made small enough, it includes only one velocity. Then there is no destructive interference reducing the signal, and the phase gives the velocity.

7 RESOLUTION, S/N, AND IMAGING TIME

7.1 Resolution and Field of View

Image quality will be affected by its resolution, S/N, and imaging time.[35,60] The resolution in MRI is measured by the voxel dimensions used in the image. It is determined by the frequency bandwidth of the rf excitation and reception, and the strength of the magnetic field gradients. Useful achievable resolution in a whole body image is 0.5 × 0.5 × 2 mm. Despite increasing capabilities of the hardware, there are other limitations to the minimum voxel dimension. As the voxel size decreases, signal strength decreases in proportion to the reduction in the number of nuclei it contains. The S/N becomes a practical limitation. Even with improvements in noise reduction techniques, thermal motion and diffusion within a voxel may become a more fundamental constraint. Another consideration is the relationship between resolution, the size of the field-of-view (FOV) and the imaging time. For a fixed matrix size and imaging time, the FOV will be reduced in proportion to the reduction in voxel size. To

maintain the FOV at the higher resolution, additional measurements would be necessary. If they are taken in the phase-encoding direction, the imaging time increases proportionally. If the FOV is reduced, one risks the problem of aliasing.

For example, in a head image for which the FOV in the anterior–posterior direction is smaller than the size of the head, the signal from the anterior of the head that is above the FOV will appear at the bottom of the image, overlapping the posterior segment of the image. This can be overcome by eliminating signal from outside tissue using selective irradiation or presaturation.

7.2 Signal-to-Noise Ratio

The S/N is another important contributor to image quality. Parameters of the imaging sequence such as *TR*, *TE*, and flip angle will all affect the total signal. Increasing *TR*, decreasing *TE*, and using a flip angle of 90° with a long *TR* will all increase the total signal but may be undesirable from the standpoints of contrast and imaging time. Reduction of the voxel size provides an improvement in resolution but proportionally reduces the number of signal generating spins while noise remains the same. If more measurements are taken to provide the resolution, the extra measurements bring back some S/N. Another important determinant of signal is the frequency bandwidth of the spectrum of the voxel. Distributing the voxel signal over a larger bandwidth reduces the S/N by increasing the noise included in the image. Increasing the FOV, total bandwidth, and number of elements by the same factor has no impact on the S/N because individual voxel bandwidth does not change.

For a fixed imaging sequence, the signal intensity will also be affected by the operating frequency of the magnet. Signal increases as the square of frequency, ignoring variations in relaxation times. The noise dependence is not as easily quantified. Theory shows that at high frequency, noise increases in proportion to frequency while at low frequency it is proportional to the square root of frequency.[60] The dependence of the S/N on operating frequency has been reported experimentally to vary to the first power or less. For a well tuned system, the body itself is the biggest noise source because random currents in the body are picked up as noise by the receiver coil. The T_1 relaxation time of most tissues increases with field strength.[61,62] Thus, the imaging parameters must change with field strength to achieve the best contrast.

7.3 Imaging Time

To acquire a full data set, excitation, and readout are repeated after *TR* for each point, line or projection. An $N \times N$ point scan then takes $N^2 \times TR$. Line scans, projection reconstruction, and Fourier imaging measure a line or projection every *TR*. Repeated measurements of the same line or projection may also be obtained in order to improve the S/N using signal averaging. In this case

$$\text{total time} = (TR)N_{\text{lines}}N_{\text{acq}} \tag{32}$$

where N_{acq} is the number of repetitions of each line or projection, and

$$\text{S/N} \propto \sqrt{N_{\text{acq}}} \tag{33}$$

Thus, improving the S/N by increasing N_{acq} requires a large increase in imaging time. For projection reconstruction and Fourier imaging the S/N also improves by

$$\text{S/N} \propto \sqrt{N_{\text{lines}}} \tag{34}$$

This efficient S/N performance is one of the main reasons for their success.

8 CONCLUSION

A number of imaging methods have been described. Early imaging development concentrated on increasing image quality in terms of the S/N, resolution, and contrast. Today, these items are sufficient for clinical medical needs and attention is moving to reducing imager cost and imaging time. Cost reduction is dominated by imager system design trade-offs. On the imaging time front, we have seen that reducing *TR* is one way to speed up imaging. Another is to collect multiple projections in every *TR* interval. Echo planar imaging[63,64] pushes speed to the limit in this direction by acquiring all phase-encoded projections in a train of spin echoes (typically 64 echoes). By taking only some of the projections in repeated echo trains one can trade off time, the S/N, and resolution over broad ranges. This is the challenge of MRI, finding the technique and combination of parameters that best solve a given imaging problem.

9 RELATED ARTICLES

Gradient Coil Systems; Health and Safety Aspects of Human MR Studies; Low-Field Whole Body Systems; Resistive and Permanent Magnets for Whole Body MRI; Whole Body Magnetic Resonance Angiography; Whole Body Magnetic Resonance Spectrometers: All-Digital Transmit/Receive Systems.

10 REFERENCES

1. A. N. Garroway, P. K. Grannell, and P. Mansfield, *J. Phys. C.*, 1974, **7**, 457.
2. D. Hoult, *J. Magn. Reson.*, 1979, **35**, 69.
3. D. I. Hoult, *J. Magn. Reson.*, 1980, **38**, 369.
4. P. Mansfield, A. Maudsley, P. Morris, and I. Pykett, *J. Magn. Reson.*, 1979, **33**, 261.
5. M. S. Silver, R. I. Joseph, and D. I. Hoult, *J. Magn. Reson.*, 1984, **59**, 347.
6. S. Conolly, D. Nishimura, and A. Macovski, *IEEE Trans. Med. Imaging*, 1986, **5**, 106.
7. J. W. Carlson, *J. Magn. Reson.*, 1992, **97**, 65.
8. P. C. Lauterbur, *Nature*, 1973, **242**, 190.
9. A. Kumar, D. Welti, and R. Ernst, *J. Magn. Reson.*, 1975, **18**, 69.
10. W. A. Edelstein, J. M. S. Hutchison, G. Johnson, and T. Redpath, *Phys. Med. Biol.*, 1980, **25**, 751.
11. D. A. Ortendahl, N. M. Hylton, L. Kaufman, J. C. Watts, L. E. Crooks, C. M. Mills, and D. D. Stark, *Radiology*, 1984, **153**, 479.

12. W. A. Edelstein, P. A. Bottomley, H. R. Hart, and L. S. Smith, *J. Comput. Assist. Tomogr.*, 1983, **7**, 391.
13. W. S. Hinshaw, *J. Appl. Phys.*, 1976, **47**, 3709.
14. L. Kaufman, L. E. Crooks, and A. R. Margulis, eds., 'Nuclear Magnetic Resonance Imaging in Medicine', Igaku Shoin, New York, 1981.
15. P. G. Morris, 'Nuclear Magnetic Resonance Imaging in Medicine and Biology', Clarendon, Oxford, 1986.
16. C. L. Partain, J. A. Patton, M. V. Kulkarni, and A. E. James, eds., 'Magnetic Resonance Imaging', Saunders, Philidelphia, Vol. 2, 1988.
17. W. P. Aue, S. Muller, T. A. Cross, and J. Seelig, *J. Magn. Reson.*, 1984, **56**, 350.
18. P. A. Bottomley, *Ann. N.Y. Acad. Sci.*, 1987, **508**, 333.
19. J. Frahm, K.-J. Merboldt, and W. Hanicke, *J. Magn. Reson.*, 1987, **72**, 502.
20. R. Damadian, L. Minkoff, M. Goldsmith, M. Stanford, and J. Koutcher, *Science*, 1976, **194**, 1430.
21. L. E. Crooks, T. P. Grover, L. Kaufman, and J. R. Singer, *Invest. Radiol.*, 1978, **13**, 63.
22. R. Damadian, M. Goldsmith, and L. Minkoff, *Physiol. Chem. Phys.*, 1978, **10**, 285.
23. E. R. Andrew, P. A. Bottomley, W. S. Hinshaw, G. N. Holland, W. S. Moore, and C. Simaroj, *Phys. Med. Biol.*, 1977, **22**, 971.
24. G. N. Holland, W. S. Moore, and R. C. Hawkes, *J. Comput. Assist. Tomogr.*, 1980, **4**, 1.
25. P. Mansfield, A. A. Maudsley, and T. Baines, *J. Phys. E*, 1976, **9**, 271.
26. P. Mansfield, I. L. Pykett, and P. G. Morris, *Br. J. Radiol.*, 1978, **51**, 921.
27. L. E. Crooks, *IEEE Trans. Nucl. Sci.*, 1980, **NS-27**, 1239.
28. L. E. Crooks, J. C. Hoenninger, M. Arakawa, L. Kaufman, R. McRee, J. Watts, and J. Singer, *Radiology*, 1980, **136**, 701.
29. J. Hutchison, W. Edelstein, and G. Johnson, *J. Phys. E*, 1980, **13**, 903.
30. W. S. Hinshaw, P. A. Bottomley, and G. N. Holland, *Nature*, 1977, **270**, 722.
31. W. S. Hinshaw, E. R. Andrew, P. A. Bottomley, G. N. Holland, W. S. Moore, and B. S. Worthington, *Br. J. Radiol.*, 1978, **51**, 273.
32. P. A. Bottomley, *Cancer Res.*, 1979, **39**, 468.
33. G. Hansen, L. E. Crooks, P. L. Davis, J. Degroot, R. Horfhuns, A. R. Margulis, C. Gooding, L. Kaufman, J. Hoenninger, M. Arakawa, R. McRee, and J. Watts, *Radiology*, 1980, **136**, 695.
34. G. K. von Schulthess, M. Fisher, L. E. Crooks, and C. B. Higgins, *Radiology*, 1985, **156**, 125.
35. P. Brunner and R. R. Ernst, *J. Magn. Reson.*, 1979, **33**, 83.
36. T. F. Budinger, S. E. Derenzo, G. T. Gulberg, W. L. Greenberg, and R. H. Huesman, *J. Comput. Assist. Tomogr.*, 1977, **1**, 131.
37. G. H. Glover and J. M. Pauly, *Magn. Reson. Med.*, 1992, **28**, 275.
38. W. V. House, *IEEE Trans. Nucl. Sci.*, 1980, **NS-27**, 1220.
39. G. N. Holland, R. C. Hawkes, and W. S. Moore, *J. Comput. Assist. Tomogr.*, 1980, **4**, 429.
40. R. C. Hawkes, G. N. Holland, W. S. Moore, and B. S. Worthington, *J. Comput. Assist. Tomogr.*, 1980, **4**, 577.
41. L. E. Crooks, M. Arakawa, J. C. Hoenninger, J. Watts, R. McRee, L. Kaufman, P. L. Davis, A. R. Margulis, and J. Degroot, *Radiology*, 1982, **143**, 169.
42. D. I. Hoult, Proceedings of the 19th Experimental NMR Conference, Blacksburg, Virginia, 1978.
43. P. C. Lauterbur, D. M. Kramer, W. V. House, and C.-N. Chen, *J. Am. Chem. Soc.*, 1975, **97**, 6866.
44. P. Bendel, C. M. Lai, and P. C. Lauterbur, *J. Magn. Reson.*, 1980, **38**, 343.
45. T. R. Brown, B. M. Kincaid, and K. Ugurbil, *Proc. Natl. Acad. Sci. USA*, 1982, **79**, 3523.
46. R. Sutherland and J. Hutchison, *J. Phys. E*, 1978, **11**, 79.
47. G. Johnson, J. M. S. Hutchison, T. W. Redpath, and L. M. Eastwood, *J. Magn. Reson.*, 1983, **54**, 374.
48. J. Carlson, L. Crooks, D. Ortendahl, D. M. Kramer, and L. Kaufman, *Radiology*, 1988, **166**, 266.
49. D. M. Kramer, L. Kaufman, P. Rothschild, J. Hale, J. Wummer, and K. K. Hake, *IEEE Trans. Med. Imaging*, 1991, **10**, 382.
50. P. C. Lauterbur and C. M. Lai, *IEEE Trans. Nucl. Sci.*, 1980, **27**, 1227.
51. D. M. Kramer, J. S. Schneider, A. M. Rudin, and P. C. Lauterbur, *Neuroradiology*, 1981, **21**, 239.
52. M. A. Heneghan, T. M. Biancaniello, E. Heidelberger, S. B. Peterson, M. J. Marsh, and P. C. Lauterbur, *Radiology*, 1982, **143**, 183.
53. L. Kaufman, L. E. Crooks, P. E. Sheldon, W. Rowan, and T. Miller, *Invest. Radiol.*, 1982, **17**, 554.
54. S. D. Wolff and R. S. Balaban, *Magn. Reson. Med.*, 1989, **10**, 135.
55. G. B. Pike, B. S. Hu, G. H. Glover, and D. R. Enzmann, *Magn. Reson. Med.*, 1992, **25**, 372.
56. E. L. Hahn, *J. Geophys. Res.*, 1960, **65**, 776.
57. T. Grover and J. R. Singer, *J. Appl. Phys.*, 1971, **42**, 938.
58. A. N. Garroway, *J. Phys. D: Appl. Phys.*, 1974, **7**, L159.
59. P. R. Moran, *Magn. Reson. Imaging*, 1982, **1**, 197.
60. D. I. Hoult and P. C. Lauterbur, *J. Magn. Reson.*, 1979, **34**, 425.
61. L. E. Crooks, M. Arakawa, J. C. Hoenninger, B. McCarten, J. C. Watts, and L. Kaufman, *Radiology*, 1984, **151**, 127.
62. J.-H. Chen, H. E. Avram, L. E. Crooks, M. Arakawa, L. Kaufman, and A. C. Brito, *Radiology*, 1992, **184**, 427.
63. P. Mansfield and I. L. Pykett, *J. Magn. Reson.*, 1978, **29**, 355.
64. P. Mansfield, *Br. Med. Bull.*, 1984, **40**, 187.

Acknowledgements

The author thanks Philip Sheldon for contributions to the illustrations.

Biographical Sketch

Lawrence E. Crooks. *b* 1949. B.S., 1971, M.S., 1973, and Ph.D., 1978, Electrical Engineering and Computer Science, University of California, Berkeley. Introduced to NMR by J.R. Singer. Faculty in Radiology, University of California, San Francisco, 1976–1993. Research fellow at Toshiba America MRI 1994–present. More than 100 papers and 14 patents on MR imaging. Research interests are the use of MR for medical imaging and the associated instrumentation.

Motion Artifacts: Mechanism and Control

Michael L. Wood
University of Toronto, Toronto, Ontario, Canada

1 INTRODUCTION

The acquisition of data for magnetic resonance (MR) images usually takes too long to freeze motion in the human body, such as the abdomen which moves during breathing. Motion during data acquisition blurs MR images and repetitive motion also generates ghost-like replicas of moving structures (Figure 1).[1,2] Ghosts can mask or mimic lesions and otherwise degrade image quality. Motion also hinders the quantitative analysis of images by changing the intensity of moving anatomic structures.[3,4]

Motion causes artifacts in MR images through several mechanisms, depending on the characteristics of motion, intensity of moving structures, and the pulse sequence, particularly the configuration of magnetic field gradient pulses. The purpose of this article is to review the mechanisms behind motion artifacts and the most successful ways to control the artifacts. The article focuses on respiratory motion in two-dimensional (2D) Fourier transform MR imaging, although the principles apply generally to other types of motion (see ***Pulsatility Artifacts Due to Blood Flow and Tissue Motion and Their Control*** and ***Spin Warp Data Acquisition***). Some of the principles also apply to imaging techniques, such as echo planar imaging, spiral scanning, line scanning, and fast spin echo imaging, but specific reports should be consulted for more detail.[5–8] (See also ***Echo-Planar Imaging***; ***Image Formation Methods***; ***Projection–Reconstruction in MRI***; ***Spiral Scanning Imaging Techniques***.)

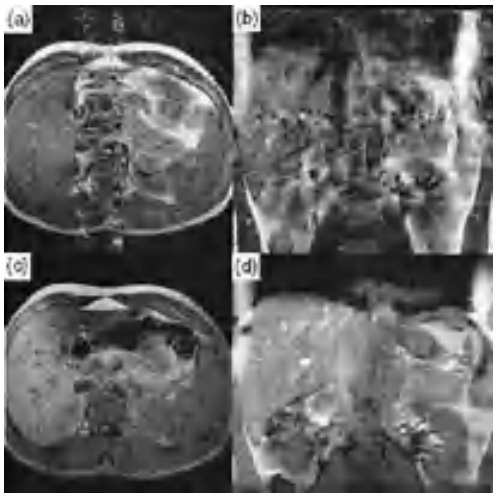

Figure 1 Ghosts and blurring caused by respiratory motion and also blood flow during 2D MR imaging of a normal patient: (a) and (b) are slices in the transverse and coronal orientations, respectively, acquired during normal breathing on a commercial 1.5 T MRI system using a spin echo pulse sequence with *TR*/*TE* (repetition time/echo time) = 300/12 ms, slice thickness = 10 mm, field-of-view (FOV) = 350 mm, and data matrix = 256 × 256. The same patient held his breath during the acquisition of (c) and (d), each of which required 13 s using a spoiled gradient echo pulse sequence with *TR*/*TE* = 50/4 ms, rf tip angle = 60°, inferior and superior spatial presaturation, and otherwise identical imaging conditions

2 RESPIRATORY MOTION

Various physiologic motions and body movements degrade MR images. The most problematic physiologic motions include blood flow, cerebrospinal fluid (CSF) pulsation, respiratory motion, cardiac motion, and gastrointestinal peristalsis. Blood flow can cause intense ghosts and inconsistent image intensity within vessels, which can mimic dissections and thrombi or mask pathology (see ***Pulsatility Artifacts Due to Blood Flow and Tissue Motion and Their Control***). Body movements, such as nodding of the head or shifting of position, are encountered frequently during MR imaging of uncomfortable or disoriented patients and infants and children. Breathing is the main problem for abdominal MRI, causing the liver, spleen, pancreas, and kidneys to move craniocaudally and anteroposteriorly (see ***Abdominal MRA***). The amplitude, period, and pattern of respiratory motion vary considerably between individuals. Furthermore, various diseases of the heart or lungs result in abnormal and exaggerated breathing (see ***Lung and Mediastinum MRI***). Nevertheless, certain trends are recognized.

In the upper abdomen, the most displacement tends to occur craniocaudally, averaging about 20 mm, but approaching 100 mm during deep breathing.[9–11] In the transverse plane, the displacement of the abdominal wall generally is only about one-sixth that of the longitudinal displacement of the abdominal contents.[9] The thorax, through the action of the intercostal muscles, can experience substantial displacement in the transverse plane. Motion of the diaphragm during breathing also tends to flare the base of the rib cage.

3 MODULATION OF *k*-SPACE

Data from Fourier imaging correspond to the coordinates k_x and k_y of *k*-space, which are associated with frequency encoding and phase encoding, respectively (see ***Image Formation Methods*** and ***Spin Warp Data Acquisition***). Images are obtained simply by inverse Fourier transforming the *k*-space data. Each row of *k*-space has a distinct value of k_y, depending on the phase-encoding gradient pulse. Typically, 256 values of k_y are acquired to produce 256 pixels in the phase-encoding direction. As illustrated in Figure 2, there is a much longer time between consecutive k_y values than between consecutive k_x.

Ghosts arise when motion causes a periodic modulation of the magnetization measured as data for an MR image.[12–15] Motion affects the magnitude or the phase of the magnetization, which disrupts the Fourier transform relationship between *k*-space and image. Respiratory motion tends to modulate *k*-space periodically or at least quasiperiodically. The inverse

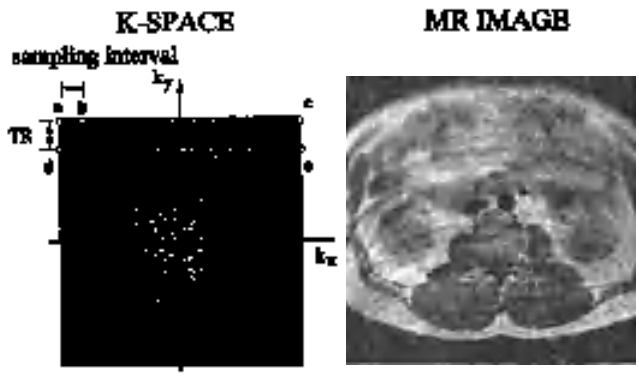

Figure 2 Ghosts along phase-encoding direction of Fourier MR images, due to much longer time between consecutive values of k_y than k_x. Typical 2D Fourier pulse sequences fill *k*-space row by row where each row has a distinct k_y, corresponding to a phase-encoding gradient pulse of different amplitude. Sample a is the first sample in the echo after the strongest phase-encoding gradient pulse. Sample b follows approximately 10 μs later. The echo reaches its peak at $k_x = 0$ and the last sample from this first echo is stored at position c. The time between samples a and c is the sampling time, which is typically about 10 ms. The next row is filled with samples from the next echo, for which the amplitude of the phase-encoding gradient is reduced slightly. The time between samples a and d is the repetition time, *TR*, which typically is on the order of 1 s

Fourier transform of the function describing the modulation is a series of peaks corresponding to harmonics in the modulation function. These peaks can be characterized by a point spread function (PSF).[2] Inverse Fourier transforming the *k*-space data yields an image with ghosts, which are the average magnetization convolved with the peaks associated with modulation.

Respiratory motion is not rapid enough to modulate the data for different k_x and the same k_y. When *TR* is on the order of 1 s, respiratory motion can modulate the k_y direction, thereby producing ghosts along the phase-encoding direction of an MR image. Incidentally, 3D MR images have two phase-encoding directions and ghosts propagate along both.[2]

The phase-encoding direction can be chosen to redirect ghosts—but not to eliminate them, because motion in any direction causes artifacts in MR images.[12] The anteroposterior direction in Figure 1(a) was resolved by phase encoding. Ghosts from blood flow through the aorta interfere with the left lobe of the liver. If the left–right direction had been phase encoded instead, the column of ghosts from the aorta would have been rotated 90° and these ghosts would have interfered with the right lobe of the liver. Thus, the phase-encoding direction influences the overlap of ghosts with other structures. The preferred choice depends on the anatomic site and the slice orientation.

4 MOTION-INDUCED PHASE SHIFTS DURING *TE*

4.1 Mechanism

Movement during the application of gradient pulses used for spatial encoding can affect the phase of the magnetization adversely. The phase, $\phi(TE)$, that accumulates after a radiofrequency (rf) pulse at time $t = 0$ until the center of an echo at time *TE* is particularly relevant to spatial encoding and is given by the following equation:

$$\phi(TE) = \gamma \int_0^{TE} \boldsymbol{r}(t) \cdot \boldsymbol{G}(t)\, \mathrm{d}t \tag{1}$$

where γ is the gyromagnetic ratio and $\boldsymbol{r}(t)$ and $\boldsymbol{G}(t)$ are time-dependent vectors representing the position of the spins and the three gradient waveforms, respectively.

4.1.1 *Gradient Moments*

The configuration of gradient pulses and the position of the spins need to be known to calculate $\phi(TE)$. It is simplest to consider one direction at a time, because motion along each direction contributes separately to $\phi(TE)$. Let $r(t)$ denote the component of $\boldsymbol{r}(t)$ along a particular direction of interest. Since *TE* is usually brief relative to movements in the body, it is useful to expand $r(t)$ in the following Taylor series:

$$r(t) = r_0 + v_0 t + \tfrac{1}{2} a_0 t^2 + \ldots \tag{2}$$

The symbols r_0, v_0, and a_0 represent the position, velocity, and acceleration, respectively, at time $t = 0$. This Taylor series expansion is useful when only two or three terms are significant. After substituting equation (2) into equation (1), $\phi(TE)$ becomes the following:

$$\phi(TE) = \gamma \left[r_0 \int_0^{TE} G(t)\, \mathrm{d}t + v_0 \int_0^{TE} tG(t)\, \mathrm{d}t + (1/2)a_0 \times \int_0^{TE} t^2 G(t)\, \mathrm{d}t + \ldots \right] \tag{3}$$

The integrals in equation (3) are defined as the zeroth, first, and second moments of the gradient waveform, $G(t)$. Normally, the slice selection and frequency-encoding gradient waveforms are configured so that $\phi(TE)$ vanishes. Two identical pulses in a gradient waveform contribute equally to the zeroth moment, but the later pulse influences higher order moments more. If a gradient waveform has a large first moment, equation (3) indicates that a given velocity will contribute more to $\phi(TE)$. Assuming that the time between the two pulses in Figure 3 is negligible, motion of constant velocity, v, along this direction would make $\phi(TE)$ nonzero by $\frac{1}{2}\gamma G v TE^2$, which is a motion-induced phase shift. Larger phase shifts occur for faster motion or longer *TE*. Similarly, acceleration influences $\phi(TE)$ in proportion to the second moment. Thus, gradient moments characterize the sensitivity of a gradient waveform to motion.

Phase shifts induced by motion during *TE* present three problems for MR images—ghosts, intravoxel phase dispersion, and spatial misregistration. Ghosts arise if the velocity changes during different *TE* intervals, which is usually the case. Intravoxel phase dispersion, which arises when a distribution of velocities exists within a voxel, weakens the net magnetization within the voxel. Misregistration of flowing blood within a vessel can occur when the vessel courses obliquely within a slice, because frequency encoding and phase encoding are separated by a few milliseconds.[16]

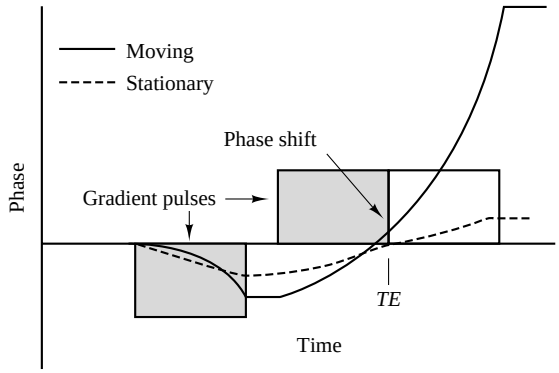

Figure 3 Phase shift at time *TE*, as a result of motion during application of gradient pulses. The phase of the magnetization from a stationary structure and one moving at constant velocity along the frequency-encoding direction are shown for a two pulse gradient waveform, such as that used for frequency encoding in a gradient echo pulse sequence. The gradient waveform is designed to yield an echo midway through the second pulse, at which time, *TE*, the cumulative time integral or area vanishes. Motion makes the magnetization phase at *TE* nonzero, because the phase accumulates at a position-dependent rate

4.2 Control

4.2.1 Gradient Moment Nulling

Motion-induced phase shifts can be reduced by configuring a gradient waveform to make its first and possibly higher moments vanish at the time *TE*.[17–19] (see also ***Pulsatility Artifacts Due to Blood Flow and Tissue Motion and Their Control***). This procedure is called gradient moment nulling (GMN), motion artifact suppression technique (MAST), flow compensation, gradient motion rephasing (GMR), gradient moment compensation (GMC), and other names.[20] According to equation (3), first-order nulling, in which the first moment of a gradient waveform becomes zero, prevents motion of constant velocity from time t = 0 to *TE* from shifting the magnetization phase. In implementing GMN, usually another pulse needs to be added to the gradient waveform. Seldom are gradient moments higher than the first nulled. Usually, GMN is applied to the frequency-encoding and slice selection gradient waveforms. Occasionally, GMN is incorporated into the phase encoding gradient waveform to eliminate oblique-flow artifacts.

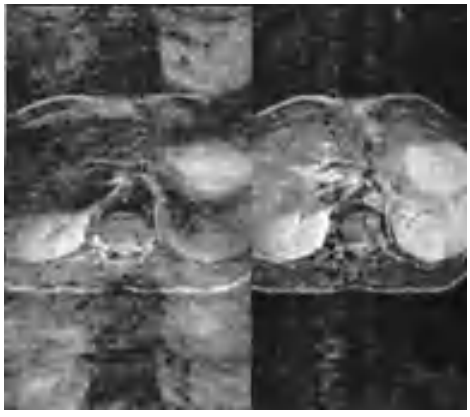

Figure 4 Demonstration of GMN in reducing ghosts in 1.0 T abdominal MR image. First-order GMN in both the slice selection and frequency-encoding directions was used for the right-hand image, but not the left-hand image. All other imaging conditions were the same for both images, including *TR*/*TE* = 2000/45 ms. The phase-encoding direction was anteroposterior. Note the bright blood vessels in the liver in the left-hand image. (Reproduced by permission of the American Institute of Physics from M. L Wood and Q. S. Xiang, in 'Medical Physics Monograph No. 21: The Physics of MRI: 1992 AAPM Summer School Proceedings', eds. M. J. Bronskill and P. Sprawls, 1993, p. 383)

Attributes of GMN include a sometimes dramatic reduction of ghosts and a return of the image intensity to the expected level, as illustrated in Figure 4. Once GMN has been implemented into a pulse sequence, its use is simple and it does not prolong patient preparation or data acquisition. It applies to all types of motion and all pulse sequences. Unfortunately, the extra gradient pulses required by GMN prolong the minimum *TE* that can be achieved. This is a serious limitation for essentially every pulse sequence. Moreover, hepatic blood vessels made bright by GMN might be mistaken for pathology on long *TR*/long *TE* images.

5 INTENSITY OF MOVING STRUCTURES

5.1 Mechanism

When structures that move are more intense, their ghosts are correspondingly more intense. The intensity of any ghost is proportional to the intensity of the moving anatomic structure that created it. The intensity of a particular structure relative to the background noise depends on the pulse sequence and its parameters, such as *TR* and *TE*, and general conditions, such as the signal-to-noise ratio (S/N), which depend on other factors, such as the magnetic field strength and receiver coil sensitivity. For example, adipose tissue in short *TR*/short *TE* spin echo pulse sequences tends to be the most intense structure, in which case the transverse movement of the abdominal wall during breathing creates conspicuous ghosts. Blood flowing through single slice, gradient echo images usually is much more intense than in spin echo images, in which case the ghosts are also more intense. High-field images tend to have conspicuous ghosts, principally because these images have less random noise to hide ghosts and also greater contrast between adipose tissue and other tissues.[12,13] Positioning a surface coil near a moving structure can also cause ghosts to be more intense than if a coil with lower sensitivity had been used.

5.2 Control

Reducing the intensity of a moving structure reduces the intensity of the associated ghosts. Such an action is acceptable only if the structure need not be imaged. Several methods for reducing the intensity of certain anatomic structures have been advanced, including spatial presaturation, spectral presaturation, short T_1 inversion recovery (STIR), and surface-coil imaging. Each is explained below, beginning with spatial presaturation, which is the most widely used.

5.2.1 Spatial Presaturation

A few milliseconds before each rf excitation, one or more spatially selective rf pulses can be applied to tip longitudinal magnetization in a designated region into transverse magnetization.[12,19] Ideally, this so-called spatial presaturation would leave no longitudinal magnetization in the region for an rf excitation pulse to tip into transverse magnetization and thereby elicit an MR signal. Spatial presaturation can affect a strip in any orientation. Presaturation seems to be implemented on every commercial MRI system and identified by many different acronyms, including SAT, REST, PRE-SAT, PRESAT, BFAST, and SATURATION.[20]

Spatial presaturation is compatible with essentially every pulse sequence and generally does not prolong data acquisition or require any special preparations. However, presaturation increases the time to prepare each MR signal, such that fewer slices can be imaged during the same *TR*. The rf pulses required by presaturation also increase the power deposited during data acquisition. These disadvantages of presaturation are usually tolerable given its attributes.

There are many useful applications of presaturation, one of which is to reduce the intensity of the abdomen in images of the spine, so that ghosts from abdominal motion cause less interference. Ghosts caused by the pulsatile flow of blood through a slice can be reduced by presaturating regions on both sides of the slice, as illustrated in Figure 1. Incidentally, presaturation can also restrict the field-of-view (FOV) and help distinguish between arteries and veins (see ***Time-of-Flight Method of MRA***).

5.2.2 Spectral Presaturation

The objective of spectral presaturation is to reduce the intensity of either fat or water, based on their characteristically different Larmor frequency. At 1.5 tesla (T), the Larmor frequency of water is about 225 Hz greater than the Larmor frequency of fat. Spectral presaturation is similar to spatial presaturation, except that the rf pulse is spectrally selective rather than spatially selective. The rf pulse for presaturating fat at 1.5 T would have a frequency about 225 Hz less than the rf pulse for generating an MR signal from water. Spectral presaturation is implemented on many commercial MRI systems and identified by acronyms, including FATSAT, SPIR, and ChemSat.[20] The attributes and limitations of spectral presaturation are similar to those of spatial presaturation, but an additional limitation is that spectral presaturation requires a homogeneous magnetic field. The field can be made more homogeneous through shimming, although shimming takes time.

5.2.3 STIR

Short T_1 inversion recovery (STIR)[21] is an inversion–recovery pulse sequence in which the inversion time is chosen such that longitudinal magnetization from adipose tissue reaches zero when each rf excitation pulse is applied. The short T_1 of adipose tissue allows STIR to zero its image intensity and still achieve good contrast between other tissues. Unfortunately, STIR gives fluids a high intensity and their motion can generate more conspicuous ghosts. The concept of selecting the inversion time to null a tissue with a characteristic T_1 applies also to tissues other than adipose.

5.2.4 Surface-Coil Imaging

The sensitivity of surface coils decreases with distance from the coil (see ***Surface and Other Local Coils for In Vivo Studies***). Although this compromises image uniformity, it is beneficial when the lowest sensitivity is near a moving anatomic structure that does not need to be imaged. For example, the spine coil used for most spine images makes the intensity of the anterior region of the abdominal wall much less than that of the posterior region close to the coil. Consequently, ghosts from movement in the anterior region are much less intense than in images acquired using the body coil.

6 DISPLACEMENT DURING *TR*

6.1 Mechanism

The amount of movement during data acquisition affects the intensity of ghosts. Greater displacement (pixels rather than centimeters) causes more modulation of the *k*-space data. When the displacement is more extensive, ghosts located farther from moving structures tend to become more intense.[12]

6.2 Control

Displacement during *TR* can be controlled by several methods, including restraining, breath-holding, gating, triggering, retrospective gating, and postprocessing, each of which is outlined below.

6.2.1 Restraining

Restraining could be considered insurance against extensive displacement. Restraining applies to a wide variety of MRI examinations, although the exact procedure depends on the anatomic site, resourcefulness of the operator, and cooperation of the patient. The anterior–posterior movement of the abdomen can be restricted using an inflexible band wrapped around the abdomen. However, a tight band might lead to an altered pattern of breathing with more displacement in the craniocaudal direction, which would be counterproductive.

6.2.2 Breath Holding

Images acquired rapidly can sometimes capture anatomic structures while they are essentially stationary (see ***Echo-Planar Imaging***; ***Spiral Scanning Imaging Techniques*** and ***Whole Body Magnetic Resonance: Fast Low-Angle Acquisition Methods***). Respiratory motion was frozen during the 13-s data acquisition for Figures 1(c) and (d). However, the left lobe of the liver seemed to be affected by heart motion transmitted through the diaphragm. Misregistration of anatomy is a problem in images acquired during repeated breath holding periods. Although techniques for producing MR images rapidly continue to improve, they still provide less contrast and S/N than more time-consuming techniques. Certain rapid imaging techniques are prone to degradation caused by abrupt changes in magnetic susceptibility, chemical shift, and other resonance offsets. Nevertheless, further technical developments are anticipated.

6.2.3 Gating

The principle behind gating is to allow data acquisition to proceed only if the displacement does not exceed a predetermined limit.[22,23] Otherwise, data are rejected and data acquisition is repeated until the displacement becomes acceptable. By rejecting data acquired during extreme displacements, gating reduces ghosts and blurring and makes it appear as if less motion actually occurred. Gating has been applied to overcome respiratory motion for MR imaging of the abdomen and thorax, although now it is rarely used.

The most significant limitation of gating is that it requires data acquisition to be repeated, which typically doubles or triples the data acquisition time. Data acquisition need not take as long if only the most extreme displacements are rejected or if gating is used for only a fraction of data acquisition.[24] Another limitation is that gating relies on measurements of displacement, typically provided by a transducer, although MR signals can also be used to monitor position.[25] The use of a transducer prolongs patient preparation and also adds complexity to the procedure.

6.2.4 Triggering

Data acquisition can be triggered to a specific phase of a repetitive motion.[12] Triggering has been used effectively for imaging of the heart, blood vessels, and the spine, in which the pulsatile flow of CSF causes ghosts (see ***Cardiac Gating Practice*** and ***Pulsatility Artifacts Due to Blood Flow and Tissue Motion and Their Control***). These movements are periodic and correlated with the electrocardiogram (ECG) or a peripheral pulse, which can be monitored and used as the data acquisition trigger. Data for separate images can be acquired at different delays after the trigger is detected. Triggering reduces ghosts and blurring, to the extent that the data for each image are acquired at the same phase of a periodic motion. If the trigger is irregular, *TR* varies, which in itself causes ghosts.[23,24] Irregular triggers and the lack of a convenient physiologic trigger limit the usefulness of triggering at controlling respiratory motion.

6.2.5 Retrospective Gating

Retrospective gating monitors a signal correlated to motion and uses it later to sort the data measurements into groups acquired approximately at the same time relative to this signal.[26] (See also ***Cardiac Gating Practice***.) The time that each echo is measured relative to the trigger is recorded with the data. After the data have been acquired, they are sorted so that separate images can be reconstructed from data acquired at similar stages of motion. Cardiac imaging is the best known application of retrospective gating, but it could be extended to control respiratory motion.

6.2.6 Postprocessing

Data that have already been collected can be processed to undo the degradation caused by motion.[27] A realistic model of the motion is needed for effective postprocessing. Several strategies for extracting information about motion during data acquisition have been explored, including the use of navigator echoes interleaved with the echoes intended for imaging.[28] One important attribute is that postprocessing can reduce both the ghosts and blurring caused by motion. Postprocessing is difficult for respiratory motion because the associated displacement varies within the abdomen.[29,30]

7 PERIODICITY OF MOTION

7.1 Mechanism

Repetitive motion, such as respiratory motion, causes ghosts in MR images. Although respiratory motion has a range of frequencies, often one frequency dominates. Usually, the phase-encoding gradient is incremented monotonically, in which case single frequency motion yields a pattern of regularly spaced ghosts, with the separation, Δy, given below:[2]

$$\frac{\Delta y}{\mathrm{FOV}} = F \cdot NSA \cdot TR \tag{4}$$

where FOV is the field-of-view, *NSA* is the number of data measurements averaged, *TR* is the repetition time, and *F* is the frequency of motion. The product of *NSA* and *TR* is the time after which the amplitude of the phase-encoding gradient is changed. Ghosts that would extend beyond the *FOV* are folded back into MR images from the opposite side, as a result of aliasing.

7.2 Control

Methods to control the periodicity of motion include averaging, pseudogating, ordered phase encoding, and ghost interference. Each of the remedies are explained below, beginning with averaging, because it is the most versatile and widely used.

7.2.1 Averaging

Multiple sets of data can be averaged. The number of repetitions is called the number of signal averages (*NSA*) or acquisitions, data sets, averages, excitations, repetitions, projections, views, and profiles.[20] Averaging reduces random noise in MR images and it can also reduce ghosts if the motion is in a different phase when repeated data are acquired. The pattern of ghosts that would arise from separate reconstruction of these data would be similar, except for the phase of each ghost.[24] Averaging the data, or equivalently, images, allows cancellation of ghosts that have different phase.

Two alternative strategies for collecting repeated data are known as parallel and serial averaging.[31] In parallel averaging, data for each particular k_y are repeated before collecting data for a new k_y. Serial averaging collects complete sets of *k*-space serially. Equation (4) applies explicitly to parallel averaging. The factor *NSA* does not affect the separation of ghosts in serial averaging. Serial averaging is advantageous for reducing ghosts because it provides a much longer time between repeated data, so that a moving structure is more likely to be in a new position for the repeated data.

Averaging is easy to use, versatile, and reasonably effective at suppressing ghosts. However, averaging prolongs data acquisition by the factor *NSA*, making it more practical for shorter *TR*. Attempts at making averaging less time-consuming have been proposed, such as repeating only part of the data. It is difficult to suppress ghosts completely by averaging, because the intensity of ghosts generally decreases only as $\sqrt{(NSA)}$.[32] Data

acquisition would need to become four-times longer to reduce ghosts in one-half. Moreover, averaging fails to reduce the blurring caused by repetitive motion. In spite of these limitations, averaging is a useful remedy for motion artifacts, because of its simplicity and versatility.

7.2.2 Pseudogating

Pseudogating uses aliasing to superimpose all of the ghosts back on the moving structure or at a distance of one-half of the FOV from the moving structure. A deliberate attempt at pseudogating consists of choosing *NSA* and *TR* so that $\Delta y = n \cdot \text{FOV}/2$, where n is a positive integer.[24,33] Pseudogating is not widely used to control respiratory motion, because it is difficult to choose the proper *TR* and *NSA* and the choice tends to require a long data acquisition time.

7.2.3 Ordered Phase Encoding

Ordered phase encoding (OPE) alters the sequence in which data for different k_y are acquired, depending on the position of a patient.[29,34,35] Ordered phase encoding is referred to as ROPE, COPE, POPE, respiratory compensation (RESCOMP), respiratory-sorted phase encoding (RSPE), phase-encoded artifact reduction (PEAR), phase reordering, and FREEZE.[20] Prior to the start of data acquisition, OPE requires information about the pattern of motion, which is usually provided by a transducer attached to the patient. Prior to each rf excitation, the position is measured to choose the particular value of k_y to acquire. In practice, end expiration, end inspiration, and positions in between these two extremes are assigned blocks of *k*-space (see Figure 5).

If successful, OPE makes it appear as if a patient simply inhaled once during data acquisition, even though many cycles of respiratory motion occurred. The resulting images should be free of ghosts, because the motion modulates the data monotonically, rather than periodically. Unlike gating, OPE does not interrupt data acquisition, so it should not prolong data acquisition. However, OPE is technically difficult to implement and requires special patient preparation. Consequently, the success of OPE relies on the cooperativeness of the patient and the expertise of the MRI operator. Ordered phase encoding applies to a specific movement, usually respiratory motion. It does not generally reduce ghosts from other movements simultaneously and it fails to decrease the blurring caused by movement.

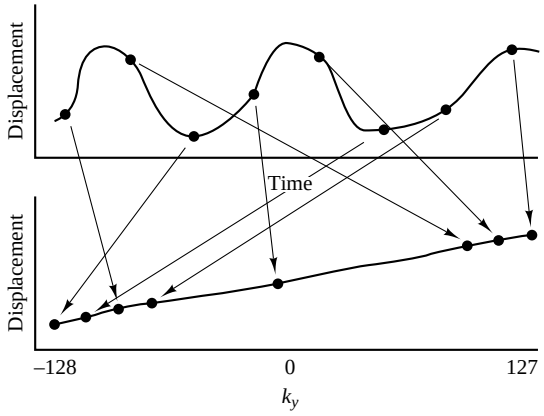

Figure 5 Mechanism of ordered phase encoding. The curve represents the position of the chest during breathing and the points demarcate times when data for a few values of k_y are sampled. These repetitive displacements become monotonic in k_y if the k_y are acquired in the order indicated. (Reproduced by permission of the American Institute of Physics from M. L Wood and Q. S. Xiang, in 'Medical Physics Monograph No. 21: The Physics of MRI: 1992 AAPM Summer School Proceedings', eds. M. J. Bronskill and P. Sprawls, 1993, p. 383)

7.2.4 Ghost Interference

A complex-valued image with ghosts can be decomposed into a ghost mask superimposed on an ideal image representing the time-averaged magnetization. Unlike the ideal image, the phase of the ghost mask depends on the phase of the periodic motion. Consequently, data for two or three images can be acquired interleaved and with the order of the phase-encoding steps shifted.[36] These data are modulated by motion differing only in phase, so the associated images have a similar pattern of ghosts but with different phase. Images from the data can be combined to generate a ghost-free image. This ghost-interference method is simple, because it does not need patient monitoring or detailed knowledge of the motion. Ghosts cancel, provided that the motion is at least quasiperiodic. The primary drawbacks are a doubling or tripling of the data acquisition time and the assumption of quasiperiodic motion.

8 SUMMARY

Respiratory motion remains troublesome for MRI in spite of a decade of research directed at understanding and controlling the associated artifacts. Respiratory motion is repetitive, so it generates blurring and ghosts in MR images. Blurring is undesirable because it degrades spatial resolution and contrast by spreading structures over a broader range of pixels than warranted. The ghosts are distributed along the phase-encoding direction of MR images, regardless of the direction of motion. Ghosts in MR images are undesirable because they can mask pathology or mimic it.

Many methods to control respiratory motion artifacts have been advanced, although none are always completely effective. Some methods, such as spatial presaturation, reduce the intensity of ghosts by reducing the intensity of moving anatomic structures. Other methods reduce the displacement during data acquisition or exploit the periodicity of respiratory motion. All of the methods reduce ghosts and some of them also decrease blurring. Methods that do not prolong data acquisition or patient preparation are also desirable. Every one of the methods has a deficiency, but fortunately they are not the same. Most of the methods to control motion artifacts are not mutually exclusive so they can be combined for greater artifact suppression. The best combination is debatable, but it probably depends on the anatomic region, pulse sequence, and MRI system.

9 RELATED ARTICLES

Abdominal MRA; Cardiac Gating Practice; Echo-Planar Imaging; Image Formation Methods; Lung and Mediastinum

MRI; Projection–Reconstruction in MRI; Pulsatility Artifacts Due to Blood Flow and Tissue Motion and Their Control; Spin Warp Data Acquisition; Spiral Scanning Imaging Techniques; Surface and Other Local Coils for In Vivo Studies; Time-of-Flight Method of MRA; Whole Body Magnetic Resonance Artifacts; Whole Body Magnetic Resonance: Fast Low-Angle Acquisition Methods.

10 REFERENCES

1. C. L. Schultz, R. J. Alfidi, A. D. Nelson, S. Y. Kopiwada, and M. E. Clampitt, *Radiology*, 1984, **152**, 117.
2. M. L. Wood and R. M. Henkelman, *Med. Phys.*, 1985, **12**, 143.
3. R. L. Ehman, M. T. McNamara, R. C. Brasch, J. F. Felmlee, J. E. Gray, and C. B. Higgins, *Radiology*, 1986, **159**, 777.
4. A. M. Aisen, G. M. Glazer, P. L. Carson, and D. O. Hearshen, *Magn. Reson. Imaging*, 1986, **4**, 207.
5. A. Kumar, D. Welti, and R. R. Ernst, *J. Magn. Reson.*, 1975, **18**, 69.
6. G. H. Glover and J. M. Pauly, *Magn. Reson. Med.*, 1992, **28**, 275.
7. J. L. Duerk and O. P. Simonetti, *J. Magn. Reson. Imaging*, 1991, **1**, 643.
8. D. C. Ailion, K. Ganesan, T. A. Case, and R. A. Christman, *Magn. Reson. Imaging*, 1992, **10**, 747.
9. J. T. Sharp, N. B. Goldberg, W. S. Druz, and J. Danon, *J. Appl. Physiol.*, 1975, **39**, 608.
10. P. H. Weiss, J. M. Baker, and E. J. Potchen, *J. Nucl. Med.*, 1972, **13**, 758.
11. R. L. Ehman, J. P. Felmlee, H. W. Korin, and S. J. Riederer, *Magn. Reson. Imaging*, 1990, **8**, 26.
12. M. L. Wood and Q. S. Xiang, in 'Medical Physics Monograph No. 21: The Physics of MRI, 1992 AAPM Summer School Proceedings', eds. M. J. Bronskill and P. Sprawls, American. Institute. Physics, Washington, DC, 1993, p. 383.
13. M. L. Wood and R. M. Henkelman, in 'Magnetic Resonance Imaging', 3rd edn., eds. D. D. Stark and W. G. Bradley, Mosby Year Book, Inc., St. Louis, MO, 1998, Vol. 1, chap. 10.
14. Q. S. Xiang and R. M. Henkelman, *Magn. Reson. Med.*, 1993, **29**, 422.
15. M. L. Lauzon and B. K. Rutt, *Magn. Reson. Med.*, 1993, **30**, 438.
16. D. G. Nishimura, J. I. Jackson, and J. M. Pauly, *Magn. Reson. Med.*, 1991, **22**, 481.
17. P. M. Pattany, J. J. Phillips, L. C. Chiu, J. D. Lipcomon, J. L. Duerk, J. M. McKelly, and S. M. Mohapetra, *J. Comput. Assist. Tomogr.*, 1987, **11**, 369.
18. E. M. Haacke and G. W. Lenz, *Am. J. Roentgenol.*, 1987, **148**, 1251.
19. R. L. Ehman and J. P. Felmlee, *Magn. Reson. Med*, 1990 **14**, 293.
20. M. L. Wood, M. J. Bronskill, R. V. Mulkern, and G. E. Santyr, *J. Magn. Reson. Imaging*, 1993, **3(S)**, 19.
21. G. M. Bydder and I. R. Young, *J. Comput. Assist. Tomogr.*, 1985, **9**, 659.
22. V. M. Runge, J. A. Clanton, C. L. Partain, and A. E. James, Jr., *Radiology*, 1984, **151**, 521.
23. C. E. Lewis, F. S. Prato, D. J. Drost, and R. L. Nicholson, *Radiology*, 1986, **160**, 803.
24. M. L. Wood and R. M. Henkelman, *Med. Phys.*, 1986, **13**, 794.
25. Y. L. Liu, S. J. Riederer, P. J. Rossman, R. C. Grimm, J. P. Debbins, and R. L. Ehman, *Magn. Reson. Med.*, 1993, **30**, 507.
26. G. W. Lenz, E. M. Haacke, and R. D. White, *Mag. Reson. Imaging*, 1989, **7**, 445.
27. M. L. Wood, P. L. Stanchev, and M. J. Shivji, *J. Magn. Reson. Imaging*, 1995, **5**, 57.
28. R. L. Ehman and J. P. Felmlee, *Radiology*, 1989, **173**, 255.
29. E. M. Haacke and J. L. Patrick, *Magn. Reson. Imaging*, 1986, **4**, 359.
30. E. Atalar and L. Onural, *IEEE Trans. Med. Imaging*, 1991, **10**, 11.
31. W. T. Dixon, M. E. Brummer, and J. A. Malko, *Magn. Reson. Imaging*, 1988, **6**, 74.
32. M. L. Wood, *J. Magn. Reson. Imaging*, 1991, **1**, 593.
33. E. M. Haacke, G. W. Lenz, and A. D. Nelson, *Magn. Reson. Med.*, 1987, **4**, 162.
34. D. R. Bailes, D. J. Gilderdale, G. M. Bydder, A. G. Collins, and D. N. Firmin, *J. Comput. Assist. Tomogr.*, 1985, **9**, 835.
35. H. W. Korin, S. J. Riederer, A. E. H. Bampton, and R. L. Ehman, *J. Magn. Reson. Imaging*, 1992, **2**, 687.
36. Q. S. Xiang and R. M. Henkelman, *J. Magn. Reson. Imaging*, 1991, **1**, 633.

Biographical Sketch

Michael L. Wood. *b* 1960. B.Sc., 1982, physics, McGill University, Canada, Ph.D., 1986 (supervisor R. M. Henkelman), medical biophysics, University of Toronto, Canada. Assistant professor and staff physicist, Departments of Radiology and Radiation Oncology, Tufts University and New England Medical Center Hospitals, USA, 1986–91. Director of Research, Department of Medical Imaging, and Associate Professor, Departments of Medical Imaging and Medical Biophysics, University of Toronto, 1992–present. Co-Director, Centre for Magnetic Resonance Imaging, University of Toronto. Physicist, St. Michael's Hospital, Toronto and staff scientist, Toronto Hospital, Toronto, 1991–present. Approx. 50 publications. Current research specialty: reduction of MRI motion artifacts, wavelets, pulse sequences for rapid MRI, 3D MRI, and velocity quantification.

Multi Echo Acquisition Techniques Using Inverting Radiofrequency Pulses in MRI

Jürgen K. Hennig
Universität Freiburg, Germany

1 INTRODUCTION

Fast multi echo acquisition techniques comprise a family of MRI sequences, which are meant to reduce the total acquisition time of an MRI examination (see ***Echo-Planar Imaging*** and ***Whole Body Magnetic Resonance: Fast Low-Angle Acquisition Methods***). By sampling more than one line of *k*-space per excitation of the spin system, the saturation effects of multi-excitation techniques are avoided. In conventional techniques, one line of *k*-space is sampled per excitation of the spin system. For imaging of protons in living tissues repetition times of the order of 500 ms or more are required between successive excitations in order to avoid saturation of spins. Although images from several different sections of the body can be acquired in one such data collection period by means of multi-slice acquisition, and although images of different contrast can be obtained using multi echo techniques, the resulting acquisition times are in the region of several minutes, which is rather long compared with physiological timescales. Motion due to cardiac action, respiration and peristalsis will lead to artifacts; involuntary motion is a severe problem in uncooperative patients such as small children. This and the high cost of MRI equipment has led to intensive research into faster imaging techniques.

The possibility of scanning more than one line of *k*-space after a single excitation has been proposed by Mansfield in his paper on echo planar imaging[1] (see ***Echo-Planar Imaging***). The technological problem with the proposed method is that the timescale for scanning *k*-space by gradient reversal is given by the field inhomogeneity dependent signal decay time T_2*, which for in vivo applications typically lies in the range 20–50 ms. To sample 256×256 data points on such a timescale requires extremely strong and fast gradients, which only recently have become available outside of research laboratories (see ***Gradient Coil Systems***). An additional problem is the high bandwidth that has to be used for fast data sampling, which results in a considerable decrease in the signal-to-noise ratio. Finally, it should be mentioned that the physiological thresholds for nerve stimulation by fast gradient switching do allow reasonably fast acquisition times of medium resolution images (60 ms for a 128×128 image matrix). However, it is questionable whether high resolution imaging with matrices of 256×256 or 512×512 with the same or even lower acquisition times would be tolerable, even if it were technically feasible.

Mansfield mentioned in his original paper[1] the possibility of supplementing refocusing by gradient inversion by rf refocusing using 180° pulses. Although this is an intrinsically slower procedure, because gradient switching is faster than the application of a refocusing pulse under in vivo conditions, it has the intrinsic advantage that the signal decay of spin echoes is given by the relaxation time T_2, which is considerably longer than the field inhomogeneity dependent time T_2*. An additional benefit of rf refocusing is the fact that spin echoes are self-compensating for a large number of imperfections arising from susceptibility effects (see ***Susceptibility Effects in Whole Body Experiments***), dephasing due to chemical shift, motion (see ***Motion Artifacts: Mechanism and Control***), etc. Imaging techniques based on spin echo formation are therefore intrinsically more stable and reproducible under the nonperfect conditions of a clinical examination, which is of considerable interest for the radiologist, who has to base a diagnosis on the resulting images.

In spite of these apparent advantages of spin echo refocusing, it was several years before a practical MRI experiment was done using this concept. The problems in implementing the apparently simple concept are discussed in Section 2. After the first demonstration of the rapid acquisition with relaxation enhancement (RARE) experiment,[2] it was another 5–6 years before a routine whole body system finally met the strict requirements of the sequence regarding the temporal stability against eddy current effects induced by the switched gradient fields.

After the proliferation of the use of the sequence, under various acronyms (FAISE, FSE, TSE, etc.), on routine whole body scanners, RARE made a tremendous impact on the way in which a routine diagnostic examination was performed. Previously, conventional spin echo sequences with short recovery times of around 500 ms had been the basis of diagnostic MRI (see ***MRI in Clinical Medicine***). The poor contrast of this T_1-weighted sequence for many pathologies was compensated for by the abundant use of MRI contrast agents (see ***Contrast Agents in Magnetic Resonance: Operating Mechanisms***). With RARE, T_2-weighted imaging, with its intrinsic high contrast for many pathological conditions, suddenly became routinely available due to the considerable time savings compared with conventional T_2-weighted experiments afforded by the acquisition of several *k*-space lines per excitation. Currently, in most applications the experiment is performed in several excitation cycles with the acquisition of 3–48 differently phase-encoded echoes per excitation. Single shot implementations with echo times of 10–25 ms have led to new applications such as MR RARE myelography,[3] urography,[4,5] and cholangiography,[6] the unique contrast behavior of which has opened up new avenues for clinical diagnosis using MRI.

With the current introduction of fast gradient systems into clinical MRI, single shot RARE applications with acquisition times below 1 s have become feasible. With the availability of fast gradient systems, the rf power deposition due to the rapid repetition of refocusing pulses has become the limiting factor for acquisition speed. An echo interval of around 3.5–5 ms appears to be minimal for routine clinical applications. Various developments based on fast gradient systems are discussed in Section 3.3.

2 METHODOLOGY

The Carr–Purcell–Meiboom–Gill sequence makes use of an excitation pulse followed by a sequence of equally spaced 180°

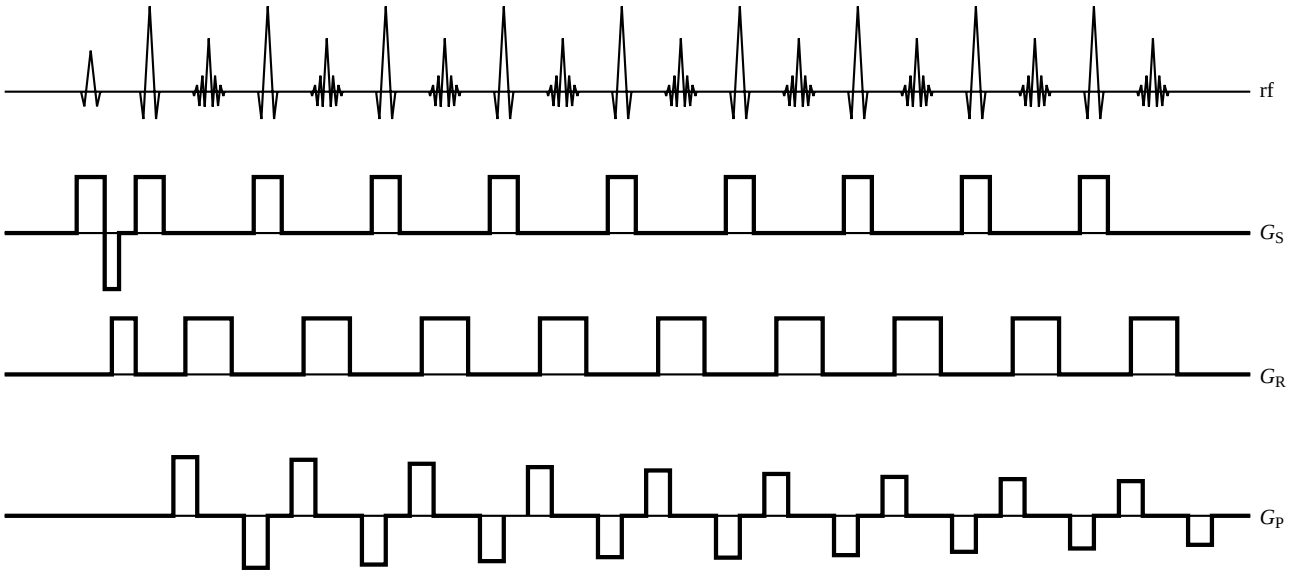

Figure 1 Scheme of the RARE imaging sequence. rf, rf pulses and signals; G_S, G_R and G_P, the slice selection, readout, and phase-encoding gradients, respectively

refocusing pulses.[7] If the phase of the refocusing pulses is shifted by 90° with respect to the excitation pulse, and if the spacing between refocusing pulses is twice the time between the excitation pulse and the first refocusing pulse, this sequence is self-refocusing against effects from imperfect pulse flip angles, in the sense that the resulting errors do not accumulate over the length of the echo train, but rather average out to some steady state contribution. The problem in using this sequence as the basis of a MRI experiment lies in the difficulties in preserving the self-refocusing properties under the conditions of switched gradient fields. It has been demonstrated that this requires the use of gradients such that the spin dephasing caused by the phase-encoding gradient in each refocusing period is equal to twice the dephasing caused by the same gradient in the interval between the excitation pulse and the first refocusing pulse. The application of this principle has led to the introduction of the RARE sequence[2,3] shown in Figure 1. The dephasing caused by the phase-encoding gradient between two successive rf pulses is brought to zero by means of a phase-encoding rewinding gradient after each echo and before the following rf pulse. The disastrous image artifacts that arose in previous attempts to perform multi echo acquisition are thus avoided.

It has also been demonstrated that flip angles of the refocusing pulses as low as 60° can be used, which significantly reduces the rf absorption problems mentioned above.[8] A thorough description of the behavior of spin systems in multipulse sequences under the conditions of time-variable magnetic field gradients based on the papers of Hahn[9] and Woessner[10] is given by Ahn et al.[11] It should be noted that artifact-free images can only be generated if the total phase of the spin system under observation is brought to exactly the same state prior to each refocusing pulse. Temporal variations in the magnetic field caused by eddy currents arising from the effect of the switched magnetic field gradients are disastrous for the stability of the sequence. This factor delayed the widespread clinical use of the sequence until the beginning of the 1990s.

The assessment of the contrast in RARE images is somewhat complicated by the fact that data are acquired at different echo times. This leads to an unequal T_2-weighting of different k-space lines, which not only affects the final pixel intensities, but also the point spread function of different structures. Since most of the signal intensity in a typical clinical image is concentrated around the lower order phase-encoding steps, the overall image contrast is determined by the T_2-weighting of the corresponding echoes.[2,12,13] Narrow structures with a more even distribution of signal intensities over k-space are affected differently than broad structures with a corresponding narrow intensity distribution in k-space. In general, RARE sequences produce some edge enhancement, thus overemphasizing narrow structures and interfaces between tissues.

The distribution of k-space data over the various echoes occurring at different times is thus a very important factor influencing the image contrast. Figure 2 shows a series of images, all of which were acquired with identical parameters except for the distribution of phase-encoding steps. In all images, phase encoding was applied such that the distribution of T_2-weighting of the data in k-space was as smooth as possible. The difference in contrast in the images shown arises from a shift of the phase-encoding zero point along the echo train. Phase encoding zero in late echoes leads to heavier T_2-weighting. An interleaved consecutive phase-encoding scheme was proposed in the original RARE paper.[2] Later, a corresponding centric phase-encoding approach was demonstrated as an alternative.[12,13] Both strategies allow a wide variation of the image contrast.

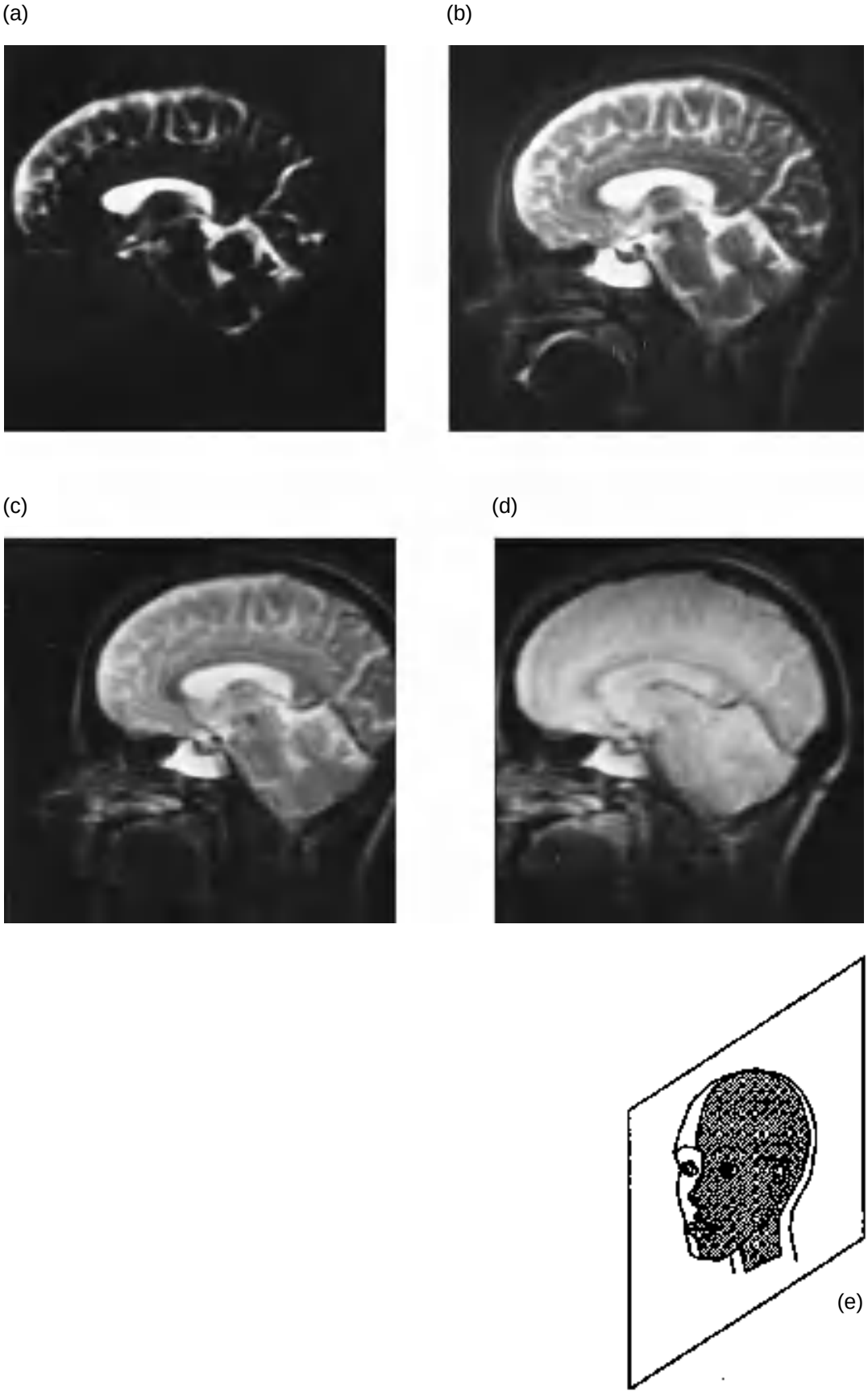

Figure 2 A series of sagittal RARE images acquired with identical timing parameters (echo interval 20 ms, 8 echoes per excitation, 2800 ms recovery time) but different phase-encoding schemes. The phase encoding zero point was placed at $TE = 140$ ms (a), 80 ms (b), 60 ms (c), and 40 ms (d). (e) The anatomical position of the images. (2 T, Bruker S 200 F, University Freiburg)

Figure 3 RARE image of a patient with an extensive glioblastoma. The main anatomical features are depicted in the drawing. (a) Cerebrum; (b) tumor, (c) brainstem, (d) cerebellum. ($TR/TE = 2800/25$, 8 echoes per excitation; 2 T, Bruker S 200 F, University Freiburg)

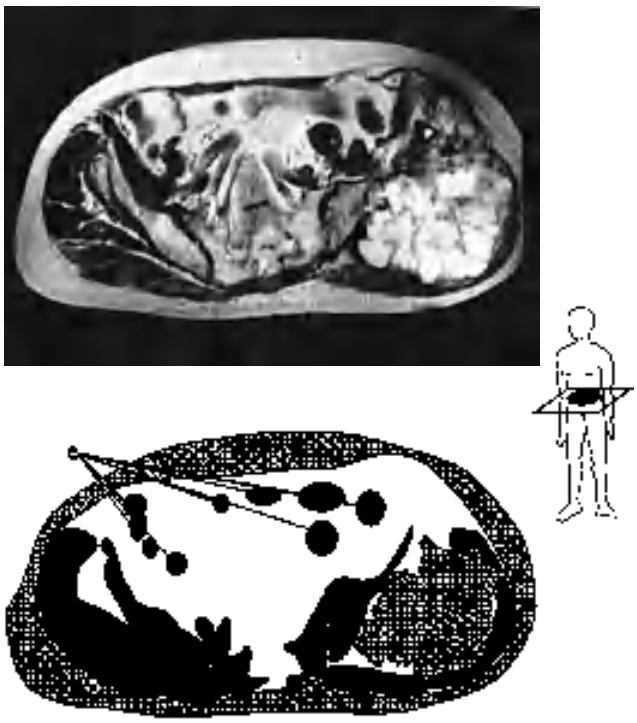

Figure 4 RARE (TSE) image of a patient with a chondrosarcoma. (a) Pelvic bones, (b) muscles, (c) subcutaneous fat, (d) tumor, (e) bowel. ($TR/TE = 4650/16$, 25 echoes per excitation; 1 T, Siemens Magnetom, University Freiburg)

3 APPLICATIONS

3.1 Clinical Applications using Segmented Acquisition

Although the clinical usefulness of RARE images has been demonstrated since 1986,[3,14] the widespread proliferation of RARE sequences into routine clinical practice began only in 1990, aided by the availability of actively shielded gradient systems (see ***Gradient Coil Systems***)[11–13,15–31] and originating in the work done by Jolesz, Mulkern and their co-workers. With the echo times of 10–20 ms achievable at that time, it was clear that segmented acquisition was the best option for achieving a contrast relevant effective echo time of 60–100 ms. Between 3 and 8 echoes per excitation are commonly used in this acquisition mode, leading to a time saving of roughly the same factor. For multislice applications, where the recovery time between successive excitations of the same slice is filled with measurements in adjacent slices, the time saving may be less, since the repetition time might have to be increased in order to accommodate the longer acquisition time per slice resulting from the long echo train.

Clinically, the most relevant area of application for this experiment is the diagnosis of lesions in the central nervous system (see ***Intracranial Infections***; ***Head and Neck Investigations by MRI***; ***Magnetic Resonance Imaging: A Historical Overview***). Most tumors and metastasis show up brightly in T_2-weighted scans, as do demyelinating lesions, edema and various types of inflammatory lesions. An example is shown in Figure 3. For examinations of the abdomen, T_2-weighted scans also deliver important diagnostic information, as shown in Figure 4. For imaging of the extremities, a stronger T_1 contrast is normally used (Figure 5). Acquisition times below 20 s, which allow the examination to take place within one breathhold, are especially important for examinations of the upper abdomen. With state-of-the-art gradient systems, such applications have become feasible (Figure 6). High-resolution multislab three-dimensional examinations with a 512×512 matrix have also been demonstrated to be feasible with short

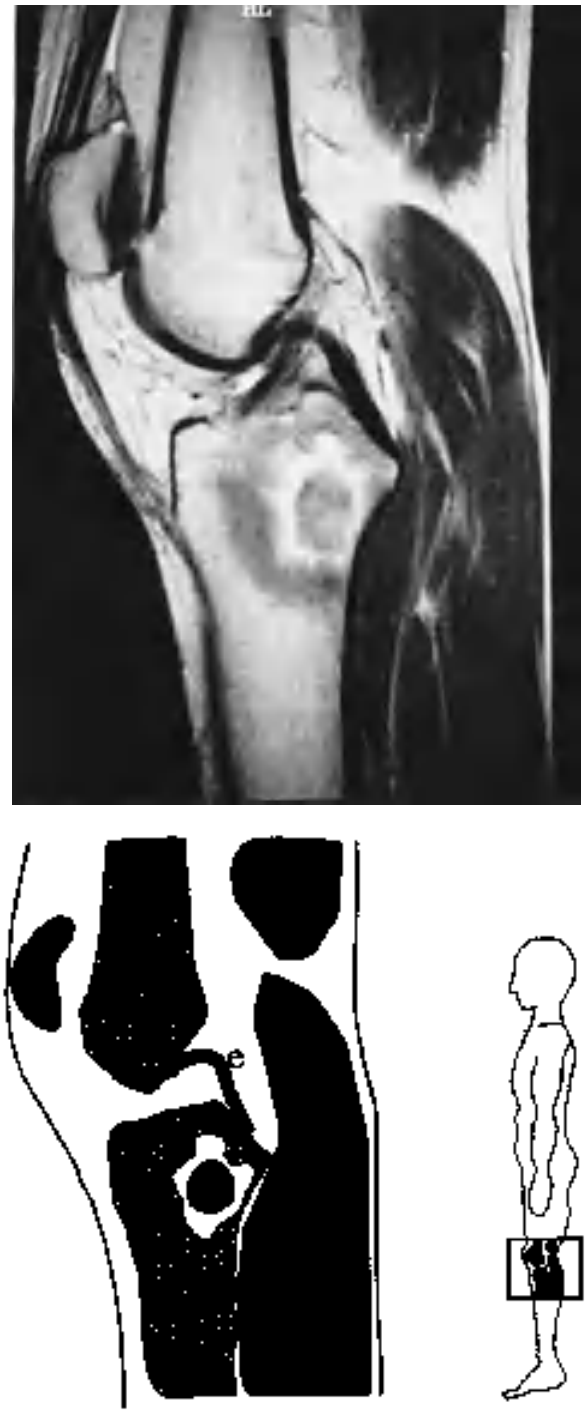

Figure 5 RARE (TSE) image of the knee showing a metastasis of a lymphoma (f) in the tibia. (a) Femur, (b) tibia, (c) patella, (d) muscles, (e) crucial ligament. ($TR/TE = 600/15$, 3 echoes per excitation; 1 T, Siemens Magnetom, University Freiburg)

acquisition times.[24] In addition, dual-contrast sequences, which use groups of early echoes for the reconstruction of more spin density weighted images and groups of late echoes for T_2-weighted imaging,[15] have been used successfully.

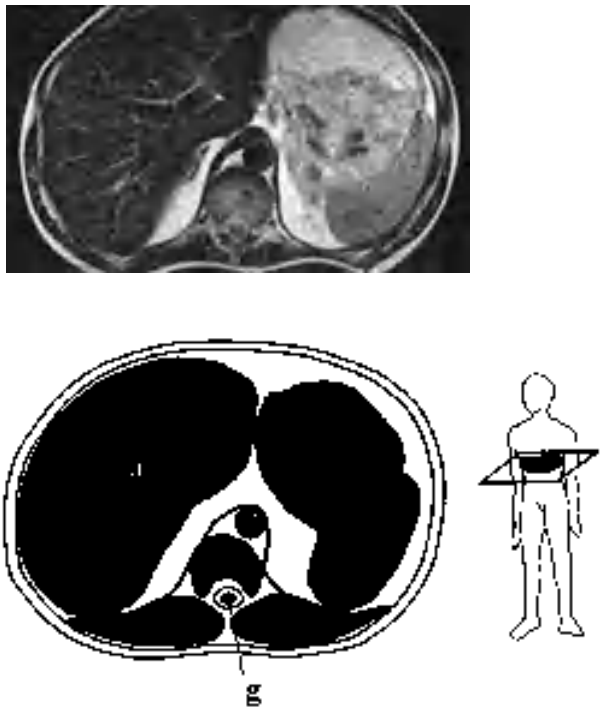

Figure 6 RARE (FSE) image of the abdomen acquired within one breathhold, illustrating the lack of respiratory artifact. (a) Liver, (b) stomach, (c) spleen, (d) muscles, (e) vertebra, (f) aorta, (g) spinal canal with spinal chord. (1.5 T, G E Signa, Children's Hospital, Boston.) (Courtesy of R. V. Mulkern)

3.2 RARE Myelography, Urography, and Cholangiography

Segmented RARE imaging delivers images with an information content which is (nearly) identical to that of a conventional T_2-weighted image. The advantage of RARE lies in its considerable time saving. Applications of multi echo acquisition, for which no reasonable conventional technique appears to be feasible, are described in Section 3.3. In these experiments, multi echo acquisition is achieved by creating one long echo train after a single excitation of the spin system.[2,3] By placing the zero phase-encoding step into an echo occurring at 500–1000 ms after excitation, all the signal from soft tissue is suppressed to well below 0.001% due to its typical relaxation time of 50–100 ms. Signals from body fluids, however, will appear bright because their T_2 is 1–3 s. The acquisition therefore selects fluid filled parts of the body. This allows acquisition without slice selection (Figure 7), which is of particular importance for structures of highly complicated geometric shape such as the cerebrospinal spaces[3,30] (Figure 8), the urinary tract[4,5] (Figure 9), and the hepatobiliary system[6] (Figure 10), which are notoriously difficult to image using any slice selective technique.

The short acquisition times of 2–3 s per image allow the generation of views under different projection angles within very short total acquisition times, as well as studies of temporal changes over several seconds. The application of this experiment to three-dimensional acquisition has also been demonstrated.[13,32]

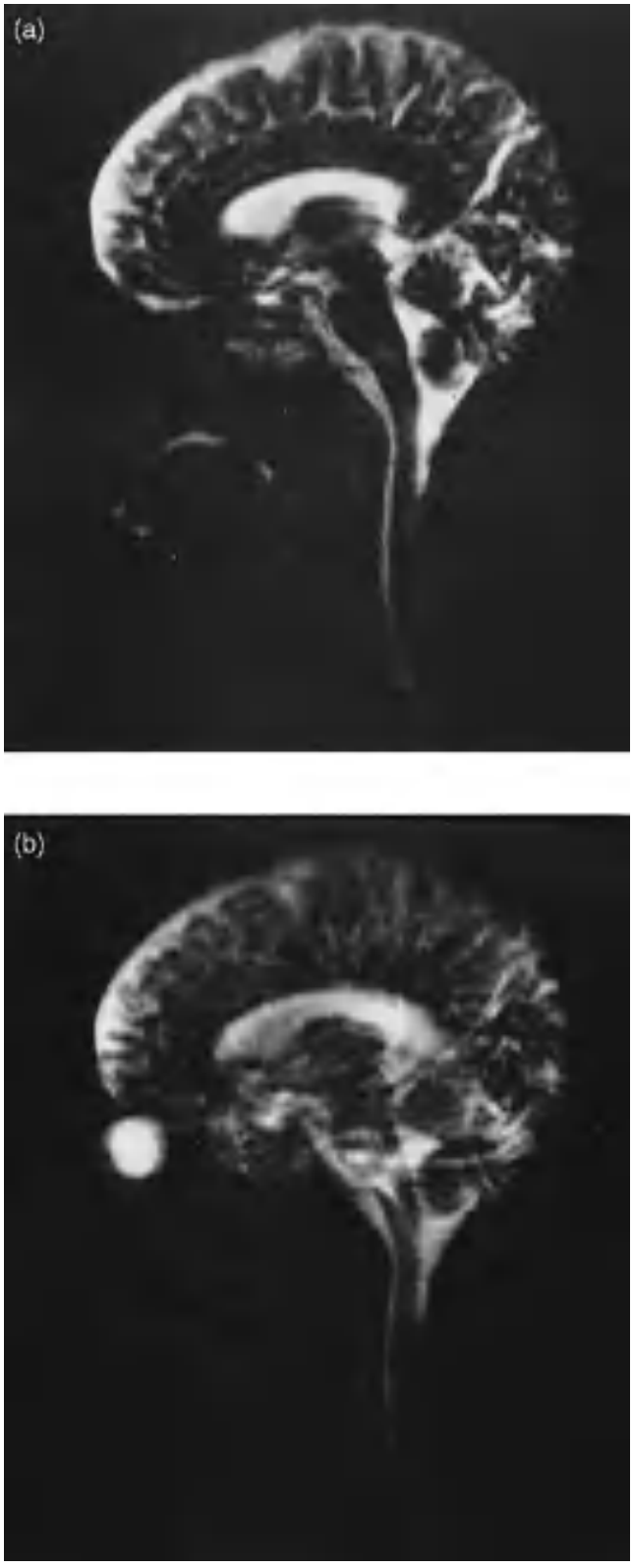

Figure 7 Single shot RARE images acquired with (a) and without (b) slice selection, demonstrating the suppression of soft tissue signals which allow the imaging of the cerebrospinal fluid filled spaces in the projection mode. The signal from the eyes is also shown, due to the long T_2. (0.23 T, Bruker R 23, University Freiburg; anatomical position as in Figure 2)

Figure 8 Single shot RARE myelogram of a patient with a large subarachnoidal cyst. (a) Cerebrum, (b) cerebellum, (c) brainstem, (d) cyst, (e) eye. (0.23 T, Bruker R 23, University Freiburg)

3.3 Recent Developments

The faster gradients that are now becoming available allow a reduction of the echo time. The use of such fast gradients for the generation of a multislice dataset acquired within one breathhold has already been mentioned. For multislice applications it should be noted that it might not be the optimum solution to acquire images in consecutive single shots mode. An interleaved sequential acquisition using the same total acquisition time might be preferable in terms of image contrast and signal-to-noise ratio. An example of a volunteer image acquired with a single scan using an echo interval of 6 ms is shown in Figure 11.

Faster acquisition times are feasible if more than one signal is produced between successive refocusing pulses by gradient inversion.[33] The resulting GRASE sequence has been demonstrated to produce high-resolution images within very short acquisition times (Figure 12). The penalty for the decreased acquisition time is the sensitivity of GRASE images to T_2* effects (see above), although to a lesser degree than that of pure echoplanar imaging. Clinical practice will show whether

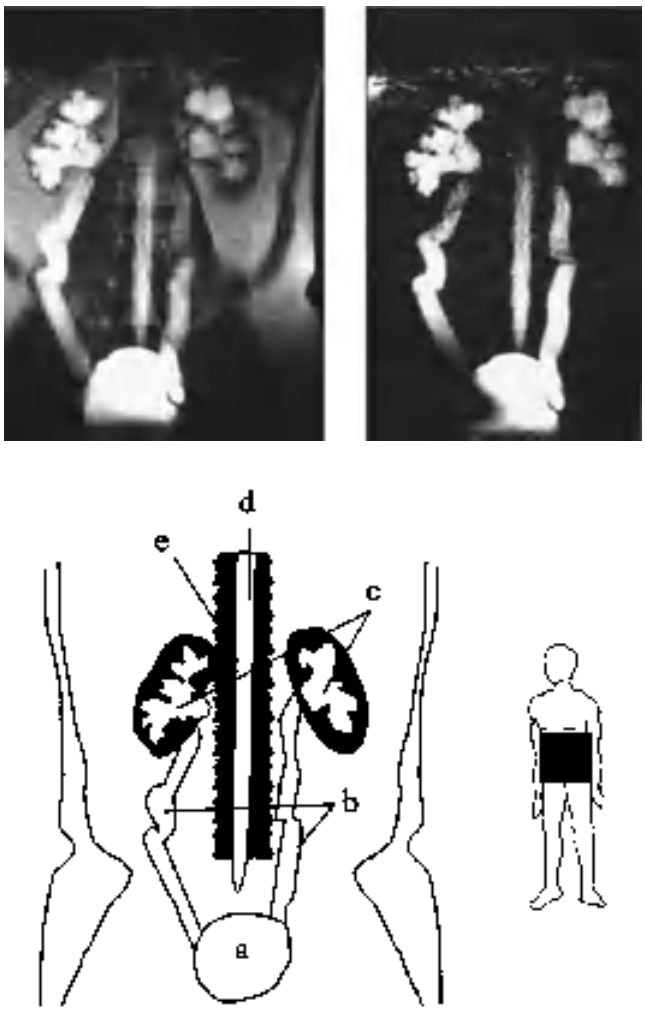

Figure 9 Urogram of a patient with stenosis of both urethras due to a bladder tumor. (a) Bladder, (b) dilated urethras, (c) renal pelvis, (d) spinal canal, (e) spinal column. (0.23 T, Bruker R 23, University Freiburg)

Figure 10 Single shot RARE cholangiogram of a patient with a benign restriction of the common bile duct. (a) Liver (not shown on the image), (b) dilated bile duct, (c) common bile duct, (d) bile injected into the small bowel, (e) spinal canal, (f) nerve roots, (g) dural diversion, (h) subphrenic effusion, (i) liver cysts, (j) intrahepatic bile ducts

applications can be found where the higher speed of GRASE outweighs the reliability and robustness of the RARE sequence.

Other recent developments in multi echo acquisition techniques use various schemes in order to introduce additional contrast mechanisms into the basic sequence. This includes prepulses for T_1 weighting by inversion–recovery[34,35] for the suppression of signal from cerebrospinal fluid (brain water) for the better discrimination of lesions (Figure 13). A different approach called U-FLARE was pioneered by Norris[36] on an animal scanner. It uses various preparation sequences leading to magnetization transfer, motion, and diffusion weighting or additional spatial selection. The application of these experiments to whole body systems presents the very promising possibility of combining contrast manipulation with the inherently robust and self-refocusing properties of the RARE experiment. The resulting image contrast has been demonstrated to be highly relevant for applications such as early diagnosis of infarcts and asphyxia, and for novel applications such as functional imaging of brain activity (see ***Brain Parenchyma Motion Observed by MRI*** and ***Susceptibility Effects in Whole Body Experiments***). Further modifications of the RARE sequence have been proposed for the study of the flow of cerebrospinal fluid,[8] for examining the relative pro-

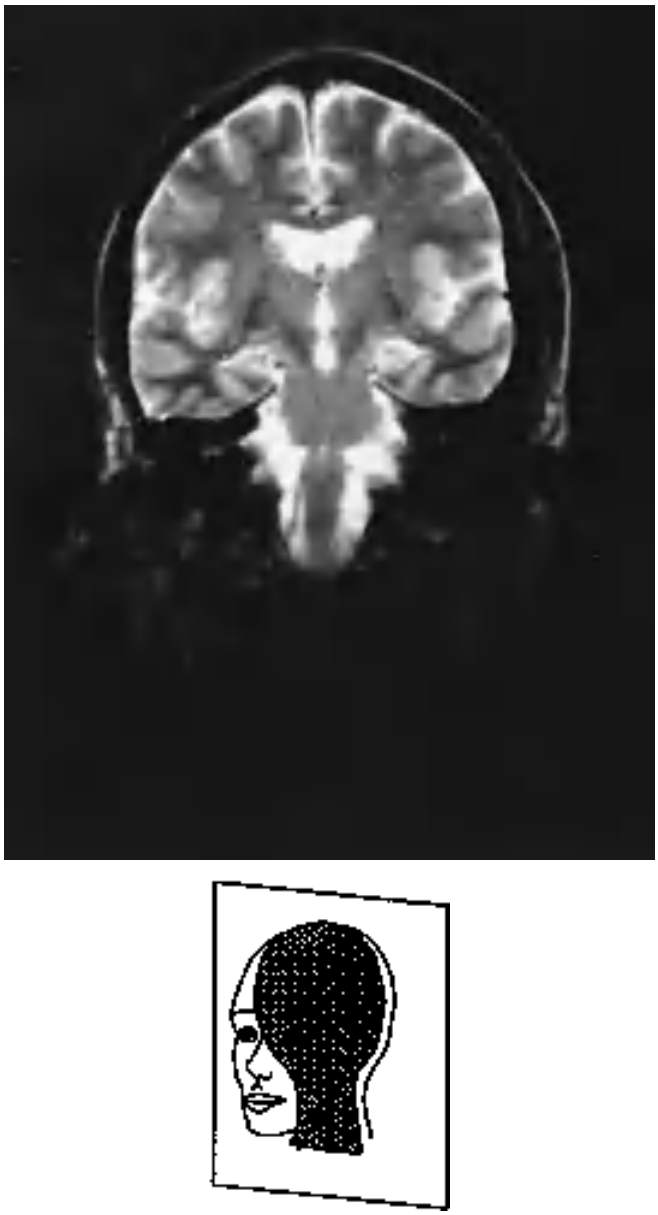

Figure 11 Single shot RARE image with an echo interval of 6 ms showing the feasibility of producing T_2-weighted soft-tissue images with reasonable resolution (160 echoes, total acquisition time 960 ms; 2 T, Bruker S 200 F, University Freiburg)

Figure 12 GRASE image of the head of a volunteer (512×512, $TR/TE_{\text{eff}} = 3500$ ms/110 ms, total acquisition time-2 min 50 s). (a) Eyes, (b) orbit, (c) brainstem, (d) cerebrum. (1 T, Siemens Magnetom, New York University Medical Center.) (Courtesy of D. Feinberg)

portions of fat and water in tissues,[37] and for performing fat-suppressed RARE imaging.[11] The high sampling efficiency of multi echo acquisition has also been used for chemical shift imaging.[22]

4 RELATED ARTICLES

Brain Parenchyma Motion Observed by MRI; Central Nervous System Degenerative Disease Observed by MRI; Contrast Agents in Whole Body Magnetic Resonance: An Overview; Echo-Planar Imaging; Gradient Coil Systems; Head and Neck Investigations by MRI; Intracranial Infections; Ischemic Stroke; Magnetic Resonance Imaging: A Historical Overview; Motion

Figure 13 Comparison of an inversion–recovery RARE image (a) ($TI = 1500$ ms) with a conventional RARE image (b) acquired with otherwise identical parameters ($TR = 4500$ ms, $TE = 20$ ms). The demyelinating lesions are much better visualized on the cerebrospinal fluid suppressed inversion–recovery image. (a) Cerebrum, (b) ventricle, (c) demyelinating lesions

Artifacts: Mechanism and Control; MRI in Clinical Medicine; Susceptibility Effects in Whole Body Experiments.

5 REFERENCES

1. P. Mansfield, *J. Phys. C, Solid State Phys.*, 1977, **10**, L55.
2. J. Hennig, A. Nauerth, and H. Friedburg, *Magn. Reson. Med.*, 1986, **3**, 823.
3. J. Hennig, H. Friedburg, and B. Stroebel, *J. Comput. Assist. Tomogr.*, 1986, **10**, 375.
4. G. Sigmund, B. Stoever, L. B. Zimmerhackl, A. Frankenschmult, E. Nirzsche, J. U. Leititis, F. E. Struve, and J. Hennig, *Pediatr. Radiol.*, 1991, **21**, 416.
5. G. Sigmund, B. Stoever, L. B. Zimmerhackl, A. Frankenschmult, E. Nitzsche, J. U. Leititis, F. E. Struve, and J. Hennig, *Eur. J. Radiol.*, 1991, **1**, 27.
6. J. Laubenberger, M. Büchert, B. Schneider, U. Blum, J. Hennig, and M. Langer, *Magn. Reson. Med.*, 1995, **33**, 18.
7. S. Meiboom and D. Gill, *Rev. Sci. Instrum.*, 1958, **29**, 688.
8. J. Hennig, *J. Magn. Reson.*, 1988, **78**, 397.
9. E. L. Hahn, *Phys. Rev.*, 1950, **80**, 580.
10. D. E. Woessner, *J. Chem. Phys.*, 1961, **34**, 2057.
11. S. S. Ahn, M. T. Mantello, K. M. Jones, R. V. Mulkern, P. S. Melke, N. Higuchi, and P. D. Barnes, *Am. J. Neuroradiol.*, 1992, **13**, 1169.
12. P. S. Melki, F. A. Jolesz, and R. V. Mulkern, *Magn. Reson. Med.*, 1992, 26, 328 and 26, 342.
13. R. V. Mulkern, S. T. S. Wong, C. Winalski, and J. A. Jolesz, *Magn. Reson. Imaging*, 1990, **8**, 557.
14. J. Hennig and H. Friedburg, *Magn. Reson. Imaging*, 1988, **6**, 391.
15. S. S. Ahn, M. T. Mantello, K. M. Jones, R. V. Mulkern, P. S. Melki, N. Higuchi, and P. D. Barnes, *Am. J. Neuroradiol.*, 1992, **13**, 1169.
16. D. Chien and R. V. Mulkern, *J. Magn. Reson. Imaging*, 1992, **2**, 483.
17. N. Higuchi, K. Hiramasu, and R. V. Mulkern, *Magn. Reson. Med.*, 1992, **27**, 107.
18. K. M. Jones, R. V. Mulkern, M. T. Mantello, P. S. Melki, S. S. Ahn, P. D. Barnes, and F. A. Jolesz, *Radiology*, 1993, **182**, 53.
19. K. M. Jones, R. V. Mulkern, R. B. Schwartz, K. Oshio, P. D. Barnes, and F. A. Jolesz, *Am. J. Roentgenol.*, 1992, **158**, 1313.
20. P. S. Melki, R. V. Mulkern, L. P. Panych, and F. A. Jolesz, *J. Magn. Reson. Imaging*, 1991, **1**, 319.
21. P. S. Melki and R. V. Mulkern, *Magn. Reson. Med.*, 1992, **24**, 189.
22. R. V. Mulkern, P. S. Melki, H. S. Lilly, and F. A. Hoffer, *Magn. Reson. Imaging*, 1991, **9**, 909.
23. R. V. Mulkern, P. S. Melki, P. Jakb, N. Higuchi, and F. A. Jolesz., *Med. Phys.*, 1991, **18**, 1032.
24. K. Oshio, F. A. Jolesz, P. S. Melki, and R. V. Mulkern, *J. Magn. Reson. Imaging*, 1991, **1**, 695.
25. R. C. Smith, C. Reinhold, R. C. Lange, T. R. McCauley, R. Kier, and S. McCarthy, *Radiology*, 1993, **184**, 665.
26. G. Sze, M. Merriam, K. Oshio, and F. A. Jolesz, *Am. J. Neuroradiol.*, 1992, **13**, 1383.
27. H. M. Tice, K. M. Jones, R. V. Mulkern, R. B. Schwartz, P. Kalina, S. S. Ahn, P. B. Barnes, and F. A. Jolesz, *J. Comput. Assist. Tomogr.*, 1993, **17**, 425.
28. R. D. Tien, G. J. Felsberg, and J. MacFall, *Neuroradiology*, 1992, **35**, 38.
29. P. Vinee, B. Stoever, G. Sigmund, J. Laubenberger, K. H. Hauenstein, G. Weyrich, and J. Hennig, *J. Magn. Reson. Imaging*, 1992, **2**, 593.
30. A. K. Wakhloo, V. van Velthoven, M. Schumacher, and J. K. Krauss, *Acta Neurochir.*, 1991, **111**, 119.
31. G. H. Zoarski, J. K. Mackey, Y. Anzai, W. N. Hanafee, P. S. Melki, R. V. Mulkern, F. A. Jolesz, and R. B. Lufkin, *Radiology*, 1993, **188**, 323.

32. J. Hennig, H. Friedburg, and D. Ott, *Magn. Reson. Med.*, 1987, **5**, 380.
33. K. Oshio and D. A. Feinberg, *Magn. Reson. Med.*, 1991, **20**, 344.
34. B. De Coene, J. V. Hajnal, P. Gatehouse, D. B. Longmore, S. J. White, A. Oatridge, J. M. Pennock, I. R. Young, and G. M. Bydder, *Am. J. Neuroradiol.*, 1992, **13**, 1555.
35. D. Panush, R. Fulbright, G. Sze, R. C. Smith, and R. T. Constable, *Radiology*, 1993, **187**, 421.
36. D. G. Norris, P. Börnert, T. Reese, and D. Leibfritz, *Magn. Reson. Med.*, 1992, **27**, 142.
37. K. Oshio and R. V. Mulkern, *J. Magn. Reson. Imaging*, 1992, **2**, 601.

Biographical Sketch

Jürgen K. Hennig. *b* 1951. Dipl.chem., 1977, Dr.rer.nat., 1980. Postdoctorate 1981–83 (with Prof. H. Fischer), University Zürich), working on NMR of photokinetic reactions. Professor of Medical Physics at the Albert-Ludwigs-Universität, Freiburg; research in clinical MRI, 1983–present. Approx. 100 publications. Research specialties: fast imaging, Ifaster imaging techniques, in vivo proton spectroscopy, functional imaging and spectroscopy.

Multiple Quantum Coherence Imaging

Timothy J. Norwood and Laurie D. Hall
Cambridge University, UK

1 INTRODUCTION

In both NMR spectroscopy and imaging, the precessing nuclear magnetization of the sample is detected. This magnetization corresponds to single quantum coherence, that is those coherences between pairs of states for which $\Delta M_T = \pm 1$, where ΔM is the overall change in magnetic quantum number between those two states. Multiple quantum coherences[1,2] are all those coherences for which $\Delta M_T \neq \pm 1$, and which are consequently 'spin forbidden' and cannot be either excited or detected directly. For spin-$\frac{1}{2}$ nuclei, multiple quantum coherences can only be excited between a group of interacting spins (two for a zero or double quantum coherence, three for a triple quantum coherence), since for a single spin $\Delta m = \pm 1$.

A diagram of a system of two interacting spin-$\frac{1}{2}$ nuclei is given in Figure 1. In addition to the four allowed single quantum transitions (solid lines), this spin system contains a zero quantum transition, for which $\Delta M_T = 0$ (diagonal dashed line), and a double quantum transition (vertical dashed line), for which $\Delta M_T = \pm 2$. For nuclei with spins greater than $\frac{1}{2}$, some multiple quantum coherences can be excited from a single spin; for example, double as well as single quantum coherence can be excited from a spin-1 nucleus.

Interest in multiple quantum coherences arises from the fact that their properties are different from, yet complementary to, those of single quantum coherence.[2] In general, the precessional frequency of a coherence is given by:

$$\omega_{MQC} = \sum_k \Delta m_k (1 - \sigma_k)\gamma_k B_0$$

$$= \sum_k \Delta m_k \omega_k \qquad (1)$$

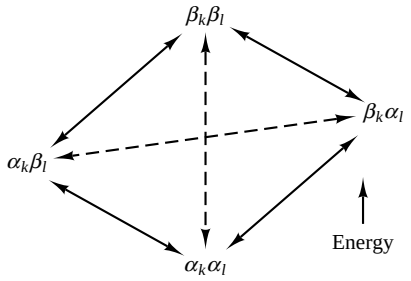

Figure 1 Energy level diagram of an AX spin system. In addition to the four allowed single quantum transitions there are two forbidden transitions: a zero quantum transition (diagonal dashed line) and a double quantum transition (vertical dashed line)

where Δm_k is the change in magnetic quantum number of the spin k between the two states, and $\omega_k = (1 - \sigma_k)\gamma_k B_0$. Consequently, it can be seen that the precessional frequency of a multiple quantum coherence will be a linear combination of those of its active spins k. For example, a zero quantum coherence between spins l and m will precess at $(\omega_l - \omega_m)$.

If the effect of a spatially dependent variation in B_0, $\Delta B(r)$, is included, equation (1) becomes:

$$\omega_{MQC} = \sum_k \Delta m_k [\omega_k + (1 - \sigma)_k \gamma_k \Delta B(r)] \qquad (2)$$

Since $\sigma << 1$ and, usually, $\Delta B(r) << B_0$, equation (2) can be reduced to:

$$\omega_{MQC} = \sum_k \Delta m_k [\omega_k + \gamma_k \Delta B(r)] \qquad (3)$$

It can be seen from equation (3) that the sensitivity of a homonuclear coherence to $\Delta B(r)$ will be directly proportional to its order. Thus, while a single quantum coherence will experience $\gamma\Delta B(r)$, a double quantum coherence will experience $2\gamma\Delta B(r)$, and a zero quantum coherence is completely unaffected. $\Delta B(r)$ may equally well be due to variations in the static magnetic field $\boldsymbol{B}_0$, or an applied magnetic field gradient. While a magnetic field gradient may be useful for encoding spatial information in an image, in a spectrum it is a nuisance, causing lines to broaden and thus decreasing resolution. While variations in the magnetic field will broaden double quantum lines twice as much as those of single quantum coherences, the zero quantum spectrum will be completely unaffected, and will consequently remain at high resolution.

The scalar couplings of multiple quantum coherences are also linear combinations of those of their active spins:

$$J_{MQC} = \sum_k \Delta m_k J_{kl} \qquad (4)$$

where l is a passive spin. Multiple quantum coherences do not exhibit scalar couplings between their active spins.

2 MULTIPLE QUANTUM EXPERIMENTS

As noted above, multiple quantum coherences are 'spin forbidden' and consequently cannot be excited directly by the application of a single nonselective rf pulse to the equilibrium magnetization of a spin system, nor can they be detected directly since they have no net magnetization associated with them. Consequently, both these processes are usually achieved indirectly using a sequence of pulses. A multiple quantum pulse sequence can be regarded as consisting of four modules: an excitation module, an evolution module, a mixing module, and a detection module. During the excitation module, multiple quantum coherence is created from the equilibrium magnetization of the spin system, while during the evolution module it is allowed to evolve, sampling its environment. During the mixing module, the multiple quantum coherence is reconverted into an observable single quantum coherence which is subsequently detected. To obtain a multiple quantum spectrum it is necessary to repeat the experiment a number of times, systematically incrementing the length of the evolution module t_1.

This introduces a modulation into the observed signal as a function of t_1 and the multiple quantum frequency, and consequently Fourier transformation with respect to t_1 will yield the multiple quantum spectrum.

The excitation module typically consists of the pulse sequence:

$$90^\circ_x(\tau/2)180^\circ_y(\tau/2)90^\circ_\theta$$

where $\theta = x$ if even orders of coherence are to be excited, and $\theta = y$ when odd orders are required. Typically, $\tau = (\frac{1}{4}J)$. The effect of this pulse sequence, when $\theta = x$, on the magnetization of a spin k coupled to a spin l is, in the product operator formalism:[3]

$$I_{kz} \xrightarrow{90^\circ_x} -I_{ky} \xrightarrow{\tau} 2I_{kx}I_{lz} \xrightarrow{90_x} -2I_{kx}I_{ly}$$

where I_{ky} corresponds to in-phase y magnetization of spin k, $2I_{kx}I_{lz}$ corresponds to x magnetization of spin k antiphase due to its scalar coupling to spin l, and $2I_{kx}I_{ly}$ describes a linear combination of zero quantum and double quantum coherence with active spins k and l. The first 90° pulse excites in-phase magnetization which subsequently becomes antiphase during τ due to any scalar couplings present. This antiphase single quantum coherence is converted into multiple quantum coherence by the second 90° pulse. The 180° pulse refocuses chemical shift evolution and any dephasing due to magnetic field inhomogeneity during τ. For spin-$\frac{3}{2}$ nuclei in the slow tumbling regime, relaxation may take the place of scalar coupling evolution during τ in converting in-phase into antiphase magnetization.

The evolution module typically consists of a single delay t_1 which may be incremented in consecutive experiments when multiple quantum spectra are to be acquired (see above) or set to zero when the sequence is being used solely to achieve multiple quantum filtration (see below). The mixing module is essentially the reverse of the excitation period, except that it converts the multiple quantum coherence back into transverse instead of longitudinal magnetization. The FID is observed during the detection module.

Usually, a single order of coherence is selected during the evolution module. This is achieved by using either phase cycling or magnetic field gradient pulses. The latter has the advantage that only a single experiment is required to achieve selection, which is often much cleaner than the corresponding phase cycled experiment, although up to half of the signal may be lost.

3 PRACTICAL CONSIDERATIONS

The nature of multiple quantum coherences dictates the structure of pulse sequences suitable for multiple quantum NMR. This structure, and in particular the necessity of using multiple pulse excitation and mixing sequences, has important consequences for the practicality of multiple quantum techniques in the context of NMR imaging and in vivo spectroscopy.

The efficiency of the excitation sequence in particular is parameter dependent. As noted in the previous section, the length of the excitation sequence is usually set to $\frac{1}{4}J$ since, although this does not produce the maximum intensity of any particular coherence, it does, in principle, produce a relatively uniform distribution of coherence intensities. However, in practice, the size of scalar couplings may vary considerably and as a consequence so will coherence intensities. Furthermore, transverse relaxation times in vivo are frequently short, resulting in an additional loss of signal intensity during the excitation and mixing sequences. These two factors—the limited efficiency of multiple quantum excitation (and to a more limited degree reconversion of multiple quantum into single quantum coherence during the mixing module) and transverse relaxation—combine to limit the usefulness of multiple quantum techniques in many applications. Imaging magnets are usually of relatively low magnetic field strengths (typically no more than 2 T). Consequently, sensitivity is at a premium, and additional losses, such as those arising during multiple quantum experiments, can ill be afforded.

4 APPLICATIONS

4.1 Zero Quantum Coherence Chemical Shift Imaging

The samples studied by NMR imaging are often both large and heterogeneous compared to their high resolution counterparts. As a consequence, variations in the static magnetic field B_0 and internal magnetic field gradients arising from susceptibility variations across the sample may both cause a broadening of the transitions in the conventional single quantum spectrum. As a result of this, peaks in the single quantum spectrum may overlap, making it impossible to obtain separate chemical shift resolved images of different chemical species.

Homonuclear zero quantum coherence offers a solution to this problem, since it is intrinsically independent of magnetic field inhomogeneity. By replacing the encoding of single quantum with zero quantum chemical shift it is possible in a chemical shift resolved imaging experiment to produce resolved images of different chemical species, independent of any variations in the magnetic field.[4,5] The pulse sequence for a zero quantum coherence chemical shift resolved imaging experiment is shown in Figure 2. As with most subsequent multiple quantum imaging experiments, spatial encoding takes place in the mixing and detection periods. The slice selection gradient is pulsed during the evolution period to dephase the nonzero quantum coherences. An example of the application of this experiment using a phantom is given in Figure 3. While a three-dimensional data set correlating two spatial dimensions against zero quantum chemical shift can be obtained by incrementing the zero quantum evolution period t_1 independently of the phase-encoding gradient, in this example the two have been incremented simultaneously to produce a series of images displaced by the relevant zero quantum frequency in the F_1 dimension. A disadvantage of this technique, common to all zero quantum experiments, is the presence of an intense peak at $F_1 = 0$ arising, not from zero quantum coherence, but from magnetization that is longitudinal during the evolution period; the two cannot be separated by using either phase cycling or magnetic field gradient pulses, since they have identical phase properties.

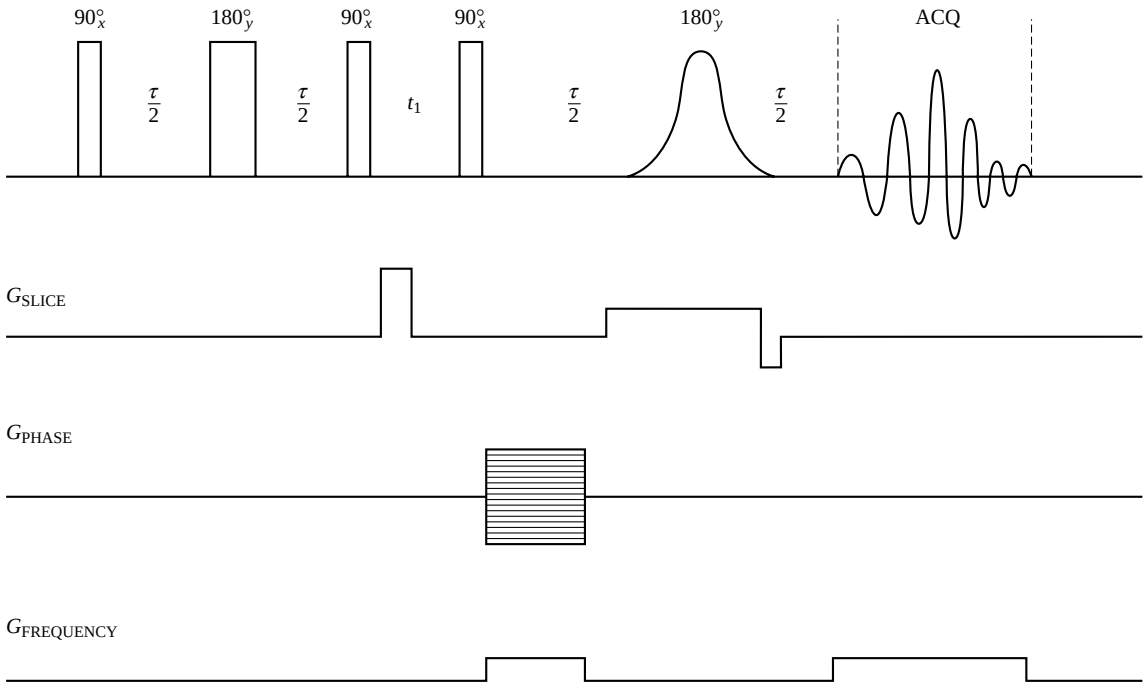

Figure 2 Pulse sequence for zero quantum coherence chemical shift resolved imaging. t = $(\frac{1}{4}J) - (\frac{1}{2}J)$ coherence transfer pathway selection is achieved using the magnetic field gradients

4.2 Double Quantum Coherence Phase Encoding

The sensitivity of multiple quantum coherences to magnetic field gradients is put to further use in an experiment which uses double quantum coherence for phase encoding[6] (Figure 4). Unlike the experiment described above where zero quantum coherence may be used because of its insensitivity to magnetic field gradients, here double quantum coherence is used because of its increased sensitivity with respect to single quantum coherence. Since double quantum coherence is twice as sensitive to magnetic field gradients as is single quantum coherence, a phase-encoding gradient applied to it need only be half the amplitude or half as long as one applied to the latter to achieve the same effect. However, any advantage gained through this procedure would seem to be lost in the increased length of the experiment resulting from multiple quantum excitation, unless a particularly long delay is required for T_2-weighting or if double quantum T_2-weighting is required.

In the pulse sequence shown in Figure 4 a magnetic field gradient rather than phase cycling was used to select the desired coherence transfer pathway. The double quantum coherence is dephased by pulsing the frequency-encoding gradient. After reconversion into single quantum coherence, a coherence transfer echo is formed in the presence of the final frequency-encoding gradient, which is observed. Magnetization that followed other pathways will form echoes at different times, and consequently coherence transfer pathway selection can be achieved in a single scan. It should be noted that the signal intensity will only be half of that obtained using phase cycling.

4.3 Multiple Quantum Filtration

Multiple quantum filtration provides a quick and easy to implement method of separating out the magnetization of nuclei according to the number of scalar coupling partners that they have. Unlike most other techniques used for in vivo spectroscopy and imaging, no prior knowledge of the frequencies of individual resonances and no soft pulses (except for spatial localization, where applicable) are required. Three types of multiple quantum filtration experiment have been demonstrated: double quantum filtration of spin-$\frac{1}{2}$ nuclei, double quantum and triple quantum filtration of spin-$\frac{3}{2}$ nuclei, and heteronuclear zero quantum and double quantum filtration of ^{1}H magnetization coupled to ^{13}C.

Double quantum filtration of spin-$\frac{1}{2}$ nuclei has been used for both ^{1}H spectroscopy and imaging.[7,8] While both phase cycling and magnetic field gradient pulses can be used to select the relevant coherence transfer pathways, the latter are often preferred because, although their use results in an additional reduction in signal intensity, they are quicker since no signal averaging is required, and they are less sensitive to motion artifacts. The main rationale for the use of double quantum filtration is as a form of water suppression. It has the advantage over most other types of water elimination procedure in that the lines in the spectrum do not have to be resolved from each other and no selective pulses are required in the procedure. Furthermore, unlike most other techniques, any signal from coupled nuclei underneath the water signal is not suppressed. A typical double quantum filtered imaging sequence is shown in Figure 5. Spatial encoding is accomplished in the period following

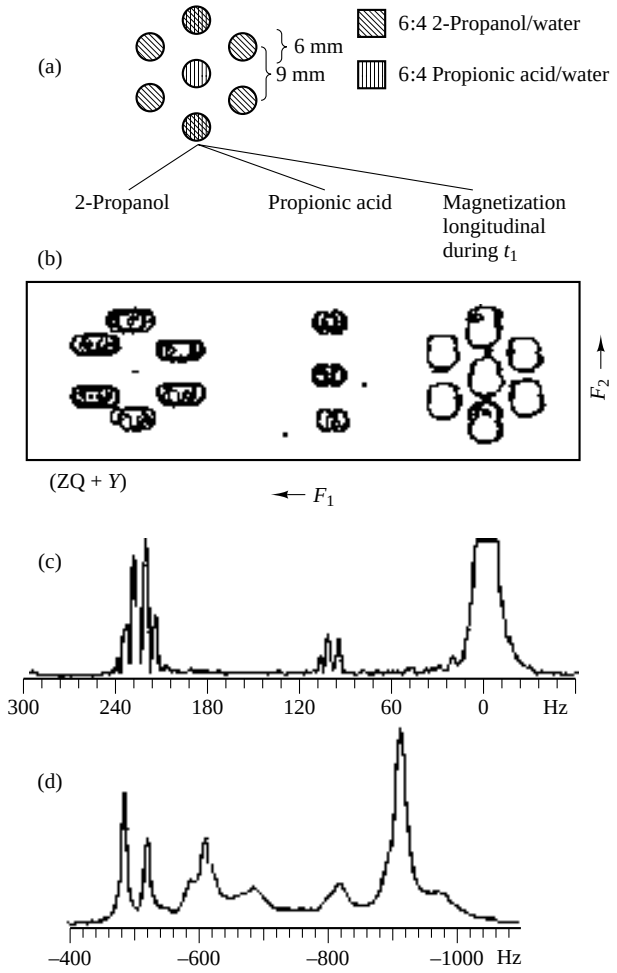

Figure 3 ^{1}H zero quantum image of a phantom consisting of vials of 2-propanol, propionic acid, and water obtained using the pulse sequence given in Figure 2. The zero quantum evolution period t_1 and the phase-encoding gradient were incremented simultaneously to produce images of each chemical species centered on its zero quantum chemical shift

reconversion of double quantum into single quantum coherence. The gradient pulses during the preparation period serve to dephase magnetization not following the desired coherence transfer pathway. The 180° pulse during the multiple quantum evolution period reverses chemical shift evolution and dephasing due to magnetic field inhomogenities. An example of data acquired with this pulse sequence is given in Figure 6. A two-step phase cycle is used; adding data from the two steps produces a single-quantum image, while subtraction produces a multiple-filtered image.

Double quantum and triple quantum filtration has been used to separate the signals from intracellular and extracellular sodium.[9–11] The nature of the intracellular milieu tends to give rise to long correlation times, which in the cast of spin-$\frac{3}{2}$ nuclei results in biexponential relaxation. Multiexponential relaxation in spin-$\frac{3}{2}$ nuclei such as ^{23}Na has a similar effect to scalar couplings in spin-$\frac{1}{2}$ nuclei—it causes evolution between in-phase and antiphase magnetization. Antiphase magnetization, whatever its origin, can be converted into multiple quantum coherence. Consequently, intracellular ^{23}Na will be passed by double quantum and triple quantum filtration, while extracellular sodium, which relaxes monoexponentially, will not. These effects have been used to produce both edited spectra and images of intracellular sodium.

Heteronuclear multiple quantum filtration has been used to produce spectra and images of ^{1}H magnetization coupled to ^{1}X; ^{1}H magnetization that does not meet this criterion is removed.[12,13] Editing is achieved with a one-dimensional version of the heteronuclear multiple quantum coherence (HMQC) experiment in which heteronuclear zero quantum and double quantum coherence is excited. While, for reasons of sensitivity due to the low natural abundance of ^{13}C this has not yet been used in vivo, it is likely to be a useful tool when used in conjunction with ^{13}C labeling.

5 RELATED ARTICLES

Systemically Induced Encephalopathies: Newer Clinical Applications of MRS; Image Formation Methods; Sodium-23 Magnetic Resonance of Human Subjects.

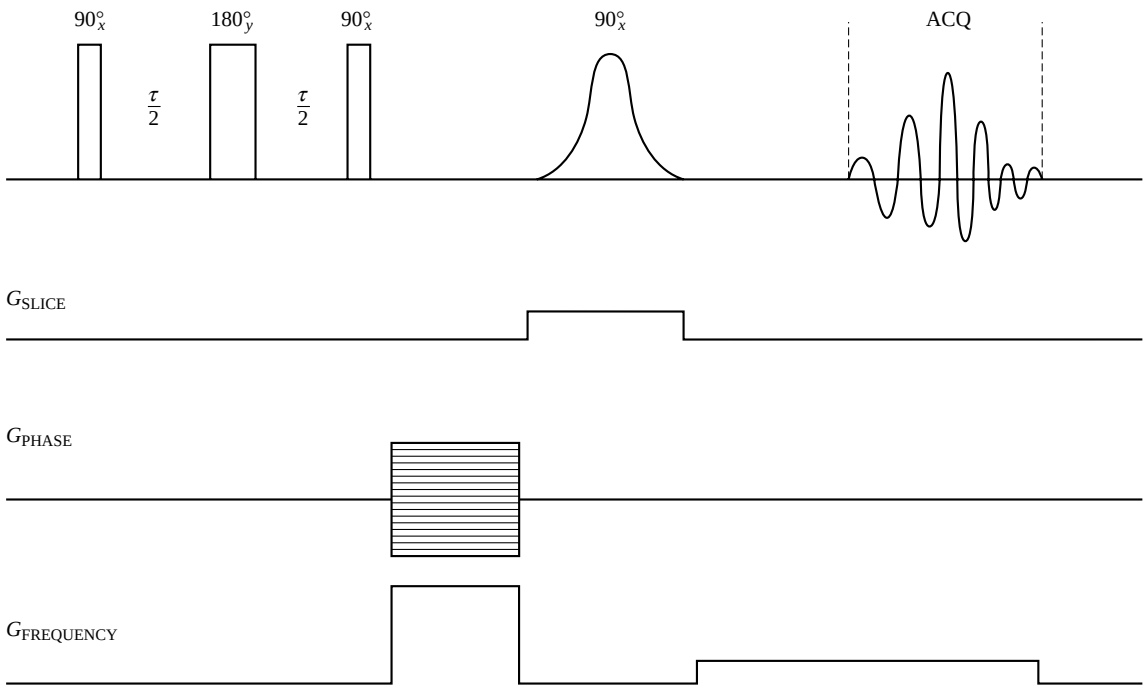

Figure 4 Imaging pulse sequence incorporating double quantum phase encoding t = $(\frac{1}{4}J) - (\frac{1}{2}J)$. Coherence transfer pathway selection is acheived by the use of magnetic field gradients

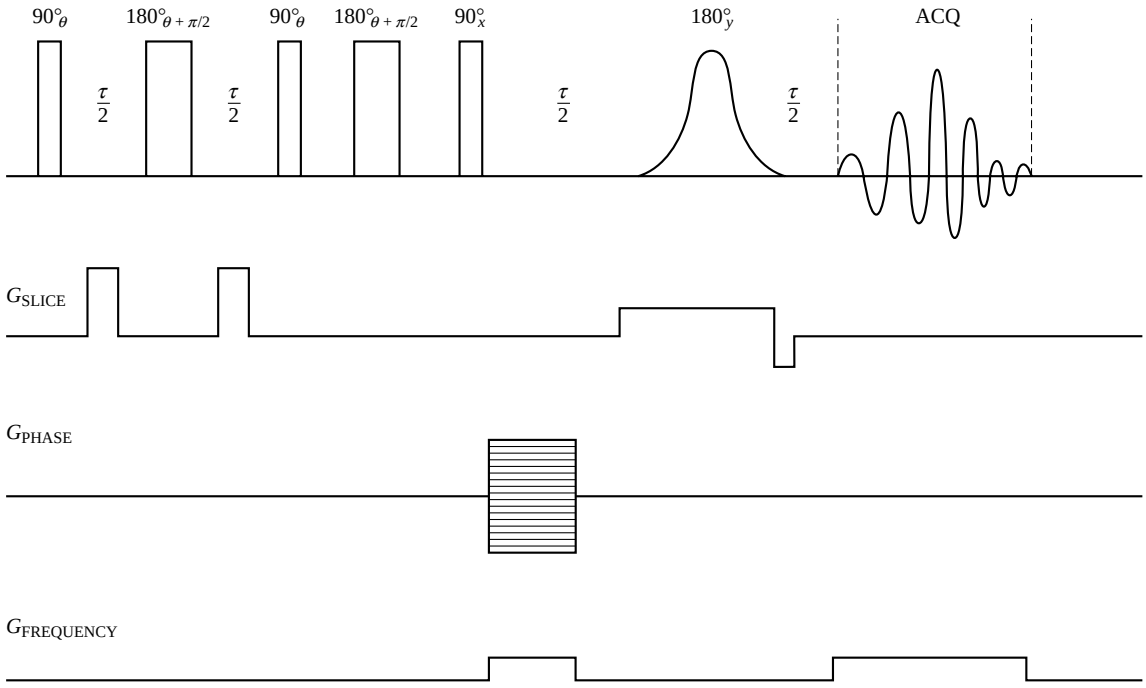

Figure 5 Pulse sequence for double quantum filtered imaging t = $(\frac{1}{4}J) - (\frac{1}{2}J)$. Data are acquired with q = x and y. Adding the two data sets results in a single quantum image, while subtracting them results in a double quantum image

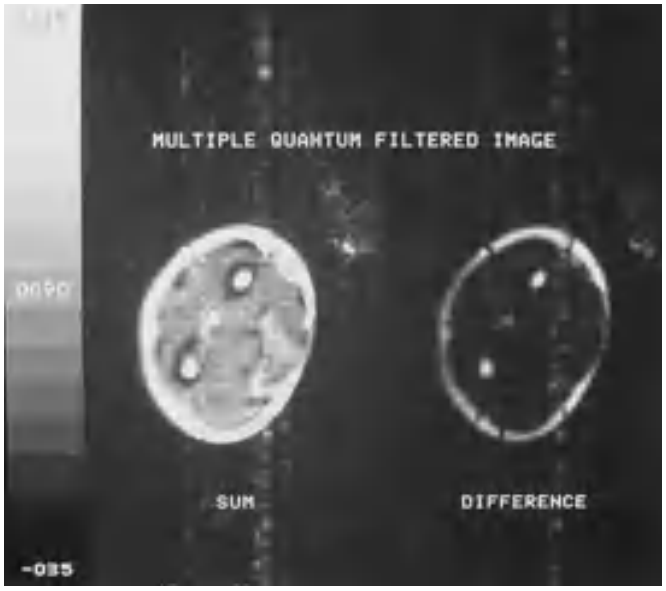

Figure 6 ^{1}H images of a human forearm acquired using the pulse sequence given in Figure 5. The left image is a single-quantum and the right image a double-quantum image

6 REFERENCES

1. R. R. Ernst, G. Bodenhausen, and A. Wokaun, 'Principles of Nuclear Magnetic Resonance im One and Two Dimensions', Clarendon, Oxford, 1987.
2. T. J. Norwood, *Prog. NMR Spectrosc.*, 1992, **24**, 295.
3. O. W. Sorensen, G. W. Eich, M. H. Levitt, G. Bodenhausen, and R. R. Ernst, *Prog. NMR Spectrosc.*, 1983, **16**, 163.
4. L. D. Hall and T. J. Norwood, *J. Magn. Reson.*, 1986, **67**, 382.
5. L. D. Hall and T. J. Norwood, *J. Magn. Reson.*, 1986, **69**, 391.
6. N. M. Szeverenyi and E. M. Haacke, *J. Comput. Assist. Tomogr.*, 1986, **10**, 484.
7. C. L. Dumoulin and D. Vatis, *Magn. Reson. Med.*, 1986, **3**, 282.
8. A. A. de Graaf, P. R. Luyten, J. A. den Hollander, W. Heindel, and W. M. H. J. Bovée, *Magn. Reson. Med.*, 1993, **30**, 231.
9. R. H. Griffey, B. V. Griffey, and N. A. Matwiyoff, *Magn. Reson. Med.*, 1990, **13**, 305.
10. J. Pekar and J. S. Leigh, *J. Magn. Reson.*, 1986, **69**, 582.
11. G. Jaccard, S. Wimperis, and G. Bodenhausen, *J. Chem. Phys.*, 1986, **85**, 6268.
12. A. Knuttel, R. Kimmich, and K. H. Spohn, *J. Magn. Reson.*, 1990, **86**, 526.
13. A. Knuttel, K. H. Spohn, and R. Kimmich, *J. Magn. Reson.*, 1990, **86**, 542.

Biographical Sketches

Timothy J. Norwood. *b* 1962. B.Sc. (Hons), 1983, King's College, University of London; M.Sc., 1985, University of British Columbia (where introduced to NMR by Laurie Hall), Ph.D., 1989, Cambridge University. Research interests: the development and application of NMR techniques for addressing biological problems in vitro and in vivo.

Laurie D. Hall. *b* 1938. B.Sc. 1959, Ph.D. 1962, Chemistry, University of Bristol, UK. Postdoctoral Fellow (with F. A. L. Anet) Ottawa University, 1962–63. Successively, instructor, and assistant, associate and Full Professor, Department of Chemistry, University of British Columbia, Vancouver Canada, 1962–84. Currently first holder of the Herchel Smith Chair of Medicinal Chemistry, University of Cambridge, UK (1985–present) Approx. 400 publications. Research specialities: carbohydrate chemistry, high-resolution NMR spectroscopy, and medical and nonmedical applications of magnetic resonance imaging.

Partial Fourier Acquisition in MRI

Paul M. Margosian, Gordon DeMeester, and Haiying Liu
Picker International, Highland Heights, OH, USA

1 INTRODUCTION

The original motivation for exploring partial Fourier image reconstruction methods for MRI was the possibility of completing an acquisition in roughly half the normal time. For standard multislice spin echo methods, this means that a typical acquisition might be reduced from 10 to 5 min. Such possibilities offer the potential of increasing the efficiency, both clinical and economic, of a commercial magnetic resonance (MR) imager.

The most basic partial Fourier acquisition is to acquire the central 128 lines of the raw data space, zero fill the outer lines [Figure 1(a)], and take the amplitude of the Fourier transform (FT) to make a 256 × 256 image which has sacrificed spatial resolution in the phase-encode direction. This is a basic property of FTs,[1] and is equivalent to making a sinc interpolation of a 128 × 256 image up to full size.[2]

Another basic manipulation is to acquire only every second phase-encode line (Figure 1(b)) of a normal set of 256, and

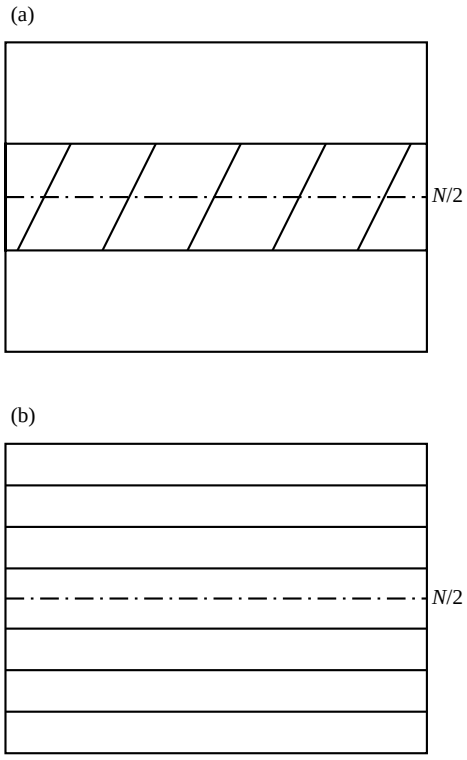

Figure 1 (a) Center 128 data lines; (b) all other data lines

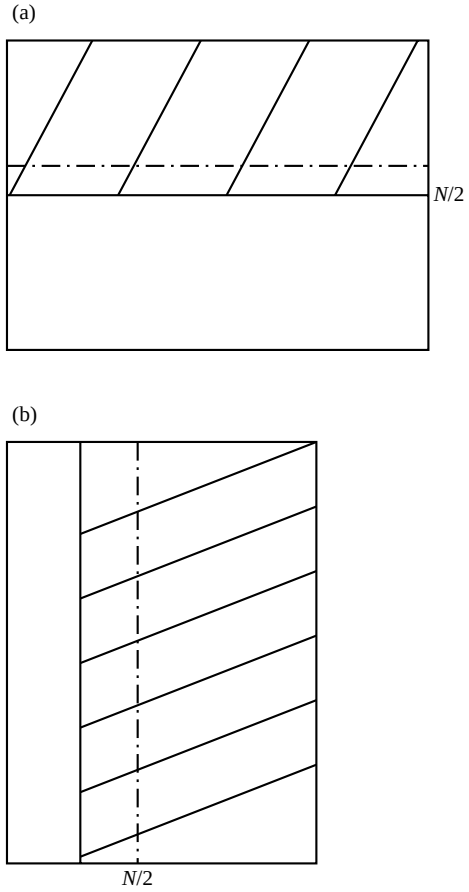

Figure 2 $N/2 + L$ data lines in (a) the phase-encode direction and (b) the read direction

seek various interpolation methods to approximate the missing data lines in an attempt to maintain full spatial resolution. Such an attempt is doomed to failure by the sampling theorem;[1] the result of such an experiment is invariably an image with accompanying ghost images that may overlap the main image, the relative amplitude of which reflects the importance of the spatial frequencies that could not be faithfully reproduced. Only iterative methods which insert additional constraints and a priori information are suitable to make such a strategy work.

The most widely used partial Fourier methods take advantage of the fundamental redundancy of complex samples of the signals acquired to provide a full resolution reconstruction from half the raw data, using all the samples on one side of the echo (in either the phase-encode direction [Figure 2(a)] or the readout direction [Figure 2(b)]. Of the most commonly used 'single-pass' methods, one is based on an approximate deconvolution of the data 'blanking' function which represents missing data,[3,4] while the other is based on explicit calculation of missing raw data by assuming that the full data set (of which only half has been acquired) is Hermitian[5] and therefore that the image is strictly real. These methods achieve full spatial resolution at the cost of a loss of approximately a factor of $\sqrt{2}$ in the signal-to-noise ratio. They require acquisition of a few more than half the normal number of data lines in order to allow generation of a low-frequency phase correction which is

needed in order to remove the effects of practical instrument imperfections from the raw data. More elaborate iterative methods have been reported[6–9] which seek to overcome more complicated errors at the cost of much increased computation time; an exposition of such algorithms in the more general context of constrained reconstruction methods is given by Liang et al.[10]

This article describes the two most commonly used 'single pass' half Fourier methods and provides an example of one type of iterative method. These methods are sometimes referred to as 'phase constrained' reconstructions.

2 MATHEMATICAL BACKGROUND

2.1 General Considerations

For the ideal MRI application, the spin system of the imaged object (the patient) is a real function. First-order gradients of a z directed magnetic field phase-encode the data as the FT of the excited spin system. Such measurements form a two- or three-dimensional k-space, or spatial frequency space, representation of the object.

In practice, the phase-encoding process, and consequently the k-space data, are not ideal. Possible errors include uncorrected time dependence of the gradient field as with eddy currents. Furthermore, signal from the spin system is likely to decay with time constants such as T_2 and T_2^* in the read direction. Even rf imperfections can disturb the phase. Such errors cause uncontrolled phase variations across the k-space, but preserve the amplitude. This means that the phase of a complex MR image is not really zero and that partial Fourier reconstruction algorithms which appeal to the special kind of symmetry of ideal data will be distorted unless an appropriate phase correction is devised.

2.2 Notation

The partial Fourier methods discussed all seek to recover an image from slightly more than half of k-space (Fourier encoded raw data in Cartesian coordinates). In principle, it does not matter if the data set is one-, two-, or three-dimensional, as long as it is incomplete in only one spatial frequency coordinate, and it is equivalent for the data to be incomplete in either a phase-encode direction or a read direction. In practice, however, data variations in the phase direction are more nearly ideal than in the read direction. The acquired data are represented by $D(k_1, k_2, k_3)$, where the data are assumed to be complete in the k_1 and k_2 spatial frequency dimensions, and incomplete in the k_3 direction. When discussing Fourier reconstruction, the corresponding spatial variables are x_1, x_2, and x_3, respectively; the transforms are done sequentially for the axes having complete data (k_1 and k_2), and the partial Fourier algorithms are applied only to the incomplete (k_3) axis. The notation used to denote the partially transformed data is $D(x_1, x_2, k_3)$, where

$$D(x_1,\ x_2,\ k_3) = \mathrm{IFT}_{(k1,\,k2)}[D(k_1,\ k_2,\ k_3)] \tag{1}$$

and IFT is the inverse Fourier transformation. Reduction to two dimensions is straightforward.

In all the algorithms described for completing the transformation in the k_3 direction, the number of data lines acquired is described as $N/2 + L$, where N is the (full) image matrix size, and L is the number of extra lines which has been taken past the center of k-space. The central $2L$ data lines are used to generate a low-frequency phase estimate of the completed complex image.

2.3 Minimizing Ringing Artifacts

Truncation of k-space is always a problem with digital data acquisition because of the limited extent of the sampling; the presence of significant object information beyond the end of k-space sampling will cause Gibbs ringing.[2] This kind of artifact is best controlled by sampling far enough in k-space to satisfy the sampling theorem for the data present. In the cases discussed here, there are always too few samples in one dimension and, therefore, truncation artifacts are minimized by using the Hanning filter $H(k_3)$ which varies smoothly from one to zero over $L + 1$ points.[2] Exact details of the application of this filter are given with each partial Fourier algorithm.

2.4 Phase Correction Method

All partial Fourier methods to be discussed require at least a low-frequency phase correction to the MRI data for proper functioning. Typical phase errors consist of an arbitrary overall phase constant plus a limited excursion of a few π across a complex image. Thus it is reasonable to estimate phase variations by a phase map generated from the central 8–15% of the data lines of k-space; the exact number of lines is an adjustable parameter. A low-resolution phase correction is generated as described below.

The phase map estimate $\phi_L(x_1, x_2, x_3)$ is determined from the central $2L$ lines of k-space with zero padding. A Hanning weighting $H(k_3)$ is applied to these central data in order to minimize the potential for ringing artifacts. The raw data P are used for the phase correction:

$$P(x_1,\ x_2,\ k_3) = D(x_1,\ x_2,\ k_3) * H(k_3) \qquad -L \le k_3 \le +L \tag{2a}$$

$$P(x_1,\ x_2,\ k_2) = 0.0 \qquad \text{Elsewhere} \tag{2b}$$

where we have followed the notation established in Section 2.2. The inverse FT in the k_3 variable is then calculated:

$$p(x_1,\ x_2,\ x_3) = \mathrm{IFT}_{k3}[P(x_1,\ x_2,\ k_3)] \tag{2c}$$

A low-frequency phase map can be formed from p:

$$\phi_L(x_1,\ x_2,\ x_3) = \arctan\left[\frac{\mathrm{Im}(p[x_1,\ x_2,\ x_3])}{\mathrm{Re}(p[x_1,\ x_2,\ x_3])}\right] \tag{3}$$

Note that this phase map exists in the complex image domain (i.e. the independent variables are spatial coordinates, not spatial frequencies). An alternative way to accomplish the desired phase correction is to compute a normalized version u of the (blurry) complex image $p(x_1, x_2, x_3)$:

$$u(x_1,\ x_2,\ x_3) = p(x_1,\ x_2,\ x_3)/|p(x_1,\ x_2,\ x_3)| \tag{4}$$

The complex conjugate of u, u^*, can be used to make an approximate phase correction to complex images made from the

acquired data. The function u itself is used to correct phases of data sets synthesized by Hermitian conjugation. The effect of such a correction is to make the complex image more nearly real.

3 HALF FOURIER, DECONVOLUTION APPROACH

3.1 Theory for the Ideal Case

The half Fourier method is a technique for recovering an image from slightly more than half of k-space data coverage, in which one treats the problem of recovering the full image as equivalent to deconvolving the effects of the data truncation from the complex image domain.

Assume that exactly half of a three-dimensional data set exists. Then each of the (partially transformed) data lines $D(x_1, x_2, k_3)$ can be thought of as the product of the object data $O(x_1, x_2, k_3)$ and a unit step function $S(k_3)$:

$$D(x_1,\ x_2,\ k_3) = O(x_1,\ x_2,\ k_3) * S(k_3) \tag{5}$$

The image recovery process includes the FT of the data:

$$d(x_1,\ x_2,\ x_3) = \mathrm{IFT}_{k3}[D(x_1,\ x_2,\ k_3)] \tag{6}$$

Using the convolution theorem with equations (5) and (6) gives the result

$$d(x_1,\ x_2,\ x_3) = O(x_1,\ x_2,\ x_3) \otimes s(x_3) \tag{7}$$

where $o(x_1, x_2, x_3)$ is the desired object information and the FT of the step function is

$$s(x_3) = \tfrac{1}{2}\{\delta(x_3) + \mathrm{i}/\pi x_3\} \tag{8}$$

and δ is the Dirac delta function. Now assume that we can find a phase map $\phi(x_1, x_2, x_3)$ for the object $o(x_1, x_2, x_3)$ that reduces this complex image to a real image $r(x_1, x_2, x_3)$:

$$r(x_1,\ x_2,\ x_3) = o(x_1,\ x_2,\ x_3) * \exp[-\{\mathrm{i}\phi(x_1,\ x_2,\ x_3)\}] \tag{9}$$

This phase map (Section 2.4) is that which would be generated from the data of the object $O(x_1, x_2, x_3)$ if it existed. Finally,

$$\begin{aligned} &d(x_1,\ x_2,\ x_3) * \exp[-\{\mathrm{i}\phi(x_1,\ x_2,\ x_3)\}] \\ &\quad = r(x_1,\ x_2,\ x_3) \otimes s(x_3) \\ &\quad = r(x_1,\ x_2,\ x_3)/2 - \mathrm{i}\{r(x_1,\ x_2,\ x_3) \otimes 1/2\pi x_3\} \end{aligned} \tag{10}$$

The image that we wish to recover is $r(x_1, x_2, x_3)$. It can be determined from

$$r(x_1,\ x_2,\ x_3) = \mathrm{Re}[d(x_1,\ x_2,\ x_3) * \exp[-\{\mathrm{i}\phi(x_1,\ x_2,\ x_3)\}] \tag{11}$$

3.2 Practical Implementation

The half Fourier method follows the ideal theory except in the details of the Hanning filtering of the central lines in order to avoid truncation effects.

1. Acquire the data set, inverse FT in the complete data directions.
2. Find the phase map ϕ, or normalized correction function u, as in Section 2.4.
3. Recover the image. This requires both the phase estimate and a Hanning roll-off filter. The filtered data, D_f are formed by using weight factors that range from one for the element $-L$ down to zero for the element $+L$:

$$D_\mathrm{f}(x_1,\ x_2,\ k_3) = D(x_1,\ x_2,\ k_3) \qquad -N/2 \le k_3 < -L \tag{12a}$$

$$D_\mathrm{f}(x_1,\ x_2,\ k_3) = D(x_1,\ x_2,\ k_3) * H(k_3) \qquad -L \le k_3 < +L \tag{12b}$$

$$D_\mathrm{f}(x_1,\ x_2,\ k_3) = 0.0 \qquad \text{Elsewhere} \tag{12c}$$

Now inverse FT the filtered data:

$$d(x_1,\ x_2,\ x_3) = \mathrm{IFT}_{k3}[D_\mathrm{f}(x_1,\ x_2,\ x_3)] \tag{13}$$

Finally, recover the desired image by applying equation (11):

$$\begin{aligned} r(x_1,\ x_2,\ x_3) &= \mathrm{Re}[d(x_1,\ x_2,\ x_3) * u^*(x_1,\ x_2,\ x_3)] \\ &= \mathrm{Re}[d(x_1,\ x_2,\ x_3) * \exp[-\{\mathrm{i}\phi_L(x_1,\ x_2,\ x_3)\}] \end{aligned} \tag{14}$$

The result is a simple and fast method of making images from slightly more than half the data. The signal-to-noise ratio is proportional to the number of phase-encode lines acquired; therefore, with half Fourier imaging we expect the signal-to-noise in the image to be reduced by $1/\sqrt{2}$ compared with a conventional complete data set.

4 CONJUGATE SYMMETRY APPROACH

4.1 Theory for the Ideal Case

Ideally, the spin system of the imaged object or patient is real, and therefore its FT is conjugate symmetric (Hermitian). The conjugate symmetry relation for an ideal three-dimensional data set $D(k_x, k_y, k_z)$ can be written as

$$D(k_x,\ k_y,\ k_z) = D^*(-k_x,\ -k_y,\ -k_z) \tag{15}$$

It is clear from equation (15) that half the ideal k-space data are redundant. A statement of conjugate symmetry at an intermediate step of processing is

$$I(x_1,\ x_2,\ k_3) = I^*(x_1,\ x_2,\ -k_3) \tag{16}$$

4.2 Practical Implementation

The conjugate symmetry algorithm uses the conjugate symmetry relation in one dimension, a Hanning filter, and the phase estimate. The Hanning filter, whose weights vary from one to zero over $L + 1$ data lines, is used when synthesizing a complete data line. The method of combining these elements to generate the desired image $c(x_1, x_2, x_3)$ is described below.

1. Calculate the intermediate image $I(x_1, x_2, k_3)$ as in equation (16). This image spans the range of the variables x_1 and x_2 as well as variable k_3.
2. Produce the phase estimate function u, as in Section 2.4.
3. Produce a partial image $a(x_1, x_2, x_3)$ from the acquired data:

$$A(x_1,\ x_2,\ k_3) = I(x_1,\ x_2,\ k_3) \qquad -N/2 \le k_3 < 0 \qquad (17a)$$
$$A(x_1,\ x_2,\ k_3) = H(k_3) * I(x_1,\ x_2,\ k_3) \qquad 0 \le k_3 \le L \qquad (17b)$$
$$A(x_1,\ x_2,\ k_3) = 0.0 \qquad k_3 > L \qquad (17c)$$

Now inverse FT on the k_3 variable:

$$a(x_1,\ x_2,\ x_3) = \mathrm{IFT}_{k3}[A(x_1,\ x_2,\ k_3)] \qquad (18)$$

The complex image $a(x_1,\ x_2,\ x_3)$ is then multiplied point by point by the complex conjugate of the phase image $u(x_1,\ x_2,\ x_3)$:

$$au(x_1,\ x_2,\ x_3) = a(x_1,\ x_2,\ x_3) * u^*(x_1,\ x_2,\ x_3) \qquad (19)$$

4. Now use the conjugate symmetry relation to generate a partial image from the data that were not acquired,

$$B(x_1,\ x_2,\ k_3) = 0.0 \qquad -N/2 \le k_3 < 0 \qquad (20a)$$
$$B(x_1,\ x_2,\ k_3) = \{1.0 - H(k_3)\} * I^*(x_1,\ x_2,\ -k_3) \qquad 0 \le k_3 \le L \qquad (20b)$$
$$B(x_1,\ x_2,\ k_3) = I^*(x_1,\ x_2,\ -k_3) \qquad k_3 > L \qquad (20c)$$

and then FT in k_3 to make a partial image from the missing data,

$$b(x_1,\ x_2,\ x_3) = \mathrm{IFT}_{k3}[B(x_1,\ x_2,\ k_3)] \qquad (21)$$

This intermediate image also needs to be multiplied by the phase map; use the unit phase map and not its complex conjugate for the point-by-point product:

$$bu(x_1,\ x_2,\ x_3) = b(x_1,\ x_2,\ x_3)u(x_1,\ x_2,\ x_3) \qquad (22)$$

5. Compute the final image from the complex sum of the two intermediate images formed in steps 3 and 4 above:

$$c(x_1,\ x_2,\ x_3) = |au(x_1,\ x_2,\ x_3) + bu(x_1,\ x_2,\ x_3)| \qquad (23)$$

Because of the use of the complex phase map the final image $c(x_1,\ x_2,\ x_3)$ is nearly real, therefore one may choose this presentation as an alternative to a standard magnitude image. The noise in a real image is not required to be positive, as with a magnitude image, so it maintains a zero mean Gaussian behavior near zero. The effectiveness of the phase map corrections may be estimated by looking at the residual imaginary image.

The signal-to-noise ratio in a full data set varies as $\sqrt{N}$. For the partial data set, the noise is averaged down inversely as the number of lines acquired. Since the region between $N/2 + 1$ and $N/2 + 1 + L$ is only weighted on average by $\frac{1}{2}$, the predicted signal-to-noise ratio (S/N) will scale as:

$$\mathrm{S/N} \propto (N/2 + L/2 + 1)^{1/2} \qquad (24)$$

5 ITERATIVE RECONSTRUCTION

When half or more of the data are acquired in any direction, iterative techniques can be devised to substitute, sequentially, synthesized data subjected to constraints for the missing data. One such method is referred to as the 'Cuppen-POCS iterative method'.[6]

The theoretical development is similar to that used in the half Fourier or deconvolution method. However, the physical object is no longer represented by a real function but by the magnitude of a complex function. This would not be correct for the noise surrounding the object or for inversion–recovery imaging, but otherwise it is a reasonable constraint. The steps in the projection onto convex sets (POCS) method are as follows.

1. Acquire the partial Fourier data set $D(k_1,\ k_2,\ k_3)$ which is truncated in the k_3 direction.
2. Develop a phase map from the data lines $-L$ to $+L$, as in Section 2.4.
3. For the first iteration $m = 1$, replace the missing data with zero. For all subsequent iterations $m > 1$, replace the missing data with synthesized data $R(x_1,\ x_2,\ k_3)$ from the last iteration:

$$D_m(x_1,\ x_2,\ k_3) = D(x_1,\ x_2,\ k_3) \qquad -N/2 \le k_3 \le +L \qquad (25)$$

Then, for the first iteration

$$D_1(x_1,\ x_2,\ k_3) = 0.0 \qquad +L < k_3 \le N/2 \qquad (26)$$

and for subsequent iterations

$$D_m(x_1,\ x_2,\ k_3) = R_{m-1}(x_1,\ x_2,\ k_3) \qquad +L < k_3 \le N/2 \qquad (27)$$

4. Now take the inverse FT of the completed data set and apply the phase map $\phi_L(x_1,\ x_2,\ x_3)$ determined in step 2 above:

$$d_m(x_1,\ x_2,\ x_3) = \mathrm{IFT}_{k3}[D_m(x_1,\ x_2,\ k_3)] \qquad (28)$$

$$r_m(x_1,\ x_2,\ x_3) = |d_m(x_1,\ x_2,\ x_3)| * \exp[-\{\mathrm{i}\phi_L(x_1,\ x_2,\ x_3)\}] \qquad (29)$$

5. The data to replace the original missing data from $+L$ to $N/2$ are determined from the FT of $r_m(x_1,\ x_2,\ x_3)$:

$$R_m(x_1,\ x_2,\ k_3) = \mathrm{FT}_{x3}[r_m(x_1,\ x_2,\ x_3)] \qquad (30)$$

For the data replacement in step 3, only the values of k between L and $N/2$ will be used. For the last iteration a linear weighting scheme is used to 'feather', or merge, the replacement data with the original data in step 3. In this case a number of points before the boundary are used for the merge.

6. The desired image is $r(x_1,\ x_2,\ x_3)$, the output of step 4 after the desired number of iterations (typically three or four) is completed.

This sort of process has proven superior to both half Fourier and conjugate symmetry methods for partial Fourier reconstruction of gradient echo acquisitions where phase errors are severe. In this framework, it is also easier to incorporate more phase constraints into the image reconstruction. This procedure is somewhat more computationally intensive than are the one-pass methods.

6 CONCLUDING REMARKS

All three partial Fourier methods impose a phase correction determined from data near the center of k-space. Differences between the low-frequency phase map and the phase map

determined from a full (ideal) data set limit the accuracy of the techniques.

Both the half Fourier method and the conjugate symmetry methods assume a real object and use the same phase map, but are quite different operationally. Both methods use a Hanning filter, but in different ways: the half Fourier method applies this weight such that the center of k-space has a weight of 0.5, thus exacting a slight signal-to-noise penalty; the conjugate symmetry method applies the Hanning filter to weight the data from the center of k-space out to L. The conjugate symmetry method requires two inverse FTs, whilst the half Fourier method needs only one.

The three methods use assumptions about a real object differently. The half Fourier method requires that the imaginary part of the final image be discarded. The conjugate symmetry method generates a complex image with a small imaginary part, so a magnitude operation is performed. This imaginary part arises because the phase of the acquired data does not exactly match the low-frequency phase map. The iterative method also generates a complex image because the phase constraint is applied to the magnitude of the image. None of these methods properly reconstructs nonreal object features (in the Fourier representation) such as motion or susceptibility.

7 RELATED ARTICLES

Projection–Reconstruction in MRI; Spin Warp Data Acquisition; Spiral Scanning Imaging Techniques.

8 REFERENCES

1. R. N. Bracewell, 'The Fourier Transform and its Applications', McGraw-Hill, New York, 1986.
2. R. W. Hamming, 'Digital Filters', Prentice-Hall, Englewood Cliffs, NJ, 1977.
3. P. Margosian and M. Deimling, in *Proc. Vth Ann Mtg. Soc. Magn. Reson. Med.*, Montreal, 1986, p. 834.
4. P. Margosian, F. Schmitt, and D. E. Purdy, *Hlth Care Instrum.*, 1980, **1**, 195.
5. G. DeMeester, G. N. Holland, J. L. Patrick, and K. S. Denison, in *Proc. VIth Ann Mtg. Soc. Magn. Reson. Med.*, New York, 1987, p. 804.
6. J. J. Cuppen and A. Van Est, in 'Topical Conference on Fast MRI Techniques', Cleveland, OH, 1987.
7. E. M. Haacke, E. D. Lindskog, and W. Lin, *J. Magn. Reson.*, 1991, **92**, 126.
8. D. Purdy, in *Proc. VIth Ann Mtg. Soc. Magn. Reson. Med.*, New York, 1987, p. 379.
9. D. Purdy, in *Proc. Xth Ann Mtg. Soc. Magn. Reson. Med.*, San Francisco, 1991, p. 742.
10. Z. P. Liang, F. Boada, R. Constable, E. M. Haacke, P. Lauterbur, and M. Smith, *Rev. Magn. Reson. Med.*, 1992, **4**, 16.

Biographical Sketches

Paul M. Margosian. *b* 1940. B.S., 1962, Notre Dame. M.S., 1965, John Carroll University; Ph.D., 1974, MIT.

Gordon DeMeester. *b* 1942. B.S.E.E., 1964, Michigan State University; M.S., Ph.D., 1971, University of Michigan.

Haiying Liu. *b* 1963. B.S., 1984, Jilin University; Ph.D., 1990, University of Minnesota.

Projection–Reconstruction in MRI

Gary H. Glover and John M. Pauly
Stanford University, Stanford, CA, USA

1 INTRODUCTION

Projection–reconstruction (PR) refers to a family of magnetic resonance (MR) imaging techniques that scan through acquisition data space (*k*-space) along radial trajectories, rather than along the rectangular Cartesian trajectories of Fourier transform (FT) methods. The first MR images were made using 2D projection–reconstruction (2D PR).[1] PR methods remained dominant in MR imaging research until the advent of FT methods,[2] and in particular spin warp.[3] The FT methods have significant advantages in off-resonance response, tolerance for nonideal gradient response, and ease of reconstruction. PR has more exacting hardware requirements, has difficulties with off-resonance spins, and is less efficient in its use of scan time. Recently, imaging hardware and reconstruction methods have improved to the point that PR methods are once again the subject of active research. PR methods have some unique capabilities that outweigh their disadvantages for particular applications. Some of these advantages are short echo times for imaging short T_2 species, and reduced flow and motion artifacts.

There are several different versions of PR imaging, each with different areas of application. All PR methods collect data along radial lines in *k*-space. One major distinction is whether the whole volume or a slice is imaged. In the latter case, some form of slice selection must be incorporated, which has implications for minimum echo time. The other distinction is whether a full diameter is collected, or only a radius. Collecting full diameters is more efficient in scan time, while collecting radii allows much shorter echo times.

One of the applications for PR methods is in imaging with very short echo times. In 3D PR a single hard pulse excitation is followed immediately with the PR acquisition gradients. There are no phase-encoding gradients to delay acquisition, as in FT methods. These very short echo times are essential for imaging intracellular ^{23}Na[4] and ^{11}B,[5] which have very short T_2 values. The low sensitivity and short T_1 values of these nuclei make 3D imaging the natural choice. For ^{1}H the case is slightly different owing to the high sensitivity and desired resolution of proton images. Three-dimensional PR ^{1}H imaging would require prohibitively long scan times and result in very large data sets. In this case slice selection is desirable. This can be accomplished without increasing the echo delay using interleaved half pulses.[6] Applications include imaging lung parenchyma, which has short T_2* due to susceptibility dephasing and short T_2 due to diffusion.[7] (See ***Lung and Mediastinum: A Discussion of the Relevant NMR Physics*** and ***Sodium-23 Magnetic Resonance of Human Subjects***.)

The other area where PR methods excel is in the nature of the artifacts produced by motion. With FT methods, respiratory, cardiac, or other forms of physiological motion cause ghost artifacts. These artifacts spread in the phase-encoding direction and result from either phase or amplitude inconsistencies from one acquisition (view) to the next.[8] The artifacts are well focused into discrete ghosts when the motion is highly periodic, but can smear uniformly when the motion is random. Projection–reconstruction methods have been found to be more robust with respect to motion, often providing superior performance when imaging moving structures.[9] This is true whether full diameters or radii are collected. Flow artifacts are also reduced with PR, because short echo times eliminate most spin dephasing. FT methods exhibit a displacement artifact when imaging oblique vessels due to the different times that the x and y positions are encoded, while simultaneous encoding in PR eliminates such artifacts.[10] (See ***Pulsatility Artifacts Due to Blood Flow and Tissue Motion and Their Control***; ***Whole Body Magnetic Resonance Artifacts***.)

Thus, PR methods find applications either when imaging species with short transverse magnetization decay times or when motion artifacts are an issue.

2 THEORY OF PROJECTION–RECONSTRUCTION

2.1 Central Slice Theorem

Consider an object with a (possibly complex) distribution $m(x, y)$ as shown in Figure 1(a). In addition to the spin density, $m(x, y)$ includes relaxation weighting and phase factors which result from off-resonance excitation. Projections of the object are obtained at many angles θ in the frame (r, l), where the projection is defined as the line integral

$$P_\theta(r) = \int_C m(x, y)\, \mathrm{d}l \tag{1}$$

in which C is the path described by

$$x \sin\theta - y \cos\theta = r \tag{2}$$

and the integration extends along C through the object. Taking the Fourier transform of P in equation (1) yields

$$\begin{aligned} \hat{M}_\theta(k) \equiv \mathcal{F}(P_\theta(r)) &= \int P_\theta(r) \mathrm{e}^{\mathrm{i}kr}\, \mathrm{d}r \\ &= \int \mathrm{e}^{\mathrm{i}kr}\, \mathrm{d}r \int_C m(x, y)\, \mathrm{d}l \end{aligned} \tag{3}$$

Since the transformation between the (x, y) and (r, l) frames has unity Jacobian, equation (3) becomes

$$\hat{M}(k_x, k_y) = \int \mathrm{e}^{\mathrm{i}(k_x x + k_y y)} m(x, y)\, \mathrm{d}x\, \mathrm{d}y \tag{4}$$

where equation (2) has been substituted for r, and

$$\left.\begin{aligned} k_x &\equiv k \cos\theta \\ k_y &\equiv k \sin\theta \end{aligned}\right\} \tag{5}$$

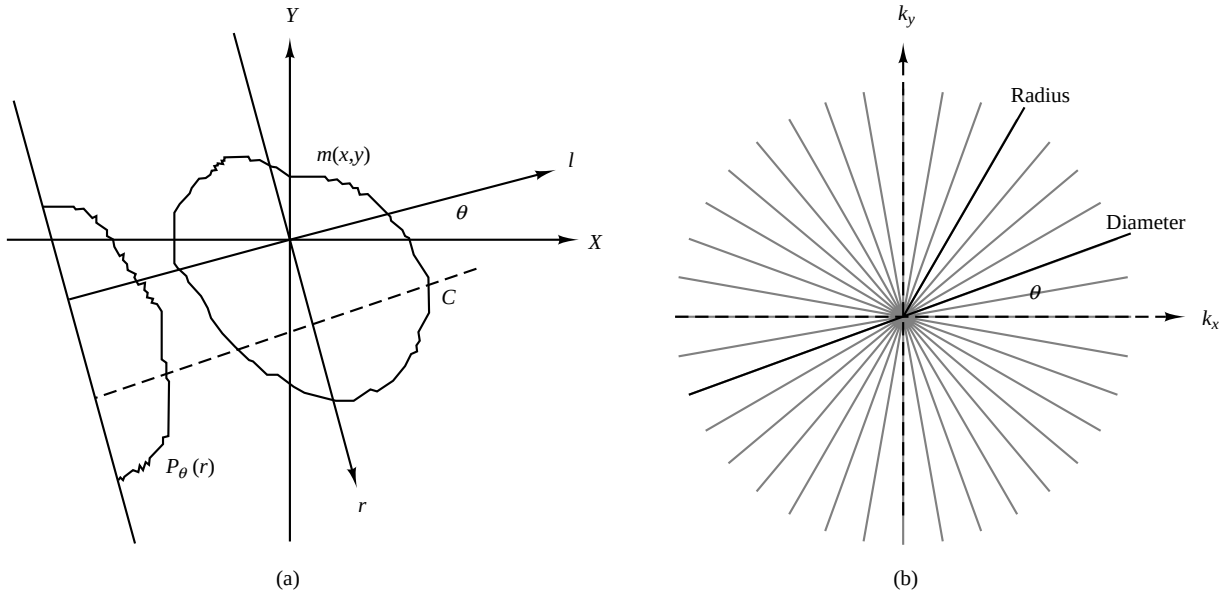

Figure 1 Projection–reconstruction geometry. (a) Projection $P_\theta(r)$ of an object with a distribution $m(x, y)$ consists of line integrals along parallel rays C at angle θ. (b) Corresponding k-space representation of projection data, collected either as a diameter or radius

Equation (4) will be recognized as the two-dimensional Fourier transform of m evaluated at (k_x, k_y) in k-space. Note that points along (k_x, k_y) are diameters in k-space, as shown in Figure 1(b). Therefore, each projection (or view) contributes data along a diameter in k-space at the angle θ. This is a conclusion of the Central Slice theorem.[11] If the incremental angle between views is fine enough, the k-space distribution will be adequately sampled and the object can be reconstructed.

Thus, k-space is covered in a radial fashion for PR, as contrasted with the rectilinear coverage obtained in 2D FT methods. The consequences of this will be examined below in conjunction with the discussions of motion artifacts and S/N efficiency.

2.2 Projection–Reconstruction in MRI

Consider the 2D PR pulse sequence in Figure 2 which uses a selective excitation pulse requiring no refocusing.[6] Projection data are collected at an angle θ during the simultaneous application of x and y gradients with amplitudes $G_{x0} = G_0 \cos\theta$, $G_{y0} = G_0 \sin\theta$, respectively. The signal is given by

$$S(t) = \int e^{i\gamma \int_0^t \boldsymbol{G}(t')\cdot\boldsymbol{r}\,dt'} m(x,y)\,dx\,dy \tag{6}$$

where $\boldsymbol{G}$ and $\boldsymbol{r}$ denote vectors with components (G_x, G_y) and (x, y), respectively. Define

$$\left.\begin{aligned} k_x(t) &\equiv \gamma \int_0^t G_x(t')\,dt' \\ k_y(t) &\equiv \gamma \int_0^t G_y(t')\,dt' \end{aligned}\right\} \tag{7}$$

then

$$\gamma \int_0^t \boldsymbol{G}(t')\cdot\boldsymbol{r}\,dt' = k_x x + k_y y \tag{8}$$

so equation (6) becomes

$$S(t) = \int_{-k_{max}}^{k_{max}} \int_{-k_{max}}^{k_{max}} e^{i(k_x(t)x + k_y(t)y)} m(x,y)\,dx\,dy \tag{9}$$

Thus the signal corresponds to a two-dimensional FT of the object's distribution, sampled along the k-space trajectory $\boldsymbol{k}(t) = (k_x(t), k_y(t))$ defined by equation (7). This trajectory is shown as a radial line in Figure 1(b). Note that samples begin at the center of k-space, and that the 'echo time' (defined as the time at which the center of k-space is sampled) can thereby, in principle, be made arbitrarily small.

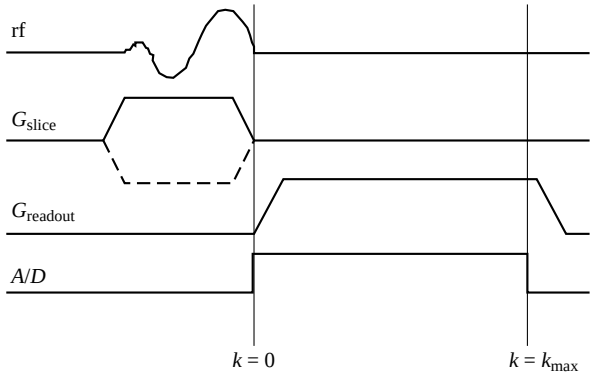

Figure 2 Pulse sequence for PR acquisition of one radial line in k-space starting at $k = 0$ (origin). Minimal echo delay is obtained using a self refocused rf pulse, which requires averaging of the signals from two excitations with inverted polarity of G_{slice}. The readout gradient is derived from vectorial combination of two or three gradients. If a k-space diameter is to be collected, a dephasing gradient pulse (not shown) is needed before readout, which lengthens the echo delay time

2.3 Resolution and Sampling Considerations

The pixel size and field-of-view (FOV) in an image reconstructed by Fourier transformation from data sampled in a Cartesian k-space matrix are determined by the extent and granularity of the sampling. For inversion of an $N \times N$ matrix, the pixel size p is related to the extent of coverage, measured by $\pm k_{max}$ in Figure 3, as

$$p = \pi / k_{max} \tag{10}$$

while the FOV, D, is given by

$$D = 2\pi / \Delta k \tag{11}$$

where $\Delta k = 2k_{max}/N$ is the spacing between Cartesian samples.

Now suppose the k-space data are obtained by PR acquisition with each projection recorded as N_s uniformly spaced samples along a path starting at $\boldsymbol{k} = 0$, with a radius k_{max}, as shown in Figure 3. The data may be interpolated onto the Cartesian grid with no loss of information if the spacing between the grid lines Δk is equal to the radial spacing between samples in the projection, $\Delta k_s = k_{max}/N_s$, and the number of projections N_{views} is chosen so that the increment between angles $\Delta\theta$ satisfies

$$\Delta\theta k_{max} = \Delta k = 2k_{max}/N \tag{12}$$

Under these conditions, the Cartesian sampling will just match the radial sampling intervals at the periphery where $k = k_{max}$, and will be oversampled for $|k| < k_{max}$. This occurs when $N_{views} = \pi N$. If the signal sampling duration is T_{ad}, the gradient strength required for all imaging axes is given by

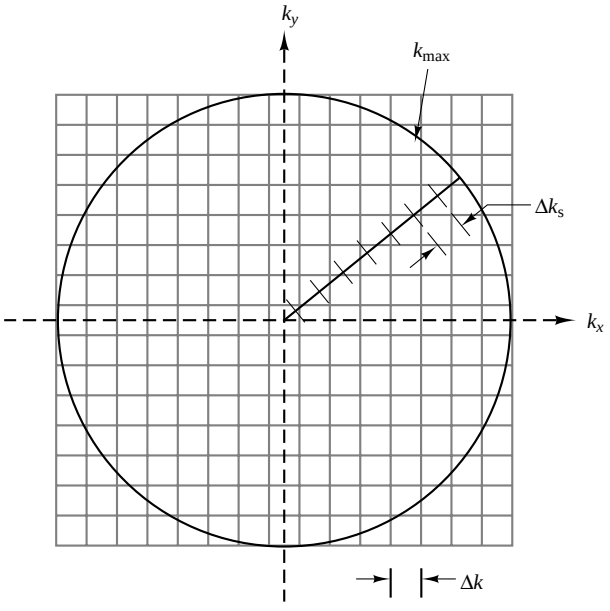

Figure 3 2D interpolation algorithms resample PR data onto a square output grid with a spacing Δk and a size $2k_{max} \times 2k_{max}$ for Fourier inversion. With gridding methods, each input measurement contributes to nearby output grid elements according to a kernel the values of which decrease with distance from the input point

$$k_{max} = \gamma \int_0^{T_{ad}} G(t')\, dt' \tag{13}$$

$$= \gamma G_0 (T_{ad} - T_r/2) \tag{14}$$

for the ramped gradient in Figure 2.

The preceding development has assumed that the data are collected as radii. If diameters are to be collected (using a pulse sequence with a dephasing gradient before the readout), appropriate changes must be made, e.g., $N_{views} = (\pi/2)N$. In addition, k-space symmetry can be used if the object is real to halve the minimum number of views required since $M_{\theta+\pi}(k) = M_\theta^*(k)$ [from equation (3) and Brooks and Di Chiro[12]]. This may have certain advantages from the standpoint of motion; however off-resonance causes phase shifts whose effects may be reduced by the full view acquisition. The rest of this development assumes that conjugate symmetry is not used.

2.4 Signal-to-Noise Ratio (S/N)

The S/N is a complex function depending on the polarizability of the nuclei, Larmor frequency, coil efficiency, T_1 and T_2 relaxation weighting, and k-space sampling considerations. In this section we will only consider the impact of the k-space trajectory on the S/N value, and compare PR and FT methods. The measured signal for a view or projection is

$$y(t) = S(t) + n(t) \tag{15}$$

where $S(t)$ is the signal given by equation (9) and $n(t)$ is assumed to be white noise (over $|k| \leqslant k_{max}$). We need only consider a reconstructed image of the signal and noise for a point object, and accordingly let $m(x, y) = m_0\delta(x)\delta(y)$. Then using equations (19) and (20) below, one can show that the image intensity I and variance σ^2 at the origin for 2D FT and radial-sampled 2D PR are given by[13,14]

$$\left.\begin{aligned} I_{FT} &= 4m_0k_{max}^2 \\ \sigma_{FT}^2 &= 2\sigma_0^2k_{max}^3/N_y \end{aligned}\right\} \tag{16}$$

and

$$\left.\begin{aligned} I_{PR} &= \pi m_0k_{max}^2 \\ \sigma_{PR}^2 &= 4\pi^2\sigma_0^2k_{max}^3/3N_{views} \end{aligned}\right\} \tag{17}$$

where N_y is the number of phase-encoding views for the 2D FT acquisition, σ_0^2 is the variance of the noise in a view or projection, and constant factors have been dropped for convenience. Letting S/N = I/σ for each method,

$$\frac{S/N(PR)}{S/N(FT)} \equiv R = \sqrt{3N_{views}/8N_y} \tag{18}$$

If $N_y = N$ and $N_{views} = \pi N$ (i.e., minimum sampling requirement), $R = \sqrt{3\pi/8} \approx 1.08$. Thus, the radial PR technique takes π times longer to scan for the same resolution, but provides a slight S/N advantage. However, the efficiency disadvantage of PR is apparent if the S/N is calculated for constant scan time (using more averaging for the FT case than the minimum), and one finds that in this case $R = \sqrt{3/8} \approx 0.61$. However, this disadvantage is

often offset by the gain in motion immunity afforded by the redundant low-frequency sampling.

3 PULSE SEQUENCE CONSIDERATIONS

3.1 Radiofrequency Pulse

One of the motivations for using PR is to image materials with short T_2 values. In this case, it is desirable to minimize the time between the end of the excitation pulse and the beginning of the readout. In the case of 3D imaging, a short nonselective excitation pulse may be employed,[5] while for 2D applications, three approaches are available. The first is to precede a short nonselective excitation pulse with a spatially-selective saturation pulse which leaves only the desired slice plane unperturbed.[15] The second is to use a selective pulse that requires no refocusing, i.e., ends with the transverse magnetization in phase. This may be accomplished using half pulses which require two excitations/view, where each excitation scans half of the excitation k-space.[6] The sequence in Figure 2 shows an example of the use of this kind of pulse. The third approach is the use of self-refocused spin echo pulses. Such pulses incorporate both a 90° and a 180° pulse in one composite envelope and produce an rf refocused echo at a specifiable time after the end of the pulse. This time can be made coincident with the end of the pulse for short T_2 imaging, and although the echo time cannot be made zero, there may be advantages for ultrashort rf-refocused echoes over gradient-recalled echoes.[16]

3.2 Field-of-View Considerations

In PR, it is important that all projections contain the entire cross-section of the subject without aliasing to avoid artifacts. In axial slices this is accomplished by making the FOV big enough; however, in sagittal or coronal orientations this may not be feasible for whole torso applications, because views with rays parallel to the magnet axis may include only part of the spins contained in views perpendicular to the axis. One technique to minimize deleterious effects which arise from such inconsistencies is to use rf coils (surface or volume) with a suitably limited sensitive region. A second approach is to use multidimensional excitation or saturation pulses to define only an inner volume of interest[17] which can be wholly contained in the FOV.

4 RECONSTRUCTION TECHNIQUES

The PR image reconstruction is performed conceptually by inverting the FT of the k-space data. From equation (4), the image is given by the FT of the measured signal $M(k_x, k_y)$:

$$I(x,y) = \int M(k_x,k_y)\mathrm{e}^{-\mathrm{i}(k_x x + k_y y)}\,\mathrm{d}k_x\,\mathrm{d}k_y \qquad (19)$$

Transferring to cylindrical coordinates in both image space and k-space and using equation (3),

$$I(\rho,\phi) = \int_\theta^{2\pi} \mathrm{d}\theta \int_0^{k_{\max}} \hat{M}_\theta(k)\mathrm{e}^{-\mathrm{i}k\rho\cos(\theta-\phi)}k\,\mathrm{d}k \qquad (20)$$

Here the radially sampled projection data $M_\theta(k)$ are related to the measured signal $S(t)$ by a coordinate transform between time t and k-space radius from the origin, given by equation (7).

There are two general methods for implementing equation (20). The first is filtered back projection.[11] This technique is widely used for X-ray CT because it allows convenient incorporation of source-to-detector intensity factors for the divergent-ray geometries commonly employed, and much has been written about this broad class of methods in the CT context. In fact, the early NMR imaging experiments used this approach,[1] and the relative merits of back projecting magnitude versus complex amplitude projections have been debated.[9,18] However, back projection reconstruction has not been used as much for MR applications as the second method, which uses interpolation of the raw data onto a rectangular matrix for FT inversion.

Interpolation methods can use a variety of techniques to resample the radially gathered raw data into elements of a Cartesian output matrix, following which a 2D or 3D FT inversion is performed to create the image(s). Interpolation algorithms can use bi/tri-linear or higher order methods, where each output datum is calculated from a suitable combination of nearby k-space input data.[11] Alternatively, a gridding technique can be employed for greater effectiveness.[19] In gridding, each input datum is multiplied by elements of a multidimensional filter and the results summed into all nearby output grid points according to the prescribed kernel weighting, which varies according to the distance of the output point from the input point. The fractional contribution that each output element receives is recorded and used to normalize the sampling density. This correction automatically accounts for the oversampling at the origin of k-space ($|k|$ or $|k|^2$ weighting for 2D or 3D acquisitions, respectively), as well as for nonuniform sampling of the projection data during gradient ramp-up.

5 ARTIFACTS IN PROJECTION–RECONSTRUCTION

5.1 Motion Effects

The motion of structures causes artifacts in conventional FT imaging. The artifacts appear either as ghosts or streaks, displaced in the phase-encoding direction, and can be accompanied by blurring of the moving structures. (See ***Pulsatility Artifacts Due to Blood Flow and Tissue Motion and Their Control***; ***Whole Body Magnetic Resonance Artifacts***.)

Projection–reconstruction methods, in addition to allowing negligible delay time before the collection of data, often have superior motion characteristics because of two mechanisms.[9] The first mechanism is that the low spatial frequencies are heavily oversampled, since each projection either starts at, or crosses through, $\boldsymbol{k} = 0$. This provides an intrinsic averaging of

the spectral components which contribute most of the signal power to the image, and therefore motion artifacts are substantially attenuated. The second mechanism is that motion artifacts are manifested with PR as streaks emanating from the moving structures, rather than as ghosts. The streaks tend to lie along rays perpendicular to the displacement direction. In abdominal scans, for example, the motion of the abdominal wall causes horizontal streaks which lie largely outside the torso in the image. Moreover, streaks from quasiperiodic motion are often not evident close to the moving structure, but become apparent only at some distance in the image. This occurs because of diffraction between adjacent streaks which causes cancellation of the inconsistent energy close to the moving structures.

Despite the relative immunity of PR methods to motion, inconsistencies remain which cause streak artifacts. One method of reducing artifacts further is the use of an algorithm which prospectively chooses the view angles depending on the motion (Retrospective Ordered View Angulation, or ROVA).[9] In axial abdominal scans this occurs, for example, by requiring the projection rays to be aligned with the anterior–posterior direction of the patient during peak inspiration, when the respiratory motion is most rapidly evolving. A second method uses consistent projection–reconstruction (CPR) algorithms, which create a set of raw data from the scan data that is consistent with a stationary object.[20] The resulting reconstruction shows diminished streaks, although the blurring remains.

Thus, PR methods often have smaller artifacts from misplaced signal energy than FT methods, but motion nevertheless causes blurring of the moving structures as in FT methods. Usually blurring is less deleterious than the overlaid ghosting, and PR is therefore more robust in the presence of physiological motion.

5.2 Off-resonance Effects

Chemical shift or field heterogeneity can cause off-resonance effects during acquisition. With FT methods, this results in a spatial shift of the depicted structures along the readout direction. In PR methods, the result is blurring. This may be easily demonstrated by calculating the reconstruction of a point at the origin, for projections acquired as radii. The effect of a loss of resonance is to shift every projection by an amount $\delta r = \delta\omega / \gamma G_o$ dependent on the offset frequency $\delta\omega$ and the readout gradient amplitude. For a point object, the FT of the offset-shifted projection is given by $M_\theta(k) = \exp(ik\delta r)$. The reconstruction will be cylindrically symmetric, and equation (20) becomes

$$I(\rho) = \left.\begin{aligned} &\int_\theta^{2\pi} d\theta \int_0^{k_{max}} e^{ik\delta r} e^{-ik\rho\cos\theta} k\, dk \\ &= \begin{cases} 2\pi\delta r((\delta r)^2 - \rho^2)^{-3/2} & (\rho < \delta r) \\ i2\pi\delta r(\rho^2 - (\delta r)^2)^{-3/2} & (\rho > \delta r) \end{cases} \end{aligned}\right\} \quad (21)$$

It may be seen that the point object has been reconstructed with its intensity peaked sharply at a circle with radius equal to the offset δr, and the point has thus been blurred.

Off-resonance therefore causes a loss of resolution in non-Cartesian methods such as PR. If the offset is spatially uniform, a simple phase correction to the data will remove the blurring. However, if the offset is spatially variant but the distribution is known from a field heterogeneity map, regional corrections can be applied by reconstructing the image at resonance offsets appropriate to each region of the imaging volume and piecing the image together. The field map can be obtained by separate acquisitions or by inference from a regional blurring cost function such as minimizing the imaginary component of the image.[21]

6 SPIRAL TECHNIQUES

The PR methods have advantages with respect to motion robustness and short T_2 imaging. However, the number of views needed to obtain a specified resolution is about 1.5–3 times greater than that for a 2D FT method. One related alternative that has the advantages of PR but is more efficient is spiral k-space trajectory acquisitions.[22] The acquisition begins radially at $\boldsymbol{k} = 0$, but quickly becomes predominantly azimuthal and is therefore more efficient because there is less redundant sampling of the low-spatial frequencies, and the gradients can be operated at the maximum value for most of the readout duration. An added advantage of these trajectories is that the gradient moments start at zero, and periodically return to zero, which provides intrinsic moment compensation for additional motion insensitivity. (See ***Spiral Scanning Imaging Techniques***.)

7 APPLICATIONS AND EXAMPLES

Figure 4 illustrates the use of 2D PR for imaging lung parenchyma, and compares the results with an image obtained in the same scan time using a conventional 2D FT method. In this application, both the immunity from motion artifacts and the short effective echo time are a significant advantage for PR.[23] A comparison of PR and FT for abdominal scanning is shown in Figure 5. Again the advantage of PR in the presence of respiratory motion is clear. Another application for PR is in diffusion weighted imaging, where flow artifacts are especially severe with FT imaging but are minimal with PR.[18]

Other applications for PR utilize the short echo time, and include imaging of ^{23}Na, for which the intracellular compartment has a transverse relaxation component with $T_2 < 10$ ms, ^{11}B with $T_2 < 1$ ms for boron neutron capture therapy, and lipid components in atherosclerotic plaque.[24]

In BOLD-contrast brain activation imaging[25] with conventional FT techniques, subtle motion of the brain from vasculature can cause artifacts which mask the relatively weak activation signal. This has driven the use of echo planar methods,[26] but these 'snapshot' acquisitions suffer from limited spatial resolution. Projection–reconstruction and spiral acquisitions have been found to be highly effective for this application, using conventional MR scanners.[27] (See ***Echo-Planar Imaging***.)

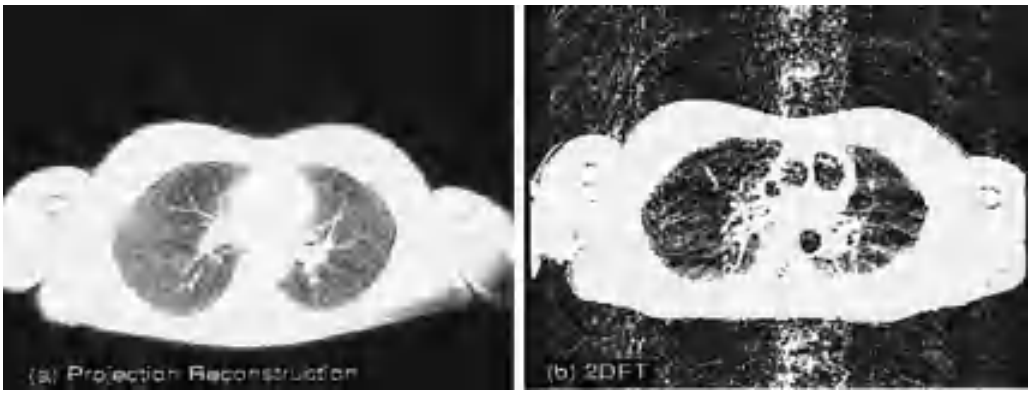

Figure 4 Images gathered at 1.5 T with PR (*TE* = 0.25 ms) and spin echo 2D FT (*TE* = 20 ms), using the same total scan time. Respiratory motion and short T_2* (<8 ms) causes poor visualization of lung parenchyma with the conventional method

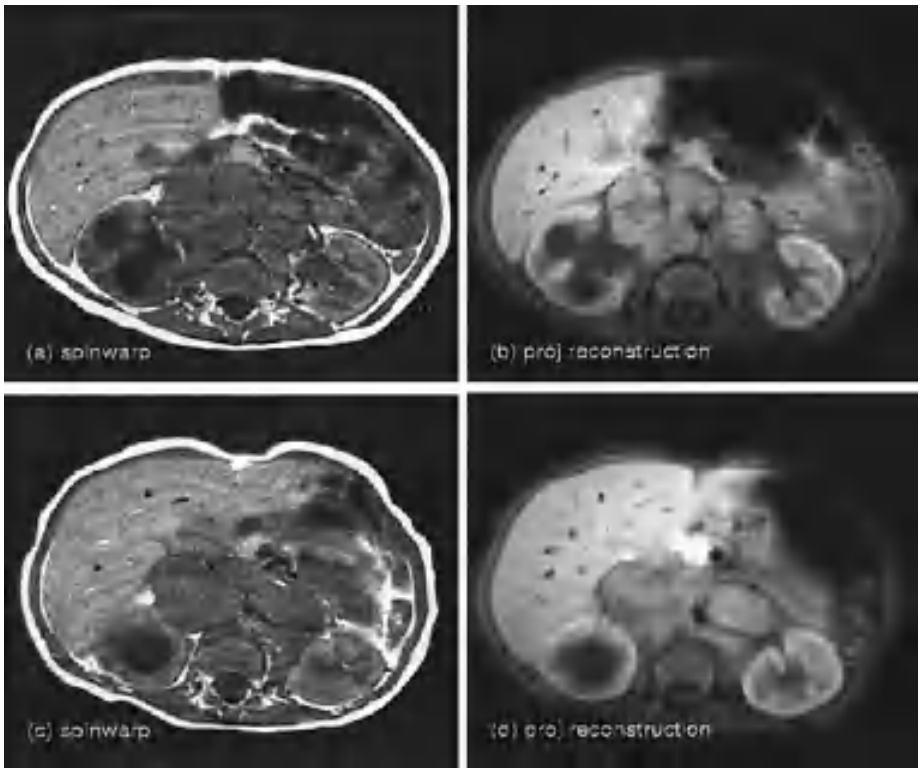

Figure 5 Comparison of T_1-weighted spin echo images with a conventional 2D FT technique (a, c) and PR technique (b, d). Scan time and *TE* were the same. Fat saturation was applied in the PR scans to reduce the effect of off-resonance

8 RELATED ARTICLES

Echo-Planar Imaging; Image Formation Methods; Lung and Mediastinum: A Discussion of the Relevant NMR Physics; Pulsatility Artifacts Due to Blood Flow and Tissue Motion and Their Control; Sodium-23 Magnetic Resonance of Human Subjects; Spin Warp Data Acquisition; Spiral Scanning Imaging Techniques; Whole Body Magnetic Resonance Artifacts.

9 REFERENCES

1. P. Lauterbur, *Nature (London)*, 1973, **242**, 190.
2. A. Kumar, D. Welti, and R. R. Ernst, *J. Magn. Reson.*, 1975, **18**, 69.
3. W. A. Edelstein, J. M. Hutchison, G. Johnson, and T. Redpath, *Phys. Med. Biol.*, 1980, **25**, 751.
4. J. B. Ra, S. K. Hilal, and Z. H. Cho, *Magn. Reson. Med.*, 1986, **3**, 296.
5. G. H. Glover, J. M. Pauly, and K. M. Bradshaw, *J. Magn. Reson. Imag.*, 1992, **2**, 47.
6. J. M. Pauly, S. I. Conolly, D. Nishimura, and A. Macovski, *Proc. VIIIth Ann Mtg. Soc. Magn. Reson. Med.*., Amsterdam, 1989, p. 28.
7. C. J. Bergin, D. C. Noll, J. M. Pauly, G. H. Glover, and A. Macovski, *Radiology*, 1992, **183**, 673.

8. L. Axel, R. M. Summers, H. Y. Kressel, and C. Charles, *Radiology*, 1986, **160**, 795.
9. G. H. Glover and J. M. Pauly, *Magn. Reson. Med.*, 1992, **28**, 275.
10. D. G. Nishimura, J. I. Jackson, and J. M. Pauly, *Magn. Reson. Med.*, 1991, **22**, 481.
11. G. T. Herman, 'Image Reconstruction from Projections', Springer-Verlag, New York, 1979, Vol. 32.
12. R. A. Brooks and G. Di Chiro, *Phys. Med. Biol.*, 1976, **21**, 689.
13. A. Macovski, 'Medical Imaging Systems', Prentice-Hall, Englewood Cliffs, NJ, 1983.
14. K. F. King and P. R. Moran, *Med. Phys.*, 1984, **11**, 1.
15. P. Mansfield and P. Morris, 'NMR Imaging in Biomedicine', Academic Press, New York, 1982.
16. J. M. Pauly, B. S. Hu, S. J. Wang, D. G. Nishimura, and A. Macovski, *Magn. Reson. Med.*, 1993, **29**, 2.
17. J. M. Pauly, D. G. Nishimura, and A. Macovski, *J. Magn. Reson.*, 1989, **81**, 43.
18. K. J. Jung and Z. H. Cho, *Magn. Reson. Med.*, 1991, **19**, 349.
19. J. I. Jackson, C. H. Meyer, D. G. Nishimura, and A. Macovski, *IEEE Trans. Med. Imag.*, 1991, **10**, 473.
20. G. H. Glover and D. C. Noll, *Magn. Reson. Med.*, 1993, **29**, 345.
21. D. C. Noll, J. M. Pauly, C. H. Meyer, D. G. Nishimura, and A. Macovski, *Magn. Reson. Med.*, 1992, **25**, 319.
22. C. H. Meyer, B. S. Hu, D. G. Nishimura, and A. Macovski, *Magn. Reson. Med.*, 1992, **28**, 202.
23. C. J. Bergin, J. M. Pauly, and A. Macovski, *Radiology*, 1991, **179**, 777.
24. G. E. Gold, J. M. Pauly, G. H. Glover, J. C. Moretto, A. Macovski, and R. J. Herfkens, *J. Magn. Reson. Imag.*, 1993, **3**, 399.
25. S. Ogawa, T. M. Lee, A. R. Kay, and D. W. Tank, *Proc. Natl. Acad. Sci. USA*, 1990, **87**, 9868.
26. P. Mansfield and A. A. Maudsley, *J. Magn. Reson.*, 1977, **27**, 101.
27. G. H. Glover, A. T. Lee, and C. H. Meyer, *Proc. XIIth Ann Mtg. Soc. Magn. Reson. Med.*, New York, 1993, p. 197.

Biographical Sketches

Gary H. Glover. *b* 1942. Ph.D., 1969, University of Minnesota. Physicist, GE Corp. Res. & Dev. Center, Schenectady, NY, 1969–76; Senior Physicist, GE Medical Systems, Milwaukee, WI, 1977–89; Faculty, Stanford University, 1990–present. Approx. 95 publications, 35 patents. Present research interests include MRI with non-Cartesian trajectories and functional brain imaging.

John M. Pauly. *b* 1958. Ph.D., 1990, electrical engineering, Stanford University, where he is currently a research associate. Research interests: rf pulse design, image reconstruction algorithms, spectroscopic localization, and fast imaging.

Pulsatility Artifacts Due to Blood Flow and Tissue Motion and Their Control

Pradip M. Pattany
University of Miami, Miami, FL, USA

1 INTRODUCTION

The most common method used for MR imaging is 2D FT imaging; in this method, the frequency and phase of the spin within a given slice determines its spatial location along the frequency and phase-encoding directions. However, the standard 2D FT imaging technique does not take into account the effects of motion and flow. It has been shown that in 2D FT imaging, motion and flow occurring in any direction result in inappropriate distribution of the signal (i.e., artifacts) in the phase-encoding direction.[1,2] The majority of artifacts in clinical imaging are due to physiologic motion and to flow.

The most frequently encountered types of physiologic motion are respiratory and cardiac. These motions are periodic; hence, they can be monitored and the data acquisition can be synchronized to occur when motions are at a minimum. This is the approach used in gating methods[3] (see also ***Cardiac Gating Practice***) to suppress motion artifacts. In these methods, motion occurring between data acquisition and the following 90° excitation pulse (known as view-to-view motion) is taken into consideration. There is a considerable time penalty associated with respiratory gating (see ***Motion Artifacts: Mechanism and Control***); however, this has been overcome by the use of the ROPE[4] (respiratory ordered phase encoding) technique, which orders the phase-encoding steps in a way that motion appears to execute a monotonic progression over the complete image acquisition.

Another approach to the reduction of artifacts due to flow or motion is to obtain several acquisitions for each phase-encoding step. This averages out the differences in accumulated phase due to flow and motion, thus reducing the artifacts. This method is called signal averaging. As data acquisition methods are becoming shorter, to the point where data can be obtained in hundreds of milliseconds, one could suspend motion during the data acquisition (in particular, respiratory motion). This is known as the breath-hold method.[5]

There are other types of physiologic motions that are not periodic, such as peristaltic, swallowing, tongue, and rapid eye motions. All these motions are involuntary and random in nature. While peristaltic motion can be controlled by glucagon, the duration of action of the drug is short compared with the total scan time. Therefore, glucagon has not proved useful for motion artifact reduction. In order to eliminate artifacts generated by all types of physiologic motions, one needs to use a different approach.

Most of the methods used for suppression of motion artifacts fail to consider the interaction of moving spins with the pulsed imaging gradients. The motion occurring between the 90° excitation pulse and data acquisition (known as within-view motion) can lead to accumulation of phase, which results in artifacts along the phase-encoding direction. When spins are moving in time, the gradients they experience change with time owing to the changes in their spatial positions. The rate at which the changes in gradients are observed depends on the direction of motion and the speed of the moving spins. In order to minimize the accumulation of added phase due to motion, additional pulses are applied to standard 2D FT imaging gradients. This is accomplished by expanding the motion as a power series in terms of position, velocity, acceleration, and pulsatility (higher-order terms), and incorporating these terms into the design of the imaging gradient.

2 THEORY

Any within-view motion or flow occurring along the frequency-encoding gradient and the slice selection gradient direction between the 90° rf pulse and data collection leads to incomplete rephasing of the moving spins at the center of the data collection in the standard frequency-encoding gradient, and at the end of the slice selection gradient. This added random phase term in 2D FT MR imaging leads to signal loss and to artifacting in the phase-encoding direction.[6]

The motion or flow occurring in the phase-encoding direction does not lead to signal loss and artifacting, because the length of time for which the phase encode is applied is very small compared with the frequency-encoding and slice selection gradients. Thus, the random phase accumulated over that time period is minimal. Secondly, the maximum signal occurs near the central phase-encoding views. Thus, the expected artifacts due to motion would be high in signal intensity. However, the amplitude of the phase-encoding gradient is close to zero. Therefore, there is little or no artifacting associated with flow or motion in the phase-encoding direction. The excited signal in the transverse plane is expressed in equation (1a), where it is clearly seen that the signal would indeed be affected by the phase of the excited spins in the transverse plane:

$$S(t_x, t_y) = \iint \bar{\rho}(x,y) \mathrm{e}^{-\mathrm{i}2\pi(\phi_x(t_x)+\phi_y(t_y))}\,\mathrm{d}x\,\mathrm{d}y \tag{1a}$$

where $S(t_x,t_y)$ is the signal in the (x,y) transverse plane, $\bar{\rho}(x,y)$ is the spin density in the transverse plane, $_x(t_x)$ and $\phi_y(t_y)$ are the phases at times t_x and t_y, and

$$\bar{\rho}(x,y) = \int \bar{\rho}(x,y,z) \mathrm{e}^{-\mathrm{i}2\pi\phi_z(t_z)}\,\mathrm{d}z \tag{1b}$$

$$\bar{\rho}(x,y,z) = \rho(x,y,z)(1 - \mathrm{e}^{-TR(x,y,z)/T_1}) \tag{1c}$$

Partial volume effects due to finite slice thickness are contained within $\bar{\rho}(x,y)$ as a result of integration along dz.

In order to obtain maximum signal at the echo time in the transverse (x,y) plane following a selective 90° rf pulse, the exponential term in equation (1b) must be equal to one:

$$e^{-i2\pi\phi_z(t_z)} = 1 \tag{2}$$

This occurs when $\phi_z(t_z) = 0$, which implies that the spins in the transverse plane are completely rephased at the echo time. The phase term $\phi_z(t_z)$ in equation (2) can be expressed as

$$\phi_z(t_z) = \gamma \int \bar{G}_z(t_z) Z(t_z)\, dt_z \tag{3}$$

where $\phi_z(t_z)$ is the phase of the magnetization at time t_z, γ is the magnetogyric ratio, $\bar{G}_z(t_z)$ is the gradient amplitude at time t, and $Z(t_z)$ is the position of the excited spins at time t. The position term $Z(t_z)$ can be expanded in a Taylor series:

$$Z(t_z) = Z_0 + \sum_{j=1}^{\infty} \frac{t_z^j Z_0^{(j)}}{j!} \tag{4}$$

where $Z_0{}^{(j)}$ is the jth derivative of Z_0.

Each of the terms of the expanded $Z(t_z)$ expression in equation (4) is integrated separately in equation (3), and the phase ϕ_z associated with each term is brought to zero at the end of the slice selection gradient waveform. A similar expression for the frequency-encoding gradient requires that the phase be brought to zero at the center of the data collection gradient lobe. When the term $Z_0{}^{(j)}$ in equation (4) is expanded up to its third derivative, the term $Z(t_z)$ can be expressed as

$$Z(t_z) = Z_0 + \frac{t_z}{1!}\frac{dz}{dt} + \frac{t_z^2}{2!}\frac{d^2z}{dt^2} + \frac{t_z^3}{3!}\frac{d^3z}{dt^3} \tag{5}$$

On the right-hand side, the first term Z_0 for static spins is of zeroth-order (zeroth moment). The second term dz/dt is for the spins moving with constant velocity, and is of first order (first moment). The third term d^2z/dt^2 is for the spins moving with constant acceleration, and is of second order (second moment). The fourth term d^3z/dt^3 is for the spins moving with pulsatility, and is of third order (third moment).

Equation (5) can be substituted into equation (3), which now becomes

$$\phi_z(t_z) = \gamma \int \bar{G}_z(t_z)\left(Z_0 + \frac{t_z}{1!}\frac{dz}{dt} + \frac{t_z^2}{2!}\frac{d^2z}{dt^2} + \frac{t_z^3}{3!}\frac{d^3z}{dt^3}\right) dt_z \tag{6}$$

For complete rephasing of the moving spins (velocity, acceleration and pulsatility) at the end of the slice selection gradient, and at the center of data sampling for the frequency-encoding gradient, each of the Z terms in equation (6) must be integrated separately, and the $\phi_z(t_z)$ term has to be equated to zero for a given gradient waveform. This can be expressed as a set of equations for the $\phi_z(t_z)$ phase associated with each order of $Z(t_z)$ as follows:

$$\phi_z(t_z) = \gamma \int \bar{G}_z(t_z)\, dt_z = C_0 = 0 \tag{7a}$$

$$\phi_z(t_z) = \gamma \int \bar{G}_z(t_z)\frac{t_z}{1!}\, dt_z = C_1 = 0 \tag{7b}$$

$$\phi_z(t_z) = \gamma \int \bar{G}_z(t_z)\frac{t_z^2}{2!}\, dt_z = C_2 = 0 \tag{7c}$$

$$\phi_z(t_z) = \gamma \int \bar{G}_z(t_z)\frac{t_z^3}{3!}\, dt_z = C_3 = 0 \tag{7d}$$

$$\phi_z(t_z) = \gamma \int \bar{G}_z(t_z)\frac{t_z^j}{j!}\, dt_z = C_j = 0 \tag{7e}$$

This set of equations can be expressed in terms of a matrix equation

$$\{t^j\}\{G^j\} = \left\{\frac{\phi}{Z_0^j \gamma}\right\} - \left\{\sum_k G^k\right\} \tag{8}$$

where $\{t^j\}$ are the specified times of the unknown gradient lobes, expressed as a $j \times j$ matrix, $\{G^j\}$ are the amplitudes of the unknown gradient lobes that are to be calculated, expressed as a $j \times 1$ matrix, $\{\phi/Z_0^j\gamma\}$ are the desired phases of the spins divided by the derivative of Z_0 and the magnetogyric ratio, expressed as a $j \times 1$ matrix, and $\{\sum_k G^k\}$ is the summation of the known gradient lobes with amplitude and times specified (e.g., the gradient lobes applied during the 90° and 180° rf pulses to give a correct slice thickness), expressed as a $j \times 1$ matrix.

Each gradient lobe in a given gradient waveform has finite rise and fall times. Therefore, each gradient lobe is a trapezoidal profile, rather than the rectangular profile assumed in equation (8). This leads to the accumulation of random phase during rise and fall times, owing to motion or flow, particularly in the higher order terms (acceleration and pulsatility), because the term t_z in the integrals in equations (7c) and (7d) is t^2 and t^3, respectively. The rise and fall times of the trapezoid can be approximated as a series of contiguous short-duration rectangular pulses, of increasing amplitude on the rising ramp of the trapezoid, and decreasing amplitude on the falling ramp. With the inclusion of rise and fall ramps, the phase term $\phi_z(t_z)$ in equation (3) now becomes

$$\begin{aligned}\phi_z(t_z) = &\sum_{i=1}^{\eta_r} \int_{t_1+(i-1)t_r/\eta_r}^{t_1+it_r/\eta_r} \gamma G_r(t_z) Z(t_z)\, dt_z \\ &+ \int_{t_1+t_r}^{t_2-t_f} \gamma G_z(t_z) Z(t_z)\, dt_z \\ &+ \sum_{i=\eta_f-1}^{0} \int_{t_2-(i-1)t_f/\eta_f}^{t_2-it_f/\eta_f} \gamma G_f(t_z) Z(t_z)\, dt_z\end{aligned} \tag{9}$$

where η_r is the number of steps for the rising ramp, η_f is the number of steps for the falling ramp, t_1 is the starting time of the trapezoid, $t_1 + t_r$ is the end of the rising ramp and the beginning of the plateau or constant section, $t_2 - t_f$ is the end of the plateau or constant section and the beginning of the falling ramp, t_2 is the end of the falling ramp, t_r is the total time of the rising ramp, and t_f is the total time of the falling ramp. Equation (9) is shown diagrammatically in Figure 1.

When the gradient profiles are generated using equation (9), the numbers of steps η_r and η_f are defined to be very large for given t_r and t_f. Thus, the rising and falling ramps could be con-

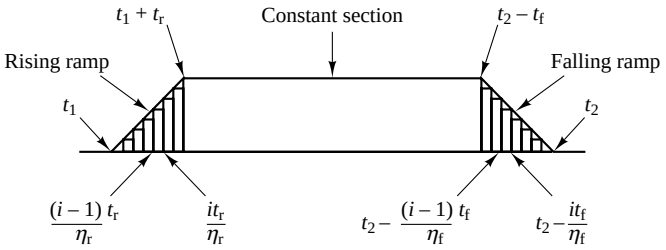

Figure 1 Trapezoidal waveform for each gradient pulse in a given gradient waveform

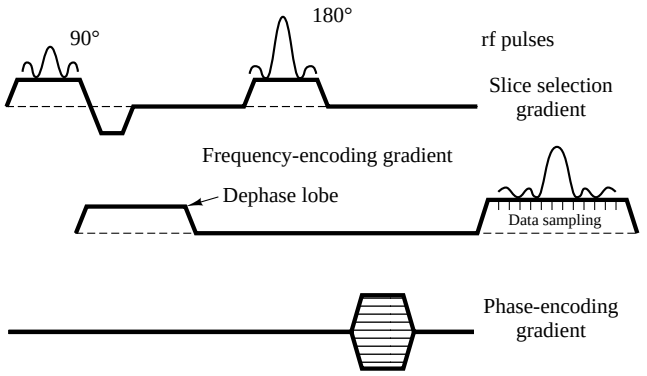

Figure 2 A standard 2D FT spin echo imaging sequence

sidered as linear ramps, rather than discrete steps of rectangles, increasing or decreasing in amplitude. In equation (9), one can see that the first term corresponds to the integral summation of the rising ramp. The second term corresponds to the integral of the plateau, or constant section of the trapezoid. The third term corresponds to the integral summation of the falling ramp. Therefore, equation (9) is the one that is used in the matrix in equation (8).

The values of the $\{t^j\}$, $\{\phi/Z_0{}^j\gamma\}$, and $\{\sum_k G^k\}$ terms in equation (8) are specified for a given gradient waveform. The $\{G^j\}$ term, for amplitude values of the unknown j gradient lobes, can be calculated by solving the $j \times j$ matrix $\{t^j\}$ in terms of the specified times, and dividing it into either side of equation (8), which now becomes

$$\{t^j\}^{-1}\{t^j\}\{G^j\} = \left(\left\{\frac{\phi}{Z_0^j\gamma}\right\} - \left\{\sum_k G^k\right\}\right)\{t^j\}^{-1} \qquad (10)$$

$$\{G^j\} = \left(\left\{\frac{\phi}{Z_0^j\gamma}\right\} - \left\{\sum_k G^k\right\}\right)\{t^j\}^{-1} \qquad (11)$$

All the terms on the right-hand side are known, and therefore the amplitude values for G can be calculated for j unknown gradient lobes. The resultant waveform will rephase the $(j-1)$th order of motion.

3 GRADIENT WAVEFORM PATTERNS

To rephase completely the moving spins in the slice selection and frequency-encoding directions, the standard spin echo imaging sequence shown in Figure 2 (see ***Spin Warp Data Acquisition***) is modified for within-view motion correction as shown in Figure 3. To rephase terms of zeroth-order (static) through to third order (pulsatility) in the slice selection gradient waveform, four unknown (A, B, C, D) gradient lobes are applied at specified time intervals in a slice selection gradient waveform. The time zero, $t_0 = 0$, is considered to be the center of the 90° rf pulse, as is the case when refocusing the static spins in conventional imaging sequences.

The amplitude and the times of the slice selection lobes, applied during 90° and 180° rf pulses (denoted by the solid lines in Figure 3), must be known in order to give a correct slice thickness and echo time. Therefore the gradient lobes with known amplitude and times are included in the $\{\sum_k G^k\}$ terms in equation (8). If all the terms from zeroth-order through to third order are completely refocused at time t_6 then the term $\{\phi/Z_0{}^j\gamma\}$ is equal to zero. The term $\{t^j\}$ in the equation includes all the specified time values (t_1, t_2, t_3, t_4, t_5, t_6), of the unknown gradient lobes. Therefore a 4×4 matrix $\{t^j\}$ is solved in terms of the specified time intervals. It is then inverted and multiplied into both sides of equation (8), which now becomes equation (10). For simplification, put

$$\left\{\frac{\phi}{Z_0^j\gamma}\right\} - \left\{\sum_k G^k\right\} = \{K^j\} \qquad (12)$$

Then equation (10) can be written as

$$\{G^j\} = \{K^j\}\{t^j\}^{-1} \qquad (13)$$

All the known values are on the right-hand side of equation (13). Therefore, the $\{G^j\}$ term can be solved for the amplitudes of the unknown gradient lobes (A,B,C,D) in the slice selection gradient waveform by multiplying the matrix $\{K^j\}$ by the matrix $\{t^j\}^{-1}$.

Similarly, the method can be applied to the frequency-encoding gradient waveform, since the time and the amplitude of the data collection gradient lobe (denoted by a solid line in Figure 3) is known. Four unknown gradient lobes (a, b, c, d)

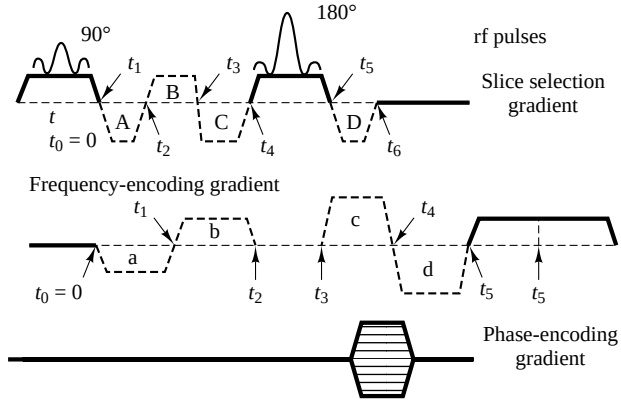

Figure 3 A 2D FT spin echo imaging sequence with motion compensation up to pulsatility applied to the slice selection and frequency-encoding gradients

are applied to the frequency-encoding gradient, as shown in Figure 3. The data collection gradient lobe is the term $\{G^k\}$, in which the amplitude and the times must be known in order to give a correct echo time and field of view. The term $\{\phi/Z_0{}^j\gamma\}$ is specified to be zero, if all the terms from zeroth-order through to third order are to be completely rephased at the echo time. The term $\{t^j\}$ gives the times (t_1, t_2, t_3, t_4, t_5) of the unknown gradient lobes, which are specified as in Figure 3.

Again, a 4×4 matrix $\{t^j\}$ is solved, inverted, and multiplied by $\{K^j\}$ as in equation (13) to determine the amplitudes of the a, b, c, and d pulses, which result in complete rephasing of the static through to the pulsatile spins moving in the frequency-encoding direction.

4 TYPICAL PERFORMANCE

A set of images were obtained on a volunteer, with a 1.5 T whole body MRI system. A quadrature body coil was used for excitation and a quadrature lumbar spine coil as a receiver. A standard spin echo sequence and a modified sequence (within-view motion compensation up to pulsatility in frequency-encoding and slice selection gradient direction) were run consecutively with the following scan parameters: echo time of 100 ms, repetition time of 2000 ms, 2 acquisitions per phase-encoding step, 256 phase-encoding steps, and a 27 cm field-of-view. Both images were acquired without using cardiac and/or respiratory gating devices.

The set of images shown in Figures 4 and 5 were acquired from the lumbar spine region. As can be seen in Figure 4, there is noticeable signal loss and artifacting across the image. This is due to cerebrospinal fluid (CSF) flow and peristaltic motion of the intestine. The presence of these artifacts degrades image quality and obscures delineation of the spinal cord and the nerve roots in the spinal canal, and the anatomical structures anterior to the vertebral body are completely obscured by the artifacts.

Figure 4 Image of lumbar spine acquired with a standard 2D FT spin echo imaging sequence

Figure 5 Image of lumbar spine acquired using a 2D FT sequence with motion compensation up to pulsatility applied to the slice selection and frequency-encoding gradients

In Figure 5, the artifacts due to peristaltic motion and CSF flow are eliminated. Visualization of the structures within the abdomen anterior to the spine is improved. Also, the spinal cord and nerve roots are now well delineated against the bright signal from the CSF.

5 DISCUSSION

The proposed method for within-view correction of motion in the frequency-encoding and slice selection directions completely rephases the signal from the moving spins with velocity, acceleration, and pulsatility. For within-view motion, the relative significance of motion of the imaging axes and the effects of spins moving during application of NMR imaging gradients has been assessed.[6] Dephasing due to motion and flow occurring along the slice selection, frequency-encoding, and phase-encoding directions has been investigated. A flow phantom under constant flow conditions was used in experiments to study the method. The within-view motion correction method was used to rephase signals along various combinations of imaging axes, applying variable terms from the Taylor expansion of motion along them. The results indicated that motion along any imaging axis can be rephased effectively when within-view motion correction is used only along the slice selection and frequency-encoding directions.

The improvement in image quality in the areas of head, abdomen, chest, and spine was assessed on patients using the within-view motion correction method.[7] There is an increase in signal intensity and anatomical details in the presence of flow and motion. The technique reduced the practical difficulty of obtaining clinically diagnostic T_2 weighted images in a reasonable acquisition time without having to perform multiple signal

averaging. It has also been shown that signal loss and the resulting artifacts due to flow, orbit, tongue, swallowing, peristaltic, and respiratory motions are eliminated, and that this method is also applicable to other 2D FT imaging sequences.[7,8]

The image quality assessment has been extended to various sequences on a larger patient population.[9] There was considerable improvement in image quality: the CSF flow artifacts were eliminated, and body and spine images had reduced blood flow and motion artifacts. The blood vessels gave an increased signal, which would be useful in cardiovascular imaging.

The within-view motion correction method has been used on patients at 0.5 and 1.5 T field strengths,[10] and it has been found that there is a more significant reduction in motion and flow artifacts than that achieved by even echo rephasing alone.[11]

The most commonly used gradient waveforms are composed of trapezoidal or sinusoidal pulses. However, given hardware constraints and the sequence parameter objectives, one could use a numerical approach to gradient waveform design. It has been shown that the amplitude of the gradient pulses can be calculated on a point-to-point basis to achieve within-view motion correction.[12]

Theoretically, solving for terms of increasingly higher order will continue to reduce the degree of signal loss and artifacting, providing the higher order terms are dominant in the moving anatomical regions. From clinical evaluation, higher order terms (higher than pulsatility) have negligible, if any, effect on image quality.

6 RELATED ARTICLES

Cardiac Gating Practice; Heart: Clinical Applications of MRI; Motion Artifacts: Mechanism and Control; Spin Warp Data Acquisition; Time-of-Flight Method of MRA; Whole Body Magnetic Resonance Angiography.

7 REFERENCES

1. M. L. Wood and R. M. Henkelman, *Med. Phys.*, 1985, **12**, 143.
2. C. L. Schultz, R. J. Alfidi, A. D. Nelson, S. Y. Kopiwada, and M. E. Clampitt, *Radiology*, 1984, **152**, 117.
3. C. E. Lewis, F. S. Prato, D. J. Drost, and R. L. Nicholson, *Radiology*, 1986, **160**, 803.
4. D. R. Bailes, D. J. Gilderdale, G. M. Bydder, A. G. Collins, and D. N. Firmin, *J. Comput. Assist. Tomogr.*, 1985, **9**, 835.
5. R. R. Edelman, P. F. Hahn, R. Buxton, J. Wittenberg, J. T. Ferrucci, S. Saini, and T. J. Brady, *Radiology*, 1986, **161**, 125.
6. J. L. Duerk and P. M. Pattany, *Magn. Reson. Imag.*, 1989, **7**, 251.
7. P. M. Pattany, J. J. Phillips, L. C. Chiu, J. D. Lipcamon, J. L. Duerk, J. M. McNally, and S. N. Mohapatra, *J. Comput. Assist. Tomogr.*, 1987, **11**, 369.
8. E. M. Haacke and G. W. Lenz, *Am. J. Roentgenol.*, 1987, **148**, 1251.
9. P. M. Colletti, J. K. Raval, R. C. Benson, P. M. Pattany, C. S. Zee, W. D. Boswell, S. L. Norris, P. W. Ralls, and H. D. Segall, *Magn. Reson. Imag.*, 1988, **6**, 293.
10. R. M. Quencer, R. S. Hinks, P. M. Pattany, M. Horen, and M. J. Post, *Am. J. Neuroroentg.*, 1988, **9**, 431 (or *AJR*, 1988, **151**, 163).
11. V. Waluch and W. G. Bradley, *J. Comput. Assist. Tomogr.*, 1984, **8**, 594.
12. O. P. Simonetti, J. L. Duerk, and V. Chankong, *Magn. Reson. Med.*, 1993, **29**, 498.

Biographical Sketch

Pradip M. Pattany. *b* 1958. B.Tech., 1982, University of Bradford, UK; M.Sc., 1983, University of Manchester Institute of Science and Technology; Ph.D., 1992 University of Lyon. Scientist/systems engineer in Advance Development Group, Picker International NMR division, UK 1983–85. Staff scientist in Clinical Research Group, Picker International NMR division USA, 1985–88. Director of Research and Development, MRI of Colorado, 1988–93. Assistant Clinical Professor, University of Colorado Department of Radiology, 1988–present. Research assistant professor, University of Miami School of Medicine, Department of Radiology, 1993–present. Approx. 40 publications. Research specialties: assessment of motion and flow, flow quantification, and diffusion imaging.

Selective Excitation in MRI and MR Spectroscopy

Andrew A. Maudsley and Gerald B. Matson

University of California San Francisco and VA Medical Center, San Francisco, CA, USA

1 INTRODUCTION

With the continuous wave methods used in the early days of NMR, the ability selectively to excite specific frequencies was inherently available, and the ideas of selective excitation were widely used to elucidate spin and dipolar couplings and multiple quantum transitions.[1,2] The advent of Fourier transform (FT) NMR provided for simultaneous excitation over a broad frequency span and yielded greatly improved sensitivity, but complicated the process of selective excitation of spins. This nonselectivity of the FT NMR excitation methods brought the need for solvent suppression into prominence for high-resolution studies, and the application of NMR to ever increasingly more complicated spin systems has spawned a variety of selective excitation methods designed for spectral simplification to enhance identification of individual spin systems.[3]

For FT NMR, a broadband excitation of the spin system is readily provided by a short rf pulse. Excitation over only a limited frequency region can be obtained by lengthening the rf pulse such that the excitation profile is narrowed; however, this approach is limited since the excitation profile in the frequency domain is described by a sinc function rather than the ideal, trapezoidal shape depicted in Figure 1(a). Improved frequency excitation profiles can be obtained by suitable amplitude shaping of the rf pulse, or more generally by using a suite of closely spaced rf pulses with different parameters (amplitude, phase, frequency, intra- or inter-pulse intervals).

In modern high-resolution NMR, applications of selective excitation techniques include elucidation of spin couplings, measurement of dipolar couplings (i.e., nuclear Overhauser enhancements), exploration of multiple quantum coherences, and solvent suppression (see ***Water Suppression in Proton MRS of Humans and Animals***), as well as spectral simplification. In the presence of a magnetic field gradient, frequency selective excitation is translated into spatially selective excitation. This is illustrated in Figure 1(b), where irradiation using the frequency profile shown in Figure 1(a), results in excitation of spins within a slice through the object [Figure 1(b)]. In this example the X gradient was applied resulting in excitation of a plane perpendicular to X (i.e., over the YZ plane). In this article we describe the development of frequency selective excitation methods for spatially selective excitation, which is required for MRI and for spatially resolved spectroscopy (see ***Single Voxel Localized Proton NMR Spectroscopy of Human Brain In Vivo***). For these applications the usual requirement is for slice selection (i.e., excitation or inversion of spins within a region bounded by parallel planes). In the ideal case the excitation would be flat over some predefined region, with sharp transitions and zero excitation outside of that region, as illustrated in Figure 1(a).

2 BACKGROUND

Tomlinson and Hill[4] introduced ideas of selective excitation for FT NMR using inverse FT of the frequency band to be excited as the basis for generating the pulse train producing the selective excitation. Limitations of this approach due to the nonlinearity of the Bloch equations were realized in this early work, and, because of phase dispersal of the transverse magnetization produced by their formalisms, the selective excitation was not proposed for direct observation of selectively excited spins. Instrumentation limitations of commercial FT NMR spectrometers restricted the utilization of the Tomlinson–Hill selective excitation approach and it was not until Morris and Freeman[5] introduced the DANTE pulse scheme that selective excitation became readily available on commercial FT NMR spectrometers. Although widely used, the DANTE scheme still produced a sinc-shaped excitation profile.

Early applications of selective excitation for spatial selection were demonstrated by Garroway et al.[6] and Mansfield et al.[7]

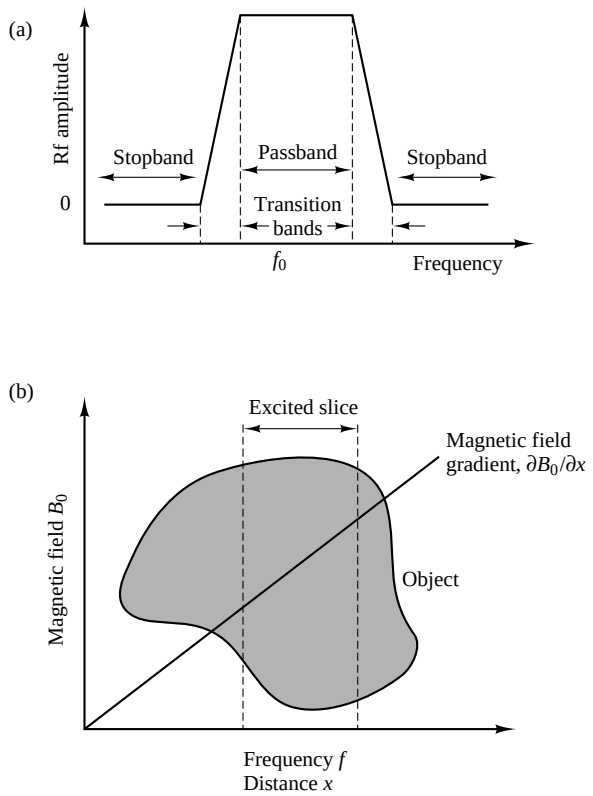

Figure 1 (a) Ideal frequency selection or slice profile. The ideal frequency selective excitation pulse produces uniform excitation over the passband, and no excitation in the stopbands. In addition, in the ideal case the transition bands are narrow compared with the passband. (b) Depiction of the action of a frequency selective pulse in the presence of a magnetic field gradient. In the presence of a magnetic field gradient, frequency selection is translated into spatial selection, so that the frequency selection depicted in (a), in the presence of a magnetic field gradient in the X direction, excites the slice depicted in (b)

for line scan imaging. Here the selective rf pulse was applied together with a magnetic field gradient across the sample, thereby causing only those spins which resonated at the frequencies within the excitation band of the selective pulse to be affected, and the resultant spin excitation was limited to a well-defined region of the object [Figure 1(b)]. Negative amplitudes produced by the FT formalism were accommodated by 180° phase reversal of the rf pulse and the gradient was switched on prior to application of the rf pulse, and held constant during the pulse. This use of a linear magnetic field gradient, referred to as the slice-selection gradient, produced a direct relationship between the selected region and the excitation frequency. The thickness of the excited slice depended on the strength of the slice-selection gradient as well as the frequency range excited by the selective pulse. The quality of the slice selection was a function of the length and shape of the rf pulse.

The early imaging articles lacked specifics as to the action of selective pulses;[7,8] however, it was later demonstrated by Hutchison et al.[9] and Hoult[10] that at the end of an excitation pulse the spins were excited with a spatially dependent phase, and that in order to recover the full magnetization it was necessary to reverse the applied gradient after the end of the pulse. The earlier formalism of Morris and Freeman[5] also anticipated this result. More rigorous treatments of selective pulses using the Bloch equations followed,[10,11] which showed that the integral of the refocusing gradient was approximately half that of the slice-selection gradient. These analyses also demonstrated that since the spin response to rf excitation is nonlinear, in the sense that the amount of transverse magnetization generated is not a linear function of amplitude of the applied rf, the FT methods for selective pulse generation were rigorous only in the limit of small tip angles. However, the errors in this approach do not become prohibitive until tip angles exceeding 90° are used, and sinc-shaped pulses, smoothed with a Gaussian (or other filter function) to reduce ringing effects, became commonly used in MRI and localized spectroscopy for 90° excitation of a slice through an object. Figure 2 shows a sinc–Gauss pulse shape [Figure 2(a)] and the resultant observed transverse magnetization across the selected slice [Figure 2(b)] following application of a 90° sinc–Gauss pulse together with the necessary refocusing gradient. It can be seen that significant magnetization is excited outside of the selected slice and the resultant phase after refocusing exhibits deviation from zero.

The selective pulses discussed above were, for the most part, amplitude modulated with phase reversal taking the place of negative rf amplitude. Selective excitation using frequency (or phase) modulation is also possible, and in the early 1980s two separate groups demonstrated similar formalisms for generation of inversion pulses with immunity to B_1 inhomogeneity.[12–16] These inversion pulses were analogous to adiabatic fast passage in high-resolution NMR, and once a threshold value of the rf strength was exceeded, the inversion became virtually independent of rf power. The second of these pulses, the hyperbolic secant pulse,[14–16] was shown to have reasonable frequency selectivity characteristics. Although the hyperbolic secant pulse was cast theoretically in terms of frequency and amplitude modulation, it could equivalently be implemented as an amplitude and phase modulated pulse.[17]

While the hyperbolic secant pulse had the advantage of being immune to rf inhomogeneity, it did not perform as a

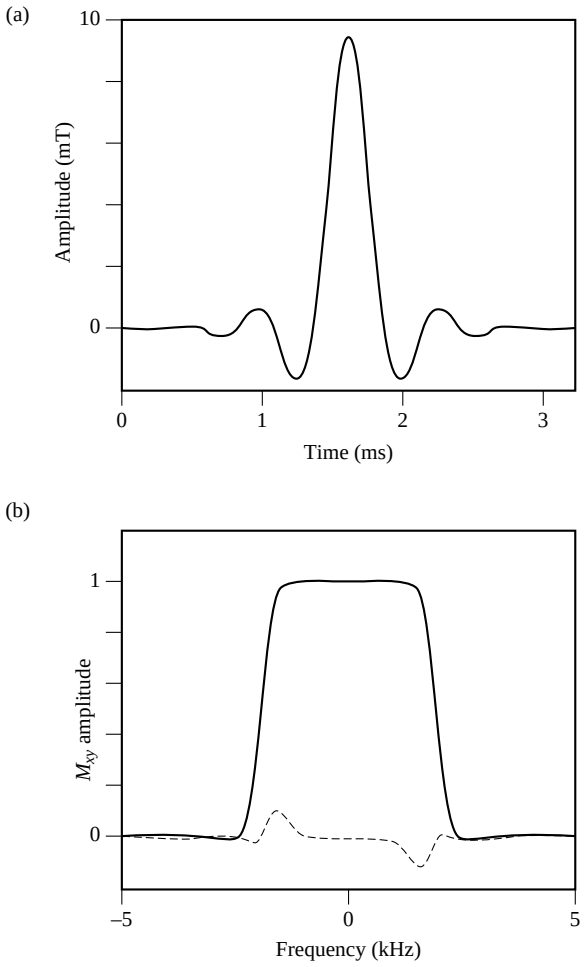

Figure 2 (a) A sinc-shaped 90° excitation pulse with Gaussian apodization. The Figure shows a 128-step 90° pulse derived from a sinc shape with Gaussian apodization. (b) Resultant slice profile from the pulse of (a). The solid line shows the in-phase signal after gradient refocusing. Although the excitation is uniform over the passband, significant excitation is evident in the stopbands. The broken line shows the quadrature signal, which exhibits significant deviation from zero

180° refocusing pulse, and in the early 1980s the demands of MRI and localized spectroscopy created a clear need for large tip angle rf pulses (including spin echo pulses) with improved slice profiles, and pulses with immunity to rf inhomogeneity. The need for multidimensional pulses exciting, for instance, simultaneously in two directions, became apparent in the latter half of the 1980s, and this class of pulse is discussed near the end of this article.

3 AMPLITUDE MODULATED PULSES

3.1 Early RF Pulse Design

For slice selective pulses the 'ideal' selection profile is one which has a flat excitation over the slice, narrow transition regions, and minimal excitation outside of the slice (Figure 1).

Although early pulse shaping relied on the Fourier time–frequency relationship, as noted above this approach is not rigorous outside of the small tip angle regime. Subsequent work showed that amplitude modulation is sufficient for generation of excellent excitation profiles as long as the rf field is homogeneous.[18] When significant rf inhomogeneity is present, it turns out that frequency modulated designs may be used with inversion or refocusing pulses to provide variable degrees of immunity to rf inhomogeneity,[17] although a price in pulse length or excitation profile is inevitably required. This class of pulse is discussed in the next section. Finally, selective pulse generation always involves tradeoffs of overall pulse duration and, in some cases, pulse amplitude, and acceptable excitation profile. That is, increasing pulse duration may provide an improved selection profile, but lengthens the experiment and may incur profile degradation due to relaxation during the pulse.[19–21] In addition, reducing the transition region at constant pulse duration invariably has its cost in increased deviations over the desired profile.

The difficulty of generating desired trapezoidal excitation bands was highlighted by theoretical analyses of selective pulse shapes[10,11] developed prior to 1980, which pointed out that the Bloch equations are nonlinear. Thus, in general, the problem of finding the amplitude modulation that best approaches a desired excitation profile (for a given overall pulse duration) is nonlinear, and requires an iterative approach for solution.

A number of approaches to pulse optimization appeared in the middle 1980s. Silver et al.[14] showed that the Bloch–Ricatti equation could be used as a basis for optimization of a 90° pulse. The work of Warren showed how pulse profiles could be improved starting with a particular class of pulse shape.[22] The approach of Carlson[23] provided for improved excitation pulse profiles, while that of Adams and O'Donnell[24] provided for improved spin echo pulses. Using a simplex method, Lurie showed that sinc-shaped rf pulses could be reshaped to provide improved excitation, inversion, and spin echo pulses.[25]

3.2 Optimal Control Theory

More general methods for pulse optimization were demonstrated in the optimal control theory approaches of Conolly et al.[18] and Murdoch et al.[17] which provided for optimization of excitation, inversion, and spin echo pulses. Both of these approaches used a penalty function for rf power so that, within the other pulse constraints, the optimization process produced the lowest power pulse. These approaches demonstrated that optimal control theory provided a robust, albeit time-consuming, approach to generation of amplitude modulated pulses.

The approach of Murdoch et al.[17] is described with the aid of Figure 1(a), which here represents the target profile. An initial pulse shape was run through the Bloch equations, and the square of the deviation from the target profile function calculated, which represented the error or 'cost' parameter to be minimized. In the Murdoch formulation, deviations in the transition region were ignored, and other 'costs' to be minimized included a cost factor for the amount of rf power, and at times a cost for 'jaggedness'.[17] Relative weights for these costs were determined by trial and error. A conjugate-gradient minimization routine was used to minimize the cost function. Other optimal control methods were approached in similar fashion.[18,26,27] A relatively comprehensive review of these early approaches is available.[28]

3.3 Shinnar–Le Roux (SLR) Pulse Design

The primary disadvantages of the optimal control theory approach were that the optimization was computationally intensive, and that it left some uncertainty as to whether or not a truly optimal design had been achieved. Thus, efforts continued to achieve more efficient algorithms for generation of amplitude modulated selective pulses. Noteworthy approaches include a unique approximation for linearizing the Bloch equations by Ngo and Morris,[29] and, more recently, approaches making use of inverse scattering theory.[30–32] Still another approach was developed based on the use of digital filter design methods[33–38] culminating in what has been termed the SLR algorithm.[39] Quite recently, Buonocore has demonstrated that the inverse scattering theory approaches and SLR algorithms are, roughly speaking, computationally equivalent.[40]

In spite of their computational similarities, the SLR method appears to offer distinct advantages in that the digital filter design parameters can be interpreted in terms of rf pulse slice profile, so that the results of the design are known to a reasonable approximation even before the design is performed.[39] This prior knowledge facilitates the rf pulse design process. A brief overview of the SLR approach to rf pulse design is presented with the aid of Figure 3, which depicts a digital filter with equal ripple amplitudes in the passband and stopbands. The optimal filter, defined in terms of a polynomial in powers of inverse frequency, is one in which the ripple amplitudes are minimal given the length (order) of the polynomial and the width of the transition bands[41] (Figure 3). The filter coefficients are associated with the rf amplitude steps.[39] The (iterative) solution for the polynomial coefficients is facilitated by prior knowledge of the number of ripple alternations, and approximation formulas exist predicting the ripple amplitudes given the other parameters of the filter.[39]

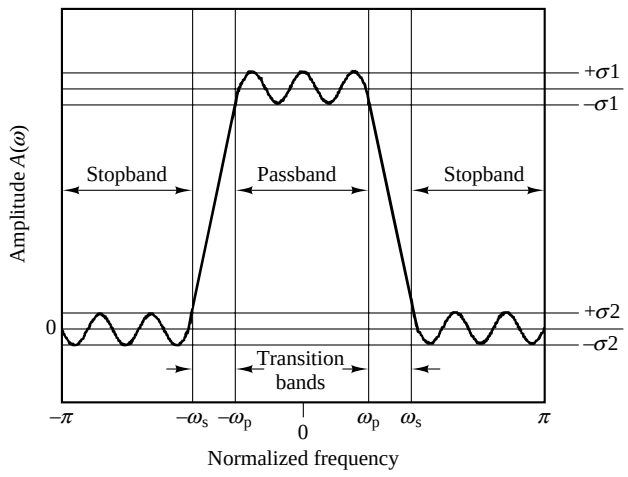

Figure 3 Depiction of an equal-ripple digital filter, which is used as a basis for the SLR algorithm for generation of amplitude modulated frequency selective pulses. The amplitudes of the stopband ripples are not necessarily equal to those of the passband ripples

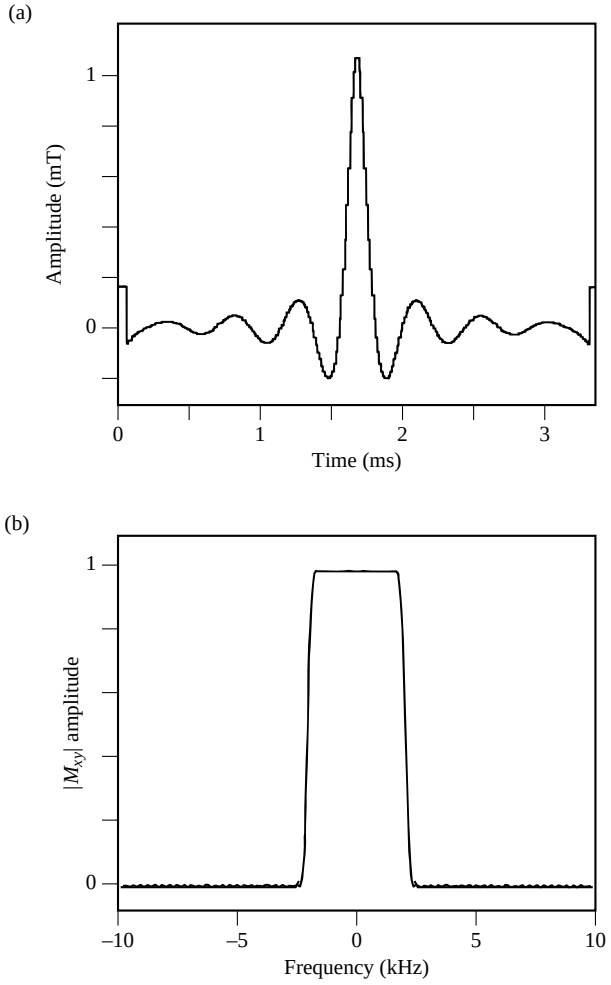

Figure 4 (a) An SLR-optimized 256-step 180° spin echo pulse. The symmetric pulse shape is required for a linear phase pulse, which is necessary for excitation or refocusing. (b) The resultant slice profile from the pulse in (a). The theoretical profile assumes that unit magnetization existed in the transverse plane prior to application of the pulse, and further assumes the presence of crusher gradients. (Reproduced with the computer program described in Matson[19])

Finally, magnetization ripples in the slice profile can be estimated from the filter ripples, and the filter coefficients converted to a linear phase (necessary for refocusing) rf pulse through the SLR transform.[39] In addition, pulses producing nonlinear phase distributions (maximum or minimum phase[39]) are also obtainable. Figure 4 illustrates a 180° rf pulse and resulting (theoretical) slice profile obtained by the SLR algorithm, while Figure 5 shows a maximum phase 180° inversion pulse along with its slice profile.[19]

3.4 Self-Refocused Pulses

In contrast to imaging and localized spectroscopy, where gradients are used to generate a range of frequencies across the object, excitation in high-resolution NMR spectroscopy is done in the absence of gradients. Thus, gradient refocusing is not possible, and self-refocused pulses are necessary for direct observation of the selectively excited spins. A surprising variety of methods have been used for generation of self-refocusing or (prefocused) pulses.[29,42–46] In some situations self-refocusing may be advantageous in imaging and localized spectroscopy as well, for instance in measurement of short T_2 species where the time for gradient refocusing would be detrimental.

4 FREQUENCY MODULATED PULSES

When rf inhomogeneity is small, optimized amplitude modulated pulses as discussed above can provide excellent selectivity with constant tip angle over the selected frequency range; however, these pulses are inherently sensitive to rf inhomogeneity. An advantage of the class of pulses based on the adiabatic sweep principle is that they are able to maintain both tip angle and selectivity over a range of rf power. This class of pulses is referred to as frequency modulated or adiabatic pulses. Unlike the amplitude modulated pulses, traditional adiabatic pulses operate on a spin locking mechanism, in which the spins follow the direction of the effective $\boldsymbol{B}_1$ field. One of these selective pulses was the hyperbolic secant pulse, an inversion pulse whose form was obtained from the Bloch–Ricatti

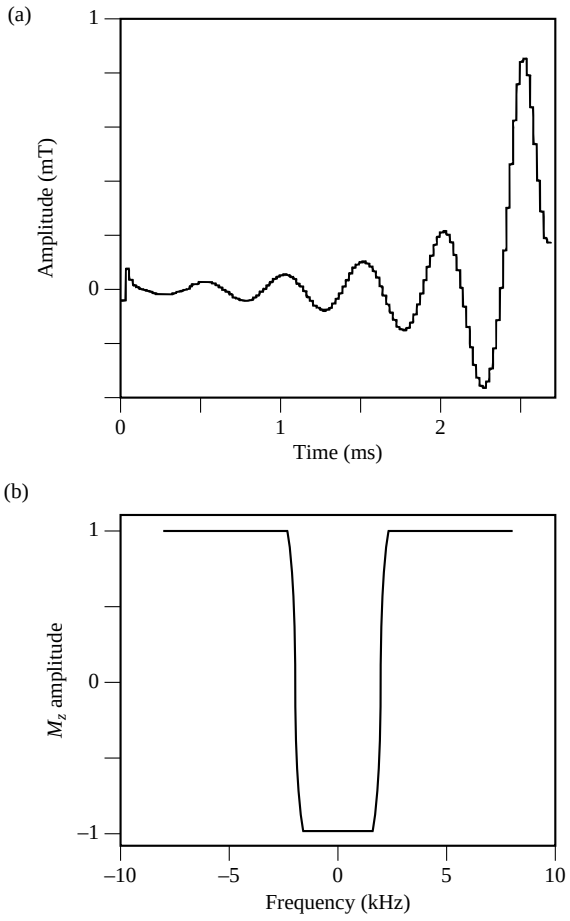

Figure 5 (a) An SLR-optimized 256-step 180° maximum phase inversion pulse. A symmetric pulse shape (for linear phase) is not required, and the maximum (or minimum) phase pulse produces a superior profile (as compared with a linear phase pulse) for inversion or saturation. (b) The resultant slice profile from the pulse in (a). (Reproduced with the computer program described in Matson[19])

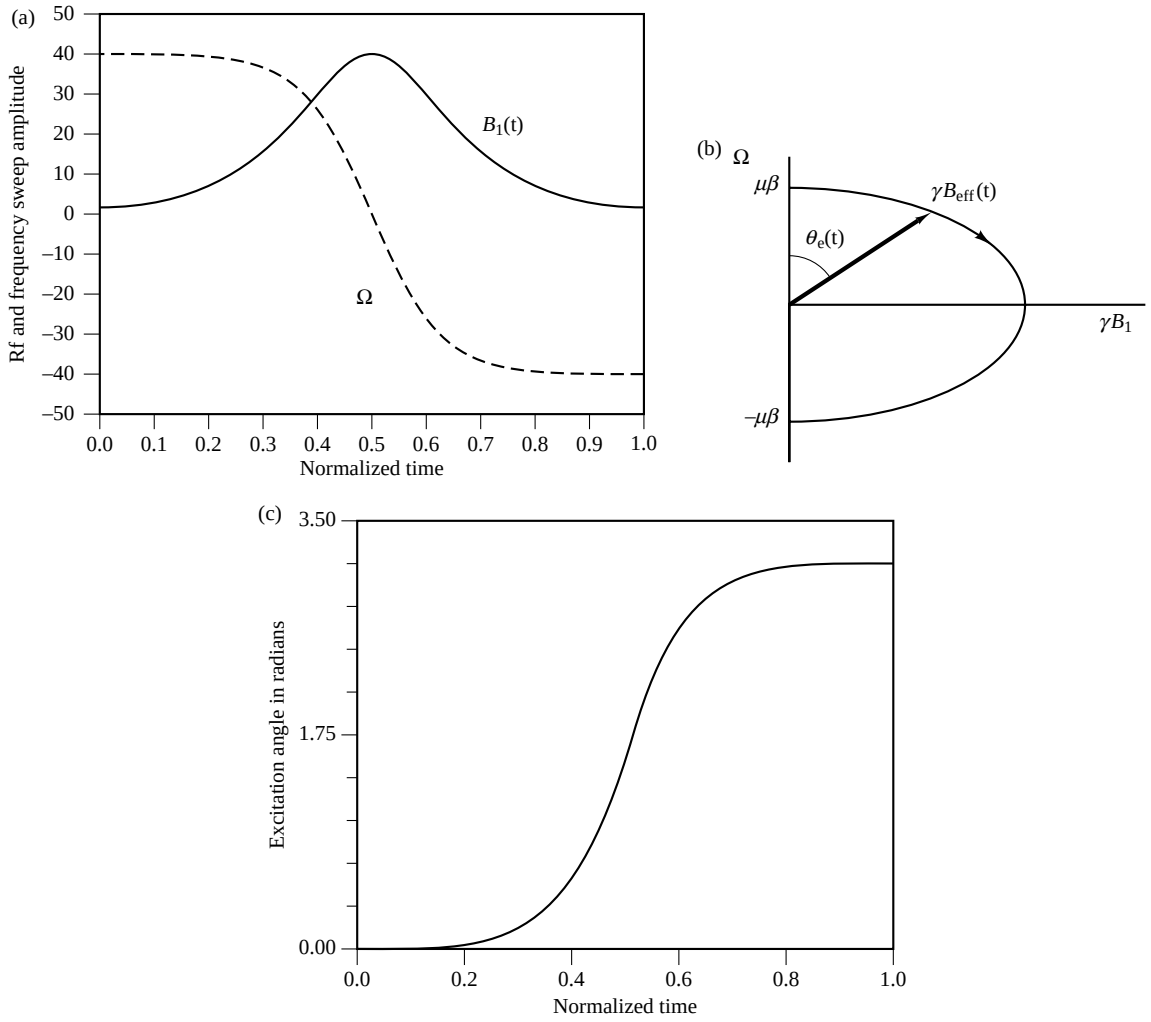

Figure 6 (a) Radiofrequency amplitude (B_1) and frequency (Ω) sweeps for the hyperbolic secant inversion pulse. (b) Parametric plot of the locus of points touched by the tip of the effective field (scaled in units of frequency). (c) The angle between the z axis and the excitation vector at $\gamma q_z = 0$. The Figure shows the effective field for spins in the center of the inverted slice. For spins outside of the selected slice, the origin for the effective field would be offset in Ω such that the effective field would not change sign during the sweep. As discussed in the text, the spins follow the effective field; thus, only those spins experiencing a sign change in the effective field are inverted. (Reproduced by permission of Academic Press from Conolly et al.[53])

equation,[14–16] and this pulse became widely used, particularly for surface coil experiments. As first noted[47,48] and then aptly demonstrated with the image-selected in vivo spectroscopy (ISIS) experiment,[49] multiple acquisitions with different combinations of inversion pulses can be used to achieve localization.

The price paid for B_1 immunity was time and power. Following the introduction of the hyperbolic secant pulse, considerable work was done with frequency modulated pulses to shorten pulse lengths, reduce power requirements, improve immunity to B_1 inhomogeneity, or provide the capability for spin echo and additional tip angle pulses. Although the majority of this work was not aimed at developing good slice selection, there were a number of exceptions. Murdoch et al.[17] showed that the slice profile of the hyperbolic secant pulse could be improved, albeit at the expense of reduction of B_1 immunity, and that somewhat analogous spin echo slice selective pulses could be defined. Ideas introduced initially by Ugurbil et al.[50] were extended by Conolly et al.[51–53] to generate slice-selective, adiabatic spin echo pulses. Figure 6 illustrates the action of a frequency modulated (adiabatic) inversion pulse.[53] A variety of adiabatic slice-selective excitation pulses have also been demonstrated, but all have drawbacks, including the need for two acquisitions to achieve the slice excitation,[54] perturbation of the out-of-slice magnetization,[55] or the requirement of complicated modulation of the gradients along with the rf waveform.[56]

5 MISCELLANEOUS

5.1 Selective Pulses with Modulated Gradients

Practical considerations may limit the implementation of a desired selective rf pulse, namely: excessive power deposition

in the sample (SAR), maximum rf power available from the instrument or limits in the power handling capabilities of the probe, and available gradient strengths. As higher gradient strengths have become available the rf power considerations have become most important. To address these problems, as well as to make better utilization of the available gradient strength, Conolly et al.[57] proposed using variable rate selective excitation (VERSE) pulses where the gradient strength was varied during the selective pulse. In essence, the idea was to refabricate (or reformulate) the selective pulse by using increased gradients (and rf power) in regions where the original rf power was low, and reduced gradient strength (and rf power) where the original rf power was high. Since the SAR is proportional to the square of the integrated B_1 strength, reducing the peak power of a pulse yields reduced SAR.

In the VERSE technique the modified rf and gradient waveforms were determined by nonlinear constrained minimization methods which included constraints for gradient strength and slew rate limitations. Other implementations have since appeared.[19,58] One limitation encountered with these pulses arises from chemically shifted resonances. As described below, the selected slice position differs for different chemically shifted species. With reformulated pulses, the applied gradient varies, resulting in smearing of the selected slice profile for chemically shifted resonances.[19,57] The idea of reformulated pulses is demonstrated with Figure 7, which shows the gradient and rf waveforms for a reformulated version[19] of the spin echo pulse of Figure 4.

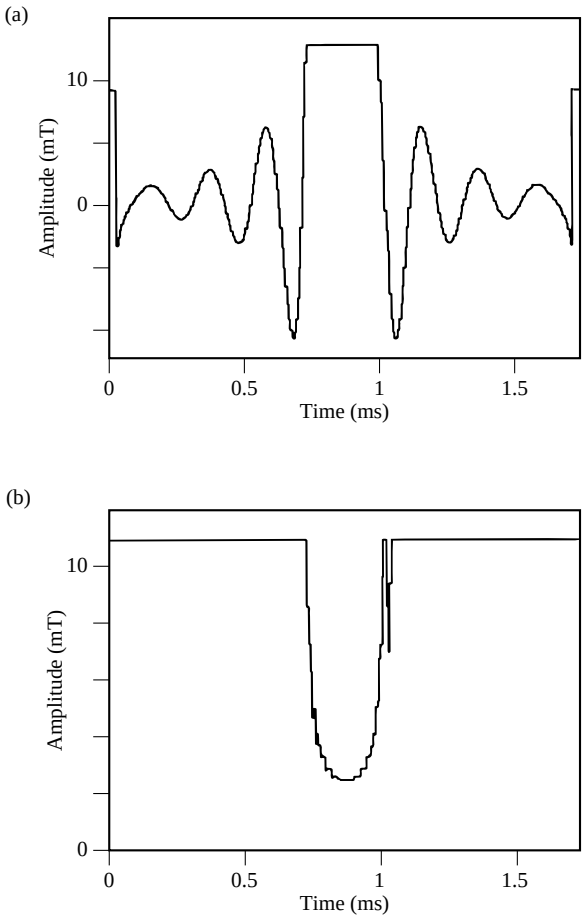

Figure 7 Reformulated spin echo pulse from Figure 4(a). (a) Radiofrequency waveform of the reformulated pulse. The amplitude is increased and the time shortened compared with Figure 4(a); however, when executed with the gradient waveform of Figure 7(b), the slice profile is unchanged from Figure 4(b). (b) Gradient waveform for the reformulated pulse. The gradient dips at the center of the pulse to prevent the rf amplitude from exceeding a preset value (12 mT). The sharp dip at just over 1 ms is a resynchronization adjustment to maintain symmetry at the beginning and ends of the reformulated pulse.[19] (Reproduced with the computer program described in Matson[19])

5.2 Multidimensional Pulses

Multiple applications of selective excitation pulses in a single pulse sequence permit observation of signals from a small, well-defined volume. This approach has been used for localized spectroscopy studies, such as ISIS,[49] stimulated echo acquisition method (STEAM),[59] and point-resolved spectroscopy (PRESS).[60,61] An alternative approach is to integrate gradient waveform modulation into the rf pulse design so that multidimensional spatial selectivity can be achieved in a single pulse. Unfortunately for spectroscopic applications this approach has limitations for excitation of multiple chemically shifted species, though other more suitable applications include excitation or suppression of flowing spins,[62] and spectral–spatial excitation where simultaneous spatial and spectral selectivity is achieved in a single pulse.

One of the first approaches to multidimensional pulses was proposed by Bottomley and Hardy[63] to provide inversion of spins within a two-dimensional localized volume. This pulse applied a rotating gradient during the rf to invert a roughly cylindrical volume. Pauly et al.[64] have shown how an analysis of *k*-space trajectories can be used to design selective excitation pulses, and have applied these methods to large tip angle multidimensional pulses. The power of this approach is that the final two-dimensional pulse may be considered to be composed of concatenated, shallow tip angle pulses, so that linear FT analysis applies. This enables lengthy optimization procedures to be avoided. Suitable gradient waveforms have included spiral or pinwheel[64–66] trajectories. Pulse shapes for excitation, inversion, and spin echo pulses have been optimized using approaches similar to those previously described, including simulated annealing methods,[67] and others.[64,68]

The gradient waveforms necessary for multidimensional pulses can require significant gradient power to be practical. By combining a two-dimensional selective pulse with an additional selectivity using blipped gradients, described as an echo planar (see ***Echo-Planar Imaging***) pulse, Pauly et al.[62] have demonstrated three-dimensional localization using conventional MRI gradient systems. The echo planar pulse consists of a sequence of subpulses, each selective about one axis, which are modulated by an envelope that is selective along another. To make this three-dimensional, each of the subpulses are made up of a two-dimensional spiral pulse. The ideas of two- and three-dimensional pulses are illustrated in Figures 8 and 9.

Spectral–spatial excitation is also possible;[69] this class of pulse provides selective excitation along one or two spatial axes while simultaneously exciting only those spins resonating over a specific frequency range. One application of these pulses is to provide fat suppression with slice-selective excitation of

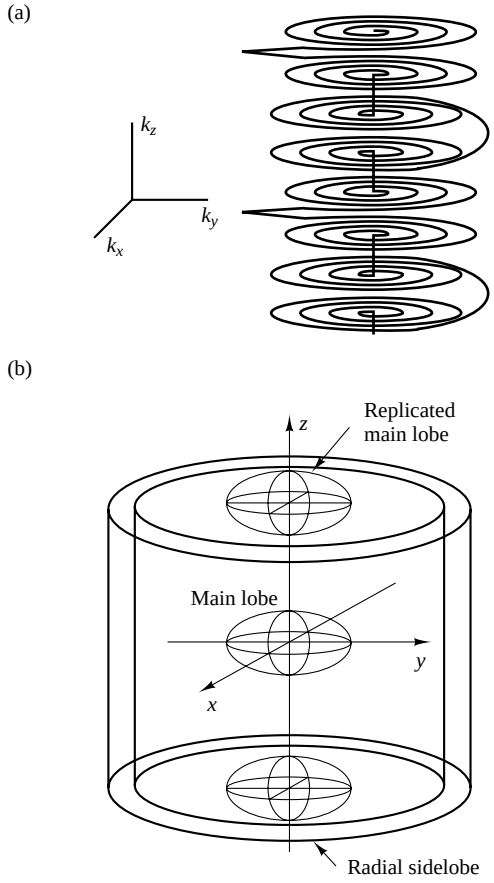

Figure 8 Depiction of k-space trajectory of a three-dimensional selective pulse, along with the sidelobe structures produced by the pulse. (a) The series of eight disks in k_x–k_y, covered by three-turn constant-slew-rate spirals. (b) The sidelobe structure, showing the replicated main lobes along z and the radial sidelobe. The sidelobes are depicted closer than they actually occur. (Reproduced by permission from Pauly et al.[62])

the water signal, which is a requirement for echo planar imaging. Another application is to provide water suppression, which was used by Spielman et al.[70] for the refocusing pulse in a spectroscopic imaging experiment (see ***Chemical Shift Imaging***). This same study also provides a practical demonstration of a two-dimensional pulse used to excite a large elliptical volume within the brain while excluding signal from the lipid regions near the edges of the head.

5.3 Chemical Shift Effects

An additional consideration for selective excitation occurs for chemically shifted resonances. In the presence of a constant applied gradient, slice-selective excitation produces a spatial shift for each chemically shifted resonance. If ω is the frequency separation between two resonances, then the shift between the slice selected for each resonance, Δ, will be given by $\Delta = G\omega/\gamma$, where G is the applied slice-selective field gradient. For example, for volume selective ^{31}P spectroscopy at a field strength of 1.5 T and with a field gradient of 5 mT m^{-1}, the relative localization error for the 23 ppm range between monophosphate and β-ATP resonances is 6 mm in each gradient direction. Clearly this localization error can be reduced by using larger gradient strengths. These spatial errors become more significant for higher magnetic field studies, for observation of nuclei such as ^{13}C, which have wide chemical shift ranges, and for slice selection with narrow slice width.

When the gradient is nonconstant, as in reformulated and multidimensional pulses, the spatial shift is not constant during

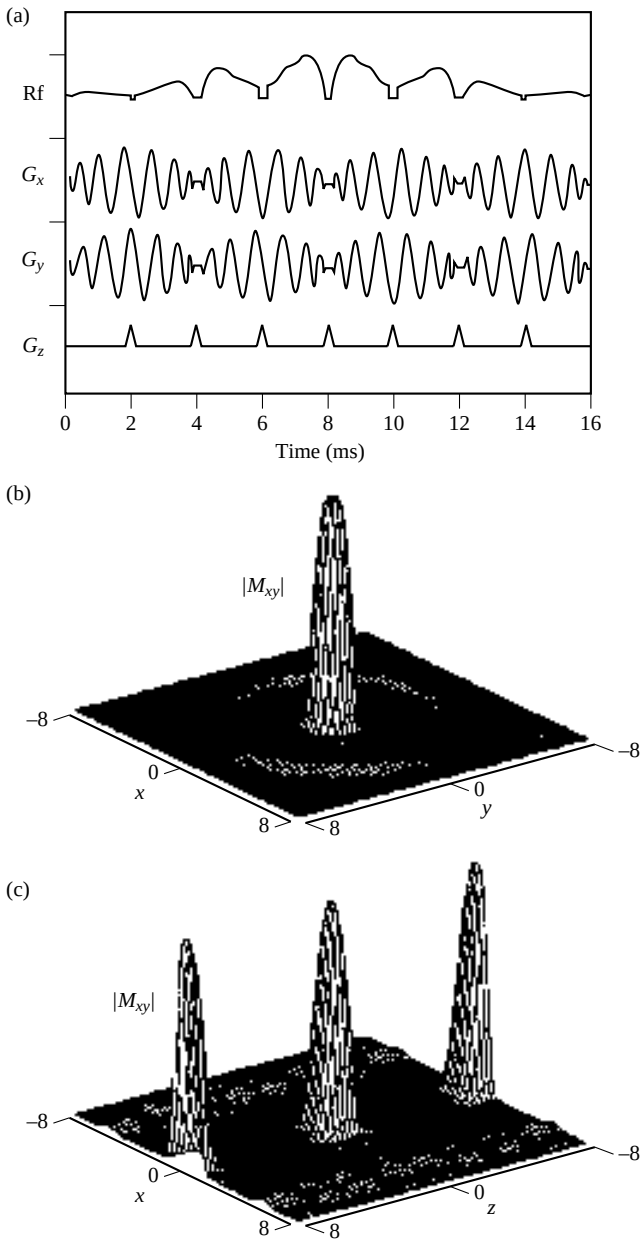

Figure 9 Radiofrequency and gradient waveforms and resulting spin echo profiles for the pulse depicted in Figure 8. (a) Radiofrequency and gradient waveforms for the spin echo pulse. The blips in G_z provide the steps from one disk to another in Figure 8(a). (b) Simulated spin echo profile in the xy plane. The radial sidelobe is apparent in the simulation. (c) Simulated spin echo profile in the xz plane. The replicated main sidelobes are apparent in this orientation. (Reproduced by permission of Waverley from Pauly et al.[62])

the pulse, and degradation of the selection profile can occur.[19,57,63,70] While an approach has been demonstrated for elimination of the spatial shift in slice-selective pulses,[71] the length and complexity of this approach probably precludes its use in in vivo imaging and spectroscopy applications.

6 CONCLUSIONS

The field of RF pulse design has evolved to the point that a large number of computer-optimized pulses are available for a wide variety of MRI and MRS applications. Improved pulse design methods make use of the increased computational capabilities that have become available as well as new algorithmic methods. To summarize the current state of optimized pulse design for selective excitation:

1. Algorithms for amplitude modulated pulses have evolved to the point that it is feasible to perform the pulse design at run time with modern computer workstations, permitting the excitation profiles to be specifically tailored to the application. Unfortunately, the same is not yet true for tailoring frequency modulated pulses.
2. Little use has been made to date of reformulated or remapped pulses though the FOCI pulses,[72] which were presented as improved pulses for the ISIS experiment, represent a class of remapped pulses. In addition, the increased flexibility, speed, and strength of the gradient systems being introduced and implemented on state-of-the-art MRI systems should accelerate the use of this class of pulses.
3. Multidimensional pulses, whose implementation and performance are also greatly facilitated by improved gradient systems, remain an unknown in terms of general use. A recent report demonstrates that they can be used to advantage in long TE PRESS localized spectroscopy to suppress lipid signals.[73] However, although they enable multidimensional selectivity within a single pulse, the pulses are long and lack the sharp profiles of the single-dimension selective pulses. Undoubtedly, their use will accelerate along with the improvements in gradient systems.
4. One area where current pulse designs are still lacking is a slice excitation pulse with immunity to B_1 inhomogeneity.
5. Other important areas for further investigation include faster algorithms for frequency modulated pulses which would allow for transition width to be traded off against immunity to B_1 inhomogeneity, and more efficient algorithms for generation of multidimensional pulses. The use of a small number of pulse parameters to be optimized may prove useful for speeding up optimization.[63]

7 RELATED ARTICLES

Chemical Shift Imaging; Complex Radiofrequency Pulses; Echo-Planar Imaging; Image Formation Methods; Selective Excitation Methods: Artifacts; Single Voxel Localized Proton NMR Spectroscopy of Human Brain In Vivo; Single Voxel Whole Body Phosphorus MRS.

8 REFERENCES

1. J. A. Pople, W. G. Schneider, and H. J. Bernstein, 'High Resolution NMR', McGraw-Hill, New York, 1959.
2. J. W. Emsley, J. Feeney, and L. H. Sutcliffe, 'High Resolution NMR', Macmillan, New York, 1966.
3. R. R. Ernst, J. Bodenhausen, and A. Wokaun, in: 'Principles of Nuclear Magnetic Resonance in One and Two Dimensions', Clarendon Press, Oxford, 1987.
4. B. L. Tomlinson and H. D. Hill, *J. Chem. Phys.*, 1973, **59**, 1775.
5. G. A. Morris and R. Freeman, *J. Magn. Reson.*, 1978, **29**, 433.
6. A. N. Garroway, P. K. Grannell, and P. Mansfield, *J. Phys. C*, 1974, **7**, L457.
7. P. Mansfield, A. A. Maudsley, and T. Baines, *J. Phys E*, 1976, **9**, 271.
8. P. C. Lauterbur, D. M. Kramer, W. V. House, Jr., and C.-N. Chen, *J. Am Chem. Soc.*, 1975, **97**, 6866.
9. J. M. S. Hutchison, R. J. Sutherland, and J. R. Mallard, *J. Phys. E*, 1978, **11**, 217.
10. D. I. Hoult, *J. Magn. Reson.*, 1979, **35**, 69.
11. P. Locher, *Phil. Trans. R. Soc. London, Ser. B*, 1980, **289**, 537.
12. J. Baum, R. Tycko, and A. Pines, *J. Chem. Phys.*, 1983, **79**, 4643.
13. J. Baum, R. Tycko, and A. Pines, *Phys. Rev. A*, 1985, **32**, 3435.
14. M. S. Silver, R. I. Joseph, and D. I. Hoult, *J. Magn. Reson.*, 1984, **59**, 347.
15. M. S. Silver, R. I. Joseph, C.-N. Chen, V. J. Sank, and D. I. Hoult. *Nature (London)*, 1984, **310**, 681.
16. M. S. Silver, R. I. Joseph, and D. I. Hoult, *Phys. Rev. A*, 1985, **31**, 2753.
17. J. B. Murdoch, A. H. Lent, and M. R. Kritzer, *J. Magn. Reson.*, 1987, **74**, 226.
18. S. Conolly, D. Nishimura, and A. Macovski, *IEEE Trans. Med. Imaging*, 1986, **2**, 106.
19. G. B. Matson, *Magn. Reson. Imaging*, 1994, **12**, 1205.
20. D. G. Norris, H. Ludemann, and D. Leibfritz, *J. Magn. Reson.*, 1991, **92**, 94.
21. P. J. Hajduk, D. A. Horita, and L. E. Lerner, *J. Magn. Reson.*, 1993, **103**(A:1), 40.
22. W. S. Warren, *J. Chem. Phys*, 1984, **81**, 5437.
23. J. W. Carlson, *J. Magn. Reson.*, 1986, **67**, 551.
24. M. O'Donnell and W. J. Adams, *Magn. Reson. Imaging*, 1985, **3**, 377.
25. D. J. Lurie, *Magn. Reson. Imaging*, 1985, **3**, 235.
26. J. Mao, T. H. Mareci, K. N. Scott, and E. R. Andrew, *J. Magn. Reson.*, 1986, **70**, 310.
27. J. Mao, T. H. Mareci, and E. R. Andrew, *J. Magn. Reson.*, 1988, **79**, 1.
28. W. S. Warren and M. S. Silver, *Adv. Magn. Reson.*, 1988, **12**, 248.
29. J. T. Ngo and P. G. Morris, *Magn. Reson. Med.*, 1987, **5**, 217.
30. D. E. Rourke and P. G. Morris, *J. Magn. Reson.*, 1992, **99**, 118.
31. J. W. Carlson, *J. Magn. Reson.*, 1991, **94**, 376.
32. J. W. Carlson, *J. Magn. Reson.*, 1992, **97**, 65.
33. V. H. Subramanian, S. M. Eleff, S. Rehn, and J. S. Leigh, Jr., *Proc. 5th Ann. Mtg. Soc. Magn. Reson. Med.*, Montreal, 1986, pp. 1452–1453.
34. S. M. Eleff, V. H. Subramanian, M. Shinnar, S. Renn, and J. S. Leigh, Jr., *J. Magn. Reson.*, 1987, **72**, 298.
35. M. Shinnar and J. S. Leigh, Jr., *J. Magn. Reson.*, 1987, **75**, 502.
36. M. Shinnar, S. Eleff, H. Subramanian, and J. S. Leigh, *Magn. Reson. Med.*, 1989, **12**, 74.
37. M. Shinnar, L. Bolinger, and J. S. Leigh, *Magn. Reson. Med.*, 1989, **12**, 81.
38. M. Shinnar, L. Bolinger, and J. S. Leigh, *Magn. Reson. Med.*, 1989, **12**, 88.

39. J. Pauly, P. Le Roux, D. Nishimura, and A. Macovski, *IEEE Trans. Med. Imag.*, 1991, **10**, 53.
40. M. H. Buonocore, *Magn. Reson. Med.*, 1993, **29**, 470.
41. A. V. Oppenheim, and R. W. Schafer, 'Discrete-Time Signal Processing', Prentice-Hall, Englewood Cliffs, NJ, 1989.
42. P. G. Morris, J. O. McIntyre, D. E. Rourke, and J. T. Ngo, *Magn. Reson. Med.*, 1989, **11**, 167.
43. F. Loaiza, M. A. McCoy, S. L. Hammes, and W. S. Warren, *J. Magn. Reson.*, 1988, **77**, 175.
44. H. Geen and R. Freeman, *J. Magn. Reson.*, 1991, **93**, 93.
45. H. Geen, S. Wimperis, and R. Freeman, *J. Magn. Reson.*, 1989, **85**, 620.
46. T. P. L. Roberts, T. A. Carpenter, and L. D. Hall, *J. Magn. Reson.*, 1990, **89**, 595.
47. R. Tycko and A. Pines, *J. Magn. Reson.*, 1984, **60**, 156.
48. A. J. Shaka and R. Freeman, *J. Magn. Reson.*, 1985, **63**, 596.
49. R. J. Ordidge, A. Connelly, and J. A. B. Lohman, *J. Magn. Reson.*, 1986, **66**, 283.
50. K. Ugurbil, M. Garwood, A. R. Rath, and M. R. Bendall, *J. Magn. Reson.*, 1988, **78**, 472.
51. S. Conolly, D. Nishimura, and A. Macovski, *J. Magn. Reson.*, 1989, **83**, 324.
52. S. Conolly, G. Glover, D. Nishimura, and A. Macovski, *Magn. Reson. Med.*, 1991, **18**, 28.
53. S. Conolly, D. Nishimura, and A. Macovski, *J. Magn. Reson.*, 1989, **83**, 549.
54. A. J. Johnson, M. Garwood, and K. Ugurbil, *J. Magn. Reson.*, 1989, **81**, 653.
55. J. Shen and D. L. Rothman, *J. Magn. Reson.*, 1997, **124**, 72.
56. R. A. de Graaf, K. Nicolay, and M. Garwood, *Magn. Reson. Med.*, 1996, **25**, 652.
57. S. Conolly, D. Nishimura, A. Macovski, and G. Glover, *J. Magn. Reson.*, 1988, **78**, 440.
58. J. Slotboom, J. W. Gunning, A. F. Mehlkopf, and W. M. M. J. Bovee, *J. Magn. Reson.*, 1993, **101**, 257.
59. J. Frahm, K. D. Merboldt, and W. Hanicke, *J. Magn. Reson.*, 1987, **72**, 502.
60. R. J. Ordidge, M. R. Bendall, R. E. Gordon, and A. Connelly, in 'Magnetic Resonance in Biology and Medicine', eds. G. Govil, C. L. Khetrapal, and A. Saran, Tata McGraw-Hill, New Delhi, 1985, pp. 387–397.
61. P. R. Luyten, A. J. H. Marien, W. Heindel, P. H. J. van Gerwen, K. Herholz, J. A. den Hollander, G. Friedmann, and W. Heiss, *Radiology*, 1990, **176**, 791.
62. J. M. Pauly, B. S. Hu, S. J. Wang, D. G. Nishimura, and A. Macovski, *Magn. Reson. Med.*, 1993, **29**, 2.
63. P. A. Bottomley and C. J. Hardy, *J. Magn. Reson.*, 1987, **74**, 550.
64. J. Pauly, D. Nishimura, and A. Macovski, *J. Magn. Reson.*, 1989, **82**, 571.
65. C. J. Hardy and P. A. Bottomley, *Magn. Reson. Med.*, 1991, **17**, 315.
66. J. B. Ra, C. Y. Rim, and Z. H. Cho, *Magn. Reson. Med.*, 1991, **17**, 423.
67. C. J. Hardy, P. A. Bottomley, M. O'Donnell, and P. Roemer, *J. Magn. Reson.*, 1988, **77**, 233.
68. P. G. Morris, D. J. O. McIntyre, D. E. Rourke, and J. T. Ngo, *Magn. Reson. Med.*, 1991, **17**, 33.
69. C. H. Meyer, J. M. Pauly, A. Macovski, and D. Nishimura, *Magn. Reson. Med.*, 1990, **15**, 287.
70. D. Spielman, C. Meyer, A. Macovski, and D. Enzmann, *Magn. Reson. Med.*, 1991, **18**, 269.
71. D. S. Williams and I. J. Lowe, *J. Magn. Reson.*, 1991, **91**, 57.
72. R. J. Ordidge, M. Wylezinska, J. W. Hugg, E. Butterworth, and F. Franconi, *Magn. Reson. Med.*, 1996, **36**, 562.
73. J. Star-Lac, D. B. Vigneron, J. Pauly, J. Kurhanewicz, and S. J. Nelson, *J. Magn. Reson. Imaging*, 1997, **7**, 745.

Biographical Sketches

Andrew A. Maudsley. *b* 1952. B.Sc. 1973, Ph.D., 1976, physics, University of Nottingham, UK. 1987–present, Professor of Radiology, University of California, San Francisco. 78 Publications Research specialties; development of data acquisition and processing methods for MR spectroscopic imaging, and application of these methods for biomedical studies.

Gerald B. Matson. *b* 1938. Ph.D. 1967, physical chemistry, University of Wisconsin. 1986–present, Facilities Manager, MR Unit, Department of Veterans Affairs Medical Center, San Francisco, and Adjunct Professor, Department of Pharmaceutical Chemistry, University of California, San Francisco. 76 publications. Research specialties; development of methods for in vivo magnetic resonance studies of human brain, including selective excitation and localization methods, and NMR probe design.

Selective Excitation Methods: Artifacts

Ian R. Young

The Robert Steiner MRI Unit, Hammersmith Hospital, London, UK

1 INTRODUCTION

This article describes some of the artifacts that arise in the process of selective excitation and from the use of gradient pulses to spoil (i.e. eliminate) transverse magnetization. It assumes that the pulse profiles intended by the user have been implemented correctly, and that the machine is performing well (so that if, for example, a certain rf pulse profile was designed to produce a 90° spin precession then, in fact, the right amount of rf field was delivered to the sample for the correct time). This section aims to suggest some of the ways in which errors can creep into apparently well-designed processes, the aim of which is to excite an accurate quantity of magnetization in the correct location.

Many of the problems described were most pernicious in the earlier stages of whole body MR, and can be avoided by some of the more sophisticated methods developed later (see ***Selective Excitation in MRI and MR Spectroscopy***). However, problems with selection have contributed very substantially to the difficulties of measurement in whole body MR (see ***Relaxation Measurements in Imaging Studies***) and, so, an understanding of the artifacts that can develop is an essential precursor to proper quantitation.

Clearly an evaluation of the detailed problems with any one form of data acquisition has to be left to its designer and users: a detailed survey of all problems is impracticable. This article can only point out potential sources of trouble.

2 APPEARANCE OF ARTIFACTS

It is important to note that what may be an artifact to one observer, may appear quite unimportant, or even be useful, to another. Thus, as long as the shape of its slice is not too distorted, a radiologist may still find an image quite usable: though be very suspicious of the presence of an unusual structure in it. A scientist might well not recognize the latter as existing or relevant, but might be very concerned about errors introduced by imperfections in the slice into his numerical values. Frequently, the only clue to the presence of such artifacts are seemingly anomalous numerical values. Subtle artifacts are the source of many concerns about measurement accuracy. An analogy can be drawn with spectroscopy where motion artifacts generally cause an apparent loss of signal-to-noise ratio, without producing an apparently erroneous spectral pattern that would immediately suggest the likely cause of the abnormality.[1]

3 SLICE SELECTION ARTIFACTS

3.1 Impact of Flow and Motion

Flow effects (principally due to blood) are extremely common in any form of localized in vivo MR, and were exploited very early in the development of MRI.[2] Simplistically, if some fraction f of the blood in a slice is replaced in the sequence repetition time TR, the signal which results S is given by:

$$S = S_{0B}\exp\left(-\frac{TE}{T_{2B}}\right)\left\{(1-f)\left[1-\exp\left(-\frac{TR}{T_{1B}}\right)\right]+f\right\} \quad (1)$$

where S_0 is the total fully relaxed blood signal and the additional B subscripts refer to blood parameters. In practice, of course, the voxel may also include parenchymal signal leading to the fuller relationship:

$$\begin{aligned} S = {} & xS_0\exp\left(-\frac{TE}{T_{2B}}\right)\left\{(1-f)\left[1-\exp\left(-\frac{TR}{T_{1B}}\right)\right]+f\right\} \\ & +(1-x)S_0\exp\left(-\frac{TE}{T_{2P}}\right)\left[1-\exp\left(-\frac{TR}{T_{1P}}\right)\right] \end{aligned} \quad (2)$$

where subscript P refers to the parenchyma, and x is the fractional contribution of blood the magnetization of which has reached a steady state saturation at the TR used to the fully recovered overall signal. Many of these parameters are difficult to determine even with good slice shapes, and are largely unresolvable with bad.

Very frequently (usually when cardiac gating is not used; not infrequently when it is) f is unstable, and characteristic ghosting artifacts develop. (See ***Cardiac Gating Practice***; ***Motion Artifacts: Mechanism and Control*** and ***Whole Body Magnetic Resonance Artifacts***.) These can be minimized in general with gating, and the use of sequences such as even echo rephasing,[3] and motion artifact suppression technique[4] (see ***Pulsatility Artifacts Due to Blood Flow and Tissue Motion and Their Control***), though complete elimination is rarely achieved.

Another motion artifact arises where the region being imaged moves through the slice (as in a transverse image of the liver). In this case, again, variable degrees of saturation develop even in nominally homogeneous regions of tissue as predicted by equation (2), though with variable fractions of unsaturated magnetization affecting both blood and parenchyma signals.

3.2 Time Constant Dependent Effects

Any degeneration in slice form tends to exacerbate the effects just described. Apart from machine maladjustment, the major slice selection artifacts arise from the impossibility of exciting all the spins in a region exactly to the degree required, while having no effect at all on those outside it. If a selected region is excited repetitively at a TR which is relatively short compared with T_1 there is likely to be enhanced signal from its edges. The original analyses were for the simple partial saturation (PS, or α-TR-α) sequence (where α is the flip angle).

Solving the Bloch equations in the presence of a gradient and rf pulse yields ultimately:[5]

$$M_{xyr} = \left\{ M_0 \left[1 - \exp\left(-\frac{TR}{T_1} \right) \right] \exp\left(-\frac{t_r}{T_2} \right) \sin \alpha_r \right\} \times \left\{ \left[1 - \exp\left(-\frac{TR}{T_1} \right) \cos \alpha_r \right] + \exp\left(-\frac{TR}{T_2} \right) \times \left[\exp\left(-\frac{TR}{T_1} \right) - \cos \alpha_r \right] \right\}^{-1} \quad (3)$$

where α_r is the precession angle of the rf pulse at a distance r from the reference plane; t_r is the time of the observation (post-rf pulse) and M_0 is the available, and M_{xy} the transverse, magnetization respectively. The value of α_r is derived from the Fourier transform of the pulse profile in conjunction with the applied gradient. Thus if the pulse profile is $P(t)$ for the duration (t_P) of the rf pulse, then

$$\int_{\omega=0}^{\infty} I_\omega \mathrm{d}\omega = F\left\{ \int_{t=0}^{t_p} P(t)\, \mathrm{d}t \right\} \quad (4)$$

where I_ω is the intensity of the rf at frequency ω. α_r is then defined by:

$$\alpha = \gamma I_{\omega_r} t_P \quad (5)$$

where $\omega_r = \gamma Gr$ relative to the reference.

Equation (3) can be simplified in general, except for short TR sequences (see ***Whole Body Magnetic Resonance: Fast Low-Angle Acquisition Methods***), when $TR >> T_2$, to give at the conventional echo at the center of data acquisition:

$$M_{xyr} = \frac{M_0 \left[1 - \exp\left(-\frac{TR}{T_1} \right) \right] \exp\left(-\frac{TE}{T_2} \right) \sin \alpha_r}{\left[1 - \exp\left(-\frac{TR}{T_1} \right) \cos \alpha_r \right]} \quad (6)$$

This relationship is that derived by Ernst and Anderson[6] in their original description of Fourier transform MR, and yields the relationship:

$$\cos \alpha_M = \exp\left(-\frac{TR}{T_1} \right) \quad (7)$$

where α_M is the precession angle which results in the optimum signal-to-noise ratio per unit time for a sample with longitudinal relaxation time constant T_1 in an experiment with a sequence repetition time TR. Figure 1 illustrates the patterns that can develop, while Figure 2 is a practical demonstration of the predictions.

In Figure 1 a series of profiles are plotted for different ratios of TR/T_1 for the simple partial saturation experiment, using a slice the ideal form of which is given in Figure 1(a). The increasingly large fraction of the signal contribution from the slice edges as the ratio is reduced is apparent. Reducing α (the nominal precession angle) can improve slice shape. Notice that at $TR/T_1 = 0.1$, equation (8) predicts that $\alpha_M = 25.2°$. Figure 2 shows how experiment confirms the theoretical predictions very exactly.

Similar problems exist with other sequences to some extent, as long as all the rf pulses in them are selective (each defining a similar width of slice, such as might be needed for a multi-slice acquisition with contiguous, or closely adjacent, slices).

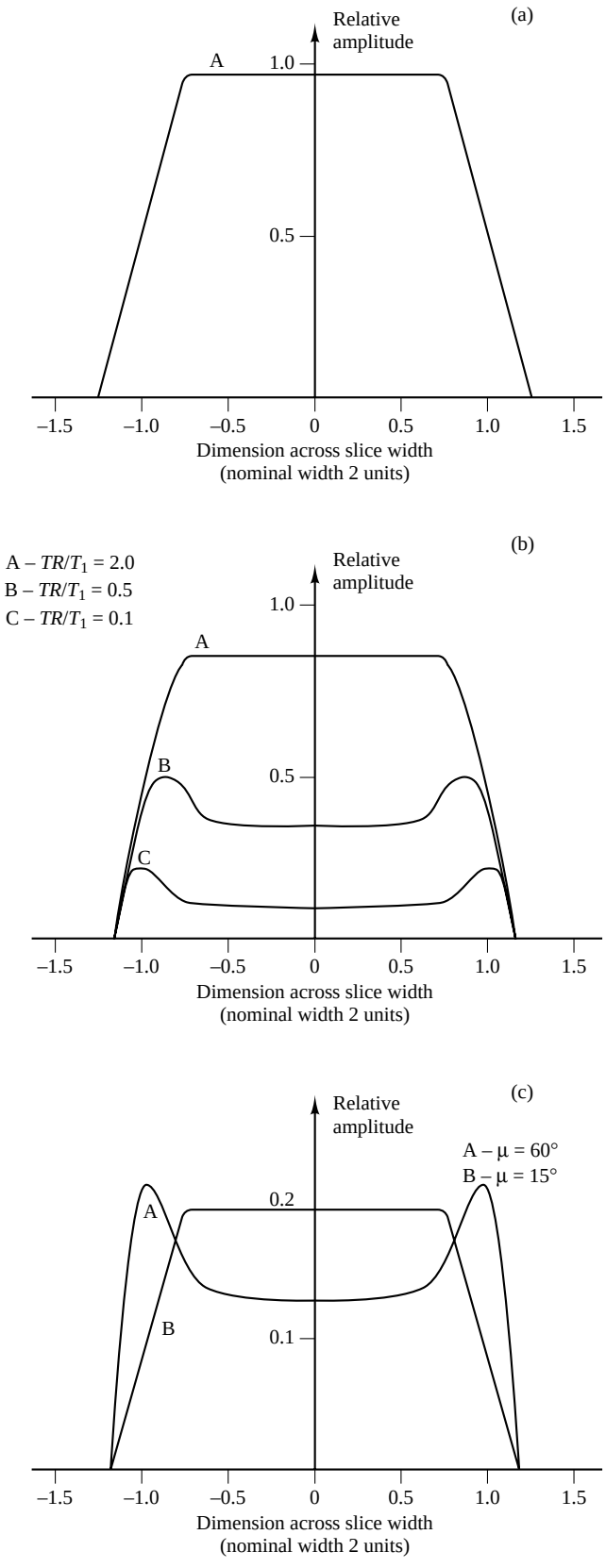

Figure 1 Predicted profile forms across a slice. (a) Desired slice form with $TR/T_1 \rightarrow \infty$ ($\alpha = 90°$). (b) Predicted signal amplitude across the slice in Figure 1(a) for $TR/T_1 = 2$; $TR/T_1 = 0.5$; and $TR/T_1 = 0.1$ (all with nominal $\alpha = 90°$). (c) Predicted amplitudes for $TR/T_1 = 0.1$, but with nominal values of $\alpha = 60°$ and $15°$ respectively. T_2, TE assumed constant in all experiments; M_0 taken as unity

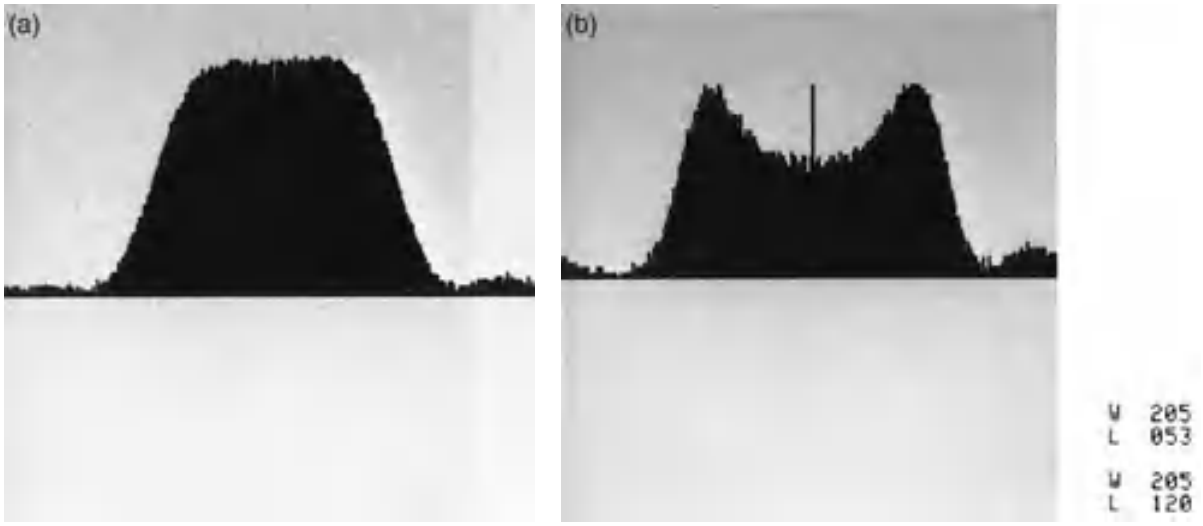

Figure 2 Pair of images showing the actual form of slices. (a) $TR/T_1 = 5$ ($\alpha = 90°$); (b) $TR/T_1 = 0.2$ ($\alpha = 90°$). The images were taken by using a conventional slice-selection gradient pulse with a sinc rf pulse, truncated at the third duration on either side of zero. Rf pulse duration was 4 ms; nominal slice width 8 mm. The normal duration of the rephasing pulse was extended, and then the gradient reversed, to form an echo, during which data was sampled. The process was repeated 64 times to improve the signal-to-noise ratio, and the results collected, zero filled to 256 points, Fourier transformed, and displayed. (Reproduced with permission of Academic Press from Young, Bryant, and Payne, *Magn. Reson. Med.*, 1985, **2**, 361)

Sequence variants in which nonselective inverting pulses are used tend to minimize the problem.

From a practical point of view, it is apparent that in the body, where T_1 values for different tissues vary by the best part of an order of magnitude, slice shape can change quite markedly from place to place in it. Partial volume effects, meaning that issues with significantly different T_1 values occupy opposite sides of the slice in the same location in the plane, can result in the slice profile being quite different from one side to the other.

3.3 Consequence for Measurement

It is also clear from the foregoing how the accuracy of measured values can be destroyed. Generally speaking, techniques in which partial saturation sequences are used result in an underestimate of the T_1 of slowly relaxing tissues. However, because they are relatively fast, a number of attempts have been made to exploit them, particularly in the early 1980s.[7] Examination of the problems found with their use are instructive in showing how hard it can be to destroy unwanted magnetization by gradient spoiling pulses.[8]

The principle of gradient spoiling assumes that the net signal from a region is given by:

$$S = \int_{r=-\infty}^{+\infty} S_r \sin \gamma G r t_P \, dr = 0 \qquad (8)$$

where t_P is the duration of the pulse application, G the gradient, and S_r the available signal in a strip of width δr at distance r from the center of the slice. Clearly, if S_r is nearly constant, $S \rightarrow 0$ more quickly than if S_r is significantly nonuniform (particularly if it has large symmetrical peaks in it).

Similarly apparently efficient saturation techniques such as the use of a group of rf pulses, even nonselective ones, interleaved with gradient pulses can result in complex modulation patterns which, ultimately, make proper destruction of the magnetization (the actual aim of saturation) very difficult to achieve. This is illustrated in Figure 3 which shows the magne-

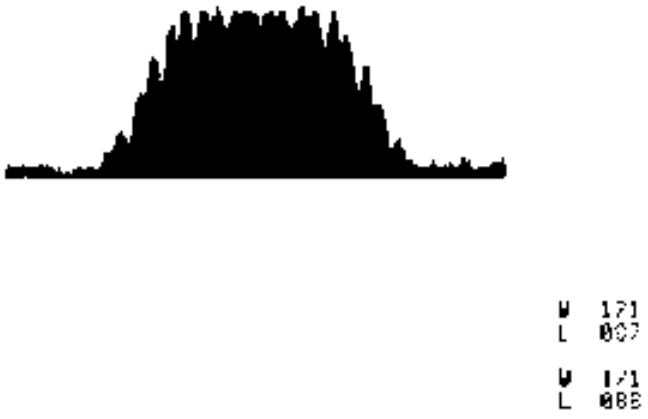

Figure 3 Magnetization excited by a nominally 10 mm-wide slice in a phantom of T_1 of 1600 ms, 200 ms after the start of a burst saturation sequence (three rf pulses each 1 ms long, each followed immediately by a gradient pulse with 1 ms rising and falling edges, and 5 ms period at 15 mT m^{-1} amplitude). (Reproduced with permission of Academic Press from Young, Bydder, and Bryant, *Magn. Reson. Med.*, 1985, **11**, 129)

tization excited by a selective 90° excitation, 200 ms after the commencement of a burst of three nonselective rf pulses with interleaved spoiling gradients. The magnetization pattern can be predicted theoretically through the process but the evaluation of coherence pathways is only really instructive as a didactic exercise.

3.4 Chemical Shift Effects

These are discussed more fully elsewhere (see ***Selective Excitation in MRI and MR Spectroscopy***) and are described here only for completeness.

If there are two moieties with a chemical shift of δ between them in a region where a slice is selected using a gradient of strength G, then the effective centers of the two slices formed, one for each component, are offset by a distance d given by

$$d = \frac{\delta}{\gamma G} \tag{9}$$

The effects of this artifact are much more pronounced with nuclei other than hydrogen such as ^{13}C, where the spectral dispersion is much greater, or phosphorus (see ***Whole Body Studies: Impact of MRS***), particularly in methods where multiple selective excitations are used such as Image-Selected In Vivo Spectroscopy.[9] At 1.5 T, the magnitude of the offset for a chemical shift of 10 ppm in a selective gradient of 5 mT m^{-1} is around 0.3 mm, and the problem can be substantially discounted in most proton work.

4 EFFECTS OF MULTISLICE AND MULTIECHO ACQUISITIONS

Because of the relative efficiency with which these methods use available time, their application is very widespread. However, as has emerged lately, details of the way in which they are implemented can introduce changes in the magnetization that have significant impact on the accuracy of data acquired using them. The notes which follow are designed only to give guidance as to where there may be problems, and readers should consult related articles for further explanation and understanding.

4.1 Artifacts in Multislice Acquisitions

4.1.1 Direct Contamination of One Slice by Another

If the slice shape is poor, with significant excitation of sidelobes, it is likely that some fraction of the spins in a slice will have been excited at a time other than (and less than) the intended *TR*. Depending on the order in which slices are interrogated this results in both a reduction in available signal, and a distortion of expected partial volume effects, as the near neighbors on one side of a slice will inevitably be excited at different times from those on the other.

4.1.2 Off-Resonance Irradiation Effects

As was pointed out by Dixon et al.,[10] the on-resonance excitation of one slice is an off-resonance perturbation of its neighbors. This results in a degree of saturation of the broad spectral line of the cell wall proteins, and some attenuation, potentially, and change of effective time constants, of the narrow water line (which is what is observed) (see ***Magnetization Transfer between Water and Macromolecules in Proton MRI*** and ***Magnetization Transfer and Cross Relaxation in Tissue***). The model used here is discussed fully in those articles.

The behavior of a two-pool system was modeled by Försen and Hoffman,[11] to give the relationship:

$$S_A = \left[S_{0ASAT} + (S_{0A} - S_{0ASAT}) \exp\left(-\frac{t}{T_{1ASAT}}\right)\right] \times \exp\left(-\frac{TE}{T_2}\right) \tag{10}$$

where subscript A refers to signals from the visible pool, and the observation is made just after a period t of off-resonance irradiation. S_{0A} is the available signal after an extended recovery period; S_{0ASAT} that available after prolonged irradiation, and T_{1ASAT} the effective time constant of the evolution of the saturated situation.

If the slice to be observed is the xth in the series, its signal is then given by assuming the rf pulse durations are short compared with T_1 of the visible pool:

$$S_{xobs} = \left[S_0 - \exp\left(-\frac{TR_x}{T_{1(x-1)}}\right)(S_0 - S_{(x-1)})\right] \times \exp\left(-\frac{TE}{T_2}\right) \tag{11}$$

where $S_{(x\ -\ 1)}$ is the magnetization available after the previous excitation. $T_{1(x\ -\ 1)}$ is the effective relaxation time of the magnetization in the state it had reached after the recovery of the $(x - 1)$th slice, determined by the order and timing of acquisition of previous nearby slices. TR_x is the time since the last slice was acquired. S_0 is the fully recovered magnetization of the slice. In practice there are no long recovery periods and some sort of steady state develops which is dependent on the pulse pattern in use. As has been observed from the first in vivo experiment,[12] magnetization transfer effects in tissue are substantial, so that artifacts from this source are a real problem.

4.2 Artifacts of Multiecho Acquisitions

4.2.1 Stimulated Echo Effects

Any multiple pulse train such as that used in a multiecho data acquisition can result in the generation of multiple complex echoes, which can develop to produce interference-like patterns on the resultant images. Stimulated echoes[13] are only one significant aspect of effects produced by more or less adequate rf pulses in the presence of complicated gradient patterns.

4.2.2 Magnetization Transfer Artifacts

As was pointed out by Constable et al.,[14] magnetization transfer effects also contaminate sequences in which many rf refocused echoes are used [such as, for example, 'rapid acquisition with relaxation enhancement' (RARE[15]) and its variants (see ***Multi Echo Acquisition Techniques Using Inverting Radiofrequency Pulses in MRI***)]. Because the relative time-

constant weighting in such sequences is readily modified by the phase encoding order selected from one data acquisition to another, the relative extent of saturation at the time of formation of the echoes at the center of *k*-space is also variable if it is appreciated that a succession of rapid spin-inverting pulses has a quasisaturating effect on the system. The arguments involved are similar to those deployed in Section 4.1.2 above, and, in any event, are much more extensively described in Constable et al.[14]

4.2.3 Unintentional Diffusion Weighting

Another problem to which multiple acquisition sequences can easily become exposed is an over exuberant use of gradients for spoiling out-of-slice and other unwanted magnetization. Modern machines can have very powerful gradients, and putting a couple of large spoiling pulses on either side of a slice-selective 180° pulse seems to require little time (which can generally be used profitably for other, phase encoding, purposes, for example) and is a useful precaution.

Following the Stejskal and Tanner pulsed gradient spin echo experiment,[16] and assuming no significant contribution from the central gradient pulse (present during the rf inversion pulse) the resulting signal S_n (after the nth inverting pulse) of an acquisition with a very long TR preceding it is given by:

$$S_n = S_0 \exp\left[-\frac{TE_n}{T_2} - nD\gamma^2 G^2 \delta^2 (\Delta - \delta/3)\right] \qquad (12)$$

where the spoilers round each rf pulse are assumed identical, of amplitude G, duration (effective) δ, and with a leading edge separation of Δ.

If $G = 20$ mT m^{-1}; $\delta = 3$ ms; $\Delta = 6$ ms; $D = 3 \times 10^{-3}$ mm^2 s^{-1}, and $n = 16$, then the signal (S_{16}) is about 6% smaller than it would be in the absence of the spoiling pulses. While this effect is small, an increase to 25 mT m^{-1} increases the effect to 9.2%, and it is clear that care must be taken in designing sequences for quantitative studies.

Large spoilers in any in vivo studies (including spectroscopy) must be applied with care, particularly when studies of tissues with marked known anisotropies (as in the brain[17,18] and muscle[19]) are being undertaken.

5 CONCLUSION

The foregoing can only be an illustration of the artifacts arising from sequence design and implementation in vivo. Tissue is a very complex system and many artifacts are a function of the tissue parameters present in the region being studied. Thus, for example, a slice which straddles a region containing normal and abnormal tissue can have significantly different profile shape at either side of the same planar location.[5] It is only by considering all the likely contaminating circumstances built into the data acquisition that useful quantitative MRI (or localized MRS) can be expected. In the majority of cases clinical imperatives (the need for multiple data acquisitions while at the same time maintaining high patient throughput) militate against the prolonged recovery times and single slice procedures optimal for measurement accuracy.

6 RELATED ARTICLES

Anisotropically Restricted Diffusion in MRI; Cardiac Gating Practice; Magnetization Transfer and Cross Relaxation in Tissue; Magnetization Transfer between Water and Macromolecules in Proton MRI; Motion Artifacts: Mechanism and Control; Multi Echo Acquisition Techniques Using Inverting Radiofrequency Pulses in MRI; Pulsatility Artifacts Due to Blood Flow and Tissue Motion and Their Control; Relaxation Measurements in Imaging Studies; Selective Excitation in MRI and MR Spectroscopy; Selective Excitation Methods: Artifacts; Single Voxel Whole Body Phosphorus MRS; Whole Body Magnetic Resonance Artifacts; Whole Body Magnetic Resonance: Fast Low-Angle Acquisition Methods; Whole Body Studies: Impact of MRS.

7 REFERENCES

1. I. R. Young, I. J. Cox, G. A. Coutts, and G. M. Bydder, *NMR Biomed.*, 1989, **2** (5/6), 329.
2. I. R. Young, A. S. Hall, A. G. Collins, J. M. Pennock, D. H. Spencer, and G. M. Bydder, *Proc. Soc. Photo-Opt. Instrum. Eng.*, 1982, **347**, 254.
3. G. L. Nayler, D. N. Firmin, and D. B. Longmore, *J. Comput. Assist. Tomogr.*, 1986, **10(5)**, 715.
4. P. M. Pattany, J. J. Philips, L. C. Chiu, J. D. Lipcamon, J. L. Duerk, J. M. McNally, and S. N. Mohapatra, *J. Comput. Assist. Tomogr.*, 1987, **11(3)**, 369.
5. I. R. Young, D. J. Bryant, and J. A. Payne, *Magn. Reson. Med.*, 1985, **2**, 355.
6. R. R. Ernst and W. A. Anderson, *Rev. Sci. Instrum.*, 1966, **37**, 93.
7. D. S. Hickey, D. Checkley, R. M. Aspden, A. Naughton, J. P. R. Jenkins, and I. Isherwood, *Br. J. Radiol.*, 1986, **59**, 565.
8. I. R. Young, G. M. Bydder, and D. J. Bryant, *Magn. Reson. Med.*, 1989, **11(1)**, 127.
9. R. J. Ordidge, A. Connelly, and J. A. B. Lohman,. *J. Magn. Reson.*, 1986, **66(2)**, 283.
10. W. T. Dixon, H. Engels, M. Castillo, and M. Sardashti, *Magn. Reson. Imaging*, 1990, **8** (4), 417.
11. S. Försen and R. A. Hoffman, *J. Chem. Phys.*, 1963, **39(11)**, 2892.
12. S. D. Wolff and R. S. Balaban, *Magn. Reson. Med.*, 1989, **10(1)**, 135.
13. E. L. Hahn, *Phys. Rev.*, 1950, **80(4)**, 580.
14. R. T. Constable, A. W. Anderson, J. Zhong, and J. C. Gore, *Magn. Reson. Imaging*, 1992, **10(4)**, 497.
15. J. Hennig, A. Nauerth, and H. Friedburg, *Magn. Reson. Med.*, 1986, **3(6)**, 823.
16. E. O. Stejskal and J. E. Tanner, *J. Chem. Phys.*, 1965, **42**, 288.
17. M. E. Moseley, J. Kucharczyk, H. S. Asgari, and D. Norman, *Magn. Reson. Med.*, 1991, **19(2)**, 321.
18. J. V. Hajnal, M. Doran, A. S. Hall, A. G. Collins, A. Oatridge, J. M. Pennock, I. R. Young, and G. M. Bydder, *J. Comput. Assist. Tomogr.*, 1991, **15(1)**, 1.
19. F. A. Howe, A. G. Filler, B. A. Bell, and J. R. Griffiths, *Magn. Reson. Med.*, 1992, **28(2)**, 328.

Biographical Sketch

Ian R. Young. *b* 1932. B.Sc., 1954, Ph.D., Aberdeen, 1958. No involvement with NMR until joining EMI in 1976, where charged with leading the engineering group developing first a resistive, then a cryogenic machine, installed at Hammersmith Hospital in 1980–1. Approx. 150 papers and 30 patents in whole body NMR and related aspects. Research interests: obtaining better images and spectra in vivo.

Spatial Encoding Using Multiple rf Coils: SMASH Imaging and Parallel MRI

Daniel K. Sodickson

Beth Israel Deaconess Medical Center and Harvard Medical School, Boston, MA, USA

1 INTRODUCTION

The speed of MR image acquisition has increased dramatically since the 1980s through a combination of technological and methodological advances. Nevertheless, many clinical applications of MRI continue to require motion compensation in some form. In body regions containing moving structures such as the heart or diaphragm, serious artifacts can arise if scan times exceed the characteristic time scales of physiologic motion. Accurate tracking of dynamic processes, such as cardiac contraction or the arrival and uptake of intravenous contrast agents, may require high temporal resolutions without undue sacrifices in spatial resolution. Meanwhile, the fastest imaging sequences and the most state-of-the-art scanners are approaching certain basic limits of imaging speed. These limits, which have both a technological and a physiological component, are related to the maximum switching rates of magnetic field gradients and rf pulses. Most of the fast imaging sequences now in use – echo planar imaging (EPI), fast low angle shot (FLASH), turbo spin echo (TSE), spiral, or BURST, for example – achieve their high speeds by optimizing the strengths, the switching rates, and the patterns of applied gradients and pulses. Beyond a certain threshold, however, rapidly switched field gradients are known to produce neuromuscular stimulation, while excessively dense rf pulse trains can lead to unacceptable levels of rf energy deposition and heating of tissue. One common feature of fast imaging sequences is that they all acquire data in a sequential fashion. Regardless of the particular sequence the acquisition follows, the MR signal is always acquired one point and one line at a time, with each separate line of data requiring a separate application of field gradients and/or rf pulses. Therefore, imaging speed is generally limited by the maximum switching rates compatible with scanner technology and patient safety.

Recently, a new paradigm of parallel MRI has been used to increase imaging speeds beyond the basic limits just described. The term 'parallel MRI' may be used to describe any MRI strategy in which multiple MR signal data points are acquired *simultaneously*, rather than one after the other. Parallel imaging strategies in general require the use of multiple distinct detectors, with each detector providing some component of distinct spatial information to the image. (A many-detector CCD camera is a familiar optical example of a parallel imaging device while a FAX machine is an example of a sequential line-scanning device.) For MRI in particular, some of the burden of spatial encoding traditionally accomplished by field gradients may be shifted instead to arrays of rf coils. Recent work has shown that coil arrays may be used, in combination with appropriate image reconstruction strategies, to encode and detect multiple MR signal or image components simultaneously and thereby to multiply the speed of existing imaging sequences *without* increasing gradient switching rate or rf power deposition.

2 THE HISTORY OF PARALLEL MRI

Radiofrequency coil arrays were first developed for use in MRI in the late 1980s. Prior to that time, single volume or surface coils were typically used for signal detection, or else pairs of coils were arranged in quadrature to increase signal-to-noise ratio (SNR). Work by Roemer and co-workers demonstrated that arrays of suitably decoupled surface coils could be used to achieve further substantial SNR increases[1,2] (see ***Whole Body Machines: NMR Phased Array Coil Systems***). When used in combination with traditional gradient-encoding sequences, coil arrays increased the achievable SNR for any given field of view (FOV) in any given imaging time, but ultimate imaging speed was still governed by the imaging sequence and the gradient hardware.

The fact that spatial information from coil arrays might also be used directly for the encoding and decoding of images was realized in principle relatively early in the development of MR-compatible arrays. The simplest manifestation of the parallel imaging principle was the use of spatially separated coils to image distant and nonoverlapping body regions simultaneously. More challenging was the prospect of imaging a continuous FOV rapidly using detectors overlapping in space and/or sensitivity. An early theoretical proposal by Carlson suggested that the Fourier coefficients of signal voltages in multiple coils disposed around a cylinder could be used to calculate multiple *k*-space lines for magnetization within that cylinder.[3] Hutchinson and Raff suggested in 1988 that a large array of narrow loops surrounding an object could, in principle, be used to acquire an image without the use of any phase-encoding gradients at all.[4] Other proposals followed, and these proposals fall into two general categories: massively parallel and partially parallel strategies.

In massively parallel strategies, the number of detectors approaches the number of data points or lines. These techniques aim to replace gradient encoding entirely, with resulting dramatic improvements in imaging speed. The original massively parallel proposal of Hutchinson and Raff was intended to show theoretical feasibility, and no direct practical implementation was suggested.[4] A subsequent proposal for massively parallel imaging was made by Kwiat, Einav, and Navon in 1991.[5] Their study included a more detailed investigation of practical issues, though no images were presented. A preliminary array design based on the general principles of this proposal was presented in 1995.[6]

In partially parallel imaging strategies, the number of detectors is significantly smaller than the number of data points. Spatial encoding using multiple rf coils is used to supplement the spatial encoding normally accomplished using magnetic field gradients. Kelton, Magin, and Wright,[7] and later Ra and Rim[8,9] described a 'subencoding'[9] approach by which aliased

Table 1 Parallel MRI techniques

Technique	Sensitivity calibration	Image reconstruction
Partially parallel		
k-space techniques		
Carlson and Minemura (1993)[10]	Known volume coil sensitivities	*k*-space series expansion
SMASH[a] (1996)[11]	Surface coil sensitivity reference (phantom, in vivo, AUTO-SMASH)	*k*-space linear combination (spatial harmonics)
Image domain techniques		
Kelton, Magin, and Wright (1989)[7]	Pixel-by-pixel sensitivity reference	Pixel-by-pixel matrix inversion (subencoding)
Ra and Rim (1991, 1993)[8,9]	Pixel-by-pixel image reference	Pixel-by-pixel matrix inversion (subencoding)
SENSE[a] (1997)[12]	Pixel-by-pixel sensitivity extraction from full reference images	Pixel-by-pixel matrix inversion (subencoding)
Massively parallel		
Hutchinson and Raff (1988)[4]	Not discussed	Inverse source
Kwiat, Einav, and Navon (1991)[5]	Point source references	Inverse source

SMASH, simultaneous acquisition of spatial harmonics; SENSE, sensitivity encoding technique.
[a]In vivo results have been published for this technique.

component coil images acquired rapidly with reduced phase encoding may be 'unaliased' using information about component coil sensitivities. Carlson and Minemura proposed using nested volume coils with differing sensitivity patterns to approximate multiple *k*-space lines from a series expansion.[10] In 1997, SiMultaneous Acquisition of Spatial Harmonics (SMASH)[11] was introduced, and the first accelerated in vivo MR images using a parallel imaging strategy were obtained. The SMASH technique uses linear combinations of component coil signals from a surface coil array to replace time-consuming gradient steps directly. Following the introduction of SMASH, the subencoding principle was revisited and refined in the SENSitivity Encoding technique (SENSE) of Prüssmann, Weiger, and co-workers,[12] which has also been used recently to obtain accelerated in vivo images. At the present time, various other research groups both in academia and in industry have also begun to investigate parallel imaging strategies.

Table 1 lists the various proposed parallel MRI techniques, further categorized by coil sensitivity calibration and image reconstruction method. The principal message of this table is that there are numerous ways to extract spatial information from an array of rf detectors. We will now discuss some of these methods in greater detail, emphasizing approaches for which in vivo results have already been published, and which are likely to be well suited for clinical MRI. We will begin with the SMASH technique,[11] for which the broadest range of in vivo results have been achieved to date. We will then discuss the image-domain subencoding reconstruction techniques.

3 SMASH IMAGING

3.1 Theory

The SMASH technique exploits sensitivity variations in a surface coil array to substitute for spatial modulations normally produced by phase-encoding gradients.[11] This use of coil encoding in place of gradient encoding allows the whole of *k*-space to be traversed using a reduced number of phase-encoding gradient steps, thereby reducing image acquisition times.

The function of phase-encoding gradients is to impose sinusoidal modulations of magnetization across the image plane. The MR signal integrated against these sinusoids then corresponds to spatial Fourier components of the image, or the familiar *k*-space lines. Figure 1 illustrates schematically this well-known effect. In the figure, sinusoidal modulations of varying spatial frequency, resulting from spin evolution in phase-encoding gradients of varying strength, are shown next to their associated *k*-space lines. In the SMASH technique, some of these sinusoidal modulations, or 'spatial harmonics', are generated by manipulations of component coil sensitivities, rather than by gradient-induced modulations of magnetization.

An array of rf coils contains spatial information in the form of its component coil sensitivities (Figure 2). In a linear surface coil array with adjacent components, each coil j has a distinct but overlapping sensitivity $C_j(x, y)$. By forming appropriate linear combinations of component coil signals (Figure 3), we may generate composite sensitivity profiles C^{tot} which oscillate in

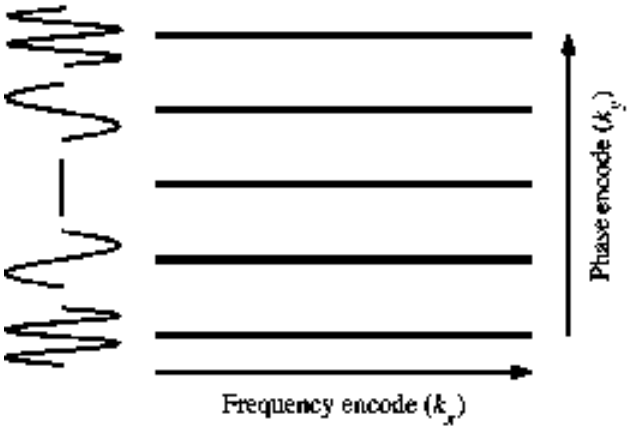

Figure 1 A *k*-space schematic, indicating the spatial modulations resulting from phase-encoding gradients. Gradient steps on either side of the central $k = 0$ line correspond to various harmonics of spin modulation across the image plane

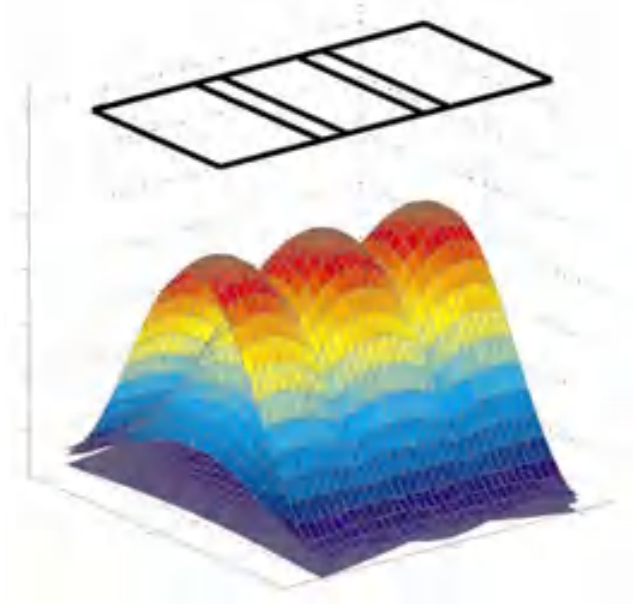

Figure 2 The rf sensitivities of a linear coil array. Each of the three overlapping sensitivity distributions corresponds to one of the three component coils in the array pictured at the top. (The conductor paths of adjacent component coils are also typically overlapped, as shown in this example, to minimize inductive coupling between coils.) Only sensitivity magnitudes are shown here. In practice, coil sensitivities may also have spatially varying phase distributions

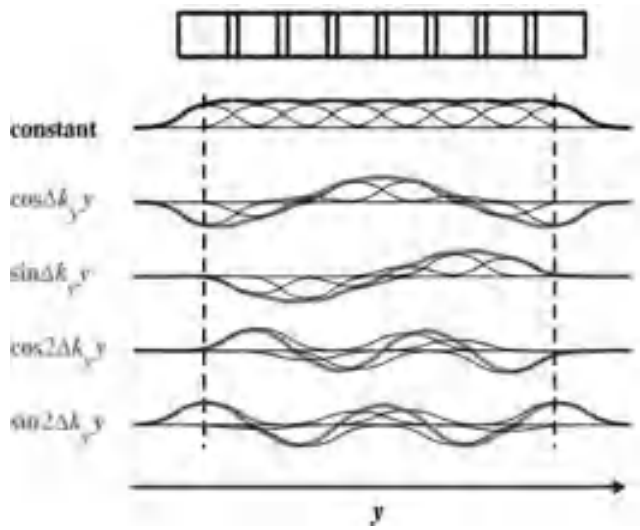

Figure 3 Multiple spatial harmonic profiles derived by linear combination of component coil sensitivities in an eight-element array

much the same way as the gradient-induced modulations of Figure 1:

$$C^{\text{tot}}(x,y) = \sum_j n_j C_j(x,y) \approx \exp(im\Delta k_y y) \qquad (1)$$

where n_j are complex weight factors, m is an integer, and $k_y = 2\pi/\text{FOV}$ is the minimum k-space interval corresponding to the desired FOV.

If a composite sensitivity profile generated in this way forms an accurate spatial harmonic pattern, the same k-space step is produced as would have resulted from a traditional gradient step.[11] In other words, each combined signal S^{tot}, generated from linear combinations of component coil signals S_j using the weights n_j from Equation (1), is shifted in k-space by an amount $(-m\Delta k_y)$:

$$S_j(k_x,k_y) = \int\int \mathrm{d}x\,\mathrm{d}y\, C_j(x,y)\rho(x,y)\exp\{-ik_x x - ik_y y\}$$

$$\begin{aligned} S^{\text{tot}}(k_x,k_y) &= \sum_j n_j S_j(k_x,k_y) \\ &= \int\int \mathrm{d}x\,\mathrm{d}y \sum_j n_j C_j(x,y)\rho(x,y)\exp\{-ik_x x - ik_y y\} \\ &= \int\int \mathrm{d}x\,\mathrm{d}y\, C^{\text{tot}}(x,y)\rho(x,y)\exp\{-ik_x x - ik_y y\} \\ &\approx \int\int \mathrm{d}x\,\mathrm{d}y\,\rho(x,y)\exp\{-ik_x x - i(k_y - m\Delta k_y)y\} \\ &\approx \tilde{\rho}(k_x, k_y - m\Delta k_y) \end{aligned} \qquad (2)$$

where $\rho(x, y)$ represents the spatial distribution of spin density in the image plane and $\tilde{\rho}$ is its spatial Fourier transform. This k-space shift is precisely the same shift as would be produced by evolution of spins with gyromagnetic ratio γ for time t_y in a y gradient of magnitude G_y, with $\gamma G_y t_y = -m\Delta k_y$.

Such a coil-encoded k-space step combines naturally with any gradient-encoded k-space steps. When a coil array with multiple elements is used, multiple harmonics may be generated from a single data set (Figure 3). The result is that a reduced number of phase-encoded lines (thick lines in Figure 4) may be acquired in a reduced acquisition time, and the remaining lines of k-space (thin lines in Figure 4) may be reconstructed using linear combinations of component coil signals. If a total of M spatial harmonics are generated, then M lines of k-space may be reconstructed for each application of a phase-encoding gradient. The full signal matrix may, therefore, be generated in a fraction $1/M$ of the usual acquisition time.

3.2 Implementation

An important first step in a practical SMASH implementation is to measure the rf sensitivities of the various array elements. These sensitivities may be extracted in a straightforward manner from images of homogeneous phantoms, since any intensity variations in such images may be traced to variations in coil sensitivity. Typically, intensity profiles across an image plane of interest are extracted from a stored phantom data set and are used as sensitivity references. (Often, intensity profiles along a single central line of the image plane suffice for calibration.) For cases in which phantom sensitivity reference measurements are cumbersome or inaccurate (for example when flexible coil arrays are used, the particular conformations of which for any given patient are not known a priori), sensitivity profiles may also be obtained in vivo by examining component coil images in regions of comparatively uniform spin density such as the spine. Alternative in vivo sensitivity calibration procedures, such as the self-calibrating approach

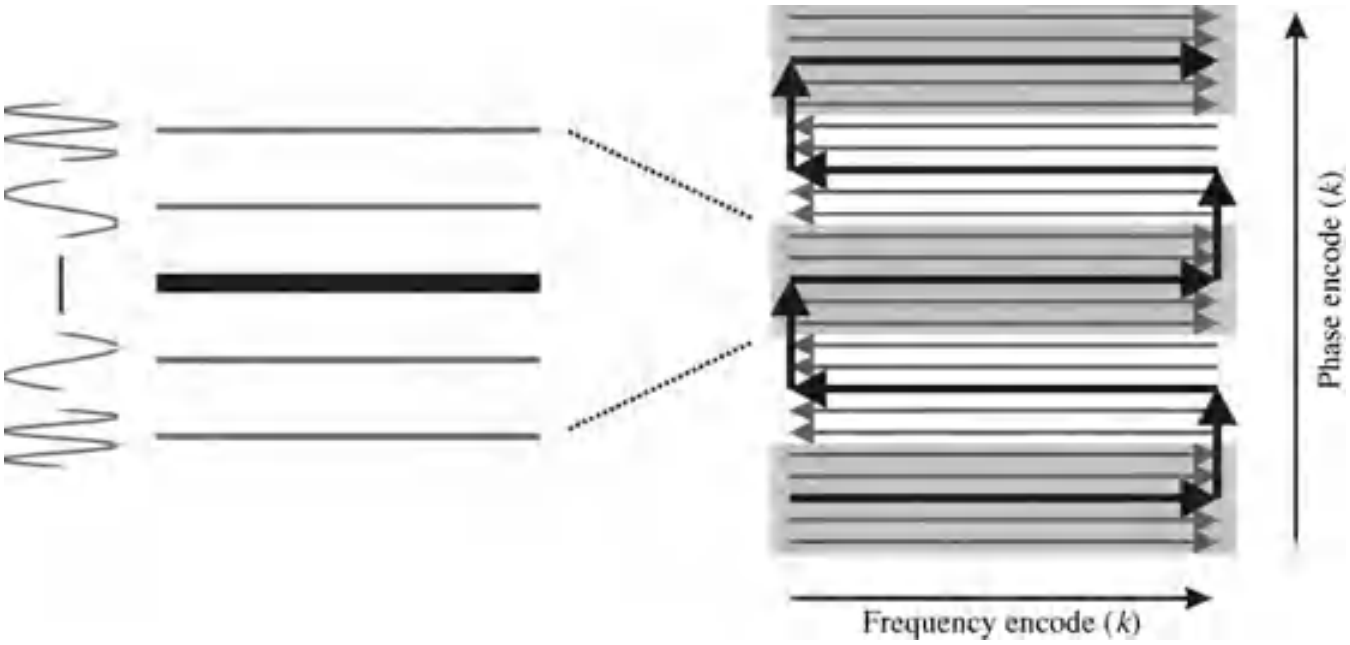

Figure 4 Schematic *k*-space trajectory for a partially parallel acquisition using five spatial harmonics. Thick lines represent *k*-space lines corresponding to applied phase-encoding gradient steps, while thin lines represent additional *k*-space lines reconstructed using the linear combinations shown in Figure 3. The additional reconstructed lines substitute for omitted phase-encoding gradient steps

called AUTO-SMASH,[13] may be used for imaging in regions of heterogeneous spin density such as the thorax, where large differences in signal between the heart and lungs preclude straightforward estimation of rf sensitivity. In AUTO-SMASH, a small number of reference *k*-space lines are added to the acquisition, and the relation between these reference lines and the usual MR signal data lines are used to 'train' SMASH reconstructions directly in *k*-space.

Following sensitivity calibration, the sensitivity profiles are fitted to the desired spatial harmonic functions, using a numerical optimization algorithm with the complex weight factors n_j as fitting parameters. For favorable array geometries, the resulting fits can, in practice, be quite as good as the schematic fits shown in Figure 3.

The remaining steps in the SMASH reconstruction procedure are summarized in Figure 5. The left-hand side of Figure 5 shows a *k*-space schematic, and the right-hand side shows image data from a water phantom at each of the corresponding stages of reconstruction. With the necessary weights in hand, MR signal data are acquired simultaneously in the coils of the array. A fraction $1/M$ of the usual number of phase-encoding steps are applied, with M times the usual spacing in *k*-space (Figure 5A, left). The component coil signals acquired in this way correspond to images with a fraction $1/M$ of the desired FOV (Figure 5A, right). With $1/M$ times fewer phase-encoding steps, only a fraction $1/M$ of the time usually required for this FOV is spent on data collection.

Next, the appropriate M linear combinations of the component coil signals are formed to produce M shifted composite signal data sets (Figure 5B). The composite signals are then interleaved to yield the full *k*-space matrix (Figure 5C, left), which is Fourier transformed to give the reconstructed image (Figure 5C, right).

The schematic summary in Figure 5 shows a SMASH reconstruction with acceleration factor $M = 2$ using a 3-element rf coil array. Substantially larger factors are possible, however, when coil arrays with larger numbers of elements are used. In fact, for favorable image plane and coil array geometries, the maximum achievable SMASH acceleration factor M is equal to the number of independent component coils in the array, since a maximum of M distinct harmonics may be generated using a total of M independent coils. Since generation of spatial harmonics does not depend upon how the gradient-encoded *k*-space lines were generated, the SMASH reconstruction is to a large extent sequence independent. Nearly all existing rapid imaging sequences may be accelerated in this manner, and, to date, SMASH has been successfully tested with a wide range of sequence types. Both two-dimensional and three-dimensional acquisitions are amenable to acceleration using SMASH, provided distinct coil sensitivity information is available along one or more phase-encoding directions.

3.3 In Vivo Results

The improvements in imaging efficiency afforded by a parallel imaging strategy may be put to use in a number of ways. The following examples demonstrate some of the applications for which SMASH imaging has been used to increase imaging speed and improve image quality.

Reductions in breath-hold duration for scans requiring breath-holding can be achieved, which increases patient comfort and compliance and allows scans free of respiratory motion artifact in patients incapable of prolonged breath-holds. Figure 6 demonstrates a twofold reduction in breath-hold duration for abdominal MR imaging.

Improvements in spatial resolution can be achieved in any given imaging time: images of increased spatial resolution may

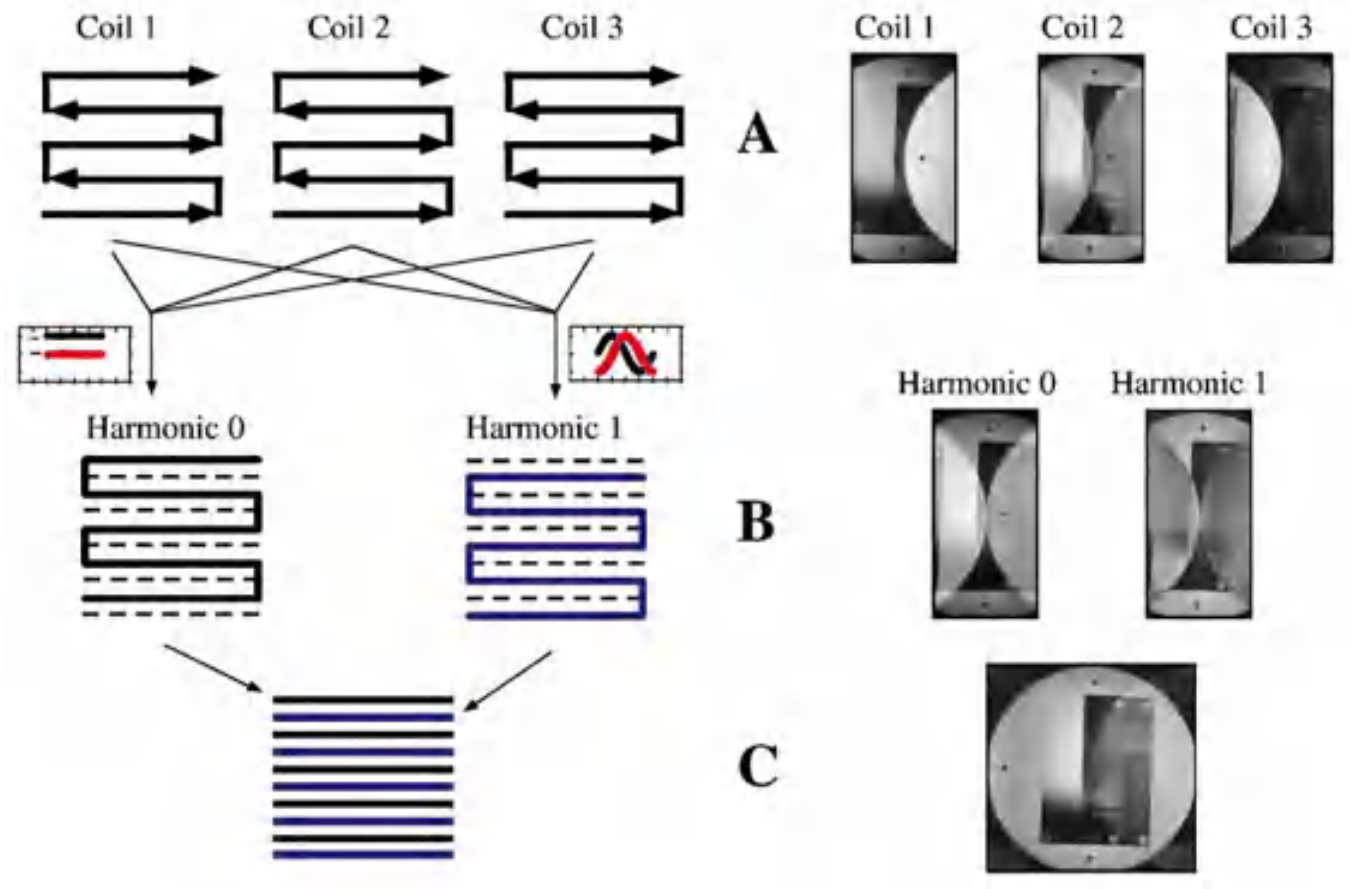

Figure 5 Schematic representation of the SMASH reconstruction procedure (left: *k*-space cartoon, right: corresponding phantom images). (A) Acquisition of data with reduced phase encoding. (B) Formation of shifted data sets using spatial harmonic combinations. (C) Interleaving of shifted data sets to generate a full signal matrix, corresponding to an image with full FOV

be generated in a given acquisition time by carrying the faster SMASH acquisition farther out in *k*-space. Figure 7 shows the use of SMASH for spatial resolution enhancement in a cardiac scan. Additional resolution benefits can result from the use of SMASH or other partially parallel techniques in single-shot imaging sequences such as HASTE (half-Fourier single-shot turbo spin echo), EPI, or BURST.[14] Indeed, single-shot images with both reduced acquisition time *and* increased spatial resolution compared with the corresponding reference images have been obtained. This is possible because a reduced aquisition time also entails reduced relaxation, and hence reduced attenuation of high spatial frequencies in single-shot sequences.[14]

Improvements in temporal resolution (i.e., reductions in image-acquisition interval for gated or ungated scans) minimize undesired effects of physiologic motion while allowing accurate tracking of time-dependent phenomena. Figure 8 illustrates a twofold and a fourfold reduction in acquisition window at fixed spatial resolution in cardiac MR images. These progressive increases in temporal resolution result in progressively reduced motional blurring of the right coronary artery and other cardiac structures in the SMASH images. SMASH has also been used to increase true frame rate in real-time cardiac MR scans up to and beyond current two-dimensional echocardiographic frame rates.

Reductions in the overall duration of long MR scans increase patient comfort and compliance and also increase the throughput of clinical MR scanners and the cost-effectiveness of MR diagnosis. Noncontrast MR coronary angiograms obtained using SMASH are shown in Figure 9. Reduction in overall acquisition time in these navigator-gated scans has the further advantage of reducing long-term diaphragmatic drift over the course of the scans.

4 IMAGE-DOMAIN SUBENCODING TECHNIQUES

4.1 Theory

A subencoding image reconstruction begins at the same starting point as a SMASH reconstruction – namely, with a set of component coil signals acquired using a reduced number of phase-encoding gradient steps. Fourier transformation of these signal sets results in aliased component coil images like those shown in Figure 5A. From that point on, the subencoding reconstruction operates entirely in the image domain.

The basis of the technique lies in the fact that each pixel in an aliased image is in fact a superposition of multiple pixels

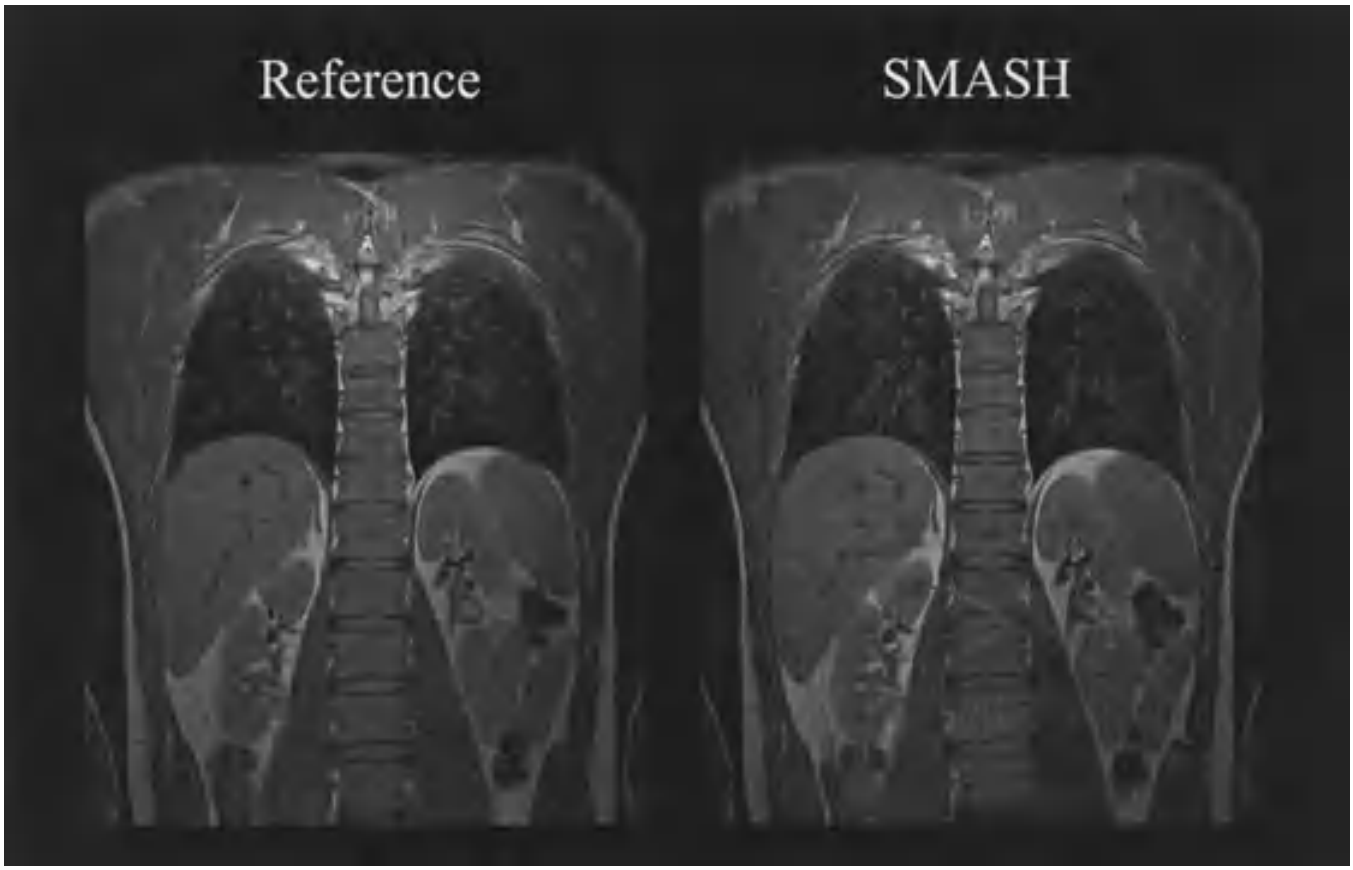

Figure 6 Turbo spin echo (TSE) images taken along the thoracic and lumbar spine of a healthy adult volunteer, demonstrating the use of SMASH imaging for reduction of breath-hold times in vivo (*TR* 700 ms, *TE* 32 ms, 9 echoes per excitation, in-plane spatial resolution 1.9 mm×1.0 mm). These images were obtained using four active elements of a six-element circularly polarized spine array on a 1.5 T Siemens Vision imaging system. The reference image was obtained in a breath-hold lasting 22 s and reconstructed using a standard sum of squares combination of component coil images.[1] The SMASH image with the same final spatial resolution and FOV was obtained in only 11 s

from a corresponding full unaliased image (Figure 10). In other words, as a result of Nyquist aliasing, an *M*-times aliased image I^{fold} is related to the full image I^{full} as follows:

$$I^{\text{fold}}(x,y) = I^{\text{full}}(x,y) + I^{\text{full}}(x,y+\Delta y) + I^{\text{full}}(x,y+2\Delta y) + \cdots = \sum_{m=0}^{M-1} I^{\text{full}}(x,y+m\Delta y) \tag{3}$$

When I^{fold} is acquired using a single coil, this superposition cannot be 'unfolded' without a priori knowledge of the full image.

The situation changes when an array of coils is used. The full image I_j^{full} in each coil j is actually made up of two pieces: the spin density ρ, and the coil sensitivity function C_j:

$$I_j^{\text{full}}(x,y) = C_j(x,y)\rho(x,y) \tag{4}$$

and in an array, each component coil j has a different sensitivity C_j. Therefore, we now have multiple 'views' of the aliasing that can be used to deduce just how much of each aliased pixel belongs at any position in the full image. Substituting Equation (4) into Equation (3) gives

$$I_j^{\text{fold}}(x,y) = \sum_{m=0}^{M-1} I_j^{\text{full}}(x,y+m\Delta y) = \sum_{m=0}^{M-1} C_j(x,y+m\Delta y)\rho(x,y+m\Delta y) \tag{5}$$

For any particular aliased pixel (x,y), this may be written as follows:

$$I_j^{\text{fold}} = \sum_{m=0}^{M-1} I_{jm}^{\text{full}} = \sum_{m=0}^{M-1} C_{jm}\rho_m \tag{6}$$

where $I_{jm}^{\text{full}} \equiv I_j^{\text{full}}\ (x,y+m\Delta y)$, $C_{jm} \equiv C_j(x,y+m\Delta y)$, and $\rho_m \equiv \rho\ (x,y+m\Delta y)$.

Let us study the particular example (illustrated in Figure 11) in which a four-coil array is used with a factor of three aliasing. We may write

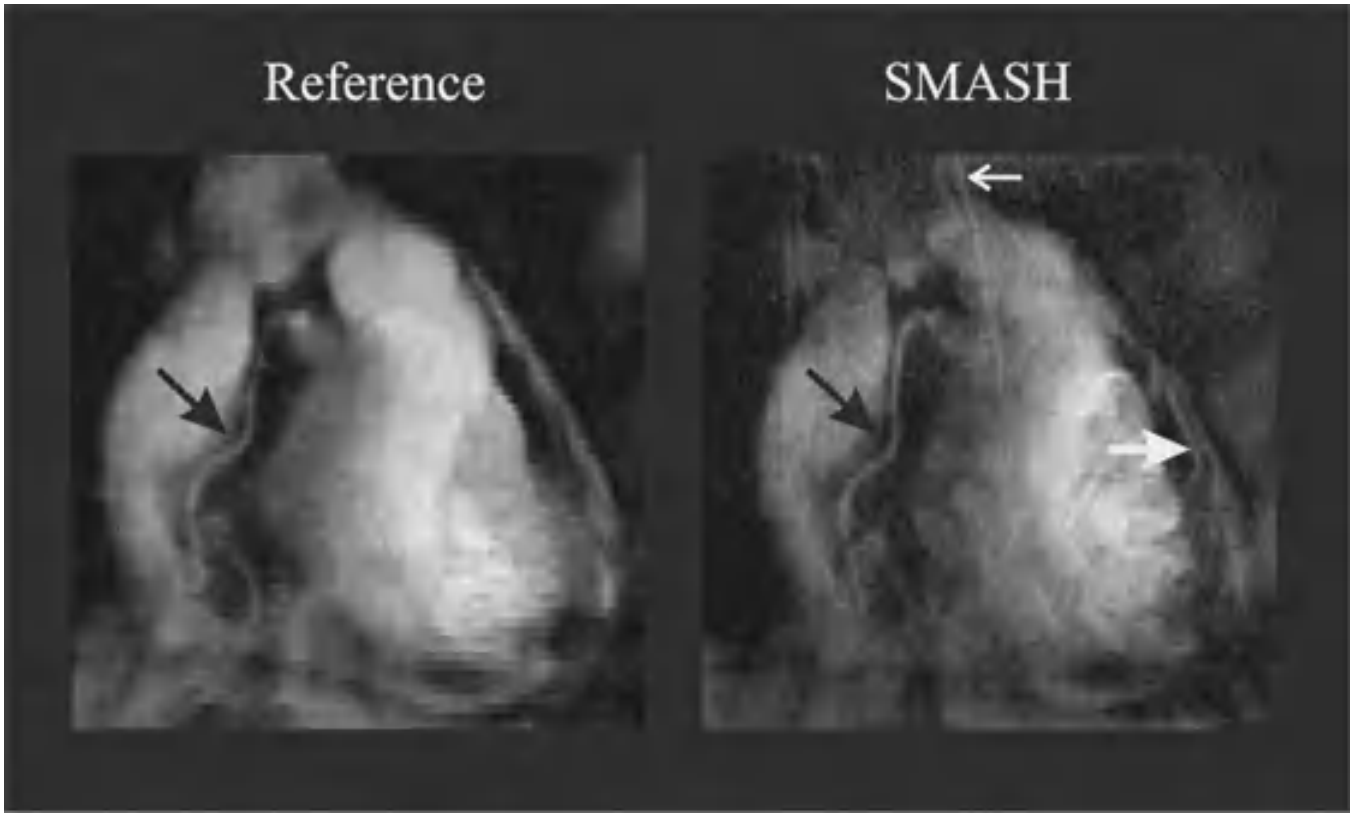

Figure 7 Coronal cardiac images showing the use of SMASH for increased spatial resolution (2D segmented-*k*-space FLASH, 9 echoes per segment, *TR* 14.4 ms, *TE* 7.3 ms, custom-designed four-element array, Siemens Vision scanner). The reference image has a matrix size of 144×256, corresponding to an in-plane resolution of 2.2 mm×1.2 mm. The SMASH image has double the spatial resolution in both dimensions (288×512 matrix size, in-plane resolution 1.1 mm×0.6 mm). Both images were obtained in a breath-hold lasting 16 cardiac cycles. A long segment of the right coronary artery (thick black arrows) may be seen in both images but is notably sharper in the higher-resolution SMASH image. Branches of the left coronary system (thick white arrow) may also be discerned in the SMASH image, whereas they are not seen in the reference image. Finally, internal mammary arteries (thin white arrow), invisible in the reference image, may just be discerned running down the center of the SMASH image

$$\begin{aligned} I_1^{\text{fold}} &= C_{11}\rho_1 + C_{12}\rho_2 + C_{13}\rho_3 \\ I_2^{\text{fold}} &= C_{21}\rho_1 + C_{22}\rho_2 + C_{23}\rho_3 \\ I_3^{\text{fold}} &= C_{31}\rho_1 + C_{32}\rho_2 + C_{33}\rho_3 \\ I_4^{\text{fold}} &= C_{41}\rho_1 + C_{42}\rho_2 + C_{43}\rho_3 \end{aligned} \tag{7}$$

This equation may be rewritten in matrix form as

$$\begin{bmatrix} I_1^{\text{fold}} \\ I_2^{\text{fold}} \\ I_3^{\text{fold}} \\ I_4^{\text{fold}} \end{bmatrix} = \begin{bmatrix} C_{11} & C_{12} & C_{13} \\ C_{21} & C_{22} & C_{23} \\ C_{31} & C_{32} & C_{33} \\ C_{41} & C_{42} & C_{43} \end{bmatrix} \cdot \begin{bmatrix} \rho_1 \\ \rho_2 \\ \rho_3 \end{bmatrix} \tag{8}$$

or, in other words,

$$\mathbf{I}^{\text{fold}} = \mathbf{C}\rho \tag{9}$$

As long as the number of coils N_c is greater than or equal to the aliasing factor M (as in our exemplary case for which $N_c = 4$, $M = 3$), Equation (9) may be inverted:

$$\rho = \mathbf{C}^{-1}\mathbf{I}^{\text{fold}} \tag{10}$$

and the unaliased spin density over the full FOV may be determined. This 'unaliasing' approach bears some kinship with the principle of computed tomography, in the sense that multiple different 'views' or projections are used to extract full two-dimensional image information.

4.2 Implementation

Subencoding implementations differ from SMASH implementations primarily in their approaches to sensitivity calibration and in the nature and numerical stability of their image reconstruction algorithms. Sensitivity estimates at each pixel of the full FOV are generally required to perform the pixel-by-pixel subencoding matrix inversion of Equation (10). Ra and Rim describe the use of an in vivo sensitivity reference in the form of full-FOV component-coil images of the target image plane, manipulated in the reconstruction in such a way that the spin density divides out.[9] The SENSE technique incorporates a different in vivo sensitivity calibration method in which full-FOV component coil images are divided by an additional full-FOV body coil image, and the quotient images are then subjected to several stages of interpolation, filtering, and thresholding.[12] Phantom sensitivity references can also, in principle, be used for subencoding reconstructions.

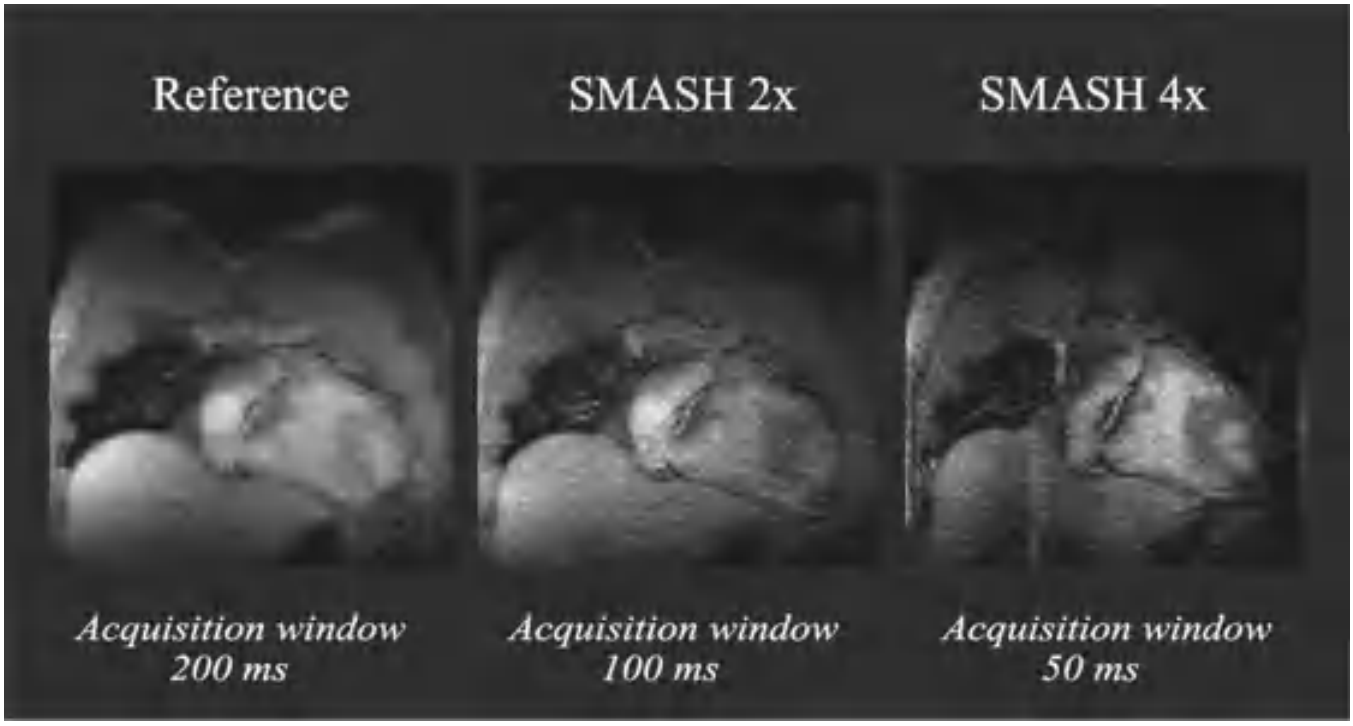

Figure 8 Coronal cardiac images from a 3D data set demonstrating the use of SMASH to increase temporal resolution at fixed spatial resolution (3D turbo field echo, *TR* 8.8 ms, *TE* 2.4 ms, in-plane spatial resolution 1.5 mm×1.5 mm, with fat suppression, T_2 preparation, electrocardiogram triggering, and navigator gating/correction using a 6-element linear coil array on a 1.5 T Philips NT scanner). The reference image (sum of squares reconstruction) has an acquisition window of 200 ms per cardiac cycle. The twofold- and fourfold-accelerated SMASH images show progressively reduced motional blurring and improved visualization of the right coronary artery running near the midline of the images

Whereas the quality of SMASH reconstructions is governed by the 'goodness' of spatial harmonic fits, the principal algorithmic concern of subencoding reconstructions is the numerical stability of the inverse $\mathbf{C}^{-1}$. For $N_c > M$, the inverse may be implemented, for example, as a Moore–Penrose pseudoinverse, resulting in a least squares solution to the overdetermined problem for each pixel. For $N_c = \mathrm{M}$, a standard matrix inverse may be used. The use of a pixel-by-pixel inversion affords the advantage of fine regional control over the reconstruction: it does not, for example, require a global spatial harmonic fit. A disadvantage of the pixel-by-pixel approach, however, is that in regions of low actual or apparent coil sensitivity, the matrix $\mathbf{C}$ may be poorly conditioned, and error propagation through the inverse may amplify the effects both of noise and of sensitivity miscalibrations.

4.3 In Vivo Results

Image-domain subencoding techniques can be used for many of the same applications as were demonstrated with SMASH in Section 3.3. The resulting images will resemble accelerated SMASH images, with some particular differences in image artifacts and noise distribution resulting from the different approaches to sensitivity calibration and image reconstruction. In vivo SENSE images in the brain and the heart with two- to threefold accelerations have been presented.[12,15] An in vivo sensitivity calibration method similar to that suggested by Ra and Rim has also been used by the SMASH group to obtain accelerated subencoding images for direct comparison with SMASH reconstructions of the same data sets. Figures 12 and 13 compare reference, SMASH, and subencoding images from contrast-enhanced angiography and real-time cardiac MR imaging studies.

5 A RECIPE FOR PRACTICAL PARALLEL IMAGING

The following is a list of essential elements needed for effective implementations of partially parallel imaging strategies such as SMASH or subencoding.

1. *rf coil array*. Arrays should be designed with overall dimensions appropriate to the desired FOV for imaging applications of interest. Inductive decoupling of array elements is helpful for improved SNR and for increased spatial selectivity of the sensitivity profiles, although some degree of coupling between array elements can generally be tolerated. The imaging system must be equipped with a sufficient number of receiver channels to allow simultaneous data acquisition in the various component coils of the array. Alternative data-reception schemes such as time-domain multiplexing may also be used.[16,17]

2. *Sensitivity calibration*. Accurate coil sensitivity calibration is crucial for all parallel imaging techniques. A great deal of effort has been devoted over the years to the understanding and calibration of gradient waveforms in MR scanners. Since parallel imaging strategies use rf coils in place of gradients for spatial encoding, it is not surprising that some

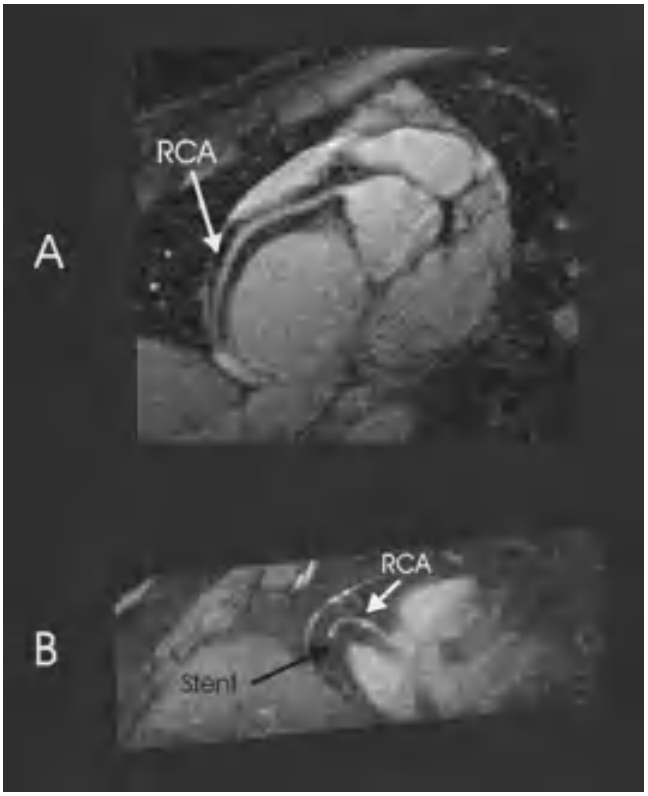

Figure 9 Noncontrast MR coronary angiograms obtained in reduced total scan time using SMASH (same basic sequence, coil array, and MR scanner as in Figure 8, with an acquisition window of 70 ms and an in-plane resolution of 0.7 mm×1.0 mm). Double oblique image planes were planned along the major axis of the right coronary artery (RCA). (A) A 7.5 cm length of the native RCA in a healthy adult volunteer is seen in this high-resolution image. The 3D data set from which this image was taken was obtained during free breathing in a total of 11 min using a SMASH acceleration factor of two. (B) The RCA is interrupted by a region of signal dropout from a coronary stent in this local maximum intensity projection of a twofold-accelerated 3D SMASH image set (11 min free-breathing acquisition) in a patient with coronary artery disease

degree of analogous effort must go into the calibration of coil sensitivities.

3. *Scan planning*. After a target image plane and FOV have been selected, all that is required on most MR scanners to plan a SMASH or subencoding scan is a simple FOV reduction in the phase-encode direction. The need to perform spatial encoding with the rf coil array places some limitations on the choice of image plane position and orientation. For example, phase encoding must be performed along a direction in which the sensitivities of different array elements are sufficiently distinct. Substantial angulations between the image plane and the coil array are often possible (see, for example, the double-oblique images in Figures 9 and 13), though some penalty in SNR may be incurred.

4. *Image reconstruction*. Signal and image processing requirements are modest, but some capabilities for variable component coil signal combinations are required, whether in the MR scanner itself or in offline processors with access to the raw MR signal data. Details of software and/or hardware implementations will depend upon which parallel reconstruction strategy is elected.

Occurring as they do on either side of the Fourier transform, the *k*-space and the image-domain reconstructions bear a theoretical kinship, but their practical specifications differ. The choice of reconstruction strategy may be influenced by a number of factors:

(a) *Ease of implementation*. SMASH uses a small number of weight factors (a minimum of one per component coil per spatial harmonic), and operates in *k*-space prior to Fourier transformation. Consequently, it is particularly amenable to in-line implementations in which the coil-encoded *k*-space data are generated as soon as each gradient-encoded data point is read out. By contrast, the large numbers of weight factors in subencoding (one per component coil per image pixel) provide finer pixel-by-pixel control at the expense of increased calibration and reconstruction time. In the future, compromises between these two extremes may be anticipated, using various extrapolation schemes.

(b) *Image artifacts*. In SMASH, residual aliasing artifacts result from errors in sensitivity calibration or spatial harmonic fitting.[11] In subencoding images, localized pixel-by-pixel artifacts are more commonly seen as a result of pixel-by-pixel errors in the coil sensitivity references. (These local artifacts may be accompanied by global aliasing artifacts when there are systematic errors in sensitivity calibration.) In some circumstances, however, both techniques can actually lead to artifact *reduction*. Not only can accelerated acquisitions reduce motion artifacts, but they have also been shown to reduce geometrical distortions in single-shot SMASH EPI images through reduced

Figure 10 Superposition of pixels (white squares) in an aliased image

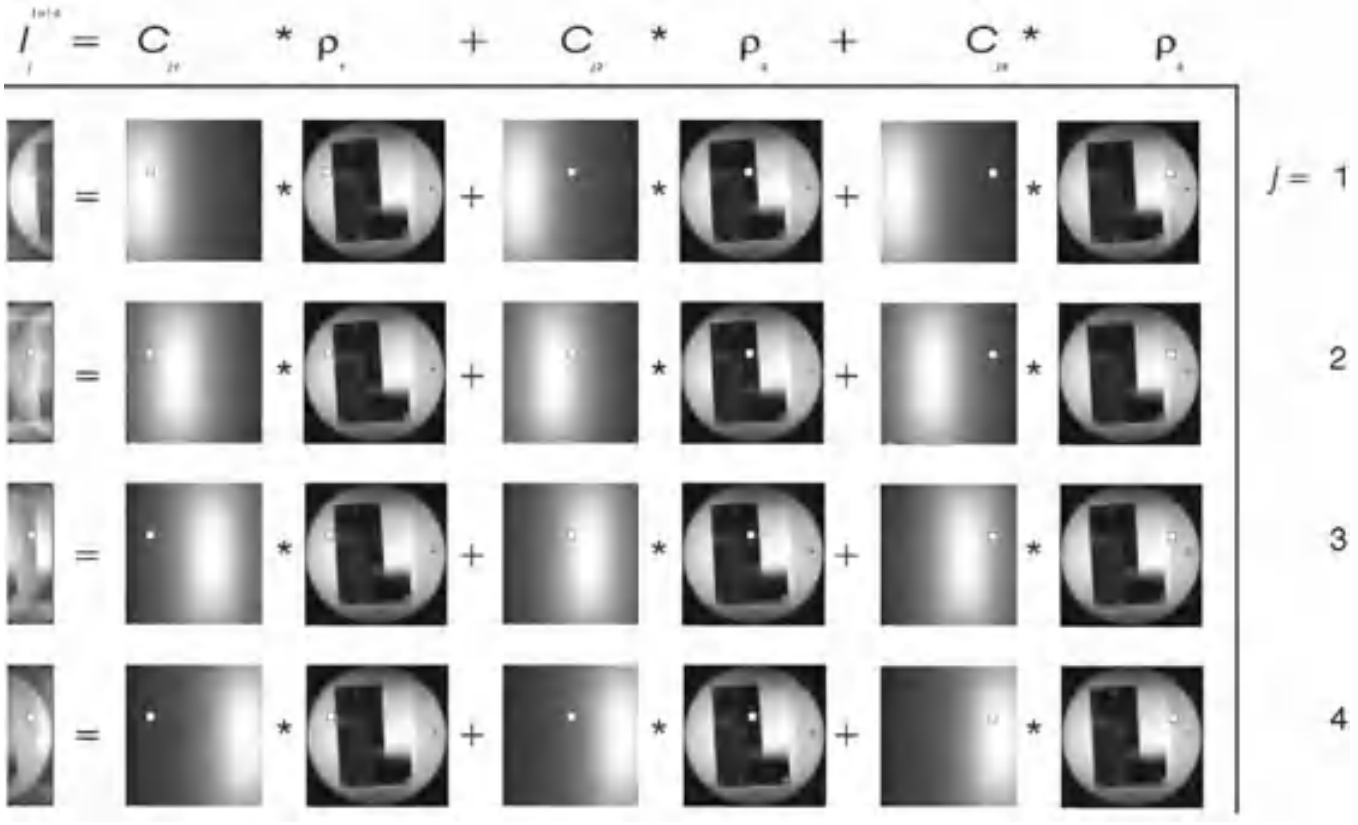

Figure 11 Superposition of pixels (white squares) in an aliased or subencoded image set from an array, corresponding to Equation (7). The inversion of this equation, and hence the unraveling of pixel-by-pixel superpositions, forms the basis of the image-domain subencoding techniques

accumulation of phase discrepancies in the shortened acquisition time.

(c) *SNR*. The SNR in a partially parallel image reconstruction is a balance between coil-specific, reconstruction-specific, and sequence-specific effects. Theoretical and experimental studies of SNR in SMASH imaging have been reported.[18] Generally speaking, both SMASH and subencoding techniques are bound by the well-known limit that SNR scales as the square root of the acquisition time for any given coil and sequence. With either class of technique, then, there is some expected loss of SNR compared with optimal combinations[1] of traditionally acquired full data sets in the same array, though parallel acquisitions may still show improved SNR when compared with sequential acquisitions using single surface coils spanning the same FOV. For certain imaging sequences, furthermore, some additional SNR beyond the square root limit may be recovered through reduced relaxation in the shortened acquisition times.

6 THE FUTURE OF PARALLEL MRI

Since the initial demonstration in 1997 of twofold-accelerated in vivo images using SMASH, new in vivo work has shown up to fourfold increases in acquisition speed, and as much as eightfold improvements have been achieved in phantoms using specialized rf hardware.[17] What future progress may be expected, and what are the key technical and methodological hurdles to further development?

Coil array design and rf sensitivity calibration top the list of developments that will be crucial for future improvements in parallel imaging, since array geometry and sensitivity characteristics determine the degree of spatial encoding which may be accomplished in any particular region of interest. The design of tailored arrays and the availability of increased numbers of receiver channels will greatly facilitate the optimization of image quality and SNR, and the maximization of achievable acceleration factors. In-line reconstruction hardware will be of benefit for real-time imaging applications. When the necessary weight factors are known in advance, the use of onboard analog signal combiners prior to digitization may even allow large 'smart' arrays to be interfaced to existing MR scanners with limited numbers of receivers. Methodological advances further in the future may also allow a return to the principle of massively parallel imaging. The potential gains of massively parallel imaging approaches are dramatic (they include the possibility of acquiring an entire image in a single echo, for example), but serious technological and theoretical hurdles remain to be overcome in areas such as electric decoupling of large arrays, massively parallel data reception, and SNR.

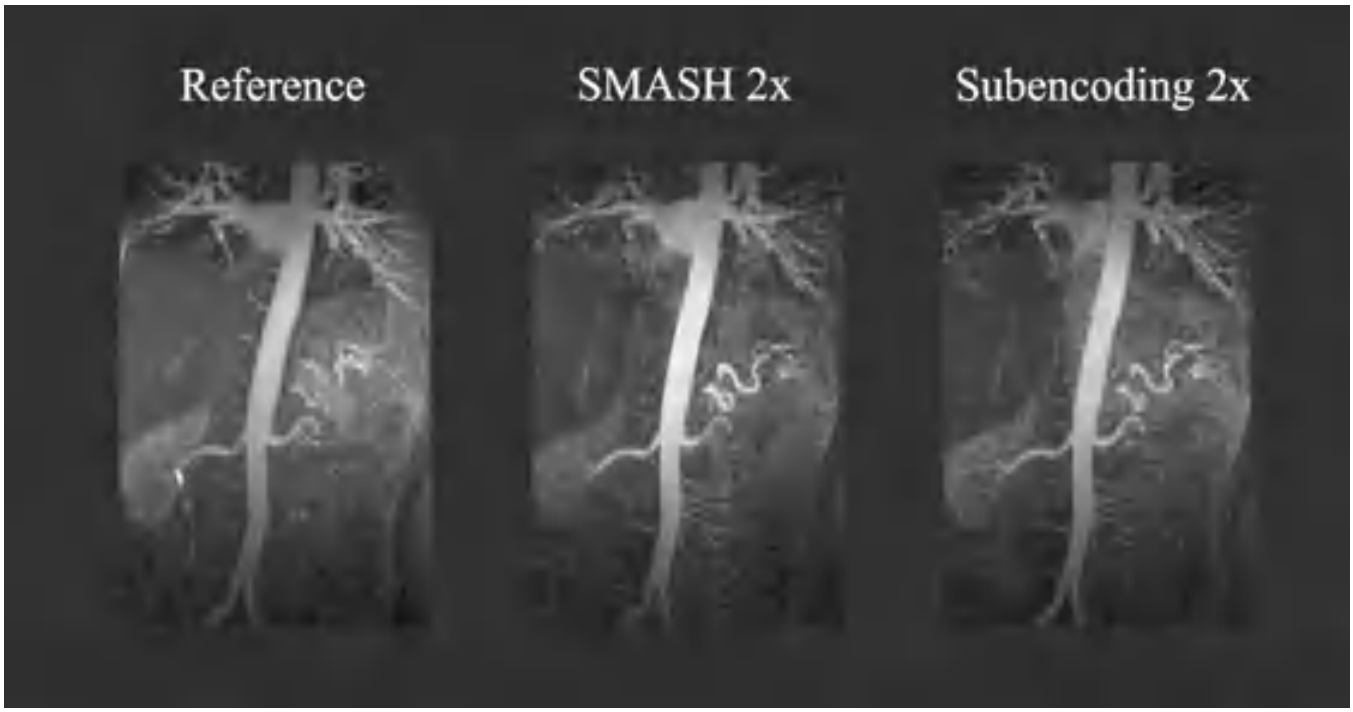

Figure 12 Maximum intensity projections of contrast-enhanced 3D MR angiograms of the abdominal aorta and renal arteries in a healthy adult volunteer (3D T_1-weighted rf-spoiled gradient-echo imaging sequence, *TE* 1.5 ms, *TR* 7.0 ms, in-plane spatial resolution 2.7 mm×1.4 mm, 6-element array, Philips NT scanner). The reference image set was obtained in a 23 s breath-hold following gadolinium injection, whereas the twofold accelerated data set used for SMASH and subencoding reconstruction was obtained in 11.5 s

In the meantime, clinical implementation of partially parallel imaging is possible now using existing arrays and receiver systems. Indeed, clinical studies in selected patient populations are now being initiated using parallel acquisition techniques. Particularly for applications with stringent requirements on imaging speed, parallel imaging can be a useful tool to enhance image quality, to improve imaging efficiency, and, in general, to overcome the acquisition speed limit in magnetic resonance imaging.

7 RELATED ARTICLES

Image Formation Methods; Radiofrequency Systems and Coils for MRI and MRS; Spin Warp Data Acquisition; Surface and Other Local Coils for In Vivo Studies; Whole Body Machines: NMR Phased Array Coil Systems.

8 REFERENCES

1. P. B. Roemer, W. A. Edelstein, C. E. Hayes, S. P. Souza, and O. M. Mueller, *Magn. Reson. Med.*, 1990, **16**, 192.
2. C. E. Hayes and P. B. Roemer, *Magn. Reson. Med.*, 1990, **16**, 181.
3. J. W. Carlson, *J. Magn. Reson.*, 1987, **74**, 376.
4. M. Hutchinson and U. Raff, *Magn. Reson. Med.*, 1988, **6**, 87.
5. D. Kwiat, S. Einav, and G. Navon, *Med. Phys.*, 1991, **18**, 251.
6. D. Kwiat and S. Einav, *Med. Eng. Phys.*, 1995, **17**, 257.
7. J. R. Kelton, R. L. Magin, and S. M. Wright, *Proc. VIIIth Annu. Mtg Soc. Magn. Reson. Med.*, Amsterdam, 1989, p. 1172.
8. J. B. Ra and C. Y. Rim, *Proc. Xth Annu. Mtg Soc. Magn. Reson. Med.*, San Francisco, 1991, p. 1240.
9. J. B. Ra and C. Y. Rim. *Magn. Reson. Med.*, 1993, **30**, 142.
10. J. W. Carlson and T. Minemura, *Magn. Reson. Med.*, 1993, **29**, 681.
11. D. K. Sodickson and W. J. Manning, *Magn. Reson. Med.*, 1997, **38**, 591.
12. K. P. Pruessmann, M. Weiger, M. B. Scheidegger, and P. Boesiger, *Proc. VIth Sci. Mtg (Int.) Soc. Magn. Reson. Med.*, Sydney, 1998, p. 579.
13. P. M. Jakob, M. A. Griswold, R. R. Edelman, and D. K. Sodickson, *MAGMA*, 1998, **7**, 42.
14. M. A. Griswold, P. M. Jakob, Q. Chen, J. W. Goldfarb, W. J. Manning, R. R. Edelman, and D. K. Sodickson, *Magn. Reson. Med.*, 1999, **41**, 1236.
15. M. Weiger, K. P. Pruessmann, M. B. Scheidegger, and P. Boesiger, *Proc. VIth Sci. Mtg (Int.) Soc. Magn. Reson. Med.*, Sydney, 1998, p. 803.
16. J. R. Porter, S. M. Wright, and N. Famili, *Magn. Reson. Med.*, 1994, **32**, 499.
17. D. K. Sodickson, J. A. Bankson, M. A. Griswold, and S. M. Wright, *Proc. VIth Sci. Mtg (Int.) Soc. Magn. Reson. Med.*, Sydney, 1998, p. 577.
18. D. K. Sodickson, M. A. Griswold, P. M. Jakob, R. R. Edelman, and W. J. Manning, *Magn. Reson. Med.*, 1999, **41**, 1009.

Biographical Sketch

Daniel K. Sodickson. *b* 1966. B.Sc. (Physics) and B.A. (Humanities), 1988, Yale college, Ph.D., 1994, Massachusetts Institute of Technol-

ogy, M.D., 1996, Harvard Medical School. Graduate work in solid-state NMR involved methodological developments for molecular structure determination and studies of the classical and quantum physics underlying spin diffusion in lattices. Appointed Research Associate, Beth Israel Deaconess Medical Center, Boston, MA, 1996. Appointed Instructor in Medicine, Harvard Medical School, 1997. Developed the SMASH imaging technique at Beth Israel Deaconess Medical Center in 1996. Approx. 10 papers and 1 patent in areas related to NMR. Primary research interests: parallel acquisition strategies in MRI, rapid MRI, cardiovascular MRI.

Spin Warp Data Acquisition

James M. S. Hutchison
University of Aberdeen, Aberdeen, UK

1 PRINCIPLES

1.1 Fourier Transform Methods

The Fourier transform (FT) group of imaging techniques derives from an idea presented by Kumar et al.[1] The fundamental idea is that the simple 1D projection is a Fourier transform of the *free induction signal* (FIS) as it evolves with time in the presence of a field gradient. If a second 'dimension' of time could be introduced in which the signal effectively evolved in the presence of another gradient at right angles to the first then a 2D Fourier transform of the signal, expressed as a function of ordinary time and 'pseudotime' (the second dimension), would produce a 2D image. In principle, one could extend the idea to many dimensions.

Now, higher dimensions of time do not exist, but a useful approximation can be obtained by appropriate subdivision of real time. For example, a TV video signal is a single valued function of real time alone, yet it can encode two spatial dimensions as well as time in the range of human activity. It does this by using a finite but adequate number of horizontal picture lines, and individual static image frames presented at a rate adequate to simulate movement. In FT imaging, the real-time evolution of the free induction signal in one field gradient is repeated many times, incrementing pseudotime between each repetition. With each repetition, a second field gradient is applied in such a way that its effect increases linearly with increasing pseudotime.

In the original method of Kumar et al.,[1] each new rf pulse and FIS sequence constitutes one increment of pseudotime. The second field gradient is applied immediately after the 90° pulse and immediately before the readout gradient, in which the signal evolves in real time. The second gradient has a constant amplitude, but its duration increases with each succesive pulse–FIS sequence, that is, with the progress of pseudotime. The main disadvantage of the method is that the time between the 90° pulse and the observed signal varies, and hence the effects of transverse (spin–spin) relaxation and main field inhomogeneity increase with pseudotime, degrading the final image.

1.2 Spin Warp Imaging

If the second field gradient is applied for a fixed duration, but the amplitude varies linearly with the progress of pseudotime, then the above disadvantages are overcome. This is the principle of the *spin warp method*,[2] developed at the University of Aberdeen. The sequence of rf and gradient pulses is shown in Figure 1. We shall use a generalized coordinate system with axes s, r and c, representing the directions of the slice-selection gradient G_s, the readout gradient G_r, and what is called the *phase encoding gradient*, G_c, respectively. G_c is then the gradient that varies with pseudotime. The selection gradient G_s, in combination with the shaped rf pulse, normally defines a slice in and close to the plane $s = 0$. In most imagers, the main field direction (z) is horizontal, along the head–foot axis of the patient, and y is vertical by convention. Thus, if we assign $x = r$, $z = s$, and $y = c$, a transaxial image will be produced. Sagittal or coronal images can be produced by interchanging the designations of the three gradients.

To understand why one may use a fixed duration, variable amplitude gradient, let us first consider the action of the ordinary readout gradient G_r on a spin packet (isochromat) at position (r, c). The magnetization vector $\boldsymbol{M}$, viewed in the rotating frame, will rotate about the main field axis (z) by an angle Φ, and hence shift the phase of the induced signal by the same Φ, where

$$\Phi = \gamma \int_{t_0}^{T} rG_r \, \mathrm{d}t = r\gamma \int G_r \, \mathrm{d}t \tag{1}$$

which reduces to $\Phi = \gamma r G_r (T - t_0)$ for a constant gradient. Here T is real time and γ is the gyromagnetic ratio.

The gradient G_c also produces a phase shift over interval 2 in Figure 1, given by

$$\Phi_2 = \gamma \int_{(2)} cG_c \, \mathrm{d}t = c\gamma \int_{(2)} G_c \, \mathrm{d}t \tag{2}$$

but the requirement of the FT method is that this phase shift be

$$\Phi_2 = \gamma c G_c' T' \tag{3}$$

where T' is pseudotime and G_c' is the effective gradient in pseudotime. Hence,

$$\int_{(2)} G_c \, \mathrm{d}t = G_c' T' \tag{4}$$

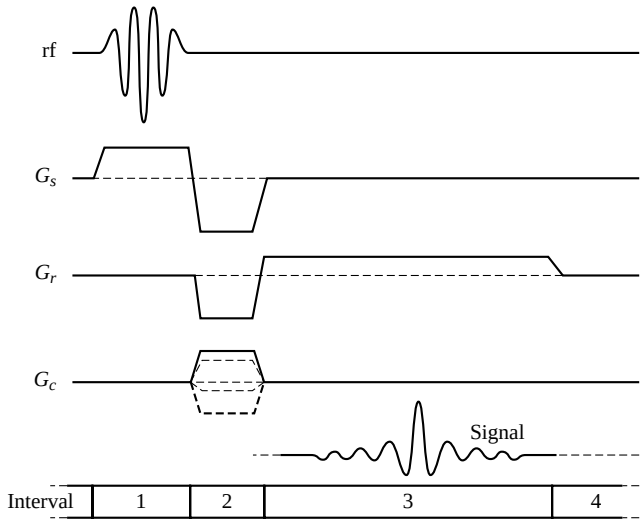

Figure 1 The spin warp imaging sequence

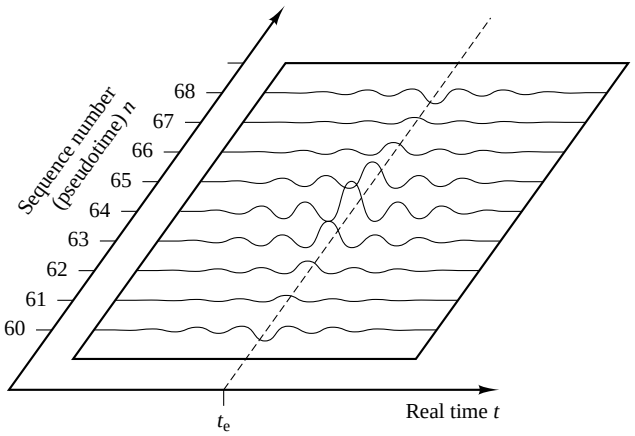

Figure 2 The pattern of free induction signals versus real time and pseudotime. t_e is the expected echo time

Since interval 2 is fixed, G_c must be proportional to T'. The shape of G_c is not critical; in practice, the rising and falling edges of the waveform may be slanted and rounded for ease of generation. It is also advantageous to employ both negative and positive G_c pulses, so that the range of T' is symmetrical about zero. In effect, this produces an 'echo' in pseudotime.

The individual amplitudes of the G_c pulses of duration t_0 then vary linearly with sequence number n according to the formula

$$\int_{(2)} G_c \, \mathrm{d}t = G_0[n - \tfrac{1}{2}(N+1)]t_0 \quad \text{for } n = 1, \ldots, N \tag{5}$$

where G_0 is a constant. Figure 2 illustrates the pattern of FIS obtained as n is stepped through consecutive values, and when presented two-dimensionally like this, it can be seen that n does in fact behave as a pseudotime variable. For example, if t is held constant and n varied, we obtain a kind of spin echo in pseudotime, equivalent to interchanging the roles of G_r and G_c. It is as if we were using a readout gradient G_0 in the c direction. In fact, the image formation procedure is simply to carry out a two-dimensional Fourier transform of the free induction signal S as a function of real time t and pseudotime n. The spin density image can be expressed as P, a function of the r and c coordinates:

$$P(r,c) = k' \left| \int\int S(t,n) \exp(-\mathrm{i}rt\gamma G_r) \exp(-\mathrm{i}cn\gamma G_0) \, \mathrm{d}t \, \mathrm{d}n \right| \tag{6}$$

where k' is a suitable multiplying constant.

Note the modulus symbol around the expression for P. If the main field $\boldsymbol{B}_0$ were completely homogeneous then the echo signal would be perfectly symmetrical about the echo time TE (ignoring T_2 decay), and its Fourier transform would have no imaginary components. In other words, all the frequencies present in the spin echo would have exactly the same phase, and we should get complete rephasing at the field echo time TE. In such an ideal case, there would be no need to include any modulus sign, since P would be real over the entire image plane. The phase of P contains information about the inhomogeneity of $\boldsymbol{B}_0$ and chemical shift of the nuclei, but it contributes nothing to the density image, and is best discarded by using only the amplitude (modulus) of P. In some types of image, such as inversion–recovery (IR), the sign of the NMR signal may be reversed in certain regions of the object, but the corresponding amplitude image will not show the reversal. This problem is discussed by Young et al.[3] and Park et al.[4]

1.3 Phase Encoding and Frequency Encoding

An alternative approach to the action of spin warp imaging is to consider the pulse of the third gradient, G_c, introduced during interval 2, as producing a phase twist or 'warp' into each column (the c direction) of spins prior to collecting the FIS. It may be regarded as producing a phase encoding of the spin density before projection onto the r axis. In effect, the G_c pulse maximizes the response to a particular spatial frequency in the c direction, namely, that of the warp. It is for this reason that the c direction is usually referred to as the *phase-encoding direction*. The readout direction (r) is also commonly known as the *frequency-encoding direction*, after the essential function of a field gradient, namely that of causing the Larmor precession frequency to become a linear function of distance. The phase-encoding gradient G_c could also be regarded as encoding for 'pseudofrequency', that is, frequency on the scale of pseudotime.

1.4 *k*-Space

Almost all imaging techniques in use today employ the Fourier transform method in one form or another. The essential features of a single slice Fourier imaging technique are

1. a slice selection and spin excitation;
2. a readout gradient, during which the NMR signal is collected;
3. a phase-encoding gradient, applied between the excitation and the readout periods.

This classification of the separate functions of the three orthogonal gradients is adequate for the simpler FT imaging schemes, and is helpful in understanding the principles behind FT imaging. However, it is unnecessarily restrictive, and may have delayed the invention of some of the more esoteric sequences that have appeared in recent years. In particular, the functions of readout and phase encoding can be mixed, and may involve all three gradients (x, y, and z). The most convenient way to study the evolution of the spin system after excitation is by invoking reciprocal space or $\boldsymbol{k}$-space as it is usually known.

$\boldsymbol{k}$-space is really the Fourier transform domain of ordinary space.[5] The relationship between the two is the same as that between (angular) frequency and time, which is probably a more familiar concept to many people. The $\boldsymbol{k}$ stands for the wavenumber, which is 2π times the number of wavelengths in unit distance. $\boldsymbol{k}$-space has three components, as one might expect, so the vector $\boldsymbol{k}$ represents a single point in $\boldsymbol{k}$-space, with components k_x, k_y, and k_z. In real space, it corresponds to a sine wave pattern of wavelength $\lambda = 2\pi/|\boldsymbol{k}|$, with the direction of the normal to the wavefronts being the direction of $\boldsymbol{k}$.

The action of the phase-encoding gradient pulse is such as to impose a 'twist' on a column of spins, so that their phases change linearly with distance along the c axis. In other words,

we have imposed a wave structure on the spins, with a characteristic wavelength λ, and hence a wavenumber k in the c direction. We have

$$\Phi(c) = \gamma c \int_0^T G_c \, \mathrm{d}t \tag{7}$$

so that

$$k_c = \gamma \int_0^T G_c \, \mathrm{d}t \tag{8}$$

Similar formulas are, of course, also true for the other two orthogonal components, so we can write a more general vector formula

$$\boldsymbol{k} = \gamma \int_0^T \boldsymbol{G} \, \mathrm{d}t \tag{9}$$

This formula represents the point in $\boldsymbol{k}$-space reached by the spin system at time T, assuming that the spins are all in phase at time $t = 0$. Generally speaking, it is unlikely that a given spin system will start out all in phase; if it has a particular phase distribution at time zero, this can be represented by a term $\boldsymbol{k}_0$ that may be added to the right-hand side of equation (9) as a constant of the integral.

By applying this formula to a field gradient sequence, we can trace out a path in $\boldsymbol{k}$-space. The important parts of the path or paths are where the NMR signal is being collected for processing into an image. In a straightforward FT imaging procedure, the whole track in $\boldsymbol{k}$-space should be a rectilinear scan, preferably with a square aspect ratio, since this implies equal spatial resolution along both axes.

The spin density distribution over the imaged region (the slice) can also be translated into a $\boldsymbol{k}$-space distribution. We can then regard the NMR image as being the result of sampling this distribution via the sequence's track in $\boldsymbol{k}$-space. Now the spin density distribution in real space is a real value (i.e., it has no imaginary part), so the true $\boldsymbol{k}$-space map would be symmetrical about the origin. This means that it is only necessary to sample one half of $\boldsymbol{k}$-space, since the other contains no extra information. In practice, this means that we could, say, collect only one side of our gradient or spin echo, while covering both negative and positive phase encoding. Alternatively, we might collect all the echo, but dispense with one half of the phase-encoding set. The latter is often used to cut down total collection time. However, unless the main field $\boldsymbol{B}_0$ is perfectly homogeneous, one must always cover slightly more than half of $\boldsymbol{k}$-space, and use sophisticated computer algorithms to correct the results (see ***Partial Fourier Acquisition in MRI***).

1.5 Transforming the Signal

So far, we have casually assumed that P is a continuous function of r and c, as implied by the integral representation. Obviously, n is not a continuous variable, but neither is t in practice. In order to process the signal digitally, S must be sampled M times at intervals of t_s, and our double integral becomes a double summation, which is just a two-dimensional discrete Fourier transform (DFT). Thus, P is only defined at discrete points (k, l) of an $M \times N$ array

$$P(p,q) = k' \left| \sum_{m=1}^{M} \sum_{n=1}^{N} S(m,n) \times \exp\left(-\frac{2\pi \mathrm{i} p m}{M}\right) \exp\left(-\frac{2\pi \mathrm{i} q n}{N}\right) \right| \tag{10}$$

Each of these points, or *pixels*, corresponds to an element of volume in the original subject (the patient), known as a *voxel*. The image can be mapped onto a region of real space containing an array of $M \times N$ voxels (the object slice), whose overall dimensions are R in the readout direction (r) and C in the phase encoding direction (c), given by

$$R = \frac{2\pi}{\gamma G_r t_s}, \quad C = \frac{2\pi}{\gamma G_0} \tag{11}$$

It is important that R and C correspond to the intended dimensions of the frame of interest, so that the image geometry is correct.

2 PRACTICAL ASPECTS

For a detailed review of these, the reader should refer to the article by Johnson and Hutchison.[6]

2.1 Demodulating the Signal

After suitable amplification, the NMR free induction signal (FIS) is demodulated into two components in phase quadrature. In effect, these represent the magnetization components in the rotating frame, M_x' and M_y'. The (angular) rotation frequency ω_0 is that of the system reference oscillator, and would normally be the same as the actual Larmor precession frequency in the absence of field gradients. Full quadrature demodulation is necessary if we are to collect all the information in the FIS. Demodulation consists essentially of multiplication of the FIS by cosine and sine waves of the reference frequency, respectively, followed by low-pass filtering. Suppose the FIS from some spin packet is $A \sin(\omega t + \phi)$. The in-phase demodulator then multiplies the FIS by a reference signal $\cos \omega_0 t$, giving

$$S_\mathrm{R} = \tfrac{1}{2} A \sin(\omega - \omega_0)t + \tfrac{1}{2} A \sin[(\omega - \omega_0)t + \phi] \tag{12}$$

while the quadrature one multiplies it by $\sin \omega_0 t$, giving

$$S_\mathrm{I} = \tfrac{1}{2} A \cos(\omega - \omega_0)t - \tfrac{1}{2} A \cos[(\omega + \omega_0)t + \phi] \tag{13}$$

In each case, the low-pass filter removes the component at the sum frequency, leaving only the first term, that is, the difference frequency. Note that the two demodulated signals are now in quadrature, but both retain the phase term ϕ from the original FIS. The two signals, S_R and S_I, represent the components M_x' and M_y' of the magnetization vector in the rotating frame.

The multiplying device is variously known as a *phase-sensitive detector* (PSD), *double balanced modulator* (DBM), and *synchronous detector*, among other names. DBMs and PSDs are basically the same device, the difference lying in their application. A popular implementation as an integrated circuit is

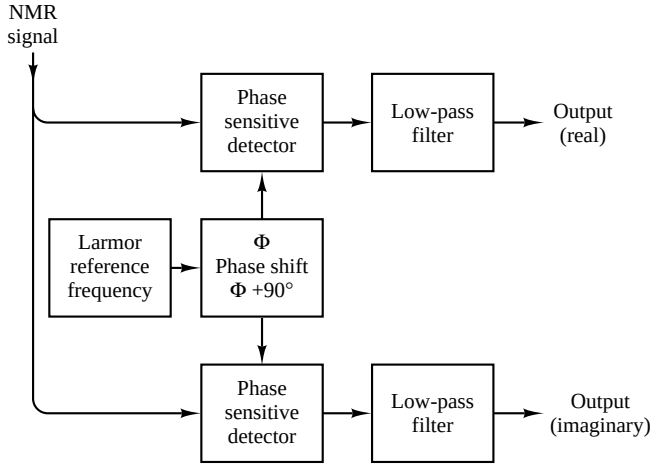

Figure 3 Quadrature demodulator

available under the generic label '1496' (e.g., LM1496 and MC1496), and will function satisfactorily up to about 20 MHz.

When the Larmor frequency is higher than about 20 MHz, it may be necessary to make the receiver a *superheterodyne* system. Here the original FIS is shifted down in frequency to something more convenient, say about 10 MHz. This is again done using a balanced modulator driven by a *local oscillator*; the output is then the difference between the Larmor frequency and the local oscillator frequency, and is generally known as the *intermediate frequency* (IF). A further advantage of superheterodyne operation is that the working Larmor frequency can be altered simply by retuning the local oscillator; the main amplification and demodulation is carried out at the fixed intermediate frequency. The same principle can be used in reverse to produce the rf excitation pulses; the generation and shaping is done at the intermediate frequency, then shifted up to the Larmor frequency using the same local oscillator to drive another balanced modulator, except that this time the sum frequency is extracted.

Figure 3 is a block diagram of a typical quadrature demodulation system. It is essential that the reference signals sent to the two demodulators be 90° out of phase, and that the two channels have the same gain. As a general rule, the phase error should not exceed 1°, and the gain imbalance should not exceed 1%, otherwise image aliases will appear (see ***Spin Warp Method: Artifacts***).

The low-pass filters do not simply remove components at and above the Larmor frequency f_0. They must also act as *anti-aliasing filters* prior to digitizing the signals. For this purpose, they should have a well-defined cut-off frequency f_{max}, corresponding to the spread of Larmor frequencies expected under the action of the readout gradient (from $f_0 - f_{max}$ to $f_0 + f_{max}$). When this signal is subsequently sampled for digitization, the Nyquist criterion states that the sampling rate f_s must be at least $2f_{max}$. If $f_s < 2f_{max}$ then a signal at a frequency $f > \frac{1}{2}f_s$ can still be within the filter's passband, but will appear, in its digitized form, to be at a lower frequency $f_s - f$, commonly referred to as an *alias*. The best gain versus frequency characteristic for an antialias filter is afforded by a maximally flat or *Butterworth* filter, which can be implemented using operational amplifiers configured as active filter building blocks.

A more versatile approach is to use *switched capacitor filters*; these are readily available as integrated circuits, ranging from basic two-pole building blocks to complete filters such as six-pole Butterworth or more sophisticated 'elliptic' filters. The big advantage of switched capacitor filters is that their cut-off frequency can be changed easily by changing the rate of the clock drive pulses. Conventionally, the clock rate is 50 times the required cut-off frequency, although there is nothing sacred about this ratio. Thus, a 10 kHz cut-off would need a 500 kHz clock. This feature is extremely useful when several different types of pulse sequence are being used in rapid succession, since the filters can be changed automatically under software control. Moreover, by using the same clock for both filters, their frequency responses change together and preserve the matching of the two channels.

In order to avoid the problems of matching the two demodulators and keeping the phases of their reference inputs exactly 90° apart, some workers[7] have tried *offset carrier demodulation*. Figure 4 illustrates the method. The reference frequency f_c for the single demodulator is offset from the central Larmor frequency f_0 sufficiently to ensure that all NMR signal components lie on one side of it only. In the conventional setup, the second demodulator is needed to distinguish between positive and negative demodulated frequencies; in this case, however, all demodulated frequencies have the same sign, so it is unnecessary. The primary disadvantage is that the ADC must sample the signal much faster, i.e. at a rate of at least $2\,\Delta f_{max}$, although only one ADC is required. Also, although the mirror frequency range (the second channel, as it is called) contains no NMR signals, it may still contain noise, so a good selective filter is required before the demodulator[8] (see also ***Whole Body Magnetic Resonance Spectrometers: All-Digital Transmit/Receive Systems***).

One rather important point to consider is how much gain should be applied to the FIS before it is presented to the demodulators. In theory, the maximum FIS should occur when all the spins in the selected slice are in phase, that is, when all the gradient integrals are zero. For a spin echo sequence, this should happen at the 'official' spin echo time, and when the phase-encoding gradient is zero. The peak signal is that due to all the spins in the slice, and may be estimated from the slice volume and the mean proton density. We shall denote this largest signal, as presented to the demodulators, by S_{max}. Ideally, the whole receiver chain should behave linearly towards any signals up to an amplitude of S_{max}. In the case of a field echo, main field inhomogeneity will normally prevent the spins all coming into phase at one time, thus reducing S_{max} and making

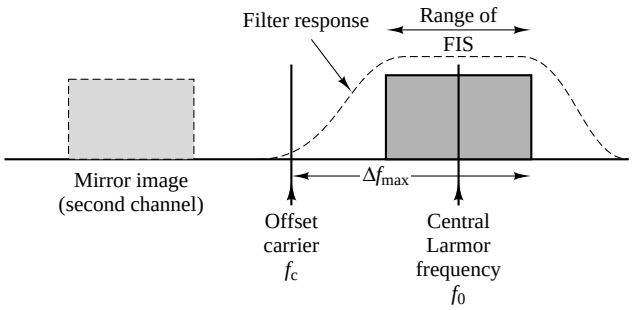

Figure 4 Spectral diagram illustrating the offset carrier method of signal acquisition

the job of signal acquisition easier. This is one of the few cases where lack of field homogeneity is an advantage! Some experimental groups[9,10] have tried to overcome this problem by deliberately imposing a nonlinear distribution of phase on the precessing spins, by the use of higher order field gradients. Although the method works in principle, it requires the installation of one or more sets of additional windings to create these higher order fields. Some method that could use the existing hardware would be much more acceptable.

It is also important that the overall receiver gain does not change over the duration of a scan. Nevertheless, it is desirable to adjust the gain prior to each scan to make allowances for changes in slice width, pixel size, rf coil sensitivity, and so on. In some commercial imagers, a short dummy run is carried out, covering the middle range of phase encoding steps, where the conditions likely to produce S_{max} occur. Then the appropriate gain setting is selected automatically and the full scan carried out. This sophisticated procedure should not be confused with the so-called *automatic gain control* (AGC) incorporated into most radio receivers. AGC simply adjusts the gain so that the mean rf signal level at the detector remains fairly constant, which is not what we require. It should also be noted that many of the simpler electronic gain control circuits are not particularly stable when removed from the stabilizing influence of the AGC feedback loop. Gain control circuits suitable for imager use need rather careful design.

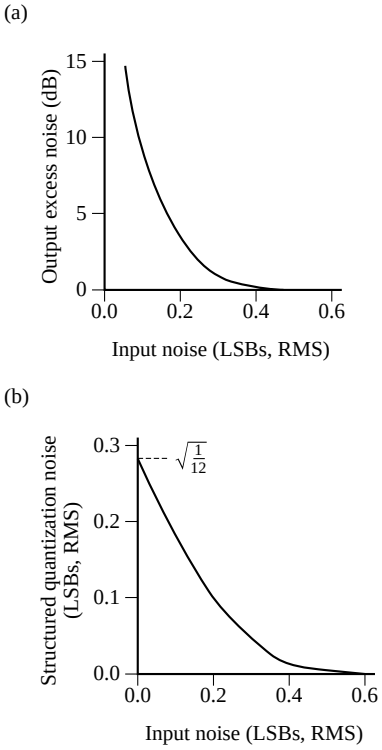

Figure 5 ADC performance as a function of input RMS noise level in LSBs: (a) excess output noise; (b) 'structured' quantization noise

2.2 Signal Digitization

The two low-frequency signals S_R and S_I emanating from the demodulator and filter must be sampled at intervals of t_s and each converted to digital form by an analog-to-digital converter (ADC). For the simple single slice imaging sequences, a digitization rate of 10 kHz (t_s = 100 μs) is adequate. However, most of the FAST sequences and the majority of multislice sequences require much faster conversion, perhaps up to 100 kHz. It is essential that both signal channels be sampled simultaneously, since any delay between sampling one channel and the other is equivalent to a phase error, and will give rise to image aliases.

Probably the single most important consideration in choosing an ADC is the wordlength, or resolution in bits. This sets the dynamic range of the signal that the ADC can handle. Obviously, if the signal is too large, it cannot be represented by the number of bits available, and most ADCs will simply output the maximum possible number (all bits = 1) if the signal is too large, or all bits = 0 if the signal is too negative. The results of such 'clipping' on the image are described in ***Spin Warp Method: Artifacts***.

If the signal is too small, the ADC can only choose the nearest discrete level, so that we can expect an error of up to half the value of the least significant bit (LSB). Supposing that our signal is a low-level sine wave, the digitized version will be chopped up into discrete levels, resulting in a staircase-like waveform. Any attempt to Fourier transform this will result in the appearance of unwanted harmonics. This type of error is known as *quantization noise*, and, because of its tendency to be structured and signal-dependent instead of random, it can give rise to structured noise on the final image. Quantization noise can be rendered much less troublesome by introducing *dither* on the signal, that is, an extra signal with an amplitude of about $\frac{1}{2}$LSB, which does not clash with the wanted signal. It happens that the best dither is provided by white noise, which is normally present on the signal anyway. Figure 5 shows the effects of increasing the level of random noise on the signal. In theory, quantization noise imposes an error whose RMS amplitude is $\frac{1}{12}$LSB. Once the input noise exceeds this amount, the staircase structuring is fairly well masked, and when the input noise reaches $\frac{1}{2}$LSB (RMS), the extra noise produced by the digitization process is negligible.

Effects similar to those of quantization noise can be produced by nonlinearity in the ADC, except that they are not reduced by white noise dither. In bad cases, harmonics would be generated, and show up as aliases on an image. In practice, the standard linearity of $\pm\frac{1}{2}$LSB is quite adequate for imaging work. This is in contrast to spectroscopy, where even tiny levels of harmonics are manifest as unreal spectral lines.

If the entire field of view were filled with active spins and the main field $\boldsymbol{B}_0$ was perfectly uniform, the NMR signal would be concentrated so that it occurred entirely within one ADC sample. Then, for example, if the image signal-to-noise ratio S/N was 50:1 and the image matrix 256 × 256, the peak S/N should be 12 800:1. Given that the noise should be equivalent to about 1 LSB, we can see that the ADC needs at least 15-bit resolution (32 768 levels) to fit this signal in, whether it be positive or negative. However, taking account of various mitigating factors, such as imperfect field homogeneity and the improbability of ever filling the entire field with spins, we find in practice that, for 2D imaging, a 12-bit ADC is generally adequate. These are standard commercial items, available with a range of conversion times from 100 μs down to less than 2 μs. The price is almost inversely proportional to the conversion time.

The most severe demands on dynamic range are made by 3D imaging techniques. Here it may be necessary to employ 16-bit ADCs to accommodate the full range of signal amplitudes. Such high-resolution ADCs have been developed recently as part of the 'digital audio' revolution, but the fastest conversion time is limited to about 10 μs. To get the full advantage of a 16-bit ADC, very careful circuit design and layout is needed to avoid pickup of spurious signals. The full-scale input for such an ADC would typically be 10 V peak-to-peak, so that one LSB represents a mere 150 μV, a signal that cannot be seen on most oscilloscopes!

A different approach to the problem of wide dynamic range is the recent appearance of a device known as a *floating point ADC*. The first stage of conversion consists of changing the gain of a precision preamplifier in steps of two until the signal is within the range of the actual ADC. The output then consists of an exponent denoting the chosen amplifier gain, and a mantissa representing the ADC output. Using a 12-bit mantissa (i.e., a 12-bit actual ADC) and a 3-bit exponent, a dynamic range equivalent to 20 bits (one million to one) can be achieved.

3 RELATED ARTICLES

Echo-Planar Imaging; Image Formation Methods; Partial Fourier Acquisition in MRI; Projection–Reconstruction in MRI; Spin Warp Method: Artifacts; Spiral Scanning Imaging Techniques; Whole Body Magnetic Resonance Artifacts; Whole Body Magnetic Resonance Spectrometers: All-Digital Transmit/Receive Systems.

4 REFERENCES

1. A. Kumar, D. Welti, and R. R. Ernst, *J. Magn. Reson.*, 1975, **18**, 69.
2. W. A. Edelstein, J. M. S. Hutchison, G. Johnson, and T. W. Redpath, *Phys. Med. Biol.*, 1980, **25**, 751.
3. I. R. Young, D. R. Bailes, and G. M. Bydder, *Magn. Reson. Med.*, 1985, **2**, 81.
4. H. W. Park, M. H. Cho, and Z. H. Cho, *Magn. Reson. Med.*, 1986, **3**, 15.
5. R. N. Bracewell, 'The Fourier Transform and its Applications', McGraw-Hill, New York, 1978.
6. G. Johnson and J. M. S. Hutchison, *J. Phys. E: Sci. Instrum.*, 1981, **14**, 1131.
7. A. F. Mehlkopf and J. H. den Boef, *Proc. VIIth Ann Mtg. Soc. Magn. Reson. Med.*, San Francisco, 1988, p. 857.
8. G. N. Holland and J. R. MacFall, *J. Magn. Reson. Imaging*, 1992, **2**, 241.
9. P. Hanley and R. E. Gordon, *J. Magn. Reson.*, 1981, **45**, 520.
10. C. H. Oh, S. K. Hilal, Z. H. Cho, and I. K. Mun, *Magn. Reson. Med.*, 1991, **18**, 63.

Biographical Sketch

James M. S. Hutchison. *b* 1940. B.Sc., 1962, Ph.D., 1968, St Andrews, UK. F.R.S.E., 1996. Department of Biomedical Physics, University of Aberdeen, UK, 1968–present. Approx. 75 publications. Research interests: electrical impedance tomography, physics and instrumental aspects of MRI.

Spin Warp Method: Artifacts

James M. S. Hutchison
University of Aberdeen, Aberdeen, UK

1 INTRODUCTION

In imaging technology, an artifact is a feature appearing on the image which does not correspond to the properties of the subject in the corresponding region. An artifact may arise from the equipment itself, from some unwanted interaction between the subject and the imaging equipment, or from an external cause. In NMR imaging, the artifact may be manifest as a local error in the parameter(s) being imaged, or as a feature displaced from its supposed 'correct' position. This second type of artifact is commonly known as an 'alias', particularly if it is fairly discrete and has some recognizable geometric similarity to the true image.

It should be expected that anything which distorts or changes the main magnetic field will cause artifacts. Temporal variations of the magnetic field also cause artifacts. These variations often arise in resistive magnets from instability of the power supply, or temperature changes in the magnet and/or its connecting leads. Superconducting magnets are much less prone to such variation, although movement of large ferromagnetic objects (e.g. trolleys, elevators) near the imager can affect the field. Random field variation over the timescale of the data collection for one image will tend to give a smearing artifact in the phase-encoding direction.

2 DISCRETE ALIASES

Discrete aliases are most often produced from misplacing of the patient, or choosing an object frame size which is too small, so that the patient overlaps the sides. In the spin warp method, this will cause image wrap around, either in the phase-encoding or the frequency-coding direction. This is more serious when the patient overlaps the frame in the phase-encoding direction, since there is no way to prevent wrap around except by repositioning. However, if the total extent of the patient section is less than that of the frame, the image can be 'unwrapped' quite easily; an example is shown in Figure 1. Wrap-around aliasing in the frequency-coding direction can be controlled either by the use of a sharp cutoff low-pass filter following the demodulators, or by oversampling the free induction signal. The former attempts to remove NMR signals the precession frequencies of which are too far from the central reference frequency, i.e. those which arise from tissues too far off-center in the readout gradient. Demodulated signals whose frequency f_m is more than half the sampling rate f_s of the analog-to-digital converter (ADC) become aliased to a new, lower frequency of $f_s - f_m$. Oversampling the ADC, say at twice the original rate, is a more satisfactory solution, although it is then necessary to FT twice as many points. The result is a double-width image frame of which only the central half is relevant.

Discrete aliases of different types arise from anything in the subject which changes in a regular cyclic manner, particularly if its frequency is harmonically related to the imaging sequence's basic repetition rate (*TR*). Heart motion and relaxed breathing are the main causes of such artifacts. Figure 2 shows discrete aliases of the anterior abdominal wall, caused by regular breathing motion.

Irregular motion, such as fidgeting by the patient, causes a more featureless smear in the phase-encoding direction. The extent of the smear is usually much greater than that of the patient's movement. It can also be caused by faulty cushioning, which slowly sinks under the weight of the patient during a

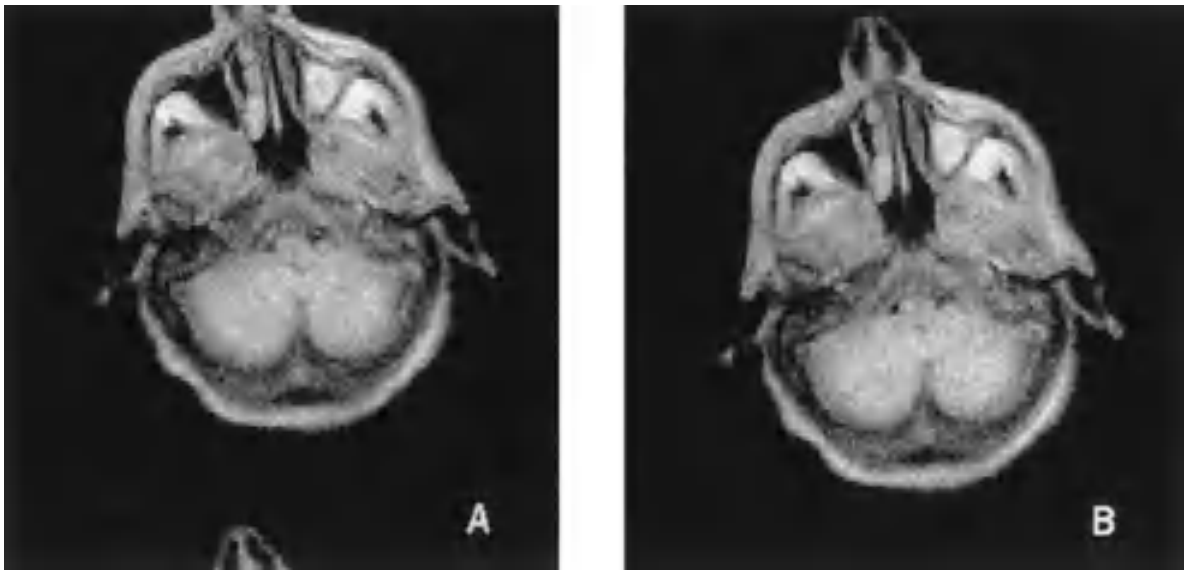

Figure 1 (a) Vertical image 'wrap around' shown on a transaxial head section. (b) Image unwrapped by postprocessing

Figure 2 A sagittal abdominal section, showing regular aliases of the anterior abdominal wall, caused by regular breathing motion

scan, even though the patient is well behaved. In many ways, irregular patient motion produces artifacts which are very similar to those due to field instability.

3 FLOW

Blood flow in major vessels and the heart can give rise to a number of different artifacts in normal imaging. Many of the effects of flow have been put to good use in flow imaging and measurement techniques. Briefly, constant flow tends to produce only changes of intensity; for example, saturation recovery (SR) images show brightening of flowing blood due to refreshment of spins within the slice in the time between consecutive rf pulses (*TR*).

On the other hand, pulsatile flow, such as that in arteries and the chambers of the heart, produces aliases similar to those due to cyclic motion. Figure 3 shows a transaxial thoracic section taken with an SR 200 sequence, where the heart rate was almost exactly one-third of the NMR pulse rate. Discrete aliases of the aorta and other blood-filled structures can be seen displaced vertically (the phase-encoding direction) by one-third of the full image frame height. Aliases of this nature may be interesting, but they can be very confusing in clinical routine, since they can occur within the boundary of the body and be wrongly interpreted.

4 CHEMICAL SHIFT ARTIFACTS

In high-field imagers, the chemical shift between water and fat may cause the 'water' and 'fat' images to be slightly displaced from each other in the frequency-coding direction. At 1.5 T, the two Larmor frequencies differ by about 200 Hz, equivalent to several pixels of shift. Clinically, this can be very confusing and is wide open to misinterpretation. Examples include kidneys displaced relative to perinephric fat, apparent displacement of intervertebral discs, the optic nerve relative to postorbital fat, and so on. Similar but less predictable positional shifts can occur from magnetic susceptibility effects. In particular, gas pockets within the body can produce nearby field changes of the same order of magnitude as chemical shift, with consequent distortion of the image. Both effects can also occur in the slice-selection direction; thus the 'water' and 'fat' components may not even be in the same actual slice. The problems of these shifts constitute one of the few realistic arguments against the use of high fields for imaging.

In the spin warp method, this chemical shift also produces a substantial phase shift between the water and fat components at the time of the gradient echo. In fact, this is the basis of Dixon's method[1] for separating out the fat and water components. As an example, a gradient echo at 8 ms after the rf pulse will incur a phase difference of over 600° in a 1.5 T imager. Dixon's method requires two images in which the fat–water phase shift differs by 180°, and is usually achieved using spin echo sequences in which the 180° pulse is asymmetrically placed, rather than gradient echoes which produce too large an effect.

5 MACHINE-GENERATED ARTIFACTS

We come now to the set of machine-generated artifacts, which covers a very wide range, including machine-specific artifacts, i.e. those which are peculiar to one make and type of

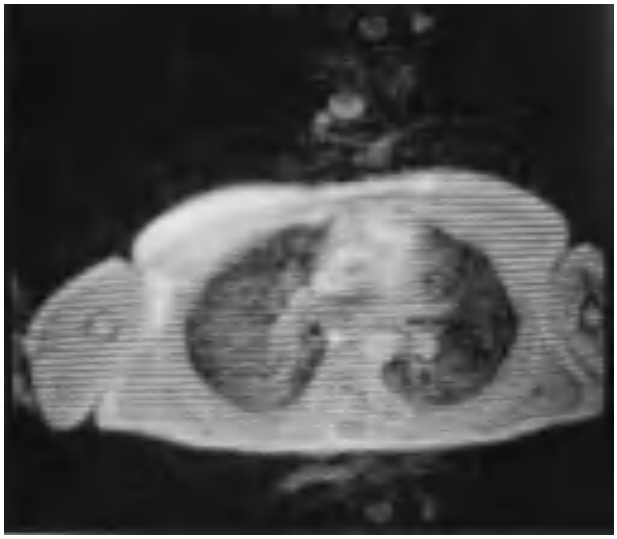

Figure 3 Transaxial thoracic section from an SR 200 sequence, showing discrete aliases of the vessels around the heart

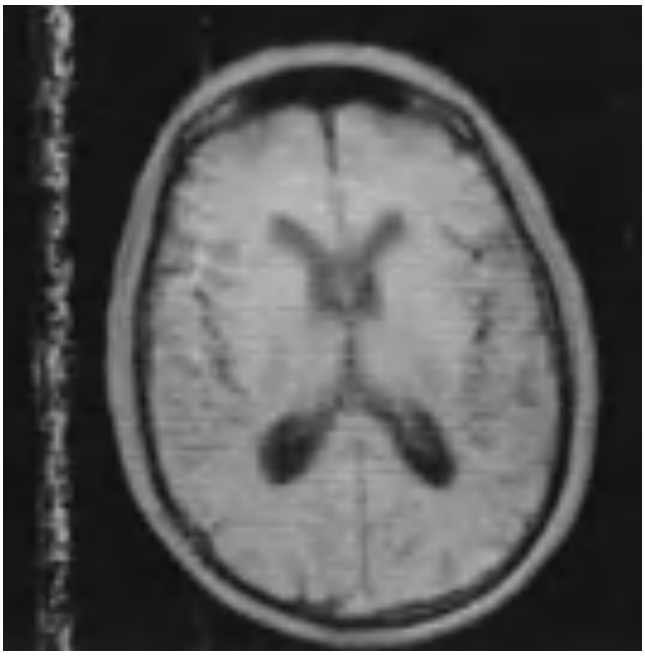

Figure 4 Vertical banding on a head image caused by severe RFI from an unstable oscillator

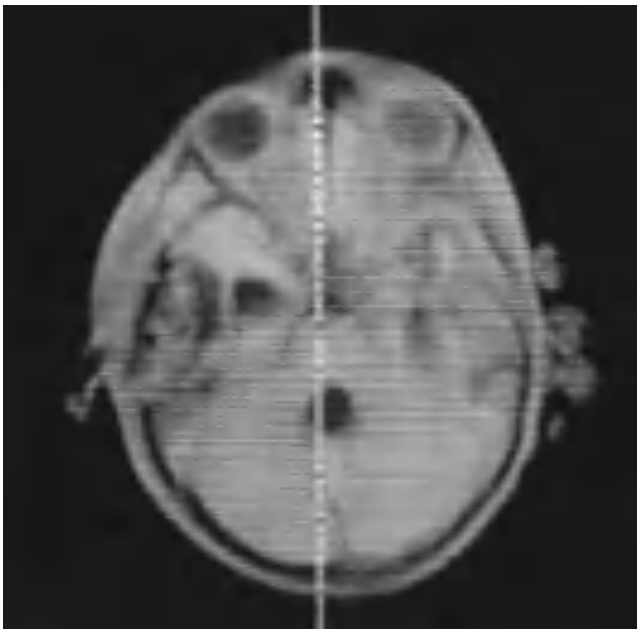

Figure 5 Central 'zipper' artifact resulting from breakthrough of a non-phase-encoded FID

imager only. We shall ignore machine-specific artifacts here, and describe some of the commoner effects that may arise on any imager.

A common source of unwanted features on an image is rf interference (RFI) entering the signal receiver. RFI may arise from external sources or from components of the imager itself, such as the data-processing computer. If the source is a very stable single frequency close to the imager's reference frequency, it may result in a single bright dot on the image. Many radio transmitters exhibit the necessary frequency stability to produce such dot artifacts. If the source is slightly less stable, say varying by a few hertz, the dot will extend into a line in the phase-encoding direction. Further instability, or strong modulation of the source, may produce a wider band on the image (Figure 4). Slow drifting of the source frequency is manifest as changes in the position of the interference band on consecutive images. Transient interference from, for example, light switches, thermostats, or electric sparks, may produce large errors in one or two signal data values; the result is often a characteristic 'herringbone' pattern across the image. Many commercial imagers have facilities to detect such signal spikes on any one 'line' of data, and to repeat the acquisition of that line. Doing 257 pulse sequences (lines) instead of 256 is a negligible burden when compared with a spoilt image.

Spin echo images can suffer from what is known as a central 'zipper' artifact. The central line in the frequency-coding direction contains incorrect and apparently random intensity values, as shown in Figure 5. This is the image line corresponding to no phase encoding, and the spurious data arise from the FID following the 180° pulse overlapping into the echo signal acquisition window. This FID is not subject to phase encoding and so is the same for each sequence repetition. The effect can be reduced by the use of spoiler gradient pulses, or moved to the outer edge of the image by phase alternating the 180° pulses. Gradient echo (field echo) images do not suffer from this effect

Errors occurring in the signal processing circuits of the imager can also produce artifacts. Imbalance of the two channels of the quadrature detector, either in phase (deviation from 90°) or amplitude, will give ghost image aliases of the true image, mirrored about the center of the image frame; i.e. if the true image is at (x, y), a faint ghost will occur at $(-x, -y)$.

Generally the NMR signal consists of a lot of low level signal not greatly exceeding noise level, and a few relatively large and short echo peaks. To accommodate both the low level signals and the peaks, the ADC must have a wide dynamic range. If the system gain is set too high, it may happen that the ADC

Figure 6 Image intensity distortion resulting from signal overload at the ADC

is overloaded on the largest of the peaks, resulting in truncation of the data value. The typical effect on an image is shown in Figure 6. The outer background level is no longer zero, nor even constant; edge ringing is more pronounced, and fringing may appear in the outer regions, arising from diffraction-type interference between the NMR signals and the effective truncation 'spike'.

This has necessarily been a brief summary of artifacts. For a detailed and comprehensive review of imaging artifacts the reader is recommended to study the paper by Henkelman and Bronskill.[2]

6 RELATED ARTICLES

Image Formation Methods; Multi Echo Acquisition Techniques Using Inverting Radiofrequency Pulses in MRI; Motion Artifacts: Mechanism and Control; Selective Excitation Methods: Artifacts; Spin Warp Data Acquisition; Whole Body Magnetic Resonance Artifacts.

7 REFERENCES

1. W. T. Dixon, *Radiology*, 1984, **153**, 189.
2. R. M. Henkelman and M. J. Bronskill, *Rev. Magn. Reson. Med.*, 1987, **2**, 5.

Biographical Sketch

James M. S. Hutchison. *b* 1940. B.Sc., 1962, Ph.D., 1968, St Andrews, UK, F.R.S.E., 1996. Department of Biomedical Physics, University of Aberdeen, UK, 1968–present. Approx. 75 publications. Research interests: electrical impedance tomography, physics and instrumental aspects of MRI.

Spiral Scanning Imaging Techniques

Albert Macovski and Craig H. Meyer
Stanford University, CA, USA

1 INTRODUCTION

Unlike other imaging modalities, MRI sequentially collects imaging data in the Fourier domain, or ***k***-space, rather than in object space. The format of ***k***-space scanning is determined by the integral of the applied magnetic gradients. At any time during the readout interval, the position in ***k***-space is given by the time integral of these gradient waveforms (see also ***Image Formation Methods*** and ***Spin Warp Data Acquisition***). Within limits imposed by the gradient amplifiers, and the dB/dt limits based on neural stimulation, any gradient waveform can be used. A spiral format, starting at the center of ***k***-space and spiraling outward, is a natural approach with a large number of performance advantages. These include minimal flow dephasing, rapid coverage of ***k***-space, efficient utilization of the available gradient power, and a well-behaved impulse response in the presence of T_2 decay.

The entire region of interest in ***k***-space can be covered in a single spiral scan. However, this would require very high power gradient amplifiers and would reduce the signal-to-noise ratio (S/N). We first discuss the basic interleaved spiral imaging technique and some of its properties. We then discuss important applications, including coronary artery imaging, abdominal imaging, and fluoroscopy.

Spiral ***k***-space trajectories were perhaps first mentioned as an alternative to Mansfield's original echo planar trajectory[1] by Likes.[2] Ljunggren[3] independently mentioned spiral trajectories and pointed out that a spiral trajectory would lead to an isotropic impulse response in the presence of T_2 decay, as compared to the anisotropic impulse response of the echo planar trajectory. Ahn et al.[4] published the first spiral images. They used a sequence that traced a spiral with constant angular velocity, and reconstructed the images using a convolution backprojection algorithm. At Stanford, we showed that a spiral with constant linear velocity in ***k***-space is optimal from an S/N standpoint.[5] In our spiral experiments we have tried to approach this ideal of constant linear velocity in ***k***-space, subject to gradient rise-time constraints.[5,6] We also studied interleaving and square-spiral imaging, which has the advantage of only requiring one-dimensional interpolation and a fast FT for reconstruction.[5–7]

2 INTERLEAVING

A spiral ***k***-space trajectory can, in theory, be traversed in a single-shot mode, similar to the way in which echo planar trajectories have been successfully employed[1,8–10] (see ***Echo-Planar Imaging***). We have concentrated on interleaved spirals because they can be readily implemented on standard commercial scanners. A set of interleaved spiral ***k***-space trajectories is shown in Figure 1. The principal advantage of interleaving is practical: to traverse N interleaved spirals after N excitations, the required gradient power drops by about $1/N^2$, the required data collection bandwidth drops by $1/N$, and the S/N goes up

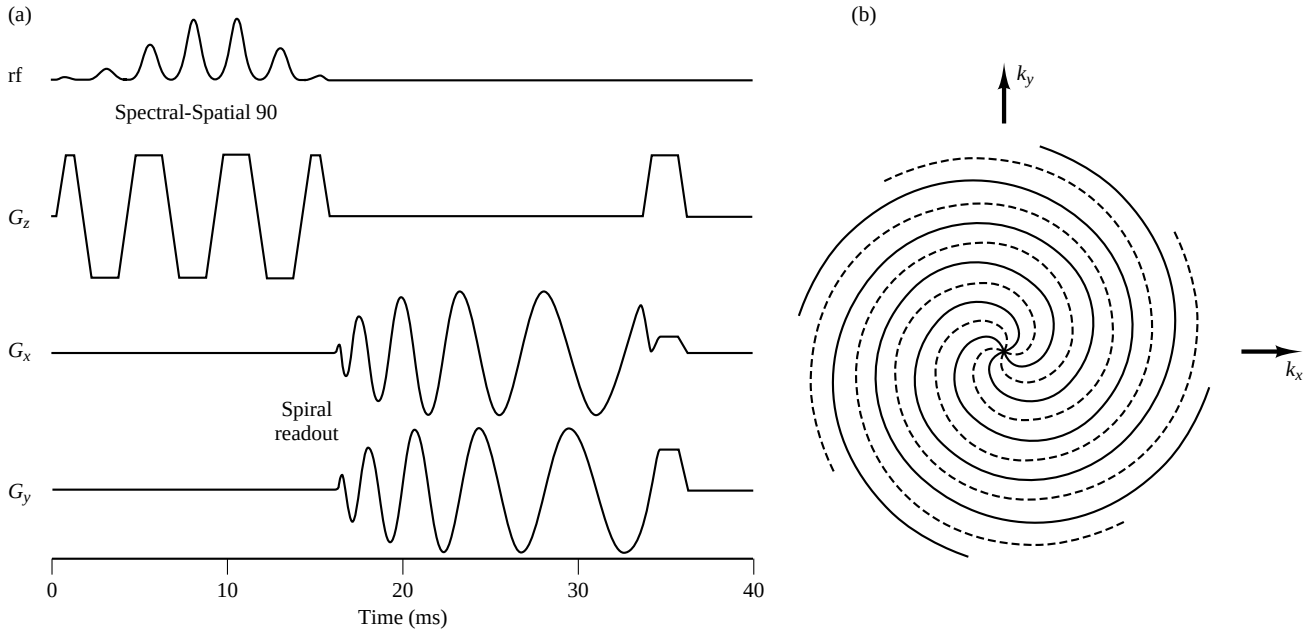

Figure 1 (a) A fast interleaved spiral pulse sequence. There is a spectral–spatial excitation pulse for fat suppression followed by spiral readout gradients. (b) Interleaved spiral ***k***-space trajectories. The first section of the readout gradients on the left traces out one of these interleaves, and the other interleaves are traced out on subsequent readouts by rotating the readout gradients with a hardware rotation board

by $\sqrt{N}$, as compared to a single-shot scan. Interleaving reduces the gradient power requirements to a degree that enables the images to be acquired using standard commercial systems. The gradient power advantage of interleaving is also important in light of studies that have shown that strong echo planar gradients can induce physiological effects.[11,12] Using cardiac gating, interleaved spiral imaging appears to be well suited to breath-hold coronary artery imaging, which is one of the major applications of this technique.

3 SPIRAL GRADIENT GENERATION

The radius at any point on an Archimedean spiral is proportional to the cumulative angle traced out to that point. A spiral $\boldsymbol{k}$-space trajectory is thus given by

$$\boldsymbol{k}(t) = \boldsymbol{A}\tau(t)e^{i\omega\tau(t)} \quad (1)$$

where $\tau(t)$ is some function of time. Setting $\tau(t) = t$ leads to the constant angular velocity spiral of Ahn et al.,[4] with $\boldsymbol{g}(t) = i\boldsymbol{A}\omega te^{i\omega t} \approx d\boldsymbol{k}/dt$. A constant angular velocity spiral is undesirable from an S/N standpoint, because more time is spent near the center of $\boldsymbol{k}$-space than near the edge. Assuming that the readout time is held constant, one must weight the data unequally in the reconstruction, which reduces the S/N. When one is trying to complete the scan as quickly as possible, a constant angular velocity spiral is also undesirable, because the readout gradients only reach their maximum amplitude at the end of the scan. Setting $\tau(t) = \sqrt{t}$ leads to a constant linear velocity spiral (ignoring the singularity at the origin), with $\boldsymbol{g}(t) \approx i\frac{1}{2}\boldsymbol{A}\omega\exp(i\omega\sqrt{t})$. Since $\boldsymbol{g}(t)$ is proportional to the $\boldsymbol{k}$-space velocity, it is evident from this equation that the magnitude of the $\boldsymbol{k}$-space velocity is constant. The $\sqrt{t}$ term appears in the equation for $\boldsymbol{k}(t)$, but not for $\boldsymbol{g}(t)$. Unfortunately, this gradient waveform is impossible to generate on a scanner, because it starts at full amplitude, and gradient subsystems have rise-time constraints.

To deal with gradient limitations we choose $\tau(t) = \sqrt{t}$, except where such a choice violates gradient rise-time constraints. The resulting gradient will be rise-time limited during the first part of the scan and then will be constant amplitude for the rest of the scan. The problem of generating a rise-time limited spiral has been studied in the context of two-dimensional selective excitation.[13,14] These algorithms have been adapted to generate spirals under both rise-time and amplitude constraints. The gradients shown in Figure 1 were designed using this algorithm; they are rise-time limited for the first 5 ms of the scan and amplitude limited for the remaining 12.5 ms. For a given field-of-view (FOV), increasing the number of interleaves allows the gradients to reach a given amplitude faster. For a given number of interleaves, decreasing the imaged FOV also has a similar effect. Each of these effectively reduces ω in equation (1). Note that the complex magnitude of the gradients is constrained to meet the rise-time and amplitude constraints, so that these constraints are not violated when the gradients are rotated during interleaving. For a non-interleaved spiral, some time savings can be achieved by optimizing the x and y axis gradients separately.

4 FLOW PROPERTIES

Spiral readouts have surprisingly good resistance to flow and motion artifacts. Some of the spiral advantages accrue from the fact that the scan begins at the $\boldsymbol{k}$-space origin. Flow dephasing occurs where material moving along a magnetic gradient produces phase shifts. These are often sufficiently large to cause loss of signal within a voxel. When a scan starts at the $\boldsymbol{k}$-space origin, it ensures that the low-frequency high-energy components will not have time to accrue any significant phase shift. Thus the spiral format does not exhibit drop-outs in regions of complex flow. This can be seen by studying the various gradient moments $M_n(t)$ as given by

$$M_n(t) = \int_0^t \tau^n G(\tau)d\tau \quad (2)$$

Echo planar gradients that collect all of $\boldsymbol{k}$-space are known to be susceptible to flow-related dropouts and artifacts.[15,16] With spirals, the center of $\boldsymbol{k}$-space is collected at the start of the scan and thus with zero transverse moments of all orders. Also, the symmetrical nature of spiral scanning means that spiral readouts do not suffer from the oblique flow artifact that two-dimensional FT sequences do.[17]

Another advantage of spiral gradients is that the moments of all orders in a particular direction periodically return to zero together during the readout, thus further reducing flow-related dropouts. Figure 2 shows the first three x axis moments of the gradients shown in Figure 1. The zero crossing points of the the zeroth moment (k_x) are nearly coincident with those of the first and second moments. (The first moment is related to velocity sensitivity and the second moment is related to acceleration sensitivity.) One benefit of this moment behavior is that there is no cumulative buildup of these moments during the scan. Another benefit is that the flow sensitivity is quite

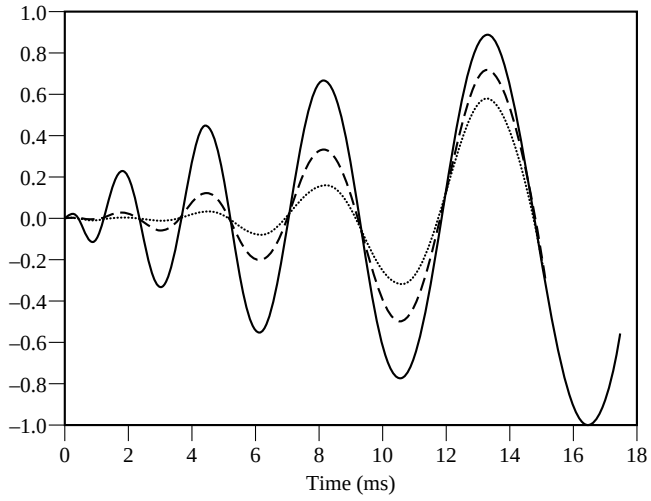

Figure 2 The first three moments of the G_x shown in Figure 1. Each moment is normalized to have the same maximum magnitude on the plot. The solid line is the zeroth moment (i.e. k_x), the dashed line is the first moment, and the dotted line is the second moment. Note that all three moments return to near zero each time k_x returns to zero, which means that the gradients are relatively insensitive to motion during the scan

low in the direction perpendicular to the direction of flow, which is the important direction for resolving the edges of a vessel. (The flow sensitivity along the direction of flow is quite benign as well, being predominately a blur related to the distance a spin travels during the readout window.)

5 RECONSTRUCTION CONSIDERATIONS

Reconstructing spiral images is of course more complicated than reconstructing two-dimensional FT images. The collected data points do not, in general, fall on a two-dimensional grid and so some operations must be performed in addition to a fast FT (see also ***Projection–Reconstruction in MRI***). We use a gridding algorithm related to algorithms first used in radio-astronomy.[18–20] The basic idea of the algorithm is to convolve the density-compensated $\boldsymbol{k}$-space data into a two-dimensional grid, perform a two-dimensional fast FT, and then to compensate for the image intensity variations introduced by the convolution operation. An outline of the algorithm is as follows:

1. Determine the receiver offset frequency Δf. One method for doing this is to collect a FID with no readout gradients and to determine the peak of the spectrum of this FID.
2. Multiply the data points by $\exp(i2\pi\Delta f t)$ to demodulate at the offset frequency determined in step (1).
3. Multiply the data points by $|\boldsymbol{g}(t)| \cdot |\sin[\arg\{\boldsymbol{g}(t)\} - \arg\{\boldsymbol{k}(t)\}]|$ to compensate for the varying density of the data points in $\boldsymbol{k}$-space. The first term in this equation compensates for the varying $\boldsymbol{k}$-space velocity, and the second term compensates for the increased density of the spirals near the origin.
4. Convolve the data into the two-dimensional array. This is done by multiplying each density-compensated data point by a Kaiser–Bessel window a few grid points in width, evaluating the result at each grid point within the window, and adding the result into the array. An auxiliary array is used to keep track of the amount of energy put into each grid point, which is the product of the density-compensation factor and the Kaiser–Bessel function evaluation.
5. Normalize the energy in each grid point by dividing by the auxiliary array. If the density compensation of step (3) is done properly, this step results in only a minor correction.
6. Perform a complex two-dimensional fast FT.
7. Divide by the transform of the Kaiser–Bessel window to remove the apodization resulting from the convolution of step (4).
8. Take the magnitude of the result.

6 OFF-RESONANCE CONSIDERATIONS

One of the disadvantages of spiral imaging is that the impulse response off-resonance is broadened, instead of just shifted as in two-dimensional FT imaging[7,21] (see also ***Susceptibility Effects in Whole Body Experiments***). Also, spiral readout times are typically longer than two-dimensional FT readout times, which allows more time for phase accrual. Because of these factors, it is necessary to take steps to minimize the off-resonance artifacts. The steps include the following: (1) suppressing fat, because fat and water will not simultaneously be in focus at 1.5 T; (2) designing the gradients to reach maximum gradient amplitude as quickly as possible; (3) using as many interleaves as possible for the application, because the blurring is related to the time it takes to reach a particular radius in $\boldsymbol{k}$-space; and (4) reconstructing at the proper frequency for the region of interest. It is also possible to deblur spiral images in postprocessing, both with and without a phase map.[21]

The fat suppression in our sequence is provided by a spectral–spatial excitation pulse, i.e. a pulse with an oscillating gradient that is simultaneously selective in space and frequency.[22]

The deblurring process referred to is based on the simple premise that, in each region of the object, there is a desired demodulation frequency based on the local magnetic field. To choose the correct frequency for each region we create a frequency map by subtracting two images taken at different echo times. From the resultant phase difference we compute the frequency error.

Motion between field map collection and imaging can reduce the effectiveness of the deblurring. We minimize this by rapidly collecting a low-resolution field map immediately before imaging. Alternatively, the field map collection can be eliminated entirely. In this method, a sequence of images is created using different demodulation frequencies. For each incremental region of the object, we sequence through the stored images to find the one which minimizes the imaginary component resulting from phase shift. This has produced significantly improved images.

7 SPIRAL SCAN VARIATIONS

7.1 Square Spirals

A 'square' spiral, as the name implies, consists of a sequence of expanding squares in $\boldsymbol{k}$-space.[5] With an ideal gradient system, the gradient waveforms would simply consist of a series of rectangular pulses alternating in polarity and alternating between the x and y axes, which are incremented in width following each cycle. The magnitude of such gradients is constant, again providing a constant velocity in $\boldsymbol{k}$-space. The principal advantage of the square spirals is that the scan format forms a rectangular grid of samples, which can be rapidly reconstructed using the classical two-dimensional fast FT approach. In our practical implementations of square-spiral scanning, we replaced the ideal rectangular pulses with triangular and trapezoidal pulses, because of gradient rise-time constraints.[6,7] The resulting trajectory is still a square spiral, but it is not quite constant velocity and one-dimensional interpolations are necessary before the two-dimensional fast FT is undertaken. The major disadvantage of practical square-spiral scanning is that it is less efficient than round-spiral scanning, because the average gradient amplitude is lower and because the unneeded corners of $\boldsymbol{k}$-space are collected.

7.2 RARE Spirals

A recent improvement has provided an additional approach to the problem of inhomogeneity. It is based on the rapid ac-

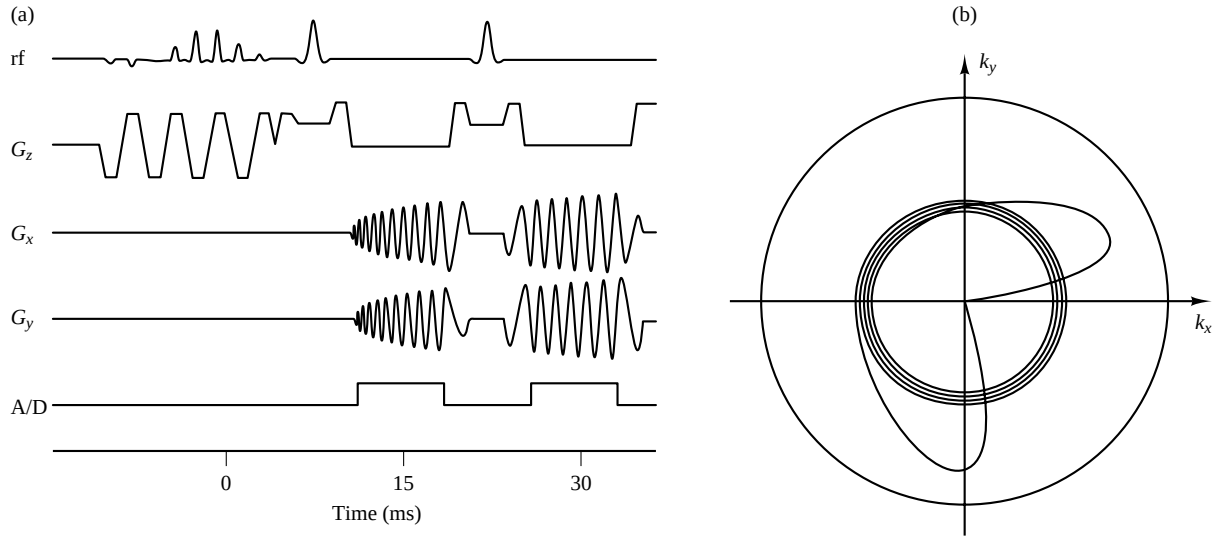

Figure 3 (a) Initial part of a single-shot RARE spiral pulse sequence. (b) The ***k***-space trajectory of the fourth spiral segment. The trajectory starts and ends at the origin to preserve the Carr–Purcell–Meiboom–Gill (CPMG) condition on which RARE depends. (Reproduced with permission of Dr John Pauly)

quisition with relaxation enhancement (RARE) sequence[23] which involves scanning different regions of ***k***-space interspersed with a sequence of 180° refocusing pulses. This enables an acquisition time of the order of T_2. The spiral version uses a sequence of concentric spiral sections each separated by a 180° refocusing pulse.[24] This improves both the S/N and the immunity to inhomogeneity. The spiral section at the origin determines the contrast, so it is chosen for the desired T_2 sensitivity. The remainder of the spiral sections are chosen to ensure a smooth frequency domain, with a resulting well-behaved impulse response. The gradient sequence and ***k***-space representation are shown in Figure 3.

7.3 Fluoroscopy

MRI is, in one sense, particularly well adapted for use in fluoroscopy because of its lack of ionizing radiation. Unfortunately, dB/dt considerations and existing gradient systems make it very difficult to cover all of ***k*** space in a typical frame time with sufficient resolution. Using spiral techniques, however, interleaved formats can be derived which present an effective dynamic presentation to the observer. Two techniques are employed, both of which are based on the premise that the human visual system has limited acuity to objects in motion. Firstly, we use a sequence of interleaved spirals at the desired frame rate. These are combined so that each output frame includes the sum of an interleaved set, providing full resolution. In this way, some of ***k***-space, including the origin, is updated every frame. For a smoother presentation we combine the interleaves in a weighted fashion to provide an improved temporal impulse response. A triangular weighting has proven effective in our experiments.[25]

In addition, each interleaf can be structured so as to repeat fully the low spatial frequencies and interleave only the higher spatial frequencies.[25,26] This is completely in accord with known visual physiology and is being considered in the formulation of high definition television.[27] A representative interleaf is shown in Figure 4, demonstrating the repeated low frequencies and the interleaved high frequencies.

7.4 In–Out Spirals

In spin echo imaging it is advantageous to collect data on both sides of the spin echo. One approach to collecting both sides of a spin echo with spirals is the use of spiral-in/spiral-out trajectories. Any T_2 decay is opposite on each portion, thus

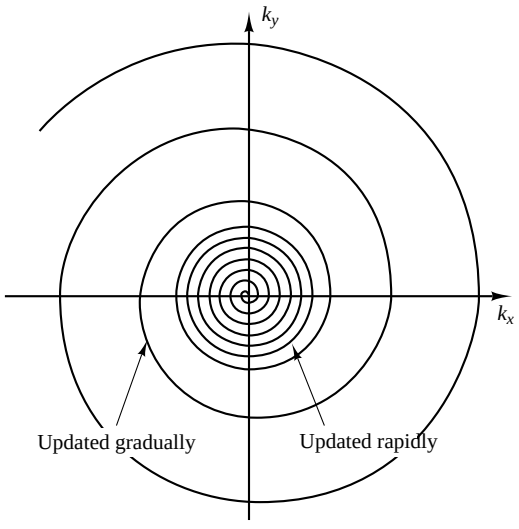

Figure 4 The ***k***-space sampling for a variable-density spiral used for continuous fluoroscopic acquisition. The center of ***k***-space is sampled more rapidly than the edges, to match the spatiotemporal properties of the human visual system

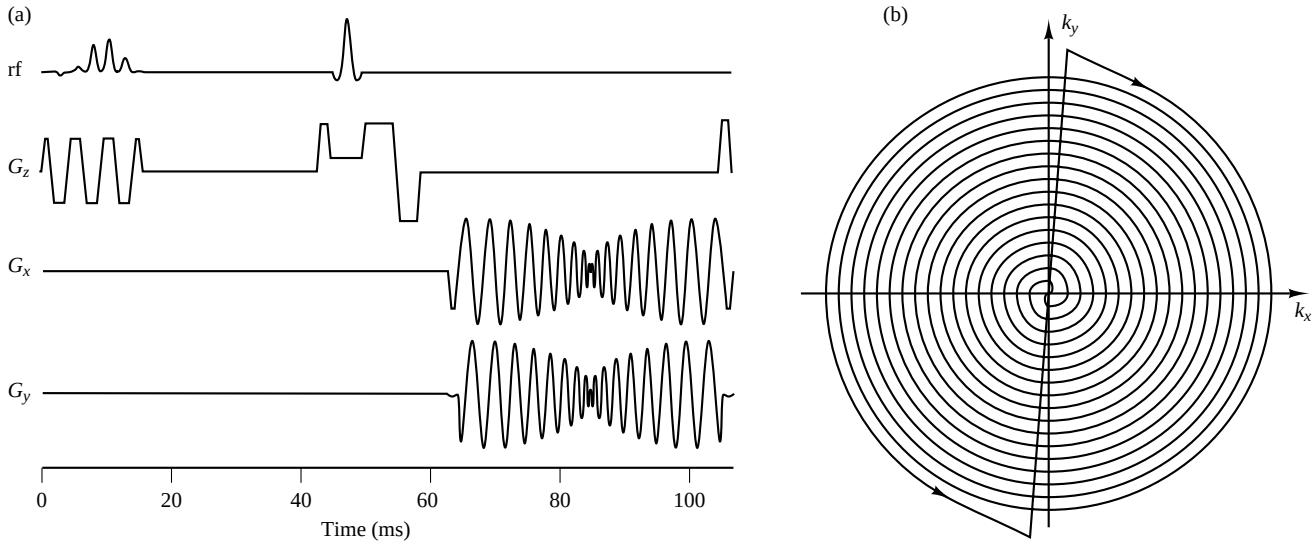

Figure 5 (a) A full echo T_2-weighted spiral sequence. (b) One interleaf of the corresponding spiral-in/spiral-out ***k***-space trajectory

providing first-order cancellation when the two sections are combined in the reconstruction. In addition, for some spiral-in/spiral-out formats the phase buildup due to inhomogeneity is opposite on each portion, resulting in a real frequency spectrum with mild cosine weighting. The gradient waveforms and ***k***-space format are shown in Figure 5.

8 SPIRAL SCAN APPLICATIONS

8.1 Coronary Artery Imaging

Spiral scans enable the efficient imaging of a section in the myocardium containing the desired coronary vessel (see ***Heart: Clinical Applications of MRI***). The interleaved spiral sequence used for this work is shown in Figure 1. It consists of a 15.5 ms spectral–spatial excitation pulse and 17.5 ms spiral readout gradients, followed by transverse gradients to return to the origin in ***k***-space and a spoiler gradient along the z axis. The spectral–spatial pulse suppresses fat, while simultaneously selecting a slice; the spatial profile is Gaussian and the spectral profile is minimum-phase to minimize spectral dephasing during the pulse.[28] The readout gradients are designed to image a 20 cm FOV in 20 interleaves. The gradients shown correspond to one of the interleaves; the other interleaves are traced by rotating the readout gradients.

We used the fast spiral sequence shown in Figure 1 to image the coronary arteries of normal volunteers and patients. The images were acquired in 20-heartbeat breath-holds with 17.5 ms readout windows using a 13 cm receive-only surface coil positioned on the chest of the supine subjects. The acquired resolution was 1.08 mm $\times$ 1.08 mm (186 $\times$ 186 pixels over 20.0 cm). The flip angle was 90° for the static images, and fat was suppressed using a spectral–spatial excitation pulse.

Figure 6 shows a right anterior oblique image of the right coronary artery of a normal volunteer. The slice was prescribed to be tangent to the heart in the axial scout scans. Figure 7 shows an oblique axial, or Grüntzig, view of the left coronary artery of a normal volunteer. The left main coronary artery, the left anterior descending coronary artery (LAD) and several branches of the LAD are visible.

Other coronary artery studies done with spirals include movies and multiple-slice imaging. In the movie, each interleaf acquisition is repeated throughout the cardiac cycle. Complete images corresponding to each portion of the cycle are then assembled and presented in movie form. In multiple-slice ima-

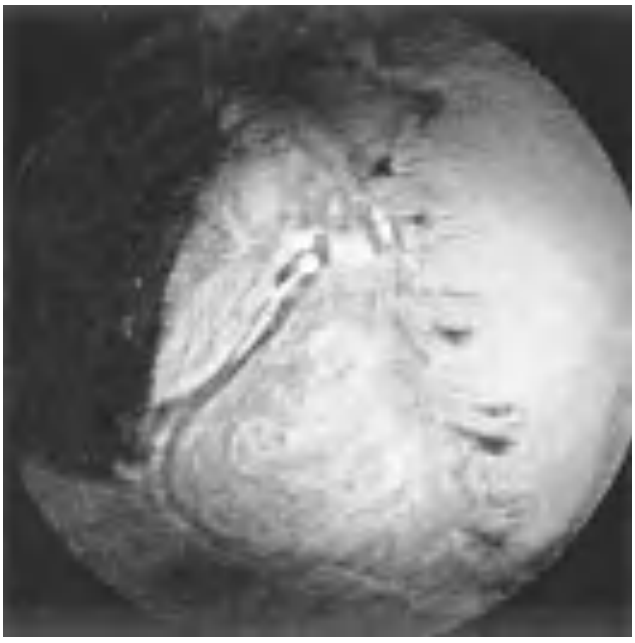

Figure 6 A right anterior oblique image of the right coronary artery of a normal volunteer. The image was acquired during a single breath-hold using the pulse sequence shown in Figure 1

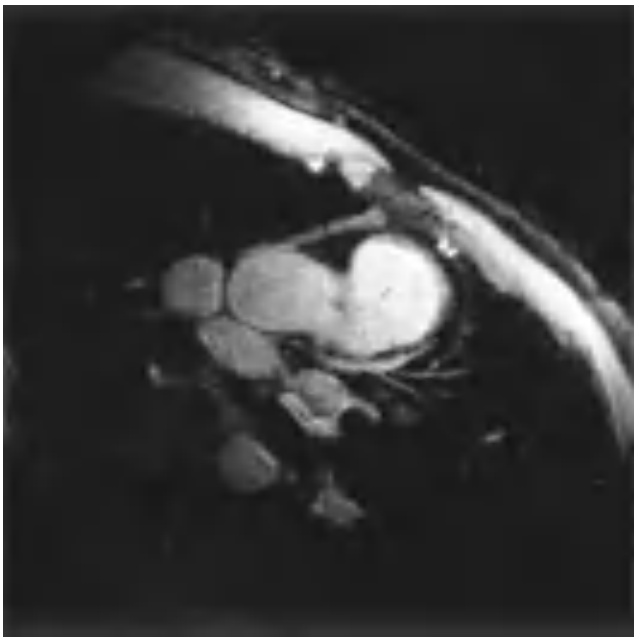

Figure 7 Oblique axial (Grüntzig) view of the left coronary artery of a normal volunteer. The left main coronary artery, left anterior descending coronary artery (LAD), and several diagonal branches of the LAD are visible. The image was acquired during a single breath-hold using the pulse sequence shown in Figure 1

ging, during diastole, interleaves from successive slices are acquired to provide a complete volume of the heart. Using fat and muscle suppression, the coronary vessels can be readily visualized.

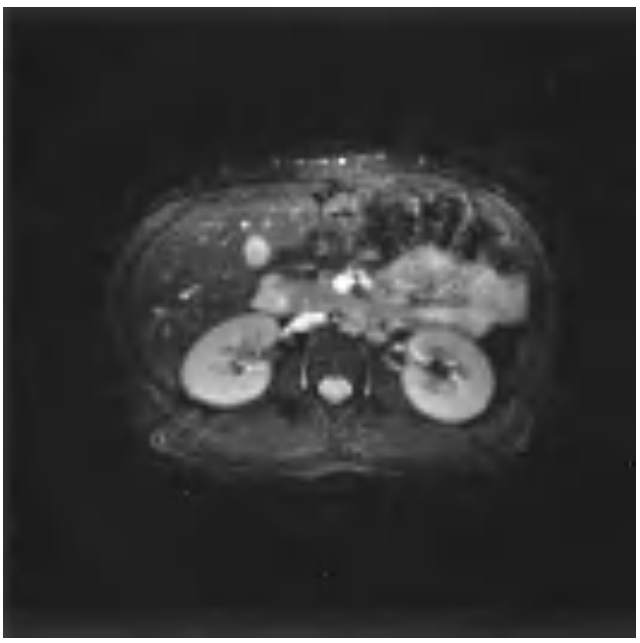

Figure 8 Breath-hold spiral-in/spiral-out image of a patient with no visible pathology. This image was acquired using the sequence shown in Figure 5 and a four-coil phased array was used for signal reception, accounting for the variations in signal intensity across the image

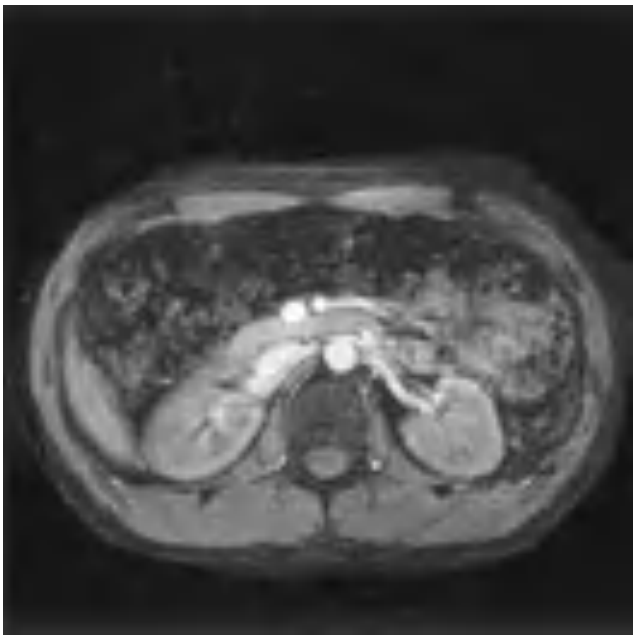

Figure 9 Breath-hold T_1-weighted interleaved spiral image of a normal volunteer

8.2 Abdominal Imaging

Abdominal imaging has been plagued by respiratory motion. Conventional T_2-weighted sequences suffer from long imaging times, motion artifacts and low S/N. In recent years a number of high-speed, T_2-weighted techniques have enabled abdominal imaging in a breath-holding interval (see also ***Liver, Pancreas, Spleen, and Kidney MRI***). For the most part these techniques have required special gradient hardware or suffered from low SNR, low resolution, or image artifacts. The interleaved spiral sequence shown in Figure 5 enables high-speed imaging with T_2-weighting. The preferred sequence uses 12 interleaves with TR = 2000 ms, 24 s scan time, and a 36 cm field-of-view, resulting in a 196 $\times$ 196 image. A representative breath-hold image is shown in Figure 8. Spiral acquisitions can also be used to produce T_1-weighted images. Figure 9 shows a 256 $\times$ 256 breath-hold T_1-weighted image.

9 RELATED ARTICLES

Echo-Planar Imaging; Heart: Clinical Applications of MRI; Image Formation Methods; Liver, Pancreas, Spleen, and Kidney MRI; Projection–Reconstruction in MRI; Spin Warp Data Acquisition; Susceptibility Effects in Whole Body Experiments.

10 REFERENCES

1. P. Mansfield, *J. Phys. C: Solid State Phys.*, 1977, **10**, L55.
2. R. S. Likes, US Patent 4 307 343, 1981.
3. S. Ljunggren, *J. Magn. Reson.* (1983) **54**, 338.
4. C. B. Ahn, J. H. Kim, and Z. H. Cho, *IEEE Trans. Med. Imaging*, 1986, **MI-5**, 2.

5. A. Macovski and C. Meyer, in 'Works in Progress, Fifth Annual Meeting of the Society of Magnetic Resonance in Medicine', 1986, p. 156.
6. C. H. Meyer, A. Macovski, and D. G. Nishimura, in *Proc. VIIIth Ann Mtg. Soc. Magn. Reson. Med.*, Amsterdam, 1989, p. 362.
7. C. H. Meyer and A. Macovski, in *Proc. VIth Ann Mtg. Soc. Magn. Reson. Med.*, New York, 1987, p. 230.
8. R. J. Ordidge, A. Howseman, R. Coxon, R. Turner, B. Chapman, P. Glover, M. Stehling, and P. Mansfield, *Magn. Reson. Med.*, 1989, **10**, 227.
9. R. R. Rzedzian and I. L. Pykett, *Am. J. Roentgenol.*, 1987, **149**, 245.
10. F. Schmitt, M. Stehling, R. Ladebeck, D. Atkinson, and M. Fang, in *Proc. Xth Ann Mtg. Soc. Magn. Reson. Med.*, San Francisco, 1991, p. 841.
11. M. S. Cohen, R. M. Weisskoff, R. R. Rzedzian, and H. L. Kantor, *Magn. Reson. Med.*, 1990, **14**, 409.
12. T. F. Budinger, H. Fischer, D. Hentschel, H.-E. Reinfelder, and F. Schmitt, *J. Comput. Assist. Tomogr.*, 1991, **15**, 909.
13. J. M. Pauly, Ph.D. thesis, Stanford University, CA, 1989.
14. C. Hardy and H. Cline, *J. Appl. Phys.*, 1989, **66**, 1513.
15. J. L. Duerk and O. P. Simonetti, *JMRI*, 1991, **1**, 643.
16. R. Weisskoff, A. Crawley, and V. Wedeen, in *Proc. IXth Ann Mtg. Soc. Magn. Reson. Med.*, New York, 1990, p. 398.
17. D. Nishimura, J. Jackson, and J. Pauly, *Magn. Reson. Med.*, 1991, **22**, 481.
18. J. O'Sullivan, *IEEE Trans. Med. Imaging*, 1985, **MI-4**, 200.
19. R. B. Marr, in 'Works in Progress, Sixth Annual Meeting of the Society of Magnetic Resonance in Medicine', 1987, p. 25.
20. J. Jackson, C. Meyer, D. Nishimura, and A. Macovski, *IEEE Trans. Med. Imaging*, 1991, **10**, 473.
21. D. C. Noll, C. H. Meyer, J. M. Pauly, D. G. Nishimura, and A. Macovski, *IEEE Trans. Med. Imaging*, 1991, **10**, 629.
22. C. H. Meyer, J. M. Pauly, A. Macovski, and D. G. Nishimura, *Magn. Reson. Med.*, 1990, **15**, 287.
23. J. Hennig, A. Neureth, and H. Friedburg, *Magn. Reson. Med.*, 1986, **3**, 823.
24. J. M. Pauly, D. Spielman, C. H. Meyer, and A. Macovski, in *Proc. XIIth Ann Mtg. Soc. Magn. Reson. Med.*, New York, 1993, p. 1258.
25. C. H. Meyer, D. Spielman, and A. Macovski, in *Proc. XIIth Ann Mtg. Soc. Magn. Reson. Med.*, New York, 1993, p. 475.
26. D. Spielman, J. M. Pauly, and C. H. Meyer, in *Proc. XIIth Ann Mtg. Soc. Magn. Reson. Med.*, New York, 1993, p. 1261.
27. W. E. Glenn, K. G. Glenn, and C. J. Bastian, *Proc. Soc. Information Display*, 1985, **26**, 71.
28. C. H. Meyer, A. Macovski, and D. G. Nishimura, in *Proc. IXth Ann Mtg. Soc. Magn. Reson. Med.*, New York, 1990, p. 32.

Biographical Sketches

Albert Macovski. *b* 1929. B.E.E., 1950, CCNY; Ph.D., 1968, Stanford. Studied television systems at RCA Labs, 1950–60. Worked on variety of imaging systems at SRI, 1960–1972. Faculty in Electrical Engineering and Radiology, 1973–present. Approx. 170 publications and a book, *Medical Imaging Systems*. Research interests: systems aspects of medical imaging, in particular, MRI.

Craig H. Meyer. *b* 1959. B.S., 1982, University of Missouri; Ph.D., 1995, Stanford University. Research associate in electrical engineering. Approx. 50 publications. Research interests: high-speed imaging, multidimensional excitation, and efficient postprocessing techniques.

Stray Field (STRAFI) NMR: Imaging in Large Field-Gradients

Edward W. Randall

Queen Mary, University of London, London, UK

1 Introduction 1
2 The Magnetic Flux-Density and the Gradient-Strength 1
3 STRAFI-Work in the Sensitive Slice 3
4 STRAFI-Imaging in 1-Dimension 10
5 STRAFI-Studies in 2- and 3-Dimensions 12
6 Applications 12
7 Prospects 14
8 References 14

1 INTRODUCTION

The only new component which we need to consider in this article, additional to the normal complement of experimental factors for NMR experiments, is the presence of a large fixed gradient, **G**, in the magnetic flux-density, **B**. Normally in high resolution spectrometers we have the presence of a high degree of homogeneity in the magnetic flux-density, the 'magnetic field', to the tune of say 1 in 10^9, over a sample about 5 mm in diameter in a flux of about 10 T or more. In other words the field variation across the sample is of the order of $2 \times 10^{-6}\,\mathrm{Tm}^{-1}$. In conventional imaging instruments a gradient is introduced which is of the order of $10^{-3}\,\mathrm{Tm}^{-1}$. The sample size may be as large as 1 m in clinical instruments, and the Zeeman polarizing field, **B**, about 1 T.

The magnitude of the gradient we shall be considering here on the other hand is in the region of $50\,\mathrm{Tm}^{-1}$ for a basic polarizing Zeeman-field of about 5 T. In other words the value of the ratio of **G** to **B** is about $10\,\mathrm{m}^{-1}$, whereas it is effectively zero in normal NMR spectroscopy, and about $10^{-3}\,\mathrm{m}^{-1}$ in conventional imaging experiments. This large gradient is to be found at the edge of a super-conducting solenoid in the so called stray field (STRAFI).

The consequences in the spin-physics of using a large gradient turn out to be rather more wide-ranging than one might initially expect. The first effect, of course, is that the radio-frequency field, $\mathbf{B_1}$, excites only a very narrow slice of the sample, the so-called 'sensitive slice' of Samoilenko.[1] This is normally about 50 μm thick for protons – the exact value depending on the length of the pulse, the pulse-shape and the line-width, W, of the sample. The main advantage which accrues is that Hahn spin-echoes can be produced from almost *any* sample for any tip-angle, so that it becomes easy to image any small object even one which gives rise to broad lines. Solids may now be visualized even if they contain quadrupolar nuclides, or are paramagnetic, albeit at a spatial resolution limited normally by the spectral line-width. Liquids, liquids in solids, and solids are simultaneously accessible. The attainable spatial resolution for protons is in the region of between 1–100 μm depending on the conditions.

An additional great advantage of the STRAFI-technique is that the effects of distortion of the image, caused by variations in susceptibility producing local variations of **B**, are reduced in proportion to **G**.[2,3] There is no need with STRAFI-imaging to operate at low Zeeman-fields as in conventional imaging to avoid this effect.

Also, of course, in very large gradients, the effects of diffusion become increasingly important, so that very small diffusion-coefficients, of the order of $10^{-15}\,\mathrm{m}^2\,\mathrm{s}^{-1}$, come within measuring range.[4,5] Normally in experiments conducted with short pulses and with small pulse-gaps of the order of say 10 μs the effects of diffusion may be neglected on the first few echoes.

The topic of STRAFI-diffusion studies has been discussed recently by Geil.[6] The concepts in STRAFI-imaging have been covered briefly by Randall,[7] and both the theory and many applications have been reviewed.[8,9]

2 THE MAGNETIC FLUX-DENSITY AND THE GRADIENT-STRENGTH

If one has a conventional spectrometer or imager, the easiest way to introduce a very large gradient is to move the area of NMR operation away from the central region of the magnet, where the field-homogeneity is very high and the field gradients are very low, to the stray field, alternatively referred to as the fringe-field.[4,5] For super-conducting solenoids in conventional instruments the area of largest gradient is near the edge of the super-conducting coils. This was part of Samoilenko's original idea.[1] The spectrometer he employed was a Bruker MSL 300. The position used in the stray field was chosen to be that at which the normal ^{31}P frequency in the central field, 121 MHz, and its associated electronic hardware, could be used for protons in the fringe-field. At this spot the gradient was about $37.5\,\mathrm{T\,m}^{-1}$ and the corresponding field was 2.89 T.

Normally super-conducting solenoids as used in NMR spectrometers have a complex arrangement of coils which vary from one manufacturer and magnet to the next. It is sufficient for our illustrative purposes, however, to consider a simple solenoid consisting of a single uniformly wound cylinder of length, $\boldsymbol{l}$, and radius $\boldsymbol{r}$, in the limit where $\boldsymbol{l} \gg \boldsymbol{r}$. carrying a current $\boldsymbol{I}$ in **n** turns. The magnetic field, $\mathbf{B_z}$, at a point P on the z-axis (the cylinder axis) is given by

$$\mathbf{B_z} = 2\pi\,\mathbf{n}\boldsymbol{I}\,(\cos\boldsymbol{\phi} - 1) = \mathbf{A}(\cos\boldsymbol{\phi} - 1)$$

where $\boldsymbol{\phi}$ is the angle between the z-axis and a line from P to the end of the coil. On axis at the end of the coil, taken as z = 0, $\boldsymbol{\phi} = 90$, so cos $\boldsymbol{\phi} = 0$, and

$$\mathbf{B_{stray}} = 2\pi\,\mathbf{n}\boldsymbol{I} = \mathbf{A}$$

The field at the center of the solenoid is double this.

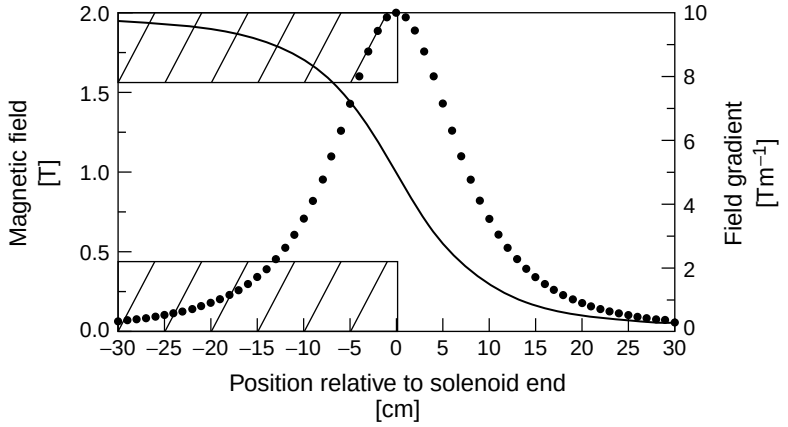

Figure 1 Variation of **B** (full line) and **G** (dotted line) with distance for a simple infinitely long cylindrical solenoid (see text). (Courtesy of Dr. A. R. Preston)

The maximum gradient $\mathbf{G_{max}}$ occurs at $z = 0$ and is given by

$$\mathbf{G_{max}} = 2\pi \frac{\mathbf{n}I}{r} = \frac{\mathbf{A}}{r}$$

So if $\mathbf{A} = 1\,\mathrm{T}$, then $\mathbf{B_{stray}} = 1\,\mathrm{T}$, at $z = 0$, and for $r = 10\,\mathrm{cm}$, $\mathbf{G_{max}} = 10\,\mathrm{Tm}^{-1}$. At the center of the magnet, where **G** is zero, $\mathbf{B_{center}}$ is 2 T.

The functions **B**(z) and **G**(z) are shown in Figure 1. **B**(z) is nearly linear at the edge of the solenoid, i.e., when $z = 0$.

The exact position of the excited slice may be chosen by selection of the resonance frequency, ν, (or the field **B**). Because of the cylindrical symmetry of the solenoid the slice is actually saucer-shaped. The ideal position for locating it occurs at a position $P_{optimum}$ where the saucer is a nearly planar disc and shows negligible curvature for some way off the z-axis in the xy-plane.

The situation may be represented by Figure 2 in which lines of equi-potential are shown. These are normal to the z-axis for some distance into the xy-plane at positions far from the end of the solenoid. Inside the cylinder closer to the end, the lines become concave but far outside it the lines are convex. In between lies the nearly flat disc. In theory at great resolution the disc is never quite flat but if the curvature is sufficiently small, compared with the resolution, this is not a major factor in determining the optimum position for STRAFI-studies. $P_{optimum}$ occurs near the position of maximum gradient.

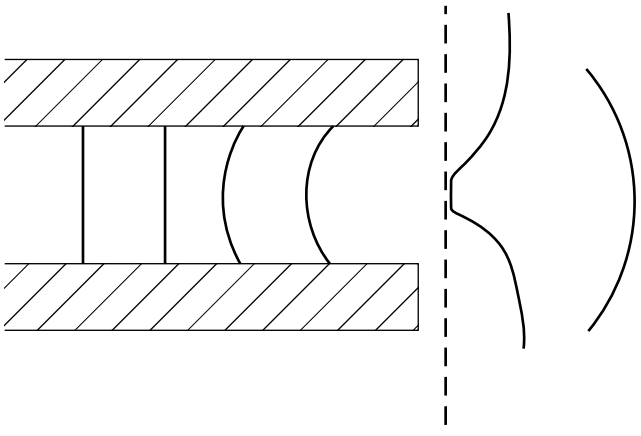

Figure 2 Lines of equi-potential for a horizontal solenoid showing concave and convex regions and their near cancellation at the edge of the solenoid resulting in a nearly flat disc (after Samoilenko)

The situation for commercial NMR spectrometers is more complicated than for the simple solenoid, since the superconducting solenoids are complex. As a consequence the literature contains a variety of magnetic characteristics depending on the exact details of the magnet designs, which are not generally revealed. Most of the values reported in the literature for STRAFI-studies are shown in Table 1.

The effect of r may be seen from the table in two instances: of the two spectrometers with $\mathbf{B_0} = 4.7\,\mathrm{T}$, the one with the smaller radius has the higher value for the STRAFI-gradient, $\mathbf{G_s}$, and the same is true for the two spectrometers with $\mathbf{B_0} = 14.1\,\mathrm{T}$. We may see, however, that the gradient in the last case is lower than expected.

The MSL 300 systems (third entry) have STRAFI-resonance frequencies which are rather low, as can be seen from the table, since they utilize center-field ^{31}P electronic hardware for protons in the stray field.

The high field magnet with a central field of 19.7 T is the latest addition to the STRAFI-family of instruments. It is located at the National High Magnetic Field Laboratory (NHMFL) in Tallahassee, Florida.

The main STRAFI centers for imaging until now have been Moscow (MSL 300, Samoilenko), Karlsruhe (Bruker MSL 400, Zick and Samoilenko), Lisbon (MSL 300, Nunes), Surrey (Chemagnetics 400, McDonald), and London (Varian 4.7 T, 30 cm., Kinchesh and Randall). Each of the instruments used takes samples about $1\,\mathrm{cm}^3$ and has a vertical solenoid, except the last which is designed for $5\,\mathrm{cm}^3$ samples, and has a horizontal bore-system. In all systems except that at Surrey both the sample and the STRAFI-probe move as a unit, whereas in Surrey only the sample moves. Many landmark developments were made at Bruker GmbH, Rheinstetten: the extension of STRAFI-1D-imaging to 2- and 3-dimensions, FT-STRAFI-imaging and micro-imaging. Accounts of these appeared in various Bruker Reports, but fortunately now they are referred to in the open literature, notably in the excellent review of Newling and McDonald.[9]

It was not until recently that magnets were designed specifically for their gradients rather than for the homogeneity

Table 1 Typical values for the central field, $\mathbf{B_0}$, the stray field, $\mathbf{B_s}$, the stray field gradient, $\mathbf{G_s}$, and proton resonance frequencies

Central field $\mathbf{B_0}$/T	Center ^{1}H frequency ν/MHz	Bore r/mm	Stray Field $\mathbf{B_s}$/T	STRAFI frequency ν_s/MHz	Gradient $\mathbf{G_s}$/Tm^{-1}
4.7	200	400	1.86	79	9.0
4.7	200	300	2.61	111	12.0
7.05	300	89	2.94	125	37.5
9.4	400	89	5.52	235	58.5
14.1	600	89	9.66	411	52.9
14.1	600	54	8.9	380	90.0
19.6	833	32	11.2	477	75.7

of their central fields. A magnet with a very large gradient (200 Tm^{-1}), the product of two anti-Helmholz coils, has been described for STRAFI-diffusometry. The field at the center of the coils is zero so a position off-center, where the field is 2 T and the gradient is 180 Tm^{-1} is used for the diffusion measurements.[10] An ingenious design for a horizontal permanent magnet for STRAFI-work informally known as GARField (Gradient at right angles to field) has been described. The pole-pieces are shaped to give planes of constant $|\mathbf{B}|$ in the horizontal direction – the magnetic lines of force are approximately parallel and horizontal – but with a strong *ortho-normal* gradient. In this case $\mathbf{B_1}$ and $\mathbf{G}$ are parallel and vertical (with $\mathbf{B}$ at right angles), whereas in the conventional STRAFI-arrangement $\mathbf{B}$ and $\mathbf{G}$ are parallel (and $\mathbf{B_1}$ is at right angles). GARField operates at a field of 0.8 T and a gradient of 20 Tm^{-1}. $|\mathbf{B}|$ has a curvature of less than $+/-5\,\mu$m over an area of 5×5 mm. The rf-coil is mounted underneath the sample which is placed on a glass cover slip. The rf-assembly may be adjusted to lie in the horizontal plane to better than 10 μm. GARField is ideal for the study of thin films and coatings at high spatial resolution.[11]

Another type of system which operates in strong gradients is the MOUSE (Mobile Universal Surface Explorer). It is an example of a portable, 'inside-out' NMR system. The system has a very small permanent magnet which is applied externally to an object of interest. The magnet consists of two parallel opposed permanent magnets joined by a yoke at one end. At the other end an rf-solenoidal surface-coil is placed in the gap between the two magnets, so that the static field $\mathbf{B}$ and $\mathbf{B_1}$ are approximately at right angles.[12] A major difference from the super-conducting magnet systems is in the use of surface-coils which give a variation of $\mathbf{B_1}$ across the sample. The arrangement is similar to the NMR equipment used for oil well logging. Although the fields and gradients of both of these systems are lower than for the STRAFI-systems utilizing super-conducting solenoids, there is a similarity in the ratio $\mathbf{G/B_s}$, which is about 10 m^{-1} in all three cases.

3 STRAFI-WORK IN THE SENSITIVE SLICE

The ***location* of the sensitive slice** can be chosen for a given nucleus by an appropriate choice of the resonance frequency, ν, according to the basic resonance equation, which is simply given by

$$2\pi\nu = \gamma\mathbf{B} \tag{1}$$

where γ is the gyromagnetic ratio. Alternatively of course, if $\mathbf{B}$ can be varied, one can operate at fixed frequency and change $\mathbf{B}$. We neglect for the moment considerations of the screening constant, $\boldsymbol{\sigma}$, the coupling constants, $\mathbf{J}$ and $\mathbf{D}$, between the nuclear magnetic dipoles, paramagnetic effects, and the electric quadrupole coupling constant, $\boldsymbol{\chi}$. Additionally we may note in passing that in neglecting $\mathbf{D}$ and paramagnetic dipoles, we shall be ignoring the complications of the *dipolar field*, which is alternatively but less satisfactorily referred to as the *demagnetizing field*. In other words, we shall adopt, initially at least, what is called the high field approximation: which assumes that the *induced* field due to the polarized dipoles can be neglected relative to $\mathbf{B}$.

It is interesting to compare the positions of the sensitive slices for two different types of nuclides which have different gyro-magnetic ratios. The first such pair to be considered was ^{1}H and ^{19}F at a constant frequency.[13]

The separation, $\mathbf{d}$, of the sensitive planes is easily calculated for a fixed resonance frequency, ω_s, and is

$$\mathbf{d} = \frac{\omega_s}{\mathbf{G_s}}[\gamma_F^{-1} - \gamma_H^{-1}] \tag{2}$$

in which γ is the gyro-magnetic ratio and ω_s is the STRAFI-frequency in angular units. The value of $\mathbf{d}$ depends on the ratio of $\mathbf{G_s}$ to $\mathbf{B_s}$ for the instrument being considered. We may refer to this separation as the γ-shift by analogy with the chemical shift. Shift effects may be included in equations (1) and (2) by the introduction of the screening constant: it is normally too small, however, to affect the experiment. For paramagnetic compounds on the other hand large shift effects due to hyperfine interactions may become significant. We have observed one such effect: the ^{31}P-sensitive plane and therefore the ^{31}P 1-D profile of cobaltous phosphate is shifted relative to the profile of calcium phosphate because of a hyperfine shift of 1.5 MHz. Even in diamagnetic compounds we may expect that in the case of heavy atoms which have very large chemical shifts, chemical shift displacements may be observed in images.

For the MSL 300, $\mathbf{d}$ is about 4.9 mm for the ^{1}H-^{19}F pair, whereas on the lower field Varian system at Queen Mary, University of London, it is 13.6 mm.

For any other pair of nuclides which have values of γ which are nearly equal the γ-shift is smaller and the images of the nuclides may overlap (see later). Examples are: ^{7}Li, ^{11}B and ^{31}P; ^{23}Na and ^{27}Al (and ^{51}V); ^{63}Cu and ^{65}Cu; ^{75}As and ^{115}In. In these cases the experiment cannot distinguish between the signals from the different nuclides in the overlapping region of the images, except by means of differential relaxation weighting. This overlap-factor may prove to be one of the main limitations of the STRAFI-method for multinuclear situations.

The ***thickness* of the sensitive slice**, $\boldsymbol{\Delta}$, depends on two factors: the width, **P**, of the excitation pulse, or more correctly the pulse-shape, and the width, **W**, of the transition or NMR line, or again the shape of the resonance. It is given simply by the convolution of the two functions in the frequency domain.[7,14]

$$\Delta = \mathbf{P} * \mathbf{W} \tag{3}$$

The easiest case for consideration is the uncommon one in which the pulse has a sinc form in the time-domain and consequently gives a simple square or top-hat shape in the frequency-domain for **P**. Lines whose centers lie outside this excitation envelope but which overlap it, will contribute to the magnetization. The width, **W**, of the transition is given by the 'homogeneous' line-shape and the relaxation time, T_2, for liquids. If we introduce considerations of screening constants, and the dipolar and quadrupolar interactions, the appropriate line-shape for a solid will depend on the nature of the solid: for a powder the 'heterogeneous' powder line-shape is relevant.

The effect of **W** on the thickness of the excited slice, and hence on the initial magnetization, was shown by a comparison of the deuterium signals from heavy ice and heavy water: the former was about 3 times larger than the latter because of the line-width effect, despite the much smaller T_2 for the solid.

The ***magnetization* of the sensitive slice** is complex: it is the sum, or rather the integral, of the magnetizations across the slice. These differ because the field at each position varies across the slice. In other words there is a large field-offset which is about 5×10^{-4} T for a 100 μm slice and a gradient of 50 Tm^{-1}. In frequency terms this is 0.02 MHz, or 20 kHz for protons. The consequence of this large offset for STRAFI-studies is that the tip-angle varies across the slice: if it is 90° at the slice-center it is much different at the extremes of the slice. The observed total magnetization may therefore be viewed as a superposition of the responses to a varying tip-angle and phase.

In accurate simulations of the response of the system to the pulses, therefore, it is necessary to sum the calculations across the slice. Otherwise the alternative is to use the 'delta approximation' in which it is assumed that the tip-angle is constant.

For quadrupolar samples the electric quadrupolar interaction can be large, much larger than the dipolar interactions, and may become the dominant factor in the determination of $\boldsymbol{\Delta}$.[15] This is shown in the Figure 3: at low values of the electric quadrupolar coupling constant, $\boldsymbol{\chi}$ (or $\mathbf{C_p}$), the pulse duration and shape are the main factors but above about $\mathbf{C_p} = 1$ MHz, **W** dominates.

3.1 Calibration of the Gradient Strength

Equation 2 gives a method for the easy calibration of the STRAFI-gradient strength, $\mathbf{G_s}$, by accurate measurement of **d** since all other terms in the equation are known to a high order of accuracy.[16] A good alternative method is by field-profiling, that is by simply measuring the resonance frequency as a function of position. One problem with this is that the frequency range to be covered is very high and the probe needs to tuneable over the desired range. Both methods have the advantage that they are 'primary methods' and do not need knowledge of a parameter determined elsewhere, such as a diffusion constant in the diffusion method of calibration, which can be regarded as a secondary method and requires careful matching of experimental conditions, such as the temperature of the both sample and a standard substance.

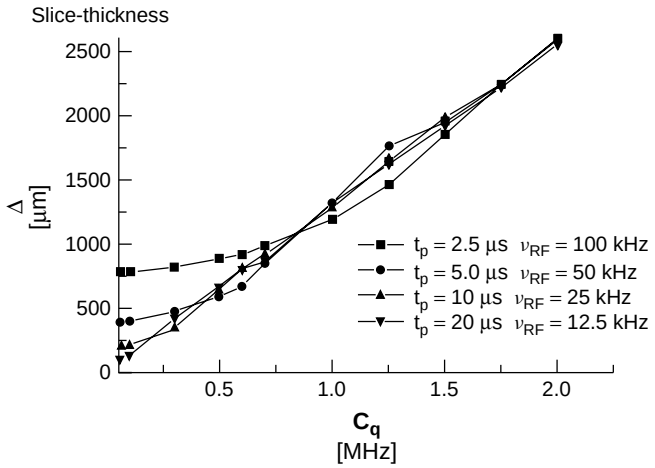

Figure 3 The slice-thickness as a function of pulse-duration and strength of the $\mathbf{B}_1$-field, ν_{RF}, and $\mathbf{C_q}(\boldsymbol{\chi})$ for a spin with $I = 3/2$, at a constant tip-angle of 90°. The pulse-delay, τ, is 50 μs for sequence 4 with two pulses in quadrature

Generally the manufacturer's calculated field-plots are sufficiently good and give accurate enough values for the gradient for most purposes. In general the most accurate calibration is required only for measurements of diffusion-constants to a high order of accuracy.

3.2 Spin-Echoes in STRAFI

STRAFI-experiments are invariably conducted with spin-echoes in order to overcome the effects of the large gradient: collection of the initial FID with present electronics is not possible, since the dead-time is normally too short. The echo-width is determined mainly by the dominant interaction which is the gradient, and is very narrow.

Hahn's original experiments, reported in 1950, were conducted with 90 degree pulses which had no specific phase relation to each other, and in magnetic fields which were not very homogeneous. The samples were restricted to protons in liquids, except for one sample, paraffin.[17] In other words the main de-focussing agency was the inhomogeneity, and neither a dipolar interaction nor a quadrupolar. This is the general sense in which we shall use the term Hahn-echo for STRAFI-echoes since even for dipolar solids the main term is the STRAFI-gradient. In Hahn's case the inhomogeneity was not so great that chemical shift effects were obscured unlike the situation in most STRAFI-experiments.

The basic two-pulse Hahn sequence (sequence 1) was $90 - \tau - 90$, and this led to an echo at time 2τ. The echo is caused by a re-focussing of the magnetization vectors. These are diverging after the first pulse, since different spin-packets experience different magnetic fields because of the natural width of the line and the different fields, $\mathbf{B_0}$, across the sample caused by the inhomogeneity. The explanation of the re-focussing after the second pulse, which was ascribed by Hahn to Purcell, was by a motion of the spin vectors in

the rotating frame, which had the shape of a Figure 8, the so-called eight-ball of pool. In fact *any* two pulses, not only those with tip-angles of 90 degrees, will give some re-focussing, the amount depending on the value of the tip-angle, α: Hahn's original 90 degree pulses re-focus only half the magnetization.

The sequence $90 - \tau - 180$ (sequence 2), on the other hand, will re-focus *all* the magnetization, apart from any lost because of relaxation. Moreover the re-focussing in this case is easier to represent and to visualize than the eight-ball so that for many *it* has become known as the Hahn sequence. It was actually Carr and Purcell who proposed it: for the measurement of T_2 by observation of the decay of the echo-amplitudes as a function of τ.[18] The field inhomogeneities, which give rise to an apparently shortened T_2, referred to as T_2^*, are exactly re-focussed at the top of each echo, so the echo-tops decay according to the true T_2.

Hahn also used more than just two pulses and produced echo-trains. He had, however, no control over the phase of the pulses. He generated stimulated echoes as well as direct echoes and separated them by using more than one value of τ between the pulses.

Later in 1958 Solomon, in a little noted piece of work, produced echoes from a quadrupolar solid, nowadays referred to as quadrupolar echoes.[19] The sequence used was

$$\alpha_x - \tau - \alpha_x \quad \text{(sequence 3)}$$

An important breakthrough was made for dipolar solids in 1965 by Powles and Mansfield with two sequences which differed in the phases, an advance on Hahn's original work[20]

$$90_x - \tau - 90_y \quad \text{(sequence 4)}$$

and the in-phase sequence

$$90_x - \tau - 90_x \quad \text{(sequence 5)}$$

In sequence 4 the pulses are said to be in quadrature, so this sequence is called a quadrature sequence, whereas sequence 5, which has no phase-change between the pulses is referred to as an in-phase sequence.

Sequence 4 produces the dipolar echo from dipolar solids, commonly referred to as the 'solid-echo', whereas sequence 5 did not. In view of the fact that the first echo from a solid sample was the quadrupolar echo observed by Solomon, we shall avoid using the term solid-echo and solid echo-sequence to refer and sequence 4.

It is an important feature of STRAFI-work in large gradients that *both* sequences 4 and 5 produce echoes from *either* solids or liquids.

Simulations with the GAMMA-platform (a suite of consistent NMR programs[21]) extended to STRAFI-calculations show this: see Figure 4. The spin-system is simply treated as spin-half dipolar. The calculations reproduce the different results of Powles and Mansfield when $\mathbf{G} = 0$ for the two sequences, but they show that at large values for $\mathbf{G}$ the quadrature and in-phase echoes are virtually indistinguishable. The explanation is simply that when $\mathbf{G}$ is large the effect of the dipolar term in the Hamiltonian is negligible in comparison with the gradient term, as noted earlier. This may be referred to as the high magnetic field-gradient approximation in which all terms in the Hamiltonian are smaller than the gradient term.[22] Exceptions to this approximation so far noted are for interactions which may be large, of the order of MHz, namely quadrupolar couplings and hyperfine interactions.

3.3 STRAFI-Echo-Shapes

STRAFI-echo-shapes differ from the shapes for the same pulse sequence in the absence of the gradient because of the effects of offset. For an assumed rectangular pulse-shape the echo-shapes for differing nominal tip-angles are shown in Figure 5 for sequence 4. These data have been computed by use of GAMMA-STRAFI which sums the echoes from each position in the sensitive slice: the number of subsystems was set at 2 per micron over 25 microns.[23] The effect of the gradient is easily seen for a tip-angle of 180 degrees. When $\mathbf{G} = 0$ one expects no echo, but the effect of the assumed gradient of $50\,\mathrm{Tm}^{-1}$ gives an echo which is zero only at its center: at either side of center the echo is finite and has opposite signs. Different echo-shapes are produced when the pulse-shape is changed from rectangular to sinc or Gaussian. These calculations give very accurate methods for the calibration of the tip-angle (see below).

3.4 Many Pulses: Long Echo-Trains

Both the Mansfield and the Waugh groups used many pulses in an extension of the quadrature Powles-Mansfield sequence:

$$90_x - (\tau - 90_y - \tau - \text{echo}-)_n \quad \text{(sequence 7)}$$

They observed that the echoes did not decay as T_2 but that the echo train was lengthened. The deduction that some line-narrowing had occurred was a most useful result for the spectroscopy of solids.[24,25] The work developed into other sequences which produced even more line-narrowing.

In the case of sequence 7, a ready explanation at hand makes use of the concept of spin-locking. Strictly spin-locking is defined in the continuous wave limit, where the second pulse can be regarded as infinitely long. Then one may consider that at resonance the magnetization is locked in the xy-plane of the rotating frame. In this case the relaxation is not according to T_2, but is referred to as T_1 in the rotating frame, and given the symbol, $T_{1\rho}$. This is longer than T_2, so the line is narrower, and shorter than T_1. In actual pulse-cases the extent of the spin-locking depends on the duty-cycle and is maximized when τ is short.

If there is no phase-change as in sequence 8

$$90_x - (\tau - 90_x - \tau - \text{ echo}-)_n \quad \text{(sequence 8)}$$

then there is no spin-locking. Also some echoes are negative whereas all echoes from the quadrature sequence 8 are positive, see Figure 6. Both of these sequences are very useful in STRAFI-studies.

Figure 6 also shows the Hahn-nature of the STRAFI-echoes since echo-trains are obtained from both a solid and a liquid for each of the sequences 7 and 8.[26]

Clearly the echoes from water cannot be classed as dipolar echoes, and the echoes produced by the in-phase sequence for the solid also are not dipolar in nature. All STRAFI-echoes are now classified therefore as Hahn spin-echoes.

Both sequences 7 and 8 have been considered theoretically by Bain and Randall using a density matrix treatment with and

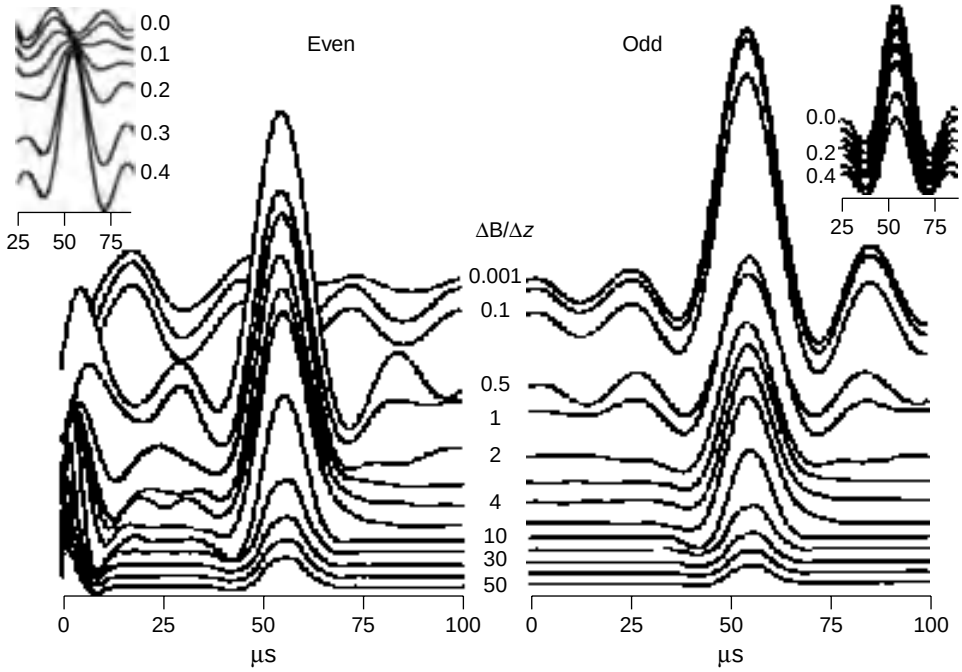

Figure 4 Simulated Echoes using the GAMMA-STRAFI for a dipolar solid for each of the sequences 4 and 5 (in-phase and quadrature, here referred to as EVEN and ODD, respectively), as the gradient strength ($\Delta B/\Delta z$) increases. The system consisted of two protons set to resonance at 300 MHz with a dipolar coupling of 50 kHz. The pulses were rectangular with a duration of 10 μs and a τ-delay of 50 μs. A 2 kHz apodisation was applied and powder averaging was included in the calculation. The inset at top left reveals the absence of a dipolar echo and the emerging Hahn-echoes for the EVEN sequence, and the top-right inset shows the same region of critical gradient strengths where the dipolar and Hahn-echoes compete. (Courtesy of Dr. S. A. Smith)

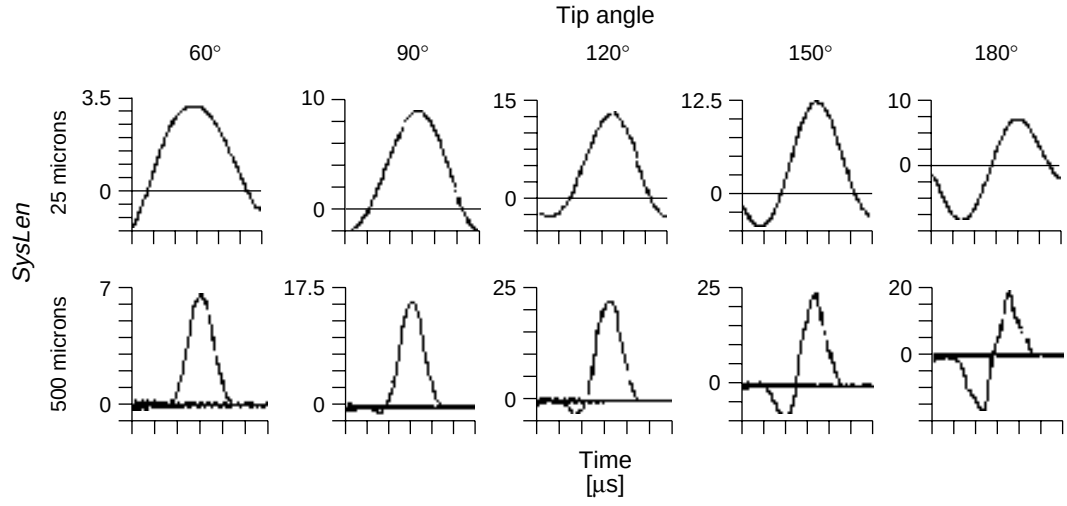

Figure 5 GAMMA-STRAFI calculations of the shape of the first echo as a function of the tip-angle for the slice-center. Rectangular pulses were assumed for the quadrature sequence: $\nu = 300$ MHz and $G = 50\ Tm^{-1}$. A single proton system was assumed. SysLens is the length over which summation of the subsystems is made within the sensitive slice. The number of subsystems was set at 2 per micron. Notice the echo broadens as SysLens decreases: it will be maximum for the central subsystem. (Courtesy of Drs. P. Kinchesh and S. A. Smith)

without the gradient.[27] They showed that all echoes after the first are composite echoes, most of which are governed partly by T_1 (see later).

This T_1-weighting is very useful for cases where T_1 is long, such as it frequently is for, say ^{15}N, ^{29}Si, and ^{31}P, particularly in solids. The idea is simply to collect the echo-tops, and sum all the values. This has been common in most STRAFI-experiments, but initially only for a modest number of echoes up to about n = 64 or less. Recently the advantage of using very long echo-trains, with n in the region of thousands, has been pointed out, since large time-savings may be achieved. The effect is quite general. Published examples so far include solids containing ^{2}H, ^{14}N or ^{31}P.[14,28,29] We should note that the technique, called Long Echo-Train Summation, LETS, should be applicable to spectroscopic studies in homogeneous fields for either solids or liquids. In these cases the whole of the

echo should be summed since Fourier transformation should then give the spectrum. The achievable spectral resolution, however, will be determined by τ since this limits the echo-sampling time.

3.5 Primary Hahn-Echoes: the Dipolar Field

STRAFI-work on solids has shown the many spin echoes, which we refer to as Primary echoes, are obtained also from just two pulses only[30] (Figure 7). This effect is due to non-linear effects and the breakdown of the high-field approximation, i.e., the induced dipolar field is not negligible. It is accounted for by the fact that the initial magnetization in the vector model forms a spiral in the rotating frame. This is just the large offset and variation in phase angle across the slice which we have discussed above.

This effect was first observed as long ago as 1974 for solid helium in modest gradients.[31] The echoes continue to be referred to, rather misleadingly, as Multiple Spin-Echoes (MSEs). The sample was solid helium at first but the work was then extended to liquid helium. At the time it was forecast that the results would not be extended to other solids and liquids. The argument was that for solids the lines would be too broad and the relaxation times too short. Solid helium was thought to be a special case: the spectral lines are narrow because of an exchange interaction, peculiar to helium. Although liquids in general give narrow lines and have long relaxation times the reasoning was that because of diffusion effects, only one echo would be obtained.

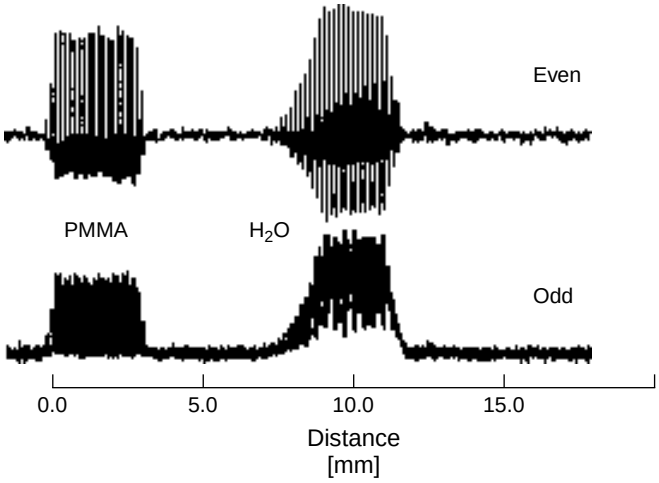

Figure 6 Spatially separated echo-trains for the protons in a phantom consisting of poly(methyl methacrylate), PMMA, and water, for both the in-phase sequence 7 and the quadrature sequence 8 (here called EVEN and ODD respectively). The water-meniscus is clearly seen on the water image. Conditions were: $\nu = 123.4\,\mathrm{MHz}$; $\mathbf{G} = 37.5\,\mathrm{Tm}^{-1}$; $t_p = 10\,\mu\mathrm{s}$; $\tau = 25\,\mu\mathrm{s}$; repetition time 1 s; number of sampled echoes = 32; 100 echo-trains accumulated

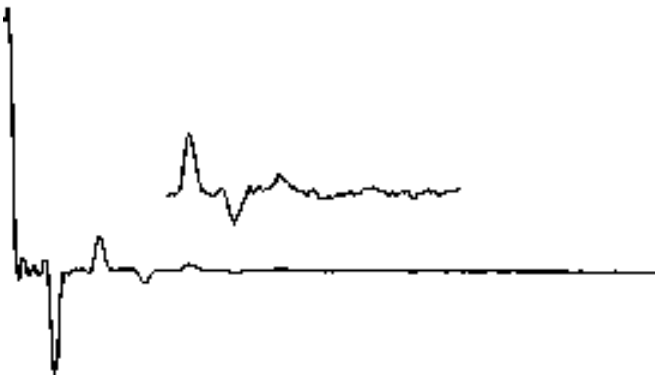

Figure 7 Multiple primary Hahn-echoes from protons in a sample of silicone rubber. Conditions were: $\nu = 123.4\,\mathrm{MHz}$; $t_p = 8\,\mu\mathrm{s}$; $\tau = 7.7\,\mu\mathrm{s}$; repetition time 10 ms

Both of these arguments were shown subsequently not to be valid. Firstly, for liquids Bowtell et al.[32] and Morris et al.[33] produced many echoes from just two pulses with modest gradients on conventional spectrometers, but it was not until 21 years after the first observation that the effect was experimentally generalized to all samples, solids as well as liquids, by STRAFI-experiments.[30] Primary Hahn Echoes are becoming fashionable in the imaging of liquids. Extension of this type of imaging to solids will require application of STRAFI-techniques. For STRAFI-cases in which many pulses are used it has been shown that the effects of the dipolar field are small so that the contribution of the MSEs to the STRAFI-echoes may be neglected.[29]

It has been pointed out by Okibo et al. that sufficient relaxation delays must be used between repetitions of sequences 4 or 5, other wise effectively the actual sequences are not simple two pulse due to a storage effect.[34]

3.6 STRAFI-Relaxation

The relaxation behavior of the STRAFI echo-train is very complex even if diffusion is not included. The reason is that the total echo-train is *the sum of the echo-trains of the isochromats at each position of the slice*. For example if there is spin-locking, not only does the initial magnetization of one component of the train vary with the pulse-angle, α, but so also does the *length* of its echo-train. For example for $\alpha = 45°$ the initial magnetization, $\mathbf{M_{45}}$, is less than $\mathbf{M_{90}}$ for $\alpha = 90°$, but the length of the train is longer, so that the two trains cross. All the other isochromats must be added in.[29] If long echo-trains are being observed then diffusion-effects should be considered, especially for liquids.

For either of the sequences 7 or 8 the first echo of the echo-train, whether a gradient is present or not, has only one coherence pathway and consequently its relaxation characteristics are governed by T_2 only (if the diffusion-term is small as it is for small values of τ). Consequently T_2 may be determined by arraying τ and observing the first echo as in Hahn's original experiments. The second echo formed by the application of three pulses, however, has two coherence pathways and the T_2-contribution is only 1/2, the rest being T_1. (This may be contrasted with the CPMG case where the pulses after the first 90° have $\alpha = 180°$ and there is no T_1-contribution).

The number of coherence pathways for the (n + 1)th echo is the sum of the coefficients of s^{n-1} and s^n in the expansion of the generating function

$$(1 + s + s^2)^n = \frac{(1 - s^3)^n}{(1 - s)^n}$$

The number of pathways increases from the first to the tenth echo in the sequence

1, 2, 5, 13, 35, 96, 267, 750, 2123, 6049

The second echo for sequence 7 has an intensity of 3/2 relative to the intensity of the first echo, whereas for sequence 8 it is only 1/2 when $\alpha = 90°$.

The T_1-weighting, which occurs with or without a gradient, means that the echo-train does **not** decay as T_2. The echo-magnetizations for the two sequences 7 and 8 are shown in Figure 8.

The lengths of the calculated echo-trains are different for the two sequences even though relaxation is not included: the echo-train from sequence 8 converges to zero, *whereas the quadrature sequence 7 produces a finite echo-asymptote*, approximately $\sqrt{2}$ times the initial magnetization.[27] An analogy may be drawn with constructive and destructive interference. The quadrature sequence is consequently the most commonly used one in STRAFI-imaging experiments.

3.7 Calibration of the Tip-Angle in STRAFI-Work

This is not trivial in the STRAFI-field since the tip-angle varies across the slice as shown by the occurrence of Primary Hahn echoes. Nevertheless one can employ a 'nominal' tip-angle, which is effectively the angle for the center of the slice.

In the first STRAFI pulse-calibration method, a value of 120° was taken as the angle, α_{max}, corresponding to maximum signal when the quadrature sequence 7 was used. This followed from calculations which used the Bloch treatment and assumed the delta-approximation.[35] It is interesting that Hahn gave $\alpha = 120°$ as the condition for maximum amplitude of the echo in the $\mathbf{G} = 0$ case, hence the result above. GAMMA-STRAFI calculations, which use the density matrix approach and in which proper summation across the slice is carried out, give $\alpha_{max} = 140°$.

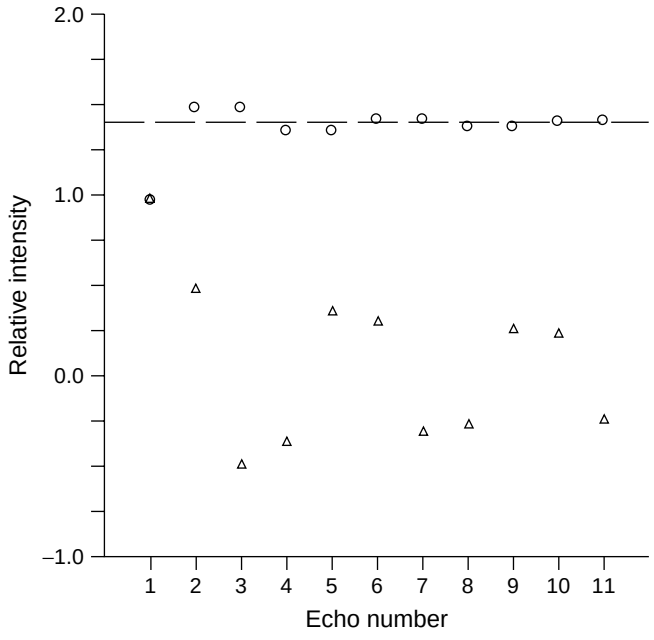

Figure 8 Calculated echo-amplitudes as a function of echo-number for the 90° quadrature sequence 7 (circles) and the in-phase sequence 8 (triangles). Relaxation and diffusion effects are ignored. The amplitude of the first echo is the same in both cases

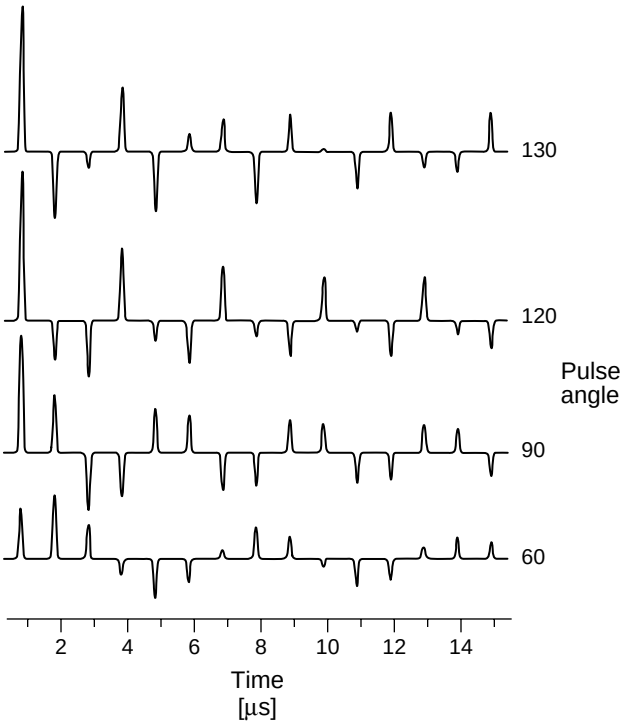

Figure 9 GAMMA calculated echoes from the in-phase sequence as the tip-angle is changed. The up-down pattern has three up and three down for 60°, two up and two down for 90°, and (not shown) 4 up and 4 down for 45°. Single proton; $\nu = 300\,\text{MHz}$; $t_p = 10\,\mu\text{s}$; $\tau = 50\,\mu\text{s}$, $\mathbf{G} = 50\,\text{Tm}^{-1}$, SysLen $= 5\,\mu\text{m}$, 3000 subsystems. (Courtesy of Dr. S. A. Smith)

A preferred method for calibration uses pulse-sequence 8. This leads to an up-down sequence of echoes: two up and two down signifies that the tip-angle is 90°; three up and three down indicates 60°; and so on, the general formula being 180/m where m is an integer.[36] The method is convenient since an immediate if approximate assessment of the pulse-angle is obtained for any initial angle. GAMMA-STRAFI calculations reproduce the experimental results: see Figure 9.

Alternatively one can use the shape of the first echo for calibration: GAMMA-simulations are shown in Figure 5. This method is probably the most accurate since it minimizes both relaxation and diffusion effects on the echo-intensities. The shape of the echo can be parameterized and a look-up table incorporated in the spectrometer computer to deduce the pulse-duration, δt, for say a 90° pulse, from an array of spectra as a function of δt.

3.8 Quadrupolar Nuclei: Half Integral Spin

Many quadrupolar nuclei having half-integral ($I = n/2$) spins have been studied in STRAFI-gradients. Examples include all odd values of n from 3 to 9.

It has been shown both by computation, see Figure 10, and by experiment that the echo-shape depends upon the electric quadrupolar coupling constant.[37] The different contributions to

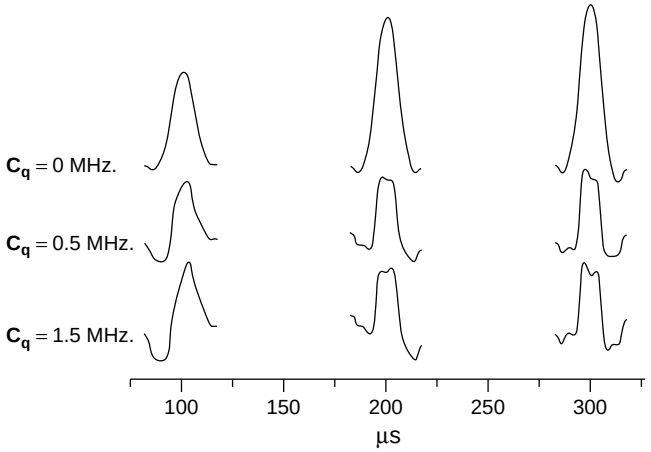

Figure 10 The first three calculated echoes for sequence 7 as a function of the assumed quadrupolar coupling constant for a powder containing a spin 3/2 nucleus. (Courtesy of P. R. Bodart)

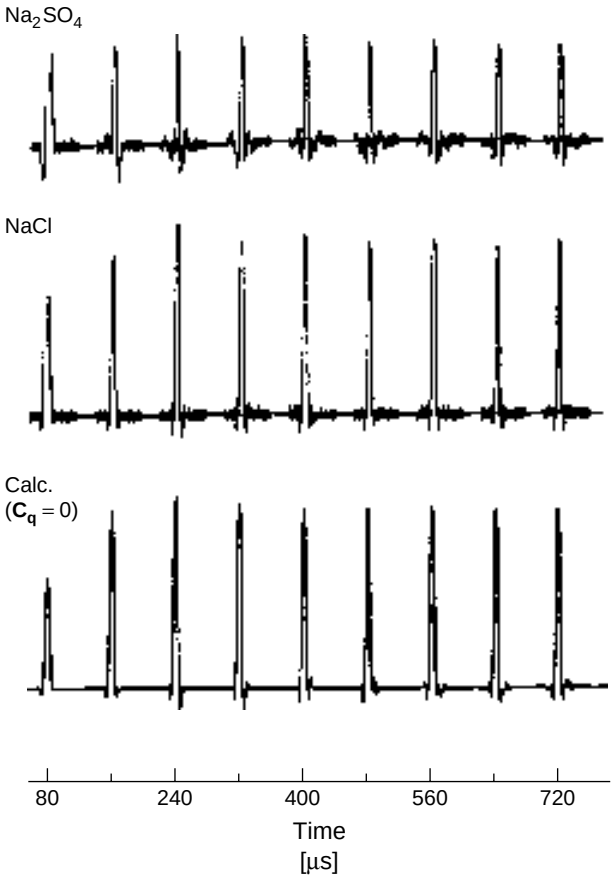

Figure 11 Responses to pulse-sequence 7 of ^{23}Na ($I = 3/2$) in powders of NaCl ($\mathbf{C_q} = 0$) and Na_2SO_4 ($\mathbf{C_q} = 2.6$ MHz and the asymmetry parameter = 0.6): $\nu = 32.2$ MHz; $t_p = 4.7$ μs; $\tau = 40$ μs; $\mathbf{B_1} = 50$ kHz; recycle time = 40 s; number of scans = 880; $\mathbf{G} = 37.5\,\mathrm{Tm}^{-1}$

the STRAFI-signal from different transitions have also been computed. Experimental STRAFI-echoes for ^{23}Na, for which $I = 3/2$, were obtained for both solid sodium chloride and sulfate, which have χ values of 0 and 2.6 MHz, respectively,

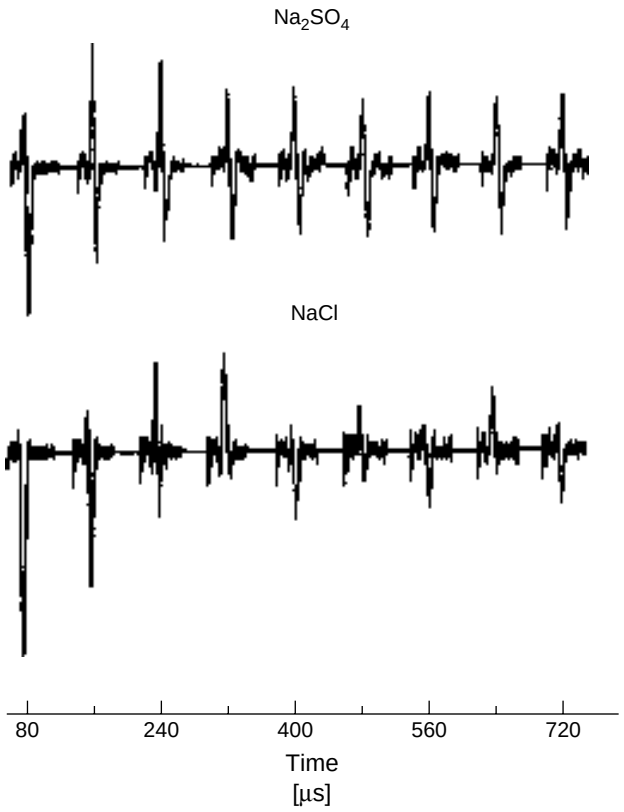

Figure 12 As for Figure 11 except the sequence is the in-phase sequence 8, and the number of scans was 1,500

and asymmetry parameters of 0 and 0.6. Figure 11 shows the experimental echoes from the quadrature sequence 7 for each of the two solids and the calculated echo-train for NaCl, whereas Figure 12 contrasts the results for the in-phase sequence 8. In the latter case it can be noted that the large quadrupolar coupling constant for the sodium sulfate disturbs the results so that the normal use of sequence 8 for pulse-calibration is not possible. Effects of the coupling can be seen too in Figure 12 in the contrast between the echo-trains. The excellence of the calculations in matching the experimental results, for example in Figure 13, shows that such comparisons, with iteration of the value of the coupling constant in the calculations, could constitute a new method for measurement of the electric-quadrupolar coupling. This may be particularly useful for paramagnetic samples, which present little difficulty for STRAFI-measurements (see below).

3.9 Quadrupolar Nuclei: Integral Spin

Two cases of nuclides having integral spins ($I = 1$) have been reported: ^{2}H and ^{14}N.[14,28] In each of these cases very long STRAFI echo-trains were obtained with thousands of echoes, even though in the nitrogen study the electric quadrupolar coupling constants varied from close to zero for ammonium nitrate to 4.9 MHz for sodium nitrite. Initial experiments on ^{14}N using an MSL 300 failed because the STRAFI-resonance frequency of about 9 MHz was too low. Success came with the use of a Bruker DMX 600 in the NHMFL in Tallahassee.[14] The higher stray field gave a resonance frequency of 33.2 MHz.

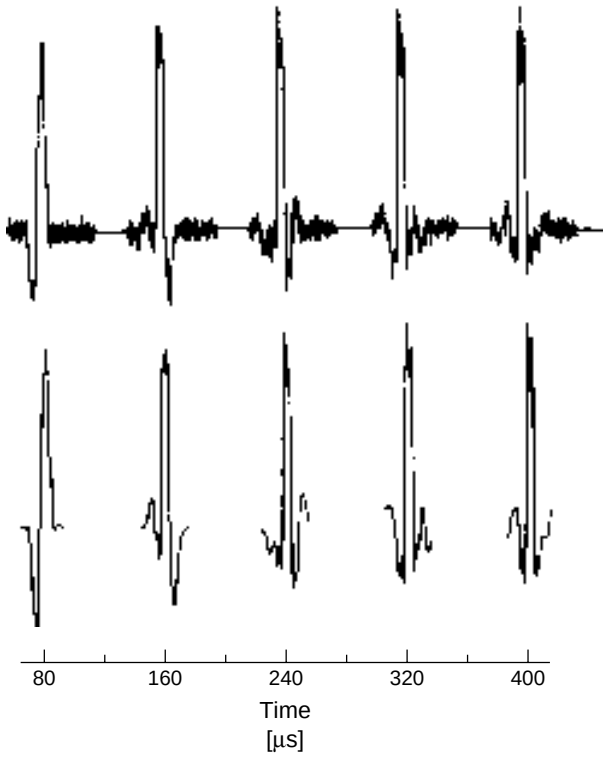

Figure 13 Comparison of the experimental STRAFI-echoes for Na_2SO_4, expanded from Figure 11, and echoes calculated using the known quadrupolar parameters

3.10 Paramagnetic Samples

So far there has been no problem in the production of STRAFI-echoes from paramagnetic samples. The first cases were proton-echoes from copper sulfate pentahydrate, diphenylpicrylhydrazyl monohydrate, tri (acetyacenato) cobalt and vanadyl bis (acetylacenate), each of which easily produced echoes provided short pulse-durations and echo-times in relation to T_2 were used.[38] The T_2 values are not greatly affected by the paramagnetism, at least at room temperature, in contrast to the much greater shortening of T_1. Consequently the proton line-width in copper sulfate pentahydrate is governed by the nuclear dipole dipole interaction, as for diamagnetic hydrates.

Both ^{19}F and ^{1}H nuclides in organic ligands co-ordinated to a variety of lanthanide metals, including holmium, which has a larger paramagnetic susceptibility (10 Bohr magnetons) than the other members of the series do, also gave no problems.[39]

More surprisingly and significantly both the paramagnetic and quadrupolar nature of vanadium ($I = 7/2$) in vanadyl bis aceto acetylacetate did not interfere with echo-formation for ^{51}V. Similarly for ^{59}Co ($I = 7/2$), STRAFI-resonances have been obtained from a variety of paramagnetic (Co II) cobalt samples, as well as diamagnetic (Co III) complexes. Generally the intensities are lower for the former presumably because of shorter T_2 values. STRAFI-methods may therefore prove to be very useful for the study of paramagnetic compounds with quadrupolar nuclides.

3.11 Enhancements: Double Resonance

In conventional imaging of liquid samples, as in spectroscopy, double resonance (DR) has been usefully employed to enhance the signal of one nuclide by cw irradiation or pulsed-irradiation of the transitions of another. Both direct and indirect (inverse) methods have employed such as the Nuclear Overhauser Effect in ^{1}H-$\{^{15}N\}$ experiments, or narrowing of lines broadened by a coupling to a quadrupolar nucleus as in ^{1}H-$\{^{14}N\}$ experiments.[40,41] 'Edited' images of only those protons attached to nitrogen are produced in each case. Concerning the imaging of solids, successful ^{1}H-^{31}P cross-polarization imaging experiments in modest gradients on chicken-bone have been reported.[42] The DR-technique therefore holds out hope of reducing the long experiment times necessary in STRAFI- cases which are caused by the large band-widths and the single-point nature of the experiments. The band-width problem could be overcome by the use of line-narrowing techniques.

Preliminary STRAFI-DR results have been obtained in the case of solid KPF_6. Modest ^{31}P enhancements have been reported for ^{19}F pre-saturation (26%), and cross polarization (16%).[29] Initial attempts at line-narrowing failed, however.

4 STRAFI-IMAGING IN 1-DIMENSION

The imaging experiment in one spatial dimension may be performed in four main ways depending on the size of the phantom. These techniques are:

Fourier Transformation
Frequency sweep
Field sweep
Sample translation

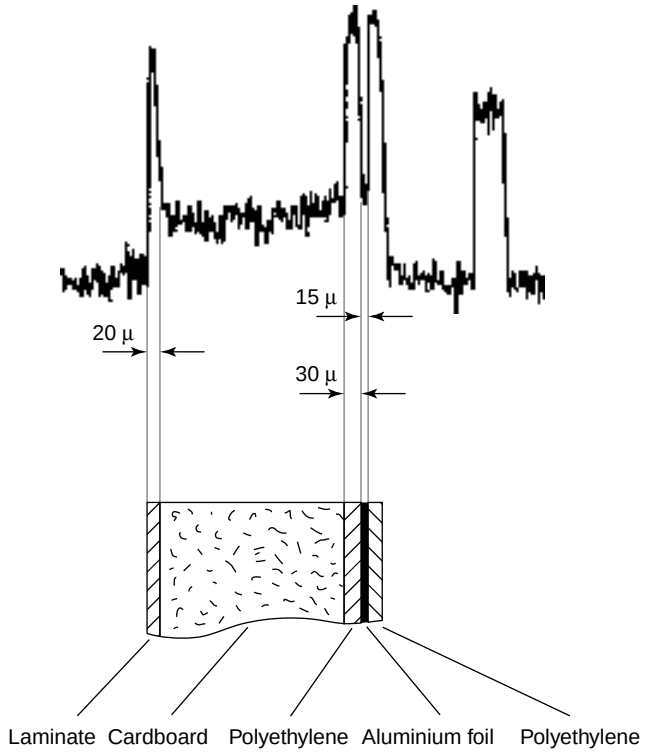

Figure 14 STRAFI-FT of the protons in the material of a container of fruit juice. The right hand signal is from a marker. (Courtesy of Dr. A. A. Samoilenko)

If the sample size is less than the excited slice-thickness then the whole of the phantom may be excited by the rf if very short pulses are used. Fourier transformation of the signal then yields the 1-D projection. This *FT-method* is useful for thin objects and has been exploited extensively for thin films, wafers and sheets. An example is shown in Figure 14. For protons a spatial resolution of about 5 μm for solids has been demonstrated for a gradient strength of 37.5 Tm^{-1}. The resolution is capable of improvement at higher values of G.

In other cases where the phantom is larger than the thickness of the excited slice, there are three basic methods for imaging: frequency-sweep, field-sweep, and translation of the sample. The problem with *the frequency-sweep method* is that large sweep-widths of the order of MHz are needed and the coil does not remain in tune unless the Q is unacceptably small. *The field-sweep method* requires a spectrometer which has the appropriate field-sweep coils, either built-in or added.[43] Built-in sweep-coils are not very common for superconducting solenoids. Although both of these methods have been demonstrated it is the fourth one, *sample translation*, the one originally used by Samoilenko, which has been most commonly used.

4.1 Sample Translation

This method is normally employed with the quadrature pulse-sequence with sampling of the echo-tops. The sample is then moved step-wise through the position of the sensitive plane. The step-size is of the order of the slice-thickness for the best resolution: if it is larger then the resolution is degraded. An alternative method, 'on the fly', has a continuous motion of the sample. In this case the motion has to be slow enough not to introduce phase-shifts. There is no FT: the magnetization at each position is simply summed and recorded.

4.2 Accumulation

There is a choice between repeating the echo-trains at each position in the traverse, with a delay between each, and taking only one traverse, or, more commonly, moving the sample after the collection of a train from one slice to the next slice without a delay, and making many traverses. Since one complete traverse and return of the sample to the initial position takes a time Θ, which is of the order of one or two seconds, this second method allows Θ to be used as part of a T_1-relaxation delay. In either case many pulses may be used in each sequence to yield long echo-trains. These are T_1-weighted and may be summed in the method of Long Echo-Train Summation (LETS). Solids are normally endowed with large T_1 values so this method of accumulation is of considerable advantage in STRAFI-studies.

4.3 Quadrupolar Nuclides

Examples of 1-D profiles from a selection of quadrupolar nuclides are shown in Figure 15, as well as the spin-half example of ^{31}P (in red phosphorus), for which an example of a moderately long echo-train is shown since the STRAFI-decay is long. In each case the phantom was divided into two volumes with a spacer of thickness 0.65 mm. The spacer is clearly resolved. In some cases it can be seen that profiles for

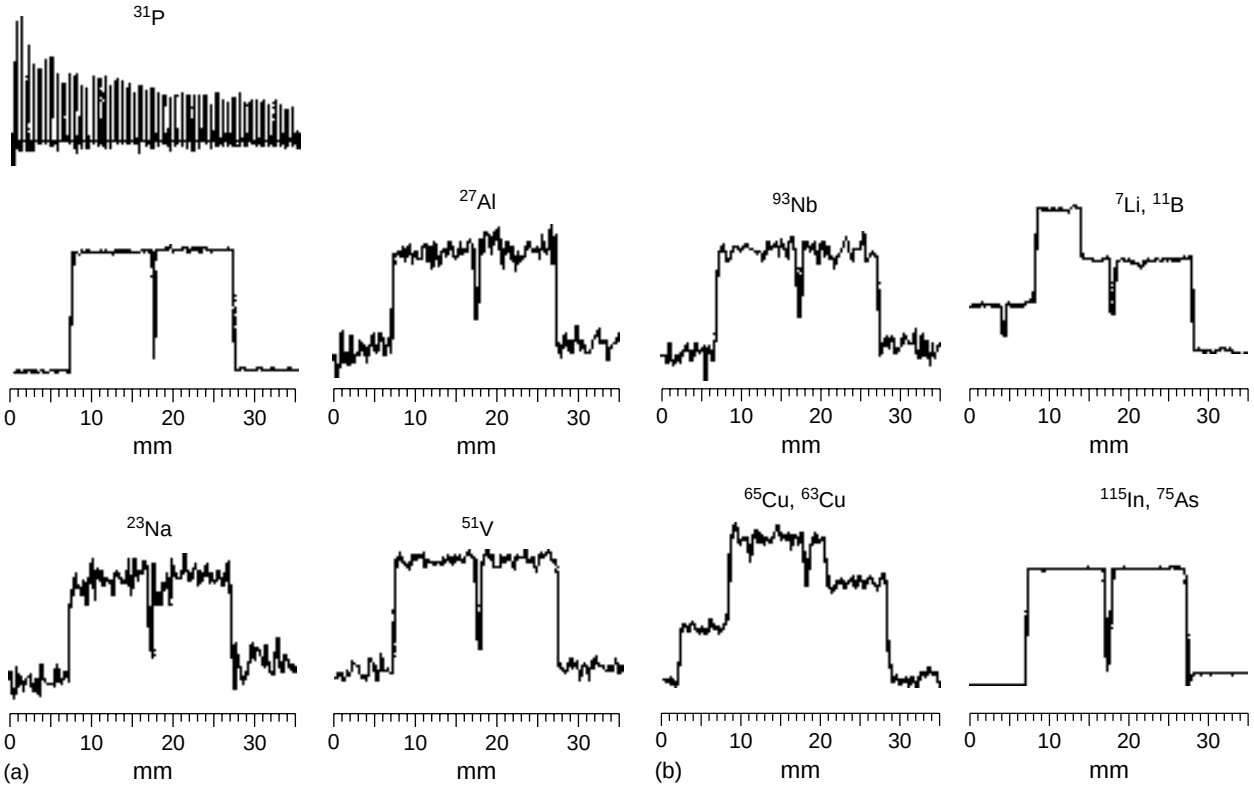

Figure 15 1-D profiles for ^{31}P and a variety of quadrupolar nuclides taken using the translation method (see text). The gap is 0.65 mm in each case. (Courtesy of Dr. A. A. Samoilenko)

different nuclides overlap, because of the closeness of their γ-values (see equation (2)).

4.4 Multinuclear Profiles

Separate ^{11}B and ^{1}H profiles of a phantom containing sodium borohydride, sodium borofluoride, and sodium borate decahydrate have been reported,[44] and more recently ^{31}P and ^{1}H profiles of the same section of dried chicken bone have been obtained.

There are several examples of *simultaneous* procurement of profiles of pairs of nuclides which have γ-values which are close to each other, in addition to those noted above for quadrupolar nucleides.

The examples are mainly for the proton-fluorine pair, including one involving dental cement.[45] The original study[13] included three experiments: one with solid discs of the polymers PMMA and PTFE (spatial separation of H and F); the second had a disc of nylon being ingressed by 2,2,2 trifluoroethanol (H in the solid, and both H and F in the same liquid); and the third had a fluorine-free polymer (used as a cement for bone prostheses), being ingressed by a perfluorinated solvent, hexafluorobenzene.[13] In each case both the ^{1}H and ^{19}F images are obtained in one traverse with the Bruker probe. The appearance of the image depends on whether the F- or the H-containing parts of the phantom enter the fringe-field first: the maximum separation of the ^{1}H and ^{19}F images occurs when it is the proton: see Figure 16.

The only other pair noted so far is ^{7}Li and ^{31}P. The displaced profiles were obtained from a number of ceramics and glasses on the high field Tallahassee system at 202 MHz, at which frequency the relative γ-displacement is 6.45 mm.

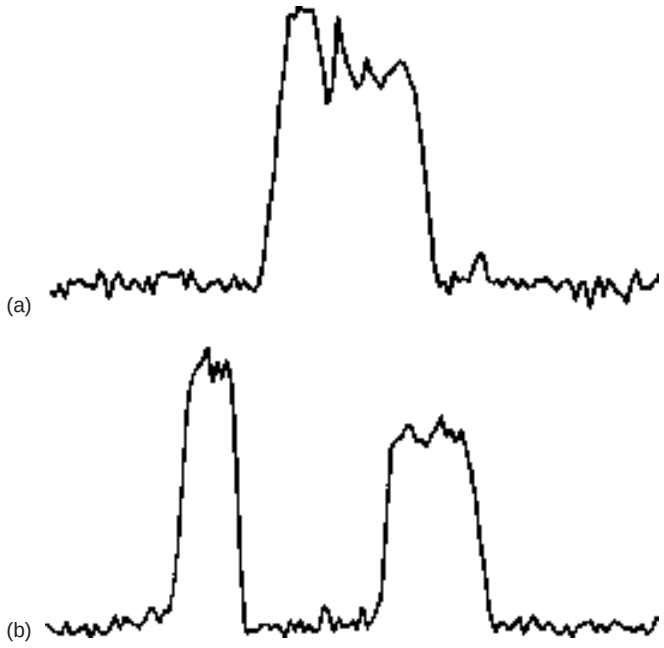

Figure 16 1D-profiles for ^{1}H- in a PMMA disc of height 2 mm and 19 F in a PTFA disc 3 mm high showing the γ-shift (see text). The discs are in contact and the separation of the sensitive planes is about 4.9 mm. The top scan (a) was taken with the fluorine disc entering the STRAFI-region first. The bottom scan (b) was after a 180° rotation of the phantom. $\nu = 123.4$ MHz and $\mathbf{G} = 37.5\,\mathrm{Tm}^{-1}$

5 STRAFI-STUDIES IN 2- AND 3-DIMENSIONS

Most STRAFI-studies employing sample movement have been accomplished in one dimension and have involved a simple translation of the phantom. Since in this mode the STRAFI-technique is essentially a single point method and because of the large band-width for solids, it is time-consuming. In general it has been more advantageous to design the experiment to yield the desired information from one dimension than to use 2- or 3D-STRAFI-imaging. Of course this is not always possible, for example for bones and many other materials.

The translation method in which the sample is moved along the z-axis of the solenoid along which **G** varies may be extended to a second spatial dimension by a rotation around an axis perpendicular to z, say around the x-axis, and to a third dimension by a second orthogonal rotation around the y-axis. There is a 3D proton STRAFI-study of an extracted first mandibular tooth.[46] For very small samples for which the 1-D FT method may be applied, i.e., for which the excited slice is potentially wider than the sample in any orientation, a second dimension may be obtained by one rotation, as has been achieved by Newling. It is possible to add a third dimension by a second orthogonal rotation as for the extension of the translation method.

6 APPLICATIONS

Most reported STRAFI-applications have been confined to proton work in one dimension, and most of these have employed the method of sample translation, although an increasing number employ the FT-method. Many of the applications only mentioned briefly below have been comprehensively reviewed by Newling and McDonald.[9]

A seminal STRAFI-study was the examination of acetone ingressing into poly(vinyl chloride), PVC.[47] For the first time protons in all three environments, polymer, softening polymer and ingressing liquid, were imaged at high spatial resolution, about 80 μm. Results from relaxation-weighting and per-deuteriated acetone experiments allowed discrimination of the overlapping contributions of liquid and softening polymer. The mechanism of ingression and the rates of softening of the polymer were reported. Great pains were taken by the Surrey group to yield phantoms suitable for 1-D studies. A number of PVC samples were placed in acetone atmospheres at different partial pressures of acetone and different temperatures. In each case the sample was then frozen to stop the process and the frozen solid was machined down to 10 mm cubes to yield a phantom which had only one surface exposed to the acetone. In other words the ingression was not followed on one sample, as in subsequent work. Each profile took about 30 minutes to one hour to acquire.

The STRAFI-method is very useful for such temporal studies because of its non-invasive nature. Subsequently there have been many similar studies on organic polymers such as with mixed solvents, for example methanol and acetone with poly(methylmethacrylate).[48] Other polymers investigated by the STRAFI-method include poly(ester) and epoxide resins,[49] extruded poly(propylene),[50] microbial poly(saccharides),[51] and polystyrene.[52] A 3-D study was used on poly(ethylene glycol) and poly(vinyl alcohol) binders.[53] Other classes of mainly

organic materials are glues and coatings, latex paint, creaming of emulsion layers, adhesive tapes, and photographic films.

The class of porous inorganic minerals and materials has also been studied quite extensively. These are heterogeneous and suffer in normal imaging studies from short T_2-values, and from the effects of magnetic susceptibility variations, neither of which affect STRAFI-imaging to the same extent as conventional studies. All categories of protons may be detected. In the case of water detection of all types and conditions is possible: from bound or co-ordinated water, ice, water in pores and capillaries, to more mobile water in

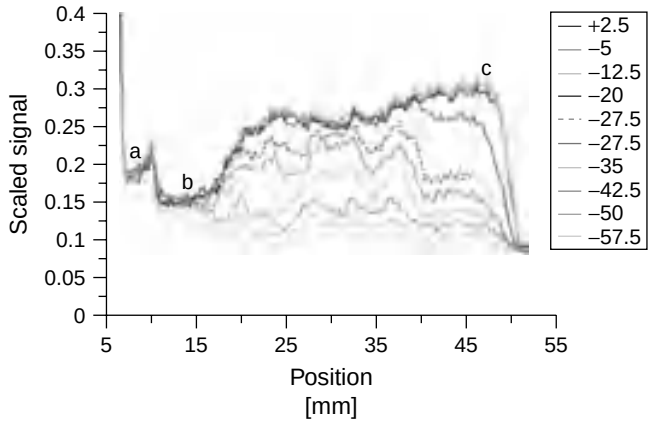

Figure 17 STRAFI-profiles for water-protons in a soil sample being drained to various matric potentials. Bulk water is shown at the left at a and is given unit intensity. The water and the wet soil are separated by a porous disc at b. The matric potentials are given in hPa. Each image is from 146 slices 360 μm apart and each point is the sum of the total intensity of an echo-train 32 echoes long. $\nu = 111$ MHz and $\mathbf{G} = 12.0\,\mathrm{Tm}^{-1}$. (Courtesy of Dr. A. R. Preston)

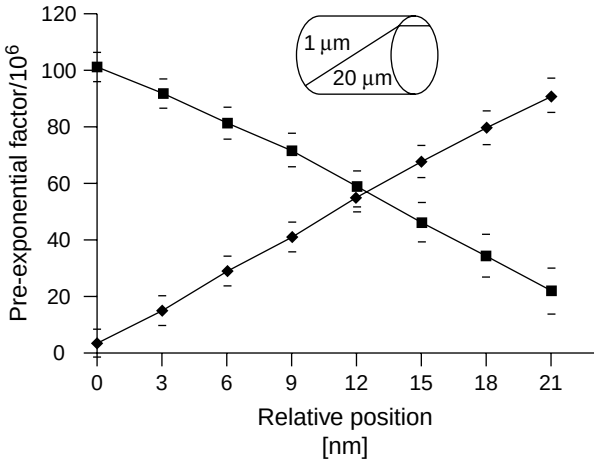

Figure 18 Spatial dependence of the amplitudes of two exponential decay-terms needed to fit the water-proton peak-amplitudes from a series of positions along a bi-wedge (inset). The cylindrical bi-wedge has a diameter of 31 mm and length of 24 mm. Its two parts are separated by an acetate sheet. Each part was cut from a Coralith ceramic having pores characterized by a single-size pore-diameter: 1 μm and 20 μm respectively. The relaxation time of the pore-water depends on the pore-size. $\nu = 111$ MHz and $\mathbf{G} = 12.0\,\mathrm{Tm}^{-1}$. (Courtesy of Dr. A. R. Preston)

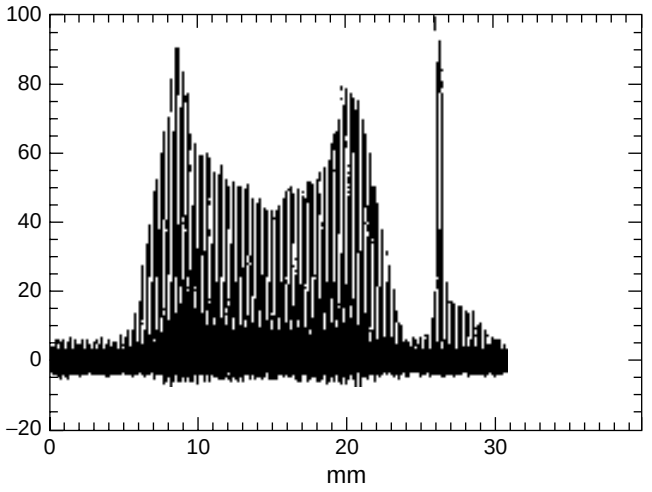

Figure 19 Spatially resolved echo-trains for protons in a section of dry chicken bone without marrow. Results were from the Surrey STRAFI-system. $\nu = 236.6$ MHz; $\mathbf{G} = 58.5\,\mathrm{Tm}^{-1}$; $t_p = 8\,\mu$s; $\tau = 60\,\mu$s; number of echoes, 128 in each train, recycle time 0.1 s. Signal at the right is from the glue holding the glass container. (Courtesy of Dr. J. Godward and Dr. D. G. Gillies)

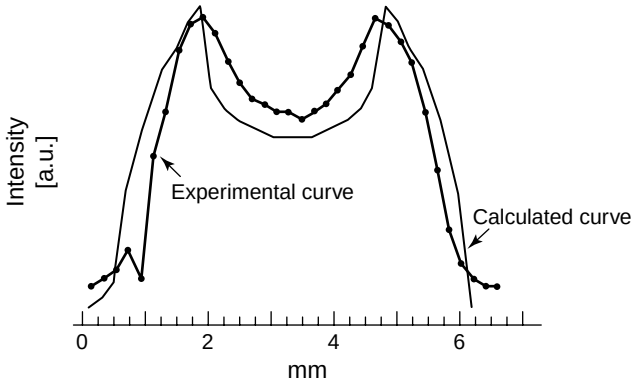

Figure 20 Experimental and calculated points for a 1-D profile of an electrical insulating disc (outer and inner diameters of 6.4 and 3.0 mm respectively, height 15 mm) made of aluminium oxide. The gradient was $75.7\,\mathrm{Tm}^{-1}$ that of a Magnex magnet of bore 31.6 mm with center field of 19.6 T. The STRAFI-nucleus was ^{27}Al; $\nu = 124.3$ MHz; $t_p = 4\,\mu$s; $\tau = 103\,\mu$s; recycle delay of 0.2 s; 100 scans for each position. Only two pulses were used each time giving a single echo. (Courtesy of Dr. V. Soghomonian and A. R. Samoilenko)

gels or in free water. Rocks, soils, cements and other building materials, such as tiles, may be studied advantageously by the STRAFI-method, which can yield not only images but spatial variation of relaxation parameters and diffusion constants.

There is only a small number of STRAFI studies in 3D. Two early studies were of water: firstly in a narrow tube surrounded by nickel sulphate crystals, which severely distorted a conventional image taken in the center field because of susceptibility effects but not the STRAFI-results;[2] and then a study of water and plant-material in soil.[3] Other 3D-work, in addition to the investigation of a mandibular tooth[46] includes Zick's imaging of a poly-carbonate plug, and Wang's study of unsintered green ceramics.[9]

Figure 21 The STRAFI-system at Queen Mary, University of London. The stepper motor is mounted on a table bolted to the floor. The sliding carriage is shown in close-up together with the coil-system (5 cm bore), a copper shielding box, and a phantom surmounted by a rubber bung contained in a glass cylinder. (Courtesy of Dr. P. Kinchesh)

Soil-water, including the pore-size distribution, is now being studied as a function of matric potential (hydrostatic pressure) see Figure 17, a possibility which may be extended to other materials.[54] The advantage of STRAFI-work is that it can reach water even in the smallest pores and also bound water. A problem even with the STRAFI-technique in investigations of ice, whether in bulk or in pores, is the complication of the very short T_2 which is of the order of $5\,\mu s$ for ^1H: very short pulse-durations and echo-times are required. Nevertheless both heavy water and heavy ice,[28] and water and ice, have been studied by Nunes et al. An illustrative example of work on water in porous ceramics is shown in Figure 18.[55]

Work with medical potential, in addition to that on dental materials, is STRAFI-work on bones: one may use either ^{31}P or ^1H. Proton-work on bone is illustrated in Figure 19, which shows the STRAFI-profile, in the form of spatially separated echo-trains, of a section of dry chicken-bone without the marrow.

Work on other nuclei may be contemplated, such as ^{27}Al in cements provided ^{23}Na does not interfere. Lastly we conclude with a high field example of STRAFI-work on ^{27}Al in an electrical insulating disc of aluminium oxide as shown in Figure 20. Other exploratory work on this 19.6 T system at the NHMFL was with the nuclides 1H, 2H, ^7Li, ^{23}Na and ^{31}P.

7 PROSPECTS

STRAFI-work has been curiously slow to spread, despite its strengths as demonstrated for example by the applications published by the Surrey and Lisbon groups.[9] Nevertheless its worth is being increasingly appreciated particularly by the materials community. One disadvantage is that currently there is no commercial STRAFI-package available, indeed only Bruker, where the technique was largely developed, has ever offered a commercial STRAFI-system. The STRAFI-additions to instruments at Surrey, Tallahassee and Queen Mary, have each been made in-house. The STRAFI-apparatus, developed at Queen Mary around a Varian/Sisco system with an Oxford magnet, to a STRAFI-design by Andre Samoilenko, is shown in Figure 21.

8 REFERENCES

1. A. A. Samoilenko, D. Yu. Artemov, and A. L. Sibel'dina, *JEPT Lett.*, 1988, **47**, 348.
2. P. Kinchesh, E. W. Randall, and K. Zick, *J. Magn. Reson.*, 1992, **100**, 411–415.
3. P. Kinchesh, E. W. Randall, and K. Zick, *Magn. Reson. Imaging*, 1994, **12**, 305–307.
4. R. Kimmich, W. Unrath, G. Schnur, and E. Rommel, *J. Magn. Reson.*, 1991, **91**, 136–140.

5. R. Kimmich and E. Fischer, *J. Magn. Reson.*, 1994, **A106**, 229–235.
6. B. Geil, *Concepts NMR*, 1999, **10**, 299–321.
7. E. W. Randall, in 'Encylopedia of Spectroscopy and Spectrometry', eds J. C. Lindon, G. E. Tranter, and J. L. Holmes, Academic Press, 2000, 1396–1403.
8. P. J. McDonald, *Prog. NMR*, 1997, **30**, 69–99.
9. B. Newling and P. J. McDonald, *Rep. Prog. Phys.*, 1998, **61**, 1441–1493.
10. I. Chang, F. Fujara, B. Geil, G. Hinzer, H. Sillescu, and A. Tölle, *J. Non-Crystalline Solids*, 1994, **172**, 674–681.
11. P. Glover, P. S. Aptaker, J. R. Bowler, E. Ciampi, and P. J. McDonald, *J. Magn. Reson.*, 1999, **139**, 90–97.
12. F. Balibanu, K. Hailu, R. Eymael, D. E. Demco, and B. Blümich, *J. Magn. Reson.*, 2000, **145**, 246.
13. E. W. Randall, A. A. Samoilenko, and T. Nunes, *J. Magn. Reson.*, 1995, **A117**, 317–319.
14. E. W. Randall, A. A. Samoilenko, and R. Fu, *Solid State NMR*, 1999, **14**, 173–179.
15. P. Bodart, T. Nunes, and E. W. Randall, *Appl. Mag. Reson.*, 1997, **12**, 269–273.
16. A. R. Preston, P. Kinchesh, and E. W. Randall, *J. Magn. Reson.*, 2000, **146**, 359–362.
17. E. L. Hahn, *Phys. Rev.*, 1950, **80**, 580.
18. H. Y. Carr and E. M. Purcell, *Phys. Rev.*, 1954, **94**, 630.
19. I. Solomon, *Phys. Rev.*, 1958, **100**, 61.
20. J. G. Powles and P. Mansfield, *Phys. Lett.*, 1965, **2**, 58.
21. S. A. Smith, T. O. Levante, B. H. Meier, and R. R. Ernst, *J. Magn. Reson.*, 1994, **A106**, 75–105.
22. E. W. Randall, A. A. Samoilenko, and T. Nunes, *J. Magn. Reson.*, 1995, **A116**, 122–124.
23. P. Kinchesh, S. A. Smith, A. R. Preston, and E. W. Randall, *J. Magn. Reson.*, 2002, **154**, 1–9.
24. P. Mansfield and D. Ware. *Phys. Lett.*, 1966, **22**, 133–135; *Phys. Rev.*, 1968, **168**, 318–334.
25. E. D. Ostroff and J. S. Waugh, *Phys Rev. Lett.*, 1966, **16**, 1097–1098; J. S. Waugh and C. H. Wang, *Phys. Rev.*, 1967, **162**, 209–216.
26. E. W. Randall, A. A. Samoilenko, and T. Nunes, *Q. Mag. Reson. Biol. Med.*, 1995, **2**, 299–300.
27. A. D. Bain and E. W. Randall, *J. Magn. Reson.*, 1996, **A123**, 49–55.
28. E. W. Randall, T. G. Nunes, G. Guillot, and P. R. Bodart, *Solid State NMR*, 1999, **14**, 165–172.
29. D. G. Gillies, B. Newling, and E. W. Randall, *J. Magn. Reson.*, 2001, **151**, 235–241.
30. E. W. Randall, A. A. Samoilenko, and T. Nunes, *J. Magn. Reson.*, 1995, **A116**, 259–261.
31. G. Deville, M. Bernier, and J. M. Delrieux, *Phys. Rev. B*, 1979, **19**, 5666.
32. R. Bowtell, R. M. Bowley, and P. Glover, *J. Magn. Reson.*, 1990, **88**, 643–651.
33. J. C. Waterton, R. P. O. Jones, and G. A. Morris, *J. Magn. Reson.*, 1992, **97**, 218–221.
34. N. Okibo, T. Suzuki, and T. Aokit, *Phys. Lett.*, 1998, **A248**, 463–467.
35. P. Benson and P. J. McDonald, *J. Magn. Reson.*, 1995, **A112**, 17–23.
36. E. W. Randall, *Solid State NMR*, 1997, **8**, 179–183.
37. P. Bodart, T. Nunes, and E. W. Randall, *Solid State NMR*, 1997, **8**, 257.
38. E. W. Randall, A. A. Samoilenko, and T. Nunes, *J. Magn. Reson.*, 1995, **A116**, 122–124.
39. E. W. Randall, *Solid State NMR*, 1997, **8**, 173–178.
40. P. Kinchesh, E. W. Randall, and S. R. R. Williams, *J. Magn. Reson.*, 1993, **A103**, 234–237.
41. P. Kinchesh, E. W. Randall, and S. R. R. Williams, *J. Magn. Reson.*, 1993, **B105**, 253–255.
42. J. R. Moore, L. Garrido, and J. J. Ackerman, *Magn. Reson. Med.*, 1995, **33**, 293–299.
43. M. J. D. Mallet, M. R. Halse, and J. H. Strange, *J. Magn. Reson.*, 1998, **132**, 172–175.
44. D. G. Gillies and E. W. Randall, *J. Magn. Reson.*, 1996, **A121**, 217–220.
45. C. H. Lloyd, S. N. Scrimgeour, G. Hunter, J. A. Chudek, D. M. Lane, and P. J. McDonald, *J. Mat. Sci.: Mat. Med.*, 1999, **10**, 369–373.
46. M. A. Baumann, G. M. Doll, and K. Zick, *Oral Surg. Oral Med. Oral Pathol.*, 1993, **75**, 517–522.
47. K. L. Perry, P. J. McDonald, E. W. Randall, and K. Zick, *Polymer*, 1997, **38**, 2744–2748.
48. D. M. Lane and P. J. McDonald, *Polymer*, 1994, **35**, 2329–2335.
49. S. N. Scrimgeour, G. Hunter, W. J. Harvey, C. H. Lloyd, D. M. Lane, and P. J. McDonald, in 'Spatially Resolved Magnetic Resonance', eds P. Blümler, B. Blümich, R. Botto, and E. Fukushima, Wiley-VCH: Weinheim, 1998, pp 281–286.
50. R. J. Abbott, J. A. Chudek, G. Hunter, R. L. Mackay, and L. Squires, in 'Spatially Resolved Magnetic Resonance', eds P. Blümler, B. Blümich, R. Botto, and E. Fukushima, Wiley-VCH: Weinheim, 1998, pp 253–258.
51. T. D. Hart, A. H. L. Chamberlain, J. M. Lynch, B. Newling, and P. J. McDonald, *Enzyme Microbiol. Technol.*, 1999, **24**, 339–347.
52. P. J. McDonald, J. Godward, R. Sackin, and R.P. Sear, *Macromolecules*, 2001, **34**, 1048–1057.
53. P. S. Wang, D. B. Minor, and S. G. Malghan, *J. Mat. Sci.*, 1993, **28**, 4940–4943.
54. A. R. Preston, P. Kinchesh, E. W. Randall, N. R. A. Bird, and W. R. Whalley, *Magn. Reson. Imaging*, 2001, **19**, 561–563.
55. P. Kinchesh, A. A. Samoilenko, A. R. Preston, and E. W. Randall, *J. Environ. Quality*, 2002, **31**, 444–459.

Acknowledgements

I am grateful particularly to Andrei Samoilenko, the father of the technique, for our stimulating periods of work together, to Teresa Nunes in Lisbon and Peter McDonald in Surrey for making me so welcome in their respective laboratories, and indeed to all my STRAFI-collaborators from the first, Paul Kinchesh and Klaus Zick, to Alex Bain, Scott Smith and Philippe Bodart for computations, and to the latest, Alasdair Preston, for enlightenment. I am greatly obliged to collaborators for permission to include work which is not in the open literature or is not yet published. Thanks too, to Dr. Nathalie Mahieu and Alasdair Preston for help with the figures.

Biographical Sketch

Edward Randall, *b* 1933 in Liverpool and educated at Magdalen College Oxford. He began research in magnetic resonance as a post-doctoral fellow at Harvard (1959–61) with some of the first double resonance studies, which he continued at Queen Mary College. There he ran a National NMR Service on the first commercial pulse-FT spectrometer in the UK beginning in 1970. His own group specialized in 15N studies including the first studies of peptides, and 13C and 17O work on organometallics. He began imaging in 1991 using both direct and new indirect spin-echo techniques for both 14N and 15N in liquids. He then turned to the difficult task of imaging solids and was one of the first to use and adopt the STRAFI-technique in 1992. Working in Lisbon, Surrey, and more recently in Tallahassee, he has published more than 30 STRAFI-papers in which he showed that any nucleus in virtually any solid can be imaged.

Wavelet Encoding of MRI Images

Lawrence P. Panych and Ferenc A. Jolesz

Brigham and Women's Hospital and Harvard Medical School, Boston, MA, USA

1 INTRODUCTION

In Fourier transform MRI, the raw image data can be expressed mathematically as samples of the Fourier transform of a spatially dependent density function that is proportional to the magnitude distribution of the transverse magnetization. Thus, the raw Fourier image data represent a spatial frequency decomposition of the density function. In wavelet encoding of MRI images, one attempts to image in such a way that the raw image data can be expressed as samples of the wavelet transform of the density function along at least one spatial dimension. The raw wavelet image data have some characteristics of a spatial frequency decomposition, but they also retain features of the spatial domain representation.

More formally, let $s(x)$ represent the density function. The Fourier transform of $s(x)$ is a function $S(k)$ of the spatial frequency parameter k, and $|S(k)|^2$ gives a measure of the 'energy' content in $s(x)$ at the spatial frequency k (in cm^{-1}). The wavelet transform of $s(x)$ is a function $S_w(v,u)$ of two parameters: a 'scale' (spatial frequency band) parameter v and a location parameter u. $|S_w(v,u)|^2$ gives a measure of the 'energy' content in $s(x)$ at the scale v (in cm^{-1}) in the vicinity of the location u (in cm).

In Fourier transform MRI, the raw Fourier domain data are produced by manipulation of the phase angle of the transverse magnetization. In wavelet MRI, on the other hand, it is the angle of the magnetization vector between the longitudinal axis and the transverse plane that is manipulated. In other words, the amount of the magnetization tilted into the transverse plane is modulated according to wavelet-shaped excitation profiles. This is done by modifying the rf excitation pulses on each encoding step.

In this article, wavelet encoding in one of the dimensions of a two-dimensional imaging method is described. The second dimension is Fourier-encoded because, during the data acquisition period of an imaging sequence, it is not possible to manipulate the flip angle of the spins, nor is it possible (with linear gradients) to wavelet-encode the phase angle of the transverse magnetization. Thus, the so-called frequency-encoding dimension must be Fourier-encoded. Figure 1 shows a modified line scanning sequence that has been used[1,2] to encode two-dimensional images with wavelet encoding along one of the dimensions (y). The wavelet encoding method using this sequence applies ideas first proposed by Healy and Weaver.[3,4] Wavelet encoding has also been implemented in the slice-select direction using a multislice gradient echo sequence with wavelet-shaped slice profiles.[5]

2 WAVELET TRANSFORM THEORY

2.1 Continuous and Discrete Wavelet Transform

A wavelet transform[6] $F_\Psi(v,u)$ of the real-valued finite-energy function $f(x)$ is defined by

$$F_\Psi(v,u) = |v|^{-1/2} \int f(x)\Psi\left(\frac{x-u}{v}\right) \mathrm{d}x \quad v \neq 0 \tag{1}$$

$\Psi(x)$ is the real-valued 'basic' wavelet function, and is a window on $f(x)$ that is both scaled (v) and translated (u). For practical applications such as imaging, it is important to know if a function can be recovered from a discrete and finite sampling of its wavelet transform space. When the sampling is exponential as expressed by

$$v = 2^j, \quad u = 2^j n, \quad \text{where } j \text{ and } n \text{ are integers} \tag{2}$$

a family of 'dyadic' wavelets $\{\Psi_{j,n}(x)\}$ is produced as defined by

$$\Psi_{j,n}(x) \equiv 2^{-j/2}\Psi(2^{-j}x - n) \tag{3}$$

$\Psi(x)$ have been found such that the set of dyadic wavelets defined by equation (3) is orthonormal, and arbitrary functions can be represented by a series with the same number of terms used in a Fourier expansion. In fact, for functions with distinct edges (as are typical in MRI), even fewer terms are generally needed in the wavelet representation. Figure 2 demonstrates how a set of dyadic wavelets is constructed by scaling of the basic wavelet and then translating (in steps of $2^j \Delta x$) each of the scaled wavelets.

2.2 Wavelet Multiresolution Analysis

Multiresolution analysis[7] provides an elegant interpretation of the dyadic wavelet expansions. The central idea of multiresolution analysis is that the space of finite-energy functions can be decomposed into a hierarchy of subspaces $\{\mathbf{V}^{[j]}\}$ where $\mathbf{V}^{[j]}$ is the space of all approximations of the finite-energy functions at the resolution $2^j \Delta x$ (j integer). Resolution is defined such that, at the resolution $2^j \Delta x$, a function $f(x)$ is approximated by evenly spaced samples of width $2^j \Delta x$. Note that, by the convention adopted here, a higher index j corresponds to a poorer (coarser) resolution.

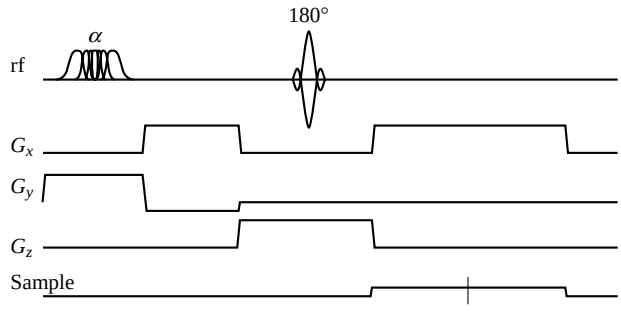

Figure 1 Pulse sequence for wavelet encoding in the y dimension

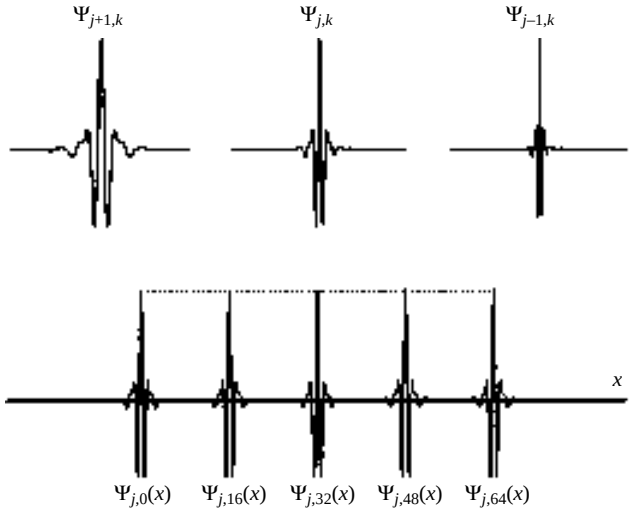

Figure 2 A wavelet basis is constructed by scaling the basic wavelet. The top row of plots shows Battle–Lemarie wavelets at three dyadic scales. At each scale, the wavelets are translated in increments of $2^j \Delta x$ as shown in the bottom row of plots for the scale j. In this figure, only every 16th translate is plotted, and the positions of all other translates are shown with tick marks

Approximation spaces are defined such that $\mathbf{V}^{[j+1]}$ is completely contained within the finer resolution subspace $\mathbf{V}^{[j]}$. The extra detail found in $\mathbf{V}^{[j]}$ that is not also found in $\mathbf{V}^{[j+1]}$ is included within the detail space $\mathbf{W}^{[j+1]}$ as formalized by

$$\mathbf{V}^{[j]} = \mathbf{W}^{[j+1]} \cup \mathbf{V}^{[j+1]} \tag{4}$$

Each of the approximation subspaces $\mathbf{V}^{[j]}$ is spanned by a family of scaling functions, $\{\Phi_{j,n}(x)\}$, as defined by

$$\Phi_{j,n}(x) = 2^{-j/2}\Phi(2^{-j}x - n\,\Delta x), \quad \text{where } j \text{ and } n \text{ are integers} \tag{5}$$

and where Δx is the width of the basic scaling function[6] $\Phi(x)$. Each detail space $\mathbf{W}^{[j]}$ is spanned by a family of wavelets $\{\Psi_{j,n}(x)\}$ defined by

$$\Psi_{j,n}(x) = 2^{-j/2}\Psi(2^{-j}x - n\,\Delta x), \quad \text{where } j \text{ and } n \text{ are integers} \tag{6}$$

Figure 3 shows examples of basic scaling functions and wavelets used to build orthonormal bases.

A wavelet transform decomposes a function into an expansion in terms of functions built from the scaling functions and wavelets as follows. Assume that the function of interest is contained within the approximation space $\mathbf{V}^{[0]}$. Any function in $\mathbf{V}^{[0]}$ can be expressed as a weighted sum of the scaling functions $\{\Phi_{0,n}\}$ that span $\mathbf{V}^{[0]}$. However, since $\mathbf{V}^{[0]} = \mathbf{W}^{[1]} \cup \mathbf{V}^{[1]}$, it can also be expressed as a weighted sum of the scaling functions $\{\Phi_{1,n}\}$ and the wavelets $\{\Psi_{1,n}\}$ that span the subspaces. Further, since $\mathbf{V}^{[1]} = \mathbf{W}^{[2]} \cup \mathbf{V}^{[2]}$, any function in $\mathbf{V}^{[0]}$ can also be expressed as a weighted sum of the scaling functions $\{\Phi_{2,n}\}$ and the wavelets $\{\Psi_{2,n}\}$ and $\{\Psi_{1,n}\}$. The wavelet decomposition can be continued to an arbitrary scale J, so that the approximation of $f(x)$ in $\mathbf{V}^{[0]}$ is expressed as a weighted sum of wavelets $\{\Psi_{1,n}\}$, $\{\Psi_{2,n}\}, \ldots, \{\Psi_{J,n}\}$ and the scaling functions $\{\Phi_{J,n}\}$.

On a finite interval of length $N\Delta x$, J cannot be greater than $\log_2 N$. Each set of wavelets $\{\Psi_{j,n}\}$ or scaling functions $\{\Phi_{j,n}\}$ contains $N/2^j$ functions, since the translation step size for each scale j is $2^j \Delta x$. Problems at the edges of finite intervals are avoided if it is assumed that the basis functions wrap around at the edges.

The approximation of $f(x)$ in $\mathbf{V}^{[0]}$ on the finite interval of length $N\Delta x$ can be expressed by the wavelet series expansion

$$f^{[0]}(x) = \sum_{j=1}^{J} \sum_{k=0}^{N/2^j-1} D_{j,k}\Psi_{j,k}(x) + \sum_{l=0}^{N/2^J-1} A_{J,l}\Phi_{J,l}(x) \tag{7}$$

where the total number of terms in the expansion is N and the weights $A_{j,n}$ and $D_{j,n}$ are defined by

$$A_{j,n} = \int f(x)\Phi_{j,n}(x)\,\mathrm{d}x, \quad D_{j,n} = \int f(x)\Psi_{j,n}(x)\,\mathrm{d}x \tag{8}$$

2.3 Multiresolution Wavelet Reconstruction

The sets $\{D_{1,k}\}, \ldots, \{D_{J,k}\}$ and $\{A_{J,l}\}$ in equation (7) are the coefficients of a discrete wavelet transform of $f(x)$. Reconstruction begins with the data sequences $\{A_{J,l}\}$ and $\{D_{J,l}\}$. The multiresolution interpretation says that the sequence $\{A_{J,l}\}$ represents the coarsest approximation of $f(x)$, and $\{D_{J,l}\}$ represents the detail between the coarsest approximation and an approximation one level finer.

To move to a finer level of approximation, zeros are inserted between each value in the two sequences. The zero-padded sequences are then individually convolved with the impulse response of a low- and a high-pass filter,[7] and the convolution results are added. In this way, the sequence $\{A_{J-1,k}\}$ is produced. It has twice as many values as $\{A_{J,l}\}$, and represents a discrete approximation of $f(x)$ at the second coarsest resolution. To move to another scale, $\{A_{J-1,k}\}$ and $\{D_{J-1,k}\}$ are padded with zeros and convolved with the same low- and high-pass filters, and $\{A_{J-2,k}\}$ is produced. The process is continued until all of the detail sequences are merged and the N-element sequence $\{A_{0,k}\}$ is the final result. $\{A_{0,k}\}$ represents a discrete approximation of $f(x)$ at the resolution Δx.

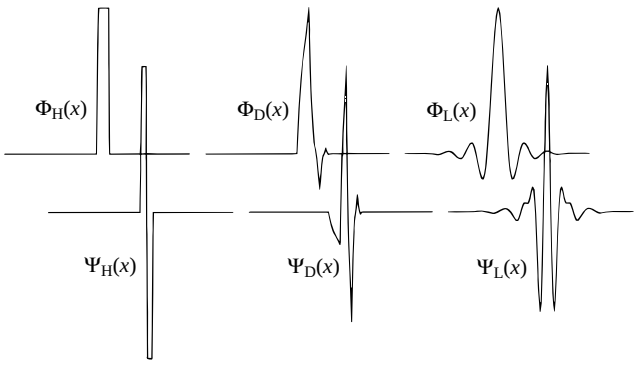

Figure 3 Basic scaling functions and wavelets for the Haar basis (Φ_H, Ψ_H), a Daubechies basis (Φ_D, Ψ_D), and the Battle–Lemarie basis (Φ_L, Ψ_L)

3 MR ENCODING BY SPATIALLY SELECTIVE EXCITATION

Assume that the modified line scan sequence shown in Figure 1 is used and, on each of N excitations, a set of profiles, $\{\phi_{0,n}(y)\}$, defined by

$$\phi_{0,n}(y) = \phi(y - n\Delta y), \quad n = 0, 1, \ldots, N-1 \tag{9}$$

is excited, where $\phi(y)$ is centered at $y = 0$, has a width of Δy, and is mostly positive. The general form of the echo data from the nth excitation, $S_n(k_x)$, is expressed by

$$S_n(k_x) = \int\int s(x,y)\phi_{0,n}(y)e^{ik_x x}\,dx\,dy \tag{10}$$

where $s(x,y)$ is the magnetization density function introduced in Section 1.

Assume that N (k-space) samples are taken from each echo. After performing an inverse fast Fourier transform (FFT) on each of the N sets of echo data with respect to k_x, the partially transformed data set $\{s_{m,n}\}$ can be expressed by

$$s_{m,n} = \int\int s(x,y)\mathrm{sinc}\left[\frac{\pi}{\Delta x}(x - m\,\Delta x)\right]\phi_{0,n}(y)\,dx\,dy$$
$$m, n = 0, 1, \ldots, N-1 \tag{11}$$

where the sinc function represents the point spreading due to finite k-space sampling. Clearly, $\{s_{m,n}\}$ is a discrete approximation of $s(x,y)$, since $\phi_{0,n}(y)$ in equation (11) also acts like a point-spread function. In fact, if $\phi(y)$ is a sinc function and $\Delta y = \Delta x$ then the N^2 values of $\{s_{m,n}\}$ should be identical to an image obtained using phase encoding.

Now, suppose that $\phi(y)$ is a scaling function $\Phi(y)$ such as one of those shown in Figure 3. In this case, $\{s_{m,n}\}$ is also a discrete approximation of $s(x,y)$, but with a different point-spread function in the y direction. If equation (11) is rewritten as

$$s_{m,n} = \int \bar{s}(m\,\Delta x, y)\Phi_{0,n}\,dy \tag{12a}$$

where

$$\bar{s}(m\,\Delta x, y) \equiv \int s(x,y)\mathrm{sinc}\left[\frac{\pi}{\Delta x}(x - m\,\Delta x)\right]dx \tag{12b}$$

and compared with the definition of $A_{j,n}$ in equation (8), it is clear that $s_{m,n}$ has the same form as $A_{0,n}$. For any x-location index m, $\{s_{m,0}, s_{m,1}, \ldots, s_{m,N-1}\}$ represents a set of coefficients $\{A_{0,n}\}$, and can be interpreted as a discrete approximation of $\bar{s}(m\,\Delta x, y)$.

At low flip angles, a scaling-function-shaped profile $\Phi(y)$ can be excited using an rf pulse whose shape is given by the Fourier transform of $\Phi(y)$. In order to translate the profiles across the field of view in steps of Δy, the rf offset frequency must be changed, on each excitation, in steps of $\Delta\omega = \gamma G_y \Delta y$, where G_y is the strength of the y gradient during the rf excitation. If $T_{3\,\mathrm{dB}}$ is the half-power (3 dB) duration of the rf pulse [see RFS(0) in Figure 4] then the width of the excitation profile is $(\gamma G_y T_{3\,\mathrm{dB}})^{-1}$, since the rf pulse excites a region proportional to its bandwidth. The translation step size Δy must be equal to the width of the excitation profile $\Phi(y)$; therefore, $\Delta\omega = 1/T_{3\mathrm{dB}}$.

For a fixed gradient strength and fixed total rf pulse duration T_{rf}, the achievable resolution Δy is strongly dependent on the type of scaling function. The best resolution is achieved when the ratio $r = T_{3\,\mathrm{dB}}/T_{\mathrm{rf}}$ approaches 1. To produce the sharp edges of the Haar scaling function, many sidelobes of a sinc-shaped rf pulse must be included, and r will be much less than 1. On the other hand, r for the Battle–Lemarie scaling function is $\frac{2}{3}$, and the resolution will be closer to the maximum, which is obtained when the rf pulse is box-shaped.

4 AN IMPLEMENTATION OF WAVELET-ENCODED MRI

4.1 Excitation Profiles and rf Pulses

From the multiresolution interpretation of the wavelet transform, we know that any function that can be represented by a weighted sum of scaling functions $\{\Phi_{0,n}(y)\}$ can also be represented by a weighted sum of the set of wavelets at the J scales and the set of scaling functions at scale J. For wavelet encoding, then, the pulse sequence shown in Figure 1 is used to excite specially shaped excitation profiles on each of N separate excitations in the same manner as in Section 3. In the wavelet case, however, the excitation profiles will be the $N/2$ wavelets $\{\Psi_{1,n}(y)\}$, the $N/4$ wavelets $\{\Psi_{2,n}(y)\}, \ldots,$ the $N/2^J$ wavelet(s) $\{\Psi_{J,n}(y)\}$, and the $N/2^J$ scaling function(s) $\{\Phi_{J,n}(y)\}$.

To generate wavelets at different scales, there are two choices:

1. use a constant gradient strength while varying the duration of the rf pulse at each scale; or
2. use an rf pulse of constant duration while varying the gradient strength at each scale.

Figure 4 shows a set of rf pulses to be used for wavelet encoding ($J = 3$) in the Battle–Lemarie basis using the constant gradient method. Note that RFS(0) is not needed for wavelet encoding. The rf pulses are shown as magnitude-normalized; however, if it is desired to maintain a constant flip angle at all scales, rf pulse amplitudes will be scale-dependent. Figure 4 also shows the (magnitude-normalized) profiles excited by each pulse. In the variable-gradient method, independent of the number of scales, only two different rf waveforms are needed (one for scaling functions and one for wavelets). If this method is used, however, gradient-strength-dependent imperfections such as eddy currents may result in image artifact.

4.2 Image Reconstruction

Assume that N wavelet-shaped profiles, as described in Section 4.1, are excited using the pulse sequence shown in Figure 1, and that N samples are collected on each echo. An inverse FFT is performed on each of the N sets of echo data, and the partially transformed data can be expressed as in equations (11) and (12a,b), with the exception that wavelet functions at the J scales and scaling function(s) at scale J replace the set of functions $\{\phi_{0,n}\}$ or $\{\Phi_{0,n}\}$. The expression for the partially transformed data has the same form as the definitions of $A_{j,n}$ and $D_{j,n}$ in equation (8). Thus, for any x-location index m, the N transformed data values represent the coefficients

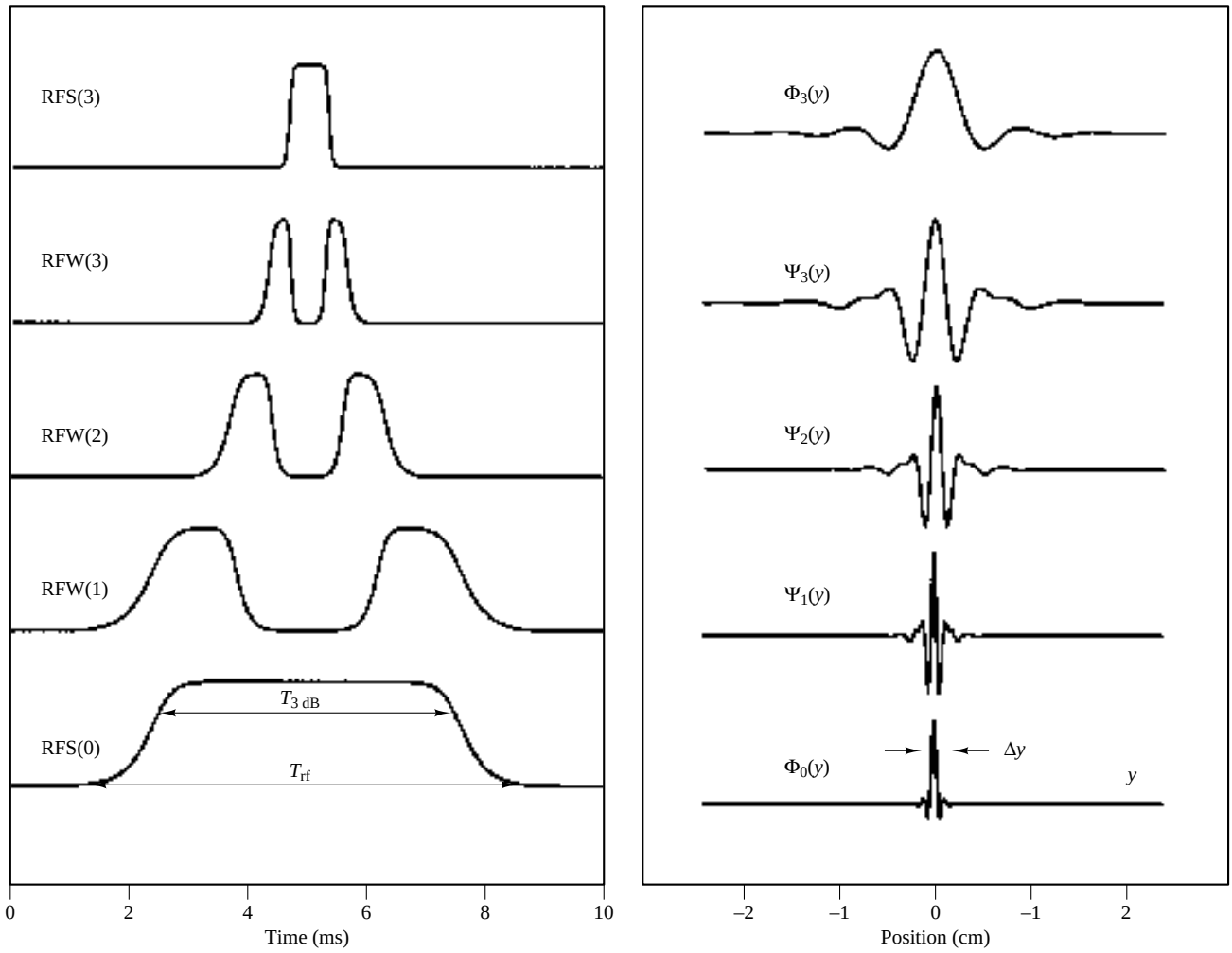

Figure 4 The top four pairs of plots are (amplitude-normalized) rf pulses and excitation profiles for a three-level wavelet encoding. See Section 3 for a discussion of RFS(0) and $\Phi_0(y)$. All profiles are computed assuming a gradient strength of $10\,\mathrm{mT\,m^{-1}}$

$\{D_{1,k}\},\ldots,\{D_{J,k}\}$ and $\{A_{J,k}\}$, which can be interpreted as a discrete wavelet transform of $\bar{s}(m\,\Delta x,y)$.

The reconstruction procedure outlined in Section 2.3 is used to transform the wavelet coefficient data for each x-location index m into a set $\{A_{0,n}\}$, which represents a discrete approximation of $\bar{s}(m\,\Delta x,y)$ of resolution Δy. In theory, then, the result obtained after complete reconstruction should be the same as if the pulse RFS(0) shown in Figure 4 had been used to excite the scaling function profiles $\{\Phi_{0,n}\}$.

5 SIGNAL-TO-NOISE RATIOS

It has previously been noted[4,8] that wavelet encoded images suffer a disadvantage in terms of signal-to-noise ratio (ratio of signal energy to noise energy) when compared with standard phase-encoded images. The intuitive explanation for this is that all spins participate in each phase encode, whereas only a small portion of the spins are, on average, involved during each wavelet encode. When wavelet encoding, on $N/2$ of the encoding steps $2/N$ of the spins are excited, on $N/4$ of the steps $4/N$ are excited, on $N/8$ of the steps $8/N$ are excited, and so on. It can be shown[9,10] that the signal-to-noise ratio for wavelet encoding is only $3/N$ of that obtained when phase encoding. Of course, since wavelet encoding generally involves only a small portion of the spins, there is a possibility that many wavelet encodes can be interleaved in a TR period, and the loss in signal-to-noise ratio may be compensated by an increase in the information rate.

If wavelet packets[6] are used instead of standard wavelets then the signal-to-noise ratio in the wavelet case can be made to approach the signal-to-noise ratio of Fourier imaging.[8,9] Wavelet packets are built from linear combinations of the standard wavelets, and can be designed to involve much larger portions of the field-of-view than the standard wavelets. When wavelet packet functions are used for encoding, more spins on average will be involved on each encoding step, and the signal-to-noise ratio increases accordingly. Of course, since the wavelet packet functions cover larger portions of the field-of-view, spatial selectivity is traded for the increase in signal-to-noise ratio.

6 LIMITATIONS AND APPLICATIONS

Because wavelet encoding is implemented by exciting wavelet-shaped profiles, the resolution when encoding along more than one dimension is limited by the ability to excite multidimensional profiles of sufficient spatial selectivity. A new digital encoding methodology,[11] however, exploits a more general approach to encoding with selective excitation[12] and thereby offers greater flexibility for multidimensional wavelet encoding. The digital approach is to excite linear combinations of basic volumes, such as slices or strips, with the combinations being defined by an encoding matrix. The actual spatial profiles in digital wavelet encoding need not have true wavelet shapes, thereby giving greater flexibility in choosing the wavelet-encoding matrix.

A further limitation of wavelet encoding is that some standard fast imaging approaches may not be fully compatible. Echo-planar or fast spin-echo methods can be used to encode the third (normally slice-select) dimension. There are, however, no reports of implementations of fast single-slice two-dimensional wavelet methods. Wavelet-encoded, low flip-angle gradient-echo imaging could be used for fast two-dimensional imaging, however, only if combined with saturation techniques for slice selection in the third dimension.

The most promising application that we see for wavelet encoding of MRI images is in the development of adaptive imaging methods.[10] An imaging method is adaptive if the image acquisition strategy is modified according to that which is learned about the image during data acquisition. Adaptive methods can be very effective in reducing redundancy in data acquisition and increasing response time in dynamic imaging applications. As an example of a dynamically adaptive imaging strategy based on wavelet encoding,[10] data are acquired beginning with the coarsest resolution. Acquired data values are then examined to determine if a change has occurred since the last time the same coefficients were encoded. Only if change occurs at the coarser resolution are the finer detail coefficients then acquired in a region. Since the number of wavelet encodes grows (by a factor of 2) at each level of detail, this strategy leads to a very significant reduction in the number of encodes necessary to update an image when spatially localized change occurs. This type of multiresolution strategy has been applied in functional MRI in order to target regions of neuronal activation.[14]

Wavelet-based adaptive methods exploit the ability, when wavelet encoding, to produce images with spatially variable resolution. This ability is useful in any application, adaptive or not, where it is desired to resolve highly only a small region of interest leaving the rest of the field of view less resolved. The ability to resolve images selectively in this way, which derives from the nature of the wavelet transform as a spatially selective multiscale decomposition, is a feature that is unavailable with standard Fourier encoding.

7 RELATED ARTICLES

Echo-Planar Imaging; Magnetic Resonance Imaging: A Historical Overview; Selective Excitation in MRI and MR Spectroscopy; Whole Body Magnetic Resonance: Fast Low-Angle Acquisition Methods.

8 REFERENCES

1. L. P. Panych, P. D. Jakab, and F. A. Jolesz, *J. Magn. Reson. Imaging*, 1993, **3**, 649.
2. R. D. Peters and M. L. Wood, *J. Magn. Reson. Imaging*, 1996, **6**, 529.
3. D. M. Healy and J. B. Weaver, *IEEE Trans. Inf. Theory*, 1992, **38**, 840.
4. J. B. Weaver, Y. S. Xu, D. M. Healy, and J. R. Driscoll, *Magn. Reson. Med.*, 1992, **24**, 275.
5. N. Gelman and M. L. Wood, *Magn. Reson. Med.*, 1996, **36**, 613.
6. C. K. Chui, 'An Introduction to Wavelets', Academic Press, San Diego, 1992.
7. S. G. Mallat, *IEEE Trans. Pattern Anal. Machine Intell.*, 1989, **11**, 674.
8. D. M. Healy and J. B. Weaver, in 'Proceedings of the IEEE International Symposium on Time–Frequency and Time-Scale Analysis', Victoria, British Columbia, Canada, October 1992, p. 133.
9. J. B. Weaver and D. M. Healy, *J. Magn. Reson. A*, 1995, **113**, 10.
10. L. P. Panych, *IEEE Trans. Med. Imaging*, 1996, **15**, 141.
11. L. P. Panych, G. P. Zientara, P. Saiviroonporn, S.-S. Yoo and F. A. Jolesz, *J. Magn. Reson. Imaging*, 1998, **8**, 1135.
12. L. P. Panych, G. P. Zientara and F. A. Jolesz, *Int. J. Imag. Sci. Technol.*, 1999, **10**, 143.
13. L. P. Panych, F. A. Jolesz, *Magn. Reson. Med.*, 1994, **32**, 738.
14. S.-S. Yoo, L. Zhao, P. Saiviroonporn, C. R. G. Guttmann and L. P. Panych, in *Proc. VIth Ann Mtg. Int. Soc. Magn. Reson. Med.*, Sydney, 1998, p. 303.

Biographical Sketches

Lawrence P. Panych *b* 1950. B.Eng., 1979, McGill University; M.S., 1983, University of British Columbia; Ph.D., 1993, Massachusetts Institute of Technology 1993. Currently Assistant Professor of Radiology at Harvard Medical School and Brigham and Women's Hospital. Approx. 30 publications. Research specialties: dynamic MRI and novel encoding techniques.

Ferenc A. Jolesz *b* 1946. M.D., 1971, Semmelweis Medical School, Budapest; M.S., 1975, Kando College of Electrical Engineering, Budapest. Research fellowships in neurology at Massachusetts General Hospital and in physiology at Harvard Medical School. Currently B. Leonard Holman and the Image-Guided Therapy Program Professor of Radiology at Harvard Medical School and Director of the Division of MRI at Brigham and Women's Hospital, Boston. Approx. 170 publications. Research specialties: interventional MRI, image processing, demyelination, multiple sclerosis and Alzheimer's disease.

Whole Body Magnetic Resonance Artifacts

R. Mark Henkelman

Sunnybrook Health Science Center and University of Toronto, Toronto, ON, Canada

1 INTRODUCTION

One would hope that an NMR image would show an exact one-to-one correspondence to the object being imaged. This, however, is not the case. There are many 'structures' that are observed in MR images for which there is no corresponding structure in the actual object. Because these unreal 'structures' are the product of human workmanship, they are called artifacts. Artifacts often arise from imperfections in the practical implementation of ideal imaging concepts. In this case, an understanding of the artifacts and their causes can often lead to improved imaging technique. Sometimes, artifacts are intrinsic to even an ideal imaging system, and are thus not correctable. In either case, an ability to recognize some of the wide variety of artifacts that occur in MR images protects against misinterpretation of their appearances as real structures. This is particularly important in clinical MR imaging, where artifacts have sometimes been interpreted as anatomical or pathological structures, leading to unwarranted therapeutic procedures.

Since artifacts are usually first encountered in the visual image, they are described in this article in terms of how they appear. In each case, the causes of the artifacts are identified with appropriate references to other articles of this volume where the underlying science of the data acquisition and image formation are more fully described. Some prominent artifacts are subjects in their own right, and are not discussed in any detail in this article (see ***Motion Artifacts: Mechanism and Control***; ***Susceptibility Effects in Whole Body Experiments***; ***Pulsatility Artifacts Due to Blood Flow and Tissue Motion and Their Control***; ***Tissue Water and Lipids: Chemical Shift Imaging and Other Methods***; ***Chemical Shift Imaging***; ***Surface Coil NMR: Detection with Inhomogeneous Radiofrequency Field Antennas***; ***Surface and Other Local Coils for In Vivo Studies***, and ***Selective Excitation Methods: Artifacts***).

This overview of artifacts in whole body MRI is not exhaustive, since new artifacts are being identified whenever new pulse sequences and new applications are developed. However, this article introduces most of the classes of artifacts that are seen, and provides enough kinds of causes so that as new ones are identified, they can be readily understood. More detailed reviews of MRI artifacts have been published previously.[1–3]

2 IMAGE WRAP-AROUND

Figure 1 shows an image with wrap-around artifact. This is due to aliasing, in which precessional frequencies beyond the Nyquist sampling frequency appear as lower frequencies. (see ***Image Formation Methods***, and ***Spin Warp Data Acquisition***). Aliasing in the frequency-encode direction can be eliminated by over-sampling at a higher Nyquist frequency and digitally filtering the data as they are acquired (see ***Whole Body Magnetic Resonance Spectrometers: All-Digital Transmit/Receive Systems***). Over-sampling in the phase-encode direction requires extra data acquisition time, which often is not available. Selective saturation of spins that lie beyond the image boundary can be used to suppress aliased signal (see ***Selective Excitation Methods: Artifacts*** and ***Selective Excitation in MRI and MR Spectroscopy***). Aliasing can also occur in the slice selection direction when slices are phase encoded in three-dimensional acquisitions.

Images can also wrap over on themselves when attempts are made to image beyond the linear range of the gradient (see ***Gradient Coil Systems***). It is, therefore, important in whole body imaging to ensure that parts of the body that extend beyond the useful gradient are not excited by the rf system.

3 EDGE RINGING

Edge ringing appears as a series of ripples propagating away from any sharp discontinuity in signal intensity, as shown in Figure 2. Edge ringing is a truncation artifact due to inadequate sampling of the high frequencies of *k*-space (see ***Image Formation Methods***). It can be eliminated by sampling further in *k*-space with an associated increase in both image acquisition time and noise, or by low-pass filtering the acquired *k*-space data with an associated loss of image resolution. Alternatively, some postprocessing methods using predictive models of the missing data have been attempted with modest success.[4,5]

Figure 1 The top of the scalp extends beyond the upper boundary of the image frame. The image of this scalp is wrapped-around, and intrudes into the bottom of the image and overlaps the neck

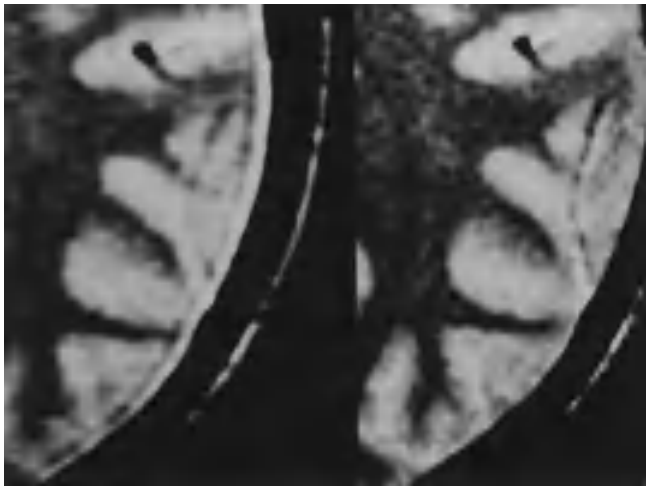

Figure 2 The left frame shows part of an axial brain image taken with 128 samples. The pattern of bright and dark rings propagating into the brain are edge ringing artifacts. On the right is the same image taken with 256 samples and then high-frequency-sampled to remove edge ringing. (Reproduced by permission of Dr. William Matthew Kelly, Department of Radiology, David Grant USAF Medical Center, CA)

Edge ringing can be particularly problematic when coarse voxel data are being acquired, as in chemical shift imaging. Here, spectral information from surrounding voxels may additively or subtractively contaminate the spectrum of the volume of interest (see ***Chemical Shift Imaging***).

Enhanced edge ringing can also arise from gradient problems. Eddy currents persisting into the data sampling window and nonlinear gradient amplifiers at high power can lead to enhanced apparent edge ringing. These are corrected by better amplifiers and self-shielded gradient designs (see ***Gradient Coil Systems***).

4 BLACK BOUNDARIES

Figure 3 shows an image with a well-defined, single-pixel-wide, black boundary between two adjacent tissues. This black line is an artifact. It results from the custom of showing MR images as magnitude images instead of as arrays of complex numbers (see ***Phase Contrast MRA***). Whenever two adjacent tissues have opposite phase, the magnitude image will present them with an artifactual black line between them. Such phase inversions can occur with inversion recovery images (see ***Inversion–Recovery Pulse Sequence in MRI***), gradient echo images of fat and water, as seen in Figure 3, or motion shear between adjacent structures. Properly phased, real reconstructions serve to present the adjacent tissues in their true contrast relationship, and hence to eliminate the perception of a discrete black boundary.

These black boundary artifacts are different from the chemical shift artifact, which appears as a black boundary on one side and a bright boundary on the other side of fat/water interfaces (see ***Tissue Water and Lipids: Chemical Shift Imaging and Other Methods***).

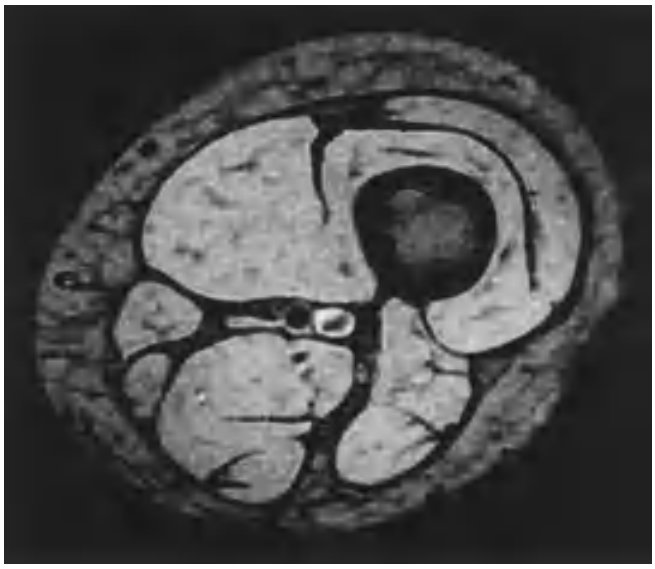

Figure 3 A gradient echo image through the thigh. The black lines between the muscle and subcutaneous fat and around the veins are artifactual black boundaries due to the fat and water signals being 180° out of phase. (Reproduced by permission of C. V. Mosby-Year Book, R. M. Henkelman, in 'Magnetic Resonance Imaging', eds. D. D. Stark and W. G. Bradley, Mosby-Year Book, St. Louis, MO, 1991, Chap. 10, p. 233)

5 STRIPING AND HERRINGBONE PATTERNS

Figure 4 shows an image with a pronounced striping artifact across it, which can be removed by correcting a single erroneous data point. When more than one data point is corrupted, the system of cross stripes gives an image with an imposed herringbone pattern. When many data points or whole data lines are corrupted, correction of the artifact using interpolation becomes less reliable.

Bad data points result from errors in the receiver analog-to-digital conversion (see ***Whole Body Magnetic Resonance Spectrometers: All-Digital Transmit/Receive Systems***). Such errors may result from ADC hardware failures, but more often are caused by electrostatic shocks into the rf receiver from the patient or blankets (see ***Quality Control and Quantification in Whole Body MRI and MRS***).

6 MOIRÉ FRINGES

Images can sometimes appear quite normal, except for an overlay of bright and dark alternating bands, often of irregular shape. These can be widely spaced, giving an appearance like stripes on a zebra, or can be closely spaced as in a moiré pattern of fringes. Such artifacts usually occur when two images overlap, such as occurs with aliasing, as shown in Figure 5. If the overlapping images have similar phase relationships, as in a spin echo image, they simply add. If, however, the images have a varying phase relationship, such as might occur with gradient echo imaging of anatomy in a large-B_0 inhomogeneity far from the center of the magnet, then the images will add constructively or destructively,

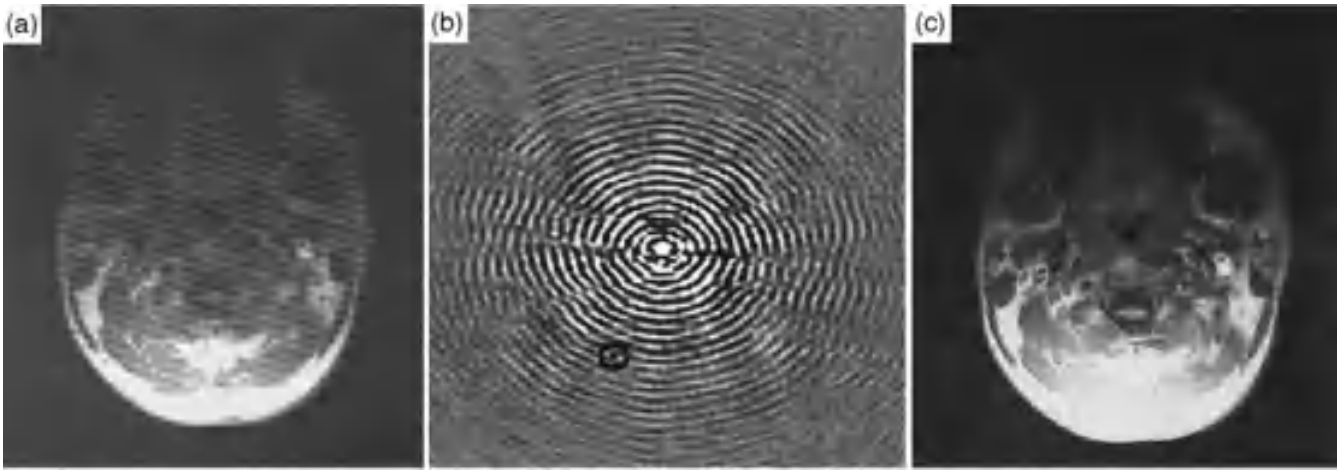

Figure 4 A bad data point. (a) An image with a pronounced diagonal striping across it. (b) Investigation of the *k*-space data from which this image was reconstructed shows a single anomalous data point (circled) at the *k*-space location corresponding to the frequency and orientation of the stripes. (c) Replacement of the bad data point by the average of its neighbors removes the artifact from the image. (Reproduced by permission of Pergamon Press, Elmsford, NY from R. M. Henkelman and M. J. Bronskill, *Rev. Magn. Reson. Med.*, 1987, **2**, 1)

depending on the relative phase. The fringing pattern is then an interference pattern between the two images with varying phase relationship.

The situation is more subtle, but the concept is the same, when the two images are geometrically identical but are generated through different coherence pathways. This can occur, for example, in a late echo, multiple spin echo image, where the stimulated echoes arising from nonideal tip angles have been arranged to superimpose on the primary spin echo. If the accumulated phase is the same for the spin echo and stimulated echo over the whole image, the addition will be constructive; if there are regions where the phase is opposite, the image will interfere, leading to fringes (see ***Multi Echo Acquisition Techniques Using Inverting Radiofrequency Pulses in MRI***; ***Selective Excitation Methods: Artifacts***).

Such interference fringes can be deliberately generated to provide a tagging grid for motion studies, particularly those of the heart (see ***Marker Grids for Observing Motion in MRI***).

Figure 5 Moiré fringing patterns from interference effects between the abdominal image and aliased anatomy from beyond the boundary of the image. (Reproduced by permission of C. V. Mosby-Year Book, from R. M. Henkelman, in 'Magnetic Resonance Imaging', eds. D. D. Stark and W. G. Bradley, Mosby-Year Book, St. Louis, MO, 1991, Chap. 10, p. 233)

7 CENTRAL POINT ARTIFACTS

The central point of the image is unique with respect to data acquired in *k*-space. For *k*-space acquisitions that begin acquiring data from the center of *k*-space (see ***Image Formation Methods***; ***Projection–Reconstruction in MRI***, and ***Spiral Scanning Imaging Techniques***), small errors in the time origin lead to bright or dark contrast pixels in the reconstructed image. Such central artifacts are almost the hallmark of radially acquired data. Removal of these artifacts requires careful time adjustment of the data acquisition or, equivalently, careful phasing of the reconstructed projection.

Even for rectangular data acquisitions (see ***Spin Warp Data Acquisition***; ***Partial Fourier Acquisition in MRI***, and ***Echo-Planar Imaging***), central artifacts occur if the rf transmitter allows the reference rf to leak through during data acquisition. Careful blanking of the rf transmitter and amplifier during all data acquisition effectively removes these central artifacts.

8 ZIPPERS

Zippers are lines of incorrect intensity that run across the image. They often appear with alternating bright and dark signal intensity, and thus can look like a 'zipper' crossing the image. The placement and orientation of such 'zippers' can be used to distinguish their various origins.

Zippers that run in the phase-encode direction (Figure 6) at any arbitrary location in the image are due to discrete rf noise.

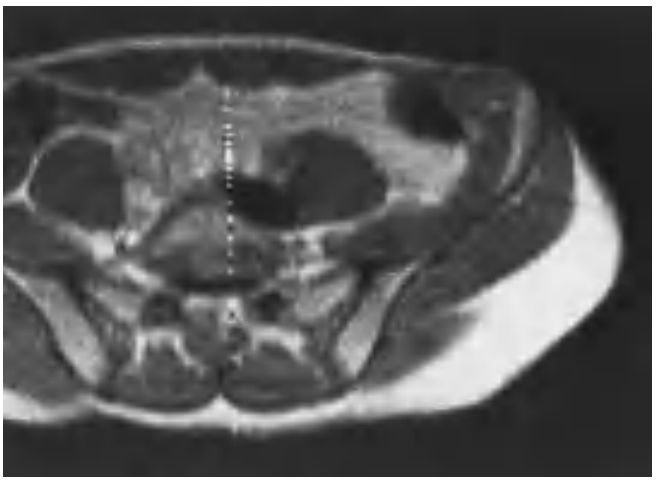

Figure 6 A 'zipper' of bright and dark signal intensity propagating in the phase-encode direction (vertical) is due to discrete rf noise from either the imager's computer systems or the environment that is being picked up by the NMR receiver coil. (Reproduced by permission of Pergamon Press, Elmsford, NY from R. M. Henkelman and M. J. Bronskill, *Rev. Magn. Reson. Med.*, 1987, **2**, 1)

They can be identified as such by shifting the magnetic field and hence the central resonant frequency of the imager, causing the rf noise zipper to shift across the image. Elimination of rf noise requires better environmental rf shielding of the MR imager or better isolation of the imager electronics from the rf receiver chain. When better shielding is not an option, shifting the resonant frequency as described above can be used to search for a clean 'window' in which to operate the MR imager.

Another type of zipper can occur through the center of the image propagating in the frequency-encode direction. The origin of these zipper artifacts is different—they arise from free induction decay or stimulated echo signal that has not been phase-encoded and hence makes a consistent contribution to each acquired data line.[6] These spurious signals usually arise from nonideal selective excitation pulses (see ***Selective Excitation Methods: Artifacts***). As imaging methods become faster, there are greater numbers of rf pulses per T_1 interval, providing many more stimulated echo pathways that can give rise to zippers. There are three methods for reducing these artifacts:

1. design of better rf-generated slice profiles (see ***Selective Excitation in MRI and MR Spectroscopy***);
2. phase cycling of alternate rf excitations to push the artifact to the boundary of the image;
3. the use of 'crusher' gradients to spoil any unwanted transverse coherence.

It should be recognized that, although the zippers discussed above are evident only in rectilinear acquisitions of *k*-space data, the physical principles from which they arise contribute unwanted signal to all data sampling schemes. For more elaborate data acquisition schemes, the resulting artifacts may be less recognizable and may even simply appear as 'noise'. This does not make it any less needful to carefully eliminate artifactual signal from the desired data.

9 IMAGE DISTORTIONS AND BLURRING

The spatial mapping in MR imaging is predicated on a fixed relationship between location and frequency. If either the magnetic field is not homogenous or the imaging gradients are not linear, this relationship is violated, and the image becomes distorted in some way.

A spin, expected to have a resonant frequency of γB_0, that has a resonant frequency of $\gamma(B_0 + \Delta B_0)$ because of a field inhomogeneity ΔB_0 will be shifted from its true location in the image along the frequency-encode direction toward higher frequency by $\Delta B_0/G_x$, where G_x is the strength of the frequency encoding gradient. It should be noted that phase encoding does not exhibit a similar displacement (see ***Spin Warp Data Acquisition***). Therefore, phase encoding in all three directions is an effective, although unrealistically slow, method to avoid magnetic field inhomogeneity distortions.

Magnetic field inhomogeneities may also be caused by magnetic susceptibility variations within the patient, as seen in Figure 7. Distortions can be minimized with increased gradient strengths and decreased acquisition bandwidths. The associated loss in signal-to-noise ratio can be recovered by judicious averaging.

Figure 7 Sagittal image of the spine of a patient with a surgically implanted metal support rod. Displacement of the spinal cord posteriorly (in the frequency encode direction) results from distortion of the main magnetic field. (Reproduced by permission of C. V. Mosby-Year Book, from R. M. Henkelman, in 'Magnetic Resonance in Medicine', eds. D. D. Stark and W. G. Bradley, Mosby-Year Book, St. Louis, MO, 1991, Chap. 10, p. 233)

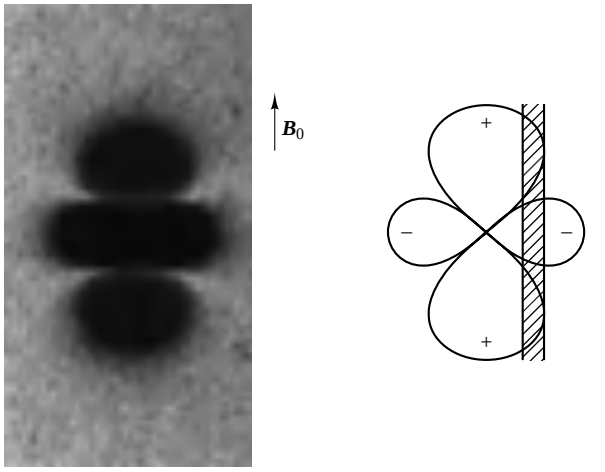

(a) (b)

Figure 8 (a) A gradient echo image from a uniform gel phantom containing a 4 mm long wire of 60 μg mass. The wire produces a dipolar field in the gel as shown in (b). The image is taken in a plane (shaded) that is parallel to the applied magnetic field and displaced from the wire. The three regions of signal loss in the image are caused by intravoxel dephasing. (Reproduced by permission of RSNA Publications, Oak Brook, IL from J. K. Kim, W. Kucharczyk, and R. M. Henkelman, *Radiology*, 1993, **187**, 735)

Even if the main field is uniform, gradient nonlinearities can produce image distortions in both the frequency *and* phase-encode directions, as well as in the slice selection direction. Gradient nonlinearities can be mapped, and images can be rerectified using postprocessing techniques.

Magnetic nonuniformities are more problematic in *k*-space acquisitions that are not unidirectional or are not rectilinear (see ***Image Formation Methods***; ***Echo-Planar Imaging***; ***Projection–Reconstruction in MRI***, and ***Spiral Scanning Imaging Techniques***). In these data acquisition strategies, points at field inhomogeneities will be mapped to several different points in the image resulting in image blur. Blur cannot be as readily corrected by postprocessing as can simple distortion, and hence elimination at the source should be attempted using stronger gradients, suppression of off-resonant spins, or some other technique.[7,8]

10 SIGNAL LOSS

Magnetic field variations not only result in image distortions, but also give rise to regions of signal loss (see ***Susceptibility Effects in Whole Body Experiments***).

In gradient echo imaging, if the phase dispersion of signal throughout an imaged voxel exceeds 2π radians, the net signal in the image will be significantly decreased. This signal loss is said to be due to intravoxel dephasing, and is illustrated in Figure 8.

Intravoxel dephasing can be reduced by using a spin echo acquisition that refocuses the spin phases at the time of echo acquisition. It can also be reduced by using short echo times (see ***Phase Contrast MRA***). It can also be improved by reducing the voxel size by moving to higher resolution images,[9] as shown in Figure 9.

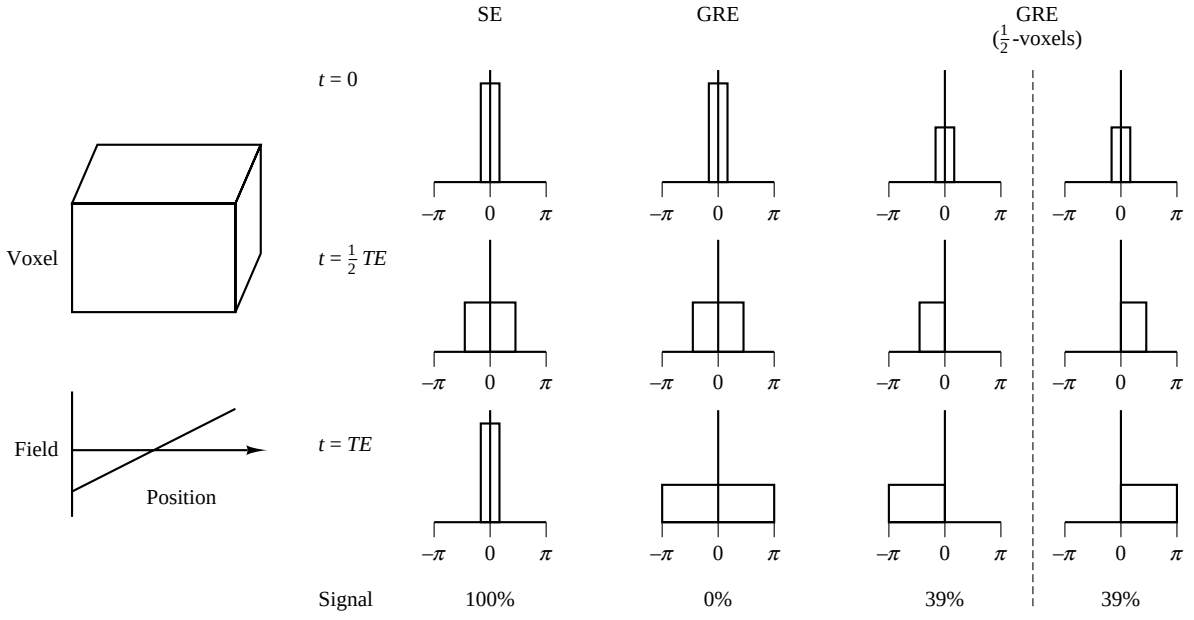

Figure 9 A single large voxel with a susceptibility-induced field gradient can be imaged in a spin echo (SE) sequence with 100% signal (left) because the dephasing at time $\frac{1}{2}TE$ is refocused at time *TE*. The same voxel imaged with a gradient-recalled echo (GRE) may show 0% signal due to intravoxel dephasing (middle). However, if the voxel size is halved with the same gradient echo sequence, each half-pixel shows 39% of the total signal. The intravoxel dephasing signal loss is diminished with higher resolution. (Reproduced by permission of C. V. Mosby-Year Book from R. M. Henkelman, in 'Magnetic Resonance in Medicine', eds. D. D. Stark and W. G. Bradley, Mosby-Year Book, St. Louis, MO, 1991, Chap. 10, p. 233)

Although signal loss is reduced with spin echo imaging, it cannot be eliminated when the spins are free to diffuse through the region of the inhomogeneity. Thus, diffusion-mediated signal loss in the presence of inhomogeneities cannot be refocused by a single spin echo. However, a train of π refocusing pulses will reduce the effects of diffusion-mediated dephasing, as in a Carr–Purcell sequence.

Finally, susceptibility-induced signal losses should not be thought of only as artifacts. These signal loss mechanisms are responsible for the contrast obtained in functional and diffusion imaging (see ***Hemodynamic Changes owing to Sensory Activation of the Brain Monitored by Echo-Planar Imaging***; ***Methods and Applications of Diffusion MRI***, and ***Anisotropically Restricted Diffusion in MRI***).

11 IMAGE GHOSTS

Ghost images are probably the most prevalent of all MRI artifacts. Ghosts are faint replications of the image or parts of images that show the correct spatial structure, but occur at the wrong location within the field of view. Three different ghost mechanisms are discussed, which can be distinguished on the basis of the ghost's position.

11.1 Quadrature Imbalance Ghosts

Central symmetric ghosts, which are a rotation of the image by 180° about its center, result from imbalance in the two quadrature receiver channels. The quadrature signal that is recorded in MR images is intrinsically complex, consisting of real and imaginary parts that are recorded by two independent channels. If the real and the imaginary channels have slightly different gains or, if the phases of the two demodulating frequencies are not separated by exactly 90°, then quadrature imbalance ghosts may be seen. Current state-of-the-art all-digital receivers are able to eliminate these ghosts (see ***Whole Body Magnetic Resonance Spectrometers: All-Digital Transmit/Receive Systems***).

11.2 Stimulated Echo Ghosts

Stimulated echo ghosts appear as inversions of the image about the center of the image in the phase-encode direction. In a multiecho sequence, the primary image signal is obtained from echoes for which the spins have remained in the transverse plane for the whole *TE* time, but also from stimulated echoes that may have been stored longitudinally for part of the echo times. If the stimulated echo has received some odd number ($\cdots, -3, -1, +1, +3, \cdots$) of addition phase encodes and refocusing pulses, the stimulated echo image will appear as an inverted ghost with respect to the primary image.

Such ghosts can be removed by crusher gradients (see Section 6), which spoil the stimulated echo signal. If it is desired to keep to stimulated echo signal, its polarity can be managed by ensuring that any applied phase encoding is rewound within the same interval between refocusing pulses[10] (see ***Multi Echo Acquisition Techniques Using Inverting Radiofrequency Pulses in MRI***).

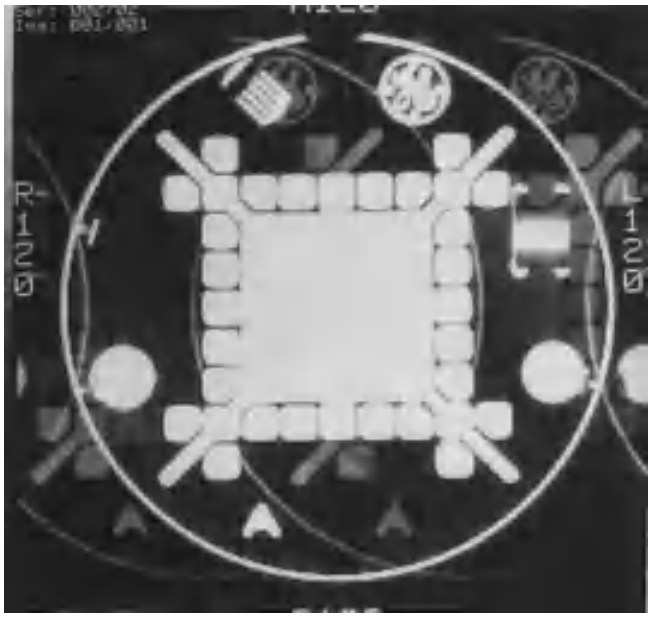

Figure 10 Ghost artifacts in an image of a quality control phantom. Ghost images are displaced in the phase-encoding direction (left and right in this case). The source of these ghosts was eventually identified as a cryopump. With each stroke, a slightly magnetic piston in the cryopump was periodically shifting the main magnet field strength. (Reproduced by permission of C. V. Mosby-Year Book, from R. M. Henkelman, in 'Magnetic Resonance Imaging', eds. D. D. Stark and W. G. Bradley, Mosby-Year Book, St. Louis, MO, 1991, Chap. 10, p. 233)

11.3 Periodic Modulation Ghosts

Displacement ghosts are replicas of parts of the image displaced in the phase-encode direction. They are the commonest type of ghost, and remain a problem in the imaging of living systems. Ghost artifacts from periodic physiological motions are discussed elsewhere (see ***Motion Artifacts: Mechanism and Control*** and ***Pulsatility Artifacts Due to Blood Flow and Tissue Motion and Their Control***).

Besides physiological motions, displacement ghosts can arise from any other type of periodic variation concurrent with the imaging process, as shown in Figure 10.

Examples include building vibration, alternating line current pickup, and amplifier oscillation, as well as cryopumps. Elimination of such ghost artifacts requires an identification of the causative periodic variation and its subsequent correction. Such a detective process can be very long and expensive.

Even if a temporal variation imposed on the imaging process is not periodic, it will still propagate signal into the phase-encoding direction, as indicated in Figure 11—but it will not be recognized as ghosts.

In nonrectilinear acquisitions of *k*-space data, there is no preferred phase-encoding direction, and misassigned signal is scattered all over the image, where it can seldom be recognized as ghosts and may simply look like noise. Nonetheless, it is still artifactual signal that must be removed if the maximum image quality is to be achieved.

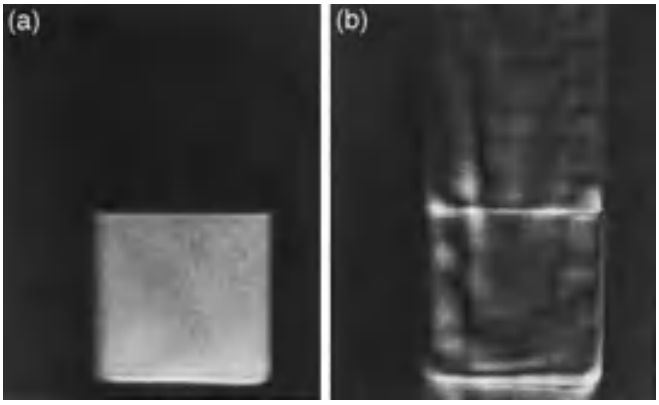

Figure 11 (a) An image of a beaker of water. (b) The same image acquisition, but after the water was stirred. Even though the motion of the water is not periodic, but rather is turbulent, signal intensity is displaced in the phase-encoding direction (up and down in this case). (Reproduced by permission of Pergamon Press, Elmsford, NY from R. M. Henkelman and M. J. Bronskill, *Rev. Magn. Reson. Med.*, 1987, **2**, 1)

12 WASHED-OUT CONTRAST

There is a very characteristic artifact that presents as an image with good spatial definition and no obviously displaced image structures, but for which the contrast is washed out and there appears to be a weak aura around the imaged structure, as seen in Figure 12. The cause is simple. The artifact occurs when the data acquisitions at the center of *k*-space exceed the range of the analog-to-digital converter (ADC). This is most likely to occur in three-dimensional data acquisitions, where the integrated signal intensity over a 256^3 acquisition typically exceeds the high-order encoded data points by 2,[11] pushing the dynamic range of conventionally employed ADCs.

The artifact can be corrected by repeating the acquisition with increased receiver attenuation. Alternatively, the data can be retrospectively corrected if they are simply aliased as in Figure 12. If the central data are lost, the image can still be salvaged by imposing reconstruction conditions of compact support.[11]

13 INTENSITY VARIATIONS IN THE IMAGE

There are many reasons why the eventual signal intensity in an image does not correspond directly to the known spin density in the object. It is the wide variety of these artifacts that has led to the very slow development of quantitative methods in MRI (see ***Relaxation Measurements in Whole Body MRI: Clinical Utility***). Three causes of intensity nonuniformity are discussed.

13.1 Slice Profile Effects

Slice-selective rf pulses are never perfect, and always exhibit some transition region through which the effective tip angle is less than that which is prescribed. While this is not a large problem for small tip angle pulses, it becomes a major source of signal intensity artifact for 180° refocusing pulses. Thus, in a slice-selective multi-echo sequence and for a phantom with an infinite T_2, there is typically a 5–10% loss in signal for each subsequent echo due only to sequential degradation of the slice profile. This needs to be borne in mind when attempting to estimate T_2 values, since there is an apparent multiecho decay rate due to slice profile degradation.

Another cause of signal loss can come from eddy currents. If the readout gradient compensation pulse immediately precedes the refocusing 180° pulse in a spin echo sequence, and if the gradient shows an eddy current that persists throughout the 180° pulse, then the slice-selective plane of the 180° pulse will be rotated with respect to the 90° slice-selective excitation. Such a situation will provide ideal refocusing at the center of the slice, but degraded signal intensity as one moves away from the center in the frequency-encode direction.

13.2 Slice Interference Effects

The single slice nonuniformities become more complicated when multiple slices in close proximity are employed.

Because selective excitation is not perfect, selective pulses affect spins beyond the nominal boundaries of the slice. This has two consequences:

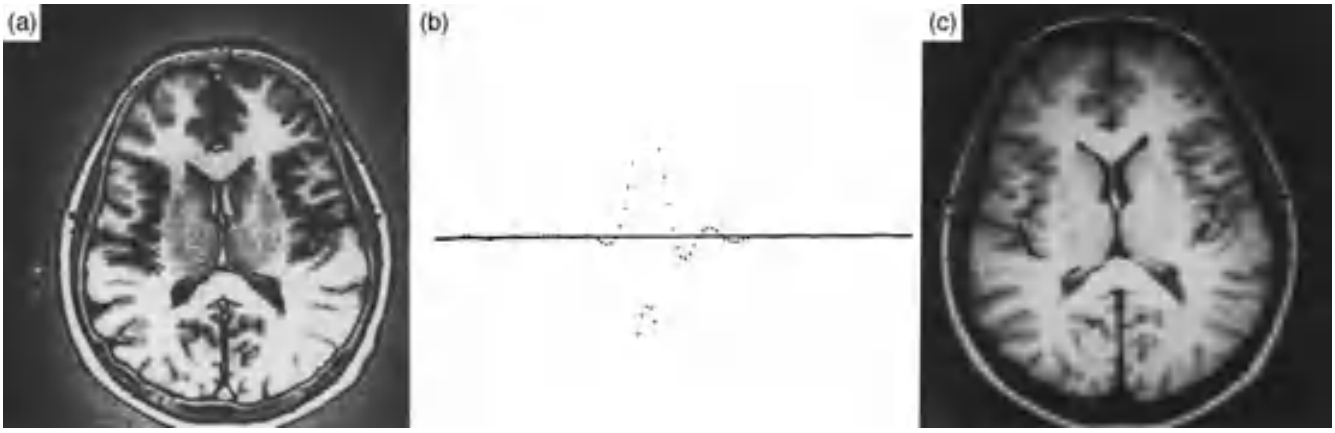

Figure 12 An axial brain image (a) with washed-out contrast and aura results from acquired *k*-space data that have exceeded the range of the analog-to-digital converter. (b) Correction of the aliased data and subsequent reconstruction results in an artifact-free image (c)

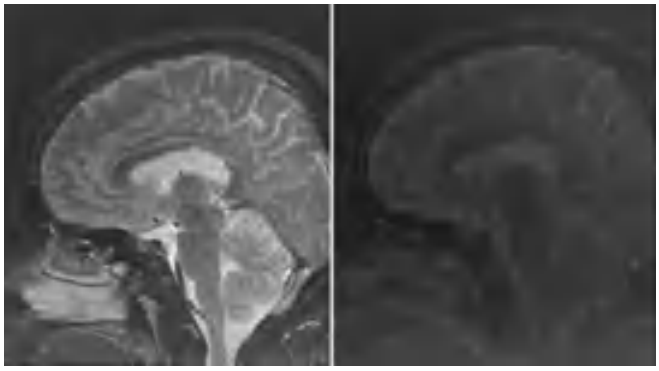

Figure 13 Sagittal head images acquired with a T_2-weighted spin echo sequence. The image on the left is a single slice whereas that on the right is the central image from a nine-slice contiguous multislice acquisition displayed with the same window and level. The multislice image shows the decreased signal intensity from slice interference and also the degraded contrast. (Reproduced by permission from W. Kucharczyk, A. P. Crawley, W. M. Kelly and R. M. Henkelman, *Am. J.N.R.* 1988, **9**, 443, American Society of Neuroradiology, Oak Brook, IL, USA)

1. direct interference from neighboring slices causes signal reduction in each slice and variation in the average signal intensity of slices throughout a multislice block, depending on the order of slice acquisition and the gap between the slices;
2. the real-time contrast within a slice is degraded owing to interference from adjacent slices, particularly for T_2-weighted images.[12]

This effect is illustrated in Figure 13. These consequences can be diminished with better selective rf pulses (see ***Selective Excitation Methods: Artifacts***) or by leaving a slice gap between slices.

A slice interference intensity artifact that is not improved with better selectivity or slice gap is that arising from magnetization transfer effects. It has been realized that excitation and refocusing rf pulses from all neighboring slices serve to satu- rate the spins of the macromolecules within the slice of interest. While these spins are not directly observed in MRI because of their short T_2 relaxation times, their saturation diminishes the signal from the liquid pool that is imaged (see ***Phosphorus-31 Magnetization Transfer Studies In Vivo***; ***Magnetization Transfer Contrast: Clinical Applications***, and ***Magnetization Transfer and Cross Relaxation in Tissue***).

13.3 Nonuniform Radiofrequency Fields

Image intensity variations also arise from nonuniformities in both the transmitted rf field and the receive sensitivities of the receiver coils.

Nonuniformities in the transmitted rf field were originally believed to impose the fundamental limit to high-field imaging (see ***High-Field Whole Body Systems***). However, although the images show slight rf shading, excellent MR images have been obtained at 4 T in whole body systems. Slight nonuniform rf intensities are seen as a left–right asymmetry on transverse abdominal images of large patients at 1.5 T.

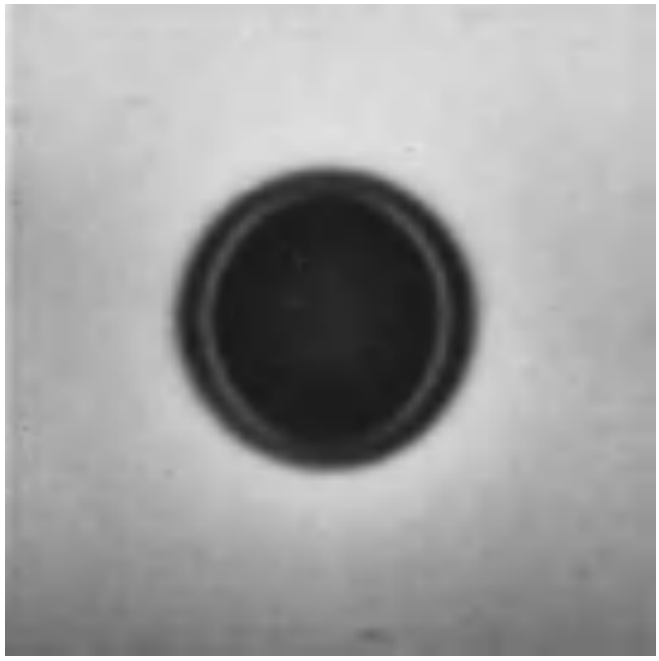

Figure 14 Spin echo image of a homogeneous doped water phantom containing a simple closed circular copper loop of 24 mm diameter. The loop serves as a secondary rf transmitter, and hence perturbs the uniformity of the transmitted rf field. The loop also plays the part of a secondary receiver, destroying the homogeneity of the rf receiver sensitivity.[13]

Nonuniformities in the sensitivities of rf receiver coils are a common experience in MRI. The image nonuniformity can hardly be considered artifactual, since the smaller localized receiver coils are used deliberately to increase the signal-to-noise ratio (see ***Surface and Other Local Coils for In Vivo Studies***; ***Whole Body Machines: NMR Phased Array Coil Systems***, and ***Surface Coil NMR: Detection with Inhomogeneous Radiofrequency Field Antennas***).

Finally, nonuniformities in signal intensity can arise from both changes in the transmitted rf field and the receive sensitivity when secondary rf conductors are included in the imaging field, as shown in Figure 14. Such secondary effects may become more of an issue with the further development of interventional MRI.

14 SUMMARY

MR imaging methods display a wide variety of image artifacts, some of which have been introduced in this article. All the artifactual signals arise from well-behaved and well-understood laws of physics, taking into account instrumental imperfection. Understanding the causes of MRI artifacts usually leads to ways of correcting, or at least avoiding them, so that images can be reliably interpreted with confidence.

15 RELATED ARTICLES

Anisotropically Restricted Diffusion in MRI; Chemical Shift Imaging; Echo-Planar Imaging; Gradient Coil Systems; Hemodynamic Changes owing to Sensory Activation of the Brain Monitored by Echo-Planar Imaging; High-Field Whole Body Systems; Image Formation Methods; Inversion–Recovery Pulse Sequence in MRI; Magnetization Transfer and Cross Relaxation in Tissue; Magnetization Transfer Contrast: Clinical Applications; Marker Grids for Observing Motion in MRI; Motion Artifacts: Mechanism and Control; Multi Echo Acquisition Techniques Using Inverting Radiofrequency Pulses in MRI; Partial Fourier Acquisition in MRI; Phase Contrast MRA; Phosphorus-31 Magnetization Transfer Studies In Vivo; Projection–Reconstruction in MRI; Pulsatility Artifacts Due to Blood Flow and Tissue Motion and Their Control; Quality Control and Quantification in Whole Body MRI and MRS; Relaxation Measurements in Whole Body MRI: Clinical Utility; Selective Excitation in MRI and MR Spectroscopy; Selective Excitation Methods: Artifacts; Spin Warp Data Acquisition; Spiral Scanning Imaging Techniques; Surface and Other Local Coils for In Vivo Studies; Surface Coil NMR: Detection with Inhomogeneous Radiofrequency Field Antennas; Susceptibility Effects in Whole Body Experiments; Tissue Water and Lipids: Chemical Shift Imaging and Other Methods; Whole Body Machines: NMR Phased Array Coil Systems; Whole Body Magnetic Resonance Spectrometers: All-Digital Transmit/Receive Systems.

16 REFERENCES

1. R. M. Henkelman and M. J. Bronskill, *Rev. Magn. Reson. Med.*, 1987, **2**, 1.
2. R. Harris and G. Wesbey, in *Magn. Reson. Annu.*, 1988, p. 71.
3. R. M. Henkelman, in 'Magnetic Resonance Imaging', eds. D. D. Stark and W. G. Bradley, Mosby-Year Book, St. Louis, MO, 1991, Chap. 10, p. 233.
4. R. T. Constable and R. M. Henkelman, *Magn. Reson. Med.*, 1991, **17**, 108.
5. Z. P. Liang, F. E. Boada, R. T. Constable, E. M. Haacke, P. C. Lauterbur, and M. R. Smith, *Rev. Magn. Reson. Med.*, 1992, **4**, 67.
6. A. P. Crawley and R. M. Henkelman, *Med., Phys.*, 1987, **14**, 842.
7. D. C. Noll, J. M. Peuly, C. H. Meyer, D. G. Nishimura, and A. Macovski, *Magn. Reson. Med.*, 1992, **25**, 319.
8. J. K. Kim, W. Kucharczyk, and R. M. Henkelman, *Radiology*, 1993, **187**, 735.
9. I. R. Young, I. J. Cox, D. J. Bryant, and G. M. Bydder, *Magn. Reson. Imag.*, 1988, **6**, 585.
10. J. Hennig, *J. Magn. Reson.*, 1988, **78**, 397.
11. J. Jackson, A. Macovski, and D. Nishimura, *Magn. Reson. Med.*, 1989, **11**, 248.
12. W. Kucharczyk, A. P. Crawley, W. M. Kelly, and R. M. Henkelman, *Am. J. Roentgenol.*, 1988, **9**, 443.
13. C. R. Camacho, D. B. Plewes, and R. M. Henkelman, *J. Magn. Reson. Imaging*, 1995, **5**, 75.

Biographical Sketch

R. Mark Henkelman. *b* 1946. B.Sc., 1969; Ph.D., 1973, University of Toronto. Faculty at the University of British Columbia, Canada, 1973–1979, working on π-meson radiotherapy at TRIUMF. Professor of Medical Biophysics, University of Toronto 1979–present; Vice-President, Research for Sunnybrook Health Science Centre 1989–present. Approx. 175 publications. Research specialties: MRI, image acquisition techniques, mechanisms of tissue contrast.

Whole Body Magnetic Resonance: Fast Low-Angle Acquisition Methods

Axel Haase

Physikalisches Institut, Universität Würzburg, Würzburg, Germany

1 INTRODUCTION

The most frequent applications of NMR imaging are within the field of biology and medical diagnosis. The inherent problem in early clinical practice was that NMR imaging was supposed to be a time-consuming technique. However, as early as 1977, a fast NMR imaging method, echo planar imaging (EPI), was described[1] (see ***Echo-Planar Imaging***). During the first decade of clinical NMR imaging, EPI was not used owing to major limitations in technical implementation. In 1985, a further fast imaging method was found, which could be immediately applied in many clinical NMR imagers, the FLASH (fast low angle shot) technique.[2] The two methods rely on different approaches to the fast sampling of NMR image data. The purpose of this work is to present the physical principles and different versions of FLASH-based fast NMR imaging.

A clear definition of 'fast NMR imaging' cannot be found in the literature. It is even more confusing that measuring times of 'fast NMR imaging techniques' cover several orders of magnitude from a few milliseconds to a few minutes. A definition of fast imaging can only be given in the context of the object and its time constants under investigation. Therefore, 'fast imaging' is understood to be 'fast' compared with the time constant of the physiological process of the biological object of interest. A fast imaging technique should freeze a time-dependent process to give a 'snapshot' of the object or the time-dependent biological function. This is the case for heart studies, when the measuring times should be less than 50 ms, or for abdominal studies, where a measuring interval of several seconds during one breath-hold is needed. For other investigations, this definition is useless (e.g., for images of joints). Here, fast imaging has a practical or economic meaning to optimize the clinical investigation and increase patient comfort (see ***Whole Body MRI: Strategies for Improving Imaging Efficiency***). Therefore, a 'fast NMR imaging' method has to cope with all the different needs of medical diagnosis, and cannot be restricted to a single measuring time interval. FLASH-based NMR imaging techniques address this goal.

The purpose of FLASH NMR imaging is to reduce all kinds of motional artifacts, for example, heart motion, breathing, and random motion by the patient. It will offer the possibility for the study of organ functions, and organ motion.[3,4] A further benefit is the ability to acquire multiparameter data sets within shorter time intervals, for example, three-dimensional imaging,[5] flow velocity information, and NMR parameter imaging.[6] A few years after its first conception in 1985, it has become generally accepted in routine clinical practice.

2 IMAGING TECHNIQUE

The physical principle of all FLASH-based techniques is the two- or three-dimensional Fourier transform, first proposed, as 'Fourier zeugmatography' in 1975[7] (see ***Image Formation Methods***). The practical question is, how to sample all necessary lines in $\boldsymbol{k}$-space as fast and efficiently as possible. First approaches for dealing with faster imaging were focused on a reduction of the number of $\boldsymbol{k}$-space lines in partial Fourier imaging (see ***Partial Fourier Acquisition in MRI***). However, this reduces the spatial resolution to a certain extent and produces (Gibbs ringing) truncation artifacts[8] (see ***Whole Body Magnetic Resonance Artifacts***). A factor of approximately two can be gained using 'half-Fourier' imaging, where only half of the data is sampled and the second half is filled later by software.[9] Partial Fourier imaging can be applied in addition to all fast techniques to reduce the measuring time further.

In principle, two methods are possible to reduce the time interval of data sampling: a reduction of the repetition time TR between the acquisition of different $\boldsymbol{k}$-space lines, or the measurement of the whole $\boldsymbol{k}$-space using a single NMR excitation followed by a series of NMR echoes. The second possibility includes the EPI methods. We focus on the first technique. However, a reduction of the repetition time has a considerable drawback. Every excitation of an NMR signal for a special $\boldsymbol{k}$-space line decreases the longitudinal magnetization to a lower value M_z. During the time interval TR, M_z recovers towards its equilibrium value M_0 by spin–lattice relaxation T_1, according to

$$M_z = M_0(1 - \mathrm{e}^{-TR/T_1}) \tag{1}$$

It can be seen that this recovery is most inefficient, as long as TR is short compared with T_1. M_z tends to zero when the excitation flip angle is 90°. Furthermore, spin echo experiments having 180° rf refocusing pulses and separated by short TR intervals give almost zero values of M_z.

The idea of reducing the repetition time TR to short values is, however, most promising. According to the above discussion, the goal can be reached when spin echo experiments are avoided and lower flip angles are used. In 1D NMR spectroscopy low flip angles are used to speed up the experiment while retaining a high level of NMR signal. It is known that, for given TR and T_1 values, an optimum flip angle, the 'Ernst angle' α_E exists where the maximum signal strength per measuring time can be expected:[10]

$$\cos\alpha_\mathrm{E} = \mathrm{e}^{-TR/T_1} \tag{2}$$

Although an 'Ernst angle' cannot be defined under imaging conditions, where many different T_1 values can be found, the idea of using a reduced flip angle is promising.

The second need resulting from the above discussion is to avoid spin echo experiments. This is done in conventional 1D NMR spectroscopy by the acquisition of the FID signal. Under imaging conditions, the FID signal is acquired with the help of the inversion of one magnetic field gradient.[11] This signal is

called a 'gradient echo'. The physical content of FLASH-based fast NMR imaging sequences is therefore fast acquisitions of gradient echoes excited by low-flip-angle NMR excitation (FLASH ≡ fast low angle shot).[2]

3 GRADIENT ECHOES

An FID signal rapidly decreases within a few milliseconds to zero in the presence of a magnetic field gradient. A gradient is needed to encode the spatial domain in the form of frequency information. Since the gradient switching process needs a certain time interval, the FID signal is already dephased at the time when the signal should be acquired in the presence of the gradient. There exists the possibility of shifting the NMR signal to a later time interval. This is achieved by an inversion of the polarity of the gradient. This gradient inversion produces a 'gradient echo'. The gradient echo appears at the time when the time integral of the negative $[G_-(t)]$ and positive $[G_+(t)]$ gradient pulses become equal:

$$\int_0^{\tau} G_+(t)\,\mathrm{d}t = \int_{\tau}^{\delta} G_-(t)\,\mathrm{d}t \tag{3}$$

Here the positive gradient pulse has a duration τ, and the negative gradient pulse until the appearance of the gradient echo a duration δ. Since this time integral can be changed by experimental parameters (gradient strength and timing), the time at which the gradient echo appears is under the control of the NMR expert. The time interval between the NMR excitation and the gradient echo is called the 'gradient echo time' *TG*.

The signal strength of the gradient echo is dependent on *TG* and the relaxation time responsible for the FID decay, T_2^*. T_2^* is much shorter than T_2. It is known that the relaxivity $1/T_2^*$ is composed of the sum of a number of contributions:

$$\frac{1}{T_2^*} = \frac{1}{T_2} + \frac{1}{T_{2\mathrm{i}}} + \frac{1}{T_{2\mathrm{s}}} + \frac{1}{T_{2\mathrm{c}}} + \cdots \tag{4}$$

Here T_2 is the spin–spin relaxation time, $T_{2\mathrm{i}}$ is given by inhomogeneities of the main magnetic field, $T_{2\mathrm{s}}$ is produced by magnetic susceptibility gradients, and $T_{2\mathrm{c}}$ is due to the chemical shift dispersion of the NMR signal. Other field inhomogeneities, and motions within the magnet, can cause further relaxation paths.

It should be emphasized that a gradient echo signal is strongly affected by magnetic field inhomogeneities. Furthermore, a gradient echo acquired at *TG* often exhibits lower signal strength than a spin echo at the same spin echo time *TE*.

In two-dimensional Fourier gradient echo imaging, the phase-encoding gradient pulse is switched on during the negative polarity of the gradient needed for the gradient echo. The theoretical minimum gradient echo time *TG* is the sum of the time intervals of the slice-selective excitation pulse, inversion of the read gradient, and half of the time interval for acquisition of the gradient echo. At least two time intervals have to be reserved for the switching processes of gradients.

In summary, the minimum *TG* is totally hardware-dependent. Minimum values of approximately 1 ms have been achieved so far. The minimum repetition time of a gradient echo imaging experiment is approximately twice as long as *TG*. Therefore, measuring times of a 128 × 128 pixel image of the order of 250 ms are possible, and have been reached by many groups. However, it should be noted that the measuring time, or the minimum repetition time *TR*, is hardware-dependent, as can be seen in Figure 1. Increasing the gradient strength results in a decreased measuring time owing to shorter data acquisition, phase encoding, and slice selection intervals. Fast switching gradient power amplifiers further reduce *TG*, *TR*, and the measuring time.

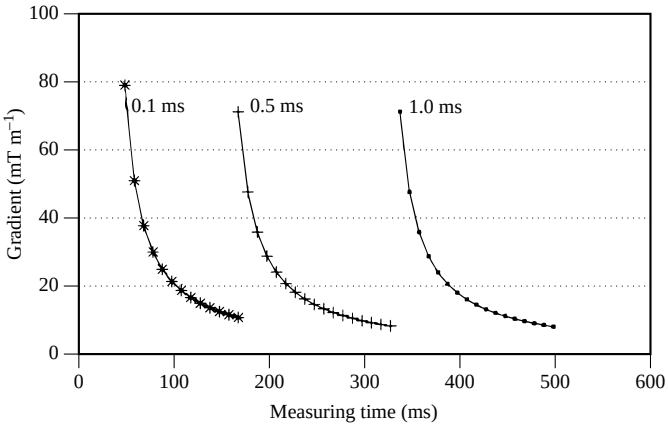

Figure 1 Dependence of the measuring time of FLASH MRI on the applied magnetic field gradient strength and switching time of the gradient pulses. Three switching time intervals are shown: 1 ms, 0.5 ms, and 0.1 ms. The curves were calculated using a 64 × 128 data matrix, slice thickness 5 mm and field of view 200 mm

Typical measurement parameters in whole body clinical scanners are a gradient switching time of 1 ms and a maximum gradient strength of 10 mT m^{-1}. Under these conditions, minimum repetition times of approximately 10 ms and gradient echo times of 5 ms are achieved with fast gradient echo imaging having a 20 cm field of view. In technologically advanced scanners repetition times of 3 ms and gradient echo times of 1.5 ms are possible. However, here, the gradient switching time must be in the range of 150 μs and maximum gradient strengths of at least 20 mT m^{-1} are needed.

4 SIGNAL INTENSITY

Fast repetitions of NMR excitations with short repetition times *TR* and low-flip-angle rf pulses need reconsideration of the signal behavior. It is known that a train of rf pulses with $TR < T_2$ generates a constant NMR signal level with an FID contribution following an rf pulse and an echo-like signal before each pulse.[12] The echo part of the signal can be destroyed by various kinds of 'spoiling' methods using gradient pulses[13] or phase scrambling of the rf pulses.[14] The echo part can be refocused, when all magnetic field gradient pulses are inverted in polarity after the acquisition of the gradient echo and before the next pulse.[15,16] The signal strength is totally dependent on the method, i.e., as between the use of 'spoiled' or 'refocused' fast gradient echo imaging.

If we assume that any transverse magnetization has been spoiled between the rf pulses, the signal will behave like

$$S \propto \frac{(1 - e^{-TR/T_1})\, e^{-TE/T_2^*} \sin\alpha}{1 - e^{-TR/T_1} \cos\alpha} \tag{5}$$

If we consider refocused experiments then the signal will behave like

$$S \propto \frac{(1 - e^{-TR/T_1})\, e^{-TE/T_2^*} \sin\alpha}{1 - e^{-TR/T_1}\, e^{TE/T_2} - (e^{-TR/T_1} - e^{-TE/T_2}) \cos\alpha} \tag{6}$$

It is interesting to note how this signal behavior changes under fast imaging conditions. Here *TR* and *TG* will be much smaller than T_1 and T_2.

For spoiled fast gradient echo imaging and large flip angles, the signal strength will behave like

$$S \propto TR/T_1 \tag{7}$$

For low-flip-angle pulses, the signal is no longer dependent on relaxation time differences, and will be dominated by spin density.

In refocused fast gradient echo imaging using large flip angles, the signal strength will behave like

$$S \propto T_2/T_1 \tag{8}$$

This parameter is relatively low in soft tissues compared with body fluids. Therefore, the most intense regions contain fluids—like CSF in the brain. Again, the signal will be dominated by the spin density contrast when using very low flip angles.

The application of fast gradient echo imaging allows great possibilities for changing the image contrast. Thus, 'refocused' gradient echo imaging can produce T_2-weighted images, according to equation (8), or 'spoiled' gradient echo images can give T_1-weighted images, according to equation (7), and both techniques result in 'spin density' images when low-flip-angle pulses are used.

The situation in the literature is rather complex, mainly because many acronyms have been used for the different contrast mechanisms in fast gradient echo imaging. Starting from the originally proposed fast gradient echo imaging using low-flip-angle pulses, FLASH, several other pulse sequences have been described using this concept:

1. 'spoiled' FLASH methods: (a) SPGR (spoiled GRASS); (b) spoiled FAST (Fourier acquired steady state); (c) FFE (fast field echo);
2. MPGR (multiplexed gradient refocusing) turbo methods: (a) Snapshot-FLASH, (b) Turbo-FLASH, (c) MPRAGE (magnetization prepared rapid acquired gradient echoes, (d) FSPGR (fast spoiled GRASS), (e) TFE (turbo FFE), (f) PFI (partial flip angle imaging);'refocused' FLASH methods: (i) FISP (fast imaging with steady precession); (ii) GRASS (gradient recalled acquisition in steady state); (iii) FAST (Fourier acquired steady state); (iv) GFE (gradient field echo); (v) CE-FAST (contrast enhanced FAST); (vi) FEER (fast field echo with even echo rephasing); (vii) GREC (gradient field echo with contrast).

It should be kept in mind that the principal idea of all these sequences is that fast NMR imaging can be achieved using gradient inversion, low-flip-angle excitations, and the acquisition of a gradient echo either with or without refocusing of transverse magnetization. The experiment has to be performed as fast as possible. The repetition time is only given by experimental or hardware constraints.

5 ARTIFACTS

Numerous artifacts can appear, but can be avoided in fast gradient echo imaging. The first, and not always visible, artifact can be a severe distortion of the slice profile. It has been known for many years that the slice profile is completely changed when using large flip angles and short repetition times.[17] In practical slice-selective imaging experiments, the flip angle varies across the slice, resulting in an often 'Gaussian-shaped' slice profile. As a consequence of this effect, large flip angles are found in the center and low flip angles at the edges of the slice profile. Higher flip angles and short repetition times *TR* will result in a heavy saturation in the center and almost no saturation at the edges of the slice profile. Therefore, high signal intensity will be found at the borders of the slice, giving strong partial volume artifacts.

This is the case when strongly T_1-weighted fast gradient echo images are needed, which can be measured according to the above discussion using short *TR* values and high flip angles in 'spoiled' imaging methods. It is therefore unrealistic to calculate T_1 maps from a series of strongly T_1-weighted images.

The most prominent feature of fast gradient echo imaging is the high-intensity signal of blood flowing perpendicular to the slice orientation. This is due to an inflow of fully relaxed magnetization during *TR*.[4] The enhancement of the signal intensity of flowing blood depends on imaging parameters (*TR*, flip angle, and slice thickness), T_1 of blood, and the flow velocity. Although this effect can be used to image blood vessels (MR angiography), it has a negative feature. Flowing spins accumulate a velocity (v)-dependent phase when flowing along a magnetic field gradient G, according to

$$\phi = \tfrac{1}{2}\gamma G v t^2 \tag{9}$$

where t is the time interval between the NMR excitation and read-out of the signal. As long as the velocity remains constant, a constant phase is obtained. However, if the velocity changes during the imaging experiment (e.g., owing to pulsatile flow), different phases are accumulated, leading to severe 'flow artifacts' of bright intensity in the phase-encoding direction. This artifact can be reduced by rephasing gradients, giving no net phase shift due to flow velocity ('flow-compensated' gradient pulses). A detailed discussion of flow NMR imaging and flow compensation can be found in ***Whole Body Magnetic Resonance Angiography***.

All gradient echo imaging experiments suffer from the common feature of FID signals, namely, T_2^* relaxation. The above discussion shows that owing to this effect, the signal intensity depends on magnetic field inhomogeneities from various sources, and chemical shift effects. If we have a magnetic field inhomogeneity given by the gradient G within a pixel of a diameter dr, a phase spread will appear during the gradient echo time *TG*:

$$\phi = \gamma G\, \mathrm{d}r\, TE \tag{10}$$

High values of ϕ give low signal intensity in gradient echo imaging. It is clear that magnetic field homogeneity effects

decrease when the spatial resolution increases and/or the gradient echo time *TG* decreases. Of course, this has technological limitations, because the gradient strength and gradient switching time has to be improved. This effect, often called the 'susceptibility' effect, appears near air–soft tissue interphases (e.g., the nasopharynx region, air-filled bowels, and lungs) (see ***Susceptibility Effects in Whole Body Experiments***).

A similar effect of signal change is observed when different chemical shift values are present in one image element. From inspection of an FID signal containing two close frequency components, we know that a beat is observed, with oscillations of the signal during T_2* decay. At periodic times, the signal vanishes—this is often called the opposed-phase signal. If the gradient echo time *TG* is exactly matched to this time, no signal can be measured from a pixel where two chemical shift components with equal intensity are present. Therefore, by a careful selection of the gradient echo time *TG*, 'in-phase' or 'opposed-phase' gradient echo images can be measured.

Since transverse magnetization remains in fast gradient echo imaging without any spoiling, a further 'center' or 'stripe' artifact can appear. This is because residual transverse magnetization accumulates phase from step to step in 2D FT imaging.

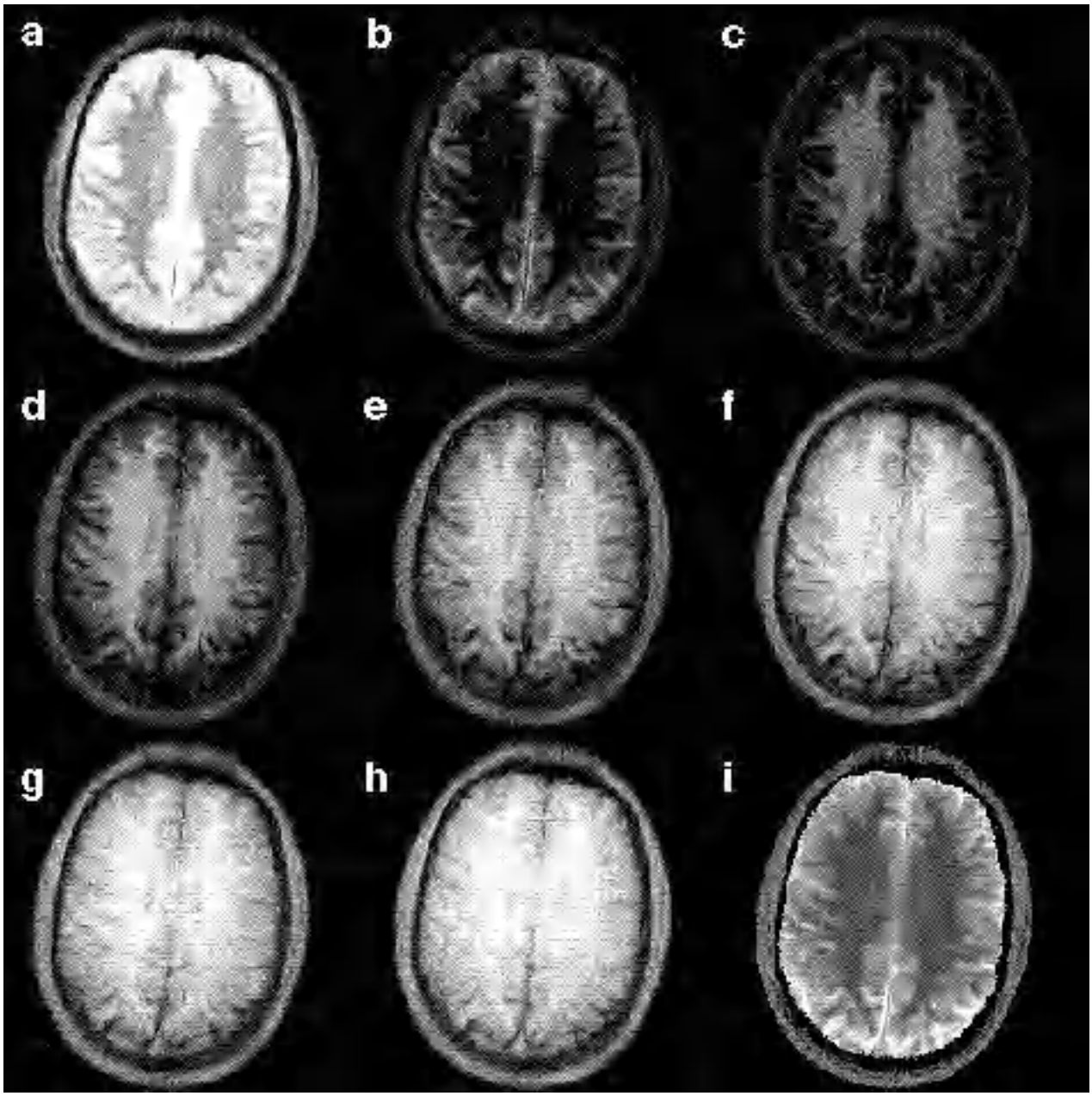

Figure 2 A series of 2 T inversion–recovery T_1-weighted snapshot-FLASH MR images of the human brain. The slice thickness was 8 mm, the data matrix 256×256, and the field-of-view 25.6 cm. The inversion–recovery delay increased from 162 ms (a) to 2281 ms (h). The calculated T_1-map is shown in (i)

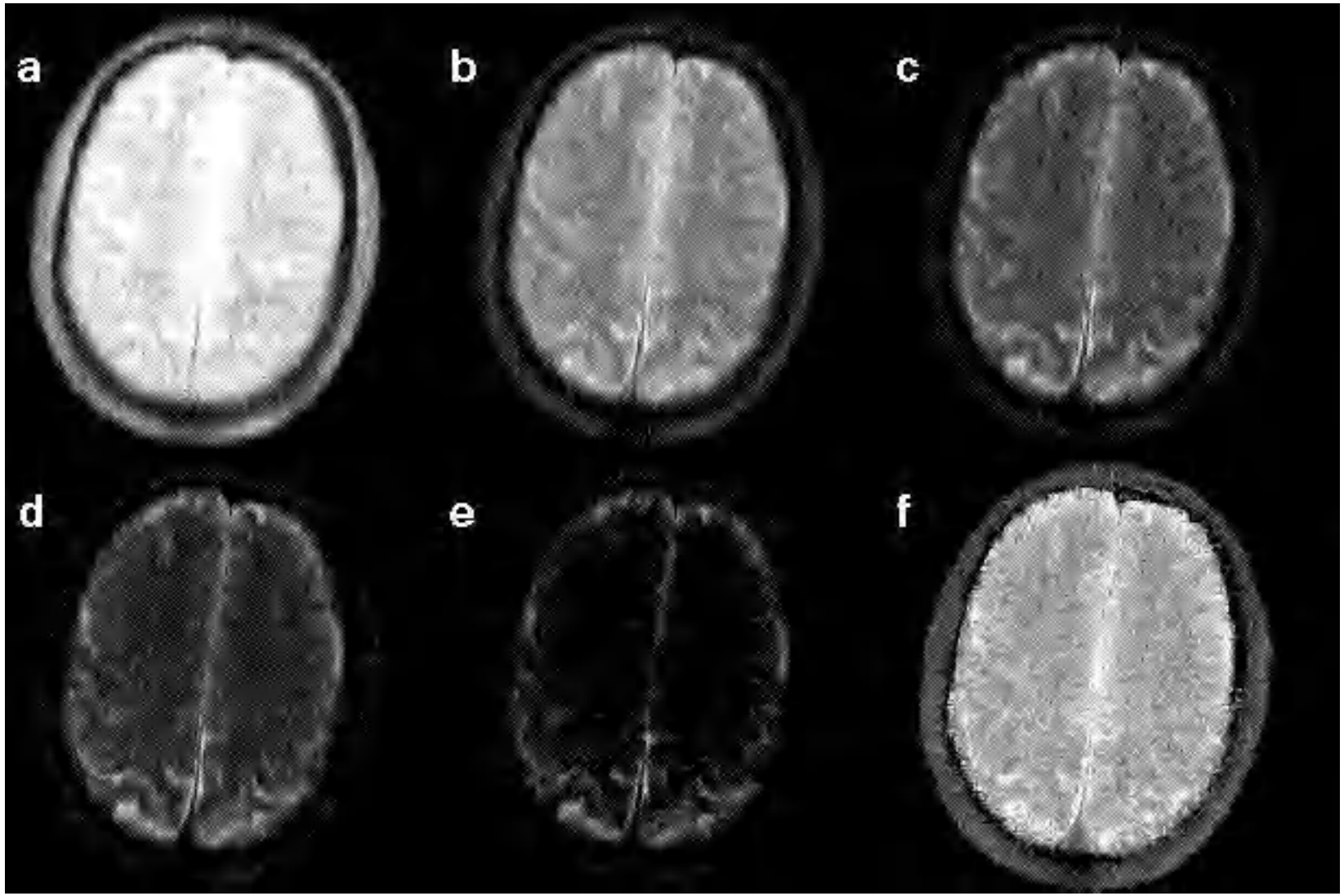

Figure 3 A series of 2 T T_2-weighted snapshot-FLASH MR images of the human brain. The slice thickness was 8 mm, the data matrix 256×256, and the field-of-view 25.6 cm. The spin echo delay 2τ in the magnetization preparation pulse sequence $90°$–τ–$180°$–τ–$90°$ increased from 1.7 ms (a) to 281.7 ms (e). The calculated T_2-map is shown in (f)

This gives a phase-encoding modulation of the signal, with low-frequency components giving a bright phase-encoding artifact in the middle of the image. The artifact can be reduced when low flip angles are used to minimize the transverse magnetization. Otherwise, either experiments with good spoiling should be selected, or random gradient spoiling, or random variation of the phase of the rf excitation pulse used.

6 QUANTITATIVE IMAGING

Fast NMR imaging should have a well-defined image contrast, and should give quantitative NMR images of relaxation times, diffusion constants, and flow velocities. However, as pointed out above, it is difficult to observe well-defined image contrast, and even more difficult to image quantitative data using fast gradient echo sequences. For example, T_1 contrast suffers from slice profile artifacts, T_2 contrast is not obtainable using 'spoiled sequences', and a mixture of T_1 and T_2 information is given by 'refocused methods'. Furthermore, flow and diffusion information needs longer gradient echo times, with adverse effects arising due to 'susceptibility artifacts'. This problematic situation changed completely when 'magnetization prepared' fast gradient echo sequences appeared. These are called 'snapshot', 'turbo', or 'MP (magnetization prepared)' gradient echo sequences.[6]

These methods gain from the fact that, because of hardware improvements, short repetition times of 5 ms or less have become possible in whole body scanners. Now, the total measuring time is less than 1 s, and therefore comparable to an average T_1 relaxation time in high magnetic fields. Magnetization preparation means that the longitudinal magnetization can be changed in a definite way before the acquisition of the whole snapshot image. The image contrast will then be dependent on the 'magnetization preparation', because this lasts for a few T_1 intervals (typically, one to three times T_1).

Magnetization preparation can be performed using a single inversion pulse for IR T_1-weighted images, a $90°$–τ–$180°$–τ–$90°$ (DEFT) pulse for spin echo T_2-weighted images ($\tau = \frac{1}{2}TE$), or a DEFT pulse combined with diffusion or flow-encoding gradients for diffusion- or flow-weighted images. This technique does not suffer from all the artifacts described previously, and gives true quantitative image data when a series of images are acquired.[6]

Figure 2 shows a series of inversion–recovery T_1-weighted snapshot-FLASH cross-sectional images of the human brain measured at 2 T magnetic field strength. These images present a sufficient data base for quantitative evaluation of a relaxation time (T_1) image. In Figure 2(i), a calculated T_1 image is shown using the images in Figure 2(a) to 2(h). The method is further demonstrated in Figure 3, where different T_2 images are displayed. The T_2-weighting was performed using a $90°$–τ–$180°$–τ–$90°$ magnetization preparation pulse sequence. The echo times, 2τ, increased from 1.7 ms to 281.7 ms. Figure 3(f) shows the calculated T_2-map.

7 APPLICATIONS AND CONCLUSIONS

A multitude of different applications have been described in the past few years since the beginning of fast gradient echo experiments. One of the most prominent applications is in the field of rapid 3D NMR imaging. Here, the total measuring time can be limited to a few minutes, and it remains a practical method for medical diagnosis. Recent software and computer improvements have helped to increase the importance of 3D NMR imaging.

A further principal application is in the field of 'functional' NMR imaging. From the beginning, dynamic contrast media studies were very helpful in organ studies. The time resolution in fast gradient echo imaging is of the order of a few seconds. The time course of a bolus injection of an NMR contrast medium can be followed easily, and kinetic data calculated. This was first done for kidney and liver studies, and later for functional NMR imaging in the brain. However, it should be emphasized that dynamic fast gradient echo imaging using contrast media acquires a time-dependent dynamic signal change. As discussed above, the signal of fast gradient echo images has a complex dependence on various parameters—relaxation times, susceptibility, etc. Therefore, the signal intensity is not clearly related to the local concentration of a contrast medium, and is strongly dependent on the imaging experiment and parameters used. It should be emphasized that quantitative data have to be acquired for quantitative contrast media studies.

The importance and applications of fast gradient echo sequences will—as in the past—gain further from hardware improvements. An important parameter in this respect is the gradient echo time. All adverse artifacts can be reduced and the signal intensity improved when this parameter is minimized. This improvement should also help with the implementation of more 'hybrid' fast imaging sequences. In a few cases, hybrids between EPI and fast gradient echo imaging can be of advantage. The ultimate limit of all fast imaging sequences, however, is not given by technological constraints but by biological effects due to nerve stimulation in rapidly switched magnetic fields.

8 RELATED ARTICLES

Contrast Agents in Magnetic Resonance: Operating Mechanisms; Image Formation Methods; Relaxation Measurements in Imaging Studies; Relaxation Measurements in Whole Body MRI: Clinical Utility; Spin Warp Data Acquisition; Susceptibility Effects in Whole Body Experiments; Whole Body Magnetic Resonance Angiography; Whole Body Magnetic Resonance Artifacts; Whole Body MRI: Strategies for Improving Imaging Efficiency.

9 REFERENCES

1. P. Mansfield, *J. Phys. C*, 1977, **10**, L55.
2. A. Haase, J. Frahm, D. Matthaei, W. Hänicke, and K.-D. Merboldt, *J. Magn. Reson.*, 1986, **67**, 258.
3. D. Matthaei, J. Frahm, A. Haase, and W. Hänicke, *Lancet*, 1985, **ii**, 893.
4. J. Frahm, A. Haase, D. Matthaei, K.-D. Merboldt, and W. Hänicke, *Magn. Reson. Med.*, 1986, **4**, 48.
5. J. Frahm, A. Haase, and D. Matthaei, *J. Comput. Assist. Tomogr.*, 1986, **10**, 363.
6. A. Haase, *Magn. Reson. Med.*, 1990, **13**, 77.

7. A. Kumar, D. Welti, and R. R. Ernst, *J. Magn. Reson.*, 1975, **18**, 69.
8. R. M. Henkelman and M. J. Bronskill, *Rev. Magn. Reson. Med.*, 1987, **2**, 126.
9. P. Margosian, F. Schmitt, and D. Purdy, *Health Care Instrum.*, 1986, **1**, 195.
10. R. R. Ernst and W. A. Anderson, *Rev. Sci. Instrum.*, 1966, **37**, 93.
11. W. A. Edelstein, J. M. S. Hutchison, G. Johnson, and T. Redpath, *Phys. Med. Biol.*, 1980, **25**, 756.
12. S. Patz, *Adv. Magn. Reson. Imaging* 1989, **1**, 73.
13. J. Frahm, K.-D. Merboldt and W. Hänicke, *J. Magn. Reson.*, 1987, **27**, 307.
14. Y. Zur, H. Israel, and P. Bendel, *Radiology*, 1987, **165**(P), 154.
15. A. Oppelt, R. Graumann, H. Barfuss, H. Fischer, W. Hartl, and W. Schajor, *Electromedica*, 1986, **1**, 15.
16. M. L. Gyngell, *Magn. Reson. Imaging*, 1988, **6**, 415.
17. I. R. Young, D. J. Bryant, and J. A. Payne, *Magn. Reson. Med.*, 1985, **2**, 355.

Biographical Sketch

Axel Haase. *b* 1952. Diploma in Physics, 1977, University of Giessen, Germany; Ph.D., 1980, working at Max-Planck-Institute, Göttingen and submitted to University of Giessen. Postdoc position, University of Oxford, with Prof. G. K. Radda, 1982. Scientist, Max-Planck-Institute in Göttingen, 1983–88. Chair of Biophysics at the University of Würzburg, Germany 1988–present. Published more than 60 articles. Present research interests are quantitative fast NMR imaging and NMR microscopy and NMR applications to cardiology and plant physiology.

Whole Body MRI: Strategies for Improving Imaging Efficiency

Felix W. Wehrli

University of Pennsylvania Medical School, Philadelphia, PA, USA

1 INTRODUCTION

Since the inception of clinical MRI at the beginning of the 1980s, the rate at which a subject can be scanned has been reduced by nearly an order of magnitude. Some of the improved scan efficiency is unrelated to a shortening of the actual data acquisition time and can be accounted for by improvements in some of the ancillary procedures such as patient set-up, rf coil placement, scan parameter entry, prescan (MRI jargon for rf carrier selection and adjustment of transmit and receive gain), and advances in digital system architecture (shortening in reconstruction times, concurrence of data acquisition and reconstruction, etc.). The focus of this article, however, will be on techniques for reducing data acquisition time, since it is this that determines patient tolerance. Scan times in excess of 5–10 min typically lead to image degradation from subject motion. Another strong motivation for shortening scan time is physiologic motion such as cardiac pulsation, respiration, and peristalsis. Clearly, if the data acquisition time could be lowered below the period of physiologic motion, the effect of motion unsharpness in the image data could effectively be suppressed. Many of the new applications, such as the assessment of organ function by monitoring the passage of a bolus of contrast agent,[1] the measurement of microcirculation,[2,3] or the study of brain function[4–6] demand temporal resolution on the order of 0.1–1 s (see also ***Contrast Agents in Whole Body Magnetic Resonance: An Overview***).

While many of the ideas for improved scan efficiency have been in existence for some time, they have become practical only in the 1990s owing to engineering advances such as digital transceiver electronics (see also ***Whole Body Magnetic Resonance Spectrometers: All-Digital Transmit/Receive Systems***) and gradient technology (see ***Gradient Coil Systems***). A case in point is echo planar imaging (EPI), which was first conceived in 1977,[7] but has only recently become commercially available. It is fair to say that the gradient system drives the modern imager's performance in that data acquisition rate (and thus imaging speed) are largely determined by the gradients' amplitude, slew rate, and duty cycle. Today, most imagers are equipped with whole-body gradients providing amplitudes and slew rates in excess of 20 mT m^{-1} and $\geqslant 150$ T m^{-1} s^{-1}, respectively. More recently, clinical systems with gradient strengths up to 40 mT m^{-1} have become commercially available.[8]

This chapter briefly reviews the concepts underlying the most important classes of rapid imaging techniques, each of which is discussed in more detail in other articles in this volume. The subject of high-speed imaging has been covered by a number of specialized texts. Haacke et al. have treated the subject of short repetition time (*TR*) gradient-echo imaging in detail.[9] EPI concepts have been covered by Cohen and Weisskoff[10] and, more recently, in a textbook by Schmitt et al.[11]

2 *k*-SPACE FORMALISM

We shall in the following resort to the classical $\boldsymbol{k}$-space formalism introduced by Ljunggren[12] and Tweig.[13] A more detailed introduction is given by Wehrli.[14] In brief, data sampling occurs in reciprocal space, referred to as '$\boldsymbol{k}$-space' or the 'spatial frequency domain'. For an object of spin density $\rho(\boldsymbol{r})$, ignoring relaxation, the spatial frequency signal $\rho'(\boldsymbol{k})$ is given by

$$\rho'(\boldsymbol{k}) = \int_{\boldsymbol{r}_1}^{\boldsymbol{r}_2} \rho(\boldsymbol{r}) \mathrm{e}^{-\mathrm{i}\boldsymbol{k}(t)\cdot\boldsymbol{r}} \, \mathrm{d}^3 r \tag{1}$$

Here $\boldsymbol{k}(t)$ is the spatial frequency vector, expressed in units of rad cm^{-1}:

$$\boldsymbol{k}(t) = \gamma \int_0^t \boldsymbol{G}(t') \, \mathrm{d}t' \tag{2}$$

where $\boldsymbol{G}(t')$ is the time-dependent spatial encoding gradient in vector format. Pictorially, the spatial frequency may be regarded as the phase rotation per unit length of the object experienced by the magnetization after being exposed to a gradient $\boldsymbol{G}(t')$ for some period t.

We further recognize from equation (1) that $\rho'(\boldsymbol{k})$ and $\rho(\boldsymbol{r})$ form a Fourier transform pair, and so

$$\rho(\boldsymbol{r}) = \frac{1}{2\pi} \int_{\boldsymbol{k}_1}^{\boldsymbol{k}_2} \rho'(\boldsymbol{k}) \mathrm{e}^{\mathrm{i}\boldsymbol{k}(t)\cdot\boldsymbol{r}} \, \mathrm{d}^3 k \tag{3}$$

The path of the spatial frequency vector during execution of the pulse sequence is determined by the time-dependent gradient waveforms.

Since $\boldsymbol{k}$-space is sampled discretely, sampling needs to satisfy the Nyquist criterion

$$\tfrac{1}{2} L_i k_{i,\max} = \tfrac{1}{2} N_i \pi \tag{4}$$

where $k_{i,\max}$ is the highest spatial frequency, L_i and N_i represent the field-of-view and number of data samples, respectively, and $i = x, y, z$. We can then write for the sampling interval Δk_i

$$\Delta k_i = \frac{k_{i\max}}{\frac{1}{2}N_i} = \frac{2\pi}{L_i} = \frac{2\pi}{N_i \Delta L_i} \tag{5}$$

with ΔL_i representing the pixel size. The factor of 2 in equation (5) arises because we collect N_i samples from $-k_{\max}$ to $+k_{\max}$ or $\frac{1}{2}N_i$ samples from 0 to $k_{\max}$.

Since the data sampling time increases with the number of data samples, one obvious approach toward shortening the

sampling time is to reduce N_i. It is readily seen from equation (5) that this can be achieved in two different ways. If we wish to maintain the pixel size, this will result in a reduction in the field-of-view and thus an increase in Δk_i. Conversely, we may want to maintain the field-of-view, in which case Δk_i remains invariant but $k_{\max}$ is lowered, and thus pixel size is increased. In the latter case, we trade spatial resolution for a reduction in sampling time.

Further, since $\Delta k \approx \gamma \Delta t\, G$, the sampling interval Δt scales inversely with the amplitude of the spatial encoding gradients. Therefore, the duration of the spatial encoding process is governed significantly by the achievable gradient amplitudes. At a given resolution, the latter essentially determine what fraction of $\boldsymbol{k}$-space can be covered following a single excitation (since the signal decays with time constant T_2). Therefore, the properties of the gradients, notably their amplitudes, and for many imaging sequences also their slew rates, are paramount in determining ultimate imaging speed.

3 CLASSIFICATION OF IMAGING TECHNIQUES

Most of the currently used imaging techniques use rectilinear $\boldsymbol{k}$-space sampling, and as such may be regarded as descendants of the spin warp technique of Edelstein et al.,[15] which itself is an outgrowth of Fourier zeugmatography, pioneered by Kumar, Welti, and Ernst.[16] Since the latter is an embodiment of two-dimensional (2D) NMR spectroscopy,[17] conceptionally all rectilinear sampling techniques may be regarded as originating from 2D NMR. By contrast, projection–reconstruction imaging[18–20] or imaging with nonperiodic time-varying gradients[21] such as spiral scanning[22,23] are not rectilinear sampling techniques, since the $\boldsymbol{k}$-space path is non-Cartesian.

Common to all rectilinear $\boldsymbol{k}$-space sampling techniques are two distinct phases of spatial encoding, a first period during which a gradient G_y is applied whose time integral determines k_y and during which no sampling occurs, followed by a second period during which a gradient G_x is applied while the free precession signal is sampled, resulting in a line S(k_x). The former is typically called 'phase encoding' and the latter 'frequency encoding'. In this manner, data are sampled along a 2D $\boldsymbol{k}$-space grid by incrementally stepping the amplitude of the phase-encoding gradient. The concept can be extended to a third dimension by phase encoding along a second spatial coordinate to afford k_z, in which case $\boldsymbol{k}$-space is three dimensional. In both back-projection and spiral scanning, two or all three spatial encoding gradients are simultaneously active while data are sampled. A generic 3D spin warp pulse sequence and $\boldsymbol{k}$-space map are shown in Figure 1.

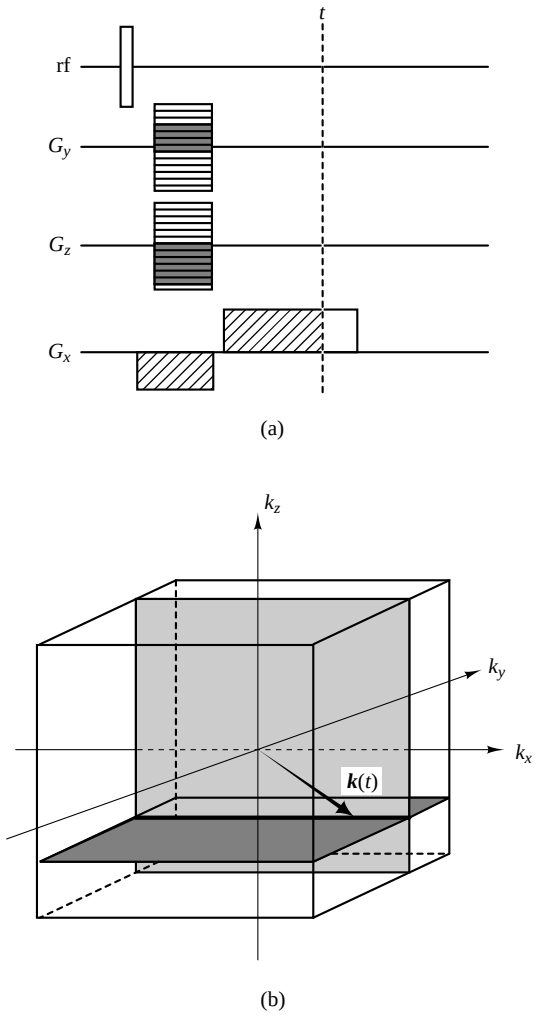

Figure 1 (a) Generic 3D spin warp imaging with phase encoding on the x and y axes and frequency encoding on z. Hatched areas indicate the spatial frequency vector at time t (b). Amplitudes of phase-encoding gradients are arbitrary. During readout, a line k_x is scanned corresponding to the intersection between the (k_xk_y) and (k_xk_z) planes (shaded areas)

4 VARIOUS EMBODIMENTS OF SPIN WARP IMAGING

4.1 Scan Time, Signal-to-Noise Ratio and Spatial Resolution

Ordinarily, only a fraction of $\boldsymbol{k}$-space is typically scanned upon creating transverse magnetization, and the process repeated multiple times, each cycle affording another $\boldsymbol{k}$-space segment. Longitudinal magnetization builds up in a recurrent fashion between cycles of period TR. The data acquisition time T_{ac} scales with TR and the number of pulse sequence cycles, the latter being a function of the number of spatial encoding steps or $\boldsymbol{k}$-space samples. It is customary to denote the frequency-encoding axis by x and the phase-encoding axis by y (or y and z, respectively, if phase encoding in an additional dimension is effected), with N_i (i = x, y, z) representing the number of data samples. Assuming further that during a frequency-encoding period a single line $k_{x,i=1,\ldots Nx}$ is sampled, T_{ac} to sample $\boldsymbol{k}$-space is given by

$$T_{\text{ac}} = N_y N_z n TR \tag{6}$$

where n represents the number of sequence repetitions (also called 'number of excitations' in imaging jargon) at given values of $\boldsymbol{k}$. At typical sampling rates, the sampling time for frequency encoding is on the order of 10 ms or less and so

does not appear in equation (6). It will, however, become critical in high-speed gradient echo imaging[24,25] and EPI and its derivatives.[26–28]

The scan time scales with the number of phase encodings (N_y in 2D, and N_y and N_z in 3D spin warp imaging), and thus a reduction in the number of phase-encoding samples entails a concomitant reduction in scan time. As previously pointed out, this can be achieved either by lowering k_{max} or by decreasing sampling density $1/\Delta k$. The former lowers resolution, the latter leads to reduced field-of-view while preserving resolution [cf. equations (4) and (5)]. Thus, the term 'matrix size' is ambiguous, though in common parlance a change in matrix implicitly implies fixed field-of-view. The two different situations, each lowering data acquisition time of a 3D image acquisition by a factor of 4, are illustrated in Figure 2.

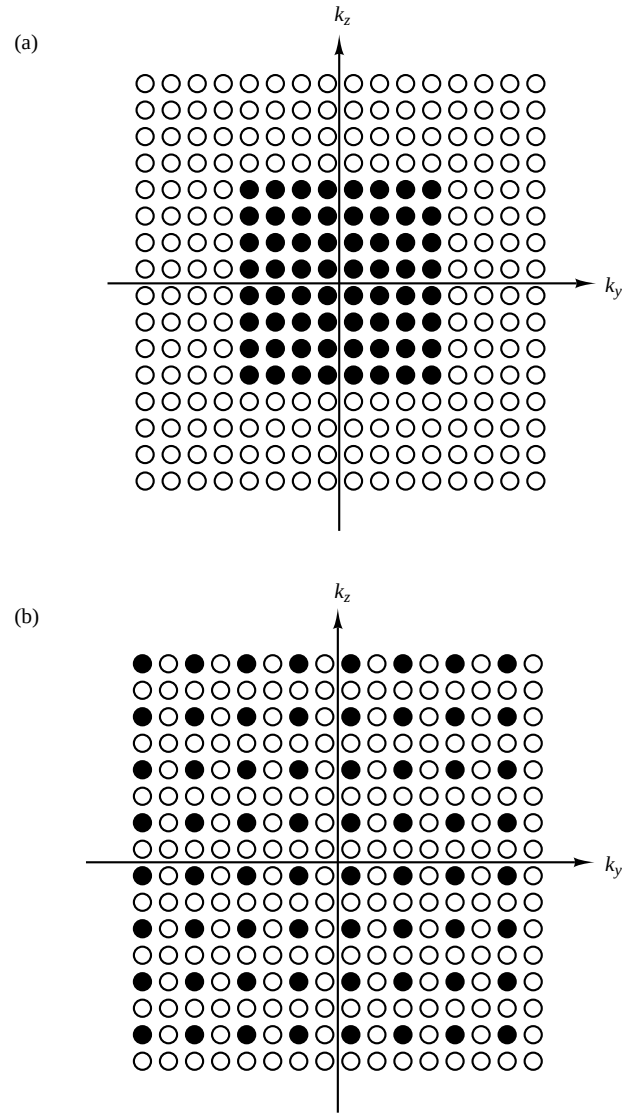

Figure 2 Halving the number of phase and slice encodings (N_y, N_z) in a 3D spin warp acquisition can be achieved by reducing either the $\boldsymbol{k}$-space area (a) or the sampling density (b), leading to lower resolution (a) or reduced field-of-view (b). Open circles represent skipped data samples

Let us now examine the signal-to-noise ratio (SNR) implications of the two different operations. The signal amplitude S scales with voxel size, i.e.,

$$S \propto \Delta x\, \Delta y\, \Delta z = \frac{L_x L_y L_z}{N_x N_y N_z} \tag{7}$$

where the product $\Delta x\, \Delta y\, \Delta z$ expresses the voxel volume; the remaining parameters have previously been defined. Further, the noise-reducing effect of sampling leads to

$$\mathrm{SNR} \propto \sqrt{n} \tag{8}$$

and thus

$$\mathrm{SNR} \propto \frac{L_x L_y L_z \sqrt{n}}{\sqrt{N_x N_y N_z}} \tag{9}$$

From equation (9), we conclude that halving the number of data samples N_y and N_z by halving $k_{y,max}$ and $k_{z,max}$ increases SNR by a factor of 2 (Figure 2a). Skipping alternate data samples, by comparison, penalizes SNR by a factor of 8 since this operation halves the field-of-view for both L_y and L_z [equation (5); Figure 2b].

4.2 Slice Multiplexing and Multiecho Acquisition

In most embodiments of 2D spin warp imaging, the period comprising slice selection, phase encoding, and frequency encoding accounts for only a fraction of the *TR* interval. Therefore, minimizing the dead time by shortening the pulse recycle time seems to be a straightforward means of optimizing scan time. However, *TR* is typically dictated by contrast requirements. Shortening of *TR* leads to progressive saturation, and thus, in spin echo imaging at least, is incompatible with proton density and T_2-weighted contrast. A solution to this problem was first implemented by Crooks et al.,[30] leading to what is commonly called '2D multislice imaging'. By making the rf pulses slice selective, only the spins in the slice of interest are stimulated. Adjacent slices are then excited in sequence without perturbing the steady state. The gain in efficiency achieved in this manner depends on *TR*, the echo time *TE*, and the time required for applying the spatial encoding gradients; it typically ranges from about 10 to 50 ms. The second important innovation was the incorporation of Carr–Purcell echoes into spin warp imaging. In this manner, images with different contrast[31] can be derived from a single acquisition. It is obvious that adding echoes reduces the number of slices that can be interrogated in a given *TR* period. Both 2D multislice and multiecho spin warp imaging, perhaps appearing trivial in hindsight, are, in historic perspective, among the most significant milestones in the quest for imaging efficiency.

4.3 Conjugate Synthesis

A salient property of $\boldsymbol{k}$-space with implications for imaging speed is its conjugate symmetry, i.e.,

$$\rho(\boldsymbol{k}) = \rho(-\boldsymbol{k}) \tag{10}$$

This implies that two data samples corresponding to spatial frequencies $\boldsymbol{k}$ and $-\boldsymbol{k}$ are complex conjugates of one another. In

principle, therefore, it suffices to acquire only half of ***k***-space. In reality, the conjugate symmetry is often not perfect. Causes of deviations are phase shifts from magnetic field inhomogeneity and motion, which require appropriate correction of the raw data before Fourier reconstruction[32] (see also ***Partial Fourier Acquisition in MRI***).

As already pointed out, sampling in the k_y and k_z directions is much slower than sampling in the k_x direction. Therefore, by exploiting the redundancy in phase-encoding lines, scan time is halved. Halving imaging time by conjugation was described by Margosian et al.[33] and also by Feinberg et al.[34] Because the phase correction requires sampling of a small number of data lines on the conjugate half, the time saving is usually somewhat less than 50%. Conjugate synthesis (also referred to as 'half-Fourier imaging') is particularly useful in EPI[10] and single-shot RARE (rapid acquisition with relaxation enhancement) imaging (discussed below).

4.4 Variable Flip Angle Imaging

In their seminal work on pulse Fourier transform spectroscopy Ernst and Anderson[30] showed that for a train of equidistant rf pulses, the extent of saturation can be controlled by adjusting the rf pulse flip angle α and further that the signal peaks for the condition

$$\alpha_{\text{opt}} = \cos^{-1}(\exp^{-TR/T_1}) \tag{11}$$

where α_{opt} is the optimum pulse flip angle (also called the 'Ernst angle'), which is valid provided that $TR >> T_2$. It is readily recognized that flip angles $< 90^\circ$ are not compatible with the simple Hahn or Carr–Purcell imaging pulse sequence, since inversion of the residual longitudinal magnetization by the subsequent phase reversal pulse would lead to a steady state of very low magnetization. Haase et al.[36] modified the original spin warp technique in which a gradient echo is sampled and showed that in this manner *TR* could be reduced at least 10-fold relative to corresponding spin echo implementations, which may have prompted the authors to the acronym FLASH (*f*ast *l*ow *a*ngle *sh*ot). Other solutions to the problem involve the idea to restore the longitudinal magnetization with a second 180° pulse.[37] An alternative solution is to select a flip angle so that $90^\circ < \alpha < 180^\circ$, followed by the usual phase-reversal 180° pulse. Since large-angle selective rf pulses are difficult to achieve, earlier work made use of composite pulses consisting of a nonselective 180° pulse followed immediately by a selective small-angle pulse of flip angle β so that $\alpha = 180^\circ - \beta$.[38,39] The motivation for spin echoes over gradient echoes is their relative insensitivity to background gradients since, in contrast to FLASH, the signal is attenuated as $\exp(-TE/T_2)$ rather than $\exp(-TE/T_2^*)$. Recent progress in rf pulse design have led to highly selective large-angle pulses that provide superior partial flip-angle imaging. The technique has been referred to as FLASE (*f*ast *l*arge-*a*ngle *s*pin *e*cho).[40]

The FLASH signal can readily be calculated from the Bloch equations to yield

$$S(TR, \alpha, TE) \propto \frac{1 - \exp(-TR/T_1)}{1 - \cos\alpha \exp(-TR/T_1)} \sin\alpha \times \exp(-TE/T_2^*) \tag{12}$$

For $\alpha = \alpha_{\text{opt}}$, equation (12) simplifies to

$$S_{\alpha_{\text{opt}}}(TE) \propto \tan(\tfrac{1}{2}\alpha) \exp(-TE/T_2^*) \tag{13}$$

The assumption implicit in equation (12), i.e., $TR >> T_2$ between successive rf pulses, is usually invalid at high pulse-repetition rates. As first described by Carr,[41] a steady-state situation arises for spins subjected to a train of rf pulses in inhomogeneous magnetic fields, with magnetization building up in a recurrent fashion from cycle to cycle. Such a stream of equidistant rf pulses forms two signals: a free induction delay (FID) and an echo. The FID follows the rf pulse whereas the echo builds up prior to the next rf pulse, reaching a maximum at the time of the pulse.[42] Both signals have been observed by various embodiments of gradient echo imaging, provided that the gradient moments are partially or fully balanced. In spin warp imaging, however, neither condition is ordinarily satisfied, since the phase-encoding gradient is stepped in an incremental fashion. The ensuing cycle-dependent phase shifts cause intensity artifacts that have a positional dependence, since the phase depends on the spins' location on the phase-encoding axis.[43] If, however, the phase imparted by the phase-encoding gradient is unwound by a gradient of opposite moment prior to the next-following rf pulse,[43,44] the spatial dependence of the steady state vanishes and the FID is observed. Common acronyms for this modification to the generic FLASH pulse sequence are GRASS (*g*radient *r*ecalled *a*cquisition in the *s*teady *s*tate) and FISP (*f*ast *i*maging with *s*teady state *p*recession). It is also possible to dephase the FID and to observe the echo, although this pulse sequence has not found widespread application.[45]

Finally, it is possible to design the pulse sequence such that both, FID and echo, occur simultaneously, which is the case when the gradients on all three axes are fully balanced, i.e. when the zeroth moment for all gradients is reset at the end of the pulse-sequence interval.[46] This pulse sequence is sometimes referred to as 'true FISP' or 'coherent steady-state imaging (CSS)' (see, for example, Haacke et al., Chapter 18[47]). A hallmark of CSS is the very strong enhancement of fluids (by virtue of their long T_2). True FISP has not been applied widely since it is very sensitive to off-resonance effects (e.g., magnetic field inhomogeneity). The signal amplitude is a function of the precession angle $\beta = \Delta\omega TR$, where $\Delta\omega$ is the (spatially dependent) resonance frequency offset that can lead to bands of low signal intensity across the image.[48] In the absence of off-resonance effects or, alternatively, if the spins precess an integral number of half-periods between successive excitations ($\beta = n\pi$), the steady-state transverse magnetization is given by:

$$M_y^{\text{ss}} = \frac{M_0 \sin\alpha}{(T_1/T_2 + 1) - \cos\alpha(T_1/T_2 - 1)} \tag{14}$$

If $\alpha = \pi/2$, equation (14) simplifies to

$$M_y^{\text{ss}} = M_0 \frac{T_2}{T_1 + T_2} \tag{15}$$

CSS images, therefore, enhance fluid proton signal to an even grater extent than the GRASS/FISP pulse sequence.[48]

From a soft tissue contrast point of view, it is often desirable to suppress transverse coherences. Application of spoiler

gradients of varying amplitude has been found to be relatively ineffective for this purpose,[49] though schemes exist that provide some spoiling efficiency.[50] Nevertheless, a more effective means of eliminating the carry-over of transverse magnetization from previous cycles is to step the rf transmit and receive phase in constant increments from cycle to cycle. Although predicted by Crawley et al.[49] rf-spoiled gradient echo imaging was developed by Matt Bernstein and his colleagues in 1989, but, unfortunately, never published.

The contrast characteristics of the two embodiments of FLASH are substantially different. In the high-flip-angle regime, GRASS affords images in which the signal scales as given in equation (14), hence favoring fluids where $T_2 \approx T_1$ (as opposed to tissues, where $T_1 >> T_2$). By contrast, with spoiling, the signal obeys equation (12), leading to a more T_1-weighted appearance.

4.5 High-Speed Gradient Echo Techniques

Combination of increased sampling frequency bandwidth and fractional echo sampling with partial Fourier processing,[51] reduction in the number of frequency-encoding samples, and other strategies such as truncated rf pulses permit shortening of pulse repetition times to 5 ms or less.[24,25]

Ultrahigh-speed imaging with *TR* values of the order of 3 ms at typical gradient amplitudes and slew rates are now possible on clinical imagers (see, for example, Epstein et al.[8]). One of the major applications of very short *TR* gradient echo imaging currently is contrast-enhanced MR angiography (CE-MRA) where a 3D volume has to be imaged within a 15–30 s breath-hold period (see, for example, Prince et al.[52] and references cited therein). This acquisition mode appears to be ideal for this application where the high repetition rate maximally suppresses signal from background tissue. At the same time, the signal from vascular protons is enhanced as a result of the drastic shortening of T_1 (~50 ms) imparted by the contrast medium. CE-MRA is performed with spoiled versions of gradient echo sequences, i.e., with complete suppression of transverse coherences.

Very recently, there has also been renewed interest in very short-*TR* steady-state imaging. Vasanawala et al. reported a fully balanced steady-state sequence in which the rf phase is alternated 90° in successive cycles.[53] In this manner, a steady state is obtained with the signal alternating between two levels and with different off-resonance properties. By judiciously selecting pulse flip angle, repetition time, and resonance offset it can be shown that lipid discrimination can be achieved in that the signal from each species is alternately suppressed and retained, thus allowing both water and fat images to be obtained in a single acquisition.

Another approach to achieve a desired contrast is to create a nonequilibrium situation by preceding the train of low-angle rf pulses by an inversion pulse for T_1-dependent contrast[54–56] or driven-equilibrium pulses to achieve T_2-weighted contrast.[57] Since, in this case, the magnetization evolves during scanning of $\boldsymbol{k}$-space, effectively filtering the data in a manner determined by the spin dynamics, the usual sequential scanning from $-k_{max}$ to $+k_{max}$ is not optimal. Remembering that the signal components pertaining to $k \approx 0$ contribute most to contrast, it is necessary to acquire these data at the desired time point during magnetization evolution (e.g., when the signal from a particular tissue is nulled). These requirements can, for example, be reconciled with a $\boldsymbol{k}$-space ordering scheme that has been called 'centric phase encoding',[55] in which data collection starts at $\boldsymbol{k}$-space center and proceeds outward. This imaging mode has proven useful in situations where strong T_1 contrast sensitivity is required while minimizing undesired signal from static material and, further, high temporal resolution is needed. A case in point is perfusion imaging based on dynamic monitoring of the passage of a bolus of contrast material. Figure 3 shows a series of images of the lungs collected with IR-prepared fast gradient echo imaging a rate of 1 s^{-1}, along with the time course of the signal from which perfusion information can be obtained.[58]

4.6 Segmentation of *k*-space and View Sharing

The need for increased scan speed is particularly stringent when imaging moving structures, the prime example being the heart. The dramatic advances in data acquisition hardware and $\boldsymbol{k}$-space scanning and reconstruction methodology have led to an explosive growth of cardiac MRI during recent years. High-speed imaging techniques now make realtime MRI of the heart a realistic possibility (see, for example, Kerr et al.[59]). Nevertheless, the speed with which the heart contracts challenges even the fastest imaging techniques. A pulse repetition time of 5 ms and collection of 128 views, resulting in a scan time of 650 ms, is more than one half of an R–R interval, i.e., far too slow to capture a particular cardiac phase. One way to deal with this problem is to divide data acquisition among several successive heart beats, which, of course, requires it to be gated to the cardiac cycle. Collecting only one view per cardiac phase would require 128 heart beats, although multiple cardiac phases can be captured in this manner. This approach is the basis of 'cardiac cine' imaging.[60,61] However the minimum scan time can be considerably shortened (albeit at some cost in temporal resolution) if, instead of a single line k_y, multiple lines are scanned per cardiac phase (here a cardiac phase is regarded as an interval of tens of milliseconds during which the heart does not move significantly). This enhancement, also termed 'segmented $\boldsymbol{k}$-space acquisition'[56] permits shortening of the data acquisition time in cardiac cine imaging to 16–24 heartbeats,[62] which is within the range of a breath-hold period, thus considerably improving cardiac image quality. The temporal resolution can be further enhanced by collecting multiple gradient echoes during each *TR* period.[8,63]

Temporal resolution can be further enhanced if only a limited number of views are updated for each temporal frame, the rationale being that not all spatial frequency components equally contribute to signal energy. Riederer et al. first proposed this concept,[64] calling it 'MR fluoroscopy' in analogy to X-ray fluoroscopy, a method used for guiding interventional procedures. Van Vaals et al. showed that by updating the central views only, while sharing the more peripheral ones, dynamic processes could be monitored with greatly increased temporal resolution.[65] In more sophisticated approaches, the frequency of temporal replacement of views is effected more gradually. While the central-most views are replaced most often, the updating frequency decreases with distance from the $\boldsymbol{k}$-space center.[66] This approach has enabled generation of multiple 3D MRA data sets following a single contrast injection

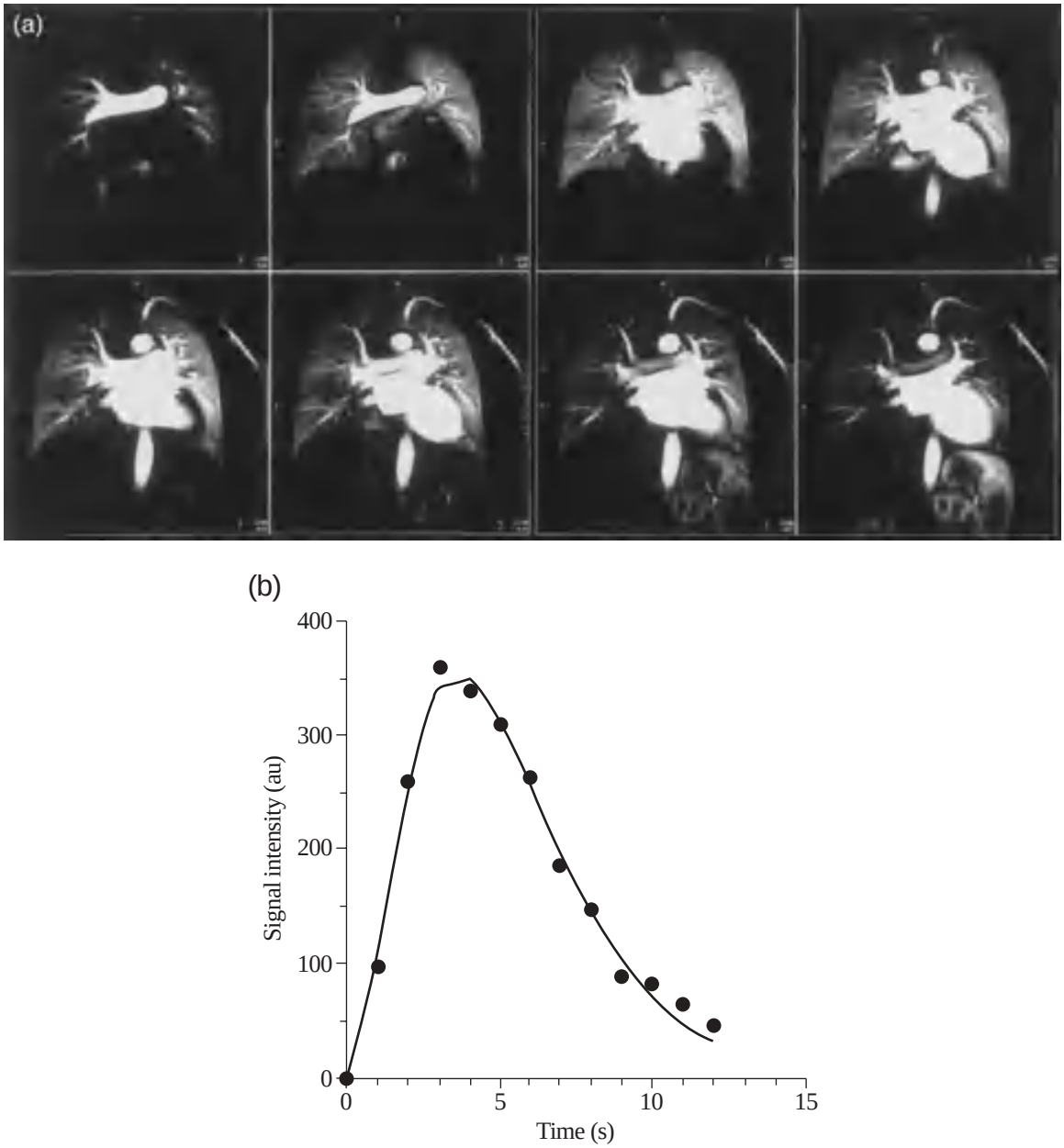

Figure 3 (a) Dynamic contrast-enhanced images of pulmonary perfusion using inversion-recovery prepared high-speed gradient echo imaging (repetition time 3.5 ms; echo time 1.4 ms; inversion time 400 ms). Forty-five images were obtained following a 1 s bolus of gadolinium-diethylenetriamine pentaacetic acid at a rate of one per second (eight images shown). (b) Time course of the parenchymal signal. (From Hatabu et al.[58] with permission)

and allows the capture of both arterial and venous phases. Images corresponding to successive temporal frames are thus reconstructed from ***k***-space data that are partly shared. Likewise, in segmented cardiac cine imaging, temporal resolution can be augmented by view sharing in that additional images are reconstructed by combining ***k***-space lines from adjacent temporal phases.[67]

Finally, there have been other developments enhancing dynamic scanning, unrelated to pulse sequence design. One of these exploits the potential of multiple-receiver coil arrays for speed enhancement (rather than for extending sensitivity over a larger volume). Recently, Sodickson and Manning showed that a modulation analogous to the one caused by exposure of the magnetization to a spatial encoding gradient can be achieved by using linear combinations of the signals from multiple receive coils.[68] In this manner, they demonstrated that the number of phase encodings needed to achieve a given resolution scales inversely with the number of coils in the array.

5 MULTILINE SCANNING TECHNIQUES

All previously discussed embodiments of spin warp imaging have in common that within one pulse sequence cycle, a single

data line is sampled. Collection of additional echoes merely replicates encoding affording images of increasing T_2 weighting. An inherently more efficient approach makes use of the idea to exploit a plurality of echoes in such a manner that each echo affords a separate k_y line.

5.1 Echo Planar Imaging

The technique of EPI, in which the entire 2D encoding process could be completed during a single FID was first proposed by Mansfield in 1977. The fundamental principle underlying the technique is to oscillate the read gradient G_x in the presence of a constant gradient G_y.[7] It is readily seen that in this manner, half of ***k***-space is traversed in a zigzag trajectory. The difficulties in reconstructing images from only half the data and nonorthogonal sampling grids were remedied with the introduction of pre-encoding gradients and discontinuous phase encoding.[27,28] In this manner, entire images of 64 × 128 data samples could be obtained in as little as 50 ms at 2 T field strength.[28,69] For an overview of the subject, the reader is referred to a review by Cohen and Weisskoff[10]. The technical aspects of high-speed imaging are also covered in recent textbooks.[11,47,70] (See also ***Echo-Planar Imaging***.)

An interesting corollary of single-shot EPI is that the pulse repetition time loses its meaning, since the data are collected in single sequence cycle. However, concatenation of individual acquisitions for the purpose of generating movies, for example, underlies the same restrictions as the conventional FLASH method, demanding adjustment of the rf flip angle to control saturation. Cohen and Weisskoff showed 16-frame cardiac movies obtained by acquiring complete images every 67 ms within a single heart beat.[10] Unlike gated techniques, where each image data set, or fraction thereof, is collected during consecutive heart beats, the method is insensitive to variations in heart rate. In contrast to the high-speed FLASH-type methods, however, EPI puts more stringent demands on instrumentation, in particular to amplitudes and slew rates of the gradients, which explains its currently limited diffusion. Some of these conditions are relaxed if only a fraction of ***k***-space is scanned from a single echo train. More recent work, however, demonstrates that hybrid techniques involving ***k***-space coverage during multiple heart beats, provide better image quality.

There are only two common clinical applications of single-shot EPI, both in the brain. The first is functional imaging where high temporal resolution is required and spatial resolution is of secondary importance size (see, for example, de Yoe et al.[71] and references therein). The second is diffusion- and perfusion-weighted imaging as a means to characterize ischemic lesions in patients with strokes.[72] Here, the significance is the short total acquisition time, which prevents artifacts that would arise from physiologic motion and that are exacerbated owing to the presence of the diffusion-sensitizing gradients.[73]

One of the inherent problems of EPI lies in the disparity in sampling rate between phase-encoding and readout direction. While each echo is read out in a fraction of a millisecond (typical sampling frequency 250–500 kHz), the duration of the echo train is on the order of 50–100 ms. The technique is, therefore, sensitive to phase accumulation from off-resonant spins in the presence of magnetic field inhomogeneity, typically arising from susceptibility effects. The obvious remedy is to shorten the echo train duration, which, without compromising resolution, would demand improved gradient hardware. Alternatively, temporal resolution can be sacrificed. Instead of collecting all ***k***-space lines from the signal of a single rf pulse, only every mth line is sampled per excitation. It, therefore, takes m separate ***k***-space traversals to cover ***k***-space but, in return, the echo train has been shortened m-fold.[74,75] The dramatic reduction in off-resonance image distortion with increasing number of interleaves is shown in Figure 4. Finally, interleaved EPI can be combined with ***k***-space segmentation, yielding a very powerful hybrid technique.[8,63] Instead of scanning only one line k_y during each of say eight TR periods per segment, four lines are obtained by collecting four echoes. This method has been shown to be capable of acquiring 16 temporal frames in as few as four heart beats (Figure 5).

Finally, it is instructive to compare the SNR of EPI with high-speed spin warp imaging. At a given resolution three parameters contribute to SNR:

1. sampling time (SNR $\propto \sqrt{t_s}$);
2. transverse relaxation losses (SNR $\propto \exp(-TE/T_2)$);
3. the fraction of magnetization available for signal creation (determined by saturation) (SNR $\propto f(TR, T_1, \alpha)$.

The following comparison may be instructive. Suppose a typical tissue such as neural white matter is scanned at 1.5 T field strength ($T_1 \approx 700$ ms, $T_2 \approx 75$ ms). Then consider a high-speed gradient echo acquisition with 128 phase encodings and 2 ms readout time, $TR = 5$ ms, $TE \approx 0$, operated at the optimum flip angle, which is 6.8°, and compare it with a single

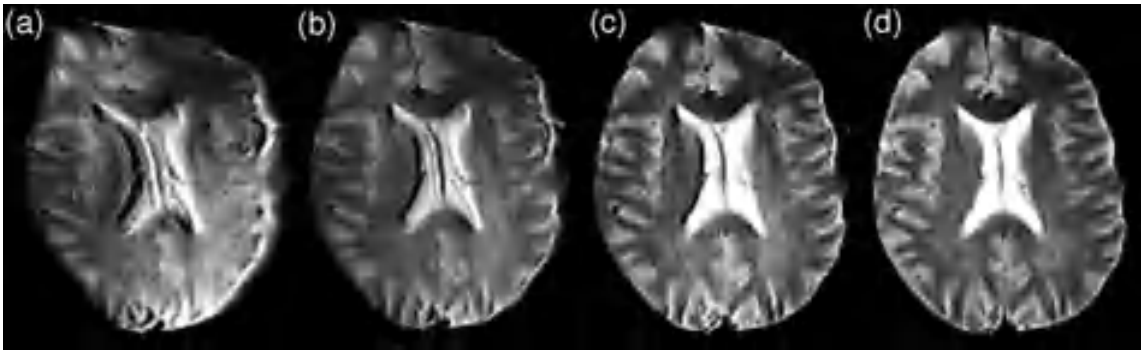

Figure 4 Dependence of magnetic field uniformity-induced image distortions on the number of ***k***-space traversals used for scanning ***k***-space in interleaved echo planar imaging. Number of interleaves: (a) 2, (b) 4, (c) 8, and (d) 16. (Images courtesy of General Electric Medical Systems)

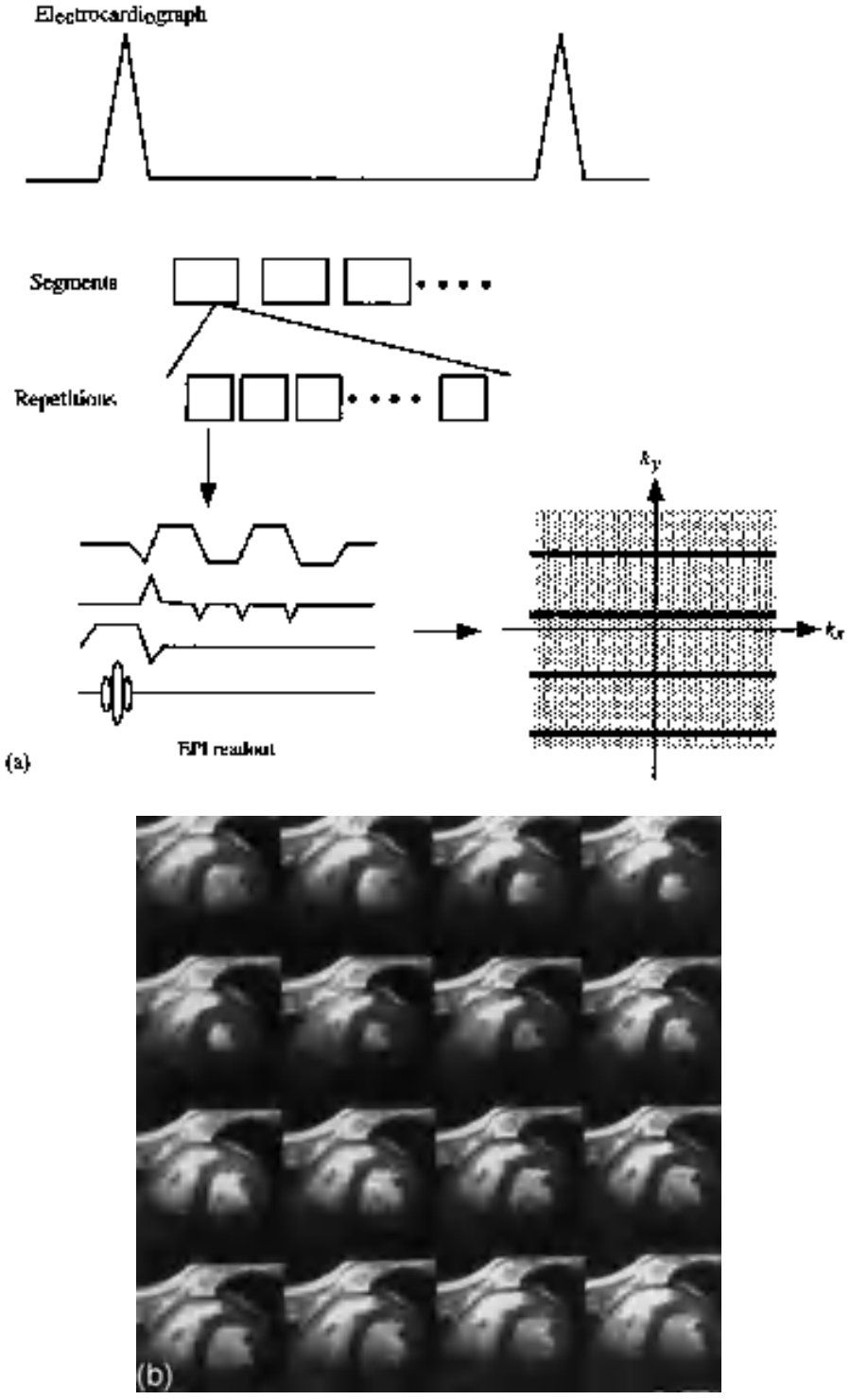

Figure 5 (a) Principle of segmented ***k***-space acquisition in cardiac cine imaging with echo planar imaging (EPI) readout: The R–R interval is divided into time periods ('segments'). During each segment multiple pulse repetitions occur, each being followed by an EPI readout during which typically four ***k***-space lines are scanned. (b) Cine images representing 16 cardiac phases. (From Epstein et al.[8] with permission)

shot EPI with 50 ms total sampling time, performed such that $k_y = 0$ is sampled at $TE = 30$ ms. The results are summarized in Table 1. They imply a net advantage of about a factor of 5 in favor of EPI, defeating the common notion that shortened scan time inevitably exacts a SNR penalty.

Similar arguments in favor of EPI have been put forward by Cohen and Weisskoff.[10] Such a comparison, however, does not withstand more rigorous scrutiny. Suppose we were to repeat the EPI scan every 640 ms, i.e., the equivalent of the FLASH data acquisition time. This would mean that the longitudinal

Table 1 Comparison of SNR in Single Shot EPI and High-Speed FLASH

	EPI	FLASH	SNR_{EPI}/SNR_{FLASH}
Sampling time (ms)	50	256	0.44
Magnetization	1	0.06	16.7
exp ($-TE/T_2$)	0.67	1	0.67
Net gain			4.9

See text for assumptions.

magnetization has only incompletely recovered, therefore requiring operation at the Ernst angle, which is 65°. Doing so reduces the transverse magnetization following the rf pulse to 0.64 [from equation (13)], thus lowering the relative SNR advantage of EPI to a (still substantial) factor of 3. This disparity in SNR may be explained by the fact that in EPI transverse magnetization is recycled (rather than quenched by spoiling as in a FLASH-type pulse sequence). Therefore, it would be more appropriate to compare EPI with steady-state free-precession techniques.

5.2 RARE

In 1986, Hennig introduced the spin echo counterpart of EPI,[76,77] initiating a development with significant impact on clinical efficiency. Surprisingly, this work did initially not elicit broad interest. The perception that the images emphasized structures with long T_2, thereby producing significantly T_2-weighted images, prompted Hennig to dub his technique 'RARE'. While obviously highly efficient, the extreme T_2 weighting appeared to limit the method to specialized applications such as imaging of cerebrospinal fluid.

Besides scan time reduction by up to an order of magnitude, the current widespread clinical use of the method owes its popularity to its spin echo nature, i.e., being insensitive to magnetic field inhomogeneities. Equally important, however, is the almost unlimited latitude in image contrast RARE provides if implemented in a hybrid mode with only a fraction of ***k***-space covered per echo train. It is interesting that the possibilities for contrast manipulation of the RARE sequence were already recognized by Hennig in his 1986 paper.[76] By ***k***-space weighting the echoes appropriately, Melki et al.[78] showed that virtually any arbitrary contrast is possible. For this purpose, they devised an algorithm for phase-encoding ordering while minimizing adverse effects from discontinuous sampling of k_y-space. For example, assigning early echoes to low spatial frequencies de-emphasizes T_2 weighting. The convolution of the data with the relaxation function, of course, may result in point spread function blurring, since high-k signals are attenuated.[79]

Since each of the n echoes generates n lines k_y, the minimum data acquisition time is lowered n-fold. Nevertheless, when assessing the method's efficiency in terms of scan time per image, one has to consider that the prolonged echo train reduces the number of slice locations that can be interleaved during the dead time following data collection. For example, at an echo train length of 250 ms consisting of 16 echoes, a TR of 3 s acquisition provides fewer than 12 slice locations, rather than about 30 s for a conventional dual echo scan with a second TE of 100 ms. Therefore, the greatly improved efficiency can be traded for improved resolution (by a factor of four in linear resolution) without adversely affecting SNR when compared with single line spin-echo imaging. Further, it enables 3D imaging with all its benefits such as retrospective data rearrangement with image display in secondary planes, which was hitherto impractical in spin echo imaging because of excessive scan time. An example of 3D RARE images is given in Figure 6.

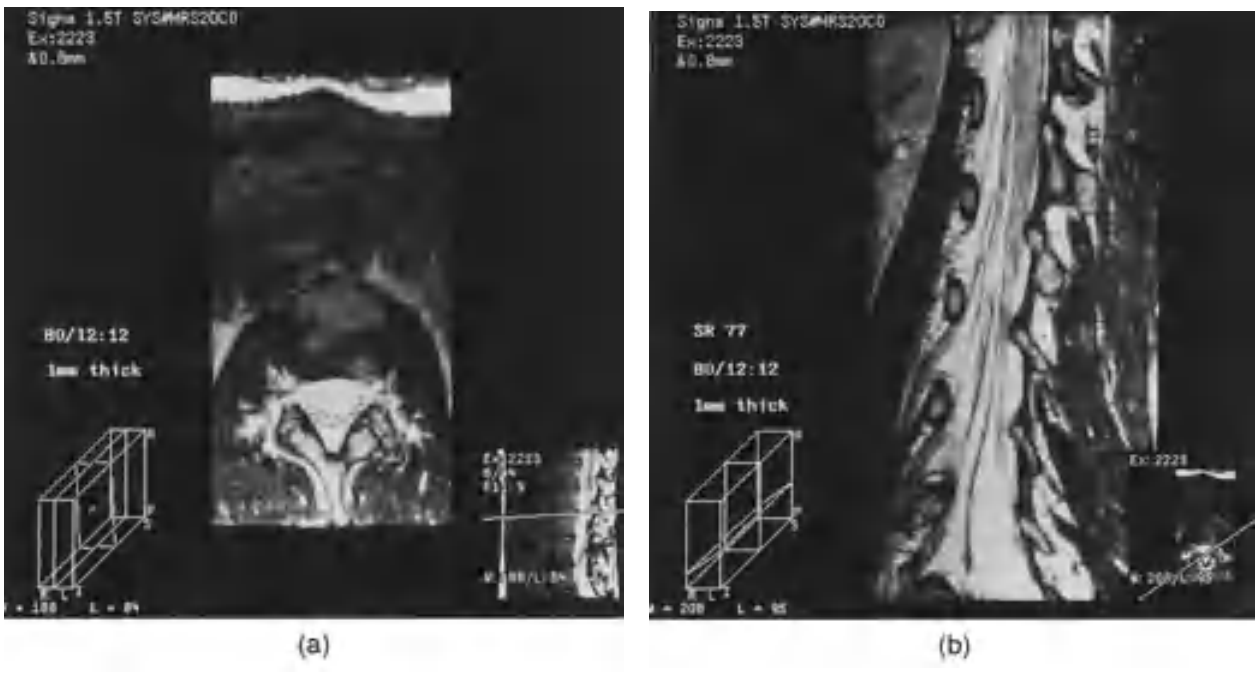

Figure 6 Three-dimensional RARE (rapid acquisition with relaxation enhancement) images of the lumbar spine: (a) axial section; (b) oblique reformation showing nerve roots. (Images courtesy General Electrical Medical Systems, Milwaukee.)

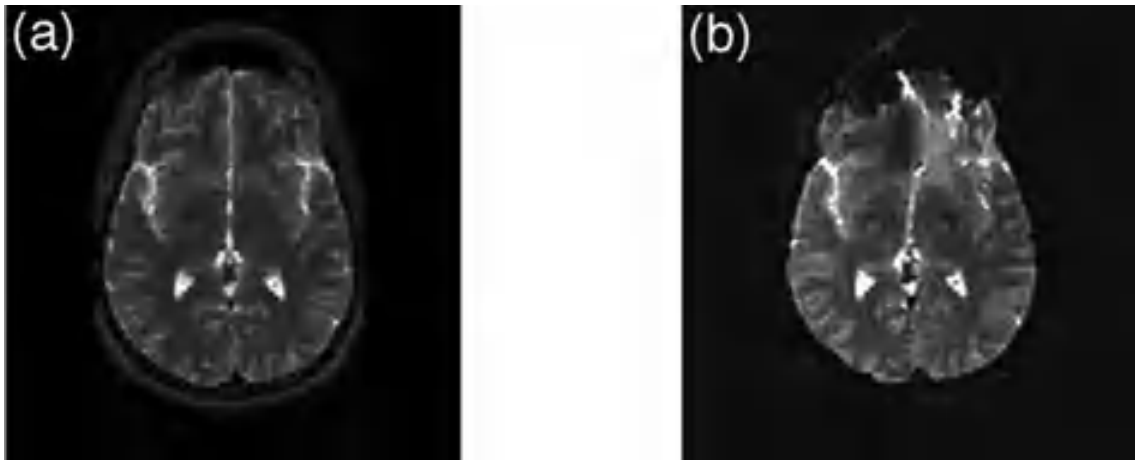

Figure 7 (a) Single-shot RARE (rapid acquisition with relaxation enhancement) image acquired in 400 ms total scan time. (b) The corresponding echo planar image collected in 110 ms. Note the spatial and intensity distortions near the frontal sinuses in (b), not present in the spin echo image. (Images courtesy Dr. D. Alsop, University of Pennsylvania Medical Center.)

The logical extension of RARE, which typically requires multiple interleaves to fill ***k***-space, is to attempt to collect all lines k_y from a single echo train, analogous to single-shot EPI. There are potential hurdles to overcome for achieving such a goal. The first is the rf heating that a closely spaced train of 180° pulses might entail, in particular in the abdomen and at high magnetic field. The second is to meet the requirement that the echoes be collected in a period short enough to avoid excessive attenuation, which otherwise can cause point spread function blurring. The first problem can be overcome by lowering the flip angle of the refocusing pulses (remembering that the power scales as the square of the flip angle), first suggested and demonstrated by Hennig.[80] One might be tempted to think that the reduction in flip angle exacts a substantial SNR penalty (just as a 90°–90° echo has only one half the amplitude of its 90°–180° counterpart). However, this is not the case, as has been shown both experimentally[80] and theoretically.[81] In fact, Alsop demonstrated recently[81] that by properly stabilizing the echo amplitude,[82] more than 95% of the maximum signal can be recovered with 90° refocusing pulses for spins with $T_1/T_2 = 10$. The reason for this apparent anomaly lies in the contribution to the echo amplitudes from stimulated echoes. Hennig had already shown that the per-unit-time SNR of single-shot RARE can be up to a factor of 100 higher than that for conventional spin echo, which again emphasizes what we have seen for EPI, i.e., that increased scan speed does not inevitably penalize SNR.

Most single-shot RARE pulse sequences use half-Fourier reconstruction[32] as a means to double resolution at a given echo train length. They are, therefore, often referred to as *h*alf-Fourier *a*cquisition *s*ingle-shot *t*urbo spin-*e*cho (HASTE).[83] This powerful imaging sequence has already proven its great potential in a number of applications such as imaging of the biliary system[84] or for such novel procedures as oxygen-enhanced lung ventilation imaging.[85,86] While only slightly slower than single-shot EPI, its main benefit is its immunity to off-resonance effects (Figure 7). Like other high-speed imaging techniques, it can be combined with various magnetization preparation schemes such as inversion recovery for fat or fluid suppression (STIR and FLAIR, respectively)[87–89] or diffusion encoding.[90]

Finally, it has also been shown that RARE and EPI principles can be combined in such a manner that gradient echoes are interwoven into a spin echo train, referred to as GRASE (*gra*dient and *s*pin *e*cho),[91,92] and, thus, the efficiency further augmented. The counterpart of single-shot RARE is single-shot GRASE, for which high-resolution images of very good quality and contrast characteristics similar to spin echo images have been demonstrated.[93] The method is likely to have significant impact in instances where acquisition speed is critical but neither contrast nor resolution can be sacrificed, such as in pediatric imaging or examination of patients who would have to be sedated for more conventional imaging protocols. Lastly, similar to RARE, 3D embodiments of GRASE have been reported. Mugler showed that excellent images can be obtained with 3D GRASE if the phase-encoding order is optimized in such a manner that the point-spread function is free of sidelobes.[94] (See also ***Multi Echo Acquisition Techniques Using Inverting Radiofrequency Pulses in MRI***).

6 OTHER METHODS OF SCANNING *k*-SPACE

An alternative ***k***-space scanning technique that, like EPI, uses oscillating gradients is spiral MRI. As implied by the term, the ***k***-space trajectory in this case is a spiral originating at the ***k***-space center. Ahn et al., who published the first spiral scan images, used a back-projection algorithm for reconstruction.[22] Most of the more recent work is based on constant-velocity interleaved ***k***-space spirals (as opposed to constant angular frequency),[23] (see ***Spiral Scanning Imaging Techniques***). This particular form of spiral MRI has the advantage that ***k***-space is covered more uniformly and that the amplitude of the oscillating gradients is constant. Compared with EPI, the gradient amplitude and slew rate requirements are less demanding, and the technique has been found to be tolerant to flow-related dephasing, an observation that was attributed to the low gradient moments near the ***k***-space center and the periodic simultaneous return to zero of all moments.[23]

Spiral scans require different reconstruction algorithms. Fourier transformation along the radial coordinate affords a series of projections, from which the image is obtained by filtered back-projection.[22] Alternatively, the data can be rearranged into a rectilinear grid by interpolation, thus allowing Fourier reconstruction.[23]

During recent years, there has been increasing interest in spiral MRI with applications targeting realtime imaging of the heart,[59] functional imaging of the brain,[95] coronary artery imaging,[96] diffusion-weighted imaging,[97] and fast spectroscopic imaging.[98] In spiral scanning, the center of $\boldsymbol{k}$-space is scanned first, as in radial scanning (projection imaging). Further, it has been shown that the first moment is smoothly varying over the $k_x k_y$ plane.[99] These properties render spiral images less sensitive to motion artifacts, properties which, incidentally, also apply to projection imaging.[100] (See also ***Spiral Scanning Imaging Techniques***.)

Another non-Cartesian sampling technique suited for high-speed imaging is projection imaging, where $\boldsymbol{k}$-space is sampled radially in two or three dimensions by simultaneous application of two or three constant-amplitude gradients that are proportional to the sine and cosine of the projection angle. In this manner, a radial path is traced, starting at the center of $\boldsymbol{k}$-space.[19,20] $\boldsymbol{k}$-space is covered by stepping the gradient amplitudes so as to increment the projection angle in successive sequence cycles. By selecting shallow rf pulses, the pulse sequence can be run at rates comparable to gradient echo spin warp imaging. Since sampling can start almost immediately following excitation, the technique is particularly suited for imaging tissues with short-T_2 times such as lung parenchyma[101] or imaging of nuclei with inherently short T_2 times such as ^{11}B.

In summary, during the past 25 years since its inception, MRI has revealed a wide spectrum of technical approaches for covering data space. Scan speed is a continuum ranging from milliseconds to minutes, with trade-offs between temporal resolution, SNR and spatial resolution. The rate at which $\boldsymbol{k}$-space can be scanned is determined significantly by the imager's hardware, in particular the achievable amplitudes of the spatial encoding gradients and their switching rates, and the receiver's bandwidth. Besides intrinsic SNR, the ultimate scan speed may be limited by adverse bioeffects, notably peripheral nerve stimulation[103] caused at increased rates of change in the magnetic flux density ($d\boldsymbol{B}/dt$) of the switched gradients.

7 RELATED ARTICLES

Echo-Planar Imaging; Gradient Coil Systems; Image Formation Methods; Multi Echo Acquisition Techniques Using Inverting Radiofrequency Pulses in MRI; Partial Fourier Acquisition in MRI; Projection–Reconstruction in MRI; Spiral Scanning Imaging Techniques; Whole Body Magnetic Resonance: Fast Low-Angle Acquisition Methods; Whole Body Magnetic Resonance Spectrometers: All-Digital Transmit/Receive Systems.

8 REFERENCES

1. A. Villringer, B. R. Rosen, J. W. Belliveau, J. L. Ackerman, R. B. Lauffer, R. B. Buxton, Y. S. Chao, V. J. Wedeen, and T. J. Brady, *Magn. Reson. Med.*, 1988, **6**, 164.
2. D. C. Alsop and J. A. Detre, *Radiology*, 1998, **208**, 410.
3. L. Ostergaard, D. A. Chester, R. M. Weisskoff, A. G. Sorensen, and B. R. Rosen, *J. Cereb. Blood Flow Metab.*, 1999, **19**, 690.
4. J. W. Belliveau, D. N. Kennedy, R. C. McKinstry, B. R. Buchbinder, R. M. Weisskoff, M. S. Cohen, J. M. Vevea, T. J. Brady, and B. R. Rosen, *Science*, 1991, 716.
5. K. K. Kwong, J. W. Belliveau, D. A. Chesler, I. E. Goldberg, R. M. Weisskoff, B. Poncelet, D. N. Kennedy, B. E. Hoppel, M. S. Cohen, R. Turner, H. Cheng, T. Brady, and B. Rosen, *Proc. Natl. Acad. Sci. USA*, 1992, **89**, 5675.
6. S. Ogawa, D. W. Tank, R. Menon, J. M. Ellerman, S. G. Kim, H. Merkle, and K. Ugurbil, *Proc. Natl. Acad. Sci. USA*, 1992, **89**, 5951.
7. P. Mansfield, *J. Phys. C*, 1977, **10**, L55.
8. F. H. Epstein, S. D. Wolff, and A. E. Arai, *Magn. Reson. Med.*, 1999, **41**, 609.
9. E. M. Haacke, P. A. Wielopolski, and J. A. Tkach, *Rev. Magn. Reson. Med.*, 1991, **3**, 53.
10. M. S. Cohen and R. M. Weisskoff, *Magn. Reson. Imag.*, 1991, **9**, 1.
11. F. Schmitt, M. K. Stehling, and R. Turner, 'Echo-planar Imaging: Theory, Technique and Applications', Springer, Berlin, 1998.
12. S. Ljunggren, *J. Magn. Reson.*, 1983, **54**, 338.
13. D. B. Twieg, *Med. Phys.*, 1983, **10**, 610.
14. F. W. Wehrli, in 'Categorical Course in MR Physics: the Basics of MR Imaging', ed. S. J. Riederer and M. L. Wood, RSNA Publications, Oak Brook, Ill, 1997.
15. W. A. Edelstein, J. M. S. Hutchison, G. Johnson, and T. Redpath, *Phys. Med. Biol.*, 1980, **25**, 751.
16. A. Kumar, D. Welti, and R. Ernst, *J. Magn. Reson.*, 1975, **18**, 69.
17. W. Aue, E. Bartholdi, and R. Ernst, *J. Chem. Phys.*, 1976, **64**, 2229.
18. P. C. Lauterbur, *Nature (Lond.)*, 1973, **243**, 190.
19. C.-M. Lai and P. C. Lauterbur, *Phys. Med. Biol.*, 1981, **26**, 851.
20. I. R. Young, D. R. Bailes, M. Burl, A. G. Collins, D. T. Smith, M. J. McDonnell, J. S. Orr, M. L. Banks, G. M. Bydder, R. H. Greenspan, and R. E. Steiner, *J. Comput. Assist. Tomogr.*, 1982, **6**, 1.
21. A. Macovski, *Magn. Reson. Med.*, 1985, **2**, 29.
22. C. Ahn, J. Kim, and Z. Cho, *IEEE Trans. Med. Imag.*, 1986, **5**, 2.
23. C. H. Meyer, B. S. Hu, D. G. Nishimura, and A. Macovski, *Magn. Reson. Med.*, 1992, **28**, 202.
24. A. Haase, *Magn. Reson. Med.*, 1990, **13**, 77.
25. J. Frahm, K. D. Merboldt, H. Bruhn, M. L. Gyngell, W. Hänicke, and D. Chien, *Magn. Reson. Med.*, 1990, **13**, 150.
26. R. Rzedzian, B. Chapman, P. Mansfield, R. E. Coupland, M. Doyle, A. Crispin, D. Guilfoyle, and P. Small, *Lancet*, 1983, **ii**, 1281.
27. B. Chapman, R. Turner, R. Ordidge, M. Doyle, M. Cawley, R. Coxon, P. Glover, and P. Mansfield, *Magn. Reson. Med.*, 1987, **5**, 246.
28. I. L. Pykett and R. R. Rzedzian, *Magn. Reson. Med.*, 1987, **5**, 563.
29. P. Brunner and R. R. Ernst, *J. Magn Reson.*, 1979, **33**, 83.
30. L. Crooks, M. Arakawa, J. Hoenninger, J. Watts, R. McRee, L. Kaufman, P. L. Davis, A. R. Margulis, and J. DeGroot, *Radiology*, 1982, **143**, 169.
31. L. E. Crooks, D. A. Ortendahl, L. Kaufman, J. Hoenninger, M. Arakawa, J. Watts, E. R. Cannon, M. Brant-Zawadzki, P. L. Davis, and A. R. Margulis, *Radiology*, 1983, **146**, 123.

32. J. R. MacFall, N. J. Pelc, and R. M. Vavrek, *Magn. Reson. Imag.*, 1988, **6**, 143.
33. P. Margosian, F. Schmitt, and D. Purdy, *Health Care Instrum.*, 1986, **1**, 195.
34. D. A. Feinberg, J. D. Hale, J. C. Watts, L. Kaufman, and A. Mark, *Radiology*, 1986, **161**, 527.
35. R. R. Ernst and W. A. Anderson, *Rev. Sci. Instrum.*, 1966, **37**, 93.
36. A. Haase, J. Frahm, and D. Matthaei, *J. Magn. Reson.*, 1986, **67**, 258.
37. J. A. Tkach and E. M. Haacke, *Magn. Reson. Imag.*, 1988, **6**, 373.
38. A. R. Bogdan and P. M. Joseph, *Magn. Reson. Imag.*, 1990, **8**, 13.
39. H. Jara, F. W. Wehrli, H. Chung, and J. C. Ford, *Magn. Reson. Med.*, 1993, **29**, 528.
40. J. Ma, F. Wehrli, and H. Song, *Magn. Reson. Med.*, 1996, **35**, 903.
41. H. Carr, *Phys. Rev.*, 1958, **112**, 1693.
42. S. Patz (ed.), 'Steady-state Free Precession: An overview of Basic Concepts and Applications', vol. 1, 'Advances in Magnetic Resonance Imaging', ed. E. Feig, Alex Publishing, Norwood, 1989, p. 73.
43. J. Frahm, K. D. Merboldt, and W. Hanicke, *J. Magn. Reson.*, 1987, **27**, 307.
44. K. Sekihara, *IEEE Trans. Med. Imag.*, 1987, **6**, 157.
45. M. L. Gyngell, *Magn. Reson. Imag.*, 1988, **6**, 415.
46. A. Oppelt, R. Graumann, H. Barfuss, H. Fischer, W. Hertl, and W. Schajor, *Electromedica*, 1986, **54**, 15.
47. E. M. Haacke, R. W. Brown, M. R. Thompson, and R. Venkatesan, 'Magnetic Resonance Imaging: Physical Principles and Sequence Design', Wiley-Liss, New York, 1999.
48. E. M. Haacke, P. A. Wielopolski, J. A. Tkach, and M. T. Modic, *Radiology*, 1990, **175**, 545.
49. A. P. Crawley, M. L. Wood, and R. M. Henkelman, *Magn. Reson. Med.*, 1988, **8**, 248.
50. H. Z. Wang and S. J. Riederer, *Magn. Reson. Med.*, 1990, **15**, 175.
51. T. K. Foo, F. G. Shellock, C. E. Hayes, J. F. Schenck, and B. E. Slayman, *Radiology*, 1992, **183**, 277.
52. M. R. Prince, T. M. Grist, and J. F. Debatin, '3D contrast MR angiography', Springer, Berlin, 1997.
53. S. Vasanawala, J. M. Pauly, and D. G. Nishimura, *Magn. Reson. Med.*, 1999, **42**, 876.
54. J. P. Mugler III and J. R. Brookeman, *Magn. Reson. Med.*, 1990, **15**, 152.
55. A. E. Holsinger and S. J. Riederer, *Magn. Reson. Med.*, 1990, **16**, 481.
56. R. R. Edelman, B. Wallner, A. Singer, D. J. Atkinson, and S. Saini, *Radiology*, 1990, **177**, 515.
57. J. P. Mugler, III, T. A. Spraggins, and J. R. Brookeman, *JMRI*, 1991, **1**, 731.
58. H. Hatabu, E. Tadamura, D. L. Levin, W. Li. Kim, P. V. Prasad, and R. R. Edelman, *Magn. Reson. Med.*, 1999, **42**, 1033.
59. A. B. Kerr, J. M. Pauly, B. S. Hu, K. C. Li, C. J. Hardy, C. H. Meyer, A. Macovski, and D. G. Nishimura, *Magn. Reson. Med.*, 1997, **38**, 355.
60. G. Nayler, D. N. Firmin, and D. B. Longmore, *J. Comput. Assist. Tomogr.*, 1986, **10**, 715.
61. G. H. Glover and N. J. Pelc, in 'Magnetic Resonance Annual', ed. H. Y. Kressel, Raven Press, New York, 1988, p. 299.
62. R. R. Edelman, W. J. Manning, D. Burstein, and S. Paulin, *Radiology*, 1991, **181**, 641.
63. S. B. Reeder, E. Atalar, A. Z. Faranesh, and E. R. McVeigh, *Magn. Reson. Med.*, 1999, **41**, 375.
64. S. J. Riederer, T. Tascyan, F. Farzaneh, J. N. Lee, R. C. Wright, and R. J. Herfkens, *Magn. Reson. Med.*, 1988, **8**, 1.
65. J. van Vaals, M. Brummer, W. Dixon, H. Tuithof, H. Engels, R. Nelson, B. Gerety, J. Chezmar, and J. den Boer, *JMRI*, 1993, **3**, 671.
66. F. R. Korosec, R. Frayne, T. M. Grist, and C. A. Mistretta, *Magn. Reson. Med.*, 1996, **36**, 345.
67. T. K. Foo, M. A. Bernstein, A. M. Aisen, R. J. Hernandez, B. D. Collick, and T. Bernstein, *Radiology*, 1995, **195**, 471.
68. D. K. Sodickson and W. J. Manning, *Magn. Reson. Med.*, 1997, **38**, 591.
69. R. R. Rzedzian and I. L. Pykett, *Am. J. Roentgenol.*, 1987, **149**, 245.
70. M. T. Vlaardingerbroek and J. A. den Boer (eds.), 'Magnetic Resonance Imaging: Theory and Practice', Springer, Berlin, 1996.
71. E. A. de Yoe, P. Bandettini, J. Neitz, D. Miller, and P. Winans, *J. Neurosci. Meth.*, 1994, **54**, 171.
72. D. Le Bihan, in 'Categorical Course in Physics: the Basic Physics of MR Imaging', ed. S. J. Riederer and M. L. Wood, RSNA, Oakbrook, Ill, 1997, p. 131.
73. M. E. Moseley, J. Kucharczyk, J. Mintorovitch, Y. Cohen, J. Kurhanewicz, N. Derugin, H. Asgari, and D. Norman, *Am. J. Neuroradiol.*, 1990, **11**, 423.
74. G. McKinnon, *Magn. Reson. Med.*, 1993, **30**, 609.
75. K. Butts, S. J. Riederer, R. L. Ehman, R. M. Thompson, and C. R. Jack, *Magn. Reson. Med.*, 1994, **31**, 67.
76. J. Hennig, A. Nauerth, and H. Friedburg, *Magn. Reson. Med.*, 1986, **3**, 823.
77. J. Hennig, H. Friedburg, and D. Ott, *Magn. Reson. Med.*, 1987, **5**, 380.
78. P. S. Melki, R. V. Mulkern, L. P. Panych, and F. A. Jolesz, *Magn. Reson. Imaging*, 1991, **1**, 319.
79. P. S. Melki, F. A. Jolesz, and R. V. Mulkern, *Magn. Reson. Med.*, 1992, **26**, 328.
80. J. Hennig, *J. Magn. Reson.*, 1988, **78**, 397.
81. D. C. Alsop, *Magn. Reson. Med.*, 1997, **37**, 176.
82. P. Le Roux and S. Hinks, *Magn. Reson. Med.*, 1993, **30**, 183.
83. R. C. Semelka, N. L. Kelekis, D. Thomasson, M. A. Brown, and G. A. Lamb, *JMRI*, 1996, **6**, 698.
84. T. Miyazaki, Y. Yamashita, T. Tsuchigame, H. Yamamoto, J. Urata, and M. Takahashi, *Am. J. Roentgenol.*, 1996, **166**, 1297.
85. R. R. Edelman, H. Hatabu, E. Tadamura, W. Li, and P. V. Prasad, *Nature Med.*, 1996, **2**, 1236.
86. H. Hatabu, J. Gaa, E. Tadamura, K. J. Edinburgh, K. W. Stock, E. Garpestad, and R. R. Edelman, *Eur. J. Radiol.*, 1999, **29**, 152.
87. G. M. Bydder and I. R. Young, *J. Comput. Assist. Tomogr.*, 1985, **9**, 659.
88. J. V. Hajnal, D. Bryant, J. L. Kasuboski, P. M. Pattany, B. de Coene, P. D. Lewis, J. M. Pennock, A. Oatridge, I. R. Young, and G. M. Bydder, *J. Comput. Assist. Tomogr.*, 1992, **16**, 841.
89. J. V. Hajnal, L. Kasuboski, N. M. deSouza, and G. M. Bydder, *Clin. Radiol.*, 1995, **50**, 1.
90. D. C. Alsop, *Magn. Reson. Med.*, 1997, **38**, 527.
91. K. Oshio and D. A. Feinberg, *Magn. Reson. Med.*, 1991, **20**, 344.
92. D. A. Feinberg and K. Oshio, *Radiology*, 1991, **181**, 597.
93. D. A. Feinberg, B. Kiefer, and G. Johnson, *Magn. Reson. Med.*, 1995, **33**, 529.
94. J. P. Mugler III, *J. Magn. Reson. Imaging*, 1999, **9**, 604.

95. Y. Yang, G. H. Glover, P. van Gelderen, V. S. Mattay, A. K. Santha, R. H. Sexton, N. F. Ramsey, C. T. Moonen, D. R. Weinberger, J. A. Frank, and J. H. Duyn, *Magn. Reson. Med.*, 1996, **36**, 620.
96. J. H. Brittain, B. S. Hu, G. A. Wright, C. H. Meyer, A. Macovski, and D. G. Nishimura, *Magn. Reson. Med.*, 1995, **33**, 689.
97. T. Q. Li, A. M. Takahashi, T. Hindmarsh, and M. E. Moseley, *Magn. Reson. Med.*, 1999, **41**, 143.
98. E. Adalsteinsson, P. Irarrazabal, D. M. Spielman, and A. Macovski, *Magn. Reson. Med.*, 1995, **33**, 461.
99. D. G. Nishimura, P. Irarrazabal, and C. H. Meyer, *Magn. Reson. Med.*, 1995, **33**, 549.
100. G. H. Glover and J. M. Pauly, *Magn. Reson. Med.*, 1992, **28**, 275.
101. C. J. Bergin, G. H. Glover, and J. M. Pauly, *Radiology*, 1991, **180**, 845.
102. G. H. Glover, J. M. Pauly, and K. M. Bradshaw, *JMRI*, 1992, **2**, 47.
103. W. Irnich and F. Schmitt, *Magn. Reson. Med.*, 1995, **33**, 619.

Biographical Sketch

Felix W. Wehrli. *b* 1941. M.S., 1967, Ph.D., 1970, chemistry, Swiss Federal Institute of Technology, Switzerland. NMR application scientist, Varian AG, 1970–79; Executive Vice President, Bruker Instruments, Billerica, 1979–82; NMR Application Manager, General Electric Medical Systems, Milwaukee, 1982–88. Currently Professor of Radiologic Science and Biophysics, University of Pennsylvania Medical School, Editor-in-Chief *Magnetic Resonance in Medicine*. Approximately 100 publications. Current research specialty: NMR imaging of connective tissues and biomaterials, specifically trabecular bone and skin.

Chemical Shift Imaging

Truman R. Brown
Fox Chase Cancer Center, Philadelphia, PA, USA

1 INTRODUCTION

This article describes chemical shift imaging (CSI), illustrating how useful it is as a tool for obtaining well-localized in vivo spectra. CSI was originally described in 1982 by Brown et al.[1,2] A similar procedure was suggested by Maudsley et al. in 1983.[3] A brief discussion of alternative localization techniques is included for comparison.

The need for a well-defined procedure for spectral localization for in vivo studies cannot be overemphasized. Unlike high-resolution NMR studies in chemistry, where the sample is placed entirely within a uniform rf field, studies in vivo are necessarily examining an inhomogeneous tissue, often with a coil which produces a spatially variable rf field. These circumstances make it very difficult to obtain a clear understanding of the relationship between observed spectra and physiology without a precise and controlled spectral localization technique: with such a technique, relationships which exist between spectral and physiological variables may be determined.

Because the wavelengths of the frequencies involved are in the 3–30 m range, no localization can be provided by the electromagnetic field directly, as in a light microscope. Instead, all localization techniques (both for imaging and spectroscopy) depend upon controlled spatial variations in either the static magnetic field or the rf magnetic field. Thus, the basic principles of localization apply equally to imaging as well as spectroscopy. The major difference is that imaging is usually concerned with localizing only a single component, generally water. In fact, the presence of two components at different frequencies, e.g. lipid and water, causes artifacts.

Spatially variable rf fields, typically arising from a surface coil,[4] will not be discussed here although they have been used extensively. They are difficult to quantify, in spite of the fact that they make it easy to acquire spectra from relatively large volumes. With carefully controlled gradients in the rf field more precise localization can be carried out,[5] although referencing them to the imaging gradients is difficult. We shall concern ourselves below only with static field gradients, used primarily as short phase-encoding pulses, which 'label' the spins at a particular position by giving them a well-defined rf phase, different at different locations. By collecting multiple FIDs each with a different gradient, mathematical reconstruction of the spatial distribution of the spins can be done by appropriately combining the FIDs. As shown below, this is generally accomplished by a Fourier transform (FT) to yield an estimate for the spin distribution. This is the same procedure used in MR imaging to reconstruct the phase-encode directions. The significant difference is the absence of a gradient during acquisition which allows a high-resolution spectrum to be acquired and then localized to particular regions or voxels.

In addition to localizing the positions of the spins with a short gradient pulse by phase encoding, gradients in the static magnetic field can be used with a selective rf pulse to excite only a limited region of the sample.[6–8] In this case, localization in three dimensions is achieved by the application of multiple gradients in three orthogonal directions. Generally such frequency-selective techniques only obtain spectra from one, or at most a few, localized regions simultaneously,[9] although complex pulse schemes do exist for multiple regions.[10] Commonly used frequency-selective techniques are ISIS[6] and STEAM,[7] the former primarily for phosphorus and the later primarily for proton spectroscopy. These techniques function well in localizing a single species of spin to a particular region. Because ISIS involves the addition and subtraction of different acquisitions there are some problems with motion sensitivity. However, the sizes of the localized region in phosphorus spectroscopy are generally large enough so that small in vivo motions are not a serious problem. As STEAM localizes the signal in a single acquisition, it does not suffer from this type of problem.

There is one artifact, however, from which all selective excitation techniques suffer. Nuclei which resonate at different frequencies are localized to different regions in space. A frequency-selective pulse will cause nuclei of different frequency to be localized to two different regions. This happens because a shift in resonant frequency of δf is the same as a shift in position of $\delta f/\gamma G$ where γ is the gyromagnetic ratio of the spins in Hz T^{-1} and G is the strength of the applied localizing gradient in mT m^{-1}. This artifact is not found in phase-encoding techniques because they only use the gradient for a short time to label the location of a spin in space with a phase factor. No frequency-selective rf is used, so no interaction with the gradient occurs and thus no frequency shift. For example, at a field of 1.5 T two nuclei, in the same or different compound separated by 20 ppm (a typical ^{31}P chemical shift), will be localized to regions shifted 1 cm with respect to each other in a gradient of 30 mT m^{-1} (twice the typical gradient available on clinical imagers before the introduction of echo planar imaging). The consequences of this can be very significant. For a cube (voxel) of side 5 cm, the two regions to which the two nuclei are localized are shifted 20% (1 cm out of 5 cm) with respect to one another in each dimension. This 20% linear shift causes nearly 50% of the two regions to be different [only $(4/5)^3 = 64/125$ of the volumes are in common]. For smaller voxel sizes the problem is even worse. For example, for a 27 cm^3 voxel ($3\times3\times3$), less than 1/3 (8/27) of the volumes would be in common. This means, for example, that much of the single voxel ^{31}P studies using these techniques need to be analyzed carefully if comparisons are being made between β-adenosine triphosphate (β-ATP) and inorganic phosphate (P_i) which are approximately 20 ppm apart.

2 THEORY OF CSI

In order to appreciate the theoretical development to follow, we need to introduce the concept of $\boldsymbol{k}$ space. This is the space of FT variables associated with the real space variables x, y, and z. This relationship is the same as that between the complementary FT variables, time and frequency. The associated variables are k_x, k_y, and k_z. The theorems of FT show that

knowledge of a function in one domain is equivalent to knowledge of a function in the other domain.[11] Thus, if we know $\bar{\rho}(\boldsymbol{k}, t)$, the spin distribution function in $\boldsymbol{k}$ space and time, we can obtain $\rho(\boldsymbol{r}, \sigma)$ the spin distribution in space and frequency. They are related by the following:

$$\bar{\rho}(\boldsymbol{k}, t) = \int \rho(\boldsymbol{r}, \sigma) \mathrm{e}^{\mathrm{i}\boldsymbol{k}\cdot\boldsymbol{r}} \mathrm{e}^{\mathrm{i}\sigma} \, \mathrm{d}\boldsymbol{r} \, \mathrm{d}\sigma \tag{1}$$

where σ is the chemical shift (frequency) variable and a 'bar' represents the transformed function.

As shown below, the fundamental theorem of NMR localization states that sampling a free induction decay is equivalent to sampling the distribution of the excited spins along a particular trajectory in $(\boldsymbol{k}, t)$ space. It was originally proved some time ago.[1] This theorem underlines all forms of imaging with NMR.

3 FUNDAMENTAL THEOREM OF NMR LOCALIZATION

The fundamental theorem we seek to prove is that the FID of the spins in a sample in a gradient is the FT of the detectable spatial spin distribution in the sample, $\bar{\rho}_{\mathrm{D}}$, evaluated along a particular trajectory in the transform space, i.e., $S(t) = \bar{\rho}_{\mathrm{D}}(\boldsymbol{k}(t), t)$. As shown below, this trajectory in $\boldsymbol{k}$ space is given by the gyromagnetic ratio, γ, times the integral of the gradient in time from the beginning of the FID. That is,

$$\boldsymbol{k}(t) = \gamma \int_0^t \boldsymbol{G}(\tau) \, \mathrm{d}\tau \tag{2}$$

Here $S(t)$ is the FID at time t, $\rho_{\mathrm{D}}(\boldsymbol{r}, \sigma)$ is the detectable concentration at position $\boldsymbol{r}$ of a spin with chemical shift σ and $\boldsymbol{G}(\tau)$ is the gradient at time τ.

To prove this, consider the evolution of a single species of spins with chemical shift σ in a sample following excitation. The FID as a function of time, $S(t)$, will be the sum of the magnetization at each point $\boldsymbol{r}$, corrected by a sensitivity factor $D(\boldsymbol{r})$ and a phase factor $\phi(\boldsymbol{r}, t)$ which measures how much the magnetization at $\boldsymbol{r}$ contributes. Mathematically,

$$S(t) = \int \rho(\boldsymbol{r}) D(\boldsymbol{r}) \mathrm{e}^{\mathrm{i}\phi(\boldsymbol{r},t)} \, \mathrm{d}\boldsymbol{r} = \int \rho_{\mathrm{D}}(\boldsymbol{r}) \mathrm{e}^{\mathrm{i}\phi(\boldsymbol{r},t)} \, \mathrm{d}\boldsymbol{r} \tag{3}$$

where $D(\boldsymbol{r})$ is simply the coil detection profile while $\phi(\boldsymbol{r}, t)$ is the rf phase of the spins at point $\boldsymbol{r}$ and time t. To calculate ϕ we need the expression for the frequency of the spins, ω, at $\boldsymbol{r}$. This is given by the instantaneous magnetic field at $\boldsymbol{r}$, $H(\boldsymbol{r}, t)$:

$$\frac{\mathrm{d}\phi}{\mathrm{d}t} = \omega(\boldsymbol{r}, t) = \gamma H(\boldsymbol{r}, t) \tag{4}$$

Integrating, we obtain

$$\phi(\boldsymbol{r}, t) = \int_0^t \omega(\boldsymbol{r}, \tau) \, \mathrm{d}\tau = \int_0^t \gamma H(\boldsymbol{r}, \tau) \, \mathrm{d}\tau \tag{5}$$

$H(\boldsymbol{r}, \tau)$ is made up of two terms, the static magnetic field H_0 and any gradient, $\boldsymbol{G}(t)$, which may be present.

Substituting $H(\boldsymbol{r}, \tau) = H_0 + \boldsymbol{G}(\tau)\cdot\boldsymbol{r}$, we find

$$\phi(\boldsymbol{r}, t) = \gamma H_0 t + \gamma \int_0^t \boldsymbol{G}(\tau) \cdot \boldsymbol{r} \, \mathrm{d}\tau \tag{6}$$

since H_0 is constant. Substituting this into equation (3) yields

$$S(t) = \int \rho_{\mathrm{D}}(\boldsymbol{r}) \exp\left\{ \mathrm{i}\left(\gamma H_0 t + \gamma \int_0^t \boldsymbol{G}(\tau) \cdot \boldsymbol{r} \, \mathrm{d}\tau \right) \right\} \mathrm{d}\boldsymbol{r} \tag{7}$$

$$= \exp\{\mathrm{i}(\gamma H_0 t)\} \int \rho_{\mathrm{D}}(\boldsymbol{r}) \exp\left(\mathrm{i}\gamma \int_0^t \boldsymbol{G}(\tau) \cdot \boldsymbol{r} \, \mathrm{d}\tau \right) \mathrm{d}\boldsymbol{r} \tag{8}$$

The first part of this expression shows the phase factor of the Larmor frequency of the spins while the second can be written, using equation (2), as

$$\int \rho_{\mathrm{D}}(\boldsymbol{r}) \mathrm{e}^{\mathrm{i}\boldsymbol{k}(t)\cdot\boldsymbol{r}} \, \mathrm{d}\boldsymbol{r} = \bar{\rho}_{\mathrm{D}}(\boldsymbol{k}(t)) \tag{9}$$

Putting the time dependence back and allowing for multiple species, we have the fundamental theorem of NMR imaging, $S(t) = \bar{\rho}_{\mathrm{D}}(\boldsymbol{k}(t), t)$, where $\bar{\rho}_{\mathrm{D}}$ is the FT in both space and frequency of the detectable spin distributions and $\boldsymbol{k}(t)$ is the integral of the gradient.

Thus a FID in the presence of a constant gradient G would sample the spatial FT of the distribution of detectable spins along the line $\boldsymbol{k} = \gamma \boldsymbol{G} t$. Hence, by sampling uniformly in time, one also samples uniformly in $\boldsymbol{k}$ space. In fact this is what is done by the readout gradient in ordinary MRI. On the other hand, immediately following a short rectangular gradient pulse of strength G and length T_0, the FID would sample the spatial FT of the detectable spin distribution at a fixed point in $\boldsymbol{k}$ space, corresponding to $\gamma G T_0$. A combination of these two approaches, namely a constant gradient in one direction and a pulse in the other, is used in standard 2D imaging to acquire a single line in $\boldsymbol{k}$ space. This is then repeated multiple times to acquire enough different lines in $\boldsymbol{k}$ space to calculate an image of the desired resolution and field of view (FOV). A CSI dataset is acquired analogously, by repeatedly acquiring multiple FIDs with gradient pulses of different strengths and directions. In CSI, unlike standard MRI, no readout gradient is employed, as the chemical shift information must be acquired in the absence of a gradient. Each FID is acquired at a single point in the $\boldsymbol{k}$ space domain. Therefore, for two spatial dimensions, one requires phase encoding in each dimension, whereas for 3D, three separate dimensions of phase encoding are needed. In this way, a complete sampling of $\boldsymbol{k}$ space can be acquired. Since the FID is acquired in the absence of a gradient except for the very early points in the FID, multiple compounds can be detected as in ordinary high-resolution pulse-acquire NMR experiments. An estimate of the original spatial and frequency distributions is then obtained by discrete Fourier transformations (DFT) in both time and space of this dataset.

Since the gradient pulse immediately follows the rf excitation, the very early time points in the FID are unusable. This can degrade broad signals if echoes are not used. On modern clinical machines the loss of the early time points is less than 1 ms, corresponding to linewidths greater than 300 Hz. This is usually broader than most peaks of interest, although certain phospholipid peaks can be observed at such widths. In such cases care must be taken in quantitation as these spectral lines can change shape as well as amplitude.

There are several properties of the DFT which are important here. First, in order to distinguish regions separated by a distance R, one needs to sample $\boldsymbol{k}$ space on the scale of $1/R$. This sets both the FOV, the largest distance to be distinguished needing the closest sampling in $\boldsymbol{k}$ space, and the spatial resolution, the smallest distance to be resolved needing the largest spread in $\boldsymbol{k}$ space, of the resultant distribution. Another important property is how the reconstructed distribution is related to the true one. This is well known from the standard theory of DFT [11] but is worth reviewing as it is so fundamental to understanding the nature of the localized spectra in CSI experiments (as well as standard MRI).

A finite sampling of $\boldsymbol{k}$ space produces effects on the reconstructed spatial distribution of the spins which is represented by a point spread function (psf) which mathematically describes how the reconstructed spectrum at a particular location, $\rho_{\text{rec}}(\boldsymbol{r})$, is related to the actual distribution, $\rho(\boldsymbol{r})$. This relationship takes the form of a convolution so that

$$\rho_{\text{rec}}(\boldsymbol{r}) = \int \rho(\boldsymbol{s})\text{psf}(\boldsymbol{r}-\boldsymbol{s})\,\text{d}\boldsymbol{s} \tag{10}$$

We now derive the form of the psf. First, from the formula of a DFT we know

$$\rho_{\text{rec}}(\boldsymbol{r}) = \sum_{n=-N/2}^{N/2-1} \bar{\rho}(\boldsymbol{k}_n)\text{e}^{-\text{i}\boldsymbol{k}_n\cdot\boldsymbol{r}} \tag{11}$$

Here, $\bar{\rho}(\boldsymbol{k}_n)$ is the FT of the true distribution at $\boldsymbol{k}_n$, assumed to range from $-(N/2)\ \Delta k$ to $(N/2-1)\Delta k$, where $\Delta k = 2\pi/L$, L being the FOV. Substituting for $\bar{\rho}(\boldsymbol{k}_n)$ in equation (11), we obtain

$$\begin{aligned}\rho_{\text{rec}}(\boldsymbol{r}) &= \sum_{n=-N/2}^{N/2-1}\left\{\int \rho(\boldsymbol{r}')\text{e}^{\text{i}\boldsymbol{k}_n\boldsymbol{r}'}\,\text{d}\boldsymbol{r}'\right\}\text{e}^{-\text{i}\boldsymbol{k}_n\cdot\boldsymbol{r}} \\ &= \int \rho(\boldsymbol{r}')\left\{\sum_{n=-N/2}^{N/2-1}\text{e}^{\text{i}\boldsymbol{k}_n\cdot(\boldsymbol{r}'-\boldsymbol{s})}\,\text{d}\boldsymbol{r}'\right\}\end{aligned} \tag{12}$$

Comparing equation (12) to equation (10), we see the psf is

$$\text{psf}(\boldsymbol{r}-\boldsymbol{s}) = \sum_{n=-N/2}^{N/2-1}\text{e}^{\text{i}\boldsymbol{k}_n\cdot(\boldsymbol{r}-\boldsymbol{s})} \tag{13}$$

In just 1D we find

$$\begin{aligned}\text{psf}(x-s) &= \sum_{n=-N/2}^{N/2-1}\text{e}^{\text{i}k_n(x-s)} &(14)\\ &= \sum_{n=-N/2}^{N/-1}\text{e}^{\text{i}n\Delta k(x-s)} \\ &= \text{e}^{-\text{i}(N/2)\Delta k(x-s)}\sum_{j=0}^{N-1}\text{e}^{\text{i}j\Delta k(x-s)} &(15)\end{aligned}$$

Using the identity

$$\sum_{j=0}^{N-1}x^j = \frac{1-x^N}{1-x}$$

with $x = \text{e}^{\text{i}\Delta k(x-s)}$, equation (15) can be evaluated to give

$$\begin{aligned}\text{psf}(x-s) &= \text{e}^{-\text{i}(N/2)\Delta k(x-s)}\frac{1-\text{e}^{\text{i}N\Delta k(x-s)}}{1-\text{e}^{\text{i}\Delta k(x-s)}} \\ &= \text{e}^{-\text{i}(1/2)\Delta k(x-s)}\frac{\sin\frac{1}{2}N\Delta k(x-s)}{\sin\frac{1}{2}\Delta k(x-s)}\end{aligned} \tag{16}$$

where $\text{e}^{\text{i}x} - \text{e}^{-\text{i}x} = 2\text{i}\sin x$ has been used to simplify the expression. Putting $\Delta k = 2\pi/L$ we find

$$\text{psf}(x-s) = \text{e}^{-\text{i}\pi(x-s)/L}\frac{\sin\pi N(x-s)/L}{\sin\pi(x-s)/L} \tag{17}$$

The real and imaginary parts of this function are plotted as a function of $\Delta = x - s$ in Figure 1 for $N = 16$.

The real part has a large peak near $\Delta = 0$ with smaller oscillations extending to the edge of the FOV, L. These oscillations cause the well-known 'sinc wiggles' found in DFT. Depending on the original distribution $\rho(\boldsymbol{r})$, the reconstructed distribution $\rho_{\text{rec}}\ (\boldsymbol{r})$ will have varying degrees of mixing of signal from outside the region. Since the function is oscillatory, these are generally small but need to be kept in mind for precise work. The imaginary part arises from the asymmetric sampling around the origin in $\boldsymbol{k}$ space ($-N/2$ to $N/2-1$).

The full 3D psf for cubic sampling is simply the product of the 1D functions:

$$\text{psf}(\boldsymbol{r}-\boldsymbol{s}) = \text{psf}(r_x - s_x)\text{psf}(r_y - s_y)\text{psf}(r_z - s_z) \tag{18}$$

A general psf can be calculated if the k-space sampling is not uniform. However it does not generally have such a simple mathematical form. In the general case, the psf is given by

$$\text{psf}(\boldsymbol{r}-\boldsymbol{s}) = \sum_{\boldsymbol{k}\text{-sampled}}\text{e}^{\text{i}\boldsymbol{k}\cdot(\boldsymbol{r}-\boldsymbol{s})} \tag{19}$$

The psf calculated above represents a cubic sampling in $\boldsymbol{k}$ space. Numerous authors have suggested spherical or high order polyhedral as sampling schemes which can take significantly less time to carry out the acquisition.[12–14] For example, the volume of a sphere inscribed inside a cube is approxi-

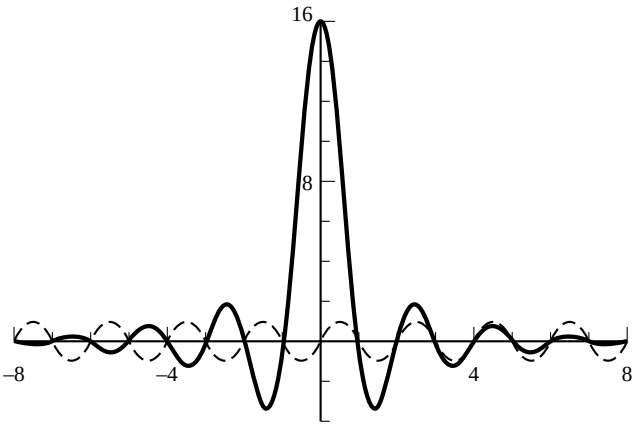

Figure 1 Point spread function for a discrete Fourier transform with $N = 16$. Solid curve is real part; dotted curve is imaginary part

mately 50% that of the cube. Thus, only one-half the time is required to sample it at equal resolution. Since the primary determinant of the resolution of the psf is the maximum separation between $\boldsymbol{k}$-space samples, such as spherical sampling will have approximately the same resolution as a cubic sampling. This has been implemented by Maudsley et al.[14]

Another potential advantage of CSI acquisition is the ability to vary the number of acquisitions at each point in $\boldsymbol{k}$ space. It has been shown by Brown and Nelson that a Weiner optimization, assuming constant noise at each point in $\boldsymbol{k}$ space, obtains the reasonable result that the $\boldsymbol{k}$ space should be sampled at a constant rate in regions where the signal-to-noise ratio (S/N) is high going smoothly to zero in regions where the S/N is low.[15] Depending upon the precise signal-to-noise ratio in a particular experimental case, a further 10% to 20% increase in sensitivity can be gathered using this procedure.

For both acquisition time considerations and spatial resolution, one generally samples only relatively small $\boldsymbol{k}$-space values in the CSI case compared with the MRI case. This is because the metabolites of interest are 1000- to 10 000-times lower in concentration than water protons. To achieve a reasonable S/N, resolutions must be on a 1 cm rather than a 1 mm scale length. Further, the three-dimensional sampling in $\boldsymbol{k}$ space required can take considerable time. For example, an $8 \times 8 \times 8$ three-dimensional grid requires 512 separate acquisitions; at a repetition time of 1 s, this is approximately 8 min.

The sampling also causes artifacts due to its finite extent if it is desired to reconstruct the distribution from the chemical shift information at a resolution more comparable to the standard MRI images. The typical way that this is accomplished is to zero-fill the datasets in $\boldsymbol{k}$ space, and then carry out a standard FT reconstruction. Note that the psf formalism [equation (10)] still describes how the reconstructed spectrum is related to the actual distribution since $\boldsymbol{r}$ can be evaluated at any point. It is clear, however, that unless two values of $\boldsymbol{r}$ are separated by a distance of the order of the size of the central peak in Figure 1 similar spectra will be obtained.

The freedom to choose any value of $\boldsymbol{r}$ for reconstruction demonstrates one of the great advantages of CSI. By obtaining information in $\boldsymbol{k}$ space the reconstructed distribution can be localized anywhere. That is to say that the psf can be centered about any point in the real space. This procedure is called voxel shifting and is accomplished by multiplying the $\boldsymbol{k}$-space distribution by a phase factor $\exp(-\mathrm{i}\boldsymbol{k}\cdot\boldsymbol{\delta})$ if we wish to shift the center of the reconstructed voxels by $\boldsymbol{\delta}$. This can be easily proven by substituting $\bar{\rho}(\boldsymbol{k}_n)\exp(-\mathrm{i}\boldsymbol{k}\cdot\boldsymbol{\delta})$ for $\bar{\rho}(\boldsymbol{k}_n)$ in the derivation of the psf given above.

This, as shown in the examples below, is a particularly convenient way to reconstruct even a single localized region because no prior localization is required and if a mistake is made it is easy to recalculate a distribution with the psf centered at a different location.

There is no easy way to overcome the difficulties of reconstruction brought about by finite sampling while using standard FT reconstruction methodology. However, there are techniques which have been proposed which work in the reverse direction. Assume a particular distribution, for example, constrained to be within the head for a head examination, calculate the forward transform from real space into $\boldsymbol{k}$ space, adjust the distribution so that the FT agrees with what has been measured at the lower $\boldsymbol{k}$-space regions while not forcing the higher $\boldsymbol{k}$-space values to be zero. The primary difficulty with methods of this type is the number of degrees of freedom in the distribution are much higher than the number of acquired data points, so that extra constraints must be imposed upon the distribution to produce a unique answer. A variety of methods can be used, e.g., correlation with the proton image[16] or the use of maximum entropy or other regularizing functions to restrict the distribution. Thus far these techniques are still in their infancy, but they have great promise for removing unwanted psf effects. They are also computationally quite expensive; as computation speeds increase, this will be less of a problem.

Finally, the sensitivity of this procedure needs to be analyzed. To do this consider two extreme cases: all the spins concentrated in a very small region and a completely uniform distribution, both observed with N gradient steps. In the first case, the only effect of the different gradient pulses will be to cause the magnetization to have a different phase in each FID. The phase factor will be $\exp(\mathrm{i}\boldsymbol{k}_n\cdot\boldsymbol{r}_0)$ for something located at $\boldsymbol{r}_0$ when the $\boldsymbol{k}$-space point $\boldsymbol{k}_n$ is observed. Thus all the DFT does is cancel these phase factors, enabling the individual FIDs to add at the location $\boldsymbol{r}_0$ as though N acquisitions had been carried out without gradients, resulting in an increase in S/N compared with a single acquisition of $N^{1/2}$. In the other case, only one FID will have any substantial signal. This is the one with zero gradient, since, with a large uniform sample, the signal from different parts will cancel even for the smallest gradient, corresponding to 1/FOV. In this case, when we carry out the DFT the only signal is from the $k = 0$ point and thus is constant everywhere. The noise, on the other hand, is in every acquisition and reduces the S/N, again compared with a single acquisition, by $N^{1/2}$. Another way of analyzing the uniform case is to realize that each reconstructed voxel corresponds to a volume of L^3/N and so as N increases, the spins contributing to the signal from each voxel decrease proportionally as N. Each of the N acquisitions contributes signal to the spins coming from the desired voxel, while the noise, being independent, adds incoherently. Thus, the final sensitivity is proportional to $N^{1/2}/N$ or $N^{-1/2}$, compared with a single acquisition.

As these examples make clear, the precise sensitivity factor depends upon details of the shape of the object and how its FT behaves in $\boldsymbol{k}$ space. If the resolution is increased by reducing the FOV while keeping the number of phase-encoding steps constant, the S/N will be reduced proportionately with the volume of the voxel if we are dealing with a uniform distribution. If, on the other hand, we are dealing with an unresolved bright spot, so that as the voxel gets smaller the number of spins within it stays the same, then so does the final sensitivity of that particular voxel. Alternatively, if we increase the resolution by keeping the same FOV and increasing N, then we will take more phase-encoding steps which will partially compensate for an increased resolution, of course at the expense of increased observation time.

Thus, as soon as the resolution is sufficient to begin to resolve objects into homogeneous regions, further increasing the resolution will result in substantial losses in S/N because the number of spins per resolution element drops as the cube of the voxel dimension. An equally valid analysis can be done in $\boldsymbol{k}$ space, once it is realized that the size of the FT of an object of dimension L rapidly falls to zero at $\boldsymbol{k}$-space values greater than $1/L$. As the resolution of the sampling is increased to provide a subdivision of the uniform object, points in $\boldsymbol{k}$

space are taken with very low signal and, thus, primarily add noise to the final result.

4 DATA ANALYSIS

One of the greatest impediments to the full application of CSI to two and three dimensions is the large size of the datasets and the hundreds of spectra which need to be analyzed. There are simply too many to be done manually; an automatic procedure is required. This problem is complicated in many cases because of the low S/N found in many in vivo CSI spectra. What is needed is a robust technique for peak identification and extraction from a noisy spectrum with variable baseline, the latter coming from the absence of the early time points in the FID during the period of the gradient pulse. Such a procedure was developed by Nelson and Brown and dubbed PIQABLE (Peak, Identification, Quantification, and Automatic Base Line Estimation).[17] It is fully described in the original paper. Briefly it relies on a statistical estimation of the probabilities of deviation of a particular spectral region under examination from a running average background. Estimates of the standard deviation are calculated from the spectrum itself. The program eliminates regions identified as peaks from noise estimation and iterates examinations of the spectrum until no further peaks are identified. It has proven to be very successful with in vivo CSI datasets and is able to deal with varying backgrounds and broad noisy peaks in a robust way. However, it is time-consuming to carry out this processing on each spectrum in every CSI dataset, thus a variety of further developments have concentrated on peak detection in specified regions.[18] This is carried out by either using a fixed frequency region or some type of localized peak search algorithm. Area estimates can then be made for each spectrum.

Several hundred numbers are still not easy to comprehend, so when one finishes analyzing a large number of spectra the problem as to how to represent these data is still present. Generally for two- and three-dimensional CSI data, image representations are an essential part of the analysis.[19] Care should be taken to examine the actual spectra as well as these images as no programs at present can be viewed as 100% reliable in converting spectra to images. Nevertheless, as a method of obtaining an overview of the entire dataset, they are excellent. Typically, different compounds, when present, are represented in different colors; this leads to a loss of gray scale sensitivity in the eye so that in cases of high sensitivity [e.g., phosphocreatine (PCr) in a skeletal muscle] a standard black and white image should be used.

Another advantage of CSI localization is that the gradients used provide the same localizing information for both the MRI proton images as well as the CSI. Thus, the MRI image and the CSI dataset are naturally in registration; no complex transformations are necessary to map from one to the other. A direct overlay of the metabolic information onto a proton image can be done as shown in several of the figures in the next section. In addition to the local metabolite concentrations, of course, one also has information regarding the specific chemical shift frequencies. By shifting compounds which are known to be independent of intracellular conditions, such as PCr, glycerolphosphocholine, etc., different regions can be aligned in frequency with the result that extremely sharp spectra can be observed from an entire organ by resuming the shifted spectra. Spatial maps of pH distribution, magnesium concentration, and other physiological variables which can shift the metabolite frequencies can also be constructed.

5 ACQUISITION

The details of acquisition of CSI sequences are generally straightforward on any standard clinical instrument. The results presented below have been acquired using a Siemens 1.5 T Magnetom. The primary criterion is the ability to generate three cycles of phase encoding which is possible on virtually all modern commercial clinical instruments. Other than that, all that is required is an excitation sequence followed immediately by a gradient pulse of as short duration as possible.

The strength of the gradient pulses can be calculated from FT considerations discussed in the previous sections. For example, a resolution of 3 cm requires the maximum distance between $\boldsymbol{k}$-space points to be sampled, $\Delta k_{\max}$, to be $2\pi \times 1/3$ cm^{-1}. From equation (10) this must be $\gamma G_{\max} T_0$ for a constant gradient which turns on and off instantly. Taking T_0 to be 1 ms and realizing $G_{\max}$ can be positive or negative, we find $G_{\max} = \frac{1}{2}\Delta k_{\max}/\gamma T_0 = 1/2 \times 2\pi \times 1/3 \times 1/10^{-3} \times 1/\gamma$; for ^{31}P this would be 6.07 mT m^{-1}(γ = 17.24 MHz T^{-1}), while for protons it would be 2.47 mT m^{-1} (γ = 42.38 MHz T^{-1}). Depending on the FOV this maximum would be divided into eight or 16 steps, corresponding to a FOV of 24 or 48 cm, respectively. Both positive and negative values in $\boldsymbol{k}$ space need to be acquired. This is required because a spatially dependent chemical shift image is a complex function, and thus both positive and negative $\boldsymbol{k}$-space information is needed to reconstruct it properly. This is not the case in proton imaging where, with a single frequency, there is no true complex information present in the image, and thus half Fourier space sampling can reduce acquisition times by a factor of two. This is not possible in a general CSI acquisition as different frequencies at different places beat with one another and thus appear as complex functions.

Note that long times are required to cycle through the $\boldsymbol{k}$-space points if three dimensions are desired. For example, a 16^3 acquisition requires 4096 acquisitions, generally requiring too long a time to be practical. It is also important to have a well-shimmed sample even using localization techniques since, for example in proton-decoupled ^{31}P spectra, the resolution required is less than 0.1 ppm in a single voxel.

One point that should be mentioned is the precise positioning of the positive and negative $\boldsymbol{k}$-space samples. Because of the finite number of points required, the sampling is often done from $-N/2$ to $N/2 - 1$ or asymmetrically around the zero point in $\boldsymbol{k}$ space. For example, if N is 8 then -4, -3, -2, -1, 0, 1, 2, and 3 will be sampled on a uniform grid. In general, this is the way imaging sampling is carried out for N values of 64–512. In this case, the difference between $N/2$ and $N/2-1$ is quite small. However, as pointed out in the theory section, the psf in this asymmetric case has a small imaginary component due to the one extra negative $\boldsymbol{k}$-space sample. Thus, in general, it is better to shift the sampling points by half of the $\boldsymbol{k}$-space grid and not sample at the precise $k = 0$ point. This produces a completely real psf with no imaginary contamination. This can be significant for broad lines since the imaginary part of the

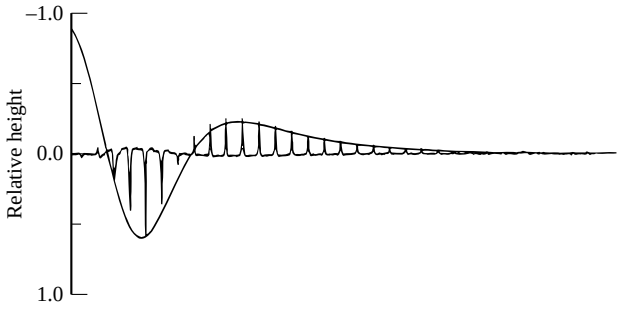

Figure 2 1D CSI experiment of a column phantom coaxial with a circular surface coil with 32 phase-encode steps. The solid curve is the theoretically expected signal. The individual peaks are the experimentally observed signal at the indicated distance from the plane of the coil

line is much wider in frequency and can thus lead to voxel contamination of a complex sort.

In addition to acquiring a single nucleus with CSI techniques, the techniques can be modified to acquire two techniques simultaneously. As shown by Gonen et al.,[20] at a slight cost in early dead time both phosphorus and proton acquisitions can be carried out in a simultaneous manner. This is accomplished by doing an early phosphorus excitation followed by part of the phase-encoding pulse, bringing the gradient to zero, exciting the protons, and finishing with another gradient pulse. The relative strengths of the gradient pulses are set so that the second pulse gives the proper proton FOV, while the combined pulses give a proper phosphorus FOV.

6 APPLICATIONS

The simplest illustration of CSI is one dimension. In this case a series of spectra is sufficient to demonstrate the localization and no complex processing or image presentation is needed to appreciate the result. Figure 2 shows the result from 32 phase-encode steps using a single turn circular surface coil with a cylinder phantom along the coil axis. A square, rectangular rf pulse, equivalent to 540° at the center of the coil, excited the spins. The FIDs were Fourier-transformed in both time and $\boldsymbol{k}$ space, and the resultant spectra were all phased the same. The gradient amplitudes and widths corresponded to a spacing of 5 mm for a total FOV of 16 cm. The experiment was carried out on a 1.5 T Siemens Magnetom at 25.6 MHz with inorganic phosphate in the phantom. The peak region surrounding the phosphate resonance was selected from each spectrum and displaced along the axis in Figure 2 a distance corresponding to where the spectrum was localized with respect to the coil. The signals were compared with those expected theoretically, $B_1(y)$ sin $\gamma B_1(y)T_0$, where $B_1(y)$ is the rf field strength at the distance y along the axis, γ is the ^{31}P gyromagnetic ratio, and T_0 is the length of the rf pulse. Since the pulse was 540° at the coil center, for the circular loop $\gamma B_1(y)T_0 = 540°a^3/(y^2 + a^2)^{3/2}$, where a is the radius of the coil. This function was calculated as a function of position (5 mm per spectrum) along the axis, scaled in the vertical direction to fit the peak heights and is plotted as the solid line in Figure 2.

As can be seen the agreement is excellent. The only adjustable parameter here was the vertical scaling of the theoretical curve. These results demonstrate the ability of CSI phase-encoding measurements to provide excellent localization in space, as would be expected from their common use in the imaging field.

In two and three spatial dimensions it becomes possible to consider alternative ways of representing this spectral information, i.e. more than simply arrays of spectra. Since we have continuous localized spectra the obvious possibility is to use an image format to represent the spatial distribution. The primary difficulty with such a procedure is the determination of the peak areas or other variables of interest from the spectra in an automatic fashion. Traditional methods of measuring area often rely on hand integration, which is unsuitable in this case since we are dealing with several hundred spectra. As discussed above, to overcome this we have developed a program, PIQABLE, which is capable of nonparametrically dividing a noisy spectrum into peak regions, slowly varying background and high-frequency noise.[17] This procedure can be applied automatically to the CSI spectra. The results of this analysis can then be presented as images. Because there are usually only 8 × 8 or 16 × 16 pixels at the original resolution in the data, we have found these data can be much better visualized if they have been zerofilled and spatially filtered so as to provide spatial smoothing, and then presented at 64 × 64 or higher resolution.

A good illustration of these techniques in two dimensions is the observation of exercise-induced changes in the high energy phosphates in human muscle. Numerous ^{31}P studies of muscle metabolism have been carried out using surface coils in order to understand the relationship between biochemical energy demand as measured by the force developed and biochemical energy supply as measured by changes in the 'high-energy' phosphates, PCr, adenosine triphosphates (ATP), and Pi which can readily be observed in a ^{31}P spectrum of muscle. The key assumption here is that one is observing changes in metabolites in the muscle which is producing the force. This is not easy to determine when only a surface coil is used for localizing the spectrum. To investigate this more carefully, CSI was used to study single finger excitation in the human forearm. A single-turn 8 cm diameter coil was placed around the forearm; the wrist was rotated to align all the major muscle groups longitudinally so that only two-dimensional localization was needed. Steady-state studies of each finger being exercised at various levels were carried out.

The full details of the study are presented elsewhere.[21] The 2D CSI data obtained from one volunteer in this study are shown in Figures 3, 4, and 5. Figure 3 shows a cross-sectional MRI of the forearm of a volunteer with a highlighted region approximately corresponding to the *flexor digitorum profundis*. Figure 4 shows three 4 × 6 arrays of spectra observed at rest (left), during exercise of the index finger (center), and of the ring and little fingers (right). Careful examination of the spectra show a very different pattern of changes in PCr and Pi in the two cases. There were no changes near the surface but substantial conversion of PCr to Pi in the deeper shaded region when the index finger was exercised while the reverse was true for the ring and little fingers.

To illustrate this, the amplitudes of the Pi peaks in the two datasets have been converted into images as discussed above.

Figure 3 Axial MRI of forearm. Highlighted region indicates approximate position of *flexor digitorium profundus*

These are shown in Figure 5 overlaid on the proton image in Figure 3 for anatomical reference. As can be seen, the metabolic activation of the muscle is localized to the deep interior of the arm during index finger exercise, while the superficial regions of the arm are activated if the ring and little finger are used. These observations suggest that many surface coil studies of the forearm need reevaluation since most surface coils used in human studies are 1–2 cm in diameter and only able to observe just beneath the surface of the arm. With such a coil, a bulb squeezing exercise without special care to use only the ring and little fingers, and not the index and middle fingers, would cause a confused picture when one tries to relate changes in high-energy phosphates with changes in physiological function, for example, Pi/PCr with workload.

Significantly different results are obtained if care is taken only to measure the work produced by the ring and little finger.[22] Without the localization provided by CSI there would be no way to separate the changes at the deeper level produced by the index finger from the changes at the superficial level produced by the ring and little fingers.

These techniques can be applied in three dimensions as well as two. The first example of this was the work of Cox et al.[23] who demonstrated the feasibility of the 3D technique in human livers using a surface coil. The technique is particularly useful in studying the brain where high-quality coils can be made to

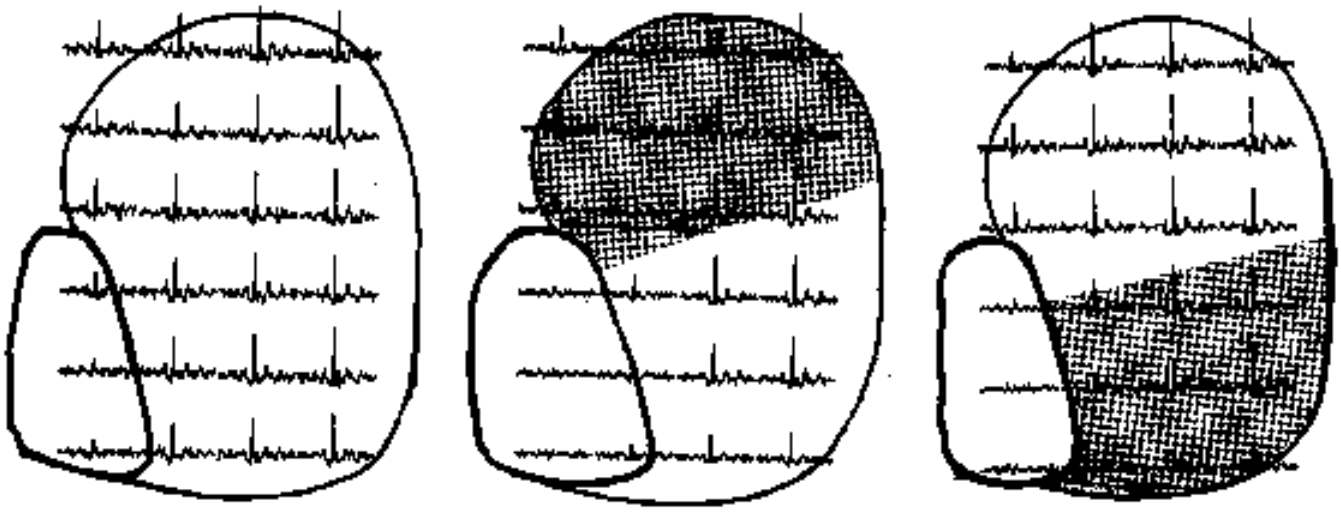

Figure 4 ^{31}P spectra from the highlighted region in Figure 3 at rest (left), during exercise of the index finger (center), and of the ring and little fingers (right)

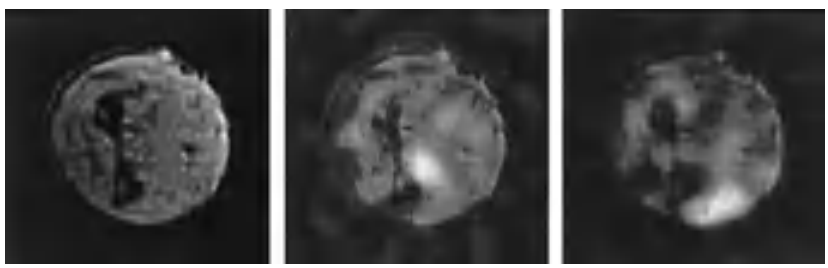

Figure 5 The image from Figure 3 (left) overlaid with a 2D CSI image calculated from the inorganic phosphate levels following excitation of only the index finger (center) and the ring and little fingers (right)

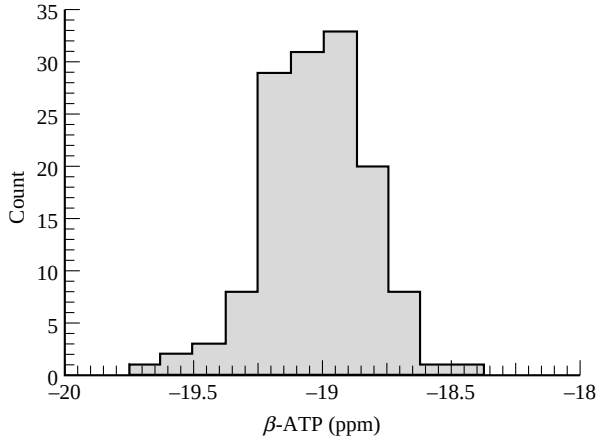

Figure 6 A histogram of the observed chemical shift of β-ATP in human brain. The data are from seven individuals and consist of measurements from 138 different voxels. The mean of the distribution is -19.03, $SD = 0.20$, corresponding to an Mg^{2+} concentration of 128 μM

encompass the entire head. Using such coils, 3D ^{31}P CSI spectra from the entire human head can be obtained with voxel sizes as small as 8 cm^3 with observation times on the order of 100 min. At lower spatial resolution, high-quality ^{31}P spectra of brain tissue can be obtained in 20–30 min.[19] This enables regional measurements of pH and pMg (from the positions of the Pi and β-ATP peaks, respectively) as well as the levels of ATP, PCr, and other phosphorylated metabolites. The Mg^{2+} levels are determined by measuring the β-ATP peak position, which is well known to titrate with Mg^{2+}.[24] Several studies have reported the intracellular brain magnesium concentration, in both normal volunteers and patients.[25,26] Interestingly, free Mg^{2+} levels in the brain appear to be substantially lower than in many other tissues.[27,28] A histogram of the position of the β-ATP peak with respect to PCr (PCr = -2.52 ppm) from normal volunteers is shown in Figure 6.

The mean is approximately -19 ppm which corresponds to a free Mg^{2+} level of about 125 μM assuming a standard titration curve for brain tissue.[29] Interestingly this value is observed to change both in brain tumors as well as cachexic patients.[30] It is too early to assign significance to these changes. Although these studies can be carried out with single voxel techniques, CSI provides both a more precise localization and a distribution of Mg^{2+} values for each individual.

Recent applications of CSI also include its use in proton spectroscopy where typically 16 $\times$ 16 2D CSI scans through the brain have achieved excellent sensitivity with voxels sizes of the order of 1 cm^3.[31–34] The applications of these techniques to proton spectroscopy are now beginning to find their way into clinical use, as they have been implemented into the latest generation of the commercial MR imagers.

The effect of proton irradiation on ^{31}P spectra from the human brain is shown in Figure 7 which compares the ^{31}P spectra from a single 42 cm^3 voxel acquired in 35 min with and without proton irradiation.[35]

It is obvious that the phosphomonoester (PME) and phosphodiester (PDE) regions of the spectrum are considerably sharpened due to the elimination of the residual proton J coupling. In both cases individual peaks can be observed corresponding to phosphorylethanolamine (PE) and phosphorylcholine (PC) in the PME region, and glycerophosphorylethanolamine (GPE) and glycerophosphorylcholine (GPC) in the PDE region. In addition there is an NOE enhancement for some peaks (e.g., approximately 50% for PCr). The additional sensitivity that proton decoupling and NOE enhancement[36] provide has enabled metabolic images of the human brain at a resolution less than 2 cm to be constructed. Figures 8 and 9 show four coronal images of a normal volunteer and the corresponding coronal slices of the PCr intensity taken from a dataset acquired in 115 min with a voxel size of 6 cm^3. At this resolution, the basal ganglia are observed as distinct anatomical objects. Whether this is due to changes in PCr concentrations in gray versus white water or PCr relaxation times is unknown at present.

CSI techniques have also been used to advantage in obtaining spectra from tumors observed with surface coils. Even though only a few localized spectra are needed in these cases, the ability to voxel-shift the final result to correspond as precisely as possible to the tumor location outweighs the added complexity of a 3D CSI acquisition. This is particularly true as time is always short in clinical studies and no extra time is needed in CSI to obtain the correct localization. Figure 10 illustrates this, showing a proton axial MRI of the groin of a patient with a lymphoma with two localized grids; the dotted one is the original unshifted one and the solid one after voxel-shifting to optimize the spectral localization to the tumor.

Figure 11 compares the initial and final spectra most closely centered on the tumor in each case. From the absence of PCr in the spectrum (and its presence in the surrounding muscle) the spectrum is well localized to the tumor.

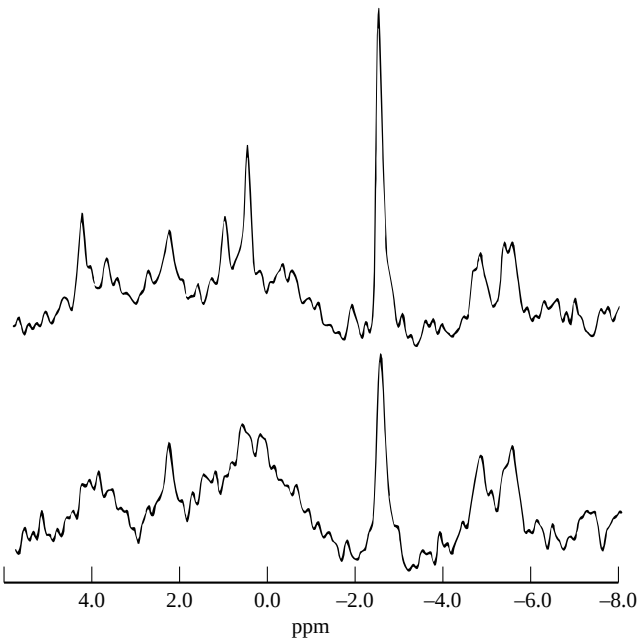

Figure 7 A comparison of proton-coupled (lower) and -decoupled (upper) ^{31}P spectra from 42 cm^3 of human brain acquired in 35 min

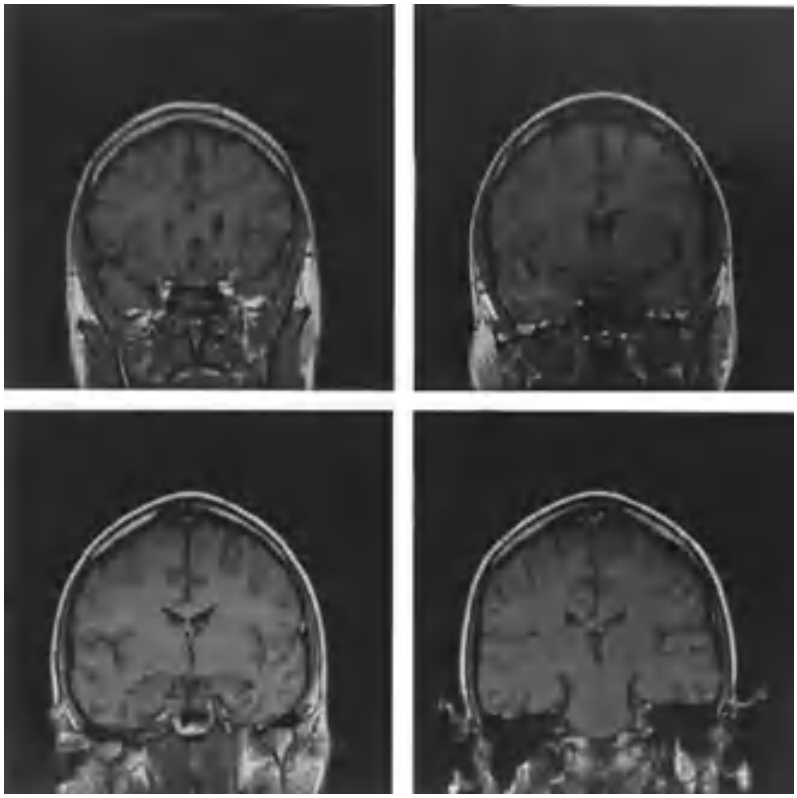

Figure 8 MRI coronal images of the brain of a human volunteer separated by 18 mm which is the voxel dimension in Figure 9

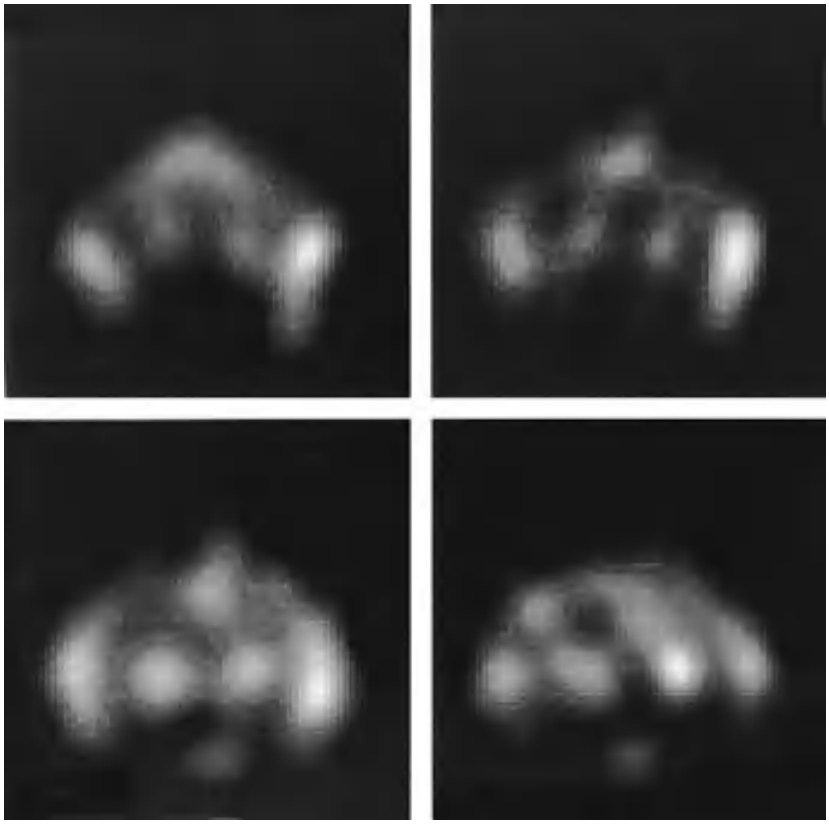

Figure 9 Adjacent phosphocreatine CSI images of the same sections as in Figure 8. Note the increased intensity in the regions of the basal ganglia as well as the superficial muscles outside the skull. These data were acquired in 115 min at a resolution of 18 mm

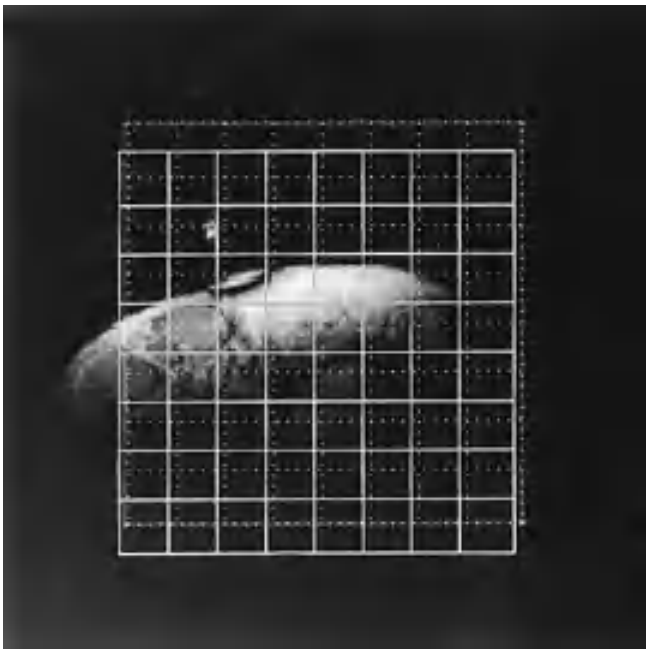

Figure 10 Axial MRI of the groin of a patient with low-grade non-Hodgkin's lymphoma with two CSI localizing grids. The dotted grid is the initial one while the solid grid is voxel shifted to align a voxel over the tumor

The ^{1}H decoupling discussed above allows clear resolution of the PME region into two components, PE and PC, with PE dominating. Without the CSI to localize the spectrum to the tumor, such detailed information is unattainable as shown by Figure 12 which is the spectrum acquired using only the surface coil for localization in the case of the patient shown in Figure 11.

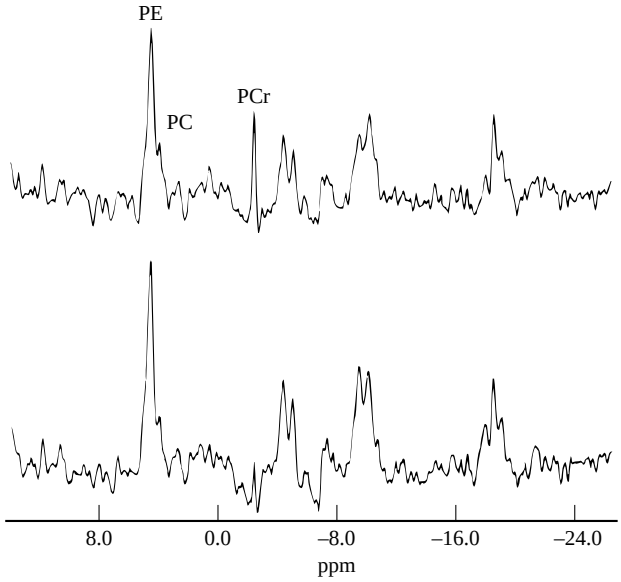

Figure 11 The localized spectra from a ^{31}P CSI measurement of the patient shown in Figure 10. The PCr in the spectrum from the initial voxel position (upper) is absent from the voxel shifted one (lower)

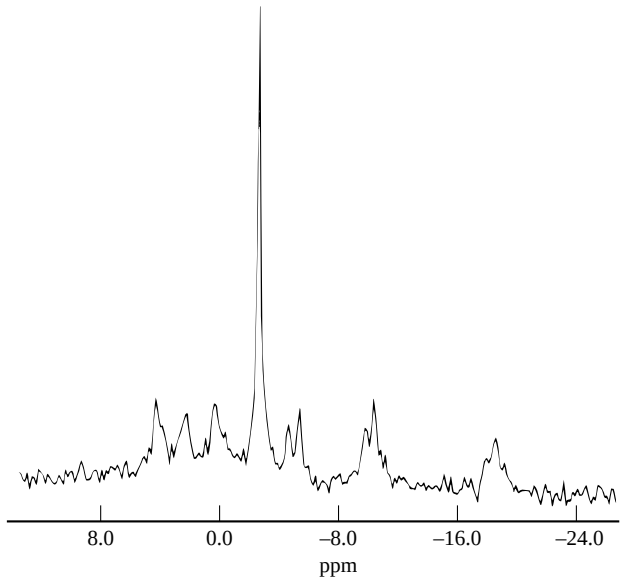

Figure 12 The nonlocalized FID from the patient shown in Figures 10 and 11

An important example of the use of CSI in spectral acquisition is its use in an autoshimming procedure. This is based upon CSI localization of the water proton signals to provide a field map; through a least-squares minimization procedure, this information is used to adjust the shim currents to produce the optimum magnetic field homogeneity. The procedure produces excellent field homogeneity, as illustrated in Figure 13 which shows ^{1}H and ^{31}P spectra following the autoshim procedure to a volunteer's head.[37]

7 DISCUSSION

As can be seen from the previous examples, CSI localization techniques have been used in a variety of circumstances, in general with great success. Summarizing their advantages, they produce signals from the entire tissue under study with a localization function that can be shifted over the sample at will, so as to optimize for the most appropriate signal from the region under investigation. Because of the well-defined properties of the FT, the difficulties due to the absence of high $\boldsymbol{k}$-space samples can be dealt with mathematically, albeit with some loss of spatial resolution. The sensitivity of these techniques is high, as high as generally possible to obtain with a particular coil and spin concentration. Nevertheless the techniques are not without disadvantages, the primary one being the acquisition time required since each point in $\boldsymbol{k}$ space acquired requires another acquisition. As pointed out above, three-dimensional acquisitions can be quite time-consuming, particularly if high-sensitivity protons are under study. In these cases, generally two-dimensional acquisitions are carried out. A further disadvantage is the loss of early time points during the gradient pulse. This can be a serious problem for low-strength gradients. However, with most modern commercial clinical instruments, the gradients are sufficiently strong that this gradient pulse is seldom more than 1 ms for resolutions of 1 cm or

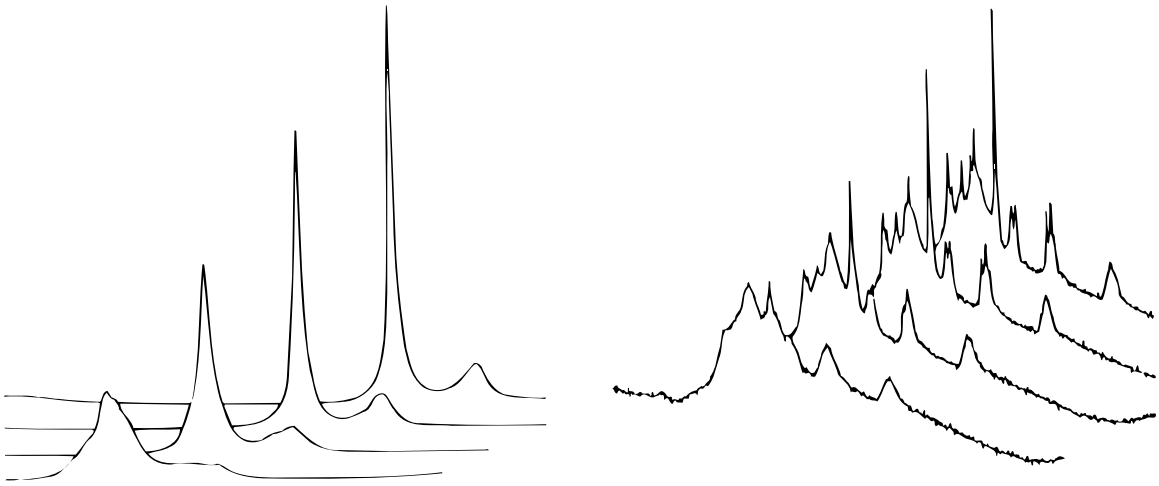

Figure 13 The ^{1}H (left) and ^{31}P (right) spectra from the whole head after several iterations of a CSI automatic shimming procedure

so, and obtaining CSI voxels significantly smaller than this is inefficient because of signal-to-noise reasons. At this short a time, only peaks with linewidths larger than 300 Hz are seriously affected, although the rolling baseline caused by even a short pulse can affect precise spectral integration procedures.

And finally, of course, is the complexity of analysis. However, with available computers the transforms can be performed in only a few minutes; the problem then becomes developing automatic analysis procedures which are able to deal with these complex data structures. This has been done and it now seems clear that it is worth the effort of dealing with these more complicated sets of spatial information. What extra information do we obtain from these observations? There is little doubt that, in many circumstances, extra biochemical or physiological information can provide a much needed insight into both physiological responses, as well as clinical questions. This is becoming clearer as more commercial instruments make it practical to carry out these types of CSI studies, and thus it is reasonable to believe that with further development, and a strong push from the user community, the instrument manufacturers will provide an integrated spectroscopy examination which is capable of easy use in a clinical setting.

This chapter has presented a brief overview of CSI and its potential. The techniques discussed here should allow a major advance in observations of metabolism in different pathological conditions. Considerable effort has been expended over the last several years to follow metabolic variations of tumors during therapeutic regimens, mostly with surface coils. Stroke and myocardial infarcts have been observed with single-voxel localization techniques which are not capable of providing as broad a picture as the multi-voxel CSI techniques discussed here. With the advent of clinical instrumentation capable of implementing these techniques, a much wider set of applications should ensue over the next few years. The ability of CSI to pinpoint metabolic changes associated with pathological states or physiological variations should provide new insights into both normal and disease processes.

8 RELATED ARTICLES

Brain MRS of Human Subjects; Brain Neoplasms in Humans Studied by Phosphorus-31 NMR Spectroscopy; In Vivo Hepatic MRS of Humans; Male Pelvis Studies Using MRI; Proton Decoupling During In Vivo Whole Body Phosphorus MRS; Single Voxel Localized Proton NMR Spectroscopy of Human Brain In Vivo; Spatial Localization Techniques for Human MRS.

9 REFERENCES

1. T. R. Brown, B. M. Kincaid, and K. Ugurbil, *Proc. Natl. Acad. Sci. USA*, 1982, **79**, 3523.
2. T. R. Brown, US Pat. 4 319 190 (9 March 1982).
3. A. A. Maudsley, S. K. Hilal, W. H. Perman, and H. E. Simon, *JMRI*, 1983, **51**, 147.
4. J. J. H. Ackerman, T. H. Grove, G. G. Wong, D. G. Gadian, and G. K. Radda, *Nature (London)*, 1980, **283**, 167.
5. R. M. Dixon and P. Styles, *Magn. Reson. Med.*, 1993, **29**, 110.
6. R. J. Ordidge, A. Connelly, and J. A. B. Lohman, *JMRI*, 1986, **66**, 283.
7. J. Frahm, H. Bruhn, M. L. Gyngell, K. D. Merboldt, W. Hanicke, and R. Sauter, *Magn. Reson. Med.*, 1989, **9**, 79.
8. R. J. Ordidge, J. A. Helpern, R. A. Knight, and K. M. A. Welch, *Proc. XIth Ann Mtg. Soc. Magn. Reson. Med.*, Berlin, 1992, p. 1925.
9. L. Bolinger and J. S. Leigh, *JMRI*, 1988, **80**, 162.
10. G. Goelman, G. Walter, and J. S. Leigh, *Magn. Reson. Med.*, 1992, **25**, 349.
11. R. N. Bracewell, 'The Fourier Transform and its Applications', McGraw-Hill, New York, 1978.
12. S. L. Ponder and D. B. Twieg, *J. Magn. Reson., Ser. B.*, 1994, **104**, 85.
13. J. C. Ehrhardt, *IEEE Trans. Med. Imag.*, 1990, **9**, 305.
14. A. A. Maudsley, G. B. Matson, J. W. Hugg, and M. W. Weiner, *Magn. Reson. Med.*, 1994, **31**, 645.
15. T. R. Brown and S. J. Nelson, *IEEE Eng. Med. Biol. Sci.*, 1990, **12**, 59.

16. S. Plevritis and A. Macovski, *Proc. XIth Ann Mtg. Soc. Magn. Reson. Med.*, Berlin, 1992, p. 3820.
17. S. J. Nelson and T. R. Brown, *JMRI*, 1987, **75**, 229.
18. S. J. Nelson and T. R. Brown, *JMRI*, 1989, **84**, 95.
19. D. B. Vigneron, S. J. Nelson, J. Murphy-Boesch, D. A. C. Kelley, H. B. Kessler, T. R. Brown, and J. S. Taylor, *Radiology*, 1990, **177**, 643.
20. O. Gonen, J. Murphy-Boesch, R. Srinivasan, J. Hu, H. Jiang, R. Stoyanova, and T. R. Brown, *J. Magn. Reson., Ser. B.*, 1994, **104**, 26.
21. J. A. L. Jeneson, S. J. Nelson, D. B. Vigneron, J. S. Taylor, J. Murphy-Boesch, and T. R. Brown, *Am. J. Physiol.*, 1992, **263C**, 357.
22. J. A. L. Jeneson, J. O. van Dobbenburgh, C. J. A. van Echteld, C. Lekkerkerk, W. J. M. Janssen, L. Dorland, R. Berger, and T. R. Brown, *Magn. Reson. Med.*, 1993, **30**, 634.
23. I. J. Cox, J. Sargentoni, J. Calam, D. J. Bryant, and R. A. Iles, *NMR Biomed.*, 1988, **1**, 56.
24. M. Cohn and T. R. Hughes, *J. Biol. Chem.*, 1962, **237**, 176.
25. N. M. Ramadan, H. Halvorsen, A. Vande-Linde, S. R. Levine, J. A. Helpern, and K. M. Welch, *Headache*, 1989, **29**, 590.
26. J. S. Taylor, D. B. Vigneron, J. Murphy-Boesch, S. J. Nelson, H. S. Kessler, L. Coia, W. Curran, and T. R. Brown, *Proc. Natl. Acad. Sci. USA*, 1991, **88**, 6810.
27. R. A. Meyer, T. R. Brown, and M. J. Kushmerick, *Am. J. Physiol.*, 1985, **248**, C279.
28. M. J. Kushmerick, P. F. Dillon, R. A. Meyer, T. R. Brown, J. M. Krisanda, and H. L. Sweeney, *J. Biol. Chem.*, 1986, **261**, 4420.
29. T. J. Mosher, G. D. Williams, C. Doumen, K. F. LaNoue, and M. B. Smith, *Magn. Reson. Med.*, 1992, **24**, 163.
30. F. Arias-Mendoza, T. Greenberg, R. Stoyanova, F. Ottery, and T. R. Brown, *Proc. XIIth Ann Mtg. Soc. Magn. Reson. Med.*, New York, 1993, p. 73.
31. C. M. Segebarth, D. F. Baleriaux, P. R. Luyten, and J. A. den Hollander, *Magn. Reson. Med.*, 1990, **13**, 62.
32. P. C. M. van Zijl, C. T. W. Moonen, J. Gillen, P. F. Daly, L. S. Miketic, J. A. Frank, T. F. DeLaney, O. Kaplan, and J. S. Cohen, *NMR Biomed.*, 1990, **3**, 227.
33. P. R. Luyten, A. J. H. Marien, W. Heindel, P. H. J. van Gerwen, K. Herholz, J. A. den Hollander, G. Friedman, and W. D. Heiss, *Radiology*, 1990, **176**, 791.
34. M. J. Fulham, A. Bizzi, M. J. Dietz, H. H. L. Shih, R. Raman, G. S. Sobering, J. A. Frank, A. J. Dwyer, J. R. Alger, and G. Di Chiro, *Radiology*, 1992, **185**, 675.
35. J. Murphy-Boesch, R. Srinivasan, L. Carvajal, and T. R. Brown, *J. Magn. Reson., Ser. B.*, 1994, **103**, 103.
36. J. H. Noggle and R. E. Shirmer, 'The Nuclear Overhauser Effect: Chemical Applications', Academic Press, New York, 1971.
37. J. Hu, T. Javaid, F. Arias-Mendoza, Z. Liu, R. McNamara, and T. R. Brown, *J. Magn. Reson.*, 1995, **108**, 213.

Acknowledgements

This work was supported by NIH Grants PO1-CA41708, RO1-CA54339, and Siemens Medical Systems. I would like to thank Fernando Arias-Mendoza, Oded Gonen, Tamela Greenberg, Jiani Hu, Tariq Javaid, Ronald McNamara, Joseph Murphy-Boesch, Sarah Nelson, William Negendank, Kristin Padavic-Shaller, Radka Stoyanova, Ravi Srinivasan, June Taylor, and Daniel Vigneron for their help and involvement in the development of the CSI techniques described here. Without the help of Doris Spindell, Jean Fink, and Lisa Siuda the chapter would never have been completed.

Localization and Registration Issues Important for Serial MRS Studies of Focal Brain Lesions

Douglas L. Arnold and Paul M. Matthews

Montreal Neurological Institute, McGill University, Montreal, Quebec, Canada

1 INTRODUCTION

Many applications have been reported illustrating the potential clinical utility of magnetic resonance spectroscopy (MRS) in the study of focal brain lesions. Examples of studies include those of brain tumors (diagnosis and monitoring response to therapy) using ^{1}H MRS[1–7] and ^{31}P MRS,[4,8–12] defining the evolution of hypoxic/ischemic brain damage in infants[13–19] and adults,[20–28] characterization of the chemical pathology and progression of focal demyelinating disease,[29–42] and localization of lesions associated with focal epilepsy, primarily using proton,[43–47] but also phosphorus,[48,49] MRS. Practical exploitation of these approaches demands: (i) the demonstration of sufficient diagnostic specificity and sensitivity; (ii) proof of the cost-effectiveness relative to current clinical test batteries for the different types of pathology; and (iii) establishment of procedures to allow studies to be reproduced with identical results at different times and with different instruments and observers. Absolute quantitation of results is desirable in the long term, but is not essential in all applications.

In this article we outline important general considerations involved in making interpretable and reproducible MRS brain studies of focal lesions. The brain is a highly heterogeneous tissue including a variety of cell types, considerable anatomic and functional specialization, and (not surprisingly, therefore) regional variations in NMR-visible metabolite resonance intensities.[32,50] Focal brain pathology is usually also anatomically, physiologically, and metabolically heterogeneous. Clinical exploitation of MRS to study focal brain lesions therefore requires that careful attention be paid to a number of fundamental problems including: (i) localization of where the magnetic resonance (MR) signals come from; (ii) registration of examinations; (iii) quantitative measurement of resonance intensities; and (iv) appropriate statistical analytical methods.

2 FUNDAMENTAL ISSUES FOR CLINICAL MRS OF FOCAL BRAIN LESIONS

2.1 Localization

The first localization problem is reliably to obtain signal only from the brain. As the fatty diploe of the skull and muscle surrounding the brain contain substantial amounts of the same compounds that are of interest in normal or pathological brain parenchyma, the ability to obtain signals from anatomically defined regions of brain without contamination from outside the volume of interest (VOI) is important. Even small proportions of signal from these regions could lead to large inaccuracies in quantitative assessment of metabolite concentrations in brain parenchyma. For example, contamination of proton brain spectra with as little as 1% of signal from extracerebral fat in the skull and scalp would lead to pathological amounts of lipid being observed in a normal brain spectrum.

Anatomical localization within the brain must also be achieved. Careful attention must be paid to potential contamination of spectra with signal from adjacent volumes having very different metabolite concentrations. Consider the problem of obtaining metabolite measurements from periventricular white matter using proton MRS, for example: periventricular white matter has a much lower lactate concentration then does cerebrospinal fluid (CSF), but concentrations of choline, creatine, and *N*-acetylaspartate are very much higher in brain parenchyma than CSF.

There are significant limitations to real spatial resolution that can be achieved using current volume-selection protocols. Understanding the degree to which selectivity is achieved in any study is critical for proper interpretation of spectroscopic data.

2.1.1 Single Voxel Localization

There are many techniques that allow spectra to be obtained from more or less well localized volumes within the brain. Here we consider only those methods most commonly used with clinical instruments. These can be divided into two types: (i) those that observe free induction decays (FIDs) rather than spin echoes and rely on cancellation of unwanted signals from regions outside the chosen VOI; and (ii) those that exploit spin echo techniques to excite only the VOI. Both utilize selective excitation in the presence of magnetic field gradients and so are subject to chemical shift artifacts. These artifacts appear because the frequency selective excitation leads to slightly different excited volumes for different metabolites because of their different resonance frequencies.

As the T_2 of brain phosphates is relatively short, single voxel phosphorus MRS studies in vivo have generally relied on techniques in which FIDs are acquired, e.g. ISIS.[51,52] This avoids the signal loss due to T_2 relaxation that accompanies use of spin echo localization sequences. However, these methods depend on accurate subtractive cancellation of the relatively large amount of signal originating from outside the VOI. In practice, this is achieved only imperfectly. If one considers, for example, the problem of selecting signal from a volume of the order of 10 cm^3 out of a whole brain volume of >1000 cm^3, it is obvious that proportionally small inaccuracies in cancellation will result in spectra that are 'contaminated' by significant amounts of signal from outside the VOI.[53,54] More recent implementations of this approach minimize this problem by employing additional methods for suppressing signal from outside the VOI.[55,56]

The class of localization sequences which rely on spin echo sequences provides more reliable localization, as they excite only the VOI. Recent improvements in hardware have enabled such sequences to be employed with sufficiently short echo

times to make them practical for phosphorus MRS studies without resulting in excessive signal loss or phase problems. Most proton studies of brain employ one of these sequences, most commonly either STEAM or PRESS. In proton MRS, measurement of the signal intensities of the most abundant compounds [e.g. choline (Cho), creatine (Cr), and *N*-acetylaspartate (NAA)] are less sensitive to echo time, as the T_2 values for these molecules are relatively large and they do not have complicated spin systems that cause phase modulation of their echoes. An additional advantage of these techniques in proton MRS is that it is easier effectively to suppress the large signals from water if one does not excite water from outside the VOI.

In proton studies spin echo sequences can be employed that use relatively long echo times to take advantage of the relatively long T_2 of some of the small soluble brain metabolites relative to fat of skin and skull in order to achieve improved localization and avoid problems from eddy currents generated by gradient coils. However, shorter echo times avoid the problem of phase modulation and allow the observation of additional metabolites with complicated spin systems and short T_2 times, e.g. amino acids and inositol.[27,57,58]

2.1.2 *Spectroscopic or Chemical Shift Imaging*

Single voxel techniques are inherently inefficient for applications in which chemical information from different regions is to be acquired at the same time (Figure 1). More recently developed spectroscopic imaging techniques approach an effective solution to this problem (Figure 2). Spectroscopic imaging sequences achieve localization with the use of phase-encoding pulse sequences, often combined with selective excitation so as to further minimize contamination from signal from outside the VOI. Phase encoding within the plane of the spectroscopic image is not associated with the chemical shift artifacts that arise from selective excitation. Spectroscopic imaging pulse sequences obtain signal from many relatively small voxels simultaneously. However, they tend to take a longer time to acquire than a single spectrum that represents a weighted average of resonance intensities from the same total volume. This is due to the number of averages required to obtain an adequate signal-to-noise ratio in the smaller voxels and the need to sample *k*-space adequately using sequences that incorporate a long sampling time in the absence of a field gradient to acquire

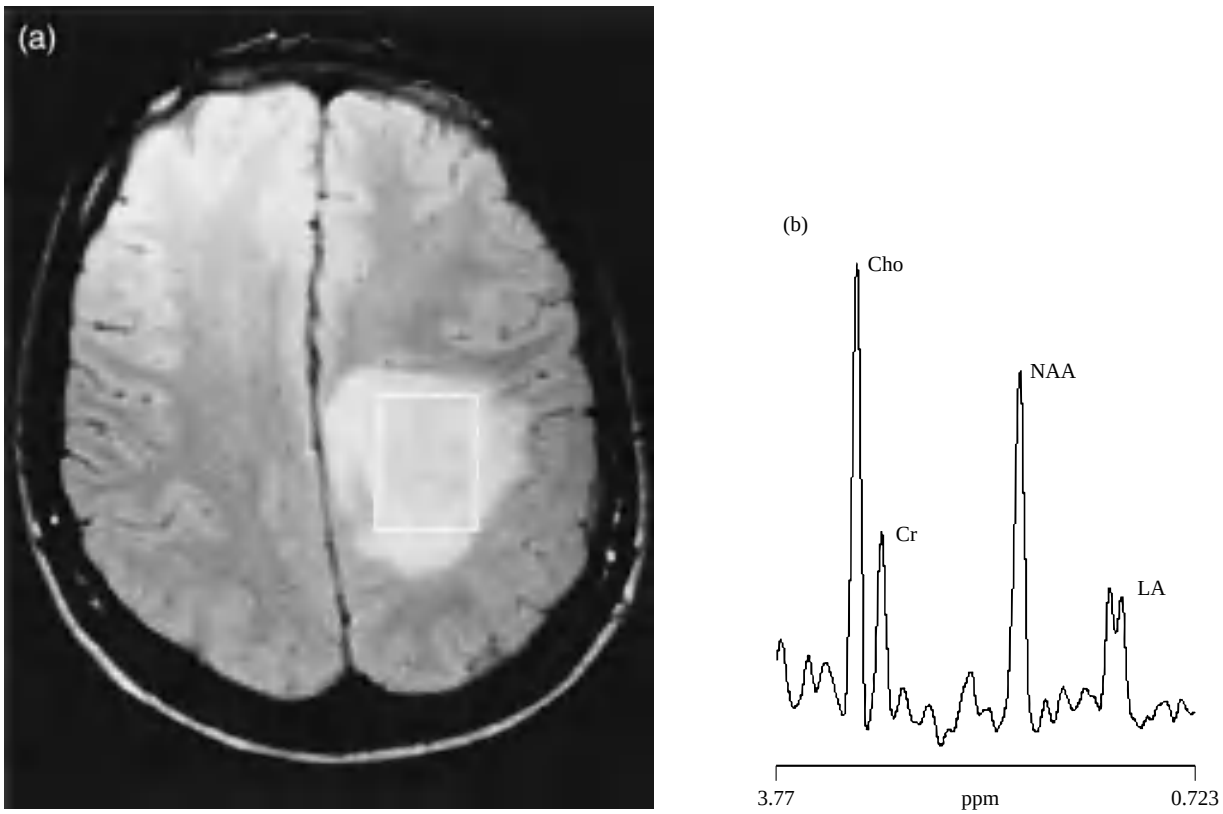

Figure 1 MRI and single voxel MRS examination of the same lesion a few days after the examination in Figure 2. The lesion appears similar on MRI (*TR* 2100, *TE* 30, slice thickness 8 mm). A single VOI for spectroscopic examination (*TR* 2000, *TE* 272, dimensions AP (anterior/posterior) 30 mm × CC (cranio/caudal) 22 mm × LR (left/right) 22 mm) is shown (in plane) in the box on the MRI. The VOI was chosen to sample as much of the lesion as possible but still accumulate essentially all of the signal selectively from within the lesion. The apparent metabolic changes represent an average over the entire volume and are therefore intermediate between those in voxels 1 and 2 in Figure 2. Quantitative comparison of the metabolic abnormalities apparent in the single voxel and MRS imaging examinations is difficult. The MRS image can be resampled in plane to correspond to the dimensions of the single voxel VOI, but the true shape of the volume from which the signal comes remains different because different techniques were used to define the voxels (i.e. phase-encoding in the MRS imaging, and selective excitation in the single voxel examination)

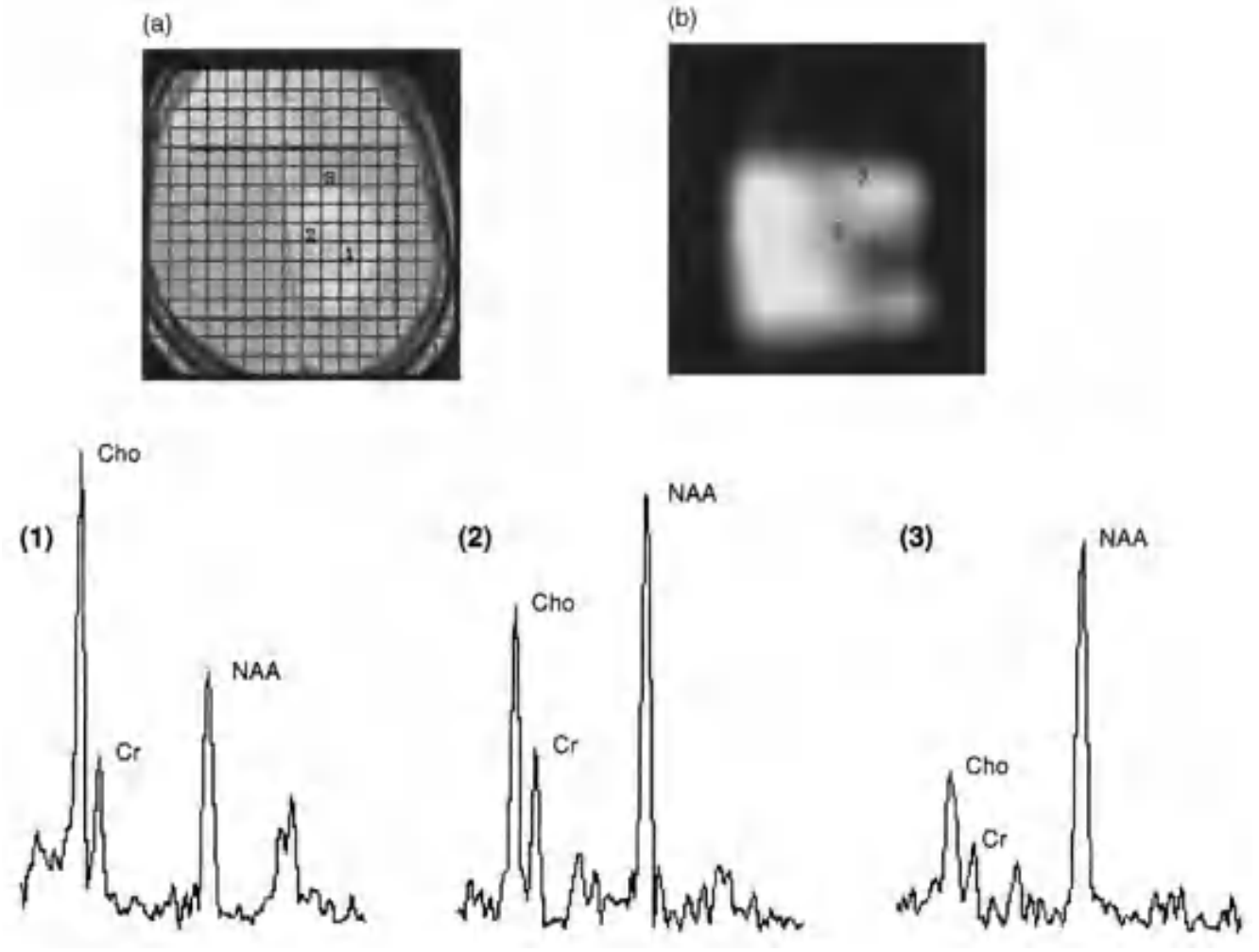

Figure 2 MRI and MRS imaging examination of a large demyelinating lesion. (a) A MRI slice through the center of the lesion (TR 2100, TE 30, slice thickness 8 mm). The phase-encoding grid for the MRS image is shown superimposed on the MRI. As long as the patient's head remains still during the entire time required for acquisition of the MR and MRS images, registration of the MRS image data is maintained. The dark and dotted lines define the VOI that was selectively excited for the MRS imaging examination. (b) The MRS image through the lesion (TR 2000, TE 272, slice thickness 20 mm). Individual spectra from voxels labeled 1, 2 and 3 are shown along the bottom of the figure. The lesion is associated with low *N*-acetylaspartate and high choline and LA. Note that the metabolic changes are different in different parts of the lesion and that abnormalities extend outside the lesion as defined on the MR image

the spectroscopic information. For proton examination in humans, current approaches allow nominal localization to volumes of about 0.5–1 cm^3 with the use of 16 × 16 or 32 × 32 phase-encoding steps (Figure 2).

Unfortunately, the relative insensitivity of phosphorus and the fact that compounds of major interest [e.g. adenosine triphosphate (ATP)] have short T_2 times, effectively limits individual voxel sizes in phosphorus MRS imaging to more than 10 cm^3, at least at 1.5 T. The large voxel size is usually combined with a low number (< 16 × 16) of phase-encoding profiles, which again tends to lead to contamination of spectra by signals adjacent to voxels.

When interpreting data from focal brain lesions it is important to appreciate that several factors cause the voxel size to be larger and less sharply defined than the nominal voxel size. It is the true shape of the excited volume that determines where signal actually comes from and, in consequence, the nature of partial volume effects. The nominal VOIs displayed on MRI images used to plan spectroscopy acquisitions may be defined very differently by different manufacturers, e.g. by the full width at half maximum amplitude of the excitation pulse or to include 90% of the excited signal. The definition of the selected volume needs to be clearly understood in terms of the percentage of signal coming from that volume versus the percentage of signal coming from outside the volume. In the case of phase-encoded spectroscopic images, the point spread function and effects of image processing also alter the voxel contours.

Defining the relationship between the volume from which the MRS signal is originating and any anatomically defined lesion on MRI is of great importance. Large focal brain lesions such as tumors, infarcts, or demyelinating plaques show wide

pathological heterogeneity. Interpretation of the data therefore poses the analytical problem of inferring (at least qualitatively) the chemical pathology of a region within the selected volume element, taking into account partial volume effects. The effects of small differences in linear dimensions on partial volume effects are easily underestimated. For example, in a single voxel study a spherical lesion filling an operator-defined 'cube' will contribute only 50% of the signal from the cube. If the 'cube' displayed on the monitor has margins that are defined by the full width at half maximum of the selection profile, then less than 25% of the signal will actually come from the lesion. Under these circumstances, given a normal variance of measurements of the order of 10%, only the most gross changes in metabolite concentrations could ever be detected as abnormal if the metabolic abnormality is spatially coextensive with the lesion seen on the MR image. In fact, for many focal lesions metabolic abnormalities are much more extensive than the associated imaging abnormalities,[29] and so significant results are obtained despite an apparently unfavorable partial volume of the lesion in the VOI.

2.2 Registration

2.2.1 Definition

The process of spatial alignment of images is referred to as 'registration'. A target image or space is defined and images to be registered with that image or space are positioned and may also be 'deformed' as necessary to match the target as closely as possible. A discussion of the methods available for registration is outside the scope of this article, but can be found in the review by Evans.[59]

2.2.2 The Importance of Registration

Registration of MRS examinations is important for at least three reasons. The first is that metabolic changes must be referred to anatomical pathology in the study of focal brain lesions in order to interpret the pathological significance of observed signal intensity changes. This type of registration is implicit in planning MRS volume acquisition parameters with respect to anatomical landmarks on MRI examinations (Figures 1–3). Common anatomical landmarks can be used to allow matching of spectroscopic VOIs in independent examinations of the same individual on different occasions (see Figures 2 and 3). Registration also can greatly facilitate appropriate comparisons of data collected from different individuals who may show regional variations in anatomy, by allowing matching of volumes from different individuals in a standard anatomical space.[59–61] Finally, averaging of anatomically correlated metabolic information increases the intrinsically low signal-to-noise ratio of single examinations, thus facilitating comparisons of groups of image data sets.[50]

2.2.3 Technical Considerations

Registration may be accomplished before or after acquisition. Preplanned registration is performed by defining volumes for spectroscopic data acquisition with respect to anatomical landmarks before the data are acquired. Even when this is done for planning purposes within the context of a single MR session, errors in registration can occur due to patient movement between or during acquisitions, as well as to chemical shift artifacts when selective excitation is used. Preplanned registration of spectroscopic examinations obtained at different times requires meticulous care and has limitations in that only translations and rotations can be matched. Thus, the method is more suitable for comparisons between studies of one individual rather than between different individuals, since it cannot compensate for different head sizes and shapes. Even minor errors in registration can have serious consequences for data quantification. For example, in a three-dimensional MRS imaging examination, shifting of 1 cm^3 voxels by 2 mm in the three axes would alter the contribution of the desired voxel to the observed metabolite signals by as much as 50%.

Registration after acquisition can correct for some errors in preplanned registration and can correct for differences in head size and shape.[59] However, effective application requires three-dimensional high resolution images. These are not usually generated by conventional MRI as the slices usually have relatively poor out-of-plane resolution, and significant image degradation occurs during resampling for the three-dimensional reconstruction.

For low resolution data like the MR single voxel or spectroscopic images, preplanned registration is essential. With single voxel data, changing or moving the VOI after data acquisition is not possible. Spectroscopic images permit manipulation of voxels after acquisition, but there are significant limitations. The severity of these limitations depends on whether data sets acquired are two or three dimensional. In the case of two-dimensional spectroscopic images (or multislice two-dimensional images), data must be acquired in the same plane in the studies being registered because the plane of the voxels cannot be shifted after acquisition. However, movement of voxels for registration within the plane of the slice is possible. In the case of three-dimensional spectroscopic images, translation of voxels in all three axes is feasible. Rotation of voxels is theoretically possible, but degrades an already low-resolution image.

2.3 Measurement of Resonance Intensities

To allow chemical changes measured by MRS to be useful as indices of pathology, methods for quantitative measurement of signal intensities are necessary. In contrast to usual clinical radiology, which is based on qualitative assessments of patterns of changes in signal across images, work to date suggests that few clinical applications of brain spectroscopy will involve significant qualitative chemical changes specific to particular pathologies.[62]

There are independent (but related) problems in quantitation of signal intensities. The first major problem is to identify methods that allow accurate and reproducible measurements of signal intensities from metabolites with varying relaxation properties and concentrations in a sample volume within which there is magnetic field inhomogeneity and, therefore, complex lineshapes. The problem is complicated in phosphorus spectra and proton spectra obtained at short echo times by the presence of overlapping and very broad peaks, which make unique fitting of peaks and the baseline impossible. Quantitative measurements with proton spectra may also be complicated by signal dynamic range problems associated with the presence of large residual signals from water. Finally, there is the problem of standardization. How can a reliable means be developed for deriving true tissue concentrations from resonance signal inten-

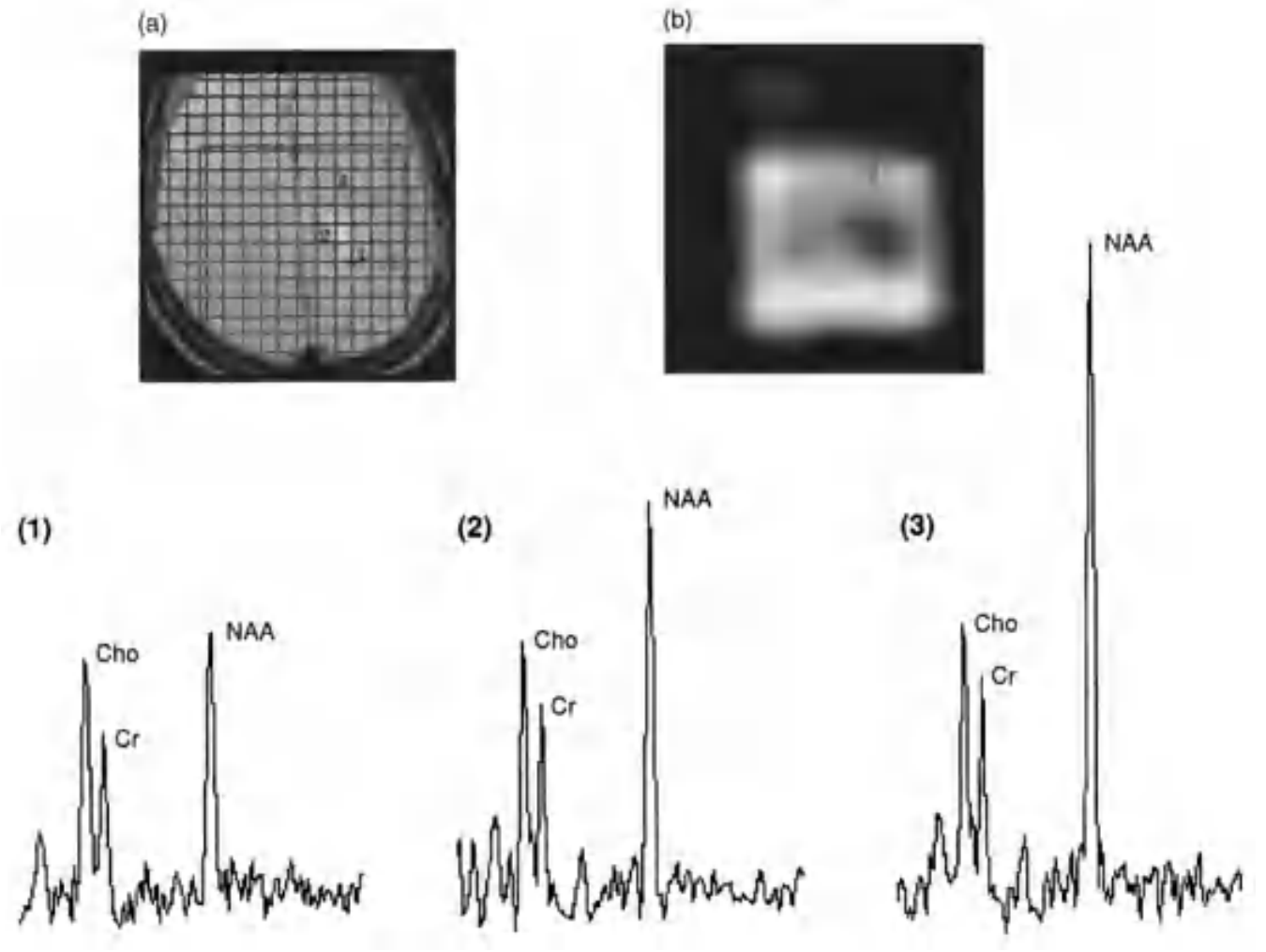

Figure 3 Follow-up MRI and MRS imaging of the same lesion as in Figure 2 approximately 1 year later, using identical acquisition techniques. The size, position, and angulation of the spectroscopic images were also matched as closely as possible to those of the first examination (Figure 2), but such a match is difficult to perform. An additional complication to registering the images is that the lesion is much smaller and the swelling which previously enlarged the hemisphere and shifted the midline towards the other side has resolved. All these factors conspire to make it unclear what the ideal volume for a single voxel spectroscopy follow-up should be. Spectroscopic images have significant advantages in this regard because of the availability of multiple small voxels. The three spectra shown are from the three voxels that most closely correspond to the three voxels chosen in the first examination (Figure 1)

sities so that data from different machines and different sites can be compared?

2.3.1 Spectral Estimation

Several methods are available for modeling either the FID or the Fourier transformed data.[63–65] The methods are generally constrained to models with limited numbers of components and generally to simple relaxation behavior as expected in a homogeneous field. These assumptions are not always well founded. Even assuming that pathological states can be modeled in the same way as normal tissue may be problematical. The nature of the constraints used in models can, in principle, significantly bias results. Differences in constraints or starting values between different clinical MRS centers could therefore be expected to limit the comparability of results. Assessment of precision of the methods is straightforward, but accuracy is difficult to evaluate because phantom systems for testing are inherently less complex physical structures than the brain.

The signal-to-noise ratio is relatively low in clinical spectra, further complicating all approaches to quantitation. The apparent signal-to-noise ratio is routinely improved by a variety of processing procedures. Signal processing can also be used to flatten baselines distorted in various ways. Effects of this processing on quantification of spectra must be taken into account.

Another problem is automation of quantitation methods. Automation facilitates evaluation by making it possible to deal with large numbers of spectra acquired in spectroscopic imaging studies. Use of prior knowledge and models facilitates automatic fitting, but introduces biases. However, these are at least consistent biases that are inherently more independent of operator bias than manually supervised methods, although they may differ between different sites if different models and approaches are used.

2.3.2 *Relative and Absolute Quantification*

Metabolite signal intensities from pathological tissue will not, in general, be useful alone. Many factors that vary from instrument to instrument, between individuals, and even during a prolonged examination determine observed signal intensities. Among them, coil quality, coupling of the sample to the coil, field ($\boldsymbol{B}_1$) inhomogeneity, and relaxation times are the most important general factors. Most approaches to controlling for variability in coil responses and coupling involve use of an external (relative to the patient) standard. To be done rigorously, the process is quite complicated. Fortunately, modern instrumentation is generally stable enough for practical methods to work. Appreciating such biases is essential in comparisons of data between different sites.

More popular has been the use of internal standards. One approach is to present data as ratios of resonance intensities relative to a signal that is assumed to be relatively invariant, e.g. use of the creatine signal as an internal reference in proton MRS, or ATP in phosphorus MRS.[31,66] This method assumes that relative relaxation rates are unchanged in the pathological volumes and that concentrations of the chosen reference signal do not vary between normal-appearing and pathological tissue (note the results in Figure 3). When comparing metabolite signal intensity ratios from different regions of the brain it is necessary to be aware of the regional variation in relative signal intensities in the normal brain or to compare only identically localized volumes (Figure 2).[32]

The validity of assumptions of invariance of internal reference signals can be tested by comparisons of absolute signal intensities with anatomically homologous volumes in the (unaffected) contralateral hemisphere. Care should be taken even with this control, however, as pathology in one hemisphere may have secondary physiological, biochemical, or anatomic effects in the contralateral hemisphere because of the extensive connectivity of the two hemispheres. With this concern in mind, absolute signal intensities can also be compared directly between lesions and normal-appearing contralateral hemispheres. While this is probably valid in some situations, it will not be in others. For example, it may be true for creatine in chronic multiple sclerosis,[30,31,42] but certainly does not hold true for brain tumors.[3,12]

2.4 Statistical Analysis of Spectroscopic Data

Single voxel methods produce a single spectrum, which simplifies the problem of data quantitation and comparisons. The data are biased by subjectivity in the volume selection, but are potentially statistically powerful.

Spectroscopic image data sets are much more difficult to analyze. Comparisons based on the subjective choice of only certain voxels within the MRS image introduces bias, as in the case of single voxel examinations. Use of more than one voxel to characterize a focal lesion is complicated because the voxels are not statistically independent measurements. An appropriate correction for their spatial correlations must be made.[67] Finally, comparisons with normal data that also consist of image data sets is complex. Objective comparisons of groups of spectroscopic images and statistical analysis of the significance of differences requires the development of a new statistical methodology that avoids sampling bias, is efficient despite a low signal-to-noise ratio, and takes into account the spatial variation and correlations in the images. However, such procedures have been developed for other applications, such as the analysis of satellite photographs.[68]

3 CONCLUSIONS

Preliminary results have demonstrated that brain MRS may be able to provide potentially important information concerning localized changes in brain chemistry associated with focal pathologies. Because focal pathologies are often the object of active treatments (e.g. for abscesses or tumors) or efforts to develop effective treatments (e.g. for stroke or multiple sclerosis), this type of pathology may provide a major justification for integration of MRS into clinical neurological and neurosurgical practice. However, at the time of writing, several fundamental problems still limit the practical availability of reproducible, quantitative spectroscopic data.

The intrinsic limitations on the signal-to-noise ratio in MRS and relaxation properties of the nuclei of interest limit spectroscopic resolution relative to water-based proton images. Despite the desirability of further increases in resolution, a practical balance is necessary between resolution and the time required for acquisition in clinical studies.

Comparisons of spectroscopic image data between individuals, individuals and groups, and between serial examinations of an individual are fundamental to clinical applications. However, they are difficult to perform rigorously. Accurate preplanned registration is likely to remain essential for spectroscopic data acquisition. Techniques that allow registration to a standard anatomical space can provide averaged normative data with a much improved signal-to-noise ratio relative to individual studies for more accurate quantitative assessment of data from pathology in an individual subject.

Application of spatial statistics[68] should facilitate efficient, unbiased assessment of spectroscopic image data. Statistical approaches such as this potentially allow meaningful comparison of data obtained from a variety of modalities. Of particular interest also is the potential for simultaneous assessment of structural and biochemical MR data.

4 RELATED ARTICLES

Brain Infection and Degenerative Disease Studied by Proton MRS; Brain MRS of Human Subjects; Brain MRS of Infants and Children; Brain Neoplasms in Humans Studied by Phosphorus-31 NMR Spectroscopy; Chemical Shift Imaging; Selective Excitation Methods: Artifacts; Selective Excitation in MRI and MR Spectroscopy; Single Voxel Localized Proton NMR Spectroscopy of Human Brain In Vivo; Surface Coil NMR: Detection with Inhomogeneous Radiofrequency Field Antennas.

5 REFERENCES

1. D. L. Arnold, E. A. Shoubridge, W. Feindel, and J. G. Villemure, *Can. J. Neurol. Sci.*, 1987, **14**, 570.

2. W. Semmler, G. Gademann, P. Bachert Baumann, H. J. Zabel, W. J. Lorenz, and G. van Kaick, *Radiology*, 1988, **166**, 533.
3. H. Bruhn, J. Frahm, M. L. Gyngell, K. D. Merboldt, H. Hanicke, R. Sauta, and C. Hamburger, *Radiology*, 1989, **172**, 541.
4. M. C. Preul, Z. Caramanos, R. Leblanc, J. G. Villemure, and D. L. Arnold, *NMR Biomed.*, 1998, **11**, 192.
5. H. Kugel, W. Heindel, R. I. Ernestus, J. Bunke, R. du Mesnil, and G. Friedmann, *Radiology*, 1992, **183**, 701.
6. C. M. Segebarth, D. F. Baleriaux, P. R. Luyten, and J. A. den Hollander, *Magn. Reson. Med.*, 1990, **13**, 62.
7. M. Preul, D. Collins, R. Ethier, W. Feindel, and D. L. Arnold, *Proc. XIIth Ann Mtg. Soc. Magn. Reson. Med.*, New York, 1993, **1**, 64 (abstract).
8. J. A. den Hollander, P. R. Luyten, A. J. Marien, C. M. Segebarth, D. F. Baleriaux, R. de Beer, and D. Van Ormondt, *Magn. Reson. Q.*, 1989, **5**, 152.
9. B. Hubesch, D. Sappey-Marinier, K. Roth, D. J. Meyerhoff, G. B. Matson, and M. W. Weiner, *Radiology*, 1990, **174**, 401.
10. D. L. Arnold, J. F. Emrich, E. A. Shoubridge, J. G. Villemure, and W. Feindel, *J. Neurosurg.*, 1991, **74**, 447.
11. W. D. Heiss, W. Heindel, K. Herholz, J. Rudolph, J. Bunke, J. Jeoke, and G. Friedmann, *J. Nucl. Med.*, 1990, **31**, 302.
12. D. L. Arnold, E. A. Shoubridge, J. Emrich, W. Feindel, and J. G. Villemure, *Invest. Radiol.*, 1989, **24**, 958.
13. D. P. Younkin, M. Delivoria-Papadopoulos, J. C. Leonard, V. H. Subramanian, S. Eleff, J. S. Leigh, Jr., and B. Chance, *Ann. Neurol.*, 1984, **16**, 581.
14. P. A. Hamilton, P. L. Hope, E. B. Cady, D. T. Delpy, J. S. Wyatt, and E. O. Reynolds, *Lancet*, 1986, **i**, 1242.
15. D. T. Delpy, M. C. Cope, E. B. Cady, J. S. Wyatt, P. A. Hamilton, P. L. Hope, S. Wray, and E. O. Reynolds, *Scand. J. Clin. Lab. Invest. Suppl.*, 1987, **188**, 9.
16. D. Azzopardi, J. S. Wyatt, E. B. Cady, D. T. Delpy, J. Baudin, A. L. Stewart, P. L. Hope, P. A. Hamilton, and E. O. Reynolds, *Pediatr. Res.*, 1989, **25**, 445.
17. T. Kato, A. Tokumaru, T. O'uchi, I. Mikami, M. Umeda, K. Nose, T. Egushi, M. Haregawa, and K. Okuyama, *Radiology*, 1991, **179**, 95.
18. E. O. Reynolds, D. C. McCormick, S. C. Roth, A. D. Edwards, and J. S. Wyatt, *Ann. Med.*, 1991, **23**, 681.
19. C. J. Peden, F. M. Cowan, D. J. Bryant, J. Sargentoni, I. J. Cox, D. K. Menon, D. G. Gadian, J. D. Bell, and L. M. Dubowitz, *J. Comput. Assist. Tomogr.*, 1990, **14**, 886.
20. K. M. Welch, S. R. Levine, G. Martin, R. Ordidge, A. M. Vande Linde, and J. A. Helpern, *Neurol. Clin.*, 1992, **10**, 1.
21. S. R. Levine, K. M. Welch, J. A. Helpern, M. Chopp, R. Bruce, J. Selwa, and M. B. Smith, *Ann. Neurol.*, 1988, **23**, 416.
22. K. M. Welch, S. R. Levine, and J. A. Helpern, *Funct. Neurol.*, 1990, **5**, 21.
23. S. R. Levine, J. A. Helpern, K. M. Welch, A. M. Vande-Linde, K. L. Sowaya, E. E. Brown, N. M. Ramadan, R. K. Devashwar, and R. J. Ordidge, *Radiology*, 1992, **185**, 537.
24. J. H. Duijn, G. B. Matson, A. A. Maudsley, J. W. Hugg, and M. W. Weiner, *Radiology*, 1992, **183**, 711.
25. M. J. Fenstermacher and P. A. Narayana, *Invest. Radiol.*, 1990, **25**, 1034.
26. J. W. Berkelbach van der Sprenkel, P. R. Luyten, P. C. van Rijen, C. A. Tulleken, and J. A. den Hollander, *Stroke*, 1988, **19**, 1556.
27. G. D. Graham, A. M. Blamire, A. M. Howseman, D. L. Rothman, P. B. Fayad, L. M. Brass, O. A. Petroff, R. G. Shulman, and J. W. Prichard, *Stroke*, 1992, **23**, 333.
28. D. L. Rothman, A. M. Howseman, G. D. Graham, O. A. Petroff, G. Lantos, P. B. Fayad, L. M. Brass, G. I. Shulman, and J. W. Prichard, *Magn. Reson. Med.*, 1991, **21**, 302.
29. D. L. Arnold, P. M. Matthews, G. S. Francis, J. O'Connor, and J. P. Antel, *Ann. Neurol.*, 1992, **31**, 235.
30. P. M. Matthews, G. Francis, J. Antel, and D. L. Arnold, *Neurology*, 1991, **41**, 1251.
31. D. L. Arnold, P. M. Matthews, G. Francis, and J. Antel, *Magn. Reson. Med.*, 1990, **14**, 154.
32. J. Frahm, H. Bruhm, M. L. Gyngell, K. D. Merboldt, W. Hanicke, and R. Sauter, *Magn. Reson. Med.*, 1989, **11**, 47.
33. H. B. Larsson, P. Christiansen, M. Jensen, J. Frederikren, A. Heltberg, J. Olesen, and O. Henriksen, *Magn. Reson. Med.*, 1991, **22**, 23.
34. T. L. Richards, *Am. J. Roentgenol.*, 1991, **157**, 1073.
35. D. H. Miller, S. J. Austin, A. Connelly, B. D. Youl, D. G. Gadian, and W. I. McDonald, *Lancet*, 1991, **337**, 58.
36. R. I. Grossman, R. E. Lenkinski, K. N. Ramer, F. Gonzalez-Scarano, and J. A. Cohen, *Am. J. Neuroradiol.*, 1992, **13**, 1535.
37. L. Fu, P. M. Matthews, N. de Stefano, K. J. Worsley, S. Narayanan, G. S. Francis, J. P. Antel, C. Wolfson, and D. L. Arnold, *Brain*, 1998, **121**, 103.
38. C. A. Davie, C. P. Hawkins, G. J. Barker, A. Brennan, P. S. Tofts, D. H. Meller, and W. J. McDonald, *Proc. XIIth Ann Mtg. Soc. Magn. Reson. Med.*, New York, 1993, **1**, 133.
39. P. A. Narayana, J. S. Wolinsky, E. F. Jackson, and M. McCarthy, *JMRI*, 1992, **2**, 263.
40. J. S. Wolinsky, P. A. Narayana, and M. J. Fenstermacher, *Neurology*, 1990, **40**, 1764.
41. C. Husted, D. S. Goodin, A. A. Maudsley, J. S. Tsuruda, and M. W. Weiner, *Neurology*, 1993, **43**, A182 (abstract).
42. D. L. Arnold, G. T. Riess, P. M. Matthews, G. S. Frances, D. L. Collins, C. Wolfson, and J. P. Antel, *Ann. Neurol.*, 1994, **36**, 76.
43. P. M. Matthews, F. Andermann, and D. L. Arnold, *Neurology*, 1990, **40**, 985.
44. A. Connely, D. G. Gadian, G. D. Jackson, J. H. Gross, M. D. King, J. S. Duncan, and F. J. Kirkham, *Proc. XIth Ann Mtg. Soc. Magn. Reson. Med.*, Berlin, 1992, **1**, 234.
45. F. Cendes, F. Andermann, M. C. Preul, and D. L. Arnold, *Ann. Neurol.*, 1994, **35**, 211.
46. J. W. Hugg, K. D. Laxer, G. B. Matson, A. A. Maudsley, and M. W. Weiner, *Ann. Neurol.*, 1993, **34**, 788.
47. F. Cendes, Z. Caramanos, F. Andermann, F. Dubeau, and D. L. Arnold, *Ann. Neurol.*, 1997, **42**, 737
48. L. Fu, C. Wolfson, K. J. Worsley, N. de Stefano, D. L. Collins, S. Narayanan, and D. L. Arnold, *NMR Biomed.*, 1996, **9**, 339.
49. J. W. Hugg, K. D. Laxer, G. B. Matson, A. A. Maudsley, C. A. Husted, and M. W. Weiner, *Neurology*, 1992, **42**, 2011.
50. D. L. Collins, L. Fu, E. Pioro, A. C. Evans, and D. L. Arnold, *Magn. Reson. Med.*, 1993, **3**, 1600.
51. R. J. Ordidge, P. Mansfield, J. A. Lohman, and S. B. Prime, *Ann. NY Acad. Sci.*, 1987, **508**, 376.
52. R. J. Ordidge, R. M. Bowley, and G. McHale, *Magn. Reson. Med.*, 1988, **8**, 323.
53. G. B. Matson, D. J. Meyerhoff, T. J. Lawry, R. S. Lara, J. Duijn, R. F. Deeken, and M. W. Weiner, *NMR Biomed.*, 1993, **6**, 215.
54. S. F. Keevil, D. A. Porter, and M. A. Smith, *NMR Biomed.*, 1992, **5**, 200.
55. S. Posse, B. Schuknecht, M. E. Smith, P. C. van Zijl, N. Herschkowitz, and C. T. Moonen, *J. Comput. Assist. Tomogr.*, 1993, **17**, 1.
56. R. J. Ordidge, *Magn. Reson. Med.*, 1987, **5**, 93.
57. B. D. Ross, *NMR Biomed.*, 1991, **4**, 59.
58. R. Kreis, N. Farrow, and B. D. Ross, *NMR Biomed.*, 1991, **4**, 109.
59. A. C. Evans, in 'Principles of Nuclear Medicine', ed. H. N. Wagner, Jr., W. B. Saunders, Philadelphia, 1995.
60. P. T. Fox, J. S. Perlmutter, and M. E. Raichle, *J. Comput. Assist. Tomogr.*, 1985, **9**, 141.
61. A. C. Evans, T. S. Marrett, D. L. Collins, and T. M. Peters, *SPIE*, 1989, Medical Imaging III, 264 (abstract).

62. Arnold D. L. and P. M. Matthews, in 'MR Spectroscopy: Clinical Applications and Techniques', ed. I. R. Young and C. Charles, Martin Dunitz, London, 1995.
63. P. R. Luyten, A. J. Marien, and J. A. den Hollander, *NMR Biomed.*, 1991, **4**, 64.
64. A. Knijn, R. de Beer, and D. van Ormondt, *J. Magn. Reson.*, 1992, **97**, 444.
65. R. de Beer, A. Van den Boogaart, D. van Ormondt, W. W. Pijnappel, J. A. den Hollander, A. J. Morien, and P. R. Luyten, *NMR Biomed.*, 1992, **5**, 171.
66. D. L. Arnold, P. M. Matthews, and G. K. Radda, *Magn. Reson. Med.*, 1984, **1**, 307.
67. K. J. Worsley, A. C. Evans, S. Marrett, and P. Neelin, *J. Cereb. Blood Flow Metab.*, 1992, **12**, 900.
68. N. A. Cressie, 'Statistics for Spatial Data', Wiley, Toronto, 1991.

Biographical Sketches

Douglas L. Arnold. *b* 1951. B.Sc. (Physiology), McGill University, M.D., Cornell University Medical College. Trained in medicine and neurology at McGill before doing a postdoctoral fellowship in NMR under the supervision of Professor G. K. Radda, Department of Biochemistry, University of Oxford, UK. Currently Professor of Neurology and Neurosurgery at McGill University. Research interests: magnetic resonance spectroscopy of disorders of brain and muscle. Approx. 100 publications, including, with P. M. Matthews, the book *Diagnostic Tests in Neurology*.

Paul M. Matthews. *b* 1956. B.A. (Chemistry), D.Phil. (Biochemistry) (supervisor G. K. Radda and D. G. Gadian), University of Oxford. General medical training at Oxford and Stanford. Trained in neurology at the Montreal Neurological Institute. Currently Professor in the Department of Neurology, University of Oxford, and Director of the Oxford Centre for Functional Magnetic Resonance Imaging of the Brain. Research interests: the chemical pathology of multiple sclerosis and mitochondrial disorders.

pH Measurement In Vivo in Whole Body Systems

Neil A. Farrow and John H. Richards
California Institute of Technology, Pasadena, CA, USA

and

Brian D. Ross
Huntington Medical Research Institutes, Pasadena, CA, USA

1 INTRODUCTION

In 1973 Moon and Richards[1] described a noninvasive approach for the determination of conditions within cells, such as pH, by observing the magnetic resonance signal of ^{31}P from intracellular phosphates whose chemical shifts vary significantly with pH (see Figure 1). In this study of the pH within erythrocytes they monitored the chemical shift of the two ^{31}P signals of intracellular 2,3-diphosphoglycerate and found that the intraerythrocytic pH of whole blood was the same as that of packed cells, as well as that of hemolysates of packed red blood cells. This and analogous approaches have since been used to study a wide variety of biological systems including ion transport in plants,[2] the metabolism of flight in insects,[3] as well as human physiology and pathology, the particular focus of this discussion.

To determine the pH of biological samples by NMR spectroscopy the presence is required of a molecule containing a nucleus with appropriate magnetic properties. The chemical shift of the nucleus in the molecule should vary significantly with pH and the molecule should have a pK_a close to that of the environment whose pH is being determined. The ^{31}P nucleus satisfies these conditions. Its spin quantum number of $\frac{1}{2}$ provides high-resolution spectra; its 100% natural abundance and inherent sensitivity give an observational sensitivity of 6.6% relative to ^{1}H; molecules that contain ^{31}P are often present in biological samples at millimolar (mM) concentrations. These factors allow the collection of one-dimensional spectra within short periods of time to determine ^{31}P chemical shifts. Inorganic phosphate can serve as a pH-sensitive indicator as the pK_a for dihydrogen phosphate is near 7 and the two differently protonated forms are in rapid exchange ($k \sim 10^9$–10^{10} s^{-1}).

$$H_2PO_4^- \rightleftharpoons HPO_4^{2-} + H^+ \qquad pK_a = 7.21$$

The chemical shifts of monohydrogen phosphate and dihydrogen phosphate differ by about 2.35 ppm. On a 500 MHz instrument (where ^{31}P nuclei resonate around 202 MHz) this corresponds to a frequency difference between the two differently protonated forms of 475 Hz, which is well below the chemical exchange rate of 10^9–10^{10} s^{-1}. In such situations one observes a single resonance for the two forms; the chemical shift represents an average weighted by the relative concentrations of the two forms. Since most biological systems normally have pH values near 7, the changing relative concentrations of these two forms with varying pH leads to a ^{31}P signal that sensitively reflects the pH of the environment.

Since features of the environment, other than pH, can also influence the chemical shifts of ^{31}P nuclei, one requires a reference signal whose chemical shift should ideally be independent of pH. For many systems phosphocreatine serves this function; it is completely ionized near physiological pH:

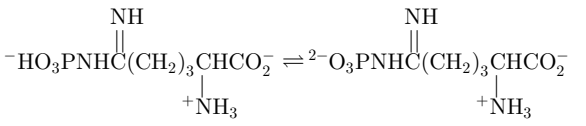

pK_a of phosphate = 4.6

and has a chemical shift 3.5–5.5 ppm away from that of inorganic phosphate in the range of physiological pH. Thus by constructing reference titration curves under conditions that simulate those of the biological sample (as shown in Figure 2) one can determine the pH of the biological system itself. In situations where no phosphocreatine signal is present, as in liver, the α-phosphate of ATP can serve as a reference, though one must recognize that its chemical shift changes with pH as shown in Figure 1. Other internal references, such as cell water[4] or an external reference, such as a vial of methylene diphosphonate, can also be used.

Nuclei other than ^{31}P can also serve as probes. For example esterified F-quene-1,[5] can enter a cell where the ester groups are then hydrolyzed. The resulting F-quene-1 cannot cross the cell membrane and becomes trapped intracellularly. The ^{19}F signal of F-quene-1 has been used to monitor the intracellular pH of rat liver, for example. The ^{1}H signal from C-4 of histidine in the hemoglobin of erythrocytes[6] and of anserine in muscle,[7] as well as the ^{13}C signal from C-3 of *sn*-glycerol 3-phosphate, have also been used as probes to determine pH.

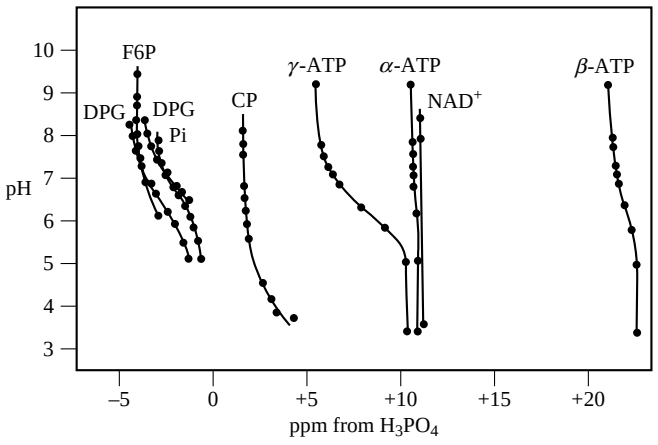

Figure 1 The pH-dependent chemical shift behavior of a variety of biological organic phosphates. Chemical shifts are reported relative to external 1.0 M phosphoric acid. F6P, fructose 6-phosphate; DPG, 2,3-diphosphoglycerate; CP, carbamyl phosphate; Pi, inorganic phosphate; ATP, adenosine triphosphate. (Reproduced by permission from R. B. Moon and J. H. Richards[1])

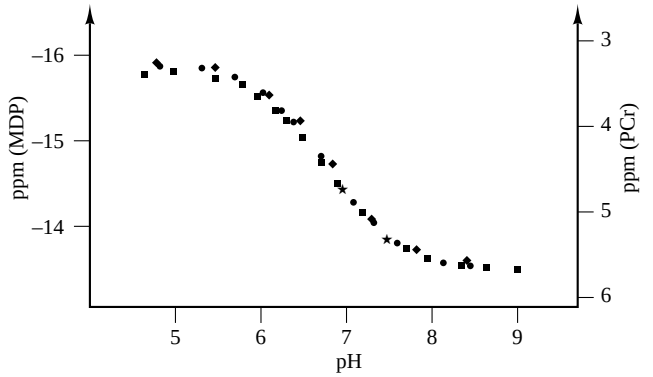

Figure 2 Variation of the chemical shift of inorganic phosphate with solution pH. The chemical shift is expressed relative to two different standards: methylene diphosphonate (MDP) and phosphocreatine (PCr) at pH 7. Solutions containing 10 mM inorganic phosphate and 10 mM phosphocreatine were adjusted to various ionic strengths by addition of KCl or NaCl and titrated at 37 °C by addition of HCl and KOH or NaOH. Symbols: ◆ 120 mM KCl; ● 160 mM KCl; ■ 200 mM KCl; ★ 160 mM NaCl. (Reproduced by permission of Clarendon Press, from D. G. Gadian, 'Nuclear Magnetic Resonance and its Applications to Living Systems', 1982, p. 32)

The introduction of wide-bore magnets and whole body spectrometers that operate at fields from 1.5 to 7 T, permit observations of perfused organs, whole animals, and humans. Surface coils[8] or localization protocols such as image-selected in vivo spectroscopy[9] and chemical shift imaging[9,10] pulse sequences have become popular methods for acquiring a ^{31}P signal from a specific volume element of the subject. Such instruments and techniques can give important information from liver, kidneys, muscle, and brain, as well as cell cultures and ex vivo tissue samples.

2 RELIABILITY

The inherent precision of MRS measurements of pH in favorable circumstances is around 0.06 pH units.[11] In real biological samples, additional sources of error arise due to partial volume effects caused by the signal from the region of interest being compromised by signal from other regions of the sample. For example, the ^{31}P spectra of in vivo liver often contain a phosphocreatine peak whose source is the surrounding muscle. Even for a signal from a homogenous tissue or cell population, the same substance in various compartments can complicate the interpretation by giving rise to more than one signal. For example, studies on various tumors[12] reveal that the signal for inorganic phosphate originates from about 65% intracellular phosphate and 35% phosphate in the extracellular space. Accordingly, an observation of inorganic phosphate in tumors reports a pH that is somewhat weighted toward the intracellular pH despite the fact that the extracellular volume of a tumor sample exceeds that of normal tissue.

Mitochondrial preparations show two signals for inorganic phosphate, one within the mitochondria, the other from the medium.[11] The different pH values arise because of pH gradients across the membranes that separate the compartments; in the cases discussed, the magnitude of the pH differences accord with Mitchell's chemosmotic hypothesis.[13] Signals can also arise from different intracellular compartments as in aerobic preparations of rat liver; one signal represents cytoplasmic phosphate, the other comes from phosphate within the mitochondria that are so abundant in such samples.

3 CANCER

One of the earlier and significant contributions of MRS pH measurements concerned the intracellular pH of tumors, which was found to be from neutral to alkaline,[12,14–16] in direct contrast with the standard belief of the day that tumors were acidic.[17,18] Tumors produce excess lactic acid (because of appreciable anaerobic metabolism) suggesting an acidic intracellular pH, a surmise which studies with microelectrodes supported.[18] Thus MRS results gave a pH in the 6.9–7.4 range, whereas microelectrodes reported pH values in the 5.6–7.6 range. In fact, tumor cells do contain unusually high amounts of anionic lactate[19] (not lactic acid as was once assumed) because they probably export the protons which then accumulate in the extracellular regions in unusually large amounts because of the incomplete equilibration that results from the compromised blood circulation in many solid tumors. In these circumstances microelectrodes report more the extracellular acidic pH than the neutral intracellular pH that MRS allows one to observe noninvasively. This result has proved significant in rational design of anticancer drugs.

4 MUSCLE

Moderate exercise of muscle leads to intracellular acidosis. Indeed the pH can drop from 7.1 to values as low as 6.0.[20] After stopping exercise, the pH recovers to normal values within 1 min. Some protocols for moderate exercise show little or no decrease in intracellular pH.[21] As one would expect, more vigorous exercise, or exercise under ischemic conditions, causes a more profound intramuscular acidosis,[22] as shown in Figure 3. Interestingly, and reassuringly for athletes and fitness fans, similar levels of exercise after training cause significantly less acidification than that for untrained individuals and this benefit extends even to those muscles not specifically trained.[20] Exercise protocols can also be used to study the pathology of various muscle diseases. For example, patients with myotonic dystrophy show a smaller decrease in intramuscular pH with exercise, and their muscles also return more rapidly to a normal value than do those of controls.[23] Furthermore, patients who lack glycogen phosphorylase (McArdles syndrome) actually manifest the expected increase in intramuscular pH due to the unmasking of the alkalinizing hydrolysis of phosphocreatine to phosphate and creatine.

5 HEART

To monitor transient ischemia, the effects on heart muscle of occlusion of the coronary artery followed by reperfusion have been monitored by ^{31}P MRS. In a perfused heart ligation, occlusion of the left anterior descending artery[24,25] caused a decrease in pH from 7 to 6.7. In a globally ischemic heart, the

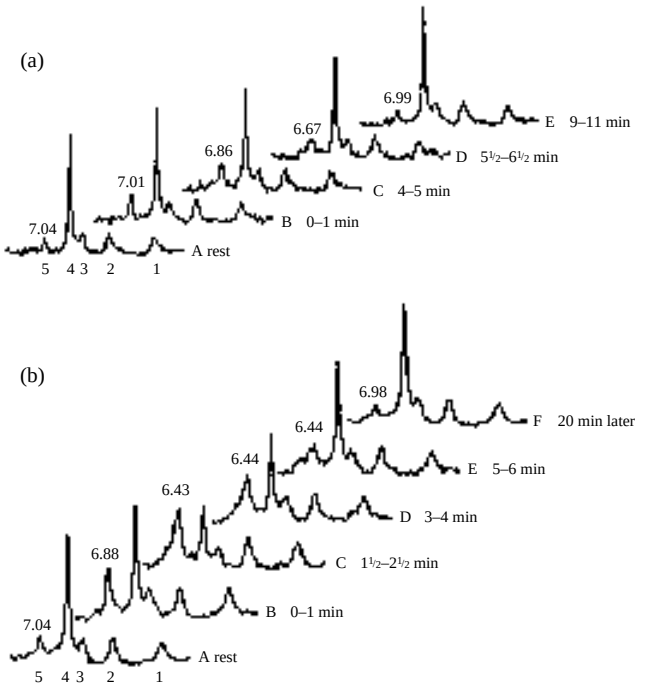

Figure 3 Phosphorus-31 NMR spectra in a control subject showing the effects of (a) normal aerobic exercise and (b) ischemic exercise. A 1.9 T, 20 cm bore magnet and a 4.5 cm surface coil were used to acquire signal from about 25 mL of the subject's flexor compartment of the forearm. Phosphorus-31 spectra were recorded at 32.5 MHz with an interpulse delay of 2 s, sweep width 4 kHz, and a line broadening of 6 Hz used before Fourier transformation. The exercise protocol involved flexion of fingers at 2 s intervals. The signals are assigned as follows: 1, 2, and 3, the β, α, and γ phosphates of ATP; 4, phosphocreatine; and 5, inorganic phosphate. The pH value given above each inorganic phosphate signal was determined from the frequency separation of the inorganic phosphate and phosphocreatine signals. (a) Zero minutes corresponds to the start of exercise and was maintained for 5 min. Spectra A and E were accumulated with 64 scans; the other spectra were accumulated with 32 scans. The pH value is an average in spectra where the inorganic phosphate signal is split into two components. (b) Zero minutes corresponds to the start of exercise and was maintained for 1.5 min. Arterial occlusion was maintained from zero minutes to 3 min with arterial flow being restored after this period. (Reproduced by permission from B. D. Ross, G. K. Radda, D. G. Gadian, G. Rocker, M. Esiri, and J. Falconer-Smith, *N. Engl. J. Med.*, 1981, **304**, 1338)

pH falls to 6.2.[26,27] In dogs, occlusion of the left descending coronary artery caused the pH to decrease to 5.9; in some cases the pH recovered spontaneously to preocclusion values presumably because of the development of collateral flow to the affected myocardium.[28] Other hearts showed more permanent changes reflecting a decreased pH that was consistent with the ischemia. These pH changes occurred within minutes of the occlusion.

One can even observe the results of exercise-induced ischemia in the human heart in vivo, despite the large ^{31}P signal from the 2,3-diphosphoglycerate in the red cells of the blood within the ventricles. Heart muscle cells have a relatively high density of mitochondria (30%) such that one might actually be able to observe the pH gradient between the mitochondria and the cytosol. Such differences have been demonstrated in other tissues, for example lineshape analysis of ^{31}P spectra leads to a pH gradient of 0.5 in skeletal muscle[29,30] and kidney.[31] In the perfused rat heart, deoxyglucose, which is unable to enter mitochondria, and upon phosphorylation becomes trapped in the cytoplasm, gives the same pH value as that determined by using inorganic phosphate.[32] This study suggested that the pH observed in heart muscle reflects that in the cytoplasm, possibly because intramitochondrial inorganic phosphate cannot be observed with present-day technology due to its low concentration and/or due to a broadened signal. Alternatively, the pH gradient may be small in heart muscle.

Calculations have shown that a pH difference of 0.3–0.4 is necessary to resolve the peaks for inorganic phosphate within or outside a cell when 65% of the observed MRS signal represents intracellular phosphate.[33] Nonetheless, separate MRS signals for Walker's tumors were unobservable even though the ΔpH was 0.6, as calculated from the distribution of lactate across the cell membrane; this failure was attributed to the poor signal-to-noise characteristic of this type of tumor.

6 BRAIN

Studies in the brain of animal models also show a similar decrease in pH due to ischemia. Unfortunately, correlation of these findings with other parameters such as preischemic glucose levels or the exogenous introduction of base to alleviate trauma, have provided inconclusive, and even in some cases contradictory, results.[34,35]

7 FUTURE

Difficulties occasioned by low signal-to-noise or poor resolution hamper many studies now being undertaken with in vivo MRS studies of human pathologies. The introduction of whole body spectrometers with higher fields, the use of alternative nuclei such as ^{15}N (spectra of which can now[36,37] be acquired in vivo), the ability to obtain high-resolution data from smaller, well-defined volume elements, the use of other endogenous metabolites or the introduction of exogenous reporting substances, provide hopeful new avenues to achieve noninvasively more reliable information about the metabolic status of organs, tissues, and other biological samples. The resulting insights will greatly broaden our understanding of the complex integrated metabolism of intact living systems. For humans, these advances can significantly enhance the power of diagnosis.

8 RELATED ARTICLES

Brain MRS of Human Subjects; Brain MRS of Infants and Children; Brain Neoplasms in Humans Studied by Phosphorus-31 NMR Spectroscopy; In Vivo Hepatic MRS of Humans; Kidney, Prostate, Testicle, and Uterus of Subjects Studied by MRS; Peripheral Muscle Metabolism Studied by MRS; Tissue Behavior Measurements Using Phosphorus-31 NMR; Whole Body Studies: Impact of MRS.

9 REFERENCES

1. R. B. Moon and J. H. Richards, *J. Biol. Chem.*, 1973, **248**, 7276.
2. C. M. Spickett, N. Smirnoff, and R. G. Ratcliffe, *Plant Physiol.*, 1993, **102**, 629.
3. G. Wegener, N. M. Bolas, and A. A. G. Thomas, *J. Comp. Physiol. B*, 1991, **161**, 247.
4. A. Madden, M. O. Leach, D. J. Collins, and G. S. Payne, *Magn. Reson. Med.*, 1991, **19**, 416.
5. J. S. Beech and R. A. Iles, *Magn. Reson. Med.*, 1991, **19**, 386.
6. F. F. Brown, I. D. Campbell, P. W. Kuchel, and D. L. Rabenstein, *FEBS Lett.*, 1977, **82**, 12.
7. S. R. Williams, D. G. Gadian, E. Proctor, D. B. Sprague, D. F. Talbot, F. F. Brown, and I. R. Young, *Biochem. Soc. Trans.*, 1985, **13**, 839.
8. J. J. H. Ackerman, T. H. Grove, G. G. Wong, D. G. Gadian, and G. K. Radda, *Nature (London)*, 1980, **283**, 167.
9. R. J. Ordidge, A. Connelly, and J. A. B. Lohman, *J. Magn. Reson.*, 1986, **66**, 283.
10. T. R. Brown, B. M. Kincaid, and K. Ugurbil, *Proc. Natl. Acad. Sci. USA*, 1982, **79**, 3523.
11. S. R. Smith, R. D. Griffiths, P. A. Martin, and R. H. Edwards, *Radiology*, 1989, **173**, 572.
12. M. Stubbs, Z. M. Bhujwalla, G. M. Tozer, L. M. Rodrigues, R. J. Maxwell, R. Morgan, F. A. Howe, and J. R. Griffths, *NMR Biomed.*, 1992, **5**, 351.
13. P. Mitchell, *Biochem. Soc. Trans.*, 1976, **4**, 399.
14. S. Ogawa, H. Rottenberg, T. R. Brown, R. G. Schulman, C. L. Castillo, and P. Glynn, *Proc. Natl. Acad. Sci. USA*, 1978, **75**, 1796.
15. J. R. Griffiths, A. N. Stevens, R. A. Iles, R. E. Gordon, and D. Shaw, *Biosci. Rep.*, 1981, **1**, 319.
16. R. A. Iles, A. N. Stevens, and J. R. Griffiths, *Prog. Nucl. Magn. Reson. Spectrosc.*, 1982, **15**, 49.
17. J. R. Griffiths, E. Cady, R. H. T. Edwards, V. R. McCready, D. R. Wilkie, and E. Wiltshaw, *Lancet*, 1983, **1**, 1435.
18. J. R. Griffiths, *Br. J. Cancer*, 1991, **64**, 425.
19. J. L. Wike-Hooley, J. Haveman, and H. S. Reinhold, *Radiother. Oncol.*, 1984, **2**, 343.
20. O. Warburg, 'The Metabolism of Tumors', Translated into English by F. Dickens, Constable, London, 1930.
21. J. R. Griffiths, Z. M. Bhujwalla, R. C. Coombes, R. J. Maxwell, C. J. Midwood, R. J. Morgan, A. H. Nras, P. Perry, M. Prior, and A. Prysor Jones, *Ann. N.Y. Acad. Sci.*, 1987, **508**, 193.
22. B. D. Ross, N. Farrow, and D. M. Freeman, '31-P MRS: A Tool for Studying Muscle Metabolism', Presented at the 8th Congress of Sports Medicine of the A.Z. ST, Brugge, Belgium, 1989.
23. G. D. Marsh, D. H. Paterson, J. J. Potwarka, and R. T. Thompson, *J. Appl. Physiol.*, 1993, **75**, 648.
24. D. J. Taylor, G. J. Kemp, C. G. Woods, J. H. Edwards, and G. K. Radda, *J. Neurolog. Sci.*, 1993, **116**, 193.
25. H. Mayr, D. M. Freeman, and B. D. Ross, *J. Appl. Cardiol.*, 1989, **4**, 153.
26. J. C. Chatham, D. M. Freeman, P. B. Barker, E. A. Moress, and B. D. Ross, *J. Appl. Cardiol.*, 1989, **4**, 117.
27. W. E. Jacobus, and M. L. Weisfeldt, *Biophys. J.*, 1981, **33**, 33.
28. P. B. Garlick, G. K. Radda, and P. J. Seeley, *Biochem. J.*, 1979, **184**, 547.
29. P. A. Bottomley, L. S. Smith, S. Brazzamano, L. W. Hedlund, R. W. Redington, and R. J. Herfkens, *Magn. Reson. Med.*, 1987, **5**, 129.
30. S. J. W. Busby, D. G. Gadian, G. K. Radda, R. E. Richards, and P. J. Seeley, *Biochem. J.*, 1978, **170**, 103.
31. D. I. Hoult, S. J. W. Busby, D. G. Gadian, G. K. Radda, R. E. Richards, and P. J. Seeley, *Nature (London)*, 1974, **252**, 285.
32. I. A. Bailey, S. R. Williams, G. K. Radda, and D. G. Gadian, *Biochem. J.*, 1981, **196**, 171.
33. A. A. Maudsley, S. K. Hilal, W. H. Perman, and H. E. Simon, *J. Magn. Reson.*, 1983, **51**, 147.
34. R. J. T. Corbett, A. R. Laptook, R. L. Nunally, A. Hassan, and J. Jackson, *J. Neurochem.*, 1988, **51**, 1501.
35. P. L. Hope, E. B. Cady, D. T. Delpy, N. K. Ives, R. M. Gardiner, and E. O. R. Reynolds, *J. Neurochem.*, 1988, **50**, 1394.
36. K. Kanamori, F. Parivar, and B. D. Ross, *NMR Biomed.*, 1993, **6**, 21.
37. K. Kanamori and B. D. Ross, *J. Neurochem.*, 1997, **68**, 1209.

Biographical Sketches

Neil A. Farrow. *b* 1966. B.Sc., 1988, Portsmouth (UK). Currently graduate student Caltech; expected graduation date 1996. One publication. Research interests include structure/function relationships of proteins with DNA, NMR spectroscopy of proteins/DNA, in vivo MRS, and electron transfer in proteins.

John H. Richards. *b* 1930. B.S., 1951, U.C. Berkeley; B.Sc., 1953, Oxford (Rhodes Scholar); Ph.D., 1955, U.C. Berkeley; Harvard, 1955–1957; Caltech 1957–present. Approx. 150 publications. Research interests include structure–function relationships in biological molecules and biophysical studies of protein function.

Brian D. Ross. *b* 1938. B.Sc., 1958, University College, London. D.Phil., 1966, University of Oxford. M.B., 1961, University College Hospital, London. F.R.C.S., 1973, Royal College of Surgeons, London. M.R.C.Path., 1976, Royal College of Pathologists, London. 1989, F.R.C.Path. University of Oxford lecturer, Metabolic Medicine. Director, Renal Metabolism Unit and Consultant Chemical Pathologist, Radcliffe Infirmary, Oxford, 1976–84. Director of Clinical Spectroscopy Programs at Radcliffe Infirmary, Oxford, 1981–84, Hammersmith Hospital, London, 1986–88, and Huntington Medical Research Institutes, Pasadena, CA, 1986–present. Visiting Associate, California Institute of Technology, 1986–present.

Phosphorus-31 Magnetization Transfer Studies In Vivo

Ruth M. Dixon

Department of Biochemistry, University of Oxford, Oxford, UK

1 BACKGROUND AND THEORY

The rates of certain chemical reactions can be studied by magnetization transfer techniques, the theory of which was first developed by Forsén and Hoffman.[1] The theory and uses of these techniques for measuring enzyme-catalyzed reaction rates are reviewed extensively elsewhere.[2–6] This article will therefore give only a brief outline of the theoretical background, concentrating on the applications of the methods in living animals, and will include the small number of studies in human subjects.

1.1 Techniques

Perturbation of the magnetization of a species in chemical exchange with others causes a change in the magnetization of the other species that depends in general not only on the exchange rate constants k_{forward} and k_{reverse}, but also on the spin–lattice relaxation times (T_1) of the exchanging species. For a reaction involving two species, A↔B, the unidirectional fluxes through the reaction are k_{forward}[A] for the forward reaction and k_{reverse}[B] for the reverse reaction. The measured rate constants (k) are always first-order, or pseudo first order, that is, for reactions involving several substrates, the apparent rate constant is a function of the concentrations of the other metabolites. Two main types of experiment may be performed to measure the forward and reverse rate constants. In the first, a continuous radiofrequency irradiation selectively saturates one of the exchanging species and the changes in the other species are observed, either as a function of the time of irradiation, or at steady state. This experiment is known as saturation transfer (ST). In the second type of experiment [inversion transfer (IT)], a selective inversion pulse is applied to one of the exchanging resonances, and the temporal changes of all of the resonances are observed. In both experiments the various recovery curves of the exchanging species are fitted to suitable solutions of the Bloch equations modified for chemical exchange.[1–6] For instance, in a steady-state ST experiment where species B is irradiated and species A is measured, the rate constant is given by:

$$k_{\text{A}\to\text{B}} = \frac{1}{T_1}\left[\frac{M_0}{M_s} - 1\right]$$

where T_1 is the longitudinal relaxation time of A in the absence of chemical exchange, M_s is the signal from A in the presence of a saturating pulse on B, and M_0 is the signal from A in the presence of a saturating pulse an equal distance on the opposite side of A. In this type of experiment, a separate determination of T_1 (with irradiation of the exchanging species) is required. (See also ***Selective Excitation in MRI and MR Spectroscopy***).

Two-dimensional (2D) techniques (analogous to NOESY experiments) give cross peaks between resonances that are in chemical exchange. The rate constants can be derived from the dependence of the cross-peak volumes on the mixing time. Selective pulses are not required, but a separate 2D experiment is required for each delay time. Two-dimensional experiments have been implemented in vivo (reviewed in Kuchel[6]) but there have been few applications in whole organisms because of time constraints.

The range of exchange rates that can be measured by magnetization transfer techniques is limited by the chemical shift difference of the exchanging species (in Hz), and by the T_1 times. For exchange rates that are fast compared with the chemical shift difference, only one resonance at an average chemical shift is observed, while for very slow reactions, where $k << 1/T_1$, relaxation will occur before significant exchange has taken place. Therefore rate constants of the same order of magnitude as $1/T_1$ are optimal for measurement by magnetization transfer.

1.2 Reactions Studied In Vivo

The reaction most widely studied in vivo is the reaction catalyzed by creatine kinase (CK):

$$\text{PCr}+\text{ADP}+\text{H}^+ \rightleftharpoons \text{Cr}+\text{ATP}$$

The phosphate of phosphocreatine (PCr) exchanges with the γ-phosphate of adenosine 5′-triphosphate (ATP γ-*P*). The role of CK is not fully understood, but various possibilities have been discussed (reviewed in Wallimann et al.[7] and by Saks et al.[8]). It may simply buffer the free ATP and adenosine diphosphate (ADP) levels during periods of energy utilization, or PCr may act particularly in muscle as a transporter for 'high-energy' phosphate groups, by diffusing from the mitochondria to the myofibrils. Since PCr and Cr have higher diffusion coefficients in vivo than ATP and ADP, and Cr concentration is much higher than that of ADP, they may facilitate the exchange between the energy-producing and energy-utilizing sites in the cell. The calculation of free ADP concentration from the NMR-measured PCr/ATP ratio, the proton concentration, and the CK equilibrium constant, assumes that the reaction is at equilibrium in each tissue of interest. Magnetization transfer measurements have been used to confirm whether this is indeed the case, using the principle that if the flux through CK is much faster than the net utilization (or production) of ATP by the cell, the enzyme may be considered to be at equilibrium. The interpretation of these studies is, however, not always straightforward, and it is suggested that not all of the Cr flux is visible to NMR as a consequence of compartmentalization and immobilization of enzymes and substrates.[9]

Other enzymatic reactions that have been studied by magnetization transfer methods in vivo are those involving ATP exchange, for instance, inorganic phosphate (Pi) → ATP γ-*P* exchange, catalyzed by the mitochondrial F_1F_0 ATPase, glyceraldehyde-3-phosphate dehydrogenase, and phosphoglycerate

kinase, and ATP γ-*P* → Pi exchange, catalyzed by various ATPases. The exchange between ADP and ATP β-phosphates is also catalyzed by many enzymes, and so an apparent exchange is often seen between ATP γ-*P* and ATP β-*P*, which is in fact due to the saturation of ADP β-*P*, at less than 1 ppm upfield of ATP γ-*P*. As yet unexplained is the apparent exchange between ATP γ-*P* and ATP α-*P* that has been seen in some systems.

A rather different set of studies, that may also be termed magnetization transfer, involves the irradiation of the broad resonance that underlies the spectra from brain, liver, and some other tissues. These are discussed in Section 4.

2 WHOLE ANIMAL STUDIES

Most ^{31}P magnetization transfer studies in vivo have involved the CK reaction in skeletal muscle, heart, and brain. Extensive investigations of isolated systems such as perfused organs, immobilized cells, and tissue slices, have also been undertaken,[2–5,10] but these are beyond the scope of this article (see also ***Cells and Cell Systems MRS***).

2.1 Skeletal Muscle

Creatine kinase is found in the skeletal muscle of all mammalian species. During exercise, ATP is hydrolyzed to ADP, and this is rephosphorylated to ATP by CK. This process is so rapid that the level of ATP generally remains constant even during severe exercise, until the PCr level falls to zero. In vitro, the rate of ATP production from PCr increases as the ADP concentration is increased, suggesting that the reaction is substrate-controlled. In studies of intact rat skeletal muscle in vivo, however, no such increase with workload and calculated [ADP] was observed.[11] Indeed in one study, the flux from PCr to ATP was significantly lowered as the workload increased, despite a calculated ninefold increase in [ADP], which would be expected to result in a 70% increase in flux.[12] The CK reaction does not appear to be obligatory for muscle metabolism, in that rats fed with an analog of creatine, β-guanidinopropionic acid (β-GPA), have a 12-fold lower flux through CK (PCr → ATP) and 10% of the normal PCr concentration, but normal physiological performance under electrical stimulation.[13] It was suggested that the results supported a role for CK in preventing sudden large changes in [ADP] (which may regulate oxidative ATP synthesis), but a role for PCr in facilitating diffusion of high-energy phosphates was not ruled out, since adaptive changes in muscle fiber type or blood flow could have occurred over the 6–10 weeks of β-GPA feeding. A more direct manipulation of CK activity was achieved by Brosnan et al.,[14] who expressed the B isozyme of CK (normally found only in brain and heart) in the skeletal muscle of transgenic mice. The normal levels of the M isozyme were also expressed, resulting in a 49% increase in total CK activity in vitro. No changes in metabolite levels were found (confirming that the reaction is at equilibrium in normal and transgenic mice) but the ATP → PCr flux (measured by saturation transfer) doubled. It is possible that this reflects the lower Michaelis constant (K_m) for ADP of the B isozyme, although earlier studies did not show a simple relationship between [ADP] and k.[11,12] Transgenic mice lacking the M isozyme of CK were produced by van Deursen et al.[15] These mice had only mitochondrial CK activity in their muscles, and normal levels of PCr and ATP, but no detectable flux through CK, measured by IT. Surprisingly, the PCr level fell during exercise and recovered with a similar timecourse to the controls, but this could have been catalyzed by the small amount of the mitochondrial isozyme, without the flux being detectable in the IT experiment. Studies of CK kinetics in transgenic mice have been reviewed by Nicolay et al.[16]

During steady state exercise and at rest, the ratio of the forward to reverse fluxes of CK should be equal, since the metabolite concentrations are constant. This was found to be the case in a study of resting rat muscle, obtained by saturation transfer.[17] In a study of rabbit muscle[18] the forward and reverse fluxes were equal when measured by fitting the initial recovery rates of an inversion transfer experiment, and the forward flux (PCr → ATP) determined by saturation transfer agreed well with the inversion recovery rates, but the reverse flux determined by saturation transfer was significantly lower. Although competing ATPase reactions would be able to account for this discrepancy, no ATP γ-*P* to Pi exchange was observed. It has been suggested that compartmentation of intracellular ATP may account for this type of discrepancy.[19] A 2D study of rat muscle found no significant differences between the forward and reverse fluxes, and no exchange between ATP γ-*P* and Pi, ATP α-*P*, or ATP β-*P*,[20] in contrast to the saturation transfer studies.[11,12] The differences arise from the fact that the 2D technique, like the IT experiment, follows the transfer of a transient pulse of magnetization, and would not detect small pools of exchanging metabolites that would be detected in the ST experiment, in which the pool is continuously labeled. A saturation transfer study of tetanically stimulated rat muscle showed that ATP turnover (Pi → ATP flux) showed an approximately linear dependence on calculated free [ADP], up to approximately an ADP concentration of about 90 μM.[21] There are difficulties with measuring the ATP β-*P* to ADP β-*P* flux, as shown by Le Rumeur et al.[22] They found that the overall rate of β-phosphoryl conversion increased with exercise in rat muscle but did not reach the expected rate, which should equal or exceed that of the reverse CK reaction, ATP→PCr (since this reaction includes β-phosphoryl conversion). The authors suggest that the flux is underestimated either because of compartmentation of ATP or because of imperfect saturation of ATP β-*P* (if its signal is broadened by binding to intracellular proteins).

Since PCr takes part only in the reaction catalyzed by CK, the forward flux (PCr → ATP) can be measured accurately by saturation of ATP γ-*P*. An image of the intensity ratio of PCr with and without irradiation of ATP γ-*P* therefore reflects localized CK activity. Such an image was produced by Hsieh and Balaban,[23] who showed that CK activity did not vary across the resting hind limb muscles of the rabbit.

2.2 Heart

The CK system has been investigated extensively in the heart, both in the isolated perfused heart and in vivo, in order to understand the metabolic coupling between oxidative phosphorylation and energy demand. Studies of perfused hearts led

to contradictory results concerning the relationship between the flux through CK and oxidative metabolism, and questions remain about the regulation in vivo.[24] Ingwall and co-workers showed that the pseudo-first-order rate constant (k) for myocardial PCr → ATP exchange in the open-chested rat correlated closely with the rate pressure product (a measure of cardiac function) whether this was depressed by hypoxia,[25] or increased by norepinephrine infusion.[26] The change in k was accompanied by significant changes in [PCr], [ATP], and calculated free [ADP]. It was concluded that the flux through CK is controlled by the availability of ATP during hypoxia, and by ADP levels during inotropic stimulation. In contrast, in the pig heart in vivo, a similar infusion of norepinephrine produced no significant increase in rate constant over a 2.5-fold increase in rate pressure product, nor any changes in [PCr] or [ATP] (and hence in calculated [ADP]).[27] Pacing the canine heart in vivo so as to double oxygen consumption, led to no changes in CK flux. The flux was estimated to be at least 10 times the flux through oxidative phosphorylation, confirming that the CK reaction is at equilibrium in this tissue.[28] The transmural variation of the CK reaction was studied recently in the open-chested dog heart by combining one-dimensional (1D) localization with saturation transfer measurements. A 61% increase in the PCr → ATP flux was observed from the endocardium to the epicardium, in the presence of constant ATP/PCr ratios. This difference could not be explained by differences in CK levels, oxygen consumption, or substrate levels, and led the authors to invoke possible differences in the rate constant of the reaction.[29] Discrepancies between the forward and reverse fluxes were found in the rat heart in situ, which could not be attributed to ATP → ADP or ATP → Pi exchange, but it was suggested that they could be due to a small pool of exchanging ATP in or near the mitochondria.[3,30]

ATP synthesis rates were measured in the intact dog heart by measuring Pi → ATP flux before and after a period of ischemia, and an estimate of the contribution of the glycolytic enzymes glyceraldehyde 3-phosphate dehydrogenase and phosphoglycerate kinase to this exchange was made.[31]

An interesting use of saturation transfer (ST) to measure myocardial pH was demonstrated in sheep, dog, and cat hearts in vivo.[32] The NMR signal from intracellular Pi in the heart is obscured by resonances from 2,3-diphosphoglycerate and Pi in the blood. ATP is in exchange with Pi in the heart, so difference spectra with and without saturation of ATP γ-P contained a resonance from myocardial Pi (a similar exchange in blood could not be demonstrated). The pH could be obtained from the chemical shift of Pi and was found to be about pH 7.0, that is, considerably lower than previous estimates (***pH Measurement In Vivo in Whole Body Systems***).

2.3 Brain

The brain also contains high levels of CK. The first study in vivo showed that the reaction is at equilibrium in the anesthetized rat brain, since the forward flux through CK (PCr→ATP) was about five times the steady state rate of ATP synthesis.[33] A lower reverse flux through CK was observed in this ST study, while a 2D study showed equal forward and reverse rates.[20] This problem was addressed by Degani et al.[34] in a study of the rabbit brain, in which IT data were compared with ST data from the same animals, and by Mora et al.[35] in the monkey brain. The forward and reverse fluxes were equal, within experimental error, when IT data were analyzed, but the reverse flux was undetectably low in an ST experiment when the PCr resonance was irradiated. These results agree with other observations that ST experiments underestimate the ATP → PCr flux when inhomogeneous tissue is studied.[4] Sauter and Rudin found that the CK forward flux (and k_{forward}) correlated linearly with the electroencephalogram intensity in rat brain when brain function was depressed or stimulated pharmacologically.[36]

Mora et al.[37] also produced a map of CK activity in the monkey brain by combining a Hahn spin echo imaging sequence with selective saturation of ATP γ-P. The difference between this image and one obtained with control irradiation showed that CK activity was approximately uniform across the monkey brain in the sagittal plane, but since no slice selection was used, each voxel contained a mixture of white and grey matter. In the developing piglet brain, the CK rate constant and the forward flux were measured by ST localized by spectroscopic imaging and were found to be higher in white than in grey matter.

2.4 Other Organs

Magnetization transfer techniques have found few applications in other organs in the whole animal. Koretsky et al.[39] studied the rat kidney in vivo with chronically implanted radiofrequency coils. The Pi → ATP rate constant was estimated to be $0.12 \pm 0.03\ s^{-1}$, somewhat less than that obtained in the isolated perfused rat kidney ($0.35 \pm 0.05\ s^{-1}$). The CK reaction has also been studied in an implanted tumor in the hind limb of a rat.[6]

3 HUMAN STUDIES

Few studies have involved human subjects, and none, so far, have involved pathological conditions in patients. In skeletal muscle at 1.9 T, Rees et al.[40] found that the PCr → ATP flux was significantly reduced with exercise to 64% of the resting value of $8.5 \pm 0.7\ mM \cdot s^{-1}$ in 12 normal subjects. This decrease was similar to that found in rat muscle,[11,12] but in contrast to the expected dependence of the flux on [ADP] and pH. More recently, Goudemant et al. found that if the exercise intensity was varied, the decrease in flux was found only at the highest workload.[41] These authors argue that the results are not consistent with a 'shuttle' role for PCr in skeletal muscle, since this would lead to a functional coupling between energy production and the CK reaction, which was not, in fact, found. Instead, the role of the CK reaction is likely to be energy buffering. They suggest that the results could be explained by the formation at high workloads of a dead-end enzyme–Cr–ADP complex, stabilized by anions such as chloride and bicarbonate, as suggested by McFarland et al. from studies of cat muscle ex vivo.[42] Walliman, however, argued that NMR may not accurately determine the total CK flux in muscle, and that these results are caused by varying degrees of compartmentalization during exercise.[9]

A 1D map of CK activity in brain was obtained by Cadoux-Hudson et al.[43] using phase-modulated rotating frame imaging combined with ST (see also ***Rotating Frame Methods for Spectroscopic Localization***). Figure 1 shows a typical data set,

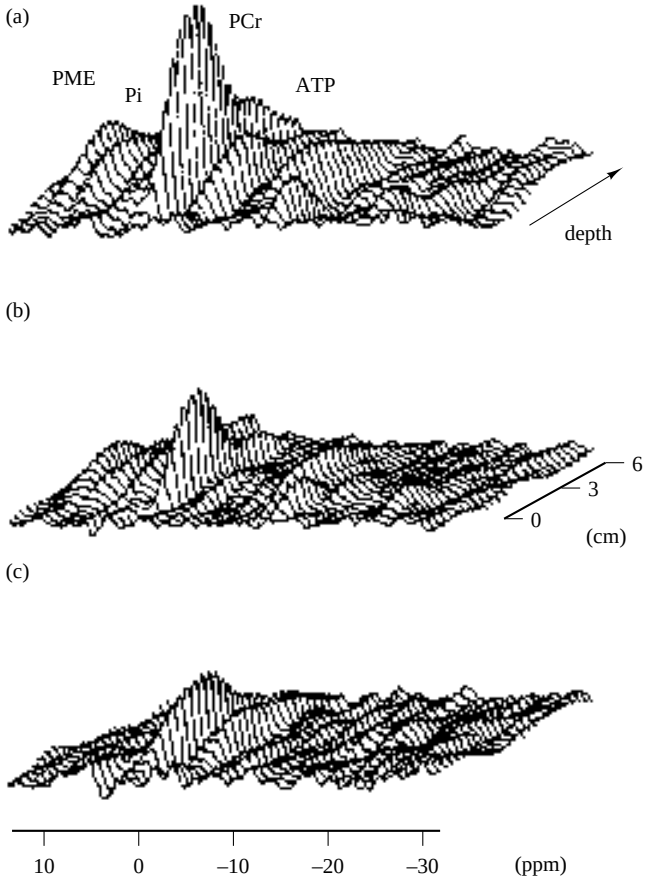

Figure 1 Stack plots of ^{31}P phase-modulated rotating frame images of human brain with (a) control irradiation; (b) irradiation of ATP γ-*P*; (c) the subtraction of (b) from (a). Repetition delay = 15 s, total number of transients for each data set = 80. (Reproduced by permission of FASEB from Cadoux-Hudson et al.[43])

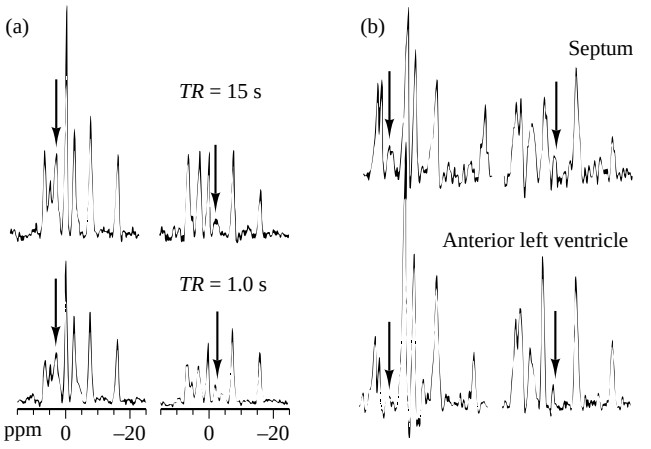

Figure 2 (a) ^{31}P NMR spectra of human brain (entire axial section) with saturating irradiation applied at ±2.7 ppm (arrows). Repetition delay (*TR*) = 1 s or 15 s. (b) Localized ^{31}P NMR spectra from 1-cm-thick sections through the anterior wall (lower) and septum (upper) of the heart in a resting volunteer with saturating irradiation applied at ±2.7 ppm. (Reproduced by permission of Academic Press, from Bottomley and Hardy[44])

with control and on-resonance irradiation. The CK activity was significantly greater in regions of predominantly gray matter ($k = 0.30 \pm 0.04$ s^{-1}, flux = 1.56 ± 0.30 mmol^{-1} L^{-1} s^{-1}) than in white matter ($k = 0.16 \pm 0.02$ s^{-1}, flux = 0.72 ± 0.12 mmol^{-1} L^{-1} s^{-1}) in six normal subjects. In contrast, Bottomley and Hardy[44] found no significant variation of CK activity with brain region in an ST 2D chemical shift imaging (CSI) experiment in one subject at 4 T ($k = 0.42$ s^{-1}, flux = 2.1 mmol^{-1} kg wet weight^{-1} s^{-1}). One-dimensional CSI with ST in the human heart resulted in a forward rate constant of 0.51 s^{-1}, and a flux of 5.6 mmol^{-1} kg wet weight^{-1} s^{-1}.[44] Figure 2 shows spectra from this study, with control and on-resonance irradiation of ATP γ-*P* in heart and brain. The decrease in PCr with irradiation of ATP γ-*P* can clearly be seen in both tissues.

The technique of functional MRI based changes dependent on blood oxygenation was recently used together with localized ^{31}P ST to measure the activation of the visual cortex during visual stimulation.[45] This study showed that the forward rate constant for PCr→ATP γ-*P* increased significantly within the visual cortex from 0.56 ± 0.19 s^{-1} (control) to 0.76 ± 0.29 s^{-1} during visual stimulation, in the absence of any detectable change in PCr/ATP or PCr/Pi ratios.

4 BASELINE FLATTENING AND PHOSPHOLIPID BILAYERS

The ^{31}P NMR spectra of brain, liver, kidney, and breast all show a broad signal in the phosphodiester region that cannot wholly be accounted for by the water-soluble phosphodiesters glycerophosphorylcholine and glycerophosphorylethanolamine. A study of liver and brain slices in vitro, and of liver in vivo, showed that this resonance was characteristic of phospholipid bilayers broadened by shielding anisotropy.[46] Irradiation of the wings of the broad resonance, 28 ppm from its maximum, completely eliminated the broad resonance from rat liver spectra in vivo, allowing the remaining resonances to be quantified more accurately.

5 RELATED ARTICLES

Cells and Cell Systems MRS; pH Measurement In Vivo in Whole Body Systems; Rotating Frame Methods for Spectroscopic Localization; Selective Excitation in MRI and MR Spectroscopy.

6 REFERENCES

1. S. Forsén and R. A. Hoffman, *J. Chem. Phys.*, 1963, **39**, 2892.
2. J. R. Alger and R. G. Shulman, *Q. Rev. Biophys.*, 1984, **17**, 83.
3. A. P. Koretsky and M. W. Weiner, in 'Biomedical Magnetic Resonance', eds. T. L. James and A. R. Margulis, Radiology Research and Education Foundation, San Franscisco, 1984, p. 209.
4. K. M. Brindle, *Prog. NMR Spectrosc.*, 1988, **20**, 257.
5. M. Rudin and A. Sauter, in 'NMR, Basic Principles and Progress', eds. P. Diehl, E. Fluck, H. Günther, R. Kosfeld, and J. Seelig, Springer, Berlin, 1992, Vol. 27, p. 257.
6. P. W. Kuchel, *NMR Biomed.*, 1990, **3**, 102.
7. T. Wallimann, M. Wyss, D. Brdiczka, K. Nicolay, and H. M. Eppenberger, *Biochem. J.*, 1992, **281**, 21.

8. V. A. Saks, Z. A. Khuchua, E. V. Vasilyeva, O. Y. Belikova, and A. V. Kuznetsov, *Mol. Cell. Biochem.*, 1994, **133/134**, 155.
9. T. Wallimann, *J. Muscle Cell Res. Cell Motil.*, 1996, **17**, 177.
10. P. G. Morris, *Annu. Rep. NMR Spectrosc.*, 1988, **20**, 1.
11. E. A. Shoubridge, J. L. Bland, and G. K. Radda, *Biochim. Biophys. Acta*, 1984, **805**, 72.
12. E. Le Rumeur, L. Le Moyec, and J. D. de Certaines, *Magn. Reson. Med.*, 1992, **24**, 335.
13. E. A. Shoubridge and G. K. Radda, *Biochim. Biophys. Acta*, 1984, **805**, 79.
14. M. J. Brosnan, S. P. Raman, L. Chen, and A. P. Koretsky, *Am. J. Physiol.*, 1993, **264**, C151.
15. J. van Deursen, A. Heerschap, F. Oerlemans, W. Ruitenbeek, P. Jap, H. ter Laak, and B. Wieringa, *Cell*, 1993, **74**, 621.
16. K. Nicolay, F. A. van Dorsten, T. Reese, M. J. Kruiskamp, J. F. Gellerich, and C. J. A. van Echteld, *Mol. Cell Biochem.*, 1998, **184**, 195.
17. J. A. Bittl, J. DeLayre, and J. S. Ingwall, *Biochemistry*, 1987, **26**, 6083.
18. P. S. Hsieh and R. S. Balaban, *Magn. Reson. Med.*, 1988, **7**, 56.
19. A. P. Koretsky, V. J. Basus, T. L. James, M. P. Klein, and M. W. Weiner, *Magn. Reson. Med.*, 1985, **2**, 586.
20. R. S. Balaban, H. L. Kantor, and J. A. Ferretti, *J. Biol. Chem.*, 1983, **258**, 12787.
21. K. M. Brindle, M. J. Blackledge, R. A. J. Challis, and G. K. Radda, *Biochemistry*, 1989, **28**, 4887.
22. E. Le Rumeur, N. Le Tallec, F. Kernec, and J. D. de Certaines, *NMR Biomed.*, 1997, **10**, 67.
23. P. S. Hsieh and R. S. Balaban, *J. Magn. Reson.*, 1987, **74**, 574.
24. F. Joubert and J. A. Hoerter, *Cell. Mol. Biol.*, 1997, **43**, 763.
25. J. A. Bittl, J. A. Balschi, and J. S. Ingwall, *Circulation Res.*, 1987, **60**, 871.
26. J. A. Bittl, J. A. Balschi, and J. S. Ingwall, *J. Clin. Invest.*, 1987, **79**, 1852.
27. J. F. Martin, B. D. Guth, R. H. Griffey, and D. E. Hoekenga, *Magn. Reson. Med.*, 1989, **11**, 64.
28. L. A. Katz, J. A. Swain, M. A. Portman, and R. S. Balaban, *Am. J. Physiol.*, 1989, **256**, H265.
29. P. M. Robitaille, A. Abduljalil, D. Rath, H. Zhang, and R. L. Hamlin, *Magn. Reson. Med.*, 1993, **30**, 4.
30. A. P. Koretsky, S. Wang, M. P. Klein, T. L. James, and M. W. Weiner, *Biochemistry*, 1986, **25**, 77.
31. P.-M. Robitaille, H. Merkle, E. Sako, G. Lang, R. M. Clack, R. Bianco, A. H. L. From, J. Foker, and K. Ugurbil, *Magn. Reson. Med.*, 1990, **15**, 8.
32. K. M. Brindle, B. Rajagopalan, D. S. Williams, J. A. Detre, E. Simplaceanu, C. Ho, and G. K. Radda, *Biochem. Biophys. Res. Commun.*, 1988, **151**, 70.
33. E. A. Shoubridge, R. W. Briggs, and G. K. Radda, *FEBS Lett.*, 1982, **140**, 288.
34. H. Degani, J. R. Alger, R. G. Shulman, O. A. C. Petroff, and J. W. Pritchard, *Magn. Reson. Med.*, 1987, **5**, 1.
35. B. N. Mora, P. T. Narasimhan, and B. D. Ross, *Magn. Reson. Med.*, 1992, **26**, 100.
36. A. Sauter and M. Rudin, *J. Biol. Chem.*, 1993, **268**, 13166.
37. B. Mora, P. T. Narasimhan, B. D. Ross, J. Allman, and P. B. Barker, *Proc. Natl. Acad. Sci., USA*, 1991, **88**, 8372.
38. D. Holtzman, R. Mulkern, M. Tsuji, C. Cook, and R. Meyers, *Dev. Neurosci.*, 1996, **18**, 535.
39. A. P. Koretsky, S. Wang, J. Murphy-Boesch, M. P. Klein, T. L. James, and M. W. Weiner, *Proc. Natl. Acad. Sci., USA*, 1983, **80**, 7491.
40. D. Rees, M. B. Smith, J. Harley, and G. K. Radda, *Magn. Reson. Med.*, 1989, **9**, 39.
41. J. F. Goudemant, M. Francaux, I. Mottet, R. Demeure, M. Sibomana, and X. Sturbois, *Magn. Reson. Med.*, 1997, **37**, 744.
42. E. W. McFarland, M. J. Kushmerick, and T. S. Moerland, *Biophys. J.*, 1994, **67**, 1912.
43. T. A. Cadoux-Hudson, M. J. Blackledge, and G. K. Radda, *FASEB J.*, 1989, **3**, 2660.
44. P. A. Bottomley and C. J. Hardy, *J. Magn. Reson.*, 1992, **99**, 443.
45. W. Chen, X. H. Zhu, G. Adriany, and K. Ugurbil, *Magn. Reson. Med.*, 1998, **38**, 551.
46. E. J. Murphy, B. Rajagopalan, K. M. Brindle, and G. K. Radda, *Magn. Reson. Med.*, 1989, **12**, 282.

Biographical Sketch

Ruth M. Dixon. *b* 1959. B.A. Churchill College, Cambridge, 1981; Ph.D. University of Warwick, 1985; Postdoctoral research fellow with Professor G. Lowe, Dyson Perrins Laboratory, University of Oxford, 1986; MRC nonclinical scientist at the MRC Biochemical and Clinical Magnetic Resonance Unit, Oxford 1986–present. Alexander von Humboldt research fellow, working with Dr. J. Frahm at the Max-Planck-Institute, Göttingen, 1992–1993. Research interests include the study of liver and brain metabolism by NMR in vivo, phospholipid metabolism in tumors and rapidly dividing tissues, and the development of techniques for NMR spectroscopy in vivo.

Proton Decoupling During In Vivo Whole Body Phosphorus MRS

Rolf M. J. N. Lamerichs and Peter R. Luyten
Philips Medical Systems, Best, The Netherlands

1 INTRODUCTION

In vivo MRS in humans started with the measurement of phosphorus spectra in muscle tissue (see also ***Whole Body Studies: Impact of MRS***). These first measurements were directed toward the assessment of muscle metabolism by using surface coils to localize the spectral information to a confined region of interest. With the advent of localization techniques, in vivo whole body phosphorus spectroscopy could also be used to study metabolism in other regions of the human body. Localized brain spectra have been used to study the metabolic changes in intracranial tumors, stroke, epilepsy, and white matter disorders. Liver and heart phosphorus spectroscopy have provided metabolic information on stress and ischemic conditions.

In spite of mature localization techniques for spatially selective phosphorus spectroscopy, the clinical efficacy of these techniques is hampered by a number of physical limitations. First, phosphorus spectroscopy is an eternal struggle for a better signal-to-noise ratio. Volumes of interest smaller than 10 cm^3 will usually result in excessive measurement times, excluding those techniques for relatively focal pathologies. Higher field strengths may overcome this fundamental problem to some extent. However, the linewidth of in vivo NMR signals is predominantly determined by tissue susceptibility, which results in broader lines at higher field strengths. This effect limits the advantages of increasing the field strengths. Another reason for poor ^{31}P signal detection is the low intensity for some ^{31}P resonances due to complex J coupling patterns with protons. Further complications may result from the overlap of resonance frequencies between different components.

One technique which may alleviate these limitations to some extent is the use of proton decoupling in combination with whole body ^{31}P spectroscopy.[1] Proton decoupling may simplify the structure of the spectrum by suppressing the heteronuclear J modulation patterns due to coupling with the spin–spin protons. Moreover, excitation or saturation of the surrounding protons in the tissue may contribute to the signal strength of the individual phosphorus signals by virtue of the nuclear Overhauser effect (NOE).[2]

The use of double resonance techniques in whole body ^{31}P MRS results in considerable signal enhancement which improves the clinical utility of ^{31}P MRS.

2 DECOUPLING OF ^{31}P SIGNALS

The limited chemical shift dispersion of in vivo ^{31}P NMR spectra obtained at the relatively low field strengths used for human applications may be the cause of poor spectral resolution. Excellent shimming over the region of interest is an absolute necessity for good in vivo spectral resolution. Depending on the relevant tissue susceptibility and volume of interest size, a homogeneity of 0.05–0.3 ppm (full width at half maximum) can be achieved. Methods to accomplish this homogeneity either employ the spatially resolved water signal in an iterative shim process or generate $\boldsymbol{B}_0$ maps obtained from phase-sensitive imaging methods. After shimming, the linewidth will be 1.5–7 Hz at 1.5 T for in vivo ^{31}P NMR resonances. These linewidths are sufficient to resolve the homonuclear ^{31}P J couplings of ±17 Hz between the three nuclear ^{31}P spins of adenosine triphosphate (ATP). Since the three-bond isotropic heteronuclear coupling between protons and phosphorus is in the range of 6–10 Hz, this coupling may become the dominant factor in the residual resonance linewidth of ^{31}P nuclei coupled to one or more protons, such as in 2,3-diphosphoglycerate (2,3-DPG), nicotinamide adenine dinucleotide (NAD^+), phosphoethanolamine (PE), phosphocholine (PC), glycerophosphoethanolamine (GPE), glycerophosphocholine (GPC), and α-ATP. Therefore, proton decoupling at a field strength of 1.5 T combined with an excellent local homogeneity can improve spectral resolution substantially, resulting in more resolved resonances and more reliable, quantitative information. At higher field strengths proton decoupling of ^{31}P MR signals will be less effective due to the increased linewidths, which may become larger than the actual J couplings.

3 THE NUCLEAR OVERHAUSER EFFECT AND ^{31}P SIGNALS

Irradiation of protons during in vivo ^{31}P spectroscopy results in signal increase due to collapse of multiplet structures into singlets. Furthermore, this irradiation may introduce NOE which also results in significant signal increase. This signal enhancement affects not only ^{31}P nuclei that are coupled to protons within the same molecule, but also noncoupled resonances, e.g. the phosphocreatine (PCr) signal, may show a substantial increase in signal intensity during saturation of the surrounding water protons. Due to the heteronuclear dipolar relaxation mechanism and the long dipolar cross-relaxation times between the ^{31}P and ^{1}H water nuclei, the NOE may be quite effective. After application in animal studies,[3] different irradiation schemes have been suggested for whole body in vivo applications that result in enhancement of the ^{31}P signal. These methods range from low-power single-frequency irradiation at the H_2O resonance, which proved to be quite effective in generating NOE in ^{31}P spectra of calf muscle,[4] to truncated driven or transient NOE techniques.[5] These methods are relatively simple to implement on a whole body MR scanner equipped with a second rf channel. Like decoupling, the NOE may result in relatively larger signal enhancements at lower field strengths. This is related to the inherent relaxation mechanisms for the ^{31}P nuclear spins. The two most important relaxation mechanisms for in vivo ^{31}P signals originate either from dipolar interactions or from the shielding anisotropy. Because this

latter relaxation mechanism is proportional to B_0^2, it becomes the predominant relaxation mechanism at higher field strengths, resulting in a decreased NOE.

4 EXPERIMENTAL IMPLEMENTATIONS

A variety of effective pulse sequences have been developed for decoupling purposes, especially for high-resolution NMR applications. A well-defined decoupling sequence requires a homogeneous decoupling field $\boldsymbol{B}_1$, whose magnitude exceeds the strength of the J couplings involved and covers the entire spectral range of the proton spectrum that has to be decoupled. Broadband decoupling techniques generally rely on repeated inversion of the proton spins. Therefore, they require inversion pulses with a repetition time that is short compared with $1/J$. For proton decoupling of in vivo ^{31}P NMR signals, these conditions are easily fulfilled with the current 1.5 T whole body technology.[1] First of all, the J couplings involved are very small, only of the order of 6–10 Hz. This allows for relatively long pulses, and concomitantly for low rf power levels to decouple sufficiently. Furthermore, the relevant in vivo proton resonances coupled to phosphorus nuclei resonate in a small chemical shift range of ±100 Hz around the H_2O resonance. This again allows for low rf power without affecting the broadband decoupling performance.

Sufficient decoupling power can be generated utilizing a WALTZ-4 sequence using a basic 90° pulse length of 900 μs, corresponding to an expected decoupling bandwidth of ±280 Hz around the water resonance. These values allow for the use of large resonators such as standard whole body ^{1}H transmission coils employed on clinical MR scanners. For NOE the conditions are even more favorable. As most NOE contributions are expected to originate from the tissue water only, a low-power single-frequency irradiation of the water protons can be sufficient to generate large NOE enhancements.

5 APPLICATIONS

As the availability of second rf channels on clinical 1.5 T scanners is limited, the number of in vivo applications is quite restricted. However, for all applications of ^{31}P MRS, especially for studies on focal pathologies, proton decoupling showed an important improvement in the sensitivity of the technique. An illustration of the effect of broadband proton decoupling is given Figure 1. The lower part shows a coupled ^{31}P spectrum of the human calf. The upper part shows the effect of proton decoupling, which clearly demonstrates how the multiplets of GPC and NAD resolve into two singlets. Another example is given in Figure 2, showing the resolved PE, GPC, and GPE resonances in the localized ^{31}P spectrum of the brain of a 6-year-old girl. These particular resonances are important indicators for membrane metabolism. These mono- and diester signals are used for the assessment of tumor metabolism and therapy response. Increased resolution will greatly enhance the potential of localized ^{31}P MRS in several important applications.

Figure 3 shows the effect of proton decoupling on the localized ^{31}P spectrum in the normal human myocardium. The lower trace shows the spectrum without any data processing,

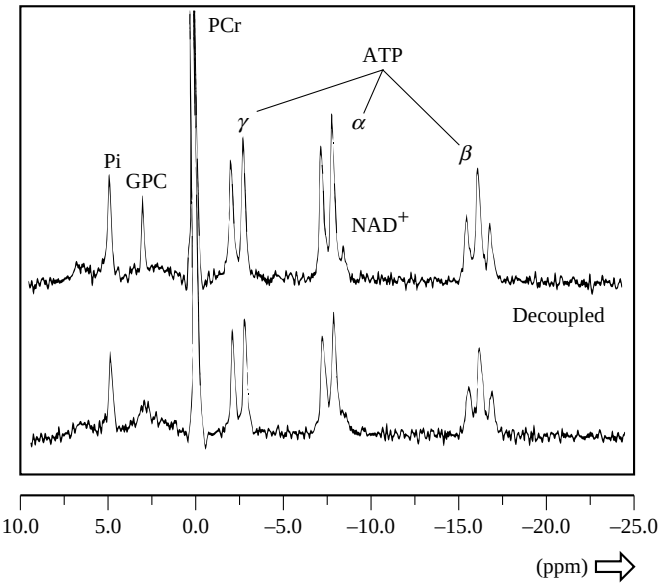

Figure 1 1.5 T ^{31}P NMR spectra of the human calf. The spectra were obtained for 64 transients and a repetition time of 3 s using a 14 cm diameter surface coil without spatial localization. (Reproduced by permission of Wiley from Luyten et al.[1])

whereas the middle spectrum is the result of a time domain fitting routine (see also ***Quantitation in In Vivo MRS***). The upper trace represents the residual signal between raw and fitted data. The spectrum shows a resolved inorganic phosphate (Pi) signal. Without any proton decoupling this signal would

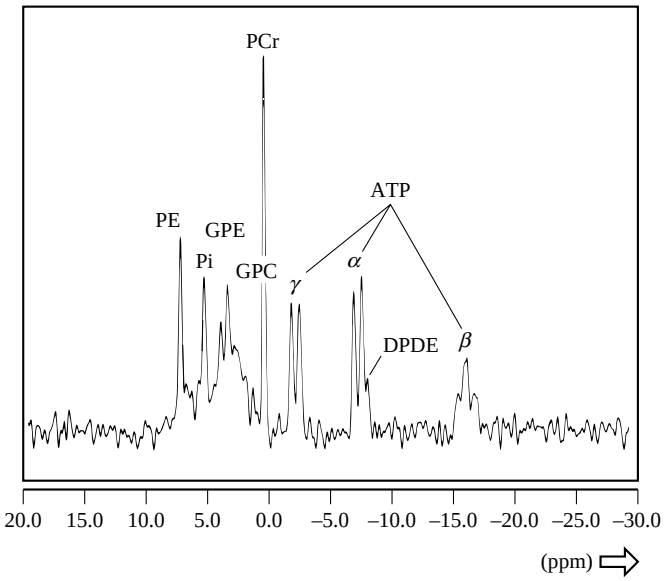

Figure 2 Proton decoupled ^{31}P NMR spectrum of the brain of a 6-year-old girl who has a history of chemotherapy for leukemia. The spectrum was acquired using a small ^{31}P NMR head coil, and a regular ^{1}H imaging head coil for decoupling. WALTZ-4 decoupling was applied; the spectrum was obtained for 256 transients, with a 3.5 s repetition time. Proton decoupling has helped to resolve resonances from GPC, GPE, PE, and NAD^+. DPDE = diphosphodiester. (Reproduced by permission of Wiley from Luyten et al.[1])

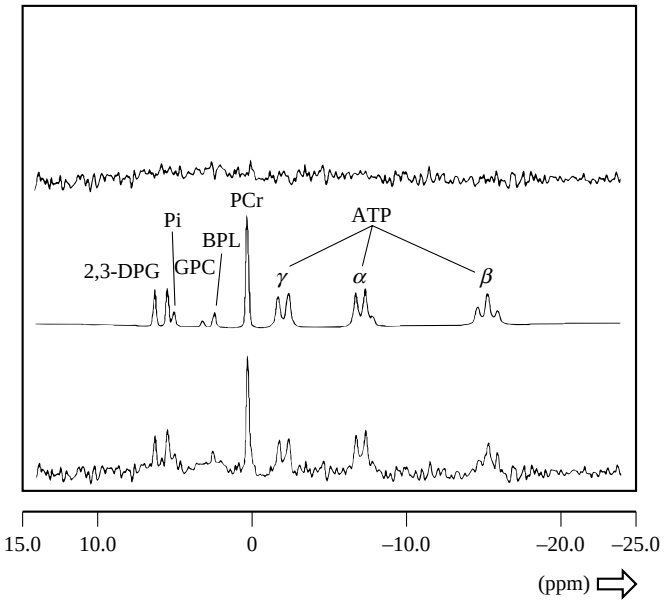

Figure 3 Proton decoupled ^{31}P spectrum of the left ventricular myocardium of a healthy subject. The acquired spectrum (bottom), simulated spectrum (middle), and the difference between the acquired and simulated spectra (top) are illustrated. Indicated are the signals from 2,3-DPG, inorganic phosphate (Pi), GPC, phospholipid signal from the blood (BPL), PCr, and ATP. Three-dimensional localization was applied by combining one-dimensional phase encoding and two-dimensional image-selected in vivo spectroscopy column selection. (Reproduced by permission of the Society of Magnetic Resonance Imaging from de Roos et al.[6])

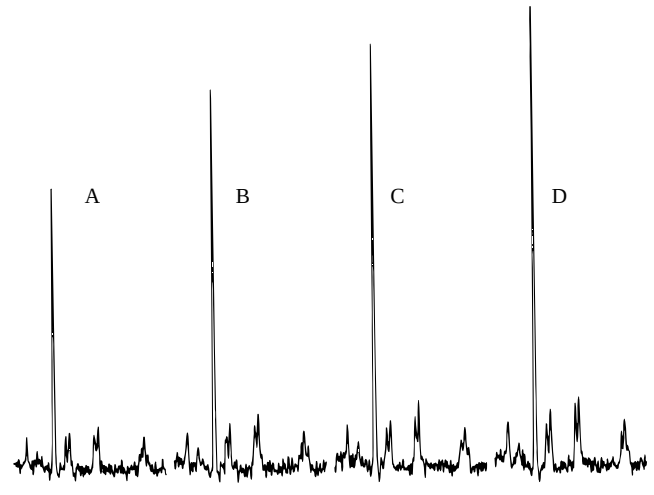

Figure 4 Proton decoupling and NOE applied to the human calf. The spectra were obtained for eight transients with a repetition time of 3 s. Spectrum A was acquired without any ^{1}H irradiation, spectrum B with proton decoupling (WALTZ-4) during acquisition of the ^{31}P signal only, spectrum C with decoupling and an inversion pulse on the ^{1}H signal 1000 ms before ^{31}P data acquisition (transient NOE), and spectrum D by combining WALTZ-4 decoupling during ^{31}P data acquisition with continuous single-frequency low-power irradiation of the water resonance during the relaxation delay

have been obscured by the overlapping 2,3-DPG signal from blood. This resolution is absolutely required to determine the intracellular pH, which is 7.15 for this particular spectrum.

Figure 4 summarizes signal enhancements that can be expected from NOE and decoupling separately. Spectrum A was obtained without the use of any proton irradiation. Broadband decoupling during ^{31}P signal acquisition was applied to obtain spectrum B, whereas spectrum C was obtained by broadband decoupling combined with an inversion pulse on the water resonance to create a transient NOE. Continuous irradiation during the entire experiment results in the largest enhancement (spectrum D): continuous low-power (5 W) single-frequency irradiation of the water resonance during all relaxation delays and broadband proton decoupling during ^{31}P acquisition were used. The NOE factors for PCr in spectra B, C, and D are 0.35, 0.50, and 0.64, respectively. For purely ^{31}P–^{1}H dipolar relaxation and under extreme narrowing conditions the maximum enhancement factor is given by $\eta = \gamma(^{1}\mathrm{H})/2\gamma(^{31}\mathrm{P}) = 1.24$. This implies that combined broadband decoupling during acquisition and single-frequency low-power irradiation at the water resonance frequency during all relaxation delays results in a substantial signal increase. This effect may have an important impact on the quantification of ^{31}P MR signals that are obtained using double resonance techniques.

6 SAFETY CONSIDERATIONS

Continuous irradiation or broadband decoupling during relatively long acquisition intervals may result in excessive sample heating. This phenomenon is well-known in high-resolution NMR, where sample cooling during the experiment is common practice. For in vivo experiments this requires extremely careful precautions to prevent tissue damage. Fortunately, proton decoupling of in vivo ^{31}P signals requires power levels which are on the safe side of the current US Food and Drug Administration safety limits for rf irradiation. The total power deposition required to obtain the result depicted in Figure 4, spectrum D, results in a continuous single-frequency power deposition of 5 W to obtain NOE enhancement, whereas the broadband decoupling consumed 150 W during the 512 ms acquisition interval. Using a *TR* of 3 s, this resulted in a worst-case average power absorption (under the assumption that all power is dissipated in the tissue, i.e. zero reflection and no cable losses) of 30 W. As these values relate to transmission with the body coil, total power absorption of this experiment is well within the safety guidelines. However, extreme precautions including a dedicated power delimiter for a second rf channel are still an absolute necessity for performing these experiments, especially when decoupling is performed with smaller (surface) coils, which may result in excessive tissue heating close to the conductors of the coil.

7 RELATED ARTICLES

Proton Decoupling in Whole Body Carbon-13 MRS; Quantitation in In Vivo MRS; Whole Body Studies: Impact of MRS.

8 REFERENCES

1. P. R. Luyten, G. Bruntink, F. M. Sloff, J. W. A. H. Vermeulen, J. I. van der Heijden, J. A. den Hollander, and A. Heerschap, *NMR Biomed.*, 1989, **1**, 177.
2. J. H. Noggle and R. E. Schirmer, 'The Nuclear Overhauser Effect', Academic Press, New York, 1971.
3. R. L. Nunnally and P. A. Bottomley, *Science*, 1981, **211**, 177.
4. P. A. Bottomley and C. J. Hardy, *Magn. Reson. Med.*, 1992, **24**, 384.
5. P. Bachert and M. E. Belleman, *J. Magn. Reson.*, 1992, **100**, 146.
6. A. de Roos, J. Doornbos, P. R. Luyten, L. J. M. P. Oosterwaal, E. E. van der Wall, and J. A. den Hollander, *J. Magn. Reson. Imaging*, 1992, **2**, 711.

Biographical Sketches

Rolf M. J. N. Lamerichs. *b* 1959. Ph.D., 1989, chemistry, University of Utrecht (thesis on two-dimensional NMR studies on protein and DNA structures). Department of MR Systems and Methods, Philips Medical Systems, 1990–present.

Peter R. Luyten. *b* 1954. Ph.D., 1984, physical chemistry, Free University of Amsterdam (dissertation on NMR relaxation studies on small solutes in liquid crystals). Visiting scholarship (1 year): University of California, San Diego, 1982; Department of MR Predevelopment, Philips Medical Systems, 1984. Currently Director of Clinical Science, Philips Medical Systems.

Proton Decoupling in Whole Body Carbon-13 MRS

Glyn A. Coutts
Marconi Medical Systems, UK

and

David J. Bryant
GEC Hirst Research Centre, Borehamwood, Herts, UK

1 INTRODUCTION

High-resolution ^{13}C NMR spectroscopy has utilized the full 200 ppm range of the ^{13}C spectrum for exploring metabolism in cells.[1] The multiplet structure of the spectrum arising from heteronuclear J coupling to protons has been exploited for the assignment of resonances. The spin-$\frac{1}{2}$ ^{13}C isotope has only 1.1% natural abundance, but by using ^{13}C-enriched labeled substrates, metabolic pathways can be followed dynamically. In vivo human spectroscopy has so far mainly been limited to studies of triglycerides in adipose tissue and glycogen storage in liver and muscle because of the very low sensitivity of the ^{13}C signal compared with that from protons or ^{31}P. In order to increase the range of metabolites accessible to ^{13}C spectroscopy, or to improve the localization within the human body, every effort has to be made to improve the S/N. One route for improvement of the S/N is to exploit the heteronuclear coupling, either through manipulation of the population of the ^{13}C energy levels through the nuclear Overhauser effect (NOE) or polarization transfer, or by collapsing the multiplet lines through direct decoupling from the protons. The gated decoupling experiment imposes stringent technical demands. The proton and carbon channels need to be well isolated, and coil systems need to be designed with a large degree of decoupling of their mutual inductances, which are adapted to the relevant anatomy and capable of delivering the decoupling energies at the required volume of tissue. However the most stringent limit in experiment design arises from the near continuous rf irradiation at proton frequencies with the requirement that the local deposition of rf energy does not exceed the various national guidelines, and presents no risk to the human subjects.

2 THE EFFECT OF PROTON IRRADIATION ON THE ^{13}C SPECTRUM

Irradiation at proton frequencies can affect the ^{13}C spectrum in two ways. The first of these is enhancement of the ^{13}C sensitivity by using the heteronuclear coupling to alter the population of ^{13}C energy levels. This further divides into two techniques: NOE[2,3] and polarization transfer. The NOE uses a continuous secondary rf (B_2) irradiation to saturate the proton levels of the coupled system, whilst cross relaxation transfers the high proton polarization to the ^{13}C levels leading to a new steady state determined by the various relaxation processes. For purely dipolar relaxation the enhancement is $1 + \gamma_H/2\gamma_C$ or a factor of 3. Polarization transfer uses rf pulses applied to the protons to create population changes which are then transferred to the carbon levels. The SINEPT (SINE-dependent polarization transfer) sequence,[4] for example, consists of two 90° pulses separated by a time determined by the coupling constant of the particular resonance to be enhanced and the proton transverse relaxation time. Although the enhancement is optimized for those multiplets exhibiting a particular J coupling, the enhancement available is γ_H/γ_C, or a factor of 4.

The second effect of proton irradiation on the ^{13}C spectrum is through coherent effects causing collapse of the multiplet lines. The idea is that if nuclear spins X, in our case the protons, of an AX coupled system are irradiated at a frequency centered on the chemical shift of X and at an intensity B_2 such that $\gamma B_2 \approx 2\pi J_{AX}$ then in the rotating frame the evolution of the A, or ^{13}C, magnetization vectors due to coupling is continually reversed and the multiplet line coalesces to a single peak. This is known as continuous wave (CW) decoupling.[5] The effectiveness of the decoupling diminishes with offset of the proton frequency from the X resonance and B_2 intensity. Broadband decoupling attempts to apply decoupling equally for all metabolites in the ^{13}C spectrum. One method of doing this is to modulate the B_2 irradiation with a noise source.[6] A second method uses composite pulses[7,8] which are designed to give inversion over a wide range of frequencies. The most commonly used of the composite pulses is the WALTZ pulse[9] consisting of the triplet 90°(+X)180°(−X)270°(+X). Phase cycling of these pulses produces WALTZ-4, WALTZ-8, or WALTZ-16 with progressively less sensitivity to errors in rf phase shifts. For full decoupling the pulses need to be applied at a frequency greater than $2J$, where J is the largest coupling constant for the metabolites under consideration, and the average B_2 energy utilization is much greater than for CW decoupling.

Switching of the B_2 irradiation, or gated decoupling, depending on whether data are being acquired, can give any combination of sensitivity enhancement or multiplet collapsing since the timescales of the former are those of the relaxation processes whilst the coherent effects are instantaneous. Suitable gating of the B_2 irradiation throughout the duty cycle is therefore useful for minimizing the overall rf power deposition.

3 HARDWARE, COIL DESIGN, AND RF DEPOSITION

For a gated decoupling experiment a second transmit channel with frequency synthesizer, phase modulator, and power amplifier is required. Most workers have also specifically designed the system of coils needed for proton transmit and carbon transmit and receive. The coil design most widely used for human in vivo ^{13}C studies consists of a planar, circular, ^{13}C transmit-receive surface coil with a butterfly or figure-of-eight proton transmit coil, the crossover point being coaxial with the carbon coil center. This arrangement minimizes the inductive coupling of the two coils, and can be easily sited over the anatomy of interest with the long axis of the proton coil parallel to $\boldsymbol{B}_0$. Distributed capacitances are of course required to prevent electrical breakdown. In addition the proton transmit coil is gen-

erally spaced off from the subject to avoid regions of large B_2 field near to the coil. Further filtering is generally required to give the high level of magnetic isolation of the two frequencies so that the carbon receive signal is not degraded by the simultaneous proton frequency irradiation. For example Bottomley et al.,[10] working at 1.5 T, using a 3-turn spiral 6.5 cm diameter ^{13}C coil and 8×13 cm air-cooled proton coil, achieved a 90 dB isolation of the 64 MHz signal at 16 MHz.

Rf power deposition in human NMR studies through the induction of eddy currents and Joule heating has long been a cause of concern and has led to guidelines limiting the specific absorption ratio (SAR) experienced by human subjects. In the USA the Food and Drug Administration (FDA) guidelines[11] are a body average SAR of 0.4 W kg^{-1} and a peak SAR of 8 W kg^{-1} in any 1 g of tissue, whilst in the UK the National Radiological Protection Board guidelines[12] are a body average SAR of 0.4 W kg^{-1} and a peak SAR of 4 W kg^{-1} in any 1 g of tissue. There is also a limit on the body temperature increase of 1°C. Bottomley and Roemer[13] have used a homogeneous tissue model to investigate the power deposition for the coil arrangement described above and have compared their model with experimental observations of power deposition on the basis of the coil Q value using $P_{\text{absorbed}} = P_{\text{total}}(1 - Q_{\text{loaded}}/Q_{\text{unloaded}})$. They concluded that, although the theoretical homogeneous models probably overestimated the local power deposition in adipose tissue close to the coils, nevertheless, without care, the guidelines for peak SAR could easily be exceeded. Bottomley et al.[10] in their studies on human limbs and chest using a noise-modulated decoupling source limited the decoupling power to below 8 W, which according to the above model limited the power deposited in tissue to 3 W. Using one-dimensional phase encoding methods in a phantom they estimated that some level of decoupling was sustained at depths of 6 cm whilst significant NOE was realized to depths of 4 cm.

Working at 4 T, Bomsdorf et al.[14] used an 11 cm diameter carbon coil and a 7×14 cm butterfly proton coil, achieving 40 dB of isolation. It was concluded that broadband decoupling would not be possible at this field strength without exceeding the SAR limits, but studies on the calves of human volunteers were performed with gated CW decoupling. Decoupling power levels of 6 W were used for subcutaneous fat at a depth of 1 cm, and 24 W for muscle at a depth of 2.5 cm. Heating sensations for one volunteer at the higher power levels were eliminated by reducing the duty cycle, i.e. increasing the recovery period between data acquisitions. In addition, these workers, by careful positioning of the carbon surface coil, were able to use the body coil for proton transmit in polarization transfer experiments, where there is no proton irradiation during data collection. In this case for a repetition time of 200 ms the SAR was estimated to be ~1 W kg^{-1} and hence well within guidelines.

Saner et al.[15] working at 1.5 T were able to use a 7 cm diameter carbon coil in combination with a standard head coil for CW decoupling, and were able to conduct polarization transfer studies without hardware modification. Applying the gated CW decoupling during a 64 ms data acquisition these authors estimated that the average SAR was 3.9 W kg^{-1} whilst the peak SAR was twice this, and thus just within FDA guidelines, but were able to demonstrate decoupling within calf muscle of a human leg.

Systems of concentric and coplanar circular coils have also been successfully used for decoupling. Beckmann et al.[16] were able to use broadband decoupling at 1.5 T with circular coils of 8 cm (carbon) and 13 cm (proton) diameter. Using a WALTZ-8 sequence intercalated throughout the 70 ms data acquisition, and interspersing rest periods within the total data acquisition time to reduce the duty cycle, they estimated that the average SAR did not exceed 2.8 W kg^{-1} and also demonstrated decoupling within the calf muscle of a human volunteer. Finally, with this coil arrangement, gated CW decoupling through a 20 ms data acquisition and a 10% duty cycle, Avison et al.[17] were able to demonstrate decoupling on a human calf muscle at 4.7 T.

4 HUMAN ^{13}C STUDIES

In whole body ^{13}C spectroscopy adipose tissue is the most accessible for study, especially if proton decoupling is required. Moonen et al.[18] showed that all the resonances in the ^{13}C spectrum are due to triglycerides, and using the resonances of the olefinic signal from unsaturated carbons (C*=C*) at 129 ppm were able to determine the relative concentrations of poly- and monounsaturated fatty acids. This noninvasive technique has the additional advantage that adipose tissue from specific sites, e.g. waist or thigh, can be studied. This study was also performed on patients with cystic fibrosis.[19] Beckmann et al.[20] by using long repetition times, were able to achieve sufficient S/N to quantify the relative concentrations of poly- and monounsaturated fatty acids in relation to dietary intake of fat without decoupling, but noted the poor resolution of the resonances at 130 ppm arising from long range couplings compared with the high resolution of the decoupled spectrum. Bryant et al.,[21] using both coupled and decoupled spectra in a study of the adipose tissue of vegans and control subjects, demonstrated by this noninvasive technique a significant increase in unsaturated fatty acid content in the vegan subjects compared with controls. Ende and Bachert,[22] using broadband decoupled ^{13}C spectroscopy of human calf and breast, sought to optimize the NOE enhancement, achieving maximum enhancements of 80%. With acquisition times of ~15 min they detected resonances other than those from triglycerides in breast tissue.

Glycogen in many ways has provided a test case for the implementation of human in vivo ^{13}C spectroscopy. It plays a central role in carbohydrate storage and metabolism in both muscle and liver, at depths of a few centimeters as far as NMR detection is concerned. Although fully NMR visible,[23] concentrations of around 84 mmol L^{-1} in muscle and up to 300 mmol L^{-1} in liver test the sensitivity of ^{13}C studies. The C-1 resonance of glycogen appears as a doublet at 95 and 106 ppm, but can be decoupled by CW decoupling, irradiating the proton spectrum at 5 ppm. In addition broadband decoupling is expected to give an S/N improvement of slightly more than 2 through the suppression of long range couplings. Short T_1 and T_2 values mean that the irradiation duty cycle times can be as short as 25 ms. Finally labeling studies can be easily and safely performed by the ingestion of ^{13}C-enriched glucose.

Decoupling and detection of the C-1 resonance of glycogen in human muscle and liver at 2.1 T was demonstrated by Jue et al. in 1987.[24] Using WALTZ-4 broadband decoupling at 1.5 T, Heerschap et al.[25] were able to follow the depletion and

recovery of glycogen in the gastrocnemius muscle of a fit volunteer following a 23 km run. They note that the broadband proton decoupling aids quantification both through narrowing the region covered by the high triglyceride signals and by allowing referencing against other metabolite signals, for example creatine, at 157 ppm. Depletion and repletion studies of glycogen in skeletal muscle following 2 h each of cycling and walking were recently performed[26] at 2.0 T without decoupling, with acquisition times to achieve quantifiable S/N of ~20 min.

A patient with glycogen storage disease has been studied by Beckmann et al.[16] Muscle and liver spectra were obtained using WALTZ-8 proton decoupling. In calf muscle not only was an elevated C-1 glycogen resonance observed, but also resonances in the region 73–77 ppm, tentatively assigned to the C-4 and C-2,3,5 resonances of glycogen. For the spectra obtained from the abdominal region the authors note the problems of localization to the liver given the intense triglyceride signals for the overlying adipose tissue. The fact that the fatty acid content of the livers of normal western subjects tends to be high, together with the general broadening of liver signals, suggests that quantification will be difficult without decoupling. They were able to demonstrate the increased C-1 glycogen signal in the patient compared with controls, as well as resonances in the region 73–77 ppm. These authors also presented the first proton-decoupled ^{13}C spectra from the human head, with a tentative assignment of a resonance at 54 ppm to creatine.

It should be noted that Saner et al.[15] have compared the enhancement of the glycogen signal in human leg by CW decoupling with that of the much less rf intensive polarization transfer using the SINEPT technique, and concluded that, in vivo, both methods gave a gain of approximately 2.5. Work has also begun in gaining improved S/N from ^{13}C signals by using labeling in conjunction with decoupling. Jue et al.[27] gave fasted volunteers a ^{13}C-enriched glucose drink and obtained CW decoupled spectra using a surface coil placed over the right lobe of the liver. With a 15 min acquisition time they were able to obtain a baseline decoupled C-1 glycogen signal, and were then able to follow the increase in this resonance following ingestion of the glucose. They were also able to observe the α- and β-glucose resonances at 93 and 96 ppm.

Beckmann et al.[28] were able to compare glycogen formation in the human liver following ingestion or intravenous infusion of nonlabeled glucose as well as [1-^{13}C]glucose with a low level of enrichment. Using WALTZ-8 decoupling the resonances of glycogen and α- and β-glucose were followed over time, showing greater glucose uptake by the oral route. Other labeling studies have also been performed. In a recent study[29] at 2.0 T, glutamine and glutamate in the human brain were observed in a ^{13}C spectrum following infusion of [1-^{13}C]glucose. Sensitivity and resolution were enhanced by the use of NOE and WALTZ-16 broadband decoupling, achieving linewidths of less than 2 Hz.

Other human in vivo ^{13}C studies have been considered. For example, in 1988 Sillerud et al.[30] working at 1.5 T were able to observe the central resonance of the C-2,5 citrate triplet at 47 ppm in the human prostate, but were unable to resolve the outer pair of signals at 54 and 38 ppm. They noted that with narrowband decoupling and NOE enhancement a factor of 9 gain in S/N would theoretically be achieved, but to date no decoupling studies have been attempted in this region. The trend has been rather to use improved technique and experience to move away from the technically demanding requirements of the gated decoupling experiment.

5 RELATED ARTICLES

Chemical Shift Imaging; In Vivo Hepatic MRS of Humans; Multifrequency Coils for Whole Body Studies; Peripheral Muscle Metabolism Studied by MRS; Proton Decoupling During In Vivo Whole Body Phosphorus MRS; Quantitation in In Vivo MRS; Radiofrequency Systems and Coils for MRI and MRS.

6 REFERENCES

1. J. B. Stothers, 'Carbon-13 NMR Spectroscopy', Academic Press, New York, 1982.
2. A. W. Overhauser, *Phys. Rev.*, 1955, **92**, 411.
3. I. Solomon, *Phys. Rev.*, 1955, **99**, 559.
4. H. S. Jakobsen, O. W. Sorensen, and H. Bilboe, *J. Magn. Reson.*, 1983, **51**, 157.
5. R. Freeman and W. A. Nelson, *J. Chem. Phys.*, 1962, **37**, 85.
6. R. R. Ernst, *J. Chem. Phys.*, 1966, **45**, 3845.
7. M. H. Levitt, *Prog. NMR. Spectrosc.*, 1986, **18**, 61.
8. J. S. Waugh, *J. Magn. Reson.*, 1982, **49**, 517.
9. A. J. Shaka, J. Keeler, and R. Freeman, *J. Magn. Reson.*, 1983, **53**, 313.
10. P. A. Bottomley, C. J. Hardy, P. B. Roemer, and O. M. Mueller, *Magn. Reson. Med.*, 1989, **12**, 348.
11. United States Food and Drug Administration (FDA), 'Guidance for Content and Review of a Magnetic Resonance Diagnostic Device 510(k) Application: Communication to Manufacturers', FDA, Rockville, MD, 1988.
12. NRPB (National Radiological Protection Board) ad hoc Advisory Group on Nuclear Magnetic Resonance Clinical Imaging, *Br. J. Radiol.*, 1983, **56**, 974.
13. P. A. Bottomley and P. B. Roemer, *Ann. N. Y. Acad. Sci.*, 1992, **649**, 144.
14. H. Bomsdorf, P. Roschmann, and J. Wieland, *Magn. Reson. Med.*, 1991, **22**, 10.
15. M. Saner, G. McKinnon, and P. Boesiger, *Magn. Reson. Med.*, 1992, **28**, 65.
16. N. Beckmann, J. Seelig, and H. Wick, *Magn. Reson. Med.*, 1990, **16**, 150.
17. M. J. Avison, D. L. Rothman, E. Nadel, and R. G. Shulman, *Proc. Natl. Acad. Sci. USA*, 1988, **85**, 1634.
18. C. T.W. Moonen, R. J. Dimand, and K. L. Cox, *Magn. Reson. Med.*, 1988, **6**, 140.
19. R. J. Dimand, C. T. W. Moonen, S. C. Chu, E. M. Bradbury, G. Kurland, and K. L. Cox, *Pediatr. Res.*, 1988, **24**, 243.
20. N. Beckmann, J.-J. Brocard, U. Keller, and J. Seelig, *Magn. Reson. Med.*, 1992, **27**, 97.
21. D. J. Bryant, J. D. Bell, E. L. Thomas, S. D. Taylor-Robinson, J. Simbrunner, J. Sargentoni, M. Burl, G. A. Coutts, G. Frost, M. L. Barnard, S. Cunnane, and R. A. Iles, *Proc. XIIth Ann Mtg. Soc. Magn. Reson. Med.*, New York, 1993, p. 1048.
22. G. Ende, and P. Bachert, *Proc. XIIth Ann Mtg. Soc. Magn. Reson. Med.*, New York, 1993, p. 84.
23. S. O. Sillerud and R. G. Shulman, *Biochemistry*, 1983, **22**, 1087.
24. T. Jue, J. A. B. Lohman, R. Ordridge, and R. G. Shulman, *Magn. Reson. Med.*, 1987, **5**, 377.

25. A. Heerschap, P. R. Luyten, J. I. van der Heyden, L. J. M. P. Oosterwaal, and J. A. den Hollander, *NMR Biomed.*, 1989, **2**, 124.
26. L. A. Domico, K. F. Kendrick, R. Reddy, B. Chance, and J. S. Leigh, in *Proc. XIIth Ann Mtg. Soc. Magn. Reson. Med.*, New York, 1993, p. 1145.
27. T. Jue, D. L. Rothman, B. A. Tavitian, R. DeFronzo, G. I. Shulman, and R. G. Shulman, *Proc. VIIth Ann Mtg. Soc. Magn. Reson. Med.*, San Francisco, 1988, p. 357.
28. N. Beckmann, R. Fried, I. Turkalj, J. Seelig, U. Keeler, and G. Stalder, *Magn. Reson. Med.*, 1993, **29**, 583.
29. R. Gruetter, E. J. Novotny, S. D. Boulware, D. L. Rothman, W. V. Tamborlane, and R. G. Shulman, *Proc. XIth Ann Mtg. Soc. Magn. Reson. Med.*, Berlin, 1992, p. 1921.
30. L. O. Sillerud, K. R. Halliday, R. H. Griffey, C. Fenoglio-Preiser, and S. Sheppard, *Magn. Reson. Med.*, 1988, **8**, 224.

Biographical Sketches

Glyn A. Coutts. *b* 1959. B.A. (Physics) University of Oxford, UK, 1980, D.Phil. University of Oxford 1985. Senior Research Associate at Picker Research UK, 1987–99. Marconi Medical Systems, UK, 1999–present. Approx. 30 publications in the field of MRI and MRS. Current interest: interventional MRI.

D. J. Bryant. *b* 1956. B.Sc., 1977, Ph.D., 1981, University of Nottingham, supervisor E. Raymond Andrew. Research fellow with Raymond Andrew, 1980–82. GEC Hirst Research Centre working in laboratory headed by Ian R. Young, 1982–present. Approx. 50 publications. Research interests: MRI and MRS on whole-body systems in the 0.15–1.5 T range.

Quantitation in In Vivo MRS

Wim M. M. J. Bovée, Ronald de Beer and Dirk van Ormondt
Delft University of Technology, Delft, The Netherlands

Peter R. Luyten
Philips Medical Systems, Best, The Netherlands

and

Jan A. den Hollander
University of Alabama, Birmingham, AL, USA

1 INTRODUCTION

The development of in vivo magnetic resonance spectroscopy (MRS) has provided a noninvasive means of chemically analyzing tissue volumes of a few cc's in the human body.[1–3] Ideally, diagnostic statements in the clinic should be based on numerical criteria derived from the measurement of absolute metabolite concentrations in normal and pathological tissue. Both the MRS measurement technique and the data analysis method may introduce substantial errors in obtaining absolute, or even relative, quantitative MRS data. For the introduction of MRS in the clinic as a standard method of diagnosis and of assessment of response to therapy, the development of a reliable user-unbiased quantitation methodology is therefore essential.

In this article, the quantitation of MRS data, rather than their acquisition, is discussed. The first step is to determine signal intensities. Ideally, the amplitude of an MRS signal of a metabolite, be it FID or echo, is proportional to the concentration of that metabolite. The method of choice for estimating the amplitude is to fit an appropriate model function to the data. This can be executed directly in the time (measurement) domain, or in the frequency domain after Fourier transformation (FT). Problem areas are, among others, low signal-to-noise ratio (S/N), coincidence of spectral frequencies, and magnetic field inhomogeneity. In the frequency domain, an additional concern may be estimation of the baseline. If no appropriate model function is available, one may either decompose the signal into a limited number of known well-behaved functions or apply integration in the frequency domain. Often the quality of quantitation can be increased dramatically by exploiting all available prior knowledge about experiment and signal. In addition, reference should be made to the fundamental limits of precision at the given S/N (Cramér–Rao bounds).

As a second step, the signal intensity ratios obtained may need corrections for the effects of relaxation, scalar coupling, several instrumental and pulse-sequence-dependent signal intensity distortions, and imperfect localization. Calibration of instrumentation and measurement methodology permits suitable correction factors to be derived, and to obtain the prior knowledge mentioned above. Relative metabolite concentrations can be obtained in this way, and in principle also absolute ones, but at the cost of much greater effort.

There are a number of reviews of quantitative NMR.[1–11]

2 DATA ANALYSIS

2.1 Model Functions

The basic signal types encountered in in vivo MRS are FIDs and echoes. Since an echo can be looked upon as two FIDs back to back, most modeling aspects pertain to both types of signals.

A FID consists of a sum of damped sinusoids. Well-known functions for modeling the damping are $\exp(\alpha t)$, $\exp(\beta t^2)$, and $\exp(\alpha t + \beta t^2)$, in which α and β are negative. The frequency-domain counterparts of these functions have Lorentzian, Gaussian, and Voigt lineshapes, respectively. In practice, more complicated damping functions may be required—for instance when modeling an unresolved multiplet by a single sinusoid. In addition, the frequency of a sinusoid may be ill defined. The latter occurs when anisotropic interactions are not properly averaged out, or when the magnetic field is inhomogeneous.[12] For brevity, we consider only two cases:

1. the exponentially damped sinusoid and its frequency domain counterpart;
2. unknown functions and shapes.

The basic exponential function suitable for describing FIDs as well as echoes is

$$\hat{x}_n = \sum_{k=1}^{K} c_k e^{(\alpha_k^{\pm} + i\omega_k)t_n + i\varphi_k}, \quad n = 0, 1, \ldots, N-1 \tag{1}$$

where c_k is the real-valued amplitude, $\alpha_k^{\pm}$ the damping factor, ω_k the angular frequency, and φ_k the phase of sinusoid k. All φ_k may be equal (an example of prior knowledge). The signal is sampled at times $t = t_n$.

If the signal is a FID, the time origin is set at the actual beginning of the precession. t_0 is the time of the first usable sample, relative to the origin just defined. In principle, t_0 can be inferred from experimental knowledge. In the absence of the latter, t_0 may be estimated along with the other unknown parameters.[10]

If the signal is an echo, the time origin is chosen such that at the echo maximum (t_{em}), $t = t_{em} = 0$. As for the damping factors, we have $\alpha_k^{\pm} \equiv \alpha_k^{+} > 0$ for $t < 0$, whereas $\alpha_k^{\pm} \equiv \alpha_k^{-} < 0$ for $t > 0$. Note that $|\alpha_k^{+}|$ and $|\alpha_k^{-}|$ need not be equal. $t_{em} - t_0$ may be known from the settings of the spectrometer. Alternatively, $t_{em} - t_0$ may be estimated along with the other unknown model parameters,[13] as mentioned in the previous paragraph.

2.2 Estimation of Model Parameters

Quantitation amounts to estimation of the model parameters appearing in equation (1). Good results are usually obtained by

nonlinear least-squares (NLLS) fitting, which includes the variable projection method.[14] If the noise is Gaussian, NLLS is identical to maximum likelihood estimation.[10] An advantage of NLLS is that available prior knowledge about model parameters can be exploited, which yields significant reduction of the errors, especially at low S/N. A disadvantage is that good starting values of the parameters have to be provided in order to ensure correct convergence. Problems related to starting values and convergence can be avoided by resorting to simulated annealing[15] or genetic algorithms,[16] but these techniques require rather more computer time.

An alternative to maximum likelihood estimation is Bayesian estimation (BE),[17] which requires prior probability distributions rather than starting values. One advantage of BE is that unwanted parameters (nuisance parameters) can be 'integrated out', and subsequently ignored. This may simplify the estimation process considerably. In addition, BE was successfully used for rendering maximum entropy (MEM) suitable for quantitation.[18]

Both NLLS and BE can be executed either directly in the time domain, or in the frequency domain following Fourier transformation (FT).[17–24] In the time domain, the sample times t_n need not be uniformly distributed, which may be useful in multidimensional experiments, for example, for time saving.[10] In addition, data truncation at either end does not affect the fit procedure. Frequency domain estimation is equally insensitive to data truncation if one obtains the model function from the discrete FT (DFT), rather than the usual continuous FT, of equation (1).[8,21] When using the continuous FT, the resulting model function does not reflect data truncation, which in turn may necessitate judicious processing of the experimental baseline.[25,26] Finally, we mention that in both domains, one can restrict the fit to only a small subset of the peaks (sinusoids), provided the frequencies in the subset differ sufficiently from those in the remainder.[4,17,27] This property can yield substantial reduction of processing time. A new, very different, method capable of the same is that of *wavelets*.[28]

If the residue of a properly converged fit clearly exhibits features above the noise, the wielded model function is evidently inadequate. In a number of cases, replacement of the Lorentzian model by the Gaussian or Voigt model may significantly improve the fit. However, notorious problem cases are the signals of, for example, water and fat, whose model functions are usually nondescript. The following two paragraphs indicate how one can still estimate the intensity of a nondescript signal, in both domains.

First, we consider the frequency domain, which is traditionally chosen for the task. If the baseline has been correctly estimated and the peak in question does not overlap with other peaks, the area of that peak is proportional to the amplitude of the related FID at the time origin. The FID amplitude, in turn, is proportional to the wanted number of molecules of interest. The gist of the method is that the peak area can be estimated by integration, without knowledge of the peak shape. Statistical and systematic errors attendant to the procedure have been treated by McLeod and Comisarov[29] and Nadjari and Grivet.[30] As with model fitting, one can restrict integration to just the peak(s) of interest. In cases where the model function is known, comparison of model fitting and integration has been done.[31] Simulations showed that statistical errors of integration can be about equal to those of model fitting. Systematic integration errors, on the other hand, can be substantial.[31]

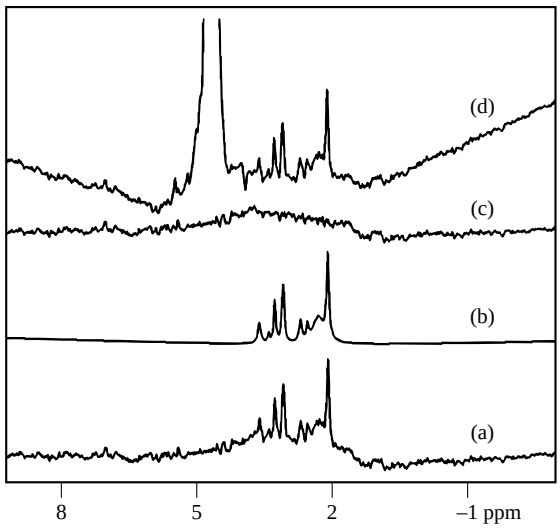

Figure 1 ^{1}H MRS STEAM signals, echo time 20 ms, from the right parietal lobe of a human brain (experiment by P. Gilligan, J. MacEnri and J. T. Ennis, The Institute of Radiological Sciences, Dublin). The signal processing comprised (1) truncation of the data record at the beginning from 1024 to 1022 points and subsequently at the end from 1022 to 512 points; (2) removal of the residual water signal by subtracting exponentially decaying sinusoids, fitted by the HLSVD method;[32] (3) quantitation in the time domain by the variable projection method,[14] thereby multiplying initial data and model function by the same weighting function in order to account for a broad background feature.[27] The figure shows the cosine DFT of (a) the experimental signal after removal of the residual water signal; (b) the fitted model function; (c) the residue (a)−(b); (d) the original experimental signal

Recently, time domain quantitation of nondescript signals has been shown to be equally feasible.[32] This is based on the fact that bell-shaped peaks of the kind encountered in spectroscopy can be represented in the time domain by a relatively small number of exponentially damped sinusoids. In agreement with intuition, the frequencies of the largest sinusoids are concentrated in the most intense region of the peak. Algorithms based on singular value decomposition (SVD) are available for the task.[33,34] In NMR, such algorithms are known as LPSVD[5–10] (linear prediction SVD), HSVD[5–10] (Hankel SVD), HLSVD[32] (Hankel–Lanczos SVD), HD[35] (Hankel diagonalization), EPLPSVD[36] (enhanced procedure LPSVD), and MV-HTLS[37] (minimum variance Hankel total least squares). The methodology is illustrated in Figure 1. Note that if the signal at hand is exponentially damped, SVD-based methods are viable alternatives to NLLS. An important advantage of these methods is that automation is easy. However, prior knowledge other than the number of sinusoids cannot be accommodated, and the S/N below which performance degradation begins (the threshold S/N) is higher than that of NLLS. However, a substantial reduction of the threshold S/N of SVD-based methods has recently been achieved.[36,37] In addition, the considerable computational load of SVD is being lowered continually.[32,38]

Table 1 Summary of Data Analysis Methods

	NLLS / BE	SVD-based	Integration
Model function	User-supplied	(see text)	—
Domain	Time/frequency	Time	Frequency
Prior knowledge	Accommodated	—	—
Starting values / distribution	User-supplied	—	—
Sampling interval	Arbitrary (time) Uniform (frequency)	Uniform	Uniform
Truncation	Accommodated (time) Baseline correction (frequency)	Accommodated	Baseline correction

Additional aspects such as robustness, computing efficiency, automation, and threshold S/N are difficult to quantitate, because they depend strongly on the particular implementation of the algorithm

2.3 Precision of the Model Parameters and Prior Knowledge

The standards against which one measures the precision of parameter estimates are the so-called Cramér–Rao bounds (CRBs).[39,40] These are the smallest possible standard deviations under the given conditions. No estimator is capable of dodging the CRBs. The CRBs are derived from

1. the model function (including the 'true' values of the model parameters);
2. the noise level;
3. the sample times;
4. prior knowledge.

Prior knowledge may pertain to, for example, relations between model parameters of overlapping members of multiplets.[13,41–43] Numerical studies of the CRBs reveal that prior knowledge is very beneficial for the precision of the remaining free model parameters. Other advantages of imposing prior knowledge are stabilization of the convergence process, lowering of the threshold S/N, and reduction of the computation time. Naturally, prior knowledge should be trustworthy.

Table 1 is a summary of data analysis techniques.

3 METABOLITE CONCENTRATIONS FROM SIGNAL INTENSITIES

3.1 Correction of Signal Intensities

Converting signal intensities to metabolite concentrations may need corrections for the effects of relaxation, scalar coupling, the applied pulse sequence, and instrumental parameters. The correction factors may be different for the separate lines.

3.1.1 Relaxation and Off-Resonance Effects

For repetition times T_r smaller than about four times the longitudinal relaxation time T_1, the signal intensity of a line j in a FID-like experiment is affected by partial saturation, and depends on T_r, T_{1j}, the total dephasing time T_{2j}*, the flip angle θ_j, and the offset frequency ω_j, in combination with the rf amplitude.[44] Corrections can be made because T_r, T_{1j}, T_{2j}*, θ_j, and ω_j are known or can be determined. Partial saturation can be avoided, at the cost of the signal-to-noise ratio per unit time, by using large T_r values or small flip angles, if the in vivo experiment allows this. With inhomogeneous rf fields, the flip angle depends on the position relative to the coil. In multipulse sequences, there is an effective flip angle depending on all applied pulses, and the signal intensity also has to be corrected for transverse relaxation during the delays. Experimental determination of T_2 values is easy for uncoupled but very difficult for strongly coupled spin systems. Metabolite T_{1j} and T_{2j} values may be age-dependent[45] and disease-dependent,[46] may show regional variations,[47,48] and may change during the development of pathologies. If a reference compound is used to calibrate the instrument (see below), the T_1 and T_2 values of this compound should also be taken into account.

3.1.2 Radiofrequency Field Inhomogeneity

This causes flip angles and signal strengths to vary over the VOI, and degrades slice profiles. Surface coils are notorious in this respect. This spatially varying sensitivity can be corrected.[11,49,50] The effects on the excitation of the spins can be minimized by using adiabatic rf pulses,[51] but remain for the detection. Correction is (especially for surface coils) more essential for magnetic resonance spectroscopic imaging (MRSI) than for single voxel MRS, because the dimensions of the field of view for MRSI are in general larger than those of the VOI for MRS. Methods used to correct effects of $\boldsymbol{B}_0$ inhomogeneity and eddy currents (see below) can easily be adapted to correct also for rf field inhomogeneity (see also ***Surface Coil NMR: Detection with Inhomogeneous Radiofrequency Field Antennas***).

3.1.3 Static Field Inhomogeneity and Eddy Currents

These effects distort the resonance frequencies, intensities, phases, widths, and shapes of the lines over the VOI, complicating the data analysis and the calculation of spectroscopic images from the line intensities in each MRSI voxel. These distortions can be derived from a reference signal and used for corrections. An example is given in Figure 2. Based on this, several methods have been proposed in the literature[12,52–54] and references cited therein.

3.1.4 Localization Effects

3.1.4.1 Radiofrequency field and $\boldsymbol{B}_0$ inhomogeneity and eddy currents. For these, see Sections 3.1.2 and 3.1.3.

3.1.4.2 Slice and VOI Profiles. In single voxel MRS, slice and VOI profiles are not perfect, and depend on the rf inhomogeneity and pulse type, and the localization method. The

Figure 2 NAA spectroscopic image of a human brain, reconstructed from a 3D in vivo ^{1}H MRSI data set (experiment by R. M. N. J. Lamerichs, P. R. Luyten, and H. van Vroonhoven, Philips Medical Systems, Best). Important steps in the signal processing comprised (1) suppression of residual water signals and correction for phase and frequency variations over the pixels by postprocessing techniques; (2) quantitation by frequency domain integration or time domain NLLS fitting, in the latter case combined with exploiting prior knowledge of spectral parameters; (3) reconstruction of spectroscopic images from frequency domain peak areas (a) or time domain amplitudes (b). Note that lipid contamination is significantly reduced by the time-domain quantitation approach

signal from the intended VOI may become increasingly contaminated with signals from outside when the VOI becomes relatively smaller, especially in add–subtraction techniques such as ISIS,[55] where all spins within the sensitive region of the coil are excited. Single shot techniques for localization are therefore to be preferred. Moreover, the exact volume of the VOI is unknown, hampering the calculation of absolute concentrations. This requires exact calibration of the actual volume of the selected regions of interest.[56]

In MRSI signal leaks from each voxel to the other voxels due to a discrete truncated sampling in $\boldsymbol{k}$-space.[57] This results in severe contamination, especially when the sample contains discontinuities or sharp edges. In this way, very intense signals (e.g., of lipids) may obscure the small metabolite signals by leaking over several voxels. Appropriate weighting in $\boldsymbol{k}$-space diminishes these effects, but decreases the spatial resolution somewhat.

3.1.4.3 Chemical shift. Slice selection with frequency-selective pulses and gradients shifts the slices of spins with different chemical shifts over a distance proportional to the ratio of their chemical shift and the gradient strength. For protons at 1.5 T, with a relevant chemical shift range of about 5 ppm, and a gradient strength of 10 mT m^{-1}, this displacement is about 1 mm. This is insignificant with respect to the VOI size of about 1 cm, but at higher field strengths, or for nuclei with larger chemical shift ranges (^{31}P and ^{13}C), this is no longer the case.

When the rf pulse bandwidth is not large compared with the chemical shift difference of coupled spins, multiplet components in different parts of the VOI are differently refocused in echo experiments, resulting in considerable signal loss.[58] Consider, for instance, lactate in the 3D PRESS experiment, with an rf pulse bandwidth of 1 kHz, and an echo time of 138 ms; at 1.5 T, 9%, and at 4 T, 24% of the CH_3 signal is lost.

It is obvious that localization errors will be more important when the sample is more heterogeneous. To minimize these errors, phantoms and spectroscopic or imaging techniques can be used to determine the size, shape and position of the selected VOI, and contamination and signal loss upon localization.[56]

3.1.5 Motions

These degrade the localization performance in single voxel single shot MRS; in multishot add–subtract experiments like ISIS[55] this effect is further increased. In MRSI,[57] motions produce large artifacts and contamination in the spectra of each voxel, and ghosting in the spectroscopic images. The effects of motions can be minimized by using single shot experiments, short echo times, and methods that trigger from the motion, as used in MRI.

3.1.6 J Modulation Effects

Transverse multiplet components of scalar-coupled spins dephase under the influence of the coupling. This dephasing is not refocused, partly refocused, or totally refocused in multipulse experiments, depending on pulse distances,[59] the offset frequencies of the spins, and the bandwidth of the refocusing pulses.[58] J modulation effects may therefore lead to complex modulation patterns in multipulse localization experiments; the several spectral components are phase and amplitude-modulated in different ways—the modulation depending on coupling constants, chemical shifts (in case of strong coupling), pulse delays and pulse angles. Moreover, if the spectral components are not all resolved then (partial) cancellation of signals with different phases may result.[43] The resulting intensity distortions therefore also depend on the $\boldsymbol{B}_0$ homogeneity; see Figure 3.

The intensity distortions can be determined experimentally on model solutions under well-defined conditions,[43] and used to correct the observed signal strengths, or as prior information in the NLLS fitting techniques to improve the accuracy. The linewidth has to be carefully controlled to keep the (partial) cancellation of signals with phase abnormalities comparable.[12,43]

3.1.7 Frequency-dependent Intensity Distortions by the Applied Pulse Sequence

Well-known examples are several water-suppressing pulse sequences. The effect can either be calculated or determined experimentally, allowing a correction.

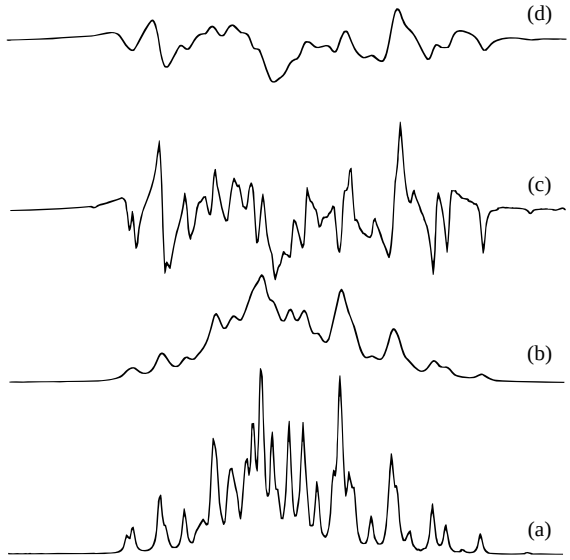

Figure 3 Real parts of the spectra obtained after FT of the 1.5 T γ and β simulated proton signals of glutamate: (a) and (b) were obtained after a single 90° pulse applied to the spin system in its equilibrium state; (c) and (d) were obtained from the echoes after a PRESS sequence with an echo time of 55 ms. In (a) and (c), the Lorentzian linewidth is 1 Hz; in (b) and (d), it is 3 Hz. The integrals of the spectra (a) and (b) are 16.4 and 16.3 (arbitrary units); the integrals of the absolute value mode signals corresponding to (c) and (d) are 13.6 and 7.8 (arbitrary units). Note the considerable signal loss in (d) as a result of phase anomalies due to *J* modulation combined with line overlap due to line broadening

3.1.8 Decoupling, Static, and Dynamic Nuclear Overhauser Effects; Exchange

Proton decoupling may result in completely different spectral patterns and intensity ratios in ^{31}P and ^{13}C spectra due to the decoupling and the heteronuclear Overhauser effect. Water suppression by selective inversion of the water resonance, followed by a relaxation delay to null the water signal, may result in distorted lineshapes and metabolite dependent intensity changes due to a dynamic nuclear Overhauser effect and/or exchange of protons. These effects can, in principle, be corrected for by determining them experimentally. See also ***Magnetization Transfer and Cross Relaxation in Tissue***; ***Proton Decoupling in Whole Body Carbon-13 MRS***; ***Proton Decoupling During In Vivo Whole Body Phosphorus MRS***.

3.1.9 Partial NMR Visibility

Metabolites with short T_2 values are visible as broad lines in the spectrum, or are totally invisible. For instance, the lipid signals in the normal brain in ^{1}H MRS are invisible, bone from the skull shows up as a broad peak in ^{31}P MRS, and glutamate is only about 65% NMR-visible in the ^{1}H spectrum of rat brain.[60] Corrections for (partial) NMR visibility are difficult.

3.2 Relative and Absolute Metabolite Concentrations

In this section, it is assumed that the corrections for distortions as described in Section 3.1 have been performed as far as possible. Relative metabolite concentrations are then obtained as signal intensity ratios, and often reported as such. This is a simple procedure, but global concentration changes are obscured. Absolute metabolite concentrations are of more clinical importance when tissue destruction or cellular damage is expected,[11] and allow better comparison of data from different studies. By acquiring, besides the metabolite signals, the signal of an internal or external reference compound with known concentration and volume, the instrument-dependent relation between signal intensity and concentration can be calibrated, and absolute concentrations obtained. Before discussing this further, some general remarks will be made.

1. To compare concentrations, the volumes occupied by the reference compound and the metabolites both have to be taken into account. These volumes can be determined by imaging. MRS localization errors may be different for the two volumes.
2. The detected NMR signal is an average over the VOI; biological tissue is heterogeneous, and the distribution over the VOI may be different for the reference and the several metabolites.
3. Signal intensity corrections as described in the previous section for both the reference and the metabolites have to be performed.
4. Loading modifies the rf field strength and coil sensitivity. By measuring the loaded and unloaded quality of the coil, or by mimicking coil loading by phantoms with conducting solutions,[11,61] a correction is possible.

3.2.1 Internal Reference

The use of an endogenous reference with a known concentration is the simplest way to obtain absolute metabolite concentrations. The PCr/Cr peak, NAA, or tissue water have been used for ^{1}H NMR, ATP, and also tissue water (as a heteronuclear reference) for ^{31}P MRS.[11,61] An internal reference has the advantages that the same experimental conditions and volume hold for reference and metabolites, making corrections for localization, rf inhomogeneity, and loading superfluous. A heteronuclear reference needs correction for the different resonance frequencies.[11] Disadvantages are that concentration and relaxation times of the reference may change with pathology and physiology. The reference peak may also contain signals from other compounds, an example being a contribution of *N*-acetylaspartylglutamate to the NAA peak.[3] The spatial distributions of reference and metabolites can be different.

3.2.2 External Reference

Several procedures have been described.[3,11] One possibility is to acquire together with the in vivo signal, a signal from a reference with known concentration and volume in a capillary close to the coil.[62] In a separate experiment, the patient is replaced by a phantom containing a known metabolite concentration. The same VOI is localized as in the in vivo experiment, acquiring signal from capillary and phantom. Relating the four signals gives the absolute concentrations. Alternative methods and corrections for partial volume effects when using water as reference can be found in the literature.[63–65]

3.2.3 Some Absolute Concentrations

The above considerations might give the impression that the determination of absolute concentrations by MRS is hardly possible. It is possible within the limitations mentioned, but it requires a lot of effort. In several studies, absolute concentrations have been reported,[3,11] and satisfactory agreement with other analysis methods was obtained. Some literature values of metabolite concentrations for normal adult human brain obtained from ^{1}H MRS are[45] (in mmol kg^{-1}) NAA 8.9 PCr + Cr 7.5, and Cho 1.3. For ^{31}P, adult human brain concentrations found were[11] (in mmol kg^{-1}) PME $\approx$ 3.5, Pi $\approx$ 2.0, PDE $\approx$ 11.0, PCR $\approx$ 4.5, and NTP (nucleotide triphosphates) $\approx$ 3.0; the corresponding values for human skeletal muscle are 2.2, 5.2, 4.2, 34, and 6.8 mmol kg^{-1}. For more data, see the review papers.[3,11,45]

4 RELATED ARTICLES

Chemical Shift Imaging; Proton Decoupling in Whole Body Carbon-13 MRS; Single Voxel Localized Proton NMR Spectroscopy of Human Brain In Vivo; Single Voxel Whole Body Phosphorus MRS; Surface Coil NMR: Detection with Inhomogeneous Radiofrequency Field Antennas.

5 REFERENCES

1. P. Diehl, E. Fluck, H. Günther, R. Kosfeld, and J. Seelig, eds. 'NMR Basic Principles and Progress' Springer-Verlag, Berlin, 1992, Vols. 26–28.
2. J. D. de Certaines, W. M. M. J. Bovée, and F. Podo eds., 'Magnetic Resonance Spectroscopy in Biology and Medicine', Pergamon Press, Oxford, 1992.
3. F. A. Howe, R. J. Maxwell, D. E. Saunders, M. M. Brown, and J. R. Griffiths, *Magn. Reson. Quart.*, 1993, **9**, 31.
4. J. C. Lindon and A. G. Ferrige, in 'Progress in Nuclear Magnetic Resonance Spectroscopy', eds. J. W. Emsley, J. Feeney, and L. H. Sutcliffe, Pergamon Press, Oxford, 1980, Vol. 14, p. 27.
5. J. C. Haselgrove, V. H. Subramanian, R. Christen, and J. S. Leigh, *Rev. Magn. Reson. Med.* 1987, **2**, 167.
6. D. S. Stephenson, 'Progress in Nuclear Magnetic Resonance Spectroscopy', 1988, Vol. 20, p. 515.
7. J. C. Hoch, *Meth. Enzymol.*, 1989, **176**, 216.
8. H. Gesmar, J. J. Led, and F. Abildgaard, 'Progress in Nuclear Magnetic Resonance Spectroscopy', eds. J. W. Emsley, J. Feeney, and L. H. Sutcliffe, Pergamon Press, Oxford, 1990, Vol. 22, p. 255.
9. R. E. Hoffman and G. C. Levy, 'Progress in Nuclear Magnetic Resonance Spectroscopy', eds. J. W. Emsley, J. Feeney, and L. H. Sutcliffe, Pergamon Press, Oxford, 1991, Vol. 23, p. 211.
10. R. de Beer and D. van Ormondt, in 'NMR Basic Principles and Progress', eds. P. Diehl, E. Fluck, A. Günther, R. Kosfeld, and J. Seelig, Springer-Verlag, Berlin, 1992, Vol. 26, p. 201.
11. E. B. Cady, in 'NMR Basic Principles and Progress', eds. P. Diehl, E. Fluck, A. Günther, R. Kosfeld, and J. Seeling, Springer-Verlag, Berlin, 1992, Vol. 26, p. 249.
12. A. A De Graaf, J. E. van Dijk, and W. M. M. J. Bovée, *Magn. Reson. Med.*, 1989, **13**, 343.
13. J. E. van Dijk, A. F. Mehlkopf, D. van Ormondt, and W. M. M. J. Bovée, *Magn. Reson. Med.*, 1992, **27**, 76.
14. G. H. Golub and V. Pereyra, *SIAM J. Numer. Anal.*, 1973, **10**, 413.
15. F. S. Digennaro, and D. Cowburn, *J. Magn. Reson.*, 1992, **96**, 582.
16. C. B. Lucasius and G. Kateman, *Chemometrics and Intelligent Laboratory Systems*, 1993, **19**, 1.
17. G. L. Bretthorst, *J. Magn. Reson.*, 1992, **98**, 501.
18. J. Skilling, *American Laboratory*, 1992, October, 32J.
19. J. S. Nelson and T. R. Brown, *J. Magn. Reson.*, 1989, **84**, 95.
20. F. Montigny, J. Brondeau, and D. Canet, *Chem. Phys. Lett.*, 1990, **170**, 175.
21. M. Joliot, B. M. Mazoyer, and R. H. Huesman, *Magn. Reson. Med.*, 1991, **18**, 358.
22. C. Burger, G. McKinnon, R. Büchli, and P. Boesiger, *Magn. Reson. Med.*, 1991, **21**, 216.
23. E. K.-Y Ho, R. E. Snyder, and P. S. Allen, *J. Magn. Reson.*, 1992, **99**, 590.
24. A. van den Boogaart, M. Ala-Korpela, J. Jokisaari, and J. R. Griffiths, *Magn. Reson. Med.*, 1994, **31**, 347.
25. A. R. Mazzeo and G. C. Levy, *Magn. Reson. Med.*, 1991, **17**, 483.
26. S. A. Rashid, W. R. Adam, D. J. Craik, B. P. Shenan, and R. M. Wellard, *Magn. Reson. Med.*, 1991, **17**, 213.
27. A. Knijn, R. de Beer, and D. van Ormondt, *J. Magn. Reson.*, 1992, **97**, 444.
28. N. Delprat, B. Escudié, P. Guillemin, R. Kronland-Martinet, P. Tchamitchian, and B. Torrésani, *IEEE Trans. Information Theory*, 1991, **38**, 644.
29. K. McLeod and M. B. Comisarov, *J. Magn. Reson.*, 1989, **84**, 490.
30. R. Nadjari and J.-P. H. Grivet, *J. Magn. Reson.*, 1991, **91**, 353.
31. R. de Beer, P. Bachert-Baumann, W. M. M. J. Bovée, E. Cady, J. Chambron, R. Domisse, C. J. A. Echteld, R. Mathur de Vré, and S. Williams, *Magn. Reson. Imaging*, 1995, **13**, 169.
32. W. W. F. Pijnappel, A. van den Boogaart, R. de Beer, and D. van Ormondt, *J. Magn. Reson.*, 1992, **97**, 122.
33. D. V. Bhaskar Rao and K. S. Arun, *Proc. IEEE*, 1992, **80**, 283.
34. A. J. van der Veen, E. F. Deprettere, and A. L. Swindlehurst, *Proc. IEEE*, 1993, **81**, 1277.
35. P. Mutzenhardt, F. Montigny, and D. Canet, *J. Magn. Reson., Ser A*, 1993, **101**, 202.
36. A. Diop, A. Briguet, and D. Graveron-Demilly, *Magn. Reson. Med.*, 1992, **27**, 318.
37. H. Chen, S. Van Huffel, C. Decanniere, and P. Van Hecke, *J. Magn. Reson., Ser. A.*, 1994, **109**, 46.
38. H. Park, S. van Huffel, and L. Eldén, in 'Proceeding of International Conference on Acoustics, Speech, and Signal Processing, Adelaide, 1994', Vol. 4, pp. 25–28.
39. J. P. Norton, 'An Introduction to Identification', Academic Press, London, 1986.
40. A. van den Bos, in 'Handbook of Measurement Science', John Wiley & Sons, Chichester, 1982, Vol. 1, p. 331.
41. A. de Roos, J. Doornbos, P. R. Luyten, L. J. M. P. Oosterwaal, E. E. van der Wall, and J. A. den Hollander, *J. Magn. Reson. Imaging*, 1992, **2**, 711.
42. J. W. C. van der Veen, R. de Beer, P. R. Luyten, and D. van Ormondt, *Magn. Reson. Med.*, 1988, **6**, 92.
43. A. A. de Graaf and W. M. M. J. Bovée, *Magn. Reson. Med.*, 1990, **15**, 305.
44. R. R. Ernst, in 'Advances in Magnetic Resonance', ed. J. S. Waugh, Academic Press, New York, 1966, Vol. 2, p. 1.
45. R. Kreis, T. Ernst, and B. D. Ross, *Magn. Reson. Med.*, 1993, **30**, 424.
46. D. Sappey-Marinier, G. Calabrese, H. P. Hetherington, S. N. G. Fisher, R. Deicken, C. van Dyke, G. Fein, and M. W. Weiner, *Magn. Reson. Med.*, 1992, **26**, 313.
47. J. Frahm, H. Bruhn, M. L. Gyngell, K. D. Merboldt, W. Hänicke, and R. Sauter, *Magn. Reson. Med.*, 1989, **11**, 47.
48. P. A. Narayana, D. Johnston, and D. P. Flamig, *Magn. Reson. Imaging*, 1991, **9**, 303.
49. G. B. Matson, D. J. Meyerhoff. T. J. Lawry, R. S. Lara, J. Duijn, R. F. Deicken, and M. W. Weiner, *NMR Biomed.*, 1993, **6**, 215.

50. K. Roth, K. Hubesch, D. J. Meyerhoff, S. Naruse, J. R. Gober, T. J. Lawry, M. D. Boska, G. B. Matson, and M. W. Weiner, *J. Magn. Reson.*, 1989, **81**, 299.
51. M. Garwood and K. Ugurbil, in 'NMR Basic Principles and Progress', eds. P. Diehl, E. Fluck, H. Günther, R. Kosfeld, and J. Seelig, Springer-Verlag, Berlin, 1992, Vol. 26, p. 109.
52. G. Johnson, K. J. Jung, E. X. Hu, and S. K. Hilal, *Magn. Reson. Med.*, 1993, **30**, 255.
53. J. R. Roebuck, D. O. Hearshen, M. O'Donnell, and T. Raidy, *Magn. Reson. Med.*, 1993, **30**, 277.
54. P. Webb, D. Spielman, and A. Macovski, *Magn. Reson. Med.*, 1992, **23**, 1.
55. R. J. Ordidge, A. Connelly, and J. A. B. Lohman, *J. Magn. Reson.*, 1986, **66**, 283.
56. W. M. M. J. Bovée, in 'Magnetic Resonance Spectroscopy in Biology and Medicine', eds. J. D. de Certaines, W. M. M. J. Bovée, and F. Foder, Pergamon Press, Oxford, 1992, p. 209.
57. M. Decorps and D. Bourgeois, in 'NMR Basic Principles and Progress', eds. P. Diehl, E. Fluck, H. Günther, R. Kosfeld, and J. Seelig, Springer-Verlag, Berlin, 1992, Vol. 27, p. 119.
58. J. Slotboom, A. F. Mehlkopf, and W. M. M. J. Bovée, *J. Magn. Reson., Ser. A*, 1994, **108**, 38.
59. A. Abragam, 'The Principles of Nuclear Magnetism', Clarendon Press, Oxford, 1961, pp. 480–510.
60. A. A. de Graaf, N. E. P. Deutz, D. K. Bosman, R. A. F. M. Chamuleau, J. G. De Haan, and W. M. M. J. Bovée, *NMR Biomed.*, 1991, **4**, 31.
61. R. Büchli and P. Boesiger, *Magn. Reson. Med.*, 1993, **30**, 552.
62. P. R. Luyten, J. P. Groen, J. W. Vermeulen, and J. A. den Hollander, *Magn. Reson. Med.*, 1989, **11**, 21.
63. T. Ernst, R. Kreis, and B. D. Ross, *J. Magn. Reson., Ser. B*, 1993, **102**, 1.
64. R. Kreis, T. Ernst, and B. D. Ross, *J. Magn. Reson., Ser. B*, 1993, **102**, 9.
65. P. Christiansen, O. Henriksen, M. Stubgaard, P. Gideon, and H. B. W. Larsson, *Magn. Reson. Imaging*, 1993, **11**, 107.

Biographical Sketches

Wim M. M. J. Bovée. *b* 1938. M.Sc., 1969, chemistry, Ph.D., 1975, physics, Delft University. Billiton Research Laboratories, Arnhem, 1969–70. Delft University 1970–present. Research specialties: MR relaxation, in vivo MRS and MRI.

Ronald de Beer. *b* 1944. M.Sc., 1967, Ph.D., 1971, physics, Delft University. Delft University 1967–present. Research specialty: signal processing for MR.

Dirk van Ormondt. *b* 1936. M.Sc., 1959, Ph.D., 1968, physics, Delft University, 1969–70, postdoc., University of Calgary with H. A. Buckmaster, 1970–71, postdoc., Clarendon Laboratory, Oxford with J. M. Baker. Delft University 1971–present. Research specialty: signal processing for MR.

Peter R. Luyten. *b* 1954. M.Sc., 1980, Ph.D., 1984, Free University, Amsterdam. Philips Medical Systems, Best, 1984–present. Research specialty: in vivo MRS.

Jan A. den Hollander. *b* 1947. M.Sc., Ph.D., physical chemistry, University of Leiden. Exchange visitor at the Biophysics Research Department, Bell Laboratories, Murray Hill, New Jersey, 1977–79. Research associate, Department of Molecular Biophysics and Biochemistry, Yale University, New Haven, Connecticut, 1979–83. Staff scientist, Max-Planck Institut für Systemphysiologie, Dortmund, Germany, 1983–84. Philips Medical Systems, Best, The Netherlands, 1984–1991. Professor of Medicine, University of Alabama at Birmingham, 1991–present.

Rotating Frame Methods for Spectroscopic Localization

Peter Styles

MRC Biochemical and Clinical Magnetic Resonance Unit, Oxford, UK

1 INTRODUCTION

Rotating frame spectroscopic localization techniques enable high-resolution spectra to be obtained from spatially resolved slices within a sample. In contrast to most localization schemes where space is encoded by means of switched gradients in the $\boldsymbol{B}_0$ field, the rotating frame method uses a gradient rf transmitter field ($\boldsymbol{B}_1$) to effect the spatial discrimination. Most applications have been in ^{31}P spectroscopy of metabolism of animals and humans. Being a one-dimensional (spatial) technique, the method is most appropriately employed in situations where the anatomy consists of approximately planar tissues.

In the late 1970s, there was great interest in developing methodologies for NMR imaging, and the concept of using a gradient $\boldsymbol{B}_1$ field to encode position was proposed by Hoult.[1] He demonstrated that a two-dimensional proton image could be produced by defining one dimension by a static $\boldsymbol{B}_0$ gradient, and the second dimension by a gradient transmitter field. A straightforward modification of this 'rotating frame zeugmatography' was to apply the method to spectroscopic localization. The $\boldsymbol{B}_0$ read gradient was omitted, preserving the chemical shift information at the expense of one dimension of spatial resolution.[2] Spatial encoding is achieved by applying, in separate data acquisitions, an incremented transmitter pulse, and performing a two-dimensional Fourier transformation to obtain a plot of chemical shift versus $\boldsymbol{B}_1$ strength. Thus, rotating frame spectroscopic imaging is a one-dimensional chemical shift imaging (CSI) technique. A second form of implementation enables spectra to be obtained from just a limited number of regions by combining data which together form a Fourier series defining the required voxel shape and position.[3]

A review article[4] provides a more comprehensive reference list than can be accommodated here.

2 PRINCIPLES OF ROTATING FRAME SPECTROSCOPIC LOCALIZATION

2.1 Rotating Frame Spectroscopic Imaging

When a nuclear spin is irradiated by a transmitter field at the Larmor frequency, then, in the rotating frame of reference, the spin precesses around the $\boldsymbol{B}_1$ field at a nutational frequency Ω given by

$$\Omega = \gamma B_1 \tag{1}$$

In a homogeneous $\boldsymbol{B}_1$ field, detection of this frequency is trivial, and is undertaken every time one determines a $\pi/2$ pulse length. Signal amplitude is measured as a function of pulse duration, and a plot of amplitude versus pulse length produces a sine wave of frequency Ω.

If, instead of using a conventional probe, we employ a transmitter coil which produces a gradient in, say, the x direction [$B_1 = f(x)$], then the nutational frequency is directly related to the position of the sample along the x axis:

$$\Omega = \gamma f(x) \tag{2}$$

Detection of Ω is again a simple matter of determining signal amplitude as a function of pulse length, but we now have a range of frequencies reflecting the distribution of the sample in the gradient field. Therefore, a Fourier transform is required to interpret the variation of amplitude with pulse length. The result of this transform is a plot of amplitude versus Ω, and so represents the signal strength as a function of $\boldsymbol{B}_1$ and hence position in the x direction.

The experimental sequence may be represented as

$$r\theta_x - \text{Acq.}\ (r = 1, \ldots, n) \tag{3}$$

where the pulse θ_x is increased by incremental steps in each of n data accumulations. In the general case, where the sample consists of various chemical species, a two-dimensional Fourier transform of these n FIDs produces a data set with chemical shift on one axis and position in the x direction on the other. The protocol is illustrated in Figure 1, and was the first to be used for obtaining chemical shift images from a human.[5]

2.2 Phase-Modulated Rotating Frame Imaging

The experiment described by sequence (3) produces signals which are amplitude modulated as a function of Ω, and this incurs an inevitable loss in sensitivity. The maximum signal is only recovered when $r\theta_x$ is an odd multiple of $\pi/2$, and passes through a null for even multiples of $\pi/2$. This disadvantage can be avoided by converting the amplitude modulation into phase modulation by using the following pulse sequence:

$$r\theta_x - (\pi/2)_y - \text{Acq.}\ (r = 1, \ldots, n) \tag{4}$$

The second pulse, which is not incremented, rotates the magnetization from the zy plane into the xy plane, and thus the maximum signal is obtained irrespective of the tip angle generated by the $r\theta_x$ pulse. This 'phase-modulated rotating frame' protocol[1,6] is illustrated in Figure 2.

One difficulty of the phase-encoded sequence is that the data generate phase twisted lines with dispersion components obscuring both spectral and spatial information. The solution is to repeat the complete sequence with the phase of one of the pulses altered by π. To process the data, each set of FIDs is separately transformed, one transform is then reversed in the spatial dimension and the two sets added. The dispersion components now subtract to obtain pure absorption spectra.

2.3 Fourier Series Methods

In certain instances, it is sufficient to obtain signals from a limited number of slices, and then the rotating frame method can be implemented in a simpler way. Instead of collecting a full two-dimensional data set, transmitter pulses may be chosen such that the region of interest experiences tip angles which are odd multiples of $\pi/2$. Appropriate combination of the several FIDs (addition or subtraction, depending on the sign of the signal) will result in the maximum signal from the region of interest, but destructive interference of signals from elsewhere. The shape and extent of the sensitive region is determined by the number of pulse angles used, and the weighting function applied to successive data acquisitions. In essence, the spatial response of each collection forms a Fourier component of the final selected region, and so the technique is usually described as the 'Fourier series window' method.[3] Provided that a reasonable number of FIDs have been collected, it is possible to combine them in different ways, thus defining more than one window from a single data set. Developments of this approach have included the use of adiabatic pulses to reduce artifacts, and a combination of $\boldsymbol{B}_0$ and $\boldsymbol{B}_1$ techniques to improve slice definition.[7]

2.4 Relaxation Time Measurements and Magnetization Transfer Sequences

The basic rotating frame sequences can be combined with saturation, inversion or spin echo pulses, thus facilitating the determination of spatially localized relaxation times, or providing a means of spectral editing. One of the benefits of $\boldsymbol{B}_1$ localization over $\boldsymbol{B}_0$ methods is that no time is lost waiting for gradient recovery, and therefore nuclear species with short relaxation times may be detected and quantitated.[8]

Magnetization transfer experiments may also be implemented,[9] giving localized measurement of certain chemical exchange processes in vivo.

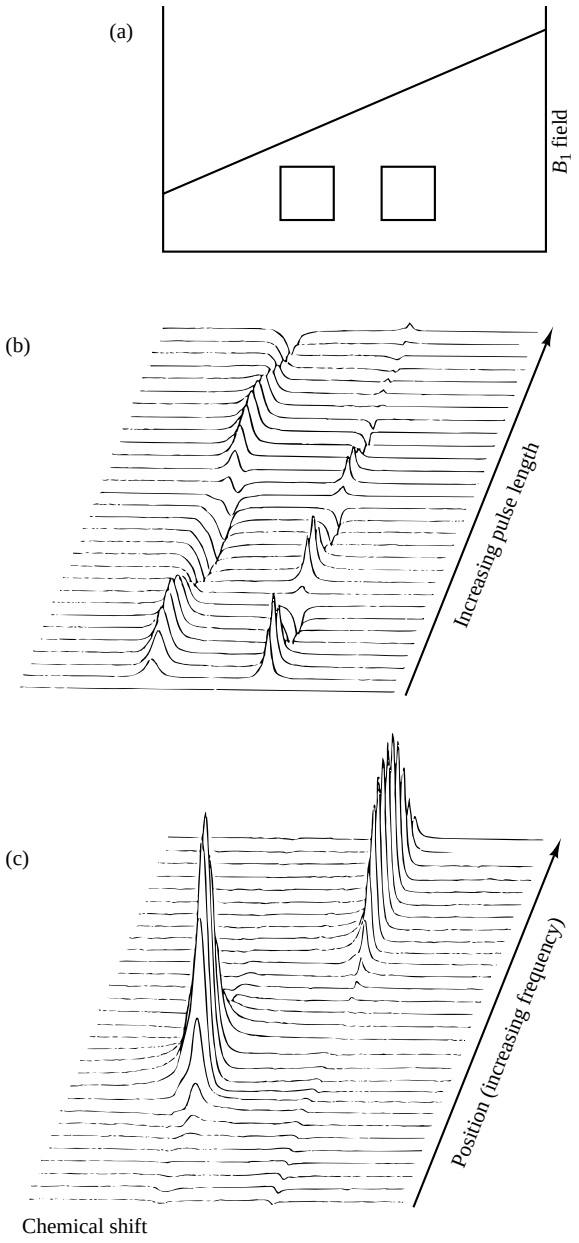

Figure 1 The acquisition of rotating frame imaging data from a phantom. (a) Schematic representation of a two-compartment phantom placed in a gradient $\boldsymbol{B}_1$ transmitter field. (b) A set of 'pulse and collect' spectra obtained from the phantom; the pulse length is incremented in successive data collections. (c) The data generated by performing a second Fourier transformation on the set of spectra shown in (b). The vertical axis represents the frequency with which the signal modulates as a function of the increasing pulse length, and therefore displays the position of the phantom in the gradient $\boldsymbol{B}_1$ field. (Reproduced by permission of Springer-Verlag from P. Diel, E. Fluck, H. Gunther, R. Kosfeld, and J. Seelig (eds), 'In Vivo Magnetic Resonance Spectroscopy. II: Localization and Spectral Editing', Berlin, 1992, p. 45)

3 ROTATING FRAME LOCALIZATION IN PRACTICE

3.1 Probes for Rotating Frame Spectroscopy

The generation of a linear gradient in the $\boldsymbol{B}_1$ field is less straightforward than in the $\boldsymbol{B}_0$ field. Hoult[1] used a saddle-shaped transmitter coil with three turns on one side and one turn, wound in the opposite sense, on the other. To perform the phase-encoded protocol, a second orthogonal transmitter coil is needed to generate the $(\pi/2)_y$ pulse. This arrangement has never been used for in vivo spectroscopy due to the excessive amounts of rf power which would be required. Instead, surface coils have been used for production of the $\boldsymbol{B}_1$ gradient. This approach is, at best, a pragmatic solution on several counts. First, a surface coil does indeed provide a gradient field, but it is only approximately linear over a restricted region of space. Secondly, although the isofield contours are relatively flat close to the axis of the coil, they curve towards the plane of the coil away from this central region. Finally, the phase encoding experiment ideally needs a homogeneous pulse in addition to the gradient pulse for spatial encoding. These problems constitute substantial drawbacks, but the particular

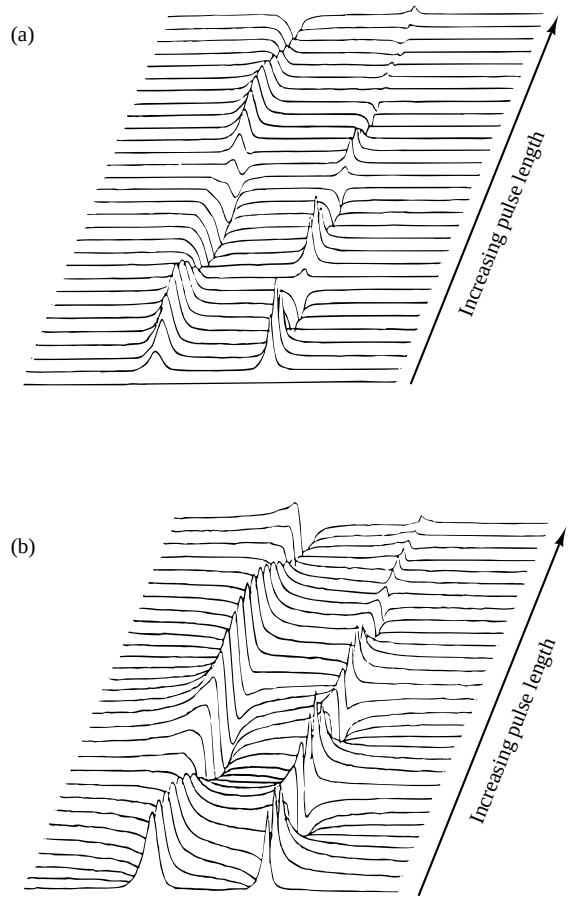

Figure 2 A comparison of spectra collected by (a) amplitude and (b) phase-modulated protocols. The data were obtained from the same phantom as in Figure 1, and are sets of individual spectra prior to the second Fourier transformation. Note that the full signal strength is obtained at all pulse lengths in the phase-modulated experiment. (Reproduced by permission of Springer-Verlag from P. Diel, E. Fluck, H. Gunther, R. Kosfeld and J. Seelig (eds), 'In Vivo Magnetic Resonance Spectroscopy. II: Localization and Spectral Editing', Berlin, 1992, p. 45)

suitability of the surface coil for in vivo spectroscopy has encouraged workers to devise methods which maintain the integrity of the experiment within acceptable bounds. Three approaches have been adopted:

1. Single surface coil transmit/receive probes can be used, provided that the sample is restricted to a region close to the coil axis. This method is not of general application, but has been used, for example, to obtain information from the excised bovine globe.
2. A single surface coil probe may be used if some other localization strategy is incorporated into the protocol to restrict the localized volume to a column bounded within the surface coil perimeter. $\boldsymbol{B}_0$ methods such as ISIS[10] can be used to define the lateral extent of the detected signal, and rotating frame localization subdivides this region into planar slices.[6]
3. Separate surface coils for transmit and receive overcome many of the difficulties encountered.[5] A surface coil transmitter produces a nearly linear field gradient over a region between about $0.3r_t$ and r_t (r_t is the radius of the transmitter coil), and close to the coil axis. If a smaller receiver coil is positioned coaxially with the transmitter, but offset by the appropriate amount, then the detected signals will come from this linear transmitter region. The two coils must, of course, incorporate suitable circuitry to avoid the electrical coupling caused by their mutual inductance.

3.2 Phase-Modulated Rotating Frame Implementation

The most efficient rotating frame protocol is the phase-modulated version, but this experiment requires a homogeneous $\pi/2$ phase-encoding pulse. In practice, the provision of yet another coil to produce this irradiation has been avoided. Instead, the phase-encoding pulse is usually applied by the gradient coil. Clearly, this will only produce an accurate $\pi/2$ rotation in a single plane. However, provided that the region of interest does not extend over too large a range of $\boldsymbol{B}_1$ field, the experiment still gives good results. Away from the optimum plane, the main consequence is a small loss of sensitivity ($\leqslant 15\%$) where the phase-encoding pulse is within the range $\pi/4$ to $3\pi/4$.

An alternative solution to this problem is to employ an adiabatic pulse in place of the hard $\pi/2$ pulse.[11] $\boldsymbol{B}_1$ insensitive plane rotation pulses are now available, their main drawback being that they are longer than hard pulses, and so introduce relaxation dependent losses into the sequence.

4 APPLICATIONS OF ROTATING FRAME METHODS

Rotating frame methods[4] are most usefully applied in situations where a surface coil provides the optimum method of data collection, and the anatomy is suited to planar localization. In humans, the heart and liver have both been studied extensively. In each case, the tissue of interest needs to be distinguished from the overlying intercostal muscles. The liver is of particular note because, unlike muscle, it contains no creatine phosphate. Thus, the efficacy of the localization can be easily tested using the liver as an 'in vivo phantom' (Figure 3). In other studies of the human, spectra have been obtained from the brain, breast, leg muscle, and several types of tumor. A variety of disorders have been investigated, including heart failure, hepatic diseases, and trauma of the brain.

Many experiments have also been performed on animal models, perhaps the most striking being the detection of metabolite concentration differences across the ventricular wall of the exposed beating heart.[12,13] Although most studies have used the phosphorus nucleus, carbon, fluorine, and sodium spectra have also been obtained.

The absence of time-consuming switched field gradients is important for the detection and measurement of short T_2 species such as the broad phosphodiester resonances in brain.[8] In the liver, proton spin echo rotating frame spectroscopy has

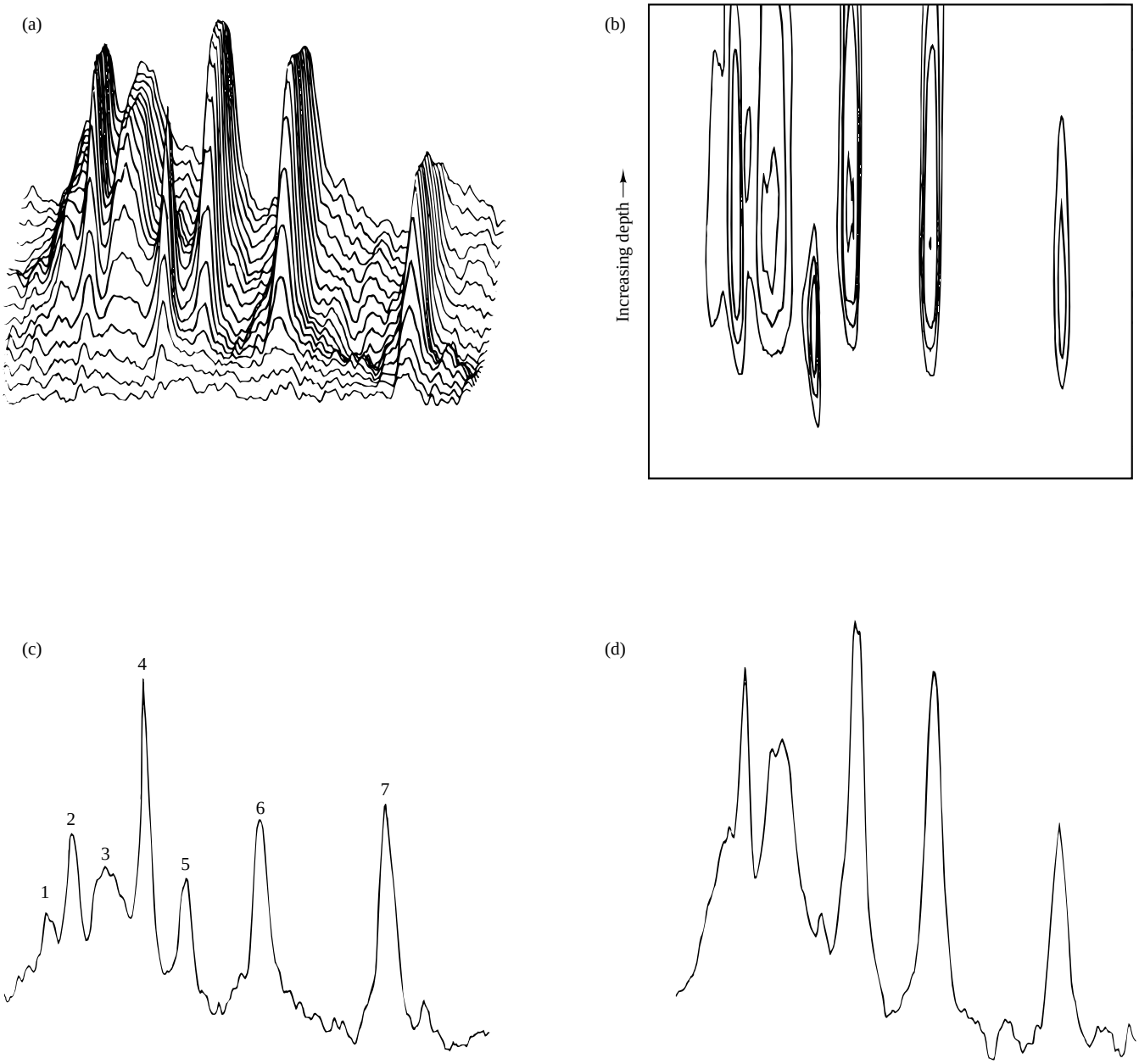

Figure 3 A phase-modulated rotating frame spectroscopic image obtained from the chest of a human subject in the region where the intercostal muscles overlie the liver. The data are presented as: (a) a stacked plot of the spectra; (b) a contour plot; (c) a single spectrum from the muscle region; (d) a single spectrum from the liver region. Peak assignment: 1, phosphomonoesters; 2, inorganic phosphate; 3, phosphodiesters; 4, creatine phosphate; 5–7, mainly adenosine trisphosphate. Note the localization of the creatine phosphate to the superficial region corresponding to the intercostal muscles

been used to quantitate iron overload,[14] which manifests itself by a dramatic decrease in the T_2 of water.

5 THE ROLE OF ROTATING FRAME TECHNIQUES

Techniques for localized spectroscopy have undergone considerable development over the last 10 years, and it is instructive to consider both the merits and disadvantages of rotating frame methods in comparison to other localization schemes.

There is no doubt that the rotating frame approach lacks the versatility of phase-encoded Fourier imaging using switched $\boldsymbol{B}_0$ field gradients. $\boldsymbol{B}_1$ methods give localization in only one dimension, suffer from off-resonance effects, and often require specialized hardware in the form of multicoil probes. Also, there is no direct correlation between the localized spectroscopic data and anatomical information obtained from an MRI image taken during the same investigation.

On the other hand, the absence of switched gradients imparts several benefits. The signal is collected immediately after the transmitter pulse, thus avoiding phasing problems and

loss of signal due to T_2 effects. The experiment is silent, which can be particularly important when a subject is nervous or young. Finally, the localization is defined relative to the probe (as distinct to the magnet), and so moving objects such as the chest wall or exposed beating heart can be scanned by attaching the probe directly to the tissue.

Therefore, rotating frame localization is a technique which does not match the generality of $\boldsymbol{B}_0$ Fourier methods, but can offer very significant advantages in specific applications such as those outlined above.

6 RELATED ARTICLES

Chemical Shift Imaging; Spatial Localization Techniques for Human MRS; Whole Body Studies: Impact of MRS.

7 REFERENCES

1. D. I. Hoult, *J. Magn. Reson.*, 1979, **33**, 183.
2. S. J. Cox and P. Styles, *J. Magn. Reson.*, 1980, **40**, 209.
3. The Fourier series experiment was described simultaneously by several workers, including: K. R. Metz and R. W. Briggs, *J. Magn. Reson.*, 1985, **64**, 172; J. Pekar, J. S. Leigh, and B. Chance, *J. Magn. Reson.*, 1985, **64**, 115; M. Garwood, T. Schleich, B. D. Ross, G. B. Matson, and W. D. Winters, *J. Magn. Reson.*, 1985, **65**, 239.
4. P. Styles, in 'In Vivo Magnetic Resonance Spectroscopy. II: Localization and Spectral Editing', ed. P. Diehl, E. Fluck, H. Günther, R. Kosfeld, and J. Seelig, Springer, Berlin, 1992, p. 45.
5. P. Styles, C. A. Scott, and G. K. Radda, *Magn. Reson. Med.*, 1985, **2**, 402.
6. M. J. Blackledge, B. Rajagopalan, R. D. Oberhaensli, N. M. Bolas, P. Styles, and G. K. Radda. *Proc. Natl. Acad. Sci. USA*, 1987, **84**, 4283.
7. P.-M. Robitaille, H. Merkle, E. Sublett, K. Hendrich, B. Lew, G. Path, A. H. L. From, R. J. Bache, M. Garwood, and K. Ugurbil. *Magn. Reson. Med.*, 1989, **10**, 14.
8. P. M. Kilby, J. L. Allis, and G. K. Radda, *FEBS Lett.*, 1990 **272**, 163.
9. T. A. D. Cadoux-Hudson, M. J. Blackledge, and G. K. Radda, *FASEB J.*, 1989, **3**, 2660.
10. R. J. Ordidge, A. Connelly, and J. A. B. Lohman, *J. Magn. Reson.*, 1986, **66**, 283.
11. K. Hendrich, H. Merkle, S. Weisdorf, W. Vine, M. Garwood, and K. Ugurbil, *J. Magn. Reson.*, 1991, **92**, 258.
12. P.-M. Robitaille, H. Merkle, B. Lew, G. Path, K. Hendrich, P. Lindstrom, A. H. L. From, M. Garwood, R. J. Bache, and K. Ugurbil, *Magn. Reson. Med.*, 1990, **16**, 91.
13. B. Rajagopalan, J. D. Bristow, and G. K. Radda. *Cardiovasc. Res.*, 1989, **23**, 1015.
14. R. M. Dixon and P. Styles, *Magn. Reson. Med.*, 1993, **29**, 110.

Biographical Sketch

Peter Styles. *b* 1946. B.Sc., 1968, University of Sussex, D. Phil., 1984. University of Oxford, Introduced to NMR by Rex Richards and David Hoult, then worked with George Radda. Initial employment as a designer of a high field spectrometer, later as an in vivo spectroscopist. Currently acting director, Medical Research Council Biochemical and Clinical Magnetic Resonance Unit, University of Oxford. Approx. 90 publications. Research interests include: instrumental and experimental aspects of in vivo spectroscopy, metabolic control in skeletal muscle, and application of MRI and MRS in clinical research.

Single Voxel Localized Proton NMR Spectroscopy of Human Brain In Vivo

Jens Frahm and Wolfgang Hänicke

Biomedizinische NMR Forschungs GmbH am Max-Planck-Institut für Biophysikalische Chemie, Göttingen, Germany

1 INTRODUCTION

The unique potential of in vivo NMR for the life sciences is based on true noninvasiveness and tremendous methodologic flexibility. A continous flow of novel techniques allows the addressing of fundamental questions related to structural, functional, and metabolic aspects of life processes within the intact human body. In particular, in vivo spectroscopy yields detailed insights into cellular metabolism of organ systems by combining the analytical strength of high-resolution NMR with image-controlled spatial localization within a three-dimensional object. Typically, localized proton NMR spectroscopy of human brain provides access to tissue metabolites with millimolar concentrations from a few milliliter volumes and within measuring times of less than 10 min.

Early studies employed surface radiofrequency (rf) coils[1] and homogeneity profiling of the static magnetic field[2] to assess bioenergetics via phosphate metabolites.[3–5] Although the simple surface coil technique was applied to other organs and nuclei including proton NMR of human brain,[6] optimum placement of a local rf antenna suffered severe limitations and often required surgical interventions as demonstrated by animal work.[7,8] With the availability of well-controllable magnetic field gradients through advances in NMR imaging, improved localization methods took advantage of the principles of spatial encoding by magnetic field gradient pulses and slice selection by frequency-selective rf excitation in the presence of a magnetic field gradient. Two complementary approaches were developed that are able to accomplish three-dimensional spatial discrimination of the NMR signal:

- chemical shift imaging (CSI) techniques that cover a column, plane, or volume in a two- (2D), three- (3D), or four-dimensional spectroscopic image where spatial information is phase encoded onto the chemical shift information of the NMR frequencies,
- single voxel spectroscopy techniques that acquire spectroscopic time-domain data directly from a restricted volume of interest (VOI) selected prior to or during rf excitation.

The aim of this contribution is to discuss the mainstream of in vivo proton NMR spectroscopy techniques based on single voxel localization. The capability of performing human studies on whole body systems is ensured by emphasizing the compliance of pertinent sequences with safety requirements and instrumental limitations, e.g. in terms of rf power. Methodologic descriptions include an outline of specific merits and pitfalls, while selected studies of human brain metabolism illustrate particularly advantageous applications.

2 LOCALIZATION TECHNIQUES

Beyond structure elucidation of biomacromolecules, NMR studies of biologic systems comprise body fluids, cell cultures, excised tissues, perfused organs, and intact living subjects (***Body Fluids***, ***Cells and Cell Systems MRS***, and ***Tissue NMR Ex Vivo***). Respective applications benefit from a widespread range of instruments and sequences and cover a large diversity of basic science and clinical questions. Even when restricting this complexity to single voxel proton NMR there are multiple factors that affect the design and outcome of localization techniques. This particularly holds true for differences in (i) hardware of small-bore high-field spectrometers and whole body instruments (see Section 2.5), (ii) relaxation times and available measuring times under in vitro and in vivo conditions, (iii) the extent of motion in nonliving materials, anesthetized animals, and human subjects, and (iv) cooperativity of healthy subjects and patients.

Thus, optimum strategies for localization sequences applicable to human subjects not only have to address relaxation losses and suppression factors, but also critically rely on practical simplicity and stability as crucial elements for ease of implementation and use as well as for the reliability of the results. Accordingly, the following sections discuss surface coil techniques and *i*mage *s*elected *i*n vivo *s*pectroscopy (ISIS) for historic reasons, while special emphasis is paid to *p*oint-*res*olved *s*pectroscopy (PRESS) and *sti*mulated *e*cho *a*cquisition *m*ode (STEAM) spectroscopy as the major localization techniques for single voxel proton NMR on whole body units.

2.1 Surface Coils and Beyond

The popularity of local rf antennae or 'surface' coils is based on the simplicity of the concept and the excellent signal-to-noise ratio (S/N; see ***Surface Coil NMR: Detection with Inhomogeneous Radiofrequency Field Antennas***). However, from a technical point of view the latter benefit is not only due to a good filling factor but is also due to a sensitive volume extending far beyond the coil radius.[9] In fact, the contributing volume is not even well-defined, since it strongly depends on the experimental parameters of the rf pulse sequence (e.g., repetition time, flip angle used) and the tissue T_1 relaxation times involved.[10]

Figure 1 depicts flip angle distributions of a single-turn surface coil for $\boldsymbol{B}_1$ field strengths yielding flip angles of either 90° (top) or 180° (bottom) at a distance $r/2$ from the center of the coil. While pertinent flip angle distributions result in inhomogeneous *excitation* of transverse magnetizations, corresponding sensitivity distributions also affect the *acquisition* of the NMR signal by surface coil reception. Thus, transmit–receive use of an inhomogeneous coil leads to a quadratic dependence on B_1 which may be reduced to a linear dependence by combining surface coil detection with homogeneous excitation using a second circumscribing coil.

Assuming a transmit–receive situation, Figure 2 describes the sensitivity σ of a single-turn surface coil as a function of TR/T_1 and rf flip angle

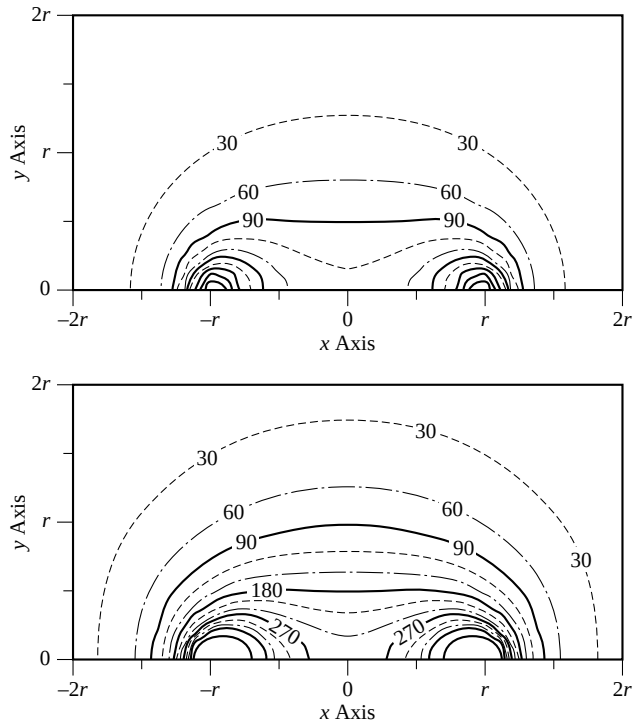

Figure 1 Flip angle distribution of a single-turn flat surface coil (radius r) in the central xy plane perpendicular to the coil for two different $\boldsymbol{B}_1$ field strengths adjusted such that the flip angle at a distance $r/2$ from the center of the coil is either 90° (top) or 180° (bottom). Iso-$\boldsymbol{B}_1$ curves are given for selected flip angles in steps of 30°. The coil is oriented parallel to the static $\boldsymbol{B}_0$ field (z axis). (Reproduced by permission of Academic Press from Haase et al.[10])

$$\sigma = \iiint B_1(x,\ y,\ z)S(x,\ y,\ z)\mathrm{d}x\ \mathrm{d}y\ \mathrm{d}z \qquad (1)$$

with $B_1(x,y,z)$ the rf field distribution as demonstrated in Figure 1. $S(x,y,z)$ denotes the local strength of the FID of a repetitive single pulse experiment with equilibrium magnetization M_0, flip angle α, repetition time TR, assuming the absence of transverse components (i.e., $TR > 3\ T_2^*$)[11]

$$S(x,\ y,\ z) = M_0 \sin\alpha(x,\ y,\ z)\frac{1-\exp(-TR/T_1)}{1-\exp(-TR/T_1)\cos\alpha(x,\ y,\ z)} \qquad (2)$$

The spatial flip angle distribution

$$\alpha(x,\ y,\ z) = \gamma B_1(x,\ y,\ z)\tau_\mathrm{p}\mu I/(2\pi) \qquad (3)$$

has to be calculated according to Biot–Savart's law with γ the magnetogyric ratio, τ_p the pulse duration, I the current, and μ the permeability of the specimen.

Obviously, the strength of the detected NMR signal predominantly reflects the size of the excited volume. Regardless of the actual measuring parameters, the nonlocalized signal from the 'total' volume ($\sigma/TR \approx 75$, upper left in Figure 2) is considerably larger than that of a near (≈ 15, lower left) or distant (≈ 8, lower right) slice of thickness $r/5$ or that of a sphere of radius $r/2$ (≈ 4, upper right) at a distance r from the coil center. Assuming $TR/T_1 = 1$ the maximum *local* signal strength is in a 90° flip angle region close to the coil. However, although outer signal strengths are much smaller, their contributions to the received signal may easily overcompensate 'high-flux' regions close to the coil by simple volume considerations. Moreover, low flip angle excitations in outer regions effectively reduce the extent of signal saturation for acquisitions with $TR < 3\ T_1$ and therefore further increase the relative contribution of unwanted signals distant from the coil. Thus, despite some gross anatomic localization of the NMR signal as given by the size and shape of the coil, it is not possible to focus properly on a desired VOI by a simple single pulse surface coil NMR experiment.

Of course, there are important biochemical questions that do not need exquisite spatial discrimination of tissue signals. Even nonlocalized experiments may provide the answer if relative changes are monitored during the course of a dynamic stimulus-driven study. Nevertheless, a number of refinements have been proposed to improve spatial selectivity of the basic surface coil experiment:

- slice-selective excitation and refocusing of the applied magnetic field gradient to select a plane parallel to the coil, *d*epth *re*solved *s*urface coil *s*pectroscopy (DRESS);[12]
- slice-selective presaturation, *f*ast *r*otating *g*radient *s*pectroscopy (FROGS),[13] and homogeneity spoiling by surface gradients[14] parallel to the coil to eliminate signal contributions from superficial tissues (fat, muscle) between the coil and the target VOI;
- phase-cycled rf excitation and composite rf pulses ('depth' pulses[15]) to reshape the sensitive volume along the $\boldsymbol{B}_1$ gradient of the coil;
- Fourier series windowed variants of the 'rotating frame imaging'[16] experiment to profile spatially the acquired NMR signal along the $\boldsymbol{B}_1$ gradient by multiple excitations with predefined flip angles (***Rotating Frame Methods for Spectroscopic Localization***).[17–19]

In summary, localization by placement of a surface coil is simple, easy to use, and provides good S/N. With single pulse rf excitation respective FID signals do not suffer T_2 relaxation losses. Potential pitfalls are (i) the uncontrolled extent of the sensitive volume as it depends on experimental parameters (TR, flip angle, tissue T_1), (ii) problems with absolute quantitation and comparability of studies, and (iii) limited or no access to inner organs. Most of these arguments also hold true for the refined versions mentioned above as they deliver one-dimensional (1D) solutions to a 3D problem.

Surface coils have mainly been applied in conjunction with phosphorus NMR studying alterations of cellular energy metabolism in skeletal muscle, liver, or heart (***Peripheral Muscle Metabolism Studied by MRS*** and ***Complex Radiofrequency Pulses***). In contrast, proton NMR studies of focal metabolism in brain require more sophisticated gradient-based localization techniques. While homogeneous rf coils are beneficial with respect to metabolite quantitation and study comparability, surface coils may still be used for sensitivity enhancement in a receive-only configuration. In fact, gradient-localized single voxel NMR techniques such as PRESS or STEAM are even possible in a transmit–receive mode. If the dimension of the VOI remains smaller than the surface coil radius, then localized

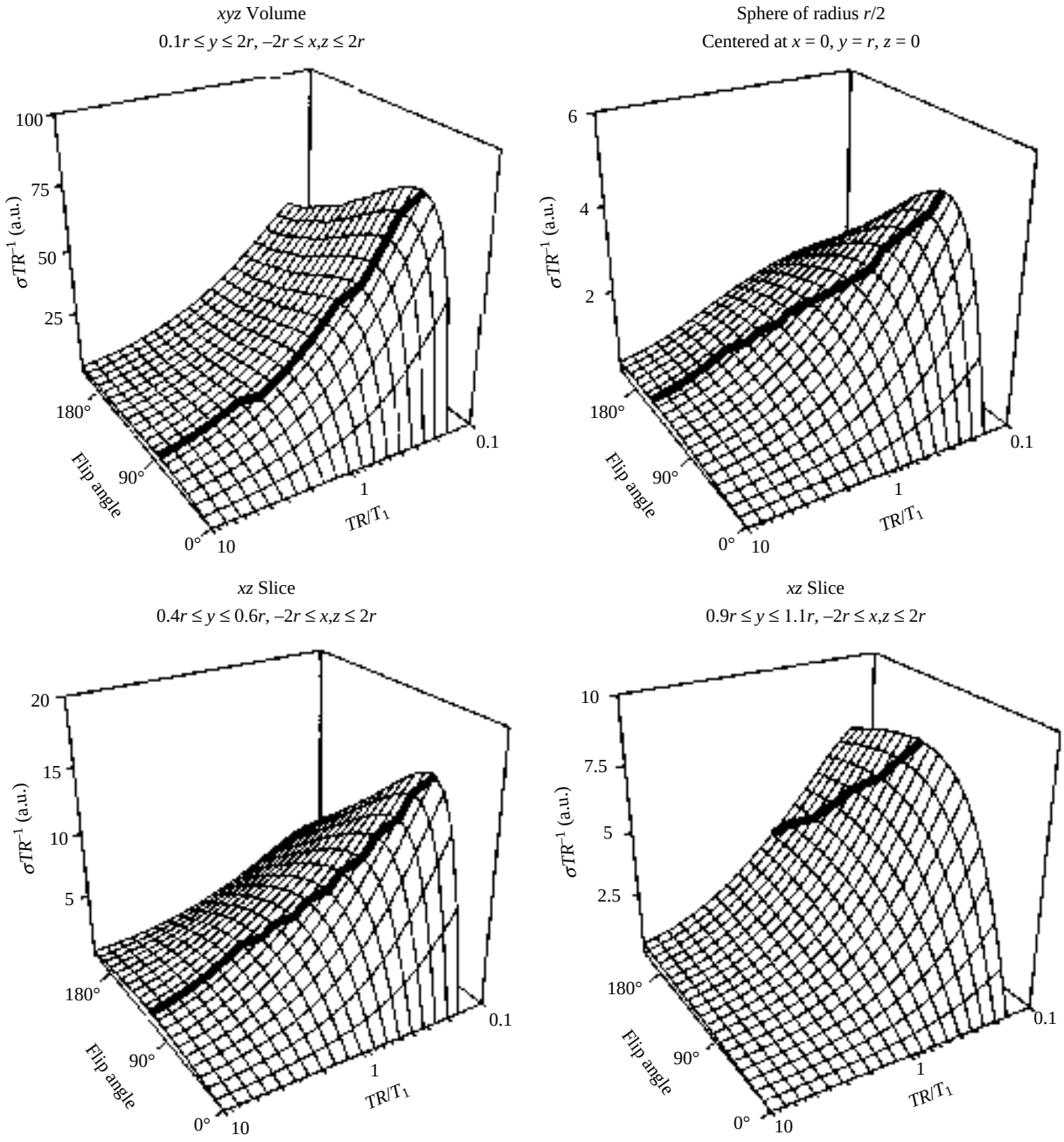

Figure 2 Sensitivity per unit time (σ/TR) as a function of TR/T_1 (logarithmic scale) and rf flip angle α for a transmit–receive single-turn flat surface coil. The NMR signal, as given in equation (1), is integrated over four different volumes: (upper left) 'total' volume covering linear dimensions of $2r$ and $4r$ perpendicular and parallel to the coil (radius r), respectively; (upper right) spherical volume of radius $r/2$ centered at a distance r from the coil center; (lower left) slice of thickness $r/5$ at a distance $r/2$ parallel to the coil; (lower right) similar slice at a distance r. The solid lines indicate maximum sensitivity. (Reproduced by permission of Academic Press from Haase et al.[10])

optimization of the rf power ensures homogeneous rf excitation and signal reception.

2.2 Image-Selected In Vivo Spectroscopy (ISIS)

Prior to nonselective excitation by a 90° rf pulse (or any other rf scheme), the ISIS sequence[20] prepares the equilibrium magnetization of a 3D object by up to three slice-selective 180° inversion pulses in the presence of orthogonal magnetic field gradients. As outlined in Figure 3 the method requires a minimum of eight successive experiments to achieve spatial localization by adding/subtracting FID signals of properly prepared longitudinal magnetizations. The individual acquisitions correspond to 2^3 combinations (on/off) of the three inversion pulses. For example, subtraction of acquisitions #1 (no 180° pulse applied, excitation of the entire object) and #4 (magnetization inversion of a plane along the first gradient axis) results

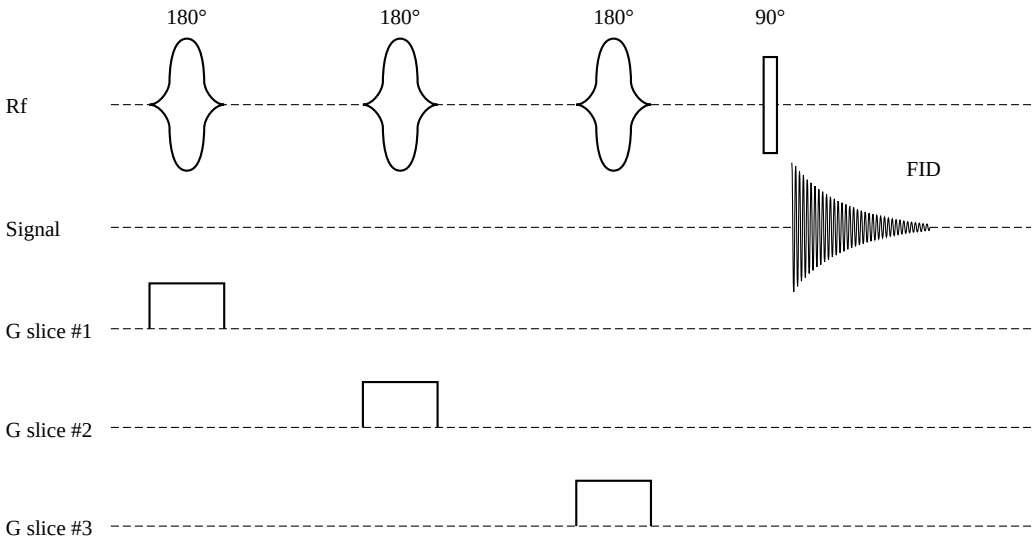

OFF	OFF	OFF	ADD
ON	ON	ON	SUBTRACT
ON	ON	OFF	ADD
ON	OFF	OFF	SUBTRACT
OFF	ON	ON	ADD
OFF	ON	OFF	SUBTRACT
ON	OFF	ON	ADD
OFF	OFF	ON	SUBTRACT

Figure 3 ISIS localization sequence comprising three slice-selective 180° inversion rf pulses along orthogonal gradient axes. A Gaussian shape has been chosen for schematic drawing only, while frequency-modulated pulses of the hyperbolic-secant type are most frequently employed. The measured NMR signal is excited by a final 90° read pulse. For full three-dimensional localization the ISIS sequence needs to be repeated at least eight times using inversion pulses on/off in all three gradient axes (2^3 combinations) with proper setting of the receiver phase (add/subtract)

in twice the signal from a plane perpendicular to the first gradient axis, whereas all signals outside the inverted area have the same phase and thus cancel.

In its original form the ISIS method is only valid for fully relaxed acquisitions with $TR > 3\ T_1$. This is due to the fact that incomplete recovery of the longitudinal magnetization prior to a subsequent preparation period affects the resulting longitudinal magnetization. Since preparation of the longitudinal magnetization is different for the eight experiments, the cancelation of unwanted signal remains incomplete and also depends on the order in which the eight acquisitions are performed. This problem may be solved by a postacquisition saturation or 'magnetization purging' pulse[21] eliminating any residual longitudinal magnetization in between ISIS acquisitions. Further improvements are due to the use of frequency-modulated 'adiabatic' inversion pulses[21,22] that sharpen the spatial profiles of the inverted planes. In addition, signal contamination from outside the VOI has been attenuated by means of outer volume suppression schemes, in particular by using noise-modulated rf excitation in combination with dephasing gradients.[23]

The main advantage of the ISIS approach is the use of the FID since it avoids signal losses for metabolite resonances with short T_2 relaxation times as frequently observed in vivo. Only very small T_1 relaxation losses occur during the initial preparation period. Effective decoupling of localization from excitation in the ISIS sequence provides potential for combinations with more complex multipulse excitation sequences including spectral editing techniques. Major disadvantages of ISIS originate from its multishot character and the fact that localization of a small VOI signal is accomplished by subtraction of large signals from almost the entire object. Thus, the technique may lead to substantial signal contamination and shows considerable sensitivity to motion-induced localization errors. Signal contamination may also arise from spins within inverted planes but outside the VOI through T_1 relaxation between inversion and excitation. Moreover, the excited though unwanted signal outside the VOI increases with decreasing size of the VOI. Finally, localized optimization of magnetic field homogeneity and water suppression as well as online monitoring of dynamic acquisitions are precluded as they require single-shot capabilities.

Despite some useful technical improvements, applications of single voxel ISIS spectroscopy have been mainly directed toward phosphorus NMR with only rare applications to proton NMR of human brain.[24–28] Figure 4 shows ISIS proton NMR spectra of a patient with chronic infarction[27] where the nonselective 90° excitation pulse has been replaced by a semiselective spin echo sequence with different echo times *TE*. The excited frequency range was centered between the methyl resonances of *N*-acetylaspartate (NAA) and lactate to improve water suppression and to eliminate homonuclear *J* modulation of the lactate doublet at 1.33 ppm weakly coupled to the nonexcited methine quartet at 4.12 ppm.

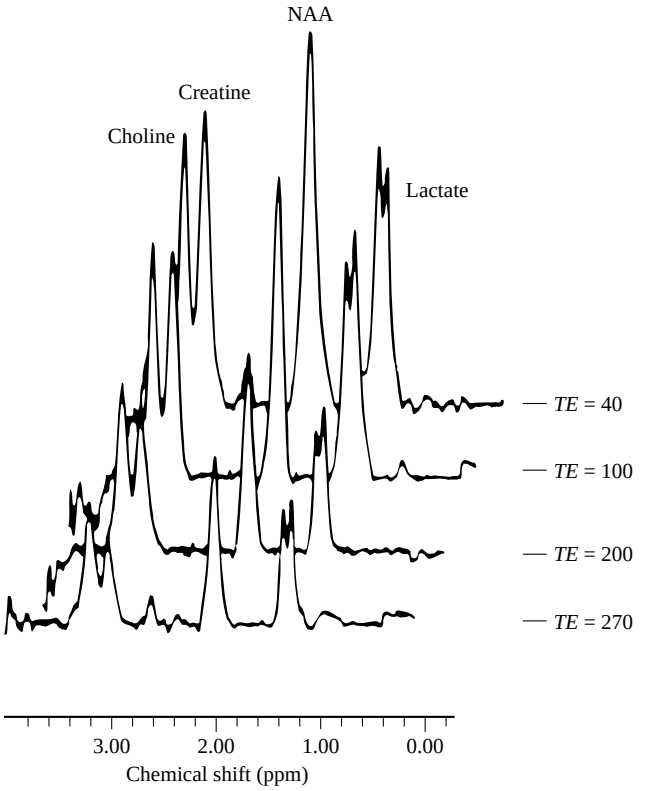

Figure 4 Localized proton NMR spectra of a patient with a chronic infarction at different echo times (*TE*) obtained using ISIS with outer volume suppression pulses and semiselective spin echo excitation. Other parameters: 2.0 T, VOI 40 × 25 × 30 mm^3, *TR* = 3000 ms, 256 transients. Frequency-selective excitation was centered between the methyl resonances of *N*-acetylaspartate (NAA) and lactate thereby eliminating *J* modulation of the lactate doublet at 1.33 ppm. Water suppression was achieved by an initial DANTE presaturation sequence. The patient spectra demonstrate a reduced NAA/creatine ratio and a strong contribution from lactate. (Reproduced by permission of Academic Press from Sappey-Marinier et al.[27])

2.3 Point-Resolved Spectroscopy (PRESS)

In vivo proton NMR spectroscopy of human brain is more demanding in terms of localization acuity and lack of outer volume contamination than usually can be fulfilled by surface coil and ISIS localization strategies. On the other hand, potential problems due to T_2 attenuation are considerably reduced since proton resonances of cerebral metabolites exhibit much longer T_2 relaxation times than in skeletal muscle, liver, and heart or are found in phosphorus NMR. PRESS and STEAM sequences therefore achieve localization by integrating slice selection and spectral excitation. Both methods directly excite the NMR signal from the desired VOI in a single 'shot' rather than attempt to saturate or subtract the much larger signal from outer volumes. In addition, PRESS and STEAM lend themselves to a user-friendly and partially automated spectroscopy examination ranging from image selection and VOI definition to spectral evaluation and quantitation.

Figure 5 shows a basic rf pulse and gradient scheme for a PRESS localization sequence[29,30] comprising slice-selective 90° rf excitation, dual slice-selective 180° rf refocusing, and acquisition of the resulting secondary spin echo (SE). The VOI is defined by the intersection of three orthogonal planes since only spins that experience all three rf pulses refocus as a SE signal at the double echo time $TE = TE1 + TE2$. To avoid multiple quantum interferences caused by imperfect slice-selective refocusing pulses with non-180° flip angles, the echo time *TE*1 of the first SE should be chosen as short as possible (see Section 3.2). Similar arguments hold true for a reduction of motion sensitivity (see Section 3.3). In most cases only the second half of the SE is acquired. This is due to the fact that proton signals of a well-shimmed VOI in brain exhibit rather long T_2^* relaxation times, so that even for long echo times such as *TE* = 270 ms the leading part of the SE signal becomes truncated by the localization sequence itself.

For proton NMR spectroscopy of metabolites the PRESS sequence has to be combined with water suppression. While a variety of techniques including differential relaxation, binomial excitation, and frequency-selective saturation by long pulses or pulse trains have been employed on spectrometers without shaped rf pulse capabilities, the most convenient method on modern NMR systems is the use of chemical shift selective (CHESS) water suppression.[31] The method is based on frequency-selective excitation of the resonance to be suppressed by an amplitude-modulated rf pulse followed by dephasing of the created transverse magnetization by spoiler gradients. For maximum water suppression several CHESS cycles may be applied immediately prior to the localization sequence.

The PRESS proton NMR spectra of parietal white matter of a normal human subject are shown in Figure 6 for a short (top) and long (bottom) echo time. Resonances have been assigned to *N*-acetylaspartate (NAA), creatine and phosphocreatine (Cr), choline-containing compounds (Cho), *myo*-inositol (*myo*-Ins), and glutamate/glutamine (Glx). The resonance at about 4.7 ppm represents the residual water proton signal which is further attenuated by T_2 relaxation at the echo time of *TE* = 270 ms.

The PRESS sequence represents a single-shot method that is easy to use on commercial whole body NMR systems including image selection and *localized* optimization of magnetic field homogeneity and water suppression. Since PRESS excites only those magnetizations that contain the desired VOI as part of an excited slice, most of the outer volume equilibrium magnetization remains unaffected. Gradient spoiling is applied to FID signals from outside the VOI that are due to the first 90° rf pulse as well as caused by imperfect 180° rf pulses. In contrast to ISIS, this problem decreases with decreasing size of the VOI as determined by three slice thicknesses. Of course, PRESS suffers from T_2 relaxation losses the extent of which depends on the chosen echo time, while coupled spins may be subject to substantial *J* modulation.

2.4 Stimulated Echo Acquisition Mode Spectroscopy (STEAM)

In close analogy to the PRESS technique, STEAM sequences define the VOI by the intersection of three planes excited by sequential application of slice-selective 90° rf pulses.[32–34] The schematic diagram shown in Figure 7 refers to a short echo time version corresponding to $TE \approx 10$–30 ms. Retransformation of transverse magnetization excited by the first pulse into longitudinal magnetization components by the

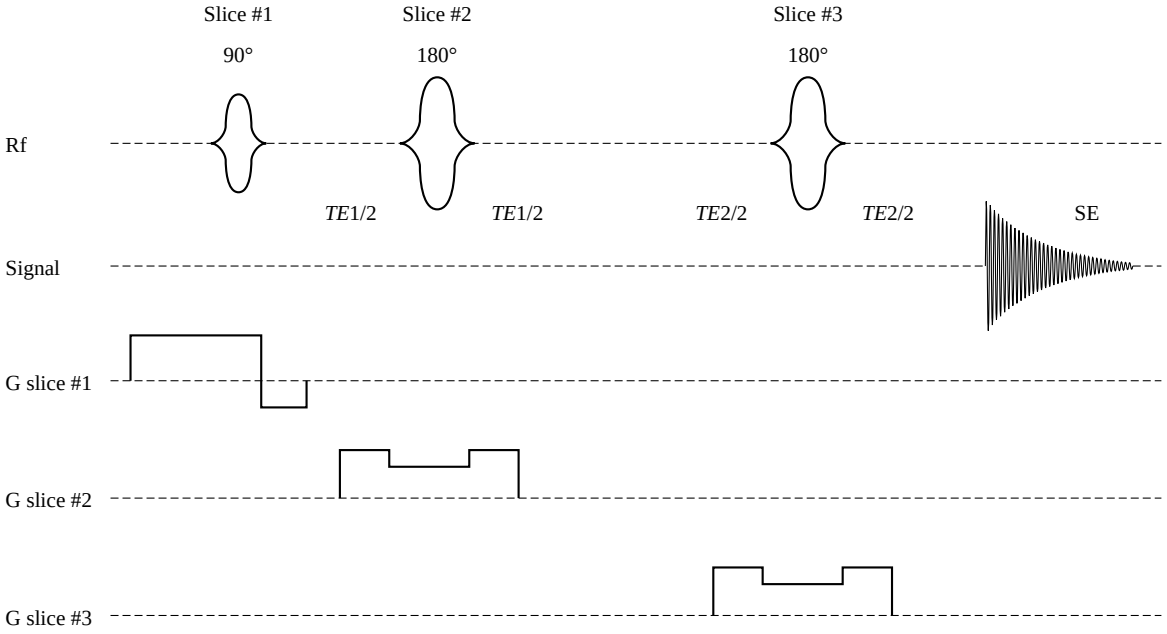

Figure 5 PRESS localization sequence comprising a slice-selective 90° rf excitation pulse followed by two slice-selective 180° rf refocusing pulses along orthogonal gradient axes. In most cases only the second half of the secondary spin echo (SE) occurring at the echo time $TE1 + TE2$ is acquired

second pulse retains the phase information acquired during *TE*/2, but subjects the signal to T_1 relaxation during the middle interval *TM*. The FID associated with the second pulse is dephased by application of spoiler gradients during *TM* that also eliminate unwanted spin echoes. Application of the third pulse leads to two types of transverse magnetization. Firstly, components that carry phase information from the first *TE*/2 interval refocus after a total echo time (*TE*) as a stimulated echo (STE) attenuated by T_2 (and T_1) relaxation. Secondly, the FID from the equilibrium magnetization of the third slice outside the VOI as well as from T_1-relaxed longitudinal magnetizations during *TM* is dephased by the gradients following the third pulse (compare Figure 7).

It is important to note that proper functioning of the STEAM sequence requires complete dephasing of the transverse magnetization prior to application of the second rf pulse. Only randomization of transverse components ensures an equal distribution of spin moments that subsequently form the SE signal from the first two rf pulses (dephased during *TM*) and the STE signal following all three pulses. In the original work on stimulated echoes[35] dephasing was fulfilled by extremely poor magnet homogeneity, but has not been mentioned as a 'necessary condition' for generation of a STE signal without modulations due to resonance offsets. In fact, in the case of complete spin rephasing during *TE*/2 and on-resonance excitation of a single resonance such as water, the first two pulses of the STEAM sequence would effectively add to yield a 180° inversion. Application of the third pulse then results in a FID of the actually recovered magnetization in very much the same way as in an inversion–recovery T_1 experiment. Of course, no STE signal would be observable.

It is for the above reason that the slice-selective gradients for the second and third pulse in Figure 7 are refocused after the third rf pulse and prefocused before the second rf pulse, respectively. Since pertinent gradient pairs encode motion by inducing phase differences, it is advisable to keep *TM* as short as possible (also helpful to avoid T_1 losses) and as long as necessary to eliminate unwanted SE and FID signals by gradient spoiling. Typical values of $TM \approx 10$–30 ms depend on system hardware (gradient strength) and eddy current performance.

For STEAM acquisitions at extremely short echo times, e.g. $TE = 3$ ms, refocusing of the initial transverse magnetization may be accomplished after the third rf pulse as demonstrated for the other two directions in Figure 7. Of course, a substantial reduction of *TE* also involves shortening of rf pulse durations which often is at the expense of slice profile (VOI) quality. Pertinent applications may be advantageous for proton NMR in the presence of unavoidable motions, e.g. in abdominal organs, or for nuclei with short T_2 relaxation times such as phosphorus.[36] At long echo times care should be taken to keep the motion sensitivity to a minimum. Independence of *TE* may be accomplished by arranging respective slice-selective gradient pairs closely around the *TM* interval.

Figure 8 shows STEAM proton NMR spectra of parietal white (top) and gray matter (bottom) of a young healthy adult. Water suppression has been accomplished by three CHESS pulses preceding the STEAM localization sequence[34] in agreement with a detailed analysis of various suppression schemes.[37] In fact, CHESS pulses may also be incorporated into the *TM* interval, where longitudinal magnetizations are already restricted to a column.[38] Although such additional water suppression pulses slightly prolong the *TM* interval, they may be advantageous when using inhomogeneous rf coils.

Major resonances in proton NMR spectra of human brain are due to NAA, *N*-acetylaspartylglutamate (NAAG), glutamate

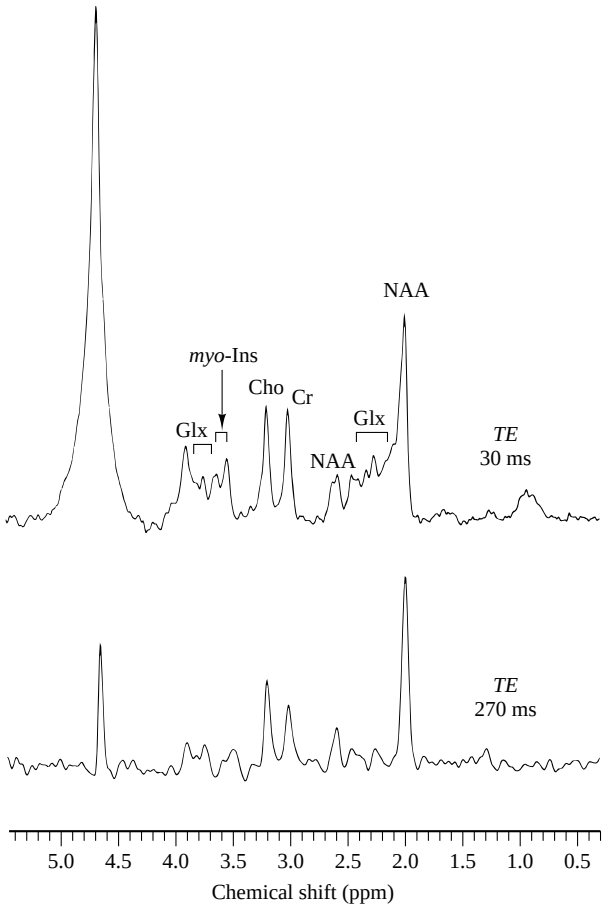

Figure 6 Localized proton NMR spectra of parietal white matter of a normal subject obtained using a PRESS sequence at $TE1 + TE2 = 30$ ms (top) and $TE1 + TE2 = 270$ ms (bottom). Other parameters: 2.0 T, VOI $25 \times 25 \times 25$ mm^3, $TR = 1500$ ms, 256 transients. Resonances are due to: *N*-acetylaspartate (NAA), creatine and phosphocreatine (Cr), choline-containing compounds (Cho), *myo*-inositol (*myo*-Ins), glutamate/glutamine (Glx), and residual water at 4.7 ppm. (Courtesy of T. Ernst and J. Hennig)

(Glu), Cr, Cho, glucose (Glc), *scyllo*-inositol (*scyllo*-Ins), and *myo*-inositol (*myo*-Ins). Resonance assignments involved high-resolution high-field NMR spectra of tissue extracts from experimental animals and human biopsies as well as investigations of model solutions under the same conditions as used in vivo.[7,39–42] Further work is required to assign unambiguously additional resonances in the aromatic part of the spectrum as well as aliphatic resonances from mobile lipids and/or cytosolic proteins, while resonances from metabolites such as lactate, glutamine, and alanine become detectable when elevated in disease states of the brain. Further examples of STEAM spectra are given in Sections 3 and 4 discussing effects of strong spin–spin coupling and advantageous applications of single voxel proton NMR as compared with CSI, respectively.

In summary, the basic advantages of STEAM localization are identical to those of PRESS sequences (see Section 2.3). A special merit stems from the excellent definition of the STEAM VOI via slice-selective 90° rather than 180° rf pulses. This feature translates into even less practical problems with signal contamination, e.g. when selecting a VOI position close to the lipid-containing skull. Moreover, STEAM sequences allow shorter echo times than PRESS when using the same hardware (gradient strength, pulse durations, etc.). This is a benefit from the *TM* interval in STEAM as opposed to the two echo intervals *TE*1 and *TE*2 in PRESS. Another advantage relative to PRESS is due to the fact that STEAM sequences result in only half the *J* modulation of PRESS sequences at the same echo time (see Section 3.1), which considerably improves the detectability of homonuclear spin-coupled resonances in short echo time proton NMR spectra of tissue metabolites. This particularly applies to strongly coupled multiplets suffering from incomplete refocusing and signal loss at longer echo times. A typical example at 2.0 T is given by the Glu methylene resonances in the 2.0–2.5 ppm range which are much more reliably resolved in the STEAM $TE = 20$ ms spectrum (Figure 8) than in the PRESS $TE = 30$ ms spectrum (Figure 6), where *J* modulation corresponds to that of a STEAM sequence at $TE = 60$ ms.

On the negative side, STEAM results in only half the signal strength of PRESS at the same echo time. Of course, this theoretical value only holds true for exactly the same VOI: improved spatial discrimination by slice-selective 90° rf pulses in STEAM should not be mistaken as loss of signal. The STEAM technique also exhibits very small T_1 relaxation losses of the order of $[1-\exp(-1/50)]$ or about 2%. Thus, PRESS sequences are recommended for acquisitions at long echo times (e.g. $TE = 135$–270 ms), while STEAM sequences demonstrate superior performance at short echo times (e.g. $TE = 20$ ms). With respect to ISIS it is worth noting that spatial discrimination of the VOI by direct excitation with PRESS and STEAM is independent of the power of the rf excitation pulses, so that deviations from 90° or 180° flip angles reduce the resulting VOI signal but do not compromise localization acuity.

2.5 Miscellaneous Methods

This section gives a brief overview of miscellaneous localization techniques that have been described in the literature. Although of theoretical interest, many sequences suffer from practical limitations and therefore have only been applied to phantom or animal studies performed on small-bore NMR systems. In particular, a whole class of experiments relies on the use of 'hard' nonselective rf pulses that require strong rf power to be of sufficiently short duration/large bandwidth for equivalent manipulation of unwanted spins outside the desired section. Pertinent localization techniques comprise a threefold application of a sequence module [A] in order consecutively to restore longitudinal magnetization within selected sections along orthogonal gradient axes. Since localization sequences of the type

$$[A]_x - [A]_y - [A]_z - \text{excitation} \tag{4}$$

decouple spatial selection and signal excitation, the final rf excitation sequence may be as simple as a 90°(nonsel)-FID sequence or comprise water suppression by frequency-selective excitation. While ISIS resembles a sequence of type (4) with use of slanted 180° inversion pulses, a parent method with

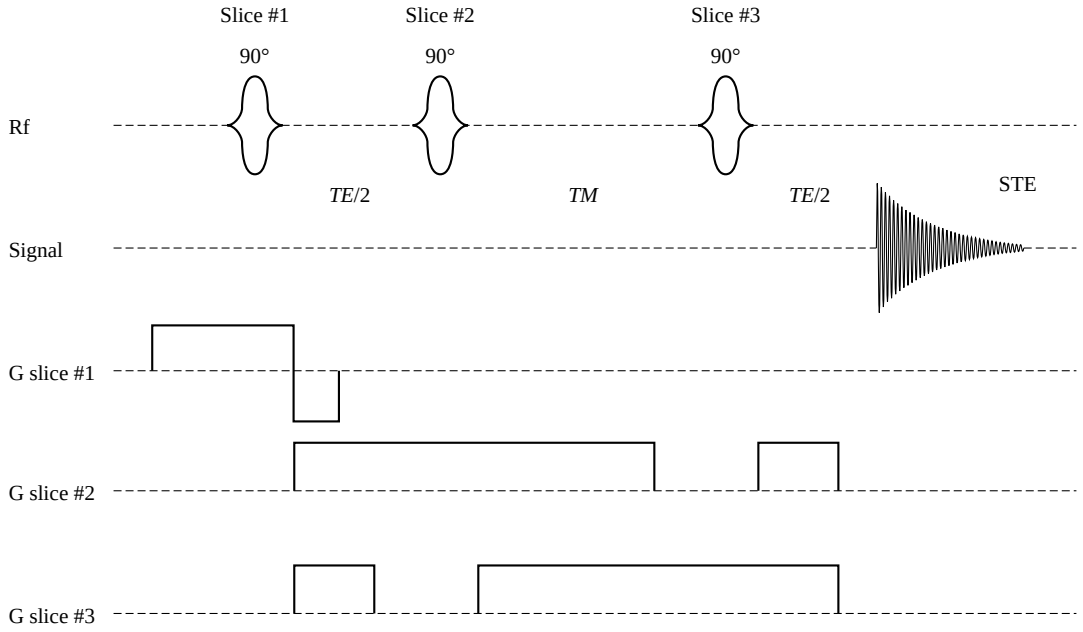

Figure 7 Short echo time STEAM localization sequence comprising three slice-selective 90° rf pulses along orthogonal gradient axes. Only the second half of the stimulated echo (STE) occurring at the echo time (*TE*) is acquired. The transverse magnetization excited by the first rf pulse is retransformed into longitudinal components by application of the second pulse, so that the intensity of the STE is subject to T_1 attenuation during the middle interval (*TM*) and to T_2 attenuation during *TE*

nonselective rf pulses is volume selective excitation (VSE).[43] The sequence employs a pulse package [A] according to[44]

$$45^\circ_{x'}(\mathrm{sel}) - 90^\circ_{-x'}(\mathrm{nonsel}) - 45^\circ_{x'}(\mathrm{sel}) \qquad (5)$$

where the two selective 45° rf pulses represent the first and second half of a symmetrically selective 90° rf pulse, e.g. an amplitude-modulated pulse of Gaussian shape. Further examples are *spa*tially *r*esolved *s*pectroscopy (SPARS),[45]

$$90^\circ_{x'}(\mathrm{nonsel}) - 180^\circ_{y'}(\mathrm{nonsel}) - 90^\circ_{-x'}(\mathrm{sel}) \qquad (6)$$

*spa*tial and *c*hemical-shift-encoded *e*xcitation (SPACE),[46]

$$90^\circ_{x'}(\mathrm{sel}) - 180^\circ_{y'}(\mathrm{nonsel}) - 90^\circ_{-x'}(\mathrm{nonsel}) \qquad (7)$$

and *s*ymmetric *p*ulses for *a*ccurate *l*oca*l*ization (SPALL),[47]

$$90^\circ_{x'}(\mathrm{nonsel}) - 180^\circ_{y'}(\mathrm{sel}) - 90^\circ_{-x'}(\mathrm{nonsel}) \qquad (8)$$

'DIGGER'[48] is an analog of VSE using frequency-modulated sin–sinc rf pulses with reduced rf power requirements.

A further class of experiment takes advantage of outer volume suppression such as *loc*alization of *u*naffected *s*pins (LOCUS),[49] where series of slice-selective 90° rf pulses with overlapping excitation profiles are required in each direction to saturate all spins outside the desired VOI. Similar ideas apply to 'ROISTER'[50] using rotating magnetic field gradients in conjunction with noise-modulated rf pulses. In general, flat saturation is very difficult to achieve.[51] This particularly holds true for water-suppressed proton NMR studies where even minor signal contributions from outside the VOI may lead to substantial spectral contamination when integrated over the entire volume. Spatial presaturation therefore seems to be restricted to applications in NMR imaging, e.g. to avoid aliasing by outer volume/plane saturation or to manipulate directional blood flow in angiography or cardiac applications.

Another category of method is formed by localization sequences combining two or more basic techniques such as DIGGER with SPACE,[52] VSE (or SPARS) with spin echo rf excitation,[53] 1D-ISIS with PRESS,[54] and spin echo rf excitation with STEAM.[55] In addition, new rf pulse designs and foreseeable improvements in magnetic field gradient performance with regard to strength, speed, and accessible waveforms promise multidimensionally selective excitation by just one rf pulse. Preliminary results have been reported for 2D selective[56,57] and even 3D selective rf pulses[58] as well as for special hardware developments such as radial gradient coils.[59] In spoiling unwanted magnetization from planar excitations by rotating gradients, the latter approaches bear similarities to spatially selective saturation techniques. Again, current results underline some potential in NMR imaging, whereas applications for localized proton NMR spectroscopy still suffer contamination problems.

Finally, mixed forms of NMR spectroscopy and imaging have been proposed that achieve spectral localization with use of optimized point spread functions reflecting the shape of a desired VOI. For example, the *s*pectral *lo*calization with *o*ptimal *p*ointspread function (SLOOP)[60] as a generalization of the *s*pectral *l*ocalization by *im*aging (SLIM)[61] results in a single voxel spectrum from an arbitrarily shaped VOI by means of a CSI acquisition with modulated phase-encoding gradients, i.e. by matched numbers of transients per gradient step. The approach is analogous to Fourier series windowing techniques[17–19] that allow focusing of a spectroscopic image in the rotating frame.

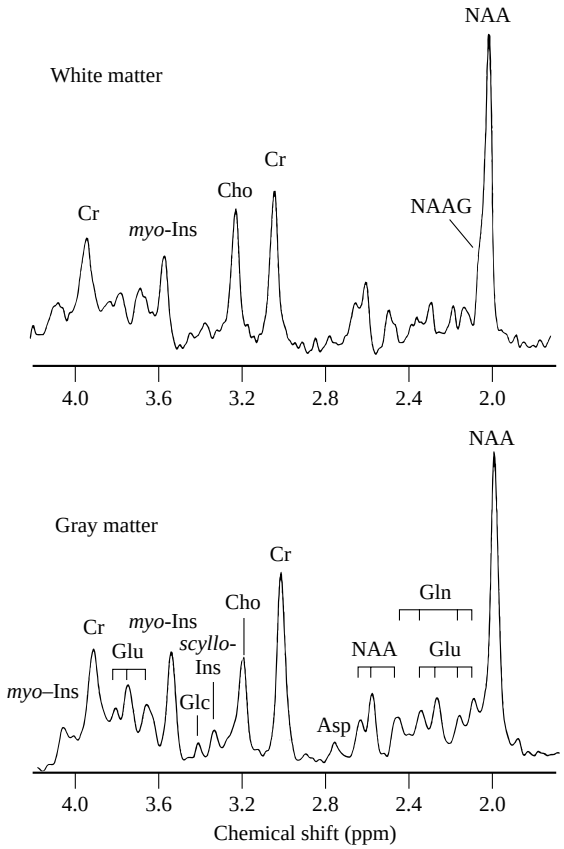

Figure 8 Localized proton NMR spectra of parietal white (top) and gray matter (bottom) of a normal subject obtained using a short echo time STEAM sequence under fully relaxed conditions. Parameters: 2.0 T, VOI $20 \times 30 \times 20$ mm^3 (white matter) and $20 \times 30 \times 30$ mm^3 (gray matter), *TR*/*TE*/*TM* = 6000/20/30 ms, 64 transients. Resonances are due to *N*-acetylaspartate (NAA), *N*-acetylaspartylglutamate (NAAG), glutamate (Glu), glutamine (Gln), aspartate (Asp), phosphocreatine and creatine (Cr), choline-containing compounds (Cho), glucose (Glc), *scyllo*-inositol (*scyllo*-Ins) and *myo*-inositol (*myo*-Ins). Chemical shifts are given in parts per million (ppm) and referenced to 2.01 ppm for the CH_3 group of NAA

3 CHARACTERISTICS OF PRESS AND STEAM

Since both PRESS and STEAM sequences excite rf refocused echoes with use of three rf pulses, respective signals are sensitive to modulation by homonuclear spin–spin couplings or lead to the evolution of multiple quantum coherences. These effects are not seen with single pulse FID acquisitions unless surface coil or ISIS techniques are extended by appropiate excitation sequences.[62] In addition, gradient-localized sequences are subject to motion-induced amplitude and phase errors that either ought to be minimized or may be exploited for motion editing and chemically specific diffusion measurements. Some of these characteristics are discussed in the following sections.

Common properties are also due to the fact that single voxel proton NMR techniques primarily focus on studies of the central nervous system. Such applications are motivated by the importance and uniqueness of a noninvasive access to cerebral metabolism and its sensitivity to pathologic alterations in disease states of the brain ranging from neoplasms and stroke to psychiatric diseases and inborn errors of metabolism. In addition, proton NMR of the living brain is facilitated by advantageous tissue properties not found in other organ systems such as small variability of magnetic susceptibilities, metabolites with long T_2 relaxation times, and minimum motions.

For human applications the minimum accessible VOI for any of the localization techniques discussed is of the order of 1 mL (e.g. $10 \times 10 \times 10$ mm^3). This estimate is based on the following assumptions: (i) a noninvasive approach with use of a circumscribing head coil, (ii) a reasonable measuring time of only a few minutes, and (iii) adequate spectral S/N. Obviously, VOI dimensions of several millimeters result in spectra comprising signals from both neural and glial structures as well as from vascular compartments and/or cerebrospinal fluid. Considerable improvements in spatial resolution will only be possible by interventional procedures using miniaturized rf coils attached to catheters.

3.1 Spin–Spin Coupling

Figure 9 shows the effect of *J* modulation on spin echo proton NMR spectra of ethanol as a function of echo time *TE*. A spin–spin coupling constant of $J = 7$ Hz and a chemical shift difference of $\delta = 245$ Hz (2.45 ppm) result in weak coupling of the methylene quartet and methyl triplet even at the low field strength of 2.35 T. Refocusing of the triplet occurs at $TE = 1/J$ or 143 ms (inversion of quartet), while both the triplet and the quartet refocus at $TE = 2/J$ or 286 ms. The central triplet resonance is not modulated due to the absence of a differential precession frequency and the well-known rephasing of resonance offsets (chemical shifts) by rf echoes.

Doublet resonances refocus at $TE = 1/J$, as frequently observed in vivo for the lactate methyl doublet in PRESS spectra of patients with cerebral disorders. This finding is in contrast to corresponding *J* modulation effects in STEAM spectra since stimulated echoes exhibit modulation frequencies of only half the value of those in spin echo sequences. Accordingly, lactate doublet resonances only refocus at $TE = 2/J$ and integer multiples thereof. Applications of echo spectroscopy to coupled spin systems have been discussed by several authors for PRESS,[63] STEAM,[64] and both localization sequences.[65,66] In principle, it is even possible to extend these sequences to localized 2D NMR spectroscopy as has been demonstrated for a 2D *J*-resolved version of STEAM.[67]

With the prominent exceptions of lactate, alanine, and ethanol, most homonuclear proton interactions lead to strong coupling ($J/\delta \geqslant 0.1$) at low field strengths and therefore give rise to marked multiplet distortions. Such resonance patterns also deviate severely from the modulation behavior of weakly coupled spin systems. In particular, the intensities of strongly coupled multiplets tend to fade out with increasing echo time rather than to rephase at selected echo times. In practical terms it therefore turns out to be best to minimize *J* modulation by using short echo times and STEAM sequences. A typical example is shown in Figure 10 for the case of *myo*-Ins. The complex multiplet pattern at 7.0 T [Figure 10(a)] is simplified to two major resonances at 3.56 ppm and 4.06 ppm [Figure

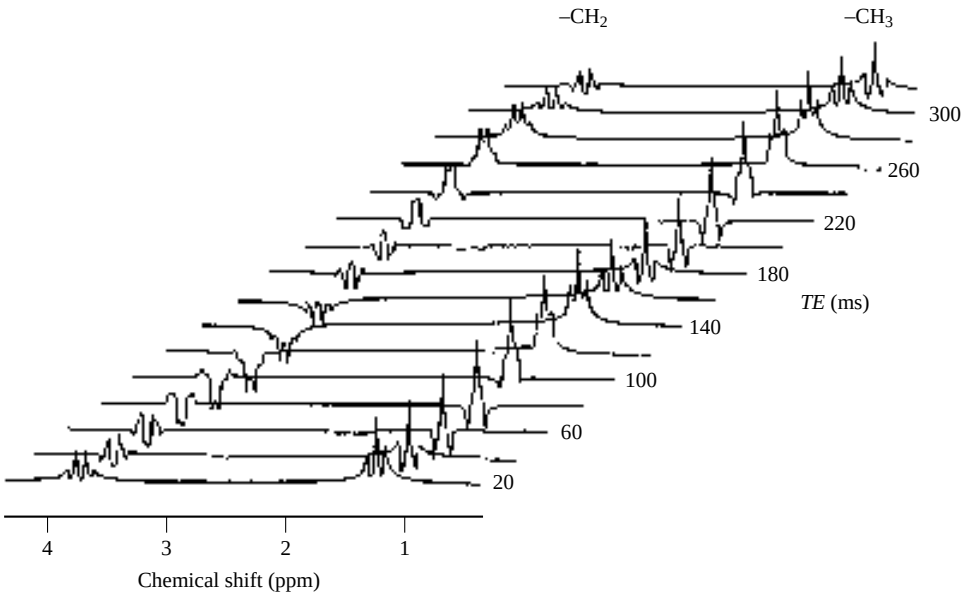

Figure 9 Proton NMR spectra of ethanol obtained using a spin echo sequence without spatial localization as a function of echo time ranging from *TE* = 20–320 ms (2.35 T). Modulation of the weakly coupled ($J/\delta = 0.03 << 1$) methyl triplet (1.20 ppm) and methylene quartet (3.70 ppm) occur with a period of $1/J$ = 143 ms (outer triplet resonances) and $2/J$ = 286 ms (central quartet resonances). The homonuclear spin–spin coupling constant is J = 7.0 Hz (Courtesy of T. Michaelis)

10(b)], whereas the true singlet resonance from the six protons of *scyllo*-Ins at 3.35 ppm remains unaffected. High levels of *myo*-Ins, *scyllo*-Ins, and Cho in white matter of a patient with a mitochondrial enzyme deficiency indicate enhanced membrane turnover and/or gliosis [Figure 10(c)]. The concomitant reduction of NAA and glutamate provides evidence for a loss of vital neuroaxonal tissue.

3.2 Multiple Quantum Effects

In addition to J modulation, stimulated echoes may be affected by the intermediate evolution of multiple quantum coherences during *TM* (***Multiple Quantum Coherence Imaging***). For example, when using an echo time of $TE = 1/J$ such as to provide antiphase magnetization for a doublet at the end of the first *TE*/2 interval, i.e. $TE/2 = 1/(2J)$, then application of the second 90° rf pulse creates zero-quantum and double-quantum coherences that evolve during the middle interval *TM*. The final read pulse converts multiple quantum coherences into detectable transverse magnetization and causes an amplitude modulation of the resulting STE signal in correspondence to the phase of the coherence acquired during *TM*. Assuming gradient switches as for the STEAM sequence shown in Figure 7 where gradients are balanced to refocus single quantum magnetizations of static spins, double quantum coherences become automatically dephased as their precession frequencies correspond to the *sum* of chemical shifts of coupled resonances, i.e. about twice the precession frequencies of transverse magnetizations. Of course, on the one hand, adjustment of gradient refocusing according to multiple quantum order provides a simple means for order selection.[68] On the other hand, zero quantum coherences survive any gradient spoiling since their precession frequencies represent the chemical shift *difference* of coupled spins and therefore are completely independent of resonance offsets and magnetic field inhomogeneities.

The effect of zero quantum modulation as a function of *TM* is demonstrated in Figure 11 for localized STEAM spectra of an aqueous solution of lactate. The *TM* interval was incremented in steps of 0.5 ms while holding the echo time constant at $TE/2 = 1/(2J) = 68$ ms. The observed zero quantum modulation of the methyl doublet (1.33 ppm) weakly coupled to the methine quartet (4.12 ppm, J = 7.1 Hz) refers to the chemical shift difference of 180 Hz at 1.5 T. It is apparent that subtraction of inverted spectra, e.g. at *TM* = 27 ms and 30 ms, would result in twice the lactate methyl doublet while eliminating all non-coupled spins as well as coupled spins with other chemical shift differences, i.e. zero quantum modulation frequencies. The approach clearly indicates potential for in vivo lactate editing[69] in the presence of strong overlap with lipid signals as in skeletal muscle and kidney. Refinements of the basic technique include 2D zero-quantum and double-quantum spectroscopy,[70,71] considerations of strong coupling,[72] and most importantly the design of single-shot multiple quantum filters for STEAM localization sequences to overcome the motion sensitivity of subtraction techniques or phase cycling schemes.[73,74]

In PRESS sequences 180° rf pulses with imperfect slice profiles subject a part of the magnetization to a stimulated echo sequence. Thus, depending on the actual echo times *TE*1 and *TE*2 and the homonuclear spin–spin couplings involved, PRESS sequences may also lead to multiple quantum modulation. Excitation of respective coherences is best avoided by not creating antiphase magnetization at the time of the second rf pulse, which requires the first half-echo interval *TE*1/2 in PRESS and *TE*/2 in STEAM to be as short as possible. This

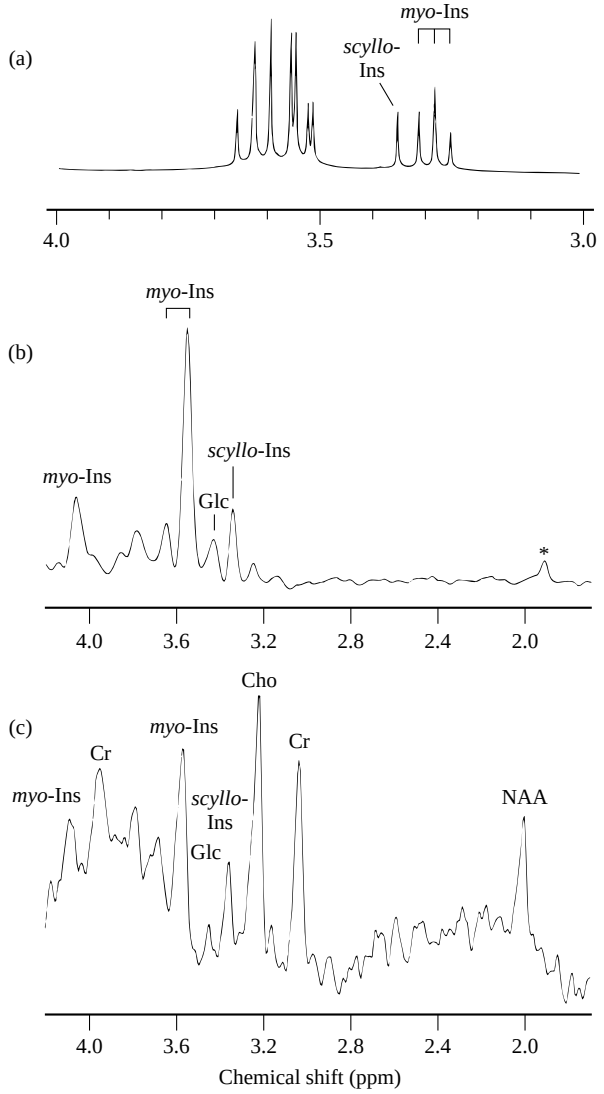

Figure 10 Proton NMR spectra of inositols (Ins) at different field strengths. (a) FID spectrum (7.0 T, TR = 10 000 ms) of a 1:18 mixture of *scyllo*-Ins (singlet at 3.35 ppm) and *myo*-Ins exhibiting a distorted triplet centered at 3.28 ppm, strongly coupled multiplets at 3.5–3.7 ppm, and a distorted triplet at 4.06 ppm (not shown). (b) Localized STEAM spectrum of a 1:12:2 mixture of *scyllo*-Ins, *myo*-Ins, and glucose (Glc) line broadened to mimic in vivo conditions (2.0 T, VOI 20 × 20 × 20 mm^3, $TR/TE/TM$ = 6000/20/30 ms, 32 transients, acetate reference). (c) Localized STEAM spectrum of left frontoparietal white matter of a patient with Leigh's disease (2.0 T, VOI 16 × 16 × 16 mm^3, $TR/TE/TM$ = 3000/20/30 ms, 128 transients). (Reproduced by permission of Wiley from Michaelis et al.[42])

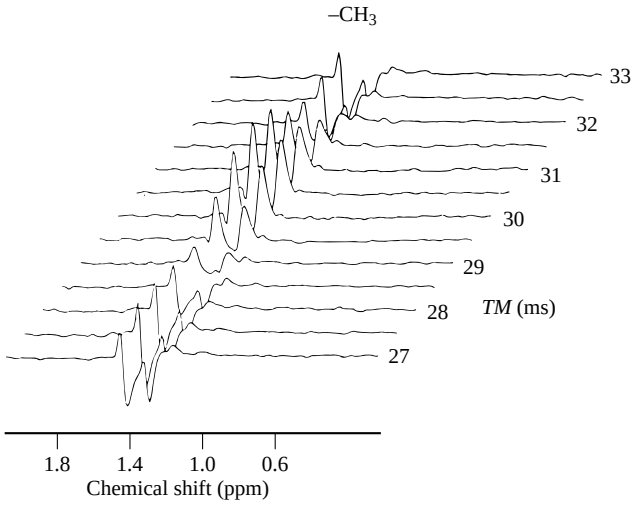

Figure 11 Localized proton NMR spectra of an aqueous solution of 100 mM lactate obtained using a STEAM sequence with a middle interval TM ranging from 27 to 33 ms. Other parameters: 1.5 T, VOI 40 × 40 × 40 mm^3, TR/TE = 3000/135 ms, 4 transients. Antiphase magnetization components at $TE/2 = 1/(2J)$ lead to multiple quantum coherences that evolve during TM. Elimination of all higher orders by magnetic field gradients as in Figure 7 results in exclusive zero quantum modulation of the methyl doublet (1.33 ppm) weakly coupled to the methine quartet (4.12 ppm, J = 7.1 Hz). The modulation period reflects the chemical shift difference of 180 Hz at 1.5 T

allows arbitrary echo times $TE2$ in PRESS and middle intervals TM in STEAM. A theoretical and experimental comparison of STEAM and PRESS sequences has addressed a number of properties including homonuclear coupling, minimum attainable TE, slice profiles, and motion/diffusion.[75]

3.3 Flow and Motion

In close analogy to NMR imaging, gradient-localized echo spectroscopy suffers from chemical shift artifacts in localization acuity, i.e. metabolite-specific positional displacements, and signal loss due to amplitude and phase changes associated with macroscopic and microscopic motions (***Whole Body Magnetic Resonance Angiography***; ***Pulsatility Artifacts Due to Blood Flow and Tissue Motion and Their Control***; ***Time-of-Flight Method of MRA***; ***Phase Contrast MRA***). For proton NMR at field strengths of 1.5–2.0 T chemical shift displacements can be overcome by strong magnetic field gradients that reduce the spatial equivalents of chemically induced frequency differences to a submillimeter scale. If residual eddy currents associated with gradient switching lead to spectral distortions, then sufficient decline of frequency fluctuations prior to data acquisition is only achieved by prolonged echo times. In general, phase distortions of spectroscopic time-domain data may be corrected with use of a reference scan.[76]

Flow effects manifest themselves in two different ways: (i) inflow/outflow of spins carrying longitudinal magnetization, and (ii) motion-induced phase errors that reflect the sensitivity of transverse magnetizations to positional displacements in magnetic field gradients with a component along the flow direction. In localized NMR spectroscopy phase changes within the VOI result in partial cancelation of individual magnetization components and thus incomplete refocusing of SE or STE signals. This particularly holds true for large VOI sizes and at long echo times. In addition, overall phase differences from scan to scan may lead to considerable signal attenuation rather than to signal accumulation during data averaging. This observation may be easily verified since the desired S/N improvement will be less than the expected factor of $\sqrt{n}$, with n the number of acquisitions.

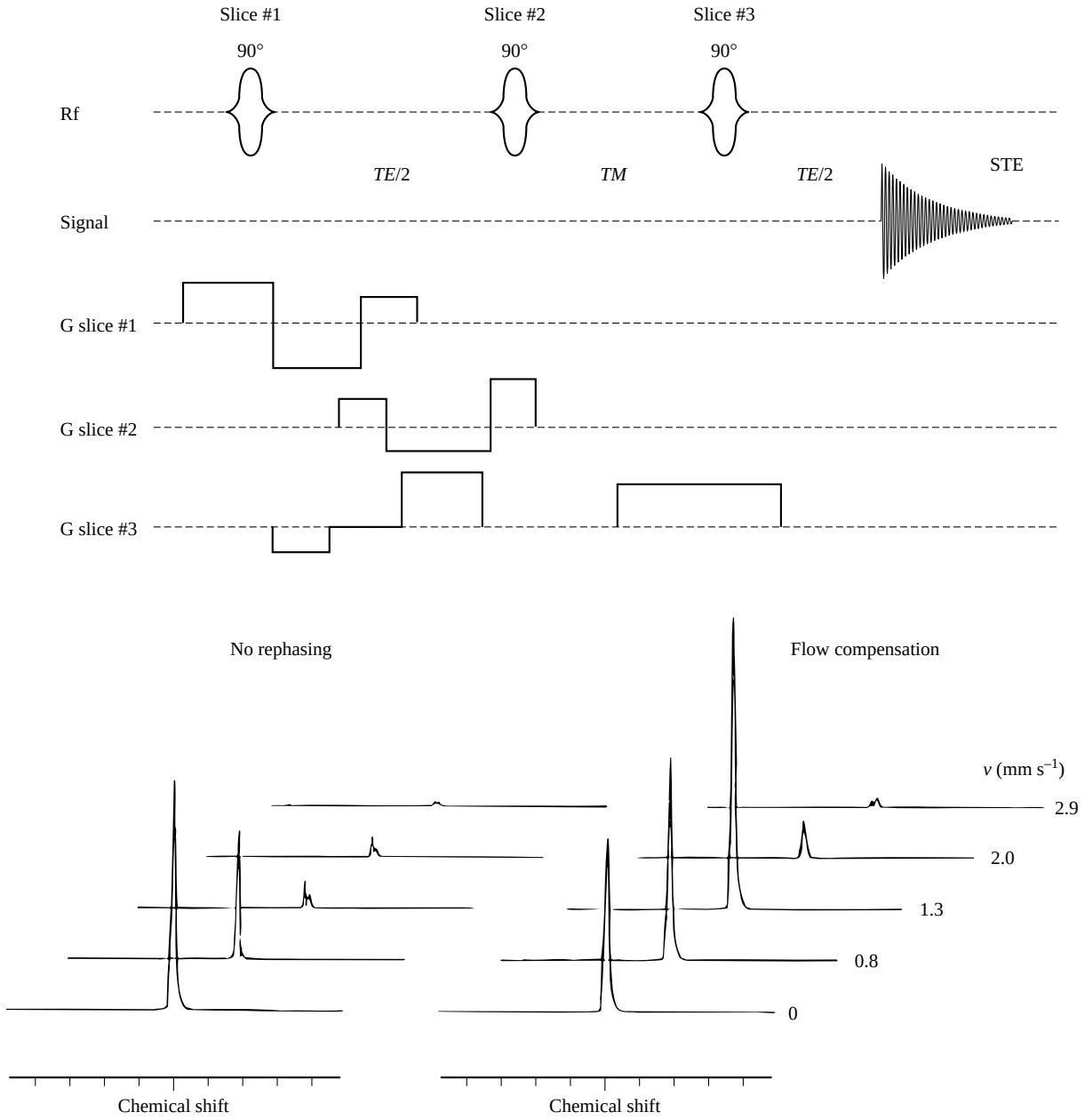

Figure 12 (Top) Long echo time STEAM localization sequence with first-order motion-rephasing gradients in all three directions. (Bottom) Localized proton NMR spectra of tap water flowing in a glass tube of 5 cm diameter at different velocities v = 0, 0.8, 1.3, 2.0, and 2.9 mm s^{-1}. The spectra were obtained using STEAM sequences in the absence (left) and presence (right) of a velocity-rephasing gradient waveform along the principal flow direction. Other parameters: 2.35 T, VOI 13 × 13 × 13 mm^3, *TR/TE/TM* = 2000/270/100 ms, 32 transients. (Reproduced by permission of Academic Press from Gyngell et al.[77])

Figure 12 demonstrates both the amplitude and the phase effect of flowing water on long echo time localized proton NMR spectra obtained with and without velocity compensated gradient waveforms.[77] Without rephasing, even very small flow velocities of the order of 1 mm s^{-1} cause substantial signal loss (bottom left). Velocity compensation not only eliminates such phase errors and associated signal losses, but also benefits from the inflow effect of unsaturated spins from outside the VOI when using short *TR* values. A corresponding signal increase is seen at a velocity of 1.3 mm s^{-1} as spectra were acquired under conditions of partial saturation (bottom right). Irreversible signal loss due to turbulent flow becomes dominant at even higher flow velocities (here at $\geqslant$ 2 mm s^{-1}).

In theory, PRESS sequences are less sensitive to motion than STEAM sequences. This is due to the gradient symmetry normally employed for the two slice-selective 180° rf pulses and thus a benefit from the rephasing properties of the secondary SE ('even echo rephasing'). However, for both sequences the best strategy emerges from avoiding flow/motion-induced phase errors with use of short echo times. In special circumstances, flowing spins may be exploited for motion editing. Discrimination of stationary metabolite signals from flowing

metabolites is a common problem in phosphorus spectroscopy of the heart where phosphate resonances from 2,3-diphosphoglycerate in blood within the cardiac chambers contribute to phosphorus spectra of myocardial tissue.[78] Further applications stem from elimination of resonance signals from flowing liquids used for temperature control in high-resolution NMR. This also holds true for studies of cell suspensions where contamination with substrates from the perfusate may be completely avoided by motion-encoding gradient pairs.[79]

3.4 Diffusion

NMR measurements of molecular self-diffusion coefficients in vivo provide insight into cellular dynamics and give hints as to intra- and extracellular structural organization (***Anisotropically Restricted Diffusion in MRI***; ***Methods and Applications of Diffusion MRI***). While diffusion-weighted NMR imaging of water protons is unable to discriminate between multiple compartments, diffusion-weighted water-suppressed spectroscopy in most cases reflects intracellular metabolite mobility. Such studies may be even more specific since metabolites such as NAA and *myo*-Ins have been found to be exclusively located in neuronal and glial cells, respectively.

The most suitable localization sequence for in vivo diffusion weighting is STEAM. It allows for long diffusion times Δ without detrimental effects due to strong T_2 attenuation in systems with $T_2 << T_1$. Thus, variable diffusion times (e.g. different *TM* intervals) may be used to study the influence of restricted diffusion when dephasing and rephasing parts of the diffusion gradient pair are separated into the first and second *TE*/2 intervals. On the other hand, to determine the free diffusion coefficient in vivo and to minimize encoding of competitive motions such as flow, diffusion weighting is best accomplished by the incorporation of a bipolar self-balanced gradient of duration δ and effective separation Δ into one of the *TE*/2 intervals of the STEAM sequence. While this strategy compensates for motion-induced phase errors as long as pertinent motions exhibit constant velocity, a further reduction of the flow/motion sensitivity of diffusion-weighted sequences is achieved by respiratory triggering and/or scan-to-scan phase alignment using postacquisition correction schemes.

Figure 13 shows diffusion-weighted localized proton NMR spectra of rat brain obtained using bipolar diffusion gradients during both *TE*/2 intervals to yield short diffusion times of $\Delta = \delta = 25$ ms at an echo time of $TE = 120$ ms.[80] The acquisition of spectra with metabolite signal intensities $S(b)$ as a function of diffusion weighting factor b allows the calculation of molecular self-diffusion coefficients D from the signal attenuation according to

$$\ln(S/S_0) = -Db \tag{9}$$

with

$$b = \gamma^2(\Delta - \delta/3)\delta^2 G^2 \tag{10}$$

and G the diffusion gradient strength. Since metabolite diffusion coefficients in vivo can only be measured in the presence of residual unavoidable/uncorrectable motions, values are expressed as apparent diffusion coefficients (ADC).

The ADC value of 0.27×10^{-3} mm^2 s^{-1} found for NAA, Cr, and Cho in rat brain is about a factor of three smaller than the water proton ADC of 0.75×10^{-3} mm^2 s^{-1}. In human subjects an ADC value of 0.65×10^{-3} mm^2 s^{-1} was obtained for water protons, while values of 0.18, 0.15, and 0.13×10^{-3} mm^2 s^{-1} were reported for NAA, Cr, and Cho, respectively.[81] The finding of smaller metabolite ADC values in human brain compared with rat brain is most likely to be due to the use of a long diffusion time of $\Delta > 200$ ms in the human study that reduces the ADC by the influence of restricted diffusion.

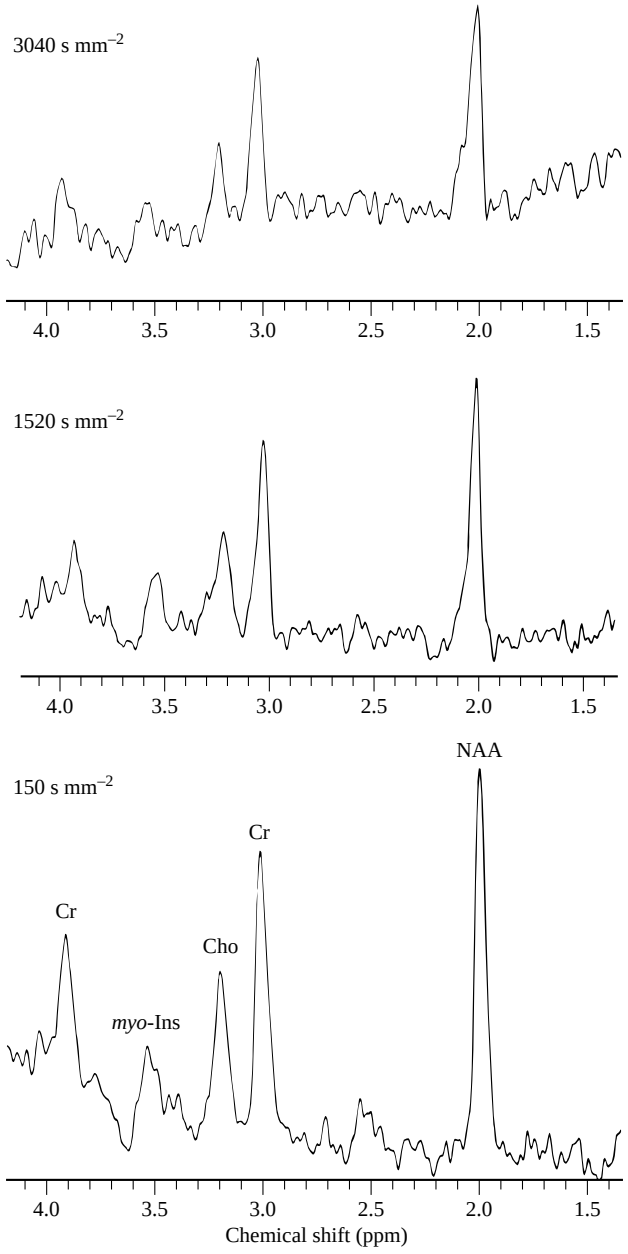

Figure 13 Diffusion-weighted localized proton NMR spectra of rat brain in vivo obtained using a STEAM sequence with bipolar diffusion gradients G in each *TE*/2 interval ($\Delta = \delta = 25$ ms). Other parameters: 2.35 T, VOI $5 \times 5 \times 5$ mm^3, *TR*/*TE*/*TM* = 3000/120/30 ms, 128 transients triggered to respiration. Spectra with increasing diffusion weighting factor b according to equation (10) are shown from bottom to top (150, 1520, and 3040 s mm^{-2}). The orientation of the diffusion gradient was along the long axis of the animal. (Reproduced by permission of Williams and Wilkins from Merboldt et al.[80])

Table 1 Absolute concentrations (mM) of major metabolites in human parieto-occipital white and parietal gray matter in vivo as obtained from fully relaxed (TR = 6000 ms) short echo time (TE = 20 ms) localized proton NMR spectra (STEAM) of young healthy adults (age 27 ± 4 years).[82] The values have been determined without user interference using a fully automated spectral evaluation program[83] and a library of localized model metabolite spectra calibrated with known concentrations.[84] VOI concentrations are given without corrections for partial volume effects and T_2 relaxation differences between in vitro and in vivo conditions.

	White matter (n = 61)	Gray matter (n = 45)
NAA + NAAG	8.2 ± 0.7	9.1 ± 0.7
NAA	6.1 ± 0.7	8.9 ± 0.8
NAAG	2.1 ± 0.7	0.3 ± 0.4
Cr + PCr	4.9 ± 0.6	6.5 ± 0.5
Cho	1.6 ± 0.2	1.2 ± 0.1
myo-Ins	4.2 ± 0.7	4.4 ± 0.6
Glu	5.8 ± 1.2	8.8 ± 1.1
Gln	1.8 ± 1.2	4.1 ± 1.3

Despite current limitations with regard to gradient strength and eddy current performance, diffusion spectroscopy is an active area of research. This is largely due to expectations that cell-specific information will contribute to the understanding of pathophysiologic events associated with stroke. In contrast to water diffusion NMR imaging, studies of intracellular metabolites may clarify the nature of the reduced water ADC observed shortly after ischemia as well as its subsequent rise to larger than normal values within 5–7 days after stroke.

4 SINGLE VOXEL LOCALIZATION OR CHEMICAL SHIFT IMAGING?

Biological NMR covers a wide range of diverse methods and applications. Thus, the absence of a 'single best' technique for a complex field such as in vivo NMR spectroscopy is not surprising. Instead, different problems will require different solutions and specific applications should ask for problem-oriented decisions as to which strategy to employ. For example, single voxel localization and CSI techniques are complementary with regard to temporal resolution and volume coverage. While CSI provides simultaneous access to the spatial distribution of metabolites in one, two, or three dimensions, the strength of a single voxel spectrum arises from a more detailed and more easily quantifiable metabolic picture, as well as from its speed. These factors are often beneficial to studies of cerebral metabolism by proton NMR spectroscopy, whereas the poor sensitivity and long measuring time of localized phosphorus NMR spectroscopy are more efficiently compensated for by CSI techniques with improved S/N per unit measuring time.

Accurate definition of the spatial origin of a spectrum is a prerequisite for its biochemical (and medical) interpretation. Single voxel techniques achieve this goal by direct slice-selective excitation of the VOI, whereas the spatial characteristics of a voxel spectrum from CSI reflect the point-spread function associated with discrete 1D, 2D, or 3D Fourier transformation. Since only small numbers of 8–32 phase-encoding steps per dimension are acquired due to time constraints of in vivo studies, the resulting sidelobes may cause significant signal contamination. Typically, a 2D CSI experiment with a 32 × 32 matrix and a repetition time TR = 2000 ms already leads to a measuring time of 34 min which is often beyond patient tolerance and hampered by motion artifacts.

Single-shot localization techniques such as PRESS and STEAM allow direct 'shimming' of the VOI. Good homogeneity improves the spectral quality in two respects: firstly, in terms of chemical shift resolution, and secondly, in terms of contrast-to-noise since the relevant parameter for detectability of a resonance is its peak-to-noise ratio rather than the signal strength as given by the resonance area. The residual linewidth of in vivo proton NMR spectra of human brain does not reflect spin–spin relaxation, but is determined by microscopic susceptibility differences resulting in inhomogeneous broadening. Another benefit from homogeneity and local parameter optimization is the excellent water suppression obtainable even for short echo times.

A most attractive aspect of single voxel proton NMR is the short measuring time of only a few minutes that may be exploited for several purposes. For example, a reliable quantitation of absolute metabolite concentrations without the need for saturation corrections may be accomplished by using long repetition times for fully relaxed acquisitions. Thus, typical recordings of localized proton NMR spectra of human brain (headcoil, 1–20 mL VOI) result in a measuring time of about 6 min assuming 64 transients with a repetition time TR = 6000 ms. The corresponding measuring time for the aforementioned 32 × 32 2D CSI experiment yields 102 min. Table 1 summarizes VOI concentrations of major metabolites in human brain in vivo from fully relaxed proton NMR spectra of white and gray matter.[82] The analysis was based on fully automated spectral evaluation[83] that takes advantage of a library of localized spectra from calibrated model metabolite solutions.[84]

Single voxel spectroscopy studies also provide immediate access to results without extensive postexamination processing as required for CSI. Control of spectra during the session improves the quality of patient studies by interactive decisions and avoids repeat studies. Most importantly, however, a temporal resolution of minutes allows monitoring of the time course of a physiological alteration or metabolic turnover via sequential acquisitions. An illustrative example is the uptake of ethanol after oral consumption of alcohol as shown in Figure 14 where proton NMR spectra from parietal gray matter reveal the methyl triplet signal only 12 min (top trace) after drinking.[85] The bottom part of Figure 14 shows the time course of the ethanol concentration in gray matter. Subsequent to a rapid increase, maximal tissue concentrations (central trace) were reached after 40–75 min (different subjects) followed by a slow decrease. Further examples of dynamic NMR spectroscopy deal with localized studies of glucose uptake and homeostasis,[28,85] glucose and lactate levels during physiologic stimulation,[25,86] and functional alterations of water proton signal strength and linewidth during brain activation.[87]

In conclusion, the selection of a localization technique should only depend on the question to be answered. In this respect, theoretical and experimental comparisons may be helpful in evaluating basic physical properties, but are of limited usefulness for a generalized judgement of relative merits. The ultimate criterion is of course given by the condition that the

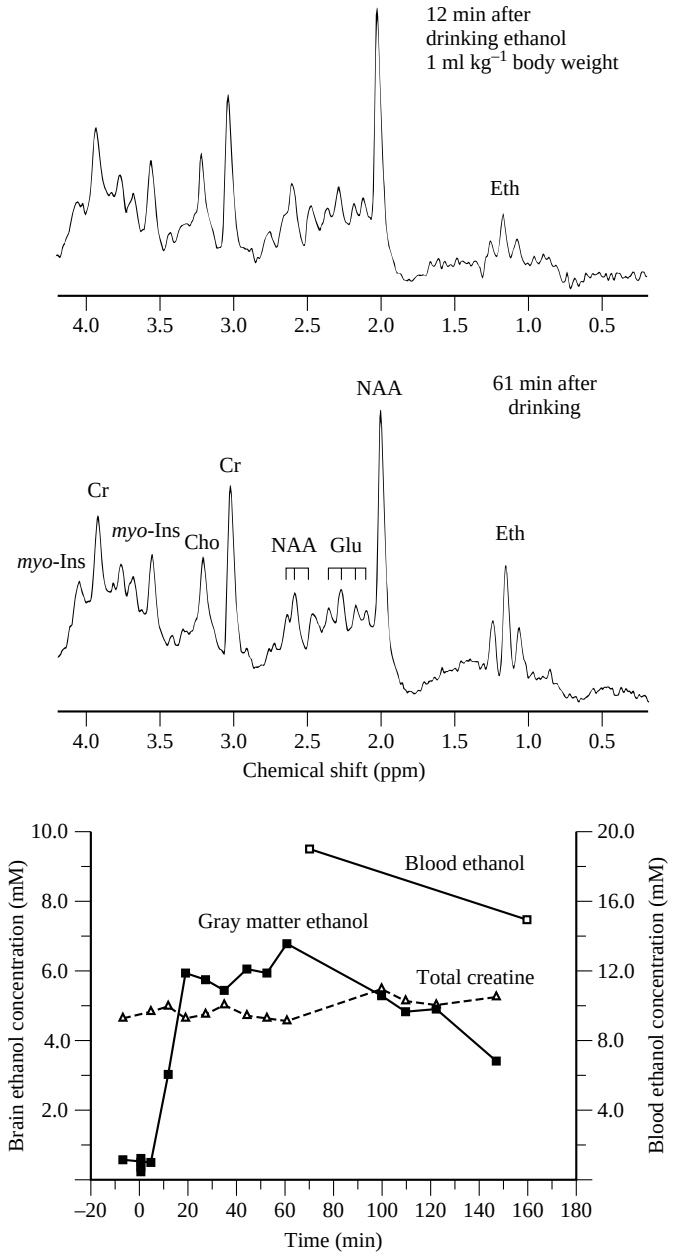

Figure 14 Uptake of ethanol (Eth) in parietal gray matter of a young healthy subject after drinking 1 mL of ethanol/kg body weight within a period of 5 min. (Upper traces) Localized proton NMR spectra reveal the presence of the methylene-coupled methyl triplet of brain ethanol at 1.20 ppm, 12 min and 61 min after drinking, respectively. Parameters: 2.0 T, VOI 16 × 30 × 30 mm^3, STEAM, *TR*/*TE*/*TM* = 3000/20/30 ms, 128 transients. (Bottom graph) Time course of ethanol and creatine levels in gray matter as evaluated by LCModel[83] in comparison with blood plasma ethanol values (right scale). Tissue concentrations are not corrected for T_1 saturation, partial volume effects, and differential T_2 attenuation between in vivo and in vitro conditions. (Reproduced by permission of Plenum Press from Frahm[85])

results of a localized NMR spectroscopy examination must be independent of the *method* chosen. Otherwise, in vivo NMR will not justify its potential as a unique noninvasive tool for both metabolic research and medical decision-making.

5 RELATED ARTICLES

Brain Infection and Degenerative Disease Studied by Proton MRS; Brain MRS of Human Subjects; Brain MRS of Infants and Children; Chemical Shift Imaging; In Vivo Hepatic MRS of Humans; Localization and Registration Issues Important for Serial MRS Studies of Focal Brain Lesions; Quantitation in In Vivo MRS; Single Voxel Whole Body Phosphorus MRS; Water Suppression in Proton MRS of Humans and Animals; Whole Body Studies: Impact of MRS.

6 REFERENCES

1. J. J. H. Ackerman, T. H. Grove, G. G. Wong, D. G. Gadian, and G. K. Radda, *Nature (London)*, 1980, **283**, 167.
2. R. E. Gordon, P. E. Hanley, D. Shaw, D. G. Gadian, G. K. Radda, P. Styles, P. J. Bore, and L. Chan, *Nature (London)*, 1980, **287**, 736.
3. B. Chance, Y. Nakase, M. Bond, J. S. Leigh, Jr., and G. McDonald, *Proc. Natl. Acad. Sci. USA*, 1978, **75**, 4925.
4. B. Chance, S. Eleff, J. S. Leigh, Jr., D. Sokolow, and A. Sapega, *Proc. Natl. Acad. Sci.*, 1981, **78**, 6714.
5. B. D. Ross, G. K. Radda, D. G. Gadian, G. Rocker, M. Esiri, and J. Falconer-Smith, *N. Engl. J. Med.*, 1981, **304**, 1338.
6. P. A. Bottomley, W. A. Edelstein, T. H. Foster, and W. A. Adams, *Proc. Natl. Acad. Sci.*, 1985, **82**, 2148.
7. K. L. Behar, J. A. den Hollander, M. E. Stromski, T. Ogino, R. G. Shulman, O. A. C. Petroff, and J. W. Prichard, *Proc. Natl. Acad. Sci.*, 1983, **80**, 4945.
8. K. L. Behar, D. L. Rothman, R. G. Shulman, O. A. C. Petroff, and J. W. Prichard, *Proc. Natl. Acad. Sci. U.S.A.*, 1984, **81**, 2517.
9. A. Haase, W. Hänicke, J. Frahm, and D. Matthaei, *Lancet*, 1983, **ii**, 1082.
10. A. Haase, W. Hänicke, and J. Frahm, *J. Magn. Reson.*, 1984, **56**, 401.
11. R. R. Ernst and W. A. Anderson, *Rev. Sci. Instrum.*, 1966, **37**, 93.
12. P. A. Bottomley, T. H. Foster, and R. D. Darrow, *J. Magn. Reson.*, 1984, **59**, 338.
13. R. Sauter, S. Müller, and H. Weber, *J. Magn. Reson.*, 1987, **71**, 167.
14. J. Hennig, C. Boesch, R. Gruetter, and E. Martin, *J. Magn. Reson.*, 1987, **75**, 179.
15. M. R. Bendall and R. E. Gordon, *J. Magn. Reson.*, 1983, **53**, 365.
16. D. I. Hoult, *J. Magn. Reson.*, 1979, **33**, 183.
17. J. Pekar, J. S. Leigh, Jr., and B. Chance, *J. Magn. Reson.*, 1985, **64**, 115.
18. K. R. Metz and R. W. Briggs, *J. Magn. Reson.*, 1985, **64**, 172.
19. M. Garwood, T. Schleich, B. D. Ross, G. B. Matson, and W. D. Winters, *J. Magn. Reson.*, 1985, **65**, 239.
20. R. J. Ordidge, A. Connelly, and J. A. B. Lohman, *J. Magn. Reson.*, 1986, **66**, 283.
21. T. J. Lawry, G. S. Karczmar, M. W. Weiner, and G. B. Matson, *Magn. Reson. Med.*, 1989, **9**, 299.
22. P. R. Luyten, J. P. Groen, J. W. A. H. Vermeulen, and J. A. den Hollander, *Magn. Reson. Med.*, 1989, **11**, 1.
23. A. Connelly, C. Counsell, J. A. B. Lohman, and R. J. Ordidge, *J. Magn. Reson.*, 1988, **78**, 519.
24. C. C. Hanstock, D. L. Rothman, J. W. Prichard, T. Jue, and R. G. Shulman, *Proc. Natl. Acad. Sci. U.S.A.*, 1988, **85**, 1821.
25. J. Prichard, D. Rothman, E. Novotny, O. Petroff, T. Kuwaborc, M. Avison, A. Howseman, C. Hanstock, and R. Shulman, *Proc. Natl. Acad. Sci. U.S.A.*, 1991, **88**, 5829.
26. D. L. Rothman, C. C. Hanstock, O. A. C. Petroff, E. J. Novotny, J. W. Prichard, and R. G. Shulman, *Magn. Reson. Med.*, 1992, **25**, 94.

27. D. Sappey-Marinier, G. Calabrese, H. P. Hetherington, S. N. G. Fisher, R. Deicken, C. van Dyke, G. Fein, and M. W. Weiner, *Magn. Reson. Med.*, 1992, **26**, 313.
28. R. Gruetter, D. L. Rothman, E. J. Novotny, G. I. Shulman, J. W. Prichard, and R. G. Shulman, *Magn. Reson. Med.*, 1992, **27**, 183.
29. P. A. Bottomley, *Ann. N.Y. Acad. Sci.*, 1987, **508**, 333; US Patent 4 480 228, 1984.
30. R. J. Ordidge, M. R. Bendall, R. E. Gordon, and A. Connelly, in 'Magnetic Resonance in Biology and Medicine', eds. G. Govil, C. L. Khetrapal, and A. Saran, Tata McGraw-Hill, New Delhi, 1985, p. 387.
31. A. Haase, J. Frahm, W. Hänicke, and D. Matthaei, *Phys. Med. Biol.*, 1985, **30**, 341.
32. J. Frahm, A. Haase, W. Hänicke, K. D. Merboldt, and D. Matthaei, German Patent DE 3 445 689, 1984.
33. J. Frahm, K. D. Merboldt, and W. Hänicke, *J. Magn. Reson.*, 1987, **72**, 502.
34. J. Frahm, T. Michaelis, K. D. Merboldt, H. Bruhn, M. L. Gyngell, and W. Hänicke, *J. Magn. Reson.*, 1990, **90**, 464.
35. E. L. Hahn, *Phys. Rev.*, 1950, **80**, 580.
36. K. D. Merboldt, D. Chien, W. Hänicke, M. L. Gyngell, H. Bruhn, and J. Frahm, *J. Magn. Reson.*, 1990, **89**, 343.
37. C. T. W. Moonen and P. C. M. van Zijl, *J. Magn. Reson.*, 1990, **88**, 28.
38. J. Frahm, K. D. Merboldt, W. Hänicke, and A. Villringer, *Proc. 6th Ann Mtg. Soc. Magn. Reson. Med.*, New York, 1987, p. 137.
39. C. Arús, Y. Chang, and M. Bárány, *Physiol. Chem. Phys. Med. NMR*, 1985, **17**, 23.
40. T. Michaelis, K. D. Merboldt, W. Hänicke, M. L. Gyngell, H. Bruhn, and J. Frahm, *NMR Biomed.*, 1991, **4**, 90.
41. J. Frahm, T. Michaelis, K. D. Merboldt, W. Hänicke, M. L. Gyngell, and H. Bruhn, *NMR Biomed.*, 1991, **4**, 201.
42. T. Michaelis, G. Helms, K. D. Merboldt, W. Hänicke, H. Bruhn, and J. Frahm, *NMR Biomed.*, 1993, **6**, 105.
43. W. P. Aue, S. Müller, T. A. Cross, and J. Seelig, *J. Magn. Reson.*, 1984, **56**, 350.
44. H. Post, D. Ratzel, and P. Brunner, German Patent P3 209 263.6, 1982.
45. P. R. Luyten, A. J. H. Mariën, B. Sijtsma, and J. A. den Hollander, *J. Magn. Reson.*, 1986, **67**, 148.
46. D. M. Doddrell, W. M. Brooks, J. M. Bulsing, J. Field, M. G. Irving, and H. Baddeley, *J. Magn. Reson.*, 1986, **68**, 367.
47. M. von Kienlin, C. Remy, A. L. Benabid, and M. Decorps, *J. Magn. Reson.*, 1988, **79**, 382.
48. D. M. Doddrell, J. M. Bulsing, G. J. Galloway, W. M. Brooks, J. Field, M. Irving, and H. Baddeley, *J. Magn. Reson.*, 1986, **70**, 319.
49. A. Haase, *Magn. Reson. Med.*, 1986, **3**, 963.
50. A. J. S. de Crespigny, T. A. Carpenter, and L. D. Hall, *J. Magn. Reson.*, 1989, **85**, 595.
51. P. A. Bottomley, C. J. Hardy, P. B. Roemer, and R. G. Weiss, *NMR Biomed.*, 1989, **2**, 284.
52. D. M. Doddrell, J. Field, I. M. Brereton, G. J. Galloway, W. M. Brooks, and M. G. Irving, *J. Magn. Reson.*, 1987, **73**, 159.
53. J. Briand and L. D. Hall, *J. Magn. Reson.*, 1988, **80**, 559.
54. J. Granot, *J. Magn. Reson.*, 1988, **78**, 302.
55. J. J. van Vaals, A. H. Bergman, J. H. den Boef, H. J. van den Boogert, and P. H. J. van Gerwen, *Magn. Reson. Med.*, 1991, **19**, 136.
56. C. J. Hardy, P. A. Bottomley, M. O'Donnell, and P. Roemer, *J. Magn. Reson.*, 1988, **77**, 233.
57. P. G. Morris, D. J. O. McIntyre, D. E. Rourke, and J. T. Ngo, *NMR Biomed.*, 1989, **2**, 257.
58. P. A. Bottomley and C. J. Hardy, *J. Magn. Reson.*, 1987, **74**, 550.
59. C. Y. Rim, J. B. Ra, and Z. H. Cho, *Magn. Reson. Med.*, 1992, **24**, 100.
60. M. von Kienlin and R. Mejia, *J. Magn. Reson.*, 1991, **94**, 268.
61. X. Hu, D. N. Levin, P. C. Lauterbur, and T. Spraggins, *Magn. Reson. Med.*, 1988, **8**, 314.
62. H. P. Hetherington, M. J. Avison, and R. G. Shulman, *Proc. Natl. Acad. Sci. U.S.A.*, 1985, **82**, 3115.
63. P. C. M. van Zijl, C. T. W. Moonen, and M. von Kienlin, *J. Magn. Reson.*, 1990, **89**, 28.
64. R. Kimmich, E. Rommel, and A. Knüttel, *J. Magn. Reson.*, 1989, **81**, 333.
65. T. Ernst and J. Hennig, *Magn. Reson. Med.*, 1991, **21**, 82.
66. A. H. Wilman and P. S. Allen, *J. Magn. Reson. B*, 1993, **101**, 102.
67. F. Desmoulin and J. Seelig, *Magn. Reson. Med.*, 1990, **14**, 160.
68. A. Bax, P. G. De Jong, A. F. Mehlkopf, and J. Smidt, *Chem. Phys. Lett.*, 1980, **69**, 567.
69. C. H. Sotak and D. M. Freeman, *J. Magn. Reson.*, 1988, **77**, 382.
70. C. H. Sotak, *Magn. Reson. Med.*, 1988, **7**, 364.
71. C. H. Sotak, D. M. Freeman, and R. E. Hurd, *J. Magn. Reson.*, 1988, **78**, 355.
72. N. Chandrakumar and F. Chandrasekaran, *J. Magn. Reson.*, 1992, **96**, 657.
73. A. Knüttel and R. Kimmich, *Magn. Reson. Med.*, 1989, **9**, 254.
74. A. Knüttel and R. Kimmich, *J. Magn. Reson.*, 1990, **86**, 253.
75. C. T. W. Moonen, M. von Kienlin, P. C. M. van Zijl, J. Cohen, J. Gillen, P. Daly, and G. Wolf, *NMR Biomed.*, 1989, **2**, 201.
76. U. Klose, *Magn. Reson. Med.*, 1990, **14**, 26.
77. M. L. Gyngell, J. Frahm, K. D. Merboldt, W. Hänicke, and H. Bruhn, *J. Magn. Reson.*, 1988, **77**, 596.
78. R. Zahler, S. Majumdar, B. Frederick, M. Laughlin, E. Barrett, and J. C. Gore, *Magn. Reson. Med.*, 1991, **17**, 368.
79. P. C. M. van Zijl, C. T. W. Moonen, P. Faustino, J. Pekar, O. Kaplan, and J. S. Cohen, *Proc. Natl. Acad. Sci.*, 1991, **88**, 3228.
80. K. D. Merboldt, D. Hörstermann, W. Hänicke, H. Bruhn, and J. Frahm, *Magn. Reson. Med.*, 1993, **29**, 125.
81. S. Posse, C. A. Cuenod, and D. Le Bihan, *Radiology*, 1993, **188**, 719.
82. P. J. W. Pouwels, K. Brockmann, B. Kruse, B. Wilkin, M. Wick, F. A. Hanefield, and J. Frahm, *Pediatr. Res.*, 1999, in press.
83. S. W. Provencher, *Magn. Reson. Med.*, 1993, **30**, 672.
84. T. Michaelis, K. D. Merboldt, H. Bruhn, W. Hänicke, and J. Frahm, *Radiology*, 1993, **187**, 219.
85. J. Frahm, *Adv. Exp. Med. Biol.*, 1993, **333**, 257.
86. K. D. Merboldt, H. Bruhn, W. Hänicke, T. Michaelis, and J. Frahm, *Magn. Reson. Med.*, 1992, **25**, 187.
87. J. Hennig, T. Ernst, O. Speck, G. Deuschl, and E. Feifel, *Magn. Reson. Med.*, 1994, **31**, 85.

Biographical Sketches

Jens Frahm, *b* 1951. Dipl.Phys., 1974, Ph.D., 1977, physical chemistry, University of Göttingen, Germany. Introduced to NMR by Hans Strehlow, research assistant at the Max-Planck-Institut für Biophysikalische Chemie in Göttingen, 1977-1992, Head of Biomedical NMR Group, 1982-1992, Head of Biomedizinische NMR Forschungs GmbH, 1993–present. Approx. 205 publications. Research specialty: NMR studies of living systems; anatomic, metabolic, and functional aspects of intact organ systems; NMR imaging, localized NMR spectroscopy. Current interests: neuroimaging.

Wolfgang Hänicke. *b* 1955. Dipl.Math., 1981, University of Göttingen, Germany. Member of the Department Molekularer Systemaufbau at the Max-Planck-Institut für Biophysikalische Chemie in Göttingen, 1978–1983; Member of the Biomedical NMR Unit, 1983–present. Approx. 120 publications. Current interests: localized in vivo proton spectroscopy, functional MRI, image processing.

Single Voxel Whole Body Phosphorus MRS

Roger J. Ordidge
University College, London, UK

Joseph A. Helpern
Nathan Kline Institute, Orangeburg, NY, USA

James W. Hugg
University of Alabama, Birmingham, AL, USA

and

Gerald B. Matson
University of California, San Francisco and VA Medical Center, San Francisco, CA, USA

1 INTRODUCTION

In vivo ^{31}P MRS has become an established research tool for studying metabolism in both animals and humans. Up to seven peaks can be identified in tissues (more if proton decoupling is employed). For muscle and brain tissue these peaks correspond to: phosphomonoesters (PME), inorganic phosphate (Pi), phosphodiesters (PDE), phosphocreatine (PCr), and the γ-, α-, and β-phosphates of adenosine 5′-triphosphate (ATP). The contribution of each peak to the total spectrum is expressed by calculating the area under each of the peaks and expressing the result as a percentage (mol%) of the total phosphate signal. The energetic state of brain tissue may be characterized by the PCr/Pi ratio, which is an approximate measure of the phosphorylation potential when the creatine kinase reaction is at equilibrium, and which decreases in situations of insufficient energy production. In vivo ^{31}P MRS also provides a noninvasive measure of pH by utilizing the dependence of the chemical shift of Pi on pH.[1] In addition, the relative chemical shifts of Pi, PCr, γ-, α-, and β-ATP can be used to estimate the concentration of free Mg^{2+} ions,[2] which play a role in membrane stability and are involved in phosphoryl transfer reactions during glycolysis. Finally, the presence of ATP is ubiquitous in all living tissues, and its depletion presages serious cell injury or, eventually, cell death. Therefore, in vivo ^{31}P MRS provides a wealth of information that is unobtainable by other noninvasive techniques.

The primary technological problem for in vivo ^{31}P MRS is a lack of sensitivity caused by the low metabolic concentrations of NMR-visible phosphorus metabolites of biological interest. The experimental complexity and the logistics of applying long NMR experimental procedures to study human disease have limited the widespread application of in vivo NMR spectroscopy in clinical diagnostic studies. It is, therefore, of utmost importance that the NMR spectrum is acquired with optimum sensitivity in order to minimize the experimental duration.

Interpretation of spatially localized in vivo ^{31}P NMR spectra depends upon a knowledge of the location and size of the tissue volume investigated in the experiment. Tissue specificity is essential to eliminate signals emanating from tissues of different type or metabolic status. For instance, contamination of the ^{31}P spectrum from brain tissue can arise from the scalp and neck muscles which are rich in high-energy phosphates, especially PCr, thereby giving a disproportionately intense contribution to the spectrum. It is the goal of any localization method to facilitate the acquisition of in vivo NMR spectra by minimizing contamination from undesired tissue volumes, and maximizing the S/N ratio to minimize experimental duration. In addition, many of the ^{31}P resonances of interest have short T_2 values, thus requiring an excitation and localization scheme which minimizes signal losses due to T_2 relaxation.

2 TECHNIQUES

2.1 Surface Coil and Related Methods

The first spatially localized in vivo ^{31}P MRS experiments were performed using surface coils,[3] which consist of a loop of wire placed in close proximity to the subject, and positioned so that a major component of the $\boldsymbol{B}_1$ field of the coil is perpendicular to the $\boldsymbol{B}_0$ field. The coils can be used for both transmission of the rf pulses and signal reception. Most of the measured signal originates from an approximately hemispherical volume of tissue of equal radius to the coil. However, the spatial sensitivity of surface coils is inherently inhomogeneous and decreases rapidly with distance from the coil. The spatial weighting of the signal in an experiment is a function of the rf pulse length and repetition time, so the spatial response pattern is both irregularly shaped in space and of variable sensitivity as a function of position. For these reasons, surface coils are often used in combination with other methods.

Although no longer being used, Topical Magnetic Resonance (TMR) provided the first three-dimensional spectroscopic localization method by generating a uniform $\boldsymbol{B}_0$ field over a limited spatial region, with a very inhomogeneous field in surrounding regions.[4] Moreover, the TMR method could be used with surface coils for improved localization. However, the spatial localization achieved by the combined method is not sharply defined, having edges which are quite diffuse. Another major disadvantage is that the region of interest is centrally located within the magnet bore assembly, having been generated by the combination of powerful Z^2 and Z^4 shim coils, and cannot be easily moved.

'Depth' pulse methods provide another approach to improved localization over that afforded by a single surface coil.[5] In brief, depth pulse methods rely on phase cycling with multiple acquisitions to obtain signals from regions experiencing a particular value of $\boldsymbol{B}_1$ field strength. Other, analogous, surface coil methods which retain signals from a region within a limited range of $\boldsymbol{B}_1$ field have also been demonstrated.[6–9] However, full, three-dimensional localization requires the use of two surface coils of differing sizes.[10]

In the middle 1980s, the availability of pulsed magnetic field gradients enabled new classes of localization experiments to be developed; namely, methods relying on the application of frequency selective rf pulses in the presence of magnetic field

gradients. The first of these methods, entitled Depth Resolved Surface coil Spectroscopy, provided for observation of a plane of material parallel to the plane of the coil.[11] Another variation of the method enabled multiple parallel slices to be simultaneously investigated.[12] A disadvantage of the method is that the selected volume is a flat disk which is not conveniently shaped for the investigation of many organs. Also, T_2 relaxation occurs during the slice selective refocussing period following the 90° rf pulse, leading to some degree of spectral distortion.

All surface coil techniques benefit from the inherent high sensitivity of signal reception from material close to the coil. However, all of the above methods suffer the disadvantage that the localized region is fixed in space, and the subject must be positioned appropriately with respect to the coil(s).

2.2 Three-Dimensional Selective Excitation Methods

The combination of three selective pulses in conjunction with pulsed magnetic field gradients applied along orthogonal axes, can be used to excite a volume of material which is defined at the intersection of all three planes. Many techniques use this principle; however, the exact nature of the spatial definition process falls into three general categories:

1. Outer volume suppression methods which selectively nutate spins in unwanted regions of the sample into the transverse plane, where the signal is dephased by applied gradients. The desired signal, which has been preserved along the longitudinal axis, is then read out using a 90° rf pulse. Examples of this principle are: Volume Selective Excitation,[13] Spatially Resolved Spectroscopy,[14] localization of unaffected spins in NMR imaging and spectroscopy (LOCUS),[15] 'SPACE',[16] and 'DIGGER'.[17]
2. Direct excitation methods in which the MR signal of interest spends some portion of the experiment evolving in the transverse plane prior to forming an echo in the signal acquisition period. Examples are Pixel-Resolved Spectroscopy (PRESS),[18,19] which uses a 90°–180°–180° selective pulse sequence and acquires a spin echo, and Stimulated Echo Acquisition Method (STEAM)[20] which uses a 90°–90°–90° sequence and acquires a stimulated echo.
3. Cancelation methods in which the entire sample volume is excited, but the signal has been previously prepared using 180° selective pulses so that spatial information is encoded in the longitudinal magnetization prior to signal acquisition, and unwanted signal is canceled following combination of the signal from a series of experiments. An example of this principle is Image Selected In vivo Spectroscopy (ISIS).[21]

The advantages of all these methods is that because of the use of selective pulses in combination with field gradients, the size and position of the selected volume can be directly related to a previously obtained MR image. The selected volume is regularly shaped (usually a cube or rhomboid), and the size and position can be easily varied with reference to an MR image by modification of the selective pulse carrier frequency and applied gradients.

A disadvantage shared by all localization schemes which employ selective excitation is the presence of a chemical shift related spatial localization error.[21] When nuclei with different chemical shifts are examined, the associated differences in NMR resonant frequency cause an erroneous displacement of the selected region for each chemical shift value. The displacement error, ΔX is given by the equation:

$$\Delta X = \frac{\sigma B_0}{G_x} \tag{1}$$

where σ is the chemical shift value relative to a suitable reference peak, B_0 is the main magnetic field strength, and G_x is the gradient strength applied in the x direction during the spatial localization procedure. This problem can be minimized by using large magnetic field gradients for spatial localization since ΔX is inversely proportional to G_x. At a field strength of 2 T, a localized ^{31}P spectrum (σ range ± 12.5 ppm) obtained with a field gradient of 1 G cm^{-1} has associated spatial localization errors of ±2.5 mm irrespective of the size of the selected region. The disadvantage of using higher gradient strengths is an increase in the rf power required to select a region of fixed size, since the bandwidth of the rf selective excitation pulse must be increased by reducing the pulse length. The rf power is ultimately limited by the rf power amplifier.

Techniques in category (1) are difficult to implement primarily because they are susceptible to signal error arising from volumes of tissue where the NMR signal has not been effectively destroyed. This can be caused by rf field inhomogeneity, insufficient rf power, or even spin–lattice relaxation during the experiment. Without exception all the techniques in category (1) benefit from phase cycling in a series of experiments to cancel the unwanted signal. Phase cycling can sometimes be achieved in two experiments; however, the most general and accurate cancelation is only achieved in eight experiments (two experiments per spatial axis).

For in vivo ^{31}P MRS, techniques in category (2) suffer from the disadvantage of signal loss due to T_2 decay. Thus, these methods have found limited application in ^{31}P studies,[22] although they are widely used for in vivo ^{1}H MRS studies.

The disadvantage of category (3) methods and specifically ISIS, is that large NMR signals often have to be canceled in order to determine the residual signal from a small selected volume surrounded by a large mass of tissue. Such cancelation is subject to errors caused by system instability, or by subject movement. The solution is to minimize the large unwanted signal components prior to application of the ISIS method, using methods which are similar in principle to the techniques in category (1).[23] Since ISIS is, at present, the most widely used method for ^{31}P MRS, it is now described in greater detail.

The ISIS technique uses selective excitation in combination with the differencing of NMR signals from a sequence of eight experiments to select a rectangular-shaped volume of tissue for spectroscopic analysis. Upon combination of the free induction decays (FIDs) from the eight ISIS experiments, signal from the desired volume adds, whereas signals from all external regions cancel. The method relies on the principle of selective inversion of the spin population prior to data acquisition. The selective inversion pulses (180° pulses) cause inversion of longitudinal magnetization in selected slices of the sample using frequency selective rf excitation pulses in combination with applied field gradients. The selective pulses are applied in sequence along the X, Y, and Z axes. The experimental sequence is illustrated in Figure 1, and the rf selective inversion pulses either applied, or withheld, in a sequence of eight experiments are shown in the accompanying table. A delay

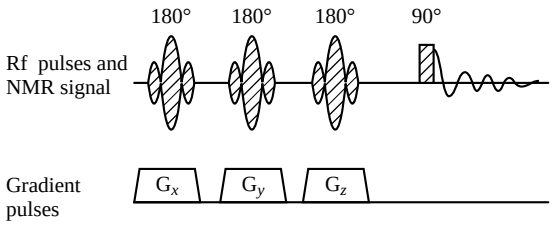

Experiment number	Selective pulse			Contribution to total spectrum
	X	*Y*	*Z*	
1	OFF	OFF	OFF	+
2	ON	OFF	OFF	−
3	OFF	ON	OFF	−
4	ON	ON	OFF	+
5	OFF	OFF	ON	−
6	ON	OFF	ON	+
7	OFF	ON	ON	+
8	ON	ON	ON	−

Figure 1 Pulse sequence used for the ISIS technique, and table indicating the order of RF pulse application during the eight experiment sequence. The addition or subtraction of relevant signals is indicated by a + or − sign

period follows application of each sequence to allow for spin–lattice relaxation.

The size of the selected region can be varied along any dimension by altering the excitation profile width of the respective rf pulse or the gradient associated with this rf pulse, thereby defining a rectangular volume. The position of the volume can be altered by adjustment of the individual frequency offset of each of the rf selective pulses. The size and position of the volume may thus be selected by reference to (and visualization with respect to) standard ^{1}H MR images of the subject.

For simplicity, the effect of a two-dimensional ISIS sequence on a two-dimensional spatial distribution of NMR spins is depicted in Figure 2. Four experiments are applied and the square array of nine elements represent three spatial regions along each axis. The hatched regions represent volumes which are inverted by ISIS prepulses in each of the four experiments. A double inversion (360° spin flip) is formed at the intersection of the inversion planes in experiment B2 (cross hatched region), and plain boxes do not receive any spin preparation prepulse. Selection of the central volume is achieved by combining the signals from the four experiments in the sequence of A1 − A2 − B1 + B2 whereupon all outer volumes correctly cancel. Three-dimensional selection (not depicted) involves extension of the scheme, and requires eight experiments, with the application of up to three selective inversion pulses, as indicated by the table which accompanies Figure 1.

The main advantage of ISIS is that signal readout immediately follows a nonselective 90° excitation pulse. This makes the method particularly useful in the study of MR signals with a short T_2 value, and specifically in the measurement of ^{31}P metabolites. Cancelation of signal outside the selected volume is accurate irrespective of the spin nutation angle experienced during each selective preparation pulse. However, selective 180° rf pulses are desirable since they provide the optimum sensitivity from spins within the ISIS volume. It is also preferable to use adiabatic, selective rf pulses such as the hyperbolic-secant selective inversion pulse proposed by Silver et al.[24] This ensures that material within the ISIS volume contributes fully in each of the eight experiments, and the optimum S/N ratio performance is achieved virtually independent of both the rf field inhomogeneity of the coil and the rf power level applied during each selective pulse. When used with adiabatic inversion pulses, the ISIS technique can be executed very effectively with surface coils to obtain improved signal sensitivity from regions close to the surface of the subject. The experiment can be made completely independent of rf power setting by replacing the 90° readout pulse with a nonselective adiabatic 90° rf pulse. Adiabatic rf pulses are commonly used in the ISIS sequence, even when the rf coil is nominally homogeneous, because they remove the need to calibrate accurately rf nutation angles.

An additional advantage of the ISIS technique is that the rectangular volume may be tilted along any axis by replacing standard Cartesian gradient pulses by mixtures of gradients, e.g. selection along a 45° axis can be achieved by simultaneous application of equal *X* and *Y* gradient pulses during the appropriate rf selection period. The ISIS volumes may also be a parallelepiped in shape if the selection gradients are applied along nonorthogonal axes.[25] The modified ISIS volume may thus be shaped to fit better within a particular region of interest, thereby increasing S/N performance.

There are several variations in the order in which the ISIS experiments may be applied. These have been devised to (i) allow optimal signal cancelation from undesired regions when there is rf inhomogeneity present and the experimental repetition delay is insufficient for complete spin–lattice (T_1) relaxation, and (ii) reduce signal cancelation errors caused by

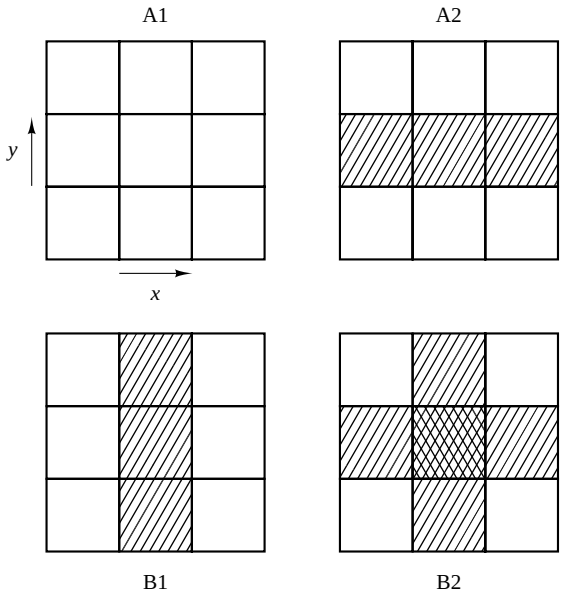

Figure 2 Diagrammatic representation of two-dimensional selection using an ISIS sequence of four experiments. The central square represents the region of interest, and is bordered along both *x* and *y* spatial dimensions by material that provides undesired signal. Inversion of a slice along *x* and *y* dimensions in experiments A2, B1, and B2 is indicated by hatched regions, and the cross hatched region (volume of interest) represents spins which have been inverted twice (e.g. 360° nutation)

subject motion. Matson et al.[26] include a 90° rf pulse following signal acquisition to ensure that T_1 relaxation commences from zero magnetization during the experimental delay period, thereby ensuring that longitudinal magnetization reaches the same state prior to each new acquisition. The experiments can then be applied in complete sequences of eight and the whole ISIS experiment is repeated successively in order to perform signal averaging. This makes the sequence less prone to movement errors and may have benefits when studying the torso. For head studies, where patient motion is not of great concern, the standard ISIS experiments may be averaged at each of the eight steps, since errors associated with relaxation will cancel upon final subtraction/coaddition of the data.[21] The absence of a 90° rf saturation pulse at the end of the signal acquisition period allows spin–lattice relaxation to proceed from the excitation pulse onwards, thus providing improved signal collection efficiency.

The method can be extended to investigate simultaneously two localized volumes centered on a common x axis but separated along the y axis. Three-dimensional ISIS with two selected cubes requires a minimum of 16 different sequences and up to four selective inversion pulses. This variation of the method is of particular use in biomedical studies since it allows simultaneous measurement of an equivalent contralateral region, thus providing an internal reference for biochemical changes in focal disease states. An example is presented in Figure 3, which shows in vivo ^{31}P brain spectra obtained from a stroke patient in the stroke-affected region and in the contralateral region for comparison.

The ISIS principle may also be extended to the simultaneous acquisition of multiple (2^n) volumes.[27] Since signal averaging is a necessity for in vivo ^{31}P spectroscopy, multiple volume spectra can be acquired with no increase in experimental duration compared with a single volume experiment. An extended sequence of selective spin inversion pulses is required in both the Hadamard transform approach[28] and the equivalent multicube ISIS method.

3 MEASUREMENT OF METABOLIC CONCENTRATIONS

Although most MRS data have been reported as spectral peak area ratios, quantitative methods have been developed for estimating molar concentrations of metabolites using in vivo MRS with single volume localization.[29,30] The principle requirements for quantitation are (a) to obtain accurate spectral integrals for the metabolite peaks of interest, (b) to determine the spatial sensitivity ($\boldsymbol{B}_1$ field distribution) of the rf transmitter/receiver coil, (c) to compare with a calibration sample of known concentration, and (d) to determine saturation and relaxation effects (T_1 and T_2) for rapidly repeated rf excitation.

The procedure typically involves measuring a ^{31}P MRS spectrum during each localization experiment from a small sample fixed to the rf coil assembly, or to the subject (e.g. containing hexamethylphosphorus triamide with a peak chemically shifted about 110 ppm downfield from PCr). This signal is used to determine rf pulse lengths, and as a reference to account for variations in coil sensitivity (Q factor) caused by variable loading. Spectral peak areas are then compared with the signal from a calibration phantom containing a known concentration of inorganic phosphate, which is measured periodically using the same spatial localization procedure. The formula used to obtain the absolute molar concentrations of metabolites might also take account of differences in the aqueous fraction between samples, (e.g. taking account of cerebrospinal fluid volume in head studies) which requires additional MRI data. The T_1 values for all metabolite resonances must also be known to obtain a saturation correction when the experimental repetition rate is high. A more complete explanation is provided in other articles (see Related Articles).

4 APPLICATIONS

In this section we present a very brief overview of some applications of single voxel whole body ^{31}P MRS in humans, with the intent of providing examples of the kinds of metabolic information available from such ^{31}P MRS studies. Many of the organs and diseases are reported on in much more detail in other chapters (see Related Articles).

4.1 Human Brain and Brain Diseases

The contralateral ^{31}P spectrum in Figure 3 is representative of normal adult brain at 3.0 T, and illustrates prominent ^{31}P resonances as identified in the figure legend. The infant brain is characterized by higher PME levels and somewhat reduced PCr. The broad hump commonly attributed to lipid resonances is less prominent at 3.0 T than at 1.5 T as a consequence of the chemical shift anisotropy relaxation mechanism. With proton decoupling, the PDE resonance splits into separate glycerophosphocholine and other PDE resonances.[31]

Phosphorus-31 MRS single voxel studies have been performed in AIDS or HIV infection, Alzheimer's disease, deep white matter lesions, epilepsy, multiple sclerosis (MS), stroke, and brain tumors. Representative trends of the ^{31}P metabolite concentration for these diseases are indicated in Table 1. Other diseases and conditions studied by ^{31}P MRS include alcoholism (and other drug use), migraines, schizophrenia and other mental disorders, and various pediatric diseases.

4.2 Heart

Although some early single volume ^{31}P MRS studies in human heart have been performed,[26,32,33] more recent studies have used more elaborate localization methods, including multiple volume methods, to combat the need to obtain very small volumes (particularly for studies of ischemia or infarction) from a moving organ.

4.3 Liver and Kidney

A ^{31}P spectrum of human liver obtained at 1.5 T is shown in Figure 4. The most notable feature, as compared with a brain spectrum, is the lack of PCr. In fact, the absence of PCr is often taken as an indication of lack of contamination from surrounding muscle tissues which contain significant concentrations of PCr. Disease conditions studied in human liver include cancers, alcoholic hepatitis and cirrhosis, and fructose intolerence. Disease typically produces a decrease in ^{31}P

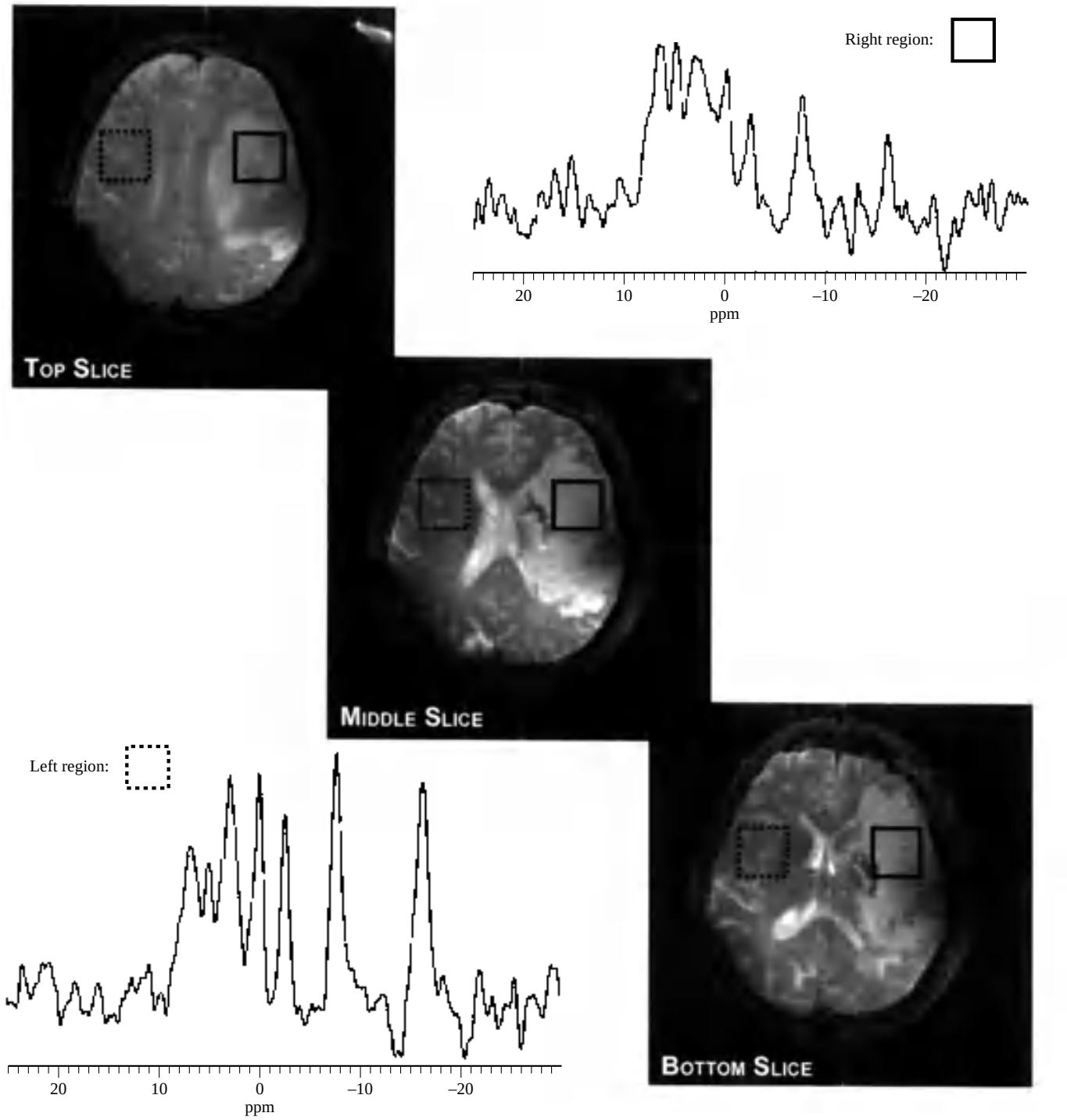

Figure 3 MR images and ^{31}P spectra obtained from a stroke patient at a field strength of 3 T using ISIS. The two regions studied using ^{31}P MRS were investigated simultaneously (*TR* = 1.5 s, number of acquisitions = 768, MRS study completed in 20 min), and incorporate tissue extending from the regions shown in the top slice through to those in the bottom slice (volume of each cube = 3 × 3 × 3 cm^3). Peaks correspond to (from left to right) phosphomonoesters (PME), inorganic phosphate (Pi), phosphodiesters (PDE), phosphocreatine (PCr) and the γ, α-, and β-phosphates of ATP. The spectrum from stroke-affected tissue (right) should be compared with that from the unaffected contralateral region (left)

metabolites, while fructose intolerance is marked by reduction in ATP following ingestion or administration of fructose.

Few ^{31}P MRS studies of normal kidney have been reported due to the depth of this organ in the body. However, transplanted kidney is typically much closer to the surface and easier to study. Several groups have made preliminary studies of transplanted kidneys and ^{31}P MRS has the potential to assess transplanted kidney metabolic health, and possibly to assist in analyzing tissue status or pathology following transplantation.

Table 1 Representative Trends of ^{31}P Metabolite Concentration for Various Diseases

Diseases	Observations
Alzheimer's	Ranges from no observable changes to reported increases in PDE and possibly PME.
Deep white matter lesions	Reductions in PME, PDE, and ATP
Epilepsy	Reduced PME, increased Pi, and decreased pH (interictal studies of focal temporal lobe epilepsy)
HIV	Reduced ATP/Pi in AIDS dementia complex
MS	Ranges from no observable changes to decreases in PDE, and reduced PME and Pi (chronic lesions)
Stroke	Reductions in all metabolites; decreased pH in acute phase; increased pH in some chronic infarcts
Tumors	Variable metabolite reductions in PDE and PCr, elevated PME, depending upon tumor type

4.4 Human Muscle

By far the largest number of ^{31}P MRS studies in humans have been performed on muscle, ranging from the study of normal muscle metabolism under various conditions of (and recovery from) exercise, to studies of the alterations of muscle metabolism in various disease states. Under light to moderate exercise, normal muscle displays a fall of PCr and a fall of pH (after an initial slight rise), with maintenance of ATP levels. Alterations of metabolic concentration with work, or under recovery conditions, may be further changed by a variety of diseases, and ^{31}P MRS has proven to be clinically useful in a number of muscle disorders. However, the localization has traditionally been accomplished by the sole use of surface coils.

4.5 Body Tumors

Tumor spectra typically display a high PME, and often reduced PCr compared with the surrounding or normal tissue. Although early studies indicated that ^{31}P MRS might have considerable potential in the assessment of tumor therapy, the investigation of tumors in the body has proved difficult. While some early studies seemed to indicate that reductions in PME heralded effective therapy, more recent studies have shown that no such simple interpretations generally prevail.

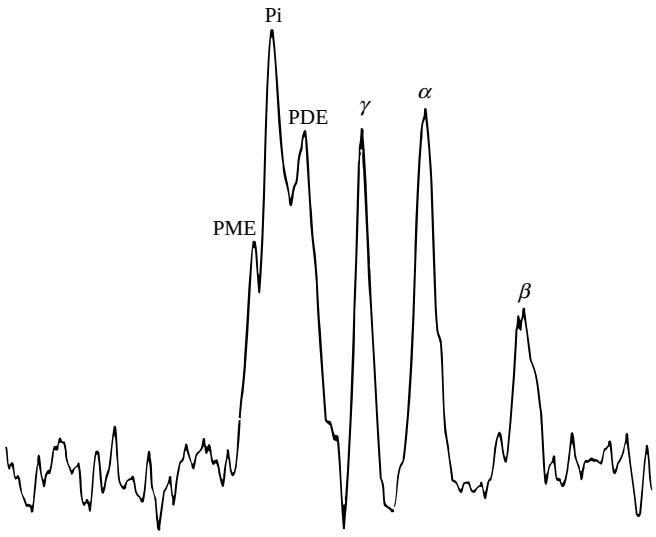

Figure 4 Human liver ^{31}P spectrum obtained at a field strength of 1.5 T using a 14 cm surface coil (number of acquisitions = 640, TR = 2 s). The 96 ml volume of tissue studied was localized using ISIS, and the ^{31}P spectrum confirms the absence of PCr in liver tissue. (Reproduced by permission of Academic Press from M. D. Boska et al.[34])

5 CONCLUSION

Single voxel whole body ^{31}P spectroscopy may be performed within acceptable experimental durations in high-field magnet systems. The most commonly used method, ISIS, while not devoid of problems, offers a reasonably robust method of localization. Two cubes may be investigated simultaneously to allow an internal comparison between different regions of biological tissue.

Application of all these single voxel localization methods requires the location of the volume to be chosen from an MR image, which assumes that the operator can either observe a region of abnormality on the image, or can identify the region from clinical symptoms. If the region of metabolic dysfunction is not known, and the contrast provided by MRI is insufficient to identify the region, chemical shift imaging (CSI) offers the advantage that all regions of the sample are investigated to produce a map of each metabolite. The region of interest may then be defined on the basis of metabolic changes following data acquisition. However, CSI methods are generally more time consuming than ISIS, and rapid experimental repetition rates result in distorted spectra which must be corrected for T_1 relaxation for the purposes of quantitation. Both approaches offer advantages and disadvantages in their application to specific studies, and appropriate choice of methodology usually involves a compromise.

6 RELATED ARTICLES

Brain MRS of Human Subjects; Brain Neoplasms in Humans Studied by Phosphorus-31 NMR Spectroscopy; Chemical Shift Imaging; In Vivo Hepatic MRS of Humans; Localization and Registration Issues Important for Serial MRS Studies of Focal Brain Lesions; NMR Spectroscopy of the Human Heart; Peripheral Muscle Metabolism Studied by MRS; Proton Decoupling During In Vivo Whole Body Phosphorus MRS; Proton Decoupling in Whole Body Carbon-13 MRS; Quantitation in In Vivo MRS; Rotating Frame Methods for Spectroscopic Localization; Surface Coil NMR: Detection with Inhomogeneous Radiofrequency Field Antennas; Systemically Induced Encephalopathies: Newer Clinical Applications of MRS; Whole Body Studies: Impact of MRS.

7 REFERENCES

1. R. B. Moon and J. H. Richards, *J. Biol. Chem.*, 1973, **248**, 7276.
2. H. Halvorson, A. M. Q. Vande Linde, J. A. Helpern, and K. M. A. Welch, *NMR Biomed.*, 1992, **5**, 53.
3. J. J. H. Ackerman, T. H. Grove, G. G. Wong, D. G. Gadian, and G. K. Radda, *Nature (London)*, 1980, **283**, 167.
4. R. E. Gordon, P. E. Hanley, D. Shaw, D. G. Gadian, G. K. Radda, P. Styles, P. J. Bore, and L. Chan, *Nature (London)*, 1980, **287**, 736.
5. M. R. Bendall, and R. E. Gordon, *J. Magn. Reson.*, 1984, **53**, 365.
6. D. I. Hoult, *J. Magn. Reson.*, 1979, **33**, 183.
7. R. Tycko and A. Pines, *J. Magn. Reson.*, 1984, **60**, 156.
8. A. J. Shaka, J. Keeler, M. B. Smith, and R. Freeman, *J. Magn. Reson.*, 1985, **61**, 175.
9. A. J. Shaka and R. Freeman, *J. Magn. Reson.*, 1985, **62**, 340.
10. M. R. Bendall, J. M. McKendry, I. D. Cresshull, and R. J. Ordidge, *J. Magn. Reson.*, 1984, **60**, 473.
11. P. A. Bottomley, T. B. Foster, and R. D. Darrow, *J. Magn. Reson.*, 1984, **59**, 338.
12. P. A. Bottomley, L. S. Smith, W. M. Leue, and C. Charles, *J. Magn. Reson.*, 1985, **64**, 347.
13. W. P. Aue, S. Muller, T. A. Cross, and J. Seelig, *J. Magn. Reson.*, 1984, **56**, 350.
14. P. R. Luyten, A. J. H. Marien, B. Sijtsma, and J. A. den Hollander, *J. Magn. Reson.*, 1986, **67**, 148.
15. A. Haase, *Magn. Reson. Med.*, 1986, **3**, 963.
16. D. M. Doddrell, W. M. Brooks, J. M. Bulsing, J. Field, M. G. Irving, and H. Baddeley, *J. Magn. Reson.*, 1986, **68**, 367.
17. D. M. Doddrell, J. M. Bulsing, G. J. Galloway, W. M. Brooks, J. Field, M. Irving, and H. Baddeley, *J. Magn. Reson.*, 1986, **70**, 319.
18. P. A. Bottomley, *Ann. NY Acad. Sci.*, 1987, **508**, 333.
19. R. J. Ordidge, M. R. Bendall, R. E. Gordon, and A. Connelly, *Magn. Reson. Biol. Med.*, 1985, 387.
20. J. Frahm, K. D. Merbolt, and W. Hanicke, *J. Magn. Reson.*, 1987, **72**, 502.
21. R. J. Ordidge, A. Connelly, and J. A. B. Lohman, *J. Magn. Reson.*, 1986, **66**, 283.
22. K. D. Merboldt, D. Chien, W. Hanicke, M. L. Gyngell, H. Bruhn, and J. Frahm, *J. Magn. Reson.*, 1990, **89**, 343.
23. R. J. Ordidge, *Magn. Res. Med.*, 1987, **5**, 93.
24. M. S. Silver, R. I. Joseph, and D. I. Hoult, *J. Magn. Reson.*, 1984, **59**, 347.
25. J. C. Sharp and M. O. Leach, *Magn. Reson. Med.*, 1989, **11**, 376.
26. G. B. Matson, D. B. Twieg, G. S. Karczmar, T. J. Lawry, J. R. Gober, M. V. Valenza, M. D. Boska, and M. W. Weiner, *Radiology*, 1988, **169**, 541.
27. R. J. Ordidge, R. M. Bowley, and G. McHale, *Magn. Reson. Med.*, 1988, **8**, 323.
28. L. Bolinger and J. S. Leigh, *J. Magn. Reson.*, 1988, **80**, 162.
29. S. Wray and P. S. Tofts, *Biochim. Biophys. Acta.*, 1986, **886**, 399.
30. K. Roth, B. Hubesch, D. J. Meyerhoff, S. Naruse, J. R. Gober, T. J. Lawry, M. D. Boska, G. B. Matson, and M. W. Weiner, *J. Magn. Reson.*, 1989, **81**, 299.
31. P. R. Luyten, G. Bruntink, F. M. Sloff, J. W. A. H. Vermeulen, J. I. van der Heijden, J. A. den Hollander, and A. Heerschap, *NMR Biomed.*, 1989, **1**, 177.
32. P. R. Luyten, J. P. Groen, J. W. A. H. Vermeulen, and J. den Hollander, *Magn. Reson. Med.*, 1989, **11**, 1.
33. S. Schaefer, J. Gober, M. Valenza, G. Karczmar, G. Matson, S. A. Camacho, E. Botvinick, B. Massie, and M. W. Weiner, *J. Am. Coll. Cardiol.*, 1988, **12**, 1449.
34. M. D. Boska, B. Hubesch, D. J. Meyerhoff, B. B. Twieg, G. S. Karczmer, G. B. Matson, and M. W. Weiner, *Magn. Reson. Med.*, 1990, **13**, 228.

Biographical Sketches

Roger J. Ordidge. *b* 1956. B.S., 1977, Ph.D., 1981, physics, University of Nothingham, UK, (supervisor Sir Peter Mansfield). Bruker Instruments, 1982–1986. Lecturer, Nottingham University, 1986–1989. Professor, Oakland University, Michigan, and Researcher, Henry Ford Hospital, Detroit, MI, 1989–1993. Professor, University College of London, 1993–present. Approximately 80 publications. Research specialties, localized spectroscopy, diffusion weighted MRI, and high speed MRI.

Joseph A. Helpern. *b* 1955. B.A., Chemistry, 1977, Case Western Reserve University, Cleveland, OH. M.A., chemistry, 1979, University of North Carolina, Chapel Hill, NC. Henry Ford Hospital, Detroit, MI, 1981, helped establish NMR Research Program. Ph.D., Medical Physics, Oakland University, Rochester, MI, 1988, supervisor, Dr. Michael Chopp. Director of NMR Research, Department of Neurology, Henry Ford Hospital, 1988–present. Over 55 publications. Research interests: cerebral metabolism, blood flow measurement, and NMR techniques for assessment of brain disorder.

James W. Hugg. *b* 1952. B.S., 1973, M.S., 1974, CalTech; M.S., 1976, Ph.D., 1978, nuclear physics, Stanford. Introduced to NMR by Felix Bloch and to Medical Imaging by Al Macovski. Petroleum industry. 1978–1988. Postdoctoral work in human brain MR spectroscopy at University of California, San Francisco, 1989–92. Rabi Young Investigator Award, 1992. Senior Staff Investigator, Neurology, Henry Ford Health Science Center (Case Western Reserve University), Detroit, MI 1992–present. Over 60 publications. Research specialties: spectroscopic imaging and diffusion imaging in human brain ischemia, epilepsy, and multiple sclerosis.

Gerald B. Matson. *b* 1938, B.A. chemistry, 1960, University of California, Ph.D., 1967, physical chemistry, University of Wisconsin. Since 1986 Facilities Manager, MR Unit, Department of Veterans Affairs Medical Center, San Francisco, Since 1989 Adjunct Professor, Department of Pharmaceutical Chemistry, University of California, San Francisco. Interests include development of MR spectroscopic imaging methods for in vivo MRS of human brain and brain diseases, MRS selective excitation and localization methods, and NMR probe design.

Spatial Localization Techniques for Human MRS

David J. Bryant and Glyn A. Coutts
GEC Hirst Research Centre, Borehamwood, Herts, UK

1 INTRODUCTION

The surface receiver coil has received widespread use in the acquisition of in vivo magnetic resonance (MR) spectra.[1–3] Its characteristic of high magnetic field ($\boldsymbol{B}_1$) flux density in close proximity to the coil provides spectra of good signal-to-noise ratio (S/N) and provides a level of spatial localization. Applications involving deep-seated organs and pathology give inferior results through lack of sensitivity and contamination from unwanted surface signals.

A number of techniques have been developed over the years in order to provide flexibility in positioning the regions from which spectroscopic data can be acquired. In this article a general description of the localization methods investigated to date are described. The predominant techniques and their applications now in use are described in the related articles listed at the end. The wide range of techniques involve manipulation of the applied magnetic field $\boldsymbol{B}_0$, either by static profiling or by the use of $\boldsymbol{B}_0$ field gradients, or the use of radiofrequency $\boldsymbol{B}_1$ field gradients. The choice of localization technique will often be as a result of the availability of specific hardware components. Radiofrequency (rf) techniques are particularly tied to the use of the surface transmit coil. The flexibility of location and size or field-of-view offered by the $\boldsymbol{B}_0$ field gradient methods places a greater premium on the control of eddy currents, high homogeneity rf coils, and rf pulse design. These additional features are also included in the related articles listed at the end of this article.

2 STATIC FIELD PROFILING

The higher order spatial harmonics of the magnetic field $\boldsymbol{B}_0$ are designed to limit the size of the homogeneous volume from which high-quality spectra can be obtained. Signals outside and on the periphery of this volume are inhomogeneously broadened and are either absent from the signal or can be removed by postprocessing. Topical magnetic resonance (TMR) has been demonstrated,[4,5] in conjunction with surface transmit and receive coils, to give high-quality spectra. The homogeneous volume from which the signal is derived is not particularly well-defined and there is very little control over its position and dimensions. Realignment of the patient is required in order to achieve this level of control.

A related approach has been suggested[6] which employs a surface $\boldsymbol{B}_0$ field gradient coil that degrades the quality of field in its close proximity. The nonlinear gradient is pulsed during the first τ interval of a spin echo sequence to ensure that only signals remote from the surface gradient coil contribute to the echo. Irreversible dephasing of surface signals has also been achieved by the use of immobilized ferrite particles with a simple pulse and collect acquisition of the data.[7] Both of these approaches give a robust method of removing the intense unwanted signals near to an rf surface receive coil.

3 RADIOFREQUENCY ($\boldsymbol{B}_1$) METHODS

This family of techniques relies upon the use of the surface coil as a transmitter system. The spatial variation in the transverse components of $\boldsymbol{B}_1$ perpendicular to the static field $\boldsymbol{B}_0$ can be manipulated to produce spatially constrained spectra. It would not be uncommon for the transmitter and receiver of the rf system to be physically different coils such that localization attributes can be optimized with the transmit coil while the reception qualities are not prejudiced.

The axial components of the B_1 field along the axis of a single current carrying loop are given by:

$$B_1(r) = \frac{\mu_0 i}{2} \cdot \frac{R^2}{(R^2 + r^2)^{3/2}} \tag{1}$$

where μ_0 is the magnetic permeability, i the current in the loop of radius R, and r the position along the axis of the coil. Assuming a square excitation pulse of duration t_p, the transverse magnetization M_{xy} at each point along the axis is proportional to $\sin\theta(r)$, where $\theta(r)$ is the spatially-dependent pulse angle given by $\gamma B_1(r) t_p$ (radians). The sinusoidal dependence of M_{xy} has been exploited in a number of ways to project the region of interest away from the proximity of the coil.

3.1 Depth and Composite Pulses

Analysis of equation (1) demonstrates that a 90° excitation is experienced at $0.77R$ when $\boldsymbol{B}_1(0)$, the field at the center of the coil, is set to 180°. Peak signal is generated at $0.58R$ for a transmit/receive surface coil arrangement where the signal is proportional to $\theta(r)\sin\theta(r)$, where $\theta(r)$ is the spatially-dependent pulse angle. Contour plots of the $\boldsymbol{B}_1$ field show that the excited volume is poorly defined.[3] However it can be considerably improved by combining several pulses together to form a composite 'depth' pulse.[8] The profile of selected M_{xy} has been demonstrated to be $\sin^n\theta(r)$, instead of $\sin\theta(r)$, where the value of n will depend upon the number of pulses that compose the depth pulse and upon the extent of phase cycling employed within the pulse. Depth pulses are often based upon the spin echo $(\theta(r);2\theta(r)(\pm x,\pm y))$, where the use of $\theta(r), 2\theta(r)$ emphasizes the spatial variability of the $\boldsymbol{B}_1$ field, ';' denotes a small time delay, and $\pm x, \pm y$ refer to the quadrature phases of the rf pulses. Analysis of the depth pulse approach involving the inversion–recovery sequence $(2\theta(r);\theta(r)(x);[2\theta(r)(\pm x,\pm y)_m];)$ has also been demonstrated allowing volume localized relaxation measurements to be carried out.[9]

Composite pulses, whose initial usage was to compensate for pulse imperfections,[10] have also been applied to the problem of spatial localization and complement the depth pulse approach.[11,12] These composite pulses excite M_{xy} and sub-

sequent 180° pulses ensure that only signals experiencing a very narrow range of $\boldsymbol{B}_1$ amplitudes actually form a spin echo. Contour plots of the inversion efficiency of these composite pulses demonstrate the potential of the method.[13,14]

The duration and extent of phase cycling for both depth and composite pulse approaches can become large as the degree of localization is improved. Comparisons of the two techniques showed that depth pulses had improved performance with respect to frequency offset although they did require more phase cycling.[15–17]

3.2 Fourier Methods

Analysis of the depth pulse described above demonstrated that the spatial profile of M_{xy} generated by the surface coil transmitter could depend on $\sin^n \theta(r)$, where n is an odd integer and $\theta(r)$ the spatially-dependent pulse angle. Pekar et al. showed that any required region at depth from the transmitter coil can be constructed from the differing spatial harmonics generated with differing pulse power in the transmitter.[18] Each harmonic is suitably weighted before accumulating a final signal response prior to Fourier transformation to obtain the localized spectrum. This harmonically analyzed sensitivity profile (HASP) technique has also been called Fourier series analysis,[19] or Fourier series windowing (FSW).[20,21] Unless each transient is accorded equal weight there is a loss of sensitivity; this loss is particularly exaggerated when the localization is required in the minimum number of transients. If unequal numbers of transients are accumulated for each of the generated harmonics, then the correct spatial profile can be obtained with no loss in sensitivity, but at the expense of increased scan acquisition time. There is the possibility of saving time by recognizing that some harmonics will not contribute greatly to the required spatial profile and need not be acquired.

The rotating frame zeugmatographic method of Hoult has been extended to the acquisition of spatially localized, high-resolution spectra.[22,23] Incrementing the rf power level through a transmitter system generating an rf gradient produces a series of spatially-encoded transients. Each transient has to be recorded and stored separately rather than weighted and coadded as in the Fourier series method described previously. The resultant two-dimensional data set can be Fourier transformed in two directions to generate planes of conventional spectra.[23–25] In this simplified method there is a loss of sensitivity of $\sqrt{2}$ since the transients are amplitude modulated by the exciting pulses and the longitudinal component of magnetization M_z remains undetected. However this loss of sensitivity can be recovered by an orthogonal 90° $\boldsymbol{B}_1$ pulse which precesses all magnetization into the transverse plane, converting amplitude spatial encoding to phase modulation.[22,26] This additional pulse should not be dependent upon the $\boldsymbol{B}_1$ field and will usually be either of a composite or adiabatic nature. It should also be noted that the same approach can be applied to the Fourier series window technique described in the preceding paragraph. Strictly, the $\boldsymbol{B}_1$ gradient should be spatially linear and Helmholtz transmitter coils have been proposed for this purpose.[22] It has been noted that the surface coil response [equation (1)] is approximately linear along its axis in the range $0.3R$ to $0.8R$ and that this linearity is insignificantly distorted for small off-axis distances ($<0.5R$).[25] More complex rf systems are required to introduce a second spatial dimension by providing an additional orthogonal linear $\boldsymbol{B}_1$ field gradient. Applications employing these Fourier rf techniques are described in ***Rotating Frame Methods for Spectroscopic Localization***.

4 $\boldsymbol{B}_0$ FIELD GRADIENT TECHNIQUES

The wider application of MRI hardware in the form of magnetic field ($\boldsymbol{B}_0$) gradient coils has allowed the development of a number of methods that provide much of the required flexibility for the acquisition of in vivo MRS data. These techniques may involve oscillatory gradients, slice selective methods, or Fourier techniques.

4.1 Sensitive Point Method

The magnetic field can be dynamically profiled by the application of sinusoidally varying $\boldsymbol{B}_0$ field gradients.[27] Non-time-dependent signals are derived only from the isocenter of a field gradient system and these can be extracted by low-pass filtering. The isocenter can be controlled by adjustment of the balance of the current between the two halves of the gradient coil set. Localization to a volume in space has been achieved by the use of three orthogonal gradients with differing time-dependences. Signal is usually sampled under the steady-state regime ($TR \leqslant T_2, T_1$) and then the rf pulse repetition rate must exceed the gradient frequency. If this is not achieved, then the gradient oscillations are superimposed upon the time domain signal and artifactual sidebands can occur in the resultant spectra. By sampling the echo rather than the FID of the steady-state signal, it has been demonstrated that these artifacts can be reduced.[28]

4.2 Slice-Selective Techniques

The degree of spatial localization offered by slice-selective pulses has led to their widespread use for in vivo MRS. Control of voxel dimension by gradient strength and rf pulse bandwidth and voxel position with rf carrier offset provide flexible positioning of regions from which signals are derived.

Common problems concern the generation of eddy currents by the pulsed gradients employed with these techniques, chemical shift artifact, and loss of initial portions of the signal. The absence of eddy currents remains an underlying strength of the $\boldsymbol{B}_1$ gradient methods described earlier. The problem has been alleviated by a number of compensation (see ***Eddy Currents and Their Control***) and correction schemes (see ***Quantitation in In Vivo MRS***) and by the development of self-shielded gradient systems (see ***Gradient Coil Systems***).

Chemical shift dispersion amongst individual resonances of a spectrum leads to a misplacement in position when pulsed $\boldsymbol{B}_0$ field gradients are employed in slice-selective procedures. The extent of this chemical shift artifact or mis-registration is given by $\delta/\gamma G$ mm, where δ is the dispersion expressed in hertz (Hz) and γG is the field gradient (Hz mm^{-1}). The positional difference becomes more pronounced as the chemical shift increases, at higher field strengths, or in ^{13}C rather than ^{1}H MRS, but can be alleviated by use of the largest gradient possible. The use of high gradient values places a requirement for wider bandwidth, higher

power rf pulses, and a greater penalty in terms of increased eddy currents. In reality, following these measures, the misplacement for in vivo ^{1}H MRS may be less than 1 mm. More detail is given in ***Selective Excitation Methods: Artifacts***.

The loss of initial data points of the digitized signal can arise through the finite time required to switch the gradient from one value to the next. Each data point lost represents a 180° phase roll across the resultant spectrum, which in poorly-resolved in vivo MRS, has proved intractable in the most rigorous sense. A number of baseline correction schemes have been suggested or, as an alternative, fitting the time domain data directly rather than introducing the artifact with the use of the Fourier transform (see ***Quantitation in In Vivo MRS***). The extent of signal loss can be reduced with greater gradient strength and switch rates, eddy current control, and sequence development. The latter provide the material for the discussion below.

Slice-selective pulses are employed in three distinct ways; the signal from the required volume may be prepared along the z axis or in the xy plane, or alternatively the magnetization from unwanted regions may be presaturated by a series of slice-selective pulses.

4.2.1 Longitudinal Spatial Preparation

A number of techniques have been described that prepare signal from the required region of interest parallel to the static field $\boldsymbol{B}_0$. During the volume-selective procedure, unwanted M_{xy} is dephased by field gradients or alternatively by a phase cycling scheme during the acquisition of the data. The required signal, which is maintained along the z axis, is observed with a single broadband pulse. Loss of signal and time delay to the start of data acquisition are kept to a minimum by this approach which can be extended to include spin echo techniques as required.

Image selected in vivo spectroscopy (ISIS) consists of three orthogonal slice-selective 180° pulses in combination with a phase cycling scheme.[29] The phase cycling and data accumulation required introduce a minimum of eight transients before the volume localized spectrum can be observed. This represents a serious inconvenience when shimming is undertaken prior to the accumulation of the data. The technique has been extended to include the multiple acquisition of several voxels simultaneously,[30] and conformation of the voxel shape to match required pathological regions.[31] ISIS, these developments, and its applications to ^{31}P MRS are described in ***Single Voxel Whole Body Phosphorus MRS***.

Volume selective excitation (VSE) is a single shot localization technique based upon a composite selective procedure (45°, 90°, 45°) where both the 45° pulses are slice selective and the 90° is broadband.[32] The required 'in-slice' material is inverted longitudinally while the unwanted magnetization is left in the transverse plane. Care must be taken to avoid the generation of stimulated echoes. Three orthogonal composite slice-selection pulses are required to define a single voxel and these are performed sequentially. VSE requires high rf power if the gradient is *not* switched during the broadband 90° pulse. VSE has been applied to the acquisition of ^{13}C and ^{31}P spectra.[33,34] A comparable technique (DIGGER)[35] has improved the off-resonance capability and does not rely upon phase cycling by paying attention to the qualities of the individual rf excitation pulses.

The solvent suppressed spatially resolved spectroscopy (SPARS) technique alleviates the high rf requirement of VSE by introducing gradient switching and the spin echo into the localization to reduce the effects of the duration of the procedure.[36] Each of the required spatially selective pulses is a 90°, 180°, 90° sandwich, where *only* the final 90° pulse is slice selective. Unwanted signal remains in the transverse plane to be dephased and its cancellation can be improved by phase cycling. A similar technique (SPACE)[37] has also been proposed that employs the same rf pulse composite as SPARS. However, in this case, the first 90° is spatially selective and subsequent pulses are phase cycled to improve the suppression of unwanted signals.

4.2.2 Transverse Spatial Preparation

These techniques prepare the required signal in the transverse plane which can make them particularly vulnerable to loss of signal through T_2^x decay unless spin echo methods are introduced. Significant initial data loss can also occur, with subsequent increase in baseline roll in the resultant spectra, without the use of the spin echo. Despite these shortcomings, these methods have been widely employed to acquire ^{31}P and ^{1}H spectra.

Depth resolved surface coil spectroscopy (DRESS) represents the simplest of localization techniques, a single slice selective 90° followed by the acquisition of the data.[38] The lateral extent of the selected plane is controlled by the use of the surface receive coil and the selected region is usually assumed to be a disk. A slice-interleaved version of DRESS (SLIT-DRESS)[39] allows more spectroscopic data to be acquired by using offset slices during the inevitable relaxation delays. DRESS methods and applications are described in ***NMR Spectroscopy of the Human Heart***.

Spin echo techniques can be introduced to alleviate time delay problems. Point resolved surface spectroscopy (PRESS) employs three selective pulses (90°, 180°, 180°) to leave M_{xy} from the required voxel to contribute to the final echo.[40] PRESS is particularly amenable to the acquisition of ^{1}H spectra where the increased echo time can be integrated into the scan as an additional suppression of unwanted fat and lipid signals. In this case the localization is preceded by a chemical shift selective (CHESS) pulse in order to presaturate the large water resonance (see ***Selective Excitation in MRI and MR Spectroscopy***). A related technique that is applicable to ^{1}H MRS, the multiple echo spectroscopic acquisition (MESA) method,[41–43] employs three mutually orthogonal slice selective pulses to define to a given region of interest. Initial transverse magnetization is generated by a binomial excitation where the large water resonance remains along the $\boldsymbol{B}_0$ axis and undetected (see ***Water Suppression in Proton MRS of Humans and Animals***). The MESA sequence (1331, 180°, 180°, 180°), like many multiecho techniques, places emphasis upon the quality of the refocusing 180° rf pulses, and unwanted signals can be substantially reduced by phase cycling.

Stimulated echo pulse sequences have been proposed to perform spectroscopic localization.[44–46] The stimulated echo acquisition mode (STEAM) sequence consists of three selective 90° pulses (90°, 90°, 90°), one in each of the three spatial orientations. During the period after the second 90° pulse, the *TM* period, the required signal is orientated along the z axis and so there is no loss in signal due to transverse relaxation. At all other points of the sequence, the required signal is in the

transverse plane and as such the STEAM sequence is included in this section. As with the multiecho PRESS sequence, ^{1}H spectra can be acquired by preceding the STEAM localization with a series of narrow band, CHESS water suppression pulses. Stimulated echoes are intrinsically half the intensity of their spin echo counterparts which would appear to be a considerable disadvantage. However voxel definition is superior, as a result of employing selective 90° rather than 180° pulses, and STEAM consistently provides shorter echo time sequences than its spin echo counterparts PRESS and MESA. In practice these features account for the widespread use of STEAM in the acquisition of ^{1}H spectra (see ***Single Voxel Localized Proton NMR Spectroscopy of Human Brain In Vivo***).

4.2.3 Spatial Presaturation

Maintaining the coherence of the signal from the required voxel can be alleviated by the use of spatial presaturation. Slice-selective pulses are used preferentially to excite the unwanted regions into the transverse plane to be dephased prior to the use of a single broadband pulse to observe the required signal. Time delays to the start of data acquisition can be reduced to a minimum suitable for shorter T_2 species.[47] This approach has been integrated into other localization schemes and has been called outer volume suppression (OVS).[48–50] This approach has been particularly useful in the acquisition of ^{1}H spectra where the spatial presaturation of high scalp fat and lipid signals is required.

4.3 Fourier Methods

In contrast to the B_1 Fourier methods described earlier, where amplitude spatial-encoding has to be converted to phase modulation in a two-step process,[22] $\boldsymbol{B}_0$ field gradients act directly upon the transverse components of magnetization and generate spatial phase modulation directly into the signal. In most other respects the $\boldsymbol{B}_0$ methods introduced here mirror those $\boldsymbol{B}_1$ techniques described earlier.

The harmonically analyzed approach to spectral localization has been described by the application of a field gradient pulse within a spin echo pulse sequence.[51] A number of transients are recorded with differing combinations of gradients in the x, y, and z directions to achieve full volume localization. Each transient can be Fourier-transformed to give spatially phase distorted spectra. Suitable weighting of each of these spectra prior to accumulation gives the desired volumetric region. The weighting factors employed are simply the Fourier coefficients of the desired region of interest. Weighting is best achieved by accumulating different numbers of transients for the various gradient permutations in order to maintain sensitivity.[52] It has also been noted that the required region may be repositioned with respect to the gradient isocenters by multiplying each time domain transient in the acquired matrix by a phase factor $\exp(-i\gamma G_r r_0 t)$, where r and r_0 may refer to either x, y, or z components of the voxel's position.

Rather than weight and accumulate signals to achieve the required level of localization, it is possible to submit the data to a multidimensional Fourier transform.[53–56] The resultant chemical shift image is a matrix of voxels, each containing a high-resolution spectrum. Chemical shift imaging or phase-encoded spectroscopy has been widely applied to the acquisition of ^{1}H, ^{19}F, ^{31}P, and ^{13}C in vivo spectra and is described in detail in ***Chemical Shift Imaging***. In situations of low S/N, which is inevitable for human MRS at low field with a poor filling factor for the remote regions of interest, this Fourier approach represents the most efficient of data acquisition procedures. In addition, since spatial resolution is expected to be low because of low concentration, the gradient usage is considerably less than the slice-selective techniques described in preceding sections with commensurate decrease in eddy current problems.

Consideration of the sensitivity, spatial response shape, and spatial location with respect to both harmonically analyzed and full Fourier approaches is given by Mareci and Brooker.[57]

4.4 Nonlinear Gradients

A method involving surface gradients has been described earlier which involves the use of nonlinear, pulsed $\boldsymbol{B}_0$ field gradients.[6] It has also been noted that slice-selective procedures in nonlinear gradients can generate multidimensional spatial localization.[58] However the development of two- and three-dimensional spatially-selective pulses and spectro-spatial-selective pulses, both with the convenience of linear gradients, may overshadow this work (see ***Complex Radiofrequency Pulses***).

5 PRACTICAL APPROACHES AND HYBRID TECHNIQUES

It is very difficult to make statements concerning the best technique for spatially-resolved in vivo MRS given the wide range of methods available. It is not surprising, given this comment, that the practical approach to spectral localization is to employ some hybrid of the techniques described beforehand. In a number of cases this hybrid approach may naturally occur through the availability of the relevant components of hardware.

The lateral spatial extent of signal, when employing a surface coil, may be controlled with any of the slice-selective techniques described earlier. This may require the use of adiabatic, hyperbolic secant[59] or frequency modulated rf pulses to compensate for the inhomogeneous $\boldsymbol{B}_1$ field if a surface transmitter coil is employed. ISIS has been employed in this manner, in combination with depth pulses, to acquire ^{1}H spectra.[60] A similar approach, employing a two-dimensional ISIS method in sequence with DRESS,[40,61,62] has been used to acquire examples of good quality ^{31}P muscle spectra. Two-dimensional ISIS, which defines a column of tissue after a four transient addition/subtraction cycle, has been employed with the B_1 Fourier series window technique.[63] In this case nine Fourier harmonics were acquired over 96 transients to obtain canine myocardia spectra in conjunction with a 29-mm surface transmit/receive coil. Phase modulation was implemented to improve sensitivity with this ISIS/FSW approach,[26,64] where additional flexibility was provided by voxel shifting the acquired data matrix to overlay the required region of interest.

Proton MRS in many ways presents the largest technical problems in spectral localization due to the intense resonances of water and lipid. This is compounded by the narrow range of ^{1}H chemical shift dispersion available at the relatively low fields offered by whole body in vivo MR systems. Robust practical approaches involve spatial presaturation (OVS), in addition to

the volume selected procedure offered by STEAM, PRESS, and MESA,[48–50] in order to control the large signals from peripheral fat layers. Water suppression may be either by narrow-band CHESS or binomial pulses. Fourier encoding has also been employed to localize further the ^{1}H signals within the defined region of interest. In a number of examinations the extent of this localization may not be fully required or warranted, but will provide a level of robustness across a number of eventualities.

The slice-selection techniques are usually introduced as single voxel methods that generate a single high-resolution spectrum from a predetermined position located by MRI. These offer the possibility of obtaining good quality spectra from regions where $\boldsymbol{B}_0$ homogeneity may not be at its best. Local shimming of these selected volumes can compensate, to an extent, for the local difficulties caused by tissue interfaces or hemorrhagic pathology for example.[65,66] The Fourier, or multivoxel, methods require a much larger volume of high-quality field since data are acquired from all voxels simultaneously with the possibility of studying a wider field of view. When S/N is low and extensive data accumulation is necessary, and local deviations in field homogeneity are small, it makes sense to employ Fourier techniques by running the required spatial encoding in parallel with the required averaging. Since signal and noise are derived with equal weight and from exactly the same tissue volume, these methods make for efficient data acquisition. However the limited number of spatial harmonics that may be acquired, particularly when localization is extended into three dimensions, means that the degree of localization is intrinsically poor. Large changes in spectral appearance, when they occur very locally, are not well perceived due to voxel bleeding.[67]

A number of comparisons have been made in relation to the variety of slice-selection methods. The use of selective 90° pulses for STEAM localization has been demonstrated to give better voxel definition than the inversion pulses of PRESS.[68] ISIS, PRESS, and STEAM have also been compared with respect to selection efficiency, selection contamination, and water suppression.[69] The minimum echo time *TE* for ISIS is much less than either STEAM or PRESS, and this tends to dominate such comparisons. The addition/subtraction requirement of ISIS was identified as a source of baseline distortion that is not readily apparent in the single-shot PRESS and STEAM techniques. Further comparisons between STEAM and PRESS have been made with respect to spin displacement (flow and diffusion effects),[68] minimum *TE*,[68] effect of *TE* upon ^{1}H spectra quality and appearance,[70] water suppression,[68] effects of rf pulse miscalibration,[68] and homonuclear coupling effects.[68,71,72]

An important point concerning rf power deposition is highlighted in a comparison between SPARS and STEAM,[73] where the broadband pulses of the SPARS method put it at a serious disadvantage. It was also noted in this work that the intrinsic insensitivity of the stimulated echo is not usually an overbearing issue since SPARS includes periods of irreversible dephasing during its localization period.

All the techniques presented previously have the attribute of acquiring conventional MR absorption spectra. Chemically shift selective pulses can be employed to excite a single resonance *within* a spectrum. Conventional and fast MRI techniques can then be employed to perform the degree of spatial localization required with greater efficiency.

6 BEYOND LOCALIZATION

A number of techniques discussed earlier, and in particular those applied to the acquisition of ^{1}H spectra, have moved beyond simple localization requirements and include additional methods for reducing the magnitude of strong, unwanted signals. In addition, a number of techniques have been investigated for the incidental or artifactual effects of flow and perfusion,[68] and homonuclear coupling phenomena.[71,72] It is likely that in vivo MRS will parallel earlier developments in high-resolution NMR by employing such dependences to improve spectral sensitivity. There have been reports of both diffusion-weighted MRS,[74,75] and editing,[76] polarization transfer,[77] and double quantum filtering.[78,79]

McKinnon and Boesinger[76] have defined the three consecutive slice-selective pulses, as employed in the MESA technique, as a volume selective refocusing (VSR) sequence that may be subsequently integrated into a wide range of existing spectral editing techniques. More recent developments in spectro-spatial pulses give potential to allow the spatial localization and editing processes to occur simultaneously (see also ***Complex Radiofrequency Pulses***) and this will further extend the quality of spectral information derived from the relatively low fields currently offered by whole body MR scanners.

7 RELATED ARTICLES

Birdcage Resonators: Highly Homogeneous Radiofrequency Coils for Magnetic Resonance; Chemical Shift Imaging; Complex Radiofrequency Pulses; Eddy Currents and Their Control; Gradient Coil Systems; Multifrequency Coils for Whole Body Studies; Multiple Quantum Coherence Imaging; NMR Spectroscopy of the Human Heart; Quantitation in In Vivo MRS; Radiofrequency Systems and Coils for MRI and MRS; Rotating Frame Methods for Spectroscopic Localization; Selective Excitation Methods: Artifacts; Selective Excitation in MRI and MR Spectroscopy; Single Voxel Localized Proton NMR Spectroscopy of Human Brain In Vivo; Single Voxel Whole Body Phosphorus MRS; Surface Coil NMR: Detection with Inhomogeneous Radiofrequency Field Antennas; Surface and Other Local Coils for In Vivo Studies; Water Suppression in Proton MRS of Humans and Animals.

8 REFERENCES

1. J. J. H. Ackerman, T. H. Grove, G. G. Wong, D. G. Gadian, and G. K. Radda, *Nature (London)*, 1980, **283**, 167.
2. R. L. Nunnally and P. A. Bottomley, *Science*, 1981, **211**, 177.
3. A. Haase, W. Hanicke, and J. Frahm, *J. Magn. Reson.*, 1984, **56**, 401.
4. R. E. Gordon, P. E. Hanley, D. Shaw, D. G. Gadian, G. K. Radda, P. Styles, P. J. Bore, and L. Chan, *Nature (London)*, 1980, **287**, 736.
5. R. D. Oberhaensli, G. J. Galloway, D. J. Taylor, P. J. Bore, and G. K. Radda, *Br. J. Radiol.*, 1986, **59**, 695.
6. M. G. Crowley and J. J. H. Ackerman, *J. Magn. Reson.*, 1985, **65**, 522.
7. Y. Geoffrion, M. Rydzy, K. W. Butler, I. C. P. Smith, and H. C. Jarrell, *NMR Biomed.*, 1988, **1**, 107.
8. M. R. Bendall and R. E. Gordon, *J. Magn. Reson.*, 1983, **53**, 365.

9. T. C. Ng, J. D. Glickson, and M. R. Bendall, *Magn. Reson. Med.*, 1984, **1**, 450.
10. M. H. Levitt and R. Freeman, *J. Magn. Reson.*, 1979, **33**, 473.
11. A. J. Shaka and R. Freeman, *J. Magn. Reson.*, 1980, **63**, 596.
12. R. Tycko and A. Pines, *J. Magn. Reson.*, 1984, **60**, 156.
13. A. J. Shaka and R. Freeman, *J. Magn. Reson.*, 1984, **59**, 169.
14. A. J. Shaka, J. Keeler, M. B. Smith, and R. Freeman, *J. Magn. Reson.*, 1985, **61**, 175.
15. M. R. Bendall and D. T. Pegg, *J. Magn. Reson.*, 1985, **63**, 494.
16. M. R. Bendall and D. T. Pegg, *J. Magn. Reson.*, 1986, **68**, 252.
17. M. R. Bendall, D. Foxall, B. G. Nichols, and J. R. Schmidt, *J. Magn. Reson.*, 1986, **70**, 181.
18. J. Pekar, J. S. Leigh, and B. Chance, *J. Magn. Reson.*, 1985, **64**, 115.
19. K. R. Metz and R. Briggs, *J. Magn. Reson.*, 1985, **64**, 172.
20. M. Garwood, T. Schleich, B. D. Ross, G. B. Matson, and W. D. Winters, *J. Magn. Reson.*, 1985, **65**, 239.
21. M. Garwood, T. Schleich, and M. R. Bendall, *J. Magn. Reson.*, 1985, **65**, 510.
22. D.I. Hoult, *J. Magn. Reson.*, 1979, **33**, 183.
23. S. J. Cox and P. Styles, *J. Magn. Reson.*, 1980, **40**, 209.
24. A. Haase, C. Malloy, and G. K. Radda, *J. Magn. Reson.*, 1983, **55**, 164.
25. P. Styles, C. A. Scott, and G. K. Radda, *Magn. Reson. Med.*, 1985, **2**, 402.
26. M. J. Blackledge, B. Rajagopalan, R. D. Oberhaensli, N. M. Bolas, P. Styles, and G. K. Radda, *Proc. Natl. Acad. Sci. USA*, 1987, **84**, 4283.
27. P. A. Bottomley, *J. Magn. Reson.*, 1982, **50**, 335.
28. K. N. Scott, H. R. Brooker, J. R. Fitzsimmons, H. F. Bennett, and R. C. Mick, *J. Magn. Reson.*, 1982, **50**, 339.
29. R. J. Ordidge, A. Connelly, and J. A. B. Lohman, *J. Magn. Reson.*, 1986, **66**, 283.
30. R. J. Ordidge, R. M. Bowley, and G. McHale, *Magn. Reson. Med.*, 1988, **8**, 323.
31. J. C. Sharp and M. O. Leach, *Proc. VIIth Ann Mtg. Soc. Magn. Reson. Med.*, San Francisco, 1988, p. 705.
32. W. P. Aue, S. Muller, T. A. Cross, and J. Seelig, *J. Magn. Reson.*, 1984, **56**, 350.
33. W. P. Aue, S. Muller, and J. Seelig, *J. Magn. Reson.*, 1985, **61**, 392.
34. S. Muller, W. P. Aue, and J. Seelig, *J. Magn. Reson.*, 1985, **63**, 530.
35. D. M. Doddrell, J. M. Bulsing, G. J. Galloway, W. M. Brooks, J. Field, M. G. Irving, and H. Baddeley, *J. Magn. Reson.*, 1986, **70**, 319.
36. P. R. Luyten, A. J. H. Marien, B. Sijtsma, and J. A. Den Hollander, *J. Magn. Reson.*, 1986, **67**, 148.
37. D. M. Doddrell, W. M. Brooks, J. M. Bulsing, J. Field, M. G. Irving, and H. Baddeley, *J. Magn. Reson.*, 1986, **68**, 367.
38. P. A. Bottomley, T. B. Foster, and R. D. Darrow, *J. Magn. Reson.*, 1984, **59**, 338.
39. P. A. Bottomley, L. S. Smith, W. M. Leue, and C. Charles, *J. Magn. Reson.*, 1985, **64**, 347.
40. P. A. Bottomley, *Ann. NY. Acad. Sci.*, 1987, **508**, 333.
41. D. Lampman, G. Hurst, J. McNally, and M. Paley, *Magn. Reson. Imag.*, 1986, **4**, 115.
42. D. K. Menon, C. Baudouin, D. Tomlinson, and C. Hoyle, *J. Comp. Assist. Tomogr.*, 1990, **14**, 882.
43. C. J. Peden, F. M. Cowan, D. J. Bryant, J. Sargentoni, D. K. Menon, D. G. Gadian, J. D. Bell, and L. M. S. Dubowitz, *J. Comp. Assist. Tomogr.*, 1990, **14**, 886.
44. J. Granot, *J. Magn. Reson.*, 1986, **70**, 488.
45. J. Frahm, K. D. Merboldt, and W. Hanicke, *J. Magn. Reson.*, 1987, **72**, 502.
46. J. Frahm, H. Bruhn, M. L. Gyngell, K. D. Merboldt, W. Hanicke, and R. Sauter, *Magn. Reson. Med.*, 1989, **9**, 79.
47. J. C. Sharp, M. O. Leach, A. Hind, V. R. McCready, H. Weber, and R. Sauter, *Proc. VIth Ann Mtg. Soc. Magn. Reson. Med.*, New York, 1987, p. 600.
48. J. H. Dujin, G. B. Matson, A. A. Maudsley, and M. W. Weiner, *Magn. Reson. Imag.*, 1992, **10**, 315.
49. S. Posse, B. Schuknecht, M. E. Smith, P. C. van Zijl, N. K. Herschkowitz, and C. T. W. Moonen, *J. Comput. Assist. Tomogr.*, 1993, **17**, 1.
50. D. C. Shungu and J. D. Glickson, *Magn. Reson. Med.*, 1993, **30**, 661.
51. T. H. Mareci and H. R. Brooker, *J. Magn. Reson.*, 1984, **57**, 157.
52. H. R. Brooker, T. H. Mareci, and J. Mao, *Magn. Reson. Med.*, 1987, **5**, 417.
53. T. R. Brown, B. M. Kincaid, and K. Ugurbil, *Proc. Natl. Acad. Sci. USA*, 1982, **79**, 3523.
54. A. A. Maudsley, S. K. Hilal, W. H. Perman, and H. E. Simon, *J. Magn. Reson.*, 1983, **51**, 147.
55. D. R. Bailes, D. J. Bryant, G. M Bydder, H. A. Case, A. G. Collins, I. J. Cox, P. R. Evans, R. R. Harman, A. S. Hall, S. Khenia, P. McArthur, A. Oliver, M. R. Rose, B. D. Ross, and I. R. Young, *J. Magn. Reson.*, 1987, **74**, 158.
56. D. R. Bailes, D. J. Bryant, H. A. Case, A. G. Collins, I. J. Cox, A. S. Hall, R. R. Harman, S. Khenia, P. McArthur, B. D. Ross, and I. R. Young, *J. Magn. Reson.*, 1988, **77**, 460.
57. T. H. Mareci and H. R. Brooker, *J. Magn. Reson.*, 1991, **92**, 229.
58. K. J. Jung, S. K. Hilal, and Z. H. Cho, *Proc. XIth Ann Mtg. Soc. Magn. Reson. Med.*, Berlin, 1992, p. 3838.
59. M. S. Silver, R. I. Joseph, and D. I. Hoult, *J. Magn. Reson.*, 1984, **59**, 347.
60. C. C. Hanstock, D. L. Rothman, T. Jue, and R. G. Shulman, *J. Magn. Reson.*, 1988, **77**, 583.
61. W. I. Jung and O. Lutz, *Z. Naturforsch.*, 1988, **43a**, 909.
62. W. I. Jung, O. Lutz, K. Muller, M. Pfeiffer, and K. Kuper, *Proc. VIIIth Ann Mtg. Soc. Magn. Reson. Med.*, Amsterdam, 1989, p. 637.
63. K. Hendrich, Y. Xu, S.-G. Kim, and K. Ugurbil, *Magn. Reson. Med.*, 1994, **31**, 541.
64. K. Hendrich, H. Liu, H. Merkle, J. Zhang, and K. Ugurbil, *J. Magn. Reson.*, 1992, **97**, 486.
65. G. A. Coutts, D. J. Bryant, A. G. Collins, I. J. Cox, J. Sargentoni, and D. G. Gadian, *NMR Biomed.*, 1989, **1**, 190.
66. I. R. Young, I. J. Cox, G. A. Coutts, and G. M. Bydder, *NMR Biomed.*, 1989, **2**, 329.
67. T. J. Lawry, D. B. Twieg, A. A. Maudsley, M. W. Weiner, and G. B. Matson, *Proc. VIIth Ann Mtg. Soc. Magn. Reson. Med.*, San Francisco, 1988, p. 944.
68. C. T. W. Moonen, M. von Kienlin, P. C. M. van Zijl, J. Cohen, J. Gillen, P. Daly, and G. Wolf, *NMR Biomed.*, 1989, **2**, 201.
69. N. M. Yongbi, G. S. Payne, and M. O. Leach, *Proc. XIth Ann Mtg. Soc. Magn. Reson. Med.*, Berlin, 1992, p. 3840.
70. R. E. Lenkinski, D. P. Flamig, and J. Listerud, *Proc. IXth Ann Mtg. Soc. Magn. Reson. Med.*, New York, 1990, p. 1073.
71. A. H. Wilman and P. S. Allen, *Proc. XIth Ann Mtg. Soc. Magn. Reson. Med.*, Berlin, 1992, p. 3842.
72. Th. Ernst and J. Hennig, *Magn. Reson. Med.*, 1991, **21**, 82.
73. P. A. Narayana, E. F. Jakson, J. D. Hazle, L. K. Fotdar, M. V. Kulkarni, and D. P. Flamig, *Magn. Reson. Med.*, 1988, **8**, 151.
74. C. T. W. Moonen, P. van Gelderen, P. C. M. van Zijl, D. DesPres, and A. Olson, *Proc. Xth Ann Mtg. Soc. Magn. Reson. Med.*, San Francisco, 1991, p. 141.
75. S. Posse, C. A Cuenod, and D. Le Bihan, *Radiology*, 1993, **188**, 719.
76. G. C. McKinnon and P. Boesiger, *Magn. Reson. Med.*, 1988, **8**, 355.
77. A. Dolle, *J. Magn. Reson.*, 1991, **94**, 596.
78. W. I. Jung and O. Lutz, *J. Magn. Reson.*, 1991, **94**, 587.
79. J. F. Shen and P. S. Allen, *J. Magn. Reson.*, 1991, **92**, 398.

Biographical Sketches

David J. Bryant. *b* 1956. B.Sc., 1977, Ph.D., 1981, University of Nottingham, supervisor E. Raymond Andrew. Research fellow with Raymond Andrew, 1980–82. GEC Hirst Research Centre working in laboratory headed by Ian R. Young, 1982–present. Approx. 50 publications. Research interests: MRI and MRS on whole body systems in the 0.15–1.5 T range.

Glyn A. Coutts. *b* 1959. B.A., 1980, Physics, D.Phil., 1985, University of Oxford, UK. Research Associate at GEC Hirst Research Centre in laboratory headed by Ian R. Young, 1987–present. Approx. 30 publications. Research interests: MRI and MRS, interventional MRI.

Water Suppression in Proton MRS of Humans and Animals

Chrit T. W. Moonen

Centre National de la Recherche Scientifique, University of Bordeaux 2, Bordeaux, France

and

Peter C. M. van Zijl

Johns Hopkins University Medical School, Baltimore, MD, USA

1 INTRODUCTION

In vivo NMR spectroscopy offers a noninvasive window on metabolism and physiology in healthy and diseased humans and animals. Most initial efforts in NMR spectroscopy of living systems were devoted to the phosphorus and carbon nuclei. Because proton NMR is more sensitive, and allows access to a range of different metabolites, attention to proton spectroscopy has been increasing. However, without specific efforts to suppress water and fat resonances, the latter compounds completely dominate the in vivo proton NMR spectrum. For example, the effective concentration of water hydrogen atoms may be as high as 110 M, whereas we wish to study metabolites in the millimolar range. Pioneering work on in vivo proton spectroscopy was performed at the laboratory of Shulman.[1,2] Recent advances are now permitting in vivo proton spectroscopy and spectroscopic imaging of the human brain in a routine examination. The topic of this review is to outline the possible strategies to suppress the water resonance, and other unwanted resonances such as those of fat (triglycerides).

The suppression of solvent resonances is an area of research that has long been in the domain of high-resolution (HR) NMR. Many techniques were well established before in vivo proton NMR was even contemplated. Recent developments such as shielded field gradient technology, and shaped rf excitation pulses have played an important role in NMR imaging. Now, these advanced tools are among the most powerful assets for water-suppressed proton spectroscopy in vivo, as well as in vitro.

When compared with HR NMR, in vivo spectroscopy has to overcome several typical problems related to $\boldsymbol{B}_0$ and $\boldsymbol{B}_1$ inhomogeneity, and motion, regardless of the nucleus being studied. These problems increase dramatically in proton spectroscopy because of the additional problem of water suppression and the narrow proton chemical shift range. For example, the range of water resonance frequencies over the human head amounts to several ppm (especially outside the brain area), comparable to the chemical shift range of most observable compounds. Therefore, chemical-shift-based water suppression cannot work unless a very high degree of localization is achieved. The use of surface coil receivers may help to avoid water signals from outside areas with a different resonance frequency. However, with the increasing attention being paid to spectroscopic imaging of large brain areas simultaneously, this solution is only of limited use. Motion effects further aggravate these problems.

Owing to limitations of space, in this article we emphasize general principles only, and highlight some important new developments. Because of the technical nature of this review, we do not restrict ourselves to human spectroscopy but also include important results in proton spectroscopy on animals. Detailed general reviews of water suppression in HR NMR and in vivo NMR have been published before.[3–6]

2 OVERVIEW OF SUPPRESSION METHODS BASED ON NMR AND OTHER BIOPHYSICAL PROPERTIES

2.1 Chemical Shift

Most suppression techniques are based on the frequency of the solvent resonance. Within this class of suppression strategies, we discriminate between methods that

1. accomplish a selective saturation of a frequency band before excitation of the spins of interest is started;[7–19] or
2. avoid altogether the excitation of a frequency band;[3,5,20,21] or
3. filter out a frequency band after signal reception.

In general, these methods have the disadvantage that all resonances of interest within the suppressed frequency band are also eliminated.

2.1.1 Selective Saturation

The general pulse sequence is

$$P_1\text{–}d_1(G_1)\text{–}P_2 \quad \text{Acq} \tag{1}$$

where P_1 is the soft rf pulse, d_1 is a short delay, preferably containing a gradient spoiling pulse G_1, and P_2 is the excitation pulse followed by acquisition time or the rest of a more complicated pulse sequence. This sequence, with a constant amplitude P_1 and a duration of the order of the solvent T_1 (the 'presaturation' method[7]) is one of the most common water suppression methods in HR NMR. It is now well established that it is more effective to employ a selective (shaped) P_1 pulse using a flip angle slightly larger than 90° to take T_1 relaxation during d_1 into account, thus nulling solvent magnetization at the time of rf pulse P_2.[8–14] The latter technique, including a spoiling gradient,[8,9] is often referred to as a CHESS sequence (chemical shift suppression). The method does not truly reflect a classical 'saturation' experiment. However, it leads to the condition of zero M_z magnetization and dephased transverse magnetization. In addition, selective magnetization inversion can be used followed by a waiting period to allow for zero M_z magnetization.[15]

The saturation procedure does not have to take place prior to the rest of the sequence. For example, a CHESS sequence can also be employed in the middle (*TM*) period of the stimulated echo sequence in in vivo NMR, when the magnetization due the resonances of interest is longitudinal. The basic

sequence can be repeated for increased efficiency. However, care should be taken that different gradient directions and powers are used to avoid unwanted echoes of the solvent resonance. A detailed analysis has been presented previously.[12] Examples are given in Figure 1.

A $\boldsymbol{B}_1$ gradient may also be helpful in suppressing a frequency band.[16–19] A combination of hard pulses followed by spin locking procedures has been proposed for in vivo NMR[18,19] The basic idea is that all off-resonance magnetization will dephase in the inhomogeneous spin locking field. In addition, a fast pulse train of hard pulses (DANTE[20]) given with an inhomogeneous $\boldsymbol{B}_1$ field has also been shown to lead to rapid effective nulling of longitudinal magnetization of solvent.[16,17] These techniques are particularly useful for surface coils.

2.1.2 Excitation Profiles with a Gap at the Water Frequency

The difference in evolution frequency of transverse magnetization between solvent and solute can be employed to create a gap in the effective excitation profile at the solvent frequency.[3,5,21] The best-known and widely used is the so-called jump–return sequence of Plateau and Guéron.[21] The sequence starts with a $\frac{1}{2}\pi$ rf pulse with the transmitter on the solvent resonance. Following an evolution period t, a second $\frac{1}{2}\pi$ rf pulse is given with opposite phase. The magnetization of the solvent resonance is thus put back along the z axis. However, for a resonance with a relative frequency of $(4t)^{-1}$ with respect to the offset, the transverse magnetization will have rotated during t exactly 90°, and thus will remain unchanged by the second rf pulse. The frequency profile of such a sequence is approximately a sine function. Instead of two rf pulses, an increasing number of rf pulses can be used to improve the frequency profile. A disadvantage is the sometimes complicated phase roll over the spectrum. Shaped, self-refocusing rf pulses can improve the phase response dramatically.[22] Guéron et al.[5] have given a detailed review of this class of suppression techniques, along with further improvements.

Continuous wave (CW) and rapid scan techniques are based on a rapid sweep of the frequency band of interest and avoidance of the solvent resonances. However, these methods are now rarely used because of their low S/N per unit time.

2.1.3 Suppression of Water Resonance Following the Complete Pulse Sequence

When radiation damping is not a problem, the solvent resonance can be suppressed following the complete pulse sequence. The disadvantage is that even a very large dynamic range analog-to-digital converter ADC can often not handle the large voltage differences due to resonances of interest and solvent[3,6] (Section 3.3).

2.2 Relaxation

Differences in relaxation times T_1 and T_2 between solutes and solvent can be exploited to achieve a relative suppression of the water resonance. T_1 and T_2 values of some brain compounds have been given by Frahm et al.[23] If the solvent suppression mechanism is entirely based on relaxation differences, signal loss for the resonances of interest can be significant, because differences in relaxation times are not dramatic. The advantage

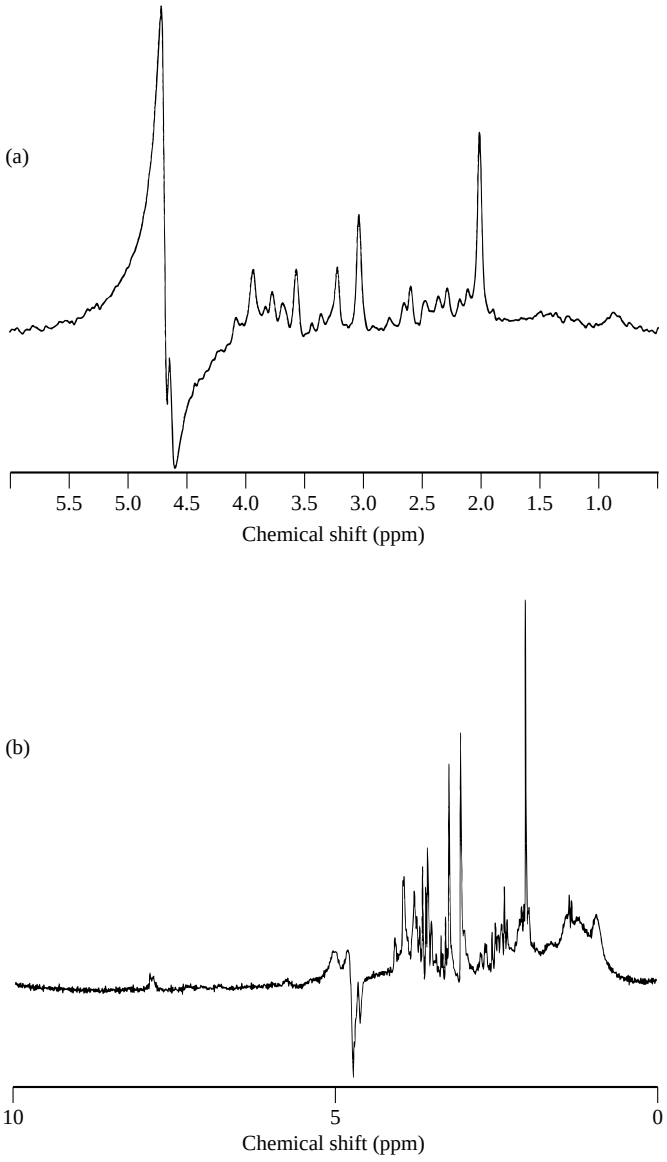

Figure 1 Examples of high quality water suppression in in vivo proton spectroscopy of (a) human and (b) animal brain. (a) In vivo proton NMR spectrum of an 18 ml volume obtained from normal gray matter of a healthy volunteer. The spectrum is obtained with STEAM localization (*TR*/*TE*/*TM* = 6000/20/30 ms), and three preceding CHESS water suppression procedures. The spectrum was obtained in approx. 6 min. A 2.0 T instrument was used, with a conventional quadrature head coil. Only exponential multiplication was used prior to FT, and no further data manipulation was applied. Courtesy of Dr. Jens Frahm, Biomedizinische NMR Forschungs GmbH, Max Planck Institut für Biophysikalische Chemie, Göttingen, Germany. (b) In vivo proton NMR spectrum from a 0.7 mL volume located in the superior part of the cat brain using STEAM localization (*TR*/*TE*/*TM* = 1000/18/80 ms). A 4.7 T instrument was used, equipped with 20 mT m^{-1} shielded gradients. A surface coil (outer diameter 48 mm) was used for transmission and reception. Three preceding CHESS water suppression sequences, and three CHESS water suppression sequences in the *TM* period were used. Lorentzian-to-Gaussian transformation was used prior to FT. For more details, see Moonen and van Zijl.[12]

of relaxation-based water suppression is that its mechanism is not frequency-selective, and therefore the method works regardless of the actual resonance frequency of water.

2.2.1 T_1-Based Methods

The general pulse sequence is as above. When P_1 in sequence 1 is a π pulse, and d_1 is a delay adjusted for zero longitudinal magnetization of water,[15,24,25] the sequence is often called a WEFT (water-eliminated Fourier transform). To avoid T_1 weighting of the resonances of interest, a selective π pulse can be used (see also Section 2.1.2). T_1-based methods require more time than CHESS-type methods to null M_z solvent magnetization (because of T_1), and are optimal only for a single T_1. In the case of more than two solvent populations with different T_1s, more inversion pulses can be used, with adjustable delays between π pulses.[25]

2.2.2 T_2-Based Methods

A general spin echo (or stimulated echo) sequence can be used, such as

$$P_1\text{–}\tau\text{–}P_2\text{–}\tau \quad \text{Acq} \tag{2}$$

where P_1 is the $\frac{1}{2}\pi$ excitation pulse, 2τ is the echo time, and P_2 is the refocusing (π) pulse. Acquisition is started at the top of the echo, or immediately following the P_2 pulse. Apart from water suppression, the spin echo sequence has the added advantage of the removal of broad resonances (owing to short T_2). The reduced overlap is often helpful for quantifying resonance intensities, for example in proton spectroscopic imaging. A disadvantage is the phase modulation due to J coupling. However, when several refocusing pulses are used, specific J modulation patterns of molecules of interest can be turned into an advantage, for example for selecting lactate and avoiding uncoupled resonances.[26]

2.3 Scalar Coupling

Many modern methods use nuclear coupling characteristics to select only coupled resonances and thus suppress the (singlet) solvent resonance automatically.[27–49] These methods are identical to many of the so-called 'editing' techniques. Some techniques can be understood in sufficient detail using a classical vector presentation, whereas some newer methods can best be treated with the modern coherence pathway formalism. We shall first explain some basic methods for heteronuclear applications (e.g. proton detection of ^{13}C-labeled compounds). For the sake of simplicity, we shall limit the discussion to weakly coupled AX systems.

2.3.1 Indirect Detection by Spin Echo Methods

The heteronuclear spin echo difference method (POCE, proton-detected carbon editing) is a two-scan experiment in which the heteronuclear π pulse is turned on/off in alternating experiments:[43,44,46,47]

$$\begin{aligned} &^1\text{H}: \tfrac{1}{2}\pi\text{–}\tau\text{–}\pi\text{–}\tau \quad \text{Acq} \\ &^{13}\text{C}: \qquad\quad \pi \quad (\text{on/off}) \end{aligned} \tag{3}$$

The optimum delay τ is $(2J)^{-1}$. The evolution of the multiplet can be easily followed in the rotating frame. If the heteronuclear π pulse is off, the coupled spins change the direction of their evolution at the time of the π pulse. As a result, the components of the multiplet rephase at the top of the echo. If both π pulses are on, the chemical shift is rephased at the top of the echo, but evolution due to the coupling has continued for a period J^{-1}. As a consequence, the multiplet has opposite phase. Subtraction thus gives resonances only for coupled spins and eliminates those for all noncoupled spins.

2.3.2 Indirect Detection by Polarization Transfer and Multiple Quantum Methods.

So far, we have discussed spin systems in terms of longitudinal and transverse magnetization. A more general treatment involves the analysis of coherence orders during the pulse sequence, and is particularly useful for the understanding of polarization transfer and multiple quantum pulse sequences. Coherence orders are denoted by p, where $p = 0, \pm1, \pm2$ for zero, single, and double quantum order, respectively. For an introduction to the coherence formalism, the reader is referred to the literature.[27–29] We shall review two fundamental heteronuclear (^{1}H–^{13}C) sequences here. Proton spins will be indicated by I, carbon spins by S. The single quantum coherences, $\hat{I}_x$ and $\hat{I}_y$, refer to the classical transverse (observable) proton magnetization, $\hat{S}_x$ and $\hat{S}_y$ to single quantum carbon magnetization. $2\hat{I}_x\hat{S}_y$ consists of double quantum coherence and zero quantum coherence, and is not directly observable. $2\hat{I}_x\hat{S}_z$ and $2\hat{I}_z\hat{S}_x$ are so-called antiphase single quantum coherences. Radiofrequency pulses may generate transitions between coherence orders, but gradient pulses cannot. The complete pulse sequence can be seen as a coherence pathway vector $\boldsymbol{p}$ with as many elements as rf pulses in which the coherence order in period i is indicated with order p_i.

As an example, we shall follow an HMQC (heteronuclear multiple quantum coherence)[38,39,48,49] experiment (for the pulse sequence see Figure 2a). Following excitation of the protons ($\hat{I}_z \rightarrow -\hat{I}_y$) by the $\frac{1}{2}\pi$ rf pulse along the x axis in the rotating frame and neglecting the chemical shift, evolution of $\hat{I}_y$ will then lead to

$$-\hat{I}_y \xrightarrow{\text{evolution}} -\hat{I}_y \cos(\pi J_{IS} t) + 2\hat{I}_x\hat{S}_z \sin(\pi J_{IS} t) \tag{4}$$

The carbon pulse after an evolution period of $(2J)^{-1}$ will transfer the antiphase single quantum coherence into a multiple quantum coherence:

$$2\hat{I}_x\hat{S}_z \xrightarrow{\frac{1}{2}\pi_x^S} -2\hat{I}_x\hat{S}_y \tag{5}$$

The π proton pulse converts the zero-quantum into a double-quantum coherence, and the double-quantum into a zero-quantum coherence. The final $\pi/2$ carbon pulse transfers the $2\hat{I}_x\hat{S}_y$ coherences into observable antiphase proton magnetization ($2\hat{I}_x\hat{S}_z$ coherence), which is first allowed to refocus and then detected.

Figure 2(b) shows an HSQC heteronuclear polarization transfer experiment (heteronuclear single quantum coher-

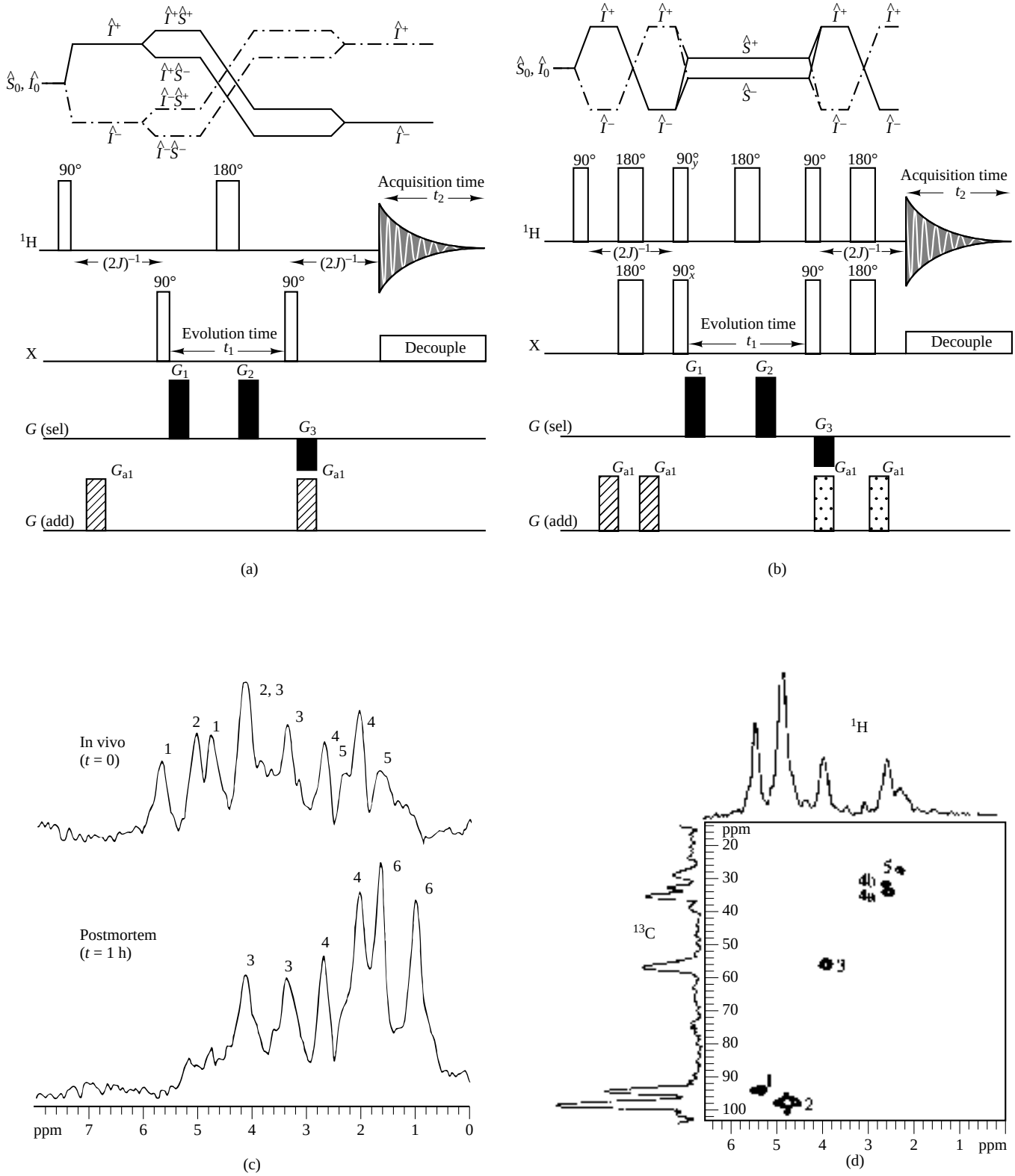

Figure 2 Coherence pathways and pulse sequences for (a) heteronuclear multiple quantum coherence (HMQC) and (b) heteronuclear single quantum coherence (HSQC) experiments. The phase of the rf pulses is irrelevant for the sequence when gradients G_{sel} and G_{add} are used for coherence selection. The phase of the rf pulses, and the multiscan phase cycle, is important when no gradients are used. Reproduced, with permission, from Ruiz-Cabello et al.[48] (c) ^{13}C–^{1}H HMQC spectra obtained from cat brain in vivo (upper spectrum), and 45 min following sacrifice (lower spectrum). Both spectra were obtained in 3 min 19 s from an 8 mm slice through the cat brain following infusion of ^{13}C-labeled glucose (final blood glucose level was 16.6 mM). Spectra are not ^{13}C-decoupled, and show ^{13}C multiplets. Note the complete absence of the water resonance. Assignments are: (1) α-[1-^{13}C]glucose; (2) β-[1-^{13}C]glucose; (3) [2-^{13}C]glutamate and glutamine; (4) [4-^{13}C]glutamate and glutamine; (5) [3-^{13}C]glutamate and glutamine; (6) [3-^{13}C]lactate. (d) Two-dimensional ^{13}C–^{1}H HMQC correlation spectrum obtained in a fully decoupled mode by incrementing the multiple quantum period. Total acquisition time was 30 min. The projections along the ^{1}H and ^{13}C axes are shown as well. Assignments are as in (c). Note the separation in peak 4 corresponding to a separation of the glutamate (peak a) and glutamine (peak b)

ence[50]). Following evolution as in the HMQC experiment [equation (4)] and refocusing of the chemical shift, the essential step is the simultaneous proton and carbon $\frac{1}{2}\pi$ pulses, which create antiphase carbon magnetization from antiphase proton magnetization ($2\hat{I}_x\hat{S}_z \rightarrow 2\hat{I}_z\hat{S}_y$). This is an effective polarization transfer from the proton spins to the coupled carbon spins. Now, the carbon nuclei can be detected with an enhanced polarization (the enhancement is γ_H/γ_C). The basic experiment is called the INEPT experiment. For maximum enhancement, a second (inverse) polarization transfer is carried out, and the sensitive hydrogen nucleus can be detected for optimum efficiency. Note the coherence pathway diagram in Figure 2(b).

When selecting a unique coherence pathway of Figure 2, noncoupled resonances are automatically eliminated. Therefore, coupled resonances under the water line can, in principle, be measured. However, note that the coherence pathway selection is generally a multiscan experiment (see Section 3.1 for important exceptions). The reason is that the rf pulses also lead to undesired coherences. This may be caused by the inhomogeneous $\boldsymbol{B}_1$ field, or by unwanted coherences that are generated even when ideal $\frac{1}{2}\pi$ pulses can be used (for example, owing to relaxation effects). In order to avoid the detection of unwanted coherences, the phase of the rf pulses and the receiver are varied using a phase cycling scheme.[27–29] For the purpose of water suppression, it is important to note that in a multiscan experiment, the ADC resolution may still be a limiting factor.

Limitations of space preclude a thorough analysis here of all hetero- and homonuclear editing pulse sequences with automatic water suppression. Generally, similar principles hold for homo- and heteronuclear coherence pathways.[27,28] However, note that single quantum evolution frequencies are similar in homonuclear sequences, whereas they are dependent on the gyromagnetic ratio of nucleus I or S in the heteronuclear case. Thus, a homonuclear editing sequence should involve either at least one rf pulse that avoids water excitation, or a multiple quantum order in part of the sequence in order to inherently eliminate the singlet solvent resonance.

In short, multipulse editing sequences, based on polarization transfer and multiple quantum coherences, can be used for 'automatic' water suppression. Multiscan phase cycling schemes are necessary for pure coherence pathway selection. In Section 3.1.3, an important exception to this rule will be reviewed, namely, the use of field gradients for single scan coherence pathway selection.

2.4 Diffusion

The diffusion constant of water is considerably higher than that of small metabolites and much higher than that of macromolecules. Pulse sequences can be sensitized to diffusion by the use of $\boldsymbol{B}_0$ magnetic field gradients without any effect on stationary molecules.[51–54] For two gradient pulses of strength G and duration δ, and with duration Δ between their starts, the attenuated signal S resulting from free diffusion can be expressed as

$$S/S_0 = \exp[-\gamma^2 G^2 \delta^2 (\Delta - \tfrac{1}{3}\delta) D] \qquad (6)$$

where S_0 is the starting signal and D is the diffusion coefficient. For long diffusion times, restrictions by cell membranes and binding to macromolecules have to be taken into account. An additional advantage for water suppression is that the permeability of cell membranes to water is generally much higher than to most other compounds. The main disadvantage is that diffusion-sensitized pulse sequences are also very sensitive to motion. Therefore, such methods appear to have more potential for HR NMR than for in vivo NMR.[52,54]

2.5 Exchange

Exchange of protons between a dissolved compound and solvent water can result in different relaxation properties of the water protons. These exchange properties can be used to attenuate the solvent resonance.[55] For example, the saturation of exchangeable spins, whether by rf irradiation, T_2 relaxation, or dephasing in a magnetic field, can be transferred to the water resonance. This exchange mechanism is the basis of the so-called 'magnetization transfer contrast' in MRI,[56] but has not been used for the specific purpose of solvent suppression in in vivo NMR.

3 ADVANCED HARDWARE AND SOFTWARE TOOLS

3.1 Pulsed Field Gradients

The development of high-quality pulsed field gradients is probably the single most important tool that has made the routine applications of proton spectroscopy possible in humans. Historically, pulsed field gradients were used in HR NMR to dephase (spoil) the transverse magnetization—hence the often used name of a homospoil pulse.[57] Although the fundamental advantages of field gradients were known,[57–60] the limited quality with respect to amplitude, ramp times, current stability, and particularly residual gradients and vibration effects, prevented their general use. The extreme demands in MRI—in particular, with respect to the very fast echo planar imaging method[61]—have dramatically accelerated hardware developments. The advent of self-shielded gradient coils with minimal residual gradients should thus be viewed as a milestone.[62,63] An outer gradient coil is used that cancels the outside field of the inner coil, thus eliminating eddy currents in the cryostat. Pulsed field gradient technology is now also becoming a routine tool in HR NMR. Field gradients are used for the following purposes:

1. rapid dephasing of transverse magnetization (homospoil pulse);
2. spatial encoding and spatially selective excitation (in conjunction with shaped rf pulses);
3. single shot coherence pathway selection;
4. creating diffusion sensitivity (Section 2.1.4).

3.1.1 Rapid Dephasing of Transverse Magnetization

Following a gradient pulse of duration δ with magnitude G_α in direction α, the phase ϕ_α at location r_α as a function of coherence order p is

$$\phi_\alpha(p) = p\gamma r_\alpha \delta G_\alpha \qquad (7)$$

Therefore, a phase dispersion results that attenuates the transverse magnetization by a factor f:

$$\frac{1}{f} = \left| \frac{1}{r_2 - r_1} \int_{r_1}^{r_2} e^{-i\varphi_\alpha} \, dr_\alpha \right| \quad (8)$$

The limits r_2 and r_1 are the voxel dimensions in the gradient direction α. Equation (8) assumes equal spin density, and a homogeneous field. Note that the attenuation works as a result of the integration of the phase over the dimension of the volume.[12] In the case of spectroscopic imaging, the integration is over the voxel dimensions, not over the full object. The attenuation is higher with a higher gyromagnetic ratio, and with a higher coherence order. Homonuclear zero quantum order will thus not be dephased by the gradient pulse. Note also that the efficiency of the gradient crusher depends on the local static field homogeneity. For a detailed account, see Moonen et al.[64] Shimming is therefore important in the full region where high efficiency of gradient crushers is necessary, not only in the region of interest.

3.1.2 *Spatial Encoding and Spatially Selective Excitation*

The essence of field gradients in imaging is the encoding of spatial information,[65] whether used for phase encoding, frequency encoding, or spatially selective excitation. In proton spectroscopy of humans, field gradients are often employed for the same purpose.[66–82] For spectroscopic imaging,[83–89] phase encoding is generally used for spatial encoding in two or three directions. In conjunction with shaped rf pulses (leading to a desired frequency profile), field gradient pulses lead to spatially selective excitation or refocusing (see Section 4.2 for a more detailed account). The importance of spatial selection for water suppression purposes is further explained in Section 4.1. Spatial and spectral selection can be combined in a single rf pulse together with a special gradient waveform.[89–91]

3.1.3 *Single Shot Coherence Pathway Selection*

Conventionally (Section 2.3), a coherence pathway is selected using a multiscan approach using specific phase cycles of rf pulses and receiver. However, this ideal result is often not reached in vivo as a result of motion or of instrumental instabilities. The selection can also be achieved using pulsed field gradients, often completely eliminating the need for phase cycling. For example, a π refocusing pulse at the end of a pulse sequence may generate transverse magnetization as a result of an inhomogeneous $\boldsymbol{B}_1$ field. Using two scans with opposite phase of the π pulse, transverse magnetization is canceled. A pair of identical gradient pulses around the π pulse will lead to cancelation of the unwanted transverse magnetization in a single scan.

We can generalize equation (7) with respect to the phase of transverse magnetization at location r as a function of coherence order p during all periods i of the pulse sequence:

$$\phi_i(r) = \left(\sum_j p_j \gamma_j \right) r G_i t_i \quad (9)$$

where p_j is the coherence order of the individual nuclei (e.g. ^{13}C, ^{1}H) in period i and all other symbols have the same meaning as in equation (7). Thus, the phase evolves as a function of coherence order and gyromagnetic ratio, and equation (9) can be used to keep track of the phase evolution during the entire pulse sequence. A certain coherence order can thus be selectively rephased if the following condition is satisfied:

$$\sum_i \phi_i(r) = 0 \quad (10)$$

In the ideal case, spins of interest are refocused after the last rf pulse, and a gradient scheme is employed that avoids any rephasing of undesired coherences.[61,62] The required gradient power depends on the signal strength of the desired versus undesired coherences.

Localization, achieved by one or more spatially selective rf pulses, can be conveniently treated as a type of coherence pathway selection.[12,64] When more rf pulses are employed during a pulse sequence, it becomes harder to ensure sufficient dephasing of all undesired coherences. However, the use of gradients in all three principal axes with different amplitudes, and using different combinations at different time points in the sequence, offers great flexibility to optimize the single scan coherence selection.

Using equation (9), it can be easily seen that a coherence pathway selection involving a double quantum evolution ($p = \pm 2$) leads to dephasing of the solvent resonance without recourse to any frequency-dependent water suppression. The example shown in Figure 3 demonstrates that resonances under the water line may be observed, such as the resonances of the biologically important glucose molecule. Heteronuclear polarization transfer can also be achieved in a single scan with complete water suppression. However, homonuclear polarization transfer or any homonuclear sequence with $p = 0, \pm 1$, without chemical-shift-selective pulses, cannot achieve this, and additional water suppression methods must be employed. However, even in such cases, the use of field gradient pulses is beneficial because of the elimination of phase cycling (less motion sensitivity), and, in conjunction with other solvent suppression techniques, decreased water signal per scan and thus fewer demands on the receiver system.[94,95]

The use of field gradients for single shot coherence selection also has some disadvantages. Most important is the loss of a factor of two in the signal (except in the case of gradient pulses around a π refocusing pulse, and in special sequences using selective refocusing pulses[37] or sensitivity-enhanced gradient experiments[96]). The reason is that only one coherence pathway is selected, whereas phase cycling allows pathways of opposite signs to be selected simultaneously. For correlated multidimensional NMR, a second disadvantage (and a consequence of the first) is that phase-sensitive 2D spectra cannot be obtained using a single scan per t_1 increment. When using a second scan with selection of coherence path with opposite sign of coherence order in the t_1 period, phased resonances can be obtained. Of course, if these disadvantages are serious, pulsed field gradients may still be used only around refocusing pulses, and thus still eliminate part of the phase cycle.

3.2 Shaped rf Pulses

Shaped rf pulses play an important role in MRI, especially in slice-selective excitation and refocusing.[90–92,97–107] To a first approximation, the frequency response resulting from a particular rf pulse shape is given by the Fourier transform of the waveform. This is known as the linear response. For flip angles close to, and above 90°, linear response theory is no longer

completely accurate, and the Bloch equations have to be used to determine the response.[5,108] Corrections to the basic sinc waveform are now commonly used in NMR imaging. In localized proton spectroscopy, shaped rf pulses are used for the same purposes. In addition, a frequency-selective excitation is often used to select a narrow frequency band at the water resonance. In contrast to slice-selective pulses, phase-coherent response is not desired for frequency-selective suppression. In other applications, it is useful to combine spatial and spectral selection in a single pulse. The different specifications in different pulse sequences clearly indicate the opportunities for a specific design of rf pulses. In modern applications, simple Fourier transform of a desired frequency profile is often used as a starting point for a shaped rf pulse. Then, an optimization routine is used to arrive at improved shapes using the complete Bloch equations. Recent advances use complex polynomials for mapping the rf pulse and then solving them analytically.[91,107]

The inhomogeneity in the $\boldsymbol{B}_1$ field (e.g., of a surface coil) has advantages and disadvantages in this respect. One can use the $\boldsymbol{B}_1$ gradient to advantage in order to arrive at a desired phase dispersal of the water magnetization following excitation (see Section 2.1.1). On the other hand, inhomogeneous $\boldsymbol{B}_1$ fields lead to loss of signal due to a spread in flip angle and to a spatially dependent population of desired and undesired coherence pathways, often necessitating the use of large gradient crushers for coherence path selection. The latter disadvantage can be overcome by using adiabatic pulses.

3.2.1 *Adiabatic rf Pulses*

Most water suppression techniques demand precise flip angles. Despite high $\boldsymbol{B}_1$ homogeneity in the modern volume coils that are now routinely available in whole body MR instruments, the range of the $\boldsymbol{B}_1$ field may still exceed the requirements—in particular, for applications of water-suppressed proton spectroscopic imaging. Accurate flip angles, independent of the local $\boldsymbol{B}_1$ field, can be achieved with adiabatic rf pulses.[92,97–106] The first such pulses accomplished excitation and spin inversion, and employed a continuous frequency ramp of the $\boldsymbol{B}_1$ field while maintaining a constant amplitude. The effect of this pulse can be visualized in the rotating frame by analyzing the direction of the effective field (a function of the $\boldsymbol{B}_1$ field and the rf frequency relative to the Larmor frequency). During the pulse, the effective field $\boldsymbol{B}_e$ rotates from the positive z axis to the negative z axis (in the case of inversion) or to the (x,y) plane (in the case of excitation). So long as the $\boldsymbol{B}_1$ field exceeds a threshold value (the adiabatic condition), the magnetization continues to rotate effectively with a small precession angle around the field $\boldsymbol{B}_e$ during the entire pulse. In other words, the magnetization $\boldsymbol{M}$ remains collinear with $\boldsymbol{B}_e$ above a threshold $\boldsymbol{B}_1$. Therefore, if we let $\boldsymbol{B}_e$ rotate by π then $\boldsymbol{M}$ will also rotate by π, and spin inversion is accomplished. The flip angle is independent of the $\boldsymbol{B}_1$ field if the rate of change of the angle of the field $\boldsymbol{B}_e$ with

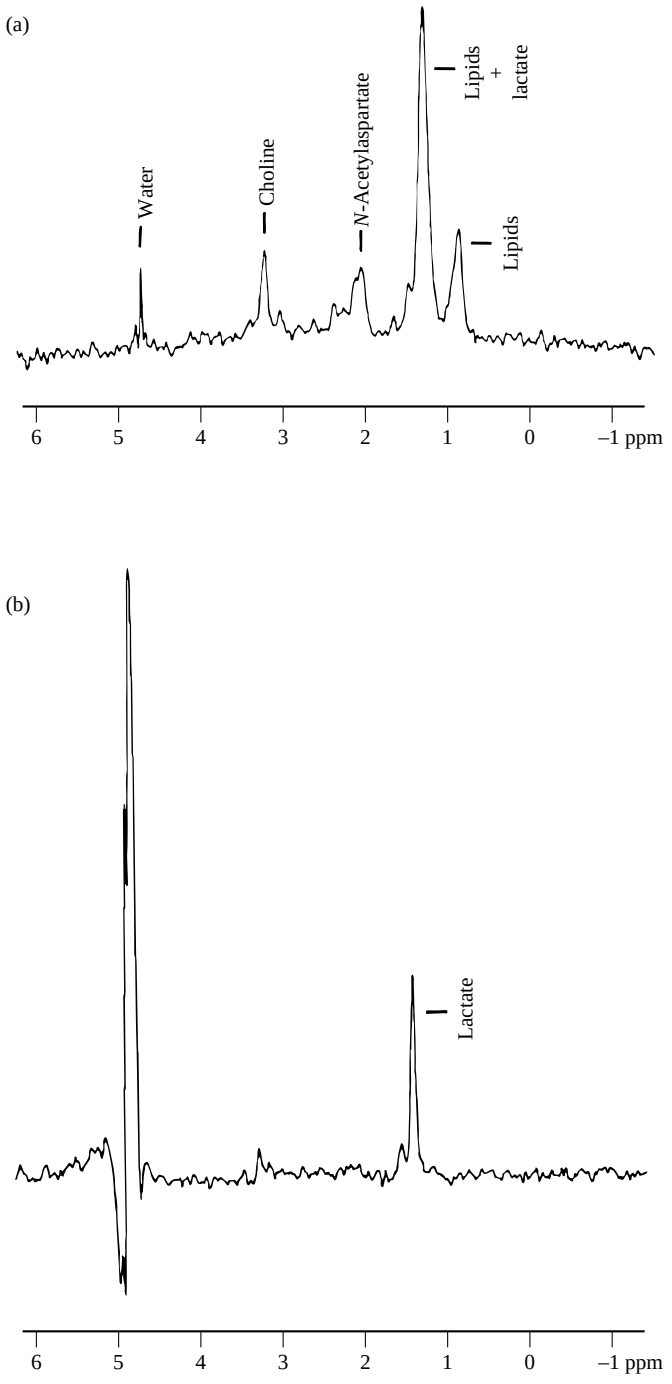

Figure 3 Unedited (a) and lactate-edited (b) localized proton spectra (volume 200 μl) of an intracerebral glioma in the rat obtained at 4.7 T with a surface coil for excitation in conjunction with adiabatic pulses (*TE*/*TR* = 272/2000 ms; 4 min acquisition time for each spectrum). The basic pulse sequence is a spin echo method with jump–return (Section 2.1.2) excitation and refocusing pulses for water suppression, combined [in (b)] with a frequency-selective inversion pulse at the resonance frequency of the C-α proton (4.1 ppm). The inversion pulse is alternated on/off, and the resulting signals are subtracted for the editing procedure.[47] All rf pulses have been replaced with adiabatic pulses. Instead of hard jump–return pulses, solvent-suppressive adiabatic pulses were used. The inversion pulse was an adiabatic DANTE pulse. To maintain better phase coherence in the editing procedure, a second (2π) adiabatic DANTE was inserted in the second $\frac{1}{2}TE$ period. Phase cycling using the EXORCYCLE procedure was performed. Localization was achieved with a modified 3D ISIS method using BIR-4 inversion pulses. Further details are given by Schapp et al.[92] and de Graaf et al.[93] Courtesy of Michael Garwood, Center for Magnetic Resonance Research, University of Minnesota, Minneapolis, MN

the z axis remains much smaller than the rotation frequency of magnetization $\boldsymbol{M}$ around the effective field $\boldsymbol{B}_e$ (i.e., the adiabatic criterion). The frequency sweep does not need to be accomplished with a linear ramp. In fact, a whole range of frequency (or phase) modulation functions have been described. The effect of the different modulation functions affect the $\boldsymbol{B}_1$ and off-resonance range where the pulse remains adiabatic. The disadvantages of these original adiabatic pulses are that

1. they do not result in good slice profiles when used for slice selection;
2. they require increased rf power;
3. plane rotation is not possible.

The latter disadvantage, in particular, has prevented many applications, especially in areas related to coherence pathway selection and water suppression. However, recent advances have made it possible to perform adiabatic plane rotations and thus refocusing. In addition, slice-selective refocusing with adiabatic pulses has been made possible by using two consecutive adiabatic inversion pulses.[109]

The problem of plane rotation using the above adiabatic pulses is that, unlike magnetization that is initially collinear with the effective field $\boldsymbol{B}_e$, magnetization perpendicular to $\boldsymbol{B}_e$ at location r will precess through an angle β depending on the actual magnitude of $\boldsymbol{B}_e$ at location r. This angle therefore varies with location, and, as a result, the possibility of $\boldsymbol{B}_1$-independent rotation is apparently lost. The central idea behind the solution of Garwood, Ugurbil and colleagues[92,102–104] is that if the effective field $\boldsymbol{B}_e$ is suddenly inverted, and if $\boldsymbol{B}_e$ is properly rotated, leading to a precession of $-\beta$ at location r, then the magnetization $\boldsymbol{M}$ will undergo an effective plane rotation. One of the most versatile of this new class of adiabatic plane rotation pulses is the so-called BIR-4 pulse.[105] The pulse consists of three sections: an adiabatic half-passage in reverse, adiabatic inversion, and adiabatic half-passage. Two inversions of $\boldsymbol{B}_e$ occur, for example, between periods one and two, and between two and three, accompanied by two discontinuous phase jumps, $\Delta\phi_1$ and $\Delta\phi_2$. The BIR-4 pulse can accomplish uniform plane rotations through any angle, the magnitude being determined by the phase jumps $\Delta\phi_1$ and $\Delta\phi_2$.

The feature of BIR-4 that is uniquely suitable for water suppression purposes or coherence pathway selection purposes is the fact that the phase jumps can be accomplished not only using the phase of the $\boldsymbol{B}_1$ field, but also by the Larmor precession frequency or by J coupling.[104,106] The first possibility is achieved simply by inserting a delay at the time of the phase jumps, leading to frequency-selective adiabatic pulses. The second possibility leads to adiabatic editing based on spin–spin coupling and adiabatic polarization transfer.[106] These elegant features can be accomplished with a high insensitivity of more than 10-fold variations in the $\boldsymbol{B}_1$ field. Figure 3 shows an example.

3.3 Postacquisition Frequency Filters

Even when the pulse sequence has resulted in water suppression of such high quality that the preamplifier has not been overloaded and the dynamic range of the ADC is sufficient with respect to the S/N of the experiment, it may be advantageous further to reduce the water line using data processing algorithms. The reason lies in some remaining disadvantages of the (suppressed but still dominating) water resonance. First, the base of the water line extends far into other regions of the spectrum. Second, insufficient apodization and truncation of the time domain can cause 'ringing' over a large portion of the spectrum. The latter problem is especially relevant if the acquisition time is short, such as in fast spectroscopic imaging using multiple spin echoes.

Several data processing methods can be used to extract the information from the raw time domain signals. Baseline corrections and convolution difference methods have been used extensively.[3–6] Much progress has been made in fitting in the time and frequency domains.[110–112] The latter methods are preferred whenever additional a priori information is available about the spectrum. A simple approach—the frequency filter—is demonstrated in Figure 4. The method is robust, fast, and automatic.[113–115] First, with water on resonance, a moving average filter over n data points is applied to generate a time domain signal from the raw data, which thus contain only data around zero frequency. Generally, a Gaussian weighting function is used, together with some extrapolation to determine the first and last $\frac{1}{2}n$ points. Second, the filter output is subtracted from the raw data. It has been shown that hardware frequency filters can also be implemented before the preamplifier stage.[116]

4 EVALUATION OF EXPERIMENTAL PROBLEMS

4.1 Spatial Selection

Most human proton spectroscopy is performed with the standard quadrature resonator. Therefore, signal detection is about equally efficient over the whole head, including the neck region. Owing to susceptibility differences over the complete sensitive volume, and also in part to nonideal shimming or magnet imperfections, water in some regions will have similar resonance frequencies to the metabolites of interest in the region to be examined. Two important conclusions can be drawn. First, frequency-based water suppression may work in a well-shimmed area, but not in the complete sensitive coil volume. Second, frequency-based water suppression only makes sense in conjunction with high-quality localization.

Localization may be performed using a surface coil for reception and transmission purposes.[117] The relatively small coil limits the sensitive area and thus the source of artifactual signals. In addition, $\boldsymbol{B}_1$ gradients generated by the surface coil can be used for additional localization.[118] Far more common is the use of $\boldsymbol{B}_0$ gradients, which are, of course, routinely available on every clinical MRI instrument. One of the first methods used a field profiling method to spoil resonances originating outside the region of interest.[119] However, most methods employ switched $\boldsymbol{B}_0$ gradients for localization—either for phase encoding or for slice selection purposes.[66–82] Slice selection in one direction is achieved similarly to common methods in MRI. Volume selection is achieved using a combination of three frequency-selective rf pulses in the presence of three mutually orthogonal gradients. This can be done in a multiscan[66–70,73–76] or single scan[10,70,71,78–81] approach. Selection in two or three different directions can also be achieved simultaneously.[90,120] Outer volume suppression may help the localization process. Because of the very high degree of localization, and the presence of motion, single shot methods are preferred. Note the important additional role of the $\boldsymbol{B}_0$ gradients in single shot localization (e.g., crushers used for coherence

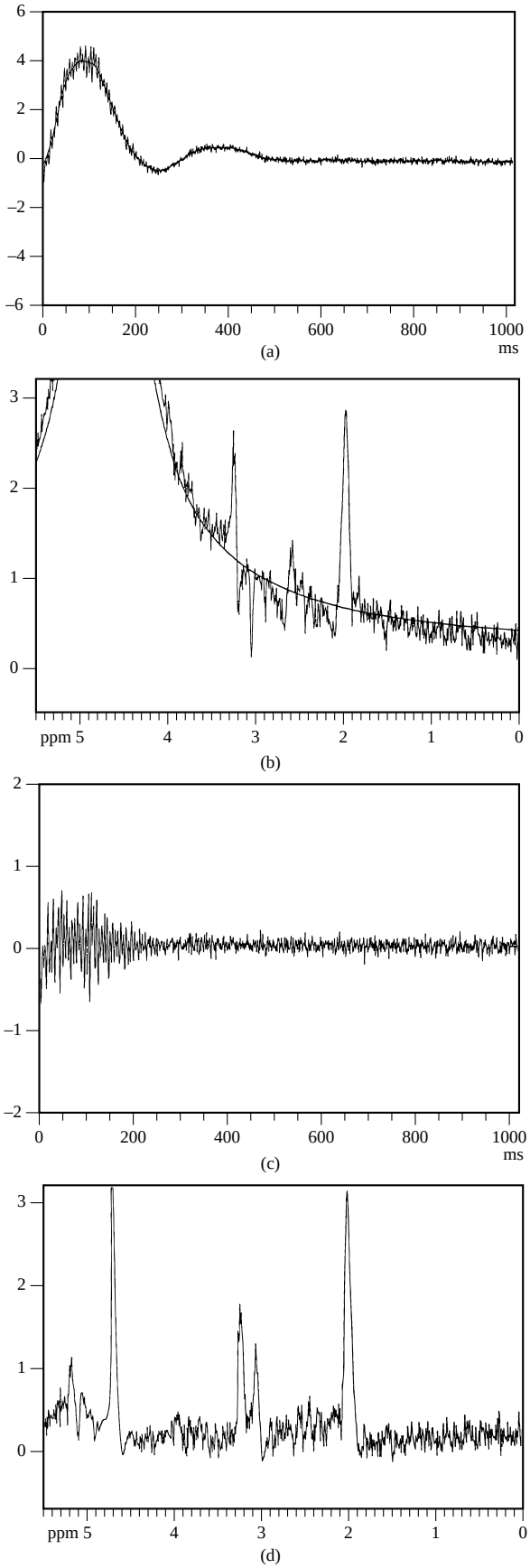

pathway selection without rf phase cycling). Phase encoding employing $\boldsymbol{B}_0$ gradients can be used for additional localization in spectroscopic imaging with Fourier transform[84] or alternative data processing methods using a priori information.[121,122] The quality of localization using phase encoding can be analyzed with the point spread function.

4.2 $\boldsymbol{B}_0$ Inhomogeneity

Perhaps the most significant problem in in vivo proton spectroscopy is the attainable homogeneity in the static magnetic field $\boldsymbol{B}_0$. Air–tissue and fat–tissue interfaces may lead to susceptibility gradients of the same magnitude as the generally used frequency range in in vivo proton spectroscopy. High-quality field homogeneity can be obtained in the brain, but is rather difficult in almost all other organs and tissues. This is the reason why proton spectroscopy is most commonly used in brain. Limited $\boldsymbol{B}_0$ homogeneity is not only detrimental to spectral appearance, but has also other disadvantages. Among these are

1. limitations in frequency-based water suppression methods;
2. errors in localization based on slice selection principles;
3. limitation in the efficiency of $\boldsymbol{B}_0$ gradients for coherence selection and for rapid dephasing;
4. echo shifting when the effect of an incompletely compensated $\boldsymbol{B}_0$ gradient is countered by the field inhomogeneity.

There are no complete solutions to the problem of limited $\boldsymbol{B}_0$ homogeneity. Partial remedies include optimal (possibly local) shimming, selecting small voxels, and using self-shielded gradients. Methods have been presented that result in sharp lines despite $\boldsymbol{B}_0$ inhomogeneities.[123] However, this result comes at the price of a severe S/N penalty.

4.3 $\boldsymbol{B}_1$ Inhomogeneity

The disadvantages of limited $\boldsymbol{B}_1$ homogeneity have been discussed in Section 2.1. In the context of water (or fat) suppression using the popular CHESS methods, the flip angle must be defined precisely. Recent advances in adiabatic pulse design may provide elegant improvements.

4.4 Motion

Motion is a common problem in MRI. Despite the much larger voxels in proton spectroscopy, it can be an even bigger problem in the latter technique—in particular, because of the extreme demands on water suppression and localization. In this regard, we may distinguish not only macroscopic motion of uncooperative patients, but also motion of arterial and venous

Figure 4 The use of a simple postprocessing frequency filter to limit detrimental effects of the suppressed but still dominant water resonance on spectral quality. The example is taken from a voxel of a water-suppressed spectroscopic image (for pulse sequence details, see Moonen et al.).[64] The raw time domain signals, and magnitude mode presentation following FT are shown in (a) and (b), respectively. The effect of the time domain frequency filter is shown on the filtered time domain (c) and the corresponding frequency spectrum (d) in magnitude mode presentation. Courtesy of Geoffrey Sobering, In Vivo NMR Research Center, NCRR, NIH, Bethesda, MD

blood, of CSF, and of brain tissue. The preferred method to minimize the detrimental effects of motion is to perform water suppression and localization in a single scan.[12] Multiscan phase cycling methods lead to incomplete suppression of unwanted signals in the presence of motion. However, single scan methods employing $\boldsymbol{B}_0$ gradients are not without problems. For example, motion during the scan may result in a phase shift of the echo. Tracking the phase using an additional echo[123] may help if the phase shift is identical for the complete voxel, but is of limited use if it is spatially dependent. In addition, if signal averaging is used, the motion sensitivity may be decreased when magnitude spectra are averaged, instead of pure phase spectra. In addition, shifts in the echo position may occur as a result of an imbalanced gradient in the presence of field inhomogeneities resulting from the motion.

4.5 Spectroscopic Imaging

The typical problems and solutions for solvent suppression in single voxels are similar to those in spectroscopic imaging methods. However, since modern spectroscopic imaging[86–91] is performed in a single session covering a large part of the brain, problems with $\boldsymbol{B}_0$ and $\boldsymbol{B}_1$ inhomogeneities are more severe. The problem of $\boldsymbol{B}_0$ homogeneity leads to the need for a larger frequency band affected by the water suppression procedure. Postprocessing water suppression (Section 3.3) is commonly used to minimize the effects of spatially dependent water suppression. Adiabatic pulses—now already routinely used for spin inversion purposes in spectroscopic imaging—may bring further improvements. Motion during spectroscopic imaging may lead to severe artifacts.

4.6 Fat Suppression

This article has dealt with suppression of the water resonance. Resonances of fat, or indeed, the family of triglycerides, can also dominate an in vivo proton NMR spectrum. Triglycerides lead to many resonances covering a large part of the useful proton spectrum. Therefore, typical frequency-selective suppression is not satisfactory. Three features of fat resonances are used for suppression purposes.

1. T_1 values are short (about 280 ms at 1.5 T), and can be used conveniently when preceding a pulse sequence with an inversion–recovery sequence.
2. In healthy brain tissue, no significant contributions originate from brain triglycerides.[2] The fat resonances arise predominantly from the skull tissue and can thus be suppressed by (a) outer volume suppression[67] (e.g., by spatial excitation of the entire skull area followed by rapid dephasing); or
   (b) avoiding excitation of skull area using accurate localization procedures (see Section 4.1).
3. Coupling patterns in trygliceride resonances, as distinct from those in the lactate doublet, are often used to separate the two compounds. Since the spatial origin of fat resonances is in the skull, phase encoding is helpful in defining the spatial origin of the fat signals, and thus suppressing the fat resonances in brain spectra.[124]

4.7 Safety Issues

The potential safety issues in water-suppressed proton spectroscopy are the same as for routine MRI. There are no specific safety issues with regard to water suppression, except in some cases heat deposition by rf irradiation when employing (semi)-continuous rf irradiation or $\boldsymbol{B}_1$ gradients to achieve scrambling of the water magnetization. However, most methods described in this article use less rf power per unit time than routinely used in multiple spin echo MRI methods.

5 SUMMARY

Solvent suppression has been, and remains, a rich area of research. Many advanced methods, developed over at least 30 years of high-resolution NMR, have been adapted for use in in vivo proton NMR spectroscopy. Water-suppressed human proton spectroscopy has now become almost a routine tool for brain NMR examination at 1.5 T. Although numerous developments have contributed to this extraordinary achievement, two fundamental technologies have been crucial:

1. the development of high-quality, fast switching, $\boldsymbol{B}_0$ gradient coils, in particular, the invention of the self-shielded gradient coil;
2. the achievement of excellent rf phase and amplitude stability and control.

The latter technology is especially relevant for adiabatic and other shaped pulses. Together with excellent progress in the field of single shot localization, these developments have made high-quality, water-suppressed proton spectroscopy of human and animal brain a reality. Solvent suppression in spectroscopic imaging is similar, but not identical, to the problem of single voxel solvent suppression. However, recent progress indicates that automated single slice and multislice spectroscopic imaging of the human brain will soon be available on standard 1.5 T instruments. The technological challenge that still remains largely unsolved is the routine use of proton spectroscopy of organs other than the brain.

6 RELATED ARTICLE

Single Voxel Localized Proton NMR Spectroscopy of Human Brain In Vivo.

7 REFERENCES

1. K. L. Behar, J. A. Den Hollander, M. E. Stromski, Y. Ogino, R. G. Shulman, O. A. C. Petroff, and J. W. Pritchard, *Proc. Natl. Acad. Sci. USA*, 1983, **80**, 4945.
2. C. C. Hanstock, D. L. Rothman, T. J. Jue, and R. G. Shulman, *Proc. Natl. Acad. Sci. USA.*, 1988, **85**, 1821.
3. P. J. Hore, *Methods Enzymol.*, 1989, **176**, 64.
4. J. E. Meier and A. G. Marshall, in 'Biological Magnetic Resonance', eds. L. J. Berliner and J. Reuben, Plenum Press, New York, 1990, Vol. 9, p. 199.
5. M. Guéron, P. Plateau, and D. Decorps, in 'Progress in Nuclear Magnetic Resonance Spectroscopy', eds. J. W. Emsley, J. Feeney

and L. H. Sutcliffe, Pergamon Press, Oxford, 1991, Vol. 23, p. 135.
6. P. C. M. van Zijl, and C. T. W. Moonen, in 'NMR Basic Principles and Progress', eds. P. Diehl, E. Fluck, and R. Kosfeld, Springer-Verlag, Berlin, 1992, Vol. 26, p. 67.
7. D. I. Hoult, *J. Magn. Reson.*, 1976, **21**, 337.
8. A. Haase, J. Frahm, W. Hänicke, and D. Matthaei, *Phys. Med. Biol.*, 1985, **30**, 341.
9. D. M. Doddrell, G. J. Galloway, W. M. Brooks, J. Field, J. M. Bulsing, M. G. Irving, and H. Baddeley, *J. Magn. Reson.*, 1986, **70**, 176.
10. J. Frahm, K. D. Merboldt, and W. Hänicke, *J. Magn. Reson.*, 1987, **72**, 502.
11. I. M. Brereton, G. J. Galloway, J. Field, M. F. Marshman, and D. M. Doddrell, *J. Magn. Reson.*, 1989, **81**, 411.
12. C. T. W. Moonen and P. C. M. van Zijl, *J. Magn. Reson.*, 1990, **88**, 28.
13. R. H. Griffey and D. P. Flamig, *J. Magn. Reson.*, 1990, **88**, 161.
14. R. J. Ogg, P. B. Kingsley, and J. S. Taylor, *J. Magn. Reson.*, 1994, **104B**, 1.
15. C. A. G. Haasnoot, *J. Magn. Reson.*, 1983, **52**, 153.
16. D. Canet, J. Brondeau, E. Mischler, and F. Humbert, *J. Magn. Reson.*, 1993, **105A**, 239.
17. W. E. Maas and D. G. Gory, *J. Magn. Reson., Ser. A*, 1994, **106A**, 256.
18. P. Blondet, M. Decorps, and J. P. Albrand, *J. Magn. Reson.*, 1986, **69**, 403.
19. D. Bourgeois and P. Kozlowski, *Magn. Reson. Med.*, 1993, **29**, 402.
20. G. A. Morris and R. Freeman, *J. Magn. Reson.*, 1978, **29**, 433.
21. P. Plateau and M. Guéron, *J. Am. Chem. Soc.*, 1982, **104**, 7310.
22. H. Liu, K. Weisz, and T. L. James, *J. Magn. Reson., Ser. A*, 1993, **105**, 184.
23. J. Frahm, H. Bruhn, M. L. Gyngell, K.-D. Merboldt, W. Hänicke, and R. Sauter, *Magn. Reson. Med.*, 1989, **11**, 47.
24. T. Inubushi and E. D. Becker, *J. Magn. Reson.*, 1983, **51**, 128.
25. J. H. Duijn, G. B. Matson, A. A. Maudsley, J. W. Hugg, and M. W. Weiner, *Radiology*, 1992, **183**, 711.
26. J. H. Duijn, J. A. Frank, and C. T. W. Moonen, *Magn. Reson. Med.* 1995, **33**, 101.
27. R. R. Ernst, G. Bodenhausen, and A. Wokaun, 'Principles of Nuclear Magnetic Resonance in One and Two Dimensions', Clarendon Press, Oxford, 1987.
28. N. Chandrakumar and S. Subramianan, 'Modern Techniques in High-Resolution FT-NMR', Springer-Verlag, New York, 1987.
29. O. W. Sørensen, in 'Progress in Nuclear Magnetic Resonance Spectroscopy', eds. J. W. Emsley, J. Feeney, and L. H. Sutcliffe, Pergamon Press, Oxford, 1989, Vol. 21, p. 503.
30. C. L. Dumoulin and D. Vatis, *Magn. Reson. Med.*, 1986, **3**, 282.
31. C. H. Sotak, D. M. Freeman, and R. E. Hurd, *J. Magn. Reson.*, 1988, **78**, 355.
32. R. E. Hurd and D. M. Freeman, *Proc. Natl. Acad. Sci. USA*, 1989, **86**, 4402.
33. D. M. Freeman, C. H. Sotak, H. H. Muller, S. W. Young, and R. E. Hurd, *Magn. Reson. Med.*, 1990, **14**, 321.
34. A. Knuttel and R. Kimmich, *Magn. Reson. Med.*, 1989, **10**, 404.
35. D. M. Doddrell, I. M. Brereton, L. N. Moxon, and G. J. Galloway, *Magn. Reson. Med.*, 1989, **9**, 132.
36. C. H. Sotak, *J. Magn. Reson.*, 1990, **90**, 198.
37. L. A. Trimble, J. F. Shen, A. H. Wilman, and P. S. Allen, *J. Magn. Reson.*, 1990, **86**, 191.
38. A. Knüttel, R. Kimmich, and K.-H. Spohn, *J. Magn. Reson.*, 1990, **86**, 526.
39. J. M. Bulsing and D. M. Doddrell, *J. Magn. Reson.*, 1986, **68**, 52.
40. C. J. Hardy and C. L. Dumoulin, *J. Magn. Reson.*, 1987, **5**, 75.
41. M. von Kienlin, J. P. Albrand, B. Authier, P. Blondet, S. Lotito, and M. Décorps, *J. Magn. Reson.*, 1987, **75**, 371.
42. A. Knüttel and R. Kimmich, *Magn. Reson. Med.*, 1989, **9**, 254.
43. D. L. Rothman, K. L. Behar, H. P. Hetherington, and R. G. Shulman, *Proc. Natl. Acad. Sci. USA*, 1984, **81**, 6330.
44. A. A. de Graaf, P. R. Luyten, J. A. den Hollander, W. Heindel, and W. M. M. J. Bovée, *Magn. Reson. Med.*, 1993, **30**, 231.
45. J. E. van Dijk, A. F. Mehlkopf, and W. M. M. J. Bovée, *NMR Biomed.*, 1992, **5**, 75.
46. D. L. Rothman, K. L. Behar, H. P. Hetherington, J. A. den Hollander, M. R. Bendall, O. A. C. Petroff, and R. G. Shulman, *Proc. Natl. Acad. Sci. USA*, 1985, **82**, 1633.
47. T. Jue, *J. Magn. Reson.*, 1987, **73**, 524.
48. J. Ruiz-Cabello, G. W. Vuister, C. T. W. Moonen, P. van Gelderen, J. S. Cohen, and P. C. M. van Zijl, *J. Magn. Reson.*, 1992, **100**, 282.
49. P. C. M. van Zijl, A. S. Chesnick, D. DesPres, C. T. W. Moonen, J. Ruiz-Cabello, and P. van Gelderen, *Magn. Reson. Med.*, 1993, **30**, 544.
50. G. Bodenhausen and D. J. Rubin, *Chem. Phys. Lett.*, 1980, **69**, 185.
51. E. O. Stejskal and J. E. Tanner, *J. Chem. Phys.*, 1965, **42**, 288.
52. P. C. M. van Zijl and C. T. W. Moonen, *J. Magn. Reson.*, 1990, **87**, 18.
53. J. Kärger, H. Pfeifer, and W. Heink, in 'Advances in Magnetic Resonance', ed. J. S. Waugh, Academic Press, New York, 1988, Vol. 12, p. 1.
54. P. C. M. van Zijl, C. T. W. Moonen, P. Faustino, J. Pekar, O. Kaplan, and J. S. Cohen, *Proc. Natl. Acad. Sci. USA*, 1991, **88**, 3228.
55. D. L. Rabenstein, S. Fan, and T. T. Nakashima, *J. Magn. Reson.*, 1985, **64**, 541.
56. S. D. Wolff and R. Balaban, *Magn. Reson. Med.*, 1989, **10**, 135.
57. R. L. Vold, J. S. Waugh, M. P. Klein, and D. E. Phelps, *J. Chem. Phys.*, 1968, **48**, 3831.
58. A. A. Maudsley, A. Wokaun, and R. R. Ernst, *Chem. Phys. Lett.*, 1978, **55**, 9.
59. A. Bax, P. G. de Jong, A. F. Mehlkopf, and J. Smidt, *Chem. Phys. Lett.*, 1980, **69**, 567.
60. P. Barker and R. Freeman, *J. Magn. Reson.*, 1985, **64**, 334.
61. P. Mansfield, *J. Phys. C*, 1977, **10**, L55.
62. P. Mansfield and B. Chapman, *J. Phys. E*, 1986, **19**, 540.
63. P. B. Roemer, W. A. Edelstein, and J. S. Hickey, *Proc. Vth Ann Mtg. Soc. Magn. Reson. Med.*, Montreal, 1986, p. 1067.
64. C. T. W. Moonen, G. S. Sobering, P. C. M. van Zijl, J. Gillen, M. von Kienlin, and A. Bizzi, *J. Magn. Reson.*, 1992, **98**, 556.
65. P. C. Lauterbur, *Nature (London)*, 1973, **242**, 190.
66. W. P. Aue, *Rev. Magn. Reson. Med.*, 1986, **1**, 21.
67. R. Sauter, S. Müller, and H. Weber, *J. Magn. Reson.*, 1987, **71**, 167.
68. P. R. Luyten, A. J. H. Mariën, B. Sijtsma, and J. A. den Hollander, *J. Magn. Reson.*, 1986, **67**, 148.
69. P. A. Bottomley, *Ann. NY Acad. Sci.*, 1987, **508**, 333.
70. R. J. Ordidge, P. Mansfield, J. A. B. Lohman, and S. B. Prime, *Ann. NY Acad. Sci.*, 1987, **508**, 376.
71. P. C. M. van Zijl, C. T. W. Moonen, J. R. Alger, J. S. Cohen, and A. S. Chesnick, *Magn. Reson. Med.*, 1989, **10**, 256.
72. C. T. W. Moonen, M. von Kienlin, P. C. M. van Zijl, J. Gillen, P. Daly, J. S. Cohen, and G. Wolf, *NMR Biomed.*, 1989, **2**, 201.
73. W. P. Aue, S. Müller, T. A. Cross, and J. Seelig, *J. Magn. Reson.*, 1984, **56**, 350.

74. P. A. Bottomley, T. H. Foster, and R. D. Darrow, *J. Magn. Reson.*, 1984, **59**, 338.
75. R. J. Ordidge, A. Connelly, and J. A. B. Lohman, *J. Magn. Reson.*, 1986, **66**, 283.
76. T. Mareci and H. R. Brooker, *J. Magn. Reson.*, 1985, **57**, 157.
77. A. Connelly, C. Counsell, J. A. B. Lohman, and R. J. Ordidge, *J. Magn. Reson.*, 1988, **78**, 519.
78. R. J. Ordidge, M. R. Bendall, R. E. Gordon, and A. Connelly, in 'Magnetic Resonance in Biology and Medicine', eds. Govil, Khetrapal, and Sran. McGraw-Hill, New Delhi, 1985, p. 387.
79. J. Granot, *J. Magn. Reson.*, 1986, **70**, 488.
80. G. McKinnon, *Proc. 5th Ann. Mtg. Soc. Magn. Reson. Med., Montreal*, 1986, p. 168.
81. R. Kimmich and D. Hoepfel, *J. Magn. Reson.*, 1987, **72**, 379.
82. J. Frahm, H. Bruhn, M. L. Gyngell, K.-D. Merboldt, W. Hänicke, and R. Sauter, *Magn. Reson. Med.*, 1989, **9**, 79.
83. T. R. Brown, B. M. Kincaid, and K. Ugurbil, *Proc. Natl. Acad. Sci. USA*, 1982, **79**, 3523.
84. A. A. Maudsley, S. K. Hilal, W. H. Perman, and H. E. Simon, *J. Magn. Reson.*, 1983, **51**, 147.
85. P. R. Luyten, A. J. H. Mariën, W. Heindel, P. H. J. van Gerwen, K. Herholz, J. A. den Hollander, G. Friedmann, and W. D. Heiss, *Radiology*, 1990, **176**, 791.
86. J. H. Duijn, G. B. Matson, A. A. Maudsley, and M. W. Weiner, *Magn. Reson. Med.*, 1992, **25**, 107.
87. J. H. Duijn, J. Gillen, G. Sobering, P. C. M. van Zijl and C. T. W. Moonen, *Radiology*, 1993, **188**, 277.
88. J. H. Duijn and C. T. W. Moonen, *Magn. Reson. Med.*, 1993, **30**, 409.
89. D. M. Spielman, J. M. Pauly, A. Macovski, G. Glover, and D. R. Enzmann, *J. Magn. Reson. Imaging*, 1992, **2**, 253.
90. P. G. Morris, in 'NMR Basic Principles and Progress', eds. P. Diehl, E. Fluck, and R. Kosfeld, Springer-Verlag, Berlin, 1992, Vol. 26, p. 149.
91. J. Pauly, P. Le Roux, D. Nishimura, and A. Macovski, *IEEE Trans. Med. Imaging*, 1991, **10**, 53.
92. D. G. Schapp, H. Merkle, J. M. Ellermann, Y. Ke, and M. Garwood, *Magn. Reson. Med.*, 1993, **30**, 1.
93. R. A. de Graaf, Y. Luo, M. Terpstra, H. Merkle, and M. Garwood, *J. Magn. Reson., Ser. B*, 1995, **109**, 184.
94. R. E. Hurd and B. K. John, *J. Magn. Reson.*, 1991, **91**, 648.
95. M. von Kienlin, C. T. W. Moonen, A. van der Toorn, and P. C. M. van Zijl, *J. Magn. Reson.*, 1991, **93**, 423.
96. J. Cavanagh, A. G. Palmer III, P. E. Wright, and M. J. Rance, *J. Magn. Reson.*, 1991, **429**, 91.
97. J. Baum, R. Tycko, and A. Pines, *J. Chem. Phys.*, 1983, **79**, 4643.
98. M. S. Silver, R. I. Joseph, and D. I. Hoult, *J. Magn. Reson.*, 1994, **59**, 347.
99. P. G. Morris, D. J. O. McIntyre, D. E. Rourke, and J. T. Ngo, *Magn. Reson. Med. Biol.*, 1989, **11**, 167.
100. S. Conolly, D. Nishimura, and A. Macovski, *J. Magn. Reson.*, 1989, **83**, 324.
101. C. J. Hardy, W. A. Edelstein, and D. Vatis, *J. Magn. Reson.*, 1986, **66**, 470.
102. K. Ugurbil, M. Garwood, and M. R. Bendall, *J. Magn. Reson.*, 1986, **72**, 177.
103. M. Garwood and K. Ugurbil, in 'NMR Basic Principles and Progress', eds. P. Diehl, E. Fluck, and R. Kosfeld, Springer-Verlag, Berlin, 1992, Vol. 26, p. 110.
104. B. D. Ross, H. Merkle, K. Hendrich, R. S. Staewen, and M. Garwood, *Magn. Reson. Med.*, 1992, **23**, 96.
105. M. Garwood and Y. Ke, *J. Magn. Reson.*, 1991, **94**, 511.
106. M. Garwood and H. Merkle, *J. Magn. Reson.*, 1990, **94**, 180.
107. M. Shinnar, L. Bolinger, and J. S. Leigh, *Magn. Reson. Med.*, 1989, **12**, 88.
108. M. Goldman, 'Quantum Description of High-Resolution in Liquids', Clarendon Press, Oxford, 1988, Chap. 1.
109. S. Connolly, G. Glover, D. Nishimura, and A. Macovski, *Magn. Reson. Med.*, 1991, **18**, 28.
110. R. de Beer and D. van Ormondt, in 'NMR Basic Principles and Progress', eds. P. Diehl, E. Fluck, and R. Kosfeld, Springer-Verlag, Berlin, 1992, Vol. 26, p. 201.
111. A. A. de Graaf, J. E. van Dijk, and W. M. M. J. Bovée, *Magn. Reson. Med.*, 1989, **13**, 343.
112. J. S. Nelson and T. R. Brown, *J. Magn. Reson.*, 1989, **84**, 95.
113. H. Barkhuijsen, R. de Beer, W. M. M. J. Bovée, and D. van Ormondt, *J. Magn. Reson.*, 1985, **61**, 465.
114. D. S. Stephenson, in 'Progress in Nuclear Magnetic Resonance Spectroscopy', eds. J. W. Emsley, J. Feeney, and L. H. Sutcliffe, Pergamon Press, Oxford, 1988, Vol. 20, p. 515.
115. D. Marion, M. Ikura, and A. Bax, *J. Magn. Reson.*, 1989, **84**, 425.
116. O. Gonen and G. Johnson, *J. Magn. Reson., Ser. B*, 1993, **102**, 98.
117. J. J. H. Ackerman, T. H. Grove, G. G. Wong, D. G. Gadian, and G. K. Radda, *Nature (London)*, 1980, **283**, 167.
118. M. R. Bendall and R. E. Gordon, *J. Magn. Reson.*, 1983, **53**, 365.
119. R. E. Gordon, P. E. Hanley, D. Shaw, D. G. Gadian, G. K. Radda, P. Styles, P. J. Bore, and L. Chan, *Nature (London)*, 1980, **287**, 367.
120. C. J. Hardy, P. A. Bottomley, M. O'Donnell, and P. Roemer, *J. Magn. Reson.*, 1988, **77**, 233.
121. X. Hu, D. N. Levin, P. C. Lauterbur, and T. Spraggins, *Magn. Reson. Med.*, 1988, **8**, 314.
122. M. von Kienlin and R. Mejia, *J. Magn. Reson.*, 1991, **94**, 268.
123. L. D. Hall and T. J. Norwood, *J. Magn. Reson.*, 1986, **67**, 382.
124. S. Posse, B. Schuknecht, M. E. Smith, P. C. M. van Zijl, N. Herscovitch, and C. T. W. Moonen, *J. Comput. Assist. Tomogr.*, 1993, **17**, 1.

Biographical Sketches

Chrit Moonen. *b* 1955. M.S., 1980, Ph.D., 1983, Agricultural University, Wageningen, The Netherlands. Introduced to protein NMR by Kurt Wüthrich, Zürich, 1979. Faculty member, Department of Biochemistry at Wageningen 1984–86; sabbatical with George Radda, Department of Biochemistry, Oxford; one year with Morton Bradbury at University of California at Davis, 1987. Head of the NIH In Vivo NMR Research Center 1987–1996. Director of Research at the Centre National de la Recherche Scientifique, University of Bordeaux 2 1997–present. Approximately 100 publications. Research interests: mapping of brain function, physiological MR, diffusion and perfusion imaging, interventional MRI, MRI guided focused ultrasound.

Peter C. M. van Zijl. *b* 1956. M.S., 1980, Ph.D., 1985, Free University, Amsterdam, The Netherlands. Postdoctoral fellow at Carnegie Mellon University, Department of Chemistry, 1985–87; visiting associate at National Institutes of Health, National Cancer Institute, 1987–90. Research assistant professor at Georgetown University, Department of Pharmacology, 1990–92; Professor at Johns Hopkins Medical School, Department of Radiology, 1992–present. Approx. 75 publications. Research interests: in vivo spectroscopy and imaging of brain function, including diffusion imaging and imaging of metabolite levels and active metabolism of magnetically labelled precursors. Mechanism of ischemia. Design of NMR technology for HR NMR.

Animal Methods in MRS

David G. Gadian

Royal College of Surgeons Unit of Biophysics, Institute of Child Health, London, UK

1 INTRODUCTION

Magnetic resonance spectroscopy studies of animal models have contributed in numerous ways to our understanding of the metabolic processes that take place in normal and diseased tissue. Applications to tumor metabolism are covered in accompanying articles (see ***Spectroscopic Studies of Animal Tumor Models***), and are therefore not discussed here. Space limitations do not allow a comprehensive review; instead, we concentrate in this article on three major themes in this research area, namely (i) ^{31}P MRS and tissue energetics, (ii) ^{1}H MRS of brain metabolites, and (iii) ^{13}C studies of intermediary metabolism, and we conclude with some illustrative examples of the role of MRS in the investigation of stroke models.

2 PHOSPHORUS-31 MRS AND TISSUE ENERGETICS

Following earlier NMR studies of cellular and tissue metabolism in the 1970s,[1] in 1980 it was reported that the use of an unusual type of radiofrequency coil, termed a surface coil (see ***Surface and Other Local Coils for In Vivo Studies***), provided a simple and effective means of probing skeletal muscle and brain metabolism noninvasively in small animals.[2] The ^{31}P spectra that were obtained in these studies (Figure 1) illustrate the type of information that is provided by ^{31}P NMR. The spectra of skeletal muscle and brain include ^{31}P signals from ATP, phosphocreatine (PCr), and inorganic phosphate (Pi), metabolites that play central roles in energy metabolism. In addition to measuring the relative concentrations of these metabolites, it is also possible to determine the intracellular pH from the chemical shift of the inorganic phosphate signal. A number of interesting points emerged from these surface coil studies. For example, the ratio of phosphocreatine to ATP was on the high side of values commonly obtained using invasive rapid freezing techniques, while the concentrations of inorganic phosphate and of free cytoplasmic ADP were lower than those measured with invasive techniques.

While the measurement of relative concentrations often provides an adequate basis for interpretation, there is increasing emphasis on the determination of absolute concentrations. A number of studies have shown that NMR and freeze clamping measurements tend to give similar values for tissue ATP concentrations.[3] In some cases, however, the two types of measurement may differ somewhat because of the presence of NMR-invisible ATP pools. Also, comparison of the two types of measurement is complicated by the fact that nucleotides other than ATP can make contributions to the triphosphate signals; in recognition of this, these signals are sometimes labeled NTP rather than ATP. In contrast to these ATP observations, the concentrations of ADP and inorganic phosphate that have been measured in various tissues using noninvasive NMR methods are often much lower than those measured by analysis of tissue extracts.[4–6] These discrepancies in the measurements of ADP and inorganic phosphate could reflect the presence of NMR-invisible intracellular fractions, resulting from tight binding to macromolecules or perhaps from sequestration within certain intracellular compartments, including the mitochondria. Alternatively, in some cases they may reflect an unavoidable breakdown of high-energy phosphates in invasive measurements, for example in human biopsy analyses where there is an inevitable delay between removal and freezing of the sample. Regardless of the precise explanation for the differences between these NMR and chemical measurements, the low levels of free inorganic phosphate and ADP have important kinetic and thermodynamic implications; in particular, these findings strongly influence our understanding of those reactions that are subject to control by inorganic phosphate and ADP.[7]

^{31}P MRS provides an excellent experimental approach to the investigation of changes in energy metabolism associated with impaired oxygen delivery, as in ischemia or hypoxia. Metabolic changes can be monitored sequentially in a single animal, for example throughout a period of ischemia and subsequent reperfusion, offering considerable advances over invasive methods of analysis. One of the main areas of interest is the evaluation of agents or procedures that may protect

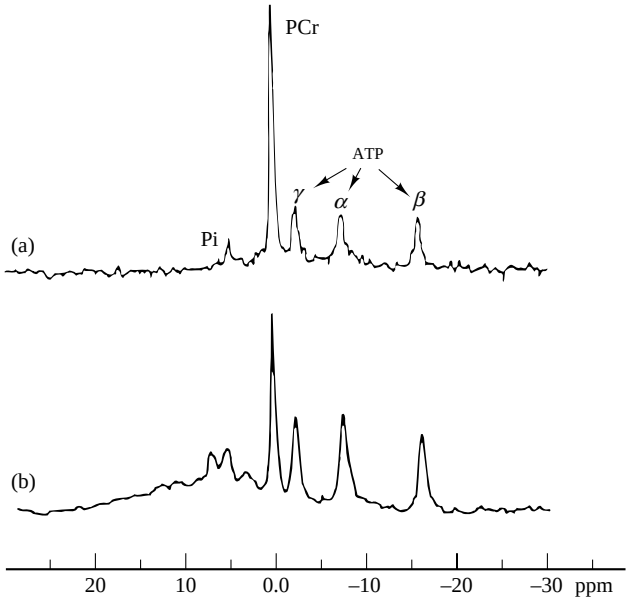

Figure 1 ^{31}P spectra obtained at 74 MHz showing signals from the α-, β-, and γ-phosphates of ATP, phosphocreatine (PCr), and inorganic phosphate (P_i) in (a) skeletal muscle and (b) the brain of an anesthetized rat. The brain spectrum also shows signals from phosphomonoesters (6–8 ppm) and phosphodiesters (2–4 ppm). (Reproduced with permission from *Nature*, Ackerman et al., *Nature (London)*, 1980, **283**, 167, Copyright (1980) Macmillan Magazines Limited)

against the damaging consequences of inadequate oxygen supply. This is of relevance to conditions such as stroke, to methods used for the preservation of organs prior to transplantation, and to cardioplegic techniques for use during open heart surgery. To exemplify this approach, a later section of this article describes some studies of experimental stroke.

Extensive studies have also been carried out of the metabolic changes that are associated with muscular exercise. While a number of such studies have been carried out in animals, the advantages of spectroscopy are most apparent for investigations in humans, where there are obvious benefits over biopsy procedures (see ***Whole Body Studies: Impact of MRS***). The large changes in energy demand and in the concentrations of the energy metabolites make it reasonable to expect that metabolites such as ADP should play a key role in the control of energy metabolism in skeletal muscle, and numerous studies have indicated that this is so. However, it is less obvious that this should be the case for other tissues such as cardiac muscle, liver, and brain which do not have such extensive variations in energy demand. Indeed, ^{31}P NMR studies of the heart (discussed more fully below), brain, and kidney have shown little correlation between the rate of oxidative phosphorylation in the steady state and the cytoplasmic concentrations of ADP, inorganic phosphate, and ATP.[7] This does not mean that these metabolites no longer have the capacity to control oxidative phosphorylation in these tissues. However, it does suggest that, at least under the conditions of these particular studies, there are other factors, including substrate and oxygen delivery, that presumably have a stronger influence on the regulation of oxidative phosphorylation.

It is difficult to measure free ADP directly from ^{31}P spectra, partly because its signals overlap with the much larger signals from ATP, but also because it is apparent that, even if overlap were not a problem, the free ADP is commonly present at such low concentrations that its signals would not be visible above the noise. The evidence for this is obtained by making use of the creatine kinase equilibrium, which permits the concentration of free ADP to be calculated on the basis of the known concentrations of the other creatine kinase reactants. While this method is feasible for skeletal muscle, cardiac muscle, and brain, it cannot be used for tissues that do not express significant amounts of creatine kinase, such as liver and kidney. An interesting means of circumventing this problem has been described by Brosnan et al.[8] who used the transgenic mouse technique to express high levels of creatine kinase in the liver. They were thus able to show that the free ADP in the liver was about 60 μmol g^{-1} wet weight. This is similar to the value previously determined by Veech et al.[9] on the basis of similar arguments involving enzymes that are believed to catalyze reactions that are near to equilibrium. Such transgenic models could clearly contribute significantly to our understanding of tissue metabolism and its control.

^{31}P NMR can make further contributions to our understanding of the kinetic and thermodynamics of oxidative phosphorylation, through its ability to monitor the unidirectional flux between ATP and inorganic phosphate in intact tissues. This measurement can be achieved by magnetization transfer techniques, in an analogous manner to the measurement of creatine kinase activity, and a particularly extensive series of studies has been carried out on cardiac muscle.[10]

These magnetization transfer studies of cardiac muscle were carried out on isolated perfused preparations. The study of cardiac muscle in vivo is a lot more difficult, partly because of the effects of motion, and also because blood can contribute significant amounts of signal, making measurements based on the phosphomonoester and inorganic phosphate signals particularly problematical. Some of the problems can be circumvented by the use of surgical procedures enabling the radiofrequency coil to be positioned adjacent to the region of interest. A number of such studies have been carried out on the dog heart in vivo. For example, a series of ^{31}P studies has been carried out examining the relationship between workload and phosphorus energy metabolites. It was found that the concentration of ADP and the phosphocreatine/ATP ratio in the heart did not change significantly despite an almost fourfold change in ATP hydrolysis, as estimated from the myocardial oxygen consumption.[11] It was subsequently found that there were no significant changes in ATP, ADP, phosphocreatine, or inorganic phosphate until the workload apparently outstripped the ability of the heart to produce ATP, because of limitations either in coronary blood flow or in oxidative phosphorylation capacity.[12] As discussed above, these findings are relevant to our understanding of metabolic control in the heart.

The spectral contributions from blood, which as mentioned above cause problems with observations based on the inorganic phosphate signal (including measurements of myocardial pH), can be eliminated or at least greatly reduced by using appropriate localization techniques. For example, Robitaille et al.[13] described the use of one-dimensional spectroscopic imaging in conjunction with an implanted surface coil to detect the transmural metabolite distribution in the dog heart. Amongst their findings, they noted that their measured pH value of 7.0–7.1 was in agreement with measurements on perfused hearts, and suggested that in some in vivo studies the pH might have been overestimated due to the contributions of 2,3-diphosphoglycerate and inorganic phosphate from the blood.

3 ^{1}H MRS AND BRAIN METABOLISM

Following earlier studies of metabolism in red blood cells,[14] the first high-resolution ^{1}H spectra of intact animals were reported by Behar et al.[15] In their studies of the rat brain, they were able to observe ^{1}H signals from a number of metabolites, including *N*-acetylaspartate, creatine + phosphocreatine, and choline-containing compounds, and they demonstrated an increase in the lactate signal on hypoxia, with a return to normal on subsequent oxygenation (Figure 2). Numerous technical developments followed, and ^{1}H MRS is now extensively used for the noninvasive detection of human brain metabolites. The range of metabolite signals that has been unequivocally identified by ^{1}H MRS has widened considerably, and a variety of animal models of disease have shown the presence of unusually high signals from specific metabolites. For example, histidine has been detected in mice with histidinemia,[16] elevated glutamine has been seen in hyperammonemic rats,[17–19] unusually high concentrations of choline-containing compounds (and in particular betaine) are present in animal models of multiple sclerosis,[20,21] and high levels of γ-aminobutyrate (GABA) have been observed in rats treated with anticonvul-

sants that act as inhibitors of GABA transaminase.[22,23] Studies of this type have pointed the way forward to analogous investigations of disordered cerebral metabolism in man; they can also aid interpretation and assignment of clinical spectra. In addition, of course, they can highlight potential pitfalls in interpretation. For example, in clinical spectroscopy the assignment of signals to brain lipids may need to be treated with some caution, in view of the demonstration that certain brain proteins can give rise to peaks that show some similarities with lipid signals.[24,25]

A number of animal studies, including some of those mentioned above, have shown that there could be many conditions in which the ^{1}H spectra are more responsive than ^{31}P signals to brain disease. However, in relating animal studies to clinical investigations, it must be appreciated that many animal models are studied in the acute phase, whereas the majority of clinical cases are investigated in the subacute or chronic phase. This is just one reason why some degree of caution must be exercised in making comparisons between studies of animal models and of man. One metabolite that is of particular relevance in this context is *N*-acetylaspartate. Several lines of evidence suggest that almost all of the *N*-acetylaspartate within the brain is neuronal, and so in clinical studies a reduction in the *N*-acetylaspartate signal is commonly interpreted in terms of neuronal loss or damage.[26] This interpretation is consistent with the spectral changes that have been observed in a number of disorders for which neuronal loss can be expected, including stroke, gliomas, AIDS, and epilepsy (see ***Brain Infection and Degenerative Disease Studied by Proton MRS***). However, extensive loss of *N*-acetylaspartate is less commonly observed in animal models, primarily because the pathological processes resulting in such loss may have a timescale of many hours or days, whereas the animal models are often studied in the acute phase. Thus in ^{1}H studies of animal stroke models, the emphasis has tended to be more on the detection of acute changes in lactate than on chronic changes in *N*-acetylaspartate. In more chronic animal models, a major loss of *N*-acetylaspartate has indeed been observed, and in kainate-induced status epilepticus this loss has been found to correlate well with neuronal injury.[27]

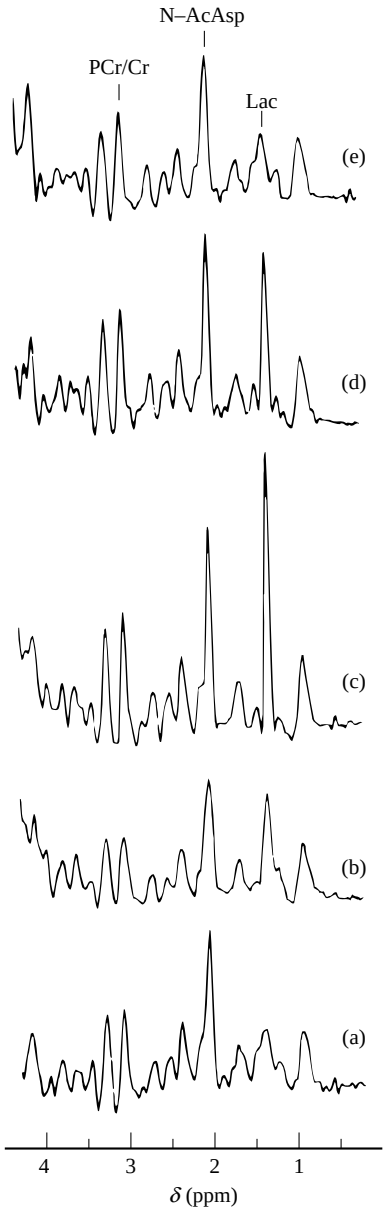

Figure 2 ^{1}H NMR spectra obtained at 360 MHz from the rat brain in vivo, showing the time course of lactate production and clearance during hypoxia and recovery. Phosphocreatine and creatine (PCr/Cr), *N*-acetylaspartate (NAc-Asp), and lactate (Lac) signals are labeled. Conditions were as follows: a, normoxic, 25% O_2; b, hypoxic, 5 min after administration of 4% O_2; c, after 17 min at 4% O_2; d, recovery, 14 min after administration of 25% O_2; e, after 41 min at 25% O_2. (Reproduced with permission from Behar et al., *Proc. Natl. Acad. Sci. USA*, 1983, **80**, 4945)

4 ^{13}C MRS AND INTERMEDIARY METABOLISM

The natural abundance of ^{13}C is only 1.1%, and this has led to the emergence of two categories of investigation. In one category, the compounds of interest are present at sufficiently high concentrations to permit detection without ^{13}C labeling. These natural abundance studies are primarily of storage compounds, in particular glycogen, since these tend to be present in the appropriate concentration range. In the early 1980s, it was reported that glycogen gives a well-resolved ^{13}C NMR spectrum in which the carbons are almost completely NMR-visible.[28] This was somewhat surprising in view of the fact that large molecules with relatively little mobility tend to give very broad signals. Presumably, glycogen has a high degree of internal mobility, as a result of which its carbons give fairly narrow signals. The high concentration of glycogen in liver and muscle means that its ^{13}C signals can be detected in these tissues without any need for isotopic enrichment. In common with other developments in spectroscopy, the main applications for the detection of glycogen may well prove to be in man.

The second category of ^{13}C studies exploits the use of ^{13}C-labeling for the investigation of specific metabolic pathways. For example, Kunnecke et al.[29] have investigated the metabolism of [1,2-$^{13}C_2$]glucose and of multiply-labeled 3-hydroxybutyrate in rat brain, obtaining spectra both in vivo and in vitro. Figure 3 shows in vivo ^{13}C spectra of rat brain before infusion (a) and during infusion of each of the two substrates (b

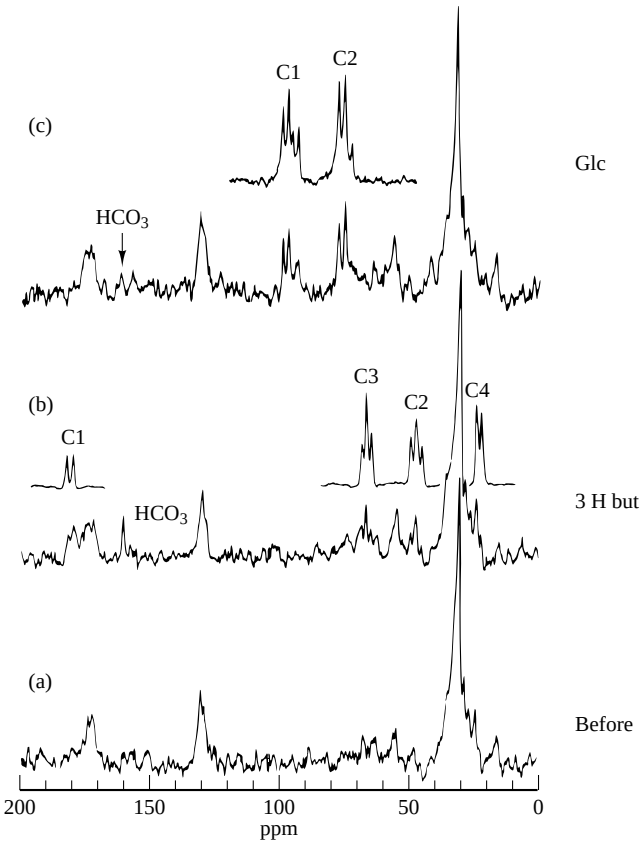

Figure 3 ^{13}C NMR spectra of rat brain obtained at 20 MHz in vivo before (a) and during the infusion of [U-$^{13}C_4$]3-hydroxybutyrate (b), or [1,2-$^{13}C_2$]glucose (c). The insets show the spectra of [U-$^{13}C_4$]3-hydroxybutyrate (b) and [1,2-$^{13}C_2$]glucose (c) in saline solution. (Reproduced with permission from Kunnecke et al., *NMR Biomed.*, 1993, **6**, 264)

and c), while Figure 4 shows the corresponding spectra obtained from perchloric acid extracts of the brain. Analysis of the spin-coupling patterns in such spectra provides detailed information about many aspects of cerebral metabolism, including the pathways of glutamate, glutamine, and GABA synthesis, and reveals various features of metabolic compartmentation that can readily be attributed to the differing metabolic characteristics of neurons and glial cells. These studies can also contribute to our understanding of the role of *N*-acetylaspartate, which was referred to above in relation to ^{1}H MRS studies of the brain. In particular, it was found that while free aspartate is ^{13}C-enriched to a similar extent as glutamate and glutamine, the labeling of the aspartyl moiety of *N*-acetylaspartate remained at the natural abundance level. In contrast, the acetyl moiety of *N*-acetylaspartate was significantly enriched, lending further support to the view that this metabolite may act as an acetyl carrier or as a storage form of acetyl-CoA.

An alternative technical approach exploits the influence of the ^{13}C spin on the signals from neighboring protons. For example, the CH_3 protons of lactate are split into a doublet if the C3 carbon is ^{13}C-labeled, and the detection of such splitting in ^{1}H spectra has formed the basis for demonstrating turnover of brain lactate in human stroke. As an extension of this indirect approach to the detection of ^{13}C label, the ^{1}H signals can be detected with and without ^{13}C-decoupling, and this provides a means of measuring fractional enrichment of the ^{13}C label. Such proton-observe-carbon-edit methods[30] have been used to measure the rate of label entry from [1-^{13}C]glucose into glutamate. Since the glucose carbon is incorporated into glutamate by rapid exchange with the tricarboxylic acid cycle (TCA) intermediate α-ketoglutarate, it is possible to use the rate of glutamate labeling to obtain an estimate of the TCA cycle activity. The method has now been extended from animal studies to humans. Since ^{1}H MRS is intrinsically more sensitive than ^{13}C MRS, it is likely that this type of approach will greatly extend the applicability of ^{13}C-labeling studies in vivo. These ^{13}C studies, and in particular their applications to humans, are discussed extensively in the article on ***Brain MRS of Human Subjects***.

5 MRS AND CEREBRAL ISCHEMIA

Ischemia refers to reduced blood flow, and has been defined as 'blood flow… too low to supply enough oxygen to support cellular function'.[31,32] One question that arises is how well one can define a threshold value for cerebral blood flow, above which energy supply is sufficient but below which energy failure ensues. The precise relationship between flow and energy metabolism has been difficult to establish because of problems in making concurrent measurements of flow and metabolism in vivo in a single animal as a function of time. These problems can be overcome with the aid of MRS measurements.

The combination of ^{1}H and ^{31}P spectroscopy, together with simultaneous measurements of regional cerebral blood flow using the hydrogen clearance technique, has demonstrated that major changes in energy metabolites occur in the gerbil brain when the flow falls from control values of about 60 mL per 100 g per min to about 20 mL per 100 g per min or below.[33] These changes reflect the characteristic metabolic features of energy failure; that is, there is a decrease in high-energy phosphates and intracellular pH, and an increase in inorganic phosphate and lactate. The flow value of 20 mL per 100 g per min is similar to that at which, in a variety of species (including man), electrical activity ceases, and is also similar to the flow level at which water accumulates in the gerbil brain. These results therefore provide evidence suggesting that the thresholds for electrical function and edema are a direct consequence of energy failure. A model such as this could also prove to be useful when examining pharmaceuticals or other forms of therapy that may influence flow and/or metabolism. For example, one might anticipate that a treatment could be beneficial if it lowers the threshold flow value from 20 to, say, 10 mL per 100 g per min, as this would imply that the brain can tolerate lower flow values without undergoing energy failure. To illustrate this point, it was shown that the decline in energy status at reduced flow values is less severe under hypothermic (30 °C) conditions than at normal body temperature, consistent with a protective effect of hypothermia.[34]

Ischemia is also associated with failure of the transmembrane ionic pumps, and this aspect of energy failure can be investigated with ^{23}Na NMR. As discussed in the article ***Cation Movements across Cell Walls of Intact Tissues Using***

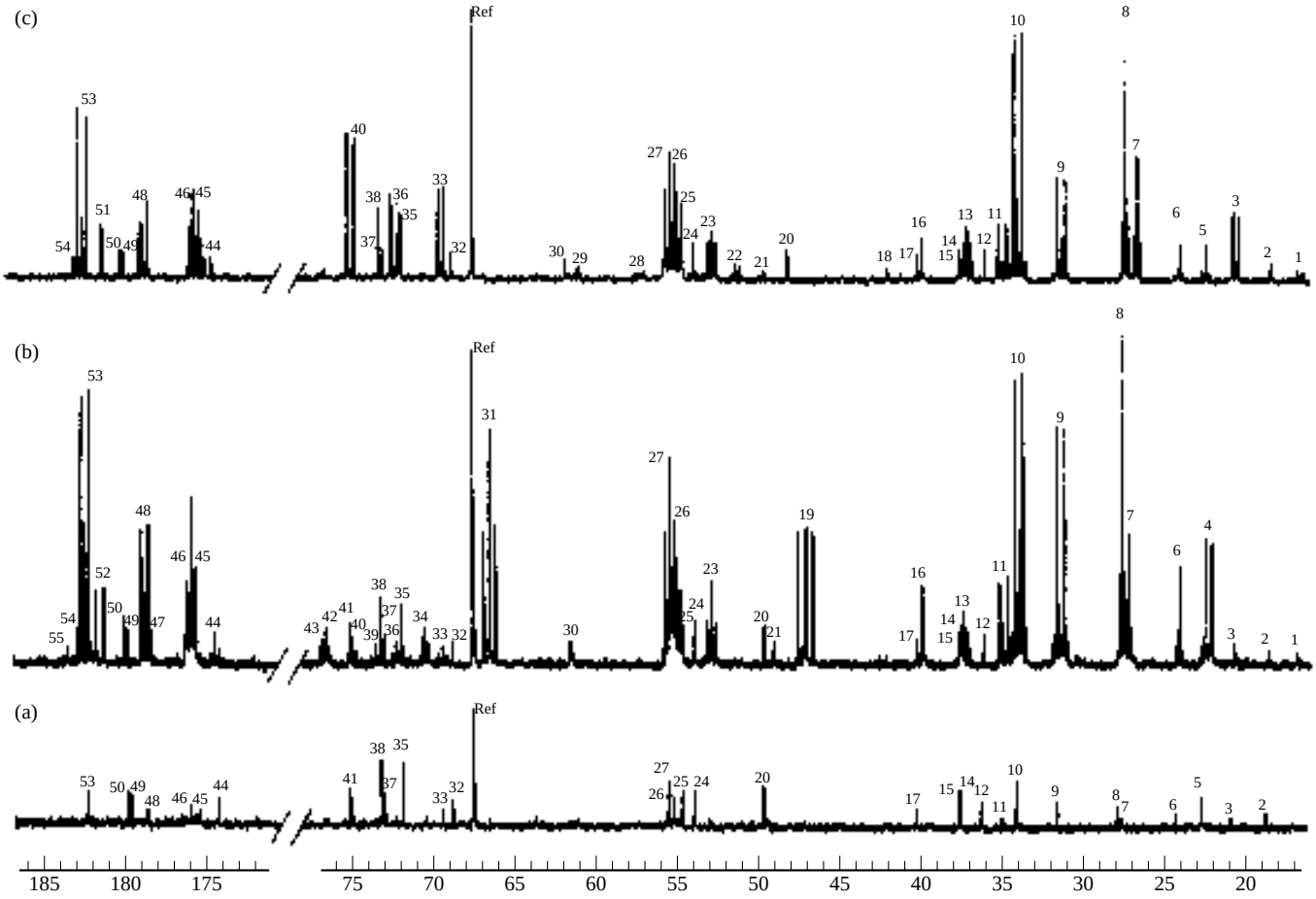

Figure 4 ^{13}C NMR spectra obtained at 100 MHz from perchloric acid extracts of rat brains after the infusion of saline solution (a), [U-$^{13}C_4$]3-hydroxybutyrate (b), and [1,2-$^{13}C_2$]glucose (c). Only the aliphatic and carboxylic regions of the spectra are shown. (Reproduced with permission from Kunnecke et al., *NMR Biomed*., 1993, **6**, 264, where the numerous spectral assignments are given)

MRS, the ^{23}Na signals of intracellular and extracellular Na^+ ions differ in their relaxation properties, and this provides a means of exploring changes in the distribution of Na^+ ions across the cell membrane. Thus the relationship of ion homeostasis to tissue energetics can be carried out by combining ^{31}P with ^{23}Na NMR.[35–37] For example, one study showed that upon production of cerebral ischemia there is a delay of approximately 2 min before the ATP level begins to fall and the intracellular Na^+ begins to rise.[37] These findings, together with the flow thresholds that have been observed for energy failure, are relevant to observations that have been made in recent years using diffusion-weighted MRI, a technique that shows remarkable sensitivity to early events in cerebral ischemia.[38,39] On the basis of the relationships between the spectroscopy and diffusion-weighted imaging findings, it appears that the diffusion-weighted imaging changes observed early after the onset of ischemia are sensitive to the disruption of tissue energy metabolism or to a consequence of this disruption, including water movements associated with loss of ion homeostasis. This has raised the interesting possibility of using diffusion-weighted imaging to visualize regions of compromised energy metabolism in man, with the spatial resolution characteristic of MRI; i.e. with much superior spatial resolution to that provided by ^{31}P or ^{1}H MRS of energy metabolites.

6 GENERAL DISCUSSION

While the focus of attention in MRS studies is inevitably moving towards noninvasive studies of tissue metabolism in man, it is apparent that studies of animal models of disease will continue to complement and aid interpretation of clinical observations. The above studies serve to illustrate the central role that animal studies can play in the investigation of tissue biochemistry and pathophysiology; they also show the importance of combining these MRS studies with in vitro analyses of tissue extracts, and with MRI investigations. It is this type of integrated approach that offers much of the excitement for the future.

7 RELATED ARTICLES

Brain Infection and Degenerative Disease Studied by Proton MRS; Brain MRS of Human Subjects; Cation Movements

across Cell Walls of Intact Tissues Using MRS; Spectroscopic Studies of Animal Tumor Models; Surface and Other Local Coils for In Vivo Studies; Whole Body Studies: Impact of MRS.

8 REFERENCES

1. Numerous articles in *Philos. Trans. R. Soc. London*, 1980, **289B**, 379.
2. J. J. H. Ackerman, T. H. Grove, G. G. Wong, D. G. Gadian, and G. K. Radda, *Nature (London)*, 1980, **283**, 167.
3. E. B. Cady, *NMR Basic Principles and Progress*, 1992, **26**, 249.
4. D. J. Taylor, P. J. Bore, P. Styles, D. G. Gadian, and G. K. Radda, *Mol. Biol. Med.*, 1983, **1**, 77.
5. D. Freeman, S. Bartlett, G. K. Radda, and B. D. Ross, *Biochim. Biophys. Acta*, 1983, **762**, 325.
6. R. A. Iles, A. N. Stevens, J. R. Griffiths, and P. G. Morris, *Biochem. J.*, 1985, **229**, 141.
7. R. S. Balaban, *Am. J. Physiol.*, 1990, **258**, C377.
8. M. J. Brosnan, L. H. Chen, T. A. van Dyke, and A. P. Koretsky, *J. Biol. Chem.*, 1990, **265**, 20 849.
9. R. L. Veech, J. W. R. Lawson, N. W. Cornell, and H. A. Krebs, *J. Biol. Chem.*, 1979, **254**, 6538.
10. P. B. Kingsley-Hickman, E. Y. Sako, P. Mohanakrishnan, P. M. Robitaille, A. H. From, J. E. Foker, and K. Ugurbil, *Biochemistry*, 1987, **26**, 7501.
11. R. S. Balaban, H. L. Kantor, L. A. Katz, and R. W. Briggs, *Science*, 1986, **232**, 1121.
12. L. A. Katz, J. A. Swain, M. Portman, and R. S. Balaban, *Am. J. Physiol.*, 1989, **256**, H265.
13. P.-M. Robitaille, H. Merkle, E. Sublett, K. Hendrich, B. Lew, G. Path, A. H. L. From, R. J. Bache, M. Garwood, and K. Ugurbil, *Magn. Reson. Med.*, 1989, **10**, 14.
14. F. F. Brown, I. D. Campbell, P. W. Kuchel, and D. C. Rabenstein, *FEBS Lett.*, 1977, **82**, 12.
15. K. L. Behar, J. A. den Hollander, M. E. Stromski, T. Ogino, R. G. Shulman, O. A. C. Petroff, and J. W. Prichard, *Proc. Natl. Acad. Sci. USA*, 1983, **80**, 4945.
16. D. G. Gadian, E. Proctor, S. R. Williams, E. B. Cady, and R. M. Gardiner, *Magn. Reson. Med.*, 1986, **3**, 150.
17. S. M. Fitzpatrick, H. P. Hetherington, K. L. Behar, and R. G. Shulman, *J. Neurochem.*, 1989, **52**, 741.
18. T. E. Bates, S. R. Williams, R. A. Kauppinen, and D. G. Gadian, *J. Neurochem.*, 1989, **53**, 102.
19. D. K. Bosman, N. E. P. Deutz, A. A. de Graaf, R. W. M. Hulst, H. M. H. van Eijk, W. M. M. J. Bovee, M. A. W. Maas, G. G. A. Jorning, and R. A. F. M. Chamuleau, *Hepatology*, 1990, **12**, 281.
20. R. E. Brenner, P. M. G. Munro, S. C. R. Williams, J. D. Bell, G. J. Barker, C. P. Hawkins, D. N. Landon, and W. I. McDonald, *Magn. Reson. Med.*, 1993, **29**, 737.
21. N. E. Preece, D. Baker, C. Butter, D. G. Gadian, and J. Urenjak, *NMR Biomed.*, 1993, **6**, 194.
22. K. L. Behar and D. Boehm, *J. Cereb. Blood Flow Metab.*, 1991, **11**, Suppl. 2, 5783.
23. N. E. Preece, S. R. Williams, G. Jackson, J. S. Duncan, J. Houseman, and D. G. Gadian, *Proc. Xth Ann Mtg. Soc. Magn. Reson. Med.*, San Francisco, 1991, p. 1000.
24. K. L. Behar and T. Ogino, *Magn. Reson. Med.*, 1993, **30**, 38.
25. R. A. Kauppinen, T. Niskanen, J. Hakumaki, and S. R. Williams, *NMR Biomed.*, 1993, **6**, 242.
26. D. G. Gadian, 'Nuclear Magnetic Resonance and its Applications to Living Systems', Oxford University Press, Oxford, 1995.
27. T. Ebisu, W. D. Rooney, S. H. Graham, Z. Wu, M. W. Weiner, and A. A. Maudsley, *Proc. XIIth Ann Mtg. Soc. Magn. Reson. Med.*, New York, 1993, p. 513.
28. L. O. Sillerud and R. G. Shulman, *Biochem. J.*, 1983, **221**, 1087.
29. B. Kunnecke, S. Cerdan, and J. Seelig, *NMR Biomed.*, 1993, **6**, 264.
30. D. L. Rothman, K. L. Behar, H. P. Hetherington, M. R. Bendall, O. A. C. Petroff, and R. G. Shulman, *Proc. Natl. Acad. Sci., USA*, 1985, **82**, 1633.
31. G. F. Mason, D. L. Rothman, K. L. Behar, and R. G. Shulman, *J. Cereb. Blood Flow Metab.*, 1992, **12**, 434.
32. N. A. Lassen and J. Astrup, in 'Protection of the Brain from Ischemia', eds. P. R. Weinstein and A. I. Faden, Williams and Wilkins, Baltimore, MD, 1990, p. 7.
33. H. A. Crockard, D. G. Gadian, R. S. J. Frackowiak, E. Proctor, K. Allen, S. R. Williams, and R. W. Russell, *J. Cereb. Blood Flow Metab.*, 1987, **7**, 394.
34. K. L. Allen, A. L. Busza, E. Proctor, M. D. King, S. R. Williams, H. A. Crockard, and D. G. Gadian, *NMR Biomed.*, 1993, **6**, 181.
35. H. Naritomi, M. Sasaki, M. Kanashiro, M. Kitani, and T. Sawada, *J. Cereb. Blood Flow Metab.*, 1988, **8**, 16.
36. S. M. Eleff, Y. Maruki, L. H. Monsein, R. J. Traystman, R. N. Bryan, and R. C. Koehler, *Stroke*, 1991, **22**, 233.
37. J. Pekar, L. Ligeti, Z. Ruttner, T. Sinnwell, C. T. W. Moonen, and A. C. McLaughlin, *Proc. Xth Ann Mtg. Soc. Magn. Reson. Med.*, San Francisco, 1991, p. 149.
38. M. E. Moseley, Y. Cohen, J. Mintorovitch, L. Chileuitt, H. Shimizu, J. Kucharczyk, M. F. Wendland, and P. R. Weinstein, *Magn. Reson. Med.*, 1990, **14**, 330.
39. A. L. Busza, K. L. Allen, M. D. King, N. van Bruggen, S. R. Williams, and D. G. Gadian, *Stroke*, 1992, **23**, 1602.

Biographical Sketch

David G. Gadian. *b* 1950. B.A. (Physics), 1971, D. Phil., 1975, University of Oxford, UK (supervisor Rex Richards). Postdoctoral research with Rex Richards and George Radda in Oxford. Moved in 1983 to the Royal College of Surgeons in London. Currently Rank Professor of Biophysics and Head of the RCS Unit of Biophysics and of the Radiology and Physics Unit at the Institute of Child Health, London. Approx. 140 publications. Research interests: development and application of magnetic resonance techniques for noninvasive investigation of brain metabolism and physiology.

Animal Models of Stroke Studied by MRI

Mark F. Lythgoe and David G. Gadian

Royal College of Surgeons Unit of Biophysics, Institute of Child Health, London, UK

1 INTRODUCTION

This chapter describes the development and adaptation of the various animal models of stroke for use with MRI and MRS. The evolution of animal models for use with MR systems has been driven by the introduction of new MR techniques and by the increasing awareness of the role of these techniques in investigating the pathophysiology and treatment of stroke.

Early research in this area used in vitro MRS of cortical and white matter tissue to investigate cerebral edema and demonstrated the potential applicability of MR for the noninvasive detection of human stroke.[1] With the advent of imaging systems in the early 1980s and the development of animal models for in vivo research, regional changes in T_1 and T_2 were observed in animal models several hours following the initial insult.[2] During this time, in vivo MRS was used to follow changes in high-energy phosphates, inorganic phosphate, intracellular pH, lactate, and changes in Na^+ distribution in various animal models of ischemia, anoxia, and hypoxia.[3] From these early experiments it became apparent that NMR, together with other techniques such as specific gravity measurements or histology, is well suited for use in the investigation and characterization of stroke.[4] Later in the 1980s, more elaborate experiments were designed, permitting the simultaneous acquisition of cerebral blood flow (CBF) and MRS data for the determination of CBF thresholds in cerebral ischemia.[5] These experiments were carried out by producing graded ischemia during the MR investigation using a remote-controlled method for gradually reducing the CBF through a series of desired levels. This novel model was subsequently used to demonstrate the relationship between diffusion-weighted imaging, energy metabolism, and CBF (Figure 1).[6,7] Even though MR systems place constraints on methodology through the confined space of the magnet bore, simultaneous physiological monitoring of electrical activity, blood gases, and blood pressure was found to be feasible.[8]

The introduction of new MRI techniques such as diffusion-weighted imaging[9] which allows the investigation of a stroke within minutes of the initial event, led to the modification of animal models to take advantage of this information about hyperacute changes. This type of animal model required remote-controlled access, that is, the ability to modulate the animal physiology from outside the MR system; this is perhaps the most challenging of adaptations (see Section 3).[10,11] Recent developments include the application of optical techniques for noninvasive cerebral metabolic monitoring and histological studies in conjunction with MR.[12] Near-infrared spectroscopy can be used to monitor hemoglobin oxygenation, the oxidation state of cytochromes, and cerebral blood volume. Laser Doppler flowmetry is used for the noninvasive measurement of CBF, and invasive bioluminescence techniques may be used to monitor metabolic disturbances. All of these methods have been interfaced with animal models of stroke and MR.[13–15]

Since the mid-1980s comprehensive reviews have described the numerous possible animals models in the investigation of cerebral ischemia.[16–20] Further, the relevance of these animal models to human disease has also been considered;[21–23] consequently, this area is not a focus for discussion in this article.

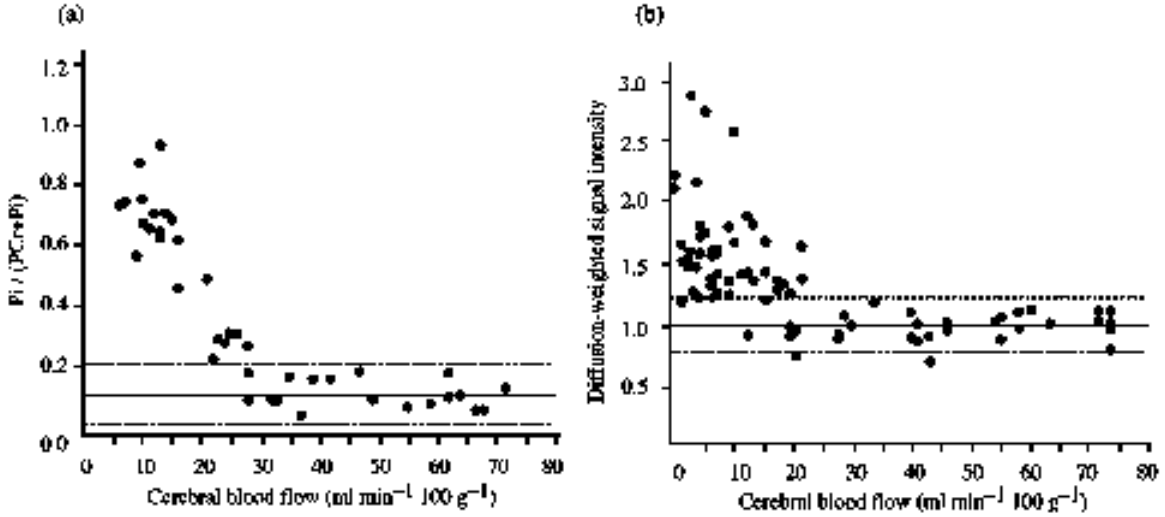

Figure 1 Remote-controlled graded ischemia produced using a snare system around both common carotid arteries in a Mongolian gerbil model. This animal model was developed to investigate the relationship between cerebral blood flow (CBF), measured with a H_2 clearance technique, diffusion-weighted MRI, and energy metabolism. CBF thresholds are similar for diffusion and for changes in Pi/(PCr+Pi). This suggests that the depletion of high-energy phosphates, leading to energy failure and an inevitable accumulation of intracellular osmotically obliged water (cytotoxic edema), results in a diffusion change through the redistribution of the water molecules. (Kindly provided by Dr Albert Busza)

The following sections contain an overview of the most widely used small animal models for MR investigations of stroke, including a discussion of the early work and subsequent modifications of these techniques for MR use.

2 FROM THE BENCH TO THE MR SYSTEM

Experimental models of cerebral ischemia may be broadly classified into global or focal models, which may, in turn, be permanent or reversible in nature. In deciding which animal model should be used to test a hypothesis, the MR researcher must take into account issues that may not be a consideration when experimenting 'on the bench'. When choosing an animal model, the investigator must consider aspects of the MR system such as the bore size of the magnet and access to the animal once it is positioned in the magnet. Another consideration is whether the magnet is horizontal or vertical, which may influence the physiology of the animal, although this is becoming less of an issue as more and more researchers use dedicated horizontal systems. Issues of temperature and its control, together with the physiological monitoring and administration of anesthetics, can also be difficult to address and must be taken into account during experimental design.

Once the choices between global and focal models, and between different animal species have been made, the issue of whether to induce the insult outside the magnet arises and whether the insult is to be treated or reversed from within the magnet. Initial experimental MR studies of stroke required that, following acquisition of the preischemia data, the animal was removed from the magnet so that the lesion could be induced on the bench, after which the animal was then replaced and the post-insult data were acquired. Improvements in design that permit remote access have allowed the investigation of the pathological consequences of the stroke immediately following the insult and have allowed direct comparison with control images without the need for image registration. This, of course, is not possible with all procedures, but the advantages are clear if remote access is achieved.

To acquire data within the MR scanner, the animal should be immobilized in a nonmagnetic probe with ear and bite bars rather like a stereotactic head holder, allowing the head to be positioned relative to the gradient coils to attain the correct imaging slice or region of interest. In MR magnets with a small bore, the use of ear and bite bars may not be possible, in which case the skull may be glued directly to the probe to reduce movement artefacts.[24] Temperature control is commonly attained through the use of warm air blown over the animal, an electrically heated mat, or warm water jacket or mat. Animals are readily anesthetized by administration of anesthetics through a nose cone for spontaneously breathing rats, by intraperitoneal injection, or by mechanical ventilation. Physiological monitoring of electrocardiographs (ECG) and respiration rate may be performed simultaneously using implanted chest electrodes.[25] Blood pressure is conventionally monitored using an intra-arterial line or, more recently, a piezo-electric pulse transducer.[26] Intravenous lines may be inserted for blood gas measurements or administration of drugs. Nonmagnetic graphite electrodes, which reduce susceptibility effects, may be used for electroencephalography (EEG).[11]

3 FOCAL ISCHEMIA

A number of experimental models of focal ischemia have been developed, including permanent, reversible, and partial occlusions (Table 1).

3.1 Permanent Middle Cerebral Artery Occlusion

Rats with permanent occlusion of the middle cerebral artery (MCA) are frequently used for exploring the pathogenesis of infarction and for the evaluation of new therapeutic agents.[54] In 1975, Robinson et al. developed a model of MCA occlusion in the rat in which the MCA was coagulated distal to the rhinal fissure, the procedure being performed through a craniotomy.[55] To improve the reproducibility of this model, Tamura et al. adopted a subtemporal approach in which the proximal MCA was occluded between the rhinal branch and the lateral striate arteries in Sprague-Dawley rats.[31] A less surgically demanding procedure was described by Chen et al., involving a more distal occlusion of the MCA above the rhinal fissure, coupled with permanent ipsilateral and temporary contralateral occlusion of the common carotid arteries (CCA).[56] Several modifications of the above model have been described in conjunction with occlusion of the MCA to increase reproducibility further, such as MCA occlusion following a brief period of hypotension[57] or permanent occlusion of the ipsilateral CCA.[58] The advantages of this type of model include its reproducible nature[16] and the ease of adaptation for MR use. However, as the occlusion is performed on the bench, the early stage of ischemia is lost because of the time taken to place the animal in the MR system from the bench, and the shimming and MR setup period. Permanent occlusion of the MCA may also be performed using the intraluminal suture approach, which has been used extensively with MR, as described below (Figure 2).[59]

3.2 Reversible Middle Cerebral Artery Occlusion

Permanent MCA occlusion models do not permit the investigator to monitor the effects of reperfusion following the initial insult. To address this problem, experimenters have developed a number of methods for occluding and reperfusing the MCA.

In 1985, Shigeno et al. placed a snare ligature around the stem of the MCA in a rat model, just distal to the lenticulostriate branches, and by pulling and releasing the thread, they occluded then reperfused the MCA.[60] This technique and many of the above are very invasive, requiring craniotomy, durotomy, and arachnoid incision, with associated drainage of cerebrospinal fluid and altered intracranial pressure. The next section describes a rat model of reversible MCA occlusion that avoids many of the above disadvantages. This type of model is now used with MR to investigate the early changes following cerebral ischemia.

In 1986, Koizumi et al. developed a new reversible focal ischemic model.[27] The MCA was occluded by a silicone rubber cylinder attached to a thread inserted through the internal carotid artery in Wistar rats. Recirculation was accomplished by pulling the thread out of the artery. This model has the advantage of avoiding craniotomy and has an important role in MR investigations of ischemia. The intraluminal thread method of

Table 1 Focal models of ischemia

Method of occlusion	Species	Remote/reversible	References	
			On bench occlusion	MR examples
Occlusion of the middle cerebral artery				
Intraluminal occlusion				
Suture	Rat	Rev	27	40
Suture	Mouse		28	41
Suture (remote)	Rat	Remote/rev	27	10
Silicon cylinder	Rat		29	42
Transorbital				
Balloon occluder	Cat	Remote/rev	30	43
Coagulation	Pig			44
Transcranial				
Coagulation	Rat		31	45
Coagulation	Mouse		32	46
Embolization				
Autologous blood clots	Rat	Remote/rev	33	47
Photothrombosis	Rat		34	48
Vasospastic occlusion with endothelin-1	Rat	Rev	35	49
Occlusion of the common carotid arteries				
Unilateral occlusion	Gerbil		36	4
Bilateral snares, graded	Gerbil	Remote/rev	36	6
Unilateral plus hypoxia	Rabbit	Rev	37	50
Unilateral plus hypoxia	Rat	Remote/rev	37	51
Unilateral plus hypoxia	Neonatal rat	Remote/rev	38	52
Both arteries, silicon cylinder	Rat		39	53

Suture, intraluminal thread (nylon monofilament), which may be coated and retractable; remote, insult may be performed from outside the magnet; rev, mechanism for insult may be reversed to control state; graded, insult may be performed in a controlled graded fashion; coagulation, electrocoagulation of vessel.

occlusion was later modified by Zea Longa et al. using a blunted nylon monofilament, in an attempt to increase reproducibility.[61]

In one study comparing these two techniques, it was suggested that there were differences in the levels of reduced CBF on occlusion, and that the Koizumi method was more reliable than that of Zea Longa.[62] However, other investigators have not supported these conclusions. The discussions for these variations focused on the degree of silicone coating of the thread, the filament size and length, and the body weight of animals.[63,64] It is interesting to note that, when comparing two uncoated 4-0 nylon monofilaments from different manufacturers, subtle differences in material and diameter resulted in variations in the final infarct size following MCA occlusion.[65] There is still much debate as to whether to coat the suture and what coating to use; one investigator has suggested that a simple coating of poly-*l*-lysine can reduce interanimal variability and increase infarct size.[66]

Two recent studies have investigated, at some length, the intraluminal suture model. Li et al., using a silicone-coated 4-0 nylon occluder adapted for remote occlusion during MRI (see below), achieved successful occlusions in 88% of animals without subarachnoid hemorrhage.[67] The failures included preocclusion damage (1/67), occluding device sliding out of the outer holding catheter (1/67), no occlusion (2/67), and arterial perforation (4/67). The other critical evaluation of the suture method, by Schmid-Elsaesser et al., indicated that a 4-0 silicone-coated suture, when compared with a 3-0 uncoated suture, produced less subarachnoid haemorrhage (8% compared with 30%).[68] However, with both these types of suture, premature reperfusion occurred in the first minutes of MCA occlusion in approximately 25% of studies, and this contributed to variability in the lesion size. Consequently, institutions using equivalent methods observe different lesion variability, which indicates the difficulty with these methods. One cannot overestimate the lengths to which a researcher must go in order to standardize the intraluminal MCA occlusion technique.

3.3 Use of Reversible Middle Cerebral Artery Occlusion with MRI

The advantage of the suture technique is that it allows remote-controlled occlusion (Figure 2) and reperfusion of the MCA from outside the magnet. Remote occlusion is essential to investigate the hyperacute MR changes postocclusion and also to allow a direct comparison of pre- and postocclusion image data.[67,69] This technique was adapted for MR use by Roussel et al. using a 2×0.25 mm silicon embolus on a nylon thread,[69] by Kohno et al. using a 3-0 monofilament coated with glue,[11] and, more recently, by Li et al. using a silicon-coated 4-0 monofilament.[67] This early work was performed in large horizontal bore imaging magnets and has been further modified for remote MCA occlusion studies in a 5 cm diameter bore vertical 8.5 T magnet.[59] This is not a trivial experiment but, as shown by Li et al., successful occlusion can be achieved in 88% of animals studied.[67]

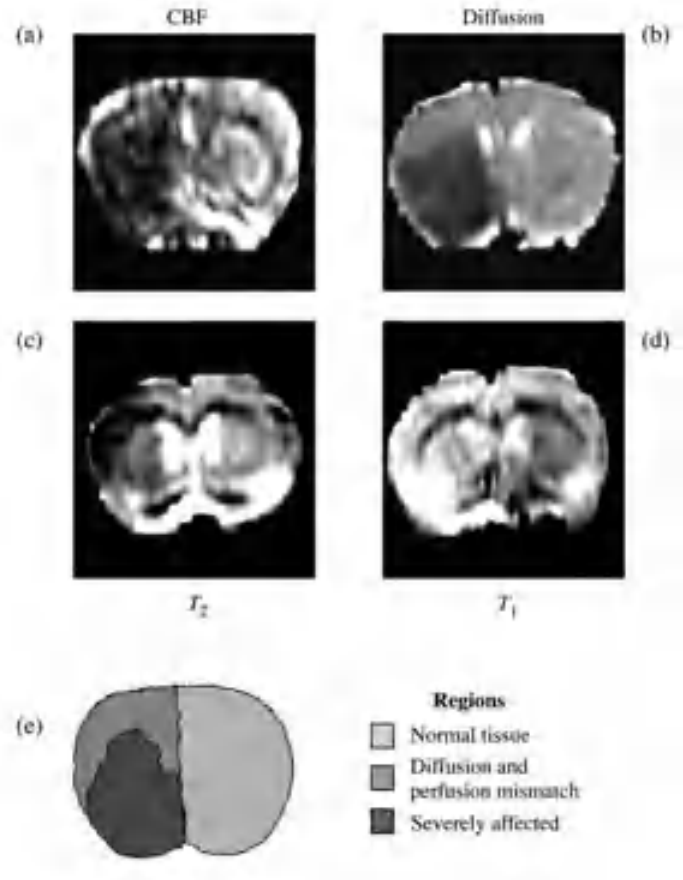

Figure 2 Remote-controlled permanent intraluminal suture occlusion of the middle cerebral artery allows MR images to be acquired throughout the acute period. (a) A map of cerebral blood flow (CBF) (measured using arterial spin labeling) with reduced flow in the occluded side (acquired 12 min postocclusion). (b) The apparent diffusion coefficient of water (25 min postocclusion) with a region of reduced diffusion indicating the area of cytotoxic edema. (c) A T_2 map (1 min postocclusion) with a region of reduced T_2. (d) A T_1 map (5 min postocclusion), with a region of increased T_1. (e) Schematic representation of the three main areas: 'normal tissue'; 'diffusion and perfusion mismatch area', with reduced CBF but normal diffusion; and 'severely affected area', in which both the CBF and diffusion were significantly reduced. (Kindly provided by Mr Fernando Calamante)

3.4 Incomplete or Partial Occlusion

Models of focal oligemia are not common, although they are finding increasing use in the investigation of the pathophysiology of penumbra, in which regions of oligemic misery perfusion are present.[70] The aim of these experimental models is to produce a large focal lesion in which the CBF is moderately reduced throughout the MCA territory (see Table 4). The degree of reduction in CBF is dependent upon the method used and the degree of stenosis or partial occlusion. In 1994, Derugin et al. developed a reversible MCA stenosis.[85] More recently, a rat model was developed for MR use in which a combination of hypotension (induced by placing the rat vertically) and electrocoagulation of the distal MCA produced a focal hypoperfusion lesion.[86] However, only the first of these models allows reperfusion to take place and neither permits occlusion from outside an MRI scanner to observe the hyperacute phase following occlusion. To avoid these problems, Thomas et al. developed a model based on the intraluminal suture method that used an undersize suture to produce a partial obstruction of the MCA and a moderate reduction in CBF throughout the MCA territory (Figure 3).[87]

3.5 Focal Lesion: Other Methods

Further methods of inducing focal ischemia that avoid a craniotomy include injection of homologous blood clot fragments[47] and intraluminal occlusion with a silicon cylinder.[39,42] Another method for producing focal infarction is the injection of rose bengal dye, followed by photochemical activation to induce focal thrombosis and cerebral ischemia.[48] This model has the advantage of being relatively noninvasive, as well as providing several cerebral locations for the placement of the lesion, although it does result in microvascular injury. Focal cerebral ischemia can also be induced using a local application of endothelin-1, a vasoconstrictive agent, which produces a blood flow decrease with a half-time of 45 to 60 min.[35] An animal model of subarachnoid hemorrhage has been produced using modification of the intraluminal suture model, which allows perforation of the circle of Willis and subsequent production of the hemorrhage (Table 3). This technique may be performed remotely and therefore monitored from the hyperacute phase onwards using MR.[88,89]

4 GLOBAL ISCHEMIA

Cardiac arrest has been extensively employed for the study of the pathological consequences of global ischemia and reperfusion (see Table 2).[20] Fischer et al. have extended this work for MR and demonstrated the feasibility of resuscitation following cardiac arrest within the magnet, thus enabling them to follow cerebral events during reperfusion.[83] As well as the cardiac arrest models, there are essentially three commonly used small animal models of global cerebral ischemia for use with MR, two in the rat and one in the gerbil. The four-vessel occlusion model in the rat produces global ischemia, while the other two models induce a bilateral forebrain ischemia. Global insults may also have both a hypoxic and ischemic component. With the aim of modeling human birth asphyxia, Thornton et al. have recently described the temporal and anatomical variation of the cerebral apparent diffusion coefficient (ADC) of water, following a hypoxic/ischemic insult in a piglet model (Figure 4).[92]

4.1 Four-vessel Occlusion Model

In 1979, Pulsinelli and Brierley introduced the four-vessel occlusion model of reversible ischemia in rats.[74] Modifications by the same group increased the proportion of successful studies.[95] Briefly, on the day before the experiment, atraumatic clasps are placed loosely around both CCAs, and the vertebral arteries are electrocauterized through the foramen alar in the first cervical vertebra. Global ischemia is induced by tightening the sutures around the CCAs. A period of between 10 and 30

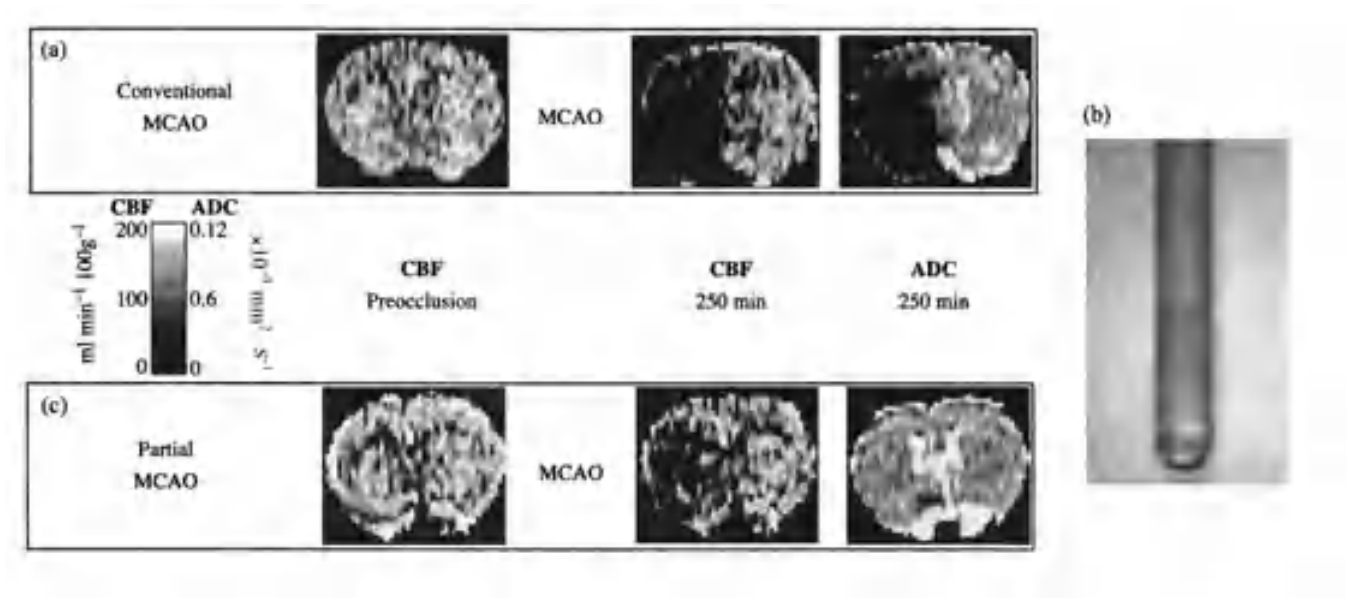

Figure 3 Intraluminal suture to produce partial and complete middle cerebral artery occlusion (MCAO). (a) Conventional MCAO in the rat using a 0.24 mm diameter nylon monofilament. Following occlusion there is a concomitant CBF and apparent diffusion coefficient (ADC) decline. (b,c) Partial occlusion of the middle cerebral artery using an undersized embolus (0.2 mm) with a bullet-shaped tip induces a moderate CBF decrease without ADC decrease

min of ischemia, followed by reperfusion, produces cell changes that provide evidence of selective vulnerability and delayed neuronal damage.[96] This technique has been used quite extensively with MR for both single and repeated occlusions,[81] and also to produce graded ischemia.[82]

4.2 Gerbil Bilateral Common Carotid Occlusion Model

In most animals, as in humans, occlusion of the CCAs will not produce ischemia. In 1966, Levin and Payen demonstrated that in gerbils there was an anomaly in the circle of Willis such that unilateral occlusion of the CCAs resulted in ipsilateral forebrain ischemia in 40% of the animals.[36] The anomaly involved the absence of the posterior communicating arteries, which connect the anterior and posterior circulation to the brain. Subsequently, it was demonstrated that almost all gerbils exhibited neurological signs of ischemia if both CCAs were ligated. This method of occlusion has been used for both single (Figure 5)[97] and graded[6] occlusion MR experiments. Early work using this model demonstrated regions of delayed tissue

Table 2 Global models in which cerebral blood flow is reduced

Method of occlusion	Species	Remote/reversible	References	
			Non-MR models	MR examples
Occlusion of the common carotid arteries				
Bilateral, remote	Gerbil	Remote/rev	71	77
Bilateral, graded	Gerbil	Remote/rev	71	7
Plus hypotension	Cat	Remote/rev	72	78
Plus hypoxia	Neonatal pig	Remote/rev		79
Occlusion of innominate and left subclavian, remote	Cat	Remote/rev	73	80
Occlusion of common carotid and vertebral arteries				
Bilateral carotid arteries, remote	Rat	Remote/rev	74	81
Bilateral carotid arteries, graded	Rat	Remote/rev	74	82
Cardiac arrest				
Fibrillation, remote	Cat	Remote/rev	75	83
With KCl	Cat	Remote		78
With KCl	Neonatal rat	Remote	76	84
Anoxia	Rat	Remote		10

See Table 1 for definition of terms.

Table 3 Other models for ischemia

Method of occlusion	Species	Remote/reversible	References	
			On bench	MR examples
Secondary energy failure				
MCA ligation plus CCAs	Rat	Rev	56	90
MCA suture occlusion	Rat	Remote/rev	27	91
Unilateral CCA plus hypoxia	Rat	Remote/rev	37	51
Unilateral CCA plus hypoxia	Neonatal rat	Remote/rev	38	52
Occlusion of CCAs/hypoxia	Piglet	Remote/rev		92
Occlusion of CCAs	Gerbil	Remote/rev	36	100
Subarachnoid hemorrhage				
Perforation of the circle of Willis	Rat	Remote	89	88

MCA, middle cerebral artery; CCA, common carotid artery; for other terms see Table 1.

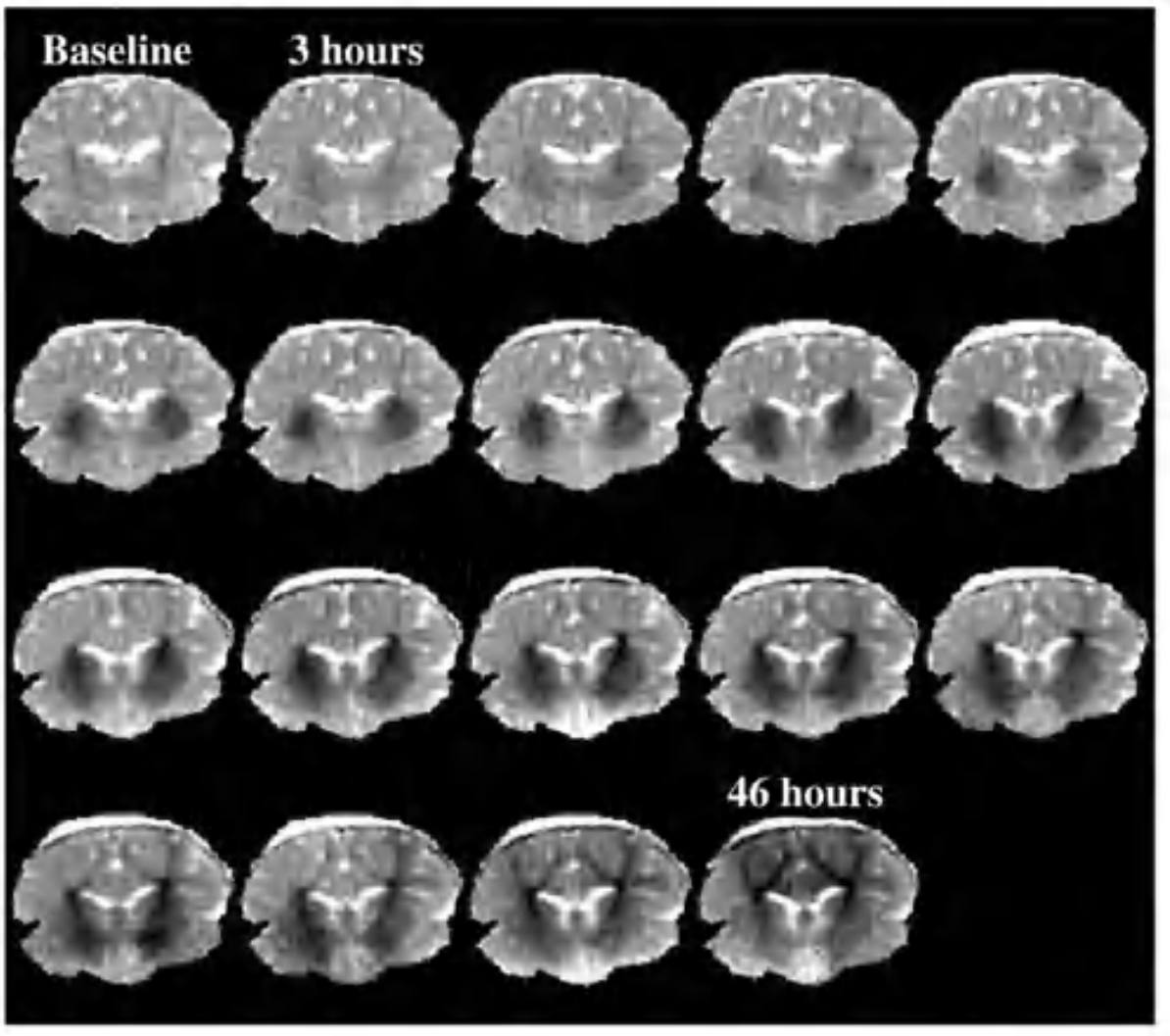

Figure 4 Coronal diffusion images (apparent diffusion coefficient maps) following a global hypoxic/ischemic insult and recovery in a piglet model of perinatal asphyxia. The initial diffusion change is limited to the basal ganglia and subsequently expands with time, apparently coincident with major white matter tracts. (Kindly provided by Dr John Thornton and Professor Roger Ordidge)

Table 4 Oligemic models of reduced cerebral blood flow

Method of occlusion	Species	Remote/reversible	References	
			On bench	MR examples
Occlusion of the middle cerebral artery				
Suture remote	Rat	Remote/rev	27	87
Stenosis	Cat	Rev	30	85
Coagulation and hypotension	Rat		56	86
Hypotension				
Hemorrhagic hypotension	Piglet	Remote/rev	93	94

See Table 1 for definition of terms.

damage following a brief period of bilateral CCA occlusion.[98] More recently, early subtle changes in diffusion imaging have been observed in regions known to present with delayed damage, indicating the gradual evolution of these lesions (Figure 6; Table 3).[99–101]

4.3 Rat Two-vessel Occlusion Model

This type of model is not commonly used by MR researchers, although it is technically easier to perform than the four-vessel model. Due to the intact circle of Willis in the rat, bilateral occlusion of the CCAs must be combined with systemic hypotension to produce reversible ischemia.[18] Hypotension is induced by bleeding[102] or with the administration of trimethaphan or phentramine.[103] This model is influenced by the need to monitor and correct for alterations in systemic hypotension, which may limit its applicability to MR studies.

4.4 Graded Global Ischemia

The methods for occlusion that have been mentioned so far do not provide any flexibility in the level of reduction of CBF. The degree of ischemia is primarily dependent on the vessel occluded, the quality of occlusion, and the collateral supply to that region. Most types of intervention give little or no control over the level of the induced ischemia. Controllable graded ischemia, however, allows investigation of cerebral tissue at the desired level of CBF. Using a gerbil model, Allen et al. have placed adjustable snares around the CCAs that can be tightened to decrease the internal diameter of the CCAs, thereby reducing the flow to the forebrain.[6] Forebrain blood

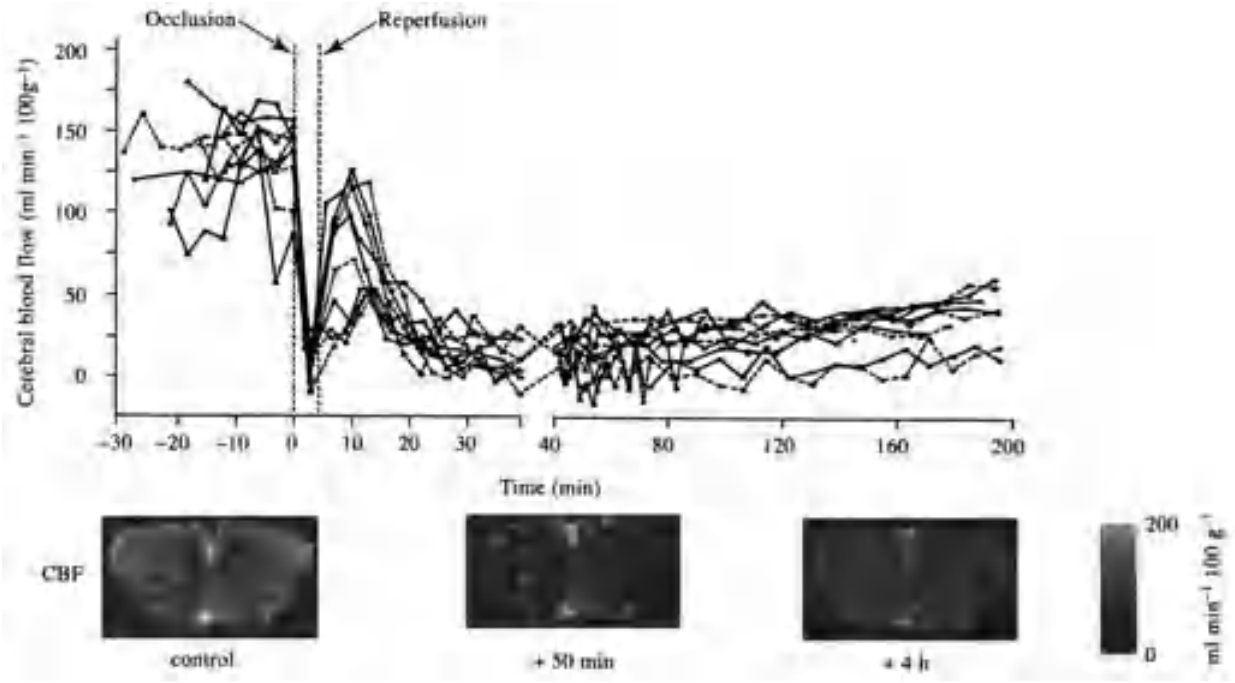

Figure 5 Forebrain ischemia induced for 5 min via remote-controlled bilateral carotid artery occlusion in a gerbil. Noninvasive MR measurement of cerebral blood flow using an arterial spin labeling technique demonstrated a prolonged and delayed hypoperfusion following reperfusion. (Kindly provided by Dr Gaby Pell)

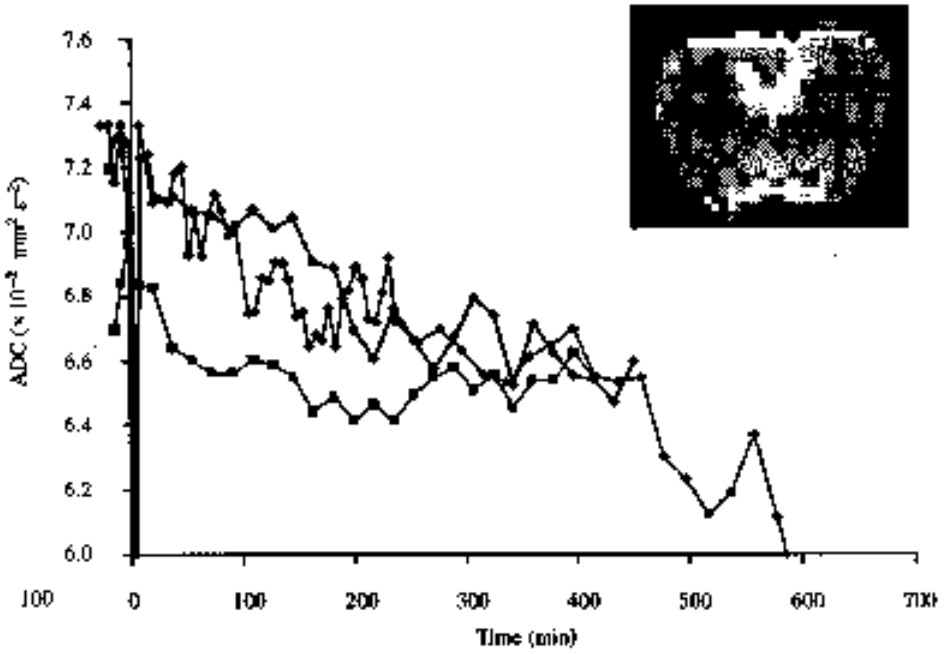

Figure 6 Diffusion (apparent diffusion coefficient, ADC) images over 10 h following 5 min of bilateral common carotid artery occlusion in three gerbils; one representative image is shown. The region of diffusion change in the image is localized to the lateral portion of the striatum, which is an area known to present with delayed tissue damage.[101] In this region a gradual diffusion decrease is observed throughout the reperfusion period

flows ranging from 80 to 8 ml min^{-1} per 100 g tissue are attainable with this method (see Figure 1).

5 CONCLUSION

Adaptation of some animal models for use with MRI is a relatively simple practice, while for others that require remote access it is technically more demanding. The ability of MR to follow time courses in single animals has promoted the development of new animal models in which data can be acquired before and after the insult without removing the animal from the magnet. The development of a range of physiological MRI techniques, including diffusion, perfusion and T_2*-weighted imaging, as well as various MRS approaches, provides new opportunities for understanding the evolving pathophysiology of lesions in these models and for evaluating novel forms of therapy.

6 RELATED ARTICLES

Anisotropically Restricted Diffusion in MRI; Cerebral Perfusion Imaging by Exogenous Contrast Agents; Ischemic Stroke; Methods and Applications of Diffusion MRI.

7 REFERENCES

1. K. Gwan and H. T. Edzes, *Arch Neurol.*, 1975, **32**, 462.
2. N. van Bruggen, T. P. Roberts, and J. E. Cremer, *Cerebrovasc. Brain Metab. Rev.*, 1994, **6**, 180.
3. S. R. Williams, H. A. Crockard, and D. G. Gadian, *Cerebrovasc. Brain Metab. Rev.*, 1989, **1**, 91.
4. K. R. Thulborn, G. H. du Boulay, L. W. Duchen, and G. K. Radda, *J. Cereb. Blood Flow Metab.*, 1982, **2**, 299.
5. D. G. Gadian, R. S. Frackowiak, H. A. Crockard, E. Proctor, K. L. Allen, S. R. Williams, and R. W. Ross Russell, *J. Cereb. Blood Flow Metab.*, 1987, **7**, 199.
6. K. L. Allen, A. L. Busza, E. Proctor, M. D. King, S. R. Williams, H. A. Crockard, and D. G. Gadian, *NMR Biomed.*, 1993, **6**, 181.
7. A. L. Busza, K. L. Allen, M. D. King, N. Van Bruggen, S. R. Williams, and D. G. Gadian, *Stroke*, 1992, **23**, 1602.
8. H. Naritomi, M. Sasaki, M. Kanashiro, M. Kitani, and T. Sawada, *J. Cereb. Blood Flow Metab.*, 1988, **8**, 16.
9. M. E. Moseley, Y. Cohen, J. Mintorovitch, L. Chileuitt, H. Shimizu, J. Kucharczyk, M. F. Wendland, and P. R. Weinstein, *Magn. Reson. Med.*, 1990, **14**, 330.
10. S. A. Roussel, N. van Bruggen, M. D. King, and D. G. Gadian, *J. Cereb. Blood Flow Metab.*, 1995, **15**, 578.
11. K. Kohno, T. Back, M. Hoehn-Berlage, and K. A. Hossmann, *Magn. Reson. Imaging*, 1995, **13**, 65.
12. M. Hoehn-Berlage, *NMR Biomed.*, 1995, **8**, 345.
13. S. Punwani, R. J. Ordidge, C. E. Cooper, P. Amess, and M. Clemence, *NMR Biomed.*, 1998, **11**, 281.
14. M. Hoehn-Berlage, D. G. Norris, K. Kohno, G. Mies, D. Leibfritz, and K. A. Hossmann, *J. Cereb. Blood Flow Metab.*, 1995, **15**, 1002.
15. O. Kloiber, T. Miyazawa, M. Hoehn-Berlage, and K. A. Hossmann, *NMR Biomed.*, 1993, **6**, 144.
16. M. D. Ginsberg and R. Busto, *Stroke*, 1989, **20**, 1627.
17. K. A. Hossman, *Cerebrovasc. Dis.*, 1991, **1**, 2.
18. S. Takaizawa, A. M. Hakim, *Cerebrovasc. Dis.*, 1991, **1**, 16.
19. T. L. C. Luvisotto and G. R. Sutherland, in 'Magnetic Resonance Spectroscopy and Imaging in Neurochemistry', eds. H. Batchelard, Plenum Press, New York, 1997, p. 117.

20. K. A. Hossmann, *Cardiovasc. Res.*, 1998, **39**, 106.
21. D. O. Wiebers, H. P. Adams, and J. P. Whisnant, *Stroke*, 1990, **21**, 1.
22. J. A. Zivin and J. C. Grotta, *Stroke*, 1990, **21**, 981.
23. C. Millikan, *Stroke*, 1992, **23**, 795.
24. M. F. Lythgoe, A. L. Busza, F. Calamante, C. H. Sotak, M. D. King, A. C. Bingham, S. R. Williams, and D. G. Gadian, *Magn. Reson. Med.*, 1997, **38**, 662.
25. N. Van Bruggen, J. Syha, A. L. Busza, M. D. King, G. W. H. Stamp, S. R. Williams, and D. G. Gadian, *Magn. Reson. Med.*, 1990, **15**, 121.
26. R. E. Widdop, and X. C. Li, *Clin. Sci.*, 1997, **93**, 191.
27. J. Koizumi, Y. Yoshida, T. Nakazawa, and G. Ooneda, *Jpn J. Stroke*, 1986, **8**, 1.
28. E. S. Connolly, C. J. Winfree, D. M. Stern, R. A. Solomon, and D. J. Pinsky, *J. Neurosurg.*, 1996, **38**, 523.
29. J. H. Turner, *Stroke*, 1975, **6**, 703.
30. M. D. O'Brien and A. G. Waltz, *Stroke*, 1973, **4**, 201.
31. A. Tamura, D. I. Graham, J. McCulloch, and G. M. Teasdale, *J. Cereb. Blood Flow Metab.*, 1981, **1**, 53.
32. F. C. Barone, D. J. Knudsen, A. H. Nelson, G. Z. Feuerstein, and R. N. Willette, *J. Cereb. Blood Flow Metab.*, 1993, **13**, 683.
33. M. Kudo, A. Aoyama, S. Ichimori, and N. Fukunaga, *Stroke*, 1982, **13**, 505.
34. B. D. Watson, W. D. Dietrich, R. Busto, M. S. Wachtel, and M. D. Ginsberg, *Ann. Neurol.*, 1995, **17**, 497.
35. J. Sharkey, I. M. Ritchie, and P. A. Kelly, *J. Cereb. Blood Flow Metab.*, 1993, **13**, 865.
36. S. Levine and H. M. Payne, *Exp. Neurol.*, 1966, **16**, 255.
37. S. Levine, *Am. J. Pathol.*, 1960, **36**, 1.
38. P. Andine, M. Thordstein, and L. Kjellmer, *Thromb. Res.*, 1990, **35**, 253.
39. T. Takeda, T. Shima, Y. Okada, S. Matsumura, Y. Nishi, and T. Uozumi, *J. Cereb. Blood Flow Metab.*, 1987, **7**, S66.
40. J. Mintorovitch, M. E. Moseley, L. Chileuitt, H. Shimizu, Y. Cohen, and P. R. Weinstein, *Magn. Reson. Med.*, 1991, **18**, 39.
41. R. Hata, G. Mies, C. Wiessner, K. Fritze, D. Hesselbarth, G. Brinker, and K. A. Hossmann, *J. Cereb. Blood Flow Metab.*, 1998, **18**, 367.
42. E. Busch, C. M., Kerskens, and M. Hoehn-Berlage, *Proc. Vth Annu. Mtg. (Int.) Soc. Magn. Reson. Med.*, Vancouver, 1997, **1**, 599.
43. A. J. de Crispigny, M. F. Wendland, N. Derugin, E. Kozniewska, and M. E. Moseley, *Magn. Reson. Med.*, 1992, **27**, 391.
44. L. Rohl, L. Ostergaard, M. Sakoh, C. Z. Simonsen, P. Vestergaard-Poulsen, R. Sangil, H. Stodkilde-Jorgensen, and C. Gyldensted, *Proc. VIIth Annu. Mtg. (Int.) Soc. Magn. Reson. Med.*, Philadelphia, 1999, **2**, 453.
45. R. A. Knight, R. J. Ordidge, J. A. Helpern, M. Chopp, L. C. Rodolosi, and D. Peck, *Stroke*, 1991, **22**, 802.
46. M. D. King, J. Houseman, D. G. Gadian, and A. Connelly, *Magn. Reson. Med.*, 1997, **38**, 930.
47. Q. Jiang, R. L. Zhang, Z. G. Zhang, J. R. Ewing, G. W. Divine, and M. Chopp, *J. Cereb. Blood Flow Metab.*, 1998, **18**, 758.
48. N. van Bruggen, B. M. Cullen, M. D. King, M. Doran, S. R. Williams, D. G. Gadian, and J. E. Cremer, *Stroke*, 1992, **23**, 576.
49. K. Fuxe, B. Bjelke, B. Andbjer, H. Grahn, R. Rimondini, and L. F. Agnati, *Neuroreport*, 1997, **8**, 2623.
50. H. E. D'Arceuil, A. J. De Crispigny, J. Rother, S. Seri, M. E. Moseley, D. K. Stevenson, and W. Rhine, *JMRI*, 1998, **8**, 820.
51. R. M. Dijkhuizen, S. Knollema, H. B. van der Worp, G. J. ter Horst, D. J. de Wildt, J. W. Berkelbach van der Spenkel, C. A. F. Tullenken, and K. Nicolay, *Stroke*, 1998, **29**, 695.
52. U. I. Tuor, P. Kozlowski, D. R. Del-Bigo, B. Ramjiawan, S. Su, K. Malisza, and J. K. Saunders, *Exp. Neurol.*, 1998, **150**, 321.
53. S. C. Jones, A. D. Perez Trepichio, M. Xue, A. J. Furlan, and I. A. Awad, *Acta Neurochir.*, 1994, **60**, 207.
54. L. Edvinsson, E. T. MacKenzie, and J. McCulloch, 'Cerebral Blood Flow and Metabolism', eds. L. Edvinsson, E. T. MacKenzie, and J. McCulloch, Raven Press, New York, 1993, p. 618.
55. R. G. Robinson, W. J. Shoemaker, M. Schlumpf, T. Valk, and F. E. Bloom, *Nature*, 1975, **255**, 332.
56. S. T. Chen, C. Y. Hsu, E. L. Hogan, H. Maricq, and J. D. Balentine, *Stroke*, 1986, **17**, 738.
57. K. A. Osborne, T. Shigeno, A. M. Balarsky, I. Ford, J. McCulloch, G. M. Teasdale, and D. I. Graham, *J. Neurol. Neurosurg. Psychiatr.*, 1987, **50**, 402.
58. S. Brint, M. Jacewicz, M. Kiessling, J. Tanabe, and W. A. Pulsinelli, *J. Cereb. Blood Flow Metab.*, 1988, **8**, 474.
59. F. Calamante, M. F. Lythgoe, G. S. Pell, D. L. Thomas, M. D. King, C. H. Sotak, A. L. Busza, S. R. Williams, R. J. Ordidge, and D. G. Gadian, *Magn. Reson. Med.*, 1999, **41**, 479.
60. T. Shigeno, G. M. Teasdale, J. McCulloch, and D. I. Graham, *J. Neurosurg.*, 1985, **63**, 272.
61. E. Longa Zea, P. R. Weinstein, S. Carlson, and R. Cummins, *Stroke*, 1989, **20**, 84.
62. R. J. Laing, J. Jakubowski, and R. W. Laing, *Stroke*, 1993, **24**, 294.
63. J. H. Garcia, *Stroke*, 1993, **24**, 1423.
64. J. P. Holland, S. G. C. Sydserff, Taylor W. A. S., and A. B. Bell, *Stroke*, 1993, **24**, 1423.
65. Y. Kuge, K. Minematsu, T. Yamaguchi, and M. Yoshihiro, *Stroke*, 1995, **26**, 1655.
66. L. Belayev, A. F. Alonso, R. Busto, W. Zhao, and M. D. Ginsberg, *Stroke*, 1996, **27**, 1616.
67. F. Li, S. Han, T. Tatlisumak, R. A. D. Carano, K. Irie, C. H. Sotak, and M. Fisher, *Stroke*, 1998, **29**, 1715.
68. R. Schmid-Elsaesser, S. Zausinger, E. Hungerhuber, A. Baethmann, and H. J. Reulen, *Stroke*, 1998, **29**, 2162.
69. S. A. Roussel, N. van Bruggen, M. D. King, J. Houseman, S. R. Williams, and D. G. Gadian, *NMR Biomed.*, 1994, **7**, 21.
70. M. F. Lythgoe, S. R. Williams, A. L. Busza, L. I. Wiebe, A. J. B. McEwan, D. G. Gadian, and I. Gordon, *Magn. Reson. Med.*, 1999, **41**, 706.
71. M. Kobayashi, W. D. Lust, and J. Passonneau, *J. Neurochem.*, 1977, **29**, 53.
72. F. A. Welsh, M. J. O'Connor, and V. R. Marcy, *J. Neurochem.*, 1977, **31**, 311.
73. E. F. Gildea and S. Cobb, *Acta Neurol. Psychiatr.*, 1930, **23**, 876.
74. W. A. Pulsinelli and J. B. Brierley, *Stroke*, 1979, **10**, 267.
75. V. Hossmann and K. A. Hossmann, *Brain Res.*, 1973, **60**, 423.
76. J. Korf, C. Klein, K. Venema, and F. Postema, *J. Neurochem.*, 1988, **50**, 1087.
77. K. L. Allen, A. L. Busza, H. A. Crockard, R. S. Frackowiak, D. G. Gadian, E. Proctor, R. W. Ross Russell, and S. R. Williams, *J. Cereb. Blood Flow Metab.*, 1988, **8**, 816.
78. D. Davis, J. A. Ulatowski, S. Eleff, M. Izuta, S. Mori, D. Shungu, and P. C. M. Van Zijl, *Magn. Reson. Med.*, 1994, **31**, 454.
79. A. Lorek, Y. Takei, E. B. Cady, J. S. Wyatt, J. Penrice, A. D. Edwards, D. Peebles, M. Wylezinska, H. Owen-Reece, V. Kirkbride, C. E. Cooper, R. F. Aldridge, S. C. Roth, G. Brown, D. T. Delpy, and E. O. R. Reynolds, *Pediatr. Res.*, 1994, **36**, 699.
80. C. Pierpaoli, J. R. Alger, A. Righini, J. Mattiello, R. Dickerson, D. Des Pres, A. Barnett, and G. di Chiro, *J. Cereb. Blood Flow Metab.*, 1996, **16**, 892.

81. B. T. Andrews, P. R. Weinstein, M. Keniry, and B. Pereira, *Neurosurgery*, 1987, **21**, 699.
82. O. H. J. Grohn, M. I. Kettunen, M. Penttonen, P. C. M. Van Zijl, and R. A. Kauppinen, *Proc. VIIth Annu. Mtg. (Int.) Soc. Magn. Reson. Med.*, Philadelphia, 1999, **2**, 329.
83. M. Fischer, K. Bockhorst, M. Hoehn-Berlage, B. Schmitz, and K. A. Hossmann, *Magn. Reson. Imaging.*, 1995, **13**, 781.
84. A. van der Toorn, E. Sykova, R. M. Dijkhuizen, I. Vorisek, L. Vargova, E. Skobisova, M. van Lookeren Campagne, T. Reese, and K. Nicolay, *Magn. Reson. Med.*, 1996, **36**, 52.
85. N. Derugin and T. P. L. Roberts, *Microsurgery*, 1994, **15**, 70.
86. O. H. J. Grohn, J. A. Lukkarinen, J. M. E. Oja, P. C. van Zijl, J. A. Ulatowski, R. J. Traystman, and R. A. Kauppinen, *J. Cereb. Blood Flow Metab.*, 1998, **18**, 911.
87. D. L. Thomas, G. S. Pell, M. F. Lythgoe, F. Calamante, C. H. Sotak, A. L. Busza, S. R. Williams, M. D. King, D. G. Gadian, and R. J. Ordidge, *Proc. Vth Annu. Mtg. (Int.) Soc. Magn. Reson. Med.*, Vancouver, 1999, p. 606.
88. E. Busch, C. Beaulieu, A. J. Crispigny, and M. E. Moseley, *Stroke*, 1998, **29**, 2155.
89. J. B. Bederson, I. M. Germano, and L. Guarino, *Stroke*, 1995, **26**, 1086.
90. M. van Lookeren Campagne, G. R. Thomas, H. Thibodeaux, J. T. Palmer, S. P. Williams, D. G. Lowe, and N. Van Bruggen, *J. Cereb. Blood Flow Metab.*, 1999, **19**, 1354.
91. M. D. Silva, F. Li, M. Fisher, and C. H. Sotak, *Proc. VIIth Annu. Mtg. (Int.) Soc. Magn. Reson. Med.*, Philadelphia, 1999, p. 52.
92. J. S. Thornton, R. J. Ordidge, J. Penrice, E. B. Cady, P. N. Amess, S. Punwani, M. Clemence, and J. S. Wyatt, *Magn. Reson. Med.*, 1998, **39**, 920.
93. P. Gygax, N. Wiernsperger, W. Meier-Ruge, and T. Baumann, *Gerontology*, 1978, **24**, 14.
94. A. R. Laptook, R. J. T. Corbett, H. T. Nguyen, J. Peterson, and R. L. Nunnally, *Pediatr. Res.*, 1988, **23**, 206.
95. T. Mima 'Central Nervous System Trauma', eds. S. T. Ohnishi and T. Ohnishi, CRC Press, New York, 1995, 107.
96. W. A. Pulsinelli, J. B. Brierley, and F. Plum, *Ann. Neurol.*, 1982, **11**, 491.
97. G. S. Pell, D. L. Thomas, M. F. Lythgoe, F. Calamante, A. M. Howseman, D. G. Gadian, and R. J. Ordidge, *J. Magn. Reson. Med.*, 1999, **41**, 829.
98. T. Kirino, *Brain Res.*, 1982, **239**, 57.
99. G. S. Pell, M. F. Lythgoe, D. L. Thomas, F. Calamante, M. D. King, D. G. Gadian, and R. J. Ordidge, *Stroke*, 1999, **30**, 1263.
100. M. F. Lythgoe, G. S. Pell, D. L. Thomas, F. Calamante, M. D. King, S. R. Williams, R. J. Ordidge, and D. G. Gadian, *Proc. VIIth Annu. Mtg. (Int.) Soc. Magn. Reson. Med.*, Philadelphia, 1999, **1**, 55.
101. B. J. Crain, W. D. Westerkam, A. H. Harrison, and J. V. Nadler, *Neuroscience*, 1988, **27**, 387.
102. B. Eklof and B. K. Siesjo, *Acta Physiol. Scand.*, 1972, **86**, 155.
103. M. L. Smith, G. Bendek, N. Dahigren, I. Rosen, T. Wieloch, and B. K. Siesjo, *Acta Neurol. Scand.*, 1985, **69**, 385.

Acknowledgements

The authors thank Dr David Thomas for his constructive suggestions during the preparation of the manuscript and Dr Gaby Pell, Mr Fernando Calamante, Dr Albert Busza and Dr John Thornton for the use of images.

Biographical Sketches

Mark F. Lythgoe. *b* 1962. M.Sc. (Behavioural Biology), Surrey, 1993, Ph.D. (Biophysics), London, 1999. Research in pediatric nuclear medicine at the Great Ormond Street Hospital: investigation of experimental cerebral ischemia using MRI. Research interests: the use of diffusion and perfusion MRI, and novel MR contrast mechanism to examine the underlying pathophysiology of stroke.

David G. Gadian. *b* 1950. B.A. (Physics) Oxford, 1971, D.Phil. Oxford, 1975. Application of NMR spectroscopy, including initial ^{31}P investigation of muscle metabolism. Current research interests: development and application of MR techniques to the investigation of brain diseases and its functional consequences, with an emphasis on disorders of childhood.

Body Fluids

Jimmy D. Bell

Imperial College School of Medicine, Hammersmith Hospital, London, UK

and

Peter J. Sadler

University of Edinburgh, UK

1 INTRODUCTION

1.1 Historical Perspective

The full potential for the use of high resolution NMR spectroscopy as applied to the study of body fluids has only become apparent in the last decade. However, Eric Odeblad, a Swedish physicist and gynecologist, used ^{1}H NMR to study body fluids as far back as 1957.[1,2] Although the spectra were relatively uninformative, he advocated the establishment of a 'department of medical research with NMR.' In the early 1970s, the introduction of Fourier transform spectroscopy, together with technical advances (field strength, coil designs, pulse sequences, and computing) enabled the use of high-resolution NMR for the detection and identification of different chemical species in biological systems. In 1979, Ohsaka et al.[3] reported high resolution proton NMR spectra of intact body fluids and attempted serodiagnosis of cancer. Their spectra consisted of sharp resonances from low-molecular-mass metabolites superimposed on broad resonances from macromolecules, with an elevated lactate signal as a criterion for diagnosis of cancer. This was closely followed by a study of high-resolution NMR spectra of urine samples from subjects with diabetes and renal failure.[4] Marked changes in the concentration of a number of then unidentified endogenous metabolites were observed. From these preliminary studies, it became clear that high resolution NMR could play an important role in the study of body fluids.

The first full clinical use of NMR to study body fluids was in a study of metabolic disorders by Bock and coworkers.[5,6] Elevated concentrations of D-lactate were detected in serum samples from human subjects following jejunoileal bypass. Full characterizations of different body fluids by high-resolution NMR and application to a wider range of biochemical and clinical problems came soon afterwards. Since then, the study of body fluids by high resolution NMR spectroscopy has become an increasingly expanding area of research.

1.2 The Range of Body Fluids

The biochemical composition of body fluids is known to reflect the metabolic status of the donor. Thus, detailed knowledge of the composition of body fluids is likely to provide good insight into the biochemical and clinical status of the donor. This has led workers to apply a variety of techniques to obtain metabolic profiles of body fluids. However, most of the standard techniques require extensive sample preparation together with careful selection of analytical conditions. This can clearly restrict the number of compounds that can be studied at a given time. Moreover, a number of fluids contain a range of molecules with diverse chemical and molecular masses, including amino acids, proteins and lipoproteins, all or some of which can be affected in disease. The nonselective nature of NMR spectroscopy makes it an ideal technique for obtaining metabolic profiles of all available body fluids. Furthermore, NMR spectroscopy can give useful insights into molecular interactions within intact fluids which are not readily available by standard biochemical techniques. Thus, NMR spectroscopy, although relatively insensitive, has been successfully applied to the detection and quantitation of a variety of molecules in intact body fluids, including blood, blood plasma, serum, urine, cerebrospinal fluid (CSF), bile, synovial fluid, seminal fluid, milk, saliva and sweat (Table 1).[7–60] Representative ^{1}H NMR spectra of some body fluids are shown in Figure 1.

The physicochemical composition of different body fluids varies widely. Fluids such as plasma, bile, CSF, seminal fluid and synovial fluid contain both macromolecules, low-molecular-mass compounds and inorganic ions. These compounds range from complex lipoproteins and glycoproteins to relatively simple organic acids, amino acids and metal ions. Less complicated body fluids include urine, aqueous humor, saliva, and sweat, which contain relatively low levels of macromolecules, but often a very large number of different low-molecular-mass metabolites (Table 1). The ^{1}H NMR chemical shifts of some common metabolites are listed in Table 2. NMR spectroscopy can provide qualitative and quantitative information about most of these body fluids components, often in just a few minutes, as well as information about molecular structures, molecular interactions and dynamics.

1.3 Sample Preparation and NMR Data Acquisition

NMR spectra can be readily obtained from intact body fluids, requiring little or no sample preparation. Samples (usually about 500 μL) can be examined untreated in the spectrometer, except that normally a small amount of a deuterated solution is added to provide a field/frequency lock (e.g. 5–10% v/v D_2O or saline). This can be added directly to the sample, or placed in a capillary tube, thus avoiding dilution of sample. Particular care should be taken with the storage of samples. For example, contaminating bacteria can introduce exogenous substances, and freezing and thawing can cause chemical changes such as precipitation and protein denaturation. Buffering can be a problem. For example, the main natural buffer in blood plasma is bicarbonate/CO_2 and the pH of samples can rise rapidly after storage due to the volatility of CO_2. This can be counteracted by adding sodium bicarbonate (25 mM) or a small amount of another buffer (e.g. phosphate).

Reasonably resolved ^{1}H NMR spectra of body fluids can be obtained on commercially available high-frequency spectrometers (>400 MHz). Higher frequency NMR spectrometers (600 and 750 MHz) give increased resolution and relative sensitivity,[21] and improve the detection and identification of body fluid components; however, these instruments are relatively expensive.

Table 1 Endogenous Metabolites detected in Body Fluids by High-Resolution ^{1}H NMR Spectroscopy[a]

Amniotic fluid
Acetate α-alanine, D-3-hydroxybutyrate, citrate, creatine, creatinine, formate, glucose, glutamate, glycerophosphorylcholine, isoleucine, lactate, lecithin, leucine, lipids, lysine, methionine, ornithine, 2-oxoisovalerate, phospholipids, proline, sphingomyelin, threonine, tyrosine, valine[55–57]
Aqueous humor
Acetate, alanine, ascorbate, citrate, creatine, formate, glucose, glutamine/glutamate, histidine, lactate, phenylalanine, threonine, tyrosine, valine[44,45]
Bile
Acetate, acetone, acetoacetate, α-alanine, cholesterol, cholesterol esters, choline, citrate, creatine, creatinine, ethanol, ergothionine, formate, glucose, glutamate, glutamine, glycine, glycocholic acid, D-3-hydroxybutyrate, isoleucine, lactate, propionate, phosphatidylcholine, taurine, taurocholic acid, urea, valine[39,40]
Blood plasma and serum
Acetate, acetone, acetoacetate, acetylcarnitine, *N*-acetyl sugars, *N*-acetyl glycoproteins, acylglycerols, alanine, aspartate, betaine, carnitine, cholesterol, cholesterol esters, choline, citrate, creatine, creatinine, dimethylamine, dimethylglycine, ethanol, ergothionine, formate, glucose, glutamate, glutamine, glycine, glycerol, histidine, D-3-hydroxybutyrate, *p*-hydroxyphenyllactate, isoleucine, lactate, leucine, lysine, lipoproteins (high density, low density, very low density), 1-methylhistidine, 3-methylhistidine, myoinositol, phenylalanine, phosphatidylcholine, pyruvate, succinate, threonine, trimethylamine *N*-oxide, tyrosine, urea, valine
Cerebrospinal fluid
Acetate, acetone, acetoacetate, α-alanine, aspartate, arginine, choline, citrate, citrulline, creatine, creatinine, dimethylamine, formate, fumarate, GABA, galactose, glucose, glutamine, glutamate, glycine, glycerol, D-3-hydroxybutyrate, histidine, indoxyl sulfate, inositol, isoleucine, lactate, leucine, lysine, mannitol, methionine, proline, pyruvate, phenylalanine, spermidine, succinate, taurine, threonine, trimethylamine *N*-oxide, tyrosine, valine.
Cystic fluid
Acetate, *N*-acetylglycoproteins, alanine, arginine, citrate, creatine, dimethylamine, ethanol, formate, glucose, glutamine, histidine, isoleucine, lactate, lysine, phenylalanine, succinate, threonine, tyrosine, urea, valine[58]
Follicular fluid
Acetate, *N*-acetyl sugars, *N*-acetyl glycoproteins, alanine, creatine, creatinine, ethanol, glucose, glycine, D-3-hydroxybutyrate, lactate, valine[49]
Gastric fluid
Histidine, tyrosine, phenylalanine[50]
Milk
Acetate, alanine, citrate, creatine, formate, glucose, lactose, lactate, lipids, taurine[51]
Saliva[41,42]
Seminal fluid
Acetate, alanine, arginine, aspartate, asparagine, D-3-hydroxybutyrate, choline, citrate, creatine, cystine, dimethylamine, formate, fumarate, fructose, glucose, glutamate, glutamine, glycine, glycerophosphorylcholine, histidine, inositol, isoleucine, lactate, leucine, lysine, methionine, phenylalanine, phosphorylcholine, proline, pyruvate, spermidine, spermine, taurine, threonine, trimethylamine *N*-oxide, tryptophan, tyrosine, uridine, valine[46–48]
Sweat
Acetate, alanine, D-3-hydroxybutyrate, citrate, glutamate, glutamine, glycine, histidine, lactate, tyrosine, valine[43]
Synovial fluid
Acetate, acetone, acetoacetate, *N*-acetyl sugars, *N*-acetyl glycoproteins, α-alanine, cholesterol, cholesterol esters, choline, citrate, creatine, creatinine, ethanol, formate, glucose, glutamine, glycine, histidine, D-3-hydroxybutyrate, lactate, lipoproteins, phenylalanine, threonine, tyrosine, valine[43,52–54]
Urine
Acetate, acetamide, acetone, acetoacetate, acetylcarnitine, *N*-acetyl sugars, α-alanine, β-alanine, allantoin, anserine, ascorbate, betaine, butanone, carnitine, choline, citrate, creatine, creatinine, dimethylamine, dimethylglycine, ethanol, formate, glucose, glutamate, glutamine, glutarate, glycine, guanine, hippurate, histidine, hydroxybenzoate, D-3-hydroxybutyrate, 2-hydroxyisocaproate, 2-hydroxyisovalerate, 2-hydroxy-3-methylvalerate, hydroxypropionate, indoxyl sulfate, inositol, isoleucine, isovalerylglycine, 2-oxoglutarate, lactate, leucine, lysine, methanol, methionine, methylamine, methylmalonate, *N*-acetylglycoproteins, 2-oxoisocaproate, 2-oxoisovalerate, 2-oxo-3-methylvalerate, phenylalanine, propionate, propionylcarnitine, propionylglycine, succinate, taurine, trimethylamine, trimethylamine *N*-oxide, threonine, tyrosine, urea, valine
Vitreous fluid
Acetate, alanine, citrate, creatine, formate, glutamine/glutamate, lactate, valine[45]

[a]References given are mostly to work not described in the text.

In general, ^{1}H NMR spectra of body fluids with good signal-to-noise ratios can be obtained within a few minutes. The acquisition of NMR spectra of body fluids requires consideration of two major factors: T_1 and T_2 relaxation, and water suppression. Fully-relaxed ^{1}H NMR spectra can usually be obtained with 35° pulses and a 3-s pulse repetition time. ^{13}C NMR spectra require up to 10 s to allow full relaxation of some lipid and protein components. For some body fluids, spin echo techniques are useful for the suppression of broad resonances from macromolecules.[12] T_2 effects, which can affect the quantitation of metabolites, must be taken into account during the analysis of these spectra.

Water suppression is crucial for ^{1}H NMR experiments on body fluids since the concentration of water protons is about 10^5 times that of the protons in the metabolites of interest. Although freeze-drying and redissolution in D_2O is very effective, volatile metabolites may be lost and the structures of some macromolecules may be altered by this process.[23] The most commonly used method for suppression is presaturation[61] (secondary irradiation during the relaxation delay, e.g. for 1 s),

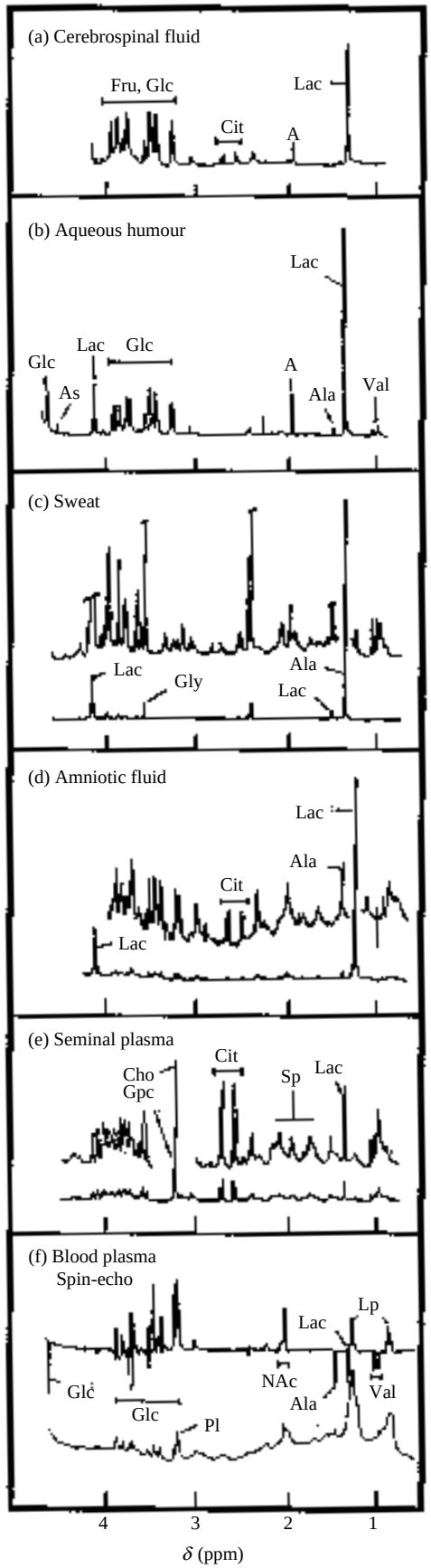

although this does not allow detection of peaks very close to the water peak. For the latter purpose the WATR method[62] (water attenuation by T_2 relaxation) is very effective. This involves addition of a water relaxation agent (e.g. NH_4C1) and use of the CPMG spin echo sequence with a short refocusing time so that normal multiplets without phase modulation are obtained. Details of other methods can be found elsewhere in this volume. Many suppression methods lead to distortions in peak intensities and this has to be checked if quantitative information is required. It seems likely that increasing use will be made of field gradient water suppression methods in future. Other advances are likely to include the use of microprobes requiring only about 50 μL of sample, and, at the other extreme, larger sample volumes (e.g. 4 mL in a 10 mM tube) which provide high sensitivity.

2 DIAGNOSIS AND MOLECULAR INTERACTIONS

2.1 Organ Dysfunction

The biochemical profile of a body fluid is known to reflect the metabolic status of the donor. Thus, the unique exploratory nature of NMR makes it an ideal technique for the study of body fluids from subjects with organ dysfunction This is clearly reflected in published work which includes analysis of plasma, CSF, urine and bile from subjects suffering from liver failure,[8,39] brain tumors,[24] organ transplant,[21] and renal failure.[16] For example, increased concentrations of aromatic amino acids have been observed in NMR spectra of plasma of subjects with hepatic failure,[8,39] while variations in plasma *N*-acetyl resonances correlate with acute heart rejection.[14]

An important area of clinical and biochemical research has been the application of high-resolution NMR spectroscopy to the study of the biochemical abnormalities associated with chronic renal failure (CRF).[16,21] Renal damage in both animals and humans has been shown to give rise to altered profiles for low-molecular-mass metabolites of urine and plasma, which in turn is reflected in the NMR spectral fingerprint. Bell et al.[16] used ^{1}H NMR to show that plasma and urine from subjects' CRF had increased levels of creatinine, trimethylamine oxide (TMAO) and dimethylamine. These amines had not been previously detected in body fluids from human subjects and have since become valuable markers to monitor renal transplant function. Since then several novel markers of renal dysfunction have been identified by NMR,[21] including TMAO, dimethylamine (DMA), dimethylglycine (DMG), 1-methylhistidine and 3-methylhistidine, thus giving a new perspective to the uremic condition and the effects of hemodialysis on body fluid composition. The contribution of NMR spectroscopy of body fluids to renal transplantation has been clearly highlighted by Foxall

Figure 1 Representative ^{1}H NMR spectra of the aliphatic regions of some human body fluids. A, acetate; Ala, alanine; As, ascorbate; Cho, choline; Cit, citrate; Fru, fructose; Glc, glucose; Gly, glycine; Gpc, glycerophosphorylcholine; Lac, lactate; Lp, lipoprotein; NAc, *N*-acetyls of glycoproteins; Pl, phospholipids; Sp, spermine; Val, valine. (Adapted from J. D. Bell, J. C. C. Brown and P. J. Sadler, *Chem. Br.* 1988, **24**, 1021)

Table 2 ^{1}H NMR Chemical Shifts of some Common Metabolites in Body Fluids at pH of about 7[a]

Metabolite	δ/ppm (multiplicity)
Acetate	1.92 (s)
N-Acetylaspartate	2.03 (s), 2.50 (dd), 2.70 (dd), 4.40 (dd)
Acetoacetate	2.29 (s)
Acetone	2.24 (s)
Adenosine	6.06 (d), 8.22 (s), 8.33 (s)
(*S*)-Adenosylmethionine	6.11 (d), 8.27 (s), 8.29 (s)
Alanine	1.47 (d), 3.76 (q)
β-Alanine	2.56 (t), 3.18 (t)
Allantoin	5.40 (s)
p-Aminohippurate	3.93 (d), 6.87 (d), 7.68 (d)
Arginine	1.66 (m), 1.91 (m), 3.24 (t), 3.75 (dd)
Asparagine	2.88 (dd), 2.95 (dd), 4.00 (dd)
Aspartate	2.68 (dd), 2.79 (dd), 3.89 (dd)
α-Hydroxy-n-butyrate	0.90 (t), 1.70 (m), 3.99 (m)
D-3-Hydroxybutyrate	1.20 (d), 2.05 (m), 2.51 (m), 4.18 (m)
Betaine	3.27 (s), 3.90 (s)
Choline	3.21 (s), 3.56 (t), 4.05 (t)
Citrate	2.67 (d), 2.80 (d)
Citrulline	1.57 (m), 1.85 (m), 3.15 (t)
Creatine	3.04 (s), 3.93 (s)
Creatinine	3.05 (s), 4.01 (s)
Cysteine	3.04 (dd), 3.12 (dd), 4.00 (dd)
Diphosphoglycerate	4.05 (m), 4.09 (m), 4.55 (dd)
Dimethylamine	2.72 (s)
EDTA	3.29 (s), 3.67 (s)
Formate	8.46 (s)
Fumarate	6.52 (s)
γ-Aminobutyrate	1.89 (m), 2.30 (t), 3.03 (t)
Galactose	β: 4.52 (d)
α-Glucose	3.41 (t), 3.53 (dd), 3.71 (t), 3.74 (m), 3.84 (m), 5.23 (d)
β-Glucose	3.24 (dd), 3.40 (t), 3.49 (t), 3.72 (dd), 3.90 (dd), 4.64 (d)
Glutamate	2.09 (m), 2.34 (dt), 3.75 (t)
Glutamine	2.14 (m), 2.45 (m), 3.77 (t)
Glycerophosphorylcholine	3.23 (s), 3.52 (dd), 3.58 (t), 3.59 (m), 3.82 (m), 4.19 (t)
Glycerol	3.56 (dd)
Glycine	3.56 (s)
Hippurate	3.97 (d), 7.64 (t), 7.84 (d)
Histidine	3.15 (dd), 3.25 (dd), 4.00 (dd), 7.11 (s), 7.89 (s)
Hydroxyproline	2.17 (m), 2.44 (m), 3.37 (d), 3.49 (dd), 4.35 (dd)
Hypoxanthine	8.19 (s), 8.22 (s)
Indoxyl sulfate	7.20 (m), 7.28 (m), 7.54 (d), 7.73 (d)
Inosine monophosphate	6.15 (d), 8.23 (s), 8.57 (s)
Inositol	3.27 (t), 3.53 (dd), 3.61 (t), 4.05 (t)
Isoleucine	0.93 (t), 1.00 (q), 1.25 (m), 1.45 (m), 1.96 (m), 3.65 (m)
α-Ketoglutaric acid	2.47 (t), 3.01 (t)
Lactate	1.33 (d), 4.11 (q)
Leucine	0.94 (d), 0.96 (d), 1.69 (m), 1.72 (m), 3.69 (t)
Lysine	1.45 (m), 1.73 (m), 3.01 (t), 3.46 (t)
Malate	2.37 (dd), 2.67 (dd), 4.30 (dd)
Mannitol	3.70 (dd), 3.82 (d), 3.90 (dd)
Methionine	2.14 (s), 2.16 (m), 2.64 (t), 3.84 (dd)
Nicotinamide	7.60 (q), 8.25 (d), 8.72 (d), 8.94 (s)
Ornithine	1.81 (m), 1.95 (m), 3.06 (t), 3.79 (t)
Oxaloacetate	2.38 (s)
Phenylalanine	3.13 (dd), 3.24 (dd), 7.31 (m), 7.44 (m)
Phosphocreatine	3.05 (s), 3.94 (s)
Phosphorylcholine	3.22 (s), 3.61 (t), 4.19 (t)
Phosphorylethanolamine	3.26 (t), 4.07 (dd)
Polyamines	1.78 (m), 2.12 (m), 3.06 (t), 3.14 (m)
Proline	2.00 (m), 2.11 (m), 2.31 (m), 3.33 (t), 3.40 (t), 4.14 (t)
Pyruvate	2.40 (s)
Sarcosine	2.74 (s), 3.61 (s)
Serine	3.84 (dd), 3.96 (dd)
Succinate	2.41 (s)
Taurine	3.26 (t), 3.42 (t)
Threonine	1.34 (d), 3.58 (d), 4.25 (m)
Trimethylamine	2.88 (s)
Trimethylamine *N*-oxide	3.27 (s)
Tyrosine	3.05 (dd), 3.15 (dd), 3.93 (dd), 6.88 (d), 7.18 (d)
Uracil	5.80 (d), 7.53 (d)
Valine	0.98 (d), 2.26 (m), 3.55 (d)

[a]Note that the shifts may vary with pH, ionic strength and temperature.

et al.[21] (Figure 2). They have shown that significantly higher concentrations of TMAO can be observed for urine collected from patients during episodes of graft dysfunction compared with urine from patients with good graft function or from healthy control subjects. Furthermore, they suggest that graft dysfunction is associated with damage to the renal medulla, which causes the release of TMAO into the urine, thus providing a novel urinary marker for posttransplant graft dysfunction.

2.2 Metabolic Disorders

The nonselective nature of NMR spectroscopy makes it the method of choice for the study of intact body fluids, especially for the study of congenital errors of metabolism. NMR spectroscopy allows rapid and accurate diagnosis of different metabolic disorders, with the added advantage that novel metabolites related to a given disease can be detected, thus improving diagnosis and possible therapy. A large number of inherited metabolic disorders have been successfully studied by NMR spectroscopy, including maple syrup urine disease, isovaleric aciduria, dicarboxylic aciduria, and tyrosinemia.[31,33,38,43] A few examples are used here to illustrate the potential of NMR spectroscopy in this area of research.

By simple NMR urinalysis, Iles and Chalmers[31] were able to monitor the progression of the disease, the fate of the therapeutic compounds and the restoration of metabolic balance in a girl with a defect in propionic acid metabolism, methylmalonic aciduria. The ^{1}H NMR spectrum of urine from this patient is shown in Figure 3. The subject was given intravenous carnitine in an attempt to resolve a severe episode of acute metabolic decompensation.

Carnitine is known to reduce the propionate pool by combining with propionyl-CoA to form propionylcarnitine. The latter is excreted in the urine. Spectra taken during this acute episode showed: (1) the range of metabolites associated with the disorder, including methylmalonate and creatine; (2) the metabolic fate of the therapeutic intervention in the form of unchanged carnitine and propionylcarnitine; and (3) the appearance of acetylcarnitine, signifying restoration of acetyl-CoA metabolism on lowering the level of intracellular propionyl-CoA. The appearance of acetylcarnitine coincided with clinical

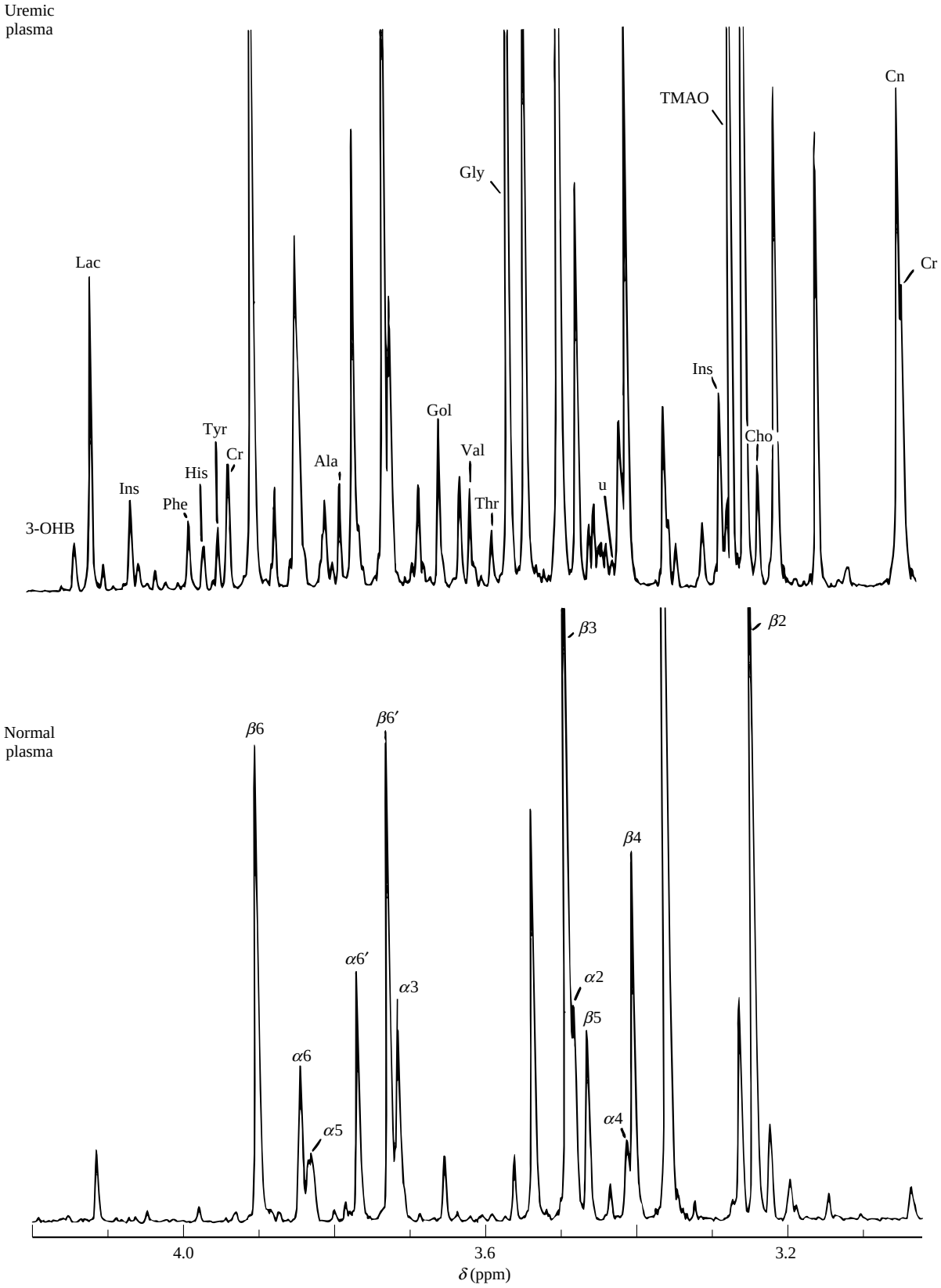

Figure 2 A 'skyline' projection of part of the aliphatic region of two-dimensional *J*-resolved 750-MHz ^{1}H NMR spectra of normal and uremic human blood plasma. α and β refer to resonances of glucose anomers. Cr, creatine; Cn, creatinine; Cho, choline; TMAO, trimethylamine *N*-oxide; Ins, myoinositol; Gly, glycine; Thr, threonine; Val, valine; Gol, glycerol; Ala, alanine; Tyr, tyrosine; His, histidine; Phe, phenylalanine; Lac, lactate; 3-OHB, D-3-hydroxybutyrate. (Adapted from P. J. D. Foxall, M. Spraul, R. D. Farrant, L. C. Lindon, G. H. Neild, and J. K. Nicholson, *J. Pharmacol. Biomed. Anal.*, 1993, **11**, 267)

improvement of the patient. Since the acquisition of an NMR spectrum from urine takes less than 3 min (at 500 MHz), this type of research opens up the possibility of 'real-time' therapeutic monitoring.

Although, ^{1}H NMR spectroscopy is the preferred method for the study of congenital errors of metabolism, dynamic metabolic studies have been carried out via ^{13}C NMR spectroscopic studies of body fluids following the infusion of ^{13}C-enriched metabolites. Tanaka et al.[63] used ^{13}C NMR urinalysis to monitor the fate of valine in methylmalonic aciduria. Following intravenous injection of DL-[1-^{13}C]- and DL-[1,2-^{13}C]valine to a boy with cobalamin-responsive methylmalonic aciduria, ^{13}C NMR spectra of urine showed that propionate was an obligatory intermediate from valine to methylmalonyl-CoA. It was previously thought that propionate was bypassed via methylmalonic semialdehyde. A similar approach was taken by Lapidot[13] in studies of glycogen storage and inherited fructose intolerance diseases in children. By means of a combination of ^{13}C NMR spectroscopy, and isotopomer analysis with gas chromatography–mass spectrometry, following nasogastrically infused [U-^{13}C]glucose, they were able to gain an insight into the biochemical alterations in specific metabolic pathways which accompany these diseases.

2.3 Proteins and Lipoproteins in Intact Fluids

Blood plasma and serum are heterogeneous fluids containing lipoprotein particles (about 5–1200 nm in diameter), macromolecules (proteins), small molecules and ions. Any of the normal anticoagulants can be used for preparing plasma for NMR studies, e.g. EDTA and lithium heparin. The former is often preferred for lipoprotein work and gives rise to peaks for CaEDTA (NCH_2 singlet at 2.57 ppm) and MgEDTA (2.76 ppm) in spectra. No interfering peaks are usually seen for heparin.

Simplification of ^{1}H NMR spectra of plasma (which are similar to those of serum) can be achieved by the use of spin echo methods to filter out the broadest resonances.[7,9,12] No resonances remain in the aromatic region with t values greater than about 30 ms. Spin echo spectra can be used to study small molecules such as valine, acetate, alanine, lactate, glucose, and the ketone bodies acetone, acetoacetate and D-3-hydroxybutyrate in cases of insulin-dependent diabetes or fasting,[7,9] as well

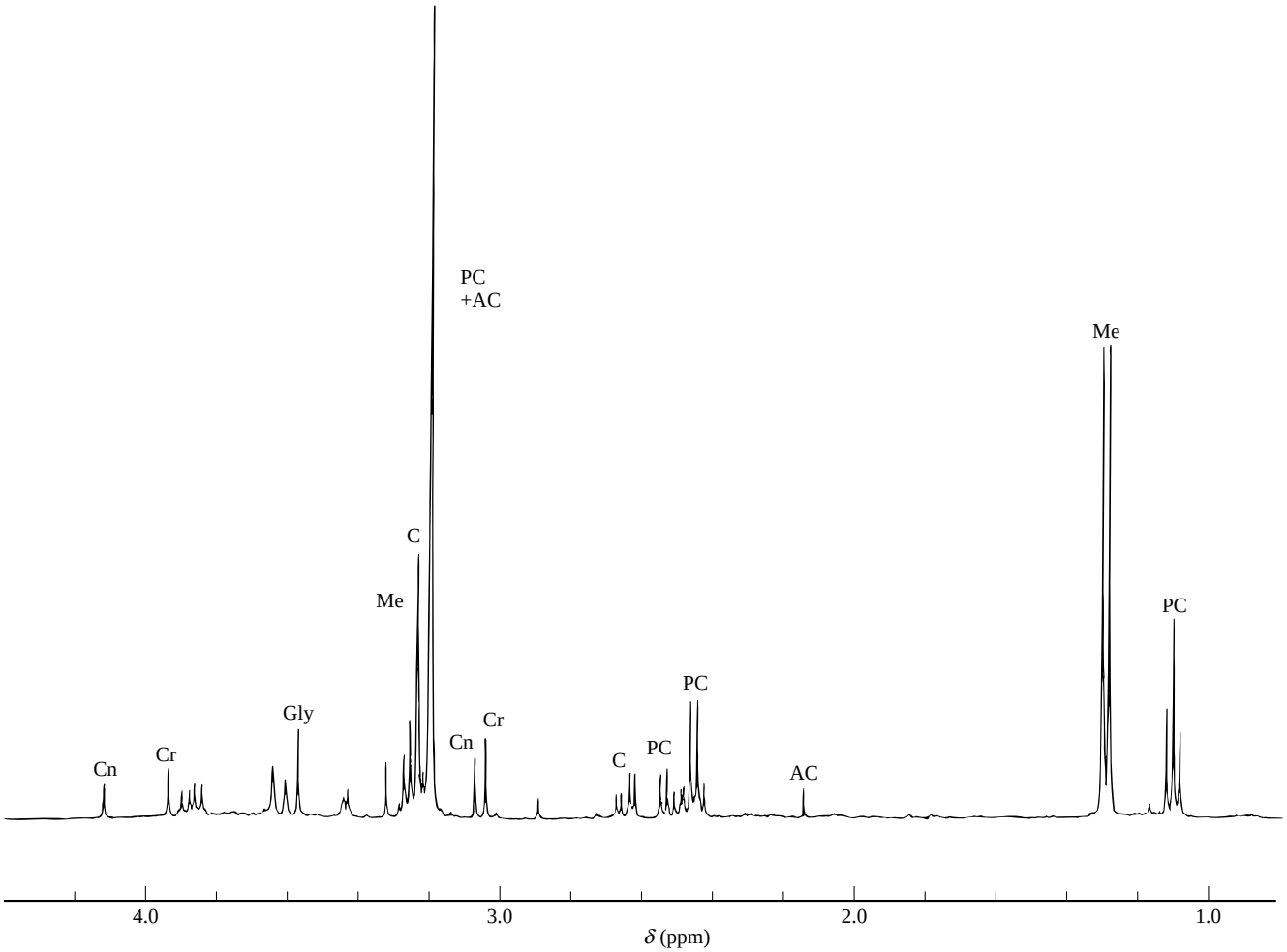

Figure 3 The 500 MHz ^{1}H NMR spectrum of urine sample from a subject with a defect in propionic acid metabolism. PC, propionylcarnitine; Me, methylmalonic acid; AC, acetylcarnitine; C, carnitine; Cr, creatine; Cr, creatinine; Gly, glycine. (Adapted from figure supplied by R. A. Iles)

as mobile segments of lipoproteins and acute-phase glycoproteins.

2.3.1 *Proteins*

Broad resonances at 2.04 and 2.08 ppm in ^{1}H NMR spectra of blood plasma have been assigned to the *N*-acetyl groups of *N*-acetylglucosamine and *N*-acetylneuramic acid residues of the glycan chains of 'acute-phase' glycoproteins such as α_1-acid glycoprotein.[64] These resonances have been used to monitor increases in maternal levels of these proteins (which are two-fold) compared with the matched neonatal cord plasma,[65] and the progress of heart transplant rejection.[66]

The application of resolution enhancement to high-field ^{1}H NMR spectra of blood plasma enables the detection of specific resonances for the major plasma protein albumin (66 kDa), including those for the N-terminal amino acids Asp1-Ala2-His3.[20] The ^{1}H NMR resonances of $H_{15}3$ of albumin can be used to monitor the state of Cys34 of albumin in blood plasma, and the formation of disulfides with, for example, the alcohol-aversive drug disulfiram and adducts with gold antiarthritic drugs.[67]

2.3.2 *Lipoproteins*

There is particular interest in the determination of lipoprotein concentrations in blood plasma on account of their association with coronary heart disease, hyperlipidemias, and possibly cancer and other diseases.

Broad resonances from the CH_2 and CH_3 groups of the fatty acid constituents of, for example, triacylglycerols, phospholipids and cholesterol esters in lipoproteins occur near 1.2 and 0.9 ppm, respectively. Comparisons of the ^{1}H NMR spectra of the individual isolated lipoproteins[10] enabled specific assignments to be made for each of the four major classes of lipoprotein (Figure 4), and suggested that ^{1}H NMR spectroscopy would allow a rapid determination of lipoproteins in intact plasma or serum. Both the CH_2 and CH_3 peaks shift slightly to high field as the density of the particle increases. The origin of the shifts is not yet clear, but may be related to susceptibility effects, protein interactions [greatest for high-density lipoprotein (HDL)], and the different types of lipid involved (higher proportion of phospholipids in denser particles). Lipoprotein classes can also be distinguished by their differing relaxation properties; in Hahn spin echo spectra, the NMe_3^+ peak from choline headgroups of phospholipids in low-density lipoprotein (LDL) and HDL decays more rapidly with increasing refocusing time for LDL than for HDL, and the CH_2 of LDL but not HDL contributes to the methyl and methylene region with longer TE values (60 ms).

Two approaches have subsequently been used to simulate the CH_2 and CH_3 regions of spectra of blood plasma and determine lipoprotein concentrations. In the first,[15] mean experimental 250 MHz spectra of isolated lipoprotein fractions have been used to construct plasma lipid CH_3 resonances using a linear least-squares fitting routine. Since this region of ^{1}H spectra of plasma from different donors is relatively similar for different donors, this procedure is reasonably successful. It has been refined[68] by including subspecies distributions within each lipoprotein class [very-low-density lipoprotein (VLDL), LDL, HDL], effectively broadening the peaks for each [Figure 5(a)]. For LDL the subspecies distributions derived from NMR correlated well with those from gradient-gel electrophoresis.

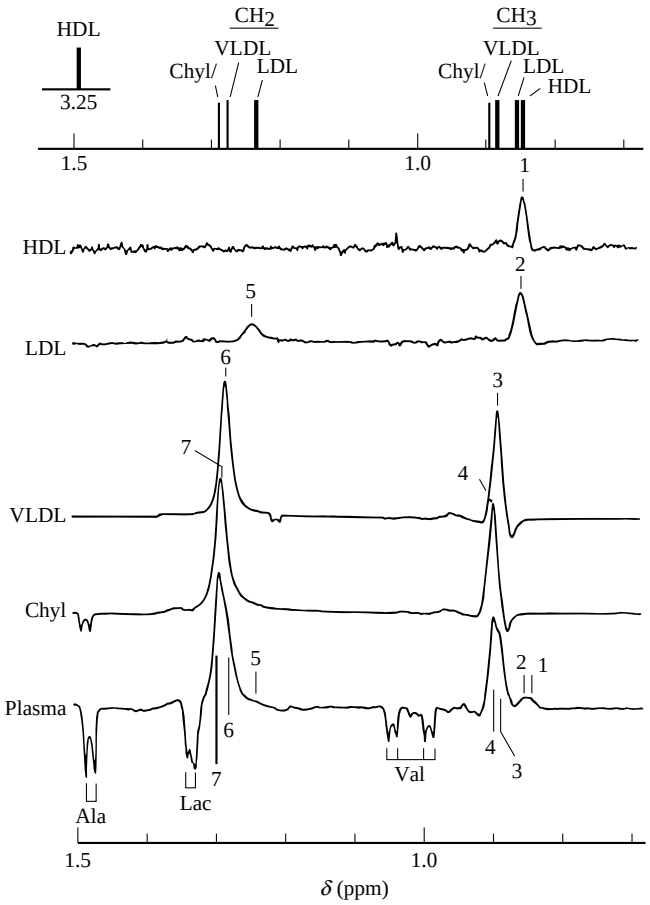

Figure 4 Assignments for the CH_3 and CH_2 ^{1}H NMR resonances of lipoproteins in Hahn spin echo spectra (TE = 60 ms). Chyl, chylomicrons; VLDL, very-low-density lipoproteins; LDL, low-density lipoproteins; HDL, high-density lipoproteins. The peak at 3.25 ppm in the insert is from the choline headgroup of HDL phospholipids. (Adapted from J. D. Bell, P. J. Sadler, P. J. Macleod, P. R. Turner, and A. LaVille, *FEBS Lett.*, 1987, **219**, 239)

These NMR measurements were carried out at 45 °C so as to avoid the problems caused by the increasing linewidth with temperature of peaks for LDL (the midpoint of the phase transition is at about 32 °C).

In a second approach the spectra of the CH_2 peaks of 400 MHz spectra of isolated individual lipoproteins at 30 °C were simulated by resolvable Lorentzian component lines:[17] two for VLDL, three for LDL, and two for HDL [Figure 5(b)]. NMR determinations of the relative amounts of each lipoprotein fraction in the plasma of normolipidemic and hyperlipidemic subjects using these model resonances gave good agreements with biochemical determinations.

Further refinements of these procedures can be envisaged involving inclusion of all the lipid peaks in the spectrum in the analysis, and consideration of modified lineshapes for lipoprotein particles with a high content of polyunsaturated fatty acids, e.g. for subjects on high fish oil content diets.[69] Halogenated anesthetics can mobilize lipids within lipoprotein particles[70] and there may also be lipophilic drugs which have such effects. ^{13}C and ^{31}P NMR analyses may be useful complements to ^{1}H work.

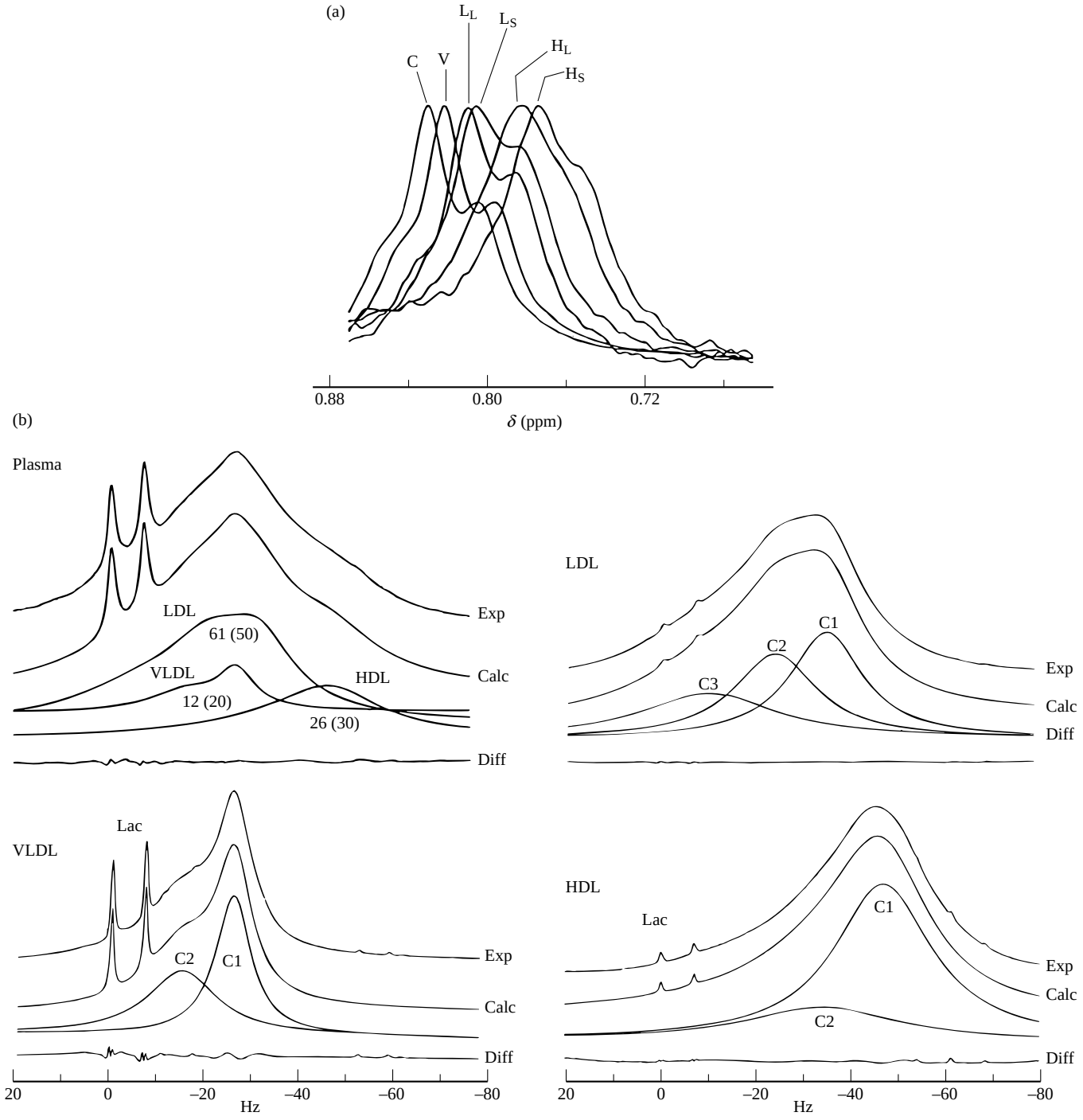

Figure 5 (a) The methyl ^{1}H NMR resonances of lipoproteins at 250 MHz, 45 °C. VLDL, very-low-density, lipoproteins; L_L and L_S, large and small LDL; H_L and H_S, large and small HDL. (Adapted from J. D. Otvos, E. J. Jeyarajah, D. W. Bennett, and R. M. Krauss, *Clin. Chem.*, 1992, **38**, 1632). (b) Experimental and calculated lipoprotein ^{1}H NMR CH_2 peaks for VLDL, LDL and HDL, and intact human blood plasma. (Adapted from M. Ala-Korpela, Y. Hiltunen, and J. Jokisaari, *NMR Biomed.*, 1993, **6**, 225)

Figure 6 (a) Lactate binding in blood plasma. 500 MHz single pulse (bottom) and Hahn spin echo (TE = 60 ms) ^{1}H NMR spectra (top) of human blood plasma before and after addition of ammonium chloride. The increase in intensity of the lactate methyl resonance with ammonium chloride concentration is plotted in the inset. (Adapted from J. D. Bell, J. C. C. Brown, G. Kubal, and P. J. Sadler, *FEBS Lett.*, 1988, **235**, 81.) (b) Ni^{2+} binding to the N-terminus of albumin in human blood plasma. Resolution-enhanced (combined exponential and sine-bell functions) 500 MHz ^{1}H NMR spectra of the aromatic region of human blood plasma before (lower) and after (upper) addition of Ni^{2+} (0.5 equivalents with respect to albumin). Alb-His3 refers to the third residue in albumin. Ni^{2+} binds to the N-terminal Aspl-Ala2-His3 residues forming a square-planar, diamagnetic complex. (Adapted from S. U. Patel, P. J. Sadler, A. Tucker, and J. H. Viles, *J. Am. Chem. Soc.*, 1993, **115**, 9285)

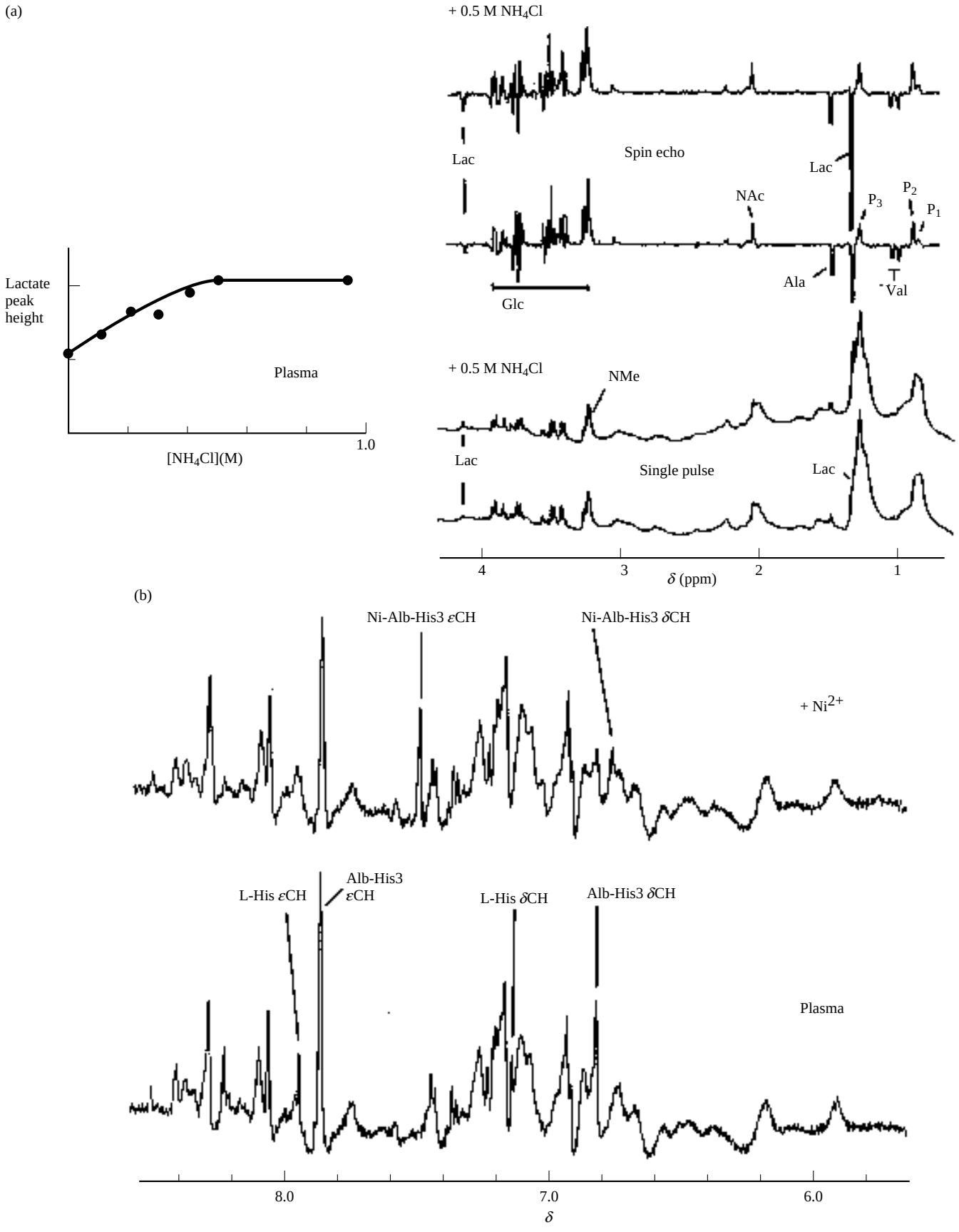
(a)
Lactate peak height
Plasma
1.0
[NH4Cl](M)
+ 0.5 M NH4Cl
Lac
Spin echo
Lac
NAc
P3
P2
P1
Ala
Val
Glc
+ 0.5 M NH4Cl
NMe
Lac
Single pulse
Lac
4
3
2
1
δ (ppm)
(b)
Ni-Alb-His3 εCH
Ni-Alb-His3 δCH
+ Ni2+
L-His εCH
Alb-His3 εCH
L-His δCH
Alb-His3 δCH
Plasma
8.0
7.0
6.0
δ

A rapid method for separation of lipoproteins from plasma for NMR work is that described by Hoffman et al.,[71] which involves the use of 1.5 mL of a gel such as Sepharose 6B in a disposable Pasteur pipet eluted with a deuterated salt solution.

It should be noted that, despite initial claims,[72] there is no useful relationship between the linewidths of lipoprotein CH_2 and CH_3 ^{1}H NMR resonances and cancer diagnosis, although they are reported to be of value for monitoring heart transplant rejection.[73] The use of 'star plots' (graphical display of peak height ratios) has been advocated for the detection of metabolic modifications brought about by cancer evolution or therapy.[74]

Kaartinen et al. have demonstrated that clinically relevant lipid classifications can be obtained from self-organizing map analysis of ^{1}H NMR spectra of blood plasma.[75] It has been suggested that the pattern of resonances at 1.17, 1.18 and 1.20 ppm can be used to measure other levels of oxidized low-density lipoprotein in human serum with possible application to cardiovascular risk factor profiles.[76] The advantages of using high frequency ^{1}H (800 MHz) and ^{13}C NMR spectroscopy for improving the resolution of lipid peaks are apparent.[77]

2.3.3 *Molecular Interactions and Binding*

Considerable caution has to be exercised in the interpretation of the intensities of peaks in spin echo spectra of plasma. The long T_1 values of some small molecules have to be taken into account when pulsing conditions for quantitation experiments are chosen (e.g. acetate 3.6 s, formate 6.6 s, glycine 2.4 s, valine 1.1 s: serum, pH 7, 400 MHz, 22 °C, 0.8 M NH_4Cl added).[78] To allow the rapid quantitation of small molecules in the plasma from subjects with chronic renal failure (CRF), Grasdalen et al.[79] applied correction factors to compensate for the effects of relaxation and water irradiation on peak intensities.

Reliable quantitation can be obtained for alanine and valine with standard additions, but lactate and some other carboxylic acids bind to plasma macromolecules. Lactate has been shown to bind to both transferrin[11] and albumin[80] in slow exchange on the NMR timescale. It can be displaced from binding by addition of NH_4Cl [Figure 6(a)],[11] the antihypertensive drug Captopril,[80] and the anticonvulsant agent [Cu_2(DIPS)$_4$] (DIPS is 3,5-diisopropylsalicylate).[18] Intriguingly, there appears to be less lactate binding in plasma from subjects with CRF than in normal plasma.[16] A noncovalent interaction between Captopril and albumin has been detected in blood plasma and the *cis* isomer undergoes faster exchange between free and bound forms than does the *trans* isomer.[80] Binding of Cu^{2+} to formate and histidine in urine has been studied by NMR, and the time-course of the reaction between copper ethylenediaminetetraacetate (CuEDTA) and blood plasma has been monitored.[18] Even at relatively low levels of Al^{3+} ions (50 μM), binding to citrate can be detected, which is reversed by the therapeutic chelating agent desferrioxamine.[19] The binding of Ni^{2+} to the N-terminal site of albumin (the antigenic determinant in cases of Ni^{2+} allergy) can be studied directly in plasma[20] [Figure 6(b)]. These kinds of experiment offer promise in the metallodrugs field, since ligand exchange and redox reactions in biological media are common, and alternative methods which involve the separation of the components can lead to changes in metal speciation.

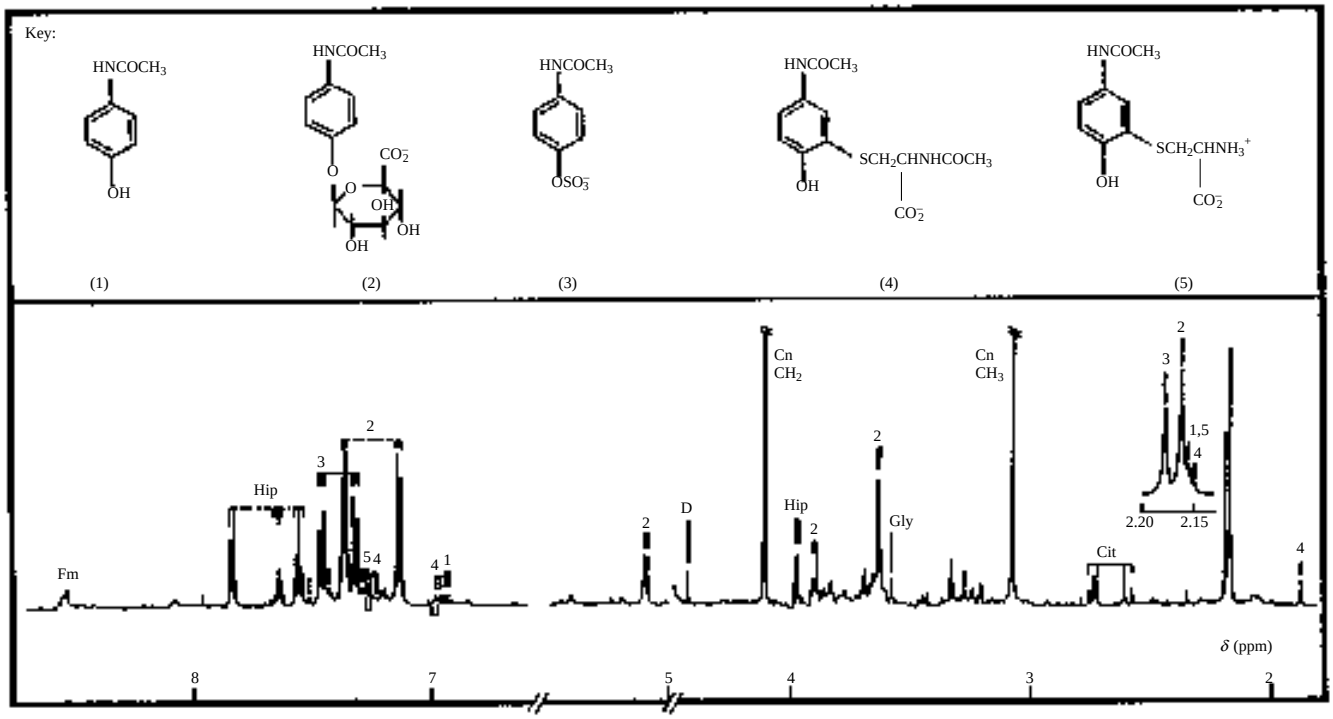

Figure 7 The 500 MHz ^{1}H NMR spectrum of human urine 6 h after a therapeutic 1 g (6.6 mmol) dose of the analgesic drug paracetamol. As well as natural metabolites (Cn, creatinine; Cit, citrate; D, dihydroxyacetone; Fm, formate; Gly, glycine; Hip, hippurate), peaks for the drug (1) and all its major metabolites (2–5) are seen. (Adapted from J. D. Bell, J. C. C. Brown, and P. J. Sadler, *Chem. Br.*, 1988, **24**, 1021)

Although a useful reference for chemical shifts and concentrations in body fluids with low levels of macromolecules, trimethylsilylpropionate (TSP) is often undetectable at <2.5 mM in ^{1}H NMR spectra of blood plasma, due to binding.[78] Similarly, resonances for phenylalanine and tyrosine are suppressed in spin echo spectra of blood plasma at normal pH compared with highly acidic pH values (<2.5). The interaction of glutamine with other components of CSF is markedly changed after freeze drying and redissolving the sample, only then are its ^{1}H NMR resonances visible.[23]

3 DRUG METABOLISM AND TOXICOLOGY

NMR spectroscopy is finding increasing uses in the study of drug metabolism and toxicology.[59] Conventional techniques require the use of radioactive labeling and extensive use of separation techniques, e.g. high-performance liquid chromatography (HPLC). Moreover, valuable information can be lost using conventional techniques since exogenous and endogenous metabolites can go undetected. NMR spectroscopy, however, allows observation of all metabolites in one experiment[27–30] (Figure 7), although it suffers from inherently low sensitivity and 'chemical noise'. Chemical noise refers to the many low-intensity resonances found in body fluids that may mask the resonances under study. In part these problems can be overcome by concentrating the samples and by the use of multidimensional/multinuclear NMR. A more recent and powerful approach is the separation of metabolites by solid-phase extraction/chromatography in conjunction with NMR (SPEC-NMR) or HPLC coupled with high-field NMR.

NMR spectroscopy has been successfully applied to the study of a variety of xenobiotics including, acetaminophen, 5-fluorouridine, ifosfamide, ibuprofen, penicillamine, flucloxacillin, ampicillin, hydrazine, *N*-methylformamide, and carboplatin.[59,81] ^{1}H and ^{19}F are usually the nuclei of choice in NMR studies of xenobiotics, although work using ^{31}P, ^{2}H and ^{15}N has been published. The advantages of ^{1}H NMR are clearly based on its high sensitivity and the fact that protons are ubiquitous to most drugs. However, ^{1}H NMR spectra often suffer from severe overlap of signals from exogenous and endogenous metabolites. On the other hand, ^{19}F NMR is particularly good for these studies in that it has high sensitivity, 100% natural abundance and no interference from naturally-occurring fluorinated compounds, and therefore no chemical noise. A good illustration of the use of NMR spectroscopy in drug metabolism is that of 5-fluorouracil (5FU).[32] The complete urinary excretion profile of cancer patients on a drug course of 5FU was followed by ^{19}F NMR spectroscopy with and without methotrexate pretreatment. The parent drug (5FU) and four of its metabolites were detected in the urine, including F^- which is produced as a degradation product. The major metabolite found in these studies was α-fluoro-β-alanine.

A new area of research has been the development of NMR of body fluids in analytical toxicology. Nicholson and coworkers[34–36] have used NMR for the rapid multicomponent analysis of body fluids following xenobiotic insults. The effects of known nephrotoxins on the NMR profiles of rat urine were investigated. The nephrotoxins consisted of sodium chromate (pars convoluta of proximal tubule), cisplatin, hexachlorobutadiene, mercury(II) chloride (pars recta of the proximal tubule), propylene imine, and 2-bromoethanamine (renal papilla). These compounds induced damage in specific regions of the rat kidney. Urinalysis by ^{1}H NMR spectroscopy showed clear biochemical fingerprints for site-specific nephrotoxic states (Figure 8). Aminoaciduria, glycosuria, and lactic aciduria were characteristic of exposure to all proximal tubular toxins (except for cisplatin), whereas papillary insult resulted in early elevations in urinary TMAO and DMA. TMAO and DMA were suggested as markers of site-specific renal papillary injury in the rat.

Toxicological studies in humans have been more limited. However, a number of cases have arisen from accidental or self-inflicted poisoning episodes, e.g. paracetamol (acetaminophen) overdose and accidental skin adsorption of phenol.[35] Although these studies are partly hampered by the lack of control of body fluids, useful clinical and biochemical information

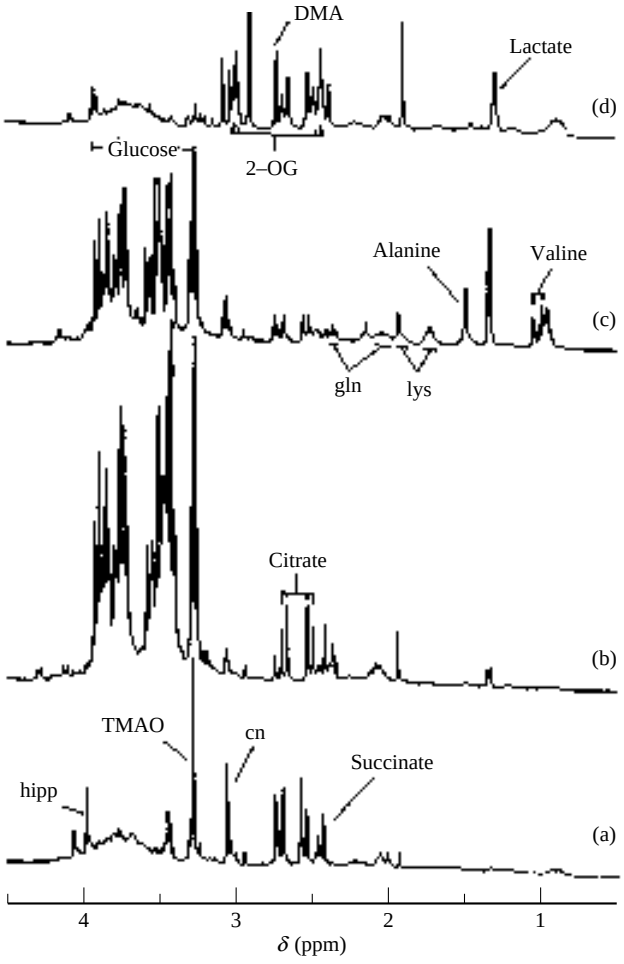

Figure 8 Effects of administration of various nephrotoxins on the ^{1}H NMR spectra (400 MHz) of rat urine. (a) Control; (b) 24–48 h after dosing with 20 mg kg^{-1} sodium chromate (pars convoluta proximal tubular toxin); (c) 24–48 h after dosing with 50 mg kg^{-1} *p*-aminophenol (pars recta proximal tubular toxin); (d) 24–48 h after dosing with 20 ml kg^{-1} propylene imine (produces renal medullary necrosis). DMA, dimethylamine; 2-OG, 2-oxyglutarate; hipp, hippurate; cn, creatine; gln, glutamine; lys, lysine; TMAO, trimethylamine *N*-oxide. (Adapted from K. P. R. Gartland, F. W. Bonner, and J. K. Nicholson, *Mol. Pharmacol.*, 1989, **35**, 242)

has been obtained. These results clearly demonstrate the strength of the NMR technique as applied to toxicological studies.

Proton NMR spectra of body fluids consist in many cases of a very large number (>100) of resonances, giving rise to a wealth of, as yet complex, information. Spectral quantitation and interpretation can thus become tedious and time-consuming. Furthermore, metabolic alterations in the body can lead to subtle, yet consistent changes in the composition profiles of some body fluids. In many cases standard quantitative and statistical analysis of the spectral data are not robust enough to detect some of these changes. Alternative computer-based pattern-recognition methods[36,59] have been applied to analyses of NMR spectra of body fluids. Preliminary results suggest that pattern-recognition methods applied to NMR data may be powerful for the characterization of metabolic abnormalities associated with diseased states and toxicological events.

4 RELATED ARTICLE

Tissue and Cell Extracts MRS.

5 REFERENCES

1. E. Odeblad and B. Westin, *Acta Radiol.*, 1958, **49**, 390.
2. E. Odeblad, *Acta Isot.*, 1961, **1**, 27.
3. A. Ohsaka, K. Yoshikawa, and T. Matuhasi, *Jpn. J. Med. Sci. Biol.*, 1979, **32**, 305.
4. K. Matsushita, K. Yoshikawa, and A. Ohsaka, *JEOL News*, 1982, **18**, 54.
5. J. L. Bock, *Clin. Chem.*, 1982, **28**, 1873.
6. M. Traube, J. L. Bock, and J. L. Boyer, *Ann. Intern. Med.*, 1983, **98**, 171.
7. J. K. Nicholson, M. J. Buckingham, and P. J. Sadler, *Biochem. J.*, 1983, **211**, 605.
8. J. R. Bales, J. D. Bell, P. J. Sadler, J. K. Nicholson, J. A. Timbrell, P. N. Bennett, R. D. Hughes, and R. Williams, *Magn. Reson. Med.*, 1988, **6**, 300.
9. J. K. Nicholson, M. P. O'Flynn, P. J. Sadler, A. F. Macleod, S. M. Juul, and P. H. Sonksen *Biochem. J.*, 1984, **217**, 365.
10. J. D. Bell, P. J. Sadler, A. F. Macleod, P. R. Turner, and A. LaVille, *FEBS Lett.*, 1987, **219**, 239.
11. J. D. Bell, J. C. C. Brown, G. Kubal, and P. J. Sadler, *FEBS Lett.*, 1988, **235**, 81.
12. D. L. Rabenstein, K. K. Millis, and E. J. Strauss, *Anal. Chem.*, 1988, **60**, 1380A.
13. A. Lapidot, *J. Inherited Metab. Dis.*, 1990, **13**, 466.
14. H. Pont, J. Vion-Dury, R. Faure, D. Maraninchi, J. R. Harle, S. Confort-Gouny, M. Sciaky, E. Fontanarava, P. Viout, and P. J. Cozzone, *Lancet*, 1991, **337**, 792.
15. J. D. Otvos, E. J. Jeyarajah, and D. W. Bennett, *Clin. Chem.*, 1991, **37**, 377.
16. J. D. Bell, J. A. Lee, H. A. Lee, P. J. Sadler, D. R. Wilkie, and R. H. Woodham, *Biochim. Biophys. Acta*, 1991, **1096**, 101.
17. M. Ala-Korpela, Y. Hiltunen, J. Jokisaari, S. Eshelman, K. Kiviniity, M. J. Savolainen and Y. A. Resaniemi, *NMR Biomed.*, 1993, **6**, 225.
18. S. W. Bligh, H. A. Boyle, A. B. McEwen, P. J. Sadler, and R. H. Woodham, *Biochem. Pharmacol.*, 1992, **43**, 137.
19. J. D. Bell, G. Kubal, S. Radulovic, P. J. Sadler, and A. Tucker, *Analyst*, 1993, **118**, 241.
20. S. U. Patel, P. J. Sadler, A. Tucker, and J. H. Viles, *J. Am. Chem. Soc.*, 1993, **115**, 9285.
21. P. J. D. Foxall, M. Spraul, R. D. Farrant, L. C. Lindon, G. H. Neild, and J. K. Nicholson, *J. Pharmacol. Biomed. Anal.*, 1993, **11**, 267.
22. O. A. C. Petroff, R. K. Yu, and T. Ogino, *J. Neurochem.*, 1986, **47**, 1270.
23. J. D. Bell, J. C. C. Brown, P. J. Sadler, A. F. Macleod, D. H. Sonksen, R. D. Hughes, and R. Williams, *Clin. Sci.*, 1987, **72**, 563.
24. F. Koschorek, H. Gremmel, J. Stelten, W. Offermann, E. Kruger, and D. Leibfritz, *AJNR*, 1989, **10**, 523.
25. B. C. Sweatman, R. D. Farrant, E. Holmes, F. Y. Ghauri, J. K. Nicholson, and J. C. Lindon, *J. Pharmacol. Biomed. Anal.*, 1993, **11**, 651.
26. F. Nicoli, J. Vion-Dury, J. M. Maloteaux, C. Delwaide, S. Confort-Gouny, M. Sciaky, and P. J. Cozzone, *Neurosci. Lett.*, 1993, **154**, 47.
27. J. R. Bales, D. P. Higham, I. Howe, J. K. Nicholson, and P. J. Sadler, *Clin. Chem.*, 1984, **30**, 426.
28. J. R. Bales, P. J. Sadler, J. K. Nicholson, and J. A. Timbrell, *Clin. Chem.*, 1984, **30**, 1631.
29. J. R. Bales, J. K. Nicholson, and P. J. Sadler, *Clin. Chem.*, 1985, **31**, 757.
30. J. Bernadou, J. P. Armand, A. Lopez, M. C. Malet-Martino, and R. Martino, *Clin. Chem.*, 1985, **31**, 846.
31. R. A. Iles and R. A. Chalmers, *Clin. Sci.*, 1988, **74**, 1.
32. W. E. Hull, R. E. Port, R. Herrmann, B. Britsch, and W. Kunz, *Cancer Res.*, 1988, **48**, 1680.
33. S. E. C. Davies, R. A. Chalmers, E. W. Randall, and R. A. Iles, *Clin. Chim. Acta*, 1988, **178**, 241.
34. K. P. R. Gartland, F. W. Bonner, and J. K. Nicholson, *Mol. Pharmacol.*, 1989, **35**, 242.
35. P. J. Foxall, M. R. Bending, K. P. R. Gartland, and J. K. Nicholson, *Hum. Toxicol.*, 1989, **8**, 491.
36. E. Holmes, F. W. Bonner, B. C. Sweatman, J. C. Lindon, C. R. Beddell, E. Rahr, and J. K. Nicholson, *Mol. Pharmacol.*, 1992, **42**, 922.
37. P. J. Foxall, G. J. Mellotte, M. R. Bending, J. C. Lindon, and J. K. Nicholson, *Kidney Int.*, 1993, **43**, 234.
38. S. E. C. Davies, D. A. Woolf, R. A. Chalmer, J. E. M. Rafter, and R. A. Iles, *J. Nutr. Biochem.*, 1993, **3**, 523.
39. K. P. R. Gartland, C. T. Eason, K. E. Wade, F. W. Bonner, and J. K. Nicholson, *J. Pharmacol. Biomed. Anal.*, 1989, **7**, 699.
40. J. P. M. Ellul, G. M. Murphy, H. G. Parkes, R. Z. Slapa, and R. H. Dowling, *FEBS Lett.*, 1992, **300**, 30.
41. H. Harada, H. Shimizu, and M. Maeiwa, *Forensic Sci. Int.*, 1987, **34**, 189.
42. A. Yamada-Nosaka, S. Fukutomi, S. Uemura, T. Hashida, M. Fujishita, Y. Kobayashi, and Y. Kyogoku, *Arch. Oral. Biol.*, 1991, **36**, 697.
43. J. D. Bell, J. C. C. Brown, and P. J. Sadler, *NMR Biomed.*, 1989, **2**, 246.
44. J. C. C. Brown, P. J. Sadler, D. J. Spalton, S. M. Juul, A. F. Macleod, and P. H. Sonksen, *Exp. Eye Res.*, 1986, **42**, 357.
45. J. V. Greiner, L. A. Chanes, and T. Glonek, *Opthalmic Res.*, 1991, **23**, 92.
46. S. Hamamah, F. Seguin, C. Barthelemy, S. Akoka, A. Le-Pape, J. Lansac, and D. Royere, *J. Reprod. Fertil.*, 1993, **97**, 51.
47. P. M. Robitaille, P. A. Robitaille, P. A. Martin, and G. G. Brown, *Comp. Biochem. Physiol. B*, 1987, **87**, 285.
48. M. J. Lynch, J. Masters, J. P. Pryor, J. C. Lindon, M. Spraul, P. J. D. Foxall, and J. K. Nicholson, *J. Pharmacol. Biomed. Anal.*, 1994, **12**, 5.
49. R. G. Gosden, I. H. Sadler, D. Reed, and R. H. Hunter, *Experientia*, 1990, **46**, 1012.

50. J. J. Powell, S. M. Greenfield, H. G. Parkes, J. K. Nicholson, and R. P. H. Thompson, *Food Chem. Toxicol.*, 1993, **31**, 449.
51. J. D. Bell and P. J. Sadler, unpublished work.
52. H. G. Parkes, M. C. Grootveld, E. B. Henderson, A. Farrel, and D. R. Blake, *J. Pharmacol. Biomed. Anal.*, 1991, **9**, 75.
53. M. Grootveld, E. B. Henderson, A. Farrell, D. R. Blake, H. G. Parkes, and P. Haycock, *Biochem. J.*, 1991, **273**, 459.
54. K. Albert, S. Michele, U. Gunther, M. Fial, H. Gall, and J. Saal, *Magn. Reson. Med.*, 1993, **30**, 236.
55. T. R. Nelson, R. J. Gillies, D. A. Powell, M. C. Schrader, D. K. Manchester, and D. H. Pretorius, *Prenatal Diagn.*, 1987, **7**, 363.
56. J. M. Pearce, M. A. Shifman, A. A. Pappas, and R. A. Komoroski, *Magn. Reson. Med.*, 1991, **21**, 107.
57. M. Dittmer, A. C. Kuesel, T. Kroft, M. Villeneuve, R. Benzeie, and I. C. P. Smith, *Proc. XIth Ann Mtg. Soc. Magn. Reson. Med.*, Berlin, 1992, Vol. 2, 3417.
58. P. J. D. Foxall, R. G. Price, J. K. Jones, G. H. Neild, F. D. Thompson, and J. K. Nicholson, *Biochim. Biophys. Acta*, 1992, **1138**, 305.
59. J. K. Nicholson and I. D. Wilson, *Progr. NMR Spectrosc.*, 1989, **21**, 449.
60. J. D. Bell, in 'Magnetic Resonance Spectroscopy in Biology and Medicine: Functional and Pathological Tissue Characterization', eds. J. D. de Certaines, W. M. M. J. Bovee, and F. Podo, Pergamon, Oxford, 1992.
61. P. J. Hore, *JMRI*, 1983, **55**, 283.
62. D. L. Rabenstein and S. Y. Fan, *Anal. Chem.*, 1986, **58**, 3178.
63. K. Tanaka, I. M. Armitage, H. S. Ramsdell, Y. E. Hsia, S. R. Lipsky, and L. E. Rosenberg, *Proc. Natl. Acad. Sci. USA*, 1975, **72**, 3692.
64. J. D. Bell, J. C. C. Brown, J. K. Nicholson, and P. J. Sadler, *FEBS Lett.*, 1988, **235**, 81.
65. J. D. Bell, J. C. C. Brown, P. J. Sadler, D. Garvie, A. F. Macleod, and C. Lowy, *NMR Biomed.*, 1989, **2**, 61.
66. J. Vion-Dury, A. Mouly-Bandini, P. Viout, M. Sciaky, S. Confort-Gouny, J. R. Monties, and P. Cozzone, *C.R. Acad. Sci. Paris*, 1992, **315**, 479.
67. J. Christodoulou, P. J. Sadler, and A. Tucker, *FEBS Lett.*, 1995, **376**, 1.
68. J. D. Otvos, E. J. Jeyarajah, D. W. Bennett, and R. M. Krauss, *Clin. Chem.*, 1992, **38**, 1632.
69. J. D. Bell and P. J. Sadler, *Chem. Br.*, 1993, **7**, 597.
70. J. D. Bell, C. Hahn, J. K. Lodge, S. U. Patel, J. Sear, and P. J. Sadler, unpublished work.
71. D. W. Hoffman, R. A. Venters, S. F. Shedd, and L. D. Spicer, *Magn. Reson. Med.*, 1990, **13**, 507.
72. E. T. Fossel, J. M. Carr, and J. McDonagh, *New Engl. J. Med.*, 1986, **315**, 1369.
73. M. Eugene, L. LeMmoyec, J. de Certaines, M. Desruennes, E. Le Reumeur, J. B. Fraysse, and C. Cabrol, *Magn. Reson. Med.*, 1991, **18**, 93.
74. J. Vion-Dury, R. Favre, M. Sciaky, M. Kriat, S. Confort-Gouny, J. R. Harle, N. Grazziani, P. Viout, F. Grisoli, and P. J. Cozzone, *NMR Biomed.*, 1993, **6**, 58.
75. J. Kaartinen, Y. Hiltunen, P. T. Koranen, and M. Ala-Korpela, *NMR Biomed.*, 1998, **11**, 168.
76. J. Jankowski, J. R. Nofer, M. Tepel, et al., *Clin. Sci.*, 1998, **95**, 489.
77. W. Wilker and D. Leibfritz, *Magn. Res. Chem.*, 1998, **36**, 579.
78. M. Kriat, S. Confort-Gouny, J. Vion-Dury, M. Sciaky, P. Viout, and P. J. Cozzone, *NMR Biomed.*, 1992, **5**, 179.
79. H. Grasdalen, P. S. Belton, J. S. Prior, and G. T Rich, *Magn. Res. Chem.*, 1987, **25**, 811.
80. D. A. Keire, S. V. Mariappan, J. Peng, and D. L. Rabenstein, *Biochem. Pharmacol.*, 1993, **46**, 1059.
81. J. D. Ranford, P. J. Sadler, K. Balmanno, and D. R. Newell, *Magn. Res. Chem.*, 1991, **29**, 125.

Biographical Sketches

J. D. Bell. *b* 1958. B.Sc. Biochemistry 1982, University of Warwick. Ph.D., (supervisor P. J. Sadler), 1987, London. Senior NMR Research Fellow (with I. Young and D. G. Gadian), Hammersmith Hospital, 1989–93. Faculty of Biochemistry, Royal Postgraduate Medical and Imperial College School of Medicine. Approx. 100 publications. Research interests include application of MRI/MRS in clinical research, and NMR spectroscopy to the chemistry of tissues and body fluids.

P. J. Sadler. *b*. 1946. B.A., 1969, M.A. D.Phil., 1972, Oxford. Introduced to NMR by R. E. Richards, H. A. O. Hill and R. J. P. Williams. MRC Research Fellow University of Cambridge and National Institute for Medical Research (NMR Unit), 1971–73. Faculty of Chemistry, Birkbeck College, University of London, 1973–96. Faculty of Chemistry, University of Edinburgh 1996–present. Approx. 280 publications. Research interests include applications of NMR spectroscopy to metallodrugs, metal transport proteins in blood plasma, and the chemistry of body fluids.

Cation Movements Across Cell Walls of Intact Tissues Using MRS

James A. Balschi
Harvard Medical School, Boston, MA, USA

Kieran Clarke
University of Oxford, UK

Laura C. Stewart
National Research Council, Ottawa, Ontario, Canada

Monique Bernard
CNRS, Marseille, France

and

Joanne S. Ingwall
Harvard Medical School, Boston, MA, USA

1 INTRODUCTION: THE IMPORTANCE OF CATION GRADIENTS FOR CELL FUNCTION

Intracellular cations play critical roles in cell division and maintaining normal cell function in both prokaryotic and eukaryotic cells, and cells actively regulate their intracellular cation levels. Large concentration gradients of the monovalent cations Na^+, K^+, and H^+, and the divalent cations Ca^{2+} and Mg^{2+}, exist across the plasma membrane. The quintessential example of the role of cation movements in normal cell function is the control of excitation–contraction coupling in striated muscle. During a twitch in skeletal muscle and during each cardiac cycle, Na^+, Ca^{2+}, H^+, and K^+ (as well as other charged species) move across the plasma membrane to initiate a sequence of events leading to contraction: Na^+ and Ca^{2+} move from the interstitium to the intracellular space while K^+ and H^+ move out of the cell. Muscle relaxation occurs when the concentrations of these critical cations (most importantly Ca^{2+}) return to baseline. Recovery of resting cell intracellular cation concentrations requires energy. Furthermore, maintenance of intracellular Na^+ and Ca^{2+} levels (Na_i and Ca_i), which in the quiescent cell are below their electrochemical equilibrium values, requires energy. The source of energy for these cation movements is the hydrolysis of ATP, either directly via membrane proteins that stoichiometrically couple ATP hydrolysis and ion translocation, or indirectly through the Na^+ gradient.

Intracellular concentrations of Na^+, K^+, H^+, and Ca^{2+} are determined by the integrated action of these membrane proteins: ion pumps, exchangers, and channels. Membrane proteins from organelles within the cell, namely the endoplasmic reticulum and mitochondria, are also important in the regulation of cation concentrations. A diagram summarizing the major components of this network is shown in Figure 1. Cation NMR has been used to examine the relative contributions of these specific components to net ion movements and how this may change in pathological states. The major advantage of using NMR to measure cation contents is that repetitive nondestructive measurements can be made for intact functioning tissue, usually over long periods of time. Moreover, some of these techniques allow simultaneous measurement of extra- and intracellular ion content, thereby permitting quantitative assessment of net ion movement.

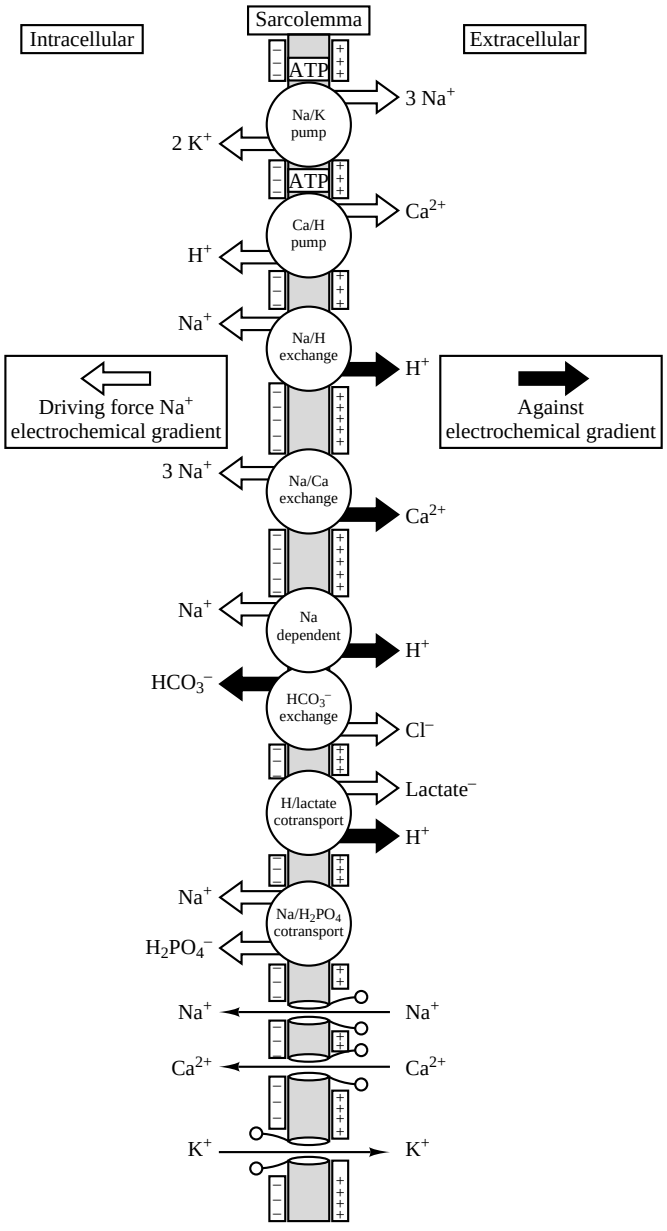

Figure 1 Diagramatic representation of the plasma membrane of a muscle cell (sarcolemma) showing the primary pathways of Na^+, K^+, and Ca^{2+} movement: the ATP-dependent Na^+ and Ca^{2+} pumps, electroneutral Na^+/H^+ exchange and electrogenic Na^+/Ca^{2+} exchange, Na^+-dependent HCO_3^- exchange, H^+/lactate and $Na^+/H_2PO_4^-$ cotransport, and the voltage-dependent Na^+, K^+, and Ca^{2+} channels. Intracellular/extracellular concentrations for Na^+(10/144 mM), K^+ (85–130/5 mM), Ca^{2+} (10–4/1.25 mM), and H^+ (pH 7.15/pH 7.40)

Table 1 NMR Properties of Selected Nuclides

Nucleus	Spin quantum number	Natural abundance (%)	Effective sensitivity[a] ($\times 10^{-2}$)	T_1[b] (ms)	T_2[b] (ms)	Resonant frequency at 8.4 T (MHz)
^{23}Na	$\frac{3}{2}$	100	9.3	70	54	95.2
^{7}Li	$\frac{3}{2}$	93	29.4	25×10^3	18×10^3	139.8
^{39}K	$\frac{3}{2}$	93	0.05	54	54	16.8
^{87}Rb	$\frac{3}{2}$	28	17.7	2.5	2.5	117.7
^{25}Mg	$-\frac{5}{2}$	10	–	–	–	22.0
^{43}Ca	$-\frac{7}{2}$	0.14	–	–	–	24.2

[a]Relative to hydrogen. [b]Measured in aqueous solution.

In this chapter we first describe the MRS methods for measuring monovalent cation contents and movements in intact organs. To illustrate their power, we then describe their application to the heart made ischemic by an abrupt cessation in blood flow. Our focus is on Na^+ because it has received the most attention experimentally.

2 METHODS FOR MEASURING CATION CONTENT AND MOVEMENTS IN VIVO

Hydrogen, Na^+ and its biological congener Li^+, K^+ and its biological congener Rb^+, Mg^{2+}, and Ca^{2+} all have nuclides that are active in NMR[1] (see Table 1). The high natural abundance, relatively high concentration in biological tissues, and short values for spin–lattice relaxation times combine to make Na^+ and K^+ amenable to direct study in biological samples using NMR. The low natural abundance of the NMR active isotopes of Mg^{2+} and Ca^{2+} precludes direct NMR observation. Because Li^+ and Rb^+ are biological congeners of Na^+ and K^+, respectively, they are also useful nuclides for the study of cation movements in biological samples. Estimates of intracellular H^+, Mg^{2+}, and Ca^{2+} contents by MRS are made using indirect techniques and are not discussed here.

2.1 MRS of ^{23}Na and ^{39}K

Because of its inherent NMR sensitivity, high natural abundance, high concentration in biological samples, and short T_1 values, ^{23}Na is the second (next to ^{1}H) most NMR-sensitive nucleus found in biological tissues (Table 1). The first ^{23}Na NMR spectrum of a biological sample was obtained in 1956; the first ^{23}Na image of tissue was obtained in 1981 for perfused heart.[1] Although it is the cation present in highest concentration in the intracellular space, low frequency and hence low sensitivity of the ^{39}K nuclide combine to make its detection by NMR difficult. The first ^{39}K NMR signal from tissue was made in 1970;[2] the first in perfused heart in 1985.[3] The ^{23}Na and ^{39}K nuclei do not exhibit any significant chemical shifts in aqueous solutions. Cations, such as Na^+ or K^+, do not bond covalently but bind electrostatically at suitable anionic sites. Hence, the electronic environment about the nucleus is relatively constant. While such binding may give rise to a small chemical shift, it is more likely to result in line broadening or intensity changes. For the most part, Na^+ and K^+ will remain as hydrated cations in aqueous solution. The electron density around the nucleus does not change, and there are no differences in chemical shift. Therefore, the resonance frequencies of intracellular and extracellular cations are indistinguishable.

Two general approaches have been attempted to discriminate between the resonances of intracellular and extracellular cations. The first approach attempts to use characteristic intrinsic properties of the cation nuclei. The ^{23}Na (and presumably all spin-$\frac{3}{2}$ nuclides) resonance of cells and tissues is predominantly homogeneous biexponential: narrow central resonance ($\frac{1}{2}-\frac{1}{2}$ transition) superimposed on two satellite coherences ($\frac{3}{2}-\frac{1}{2}$) and ($-\frac{1}{2}--\frac{3}{2}$).[4] Since spin $\frac{3}{2}$ nuclei have four nuclear spin states and three single-quantum NMR transitions, more than one relaxation rate exists in biological samples. Several investigators have explored the possibility that multiple quantum NMR can detect differences in relaxation rates of nuclei located in the intra- versus extracellular spaces in biological samples.[5–7] It is clear that more than one rate constant is required to describe observed relaxation of cations present in both the intra- and extracellular spaces. Consequently, quantitative analysis of Na^+ (or K^+) signals distributed in either intra- or extracellular spaces using a multiple quantum approach is technically problematic. However, in practical terms, changes in multiple quantum signals may reflect primarily changes in either the intra- or extracellular Na^+ (or K^+), allowing for good estimates to be made.

The second approach to discriminate between the intra- and extracellular Na^+, signals is to use hyperfine frequency-shift reagents. In the early 1980s, two groups independently developed shift reagents for cations.[8,9] Dysprosium (III) tripolyphosphate ($Dy(PPP)_2^{7-}$)[9] and triethylenetetramine-hexaacetate-dysprosium (III) ($DyTTHA^{3-}$)[10] were widely employed. More recently, another shift reagent, the thulium (III) complex of 1,4,7,10-tetraazacyclo-dodecane-*N*,*N*′,*N*″,*N*‴-tetra(methylene-phosphonate) ($TmDOTP^{5-}$) was introduced.[11] The putative structures of these three shift reagents are shown in Figure 2. These shift reagents have been successfully used to discriminate between ^{23}Na and ^{39}K NMR signals arising from the intra- and extracellular spaces in a wide variety of biological samples, ranging from single cells such as yeast[12,13] and red blood cells,[14] to isolated perfused tissues such as heart[3] and to organs within the intact animal[15–17].

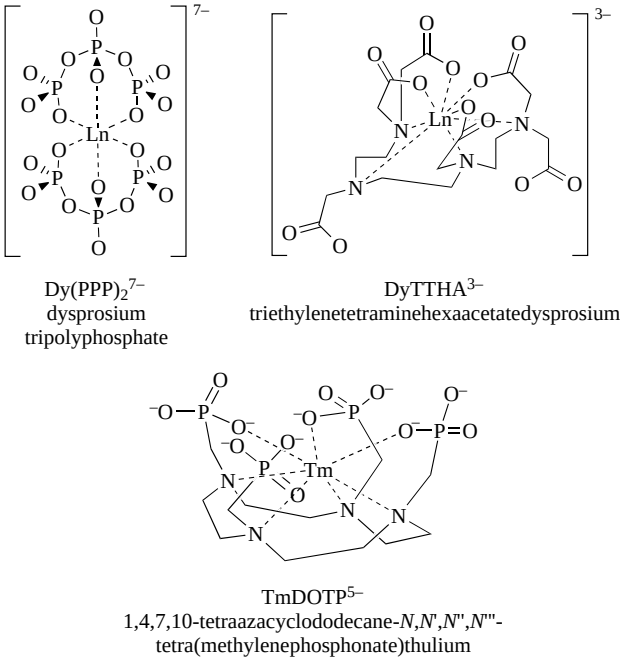

Figure 2 Putative structures for the three shift reagents currently in use to discriminate intra- and extracellular Na^+, K^+, and Li^+ NMR signals in biological systems. (Reproduced by permission of Kluwer Academic Press from J. S. Ingwall, 'Cardiovascular Magnetic Resonance Spectroscopy', 1992, Ch. 13, p. 195)

2.1.1 Properties of Frequency Shift Reagents

Aqueous shift reagents enable the spectroscopist to vary the resonance frequency of nuclei such as ^{23}Na, ^{39}K, ^{25}Mg, and ^{43}Ca. All shift reagents for cations consist of a paramagnetic ion, typically one of the lanthanides such as dysprosium, chelated to an anionic ligand (or ligands). The net negative charge on the chelated lanthanide complex is necessary for interaction between the cation and the shift reagent. The anionic character of shift reagents also minimizes binding to biological macromolecules and to membranes, essentially precluding their entry into the cell.

In general, the change of the observed chemical shift of a cation induced by the presence of a paramagnetic compound includes a diamagnetic contribution owing to a complex formation, contact hyperfine shift, and dipolar hyperfine (pseudocontact) shift. In the case of shift reagents for cations, the cation does not bond directly to the lanthanide; consequently, the contact hyperfine shift does not contribute. The complex formation shift term is negligible. As a result, the shift induced by a shift reagent is primarily from the dipolar hyperfine shift.

A magnetic dipolar interaction between the paramagnetic metal ion of the shift reagent and the cation nucleus shifts the resonance frequency of the observed nucleus. The nature of the dipolar interaction requires a specific binding site (or sites) for the cation on the complex relatively close to the paramagnetic center. The binding of the cation is relatively weak or labile; as a result, all the cationic nuclei in the sample interact briefly with the site and the lifetime of the bound cation is very short. If the average lifetime of the cation is much less than the inverse of the frequency difference between the bound and the free cation, only one resonance frequency will be observed (rapid exchange on the NMR time scale).

The direction of the observed shift, either upfield (decreasing frequency) or downfield (increasing frequency), is a characteristic of the particular shift reagent complex and the lanthanide ion. For example, substituting the lanthanide thulium for dysprosium with the same chelate results in a reversal of the direction of the observed shift. Different chelates of the same lanthanide ion can cause shifts in opposite directions. The magnitude of the observed shift for each particular shift reagent depends on the ratio of shift reagent to cation, adding more shift reagent at constant cation concentration results in a greater shift. The magnitude also depends on the total cation content. For example, adding more K^+ to a shift reagent solution decreases the observed shift in a ^{23}Na NMR spectrum. Divalent ions, such as Ca^{2+}, typically bind more strongly to the shift reagent and are, therefore, more effective at reducing the observed shift.

The dipolar shift described above is usually the dominant mechanism by which cation resonance shifts are induced by shift reagents. However, in any NMR sample the chemical shift can be affected by bulk magnetic susceptibility (BMS). The susceptibility shifts are the result of shielding effects produced by the surrounding medium, not the local electrons. Paramagnetic compounds produce large magnetic susceptibility effects. This type of paramagnetic susceptibility shift is observed in samples that have compartments that are not spherical. BMS shifts depend on differences in the susceptibility, shape, and orientation of each compartment with respect to the magnetic field. BMS shifts are predictable in certain well-defined situations.[18] Based on experiments using parallel coaxial glass cylinders,[18] simple cell suspensions,[4] and skeletal muscle containing oriented fibers,[19] it is clear that the ^{23}Na spectra of a multicompartment system in which only some of the compartments contain shift reagent are determined by a combination of hyperfine shift and BMS shifts. The BMS shifts in most biological samples are not predictable. Since the BMS shifts are variable in direction and extent, the net effect is an increase in observed linewidths.[20] The shift of intracellular resonances induced by shift reagents in other compartments is a result of the susceptibility shift.

2.1.2 Comparison of Shift Reagents

NMR properties: Each of the shift reagents currently in use to distinguish extracellular Na^+ (Na_o) and Na_i in biological samples produces spectra with both hyperfine and BMS shifts, but their relative contributions differ. For the same concentration of shift reagent, the hyperfine shift is much larger for $Dy(PPP)_2^{7-}$ than for $TmDOTP^{5-}$, which in turn is larger than for $DyTTHA^{3-}$. The contribution of BMS shift effects is smaller for $TmDOTP^{5-}$ than for $DyTTHA^{3-}$. Importantly, at concentrations of 3–10 mM, each of these shift reagents shifts the Na_o signal at least 2–4 ppm, allowing discrimination of Na_o and Na_i signals.

Physiological requirements: Shift reagents must also be compatible with the physiological requirements of the system under study. By assessing cardiac performance (heart rate, aortic pressure, left ventricular pressures) and the contents of the high-energy phosphate compounds ATP and phosphocrea-

tine (or some other sensitive marker) in vivo and in isolated hearts, short-term toxicity has been assessed. Subject to action by phosphatases, $Dy(PPP)_2^{7-}$ is not stable in most biological samples, yielding free lanthanide which is toxic. Precipitates form at physiological Ca^{2+} concentrations. Consequently, this reagent has limited biological usefulness. Neither $DyTTHA^{3-}$ nor $TmDOTP^{5-}$ disturbs heart function or high-energy phosphate content in isolated hearts provided that care is taken to maintain normal levels of extracellular cations, especially Ca^{2+}. Supplying $DyTTHA^{3-}$ (maximum concentration of 16 mM in blood)[21] to the living rat had no effects on hemodynamics or high-energy phosphate content of skeletal muscle.[15] Preservation of cardiac function and high-energy phosphate content also supports the conclusion that the sarcolemma is not permeable to these shift reagents, thereby allowing discrimination of Na_i and Na_o.

In summary, $TmDOTP^{5-}$ provides good shifts with little BMS-induced broadening. Its major limitation is loss of solubility with Ca^{2+} levels greater than 1 mM. Nonetheless, $TmDOTP^{5-}$ has been used successfully in the intact rat.[17,22] $DyTTHA^{3-}$ is quite stable in solutions containing high [Ca^{2+}]. However, it does not offer large hyperfine shifts. Moreover, the $DyTTHA^{3-}$ concentrations employed typically induce bulk magnetic susceptibility shifts, which broadens both the intra- and extracellular resonances. $DyTTHA^{3-}$ has been successfully used in the intact rat,[15] pig,[16] and dog[23,24].

2.2 Information Available from ^{23}Na NMS with Shift Reagents for Cations

2.2.1 *Information Derived from Changes in Chemical Shift*

Information derived from changes in chemical shift of Na_o resonance with time includes kinetics of shift reagent permeation into the tissue and its washout, the extent of perfusion, and the distribution volume of shift reagent. These have been described for skeletal muscle in vivo.[16,21] The chemical shift of Na_i signal in tissues perfused with shift reagents is small, typically 0.25 ppm; this shift results from BMS effects and does not provide information.

2.2.2 *Information Derived from Changes in ^{23}Na Signal Intensities*

The Na_o signal is proportional to the amount of Na in all spaces accessible to shift reagent, while the Na_i signal is proportional to the amount of free Na^+ in the compartment(s) not accessible to shift reagent. Electron probe X-ray microanalysis of heart muscle confirms the assumption that almost all cytolic Na^+ is unbound and also provides evidence that Na^+ is homogeneously distributed through the intracellular space, at least on this scale of measurement. The amounts of Na_i measured by ^{23}Na NMR with shift reagent are the volume-weighted averages over the entire cell population contained within the NMR-sensitive volume. For many tissues, there is significant heterogeneity of cell type; however, for striated muscle, myocytes comprise 80% or more of tissue volume. Therefore, changes in the Na_i signal faithfully report changes in the amount of Na_i in myocytes.

Visibility factor: The amount of Na^+ in any compartment is proportional to the product of its concentration, the volume of the compartment, and the NMR visibility factor. The NMR visibility factor is the ratio of amount of Na^+ detected by ^{23}Na NMS to the amount measured by other chemical (putatively accurate) techniques. Thus, if volume and visibility factor were known, ^{23}Na resonance areas could be converted to cation concentrations. For this reason, the history of ^{23}Na NMR is replete with attempts to establish both the NMR visibility factor of Na_i and to offer explanations for NMR 'invisibility'.

Published visibility factors for ^{23}Na in biological systems range from 0.1 to 1.0. For a system in which all the Na is the aqua ion and the ion is in a simple bulk solution, the three single quantum transitions of the spin-$\frac{3}{2}$ nuclide are degenerate and the visibility is 1.0. In contrast, for at least some biological systems, it has been thought that only the central transition is visible, yielding a visibility factor of 0.4. Others have suggested that each of the transitions were equally visible or invisible, and, therefore, signal from each transition must contribute equally to the observed signal. In an elegant theoretical and experimental analysis of all six relaxation rate constants of the Na^+ resonance obtained for a single population of isolated spins in fast exchange, Rooney and Springer demonstrated that a major determinant of the so-called 'visibility' is the delay between the hard pulse and enabling of the receiver, the 'dead time'.[4,25] The shorter the dead time, the higher the visibility factor, i.e. the more of the signal that will be captured. This dependence may explain some of the variability in literature values.

In skeletal muscle, Balschi et al. showed that the visibility factors of the interstitial and intracellular Na are essentially the same or, more precisely, that the visibility of the Na^+ which moves from the interstitium to the intracellular spaces is unchanged.[15] An analogous analysis of the Na^+ signals for the vascular compartment of an isolated perfused heart and its surrounding bath during collapse of the vasculature (caused simply by changing perfusion pressure from 100 to 0 mmHg) showed that the visibility of Na^+ moving from vascular to the bath is not altered by changing environments. Therefore, it is likely that the visibility factors are similar for interstitial and intracellular spaces (probably <1.0) and for vascular and bath (probably 1.0) in a perfused heart. By combining approaches such as these with standard curves, carefully constructed to mimic lossy environments, it should be possible to assess at least changes in visibility factors.

Calculation of concentration: There are two ways of calculating Na_i using ^{23}Na NMR spectra, the ratio method and external standard method. The ratio method takes advantage of the simultaneous measurement of Na_o and Na_i signals in ^{23}Na spectra with shift reagent. Rooney and Springer provide a strategy to quantitate intracellular sodium area (see their Figure 8c and discussion).[4] Briefly they recommend that the total resonance area of Na_i and Na_o be integrated, curve resolution being employed to integrate Na_i. The Na_i area should then be multiplied by 2.5 (this analysis predicts that only the central resonance, the $\frac{1}{2}$– $-\frac{1}{2}$ transition, is accurately quantified) to provide the total Na_i area and this area subtracted from the total to provide the Na_o area.[4] The value of Na_i can be calculated using the relationship:

$$\frac{A_{Na_i}}{A_{Na_o}} = \frac{[Na^+]_i V_i v_i}{[Na^+]_o V_o v_o} \quad (1)$$

where A_{Na_o} is the shifted peak area, A_{Na_i} is the unshifted resonance area, $[Na^+]_i$ is intracellular Na^+ concentration, $[Na^+]_o$ is extracellular interstitial Na^+ concentration, V_i is the intracellular volume, V_o is the extracellular volume, v_i is the visibility of Na_i and v_o is the visibility of Na_o. Solving for $[Na^+]_i$ yields:

$$[Na^+]_i = \frac{A_{Na_i} V_o v_o [Na^+]_o}{A_{Na_o} V_i v_i} \quad (2)$$

The ratio method is appropriate for surface coil experiments where the NMR-sensitive volume has an irregular shape. In experiments where the sample is entirely contained in the NMR-sensitive volume, an external or reference standard may be used to relate area to amount. In this case, the visibility of the compartments reported by Na_o and Na_i must be known.

In both cases, the volume of each compartment must be known. For some tissues, such as resting skeletal muscle, there is good agreement in the literature. However, for isolated organs, there is little or no information about the magnitude of the vascular bed during perfusion or how it changes with time and intervention. The approach described by Clarke and colleagues using ^{31}P-NMR to measure phenylphosphonate and dimethylmethylphosphonate in the total and extracellular water spaces in vivo provides a means to solve this problem.[26,27] Another method to measure volumes is to use $TmDOTP^{5-}$ as a combined cation shift reagent and extracellular space marker, thereby allowing quantification of $[Na^+]_i$ in vivo by NMR.[28,29].

Results from both NMR and classical experiments show that $[Na^+]_i$ differs for different striated muscles for a given species: 5 mM for rat skeletal muscle by NMR[15] and 10 mM by neutron activation analysis[30] versus ~15 mM for rat heart by ion-selective electrodes.[31] Even for the same tissue, $[Na^+]_i$ differs among species: $[Na^+]_i$ in the hearts of rat, rabbit, and guinea pig are 15, 10, and 10 mM, respectively (note that these estimates assume the visibility factor is 0.6). A more complete comparison of $[Na^+]_i$ determined by classical techniques and by ^{23}Na NMS for heart has been recently summarized.[32]

3 APPLICATION OF ^{23}Na, ^{7}Li, ^{39}K, AND ^{87}Rb MRS TO STRIATED MUSCLE: DEFINING CATION MOVEMENTS DURING ISCHEMIA IN THE RAT HEART

Cation MRS with and without shift reagents has been used to measure intra- and extracellular Na^+, Li^+, K^+, and Rb^+ contents. Many studies have examined cation changes during total global ischemia (i.e. zero flow) in isolated hearts of small mammals, typically rats. We have also examined changes in Na_i in the intact heart of the open chest pig and dog during regional ischemia. We illustrate these applications with several examples.

In the submerged isolated heart, there are five major spatial compartments that contain cations: the intracellular space, the extracellular space, the coronary vasculature, the cardiac chambers (atria and ventricles), and the volume outside the heart within the NMR tube, which we term the bath. For all calculations with this model, we assumed that the extracellular (interstitial, vascular, and chamber) ion concentration, [ion], was equal to the perfusate ion concentration during preischemia and reperfusion. For the rat heart during buffer perfusion at 37°C and 100 mmHg pressure we used the following volumes: V_i 0.48 ml g^{-1} blotted weight and V_o 1.45 ml g^{-1} blotted weight.[26]

3.1 MRS of ^{23}Na

3.1.1 Isolated Heart Studies

The basic protocol consisted of 28 min perfusion with buffer containing the shift reagent followed by 28 min of total global normothermic ischemia. The heart was bathed with ion-free buffer containing shift reagent and mannitol under control of a separate pump. The bath was used to minimize cation signal from the bath. Use of shift reagent in both the Krebs–Henseleit perfusion fluid and the mannitol bath separated the signals from Na_i and Na_o (Figure 3a). The broad resonances underlying the heart signals, ranging from 0 to 9 ppm, represent Na^+ in the mannitol-containing bath, whereas the large shifted peaks, at 1.2–5 ppm, represent buffer Na^+ in the vascular, chamber, and interstitial spaces of the heart (Na_o). The small upfield shoulder on the shifted peak at 1.2–0 ppm represents the resonance of Na_i.

During zero-flow ischemia, the large shifted peak (Na_o) moves ~2 ppm downfield because of the movement of Na^+ from the myocardial vasculature and chambers to the mannitol bath. The area of this peak decreases during the course of ischemia; concomitantly there are progressive increases in the areas of Na_i resonance and in the shifted resonances of the bath. Using the peak areas from the spectra shown in Figure 3a, we estimate that by 28 min of ischemia the Na_i signal increased to 3.6 times the preischemic values: from 9.1 ± 1.3 mM (uncorrected for visibility factor) in the preischemic rat heart to 32.1 ± 1.2 mM at 28 min ischemia. During this time, 79% of the extracellular Na^+ signal moved from the heart to the bath. Assuming that the only water movement was from the heart to the bath and that no water moved from the extracellular to the intracellular space during ischemia, the changes in $[Na^+]_i$ and V_o allow calculation of the changes in $[Na^+]_o$, which decreased from 144 mM in the preischemic heart to 108 mM after 28 min ischemia. Therefore, the ratio of $[Na^+]_o$ to $[Na^+]_i$ during preischemia was 16 (144/9.1) and after 28 min ischemia was 3.4 (108/32). Using the calculated values for $[Na^+]_o$ and $[Na^+]_i$ in the Nernst equation, these data show that $[Na^+]_i$ in the preischemic heart would be in electrochemical equilibrium with a membrane potential of +74 mV.

A number of studies have attempted to define the Na^+-transport mechanisms during global ischemia in the isolated rat heart. During both low- and zero-flow ischemia, Na_i did not increase in hearts treated with the Na^+/H^+ exchange inhibitor, 5-(*N*-ethyl-*N*-isopropyl) amiloride (EIPA).[33] During reperfusion recovery, left ventricular developed pressure was improved for zero-flow hearts treated with EIPA. These studies show that Na^+/H^+ exchange is an important mechanism for Na_i accumulation during myocardial ischemia.[33,34] After 10 min of global ischemia, lidocaine, a class IB fast Na^+ channel blocker known to protect ischemic myocardium, resulted in lower $[Na^+]_i$.[35]

Other studies have attempted to define the Na^+-transport mechanisms during reperfusion following ischemia. A study that tested the effects of limiting Na^+-K^+ ATPase activity

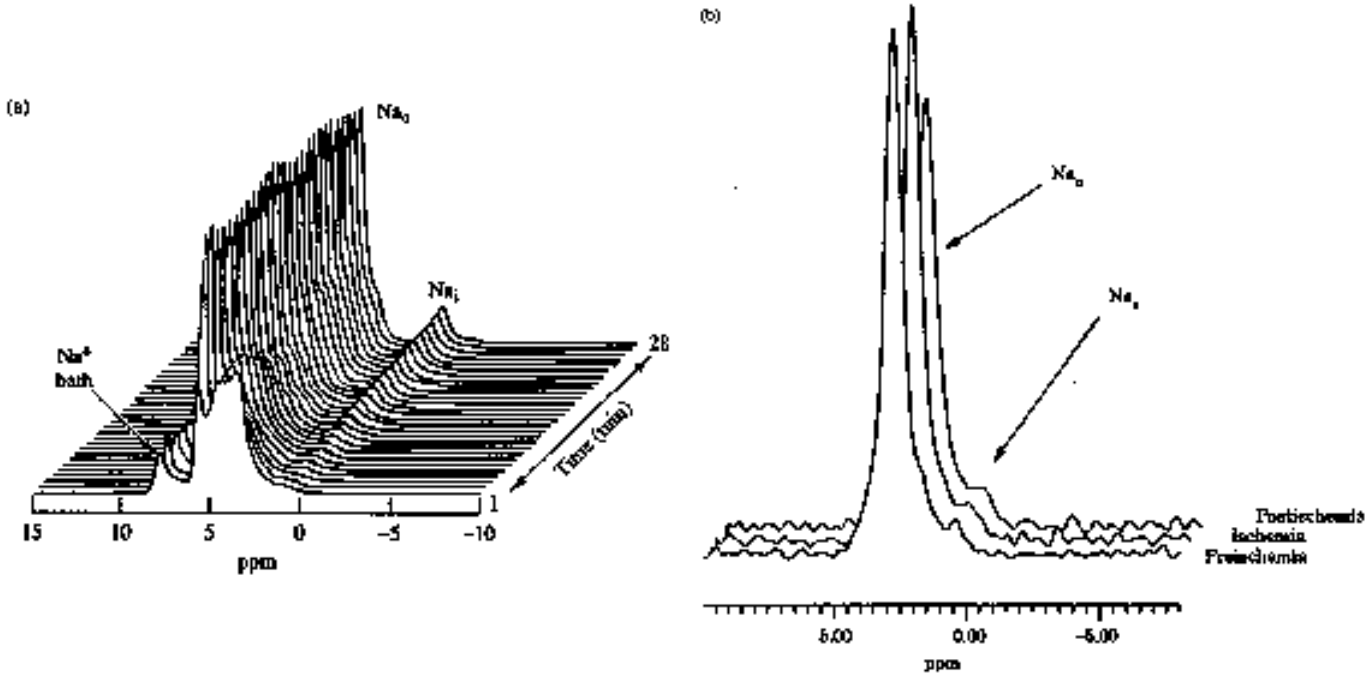

Figure 3 (a) Sodium-23 NMR spectra of an isolated buffer-perfused rat heart showing the increase in intracellular Na^+ (Na_i) during 28 min total, global ischemia. Spectra were acquired using a pulse angle of 90° and a recycle time of 250 ms. Each spectrum consisted of 240 FID, providing a time resolution of 1 min. The spectral width was ±2 kHz and 1000 data points were collected. Prior to Fourier transformation, the data were multiplied by a double exponential function (*DM* = 12, GE software) for resolution enhancement. (b) An offset stacked plot of ^{23}Na NMR spectra obtained from the in situ pig heart after infusion with the shift reagent $DyTTHA^{3-}$. The spectra are displayed from the preischemia (front), ischemia, and postischemia (rear) periods. The ^{23}Na NMR resonances of extracellular Na^+ (Na_o) and of intracellular Na^+ (Na_i) are identified

with ouabain found that Na^+_i increased upon reperfusion in hearts treated with ouabain[36] but did not increase if EIPA was also added to inhibit Na^+/H^+ exchange. This indicates the existence of a Na^+/H^+ exchange-mediated Na^+ influx upon reperfusion, which is usually masked by Na^+-K^+ ATPase activity. Another recent study has shown that altering the $[Ca^{2+}]_o$ can modify the rate at which Na_i decreases during reperfusion. Following reperfusion, low $[Ca^{2+}]_o$ slowed the decrease in Na_i while high $[Ca^{2+}]_o$ accelerated the decrease in Na_i.[37] This implicates the role of the Na^+/Ca^{2+} exchanger in reperfusion ion movements.

3.1.2 Intact Animal Studies

Isolated cells and perfused hearts are relatively well-controlled systems. There are, however, many differences between isolated systems and the in situ heart. The technical difficulty of accurately measuring Na_i in an intact heart is perhaps the main reason that few of these values for the in situ heart exist. We tested the hypothesis that Na_i increases during regional reduced pressure ischemia in the in situ pig heart. Using ^{23}Na NMR in combination with the shift reagent $DyTTHA^{3-}$ the Na_o and Na_i contents of the pig heart could be distinguished (Figure 3b). We estimated a $[Na^+]_i$ of 7 mM for the pig left ventricle prior to ischemia.[16]

In a model of reduced-pressure regional ischemia, Na_i did not change during the first 18 min of ischemia with Na_i set to 1 for preischemia. Subsequently, Na_i increased from 1.3 at 22 min to 1.6 at 38 min, the end of ischemia. Levels remained elevated during early reperfusion; after 10 min of reperfusion Na_i had increased further to 1.9. This increase of Na_i and its delayed recovery during postischemia did not arise from insufficient reperfusion because phosphorylated metabolites, measured by concomitant ^{31}P NMR, all rapidly recovered during early reperfusion while Na_i was increasing. This remarkable response of Na_i to reperfusion may reflect enhanced Na^+ influx, possibly by Na^+/H^+ exchange, with or without reduced Na^+/K^+ ATPase efflux. Levels of Na_i returned to preischemia values at 18 min of reperfusion.[16]

3.2 MRS of ^7Li

Lithium-7 is 93% abundant with an NMR sensitivity that is twice that of ^{23}Na (Table 1). These NMR properties, combined with the ability of Li^+ to replace Na^+ in the fast Na^+/H^+ exchanger (see Figure 1) makes ^7Li MRS a useful tool to study Na^+ movements in biological samples.

Lithium-7 MRS has been used to show that the Na^+/H^+ antiporter contributes to net Na^+ influx during ischemia in isolated perfused hearts.[38] Fully relaxed ^7Li NMR spectra [such as shown in Figure 4(a)] were acquired throughout the protocol. The kinetics of Li^+ uptake were determined by perfusing hearts with a buffer containing 78 mM Li^+.

Movement of Li^+ into the intracellular space of the heart is monoexponential with a rate constant of 0.068 min^{-1}, a $t_{1/2}$ value of 10.3 min, and an initial rate of increase of 5.27 mM min^{-1}. The Li^+ concentration after 24 min of control perfusion was 57 ± 7 mM. ICP–AES analysis gave an intracellular Li^+

concentration of 50 ± 2 mM after 20 min perfusion showing that NMR visibility was approximately 1. Uptake in the well-perfused heart was unaffected by the Na^+/H^+ exchange inhibitor amiloride. At the end of the 28 min ischemia, $[Li]_i$ was 84 ±10 mM. Amiloride completely prevented the uptake of Li^+ that occurred during ischemia, showing that Na^+/H^+ exchange contributes importantly to the increase in Na_i during ischemia.

3.3 MRS of ^{39}K

The ^{39}K NMR spectrum of a rat heart perfused with buffer containing shift reagent has two well-defined peaks: a large intracellular K^+ resonance and a smaller downfield extracellular resonance, the area of which is proportional to the sum of K^+ in the vascular, interstitial, and bath spaces [Figure 4(b)]. The areas of both signals remained constant throughout control perfusion. During control perfusion the K_i signal comprised 74% of the total ^{39}K signal.

During ischemia, the vasculature collapses within minutes (owing to zero perfusion pressure) and perfusate is extruded into the bath. Hence, the extracellular compartment in exchange with the intracellular compartment is primarily the interstitium. Accordingly, the interstitial K^+ signal can be calculated as the difference between the sum of vasculature and bath K^+ signals and the total extracellular K^+ signal. By 28 min of ischemia, there was no detectable change in $[K^+]_i$ but interstitial $[K^+]$ decreased. The change corresponded to an increase in the potassium membrane potential from −88 mV to −46 mV.

3.4 MRS of ^{87}Rb

Rubidium-87 is a well-established congener for K. Relatively high natural abundance and high NMR sensitivity combined with low biological abundance make ^{87}Rb a good tracer for K^+ influx and efflux studies. Unlike ^{23}Na or ^{39}K NMR studies where changes in steady-state concentrations are measured with the aid of shift reagents, the rates of influx (in the presence of extracellular Rb^+) and efflux (in the absence of extracellular Rb^+) have been measured in the absence of shift reagents.

Measured rates of influx of Rb^+ have been used to estimate Na^+/K^+ ATPase activity in living tissues using radioisotopes, atomic absorption spectroscopy, and MRS. It has been shown using ^{87}Rb MRS that, under normal physiological conditions, Rb^+ influx occurs mainly through Na^+-K^+ ATPase; the contribution of the Na^+-K^+/2Cl^- cotransporter and K^+ channels to Rb^+ influx is small.[39] Therefore, ^{87}Rb NMR can be used to assess the activity of the Na^+-K^+ ATPase in the perfused heart under normal and ischemic conditions.[40]

4 SUMMARY

MRS with ^{23}Na and ^{39}K in combination with shift reagents allows measurement of intra- and extracellular $[Na^+]$ and $[K^+]$ in biological systems. The use of ^{87}Rb MRS provides a measurement of Na^+-K^+ ATPase activity. These techniques provide unique information on the transmembrane movements of Na^+ and K^+ in intact tissues.

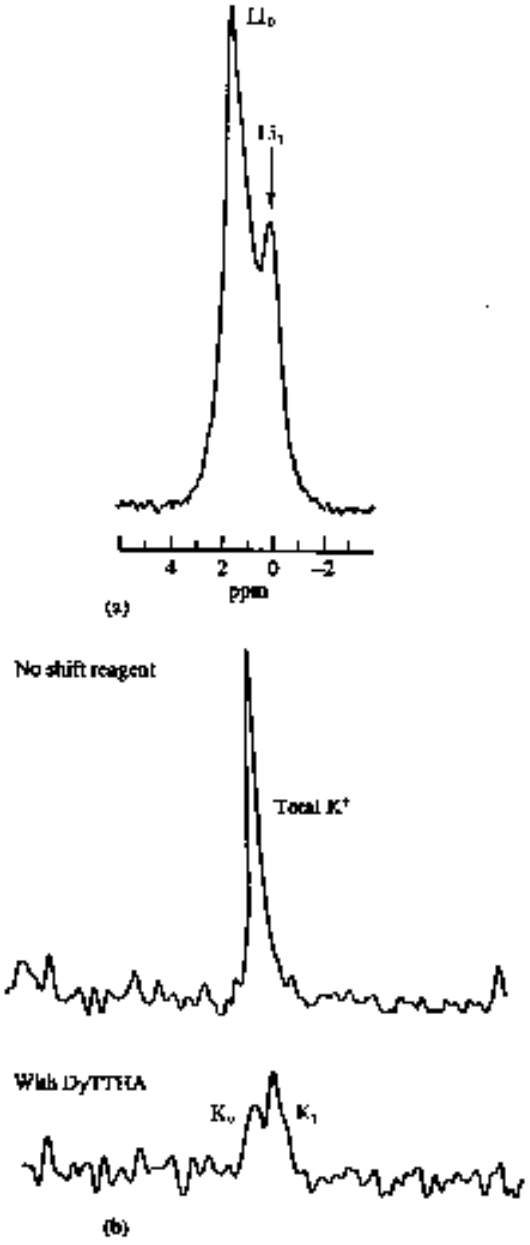

Figure 4 (a) Lithium-7 NMR spectra of a rat heart perfused with buffer containing shift reagent and 78 mM Li^+ (intracellular Li^+, Li_i; ecxtracellular Li^+, Li_o). Spectra were acquired at 8.34 T using a pulse angle of 90° and a recycle time of 45 s. Each spectrum consisted of 8 FID, providing a time resolution of 6 min. Prior to Fourier transformation, the data were multiplied by an exponential function giving a line broadening of 10 Hz for resolution enhancement. (b) Potassium-39 NMR spectra of a rat heart perfused with buffer containing the shift reagent $Dy(TTHA)^{3-}$ (intracellular K^+, K_i; extracellular K^+, K_o). Spectra were collected as described as in Figure 3. (Reproduced by permission of Springer-Verlag from J. S. Ingwall, 'Magnetic Resonance (MR) Imaging', 2nd ed., 1992, p. 131)

5 RELATED ARTICLES

Animal Methods in MRS; NMR Spectroscopy of the Human Heart; Sodium-23 Magnetic Resonance of Human Subjects.

6 REFERENCES

1. J. D. DeLayre, J. S. Ingwall, C. Malloy, and E. T. Fossel, *Science*, 1981, **212**, 935.
2. F. W. Cope and R. Damadian, *Nature (London)*, 1970, **228**, 76.
3. M. M. Pike, J. C. Frazer, D. F. Dedrick, J. S. Ingwall, P. D. Allen, C. S. Springer, Jr., and T. W. Smith, *Biophys. J.*, 1985, **48**, 159.
4. W. D. Rooney and C. S. Springer, *NMR Biomed.*, 1991, **4**, 209.
5. L. A. Jelicks and R. K. Gupta, *Magn. Reson. Med.*, 1993, **29**, 130.
6. J. M. Dizon, J. S. Tauskela, D. Wise, D. Burkhoff, P. J. Cannon, and J. Katz, *Magn. Reson. Med.*, 1996, **35**, 336.
7. J. S. Tauskela, J. M. Dizon, J. Whang, and J. Katz, *Magn. Reson.*, 1997, **127**, 115.
8. M. M. Pike, S. R. Simon, J. A. Balschi, and C. S. Springer, Jr., *Proc. Natl. Acad. Sci. USA*, 1982, **79**, 810.
9. R. K. Gupta and P. Gupta, *J. Magn. Reson.*, 1982, **47**, 344.
10. S. C.-K. Chu, M. M. Pike, E. T. Fossel, T. W. Smith, J. S. Balschi, and C. S. Springer, Jr., *J. Magn. Reson.*, 1984, **56**, 33.
11. D. C. Buster, M. C. A. Castro, C. F. G. C. Geraldes, C. R. Malloy, A. D. Sherry, and T. C. Siemers, *Magn. Reson. Med.*, 1990, **15**, 25.
12. J. A. Balschi, V. P. Cirillo, and C. S. Springer, Jr., *Biophys. J*, 1982, **38**, 323.
13. H. Hoefeler, D. Jensen, M. M. Pike, J. L. DeLayre, V. Cirillo, C. S. Springer, Jr., E. T. Fossel, and J. A. Balschi, *Biochemistry*, 1987, **26**, 4953.
14. M. M. Pike, E. T. Fossel, T. W. Smith, and C. S. Springer, Jr., *Am. J. Physiol.*, 1984, **246**, C528.
15. J. A. Balschi, J. A. Bittl, C. S. Springer, Jr., and J. S. Ingwall, *NMR Biomed.*, 1990 **3**, 47.
16. J. A. Balschi, *Basic Res. Cardiol.*, 1999, **94**, 60.
17. N. Bansal, M. J. Germann, I. Lazar, C. R. Malloy, and A. D. *JMRI*, 1992, **2**, 385.
18. S. C.-K. Chu, Y. Xu, J. A. Balschi, and C. S. Springer, Jr., *Magn. Reson. Med.*, 1990, **13**, 239.
19. S. J. Kohler, S. B. Perry, L. C. Stewart, D. E. Atkinson, K. Clarke, and J. S. Ingwall, *Magn. Reson. Med.*, 1991, **18**, 15.
20. J. A. Balschi, S. J. Kohler, J. A. Bittl, C. S. Springer, Jr., and J. S. Ingwall, *J. Magn. Reson.*, 1989, **83**, 138.
21. M. S. Albert, W. Huang, J. H. Lee, J. A. Balschi, and C. S Springer, Jr., *NMR Biomed.*, 1993, **6**, 7.
22. V. Seshan, A. D. Sherry, and N. Bansal, *Magn. Reson. Med.*, 1997, **38**, 821.
23. S. M. Eleff, I. J. McLennan, G. K. Hart, Y. Maruki, R. J. Traystman, and R. C. Koehler, *Magn. Reson. Med*, 1993, **30**, 11.
24. J. O. Hai and J. A. Balschi, *Circulation*, 1995, **92**, I-635.
25. W. D. Rooney and C. S. Springer, Jr., *NMR Biomed*, 1991, **4**, 227.
26. K. Clarke, J. F. Nedelec, S. M. Humphrey, L. C. Stewart, S. Neubauer, J. A. Balschi, A. G. Kleber, C. S. Springer, Jr., T. W. Smith, and J. S. Ingwall, *NMR Biomed.*, 1993, **6**, 278.
27. K. Clarke, R. E. Anderson, J. F. Nedelec, D. O. Foster, and A. Ally, *Magn. Reson. Med*, 1994, **32**, 181.
28. P. M. Winter, V. Seshan, J. D. Makos, A. D. Sherry C. R. Malloy, and N. Bansal, *J. Appl. Physiol*, 1998, **85**, 1806.
29. J. D. Makos, C. R. Malloy, and A. D. Sherry, *J. Appl. Physiol.,* 1998, **85**, 1800.
30. M. I. Linginger and G. J. F. Heigenhauser, *J. Appl. Physiol.*, 1987, **63**, 426.
31. M. J. Shattock and D. M. Bers, *Am. J. Physiol.*, 1989, **256**, C813.
32. J. S. Ingwall, 'Cardiovascular Magnetic Resonance Spectroscopy.', Kluwer Academic Press, Norwell, MA, 1992, Chap. 13, p. 195.
33. M. M. Pike, C. S. Luo, M. D. Clark, K. A. Kirk, M. Kitakaze, M. C. Madden, E. J. Cragoe, Jr., and G. M. Pohost, *Am. J. Physiol.*, 1993, **265**, H2017.
34. E. Murphy, M. Perlman, R. E. London, and C. Steenbergen, *Circ. Res.*, 1991, **68**, 1250.
35. N. B. Butwell, R. Ramasamy, I. Lazar, A. D. Sherry, and C. R. Malloy, *Am. J. Physiol.*, 1993, **264**, H1884.
36. J. G. van Emous, J. H. Schreur, T. J. Ruigrok, and C. J. van Echteld, *J. Mol. Cell. Cardiol.*, 1998, **30**, 337.
37. K. Imahashi, H. Kusuoka, K. Hashimoto, J. Yoshioka, H. Yamaguchi, and T. Nisimura, *Circ. Res.*, 1999, **84**, 1401.
38. C. A. Keon, J.-F. Nedelec, and K. Clarke, *Circ. Res.*, 1991, **84**, II-7.
39. V. V. Kupriyanov, L. C. Stewart, B. Xiang, J. Kwak, and R. Deslauriers, *Circ. Res.*, 1991, **76**, 839.
40. H. R. Cross, G. K. Radda, and K. Clarke, *Magn. Reson. Med.*, 1995, **34**, 673.

Biographical Sketches

James A. Balschi, *b*. 1950. B.A. 1973, Temple University, Ph.D., 1984, State University of New York at Stony Brook. Postdoctoral studies in cardiac metabolism and in vivo NMR at Harvard Medical School, 1983–86, Faculty in Medicine, Harvard Medical School and Brigham and Women's Hospital, 1986–88, University of Alabama at Birmingham, in Medicine, 1988–98, Harvard Medical School and Brigham and Women's Hospital, 1998–present. Approx. 30 publications. Current research interests: relationship between energy metabolism and cation transport studied using ^{31}P and ^{23}Na MRS.

Kieran Clarke. *b* 1951. B.Sc., 1973, Flinders University, Ph.D., 1986, University of Queensland. Postdoctoral studies in ^{31}P and ^{23}Na NMR at Harvard Medical School, 1987–89; National Research Council, Canada, 1989–91; Oxford University, UK, 1991–present. Approx. 50 publications. Research interests: use of NMR spectroscopy to study myocardial cation movements as the subcellular cause of ischemic damage and control of myocardial oxidative phosphorylation.

Laura C. Stewart. *b* 1959. B.Sc., 1982, University of Toronto, Ph.D., 1987, National Research Council. Faculty in Medicine, Harvard Medical School and Brigham and Women's Hospital, 1988–90, National Research Council, 1990–93, Science Consultant for research institutes, government and industry, 1993–present. Approx. 30 publications. Research interests: ^{31}P, ^{23}Na, ^{39}K, and ^{87}Rb NMR spectroscopy to study cation movements in striated and smooth muscles.

Monique Bernard. *b* 1958. M.S., 1980, Ph.D., 1983, University of Aix-Marseille. Faculty in Medicine, Centre National de la Recherche Scientifique, 1983–present; Faculty of Medicine, Harvard Medical School and Brigham and Women's Hospital, 1989–1990. Approx. 40 publications. Research interests: NMR applications to biological systems, energy metabolism in *E. coli* cells, myocardial protection during ischemia and reperfusion, and ^{13}C NMR conformational dynamics of proteins in solution.

Joanne S. Ingwall. *b* 1941. B.S., 1963, LeMoyne College, Ph.D., 1968, Cornell University. Postdoctoral training in Cell Biology and Biochemistry, University of California, San Francisco, 1968–73. Faculty in Medicine Biochemistry, University of California, San Diego, 1973–76, Faculty in Medicine (Physiology), Harvard Medical School and Brigham and Women's Hospital, 1977–present. Approx. 160 publications. Current research interests: regulation of cardiac energy metabolism and cation transport using ^{31}P and ^{23}Na NMR spectroscopy.

Cells and Cell Systems MRS

Jerry D. Glickson

The Johns Hopkins University School of Medicine, Baltimore, MD, USA

1 INTRODUCTION

Magnetic resonance spectroscopy (MRS) of cells and cell systems (or cellular MRS) includes studies of intact living cells or assemblies of cells. Perfused organs and tissues, and cell extracts are not included in this topic (see ***Tissue and Cell Extracts MRS***).

A key advantage of cellular MRS is that it can be conducted under well-defined and well-controlled conditions that generally cannot be achieved in the intact organism. The cellular model is often designed to facilitate the interpretation of in vivo MRS data. Systemic physiological effects, which often limit the interpretation of in vivo MRS, are absent in ex vivo cellular studies or can be systematically simulated and evaluated. However, some applications of cellular MRS focus on issues unique to the cellular system, e.g. characterization of bioreactors for production of various biological products, cell preservation, artificial organs, and microbiological studies. The range of cell systems that have been examined includes isolated bacteria and other prokaryotes, yeast, plant cells, mammalian cells, and even giant single mammalian cells. In most instances the goal is to study a uniform cell population; however, the effects of heterogeneity can be systematically investigated using multicellular assemblies such as tumor spheroids or renal microtubules. Subcellular organelles such as mitochondria and chromaffin granules have also been investigated. A variety of nuclear species have been monitored, including ^{1}H, ^{2}H, ^{3}H, ^{7}Li, ^{13}C, ^{15}N, ^{19}F, ^{23}Na, ^{31}P, ^{39}K, and ^{133}Cs, the main limitation being sensitivity and cost.

A number of excellent reviews of cellular MRS have been published.[1,2] We will limit ourselves to a description of key methods, their advantages and disadvantages, and will also present a few examples of important applications. We will note some recent developments that permit noninvasive discrimination between intracellular and extracellular metabolites. Finally, we will evaluate the potential of this method, and indicate possible areas for development.

2 PROBE DESIGN

2.1 Cell Suspensions

Early cellular NMR studies were performed on unstirred high-density suspensions of cells in conventional NMR tubes. Cells were often cooled in order to preserve viability. Spectral quality was generally poor, and cells died as substrates were depleted and toxic waste products accumulated. These methods were most suitable for nonoxygen-dependent cells that can tolerate high cell densities, such as red blood cells and anaerobic bacteria. Despite these limitations, the early studies demonstrated the potential utility of in vivo measurements of cellular metabolism.

The first cellular NMR studies were ^{13}C NMR measurements by Matwiyoff's laboratory on suspensions of blood cells[3] containing ^{13}C-labeled CO_2, CO, and CN^- and on the metabolism of [1-^{13}C]glucose by yeast.[4] Moon and Richards[5] first demonstrated the ability of ^{31}P NMR to measure intracellular pH from the chemical shift of the 2,3-diphosphodiglycerate (DPG, an intracellular metabolite) peaks and from the intracellular inorganic phosphate (Pi) resonance. Shulman's group at Bell Laboratories and later at Yale University initiated ^{31}P and ^{13}C studies of energy and carbohydrate metabolism, sodium transport and pH regulation in bacteria,[6,7] yeast,[8] liver cells,[9] and cultured tumor cells.[10] These studies had a seminal influence on the development of in vivo NMR spectroscopy, and demonstrated the unique ability of this method to examine key metabolic processes noninvasively.

Bubbling of oxygen into the NMR tube was introduced in order to oxygenate and stir the suspension, but the timing of spectral accumulations had to be adjusted to avoid intervals when bubbles were in the tube. Some of the limitations of these early methods could be overcome by using larger chambers equipped with mechanical stirrers and provided with ports for delivery of gases and sensors for monitoring temperature and pO_2; cells were examined at 37 °C for up to 2 h.[11,12] Placement of the receiver/transmitter coil inside the sample volume[12] improved sensitivity, but the apparent relaxation times were dependent on the mixing rate. Another variation of this approach is the 'airlift chamber'.[13,14] This assembly consists of a large NMR tube with a smaller-diameter concentric tube (open at both ends) inside it. A rapid stream of oxygen bubbles is delivered through a capillary located above the region of the receiver coil. This oxygenates the cells without introducing bubbles into the sampling region and causes efficient circulation of the cell suspension. Taylor and Deutsch[15] compared the airlift probe with a flow cell assembly for measuring oxygen concentrations and pH in suspensions of *Paracoccus denitrificans* (see Section 3.2). Since spectral characteristics, particularly relaxation times, depend on flow rate and bubble size, the flow and airlift systems have to be recalibrated for each experiment.

In summary, the key limitation of suspension systems is that they are applicable only to nonanchorage-dependent cells; they do not control the concentration of oxygen and vital substrates, and they allow toxic metabolic end-products to accumulate. Bubbling oxygen through the cell suspension, or mechanical stirring, often causes damage to fragile cells and modifies relaxation rates.

2.2 Perfusion Systems

2.2.1 General Characteristics

The solution to most of these problems is a perfused cell system, which allows long-term experiments to be performed on isolated cells, cell aggregates, or small organisms under conditions of well-defined medium composition. The system consists of an NMR probe in which the cells are retained by

attachment to beads, entrapment in a gel, or containment in a chamber with a semipermeable membrane. The perfusion system is attached to a reservoir that provides medium at a fixed temperature, usually 37 °C. For reasons of economy, recirculating systems are preferred when an expensive medium containing isotopically enriched substrates or expensive drugs is used. The recirculating system is adequate provided its capacity is large enough to prevent depletion of substrates or accumulation of toxic waste products; alternatively, a single-pass delivery system can be employed. Provision is generally made for delivery of gases, usually 5% CO_2/95% O_2 or air. Sterility should be maintained throughout the experiment by sterilizing the media and perfusion system, and by using large-capacity filters or closed systems. Perfusion systems have been designed for studies of both anchorage-dependent and anchorage-independent cells. Ng et al.[16] have constructed a system suitable for γ-irradiation of cells directly in the NMR tube without interruption of perfusion.

2.2.2 *Microcarrier Beads*

In 1981, Ugurbil et al.[17] introduced the first perfusion system for NMR investigation of anchorage-dependent cultured mammalian cells. Normal and transformed mouse embryo fibroblasts were grown on collagen-coated dextran microcarrier beads; at confluence the cells were transferred into a cylindrical glass chamber fitted with Plexiglas end-pieces containing nylon mesh screen filters for retention of the beads. A four-turn solenoidal coil was fitted around this sample chamber. Theoretically, a solenoid provides a 2.6-fold enhancement in sensitivity over a Helmholtz (saddle) coil.[18] However, in practice at least equivalent spectral quality can be achieved with a simpler system developed by Neeman and Degani[19] which employs a conventional 10 mm NMR tube and uses a commercial high-resolution Helmholtz coil (Figure 1). The improvement in magnetic field homogeneity of this design makes up for the higher intrinsic sensitivity of the solenoidal coil. The perfusate reservoir can easily be replaced for changing the perfusion medium, and the spectrometer can be programmed to monitor various nuclei according to a predefined protocol. Figures 2 and 3 show representative ^{31}P (202.5 MHz) and ^{13}C (125.7 MHz) spectra obtained with this system.

The key advantage of the microcarrier method is that it maintains cells in a uniform well-perfused state; several days of perfusion can be readily achieved with currently available perfusion probes (see below). The cell density is relatively low, and only a small fraction of the volume of the sample chamber is occupied by the cells (~6%). This improves homogeneity of perfusion since minimal depletion of oxygen and substrates avoids creation of local nutrient gradients.

Cell replication generally occurs, at least until the plateau phase of growth. Finding the proper conditions for attachment of cells to the beads is essential. Beads manufactured from various materials such as polyacrolein, polystyrene, glass, polyacrylamide, and agarose polyacrolein are commercially available. Coating with polylysine or collagen can be used to improve cell attachment. Gelatin beads or dextran beads covered with a layer of denatured collagen (Cytodex 3) are enzymatically degradable, which facilitates recovery of cells for assay of cell number and viability. Disadvantages of the microcarrier bead system include that it has relatively low

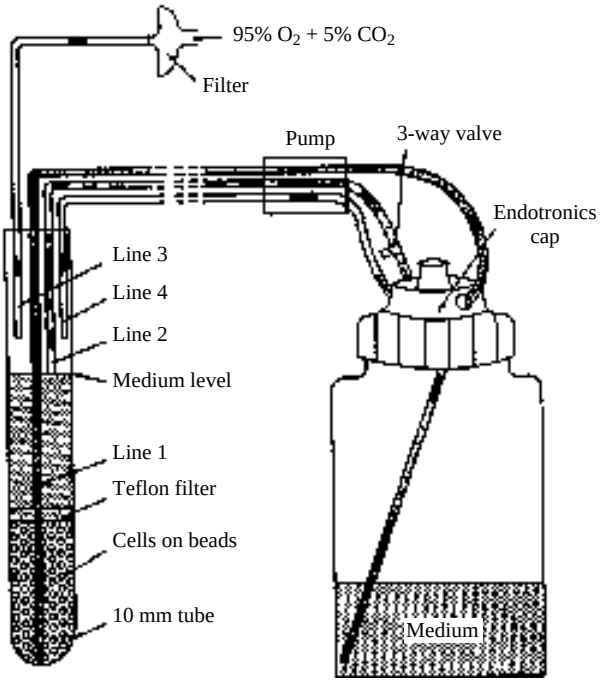

Figure 1 Schematic of perfusion system developed by Neeman and Degani[19] employing a 10 mm outer diameter NMR tube as the perfusion chamber. Line 1, inflow of perfusate; Line 2, removal of used medium mixed with 95% O_2 5% CO_2; Line 3, inflow of gas mixture; *Line 4*, additional return line. (Reproduced by permission of American Association for Cancer Research, Inc. from Neeman and Degani[19])

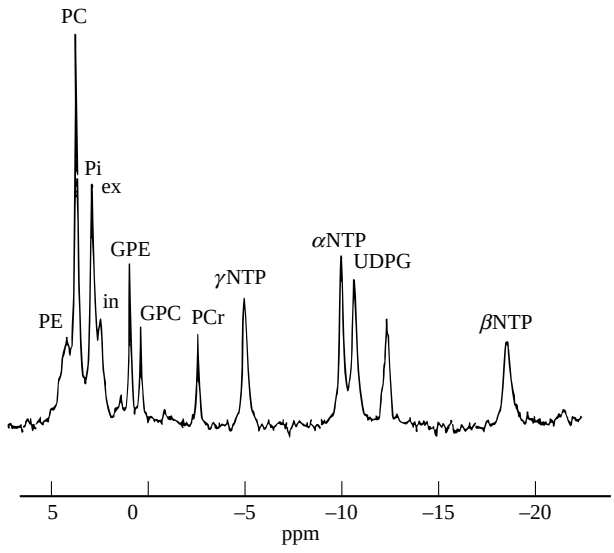

Figure 2 Fully relaxed ^{31}P spectrum of perfused T47D-clone 11 (5.2×10^7) cells treated for 5 days with 17β-estradiol (3×10^{-6} M). Each spectrum was obtained after approximately 30 min of perfusion, by accumulating 720 transients (2 h total accumulation) and processed using 10 Hz line broadening. NTP, nucleoside triphosphate; PC, phosphorylcholine; PE, phosphorylethanolamine; ex, extracellular; in, intracellular; GPE, glycerol–PE; GPC, glycerol–PC; PCr, phosphocreatine; UDPG, uridine diphosphoglucose. (Reproduced by permission of American Association for Cancer Research, Inc. from Neeman and Degani[19])

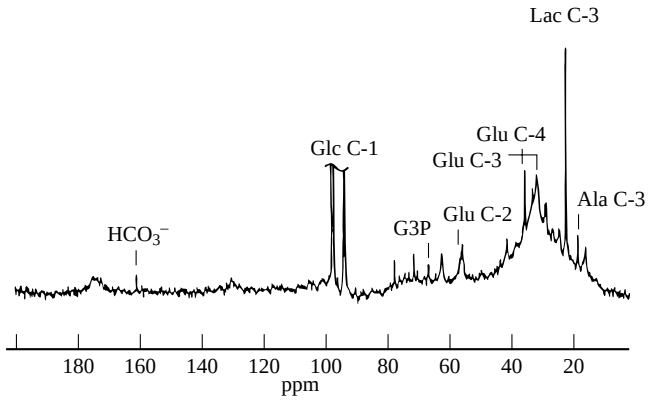

Figure 3 Carbon-13 NMR spectra of T47D-clone 11 (6.0×10^7) cells treated with estrogen as in Figure 2 after 1 h perfusion with medium containing [1-^{13}C]glucose. Spectra were Fourier transformed using 10 Hz line broadening. The designated glucose signals are due to nonenriched carbons of the glucose in the medium. (Reproduced by permission of American Association for Cancer Research, Inc. from Neeman and Degani[19])

spectral sensitivity, that it is limited to anchorage-dependent cells, and that exposure to cytotoxic agents (e.g. cancer drugs) can detach cells from the beads. Smaller beads increase the total cell volume and, hence, increase spectral sensitivity.

2.2.3 *Gels*

Cells have been immobilized by encapsulation in a variety of gelatinous materials. Encapsulation is usually simpler than attachment to microcarrier beads, and is applicable to anchorage-independent as well as to anchorage-dependent cells. An important advantage for studies of therapeutic agents is that encapsulation of the cells prevents cell detachment as a result of exposure to cytotoxic agents such as cancer drugs or γ-irradiation. The porosity of the matrix determines the rate of diffusion of substrates and metabolic end-products. The gel may also modify cellular growth characteristics. Preparation of cells for encapsulation in the gel can involve treatment with enzymes to isolate them from the primary culture system and exposure to low temperature. These procedures may modify important cellular characteristics. Removal of cells from the gel in a viable state suitable for clonogenic assay (ex vivo measurement of cellular capacity to replicate) can in some instances be difficult.

2.2.4 *Agarose Threads or Beads*

This method was first introduced by Foxall and Cohen in 1983.[20] Cells are mixed with liquid agarose in phosphate-buffered saline, and placed in a bath at 37 °C for 5–7 min to form a gel. The mixture is extruded under low pressure through 0.5 mm internal diameter tubing in an iced bath into an NMR tube containing growth medium. The solid threads are concentrated without compression at the bottom of the tube by a plastic insert. Perfusion is maintained by a peristaltic pump, and the system is aerated by diffusion of air through Teflon tubes in the system. The system is stable for more than 24 h when perfused with whole growth medium.

The agarose threads are permeable to proteins such as albumin and also to various polypeptides, thus permitting investigation of their effects on cellular metabolism and growth characteristics. The system is suitable for encapsulation of yeast, bacteria, protozoa, and a variety of mammalian cells. Small anchorage-independent cells such as lymphocytes tend gradually to wash out of (0.9%) agarose gel threads.[1] Additional limitations include the requirement for cooling cells in an ice bath and reduced cell growth rates in the agarose threads.

Encapsulation of cells in agarose beads is accomplished by mixing the cell suspension with warm liquid agarose and dispersing the suspension in paraffin oil with magnetic stirring. The mixture is cooled in an ice bath after the droplets have formed, to produce small solid cell-containing capsules, which are collected by centrifugation and placed in an appropriate medium and NMR perfusion system. This method has been used for studies of microorganisms, plant cells, and algae.[1] Entrapment in agarose did not alter metabolism, and allowed cells to proliferate. Lymphocyte proliferation has been examined in 3% agarose gel beads, but beads composed of 1.2% agarose were unstable.[21] Mouse hybridoma cells encapsulated in agarose were metabolically active and produced monoclonal antibodies.[1]

2.2.5 *Matrigel*

Growth rates of anchorage-dependent cells comparable with in vivo rates (of tumor cells) can be achieved by using a basement membrane matrix preparation extracted from a mouse tumor line (commercially available as Matrigel).[1] Cells are introduced into the liquid Matrigel in an ice bath; the suspension is warmed to 37 °C to form a gel, which is extruded through tubing to produce threads. Typically, threads are prepared at low cell density, and cells are allowed to grow in the threads before examination. Normal cells grown in Matrigel become morphologically and functionally similar to their in vivo counterparts; tumor cells simulate in vivo tumor cell growth, producing a high-density model tumor Figure 4. Nonuniform perfusion occurs in later stages of tumor growth, as it does in in vivo tumors and in spheroids (see below).

2.2.6 *Alginate Beads*

Narayan et al.[22] introduced a method for NMR studies of perfused tumor cells encapsulated in calcium alginate beads. Cells isolated from monolayer culture by trypsinization are suspended in a sodium alginate solution; beads form when droplets of this suspension are introduced into a $CaCl_2$ solution. The beads are washed with fresh medium and perfused in a system similar to the one depicted in Figure 1.

Cells perfused in alginate retain stable levels of phosphate metabolites for at least 72 h of perfusion. Some cells replicate in this medium; however, RIF-1 tumor cells do not replicate at the high cell densities used for NMR studies (7×10^7 cells/mL), even though they do at lower cell densities. Furthermore, RIF-1 tumor cells recovered by dissolving the alginate beads with sodium citrate do not retain clonogenic capacity. Exposure of cells to high concentrations of calcium could be responsible for loss of proliferative capacity.

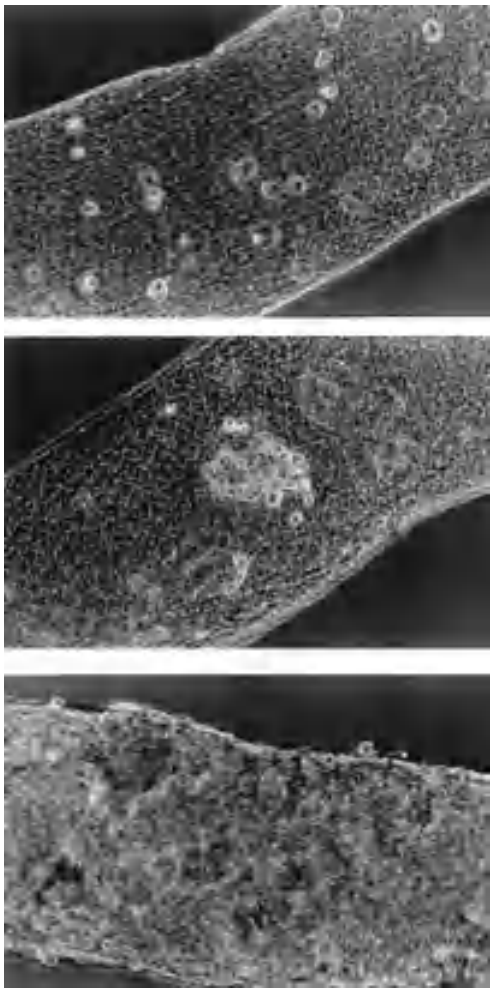

Figure 4 MDA-231 breast cancer cells growing in Matrigel threads (500 μM diameter). (Reproduced by permission of Springer-Verlag from Kaplan et al.[1])

Tumor cells, plant cells, and algae have been investigated.[1] Lymphocytes, which are too small to be retained in (0.9%) agarose threads (see above), can be studied in alginate beads.

McGovern et al.[23] introduced a technique for monitoring oxygen concentration during NMR experiments by incorporating perfluorocarbons into the alginate cell suspension. The ^{19}F spin–lattice relaxation rate of the perfluorocarbon indicates the average oxygen concentration (see Section 3.2). Mathematical modeling permits estimation of the oxygen gradient within the alginate beads. This method could readily be adapted for measuring rates of oxygen consumption and can be used in any gel-based immobilization system.

2.2.7 *Other Immobilization Matrixes*

Aiken et al.[24] used Cultisphere G-L collagen beads (Hyclone Labs, Logan, UT, USA) for studies of RIF-1 cells. The cells grow within crevices as well as on the surface of the beads. Unlike the alginate system (see above), the collagen beads allow (RIF-1) cells to replicate at a rate equivalent to that in monolayer culture. Cells are easily recovered by treating the beads with Dispase (Collaborative Research, Bedford, MA, USA); cloning efficiency of RIF-1 is similar to that of cells trypsinized from monolayer culture. This system is suitable for studying the effects of antineoplastic agents during normal cell replication.

Gamcsik (personal communication) has recently employed a 'sponge-like' collagen gel matrix, Spongostan (Ferrosan, Denmark) in NMR studies of perfused MCF-7 tumor cells. This matrix can provide more mechanical stability than Cultisphere G-L beads, which tend to settle out or move around in the perfusion chamber.

2.2.8 *Hollow Fibers*

The hollow fiber methods, first introduced by Gonzalez-Mendez et al.,[25] deliver oxygen and substrate to the cells through a compartment separated from the cells by a semipermeable membrane. These bioreactor systems are described elsewhere in detail. The key advantage of these systems is that they allow very high-density growth of tumor cells, approaching that of intact tissue. This also produces their key deficiency—the development of oxygen, nutrient, and metabolite gradients. These systems are considerably more complex than the immobilization techniques described above. Nonuniform distribution of cells can occur, and it is difficult to access the cells for counting or biological assays during the course of an experiment. However, these are the best systems for very long-term investigations, and they can achieve the highest spectral sensitivity of all the perfused cell systems.

2.2.9 *Spheroids*

Multicellular spheroids are spherical aggregates of tumor cells, which serve as models of heterogeneously perfused in vivo tumors. Cells near the external surface are well perfused, metabolically active, and rapidly proliferating; those further into the interior of the spheroid are relatively poorly perfused and metabolically and proliferatively quiescent; in larger spheroids a central core of necrotic cells is also encountered.

Lin et al.[26] introduced a very simple perfusion system for NMR study of spheroids, in which spheroids were allowed to settle at the bottom of a 10 mm NMR tube while perfusate was slowly pumped through the system for up to 80 h. No mechanical restraints were introduced into the system. This system has a number of deficiencies, the most important one being the tendency of spheroids to aggregate, which results in substantial modification of the metabolic and proliferative properties of the tumor cell.

Ronen and Degani[27] addressed this problem by encasing small MCF-7 spheroids in agarose beads. Studies were performed in the conventional perfusion system shown in Figure 1. They achieved a very high cell density (10^8 cells/1.5 mL), which permitted measurement of fully relaxed ^{31}P NMR spectra in 7.5 min. Cell growth followed Gompertzian kinetics; decreases in levels of NTP and the rate of production of ^{13}C-labeled lactate (from metabolism of [1-^{13}C]glucose monitored by ^{13}C NMR) in the plateau phase were attributed to the development of central necrosis in the spheroids.

Freyer et al.[28] have designed an efficient perfusion system for spheroids (Figure 5). It consists of a 20 mm NMR tube equipped with a mechanical stirrer and multiple inlet lines and

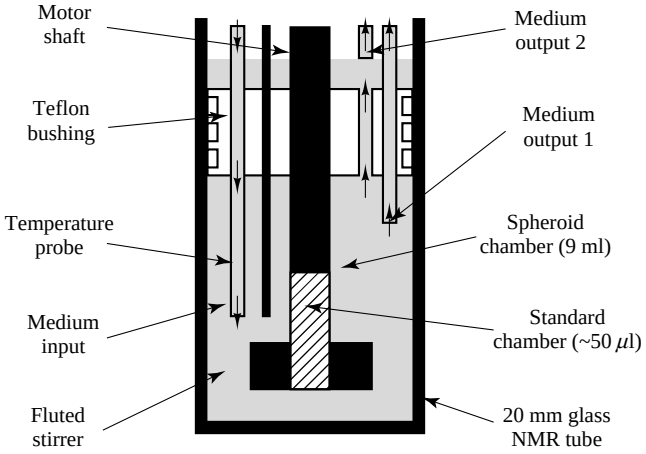

Figure 5 Diagram of the spheroid NMR perfusion chamber. The arrows indicate the direction of medium flow. The sensing volume of the NMR coil is indicated by the hatched area in the spheroid chamber. (Reproduced by permission of John Wiley and Sons from Freyer et al.[28])

sensors for oxygen concentration, pH, and temperature. EMT6/Ro spheroids are grown in the NMR tube under conditions identical to those employed in batch culture, and exhibit identical growth characteristics, cytokinetic parameters, and clonogenic viability. Except for changes due to cell growth, the system is extremely stable (<5% variation over a 24 h period in the NMR tube or in culture). Transient interruption of perfusion or stirring produces significant, largely reversible, changes in ^{31}P NMR characteristics. The cell density (~5 × 10^8 cells/9.5 mL) is substantially lower than that of the Ronen and Degani system, and the maximum medium flow rate is 34 mL min^{-1} compared with 1.5 mL min^{-1} employed by Ronen and Degani.[27] Freyer's system has two additional advantages: (i) the spheroids are uniformly distributed in the perfusion system, and (ii) the spheroids can readily be recovered for cytokinetic and radiobiological assays.

3 SPECIAL METHODS

3.1 Distinction Between Intracellular and Extracellular Metabolites

Distinction between intracellular and extracellular compartments by MRS has been accomplished on the basis of differences in chemical shifts, relaxation times, and diffusion constants of metabolites in these compartments or by the introduction of reagents that are confined to one or another compartment. In most instances this has required the introduction of special reagents, such as paramagnetic contrast agents or exploitation of unique properties of the cellular target (e.g. magnetic field gradients within erythrocytes). A more general approach to this problem which does not require introduction of reagents or unique properties in the target cell is the use of pulsed field gradients. This technique, first introduced by Andrasko[29] in 1976 for studies of Li^+ transport into red blood cells, was recently adapted to ^{1}H NMR studies of perfused cell systems by van Zijl et al.[30] It exploits differences in the effective diffusion constants of intracellular and extracellular metabolites. These investigators employed a diffusion-sensitive stimulated echo pulse sequence to isolate signals from MCF-7 cells encapsulated in agarose threads (see above). By proper choice of gradients and delays, one can determine the ratio of extracellular to intracellular volumes and eliminate the resonances of all the extracellular metabolites, which generally have a larger diffusion constant because they are flowing and are not restricted to the intracellular compartments.

This method could be extended to other nuclei such as ^{19}F, ^{31}P, ^{13}C, and ^{7}Li, but lower γ-nuclei will require proportionately steeper gradients. These are becoming available on the newer instruments.

3.2 Indicator Compounds

Many cellular parameters cannot be directly measured by NMR. Exogenous reagents have been developed to measure parameters such as intracellular and extracellular pH, concentrations of Ca^{2+}, and Na^+, as well as redox state, pO_2, cell volume, and membrane potential. Szwergold[2] has reviewed these, and they will be discussed only briefly here.

3.2.1 pH

Deutsch's laboratory[31] has developed a variety of fluorinated pH indicators that are trapped inside cells. A variety of other indicators of intracellular and extracellular pH which can be monitored by ^{31}P NMR are also available.[2]

3.2.2 Calcium Ions

Intracellular calcium concentrations can be monitored by ^{19}F NMR with the fluorinated chelator 5,5′-difluoro-1,2-bis(2-aminophenoxy)ethane-*N,N,N′,N′*-tetraacetic acid (F-BAPTA),[32] but the high calcium buffering capacity of this chelator has generated concern about its perturbing effect on cell physiology. F-BAPTA can also bind other divalent cations. The fluorinated chelator is introduced into the cell as a membrane permeable ester and is trapped inside the cell after hydrolysis by endogenous esterases. The calcium concentration is determined from the dissociation constant of the calcium complex of F-BAPTA and the ratio of intensities of resonances of the free and bound chelate.

3.2.3 Magnesium Ions

Intracellular magnesium can be measured from the chemical shift of the β-resonance of ATP, but the K_d is so low that ATP is usually saturated under physiological conditions. 4-Methyl-5-fluoroaminophenol-*N,N,O*-triacetic acid (MF-APTRA) and 5-fluoroaminophenol-*N,N,O*-triacetic acid (5F-APTRA) are fluorinated chelators with considerably greater promise because of their lower dissociation constants.[2]

3.2.4 Sodium Ions

Paramagnetic shift and relaxation reagents have been used to distinguish intracellular from extracellular sodium ions,[33,34] but these agents can be toxic and some are slowly degraded on long-term contact with cells (see ***Cation Move-***

ments across Cell Walls of Intact Tissues Using MRS). These problems can be avoided by not recycling the shift reagent (G. Elgavish, personal communication). The use of multiple quantum coherence methods to distinguish intracellular sodium has been proposed;[35] however, extracellular sodium ions that are immobilized by interaction with a gel matrix or with cell surfaces at high cell densities may also exhibit multiple quantum coherence transfer and, hence, be indistinguishable from intracellular sodium ions.

3.2.5 *Redox Potential*

Redox potentials can be determined from the ratio of oxidized to reduced forms of metabolites, using the Nernst equation and the standard reduction potential of the couple. This principle has been applied to a variety of ^{13}C-labeled couples, including lactate/pyruvate, β-hydroxybutyrate/acetoacetate, NAD(P)/NAD(P)H, and the reduced and oxidized forms of the radiation sensitizer WR3689.[2]

3.2.6 *Oxygen*

The increase in the spin–lattice relaxation rate due to paramagnetic oxygen molecules, $1/T_{1P}$, varies linearly with oxygen concentration. With proper calibration the oxygen concentration can be determined from measurements of T_{1P} of the ^{19}F resonance of perfluorocarbons.[15,23]

3.2.7 *Membrane Potential*

Membrane potentials are calculated from the ratio of intracellular and extracellular metabolites, which are in slow exchange on the chemical shift timescale. The membrane potential of erythrocytes has been measured by ^{31}P NMR using the hypophosphite ion as a probe; trifluoroacetate was employed in a ^{19}F NMR study.[2]

3.2.8 *Cell Volume*

Cell volume has been measured by ^{31}P and ^{19}F NMR, using dimethyl methylphosphonate or trifluoroacetamide as an extracellular probe, and also by ^{23}Na NMR, by utilizing the low concentration of intracellular compared to extracellular sodium.[2]

4 APPLICATIONS

Below we present a few examples of cellular NMR studies which illustrate the versatility of this method. They demonstrate its utility for studying fundamental principles of bioenergetics, for investigating mechanisms of antineoplastic agents in tumor cells, for elucidating biochemical pathways, and for evaluating mechanisms underlying therapy-induced in vivo spectral changes in tumors.

4.1 Cell Suspensions

4.1.1 *The Chemiosmotic Hypothesis*

As originally proposed by Mitchell,[36] certain membranes of microorganisms and organelles (such as mitochondria and chloroplasts) are impermeable to protons. Oxidation of substrates via the electron transport chain results in transport of protons across these membranes, generating an electrical potential ($\Delta\psi$) and a pH gradient that are coupled to the free energy, ΔG_{ATP}, for the ATP synthase reaction (Pi + ADP $\rightleftharpoons$ ATP) by the equation

$$\Delta G_{ATP} = -nF\ \Delta\psi + 2.3nRT\ \Delta\mathrm{pH} \qquad (1)$$

where F is the Faraday constant, and n is the number of protons transported per ATP molecule synthesized. When the ATP synthase-mediated reaction runs in the forward direction, protons are transported back across the membrane so as to collapse the electrochemical potential.

Ugurbil et al.[6] used ^{31}P NMR simultaneously to measure changes in ΔpH and in phosphorylation potential ([ATP]/[ADP][Pi]) in *Escherichia coli* cells grown on succinate or glucose under aerobic and anaerobic conditions. Effects of ATPase inhibitors and ATPase-deficient mutants and uncouplers were investigated. These results, together with independent determinations of the membrane potential,[37] were in qualitative agreement with equation (1), providing confirmation of the chemiosmotic hypothesis.

4.2 Perfused Cells and Spheroids

4.2.1 *Cyclophosphamide Metabolism*

Cyclophosphamide (**1**) is a potent alkylating agent used in the treatment of a wide range of human cancers. The key steps in the metabolism of this drug are depicted in Figure 6. In the liver, microsomal oxidation of (**1**) produces 4-hydroxycyclophosphamide (**2**), which is subsequently converted to aldophosphamide (**3**) in the tumor. The latter is converted to acrolein (**5**) and phosphoramide mustard (**4**), the active species which cross-links DNA. Boyd et al.[38] measured the apparent rate of alkylation of DNA in perfused tumor cells immobilized in agar threads. They incorporated (**2**) into the perfusate, monitored its conversion into (**3**) and (**4**), and then eliminated (**2**) and (**3**) by washing the cells with drug-free perfusate. Subsequent disappearance of (**4**) followed first-order kinetics, and was attributed to formation of an NMR-invisible adduct of DNA. While drug concentrations were in the millimolar range, well above clinical levels, this experiment demonstrates the unique ability of NMR spectroscopy to monitor complex pharmacological reactions inside intact tumor cells.

4.2.2 *Phospholipid Metabolism*

Ronen and Degani[39] have used ^{31}P and ^{13}C NMR spectroscopy to examine the effect of spheroid size on the metabolism of phospholipids. The largest variations occurred in levels of the phospholipid precursors, phosphocholine (PC) and phosphoethanolamine (PE). Phosphatidylcholine (PhCh) is synthesized via the Kennedy pathway by which choline is phosphorylated to PC by choline kinase, then PC is combined with cytosine triphosphate (CTP) via the action of CTP-phosphocholine transferase, forming cytosine diphosphocholine, which then combines with diacylglycerol (DAG) to form PhCh. Although phosphatidylethanolamine (PhEt) can be synthesized from PE via the Kennedy pathway, if ethanolamine is limiting, an alternative pathway, decarboxylation of phosphati-

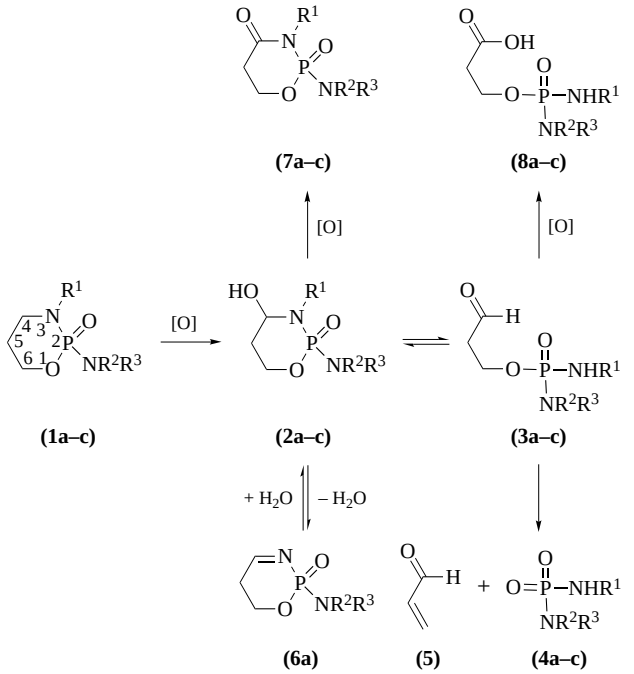

(a) $R^1 = H$; $R^2 = R^3 = CH_2CH_2Cl$
(b) $R^1 = R^2 = CH_2CH_2Cl$; $R^3 = H$
(c) $R^1 = R^2 = R^3 = CH_2CH_2Cl$

Figure 6 Generally accepted scheme for the metabolism of cyclophosphamide in the liver and tumor cells. (Reproduced by permission of American Chemical Society from Boyd et al.[38])

dylserine, may be used. The reaction effectively converts serine (which is abundant in most media) into ethanolamine, which can then be used for synthesis of PhEt.

To monitor the kinetics of these reactions Ronen and Degani[39] grew T47D human breast spheroids in the presence of [1,2-^{13}C]choline, and [1,2-^{13}C]ethanolamine and [3-^{13}C]serine. The specific pathway for phospholipid metabolism could be deduced from the labeling pattern of the metabolites in cells and in lipid extracts. They found that the ratio of PhCh to PhEt was independent of spheroid size, but the rates of the reactions in the Kennedy and serine decarboxylase pathways varied with the availability of substrates. The serine decarboxylase reaction decreased with increasing ethanolamine in the medium, and increased with spheroid size; the latter effect was attributed to decreased permeability of large spheroids to exogenous ethanolamine.

4.2.3 Mechanism of Chemotherapy- and Radiation-Induced MRS Changes in In Vivo Tumors

During untreated growth, most transplantable tumor models in rodents exhibit a progressive decline in their bioenergetic status, a decrease in levels of high-energy phosphates compared with low-energy phosphates and an acid shift in pH (see ***Spectroscopic Studies of Animal Tumor Models***).[16,24] When treated effectively with radiation or a number of chemotherapeutic agents, many of these tumors exhibit an anomalous reversal of this pattern which does not simply reflect a decrease in tumor size. These metabolic changes could result from direct effects on cellular metabolism or they could result from 'tissue effects' (changes in perfusion, cell density, etc.). To evaluate direct effects on cellular metabolism, Ng et al.[16] and Aiken et al.[24] examined the effects of γ-irradiation and of chemotherapy with 4-hydroperoxycyclophosphamide (an active derivative of cyclophosphamide), respectively, on RIF-1 cells perfused after immobilization on alginate beads or Cultisphere G-L beads (see above). The in vivo effects of these agents were not observed in the perfused cells. In fact, radiation induced a decline in bioenergetic status prior to cell death. The duration of these experiments corresponded to the timescale over which the bioenergetic 'improvements' were observed in the in vivo tumor. These data suggest that 'tissue effects' are responsible for the changes induced in this tumor by radiation and chemotherapy in vivo. This conclusion is consistent with reports that increases in tumor blood flow are correlated with radiation- and chemotherapy-induced improvements in tumor bioenergetic status.[16,24]

5 SUMMARY AND FUTURE DIRECTIONS

A wide variety of perfusion systems are available to support various applications of NMR spectroscopy to the study of cellular metabolism. Each method has distinct advantages and limitations. The particular system should be chosen to meet the needs of the application. The key advantage of NMR methods is that they permit investigation of metabolism in the intact cell. The key disadvantage of all NMR methods is limited spectral sensitivity. The examples we have chosen illustrate the utility of the method for investigation of key metabolic processes and for elucidation of mechanisms underlying in vivo spectral changes.

It is likely that major technical advances such as the use of gradient-based methods to discriminate intracellular and extracellular compartments described above will be employed in studies of cellular transport and metabolism. Multiple quantum editing techniques and imaging methods to measure diffusion constants and flow will probably be used in future cell studies. Isotopes such as ^{15}N and ^{17}O should receive more attention. Tagging of cells, multicellular organisms, or organelles with paramagnetically or isotopically labeled reagents may be used to follow embryonic development. Specialized NMR probes for monitoring oxygen in the concentration range relevant to radiation biology and respiration are likely to be developed (see ***EPR and In Vivo EPR: Roles for Experimental and Clinical NMR Studies***). Molecular biological techniques will doubtlessly have a major impact on cellular NMR studies. Overall, the field of cellular MRS, like the other MR fields, is undergoing very rapid development and is likely to continue to do so for some time.

6 RELATED ARTICLES

Cation Movements across Cell Walls of Intact Tissues Using MRS; EPR and In Vivo EPR: Roles for Experimental and Clinical NMR Studies; Spectroscopic Studies of Animal Tumor Models; Tissue and Cell Extracts MRS.

7 REFERENCES

1. O. Kaplan, P. C. M. van Zijl, and J. S. Cohen, in 'NMR Basic Principles and Progress', Springer-Verlag, Berlin, 1992, Vol. 28, pp. 3–54.
2. B. S. Szwergold, *Annu. Rev. Physiol.*, 1992, **54**, 775.
3. N. A. Matwiyoff and T. E. Needham, *Biochem. Biophys. Res. Commun.*, 1972, **49**, 1158.
4. R. T. Eakin, L. O. Morgan, C. T. Gregg, and N. A. Matwiyoff, *FEBS Lett.*, 1972, **28**, 259.
5. R. B. Moon and J. H. Richards, *J. Biol. Chem.*, 1973, **248**, 7276.
6. K. Ugurbil, R. G. Shulman, and T. R. Brown, in 'Biological Applications of Magnetic Resonance', ed. R. G. Shulman, Academic Press, New York, 1979, pp. 537–589.
7. A. M. Castle, R. M. Macnab, and R. G. Shulman, *J. Biol. Chem.*, 1986, **261**, 7797.
8. J. K. Barton, J. A. den Hollander, J. J. Hopfield, and R. G. Shulman, *J. Bacteriol.*, 1982, **151**, 177.
9. S. M. Cohen and R. G. Shulman, *Philos. Trans. R. Soc. London Ser. B.*, 1980, **289**, 407.
10. G. Navon, S. Ogawa, R. G. Shulman, and T. Yamane, *Proc. Natl. Acad. Sci. USA*, 1977, **74**, 87.
11. R. S. Balaban, D. G. Gadian, G. K. Radda, and G. G. Wong, *Anal. Biochem.*, 1981, **116**, 450.
12. A. J. Meehan, C. J. Eskay, A. P. Koretsky, and M. M. Domach, *Biotech. Bioeng.*, 1992, **40**, 1359.
13. J. E. Jentoft and C. D. Town, *J. Cell Biol.*, 1985, **101**, 778.
14. H. Santos and D. L. Turner, *J. Magn. Reson.*, 1986, **68**, 345.
15. J. Taylor and C. Deutsch, *Biophys. J.*, 1988, **53**, 227.
16. C. E. Ng, K. A. McGovern, J. P. Wehrle, and J. D. Glickson, *Magn. Reson. Med.*, 1992, **27**, 296.
17. K. Ugurbil, D. L. Guernsey, T. R. Brown, P. Glynn, N. Tobkes, and I. S. Edelman, *Proc. Natl. Acad. Sci. USA*, 1981, **78**, 4843.
18. D. I. Hoult and P. C. Lauterbur, *J. Magn. Reson.*, 1979, **34**, 425.
19. M. Neeman and H. Degani, *Cancer Res.*, 1989, **49**, 589.
20. D. L. Foxall and J. S. Cohen, *J. Magn. Reson.*, 1983, **52**, 346.
21. M. Bental and C. Deutsch, *Magn. Reson. Med.*, 1993, **29**, 317.
22. K. S. Narayan, E. A. Moress, J. C. Chatham, and P. B. Barker, *NMR Biomed.*, 1990, **3**, 23.
23. K. A. McGovern, J. S. Schoeniger, J. P. Wehrle, C. E. Ng, and J. D. Glickson, *Magn. Reson. Med.*, 1993, **29**, 196.
24. N. R. Aiken, K. A. McGovern, C. E. Ng, J. P. Wehrle, and J. D. Glickson, *Magn. Reson. Med.*, 1994, **31**, 241.
25. R. Gonzalez-Mendez, D. Wemmer, G. Hahn, N. Wade-Jardetzky, and O. Jardetzky, *Biochim. Biophys. Acta*, 1982, **720**, 274.
26. P.-S. Lin, M. Blumenstein, R. B. Mikkelsen, R. Schmidt-Ullrich, and W. W. Bachovchin, *J. Magn. Reson.*, 1987, **73**, 399.
27. S. Ronen and H. Degani, *Magn. Reson. Med.*, 1989, **12**, 274.
28. J. P. Freyer, N. H. Fink, P. L. Schor, J. R. Coulter, M. Neeman, and L. O. Sillerud, *NMR Biomed.*, 1990, **3**, 195.
29. J. Andrasko, *J. Magn. Reson.*, 1976, **21**, 479.
30. P. C. M. van Zijl, C. T. W. Moonen, P. Faustino, J. Pekar, O. Kaplan, and J. S. Cohen, *Proc. Natl. Acad. Sci. USA*, 1991, **88**, 3228.
31. C. J. Deutch and J. S. Taylor, in 'NMR Spectroscopy of Cells and Organisms', ed. R. J. Gupta, CRC Press, Boca Raton, 1987, Vol. II, p. 55.
32. G. A. Smith, R. T. Hesketh, J. C. Metcalfe, J. Feeney, and P. G. Morris, *Proc. Natl. Acad. Sci. USA*, 1983, **80**, 7178.
33. R. K. Gupta, in 'NMR Spectroscopy of Cells and Organisms', ed. R. K. Gupta, CRC Press, Boca Raton, 1987, Vol. I, pp. 1–32.
34. C. J. Springer, *Annu. Rev. Biophys. Biophys. Chem.*, 1987, **16**, 375.
35. J. Pekar, P. F. Renshaw, and J. S. Leigh, *J. Magn. Reson.*, 1987, **72**, 159.
36. P. Mitchell, 'Chemiosmotic Coupling and Energy Transduction', Glynn Research, 1968.
37. A. M. Castle, R. M. Macnab, and R. G. Shulman, *J. Biol. Chem.*, 1986, **261**, 3288.
38. V. L. Boyd, J. D. Robbins, W. Egan, and S. M. Ludeman, *J. Med. Chem.*, 1986, **29**, 1206.
39. S. M. Ronen and H. Degani, *Magn. Reson. Med.*, 1992, **25**, 384.

Biographical Sketch

Jerry D. Glickson. *b* 1941. B.A., 1963, M. A., 1964, Ph.D., 1969, Columbia University. Introduced to NMR by Roy King at Iowa State University, USA, 1965–68. Postdoctoral fellow at DuPont Central Research with Bill Phillips and Cam McDonald, 1968–70. Faculty in Biochemistry and the Comprehensive Cancer Center, University of Alabama in Birmingham, 1970–84, Faculty in Radiology, Biological Chemistry, and Biophysics and Biophysical Chemistry, The Johns Hopkins School of Medicine, USA, 1984–present. Approx. 150 publications. Current research specialty: in vivo NMR spectroscopy of cancer.

Spectroscopic Studies of Animal Tumor Models

Simon P. Robinson, Cheryl L. McCoy, and John R. Griffiths

St George's Hospital Medical School, London, UK

1 INTRODUCTION

In the clinic, there are practical constraints on what can be done to study tumors in patients as well as ethical considerations, i.e. an untreated tumor cannot be monitored through growth. Animal tumor models allow studies of basic tumor biology, metabolic stress, and response to therapeutic regimes in large enough numbers to obtain statistical significance. For basic, routine cancer research a regular supply of reproducible tumors is required. Many tumor models have been developed; the majority are grown subcutaneously in standard laboratory rodents, and are well characterized and widely available, e.g. the RIF-1 fibrosarcoma grown in C_3H mice.[1] Such tumor models have been extensively studied by MRS, to monitor tumor biology and physiology, and also for the development of new pulse sequences or other technical improvements. The use of MRS to study experimental tumor models,[2] and general work on rodent tumor models[3] have been reviewed. Now that there are many clinical MR instruments, the noninvasive examination of rodent tumors by MRS is directly applicable to humans. In this article we consider the MR nuclei that have been observed in spectroscopic studies of animal tumor models.

2 ^{31}P MAGNETIC RESONANCE SPECTROSCOPY

The nucleus most commonly observed in MRS studies of tumors is ^{31}P which has several desirable spectroscopic properties. Phosphorus-31 is 100% abundant and is one of the more sensitive nuclei (see Table 1), and ^{31}P spectra are simple and easy to interpret. Also, several important phosphorus-containing compounds occur in living systems at high enough concentrations to be detectable by ^{31}P MRS (>0.2 mM), thus providing an ideal means of monitoring the energetic state of tumors.

In vivo ^{31}P MR spectra of animal tumors were first reported using simple surface coils and pulse-acquire protocols.[4–7] A typical spectrum taken from a mouse tumor is shown in Figure 1(a). Metabolites detected include three resonances from the α, β, and γ phosphates of NTP (predominantly ATP), inorganic phosphate (Pi), phosphocreatine (PCr), and both reduced and oxidized pyridine dinucleotides (NAD^+ and NADH) which appear as a shoulder on the high field side of α-NTP. Phospholipid metabolites observed include phosphomonoesters (PME), primarily consisting of phosphocholine (PC) and phosphoethanolamine (PE), and phosphodiesters (PDE), primarily consisting of glycerophosphocholine (GPC) and glycerophosphoethanolamine (GPE). These resonance assignments have been confirmed by ^{31}P high resolution MRS analysis of PCA extracts.[8] Intracellular tumor pH can also be derived from the chemical shift of the Pi signal.[9]

Several changes of ^{31}P spectra are consistently seen during unperturbed tumor growth. These include larger Pi resonances than observed in normal tissues, high PME resonances that increase with tumor growth, decreasing PCr levels when detectable, and a size-dependent decline in NTP relative to Pi, coupled with a decrease in tumor pH. As in nutritional deprivation in tumors, NTP decreases as Pi increases and the resultant ratio of 'high energy' to 'low energy' phosphates, i.e. NTP/Pi, is often used as a measure of metabolic state.

The decline in the bioenergetic status of the tumor is consistent with the tumor vasculature becoming incapable of providing a nutritive blood (and hence oxygen) supply to the rapidly proliferating tissue, leading to the onset and development of hypoxia.[10,11] Tumor acidification also reflects poor vascularity, as the large amounts of H^+ ions produced by glycolysis accumulate extracellularly.[12] The large PME

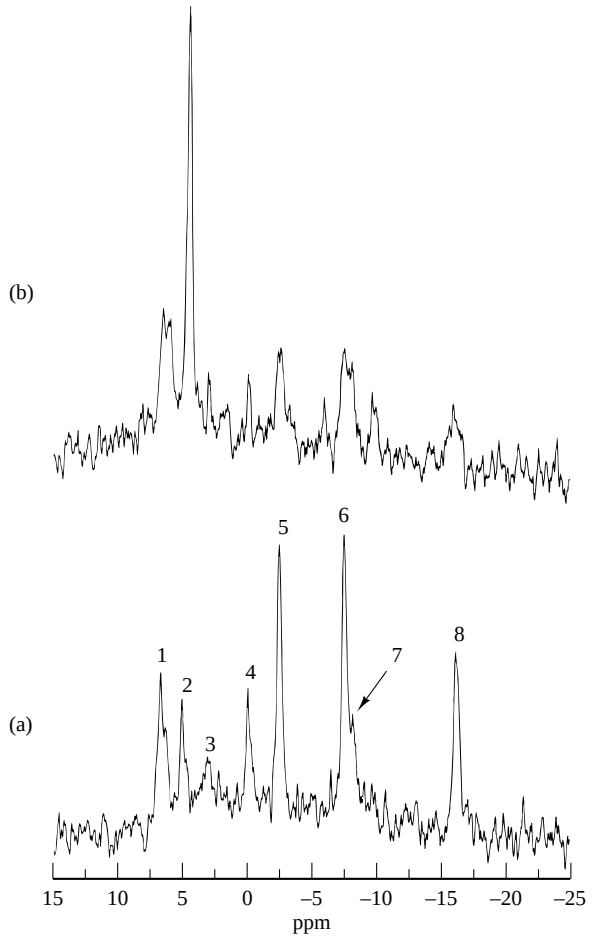

Figure 1 ^{31}P ISIS spectra of an RIF-1 fibrosarcoma in a C_3H mouse (a) before and (b) after i.v. injection of 5 mg kg^{-1} hydralazine. Peak assignments are: 1, PME; 2, Pi; 3, PDE; 4, PCr; 5, γ-NTP; 6, α-NTP; 7, NAD^+/NADH; and 8, β-NTP

Table 1

Nuclide	Sensitivity	% Natural Abundance	Chemical Shift Range (ppm)	Comments
^{1}H	1.00	100	10	amino acids, lactate
^{31}P	0.066	100	30	energy metabolism, pH, phospholipid metabolites
^{13}C	0.016	1.1	200	tumor metabolism
^{19}F	0.833	100	250	drug metabolism, blood flow
^{2}H	0.010	0.015	10	blood flow, pharmacokinetic analysis

and PDE resonances in ^{31}P spectra are related to cell membrane turnover in tumors. As both PC and PE are membrane synthesis substrates and GPC and GPE are membrane breakdown products, changes in the PME/PDE ratio may correspond to high rates of membrane synthesis within rapidly proliferating tissue or membrane decomposition within necrotic regions.[13]

Phosphorus-31 MR spectroscopy has also revealed alterations in the energy and phospholipid metabolism of tumors during response to treatment. The first use of ^{31}P MRS to monitor the response of animal tumors to radiotherapy showed an increase in intensity of the PCr resonance at 28 and 40 h post irradiation.[6] Subsequent studies have shown a common pattern of response to radiation therapy, with an observed increase in PCr/Pi, NTP/Pi, and intracellular pH, the extent of response being dose dependent and not a systemic response to radiation toxicity.[14] This observed improvement in energetic status is consistent with tumor reoxygenation, i.e. the reacquisition of radiosensitivity of cells that have survived irradiation because they were hypoxic at the time of exposure; it may result from increases in tumor blood perfusion after irradiation.[15] Another possible explanation for the improvement in cell energy status is the reduced oxygen demand, which is a consequence of cessation of growth, as well as an improved blood supply as the tumor shrinks.[16]

The response of animal tumors to a range of chemotherapeutic agents has also been observed by ^{31}P MRS. Agents such as cyclophosphamide and 1,3-bis(2-chloroethyl)-1-nitrosourea (BCNU) increase the levels of high-energy phosphates,[16,17] the reverse of the ^{31}P trends seen during unperturbed tumor growth. This response is accompanied by a decrease in tumor volume, yet the changes in ^{31}P MR spectra are detectable early after initiation of treatment, before measurable changes in tumor size are evident.[16] Other agents such as flavone acetic acid (FAA) induce metabolic deactivation of animal tumors as observed by ^{31}P MRS, i.e. decreased NTP levels. FAA causes a reduction in perfusion by causing vascular collapse, though the exact mechanism of action, as with many of these drugs, is still unclear.[18]

Improving or decreasing tumor blood flow, and hence tumor oxygenation, could facilitate tumor therapy. Acute manipulation of tumor blood flow by a range of noncytotoxic modifiers has been studied by ^{31}P MRS. Injection of agents such as nicotinamide or administration of 100% oxygen have led to improved bioenergetic status as seen by ^{31}P MRS, thus potentially rendering the tumor more susceptible to radiotherapy or improving drug delivery.[19,20] Conversely, modifiers such as hydralazine, a vasodilator acting directly on host vascular smooth muscle, decrease tumor perfusion, resulting in a decrease in NTP/Pi and pH in transplanted tumors, as depicted in Figure 1(b). These changes occur as blood is 'stolen' from the tumor, leading to vascular collapse. Such a response, however, has not been observed in spontaneous animal tumor models.[21]

The marked changes in energy metabolism seen in animal tumors are rarely observed in patients. However, the PME peak does change markedly in tumors in patients; it rises during tumor growth and decreases after successful therapy.[22] Such changes have also been observed and studied in animal models.[23]

3 ^{2}H MAGNETIC RESONANCE SPECTROSCOPY

The use of ^{2}H in spectroscopic studies of animal tumors has centered upon the observation of the uptake or clearance of the freely diffusible, nonradioactive tracer deuterium oxide ($^{2}H_2O$) to measure tumor blood flow (TBF).[24] Tumor blood flow is an important determinant of the response of solid tumors to treatment and can also be altered by treatment.

Two distinct approaches have been used. Initially, $^{2}H_2O$ clearance after a direct intratumor bolus injection was measured to give information on local TBF.[25] This method is easy to implement and generates numerical values in mL (100 g min^{-1}) for TBF by fitting the data to an appropriate model, but it only measures TBF in the local area of injection and the injection itself may disrupt the tumor vasculature. Alternatively, $^{2}H_2O$ uptake by the tumor after i.v. injection has been observed by ^{2}H MRS (Figure 2); this method does not directly affect the tumor tissue and reports TBF throughout the whole tumor. This latter approach is ideal for measuring relative TBF and the response to blood flow modifiers, though quantification of TBF is more complicated and requires knowledge of the arterial input function, i.e. the $^{2}H_2O$ concentration in the arterial blood.[26]

Administration of $^{2}H_2O$ allows repeated measurements to be made on the same tumor; hence changes in TBF in response to therapy or blood flow modifiers can be easily assessed. For example, relative TBF in response to hyperthermia showed a significant difference at 45 °C compared with control tumors at

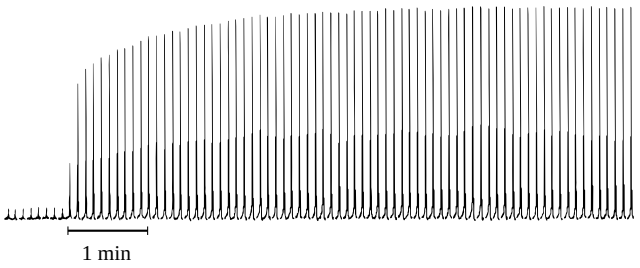

Figure 2 Uptake of ^2H_2O into a GH3 prolactinoma in a Wistar Furth rat as a function of time. Eight background FIDs collected prior to a bolus injection of 300 μl ^2H_2O

37 °C.[26] Relative TBF was also shown to decrease in response to the vasodilator hydralazine, as observed by ^{2}H MRS.[27]

Adaptation of these techniques to a ^{2}H imaging experiment has also been accomplished, and imaging the distribution of uptake of ^2H_2O provides an indication of tumor vascularity. From measurement of ^2H_2O accumulation into each pixel, a map of the spatial blood flow distribution can be created which is useful in assessing the characteristic heterogeneity of tumor blood flow.[28] Deuterium MRS provides reliable data on TBF when used with caution and provides a useful, noninvasive method of assessing an important determinant of tumor physiology.

Hydrogen-2 MRS has also been used for the direct in vivo measurement of drug concentrations. Using deuterated drugs such as ^{2}H-misonidazole, the concentration of the drug can be determined from a single ^{2}H NMR spectrum with a limit of detection of approximately 0.5 mM for a drug labeled with three equivalent deuterons.[29]

4 ^{13}C MAGNETIC RESONANCE SPECTROSCOPY

Carbon-13 MRS has been little used to study cancer. This is due in part to the relatively low natural abundance and sensitivity of the ^{13}C nucleus relative to ^{1}H (see Table 1) which causes two problems: (i) it is necessary to use high concentrations of ^{13}C labeled substrates, which can be expensive to synthesize; and (ii) the large amount of the compound that is administered may alter tumor metabolism. In spite of these limitations, the use and application of both enrichment studies and natural abundance ^{13}C studies to monitor tumor biochemistry has progressed. Most ^{13}C studies in animals have used labeled substrates injected directly into a tumor to increase the signal-to-noise ratio. Also, more efficient probe designs have been developed to overcome the limitations associated with ^{13}C MRS.[30]

The major application of in vivo ^{13}C MRS for studying cancer is to monitor glycolysis and the rate of energy utilization of tumors relative to normal tissue. Compounds such as glucose, citrate, and alanine can be detected. The presence (or absence) of several compounds can be detected, along with their concentration, mobility, and relaxation characteristics, simultaneously and noninvasively in one animal.

In vivo ^{13}C studies are routinely performed to obtain a background spectrum before injection of labeled substrates (see below). Typical studies take several minutes using ^{1}H decoupling (which increases the ^{13}C spectral resolution by removing the coupling interactions with neighboring protons whilst allowing NOE) to obtain spectra with adequate signal-to-noise ratios. For example, natural abundance ^{13}C MRS of Dunning rat tumors, a model for human prostate cancer, was used to examine the relationship between prostatic tumors and the presence or absence of citrate.[31]

Recently, ^{13}C MRS has been used in combination with ^{31}P MRS and traditional biochemical methods to examine glucose metabolism in RIF-1 tumors.[32,33] Natural abundance ^{13}C spectra were acquired from tumors to obtain a background signal from endogenous lipids ($-CH_2-$) which was used as an internal chemical shift marker; the mice were then injected intratumorally with ^{13}C labeled glucose and proton-decoupled ^{13}C spectra were acquired for 70 min. The levels of 3-^{13}C lactate and 3-^{13}C alanine were increased and the level of lactate approached a steady state at approximately 40 min after injection.

Carbon-13 MRS has also been used after intraperitoneal and intravenous administration of glucose to study tumor metabolism (Figure 3) and to monitor the generation of lactic acid. In addition to the study of subcutaneous (s.c.) tumors, brain tumor metabolism has also been examined with ^{13}C MRS.[34]

So far, ^{13}C MRS has been used to study the relationship between glucose availability and tumor metabolism. Although these natural abundance and enrichment studies demonstrate the feasibility of oncological applications of in vivo ^{13}C MRS, to date, there have been no reported studies in which it has been used to monitor tumor metabolism after therapy.

Another application of ^{13}C MRS is to follow the pharmacokinetics of ^{13}C-labeled chemotherapeutic agents. This labeling is attractive as most drugs contain carbon and usually there is one position that can be labeled during drug synthesis, thus removing the need for a label that might modify drug activity (e.g. ^{19}F). However, detection of the drug in vivo presents a challenge because of the poor sensitivity. One study has demonstrated the detection of a ^{13}C label on the active methyl group of the methylating agent temozolamide in RIF-1 fibrosarcomas with sufficient sensitivity to determine a halflife for elimination from the tumor.[35]

5 ^{19}F MAGNETIC RESONANCE SPECTROSCOPY

The ^{19}F nucleus is an excellent nuclide to monitor by MRS because it is 100% naturally occurring and has a sensitivity nearly equal to that of ^{1}H (see Table 1) and there is no background signal in vivo. The noninvasive nature of ^{19}F MRS also makes it a useful tool for monitoring in vivo drug metabolism since it is not necessary to sacrifice a large number of animals and each animal can serve as its own control.

Flourine-19 MRS has been extensively used in oncology. Most of the work has used fluorine-substituted chemotherapeutic drugs such as the fluoropyrimidines. There has also been work done using perfluorocarbons (hydrocarbons whose protons have been replaced with fluorine nuclei), which are ideal candidates for both spectroscopy and imaging. Other applications of ^{19}F MRS in cancer research in murine tumors include the use of compounds containing ^{19}F as probes for tumor hypoxia,[36,37] intracellular pH,[38] and for monitoring tumor therapy.[39]

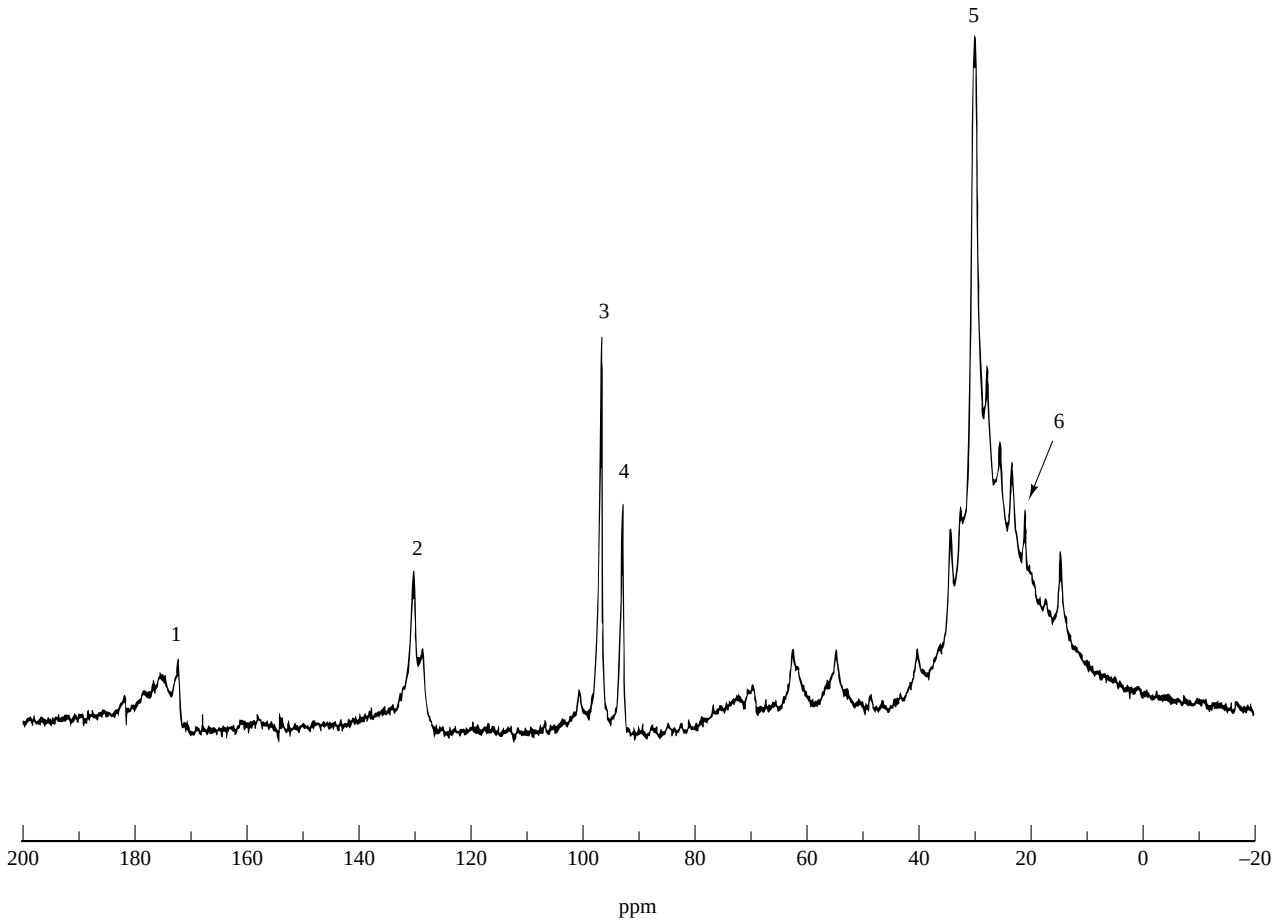

Figure 3 $^{13}C\{^{1}H\}$ MR spectrum of an RIF-1 tumor in a C_3H mouse after i.v. injection of 7 mg kg^{-1} 1-^{13}C-glucose. Peak assignments are: 1, carbonyl carbons (C=O); 2, alkene carbons (C=C); 3, β-glucose; 4, α-glucose; 5, methylene carbons (CH_2), and 6, lactate. Figure supplied by Dr R. J. Maxwell

The fluoropyrimidine that has been most widely studied by ^{19}F MRS is 5-fluorouracil (5-FU), an effective anticancer agent that has been used clinically since 1957.[40] 5-FU was synthesized as an antimetabolite of uracil and is almost always metabolized similarly to uracil and its breakdown products (Figure 4). It is commonly used in combination chemotherapy with agents such as methotrexate or adriamycin.[41] The first reported study monitored 5-FU metabolism in the livers and tumors of mice via ^{19}F MRS.[42] A more recent review explores the potential of ^{19}F MRS of fluoropyrimidines for monitoring the therapy of single chemotherapeutic agents or combinations.[43] There have also been studies using ^{19}F MRS to monitor 5-FU therapy in patients.[44]

Recently, ^{19}F MRS of perfluorocarbon emulsions has been used to examine changes in the oxygenation status of mouse RIF-1 tumors in response to treatment with nicotinamide.[45] Consistent with the hypothesis that nicotinamide improves tumor oxygenation (see above), there was a significant increase in pO_2 for treated tumors versus control tumors. The perfluorocarbon emulsions have several features that make them ideal candidates for ^{19}F MRS measurements of tumor oxygenation status: (i) they are selectively sequestered in solid tumors; (ii) oxygen binding changes the spin–lattice (T_1) relaxation time of the fluorocarbon; and (iii) there is a linear correlation between the T_1 value of the perfluorocarbon in the tumor and the tumor oxygenation.[45,46]

^{19}F MRS can also be used to observe the behavior of organofluorides such as halothane in vivo. The inhalant anaesthetic, halothane, is a hydrophobic probe that can be used for monitoring plasma membrane alterations and thus may have potential for determining the effectiveness of treatments such as hyperthermia.[47]

6 ^{1}H MAGNETIC RESONANCE SPECTROSCOPY

Studies of animal tumors by ^{1}H MRS are few, even though protons are naturally occurring and ^{1}H is the most sensitive nucleus (Table 1). Although ^{1}H MRS allows observation of several metabolites that are not detected by MRS of other nuclei, and nearly every compound in living tissues contains hydrogen atoms, there are several disadvantages associated with its application in vivo. The major obstacles are the high concentrations of tissue water (ca. 40 M) and lipids (ca. 1 mM)

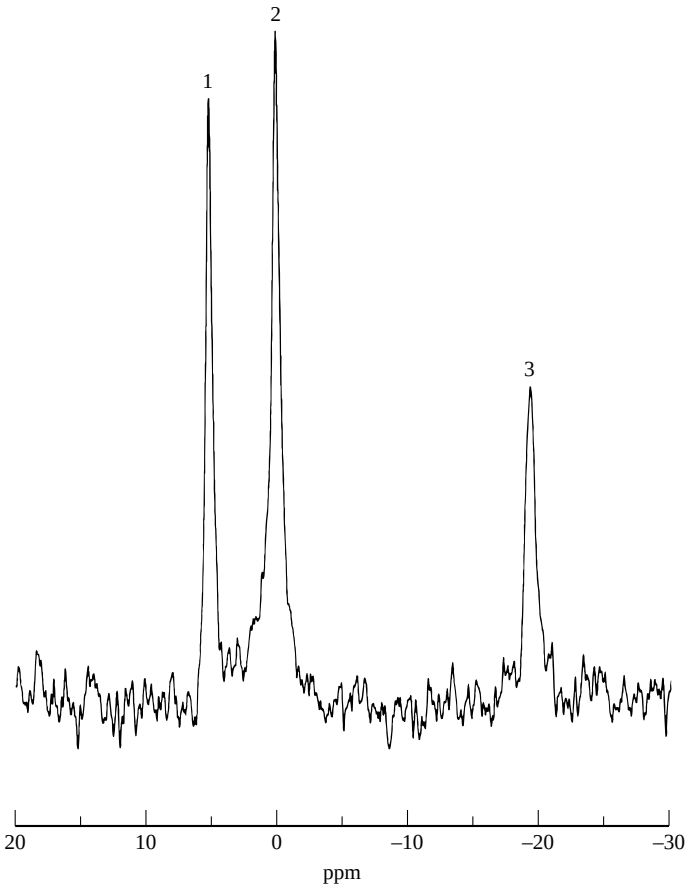

Figure 4 ^{19}F spectrum showing uptake of 5-FU into a GH3 prolactinoma in a Wistar Furth rat after i.v. injection of 60 mg kg^{-1} 5-FU. Peak assignments are: 1, fluoronucleotides; 2, 5-fluorouracil; and 3, fluoro-β-alanine. Figure supplied by Dr R. J. Maxwell

which produce intense background signals that must be suppressed to observe the metabolites of interest. The small chemical shift range of ^{1}H signals means the $\boldsymbol{B}_0$ field must be shimmed precisely. Local hemorrhaging within the tumor, or motion, can degrade spectral resolution.[48] Because of these problems, most of the studies to date have been limited to intracranial (brain) tumor models which have very little motion and less intense lipid signals.[49,50]

The resonances that appear in a water-suppressed ^{1}H spectrum differ, depending on the echo time that is used. Typical resonances observed at 'long' echo times (e.g. 240–270 ms) may include total creatines, total cholines, and lactate. Resonances attributed to inositol, glucose, and mobile lipids may appear at 'short' echo times (e.g. 20–50 ms).

Recently, water- and lipid-suppressed ^{1}H spectra of subcutaneous RIF-1 and EMT-6 tumors have been published.[51] There were no changes in metabolite levels during untreated tumor growth, and tumor response to treatment with 5-FU resulted in a decrease in all metabolites. Acute TBF reduction by hydralazine (see above) caused a twofold increase in lactate. Also, ^{1}H spectroscopic images of RIF-1 tumors showed that radiotherapy significantly decreased lactate levels.[52,53] These experiments demonstrate the feasibility of ^{1}H MRS outside the brain.

Preliminary ^{1}H MRS studies in animal tumors demonstrate the wealth of information that can be exploited once the technical obstacles have been overcome. Such approaches may therefore be extrapolated into the clinical arena.

7 SUMMARY

Animal tumor models have already been extensively studied by MRS: a recent review cites more than 100 papers on ^{31}P MRS alone.[23] The ability to monitor endogenous intracellular metabolism, drug metabolism, tumor blood flow, or tumor intracellular pH repeatedly and noninvasively in a single animal, and to combine various monitoring procedures in a single experiment, has provided a great advance in experimental oncology.

8 RELATED ARTICLES

Animal Methods in MRS; Applications of ^{19}F-NMR to Oncology; Brain Neoplasms in Humans Studied by Phosphorus-31 NMR Spectroscopy; Brain Neoplasms Studied by MRI; Cells and Cell Systems MRS; Fluorine-19 MRS: General Overview and Anesthesia; MRI of Musculoskeletal Neoplasms; Single Voxel Localized Proton NMR Spectroscopy of Human Brain In Vivo; Single Voxel Whole Body Phosphorus MRS.

9 REFERENCES

1. P. R. Twentyman, J. M. Brown, J. W. Gray, A. J. Franko, M. A. Scoles, and R. F. Kallman, *J. Natl. Cancer Inst.*, 1980, **64**, 595.
2. J. Denekamp, *NMR Biomed.*, 1992, **5**, 234.
3. 'Rodent Tumor Models in Experimental Cancer Therapy', ed. R. F. Kallman, Pergamon Press, Oxford, 1987, pp. 1–310.
4. J. R. Griffiths, A. N. Stevens, R. A. Iles, R. E. Gordon, and D. Shaw, *Bioscience Rep.*, 1981, **1**, 319.
5. J. R. Griffiths and R. A. Iles, *Bioscience Rep.*, 1982, **2**, 719.
6. T. C. Ng, W. T. Evanochko, R. N. Hiramoto, V. K. Ghanta, M. B. illy, A. J. Lawson, T. H. Corbett, J. R. Durant, and J. D. Glickson, *J. Magn. Reson.*, 1982, **49**, 271.
7. W. T. Evanochko, T. C. Ng, J. D. Glickson, J. R. Durant, and T. H. Corbett, *Biochem. Biophys. Res. Commun.*, 1982, **109**, 1346.
8. W. T. Evanochko, T. T. Sakai, T. C. Ng, N. R. Krishna, H. D. Kim, R. B. Zeidler, V. K. Ghanta, R. W. Brockman, L. M. Schiffer, P. G. Braunschweiger, and J. D. Glickson, *Biochim. Biophys. Acta*, 1984, **805**, 104.
9. R. B. Moon and J. H. Richards, *J. Biol. Chem.*, 1973, **248**, 7276.
10. P. Vaupel, F. Kallinowski, and P. Okunieff, *Cancer Res.*, 1989, **49**, 6449.
11. P. Okunieff, J. A. Koutcher, L. Gerweck, E. McFarland, B. Hitzig, M. Urano, T. Brady, L. Neuringer, and H. D. Suit, *Int. J. Radiat. Oncol. Biol. Phys.*, 1986, **12**, 793.
12. J. R. Griffiths, *Br. J. Cancer*, 1991, **64**, 425.
13. P. F. Daly, R. C. Lyon, P. J. Faustino, and J. S. Cohen, *J. Biol. Chem.*, 1987, **262**, 14 875.
14. S. S. Rajan, J. P. Wehrle, S.-J. Li, R. G. Steen, and J. D. Glickson, *NMR Biomed.*, 1989, **2**, 165.
15. G. M. Tozer, Z. M. Bhujwalla, J. R. Griffiths, and R. J. Maxwell, *Int. J. Radiat. Oncol. Biol. Phys.*, 1989, **16**, 155.
16. R. G. Steen, *Cancer Res.*, 1989, **49**, 4075.

17. S.-J. Li, J. P. Wehrle, S. S. Rajan, R. G. Steen, J. D. Glickson, and J. Hilton, *Cancer Res.*, 1988, **48**, 4736.
18. J. L. Evelhoch, M.-C. Bissery, G. G. Chabot, N. E. Simpson, C. L. McCoy, L. K. Heilbrun, and T. H. Corbett, *Cancer Res.*, 1988, **48**, 4749.
19. P. J. Wood, C. J. R. Counsell, J. C. M. Bremner, M. R. Horsman, and G. E. Adams, *Int. J. Radiat. Oncol. Biol. Phys.*, 1991, **20**, 291.
20. P. Okunieff, E. McFarland, E. Rummeny, C. Willett, B. M. Hitzig, L. Neuringer, and H. D. Suit, *Am. J. Clin. Oncol.*, 1987, **10**, 475.
21. S. B. Field, S. Needham, I. A. Burney, R. J. Maxwell, J. E. Coggle, and J. R. Griffiths, *Br. J. Cancer*, 1991, **63**, 723.
22. W. G. Negendank, *NMR Biomed*, 1992, **5**, 303.
23. J. D. de Certaines, V. A. Larsen, F. Podo, G. Carpinelli, O. Briot, and O. Henriksen, *NMR Biomed.*, 1993, **6**, 345.
24. J. J. H. Ackerman, C. S. Ewy, N. N. Becker, and R. A. Shalwitz, *Proc. Natl. Acad. Sci. USA*, 1987, **84**, 4099.
25. S.-G. Kim and J. J. H. Ackerman, *Cancer Res*, 1988, **48**, 3449.
26. J. Mattiello and J. L. Evelhoch, *Magn. Reson. Med.*, 1991, **18**, 320.
27. I. A. Burney, R. J. Maxwell, S. B. Field, C. L. McCoy, and J. R. Griffiths, *Acta Oncol.*, 1995, **34**, 367.
28. J. B. Larcombe McDouall and J. L. Evelhoch, *Cancer Res.*, 1990, **50**, 363.
29. J. L. Evelhoch, C. L. McCoy, and B. P. Giri, *Magn. Reson. Med.*, 1989, **9**, 402.
30. R. C. Lyon, R. G. Tschudin, P. F. Daly, and J. S. Cohen, *Magn. Reson. Med.*, 1988, **6**, 1.
31. L. O. Sillerud, K. R. Halliday, J. P. Freyer, R. H. Griffey, and C. Fenoglio-Preiser, in 'Magnetic Resonance in Experimental and Clinical Oncology', eds. J. L. Evelhoch, W. Negendank, F. A. Valeriote, and L. H. Baker, Kluwer Academic, Boston, 1990, p. 149.
32. I. Constantinidis, J. C. Chatham, J. P. Wehrle, and J. D. Glickson, *Magn. Reson. Med.*, 1991, **20**, 17.
33. Z. M. Bhujwalla, I. Constantindis, J. C. Chatham, J. P. Wehrle, and J. D. Glickson, *Int. J. Radiat. Oncol. Biol. Phys.*, 1992, **22**, 95.
34. B. D. Ross, R. J. Higgins, J. E. Boggan, J. A. Willis, B. Knittel, and S. W. Unger, *NMR Biomed.*, 1988, **1**, 20.
35. D. Artemov, Z. M. Bhujwalla, R. J. Maxwell, J. R. Griffiths, I. R. Judson, M. O. Leach, and J. D. Glickson, *Magn. Reson. Med.*, 1995, **34**, 338.
36. J. A. Raleigh, A. J. Franko, L. A. Trimble, and P. S. Allen, *Chem. Mods. Cancer Treat., 6th Annu. Conf.*, Paris, 1–2, 1988.
37. R. J. Maxwell, P. Workman, and J. R. Griffiths, *Int. J. Radiat. Oncol. Biol. Phys.*, 1989, **16**, 925.
38. A. Joseph, C. Davenport, L. Kwock, C. T. Burt, and R. E. London, *Magn. Reson. Med.*, 1987, **4**, 137.
39. W. E. Hull, W. Kunz, R. E. Port, and N. Seiler, *NMR Biomed.*, 1988, **1**, 11.
40. C. Heidelberger, in 'Antineoplastic and Immunosuppressive Agents', eds. A. C. Sartorelli and D. G. Johns, Springer Verlag, New York, 1974, Vol. 38, p. 193.
41. D. Cunningham, *Br. J. Cancer*, 1988, **58**, 695.
42. A. N. Stevens, P. G. Morris, R. A. Iles, P. W. Sheldon, and J. R. Griffiths, *Br. J. Cancer*, 1984, **50**, 113.
43. P. M. J. McSheehy and J. R. Griffiths, *NMR Biomed*, 1989, **2**, 133.
44. A. El-Tahtawy and W. Wolf, *Cancer Res.*, 1991, **51**, 5806.
45. P. S. Hees and C. H. Sotak, *Magn. Reson. Med.*, 1993, **29**, 303.
46. C. H. Sotak, P. S. Hees, H. N. Huang, M. H. Hung, C. G. Krespan, and S. Raynolds, *Magn. Reson. Med.*, 1993, **29**, 188.
47. C. T. Burt, R. R. Moore, and M. F. Roberts, *NMR Biomed.*, 1993, **6**, 289.
48. F. A. Howe, R. J. Maxwell, D. E. Saunders, M. M. Brown, and J. R. Griffiths, *Magn. Reson. Q.*, 1993, **9**, 31.
49. H. Bruhn, T. Michaelis, K. D. Merboldt, W. Hanicke, M. L. Gyngell, C. Hamburger, and J. Frahm, *NMR Biomed.*, 1992, **5**, 253.
50. C. Remy, M. von Kienlin, S. Lotito, A. Francois, A. L. Benabid, and M. Decorps, *Magn. Reson, Med.*, 1989, **9**, 395.
51. D. C. Shungu, Z. M. Bhujwalla, J. P. Wehrle, and J. D. Glickson, *NMR Biomed.*, 1992, **5**, 296.
52. Z. M. Bhujwalla, D. C. Shungu, and J. D. Glickson, *Magn. Reson. Med.*, 1996, **36**, 204.
53. Z. M. Bhujwalla and J. D. Glickson, *Int. J. Radiat. Oncol. Biol. Phys.*, 1996, **36**, 635.

Biographical Sketches

S. P. Robinson. *b* 1969. B.Sc. (Hons) 1991, City University, Ph.D., 1995, London University. Introduced to in vivo MR by Dr D. G. Reid. Research specialties: tumor oxygenation, perfusion and bioenergetics, development of more clinically relevant tumor models in animals.

C. L. McCoy. B.S., 1983, Fisk University, Ph.D., 1991, Wayne State University. Introduced to in vivo MR by Dr J. L. Evelhoch. Research specialties: tumor oxygenation, blood flow.

J. R. Griffiths. *b* 1945. M.B., B.S., 1969, London, D. Phil. (Biochemistry), 1974, Oxford. Studied ESR with George Radda 1970–74 and ^{31}P MRS of livers with David Gadian and Richard Iles, 1979–80. Approx. 140 publications. Research specialty: MRS as applied to cancer, latterly MRI of nerves.

Tissue and Cell Extracts MRS

Patrick J. Cozzone, Sylviane Confort-Gouny, and Jean Vion-Dury

Centre de Résonance Magnétique Biologique et Médicale, Faculté de Médecine, Marseille, France

1 INTRODUCTION

Biochemistry has been based for a long time on the identification of molecules involved in the complex architecture and organization of living systems. Prerequisites to the identification of these molecules are their extraction from cells, their chemical and structural analysis, and their quantitation. High-resolution magnetic resonance spectroscopy (MRS) of tissue and cell extracts has been playing a growing role over the past 15 years in the identification of key molecules participating in biochemical processes (metabolism). In the 1990s, studies by MRS of extracts have generated more than 100 publications per year and are often considered as a required complement to in vivo and ex vivo experiments.

MRS of extracts is gradually developing into a major analytical technique. It combines the most advanced magnetic resonance technology (spectrometers) and methods (pulse sequences) with the methods of biochemical extraction and separation based on chemical and physicochemical properties of molecules. In most cases, the MR spectrometer analyses complex mixtures of compounds in a way which is similar to the detector of a gas chromatograph or the chamber of a mass spectrometer. In some cases, chromatographic separation and subsequent analysis of compounds by MRS have been combined online in the same apparatus as in the coupling of a MR spectrometer with a high-performance liquid chromatograph.

There are many compelling reasons for an MR spectroscopist to analyze tissue and cell extracts. The first pertains to the assignments of resonances in spectra recorded ex vivo and in vivo on organs, animals, and humans, accounting for about 20% of publications on the subject. The second reason of interest is the description and monitoring of normal and pathological metabolism in cells and organs (respectively 34% and 21% of publications), essentially using isotope labeling. Attempts at diagnosing pathologies based on the analysis of human tissue extracts are being made (6% of publications). Finally, the field of pharmacology (bioconversion of drugs, pharmacokinetics, effect of drugs on metabolism) benefits significantly from the MRS analysis of extracts (19% of publications).

In this chapter, we are not aiming to cover exhaustively the field of MRS of extracts. Instead of presenting a comprehensive review, we will try to illustrate what is unique to MRS of tissue and cell extracts in the general context of analytical techniques and modern studies of metabolism.

2 TECHNICAL ASPECTS

The extraction of compounds to be analyzed by MRS has to meet two requirements. It must be *selective* in order to separate molecules of interest from unwanted compounds or cellular substructures (cell debris, membranes etc.). Also, the extraction procedure has *to avoid/limit the degradation and chemical transformation* of molecules. Treatment by perchloric acid is a widely used general method of extraction of water-soluble metabolites.[1] This method requires neutralization and allows removal of salts and proteins by centrifugation (pellet). Perchloric extraction usually follows freeze-clamping of tissues to stop metabolism. It is routinely conducted at a temperature below 5 °C in order to avoid/limit enzymatic or chemical degradation of extracted metabolites. In some cases, inhibitors of enzymatic activity can be added in the supernatant. Other methods are more specific of particular metabolites. For example, extraction by NaOH is used to obtain glycogen and extraction of lipids requires an organic phase such as a 2:1 mixture of chloroform and methanol.[2]

Extracts have to be stored at very low temperature (deep freezer at −80 °C or liquid nitrogen) to limit degradation. Progressive thawing is also critical since chemical modifications of metabolites may occur during this process.

It should be kept in mind that extraction procedures may give a distorted image of the biological reality. Aggressive procedures such as extraction by strong acids or organic solvents modify very significantly the physicochemical environment of metabolites, as compared with the one they experience in the integer cell. As an example, the ionic environment is modified at very low pH (perchloric acid) or when protons and water molecules are lost in organic phases.

Finally, all metabolites are not equal with respect to extraction procedures. They display wide variations in chemical stability, binding properties, conformational rearrangement etc. Hence, one should exert caution when comparing metabolic profiles obtained by in vivo MRS with results obtained on extracts by in vitro MRS. The comparison can be at best misleading if appropriate control experiments are not run since the information offered by extracts is, in essence, different from the information obtained by localized in vivo MR spectroscopy.

MRS of extracts does not require customized MR spectrometers. Standard high-field spectrometers (4.7–18 T) can be used with either narrow-bore or wide-bore magnets. No specific developments in the hardware or software are necessary and MRS of extracts can be performed at any MR laboratory with a basic knowledge of NMR techniques.

3 TISSUE EXTRACTS FOR RESONANCE ASSIGNMENTS

Specific assignment of the resonances recorded in vivo on an MR spectrum remains a critical issue, and a growing one, in consideration of the multiplicity of new applications of MRS in metabolic, pharmacological, and medical studies. Assignment is undoubtedly facilitated by the analysis of extracts using data banks (chemical shifts, coupling patterns, coupling constants), pH titration, and selective addition of authentic compounds to extracts.[3] Also, one can use the whole arsenal of pulse sequences and multinuclear approaches that the chemists have

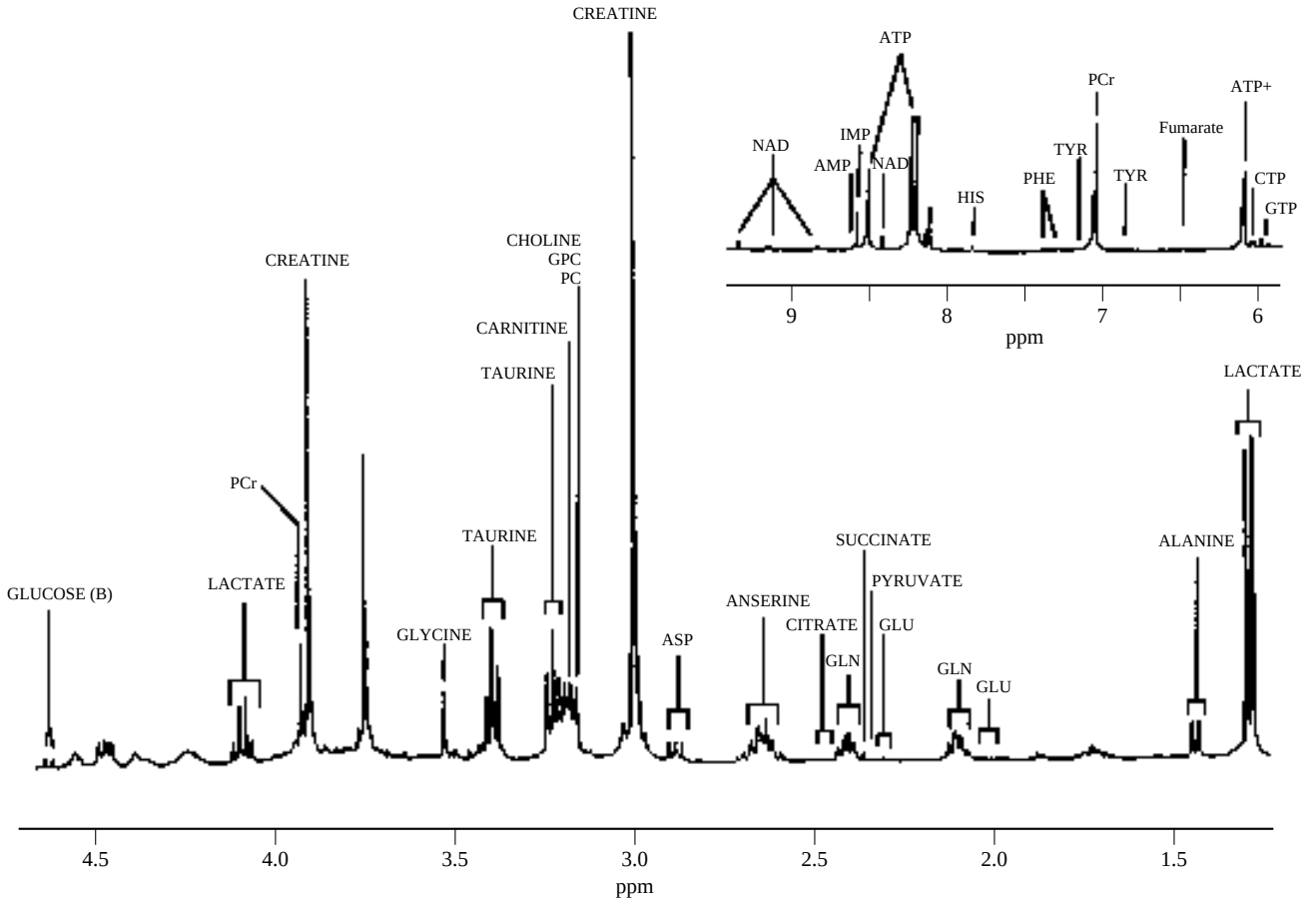

Figure 1 Proton MR spectrum (400 MHz) of a perchloric extract of rat gastrocnemius muscle obtained after freeze-clamping. The supernanant is lyophilized in order to eliminate water. Then the metabolites are dissolved in D_2O. Main Figure: aliphatic region of the spectrum (0–5 ppm). Inset: aromatic region of the spectrum (5–12 ppm). Abbreviations: PC, phosphorylcholine; GPC, glycerophosphorylcholine; PCr, phosphocreatine; ASP, aspartate, GLN, glutamine; GLU, glutamate; NAD, nicotinamide-adenine dinucleotide; AMP, adenosine monophosphate; IMP, inosine monophosphate; HIS, histidine; PHE, phenylalanine; TYR, tyrosine; CTP, cytidine 5′-triphosphate; GTP, guanosine 5′-triphosphate; ATP, adenosine triphosphate

developed in high-resolution MRS of organic compounds.[4–6] With the limitation already mentioned, in vitro MRS of extracts provides the best basis for the assignments of in vivo and ex vivo spectra. (See Figure 1.)

Extracts reflect a ‘frozen situation’ in cell metabolism which is often an advantage. Spectral resolution is always superior in vitro vs. in vivo and ex vivo by several orders of magnitude and facilitates the interpretation of spectra recorded on living cells, tissues, and organs. Interestingly, assignments of resonances in extracts have revealed the presence of unexpected compounds in plants, yeasts, bacterias, and human tissues,[7,8] the identification of which has required chromatographic separation and chemical structure identification by standard analytical techniques, including high-resolution MRS. In these instances, MRS of extracts has directly contributed to a better understanding of metabolic events occurring in the cell.

4 TISSUE EXTRACTS IN METABOLIC STUDIES

MRS of tissue extracts has played a major role in the study of metabolism of cells and organs. Two strategies have been used. The first strategy is ‘passive’ and consists of the detection and dosage of the metabolites present in the tissue extract reflecting, as a snapshot, the metabolic status of the living tissue at the time of extraction. Quantitation can be achieved with respect to wet weight of tissue, protein content, or an internal reference (e.g., an endogenous compound of known concentration). Proton and ^{13}C MR spectra bear information on the intermediary metabolism (amino acids, lipids, Krebs cycle intermediates, etc.). Phosphorus-31 MR spectra carry different information depending on the type of extraction. Aqueous extracts contain phosphorylated molecules of energy metabolism (ATP, creatine phosphate, phosphomonoesters and phosphodiesters, inorganic phosphate, etc.). (See Figure 2.) The polar head groups of many phospholipids can be assayed on lipidic extracts. In fact, ^{31}P MRS provides a viable alternative to the quantitative assay of phospholipids. (See Figure 3.)

The second strategy is ‘active’ and involves the perfusion of a selectively ^{13}C-enriched substrate prior to the freeze of metabolic activity and subsequent extraction. By choosing appropriately both the enriched molecule and the chemical site of the enrichment on the molecule, specific metabolic pathways can be singled out and monitored and metabolic fluxes can be

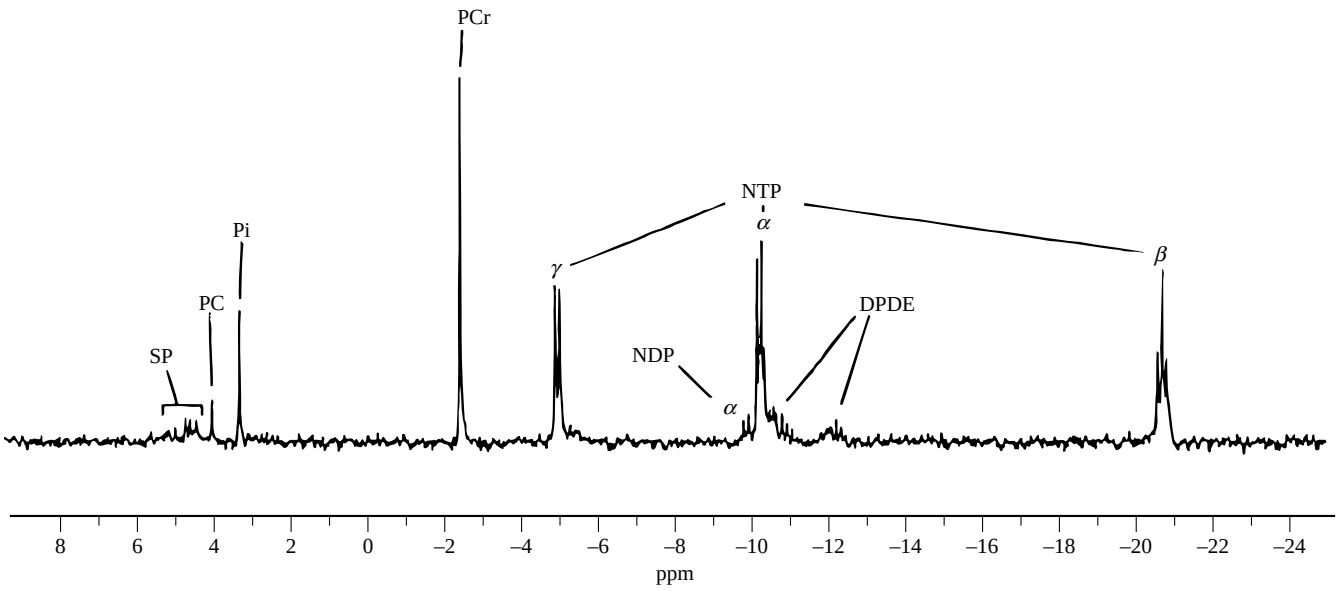

Figure 2 Phosphorus-31 MR (162 MHz) spectrum of a perchloric extract of RINm5F cells cultured in Dulbecco's Modified Eagle's Medium containing glucose. This spectrum (sum of 4800 scans, with complete proton decoupling) corresponds to the perchloric extract of 6×10^8 RINm5F cells cultured in flasks. Abbreviations: PC, phosphorylcholine; SP, sugar phosphate; PCr, phosphocreatine; DPDE, diphosphodiesters; NTP, nucleoside triphosphates; NDP, nucleoside diphosphates

quantitated under a variety of conditions, in relation to pathological state, cell differentiation,[9] cell growth, aging etc. This approach is widely used on perfused organs and cultured cells. In these experiments, extracts are prepared and analyzed at specific times to follow up the conversion and biodistribution of the ^{13}C marker. Basic metabolic events have been documented such as the phosphorylation status of liver under normal conditions[10] or in the presence of ethanol, the metabolism of acetate,[11] or the redox state of the brain,[12,13] etc.

Cellular compartmentation can also be studied from a metabolic standpoint and particularly interesting information has been obtained in brain tissue to shed additional light on the respective role of glial and neuronal cells.[14]

Particular attention has been devoted to the study of metabolic disorders in relation to cancer. The reader is referred to the abundant literature on this subject[15,16] which illustrates the large extent to which MRS of extracts has become an indispensable analytical tool to study normal and pathological metabolism in cells and tissues.

5 APPLICATIONS TO PHARMACOLOGY

Besides the study of cell metabolism, and naturally occurring metabolites, MRS of extracts can document the metabolic fate and the metabolic impact of xenobiotics. Bioconversion of drugs can be readily studied with unsurpassed accuracy. The same MRS analysis can detect, identify (structure), and quantitate the metabolites to which a drug is converted and the kinetics of their appearance.[17]

Prototype studies have been conducted on antimitotic, antifungal, and antiviral drugs.[18,19] The analysis of drug metabolites benefits from the use of selective isotope labeling and multinuclear (^{31}P, ^{19}F, ^{13}C, ^{2}H) and multidimensional MRS experiments.

A second pharmacological application of MRS of extracts is the evaluation of the metabolic changes induced by the administration of a drug. As an example, the impact of the different interleukins on cell metabolism is not well known. However, obtaining additional information is critical to develop, adapt, and optimize anticancer treatment using this new family of molecules. MRS plays a key role in evaluating the effect of these peptides on the general metabolism of the patient toward eliciting the adequate immune response to the presence of a cancer.[20] Drug resistance, another new problem of public health, is currently tackled by MRS of extracts in bacterial and eukaryotic cells, animal models, and even patients in an attempt to establish some metabolic basis to the alarming decrease in therapeutic efficacy of a number of antibiotic and antimitotic drugs.[21,22]

6 NEW DIRECTIONS: TOWARD MEDICAL DIAGNOSIS BY MRS OF TISSUE EXTRACTS

Tissue characterization in medicine is essentially based on the methods developed in pathology and cytology with a large role devoted to optical and electronic microscopy, and the use of selective dyes and immunological labeling. Biochemical studies of excised tissues is not common at the hospital, with the exception of blood and some body fluids. The analysis of tissue biopsies is a growing area of application for the MRS of extracts. Muscle and brain biopsies have been studied but most of the work done to date has focused on human tissues biopsies: breast cancer,[23] uterus,[24] colon.[25] As a matter of fact, the knowledge of the metabolic features of a cancer tumor is of the utmost interest in diagnosis, prognosis and therapeutic decisions.[26] Specific metabolic profiles are observed from extracts of malignant tumors with deviations in the metabolism of amino acids and lipids/phospholipids.[24,27] (See Figure 3.)

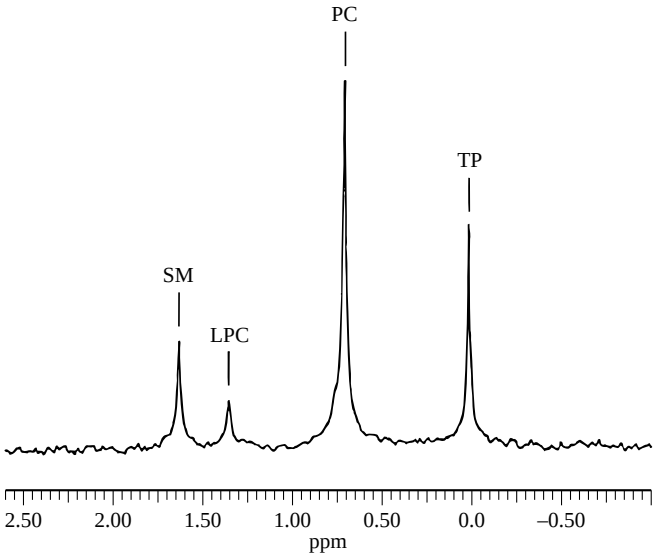

Figure 3 Phosphorus-31 MR (162 MHz) spectrum of a control plasma lipid extract. A line broadening of 4 Hz was applied. Abbreviations: SM, sphingomyelin; PC, phosphatidylcholine; LPC, lysophosphatidylcholine; TP, triethyl phosphate

The wealth of information that is available on the spectra (usually proton spectra) of biopsy extracts has prompted new strategies for data processing and analysis, based on pattern recognition, neural networks, and chemometrics.[28,29] This integrated and automated approach to spectral processing should facilitate very significantly the acceptance of MRS of biopsy extracts in routine medical diagnosis.

7 CONCLUSIONS

Obviously, MRS of extracts is not 'the MRS of the poor' that scientists and clinicians use when they do not have access to sophisticated methods of in vivo spectroscopy. It is making a definite contribution to the understanding of normal and pathological cell metabolism when it is submitted to a variety of perturbations. MRS of extracts is a cost-effective, highly informational, easy-to-use analytical procedure which is now entering the field of clinical biology by providing unique information that the medical profession can readily use for diagnosis, treatment, and prognosis. (See Figure 4.)

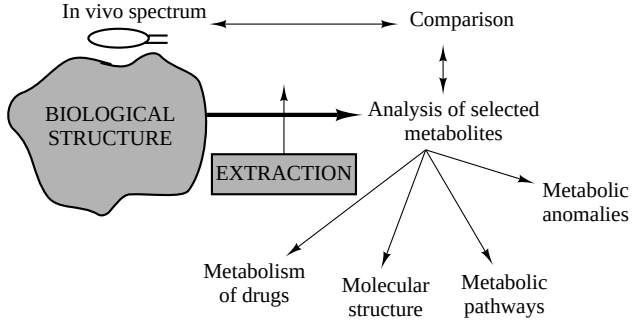

Figure 4 Synthetic scheme summarizing the position of extracts in analysis of biological activity

8 RELATED ARTICLES

Body Fluids; Cells and Cell Systems MRS; Whole Body Studies: Impact of MRS.

9 REFERENCES

1. M. Leach, L. Le Moyec, and F. Podo, in 'Magnetic Resonance Spectroscopy in Biology and Medicine', eds. J. De Certaines, W. M. M. J. Bovée, and F. Podo, Pergamon Press, Oxford, 1992, Chap. 18.
2. J. Folch, M. Lees, and G. H. S. Stanley, *J. Biol. Chem.*, 1957, **226**, 497.
3. O. Kaplan, Van Zijl, and J. S. Cohen, in 'NMR Basic Principles and Progress', eds. P. Diehl, E. Fluck, H. Günther, R. Kosfeld, and J. Seelig, Springer, Berlin, 1992, Vol. 28, Chap. 1.
4. G. Navon, T. Kushnir, N. Askenasy, and O. Kaplan. in 'NMR Basic Principles and Progress', eds. P. Diehl, E. Fluck, H. Günther, R. Kosfeld, and J. Seelig, Springer, Berlin, 1992, Vol. 27, Chap. 10.
5. C. Arus, Y. C. Chang, and M. Barany, *Physiol. Chem. Phys. Med. NMR*, 1985, **17**, 23.
6. M. Barany, C. Arus, and Y. C. Chang, *Magn. Reson. Med.*, 1985, **2**, 289.
7. N. De Tomasi, S. Piacente, F. De Simone, C. Pizza, and Z. L. Zhou, *J. Nat. Prod.*, 1993, **56**(10), 1669.
8. F. H. Kormelink, R. A. Hoffmann, H. Gruppen., A. G. Voragen, J. P. Kamerling, and J. F. Vliegentart. *Carbohydr. Res.*, 1993, **249**(2), 369.
9. J. P. Galons, J. Fantini, J. Vion-Dury, P. J. Cozzone, and P. Canioni. *Biochimie*, 1989, **71**, 949.
10. R. A. Iles, A. N. Stevens, J. R. Griffiths, and P. G. Morris. *Biochem J.*, 1985, **229**, 141.
11. S. R. Williams, E. Proctor, K. Allen, D. G. Gadian, and H. A. Crockard. *Magn. Reson. Med.*, 1988, **7**, 425.
12. O. Ben-Yosef, S. Badar-Goffer, P. G. Morris, and H. S. Bachelard. *Biochem. J.*, 1993, **291**, 915.
13. C. Remy, C. Arus, A. Ziegler, E. Sam Lai, A. Moreno, Y. Le Fur and M. Décorps. *J. Neurochem.*, 1994, **62**(1), 166.
14. J. Urenkak, S. R. Williams, D. G. Gadian, and M. Noble. *J. Neurosci.*, 1993, **13**(3), 981.
15. C. E. Mountford, C. L. Lean, and W. B. Mackinnon. *Annu. Rep. NMR Spectrosc.*, 1993, **27**, 174.
16. M. Czuba and I. C. P. Smith. *Pharmacol. Ther.*, 1991, **50**, 147.
17. J. Vion-Dury, S. Confort-Gouny, and P. J. Cozzone, in 'Human Pharmacology', eds. H. Kuemmerle, T. Shibuya, and J. P. Tillement, Elsevier, Amsterdam, 1991, Chap. 13.
18. M. O. F. Fasoli, D. Kerridge, P. G. Morris, and A. Torosantucci. *Antimicrob. Agents Chemother.*, 1990, **34**(10), 1996.
19. R. A. Vere-Hodge, S. J. Darlinson, and S. A. Readshaw. *Chirality*, 1993, **5**(8), 577.
20. E. Prioretti., F. Belardelli., G. Carpinelli, M. Di Vito, D. Woodrow, J. Moss, P. Sestelli, W. Fiers, I. Gresser and F. Podo. *Int. J. Cancer*, 1988, **42**, 582.
21. A. Ferretti, L. L. Chen, M. Di Vito, S. Barca, M. Tombesi, M. Cianfriglia, A. Bozzi, R. Srom, and F. Podo. *Anticancer Res.*, 1993, **13**, 867.
22. G. L. May, L. C. Wright, M. Dyne, W. B. Mackinnon, R. M. Fox, and C. E. Mountford. *Int. J. Cancer*, 1988, **42**, 728.
23. T. A. D. Smith, C. Bush, C. Jameson, J. C. Titley, M. O. Leach, D. E. V. Wilman, and V. R. McCready. *NMR Biomed.*, 1993, **6**, 318.
24. C. E. Mountford, E. J. Delikatny, M. Dyne, K. T. Holmes, W. B. Mackinnon, R. Ford, J. C. Hunter, I. D. Truskett, and P. Russell. *Magn. Reson. Med.*, 1990, **13**, 324.

25. A. Moreno, M. Rey, J. M. Montane, J. Alonso, and C. Arus. *NMR Biomed.*, 1993, **6**, 111.
26. D. G. Gadian, T. E. Bates, S. R. William, J. D. Bell, S. J. Austin, and A. Connelly. *NMR Biomed.*, 1991, **4**, 85.
27. M. Kriat, J. Vion-Dury, S. Confort-Gouny, R. Favre, P. Viout, M. Sciaky, H. Sari, and P. J. Cozzone. *J. Lipid Res.*, 1993, **34**, 1009.
28. S. L. Howells, R. J. Maxwell, and J. R. Griffiths. *NMR Biomed.*, 1992, **5**, 59.
29. S. L. Howells, R. J. Maxwell, A. C. Peet, and J. R. Griffiths. *Magn. Reson. Med.*, 1992, **28**, 214.

Biographical Sketches

Patrick J. Cozzone. *b* 1945. Ph.D., 1971, University of Marseille, MBA, University of Chicago. Professor of Biochemistry, University of Marseille, 1975–90; Professor of Biophysics, Faculty of Medicine, Marseille, 1990–present; Director, Centre de Résonance Magnétique Biologique et Médicale (CRMBM), 1986–present.

Sylviane Confort-Gouny. *b* 1957. Ph.D., 1984, University of Grenoble, MRS instrumentation. Research engineer, Centre National de la Recherche Scientifique; in charge at Centre de Résonance Magnétique Biologique et Médicale, Marseille, of methodological developments and clinical transfers of MRS preclinical protocols, 1986–present.

Jean Vion-Dury. *b* 1956. M.D. 1983, School of Medicine of Marseille, Ph.D., 1988, University of Marseille. Assistant Professor of Biophysics, Faculty of Medicine, Marseille, 1994–present. NMR research at the Centre de Résonance Magnétique Biologique et Médicale, 1986–present.

Tissue NMR Ex Vivo

Ian C. P. Smith and Tedros Bezabeh
National Research Council of Canada, Winnipeg, Canada

1 INTRODUCTION

NMR of tissue specimens is now an established, powerful adjunct to histopathology for classification of human cancers. The present article is an update of earlier reports.[1,2] The initial study that provided insight into the potential of NMR for the early detection and diagnosis of cancer was reported in 1980 for mouse thymus.[3] Spectral changes preceded the cellular changes observed by histopathology, suggesting that the tissue NMR method could detect preinvasive changes prior to any morphological manifestation. This was supported by a study of a rat mammary model for adenocarcinoma metastasis.[4] Spectra from the excised tumor closely resembled those from suspensions of the same cells grown in vitro. The T_2 relaxation time for the strong peak at 1.3 ppm correlated well with the metastatic potential of this tumor in the rat.

This early success with a rat model led to similar studies with human tissues. Human colorectal tumors yielded spectra with some parameters similar to those obtained from rat mammary adenocarcinoma. Over 90% of the human colorectal tumors gave long T_2 relaxation values for the resonance at 1.3 ppm, implying a high metastatic potential.[5] Patient follow-up showed no false positives; that is, no patients whose tumor generated only a short T_2 relaxation value for the resonance at 1.3 ppm developed secondary tumors.[6] Many of those with long T_2 relaxation values did develop secondary tumors.

From these studies it was apparent that the strong signals from fat were superimposed upon those of potentially diagnostic species present in the spectra from colorectal biopsies, a problem now known to exist also for lymph node and breast tissues. The implementation of two-dimensional (2D) NMR spectroscopy was a valuable complement, especially when 1D spectra were complex.[7]

Tissue NMR ex vivo has so far been primarily performed on ^{1}H nuclei. This is mainly because of the high sensitivity of ^{1}H NMR spectroscopy and the stability of the proton-containing compounds/metabolites in an excised tissue that are of diagnostic interest. Natural abundance ^{13}C NMR spectroscopy would take unreasonably long acquisition time and, therefore, is not ideal for a study of an excised/isolated piece of tissue. The instability (hydrolysis) of the high-energy phosphates [e.g., phosphocreatine (PCr), ATP] after the removal of the tissue from the system makes the use of ^{31}P NMR spectroscopy impractical.

Tissue NMR ex vivo offers an advantage over NMR of cell cultures and extracts in that it provides a situation similar to that in vivo. In particular, it helps in the examination of the biological properties of tissue that are dependent on architecture and morphology, which is impossible to do with extracts and isolated cells. Another advantage of tissue NMR ex vivo is its nondestructive character; the tissue can be submitted for histopathological assessment following the NMR experiment, enabling a direct correlation between the histopathological and MR spectral features of the same tissue specimen. As a result, no additional biopsy need be taken for the study since the clinical diagnosis can be made on the MRS sample, with no compromises or artifacts.

2 METHODS

All successful studies of viable tissues have relied heavily on careful sample handling prior to ^{1}H MRS experiments.[8] Tissues are placed into sterile tubes immediately after excision, immersed in liquid nitrogen, and stored at $-70\,^{\circ}$C. Either a glass wool platform supports the sample surrounded by buffer,[7] or the specimen is inserted into a capillary containing buffer,[8] which in turn is inserted into an NMR tube containing the same buffer and a reference. This latter method of sample positioning has several advantages including measurable volume for quantification and easier homogeneity adjustment (Figure 1).

Time constraints imposed by the limited viability of cell and tissue specimens dictate careful selection of acquisition parameters for 2D NMR spectroscopy. In order to obtain a pathological assessment of the sample used for NMR, time in the instrument must be minimized. Therefore, the trade-off between signal strength, spectral resolution, and sample viability must be addressed for each tissue type. Cells and tissues contain a variety of biochemical species at a range of concentrations, with T_2 relaxation times ranging from <100 ms to >1 s and, therefore, care must be taken with signal processing. It is imperative that histological examination be undertaken on the NMR specimen itself, rather than relying upon the routine

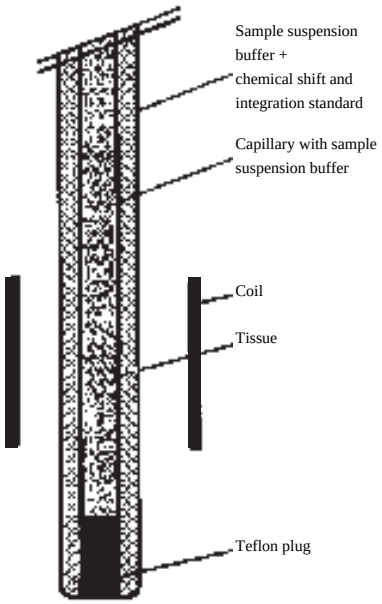

Figure 1 Schematic of the positioning of a small tissue specimen in a capillary tube. (Reproduced with permission from Kuesel et al., *Magn. Reson. Med.*, 1992, **27**, 349–355. Copyright © 1992, Wiley-Liss)

hospital report. Spectral analysis is best made by nonsubjective multivariate methods (see below).

We describe below studies on tissue from a variety of organs, each representing a solution to different technical/clinical problems: (1) the distinction between preinvasive and invasive cancers; (2) the presence of significant levels of fat, obscuring signals of interest; and (3) the detection of cellular abnormalities which are not morphologically manifest.

3 CERVIX

Cervical epithelium has preinvasive states that are well documented by histopathology. Independent clinical studies in two laboratories have shown that ^{1}H NMR can distinguish between preinvasive lesions, including carcinoma in situ (CIS), and frankly invasive cervical cancer with $p < 0.0001$ (Student t-test).[7–9] The ^{1}H NMR acquisitions are completed in 15 min, and the tissue is not subject to the vagaries of sampling since the entire punch biopsy specimen is examined. Two different approaches have been used for spectral analysis. In one, manual measurements of peak heights were performed. Typical spectra of preinvasive and invasive cervical epithelium are characterized by intense lipid resonances at 0.9, 1.3, and 5.2 ppm. In contrast, spectra of preinvasive lesions are free of signals from high-resolution lipid.[9] A second spectral region which provides diagnostic information lies between 3.4 and 4.2 ppm. The ratio of the strongest resonance between 3.4 and 4.2 ppm and the methylene resonance at 1.3 ppm, is plotted against the ratio of the methylene to methyl resonances at 1.3 and 0.9 ppm, respectively (Figure 2). The separation between the mean ratio values for CIN3 and invasive cancer is significant. The p values obtained when comparing invasive cancer to the low, moderate, or severe levels of dysplasia are all <0.0001, with a specificity of 0.94 and sensitivity of 0.98.[9]

Alternatively, a mathematical treatment of the data sets may be used. A variety of multivariate analyses, such as linear discriminant analysis, neural nets, and genetic programming were applied to these data. Using a consensus approach for a series of 150 spectra of cervical tissue, spectra were allocated to characteristic groups. Groupings were then compared with the data from histopathology,[10] and yielded sensitivities and specificities greater than 0.99 for the various levels of dysplasia. In a recent study of 196 cervical punch biopsies (nondysplastic and dysplastic of varying grades), it was found that classification of the spectra into four diagnostic groups (i.e., nondysplastic, CIN1, CIN2, and CIN3) was difficult.[11] This could be because the inter-class biochemical changes that help to differentiate between these groups are very small compared with the sensitivity of NMR spectroscopy. However, multivariate classification of the spectra into two groups, i.e., nondysplastic and CIN1 versus CIN2 and CIN3, yielded a much better classification accuracy.

Chemical shift imaging (CSI) has the potential to revolutionize the detection of cancers since it can provide information on the biochemical composition and distribution, and the spatial location, of neoplasms. In CSI the image is constituted from a single specific frequency. Water-based CSI images (excitation at 4.8 ppm) of cervical punch biopsies from invasive adenocarcinoma and low-grade squamous dysplasia show that both biopsies appear with equal intensity. However, when a lipid-based CSI (excitation at 1.3 ppm) is performed on the biopsies, only the malignant specimen shows a substantial accumulation of MR-visible lipids.[12]

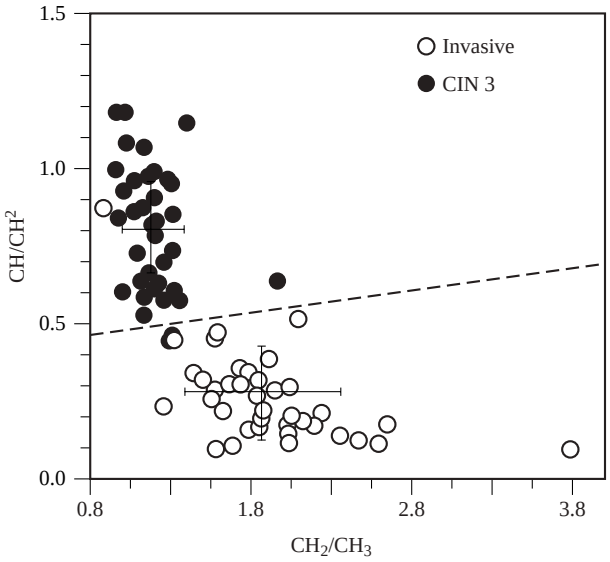

Figure 2 Peak height ratios from one-dimensional ^{1}H NMR spectra.[12] Severely dysplastic epithelium (CIN3) is compared with invasive carcinoma. The cross bars show the mean ± standard deviation. (Reproduced with permission from Delikatny et al., Proton NMR and human cervical neoplasia: ex vivo spectroscopy allows distinction of invasive carcinoma of the cervix from carcinoma in situ and other preinvasive lesions. *Radiology*, 1993, **188**, 791–796)

4 THYROID

The thyroid is the first organ where NMR has distinguished between benign adenoma and carcinoma which are morphologically identical under the light microscope.[13] Histological diagnosis of follicular thyroid cancer relies upon visualization of capsular invasion or the patients having demonstrated secondary tumors. Therefore, the morphological similarity of malignant and benign follicular cells leads to surgery solely for diagnostic purposes. One-dimensional ^{1}H NMR spectroscopy clearly distinguishes normal thyroid tissue from morphologically distinct invasive papillary carcinoma, based on differences in the relative intensities of resonances at 1.7 and 0.9 ppm,[14] demonstrating the potential to distinguish genuinely benign follicular adenomas from follicular carcinomas. The MR parameters separated follicular neoplasms into two categories, each of which was directly comparable with either normal thyroid or papillary carcinoma. The patients with clinically proven or histologically invasive follicular carcinoma were categorized by ^{1}H MR together with papillary cancers, as were a number of patients with clinically or morphological atypical neoplasms. It was subsequently established that the same diagnostic information could be obtained from fine needle aspiration biopsies, without recourse to surgery.[15] Multivariate analysis undertaken in a blind study delineated five out of six patients with follicular carcinoma (identified clinically by the

presence of secondary tumors).[13] A clinical trial is underway in Australia where patients with normal NMR profiles from fine needle aspiration biopsies are given the option not to undergo surgery for diagnostic purposes.

Although the 1.7/0.9 ppm intensity ratio can distinguish thyroid cancer from normal tissue with a high sensitivity,[16] its specificity is relatively low. The probability of correctly identifying patients without cancer was significantly raised by using the 2.05/0.9 intensity ratio.[17] Furthermore, 2D NMR spectroscopy yielded an increased incidence of cross-peaks from cholesterol/cholesteryl esters and di-/triglycerides and a decreased incidence of two unassigned cross-peaks, unique to the thyroid, for cancer specimens.[17] The best accuracy was obtained via a computed consensus diagnosis (see section 9.5 below). Analysis of 107 thyroid biopsies resulted in 100% sensitivity and specificity in the training set, and 100% specificity and 98% sensitivity on samples of known malignancy in the test set.[13]

5 COLON

Colon tissue presents the technical difficulty of naturally high levels of fat,[6] necessitating 2D NMR spectroscopy,[6] or T_2 relaxation filters[18] or very careful sample preparation[19] to define the diagnostic resonances. The 2D ^{1}H–^{1}H COSY spectra of colon-invasive adenocarcinoma indicate such diagnostic parameters as choline, choline-based metabolites, and altered lipid profiles (Figure 3). Tissues histopathologically classified as normal, while remaining distinct from the malignant spectral profile, were found to fit into two categories, one of which had some of the spectral characteristics of malignancy.[18] These results suggest that ^{1}H MRS identifies colorectal mucosa with abnormality that is not morphologically manifest.

The NMR studies of colorectal cancer biopsies have relied heavily on the correlation of biological and genetic information with the NMR data from cultured cell lines.[20] It was shown that 2D NMR data for cell surface fucosyl residues identified the various preinvasive states as well as a feature unique to the carcinoma in situ.[21] These pathological states, identifiable by NMR, include the distinction between malignant tumors and normal tissue; carcinoma in situ and frankly invasive adenocarcinoma; and the extents of dysplasia in preinvasive polyps.

Colon tumor and morphologically normal specimens were examined recently by ^{1}H NMR.[22] The spectra from 55 specimens were subjected to multivariate analysis: classification accuracy of 100% was obtained in both the training and the test sets. The concern with surgical specimens of colon has been the contamination of the sample with the nonmucosal layers of the colonic wall.[19,23] Of particular interest is the submucosal layer, which gives rise to intense lipid signals that have no diagnostic value but mask other potentially useful metabolites present at lower concentrations. Therefore, in such studies an effort must be made to examine only the mucosa. Another way to circumvent this problem is to study endoscopic biopsies where the composition is dominantly mucosal. A recent study of such biopsies aimed to differentiate between ulcerative colitis and Crohn's disease, two distinct forms of inflammatory bowel disease (IBD) sharing many similar etiologic, clinical and pathological features. A strong similarity between these two diseases poses difficulty in making an accurate differential clinical diagnosis. To date, there are no definitive methods available to distinguish Crohn's disease from ulcerative colitis, especially when the endoscopy, radiology and histology are equivocal. Preliminary results showed that ^{1}H NMR spectroscopy can differentiate between these two diseases with a good classification accuracy.[24]

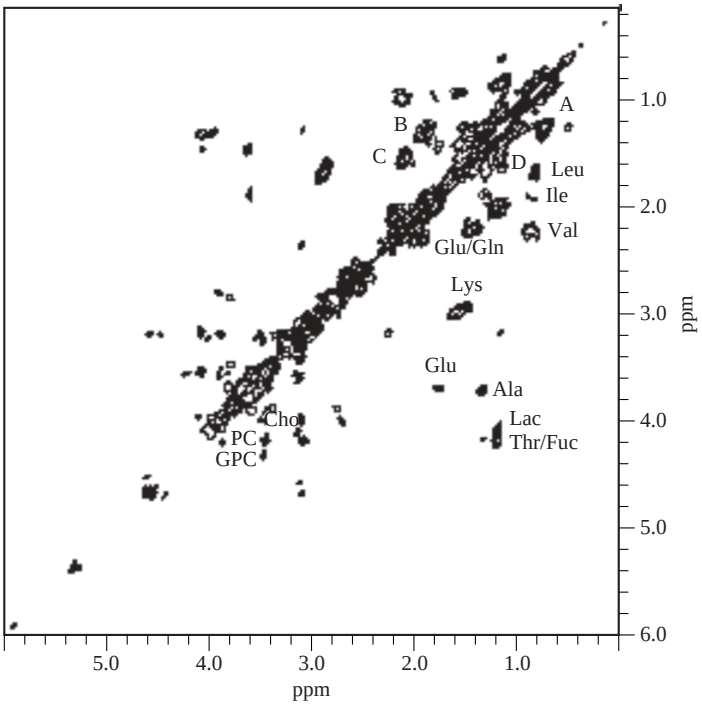

Figure 3 Proton 360 MHz NMR symmetrized COSY spectrum of colon tumor in phosphate-buffered saline/D_2O, 37 °C. Lac, lactic acid; Leu, leucine; Val, valine; Glu/Gln, glutamic acid/glutamate; Lys, lysine; Ile, isoleucine; Ala, alanine; Thr, threonine; Fuc, fucose; Cho, choline-containing compounds; PC, phosphatidylcholine; GPC, glycerophosphorylcholine; A, B, C, and D, triacylglycerols

Another useful contribution of tissue NMR ex vivo has been in providing an insight into premalignant colon tissue. A study performed on rat colon tissue showed that the NMR spectra of aberrant crypt foci (preneoplastic lesions in the colon) have spectral features intermediate between those of normal mucosa and tumor, supporting the widely held adenoma–adenocarcinoma sequence in colorectal cancer.[25] Similar studies are also underway on human polyps in our laboratory.

CSI performed on normal human colon tissue helped to characterize the different layers of the colon wall.[26] Whereas the water-based image helped to delineate the mucosal layer, the submucosal layer was identified on a lipid-based image. The presence of high levels of neutral lipid distributed in the submucosal layer agrees with the spectral profile of specimens largely composed of submucosa (i.e., with intense lipid resonances).[19,20,27]

6 PROSTATE

Distinction between benign and malignant abnormalities of the prostate is sometimes difficult. Human prostate tissue con-

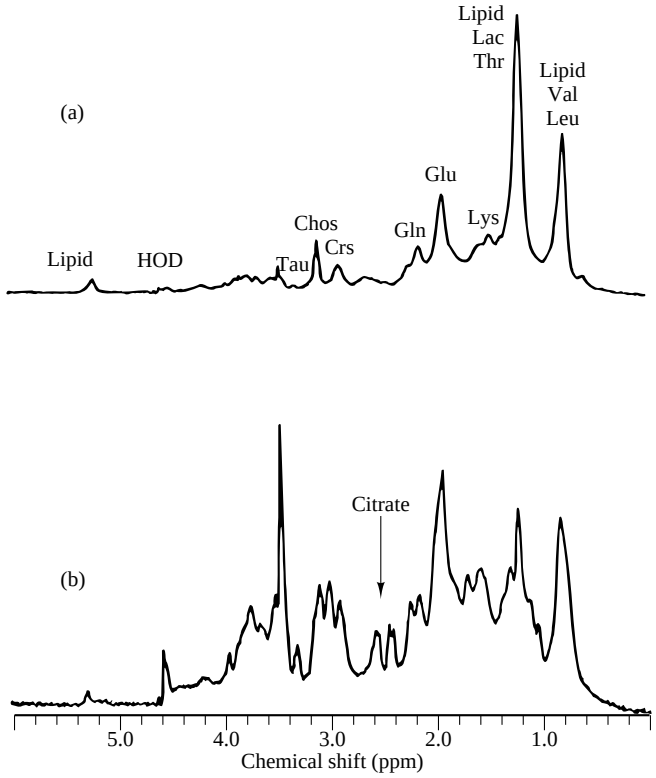

Figure 4 Proton MR spectra (360 MHz) of prostate tissue specimens. (a) Cancer (Gleason grade 3 + 3); (b) benign prostatic hyperplasia. Chos, choline-containing compounds; Crs, creatines; Gln, glutamine; Glu, glutamic acid; Leu, leucine; Lys, lysine; Tau, Taurine; Thr, threonine; Val, valine. Assignments do not imply that these are the only substances contributing to a particular resonance. (Reproduced with permission from Hahn et al., Classification of benign and malignant human prostate tissue by multivariate analysis of ^{1}H magnetic resonance spectra. *Cancer Res.*, 1997, **57**, 3398)

tains many metabolites that are detectable using NMR. It is particularly rich in the citrate anion. Human prostate tissue specimens obtained from either radical prostatectomy (complete removal of the prostate) or transurethral resection of the prostate have been examined by ^{1}H NMR.[28] Comparison of the spectra from benign prostatic hyperplasia (BPH) and prostatic adenocarcinoma indicated significant differences. As shown in Figure 4, the resonance of the citrate anion (at ~2.5 ppm) has the potential to discriminate between the two classes. As indicated in the figure, citrate levels become significantly reduced (almost to below detection levels) in prostatic adenocarcinoma. Whether the citrate levels show any correlation with the grade or stage of the cancer is yet to be determined.

Other NMR-visible metabolites with diagnostic potential in the prostate include glutamic acid, taurine and choline. The use of computed multivariate methods of tissue NMR data analysis developed at our Institute has given highly accurate results with a sensitivity and specificity of 100 and 95.5%, respectively, in classifying benign from malignant prostatic tissue.[28]

Benign prostatic hyperplasia, which is an age-related enlargement of the prostatic gland, may derive from two different types of tissue: stromal and glandular. Knowing the type of BPH in a particular patient, however, is critical for the proper management of the disease. Proton NMR of tissue obtained from dominantly glandular and stromal specimens have indicated significantly higher levels of citrate anion in the glandular cases (Figure 5).[28]

Besides its value in solving diagnostic problems, tissue NMR ex vivo may also have a role to play in assessing treatment responses and post-therapy recurrences. For example, one of the problems in assessing post-radiotherapy response is distinguishing between radiation necrosis and recurring tumor. We are currently examining prostate biopsies obtained by transrectal ultrasound guidance from patients who underwent radiation therapy 2 years previously.

Other studies of fresh tissue prostate specimens have also indicated higher levels of spermine (a polyamine with NMR resonances at 1.8, 2.1 and 3.1 ppm) in both normal and benign hyperplasia compared with tumors. However, these resonances may not be present in tissue specimens that have been frozen and thawed since the positively charged spermine may bind to negatively charged macromolecules (DNA/RNA, lipids) and become invisible to NMR.[29]

Kurhanewicz et al. have been able to perform in vivo MR spectroscopic studies of the human prostate using an endorectal coil.[30–32] Although their spectra have lower resolution than that of the ex vivo spectra, they were able to see discrete resonances from some of the diagnostically useful metabolites such as the citrate anion. By comparing MRI and MR spectroscopy plus MRI, they were able to show that the specificity and sensitivity of detecting cancer in the prostate gland, and the

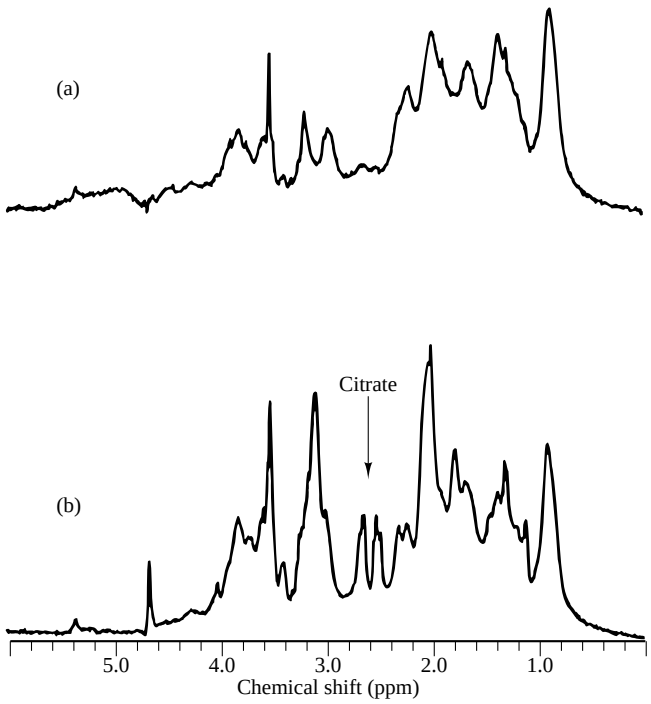

Figure 5 Proton MR spectra (360 MHz) of tissue specimens from benign prostatic hyperplasia. (a) 95% stromal, 5% glandular; (b) 90% glandular, 10% stromal. (Reproduced with permission from Hahn et al., Classification of benign and malignant human prostate tissue by multivariate analysis of ^{1}H magnetic resonance spectra. *Cancer Res.*, 1997, **57**, 3398)

estimation of the extracapsular extension of the cancer, improve significantly when the combined approach is used.[31,32]

7 BREAST

The combination of physical examination, mammography, and fine-needle aspiration cytologic analysis is currently the most sensitive method for the preoperative diagnosis of breast lesions. While the sensitivity of such a diagnostic approach is satisfactory, its specificity remains inadequate. Proton NMR spectroscopy of tissue biopsies has the potential to augment/complement this triple assessment method and to increase both the sensitivity and the specificity. Experiments performed on fine-needle biopsies obtained from patients undergoing diagnostic biopsy or definitive treatment (lumpectomy, quadrantectomy, or mastectomy) for histologically proven invasive breast cancer indicate significantly higher ratios of the peak height intensities of spectral resonances at 3.25 to 3.05 ppm for infiltrating/invasive carcinoma compared with benign lesions (Figure 6). While the 3.25 ppm resonance results from choline-based metabolites, the 3.05 ppm resonance could be from creatine or lysine. Using this spectral ratio, the sensitivity and specificity obtained in differentiating between benign and malignant breast lesions were 95% and 96%, respectively.[33] The increase in this ratio may be primarily a consequence of the elevation of choline metabolites in malignant tissues, consistent with what has been observed in other tissue types (e.g., brain, and colon). Interestingly, all atypical or suspicious fine-needle aspiration cytologic results, in subsequently confirmed benign specimens, had NMR spectroscopic ratios indicating benign disease.

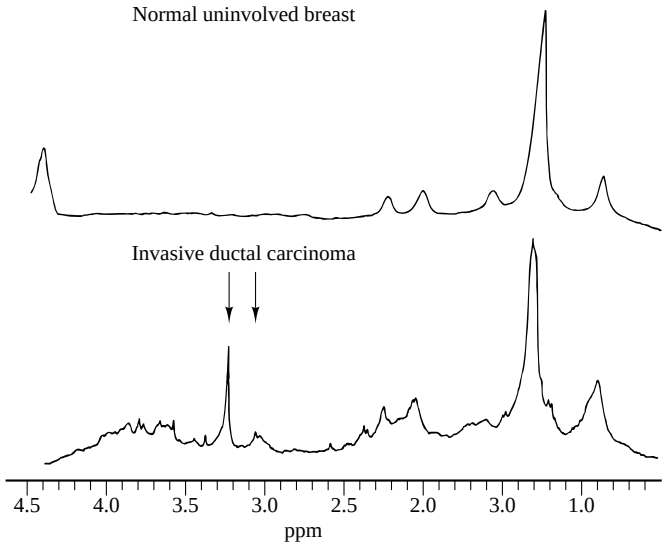

Figure 6 One-dimensional ^{1}H MR spectra in fine-needle biopsy specimens obtained in a patient who underwent mastectomy. Spectra for a normal uninvolved breast and a breast with invasive ductal carcinoma. The distinction between normal breast and invasive carcinoma is based on an increase in the *N*-trimethyl resonance at 3.25 ppm normalized to that of creatine at 3.05 ppm (peaks indicated by arrows). (Reproduced with permission from Mackinnon et al., Fine-needle biopsy specimens of benign breast lesions distinguished from invasive cancer ex vivo with proton MR spectroscopy. *Radiology*, 1997, **204**, 661)

NMR spectroscopy performed before cytologic analysis of aspirates may well be a valuable adjunct because it improves the specificity of diagnosis. Therefore, NMR spectroscopy of fine-needle biopsy specimens could reduce the number of biopsies performed in benign lesions and could lead to a more conservative approach, such as continued observation or surveillance with repeat fine-needle aspiration cytologic analysis and NMR spectroscopy. Breast tissue is naturally rich in fat; suppression of the fat signal may be critical to detect other metabolites that may have diagnostic potential but are present at low concentrations.

8 OVARY

Two of the most crucial issues in ovarian cancer are the frequent late detection of the disease and the resistance of most of these tumors to current therapeutic modalities. Proton NMR spectroscopy of ovarian tissue obtained during surgery has been performed to address these issues.[34] Multivariate analysis was performed on the data to maximize the sensitivity and specificity of the classification; a sensitivity of 100% and a specificity of 95% were obtained in distinguishing ovarian cancer from normal ovarian tissue. Moreover, the multivariate analysis was able to distinguish untreated ovarian cancer from recurrent ovarian cancer with a sensitivity of 92% and a specificity of 100%. A 2D study of ovarian tissue showed the presence of multiple cross-peaks in cancer specimens[35] attributable to cell surface fucosylation.[20] The complexity of this fucosylation correlated with tumor grade and loss of cellular differentiation. Such multiple cross-peaks were absent in both normal and benign ovarian specimens.[35]

9 METHODOLOGICAL CONSIDERATIONS

9.1 Magnetic Field Strength

Most of the work reported in this review was performed at magnetic field strength of 8.5 T (360 MHz for ^{1}H). Although higher magnetic fields would undeniably generate spectra with better detection sensitivity and resolution, sufficient diagnostic information appears to be available at this moderate field strength. Higher magnetic fields with gradient echo-editing capabilities would be preferable for 2D NMR experiments in order to increase the detection sensitivity and resonance dispersion, shorten the acquisition time, and reduce the effects of T_1 noise.

9.2 Tissue Spectral Stability

In our studies, tissue MR spectral profiles were found not to change significantly over the duration of the NMR experiment. This is particularly true for 1D experiments where the total time the tissue stays inside the magnet (for set up and data acquisition) does not exceed 1 hour. Another factor related to tissue spectral viability is the temperature at which the experiment is performed. Most of the studies reported here were

performed at 37 °C, in order to mimic the in vivo physiological condition. However, lower temperatures could be used for experiments requiring longer acquisition times in order to preserve the tissue integrity/viability.

9.3 Fresh versus Frozen Tissue

Although it may be better to use fresh tissue specimens for such NMR experiments, comparison between spectra obtained from fresh and frozen tissue specimens (at −70 °C) has shown few differences. In a multivariate data analysis where the computer training was carried out with spectra from fresh specimens and tested on spectra from frozen specimens, and vice versa, classification accuracies were comparable.[36] Therefore, since performing the NMR experiments on freshly obtained tissue may be difficult for logistical/practical considerations, experiments performed on frozen tissue would be equally useful but more convenient. It is our experience that tissue specimens can be left frozen for as long as about 6 weeks without any significant biochemical alteration or degradation.

9.4 Magic Angle Spinning (Spectral Resolution)

Recently, the use of magic angle spinning was introduced to tissue NMR ex vivo by Cheng et al.[37] with the objective of improving the spectral resolution over that obtained using standard high-resolution NMR techniques. The technique, which is widely used in solid-state NMR spectroscopy, involves mechanically spinning the sample at the 'magic' angle of 54°44′ (which meets the requirement $3\cos^2\theta - 1 = 0$, where θ is the angle between the static magnetic field and the internuclear vector). By doing so, the contribution from such interactions, as dipole–dipole couplings and chemical shift anisotropy, which produce spectral broadening, are reduced. Such studies have already been successfully applied to breast and brain tissues and yielded useful clinical information.[38,39] A potential disadvantage of this technique, however, is that it adds many resonances to an already crowded spectrum, possibly decreasing the discriminating power.

9.5 Data Analysis

Although tissue NMR spectra are rich with biodiagnostic information, advanced methods of data analysis are required to extract all available information reliably. Conventionally, peak height/area ratios of preselected resonances/metabolites have been used to analyze the data. However, such an approach does not make use of the entire information content. Multivariate methods of analysis that are robust, nonsubjective and make use of all spectral information have been successfully employed to classify normal and cancerous tissue spectra of different organs, namely, colon, prostate, brain, cervix and ovary.[10,11,22,28,34,40] Adequate data set size and proper data preprocessing/reduction are essential requirements for a successful multivariate analysis. The use of computed consensus diagnosis, which involves the cross-validated training of several classifiers (linear discriminant analysis, neural net-based methods and genetic programming) on the same data and subsequently combining their outcomes, has been successfully used in the classification of thyroid neoplasms.[13] The use of such a consensus diagnostic approach resulted in higher sensitivity and specificity than that obtained with a single classifier. It is also worth noting here that it was difficult to reach conclusive diagnoses by simply using the peak height ratio approach. In a similar study of prostate tissue specimens, comparison between the sensitivity and specificity obtained by multivariate analysis and by using the peak height ratios shows the former to be far superior.[28]

10 CONCLUSIONS

It has now been established that the tissue NMR parameters allow pathological and in some cases clinical classification of human cancers. More importantly, it has been demonstrated that ^{1}H NMR can discern changes to the cellular chemistry in human tissues prior to their histological manifestation. This has significant implications for identifying the extent of cellular abnormality in the preinvasive states, subjects with a predisposition to cancer, and pathologies that have to date eluded the light microscope.

Recent studies show that tissue NMR ex vivo studies using a portable bench top spectrometer could be clinically useful by providing histopathological information that is not evident to the pathologist.[41] With the help of multivariate classifiers, it would be convenient to obtain the NMR spectrum of the tissue immediately after the biopsy procedure and perform the classification/diagnosis nonsubjectively. This would be useful for rapid and inexpensive early detection of abnormalities and for making/confirming the diagnoses of borderline cases. By obviating unnecessary surgery, such a technique will help to develop a more conservative and efficient strategy for disease diagnosis and management.

The ^{1}H NMR spectra of biopsy specimens have demonstrated powerful diagnostic strength. The next step in the application of the technique to human medicine is in vivo spectroscopy. As will be seen in other chapters, the in vivo studies are considerably more difficult, especially since they are usually performed at much lower magnetic field values (1.5 to 3.0 T). Difficulties with radiofrequency field homogeneity, volume localization, detection of resonances with short T_2 values, and lower dispersion of resonances remain a challenge. However, the ultimate goal of accurate diagnosis in vivo is now within reach, based on the expansive data set obtained by ^{1}H NMR ex vivo.

11 RELATED ARTICLES

Body Fluids; Cells and Cell Systems MRS; Kidney, Prostate, Testicle, and Uterus of Subjects Studied by MRS; Tissue and Cell Extracts MRS.

12 REFERENCES

1. I. C. P. Smith and C. E. Mountford, 'Encyclopedia of NMR', 1995, Vol. 8, 4776.
2. I. C. P. Smith and D. E. Blandford, *Biochem. Cell Biol.*, 1998, **76**, 472.
3. C. E. Mountford, G. Grossman, P. A. Gatenby, and R. M. Fox, *Br. J. Cancer*, 1980, **41**, 1000.

4. C. E. Mountford, W. B. Mackinnon, M. Bloom, E. E. Burnell, and I. C. P. Smith, *J. Biochem. Biophys. Methods*, 1984, **9**, 323.
5. C. E. Mountford, G. L. May, P. G. Williams, M. H. N. Tattersall, P. Russell, J. K. Saunders, K. T. Holmes, R. M. Fox, I. R. Barr, and I. C. P. Smith, *Lancet*, 1986, **i**, 651.
6. I. C. P. Smith, E. J. Princz, and J. K. Saunders, *J. Can. Assoc. Radiol.*, 1990, **41**, 32.
7. C. E. Mountford, E. J. Delikatny, M. Dyne, K. T. Holmes, W. B. Mackinnon, R. Ford, J. C. Hunter, I. D. Truskett, and P. Russell, *Magn. Reson. Med.*, 1990, **13**, 324.
8. A. C. Kuesel, T. Kroft, J. K. Saunders, M. Préfontaine, N. Mikhael, and I. C. P. Smith, *Magn. Reson. Med.*, 1992, **27**, 349.
9. E. J. Delikatny, P. Russell, J. C. Hunter, R. Hancock, K. H. Atkinson, C. van Haaften-Day, and C. E. Mountford, *Radiology*, 1993, **188**, 791.
10. R. L. Somorjai, A. E. Nikulin, A. C. Kuesel, M. Préfontaine, N. Mikhael, and I. C. P. Smith, *Proc. XIth Ann Mtg. Soc. Magn. Reson. Med.*, Berlin, 1992, **1**, 56.
11. L. Friesen, Ph.D. Thesis, University of Manitoba, Winnipeg, Canada, 1999.
12. B. Kunnecke, E. J. Delikatny, P. Russell, J. C. Hunter, and C. E. Mountford, *J. Magn. Reson.*, 1994, **10**, 135.
13. R. L. Somorjai, A. E. Nikulin, N. Pizzi, D. Jackson, G. Scarth, B. Dolenko, H. Gordon, P. Russell, C. L. Lean, L. Delbridge, C. E. Mountford, and I. C. P. Smith, *Magn. Reson, Med.*, 1995, **33**, 257.
14. P. Russell, C. L. Lean, L. Delbridge, G. L. May, S. Dowd, and C. E. Mountford, *Am. J. Med.*, 1994, **96**, 383.
15. C. L. Lean, P. Russell, L. Delbridge, G. L. May, S. Dowd, and C. E. Mountford, *Proc. XIIth Ann Mtg. Soc. Magn. Reson. Med.*, New York, 1993, **1**, 71.
16. L. Lean, L. Delbridge, P. Russell, G. L. May, W. B. Mackinnon, S. Roman, T. J. Fahey III, S. Dowd, and C. E. Mountford, *J. Clin. Endocrinol. Metab.*, 1995, **80**, 1306.
17. W. B. Mackinnon, L. Delbridge, P. Russell, C. L. Lean, G. L. May, S. Doran, S. Dowd, and C. E. Mountford, *World J. Surg.*, 1996, **20**, 841.
18. C. L. Lean, R. C. Newland, D. A. Ende, E. L. Bokey, I. C. P. Smith, and C. E. Mountford, *Magn. Reson. Med.*, 1993, **30**, 525.
19. K. M. Briere, A. C. Kuesel, R. B. Bird, and I. C. P. Smith, *NMR Biomed.*, 1995, **8**, 33.
20. C. L. Lean, W. B. Mackinnon, E. J. Delikatny, R. H. Whitehead, and C. E. Mountford, *Biochemistry*, 1992, **31**, 11 095.
21. D. A. Ende, C. L. Lean, W. B. Mackinnon, P. Chapuis, R. Newland, P. Russell, E. L. Bokey, and C. E. Mountford, *Proc. XIIth Ann Mtg. Soc. Magn. Reson. Med.*, New York, 1993, **2**, 1033.
22. T. Bezabeh, I. C. P. Smith, E. Krupnik, R. L. Somorjai, D. G. Kitchen, C. N. Bernstein, N. M. Pettigrew, R. P. Bird, K. J. Lewin, and K. M. Briere, *Anticancer Res.*, 1996, **16**, 1553.
23. A. Moreno, M. Rey, J. M. Montane, J. Alonso, and C. Arús, *NMR Biomed.*, 1993, **6**, 11.
24. T. Bezabeh, C. N. Bernstein, R. L. Somorjai, and I. C. P. Smith, *Proc. Vth Ann Mtg. (Int.) Soc. Magn. Reson. Med.*, Vancouver, 1997, **2**, 1279.
25. E. Krupnik, K. M. Briere, R. P. Bird, C. Littman, and I. C. P. Smith, *Anticancer Res.*, 1999, **19**, 1699.
26. D. Ende, A. Rutter, P. Russell, and C. E. Mountford, *NMR Biomed.*, 1996, **9**, 179.
27. C. E. Mountford, W. B. Mackinnon, P. Russell, A. Rutter, and E. J. Delikatny, *Anticancer Res.*, 1996, **16**, 1521.
28. P. Hahn, I. C. P. Smith, L. Leboldus, C. Littman, R. L. Somorjai, and T. Bezabeh, *Cancer Res.*, 1997, **57**, 3398.
29. M. van der Graaf, R. G. Schipper, G. O. N. Oosterhof, J. A. Schalken, A. A. J. Verhofstad, and A. Heerschap, *Proc. VIth Ann Mtg. (Int.) Soc. Magn. Reson. Med.*, Sydney, 1998, **1**, 613.
30. J. Kurhanewicz, D. B. Vigneron, S. J. Nelson, H. Hricak, J. M. Macdonald, B. Konety, and P. Narayan, *Urology*, 1995, **45**, 459.
31. R. Males, D. Vigneron, S. Nelson, J. Scheider, H. Hricak, P. Carroll, and J. Kurhanewicz, *Proc. VIth Ann Mtg. (Int.) Soc. Magn. Reson. Med.*, Sydney, 1998, **1**, 487.
32. J. Kurhanewicz, R. Males, D. Sokolov, S. Nelson, J. Scheidler, K. Yu, H. Hricak, P. Carroll, and D. Vigneron, *Proc. VIth Ann Mtg. (Int.) Soc. Magn. Reson. Med.*, Sydney, 1998, **2**, 967.
33. W. B. Mackinnon, P. A. Barry, P. L. Malycha, D. J. Gillett, P. Russell, C. L. Lean, S. T. Doran, B. H. Barraclough, M. Bilous, and C. E. Mountford, *Radiology*, 1997, **204**, 661.
34. J. C. Wallace, G. P. Raaphorst, R. L. Somorjai, C. E. Ng, M. Fung Kee Fung, M. Senterman, and I. C. P. Smith, *Magn. Reson. Med.*, 1997, **38**, 569.
35. W. B. Mackinnon, P. Russell, G. L. May, and C. E. Mountford, *Int. J. Gynecol. Cancer*, 1995, **5**, 211.
36. R. L. Somorjai, D. Kitchen, B. Dolenko, A. Nikulin, G. Scarth, D. Ende, R. Newland, P. Russell, C. E. Mountford, T. Bezabeh, K. Briere, C. N. Bernstein, N. M. Pettigrew, K. J. Lewin, and I. C. P. Smith, *Proc. IIIrd Ann Mtg. (Int.) Soc. Magn. Reson. Med.*, Nice, 1995, **3**, 1938.
37. L. L. Cheng, M. J. Ma, L. Becerra, T. Ptak, I. Tracey, A. Lackner, and R. G. Gonzalez, *Proc. Natl. Acad. Sci., U.S.A.*, 1997, **94**, 6408.
38. L. L. Cheng, I. W. Chang, B. L. Smith, and R. G. Gonzalez, *J. Magn. Reson.*, 1998, **135**, 194.
39. L. L. Cheng, I. W. Chang, D. N. Louis, and R. G. Gonzalez, *Cancer Res.*, 1998, **58**, 1825.
40. R. L. Somorjai, B. Dolenko, A. K. Nikulin, N. Pizzi, G. Scarth, P. Zhilkin, W. Halliday, D. Fewer, N. Hill, I. Ross, M. West, I. C. P. Smith, S. M. Donnelly, A. C. Kuesel, and K. M. Brière, *JMRI*, 1996, **6**, 437.
41. C. E. Mountford, S. Doran, C. L. Lean, and P. Russell, *Biophys. Chem.*, 1997, **68**, 127.

Biographical Sketches

Ian C. P. Smith. *b* 1939. B.Sc. 1961, M.Sc. 1962, Manitoba; Ph.D. Cambridge, 1965 (Research Director, Alan Carrington); Fil. Dr. (H.C.) Stockholm, 1986; D.Sc. (H.C.) Winnipeg, 1990. Introduced to NMR by W. G. Schneider, NRC, Ottawa, 1960. Postdoctoral work with H. M. McConnell, Stanford, 1965–66 and R. G. Shulman, Bell Labs, 1966–67. Research Officer, Institute for Biological Sciences, NRC, 1967–87; Director-General, 1987–91; Director-General, Institute for Biodiagnostics, NRC, 1992–present. Approx. 400 publications. Research specialty: applications of modern spectroscopic and computational methods in medicine, with emphasis on magnetic resonance spectroscopy.

Tedros Bezabeh. *b* 1965. B.Sc. 1986, Asmara, Eritrea; M.A. 1989, Ph.D. 1993, Washington University in St Louis (Thesis Advisor: Joseph J. H. Ackerman). Postdoctoral work with Ian C. P. Smith, Institute for Biodiagnostics, National Research Council of Canada, 1993–98. Research Officer, Institute for Biodiagnostics, National Research Council of Canada, 1998–present. Approx. 10 publications. Research specialty: applications of NMR spectroscopy in the diagnoses of diseases, with emphasis on cancer.

Ceramics Imaging

David G. Cory

Massachusetts Institute of Technology, Cambridge, MA, USA

1	Introduction	1
2	An Overview of Imaging Methods	2
3	Imaging of Green-State Ceramics	3
4	Imaging of Sintered Ceramics	3
5	Imaging of Fluids in Ceramics	4
6	Local Measurements	4
7	Conclusions	4
8	Related Articles	5
9	References	5

1 INTRODUCTION

NMR imaging of ceramics provides a wide range of opportunities for microscopic imaging of both liquids[1–3] (***Image Formation Methods***) and solids[4–6] (***Imaging Techniques for Solids and Quasi-Solids***). Techniques for imaging macroscopic samples of liquids are well developed and finding wide application in medical imaging. Techniques that are appropriate at the microscopic scale and for solid objects are only now being developed, however. Part of the reason these areas lag behind medical imaging is due to difficulties associated with the broad linewidth of solids, the low sensitivity of small samples (see also ***NMR Microscopy: Resolution***), the large signal attenuation from molecular diffusion in a strong magnetic field gradient[7] (see also ***Diffusion and Perfusion in MRI***), and the susceptibility shifts from small heterogeneities within a sample[8] (see also ***Susceptibility and Diffusion Effects in NMR Microscopy***). The underlying cause, however, is the widespread realization that many of the most pressing imaging applications are in the medical arena. This difference is apparent in the way new techniques are being developed; most techniques for medical imaging are developed for specific applications, while many of the developments in solid state imaging and microscopy are focused on a challenging NMR problem. Structural ceramics, however, present a set of important real-world problems in processing that require imaging techniques, both to characterize the general processing conditions and for nondestructive evaluation (NDE) of critical components.[9,11]

Although high performance structural ceramics possess superior mechanical and chemical properties, they are subject to catastrophic failure, and it is this failure mechanism that limits their applicability. These failures arise from defects in the sintered ceramic. A goal of ceramic imaging is to detect those defects that are larger than a critical size of approximately 100 μm. It is interesting to contrast ceramics to polymers, where imaging is primarily directed towards characterizing conditions of processing. Even though most imaging studies of solids are of organic polymers (see also ***Polymer MRI***), there are extremely few applications where the costs of MRI NDE methods could be supported by a polymer product. In ceramics, however, a piece can be costly to manufacture and it may be critical that it does not fail. Under these conditions, it is reasonable to consider using MRI as a method for NDE.

Ceramics are formed by complex thermal and chemical processing. First, ceramic powder is combined with an organic binder, which is mixed to form a solid green-state ceramic. These green-state ceramics can then be shaped prior to sintering. Often the sintered ceramic is nearly the finished product, and only a final finishing or machining step is required. The binder, or mixture of binder and plasticizer, has as its primary component a waxy organic polymer. These materials have T_2 values for ^{1}H of a few to 10 ms at room temperature and T_1 values of a few hundred milliseconds. The green-state ceramic can therefore be easily characterized by NMR techniques that, while not of high resolution, are certainly not in the solid state regime. After the sample is sintered, the ^{1}H content of the ceramic is minimal, and heteronuclear solid state techniques must be employed (see also ***Ceramics***).

The successful manufacture of a structural ceramic requires that the inevitable flaw content be controlled. These flaws include cracks, voids, inclusions, and density variations. The idea of NDE in ceramic processing is to intercept defective pieces early in the manufacturing process, since each successive stage tends to be more costly. A green-state ceramic is relatively inexpensive and easily formed, but the energy costs of densification and sintering the material are quite significant. Finally, the labor costs associated with finishing a complex part can be very high. Ideally then there should be at least two NDE steps, one of the green-state material and a second of the sintered material. Since the NMR properties of the ceramic are very different in these two states, the imaging methods will also vary.[12]

An obvious question is why employ NMR to characterize the sintered material rather than X-ray computed tomography (CT) methods? The sintered sample is a complex mixture; in addition to the ceramic matrix there may be ceramic fibers, or whiskers added to the material to improve the strength and prevent catastrophic failure, and one needs to distinguish between sintered ceramic and agglomerates of additives, as well as detecting voids and variations in density. The material is therefore too complex for simple analysis by X-ray CT. Energy selected X-ray techniques are applicable, but these methods are not widely available. With NMR there is a great potential for chemical selectivity, particularly with regard to many of the quadrupolar nuclei that are used in ceramics, and it is the information content that drives the continuing development of NMR materials-imaging techniques.

Imaging techniques are not restricted to observing the ceramic matrix directly since the ceramics contain voids (both in the sintered and in the green state), and these voids may be filled with fluids which are observable via liquid state techniques.[13–15] Additionally, the binder in the green state can be swelled by a solvent that then facilitates the imaging of the binder distribution, by reducing its linewidth, or can be observed itself. There are similarities between imaging liquids in ceramics and oil core imaging (see also ***Oil Reservoir Rocks Examined by MRI*** and ***Well Logging***), but ceramics have the benefit of magnetic purity, while oil cores often suffer from large concentrations of magnetic material.

Instead of measuring an image to obtain the absolute concentration of a species throughout the sample, it is occasionally

desired to record statistical information regarding the entire sample, such as the porosity, the pore size distribution, or the tortuosity.[16] These quantities and others can be measured via a variety of diffusive scattering techniques (see also ***Diffusion in Porous Media***). Since these measurements are average properties of the entire sample, the sensitivity is good, and spatial information may be obtained at much finer resolution than is possible with imaging methods.

One difficulty that has yet to be adequately addressed in ceramic imaging (or in materials imaging in general) is that of sample size. For solid state methods, it is usually the case that the rf field needs to be sufficiently large to dominate the variation of the local field across the sample. Therefore the samples tend to be small, and almost all solid state imaging has been performed on samples of less than 1 cm in diameter. A similar problem is encountered in microscopy where the sample is constrained to be sufficiently small that effective magnetic coupling of the spin response and the receiver is maintained. However, the critical size of defects does not scale with the sample size, and so, regardless of the size of the piece, image resolution needs to be at the sub-100 μm scale.

Not all ceramics are synthetic; bone and teeth have many properties in common with the synthetic structural ceramics discussed here, and these have also been studied.[17,18]

2 AN OVERVIEW OF IMAGING METHODS

Much of the power of NMR spectroscopy and imaging arises from the flexibility to tailor an experiment to the sample and the information desired. Therefore, there is a broad spectrum of methods that may be chosen to optimize the resolution, sensitivity, and contrast of an image (see also ***Image Formation Methods***). Here the various methods used in imaging ceramics will be introduced. Ceramic samples range from liquids in porous materials through waxy solids to rigid solids, and the techniques used in imaging are similarly diverse.

Nearly all imaging experiments involve a precession period in the presence of a magnetic field gradient. Since the normally dominant Zeeman interaction is directly proportional to the magnetic field strength, this precession labels the spins according to their location within the gradient field. It is useful to distinguish between encoding by phase and by frequency. Data are not acquired until the end of the phase encoding period, and so it is only the overall phase angle of spin precession that is observable. In frequency encoding, data are acquired continuously, and the periodicity of data acquisition allows the frequency of spin precession to be determined. The criteria for resolution and sensitivity are different for these two approaches. For frequency encoding, the resulting image is a convolution of the spin density and the NMR spectrum, so the NMR linewidth acts as the system point-spread function and limits the obtainable resolution, the resolution being given by the linewidth divided by the gradient strength. If the gradient is increased to obtain a higher resolution, the frequency spread of the resolution element is broadened and the experimental sensitivity is correspondingly reduced. In phase encoding (which we will limit here to constant-time methods),[19] the NMR linewidth is decoupled from the image representation, and a true spin density can be measured. This result is a consequence of being at high field where the internal spin Hamiltonians and the gradient Hamiltonian commute. The overall spin evolution is then simply the sum of the evolution due to the internal interactions and that due to the gradient. In a constant-time experiment the internal Hamiltonians are constant and the spin evolution due to them is reproducible. The linewidth still limits the sensitivity, however, since the NMR signal decays over the time period of the spatial encoding.

One approach to obtaining higher resolution is to increase the gradient strength and accept the loss in sensitivity. An appealing alternative is to use line-narrowing methods that can recover both sensitivity and resolution[20] (see also ***Line Narrowing Methods in Solids Imaging of Wide-Band Systems by Line-Narrowing Methods***). A good line-narrowing method may reduce the linewidth by a factor on the order of 1000, while preserving the full sensitivity. For an imaging experiment, the resolution is increased as the reduction in the linewidth, and the sensitivity also increases due to the reduction in the bandwidth.

There are two general classes of coherent averaging techniques for reducing the NMR linewidth: those that manipulate the spin state of the system through a series of rf pulses (see also ***Average Hamiltonian Theory***); and those that manipulate the spatial orientation of the spin system so as to average anisotropic contributions to the linewidth (see also ***Magic Angle Spinning***). The two approaches may also be applied simultaneously (see also ***CRAMPS***). All three methods have been applied to solid state imaging.[5] These coherent averaging techniques are, however, often complex to apply, and the result is somewhat sample dependent. Coherent averaging of internal interactions reduces the linewidth by modulating effective spin interactions such that the time average is either reduced or zero. The success of these methods depends on the accuracy of the modulation scheme and on the absence of competing modulations (particularly those from random molecular motions). Coherent averaging is very useful where there is little molecular motion (such as for engineering plastics, where these methods have been widely applied), or where there is high-frequency motion of limited angular displacements (such as in elastomers). One can expect that imaging of sintered ceramics will greatly benefit from line narrowing,[21,22] but the case is not so clear for the waxy binder of green-state ceramics.

There are a variety of contributions to the solid state linewidth (see also ***Internal Spin Interactions and Rotations in Solids***). Most coherent averaging methods have aimed at removing homonuclear dipolar coupling (particularly for ^{1}H imaging), chemical shift anisotropies, inhomogeneous interactions, and all of the above via time-suspension cycles. Heteronuclear line narrowing experiments have also been performed with broadband ^{1}H decoupling. In the special case of half-integer quadrupolar nuclei, which have $m = -\frac{1}{2}$ to $m = +\frac{1}{2}$ transitions, the same methods that sharpen homonuclear dipolar couplings will remove the second-order quadrupolar broadening.[22] The first-order quadrupolar terms do not broaden this transition (see also ***Quadrupolar Nuclei in Solids***).

Nearly every ceramic imaging study requires some specialized instrumentation, either in the form of strong gradients, or as a setup for coherent averaging methods. Magnetic field gradients of a few tesla per meter are difficult to achieve over large volumes, typically have long switching times and large induced

eddy currents, as well as being difficult to contain mechanically, and to cool. For these reasons back-projection methods are often used to avoid the necessity of gradient switching (see also ***Projection–Reconstruction in MRI***). The stray field imaging experiment[23] is a variation of the large gradient back-projection method where each one-dimensional projection of the spin density is mapped out successively while translating the sample through the strong gradient which exists in the fringe field of a high field magnet. The resolution is dependent on the excitation bandwidth of the experiment and can be quite high, although the sensitivity of the experiment is generally low. This is an incoherent, constant-time imaging technique. Line-narrowing techniques typically require only very modest gradient strengths, but often need better than average rf control and setup, and for optimal results extremely short (5 μs) gradient pulses.[24] Since the spin state of the system is being modulated, the gradient Hamiltonian no longer commutes with the effective internal Hamiltonians. Therefore, the gradient must be carefully applied to avoid the gradient interfering with the line narrowing.

3 IMAGING OF GREEN-STATE CERAMICS

NMR imaging techniques are being actively developed in the area of nondestructive evaluation of green-state ceramics.[25–28] The goal of the method would be to acquire a correct spin density image of the binder distribution throughout a modest sized sample to help detect any nonuniformity in the binder distribution and to locate cracks, voids, and other defects.

For the purposes of ^{1}H NMR, green-state ceramics are waxy solids, and far from ideal samples. They have too little motion to exhibit sharp resonances, and yet sufficient motions that coherent averaging schemes tend to fail. Examples of binder material include low-molecular-weight poly(ethylene oxide), poly(vinyl alcohol), and poly(ethylene terephthalate). Although waxy materials are often compared to elastomeric materials, there is a large difference in the NMR properties. Elastomers tend to have restricted molecular motions, which are fast on the NMR timescale. Modulation rates in coherent averaging methods tend to be in the region of kilohertz to a few tens of kilohertz. Molecular motions in elastomers are significantly faster than this. Waxy materials tend to have less well-defined motions that have a broad frequency spectrum with significant contributions in the appropriate range for coherent averaging. The residual linewidth in an elastomer arises from an incomplete averaging of internal Hamiltonians based on fast but restricted motions. The linewidth in waxy materials arises from an incomplete averaging based on both restricted motions and slower motions. Elastomers are therefore easily line narrowed since in the NMR experiment the residual Hamiltonians from the fast motions are static and of modest size. Waxes are more difficult to line narrow since the residual interactions are time dependent.

There are three apparent options to recording high-resolution images of green-state ceramics:

1. Use large magnetic field gradients with the sample at room temperature to achieve the desired resolution at a sacrifice of sensitivity.
2. Heat the sample until the line sharpens and use liquid state techniques.
3. Cool the sample to freeze out molecular motions and then use solid state techniques.

The use of large gradients has the advantage of least impact on the sample, as well as of avoiding artifacts. Heating the sample must be performed with care to stay below the temperature where sample integrity is lost. Reducing the linewidth increases the sensitivity, but note that the entire binder may not narrow. Perhaps only a fraction (such as a plasticizer, or the low-molecular-weight cut) will narrow, and then the image will not yield a true representation of the spin density. Cooling the sample and employing solid state techniques has the advantage of preserving the true spin density; however, the spin–lattice relaxation time is also dependent on molecular motions and may lengthen appreciably. Also care must be taken to ensure that the binder does not phase separate or crystallize.

To date the preferred methods have been to employ modestly strong gradients, but the resolutions required for NDE applications have not been achieved. The progress in this area has been recently reviewed.[9] Some examples are two-dimensional (2D) images of a 2.54 cm diameter green-state ceramic with both Fourier imaging and constant-time techniques.[25] The sample contained 15.5% by weight of binder, and using a gradient of 0.033 T m^{-1} with an encoding time of 1.98 ms; a resolution of 552 μm was achieved in the Fourier imaging experiment and of 326 μm in the constant-time experiment. The Fourier image was acquired in 25 min and, as expected, the constant-time experiment took much longer, requiring 220 min. Back-projection techniques were employed[11] to acquire images of a 2.5% by weight green-state ceramic with 0.35 T m^{-1} gradients at a resolution of 175 μm.[3] However, the data required a collection time of 18 h. These experiments do as much to point out the remaining difficulties as they do to show the promise of the method. Clearly, much work is still required to increase both the resolution and the sensitivity of the methods.

4 IMAGING OF SINTERED CERAMICS

Probably the most underexplored area of ceramic imaging is of the final sintered piece. Since the proton content of the sintered ceramic is extremely low, many of the methods for solid state imaging that have been developed for proton-rich solid polymers are not directly applicable. To characterize the sample by direct observation of the solid ceramic matrix, the available nuclei are predominantly Al, Si, B, N, and P. It is expected that the sensitivity will be lower than seen in ^{1}H images of bulk solid polymers due to a combination of low spin concentration, low magnetogyric ratios, and quadrupolar interactions. For now, both Si and N can be excluded on sensitivity grounds: ^{29}Si has low abundance and has unacceptably long T_1 values in the solid state, and ^{15}N has low abundance and a low magnetogyric ratio. While ^{14}N is reasonably abundant, it has spin = 1 with an appreciable quadrupole coupling constant and a large chemical shift anisotropy.

The other three nuclei, ^{27}Al, ^{11}B, and ^{31}P, are all reasonable candidates for solid state imaging experiments, and some preliminary results have been reported for each.[29,30]

Phosphorus-31 is 100% abundant with spin = $\frac{1}{2}$, so where it is present in the ceramic the imaging approach is reasonably

straightforward. The linewidth is dominated by homonuclear dipole–dipole couplings and chemical shift anistropy, so here techniques very similar to those used for multiple-pulse proton imaging will apply. Phosphorus-31 images have been recorded of biologically significant solid calcium phosphates where there was an appreciable proton content.[29] The ^{31}P linewidth was dominated by ^{1}H dipolar interactions, a facet which was used to increase the sensitivity via cross polarization and then decoupled during acquisition to reduce the linewidth. An important feature of the cross polarization experiment is that the recycle time is dependent on the T_1 of ^{1}H and not on the longer T_1 of ^{31}P.

Aluminum-27 and ^{11}B are both half-integer quadrupolar nuclei and hence both have an $m = -\frac{1}{2}$ to $m = +\frac{1}{2}$ transition which can be conveniently observed. These are attractive nuclei for imaging since the central transition is not broad compared to the spectral width of broadcast and receive channels of solid state spectrometers, and can be further sharpened by multiple pulse methods.[22] Another virtue of the quadrupole interaction is that it leads to short T_1 values, so the experiment can be efficient in terms of data acquisition. Strong gradient methods have been used to record images of phantoms using both of these nuclei,[30] including a 2D ^{11}B image of a borosilicate glass sample (6 mm field of view) at a resolution of 520 μm using a gradient of 1.55 T m^{-1} and an experimental time of 133 min. For a similar phantom composed of γ-alumina, an image of ^{27}Al was obtained at the same resolution in 90 min with a gradient of 2.25 T m^{-1}.

The apparent nutation frequency of the central transition of half-integer quadrupole nuclei is dependent on the strength of the quadrupole coupling constant (see also ***Nutation Spectroscopy of Quadrupolar Nuclei***), and hence the nutation frequency can be used to introduce contrast into an image. In this way pure images of the alumina and aluminate fractions were obtained from a composite phantom.[30]

5 IMAGING OF FLUIDS IN CERAMICS

Fluids can be introduced into either sintered ceramics or green ceramics. In the case of sintered materials the fluid may be vacuum impregnated and the fluid imaged to look for defects. In the case of green ceramics, the fluid can either swell the binder, or be introduced into the pore structure of the material. It has been suggested that the fluid can be removed for NDE, although this addition of extra processing steps is undesirable. The spin density image allows one to characterize the porosity of the material and to easily find defects into which the fluid can flow. A perhaps surprising result is that the image of the fluid can provide information about defects that are inaccessible to the fluid, based on local variations in the bulk magnetic susceptibility (see also ***Susceptibility and Diffusion Effects in NMR Microscopy***). The variation in the bulk magnetic susceptibility throughout a heterogenous sample implies that, when placed in a magnetic field, the magnetic field inside the sample will be spatially varying. The result is a complex local distortion of the magnetic field in the vicinity of boundaries. If a defect in a ceramic material has a susceptibility that is significantly different than that of the bulk of the sample, the presence of the defect will appear as a resonance shift for spins that are adjacent but not in direct contact with the defect. In this fashion voids that are not filled with fluid can still be detected via liquid state imaging. In favorable cases even agglomerates of fibers or other fillers may be detected.

Areas of susceptibility variations introduce distinct image distortions that are readily identifiable. It is also quite straightforward to test for their presence either by reorienting the sample in the field and repeating the experiment, or by employing an imaging experiment that is insensitive to susceptibility artifacts, such as constant-time imaging and refocused gradient imaging experiments.

Liquid state imaging methods have been used to follow the drying of slipcasting, and the uniformity of the resulting compact.[31] Benzene that was vacuum impregnated into a green ceramic has been imaged in a matter of a few minutes at a resolution of 380 μm $\times$ 350 μm for a 2 mm thick slice.[12] From these images the overall porosity could be observed along with some rather large defects that were intentionally introduced into the sample. These are relatively early results that have not been revisited and the low resolution was a result of the small gradient strengths employed at that time.

6 LOCAL MEASUREMENTS

Imaging allows the absolute spatial properties of a selected spin system to be recorded at a resolution of up to approximately 10 μm by spreading the resonance line with a sufficiently strong gradient such that each volume element is resolved from its neighbors. Much below about 10 μm, diffusional losses and the limited number of spins in a selected cubic volume element greatly reduce the signal intensity. Therefore, absolute spatial information is not, presently, available at this and higher resolutions. Average local geometries may be characterized, however, by observing the temporal evolution of spin transport of all spatially distributed mobile spins simultaneously, thus avoiding the signal-to-noise limit on resolution. The resolution limits of these studies are only dependent on the gradient strength, the diffusion coefficient and relaxation times. For many samples the lower limit to resolution may be extended a factor of 100 below that of imaging methods. Some examples of the types of information that are available from these spin transport studies include: (1) self-diffusion constants, (2) compartment sizes and distributions, (3) eccentricities and volumes of compartments, (4) fluxes through semipermeable membranes, and (5) the existence and nature of wall relaxation. These quantities may be of interest in characterizing the packing of ceramic powders[16] (see also ***Diffusion in Porous Media***).

7 CONCLUSIONS

While much work still remains to be done, high performance structural ceramics is an area that can clearly benefit from techniques of high resolution NMR imaging. The problems that remain are to devise methods that increase the sensitivity and resolution for waxy solids, and to devise methods of studying relatively large solid samples while preserving high resolution.

8 RELATED ARTICLES

Average Hamiltonian Theory; Ceramics; CRAMPS; Diffusion and Perfusion in MRI; Diffusion in Porous Media; Image Formation Methods; Imaging Techniques for Solids and Quasi-Solids; Internal Spin Interactions and Rotations in Solids; Line Narrowing Methods in Solids; Imaging of Wide-Band Systems by Line-Narrowing Methods; Magic Angle Spinning; NMR Microscopy: Resolution; Nutation Spectroscopy of Quadrupolar Nuclei; Oil Reservoir Rocks Examined by MRI; Polymer MRI; Projection–Reconstruction in MRI; Quadrupolar Nuclei in Solids.

9 REFERENCES

1. P. T. Callaghan *Principles of NMR Microscopy*, Clarendon, Press, Oxford, 1991.
2. P. Mansfield and E. L. Hahn, *NMR Imaging*, The Royal Society, London, 1990.
3. B. Blümich and W. Kuhn (ed.), *Magnetic Resonance Microscopy*, VCH, Weinheim, 1992.
4. P. Jezzard, J. J. Attard, T. A. Carpenter, and L. D. Hall, *Prog. NMR Spectrosc.*, 1991, **23**, 1.
5. D. G. Cory, *Annu. Rep. NMR Spectrosc.*, 1992, **24**, 88.
6. P. Blümler and B. Blümich, *NMR Basic Principles Prog.*, 1993, **30**, 209.
7. C. D. Eccles and P. T. Callaghan, *J. Magn. Reson.*, 1986, **68**, 393.
8. P. T. Callaghan and C. D. Eccles, *J. Magn. Reson.*, 1987, **71**, 426.
9. W. A. Ellingson, P. S. Wong, S. L. Dieckman, J. L. Ackerman, and L. Garrido, *Ceram. Bull.*, 1989, **68**, 1180.
10. J. L. Ackerman, L. Garrido, J. R. Moore, B. Pfleiderer, and Y. Wu, in *Magnetic Resonance Microscopy*, ed. B. Blümich and W. Kuhn, VCH, Weinheim, 1992, p 237.
11. N. Gopalsami, S. L. Dieckman, W. A. Ellingson, R. E. Botto, P. S. Wong, H. C. Yeh, and J. P. Pollinger, Nuclear Magnetic Resonance Imaging of Green-State Ceramics Report ANL-90/27, Argonne National Laboratory, Argonne, IL 1990.
12. J. L. Ackerman and W. A. Ellingson, Advanced Tomographic Imaging Methods for the Analysis of Materials, *Materials Research Society Symposium Proceedings*, Materials Research Society, Pittsburgh, 1991, Vol. 217.
13. K. Hayashi, K. Kawashima, K. Kose, and T. Inouye, *J. Phys. D.*, 1988, **21**, 1037.
14. W. A. Ellingson, J. L. Ackerman, L. Garrido, J. D. Weyand, and R. A. DiMilia, *Ceram. Eng. Sci. Proc.*, 1987, **8**, 503.
15. J. L. Ackerman, L. Garrido, W. A. Ellingson, and J. D. Weyand, in *Proceedings of the Joint Conference on Nondestructive Testing of High Performance Ceramics, Boston, MA, 25–27 August 1987*, ed. A. Vary and J. Snyder, American Ceramic Society, p. 88.
16. L. Garrido, J. L. Ackerman, and B. Pfleiderer, *Ceram. Eng. Sci. Proc.*, 1991, **12**, 2042.
17. J. L. Ackerman, Personal communications, MGH, 1994.
18. K. Zick, Personal communications, Bruker Instruments, Inc., 1993.
19. S. Emid and J. Creyghton, *Physica*, 1985, **125B**, 81.
20. P. Mansfield and P. Grannel, *Phys. Rev. B.*, 1975, **12**, 3618.
21. M. S. Conradi, *J. Magn. Reson.*, 1991, **93**, 419.
22. J. Listerud, S. W. Sinton, and G. P. Drobny, *Anal. Chem.*, 1989, **61**, 23.
23. A. Samoilenko, D. Yu Artemov, and L. Sibel'dina, Russ, *J. Phys. Chem.*, 1987, **61**, 1623.
24. J. B. Miller, D. G. Cory, and A. N. Garroway, *Chem. Phys. Lett.*, 1989, **164**, 1.
25. L. Garrido, J. Ackerman, and W. A. Ellingson, *J. Magn. Reson.*, 1990, **88**, 340.
26. S. L. Dieckman, P. Rizo, N. Gopalsami, and R. Botto, in *Materials Research Society Symposium Proceedings*, 1991, Vol. **217**, p. 169.
27. N. Gopalsami, S. L. Dieckman, W. A. Ellingson, R. E. Botto, and H. Yeh, in *Review of Progress in Quantitative NDE*, ed. D. O. Thompson and D. E. Chimenti, Plenum, New York, 1990, Vol. 10B, p. 1215.
28. L. Garrido, J. Ackerman, W. Ellingson, and J. D. Weyand, *Ceram. Eng. Sci. Proc.*, 1988, **9**, 1465.
29. J. L. Ackerman, D. P. Raleigh, and M. J. Glimcher, *Magn. Reson. Med.*, 1992, **25**, 1.
30. J. R. Moore, L. Garrido, and J. Ackerman, *Ceram. Eng. Sci. Proc.*, 1990, **11**, 1302.
31. K. Hayashi, K. Kawashima, K. Kose, and T. Inouye, *J. Phys. D.*, 1988, **21**, 1037.

Biographical Sketch

David G. Cory. *b* 1958. B.A., Ph.D. (supervisor William M. Ritchey), Chemistry, Case Western Reserve University. Postdoctoral work at the University of Nijmegen, The Netherlands (with Wiebren Veeman), and at the Naval Research Laboratory, Washington, DC (with Al Garroway and Joel Miller), followed by a period as a senior research and development scientist with Bruker Instruments, Inc., Billerica, MA. Currently Assistant Professor of Nuclear Engineering, Massachusetts Institute of Technology, Cambridge. Approx. 55 publications. Research interests: new NMR methodologies and instrumentation. Current projects include: solid state imaging, rf gradient spectroscopy, and diffusive scattering methods.

Foods and Grains Studied by MRS and MRI

Suzanne L. Duce and Laurie D. Hall
University of Cambridge, UK

1	Introduction	1
2	Equipment	1
3	Spectroscopy	1
4	Imaging	1
5	Future Prospects	2
6	Related Articles	2
7	References	2

1 INTRODUCTION

From a chemical structure viewpoint, the building blocks of food are water, carbohydrates (particularly polysaccharides), lipids, and proteins. From the viewpoint of physical chemistry or materials science, these substances are combined together in a rich variety of structures ranging from essentially pure liquids, to solutions, gels, emulsions, foams, suspensions, solids, and porous media containing large amounts of water (as in fruit) and others which are dry or nearly so (e.g. biscuits). Furthermore, the molecules themselves contain one or more NMR-active nuclide (e.g. ^{1}H, ^{2}H, ^{13}C, ^{23}Na, or ^{31}P). As a result, foods are amenable to investigation by essentially the entire array of NMR methodology, including both solution- and solid state spectroscopy and NMR imaging.

2 EQUIPMENT

Whilst most of the NMR research in food science has been performed using high-resolution or solid state instrumentation, many industrial applications use low-cost, benchtop instruments specifically designed for a limited range of highly optimized applications.[1] The most widely used device is made by Bruker and operates at 10 and 20 MHz for samples up to 18 mm in diameter. Typical applications using such systems involve the determination of the solid-to-liquid ratio of fats, or the quantitation of water in foods. NMR imaging of food has mainly been done using 31-cm bore magnets operating at 2 T, or whole body clinical systems. The key technical requirement is that the gradient system be capable of implementing sequences with spin echo times of 5 ms or less.

3 SPECTROSCOPY

The most widespread use of proton spectroscopy in the food industry continues to be the determination of the solid-to-liquid ratio of fats.[2,3] The technique exploits the differences in the spin–spin relaxation times of protons in liquid and solid domains; such measurements are routinely performed using low field strength magnets. This is a rapid and reliable method for determining the oil and water content of seeds and can be used in breeding experiments and in optimizing storage and processing conditions.[4] Much of the early work on food involved ^{1}H relaxation studies of water[5,6,7] which gave insight to the location and mobility of water associated with foods, especially carbohydrates such as starch, and proteins. The diffusion coefficients of water and lipids can be determined by pulse field gradient NMR.[8] These experiments can also be used to investigate restrictions to free diffusion, and thereby allow the size of water domains in complex structures to be estimated (e.g. the size of water droplets in emulsions).

Measurements made at high field strengths of the deuteron resonances of wine and fruit juices have recently been used as a new approach to 'food authentication'. This elegant approach, called site-specific natural isotope fractionation (SNIF) NMR, is based on the fact that the distribution and ratio of ^{1}H and ^{2}H isotopes of low molecular weight molecules such as glucose, ethanol, and acetic acid depend on their biochemical origin.[9] For example, SNIF NMR can differentiate between ethanol produced from the sugar of grains and that from grape juice. Consequently, addition of beet or cane sugar to supplement a low sugar content grapes can be detected.

High field strength, highly homogeneous magnets are necessary for high-resolution, solution state NMR. This method is used to elucidate chemical structure. Typically, ^{1}H and ^{13}C spectra are acquired; however, ^{31}P, ^{23}Na, and ^{15}N nuclei are also useful in certain situations. For example, ^{31}P NMR is used to investigate metabolism in vivo as well as allowing cellular pH to be estimated.[10] Solid samples usually give rise to very broad featureless spectra; however, it is possible to acquire high-resolution spectra by cross polarization, magic angle spinning (CP MAS) NMR. Solution- and solid state ^{13}C NMR have been used to study whole intact seeds.[11,12] ^{15}N cross-polarization spectra have also been reported; for example, soya beans grown in ^{15}N enriched ammonium nitrate and amino acids have been studied.[13] High resolution solution- and solid state ^{13}C spectroscopy can be combined with ^{1}H relaxation studies to elucidate the microdynamics of the various domains in complex heterogeneous systems such as wheat gluten.[14]

4 IMAGING

It is relatively easy to obtain magnetic resonance (MR) images from most food products,[15–21] providing that the container is transparent to radiofrequency waves and is free of ferromagnetic components. Consequently, it is feasible to study food storage in the marketing container completely noninvasively. In addition to obtaining well-resolved NMR images of the internal structure of foods, the food scientist would like to make measurements from the images, for example correlating image intensity with a physical parameter such as water content, diffusion coefficient, or flow velocity. The ease with which a quantitative image[22] can be generated depends not only on the quantity of the NMR species present and their ^{1}H relaxation times, but also on the value of the echo time available. Thus it is relatively straightforward to produce proton density T_1 and T_2 maps for high water content foods such as fruit, vegetables, and many dairy and meat

products. Furthermore, since the water protons have relatively long T_2 values, their linewidths are sufficiently narrow that at 2 T or more chemical shift resolution between water and lipid resonances can be achieved by selective excitation.[23] By comparison, low moisture content foods, such as pasta, generally give such broad water resonances that the resolution of water from lipid signals is impossible; in most biscuits, for example, the MR image is dominated by the signal from the lipid.

Given the known dependence of NMR parameters on the physicochemical environment of the water and lipid molecules, it is clear that MRI should provide invaluable insight to structural changes that accompany food processing.[24,25] Examples to date include baking, freezing/thawing, drying, hydration, curing, heating in thermal or microwave ovens, or frying in oil. In addition, it is possible to visualize and quantitate the flow of liquids, including suspensions.[26] The circulation and diffusion of water within wheat grains has also been studied.[27,28]

MRI of fruits and vegetables provides excellent definition of the internal architecture of the object. Importantly, processes which disrupt the cellular structure can generally be visualized with great clarity. For example, bruising of fruit[16] and freeze/thawing[29] leads to a change in image contrast in the sample. Both these effects reflect two important changes. First, there is the local change in water distribution from intra- to intercellular space, which displaces air and thereby changes the distribution of susceptibility variations in the material.[30] Second, for some systems (e.g. celery), there can be anisotropy of diffusion rates and distances in the fresh material which is disrupted by cellular damage.

As the food system becomes 'dryer', the T_2 value of the water protons decreases. Consequently, it becomes progressively more difficult to perform any form of MRI measurement, let alone determine water content. For such systems, one-dimensional projections of spin density or ^{1}H relaxation times obtained without gradient switching can provide a one-dimensional map of water distribution. Depending on the physical shape of the object, such a projection may provide invaluable insight; for example, following the migration of water during the later stages of drying of spaghetti.

A simple example of chemical shift resolved imaging involves visualizing the separation of cream from whole milk. A valuable application is the ability to measure by this technique the water and lipid content in high moisture content samples such as sunflower oil emulsions and fresh meat.[31] An important use of chemical shift resolved imaging is mapping of the water and fat content of processed foods before, during, and after cooking. For example, chemical shift resolved studies of pork pies, fish in batter, and pizza, that were cooked in a microwave or thermal oven show distinct differences in the fat and water images related to their cooking regime. A similar study of the fat uptake during frying of chips is also revealing. In contrast, it is not possible to resolve the water and fat signals in an image of a biscuit; nevertheless, even in the hardest and driest of biscuits it is relatively easy to map the lipid distribution. The signal intensity of the MR image intensity from the lipid in chocolate[19] is very sensitive to the precise crystal, or liquid crystal, morphology of the lipid, and hence of the thermal treatment used to anneal the chocolate into a stable form which has desirable 'mouth feel'.

5 FUTURE PROSPECTS

The successful use of benchtop NMR spectrometers as a source of analytical data in the food laboratory is an encouraging augury for their wider use on the factory floor. Such applications will demand further improvements in 'ruggedization', together with interfacing either to automated batch sampling or, more likely, to continuous online, flow sampling. Fortunately, the technical components for such an instrument are already available, including low cost permanent magnets with a box or C-shaped structure, through which either a pipe or conveyor belt can pass. Furthermore, the development of 'inside-out NMR' in which the magnetic field is external to the magnet, means that it is feasible to construct a complete NMR magnet and probe which could be dipped into a container of food. Although the prospects for shop floor applications of NMR imaging are less obvious at this time, it is clear that demand will come from both increasing quality control standards and the need to develop new foods and optimize their processing and storage. A stimulus for this development is public demand for healthy, quality, ready-made foods which have low fat content and can be cooked in microwave ovens, yet have the texture and appeal of their traditional equivalents.

6 RELATED ARTICLES

Plants, Seeds, Roots, and Soils as Applications of Magnetic Resonance Microscopy; Relaxation Measurements in Imaging Studies; Tissue Water and Lipids: Chemical Shift Imaging and Other Methods

7 REFERENCES

1. Bruker Minispec Application Notes.
2. K. Van Putlte and J. Van den Erden, *J. Am. Oil Chem. Soc.*, 1974, **51**, 316.
3. M. C. M. Gibnau, *Trends Food Sci. Technol.*, 1992, **3**, 186.
4. P. N. Gambhir, *Trends Food Sci. Technol.*, 1992, **3**, 191.
5. H. Weisser, *'NMR Spectroscopy in The Food Industry'*, Bruker Minispec Application Note 7.
6. L. B. Rockland and G. F. Stewart (eds), *Water Activity: Influence on Food Quality*, Academic Press, New York, 1981.
7. B. P. Hills, S. F. Takacs, and P. S. Belton, *Food Chem.*, 1990, **37**, 95.
8. J. E. Tanner and E. O. Stejskal, *J. Chem. Phys.*, 1968, **49**, 1768.
9. C. Guillov, G. Remaud, and G. J. Martin, *Trends Food Sci. Technol.*, 1992, **3**, 197.
10. D. G. Gadian, *Nuclear Magnetic Resonance and its Applications to Living Systems*, Oxford University Press, Oxford, 1982.
11. J. Schaefer and E. O. Stejskal, *J. Am. Oil Chem. Soc.*, 1975, **52**, 366.
12. D. O'Donnell, J. J. H. Ackerman, and G. E. Maciel, *J. Agric. Food Chem.*, 1981, **29**, 514.
13. J. Schaefer, E. O. Stejskal, and R. A. McKay, *Biochem. Biophys. Res. Commun.*, 1979, **88**, 274.
14. P. S. Belton, S. L. Duce, I. J. Colquhoun, and A. S. Tatham, *Magn. Reson. Chem.*, 1988, **26**, 245.

15. S. Y. Wang, P. C. Wang, and M. Faust, *Sci. Hortic.*, 1988, **35**, 227.
16. P. Chen, M. J. McCarthy, and R. Kauten, *Trans. Am. Soc. Agric. Eng.*, 1989, **32**, 1747.
17. N. Ishida, T. Kobayashi, M. Koizumi, and H. Kano, *Agric. Biol. Chem.*, 1989, **53**, 2363.
18. J. B. German and M. J. McCarthy, *J. Agric. Food. Chem.*, 1989, **37**, 1321.
19. S. L. Duce, T. A. Carpenter, and L. D. Hall, *Lebensm. Wiss. u. Technol.*, 1990, **23**, 545.
20. S. L. Duce, T. A. Carpenter, and L. D. Hall, *Carbohydr. Res.*, 1990, **205**, Cl.
21. J. R. Heil, W. E. Perkins, and M. J. McCarthy, *J. Food Sci.*, 1990, **55**, 763.
22. J. Attard, L. Hall, N. Herrod, and S. Duce, *Phys. World*, 1991, **4**, 41.
23. H. Rumpel and J. M. Pope, *Concepts Magn. Reson.*, 1993, **5**, 43.
24. M. J. McCarthy and R. J. Kauten, *Trends Food Sci. Technol.*, 1990, Dec. **1**, 134.
25. G. W. Schrader, J. B. Litchfield, and S. J. Schmidt, *Food Technol.*, 1992, **46**, 77.
26. J. M. Ding, R. W. Lyczkowski, W. T. Sha, S. A. Altobelli, and E. Fukushima, *Powder Technol.*, 1993, **77**, 301.
27. C. F. Jenner, Y. Xia, C. D. Eccles, and P. T. Callaghan, *Nature*, 1988, **336**, 399.
28. C. D. Eccles, P. T. Callaghan, and C. F. Jenner, *Biophys. J.*, 1988, **53**, 77.
29. S. L. Duce, T. A. Carpenter, and L. D. Hall, *J. Food Eng.*, 1992, **16**, 165.
30. S. L. Duce, T. A. Carpenter, L. D. Hall, and B. P. Hills, *Magn. Reson. Imag.*, 1992, **10**, 289.
31. S. L. Duce, S. Ablett, T. M. Guiheneuf, M. A. Horsfield, and L. D. Hall, *J. Food Sci.*, 1994, **59**, 808.

Biographical Sketches

Suzanne L. Duce. *b* 1963. B.Sc., 1984. Scientific Officer, Institute of Food Research, Norwich (with Prof. Peter Belton), 1984–87. Ph.D., 1991, University of Cambridge. Postdoctoral research (with Prof. Laurie Hall), Herchel Smith Laboratory for Medicinal Chemistry, 1991–93. Presently in Cardiff. Approx. 20 publications. Research specialties: nonmedical MRI; solid and solution state carbon-13 NMR, and proton relaxation, in particular their application to food systems.

Laurie D. Hall. *b* 1938. B.Sc. 1959, Ph.D. 1962, Chemistry, University of Bristol, UK. Postdoctoral Fellow (with F. A. L. Anet) Ottawa University, 1962–63. Successively, Instructor, and Assistant, Associate and Full Professor, Department of Chemistry, University of British Columbia, Vancouver, Canada, 1962–84. Currently first holder of the Herchel Smith Chair of Medicinal Chemistry, University of Cambridge, UK (1984–present). Approx. 450 publications. Research specialties: carbohydrate chemistry, high resolution NMR spectroscopy, and medical and nonmedical applications of magnetic resonance imaging.

Oil Reservoir Rocks Examined by MRI

Ken J. Packer

University of Nottingham, Nottingham, UK

1	Introduction	1
2	NMR of Fluids in Rocks	1
3	Imaging of Rocks Containing a Single Fluid Phase	3
4	Imaging of Two-Phase Fluids in Rocks	6
5	Imaging of Oil Industry Processes	9
6	Summary	10
7	Related Articles	11
8	References	11

1 INTRODUCTION

The production of hydrocarbons involves, inter alia, drilling wells into oil-bearing rock strata at selected locations and utilizing a number of production strategies, often referred to as primary, secondary, etc., where primary, for example, refers to the fluid production consequent on the release of the naturally occurring internal pressures of the reservoir, with secondary implying some form of pressurization of the reservoir through the injection of water, gas, or some similar combination. Wells are expensive and the choice of where to place them for optimum production relies on assessments based on a wide range of information. Part of this assessment utilizes samples of rock, referred to as 'cores' taken at various depths whilst drilling wells, usually at the appraisal stage of determining a reservoir's potential. This article is concerned with the use of NMR imaging to investigate and characterize the properties of such core samples. These have traditionally been subjected to laboratory measurements of the basic properties of porosity, ϕ, and permeabilities, κ, the first being the fraction of the rock volume available to contain the reservoir fluids, comprising one or more of gas and liquid hydrocarbon and aqueous phases, and the second a measure of the ability of these fluids to flow through the rock under given fluid composition, pressure gradient and temperature conditions. NMR and NMR imaging have the potential both to support the evaluation of production strategies in a given reservoir and to advance the understanding of the underlying fluid dynamic processes. In neither case has NMR yet made the impact it could. An important issue is the nature of the samples studied and the degree to which they are representative of the conditions in the reservoir. This is a more subtle issue than just a matter of temperature and pressure. On retrieving core material it may be recovered in a 'preserved' state where attempts are made to retain the fluid saturations which existed in the reservoir. Releasing the pressure and lowering the temperature will alter these and can also affect the surface characteristics or wettability of the rock surface. However, this is not uniquely a problem for NMR studies, but is a generic issue for all such studies on cores. Many measurements are made on cleaned samples where the reservoir fluids have been removed by flushing/solvent extraction followed by resaturation with chosen fluids to allow the characterization of the required properties.

NMR has had a long history of application to the problem of characterizing fluids contained within porous rocks and other solids. Many of the relevant details may be found in other articles in this Encyclopedia, in particular ***Well Logging***, ***Imaging Techniques for Solids and Quasi-Solids***, and ***Diffusion and Flow in Fluids***. This article is concerned solely with imaging of rock–fluid systems and will restrict discussion of the NMR properties of such systems to those required to understand the strengths and limitations of such investigations. No description of imaging principles is given and, again, relevant details will be found in the many articles in this Encyclopedia and in the referenced papers. Section 2 summarizes the basic NMR of fluids in rocks, whilst Sections 3 and 4 discuss the imaging of rocks saturated with one and two fluid phases, respectively. Section 5 outlines the application of NMRI to processes of importance to the oil industry.

2 NMR OF FLUIDS IN ROCKS

Most NMR studies of fluids in rocks have been carried out using ^{1}H nuclei and, unless otherwise indicated, this will be assumed. Oil reservoir rocks are of two main types: sandstones and limestones. Sandstones are predominantly comprised of silica grains which have often been considerably changed and cemented through diagenetic geological processes, such that they present a porosity which is usually less than 0.3. In addition, they may often contain many other mineral types and, in particular, clays which may be distributed within the basic silica-based porosity. There may also be a range of transition metal species present, particularly iron, and these can significantly affect the NMR response of fluids contained within the pore spaces. In sandstones, the pore spaces tend to be in the range of $0.1-100\,\mu$m, determined by the original silica grain size and the subsequent modification by geological processes. Limestones are predominantly calcium carbonate and the pore space can cover a wider range of scales, reflecting the biological origins and processes responsible for their formation. In particular, they may have some pore spaces which are as large as 1 mm in scale arising, for example, from the fossilization/dissolution of the shells of larger species trapped in the original matrix.

NMR imaging of oil reservoir rocks is carried out using the signals from the fluid phases and, to that extent, is similar to biomedical imaging. The differences lie mainly in the degree to which the solid matrix in which the fluids reside and move, together with the multiphase character of the fluids, affect their NMR properties. In addition, the fluid content is usually less than 30% of the sample by volume, which is smaller by a considerable margin than that of typical tissues imaged in biomedical studies. As a consequence, in most cases, the time required to achieve good signal-to-noise ratios will be longer. However, as long as the samples are not undergoing changes on the relevant timescale this is not a problem as rocks, unlike patients, are not concerned with how long they spend in the imaging system! The NMR properties which may be used for generating useful contrast in NMR images of fluid-filled porous rocks are, spin density, resonance frequency, spin relaxation processes, and the fluid transport processes of diffusion and flow. All of these

have been used, separately and in combination, to generate images of these systems. In the most general case, the fluids comprise gas, oil, and aqueous phases. The naturally occurring aqueous phases, usually referred to as 'formation water', have a significant ionic salt concentration which is reservoir-dependent. Typically, imaging experiments which require a replacement aqueous phase will use 3% NaCl brine. These aqueous ionic solutions can influence the tuning and quality factors of the rf coil systems and lead to rf attenuation effects within the samples. These effects should be taken into account when quantitative measurements are the goal.[1]

2.1 Magnetic Susceptibility Broadening

The principal difficulty presented by fluid/rock systems in terms of NMR imaging is that, for many such materials, the transverse relaxation of the contained fluids can be strongly affected by magnetic susceptibility variations on the scale of the pore dimensions. This, combined with diffusion of molecules through these internal gradients, may lead to very rapid transverse relaxation for the spins in the contained fluids.[2] This effect is a strong function of the magnetic field strength of the NMR system used, in the worst case giving a T_2 value which varies as ${B_0}^{-2}$. As a consequence, the specifications required of the imaging spectrometer in order to achieve a representative signal reflecting all fluid present in the rock depend on the choice of operating field and can often exceed those which are readily accessible. Thus, there are a significant fraction of sandstones in particular for which quantitative measurements will prove impossible with conventional imaging techniques. Typically, when using the slice-selected 2D Fourier transform spin echo imaging sequence, for example, an echo time of 1 ms or less can be desirable and this places demanding requirements on the switching and settling times of the gradient systems, as well as on their maximum amplitude. Even with such short echo times, for some systems, only a fraction of the fluid will be detected. The reason that this is of concern is that, unlike some aspects of medical imaging, quantitative information is the ultimate goal when studying reservoir rocks.

The choice of magnetic field strength for imaging studies of fluid-saturated rocks is a compromise between the sensitivity and resolution required and the performance needed to overcome, as much as possible, the field-dependent T_2 effects referred to above. Many imaging studies of rocks have used a field strength of 2 T, corresponding to a ^{1}H resonance frequency of 85 MHz, and excellent quality images are achieved at this frequency. It is important, however, to recognize that these may reflect the properties of only a fraction of the fluid present and, for quantitative studies, this issue must be addressed directly. A further effect of these susceptibility contributions to the linewidth is to make chemical shift based discrimination of oil and water phases increasingly difficult as they get larger.

2.2 Surface-Enhanced Relaxation

In addition to the susceptibility effects, fluids contained within the pore space of reservoir rocks often show complex spin relaxation behavior (longitudinal and transverse), which arises from enhanced relaxation when molecules find themselves at the rock–fluid interface. Diffusion is the usual process which brings molecules of a surface-wetting phase to this interface and the effect of this process is to make the relaxation times reflect the size scale of the pore space in which they are contained,[3,4] see also ***Well Logging***. The dependence of the relaxation times on this size can vary between linear and quadratic. In most sandstone rock systems it has been established that, for saturation with an aqueous phase alone, the so-called fast-diffusion limit applies[5] making the contribution of this surface-mediated relaxation have the form

$$R_1 = (T_1)^{-1} \sim \rho(S/V) \sim \rho/a \qquad (1)$$

where S/V is the surface-to-volume ratio of the pore space, a its linear dimension, and ρ the surface relaxation strength which has the units of m s^{-1}. The key relationship is that T_1 relates directly to pore size within this model. In most natural rock systems there exists a distribution of size scales within the fluid-containing space. As a consequence, the contributions of this mechanism of relaxation, particularly to spin–lattice relaxation for which it is usually dominant, generate a multiple exponential process. This can be treated in a number of ways, the choice of which will depend on the relationship between voxel size and the heterogeneity scale of the pore size distribution. At one extreme, when a voxel contains the full range of pore sizes, then if signal-to-noise (S/N) is sufficient, a regularized inversion to give a distribution of relaxation times (directly mapping onto a pore size distribution) could be used.[6] For poorer S/N ratios, a fit to a stretched exponential is an alternative.[7] At the other extreme then a single exponential fit may be appropriate, with the histogram of voxel relaxation times then revealing the distribution.

2.3 Fluid Transport

Both diffusion and flow are important processes for fluid transport within oil reservoir rocks and both can be used to generate contrast in NMR images of fluid-saturated rocks. The principles and practice of measuring diffusion effects and flow velocities may be found in a number of other articles in this Encylopedia and the interested reader should consult these for the details,[8] see, for example, ***Diffusion and Flow in Fluids***. There are two main approaches to studying these processes. The main one is to use magnetic field gradient pulses to monitor the displacement of spins in the direction of the gradients. The range of timescales over which these displacements may be observed are dictated by the relaxation properties of the spins, while the amplitude of gradients available determine the spatial scales accessed. A second approach is to image the movement of an incoming or penetrating front which may be distinguished through some distinctive NMR property either present naturally or induced (see Section 2.4). These time-of-flight methods do not reveal the microscopic details of the process but can be simpler to implement.

2.4 Phase Discrimination

Imaging of two or more phases, present together within a porous rock, requires means of discriminating the signals from

those phases and there are a number of possible approaches. The choice available depends on the detailed characteristics of both the fluids and the containing rock. The principal methods are based on chemical shift or relaxation time differences, and can be either intrinsic or introduced. The chemical shift imaging methods used to discriminate water from fat in medical applications can be used to discriminate water and oil in rocks provided that the intrinsic transverse relaxation processes do not broaden the lines significantly beyond the shift difference and the oil phase is of low viscosity. Many crude oils have high viscosity and intrinsic linewidths which prohibit chemical shift imaging although, of course, a large difference in T_2 between the oil and aqueous phase will allow the aqueous phase to be detected uniquely. An extreme example of chemical shift imaging is the use of a substitute fluid which does not contain resonant spins, such as D_2O in place of H_2O, and, say, a fluorinated oil in place of normal oil. Spin–lattice relaxation-based discrimination is possible when the two phases have well-separated relaxation time characteristics. This can usually be achieved for water-wet rocks containing either light oil or heavy oil, which tend to give relaxation times longer and shorter, respectively, than the aqueous phase. If the spin–lattice relaxation characteristics of the two phases are too similar, then one or other may be changed by the introduction of relaxation agents, e.g. Mn^{2+}, in the aqueous phase or an oil-soluble molecule containing a nitroxide radical for the oil phase. Few of these approaches have been taken in practice in other than one-off investigations, so they cannot be regarded as well-established routines.

3 IMAGING OF ROCKS CONTAINING A SINGLE FLUID PHASE

With the development of actively shielded gradient coils[9] almost all imaging of fluids in rocks has been carried out using slice-selected 2D or direct 3D imaging techniques, although some early work utilized projection–reconstruction methods.[10] Usually, these are implemented on systems with 31-cm horizontal bore magnets with gradient coil sets and rf coils which allow for samples between core plug size (2.5–4 cm diameter) and whole core (up to 10 cm diameter). Preparation and containment of samples depends on the goal of the experiment. For simple porosity/T_1 imaging, samples may be encapsulated, after saturation under vacuum/pressure treatments, with epoxy resin[11] or other plastic film coatings[12] to prevent fluid loss during imaging. Experiments which aim to study cores under dynamic or steady-state flow conditions, or under controlled temperature/pressure regimes, require the construction of core holders which can be inserted into the rf coils and, at the same time, allow the creation of the required flow/saturation conditions. Again, there is no universal design and these vary from resin-encapsulation to contain and constrain the fluid pressures and flow to more sophisticated designs employing radial hydrostatic pressure applied via a cylindrical sleeve in a so-called Hassler cell arrangement to achieve the same requirements.[13]

3.1 Imaging of Fluid Saturation/Porosity

The measurement of the spatial distribution of fluid saturation for a single phase requires the use of porosity standards as described by Edelstein et al.[14] These workers used Cu^{2+}-doped H_2O/D_2O agarose gels as standards, allowing control of the volume concentration of ^1H spins, T_1 and T_2, as required. Using slice-selected 2D spin echo imaging, with echo times between 3 and 12 ms, they showed that they could determine the spatial distribution of fluid-filled porosity by extrapolation of the image intensities back to zero time. Figure 1 shows the resulting images for four samples together with a porosity standard and a gray-scale porosity reference scale. The only real check on the quantitative accuracy of such porosity images is to integrate the data over the image slices and compare the result with bulk measurements of the NMR porosity, calibrated by an independent determination of porosity using standard laboratory methods. Chen et al.[11] extended this T_2-extrapolation approach to obtaining quantitative porosities/fluid saturations. Using as many as 15 different echo times, covering a range which gave signal attenuations greater than a decade, they investigated the use of a number of models of the transverse relaxation process, including single and multiexponential, and the stretched exponential, to perform the required extrapolation. They found, for the small number of samples they studied, that the best agreement with porosities determined gravimetrically was obtained using a double exponential model for the transverse relaxation of each voxel. There are, of course, significant time penalties to be paid to carry out such detailed multiimage extrapolations. However, if truly quantitative measurements are required, then an element of such calibration of the systems under investigation will be necessary in most cases. The use of a double exponential model was also endorsed by Fordham et al.[15]

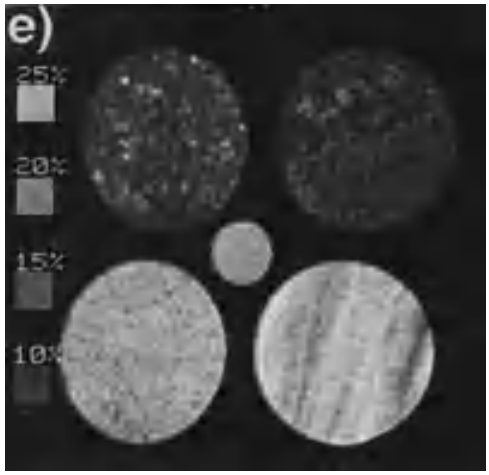

Figure 1 Porosity images of a cluster of four rock samples determined by extrapolation to zero time of a series of T_2-weighted images. Slice thickness was 3 mm. A 20% porosity standard is imaged at the center with a porosity gray scale defined at the left-hand side. (Reproduced by permission of the Society of Petroleum Engineers from Edelstein et al.[14])

Figure 2(a) is a cut-away view of a 3D porosity image of a North Sea sandstone saturated with 3% NaCl brine. This was obtained with an echo time of 1 ms and voxel dimensions of 0.3 mm. Figure 2(b) is a histogram of the distribution of porosity derived from the image in Figure 2(a) using a calibrated porosity standard without extrapolation. The mean of the distribution is 0.23 which is close to the value measured

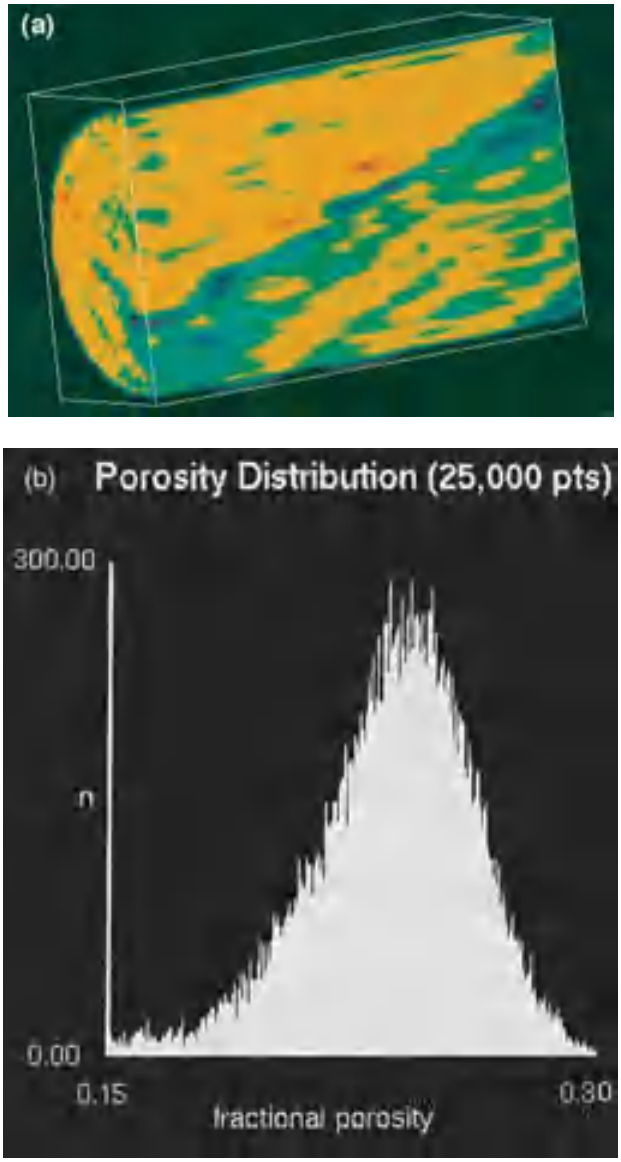

Figure 2 (a) A cut-away view of a 3D porosity image of a brine-saturated North Sea sandstone together with (b) the calibrated porosity histogram derived from the complete image. The independently-determined porosity of this sample was 23%, which agrees closely with the mean of the histogram. (Data supplied and reproduced by kind permission of A. Hardwick and D. R. Roberts, BP Research and Engineering Centre, Sunbury-on-Thames, UK)

using conventional techniques. For this sample, then, the NMR methods used are seeing essentially all the aqueous fluid contained within the rock. As already mentioned, this is by no means always the case. The histogram of Figure 2(b) gives a useful, if limited, statistical view of the nature of the spatial porosity distribution. However, as pointed out elsewhere,[16] there is a considerable amount of such information contained in the data set, of which Figure 2(a) is an example, which is not captured in any quantitative manner by these displays. A clear challenge for the future will be to characterize these complex structures, revealed by such fluid saturation spatial distributions and other image contrast mechanisms, using more sophisticated statistical treatments. The examples given in Figures 1 and 2 were of brine-saturated sandstones. Figure 3

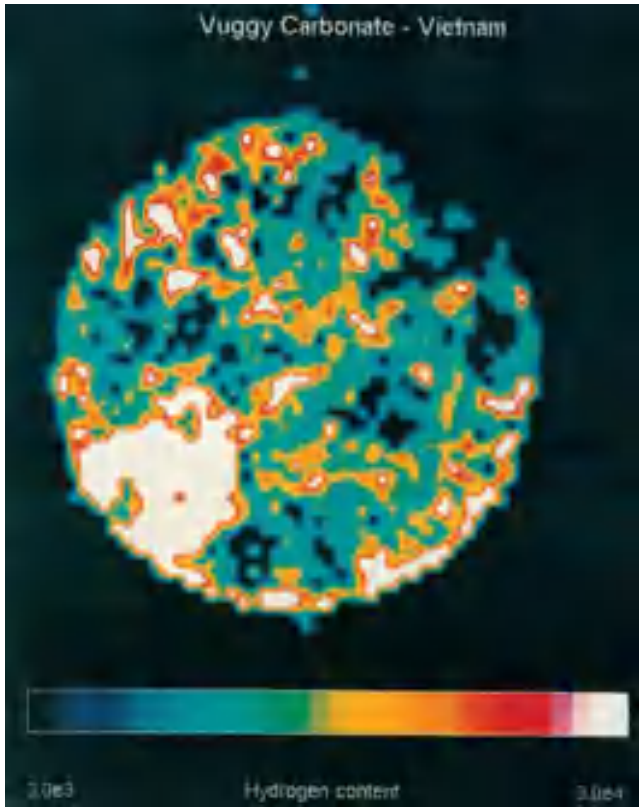

Figure 3 A 2D slice-selected ^{1}H density image of a brine-saturated carbonate rock which has a wide range of porosity, some of which is comprised of pores considerably larger than the image resolution. The porosity scale covered by this image is between 1–100%. The image resolution is 3 × 0.5 × 0.5 mm. (Data supplied and reproduced by kind permission of A. Hardwick and D. R. Roberts, BP Research and Engineering Centre, Sunbury-on-Thames, UK)

shows a porosity image of a brine-saturated carbonate. This shows very clearly the considerably greater porosity range encountered in such rock types in comparison with sandstones. The voxels in this image show porosities spanning the range 1–100%. The latter are represented by the large white areas of the image and arise from the presence of so-called vugs. A further example of imaging of larger-scale porosity in limestones is illustrated in Figure 4.[17] In this case, a 3D image data set is displayed using a computer program which enables the porosity to be viewed from different angles. On the basis of this investigation it was concluded that there was only one connected path through this particular sample, an observation which was borne out by imaging fluid flow (see Section 3.3). It should be remembered that these measurements only yield this information because, for these limestone systems, the imaging resolution can be made less than some of the pore sizes.

3.2 T_1 Imaging

The imaging of spin–lattice relaxation is of value because of the relationship between T_1 and pore size, as discussed above. The T_1 images are usually obtained by prefacing the imaging pulse sequence with either an inversion–recovery or a saturation–recovery sequence, with images being determined as a function of the recovery interval. The data for each voxel

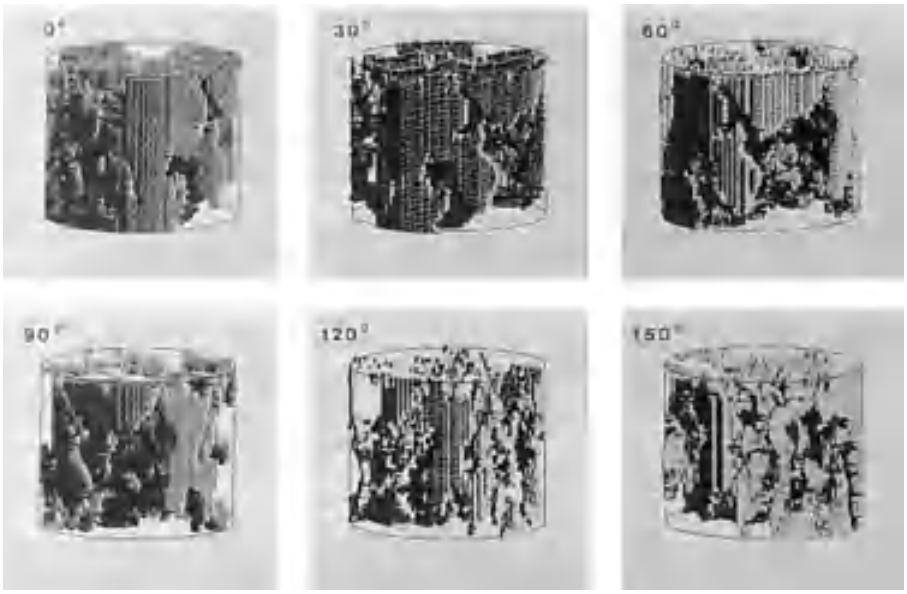

Figure 4 A 3D reconstruction of the porosity distribution inside a water-saturated limestone. Each image is of the same data but viewed from different angles by the rotations indicated. The 3D data set was constructed from a series of adjacent 2D slices. (Reproduced by permission of the publisher from Gleeson and Woessner.[17] © 1991 by Elsevier Science Inc.)

in the image can then be fitted to an appropriate model for the spin–lattice relaxation process (see Section 2.2). Figure 5(a) and (b) show corresponding T_1 and porosity images for the same brine-saturated sandstone for which the full 3D porosity image was given in Figure 2. In this case, the experimental data for each voxel have been fitted to a single exponential recovery and lead to both a T_1 and an extrapolated M_0 (porosity) value for each voxel. These images are of a central slice of the cylindrical rock sample with a slice thickness of 3 mm and an in-plane resolution of 0.5 mm. This sample has a shale band running diagonally from near 10 o'clock to around 4 o'clock and it is clear that the T_1 image reveals this with more contrast than the M_0 image. This is because the shale bed, whilst having significant porosity, has a smaller pore size on average than the other porosity. This means that although there is significant fluid content in this bed, the T_1 value is considerably reduced. Similar differences in contrast are seen in the lower left parts of these images. As indicated above, the amount of information available in such images has yet to be fully exploited in even a semiquantitative manner.[16] (The images shown in Figure 5(c) and (d) are discussed later—Sections 3.3 and 4.3.)

3.3 Diffusion and Flow Imaging

As already indicated, there are two basic approaches to the characterization of transport processes,[18] see also ***Diffusion and Flow in Fluids***. The first of these are time-of-flight methods which measure the appearance or disappearance, in a particular spatial location, of fluid spins which have been selected or saturated elsewhere. An example of this is the study of such flow-weighted imaging in a limestone.[17] Figure 6 shows the normal and flow-weighted images of the same water-saturated limestone plug. The flow-weighted image was obtained using a 2D method which saturates stationary spins and generates signal only from spins flowing into the imaged region on the repetition timescale of the sequence. It is clear from these images that only one of the several regions of significant porosity apparent from the porosity image (see Figure 4) contributes to fluid transport through this particular core plug.

Imaging of fluid velocity can, of course, be achieved directly using pulsed magnetic field gradient techniques to encode the displacements of the spins and coupling this with a suitable imaging procedure,[18] see also ***Diffusion and Flow in Fluids***. Typical results of such investigations are shown in Figure 5(c). This is a slice-selected image, obtained with a 2D FT technique incorporating two gradient pulses to encode the flow along the axis of the cylindrical rock sample, of the same sample used to generate the images of Figure 5(a) and (b). Whilst such 'velocity' images are relatively easy to measure, there are still a number of important issues which need to be addressed before quantitative data can be guaranteed. These issues are similar to those involved in the imaging of perfusion in medical applications[19–21] and relate to the time variation of velocity brought about by changes in pore size and direction of flow relative to the gradient direction. It is important to remember that this approach to characterizing fluid transport actually measures displacements (see ***Diffusion and Flow in Fluids***) with the velocity being a derived quantity. It is only in the limit that the velocity remains constant over the flow-encoding period that an unambiguous interpretation in terms of velocity can be given. These questions have been summarized by Nesbitt et al.[22] That said, the image shown in Figure 5(c) illustrates the strong heterogeneity in flow paths within this sandstone rock core and can be compared with the corresponding images in Figure 5(a) and (b). Strong similarities are apparent with both the M_0 and T_1 images, although some significant differences can be seen, particularly in the region between 7 and 9 o'clock. It should be recalled that the M_0 image reflects porosity within a voxel, while T_1 reflects pore size. Flow would be expected to reflect both of these, in that larger and connected pores will have a high conductance

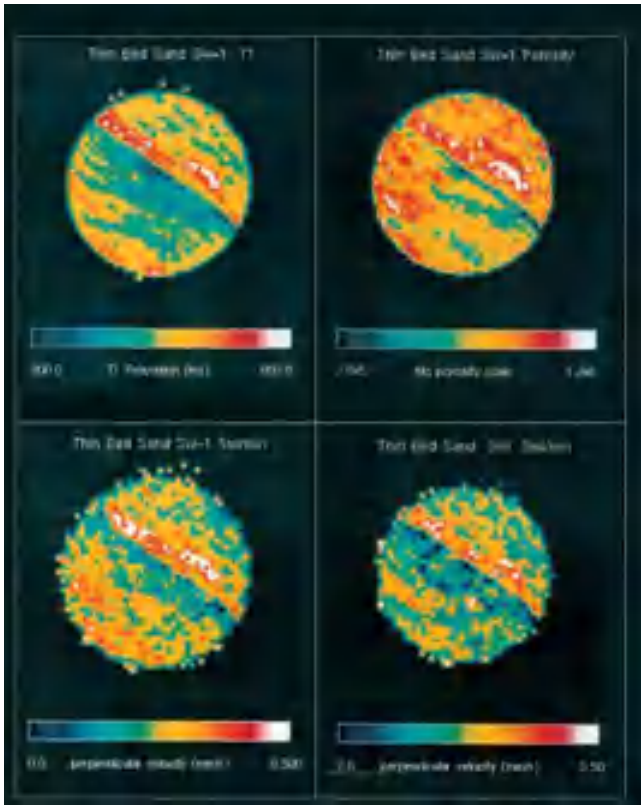

Figure 5 Images of the central slice (3-mm thick; in-plane resolution, 0.5×0.5 mm) of the brine-saturated sandstone also illustrated in Figure 2: (a) (top left) and (b) (top right) are spin–lattice relaxation time and porosity maps, respectively. These two images are constructed from a fit of each voxel magnetization recovery, measured using a saturation–recovery T_1 imaging experiment, to a single exponential process. While similar rock structures are revealed in both images, the marked differences arise because of the dependence of the T_1 value on pore size, as discussed in the text. (c) (bottom left) and (d) (bottom right) are velocity images of fluid flow in the same rock under conditions of (c) $S_w = 1$ and (d) S_{wi} (irreversible water saturation; the fractional porosity left occupied by the brine phase when displacement of this by an oil phase, under given flow conditions, has reached a steady state). The velocity is encoded along the cylindrical axis of the sample (perpendicular to the page) and was achieved by flowing the fluid at a constant rate of 5 mL min^{-1}. For (c) the fluid was the normal brine solution. For (d) the flowing fluid is a model oil, kerosene, and the signal in this case is predominantly from the oil phase. It can be seen that oil flow as visualized by comparison of these two images is less extensive, which is consistent with the presence of the residual aqueous phase. In addition, the strong similarity of (d) with (a), the T_1 image, is consistent with the water-wet characteristics of this rock which would confine the oil to larger pores. Images (c) and (d) are discussed in Sections **3.3** and **4.3**. (Data supplied and reproduced by kind permission of A. Hardwick and D. R. Roberts, BP Research and Engineering Centre, Sunbury-on-Thames, UK)

for fluid while small pores, corresponding to the shorter T_1 values, even if having similar total porosities in a voxel, are likely to have a lower fluid conductance.

The flow rates present in producing reservoirs are very low, corresponding to fluid velocities sometimes as low as 10^{-2}–10^{-1} mm s^{-1}. The measurement of such low flow rates in the presence of internal magnetic field gradients, caused by the magnetic susceptibility heterogeneities, can require special sequences of rf and gradient pulses. This can be illustrated by the use of echo planar imaging (EPI) methods to characterize the slow flow of water through porous rocks.[23] In this approach, velocity-encoding of the image for the slow fluid flow through the rock was achieved using a combination of a Carr–Purcell/Gill–Meiboom echo sequence with an applied gradient pulse sequence which allowed the build up of a cumulative phase shift of the transverse magnetization because of the flow in the applied gradients. This sequence is illustrated in Figure 7. At the same time as maximizing the phase accumulation from flow, this sequence significantly reduces the contribution to T_2 of diffusion through the internal gradients by keeping the pulse spacing small. The overall sequence for flow imaging concludes with an EPI sequence utilizing 180° rf pulses instead of the more usual gradient reversal echoes. This is required to overcome the significantly inhomogeneous nature of the lineshape. Figure 8 shows the results of the use of this sequence to image the flow of water flowing through a clean sandstone, Bentheimer.[23] In a further development of this study, Mansfield and Issa[24] have investigated the quantitative behavior of the flow velocity distributions generated as a function of the pressure difference driving the flow. They have proposed a model to explain the observed behavior which, inter alia, suggests an explanation for their observations that the precise flow pattern seen in an image slice perpendicular to the main flow direction is not reproduced in detail on stopping and restarting the flow.

Despite the importance of diffusion, and the well-documented ability of NMR to characterize both structure and transport via its effects (see ***Diffusion and Flow in Fluids***), imaging studies of fluid-saturated rocks using diffusion effects for contrast have been limited. Gibbs et al.[25] determined self-diffusion coefficient images for two brine-saturated cores (one sandstone and one limestone). They interpreted their results in terms of a reduction in the diffusion coefficient brought about by hindrance of the molecular displacements by the pore surfaces. The difficulty with diffusion imaging is that to take full advantage of the potential of the pulsed field gradient methods requires a wider range of gradient strengths than are usually found on imaging systems. This is particularly true when the intrinsic relaxation processes of the fluid spins are efficient.

4 IMAGING OF TWO-PHASE FLUIDS IN ROCKS

There are a number of approaches to obtaining spatially-resolved information from rocks containing more than one fluid phase. As already discussed, the essential discrimination methods which allow the images from the different fluid components to be separated are usually chemical shift or relaxation time differences, or some method of introducing such contrast via use of dopants or substitute fluids which, for example, give no signal.

4.1 Chemical Shift Resolved Imaging

In general, the line broadening found in rocks precludes the use of simple chemical shift imaging, although in favored cases it is possible.[14,26] Figure 9 shows oil and water images for a carbonate rock, containing both oil and water phases, obtained using standard chemical shift imaging methods.[27] It shows the

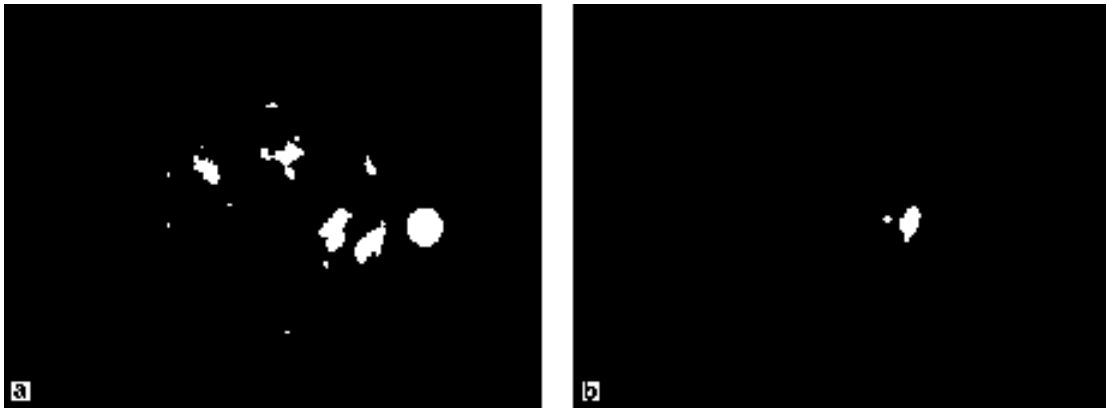

Figure 6 NMR images of the same slice of a limestone sample saturated with water showing (a) the porosity distribution and (b) the fraction of the fluid-saturated porosity which can flow under applied pressure. The method used to detect the movable fluid involved saturation of the NMR signal so that only regions of fluid receiving magnetization from outside the saturated volume on the timescale of the experiment would give a signal. (Reproduced by permission of the Society of Petroleum Engineers from Gleeson et al., *SPE Form. Eval.*, 1993, 123)

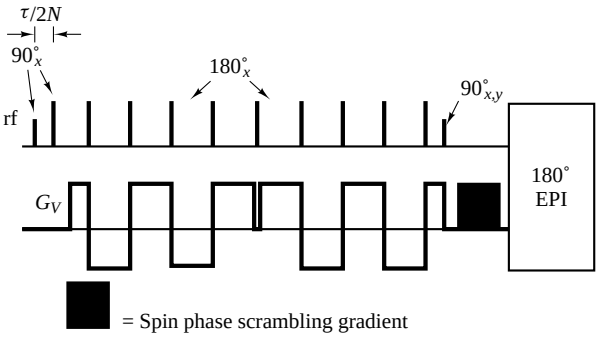

Figure 7 The flow-encoding pulse sequence used, together with an echo planar imaging sequence based on 180° rf pulses, to generate the flow image shown in Figure 8. The combination of field gradient pulse sign alternation and reflection symmetry around the midpoint, together with even echo selection in the Carr–Purcell/Gill–Meiboom rf pulse sequence, maximizes the phase shifts produced by flow through the applied gradients, eliminates phase shifts arising from flow through internal field gradients, and minimizes the effects of diffusion through the same internal field gradients. These latter are caused by the magnetic susceptibility differences within the fluid/rock system. (Reproduced with permission of Academic Press from Guilfoyle et al.[23])

presence of a large fracture which, in this case, is not cemented and hence contains fluid, predominantly water. The largely complementary nature of the two images is readily apparent. In cases such as this, chemical shift resolved imaging should be a powerful tool for characterizing the spatial distributions of both immiscible fluid saturations and, via relaxation and transport-contrast methods, the quantitative details of the pore sizes accessed by the different phases and the various displacement processes, such as imbibition, drainage, and pressure-driven flow.

In general, however, chemical shift imaging has not found extensive use because of the limitations of spectral resolution. However, a method developed by Horsfield et al.[26] has extended the scope of this approach by using a model of the line-broadening mechanism, based on the magnetic susceptibility and shape of the sample, together with an assumed form for the underlying spectrum, to estimate the best values for the separate chemically shifted images. Their method utilizes a set of images obtained for a range of free precession times (see Figure 10) which, at their extreme, produce a phase shift of 180° between the assumed oil and water resonance frequencies. Figure 11 shows a set of images reconstructed using these principles and for which the corresponding spectra were considerably overlapped.

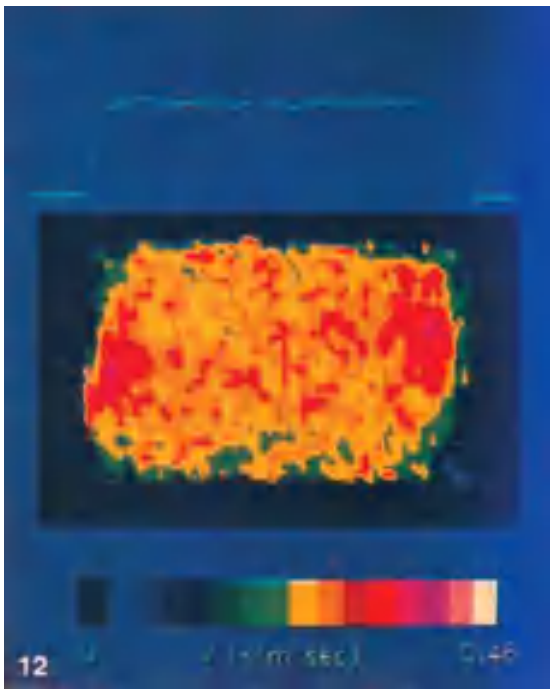

Figure 8 The fluid velocity image for a longitudinal slice (flow direction from left to right) through a cylindrical sample of Bentheimer sandstone. The saturating/flowing fluid was water. Slice thickness was 10 mm with in-plane resolution of 3 × 3 mm. The image is the result of 16 averages of the sequence shown in Figure 7 with a flow-encoding time of 42 ms. The integrated flow at each point along the image axis is shown above the image. While this is constant, significant variations are seen in the image. In particular, regions of higher velocity are seen at the either end of the sample consistent with the single entrance/exit points of the flow cell used. (Reproduced by permission of Academic Press from Guilfoyle et al.[23])

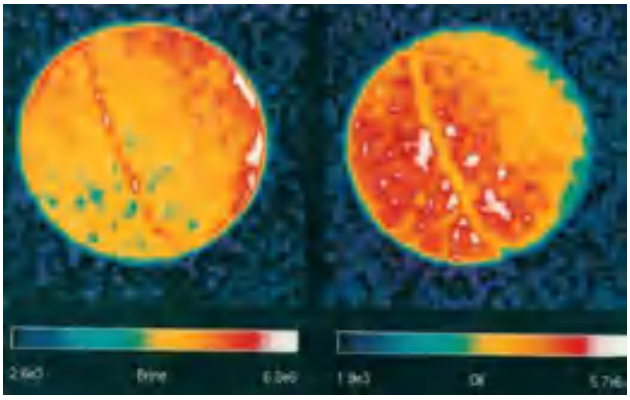

Figure 9 Chemical shift resolved images of the brine and oil phase distributions within a preserved carbonate rock core. The large fault running from top left to bottom right is shown to contain largely the aqueous phase with the smaller porosity in the rest of the sample having complementary phase contents, i.e. large oil content is associated with low water content and vice versa. (Reproduced by permission of the publisher from Davies et al.[27] © 1994 Elsevier Science Inc.)

4.2 Phase Discrimination via Spin–Lattice Relaxation

For most rock–fluid systems, the voxel size employed in imaging of core-size samples is considerably larger than the underlying pore sizes. In these circumstances, the NMR signal from each voxel, for systems saturated with two immiscible fluids, will contain contributions from each fluid. In order to separate these contributions using the spin–lattice relaxation properties, these have to be sufficiently different. In practice this means they must differ by at least a factor of three in relaxation time. Crude oils can vary very significantly in their intrinsic spin–lattice relaxation properties[28] and the aqueous phase can show a wide variation in its relaxation behavior dependent on the pore sizes, whether the rock surface is water-wet, and on the relative saturations in the rock of each phase.[29] As a consequence it is not possible to offer a general prescription and each case has to be treated individually. In some cases a clear and quantitative separation is possible and Figure 12 shows a set of spin–lattice relaxation-resolved images for the same preserved carbonate core which was used to generate the chemical shift images shown in Figure 9.[27] This sample had oil and water saturations of 0.43 and 0.56, respectively. In this case, the relaxation times of the oil and aqueous phases differ by an order of magnitude and the saturation–recovery data for each voxel were fitted to a double exponential process to extract the relaxation times for each phase. The images show clearly the considerable variation of the oil and brine saturations along the core plug. The slice shown in Figure 9 corresponds to the first slices in the middle rows of the image sets in Figure 12. It can be seen that the same features may be distinguished in both shift-resolved and relaxation-resolved images.

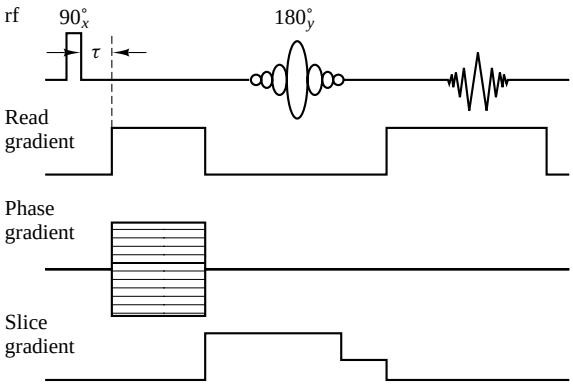

Figure 10 The pulse sequence for phase-encoded chemical shift imaging. The time interval τ allows the development of a phase shift between different precession frequencies. (Reproduced by permission of Academic Press from Horsfield et al.[26])

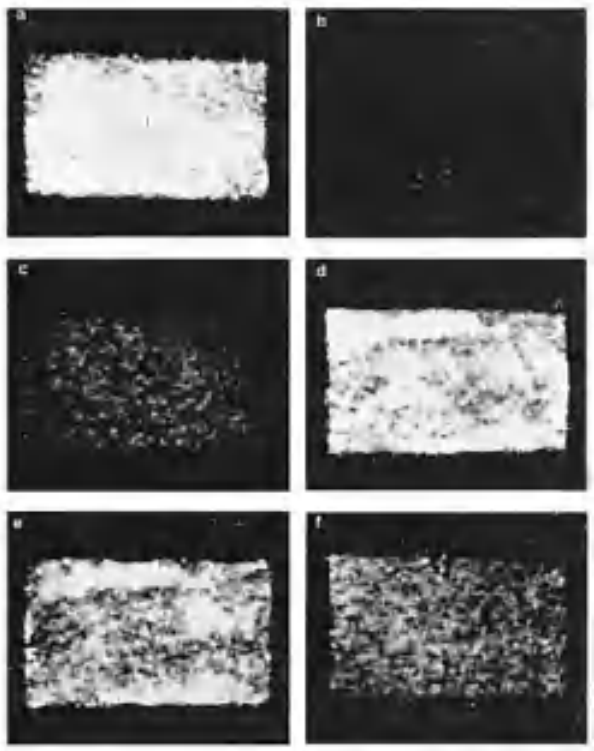

Figure 11 A series of chemical shift resolved images of a sandstone in different states of saturation, the saturating fluids being water and dodecane. The images were obtained with the sequence illustrated in Figure 10 using the modeling technique of Horsfield et al.[26] for systems with strongly overlapped spectra. Images on the left-hand side of the Figure are of the aqueous phase protons; those on the right of the dodecane protons; (a) and (b) are of the rock in its fully water-saturated state, (c) and (d) following displacement with dodecane, and (e) and (f) following further displacement with KCl solution. (Reproduced by permission of Academic Press from Horsfield et al.[26])

4.3 Flow Imaging with Two Immiscible Phases

The direct imaging of fluid displacements/velocities when two fluid phases are present requires, in principle, that separation of signals from the two phases be achieved using either of the techniques discussed in Sections 4.1 and 4.2, or the deliberate removal of the signal from one of the phases via doping with relaxation-enhancing agents or nonresonant spins. If the latter approach is adopted then this reduces the imaging experiment to effectively a single-phase measurement. Figure 5(d) is a velocity image of the same slice of the same rock used for the other images in Figure 5. In this case, the rock

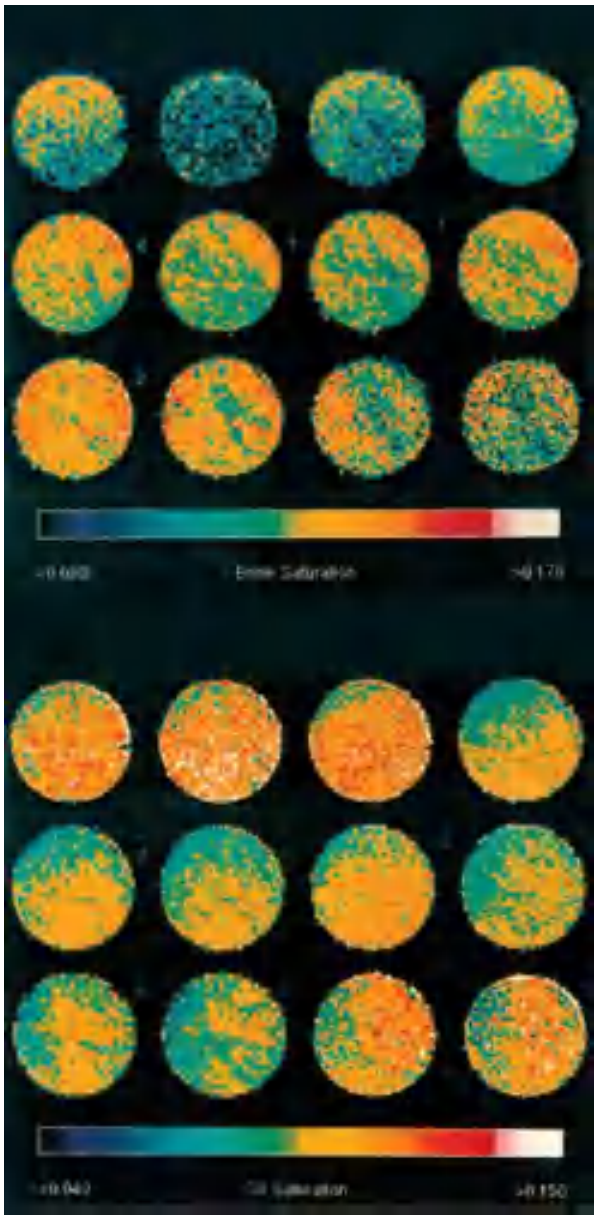

Figure 12 NMR images of oil and aqueous phase distributions in the same carbonate core sample used for Figure 9. In this case the separation of the signals from the two phases was achieved through the differences in their spin–lattice relaxation behaviors. A saturation–recovery spin–lattice relaxation imaging experiment was used to acquire the data, with the magnetization recovery for each voxel being fitted to a double exponential process. The amplitudes of these two processes can be identified with the amounts of the two phases present and are used to generate the images shown. These are a succession of transverse slices along the cylindrical sample axis. The images shown in Figure 9 correspond to the first (left-hand side) image in the middle rows of the two sets shown in this figure. (Reproduced by permission of the publisher from Davies et al.[27] © Elsevier Science Inc.)

(initially saturated with brine) has been flooded with an oil to achieve a state of irreducible water saturation (S_{wi}) at the flow rate used, 5 mL min^{-1}, which is the same flow rate used for the single-phase flow image of Figure 5(c). At S_{wi} the flowing oil has removed all the water it can and, because this is a water-wet rock, the remaining water occupies the smaller pores and will not be moving. Because of these factors this image is of the oil-phase flow only. Comparison of this image with that of Figure 5(c) shows that the oil flow is not as extensive as that of the water at $S_w = 1$ (complete saturation with brine). In addition, the oil-flow image has clear similarities with Figure 5(a), the T_1 image. This would be expected as the oil occupies, and flows through, the larger pore spaces and it is these which have the larger T_1 values.

5 IMAGING OF OIL INDUSTRY PROCESSES

In this section examples will be given of how the imaging capabilities outlined above have been used to investigate a number of processes which are utilized or encountered in oil industry operations. The industry has not, in general, taken a significant and coherent approach to the use of NMRI and the examples given in this section are the result of small groups of researchers in both industry and academic institutions who have attempted to demonstrate the ability of NMR to address phenomena and processes of importance.

5.1 Fluid Displacement

The central feature of hydrocarbon production is, of course, the relative movement of the oil and aqueous phases through the rock. This is a complex process and takes place under a range of conditions, either naturally occurring or engineered. In general, both phases coexist on a microscopic spatial scale as well as on a reservoir scale. The 'Holy Grail' for production is to move out all the oil and none of the water at very low cost! Clearly this is not an attainable goal. The processes involved in the production thus require the stimulation of the flow of the fluids and this can be driven by a natural pressure drop, or by externally applied pressures generated, for example, by pumping water and/or gas into the reservoir. The processes occurring in fluid displacement are usually characterized as being drainage or imbibition, the former being when the invading phase is nonwetting and the latter when it is the wetting phase.

Chen et al.[11] have studied both primary imbibition and drainage using a combination of 1D longitudinal profile images and 1D projections of thin-slice images, for both limestone and sandstone rocks. For a limestone core, saturated initially with the oil phase, displacement with D_2O (imbibition) was followed via measurement of longitudinal 1D projections to determine the variation with time, and the volume of injected D_2O, of the oil saturation along the displacement direction. A key observation arising from this study is that the transverse relaxation characteristics of the signal, in this case arising solely from the oil phase, depend on the oil saturation to a significant degree. This could arise from the introduction of further magnetic susceptibility inhomogeneity at the pore scale.[30] The effect is estimated to lead to a reduction in derived saturations if not properly accounted for. Figure 13 shows a set of 1D profile images obtained by projecting the signal from a thin slice perpendicular to the fluid displacement direction onto an axis in the slice plane parallel with the main bedding planes of the laminated structure of this rock. The profiles represent the oil saturations at different times in the process of imbibition of D_2O into this, originally, fully oil-saturated

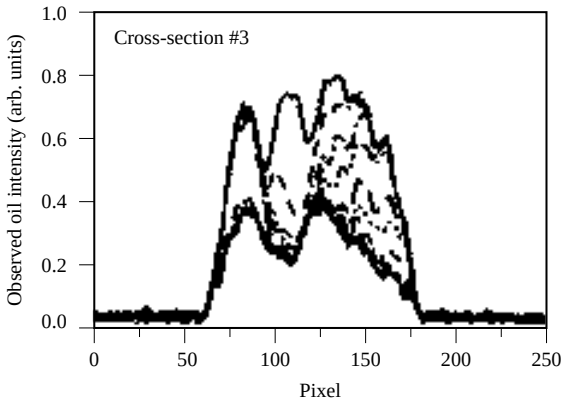

Figure 13 The evolution of 1D projection images of a laminated sandstone undergoing imbibition in which the oil phase, which gives rise to the signal, is spontaneously replaced by the wetting phase, water (D_2O). The signal decreases as the D_2O enters the slice and, because of the choice of orientation of the sample with respect to the gradient, the differential rates of transport in the different bedding planes can be discerned. The timescale spanned by the different curves is 192 min from the start of water injection. (Reproduced by permission of the Society of Petroleum Engineers from Chen et al.[11])

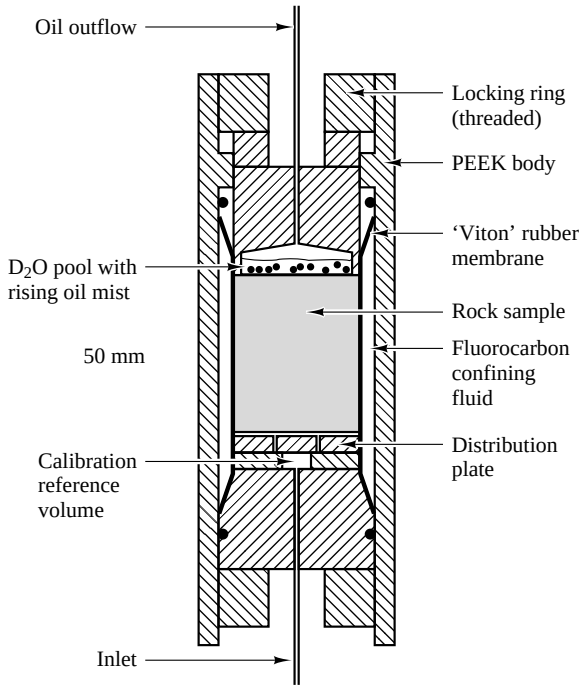

Figure 14 The sample cell used by Fordham et al.[15] to study the drainage process in a sandstone rock. The wetting phase (D_2O) is displaced by oil with the end of the sample held at $S_w = 1$. In this case the sample axis was mounted vertically within the horizontal magnet bore. The diagram shows clearly the arrangements for the generation of a reference signal, the lateral pressurized fluid containment, and the maintenance of the condition $S_w = 1$. (Reproduced by permission of the American Institute of Chemical Engineers from Fordham et al.[15] © AIChE 1993. All rights reserved)

sandstone. Analysis of the set of images from slices along the full length of the core indicated that fluid is displaced at significantly different rates in the different layers, which was interpreted as indicating significant permeability variations in the different planes of the structure. Similar slice-profile images, taken under different steady-state flow conditions, showed that for the imbibition process all the mobile oil was displaced at the lowest flow rate whereas, for the subsequent drainage process in which oil is used to displace D_2O, the oil saturation continued to increase with flow rate throughout the range investigated. It was deduced, also, that there was no significant variation of wetting behavior across the laminated structure of this sandstone.

Related investigations of fluid displacements have been carried out by other groups[12,13,15,32] and, whilst it is clear that these processes can be probed using the versatility of NMR imaging experiments, there remain the problems of signal-to-noise ratio/resolution, fast transverse relaxation, and the variation of this with saturation. These offer a considerable challenge to the NMRI/petrophysics communities if they are to capture the full potential of this combination in a quantitative manner.

A study by Fordham et al.[15] goes a long way towards meeting that challenge and, to a degree, extends the approaches of Chen et al.[11] and Enwere and Archer.[32] These workers again use D_2O together with an oil phase (*n*-dodecane) to make a quantitative study of oil saturation variations along the length of a core. In this case the displacement of the wetting phase, D_2O, by the oil phase (drainage) was investigated under the conditions that the outflow end of the rock was held at $S_w = 1$. The cell used, which was mounted vertically in the horizontal magnet bore, is shown in Figure 14 while the derived spatial variation of oil saturations and T_2 values as a function of flow rate are given in Figure 15. This study was aimed at validating a method which had been proposed for the study of two-phase flow under these conditions, which it succeeded in doing. This is probably the only example where a strong and quantitative link has been established between the complex fields of NMRI and petrophysics.

5.2 Drilling Mud Invasion/Depth Filtration

Drilling muds may contain particulates such as clays which are small enough to penetrate the rock formation being drilled. The timescale and extent of such penetration is of interest and NMRI has been used to investigate this phenomenon.[33,34] The basis of the approach is that the T_1 value of the fluid contained within the rock is reduced by the addition of fine clay particles. An earlier study of filtration[35] established the relationship between an average measure of the spin–lattice relaxation time and the local 'concentration' of the filtered solid particles. In one study[33] penetration of bentonite particles into rocks of different pore size and permeabilities were imaged and it was shown that the T_1 profiles reflected the presence of the clay and the extent of its penetration. In a further study[34] the same process was observed dynamically using a fast imaging method called 'prefocused FLASH'. Figure 16 shows a series of such images showing the time course of the penetration of the clay into the rock. The main changes occur over a time interval of 15 s and these images illustrate the potential of NMRI for the investigation of the dynamics of such processes.

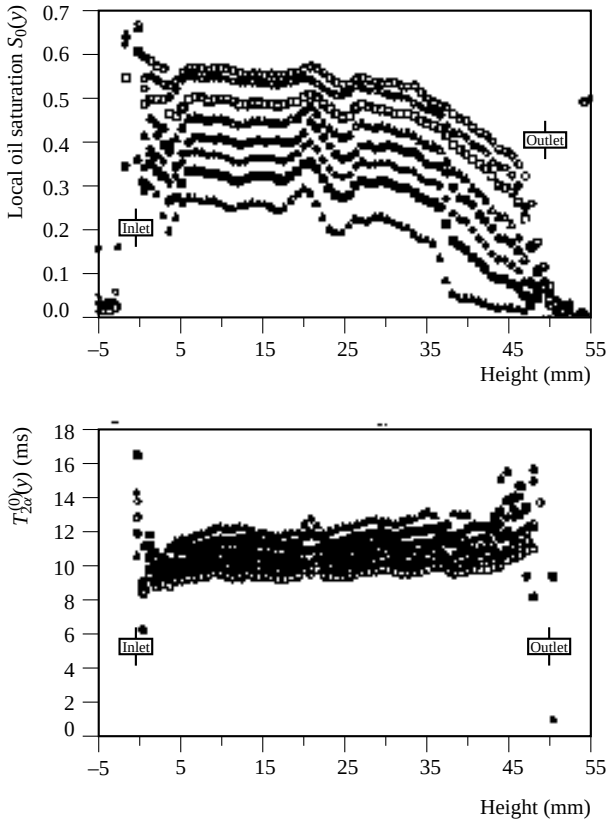

Figure 15 The 1D image profiles for the drainage process referred to in the text and in Figure 14. The upper set of profiles are the oil saturation along the length of the rock core while the lower set are of the corresponding T_2 values, each data set corresponding to different volumetric flow rates. An important observation from these data is the clear variation of T_2 of the oil phase with saturation. (Reproduced by permission of the American Institute of Chemical Engineers from Fordham et al.[15] © AIChE 1993. All rights reserved)

6 SUMMARY

NMRI studies of fluids in porous oil reservoir rocks are at a stage of development where, to a large extent, the measurement techniques with their attendant strengths and limitations have been explored and the underlying NMR physics defined in many aspects. This, coupled with studies on model and related systems,[22,36,37] will only make a real contribution to oil industry problems through a dedicated and collaborative effort between NMRI specialists and reservoir engineers and petrophysicists.

7 RELATED ARTICLES

Agriculture and Soils; Anisotropically Restricted Diffusion in MRI; Chemical Shift Imaging; Contrast Agents in Whole Body Magnetic Resonance: An Overview; Diffusion and Flow in Fluids; Diffusion Measurements by Magnetic Field Gradient Methods; Diffusion and Perfusion in MRI; Diffusion in Porous Media; Echo-Planar Imaging; Field Gradients and Their Application; Whole Body Magnetic Resonance Angiography; Imaging Techniques for Solids and Quasi-Solids; Indirect Coupling: Semiempirical Calculations; Lung and Mediastinum: A Discussion of the Relevant NMR Physics; Microporous Materials and Xenon-129 NMR; Quantitation in In Vivo MRS; Relaxation Measurements in Imaging Studies; Relaxation Measurements in Whole Body MRI: Clinical Utility; Spin Warp Data Acquisition; Susceptibility and Diffusion Effects in NMR Microscopy; Susceptibility Effects in Whole Body Experiments.

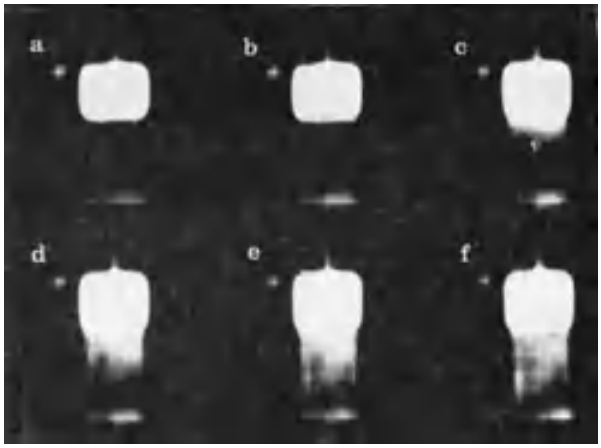

Figure 16 Rapidly acquired NMR images showing the time course of the penetration of clay particles into a rock sample. The times, from the start of the filtration process, corresponding to the successive images (a)–(f) were 7.6, 9.5, 11.4, 13.3, 15.2, and 119.7 s, respectively. The pulse sequence used was prefocused FLASH, which generates the images rapidly but at the expense of a unique image contrast mechanism, thus limiting its quantitative application in terms of local clay and fluid phase concentrations. (Reproduced by permission of the American Institute of Chemical Engineers from Fordham et al.[34] © AIChE 1991. All rights reserved)

8 REFERENCES

1. M. A. Robinson, *J. Magn. Reson.*, 1991, **95**, 574.
2. R. L. Kleinberg and M. A. Horsfield, *J. Magn. Reson.*, 1990, **88**, 9.
3. S. J. Davies and K. J. Packer, *J. Appl. Phys.*, 1990, **67**, 3163.
4. R. L. Kleinberg, *Magn. Reson. Imag.*, 1994, **12**, 271.
5. L. L. Latour, R. L. Kleinberg, and A. Sezginer, *J. Colloid Interface Sci.*, 1992, **150**, 535.
6. J. J. Howard, W. E. Kenyon, and C. Straley, *Proc. 65th Annu. Tech. Conf. Soc. Pet. Eng., 1990*, 733.
7. W. E. Kenyon, P. I. Day, C. Straley, and J. F. Willemsen, *Proc. 61st Annu. Tech. Conf. Soc. Pet. Eng., 1986*, 1.
8. P. T. Callaghan, *Principles of NMR Microscopy*, Clarendon Press, Oxford, UK, 1991.
9. P. Mansfield and B. Chapman, *J. Magn. Reson.*, 1986, **66**, 573.
10. W. P. Rothwell and H. J. Vinegar, *Appl. Opt.*, 1985, **24**, 3969.
11. S. Chen, F. Qin, K.-H. Kim, and A. T. Watson, *Proc. 67th Annu. Tech. Conf. Soc. Pet. Eng.*, 1992, 1013.
12. B. A. Baldwin and W. S. Yamanashi, *Magn. Reson. Imag.*, 1988, **6**, 493.
13. E. J. Fordham, M. A. Horsfield, C. Hall, and L. D. Hall, *Magn. Reson. Imag.*, 1991, **9**, 803.
14. W. A. Edelstein, H. J. Vinegar, P. N. Tutunjian, P. B. Roemer, and O. M. Mueller, *Proc. 63rd Annu. Tech. Conf. Soc. Pet. Eng., 1988*, 101.

15. E. J. Fordham, L. D. Hall, T. S. Ramakrishnan, M. R. Sharpe, and C. Hall, *AIChE J.*, 1993, **39**, 1431.
16. P. A. Osment, K. J. Packer, M. J. Taylor, J. J. Attard, T. A. Carpenter, L. D. Hall, N. J. Herrod, and S. J. Doran, *Philos. Trans. R. Soc. London, Ser. A*, 1990, **333**, 441.
17. J. W. Gleeson and D. E. Woessner, *Magn. Reson. Imag.*, 1991, **9**, 879.
18. A. Caprihan and E. Fukushima, *Phys. Rep.*, 1990, **198**, 195.
19. D. LeBihan, E. Breton, D. Lallemand, P. Grenier, E. A. Cabanis, and M. Laval-Jeantet, *Radiology*, 1986, **161**, 401.
20. R. Turner, in *Cerebral Blood Flow*, eds. A. Rescigno and A. Boicelli, Plenum Press, New York, 1988, p. 245.
21. R. Turner and P. Keller, *Prog. NMR Spectrosc.*, 1991, **23**, 94.
22. G. J. Nesbitt, T. W. Fens, J. S. van den Brink, and N. Roberts, in *Magnetic Resonance Microscopy*, eds. B. Blumich and W. Kuhn, VCH, Wienheim, 1992, p. 287.
23. D. Guilfoyle, P. Mansfield, and K. J. Packer, *J. Magn. Reson.*, 1992, **97**, 342.
24. P. Mansfield and B. Issa, *Magn. Reson. Imag.*, 1994, **12**, 275.
25. S. J. Gibbs, J. J. Attard, and L. D. Hall, *AIChE J.*, 1993, **39**, 689.
26. M. A. Horsfield, C. Hall, and L. D. Hall, *J. Magn. Reson.*, 1990, **87**, 319.
27. S. Davies, A. Hardwick, D. Roberts, K. Spowage, and K. J. Packer, *Magn. Reson. Imag.*, 1994, **12**, 349.
28. H. J. Vinegar, P. N. Tutunjian, W. A. Edelstein, and P. B. Roemer, *Proc. 64th Annu. Tech. Conf. Soc. Pet. Eng., 1989*, 1.
29. W. E. Kenyon, *Nucl. Geophys.*, 1992, **6**, 153.
30. S. Chen, H. K. Liaw, and A. T. Watson, *Magn. Reson. Imag.*, 1994, **12**, 201.
31. B. A. Baldwin and W. S. Yamanashi, *The Log Analyst*, 1989, 45.
32. M. P. Enwere and J. S. Archer, *Proc. 8th SPE/DOE Symp. Enhanced Oil Recovery*, 1992, 99.
33. E. J. Fordham, M. A. Horsfield, L. D. Hall, and G. C. Maitland, *J. Colloid Interface Sci.*, 1993, **156**, 253.
34. E. J. Fordham, T. P. L. Roberts, T. A. Carpenter, L. D. Hall, and C. Hall, *AIChE J.*, 1991, **37**, 1900.
35. M. A. Horsfield, E. J. Fordham, C. Hall, and L. D. Hall, *J. Magn. Reson.*, 1989, **81**, 593.
36. G. J. Nesbitt, A. de Groot, T. W. Fens, and J. H. M. Bonnie, *Magn. Reson. Imag.*, 1991, **9**, 779.
37. J.-D. Chen, M. M. Dias, S. Patz, and L. M. Schwartz, *Phys. Rev. Lett.*, 1988, **61**, 1489.

Biographical Sketch

Ken J. Packer. *b* 1938. B.Sc., 1959, Chemistry, Imperial College, London, Ph.D., 1962, Cambridge University. Introduced to NMR by making a new compound and collaborating with fellow graduate student (Robin Harris) in the analysis of its spectrum. Reinforced by a postdoctoral year with Earl Muetterties at the duPont Experimental Station, Wilmington. 1963–84, School of Chemical Sciences, University of East Anglia; 1984–93, BP Research, Chief Research Associate in Spectroscopy and latterly Chief Scientist. Currently, Research Professor in Chemistry, Department of Chemistry, University of Nottingham. Approx 120 publications including book NMR of Solid Polymers with V. J. McBrierty. Current research interests: NMR/MRI applied to heterogeneous catalysts, solid polymers, and fluid transport processes in porous solids.

Plants, Seeds, Roots, and Soils as Applications of Magnetic Resonance Microscopy

Janet S. MacFall and G. Allan Johnson
Duke University Medical Center, Durham, NC, USA

1 INTRODUCTION

Magnetic resonance imaging has been established as the 'gold standard' for many clinical diagnoses. The ability to highlight anatomical features with varied image acquisition strategies and the advent of fast scan techniques have provided new clues to the biochemical and physiological basis of many pathological conditions. In addition, functional imaging has recently generated much interest in the study of localized brain activity. As with human and animal studies, MRI can give both detailed anatomical and detailed physiological information for plant specimens.

Application of MRI to plants is not new. Many of the first imaging experiments were done with fruit or vegetable samples that provided good phantoms for engineering developments.[1] Some of the pioneers in the field applied MRI to defining plant structure in the earliest years of development.[2]

Steady improvements in the technologies have increased the spatial resolution, expanding the applications of MRI to plants. Most clinical imaging is done at resolutions >5 mm^3 ($1 \times 1 \times 5$ mm), much coarser than what is used in classical histology. The use of higher field magnets, stronger shielded gradients, and pulse sequences tailored for magnetic resonance microscopy (MRM) have made possible the routine acquisition of images with inplane resolution <10 μm. On a volume basis this translates to a resolution increase of more than 10^6 over standard clinical techniques. A variety of techniques have been used to acquire images of small samples with resolutions of <10 μm. Examples include MR images acquired of maize roots through use of implanted coils at 2 T[3] and images of geranium petioles acquired at 11.7 T with a half-Fourier technique spanning half of *k*-space.[4]

There are several critical differences between plant and animal MRI. The most obvious is the difference in movement and subject tolerance over time: plants, when properly secured, do not generally require sophisticated life support, monitoring, and gating to reduce motion artifacts. Another difference between plant and animal specimens is in water distribution and binding patterns. Most herbaceous plants contain 80–90% water, often distributed relatively homogeneously throughout the specimen. This contrasts with animal specimens in which localized tissues may have widely varied water contents, e.g. cartilage contains 28–40% water compared with skeletal muscle which contains about 79% water.[5] Finally, the fundamental structure of the plant cell is decidedly different from that of the mammalian cell, a difference that can be particularly profound at higher magnetic fields.

The contrast in MRM images of nonwoody plants is dependent on the traditional MR parameters (T_1, T_2, etc.) as well as other elements not routinely encountered in clinical studies. The existence of air spaces in plant tissues at the microscopic level has a significant effect on the contrast in MRM of plants. In geranium stems, for example, cortical parenchyma appear dark in MR images compared with the vascular bundles.[4,6,7] The parenchyma cells are larger, less tightly packed, and interspersed with intercellular air spaces compared with the tightly packed cells within the xylem, phloem, and fibrous sheath. Differences in water content between the tissues are small, however, compared with the observed differences in signal intensity. It has been demonstrated through simulations and experimentally by water infiltration of the stem that the signal loss in the cortical parenchyma is due to susceptibility from the air/cell wall interface and from diffusion-dependent dephasing rather than a proportionately lower water content.[4] Since most plant imaging is done at higher spatial resolution than in clinical applications, the stronger encoding gradients impose some diffusion contrast. In addition, most plant imaging has been performed at higher magnetic field where the susceptibility effects from the air/water interface are much more important.

In this contribution, specific applications of MRM to plant studies will be presented and discussed. This list is not exhaustive, nor intended to address all possible applications, but is designed to illustrate the utility of the technique in describing plant anatomy both from the classical viewpoint and from the view of providing unique information on correlative functional physiology.

2 DEVELOPMENTAL ANATOMY AND MORPHOLOGY

Several papers have been published describing the use of MRI for the study of plant anatomy and morphology, with resolutions and contrasts varied between specimens and image acquisition strategies. For example, the anatomy of a newly formed primary corn root can clearly be distinguished,[3] illustrating the increasing detail which can be appreciated in plant images with reduction of inplane resolution from 40 to 5 μm. Exquisite anatomical detail of plant specimens has also been seen in images acquired of other plant specimens, including geranium roots and stems,[6,8] seeds,[9] taproots of pine,[10] fruits,[11] petioles,[12] soybean nodules,[13] and leaves.[14] The majority of these studies have been performed with two-dimensional Fourier encoding. The spatial resolution in the selectively excited slice is determined by the dimensions of the encoding matrix and the field of view. Limiting the field of view through the use of selective excitation or small specimens has been essential in defining structure at higher resolution. The use of localized rf coils has been particularly effective in limiting the field of view while providing the necessary increase in sensitivity required for higher spatial resolution.[3]

Varied contrasts arising from use of alternative pulse sequences (T_1-weighted, T_2-weighted, etc.) have been very effective in defining changes in plant physiology. For example, Johnson et al. showed changes in T_1 and N(H) in different

plant tissues accompanying changes in transpiration.[15] More recently, Veres et al. showed a strong relationship between T_1 in some tissues and changes in water potential.[16] As demonstrated in cucumber stems imaged with spin echo acquisitions at varied repetition times with short *TR* values and T_1 dominated contrast, the vasculature often appears brighter than surrounding tissues. When the *TR* is lengthened, increasing contrasts are dependent on water distribution and greater signal is detected from the cortical parenchyma.[7] Other pulse sequences can also provide different and physiologically interesting contrasts. For example, gradient echo techniques may highlight magnetic susceptibility variations, such as air/cell interfaces.[4] Magnetization transfer might be expected to highlight differences in the chemical exchange of protons. These and other image acquisition protocols will become increasingly important in nondestructively 'staining' through MR contrast manipulation, reflecting differing, spatially localized physiologies or biochemistry within the tissue.

The varied contrast available in MR images of plant tissues can highlight physiologic and anatomically unique regions which are not readily distinguishable by light microscopy. For example, histological sections of a squash blossom ovary viewed with traditional light microscopy show the expected anatomy (Figure 1). The MR micrograph, however, shows very bright regions around the margin of the specimen (regions which are not highlighted in the histologic section) as well as highlighted vasculature. The difference in signal intensity in the MR image is reflective of physiological properties which are quite different from the surrounding tissue, resulting in either different water content or different binding properties and therefore different signal intensity, but which are not apparent with classical histology.

Three-dimensional Fourier transform (3D FT) encoding has allowed researchers to increase the spatial resolution along the slice axis. Extension of 3D FT encoding to very large arrays (256^3) has opened the door to MR histology of live plants, affording several unique opportunities for showing anatomical relationships and plant architecture without the artifacts associated with destructive sampling. With traditional embedding and sectioning methods as used in classical histology, plant tissues are often torn or crushed. This is particularly problematic with large specimens such as fruit and woody plant material. Additionally, by its very nature, sectioning destroys the structural integrity of the specimen, making it extremely difficult to establish anatomical connections.

An example of the importance of 3D data sets is the study of vascular structures, wherein classical histological techniques can only provide selected views dependent on the physical slice plane and not a reconstruction of the full vascular architecture. One researcher has laboriously reconstructed vascular supplies by examination of serial sections,[17] but such an approach is extremely difficult and time consuming. This destructive approach also does not allow repeated specimen examination over time which is necessary to follow vascular development with plant growth. Neither does this destructive sampling allow the specimen to be repeatedly reexamined using different protocols to enhance visualization of specific characters, such as the vasculature system or regions of photosynthate storage. Once the specimen has been sectioned and stained, it cannot be reassembled.

Three-dimensional vascular images have been acquired at 2.0 T, 7.1 T, and 9.4 T using rf refocused 3D FT encoding with 256^3 arrays.[18] The large arrays make it possible to acquire the images with isotropic resolution, i.e. with voxels with relative dimensions of 1:1:1. Short repetition times (*TR* = 200 ms) and short echo times (*TE* = 6 ms) provide excellent contrast between vascular tissues and surrounding parenchyma while allowing reasonable total acquisition times for the large arrays. Using such acquisition protocols, the conductive xylem and phloem can readily be distinguished in images of many plant specimens, including woody taproots, fruits (kiwifruit, persimmons, apples, figs, okra, kumquats), flowers, and stems. As with the squash blossom, the rapid acquisition and echo times provide spin–lattice (T_1) relaxation-time-dominated contrasts, making the vascular tissue appear brighter than the surrounding tissue.

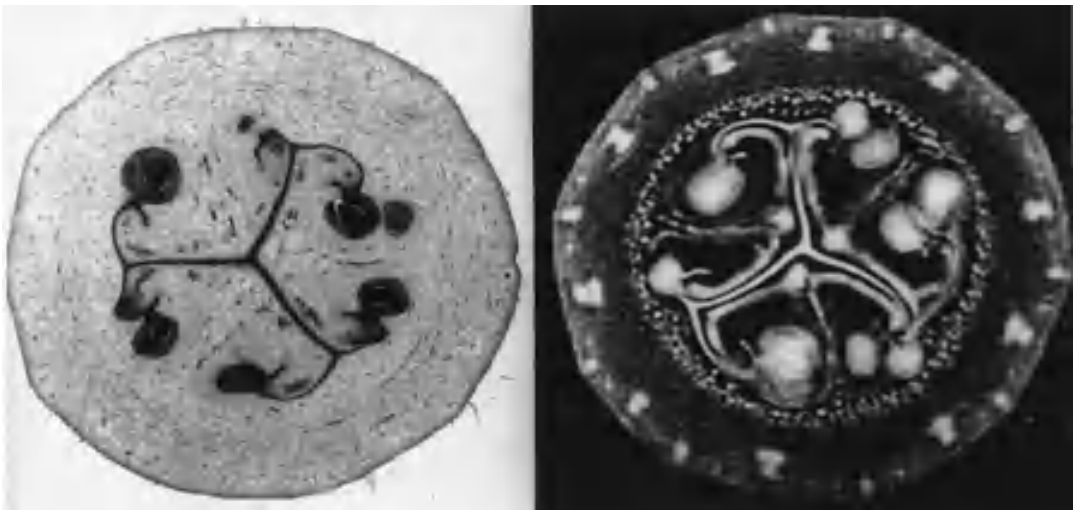

Figure 1 Single cross-sectional views through a squash blossom ovary. Left: light micrograph of an embedded and sectioned specimen. The field of view is 2958 μm. Right: spin echo image of a fresh blossom of about the same age. Note that vascular traces can clearly be distinguished around the perimeter of the specimen in the MR image, which are not readily visible in the light micrograph

A variety of display techniques are available to provide 3D perspectives of these isotropic image arrays. Many are in common use for clinical angiography, e.g. maximum intensity projection or surface rendering techniques. High-speed graphics engines (e.g. Silicon Graphics VGX) coupled to software that takes advantage of these engines (Voxel View Ultra, Vital Images, Fairfield, Iowa) now permit near real time rendering using much more computer-intensive volume-rendering techniques.[19] The vasculature can be distinguished from the surrounding tissue by interactively changing the opacity of the viewed volume so that the nonvascular tissue becomes transparent.

More sophisticated techniques employing seeding and connectivity algorithms can also be used effectively to isolate vasculature. An initial seed point is defined by the operator. The algorithm finds connected voxels within a range of signal intensities. Accepted voxels must be adjacent to previously accepted voxels, so that a contiguous network of vasculature is the final 3D digital product. The number of accepted voxels within the final vascular network is stored, providing quantitative data on the surface area and volume of the vascular structure.

An example of the anatomical detail and vascular architecture that can be studied with 3D data is seen in the apple data set in Figure 2. The longitudinal view through the volume provides a restricted view of vasculature throughout the mesocarp. The small, bright spots are the vascular traces. Single 2D views such as this, however, are limited in the information they can provide on vascular distribution throughout the specimen. Use of the segmentation algorithms to extract the vascular system (Figure 2, lower images) provides a powerful view of the connective relationships and patterns of transport throughout the fruit. The center, primary, vasculature, and connected seeds can readily be studied, and the branching order of the vascular network readily distinguished.

3 FRUIT DEVELOPMENT AND MATURATION: PHYSIOLOGICAL CHANGES

Physiological and/or biochemical changes can be seen in other plant specimens such as fruit, both between different tissues and over time as fruits develop and mature. Changes such as transport and assimilation of photosynthates, cell wall development, enzymatic changes, and changes in water content might be expected to influence image contrasts and could be tracked over time. Although chemical shift imaging of sugars, water, and lipids in plant specimens has been demonstrated,[20] careful study of changes in contrast of images acquired with different image acquisition strategies is likely to prove important in future plant studies.

One example can be seen in changes in image contrast patterns of persimmon fruit during the period of fruit development on the tree and during ripening following the final harvest (Figure 3). Images with T_2-weighted contrast clearly show dar-

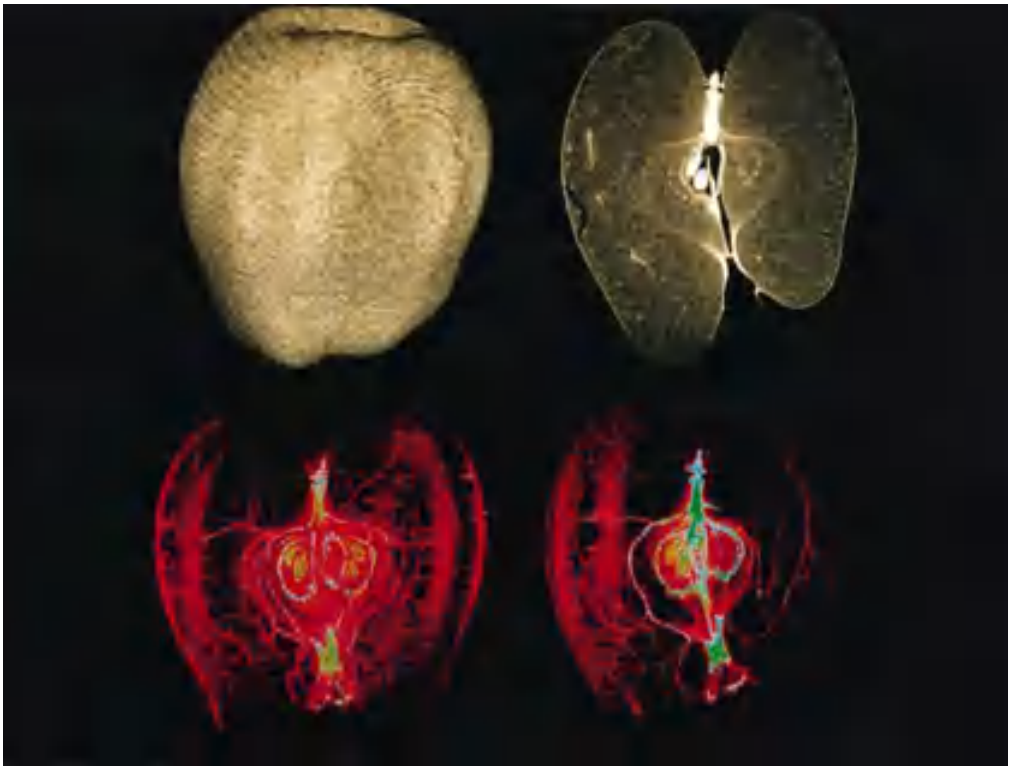

Figure 2 Top left: volume rendering of an apple fruit. Top right: longitudinal view through the center of the volume. Lower left: volume rendering of the digitally extracted vasculature. Lower right: volume rendering of the vasculature with the volume sliced in half at the same position as the longitudinal view above

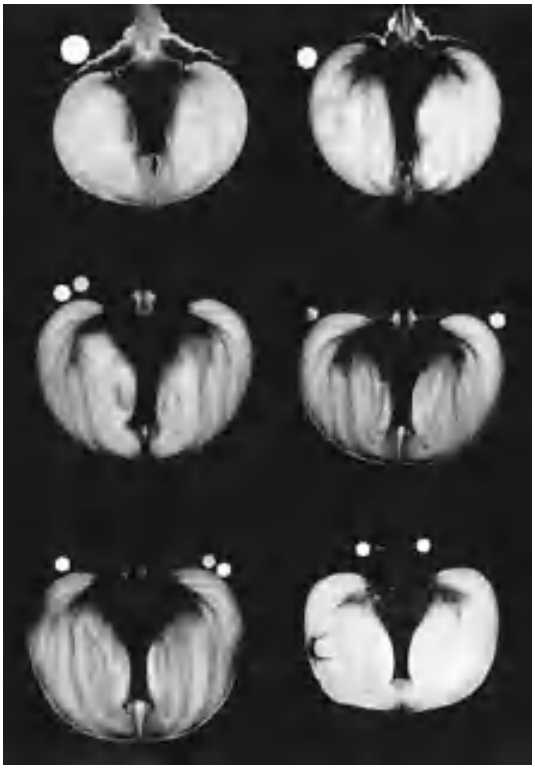

Figure 3 Spin echo images acquired with T_2-weighting (TR = 3200 ms, TE = 40 ms). Top left: persimmon fruit harvested soon after formation on a tree. Top right: persimmon fruit harvested 1 month later. Center left, center right, and lower left: persimmon fruit harvested at 1 month intervals and imaged. Lower right: same fruit as shown in lower left, but allowed to ripen for a 4 week period, then reimaged. Note the change in dark strippings through the fruit pulp. These patterns are probably reflective of photosynthate and water mobilization patterns in the developing fruit. The absence of these stripes in the ripe fruit is thought to be a result of assimilation of transported photosynthates into the mesocarp parenchyma

kened, streaked areas extending into the fruit mesocarp during fruit development. These then disappear during the 4 week ripening period following final harvest.

There are many physiological changes associated with fruit development and maturation, including sugar transport, hydrolysis, and storage, photosynthate accumulation, cell expansion, vacuole development, and tannin synthesis. Correlative studies examining the relationships of these and other physiological and biochemical properties with relaxation times and image contrasts will probably reveal properties of commercial value that can be followed by MRM.

4 ENVIRONMENTAL PHYSIOLOGY

Many plant processes that occur over shorter time periods than fruit development are also amenable to study using MRM. Plant responses to rapid environmental change, for example, stomatal closure or thigmotrophic activity, can be followed. The enclosed space of the magnet bore can be environmentally controlled through regulated gas passage, temperature, and humidity control, and lit via fiber optics placed within the bore. This makes MRM a potentially powerful tool for the repeated study of an individual specimen as it responds to defined environmental conditions.

The nondestructive nature of the technique allows acquisition of images of the specimen before, during, and after specified treatments. The ability to study the same specimen repeatedly is especially important in reducing biological variability within the experimental design. Sample sizes can be reduced as between-specimen variation with treatment is eliminated. All observations and measurements can be done on matched, registered data sets of the same specimen, an obvious advantage over having to make measurements on different specimens with different treatments.

A study examining soybean nodule response to controlled gas perfusions illustrates the power and utility of high-resolution imaging for studies following the time course of response in a single plant[13] (Figure 4). Regulation of oxygen to the center of soybean nodules is critical to their ability to perform nitrogen fixation. Activity of the nitrogenase enzyme complex within the nodule medulla requires a high flux of oxygen to maintain oxidative phosphorylation for adenosine triphosphate (ATP) production, while the enzyme complex becomes inactivated under high O_2 concentrations. These conflicting requirements make the carefully controlled flux, diffusion, and transport of O_2 from the external environment, through the nodule cortex and into the nodule center essential for nitrogen fixation to occur.

Soybean nodules were exposed first to a perfusion of O_2 gas and imaged, then perfused with N_2 gas and imaged again. T_1-calculated images, wherein the signal intensity of each pixel within the calculated image is directly proportional to the relaxation time, were made of nodules during each gas exposure.[21] Greater changes in T_1 occurred within the cortical tissue (around the nodule perimeter) between the two gas treatments than occurred in the nodule interior.[13] Several mechanisms for the physiological basis for the change have been proposed, including changes in the viscosity of the intercellular fluid from the rapid breakdown of intercellular glycoprotein, repartitioning of water between intercellular spaces and intracellular fluids, and complexation or expulsion of paramagnetic ions within the cortex resulting from the change in gas exposure. While the mechanism for the relaxation time change within soybean nodules in response to changing environmental conditions remains uncertain, these images provide strong evidence for environmentally mediated, physiological changes which are limited to the soybean nodule cortex.

5 PLANT PATHOLOGY

High-resolution MRI techniques can be used to study a variety of plant disease development and postharvest problems, illustrating both physiological as well as anatomical changes. Changing physiology, either with normal plant development or in response to biotic or abiotic stress agents, can be studied by high-resolution imaging, through either direct image examinations or evaluations of spatially defined relaxation times. Subtle changes in biochemistry are likely to alter image contrasts, although the image acquisition protocol most appropriate for highlighting specific changes must be determined.

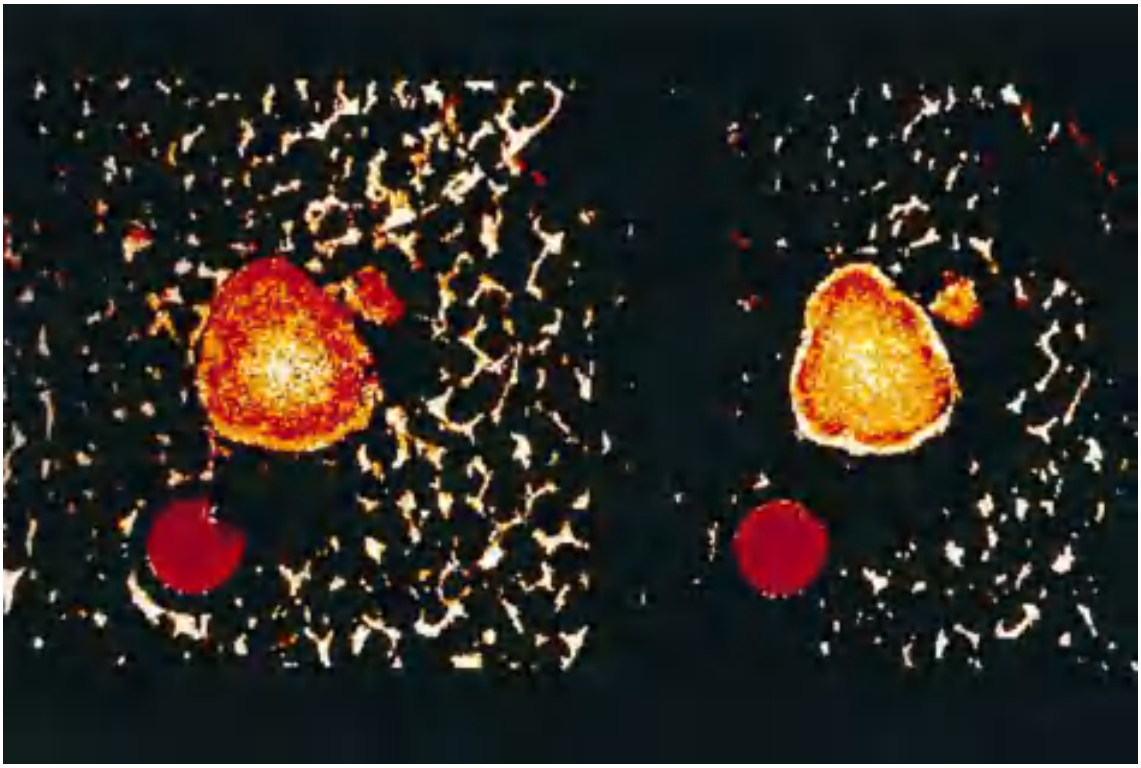

Figure 4 Spin–lattice relaxation-time-calculated images of intact soybean nodules. Left: cross-sectional view through the nodule during O_2 gas perfusion Right: cross-sectional view through the same slice position during N_2 gas perfusion. Signal intensity is proportional to relaxation times. Note the distinct change in relaxation times around the nodule perimeter (nodule cortex)

Many host–pathogen interactions can be studied directly. The ability to acquire 3D image sets is especially powerful, allowing visualization and study of anatomical and morphological change from healthy to diseased tissue. This property, combined with the ability repeatedly to image the specimen, provides both temporal and spatial information showing disease development. An example is the study of Fusiform Rust of pines, a disease caused by an obligate fungal pathogen infecting pine species of the southeastern United States. This disease is characterized by the development of swollen galls on both stems and branches of infected trees. Although there are several previously published papers which describe gall-associated hyperplasia and hypertrophy based on classical histology, no information has been available describing the impact of gall development on the fundamental process of water transport up the stem of an infected tree.

Magnetic resonance images of galls (Figure 5) have shown profound alterations in the anatomy of the stem, with replacement of the cortical parenchyma by secondary phloem, enlarged xylem rays, and an increase in the number of resin ducts. In contrast to expectations based on light micrographs, however, the MR images showed a high degree of cellular organization and relatively uninterrupted water transport through galls.[22] The region of transition from healthy to galled wood was clearly visible with a change in wood texture and water binding qualities, but the MR micrographs also clearly showed a functional water transport system through the gall. This suggests that the host–pathogen interaction has developed to promote coexistence of both host and pathogen, a concept previously unconsidered with this disease.

These images clearly demonstrate that MRM can provide a unique view into plant disease incidence and development. It gives a view of the changes in functional physiology, especially with water relations, that may develop as part of the host–pathogen interaction.

6 ROOTS AND SOILS

The opaque nature of soil makes direct, nondestructive study of plant roots and soil processes impossible without some method of remote sensing. MRM has been demonstrated to be a potential tool for the in situ study of roots both in natural and synthetic soils.[23,24] In previous studies, roots and water-filled capillary tubes about 1 mm in diameter were detectable in soils with a ferromagnetic particle content below 4%. Background signal from water held in perlite, Ottawa sand, and peat, however, made it difficult to distinguish roots. Seven native soils were identified which allowed accurate root detection and gave little background signal from soil water, regardless of soil water content.

In more recent work, water uptake by plant roots has been directly studied by MRM.[10] Repeated images acquired over time of the root system of a transpiring plant and the surround-

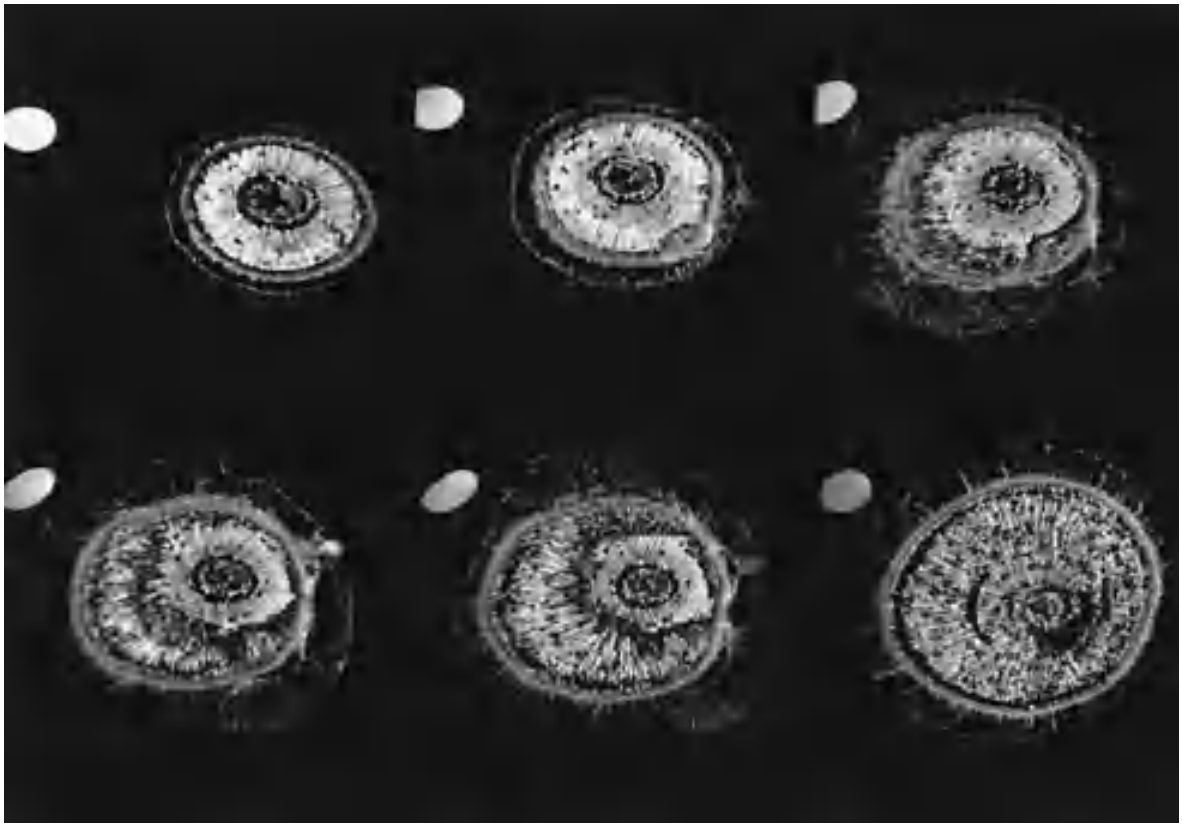

Figure 5 Cross-sectional view of a 9-month-old seedling at varied positions through a fusiform rust stem gall of pine. The reference tube (bright circle in upper left corner) was 1.12 mm in diameter. Top left: healthy stem section below gall. Top center: beginning of the transition region between the healthy and galled stem. Note the swelling of the phloem ring and proliferation of parenchyma external to the phloem. Top right: lower region of the gall, with rapid proliferation of parenchyma outside the phloem, initiation of the secondary phloem, proliferation of secondary xylem, and disruption of water transport as seen by the dark regions within the secondary xylem. Lower left: section through gall further up the stem. Note the pushed out appearance of the parenchyma external to the phloem and replacement by parenchyma and secondary phloem with a striated appearance. Region also shows further proliferation of the secondary xylem, with transport disruption. Lower center: cross section near gall center. Note the disorganized parenchyma has been nearly replaced by the 'striated' tissue, and less disruption of water transport is seen. Lower right: cross section of gall center. Note change in appearance of the secondary xylem compared with the healthy stem and the change in tissue organization external to the cambium and phloem

ing damp sand shows the development of the water depletion zone (Figure 6). The dark areas, which can be seen to form around the taproot (center bright circle) and attached lateral root (to right of taproot), are the regions from which water has been withdrawn during transpiration.

Use of fine, acid-washed sand as the medium for plant growth has allowed quantitative measurement of plant water extraction.[25] Signal from water in the sand can be normalized against a reference solution placed within the same imaging field of view.[10] A linear relationship between water content of the sand and normalized signal intensity has been described, providing quantitative measures for water uptake by the plant. Regions within the images of moist sand that appear comparatively darker are regions with a lower water content. A region of interest can be traced around the visible water depletion zones, providing a voxel count and signal intensity measurement which, in turn, allows direct calculation of the water content within the water depletion zone.

When water uptake studies are coupled with 3D image acquisition techniques, root development over time can be followed as well as root water relations (Figure 7). Image acquisition protocols can be tailored to enhance contrast between roots and the surrounding sand. Both differences in water content and relaxation times between roots and moist sand can be exploited to enhance root/sand contrast. Relaxation time differences have been measured between pine roots (500–1000 ms) and moist sand (1200 ms).[26] Water content differences between pine roots and moist sand can also provide additional contrast, as the maximum water-holding capacity of sand is about 25% (w/w) compared with 60–90% for plant tissues. In images weighted primarily with T_1 and secondarily with water-content-dominated contrasts, taproots, woody roots, and fine roots can be clearly distinguished.

With 3D acquisitions, roots can be segmented from the volume, as with the extractions of the plant vascular system previously described (Figure 7). The surrounding sand/water matrix can be rendered to be transparent, allowing visualization of an intact, in situ, root system. Thus, MRM provides root researchers with the first tool allowing direct, quantitative study of plant root growth and turnover.

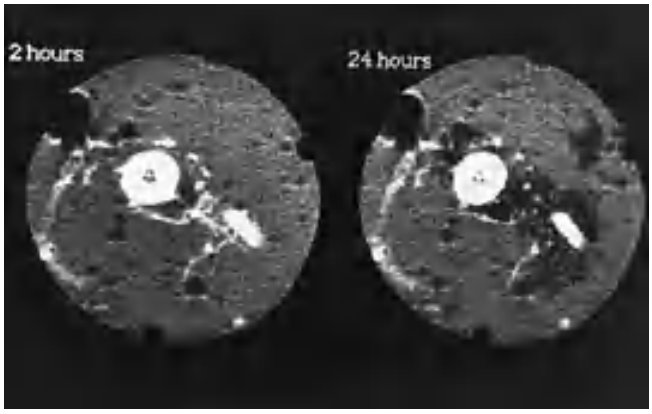

Figure 6 Cross-sectional view of a sand-filled tube containing a loblolly pine seedling. The taproot can be seen in cross section in the tube center, and a lateral root can be seen winding around the tube perimeter. The image on the left was acquired 2 h after watering. The image on the right was acquired 24 h after watering. The dark region associated with the taproot and lateral root is the water depletion zone, providing less signal because of lower water content

7 SUMMARY

The utility of MRM in plant studies has been demonstrated by many researchers. Nondestructive 3D studies of anatomy are now possible that were unimaginable only a few years ago. Functional studies of intact plants allow measurement of water movement and relations with exquisite spatial resolution. Time course studies of relaxation time changes in fruit have given new insight into the processes of ripening. Time course studies of changes induced by pathogens and environmental stress have given us new insights into plant pathology. All of these studies are based upon technologies that are robust and available today. The continued development of the technologies supporting MRM promises even more applications. High-speed imaging sequences for MRM have recently been demonstrated providing significant reduction in total acquisition times.[27] The recent demonstration of a 30× increase in sensitivity through use of a high-temperature superconducting probe will radically increase the spatial resolution routinely available.[28] There is little doubt that MRM will play an increasingly important role in the plant sciences.

Figure 7 Three-dimensional rendering of an intact loblolly pine seedling root system. The plant has been grown in a container of sand for approximately 2 months, and imaged without removal from the container. The surrounding sand/water has been rendered to be transparent

8 RELATED ARTICLES

NMR Microscopy: Resolution; Susceptibility and Diffusion Effects in NMR Microscopy; Whole Body Magnetic Resonance Angiography.

9 REFERENCES

1. P. Mansfield and P. G. Morris, in 'NMR Imaging in Biomedicine', ed. J. S. Waugh, Academic Press, London, 1982.
2. P. C. Lauterbur, *Pure Appl. Chem.*, 1974, **40**, 149.
3. G. P. Cofer, J. M. Brown, and G. A. Johnson, *J. Magn. Reson.*, 1989, **83**, 608.
4. R. Bowtell, P. Mansfield, J. Sharp, G. Brown, M. McJury, and P. Glover, in 'Magnetic Resonance Microscopy: Methods and Applications in Materials Science, Agriculture, and Biomedicine', eds. B. Blümich and W. Kuhn, VCH, New York, 1992, pp. 427–440.
5. P. T. Beall, S. R. Amtey, and S. R. Kasturi (eds.), 'NMR Data Handbook for Biomedical Applications', Pergamon, New York, 1984.
6. J. M. Brown, J. F. Thomas, G. P. Cofer, and G. A. Johnson, *Bot. Gaz. (Chicago)*, 1988, **149**, 253.
7. J. S. Veres, G. P. Cofer, and G. A. Johnson, *Am. J. Bot.*, 1991, **78**, 1704.
8. J. Brown, G. Johnson, and P. Kramer, *Plant Physiol.*, 1986, **82**, 1158.
9. C. F. Jenner, Y. Xia, C. D. Eccles, and P. T. Callaghan, *Nature (London)*, 1988, **336**, 399.
10. J. S. MacFall, G. A. Johnson, and P. J. Kramer, *Proc. Natl. Acad. Sci. USA*, 1990, **87**, 1203.
11. S. Wang, P. Wang, and M. Faust, *Scientia Hortic.*, 1988, **35**, 227.
12. P. Millard and J. Chudek, *J. Exp. Bot.*, 1993, **44**, 599.
13. J. S. MacFall, P. Pfeffer, D. Rolin, J. R. MacFall, and G. A. Johnson, *Plant Physiol.*, 1992, **100**, 1691.
14. J. S. Veres, G. P. Cofer, and G. A. Johnson, *New Phytol.*, 1993, **123**, 769.
15. G. A. Johnson, J. M. Brown, and P. J. Kramer, *Proc. Natl. Acad. Sci. USA*, 1987, **84**, 2752.
16. J. S. Veres, G. A. Johnson, and P. J. Kramer, *Am. J. Bot.*, 1991, **78**, 80.
17. M. Zimmerman, in 'Xylem Structure and the Ascent of Sap', Springer, Berlin, 1983.

18. S. A. Suddarth and G. A. Johnson, *Magn. Reson. Med.*, 1991, **18**, 132.
19. V. J. Argiro, *Pixel*, 1990, **1**, 35.
20. J. Pope, in 'Magnetic Resonance Microscopy: Methods and Application in Materials Science, Agriculture, and Biomedicine', eds. B. Blümich and W. Kuhn, VCH, New York, 1992, pp. 441–458.
21. J. R. MacFall, F. W. Wehrli, R. K. Breger, and G. A. Johnson, *Magn. Reson. Imaging*, 1987, **5**, 209.
22. J. MacFall, P. Spaine, D. RD, and G. Johnson, *Phytopathology*, 1994.
23. P. A. Bottomley, H. H. Rogers, and T. H. Foster, *Proc. Natl. Acad. Sci. USA*, 1986, **83**, 87.
24. H. Rogers and P. Bottomley, *Agron. J.*, 1987, **79**, 957.
25. J. S. MacFall, P. J. Kramer, and G. A. Johnson, *New Phytol.*, 1991, **119**, 551.
26. J. MacFall, unpublished data, 1992.
27. X. Zhou, G. P. Cofer, S. A. Suddarth, and G. A. Johnson, *Magn. Reson. Med.*, 1993, **30**, 60.
28. R. D. Black, T. A. Early, and P. B. Roemer, *Science*, 1993, **259**, 793.

Biographical Sketches

Janet S. MacFall. *b* 1955. B.S., Juniata College, 1976; M.S., University of Maryland, 1980; Ph.D., University of Wisconsin-Madison, 1988; Faculty at Duke University 1989–present. Approx. 26 publications. Research interests include study of water and nutrient mobilization in plants, and applications of high-resolution MRI and NMR in plant studies.

G. Allan Johnson. *b* 1947. B.A., 1969, Ph.D., 1974, Mathematics and Physics, Duke University. Research in medical imaging for Duke Univ. Medical Center, 1974–present, Director of Diagnostic Physics (Department of Radiology) 1982, and Professor of Radiology and Physics 1988. In 1990, established the Center for In Vivo Microscopy. Approx. 275 publications. Research specialties: magnetic resonance microscopy, its development and application.

Polymer MRI

Allen N. Garroway
Naval Research Laboratory, Washington, DC, USA

1 INTRODUCTION

Since its inception in the early 1970s, the technique of MRI has become essentially synonymous with its application to medical science and clinical practice. Reasons for the scarcity of nonmedical applications divide into two general classes:

1. the required instrumentation and methods differ substantially from those for medical studies or, in some circumstances, are not yet developed; and
2. the materials science applications are much more diverse, (arguably) less compelling, and less evolved than the medical side.

Here we consider the particular case of NMR imaging of polymers and polymeric systems, outline some of the imaging techniques, especially as they depart from conventional MRI practices, present examples of applications in polymer science, indicate present weaknesses in the technology for imaging polymers, and consider likely future improvements in the imaging technology and future applications of polymer imaging.

Review articles[1–8] specifically on NMR imaging of polymers are available; general reviews[9–21] on materials science imaging are also directly relevant to polymer imaging. A number of useful reviews relevant to polymer MRI have appeared since this article was first prepared.[22–26]

2 NMR ASPECTS OF POLYMERS: THE ROLE OF DIPOLAR COUPLING IN THE IMAGING OF POLYMERS

A polymer is a macromolecule of sufficient length that is physically entangled with others (thermoplastic) or a macromolecule that is chemically cross-linked (thermoset). Elastomers are lightly cross-linked, so they are pliable at room temperature. Most polymers of interest are organics, but some are silicon-based. Just as in medical MRI, most applications have been for hydrogen (proton) imaging, with some examples of ^{19}F, ^{13}C, and ^{29}Si imaging.

To highlight the difference between imaging of polymers and conventional medical MRI, we first consider imaging both in the time and frequency domains.

The spin echo sequence is one of the fundamental building blocks of the MRI sequence: two resonant RF pulses are applied a time τ (or *TE*) apart, and a spin echo forms at the time 2τ *provided that the spin–spin (or transverse) relaxation time* T_2 *is comparable to or longer than* 2τ (see ***Sensitivity of Whole Body MRI Experiments***). If that condition is not satisfied, the echo amplitude is substantially diminished. What determines the relevant T_2 for polymers?

For imaging abundant spin species (^{1}H or ^{19}F), in practice there can be quite strong dipolar coupling amongst the nuclei. As is well known, in a liquid the rapid molecular motions average out, both inter- and intranuclear dipolar couplings. This motional average obtains for medical imaging: there the 'mobile' species are imaged by MRI. Present whole body medical MRI scanners are designed and optimized for observing proton signals with a minimum value for *TE* of about 20 ms, and hence can image components of biological cells with values of T_2 longer than about 20 ms. However, for any material at sufficiently low temperature, the 'rigid lattice' limit applies, and the proton or fluorine NMR resonance line is quite broad, approximately 20–50 kHz. A proton linewidth of $\Delta\nu = 40$ kHz, typical for glassy polymers, corresponds to a value for T_2 of about 10 μs. (The corresponding relaxation time is estimated by $T_2 = (\pi\Delta\nu)^{-1}$; the assumption of a Lorentzian lineshape is unwarranted but numerically convenient.) *As this value of* T_2 *is three orders of magnitude less than the minimum* T_2 *accessible by conventional MRI, it is clear that some other approach must be taken for rigid polymers.*

It is useful to consider this conundrum in the frequency domain. Consider imaging a strongly coupled proton system of a nominal linewidth of 40 kHz (1 mT). Take the *gedanken* approach of imaging solids by simply increasing the gradient size. Two neighboring pixels can be resolved if their frequency separation is at least equal to their NMR linewidth. So

1. for a resolution of 100 μm, a gradient of 10 T m^{-1} (1 kG cm^{-1}) is required; and
2. for 100 pixels along a particular axis, the difference in resonance frequency (magnetic field) across the specimen must be 4 MHz (100 mT).

Thus, both the transmitter and receiver must be capable of covering this substantial bandwidth. In this naive *gedanken* approach, the transmitter intensity must be increased by a factor of 100 (a power increase of 10^4) over its value for solid state nonimaging techniques, and the bandwidth of the receiver must also be increased by a factor of 100, to at least 4 MHz. The problem of imaging solids is also treated in ***Imaging of Wide-Band Systems by Line-Narrowing Methods***.

While such large gradients and wide receiver and transmitter bandwidths have been achieved in NMR for other applications, the above brute force approach is technically extremely daunting, and suffers from the problem that excessive thermal noise is admitted into the extreme bandwidth of the receiver, degrading the signal-to-noise ratio (SNR) as well as the spatial resolution. This is the central technical challenge of polymer imaging: *broad NMR lines reduce resolution and SNR, and place extreme demands on instrumentation unless some approaches can be implemented to reduce the effects of such broad lines.*

2.1 Temperature Dependence of the Dipolar Coupling in Polymers

It is important to recognize that the linewidth (or transverse relaxation time T_2) of polymers is temperature-dependent. For polymers, the glass transition temperature T_g describes a fiducial temperature above which the mechanical bulk or shear modulus falls rapidly and the polymer becomes more pliable and may even flow. This glass transition temperature corresponds to the "point" where there is sufficient thermal motion

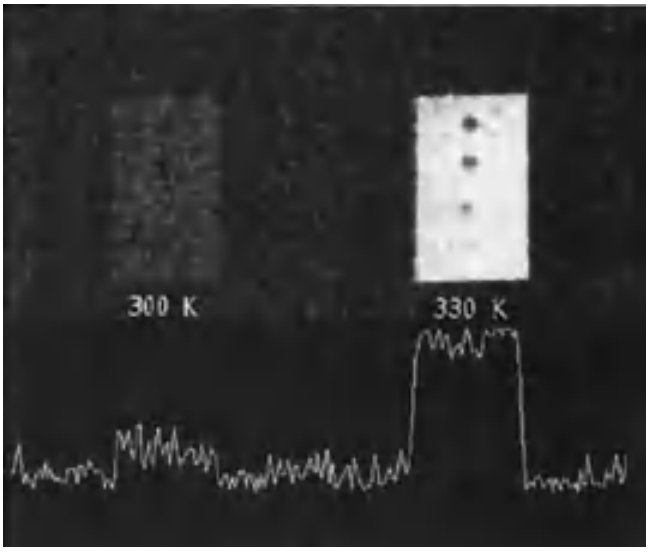

Figure 1 ^{1}H image of a 12 mm × 9 mm × 5 mm block of polypropylene at 300 and 330 K. Note that the modest increase in temperature achieves quite satisfactory spatial resolution, without the use of specialized line-narrowing sequences for this elastomer. Slice selection was not employed here. (Reproduced by permission of VCH Verlagsgesellschaft GmbH from P. Jezzard, C. J. Wiggins, T. A. Carpenter, L. D. Hall, P. Jackson, N. J. Clayden, and N. J. Walton, *Adv. Mater.*, 1992, **4**, 82)

that high molecular weight polymers can undulate by one another. (Thermosetting plastics do not flow, but do soften at the "heat distortion" temperature.) At T_g, cooperative motions of the macromolecules are on the order of seconds. From the standpoint of NMR, in order to average the intermolecular dipolar couplings motionally, the molecules must move on the timescale of the intermolecular dipolar coupling, some tens of kilohertz. Hence, the relevant timescale must be of the order of 100 μs or faster, rather than the timescale of seconds for T_g. For elastomers, the onset of motional averaging of the dipolar line typically occurs some 30–40 °C above T_g. Many commercial elastomers (with T_g values well below room temperature) exhibit substantial motional averaging at room temperature; natural rubber (*cis*-1,4-polyisoprene) has a proton dipolar linewidth of about 500 Hz at room temperature, with a T_g of −70 °C. Figure 1 provides an excellent example. The ^{1}H image[4] of a block (12 mm × 9 mm × 5 mm) of polypropylene is almost unobservable at 300 K (obtained without line narrowing techniques, with $TE = 3.8$ ms) but is well resolved at 330 K.

For many polymers of interest, substantial physical or chemical cross-linking restricts the reorientational and translational diffusion, and so motional narrowing is far less efficient than in a liquid or ordered solid. At room temperature, a polymer such as a cured epoxy may have an NMR dipolar linewidth quite comparable to its rigid lattice value.

As the dipolar coupling plays such a large role in the imaging of polymers, sometimes a parochial NMR view is taken of characterizing a polymer by its rigidity with respect to motional averaging, and not with respect to its bulk modulus, as is conventionally done in polymer science. In such argot, a 'soft' polymer has a weak dipolar coupling due to substantial motional averaging, whereas a 'rigid' polymer has a T_2 value more characteristic of its rigid lattice value.

Therefore, we see that imaging rigid solids like thermoset plastics or thermoplastics well below their glass transition involves T_2 relaxation times *three orders of magnitude shorter than for conventional MRI*. However, imaging certain elastomers at temperatures well above T_g involves relaxation times only one order of magnitude shorter than conventional MRI.

In addition to the dipolar coupling, there are other contributions to T_2 and linewidth that are important for imaging of polymers. Detailed explanations of these interactions are found elsewhere. For protons, the line-broadening mechanisms include those shown in Table 1.

The dipolar interaction, bilinear in the spin operators, is a 'homogeneous' interaction. All the other mechanisms are 'inhomogeneous' broadenings: they involve Hamiltonians that are linear in the spin operator I_z and are refocussed by spin echo techniques. The distinction between linear and bilinear operators becomes important when one seeks to remove these interactions for imaging purposes. The static field inhomogeneity is an extrinsic rather than an intrinsic broadening mechanism.

For ^{19}F imaging in polymers, the overall situation is similar to that of protons, with somewhat smaller fluorine–fluorine dipolar couplings, much larger chemical shift and chemical shift anisotropy (approx. 100 ppm), and the possible complication of fluorine–proton dipolar coupling in polymers that are not perfluorinated. For ^{13}C, the dominant interaction is the proton–carbon coupling, about 10 kHz, but one that can be removed by (heteronuclear) 'dipolar decoupling'. For ^{13}C, chemical shift and chemical shift anisotropy can range over about 200 ppm.

For highest resolution, it may be appropriate to remove all these sources of broadening. However, these mechanisms may also provide valuable sources of contrast for the imaging, and the art of solid state imaging is to remove the superfluous interactions while retaining or highlighting the desired information.

We have not touched upon the longitudinal (spin–lattice, or T_1) relaxation as it affects polymer imaging. For organic

Table 1 Contributions to Hydrogen NMR Linewidth and Transverse (T_2) Relaxation in Organic Polymers

Interaction	Typical strength	Remarks
^{1}H–^{1}H dipolar coupling	20–50 kHz	Less for polymers with motional narrowing
Chemical shift	Range of 10 ppm	
Chemical shift anisotropy	Order of 10 ppm	
Bulk susceptibility	About 1 ppm for organics	Can be quite significant for "filled" elastomers, such as rubbers filled with carbon black
Static field inhomogeneity	1–10 ppm	Depends on the details of the magnet and probe

polymers, especially those with methyl groups that provide a substantial relaxation mechanism above about 100 K, typical proton T_1 values in polymers are on the order of 0.1–1 s, not too far from the values encountered in medical MRI.

3 IMAGING TECHNIQUES FOR POLYMERS: BROAD LINES

There are some decided advantages to the examination of polymers compared with the medical applications of MRI.

1. Motion artifacts are absent.
2. Many studies may require specimen sizes less than 'whole body' size. In this regard, many 'small animal' imagers are quite suitable for polymer studies of soft polymers.
3. Long averaging times can be employed: a 48-h experiment is far more feasible on an inert specimen.
4. The experimental protocol can be much more intrusive than for in vivo imaging; temperature, chemistry, physical size, etc. can be varied over wide ranges.
5. RF power deposition and magnetic gradient strength/rise time are not limitations.

We outline the general solid state imaging strategies that have evolved to ameliorate the problem of line broadening in solid state imaging, especially polymer imaging. More details are found in reviews specifically on NMR imaging of polymers.[1–8] Other reviews on materials science imaging deal directly with NMR techniques and applications of polymer imaging.[9–21]

1. *Artificially reduce the linewidth by some form of coherent averaging*. Approaches include
   (a) averaging in spin space by RF line narrowing techniques such as MREV-8 and related sequences;
   (b) line narrowing in the rotating frame (magic angle rotating frame, MARF, imaging)
   (c) RF line narrowing by formation of magic echoes [magic sandwich echo, (MSE), and magic echo phase-encoded solid imaging, (MEPSI)];
   (d) averaging in real space by magic angle spinning, (MAS).
   (See also ***Imaging of Wide-Band Systems by Line-Narrowing Methods***.)
2. *Coherent "partial" averaging*. Here we refer to generic coherent averaging methods that are designed to remove only a part of the overall broadening. For example, terms that are linear in the spin operator I_z can be removed (or coherently averaged) by the Hahn echo or Carr–Purcell methods. See also ***Imaging Techniques for Solids and Quasi-Solids***.
3. *Perform a "constant time"*[27] *experiment in which the imaging is executed in a dimension in which the line broadening does not appear*. This approach trades off S/N for resolution; see below.
4. *Deconvolute*. Since the line broadening may be well known and independent of position, the line broadening can be removed, in principle, by deconvolution. This approach generally requires signals with high S/N, and works well when the extraneous linewidth to be deconvoluted is not much larger than the linewidth after deconvolution.
5. *Raise the temperature*. At higher temperature, increased molecular motions may be successful in reducing the undesirable line broadening.
6. *Use mobile species*. A mobile penetrant (e.g., water, cyclohexane, or xenon gas) can be employed to image the important features in a rigid polymer.
7. *Use another nucleus*. Hydrogen and fluorine have the advantage of abundance and the corresponding disadvantage of strong homonuclear dipolar coupling. Carbon-13 and silicon-29 imaging have been explored for polymers. Strong proton–carbon heteronuclear dipolar coupling is generally considered to be technically easier to remove than proton–proton homonuclear coupling.
8. *Dilute the spin system*. Deuteration is possible in certain conditions, though not of general utility.
9. *Increase the effective T_g of the polymer by addition of a plasticizer*.
10. *Use the brute force method described in the above* gedanken *approach: apply very large gradients and accept the technical limitations*. See below for a discussion of stray field imaging (STRAFI). A further approach in this vein is the use of multiple quantum coherences: as an n-quantum coherence is n-times as sensitive to the gradient as a one quantum coherence (conventional NMR signal), the size of the gradient is effectively magnified by n.

Certainly, many of these approaches can be appropriately combined. Note too that some are themselves important topics in polymer science (e.g. plasticization, molecular dynamics, and cure mechanisms) and not merely imaging methods.

We discuss in some detail the coherent averaging approaches 1 and constant time strategy 3.

3.1 Coherent Averaging for Imaging of Polymers

A series of strategies has evolved to employ coherent averaging methods. While these methods involve apparently complicated pulse sequences named by opaque acronyms, they all have evolved along a few general routes. From Table 1, it is clear that for proton NMR imaging in polymers, the dominant interaction is the homonuclear dipolar coupling, at least at 'conventional' magnetic field strengths of 2.4–11.9 T (proton Larmor frequencies of 100–500 MHz). One general class of coherent averaging sequences removes (to a high approximation) the dipolar coupling, while preserving Hamiltonians linear in the single spin operator I_z. The prototype for this approach is the multiple pulse sequence MREV-8, which removes dipolar coupling and retains a 'scaled' chemical shift term. (See ***Imaging of Wide-Band Systems by Line-Narrowing Methods***.) That straightforward method was used in the first demonstration of solid state NMR imaging.[28]

The basic MREV-8 sequence treats the chemical shift and gradient evolution essentially equivalently. But there is an important 'handle' on the magnetic gradient evolution: it can be turned off or reversed at will by removing or reversing the magnetic gradient, respectively. The overall idea is to remove the desired interactions, and then reinsert the gradient interaction that is, of course, necessary for imaging. We give some examples of this important strategy, successfully employed in polymer imaging.

One particularly simple approach, ^{13}C refocussed gradient imaging,[29,30] creates a series of spin echoes by a Carr–Purcell

sequence. When the signal is observed stroboscopically at the center of the echoes, it appears that all the chemical shift-like terms have vanished. To this sequence is added a sinusoidally varying magnetic field gradient, in synchrony with the RF pulses. As the sign of the gradient changes, the evolution in the gradient field adds constructively, rather than being canceled as are the chemical shift terms. One advantage of this approach is that other terms such as magnet inhomogeneity and bulk susceptibility also disappear. As this method is not designed to remove strong homonuclear dipolar effects, it may be classified as a 'partial' coherent averaging approach. Refocussed gradient imaging was demonstrated for ^{13}C imaging[29] of a polyacrylic specimen and a 'refocussed effective field' version, tailored to proton imaging, was implemented and demonstrated also on a polyacrylic phantom.[31]

A more general approach is to employ a 'time-suspension' sequence in which *all* time evolution of the spin system is turned off to a very high degree, and then the gradient evolution is *carefully* reintroduced. Table 2 shows the room temperature linewidth (before line narrowing) and the residual linewidth achieved with two time-suppression sequences (a 'second-averaged' MREV-8 sequence and a CMG-48 sequence) for various solids and two forms of polyethylene.[32] In the second-averaged MREV-8 sequence, evolution about a secondary axis is deliberately introduced to cause the chemical shift terms in the average Hamiltonian to cancel out over a number of 8-pulse cycles, in much the same way that higher-order error terms in the average Hamiltonian are averaged to zero in the standard MREV-8 sequence by precession about the secondary axis formed by the resonance offset. All chemical shift terms are averaged to zero over the 48-pulse CMG-48 sequence. Table 2 indicates the high efficiency of these particular line narrowing sequences: even for pressure-crystallized polyethylene with a room temperature linewidth of 59 kHz, the linewidth is reduced to 82 Hz, a reduction of almost three orders of magnitude.

Table 3 presents the proton residual linewidths under CMG-48 for a series of polymers from elastomers to glassy and crystalline polymers.[13] The linewidths range from 12 to 172 Hz, and represent a narrowing of the resonance by factors of 100–1000, *bringing the linewidths of the polymers into the regime of the liquids that are conventionally imaged by MRI*. At present, we have the techniques available to image even the most rigid of polymers, to a resolution that is, in principle, comparable to that achieved by conventional MRI approaches on more liquid-like specimens. As yet, however, most of these techniques are rather specialized, and are not generally provided on commercial instrumentation.

Table 3 Residual ^1H Linewidth for Representative Polymers under Time Suspension Sequence CMG-48 (reproduced by permission of Academic Press from D. G. Cory, "Annual Reports on NMR Spectroscopy", ed. G. A. Webb, Academic Press, London, 1992, Vol. 24, p. 87)

Polymer	Linewidth (Hz)
cis-Polybutadiene	12
Polycarbonate	40
Polyether sulfone	40
Polyacetal (Delrin)	44
Ultem	48
Poly(dimethylphenylene oxide)	52
Poly(butyl methacrylate)	65
Poly(ethylene terephthalate)	65
Cellulose acetate	65
Polystyrene	72
Polycaprolactone	72
Polyethylene, high-density	72
Polysulfone	85
Poly(methyl methacrylate)	86
Poly(vinyl acetate)	98
Ethyl cellulose	102
Polyacrylamide	116
Poly (α-methylstyrene)	117
Nylon-6,6	119
Poly(4-methyl-1-pentene)	120
Nylon-12	126
Nylon-6	142
Nylon-6,12	142
Polypropylene	143
Isotactic poly(1-butene)	172

Figure 2 shows slices from a three-dimensional ^1H image[33] of a Delrin phantom (approx. 5 mm linear dimensions) under the CMG-48 pulse sequence. The highly efficient line narrowing allows for the (relatively) high spatial resolution achieved here: the voxel size is $92\,\mu m \times 92\,\mu m \times 625\,\mu m$.

3.1.1 *Molecular Motion and Coherent Averaging in Polymer Imaging*

In imaging, especially polymer imaging, molecular motions present a two-edged sword: while motional averaging can narrow the resonance line, there is also a temperature regime in which motion interferes with the coherent averaging. When the timescale of the random molecular motions becomes comparable to the cycle time over which a particular interaction is

Table 2 ^1H Linewidths under Multiple Pulse Time Suspension Sequences for Representative Polymers and Other Solids (adapted by permission of Academic Press from D. G. Cory, J. B. Miller, and A. N. Garroway, *J. Magn. Reson.*, 1990, **90**, 205)

Compound	Dipolar linewidth (kHz)	MREV-8 (second-averaged) (Hz)	CMG-48 (Hz)
Adamantane	13	34	3.5
Ferrocene	19	45	5.5
Hexamethylbenzene	21	29	8
Oxalic acid	58	234	67
Gypsum (single crystal)	46	176	51
Polyethylene (high-density)	25	94	66
Polyethylene (pressure-crystallized)	59	335	82

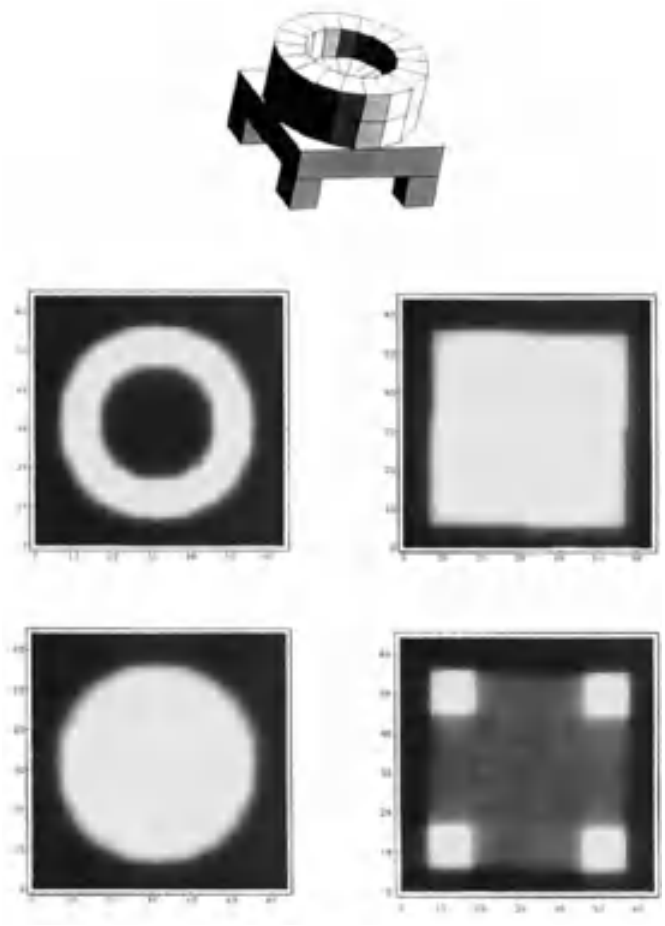

Figure 2 ^{1}H image of a Delrin phantom, with a CMG-48 time suppression pulse sequence at 400 MHz. The specimen (inset) is about 5 mm on a side and the voxel size is 92 μm × 92 μm × 625 μm. Owing to the substantial proton–proton dipolar broadening in this material, rf line-narrowing techniques such as CMG-48 must be employed to obtain an NMR image. (Reproduced by permission of D. G. Cory (unpublished results))

averaged out by a coherent averaging sequence, the efficiency of the coherent averaging is reduced. This general phenomenon may be thought of as an example of 'chemical exchange' broadening.

Consider the simple case of two-site exchange with correlation time τ_c between two chemical species separated by a frequency $\Delta\omega$. At low temperature, a spectrum of two narrow lines is observed; at high temperature, the sites are in rapid exchange, and a single narrow resonance line obtains. However, when the characteristic frequency of exchange τ_c^{-1} becomes comparable to $\Delta\omega$ (i.e., $\tau_c\Delta\omega \approx 1$), the spectrum of the two-site system is 'exchange-broadened' and the two separate lines merge into a central broad line, of width comparable to $\Delta\omega$. Apply a coherent averaging sequence, say a Carr–Purcell sequence, to this spin system. At low temperatures, there is no exchange, and the line narrowing works well on the "rigid-lattice" spectrum. At very high temperature, the lines are motionally narrowed (chemical-exchange-narrowed in this example), and coherent averaging is superfluous. But, at some intermediate regime, random molecular motions interfere with the averaging process when the timescale of the motional fluctuations, τ_c, becomes comparable to the time τ between pulses of the Carr–Purcell sequence. In a polymer, there is a rich environment of molecular motions that may be described by a broad distribution of relaxation times; consequently, the temperature range over which this "exchange broadening" occurs can be quite wide, in contrast to the narrow range expected in a simple liquid or a crystalline specimen.

Such temperature effects are seen indirectly in the linewidth data of Tables 2 and 3: while the line-narrowing ability of CMG-48 is very good for the strongly dipolar-coupled polyethylene (82 Hz residual interaction), the Nylons (Nylon-12, Nylon-6, and Nylon-6,12) have reported linewidths of 126–142 Hz. The greater residual linewidth for the Nylons most likely arises from the increase in slow (10 kHz) molecular motions at room temperature, compared with polyethylene. If motional broadening does actually present a severe problem for imaging in a given polymer then lowering the temperature may be an alternative.

3.2 Constant Time Approaches in Imaging

The constant time sequence[27] is a useful imaging approach that 'decouples' the spin system's evolution in the imaging gradient from its evolution under a dipolar (or other) Hamiltonian. In a fixed interval τ, the Hamiltonians operating will scramble the phase of the magnetization. If this scrambling is not too severe (for example, provided the timescale of the experiment is short compared with T_2) then one can hold constant that time interval and apply successively larger gradients in that fixed interval. Such a method of 'phase-encoding' by the gradient is exploited in liquid state two-dimensional imaging. However, unless some linenarrowing techniques are used for solid state imaging, the duration τ is restricted to a time less than T_2, and hence any gradients applied in that interval can only cause phase gains over that restricted timescale. To resolve spins a distance Δz apart (separate them in phase by π), the gradient g must be sufficiently large that $\gamma g\,\Delta z\,\tau \geqslant \frac{1}{2}$; with $\tau \leqslant T_2$, this condition becomes $\gamma g\,\Delta z\,T_2 \geqslant \frac{1}{2}$. But this condition is essentially the condition inferred above for brute force imaging, for which the spins a distance Δz apart must be separated by a frequency difference $\gamma g\,\Delta z$ greater than the linewidth $(\pi T_2^*)^{-1}$. For many polymers of interest with strong dipolar coupling, the 'apparent' transverse relaxation time T_2^* describing the linewidth is equal to the spin–spin relaxation time T_2. In very favorable cases, when the signal-to-noise ratio is extremely high, one can allow τ to exceed T_2 substantially and hence trade off S/N with spatial resolution.

The approach of constant time imaging that decouples the imaging evolution from the dipolar evolution is quite attractive in the circumstance that $T_2^* << T_2$, which applies in many elastomers. There a constant time interval, perhaps with a single π pulse or Carr–Purcell sequence to remove chemical shift-like terms (partial coherent averaging as discussed above), can extend the constant time interval out to T_2, and improve the spatial resolution by the factor T_2/T_2^*.

4 CONTRAST MECHANISMS IN POLYMERS

So far, the discussion of imaging polymers has concentrated on how to overcome the unwanted line broadening in produ-

cing a spin density map. But a spin density map is useful only to observe overall morphology. Just as in MRI, one must find an appropriate method of image contrast to highlight those areas that are of physical interest and suppress the rest, for example, to highlight regions of an epoxy that are not properly cured. In this regard, the interactions in Table 1 are not necessarily undesirable, and they can provide an important contrast mechanism if appropriately incorporated into the imaging procedure.

Methods of imposing contrast fall into two related categories:

1. precede the pulse sequence with a sort of NMR 'filter' designed to 'pass' the signals of interest, based on some selection of NMR relaxation times, dipolar couplings, chemical shift, proximity to other heteronuclei, etc.;
2. use the imaging sequence to perform this selectivity, for example, by adjusting the cycle time of an MREV-8 sequence to discriminate against strongly dipolar coupled spin species.

A good description of this relaxation time filter approach is found in Blümich and Blümler.[1]

5 IMAGING: PICTURES VERSUS STATISTICS

In regard to what should be imaged, it is useful to compare medical MRI with materials imaging. In the prototypical medical application, the overall morphology is already well known, and the radiologist looks for a few areas of departure from the norm: in medical MRI, there are only a few or no 'defects' to be examined, and their location is centrally important. In a notional organic matrix composite polymer, for example, there may be thousands of small-scale defects. The precise location of each of these defects is perhaps not important, but their size distribution and the details of that size distribution may be more relevant for deciding whether a fabricated part is viable. For example, one study[8,34] of a pultruded rod, a composite of glass fibers in a Nylon matrix, shows a class of tubular-shaped voids in the NMR image: these tubular defects are ascribed to entrainment of air in the pultrusion process, and could lead to potentially weaker structural components. While one approach to cataloguing such a distribution of defects is to execute a full three-dimensional image and then perform a statistical analysis on the resolved defects, a more desirable approach is to obtain such a statistical distribution directly. Moreover, such an approach overcomes, in principle, the signal-to-noise limitation that requires that the S/N of the individual defect be sufficiently large that the defect can be individually resolved.

There is not yet a general solution to this important problem in polymer imaging. A few steps have been taken towards this goal of directly generating the distribution function. One involves a statistical treatment[35] of the free induction decay, in which some general features of the distribution can be obtained. Another[36] is appropriate to the specialized circumstance of restricted diffusion for which the average linear molecular displacement reports the size of the compartment presenting a restriction to free diffusion.

6 APPLICATIONS OF POLYMER IMAGING

At present, there are few significant applications of polymer imaging. The following examples may suggest more important future applications.

Figure 3 presents an example of elastomer aging visualized by NMR. As a demonstration, a car tire was operated at high speed under a condition of deliberately misadjusted camber, so that one side of the tire (I, Figure 3) was worn heavily, while the other side (II) was barely worn. Specimens (approx. 5 mm) were taken from both sides of the tire: each included laminates of natural rubber (NR) and synthetic rubber (styrene butadiene rubber, SBR). Carbon-13 MAS spectra (not shown) do not suggest any large-scale chemical disparities between the two specimens. To highlight differences in molecular motions in

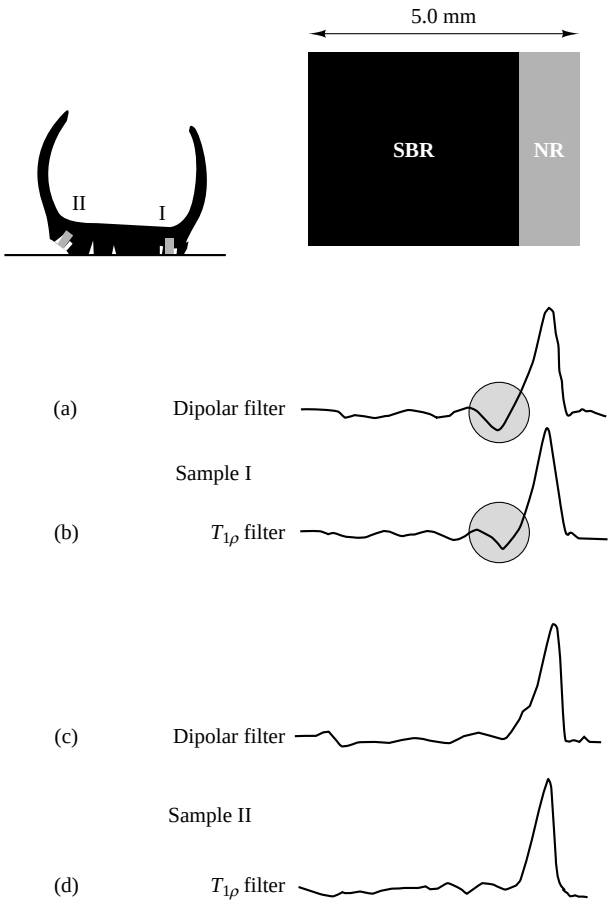

Figure 3 Accelerated physical aging in elastomers. Sections I and II were taken from a tire run under a condition of severe camber. One-dimensional ^{1}H difference images are shown, with dipolar and rotating frame ($T_{1\rho}$) filtering for specimens I and II, respectively. Filter parameters were chosen so that the dipolar- and $T_{1\rho}$-filtered difference images are sensitive to molecular motions in the range 0.8–8 kHz and around 1 kHz, respectively. Note that in the interface region between the natural rubber (NR) and styrene butadiene rubber (SBR), the image intensity is weaker for specimen I than for II, signifying reduced values of T_2 and $T_{1\rho}$, ascribed to restricted mobility brought on by accelerated physical (thermomechanical) aging. (Adapted and reproduced by permission of Dr. Alfred Hüthig Verlag GmbH from P. Blümler, B. Blümich, and H. Dumler, *Kautsch. Gummi, Kunstst.*, 1992, **45**, 699)

the range 1–10 kHz, two separate hydrogen images were obtained with dipolar filters selected to provide signal from spins whose dipolar couplings are modulated by molecular motions with frequencies up to 0.8 kHz and up to 8 kHz, respectively. A 'bandpass'-filtered image [Figure 3(a) and (c)] tuned to motions in the range 0.8–8 kHz was obtained by forming the difference between these two 'low-pass' filtered images. Similarly, a '$T_{1\rho}$-filtered' difference image [Figure 3(b) and (d)], sensitive to motions around 1 kHz, was created. In Figure 3(a),(b) the lack of signal in these two 'mobility-filtered' difference images in the interface region between the NR and SBR for the worn specimen (I) is interpreted as evidence for thermomechanical curing: the increased heat in this region has further cured the elastomer and increased the local chain packing, reducing molecular mobility and decreasing the relaxation times T_2 and $T_{1\rho}$.[37]

Polymer binders have been imaged in green (unfired) ceramics.[38] In principle, early identification of casting defects, before firing, can provide an economic advantage.

Polymerization has been followed by imaging.[39] In a study[40] of the polymerization of methyl methacrylate, the reduction in T_2 on polymerization provides a strong contrast mechanism. The polymerization wavefront of methacrylic acid initiated by benzoyl peroxide has been visualized by NMR imaging.[41]

Stress and strain distributions have been indirectly observed in the imaging of polymers. Localized strain reduces molecular mobility of the elastomer, reducing the transverse relaxation time. Separate NMR experiments provide the connection between the imposed strain and the measured T_2 values. With that information, the T_2 image of a stretched filled poly(dimethylsiloxane) elastomer notched by a small cut has been recalibrated as a strain image (Figure 4).[42] In the figure, the gray scale levels (dark to light) indicate strain from 0 to 200%, respectively. Note the increased strain in the region interior to the cut, and unstrained lips of the cut that have apparently peeled back from the initial cut. Other localized high-strain regions are interpreted as build up of strain near the sites of the filler material. Separate mechanical measurements on this elastomer relate stress to strain for this sample geometry, and the strain image can be recast into a stress distribution image (not shown[42]). It is recognized that parameterization of stress and strain tensors by a scalar, a single NMR relaxation time, is a severe simplification, but one that provides for a qualitative visualization of the important problem of mechanical load transfer in inhomogeneous, highly anisotropic materials.

Figure 4 The strain image of a polysiloxane elastomer, stretched to 200% elongation. A value of T_2 was determined for each pixel, and then, by a separate calibration, the T_2 data were converted to strain. The gray scale (dark to light) in the resulting strain image corresponds to local elongation of 0–200%, respectively. Note the strain concentrations just interior to the shallow cut (center of top surface) and also at the sites of filler particles. Note too the lips of the cut that have snapped back into an unstrained state. (Reproduced by permission of VCH Verlagsgesellschaft mbH from P. Blümler and B. Blümich, *Acta Polym.*, 1993, **44**, 125)

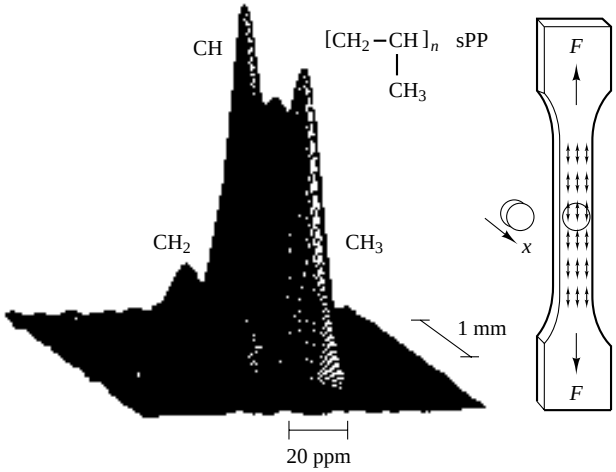

Figure 5 Carbon-13 spectroscopic one-dimensional image of a bar of syndiotactic polypropylene drawn to 500%. A section from the center was aligned with the draw axis parallel to the static field direction. Note the substantial difference in the CH_2 and, to a lesser extent, CH resonances within the core, compared with the signals from regions near the surface. This is interpreted as evidence for a denser core (compared with the outer skin) and also a broader distribution of orientations in the core interior, leading to a broader chemical shift anisotropy. (Reproduced by permission of the American Chemical Society from E. Günther, B. Blümich, and H. W. Spiess, *Macromolecules*, 1992, **25**, 3315)

Figure 5 shows the geometry of an injection molded bar of syndiotactic polyproplyene drawn to 500% of its initial length.[43] A spectroscopic ^{13}C image (under cross-polarization conditions) was obtained of a small section (inset) in the region that necked down; one dimension is spatial and the second dimension is the ^{13}C chemical shift. Note that the signals from the methylene and methine carbons in the core of the bar are weaker and broader than the corresponding signals nearer to the surface. This is interpreted as evidence for a denser core (compared with the outer skin) and also a broader distribution of orientations in the core interior, leading to a broader chemical shift anisotropy. The methyl peaks, partly hidden, are weak, since the methyl groups are highly mobile and the cross polarization process is inefficient under these conditions.

A further visualization[44] of stress/strain effects has been accomplished in ^{19}F spectroscopic imaging in poly(tetrafluoroethylene) (PTFE, Teflon). There, the chemical shift anisotropy (CSA) was used as an indication of preferential orientation in the crystalline regions of the polymer. Three specimens were examined (Figure 6, inset): a strained notched specimen and two fragments of notched specimens strained to failure, at strain rates of 5 and 500 mm min^{-1}. From a three-dimensional data set (two spatial and one spectroscopic dimensions), an image was extracted for crystalline phase PTFE with ^{19}F CSA tensors preferentially oriented. Figure 6 shows a ^{19}F NMR density image of the crystalline phase and also a false-color overlay onto the density images, corresponding to preferential alignment. Note the rather uniform stress in the unfractured piece (a); the high-stress region near the site of the crack in

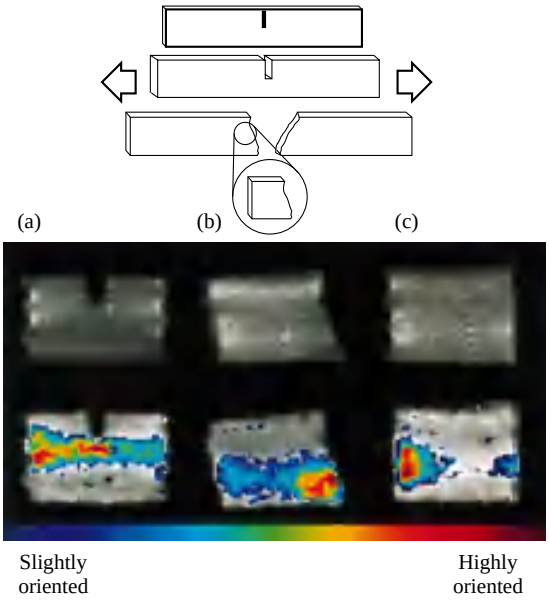

Figure 6 Notched PTFE specimens: partially strained (a); and strained to failure at 5 mm min^{-1} (b) and 500 mm min^{-1} (c). In (b) and (c), only a part of the failed specimen is imaged; see inset. In the top row are ^{19}F NMR density images of the crystalline regions. In the bottom row, false colors corresponding to preferential molecular orientation have been superposed. Note the general stress buildup, signaled by preferential orientation, in (a) near the crack and the grips of the mechanical tester; the stress buildup at the crack tip in the fractured specimen (b); and in (c) the absence of stress at the crack tip, suggesting that the strain rate in (c) was too rapid for stress to build up in this viscoelastic material. (Adapted by permission of Academic Press from M. A. Hepp and J. B. Miller, *J. Magn. Reson., Ser. A*, 1994, **111**, 62)

(b); and the absence of a high-stress region near the crack tip in (c), interpreted as evidence that the strain built up too rapidly for the stress to redistribute in that specimen.

Physical and chemical cross-linking also reduce molecular mobility, and T_2-weighted imaging or T_2-filtering is one approach for providing images of cross-link density. A recent example is shown in Figure 7. There, a model system of fiberglass (D-glass) rods in a matrix of a bisphenol-A epoxy resin was cured with an aliphatic polyamine curing agent.[45] The proton images indicate that the curing, signified by less signal intensity and hence by a reduced value of T_2, is more rapid near the glass rod. This particular image was obtained without invoking the line narrowing approaches discussed above. Related work on Kevlar fibers in the same epoxy matrix showed, by FTIR spectroscopy, the chemical details of the cure mechanism at the fiber site.[45]

7 POLYMER IMAGING: LIMITATIONS AND OUTLOOK

To date, much of the effort in polymer imaging has been devoted to the technique and technology of imaging, with only a few substantial indications of the potential for the field, and many of those applications are in the area of elastomers. Elastomers are easier to image (since their dipolar couplings are substantially motionally averaged), and, more importantly, the commercial elastomer industry is quite significant.

Coherent averaging, with various rf pulse sequences, has been quite useful in imaging polymers with strong dipolar couplings. However, these techniques impose an implicit size requirement for the specimen.

For the rf line narrowing techniques, peak power levels of about 1 kW are employed for specimens about 1 cm in diameter. The power requirements are dictated by the need to produce rf pulses of amplitude B_1 larger than the local magnetic field, of order 1 mT. For constant coil Q and constant B_1, the required rf power scales as the coil volume, and hence as the *cube* of the coil's linear dimension. While one wishes and anticipates improvements in coil efficiency and in pulse sequences that work well with smaller rf field strengths, it is unlikely that the present rf line narrowing approach can be scaled up for specimens with linear dimensions much larger than 10 cm. However, there are a few specially favorable geo-

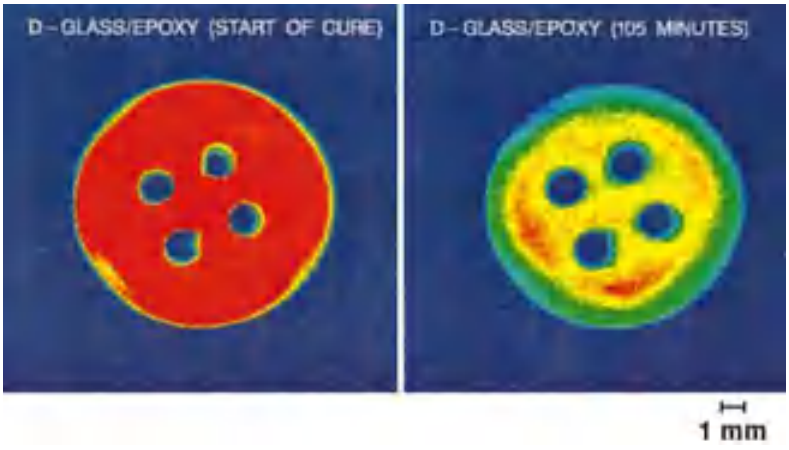

Figure 7 ^{1}H images of D-glass rods in a bisphenol-A epoxy resin with an aliphatic polyamine curing agent: (a) start of the cure; (b) after 105 min. Note that the dark regions about the four D-glass rods have increased in size, indicating that the epoxy is preferentially curing near the glass rods. (Reproduced by permission of Gordon and Breach Science Publishers AS from A. Mavrich, F. Fondeur, H. Ishida, J. L. Koenig, and H. D. Wagner, *J. Adhes.*, 1994, **46**, 91)

metries: rf methods are dependent on volume, so that large, thin (two-dimensional) structures can be assessed.

While MAS can remove modest homonuclear dipolar interactions, for imaging it is generally combined with an rf line narrowing sequence to remove larger dipolar couplings while preserving the isotropic chemical shift. There are strong limitations on the physical size of specimens suitable for MAS. For (nonimaging) MAS, a typical sample diameter is 8 mm for 5 kHz spin rates; larger (15 mm), lower-speed (2 kHz) spinners were used in the 1970s. It is difficult to imagine a MAS system for imaging that could accommodate samples with linear dimensions beyond 5 cm. One possible alternative to MAS is to replace the continuous reorientation about the magic angle by a discrete sequence of "flips" of the specimen to perform a discrete averaging about the magic angle. Here, the requirement is that the complete flipping cycle take place on a timescale less than T_1 and also less than T_2. As typical times to physically rotate a 1 cm sample through 90° are on the order of 10–100 ms, the flipping approach is not useful for removing a strong homogeneous dipolar coupling, but is certainly helpful to remove the inhomogeneous interactions linear in I_z.

Of course, to the extent the specimen has NMR characteristics similar to those of a liquid, MRI medical approaches can be used, and, at present, MRI accommodates specimens on an anthropomorphic scale, of about 1 m.

How can larger structures be imaged by NMR?

Coherent line narrowing techniques at present require the specimen to be contained within the apparatus: within the magnet and within the rf coil. A step towards solid state imaging of large-scale structures is the demonstration[46] of coherent line narrowing methods using the inhomogeneity of a surface coil to create a one-dimensional image. A sequence of composite π inversion pulses, specially designed to remove the dipolar coupling was employed: signal is obtained only from those spins that see exactly a π or an $n\pi$ inversion. With this method, a one-dimensional image (with a spectroscopy dimension of the proton chemical shift) was obtained of a stack of polyacrylic sheets.[46] Imaging of polyurethane foam by a surface coil has also been demonstrated:[47] there, because of the weaker dipolar coupling, only a two pulse spin echo sequence was required.

We also wish to overcome the limitation that the specimen has to be contained within the magnet. A step in that direction is the method of stray field imaging (STRAFI),[48–50] using the stray field of a superconducting magnet to provide large magnetic gradients. Figure 8 is the NMR image of an integrated circuit (IC) socket, with the metal pins present, obtained by this method. The specimen is just outside the bore of the magnet, but contained within the rf coil. This STRAFI approach is presently designed to produce three-dimensional images by physically stepping the orientation of the specimen, and, as such, is not directly suitable for imaging large objects.

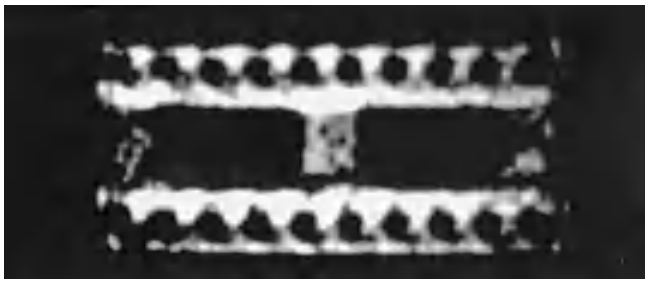

Figure 8 ^{1}H image of a plastic integrated circuit (IC) socket by the method of STRAFI (stray field imaging). In this geometry, the sample is just outside the bore of the superconducting magnet, in a region of very high magnetic field gradient. (Reproduced by permission of K. Zick (unpublished results))

In addition to these geometrical constraints, there are other limitations of the imaging technique: the rf fields must penetrate the specimen. As is well known, in medical MRI, there is some modest attenuation at higher frequencies due to eddy currents induced in the human body. For conducting media such as graphite-reinforced epoxy composites, the attenuation is quite severe in composites with a high degree of fiber loading.[51] For lesser degree of fiber loading and for small sections of a composite, the rf energy can penetrate and images can be obtained.[52,53] It has been shown that rf attenuation can be used as a method of imaging within the skin depth of a good conductor; with this specialized method, depth resolution on the scale of micrometers has been demonstrated.[54]

8 CONCLUSIONS

Progress in MRI of polymers has proceeded much more slowly than in medical areas. Technical obstacles, such as the strong proton dipolar coupling in rigid polymers, have recently been largely overcome, but, to date, imaging rigid polymers requires specialized instrumentation. So far, elastomers have provided the best examples of the potential of the imaging technique.

Most commercial polymer products are low-value, high-volume commodities, although there are some high-value applications for which hours or days of imaging time could be economically justified to ensure the integrity of a single manufactured part. As such, the use of MRI in the quality control of polymer manufacturing is likely to be rather limited. Likely quality control applications will involve very specialized NMR instrumentation, rather than the general instruments used in medical MRI.

In addition to possible quality control applications, NMR imaging for polymers may provide a means of visualizing important three-dimensional problems not amenable to other techniques. Examples include mechanical processing of thermoplastics, cure heterogeneity in large complex thermosets, the mixing process in solid phase mixtures, and the mechanics of stress and strain in heterogeneous anisotropic polymeric structures. In those areas, we anticipate that MRI of polymers may well have a significant impact.

9 RELATED ARTICLES

Image Formation Methods; Imaging Techniques for Solids and Quasi-Solids; Relaxation Measurements in Imaging Studies; Relaxation Measurements in Whole Body MRI: Clinical Utility; Sensitivity of Whole Body MRI Experiments; Spin Warp Data Acquisition; Susceptibility and Diffusion Effects in

NMR Microscopy; Tissue NMR Ex Vivo; Tissue Water and Lipids: Chemical Shift Imaging and Other Methods.

10 REFERENCES

1. B. Blümich and P. Blümler, *Makromol. Chem.*, 1993, **194**, 2133.
2. D. G. Cory and W. E. Maas, *Bull. Magn. Reson.*, 1993, **15**, 160.
3. P. Jackson, N. J. Clayden, J. A. Barnes, T. A. Carpenter, L. D. Hall, and P. Jezzard, in 'Advanced Materials: Cost Effectiveness, Quality Control, Health and Environment', eds. A. Kwakernaak and L. van Arkel, SAMPE/Elsevier, Amsterdam, 1991, p. 277.
4. P. Jezzard, C. J. Wiggins, T. A. Carpenter, L. D. Hall, P. Jackson, N. J. Clayden, and N. J. Walton, *Adv. Mater.*, 1992, **4**, 82.
5. J. L. Koenig, in 'Polymer Spectroscopy', A. J. Fawcett, ed., Wiley, Chichester, 1996, Chap. 6.
6. J. L. Koenig, 'Spectroscopy of Polymers', American Chemical Society, Washington, DC, 1992, Chap. 11.
7. J. L. Koenig, in 'Magnetic Resonance Microscopy', eds. B. Blümich and W. Kuhn, Verlag Chemie, Weinheim, 1992, p. 189.
8. J. L. Koenig, in 'Solid State NMR of Polymers', ed. L. Mathias, Plenum Press, New York, 1991, Chap. 3.
9. J. L. Ackerman and W. A. Ellingson (eds), 'Advanced Tomographic Imaging Methods for the Analysis of Materials', Materials Research Society, Symposium Proceedings, Materials Research Society, Pittsburgh, PA, 1990, Vol. 217.
10. B. Blümich and W. Kuhn (eds), 'Magnetic Resonance Microscopy', Verlag Chemie, Weinheim, 1992. This conference proceedings includes useful reviews on aspects of materials imaging.
11. P. Blümler and B. Blümich, in 'NMR, Basic Principles and Progress', eds. P. Diehl, E. Fluck, and R. Kosfeld, Springer-Verlag, Berlin, 1994, Vol. 30, p. 209.
12. B. Blümich, *Adv. Mater.*, 1991, **3**, 237.
13. D. G. Cory, in 'Annual Reports on NMR Spectroscopy.', ed. G. A. Webb, Academic Press, London, 1992, Vol. 24, p. 87. This is a comprehensive review on solid state imaging.
14. W. S. Veeman and D. G. Cory, *Adv. Magn. Reson.*, 1989, **12**, 43.
15. P. Jezzard, J. J. Attard, T. A. Carpenter, and L. D. Hall, *Prog. Nucl. Magn. Reson. Spectrosc.*, 1991, **23**, 1.
16. W. Kuhn, *Angew. Chem., Int. Ed. Engl.*, 1990, **29**, 1.
17. J. M. Listerud, S. W. Sinton, and G. P. Drobny, *Anal. Chem.*, 1989, **61**, 23A.
18. P. Mansfield and E. L. Hahn (eds), 'NMR Imaging', The Royal Society, London, 1990; also published in *Phil Trans. R. Soc. Lond., Ser. A*, 1990, **333**.
19. S. Matsui, in 'Shin-Koubunshijikkengaku', I. Ando, ed., Kyouritsu-shuppan, Tokyo, 1995, Vol. 5, Chap. 5.
20. J. B. Miller, D. G. Cory, and A. N. Garroway, *Phil. Trans. R. Soc. London Ser. A*, 1990, **333**, 413.
21. J. B. Miller, *Trends Anal. Chem.*, 1991, **10**, 59.
22. J. B. Miller, *Prog. Nucl. Magn. Reson. Spectrosc.*, 1998, **33**, 273.
23. W. M. Ritchey, L. Maylish-Kogovsek, and A. S. Wallner, *Appl. Spectrosc. Rev.*, 1994, **29**, 233.
24. T. Watanabe, *Nucl. Magn. Reson.*, 1997, **26**, 447.
25. W. S. Veeman, *NATO ASI Ser.*, Ser. C, 1994, **447**, 563.
26. D. D. Parker and J. L. Koenig, *Curr. Trend. Polym. Sci.*, 1996, **1**, 65.
27. S. Emid and H. H. N. Creyghton, *Physica*, 1985, **81**, 1253.
28. P. Mansfield and P. K. Grannell, *J. Phys. C*, 1973, **6**, L422.
29. J. B. Miller and A. N. Garroway, *J. Magn. Reson.*, 1989, **85**, 255.
30. P. Bendel, *IEEE Trans. Med. Imaging*, 1985, **MI-4**, 114.
31. J. B. Miller and A. N. Garroway, *J. Magn. Reson.*, 1989, **82**, 529.
32. D. G. Cory, J. B. Miller, and A. N. Garroway, *J. Magn. Reson.*, 1990, **90**, 205.
33. D. G. Cory, unpublished results.
34. K.-P. Hoh, B. Perry, G. Rotter, H. Ishida, and J. L. Koenig, *J. Adhes.*, 1989, **27**, 245.
35. G. A. Barrall, L. Frydman, and G. C. Chingas, *Science*, 1992, **255**, 714.
36. D. G. Cory and A. N. Garroway, *Magn. Reson. Med.*, 1990, **14**, 435.
37. P. Blümler, B. Blümich, and H. Dumler, *Kautsch. Gummi, Kunstst.*, 1992, **45**, 699.
38. L. Garido, J. L. Ackerman, and W. A. Ellingson, *J. Magn. Reson.*, 1990, **88**, 340.
39. T. A. Carpenter, L. D. Hall, P. Jezzard, C. J. Wiggins, N. J. Clayden, P. Jackson, and N. Walton, in 'Magnetic Resonance Microscopy', eds. B. Blümich and W. Kuhn, Verlag Chemie, Weinheim, 1992, p. 267.
40. P. Jackson, N. J. Clayden, N. J. Walton, T. A. Carpenter, L. D. Hall, and P. Jezzard, *Polym. Int.*, 1991, **24**, 139.
41. B. J. Balcom, T. A. Carpenter, and L. D. Hall, *Macromolecules*, 1992, **25**, 6818.
42. P. Blümler and B. Blümich, *Acta Polym.*, 1993, **44**, 125.
43. E. Günther, B. Blümich, and H. W. Spiess, *Macromolecules*, 1992, **25**, 3315.
44. M. A. Hepp and J. B. Miller, *J. Magn. Reson., Ser. A*, 1994, **111**, 62.
45. A. Mavrich, F. Fondeur, H. Ishida, J. L. Koenig, and H. D. Wagner, *J. Adhes.*, 1994, **46**, 91.
46. J. B. Miller and A. N. Garroway, *J. Magn. Reson.*, 1989, **85**, 432.
47. F. Weigand, C. Fülber, B. Blümich, and H. W. Spiess, *Magn. Reson. Imaging*, 1994, **12**, 301.
48. A. A. Samoilenko, D. Yu. Artemov, and L. A. Sibel'dina, *Russ. J. Phys. Chem.*, 1987, **61**, 1623.
49. A. A. Samoilenko, D. Yu. Artemov, and L. A. Sibel'dina, *JETP Lett.*, 1988, **47**, 417.
50. K. Zick, unpublished results.
51. A. C. Lind, C. G. Fry and C. H. Sotak, *J. Appl Phys.*, 1990, **68**, 3518.
52. P. Jackson, J. A. Barnes, N. J. Clayden, T. A. Carpenter, L. D. Hall, and P. Jezzard, *J. Mater. Sci. Lett.*, 1990, **9**, 1165.
53. P. Jezzard, C. J. Wiggins, T. A. Carpenter, L. D. Hall, J. A. Barnes, P. Jackson, and N. J. Clayden, *J. Mater. Sci.*, 1992, **27**, 6365.
54. U. Skibbe and G. Neue, *Colloids Surf.*, 1990, **45**, 235.

Biographical Sketch

Allen N. Garroway. *b* 1943. B.S., 1965, physics, Rensselaer Polytechnic Institute, Ph.D., 1972, experimental solid-state physics, Cornell University (supervisor Robert M. Cotts). Postdoctoral research at University of Nottingham (Peter Mansfield) and US Naval Research Laboratory (Henry A. Resing). Research physicist, Chemistry Division, US Naval Research Laboratory, 1976–present. Research specialties: solid state NMR imaging, polymer properties and dynamics, non-traditional applications of nuclear quadrupole resonance (NQR).

Well Logging

Robert L. Kleinberg

Schlumberger-Doll Research, Ridgefield, CT, USA

1	Introduction	1
2	NMR Relaxation Processes in Rocks	1
3	Practical Importance of NMR Measurements	4
4	Instrumentation for Well Logging	5
5	Related Articles	9
6	References	9

1 INTRODUCTION

Well logging is the means by which physical properties of subsurface earth formations are measured in situ. The most important, and the most technically challenging, application of well logging is to the characterization of hydrocarbon reservoirs. Oil and gas are found up to 10 km underground in beds of sedimentary or other porous rock. Only a part of a typical sedimentary rock is solid mineral matter. The pore space, which accounts for up to 30% of the volume, can be filled by combinations of oil, water, or natural gas. Well logging is directed toward understanding these fluids and their relationship to the solid mineral matrix. A large variety of electromagnetic, acoustic, and nuclear borehole instruments are used for various purposes. Each technique has drawbacks and limitations, and no one logging device ('tool') is adequate to give a complete description of an earth formation.[1,2]

Measuring properties of earth formations in situ by NMR obviously requires apparatus very different than that commonly used in the laboratory. Instead of placing the sample inside the apparatus, the apparatus is placed inside the 'sample', which is in fact the earth. Thus 'inside-out' NMR equipment is required: large static magnetic fields and high-frequency oscillatory magnetic fields must be projected outside of the apparatus and into the surrounding rock formations. Moreover, the apparatus is normally in motion during the measurement.

The amplitude of the proton NMR signal is proportional to the fluid content of the rock, and relaxation times give information on the pore size distribution and, under favorable conditions, the amount and type of oil. These measurements are used by the oil industry to estimate the quantity of hydrocarbon in a reservoir and the rate at which it can be economically extracted. The application of NMR to well logging is the subject of an extensive bibliography, covering 1946–1990, compiled by Jackson and Mathews.[3] The reader also is referred to review articles[4,5] and proceedings of international conferences.[6]

Owing to limitations of signal-to-noise ratio, the only nucleus accessible to borehole NMR is hydrogen. Throughout this article, all statements refer to proton NMR. Nonuniformity of the static magnetic field precludes the acquisition of chemical shift spectra.

2 NMR RELAXATION PROCESSES IN ROCKS

2.1 Surface-Limited and Diffusion-Limited Regimes

NMR relaxation rates of fluids in porous media are enhanced by relaxation at the pore–grain interface.[7,8] Fluid molecules diffuse, eventually reaching a grain surface, where they have a finite probability of being relaxed. The rate-limiting step can either be the relaxation process at the surface or the transport of unrelaxed spins to the surface.

If the rate-limiting step is relaxation at the surface, the nuclear magnetization in a pore is uniform. Therefore the magnetization decay in the pore is monoexponential and does not depend on pore shape but only on the surface-to-volume ratio of the pore. This is referred to as the 'fast diffusion' or 'surface-limited' regime.[9]

In the opposite case, magnetic relaxation occurs at the grain surface, but the decay of macroscopic magnetization is controlled by the transport of molecules to the surface. This is possible when pores are relatively large and/or surface relaxation is strong. This is called the 'slow diffusion' or 'diffusion-limited' regime. In this regime, magnetization in the pore is not uniform. This gives rise to a magnetization decay, which, in each pore, has multiexponential character, and which depends on the shape of the pore.[10]

Support for the surface-limited hypothesis comes from measurements of the temperature dependence of relaxation times in rocks.[11] Remarkably, T_1 and T_2 are nearly independent of temperature over the range 25–175 °C, at least for the modest number of rock samples studied. If NMR relaxation were in the diffusion-limited regime, the relaxation time would depend on the diffusion coefficient of the pore fluid, which is very temperature-dependent. The lack of temperature dependence is a mark of the surface-limited regime.

2.2 Surface Relaxation Mechanisms

The basic principles of NMR relaxation of fluids at solid surfaces in porous media were established by Korringa, Seevers, and Torrey (KST).[12] Two surface processes were identified. One occurs at all sites on the surface and the other is associated with dilute paramagnetic metal ion impurities on the surface. The relaxation process associated with nonmagnetic sites is much too weak to account for the observed relaxation of water in rocks.[13] Paramagnetic ions, such as iron, manganese, nickel, and chromium, are particularly powerful relaxers, and tend to control the rate of relaxation whenever they are present. Rocks primarily composed of silica (sandstones) generally have an iron content of about 1%, and also frequently contain manganese in significant concentrations; these ions make fluid proton relaxation fairly efficient. Occasionally, sandstones contain grains of magnetic minerals such as magnetite (Fe_3O_4), which are sites of relaxation. In carbonate rocks, which are composed of calcite ($CaCO_3$) and related minerals, the rate of fluid relaxation tends to be lower than in sandstones.

Considering only relaxation by dilute paramagnetic ions, the KST equations for surface relaxation in a single pore reduce to

$$\frac{1}{T_1} = \frac{Sh}{V}\frac{n_M}{T_{1M}} = \rho_1 \left(\frac{S}{V}\right)_{pore} \tag{1}$$

where S and V are the surface area and volume of the pore, h is the thickness of the surface layer within which relaxation can take place, n_M is the proportion of surface sites occupied by paramagnetic metal ions, and T_{1M} is the relaxation time of protons in molecules coordinated with paramagnetic ions. All material constants are included in the surface relaxivity parameter ρ_1, which has dimensions of m s^{-1}.

KST do not discuss T_2 in porous media. T_2 is shortened by > molecular diffusion in the inhomogeneous magnetic field arising from the magnetic susceptibility contrast between grains and pore fluid (see Section 2.3), which is unrelated to surface relaxation. However, for proton Larmor frequencies below 5 MHz and for Carr–Purcell echo spacings less than about one millisecond, the enhancement of T_2 decay coming from diffusion in inhomogeneous local fields is often negligible compared with the surface relaxation mechanism. Then[14]

$$\frac{1}{T_2} = \frac{Sh}{V}\frac{n_M}{T_{2M}} = \rho_2\left(\frac{S}{V}\right)_{pore} \tag{2}$$

The surface relaxation mechanism is treated in detail by Kleinberg, Kenyon, and Mitra.[14] Briefly, the relaxation of fluid protons at paramagnetic ion sites on the surface of rock grains is controlled by the dipolar and scalar interactions between the ion and nuclear moments. Among other things, the theory explains why T_1 and T_2 are correlated at low frequency: $T_1 \approx 1.6\ T_2$.

2.3 Molecular Diffusion in Magnetic Field Gradients

A second contribution to transverse relaxation is the diffusion of spins in static magnetic field gradients. In a uniform B_0 gradient, the contribution of this mechanism is

$$\left(\frac{1}{T_2}\right)_D = \tfrac{1}{12}D(\gamma G T_E)^2 \tag{3}$$

where D is the molecular diffusion coefficient, γ is the gyromagnetic ratio of the proton, G is the gradient strength in T m^{-1}, and T_E is the Carr–Parcell echo spacing. This equation is applicable to bulk liquids, for which the diffusion coefficient is a constant. In porous media, the diffusion coefficient is time-dependent,[15] and equation (3) must be modified.

A further complication is the presence of local magnetic field gradients, which result from the magnetic susceptibility contrast between grain material and pore fluid. Rocks typically have paramagnetic ion contents of about 1%, and grain volumetric susceptibilities (SI dimensionless) are typically $\chi_g = +10^{-4}$; grain susceptibilities of the magnetic minerals are much higher. Pore fluids are usually diamagnetic. The internal gradient is proportional to B_0. It also depends on the details of the pore geometry, and therefore varies from point to point within the pore space; some realistic models have been developed.[16,17]

The Carr–Purcell–Meiboom–Gill (CPMG) method mitigates the effect of diffusion in a magnetic field gradient. Keeping both the CPMG echo spacing and the applied magnetic field to a minimum reduces the contribution of diffusion to T_2 relaxation. At low values of B_0 typical of borehole logging tools, in the absence of an applied field gradient, and for closely spaced pulses in the CPMG measurement sequence, T_2 is dominated by surface relaxation. Diffusion effects become important when substantial field gradients are applied, and/or longer pulse spacings are used.

2.4 Bulk Fluid Processes

The last relaxation process is that of the bulk fluid itself. This occurs in the absence of grain surfaces and internal field gradients, and is unaffected by them. Bulk relaxation often can be neglected, but it is important when fluid is in very large pores and therefore is little affected by a surface. Bulk relaxation can also be important for very viscous fluids, such as heavy oils, and also can be the dominant process when the pore fluid has a high concentration of paramagnetic ions. For example, chromium lignosulfonate is a common additive in drilling fluids; chromium ion that enters the pore fluid from the borehole can dramatically reduce the observed relaxation time.

Fine particulates from the borehole can also enter the pore space. When in suspension they also reduce the fluid relaxation time, by making 'floating' solid surface area available for fluid molecules to encounter. However, it has been shown, using a novel NMR imaging technique, that this is not likely to be a problem for NMR logging tools.[18]

2.5 Pore Size Distributions and Distributions of Relaxation Times

Rocks tend to have very broad distributions of pore sizes, and therefore magnetization decays of fluids in rocks are nonexponential. In early work,[19] NMR data were analyzed in terms of two- or three-exponential decays. Later, magnetization decays of water in rock were fitted to stretched exponentials,[20] which assumes a particular form of pore size distribution. The most general way to analyze relaxation data is with a distribution (spectrum) of relaxation times: a plot of signal intensity versus relaxation time. In the following discussion, we assume that the transverse relaxation is controlled by the surface relaxation mechanism and that relaxation is surface-limited. The magnetization decay in an individual pore is then monoexponential, and does not depend on pore shape but only on the surface-to-volume ratio:

$$M(t) = M_0 \exp\left(-\frac{t}{T_2}\right) = M_0 \exp\left[-\rho_2\left(\frac{S}{V}\right)_{pore} t\right] \tag{4}$$

The time evolution of the magnetization of a sample having a distribution of pore sizes can be expressed as a sum of exponential decays:

$$M(t) = \sum_i m_i \exp\left(-\frac{t}{T_{2i}}\right) = \sum_i m_i \exp\left[-\rho_2\left(\frac{S}{V}\right)_i t\right] \tag{5}$$

where m_i is proportional to the volume of fluid relaxing at the rate $1/T_{2i}$. The sum of the volumes is proportional to the porosity ϕ:

$$M_0 = \sum_i m_i \propto \phi \tag{6}$$

Thus, in this model, there is a direct mapping from the spectrum of pore sizes, or more precisely the spectrum of surface-to-volume ratios, to the spectrum of relaxation times.

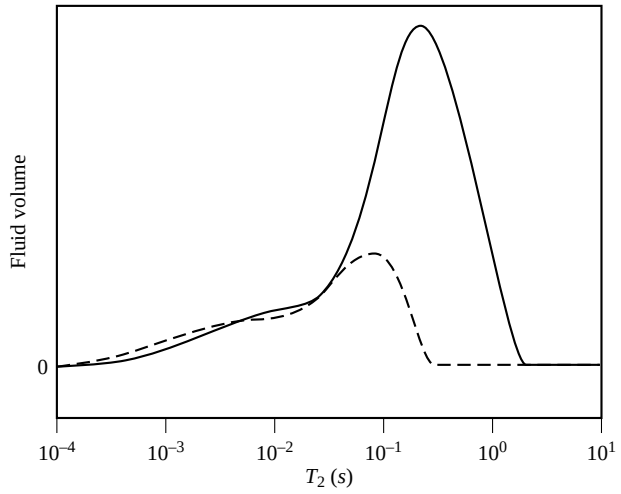

Figure 1 Distribution of relaxation times for a sedimentary rock. The spectrum is a plot of fluid volume as a function of relaxation time. Solid curve: rock fully saturated with water. Dashed curve: the same rock after centrifuging. Centrifugation drains the largest pores, and the corresponding part of the relaxation time distribution disappears. Fluid content before and after centrifuging is directly proportional to the area under the respective curve

Implicit in this discussion is the assumption that pores exist as identifiable entities. On the basis of steady state measurements such as hydraulic permeability and electrical conductivity, it is known that the pore space in rocks is well connected. However, pulse NMR is not a steady state measurement. Molecules only sample a limited volume of pore space before they are relaxed.[21] The radius of the volume sampled is approximately the root mean square distance the molecule diffuses in the NMR relaxation time, $\sqrt{6DT_1}$, the diffusion coefficient, is itself a function of observation time in porous media.[15] If there is significant coupling of pores of different sizes, the relaxation time distributions will be narrowed.[22]

A confirmation of the connection between pore size and NMR relaxation time was provided by Straley et al.[23] Rock specimens were fully saturated with water, and the spectrum of longitudinal relaxation times was determined. Then each rock was centrifuged at a number of rotor speeds. At successively higher speeds, water was progressively expelled from the samples as the centrifugal pressure overcame the capillary pressure of successively smaller pore spaces. At each step, the NMR relaxation spectrum was remeasured. At low centrifuge speed, the components with the longest T_1 disappeared from the spectrum, while the short-T_1 components were unaffected, indicating that only the largest pores had drained. As the centrifuge speed was increased, smaller pores drained and shorter components disappeared. A typical result of a similar T_2 measurement is shown in Figure 1.

The extraction of the values of m_i from the measurement data $M(t)$ poses significant mathematical problems. The inversion is not unique when $M(t)$ is noisy or when the mathematical computation has finite precision. In the past, either the number of terms in equation (5) was limited to two or three—a sparse spectrum indeed—or many terms were used, resulting in spiky, unphysical spectra. This problem can be solved by the use of regularization.[24] Regularization has the effect of smoothing the spectrum, which removes spikes and makes the inversions reproducible. The obvious disadvantages are that the distributions are artificially broadened and that real, narrow features can be filtered out of the results. To avoid problems of arbitrary smoothing, it is essential to use an algorithm that selects the regularization parameter in a data-dependent but objective manner. One such algorithm is that of Butler, Reeds, and Dawson.[25] This automatically selects a regularization parameter based on the signal-to-noise ratio of the measurement data to obtain a minimally broadened, but reproducible, inversion.

2.6 Determination of Surface Relaxivity

To relate quantitatively the NMR relaxation rate spectrum to the pore size spectrum, it is necessary to know the coefficient ρ in equations (1) and (2). Determination of the strength of the surface relaxation has proved to be elusive, because it is difficult to obtain independent information on pore size distributions of sedimentary rock.

The first problem is that the connection between a surface-to-volume distribution and a pore size distribution is poorly defined for rocks. The pore space of rocks has been modeled as spheres connected by throats, an interconnected network of tubes, and an interconnected network of sheets. None of these models has universal applicability. Thus the term 'pore size' should be understood to mean a quantity inversely proportional to the surface-to-volume ratio of a locality in the pore space.

Even more importantly, grain surfaces can have fractal character.[26] That is, the apparent surface area depends on the characteristic scale length η of the measurement. Relaxation time measurements also have characteristic scale lengths: the distance a molecule can diffuse in the shortest recovery time of an inversion-recovery measurement of T_1, or before the first spin echo of a CPMG determination of T_2.

Surface area determinations based on low-temperature adsorption of gas, e.g., the BET method,[27] probe the surface at molecular scale and are dominated by the finest features of grain surfaces. Optical microscopy of thin sections has a resolution of about $\eta = 5\,\mu$m: large pores appear to have smooth surfaces and small pores are invisible. It is not unusual to find that the surface-to-volume ratio determined by a combination of BET and buoyancy porosity methods is orders of magnitude larger than that determined by optical imaging measurements. An interesting new technique measures the surface-to-volume ratio by pulsed field gradient NMR measurements of diffusion.[28] The scale length is determined by the distance fluid molecules diffuse during the finite-length gradient pulses that tag the spins; in recent experiments,[29] $\eta = 2\,\mu$m.

The ambiguity in the determination of surface-to-volume ratio results in an ambiguity in the determination of ρ_1 and ρ_2. When the BET method is used to measure surface area and the relaxation time is determined by the initial slope method, for which $\eta < 1\,\mu$m,[21] ρ_1 is found to be in the range $0.1–0.8\,\mu$m s^{-1}. The pulsed field gradient diffusion measurements[29] yield ρ_1 in the range $3–40\,\mu$m s^{-1}. From optical imaging,[30] ρ_1 is $30–300\,\mu$m s^{-1}.

Yet another technique for determining ρ is based on capillary pressure measurements.[27,31] Differential mercury intrusion porosimetry measures a pore size distribution, on the assumption that the pore space is composed of a well-connected network of tubes of various diameters. For many

sandstones, the pore size distribution deduced from mercury porosimetry overlays the NMR relaxation time distribution.[32] These comparisons indicate that $\rho_1 = 4\,\mu\text{m s}^{-1}$ and $\rho_2 = 7\,\mu\text{m s}^{-1}$.

The relatively high values of ρ_1 found using the optical microscopy, PFG NMR, and capillary pressure methods reflect the fact that they measure not $(S/V)_{\text{pore}}$ but pore size, from which are calculated *effective* relaxivities. Sandstones can have significant amounts of clay or microporosity, which have large surface areas. BET measurements include this surface area while other methods miss it. Since large pore spaces are the dominant passages for fluid flow, the effective relaxivity ρ_{eff} is the appropriate quantity to use to convert relaxation times to pore sizes for many petrophysical applications.

3 PRACTICAL IMPORTANCE OF NMR MEASUREMENTS

3.1 T_1 versus T_2

Relaxation measurements can provide valuable information about rock formations. Unfortunately, measurements of T_1 and T_2 both have serious problems, though the problems are of very different natures. T_2 of fluids in rocks is dominated by molecular diffusion in random internal magnetic field gradients when the Larmor frequency is 10 MHz and above. This makes 'high-field' T_2 difficult to interpret. In contrast, T_1 is generally controlled by the surface relaxation mechanism, because it is unaffected by diffusion in gradients; thus interpretation of T_1 measurements is usually straightforward. However, determination of the longitudinal decay curve requires a time-consuming series of inversion–recovery measurements. For practical reasons, the time available for NMR measurements in an oil well is very limited (see Section 4.1). A CPMG determination of T_2 is much faster, and is therefore preferred.

Fortuitously, the borehole tools are not able to generate high static magnetic fields, and therefore do not generate large internal magnetic field gradients. Static field gradients are either known apparatus constants or are negligible (see Section 4). Under these conditions, transverse relaxation times are readily interpretable. Therefore, most recent work related to borehole NMR has focused on T_2 at frequencies of 2 MHz and below.

3.2 Porosity

Porosity, defined as the fraction of rock volume that can be occupied by fluid, is one of the most important parameters characterizing a hydrocarbon reservoir. In economically significant reservoirs, porosities generally range from 5% to 30%. There are many ways of measuring porosity in situ.[1,2] The speed of compressional sound waves, the scattering of neutrons, and the scattering of gamma rays are commonly measured for this purpose. However, these techniques require knowledge of the mineralogy of the solid matrix to make a determination of porosity.

NMR has the unique capability of measuring fluid-filled porosity without the need to know anything about the solid matrix. The amplitude of a proton NMR measurement is directly proportional to the amount of hydrogen in the material investigated. Protons are present in both oil and water (in approximately equal concentrations), in water associated with clay minerals, and in some matrix minerals such as gypsum (calcium sulfate hydrate). T_2 is sufficiently short in solid matrix materials, on the order of 10 μs, that the signal from protons in the matrix is lost in the deadtime of the borehole instruments. Protons in clay-bound water relax in a millisecond or less, so these generally are lost in the noise of the first one or two CPMG echoes of the borehole tools. On the other hand, relaxation times of protons in the fluids are usually greater than 10 ms, so these protons contribute significantly to the long echo trains collected by the downhole apparatus.

Pore fluids can be further subdivided into capillary-bound fluid and producible fluid. The partition depends on the pressure difference that drives fluids from the rock formation to the wellbore. This pressure is commonly around 0.7 MPa. It has been found that centrifuging sandstones at a differential pressure of 0.7 MPa depletes them of all water protons with $T_1 > 50$ ms.[23] Thus protons with $T_1 > 50$ ms (or $T_2 > 30$ ms) are associated with large pores containing 'unbound' or 'free' fluid. Although the total porosity measurement is independent of rock type, the 50 ms partition between bound and free fluid is merely typical, and depends on the surface relaxivity (see Section 2.2). Nonetheless, the estimation of producible fluid is a unique and valuable capability of NMR logging tools.

3.3 Permeability to Fluid Flow

Hydraulic permeability is one of the most difficult rock properties to estimate, because it depends sensitively on pore sizes and connectivities, which are themselves hard to measure. In simple models of porous media, the permeability is inversely proportional to the square of the surface-to-volume ratio and therefore directly proportional to the square of the NMR relaxation times, a hypothesis that has been substantiated by a large body of laboratory experiments on water-saturated sandstones.[20,33] The correlation between hydraulic permeability and NMR relaxation time appears to depend on limited variability of the surface relaxivity. Attempts to establish similar correlations for carbonates have been less successful, probably because their microgeometry is much more diverse than that of sandstones.

3.4 Measurement of Oil Content

Oil and water are generally found together in reservoir rocks. Many factors affect the NMR response of oil and water mixed in porous media:

1. the relative amounts of each phase;
2. the wettability of the grain surfaces;
3. the surface relaxivity;
4. the bulk relaxation times of each phase;
5. the extent to which the original formation fluids have been replaced by borehole fluid filtrate.

When magnetic field gradients are present (see Section 4.5), the restricted diffusion coefficients of the phases are also a factor.

The water–oil interface does not assist relaxation, so if a fluid is not in contact with grain surface, it relaxes at its

bulk liquid relaxation rate. The bulk relaxation time of oil depends on its viscosity, while the bulk relaxation time of water depends primarily on the concentration of paramagnetic ions. The proton density of an oil is generally within 10% of that of water, so its contribution to the relaxation time distribution is simply weighted by concentration.

Most reservoir rocks are thought to be hydrophilic. In such cases, droplets of oil sit in the center of pores and are unaffected by the surface. Therefore they relax at their bulk liquid relaxation time, which can be rather long if the oil has a low viscosity. In many cases, the water in contact with the grains will relax considerably faster, and there can be two distinct peaks in the relaxation time spectrum.[23] Then the amount of oil in the rock can be determined quantitatively.

When the oil is very viscous, its bulk relaxation time is shorter than the tool deadtime, and it will not be detected. Then the NMR porosity is just the water-filled porosity.[34] By subtracting the NMR porosity from a porosity measurement that is insensitive to the material properties of the oil, the quantity of oil can be obtained.

Borehole NMR measurements probe the formation to depths of 10 cm or less. In many cases, original formation fluids are flushed away from the rock near the well bore and replaced by borehole fluids ('invasion' by 'mud filtrate'). In these cases, NMR does not give information about the quantity of original oil in place. It can, however, estimate the amount of oil that will be retained in the formation after the usual recovery processes: water floods that, in fact, resemble invasion by mud filtrate, but on a larger scale. This information is useful in planning enhanced oil recovery projects.

4 INSTRUMENTATION FOR WELL LOGGING

4.1 The Borehole Environment and Field Operations

The borehole environment is unusually harsh. Boreholes drilled to extract oil are typically 20 cm in diameter and 1–10 km deep. The geothermal gradient of the Earth can give rise to temperatures of 175 °C or more, and pressures range to 140 MPa. Borehole logging tools must not only survive but must make quantitative measurements under these conditions. The requirements on electronic components exceed military specifications by a wide margin.

Borehole NMR tools must be rugged enough to survive transport in arctic, tropical, desert, and marine environments, and then a 1 m drop onto a steel surface, which typically produces a shock of $500g$. They must survive the abrasion resulting from being dragged over kilometers of rough rock face in the well bore. They must comply with laws regulating transport by aircraft and helicopter, which is of particular significance for NMR equipment containing strong permanent magnets. The conditions and space constraints are in many respects more severe than those encountered in the exploration of outer space or the ocean bottom.

During well logging operations, the drilling rig is idle. Since rig charges can be $10 000 to $100 000 per day, oil companies wish to minimize logging time. This poses a significant constraint on practical logging operations. Typically, data might be required over a depth interval of 300 m or more, with a vertical resolution of 50 cm. To be economically viable, the NMR apparatus must move continuously past the formation at a rate of 300 m h^{-1}. This means that it is necessary to measure signal amplitude and a distribution of relaxation times in 6 s, while the sample and apparatus are in motion relative to each other, at low field, and with an unprecedentedly small coil filling factor.

Skilled NMR specialists are not available for logging operations. The borehole NMR tool must be maintained, set up, and operated by field engineers, who also are responsible for other electromagnetic, acoustic, and nuclear radiation instruments that are being run simultaneously. Thus there is a large premium on instruments that can operate autonomously under conditions of continuously changing environmental conditions, including radical excursions in temperature. The NMR and electromagnetic properties of the materials presented to the apparatus also vary radically, on a timescale of seconds.

Logging tools are generally transported to the wellsite on a truck, which also carries 10 km of 7-conductor armored cable ('wireline') used to lower a string of several tools into the borehole. In present practice, the cable carries nothing but 1 kW of power and 500 kilobits s^{-1} of digital telemetry. The power budget for an individual tool is normally around 100 W, which for an NMR tool must be apportioned among transmitter, receiver, auxiliary sensors, and a downhole computer.

Laboratory NMR apparatus consists of a magnet that provides a strong, steady magnetic field that is as uniform as possible, and a radiofrequency coil that produces an oscillating magnetic field perpendicular to the static field direction. A relatively small, compact sample (which may be a human being) is placed inside the coil. It requires a leap of imagination to see how NMR measurements can be made 'inside-out' on a sample external to the apparatus.

4.2 Early Work

It was recognized at an early date that nuclear magnetic resonance could contribute to the in situ investigation of earth formations. Laboratory NMR studies of fluids in rocks, of clays, and in other porous media started in the 1950s at a number of oil company research laboratories, most notably those of Chevron and Mobil. More than three dozen patent applications for borehole NMR devices were filed between 1950 and 1960, representing work sponsored by Chevron, Schlumberger, Mobil, Texaco, and Varian. Efforts accelerated in the 1960s and 1970s. A chronological bibliography[3] is an excellent guide to the early patents and publications.

4.3 Chevron Tool

The first practical NMR borehole logging device did not use magnets and an rf coil, but instead employed free precession in the Earth's magnetic field. It was invented at the Chevron research laboratory,[35] and was subsequently commercialized by Schlumberger as the Nuclear Magnetism Tool (NMT). The NMT contains a large coil of 1000 turns of wire energized by 1 kW direct current; the power consumption prevents other tools from being used at the same time as the NMT. The current produces a spatially inhomogeneous magnetic field in the formation. The current is left on for several seconds, long enough to polarize the proton spins of the formation fluids. The

magnetization varies in magnitude and direction from point to point in the earth formation, but over a large volume the polarization is substantially greater than that associated with the Earth's field alone.

The coil current is then turned off rapidly, and the spins precess around the Earth's field direction.[36] A signal is coupled into the same coil used to polarize the spins. A bandpass filter selects the signal from hydrogen, which in any event is by far the largest signal of nuclear origin. The proton Larmor frequency in the Earth's magnetic field varies considerably with geographical location: 2.6 kHz in Canada and 1.0 kHz in Argentina. The free induction decay is often controlled by the T_2 of the rock. It can also be affected by small perturbations in the local Earth's field, such as might be caused by grains of magnetic minerals in the formation.

The deadtime of the NMT, controlled by the decay of coil current after the polarizing pulse, is about 25 ms. Most of the signal from clay-bound and capillary-bound fluid has decayed by then, so the amplitude of the remaining signal, extrapolated back to the turn-off time, is directly proportional to the producible fluid porosity ('free fluid index'). The formation response is spatially weighted and decreases rapidly with distance from the coil. Therefore the tool is calibrated in a large tank of water-saturated sand, representing a uniform formation of known porosity.

The borehole is always full of water or oil. In the absence of precautions, the received signal would be dominated by protons in the borehole, which are both closer and more numerous than those in the surrounding rock formation. To solve this problem, the borehole is 'doped' with magnetite (Fe_3O_4) grains. The magnetic grains rapidly relax protons in the wellbore. Since the grains cannot enter the formation, relaxation of protons in the pore fluid is unaffected.

The tool can make neither continuous wave nor pulsed NMR measurements. Neither T_2* not T_2 is measured with this device. T_1 can be measured by varying the polarization time, and measuring the signal amplitude at subsequent field turn-offs.

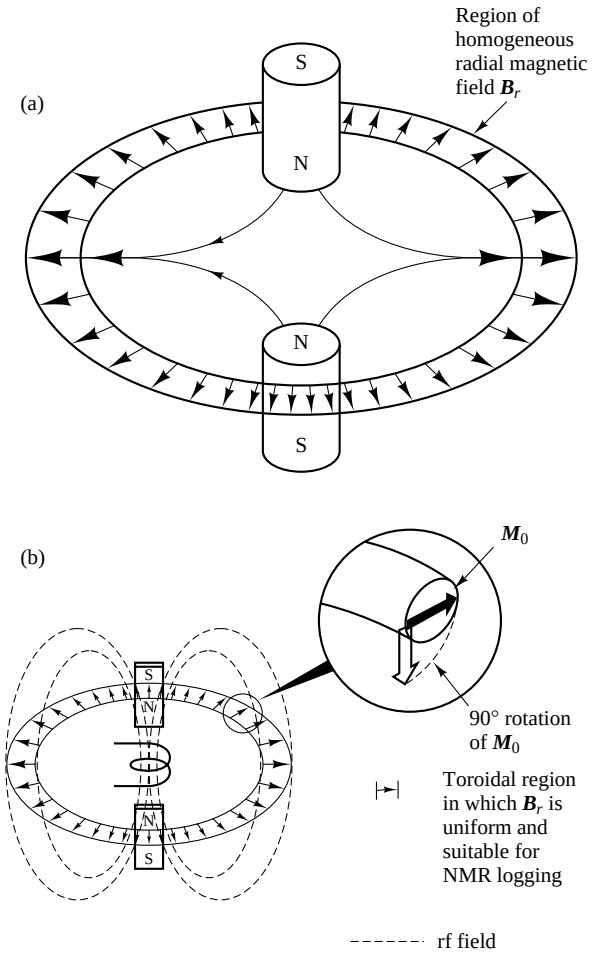

Figure 2 Schematic views of Los Alamos NMR well logging tool. (a) Static field generation. (b) rf field generation. The inset shows a cross section of the toroidal resonance region, where $\boldsymbol{B}_0$ is perpendicular to $\boldsymbol{B}_1$. (Reproduced by permission of Academic Press from J. A. Jackson et al., *J. Magn. Reson.*, 1980, **41**, 411)

4.4 Los Alamos Tool

An 'inside-out NMR' device was designed and built at Los Alamos National Laboratory (LANL);[37] the basic idea is illustrated in Figure 2. The apparatus contains two axially magnetized cylindrical bar magnets. These are placed with like poles facing each other in a cylindrical housing ('sonde'). The radial magnetic field in the transverse symmetry plane is a maximum at a distance from the sonde axis that depends on the radius and spacing of the magnets. A toroidal region of relatively uniform static magnetic field strength is created. A prototype instrument generated a static field of 12 mT in a toroid having a major diameter of 28 cm.

A radiofrequency coil is placed between the magnets, and irradiates the resonance region. In the resonance region, the rf field is perpendicular to the static magnetic field. When driven by 1 kW peak power, the coil generates an oscillating magnetic field of 0.1 mT in the resonance region. The same coil detects the NMR response of the earth formation.

Unlike the field turn-off scheme of the NMT, the LANL tool is capable of performing a variety of pulsed NMR measurements. Both inversion–recovery and Carr–Purcell–Meiboom–Gill measurements are easy to implement. Pulse lengths are comparable to those of laboratory instruments, and the 200 μs deadtime achieved at Los Alamos is adequate for relaxation measurements on rock formations.

Although the Los Alamos design was never commercialized, it attracted considerable interest in the geophysical community, and was an inspiration for a number of other tool design efforts.

4.5 NUMAR Tool

Shtrickman and Taicher invented another NMR borehole logging tool,[38] and a small company (NUMAR) commercialized the technology. A cylindrical ferrite magnet roughly 1 m long is magnetized perpendicular to its long axis. A cross-sectional view is shown in Figure 3. The field outside the magnet is purely dipolar in the transverse plane; thus the magnitude of $\boldsymbol{B}_0$ is independent of azimuth and depends only on radius.

The radiofrequency field $\boldsymbol{B}_1$ is provided by a coil wound longitudinally around the magnet, so that $\boldsymbol{B}_1$ is also transverse to the tool's long axis. Whereas a metallic magnet would

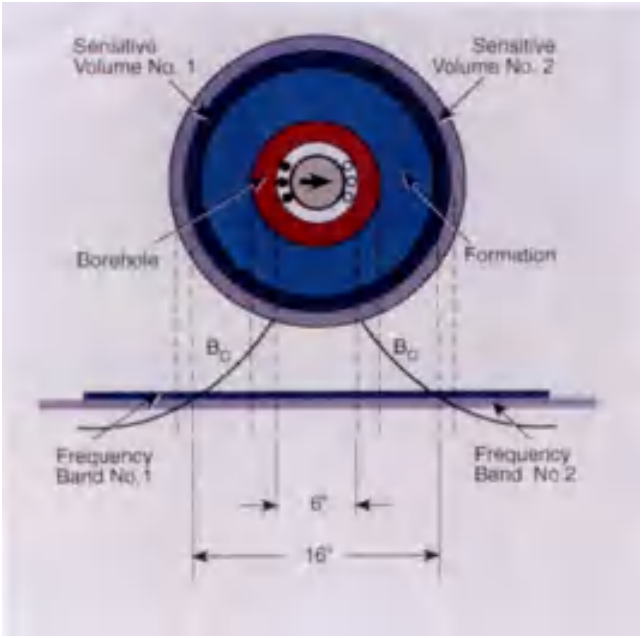

Figure 3 Cross-sectional view of the NUMAR tool. The permanent magnet is magnetized in the direction of the arrow. The tool is centered in the borehole, and the resonance region is a thin cylindrical shell. $\boldsymbol{B}_0$ is perpendicular to $\boldsymbol{B}_1$ everywhere in space. (Courtesy of NUMAR Corp.)

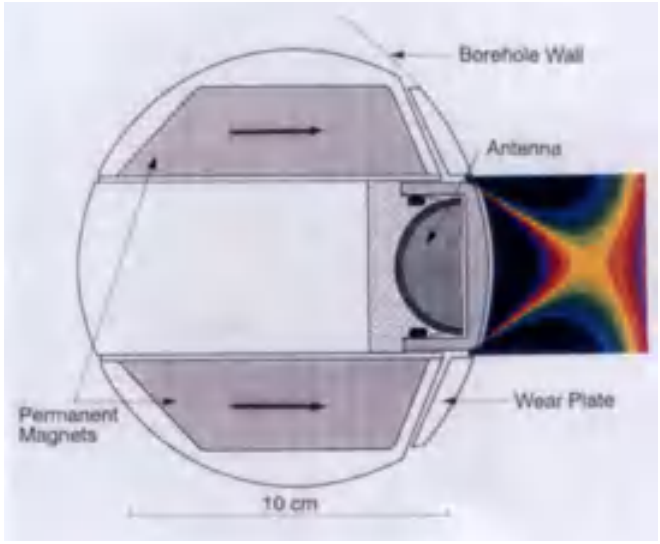

Figure 4 Cross-sectional view of the Schlumberger tool. The permanent magnets are magnetized in the direction of the arrows. The sonde is pressed against the borehole wall, and $\boldsymbol{B}_0$ is directed radially into the formation. A region of relatively homogeneous magnetic field is located inside the formation. Colors code for static field strengths: the resonance region is coded in yellow, stronger fields are coded in greens, weaker fields in reds. The antenna is in a semicircular cavity under a nonmetallic wear plate

exclude the rf field from its interior, the ferrite magnet allows free penetration of the field, improving efficiency in both transmission and reception. The windings are spaced so as to produce a dipolar field, and so, like $\boldsymbol{B}_0$, the magnitude of $\boldsymbol{B}_1$ is independent of azimuth. Because the dipoles are perpendicular to each other, $\boldsymbol{B}_1$ is perpendicular to $\boldsymbol{B}_0$ at every point in space.

The NUMAR tool is unusual in that it does not produce a region of uniform static magnetic field; to be more precise, there is no place outside the magnet where all spatial derivatives of $\boldsymbol{B}_0$ vanish. The coil may be energized at any frequency: selecting a frequency selects a thin cylindrical shell on which the resonance condition is satisfied. The cylindrical resonant shell has thickness because spin tipping is effective where $B_1 > |\boldsymbol{B}_0(r) - \boldsymbol{B}_0(r_0)|$, where $\boldsymbol{B}_0(r)$ is the static magnetic field at radius r, and r_0 is the radius at which the resonance condition is exactly satisfied. Thus, the larger the B_1, the thicker the shell from which signal is obtained. The resonance frequency is selected to be between 0.5 and 1 MHz, with resonant shell radii $r_0 = 0.23$ and 0.18 m, respectively. $\mathrm{d}B_0(r_0)/\mathrm{d}r = 0.25\,\mathrm{T\ m^{-1}}$, and the shell is 2.5 mm thick. Volume selection allows CPMG sequences to be collected continuously without waiting for longitudinal recovery: the tool hops between two or more frequencies, resonating separate shells during successive sequences.

The applied gradient of $0.25\,\mathrm{T\ m^{-1}}$ is considerably larger than typical internal gradients due to magnetic susceptibility contrast between grains and pore fluids of rocks. Diffusion in the magnetic field gradient is an important contribution to transverse relaxation, and must be taken into account explicitly in understanding the measurements. Since the magnetic field gradient is known, an effective diffusion coefficient can be estimated by varying the CPMG pulse spacing. Extrapolating the pulse spacing to zero allows estimation of the part of T_2 that is due to surface relaxation.

4.6 Schlumberger Tool

Schlumberger has developed a novel tool design for NMR logging.[39] Unlike the other tools, the sonde is pressed against the borehole wall; the length of the wall-engaging section is about 40 cm. A cross sectional view of the Schlumberger logging sonde is shown in Figure 4. Two samarium cobalt magnets are magnetized in the same direction, transverse to the sonde axis. The static magnetic field is predominantly radial into the formation. The figure shows a contour plot of the total field strength in the plane transverse to the borehole axis. The field has a saddle point about 25 mm inside the formation; at this location, all three spatial derivatives of $\boldsymbol{B}_0$ are zero. The field strength in the resonant region is 55 mT, so the Larmor frequency is 2.3 MHz.

The antenna used to radiate the formation at the resonance frequency is placed in a semicircular cylindrical cavity on the face of the sonde. The antenna is essentially a half coaxial cable 15 cm long that irradiates the formation with a field transverse to the static field. It is loaded with ferrite and has a high Q, which is desirable for the reception of weak signals from the nuclear spin system. The field produced by the antenna is not particularly homogeneous over the resonance region; inhomogeneity of $\boldsymbol{B}_1$ is acceptable, so long as error-correcting pulse sequences such as the Carr–Purcell–Meiboom–Gill sequence are used. The antenna resides underneath a wear plate, which is the only nonmetallic surface on an otherwise all-metal sonde. Magnetoacoustic ringing of metal structures, which would increase the deadtime of the instrument, is suppressed.

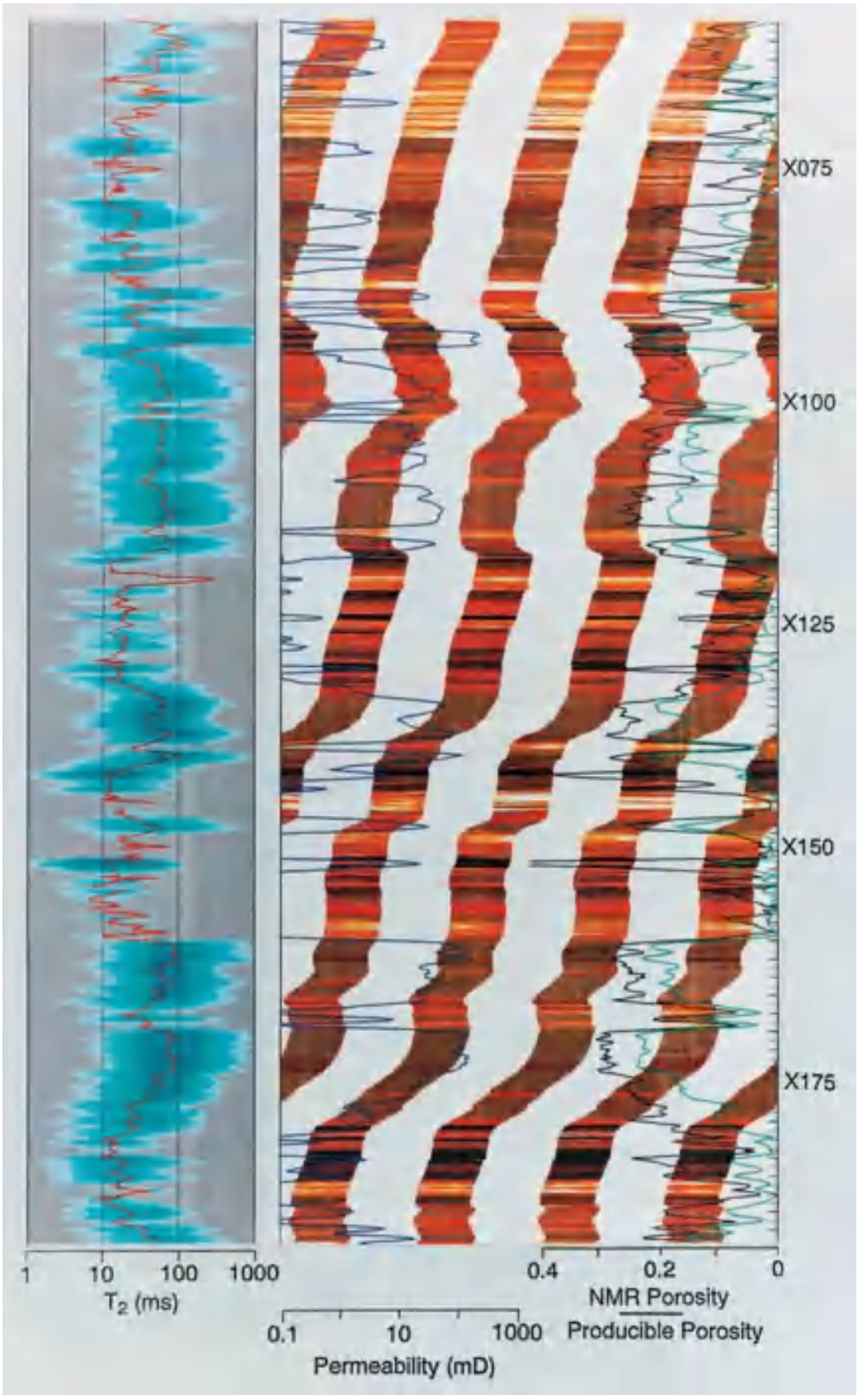

Figure 5 NMR well log. Left panel: A log of the transverse relaxation time distribution is shown in blue, darker color indicating higher amplitude. The red line is the logarithmic mean of T_2. Right panel: The variegated orange and brown background is an unwrapped electrical image of the borehole wall, showing fine statigraphic features. NMR porosity is shown as a black curve, producible fluid porosity is shown as a green curve, and permeability to fluid flow is shown as a blue curve. The curves are explained fully in the text. The depth scale is in feet; the most significant figure has been replaced by X (Reproduced by courtesy of Schlumberger)

4.7 Log Example

A well log consists of the readings of one or more borehole logging tools plotted as a function of depth. Figure 5 is an example of an NMR well log. The vertical scale is depth, marked in feet. The left panel is a presentation of the spectrum of transverse relaxation times; the horizontal scale is T_2 in milliseconds. Higher amplitude is coded as darker color. This is an indicator of pore size distribution: for example, high amplitude at short relaxation times indicates a formation with relatively small pores. The red line is the logarithmic mean of T_2, $T_{2\mathrm{LM}}$:

$$T_{2\mathrm{LM}} = \exp\langle \log T_2 \rangle = \exp\left(\frac{\sum_i m_i \log T_{2i}}{\sum_i m_i} \right) \tag{7}$$

On the right panel is an electrical image of the borehole created by the Formation Microscanner (FMS). The FMS measures the local electrical conductivity using a number of small electrodes placed in contact with the borehole wall by retracting arms. Darker colors indicate high electrical conductivity, usually associated with the presence of saline water or clay. Lighter colors indicate low conductivity, and suggest low porosity or the presence of oil. The resulting electrical image of the borehole is unwrapped: the 0° azimuth is at the left edge of the panel and the 360° azimuth is at the right. The blank stripes represent areas of the borehole wall that are not in contact with the four arms of the tool. The stripes change azimuth slowly because the tool rotates as it is pulled up.

The NMR logs overlay the FMS image. By convention, porosity is plotted on the right-hand side of the panel and increases to the left, while hydraulic permeability is plotted on the left-hand side of the panel and increases to the right. The total NMR porosity is shown in black and the producible fraction of the porosity in green. Zones with small pores have low producible porosity, even when the total porosity is high. The permeability to fluid flow (measured in millidarcies, mD) is computed using the empirical equation

$$k = (2.25 \times 10^6 \text{ mD s}^{-2})\phi^4 T_{2\mathrm{LM}}^2 \tag{8}$$

where ϕ is the porosity. The permeability is plotted on a logarithmic scale, and changes by orders of magnitude from one zone to the next. In this powerful combination of measurements, the FMS gives a high-resolution stratigraphic image of the subsurface, while NMR provides quantitative producibility information.

5 RELATED ARTICLES

Diffusion in Porous Media; Microporous Materials and Xenon-129 NMR; Oil Reservoir Rocks Examined by MRI; Terrestrial Magnetic Field NMR.

6 REFERENCES

1. J. R. Hearst and P. H. Nelson, *Well Logging for Physical Properties*, McGraw-Hill, New York, 1985.
2. D. V. Ellis, *Well Logging for Earth Scientists*, Elsevier, New York, 1987.
3. J. A. Jackson and M. Mathews, *Log Anal.*, 1993, **34**(3), 35.
4. C. Chardaire-Riviere and J.C. Roussel, *Rev. Inst. Fr. Pet.*, 1992, **47**, 503.
5. W. E. Kenyon, *Nucl. Geophys.*, 1992, **6**, 153.
6. *Magn. Reson. Imaging*, 1991, **9**(5), entire issue; *Magn. Reson. Imaging*, 1994, **12**(2), entire issue.
7. F. Bloch, *Phys. Rev.*, 1951, **83**, 1062.
8. R. J. S. Brown and I. Fatt, *Petrol. Trans. AIME*, 1956, **207**, 262.
9. M. H. Cohen and K. S. Mendelson, *J. Appl. Phys.*, 1982, **53**, 1127.
10. K. R. Brownstein and C. E. Tarr, *Phys. Rev. A*, 1979, **19**, 2446.
11. L. L. Latour, R. L. Kleinberg, and A. Sezginer, *J. Colloid Interface Sci.*, 1992, **150**, 535.
12. J. Korringa, D. O. Seevers, and H. C. Torrey, *Phys. Rev.*, 1962, **127**, 1143.
13. F. D'Orazio, S. Bhattacharja, W. P. Halperin, K. Eguchi, and T. Mizusaki, *Phys. Rev. B*, 1990, **42**, 9810.
14. R. L. Kleinberg, W. E. Kenyon, and P. P. Mitra, *J. Magn. Reson., Ser. A*, 1994, **108**, 206.
15. L. L. Latour, P. P. Mitra, R. L. Kleinberg, and C. H. Sotak, *J. Magn. Reson., Ser. A*, 1993, **101**, 342.
16. P. Le Doussal and P. N. Sen, *Phys. Rev. B*, 1992, **46**, 3465.
17. R. J. S. Brown and P. Fantazzini, *Phys. Rev. B*, 1993, **47**, 14 823.
18. E. J. Fordham, A. Sezginer, and L. D. Hall, *J. Magn. Reson., Ser. A*, 1995, **113**, 139.
19. A. Timur, *J. Petrol. Tech.*, 1969, **21**, 775.
20. W. E. Kenyon, P. I. Day, C. Straley, and J. F. Willemsen, *Soc. Petrol. Eng. Form. Eval.*, 1988, **3**, 622; erratum: *Soc. Petrol. Eng. Form. Eval.*, 1989, **4**, 8.
21. W. P. Halperin, F. D'Orazio, S. Bhattacharja, and J. C. Tarczon, in *Molecular Dynamics in Restricted Geometries*, eds. J. Klafter and J. M. Drake, Wiley, New York, 1989, Chap. 11
22. K. R. McCall, D. L. Johnson, and R. A., Guyer, *Phys. Rev. B*, 1991, **44**, 7344.
23. C. Straley, C. E. Morriss, W. E. Kenyon, and J. J. Howard, in *Transactions of the SPWLA 32nd Annual Logging Symposium, 1991*, Paper CC.
24. D. P. Gallegos and D. M. Smith, *J. Colloid Interface Sci.*, 1988, **122**, 143.
25. J. P. Butler, J. A. Reeds, and S. V. Dawson, *SIAM J. Numer. Anal.*, 1981, **18**, 381.
26. A. H. Thompson, *Annu. Rev. Earth Planet. Sci.*, 1991, **19**, 237.
27. S. Lowell and J. E. Shields, *Powder Surface Area and Porosity*, Chapman and Hall, New York, 1984.
28. P. P. Mitra, P. N. Sen, L. M. Schwartz, and P. Le Doussal, *Phys. Rev. Lett.*, 1992, **68**, 3555.
29. M. D. Hurlimann, K. G. Helmer, L. L. Latour, and C. H. Sotak, *J. Magn. Reson. Ser. A*, 1994, **111**, 169.
30. J. J. Howard, W. E. Kenyon, and C. Straley, *Soc. Petrol. Eng. Form. Eval.*, 1993, **8**, 194.
31. J. D. Loren and J. D. Robinson, *Soc. Petrol. Eng. J.*, 1970, **10**, 268.
32. C. E. Morriss, J. MacInnis, R. Freedman, J. Smaardyk, C. Straley, W. E. Kenyon, H. J. Vinegar, and P. N. Tutunjian, in *Transactions of the SPWLA 34th Annual Logging Symposium, 1993*, Paper GGG.
33. G. C. Borgia, G. Brighenti, P. Fantazzini, G. D. Fanti, and E. Mesini, *Soc. Petrol. Eng. Form. Eval.*, 1992, **7**, 206.
34. C. H. Neuman and R. J. S. Brown, *J. Petrol. Tech.*, 1982, **34**, 2853.
35. R. J. S. Brown and B. W. Gamson, *Petrol. Trans. AIME*, 1960, **219**, 199.

36. A. Abragam, *Principles of Nuclear Magnetism*, Clarendon Press, Oxford, 1961, p. 64–65.
37. R. K. Cooper and J. A. Jackson, *J. Magn. Reson.*, 1980, **41**, 400; L. J. Burnett and J. A. Jackson, *J. Magn. Reson.*, 1980, **41**, 406; J. A. Jackson, L. J. Burnett, and J. F. Harmon, *J. Magn. Reson.*, 1980, **41**, 411.
38. Z. Taicher, G. Coates, Y. Gitartz, and L. Berman, *Magn. Reson. Imaging*, 1994, **12**, 285.
39. R. L. Kleinberg, A. Sezginer, D. D. Griffin, and M. Fukuhara, *J. Magn. Reson.*, 1992, **97**, 466.

Biographical Sketch

Robert L. Kleinberg. *b* 1949. B.S., 1971, chemistry, University of California, Berkeley. Ph.D., 1978, physics, University of California, San Diego. Postdoctoral physicist, Exxon Research, 1978–80. Schlumberger-Doll Research, 1980–present. Approx. 50 publications, 10 US patents. Research specialties: borehole instrumentation (ultrasonics, electrical resistivity, nuclear magnetic resonance, gravimetry) and NMR properties of rocks and other porous media.

Laser Devices in NMR: Routes to Chaos

E. Brun

University of Zürich, Zürich, Switzerland

1	Introduction	1
2	Time Series and Embeddings	1
3	Chaos in the Parameter Modulated Laser	2
4	Control of Chaotic Flow	5
5	Summary and Outlook	7
6	Related Articles	8
7	References	8

1 INTRODUCTION

It has been a remarkable finding that low-dimensional nonlinear systems, upon sweeping a control parameter, show a rich variety of modes of collective behavior. Besides fixed points and limit cycles, seemingly irregular behavior can often be observed in various regions of the parameter space. This so-called chaos is highlighted by the fact that the detected noise-like irregularities are a form of order which can be reached over universal routes: period-doubling bifurcations, intermittency, and quasi-periodicity—the scenarios of deterministic chaos.[1,2]

Noisy behavior arising from stochastic driving forces—mechanical, electrical, thermal fluctuations, for example—is a common facet of daily laboratory practice. However, the phenomena to be discussed in this article concern deterministic chaotic behavior. Noise and chaos are both related to randomness. A seeming paradox is that the chaotic randomness is generated by fixed rules without any element of chance. In principle, the future of a chaotic but noiseless dynamical system is predictable from the past; however, in practice small initial uncertainties are strongly amplified so that even if the behavior is predictable in the short term, it is unpredictable in the long term. That sensitivity to initial conditions is the crucial feature of chaotic behavior. The paradigm of chaos thus means that two orbits starting at a distance, ε, much smaller than the typical size of the region visited during the motion, diverge exponentially in time, so that their separation after a time t will be of the order of $\varepsilon e^{\lambda t}$ with λ a positive, real number. This makes long-time predictions virtually impossible. A suitable average of the exponential growth rate λ, the Lyapunov exponent, represents one of the most common indicators of chaotic behavior.[3] This instability does not prevent the system trajectories from remaining confined in a bounded domain of phase space when the nonlinearity provides a sufficiently strong folding mechanism. Hence, chaotic motion does admit contraction: accordingly, each of the d directions of phase space carries a Lyapunov exponent λ_i ($i = 1, \ldots, d$). The signature for chaos is the positivity of at least one of them. The sum γ of the Lyapunov exponents represents the volume variation rate in time as $V(t) \approx V(0) \exp(\gamma t)$. Conservative motion is characterized by $\gamma = 0$, and dissipation by $\gamma < 0$.

The combined effect of stretching and folding in dissipative systems, such as lasers, is responsible for the creation of strange attractors. These objects are invariant under the dynamics and exhibit a dimension D which, besides being smaller than that of the phase space, can take noninteger values. The evaluation of such a fractal dimension[4] has been one of the most popular characterizations of strange attractors in the last decade.[5,6]

Related to the values of Lyapunov exponents and dimensions is the Kolmogorov–Sinai or metric entropy. This chaos indicator is a measure of the average information about the initial conditions obtained by observing the motion on a strange attractor in a unit time. In fact, all initial conditions belonging to a small domain of size $\varepsilon > 0$ will evolve into distinguishable states after a finite time t, because of the exponential divergence of nearby orbits.

The above average indicators (Lyapunov exponents, fractal dimensions, and metric entropies) provide just a global characterization of the dynamics. In order to gain more detailed information about the chaotic behavior, one thus started to look for the recurrent properties of strange attractors, in particular by considering its unstable periodic orbits.[7] In fact, chaotic motion can be seen as an aperiodic wandering among an infinity of unstable periodic orbits, remnants of attracting cycles that bifurcated as a consequence of some parameter change in the system. The newly generated stable cycles undergo the same fate upon further variation of the external conditions until a strange attractor is left. The unstable cycles can be seen as a sort of skeleton supporting the dynamics in phase space. In particular, they provide an invariant topological characterization of the dynamics. It has been proposed to use their knowledge to obtain a more accurate and complete description of the system. To this end, the unstable periodic orbits are encoded by means of sequences of symbols from a finite alphabet and on a hierarchical ordering of them, yielding a symbolic dynamics.

In this article, we review the status of quantitative chaos analysis using the NMR laser (see ***Ruby NMR Laser***) as a test system. The systematic research started in 1982 after the first observation of chaos in that device.[8] The proof of the existence of low-dimensional chaos requires from the experimenter the quantitative determination of the discussed numerical and topological properties. Since noise can never be excluded in real world systems, the aims of the studies have been directed towards the clear distinction between stochastic and deterministic irregular behavior. However, the separation of noise and chaos in experiments or simulations is not a straightforward task. Testing the chaos quantitatively needs not only a well behaved physical system but sophisticated computer tools for executing the measurements, recording the data, and analyzing and displaying the experimental results. The ruby NMR laser has been found to be an almost ideal system that meets the requirements to separate deterministic behavior from thermal noise.

In the course of time we have studied various NMR laser devices showing typical routes to chaos.[9–11] Among them we have the laser with delayed feedback (LDF), the laser with an injected (rf) signal (LIS), and, in particular, the parametrically modulated laser (PML), which will be discussed at some length in the following sections. We want to demonstrate the excellent agreement between theoretical modeling and experiment.

2 TIME SERIES AND EMBEDDINGS

The quantitative analysis of the regular (periodic) and chaotic (nonperiodic) output of the NMR laser is performed on its stroboscopically observed amplitude. To this end, the rf laser signal is rectified, and its value $v(t)$ is measured at discrete time coordinates t_k. This way, a time series $\{x_k\}$ is formed, where $x_k = v(k\ \Delta t)$ is the value of the sampled output v at the time $t_k = k\ \Delta t$, $k = 1, 2, \ldots$. with Δt an appropriate strobing time unit. $\{x_k\}$ is stored in a computer memory for further analysis and display. Figure 1 shows the time plot of a chaotic time series from the NMR laser.

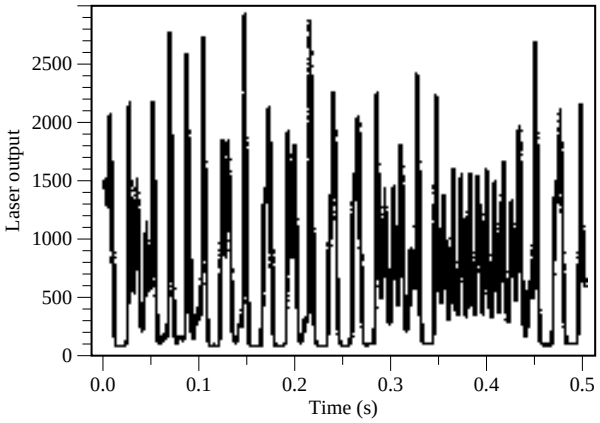

Figure 1 Real time dependence of the output $v(t)$ of the NMR laser with Q modulation

A faithful reconstruction of the dynamics is obtained by embedding the scalar time series in a Euclidean space with a sufficiently large dimension E.[12] This is usually achieved by forming vectors of the type $\boldsymbol{x}_k = (x_k, x_{k\pm\tau}, x_{k\pm2\tau}, \ldots, x_{k\pm(E-1)\tau})$. Their coordinates are time delayed values of a single observable with τ a suitable time delay index. With an infinite amount of noise-free data, this representation is diffeomorphic to the original phase space if $E \geq 2D + 1$, where D is the dimension of the strange attractor. Limitations in both precision and number of the data require a careful choice of the delay time τ. Usually, a good compromise is $\tau \approx T_0/(4\ \Delta t)$, where T_0 is the shortest characteristic time of the deterministic (i.e. noise-free) dynamics: for example, the length of the shortest unstable periodic orbit. In systems subjected to a periodic external force $\boldsymbol{A}(t)$, T_0 is just the natural period of $\boldsymbol{A}$.

3 CHAOS IN THE PARAMETER MODULATED LASER

The discussions in the related article ***Ruby NMR Laser*** indicate that the onset of chaos in the NMR laser is prevented within the accessible parameter space of the system. In fact, the system can be described by a set of only two ordinary differential equations. However, if an external driving is applied, for example in the form of a sinusoidal modulation of a system parameter, the additional degree of freedom makes chaotic behavior possible. Experimentally, this has been

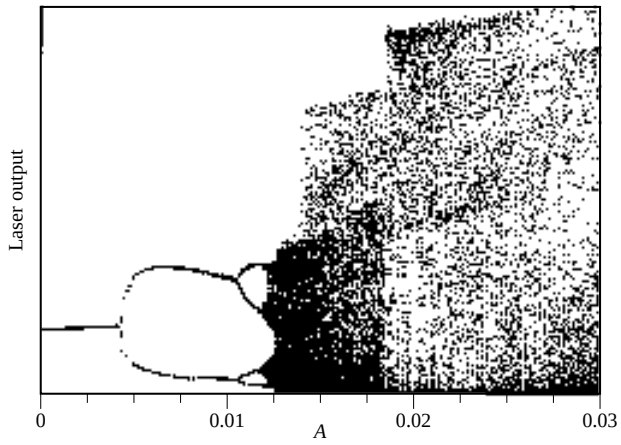

Figure 2 Bifurcation diagram for the Q-modulated NMR laser obtained by sweeping down the forcing amplitude A

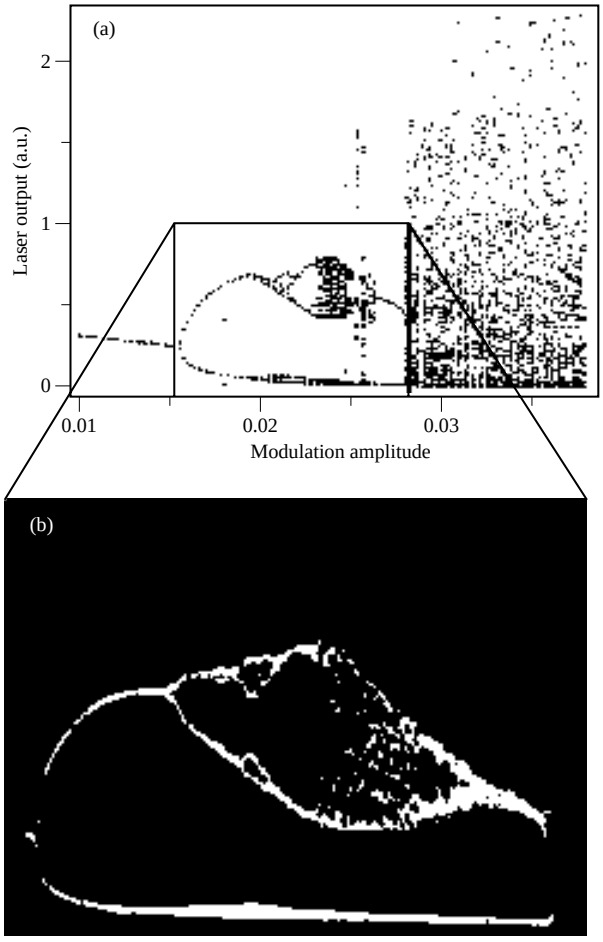

Figure 3 Bifurcation diagrams, as in Figure 2, but with a different forcing frequency. The diagram from the EBL model (a) should be compared with an early experimental one (b) observed on the oscilloscope screen

realized by varying a system parameter p in time according to $p(t) = p_0(1 + A \cos \omega_m t)$, where the modulation frequency $\nu_m = \omega_m/2\pi$ is chosen in the range [20,150] Hz, i.e. close to the

relaxation frequency $\nu_{rel} \approx 67.7$ Hz of the free running laser. The response of the driven laser has mainly been studied by modulating the quality factor Q. This offers favorable running conditions where rather weak forcing signals may lead to chaos. In fact the amplitude A lies in the range [0,0.03]. In this work, we survey experiments conducted with the Q-modulated NMR laser which is called PML. This type of forcing is accomplished by varying the resistance of the NMR circuit. In the rescaled variables (x,y,z) of equation (14) in ***Ruby NMR Laser***, the extended Bloch laser (EBL) model takes the form

$$\dot{x} = -\sigma(x/f(t) - y) \tag{1a}$$

$$\dot{y} = -y(1 + ay) + rx - xz \tag{1b}$$

$$\dot{z} = -bz + xy \tag{1c}$$

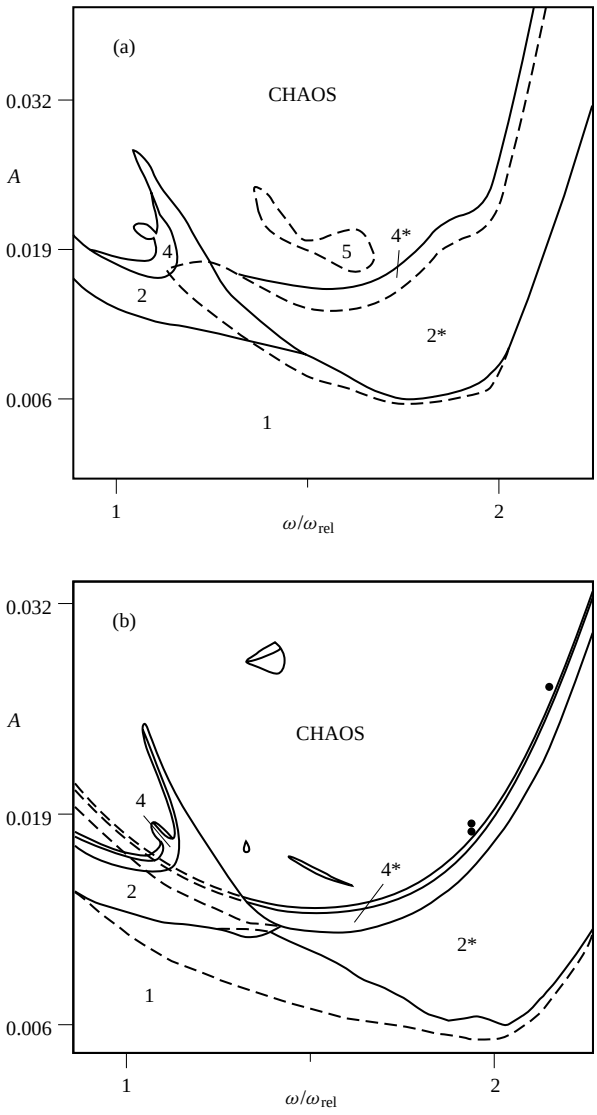

Figure 4 Phase diagrams for the Q-modulated NMR laser: (a) experiment and (b) EBL model. The lines depict boundaries between different attractors in the (A,ω) plane. The main regions with stable periodic motion are indicated. The periods 2 and 4 labeled by an asterisk are distinct from the unlabeled ones. Notice the coexistence of different types of motion in a few regions. The solid circles in (b) indicate the parameter values for which the periodic orbit analysis of chaos has been carried out

where $f(t) = 1 + A \cos \omega t$ and $\omega = \omega_m/\gamma_\perp$ is the rescaled modulation frequency. Equation (1a)–(1c) are the basis to model PML chaos.

3.1 Conventional Analysis of PML Chaos

A common visualization of the transition to chaos consists of a bifurcation diagram, where values $v(t_k)$ of the output, measured at equally spaced times $t_k = k\ \Delta t$, are reported as a function of the control parameter, after transients have died out. The plot in Figure 2 has been obtained by sweeping the amplitude A at a fixed frequency ω. A period-doubling cascade is clearly visible, with the first bifurcations occurring at $A \approx 0.0047$ (period $1 \rightarrow 2$), $A \approx 0.0105$ (period $2 \rightarrow 4$), and $A \approx 0.0117$ (period $4 \rightarrow 8$). The abrupt expansions of the region visited by the trajectory (at $A \approx 0.014$ and $A \approx 0.018$) are crises. Very similar diagrams have been obtained from the EBL model. In Figure 3, an early experimental observation on the oscilloscope screen [Figure 3(b)] can be compared with the corresponding simulation [Figure 3(a)]. The agreement between experiment and the EBL model is once more confirmed.

A more significant test is provided by the comparison between phase diagrams, i.e. graphical representations of the types of motion (either stable periodic or chaotic) exhibited

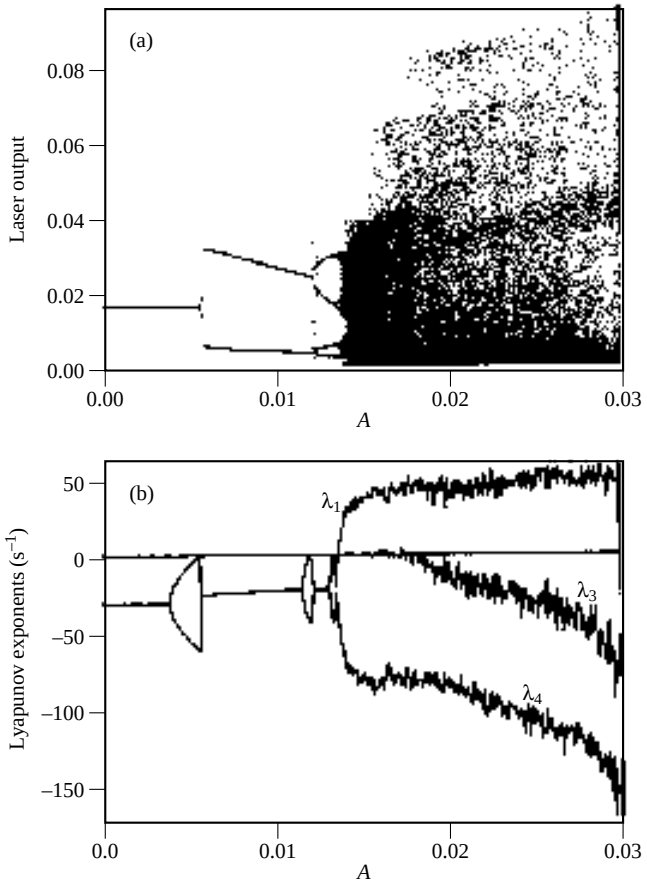

Figure 5 Computed bifurcation diagram (a) for the Q-modulated NMR laser and the corresponding average Lyapunov exponents (b) from the EBL model. The second Lyapunov exponent λ_2 (not indicated) is identically zero

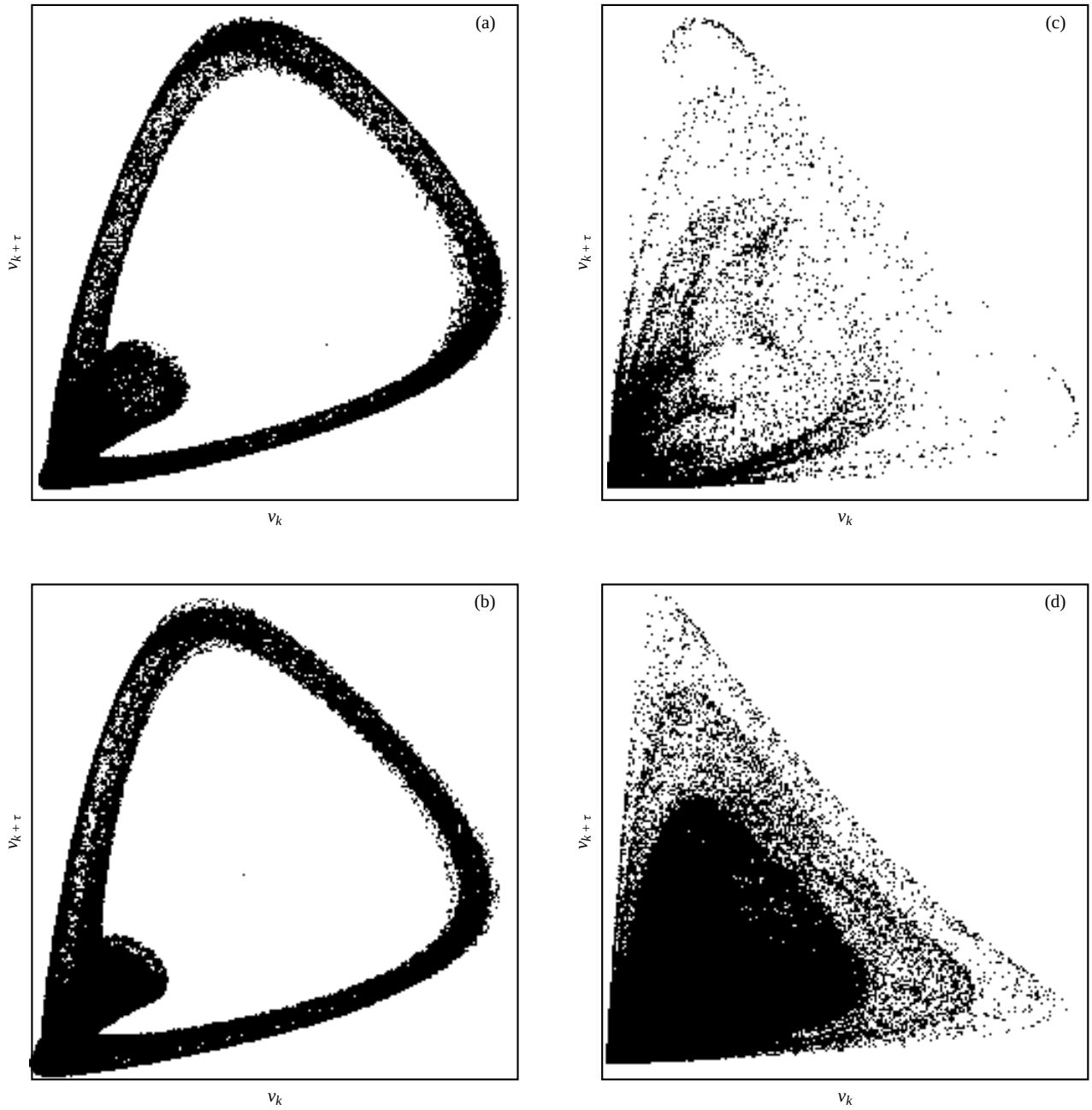

Figure 6 Comparison of two-dimensional projections ($v_{k+\tau}$ versus v_k) from (a, c) the PML and (b, d) the EBL model

by the system in an extended portion of the (ω,A) plane. In Figure 4, we report experimental and EBL diagrams, where the main islands of stable periodic behavior are indicated together with the large chaotic region. Multistability occurs quite often. Most of the structure in the two parts of Figure 4 coincides, although some discrepancy exists (probably caused by uncertainty about the value of the other model parameters).

The experimental bifurcation behavior of the PML renders data for more severe tests of the EBL model. To this end, we performed simulations of bifurcations along the roads to chaos using the same strategy and parameters as in the experiments. The EBL equations [equation (1)] were numerically solved and the results analyzed for comparison with experimental data. Figure 5(a) depicts the computed bifurcation diagram, where A is swept up in small sequential steps $\Delta A = 0.0002$ in the interval [0,0.03]. Indeed, the EBL model yields the main chaotic features that can be observed in the experiment shown in Figure 2.

In addition to the bifurcation diagram, the behavior of the Lyapunov exponents (λ_1,λ_2,λ_3) was also determined from the EBL model when A is varied in the range [0,0.03]. The result is shown in Figure 5(b). The largest Lyapunov exponent λ_1 gets positive: $\lambda_1 \approx 40\,\mathrm{s}^{-1}$ for $A \geq 0.0148$, which indicates the onset of deterministic chaos. Note in Figure 5(b) the splitting of λ_1 and λ_3 ($\lambda_2 = 0$) at $A = 0.0038$ and $A = 0.0118$, respectively, reflecting a precursor of a bifurcation with $\lambda_1 = 0$ at some higher value of A. The value $\lambda_1 = 40\,\mathrm{s}^{-1}$ obtained from the EBL model has been confirmed experimentally. It agrees with

the Lyapunov exponent derived from an embedded time series recorded directly from the NMR laser at $A \approx 0.0145$.

The methods of determining the conventional chaos indicators for the NMR laser (Lyapunov exponents, fractional dimensions, and metric entropies) cannot be discussed in this article. The interested reader should consult the respective literature.[13–15]

The large chaotic region in Figure 4 is not uniform. Chaotic attractors of a quite different geometrical structure and with fractal information dimensions D_1 between 2.10 and 2.60 can be found. The distinct geometrical features may be visualized with two-dimensional projections in the embedding space. To this end, we show in Figure 6 the signal ($v_{k+\tau}$ versus v_k) obtained from the experiment [Figure 6(a) and (c)] and the EBL equations [Figure 6(b) and (d)]. The scaled attractor in Figure 6(a) and (b) is roughly of the same size as the high density region in Figure 6(c) and (d). Figure 6(a) and (b) illustrate the marginal chaos after a sequence of period-doubling bifurcations (the Feigenbaum scenario), whereas Figure 6(c) and (d) show the same attractor after two crises. Again simulation and experiment show a remarkable agreement: not in the details but in the topology.

3.2 Periodic Orbit Analysis

The motion on a strange attractor is deeply influenced by the existence of an infinity of unstable periodic orbits. The aperiodic trajectory describing the evolution of the system is attracted to any one of these when it approaches the stable manifold and is repelled to some other region when it finds itself in the vicinity of the unstable one. Because of its invariance under smooth coordinate changes, the set of unstable periodic orbits provides a topological characterization of the dynamics which facilitates the testing of a faithful mathematical model from the observation of even a single scalar time series. Not only must the number and length of the periodic orbits agree, but also their shape and the probability with which the aperiodic trajectory of the chaotic system visits their neighborhoods.

The periodic orbit analysis has been applied simultaneously to the NMR laser and its EBL model. Time series of the laser output, consisting of $N = 8 \times 10^5$ points, have been recorded with a sampling rate $\nu_s = 25/T_0$, where $T_0 = 2\pi/\omega$ is the period of the forcing term: hence, we collected $n_p = 25$ points per driving period. The dimensionless delay time index for the embedding was $\tau = 5$. Hence, the embedding window $E\tau$ covers just one period for an embedding dimension $E = 5$. All unstable periodic orbits up to order 9 (i.e. of period $9T_0$) have been located. For illustration, we show in Figure 7 a period-5 orbit superimposed on the underlying strange attractor.

A Newton method has been used to detect the periodic orbits of the EBL model. All cycles up to order 9 have been compared with the experimental ones and found to agree very well for all E between 6 and 16.[16]

In a first step towards a hierarchical classification of the dynamics of the NMR laser, we have constructed Poincaré sections Σ in embedding space by considering points $\boldsymbol{x}_i$ which lie n_p time units apart from one another. Two-dimensional projections of the strange attractor in Σ are shown in Figure 8. The coordinates from the experimental [Figure 8(a) and (a′)] and numerical [Figure 8(b) and (b′)] time series are shown for

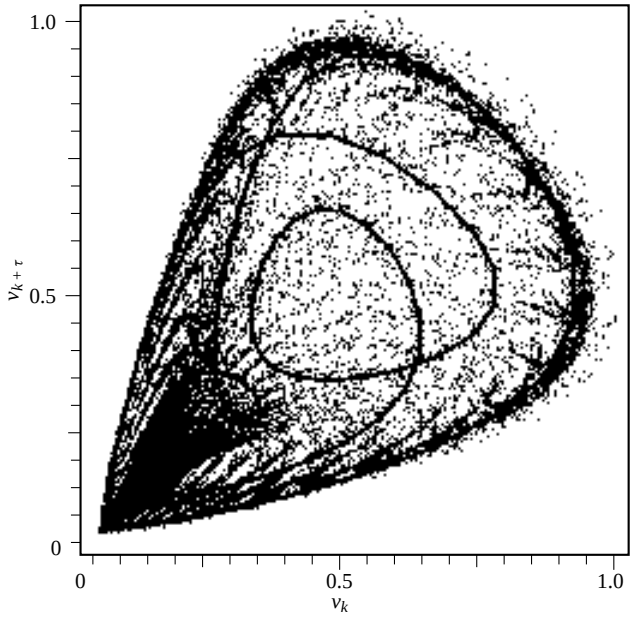

Figure 7 Two-dimensional projection of the unstable period-5 orbit superimposed on the strange attractor

$A = 0.018$ and $\omega = 0.03168$. The intersection points of a period-3 orbit [Figure 8(a) and (b)] and of a period-9 orbit [Figure 8(a′) and (b′)] with Σ are indicated by open circles. Notice the striking similarity between the two data sets.

The identification of unstable periodic orbits may also be used for the study of so-called crises.[17,18] These are sudden changes, as seen in Figure 2, occurring in strange attractors when a control parameter reaches some critical value A_c. It has already been mentioned that the NMR laser shows several phenomena of this type when the control parameter A is slowly increased, and this in a wide range of frequency values.

4 CONTROL OF CHAOTIC FLOW

The knowledge of the periodic orbit structure makes it possible to constrain the motion on a strange attractor to the close neighborhood of some unstable periodic orbit. This practice is called intelligent control, and is usually carried out by applying small, carefully chosen, perturbations to a control parameter. The method, originally proposed by Ott, Grebogi, and Yorke (OGY),[19] requires that the displaced trajectory lies as close as possible to the stable manifold of the target orbit γ. In a practical implementation, after having located the selected orbit in a suitable embedding space, it is necessary to approximate the flow around it by means of a matrix $\mathbf{M}$ (usually estimated through a least squares fit). It is further assumed that the target orbit is of the saddle type, so that its invariant manifolds can be identified with the eigendirections of the matrix $\mathbf{M}$ in an ε ball centered at some reference point x_F on γ. The dependence of the motion on a control parameter p is simply evaluated by comparing $\gamma(p = 0)$ with the perturbed orbit $\gamma(p)$ which is also to be extracted from the observed data. This method presents a few distinctive features: the knowledge of the underlying exact equations is not needed, although effective use of the linearized dynamics

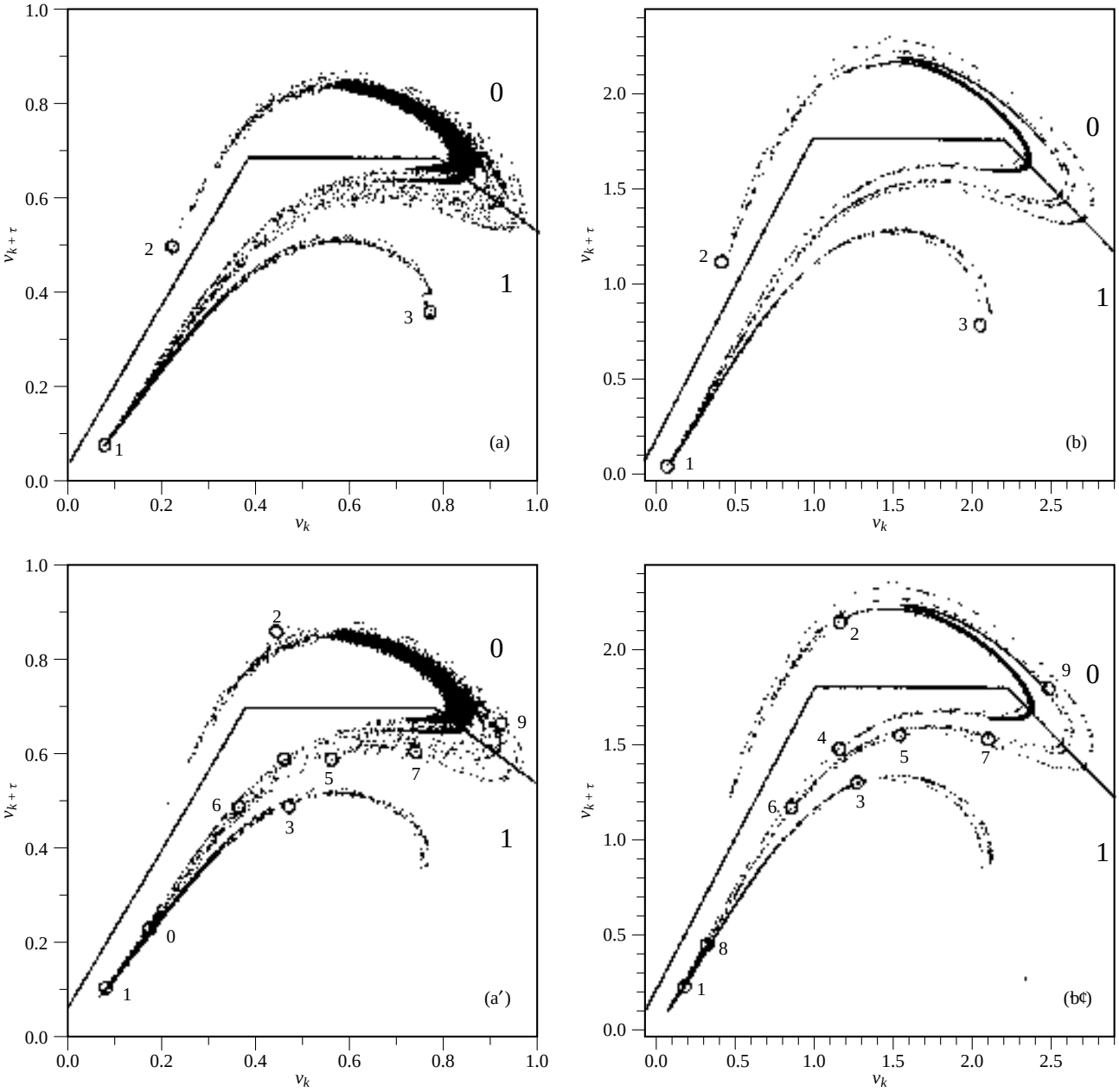

Figure 8 Two-dimensional projections of the Poincaré section for $A = 0.018$ and $\omega = 0.03168$. The intersection points of the period-3 (a, b) and of a period-9 (a′, b′) cycle are labeled in order of their occurrence: (a, a′) experiment, (b, b′) EBL model. The solid line represents the binary partition with elements labeled 0 and 1. The primed figures correspond to the EBL model

in embedding space is made; the target orbit can be explicitly chosen and the computations involved are relatively simple. However, the method becomes inappropriate as soon as several unstable or complex eigenvalues occur. An extension to the higher-dimensional case is nevertheless possible although the procedure becomes rather cumbersome.

Therefore, while retaining the positive characteristics of the method, we implemented an alternative technique which is affected neither by the occurrence of more than one unstable direction nor by the possible complexity of the eigenvalues. The control condition is obtained by requiring that the expected deviation of the orbit from the target be minimized by our choice of the control signal [minimal expected deviation (MED) method]. The procedure is based on the same matrix **M** as for the OGY method, although the dynamics may now be approximated by a more general nonlinear map as well. No estimate of the eigenvalues and of the corresponding contravariant vectors is needed, thus yielding higher reproducibility of the control. Finally, the new method may easily be implemented with several control stations along the target orbit.

We applied both the OGY and MED methods to the NMR laser operating with a modulation frequency $\nu_m \in (100, 120)$ Hz.[20] Although the embedding dimension was $E = 6$ and the operating frequency about 120 times higher than that of previous experiments,[21] control has been achieved under several conditions for the lowest-order periodic orbits. Another important difference is the higher embedding dimension used

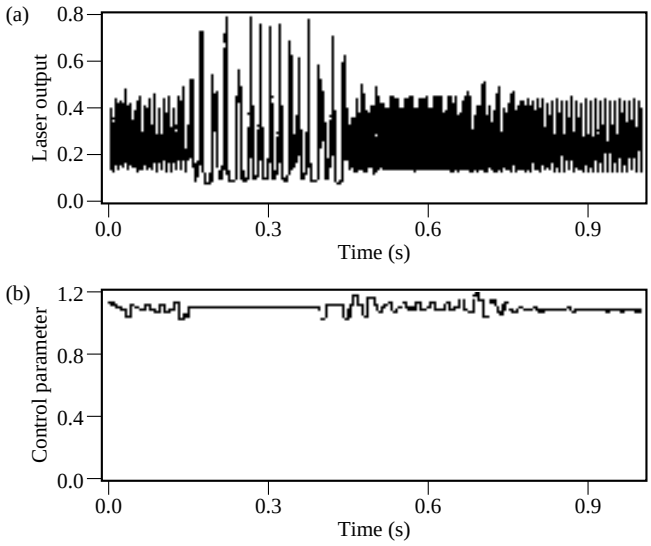

Figure 9 Time plot of (a) the controlled period-1 orbit and (b) the controlling signal as produced by the OGY method. The control was switched off at $t = 0.15$ s and restarted at $t = 0.4$ s

in the present work and the high precision required for a close return to be accepted. Time series of length $N = 1.5 \times 10^5$ have been analyzed and the unstable periodic orbits up to order 6 have been located during the acquisition of data points. The dynamics around an interactively chosen unstable orbit γ has been approximated by means of one or more linear maps. For detailed information about these controlling schemes, we refer to the work by Reyl et al.[20]

For illustration, we show in Figure 9 a portion of the time series $v(t)$ and the corresponding controlling signal during the stabilization of the period-1 orbit with the method by OGY; in Figure 10, we report three-dimensional projections of the strange attractor and of the controlled orbit.

The minimal expected deviation technique proved to be more efficient than the OGY method for the period-1 cycle, even. The period-2 orbit could be stabilized in a reproducible way, as well as a period-4 cycle. In both cases, it was sufficient to apply a rather small relative perturbation $A \rightarrow A + p$, with $|p| \leq p_{\max}$ and $p_{\max}/A \leq 0.02$. No spontaneous outbursts have been observed for times of the order of 2 hours or more. This technique appears to be less sensitive to noise.

5 SUMMARY AND OUTLOOK

The characterization of low-dimensional chaotic systems has gradually moved from the evaluation of simple, global indicators, such as Lyapunov exponents, fractal dimensions, and entropies, to the identification of periodic orbits. In the presented work, we reviewed the analysis of experimental chaotic time series, inspired by this evolution. In particular, we discussed the requirements that measurements must satisfy in terms of precision and statistics in order for an accurate analysis to be feasible. The role of noise has also been considered. We illustrated a method for the location of the unstable periodic orbits in embedding space, with special care for reliability tests.

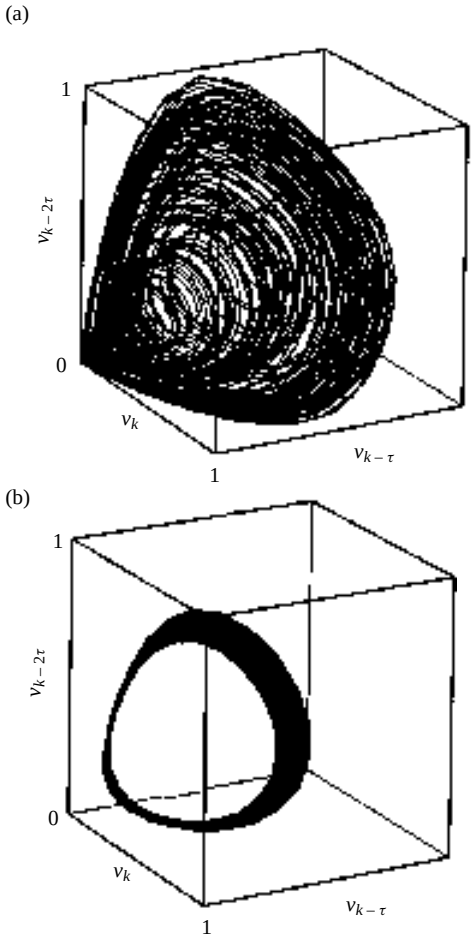

Figure 10 Three-dimensional phase portraits of the strange attractor (a) without control and (b) of the controlled period-one orbit

The important result of the analysis was the identification of an extremely accurate differential model for the dynamics, an extension of the conventional Bloch-type description. A similar modification might prove effective in optical lasers as well.[22] We have further illustrated the superiority of a periodic orbit analysis over conventional techniques with a quantitative study of a heteroclinic crisis. Finally, a control method has been applied to the NMR laser to show how the precise location of the unstable orbits and a careful local modeling of the dynamics can be used to constrain the motion in the vicinity of a periodic orbit, in spite of its repulsivity. The method was successful for low-order orbits (up to period 4), notwithstanding the high 'speed' of the system (about 100 Hz).

It appears that a careful analysis based on periodic orbits and symbolic dynamics[23] can be helpful in understanding more general questions, such as the nature of complexity, at least in relatively elementary dynamical models, such as cellular automata.

Another class of systems that goes beyond that of simple low-dimensional chaos consists of delayed-feedback processes in which the future state depends on the position at the current time and at a previous one. Hence, a description in terms of differential equations requires knowledge of all variable values in a whole time interval, so that the dimension of the system is infinite. This is suggestive of new phenomenology although it can be shown that the dimension of the attractors is

always bounded. Therefore, we started an investigation of the LDF, as a first step towards a higher-dimensional dynamics. The LDF dynamics exhibits quite an interesting behavior, including motion on incommensurate tori or strange attractors with dimension $D > 3$ or 4. The transition to chaos and, especially, the symbolic dynamics of such systems have not been studied yet. The experimental arrangement is obtained by rendering the quality factor Q dependent on the laser output signal, suitably delayed with an electronic device. The system is now autonomous (i.e. no external periodic forcing is needed for the onset of chaos), so that the periodic orbits do not have time lengths that are multiples of a fundamental one and, in general, a distribution of characteristic times is expected at each given order. Again, the agreement of the EBL modeling and experiment is excellent in the case of conventional chaos analysis.

6 RELATED ARTICLES

Ruby NMR Laser; Quantum Optics: Concepts of NMR.

7 REFERENCES

1. P. Bergé, Y. Pomeau, and C. Vidal, *Order within Chaos*, Wiley, New York, 1986.
2. H. G. Schuster, *Deterministic Chaos*, VCH, Weinheim, 1988.
3. J.-P. Eckmann and D. Ruelle, *Rev. Mod. Phys.*, 1985, **57**, 617.
4. B. B. Mandelbrot, *The Fractal Geometry of Nature*, Freeman, San Francisco, 1982.
5. P. Grassberger and I. Procaccia, *Phys. Rev. Lett.*, 1983, **50**, 346; P. Grassberger and I. Procaccia, *Physica D*, 1984, **13**, 34.
6. R. Badii and A. Politi, *Phys. Rev. Lett.*, 1984, **52**, 1661; R. Badii and A. Politi, *J. Stat. Phys.*, 1984, **40**, 725.
7. D. C. Auerbach, P. Cvitanović, J.-P. Eckmann, G. Gunaratne, and I. Procaccia, *Phys. Rev. Lett.*, 1987, **58**, 2387.
8. D. Meier, R. Holzner, B. Derighetti, and E. Brun, *Evolution of Order and Chaos in Physics, Chemistry, and Biology*. *Springer Series in Synergetics*, Springer-Verlag, Berlin, 1982, vol. 17, p. 146.
9. E. Brun, B. Derighetti, R. Holzner, and D. Meier, *Helv. Phys. Acta*, 1983, **56**, 825.
10. E. Brun, B. Derighetti, D. Meier, R. Holzner, and M. Ravani, *J. Opt. Soc. Am. B*, 1985, **2**, 156.
11. E. Brun, B. Derighetti, M. Ravani, G. Broggi, P. F. Meier, R. Stoop, and R. Badii, *Phys. Scr. T*, 1986, **13**, 119.
12. E. Ott, *Chaos in Dynamical Systems*, Cambridge University Press, Cambridge, 1993.
13. G. Broggi, *J. Opt. Soc. Am. B*, 1988, **5**, 1020.
14. M. Ravani, B. Derighetti, G. Broggi, E. Brun, and R. Badii, *J. Opt. Soc. Am. B*, 1988, **5**, 1029.
15. R. Stoop and P. F. Meier, *J. Opt. Soc. Am. B*, 1988, **5**, 1037.
16. L. Flepp, R. Holzner, E. Brun, M. Finardi, and R. Badii, *Phys. Rev. Lett.*, 1991, **67**, 2244.
17. C. Grebogi, E. Ott, F. Romeiras, and J. A. Yorke, *Phys. Rev. Lett.*, 1987, **36**, 5365.
18. M. Finardi, L. Flepp, J. Parisi, R. Holzner, R. Badii, and E. Brun, *Phys. Rev. Lett.*, 1992, **68**, 2989.
19. E. Ott, C. Grebogi, and J. A. Yorke, *Phys. Rev. Lett.*, 1990, **64**, 1196.
20. C. Reyl, L. Flepp, R. Badii, and E. Brun, *Phys. Rev. E*, 1993, **47**, 267.
21. W. L. Ditto, S. N. Rauseo, and M. L. Spano, *Phys. Rev. Lett.*, 1990, **65**, 3211.
22. C. O. Weiss and R. Vilaseca, *Dynamics of Lasers* VCH, Weinheim, 1991.
23. R. Badii, E. Brun, M. Finardi, L. Flepp, R. Holzner, J. Parisi, C. Reyl, and J. Simonet, *Rev. Mod. Phys.*, 1994, **66**, 1389.

Biographical Sketch

E. Brun. *b* 1927. Diploma in physics, 1952. Ph.D., 1954, University of Zürich. Introduced to NMR by H. H. Staub and C. D. Jeffries. Research associate, W. E. Meierhof, Stanford University, 1955–56. Privatdozent, 1957. Extraordinarius, University of Zürich, 1958. Guest professor, University of Colorado, 1961–62. Full Professor for Experimental Physics, University of Zürich, 1963–present. Dean of faculty, 1970–72. Director of the Physics Institute, 1973–92. Retirement, 1993. Research interests include nuclear magnetism and its applications to solid state physics, spin dynamics at low temperature, nonlinear dynamics, synergetics, order and disorder in lasers, and the transitions to chaos.

Nuclear Spin Properties and Conventions for Chemical Shifts (IUPAC Recommendations 2001†)

Robin K. Harris,[1]* Edwin D. Becker,[2] Sonia M. Cabral de Menezes,[3] Robin Goodfellow,[4] and Pierre Granger[5]

[1] *Department of Chemistry, University of Durham, South Road, Durham, UK*
[2] *National Institutes of Health, Bethesda, MD, USA*
[3] *PETROBRAS/CENPES/QUÍMICA, Ilha do Fundão, Cidade Universitária, Rio de Janeiro, Brazil*
[4] *School of Chemistry, University of Bristol, Cantock's Close, Bristol, UK*
[5] *Institut de Chimie, Université Louis Pasteur de Strasbourg, 1 rue Blaise Pascal, Strasbourg, France*

1	Introduction	5
2	Nuclear Spin Properties	5
3	Chemical Shifts	10
4	Summary of Recommendations	17
5	Appendix	18
6	Related Article in this Volume	18
7	References	18

ABSTRACT: A unified scale is recommended for reporting the NMR chemical shifts of *all* nuclei relative to the ^{1}H resonance of tetramethylsilane. The unified scale is designed to provide a precise ratio, Ξ, of the resonance frequency of a given nuclide to that of the primary reference, the ^{1}H resonance of tetramethylsilane (TMS) in dilute solution (volume fraction, $\varphi < 1\%$) in chloroform. Referencing procedures are discussed, including matters of practical application of the unified scale. Special attention is paid to recommended reference samples, and values of Ξ for secondary references on the unified scale are listed, many of which are the results of new measurements.

Some earlier recommendations relating to the reporting of chemical shifts are endorsed. The chemical shift, δ, is redefined to avoid previous ambiguities but to leave practical usage unchanged. Relations between the unified scale and recently published recommendations for referencing in aqueous solutions (for specific use in biochemical work) are discussed, as well as the special effects of working in the solid state with magic-angle spinning. In all, nine new recommendations relating to chemical shifts are made.

Standardized nuclear spin data are also presented in tabular form for the stable (and some unstable) isotopes of all elements with non-zero quantum numbers. The information given includes quantum numbers, isotopic abundances, magnetic moments, magnetogyric ratios and receptivities, together with quadrupole moments and linewidth factors (where appropriate).

1 INTRODUCTION

A distinguishing feature of nuclear magnetic resonance (NMR) is that signals are isotope-specific. In other words each signal can be firmly linked to a particular element and nuclide. Two features follow: Firstly there is a close connection with chemistry and, in particular, with the Periodic Table, since almost all elements can be studied; secondly, the spin properties of each isotope need to be clearly tabulated and firmly understood. It is a principal purpose of this document to provide such information.

Any scientific discipline relies for its effectiveness upon communication of ideas and results, which can only occur if there is an agreed basis for the meaning of the terminology used. The process of communication is greatly eased if there are universally-recognized conventions for measurement and reporting of quantities with their units and symbols. The aim of this document is to set down such a set of meanings and conventions in relation to chemical shifts (and shielding) and to list resonance frequencies for reference signals for each magnetically active nucleus.

Within IUPAC, Commission I.5 has been responsible for Molecular Structure and Spectroscopy. Until now, this Commission has produced only three reports[1–3] specifically relating to NMR. The two earlier ones of these refer to chemical shifts. The more recent of these two publications is 25 years old, and the NMR world has changed beyond recognition since then. Recently, however, conventions for chemical shifts of five nuclei of wide biochemical interest have been included in *Recommendations for the Presentation of NMR Structures of Proteins and Nuclei Acids*[4] by Commission I.7, Biophysical Chemistry. The current document addresses the same issue for general chemical usage and extends the conventions to the entire range of active nuclei, providing a more comprehensive guide to the factors important in chemical shift referencing. A unified list of properties of NMR-observable nuclei is also included herein.

2 NUCLEAR SPIN PROPERTIES

The phenomenon of NMR is based upon the magnetic properties of various isotopes of elements in the Periodic Table. It is therefore important to have an accessible unified list of these properties. These are contained in Tables 1–3 of this article which include the following for each stable isotope and each long-lived radioactive isotope with non-zero spin:

* To whom correspondence should be addressed: *E-mail*: r.k.harris@durham.ac.uk

† The original article may be freely accessed at (and reproduced from): http://www.iupac.org/publications/pac/2001/7311/7311×1795.html. Membership of the relevant IUPAC Commission during the preparation of the report is listed therein.

Table 1 The Spin Properties of the Spin-1/2 Nuclei[a]

Isotope[b]	Natural abundance,[c] x/%	Magnetic moment,[d] μ/μ_N	Magnetogyric ratio,[d] $\gamma/10^7$ rad s^{-1} T^{-1}	Frequency ratio,[e] Ξ/%	Reference compound	Sample conditions[f]	Literature for Ξ	Relative receptivity[g] D^p	Relative receptivity[g] D^C
^{1}H	99.9885	4.837 353 570	26.752 2128	100.000 000[h]	Me_4Si	$CDCl_3$, $\varphi = 1\%$	–	1.000	5.87×10^3
^{3}H[i]	–	5.159 714 367	28.534 9779	106.663 974	Me_4Si-t_1	[j]	**10**	–	–
^{3}He	1.37×10^{-4}	−3.685 154 336	−20.380 1587	76.179 437	He	gas	**11**	6.06×10^{-7}	3.56×10^{-3}
^{13}C	1.07	1.216 613	6.728 284	25.145 020	Me_4Si	$CDCl_3$, $\varphi = 1\%$	**12,13**	1.70×10^{-4}	1.00
^{15}N	0.368	−0.490 497 46	−2.712 618 04	10.136 767	$MeNO_2$	neat/$CDCl_3$[k]	**9**	3.84×10^{-6}	2.25×10^{-2}
^{19}F	100	4.553 333	25.181 48	94.094 011	CCl_3F	[j]	**14**	0.834	4.90×10^3
^{29}Si	4.6832	−0.961 79	−5.3190	19.867 187	Me_4Si	$CDCl_3$, $\varphi = 1\%$	**15**	3.68×10^{-4}	2.16
^{31}P	100	1.959 99	10.8394	40.480 742	H_3PO_4	[j]	**16**	6.65×10^{-2}	3.91×10^2
^{57}Fe	2.119	0.156 9636	0.868 0624	3.237 778	$Fe(CO)_5$	C_6D_6[l]	**9**	7.24×10^{-7}	4.25×10^{-3}
^{77}Se	7.63	0.926 775 77	5.125 3857	19.071 513	Me_2Se	neat/C_6D_6[k]	**9**	5.37×10^{-4}	3.15
^{89}Y	100	−0.238 010 49	−1.316 2791	4.900 198	$Y(NO_3)_3$	H_2O/D_2O[m]	**9**	1.19×10^{-4}	0.700
^{103}Rh	100	−0.1531	−0.8468	3.186 447[n,o]	$Rh(acac)_3$[p]	$CDCl_3$, sat.	**18**	3.17×10^{-5}	0.186
(^{107}Ag)	51.839	−0.196 898 93	−1.088 9181	4.047 819	$AgNO_3$	D_2O, sat.	**9**	3.50×10^{-5}	0.205
^{109}Ag	48.161	−0.226 362 79	−1.251 8634	4.653 533	$AgNO_3$	D_2O, sat.	**9**	4.94×10^{-5}	0.290
(^{111}Cd)	12.80	−1.030 3729	−5.698 3131	21.215 480	Me_2Cd	neat[j]	**19**	1.24×10^{-3}	7.27
^{113}Cd[q]	12.22	−1.077 8568	−5.960 9155	22.193 175	Me_2Cd	neat[j]	**19**	1.35×10^{-3}	7.94
(^{115}Sn)	0.34	−1.5915	−8.8013	32.718 749	Me_4Sn	neat/C_6D_6[k]	**9**	1.21×10^{-4}	0.711
(^{117}Sn)	7.68	−1.733 85	−9.588 79	35.632 259	Me_4Sn	neat/C_6D_6[k]	**9**	3.54×10^{-3}	20.8
^{119}Sn	8.59	−1.813 94	−10.0317	37.290 632	Me_4Sn	neat/C_6D_6[k]	**9**	4.53×10^{-3}	26.6
(^{123}Te)	0.89	−1.276 431	−7.059 098	26.169 742	Me_2Te	neat/C_6D_6[k]	**9**	1.64×10^{-4}	0.961
^{125}Te	7.07	−1.538 9360	−8.510 8404	31.549 769	Me_2Te	neat/C_6D_6[k]	**9**	2.28×10^{-3}	13.4
^{129}Xe	26.44	−1.347 494	−7.452 103	27.810 186	$XeOF_4$	neat[j]	**20,21**	5.72×10^{-3}	33.6
^{183}W	14.31	0.204 009 19	1.128 2403	4.166 387	Na_2WO_4	D_2O, 1 M	**11**	1.07×10^{-5}	6.31×10^{-2}
^{187}Os	1.96	0.111 9804	0.619 2895	2.282 331	OsO_4	CCl_4, 0.98 M	**22**	2.43×10^{-7}	1.43×10^{-3}
^{195}Pt	33.832	1.0557	5.8385	21.496 784[n]	Na_2PtCl_6	D_2O, 1.2 M	**9**	3.51×10^{-3}	20.7
^{199}Hg	16.87	0.876 219 37	4.845 7916	17.910 822	Me_2Hg[r]	neat	**11**	1.00×10^{-3}	5.89
(^{203}T1)	29.524	2.809 833 05	15.539 3338	57.123 200[s]	$T1(NO_3)_3$	[j]	**24**	5.79×10^{-2}	3.40×10^2
^{205}T1	70.476	2.837 470 94	15.692 1808	57.683 838	$T1(NO_3)_3$	[j]	**25**	0.142	8.36×10^2
^{207}Pb	22.1	1.009 06	5.580 46	20.920 599	Me_4Pb	neat/C_6D_6[k]	**9**	2.01×10^{-3}	11.8

[a] A complete list for stable nuclei, but excluding the lanthanides, the actinides and most radioactive isotopes.
[b] Nuclei in parentheses are considered to be not the most favorable of the element concerned for NMR.
[c] Data are 'representative isotopic compositions', taken from Rosman et al.,[8]. For the error limits, see Rosman et al.[8]
[d] Data derived from the compilation in Mills et al.,[6] pp. 98–104, which lists values of $\mu_{max}/\mu_N = \gamma\hbar I/\mu_N$. For the error limits, see Mills et al.[6]
[e] Ratios of the resonance frequency of the reference to that of the protons of TMS at infinite dilution (in practice at $\varphi = 1\%$) in $CDCl_3$.
[f] M ≡ molarity in mol dm^{-3} (solution); m ≡ molality in mol kg^{-1} (solvent). Some results from Ref.[9] were initially referenced[7] to a TMS concentration of 4.75 m in $CDCl_3$, but the values are corrected to refer to a dilute ($\varphi = 1\%$) solution of TMS in $CDCl_3$.
[g] D^p is the receptivity[5] relative to that of ^{1}H whereas D^C is relative to ^{13}C.
[h] Value by definition (see the text).
[i] Radioactive (half-life 12 y).
[j] See literature cited.
[k] Small amount of lock substance ($\varphi < 10\%$) in neat liquid.
[l] $\varphi = 20\%$ of C_6D_6 in $Fe(CO)_5$.
[m] H_2O/D_2O solution, concentration not reported.
[n] Alternatively, the precise values 3.160 000 MHz and 21.400 000 have been suggested[17] as the references for ^{103}Rh and ^{195}Pt, respectively.
[o] Subject to considerable variation with temperature.
[p] acac ≡ acetylacetonato.
[q] Long-lived radioactive isotope.
[r] The high toxicity of this compound means its direct use should be strongly discouraged.[23]
[s] Deduced from Refs.[24,25]

Table 2 The Spin Properties of Quadrupolar Nuclei[a]

Isotope[b]	Spin[c]	Natural abundance,[c] x/%	Magnetic moment,[d] μ/μ_N	Magnetogyric ratio,[d] $\gamma/10^7$ rad s^{-1} T^{-1}	Quadrupole moment,[e] Q/fm^2	Frequency ratio,[f] Ξ/%	Reference sample	Sample conditions[g]	Literature for Ξ	Line-width factor,[h] ℓ/fm^4	Relative receptivity[i]	
											D^p	D^C
^{2}H[j]	1	0.0115	1.212 600 77	4.106 627 91	0.2860	15.350 609	$(CD_3)_4Si$	$CDCl_3$, $\phi = 1\%$	**15**	0.41	1.11×10^{-6}	6.52×10^{-3}
^{6}Li	1	7.59	1.162 5637	3.937 1709	−0.0808	14.716 086	LiCl	D_2O, 9.7 m	**9**	0.033	6.45×10^{-4}	3.79
^{7}Li	3/2	92.41	4.204 075 05	10.397 7013	−4.01	38.863 797	LiCl	D_2O, 9.7 m	**9**	21	0.271	1.59×10^{3}
^{9}Be	3/2	100	−1.520 136	−3.759 666	5.288	14.051 813	$BeSO_4$	D_2O, 0.43 m	**9**	37	1.39×10^{-2}	81.5
^{10}B	3	19.9	2.079 2055	2.874 6786	8.459	10.743 658	$BF_3{\cdot}Et_2O$	$CDCl_3$[k]	**29**	14	3.95×10^{-3}	23.2
^{11}B	3/2	80.1	3.471 0308	8.584 7044	4.059	32.083 974	$BF_3{\cdot}Et_2O$	$CDCl_3$[k]	**29**	22	0.132	7.77×10^{2}
^{14}N[j]	1	99.632	0.571 004 28	1.933 7792	2.044	7.226 317	CH_3NO_2	neat/$CDCl_3$[l]	**9**	21	1.00×10^{-3}	5.90
^{17}O	5/2	0.038	−2.240 77	−3.628 08	−2.558	13.556 457	D_2O	neat	**9**	2.1	1.11×10^{-5}	6.50×10^{-2}
^{21}Ne	3/2	0.27	−0.854 376	−2.113 08	10.155	7.894 296[m]	Ne	gas, 1.1 MPa	**9**	140	6.65×10^{-6}	3.91×10^{-2}
^{23}Na	3/2	100	2.862 9811	7.080 8493	10.4	26.451 900	NaCl	D_2O, 0.1 M	**9**	140	9.27×10^{-2}	5.45×10^{2}
^{25}Mg	5/2	10.00	−1.012 20	−1.638 87	19.94	6.121 635	$MgCl_2$	D_2O, 11 M	**9**	130	2.68×10^{-4}	1.58
^{27}Al	5/2	100	4.308 6865	6.976 2715	14.66	26.056 859	$Al(NO_3)_3$	D_2O, 1.1 m	**9**	69	0.207	1.22×10^{3}
^{33}S	3/2	0.76	0.831 1696	2.055 685	−6.78	7.676 000	$(NH_4)_2SO_4$	D_2O, sat.	**9**	61	1.72×10^{-5}	0.101
^{35}Cl	3/2	75.78	1.061 035	2.624 198	−8.165	9.797 909	NaCl	D_2O, 0.1 M	**9**	89	3.58×10^{-3}	21.0
^{37}Cl	3/2	24.22	0.883 1998	2.184 368	−6.435	8.155 725	NaCl	D_2O, 0.1 M	**9**	55	6.59×10^{-4}	3.87
^{39}K	3/2	93.2581	0.505 433 76	1.250 0608	5.85	4.666 373	KCl	D_2O, 0.1 M	**9**	46	4.76×10^{-4}	2.79
(^{40}K)	4	0.0117	−1.451 3203	−1.554 2854	−7.3	5.802 018	KCl	D_2O, 0.1 M	**31**	5.2	6.12×10^{-7}	3.59×10^{-3}
(^{41}K)	3/2	6.7302	0.277 396 09	0.686 068 08	7.11	2.561 305[n]	KCl	D_2O, 0.1 M	**31**	67	5.68×10^{-6}	3.33×10^{-2}
^{43}Ca	7/2	0.135	−1.494 067	−1.803 069	−4.08	6.730 029°	$CaCl_2$	D_2O, 0.1 M	**32**	2.3	8.68×10^{-6}	5.10×10^{-2}
^{45}Sc	7/2	100	5.393 3489	6.508 7973	−22.0	24.291 747	$Sc(NO_3)_3$	D_2O, 0.06 M	**9**	66	0.302	1.78×10^{3}
^{47}Ti	5/2	7.44	−0.932 94	−1.5105	30.2	5.637 534	$TiCl_4$	neat[p]	**9**	290	1.56×10^{-4}	0.918
^{49}Ti	7/2	5.41	−1.252 01	−1.510 95	24.7	5.639 037	$TiCl_4$	neat[p]	**9**	83	2.05×10^{-4}	1.20
(^{50}V)[q]	6	0.250	3.613 7570	2.670 6490	21.0	9.970 309	$VOCl_3$	neat/C_6D_6[l]	**9**	17	1.39×10^{-4}	0.818
^{51}V	7/2	99.750	5.838 0835	7.045 5117	−5.2	26.302 948	$VOCl_3$	neat/C_6D_6[l]	**9**	3.7	0.383	2.25×10^{3}
^{53}Cr	3/2	9.501	−0.612 63	−1.5152	−15.0	5.652 496	K_2CrO_4	D_2O, sat.	**9**	300	8.63×10^{-5}	0.507
^{55}Mn	5/2	100	4.104 2437	6.645 2546	33.0	24.789 218	$KMnO_4$	D_2O, 0.82 m	**9**	350	0.179	1.05×10^{3}
^{59}Co	7/2	100	5.247	6.332	42.0	23.727 074	$K_3[Co(CN)_6]$	D_2O, 0.56 m	**9**	240	0.278	1.64×10^{3}
^{61}Ni	3/2	1.1399	−0.968 27	−2.3948	16.2	8.936 051	$Ni(CO)_4$	neat/C_6D_6[l]	**33**	350	4.09×10^{-5}	0.240
^{63}Cu	3/2	69.17	2.875 4908	7.111 7890	−22.0	26.515 473	$[Cu(CH_3CN)_4][ClO_4]$	CH_3CN, sat.[r]	**9**	650	6.50×10^{-2}	3.82×10^{2}
^{65}Cu	3/2	30.83	3.074 65	7.604 35	−20.4	28.403 693	$[Cu(CH_3CN)_4][ClO_4]$	CH_3CN, sat.[r]	**9**	550	3.54×10^{-2}	2.08×10^{2}
^{67}Zn	5/2	4.10	1.035 556	1.676 688	15.0	6.256 803	$Zn(NO_3)_2$	D_2O, sat.	**9**	72	1.18×10^{-4}	0.692

(*continued overleaf*)

Table 2 (*Continued*)

Isotope[b]	Spin[c]	Natural abundance,[c] x/%	Magnetic moment,[d] μ/μ_N	Magnetogyric ratio,[d] $\gamma/10^7$ rad s^{-1} T^{-1}	Quadrupole moment,[e] Q/fm^2	Frequency ratio,[f] Ξ/%	Reference sample	Sample conditions[g]	Literature for Ξ	Line-width factor,[h] ℓ/fm^4	Relative receptivity[i]	
											D^p	D^C
(^{69}Ga)	3/2	60.108	2.603 405	6.438 855	17.1	24.001 354	$Ga(NO_3)_3$	D_2O, 1.1 m	**34**	390	4.19×10^{-2}	2.46×10^2
^{71}Ga	3/2	39.892	3.307 871	8.181 171	10.7	30.496 704	$Ga(NO_3)_3$	D_2O, 1.1 m	**34**	150	5.71×10^{-2}	3.35×10^2
^{73}Ge	9/2	7.73	−0.972 2881	−0.936 0303	−19.6	3.488 315	$(CH_3)_4Ge$	neat[s]	**35**	28	1.09×10^{-4}	0.642
^{75}As	3/2	100	1.858 354	4.596 163	31.4	17.122 614	$NaAsF_6$	CD_3CN, 0.5 M	**9**	1300	2.54×10^{-2}	1.49×10^2
(^{79}Br)	3/2	50.69	2.719 351	6.725 616	31.3	25.053 980	NaBr	D_2O, 0.01 M	**9**	1300	4.03×10^{-2}	2.37×10^2
^{81}Br	3/2	49.31	2.931 283	7.249 776	26.2	27.006 518	NaBr	D_2O, 0.01 M	**9**	920	4.91×10^{-2}	2.88×10^2
^{83}Kr	9/2	11.49	−1.073 11	−1.033 10	25.9	3.847 600[t]	Kr	gas	**36**	50	2.18×10^{-4}	1.28
(^{85}Rb)	5/2	72.17	1.601 3071	2.592 7050	27.6	9.654 943	RbCl	D_2O, 0.01 M	**9**	240	7.67×10^{-3}	45.0
^{87}Rb[q]	3/2	27.83	3.552 582	8.786 400	13.35	32.720 454	RbCl	D_2O, 0.01 M	**9**	240	4.93×10^{-2}	2.90×10^2
^{87}Sr	9/2	7.00	−1.209 0236	−1.163 9376	33.5	4.333 822	$SrCl_2$	D_2O, 0.5 M	**37**	83	1.90×10^{-4}	1.12
^{91}Zr	5/2	11.22	−1.542 46	−2.497 43	−17.6	9.296 298	$Zr(C_5H_5)_2Cl_2$	CH_2Cl_2, sat.[r]	**9**	99	1.07×10^{-3}	6.26
^{93}Nb	9/2	100	6.8217	6.5674	−32.0	24.476 170	$K[NbCl_6]$	CH_3CN, sat.[u]	**9**	76	0.488	2.87×10^3
^{95}Mo	5/2	15.92	−1.082	−1.751	−2.2	6.516 926	Na_2MoO_4	D_2O, 2 M[v]	**9**	1.5	5.21×10^{-4}	3.06
(^{97}Mo)	5/2	9.55	−1.105	−1.788	25.5	6.653 695	Na_2MoO_4	D_2O, 2 M[v]	**9**	210	3.33×10^{-4}	1.95
^{99}Tc[q]	9/2	–	6.281	6.046	−12.9	22.508 326	NH_4TcO_4	D_2O[w]	**9**	12	–	–
^{99}Ru	5/2	12.76	−0.7588	−1.229	7.9	4.605 151	$K_4[Ru(CN)_6]$	D_2O, 0.3 M	**9**	20	1.44×10^{-4}	0.848
^{101}Ru	5/2	17.06	−0.8505	−1.377	45.7	5.161 369	$K_4[Ru(CN)_6]$	D_2O, 0.3 M	**9**	670	2.71×10^{-4}	1.59
^{105}Pd	5/2	22.33	−0.760	−1.23	66.0	4.576 100	K_2PdCl_6	D_2O, sat.	**22**	1400	2.53×10^{-4}	1.49
(^{113}In)	9/2	4.29	6.1124	5.8845	79.9	21.865 755	$In(NO_3)_3$	D_2O, 0.1 M[x]	**34**	470	1.51×10^{-2}	88.5
^{115}In[q]	9/2	95.71	6.1256	5.8972	81.0	21.912 629	$In(NO_3)_3$	D_2O, 0.1 M[x]	**34**	490	0.338	1.98×10^3
^{121}Sb	5/2	57.21	3.9796	6.4435	−36.0	23.930 577	$KSbCl_6$	CH_3CN, sat.[u]	**9**	410	9.33×10^{-2}	5.48×10^2
(^{123}Sb)	7/2	42.79	2.8912	3.4892	−49.0	12.959 217	$KSbCl_6$	CH_3CN, sat.[u]	**9**	330	1.99×10^{-2}	1.17×10^2
^{127}I	5/2	100	3.328 710	5.389 573	−71.0	20.007 486	KI	D_2O, 0.01 M	**9**	1600	9.54×10^{-2}	5.60×10^2
^{131}Xe[j]	3/2	21.18	0.893 1899	2.209 076	−11.4	8.243 921[y]	$XeOF_4$	neat		170	5.96×10^{-4}	3.50
^{133}Cs	7/2	100	2.927 7407	3.533 2539	−0.343	13.116 142	$CsNO_3$	D_2O, 0.1 M	**9**	0.016	4.84×10^{-2}	2.84×10^2
(^{135}Ba)	3/2	6.592	1.081 78	2.675 50	16.0	9.934 457	$BaCl_2$	D_2O, 0.5 M	**9,38**	340	3.30×10^{-4}	1.93
^{137}Ba	3/2	11.232	1.210 13	2.992 95	24.5	11.112 928	$BaCl_2$	D_2O, 0.5 M	**9,38**	800	7.87×10^{-4}	4.62
^{138}La[q]	5	0.090	4.068 095	3.557 239	45.0	13.194 300	$LaCl_3$	D_2O/H_2O[z]	**39**	120	8.46×10^{-5}	0.497
^{139}La	7/2	99.910	3.155 6770	3.808 3318	20.0	14.125 641	$LaCl_3$	D_2O, 0.01 M	**11**	54	6.05×10^{-2}	3.56×10^2
^{177}Hf	7/2	18.60	0.8997	1.086	336.5	(4.007)[A]	–	–		1.5×10^4	2.61×10^{-4}	1.54
^{179}Hf	9/2	13.62	−0.7085	−0.6821	379.3	(2.517)[A]	–	–		1.1×10^4	7.45×10^{-5}	0.438
^{181}Ta	7/2	99.988	2.6879	3.2438	317.0	11.989 600[B]	$KTaCl_6$	CH_3CN, sat.	**40**	1.4×10^4	3.74×10^{-2}	2.20×10^2

(^{185}Re)	5/2	37.40	3.7710	6.1057	218.0	22.524 600[B]	$KReO_4$	D_2O, 0.1 M	**40**	1.5×10^4	5.19×10^{-2}	3.05×10^2
^{187}Re[q]	5/2	62.60	3.8096	6.1682	207.0	22.751 600[B]	$KReO_4$	D_2O, 0.1 M	**40**	1.4×10^4	8.95×10^{-2}	5.26×10^2
^{189}Os[j]	3/2	16.15	0.851 970	2.107 13	85.6	7.765 400[B]	OsO_4	CCl_4, 0.98 M	**22**	9800	3.95×10^{-4}	2.32
(^{191}Ir)	3/2	37.3	0.1946	0.4812	81.6	(1.718)[A]	–	–		8900	1.09×10^{-5}	6.38×10^{-2}
^{193}Ir	3/2	62.7	0.2113	0.5227	75.1	(1.871)[A]	–	–		7500	2.34×10^{-5}	0.137
^{197}Au	3/2	100	0.191 271	0.473 060	54.7	(1.729)[A]	–	–		4000	2.77×10^{-5}	0.162
^{201}Hg[j]	3/2	13.18	−0.723 2483	−1.788 769	38.6	6.611 583[C]	$(CH_3)_2Hg$[D]	neat	**41**	2000	1.97×10^{-4}	1.16
^{209}Bi	9/2	100	4.5444	4.3750	− 51.6	16.069 288	$Bi(NO_3)_2$	$HNO_3/D_2O/H_2O$[E]	**9**	200	0.144	8.48×10^2

[a] Excluding the lanthanides, the actinides and most radioactive isotopes.
[b] Nuclei in parentheses are considered to be not the most favorable of the element concerned for NMR.
[c] Data are 'representative isotopic compositions', taken from Rosman et al.,[8]. For the error limits on the natural abundances, see Rosman et al.[8]
[d] Data derived from the compilation in Mills et al.,[6] pp. 98–104, which lists values of $\mu_{max}/\mu_N = \gamma\hbar I/\mu_N$. For the error limits, see Mills et al.[6]
[e] Data from Mills et al.,[6] pp. 98–104 (taken mostly from Pyykko[26] and Raghavan[27]) and updated from Pyykko.[28] It should be noted that reported values of Q may be in error by as much as 20–30%. For the error limits, see Pyykko.[28]
[f] Ratio of the resonance frequency of the reference to that of the protons of TMS at infinite dilution (in practice at $\varphi = 1\%$) in $CDCl_3$.
[g] M ≡ molarity in mol dm^{-3} (solution); m ≡ molality in mol kg^{-1} (solvent). Some results from Ref.[9] were initially referenced[7] to a TMS concentration of 4.75 m in $CDCl_3$, but the values are corrected to refer to a dilute ($\varphi = 1\%$) solution of TMS in $CDCl_3$.
[h] $\ell = (2I + 3)Q^2/I^2(2I - 1)$ (Ref.[5]). The values are quoted, arbitrarily, to 2 significant Figures.
[i] D^p is the receptivity[5] relative to that of ^{1}H whereas D^C is relative to ^{13}C. The values are given to three significant figures only.
[j] A useful isotope of $I = 1/2$ exists.
[k] 15% by volume of $BF_3{\cdot}Et_2O$ in $CDCl_3$.
[l] Small amount of lock substance ($\varphi \leq 10\%$) in neat liquid, except for ^{61}Ni (where φ = ca. 20% of C_6D_6 is involved).
[m] Ξ In reasonable agreement with a value deduced from a ratio given in Ref.[30]
[n] Ξ Deduced from data in Ref.[31]
[o] Ξ Deduced from a ratio given in Ref.[32]
[p] Plus C_6D_{12} ($\varphi = 10\%$) for field/frequency lock purposes.
[q] Radioactive, with a long half-life.
[r] Containing a little C_6D_6 ($\varphi < 10\%$).
[s] With conversion factors applied by Granger.
[t] The data in Ref.[36] are only accurate to 4 decimal places. The proposal herein is that Ξ (^{83}Kr) is defined to the 6 decimal places given.
[u] In CH_3CN/CD_3CN for ^{93}Nb, ^{121}Sb and ^{123}Sb.
[v] Plus a small quantity of NaOH.
[w] Semi-saturated in H_2O/D_2O.
[x] Plus 0.5 M DNO_3.
[y] Calculated from the value for ^{129}Xe via the ^{129}Xe : ^{131}Xe frequency ratio.
[z] For the solution conditions, see the reference.
[A] Value calculated from literature data on nuclear magnetic moments.
[B] The proposal herein is to define to 6 decimal places, but linewidths are generally such that this is unnecessarily accurate.
[C] Deduced from the ^{201}Hg : ^{199}Hg ratio given in Ref.[41]
[D] The high toxicity of this compound means its direct use should be strongly discouraged.[23]
[E] Saturated in conc. HNO_3, then diluted with an equal volume of D_2O.

(i) The nuclear spin quantum number, I, of the ground state of the nucleus.* This defines the magnitude of the spin angular momentum vector (and hence magnetic dipole moment – see below). The z-component quantum number is then denoted by m_I.

(ii) The standard isotopic natural abundance, x, expressed as a mole fraction in %.

(iii) The magnetic dipole moment, μ, of the nuclide, in terms of the nuclear magneton, μ_N. It should be noted that we have chosen to use the full vector magnitude of μ, given by:

$$|\mu|/\mu_N = |\gamma|\hbar[I(I+1)]^{1/2}/\mu_N \quad (1)$$

where γ is the magnetogyric ratio and $\hbar$ is the Planck constant divided by 2π. Many lists prefer to give only the maximum value of the z-component of μ, namely $\mu_z = \gamma\hbar I$, frequently without explicitly stating this fact. The sign of μ given in Tables 1–3 refers to its direction compared to the related spin angular momentum vector.

(iv) The magnetogyric ratio, γ (sometimes called the gyromagnetic ratio). The SI base units of this quantity are (angular frequency)/(magnetic induction), normally given as rad s^{-1} T^{-1}.

(v) The receptivity, of a nucleus in natural abundance, which influences the NMR signal strength. A common definition[5] involves the proportionality of receptivity to $\gamma^3 x I(I+1)$. In practice it is useful to list such receptivities relative to those of the commonly-used nuclei ^{1}H (proton) and ^{13}C, giving receptivity ratios D^p and D^C respectively. Both these quantities are given in Tables 1 and 2.

(vi) The quadrupole moment, Q, for nuclei with spin quantum number $I > 1/2$ (Tables 2 and 3 only). These data fall naturally in the region of 10^{-30} m^2, i.e., fm^2. However quadrupole moments are often expressed in units of 10^{-28} m^2, called a barn, where 1 barn = 100 fm^2.

(vii) The line-width factor, ℓ, for quadrupolar nuclei. This is defined[5] by:

$$\ell = Q^2(2I+3)/[I^2(2I-1)] \quad (2)$$

When taken in conjunction with the relative receptivity (e.g., as D^C/ℓ), this quantity gives a guide to the ease with which spectra can be obtained for different quadrupolar nuclei in solution for similar site symmetries and molecular mobilities. However, in practice, both symmetry and mobility may vary widely, thus introducing variations that may amount to several powers of ten.

Table 1 gives the data for the spin-1/2 nuclei in the Periodic Table, whereas Table 2 refers to quadrupolar nuclei. These two tables omit the lanthanide and actinide nuclei, which are separately listed in Table 3. Many of the data in Tables 1–3 have been taken from the IUPAC 'Green Book',[6] but additional information is included (particularly on resonance frequencies and quadrupole moments). A version of Tables 1–3 has been published.[7] However, the tables given here contain revised resonance frequencies for consistency with the recommended primary reference, as described in Section 3.5. In addition, some new measurements of resonance frequencies are reported in Tables 1–3, and information about solution conditions and relevant references has been added.

* NMR is entirely concerned with the nuclear spin in the lowest-energy nuclear state, though Mössbauer spectroscopy involves values of I in higher-energy nuclear states.

3 CHEMICAL SHIFTS

3.1 Background

Since the discovery of the chemical shift in 1950, NMR spectroscopy has become of vital importance to chemistry and related disciplines. The term chemical shift refers to a difference in resonance frequency (conventionally expressed as a fraction – see below) between nuclei in different chemical sites (or for samples under different physical conditions). Such effects are caused by variations in shielding by the electronic environment of the nuclei in question, and the concept of chemical shift is described by equation (3):

$$\nu = \frac{\gamma}{2\pi} B_0(1-\sigma) \quad (3)$$

In this equation, the resonance frequency ν (normally in the radiofrequency region) is related to the applied magnetic flux density B_0 by the magnetogyric ratio of the nucleus and the shielding constant σ. In the SI, ν is expressed in hertz, Hz, (and is normally in the range of tens or hundreds of MHz), B_0 is in tesla, T, and σ is a dimensionless fraction (generally reported in parts per million, ppm). Equation (3) is usually applied to the situation in isotropic media (liquids, solutions and gases), for which σ can be represented as a scalar quantity. However, the value of σ depends on molecular orientation in the applied magnetic field and can be represented by a scalar quantity only because of the averaging caused by rapid isotropic molecular tumbling. Therefore, σ is a second-rank tensor and must be used in that form for many situations in the solid state and in liquid crystals (and their solutions).

Whereas frequencies can be measured very precisely, the same cannot be said of B_0. Thus, although in principle chemists would like to know the absolute value of σ, it has long been recognized that only relative values can normally be obtained with precision. Therefore, from the early days of NMR the concept of a standard reference signal has been developed. This requires a number of choices, among which are:

(i) whether to base chemical shifts on resonance frequencies or on shielding

(ii) which compound to use as a reference

(iii) what further conditions to specify for the reference situation

(iv) whether to use separate references for different nuclei or to attempt to link them.

These matters will be dealt with in detail below.

In the early days of NMR, resonance was normally achieved by varying the applied field B_0. It therefore seemed natural for positive chemical shifts to refer to situations where the sample resonated at higher field than that of the reference. Equation (3) shows that this corresponds to greater shielding for the sample than for the reference – a convention that was popular with theoreticians, who are principally concerned

Table 3 The spin properties of lanthanide and actinide nuclei[a]

Isotope	Spin	Natural abundance x/%	Magnetic moment μ/μ_N	Magnetogyric ratio $\gamma/10^7$ rad s^{-1} T^{-1}	Quadrupole moment[b] Q/fm^2	Frequency ratio[c] Ξ/%
^{141}Pr	5/2	100	5.0587	8.1907	−5.89	(30.62)
^{143}Nd	7/2	12.2	−1.208	−1.457	−63.0	(5.45)
^{145}Nd	7/2	8.3	−0.744	−0.898	−33.0	(3.36)
^{147}Sm[d]	7/2	14.99	−0.9239	−1.115	−25.9	(4.17)
^{149}Sm	7/2	13.82	−0.7616	−0.9192	7.4	(3.44)
^{151}Eu	5/2	47.81	4.1078	6.6510	90.3	(24.86)
^{153}Eu	5/2	52.19	1.8139	2.9369	241.2	(10.98)
^{155}Gd	3/2	14.80	−0.332 08	−0.821 32	127.0	(3.07)
^{157}Gd	3/2	15.65	−0.435 40	−1.0769	135.0	(4.03)
^{159}Tb	3/2	100	2.600	6.431	143.2	(24.04)
^{161}Dy	5/2	18.91	−0.5683	−0.9201	250.7	(3.44)
^{163}Dy	5/2	24.90	0.7958	1.289	264.8	(4.82)
^{165}Ho	7/2	100	4.732	5.710	358.0	(21.34)
^{167}Er	7/2	22.93	−0.63 935	−0.77 157	356.5	(2.88)
^{169}Tm	1/2	100	−0.4011	−2.218	–	(8.29)
^{171}Yb	1/2	14.28	0.855 06	4.7288	–	17.499 306[e]
^{173}Yb	5/2	16.13	−0.804 46	−1.3025	280.0	(4.821)
^{175}Lu	7/2	97.41	2.5316	3.0552	349.0	(11.404)
^{176}Lu[d]	7	2.59	3.3880	2.1684	497.0	(8.131)
^{235}U[d]	7/2	0.7200	−0.43	−0.52	493.6	1.841 400[f]

[a]These nuclides are sufficiently little used that values for linewidth factors and relative receptivities are not listed here. However, for ^{169}Tm, $D^p = 5.70 \times 10^{-4}$ and $D^C = 3.35$, while for ^{171}Yb, $D^p = 7.89 \times 10^{-4}$ and $D^C = 4.63$.
[b]For the limits of accuracy, see Ref.[28]
[c]Values in brackets are approximate (calculated from the magnetogyric ratios).
[d]Long-lived radioactive isotope.
[e]Reference: Yb(η-$C_5Me_5)_2$(THF)$_2$, 0.171M in THF solution (THF ≡ tetrahydrofuran).[42]
[f]Reference: UF_6(with $\varphi = 10\%$ of C_6D_6).[43]

with σ. The first clear consensus on an experimental reference compound for proton NMR (by far the most popular nucleus at the time because of its high sensitivity) was tetramethylsilane (TMS), introduced in 1958 by Tiers.[44] However, both for proton NMR and for other nuclei various chemical shift scales were used, with some increasing in the direction of increasing magnetic field and others increasing in the direction of decreasing field (which corresponds to increasing frequency).

The convention recommended by IUPAC in the 1972 document,[1] which mostly concerned proton NMR, was that given in equation 4:

$$\delta_{X,sample} = \left(\frac{\nu_{X,sample} - \nu_{X,reference}}{\nu_{X,reference}} \right) \times 10^6 \qquad (4)$$

in which the chemical shift of a resonance for nucleus X is defined. For protons referenced to TMS this convention gives positive values with increasing frequency, and most proton chemical shifts then turn out to be positive. A second IUPAC report[2] in 1976 extended the recommendations to include nuclei other than protons, always with a high-frequency-positive convention.

Of course, since σ is, in principle, a tensor quantity, so is δ. However, the present document deals only with the isotropic average value of δ, which is the usual value of relevance for solution-state NMR. The tensor properties of σ and δ may be the subject of a later document.

3.2 Recommendations Endorsed

At this point it is appropriate to list those recommendations of the previous two IUPAC reports on NMR which relate to chemical shifts[1,2] (including presentation of spectra) and which we endorse, with one exception noted under item 6. These relate to notational matters and are particularly directed at publications in chemical journals. In several places we use different wording from the original reports and in some cases extended meanings:

1. The nucleus giving rise to the spectrum concerned should always be explicitly stated in full or in abbreviation (e.g., ^{10}B NMR or boron-10 NMR). The isotopic mass number should be given except in cases without ambiguity. In the case of hydrogen NMR the *de facto* usage is proton NMR, deuterium NMR or tritium NMR, in spite of the inconsistency of the wording. Abbreviations such as PMR for proton NMR are strongly discouraged. The term multinuclear NMR is clumsy (a repeated word 'nuclear') and so is also to be discouraged. Where reference to a variety of nuclei is required, multinuclear magnetic resonance should be written in full.
2. The graphical presentation of spectra should show frequency increasing to the left and positive intensity increasing upwards.
3. The dimensionless scale for chemical shifts should be tied to a reference, which should be clearly stated. The procedures used must be carefully defined.

4. The dimensionless scale factor for chemical shifts should generally be expressed in parts per million, for which ppm is the appropriate abbreviation. The radiofrequency of the reference, appropriate to the nucleus in question and to the spectrometer in use, should always be quoted, with sufficient accuracy in relation to the numerical values of shifts listed. Unfortunately, older software supplied by manufacturers to convert from frequency units to ppm in FT NMR sometimes uses the carrier frequency in the denominator instead of the true frequency of the reference, which can lead to significant errors.
5. The chemical shift scale should be defined with respect to resonance frequencies, with the appropriate sign convention (i.e., a positive sign should imply the sample resonates to high frequency from that of the reference). In order to avoid ambiguities of sign, the term 'chemical shift' should *not* be used to describe variations in shielding.
6. The symbol δ (lower case Greek delta) should be used for chemical shift scales with the sign convention given above. Such a symbol should *never* be used to refer to shielding. These recommendations cohere with the definition of the δ-scale adopted in References.[1,2] The definition of δ in equation 4 leads to a value with no units, and the 1972 document recommended that 'ppm' be not stated explicitly (e.g., $\delta = 5.00$, *not* $\delta = 5.00$ ppm). However, this convention is widely ignored. Therefore we do *not* endorse the omission of 'ppm' in reporting values of δ (see Section 3.3).
7. The nucleus in question should be indicated as a subscript or in brackets, e.g., δ_C or $\delta(^{13}\mathrm{C})$, unless there is no ambiguity.
8. As far as possible full information should be given in publications regarding any factor that might influence chemical shifts, such as:

   (i) The physical state of the sample (solid, liquid, solution or gas), with additional relevant facts where necessary.
   (ii) For solutions, the name of the solvent and the concentration of solute.
   (iii) The nature of the referencing procedure, e.g., internal, external (coaxial tubes or substitution), absolute frequency. (This aspect is discussed in detail in later sections of this article.)
   (iv) The name of the secondary reference compound local to the nucleus in question and its concentration. Note, however, that no reference compound needs to be added to the sample if the unified scale described in Section 3.5 is used, though a chemical shift value with respect to a recommended secondary reference compound, obtained via the unified scale, may still be quoted. In exceptional cases, where an isotope-specific secondary reference compound must be used in the experimental measurement, a clear description of the referencing procedure should be given.
   (v) The temperature and (if different from ambient) the pressure of the sample.
   (vi) Whether oxygen and other gases have been removed from the sample.
   (vii) Any chemicals present in the sample, in addition to the solvent and the compound under investigation, and details of their concentrations.

3.3 Definition and Reporting of δ Scales

As mentioned above, the IUPAC Recommendation[1] dating from 1972 defined the proton chemical shift scale in such a way that δ has no quoted units but is presumed to be in ppm. However, this recommendation not to use 'ppm' has *not* received acceptance in practice. It is a simple matter to rewrite equation 4 in a general way that can lead validly to the units of ppm. We now *define* the chemical shift (for any nucleus X, using its local reference substance) by equation 5:

$$\delta_{\mathrm{X,sample}} = (\nu_{\mathrm{X,sample}} - \nu_{\mathrm{X,reference}})/\nu_{\mathrm{X,reference}} \qquad (5)$$

that is, *without* the factor of 10^6. This leads, in general, to a very small number, $M \times 10^{-n}$. Normal practice has been and will doubtless continue to be to use $n = 6$ and thus to express δ in ppm. With equation 5 as the *definition* of δ, equation 6 provides a simple procedure for *calculating* the value of δ in ppm from measured frequencies:

$$\delta_{\mathrm{X,sample}}/\mathrm{ppm} = \frac{(\nu_{\mathrm{X,sample}} - \nu_{\mathrm{X,reference}})/\mathrm{Hz}}{\nu_{\mathrm{X,reference}}/\mathrm{MHz}} \qquad (6)$$

where the factor of 10^6 difference in the units of numerator and denominator is appropriately represented by the units ppm.

This re-definition allows values to be quoted also in parts per billion, ppb $= 10^{-9}$, (as is appropriate for some isotope effects) by expressing the numerator in equation 6 in millihertz (mHz). Alternatively, the units of equation 6 could be altered to give % (relevant for some heavy-metal chemical shifts), but ppm will undoubtedly remain as the most common usage. *IUPAC therefore recommends that the chemical shift δ be defined by equation 5 and that δ normally be expressed in ppm.*

3.4 Referencing Procedures

Accurate and consistent referencing is easy to visualize but hard to implement. For mobile isotropic media (liquids, solutions and gases) there are several possible methods:

(a) *Internal referencing*, where the reference compound is added directly to the system under study. This method is used almost universally for ^{1}H and ^{13}C NMR. However, it is clearly limited by the solubility, miscibility or mutual reactions of the sample components and may be difficult to implement for many samples in which a variety of nuclei are studied.
(b) *External referencing*, involving sample and reference contained separately in coaxial cylindrical tubes. A single spectrum is recorded, which includes signals from both the sample and the reference compound.
(c) *Substitution method*: The use of separate cylindrical tubes for the sample and reference compound, with (in principle) spectra recorded individually for each. It is similar to external referencing in that sample and reference materials are not mixed, but there are significant differences in the two procedures, as described later, which arise because of the common use of precise field/frequency locking (usually *via* the ^{2}H signal of a deuterated solvent). If locking is not used, the magnet should not be re-shimmed between running the sample and reference solutions, since this changes the applied magnetic field.

(d) Referencing *via* direct measurement of the absolute frequency of the field/frequency lock signal, usually provided by the ^{2}H resonance of an internally-contained deuterated compound (frequently the solvent). This method is discussed more fully in Section 3.6.
(e) Application of magic-angle spinning, usually with the substitution method, but also conceivably with coaxial tubes – see Section 3.8.

These methods all have various advantages and disadvantages. For (a) the shielding of the reference nucleus depends, to a greater or lesser extent, on the solvent, on the solute under study, and on the concentration of both solute and reference because of the effects of intermolecular interactions. These effects may be minimized by a judicious choice of solvent and reference compound, but they cannot be eliminated. External reference procedures (b) generally require corrections arising from differences in bulk magnetic susceptibility between sample and reference. These corrections depend on the geometry employed for the sample containers. For the usual coaxial cylindrical arrangement, the correction is[45]

$$(\delta_{\text{true}} - \delta_{\text{obs}}) = k(\kappa_{\text{sample}} - \kappa_{\text{reference}}) \tag{7}$$

where κ refers to the relevant volume magnetic susceptibility (in rationalized units) and ideally $k = +1/6$ for a tube perpendicular to B_0, $k = -1/3$ for a tube parallel to B_0 (as is usual for a superconducting magnet), and $k = 0$ for a tube inclined at the magic angle. These theoretical factors are calculated for infinite cylinders. In practice they depend on the length of the liquid column and other geometrical factors which are not always under control. No correction is needed for spherical samples, but the production of a truly spherical sample cell is generally not feasible. (Equation 7 is consistent with SI notation. A corresponding expression in the cgs system would substitute $k_{\text{cgs}} = 4\pi k_{\text{SI}}$ along with a $\Delta\chi_V$ term numerically equal to $\Delta\kappa/4\pi$. Many listings of susceptibility data give χ_V rather than κ.)

The substitution method uses the fact that, with the advent of stable, internally solvent-locked spectrometers, it has become feasible to obtain accurate data by measuring the spectra of sample and reference in two separate experiments. If the sample and the reference compound are each dissolved in the same solvent at low concentration (which, where feasible, we recommend), the substitution method is equivalent to use of an internal reference except that the reference substance does not contaminate the sample or interact with it, chemically or physically. If the reference compound is a nearly neat liquid with only a small amount of the deuterated 'solvent' to serve as a lock, the measured chemical shifts may be slightly different from those obtained with an internal reference because of differing molecular interactions. It might appear that a magnetic susceptibility correction would be needed if the susceptibilities of sample and reference differ, but this is not the case. With the field/frequency lock established via the deuterated solvent, the applied magnetic field simply shifts slightly to maintain the magnetic induction inside the sample tube constant so as to keep the ^{2}H nuclei on resonance. There is thus a distinct difference between the commonly used *internally locked* system, in which the magnetic induction B_0 is maintained constant and an *unlocked* (or *externally locked*) system in which the applied field H_0 is constant.

If the lock signal of the sample differs from that of the reference, a lock correction may need to be applied according to:

$$\delta_{\text{true}} = \delta_{\text{measured}} + \left(\delta^{\text{lock}}_{\text{sample}} - \delta^{\text{lock}}_{\text{reference}}\right) \tag{8}$$

Except for very strongly hydrogen-bonded systems,[46–48] no primary isotope effects between proton and deuterium have been firmly established, and none are expected on theoretical grounds. Hence, the difference between deuterium lock frequencies in equation (8) may be obtained from a table of proton chemical shifts. However, when polyhydrogenated groups are involved, corrections may be needed for secondary isotope effects[46] arising from $^1\text{H} \rightarrow {}^2\text{H}$ replacement. When high precision is required, the measurement of the shift difference between the locks may be obtained via direct observation of the deuterium spectrum of the two solvents, placed in coaxial tubes.

However, for most modern spectrometers the manufacturers have incorporated compensating procedures for lock changes, largely for the users' convenience of retaining the spectral window in the same position on the screen or chart. Unfortunately these procedures vary between manufacturers and between spectrometers of different ages from the same manufacturer, so no completely general comments on this question can be made here. NMR spectroscopists must refer to the relevant operating manual for details. In most cases with modern instruments the effect is to keep the magnetic field inside the samples constant when different lock compounds are used. In such situations the correction term in brackets in equation 8 is not necessary. Of course, the accuracy of the result clearly depends on what the manufacturers use for the term in brackets, generally present in a 'look-up' table in the spectrometer software. *We recommend that manufacturers give clear, explicit and accurate guidance on their procedures in this matter and quote their 'look-up' tables prominently.*

Another situation where isotope shifts have some effect is when signals of the reference compound are affected, for instance for ^{19}F measurements. In this case the signal is split into four lines with intensities approximately 27 : 27 : 9 : 1 because the natural-abundance isotopic ratio $^{35}\text{Cl} : {}^{37}\text{Cl}$ is ca. 3 : 1. Since $CFCl_3$ is firmly accepted as the local reference for ^{19}F, it is not reasonable to suggest a new alternative. It is recommended that the reference signal is that of $CF(^{35}Cl)_2(^{37}Cl)$.

Earlier IUPAC documentation[1,2] did not suggest any specific composition for the reference sample, or choice of solvents. Ideally, for most referencing methods, a non-polar solvent consisting of nearly spherical molecules should be used, and measurements should be extrapolated to zero reference concentration. Clearly such procedures are not generally feasible, so that caution always needs to be exercised when comparing shift data from different sources.

3.5 A Unified Scale

As NMR studies of various nuclei were initiated, each was, of necessity, treated independently, with some substance containing the nuclide being studied selected as a reference compound. The result is a vast collection of data in the literature for multinuclear magnetic resonance based on a large array of reference compounds. The proliferation of

reference substances is, however, unnecessary and in some ways unhelpful. In a given magnetic field all resonance frequencies form a single spectral range, and it is only because different nuclides resonate at markedly different frequencies that use of separate references has arisen. With modern instruments, in which all frequencies are derived from a single source, it is therefore possible to relate the observed frequencies of all nuclides in a particular sample to that of a single primary reference – preferably the proton resonance of TMS.[#]

There are, however, two reasons for wishing to retain the concept of a separate reference for each nucleus: (i) It is convenient to speak of, say, an aromatic ^{13}C resonance at x ppm from the ^{13}C line of TMS, rather than always quoting a frequency to many significant figures, and (ii) many data tabulations are available with values only expressed relative to separate heteronuclear references. Thus, for a unified scale to be of practical use, there must be agreed frequency relations between a set of commonly used secondary (heteronuclear) references and the primary reference. Measurements of such relations have been reported sporadically since the time of early double-resonance experiments,[49] and it has been proposed to relate the separate reference frequencies to a primary standard originally defined for a magnetic field such that the ^1H TMS signal is at exactly 100 MHz. These frequencies have been given[49] the symbol Ξ (capital Greek xi), and some tabulations have been presented.[5,14,50–52] However, it is clearer and more appropriate for users of modern high-field NMR spectrometers simply *to define Ξ as the ratio of the secondary (isotope-specific) frequency to that of ^1H in TMS in the same magnetic field. Therefore, it is convenient to express Ξ as a percentage* by the use of equation 9:

$$\Xi/\% = 100(\nu_X^{obs}/\nu_{TMS}^{obs}) \quad (9)$$

where ν_{TMS}^{obs} is the measured ^1H frequency of TMS. The use of percentage ensures that values of Ξ with this recommendation are numerically identical to those based on the earlier[49] definition.

Recently, the question of a unified reference has been addressed for multinuclear studies in biomolecular NMR: Wishart et al.[53] surveyed the relevant literature, pointed out inconsistencies in existing practices, and proposed the use of a single internal reference – for their purposes, one that is highly soluble in water (sodium 2,2-dimethyl-2-silapentane-5-sulfonate, DSS[#], preferably deuterated at the CH_2 positions). Operationally, as discussed in the following sections, it is often easier to obtain the necessary heteronuclear frequency data directly via the lock signal than to make additional measurements with various reference materials for different nuclei.

IUPAC recommends that a unified chemical shift scale for all nuclides be based on the proton resonance of TMS as the primary reference. This recommendation is in line with the *Recommendations for Presentation of NMR Structures of Proteins and Nucleic Acids*, recently promulgated[4] by IUPAC in conjunction with the International Union of Biochemistry and Molecular Biology and the International Union of Pure and Applied Biophysics, which include recommended Ξ values for several nuclei of importance in such studies for aqueous solutions, but which uses the proton resonance of DSS as the primary standard because of its solubility in water (see Section 3.9).

In conformity with other areas in physical chemistry, it would be desirable to define a precise standard state – for example, pure liquid TMS or TMS at infinite dilution in $CDCl_3$ at 293 K and 1 bar. [Indeed, in principle a better standard might be ^3He or ^{129}Xe in the gaseous state at a very low pressure (see Ref.[55] and references therein), but this is not practicable.] However, in this document we concentrate on aspects that are of immediate practical utility.

Temperature and pressure effects on chemical shifts for solutions and solid samples are sufficiently small for the lighter elements to be generally ignored for most chemical usage of NMR (largely carried out at ambient probe temperature and pressure), so we make no detailed recommendations regarding these parameters. References[55,56] contain some data on the temperature dependence of ^1H and ^{13}C resonances for TMS. Variation of solvent and/or change in sample concentration are known to have important effects on many chemical shifts, but they are relatively small for a symmetrical, non-polarizable molecule like TMS.

To assess the magnitude of the concentration effect, measurements have been obtained[12] of the proton chemical shift for TMS in solutions of volume fractions, $\varphi = 0.01\%$, 1% and 80% in $CDCl_3$ (see the Appendix). The ^1H NMR frequency of TMS ($\varphi = 1\%$) in chloroform is essentially at the infinite dilution level, the value for a $\varphi = 0.01\%$ solution differing by of the order of $10^{-7}\%$ in Ξ, which is normally reported to only $10^{-6}\%$. However, for a $\varphi = 80\%$ solution Ξ is $9 \times 10^{-6}\%$ larger than for a $\varphi = 1\%$ solution. *Therefore, for the primary reference in multinuclear magnetic resonance we recommend a dilute solution (approximately $\varphi = 1\%$ or less) of TMS in $CDCl_3$.* This recommendation does not preclude the use of TMS in other solvents as an alternative internal reference for ^1H NMR, and it is consistent with the use of DSS in aqueous solution (see Section 3.7).

These recommendations should not be taken in any way to preclude the design and implementation of experiments to measure specific properties, such as very high precision relative frequency measurements and special sample arrangements designed to minimise certain molecular interactions. Data will continue to be reported in the most effective way for the purpose at hand, but we believe that adoption of the unified chemical shift scale will facilitate comparison of the vast majority of NMR frequency measurements. The choice of the base reference as the proton signal of TMS is in accord with the virtually universal use of this signal as a reference for proton NMR.[#]

[#] TMS has a low boiling point (28 °C), which can be advantageous in facilitating removal from non-volatile samples after use, but can in other circumstances be a severe disadvantage. To overcome this problem, a substance such as $[(CH_3)_3Si]_4C$ (m.p. 267 °C), can be used as a reference[54] and the results converted to the TMS standard.

[#] The name sodium 3-(trimethylsilyl)propane-1-sulfonate is strictly the correct one for this compound.

[#] With hindsight it might have been better to choose the ^{29}Si signal of TMS since that is arguably even less susceptible to outside influence than the ^1H resonance (silicon being at the symmetry center of the molecule). However, because of the large amount of literature based on the proton signal, we recommend that the primary reference remain the ^1H signal of TMS.

If the recommendation for use of a unified scale is widely adopted, future measurements should be reported as Ξ values. However, to assure consistency with data already in the literature, it is important to have a set of Ξ values of sufficient accuracy to permit conversion between the primary TMS reference and at least one secondary homonuclear reference for each nuclide (other than ^{1}H). Tables 1–3 list values of Ξ for a number of commonly used secondary references, which are hereby recommended for further use. These values come from a number of sources, as indicated in the tables. However, it should be noted that a number of these compounds are hazardous (for example: Me_2Se, Me_2Te, $Ni(CO)_4$ and, especially, Me_2Hg). The unified scale has the advantage that its use avoids direct handling of any secondary references (see Section 3.6). For most of the nuclides listed in Table 3, there are few data available, and the values of Ξ are simply approximations based on magnetogyric ratios.

However, for Tables 1 and 2, values of Ξ are stated for almost all nuclides to 10^{-6}%. For 69 of the most commonly studied nuclides, careful measurements of Ξ have been made specifically for the purpose of this tabulation. The frequencies of ^{13}C and ^{29}Si were determined for samples of TMS in dilute solution in $CDCl_3$.[12,13,15] The remaining 67 measurements were made[9] by the substitution method (as described in the Appendix). Since all observation frequencies and the ^{2}H lock frequency are derived from a single source, the measured frequencies (Ξ) are reproducible to better than 10^{-7}% and are reported to 10^{-6}%. Experimental details are given in the Appendix. Values of Ξ for the remaining 30 nuclides in Tables 1 and 2 are taken from published values, which have been converted to be consistent with the choice of the ^{1}H signal for TMS in very dilute solution as the primary reference. The literature cited should be consulted for details of the experimental procedure and for estimates of experimental precision and accuracy.

For ^{1}H and ^{13}C NMR, internal referencing has been used almost exclusively, primarily to avoid bulk magnetic susceptibility effects, which can be of the same magnitude as some chemical shift differences that are interpretable with regard to chemical structure. The recommended reference for these nuclides is therefore TMS in a dilute solution in $CDCl_3$, and for consistency this reference is recommended also for ^{29}Si. For most other nuclides, magnetic susceptibility effects are small relative to chemical shift differences, and many of the published data have been reported relative to an external or replacement reference, often a neat liquid where feasible. To provide maximum utility, most of the entries in Tables 1 and 2 refer to such neat liquids or concentrated solutions, usually with a minimum amount of deuterated substance added to provide a stable lock. Of course, a very large number of such reference materials and lock substances could be used, but as described in Section 3.6, it is relatively simple to convert from one to another if necessary.

Values of Ξ can generally be determined to 10^{-6}%, which represents resonance measurement differences of only 0.01 ppm for nuclides with large values of γ to 0.5 ppm for nuclides with very low γ values (an imprecision which is usually negligible compared with their generally large chemical shift ranges). Under the unified scale, chemical shifts can thus be reported to a precision that is often dependent on linewidth or other sample-related factors, rather than instrumental factors. Since literature data for a number of nuclides are usually referred to a secondary reference and hence are often of considerably lower precision, small discrepancies in values of Ξ are of little practical consequence in most instances.

3.6 Practical Application of the Unified Scale

Modern NMR spectrometers invariably include field/frequency locking and frequency synthesizers, so that all frequencies are reliably interrelated by locking to a master clock frequency. There are two ways in which this fact can be used to determine chemical shifts, either directly on the Ξ scale or with respect to a recognized reference for the nucleus in question. These two ways are equivalent to the use of the conventional internal reference and substitution methods, respectively. In the former case, if a nucleus X is to be studied, and the sample can be prepared with a small amount of TMS, then two direct frequency measurements made whilst maintaining the same ^{2}H locking conditions will provide the chemical shift of X on the unified scale according to equation 9. If this procedure is applied to a series of samples, the effect is to replace 'medium effects' on the shielding of X (given by measurements using a reference compound containing the nuclide X) by 'medium effects' on the shielding of ^{1}H in TMS. In general, this should result in a reduction of 'medium effects' due to the referencing procedure, which is desirable. Clearly, the substitution method can be used similarly and is particularly valuable when it is not convenient to add TMS to the sample. Equation (9) is still pertinent. However, as noted in Section 3.4, medium effects may vary to some extent if different concentrations of sample and reference are used.

In the future, reporting of chemical shift data as Ξ values may become more common and acceptable. Conversion of Ξ values to conventional chemical shifts relative to a reference of an X-containing compound requires only subtraction of the Ξ value of a suitable homonuclear reference, as given in Tables 1 and 2, followed by division by the Ξ value of the homonuclear reference. Thus:

$$\delta_X/\text{ppm} = 10^6(\Xi_{X,\text{sample}} - \Xi_{X,\text{reference}})/\Xi_{X,\text{reference}} \qquad (10)$$

The widespread use of a ^{2}H lock for NMR measurements on isotropic samples suggests a modification of the substitution approach, since the relevant reference frequency should not vary with time. Thus the chemical shifts of the X nuclei can, in principle, be determined on the unified (TMS-based) scale merely by measuring the resonance frequency of the sample and using a predetermined reference frequency for the nuclide in question. Thus only one (sample) tube is required and no reference substance needs to be added. The predetermined reference frequency is obtained by measuring the proton resonance of TMS under similar conditions to the sample (i.e., with the same lock compound) in a single experiment for the spectrometer being used. Then the frequency of the usual secondary reference for the X nucleus can be calculated using the pre-determined value of ν_{TMS}:

$$\nu_{\text{reference}} = \nu_{TMS} \times \Xi_{\text{reference}}/100\% \qquad (11)$$

where $\Xi_{\text{reference}}$ takes the appropriate value given in Tables 1–3. Thence the chemical shift (or the value of Ξ_X) for the sample can be readily derived. If the lock substance in

the sample solution is not the same as that of the reference solution, a lock correction must be applied (equation (8)).

As an example, suppose that a ^{77}Se resonance has been measured on a compound dissolved in acetone-d_6, resulting in a value:

$$\nu_{\text{sample}} = 76\,344\,378\,\text{Hz}$$

On this spectrometer, the ^{1}H resonance of a $\varphi = 1\%$ solution of TMS in $CDCl_3$ has been found at 400 103 342 Hz when the spectrometer was installed. The reference frequency of selenium is then, from Table 1:

$$400\,103\,342\,\text{Hz} \times 19.071\,513 \div 100 = 76\,305\,761\,\text{Hz}$$

The proton chemical shifts of the resonances of the lock compounds are:

$$\delta_{\text{H}}(\text{CHCl}_3) = 7.27\,\text{ppm and } \delta_{\text{H}}(\text{acetone}) = 2.17\,\text{ppm}$$

Then:

$$\delta_{\text{Se,sample}} = (76\,344\,378 - 76\,305\,761)/76.305\,761 + (2.17 - 7.27) = 501.0\,\text{ppm}$$

Since this is still basically a substitution method, an error will arise if the ^{2}H frequency of the solvent has been influenced by the particular sample used. For many samples which consist of dilute solutions the error is small, and for many nuclei with large chemical shift ranges the error introduced in this way is probably smaller than would occur if a homonuclear (X) reference were used in the conventional manner.

Reporting of Ξ_{X} and δ_{X} measurements in future heteronuclear magnetic resonance studies will ultimately lead to a large set of consistent data, provided that values of $\Xi_{\text{X,ref}}$ are established and used consistently in all future work. Therefore, particularly for comparison with chemical shifts reported relative to a homonuclear (X) reference via conventional internal referencing procedures, it is essential that the values of Ξ in Tables 1 and 2 represent the accepted values for the substances listed (which are the 'best' available at the present time). *We therefore recommend that the defined local chemical shift scale zero values are established as those listed in Tables 1 and 2, and that such definitions are not subject to future change arising from remeasurement even where this results in increasing accuracy for the reference compound in question.* However, the values of Ξ for 'rare earth' nuclei in Table 3 should be regarded as provisional, pending more accurate measurement.

The Unified Scale offers many advantages over other methods of referencing. However, serious errors can occur in reading and displaying frequencies in some spectrometers unless care is taken. The software in NMR spectrometers is continually evolving, and even some spectrometers of relatively recent vintage are configured to display frequencies that are rounded off or that appear with many digits that do not correctly represent the frequency of a peak indicated by the cursor. The correct information is available in the appropriate parameter tables, but the authors of this document have found that in instruments which are several years old it may be necessary to seek the correct file and not rely on what appears to be an 'obvious' display. Although the situation has improved with the latest version of commercial instruments, *we strongly recommend that each user verify that his/her own instrument correctly determines one or more values of Ξ as given in Tables 1–3.*

3.7 Alternative Reference Compounds

Many of the elements have more than one proposed reference compound for the chemical shift scale mentioned in the literature. The majority are secondary reference standards chosen for convenience. Although our recommendation stands for the compounds listed in Tables 1 and 2, there are some situations where an alternative reference has to be used. One of these cases occurs when ^{1}H, ^{13}C, ^{15}N, ^{29}Si and other nuclei have to be referenced in highly polar solvents such as water, where TMS is only very sparingly soluble. For those situations, DSS or its partially deuterated form, $Me_3SiCD_2CD_2CD_2SO_3Na$, is the recommended primary reference.[53,57] [Sodium 3-(trimethylsilyl)propanoate (TSP) is another salt that has been suggested.[58]] When DSS is used as a reference, it has been recommended[4] that ^{1}H chemical shifts be denoted by the symbol δ_{DSS} to distinguish them from those referenced to TMS. However, the resonances of DSS and TMS, *both dissolved in the same solvent*, are very close: On the scale with TMS as zero, DSS has a chemical shift of $\delta = 0.0173$ ppm in dilute aqueous solution, while in dilute solution in di[($^2H_3$)methyl] sulfoxide (DMSO-d_6), the chemical shift of DSS is $\delta = -0.0246$ ppm[4]. For most purposes these differences are negligible (falling well below the anticipated range of solvent effects), and *data from the TMS and DSS scales may be validly compared without correction for the different ^{1}H reference*.

Table 4 repeats the recommended values of Ξ from Reference,[4] along with data for additional references proposed in the literature for nitrogen, and compares them with our recommendations in Tables 1 and 2. For ^{13}C studies in aqueous solution, Reference[4] recommends using the ^{13}C methyl resonance of DSS, rather than that of TMS, as the secondary reference. Carbon-13 chemical shifts based on DSS and TMS differ by about 2 ppm, which can cause confusion if not clarified. *We recommend that when ^{13}C chemical shifts are referenced to DSS, that point should be made clear by using a notation such as $\delta_{\text{DSS}}(^{13}\text{C})$.*

Reference[4] recommends use of trimethyl phosphate (internal) as a secondary reference for ^{31}P studies in aqueous solution, whereas Table 1 recommends 85% phosphoric acid (external), which has been used more widely, particularly for chemical systems where use of an internal reference is not feasible. The two secondary references differ by about 3 ppm, so *it is important to specify which is being used.*

Several reference compounds have been used historically for nitrogen NMR, partly resulting from the very different properties and natural abundances of the two nuclides (^{14}N and ^{15}N). Nitromethane as either an internal or external reference has been the most widely used for ^{14}N and to some extent for ^{15}N, while liquid ammonia has been a popular external reference for ^{15}N. Ammonium and tetramethylammonium salts have been used as internal references for both ^{14}N and ^{15}N. Reference[4] recommends liquid NH_3 as a secondary reference for ^{15}N in aqueous solutions, since most biochemical applications of ^{15}N NMR have used this reference. In Tables 1 and 2 *we recommend nitromethane as a reference*, in line with common usage in many other applications. The values of Ξ

Table 4 Alternative Secondary References

Isotope	Alternative secondary references				Recommended Secondary references[a]		
	Reference compound	Sample conditions	Frequency ratio	Literature Ξ/%	Reference compound	Sample conditions	Frequency ratio
^{1}H	DSS	Internal	100.000 000	**4**	TMS	Internal[b]	100.000 000
^{2}H	DSS	Internal	15.350 608	**4**	TMS	Internal[b]	15.350 609
^{13}C	DSS	Internal	25.144 953	**4**	TMS	Internal[b]	25.145 020
^{31}P	$(CH_3O)_3PO$	Internal	40.480 864	**4**	H_3PO_4 (85%)	External	40.480 742
^{15}N	NH_3 (liquid)	External	10.132 912	**4**	CH_3NO_2	External	10.136 767
^{15}N	$[(CH_3)_4N]I$	Internal[c]	10.133 356	**59,60**			
^{14}N	$[(CH_3)_4N]I$	Internal[c]	7.223 885	**59**	CH_3NO_2	External	7.226 317

[a]See Tables 1 and 2.
[b]Volume fraction $\varphi = 1\%$ in $CDCl_3$.
[c]0.075 M in DMSO-d_6.

for different nitrogen reference compounds are presented in Table 4, along with those for tetramethylammonium iodide, which has been suggested as an internal reference for both ^{14}N and ^{15}N since the tetrahedral geometry results in sharp lines for both isotopomers.

For most of the nuclei listed in Tables 1 and 2, Ξ values are listed for only one homonuclear reference, since conversions to other reference compounds can be readily made from literature values.

3.8 Magic-angle Spinning

It has been shown[61–63] that in theory bulk isotropic magnetic susceptibility effects are eliminated by spinning an infinitely-long cylindrical sample with its axis at the magic angle (54.7°) to the static magnetic field of an NMR spectrometer. Therefore, in principle, magic-angle spinning (MAS) can be used in the external referencing method to obtain chemical shifts free from bulk susceptibility problems. Whereas this technique was proposed in the context of solid-state NMR (see below), its utility applies equally well to the solution state.[64,65] In practice an infinitely long cylinder is not necessary to reduce bulk susceptibility effects on chemical shifts to an acceptable level. Strictly speaking, to correct for *isotropic* bulk magnetic susceptibility effects, it is also not necessary to spin at the magic angle, but merely to orient the cylinder containing the sample at the magic angle (see equation (7)). However, spinning may narrow the lines significantly and so is normally essential for accurate chemical shift measurement.

3.9 Solids

Sample-handling procedures differ substantially for solids from those appropriate for solutions, and there are clear advantages to using suitable solids as secondary references. This is almost always done using sample replacement. However, the spectrometers are generally used without field/frequency locking, so that the resulting chemical shifts are inevitably less accurate than those for solutions. This is not a significant problem, because linewidths are usually substantially greater than those for solutions and they impose an upper limit to accuracy. High-resolution NMR of solids almost invariably relies on magic-angle spinning, and, as discussed in Section 3.8, this eliminates the effects of differences in bulk isotropic magnetic susceptibilities. Early papers[61,62] addressed this matter, and a recent review by VanderHart,[45], which refers to both liquids and solutions, further discusses the influence of MAS for referencing spectra. Unfortunately, the situation is simple only for systems with isotropic magnetic susceptibility. VanderHart[45] discusses the case of anisotropic susceptibility, but there has been to date little experimental work in this area. However, in general it may be taken that, within the accuracy of measurement, referencing by sample replacement under MAS conditions in an unlocked but stable spectrometer is to a good approximation equivalent to the substitution method as described in Section 3.5.

Several papers[66–68] take advantage of the MAS technique to suggest secondary solid standards for practical use in solid-state NMR. For example the ^{13}C signals of solid adamantane, glycine, hexamethylbenzene and $[(CH_3)_3Si]_4Si$ have been referenced to those for liquids and solutions using MAS, and data were reported to accuracies in the region of 0.004–0.04 ppm.

Chemical shift referencing for solid-state NMR is not yet at the stage where much further discussion is warranted here, so the only recommendation that we make is for referencing procedures to be always clearly and carefully stated in publications.

4 SUMMARY OF RECOMMENDATIONS

In addition to the endorsements of earlier Recommendations stated in Section 3.2 above, IUPAC recommends the following:

(a) Equation (5) should be used to define chemical shift scales, with symbol δ and with ppm (or ppb or %, as appropriate) explicitly stated after the numerical values. Equation (6) provides a simple way to calculate chemical shift values in ppm.
(b) The ^{1}H signal of tetramethylsilane in dilute solution (ca. volume fraction $\varphi = 1\%$ in $CDCl_3$) should be used as the primary *internal* or substitution reference for the resonance frequencies (and hence chemical shifts) for *all* nuclei. However, for aqueous solutions the recommendations of Ref.[4] are supported.
(c) The secondary references listed in Tables 1 and 2 may be used for the nuclei of the various elements, with their Ξ taking the fixed values given (not subject to revision).
(d) Internal referencing may be used for solutions but its limitations should be recognized.

(e) For solution-state measurements, referencing via an internal ^{2}H lock signal may be used, either to give the value of Ξ directly or to calculate the chemical shift with respect to the relevant secondary reference (via equation (8) where relevant).
(f) Referencing by the substitution method with field/frequency lock spectrometers may also be used for solutions.
(g) External referencing for either liquids or solids may be carried out with magic-angle spinning.
(h) External referencing by means other than (f) and (g) is to be discouraged unless corrections are applied for bulk magnetic susceptibility effects.
(i) In all circumstances, and especially where strict adherence to these Recommendations is not feasible, details of experimental procedures should be given clearly so that results may be validly intercompared.

Acknowledgements

We thank H. J. C. Yeh (National Institutes of Health), A. M. Kenwright (University of Durham) and B. Ancian (Université de Paris VII) for measurements of Ξ for ^{13}C and ^{29}Si in solutions of TMS in $CDCl_3$. Other special measurements of Ξ have also been made by C. Brevard, R. Hoffman, J. Raya, M. Bourdonneau, T. Meersmann, B. Ancian and L. Helm. We are also grateful to W. Bremser, who participated in some of the early discussions on the topic of these recommendations, and to J. Kowalewski and G. Martin for comments and encouragement. Specific comments were received from members of IDCNS (W. V. Metanomski, K. Hatada, A. D. Jenkins, J. W. Lorimer, W. H. Powell, S. E. Schwartz, A. J. Thor, H. A. Favre, T. Cvitaš) and a wide range of NMR experts and others (A. D. McNaught, D. L. Van der Hart, D. T. Burns, M. Duteil, J. R. Everett, B. E. Mann, W. McFarlane, P. S. Pregosin, B. Mandava, W. von Philipsborn, T. D. W. Claridge, C. Ye, D. Neuhaus, P. Jonsen, G. Hägele, J. C. Lindon, P. E. Meadows, B. Wrackmeyer, D. L. VanderHart, K. Mizuno, T. Richert); we are very grateful for their assistance and guidance. P. Pyykko very helpfully supplied details of his review of quadrupole moments in advance of publication, and R. Hoffman not only supplied data for Ξ on several nuclei but also made many pertinent and useful suggestions.

5 APPENDIX

As noted in the body of this document, a number of new experimental measurements have been made to verify values of Ξ for various nuclides. Experimental details are given here.

Concentration dependence of δ_H (TMS).[12] Measurements were made with a Varian VXR-500S spectrometer, sample at ambient probe temperature (about 23 °C), locked onto the signal for $CDCl_3$. Measured ^{1}H frequencies were as follows:

$$\varphi = 0.01\% : 499.872\,5048\ \text{MHz}$$

$$\varphi = 1\% : 499.872\,5054\ \text{MHz}$$

$$\varphi = 80\% : 499.872\,5495\ \text{MHz}$$

Ξ for ^{13}C and ^{29}Si. Three measurements were made of Ξ (^{13}C) for TMS in $CDCl_3$ at $\varphi = 1\%$, all at ambient probe temperature using the following spectrometers: – Varian VXR-500S,[12] $\Xi = 25.145\,0188\%$; Varian Unity-300,[13] $\Xi = 25.145\,0202\%$; and Varian Inova-500,[13] $\Xi = 25.145\,0196\%$. The reported value[15] (Table 1) of Ξ (^{29}Si) for TMS in $CDCl_3$ at $\varphi = 1\%$ was obtained at ambient probe temperature using a Bruker Avance-400 spectrometer.

Other values of Ξ. Most of the remaining 67 new measurements presented in Tables 1 and 2 were made by the substitution method (as described above) with a Bruker Model MSL spectrometer, operating at a nominal frequency of 300 MHz for ^{1}H, and with corrections applied for the lock signals (see equation 8).[9] However, Ξ was measured for the following nuclei using a Bruker Avance-400 spectrometer: ^{2}H, ^{17}O, ^{45}Sc, ^{47}Ti, ^{49}Ti, ^{55}Mn, ^{75}As, ^{81}Br, ^{87}Rb, ^{127}I, ^{131}Xe, ^{133}Cs, ^{135}Ba, and ^{137}Ba. The ^{21}Ne value was measured[9] using a Chemagnetics Infinity 600 spectrometer. All 67 measurements were made at ambient probe temperature, approximately 298–300 K. The replacement reference samples used were either a concentrated solution ($m = 4.75\,\text{mol kg}^{-1}$, $\varphi = 80\%$) of TMS in $CDCl_3$, or a $\varphi = 1\%$ solution of TMS in $CDCl_3$. In the former case, the values have been converted to refer to TMS ($\varphi = 1\%$) in $CDCl_3$ (see above).

6 RELATED ARTICLE IN THIS VOLUME

Parameters and Symbols for Use in Nuclear Magnetic Resonance (IUPAC Recommendations 1997). The reader should note that together these two articles in this volume, Nuclear Spin Properties and Conventions for Chemical Shifts (IUPAC Recommendations 2001) and Parameters and Symbols for Use in Nuclear Magnetic Resonance (IUPAC Recommendations 1997), essentially replace the article Nuclear Spin Properties and Notation in volume 5 of the Encyclopedia. In fact some of the numbers in the tables have been changed from that article by updating and because the primary standard has been rebased from 4.75 m in $CDCl_3$ to 1% in $CDCl_3$.

7 REFERENCES

1. Recommendations for the Presentation of NMR Data for Publication in Chemical Journals, *Pure Appl. Chem.*, 1972, **29**, 627.
2. Presentation of NMR Data for Publication in Chemical Journals – B. Conventions relating to Spectra from Nuclei other than Protons, *Pure Appl. Chem.*, 1976, **45**, 217.
3. R. K. Harris, J. Kowalewski, and S. C. de Menezes, Parameters and Symbols for Use in Nuclear Magnetic Resonance, *Pure Appl. Chem.*, 1997, **69**, 2489.
4. J. L. Markley, A. Bax, Y. Arata, C. W. Hilbers, R. Kaptein, B. D. Sykes, P. E. Wright, and K. Wüthrich, Recommendations for the Presentation of NMR Structures of Proteins and Nucleic Acids, *Pure Appl. Chem.*, 1998, **70**, 117.
5. 'NMR and the Periodic Table', eds R. K. Harris and B. E. Mann, Academic Press: 1978.
6. I. Mills, T. Cvitas, K. Homann, N. Kallay, and K. Kuchitsu, 'Quantities, Units and Symbols in Physical Chemistry', 2nd edn., published for IUPAC by Blackwell Scientific Publications: 1993.
7. R. K. Harris, in 'Encyclopedia of NMR', eds D. M. Grant and R. K. Harris, Wiley: Chichester, 1996, vol. 5, p 3301.
8. K. J. R. Rosman and P. D. P. Taylor, *Pure Appl. Chem.*, 1998, **70**, 217.
9. P. Granger, J. Raya, M. Bourdonneau, L. Helm, and T. Meersmann, measurements previously unpublished in the primary literature. See the Appendix for details.
10. J. P. Bloxsidge, J. A. Elvidge, J. R. Jones, R. B. Mane, and M. Saljoughian, *Org. Magn. Reson.*, 1979, **12**, 574.
11. R. Hoffman, private communication.

12. H. J. C. Yeh, previously unpublished work.
13. A. M. Kenwright, previously unpublished work.
14. S. Brownstein and J. Bornais, *J. Magn. Reson.*, 1980, **38**, 131.
15. B. Ancian, previously unpublished work.
16. H. T. Edzes, *Magn. Reson. Chem.*, 1992, **30**, 850.
17. P. L. Goggin, R. J. Goodfellow, and F. J. S. Reed, *J. Chem. Soc. Dalton*, 1974, 576; S. J. Anderson, J. R. Barnes, P. L. Goggin, and R. J. Goodfellow, *J. Chem. Res. (M)*, 1978, 3601.
18. R. Benn and A. Rufinska, *Angew. Chem., Int. Ed. Engl.*, 1986, **25**, 861.
19. J. D. Kennedy and W. McFarlane, *J.C.S. Perkin II*, 1977, 1187.
20. M. Gerken and G. J. Schrobilgen, *Coord. Chem. Rev.*, 2000, **197**, 335.
21. G. A. Schumacher and G. J. Schrobilgen, *Inorg. Chem.*, 1984, **23**, 2923.
22. C. Brevard, previously unpublished work.
23. M. B. Blayney, J. S. Winn, and D. W. Nierenberg, *C & E News*, May 12, 7 1997; T. Y. Yoribara, T. W. Clarkson, and D. W. Nierenberg, *C & E News*, June 16, 6 1997; D. Live, *C & E News*, July 14, 7 1997; R. K. Harris, *C & E News*, July 14, 7 1997.
24. J. F. Hinton, G. L. Turner, G. Young, and K. R. Metz, *Pure Appl. Chem.*, 1982, **54**, 2359.
25. J. F. Hinton and R. W. Briggs, *J. Magn. Reson.*, 1977, **25**, 555.
26. P. Pyykko, *Z. Naturforsch.*, 1992, **47A**, 189.
27. P. Raghavan, *At. Data Nucl. Data Tables*, 1989, **42**, 189.
28. P. Pyykko, *Mol. Phys.*, 2001, **99**, 1617.
29. J. D. Kennedy, in 'Multinuclear NMR', ed J. Mason, Plenum Press, Ch. 8, p 221, 1987.
30. J. T. LaTourrette, W. E. Quinn, and R. F. Ramsey, *Phys. Rev.*, 1957, **107**, 1202.
31. W. Sahm and A. Schwenk, *Z. Naturforsch.*, 1974, **29a**, 1754.
32. O. Lutz, A. Schwenk, and A. Uhl, *Z. Naturforsch.*, 1975, **30a**, 1122.
33. N. Hao, M. J. McGlinchey, B. G. Sayer, and G. J. Schrobilgen, *J. Magn. Reson.*, 1982, **46**, 158.
34. J. Kodweiss, O. Lutz, W. Messner, K. R. Mohn, A. Nolle, B. Stütz and D. Zepf, *J. Magn. Reson.*, 1981, **43**, 495.
35. J. Kaufmann, W. Sahm, and A. Schwenk, *Z. Naturforsch.*, 1971, **26A**, 1384.
36. D. Brinkman, *Helv. Phys. Acta*, 1968, **41**, 367.
37. W. Sahm and A. Schwenk, *Z. Naturforsch.*, 1974, **29a**, 1763.
38. O. Lutz and H. Oehler, *Z. Physik A*, 1978, **288**, 11.
39. O. Lutz and H. Oehler, *J. Magn. Reson.*, 1980, **37**, 261.
40. C. Brevard and P. Granger, 'Handbook of High Resolution Multinuclear NMR', Wiley: 1981.
41. G. Wu and R. E. Wasylishen, *Magn. Reson. Chem.*, 1993, **31**, 537.
42. A. G. Avent, M. A. Edelman, M. F. Lappert, and G. A. Lawless, *J. Am. Chem. Soc.*, 1989, **111**, 3423.
43. H. LeBail, C. Chachaty, P. Rigny, and R. Bougon, *C.R. Acad. Sci.*, 1983, **297**, 451.
44. G. V. D. Tiers, *J. Phys. Chem.*, 1958, **62**, 1151.
45. D. L. VanderHart, in 'Encyclopedia of NMR', eds D. M. Grant and R. K. Harris, Wiley: Chichester, 1996, vol. 5, p 2938.
46. P. E. Hansen, *Prog. Nucl. Magn. Reson. Spectrosc.*, 1988, **20**, 207.
47. D. F. Evans, *J.C.S. Chem. Commun.*, 1982, 1226.
48. L. J. Altman, D. Laungani, G. Gunnarson, H. Wennerström, and S. Forsen, *J. Am. Chem. Soc.*, 1978, **100**, 8264.
49. W. McFarlane, *Proc. R. Soc. (London) A*, 1968, **306**, 185 and references therein.
50. W. McFarlane, *Annu. Rev. NMR Spectrosc.*, 1968, **1**, 135.
51. R. K. Harris and B. J. Kimber, *J. Magn. Reson.*, 1975, **17**, 174.
52. D. Canet, C. Goulon-Ginet and J. P. Marchal, *J. Magn. Reson.*, 1976, **22**, 537.
53. D. S. Wishart, C. G. Bigam, J. Yao, F. Abildgaard, H. J. Dyson, E. Oldfield, J. L. Markley, and B. D. Sykes, *J. Biomol. NMR*, 1995, **6**, 135.
54. N. N. Zemlyanskii and O. K. Sokolikova, *Russ. J. Anal. Chem.*, 1981, **36**, 1421.
55. C. J. Jameson, A. K. Jameson, and S. M. Cohen, *J. Magn. Reson.*, 1975, **19**, 385.
56. F. G. Morin, M. S. Solum, J. D. Withers, and D. M. Grant, *J. Magn. Reson.*, 1982, **48**, 138.
57. G. V. D. Tiers and A. Kowalewsky, paper presented to the Division of Physical Chemistry, 137th National Meeting ACS, Cleveland, Ohio, 1960, Abstracts, p. 1712; G. V. D. Tiers and R. I. Coon, *J. Org. Chem.*, 1961, **26**, 2097.
58. G. V. Tiers and A. Kowalewsky, Division of Physical Chemistry, 137th ACS National Meeting, Cleveland, Ohio, 1960; L. Pohl and M. Ecke, *Angew Chem., Int. Ed. Engl.*, 1969, **8**, 381; D. H. Live and S. I. Chan, *Org. Magn. Reson.*, 1973, **5**, 275.
59. E. D. Becker, *J. Magn. Reson.*, 1971, **4**, 142.
60. E. D. Becker, R. B. Bradley, and T. Axenrod, *J. Magn. Reson.*, 1971, **4**, 136.
61. D. Doskočilová and B. Schneider, *Macromolecules*, 1972, **5**, 125.
62. D. Doskočilová, D. D. Tao, and B. Schneider, *Czech. J. Phys. B*, 1975, **25**, 202.
63. W. L. Earl and D. L. VanderHart, *J. Magn. Reson.*, 1982, **48**, 35.
64. A. N. Garroway, *J. Magn. Reson.*, 1982, **49**, 168.
65. S. Hayashi, M. Yanagisawa, and K. Hayamizu, *Anal. Sci.*, 1991, **7**, 955.
66. S. Hayashi and K. Hayamizu, *Bull. Chem. Soc. Jpn.*, 1989, **62**, 2429.
67. S. Hayashi and K. Hayamizu, *Bull. Chem. Soc. Jpn.*, 1991, **64**, 685.
68. S. Hayashi and K. Hayamizu, *Bull. Chem. Soc. Jpn.*, 1991, **64**, 688.

Orientationally Broadened NMR Spectra: Analysis by Special Processing Methods

Frederick G. Vogt

GlaxoSmithKline Research and Development, King of Prussia, PA, USA

&

Karl T. Mueller

The Pennsylvania State University, PA, USA

1	Introduction	1
2	Theoretical Background	1
3	Methods of Spectral Analysis	4
4	Applications	7
5	Conclusions and Future Directions	12
6	Related Article in this Volume	12
7	Related Articles in Volumes 1–8	12
8	References	12

1 INTRODUCTION

NMR signals are usually analyzed for frequency content by way of the discrete Fourier transform (DFT).[1,2] The goal of this analysis is to extract and separate the parameters describing the various NMR interactions, such as isotropic chemical shift values or coupling constants. The DFT is the method of choice for signals that are sinusoidal in nature, but is also commonly used to analyze other oscillatory NMR signals that inherently contain a wide range of frequencies. An example is provided by the destructive interference effect that accompanies anisotropic interactions in solid-state NMR, in which the signals from molecules oriented differently with respect to the magnetic field will often cancel each other in the time domain. This results in a DFT spectrum containing broadened lineshapes and a wide range of frequencies, but which may still retain some sharp structural features. The breadth of these so-called 'powder patterns' can often lead to spectral overlap. This is an obvious hindrance to the extraction of relevant information from the NMR spectrum. If the spectrum happens to be dominated by a single strong interaction, the powder lineshape can usually be fitted in the time or frequency domain to extract out the anisotropic parameters. The fitting procedure works well for simple situations yielding signals with good signal-to-noise ratios, and has the advantage of being easy to visualize. However, as more interactions complicate the spectrum, this nonlinear fitting approach requires more variables and quickly becomes intractable. Even in simple cases, there are other disadvantages of the fitting approach caused by the choices involved in fitting to a model. An example is the decision to include or ignore relaxation effects in the fitting procedure.

In the case of multiple overlapping interactions, the task of extracting the relevant coupling constants or chemical shift parameters can be often tackled by using 'special' processing schemes that supplement or replace the DFT. These schemes are the subject of the present article. They offer a more capable analysis that resembles the DFT in its linearity towards multiple overlapping signals. An important requirement for these special methods is that the signals under analysis must all be of the same form, which usually implies that they arise from the same type of interaction. Thus, the interactions of interest must either dominate all other interactions in the spectrum, or be separated out in an appropriate multidimensional NMR experiment. A second fundamental assumption behind the special processing schemes discussed here is that the theoretical form of the signal is known and is at least reasonably well understood. When these assumptions are met, two distinct application classes are possible. The first occurs in microcrystalline or amorphous powders, where the orientational distributions are known to be random and the desired information is the strength of the interaction. This case, commonly known as the 'powder average', presently encompasses the majority of applications and will thus receive the most attention. However, another important situation occurs when the magnitude of the interaction (e.g., the coupling constant) is known and an orientational distribution is sought. Examples of this situation will also be considered, and include studies of ordering in a sample or analyses of anisotropic molecular motion.

2 THEORETICAL BACKGROUND

Orientationally averaged NMR signals can be theoretically analyzed in a fairly consistent manner, even in situations where sample spinning and other mechanical reorientations of the axis system are employed. A mathematical analysis of the theoretical time or frequency domain signal is the first step in the process. This is at the root of many useful processing schemes for powder averaged signals, where the reduction of integrals to simplified analytical forms saves enormous amounts of computational time and offers greater insight into signal behavior. An illustrative and pertinent example is the static (i.e., non-spinning) powder signal produced by isolated spin-1 nuclei under the influence of an axially symmetric first-order quadrupolar Hamiltonian. This signal is equivalent to that from an isolated dipolar-coupled pair of spin-1/2 nuclei, and results in the well-known Pake pattern upon Fourier transformation.[3,4] The Pake signal is also closely related to that arising from an axially-symmetric chemical shift or Knight shift interaction. In these cases the single transition that produces the signal yields only 'half' of the Pake frequency-domain powder pattern.[3] In the more common dipolar and quadrupolar cases, the frequencies produced by an interaction i will mathematically scale as

$$\omega_i(\theta) = \pm\omega_i^0 P_2(\cos\theta) = \pm\tfrac{1}{2}\omega_i^0(3\cos^2\theta - 1) \qquad (1)$$

where θ is the angle between the static applied magnetic field and the principal axis system (PAS) of the interaction. The function P_2 represents a Legendre polynomial, and the

frequency ω_i^0 (where $\omega_i^0 = 2\pi\nu_i^0$) contains the fundamental strength of the interaction, obtained at $\theta = 0$, in units of radians per second.[5] In the case of a through-space dipolar coupling ($i = D$), the PAS is defined by the internuclear vector, and in the case of an axially symmetric quadrupolar interaction ($i = Q$), the unique axis of the PAS is the symmetry axis of the interaction. When the interaction of interest is an axially symmetric chemical shift, equation (1) is of the same form but its magnitude is given by the difference between the parallel and perpendicular components of the shift tensor (see **Chemical Shift Tensors,** Volume 2 Section 4.2).

The analysis of the Pake signal starts with the traditional time-independent dipolar Hamiltonian, averaged over all possible angles. Because many experiments that produce this signal yield spectra that are symmetric about their center (or are independent of the signal phase), the propagation of the signal is often confined to the real portion

$$S_{Pake}(\omega_i^0, t) = \frac{1}{2}\int_0^{\pi} \sin\theta d\theta \cos[\omega_i^0 P_2(\cos\theta)t] \qquad (2)$$

Evaluation of this integral for a series of time (t) values yields the time domain form of the Pake signal, which shows a characteristic decay caused by interfering signal contributions. This is illustrated by the time domain signal (Figure 1a) for the case of a heteronuclear dipolar signal. The Fourier transform of this signal (i.e., the Pake pattern) is shown in Figure 1(b). Note that the frequency difference between the maxima and the width of the entire pattern reflect the magnitude of the interaction.

The numerical integration in equation (2) can be accomplished by summing the integral over an evenly-spaced array of values, or by using other well-known numerical integration methods. For some time-independent Hamiltonians, numerical integration may be the only way to simulate spectra in the time domain. (Explicitly time-dependent Hamiltonians require a more sophisticated approach and are not discussed here.) The signal of equation (2) can also be analytically integrated to yield a compact form

$$S_{Pake}(\omega_i^0, t) = \frac{\sqrt{\frac{\pi}{3}}\left(\cos\left(\frac{1}{2}\omega_i^0 t\right) C\left(\sqrt{\frac{3}{\pi}}\sqrt{\omega_i^0 t}\right) + \sin\left(\frac{1}{2}\omega_i^0 t\right) S\left(\sqrt{\frac{3}{\pi}}\sqrt{\omega_i^0 t}\right)\right)}{\sqrt{\omega_i^0 t}} \qquad (3)$$

In equation (3), C and S represent the cosine and sine Fresnel integrals, which are defined as[5]

$$S(x) = \int_0^x \sin\left(\frac{\pi t^2}{2}\right)dt \quad C(x) = \int_0^x \cos\left(\frac{\pi t^2}{2}\right)dt \qquad (4)$$

(Note that other definitions for C and S exist; those used here are prevalent in the physical sciences).[5–7] These special functions can be directly calculated for larger arguments of x via efficient numerical algorithms that rely on the evaluation of continued fractions.[7] Simulation of Pake-type signals is greatly facilitated by the form in equation (3), as the aforementioned numerical integration and its attendant computational complexities are avoided.

Other representations of the Pake signal that can yield even faster computational results are also available. A different approach to the integration of equation (2) yields a series representation of the signal in terms of integer-order Bessel functions:

$$S_{Pake}(\omega_i^0, t) = \cos\left(\frac{1}{4}\omega_i^0 t\right) J_0\left(\frac{3}{4}\omega_i^0 t\right) - 2\sum_{k=1}^{\infty} \cos\left(\frac{1}{4}\omega_i^0 t + \frac{k\pi}{2}\right)\left(\frac{J_k(\frac{3}{4}\omega_i^0 t)}{4k^2 - 1}\right) \qquad (5)$$

where the J represent Bessel functions of the first kind.[5,8] The derivation is based on the Jacobi-Anger expansion of a plane wave into cylindrical waves, and offers some insight into the individual components that make up the Pake signal.[9] Computationally, equation (5) yields accurate results when the series is truncated at values of k ranging from 5 to 20, and usually has significant computational advantages over the evaluation of equation (3). The increased performance results from the availability of fast algorithms for the numerical determination of sequential integer-order Bessel functions.[7]

Another type of expansion can be used to obtain further theoretical insights into the Pake signal and many other relevant signals.[10] This expansion has been developed in the literature for the more general complex form of equation (2):

$$S_{Pake}(\omega_i^0, t) = \frac{1}{2}\int_0^{\pi} \sin\theta d\theta \exp\left[-i\omega_i^0 P_2(\cos\theta)t\right] \qquad (6)$$

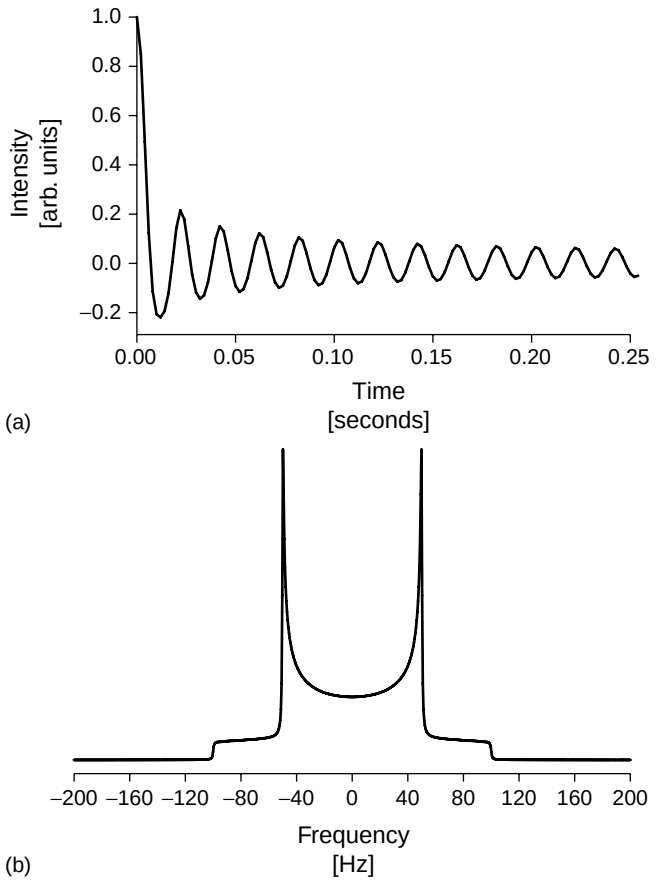

Figure 1 The Pake signal in the time and frequency domains. (a), the time evolution of a Pake signal produced by a 100 Hz heteronuclear dipolar coupling is shown. The singularities in the Fourier transform of this signal, shown in (b), are separated by 100 Hz. Note that the frequency domain spectrum is symmetric about 0 Hz

The expansion then proceeds by expanding the exponential function into a power series, the polynomial terms of which are then further expanded into Legendre polynomials

$$\exp\left[-i\omega_i^0 P_2(\cos\theta)t\right] = \exp(-i\omega_i^0 t)\sum_{k=0}^{\infty} c_{2n}\left(\frac{3}{2}\omega_i^0 t\right) P_{2n}(\cos\theta) \quad (7)$$

The scaling coefficients are found from the coefficients of both series expansions, and may be compactly written in terms of a Whittaker function (M)[5]

$$c_{2n}\left(\frac{3}{2}\omega_i^0 t\right) = \frac{\exp(\frac{i}{4}\omega_i^0 t)}{(n+\frac{1}{2})_n(\frac{3}{2}i\omega_i^0 t)^{3/4}} M_{1/4,n+1/4}\left(\frac{3}{2}i\omega_i^0 t\right) \quad (8)$$

The subscripted n in the $(n+1/2)_n$ term represents a Pochhammer symbol.[9] The key feature of this generalized representation is that the orientational dependence of the signal is separated from the time and frequency dependence, in analogy to the irreducible tensor notation for spin interactions (see **Internal Spin Interactions & Rotations in Solids,** Volume 4). Equation (7) has special advantages if additional reorientations are to be included at a later stage in the analysis (i.e., for more complex experiments or for partially ordered samples). The Pake signal can be quickly identified from this form after the expansion coefficients are found via simple overlap integrals. Only the $n = 0$ coefficient contributes to this third form for the Pake signal, which differs from the previous forms in that it is written in complex notation and is found without explicit integration

$$S_{Pake}(\omega_i^0, t) = c_0\left(\frac{3}{2}i\omega_i^0 t\right) = \frac{\exp(\frac{i}{4}\omega_i^0 t)}{(\frac{3}{2}i\omega_i^0 t)^{3/4}} M_{1/4,1/4}\left(\frac{3}{2}i\omega_i^0 t\right) \quad (9)$$

Evaluation of the real component of equation (9) produces a signal equivalent to that of equation (3), as there is a direct connection between the two via the imaginary error function.[5] Further discussion of the expansion shown in equation (7) and its applications is given in the literature.[10]

The Pake signal can also be treated completely in the frequency domain, by considering the powder spectrum as a weighted sum of contributions from the range of angles.[11–13] The analysis of the powder pattern can be made by determining its theoretical form from the analytical Fourier transform of equation (3), or by a more direct substitution method in which the derivative of equation (1) is used to find a frequency domain signal

$$S_{Pake}(\omega_i^0, \omega_i) = \frac{1}{\sqrt{3\omega_i^0\left(2\omega_i + \omega_i^0\right)}}, \quad -\frac{1}{2} < \frac{\omega_i}{\omega_i^0} \leq 1 \quad (10)$$

where S_{Pake} is zero outside the specified region. (For the details of this derivation, see Gerstein and Dybowski or **Chemical Shift Tensors,** Volume 2 Section 4).[14] This expression has the advantage of simplicity; however, a potential problem exists because of the singularity occurring at $\omega_i^0 = 0$, which affects the function in a manner that can lead to numerical difficulties. This issue is discussed in more detail in the following sections.

Besides the Pake signal, a number of other signals have been extensively studied, including those obtained in conjunction with the magic-angle spinning (MAS) technique. The use of MAS greatly simplifies spectral interpretation by partially or fully averaging away the anisotropic information contained in powder lineshapes (see **Magic Angle Spinning,** Volume 5). However, this loss of information can be circumvented by 2D approaches that use RF pulse sequences to reintroduce and separate interactions into different dimensions.[1,3] The signals acquired in the indirectly detected dimensions usually retain an orientationally averaged form that is further influenced by both the sample spinning and the particular RF pulse sequence. A relevant example is the rotational-echo double resonance (REDOR) experiment, a popular MAS method of separating chemical shift and heteronuclear dipolar interactions.[15] It is used for the determination of dipolar coupling constants and thus internuclear distances between spin-1/2 heteronuclei in a variety of situations (see **REDOR & TEDOR,** Volume 6). The reintroduced dipolar signal observed in most implementations of the REDOR experiment can be found from an average Hamiltonian analysis

$$S_{REDOR}(\omega_D^0, t) = \frac{1}{4\pi}\int_0^{2\pi} d\alpha \int_0^{\pi} \sin\beta\, d\beta \times \cos\left[\pm\frac{2\sqrt{2}}{\pi}\omega_D^0 t(\sin\beta\cos\beta\sin\alpha)\right] \quad (11)$$

The angles α and β represent the azimuthal and polar angles that describe the orientation of the dipolar internuclear vector (i.e., the principal axis system) within the MAS spinner.

The double integral in equation (11) adds to the computational complexity of numerical integration, although more sophisticated and effective powder integration routines yield major performance gains for problems of this sort.[16–18] However, numerical evaluation of equation (11) is not necessary because of the availability of a simple analytical form for the REDOR signal.[19–21] This form can be efficiently derived using tabulated integral forms.[21] The integration over α is first performed using an integral representation of the zeroth-order Bessel function of the first kind, followed by the use of a second form for the integration over β.[22,23] The compact form for the REDOR signal is then found

$$S_{REDOR}(\omega_D^0, t) = \frac{\sqrt{2}\pi}{4} J_{1/4}\left(\frac{\omega_D^0 t}{\sqrt{2}\pi}\right) J_{-1/4}\left(\frac{\omega_D^0 t}{\sqrt{2}\pi}\right) \quad (12)$$

in which $J_{1/4}$ represents a quarter-integer order Bessel function of the first kind.[5] This signal is also equivalent to that measured in dipolar dimensions of the homonuclear MELODRAMA, rotational resonance, and RFDR experiments.[24–27] In addition, a closely related signal is observed in the heteronuclear transferred-echo double resonance (TEDOR) experiment. The details of this signal and its analytical form are given in the references.[8,28,29]

As previously noted, different RF pulse sequences can produce different average Hamiltonians and hence different observed signals. A well-known example is the cross-polarization (CP) pulse sequence commonly used in conjunction with MAS (see **Cross Polarization in Solids,** Volume 3 and **Cross Polarization in Rotating Solids: Spin-1/2 Nuclei,** Volume 3). The case of interest here is rather rare in practice, but occurs when CP-MAS is used to transfer polarization

between two isolated heteronuclear spins. An average Hamiltonian calculation for this case results in an effective dipolar magnitude of

$$\omega_D = \frac{\omega_D^0}{2\sqrt{2}} \sin(2\beta) \tag{13}$$

where β is an angle that relates the rotor frame to the I-S internuclear vector.[30,31] The dipolar signal as a function of time is calculated from the weighted propagator

$$S_{CP}(\omega_D^0, t) = \frac{1}{2}\left[1 - \frac{1}{2}\int_0^{\pi} d\beta \sin(\beta) \cos\left(\frac{\omega_D^0}{2\sqrt{2}} \sin(2\beta) t\right)\right] \tag{14}$$

Direct integration of equation (14) leads to concise forms for this signal

$$\begin{aligned} S_{CP}(\omega_D^0, t) &= -\frac{1}{8}\left[s_{-1,1/2}\left(\frac{\omega_D^0 t}{2\sqrt{2}}\right)\right] \\ &= \frac{1}{2}\left[{}_1F_2\left(1; \frac{3}{4}, \frac{5}{4}; \frac{(\omega_D^0 t)^2}{32}\right)\right] \end{aligned} \tag{15}$$

where $S_{-1,1/2}$ represents a Lommel function and ${}_1F_2$ represents the generalized hypergeometric function.[5,32] A more computationally efficient series representation in terms of Bessel functions, similar in nature to the Pake signal in equation (5), can be found via the Jacobi-Anger expansion and subsequent integration:[24]

$$S_{CP}(\omega_D^0, t) = \frac{1}{2} J_0\left(\frac{\omega_D^0 t}{2\sqrt{2}}\right) - \sum_{k=1}^{\infty} \frac{1}{16k^2 - 1} J_{2k}\left(\frac{\omega_D^0 t}{2\sqrt{2}}\right) \tag{16}$$

This signal is theoretically observed in a variety of dipolar experiments on spin pairs. These include certain heteronuclear double cross-polarization (DCP) experiments, and the C7 and DQ-HORROR homonuclear dipolar pulse sequences.[31,33,34] In these cases equation (16) is measured as a function of the dipolar mixing period and may require time domain correction for relaxation effects. A computationally efficient, truncated form of this series is useful for processing the data obtained from these experiments.[24] It should be noted that in several of the aforementioned experiments, equation (16) represents the form of the signal predicted by zeroth-order average Hamiltonian theory, but other strong interactions can alter the signal by contributing high-order terms to the Hamiltonian.

Asymptotic forms for several of the aforementioned time domain signals also impart some insight into the development of processing methods. Two asymptotic approximations that lead to important simplifications are available for the Fresnel integrals and the Bessel function:[5,10]

$$C(x) \approx S(x) \approx \frac{1}{2}, \text{ as } x \to \infty \tag{17}$$

$$J_k(x) \approx \sqrt{\frac{2}{\pi x}} \cos\left(x - \frac{1}{2}k\pi - \frac{1}{4}\pi\right), \text{ as } x \to \infty \tag{18}$$

These asymptotic expressions are only valid at larger x values, which in the present case usually implies longer acquisition times or larger interaction strengths. (Asymptotic expressions for smaller values of x and for other special functions are also available.) By substitution of equation (17) into equation (3), the asymptotic form of the Pake signal can be determined (after manipulation of the relative phase of the positive and negative frequency components)[10,35,36]

$$S_{Pake}^a(\omega_i^0, t) = \frac{\sqrt{\frac{\pi}{3}} \cos(\frac{1}{2}\omega_i^0 t - \frac{\pi}{4})}{\sqrt{\omega_i^0 t}} \tag{19}$$

For the REDOR signal, the asymptotic form is found by use of equations (12) and (18)[24]

$$S_{REDOR}^a(\nu_D, t) = \frac{\sin(2\sqrt{2}\nu_D t)}{4\sqrt{2}\nu_D t} \tag{20}$$

The simplicity of these versions of the Pake and REDOR signals is especially useful in the design of specialized algorithms for spectral analysis.

In the case of problems for which the magnitude of the interaction is known and the orientational distribution is desired, the signal takes on a different appearance. Since an angle or a range of angles is the desired quantity, the need for integration is usually removed and there is no need for a mathematical reduction to an analytical form. Many different signals can be studied for their orientational distribution; however, their derivation is highly specific to the problem at hand.

3 METHODS OF SPECTRAL ANALYSIS

Analytical forms for powder averaged signals can lead to obvious enhancements in traditional fitting methods in either the time or frequency domain, as there is no longer a need for the numerical evaluation of integrals. However, another great benefit of analytical forms is the direct link that they provide to improved signal analysis schemes. Drawing on the theoretical information presented in the previous section, special processing methods can be constructed that seek to provide a more understandable and reliable representation of the information in these signals than that obtainable from nonlinear fitting analyses or from powder patterns. The desired result is a spectrum showing sharp peaks at relevant frequencies or specific orientations. The processing method should also be linear, in that a sum of input signals should be faithfully broken into its constituent parts (as in the Fourier transform).[12]

Most of the methods that will be discussed here attempt to solve a problem known as a Fredholm integral equation of the first kind

$$f(t) = \int_{\nu_1}^{\nu_2} K(\nu, t) F(\nu) d\nu \tag{21}$$

The Fredholm equation shown here is formulated for the common case of a time domain measurement $f(t)$ and a desired result in the frequency domain $F(\nu)$ (i.e., the domain of the interaction strength). The kernel function K relates the two domains, and is constructed from the expected form of the signal. A great number of methods for extracting $F(\nu)$ are available; however, only those that are successful in NMR analyses are given attention herein.

An additional class of spectral analysis method presented here relies on information extracted from the asymptotic form of a signal. This information is indirectly used to 'solve' equation (21) by way of time and frequency domain weighting procedures. A suitable and reliable asymptotic form (which may not be available) is a prerequisite for these methods, which feature significant performance advantages but are also subject to undesirable spectral artifacts.

3.1 Analytical Transforms

The analysis of an orientationally averaged signal can be accomplished if the Fredholm equation in equation (21) can be solved. Conceptually, the simplest procedure for obtaining the solution is to find an analytical inverse for the kernel function. This can be used to find the frequency domain solution by way of the inverted form of equation (21):

$$F(\nu) = \int_{t_1}^{t_2} K^{-1}(\nu, t) f(t) dt \tag{22}$$

where K^{-1} represents the analytical inverse of K. In practice, NMR data are measured at a finite number of points, and this operation (known as a discrete integral transform) must be rewritten as

$$F_k = \sum_{j=1}^{n} K_{kj}^{-1} f_j \tag{23}$$

where k and j are vector and matrix indices, and n is the number of data points. (The discrete transform is written here for the usual case of a square kernel matrix.) The Fourier transform is an example of a discrete integral transform, in which the kernel is given by a complex sinusoidal function. In the case of the DFT, the procedure normally does not occur via the explicit form of equation (23), but instead takes advantage of special kernel features with fast algorithms (i.e., the fast Fourier transform or FFT).[2,7,37]

Presently, the only signal of interest here with a known analytical inverse is the REDOR signal of equation (12). This was found from a published expression for the inverse of quarter-integer order Bessel functions.[19,20] The analytical inverse is written here for the common case of the dipolar coupling ν_D

$$\begin{aligned} K_{REDOR}^{-1}(\nu_D, t) = \sqrt{2}\nu_D t \left[J_{1/4}(\sqrt{2}\nu_D t)^2 - J_{-1/4}(\sqrt{2}\nu_D t)^2 \right] \\ + 2(\nu_D t)^2 \left[J_{-3/4}(\sqrt{2}\nu_D t) J_{1/4}(\sqrt{2}\nu_D t) \right. \\ \left. - J_{-5/4}(\sqrt{2}\nu_D t) J_{-1/4}(\sqrt{2}\nu_D t) \right] \\ + 2(\nu_D t)^2 \left[J_{-1/4}(\sqrt{2}\nu_D t) J_{3/4}(\sqrt{2}\nu_D t) \right. \\ \left. + J_{1/4}(\sqrt{2}\nu_D t) J_{5/4}(\sqrt{2}\nu_D t) \right] \end{aligned} \tag{24}$$

A highly effective algorithm for the REDOR transform is then constructed by substitution of this inverse kernel function into equation (23). An asymptotic relationship for this kernel function can also be obtained[19–21]

$$\lim_{\nu_D t \to 0} K_{REDOR}^{-1}(\nu_D, t) \propto \nu_D t \sin(2\sqrt{2}\nu_D t) \tag{25}$$

The asymptotic inverse REDOR kernel is not normally used in actual computations because of the availability of the simpler and faster asymptotic rescaling procedure discussed in Section 3.4. However, the asymptotic inverse kernel can be used to obtain a sampling theorem for the REDOR transform (analogous to the Nyquist theorem for the Fourier transform).[2] The primary frequency component of this kernel is revealed by Fourier transformation of equation (25), which then gives the following approximate sampling theorem

$$\nu_{\max} = \frac{\pi}{2\sqrt{2}\Delta t} \tag{26}$$

where $\nu_{\max}$ is the critical frequency (or spectral width) and Δt is the REDOR sampling rate (determined by the rotor speed and the number of rotor periods between sampling points).[19–21] Expressions for the resolution of a dipolar spectrum also follow from this analysis.[21] Similar results can be obtained from further study of the asymptotic REDOR signal (see Section 3.4).[24]

The REDOR kernel diverges with increasing D or t, so that the multiplicative process inherent in the transform tends to amplify the part of the time domain REDOR signal where noise is most noticeable. In practice, strong apodization of the time domain signal is needed to counteract this effect. Use of the Blackman-Harris and Kaiser-Bessel window functions has proved effective.[19–21,38] (The need for this type of apodization function is rooted in the 'ill-posed' nature of this type of problem, which is discussed in more detail in Section 3.3.) The REDOR transform is computationally expensive to perform because of the large number of Bessel functions in the kernel and the n^2 operations count of the matrix-vector multiplication. Unfortunately, the kernel function does not have the proper form that would make it amenable to solution via an FFT-like algorithm.[37] A substantial improvement in performance can still be obtained for signals with the same number of points and spectral parameters by preparing a desired inverse kernel once and storing it for subsequent usage. Thus analytical transforms have numerous advantages and disadvantages; however, their most significant drawback is the current unavailability of inverse functions for other signals.

3.2 Numerical Inversion Methods

In those cases where an analytical inverse is not available, such as that of the Pake signal, the well-developed numerical methods of inverse theory can be used to invert the Fredholm equation and obtain the desired spectrum. Equation (21) is then best written in its discrete form

$$f_k = \sum_{j=1}^{n} K_{kj} F_j \tag{27}$$

The solution vector F_j, which could be a frequency domain spectrum of coupling strengths, is then sought by numerical means. Several methods are available for solving this set of linear algebraic equations. A few of the more popular computational procedures have been applied to NMR problems, including the singular-value decomposition (SVD) and non-negative least squares (NNLS) methods.[10,37] The SVD procedure, which usually utilizes the Golub-Reinsch algorithm, is designed to handle 'singular' (or semi-degenerate) kernel

functions.[37] The NNLS algorithm in common use has been given by Lawson and Hanson.[39] It includes the feature of a constrained non-negative solution, which is useful in cases where the spectrum is known to be positive. Both the SVD and NNLS algorithms are robust and are theoretically guaranteed to produce a solution. Other promising solution methods exist but have not been widely demonstrated; an example is the preconditioned conjugate gradient method.[37] It is important to note that several other well-known methods for solving linear algebraic systems, especially those that utilize the so-called normal equations, can potentially fail to achieve a solution and should not generally be used for this sort of analysis.

When inverse methods are applied to the Pake problem in either the time or frequency domain – by using a K constructed from equations (3), (5) or (10) – the result is a spectrum with no Pake-style powder broadening. Thus these and all other methods for achieving this representation have earned the name 'dePakeing'. A third method, a customized iterative scheme for dePakeing, has also been widely used for this type of analysis.[11,12] It achieves the same net result as the SVD and NNLS algorithms, but considers the effect of each frequency separately, which corresponds to use of one row of K at a time. The iterative method has not been studied as thoroughly as the SVD and NNLS methods, and it is not known whether it will converge correctly in all cases, although in practice it seems to be quite robust.[11–13] In comparisons of the three methods applied to the Pake problem, the SVD and NNLS algorithms yield somewhat improved spectral clarity, and the non-negativity constraint of NNLS further enhances its capability.[13] The SVD, NNLS, and iterative methods have all been successfully applied to the Pake problem in both theoretical and experimental situations.

3.3 Regularization Methods

Despite their numerous advantages, inverse methods do have a significant drawback. As was noted previously, the SVD and NNLS methods will always find a solution to an inverse problem. There is no guarantee, however, that this solution will be the 'correct' solution. Specifically, in the presence of experimental noise, the actual Fredholm equation to be solved is not equation (21) but is instead

$$f(t) = \int_{\nu_1}^{\nu_2} K(\nu, t)F(\nu)d\nu + \varepsilon(t) \tag{28}$$

where $\varepsilon(t)$ represents the noise intensity that affects all experimental NMR data. In its discrete form, equation (28) is written as

$$f_k = \sum_{j=1}^{n} K_{kj}F_j + \varepsilon_k \tag{29}$$

for n points of data where k and j are indices of summation, and the F_j again represent the desired solution. The possibility of an incorrect solution from a traditional numerical inversion method arises from the Riemann-Lebesgue lemma[40–42]

$$\lim_{y\to\infty} \int_{\nu_1}^{\nu_2} K(\nu, t)\sin(y\nu)d\nu = 0 \tag{30}$$

If $F(\nu) + A\sin(y\nu)$ is substituted into equation (28) in place of $F(\nu)$, one finds

$$f(t) = \int_{\nu_1}^{\nu_2} K(\nu, t)F(\nu)d\nu + \int_{\nu_1}^{\nu_2} K(\nu, t)A\sin(y\nu)d\nu + \varepsilon(t) \tag{31}$$

Thus, the Riemann-Lebesgue lemma indicates that even for small noise intensity $\varepsilon(t)$ and an arbitrarily large scaling factor A, there will still be a y that will reduce equation (31) to equation (28). In other words, $F(\nu) + A\sin(y\nu)$ will be indistinguishable from $F(\nu)$ and oscillatory terms can 'hide' in the noise intensity. The error in the solution is unbounded, and the variability of y yields a large number of possible solutions.[40–42] Methods utilizing an exact analytical inverse formula or numerical inversion, such as the REDOR transform or any of the aforementioned dePakeing methods, by their nature ignore the noise values and can only determine the correct solution when $\varepsilon(t)$ is zero at all times. If $\varepsilon(t) > 0$, these methods will arbitrarily select one of solutions to $F(\nu)$, which is statistically unlikely to be the best estimate of the spectrum. While the theory behind this situation is obviously quite detailed, its manifestation is simple and usually consists of the appearance of strong oscillations in the resulting spectrum, particularly at higher frequencies.[40–42]

The problem described here has been given the title of 'ill-posedness', implying that the solution is overly sensitive to perturbations in the input data. The severity of an ill-posed problem depends on the kernel function. A strongly ill-posed kernel function will be measurably ill-conditioned, and yield larger L_1 condition numbers and a more singular kernel matrix.[37] (Specialized algorithms are available for the estimation of condition numbers.)[43,44] The Pake kernel typically shows a relatively low condition number, and hence is usually solvable by the inverse methods.[24] However, upon closer examination, it is found that noise sensitivity issues do affect the Pake analyses.[45] Other kernels (including the REDOR kernel) are often very ill-conditioned and cannot usually be solved by traditional inverse methods.[24] The problem of an ill-posed kernel function also affects the REDOR transform, although the availability of the analytical inverse avoids many of the noise sensitivity issues associated with numerical inversion methods.

If the ill-posedness of the problem causes difficulty in an analysis, then methods explicitly designed to handle this issue should be considered. The problems of ill-posed Fredholm equations and their noise sensitivity have afflicted many areas of science and engineering, and led to the development of a branch of numerical analysis known as regularization.[40–42] In general, a regularization algorithm finds an approximate solution to an ill-posed Fredholm equation from a neighboring group of well-posed equations by optimizing an expanded least squares problem. Like NNLS algorithms, the least-squares problem allows regularization software to impose known constraints (such as positivity requirements) on the solution and thus gain an additional advantage in these cases. However, the most important feature of regularization, which is lacking in the other inverse methods, is based on its use of a principle called parsimony. This refers to the process of selecting the simplest member of the set of solutions given by the least squares method, such as the smoothest solution with the fewest number of peaks.

The Tikhonov regularization method (also known as Linear or Twomey-Phillips regularization) and the maximum entropy

regularization method (MaxEnt) are two of the most popular and effective methods for regularization. (Other methods, such as the Backus-Gilbert method, are not discussed here.)[7] The Tikhonov and MaxEnt regularization methods differ in their choice of a regularization operator, which is the mathematical tool used to actually select the 'best' solution. Understanding the role of the regularization operator requires knowledge of the details of the regularization method, which minimizes a least-squares problem

$$\Psi(\lambda) = \sum_{j=1}^{n} \frac{1}{\sigma_j} \left((f_k + \varepsilon_k) - \int_{\nu_1}^{\nu_2} K(\nu, t) F(\nu) d\nu \right)^2 + \lambda R(F(\nu)) \tag{32}$$

Here Ψ is the function being minimized and the variable λ represents the regularization parameter that scales the operator R and controls its effectiveness. The σ_j are determined by the noise model (usually a Gaussian distribution), and the quantity $f_k + \varepsilon_k$ refers to the combination of the time domain signal and the experimental noise. For the Tikhonov method, the regularization operator is the second derivative operator (D)[40–42]

$$R(F(\nu)) = \|DF(\nu)\|^2 \tag{33}$$

where the vertical bars designate a norm, which is a measure of distance in matrix space.[37] The operator for MaxEnt is the negentropy operator

$$R(F(\nu)) = -\int_{-\infty}^{+\infty} F(\nu) \ln\left(\frac{F(\nu)}{F_N}\right) d\nu \tag{34}$$

The second derivative operator tends to smooth data more effectively than the negentropy operator, because the derivative takes into account the connectivity of neighboring discrete spectral points. This helps prevent noise from being mistaken for peaks, and is especially useful in cases where a few broad peaks are expected (as in solid-state NMR). The second derivative operator used by Tikhonov regularization also allows for a linear least squares solution to equation (32), as opposed to the more complicated nonlinear solution needed by MaxEnt regularization. Tikhonov regularization thus has two advantages over MaxEnt regularization for the spectra typically seen in solid-state NMR applications, and has so far seen the majority of applications to orientationally-averaged signals, although alternative methods are likely to be introduced in the future.

In the case of Tikhonov regularization, equation (32) has the discrete form

$$\Psi(\lambda) = \sum_{j=1}^{n} \frac{1}{\sigma_j} \left\| (f_k + \varepsilon_k) - \sum_{k=1}^{n} K_{kj} F_j \right\|^2 + \lambda \|DF_j\|^2 \tag{35}$$

A number of fast algorithms are available for obtaining the solution by minimization of equation (35).[40–42,46,47] The selection of the regularization parameter is an important contributor to the success of the regularization procedure. If λ is too large, the result will be a featureless, overly smoothed spectrum. If λ is too small, the problem will approach a standard linear least squares solution, and will yield unrecognizable oscillations and spurious peaks for the reasons discussed above. One popular method for the estimation of λ is the self-consistent (SC) method.[46,47] Many other statistically derived methods for selection of the regularization parameter are also in use.[7,40]

3.4 Rescaling of Signals using Asymptotic Forms

The asymptotic forms of orientationally averaged signals can, in certain cases, be used to algebraically rescale or weight an acquired signal so that the broadening observed in the frequency domain is avoided. For example, in the case of the Pake signal, the approximation given in equation (19) suggests that a co-sinusoidal signal could be obtained by multiplying the signal by the square root of time (while in the time domain), followed by multiplication by the square root of frequency (in the frequency domain).[13,35,36] The required transformation between domains is easily accomplished using the FFT upon the remaining scaled sinusoidal signal. The operation is completed by a $\pi/4$ phase shift, to offset the constant term inside the cosine function of the asymptotic expression in equation (19). A similar procedure can be applied to the REDOR signal, whose asymptotic form, given in equation (20), requires multiplication by time and dipolar frequency (in their respective domains), with a subsequent phase shift of $\pi/2$.[24] The REDOR asymptotic rescaling procedure is referred to herein as the REDOR-AR method. In both cases, the net result of returning these signals to a co-sinusoidal form is to make them interpretable via a Fourier transform.

At first glance, the asymptotic rescaling methods should theoretically not suffer from the ill-posed nature of these problems because of the relative stability of the FFT.[38] However, the weighting procedure strongly amplifies the noise present at later portions of the time domain signal (more so for the REDOR signal than for the Pake signal). This noise is carried through the FFT, where it accumulates at higher frequencies, and is then further amplified by the frequency-domain weighting. The result is significant noise effects in the final spectrum, which are comparable to those observed using analytical transforms or inverse methods.[24]

The simple spectral multiplication procedure and the efficiency of fast DFT algorithms makes asymptotic rescaling the computationally fastest method of those discussed here. Its dominant operations count, $O(n)$, is governed by the FFT and is thus $n \log(n)$, where n is the number of data points.[7] However, there are a number of drawbacks to the procedure, most notably the artifacts that may be observed in the resulting spectra because of deviations of the true signal from the asymptotic form. These deviations are known to cause small spurious peaks in the frequency domain spectrum (for the Pake signal) or other minor spectral distortions (for the REDOR case).[10,24,36] Finally, the lack of simple and reliable asymptotic forms has prevented application of this technique to other signals.

4 APPLICATIONS

4.1 DePakeing of Static Quadrupolar Spectra

The earliest application of the techniques discussed here was to the removal of quadrupolar powder broadening in static ^{2}H NMR spectra.[11] These wideline spectra can yield valuable information about molecular motion and order in solid

materials. Deuterium spectral features are often dominated by broad first-order quadrupolar coupling interactions that commonly exhibit axial symmetry (see **Deuterium NMR in Solids,** Volume 3). Static ^{2}H experiments that measure these interactions, usually via the quadrupolar-echo pulse sequence, have been in use for some time. The resulting spectra contain Pake patterns with singularities that are separated by $3/4\nu_Q^0$. These spectra are amenable to the dePakeing procedure as a means to improve both resolution and quantitation. The pure quadrupolar spectrum produced by dePakeing methods is often referred to as an 'oriented' spectrum. It is the spectrum that would be experimentally measured from a single crystal sample with a PAS aligned with the static magnetic field. Note that ^{2}H applications, which have received the majority of attention to date, will be discussed in detail here. The spectral analysis of other quadrupolar nuclei may also benefit from the methods discussed above. Examples of the dePakeing procedure applied to ^{23}Na and ^{27}Al spectra (which did not exhibit significant second-order quadrupolar effects) have appeared in the literature.[48]

All of the aforementioned spectral analysis methods have been applied to the dePakeing of deuterium NMR spectra. As was previously noted, the first method used was the iterative frequency-domain process.[11,12] An example of its use, in an application to perdeuterated tetradecanol in a phospholipid-water dispersion, is shown in Figure 2.[13,49] The dePakeing procedure allowed for a complete study of this system, and direct observation of its temperature-dependent phase changes.

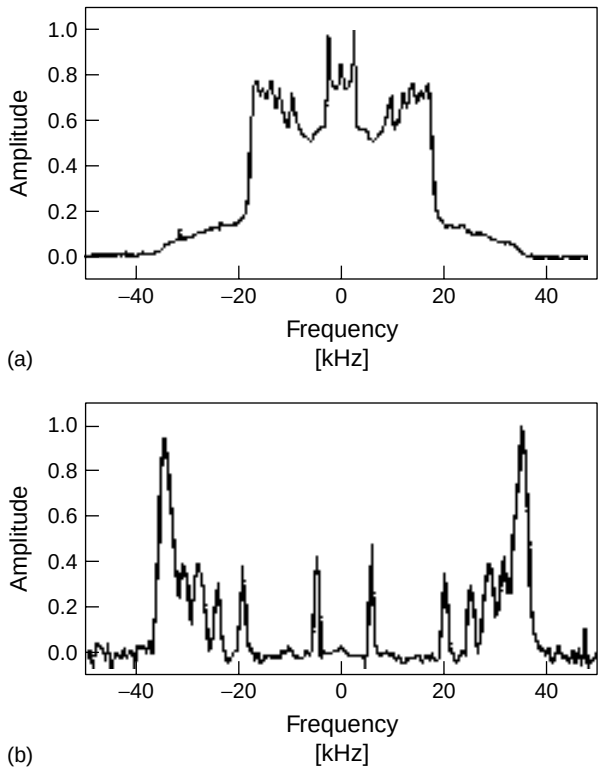

Figure 2 The dePakeing procedure applied to static ^{2}H NMR spectra of perdeuterated tetradecanol in a phospholipid-water dispersion. The powder spectrum is shown in (a), and the results of the dePakeing procedure are shown in (b). Note the greatly enhanced resolution of the bottom spectrum (often referred as the oriented spectrum), which contains sharp peaks at different quadrupolar coupling frequencies

The newer and more capable SVD and NNLS dePakeing methods were also demonstrated on this same experimental data.[16] These dePakeing methods have proven their value in a wide variety of applications to ^{2}H NMR. These include studies of amphiphilic dispersions and membranes (such as phospholipid bilayers) in which the orientation order of acyl chains is studied.[49–59] The phase transitions of these systems are often of interest, as are the effects of surfactants. A study of a ferroelectric transition and its thermal hysteresis in a deuterated and fluorinated copolymer has also been reported, and underscores the potential of dePakeing analyses for materials science problems.[60]

Because of the relatively stable nature of the kernel, the ill-posedness of the Pake problem was not addressed until 1995, when Tikhonov regularization was shown to significantly reduce noise artifacts in dePaked spectra.[45] A comparison of the spectra resulting from the iterative, SVD, NNLS, and Tikhonov regularization methods applied to a simulated test signal is shown in Figure 3. The Tikhonov regularization procedure aids in removal of noise artifacts, which could obscure features in ^{2}H spectra with lower signal-to-noise ratios. The Tikhonov procedure is also fast and robust,

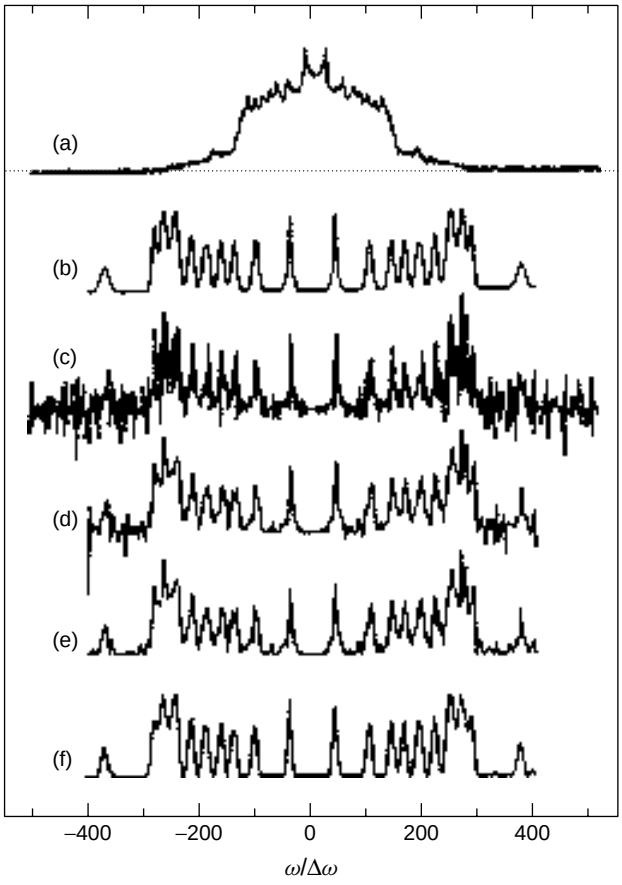

Figure 3 Comparison of methods used to process Pake signals. In (a), a simulated ^{2}H powder spectrum is shown. This was created by addition of a small amount of Gaussian noise to the simulated oriented spectrum in (b). The results of the iterative dePakeing procedure (c), the SVD solution (d), the NNLS solution (e), and the Tikhonov regularization method (f) are also shown. The Tikhonov regularization method displays superior noise-handling characteristics. Note that the FFT dePakeing method is not shown in this figure

and presently is the method of choice for most dePakeing applications.[45] A fast dePakeing procedure was also developed based on the asymptotic form of the Pake signal. This method, known as 'FFT dePakeing', has seen some initial applications to biochemical systems.[35,36] A simple example of its use is illustrated by the analysis of the ^{2}H spectrum of polycrystalline ^{2}H-labeled palmitic acid shown in Figure 4, where the results of the FFT dePakeing method are compared with those of the iterative method.[35] The oriented, pure quadrupolar ^{2}H spectra are similar, but FFT dePakeing achieved its result in less than 0.5% of the computational time needed by the iterative method. This performance gain far exceeds other available methods, but at the expense of significant spectral artifacts caused by the use of an inexact asymptotic form.[10,24,36] Nevertheless, for large data sets, the performance gain conferred by FFT dePakeing is an important element in the choice of a processing scheme, as is the exceptional simplicity of its implementation.

4.2 Measurement of Dipolar Coupling Constants

Analyses of dipolar powder spectra represent a second major area of application for specialized processing methods. The through-space dipolar coupling between two nuclear spins scales as the inverse third power of the internuclear distance. In static samples, the dipolar coupling manifests itself as a Pake pattern in which the singularities are separated by the dipolar coupling or 1.5 times the dipolar coupling, depending on whether the coupling is heteronuclear or homonuclear in origin. An early application of the iterative dePakeing procedure to dipolar spectra has demonstrated its applicability to these problems.[61] The analysis was directed towards simulated and experimental high-field static ^{13}C spectra containing additional broadening from strong chemical shift interactions. Because of the chemical shift anisotropy, the dePakeing procedure was unable to produce a true dipolar spectrum. Nevertheless, it did sharpen spectral features and allowed for an easier measurement of dipolar splitting, which in turn was used to aid in a fit of the spectra in the frequency-domain. This work demonstrates the tendency of dipolar interactions to be obscured, and points to the potential of multidimensional experiments that separate interactions. A well-known separation experiment has been given the acronym of SEDOR (for spin-echo double resonance), and produces a Pake signal in its indirectly-detected dimension.[3,62,63] Despite the use of SEDOR on suitable spin-pair systems, the potentially useful combination of this experiment and the dePakeing procedure has not yet appeared in the literature, although the fitting of experimental time domain data using equation (5) has been demonstrated.[8,64]

The resolution limitations of solid-state NMR have pushed dipolar spectroscopy into the MAS regime, where newer experiments have become very widely used. In particular, the previously discussed REDOR experiment is often run in a 2D fashion with an indirectly-detected dipolar dimension. While time domain fitting of the dipolar dephasing signal can be used in cases of a single dipolar coupling, multiple internuclear distance measurements are best achieved by special processing techniques. Most published examples have used the REDOR transform to accomplish this task. The initial experimental example was carried out on REDOR data taken from a sample of two small cyclic 9-residue polypeptides.[65] Both peptides were bound to a resin, but each was labeled differently at an internal glycine residue. The expected dipolar frequencies of 200 and 900 Hz were obtained from the dipolar dimension via the REDOR transform, as shown in Figure 5.

Other applications of the REDOR transform to multiple coupling situations have also appeared. A REDOR study of an organolithium complex utilized the ^{6}Li-^{13}C spin pair and the REDOR transform to measure multiple distances, which were used to locate lithium cations within a fluorenyl framework.[66] Other studies have used the REDOR transform to study multiple spin interference effects and their avoidance.[67,68] It should again be emphasized that the REDOR transform and all other techniques discussed herein rely on the signal being in the expected form of equation (12). The Pake, REDOR, and other signals derived above, when viewed in the dipolar context, must arise from *isolated* spin pairs. If this condition is not met, additional local interference effects will occur and the methods discuss herein must be supplied with a different kernel function to complete the analysis. Hence, the REDOR transform and dipolar dePakeing methods are only linear for systems that consist of well-separated interacting spin pairs, a fact which has been well-documented and demonstrated.[67,68]

A comparison of the available dePakeing methods has already been discussed for the quadrupolar case (Figure 3); these results, while not explicitly demonstrated, are also likely to be applicable to the static Pake-type dipolar signals.[45] For the more strongly ill-posed REDOR signal, the comparison of the available methods requires some further consideration. We note that the availability of the inverse REDOR kernel makes every method discussed herein applicable to the REDOR signal. However, since inverse theory methods usually fail completely for data containing even small amounts of noise, they will be dropped from the present discussion.[24] The available methods, namely the REDOR transform, REDOR-AR, and Tikhonov regularization, have been compared by analysis of a simulated signal to which a small amount of Gaussian noise has been added.[24] This comparison is depicted in Figure 6.

The results of the REDOR transform and the REDOR-AR procedure show the effects of noise upon the dipolar spectrum when the ill-conditioned problem is not treated as such. The computational performance of the REDOR-AR method greatly exceeds that of the REDOR transform, but the use of an inexact asymptotic form again introduces spectral artifacts. However, the artifacts are not as serious as those arising in FFT dePakeing owing to the superior approximation provided by the Bessel function asymptotic. As is clear from Figure 6, the excellent noise-handling capabilities of the Tikhonov regularization method and its lack of a requirement for an analytical inverse make this method theoretically the most preferable for processing experimental dipolar signals. The Tikhonov regularization procedure is computationally fast and benefits from its use of the simple direct kernel of equation (12), although it is not as fast as the REDOR-AR procedure.[24] The regularization method does have the drawback of being a more complicated algorithm that also requires a serviceable estimate of the regularization parameter. The REDOR-AR procedure and the Tikhonov regularization method have also been applied experimentally, but as of yet only to simpler REDOR-based dipolar coupling measurements.[24,29]

Further applications of the special processing techniques to dipolar coupling measurements seem likely given the extent of scientific interest in this area. The current synthetic abilities of the isotopic labeling field, coupled with relevance of the ^{2}H,

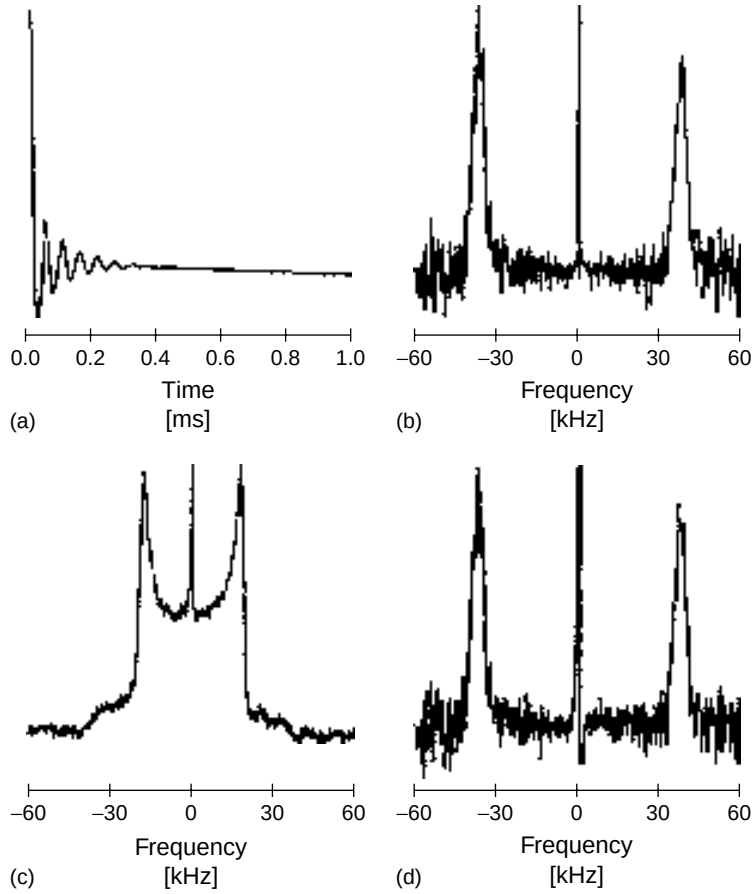

Figure 4 The FFT dePakeing procedure applied to static ^{2}H spectra of polycrystalline ^{2}H-labeled palmitic acid. In (a) the time domain decay of the Pake signal is shown, and in (b) the results of the FFT dePakeing procedure are illustrated. In (c) and (d), the Fourier transform and the iteratively dePaked spectra are shown for comparison

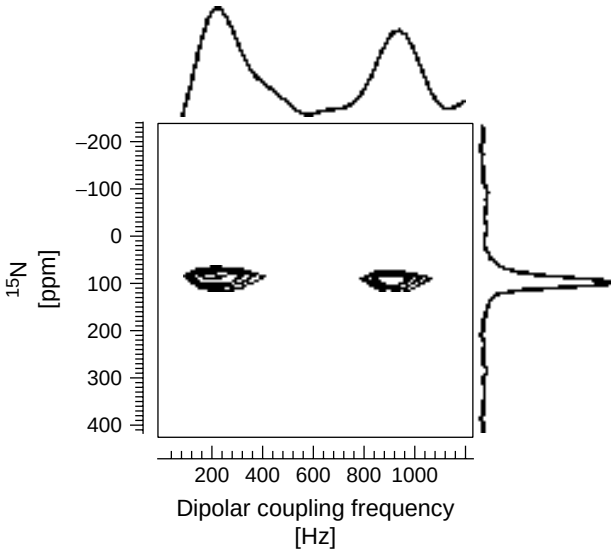

Figure 5 The 2D-REDOR results obtained from two cyclic peptides, each doubly ^{13}C and ^{15}N labeled at a glycine residue (see text for details). The data is shown after Fourier transformation of the directly-detected dimension and REDOR transformation of the dipolar dimension. The measured dipolar frequencies of 200 and 900 Hz correspond to the two known internuclear distances in each type of glycine residue

^{13}C, ^{15}N, ^{31}P, ^{19}F, and numerous other nuclei to many biochemical and materials science problems, is likely to ensure a steady supply of prospective data. Experimental demonstrations of these processing techniques for other types of signals, such as the CP signal, has not yet been accomplished, although simulations have shown their viability.[24] Finally, it is noted that all of the MAS applications discussed here have been heteronuclear dipolar experiments. Homonuclear dipolar MAS experiments are technically and theoretically more demanding. As previously noted, analytical forms have been determined for the dipolar signals produced by these experiments, but experimental applications of the special processing methods have yet to appear.

4.3 Analysis of Anisotropic Chemical Shift Interactions

The dePakeing process has also been applied to cases of axially-symmetric chemical shift tensors, namely those that are sometimes found in static ^{31}P solid-state NMR. Most applications have been to phospholipid bilayers and membranes. The data obtained often complement the more common ^{2}H NMR results, since the ^{31}P spectra report on polar head group motion and the ^{2}H data are indicative of chain motion. The ^{31}P spectra, because of their origin in the single-transition spin-1/2 chemical shift, are not symmetric; hence the resulting dePaked data is sign-sensitive (unlike the case for ^{2}H

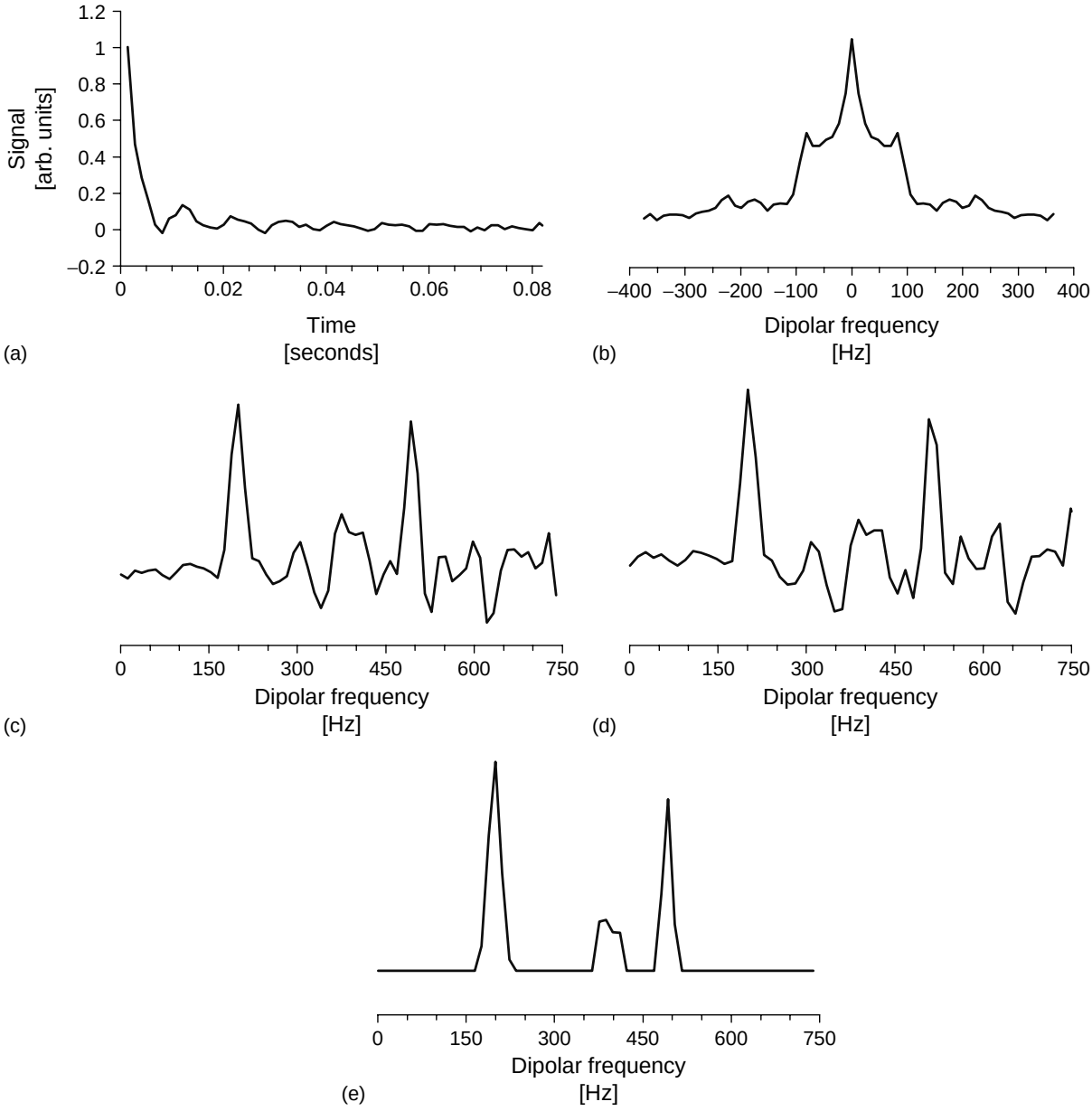

Figure 6 Comparison of methods for processing REDOR signals. In (a), a simulated 64-point REDOR time-domain signal is shown. This additive signal was constructed from three signals of 200, 400 and >500 Hz with relative intensities of 3 : 1 : 2, and was sampled every 0.000333 > s. The signal also contains random Gaussian noise having a standard deviation equal to 1% of the magnitude of the first time domain data point. The results of various processing methods on this signal are also illustrated: (b) the complex Fourier transform, (c) the REDOR Transform, (d) REDOR asymptotic rescaling, and (e) Tikhonov regularization using positivity constraints

and dipolar measurements).[49] Several studies that have utilized ^{31}P chemical shift dePakeing have been reported.[49,55,56]

Axially symmetric shift tensors are a somewhat specialized occurrence in solid-state NMR. The usual case is the non-axially symmetric shift tensor, where the frequencies scale as

$$\omega_{CS}(\theta, \phi) = \omega_0 \zeta [\tfrac{1}{2}(3\cos^2\theta - 1) + \tfrac{1}{2}\eta \sin^2\theta \cos 2\phi] \qquad (36)$$

where ω_0 is the Larmor frequency, ζ represents the anisotropy of the chemical shift tensor, and η denotes the asymmetry parameter, which can vary from zero to unity (see **Chemical Shift Tensors,** Volume 2). Note that equation (36) reduces to the single-transition form of equation (1) in cases of axially symmetric shift interactions (where $\eta = 0$). Powder averaging of equation (36) obviously does not result in the Pake signal; nevertheless, applications of the dePakeing procedure to static shift tensors of varying asymmetry have been attempted.[15] The results are complex and do not approach the desired $\delta-$function spectra; nevertheless, estimates of spectral parameters are possible by identification of distinct features.

A true chemical shift 'transform' (or inverse analysis) would extract the parameters in the same way as a linear transform; i.e., like the Fourier transform, the dePakeing methods, and the REDOR transform and related procedures. The goal of the chemical shift transform is twofold, since it

provides a more easily interpretable estimate of chemical shift parameters while also increasing the resolving capabilities of traditional, isotropic chemical shift NMR experiments. For example, two ^{13}C sites may have isotropic shifts that differ by a value less than their linewidths, and hence would not be resolvable in a ^{13}C CP-MAS experiment. However, the sites may have differing anisotropies or asymmetry parameters, which when resolved in a multidimensional experiment would allow for discrimination between the two ^{13}C environments. Several approaches to a chemical shift analysis that would facilitate these two goals have already been attempted.

Another method is to analyze chemical shift spectra using an adjustable model for the asymmetric chemical shift. This could be achieved in principle by a modified Tikhonov regularization method, in which the usual minimization is carried under the control of an secondary minimization of the asymmetry parameter, using the residuals for a convergence criteria.[45] The kernel function would thus adapt itself to the experimental data, and the result would report both the asymmetry parameter and the anisotropy of the shift. A more direct method employs a special transform to project the chemical shift Hamiltonian onto orthogonal axes.[69,70] This procedure is powerful but is hindered by a t^3 scaling factor that strongly enhances the effect of noise on the spectrum; the problem is thus strongly ill-posed and requires strong apodization or a regularization approach. In addition, the actual experiment used to obtain the data is sensitive to pulse imperfections.[70] Future developments and experimental improvements are expected in this area. Presently, most chemical shift analyses are still accomplished by reliable non-linear fitting routines such as the Herzfeld-Berger method or the more recent time domain method (see **Spinning Sideband Analysis for Spin-1/2 Nuclei**), often in combination with the 2D-PASS experiment.[71,72] Another chemical shift analysis method that yields valuable results is the TIGER processing scheme in combination with the 2D-PHORMAT experiment.[73,74] The TIGER method relies on a guide spectrum to increase the resolution and signal-to-noise of a 2D isotropic/anisotropic chemical shift correlation spectrum. As such, it is not a true chemical shift transform, but like the Herzfeld-Berger approach, it is highly practical and applicable to a variety of chemical problems.

4.4 Extraction of Orientational Distributions

Several other applications of the special processing techniques discussed here have also appeared. These can be loosely classified as orientational distribution problems, in which angular parameters are extracted from NMR data (and not the parameters defining the magnitude of an NMR interaction). Simpler examples of these problems are illustrated by NMR studies of oriented systems, such as nematic liquid crystals and lyotropic liquid crystals of surfactant and water.[75,76] For example, spectra of a nematic mixture in a membrane were obtained at different orientations with respect to the Zeeman field. The data were then analyzed to produce orientational distributions, as the membrane tends to orient the liquid crystal.[75] An application to 2D ^2H exchange spectroscopy has also been given.[77] In this case the signal function is defined by a multitude of parameters, some of which must be estimated from an additional specialized experiment. The Tikhonov regularization procedure can then be used to estimate the reorientational angle distribution.[77] Practical uses for this particular combination of experiment and data processing include estimates of slow dynamics in solids, such as the jump and chain motion experienced by organic molecules and polymers. The magnetic resonance line shape obtained by the ENDOR technique in proton containing glasses has also been analyzed by Tikhonov regularization, in order to determine the polarization distribution.[3,78] This work used a lineshape function for a system undergoing chemical exchange in an asymmetric potential, which is useful as a model for hydrogen bonding. The kernel function requires an additional variable, so that iteration over the range of this variable and minimization of the overall error is required.

5 CONCLUSIONS AND FUTURE DIRECTIONS

The methods discussed here are applicable to a wide variety of problems encountered in NMR spectral analysis, particularly those presented by solid-state systems. There are also a number of parallels between the extraction of information shown here and the determination of diffusion coefficients from gradient-assisted solution-state NMR. Since these signals acquire their unique form through diffusional effects instead of orientational averages, they are not discussed in the present article (see **Diffusion Measurements by Magnetic Field Gradient Methods,** Volume 3). However, the Laplace transform used in these analyses is built around an exponential kernel function, and may find use in solid-state NMR analyses.

In the past, choice of a given method was greatly dependent on the penalty one was willing to pay in computer time. Presently, this is no longer as serious of a concern, and methods can often be chosen freely based on their merits. However, large multidimensional data sets may still require expensive amounts of computer time. In any case, the expense in computer time is usually worth the improvement in data analysis that these special methods provide. As NMR instrumentation becomes more costly, these methods will become more valuable as a way of extracting out every possible bit of information from an NMR spectrum.

6 RELATED ARTICLE IN THIS VOLUME

Spinning Sideband Analysis for Spin-1/2 Nuclei.

7 RELATED ARTICLES IN VOLUMES 1–8

Average Hamiltonian Theory, Volume 2; Chemical Shift Tensors, Volume 2; Cross Polarization in Rotating Solids: Spin-1/2 Nuclei, Volume 3; Cross Polarization in Solids, Volume 3; Deuterium NMR in Solids, Volume 3; Diffusion Measurements by Magnetic Field Gradient Methods, Volume 3; Homonuclear Recoupling Schemes in MAS NMR, Volume 4; Internal Spin Interactions & Rotations in Solids, Volume 4; Magic Angle Spinning, Volume 5; Magic Angle Turning & Hopping, Volume 5; REDOR & TEDOR, Volume 6.

8 REFERENCES

1. R. R. Ernst, G. Bodenhausen, and A. Wokaun, 'Principles of Nuclear Magnetic Resonance in One and Two Dimensions', Clarendon Press: Oxford, 1987.

2. J. C. Hoch and A. S. Stern, 'NMR Data Processing', Wiley-Liss: New York, 1996.
3. C. P. Slichter, 'Principles of Magnetic Resonance', 3rd edn., Springer-Verlag: New York, 1996.
4. G. E. Pake, *J. Chem. Phys.*, 1948, **16**, 327–336.
5. M Abramowitz and I. A. Stegun, 'Handbook of Mathematical Functions', NBS Applied Mathematics Series, Vol. 55, Dover: New York, 1972.
6. I. S. Gradshteyn and I. M. Rhyzik, in 'Tables of Integrals, Series and Products', 5th edn., ed A. Jeffrey, Academic Press: San Diego, 1994, p xxxvi.
7. W. H. Press, B. P. Flannery, S. A. Teukolsky, and W. T. Vetterling, 'Numerical Recipes in C', 2nd edn., Cambridge University Press: Cambridge, 1991.
8. K. T. Mueller, *J. Magn. Reson.*, 1995, **113A**, 81–93.
9. G. B. Arfken and H. J. Weber, 'Mathematical Methods for Physicists', 4th edn., Academic Press: San Diego, 1995.
10. D. C. Douglass, *J. Magn. Reson.*, 1994, **110A**, 146–169.
11. M. Bloom, J. H. Davis, and A. L. MacKay, *Chem. Phys. Lett.*, 1981, **80**, 198–202.
12. E. Sternin, M. Bloom, and A. L. MacKay, *J. Magn. Reson.*, 1983, **55**, 274–282.
13. K. P. Whittall, E. Sternin, M. Bloom, and A. L. MacKay, *J. Magn. Reson.*, 1989, **84**, 64–71.
14. B. C. Gerstein and C. R. Dybowski, 'Transient Techniques in NMR of Solids', Academic Press: San Diego, 1985, pp 113–119.
15. T. Gullion and J. Schaefer, *Adv. Magn. Reson.*, 1989, **13**, 57–83.
16. D. W. Alderman, M. S. Solum, and D. M. Grant, *J. Chem. Phys.*, 1986, **84**, 3717–3725.
17. M. Bak and N. C. Nielsen, *J. Magn. Reson.*, 1997, **125**, 132–139.
18. M. Edén and M. H. Levitt, *J. Magn. Reson.*, 1998, **132**, 220–239.
19. K. T. Mueller, T. P. Jarvie, D. J. Aurentz, and B. W. Roberts, *Chem. Phys. Lett.*, 1995, **242**, 535–542.
20. K. T. Mueller, T. P. Jarvie, D. J. Aurentz, and B. W. Roberts, *Chem. Phys. Lett.*, 1995, **254**, 281–282.
21. J. B. D. de la Caillerie and C. Fretigny, *J. Magn. Reson.*, 1998, **133**, 273–280.
22. M Abramowitz and I. A. Stegun, 'Handbook of Mathematical Functions', NBS Applied Mathematics Series, Vol. 55, Dover: New York, 1972, p 360, equation 9.1.18.
23. I. S. Gradshteyn and I. M. Rhyzik, 'Tables of Integrals, Series and Products' 5th edn., ed A. Jeffrey, Academic Press: San Diego, 1994, p 756, equation 6.681.8.
24. F. G. Vogt, D. J. Aurentz, and K. T. Mueller, *Mol. Phys.*, 1998, **95**, 907–919.
25. B. Q. Sun, P. R. Costa, D. Kocisko, P. T. Lansbury, and R. G. Griffin, *J. Chem. Phys.*, 1995, **102**, 702–707.
26. M. H. Levitt, D. P. Raleigh, F. Creuzet, and R. G. Griffin, *J. Chem. Phys.*, 1990, **92**, 6347–6364.
27. A. E. Bennett, C. M. Rienstra, J. M. Griffiths, W. Zhen, P. T. Lansbury, and R. G. Griffin, *J. Chem. Phys.*, 1998, **108**, 9463–9479.
28. A. W. Hing, S. Vega, and J. Schaefer, *J. Magn. Reson.*, 1993, **103A**, 151–162.
29. F. G. Vogt, S. M. Mattingly, J. M. Gibson, and K. T. Mueller, *J. Magn. Reson.*, 2000, **147**, 26–35.
30. L. Müller, A. Kumar, T. Baumann, and R. R. Ernst, *Phys. Rev. Lett.*, 1974, **32**, 1402–1406.
31. B. Q. Sun, P. R. Costa, and R. G. Griffin, *J. Magn. Reson.*, 1995, **112A**, 191–198.
32. I. S. Gradshteyn and I. M. Rhyzik, 'Tables of Integrals, Series and Products', 5th edn., ed A. Jeffrey, Academic Press: San Diego, 1994, p 441, equation 3.715.8.
33. Y. K. Lee, N. D. Kurur, M. Helmle, O. G. Johannessen, N. C. Nielsen, and M. H. Levitt, *Chem. Phys. Lett.*, 1995, **242**, 304–309.
34. N. C. Nielsen, H. Bildsøe, H. J. Jakobsen, and M. H. Levitt, *J. Chem. Phys.*, 1994, 1805–1812.
35. M. A. McCabe and S. R. Wassall, *J. Magn. Reson.*, 1995, **106B**, 80–82.
36. M. A. McCabe and S. R. Wassall, *Solid State NMR*, 1997, **10**, 53–61.
37. G. H. Golub and C. F. Van Loan, 'Matrix Computations', Johns Hopkins University Press: Baltimore, 1996.
38. F. J. Harris, *Proc. IEEE*, 1978, **66**, 51–83.
39. C. L. Lawson and R. J. Hanson, 'Solving Least Squares Problems', Prentice Hall: Englewood Cliffs, NJ, 1974.
40. S. W. Provencher, *Comput. Phys. Commun.*, 1982, **27**, 213–227.
41. H. W. Engl, M. Hanke, and A. Neubauer, 'Regularization of Inverse Problems', Kluwer Academic Publishers: Dordrecht, 1996.
42. A. N. Tikhonov, A. V. Goncharsky, V. V. Stepanov, and A. G. Yagola, 'Numerical Methods for the Solution of Ill-Posed Problems', Kluwer Academic Publishers: Dordrecht, 1995.
43. J. J. Dongarra, J. R. Bunch, C. B. Moler, and G. W. Stewart, 'LINPACK User's Guide', Philadelphia: SIAM, 1979.
44. A. K. Kline, C. B. Moler, G. W. Stewart, and J. H. Wilkinson, *SIAM J. Numer. Anal.*, 1979, **16**, 368.
45. H. Schäfer, B. Mädler, and F. Volke, *J. Magn. Reson.*, 1995, **116A**, 145–149.
46. J. Honerkamp and J. Weese, *Continuum Mech. Thermodyn.*, 1990, **2**, 17.
47. J. Weese, *Comput. Phys. Commun.*, 1992, **69**, 99–111.
48. E. Oldfield, H. K. C. Timken, B. Montez, and R. Ramachandran, *Nature*, 1985, **318**, 163–165.
49. E. Sternin, B. Fine, M. Bloom, C. P. S. Tilcock, K. F. Wong, and P. R. Cullis, *Biophys. J.*, 1988, **54**, 689–694.
50. M. R. Paddy, F. W. Dahlquist, E. A. Dratz, and A. J. Deese, *Biochemistry*, 1985, **24**, 5988–5995.
51. J. L. Thewalt and R. J. Cushley, *Biochim. Biophys. Acta*, 1987, **905**, 329–338.
52. M. Lafleur, B. Fine, E. Sternin, P. R. Cullis, and M. Bloom, *Biophys. J.*, 1989, **56**, 1037–1041.
53. M. B. Sankaram and D. Marsh, *Biophys. J.*, 1989, **56**, 1043–1044.
54. P. O. Eriksson, L. Rilfors, A. Wieslander, A. Lundberg, and G. Lindblom, *Biochemistry*, 1991, **30**, 4916–4924.
55. T. Brumm, A. Moeps, C. Dolainsky, S. Brueckner, and T. M. Bayerl, *Biophys. J.*, 1992, **61**, 1018–1024.
56. D. B. Fenske and P. R. Cullis, *Biophys. J.*, 1993, **64**, 1482–1491.
57. M. R. Morrow, J. Perez-Gill, G. Simatos, C. Boland, J. Stewart, D. Absolom, V. Sarin, and K. M. W. Keough, *Biochemistry*, 1993, **32**, 4397–4402.
58. L. L. Holte, S. A. Peter, T. M. Sinnwell, and K. Gawrisch, *Biophys. J.*, 1995, **68**, 2396–2403.
59. A. E. Drobnies, B. van der Ende, J. L. Thewalt, and R. B. Cornell, *Biochemistry*, 1999, **38**, 15 606–15 614.
60. C. Perry, E. A. Dratz, Y. Ke, V. M. Schmidt, J. M. Kometani, and R. E. Cais, *Ferroelectrics*, 1989, **92**, 55–63.
61. R. D. Curtis, P. J. Tonge, I. C. P. Smith, and H. C. Jarrell, *J. Magn. Reson.*, 1993, **102**, 110–113.
62. D. E. Kaplan and E. L. Hahn, *J. Phys. Radium*, 1958, **19**, 821.
63. M. Emshwiller, E. L. Hahn, and D. Kaplan, *Phys. Rev.*, 1960, **118**, 414–424.
64. N. P. Kenaston, A. T. Bell, and J. A. Reimer, *J. Phys. Chem.*, 1994, **98**, 894–896.
65. T. P. Jarvie, G. T. Went, and K. T. Mueller, *J. Am. Chem. Soc.*, 1996, **118**, 5330–5331.
66. P. O. Quist, H. Forster, and D. Johnels, *J. Am. Chem. Soc.*, 1997, **119**, 5390–5397.
67. T. Gullion and C. H. Pennington, *Chem. Phys. Lett.*, 1998, **290**, 88–93.
68. O. Liivak and D. B. Zax, *J. Chem. Phys.*, 2000, **113**, 1088–1096.
69. T. M. de Swiet, *J. Chem. Phys.*, 1999, **110**, 5231–5237.
70. T. M. de Swiet, *J. Chem. Phys.*, 2000, **112**, 8567–8572.
71. J. Herzfeld and A. E. Berger, *J. Chem. Phys.*, 1980, **73**, 6021–6030.

72. O. N. Antzutkin, Y. K. Lee, and M. H. Levitt, *J. Magn. Reson.*, 1998, **135**, 144–155.
73. G. McGeorge, J. Z. Hu, C. L. Mayne, D. W. Alderman, R. J. Pugmire, and D. M. Grant, *J. Magn. Reson.*, 1997, **129**, 134–144.
74. D. W. Alderman, G. McGeorge, J. Z. Hu, R. J. Pugmire, and D. M. Grant, *Mol. Phys.*, 1998, **95**, 1113–1126.
75. H. Schäfer and R. Stannarius, *J. Magn. Reson.*, 1995, **106B**, 14–23.
76. J. Winterhalter, D. Maier, D. A. Grabowski, J. Honerkamp, S. Müller, and C. Schmidt, *J. Chem. Phys.*, 1999, **110**, 4035–4046.
77. D. Grabowski and J. Honerkamp, *J. Chem. Phys.*, 1992, **96**, 2629–2632.
78. H. Schäfer and H. Bauch, *Phys. Lett.*, 1995, **199A**, 93–98.

Biographical Sketches

Frederick G. Vogt, *b* 1973. B.Sc., 1994, Chemistry, Ursinus College, Ph.D., 2000, Chemistry, The Pennsylvania State University (Research advisors: A. J. Benesi and K. T. Mueller). Analytical Chemist, Corporate R&D Spectroscopy Group, Betz Laboratories, Inc., 1994–1995. Research Investigator, Small Molecule NMR Group, GlaxoSmithKline R&D, 2000–present. Research interests: structural measurements and spectroscopic problem solving using solution and solid-state NMR, theoretical NMR simulations, data processing and algorithms, pulse sequence development, solid-state NMR and LC-NMR of pharmaceuticals and related compounds.

Karl T. Mueller, *b* 1964. B.Sc., 1985, Chemistry, University of Rochester, Ph.D., 1991, Chemistry, University of California, Berkeley. Assistant and later Associate Professor of Chemistry, The Pennsylvania State University, 1994–present. Worked on development of dynamic-angle spinning while in graduate school. Postdoctoral work on cross-polarization between quadrupolar and spin-1/2 nuclei. Approximately 45 publications on the development of solid-state NMR methods and applications to complex materials. Research interests: solid-state NMR studies of glasses, zeolites, and biomolecules as well as the development of alternative processing techniques.

Rapid Scan Correlation Spectroscopy

Raj K. Gupta
Albert Einstein College of Medicine, Bronx, NY, USA

and

James A. Ferretti and Edwin D. Becker
National Institutes of Health, Bethesda, MD, USA

1	Introduction	1
2	Description of the Technique	2
3	Selected Applications	4
4	Future Prospects	5
5	Related Articles	5
6	References	5

1 INTRODUCTION

During the late 1960s and early 1970s, fairly extensive searches were carried out to find new methods for obtaining the highest sensitivity in NMR experiments. These searches were primarily applied to optimization of high-resolution NMR spectra. It was recognized at a very early stage in the development of modern NMR that the original continuous wave (CW) method was usually inefficient in terms of both the time required to obtain a single NMR scan and the magnitude of the signal produced per scan. In CW experiments, the magnetization vector is tipped only slightly from its equilibrium value, thus producing a relatively weak signal. The necessity of maintaining a small tip or effective flip angle arises because nuclear spin systems become nonlinear in their response at high applied rf field. To record CW spectra properly, it was necessary to approximate slow passage conditions to produce spectral lines that were undistorted by such effects as frequency oscillations in the tails of the spectral lines (ringing), relaxation, and the inability of the detector to respond to the 'ringing'. Because of the necessity of obeying these slow passage conditions, attempts to tip the magnetization vector by a significant amount resulted in a reduction of the total intensity or 'saturation' of the resonance lines. These limitations provided the driving force behind attempts to develop alternative techniques to maximize the sensitivity of the NMR experiment.

Several alternative methods were proposed and developed that allowed rapid acquisition of an entire spectrum as well as the use of a large nutation angle, thus reducing the time required to obtain a single scan while also producing an enhanced signal per scan. The most popular of these methods is the pulse Fourier transform technique, on which almost all modern NMR spectrometers are based. A second method involves stochastic excitation, for which there have been several recent developments that appear quite promising. These two methods rely on simultaneous excitation of the different resonance transitions of a nuclear spin system. A third method is the rapid scan correlation technique, in which the entire spectrum is traversed under fast passage conditions where typical circumstances involve tipping the magnetization vector into the (x,y) plane. Here each transition is excited successively in a fast sequence. If the field or the frequency is swept rapidly enough, constructive and destructive oscillations characteristic of the spectrum occur. The origin of these frequency oscillations was understood 30 years ago. It was recognized then that all of the available spectral information is in the frequency oscillations found in the tails of resonance lines obtained by rapidly scanning the spectrum. However, the proper analysis procedure for extracting the corresponding undistorted spectra remained elusive for many years. Several papers were published about 20 years ago describing the mathematical procedures for obtaining the undistorted spectrum, and pointing out that this rapid scan technique is capable of producing spectra with sensitivity comparable to the pulse Fourier transform technique. The technique was initially referred to both as rapid scan Fourier transform NMR spectroscopy and correlation NMR spectroscopy, because of the nature of the experiment and because the procedure for obtaining the undistorted spectrum may involve cross correlation. Ultimately, it was named rapid scan correlation spectroscopy. The purpose here is to examine the historical development of the method, review some applications of the technique, and speculate on future developments. Interestingly, the original discovery of NMR by Bloch was a rapid scan experiment where the signal was observed when the field was rapidly changing as the magnet was turned off, after a frustrating failed slow passage search for an NMR signal.

Dadok originally pointed out at the 1972 Experimental NMR Conference in Asilomar, CA that the true undistorted high-resolution NMR spectrum can be obtained from a rapidly scanned response by cross correlation with the response obtained under identical sweep conditions from a single 'reference' line.[1a] The quality of the spectra was quite good, but suffered from several inherent disadvantages. First of all, the correlated spectra showed broadened lines with widths that were the sums of the inherent linewidths and the width of the single reference line used in the cross-correlation operation. Secondly, any additional spectral lines (e.g., from impurities) present in the reference sample produced additional spectral lines in the correlated spectra. Subsequently, the theoretical basis of this method was examined, and it was shown that the undistorted spectra could be obtained with no added linewidth by Fourier transforming the fast passage response and multiplying it with an analytical function of the form $\exp(-\frac{1}{2}ibT^2)$, where b is the sweep rate and T is the running variable in the time domain.[1b,2] It was also shown that the data are easily obtained using a spectrometer–computer interface, just as all modern FT spectra are acquired and processed. It was shown that rapid scan correlation FT NMR offers an alternative to pulse methods for rapid acquisition of NMR spectral information. The sensitivity of the rapid scan method was shown to be comparable to that of the pulse Fourier transform method. However, two potential advantages of rapid scan FT over the pulse technique were recognized:

1. the ease with which a portion of the spectrum can be scanned without recording large peaks such as H_2O or

HDO, which cause dynamic range problems and severely limit the sensitivity of pulse FT NMR;
2. the ability to study selectively in a multiline spectrum the spectral properties of some spins without perturbing others, thus avoiding complications due to cross relaxation or chemical exchange.

At that time, another distinct advantage appeared to be that no new spectrometer hardware was required and no high-power pulse equipment was needed. Furthermore, for heteronuclei with large chemical shift dispersion, or for protons in paramagnetic systems, the rapid scan technique offered a simple straightforward procedure to obtain spectra of a chemical shift region of particular interest. The typical problems associated with foldover that are often encountered in pulse FT were avoided.

2 DESCRIPTION OF THE TECHNIQUE

2.1 Slow Passage Spectrum from the Rapid Scan Response

In the rapid scan technique,[1,2] the entire spectrum is traversed under fast passage conditions such that the magnetization corresponding to each line produces pronounced ringing (wiggles), which persists a time of the order of $3T_2$*, and results in badly distorted spectral lines. The true spectrum is then obtained from such a fast scan response by cross correlating the response with that obtained from a reference consisting of only a single sharp NMR line scanned under identical conditions, or alternatively by applying to the Fourier-transformed response an analytical function $\exp(\frac{1}{2}\mathrm{i}bT^2)$. Unlike pulse FT NMR, where the different resonance conditions of a complex spin system are satisfied simultaneously, in rapid scan correlation NMR, as in CW NMR, the resonance conditions are met sequentially.

Cross correlation of two complex functions G and H defined mathematically as

$$\int_{-\infty}^{\infty} H^*(\tau)G(t+\tau)\,\mathrm{d}\tau \tag{1}$$

where H* is the complex conjugate of H, has the physical meaning of one function searching for itself in another function, and is useful in picking out hidden periodicities. The property that cross correlation in one domain is equivalent to complex conjugate multiplication in the Fourier domain is used to simplify data handling considerably.

The detailed theory of rapid scan correlation NMR treats the spins as a linear time-independent system. The frequency response function $Y(\omega)$ of such a system and the corresponding impulse response $h(T)$ form a Fourier transform pair. In rapid passage experiments, the frequency ω is scanned rapidly ($\omega_t = bt$) and the response $Y(\omega_t)$ is observed as a function of time (frequency), giving rise to the well-known transient effects as wiggles or ringing following passage through a resonance. The linear response $R(t)$ of the spins to a swept rf field $E(t) = \exp(\frac{1}{2}\mathrm{i}bt^2)$ is given by the convolution integral

$$R(t) = \int_{-\infty}^{\infty} h(\tau)E(t-\tau)\,\mathrm{d}\tau \tag{2}$$

so that the detected NMR signal $Y(\omega_t)$, which is the component of the response in phase with the rf field, is given by

$$\begin{aligned} Y(\omega_t) &= R(t)\exp(-\tfrac{1}{2}\mathrm{i}bt^2) \\ &= \int_{-\infty}^{\infty} h(\tau)\exp[\tfrac{1}{2}\mathrm{i}b(\tau^2 - 2t\tau)]\,\mathrm{d}\tau \end{aligned} \tag{3}$$

It is straightforward to show that the inverse Fourier transform $F(T)$ of this response is given by

$$F(T) = h(T)\exp(\tfrac{1}{2}\mathrm{i}bT^2) \tag{4}$$

where T is the running variable of the time domain. This result for the Fourier transform of the rapid scan signal can also be obtained from the usual Bloch equations,[2] as well as the Bloch equations modified to include chemical exchange,[3] provided that spin saturation is avoided. However, nonlinearities due to spin–spin couplings can modify the observed response.[4]

It is clear from the expression for the inverse Fourier transform $F(T)$ of the rapid scan response that multiplication of $F(T)$ by $\exp(-\frac{1}{2}\mathrm{i}bT^2)$ gives the impulse response of the system $h(T)$, from which the slow passage spectrum is readily obtained by another (forward) Fourier transformation (Figure 1). Because of the extensive use of Fourier transformations for rapid data processing, we suggested that the technique be named rapid scan FT NMR, despite the fact that the resulting slow passage spectrum and the initial rapid scan response are in the same Fourier domain.

Use of an experimental reference involves cross correlation of an unknown rapid scan response with the rapid scan response of a single narrow reference resonance. Cross correlation is carried out most efficiently by Fourier transforming both the reference and the unknown responses and then multiplying the Fourier transform of the unknown response, $h(T)\exp(\frac{1}{2}\mathrm{i}bT^2)$, with the complex conjugate of the Fourier

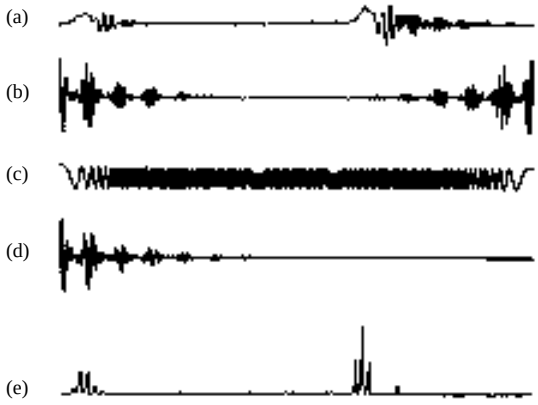

Figure 1 Signals at various stages of analysis in rapid scan correlation NMR. (a) Rapid scan data, showing the proton resonances of the CH_2 and CH_3 groups of ethylbenzene at a scan rate of 200 Hz s^{-1}. (b) Inverse cosine Fourier transform of (a). (c) The real part of the function $\exp(-\frac{1}{2}\mathrm{i}bT^2)$ for $b/2\pi$ = 200 Hz s^{-1}. (d) The result of multiplying (b) and (c), followed by zeroing of half of the data points. (e) The Fourier transform of (d), with phase correction applied if necessary.

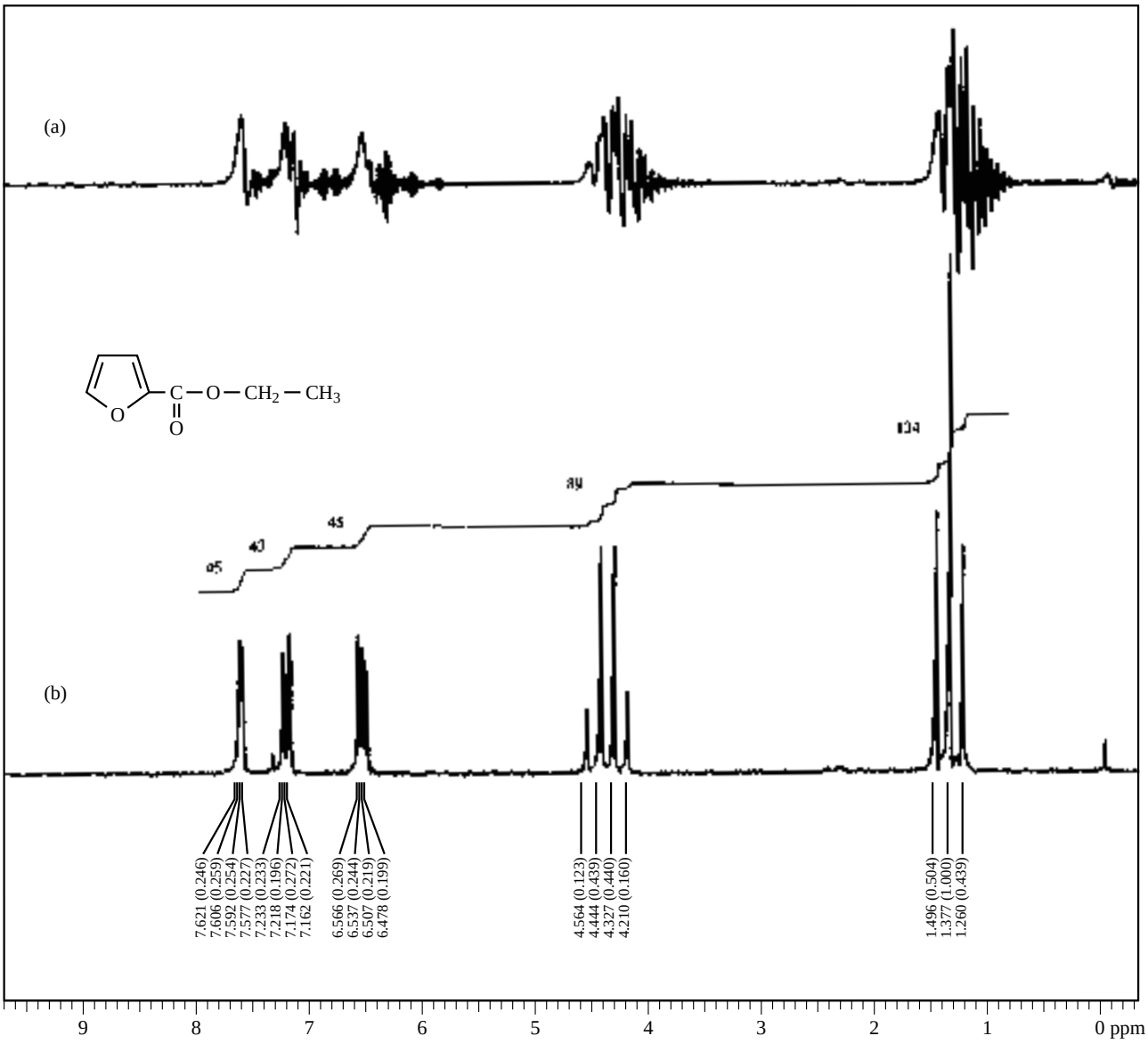

Figure 2 Rapid scan (a) and correlated spectrum (b) obtained at 60 MHz on a Hitachi Instruments, Inc. Model R-1200 rapid scan NMR spectrometer

transform of the reference response, $h_{\text{ref}}^*(T)\exp(-\frac{1}{2}ibT^2)$, to obtain $h_{\text{ref}}^*(T)h(T)$. The Fourier transform of this product is then taken as an approximation to the slow passage spectrum (Figure 2). The linewidths of the resulting spectrum in this case will be the sums of the true linewidths and the width of the reference line. When using the reference line approach, the final slow passage spectrum is properly phased, provided that the same phase setting is used for both the reference and the unknown. Also, the frequency axis of the final spectrum is shifted so as to set the reference line to zero frequency. In using the theoretical function approach, an adjustment of the spectral phase may be needed to produce a pure absorption signal, if the initial rapid scan response was not properly phased. However, when the theoretical function is used, the resonance positions remain unchanged with respect to their original positions in the rapid scan response. Cross correlation using the experimental reference results in slightly broader resonances, but this broadening could be minimized by choosing a very narrow reference line such that the broadening effect will be negligible for lines whose widths are greater than 1–2 Hz. With a strong reference signal, the additional noise introduced by cross correlation is normally very small, and the decay constant inherent in h_{ref} leads in effect to exponential filtering, which improves the signal-to-noise ratio. It was noted that TMS is not the most suitable reference since its NMR response shows observable ^{29}Si satellites. It was suggested that a sample of degassed benzene or cyclohexane would be better.[2]

It is interesting to note that just before the final Fourier transformation, the data in the rapid scan technique are analogous to a simple free induction decay (see Figure 1). Thus, digital filtering techniques (e.g., resolution and sensitivity enhancement) to manipulate the quality of the final spectrum can be used just as in pulse FT NMR. The maximum intensity of the absorption signal in the rapid scan mode has been shown to be equal to the equilibrium magnetization, and it has been shown that the sensitivity of the rapid scan technique is comparable to that of the pulse FT technique. However, a necessary condition to be satisfied for the spin

system to be driven into the rapid passage region is that the sweep rate be greater than $1/2\pi T_2^{*2}$.

2.2 Nonlinear Effects in Rapid Scan Correlation Spectroscopy of Coupled Spin Systems

The existence of spectral distortions due to nonlinear effects in rapid scan correlation NMR of coupled spin systems has been described in the literature.[4] These distortions depend strongly on the applied sweep rate and the rf power level where the effective flip angle may be close to 90°. The resultant spectra can show serious variations in resonance lineshapes (both phase and intensity), which depend upon the sweep rate, power level, and the initial state of the spin system, although the resonance frequencies remain essentially unaltered. These effects occur when the spin system does not completely recover in the time between passage through adjacent resonance lines owing to incomplete transverse and/or longitudinal relaxation. Under rapid passage conditions, the transverse magnetization components of the first scanned lines will be mixed by later passage through any connected resonance transitions, causing distortion of the resonances traversed first, while the later lines show normal behavior (e.g., for certain sweep rates in Figure 3, the first two lines are badly distorted). Maximum distortion of the spectrum of a weakly coupled two-spin system was found to occur for values of the sweep rate (in radians per second squared) $b = 2J(\omega_1 - \omega_2)$ where J is the coupling constant (in hertz), and $(\omega_1 - \omega_2)$ is the chemical shift difference (in radians per second). Effects of incomplete longitudinal relaxation manifest themselves as flip angle dependent anomalies in the intensities of the spectral lines that are observed when the spin system is initially in a nonequilibrium state. The above nonlinear effects should be kept in mind in interpreting the results of rapid scan correlation experiments with coupled spin systems.

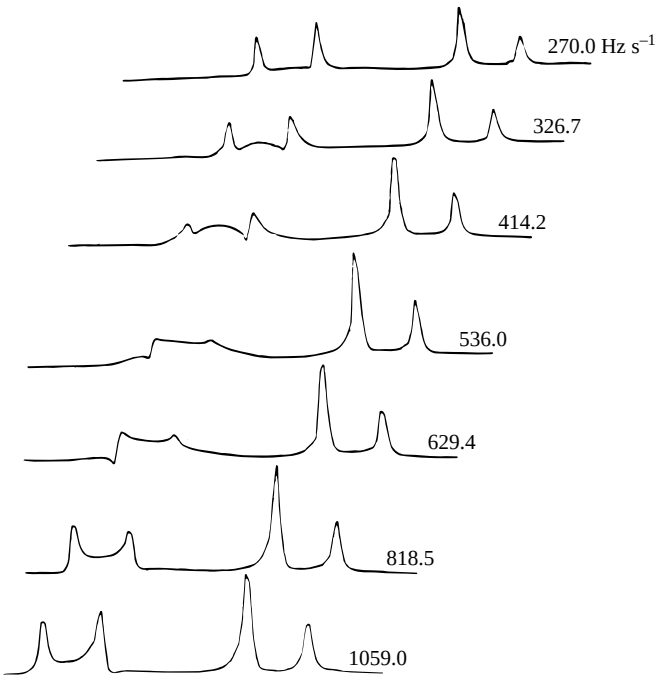

Figure 3 Rapid scan correlation spectra of 2,3,4-trichloronitrobenzene at different scan rates.

2.3 Spin–Lattice Relaxation Measurements

An analog of the progressive saturation experiment well known in CW and pulsed FT works well in rapid scan spectroscopy.[2] The entire spectrum or a part of it is repetitively scanned and a steady state is established where there is a dynamic balance between the passages through the resonances. It is important to make optimum adjustments such that the spin magnetization following passage through a resonance ends up in the (x, y) plane. This requires careful adjustment of rf power and sweep rate. Further, this technique is limited to relatively long T_1 values.

A different approach, somewhat analogous to the saturation recovery pulse method, is applicable for measurement of both long and short T_1s using rapid scan FT NMR.[5] Here, the initial state of the spin system is established by applying a saturating rf field to the spectral lines to be studied. Such an rf field causes essentially complete demagnetization of the spins in a time of the order of a few times $T_{1\rho}$. The saturating rf is then turned off, and, after a variable delay time, the partially relaxed spins are rapidly scanned under fast passage conditions with another rf field of appropriate strength. The fast passage response thus obtained is cross correlated or treated with an analytical function to yield a partially relaxed slow passage spectrum. Repetition of saturation and observation sequence permits the determination of T_1 for each saturated line from its exponential recovery. In a multiline spectrum, T_1 values in the range 0.7–10 s were easily measured by this technique.[5]

3 SELECTED APPLICATIONS

3.1 Observation of Hyperfine Shifted Resonances in Hemoproteins

Ho and co-workers[6] used rapid scan correlation spectroscopy at 250 MHz to obtain proton nuclear magnetic resonance spectra of human deoxyhemoglobin in D_2O in the region from 6 to 20 ppm downfield from the proton resonance of residual water, showing a number of hyperfine shifted resonances due to groups on or near the α- and β-hemes. They showed, by the use of correlation spectroscopy, that at least two resonances, one at about 18 ppm downfield from HDO due to the β chain and the other at about 12 ppm downfield due to the α chain, can be used to study the binding of oxygen to the α and β chains of hemoglobin. They also used rapid scan correlation proton NMR in H_2O to investigate the conformations of proximal histidyl residues in human deoxyhemoglobin and its mutants.[7] Two resonances sensitive to the quaternary state of hemoglobin that occur between 58 and 76 ppm, far downfield from the water proton signal, could be readily observed and assigned to the hyperfine-shifted proximal histidyl NH-exchangeable protons of the α and β chains of deoxyhemoglobin. The biochemical information derived from these hyperfine-shifted proximal histidyl NH-exchangeable proton resonances complemented that obtained from the other hyperfine-shifted exchangeable and nonexchangeable proton resonances of deoxyhemoglobin in the spectral region from 5 to 20 ppm downfield from H_2O.

These studies made use of the ability of the rapid scan correlation technique to observe selected spectral regions, in the

presence of a large chemical shift dispersion, without perturbing other regions of the proton spectrum. No presaturation of the water resonance was necessary.

3.2 Transfer of Saturation from Water and 'Underwater' Decoupling

In several studies of biologically important peptides,[8–12] the rapid scan correlation technique provided well-resolved proton NMR spectra with signal-to-noise ratios significantly better than those obtainable using the CW but comparable to those obtained with the pulse FT technique. Furthermore, when protonated solvents were used, rapid scan correlation spectroscopy provided distinct advantages over the short pulse method because of its ability to avoid interference from the overwhelmingly large solvent signal. Peptide NH resonances of individual amino acids could be assigned by the correlation method using 'underwater decoupling' (i.e., decoupling from the corresponding C-α proton resonances, which are buried beneath the intense water peak). These experiments could be done maintaining good signal-to-noise ratio and resolution. Solvent exposure of specific hydrogens and exchangeability of NH protons could be studied by comparing peptide proton spectra in H_2O, with and without rf saturation of the large water resonance. Such experiments would have been difficult to perform using the pulse FT technique, since the latter requires saturation of water as a precondition for spectral data acquisition. Underwater decoupling experiments are useful for assignment of peptide NH resonances, while transfer of saturation from water measures solvent exposure of specific nuclei in the biomolecule.

As an example of the above, peptide NH resonances in the 250 MHz NMR spectrum of oxytocin in H_2O were assigned to specific amino acid residues by the 'underwater decoupling' technique.[12] Exposure to solvent of specific hydrogens of oxytocin in H_2O could be studied by monitoring intensity changes of peptide resonances when the solvent peak was saturated. Positive nuclear Overhauser effects (NOEs) of sizeable magnitude were observed for the Tyr *ortho*-CH and *meta*-CH resonances, indicating intimate contact between water and the aromatic CH hydrogens of the Tyr side chain. Transfer of saturation from water to NH protons reflected acid–base catalysis of the proton exchange reaction. There was no indication that any NH protons were substantially shielded from the solvent, which pointed to the need for avoiding solvent saturation to observe true resonance intensities.

3.3 Nonexchangeable Protons in Proteins

The rapid scan correlation technique has also been used for routine observation of one-dimensional protein proton NMR spectra as an alternative to pulse techniques with comparable signal-to-noise ratio and resolution.[13–15] For example, Markley and co-workers[14] used the technique at 250 MHz to measure titration curves of the three histidine residues of staphylococcal protease, while Arata and co-workers[13] applied it to lysozyme. Bothner-By and co-workers[15] used rapid scan correlation at 600 MHz to study glucocerbrosidase activator protein from Gaucher spleen. The upfield ring current shifted aliphatic region and the downfield aromatic region were examined using NOE methods in the correlation mode.

3.4 Applications in Food Chemistry

Since the rapid scan correlation NMR technique combines the sensitivity advantage of pulse FT NMR with the dynamic range advantage of the CW method, it has found recent applications in the analysis of food products.[16] Results of qualitative as well as quantitative studies from a variety of foods and food-related systems have been reported. The rapidity and noninvasiveness of the technique are important considerations in such applications. A quantitative analysis of the ethanol content of various wines has also been carried out with this technique.[17]

4 FUTURE PROSPECTS

Even though rapid scan correlation spectroscopy showed significant promise in 1970s, it was soon overtaken by the rapid developments in the pulse FT method. With the advent of the new generation of pulse Fourier transform spectrometers, the advantage of not requiring new instrumental hardware for the rapid scan method disappeared. Eventually, most NMR manufacturers discontinued producing spectrometers capable of performing swept field or frequency experiments. Also, it is quite difficult to envision numerous heteronuclear and homonuclear multidimensional applications, now known for pulse FT NMR. Nevertheless, Hitachi Instruments, Inc. manufactures a spectrometer operating at 60 MHz that functions exclusively in the rapid scan correlation mode. Recent applications of the technique seem to have been in the area of quality control in food chemistry and in the study of biomolecules in H_2O solution. The ability to avoid overdriving the dynamic range of the spectrometer, which is still problematical on modern NMR spectrometers, implies that the rapid scan correlation technique is still a useful complement to pulse FT NMR. Also, one can envision applications in magnetic resonance imaging that might be advantageous in terms of rf power requirements. One purpose of this review is to remind the NMR community of the existence of this potentially powerful alternative to pulse techniques.

While we do not envision any widespread resurgence in the use of the rapid scan method, the technique is likely to continue to be useful for routine one-dimensional NMR analyses and for specific applications in the study of biomolecule–water interactions. Possible applications of the rapid scan technique in imaging and in vivo proton spectroscopy may still result in the future.

5 RELATED ARTICLES

Biological Macromolecules; Fourier Transform Spectroscopy; Selective Pulses; Stochastic Excitation; Water Signal Suppression in NMR of Biomolecules.

6 REFERENCES

1. (a) J. Dadok, R. F. Sprecher, and A. A. Bothner-By, *13th Experimental NMR Conference, Asilomar, Pacific Grove, California, 1972*. (b) J. Dadok and R. F. Sprecher, *J. Magn. Reson.*, 1974, **13**, 243.

2. R. K. Gupta, J. A. Ferretti, and E. D. Becker, *J. Magn. Reson.*, 1974, **13**, 275.
3. J. Jen, *J. Magn. Reson.*, 1981, **45**, 257.
4. J. A. Ferretti and R. R. Ernst, *J. Chem. Phys.*, 1976, **65**, 4283.
5. R. K. Gupta, J. A. Ferretti, and E. D. Becker, *J. Magn. Reson.*, 1974, **16**, 505.
6. G. Viggiano, N. T. Ho, and C. Ho, *Biochemistry*, 1979, **18**, 5238.
7. S. Takahashi, A. K. Lin, and C. Ho, *Biophys. J.* 1982, **39**, 33.
8. J. D. Glickson, J. Dadok, and G. R. Marshall, *Biochemistry*, 1974, **13**, 11.
9. T. P. Pitner, J. D. Glickson, J. Dadok, and G. R. Marshall, *Nature (London)*, 1974, **250**, 582.
10. J. D. Glickson, J. Dadok, and G. R. Marshall, *Biochemistry*, 1974, **13**, 11.
11. W. A. Gibbons, C. F. Beyer, J. Dadok, R. F. Sprecher, and H. R. Wyssbrod, *Biochemistry*, 1975, **14**, 420.
12. J. D. Glickson, R. Rowan, T. P. Pitner, J. Dadok, A. A. Bothner-By, and R. Walter, *Biochemistry*, 1976, **15**, 1111.
13. Y. Arata, H. Ogawa, T. Ogino, and S. Fujiwara, *Pure Appl. Chem.*, 1978, **50**, 1273.
14. J. L. Markley, W. R. Finkenstadt, H. Dugas, P. Leduc, and G. R. Drapeau, *Biochemistry*, 1975, **14**, 998.
15. L. Sheh, R. H. Glew, A. A. Bothner-By, and P. K. Mishra, 1985, **24**, 6645.
16. H. Barjat, P. S. Belton, and B. J. Goodfellow, *Food Chem.*, 1993, **48**, 307.
17. H. Barjat, P. S. Belton, and B. J. Goodfellow, *Analyst (Cambridge, UK)*, 1993, **118**, 73.

Biographical Sketches

Raj K. Gupta. *b* 1943. Ph.D., 1969, Indian Institute of Technology, Kanpur. Introduced to NMR by A. G. Redfield. Professor of Physiology & Biophysics, and of Biochemistry, Albert Einstein College of Medicine, NYC, 1982–present. Approx. 200 publications. Research interests include applications of NMR in physiology and biochemistry, especially in the measurement of intracellular ions.

James. A. Ferretti. *b* 1939. Ph.D., 1965, University of California at Berkeley. NIH, 1966–present, currently Chief of the Structural Biophysics Section, Laboratory of Biophysical Chemistry, National Heart, Lung & Blood Institute, Bethesda, MD. Approx. 100 publications. Research interests include 3D solution structures of peptides and proteins.

Edwin D. Becker. *b* 1930. B.S., 1952, University of Rochester, Ph.D., 1955, chemistry, University of California, Berkeley, USA. National Institutes of Health, 1955–present; Laboratory Chief (1972–80, 1988–present); Associate Director for Research Services (1980–88). Concurrent position on Faculty, Georgetown University, 1959–present. Books on NMR. Research interests and publications: hydrogen bonding, molecular structure elucidation, technique development in NMR and other areas of molecular spectroscopy.

Reference Deconvolution

Gareth A. Morris

University of Manchester, Manchester, UK

1 Introduction 1
2 Historical Background 2
3 Theory 2
4 Applications 4
5 Related Article in this Volume 6
6 Related Articles in Volumes 1–8 6
7 References 6

1 INTRODUCTION

All experiments are imperfect. Advances in the engineering and design of NMR spectrometers mean that NMR experiments have steadily improved in quality over the last 50 years, and are certainly closer to perfection than many other types of spectroscopic measurement, but nevertheless all NMR measurements carry internal evidence of the shortcomings of the experimental equipment and techniques used. Some sources of imperfection are inevitable: any electronic measurement that takes place above absolute zero contains random noise originating in the thermal motion of charge carriers. Many other sources could be avoided in an ideal NMR instrument: line broadening or spinning sidebands caused by static magnetic field inhomogeneity, difference artifacts caused by instabilities in field-frequency ratio, and phase errors caused by impure radiofrequency sources. One feature shared by all the members in this list is that they affect all the signals in a spectrum in the same way: each can be described as a multiplication of the expected free induction decay by some sort of error function. It is therefore possible in principle to correct for the effects of these sources of imperfection by using prior knowledge of the form expected for a given line in the spectrum. This is the basis of reference deconvolution,[1] in which the experimental spectrum is deconvoluted with the experimental form of a reference signal and reconvoluted with the theoretical ideal form, to yield a spectrum in which instrumental distortions are suppressed for all signals. In keeping with its original use for the correction of lineshapes, the method is often referred to by the acronym FIDDLE (Free Induction Decay Deconvolution for Lineshape Enhancement), although strictly it is the experimental spectrum, rather than the free induction decay, that is deconvoluted.

The basic principles of reference deconvolution are illustrated in Figure 1, which uses data from a 300 MHz proton experiment in which the homogeneity of the static field was deliberately perturbed. The spectrum contains a signal from acetone which should be a simple singlet, but which in common with all the other signals in the spectrum shows severe lineshape errors and spinning sidebands because of the combination of poor B_0 homogeneity and sample spinning. If the Fourier transform of the raw experimental free induction decay, Figure 1(b), is treated by zeroing all the spectrum apart from the region containing the acetone signal, inverse Fourier transformation of this windowed spectrum will yield a time-domain signal which is that component of the original free induction decay attributable to the acetone reference signal. This time-domain acetone signal is the product of the signal that would have been recorded by a perfect instrument, multiplied by a complex time-dependent envelope function which describes the modulation of the signal by the spatially and temporally varying magnetic field experienced by different parts of the sample, and supplemented by a background of random noise.

The ideal form of the signal expected from theory is straightforward: in the frequency domain, a Lorentzian line centered on the acetone chemical shift, and in the time domain, a complex exponential that rotates at the acetone chemical shift and decays exponentially. It is thus possible both to deduce the form of the error modulation experienced by the experimental signal, and to produce a spectrum corrected for its effects, by taking the complex ratio of the theoretical and experimental forms of the reference signal. Multiplying the original experimental free induction decay by this time-dependent complex ratio yields a corrected signal, shorn of the unwanted modulation, which can be Fourier transformed to yield a corrected spectrum with ideal lineshapes (Figure 1b). The price paid is a small increase in the complexity of data processing, and an increased (and non-white) noise background.

Reference deconvolution is not limited to the correction of lineshape errors: many different instrumental errors are multiplicative in the time domain and hence susceptible to

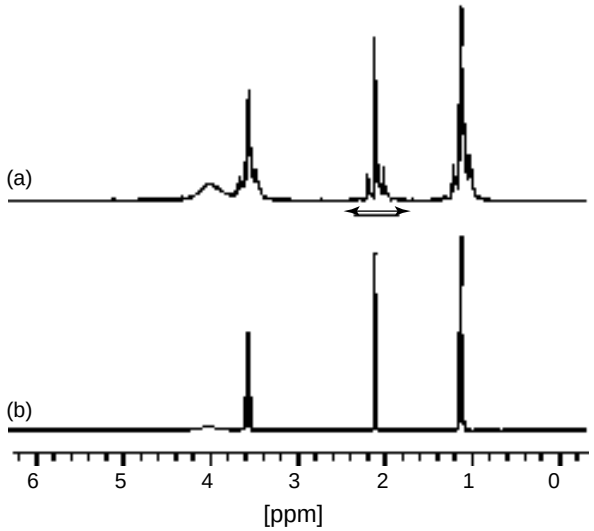

Figure 1 Schematic illustration of simple reference deconvolution. Deconvoluting the raw experimental spectrum (a) with the acetone lineshape contained in the arrowed frequency range and reconvoluting with a 1 Hz wide Lorentzian gives the corrected spectrum (b), in which signals have essentially perfect lineshapes. (Adapted from 'Progress in Nuclear Magnetic Resonance Spectroscopy', Vol. 31, G. A. Morris, H. Barjat and T. J. Horne, Reference Deconvolution Methods, pp 197–257, Copyright (1997), with permission from Elsevier Science)

correction in this way. Examples include changes in receiver gain, field-frequency ratio, receiver phase, and many of the sources of t_1-noise in 2D NMR spectroscopy. Unlike other post-processing methods for improving the interpretability of NMR data, such as maximum entropy reconstruction or linear prediction, reference deconvolution is essentially a linear process. Prior knowledge of the theoretical form of the reference signal is used to allow the experimental signal(s) to be factorized into a corrected spectrum and an experimental lineshape, with no change in the overall information content. This linearity represents both a strength and a weakness. The risk of over-interpretation of the experimental evidence, ever present with nonlinear methods, is small. However, reference deconvolution cannot produce corrected data where there is no experimental evidence. The range of experimental imperfections that may be corrected is thus finite: if the time-domain envelope of an experimental signal touches zero, division of the ideal time-domain signal by its experimental form will produce a singularity. In such circumstances there is a choice between restricting the correction of the signal to times before the experimental signal disappears, and invoking nonlinear methods.

2 HISTORICAL BACKGROUND

Experimental spectroscopists frequently use the principle of reference deconvolution implicitly: if a small shoulder appears on one side of an NMR line, the immediate reaction is to check for the same feature elsewhere in the spectrum. If absent, the shoulder represents a real signal; if present throughout, it probably indicates a shimming error and can safely be ignored. Giving this principle quantitative form, numerical fitting of complex multiplets with an experimental lineshape dates back at least to 1966.[2,3] Reference deconvolution proper has been independently proposed at least four times in different guises, for correcting pulse Fourier Transform FT NMR,[4,5] correlation NMR[6] (Reference Lineshape Adjustment, RLSA) and in vivo NMR[7] (Quantification Improvement by Converting Lineshapes to the Lorentzian Type, QUALITY) data. Although the algorithms proposed differ somewhat in detail, all share the same basic features. In addition to these methods, which seek to use all the experimental information available in the correction process, a variety of less general methods have been proposed which seek to correct just one or two classes of error. Examples include time-dependent phase correction in in vivo experiments using pulsed field gradients,[8] and phase[9] or phase and amplitude[10] tracking for t_1-noise reduction in 2D NMR experiments.

3 THEORY

The basic algorithm described in the Introduction can be quite effective, but in all but the simplest spectra it suffers from a significant disadvantage. In order to obtain the experimental free induction decay for the reference signal alone it is necessary to filter out contributions from all other signals. At first sight this is straightforward; zeroing all but the arrowed reference signal region of Figure 1(a) should have the desired effect. However, in order to obtain the complete time-domain reference signal it is necessary to use both real (absorption mode) and imaginary (dispersion) mode parts of the raw experimental spectrum. Because the dispersion mode signal falls off only hyperbolically with frequency offset, it is much more difficult to choose a reference region which neither truncates the dispersion mode reference signal nor includes signal from other resonances. The solution is to perform the filtering of the experimental spectrum on the absorption mode signal alone, and reconstruct the missing contribution from the dispersion signal using the Hilbert transform relationship between the two. Provided that the raw experimental free induction decay is zero-filled at least once before Fourier transformation, no net loss of information results.

A practical algorithm for reference deconvolution proceeds as follows. The raw experimental free induction decay $s_e(t)$ is zero-filled once, Fourier transformed and phase corrected to yield an experimental spectrum $S_e(\omega)$. The experimental free induction decay for the reference signal $s_r(t)$ alone may be obtained by taking the first half of the inverse Fourier transform of the windowed spectrum:

$$s_r(t) = \mathrm{FT}^{+}[\mathrm{Re}\{S_e(\omega)\} \prod(\omega_R, \omega_L)] \prod(0, t_{max}) \qquad (1)$$

Here FT^{+} and FT^{-} indicate inverse Fourier transformation and Fourier transformation respectively:

$$\mathrm{FT} \pm [A(\omega)\} = \frac{1}{2\pi} \int_{-\infty}^{+\infty} A(\omega) e^{\pm i\omega t} d\omega \qquad (2)$$

the window function $\Pi(a,b)$ is unity between a and b and zero elsewhere, the reference signal (and nothing else) is entirely contained within the frequency range ω_R to ω_L, and t_{max} is the time for which the experimental free induction decay is recorded. The windowing $\Pi(0,t_{max})$ is necessary because transforming only the real part of $S_e(\omega)$ generates a time-symmetric function consisting of the required signal followed by its reflection. The use of zero-filling before the initial Fourier transformation ensures that no information is lost when this reflection is discarded.

The next step is to calculate the ideal form $s_i(t)$ of the ideal reference signal. This may be done either by direct calculation in the time domain, or by inverse Fourier transformation of the theoretical spectrum; in both cases it is necessary to include explicitly any known satellite signals, isotope shifts etc. The choice of lineshape for the ideal reference signal is critical. The obvious choice, the natural lineshape, is almost always far too ambitious: because most experimental spectra are significantly broadened by field inhomogeneity, setting a target lineshape which is much narrower than the experimental lineshape generally yields unacceptably low signal-to-noise ratio. As with other forms of resolution enhancement, the uninformative limit is an infinitely sharp spectrum with zero signal-to-noise ratio. The solution is to select a target lineshape, typically Lorentzian, Gaussian, or some mixture of the two, which gives a suitable compromise between resolution and signal-to-noise ratio in the corrected spectrum. In general the ideal reference signal can be described as a sum of rotating complex exponentials multiplied by an envelope function $W(t)$:

$$s_i(t) = \sum_{j=1}^{n} a_j \exp(i\omega_j t) \times W(t) \qquad (3)$$

where the summation is over the known components of the reference signal, and $W(t)$ typically has the form

$$W(t) = \exp\left[-\frac{t}{t_e}\right]\exp\left[-\frac{t^2}{t_g^2}\right] \quad (4)$$

with exponential and Gaussian components defined by the time constants t_e and t_g receptively.

The correction function required is then the complex ratio $c(t)$ between the theoretical and experimental reference free induction decays:

$$c(t) = \frac{s_i(t)}{s_r(t)} \quad (5)$$

Since the experimental reference free induction decay is derived from a phase-corrected spectrum (in order to avoid dispersion mode contributions), any frequency-dependent component of the phase correction will have had the effect of giving a small time shift to the time-domain signal. Therefore to ensure exact time correspondence between the full and the reference experimental free induction decays, a time-shifted version $s'_e(t)$ of the former should be produced:

$$s'_e(t) = \mathrm{FT}^+[\mathrm{Re}\{S_e(\omega)\}]\prod(0, t_{max}) \quad (6)$$

The corrected spectrum is finally obtained by Fourier transforming the product of the time-shifted full experimental free induction decay and the correction function $c(t)$:

$$S_c(\omega) = \mathrm{FT}^-[s'_e(t)c(t)] \quad (7)$$

The complete process is summarized in Figure 2. The raw experimental free induction decay (a) is zero-filled, Fourier transformed and phase corrected (b), and then inverse Fourier transformed with (d) and without windowing to yield the reference free induction decay (c) $s_r(t)$ and the time-shifted (phase-corrected) full free induction decay (i) $s'_e(t)$. The ideal reference signal (e) $s_i(t)$ is calculated either directly or by inverse Fourier transformation of the ideal spectrum (f). Finally the time-shifted signal (i) is divided by the experimental reference signal (c) and multiplied by the ideal reference signal (e) to give the corrected free induction decay (g), which may be transformed to give a corrected spectrum (h) $S_c(\omega)$.

Not all experimental spectra contain a suitable singlet reference signal. There is a fundamental difficulty in using reference signals which are simple multiplets, in that such signals contain zeroes in the time domain. It is however still possible to use such signals in spectra with good signal-to-noise ratio, by interpolating the correction function $c(t)$ over the gaps in the experimental data. Although this compromises slightly the linearity of the process, in practice the extra information generated is a very small proportion of the whole, and the interpolation works well. The principal problem is the need for the ideal reference signal to be very accurately characterized, as visible artifacts can result from errors of just a few MHz in coupling constant or a fraction of a percent amplitude asymmetry. Fortunately the effects of such errors are simple and predictable (spurious sidebands at harmonics of the multiplet splitting), and iterative minimization of such sidebands can be used to refine the form of the ideal signal. Provided care is taken, very good results can be obtained with doublet reference signals.[11]

Reference deconvolution is not restricted to one-dimensional spectra, but different multidimensional experiments may

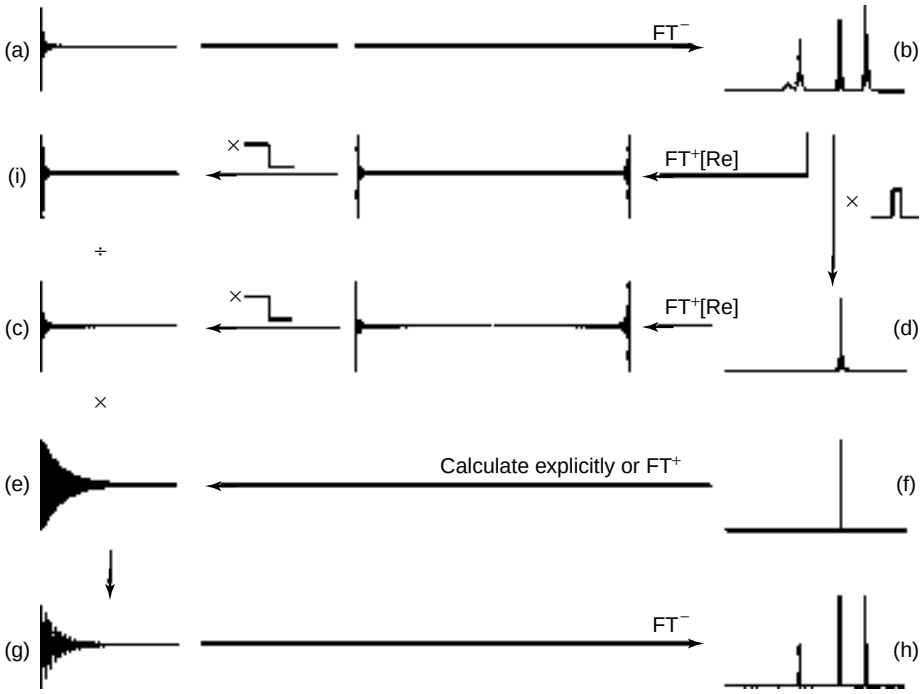

Figure 2 Schematic summary of a practical algorithm for reference deconvolution. (Reprinted from 'Progress in Nuclear Magnetic Resonance Spectroscopy', Vol. 31, G. A. Morris, H. Barjat and T. J. Horne, Reference Deconvolution Methods, pp 197–257, Copyright (1997), with permission from Elsevier Science)

require different implementations. The discussion which follows concerns the application to 2D NMR, but similar considerations apply to all multidimensional NMR experiments. Reference deconvolution for the simple correction of lineshape errors can be applied to any 2D experiment by using a correction function derived from a conventional 1D experiment. The same correction function is applied to every experimental free induction decay, correcting the lineshape in F_2; where appropriate, the same correction can be used in F_1. A much more powerful use of reference deconvolution in 2D NMR is for the correction of t_1-noise, but here two complications intrude. The first is that reference deconvolution only corrects for instrumental errors which affect all signals equally; in 2D NMR, this can effectively limit reference deconvolution to correcting a single coherence transfer pathway. The second problem is that reference deconvolution cannot be used where there is no reference signal, preventing (or at least greatly complicating) its application to experiments in which the reference signal is amplitude modulated as a function of t_1.

Reference deconvolution has been applied very successfully to two different classes of 2D experiment: those in which t_1-noise is dominated by a single unwanted pathway (e.g., HMBC (heteronuclear multiple bond coherence)), and those in which pulsed field gradients are used to ensure that only a single coherence transfer pathway survives (e.g., gradient enhanced COSY (correlation spectroscopy), gradient NOESY (nuclear Overhauser effect spectroscopy)). In the former case, the normal phase cycle is split into two halves in which the unwanted signals are of opposite phase, and reference deconvolution is used to ensure that the reference signal is nulled when data for the two halves are combined.[12] In the latter case, reference deconvolution is used as normal except that the ideal reference signal is phase-modulated as a function of t_1, and the extraction of the experimental reference signal requires automatic phase and baseline adjustment of the reference region of the (t_1,F_2) spectra.[13]

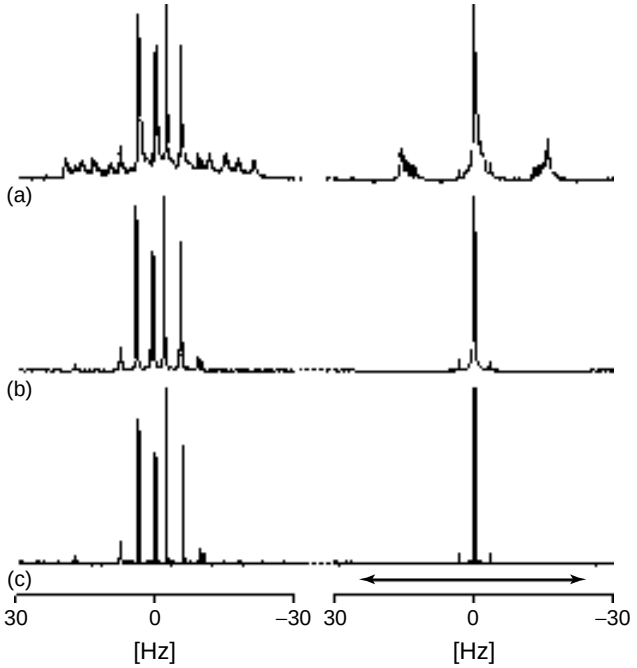

Figure 3 Reference deconvolution of a 300 MHz proton spectrum of a solution of orthodichlorobenzene and TMS in deuterioacetone. (a) Raw spectrum; (b) after reference deconvolution with a target lineshape of a 0.2 Hz wide Lorentzian; and (c) after reference deconvolution with a target lineshape of a 0.2 Hz wide Gaussian. The horizontal arrow indicates the reference region used. (Adapted from Progress in Nuclear Magnetic Resonance Spectroscopy, Vol. 31, G. A. Morris, H. Barjat and T. J. Horne, Reference Deconvolution Methods, pp 197–257, Copyright (1997), with permission from Elsevier Science)

4 APPLICATIONS

4.1 Lineshape Correction

One of the earliest applications of reference deconvolution, and still the most widespread, is for the correction of instrumental errors in lineshape. Figure 3 offers an extreme example, in which a 300 MHz proton spectrum of a sample of orthodichlorobenzene and tetramethylsilane (TMS) was acquired under conditions of sample spinning and poor shimming. The raw spectrum of Figure 3(a) shows severe lineshape asymmetry and spinning sidebands. Reference deconvolution with a target lineshape of a 0.2 Hz wide Lorentzian ($t_e = 5/\pi$ s, $t_g = \infty$ in equation 4) using a 50 Hz wide region of the spectrum containing the TMS signal yielded the corrected spectrum of Figure 3(b), while setting a target lineshape of a 0.2 Hz Gaussian ($t_e = \infty$, $t_g = 2.65$ s in equation 4) gave the spectrum of Figure 3(c). Note the ^{29}Si and ^{13}C satellites visible in the TMS region of Figures 3(b) and 3(c); if these are omitted from the ideal reference signal, spurious negative sidebands appear in the corrected spectrum.

Figure 3 is illustrative of the sort of improvement obtainable, at relatively modest cost in signal-to-noise ratio, even where there are severe lineshape distortions. In spectra where the natural widths of the lines of interest are significantly greater than that of the reference signal, as is generally the case, resolution enhancement is easily obtained by using a negative time constant t_e and a positive t_g in equation (4). This leads to over-enhancement of the reference line, generating negative side-lobes, but enhanced resolution for the remainder of the spectrum. The application of reference deconvolution is not restricted to spectra, such as that of Figure 3, which have relatively high signal-to-noise ratio. The basic requirement is that the signal-to-noise ratio of the reference signal be at least as good as that of the signals of interest, as otherwise the noise in the reference region would lead to visible noise being convoluted onto the remainder of the spectrum. Reference deconvolution is not uniformly successful; in the small minority of situations where there is significant multiplet character to the experimental lineshape, so that nodes appear in the time-domain signal, the width of target lineshape for which clean results are obtained is limited by the time at which the first zero appears in the experimental signal envelope.

Lineshape correction by reference deconvolution finds a wide variety of uses in NMR. It is particularly helpful in dynamic NMR, where instrumental contributions to the experimental lineshape interfere with attempts to extract dynamic information by bandshape fitting;[14] in diffusion-ordered spectroscopy, where small magnetic field perturbations following the application of field gradient pulses can distort lineshapes and lead to overestimation of diffusion coefficients;[15] and in

in vivo NMR,[7] where accurate shimming is frequently impossible. It has also been used in single crystal solid state NMR, and for the suppression of unwanted sidebands from a variety of sources. Although not strictly an application of lineshape correction, examination of the correction function $c(t)$ for 1D spectra can be a valuable diagnostic tool in tracking down instrumental problems.

4.2 Difference Spectroscopy

One of the families of NMR techniques most susceptible to instrumental irreproducibility is that of difference spectroscopy. The most common example is the NOE (nuclear Overhauser effect) difference technique, in which a difference is typically taken between an unperturbed spectrum and one acquired following selective saturation of a particular proton signal. Because Overhauser effects are typically small for small molecules in mobile solution, this technique is normally carried out only on samples with strong signals. This has the result that almost all such spectra show substantial difference artifacts, typically in the form of spurious signals which appear to be in dispersion mode. In fact such artifacts usually arise from small frequency differences between the saturated and unperturbed spectra, and hence cannot be adjusted to pure absorption mode. Although frequency errors frequently dominate, small changes in lineshape (especially if there is some probe heating as a result of the saturating irradiation), pulse phase errors etc., also contribute. All of these ills can be treated by using reference deconvolution to ensure that the reference signal has the same frequency, amplitude, phase and shape in both spectra. Provided that precautions are taken to avoid frequency-dependent perturbations of the spectra, the resultant difference spectra can be extremely clean.[16]

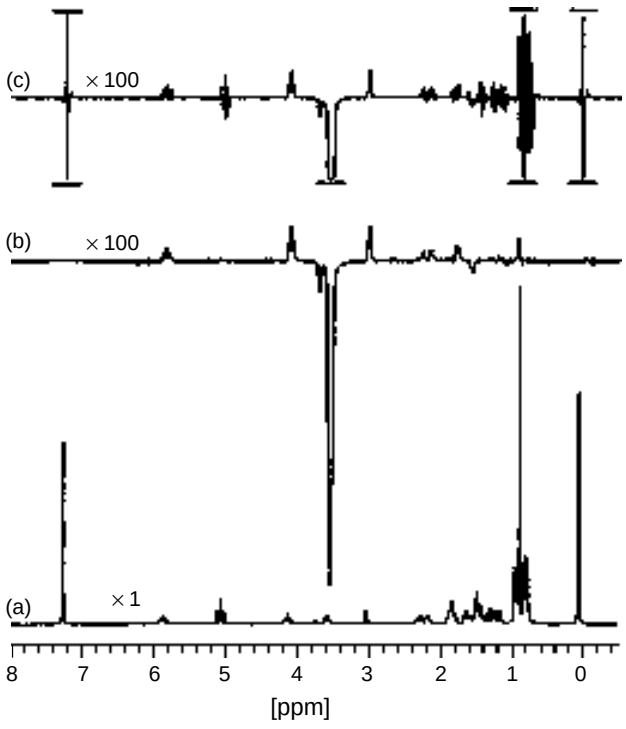

Figure 4 300 MHz proton spectra of compound **1**. (a) Normal spectrum; (b) NOE difference spectrum corrected by reference deconvolution using a 140 Hz wide reference region centered on the chloroform signal at 7.24 ppm, and expanded vertically ×100; and (c) uncorrected difference spectrum, with the same expansion but truncated as indicated by the horizontal bars

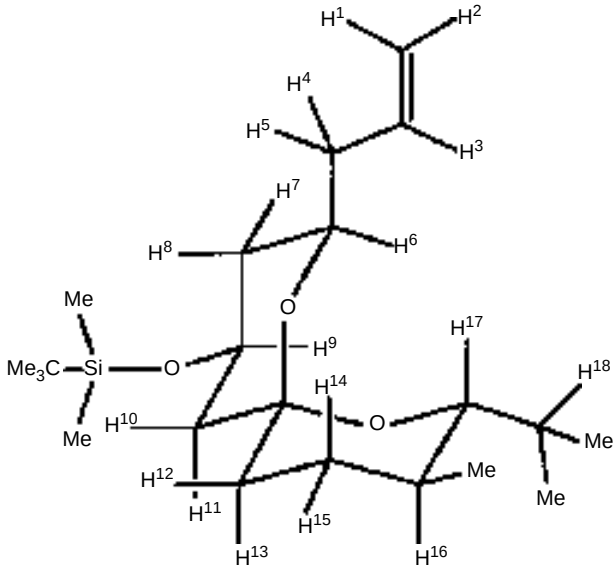

(1)

Figure 4(a) shows the normal spectrum of the species **1**, Figure 4(b) a hundred-fold vertical expansion of the corrected NOE difference spectrum following irradiation of proton 6, and Figure 4(c) the uncorrected difference spectrum. At such an expansion the uncorrected spectrum shows severe difference artifacts, but these are almost completely absent in the corrected spectrum. In the uncorrected spectrum only Overhauser effects greater than about 1% can be identified unequivocally, whereas the corrected spectrum shows a clean 0.5% NOE to the methyl signal at 0.9 ppm. The complete nulling of the signal of the trimethylsilyl blocking group, which is not expected to show any NOE, is particularly gratifying. This shows that the reference deconvolution process matches the signal amplitudes in the two parent spectra to better than 1 part in 10^4, or in other words would allow the detection of NOE's as small as 0.01% for such a signal.

4.3 2D NMR

Considerable improvements in spectral quality can be obtained by the use of reference deconvolution to correct the t_1-noise that results when instrument instability causes – as it inevitably does – different increments of a 2D NMR experiment to be acquired under slightly different conditions. If reference deconvolution is to correct in 2D NMR all of the errors that it can correct in 1D, it is necessary that all the signals of interest follow the same coherence transfer pathway, as otherwise any errors in pulse phase will have different effects on signals following different pathways. Of course, in experiments where other sources of t_1-noise that do not affect the relative phases of pulses and signals are dominant, the requirement of a single pathway may be relaxed.

The simplest example of a single pathway 2D experiment is gradient-enhanced COSY,[17] in which field gradient pulses

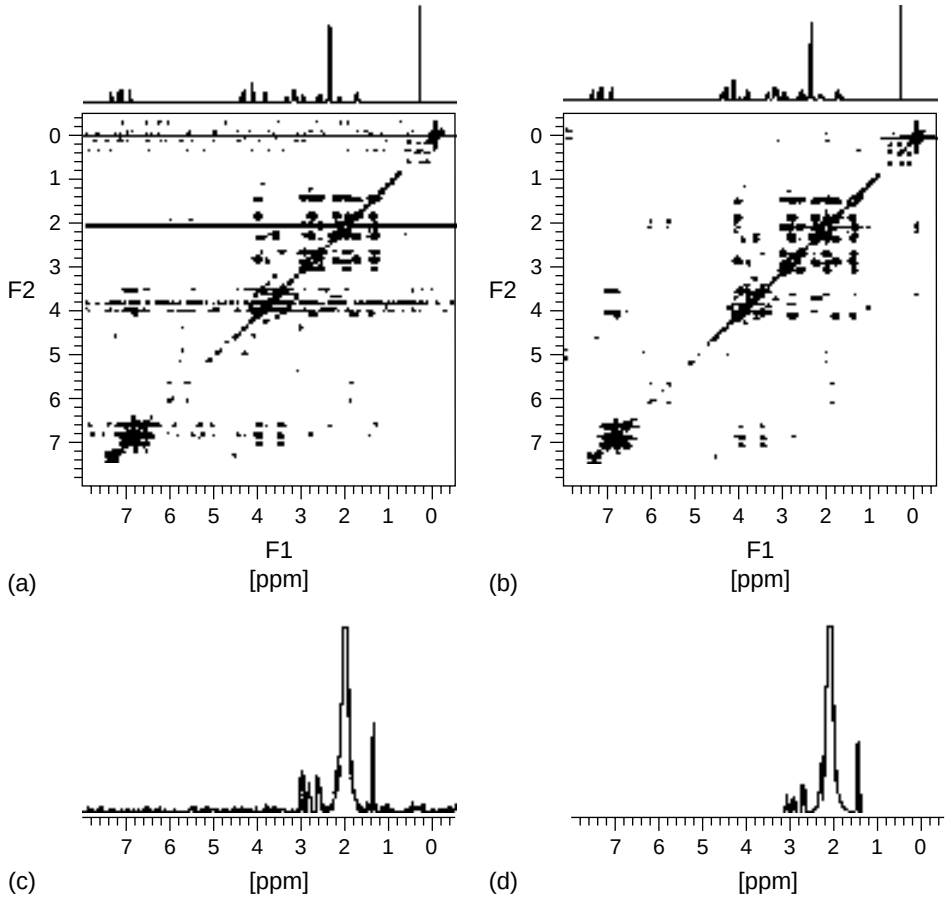

Figure 5 500 MHz gradient COSY spectra of compound 2. (a) Raw and (b) corrected COSY spectra, with (c) and (d) vertical expansions of the corresponding F_1 cross-sections through the residual proton signal from the solvent. (Adapted from T. J. Horne and G. A. Morris, *J. Magn. Reson. Ser A*, 1996, **123**, 246, by permission of Academic Press)

either side of the mixing pulse are used to enforce either the coherence transfer echo or the antiecho pathway.

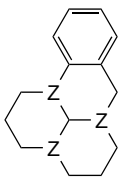

(2)

Figure 5 shows the results of a simple gradient COSY experiment on a solution of the tetracyclic orthoamide **2** in deuterioacetone with TMS as reference. To correct the experimental data, the raw free induction decays were treated with a mild Gaussian weighting to prevent truncation artifacts, zero-filled, and Fourier transformed with respect to t_2. Each of the resultant spectra was then subjected to reference deconvolution using an 88 Hz wide region around the TMS signal, and the corrected free induction decay stored. Automatic zero-order phase and linear baseline correction were applied to the reference region, and a target lineshape of a 3 Hz wide Lorentzian, phase modulated as a function of t_1 at the TMS offset from resonance, was used. The 2D spectra of Figure 5(a) and (b) show the raw and corrected data respectively, following sinebell multiplication, zero-filling and double Fourier transformation. The corresponding F_1 cross-sections Figure 5(c) and (d) through the residual solvent peak at 2.04 ppm show the reduction in t_1-noise achieved by reference deconvolution. The signal-to-t_1-noise ratio increases from 2600 : 1 to 110 000 : 1, a 40-fold improvement. Interestingly, the reduction in the noise level reveals some small signals attributable to dipolar demagnetization field effects, which are not normally seen in spectra of relatively dilute samples.

5 RELATED ARTICLE IN THIS VOLUME

Diffusion-Ordered Spectroscopy (DOSY).

6 RELATED ARTICLES IN VOLUMES 1–8

COSY Two-Dimensional Experiments, Volume 3, Data Processing, Volume 3, Maximum Entropy Reconstruction, Volume 5, Nuclear Overhauser Effect, Volume 5.

7 REFERENCES

1. H. Barjat, T. J. Horne, and G. A. Morris, *Prog. Nucl. Magn. Reson. Spectrosc.*, 1997, **31**, 197.

2. W. D. Keller, T. R. Lusebrink, and C. H. Sederholm, *J. Chem. Phys.*, 1966, **44**, 782.
3. R. R. Ernst, R. Freeman, B. Gestblom, and T. R. Lusebrink, *Mol. Phys.*, 1967, **13**, 283.
4. J. Taquin, *C.R. Acad. Sci. Paris*, 1975, **280B**, 485; *C.R. Acad. Sci. Paris*, 1976, **283B**, 257; *Rev. Phys. Appl.*, 1979, **14**, 669.
5. G. A. Morris, *J. Magn. Reson.*, 1988, **80**, 547.
6. J. M. Wouters and G. A. Petersson, *J. Magn. Reson.*, 1977, **28**, 81; J. M. Wouters, G. A. Petersson, W. C. Agosta, F. H. Field, W. A. Gibbons, H. Wyssbrod, and D. Cowburn, *J. Magn. Reson.*, 1977, **28**, 93.
7. A. A. DeGraaf, J. E. van Dijk, and W. M. M. J. Bovée, *Magn. Reson. Med.*, 1990, **13**, 343.
8. R. J. Ordidge and I. D. Cresshull, *J. Magn. Reson.*, 1986, **69**, 151.
9. G. A. Zhu, A. Renwick, and A. Bax, *J. Magn. Reson. Ser. A*, 1994, **110**, 257.
10. A. Ziegler, M. Izquierdo, C. Rémy, and M. Décorps, *J. Magn. Reson. Ser. B*, 1995, **107**, 10.
11. H. Barjat, G. A. Morris, A. G. Swanson, S. Smart, and S. C. R. Williams, *J. Magn. Reson. Ser. A*, 1995, **116**, 206.
12. A. Gibbs, G. A. Morris, A. G. Swanson, and D. Cowburn, *J. Magn. Reson. Ser. A*, 1993, **101**, 351.
13. T. J. Horne and G. A. Morris, *J. Magn. Reson. Ser. A*, 1996, **123**, 246.
14. D. V. S. Green, I. H. Hillier, G. A. Morris, and L. Whalley, *Magn. Reson. Chem.*, 1990, **28**, 820.
15. H. Barjat, G. A. Morris, S. Smart, A. G. Swanson, and S. C. R. Williams, *J. Magn. Reson. Ser. B*, 1995, **108**, 170.
16. G. A. Morris and D. Cowburn, *Magn. Reson. Chem.*, 1989, **27**, 1085.
17. R. E. Hurd, *J. Magn. Reson.*, 1990, **87**, 422.

Biographical Sketch

Gareth A. Morris, *b* 1954. M.A. (Nat. Sci.), Ph.D. (supervisor Ray Freeman) 1978, Oxford University, UK. Fellow by Examination, Magdalen College, Oxford, 1978–1981; Izaak Walton Killam Postdoctoral Fellow, University of British Columbia (with Laurie Hall) 1978–1979. Lecturer (1982–1989) and Reader (1989–1997) in Chemistry, Professor of Physical Chemistry (1998 to date), University of Manchester, UK. Approx. 130 publications. Current research interests: development of novel NMR techniques and their application to problems in chemistry, biochemistry and medicine.

Spin Echo Spectroscopy of Liquid Samples

Anthony G. Avent
University of Sussex, Brighton, UK

1	Introduction	1
2	The Spin Echo in Liquids	1
3	Calculation of Spin Echoes	4
4	Spin Echo Spectroscopy in Liquid Crystals	5
5	Related Articles	6
6	References	6

1 INTRODUCTION

The first use of an intense rf pulse to stimulate a transient response in NMR was reported by Erwin Hahn in 1950,[1] just a few years after the first NMR signals had been observed.[2,3] And it was Hahn again who, shortly afterwards, investigated the effect of applying two rf pulses separated by a period of free precession, and thereby demonstrated the generation of the spin echo.[4] This was the first multipulse NMR experiment and hence may be regarded as the precursor of the myriad of such experiments that are in current use in NMR spectroscopy.

The significance of the experiment lay in the discovery that the different interactions that determine the NMR spectrum responded to the two pulse sequence in different ways. As a result, spin echo spectroscopy can be used to distinguish, for example, field inhomogeneity and molecular diffusion effects from spin–spin relaxation, and chemical shifts, and heteronuclear couplings from homonuclear couplings. Indeed it was this experiment that first demonstrated to NMR spectroscopists that they did not have to accept meekly the NMR spectrum that nature provides, but rather they may intervene actively to mould the spectrum to their own requirements. This intervention may involve, as here, multipulse sequences, or it may involve the use of decoupling fields or the physical rotation of the sample. In all cases, however, the object is the same, to suppress effects that are of no interest or which are obscuring the effects that are of interest, in order to maximize the useful information content of the spectrum. These techniques have been vital to the establishment of NMR in its present preeminent position and all may be traced back to Hahn's original 1950 experiment with two rf pulses.

Any experiment in transient NMR that uses more than one rf pulse will generate a spin echo, and as such echoes are near ubiquitous in modern NMR. They have found applications in the NMR of gases, liquids, liquid crystals, solids, heterogeneous systems, biological systems and, latterly, in MRI. In this article we are concerned only with the liquid and liquid crystalline phases, but even here there are a vast number of multipulse experiments in use, all of which generate spin echoes; this article is then further restricted to those experiments in which the spin echo is studied for itself rather than those in which the echo is generated incidentally or as a means to some other end such as polarization transfer or multiple quantum coherence generation.

2 THE SPIN ECHO IN LIQUIDS

In 1950, Hahn demonstrated that the dephasing of the coherent magnetization which arises from field inhomogeneity is reversible.[4] He showed that a second pulse, applied a time τ after the first, produced a rephasing of the coherence a further period τ later. This refocused packet of magnetization was called a 'spin echo'.

The generation of a spin echo from the magnetization of a single site in a molecule is illustrated in Figure 1(a). Though in Hahn's original work the second pulse was of 90°, we consider here a second pulse of 180°, as this is conceptually simpler. This modification was first proposed by Carr and Purcell.[5] The first pulse produces a rotation of 90° about the x axis of the off-resonance rotating frame that converts the equilibrium z magnetization into a coherence along the y axis. This then precesses about the z axis at a frequency determined by its chemical shift offset, which is directly proportional to the static field $\boldsymbol{B}_0$. If the field is inhomogeneous there is a spread of $\boldsymbol{B}_0$ values which produces a corresponding spread in precession frequencies. This variation is represented in Figure 1(a) by two vectors labeled ***f*** and ***s***; the first represents magnetization from nuclei in regions of high magnetic field which precesses faster than the norm, and the second nuclei in regions of low field whose magnetization precesses slower. After a time τ a second pulse is applied which rotates the vectors through 180° about the y axis. If the nuclei do not move out of their original regions of field strength, then the fast and slow vectors will come together a time τ later along the y axis.

If this sequence is repeated for different values of τ and the magnetization sampled only at 2τ, then it will appear to be permanently fixed along the y axis. Any decrease in the intensity of the signal is then due solely to the entropy driven spin–spin relaxation processes characterized by the time constant T_2, upon which this sequence has no effect. Note also that the effect of chemical shift has been removed by the echo.

Figure 1(b) shows the effect of the echo sequence on the magnetization from the A spins of an AX spin system, where X is a nonresonant, usually heteronuclear, spin. The A magnetization is split into two components during precession, depending upon the state, α or β, of the X spin. The second pulse rotates these vectors into positions such that a further time τ later they refocus along the y axis, so that observations made at 2τ will not detect the effect of the heteronuclear coupling. That is, the X spins will appear to have been decoupled from the A spins.

Figure 1(c) shows the fate of the A magnetization in an AX spin system where X is a resonant, homonuclear spin. This splits during the first period of precession, as in the heteronuclear case, and the second pulse rotates the vectors as before but, in addition, because the X spin is also resonant, it flips the state of the spin and the vectors are interchanged. They now no longer refocus at 2τ; indeed, the splitting continues to develop as if the second pulse had not been applied. The effects of chemical shift and field inhomogeneity continue to refocus and observations made at 2τ will show a signal that is modulated only by the homonuclear coupling.

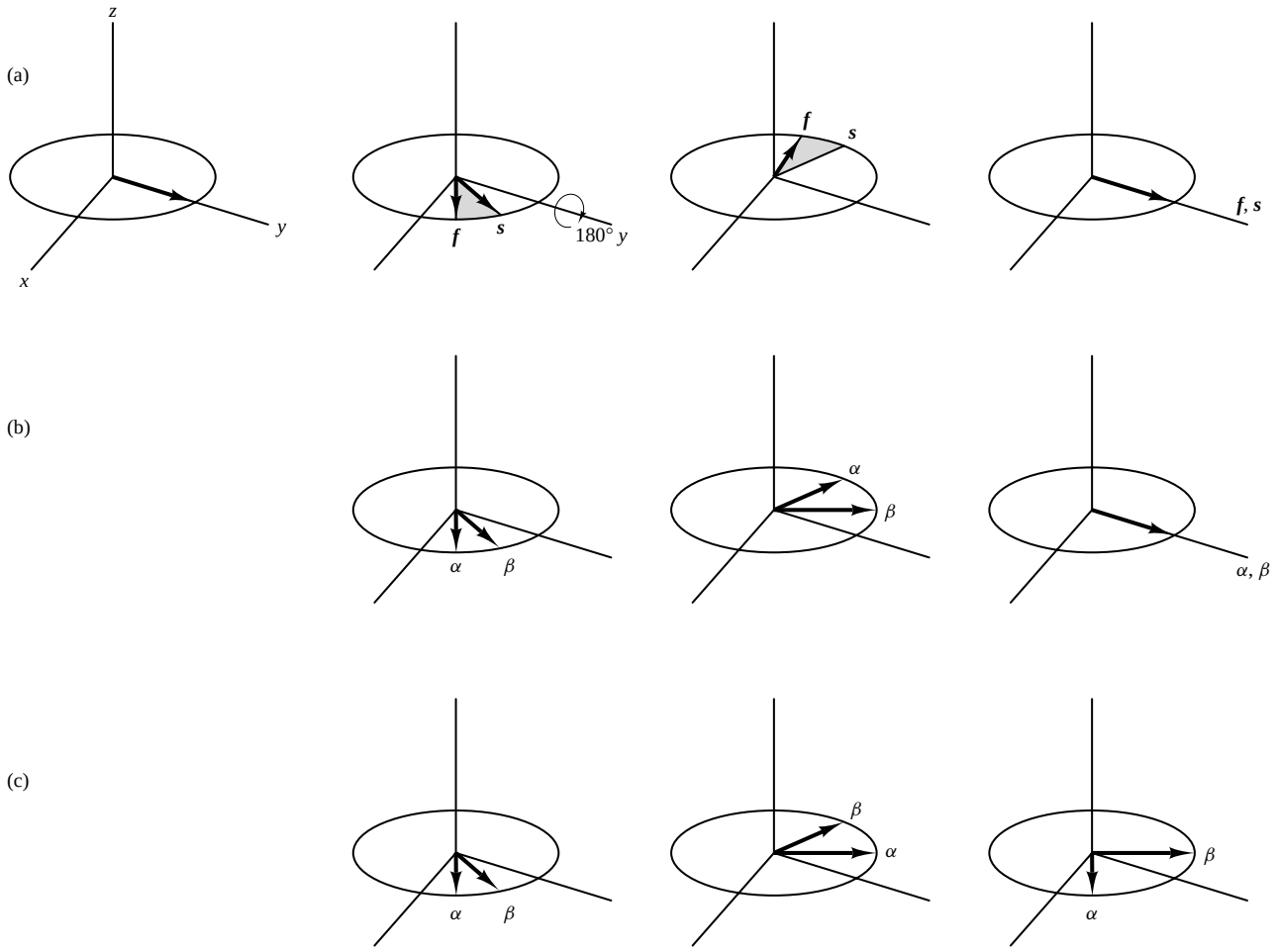

Figure 1 The effect of the 90 °−τ−180 °−τ sequence on (a) field inhomogeneity, (b) the A spins of a heteronuclear AX spin system, and (c) the A spins of a homonuclear AX spin system

To summarize, the spin echo removes the effects of field inhomogeneity but not spin–spin relaxation, and removes the effects of chemical shift and heteronuclear couplings but not homonuclear couplings; almost all applications of the spin echo in liquids exploit these differentiations.

So far the systems considered have been first order, if there is any significant second-order character to the system then this simple vector picture breaks down and to predict the echo amplitudes a full density matrix treatment is required. This is considered below.

In the early days of NMR, before magnets achieved their present level of homogeneity, the principal value of the spin echo technique was its ability to remove the effects of field inhomogeneity. This, combined with the effect of spin–spin coupling on the echo led to the discovery of J couplings, by Hahn, as a modulation in an echo experiment.[4] The molecule involved was ethanol, and a contemporary state of the art CW spectrum of the same molecule showed only three broad resonances corresponding to the three chemical environments of the protons.

The original Hahn echo experiment involved performing the pulse sequence for one value of τ, allowing the system to relax (a period that should be $>5T_1$) and repeating with a different value of τ until sufficient data had been accumulated. This is time consuming, and in experiments to measure T_2 was found to give incorrectly short values, especially where T_2 was long. This is because of molecular diffusion which means that molecules which, for example, start out in regions of relatively high magnetic field can diffuse during the course of the echo sequence into regions of low field, with the result that the effect of field inhomogeneity is not completely removed and contributes to the observed T_2.

A method that avoids this problem, and also speeds up the accumulation of data was put forward by Carr and Purcell[5] who, in addition to suggesting the use of 180° refocusing pulses, proposed the 'echo train'. This is a sequence of the kind:

$$90^\circ - [\tau - 180^\circ - \tau - \text{Sample}-]_n$$

If τ is short compared to the rate of molecular diffusion, then its effects on the observed magnetization are negligible. However, having solved one problem, Carr and Purcell were confronted with another, in that any imperfections in the 180° pulses have a cumulative effect along the echo train and lead to serious degradation of the signal.

The sources of pulse imperfections include jitter in their timing and, probably most serious, inhomogeneity in the rf field $\boldsymbol{B}_1$. This variation in $\boldsymbol{B}_1$ across the sample leads to variations in the angles of rotation produced by the refocusing pulse, which in turn leads to a distribution of magnetization

around the axis onto which it should be accurately refocused, and hence to a shortening of the apparent T_2. In systems without homonuclear coupling this problem can be overcome by phase shifting the refocusing pulses by 90° with respect to the initial pulse. This was first proposed by Meiboom and Gill[6] who showed that in this case the imperfection of the second refocusing pulse cancelled out that of the first, so that if the echo is sampled at alternate maxima a reliable result is achieved. The sequence used is then:

$$90^\circ_x - [[\tau - 180^\circ_y - \tau]_2 - \text{Sample}]_n$$

Where there is modulation by homonuclear coupling, the best solution is to improve the accuracy of each individual 180° pulse by using a composite pulse, which ensures a high quality refocusing at each echo maximum[7] (see ***Composite Pulses***).

The Carr–Purcell–Meiboom–Gill (CPMG) sequence has become established as the standard method for investigating spin–spin relaxation and related phenomena such as molecular diffusion and chemical exchange.[8]

The CPMG sequence as given above can only be used for systems that only contain, or are dominated by, a single peak, such as the protons of benzene or chloroform, or biological systems dominated by water. For multicomponent systems, such as for example, the ^{13}C nuclei of a complex organic molecule, the technique used is to apply the echo train and then sample an entire FID from the top of the final echo. This is repeated for echo trains of different lengths and the Fourier transformation of the resulting set of FIDs reveals the rate of decay of each component in the system. For systems involving homonuclear coupling the problem of echo modulation has also to be addressed. As we shall see below, one method is to pulse rapidly, but a more satisfactory method is to proceed as for multicomponent systems but with the accumulation of the whole of the final echo. That is, acquisition of data begins immediately after the final 180° pulse rather than from the top of the final echo. Fourier transformation of this whole echo combined with an absolute value mode of display then serves to eliminate the effect of modulation.[9]

In the case of molecular diffusion, the decay in the amplitude of the echo $E(2\tau)$ is given by:

$$E(2\tau) \propto \exp[-(2\tau/T_2) - 2\gamma^2 G^2 D\tau^3/3] \quad (1)$$

where τ is the echo spacing, D is the diffusion constant, G is the spatial magnetic field gradient, and γ is the magnetogyric ratio.

Note the τ^3 dependence, which explains the rapidly increasing effect diffusion has on long T_2 times. For a spectrometer in its normal mode of operation, G may be regarded as a measure of the inhomogeneity of the magnetic field, but where the echo technique is used to measure diffusion the experimenter can introduce a field gradient of known size across the sample and, by observing the effect this has on the echo amplitude, measure D[10] (see ***Diffusion Measurements by Magnetic Field Gradient Methods***).

Another source of broadening in NMR is chemical exchange, and this has also been studied by means of the spin echo technique. The echo does not remove the broadening, which is analogous to diffusion where spins move between regions of different local field strength, thus preventing the echo from refocusing properly. Here, the spins move between chemical sites of different precession frequencies, with the same result. When a system is close to either the fast or slow exchange limits, the amount of broadening caused by the exchange is small, and the spin echo can distinguish such small effects from those of field inhomogeneity better than the conventional spectrum. It can also allow the effects of small couplings to be observed at temperatures at which otherwise they are lost in the broadening linewidths.[11] Nonetheless, it must be said that the additional information produced by the echo technique is marginal when compared to the vast amount that is available from bandshape analysis and magnetization transfer experiments (see ***Chemical Exchange Effects on Spectra*** and ***Relaxation Effects of Chemical Exchange***).

As we have seen, homonuclear couplings were first observed in an echo experiment and, even at a time when CW spectrometers were well able to resolve proton–proton couplings, the echo method continued to be used. A study by Hahn and Maxwell[12] of the fluorine atoms in 1-fluoro-1,2,2-trichloroethane and 1,1-difluoro-2,2-dichloroethane was notable for providing the first example of echo modulation arising from strong coupling from nonresonant spins. Theoretical calculations of the response of various simple spin systems to the echo train were also made; these are considered in the next section. The principal difficulty with the technique lay in having to analyze complex modulations without the benefit of computerized Fourier transformation. When this became available with the advent of the computer driven spectrometer, it was first applied to the spin echo by Freeman and Hill.[13]

Their elegant experiment performed the same function as the original Hahn experiment, i.e. the removal of the effect of field inhomogeneity so as to reveal couplings otherwise obscured. Of course, given the improvements in magnet homogeneity in the intervening years, the couplings so revealed were very much smaller. The example given was of the molecule 2-bromothiophene-4-aldehyde. The Carr–Purcell echo train was used and tailored to excite selectively the aldehyde proton; the resulting echo envelope was Fourier transformed to give a 'J spectrum' consisting of a doublet of doublets showing the four- and five-bond couplings to the two ring protons (1.36 and 0.05 Hz, respectively). In addition, the linewidths of the J spectrum, in this case 0.03 Hz, provide an accurate measure of the spin–spin relaxation time of the nucleus. Selective excitation was used because, with the effect of chemical shifts removed, all the multiplets are crowded around the transmitter frequency and for systems of any size the resulting overlaps make analysis unrewarding. However, selective excitation cannot be used if the multiplets are too close together or if there are second-order effects. These drawbacks greatly restricted the use of the technique until the arrival of two-dimensional spectroscopy, which solved the overlap problem by spreading the signals into a second dimension (see ***Two-Dimensional J-Resolved Spectroscopy***).

Returning to one dimension and the echo train, a further problem or, in some cases, opportunity, arising from the experiment is that the echo amplitudes can be affected by the repetition rate of pulsing within the train, with fast repetition rates 'pulsing out' some phenomena. One example of this that has already been discussed is the removal of molecular diffusion effects; it has also been shown that chemical exchange effects are influenced by pulse rate. Furthermore, it has been shown that the modulation of the echo by

homonuclear couplings can be removed, for both first- and second-order spin systems, if the pulse rate is fast with respect to both the couplings and the chemical shift offsets of the system. For example, Freeman and Hill[8] have shown that for the molecule 1,1,2-trichloroethane, the spectrum of which consists of a triplet and a doublet (J = 7 Hz) separated by a shift difference of about 200 Hz, a pulse repetition rate such that 2τ = 2 ms is sufficient to eliminate any modulation from the echo. This effect arises because, if the repetition rate is fast compared to the offsets of the magnetization vectors from the transmitter frequency, then they are unable to precess far from the y axis onto which they were deposited by the initial 90°_x pulse, before being rotated round by a 180° pulse. Indeed, the effective field experienced by the vectors is along the y rather than z axis. The vectors are then locked onto the y axis so that phase differences are unable to build up. Such spin echo trains have a close relationship with the spin locking experiment, and it should be noted that any transverse relaxation times measured in these experiments are not true T_2 times, but rather are related to the $T_{1\rho}$ relaxation time (see ***Rotating Frame Spin–Lattice Relaxation Off-Resonance***).

3 CALCULATION OF SPIN ECHOES

For first-order spin systems the effect of the spin echo sequence can be calculated simply in terms of vector diagrams such as that shown for the AX case in Figure 1(c). Here it is clear that, with the effect of chemical shift removed but with that of homonuclear coupling left unchanged, the amplitude of the echo will be modulated as a function of τ by $\cos 2\pi J\tau$. Other first-order systems can be considered in the same way, though the results will be more complex. If the system is not first order, however, then a more rigorous approach using the density matrix formalism is required.

Before embarking on this, and to give the reader a feel for what the calculation entails, I shall begin by simply quoting the result for the simplest second-order spin system AB. An analytical equation for the echo amplitude $E(\tau)$ is possible and has been given by Abragam:[14]

$$E(2\tau) = (\delta^2/\Delta^2)\cos 2\pi J\tau + (J^2/\Delta^2)\cos 2\pi\Delta\tau\cos 2\pi J\tau + (J/\Delta)\sin 2\pi\Delta\tau\sin 2\pi J\tau \quad (2)$$

where δ is the shift difference between A and B (in hertz) and $\Delta = (J^2 + \delta^2)^{\frac{1}{2}}$.

Note that where $J \ll \delta$, equation (2) tends to $\cos 2\pi J\tau$, as in the AX case, but generally, and notwithstanding all that has been said above, the echo amplitude does now depend on chemical shifts. To see why this should be the case, consider first the AX spin system, the response of the A spins of which to the echo sequence is shown in Figure 1(c). The spectrum consists of four peaks at (1) $\nu_A + \frac{1}{2}J$, (2) $\nu_A - \frac{1}{2}J$, (3) $\nu_X + \frac{1}{2}J$, and (4) $\nu_X - \frac{1}{2}J$, and we can say that the two peaks around ν_A involve the flipping of the A spin and the two around ν_X the flipping of the X spin. Furthermore, when the system is subjected to the second pulse of the spin echo sequence, the magnetization associated with transition (1) is carried cleanly and completely into transition (2), and vice versa, and the same is true for transitions (3) and (4); this is implicit in Figure 1(c). The modulation of the echo then arises from the frequency difference between (1) and (2) and between (3) and (4), which is J. Moving on to the AB case, the situation is more complex because the stationary states of the system can no longer be described by the simple product basis set ($\alpha\alpha$, $\alpha\beta$, $\beta\alpha$, $\beta\beta$), the two central energy levels being now described by states that are linear combinations of $\alpha\beta$ and $\beta\alpha$. In turn, this means that the four transitions observed can no longer be regarded as corresponding to the flip of either the A or the X spin, but as a combination of both. So, though the transitions may still be regarded as 'A like' or 'X like', they carry an admixture of the character of the other spin. When the second pulse of the echo sequence is applied, there is now no longer a simple transfer of magnetization between well defined pairs of transitions, but rather there is a nonzero probability of transfer of magnetization from 'A like' to 'X like' transitions. It is this magnetization that gives rise to the chemical shift terms in equation (2).

We can now see that our task in calculating the response of a complex spin system to the echo sequence is firstly to calculate the frequencies and intensities of all the transitions, just as in the analysis of conventional spectra (see ***Analysis of High-Resolution Solution State Spectra***), but then we must calculate for each pair of transitions the efficiency with which they are mixed by the second and subsequent pulses.

The density matrix describes a system in the sense that the expectation value of any experimentally observable property of the system can be found by multiplying the density matrix by the matrix operator of the observable and taking the trace of the product. In this case we are interested in the magnetization in the y direction, so:

$$\langle \hat{I}_y \rangle = \mathrm{Tr}(\rho \hat{I}_y) \quad (3)$$

We now calculate the density matrix at the end of the echo sequence, $90^\circ_x - \tau - 180^\circ_y - \tau$, following the treatment of Allerhand.[15] For this we start with the time dependent form of the Schrödinger equation:

$$\mathrm{d}\hat{\rho}/\mathrm{d}t = \mathrm{i}[\hat{\rho}, \hat{\mathcal{H}}] \quad (4)$$

For a system of N spins, the static Hamiltonian $\hat{\mathcal{H}}$ is represented by a $2^N \times 2^N$ matrix which is constructed originally in the simple product basis set but is then diagonalized to give a matrix whose elements give the energies of the 2^N states of the system.

In isotropic liquids the Hamiltonian has chemical shift and J coupling terms; for liquid crystalline systems, these are supplemented by dipolar and, where appropriate, quadrupolar coupling terms. If relaxation effects are ignored, $\hat{\mathcal{H}}$ is time independent and the solution of equation (4) is

$$\rho(t) = \exp(-\mathrm{i}\hat{\mathcal{H}}t)\rho(0)\exp(2\mathrm{i}\hat{\mathcal{H}}t) \quad (5)$$

These operators can be easily derived from $\hat{\mathcal{H}}$, as the exponential of a diagonal matrix is a matrix containing the exponentials of each element.

If the rf field that provides the pulses is intense, their effect may be represented by simple rotation operators.[16] Thus the density matrix immediately after the initial 90°_x pulse, $\rho(+)$, is given by

$$\rho(+) = \exp(-\tfrac{1}{2}\mathrm{i}\pi\hat{I}_x)\rho(\mathrm{eq})\exp(\tfrac{1}{2}\mathrm{i}\pi\hat{I}_x) \quad (6)$$

The matrices representing $\hat{I}_x$, $\hat{I}_y$, and these exponential operators are constructed by taking tensor products of the

single spin operators N times, and then performing the same transformation that was required to diagonalize $\hat{\mathcal{H}}$, so as to bring them into the stationary state basis set.

Here $\rho(\text{eq})$ is the density matrix at equilibrium, which in the high-field and high-temperature approximations is proportional to $\hat{I}_z$ + Constant. Applying the rotation of equation (6) then gives:

$$\rho(+) \propto \text{Constant} + \hat{I}_y \tag{7}$$

If we now apply equation (5) for the first period of the echo, followed by an appropriate version of equation (6) for the 180°_y pulse and then equation (5) again for the second half of the echo, we have for the density matrix at the top of the echo $\rho(2\tau)$:

$$\rho(2\tau) \propto \exp(-\mathrm{i}\hat{\mathcal{H}}\tau)\exp(-\mathrm{i}\pi\hat{I}_y)\exp(-\mathrm{i}\hat{\mathcal{H}}\tau)\rho(+)\exp(\mathrm{i}\hat{\mathcal{H}}\tau) \times \exp(\pi\hat{I}_y)\exp(\mathrm{i}\hat{\mathcal{H}}\tau) \tag{8}$$

Inserting equation (8) into equation (3) and multiplying out gives the following expression for the observable magnetization at the top of the echo:

$$\langle\hat{I}_y\rangle \propto \sum_{k<l,m>n} \hat{I}_{ynm}\hat{I}_{xkl}R^{-1}_{ymk}R_{yln}\exp(\mathrm{i}2\omega_{klmn}\tau) \tag{9}$$

where

$$R_y = \exp(-\mathrm{i}\pi\hat{I}_y) \tag{10}$$

and where k, l, m, and n represent the 2^N states of the system and the sum is over all these states, ω_{klmn} represents a packet of magnetization that in the first half of the echo forms a coherence between the k and l states and which is then carried over by the second pulse to the transition between the m and n states.

On Fourier transformation, this gives a sum of δ functions at frequencies given by $[(E_l - E_k) - (E_m - E_n)]/2$, where E_l is the energy of state l, etc., with intensities given by the appropriate elements of $\hat{I}_x$, $\hat{I}_y$, ${R_y}^{-1}$, and R_y, which give a 'supertransition probability' which combines the normal transition probability of each coherence with the efficiency with which they are mixed by the rotation operator. A computer program for performing these calculations has been written by Turner;[17] its greatest challenge is to tackle the immensely complex results generated by spin echo spectroscopy of liquid crystalline phases.

4 SPIN ECHO SPECTROSCOPY IN LIQUID CRYSTALS

The unique features of the NMR spectroscopy of liquid crystalline phases are dealt elsewhere (see ***Liquid Crystals: General Considerations***). For our purposes here, the following summary is sufficient. The liquid crystalline state is characterized by long-range orientational order and by rapid relative translational motion of molecules. The orientational order gives rise to the crystalline character, and the rapid motion gives rise to the liquid like character. Molecules that form liquid crystals tend to be either long rod-like molecules or flat plate-like ones. At the local level the molecules align themselves with rods or plates parallel. This direction of preferred alignment is called the 'mesophase director' and, in the absence of any external restraint, such directors are isotropically distributed within the sample. In the presence of a magnetic field, however, the interaction between the field and the anisotropy of the bulk diamagnetic susceptibility of the system causes the local directors to become aligned with the field, thus amplifying local order into macroscopic order.

The consequences for the NMR of these systems is that anisotropic interactions such as the dipolar coupling and, for spins $>\frac{1}{2}$, quadrupolar coupling, which in ordinary liquids average to zero, are now averaged to a single, generally nonzero, value. The rapid motions of molecules within the sample ensure that resolution is still high and that any intermolecular interactions are averaged to zero. Dipolar couplings are much larger than J couplings (ranging up to a few thousand hertz), so almost all spectra are highly second order and there are significant couplings between widely separated nuclei. In addition, couplings are observed between magnetically equivalent spins so that, for example, the spectrum of water in a liquid crystalline phase is a doublet. These factors taken together mean that the spectra obtained are far more complex than those from isotropic media, to the point where the difficulty of analysis becomes a limiting factor in the use of this spectroscopy (see ***Liquid Crystalline Samples: Spectral Analysis***). It is nonetheless worth going to considerable lengths to achieve a full analysis, because of the simple relationship between dipolar couplings and internuclear distances, and hence molecular structure[18] (see ***Structure of Rigid Molecules Dissolved in Liquid Crystalline Solvents***).

One method for simplifying the problem is to deuterate the molecule partially and then observe both proton and deuteron spectra from which the effect of the heteronuclei has been removed. As we have seen in connection with Figure 1(b), the spin echo removes heteronuclear couplings and so may be regarded as a decoupling technique. The fact that it also removes the chemical shifts is no great disadvantage in liquid crystal NMR where the spectral widths are mainly determined by the large dipolar or quadrupolar couplings.

The first application of the spin echo to liquid crystalline systems was by Vold and Chan[19] who demonstrated for dichloromethane dissolved in a liquid crystalline medium that dipolar couplings produce a modulation of the echo amplitude just as J couplings do.

The echo has been investigated as a decoupling technique for various combinations of heteronuclei and for both liquid crystals and small molecules dissolved in liquid crystals.[20] Because the systems are strongly second order, the effects of heteronuclear couplings are not expected to be removed completely, just as chemical shifts are not removed from the echo spectrum of the AB system. However, calculations show that, if the heteronuclear couplings are small compared with the homonuclear ones, the decoupling effect is essentially complete and the homonuclei may be analyzed alone. An example is a study of ethylbenzene dissolved in a liquid crystalline phase. The spectrum of the fully protonated species was so complex as to defy analysis, so to simplify the system the ring protons were replaced with deuterons; the proton spectrum of this species was broad and largely featureless due the heteronuclear couplings between protons and deuterons. In contrast, the spin echo spectrum, which is shown in Figure 2(a), is a well-resolved and detailed spectrum which

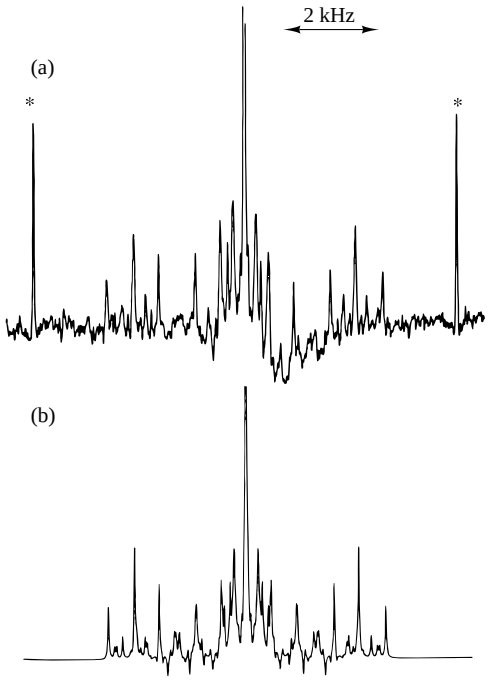

Figure 2 The experimental (a) and calculated (b) proton spin echo spectra of $C_6D_5CH_2CH_3$ dissolved in the liquid crystalline phase ZLI 1167. The peaks marked with asterisks are from water. (Reproduced by permission of the Royal Society of Chemistry from A. G. Avent, J. W. Emsley, Soon Ng, and S. M. Venables, *J. Chem. Soc., Perkin Trans. II*, 1984, 1855)

can be analyzed to give the dipolar couplings amongst the five protons of the ethyl group. The experiment used a single 180° pulse rather than an echo train in order to avoid heating the sample and pulse repetition effects. Figure 2(b) shows a computer simulation of the echo calculated using the program by Turner,[17] in which only the protons were considered. The best fit was obtained when the refocusing pulse was assumed to be 150°, which in effect allows for imperfections in the $\boldsymbol{B}_1$ field.

5 RELATED ARTICLES

Analysis of High-Resolution Solution State Spectra; Chemical Exchange Effects on Spectra; Composite Pulses; Diffusion Measurements by Magnetic Field Gradient Methods; Liquid Crystalline Samples: Spectral Analysis; Liquid Crystalline Samples: Structure of Nonrigid Molecules; Liquid Crystals: General Considerations; Relaxation Effects of Chemical Exchange; Rotating Frame Spin–Lattice Relaxation Off-Resonance; Structure of Rigid Molecules Dissolved in Liquid Crystalline Solvents; Two-Dimensional J-Resolved Spectroscopy.

6 REFERENCES

1. E. L. Hahn, *Phys. Rev.*, 1950, **77**, 297.
2. F. Bloch, W. W. Hansen, and M. Packard, *Phys. Rev.*, 1946, **70**, 474.
3. E. M. Purcell, H. C. Torrey, and R. V. Pound, *Phys. Rev.*, 1946, **69**, 37.
4. E. L. Hahn, *Phys. Rev.*, 1950, **80**, 580.
5. H. Y. Carr and E. M. Purcell, *Phys. Rev.*, 1954, **94**, 630.
6. S. Meiboom and D. Gill, *Rev. Sci. Instrum.*, 1958, **29**, 688.
7. M. H. Levitt and R. Freeman, *J. Magn. Reson.*, 1981, **43**, 65.
8. R. Freeman and H. D. W. Hill, in *Dynamic Nuclear Magnetic Resonance Spectroscopy*, ed. L. M. Jackman and F. A. Cotton, Academic, New York, 1975.
9. A. Bax, A. E. Mehlkopf, and J. Smidt, *J. Magn. Reson.*, 1979, **35**, 373.
10. P. Stilbs, *Progr. NMR Spectrosc.*, 1987, **19**, 1.
11. J. G. Powles and J. H. Strange, *Mol. Phys.*, 1964, **8**, 169.
12. E. L. Hahn and D. E. Maxwell, *Phys. Rev.*, 1952, **88**, 1070.
13. R. Freeman and H. D. W. Hill, *J. Chem. Phys.*, 1971, **54**, 301.
14. A. Abragam, *Principles of Nuclear Magnetism*, Oxford University, Oxford, 1961, p. 500.
15. A. Allerhand, *J. Chem. Phys.*, 1966, **44**, 1.
16. S. Schäublin, A. Höhener, and R. R. Ernst, *J. Magn. Reson.*, 1974, **13**, 196.
17. D. L. Turner, *J. Magn. Reson.*, 1982, **46**, 213.
18. J. W. Emsley and J. C. Lindon, *Nuclear Magnetic Resonance Spectroscopy Using Liquid Crystal Solvents*, Pergamon, Oxford, 1975.
19. R. L. Vold and S. O. Chan, *J. Chem. Phys.*, 1970, **53**, 449.
20. A. G. Avent, J. W. Emsley, Soon Ng, and S. M. Venables, *J. Chem. Soc., Perkin Trans. II*, 1984, 1855 and references therein.

Biographical Sketch

Anthony G. Avent. *b* 1956. B.A., Oxford, 1979; D.Phil., Southampton, 1983. Introduced to NMR by R. Freeman and J. W. Emsley. Manager of the NMR service at Sussex, 1983–present. Research interests: application of NMR to a wide range of organic, inorganic and organometallic chemistry, with particular recent interest in the fullerenes.

SQUIDs

Ulrike Werner-Zwanziger
Indiana University, Bloomington, IN, USA

1	Introduction	1
2	How a SQUID Works	1
3	Design of a SQUID Spectrometer	1
4	Applications	2
5	Conclusion	3
6	Related Articles	4
7	References	4

1 INTRODUCTION

Superconducting quantum interference devices (abbreviated SQUIDs) can be used as sensitive magnetic flux-to-voltage converters. In this mode they can detect NMR signals, replacing the tuned coil in a conventional NMR probe. Their primary applications include low frequency studies (below a few megahertz), observation of large spectral widths (several megahertz), and measurements at ultralow temperatures (millikelvin regime).

In conventional detection of NMR, the signal is observed as a voltage induced in a tuned coil by a changing magnetization $\mathrm{d}M/\mathrm{d}t$ (Faraday's law). This method is inefficient at low frequencies, where $\mathrm{d}M/\mathrm{d}t$ is small. The SQUID, on the other hand, directly transforms changes in the magnetization ΔM, induced by spin transitions, into voltages. Thus, SQUID detection works sensitively down to very low frequencies.[1]

SQUIDs can detect changes in both the longitudinal and transverse magnetization. SQUID measurements of the longitudinal magnetization have been used to obtain NMR,[2,3] NQR,[3,4] and EPR[5] spectra and relaxation times. There are no restrictions on the methods used to excite the transitions: techniques employed include CW excitation,[3,6,7] rf pulses,[8] and acoustic fields.[9] Applications of SQUID NMR spectrometers range from structural studies of solids[4] to thermometry,[1,10] study of enhanced nuclear moments,[11] and properties of superfluid ^{3}He.[8,12,13]

Changes in the transverse magnetization, that is, in the FID following an rf pulse, have been observed with SQUIDs both at high frequencies (30 MHz)[14] and in the low frequency regime ($<$200 kHz).[15–17] This application has great potential in that it could make use of the multitude of pulse sequences developed for high field NMR.

After sketching the principles of operation of a SQUID and the design of a SQUID spectrometer, we outline some applications of SQUID detection in NMR. We conclude with a summary of areas of future potential progress for the field.

2 HOW A SQUID WORKS

Here we briefly describe the principles of operation of SQUIDs. For a more detailed description of both operation and noise characteristics, see Meredith et al.[1] and Clarke.[18]

By combining the phenomena of fluxoid quantization in a superconducting ring and Josephson tunneling, SQUIDs convert changes in magnetic field into voltages that can be detected by conventional semiconducting electronics.[19] Fluxoid quantization in a superconducting ring restricts the magnetic flux threading the ring to $n\Phi_0$, a multiple of the flux quantum $\Phi_0 \sum h/2e \approx 2 \times 10^{-15}$ Wb. Application of an arbitrary flux Φ causes the ring to generate a supercurrent of Cooper pairs such that the self-generated flux exactly cancels Φ. To detect these flux-induced changes the superconducting ring is interrupted by one or two Josephson junctions. A Josephson tunnel junction consists of two superconducting films separated by a thin insulating layer. When a current I is passed through the junction, the Cooper pairs tunnel through the barrier. No voltage V is developed by this supercurrent until I exceeds the maximum supercurrent I_0 that the junction can sustain. Depending on whether one or two Josephson junctions interrupt the superconducting ring, one distinguishes between rf and dc SQUIDs, respectively. Direct current SQUIDs are normally operated by fixing the dc bias current across the SQUID at a constant value larger than the supercurrent I_0. Since the amount of current that travels as supercurrent through the ring depends on the flux threading the SQUID, the voltage changes periodically as a function of the applied flux with a period Φ_0. To obtain an output voltage that is proportional to the input flux even when the applied flux is less than Φ_0 or corresponds to many Φ_0, one uses a feedback circuit in which the SQUID acts as a null-flux detector.

The rf SQUID, on the other hand, consists of a superconducting loop interrupted by a single Josephson junction. The prefix 'rf' implies that the device is biased with a radiofrequency modulated flux. Both types of SQUID have been incorporated into NMR and NQR spectrometers.

3 DESIGN OF A SQUID SPECTROMETER

Despite the multitude of applications and experimental techniques exploiting the high sensitivity of a SQUID, the basic features of the spectrometers and their problems are similar. We therefore describe in some detail a particular spectrometer which uses a dc SQUID to detect the changes of the longitudinal magnetization.[3,20]

The probehead of this spectrometer is shown in Figure 1. The commercial dc SQUID (Model DBS, Biomagnetic Technologies, Inc.) operates in the flux-locked mode as a linear flux-to-voltage converter. To protect the SQUID from direct rf irradiation, the SQUID is embedded in a superconducting niobium tube (shown on the left-hand side of Figure 1), and is spatially separated from the sample environment (shown on the right-hand side of Figure 1). A superconducting flux transformer transfers the changes of magnetic flux from the sample into the SQUID. The transformer consists of two coils of equal inductance, and shunt resistors. The pickup coil holds the sample, which has a volume of roughly 100 mm^3. The second coil, the coupling coil close to the SQUID, feeds the flux change of the pickup coil into the SQUID itself. The shunt resistors in parallel with the coils at the bottom of the probehead act as a low pass filter to prevent rf from being transferred directly into the SQUID.

Changes of magnetic flux in the sample are induced by rf excitation of spin transitions. In this spectrometer, two

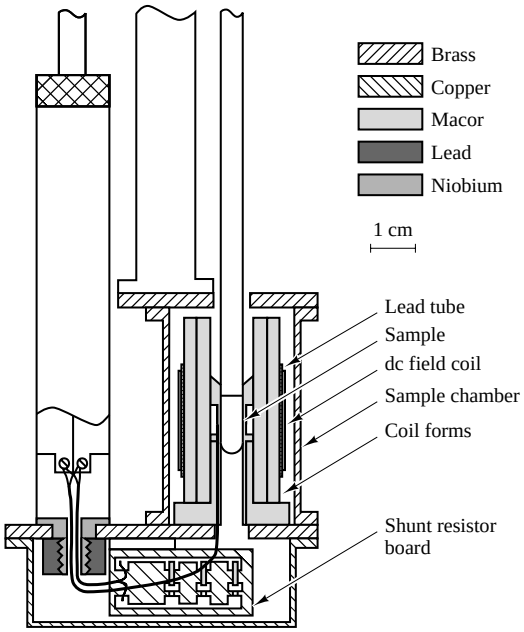

Figure 1 Cross section of the low-temperature part of the SQUID spectrometer. (Reproduced by permission of the American Institute of Physics from C. Conner, J. Chang, and A. Pines, *Rev. Sci. Instrum.*, 1990, **61**, 1059)

Helmholtz saddle coils wound orthogonally to the pickup coil emit a linearly or circularly polarized rf field to the sample (of microtesla magnitude). The exact orientation of these coils with respect to the pickup coil is one of the main factors in minimizing rf influence on the SQUID. The rf circuit is not tuned to a specific frequency, thus allowing a wide range of frequencies to be observed. Also, since the SQUID detects the slowly changing magnetization of the sample parallel to the static magnetic field, the resonance frequencies do not determine directly the sensitivity of detection. A small static magnetic field (up to about 10 mT) can be trapped in a lead tube surrounding the rf coils, the pickup coil, and the sample.

In this apparatus the probehead is immersed completely in liquid helium, giving a constant temperature of 4.2 K. The SQUID feedback circuit rests on top of the cryostat; this circuit, the cryostat, and the probehead are placed inside a cage made of copper mesh to shield them from external rf fields. The rest of the spectrometer, consisting of the rf transmitter, the remaining SQUID electronics, and the receiver is situated outside the copper cage. The rf irradiation is generated by a computer-controlled frequency synthesizer. The signal obtained from the SQUID is passed through the feedback unit to the SQUID controller (BTi Model 40). The signal is amplified, filtered, digitized, and finally transferred to a computer for storage and analysis.

4 APPLICATIONS

Early experiments using SQUIDs as part of NMR spectrometers concentrated mainly on studying the physical properties of systems. For example, Meredith et al. took advantage of the low excitation powers needed for the SQUID-based spectrometer to measure temperatures in the millikelvin regime, by determining relaxation times T_1 of a bundle of copper wires and using the Korringa relation T_1T = Constant.[1,10] Similarly, the low power requirements of the SQUID, together with the wider accessible frequency range (10 kHz to 1 GHz) allowed NMR and EPR relaxation studies of Ce^{3+} in cerium magnesium nitrate at temperatures down to 10 mK with the same spectrometer.[5] The wide available frequency range was also important for studies of the hyperfine-enhanced nuclear moment in $TmPO_4$,[11] for which an effective field 77.9 times stronger than the applied magnetic field was found. Pickens et al. presented NQR spectra and the first measurements of magnetic-field-dependent nuclear spin relaxation rates in a bulk metal (^{121}Sb and ^{123}Sb).[9] These experiments were performed using a SQUID spectrometer to detect the change of static susceptibility caused by transitions driven by acoustic energy. Webb studied the difference between the static and dynamic susceptibilities of superfluid ^{3}He–B at ultralow temperatures (1.2 K to 2 mK) and various pressures.[12,13]

Besides investigating the physical problems outlined above, SQUID spectrometers are valuable tools for obtaining answers to a wide range of chemical questions. Examples discussed below include studies of rotational tunneling in methyl groups to characterize local environments, and various quadrupole resonance experiments.

4.1 Rotational Tunneling of Methyl Groups

The tunneling frequencies of methyl groups have been used to characterize the local methyl group environments and correlate them with macroscopic properties.[2] The ground state rotation eigenfunctions of hindered methyl groups split into A and E symmetry states. The energy difference between the A and the E levels, denoted as the tunnel splitting $h\nu_T$, depends on the hindering potential given by the environment. The Pauli principle dictates that transitions between the rotational states are coupled to changes in the spin states. Unfortunately, transitions between the pure A and E states, which contain information about the environment, are symmetry forbidden in both high and zero magnetic fields. The SQUID experiments detect these transitions by applying a small magnetic field, resulting in Larmor frequencies of only a few hundred kilohertz. For methyl groups attached to sp^3 hybridized carbon, the similar size of the proton Larmor frequency, the dipole–dipole coupling constant between the protons, and the tunneling frequencies render transitions between the A and E symmetry species observable. The spectra (an example is shown in Figure 2) show maxima at the proton Larmor frequency ν_0 and twice the Larmor frequency $2\nu_0$, with their tunneling sidebands $\nu_0 \pm \nu_T$ and $2\nu_0 \pm \nu_T$. A systematic study of the dependence of the tunneling frequencies on the chain length of a series of carboxylic acids, and comparison to macroscopic properties like the heat of fusion, has led to a deeper understanding of subtle differences in crystal packing and its consequences for physical properties.[2]

4.2 NQR: Longitudinal Magnetization

NQR transitions provide chemical and structural information about the environment of the nuclei studied. In pure NQR the transition frequencies are sharply defined by the local electric

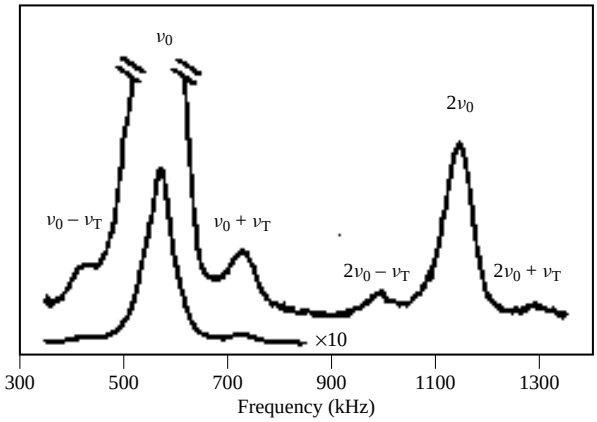

Figure 2 The proton SQUID NMR spectrum of solid hexanol in a magnetic field of 13.5 mT at 4.2 K. One frequency sweep each, from low to high frequencies and in opposite directions, were added. The insert shows the resonance at the Larmor frequency (reduced by 1/10th). The transitions at the Larmor frequencies ν_0 = 574 kHz and $2\nu_0$ = 1147 kHz are flanked by the tunneling sidebands $\nu_0 \pm \nu_T$ for a tunneling frequency ν_T = 145 ± 3 kHz. (Shown at the 33rd ENC, Asilomar, 1992, by B. Black, G. Majer, U. Werner, and A. Pines, reproduced in part by B. Black, Ph.D. Thesis, University of California, Berkeley, CA, 1993)

field gradients at the nucleus studied. However, low signal intensities due to low quadrupole transition frequencies, which can differ by several megahertz in the same sample, pose problems. These difficulties have been addressed by using a SQUID based spectrometer, both by detecting the longitudinal and transverse magnetization.

Studying NQR through the change in static susceptibility differs significantly from NQR experiments that observe the transverse magnetization either with a SQUID or a conventional detection scheme. The difference arises from the quenching of the magnetic moment of the quadrupolar eigenstates in zero field. This quenching is the result of time reversal symmetry of the quadrupole Hamiltonian.[21] For half-integer spins, the eigenstates with magnetic quantum numbers m and $-m$ ($m \neq 0$) are degenerate. For integer spins the eigenstates are either degenerate (for $\eta = 0$, where η is the asymmetry of the quadrupole interaction) or a superposition of equal contributions of the states with magnetic quantum numbers m and $-m$. In either case, exciting a transition between the pure quadrupole eigenstates with linearly polarized rf does not change the static susceptibility, and therefore no signal is induced in the SQUID. Any magnetization induced by a circularly polarized radiation is rapidly quenched by cross relaxation between the $\pm m$ manifolds. These difficulties are avoided by applying a small magnetic field to lift the degeneracy of the eigenstates and suppress cross relaxation. A frequency sweep using linearly polarized radiation through one of the resonances first excites one manifold at its resonance frequency, thereby creating a signal in the SQUID. Upon further increase of the frequency, the resonance of the corresponding negative manifold inverts the magnetization change again. Thus, the spectra resemble a square shape, possibly distorted by relaxation effects between the two resonance transitions.[4,22] This technique has been applied to a number of ^{27}Al, ^{10}B, and ^{11}B containing compounds in single crystals, and in polycrystalline and amorphous samples.[4,22]

Using circularly polarized radiation selectively excites transitions among either the $+m$ or the $-m$ manifold, depending on the sense of polarization.[22] The spectra show the sharp change of magnetization followed by the relaxation decay back to the equilibrium value. One peculiarity of this technique and other NQR measurements with a SQUID is that the sign of the observed changes in magnetization depends on the sign change of the magnetic quantum number of the transitions induced, an effect not observable by non-SQUID NMR.[9]

For integer spins, the application of a magnetic field either splits degenerate eigenstates or redistributes the weights in the superpositions of Zeeman states making up the quadrupolar eigenstates. These effects may still not be sufficient to create an observable signal in the SQUID. A study of the NQR of ^{14}N interacting with the weak electric field gradients in amino acids and small peptides[23,24] shows that the NQR transitions can be observed via cross relaxation of the ^{14}N polarization to adjacent proton spins. Properties of this technique such as the magnetic field dependence, additional signal enhancement by double irradiation, as well as application to studies of the changes of the nitrogen environment by mixing optical isomers and by combining amino acids into small peptides, are given in Werner et al.[23,24]

4.3 NQR: Transverse Magnetization

Pure NQR transitions can be detected with a SQUID by observing the FID after a rf pulse, or a spin echo created by a two-pulse sequence. The echo and a spectrum obtained by Fourier transformation for ^{14}N in NH_4ClO_4 at 1.5 K are shown in Figure 3.[16,17] The signal, a sum of 16 000 transients, shows an FID after the second pulse and the formation of a spin echo after 5 ms. For display, the echo signal was demodulated with a frequency of 35 kHz. The spectrum shows the FT of the echo obtained with a pulse spacing reduced to 4 ms. The sharp peaks at 17.4, 38.8, and 56.2 kHz are the lowest directly detected ^{14}N NQR transition frequencies. Note that these are the absolute frequencies, not those demodulated from a Larmor frequency as is done in high field NMR. The peak at 10.6 kHz was attributed to magnetoacoustic resonance of the input circuit. The three transitions allow determination of the ^{14}N NQCC $|e^2qQ/h| = \chi$ = 63.3 kHz and an asymmetry parameter η = 0.550. The absence of proton zero field NMR lines and of splittings of the ^{14}N NQR in the experimental results suggest motional averaging.

Finally, a SQUID acting as a tuned rf low noise amplifier at liquid helium temperatures was used to detect pulsed NQR at 30.686 MHz of ^{35}Cl in $NaClO_3$.[14,25] The long ring-down times after an rf pulse of the circuit, due to the high quality factor Q = 2500, was reduced using a Q spoiler consisting of a series array of Josephson tunnel junctions.

5 CONCLUSION

Detection of NMR and NQR signals using a SQUID has proven advantageous for studies at low frequencies, over large spectral widths, and at ultralow temperatures. Further technical developments should make these techniques even more widely applicable. For example, current SQUID spectrometers that

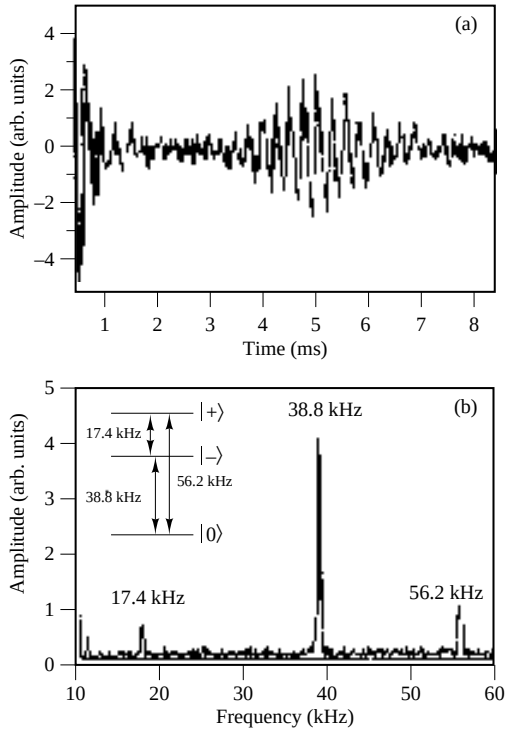

Figure 3 (a) FID after second pulse and spin echo of NH_4ClO_4 at 1.5 K. For display purposes, the real-time signal has been demodulated with 35 kHz. (b) FT of the spin echo. The inset shows the energy level diagram of ^{14}N in the presence of the electric field gradient of NH_4ClO_4. (Reproduced by permission of The American Physical Society from M. D. Hürlimann, C. H. Pennington, N. Q. Fan, J. Clarke, A. Pines, and E. L. Hahn, *Phys. Rev. Lett.*, 1992, **69**, 684)

detect the FID following an rf pulse with untuned circuits are limited by the feedback electronics to frequencies below 200 kHz. An increase in the spectral width and improved stability against rf pulses would open up the possibility for a variety of otherwise very difficult, if not impossible, single- and multi-dimensional NMR and NQR experiments at low magnetic fields using multipulse sequences. Whether detecting longitudinal or transverse magnetization, recent results show that SQUID spectrometers are becoming valuable tools for obtaining answers to a wide range of chemical and physical questions.

6 RELATED ARTICLES

Boron NMR; Cross Polarization in Solids; Field Cycling Experiments; Nitrogen NMR; Quadrupolar Interactions; Quadrupolar Nuclei in Solids; Quantum Tunneling Spectroscopy; Zero Field NMR.

7 REFERENCES

1. D. J. Meredith, G. R. Pickett, and O. G. Symko, *J. Low. Temp. Phys.*, 1973, **13**, 607.
2. B. Black, G. Majer, and A. Pines, *Chem. Phys. Lett.*, 1993, **201**, 550.
3. C. Conner, J. Chang, and A. Pines, *Rev. Sci. Instrum.*, 1990, **61**, 1059.
4. C. Conner, J. Chang, and A. Pines, *J. Chem. Phys.*, 1990, **93**, 7639.
5. R. V. Chamberlin, L. A. Moberly, and O. G. Symko, *J. Low Temp. Phys.*, 1979, **35**, 337.
6. E. P. Day, *Phys. Rev. Lett.*, 1972, **29**, 540.
7. E. P. Day, *Low Temp. Phys.-LT13, 'Proceedings, International Conference on Low Temperature Physics, 13th Meeting', Plenum Press, New York, 1972*, Vol. 4, p. 550.
8. Y. Kondo, T. Mizusaki, A. Hirai, Y. Hirayoshi, and K. Eguchi, *J. Low Temp. Phys.*, 1989, **75**, 289.
9. K. S. Pickens, D. I. Bolef, M. R. Holland, and R. K. Sundfors, *Phys. Rev. B: Condens. Matter*, 1984, **30**, 3644.
10. D. J. Meredith, G. R. Pickett, and O. G. Symko, *Phys. Lett. A*, 1972, **42**, 13.
11. H. Suzuki, Y. Higashino, and T. Ohtsuka, *J. Low Temp. Phys.*, 1980, **41**, 449.
12. R. A. Webb, *Phys. Rev. Lett.*, 1977, **38**, 1151.
13. R. A. Webb, *Rev. Sci. Instrum.*, 1977, **48**, 1585.
14. N. Q. Fan, M. B. Heaney, J. Clarke, D. Newitt, L. L. Wald, E. L. Hahn, A. Bielecki, and A. Pines, *IEEE Trans. Magn. Reson.*, 1989, **25**, 1193.
15. G. J. Ehnholm, J. P. Ekström, M. T. Loponen, and J. K. Soini, *Cryogenics*, 1979, **19**, 673.
16. N. Q. Fan and J. Clarke, *Rev. Sci. Instrum.*, 1991, **62**, 1453.
17. M. D. Hürlimann, C. H. Pennington, N. Q. Fan, J. Clarke, A. Pines, and E. L. Hahn, *Phys. Rev. Lett.*, 1992, **69**, 684.
18. J. Clarke, in *Superconducting Devices*, ed. S. T. Ruggiero and D. A. Rudman, 1st edn, Academic, San Diego, 1990, p. 51.
19. J. Clarke and R. H. Koch, *Science*, 1988, **242**, 217.
20. C. Conner, Ph.D. Thesis, University of California, Berkeley, CA, 1989.
21. G. W. Leppelmeier and E. L. Hahn, *Phys. Rev.*, 1966, **141**, 724.
22. J. Chang, C. Connor, E. L. Hahn, H. Huber, and A. Pines, *J. Magn. Reson.*, 1989, **82**, 387.
23. U. Werner, B. Black, M. Ziegeweid, and A. Pines, *Chem. Phys. Lett.*, 1993, **209**, 17.
24. U. Werner-Zwanziger, M. Ziegeweid, B. Black, and A. Pines, *Z. Naturforsch.*, 1994, **49a**, 1188.
25. C. Hilbert, J. Clarke, T. Sleator, and E. L. Hahn, *Appl. Phys. Lett.*, 1985, **47**, 637.

Biographical Sketch

Ulrike Werner-Zwanziger. *b* 1961. Diplom, 1988, Dr.rer.nat., 1991, Westfälische Wilhelms Universität Münster, Germany. DAAD fellow, 1987–88, Feodor Lynen fellow, 1991–93, with Professor A. Pines. Presently postdoctoral associate at Indiana University, Bloomington, IN, USA. 12 publications. Research interests: the structure of crystalline and disordered materials, and classical and quantum mechanical dynamics in solids.

Steady-State Techniques for Low Sensitivity and Slowly Relaxing Nuclei

Andreas Schwenk

Universität Tübingen, Tübingen, Germany

1	Introduction	1
2	Theoretical Analysis of the Steady-State Free Precession Technique	2
3	Recording of NMR Spectra with the Steady-State Technique	3
4	Measuring Techniques for Extremely Long Relaxation Times	6
5	Investigation of Nuclei with Spin–Spin Coupling	6
6	Related Articles	7
7	References	7

1 INTRODUCTION

The detection of NMR signals of low-γ nuclei with spin $I = \frac{1}{2}$ is a very difficult task in most cases, for the following reasons: owing to the low magnetic moment, the sensitivity of these nuclei is very poor, and owing to the missing electric and the small magnetic interaction of these nuclei, they are very slowly relaxing. If a sufficiently large indirect spin–spin coupling to another kind of nucleus with higher magnetogyric ratio exists, the signal of the low-γ nuclei may be enhanced by polarization transfer, or the spectrum of the low-γ nuclei may be detected indirectly by double resonance techniques; such methods are described in detail elsewhere (see ***Double Resonance*** and ***Polarization Transfer Experiments via Scalar Coupling in Liquids***). With the greater and greater static magnetic fields $\boldsymbol{B}_0$ available from superconducting magnets, the relaxation rates by chemical shift anisotropy increase proportionally to B_0^2, and the relaxation times of anisotropically shielded nuclei are sometimes reduced to a value useful for pulsed Fourier spectroscopy. In general, however, the natural widths of NMR lines $\Delta\nu_{\frac{1}{2}} = (\pi T_2)^{-1}$ of spin-$\frac{1}{2}$ low-γ nuclei are far less than the instrumental linewidth, which is due to the inhomogeneity of the magnet used for the experiment, i.e., inhomogeneously broadened lines result.

The only way to avoid such inhomogeneously broadened NMR lines and the resulting loss of signal intensity in CW spectroscopy consists in broadening the NMR lines beyond the width of the instrumental line by adding paramagnetic substances to the sample. Unfortunately, other essential properties of the sample may be changed by such paramagnetic admixtures (e.g., shifts of the NMR lines or changes in their relative intensities). Moreover, the efficiency in reduction of the relaxation times of an unknown sample by paramagnetic ingredients cannot be predicted in most cases. Pulsed Fourier spectroscopy, starting from thermal equilibrium, yields absorption lines with the same natural halfwidth, i.e., the resulting NMR lines are inhomogeneously broadened to the same instrumental linewidth. This loss of NMR signal may also be demonstrated in the time domain by the following example: the nucleus ^{109}Ag in a 1 M aqueous $AgNO_3$ solution in a field $B_0 = 2.1\,\mathrm{T}$ has a longitudinal relaxation time $T_1 > 1000\,\mathrm{s}$, whereas the decay time of the FID of such a sample contained in a cylinder of 20 mm diameter and 40 mm filling height in an optimally homogenized iron magnet is $T_2{}^* \approx 60\,\mathrm{ms}$. To observe the FID during $T_{\mathrm{ac}} \approx 200\,\mathrm{ms}$, one must wait for the build-up time of thermal equilibrium (at least $3T_1$) $T_{\mathrm{p}} \approx 1\,\mathrm{h}$; this shows clearly that the NMR signal may be received only during a small fraction $T_{\mathrm{ac}}/T_{\mathrm{p}} \approx 2 \times 10^{-4}$ of the total measuring time.

In pulsed Fourier spectroscopy, beginning with the pioneer work of Ernst and Anderson,[1] the results of a multitude of equal experiments are averaged, each of them starting from the thermal Boltzmann equilibrium, i.e. starting with the magnetization $\boldsymbol{M}_0$ in the z direction (the direction of the static field $\boldsymbol{B}_0$). In contrast to CW spectroscopy, pulsed Fourier spectroscopy offers a way to overcome the problem of these inhomogeneously broadened lines: the narrow NMR lines of very slowly relaxing nuclei may be broadened by saturation to any desired width in an exactly predictable way. To achieve this aim, the distance T_{p} between the periodically applied rf pulses must be reduced: $T_{\mathrm{p}} \ll T_2{}^*$ or $T_{\mathrm{p}} \gtrsim T_2{}^*$, with $T_2{}^* \ll T_2 \leq T_1$; then the magnetization vector $\boldsymbol{M}$ of the sample will perform a periodic motion with the period T_{p}, but $\boldsymbol{M}$ never reaches its thermal equilibrium value $\boldsymbol{M}_0$ in the z direction. In this pulsed steady state of the nuclear spin system, a refocusing effect occurs for the magnetization vectors of all different spin isochromats, which shows some analogy to the well-known spin echo techniques of Hahn[2] and Carr and Purcell,[3] with the modification by Gill and Meiboom,[4] which was also introduced to FT spectroscopy by Allerhand and Cochran[5] and called spin echo Fourier transform NMR. A spin echo technique including a steady state of the z magnetization was pointed out by Becker et al.[6] and named driven equilibrium Fourier transform spectroscopy.

In contrast to all spin echo techniques, the steady state magnetization vector $\boldsymbol{M}$ is neither in the z direction nor perpendicular to the z axis during any time interval; i.e., $\boldsymbol{M}$ shows a periodic motion with the pulse period T_{p} in all three dimensions of the space. No exact adjustment of the flip angle Θ of the periodically applied rf pulses is required; a misadjustment of Θ results in a changed steady state but it is not cumulative. But, in contrast to the normal FT spectroscopy starting from thermal equilibrium, the steady-state magnetization $\boldsymbol{M}$ depends strongly on the free precession angle of the magnetization during the pulse period in the rotating frame: $\Phi = (\omega_0 - \omega_{\mathrm{c}})T_{\mathrm{p}}$. Such a steady state of all three components of $\boldsymbol{M}$ was first observed by Bradford et al.,[7] and was analyzed in detail and demonstrated with water protons by Carr.[8] Unfortunately this steady-state technique could not be introduced into NMR spectroscopy at that time, since digital signal averagers and efficient computers to perform the Fourier transformation were not then available.

However, this situation changed when, in the second half of the 1960s signal averagers and on-line computers became available. Only a few months after the pioneer work of Ernst

and Anderson,[1] the extremely weak NMR signal of the spin-$\frac{1}{2}$ nucleus ^{187}Os, which has one of the smallest magnetic moments and which is of low natural abundance (1.64%), was detected for the first time with the aid of this steady-state free precession technique.[9,10] In the following years, the gain in sensitivity with the steady-state technique made possible the first systematic investigations or even the first detection of the NMR signal of a string of $I = \frac{1}{2}$ low-γ nuclei: ^{57}Fe, ^{107}Ag and ^{109}Ag, ^{207}Pb, ^{111}Cd and ^{113}Cd, ^{115}Sn, ^{117}Sn, and ^{119}Sn, ^{183}W, ^{89}Y, ^{103}Rh, and others (cited by Schwenk[11]).

Because of the dependence of the steady-state magnetization $\boldsymbol{M}$ on the free precession angle Φ, this simple steady-state technique cannot be used to record multiline NMR spectra; each line of such a spectrum is attenuated and distorted in a different way, as pointed out by Ernst and Anderson[1] and in more detail by Freeman and Hill.[12] To cancel these phase and intensity anomalies, the results of different experiments must be combined, in which the frequencies of the lines of the irradiated rf spectra are changed relative to the Larmor frequencies of the NMR spectrum. Two ways were proposed to reach this goal: in the scrambled steady-state technique,[12] many experiments are performed with changed pulse period T_p, i.e., the distance of the lines in the irradiated rf spectrum is changed, whereas in the Quadriga technique[13] only four experiments are performed with the carrier ν_c of the irradiated rf spectrum lowered by a quarter of the pulse repetition rate $1/T_p$ after each experiment. Ernst has pointed out a variant of the latter technique, four phase Fourier spectroscopy,[14,15] which reduces the four FT calculations, and with this the amount of data to be processed, to a single FT calculation. By an appropriate selection of the pulse period $T_p \ll T_2^*$ or $T_p \gtrsim T_2^*$, either maximum sensitivity or maximum resolution can be achieved, respectively.

Steady-state free precession techniques also offer a way to determine extremely long relaxation times T_1 and T_2 in the range from 1 s to some hours.[16] In contrast to spin echo techniques, no waiting time, either for the installation of the thermal equilibrium or for partial relaxation, is required during which no signal acquisition is possible. With the aid of these techniques the relaxation mechanisms of ^{109}Ag in the Ag^+ ion[17] and in a molecule[18] and of ^{57}Fe and ^{103}Rh in organometallic compounds[19] were detected for the first time. To separate the contributions of different relaxation mechanisms to the relaxation rate of spin-$\frac{1}{2}$ low-γ nuclei, determinations of the relaxation times T_1 in at least two quite different fields $\boldsymbol{B}_0$ must be performed. In the high fields of superconducting magnets, conventional techniques may be applied, whereas the extremely long relaxation times in the low $\boldsymbol{B}_0$ of iron magnets cannot be measured without the application of such steady-state techniques. Moreover, slowly relaxing nuclei are excellent tools to study exchange phenomena[20,21] (see ***Relaxation Effects of Chemical Exchange***).

Steady-state free precession techniques have proved to be powerful tools in NMR spectroscopy of slowly relaxing spin systems. The signal-to-noise ratio attainable in a given measuring time may be increased by orders of magnitude with the aid of such techniques. This is why steady-state techniques presently are not only applied to low-γ nuclei but also used in fast imaging techniques.[22,23] To carry out steady-state experiments on a pulsed FT NMR spectrometer requires no extra hardware—but does of course require appropriate software.

2 THEORETICAL ANALYSIS OF THE STEADY-STATE FREE PRECESSION TECHNIQUE

For the following considerations, one single species of spins with magnetogyric ratio γ may be assumed, and also the validity of the Bloch equations, i.e., the spin system can be described by the Larmor frequency $\nu_0 = \gamma B_0/2\pi$, the longitudinal relaxation time T_1, and the transverse relaxation time T_2. To establish a steady state in this spin system, equal, periodic, and coherent rf pulses of an oscillating magnetic field are applied to the sample. The repetition period T_p must be chosen to be small in comparison with the relaxation times T_1 and T_2:

$$T_p \ll T_2 \leq T_1 \tag{1}$$

In order to be able to observe the NMR signal during the most part of T_p, the duration of the rf pulses may be chosen as

$$\tau_p \ll T_p \tag{2}$$

The amplitude $2B_1$ and the carrier frequency ν_c of the oscillating rf magnetic field must fulfill the condition

$$\Delta B = \left|\frac{2\pi(\nu_0 - \nu_c)}{\gamma}\right| = \left|\frac{\omega_0 - \omega_c}{\gamma}\right| = \left|\frac{\Delta\omega}{\gamma}\right| \ll B_1 \tag{3}$$

Moreover, the rf pulses must be coherent; i.e., the rf signal necessary to produce the oscillating magnetic field must be derived with the aid of electronic switches from a generator constantly running with the frequency ν_c; the rf signal cannot be derived from an oscillator, which starts with arbitrary phase for each rf pulse. By this, it is guaranteed that one of the rotating components of the rf field is stationary (assumed in the u direction) in the coordinate system (u, v, z) rotating around the z axis with the angular velocity ω_c; during the pulse, its amplitude is B_1.

The magnetization vector $\boldsymbol{M}$ of the sample responds to these periodic, equal, and coherent rf pulses in the following ways.

1. During the rf pulse, $\boldsymbol{M}$ precesses around the u axis with angular velocity $\omega_1 = \gamma B_1$, and the total precession angle is $\Theta = \omega_1\tau_p = \gamma B_1\tau_p$. Relaxation effects may be neglected during this short time interval τ_p.
2. During the time interval of free precession (duration $T_p - \tau_p \approx T_p$), $\boldsymbol{M}$ precesses around the z axis with angular velocity $\Delta\omega = 2\pi\ \Delta\nu = 2\pi(\nu_0 - \nu_c)$; the total precession angle $\Phi = \Delta\omega\ T_p$. Superimposed on this motion are the relaxation effects: the exponential increase of the z component of $\boldsymbol{M}$ to the thermal equilibrium value $\boldsymbol{M}_0$ with the time constant T_1, and the exponential decay of the transverse component of $\boldsymbol{M}$ with the time constant T_2.

The magnetization vectors in the rotating frame (u, v, z) may be denoted as $\boldsymbol{M}(-0)$ immediately before the application of an rf pulse, $\boldsymbol{M}(+0)$ immediately after the end of this rf pulse, and $\boldsymbol{M}(-T_p)$ at the end of the following free precession period. In the steady state, which is established after a time considerably longer than T_1 [see equations (13) and (14)], $\boldsymbol{M}$ will always perform the same motion during each pulse period. In particular, the magnetization vectors immediately before the irradiation and at the end of the free precession, i.e., immediately before the next pulse, must be the same:

$$\boldsymbol{M}(-0) = \boldsymbol{M}(-T_p) \tag{4}$$

This condition leads to a linear, inhomogeneous system of equations for the steady state magnetization $\boldsymbol{M}(-0)$. The

solutions were first derived by Ernst and Anderson[1] for the general case [without the steady-state condition, equation (1)]. The special solutions for the steady state [equation (1)] and the additional condition

$$\Theta \gg T_p/T_2 \geq T_p/T_1 \tag{5}$$

are[11]

$$\left.\begin{aligned} \frac{M_u(+0)}{M_0} &= \frac{M_u(-0)}{M_0} = \frac{\sin\Theta\sin\Phi}{\Delta} \\ \frac{M_v(+0)}{M_0} &= -\frac{M_v(-0)}{M_0} = \frac{\sin\Theta(1-\cos\Phi)}{\Delta} \\ \frac{M_z(+0)}{M_0} &= \frac{M_z(-0)}{M_0} = \frac{(1+\cos\Theta)(1-\cos\Phi)}{\Delta} \end{aligned}\right\} \tag{6a}$$

where

$$\Delta = (1+\cos\Theta)(1-\cos\Phi) + 2(1-\cos\Theta)T_1/T_2 \tag{6b}$$

The steady-state transverse component of $\boldsymbol{M}$, which is responsible for the induced NMR signal, becomes

$$M_R = M_0 \frac{|\sin\Theta|\sqrt{2-2\cos\Phi}}{(1+\cos\Theta)(1-\cos\Phi) + 2(1-\cos\Theta)T_1/T_2} \tag{7}$$

The free precession angle Φ appears as argument only of harmonic functions, which are periodic in multiples of 2π; therefore, in all equations, Φ may be replaced by the excess free precession angle Φ_{ex}, which is defined by subtracting an integer multiple of 2π from Φ: $\Phi_{ex} = \Phi - 2\pi n$, so that Φ_{ex} falls in the range $0 \leq \Phi_{ex} < 2\pi$. Equation (7) shows clearly that M_R, and thus the NMR signal induced during the free precession period, depend only on the ratio T_1/T_2 but not on the absolute values of the relaxation times.

The strong dependence of M_R on the free precession angle Φ is shown in Figure 1 for the special case $T_1/T_2 = 1$. For $\Phi_{ex} = 0$, all components of the steady-state magnetization $\boldsymbol{M}$ vanish because of saturation of the spin system. This result may be seen in the frequency domain: the Fourier transform of the pulsed irradiation of the rf magnetic field is a discrete spectrum of lines with the frequencies

$$\nu_c \pm n/T_p, \quad n = 0, 1, 2, \ldots \tag{8}$$

and the amplitudes

$$A(\nu_c \pm n/T_p) \propto \frac{\sin(n\pi\tau_p/T_p)}{n\pi\tau_p/T_p} \tag{9}$$

For $\Phi_{ex} = 0$, one of the sidebands of the irradiated spectrum coincides with the Larmor frequency ν_0, the NMR transition is saturated, and all macroscopic magnetization vanishes. By considering either the frequency or time domains, it is concluded that the optimum case for a steady-state experiment is the choice of the free precession angle $\Phi_{ex} = \pi$ or the choice of the irradiation carrier frequency

$$\nu_c = \nu_0 \pm (n + \tfrac{1}{2})/T_p \tag{10}$$

This choice guarantees that the Larmor frequency ν_0 lies just in the middle between two irradiation lines, i.e., the maximum distance between ν_0 and any sideband of the irradiation spectrum.

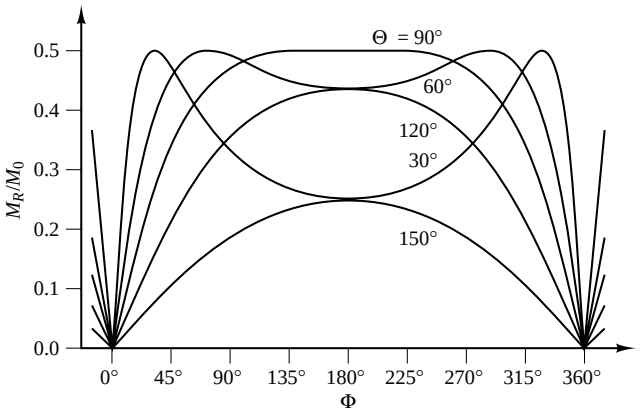

Figure 1 Steady-state transverse magnetization (proportional to the NMR signal) during the free precession period as a function of the free precession angle Φ for various flip angles Θ. A sample with T_1=T_2 is assumed

Under this optimum experimental condition, $\Phi_{ex} = \pi$ or equation (10), the maximum transverse component of the magnetization

$$M_{R,opt} = \frac{M_0}{2}\sqrt{\frac{T_2}{T_1}} \tag{11}$$

is reached, when pulses with the optimum flip angle

$$\Theta_{opt} = \arccos\frac{T_1/T_2 - 1}{T_1/T_2 + 1} \tag{12}$$

are applied.

The development of this steady state free precession [$\Phi_{ex} = \pi$ and irradiation of optimum flip angles Θ_{opt}, as given in equation (12)], starting from the unmagnetized sample $\boldsymbol{M}(t = 0) = 0$, may be described by an exponential function:[11,16]

$$M_R(t) = \frac{M_0}{2}\sqrt{\frac{T_2}{T_1}}(1 - e^{-t/T^*_{opt}}) \tag{13}$$

with the time constant

$$T^*_{opt} = \tfrac{1}{2}(T_1 + T_2) \tag{14}$$

Apart from rapidly damped oscillations, which are averaged out in a real experiment, each initial state $\boldsymbol{M}(t = 0)$ yields an exponential build-up of M_R as well as of M_z with the same time constant T^*_{opt} as given in equation (14).

3 RECORDING OF NMR SPECTRA WITH THE STEADY-STATE TECHNIQUE

In a real NMR experiment, a single species of a nucleus with one well-defined Larmor frequency is never investigated. The inhomogeneity of all magnets available today results in an inhomogeneously broadened NMR line, i.e., in a distribution of Larmor frequencies, usually characterized by its mean value $\langle\nu_0\rangle$ and the decay constant $T_2' \approx T_2^*$. Slowly relaxing spin systems are characterized by the condition $T_2^* \ll T_2$.

To achieve maximum sensitivity, the pulse period should be chosen as

$$T_p \ll T_2^* \tag{15}$$

The conditions in equations (1)–(3) are assumed to be valid, the carrier ν_c of the irradiated rf field should be chosen according to equation (10), and pulses with the optimum flip angle Θ_{opt} as given in equation (12) should be applied. Then the NMR signal is induced by a transverse magnetization M_R as described in equation (11). After mixing with the carrier ν_c, the low-frequency NMR signal is received during the free precession period:

$$S(t) = A\frac{M_0}{2}\sqrt{\frac{T_2}{T_1}}\cos[2\pi(\nu_0 - \nu_c)t + \varphi] \tag{16}$$

in the time interval $0 \le t \le \alpha T_p$, with $\alpha < 1$. A is an apparatus constant, containing all properties of the probe assembly, gain, etc. This signal is accumulated in a time-averaging computer:

$$S(n) = A'\frac{M_0}{2}\sqrt{\frac{T_2}{T_1}}\cos\left(\frac{2\pi\kappa n}{N} + \varphi\right) \tag{17}$$

where $n = 1, 2, \ldots, \alpha N$ are the computer word numbers and N is the number of words corresponding to the total pulse period T. The quantity κ, the resonance frequency in harmonics of the pulse repetition rate, is given by $\kappa = T_p(\nu_0 - \nu_c) = \Phi/2\pi$. This function $S(n)$ is Fourier transformed:

$$\tilde{I}(x) = \frac{2}{N}\int_0^{\alpha N} S(n)\cos\left(\frac{2\pi x n}{N} + \psi\right) \mathrm{d}n \tag{18}$$

Neglecting all terms with $\kappa + x$ in the denominator and adjusting the phase angle $\psi = \varphi$, the result of the Fourier transformation is the absorption curve:

$$I(x) = A'\frac{M_0}{2}\sqrt{\frac{T_2}{T_1}}\frac{\sin[2\pi\alpha(\kappa - x)]}{2\pi(\kappa - x)} \tag{19}$$

with the halfwidth $\Delta x_{\frac{1}{2}} = 0.6/\alpha$. Setting the phase adjustment ψ to be $\varphi + \frac{1}{2}\pi$ yields the corresponding dispersion curve:

$$I'(x) = A'\frac{M_0}{2}\sqrt{\frac{T_2}{T_1}}\frac{\cos[2\pi\alpha(\kappa - x)] - 1}{2\pi(\kappa - x)} \tag{20}$$

Figure 2 shows an example of a steady-state experiment of this kind with fairly good signal-to-noise ratio. Further examples with extremely low NMR signals are given by Schwenk.[11] As pointed out in detail there, the signal-to-noise ratio (S/N) attainable with the steady-state free precession technique is superior to that of the usual FID technique starting from thermal equilibrium before each pulse by a factor

$$\frac{(\mathrm{S/N})_{\text{steady state}}}{(\mathrm{S/N})_{\text{therm equil}}} = \sqrt{\frac{T_2}{T_2^*}} \tag{21}$$

i.e., all disadvantages resulting from the inhomogeneity of the static field $\boldsymbol{B}_0$ are removed.

Choosing, instead of the condition in equation (15), a pulse period

$$T_p \gtrsim T_2^* \tag{22}$$

(in practice, $T_p > 6T_2^*$), the distribution of the Larmor frequencies of all spin isochromats becomes considerably wider than the distance $1/T_p$ of the Fourier lines of the pulsed rf magnetic field; i.e., many lines of the rf spectrum fall in the range of the inhomogeneously broadened NMR line. Owing to this, the dependence of the NMR signal on the free precession angle Φ is averaged out, and the FT yields an NMR line with shape determined by the inhomogeneity of the magnet. The condition in equation (21) guarantees maximum resolution in a given magnetic field. However, the price that must be paid for this maximum resolution is a loss of signal-to-noise ratio of up to one order of magnitude in comparison with the maximum sensitivity case [the condition in equation (15)]. This approach of the steady state technique was first pointed out by Waldstein and Wallace,[24] and is described in detail with experimental hints by Schwenk.[11]

Recording a multiline NMR spectrum, the condition $\Phi_{ex} = \pi$, or equation (10), can never be fulfilled for all NMR lines simultaneously; i.e., according to equations (6) and (8) and

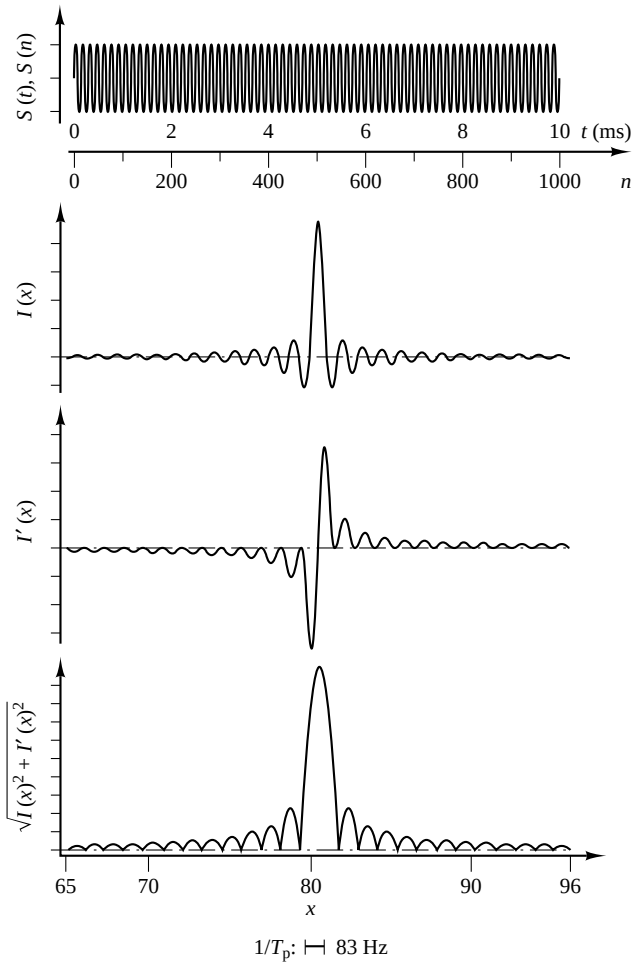

Figure 2 Steady-state ^{109}Ag NMR signal of a 8.3 M aqueous AgF solution, recorded with pulse period T_p = 12 ms, corresponding to N = 1200 channels in the time-averaging computer, i.e., α = 0.83. The carrier frequency ν_c of the irradiation spectrum was chosen $80.5/T_p$ below the Larmor frequency ν_0, i.e., κ = 80.5. The time-dependent NMR signal [equations (16) and (17)], the absorption curve $I(x)$, and the dispersion curve $I'(x)$ [equations (19} and (20)] are plotted, as well as the power spectrum

Figure 1, each line will be affected by a special phase and intensity anomaly. To get rid of these distortions in the case of maximum sensitivity [the condition in equation (15)], either the distribution $D(\Phi_{ex})$ of the free precession angles of one line of the spectrum must be enlarged far beyond the separation $1/T_p$ of the lines of the irradiation spectrum, as given in equation (8), or the irradiation spectrum must be changed sometimes during the NMR experiment, in order to average the results of experiments with different free precession angles Φ_{ex}, i.e., to give each NMR line the same chance.

The first way—the enlargement of the distribution $D(\Phi_{ex})$—may be accomplished by inserting a short homogeneity spoil pulse at an arbitrary time during the pulse period T_p. In doing this, the steady state is not destroyed at all, and all Larmor frequencies remain unchanged during the time of observation of the signal; examples and experimental hints are given by Schwenk.[11] Unfortunately, in samples of low viscosity, diffusion effects during the interval T_p between homogeneity spoil pulses may reduce the NMR signal.

The second way—the change of the irradiation spectrum—may be accomplished in two different manners. The first consists in a random variation of the pulse period T_p after a batch of pulses. In doing this, the rf spectrum [equation (8)] is stretched or compressed, with the carrier frequency ν_c as a fixed point. Outside a frequency range near ν_c, this scrambled steady-state technique[12] changes the free precession angle to be equally distributed in the range $0 \leq \Phi_{ex} \leq 2\pi$, and averaging the results of all such experiments cancels phase and intensity anomalies. The second manner of changing the irradiation spectrum consists of a linear shift of the carrier: four experiments with the carrier frequencies

$$\nu_{c,\rho} = \nu_c - \rho/4T_p, \quad \rho = 0, 1, 2, 3 \tag{23}$$

must be performed; the complete irradiation spectrum is shifted to lower frequencies by $\rho/4T_p$. The accumulated NMR signals $S_\rho(t)$ or $S_\rho(n)$, as described by equations (16) and (17), must be Fourier transformed separately to give four resonance curves $I_\rho(x)$, as described by equation (19). Shifting back these curves $I_\rho(x)$ by defining four different abscissa scales $z = x - \frac{1}{4}\rho$, the absorption curves $I_\rho(z)$ may be added, $I(z) = \sum_{\rho=0}^{3} I_\rho(z)$, to get the undistorted spectrum. This Quadriga–FT technique (QFT),[13] with only four experiments, reduces phase and intensity anomalies to less than 1% of the desired signal. Many details, experimental hints, and examples are given by Schwenk.[11] The QFT signal attainable within a given measuring time is 60% of that attainable with a normal steady-state free precession experiment ($T_p \ll T_2^*$ and $\Phi_{ex} = \pi$); this is the price to pay for the constant sensitivity throughout the total frequency range. Hence, in the case of maximum sensitivity, the QFT signal-to-noise ratio becomes

$$\frac{(S/N)_{QFT}}{(S/N)_{therm\ equil}} \approx \frac{3}{5}\sqrt{\frac{T_2}{T_2^*}} \tag{24}$$

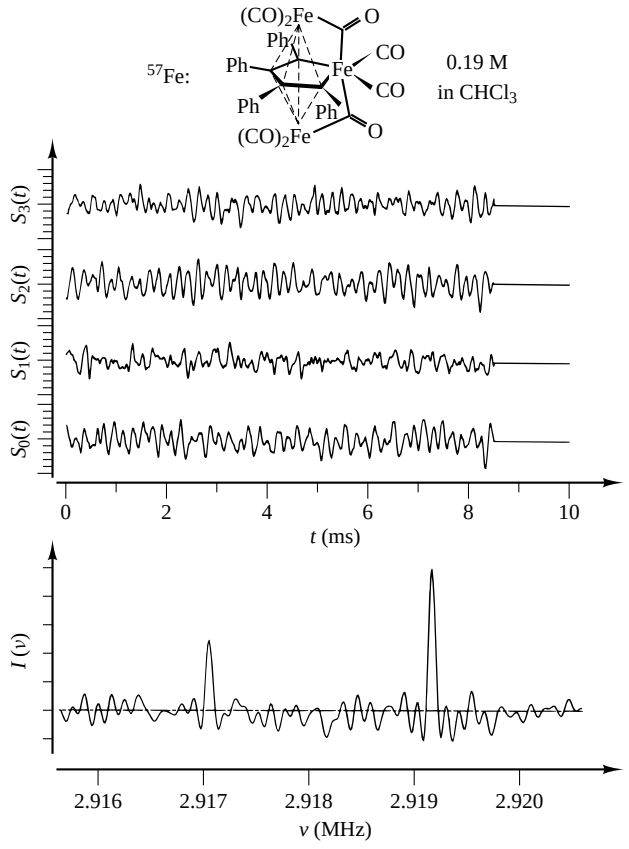

Figure 3 ^{57}Fe NMR spectrum of a three-nuclear iron complex recorded with the Quadriga–FT technique to achieve maximum sensitivity: $1/T_p$ = 83 Hz, $\Theta = 57^\circ$ (optimum for unknown ratio T_1/T_2). A measuring time of 4 × 12 h = 2 days was spent for this spectrum of the unenriched sample

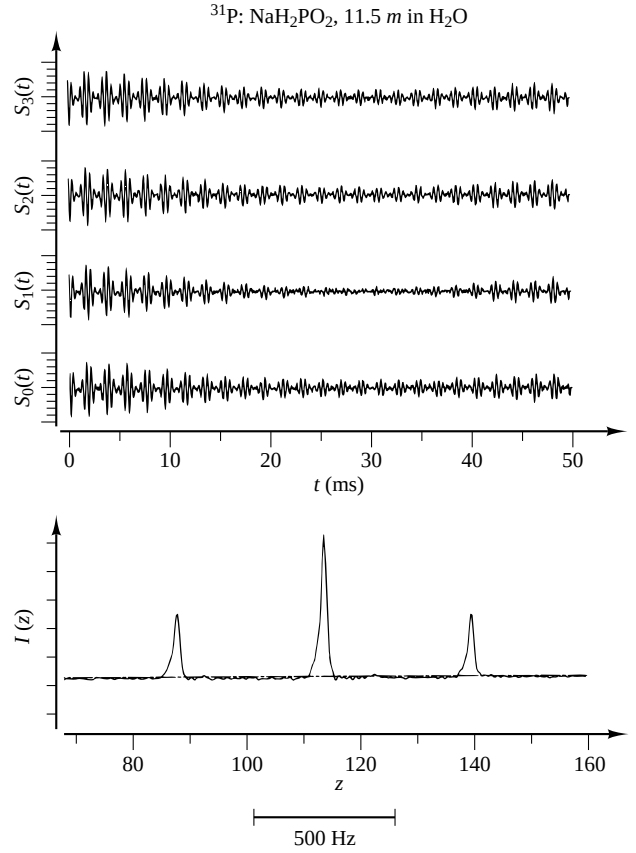

Figure 4 ^{31}P NMR spectrum of the hypophosphite ion recorded with the quadriga technique to achieve maximum resolution in a less homogeneous field $\boldsymbol{B}_0$: $1/T_p$ = 20 Hz, $\Theta = 44^\circ$ (optimum for the ^{31}P relaxation times $T_1 \approx 1$ s and $T_2 \approx 270$ ms). The total measuring time was about 4 min

Of course, this QFT technique may be applied with the condition in equation (15) to get maximum sensitivity, as well as with the condition in equation (22) to get maximum resolution. Examples of both cases are given in Figures 3 and 4.

The same four irradiation spectra may be achieved by phase shifts of the carrier signal by 0, $\frac{1}{2}\pi$, π, and $\frac{3}{2}\pi$ from pulse to pulse instead of lowering the carrier frequency ν_c. This four-phase Fourier spectroscopy, proposed by Ernst,[15] enables the coaddition of the NMR signals in time, $S_\rho(t)$, from all four experiments, and therefore requires only one Fourier transformation.

4 MEASURING TECHNIQUES FOR EXTREMELY LONG RELAXATION TIMES

The steady state magnetization $\boldsymbol{M}(t)$ is neither purely longitudinal nor purely transverse during any time interval. Therefore steady-state techniques are not suitable to study purely longitudinal or purely transverse relaxation. The results of two experiments must be combined to evaluate T_1 and T_2.

In the T_1/T_2 *experiment*, the amplitudes of the established steady state of the sample are determined for some different flip angles in the range $0° \leq \Theta \leq 90°$. Equation (7), describing the transverse component M_R of the magnetization, contains, besides the flip angle Θ and the free precession angle Φ (which should be adjusted to $\Phi_{ex} \approx \pi$), the two unknown quantities M_0 and the ratio of the relaxation times T_1/T_2. With the aid of a Gaussian least-squares fitting routine, this ratio of the relaxation times as well as the signal amplitude corresponding to the equilibrium magnetization M_0 may be evaluated. The necessary calibration of the flip angles Θ is described in detail by Kronenbitter and Schwenk[16] and Schwenk,[11] and many experimental hints and examples are given there. Figure 5 shows the results of such T_1/T_2 experiments with some nuclei in different chemical environments.

In the $T_1 + T_2$ *experiment*, the development of the transverse magnetization $M_R(t)$ starting from the totally unmagnetized state of the sample $\boldsymbol{M}(t = 0) = 0$ (or starting from any other initial state of the sample) is observed. To investigate this development of the NMR signal as a function of the time elapsed since demagnetization, the following block averaging technique is used. The signal is observed during a time interval of about $3T^*_{opt}$; this interval is split into L parts (about a dozen) of the duration T_{ac}. During the νth time interval $\nu T_{ac} \leq t \leq (\nu + 1)T_{ac}$ ($\nu = 0, \ldots, L - 1$), the NMR signal is accumulated in block ν of the memory in the time-averaging computer. Of course, this acquisition time T_{ac}, governed by the relaxation times of the sample, is far too short to achieve a sufficient signal-to-noise ratio. Therefore this development must be repeated frequently and the signal added to the corresponding block in the computer memory; i.e., a dynamic steady state is performed in the spin system. The demagnetization of the sample within the shortest time is described in detail by Kreibich and Schwenk;[25] a higher range of this dynamic steady state may be achieved by an inversion of the magnetization rather than by a destruction. This development of the transverse magnetization M_R is described in equations (13) and (14), for the special case $\Phi_{ex} = \pi$ and $\Theta = \Theta_{opt}$ [as given in equation (12)]; for the arbitrary case, see Kronenbitter and Schwenk[16] and Schwenk.[11] By a Gaussian least-squares fitting routine, the time constant T^* as well as the signal amplitude of the totally established steady state may be evaluated from the absorption maxima of $I_\nu(x = \kappa)$; equation (19), as determined by Fourier transformation of the signal in block ν of the memory. Figure 6 shows an example of such a $T_1 + T_2$ experiment.

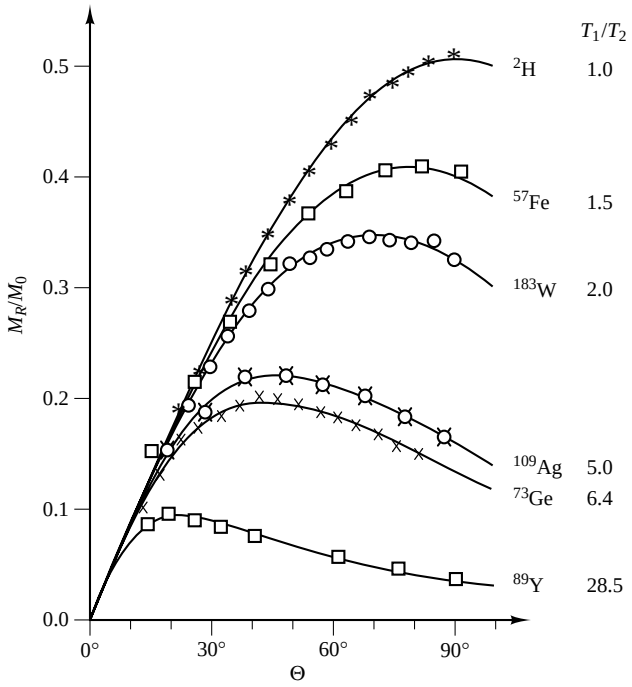

Figure 5 Results of some T_1/T_2 experiments with the following nuclei and samples: ^{2}H in D_2O; ^{57}Fe in butadiene–$Fe(CO)_3$, 2.9 M in C_6D_6; ^{183}W in WF_6, neat liquid; ^{109}Ag in a 12 M solution of $AgNO_3$ in acetonitrile at 298 K; ^{73}Ge in $GeCl_4$, neat liquid; and ^{89}Y in a 3 M aqueous solution of $Y(NO_3)_3$ with pH 1.3

A detailed description with additional examples, experimental hints and a discussion of the systematic errors caused by inhomogeneities in the fields $\boldsymbol{B}_0$ and $\boldsymbol{B}_1$ may be found in Kronenbitter and Schwenk[16] and Schwenk.[11]

5 INVESTIGATION OF NUCLEI WITH SPIN–SPIN COUPLING

Two types of scalar coupling of the $I = \frac{1}{2}$ low-γ nucleus X under investigation to another nucleus A must be distinguished.

5.1 Heteronuclear Coupling

Here, A is not the same isotope as X. In this case, nucleus A is not affected by the steady-state experiment performed with nucleus X. However, the steady state of X is affected by the longitudinal relaxation of A. A change in the eigenstate of nucleus A results in a change in the Larmor frequency of X by the coupling constant J. Owing to this, the steady state of X is disturbed, depending on the longitudinal relaxation time $T_1{}^A$ of nucleus A; the worst case is $T_1{}^A \approx T_p$. In this worst case,

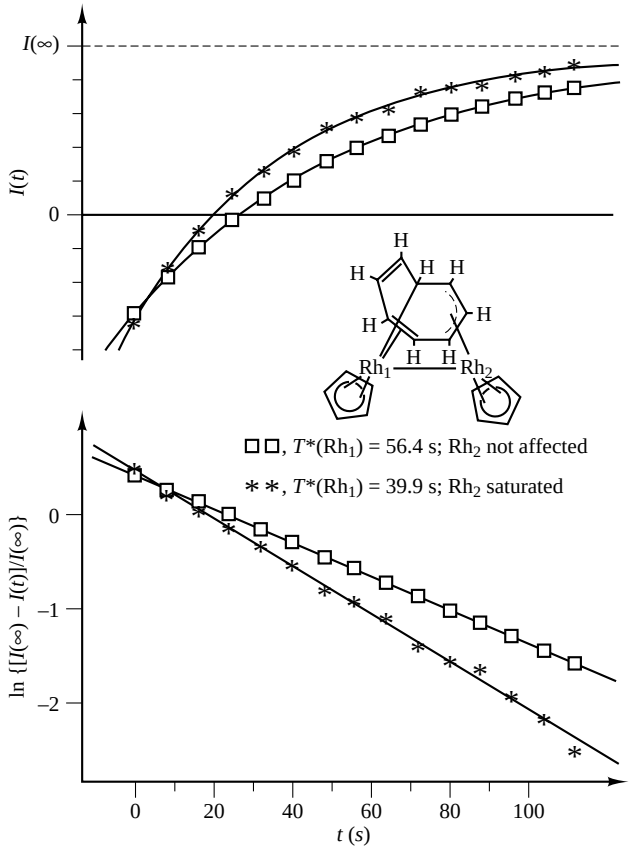

Figure 6 Results of a T_1+T_2 experiment with a binuclear Rh complex, about 0.1 M in CH_2Cl_2 at 296 K. $Rh_1 \equiv$ X and $Rh_2 \equiv$ A are weakly spin–spin coupled. Rh_1 was investigated; i.e., $\Phi_{ex}(Rh_1) = \pi$ was chosen. By application of semiselective triplet rf pulses, Rh_2 was not affected by the irradiation in the first experiment, whereas by single pulses with $\Phi_{ex}(Rh_1) = \pi$ and $\Phi_{ex}(Rh_2) = 0$ in the second experiment, the Rh_2 NMR line was saturated, resulting in a shorter $T^*(Rh_1)$ because of cross relaxation

a coupling constant J with $|J|T_p \approx 5\%$ is sufficient to destroy the steady state of X, as pointed out by Schwenk.[11] In most cases, a scalar coupling of X to an $I = \frac{1}{2}$ nucleus with high γ, e.g., to ^{19}F, ^{31}P, or a similar nucleus, destroys the steady state of nucleus X. Fortunately, such a coupling of X to an $I = \frac{1}{2}$ nucleus A with considerably stronger magnetic moment offers a way to improve the signal of spins X by spin transfer or to record the spectrum of spins X by a double resonance experiment.

5.2 Homonuclear Coupling

Here, A and X are nuclei of the same isotope in a molecule, they differ only in their chemical shifts δ_X and δ_A. In general, rf irradiation affects both nuclei X and A; i.e. a double resonance experiment is performed, which must be treated theoretically with the density matrix[26] or product operator formalism,[27] rather than with the Bloch equations. In contrast with an NMR experiment affecting only one kind of nuclei X or A, in such a double resonance experiment, not only the signal intensities of both nuclei X and A but also their relaxation times are changed. In the case of weak spin–spin coupling $|J| \ll |\delta_X - \delta_A|$, such a double resonance experiment can nearly be avoided by irradiation of semiselective rf pulses with full intensity for nuclei X and vanishing spectral intensity for nuclei A. Such semiselective pulses may be doublets[11] or triplets,[28] which (in the time domain) act on nuclei X in just the same manner as a single rf pulse, but restore the magnetization of spins A, assumed to be in the z direction immediately before the semiselective pulse, to exactly the same direction after it. Semiselective doublets allow such a restoration of $\boldsymbol{M}$ in the z direction only for one spin isochromat with distinct Larmor frequency, whereas with semiselective triplets, the same result may be achieved in a range of Larmor frequencies sufficient for a real inhomogeneously broadened NMR line. A steady state of the nuclei X stimulated with semiselective triplets consists of three pulses and three intervals of free precession and relaxation; this, of course, requires amendment of the formulas [equations (7), (13), and (14)] necessary to evaluate the relaxation experiments. Figure 6 shows two results of the T_1 + T_2 experiment performed with the ^{103}Rh nucleus shifted to lower frequency in *cis*-[$(CpRh)_2COT$] (the two ^{103}Rh Larmor frequencies differ by 960 Hz at 2.114 T and the coupling constant is $|J(Rh,Rh)| < 5$ Hz). Selective irradiation yields a considerably longer T^* than wideband irradiation, since cross relaxation is avoided (see ***Relaxation Processes in Coupled-Spin Systems*** and ***Relaxation Processes: Cross Correlation and Interference Terms***).

6 RELATED ARTICLES

Fourier Transform Spectroscopy; Germanium, Tin, and Lead NMR; Inorganic Nuclei: Low Sensitivity Transition Metals; Organometallic Compounds; Selective Pulses.

7 REFERENCES

1. R. R. Ernst and W. A. Anderson, *Rev. Sci. Instrum.*, 1966, **37**, 93.
2. E. L. Hahn, *Phys. Rev.*, 1950, **80**, 580.
3. H. Y. Carr and E. M. Purcell, *Phys. Rev.*, 1954, **94**, 630.
4. S. Meiboom and D. Gill, *Rev. Sci. Instrum.*, 1958, **29**, 688.
5. A. Allerhand and D. W. Cochran, *J. Am. Chem. Soc.*, 1970, **92**, 4482.
6. E. D. Becker, J. A. Ferretti, and T. C. Farrar, *J. Am. Chem. Soc.*, 1969, **91**, 7784.
7. R. Bradford, C. Clay, and E. Strick, *Phys. Rev.*, 1951, **84**, 157.
8. H. Y. Carr, *Phys. Rev.*, 1958, **112**, 1693.
9. J. Kaufmann and A. Schwenk, *Phys. Lett. A*, 1967, **24**, 115.
10. A. Schwenk, *Z. Phys.*, 1968, **213**, 482.
11. A. Schwenk, in *Progress in Nuclear Magnetic Resonance Spectroscopy*, eds. J. W. Emsley, J. Feeney, and L. H. Sutcliffe, Pergamon Press, Oxford, 1985, Vol. 17, p. 69.
12. R. Freeman and H. D. W. Hill, *J. Magn. Reson.*, 1971, **4**, 366.
13. A. Schwenk, *J. Magn. Reson.*, 1971, **5**, 376.
14. R. R. Ernst, personal communication, 1972.
15. R. R. Ernst, G. Bodenhausen, and A. Wokaun, *Principles of Nuclear Magnetic Resonance in One and Two Dimensions*, Clarendon Press, Oxford, 1987, p. 133.
16. J. Kronenbitter and A. Schwenk, *J. Magn. Reson.*, 1977, **25**, 147.

17. H. Pfister, A. Schwenk, and D. Zeller, *J. Magn. Reson.*, 1986, **68**, 138.
18. A. Schwenk, U. Piantini, and W. Wojnowski, *Z. Naturforsch. A*, 1991, **46**, 939.
19. A. Hafner, W. von Philipsborn, and A. Schwenk, *J. Magn. Reson.*, 1987, **74**, 433.
20. J. Kronenbitter, U. Schweizer, and A. Schwenk, *Z. Naturforsch. A*, 1980, **35**, 319.
21. L. Guinand, K. L. Hobt, E. Mittermaier, E. Rössler, A. Schwenk, and H. Schneider, *Z. Naturforsch. A*, 1984, **39**, 83.
22. A. Haase, J. Frahm, D. Matthaei, W. Hänicke, and K.-D. Merboldt, *J. Magn. Reson.*, 1986, **67**, 258.
23. P. Mansfield and P. G. Morris, *NMR Imaging in Biomedicine*, Academic Press, New York, 1982, p. 76.
24. P. Waldstein and W. E. Wallace, *Rev. Sci. Instrum.*, 1971, **42**, 437.
25. W. Kreibich and A. Schwenk, *J. Magn. Reson.*, 1987, **77**, 308.
26. R. R. Ernst, G. Bodenhausen, and A. Wokaun, *Principles of Nuclear Magnetic Resonance in One and Two Dimensions*, Clarendon Press, Oxford, 1987, Chap. 2
27. O. W. Sørensen, G. W. Eich, M. H. Levitt, G. Bodenhausen, and R. R. Ernst, in *Progress in Nuclear Magnetic Resonance Spectroscopy*, eds. J. W. Emsley, J. Feeney, and L. H. Sutcliffe, Pergamon Press, Oxford, 1983, Vol. 16, p. 163.
28. A. Melchinger and A. Schwenk, *J. Magn. Reson.*, 1991, **94**, 34.

Biographical Sketch

Andreas Schwenk. *b* 1937. Dipl.-Phys., 1963, Dr. rer. nat., 1968, Universität Tübingen. Introduced to NMR by H. Krüger. Faculty in Physics, University of Tübingen, Germany, 1977–present. Approx. 70 publications. Research specialties: investigation of slowly relaxing low-γ nuclei and development of new techniques enabling such investigations.

Ultrasonic Irradiation and NMR

John Homer

Aston University, Birmingham, UK

1	Introduction	1
2	Lattice Phonons in Solids	1
3	Relaxation Transition Probabilities	2
4	Acoustic Nuclear Magnetic Resonance in Solids	3
5	Acoustic Nuclear Magnetic Resonance in Liquids	3
6	Ultrasonically induced Changes to T_1 in Liquids and Solids	4
7	Sonically Induced Narrowing of the NMR Spectra of Solids (SINNMR)	6
8	Conclusions	9
9	Related Articles	9
10	References	9

1 INTRODUCTION

Although the relationship might not be apparent immediately, NMR spectroscopy and sound are inextricably linked. Their marriage is secured, most evidently in solids, by spin–lattice relaxation, which itself controls the utility, and limitations, of the NMR technique. While we direct quanta of electromagnetic energy at nuclear spin systems to make them do our bidding, Nature cleverly generates its own missiles, phonons. By bouncing them back and forth between the nuclear spins and their surrounding lattice, Nature can facilitate the necessary initial polarization of spins in our magnetic fields, and then undo our experimental meddling by using them to return perturbed systems to natural equilibrium.

The state of a spin system may be characterized by its so-called spin temperature, and the magnitude of this in relation to the temperature of the bulk lattice can be imagined to govern the flow of thermal energy between the spins and lattice. To conceptualize the interchange mechanism, it is convenient to refer to Debye's theory of the specific heats of solids.[1] This relies on the existence of a large number of standing elastic waves (of which sound is an example) of high frequencies that are associated with thermal lattice vibrations. Each of the quantized elastic waves has a characteristic frequency, ν (= $\omega/2\pi$), and is called a phonon which carries an energy $h\nu$. It behaves as though it has momentum, and the creation or destruction of phonons corresponds with the increase or decrease of the energy of the elastic wave. The sum total of the phonon energies is the internal energy of the solid.

By treating a solid as a continuum, Debye provided a simple theory that enables the prediction of the dependence of phonon density on frequency, as exemplified in Figure 1.

Although not revealing all of the detailed features of more precise lattice theory, it serves to illustrate two important points. First, there is a cut-off frequency above which the phonon density vanishes. Second, below the cut-off frequency there is appreciable phonon density at all frequencies. The existence of an effective continuum of phonon frequencies, and energies, creates the possibility of energy transfer between spins and the lattice either at the nuclear spin Larmor frequency, when in a magnetic field, or indirectly at other frequencies.

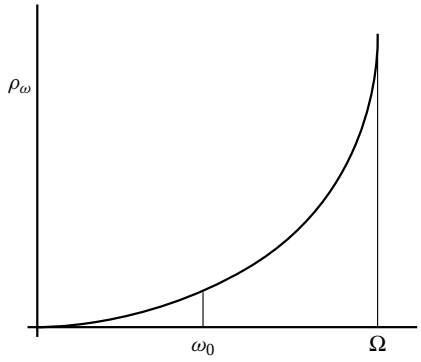

Figure 1 Variation in phonon spectral density (ρ_ω) as a function of frequency. (Adapted by permission of Academic Press (London) Ltd, from R. A. Levy, 'Principles of Solid State Physics', 1968, p. 133)

As liquids possess thermal energy that involves the motion of molecules or clusters of molecules, they can also be considered to have phonons associated with them. The greater motion in liquids than in solids results in the creation and destruction of phonons at any particular location in the liquid.

Phonons, of course, are not limited to Nature's domain and control. In addition to thermal phonons, an acoustic wave can be considered to be a beam of phonons over which the experimenter has control. Accordingly, phonons of varying energy are at our disposal by generating sound (manifest as sinusoidally varying pressure variations) at a variety of frequencies. Sound that has a frequency above about 18 kHz is referred to as ultrasound. In the terms of the rapidly increasing body of sonochemists, ultrasound with frequencies above 1 MHz is referred to as diagnostic ultrasound, while that with lower frequencies is referred to as power ultrasound.[2a] It is ultrasound with the higher frequencies that is of particular interest to those concerned with experiments that rely on, for example, ultrasonic phonon–thermal phonon and –spin interactions.

The combination of ultrasound and NMR experiments is not new, but such experiments have been confined largely to acoustic nuclear magnetic resonance (ANMR).[3] However, experiments have been reported recently that, in general terms, use ultrasound at frequencies away from the nuclear Larmor frequency in order to modify normal NMR spectral parameters.[4–6] For example, ultrasound has been used to reduce spin–lattice relaxation times in both liquids[4] and solids,[6] and separately to effect the sonically-induced narrowing of the NMR spectra of solids (SINNMR).[5,6] In the interests of both coverage and the benefits of highlighting relevant theoretical features, some attention will be paid to ANMR before covering aspects of the more recent studies. While the former subject has been treated in theoretical detail, the understanding of the principles underlying the latter studies remains largely at the empirical level and their treatment may be deemed speculative.

2 LATTICE PHONONS IN SOLIDS

Although there are a variety of mechanisms than can be considered to contribute to spin–lattice relaxation in solids, and different ways of treating these, attention will be focused here on the consequences of the thermal motions of constituents of the lattice.

The atomic constituents of a solid (the lattice) are in continual thermal agitation and the approximately elastic interatomic forces cause the disturbances to be propagated as elastic waves. Lattice oscillators with particular energies can be equated to there being appropriate numbers of lattice quanta or phonons in the lattice. As mentioned earlier, the principal features of lattice phonons can be deduced from the Debye treatment. Inevitably Abragam[7] has summarized the salient features of this and shows that the density of phonon states (ρ_ω) in a solid continuum that contains N atoms in a sample of volume V depends on the frequency (ω) according to

$$\rho_\omega = \frac{3V\omega^2}{2\pi^2 v^3} \tag{1}$$

where v is the velocity of propagation. Obviously the number of modes must be limited to the $3N$ degrees of freedom of the lattice and it is necessary to have an upper cut-off frequency (Ω) that is related to the Debye temperature (θ) by

$$k\theta = h\Omega/2\pi \tag{2}$$

The dependence of phonon density on frequency and the cut-off (typically at about 10^{13} Hz for many materials) is illustrated in Figure 1: note the approximate position corresponding to a typical nuclear spin Larmor frequency, ω_0.

3 RELAXATION TRANSITION PROBABILITIES

3.1 Solids

Bearing in mind the typical value of the cut-off frequency, Figure 1 reveals that there will be a finite phonon spectral density at the nuclear Larmor frequency (ω_0) that can, in principle, facilitate spin–relaxation transitions. These can occur by a *direct* process but phonons at other frequencies can facilitate *indirect* processes.

3.1.1 Direct

In the direct relaxation process, a spin makes a transition from one energy level to another by the emission (or absorption) of a single phonon with the resonant frequency, as illustrated in Figure 2(a). The transition probability (P_1) and the relaxation time for this process may be represented in a simplified form by

$$P_1 \sim T_1^{-1} = C B_0^2 T \tag{3}$$

where C is a constant, B_0 the applied magnetic field, and T the absolute temperature. It emerges that C, being proportional to $k\Omega^{-3}$, is exceedingly small in relation to the product of the other two terms in Equation (3) so that the transition probability is very low. The reason for this is that only phonons essentially at ω_0 contribute to the process and the spectral density of thermal energy, proportional to the number of phonons at this frequency, is very low.

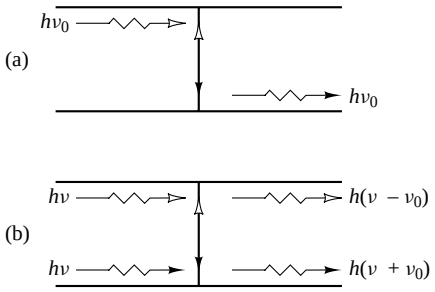

Figure 2 (a) Direct and (b) indirect relaxation transition mechanisms involving phonons. (Adapted by permission of Academic Press (Orlando), from R. T. Beyer and S. V. Letcher, 'Physical Ultrasonics', 1969, p. 290)

3.1.2 Indirect

Of the indirect relaxation processes, those sequentially involving two phonons, or the absorption or emission of two phonons, are highly improbable[7,8] because the number of pairs of phonons whose energies combine to match $h\nu_0$ is very small. Accordingly, attention is focused on the Raman process, shown in Figure 2(b), in which the spin may change levels with the simultaneous absorption and emission of phonons. If the absorbed phonon has a frequency ν, the frequency of the emitted phonon may be either $\nu + \nu_0$ (spin emission) or $\nu - \nu_0$ (spin absorption). Obviously, by reference to Figure 1, absorption can only occur when ω lies between ω_0 and Ω. However, emission can occur for any value of ω up to Ω, and has high probability. The Raman relaxation rate is independent of ω_0 and varies as T^2 for $T \geq \theta$ and as T^7 for $T \ll \theta$. Abragam[7] shows that the ratio of the probability of this type of Raman relaxation (P_2) to that of the direct process is

$$\frac{P_2}{P_1} \approx \frac{kT\Omega^2}{mv^2\omega_0^2} \tag{4}$$

and accordingly $P_2 > P_1$.

3.1.3 Other Processes

Lattice vibrations can result in the modulation of the separations of nuclear spins and in the electric field gradients at nuclei. In principle, therefore, both dipolar and quadrupolar relaxation processes may be influenced by lattice vibrations. Whereas the magnetic nuclear spin–phonon coupling relaxation mechanism turns out to be negligible, the coupling of lattice vibrations with nuclear quadrupole moments can be important. In the case of quadrupole spin–lattice relaxation, both direct and Raman processes are possible, but the probability of the latter process is some 10^{10} times more probable than the former.

3.2 Liquids

Many mechanisms may be attributed to nuclear spin relaxation in liquids. Inevitably the increased molecular motion, particularly translation and rotation, is important to the characterization of the relaxation mechanisms. Although the coupling of a spin system with the lattice can in

principle be described quantum mechanically, an alternative is to describe the lattice classically and consider the effects of fluctuating magnetic and electric fields. Accordingly, the enormous complexity of the subject is frequently camouflaged by simplistically representing the spin–lattice relaxation time in the form

$$1/T_1 = 1/T_1^{\text{trans}} + 1/T_1^{\text{rot}} \quad (5)$$

where $T_1{}^{\text{trans}}$ and $T_1{}^{\text{rot}}$ encompass contributions arising respectively from molecular translational and rotational motions that are assigned appropriate correlation times, τ. For the purposes of the following discussion this oversimplified treatment of relaxation in liquids will suffice.

The above deliberately biased treatment of selected aspects of spin–lattice relaxation leads to several interesting questions. For example: (a) if lattice phonons induce transitions of nuclear spins between allowed levels can we use sound to mimic this experimentally and detect a net NMR effect?; (b) can we use externally applied sound to modify effectively the natural phonon spectral density in a solid sample and change T_1 from its normal value?; (c) can sound be used to modulate normal molecular motion and modify T_1 values relative to their normal values in liquids?; (d) if the answer to (c) is yes, can we use sound to induce motion of small solid particles suspended in a liquid in such a way that the resulting motions resemble those of rather large molecules so that the usual dipolar and quadrupolar line broadenings from solids are reduced? Answers to these questions will now be embraced, and although not all are definitive they are included in the hope that they may stimulate work that will further enhance the already immense diagnostic capacity of NMR.

4 ACOUSTIC NUCLEAR MAGNETIC RESONANCE IN SOLIDS

If thermal phonons facilitate the net transfer of energy from a nonequilibrium spin system to the lattice, it is not unreasonable to speculate that ultrasonic phonons may be used to cause a net absorption of energy by a spin system, as proposed by Kastler[9] and Al'tshuler.[10] It is indeed possible to use ultrasound to excite vibrations in a solid lattice and concentrate energy in a narrow frequency range. If the ultrasound has the frequency ν_0 it can stimulate nuclear spin transitions by a mechanism that is directly analogous to the direct thermal relaxation process. The important difference between the natural and experimental processes stems from the fact that in the latter the spectral density at the Larmor frequency is much greater than in the former case. While this increases the rate of stimulated transitions by a factor of around 10^{11} for dipoles, it is unlikely that this is enough to make the direct process experimentally valuable in such cases. However, in the case of nuclear quadrupoles, the ultrasonic transition rates can be increased by a further factor of about 10^4, so that they can compete successfully with relaxation transitions and a net absorption of acoustic energy is observed in ANMR.

There have been many experimental demonstrations of ANMR for quadrupolar nuclei in solids. As the selection rules for allowed transitions due to quadrupole coupling are $\Delta m = \pm$ and ± 2 (but not $m = -\frac{1}{2} \leftrightarrow +\frac{1}{2}$), ANMR can be detected at both ν_0 and $2\nu_0$. Usually, ANMR is detected by monitoring the ultrasonic saturation of resonances by conventional NMR techniques. Indeed the first demonstration of ANMR by Proctor et al.[3] relied on this approach. Essentially, after applying a conventional 90° rf pulse, the sample was irradiated with a relatively long pulse of ultrasound which prevented complete restoration of M_z to $\boldsymbol{M}_0$ due to saturation, and the resulting magnetization, read by a subsequent 90° pulse, was found to be less than that obtained in the absence of ultrasound.

ANMR can also be observed without the use of rf irradiation, through the direct detection of the loss of acoustic energy to the spin system,[11] although this is by no means easy due to the low acoustic absorption coefficient.

In view of the experimental difficulties associated with ANMR [e.g. the sample may have to be specially prepared and a transducer (piezoelectric crystal[8]) bonded to it in order to enable coupling of the ultrasound with it], doubt may be cast on its value as being of other than academic interest. However, it should be pointed out that the penetration of ultrasound into metals is not restricted by skin depth problems[7,11] and the direct, non-rf, detection of ANMR can have value in this area of study.

5 ACOUSTIC NUCLEAR MAGNETIC RESONANCE IN LIQUIDS

The theoretical arguments for and against the possibility of ANMR in liquids are plentiful and diverse. For example, Kessel[12] argues that ANMR should not be observable for either dipolar or quadrupolar nuclei. On the other hand, Iolin[13] suggests that the reorientation of the axis of an anisotropic molecule by an acoustic wave could lead to narrow ANMR resonances in low viscosity liquids. Alekseev and Kopvillem[14] essentially reason that the variation in sound pressure should induce molecular motion and, if the spectral density at the resonant frequency due to this is greater than that corresponding to Brownian motion, ANMR should be possible even if the applied acoustic frequency is not at the Larmor frequency. An experiment on ^{1}H in an aqueous copper sulfate solution using ν_0 = 16 MHz with sound at 2.1 MHz and 72 W cm^{-2} showed a small signal amplitude modulation that may be interpreted to indicate that ANMR is possible in liquids with an acoustic wave frequency lower than ν_0.

The increasing evidence in support of the possibility of conducting ANMR in liquids prompted Homer and Patel[4] to attempt ^{14}N ANMR (ν_0 = 6.42 MHz) saturation experiments on acetonitrile and *N*,*N*-dimethylformamide. The results as presented in Figure 3(a) and (b) are similar. As the acoustic power (more precisely, reference should be made to the intensity of an acoustic beam which is the average rate of energy flux across unit area perpendicular to the direction of propagation, and here is derived from the number of watts delivered to immersed 5-mm diameter piezoelectric crystals) is increased at 1.12 MHz little change in the S/N ratio is observed. At 6 MHz there is some evidence of decreasing S/N ratio with increasing applied power. At 6.42 MHz only a very small residual ^{14}N signal is seen, even at low applied acoustic power. At 10 MHz the signal is again detected: similar results were obtained from corresponding studies of *N*,*N*-dimethylacetamide.[15] The implications of these experiments are that ANMR is possible for liquids. However, it must be

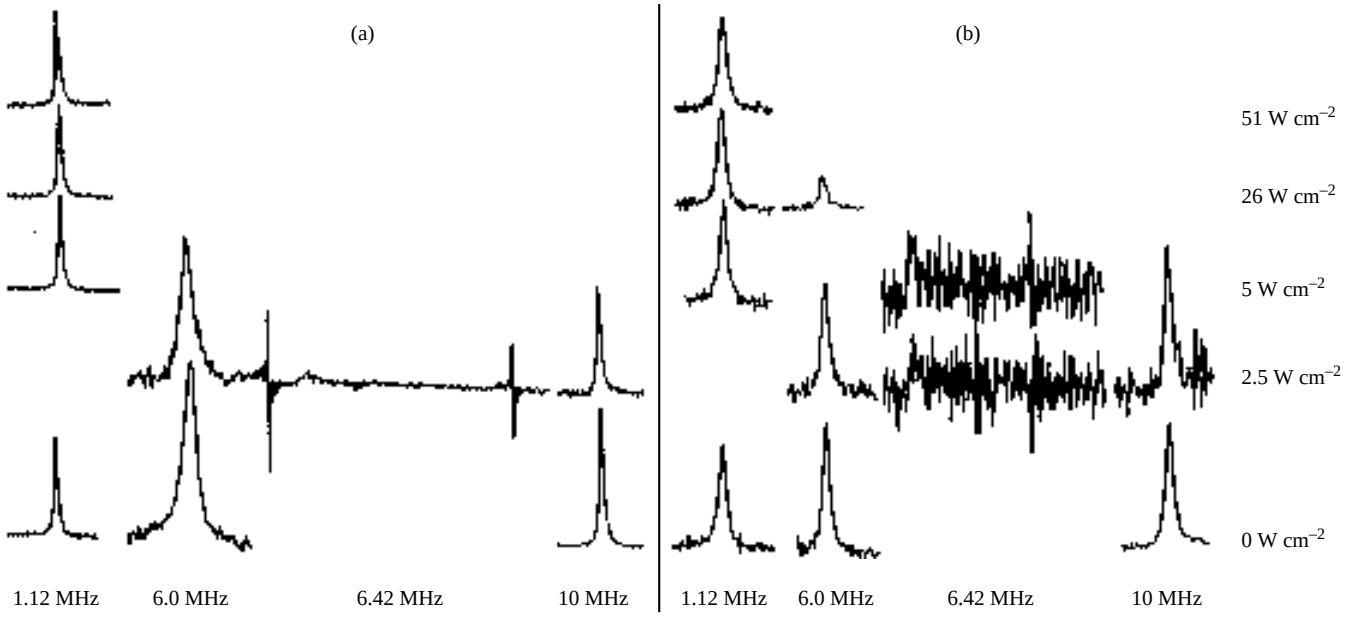

Figure 3 The effect of ultrasound at various frequencies and powers on the ^{14}N spectra of (a) acetonitrile and (b) *N*,*N*-dimethylformamide in equimolar mixtures with $CDCl_3$. (Adapted from S. U. Patel, Ph.D. Thesis, Aston University, 1989)

noted that when the acoustic frequency matches the Larmor frequency, interference beats are observed that, in principle, could reduce the S/N of the ^{14}N signal.

6 ULTRASONICALLY INDUCED CHANGES TO T_1 IN LIQUIDS AND SOLIDS

Almost three decades ago, Bowen[16] noted a reduction of T_1 during ANMR studies on an aqueous colloidal sol of As_2S_3. As discussed earlier the irradiation of solids with ultrasound may lead to reductions in T_1: if this can be achieved routinely it could have a major impact on the investigation of a range of solid materials for which magnetic resonance studies normally rely on very slowly relaxing nuclei. The indications are that such reductions might be best achieved through the indirect Raman process using acoustic frequencies less than the Larmor frequency.

In the case of liquids, there is no reason why ultrasound should not be used to reduce T_1 values if sound can be used to cause unusual relative molecular motions. However, in this case predictions become far more problematical in the absence of a detailed characterization of the structures of liquids and of acoustically induced molecular motions. A pragmatic approach may prove to be the best way forward.

Homer and Patel[4,15] have conducted extensive investigations on the effects of ultrasound at various frequencies on the T_1 values of ^1H, ^{13}C, and ^{14}N in a variety of liquids and liquid mixtures. As a detailed discussion of the data is beyond the scope of the present work, only the main conclusions will be mentioned. It is important to note at the outset that the studies were conducted using immersed piezoelectric transducers, but each component of the assemblies used was checked to ensure that it had no effect on the measured relaxation times. The T_1 values were measured using the rapid DESPOT[17] (driven equilibrium single pulse observation of T_1) technique so that the effects of direct heating of the sample were minimized. No effect was observed using low-frequency ultrasound at 20 kHz, but changes to T_1 were observed in the MHz region. Changes to T_1 were observed only for liquid mixtures, suggesting that ultrasound causes the relative motion of different molecular species and that, at least, it modifies the translational contribution to T_1. A possible reason for this observation may stem from the fact that liquid mixtures are normally inhomogeneous at the molecular level due to different interaction energies between like and unlike molecular pairs. If ultrasound modifies this local inhomogeneity, the time-average environment of a particular molecule may be changed and, therefore, the value of T_1 for a nucleus within it may also be changed. Further support for the suggestion that ultrasonically induced changes to T_1 largely originate from a translational mechanism derives from the fact that no acoustically stimulated changes to T_1 were observed[15] for ^{14}N in a conformationally rigid molecule for which intramolecular mechanisms are responsible for the relaxation characteristics of the quadrupolar nucleus. The fact that little or no changes were observed for pure liquids indicates that the effects of acoustic streaming,[8] which could enhance the effects on T_1 of molecular diffusion into and out of the NMR detector region, are unimportant. The effects of MHz ultrasound on T_1 are greater for deoxygenated than oxygenated liquids: the implication is that the ultrasonically induced changes to T_1 that were observed largely for oxygenated liquids are in fact less than the absolute effect of ultrasound on the T_1 values of the major molecular components of the mixtures. Detailed examination of the extensive results reveals that they are not totally reproducible in an absolute sense, probably due to the differing initial state of oxygenation of the samples. Nevertheless, the overall trends in the results are reproducible. Some selected results for ^1H and ^{13}C for cyclohexane/benzene/chloroform-*d* mixtures are presented in Table 1: little change in the data is observed when the ultrasound frequency is increased to 6 MHz. These data

Table 1 The Effects of 1.115 MHz Ultrasound on ^{1}H (89.56 MHz) and ^{13}C (22.5 MHz) T_1 Values for a 1:1:2 Molar Ratio of Cyclohexane/Benzene/Chloroform-*d*. (Adapted from S. U. Patel, Ph.D. Thesis, Aston University, 1989)

Power ($W\,cm^{-2}$)	T_1 Values (s)			
	Aryl ^{1}H	Aryl ^{13}C	CH_2 ^{1}H	CH_2 ^{13}C
0	4.9	12.0	3.9	10.1
2.6	4.1	10.6	3.6	9.9
5.1	3.9	10.8	2.8	9.8
10.2	2.8 (−43%)	9.8 (−18%)	2.2 (−44%)	9.6 (−5%)
25.5	4.1	10.9	3.1	9.3
51.0		11.6		11.2

serve to illustrate several important general features of the experiments.

As the power of the applied ultrasound is increased progressively, the T_1 values first decrease from their normal values to a minimum, whereafter they increase. The maximum decreases (approximate percentages are shown in parentheses) in T_1 are always larger for ^{1}H than for ^{13}C, consistent with the well-known fact that translational relative intermolecular motion influences the former more than the latter.

Whenever a process removes energy from a sound wave and returns it at an appreciable time later in the wave cycle, the acoustic energy is dissipated. Simplistically, therefore, the acoustic wave will modify normal molecular translation but processes such as molecular collisions can transfer translational energy to, for example, molecular rotational and vibrational energies. The changes to T_1, as illustrated in Table 1, may therefore also accommodate changes arising from the rotational contribution to T_1.

If resonances are normally in the extreme narrowing region with $\omega_0\tau \ll 1$, the only way that dipolar governed T_1 values can be artificially reduced at the lower ultrasound powers is for the spectral density at ω_0 to increase. This necessitates an increase in molecular correlation times to intermediate values where $\omega_0\tau \approx 1$ (see Figure 4). If, pro temp, applied ultrasound is assumed mainly to modify molecular translational motion, and the propagation of the acoustic wave is considered to be effected by almost instantaneous and sequential molecule to molecule interactions, it is not unreasonable to assume that the acoustically imposed translational correlation time is of the order of the inverse of the acoustic frequency ($\sim 10^{-6}$ s). Consequently, if nuclear relaxation rates are considered to be influenced by a normal correlation time of the order of say 10^{-10} s and an ultrasonically, and translationally, dominated correlation time of the order of 10^{-6} s is imposed in an approximately additive fashion, it is evident that the latter will have the principal effect. In this case $\omega_0\tau \approx 1$, and there will be a significant increase in the spectral density at ω_0 and result in a reduction in T_1, as observed. The fact that 20 kHz ultrasound does not change T_1 is consistent with the fact that in this case $\omega_0\tau \gg 1$ and there may be little change from the normal spectral density at ω_0. The fact that the values of T_1 ultimately increase with increasing ultrasonic power is interesting and lends support to the above speculations. As the relaxation times are dipolar controlled, the only way they can increase in the extreme narrowing limit is by a reduction in the correlation time (see Figure 4) with an accompanying decrease in the spectral density at ω_0. The implication is that now a much higher proportion of the increased translational energy available on molecular collisions is transferred to rotational energy by acoustic thermal relaxation, with a net decrease in

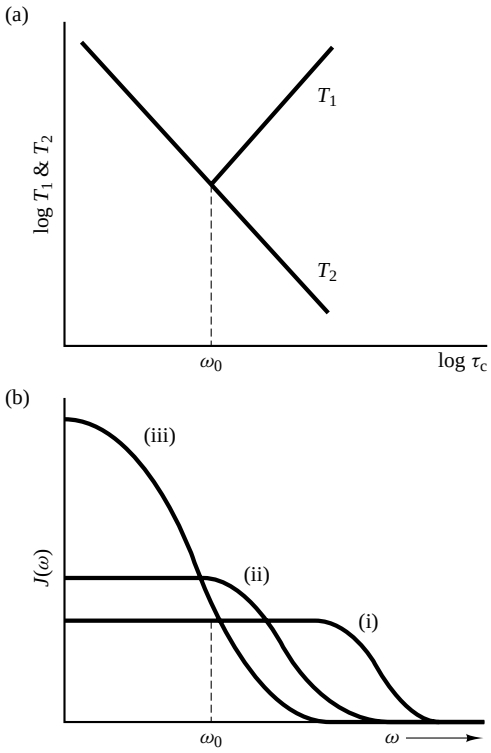

Figure 4 Variation of (a) T_1 with molecular correlation times (τ) and (b) spectral density (J_ω) with frequency (ω) [(i) short correlation times, $\omega\tau_c \ll 1$; (ii) intermediate correlation times, $\omega\tau_c \approx 1$; (iii) long correlation times, $\omega\tau_c \gg 1$]

correlation time and an increase in T_1. It must, of course, be noted that direct heating of the sample by the immersed transducer, when operating at the higher powers, could also account for a reduction in correlation times and an increase in T_1. An additional point that must be recognised is that ultrasonic effects are highly nonlinear and threshold effects are observed, such as that due to the onset of cavitation. It is possible, therefore, that minima in acoustically controlled T_1 values, such as is evident in Table 1, could simply arise because of, for example, the onset of cavitation.

It must be emphasized that the above speculative explanations regarding the effect of ultrasound ignore the various other acoustic relaxation processes that may occur. Of interest among these is the transfer of energy from the translational mode of motion to the potential energy of the rearrangement between energetically different structures. Apparently, only one successful NMR detection of such a process has been recorded.[2b,15] This was for the classical example of

N,*N*-dimethylacetamide. Progressively increasing the power of 20 kHz ultrasound was reported to result in the onset of rotation about the central N–C bond and cause the coalescence of the two ^{1}H methyl resonances that are observed at room temperature. To have produced the same effect by electrically raising the temperature would have necessitated the sample reaching about 100 °C, and normally the direct heating of a sample during ultrasonic irradiation does not result in the sample temperature exceeding about 55 °C.

7 SONICALLY INDUCED NARROWING OF THE NMR SPECTRA OF SOLIDS (SINNMR)

It is well known that the NMR spectra of mobile liquids can provide more structural information directly than can the corresponding spectra of solids. The basic reason for this is that rapid incoherent molecular motion in liquids averages out the anisotropic line-broadening effects that are present in solids. However, various experimental techniques are available to reduce line broadening for solids. Among these is the MAS NMR technique, originating from the pioneering work of Andrew et al.,[18] that involves the rapid spinning of a sample about its axis at the so-called magic angle (54.74°) to the polarizing field direction in order to remove dipolar broadening effects. Quadrupolar broadening interactions can also be minimized by rapid sample rotation about other appropriate angles, e.g., 30.56°. The simultaneous minimization of both dipolar and quadrupolar broadenings was first achieved through the elegant methods of DOR and DAS.[19a,b,20] Other relevant techniques involve rapid pulsed manipulation of magnetization vectors to place them on time average at appropriate angles to minimize the line-broadening effects, e.g., M-REV8.[21] The combination of rapid sample spinning and pulse sequences is possible through CRAMPS.[22] Essentially, all of these techniques depend on coherent motions of, or within, a sample that are induced by the experimenter. An alternative is to make solid samples undergo incoherent motion, similar to molecular motion in liquids, to effect resonance line narrowing.

Although various ways of inducing incoherent motion of solids are possible, probably the most obvious methods depend on suspending solid particles in a suitable support liquid. If the particles are extremely small, Brownian motion can be used to effect line narrowing. This was first proposed by Yesinowski,[23] and again, a decade later, by Kimura and Satoh.[24] Naturally, the preparation of sufficiently small particles capable of experiencing effective Brownian motion is not without difficulties. In order to induce incoherent motion of much larger particles, some external perturbation of them is necessary. Homer et al.[5,6] have demonstrated that 20 kHz ultrasound can be used to induce adequate incoherent motion to enable line narrowing for particles having dimensions up to 2 mm.

In principle, ultrasound can be used to induce motion of suspended particles through several mechanisms. Of these, three are particularly important and are now outlined.

The theoretical work of Dysthe[25] reveals that a single suspended anisotropic particle subject to a standing acoustic wave, with a wavelength much greater than the particle dimensions, has three possible equilibrium orientations that are not necessarily energetically equivalent. If the particle is transiently perturbed in some way from an equilibrium orientation it will rapidly reorientate to the most stable orientation, whereafter its motion will be purely translational. In a many-particle system, interparticle collisions may provide the necessary perturbation to cause incoherent particle motion.

One consequence of the passage of ultrasound through a liquid that has not been detailed so far is the production of cavities[8] in the liquid. If ultrasonic irradiation of a liquid is considered to result in the subjection of a region of the liquid to periodic compression and decompression, the latter can, in the presence of a suitable nucleation center, result in the formation of a small bubble or cavity. Subsequent decompression cycles of the acoustic wave can cause the cavity to grow in size to result in one of two types. First, a stable cavity may be formed that either resonates synchronously with the wave when the frequency of the latter is the same as the frequency of the oscillation of the cavity, or, when the two frequencies are not equal, has its oscillation frequency modulated by that of the acoustic wave. Second, an unstable cavity may be formed that can collapse violently (it is this mechanism that lies at the heart of sonochemistry and facilitates the enhancement of the rates of chemical reactions). The details of the mechanism have not been definitively characterized, but two possibilities are favored. One, the so-called 'hot spot' theory,[26] requires violent collapse of a cavity with the generation of local temperatures in excess of 2000 °C and pressures exceeding 2000 atm. The other, the electric field theory,[27] suggests that fragmentation of a cavity produces sufficient molecular ordering of the double layer at the constriction to generate intense electric fields that are capable of producing an electrical discharge (this might be expected to be modulated by magnetic fields, but preliminary studies of the effect of these on the sonochemically accelerated maleate–fumarate isomerization revealed no effect on the reaction rate in the presence and absence of a 2.3 T magnetic field[28]). Whatever the detailed mechanism of cavity collapse may be, there are two incontrovertible consequences of it. First, shock waves are generated that can cause interparticle collisions of such violence that, for certain metallic particles, fusion may occur on impact.[29] Second, if cavity collapse occurs near a solid surface, a microjet of liquid passes through the cavity and strikes the surface with speeds up to several hundreds of meters per second.[30]

If any of the above-mentioned consequences of ultrasonic irradiation of liquids causes energy dissipation on a solid along an axis tangential, or near tangential, to the surface, the particle will rotate in a fashion that will become incoherent after sufficient perturbations. Even when this is achieved it is necessary to arrange for the particles to be brought to spatial equilibrium in the NMR detector coil region. The pioneering work of Homer et al.[5,6] was restricted by access only to an iron magnet NMR spectrometer (^{1}H frequency at 89.56 MHz) in which ultrasonic irradiation of the sample was only readily possible vertically downwards from the top of the sample. Nevertheless, by using a pseudoprogressive wave, particles were appropriately positioned by balancing the forces due to the acoustic wave, gravity, buoyancy, and viscous drag. Although the original expectation was that it would be necessary to use ultrasound with frequencies in the megahertz region, the first reproducible SINNMR spectra for ^{23}Na and ^{31}P in trisodium phosphate dodecahydrate (TSP) were obtained at 20 kHz. These are compared in Figure 5

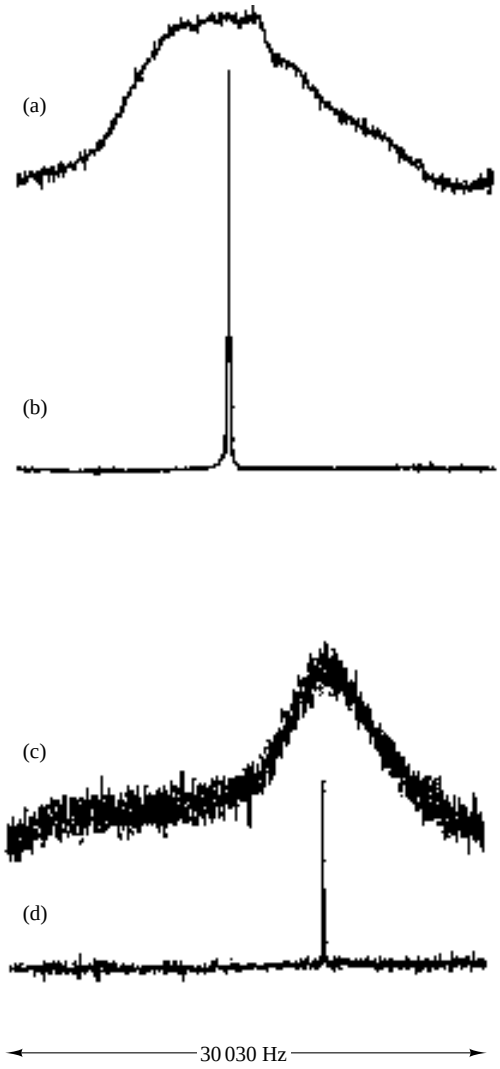

Figure 5 Sodium-23 spectra (23.64 MHz) of trisodium phosphate dodecahydrate (a) static and (b) solid suspended in a $CHCl_3/CHBr_3$ mixture and irradiated with ultrasound at 20 kHz. Plots (c) and (d) are the corresponding ^{31}P spectra (36.26 MHz). (Reproduced by permission of the Royal Society of Chemistry, from J. Homer and M. J. Howard, *J. Chem. Soc., Faraday Trans.*, 1993, **89**, 3029)

with the corresponding static powder spectra. The full width at half-maximum height (FWHM) of the SINNMR resonances are more than two orders of magnitude smaller than the corresponding bandwidths of the static sample resonances for both the quadrupolar and dipolar nuclei, and the spectra show no spinning sidebands.

Detailed investigations on TSP revealed the following important findings. SINNMR spectra can be obtained from samples with different particle sizes, but for each size the density of the support liquid (in this case mixtures of chloroform and bromoform in order to achieve sufficiently high densities relevant to the experimental configuration used) has to be appropriately adjusted to optimize the SINNMR resonance signal-to-noise ratio (S/N). If a range of particle sizes is used, the smaller particles pass through and the larger do not reach the detector coil region, and are not detected. Table 2 presents ^{23}Na SINNMR S/N and FWHM data obtained for TSP with optimized support liquid densities and the same acoustic power and NMR pulse and acquisition parameters. The interesting feature here is that for particles with dimensions less than about 100 μm, the S/N decreases dramatically while the FWHM increases. This dimension corresponds well with a resonant cavity radius $R_r \approx 95\,\mu$m calculated using[31]

$$R_r = \frac{1}{2\pi\nu}\left(\frac{3\kappa P_0}{\rho}\right)^{1/2} \quad (6)$$

with values for the acoustic frequency (ν), a polytropic constant (κ) (varying between 1 and the ratio of the specific heats), the ambient liquid pressure (P_0), and the liquid density (ρ) appropriate to the support media used. As indicated earlier, microjet action is only effective when the particle dimensions are greater than that of the resonant cavity. Taken together with the fact that SINNMR spectra were only obtained using power levels above the estimated cavity threshold of about 16 W cm^{-2}, the implications are that cavitation is important to the efficient production of SINNMR spectra at low acoustic frequencies.

Measurements of T_1 for ^{31}P in TSP were made to elucidate the motional characteristics of particles producing SINNMR spectra. A reference value of T_1 was obtained first by MAS NMR at 121.441 MHz and adjusted to give 7.1 s (incorrectly stated elsewhere[6] to be 46 s) at the SINNMR frequency of 36.26 MHz. Subsequently, T_1 was found to be 0.52 ± 0.05 s for the SINNMR resonance, whereas a value of 2.1 ± 0.2 s was obtained under identical conditions for a sonicated sample constrained in an open mesh nylon bag. These data reveal two important results. First, the reduction of T_1 under conditions of MAS NMR to that obtained by acoustically irradiating a static sample is consistent with the possibility of using Raman-type processes to reduce T_1 values, as speculated on earlier. Second, the reduction in T_1 from the value obtained for the irradiated static sample to that measured for the freely moving particles must be attributed to the motion of the particles in the latter case. The two relevant values were used with the theoretical dependence of T_1 on correlation times to deduce that in the SINNMR experiment the particles had a correlation time of the order of 4×10^{-7} s. The validity of this value was substantiated by using it to predict a ^{31}P SINNMR FWHM of 32 Hz that was in close agreement with the measured value of 31 Hz. Further detailed studies of particle correlation times[32] have revealed, surprisingly, that the larger particles move more rapidly than the smaller particles. This unexpected finding has been rationalized in terms of the relative probabilities of microjet/shock wave energy dissipation at the particle surface resulting in either particle translation or rotation; the probability of induced particle rotation being higher than translation for the larger particles with dimensions greater than that of the resonant cavity. While the investigations outlined above were specifically directed to establishing that ultrasound does in fact induce the incoherent motion of suspended solid particles that is essential to the production of SINNMR spectra, the finding that ultrasound reduces T_1 in solids may have additional important benefits in the study of materials via very slowly relaxing nuclei.

It is important to observe that throughout the SINNMR studies outlined above Homer and Howard[6] paid particular attention to the possibility that sample melting, dissolution, chemical reaction, phase changes, etc. could have been responsible for the line narrowings observed. While each of these were in fact shown to be unimportant, it was found that

Table 2 ^{23}Na SINNMR S/N and FWHM for Different Particle Size Ranges of Trisodium Phosphate Dodecahydrate[a]. (Reproduced by permission of the Royal Society of Chemistry, from J. Homer and M. J. Howard, *J. Chem. Soc., Faraday Trans.*, 1993, **89**, 3029)

Particle size range (μm)	^{23}Na signal-to-noise ratio	^{23}Na FWHM (Hz)
1000–500	110:1	88
500–210	110:1	103
210–105	102:1	121
105–90	20:1	161

[a]For each particle size range, the support medium density was optimized to ensure that particle displacement was between the limits of the NMR probe region. All acquisition parameters were identical.

ultrasound did stimulate effectively free rotation of species in the solid TSP lattice, but the resulting narrowed line contributed only about $\frac{1}{80}$th to the signal intensity in an optimized SINNMR experiment.

Encouraged by the implications of the investigations of TSP that SINNMR is a genuine phenomenon, further SINNMR investigations using 20 kHz ultrasound were conducted. For example, the major resonance in the ^{19}F spectrum of PTFE (polytetrafluoroethylene) was narrowed by a factor of about two. Normally, the narrowing of such strongly dipolar broadened resonances using MAS NMR is inefficient and pulse techniques such as M-REV8 have to be used. Greater success has been achieved with the ion exchange resin Amberlite, for which ^{1}H SINNMR studies resolved three separated major resonances at shifts corresponding to inflections in the otherwise broad resonance obtained from the static solid. A further particularly important set of SINNMR observations has also been made on aluminum and its alloys: the particles were protected by a resin matrix to prevent sonochemical reactions with the haloform support liquids or more probably with Cl_2, Br_2, HCl, or HBr generated by the sonication of the haloforms. Some results on ^{27}Al are presented in Figure 6. These reveal FWHMs in the range 350–500 Hz that are significantly less than the value of 700 Hz obtained by Andrew et al.[33] for aluminum using MAS NMR. Of particular importance is the fact that the SINNMR chemical shifts relative to aqueous $AlCl_3$ are typically Knight shifted,[34] and could not arise from reaction products but only from the metallic state. These particular results may be viewed as definitive evidence for SINNMR being a genuine phenomenon. The small shift differences for ^{27}Al between the spectra shown in Figure 6 have not yet been characterized. While they could be due to the effect of differing alloying components, it is possible that, as Knight shifts are pressure-dependent,[34] the shift differences arise from differing phonon–Fermi electron interactions.

Superficially, the foregoing discussion might be interpreted to indicate that the utility of SINNMR is limited to the study of fairly large solid particles. However, it must be appreciated that this implication stems from the use of ultrasound at the low frequency of 20 kHz. Even in the event that SINNMR relies solely on cavitational processes, reference to equation (6) reveals that the use of higher acoustic frequencies will facilitate the study of small particles. For example, if water was used as the support liquid, the use of ultrasound at 280 kHz should permit the study of 10 μm size particles. Following this prediction, studies using acoustic frequencies in the megahertz region have very recently been initiated. Unfortunately, these have so far been restricted to the acoustic irradiation of samples from the top in a conventional high-resolution iron magnet spectrometer. Nevertheless, encouraging results have been obtained, and Figure 7 provides an example of the ^{11}B SINNMR spectrum obtained by 2 MHz ultrasonic irradiation of a finely ground boron-rich glass in bromoform. The spectrum appears to reveal the chemically-shifted isotropic BO_3 and BO_4 resonances that are known from MAS NMR studies to have respective abundances of 80% and 20%.

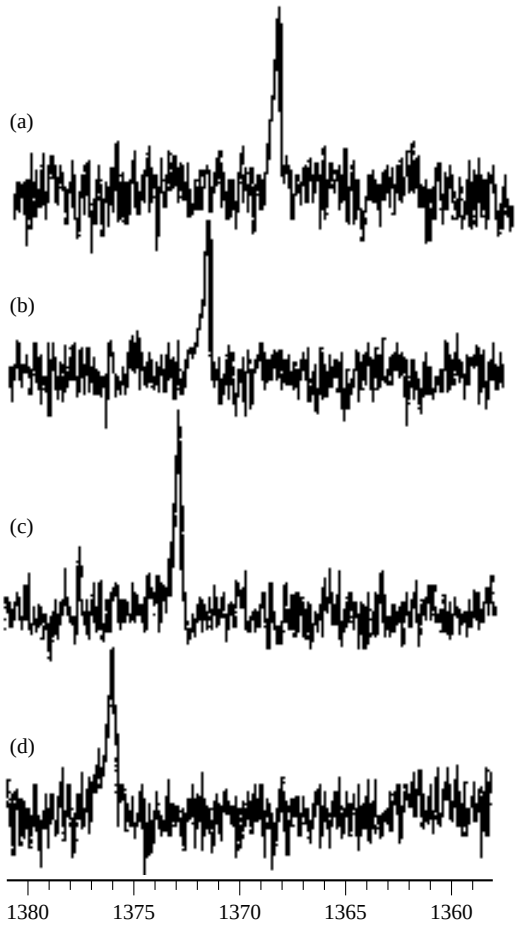

Figure 6 Aluminum-27 SINNMR spectra (23.3 MHz) of (a) Li(3%)/Al alloy, (b) Dural, (c) 99% Al, and (d) Al foil, relative to aqueous 0.05 M $AlCl_3$. (Reproduced from M. J. Howard, Ph.D. Thesis, Aston University, 1994)

An interesting finding that has been obtained during the preliminary high acoustic frequency small particle size work is that nonirradiated suspensions of particles that have been produced simply by grinding in a pestle and mortar are quite capable of yielding narrowed resonances relative to those

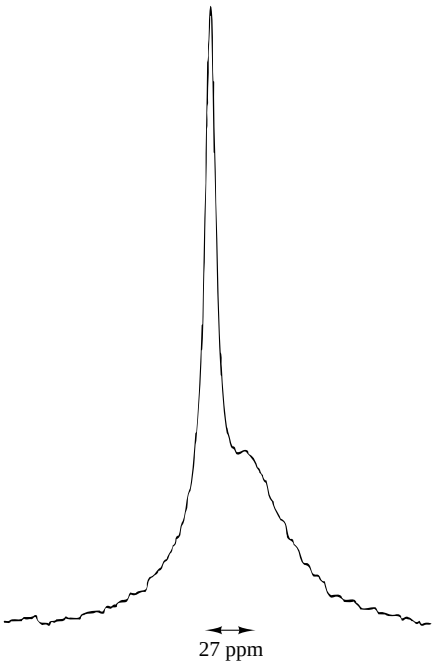

Figure 7 The ^{11}B SINNMR spectrum (28.75 MHz) of a $Na_2O/B_2O_3/Al_2O_3$ (20:70:10 mol%) glass (provided by Dr. C. Jaeger, Max Planck Institute, Mainz) from a suspension in $CHBr_3$ irradiated with 2 MHz ultrasound. (Reproduced from M. J. Howard, Ph.D. Thesis, Aston University, 1994)

of the static powder: subsequent high acoustic frequency irradiation of the samples further reduces the linewidths. Concurrent particle size measurements have revealed no detectable submicron particles, so that, strangely, it would appear that there are no sufficiently small particles present, as required by the principles implicit in the work of Yesinowski[23] and of Kimura and Satoh,[24] to be influenced by Brownian motion.

Although SINNMR shows promise as a new tool in the armory of NMR techniques, it is still in its infancy with many problems to be overcome before it becomes a readily usable and versatile method of studying structural problems. Major advances should become possible by its development to enable the levitation of particles in cryomagnet spectrometers: work is currently under way on this aspect of the technique.

8 CONCLUSIONS

NMR studies of samples simultaneously irradiated with ultrasound appear to have promise and be worthy of further development. While ANMR of solids and possibly liquids may hold little more than academic interest, it may be that its use for the study of metals, where phonons do not experience the skin depth problems of photons, may be worthy of increased attention. The fact that ultrasound can be used to modify T_1 values in liquids could be put to use in conjunction with magnetic resonance imaging, because of the ability to direct ultrasound reasonably precisely. If the strong indications that ultrasound can be used to reduce T_1 values in solids are definitively substantiated, it will undoubtedly prove beneficial to develop the approach to facilitate studies of nuclei that have naturally long relaxation times. Probably the major use of combined ultrasound and NMR investigations will lie with SINNMR. Not only does it result in the reduction of T_1 values in solids, but it also enables significant reductions in resonance line broadenings of both dipolar and quadrupolar origins to be achieved. Additionally, it has the ability to yield isotropic chemical shifts directly from spectra of solids that show resonances, often with better resolution than those obtained by MAS techniques, without spinning sidebands.

9 RELATED ARTICLES

Aluminum-27 NMR of Solutions; Boron NMR; Brownian Motion and Correlation Times; Carbon-13 Relaxation Measurements: Organic Chemistry Applications; Chemical Shift Tensors; Colloidal Systems; CRAMPS; Double Rotation; Dynamic Angle Spinning; Fluorine-19 NMR; High Speed MAS of Half-Integer Quadrupolar Nuclei in Solids; Line Narrowing Methods in Solids; Low Spin Temperature NMR; Phosphorus-31 NMR; Quadrupolar Interactions; Quadrupolar Nuclei in Glasses; Quadrupolar Nuclei in Solids; Relaxation of Quadrupolar Nuclei Measured via Multiple Quantum Filtration; Shielding: Overview of Theoretical Methods; Sideband Analysis in Magic Angle Spinning NMR of Solids; Sodium-23 NMR.

10 REFERENCES

1. See e.g. R. A. Levy, *Principles of Solid State Physics*, Academic Press, New York, 1968.
2. (a) See, for example, G. J. Price, p. 1; (b) J. Homer, S. U. Patel, and M. J. Howard, p. 136, in *Current Trends in Sonochemistry*, ed. G. J. Price, Royal Society of Chemistry, Special Publication No. 116, Cambridge, 1992.
3. W. G. Proctor and W. H. Tanttila, *Phys. Rev.*, 1956, **101**, 1757; W. G. Proctor and W. A. Robinson, *Phys. Rev.*, 1956, **104**, 1344.
4. J. Homer and S. U. Patel, *J. Chem. Soc., Faraday Trans.*, 1990, **86**, 215.
5. J. Homer, P. McKeown, W. R. McWhinnie, S. U. Patel, and G. J. Tilstone, *J. Chem. Soc., Faraday Trans.*, 1991, **87**, 2253.
6. J. Homer and M. J. Howard, *J. Chem. Soc., Faraday Trans.*, 1993, **89**, 3029.
7. A. Abragam, *Principles of Nuclear Magnetism*, Oxford University Press, New York, 1989.
8. See, for example, R. T. Beyer and S. V. Letcher, *Physical Ultrasonics*, Academic Press, London, 1969.
9. A. Kastler, *Experientia*, 1952, **8**, 1.
10. S. A. Al'tshuler, *Zh. Eksp. Teor. Fiz.*, 1953, **24**, 681; 1954, **28**, 49 (translated in *Sov. Phys. JETP*, 1955, **1**, 29; 1955, **1**, 37); S. A. Al'tshuler, B. I. Kochelaev, and A. M. Leuslin, *Usp. Fiz. Nauk*, 1961, **75**, 459 (translated in *Sov. Phys. Usp.*, 1962, **4**, 880).
11. D. I. Bolef and M. Menes, *Phys. Rev.*, 1958, **109**, 218; 1959, **114**, 1441.
12. A. R. Kessel, *Sov. Phys. Acoust.*, 1971, **16**, 425, Effect of Molecular Motion on Acoustic Resonance, (translated from *Akust. Zh.*, 1970, **16**, 497).
13. E. M. Iolin, *J. Phys. C. Solid State Phys.*, 1973, **6**, 3469; *Sov. Phys. Dokl.*, 1974, **18**, 527; E. M. Iolin and V. V. Kozlov, *Mol. Phys.*, 1978, **35**, 419.
14. A. V. Alekseev and U. K. Kopvillem, *Ultrasonics*, **1980**, 76.

15. S. U. Patel, Ph.D. Thesis, Aston University, UK, 1989.
16. L. O. Bowen, *Br. J. Appl. Phys.*, 1964, **15**, 1451; *Proc. Phys. Soc. London*, 1966, **87**, 717.
17. J. Homer and M.S. Beevers, *J. Magn. Reson.*, 1985, **63**, 287.
18. E. R. Andrew and R. G. Eades, *Proc. R. Soc. London, Ser. A*, 1953, **216**, 398; E. R. Andrew, A. Bradbury, and R. G. Eades, *Nature (London)*, 1958, **182**, 1659.
19. (a) A. Samoson, E. Lipmaa, and A. Pines, *Mol. Phys.*, 1988, **65**, 1013; (b) A. Llor and J. Virlet, *Chem. Phys. Lett.*, 1988, **152**, 248.
20. B. F. Chmelka, K. T. Mueller, A. Pines, J. Stebbings, Y. Wu, and J. W. Zwanziger, *Nature (London)*, 1989, **339**, 42.
21. P. Mansfield, *J. Phys. C: Solid State Phys.*, 1971, **4**, 1444; P. Mansfield, M. J. Orchard, D. C. Stalker, and K. H. B. Richard, *Phys. Rev. B*, 1973, **7**, 90; W.-K. Rhim, D. D. Ellerman, and R. W. Vaughan, *J. Chem. Phys.*, 1973, **58**, 1772; 1973, **59**, 3740.
22. B. C. Gerstein, R. G. Pembleton, R. C. Wilson, and L. M. Ryan, *J. Chem. Phys.*, 1977, **66**, 361.
23. J. P. Yesinowski, *20th Exp. NMR Conf., Asilomar, CA, 1979*; J. P. Yesinowski, *J. Am. Chem. Soc.*, 1981, **103**, 6266.
24. K. Kimura and N. Satoh, *Chem. Lett.*, 1989, 271.
25. K. B. Dysthe, *J. Sound Vib.*, 1969, **10**, 331.
26. V. L. Levshin and S. N. Rzhevkin, *Dokl. Akad. Nauk SSSR*, 1937, **16**, 407: B. E. Noltingk and E. A. Neppiras, *Proc. Phys. Soc. London*, 1950, **B63**, 674; 1951, **B64**, 1032.
27. V. Griffing, *J. Chem. Phys.*, 1950, **18**, 997: M. A. Margulis, *Russ. J. Phys. Chem.*, 1985, **59**, 882.
28. J. Homer, J. Reisse, and S. A. Palfreyman, unpublished results.
29. K. S. Suslick and S. J. Doktycz, in *Advances in Sonochemistry*, ed. T. J. Mason, JAI, New York, 1990, Vol. 1, pp. 197–230.
30. W. Lauterborn and H. J. Bolle, *J. Fluid Mech.*, 1975, **72**, 391.
31. See, for example, R. E. Apfel, *Methods of Experimental Physics*, ed. P. D. Edmonds, Academic Press, New York, 1981, Vol. 19, Chap. 7
32. J. Homer and M. J. Howard, unpublished results.
33. E. R. Andrew, W. S. Hinshaw, and R. S. Tiffen, *Phys. Lett. A*, 1973, **46**, 57.
34. W. D. Knight, *Solid State Phys.*, 1956, **2**, 93.

Biographical Sketch

John Homer. *b*, 1938. B.Sc., 1959, Leeds, Ph.D., 1962, Birmingham, D.Sc., 1980 Leeds. Introduced to NMR by J. A. S. Smith and interest nurtured by L. F. Thomas (Ph.D. supervisor). Albright and Wilson (MFG) Ltd., 1962–64; Aston University, 1964–present, Reader in Physical Chemistry. Approximately 100 publications. Current research interests: new techniques, either theoretical or experimental; NMR techniques including DESPOT, TIRADES, SINNMR, and PENDANT; generalization of London's dispersion theory to polyatomic molecules; generalized approach to phase equilibria (AGAPE).

Wide Lines for Nonquadrupolar Nuclei

Cecil Dybowski
University of Delaware, Newark, DE, USA
and
Günther Neue
Universität Dortmund, Dortmund, Germany

1	Introduction	1
2	CW Detection	1
3	Pointwise Detection by Spin Echoes	2
4	Excitation by Composite Pulses	2
5	Analyzing Broad Lines Using Transfer Functions	3
6	Related Articles	5
7	References	5

1 INTRODUCTION

Since the inception of NMR, one hallmark of its use has been the ability to analyze materials specifically by selectively detecting only resonances of certain nuclei in the material. Early on, the focus on protons by chemists resulted from the favorable NMR properties of this nucleus, but other spin-$\frac{1}{2}$ nuclei such as ^{13}C and ^{31}P have become routine targets because their spectroscopy addresses appropriate chemical problems with the same specificity as protons have for proton-containing organic materials.

An examination of the Periodic Table shows that approximately one-third of naturally occurring elements have at least one stable isotope with spin-$\frac{1}{2}$. Because the nuclear system of single spins $\frac{1}{2}$ has only two energy levels, these isotopes represent the simplest NMR spectroscopic systems. The proton occupies a unique position, being the spin-$\frac{1}{2}$ isotope of lowest atomic number. At the other extreme stands ^{207}Pb, the isotope of spin-$\frac{1}{2}$ having the highest atomic number. Thus, the NMR spectroscopy of this isotope logically represents the opposite extreme of NMR properties of spin-$\frac{1}{2}$ isotopes from the proton. Quite a few materials containing ^{207}Pb have been studied in solution, particularly the organolead compounds.[1] Despite its unique position, surprisingly little has been done to investigate the spectroscopy of ^{207}Pb in solid materials.

Figure 1 shows the shift ranges of several spin-$\frac{1}{2}$ nuclei. It is obvious that there is a loose correlation between the shift range of an isotope and its number of electrons. Elements with more electrons show a tendency to react more sensitively to their chemical environment than those with fewer electrons. It can be expected that similar arguments also hold for chemical shift anisotropies. The resulting broad spectra in noncubic environments lead to low signal-to-noise ratios and present problems for uniform excitation by pulses. The situation becomes even worse if the magnetogyric ratio is also low. Spin-$\frac{1}{2}$ nuclei of that type are sometimes nicknamed the 'Cinderella nuclei'.[2] Long T_1 values in solids may add to the problem.

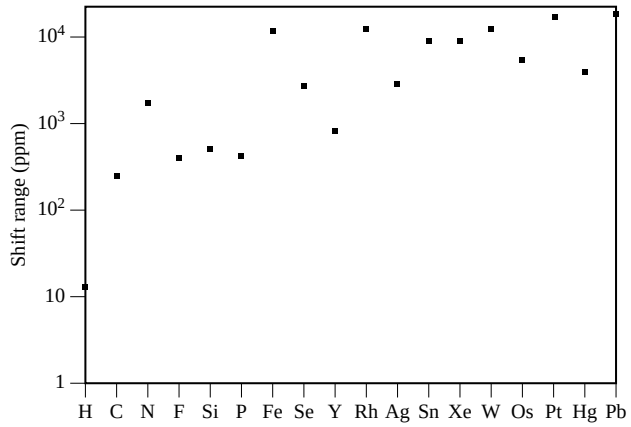

Figure 1 Shift ranges of some spin-$\frac{1}{2}$ nuclei ordered by increasing atomic number. The tendency of heavier nuclei to show larger shift ranges is clearly visible

Certainly, inherently difficult detection is a major reason for the comparatively fewer NMR studies of heavier isotopes. This article summarizes a few techniques for obtaining and analyzing spectra that consist of broad lines.

2 CW DETECTION

This old non-FT method scans a spectrum sequentially. The sensitivity is low, and therefore CW NMR has been replaced in most applications by the much more sensitive and more versatile pulse NMR. But this statement holds only for spectra consisting of narrow lines. Under such circumstances, a CW spectrometer scans detector noise of the baseline most of the time, while pulses excite all signals at once, as long as the pulse is strong enough. For liquids, the difference in the signal-to-noise ratio that can be obtained in a given time by both methods is striking (see e.g. Figure 4.3.4 on p. 157 of Ernst et al.[3]), and this characteristic boosted the development of FT NMR. However, this advantage becomes less important the broader the spectra are. For a faithful recording of very wide lines, CW spectrometers can be used. Swept CW detection always operates on resonance with a constant-amplitude rf signal. Among other things, this avoids offset effects and artifacts due to pulse imperfections. The detection of the ^{59}Co resonance in $KCoF_3$ gives an impression of what is possible with a CW wide line spectrometer.[4]

Essentially, there are two CW methods. The first is the slow passage experiment, which for a long time was the standard method for detecting NMR signals from liquids. Neglecting transient effects that result from noninfinitely slow scanning, the signal shape $g(\omega)$ depends on the amplitude of the rf field, B_1. For a Lorentzian peak with a linewidth described by T_2, one obtains[3]

$$g(\omega) \propto \gamma B_1 \frac{1/T_2}{(1+S)/T_2^2 + \omega^2} \tag{1}$$

where $S = (\gamma B_1)^2 T_1 T_2$ is called the saturation parameter. This quantity depends on both T_1 and T_2, as well as on B_1. It can be seen that there is a conflict. To maximize the

signal, B_1 has to be as big as possible, but to keep distortions low, B_1 has to be as small as possible. For solids with very long T_1 values, this may be a substantial problem. In such cases, a second CW method, the adiabatic fast passage through resonance, is useful.[5] This is based on the fact that, under certain circumstances, the nuclear magnetization always remains aligned with the effective field $\boldsymbol{B}_e = (B_1, 0, B_0 - \omega/\gamma)$ in the rotating frame. In solids, a signal can be observed if the B_1 field strength and the scanning rate $d|B_0|/dt$ fulfil the condition

$$\frac{1}{T_1} \ll \frac{1}{B_1}\frac{d|B_0|}{dt} \ll |\gamma B_1| \approx \frac{1}{T_2} \tag{2}$$

But, since the last relationship means that the nutation frequency $\omega_1 = \gamma B_1$ must be comparable to the linewidth, one has a restriction similar to that for pulse methods.

For details on both CW methods, the reader is referred to Abragam.[5] It should be noted, however, that it is becoming more and more difficult to find a commercially produced CW NMR spectrometer to use in such experiments.

3 POINTWISE DETECTION BY SPIN ECHOES

Spectra representing extremely broad shift distributions cannot be excited evenly over the whole shift range if pulses are used. Instead, only a region, which may be small compared with the total width of the spectrum, will be selected by the pulse. By using the basic idea of CW spectroscopy, sequential detection in different parts of the spectrum will outline the lineshape. In practice, one uses spin echoes to circumvent deadtime problems. The height of the echo is a direct measure of the intensity of the spectrum at the irradiation frequency. More precisely, it is a point on the true line smoothed with the excitation profile. Obviously, there are two possibilities to achieve the goal. Either the frequency or the field is changed from point to point. Field sweeps, if possible, are the better choice, because the tuning of the spectrometer can be kept constant.

With the limited availability of CW spectrometers, this method is becoming more and more the standard for observing extremely broad lines. It was, for example, extensively used for measuring the copper resonances in high-T_c superconductors.[6]

An instructive example to demonstrate the application and power of the spin echo technique is the study of the ^{195}Pt resonance of metallic Pt particles on an alumina-supported catalyst.[7,8]

Figure 2 shows a spin echo spectrum of such a catalyst with a Pt dispersion of 26% (= the percentage of surface atoms) covered by CO. The meaning of the structure of the spectrum is elucidated by a double resonance version of the spin echo experiment, where the ^{195}Pt resonance is observed while ^{13}C is irradiated. As only Pt atoms directly attached to CO can be observed, this method is surface-sensitive. By using this approach, it could be shown unambiguously that only the pronounced peak on the left side of the spectrum is due to surface atoms, while the right part belongs to resonances of ^{195}Pt atoms located within the small metal clusters.

4 EXCITATION BY COMPOSITE PULSES

To improve excitation over a wider range of frequencies, composite pulses have been used for many years.[9] The basic idea of this approach is to use a sequence of pulses that mimics the effect of a single pulse. The extra degrees of freedom in times (pulse durations, delays) and phases that are introduced by using several pulses are used to improve the properties of the equivalent pulse towards an ideal delta function pulse.

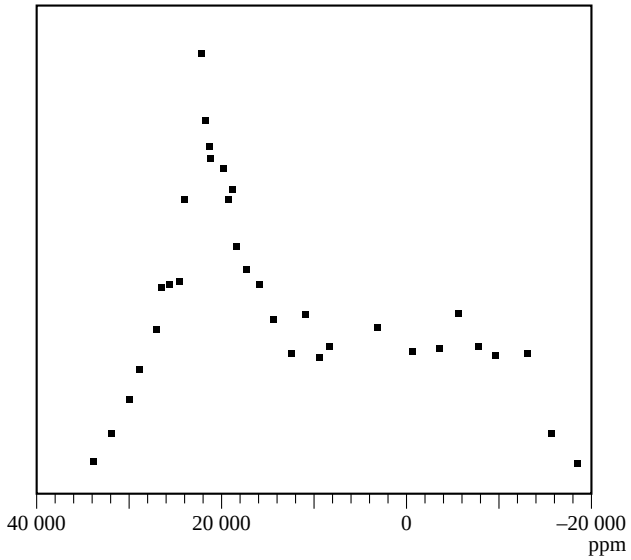

Figure 2 ^{195}Pt spin echo spectrum of small CO-covered Pt clusters on an alumina-supported catalyst. The data are taken from Makowka et al.[7]

There is a wide variety of suggestions for composite pulses. Usually, they are optimized to achieve a particular property. Many pulse sequences are designed to be tolerant to missettings of the pulse length to allow a more uniform excitation over a large sample volume with B_1 inhomogeneities.[10] Another area of successful application of composite pulses is spin decoupling.[11]

More important in the context of exciting wide lines is an optimization with respect to a minimal phase dispersion as a function of frequency offset. A well-known sequence with that property is the 'spin knotting' sequence[12]

$$(\phi_1)_{+x} - \tau_1 - (\phi_2)_{-x} - \tau_2 - (\phi_3)_{+x} \tag{3}$$

The rotation angles ϕ_i have to fulfil the condition $\phi_1 - \phi_2 + \phi_3 = 90^\circ$. The remaining four degrees of freedom can be used to optimize the performance of the sequence for each B_1 field strength by trial and error.[12] Figure 3 shows a simulated powder spectrum with shift anisotropy excited by a single $(\frac{1}{2}\pi)_{+x}$ pulse. The B_1 field strength was assumed to correspond to a nutation frequency of 10 kHz. Distortion of the lineshape is clearly visible. If the same spectrum is detected by applying the 'spin knotting' sequence with pulses of the same B_1 field strength, the result is an almost perfect powder pattern (Figure 4).

A more direct and general approach to the construction of sequences that approximate ideal pulses[13] predicts that a composite pulse

$$(385^\circ)_{+x}(320^\circ)_{-x}(25^\circ)_{+x} \tag{4}$$

is equivalent to a $(\frac{1}{2}\pi)_{+x}$ pulse with minimum phase dispersion. As this particular method uses a series expansion, higher order approximations can be found that consist of more

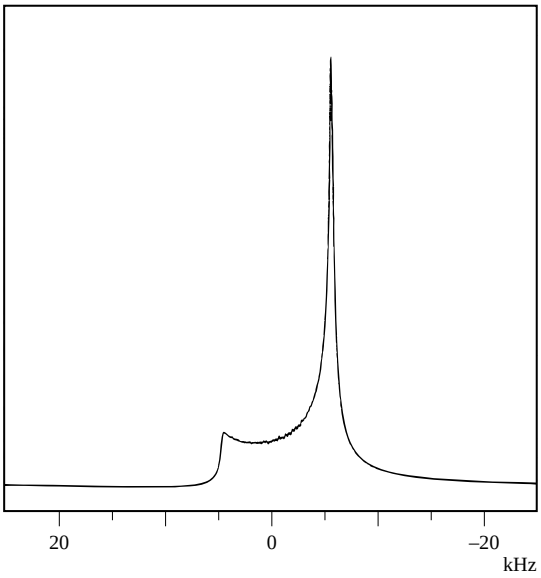

Figure 3 Simulation of a spectrum excited by a weak pulse and governed by chemical shift anisotropy. The rf pulse strength was assumed to correspond to a nutation frequency of 10 kHz

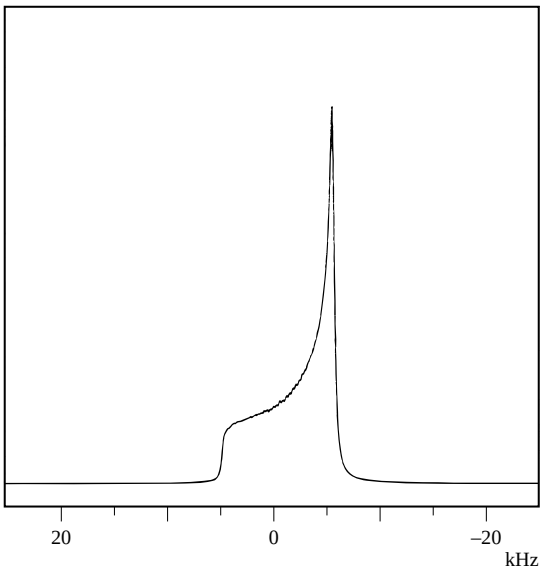

Figure 4 Simulation of the response of the same system as in Figure 3 to excitation by the spin knotting sequence with optimized parameters.[12] Again, the rf pulse strength was assumed to correspond to a nutation frequency of 10 kHz

and more pulses and that increase the spectral range over which the phases of the excitation are almost constant.

It may seem that cleverly designed composite pulses are the ultimate solution to the problem of exciting broad lines. But there are limitations. The power theorem of Fourier transforms,

$$\int_{-\infty}^{\infty} |p(t)|^2 \, \mathrm{d}t = \frac{1}{4\pi} \int_{-\infty}^{\infty} |P(\omega)|^2 \, \mathrm{d}\omega \tag{5}$$

relates the power in a pulse train as a function of time [amplitudes $p(t)$] to the power available in the spectrum as a function of the frequency [amplitudes $P(\omega)$]. In general, both amplitudes are complex functions, since one has to include the phases. By assuming a constant amplitude $|A|$ for the pulses and a flat spectrum of the pulse sequence with a constant amplitude $|B|$ (disregarding its practical realization), one obtains

$$|A|^2 \Delta t = \frac{1}{4\pi} |B|^2 \Delta\omega \tag{6}$$

where Δt is the total time during which the transmitter is on and $\Delta\omega$ is the bandwidth of the excitation. It is obvious that a larger frequency range $\Delta\omega$ can be obtained only by increasing the total lengths of the pulses, since the transmitter power $|A|^2$ is limited in practice. Note that the other quantity, $|B|$, is fixed by the condition to obtain a 90° pulse. Usually, in solids, there will be dipolar interactions that give rise to a T_2 decay of the order of a few tens of microseconds. On typical solids spectrometers $\frac{1}{2}\pi$ pulse lengths may be $5\,\mu$s. It should be observed that even simple composite pulse sequences such as those given above may last as long as typical decay times owing to dipolar interactions. Thus, in most solids, the bandwidth of ideal excitation cannot be increased much by more sophisticated and longer sequences than those given above. Similar bandwidth versus time arguments also hold for a newer development in the field of tailored excitation, namely, shaped pulses,[14] where extra degrees of freedom are obtained by modulating the amplitudes by analog signals rather than by pulses.

5 ANALYZING BROAD LINES USING TRANSFER FUNCTIONS

Despite the success of the methods described in the previous section, it might be inconvenient, difficult, or impractical to use them. Owing to the nonideal behavior of electronic circuits (finite rise times, power droop, etc.), one usually needs to adjust the pulses to optimize the operation of the sequence. Adjustments on the sample of interest may not be possible in cases of low intensities or long relaxation times. If one works with special probeheads that need insulation from the environment, like low- or high-temperature probes, then it may not be practical to substitute a calibration sample.

Very wide lines also present another problem. As discussed above, the possible bandwidth of excitation is subject to practical limitations like those imposed by relaxation. If the line extends over more than this range, application of the common composite pulse sequences destroys the wings of the line very efficiently. According to the power theorem, increasing the power in a given region of the spectrum means that, outside of that region, the excitation is reduced. In contrast to the almost rectangular excitation profile (transfer function) of a composite pulse, a simple single pulse spreads its energy over a much wider frequency range, though unevenly. This fact allows one to use another strategy for wide lines. As the transfer function is given by pulse timings, it can be calculated exactly and included in the data analysis. Under these circumstances, a simpler excitation has the advantage of giving a better signal-to-noise ratio far off resonance, allowing a better fit of data.[15] This is illustrated by Figure 5. It is clearly seen that if the lines are so broad that they cannot be covered by composite pulses, a simple pulse shows the singularities

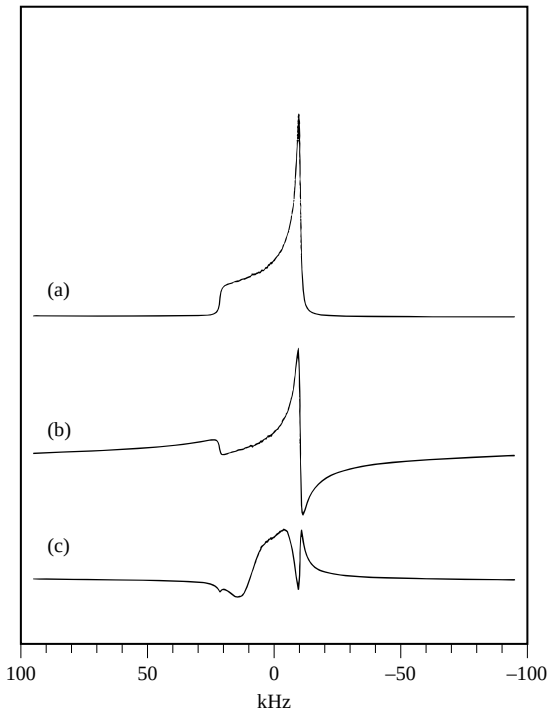

Figure 5 Simulation of the effects of different excitation methods on the appearance of spectra. (a) Ideal spectrum governed by chemical shift anisotropy. (b) Excitation by a single pulse. (c) Excitation by the spin knotting sequence. The rf pulse strength was always assumed to correspond to a nutation frequency of 10 kHz

and shoulders of powder spectra better, and the extraction of tensor elements consequently becomes more precise.

Because of receiver dead time, one cannot use a single pulse, but has to rely on spin echo techniques. Furthermore, the detection of weak signals very often suffers from acoustic ringing. A simple pulse sequence that produces a spin echo and removes acoustic ringing, as well as some other imperfections is

$$\begin{gathered}(\tfrac{1}{2}\pi)_{+x} - \tau - (\pi)_{+y} - \tau - (\mathrm{acq})_{+x} \\ (\pi)_{+x} - \tau_1 - (\tfrac{1}{2}\pi)_{+x} - \tau - (\pi)_{+y} - \tau - (\mathrm{acq})_{-x} \\ (\tfrac{1}{2}\pi)_{-x} - \tau - (\pi)_{-y} - \tau - (\mathrm{acq})_{-x} \\ (\pi)_{+x} - \tau_1 - (\tfrac{1}{2}\pi)_{-x} - \tau - (\pi)_{-y} - \tau - (\mathrm{acq})_{+x}\end{gathered} \tag{7}$$

where $(\theta)_\phi$ denotes a pulse with phase ϕ that produces a nutation by angle θ, and $(\mathrm{acq})_\phi$ stands for acquisition with receiver phase ϕ.

The effect of this sequence can be calculated by standard density matrix theory.[5,8,16] For signals governed by chemical shift anisotropy (CSA), we define the Hamiltonian in the rotating frame as

$$\hat{\mathcal{H}} = \begin{cases} -\Delta\omega_0 \hat{I}_z & \text{no pulse} \\ -\Delta\omega_0 \hat{I}_z \mp \omega_1 \hat{I}_{x,y} & \text{during pulses} \end{cases} \tag{8}$$

where $-\omega_1\hat{I}_x$ has to be used for a $(\theta)_x$ pulse, $+\omega_1\hat{I}_x$ for a $(\theta)_{-x}$ pulse, etc. As this Hamiltonian is a piecewise-constant function of time, the evolution of the density matrix $\hat{\rho}$ is given simply by[5]

$$\hat{\rho}(t) = \mathrm{e}^{-\mathrm{i}\hat{\mathcal{H}}_n t_n} \ldots \mathrm{e}^{-\mathrm{i}\hat{\mathcal{H}}_1 t_1}\, \hat{\rho}(0)\, \mathrm{e}^{\mathrm{i}\hat{\mathcal{H}}_1 t_1} \ldots \mathrm{e}^{\mathrm{i}\hat{\mathcal{H}}_n t_n} \tag{9}$$

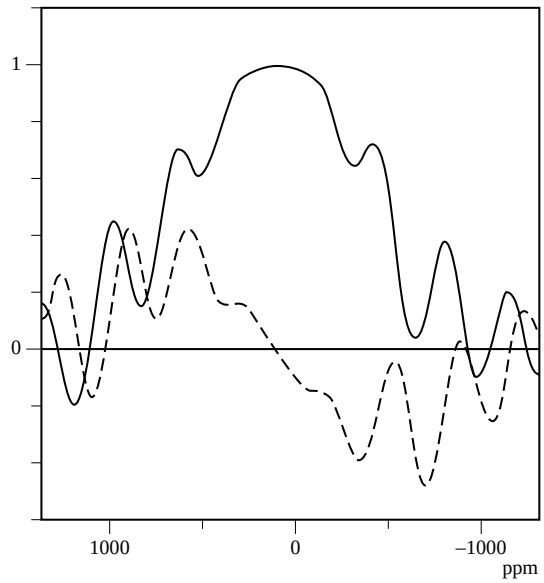

Figure 6 Complex transfer function for a pulse sequence using τ = 20 μs, $(\frac{1}{2}\pi)$ = 3.75 μs, and $\omega_0/2\pi$ = 62.60 MHz

where subscripts n label subsequent time intervals.

The numerical calculation of the evolution of the density matrix is fairly easy, since all operators of a spin-$\frac{1}{2}$ can be expressed by 2 × 2 matrices. Figure 6 shows a calculated transfer function for the excitation by the above sequence. The effect on both receiver channels of a quadrature detector was calculated. One sees the complicated distortions of amplitudes and phases as a function of offset frequency.

Least-squares fits become significantly more precise if the transfer function is included. It should be noted that no new fitting parameters are introduced, but the experiment with its

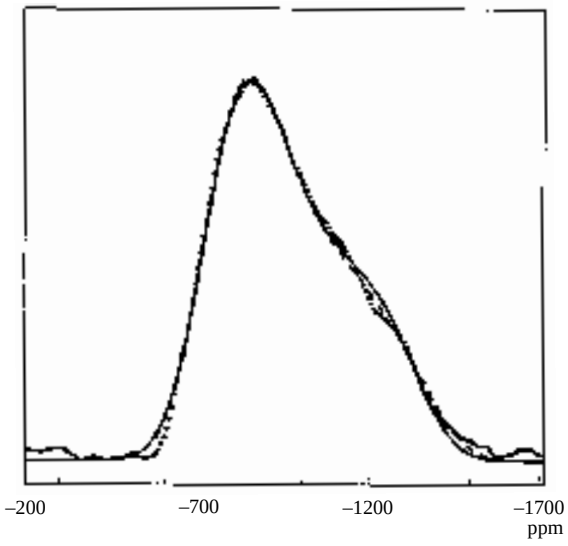

Figure 7 Experimental ^{207}Pb spectrum of $PbBr_2$ (squares) at 62.601 MHz. The rf pulse strength corresponds to a nutation frequency of 1000 ppm. The solid line represents a simple fit that assumes three shift tensor elements as well as a Gaussian broadening, while the dashed line is a best fit including the transfer function of the excitation. The ppm scale is referred to the chemical shift of $Pb(CH_3)_4$

timings of pulses and delays determines the transfer function completely.

The possible improvement is demonstrated by Figure 7. Though, at first sight, the differences seem to be small, application of the transfer function leads to a better reproduction of the almost triangular lineshape. The set of best-fit parameters changes from $\sigma_{11} = -710$ ppm, $\sigma_{22} = -849$ ppm, and $\sigma_{33} = -1350$ ppm without correction to $\sigma_{11} = -699$ ppm, $\sigma_{22} = -845$ ppm, and $\sigma_{33} = -1398$ ppm if the transfer function is included in the theoretical lineshape. The width of the line, $\sigma_{11} - \sigma_{33}$, changes by 10%, or 69 ppm, which is clearly outside the limit of statistical error. The mean-square deviation is also reduced by about 25%.

6 RELATED ARTICLES

Chemical Shift Tensor Measurement in Solids; Chemical Shift Tensors; Composite Pulses; Echoes in Solids; Fourier Transform and Linear Prediction Methods; Fourier Transform Spectroscopy; Magic Angle Turning and Hopping; Phase Cycling; Radiofrequency Pulses: Response of Nuclear Spins; Selective Pulses; Shaped Pulses; Shielding Tensor Calculations; Solid State Probe Design.

7 REFERENCES

1. B. Wrackmeyer and K. Horchler, in *Annual Reports on NMR Spectroscopy*, ed. G. A. Webb, Academic Press, London, 1990, Vol. 22, p. 249
2. B. E. Mann, in *Annual Reports on NMR Spectroscopy*, ed. G. A. Webb, Academic Press, London, 1991, p. 141.
3. R. R. Ernst, G. Bodenhausen, and A. Wokaun, *Principles of Nuclear Magnetic Resonance in One and Two Dimensions*, Oxford University Press, Oxford, 1987.
4. R. G. Shulman, *Phys. Rev. Lett.*, 1959, **2**, 459.
5. A. Abragam, *The Principles of Nuclear Magnetism*, Oxford University Press, Oxford, 1961.
6. T. Shimizu, H. Yasuoka, T. Imai, T. Tsuda, T. Takabatake, Y. Nakazawa, and M. Ishikawa , *J. Phys. Soc. Jpn.*, 1988, **57**, 2494.
7. C. D. Makowka, C. P. Slichter, and J. H. Sinfelt *Phys. Rev. Lett.*, 1982, **49**, 379; *Phys. Rev. B*, 1985, **31**, 5663.
8. C. P. Slichter, *Principles of Magnetic Resonance*, 3rd edn., Springer-Verlag, Berlin, 1990.
9. M. H. Levitt, and R. Freeman, *J. Magn. Reson.*, 1979, **33**, 473.
10. M. H. Levitt, *J. Magn. Reson.*, 1982, **48**, 234.
11. M. H. Levitt, R. Freeman, and T. Frenkiel, in *Advances in Magnetic Resonance*, ed. J. S. Waugh, Academic Press, New York, 1983, Vol. 11, p. 48.
12. R. Freeman, S. P. Kampsell, and M. H. Levitt, *J. Magn. Reson.*, 1980, **38**, 453.
13. R. Tycko, H. M. Cho, E. Schneider, and A. Pines, *J. Magn. Reson.*, 1985, **61**, 90.
14. L. Emsley and G. Bodenhausen, *J. Magn. Reson.*, 1990, **87**, 1.
15. G. Neue, C. Dybowski, M. L. Smith, and D. H. Barich, *Solid State NMR*, 1994, **3**, 115.
16. M. Mehring, *High Resolution NMR in Solids*, 2nd edn, Springer-Verlag, Berlin, 1982.

Acknowledgments

Simulations were performed using the program ANTIOPE, which was kindly provided by J. S. Waugh.

Biographical Sketches

Cecil Dybowski. *b* 1946. B.S., 1969, Ph.D., 1973, Texas. Faculty at the University of Delaware, 1976–present. Over 100 publications, including the book “Transient Techniques in the NMR of Solids” (with B. C. Gerstein). Research interests include all facets of NMR spectroscopy, the analysis of heterogeneous catalysis and catalytic processes, materials structure and function.

Günther Neue. *b* 1955. Dipl.-Chem., 1978, Dr.rer.nat., 1983, Priv.-Doz., 1988, Dortmund. Hochschuldozent, Universität Dortmund, 1988–present. Over 25 research publications. Research interests include development of analytical techniques in the fields of surface science and environmental chemistry.

Liquid Crystalline Samples: Carbon-13 NMR

Bing M. Fung

University of Oklahoma, Norman, OK, USA

1	Introduction	1
2	Anisotropic ^{13}C Chemical Shifts in Liquid Crystals	1
3	MAS and VAS	1
4	The Effect of the Local Dipolar Field	2
5	Study of ^{13}C–^{1}H Dipolar Couplings with VAS	4
6	Applications Combining Measurements of Chemical Shifts and Dipolar Couplings	5
7	Relaxation	6
8	Conclusions	6
9	Related Articles	6
10	References	7

1 INTRODUCTION

Because of the ubiquitous presence of the carbon atom in organic compounds, ^{13}C NMR has been widely used to study liquid, liquid crystalline, and solid samples. The application of ^{13}C NMR to study liquid crystals offers important information that complements that obtained from proton and deuterium NMR experiments. The most important parameters obtained in ^{13}C NMR studies of liquid crystals are anisotropic ^{13}C chemical shifts, ^{1}H–^{13}C dipolar coupling constants, and ^{13}C relaxation times. They will be reviewed in this article.

2 ANISOTROPIC ^{13}C CHEMICAL SHIFTS IN LIQUID CRYSTALS

For macroscopically oriented liquid crystal samples, the major advantage of ^{13}C NMR is the simplicity of the spectra. With broadband proton decoupling, the ^{13}C spectra of liquid crystals usually show resolvable peaks which can be assigned to individual carbon atoms, similar to the case of isotropic samples. However, because of the presence of ^{13}C chemical shift anisotropy, the chemical shifts of the observed signals (δ^{obs}) are often considerably different from those in the isotropic state (δ^{iso}):

$$\begin{aligned}\delta^{\text{obs}} &= \delta^{\text{iso}} + \delta^{\text{aniso}} \\ &= \delta^{\text{iso}} + \tfrac{2}{3}S_{zz}[\sigma_{zz} - \tfrac{1}{2}(\sigma_{xx} + \sigma_{yy})] \\ &\quad + \tfrac{1}{3}(S_{xx} - S_{yy})(\sigma_{xx} - \sigma_{yy}) \\ &\quad + \tfrac{2}{3}S_{xy}\sigma_{xy} + \tfrac{2}{3}S_{xz}\sigma_{xz} + \tfrac{2}{3}S_{yz}\sigma_{yz} \qquad (1)\end{aligned}$$

where the S_{ij} are components of the order parameter matrix, and the δ_{ij} are components of the chemical shift tensor, both being in the same axis system.

The first report on the ^{13}C NMR of liquid crystals was given by Yannoni and Whipple, who studied ^{13}C-enriched CH_3I dissolved in a liquid crystalline solvent.[1] They determined the order parameter S_{zz} of the molecule from its proton spectrum (the other components of the order parameter matrix are zero), and calculated the ^{13}C chemical shift anisotropy $\delta_{zz} - (\delta_{xx} + \delta_{yy})/2$ according to equation (1). Subsequently, similar studies of other small solute molecules have been made, using either enriched or naturally abundant compounds. Examples include acetonitrile,[2,3] hydrogen cyanide,[4] benzene,[5,6] acetylene,[7] chloroform,[3] methyl halides,[3] methanol,[3] a further study of CH_3I,[8] benzonitrile,[9] halobenzenes,[10] pyridine,[11] and diazenes.[11] Details of the determination of ^{13}C chemical shift anisotropy using liquid crystalline solvents are discussed by Jokisaari (see ***Anisotropy of Shielding and Coupling in Liquid Crystalline Solutions***), and will not be repeated here.

A much more general application of ^{13}C NMR is the investigation of bulk liquid crystals in their natural abundance. The first work of this type was reported by Pines and co-workers, who studied the ^{13}C chemical shifts of 4,4′-azoxyanisole,[12] 4-methoxybenzylidene-4′-*n*-butylaniline (MBBA)[13] and 4-alkoxyazoxybenzenes[14] as a function of temperature. Fyfe, Lyerla, and Yanonni also demonstrated the significant effect of orientational ordering on the ^{13}C chemical shifts of MBBA, 4,4′-di-*n*-hexyldiphenyldiacetylene, and 4-*n*-octyl-4′-cyanobiphenyl (8CB).[15] By using model compounds to estimate the components of the chemical shift tensors in the molecular axis system, Pines and co-workers calculated the order parameter S_{zz} of the liquid crystals from equation (1), omitting other terms.[12–14] The method of employing ^{13}C chemical shifts to estimate the order parameters of liquid crystals is rather simple and straightforward, and studies have been made on other systems. Examples include a eutectic mixture of MBBA and 4-ethoxybenzylidene-4′-*n*-butylaniline (EBBA),[16] several chiral smectic C (SmC*) compounds,[17,18] and 4-cyanobenzylidene-4′-*n*-octyloxyaniline.[19] However, because the ^{13}C chemical shift tensors are highly dependent upon the molecular structure and the nature of substituents, and their principal axis systems do not always coincide with the molecular axis system used to define the order parameters, the values obtained from model compounds may not be very accurate. Thus, the order parameters calculated are only approximations. On the other hand, calculations made by combining the ^{13}C chemical shift data with dipolar and quadrupolar splittings[20] give more reliable results.

If a liquid crystal sample is not macroscopically oriented, the ^{13}C spectrum would be a superposition of peaks, showing a ‘powder pattern’; if the sample is partially oriented, such as cholesteric or SmC* phases with the helical axes aligned along the magnetic field, the spectra exhibit ‘partial powder patterns’. In these cases, information obtained from the ^{13}C spectra is rather limited. An attempt has been made to calculate diffusion constants of two cholesteric mixtures from the lineshapes of their ^{13}C spectra,[21] but it depends on a number of assumptions and is less reliable than the pulsed field gradient method, which is discussed by Lindblom (see ***Liquid Crystalline Samples: Diffusion***).

3 MAS AND VAS

To obtain resolvable peaks in the ^{13}C spectra of liquid crystals, broadband proton decoupling must be used.[12–15] Because the proton spectra of liquid crystals have wide spectral windows, the decoupler power applied must be considerably larger than that for liquid samples. Excessive decoupler power, however, leads to rf heating, which is an extremely undesirable effect[22] because the orientational ordering of liquid crystals is very sensitive to temperature. To alleviate this problem, the MAS (magic angle spinning) and VAS (variable angle spinning) techniques can be used.

With MAS, the ^{13}C linewidths of liquid crystal samples can be greatly reduced even with rather nominal decoupler power.[23] The MAS method has been employed to investigate the conformation of liquid crystal molecules,[24–26] phase transition,[18,27] the rate process of dissolved solute molecules,[28] and lipid systems.[29–32] It should be noted that, because of the fast motions in liquid crystals, cross polarization is effective for static samples,[12–14] but much less so with MAS.[23] MAS also removes the anisotropic chemical shifts and dipolar couplings, which are often the most interesting aspects of the ^{13}C NMR of liquid crystals.

Like MAS, the VAS technique results in sharp ^{13}C peaks for bulk liquid crystals.[16,33] In addition, part of the anisotropic interactions are preserved, offering an advantage over MAS. The principles of the VAS technique are reviewed in a recent article[34] and discussed by Courtieu (see ***Spinning Liquid Crystalline Samples***). Here, the essential features pertinent to ^{13}C NMR are briefly outlined for the convenience of discussion.

Solid samples with VAS show residual 'powder patterns' in the proton-decoupled ^{13}C spectra, because the chemical shift anisotropy is not averaged to zero. On the other hand, even though residual chemical shift anisotropy is present in nematic liquid crystal samples with VAS, the ^{13}C spectra show sharp peaks due to macroscopic alignment of the director.[16,33] For a nematic liquid crystal being spun along an axis forming an angle η with respect to the magnetic field $\boldsymbol{B}_0$, the macroscopic orientation of the director is determined by a competition between the magnetic torque and the viscous torque. If the spinning rate is high enough, the nematic director of liquid crystals with a positive anisotropy of the magnetic susceptibility ($\Delta\chi > 0$) aligns along the spinning axis for $0^\circ < \eta < 54^\circ 44'$, and aligns perpendicular to the spinning axis for $54^\circ 44' < \eta < 90^\circ$. The alignment with respect to the spinning axis for liquid crystals with $\Delta\chi < 0$ is opposite to liquid crystals with $\Delta\chi > 0$.[16,33] Smectic liquid crystals can also be aligned similarly, provided that they are cooled down from the nematic phase while the sample is being spun rapidly.[23]

The macroscopic alignment of the director gives sharp peaks in the ^{13}C spectra, with scaled anisotropic chemical shifts expressed by

$$\delta^{\text{obs}} = \delta^{\text{iso}} + \frac{3\cos^2\eta - 1}{2}\delta^{\text{aniso}} \tag{2}$$

for parallel alignment, and by

$$\delta^{\text{obs}} = \delta^{\text{iso}} - \frac{3\cos^2\eta - 1}{4}\delta^{\text{aniso}} \tag{3}$$

for perpendicular alignment, where δ^{aniso} is the anisotropic part of the chemical shift, which is given in equation (1).

The spectra in Figure 1 illustrate the effect of VAS on the proton-decoupled ^{13}C NMR of 4-*n*-pentyl-4′-cyanobiphenyl (5CB). With the normal condition of $\eta = 0$, the ^{13}C peaks show large shifts [Figure 1(c)] from their isotropic values [Figure 1(a)], and the changes in the chemical shifts of different carbons are related to the corresponding chemical shift tensors. However, the peaks are not very sharp due to incomplete proton decoupling. On the other hand, the proton–proton dipolar interactions are reduced in a VAS experiment, so that much better decoupling can be achieved with a reasonable decoupler power (20–25 kHz). Thus, sharp ^{13}C peaks can be observed, with the anisotropic part of the chemical shifts scaled by the factor $(3\cos^2\eta - 1)/2$ [Figure 1(b)].

By taking advantage of the changes in ^{13}C chemical shifts with the alignment of the director, the dynamics of the realignment process of liquid crystals in a magnetic field can be studied with ^{13}C NMR. When the spinning sample is suddenly stopped, the action of the magnetic torque causes the director to realign from being parallel to the spinning axis to being parallel to the magnetic field. Consequently, the ^{13}C spectrum gradually changes from that in Figure 1(b) to Figure 1(c). The chemical shift is related to the angle β formed between the director and the magnetic field by an equation similar to equation (2) for the angle η. The time dependence of β is governed by the relationship[35,36]

$$\beta = \tan^{-1}[(\tan\eta)\,e^{-t/\tau}] \tag{4}$$

where τ is the time constant for the reorientation of the nematic director in the magnetic field. Thus, by using a least-squares fitting of the chemical shift data as a function of time after the rotor stops, the value of τ can be determined.[37] Actually, equation (4) is strictly applicable to rigid rods only. However, liquid crystal molecules are flexible and the order parameters of individual molecular segments differ along the long axis. Because the hydrodynamic behavior of liquid crystals is related to their order parameters, the reorientation times for different parts of the molecule need not be the same. For 5CB at room temperature, it was found that $\tau = 8.7$ ms for the aromatic rings and 11 ms for the methyl group.[37] The smectic A compound 8CB is much more viscous, and the corresponding τ values are about 300 times longer, being 2.4 and 3.2 s, respectively.[37]

In the application of VAS to study liquid crystals, a sufficiently high spinning rate must be used to induce macroscopic alignment with respect to the spinning axis (~1 kHz at $B_0 = 7$ T for most liquid crystals), and the critical spinning rate is proportional to the square of the magnetic field.[33,34] However, the inertial torque tends to oppose the viscous torque and the magnetic torque, and would destroy the alignment at very high spinning rates.[34] Therefore, one must be careful to balance the different torques to obtain the desired macroscopic orientation of the liquid crystalline samples.

4 THE EFFECT OF THE LOCAL DIPOLAR FIELD

In Section 2, it was pointed out that in most cases it is difficult to evaluate accurately the order parameters from ^{13}C chemical shifts because the use of equation (1) requires a

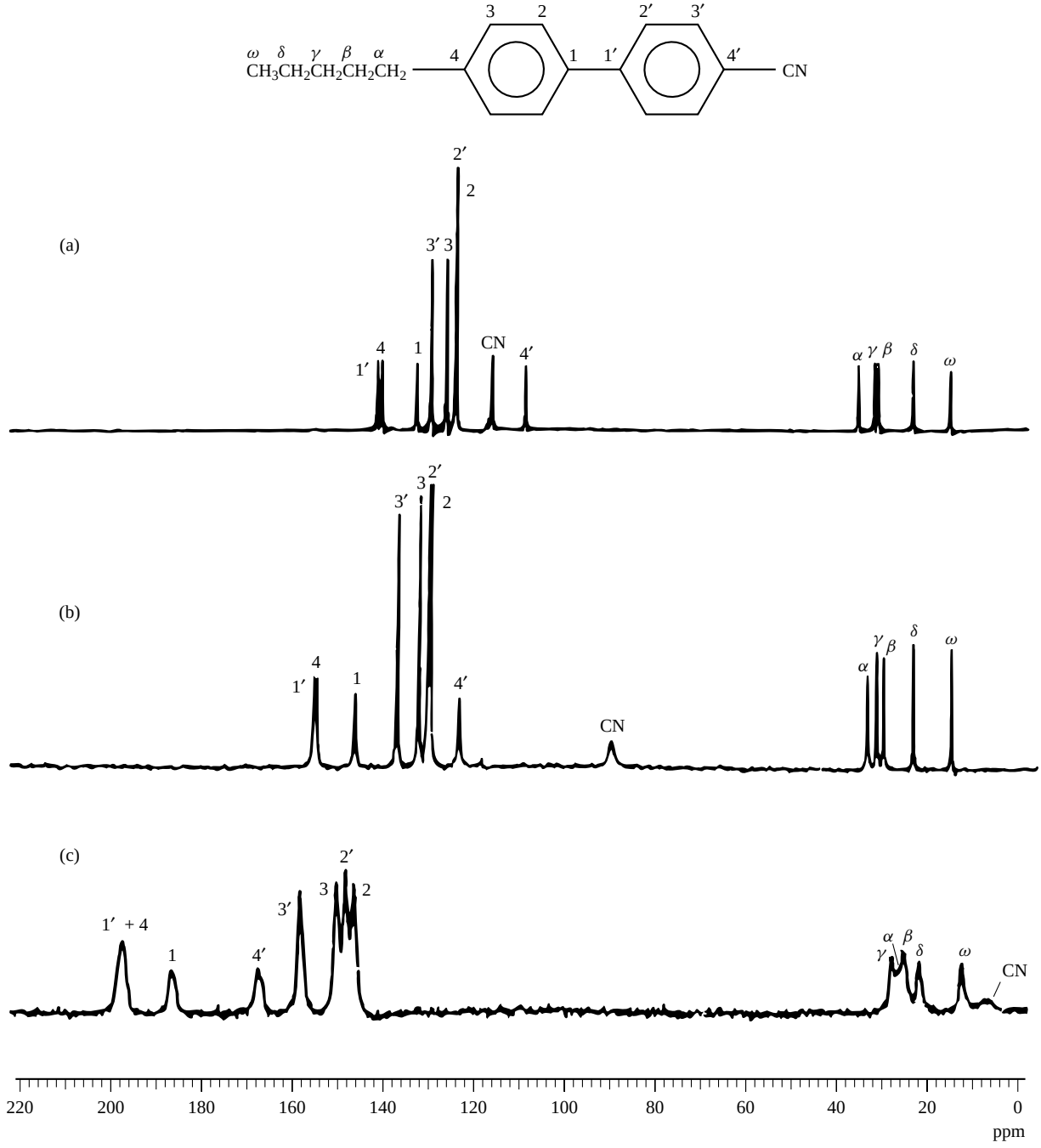

Figure 1 Proton-decoupled ^{13}C NMR spectra of 5CB at 75.43 MHz. (a) Isotropic spectrum at 37°C. (b) Anisotropic spectrum at 26°C, with a spinning angle of $\eta = 44.6°$ and a spinning rate of 1.1 kHz. (c) Anisotropic spectrum at 26°C, nonspinning

knowledge of the components of the chemical shift tensors in the molecular frame defining the ordering matrix. On the other hand, dipolar coupling constants can be used to calculate the order parameters of liquid crystals without relying on parameters estimated from model compounds. With broadband proton decoupling, dipolar coupling constants (D) between ^{13}C and ^{15}N,[38] between ^{13}C and ^{19}F,[39] and between two ^{13}C nuclei[40] can often be determined directly from the ^{13}C spectra, because the pairwise splittings are expressed by

$$\Delta\nu = 2D + J \tag{5}$$

where J is the scalar coupling constant, the anisotropy of which is usually small compared with the value of D and can be neglected. On the other hand, except for perdeuterated compounds,[41] it is less straightforward to determine $^{13}C-^{1}H$ dipolar coupling constants from the ^{13}C spectra.

To discuss this, let us first consider the example of benzene dissolved in a liquid crystalline solvent. With broadband ^{1}H decoupling, there is only a single sharp ^{13}C peak for benzene. On the other hand, the proton-coupled ^{13}C spectrum is complicated [Figure 2(a)] because the ^{13}C nucleus is coupled to six protons, which are in turn strongly coupled to each other. Although the spectrum can be analyzed exactly by

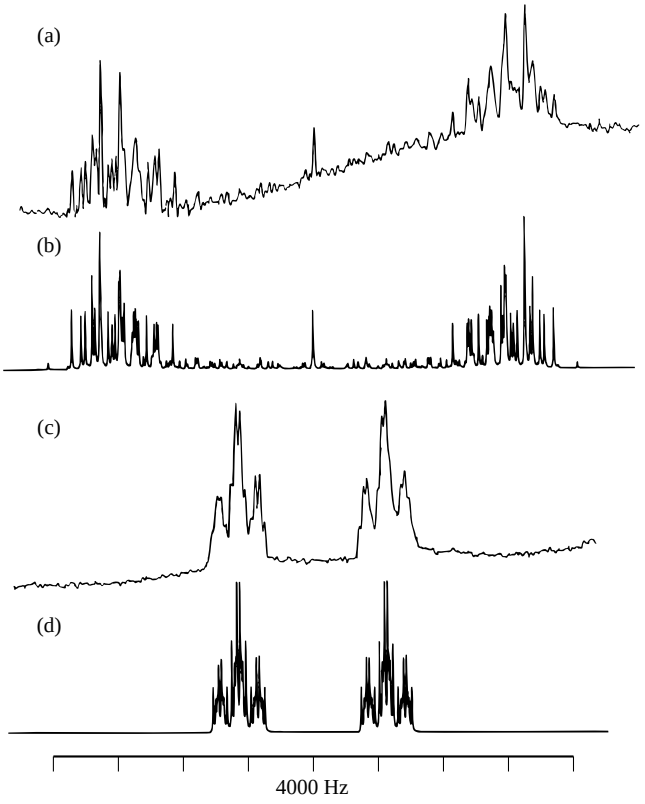

Figure 2 Carbon-13 NMR spectra of benzene dissolved in the liquid crystalline solvent ZLI 1167 at 75.43 MHz and 25°C. (a) Experimental spectrum without decoupling; the baseline is due to the solvent. (b) Calculated spectrum with complete $^1H-^1H$ and $^1H-^{13}C$ coupling. (c) Experimental spectrum with BLEW-48 decoupling and a decoupler power of 14 kHz. (d) Spectrum calculated by scaling the $^1H-^{13}C$ coupling constants obtained from case (b) and setting the $^1H-^1H$ dipolar coupling constants to zero

computer simulation [Figure 2(b)] due to the high symmetry of benzene, the spectral analyses for more complex molecules are practically intractable. This problem can be overcome by applying a special decoupling sequence to remove the $^1H-^1H$ dipolar coupling, so that the ^{13}C spectrum becomes first order in terms of $^{13}C-^1H$ coupling [Figure 2(c) and (d)].[42] Among several well known dipolar decoupling sequences introduced for the study of solids, it was found that the so-called 'BLEW-48' sequence[43] is the most effective one for liquid crystal systems.[44] The first-order splittings resulting from using a dipolar decoupling sequence is given by[45]

$$\Delta\nu = f[(3\cos^2\eta - 1)D + J] \qquad (6)$$

where f is a scaling factor determined by the $^1H-^1H$ dipolar decoupling sequence. For BLEW-48, the theoretical value is $f = 0.424$;[43] experimentally, the scaling factor varies slightly with the decoupler offset, and the best average value is $f = 0.420$.[42] Although the sign of $\Delta\nu$ cannot be determined from the spectra, several different possibilities can be distinguished by a consideration of the molecular geometry and the macroscopic orientation of the liquid crystal in the magnetic field. Thus, for the spectrum shown in Figure 2(c), the values of $\Delta\nu$ for the directly bonded and the *ortho* C–H pairs can be measured directly from the first-order splittings without computer simulation, and the corresponding values of D can be easily calculated by the use of equation (6). These values are the same as those obtained from a computer simulation of the spectrum [Figure 2(d)] within experimental error. This method is particularly useful for compounds with more complex structures, for which the completely coupled ^{13}C spectra are practically intractable by computer simulation.

For the ^{13}C spectra of bulk liquid crystals, there are many peaks in the spectra, and the $^{13}C-^1H$ splittings overlap with each other. To resolve the splitting pattern of each ^{13}C peak unambiguously, a two-dimensional (2D) method called separated local field (SLF) spectroscopy[46–49] can be applied. Like the MAS technique, the SLF method was first developed for solid state NMR. In this 2D method, the spin system is allowed to evolve with $^{13}C-^1H$ coupling and $^1H-^1H$ dipolar decoupling in the evolution period, so that information on dipolar coupling constants can be obtained from the ω_1 dimension. In the acquisition period, complete proton decoupling is applied, so that resolved peaks for individual carbon atoms can be obtained from the ω_2 dimension. Thus, 'slices' of the 2D spectra give clear splitting patterns for each chemically distinct ^{13}C peak, in the same way as the 'heteronuclear 2D J-resolved' method (see ***Two-Dimensional J-Resolved Spectroscopy***).

The first application of the SLF method to liquid crystals was the study of EBBA with the director aligned along the magnetic field.[38] However, because of the presence of large $^1H-^1H$ dipolar couplings which were not completely removed, the ^{13}C peaks in the ω_2 dimension were rather broad, and the splittings in the ω_1 dimension did not yield accurate $^{13}C-^1H$ dipolar coupling constants. Later on, the application of the SLF method to study a static sample of an SmC* liquid crystal was also reported,[50] and a similar problem was encountered. In principle, increasing the decoupling power would alleviate this problem. However, it would create excessive rf heating and a large temperature gradient, which is not acceptable for liquid crystals.[22]

5 STUDY OF $^{13}C-^1H$ DIPOLAR COUPLINGS WITH VAS

Because the use of VAS can reduce dipolar couplings by a factor of $(3\cos^2\eta - 1)/2$ [equation (2)] or $-(3\cos^2\eta - 1)/4$ [equation (3)], a combination of VAS with the SLF method solves the problem of incomplete proton dipolar decoupling. For example, $(3\cos^2\eta - 1)/2 = 0.2$ for $\eta = 46.91°$, and a nominal decoupler power (20–25 kHz) is sufficient to obtain good $^1H-^1H$ dipolar decoupling with the use of the BLEW-48 sequence. It was shown that, for the application of the SLF method to EBBA, the use of VAS[51] yielded much better first-order spectra in the ω_1 dimension than the use of a static sample.[38]

As an example of the ^{13}C spectra obtained from the VAS/SLF technique, the spectra of 4-*n*-heptyl-4′-cyanobiphenyl (7CB) at 75 MHz and 31°C are shown in Figure 3.[52] It can be seen that all seven peaks in the aliphatic chain and all nine peaks in the mesogenic core are resolved in the ω_2 dimension. The spectra in the ω_1 dimension show first-order $^{13}C-^1H$ splittings. The CH_3 group exhibits a clear quartet, and each of the CH_2 groups exhibits a triplet, with discernible

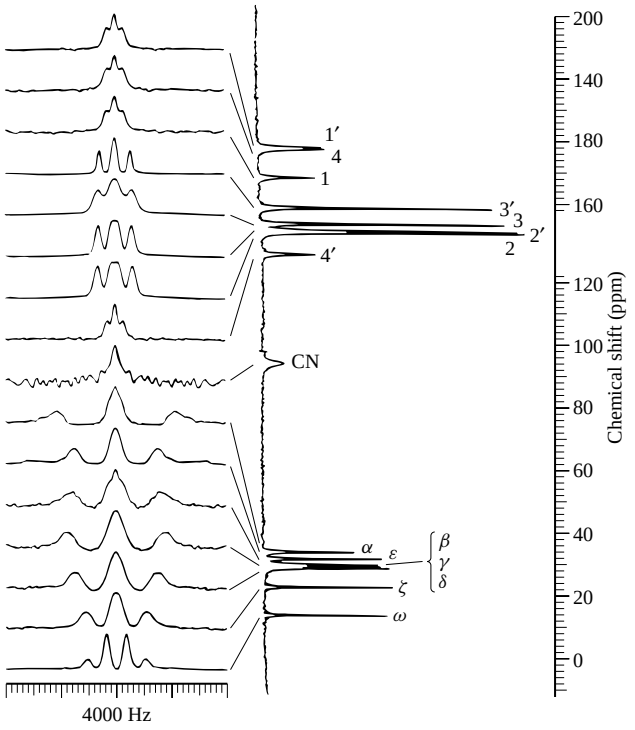

Figure 3 2D ^{13}C NMR spectra of 7CB at 75.43 MHz and 31°C obtained by the SLF/VAS method. The spectra were obtained with variable angle spinning at $\eta = 45.6°$. The spectra in the ω_1 dimension are shown on the left, and the first spectrum in the ω_2 dimension is shown on the right. (Reproduced by permission of the Royal Society of Chemistry from Foster and Fung[52])

long range splittings for the α- and β-carbons. Each peak for the quaternary carbons (1, 4, 1′, and 4′) in the phenyl rings is split into a triplet by the *ortho* protons, and each peak for the protonated carbons (2, 3, 2′, and 3′) is split into a doublet of doublets by the directly bonded and the *ortho* protons, respectively. Some of the peaks overlap slightly, but the values of $\Delta\nu$ can be readily obtained by least-squares analysis of the spectra. Then, the ^{13}C–^{1}H dipolar coupling constants can be evaluated by the use of equation (6), and the order parameters for the corresponding molecular segments can be calculated. The procedure for the calculation is briefly summarized in the following discussion.

In the nematic phase, each phenyl ring has an effective D_2 symmetry because it undergoes rapid jumps between four equilibrium positions. Therefore, two order parameters, S_{zz} and $S_{xx} - S_{yy}$, are sufficient to describe the orientational ordering of each ring. These order parameters are related to the dipolar coupling constant of each C–H pair in the ring by

$$D_{ij} = -\frac{\gamma_i \gamma_j h}{8\pi^2 r_{ij}^3}[(3\cos^2\theta_{ijz} - 1)S_{zz} + (\cos^2\theta_{ijx} - \cos^2\theta_{ijy}) \times (S_{xx} - S_{yy})] \quad (7)$$

where r_{ij} is the internuclear distance and $\theta_{ij\alpha}$ is the angle between r_{ij} and the molecular axis α. The twofold axis of the phenyl ring is taken as the z axis, and the axis perpendicular to the plane of the phenyl ring is taken as the y axis. Assuming that $r_{CC} = 0.140$ nm and $r_{CH} = 0.108$ nm, the order parameters and the bond angles can be calculated from least-squares fitting of a set of D values to equation (7). This procedure has been used to determine the order parameters of the phenyl rings in many liquid crystals.[45,52–67]

The situation is more complicated for phenyl rings with lateral substituents or compounds containing cyclohexyl rings, and more order parameters are needed to describe the orientational ordering of the rings. The cyclohexyl ring in a liquid crystal has a C_s symmetry, and an additional order parameter S_{xy} is needed to describe the orientational ordering of the ring. Unfortunately, the ^{13}C peaks in the ω_1 dimension are quite broad due to unresolved long range couplings.[55,56,66] Therefore, only approximate values of S_{zz} and $S_{xx} - S_{yy}$ were obtained by assuming $S_{xy} \approx 0$. A laterally substituted phenyl ring or a substituted cyclohexyl ring has no symmetry, and all five order parameters are nonzero.

The aliphatic chain has a large number of segmental motions, and it is difficult to define the order parameters for the whole chain. A simplified treatment can be made to define a C–H bond order parameter for each aliphatic segment, considering the C–H bond as having an approximate axial symmetry. Then, the order parameter for the C–H bond is related to the corresponding C–H dipolar coupling constant by

$$D = -\frac{\gamma_C \gamma_H h}{4\pi^2 r_{CH}^3} S_{CH} \quad (8)$$

in which the value of r_{CH} is generally assumed to be 0.110 nm.

The results for studying the orientational ordering of 5CB using the VAS/SLF technique have been compared with those obtained from deuterium NMR.[45] A good agreement was obtained, establishing the validity of the VAS/SLF method. This method has been further applied to investigate the orientational ordering of a large number of liquid crystals, including 4-*n*-alkyl-4′-cyanobiphenyls (*k*CBs, where *k* is the number of carbon atoms in the alkyl chain),[45,53,59,60] 4-*n*-alkoxy-4′-cyanobiphenyls (*k*OCBs),[54] phenylcyclohexanes,[52,55,56] bicyclohexylnitriles,[66] ferroelectric liquid crystals of the α-chloroesters of 4-alkoxy-4′-hydroxybiphenyls[57,61] and of 4′-hydroxyphenyl-4-alkoxythiobenzoates,[58] 4′-cyanophenyl-4-alkylcarboxylates,[62] 4-*n*-alkoxybenzylidene-4′-*n*-alkylanilines (*n*O.*m*s),[63] nematic compounds with four-unit links between two phenyl rings,[64,65] and liquid crystals with lateral substituents.[67]

6 APPLICATIONS COMBINING MEASUREMENTS OF CHEMICAL SHIFTS AND DIPOLAR COUPLINGS

It was mentioned in the Introduction that the use of equation (1) to determine the order parameters from anisotropic ^{13}C chemical shifts requires the knowledge of the components of the chemical shifts tensors in the axis system defining the ordering matrix. To avoid this difficulty but still take advantage of the simplicity and accuracy in the chemical shift measurement, an empirical approach has been suggested.[60] The method involves a determination of the order parameters of a liquid crystal at several temperatures by using the VAS/SLF technique as described in the previous section, and

a measurement of the ^{13}C chemical shifts for the same sample with slow spinning at $\eta = 0^\circ$. The order parameter S_{zz} for the phenyl rings or S_{CH} for the aliphatic chains is plotted against the corresponding ^{13}C chemical shifts, and it has been found that they are linearly related:

$$\delta^{obs} - \delta^{iso} = aS + b \quad (9)$$

where a and b are constants.[60] Although equation (9) is a result of equation (1), it is only an empirical relationship for the following reasons. A strict theoretical correspondence between the two equations implies that $a = 2[\sigma_{zz} - (\sigma_{xx} + \sigma_{yy})/2]/3$ and that the other order parameters are independent of temperature. The first condition requires the major axis of the chemical shift tensor to coincide with the z axis of the ring or the C–H axis in the chain. Although this is approximately true for the carbon atoms lying on the z axis of the phenyl rings, it is not necessarily so for other carbon atoms. Usually the second condition is approximately fulfilled because the values of $S_{xx} - S_{yy}$ are very small and vary randomly with temperature within experimental error, and S_{xy}, S_{xz}, and S_{yz} are zero for phenyl rings without lateral substituents. These approximations make equation (9) a semiempirical relationship; nevertheless, it has been found to work surprisingly well for many types of compounds.[60,62–65,67]

After the constants a and b in equation (9) have been determined from the experimental VAS/SLF data at several temperatures, the order parameter S at other temperatures can be calculated from the ^{13}C chemical shifts without the use of approximate values of the shift tensors estimated from model compounds. This method has several advantages. First, the chemical shifts can be obtained from 1D experiments, which require much less spectrometer and processing time than the 2D VAS/SLF method. Second, the chemical shifts can be determined more accurately than the dipolar coupling constants, and their systematic changes with temperature are less subjected to random experimental uncertainties. Third, investigators who do not have the VAS/SLF facility can obtain order parameters directly from ^{13}C chemical shifts using published values of a and b for other homologous compounds. Thus, although the order parameters determined from ^{13}C chemical shifts via the use of equation (9) is an indirect method, the study of their temperature dependence is greatly facilitated. Problems such as the effect of various solutes on the orientational ordering of liquid crystal solvents,[54] the order of phase transitions,[63] and the temperature dependence of the position of the major axis of the mesogenic core[64,65] can be studied more conveniently by this method.

7 RELAXATION

Because of the presence of orientational ordering, the translational and rotational motions of liquid crystals are highly anisotropic. As a result, their relaxation behavior is very different from that of isotropic liquids. Details of relaxation in liquid crystals are discussed in the articles by Hoatson (see ***Deuteron Relaxation Rates in Liquid Crystalline Samples: Experimental Methods***) and Nordio (see ***Liquid Crystalline Samples: Relaxation Mechanisms***). Examples of the study of ^{13}C relaxation are summarized below.

The earliest ^{13}C spin–lattice relaxation time (T_1) measurements reported were for 4,4′-azoxyanisole[68,69] and MBBA.[70] More recently, a comprehensive investigation of ^{13}C T_1 and nuclear Overhauser enhancement (NOE) of 4-*n*-alkyl-4′-cyanobiphenyls (*k*CBs; k = 5, 6, 7, and 8) as functions of temperature and at different resonance frequencies has been made by Lewis, Tomchuk, and co-workers.[71–73] They analyzed the results by considering angular fluctuations as well as director fluctuations, and concluded that at high fields the contribution of ^{13}C chemical shift anisotropy to relaxation is important, but cautioned that the quantitative analysis is not straightforward.

A better understanding of the dynamic behavior of liquid crystals can be obtained by investigating the relaxation of several kinds of nuclei in the same molecule. A small probe molecule, CH_3CN with ^{13}C enrichment, was used for such study by two groups of investigators.[74–78] Grant and co-workers measured the relaxation of ^1H and ^{13}C with non-, semi-, and completely selective excitation of individual spectral lines.[76,77] Later on, Luyten et al. carried out similar measurements, plus ^{14}N relaxation, at six different field strengths, and calculated the contributions of rotational anisotropy, random local field, and director fluctuation to the relaxation process.[78]

Multinuclei relaxation measurements including ^{13}C and other nuclei have also been made for lyotropic liquid crystal systems,[79] phospholipids,[29–31] and lead carboxylates.[80] The ^{13}C relaxation of an SmC* compound has been reported recently.[18]

8 CONCLUSIONS

In applying ^{13}C NMR to study liquid crystals, the major parameters of interest are anisotropic chemical shifts, $^{13}C–^1H$ dipolar coupling constants, and ^{13}C relaxation times. The advantages of ^{13}C NMR are its high resolution with regard to the chemical structure of the liquid crystal molecules, and the use of naturally abundant compounds without the need for special isotope substitution. However, macroscopic sample orientation is required to obtain resolvable ^{13}C peaks unless MAS is used. Therefore, ^{13}C NMR is not very informative for the study of unaligned samples generally found for higher smectic phases, discotic phases, and liquid crystal polymers. Furthermore, ^{13}C relaxation measurements do not offer as much information on relaxation mechanisms as ^2H relaxation measurements. Therefore, ^{13}C NMR and ^2H NMR complement each other, and both offer more detailed information than ^1H NMR in the study of liquid crystals.

9 RELATED ARTICLES

Anisotropy of Shielding and Coupling in Liquid Crystalline Solutions; Carbon and Nitrogen Chemical Shifts of Solid State Enzymes; Carbon-13 Relaxation Measurements: Organic Chemistry Applications; Complex Radiofrequency Pulses; Deuteron Relaxation Rates in Liquid Crystalline Samples: Experimental Methods; Liquid Crystalline Samples: Deuterium NMR; Liquid Crystalline Samples: Relaxation Mechanisms; Liquid Crystals: General Considerations; Membranes: Carbon-13 NMR; Shielding Tensor Calculations; Spinning Liquid Crystalline Samples.

10 REFERENCES

1. C. S. Yannoni and E. B. Whipple, *J. Chem. Phys.*, 1967, **47**, 2508.
2. I. Morishima, A. Mizuno, and T. Yonezawa, *Chem. Phys. Lett.*, 1970, **7**, 633.
3. B. R. Appleman and B. P. Dailey, *Adv. Magn. Reson.*, 1974, **7**, 231.
4. F. Millett and B. P. Dailey, *J. Chem. Phys.*, 1971, **54**, 5434.
5. G. Englert, *Z. Naturforsch. A*, 1972, **27**, 715.
6. B. M. Fung and P. Parhami, *J. Magn. Reson.*, 1985, **63**, 168.
7. S. Mohanty, *Chem. Phys. Lett.*, 1973, **18**, 581.
8. T. Väänänen, J. Jokisaari, and M. Seläntaus, *J. Magn. Reson.*, 1987, **72**, 414.
9. B. M. Fung, *J. Am. Chem. Soc.*, 1983, **105**, 5713.
10. B. M. Fung and C. F. Kong, *J. Am. Chem. Soc.*, 1984, **106**, 6193.
11. P. Parhami and B. M. Fung, *J. Am. Chem. Soc.*, 1985, **107**, 7304.
12. A. Pines and J. J. Chang, *J. Am. Chem. Soc.*, 1974, **96**, 5590.
13. A. Pines and J. J. Chang, *Phys. Rev. A*, 1974, **10**, 946.
14. A. Pines, D. J. Ruben, and S. Allison, *Phys. Rev. Lett.*, 1974, **33**, 1002.
15. C. A. Fyfe, J. R. Lyerla, and C. S. Yannoni, *J. Magn. Reson.*, 1978, **31**, 315.
16. R. Teeäär, M. Alla, and E. Lippmaa, *Org. Magn. Reson.*, 1982, **19**, 134.
17. M. Luzar, V. Rutar, J. Seliger, and R. Blinc, *Ferroelectrics*, 1984, **58**, 115.
18. A. Yoshizawa, A. Yokoyama, H. Kikuzaki, and T. Hirai, *Liq. Cryst.*, 1993, **14**, 513.
19. R. J. Wittebort, R. Subramanian, N. P. Kulshreshtha, and D. B. DuPré, *J. Chem. Phys.*, 1985, **83**, 2457.
20. F. Separovic, R. Pax, and B. Cornell, *Mol. Phys.*, 1993, **78**, 357.
21. R. Stannarius and H. Schmiedel, *J. Magn. Reson.*, 1985, **65**, 1.
22. B. M. Fung, *J. Magn. Reson.*, 1990, **86**, 160.
23. B. M. Fung and M. Gangoda, *J. Chem. Phys.*, 1985, **83**, 3285.
24. K. Hayamizu, M. Yanagisawa, and O. Yamamoto, *Chem. Phys. Lett.*, 1986, **127**, 566.
25. T. Kato and T. Uryu, *Mol. Cryst. Liq. Cryst. Lett.*, 1987, **5**, 17.
26. K. Hayamizu, M. Yanagisawa, and O. Yamamoto, *Liq. Cryst.*, 1989, **4**, 273.
27. M. Bose and S. Sanyal, *Mol. Cryst. Liq. Cryst.*, 1990, **185**, 115.
28. J. Afzal and B. M. Fung, *J. Chem. Phys.*, 1986, **84**, 6119.
29. J. Forbes, J. Bowers, X. Shan, L. Moran, E. Oldfield, and M. A. Moscarello, *J. Chem. Soc., Faraday Trans. 1*, 1988, **84**, 3821.
30. E. Oldfield, F. Adebodun, J. Chung, B. Montez, K. D. Park, H. B. Le, and B. Phillips, *Biochemistry*, 1991, **30**, 11025.
31. F. Adebodun, J. Chung, B. Montez, E. Oldfield, and X. Shan, *Biochemistry*, 1992, **31**, 4502.
32. K. L. Li, C. A. Tihal, M. Guyo, and R. E. Stark, *Biochemistry*, 1993, **32**, 9926.
33. J. Courtieu, D. W. Alderman, D. M. Grant, and J. P. Bayle, *J. Chem. Phys.*, 1982, **77**, 723.
34. J. Courtieu, J. P. Bayle, and B. M. Fung, *Prog. Nucl. Magn. Reson. Spectrosc.*, 1994, **26**, 141.
35. R. A. Wise, A. Olah, and J. W. Doane, *J. Phys. (Paris) Colloq.*, **1975**, 117.
36. R. Y. Dong, *Mol. Cryst. Liq. Cryst.*, 1981, **72**, 59.
37. M. L. Magnuson and B. M. Fung, *J. Chem. Phys.*, 1994, **100**, 1470.
38. A. Höhener, L. Muller, and R. R. Ernst, *Mol. Phys.*, 1979, **38**, 909.
39. M. L. Magunson and B. M. Fung, *Liq. Cryst.*, 1994, **16**, 857.
40. C. R. Sanders II and J. H. Prestegard, *J. Am. Chem. Soc.*, 1991, **113**, 1987; D. Sandström, K. T. Summanen, and M. H. Levitt, *J. Am. Chem. Soc.*, 1994, **116**, 9357.
41. E. J. Delikatny and E. E. Burnell, *Mol. Phys.*, 1989, **67**, 757.
42. B. M. Fung, *J. Magn. Reson.*, 1986, **66**, 525.
43. D. P. Burum, N. Linder, and R. R. Ernst, *J. Magn. Reson.*, 1981, **44**, 173.
44. B. M. Fung, *J. Magn. Reson.*, 1987, **72**, 353.
45. B. M. Fung, J. Afzal, T. Foss, and M.-H. Chau, *J. Chem. Phys.*, 1986, **85**, 4808.
46. J. S. Waugh, *Proc. Natl. Acad. Sci. USA*, 1976, **73**, 1394.
47. R. K. Hester, J. L. Ackerman, B. L. Neff, and J. S. Waugh, *Phys. Rev. Lett.*, 1976, **36**, 1081.
48. J. S. Waugh and S. J. Opella, *J. Chem. Phys.*, 1977, **66**, 4919.
49. E. R. Rybaczewski, B. L. Neff, J. S. Waugh, and J. S. Sherfinsky, *J. Chem. Phys.*, 1977, **67**, 1231.
50. C. D. Poon and B. M. Fung, *Liq. Cryst.*, 1989, **5**, 1159.
51. B. M. Fung and J. Afzal, *J. Am. Chem. Soc.*, 1986, **108**, 1107.
52. P. Foster and B. M. Fung, *J. Chem. Soc., Faraday Trans. 2*, 1988, **84**, 1083.
53. B. M. Fung, C. D. Poon, M. Gangoda, E. L. Enwall, T. A. D. Diep, and C. Bui, *Mol. Cryst. Liq. Cryst.*, 1986, **141**, 267.
54. C. D. Poon, C. M. Wooldridge, and B. M. Fung, *Mol. Cryst. Liq. Cryst.*, 1988, **157**, 303.
55. C. B. Frech, B. M. Fung, and M. Schadt, *Liq. Cryst.*, 1988, **3**, 713.
56. C. B. Frech, B. M. Fung, and M. Schadt, 1989, *SPIE Proc.*, 1989, **1080**, 215.
57. C. D. Poon and B. M. Fung, *J. Chem. Phys.*, 1989, **91**, 7392.
58. W. Richter, D. Reimer, B. M. Fung, R. J. Twieg, and K. Betterton, *Liq. Cryst.*, 1990, **8**, 687.
59. W. Guo and B. M. Fung, *Liq. Cryst.*, 1991, **9**, 117.
60. W. Guo and B. M. Fung, *J. Chem. Phys.*, 1991, **95**, 3917.
61. M.-S. Ho, B. M. Fung, M. Wand, and R. T. Vohra, *Ferroelectrics*, 1993, **138**, 51.
62. N. S. Balakrishnan, J. P. Bayle, M.-S. Ho, S. C. Pham, and B. M. Fung, *Liq. Cryst.*, 1993, **14**, 591.
63. B. M. Fung, M. L. Magnuson, T.-H. Tong, and M.-S. Ho, *Liq. Cryst.*, 1993, **14**, 1495.
64. J. P. Bayle, M.-S. Ho, and B. M. Fung, *New J. Chem. (Paris)*, 1993, **17**, 345.
65. J. P. Bayle and B. M. Fung, *Liq. Cryst.*, 1993, **15**, 87.
66. W. Richter, B. M. Fung, and M. Schadt, *Liq. Cryst.*, 1990, **8**, 63.
67. J. P. Bayle, P. Berdagné, M.-S. Ho, and B. M. Fung, *New J. Chem. (Paris)*, 1994, **18**, 715.
68. M. Schwartz, P. E. Fagerness, C. H. Wang, and D. M. Grant, *J. Chem. Phys.*, 1974, **60**, 5066.
69. K. Hayamizu and O. Yamamoto, *Bull. Chem. Soc. Jpn.*, 1977, **50**, 1295.
70. H. Hutton, E. Bock, E. Tomchuk, and R. Dong, *J. Chem. Phys.*, 1978, **68**, 940.
71. J. S. Lewis, J. Peeling, E. Tomchuk, W. Danchura, J. Bozek, H. M. Hutton, and E. Bock, *Mol. Cryst. Liq. Cryst.*, 1987, **144**, 57.
72. J. S. Lewis, E. Tomchuk, and E. Bock, *Liq. Cryst.*, 1989, **5**, 1033.
73. J. S. Lewis, E. Tomchuk, and E. Bock, *Liq. Cryst.*, 1993, **14**, 1507.
74. H. A. L. Cardozo, J. Bulthuis, and C. MacLean, *J. Magn. Reson.* 1979, **33**, 27.
75. H. A. L. Cardozo, J. Bulthuis, J. H. Freed, and W. M. M. J. Bovée, *Chem. Phys. Lett.*, 1979, **60**, 335.

76. J. Courtieu, N. T. Lai, C. L. Mayne, J. M. Bernassau, and D. M. Grant, *J. Chem. Phys.*, 1982, **76**, 257.
77. E. P. Black, J. M. Bernassau, C. L. Mayne, and D. M. Grant, *J. Chem. Phys.*, 1982, **76**, 265.
78. P. R. Luyten, J. Bulthuis, W. M. M. J. Bovée, and L. Plomp, *J. Chem. Phys.*, 1983, **78**, 1712.
79. O. Söderman, H. Walderhaug, U. Henriksson, and P. Stilbs, *J. Phys. Chem.*, 1985, **89**, 3693.
80. G. Feio, H. D. Burrows, C. F. G. C. Geraldes, and T. J. T. Pinheiro, *Liq. Cryst.*, 1991, **9**, 417.

Biographical Sketch

Bing M. Fung. *b* 1939. 1963, Diploma, Chung Chi College (now Chinese University of Hong Kong). Ph.D., 1967, California Institute of Technology. Faculty at the University of Oklahoma, 1972–present. Approx. 160 publications. Research interests include NMR study and synthesis of liquid crystals.

Liquid Crystalline Samples: Deuterium NMR

Ronald Y. Dong
Brandon University, Brandon, Manitoba, Canada

1	Introduction	1
2	Orientational Ordering	2
3	Spin Relaxation and Molecular Motion	4
4	Novel NMR Experiments	6
5	Related Articles	7
6	References	8

1 INTRODUCTION

Rowell and co-workers[1,2] were first to demonstrate that deuterium is an excellent spin probe for studying liquid crystalline samples. They also used selectively deuterated compounds to simplify the proton NMR spectra. Early work in this field was devoted to measuring and interpreting spin–lattice relaxation rates[3] of protons, and to revealing orientational ordering in various mesophases[4] by means of deuterium splittings and spectral patterns. While proton NMR of liquid crystals shows broad partially resolved spectra, the deuteron NMR spectra are often characterized by well resolved quadrupolar doublets[5,6] that may contain some dipolar fine structures [Figure 1(a)]. The deuteron ($I = 1$) Zeeman levels [Figure 1(b)] are perturbed by interaction of its nuclear quadrupolar moment Q with the asymmetric EFG at the deuteron site. The static Hamiltonian $\hat{\mathcal{H}}_0$ of the system is defined by

$$\hat{\mathcal{H}}_0 = \hat{\mathcal{H}}_Z + \langle \hat{\mathcal{H}}_Q(t) \rangle \tag{1}$$

where $\hat{\mathcal{H}}_Z$ is the Zeeman Hamiltonian and $\hat{\mathcal{H}}_Q$, the quadrupolar Hamiltonian, is time dependent due to thermally driven, randomly fluctuating molecular processes. Due to a nonzero $\langle \hat{\mathcal{H}}_Q(t) \rangle$ in a partially ordered system, the two nuclear transitions are displaced at equal distances from the Larmor frequency ($\omega_0/2\pi$) as shown in Figure 1. The EFG tensor for most C–D bonds is axially symmetric, with the unique principal axis along the C–D bond direction. The quadrupolar splitting for a static C–D bond can take a maximum value of $\frac{3}{2}\chi$ or about 260 kHz, which is much less than its Larmor frequency of 46 MHz in a magnetic field of 7.1 T. For comparison, dipolar splitting between two deuterons in a methylene group is at most a few kilohertz, D–H dipolar splitting for a similar geometry is about 10 kHz, and the chemical shift is of the order of 1 kHz. It is therefore possible to neglect the chemical shift dispersion and the dipolar interaction with other nuclei and to treat the deuteron as an isolated spin-1 nucleus. The theoretical analysis of such a system is relatively simple. The quadrupolar splitting $\Delta\nu_i$ of the ith C–D bond may be approximated by[7,8]

$$\Delta\nu_i = \tfrac{3}{2}\chi S_{zz} \langle 3\cos^2\theta_i - 1 \rangle / 2 \tag{2}$$

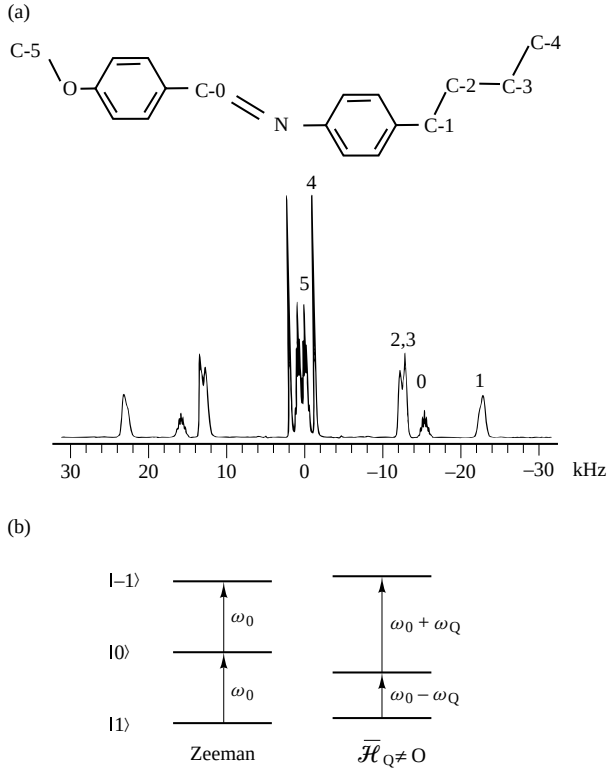

Figure 1 (a) The structure of MBBA and a typical deuterium NMR spectrum of MBBA-d_{13} in its nematic phase. (b) Energy level diagram of a deuteron spin ($\eta = 0$) in a large magnetic field. $\omega_0/2\pi$ is the Larmor frequency

where the contribution from the $S_{xx} - S_{yy}$ term is neglected, S_{zz} is the orientational order parameter of the long molecular axis with respect to the nematic director (see below), and θ_i represents the angle between the C_i–D bond and the molecular z axis. The angular brackets denote a statistical average over all allowed conformations in a flexible mesogen.

Spin relaxation has long been recognized as a useful technique for studying dynamic processes in liquid crystals.[7,8] A partial list of such processes[8] includes the order director fluctuations (ODFs), translational diffusion, order parameter fluctuations near phase transitions, molecular reorientation, and internal rotations of alkyl end chains. Deuteron is particularly suitable for getting detailed information about molecular motion in liquid crystals, since its relaxation is governed by intramolecular mechanisms, and multipulse techniques[7] may be used to determine individual spectral densities of motion from partially relaxed deuteron NMR spectra for all the resolved doublets. The quadrupolar relaxation Hamiltonian for a spin-1 system is defined by the time dependent part of $\hat{\mathcal{H}}_G(t)$ with respect to its average value $\langle \hat{\mathcal{H}}_Q(t) \rangle$:

$$\hat{\mathcal{H}}'_Q(t) = \hat{\mathcal{H}}_Q(t) - \langle \hat{\mathcal{H}}_Q(t) \rangle \tag{3}$$

The deuterium spin–lattice relaxation rates are given by[9,12]

$$\begin{aligned} \frac{1}{T_{1Z}} &= J_1(\omega_0) + 4J_2(2\omega_0) \\ \frac{1}{T_{1Q}} &= 3J_1(\omega_0) \end{aligned} \tag{4}$$

where an axially symmetric quadrupolar interaction ($\eta = 0$) is assumed. The spectral densities of motion $J_{m\mathrm{L}}$ ($m_\mathrm{L}\omega_0$) are Fourier transforms of the autocorrelation functions $G_{m_\mathrm{L}}(t)$ which involve second-rank tensor components $D^2_{m_\mathrm{L}0}(\Omega(t))$ in the relaxation Hamiltonian. The part of $\hat{\mathcal{H}}'_\mathrm{Q}(t)$ that connects spin states with $\Delta m_I = 1$ has a fluctuation spectrum described by $J_1(\omega_0)$, while the part that connects states with $\Delta m_I = 2$ is described by $J_2(2\omega_0)$. These spectral parameters and $J_0(0)$ at zero frequency (obtained in principle from one quantum spin echo or quadrupolar echo experiments) are determined without a particular choice of motional model. They must be accurately measured as a function of temperature at different Larmor frequencies, and may be used to provide critical tests of any proposed model of molecular motion. For systems with coupled deuterons, there are additional terms[13,14] in the relaxation expressions that arise from cross-correlation functions describing pairwise correlation in the motion of EFG tensor components at each deuteron. This additional information may serve as a further check of the proposed motional model.

2 ORIENTATIONAL ORDERING

One of the common features in liquid crystals is the existence of a preferred orientation of molecules along a spatial direction specified by a unit vector known as the director ***n***. Deuteron NMR spectroscopy has played a major role in establishing molecular field theories[8,15,16] for liquid crystals. These mean field theories can predict the temperature dependences of order parameters of rigid solutes and solvent molecules. The ordering of molecules in mesophases may in general be described by an orientational distribution function $f(\Omega)$ which depends on Eulerian angles $\Omega(\equiv \phi, \theta, \psi)$. The $f(\Omega)$ can be expanded in terms of Wigner rotation matrices of rank L

$$f(\Omega) = \sum_{L=0}^{\infty} \sum_{m,m'=-L}^{L} \frac{2L+1}{8\pi^2} a_{Lm'm} D^L_{m'm}(\Omega) \qquad (5)$$

where the expansion coefficients $a_{Lm'm} = \langle D^{L*}_{m'm}(\Omega)\rangle$ are the microscopic order parameters of rank L. The order parameters of rank two and four can in principle be measured, but higher rank order parameters are not as easily accessible by experiments. The potential of mean torque $V(\Omega)$ can be defined by writing $f(\Omega)$ as

$$f(\Omega) = \exp[-\beta V(\Omega)] / \int \mathrm{d}\Omega \exp[-\beta V(\Omega)] \qquad (6)$$

where $\beta = 1/k_\mathrm{B}T$. $V(\Omega)$ represents the orientational potential of a single molecule. In the Maier–Saupe theory[17,18] of nematics, $V(\Omega)$ takes on a simple form:

$$V(\cos\theta) = -\epsilon \langle P_2(\cos\theta)\rangle P_2(\cos\theta) \qquad (7)$$

where the parameter ϵ scales the strength of intermolecular interaction. The theory used a mean field approach and assumed that attractive dispersion forces among molecules are responsible for the nematic order. It was successful in predicting a first-order phase transition between a nematic and an isotropic phase, as well as the temperature dependence of the nematic order parameter $\langle P_2\rangle$ ($\equiv S_{zz}$). Using equation (2) as a first approximation, $\langle P_2\rangle$ can be calculated[1,2] from the observed quadrupolar splittings in liquid crystals. A general set of 25 rank-two order parameters[8] was defined by Saupe:

$$S^{\alpha\beta}_{ij} = \tfrac{1}{2}\langle 3 i_\alpha j_\beta - \delta_{\alpha\beta}\delta_{ij}\rangle \qquad (8)$$

where (α,β) refer to a space-fixed axis system (X,Y,Z), (i,j) refer to a molecule-fixed axis system (x,y,z), i_α denotes the projection of a unit vector ***i*** along the α axis, and the angular brackets represent an ensemble average. For uniaxial phases where ***n*** $\parallel Z$ axis, equation (8) gives the simple Saupe order matrix S_{ij} ($= \frac{1}{2}\langle 3 i_z j_z - \delta_{ij}\rangle$).

2.1 Rigid Molecules in Uniaxial Phases

For a rigid molecule (or a rigid fragment of a molecule) ordered in a uniaxial liquid crystalline phase, the partially averaged component ($\langle A_\parallel\rangle$) parallel to the director of any second rank tensor ***A*** is given by

$$\langle A_\parallel\rangle = A_0 + \tfrac{2}{3}\sum_{ij} A_{ij} S_{ij} \qquad (9)$$

where A_0 is the isotropic average of ***A***. For the EFG tensor ***q***, A_0 is zero and the splitting $\Delta\nu = \frac{3}{2}e^2Q/h\langle q_\parallel\rangle$ can be calculated using equation (9). The unknown S_{ij} elements can be determined from measuring enough independent values of $\langle q^i_\parallel\rangle$ where the superscript refers to sites in a molecule. This is usually possible for a rigid solute dissolved in a liquid crystal, where the principal axes of symmetry of the solute may be located with certainty based on its molecular symmetry. Hence deuterium NMR can provide precise measurements of S_{zz} and $S_{xx} - S_{yy}$ for a rigid molecule. Figure 2 illustrates the determination of $S_{xx} - S_{yy}$ and S_{zz} for anthracene-d_{10} in several nematogens. The solid curves are predictions based on the mean field theory of biaxial solutes where the λ parameter is a measure of the deviation in molecular symmetry of the solute from cylindrical symmetry. That the solute ordering depends on the solvent is an indication that the solute–solvent interactions cannot be dominated only by dispersion forces. For flexible mesogens, it may be possible to determine a local order matrix for a rigid fragment of the molecule provided the principal axes can be located on the fragment based on its symmetry. This is often difficult due to a lack of measurable nuclear couplings. A clear exception to this is the study of a perdeuterated fluorene group in the mesogen 2-fluorenyl-4′-tetradecyloxy benzoate-d_9 (FLOG$_4$).[20] Because of the large number (eight) of distinct deuteron sites, the location of the long molecular axis could be adjusted for the average conformer in a frame fixed to the fluorene group, and the local order parameters were unambiguously determined.

2.2 Flexible Molecules in Uniaxial Phases

Mesogenic molecules are usually composed of an aromatic core and one or more flexible alkyl chains. Due to internal

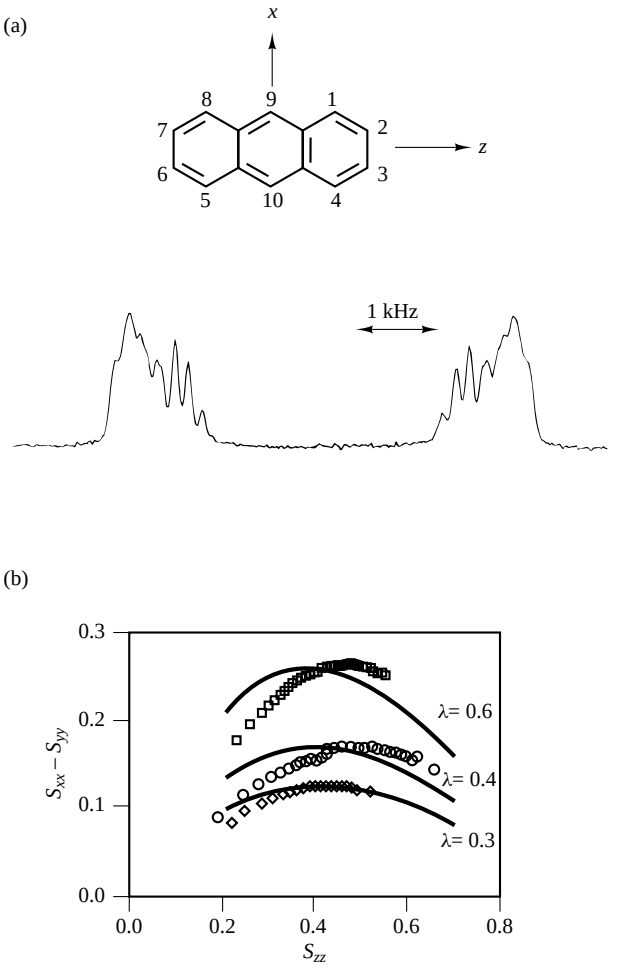

Figure 2 (a) Molecular structure of anthracene-d_{10} and the deuterium spectrum at 30.7 MHz from deuterons 1, 4, 5, 8, 9, and 10 in anthracene-d_{10} dissolved in Phase V. (b) Variation of S_{zz} with $S_{xx} - S_{yy}$ for anthracene-d_{10} dissolved in ZLI 1167 (□), E9 (○) and Phase V (◇).[19]

rotations, the chain does not always exist in an all-*trans* conformation. It is generally accepted that a single order tensor may not be enough to describe orientational ordering of different configurations. In equation (9), the average of $A_{\|}$ must also be carried out over an ensemble of molecules having all allowed configurations. The rotational isomeric state (RIS) model of Flory[21] is used to generate all chain configurations. Since a single $A_{\|}$ value would not provide quantitative information on the orientational order of the molecules, a molecular model is therefore required. Such a model using the additive potential method[15–19] was pioneered by Marcelja and later improved by Emsley and Luckhurst. The potential of mean torque which is responsible for the alignment of a conformer has its origin from the molecular field of its neighbors. It is constructed by adding up local interaction tensors of the carbon–carbon segments and the rigid aromatic core segment, which are specified by model parameters X_c and X_a, respectively. Each rigid (nth) conformer has its own order matrix $\mathbf{S}^n$ and its equilibrium probability of occurrence $P_{eq}(n)$. Equilibrium statistical mechanics is used to do the ensemble average in calculating the quadrupolar splittings $\Delta\nu_i$. The parameters X_c, X_a and E_{tg} (the energy difference between a *gauche* and a *trans* state) are varied to optimize the fits to the

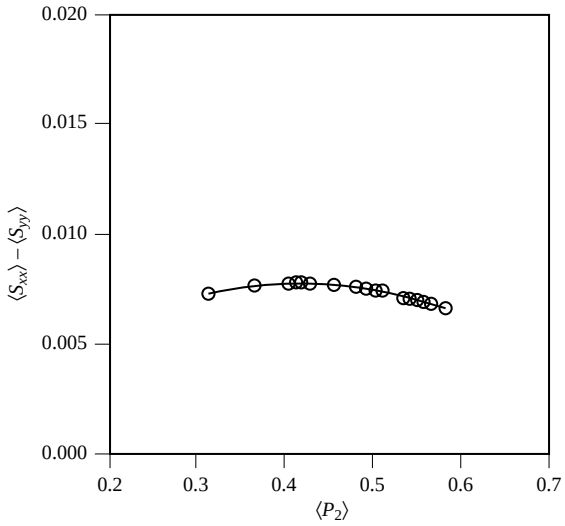

Figure 3 Plot of $\langle P_2\rangle$ versus $\langle S_{xx}\rangle - \langle S_{yy}\rangle$ for the averaged MBBA molecule.[22]

experimental splittings.[8] For example, such analysis[22] has been carried out for the splittings of MBBA (Figure 1). Knowing $S^n_{\alpha\beta}$ and $P_{eq}(n)$, it is possible to find a conformationally average order matrix $\langle\mathbf{S}\rangle$ by doing the statistical average in a common molecular frame. The principal components $\langle P_2\rangle$ and $\langle S_{xx}\rangle - \langle S_{yy}\rangle$ of the 'average' molecule can be obtained by diagonalizing the $\langle\mathbf{S}\rangle$ matrix. Figure 3 shows the plot of $\langle S_{xx}\rangle - \langle S_{yy}\rangle$ versus $\langle P_2\rangle$ of MBBA. It is interesting to note that the molecular biaxial order parameter, $\langle S_{xx}\rangle - \langle S_{yy}\rangle$, of the 'average' molecule is quite small for this flexible mesogen.

2.3 NMR in Biaxial Phases

Biaxial nematics, some smectic phases, such as S_G, and certain discotic phases[8] show phase biaxiality. Deuterium NMR may be used to detect phase biaxiality through the measurement of a nonzero motionally induced asymmetry parameter η^{LC} in the nuclear quadrupolar interaction whose EFG may have $\eta = 0$ in the solid state. Suppose that the molecule is rigid and the principal axes (X,Y,Z) of the liquid crystalline phase are chosen to coincide with the principal axes of the average EFG tensor. Letting the polar angles of the magnetic field in the (X,Y,Z) system be (θ_0, ϕ_0), the splitting is given by[8]

$$\delta\nu(\theta_0,\phi_0) = \tfrac{3}{4}\chi^{LC}\{(3\cos^2\theta_0 - 1) + \eta^{LC}\sin^2\theta_0\cos 2\phi_0\} \quad (10)$$

where χ^{LC}, a motionally averaged quadrupole coupling constant, and η^{LC} are defined by

$$\chi^{LC} = \chi\sum_m \overline{D^2_{0,m}(\theta,\psi)}D^2_{m,0}(\beta,\alpha)$$
$$\eta^{LC} = \sqrt{\tfrac{3}{2}}\frac{\chi}{\chi^{LC}}\sum_m[\overline{D^2_{2,m}(\phi,\theta,\psi)} + \overline{D^2_{-2,m}(\phi,\theta,\psi)}]D^2_{m,0}(\beta,\alpha) \quad (11)$$

where (ϕ,θ,ψ) are Euler angles that transform between a molecular frame (x,y,z) and the liquid crystalline (X,Y,Z)

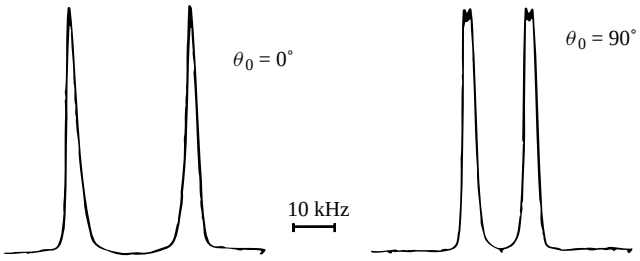

Figure 4 Experimental angular dependence of the deuterium NMR spectrum in the S_G phase of 5O.7-d_4 (aniline ring deuterated) at 31 °C.[24]

frame, and (β,α) are the polar angles of the C–D bond in the molecular frame. Phase biaxiality is reflected by $\overline{D^2_{\pm 2,m}}$ in η^{LC}, and the effect of η^{LC} on $\Delta\nu$ is maximum when the director is oriented normal to the magnetic field (i.e. $\theta_0 = 90^\circ$). It is noted that symmetry considerations involving both the nature of the molecules and of the liquid crystalline phases can considerably simplify the evaluation of the order parameters $\overline{D^2_{m',m}(\phi, \theta, \psi)}$. η^{LC} takes on a simple form if the (x,y,z) frame is chosen to be the principal frame of the order matrix. Further simplification can be made if the molecule is a cylindrical rod [$m = 0$ in equation (11)]. Then

$$\chi^{LC} = \chi S^{ZZ}_{zz}(3\cos^2\beta - 1)/2$$

$$\eta^{LC} = \sqrt{\tfrac{3}{2}}[\overline{D^2_{2,0}} + \overline{D^2_{-2,0}}]/S^{ZZ}_{zz} = (S^{XX}_{zz} - S^{YY}_{zz})/S^{ZZ}_{zz} \quad (12)$$

The $S^{XX}_{zz} - S^{YY}_{zz}$ term represents anisotropic fluctuations of the molecular z axis relative to the principal axes (X,Y,Z) of the average EFG tensor. Edge singularities (Figure 4) are predicted for the spectral pattern when $\theta_0 \neq 0$. The separation between edge singularities at $\theta_0 = 90^\circ$ is a direct measure of η^{LC}. Such a spectral pattern was first observed in an S_G phase[23] with a deuterated solute in the mesogen 6O.6. A η^{LC} value of 0.2 was obtained[24] in the S_G phase of 5O.7-d_4 (Figure 4). Phase biaxiality had been investigated in other smectic phases by Doane[25] and in discotics by Luz.[26]

3 SPIN RELAXATION AND MOLECULAR MOTION

Both nuclear spin–lattice and spin–spin relaxation rates are governed by random motion of spin-bearing molecules. Typically, a molecule remains in one state of motion for a short time (10^{-10}–10^{-12} s). After this time, it suffers a collision with one of its neighbors, which changes its state of motion. When the molecule persists in some state of motion for a time of 10^{-10} s, its motional frequency spectrum is expected to contain components ranging from zero to 10^{10} Hz, which are covered by typical NMR experiments. Several dynamic processes are known to cause deuteron spin relaxation in liquid crystals. The process known as director fluctuations is unique to liquid crystals and was first used to explain light scattering from liquid crystals. Other processes include order parameter fluctuations, molecular reorientation, and internal rotations. The latter two motions involve individual molecules as in normal liquids, while director fluctuations involve collective motions of a large number of molecules. These collective motions are influenced by macroscopic properties like elastic constants and anisotropic viscosities of the liquid crystalline medium. At best, director fluctuations can provide indirect information on the anisotropic interactions among molecules. On the contrary, molecular motion must reflect the shape of the instantaneous potential of mean torque on each molecule. Thus, it is sensitive to the nature of anisotropic interactions. Here, spin relaxation due to small cross terms between different processes will be ignored[8] for simplicity.

3.1 Solute Dynamics

To avoid dealing with internal rotations, deuterated rigid solutes dissolved in thermotropic liquid crystals were studied[7,27] by spectral density measurements. Solute reorientation and director fluctuations were used to account for the observed frequency and temperature dependences of $J_1(\omega)$ and $J_2(2\omega)$. It is now well known that director fluctuations under the small-angle approximation produce a characteristic $\omega^{-1/2}$ dependence in $J_1(\omega)$ only. Reorientation motion is often described in terms of a symmetric top reorienting in an anisotropic potential of Maier–Saupe type using a small-step rotational diffusion model.[8] This model uses a rotational diffusion tensor for the molecule which is diagonalized in a molecule-fixed frame. For weakly ordered solutes, their reorientation in a nematic solvent is often rapid to give frequency-independent spectral densities. For example, deuteron spin relaxation of p-diethynylbenzene (DEB-d_2, deuterated in the two alkynic sites) in the nematic phase of Phase V[7] clearly showed that $J_1(\omega)$ has a pronounced frequency dependence, while $J_2(2\omega)$ is essentially independent of frequency. This observation provides compelling evidence of director fluctuations in relaxing the deuterons in DEB-d_2. Smectic phases can be used to provide higher ordering of solute molecules. Similar frequency behaviors for J_1 and J_2 were obtained for DEB-d_2 in the four mesophases of 4O.8. However, J_2 showed more frequency dependence when DEB-d_2 was dissolved in 8CB.[8] A definitive explanation of the differences in these J_2 values has not yet been found. In general, analyses of experimental spectral density data would lead to rotational diffusion constants (or rotational correlation times $\tau_\parallel$, $\tau_\perp$) and a material factor A_{DF} that characterizes the strength of director fluctuations. For example, the ratio $\tau_\perp/\tau_\parallel$ is about 10 for DEB-d_2 in the nematic phase of Phase V.

3.2 Solvent Dynamics

The detection of director fluctuations in liquid crystals by means of deuteron spin relaxation in mesogens at conventional frequencies (10–50 MHz) has not met with success. This can be attributed to two factors: (1) the numerical value A_{DF} is small because most C–D bonds are oriented at an unfavorable angle to the long molecular axis; this is true for aromatic deuterons in mesogens such as 4-pentyl-4′-cyanobiphenyl (5CB), MBBA, etc., and (2) the contribution from director fluctuations to deuteron relaxation is masked by a much larger contribution due to relatively slow motions of large, sluggish molecules and fast internal motions within these molecules. To alleviate the difficulty associated with a small contribution from director fluctuations in the megahertz region, deuteron field cycling techniques have been applied[28]

to several nematogens. The techniques involve fast switching of the Zeeman field between high- and low-field levels so that detection of the NMR signal is done at a high magnetic field while the spin system is allowed to relax in a low field (in the kilohertz region). These data seem to support the findings based on the proton field cycling studies of liquid crystals that director fluctuations are slow motional processes and are effective for spin relaxation only in the kilohertz region.

To treat deuteron spin relaxation of solvent molecules in the megahertz region it is often possible to ignore the small contribution from director fluctuations. This assumption is probably necessary in modeling spectral densities of motion for various deuterated sites in flexible mesogens. In particular, correlated internal rotations in flexible chains of liquid crystals are complex to treat theoretically. Furthermore, different motional models[8] for reorientation of solvent molecules are possible. Besides the commonly used small-step rotational diffusion model, the anisotropic viscosity model of Freed and co-workers[8] is a distinct alternative. Freed used a rotational diffusion tensor that is diagonalized in the director frame to reflect the anisotropic viscosity of the liquid crystalline medium. Another motional model known as the 'third-rate' model is a simple extension of the Freed model. It has a fast rotation around the long molecular axis in addition to its motions around and toward the director. Numerous deuteron relaxation studies have been carried out in recent years to investigate molecular motion in liquid crystals. Table 1 briefly summarizes thermotropic liquid crystals in which spectral density measurements were reported.

As an example, the spectral density data of MBBA at 15.3 and 46 MHz are reproduced in Figure 5. The data are typical for thermotropic liquid crystals studied thus far. Both $J_1(\omega)$ and $J_2(2\omega)$ decrease with increasing temperature and are frequency dependent with a weaker dependence in $J_2(2\omega)$. To account for the observed site dependences of $J_1(\omega)$ and $J_2(2\omega)$, a model is required to treat internal motions in the butyl chain. A superimposed rotations model[33] was used to describe fluctuations in the orientations of the C–D bonds due to overall and internal modes of motion in the chain-deuterated nematogen 5CB. Here the internal dynamics of the pentyl chain was treated by assuming that rotations about each C–C bond are independent of each other and could be superimposed onto the rotational diffusion of the whole molecule. This motional model is, however, unrealistic and inconsistent with how quadrupolar splittings were modeled using the RIS model of Flory. The RIS model has been extended[42–44] to the time domain for liquid crystalline samples. A master equation may be used to describe transitions among all allowed configurations in the alkyl chain. The model of Nordio and co-workers[44] is inherently complex because their master equation includes configuration dependent frictional effects. The solution of the rotational diffusion problem requires a matrix representation in the full space of angular and site functions. Because of the large dimensionality of their matrix representation, the computational effort was extremely demanding. The decoupled model[42] of Dong uses three phenomenological rate constants to describe elementary jump modes: one-bond (k_1), two-bond (k_2), and three-bond (k_3) motions. The dimension of the rate matrix which is constructed in terms of these jump rate constants has the advantage of being much smaller. Both approaches,[34,42–44] however, give similar theoretical predictions for 5CB regarding site and frequency dependences of $J_1(\omega)$ and $J_2(\omega)$ as well as the observed discontinuity[33] in the spin–lattice relaxation rates at the nematic–isotropic phase transition.

The decoupled model has been successfully applied[22] to interpret the spectral densities of methylene deuterons (Figure 5) in MBBA, which are given by

$$J^{(i)}_{m_L}(m_L\omega) = \frac{3\pi^2}{2}\chi_i^2 \sum_{m_M}\sum_{n=1}^{27} c_{m_L m_M} \Big| \sum_{l=1}^{27} d^2_{m_M 0}(\beta^{(i)l}_{M,Q}) \exp[-i m_M \alpha^{(i)l}_{M,Q}] x_l^{(1)} x_l^{(n)} \Big|^2 \sum_j a^{(j)}_{m_L m_M} [(\tau^{(j)}_{m_L m_M})^{-1} + |\lambda_n|] / \{(m_L\omega)^2 + [(\tau^{(j)}_{m_L m_M})^{-1} + |\lambda_n|]^2\} \quad (13)$$

where $\beta^{(i)l}_{M,Q}$ and $\alpha^{(i)l}_{M,Q}$ are the polar angles of the C-i–D bond of the conformer l (there are 3^3 conformers in the butyl chain when the first dihedral angle at the junction of the aniline ring is allowed to sample three RISs) in a molecule-fixed frame whose z_M axis is along the ring *para* axis, λ_n and $\boldsymbol{x}^{(n)}$ are the eigenvalues and eigenvectors from diagonalizing a symmetrized rate matrix, $c_{m_L m_M}$ are the mean square of the Wigner rotation matrices, and the a, b and c coefficients are tabulated as functions of $\langle P_2 \rangle$ for a Maier–Saupe potential.[45] The correlation times $\tau^{(j)}_{m_L m_M}$ take on slightly different forms; the small-step rotational diffusion model uses

$$(\tau^{(j)}_{m_L m_M})^{-1} = [6D_\perp / b^{(j)}_{m_L m_M} + m_M^2 (D_\parallel - D_\perp)] \quad (14)$$

and the third-rate model uses

$$(\tau^{(j)}_{m_L m_M})^{-1} = h_{m_M} + [6D_\beta / b^{(j)}_{m_L m_M} + m_L^2 (D_\alpha - D_\beta)] \quad (15)$$

Table 1 Summary of Deuterium Spectral Density Measurement in Thermotropic Liquid Crystals

System	Phase	T (°C)	ν_0 (MHz)	References
1O.4 (MBBA)	N	15–40	15.3, 46	22
4O.8	N, S_A, S_B	30–79	9.2–38.4	29,30
5O.7	N, S_A, S_C, S_B	38–78	15.3, 46	31,32
5CB	N	23–35	12–46	33,34
6OCB	N	57–75.5	15.3–46	35
6OCB/8OCB	N, S_A, RN	25–78	13.8	36
1CB/5CB	N	2–28	46	37
CCH3	N	57–80	30.7	38
$FLOC_{14}$	N	130–140	38.4, 46	39
THE6	D_{h0}	68–99	46	40
8OBCAB/*n*TPCHB	N, S_A, RN	90–258	46	41

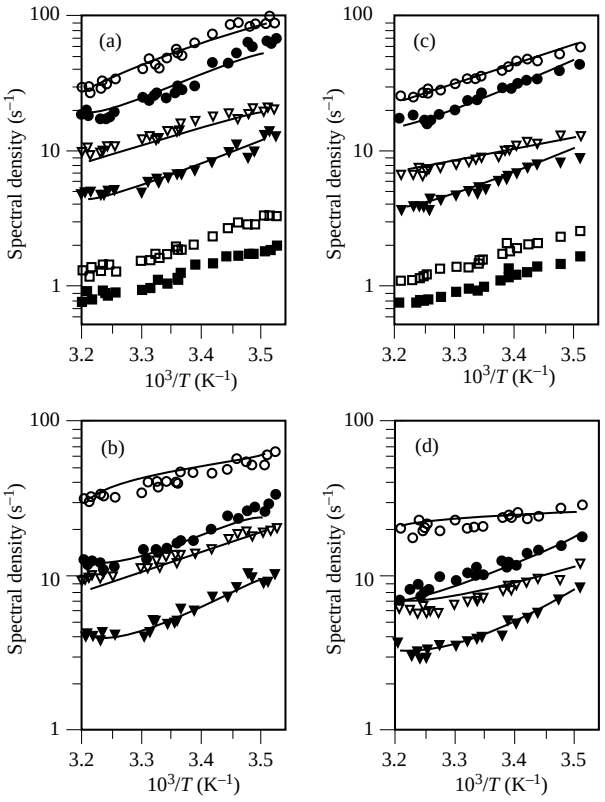

Figure 5 Plots of spectral densities versus the reciprocal temperature in the nematic phase of MBBA-d_{13}. Open symbols denote spectral densities $J_1(\omega_0)$, while solid symbols denote the corresponding $J_2(2\omega_0)$. ○ and ▽ and □ denote the C-0 and C-2 and C-4 data at (a) 15.3 MHz and (c) 46 MHz. • and ▼ denote the C-1 and C-3 data at (b) 15.3 MHz and (d) 46 MHz. Solid curves denote theoretical predictions based on the third-rate model and three jump rates for internal rotation.[22]

where $h_0 = 0$, $h_1 = D_\gamma$, and $h_2 = (3p + 1)D_\gamma$, with $p = 0$ corresponding to strong collision and $p = 1$ to small-step rotational diffusion for the γ motion. The Ds are rotational diffusion constants that are principal components of the rotational diffusion tensor of an 'average' molecule. The methine (C-0) deuteron has no internal motion, and the C-0–D bond reflects the motion of the aromatic core, giving

$$J^{(0)}_{m_L}(m_L\omega) = \frac{3\pi^2}{2}\chi_0^2 \sum_{m_M} c_{m_L m_M}[d^2_{m_M 0}(\beta_{M,Q})]^2 \times \sum_j a^{(j)}_{m_L m_M}[\tau^{(j)}_{m_L m_M}]^{-1}/[(m_L\omega)^2 + (\tau^{(j)}_{m_L m_M})^{-2}] \quad (16)$$

where $\beta_{M,Q}$ is the angle between the C–D bond and the z_M axis. Using equations (13) and (16), the fits between the calculated and experimental spectral densities are optimized by varying the rotational diffusion constants and the jump rate constants at each temperature.

Both the small-step rotational diffusion and third-rate models were examined. Both models were found to describe molecular reorientation of MBBA. The solid curves in Figure 5 are theoretical spectral densities based on equations (13) and (16) using $\tau^{(j)}_{m_L m_M}$ given by the third-rate model [equation (15)], X_a, X_c, and $\langle P_2\rangle$ given by modeling the quadrupolar splittings (E_{tg} = 2550 J mol^{-1}, $E_{g\pm g\pm}$ = 6000 J mol^{-1}). D_α and D_β are roughly the same ($\simeq 5 \times 10^7$ s^{-1} in the middle of the nematic phase), while D_γ is two orders of magnitude larger. D_α refers to the motion of the long molecular axis around the director, while D_β refers to its motion toward the director. These rotational diffusion constants decrease with decreasing temperature as expected for a thermally activated rotational process. The Nordio model has been used to derive motional parameters at different temperatures in 5CB[34] and 4-*n*-hexyloxy-4′-cyanobiphenyl (6OCB).[35] In studying the reorientation process in the smectogen 5O.7, the spectral densities of the methine and ring deuterons were measured as a function of temperature at two different Larmor frequencies in the megahertz region.[31] It was found that the large frequency dependence in $J_1(\omega)$ can only be rationalized by including director fluctuations. The third-rate model seems to produce physical rotational diffusion constants in the nematic, smectic A, and smectic C phases of 5O.7.

4 NOVEL NMR EXPERIMENTS

Some applications of newer NMR techniques to the study of liquid crystalline samples are now outlined. The proton NMR spectra of solute molecules dissolved in liquid crystals are usually complex, and iterative fitting of the NMR spectra must be used to extract dipolar couplings. Spectral simplification is possible by using partially deuterated solutes instead. When this is not practical, multiple quantum NMR spectroscopy[46] can greatly simplify spectra of complex spin systems. Multiple quantum NMR is concerned with the observation of forbidden nuclear transitions, i.e. $\Delta m_I \neq 1$. Multiple quantum coherences can only be detected indirectly. To detect all orders of multiple quantum transitions, special forms of two-dimensional NMR (2D NMR) spectroscopy are required. The high-order multiple quantum spectrum is simple due to the decrease in number of nuclear transitions with increasing order. Multiple quantum transitions of deuterons are now described.

In oriented systems, the quadrupole Hamiltonian leads to a splitting of the single quantum transitions [see Figure 1(b)]. Double quantum spectra of a deuteron (Δm_I = 2) have the advantage of eliminating quadrupolar effects. This is obvious from the deuterium energy diagram for a spin-1 system, since the quadrupolar shifts on $m_I = 1$ and $m_I = -1$ energy levels are equal. Any coherence established between these two levels will evolve at twice the Larmor frequency (as modified by chemical shift). Single- and double-quantum spectra were used[6] to study chain conformation in four members of the *n*O.7 series. It was noted that the distribution in the quadrupolar splitting is the dominant contribution to the deuteron linewidth of the single quantum spectrum. The distribution is due to a spread in the orientation of the long molecular axes in the liquid crystalline sample. Because a double quantum spectrum is not affected by quadrupolar effects, it has better spectral resolution and therefore may yield long-range dipole–dipole couplings among deuterons. Figure 6 shows a comparison of single- and double-quantum spectra of the α signal of 5O.7-αd_2 [Figure 6(a)] and the γ signal of 5O.7-$\alpha d_2 \gamma d_1$ [Figure 6(b) and (c)]. The improved resolution of the γ signal in the double quantum spectra is remarkable, and allows measurements of long-range deuterium dipolar couplings. For a two-coupled deuteron system, multiple quantum transitions can

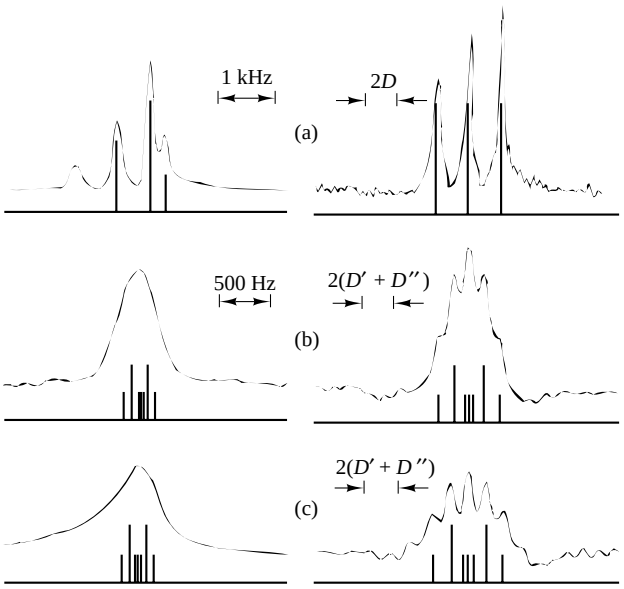

Figure 6 Single quantum (left) and double quantum (right) spectra for (a) the α signal of 5O.7-αd_2 at 57 °C, and the γ signal in 5O.7-$\alpha d_2 \gamma d_1$ at (b) 57 °C and (c) 41 °C, respectively. The stick diagrams give the corresponding theoretical spectra[6]

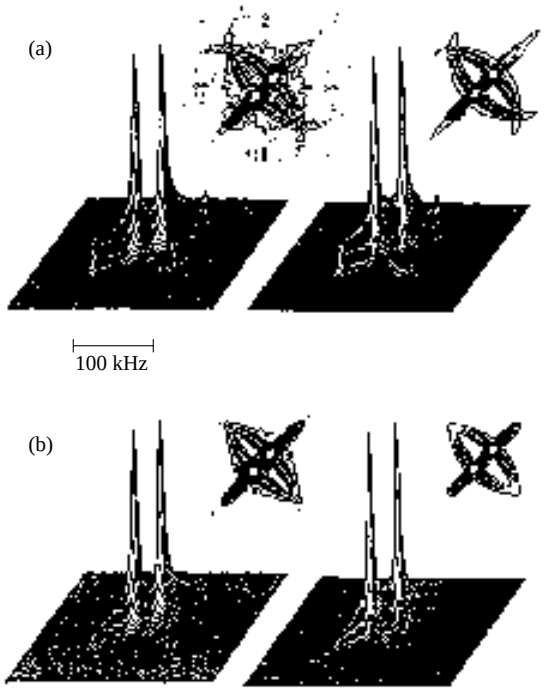

Figure 7 Experimental (left) and stimulated (right) spectra for (a) PS3 and (b) PS6 taken at 250 K with a mixing time of 100 ms. Contour plots are shown as insets[52]

reveal the correlation of relaxation mechanisms acting on two deuterium nuclei. Besides the three autocorrelation terms $J_0^{\mathrm{A}}(0)$, $J_1^{\mathrm{A}}(\omega)$, and $J_2^{\mathrm{A}}(2\omega)$, which describe the motion of the EFG tensor of either deuteron, the three cross-correlation terms $J_0^{\mathrm{C}}(0)$, $J_1^{\mathrm{C}}(\omega)$, and $J_2^{\mathrm{C}}(2\omega)$ describe correlation between the motion of the two EFG tensors. There are many relaxation studies of deuterated solutes in thermotropic liquid crystals.[13,14,27] For example, zero-, two-, and four-quantum linewidths may be used to determine the three cross-correlation terms[13,14] in acetonitrile-d_3.

2D NMR spectroscopy is now common in the study of liquid crystals. Using ^{13}C nuclei, the carbon–proton dipolar couplings can be obtained by means of the near magic angle spinning and the separated local field spectroscopy. Rapid sample spinning near the magic angle (54.7°) was incorporated to improve spectral resolution[47] so that coupling between indirectly bonded C–H pairs could be observed. A sample that has a chiral fluorinated solute dissolved in a liquid crystal was used to carry out a 2D ^{19}F spin echo[47] experiment in conjunction with the near magic angle spinning. This allows spectral analysis of small molecules to give residual dipolar coupling D_{ij} between nuclei i and j, and the isotropic spin–spin coupling J_{ij}. A deuteron 2D spin echo experiment on PAA-d_{14} allows assignment[19] of quadrupolar splittings in the NMR spectrum of perdeuterated *p*-azoxyanisole. The same technique has been used in the nematic phase of β-deuterated 5CB dispersed in polymers[48] and in model bilayer membranes[49] to determine the homogeneous linewidth of the individual lines. Another form of deuteron 2D experiment is 2D exchange spectroscopy,[50–52] which is capable of detecting slow molecular processes by monitoring the orientation of a C–D bond via its NMR frequency. A typical 2D time domain spectroscopy experiment involves four distinct periods [preparation, evolution (t_1), mixing, and detection (t_2)], leading to a time domain signal $s(t_1, t_2)$. Fourier transform of $s(t_1, t_2)$ gives $s(\omega_1, \omega_2)$, a 2D frequency spectrum. The spectrum provides information relating the frequency ω_{e} in the evolution period just before mixing and the frequency ω_{d} in the detection period just after mixing. When ω_{e} is identical to ω_{d}, this gives rise to a spectrum on the diagonal of a 2D spectrum; otherwise, off-diagonal intensity can be formed in the form of straight ridges and ellipses.[50,52] The detection of off-diagonal intensity is practical for motions that have a correlation time of the order of milliseconds or longer. As an example, deuteron 2D exchange spectroscopy in glass-forming liquid crystalline side-group polymers is described.[52] Figure 7 shows the experimental and simulated 2D spectra for poly(4-alkyloxybenzoic acid 4′-methoxyphenyl-d_4 ester)siloxane (PS*n*) with n = 3 and 6. Both PS3 and PS6 were magnetoaligned in a strong magnetic field by slow cooling from the isotropic melt into the glassy state. The glassy state of the PS6 is a frozen smectic C phase, while the glassy state of the PS3 is a frozen nematic phase. Off-diagonal intensity in the form of a partial elliptical pattern can be simulated by assuming a Gaussian distribution for the orientation distribution of the long axis of the mesogenic unit. Because the orientational order $\langle P_2 \rangle$ of PS3 is lower, the partial elliptical pattern is more pronounced for PS3 than for PS6 as seen in Figure 7. It was also found that the ring flip of 180° in PS*n* has a rather narrow angular distribution. The same technique has been used to study molecular dynamics in glass-forming discotic liquid crystals.[8]

5 RELATED ARTICLES

Amphiphilic Liquid Crystalline Samples: Nuclear Spin Relaxation; Bilayer Membranes: Deuterium and Carbon-13 NMR; Deuterium NMR in Solids; Deuteron Relaxation

Rates in Liquid Crystalline Samples: Experimental Methods; Dynamic NMR in Liquid Crystalline Solvents; Field Cycling Experiments; Liquid Crystalline Samples: Carbon-13 NMR; Liquid Crystalline Samples: Relaxation Mechanisms; Liquid Crystals: General Considerations; Lyotropic Liquid Crystalline Samples; Membranes: Deuterium NMR; Multiple Quantum Spectroscopy in Liquid Crystalline Solvents; Polymer Dispersed Liquid Crystals; Relaxation Theory: Density Matrix Formulation; Relaxation Theory for Quadrupolar Nuclei; Spinning Liquid Crystalline Samples; Two-Dimensional NMR of Molecules Oriented in Liquid Crystalline Phases.

6 REFERENCES

1. J. C. Rowell, W. D. Phillips, L. R. Melby, and M. Panar, *J. Chem. Phys.*, 1965, **43**, 3442.
2. W. D. Phillips, J. C. Rowell, and L. R. Melby, *J. Chem. Phys.*, 1964, **41**, 2551.
3. C. G. Wade, *Ann. Rev. Phys. Chem.*, 1977, **28**, 47.
4. J. W. Doane, in *Magnetic Resonance of Phase Transitions*, ed. F. J. Owens, C. P. Poole, Jr., and H. A. Farach, Academic Press, New York, 1979, Chap. 4
5. R. Y. Dong, J. Lewis, E. Tomchuk, and E. Bock, *J. Chem. Phys.*, 1978, **69**, 5314.
6. S. Hsi, H. Zimmermann, and Z. Luz, *J. Chem. Phys.*, 1978, **69**, 4126.
7. R. R. Vold, in *Nuclear Magnetic Resonance of Liquid Crystals*, ed. J. W. Emsley, Reidel, Dordrecht, 1985, Chap. 11
8. R. Y. Dong, *Nuclear Magnetic Resonance of Liquid Crystals*, Springer-Verlag, New York, 1994.
9. A. Abragam, *Principles of Nuclear Magnetism*, Oxford University Press, Oxford, 1961, Chap. 8
10. C. P. Slichter, *Principles of Magnetic Resonance*, 3rd edn., Springer-Verlag, Berlin, 1990.
11. J. P. Jacobsen, H. K. Bildsoe, and S. Schaumburg, *J. Magn. Reson.*, 1978, **23**, 153.
12. R. R. Vold and R. L. Vold, *J. Chem. Phys.*, 1977, **66**, 4018.
13. R. Poupko, R. L. Vold, and R. R. Vold, *J. Magn. Reson.*, 1979, **34**, 67.
14. D. Jaffe, R. R. Vold, and R. L. Vold, *J. Magn. Reson.*, 1982, **46**, 475.
15. G. R. Luckhurst, in *The Molecular Physics of Liquid Crystals*, ed. G. R. Luckhurst and G. W. Gray, Academic Press, London, 1979, Chap. 4
16. G. R. Luckhurst, in *Nuclear Magnetic Resonance of Liquid Crystals*, ed. J. W. Emsley, Reidel, Dordrecht, 1985, Chap. 3
17. W. Maier and A. Saupe, *Z. Naturforsch., Teil A*, 1959, **14**, 882.
18. W. Maier and A. Saupe, *Z. Naturforsch., Teil A*, 1960, **15**, 287.
19. J. W. Emsley, in *Nuclear Magnetic Resonance of Liquid Crystals*, ed. J. W. Emsley, Reidel, Dordrecht, 1985, Chap. 15
20. B. G. Wu, B. Ziemnicka, and J. W. Doane, *J. Chem. Phys.*, 1988, **88**, 1373.
21. P. J. Flory, *Statistical Mechanics of Chain Molecules*, Interscience, New York, 1969.
22. R. Y. Dong, L. Friesen, and G. M. Richards, *Mol. Phys.*, 1994, **81**, 1017.
23. T. M. Barbara and B. P. Dailey, *Mol. Cryst. Liq. Cryst.*, 1982, **87**, 239.
24. R. Y. Dong, H. Schmiedel, N. A. P. Vaz, Z. Yaniv, M. E. Neubert, and J. W. Doane, *Mol. Cryst. Liq. Cryst.*, 1993, **98**, 411.
25. J. W. Doane, in *Nuclear Magnetic Resonance of Liquid Crystals*, ed. J. W. Emsley, Reidel, Dordrecht, 1985, Chaps. 18 and 19.
26. Z. Luz, D. Goldfarb, and H. Zimmermann, in *Nuclear Magnetic Resonance of Liquid Crystals*, ed. J. W. Emsley, Reidel, Dordrecht, 1985, Chap. 14
27. R. L. Vold and R. R. Vold, *Isr. J. Chem.*, 1983, **23**, 315.
28. R. Köllner, K. H. Schweikert, F. Noack, and H. Zimmermann, *Liq. Cryst.*, 1993, **13**, 483.
29. T. M. Barbara, R. R. Vold, and R. L. Vold, *J. Chem. Phys.*, 1983, **79**, 6338.
30. T. M. Barbara, R. R. Vold, R. L. Vold, and M. E. Neubert, *J. Chem. Phys.* 1985, **82**, 1612.
31. R. Y. Dong and X. Shen, *Phys. Rev. E*, 1994, **49**, 538.
32. R. Y. Dong, *Liq. Cryst.*, 1989, **4**, 505.
33. P. A. Beckmann, J. W. Emsley, G. R. Luckhurst, and D. L. Turner, *Mol. Phys.*, 1986, **59**, 97.
34. R. Y. Dong and G. M. Richards, *J. Chem. Soc. Faraday Trans.*, 1992, **88**, 1885.
35. R. Y. Dong and G. Ravindranath, *Liq. Cryst.*, 1994, **17**, 47.
36. R. Y. Dong, G. M. Richards, J. S. Lewis, E. Tomchuk, and E. Bock, *Mol. Cryst. Liq. Cryst.*, 1987, **144**, 33.
37. G. L. Hoatson, T. Y. Tse, and R. L. Vold, *J. Magn. Reson.*, 1992, **98**, 342.
38. R. Y. Dong, J. W. Emsley, and K. Hamilton, *Liq. Cryst.*, 1989, **5**, 1019.
39. J. M. Goetz, G. L. Hoatson, and R. L. Vold, *J. Chem. Phys.*, 1992, **97**, 1306.
40. D. Goldfarb, R. Y. Dong, Z. Luz, and H. Zimmermann, *Mol. Phys.*, 1985, **54**, 1185.
41. D. Imbardelli, B. Wazynska, A. Golemme, G. Chidichimo, and R. Dabrowski, *Mol. Phys.*, 1993, **79**, 1275.
42. R. Y. Dong, *Phys. Rev. A*, 1991, **43**, 4310.
43. R. Y. Dong and G. M. Richards, *Chem. Phys. Lett.*, 1992, **200**, 541.
44. A. Ferrarini, G. J. Moro, and P. L. Nordio, *Liq. Cryst.*, 1990, **8**, 593.
45. R. R. Vold and R. L. Vold, *J. Chem. Phys.*, 1988, **88**, 1443.
46. G. P. Drobny, *Annu. Rev. Phys. Chem.*, 1985, **36**, 451.
47. J. Courtieu, J. P. Bayle, and B. M. Fung, *Prog. Nucl. Magn. Reson. Spectrosc.*, 1994, **26**, 141.
48. J. Dolinsek, O. Jarh, M. Vilfan, S. Zumer, R. Blinc, J. W. Doane, and G. Crawford, *J. Chem. Phys.*, 1991, **95**, 2154.
49. L. Müller and S. I. Chan, *J. Chem. Phys.*, 1983, **78**, 4341.
50. J. Jeener, B. H. Meier, P. Bachmann, and R. R. Ernst, *J. Chem. Phys.*, 1979, **71**, 4546.
51. C. Schmidt, B. Blümich, S. Wefing, and H. W. Spiess, *Chem. Phys. Lett.*, 1986, **130**, 84.
52. J. Leisen, C. Boeffel, R. Y. Dong, and H. W. Spiess, *Liq. Cryst.*, 1993, **14**, 215.

Acknowledgments

The financial support of the Natural Sciences and Engineering Council of Canada is gratefully acknowledged.

Biographical Sketch

Ronald Y. Dong. *b* 1942. B.A.Sc., 1966, Toronto. Ph.D. (Supervisor, Myer Bloom), 1969, University of British Columbia. Postdoctoral

work at the University of Waterloo, 1970–71, and at the National Research Council of Canada, 1971–73. Faculty in Physics, University of Winnipeg 1974–78. Faculty in Physics and Astronomy, Brandon University, 1978–present. Adjunct faculty in Physics, University of Manitoba, 1989–present. Approx. 100 publications. Research interests include solid state NMR, molecular dynamics, molecular crystals and liquid crystals.

Local Field Experiments in Liquid Crystals

Stefano Caldarelli

CRRMN Université d'Aix Marseille III, Marseille, France

1 Introduction 1
2 Definitions 1
3 Methods to Measure Dipolar Couplings 2
4 Methods for Quadrupolar Couplings (DECOR) 5
5 Related Articles in Volumes 1–8 7
6 References 7

1 INTRODUCTION

The analysis of NMR spectra of aligned liquid crystalline samples provides insight into the structure and dynamics of the molecular constituents or of dissolved molecular probes. However, the NMR spectra of ordinary liquid crystal samples are often too complicated to analyze. This is because the presence of proton-proton dipolar couplings renders the system strongly coupled. Substitution of the protons by deuterons might simplify the analysis, although the assignment of the signals remains uncertain. Separated local field methods for liquid crystals provide a tool to measure and/or assign in a straightforward manner interactions such as heteronuclear dipolar couplings or quadrupolar couplings in deuterium labeled compounds.

1.1 Relevance of the Separate Local Field Approach for Liquid Crystals

The dipolar coupling between protons is a long-range interaction, which is still active over several Angstroms. Any organic molecule is thus a system of mutually coupled spins, the size of which can become rather large already for small molecular weights. The spectral complexity increases accordingly, the number of lines for a system of N coupled spin 1/2 being

$$n_l = \left(\frac{2N}{N-1}\right)$$

For example, a system of 6 coupled spin-1/2 nuclei leads to 763 transitions. Molecular symmetry may reduce this number, but even so the problem of solving the proton spectrum becomes untractable for $N \sim 10$, where $n_l > 10\,000$. Conversely, the spectrum of diluted spins, such as ^{13}C, can be well resolved as, under ^{1}H decoupling, it is dominated by its chemical shift, the next NMR active neighbors being far in space. The separation of the local fields is a multidimensional NMR method in which the chemical shift of a diluted nucleus can be used to spread out other interactions using a two-dimensional scheme. Heteronuclear interactions can be measured and/or assigned in the second dimension in a more straightforward fashion. The ability to assign a coupling to a determined internuclear vector is not a trivial matter in liquid crystalline samples. In these materials, the size of the interaction depends on the molecular structure and orientation. In the absence of direct knowledge on the coupling partners, the assignment is carried out on the basis of the expected length and/or orientation of internuclear vectors. This approach yielded often reasonable results. However, labeling of the coupling partners by their chemical shift constitutes a sounder approach that may help for uncertain cases. Since the assignment obtained this way is model-free, the information obtained can be used to determine fine aspects of the molecular dynamics.

2 DEFINITIONS

2.1 Liquid Crystal Hamiltonians

The interactions measured by NMR in liquid crystals are average quantities, due to the presence of molecular motion:

$$\langle A \rangle = \int A(\Omega) f(\Omega) d\Omega \tag{1}$$

where the integral runs over the orientational coordinates and $f(\Omega)$ is the associated probability distribution function.

Due to motional averaging the NMR spectrum of magnetically or mechanically aligned samples, although still anisotropic in nature, does not show a powder-like line shape, but it is rather constituted of narrow lines.

In the case of molecules with some degree of internal flexibility, the average must be extended over internal (ϕ) and external orientational coordinates (Ω):

$$\langle A \rangle = \int A(\Omega, \phi) f(\Omega, \phi) d\Omega d\phi \tag{2}$$

These average quantities can be interpreted in terms of molecular dynamics, or as constraints in modeling an overall anisotropic potential, $U(\Omega, \phi)$, such as $f(\Omega, \phi) \propto e^{-U(\Omega,\phi)/kT}$ (see **Liquid Crystalline Samples: Structure of Nonrigid Molecules,** Volume 4).

The relevant NMR interactions for organic molecules (or for the organic part of an organometallic moiety) are the chemical shift, indirect scalar coupling and the magnetic dipolar coupling. Deuterium labeling is often used to simplify the spectra. In this case, the dominant interaction becomes the nuclear electric quadrupolar coupling. Chemical shift and quadrupolar couplings are often used to investigate the local order, especially as a function of the temperature in a phase diagram, capitalizing on the orientational dependence of these interactions (see **Liquid Crystalline Samples: Carbon-13 NMR,** Volume 4 and **Liquid Crystalline Samples: Deuterium NMR,** Volume 4). The dipolar coupling may play a similar role, with the additional important property of being an extremely sensitive probe of the internal dynamics, due to its dependence on the internuclear distance. In this respect, dipolar couplings between nuclei far apart are particularly useful, as their distance is more likely to vary between molecular conformations.

2.2 The Separate Local Field (SLF) Principle

The local field separation is a heteronuclear correlation two-dimensional experiment, first introduced by Waugh and coworkers.[1,2] As mentioned earlier, the resolution of the chemical shift dimension of a diluted nucleus is exploited to spread out (and measure) anisotropic interactions. A successful implementation of this scheme can be achieved only if the local fields relative to each probe nucleus are magnetically isolated from each other. That is to say, the corresponding 1D spectrum has to be the sum of distinct contributions, rather than the complicated one arising from a strongly coupled system. In practical terms, a prerequisite is the removal of long-range contacts, which in liquid crystals are provided by proton-proton dipolar couplings. The latter need to be effectively and selectively suppressed in order to implement any SLF scheme. This can be achieved either by employing dedicated pulse sequences (see **CRAMPS,** Volume 3), or chemically, by deuterium substitution. Each one of the mentioned options gives rise to a family of local field experiments, one to measure and assign short-range and long-range heteronuclear dipolar couplings, and the other to assign quadrupolar couplings.

3 METHODS TO MEASURE DIPOLAR COUPLINGS

3.1 Basic Pulse Sequences

The local fields concerned in this case are heteronuclear dipolar couplings (e.g., C–H or P–H). The measured quantity is actually a combination of a dipolar and a scalar interaction, as they share the same operator dependence. In the case of an isolated pair, the splitting of the transitions due to the heteronuclear coupling is shown in equation (3) (see **Liquid Crystalline Samples: Carbon-13 NMR,** Volume 4),

$$A = (2D + J) * f_S \tag{3}$$

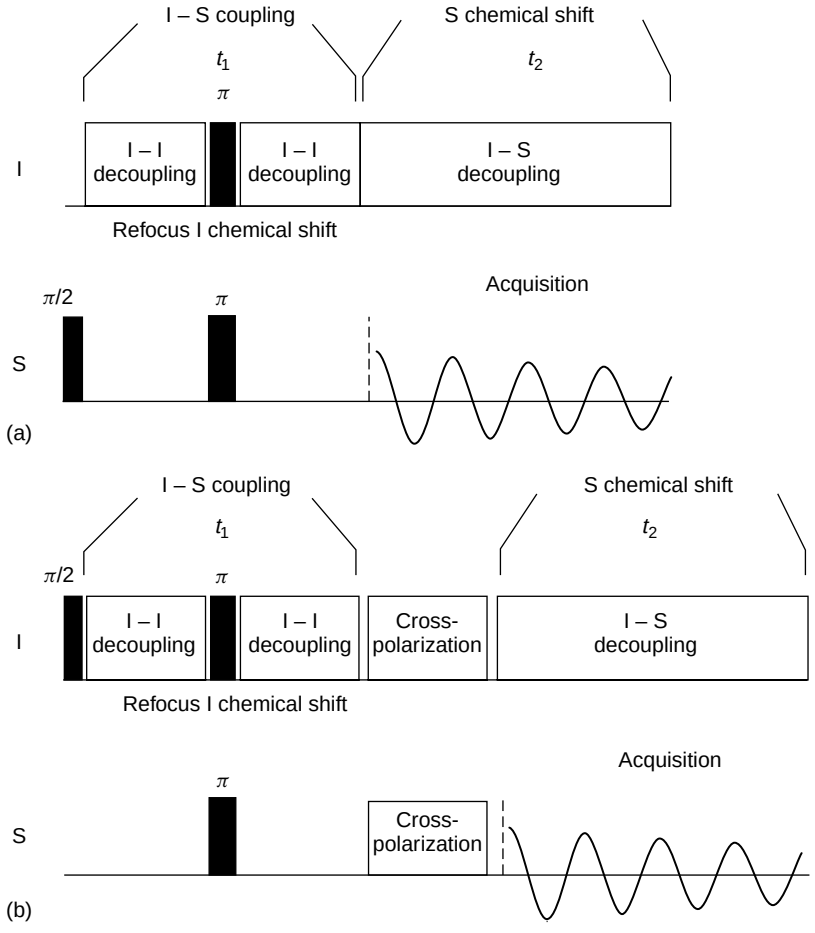

Figure 1 Pulse sequence schemes for "dipolar" separate local field experiments. (a) SLF pulse sequence. After excitation of S coherence with a $\pi/2$ pulse, evolution is allowed to occur under the pure I–S heteronuclear interaction (t_1). Other interactions are removed either by a simultaneous pair of π pulses on I and S (chemical shift) or by a dedicated irradiation scheme for selective I–I decoupling (see text). Typically, a multiple-pulse sequence is used for this purpose. This latter is encased by two extra pulses to tilt the relevant density matrix into suitable directions to achieve maximum efficiency when integrated with the other elements of the sequence. High-power I–S decoupling assures that the S chemical shift is the only active interaction during acquisition (t_2). (b) PELF (PDLF) pulse sequence. I nucleus coherence is first excited by a $\pi/2$ pulse, then allowed to evolve (t_1) under I–S coupling in analogy to the previous scheme; this same coherence is then cross-polarized onto nucleus S, which is observed during acquisition under high-power I–S decoupling. Some published sequences may include other optional elements, such as a presaturation pulse train on S or z-filters to facilitate pure-phase 2D spectroscopy. Adapted from Ref.[8], reproduced by permission of the American Chemical Society

where f_S is the scaling factor associated with the use of a multiple-pulse sequence to remove the homonuclear couplings. The largest known theoretical value for f_S is about 0.575.[3,4]

In the case of a diluted nucleus S, such as a carbon or a phosphorous atom, surrounded by many abundant (proton) I nuclei, two different ways to measure I–S coupling have been proposed (Figure 1).

In the first scheme (Figure 1(a)), the heteronuclear dipolar Hamiltonian is allowed to act on carbon coherence (created by a pulse). The relevant operators carrying the information about the heteronuclear coupling will be of the form shown in equation (4).

$$S_x \prod_k \cos(A_k t) + \sum_k 2S_y I_z \sin(A_k t) \tag{4}$$

In the second half of the sequence, only the first term is observed, under proton decoupling. In the example of an organic molecule, the presence of N protons thus split the carbon spectrum into a complex multiplet with 2^N lines. An example of application to the liquid crystal 5CB (4-*n*-pentyl-4′-cyanobiphenyl) is shown in Figure 2(a).[5]

This approach was the first to be introduced, following the original idea of local field separation as proposed by Waugh.[6,7] In the case of liquid crystal applications, this pulse sequence has been going under the simple acronym of SLF (Separate Local Field) experiment. Each trace of the 2D diagram is a combination spectrum arising from sums and differences of several heteronuclear couplings. A simultaneous fitting of all lines has to be performed in order to extract the values of the interactions. This part of the analysis may prove difficult, as it requires the resolution of all lines, especially the many ones in the center of the spectrum.

Another possible implementation of the local field separation consists in allowing the heteronuclear couplings to act upon proton coherence (Figure 1(b)).[8] In this case, the operators carrying the information on the heteronuclear coupling are in the form shown in equation (5),

$$\sum_k I_x \cos(A_k t) + \sum_k 2I_y S_z \sin(A_k t) \tag{5}$$

as it is unlikely for any proton k to have more than one coupling partner of the diluted species. The first term in equation (5) is transferred via cross-polarization into observable S_x terms. The spectrum is thus a sum of doublets, with a total of $2N$ lines. This second approach has several advantages. Firstly, the reduced number of lines ($2N$ vs 2^N) translates into a better S/N. Moreover, it is easier to measure dipolar coupling, as each doublet in the traces splits according to equation (1) (see Figure 2(b)). The lack of resolution on part of the spectrum does not affect the measurement of the other couplings. For example, in the case of C–H pairs, the measurement of the largest splitting, corresponding to directly bond partners, yields information equivalent to deuterium NMR of labeled compounds, but without chemistry required.[9] This second implementation was originally dubbed proton-detected local field (PDLF) then changed to proton-encoded local field (PELF) to avoid confusion since the actual detection in practical cases occurs on the diluted nucleus.[5,10,11]

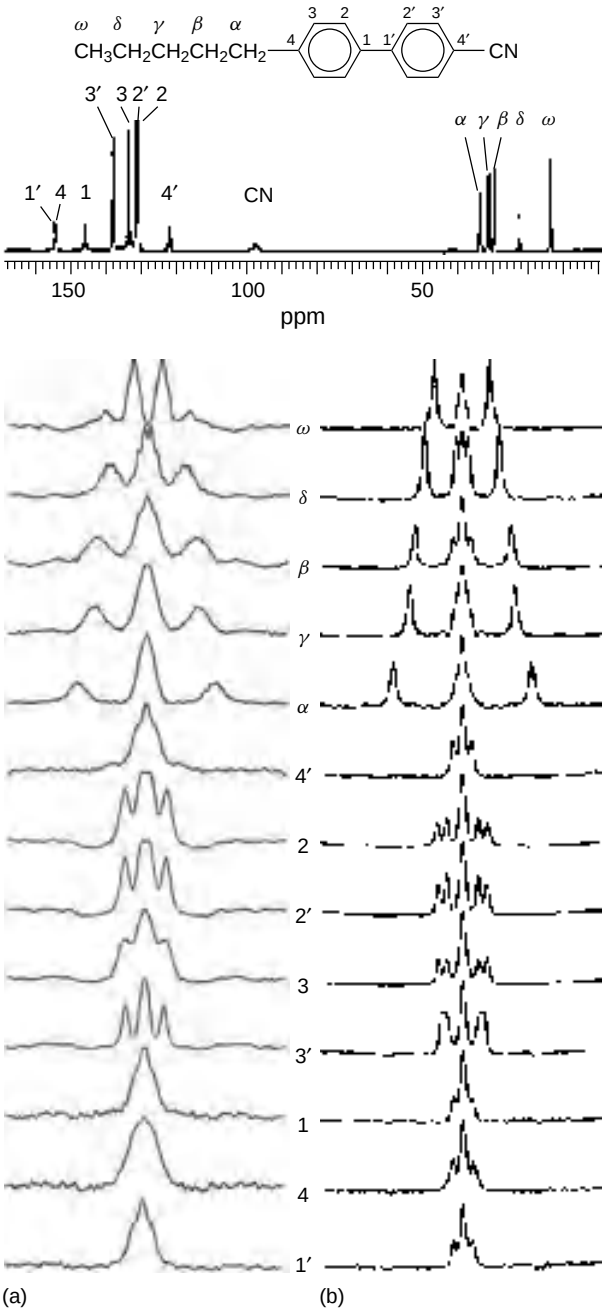

Figure 2 A comparison of the SLF and PELF methods for the nematic liquid crystal 5CB (4-*n*-pentyl-4′-cyanobiphenyl), the structure and ^{13}C NMR spectrum of which are reported on top. The left column shows traces of the 2D SLF experiment [Figure 1(a)] extracted at a chemical shift for a given carbon site. The right column (b) shows the equivalent for the PELF experiment [Figure 1(b)]. Note the different structure of the traces. SLF spectra are complex multiplets, while PELF spectra are the sum of doublets. Smaller long-range couplings produce the unresolved doublets in the center of PELF spectra. In both cases I–I decoupling was achieved by BLEW-48. Reproduced from Ref.[5] by permission of Academic Press

3.2 Off Magic-Angle (OMAS) or Variable-Angle (VAS) Spinning Experiments

Spinning of nematic liquid crystalline samples in the presence of a magnetic field introduces an additional torque

to the nematic director due to the action of viscous forces. This effect competes with magnetic alignment due to the anisotropy of the magnetic susceptibility (see **Spinning Liquid Crystalline Samples,** Volume 7) and tends to orient the directors along the axis of rotation. The 'viscosity' alignment mechanism dominates when the spinning rate is in excess of a threshold value. This kind of alignment is possible only for a given range of subtended angles between the rotor axis and the magnetic field, below or above the magic angle, depending on whether the anisotropy of the magnetic susceptibility is positive or negative, respectively. Considering that anisotropic NMR interactions depend on their orientation with respect to the magnetic field, spinning of the sample can be used to scale down the size of the heteronuclear coupling. In the case of a nematic liquid crystal, the dipolar coupling becomes as shown in equation (6),

$$D' = D\frac{(3\cos^2\beta - 1)}{2} \tag{6}$$

where β is the angle subtended between the rotor axis and the magnetic field (see **Spinning Liquid Crystalline Samples,** Volume 7). The possibility of reducing the anisotropic interactions by this effect, particularly the proton-proton dipolar couplings, has been used to facilitate the suppression of the proton homonuclear couplings. PELF or SLF experiments can be performed under OMAS, and in some cases increased resolution has been observed.[7] However, one should bear in mind that heteronuclear couplings are scaled down according to equation (6). An optimal OMAS (β) angle should be chosen in order to balance these two counteracting effects, especially if one is interested in measuring small long-range couplings. Local field experiments performed off magic-angle are often referred to as variable angle spinning (VAS) methods, since they can be performed, in principle, at different angles.

3.3 Accuracy and Precision of the Measurements

Many effects contribute to the experimental error on the measured couplings (variation of the local order, sample inhomogeneity, etc.). A pervasive source of error, typical of local field experiments, is the difficulty to accurately assess the scaling factor f_S in equation (3). The latter is theoretically known, but often depends on experimental details such as the ratio of the dipolar coupling to the RF field. Moreover, the scaling factor may not be homogeneous throughout the spectrum, as it may depend on the offset.[12,13] In the case of the SLF experiment (Figures 1 and 2(a)), either performed in a static or VAS scheme, all sources of error are mirrored by the goodness of the fit of the spectrum. In fact, the spectrum in this case is the product of combinations of many dipolar couplings involving different partners, and so the individual uncertainties propagate and combine into the line positions. Accuracy and precision of the measurements are directly related here. Conversely, precision for PELF schemes can be as high as the digital resolution of the spectrum, as the coupling is measured from the frequency difference of the lines of a doublet. This precision is expected to largely exceed the reasonable value of the accuracy. In the case when the RF coil in the VAS probe is oriented along the sample holder, the accuracy of the measurement can be evaluated by performing a series of VAS PELF spinning at different angles. By varying the rotor angle, the dipolar couplings will change according to equation (6), but the effective RF field will scale linearly. The consequent modulation of the ratio between the homonuclear proton-proton coupling and the irradiating field will affect the experimental scaling factor in a way that would mimic the variation in the effective RF field caused by the offset in a different part of the spectrum. The accuracy of the experiment can be thus inferred by a linear regression of the splitting $\Delta\nu$ measured along a series of VAS experiments to a combination of equations (5) and (6). Experimental errors measured this way showed a consistent value (about 5% in the case of MREV8) between SLF and PELF experiments.[10]

3.4 Efficiency of Homonuclear Decoupling Sequences

A crucial step toward achieving the best resolution in SLF experiments is to optimize the performance of the

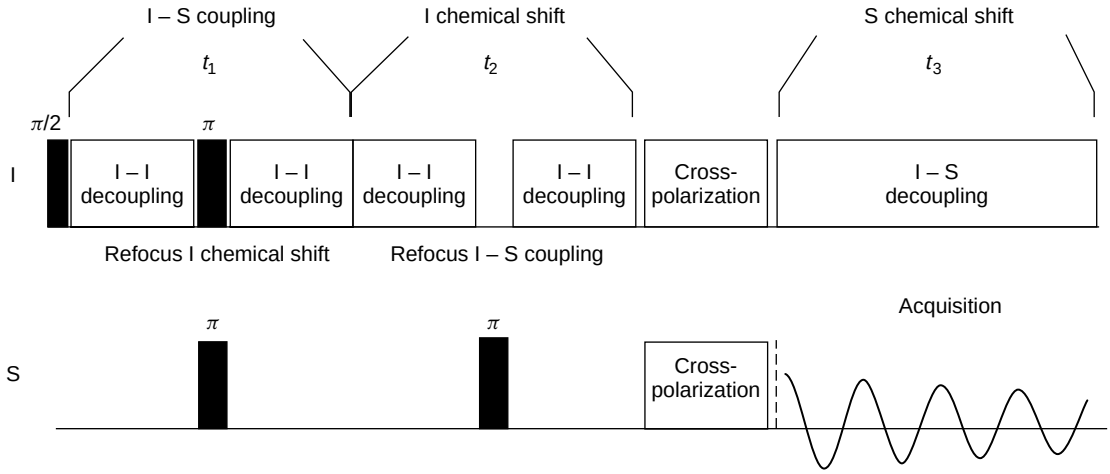

Figure 3 3D extension of the PELF (PDLF) scheme of Figure 1(a). An extra dimension, corresponding to pure I chemical shift evolution, is achieved by combining I–I decoupling and a π pulse on S, which refocuses the heteronuclear I–S couplings. In the literature, two versions of this scheme have been implemented: one in which evolution times t_1 and t_2 were incremented synchronously and the full 3D experiment. Adapted from Ref.[11] by permission of the American Chemical Society

proton homonuclear decoupling.[9,12,13] Historically, MREV8 or BLEW48 were used, but more recent and better-performing sequences can be easily integrated into the method.[9,14–16] Liquid crystal samples present the additional constraint that long, high-power pulse trains may induce thermal gradients, which could perturb the local order of the sample. This can be a serious nuisance in the case of liquid crystalline phases that are stable only over a narrow range of temperatures. Fortunately, the size of the proton-proton coupling to be removed is scaled down by the molecular motion, so that it is often not necessary to employ more than moderate power levels for homonuclear decoupling. If possible, a sequence providing a large and homogeneous (as a function of the offset) scaling factor should be chosen.

3.5 3D Methods for Long-range Couplings

Long-range dipolar couplings are particularly useful as constraints in the study of the dynamics of flexible molecules, as they are extremely sensitive to conformational modifications. It is apparent from Figure 2(b) that the PELF method can provide a reliable measurement for long-range couplings, associated to the many resolved doublets toward the center of the traces. However, these interactions cannot be fully assigned, as the carbon chemical shift only provides a label for one of the partners of the coupling. A possible ploy to avoid recourse to geometrical models is the 'natural' development to a three-dimensional extension of the PELF method, adding as a third dimension the proton chemical shift (Figure 5), which makes the assignment complete.[17,18] Although in principle being the perfect method, the performance of the 3D version of the PELF relies upon a good resolution of the proton spectrum. It is thus relatively easy to distinguish couplings between a given carbon and well-resolved protons, for instance belonging to an aromatic or aliphatic part of the molecule. Another good candidate, as shown in Figure 4, is the tail of an aliphatic chain, as the methyl proton resonance is usually well isolated. Couplings between partners of up to 4 bonds away can be measured in the case of the liquid crystal 5CB (Figure 3). On the other hand, assignment of couplings inside an aliphatic chain may prove more difficult.

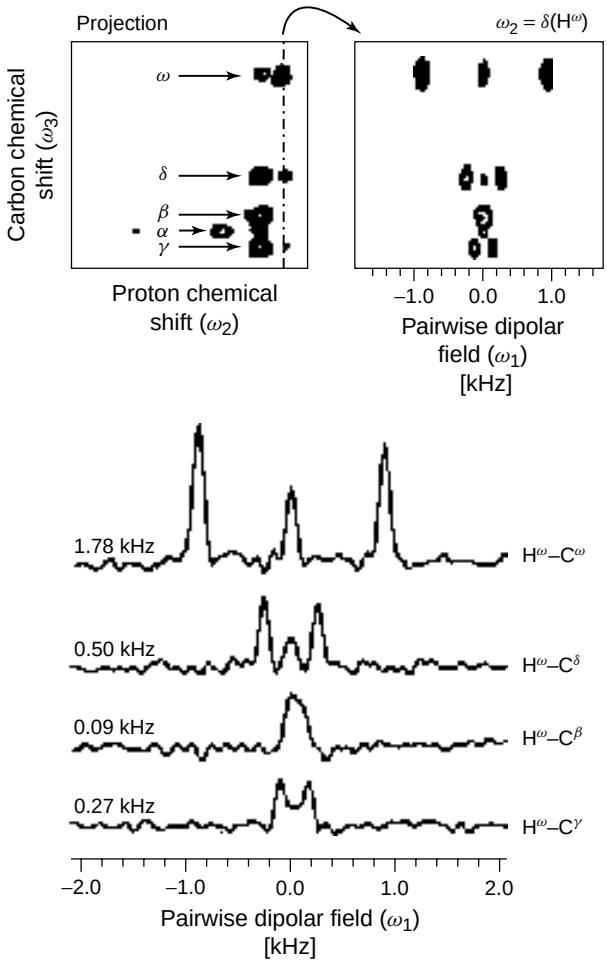

Figure 4 3D PELF spectrum of the aliphatic region of the liquid crystal 5CB. The ω_2/ω_3 plane projection yields an heteronuclear correlation spectrum (upper left). In the proton dimension, the α and ω sites are well resolved, while all other signals overlap. The methyl protons show dipolar contacts with several carbon atoms, the details of which are unveiled in the corresponding ω_2 plane (upper right), in which the size of the H_ω–C^X ($X = \alpha, \ldots, \omega$) interaction is proportional to the splitting (equation (1)). The corresponding traces are shown in the lower part of the figure. The small H^ω–C^β coupling, corresponding to a partially unresolved splitting, was evaluated by fitting of the line shape. Reproduced from Ref.[11] by permission of the American Chemical Society

4 METHODS FOR QUADRUPOLAR COUPLINGS (DECOR)

Spectral simplification in organic liquid crystals can be achieved by isotopic substitution of protons with deuterium (see **Liquid Crystalline Samples: Deuterium NMR,** Volume 4). The spectrum of a spin-1 nucleus is dominated by the quadrupolar interaction, and the dipolar couplings between hydrogens are scaled down by a factor of about 36 (by γ_H^2/γ_D^2) upon isotopic substitution. Consequently the spectrum is constituted of quadrupolar doublets, split by twice the quadrupolar frequency ω_Q, with residual dipolar couplings acting as a fine, often unresolved structure. The deuterium spectrum is usually well resolved for molecules of moderate size. However, similar to the case of dipolar spectra, the assignment of uniformly labeled compounds is obtained on the basis of geometric arguments. In the case of molecules with some degree of internal flexibility, such an assumption implies prior knowledge of the average molecular shape in solution and its correlation with the orientation. An independent way of assigning a deuterium site to a specific C–D bond is to use the ^{13}C chemical shift as a label, analogously to the PELF idea for heteronuclear dipolar couplings. Deuterium-carbon correlation can be achieved using a pulse scheme analogous to PELF (Figure 5), but simplified because of the absence of a strongly coupled network of deuterium nuclei.[19,20]

This method has been dubbed DECOR (DEuterium CORrelation spectroscopy). The (optional) 180 degree pulse on deuterium during t_1 (Figure 5) is sufficient in this case to remove the (reduced) C–D dipolar coupling. The latter may otherwise be revealed (and measured) as a splitting or line broadening (see Figure 4) in the DECOR spectra.

Besides providing a way for assigning deuterium spectra, this technique can be helpful in measuring quadrupolar couplings that are not resolved in the one-dimensional spectrum.

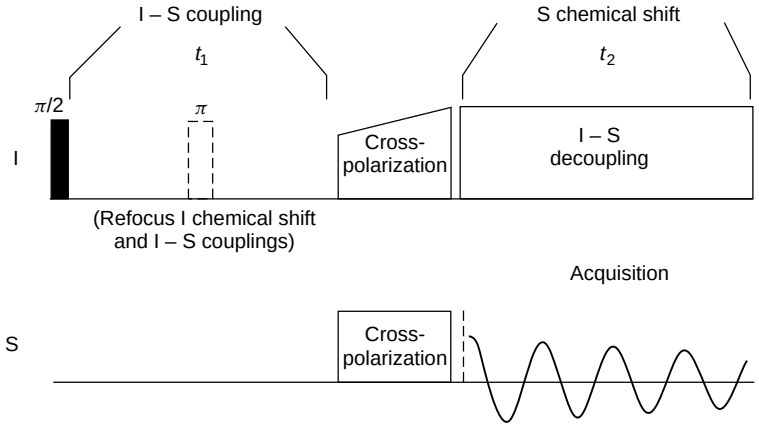

Figure 5 Pulse sequence for the separate local field experiments involving quadrupolar nuclei. In liquid crystals this concerns assignment of quadrupolar couplings in deuterated samples, and for this reason it was dubbed DECOR (DEuterium CORrelation spectroscopy). The first dimension (t_1) is simply the deuterium (I) evolution, with an optional π pulse to refocus I–S (i.e., deuterium–carbon) couplings and I chemical shift to obtain a purely quadrupolar dimension. Acquisition takes place on the S spins under I–S decoupling, after cross polarization. The latter requires special care to insure a match condition sufficiently broad to cover all C–D pairs. In the example in Figure 6, only one of the two lines of the quadrupolar doublet was used for the transfer (single-quantum cross-polarization). Even with this restriction, variable-amplitude spin-lock was still required to further broaden the match condition. Adapted from Ref.[19] by permission of the American Chemical Society

4.1 Deuterium to Carbon Cross-polarization

A delicate part in the DECOR pulse sequence is the cross-polarization step due to the large span of the deuterium spectrum, which defies the ability of a RF field to spin-lock the magnetization ($\omega_{RF} \ll \omega_Q$). Efficient cross-polarization with weak RF fields can be recovered by focussing on half of the symmetrical spectrum typical of the spin-1 deuterium. That is to say, only one of the two single-quantum transitions (i.e., one of the two lines of the doublet) is used to cross-polarize to the carbons, without loss of information. In fact, the main cause of spectral dispersion for a typical liquid crystal sample is the dispersion of the average quadrupolar couplings, essentially due to differences in mobility or average orientation of the molecular segments. The spectrum can be seen as two almost symmetrical groups of lines, in most cases well separated. In fact, single-quantum transitions are further shifted by the chemical shift and split by the dipolar coupling, which are usually much weaker interactions than the quadrupolar coupling ($\omega_{CS}, \omega_D \ll \omega_Q$). One can thus focus on half of the spectrum without losing any site resonance. The match condition for cross-polarization modifies accordingly: $\omega_S = \sqrt{2}\omega_I$.[19,20] The spectral breadth of the ensemble of the SQ-transitions can still be too large to be effectively spin-locked ($|\omega_Q^{max} - \omega_Q^{min}| > \omega_{RF}$), depending on the experimental conditions.[21] In the original experiment, a variable-amplitude cross-polarization scheme was necessary to broaden the match condition enough to achieve a homogeneous transfer over the entire spectrum.[22]

As a consequence of the use of only one SQ transition, in the DECOR 2D diagrams (see Figure 4) only half of the 1D deuterium spectrum correlates with the ^{13}C spectrum. This is sufficient to assign the deuterium spectrum, due to its mirror symmetry (neglecting to first order the effect of chemical shift).

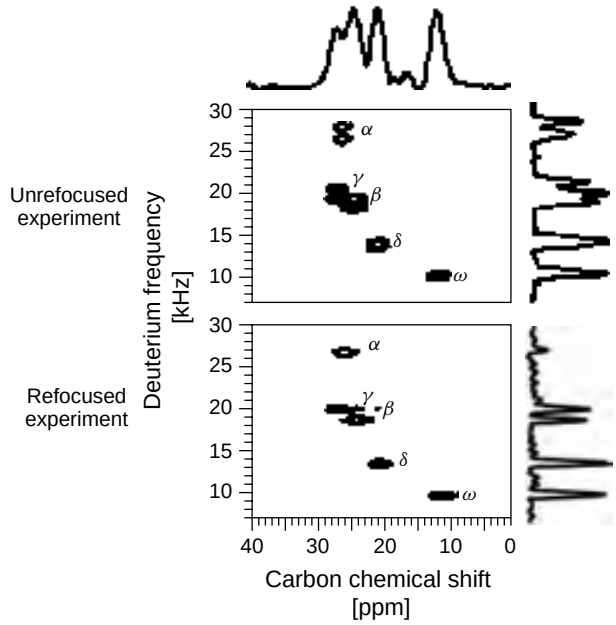

Figure 6 DECOR spectrum of the aliphatic region of a fully deuterated sample of 5CB, using the pulse sequence in Figure 5. The deuterium frequency dimension shows only half of the characteristic quadrupolar doublets because of the selective single-quantum deuterium to carbon cross-polarization scheme used (see text). The effects of the 180 degree pulse on deuterium at $t_1/2$ are demonstrated by the further splitting of some of the peaks in the upper spectrum as compared to the lower one. The effect, as the C–D dipolar coupling, scales with the quadrupolar frequency, since the two interactions are co-linear. Reproduced from Ref.[20] by permission of the American Chemical Society

4.2 Exploiting Long-range Correlations to Resolve Assignment Ambiguities

In some cases, the dipolar coupling between a directly bonded C–D pair and a pair of second neighbors may assume similar values, because of particular orientation effects. For instance, the C–D coupling of directly bonded pairs in the aromatic ring of perdeuterated 5CB is severely reduced as the bond aligns close to the magic angle with respect to the magnetic field. As a consequence, its size becomes comparable

with that of the coupling relative to next neighbors. A same quadrupolar signal in the deuterium dimension can thus correlate to two carbon signals in a DECOR experiment. This kind of ambiguity in the assignment can be lifted by using longer mixing times in the CP transfer, by which the search for correlations is pushed further to smaller couplings, and thus farther neighbors.

5 RELATED ARTICLES IN VOLUMES 1–8

CRAMPS, Volume 3; Liquid Crystalline Samples: Carbon-13 NMR, Volume 4; Liquid Crystalline Samples: Deuterium NMR, Volume 4; Liquid Crystalline Samples: Spectral Analysis, Volume 4; Liquid Crystalline Samples: Structure of Nonrigid Molecules, Volume 4; Liquid Crystals: General Considerations, Volume 4; Spinning Liquid Crystalline Samples, Volume 7

6 REFERENCES

1. R. K. Hester, J. L. Ackermann, B. L. Neff, and J. S. Waugh, *Phys. Rev. Lett.*, 1976, **36**, 1081.
2. S. J. Opella and J. S. Waugh, *J. Chem. Phys.*, 1977, **66**, 4919.
3. M. Lee and W. I. Goldburg, *Phys. Rev.*, 1965, **A140**, 1261.
4. A. Bielecki, A. C. Kolbert, and M. H. Levitt, *Chem. Phys. Lett.*, 1989, **155**, 341.
5. B. M. Fung, K. Ermolaev, and Y. Yu, *J. Magn. Reson.*, 1999, **138**, 28.
6. B. M. Fung and J. Afzal, *J. Am. Chem. Soc.*, 1986, **108**, 1107.
7. B. M. Fung and J. Afzal, *J. Chem. Phys.*, 1986, **85**, 4808.
8. K. Schmidt-Rohr, D. Nanz, L. Emsley, and A. Pines, *J. Phys. Chem.*, 1994, **98**, 6668.
9. C. Canlet and B. M. Fung, *J. Phys. Chem.*, 2000, **B104**, 6181.
10. M. Hong, K. Schmidt-Rohr, and A. Pines, *J. Am. Chem. Soc.*, 1995, **117**, 3310.
11. S. Caldarelli, M. Hong, L. Emsley, and A. Pines, *J. Phys. Chem.*, 1996, **100**, 18 696.
12. B. M. Fung, *J. Magn. Reson.*, 1986, **66**, 525.
13. B. M. Fung, *J. Magn. Reson.*, 1987, **72**, 353.
14. P. Mansfield, *J. Phys. Chem.*, 1971, **4**, 1444.
15. W. K. Rhim, D. D. Elleman, and R. W. Vaughn, *J. Chem. Phys.*, 1972, **59**, 3740.
16. D. P. Burum, N. Linder, and R. R. Ernst, *J. Magn. Reson.*, 1981, **44**, 173.
17. M. Hong, S. Caldarelli, and A. Pines, *J. Phys. Chem.*, 1996, **100**, 14 815.
18. S. Caldarelli, A. Lesage, and L. Emsley, *J. Am. Chem. Soc.*, 1996, **118**, 12 224.
19. C. Auger, A. Lesage, S. Caldarelli, P. Hodgkinson, and L. Emsley, *J. Am. Chem. Soc.*, 1997, **119**, 12 000.
20. C. Auger, A. Lesage, S. Caldarelli, P. Hodgkinson, and L. Emsley, *J. Phys. Chem.*, 1998, **102**, 3718.
21. P. J. Hodgkinson, C. Auger, and L. Emsley, *J. Chem. Phys.*, 1998, **109**, 1873.
22. G. Metz, X. Wu, and S. O. Smith, *J. Magn. Reson.*, 1994, **A110**, 219.

Biographical Sketch

Stefano Caldarelli, *b* 1962 in Spoleto, Italy. Ph.D., 1992 Pisa, Italy. Approx. 30 papers. After a beginning as an organometallic chemist, he quickly found his way into NMR of liquid crystals. An initial stay in the Pines' group in Berkeley expanded his research interests to cover all aspects of NMR for materials sciences: gas, liquids, interfaces, surfaces and solids. His scientific peregrination led him from Pisa, Italy, through Berkeley, USA, Lausanne, Switzerland and Lyon, France to the temporary permanent settlement as a chemistry professor in Marseille, France.

Multiple Quantum Spectroscopy in Liquid Crystalline Solvents

Leslie D. Field
Sydney University, NSW, Australia

1	Introduction	1
2	Multiple Quantum NMR of Samples Dissolved in Liquid Crystalline Solvents	1
3	Excitation of Multiple Quantum Coherences	2
4	Detection of Multiple Quantum Coherences	3
5	Methods of Spectral Analysis and Spectral Simulation	5
6	Applications of MQ NMR to Samples Dissolved in Liquid Crystalline Solvents	5
7	Related Articles	8
8	References	8

1 INTRODUCTION

Liquid crystals can be loosely defined as materials with properties intermediate between those of solids and liquids (mesophases). Liquid crystals typically flow like viscous liquids but the phase exhibits some degree of molecular packing or structure whereby individual molecules tend to align, making the mesophase anisotropic.

1.1 NMR in Liquid Crystalline Solvents

Most molecules that form a nematic mesophase are able to dissolve a small amount of solute compound without destroying the mesophase. Since the first reports of using liquid crystals as solvents for NMR spectroscopy, high resolution NMR in liquid crystalline solution has developed into an important area.[1] The amount of solute that can be dissolved in a nematic mesophase depends on the mesophase and the solute, but solute concentrations of 5 wt % are common and concentrations of 10–15 wt % are sometimes achievable without disrupting the liquid crystalline properties of the solvent.

The motion of solute molecules dissolved in a nematic mesophase is restricted by the arrangement of the mesophase molecules. The anisotropy of the arrangement of the solvent molecules induces anisotropy in the movement of the solute molecules via dispersion forces. A solute dissolved in an oriented mesophase is forced to undergo nonrandom (anisotropic) motion because of its interactions with the aligned solvent. If the nematic mesophase is aligned in a magnetic field then alignment of the mesophase is reflected in the anisotropy of the motion of the solute molecules.

The rapid motion of molecules in an oriented mesophase results in the averaging of the intermolecular dipolar interactions to zero. However, the intramolecular dipolar interactions have a nonzero average.

Qualitatively the NMR spectra of solutes oriented in mesophases are more complex than the spectra obtained in isotropic solvents, for two reasons (see ***Liquid Crystalline Samples: Spectral Analysis***):

1. The nonzero averaging of dipolar couplings results in many more coupling constants (splittings) being expressed in the spectrum. A dipolar coupling constant appears for every pair of interacting nuclei.
2. The magnitude of the dipolar coupling constants (D_{ij}), between a pair of interacting nuclei is generally large (up to a few kilohertz) compared with the indirect coupling constants (typically a few hertz). This results in virtually all spectra of solutes dissolved in an oriented mesophase being highly second order and adds to the spectral complexity.

2 MULTIPLE QUANTUM NMR OF SAMPLES DISSOLVED IN LIQUID CRYSTALLINE SOLVENTS

The signals observed in a conventional NMR spectrum (single rf pulse followed by signal acquisition and FT of the resulting FID) are governed by selection rules which dictate that transitions can only be induced between energy levels differing in total spin quantum number by $\Delta M = \pm 1$ (single quantum transitions). Multiple quantum NMR (MQ NMR)[2] is concerned with the observation of nuclear transitions where $\Delta M \neq \pm 1$.

The number of transitions in the single quantum NMR spectrum of a solute dissolved in an anisotropic solvent increases rapidly with the number of coupled spins. A molecule with a single proton would have a ^{1}H spectrum with only one transition. A system containing two protons would have four possible transitions, and a spin system composed of three nonequivalent protons has 15 transitions.

The number of transitions for an unsymmetrical spin system (disregarding symmetry considerations) can be calculated as[3]

$$\text{No. single quantum transitions} = (2N)!/[(N-1)!(N+1)!] \quad (1)$$

This is an exponential function where the number of transitions increases dramatically as the number of interacting spins increases (Figure 1). In an 8-spin system there would be 1.14×10^3 transitions in the single quantum spectrum; in a 10-spin system there would be 1.67×10^5 transitions.

If there is symmetry present in the spin system (i.e. chemically or magnetically equivalent nuclei) the number of transitions is reduced. For the symmetrical six proton spin system of benzene there are 72 transitions, compared with 792 transitions in a six proton system with no symmetry.

Given a reasonable linewidth for each transition, substantial overlap occurs in the single quantum spectrum of a large spin system, and the spectrum rapidly degenerates to an unresolved broad lump. In higher spin systems, it becomes impossible to resolve or assign individual transitions for an iterative computer analysis. MQ NMR can considerably reduce the complexity of the spectrum of a solute dissolved in a liquid crystalline solvent, and the main benefit of MQ NMR lies in the fact that there are fewer transitions in the very high MQ spectra.

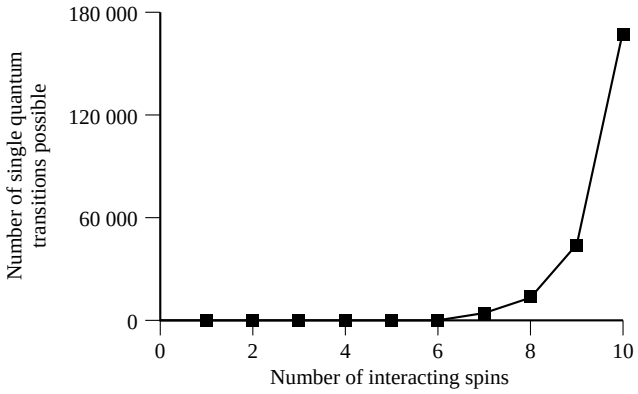

Figure 1 The number of single quantum transitions as a function of the number of interacting nuclei ($I = \frac{1}{2}$)

The number of M quantum transitions in a system of N nuclei ($I = 1/2$), neglecting symmetry, is given by

$$\text{No. of } M \text{ quantum transitions} = (2N)!/[(N - M)!(N + M)!] \quad (2)$$

Representative values are summarized in Table 1.

In the N quantum spectrum of an N-spin system, there will always be only one transition. The $(N - 1)$ quantum spectrum of an N-spin system will contain only $2N$ transitions. For large N, the $N - 1$ and $N - 2$ quantum spectra will contain only a few transitions and will be much less complex and more easily analyzed than the single quantum spectrum.

3 EXCITATION OF MULTIPLE QUANTUM COHERENCES

Coherence between states separated by $\Delta M \neq 1$ cannot be observed directly, but is usually detected indirectly by its modulation of single quantum coherence in a two-dimensional NMR experiment. A two-dimensional NMR experiment[4] for exciting and detecting MQ spectra can be divided schematically into five time frames, as shown in Table 2.

Providing that MQ coherences (MQCs) can be produced by a suitable preparation sequence, and mixed to observable single quantum coherence with an appropriate 'mixing' sequence, the MQ frequencies of a spin system can be obtained by systematically varying the duration of the 'evolution' period (t_1) followed by Fourier transformation over t_1. Compared with samples in isotropic solution, MQCs can be excited relatively easily in samples dissolved in liquid crystalline solution. The large dipolar coupling constants expressed ensure that coherences evolve rapidly and MQC can be excited efficiently before the effects of relaxation complicate coherence development in the spin system.

3.1 Nonselective Excitation

The most common (and simplest) method for preparing MQC is by use of two $\pi/2$ pulses separated by a fixed delay. The simplest mixing sequence is a single $\pi/2$ pulse and this means that a three-pulse sequence (Figure 2) can be used to record multiple quantum spectra.

The sequence of two hard pulses in the preparation part in Figure 2 nonselectively generates coherence of all orders possible in the spin system. Coherences are not excited uniformly and the efficiency with which MQC is excited depends specifically on the couplings and chemical shifts of the nuclei in the spin system and the choice of the interval d_1. Broad band excitation techniques have been proposed[5] where the value of d_1 in the preparation sequence is varied either in a pseudorandom or systematic fashion to achieve a more uniform excitation in the multiple quantum domain. Weitekamp et al.[6] have devised an experimental search procedure for optimizing the delays in the preparation period of the MQ excitation sequence.

Table 1 The Number of Transitions in the M Quantum Spectra as a Function of the Number of Interacting Nuclei ($I = \frac{1}{2}$)

	Number of spins ($I = \frac{1}{2}$)						
ΔM	2	4	6	8	10	15	20
1	4	56	792	11440	1.68×10^5	1.45×10^8	1.31×10^{11}
2	1	28	495	8008	1.26×10^5	1.19×10^8	1.13×10^{11}
4		1	220	1820	38760	5.46×10^7	6.28×10^{10}
6			1	120	4845	1.43×10^7	2.32×10^{10}
8				1	190	2.04×10^6	5.58×10^9
10					1	1.42×10^5	8.48×10^8
15						1	6.58×10^5
20							1

Table 2 The Five Time Frames in the Two-dimensional MQ NMR Experiment[a]

Relaxation	Preparation	Evolution	Mixing	Detection
Spin system relaxes between experiments	Generate MQC in the coupled spin system	MQC evolves with time (t_1)	Mixes MQC to observable SQC	Detect SQC as a FID (t_2)

[a]MQC, multiple quantum coherence; SQC, single quantum coherence.

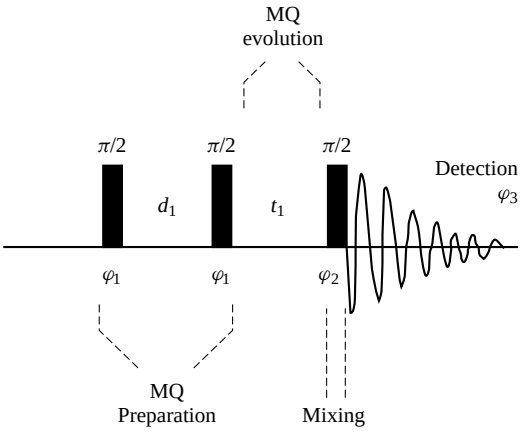

Figure 2 Three-pulse sequence for the observation of MQ spectra

3.2 Selective Excitation

Nonselective excitation of MQC excites all possible coherences, but leaves most of the spectral intensity in the single quantum and low multiple quantum spectra because these spectra have the most transitions.[3b] As a result, the simpler high-order coherences are comparatively weak. An alternative approach to the excitation of MQC is selectively to excite only a few orders of coherence and more effectively channel or focus the available signal into one order (or a few selected orders).

Order selective excitation has been achieved by the use of phase-cycled sequences of rf pulses[7] and composite pulse trains.[8] Pines et al.[7,9] have established that an nk quantum selective excitation sequence ($k = 0, \pm1, \pm2, \cdots$) can be constructed by repeating an appropriate sequence with a phase increment $2\pi/n$ between repetitions:

$$\varphi = 0 \quad \varphi = 2\pi/n \; \varphi = 4\pi/n \quad \varphi = 2(n-1)\pi/n$$
$$[p_1 \ldots p_q]\,[p_1 \ldots p_q]\,[p_1 \ldots p_q] \ldots [p_1 \ldots p_q]$$

The pulse sequences $[p_1 \cdots p_q]$ employed in each section of the sequence can be nonselective; however, only certain sequences are effective in efficiently generating the desired orders of MQC. Sequences involving several thousand cycled pulses have been explored.[7,9] An upper limit on the length of the excitation sequence is set by relaxation processes in the spin system. Effective phase-cycled excitation sequences must generate MQC efficiently and compensate for the effects of imperfect rf hardware and pulses.

4 DETECTION OF MULTIPLE QUANTUM COHERENCES

The frequencies of MQCs are obtained indirectly using two-dimensional NMR sequences whereby the multiple quantum frequencies modulate the observable single quantum spectrum. The two-dimensional spectrum contains multiple quantum frequencies in F_1 and single quantum frequencies in F_2. The frequencies of the multiple quantum spectrum are most conveniently obtained as F_1 projections from the two-dimensional spectrum.

It is not necessary to acquire an entire two-dimensional data set to obtain the multiple quantum frequencies. MQ spectra can be obtained by acquiring a single point in t_2 (at $t_2 = 0$ or some other value) and then transforming the resulting one-dimensional sequence of points as a function of t_1. In theory, the FT of the $t_2 = 0$ row of a two-dimensional data set is identical to the F_1 projection of the entire two-dimensional data set.[10]

If the MQ preparation sequence does not perfectly select coherences from an individual MQ order, then the MQ spectrum detected will be a complex superposition of subspectra from the various MQCs excited. There are several methods available to filter or separate the MQ spectra of various orders.

4.1 Order Selective Detection

4.1.1 Dependence on Resonance Offset

n Quantum coherence evolves n-fold more rapidly during the t_1 evolution period of the MQ experiment than does single quantum coherence. If the single quantum spectrum is centered at a frequency approximately $\Delta\omega$ from the rf transmitter, transitions in the n quantum spectrum are centered at a frequency $n\Delta\omega$. With nonselective excitation, multiple quantum spectra are separated by $\Delta\omega$ and by judicious selection of the transmitter offset, the spectra of various multiple quantum orders can be cleanly separated (Figure 3) in the frequency domain.

The main disadvantages of using transmitter offsets to separate various orders of MQC are: (i) offset frequencies of 10–30 kHz are often required to obtain clean separation of the coherence orders and the large offset results in nonuniform rf distribution and homogeneity across the spectrum: and (ii) for a nonselective experiment where all orders of coherence (up to $\pm N$ orders in an N-spin system) are detected, the total sweep width required in F_1 is prohibitively large. The F_1 sweep width is approximately $N*SW$, where SW is the approximate spectral width of any of the orders of coherence in the spin system; SW may be 100–300 kHz and necessarily gives rise to poor digital resolution.

4.1.2 Time Proportional Phase Incrementation

Time proportional phase incrementation (TPPI) enables the separation of spectra of various coherence orders. If the phase of the excitation radiation is incremented by $\Delta\phi = \Delta\omega{\cdot}\Delta t_1$ each time that t_1 is incremented by Δt_1, the n quantum spectrum is centered at a frequency $n\Delta\omega$ from the transmitter in the two-dimensional MQ NMR spectrum. MQ orders are separated in frequency by $\Delta\omega$ in the same fashion as if an offset had been employed.

4.1.3 Order Selective MQ Filtration Using Phase Cycling

Order selective detection of the spectrum of a desired order n is achieved by coadding $4n$ FIDs at each value of τ_1 with the phase of the preparation rf radiation (φ_1 in Figure 2) incremented from $2\pi/4n$ to 2π in steps of $2\pi/4n$ with the receiver phase (φ_3 in Figure 2) incremented by $\pi/2$ at each step.[11] Two-dimensional Fourier transformation over τ_1 and τ_2 affords a two-dimensional spectrum which has the MQ

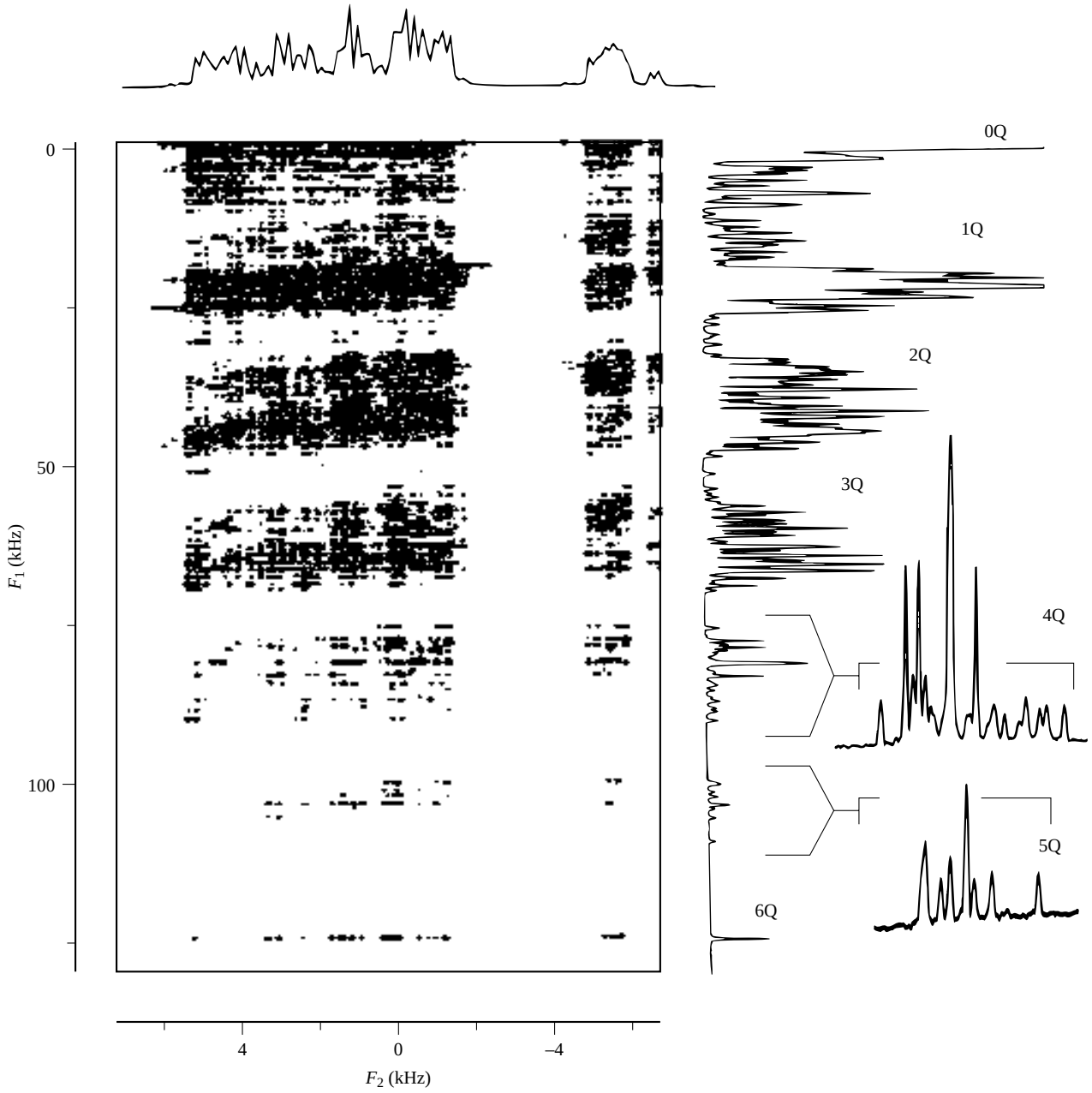

Figure 3 The separation of MQ spectra by employing a transmitter offset: ^{1}H spectrum of 2-methylthiophene aligned in a liquid crystalline solvent. The spectrum was acquired with the pulse sequence shown in Figure 2 with the transmitter offset approximately 20.7 kHz from the center of spectrum. The full spectrum is symmetrical about $F_1 = 0$ and only half of the spectrum is shown. Frequencies in the MQ spectrum are obtained from an F_1 projection of the two-dimensional data set

frequencies of the desired order of MQC in F_1 and the MQ filtered single quantum spectrum in F_2.

4.1.4 Coherence Echo Filtration

Order selective detection of the spectrum of a desired order n has been achieved by exploiting the phase properties of MQC transfer echoes. An additional (fixed) period d_e is inserted in the MQ pulse sequence, prior to the mixing pulse of the MQ pulse sequence (Figure 4). The delay d_e results in the MQCs evolving beyond the normal τ_1 period and coherence transfer echoes of the n quantum coherences maximize in the detection period at nd_e.[12] Different coherence orders give rise to echoes which maximize at different times in the detection period. The spectra derived from individual orders of coherence can be obtained by selecting a detection window to coincide with the maximum signal of the desired order of coherence.

4.1.5 Use of Magnetic Field Gradients

Order selective detection of the spectrum of a desired order n has been achieved by using field gradients.[13] A field gradient pulse of amplitude g is applied at the end of the MQ evolution

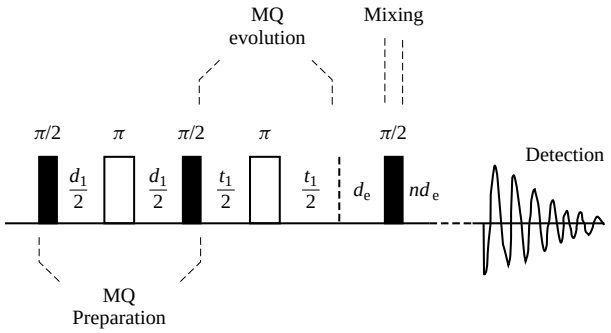

Figure 4 Pulse sequence for selectively observing MQC transfer echoes

period, prior to the mixing section of the MQ pulse sequence (Figure 5). A refocusing gradient of amplitude *ng* immediately after the mixing sequence selects only signals from the *n*-quantum spectrum.[12a,14]

4.1.6 Phase Sensitive MQ Spectra

A disadvantage of most simple mixing sequences which convert MQCs to detectable single quantum coherence is that the detectable single quantum spectrum has both absorption and dispersion components. As spin systems become larger, the single quantum spectrum degenerates to a mass of overlapping resonances, and any mixing sequence which results in signals of differing phase causes signal cancellation. In larger, more complex spin systems, the single quantum spectrum becomes weaker and inherently more difficult (or impossible) to detect. Pines et al.[15] have developed a general class of MQ experiments where the MQ preparation sequence is matched with a mixing sequence (a time reversal sequence) to give a single quantum spectrum which is in-phase. There are a number of matched preparation/mixing sequences and these have been used to observe high-order MQ spectra, including those in solids.

Another consequence of simple MQ sequences is that the MQ spectra obtained are obtained as spectra that cannot be phased. Most MQ spectra which have been recorded from samples dissolved in liquid crystalline solution have been transformed as magnitude spectra. Using appropriately matched preparation and mixing sequences, pure absorption spectra

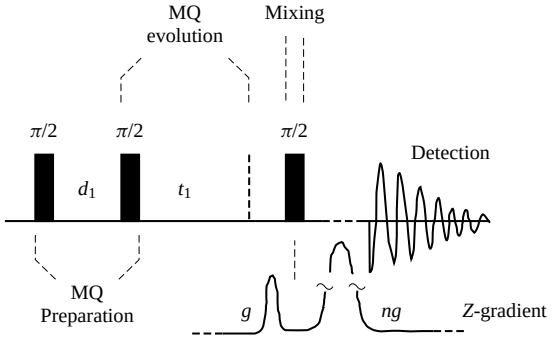

Figure 5 Pulse sequence for selectively observing MQC using field gradient filtration

have been recorded,[2b,16] and these show improved sensitivity and resolution compared with corresponding magnitude spectra.

5 METHODS OF SPECTRAL ANALYSIS AND SPECTRAL SIMULATION

The energy levels of an *n*-spin system can be calculated if the dipolar coupling constants D_{ij}, scalar coupling constants J_{ij}, chemical shifts ν_i, and quadrupolar coupling constants q_{ij} are known. The energy levels are grouped into manifolds according to their Zeeman quantum number (M) and irreducible symmetry representations. m Quantum transitions occur between energy levels of the same symmetry where $\triangle M = m$. The frequencies of MQ transitions are not difficult to calculate and the frequencies in experimental MQ spectra have been fitted iteratively to calculated frequencies using modifications of LAOCOON type[17] computer algorithms. The calculation of the correct intensities of MQ transitions is more demanding since the transition intensities are a complex function of the specific pulse sequence used to generate the spectrum. Transition intensities in MQ spectra derived from a simple three-pulse sequence (Figure 2) have been estimated using a statistical approach whereby all symmetry-allowed transitions are assumed to be equally excited. Averaging over a range of d_1 values, the integrated intensity per order decreases as $\triangle M$ increases, but the average intensity per transition increases as $\triangle M$ increases.[3b] The estimation of transition intensities in MQ spectra has been extended to excitation sequences involving order selective composite pulse excitation, and the calculations provide a reliable means for theoretically optimizing the efficiency of the excitation sequence.[18]

6 APPLICATIONS OF MQ NMR TO SAMPLES DISSOLVED IN LIQUID CRYSTALLINE SOLVENTS

6.1 Structural Studies

In the spectra of compounds dissolved in liquid crystalline solution, dipolar interactions between nuclei are not averaged to zero and the spectra can, in principle, be analyzed to obtain values for the dipolar coupling constant D_{ij} between each pair of nuclei (i and j) in the solute spin system. Since the D_{ij} are inversely proportional to the cube of the internuclear distances r_{ij} [equation (3)], the relative positions of the nuclei in the spin system can be determined and the shape of the molecule as well as its average orientation in the magnetic field can be deduced, providing enough independent D_{ij} values can be measured. For a system of coupled $I = 1/2$ nuclei, the transition frequencies in the MQ spectra are determined by the dipolar coupling constants, the scalar coupling constants, and the chemical shifts of the nuclei. In theory, the spectra of order $n - 1$ and $n - 2$ contain sufficient transitions to measure all the dipolar coupling constants and chemical shifts in an *n*-spin system:

$$D_{ij} = -(h\gamma_H^2/4\pi^2)S_{ij}/r_{ij}^3 \qquad (3)$$

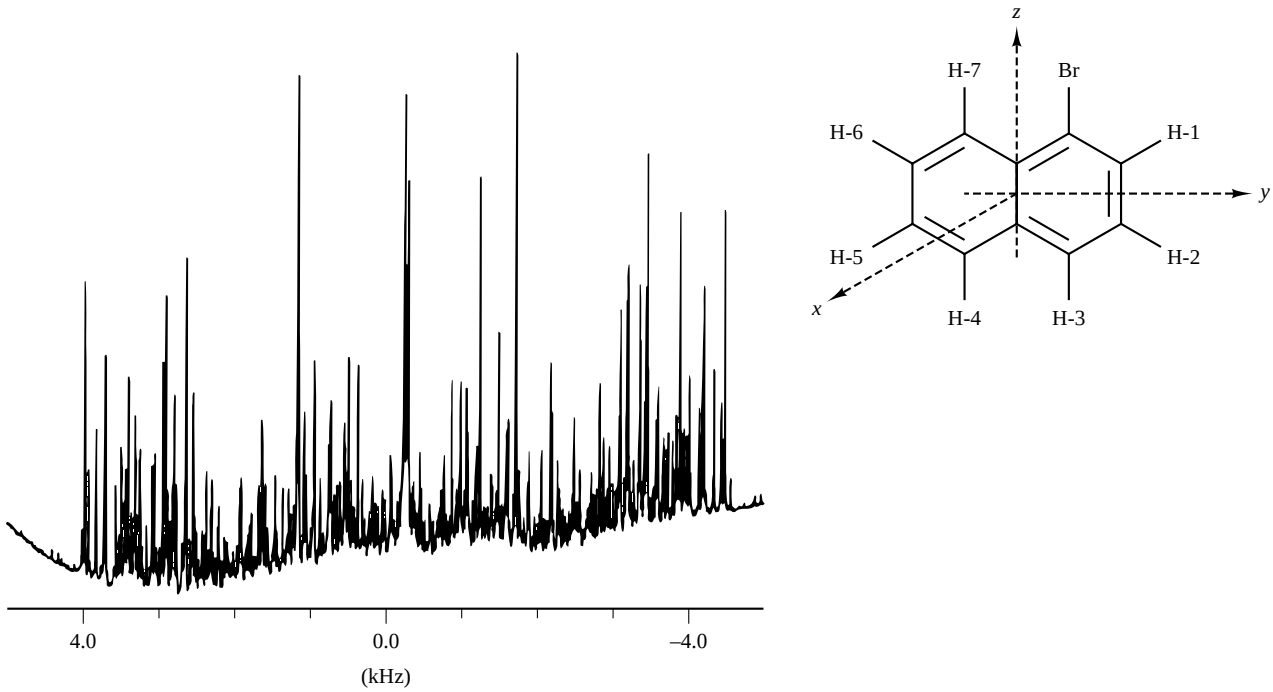

Figure 6 Single quantum proton spectra of 1-bromonaphthalene aligned in liquid crystalline solution. Reproduced by permission of Academic Press from Reference [20a]

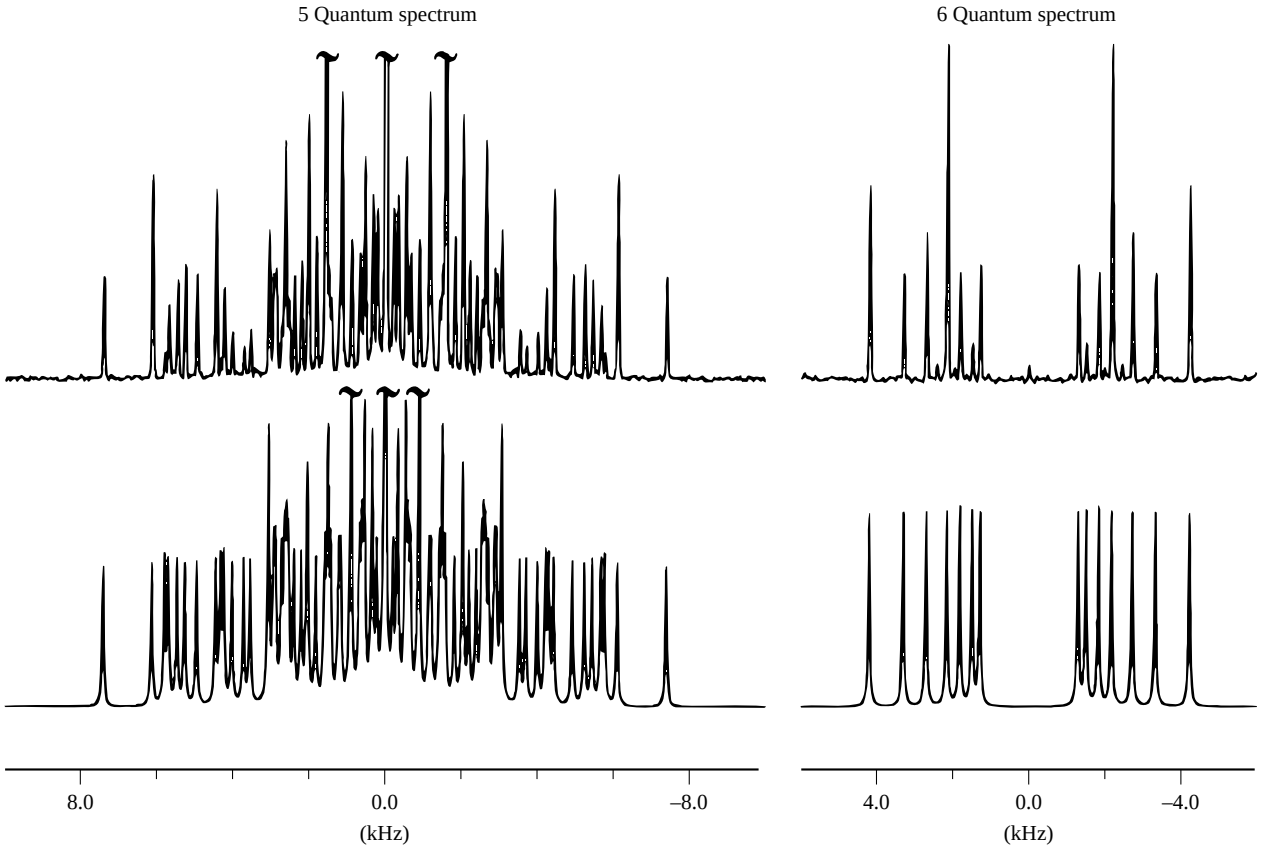

Figure 7 Experimental (upper) and simulated (lower) multiple quantum spectra of 1-bromonaphthalene aligned in liquid crystalline solution. Experimental spectra were acquired with chemical shift refocusing in F_1 and spectra were symmetrized about $F_1 = 0$. Simulations assume all transitions have the same intensity. Reproduced by permission of Academic Press from Reference [20a]

where γ_H is the proton magnetogyric ratio, r_{ij} is the internuclear distance between protons i and j, and S_{ij} is the order of the internuclear vector between i and j.[19] There have been only a few studies in which the geometry of a spin system has been established using MQ NMR.

6.1.1 Structure of Rigid Molecules: Structure of 1-Bromonaphthalene

1-Bromonaphthalene has a proton spin system containing seven nonequivalent spins. In liquid crystalline solution the ^{1}H NMR spectrum contains more than 3000 transitions (Figure 6).[20] The five and six quantum spectra have been recorded and solved simultaneously (Figure 7) to give values for the 21 independent dipolar coupling constants, and from the D_{ij} values the geometry of the planar seven spin system was determined.[20]

6.1.2 Chain Mobility in n-Hexane-d_6

MQ NMR has been employed to study chain mobility in alkanes dissolved in liquid crystalline solution. Drobny[2b] has reported the MQ spectra of *n*-hexane-d_6 (deuterated in the terminal methyl groups) dissolved in a nematic solvent. MQ spectra were recorded and the high quantum spectra (six and seven quantum) analyzed to give dipolar couplings. The six quantum proton spectrum contains 36 transitions and the seven quantum spectrum contains four transitions, as expected for an eight proton spin system with C_{2h} symmetry. The best fit of theoretically generated MQ NMR spectra to the experimental spectra was obtained with a model where only the minimum energy conformations of the alkane chain were appreciably populated.

6.1.3 Structure of 4-Cyano-4′-n-pentylbiphenyl

4-Cyano-4′-*n*-pentylbiphenyl is a nematic liquid crystal at room temperature. The five, six, and seven quantum MQ NMR spectra of the eight proton spin system of a partially deuterated compound (with the pentyl side chain completely deuterated) have been analyzed to give the interproton dipolar couplings in the biphenyl core of the molecule.[21] The best match between the experimental and simulated MQ NMR spectra were obtained when the biphenyl system was not planar, but when there was an angle of about 32° between the linked phenyl groups.

6.2 Counting Spins in Clusters

In MQ NMR, individual spins become correlated with each other over time through their dipolar couplings. The rate at which MQCs develop is a complex function of the coupling constants present in the spin system. In solids, where the distribution of dipole coupled spins is effectively infinite, the correlations between spins develop in a monotonic fashion. As time progresses, more spins can absorb more quanta and high order MQC can be generated.[22] In systems where there are effectively isolated clusters of spins (e.g. liquid crystals, molecules dissolved in liquid crystalline phases, and polycrystalline solids) the time development of MQC is interrupted and the system can only support MQC up to the size of coupled spin clusters. In the 21-spin system of the liquid crystal 4-cyano-4′-heptylbiphenyl, the effective spin system size increases to a maximum of 21 spins as the preparation time for MQC increases (Figure 8).

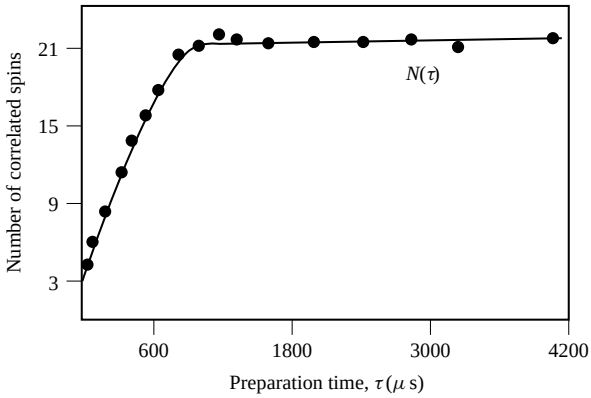

Figure 8 The effective system size $N(\tau)$ as a function of the preparation time τ for the liquid crystal 4-cyano-4′-heptylbiphenyl. After an induction period of approximately 1000 μs, $N(\tau)$ levels off to a value of 21, reflecting the number of spins in the isolated molecular cluster. Reprinted by permission of the American Chemical Society from Baum and Pines[22]

The rate of MQC development in a mixture of liquid crystalline materials has also been used to identify and observe distinct subsections of molecules comprising the liquid crystals. Separate MQ signals were observed for effectively isolated spin pairs (phenyl rings) and weakly coupled multispin clusters (alkyl tails)[23] in a mixture of 4-cyanophenyl 4′-butylbenzoate and 4-cyanophenyl 4′-heptylbenzoate.

6.3 Measurements of Diffusion

MQC has been used to extend the normal NMR spin echo measurement of diffusion. In typical spin echo experiments, molecules are labeled by their position in a magnetic field gradient after an initial rf pulse and diffusion is measured by monitoring the amplitude of the spin echo following a second pulse. MQ NMR spectroscopy exploits the fact that *n* quantum coherence dephases *n*-times more quickly than does single quantum coherence, so higher quantum coherences are significantly more sensitive to diffusion.

Martin et al.[24] measured the diffusion of dichloromethane (CH_2Cl_2) in various liquid crystal solvents by following the decay of the double quantum coherence. In measurements of the diffusion of benzene in a nematic liquid crystal, Zax and Pines[25] used a pulse sequence [Figure 9(a)] to excite MQC nonselectively and then selectively monitored the decay of the coherence echo of the $n = 1$ to $n = 6$ orders of coherence following field gradient pulses. The amplitude of echo decay for all orders of coherence was fitted to a modified Stejskal–Tanner equation[26] (Figure 9), thus verifying that the rate of echo decay is proportional to n^2.

6.4 Molecular Motion and Relaxation

The spectral densities of molecule motion $J_q(\omega)$ are usually estimated by simultaneously analyzing a combination of

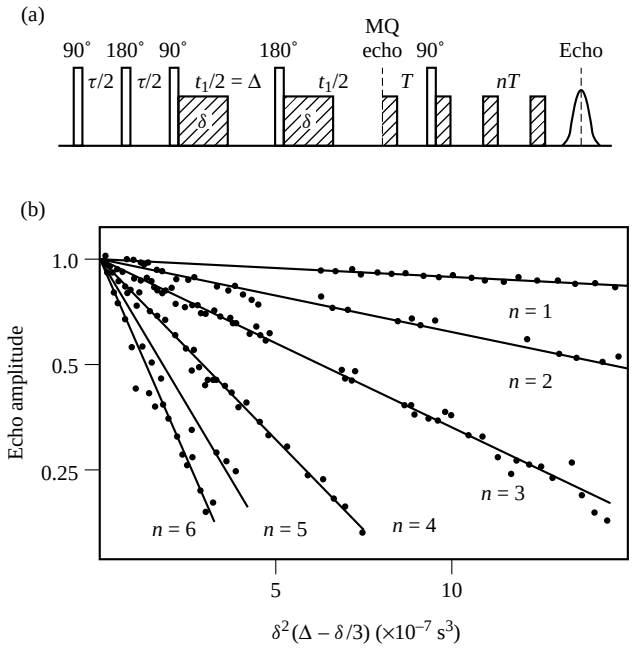

Figure 9 (a) Pulse sequence for an NMR pulsed field gradient experiment. (b) Normalized echo amplitudes plotted against the gradient pulse timing parameter $[\delta^2(\Delta - \delta/3)]$ of the Stejskal–Tanner equation.[26] (Reproduced by permission from D. Zax and A. Pines, *J. Chem. Phys.*, 1983, **78**, 6333)

relaxation measurements. Spectral densities may be measured from the decay of MQC and, particularly in $I = 1$ systems where the relaxation mechanism is dominated by the nuclear quadrupole, the relaxation of zero, double, triple and higher order coherences have been used to determine the spectral densities of motion for small deuterated organic molecules ($CDCl_3$,[27] $D{-}C{\equiv}C{-}C{\equiv}N$,[27b] CD_2Cl_2,[28] and $CD_3{-}C{\equiv}N$,[29]) dissolved in liquid crystalline solution. The relaxation of the two and three quantum resonances of ^{23}Na ($I = \frac{3}{2}$) and the four and five quantum resonances of ^{17}O ($I = \frac{5}{2}$) have been measured in lyotropic liquid crystals.[30]

6.5 Heteronuclear MQC

Heteronuclear MQC (HMQC) (coherence involving spins of different type, e.g. $^1H/^2H$ or $^1H/^{15}N$) have been used to study molecules in liquid crystal solution. Minoretti et al.[31] have demonstrated that there is a significant sensitivity advantage when the MQCs of a relatively insensitive nucleus (e.g. ^2H) can be detected indirectly by observing ^1H nuclei coupled to the heteronuclear spin system.

7 RELATED ARTICLES

Amphiphilic Liquid Crystalline Samples: Nuclear Spin Relaxation; Liquid Crystalline Samples: Deuterium NMR; Liquid Crystalline Samples: Diffusion; Liquid Crystalline Samples: Relaxation Mechanisms; Liquid Crystalline Samples: Spectral Analysis; Liquid Crystalline Samples: Structure of Nonrigid Molecules; Liquid Crystals: General Considerations; Lyotropic Liquid Crystalline Samples; Multidimensional Spectroscopy: Concepts; Multiple Quantum NMR in Solids; Multiple Quantum Spectroscopy of Liquid Samples; Structure of Rigid Molecules Dissolved in Liquid Crystalline Solvents; Two-Dimensional NMR of Molecules Oriented in Liquid Crystalline Phases.

8 REFERENCES

1. For leading references on NMR in liquid crystalline solvents see: (a) J. W. Emsley and J. C. Lindon, *NMR Spectroscopy Using Liquid Crystal Solvents*, Pergamon, Oxford, 1975; (b) J. W. Emsley (ed.), *Nuclear Magnetic Resonance of Liquid Crystals*, Riedel, Dordrecht, 1985.
2. For leading references on multiple quantum NMR spectroscopy, including studies of molecules in ordered phases see: (a) M. Munowitz and A. Pines, *Adv. Chem. Phys.*, 1987, **66**, 1; (b) G. P. Drobny, *Ann. Rev. Phys. Chem.*, 1985, **36**, 451; (c) D. Weitekamp, *Adv. Magn. Reson.*, 1983, **11**, 111; (d) G. Bodenhausen, *Progr. NMR Spectrosc.*, 1981, **14**, 137.
3. (a) S. Sinton, *Ph.D. Thesis*, University of California, Berkeley, 1982; (b) J. B. Murdoch, W. S. Warren, D. Weitekamp, and A. Pines. *J. Magn. Reson.*, 1984, **60**, 205; (c) A. Wokaun and R. R. Ernst, *Mol. Phys.*, 1978, **36**, 317; (d) R. A. Hoffman, *Adv. Magn. Reson.*, 1970, **4**, 87.
4. For general references to two-dimensional NMR spectroscopy see, for example: (a) A. E. Derome, *Modern NMR Techniques for Chemistry Research*, Pergamon, Oxford, 1989; (b) R. R. Ernst, G. Bodenhausen, and A. Wokaun, *Principles of Nuclear Magnetic Resonance in One and Two Dimensions*, Clarendon, Oxford, 1987.
5. (a) G. Drobny, A. Pines, S. Sinton, D. P. Weitekamp, and D. Wemmer, *Faraday Div. Chem. Symp.*, 1979, **13**, 49; (b) L. Braunschweiler, G. Bodenhausen, and R. R. Ernst, *Mol. Phys.*, 1983, **48**, 535; (c) O. W. Sorenson, M. Levitt, and R. R. Ernst, *J. Magn. Reson.*, 1983, **55**, 104.
6. D. P. Weitekamp, J. R. Garbow, and A. Pines, *J. Magn. Reson.*, 1982, **46**, 529.
7. (a) W. S. Warren and A. Pines, *J. Chem. Phys.*, 1981, **74**, 2808; (b) W. S. Warren, S. Sinton, D. P. Weitekamp, and A. Pines, *Phys. Rev. Lett.*, 1979, **43**, 1791; (c) W. S. Warren, D. P. Weitekamp, and A. Pines, *J. Magn. Reson.*, 1980, **40**, 581; (d) W. S. Warren, D. P. Weitekamp, and A. Pines, *J. Chem. Phys.*, 1980, **73**, 2084; (e) W. S. Warren and A. Pines, *Chem. Phys. Lett.*, 1982, **88**, 441.
8. T. M. Barbara, R. Tycho, and D. P. Weitekamp, *J. Magn. Reson.*, 1985, **62**, 54.
9. G. Drobny, A. Pines, S. Sinton, W. S. Warren, and D. P. Weitekamp, *Phil. Trans. R. Soc. London, Ser. A*, 1981, **299**, 585.
10. K. Nagayama, P. Bachmann, K. Wurthrich, and R. R. Ernst, *J. Magn. Reson.*, 1978, **31**, 133.
11. Order Selective detection: (a) A. Wokaun and R. R. Ernst, *Chem. Phys. Lett.*, 1977, **52**, 407; (b) G. Drobny, *Chem. Phys. Lett.*, 1984, **109**, 132.
12. Coherence transfer echoes: (a) A. Bax, P. G. DeJong, A. F. Mehlkopf, and J. Schmidt, *Chem. Phys. Lett.*, 1980, **69**, 567; (b) Y. S. Yen and D. P. Weitekamp, *J. Magn. Reson.*, 1982, **47**, 476; (c) D. P. Weitekamp, J. R. Garbow, and A. Pines, *J. Chem. Phys.*, 1982, **77**, 2870.
13. G. K. Pierens, T. A. Carpenter, L. D. Colebrook, L. D. Field, and L. D. Hall, *J. Magn. Reson.*, 1992, **99**, 398.
14. (a) R. L. Vold, J. S. Waugh, M. P. Klein, and D. E. Phelps, *J. Chem. Phys.*, 1968, **48**, 3831; (b) J. F. Martin, L. S. Selwyn, R. R. Vold, and R. L. Vold, *J. Chem. Phys.*, 1982, **76**, 2632; (c)

D. Zax and A. Pines, *J. Chem. Phys.*, 1983, **78**, 6333; (d) A. A. Maudsley, A. Wokaun, and R. R. Ernst, *Chem. Phys. Lett.*, 1978, **55**, 9.

15. Time reversal sequences: (a) W. S. Warren, S. Sinton, D. P. Weitekamp, and A. Pines, *Phys. Rev. Lett.*, 1979, **43**, 1791; (b) W. S. Warren, D. P. Weitekamp, and A. Pines, *J. Magn. Reson.*, 1980, **40**, 581; (c) W. S. Warren, D. P. Weitekamp, and A. Pines, *J. Chem. Phys.*, 1980, **73**, 2084.
16. G. Drobny and J. Listerud, *Mol. Phys.*, 1986, **58**, 1021.
17. (a) S. Castellano and A. A. Bothner-By, *J. Chem. Phys.*, 1964, **41**, 3863; (b) J. A. Ferretti, R. K. Harris, and R. B. Johannesen, *J. Magn. Reson.*, 1970, **84**, 3.
18. W. S. Warren, J. B. Murdoch, and A. Pines, *J. Magn. Reson.*, 1984, **60**, 236.
19. P. Diehl and C. L. Khetrapal, in *NMR, Basic Principles and Progress*, ed. P. Diehl, E. Fluck, and R. Kosfeld, Springer, Berlin, 1969, Vol. 1.
20. (a) L. D. Field, G. K. Pierens, K. J. Cross, and M. L. Terry, *J. Magn. Reson.*, 1992, **97**, 451; (b) L. D. Field and M. L. Terry, *J. Magn. Reson.*, 1986, **69**, 176.
21. (a) S. W. Sinton, D. Zax, J. B. Murdoch, and A. Pines, *Mol. Phys.*, 1984, **53**, 333; (b) S. W. Sinton and A. Pines, *Chem. Phys. Lett.*, 1980, **76**, 263.
22. J. Baum and A. Pines, *J. Am. Chem. Soc.*, 1986, **108**, 7447.
23. W. V. Gerasimowicz, A. N. Garroway, and J. B. Miller, *J. Am. Chem. Soc.*, 1990, **112**, 3726.
24. J. F. Martin, L. S. Selwyn, R. R. Vold, and R. L. Vold, *J. Chem. Phys.*, 1982, **76**, 2632.
25. D. Zax and A. Pines, *J. Chem. Phys.*, 1983, **78**, 6333.
26. E. O. Stejskal and J. E. Tanner, *J. Chem. Phys.*, 1965, **42**, 288.
27. (a) R. R. Vold and R. L. Vold, *J. Chem. Phys.*, 1977, **66**, 4018; (b) R. R. Vold, R. L. Vold, and N. Szerverenyi, *J. Phys. Chem*, 1981, **85**, 1934.
28. (a) R. Poupko, R. R. Vold, and R. L. Vold, *J. Magn. Reson.*, 1979, **34**, 67; (b) G. Bodenhausen, R. R. Vold, and R. L. Vold, *J. Magn. Reson.*, 1980, **37**, 93; (c) R. R. Vold, R. L. Vold, R. Poupko, and G. Bodenhausen, *J. Magn. Reson.*, 1980, **38**, 141.
29. (a) D. Jaffe, R. R. Vold, and R. L. Vold, *J. Magn. Reson.*, 1982, **46**, 475; (b) D. Jaffe, R. R. Vold, and R. L. Vold, *J. Magn. Reson.*, 1982, **46**, 496; (c) D. Jaffe, R. R. Vold, and R. L. Vold, *J. Chem. Phys.*, 1983, **78**, 4852.
30. I. Furo and B. Halle, *Mol. Phys.*, 1992, **76**, 1169.
31. A. Minoretti, W. P. Aue, M. Reinhold, and R. R. Ernst, *J. Magn. Reson.*, 1980, **40**, 175.

Biographical Sketch

Leslie D. Field. *b* 1953. B.Sc., 1975, Ph.D., 1979, Sydney. Faculty in Chemistry, Sydney University, 1982–present. Approx. 100 publications. Research interests: organometallic chemistry (C–H bond activation, catalytic activation of hydrocarbons, organometallic polymers, the mechanism of organometallic reactions); organic, organometallic, and inorganic synthesis; chemical applications of multinuclear MR spectroscopy, multiple quantum NMR spectroscopy, and NMR spectroscopy of molecules aligned in ordered solvents.

Spinning Liquid Crystalline Samples

Jacques Courtieu

University of Paris-Sud, Orsay, France

1	Introduction	1
2	NMR Implications of Tilting the Director from B_0	2
3	The Slow Sample Rotation Technique	2
4	Spinning at Various Angles	4
5	Application of VAS to the NMR of Dissolved Molecules	5
6	Perspectives	7
7	Related Articles	7
8	References	7

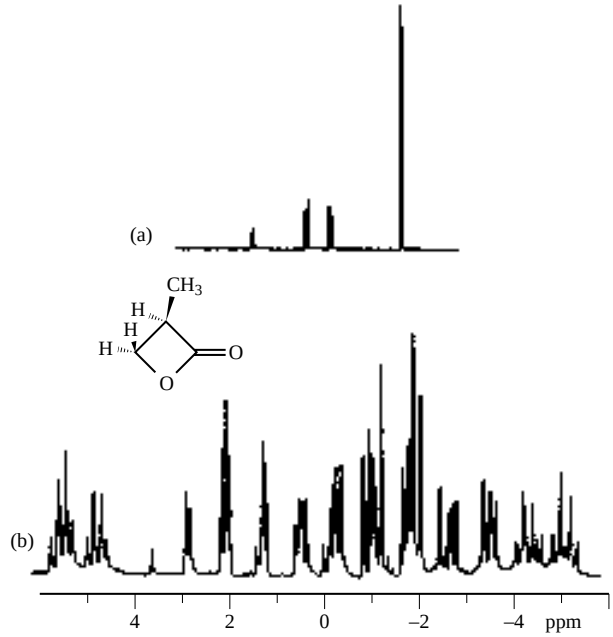

Figure 1 ^{1}H NMR spectra of β-butyrolactone at 250 MHz and 20 °C: (a) Spectrum of an isotropic solution in $CDCl_3$: (b) Spectrum of an anisotropic solution in the liquid crystal solvent ZLI 1167. Many overlapping peaks are not resolved in this experimental spectrum

1 INTRODUCTION

The analytical power of the use of nematic liquid crystals as solvents in high-resolution NMR, due primarily to the pioneering work of Saupe and Englert,[1–3] has excited a part of the NMR community since 1963. The basic phenomenon is that molecules dissolved in these ordered media are partially oriented in such a way that, while the intermolecular interactions are still averaged to zero through rapid molecular motions, all the intramolecular anisotropic interactions are no longer averaged to zero. This effect gives chemists a very powerful tool to measure, among others, shielding anisotropies, internuclear dipole–dipole interactions, quadrupolar interactions, and the anisotropic parts of the scalar coupling constants. Special emphasis must be given to the dipole–dipole interaction, because its classical relationship to molecular geometry through the well-known equation

$$D_{ij} = -\frac{h\gamma_i\gamma_j}{8\pi^2}\left\langle \frac{3\cos^2\theta - 1}{r_{ij}^3} \right\rangle \qquad (1)$$

provides a very precise method of investigating the geometry of the dissolved molecules. In this equation, h is Planck's constant, D_{ij} is the dipolar coupling constant between nuclei i and j, γ_i and γ_j are their magnetogyric ratios, r_{ij} is the magnitude of the internuclear vector $\boldsymbol{r}_{ij}$, θ is the angle between $\boldsymbol{r}_{ij}$ and the magnetic field, and the angle brackets indicate the time average. Several reviews have been written on the subject,[4–9] and readers who are not familiar with this kind of nonclassical NMR should refer to these. In spite of this great advantage, NMR studies using liquid crystal solvents have declined somewhat since the late 1970s, the reasons for which can be understood by considering the following.

Although the spectra of molecules dissolved in ordered media are much more informative than those in isotropic solvents, they are also considerably more complicated for two reasons. First, many of the residual dipolar couplings are generally much larger than the resonance frequency differences, often having values of 2 or 3 kHz. Consequently, the classical first-order approximation, which can be used when the couplings are small compared with the $\Delta\nu_i$, is no longer valid, even at high fields. Second, the appearance of the partially averaged dipolar couplings lifts the degeneracies among spin systems containing chemically or magnetically equivalent nuclei. Thus, for molecules dissolved in a nematic medium, one generally obtains second-order spectra that are difficult and sometimes even impossible to analyze by calculations using the spin Hamiltonian.

The complexity of this kind of nonclassical NMR is well illustrated by the spectra of β-butyrolactone shown in Figure 1. The isotropic spectrum shows a simple $AMKX_3$ pattern, which can be easily recognized. On the other hand, the anisotropic spectrum is very complicated, and has hundreds of transitions, many of which overlap in the experimental spectrum. Such a spectrum could be analyzed, and consequently the geometric parameters derived. However, the analysis would require a good computer, some skill, and weeks of effort. The reader should be aware of the fact that if the molecule under investigation does not possess any element of symmetry and the number of spins is larger than six, its spectrum would often become impossible to calculate. Our drawers are full of spectra that we have never been able to calculate, and the situation is probably the same in many specialized laboratories around the world. Finally, perhaps the most important point is the fact that we have not found in the scientific literature a geometrical analysis of a chiral molecule through this otherwise very precise method, which allows internuclear distances to be evaluated with a precision within the amplitude of bond vibrations.

The limitations mentioned above have become a challenge, and many investigators in this field have tried to overcome them. Their basic idea is as follows: if it is possible to reduce the magnitude of the dipolar couplings to make them smaller than the frequency shift differences, or even comparable in magnitude to the isotropic part of the scalar couplings, it would be possible to convert the very strong second-order pattern

commonly shown in the spectra into a first-order spectrum analyzable by any NMR spectroscopist. It has been known from the very beginning of the NMR study of liquid crystals that this can be achieved when the director is tilted at an angle β from the magnetic field. Section 2 is devoted to showing this effect. Then it will be shown that, in some circumstances, it is possible to tilt the director from the magnetic field through sample rotation.

The first experiments on the rotation of a nematic liquid crystal around an axis perpendicular to the magnetic field were performed by the physicists Tsvetkov[10] and Lippmann.[11] Then, Snyder[12] in 1965 and Diehl and Khetrapal[13] in 1967 applied this old idea to the NMR study of liquid crystals. The details of the effects of this technique, which we shall refer to as the slow sample rotation experiment, were first studied by Leslie, Luckhurst, and Smith for EPR[14] and by Emsley, Lindon, Luckhurst, and Shaw for applications in NMR.[15] This experiment will provide us with a starting point, which will be the content of Section 3. The reason to begin our discussion with tilting the axis of rotation by 90° is not only because of the historical chronology but also because it contains all of the main ingredients to introduce the variable angle spinning technique. Unfortunately, there are two serious limitations to this approach: first, it is theoretically impossible to reduce the anisotropic interactions by more than a factor of four; second, the reduction is accompanied by an increase in linewidth, which further limits the useful reduction factor to barely one-half.

In Section 4, we shall derive the behavior of the director of a nematic when it is spun around an axis tilted at an angle β from the magnetic field, which constitutes the basis of variable angle sample spinning (VAS). The first idea of spinning nematics neither parallel nor perpendicular to the magnetic field but in between as a means to reorient the director was due to Hornreich[16] in 1977, and the technique was first applied in EPR by Yo, Poupko, and Hornreich[17] in 1978. The NMR applications were worked out by ourselves[18] in 1981, and independently by Lippmaa et al. at Tallinn[19] in 1982. Then, a detailed theoretical analysis[20] and a review[21] were given shortly after the initial experimental demonstrations of VAS.

Section 5 will be devoted to the principal applications of the technique to the NMR of molecules dissolved in nematics. Applications to the NMR of liquid crystals themselves are described in ***Liquid Crystalline Samples: Carbon-13 NMR***.

In the concluding Section 6, we shall try to evaluate the prospects of the VAS method for the near future, which may help the further development of one of the most fascinating aspects of NMR in chemistry, namely the structural and dynamic analysis of molecules in an anisotropic environment.

2 NMR IMPLICATIONS OF TILTING THE DIRECTOR FROM B_0

The arguments presented here are based on the assumption that the nematic sample is placed in a magnetic field of 1 T or more, so that nuclear magnetic moments are quantized along this field and that nematic director dynamics are dominated by magnetic field interactions and the mechanical motion of the sample. It will also be assumed that the rotational motions of individual molecules are fast on the NMR timescale, so that interactions can be expressed as averages.

Molecules dissolved in liquid crystals tumble rapidly but with unequal orientational probabilities, so that anisotropic intramolecular interactions are averaged to nonzero values. Only the averages of these second-rank tensorial properties in the direction of spin quantization are measurable. Quantization is along the externally applied magnetic field, which is arbitrarily defined as the laboratory z axis. We have

$$\bar{T}_{zz} = \tfrac{1}{3}(T_{11} + T_{22} + T_{33}) + \frac{2}{3}\sum_{\alpha,\beta} \tfrac{1}{2}\langle 3\cos\theta_\alpha^z \cos\theta_\beta^z - \delta_{\alpha\beta}\rangle T_{\alpha\beta} \qquad (2)$$

where T_{zz}, the z component of a tensorial property T, corresponds to our measure along the magnetic field. $\frac{1}{3}(T_{11} + T_{22} + T_{33})$ is the isotropic average of the interaction, often referred to as T^{iso}. The sum, which depends on the orientation through the angles

$$\theta_\alpha^z$$

between the molecular axes $(\alpha,\beta) \equiv (1,2,3)$ and the magnetic field, is the anisotropic part of the interaction ΔT.

In uniaxial liquid crystals such as nematics it has been shown[12] that the anisotropic part is sensitive to the angle β between the axis of orientation, the director, and the magnetic field through the simple equation

$$\bar{T}_{zz} = T^{\text{iso}} + \tfrac{1}{2}(3\cos^2\beta - 1)\Delta T \qquad (3)$$

which indicates that the average property measured along the z magnetic field is made up of two terms. The first term is the invariant under the rotation of T, and the second term is the anisotropic contribution scaled by the factor $\frac{1}{2}(3\cos^2\beta - 1)$. In other words, this equation means that if it is possible to orient the director of a uniaxial liquid crystal at an angle β to the magnetic field then the anisotropic part of the interaction will be reduced by a factor $\frac{1}{2}(3\cos^2\beta - 1)$, which lies between 1 and -0.5 for $0 > \beta > \frac{1}{2}\pi$. This is true for the shielding anisotropy, the anisotropy of the scalar coupling, and for the dipolar and quadrupolar couplings that are purely anisotropic interactions.

Of course, the difficulty is that the angle β must be the same all over the sample. If this is not the case then the spectrum will not be high-resolution but a powder pattern. In other words, a homogeneous orientation is needed. This can be obtained by spinning the sample.

Having established the NMR consequences when the director is tilted from the magnetic field, we must now describe how it is possible to move the director from its equilibrium position.

3 THE SLOW SAMPLE ROTATION TECHNIQUE

3.1 Magnetic Torque Against Viscous Torque

When subjected to an external magnetic field $\boldsymbol{B}_0$ of sufficient magnitude (usually about 0.5 T or higher), the local order directors of a nematic liquid crystal have a uniform alignment, producing a single well-defined bulk nematic director $\boldsymbol{n}$. This is due to the interaction between the external field and the anisotropy of the diamagnetic susceptibility, which is defined as

$$\Delta\chi = \chi_{\parallel} - \chi_{\perp} \qquad (4)$$

where $\chi_{\parallel}$ and $\chi_{\perp}$ are the susceptibilities parallel and perpendicular to $\boldsymbol{n}$, respectively. Although $\Delta\chi$ is relatively small, the collective effect in the bulk sample is sufficient to overcome thermal disordering motions. Quantitatively, this can be expressed as a change in the potential energy P of the system:[22]

$$P = -\tfrac{1}{3}\Delta\chi B_0^2 \tfrac{1}{2}(3\cos^2\beta - 1) \tag{5}$$

where β is the angle between the director and the magnetic field. For many nematics, $\Delta\chi$ is positive, so the potential energy is minimum for $\beta = 0^\circ$, and the equilibrium alignment of $\boldsymbol{n}$ will be along $\boldsymbol{B}_0$. For a few liquid crystals, most of which have no aromatic rings, $\Delta\chi$ is negative and P is minimum for $\beta = 90^\circ$; therefore, $\boldsymbol{n}$ will tend to be perpendicular to $\boldsymbol{B}_0$. Since nematics are moderately viscous fluids, the alignment of $\boldsymbol{n}$ is not instantaneous, but requires some time to reach equilibrium. This is governed by the competition between the viscous torque and the magnetic torque.

The potential energy gives rise to a magnetic torque τ_m on the liquid crystal director whose magnitude per unit volume is

$$\tau_m = \Delta\chi B_0^2 \cos\beta \sin\beta \tag{6}$$

According to Leslie,[23,24] the viscous torque τ_v can be written as

$$\tau_v = \gamma_1 \dot{\beta} \tag{7}$$

where γ_1 is the Leslie rotational twist coefficient and $\dot{\beta}$ is the time rate of change of β.

The return of $\boldsymbol{n}$ to its equilibrium condition is related to a characteristic motional frequency expressed as ω_c, which is a function of these competing torques. Equating τ_v and τ_m in equations (6) and (7), an expression for ω_c can be obtained:

$$\gamma_1\dot{\beta} = \Delta\chi B_0^2 \cos\beta \sin\beta \tag{8}$$

$$\dot{\beta} = \omega_c \cos\beta \sin\beta \tag{9}$$

with

$$\omega_c = \frac{\Delta\chi B_0^2}{\gamma_1} \tag{10}$$

For typical nematic liquid crystals, $\omega_c/{B_0}^2$ is of the order of 4.8 Hz T^{-2}, which means that ω_c is approximately 30 Hz at 2.35 T (100 MHz proton NMR), 200 Hz at 5.87 T (250 MHz), and 1.1 kHz at 14.10 T (600 MHz).

3.2 Slow Spinning Perpendicular to the Magnetic Field

The behavior of a nematic mesophase of $\Delta\chi > 0$ being spun around an axis perpendicular to the director was first studied by Lippmann,[11] but it was the EPR and NMR spectra of probes dissolved in nematic phases that provided a detailed description of the director behavior.[14,15,25–29]

The quantitative relation can be easily derived from the equality of the two torques expressed in Equation (8). According to this, at equilibrium, the director adopts an angle β relative to $\boldsymbol{B}_0$ given by

$$\sin 2\beta = \frac{2\gamma_1\omega_r}{\Delta\chi B_0^2} \tag{11}$$

where $\omega_r = \dot{\beta}$ is the angular velocity of the spun sample. From equation (11), it can be seen that the maximum theoretical value for β is 45°, which is achieved when ω_r reaches a critical angular velocity that is half of the characteristic motional frequency defined in equation (10):

$$\omega_r^{\text{critical}} = \frac{\Delta\chi B_0^2}{2\gamma_1} = \tfrac{1}{2}\omega_c \tag{12}$$

For $\omega_r < \frac{1}{2}\omega_c$, the director will reach an equilibrium angle

$$\beta = \tfrac{1}{2}\sin^{-1}\left(\frac{2\omega_r}{\omega_c}\right) \tag{13}$$

When $\omega_r > \frac{1}{2}\omega_c$, it can be shown that the director rotates about the spinning axis.

3.3 Experiments and Limitations

The 94.1 MHz fluorine spectra of CF_3COOH dissolved in Phase V, obtained at various rotation speeds by Emsley and Lindon,[6] provide a nice way to show the power and the limitations of the slow spinning technique, Figure 2. In this A_3 spin system, the line positions are determined by the F–F dipolar coupling and the electronic shielding $\sigma_F^{iso} + \Delta\sigma_F$. Compared with the static spectrum (a), the reduction of the dipolar interaction in spectrum (b) is clear, together with a shift of the central line due to the reduction of the shielding anisotropy. Unfortunately, it must also be noted that this spectrum is no longer a simple 1–2–1 triplet, and the outer lines are broadened. This effect is more pronounced in spectrum (c), where $\omega_r = \frac{1}{2}\omega_c$. Spectra (c) and (d) show clear

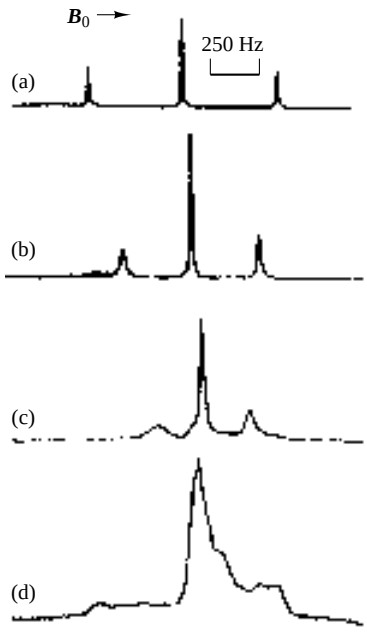

Figure 2 ^{19}F NMR spectra of CF_3COOH dissolved in the nematic liquid crystal Merck Phase V at 94.1 MHz, with ω_r(critical) = 11.8 Hz. The sample was rotated about an axis perpendicular to the magnetic field, and values of the rotation rate ω were (a) 0.0 Hz,; (b) 9.3 Hz; (c) 11.8 Hz; (d) 14.4 Hz

evidence of being weighted sums of spectra with values of β lying in a wide range between 0° and 90°. The distribution of the values of β was first analyzed in the ESR spectra of spin probes dissolved in rotating nematic phases by Carr et al.[25] They showed that the results are consistent with an elliptical distribution of the angle β.

Although slow sample rotation is limited to small tilting angles of the director, where the value of the reduction factor $\frac{1}{2}(3\cos^2\beta - 1)$ is not very different from unity, this technique has been used by Emsley and Lindon[27,28] to separate the anisotropic from the isotropic interactions, such as J^{iso} from D, or σ^{iso} from $\Delta\sigma$. However, the original goal, which is to reduce the dipolar interaction to such an extent that a first-order spectrum can be obtained, cannot be reached by this method. On the other hand, the beauty of the VAS technique, which we are going to describe in the next section, is to actually narrow the lines as the tilt angle between the magnetic field and the director increases. Because the slow sample rotation technique was discovered first, and all the necessary theoretical backgrounds have been discussed, the equations developed in this section will be found useful below.

4 SPINNING AT VARIOUS ANGLES

The work on slow spinning samples was done very early—most probably because many of the experiments were performed on conventional spectrometers with electromagnets, in which the probes are designed to spin the samples about an axis perpendicular to $\boldsymbol{B}_0$. There is another well-known situation in these electromagnets, namely the case of nematics with negative $\Delta\chi$. These orient spontaneously with the director perpendicular to the magnetic field. In this case, it is commonly said that rotation does not affect the orientation of a nematic; but this is not true. If the sample is kept static in the field, the directors distribute in a plane perpendicular to $\boldsymbol{B}_0$. When the sample is rotated, the directors reorient about the unique rotation axis, which remains perpendicular to $\boldsymbol{B}_0$. This, of course, would not change the NMR measurement, but the interesting point is that the difference of the director behavior between the two cases indicates the roles of $\boldsymbol{B}_0$, $\Delta\chi$, and the rotation axis in this problem.

In the following discussion, the derivation of Hornreich[16] together with that of Courtieu et al.[20] are followed.

4.1 Average Potential Theory

If the liquid crystal were spun around an axis tilted from $\boldsymbol{B}_0$ by an angle β at an angular velocity larger than ω_c, the director would not have time to orient parallel to the field, but would orient in such a way that the average of the potential energy over one cycle of the rotation is minimum. This average potential energy P is obtained from Equation (5) by averaging $\cos^2\beta$ over one cycle of the rotation. To calculate the average of $\cos^2\beta$, consider a reference frame fixed relative to the bulk of the liquid crystal, with the polar axis along the spinning axis as shown in Figure 3. Here we denote the principal axis of the bulk liquid crystal as $\boldsymbol{R}$, which will be defined as the spinning axis later.

Assume that the director is stationary relative to the bulk liquid and is described by a polar angle δ and an azimuthal angle ϕ. Since the angle between the spinning axis and the magnetic field is η, in this frame the magnetic field has a constant polar angle η and a constantly changing azimuthal angle $\phi_m = \omega_r t$. The cosine of the angle β between the director and the magnetic field is

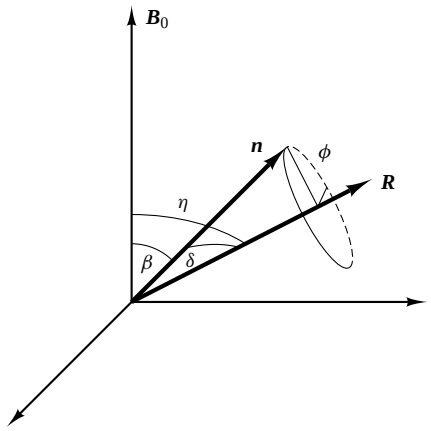

Figure 3 Definition of the axes and angles used in the text: $\boldsymbol{B}_0$, $\boldsymbol{n}$, and $\boldsymbol{R}$ are the magnetic field, the director, and the spinning axis, respectively; β is the angle between $\boldsymbol{B}_0$ and $\boldsymbol{n}$, η is that between $\boldsymbol{B}_0$ and $\boldsymbol{R}$, and δ is that between $\boldsymbol{n}$ and $\boldsymbol{R}$

$$\cos\beta = \cos\eta\cos\delta + \sin\eta\sin\delta\cos(\phi_m - \phi) \tag{14}$$

The average of $\cos^2\beta$ over one cycle of the rotation is

$$\cos^2\beta = \cos^2\eta\cos^2\delta + \tfrac{1}{2}\sin^2\eta\sin^2\delta \tag{15}$$

Inserting this into Equation (5) and simplifying the result, the average potential energy is obtained:

$$\begin{aligned}\bar{P} &= -\tfrac{1}{3}\Delta\chi B_0^2[\tfrac{1}{2}(3\cos^2\eta - 1)][\tfrac{1}{2}(3\cos^2\delta - 1)] \\ &= \tfrac{1}{3}\Delta\chi B_0^2 f(\eta,\delta)\end{aligned} \tag{16}$$

The angular part of the function $f(\eta,\delta)$ is plotted in Figure 4 for different values of η. Defining the magic angle as $\theta_m = \arccos(\frac{1}{3})^{1/2} = 54°\ 44'$, it can be analyzed in the following way for $0° \le \eta \le 90°$.

1. For nematics with $\Delta\chi > 0$, (a) when $\eta < \theta_m$, the potential energy is minimum at $\delta = 0°$, and the director tends to align along the rotation axis; (b) when $\eta = \theta_m$, the potential energy is independent of δ, which means that the director has no preferred orientation; (c) when $\eta > \theta_m$, the potential energy is minimum at $\delta = 90°$, and the director is distributed in a plane perpendicular to the rotation axis.
2. For nematics with $\Delta\chi < 0$, the situation of the minimum potential changes so that, (a) when $\eta < \theta_m$, the director is distributed in a plane perpendicular to the rotation axis; (b) when $\eta = \theta_m$, the director does not show a preferred orientation; (c) when $\eta > \theta_m$, the director aligns along the rotation axis.

The average potential treatment presented above is semi-quantitative, and holds only for high spinning speed. However, it does give a simple understanding of the phenomenon. A complete mechanistic analysis been given by Hornreich[16] and by Courtieu et al.[20] It leads to the conclusion that the theoretical situation described in Sections 2 and 3 can be achieved through sample spinning at an angular frequency five or more

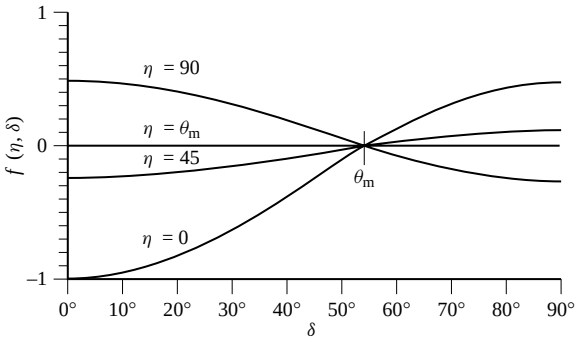

Figure 4 Plot of the function $f(\eta,\delta) = -\frac{1}{4}(3\cos^2\eta - 1)(3\cos^2\delta - 1)$

time the critical spinning rate. In this situation, the angle β reaches a steady-state position where the director is homogeneously aligned on the rotation axis, $\beta \approx \eta$, as long as we are inside the region of stability. The latter depends only on the sign of the diamagnetic susceptibility anisotropy. The next section will be devoted to the experimental confirmation of the above derivation using NMR.

5 APPLICATION OF VAS TO THE NMR OF DISSOLVED MOLECULES

In this section, we shall show some examples of the application of VAS to study the NMR of small molecules dissolved in nematic solvents. The basis of these applications is the ability of VAS to reduce various anisotropic interactions by a factor of $\frac{1}{2}(3\cos^2\beta - 1)$, as expressed by Equation (3). Actually, the tremendous advantage of the VAS technique in reducing H–H dipolar couplings has found another important application in the simplification of the ^{1}H and ^{13}C spectra of liquid crystals (see ***Liquid Crystalline Samples: Carbon-13 NMR***).

5.1 Practical Considerations for VAS

We have seen in Section 4 that in VAS, the orientation of the nematic director is dependent on the spinning angle η, the spinning rate, and the magnetic anisotropy $\Delta\chi$. When the spinning rate is fast, for a liquid crystal with $\Delta\chi > 0$, the director orients along the spinning axis for $0^\circ < \eta < \theta_m = 54^\circ\,44'$, lies around a cone about the spinning axis for η near the magic angle, and is distributed perpendicular to the spinning axis for $\theta_m < \eta < 90^\circ$. The situation is opposite for a liquid crystal with $\Delta\chi < 0$. However, when the spinning angle is near θ_m, the situation is more complicated. For example, for a nematic liquid crystal with $\Delta\chi < 0$, the director orients perpendicular to the spinning axis when η is between 0° and 52°, but lies around a cone in the vicinity of the magic angle, and spinning sidebands become a prominent feature of the spectra.[29] The patterns and intensities of the sidebands depend upon the dipolar interactions and frequency shifts of the system as well as the spinning rate and spinning angle. A study of these effects was made by studying the ^{19}F spectra of CF_2ClCCl_3 in two liquid crystal solvents (Merck ZLI 2334, $\Delta\chi > 0$; ZLI 1167, $\Delta\chi < 0$). The details of the theoretical analysis will not be repeated here; it is sufficient to say that the results agree quite well with the experimental data.

The spinning sidebands are, of course, not desirable in most applications of the VAS method. Fortunately, they can be avoided and even totally eliminated by setting the spinning rate fast enough and the angle η far away enough from the magic angle. In the experiments described in the rest of this section, the conditions were such that the fast spinning limit is reached. However, other complications would appear at very high spinning rates, where inertial forces become important.[21]

5.2 Reduction of Dipolar Interactions

The original goal of the VAS technique was to reduce the dipolar interaction and change second-order spectra into first-order ones. This goal was successfully reached,[20] and the result is illustrated in Figure 5, which shows the change in the ^{19}F spectra of $CF_2{=}CFBr$ dissolved in a nematic solvent. When the sample is stationary or spun at $\eta = 0^\circ$, the spectrum is of the ABC type, because the D_{ij} values are of the same order of magnitude as the frequency shifts. Tilting the spinning axis reduces D_{ij} more than the frequency shift differences, and the second-order spectrum gradually changes into a first-order one when η increases. At $\eta = 51^\circ$, the ABC pattern is converted

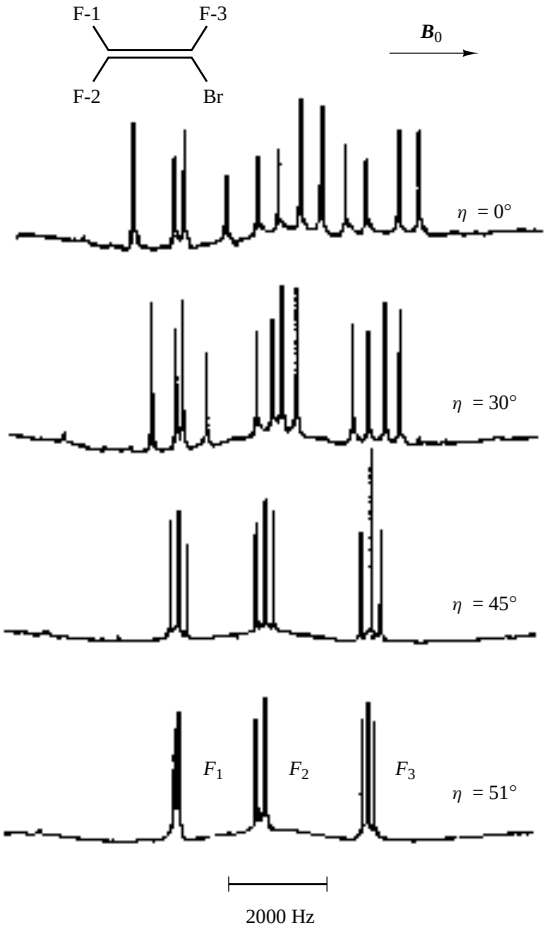

Figure 5 ^{19}F NMR spectra of $CF_2{=}CFBr$ dissolved in the nematic liquid crystal *p*-*n*-pentylphenyl 2-chloro-4-(*p*-*n*-pentylbenzoyloxy)benzoate at 75.25 MHz and 31 °C. The spinning rate was 75 Hz, and values of the spinning angle η are indicated in the spectra

into an AMX pattern, from which the values of the couplings can be obtained directly. An analysis of the spectra yields the relative signs of D_{ij} and J_{ij}. In the limit of $\eta = \theta_m$, only the isotropic scalar couplings remain, and the centers of the multiplets give the isotropic shielding in the liquid crystal solvent.

A reduction of the dipolar coupling constants, of course, also simplifies the ^{1}H spectrum of solute molecules in liquid crystal solvents. For example, the ^{1}H spectrum of norbornadiene, an eight-spin system, is quite complicated and difficult to analyze, but it becomes essentially first-order when the system is spun at $\eta = 45.2^\circ$.[30] Some peaks in the VAS spectrum overlap with each other because the order parameters are quite small, but the three largest coupling constants can be immediately obtained from the spectrum with VAS. From these data, very good initial estimates of the order parameters were made to aid the analysis of the complicated spectrum for $\eta = 0^\circ$. A simplification of the spectra of thiophene dissolved in two nematic solvents, one with $\Delta\chi > 0$, and the other with $\Delta\chi < 0$, was also observed.[31] The proton dipolar coupling constants of these systems were measured, and it was confirmed that in both cases, the coupling constants are scaled by the angular factor predicted by the theory discussed in the previous section.

In a VAS experiment, it is essential to determine the angle η between the spinning axis and the magnetic field accurately. The determination can be made by the use of an optical pointer.[32] Another way of determining η is to take advantage of the reduction in the dipolar coupling constant by comparing the dipolar splittings of a solute molecule with and without sample spinning. If the director of the liquid crystalline solvent aligns along the spinning axis, the ratio between the dipolar splittings in the two cases is $\frac{1}{2}(3\cos^2\eta - 1)$; if it aligns perpendicularly to the spinning axis, the factor is $-\frac{1}{4}(3\cos^2\eta - 1)$. The ^{1}H signal of CH_2Cl_2,[33] the ^{19}F signal of CF_2ClCCl_3,[34] and the ^{13}C signals of CH_2I_2[20] and $CHCl_3$[35] have been used for this purpose.

5.3 Shielding Anisotropy

The use of liquid crystals as solvents to determine the shielding anisotropy of solute molecules is a well-known method[36] (see ***Anisotropy of Shielding and Coupling in Liquid Crystalline Solutions***). The principle of the technique is to follow the resonance frequencies of the solute as its molecular orientation changes. This change can be induced by several methods, including changes of phase, solute concentration, or temperature. However, each has its own disadvantage, leading to various uncertainties in the results.[36] On the other hand, the VAS method does not require any internal change in the system itself, and may avoid some of these problems.

Väänänen et al. have demonstrated the use of the VAS technique to determine the shielding anisotropy in CH_3I.[32] To do this, it should be recalled that Equation (3) is applicable to both the dipolar coupling constant and the shielding anisotropy. By taking the ratio of these two kinds of interactions, the factor $\frac{1}{2}(3\cos^2\beta - 1)$ can be eliminated to give

$$\sigma^{\exp} = \sigma^{\mathrm{iso}} + \tfrac{2}{3}\Delta\sigma_H S_{zz}\frac{D^{\eta}_{HH}}{D^{0}_{HH}} \tag{17}$$

where $\sigma^{\exp}$ is the experimental electronic shielding. Then, the shielding anisotropy $\Delta\sigma_H$ was obtained from the slope of the plot of $\sigma^{\exp}$ versus the observed dipolar coupling constant D^{η}_{HH} as the angle was varied gradually. Using this approach, it was found that $\Delta\sigma_H$ was dependent on the liquid crystal solvent, which could be caused by the anisotropy of the local effects on $\sigma^{\exp}$ and different deformational effects of the liquid crystal solvents on the methyl groups of methyl iodide and the reference molecule, tetramethylsilane. This observation confirms similar results reported earlier that both the ^{1}H and the ^{13}C shielding anisotropies of CH_3CN are dependent on the liquid crystal solvent, and that they are linearly related to each other.[37]

5.4 Quadrupolar Interactions

When VAS is used to cause the nematic director to align along an axis forming an angle β with respect to $\boldsymbol{B}_0$, the quadrupolar interaction is also scaled by a factor of $\frac{1}{2}(3\cos^2\beta - 1)$. This causes the NMR peaks of quadrupolar nuclei to be much sharper and the splittings to be less. Taking advantage of this effect and following the example of an earlier study by proton NMR,[38] Kumar et al.[39,40] used deuterochloroform as a probe to investigate the effect of very small $\Delta\chi$, which was reached by mixing liquid crystals with positive and negative values of $\Delta\chi$ in proper ratios, on the orientation of the nematic directors in VAS experiments. To do this, they measured the deuterium NMR spectra of $CDCl_3$ in several mixtures of liquid crystals with different values of $\Delta\chi$. Their results show that, for a liquid crystal with a positive $\Delta\chi$ spinning along an axis with $\beta < 54^\circ\,44'$, the director orients parallel to the spinning axis above a critical spinning rate, as discussed in the previous section. However, for a system with nearly zero but positive $\Delta\chi$, the nematic director orients along the spinning axis at low spinning speeds, but orients perpendicularly to the spinning axis at high speeds, for $\beta < \theta_m = 54^\circ\,44'$. For a system with a very small but negative value of $\Delta\chi$, the behavior is similar for $\eta > 54^\circ\,44'$, but no change in the director orientation with spinning speed was observed for $\beta < 54^\circ\,44'$, but some spinning sidebands were observed indicating director reorientation.

A rather different application of VAS to deuterium NMR is the study of side-chain nematic liquid crystal polymers.[41,42] Because these polymers have very high rotational viscosities, ω_c is of the order of 0.001–0.1 Hz at $B_0 = 7.1$ T [see Equation (10)], so that very slow spinning was used to study the systems. However, it takes these liquid crystal polymers a very long time to reach equilibrium because of their high viscosities. Therefore, the initial stage of the time dependence of the deuterium NMR spectra were investigated, using synchronized data acquisition with the sample rotation. The kinetic results were used to measure the rotation viscosities[41] and study the convection director structures.[42]

5.5 Two-Dimensional NMR with VAS

Two-dimensional NMR of solute molecules in liquid crystal solvents has not enjoyed the success of that for isotropic solutions. This is mainly because the large dipolar interactions make the spectra second order, so that correlation relations, which are the essential features in 2D NMR, are usually not very informative. This problem can be overcome partly by symmetry filtering,[43–45] but the scope is still rather limited.

On the other hand, because the VAS method can simplify a second-order spectrum into a first-order one, it has a potential application in the 2D NMR of liquid crystal solutions.

As an example of this application, the ^{19}F spin echo spectra of the chiral molecule $CF_3CFBrCF_2Br$ dissolved in a liquid crystal with a negative $\Delta\chi$ (Merck ZLI 2806) was studied.[21] The normal 1D spectrum is a complicated ABC_3X type and very difficult to analyze, and the 2D spin echo spectrum is practically impossible to interpret. However, the spectrum turned into an ABM_3X type when the sample was spun at η = 63.9° or 58.4°.[46] The 2D spin echo spectra can be regarded as first-order J-resolved spectra, where the residual dipolar couplings appear in the ω_1 dimension, and the resonance frequencies in the ω_2 dimension. The analysis of the spectra in the ω_1 dimension then yielded the values of D_{ij} for this chiral molecule.

6 PERSPECTIVES

The most important characteristic of liquid crystals is the presence of orientational ordering without long-range positional ordering. Various kinds of anisotropic interactions, including dipolar couplings, quadrupolar couplings, and electronic shielding, can be used to study the orientational ordering and dynamics of liquid crystals, as well as the structures and motions of solute molecules. However, these interactions are often so large that the NMR spectra are either too broad or too complicated to be tractable. When liquid crystals are spun at high speeds along the magic angle, the NMR linewidths can be greatly reduced, just like those for solids, but information on anisotropic interactions is lost. On the other hands, the use of VAS can reduce the anisotropic interactions to yield simplified spectra, and in the mean time preserve the valuable anisotropic interactions, which are scaled by a proper factor. Solute spectra are greatly simplified, and the linewidths of bulk liquid crystals are reduced, bringing important advantages for the spectral analysis. So far, the potential of using VAS for the structural determination of complex solute molecules has not been fully realized, but investigations of the order parameters of various types of liquid crystals have been very successful.

It must be pointed out again that the reduction of the anisotropic interactions in liquid crystals by VAS is not a time-averaging effect as in MAS experiments for solids, but an effect of the alignment of the director. Therefore, a fundamental requirement for VAS experiments to be effective is the presence of macroscopic ordering of the liquid crystal director along the magnetic field in a static situation. This situation is fulfilled for nematic liquid crystals at $B_0 > 0.5\,T$, and for smectics that can be aligned through cooling from the nematic phase. However, for cholesterics and chiral smectics that have short pitches, and for smectics that have no or very short nematic ranges, powder patterns are often obtained, and the VAS technique is not very useful. In these cases, deuterium NMR without sample spinning is most advantageous. (See ***Liquid Crystalline Samples: Deuterium NMR***).

7 RELATED ARTICLES

Liquid Crystalline Samples: Carbon-13 NMR; Liquid Crystals: General Considerations; Structure of Rigid Molecules Dissolved in Liquid Crystalline Solvents.

8 REFERENCES

1. A. Saupe and G. Englert, *Phys. Rev. Lett.*, 1963, **11**, 462.
2. G. Englert and A. Saupe, *Z. Naturforsch. A*, 1964, **19**, 172.
3. A. Saupe, *Angew. Chem., Int. Ed. Engl.*, 1968, **7**, 107.
4. A. D. Buckingham and K. A. Mc Lauchlan, in *Progress in Nuclear Magnetic Resonance Spectroscopy*, eds. J. W. Emsley, J. Feeney, and L. H. Sutcliffe, Pergamon Press, Oxford, 1967, Vol. 2, p. 63.
5. P. Diehl and C. L. Khetrapal, in *NMR Basic Principles and Progress*, eds. P. Diehl, E. Fluck, and R. Kosfeld, Springer-Verlag, Berlin, 1969, Vol. 1, p. 1.
6. J. W. Emsley and J. C. Lindon, *NMR Spectroscopy Using Liquid Crystal Solvents*, Pergamon Press, Oxford, 1975.
7. C. L. Khetrapal and A. C. Kunvar, in *Advances in Magnetic Resonance*, ed. J. S. Waugh, Academic Press, New York, 1977, Vol. 9, p. 302.
8. C. Zannoni, in *Nuclear Magnetic Resonance of Liquid Crystals*, ed. J. W. Emsley, Reidel, Dordrecht, 1985, p. 1.
9. P. Diehl, in *Nuclear Magnetic Resonance of Liquid Crystals*, ed. J. W. Emsley, Reidel, Dordrecht, 1985, p. 147.
10. V. Tsevtkow, *Zh. Eksp. Theor. Fiz.*, 1935, **9**, 603.
11. H. Lippmann, *Ann. Phys. (Leipzig)*, 1958, **1**, 157.
12. L. C. Snyder, *J. Chem. Phys.*, 1965, **43**, 4041.
13. P. Diehl and C. L. Khetrapal, *Mol. Phys.*, 1967, **14**, 283.
14. F. M. Leslie, G. R. Luckhurst, and H. J. Smith, *Chem. Phys. Lett.*, 1972, **13**, 368.
15. J. W. Emsley, J. C. Lindon, G. R. Luckhurst, and D. Shaw, *Chem. Phys. Lett.*, 1973, **19**, 345.
16. R. M. Hornreich, *Phys. Rev. A*, 1977, **15**, 1767.
17. C. H. Yo, R. Poupko, and R. M. Hornreich, *Chem. Phys. Lett.*, 1978, **54**, 142.
18. J. Courtieu, D. W. Alderman, and D. M. Grant, *J. Am. Chem. Soc.*, 1981, **103**, 6783.
19. R. Teeaar, M. Alla, and E. Lippmaa, *Org. Magn. Reson.*, 1982, **19**, 134.
20. J. Courtieu, D. W. Alderman, D. M. Grant, and J. P. Bayle, *J. Chem. Phys.*, 1982, **77**, 723.
21. J. Courtieu, J. P. Bayle, and B. M. Fung, in *Progress in Nuclear Magnetic Resonance Spectroscopy*, eds. J. W. Emsley, J. Feeney, and L. H. Sutcliffe, Pergamon Press, Oxford, 1994, Vol. 26, p. 141.
22. P. G. de Gennes, *The Physics of Liquid Crystals*, Clarendon Press, Oxford, 1976.
23. F. M. Leslie, *Q. J. Mech. Appl. Math.*, 1966, **19**, 357.
24. F. M. Leslie, *Arch. Rat. Mech. Anal.*, 1968, **28**, 265.
25. S. G. Carr, G. R. Luckhurst, R. Poupko, and H. J. Smith, *Chem. Phys.*, 1975, **7**, 278.
26. S. D. Goren, S. B. Stephen, and R. Potashnik, *Chem. Phys. Lett.*, 1974, **28**, 400.
27. J. W. Emsley and J. C. Lindon, *Chem. Phys. Lett.*, 1974, **26**, 361.
28. J. W. Emsley and J. C. Lindon, *Mol. Phys.*, 1974, **28**, 1253.
29. J. P. Bayle, A. Khandar, P. Gonord, and J. Courtieu, *J. Chim. Phys.*, 1986, **83**, 177.
30. W. A. Heeschen, D. W. Alderman, and D. M. Grant, *J. Phys. Chem.*, 1988, **92**, 6504.
31. T. Väänänen, J. Jokisaari, and M. Seläntaus, *Chem. Phys. Lett.*, 1986, **129**, 399.
32. T. Väänänen, J. Jokisaari, and M. Seläntaus, *J. Magn. Reson.*, 1987, **72**, 414.
33. B. M. Fung and J. Afzal, *J. Am. Chem. Soc.*, 1986, **108**, 1107.
34. W. Richter, D. Reimer, B. M. Fung., R. J. Twieg, and K. Betterton, *Liq. Cryst.*, 1990, **8**, 687.

35. C. L. Khetrapal, B. S. A. Kumar, K. V. Ramanathan, and N. Suryaprakash, *J. Magn. Reson.*, 1987, **73**, 516.
36. J. Lounila and J. Jokisaari, in *Progress in Nuclear Magnetic Resonance Spectroscopy*, eds. J. W. Emsley, J. Feeney, and L. H. Sutcliffe, Pergamon Press, Oxford, 1982, Vol. 15, p. 249.
37. P. Diehl, J. Jokisaari, and F. Moia, *J. Magn. Reson.*, 1982, **49**, 498.
38. J. P. Bayle, A. Khandar, and J. Courtieu, *Liq. Cryst.*, 1986, **1**, 189.
39. B. S. A. Kumar, N. Suryaprakash, K. V. Ramanathan, and C. L. Khetrapal, *Chem. Phys. Lett.*, 1987, **136**, 227.
40. B. S. A. Kumar, K. V. Ramanathan, and C. L. Khetrapal, *Chem. Phys. Lett.*, 1988, **149**, 306.
41. D. Van der Putten, N. Schwenk, and H. W. Spiess, *Liq. Cryst.*, 1992, **12**, 735.
42. N. Schwenk, C. Boeffel, and H. W. Spiess, *Liq. Cryst.*, 1989, **4**, 341.
43. D. L. Turner, *J. Magn. Reson.*, 1982, **46**, 213.
44. A. G. Avent, J. W. Emsley, and D. L. Turner, *J. Magn. Reson.*, 1983, **52**, 57.
45. K. Rukmani and A. Kumar, *Chem. Phys. Lett.*, 1987, **133**, 485.
46. Nguyen Thoi Lai, J. P. Bayle, J. H. Ouvrard, and J. Courtieu, *Liquid Crystals*, 1988, **3**, 745.

Biographical Sketch

Jacques Courtieu. *b* 1944. Ph.D., 1974, University of Paris. Introduced to NMR by David M. Grant, U. of Utah, 1975–76. Faculty in Chemistry at the University of Orsay, 1969–present. Approx. 100 publications. Research interests: theory, practice and applications of liquid crystal NMR: dipolar couplings and molecular topology, relaxation in coupled systems, coherent averaging in spin space and in physical space, chiral recognition in cholesterics.

Two-Dimensional NMR of Molecules Oriented in Liquid Crystalline Phases

Anil Kumar

Indian Institute of Science, Bangalore, India

1	Introduction	1
2	Two-Dimensional Spin Echo Resolved Spectroscopy	1
3	Two-Dimensional Correlation Spectroscopy	2
4	Experiments Utilizing Longitudinal Spin Order	7
5	Other Studies	8
6	Related Articles	9
7	References	9

1 INTRODUCTION

The direct dipole–dipole interaction between nuclear spins plays a dominant role in magnetic resonance. Several kilohertz in magnitude, it causes severe line broadening of NMR lines in solids owing to the presence of a large number of coupled spins. Anisotropic reorientation coupled with translational diffusion of molecules embedded in ordered matrices, such as a liquid crystalline medium, yields extremely interesting NMR spectra.[1] In such cases, the intermolecular dipolar interactions are averaged to zero, and the intramolecular interactions, scaled by the order parameter, are reduced to a few hundreds of hertz. As a result, only a finite number of spins are dipolar-coupled, yielding a large number of sharp and often well-resolved spectral lines. These dipolar-coupled spectra are extremely useful, and contain detailed information on the conformation, symmetry and anisotropy of reorientation of the molecules. However, since the dipolar couplings are often large compared with the chemical shifts, the spectra exhibit strong coupling features, making the analysis of such spectra nontrivial.[2–5] Only in some simple spin systems is the Hamiltonian analytically diagonalizable, allowing straightforward interpretation of the spectra. In most cases, one has to perform a numerical analysis using iterative computer programs such as LAOCOON[6] and its various modifications.[4,7,8] The input to these programs comprises the line frequencies, intensities, and initial parameters of the Hamiltonian. Trapping of the algorithm into local minima is a frequently encountered problem, and any additional information about the spectrum, the spin system, and the molecular reorientations is extremely useful.

Two-dimensional (2D) NMR spectroscopy has played a significant role in simplifying spectra and in often providing the key information. The various 2D NMR studies of oriented molecules discussed in this article are classified into the following categories:

1. resolved spectroscopy;
2. experiments utilizing transverse spin orders using single and multiple quantum coherences;
3. experiments utilizing longitudinal spin orders such as NOESY and Z-COSY.

The emphasis in this article is on proton spectra of small molecules oriented in liquid crystal matrices. Reference may be made to a review on this subject,[9] and periodic reviews of NMR of oriented molecules.[10]

2 TWO-DIMENSIONAL SPIN ECHO RESOLVED SPECTROSCOPY

The spin echo 2D resolved experiment utilizes a pulse sequence (90°, $\frac{1}{2}t_1$, 180°, $\frac{1}{2}t_1$, t_2). The 180° pulse reverses the sign of all terms linear in spin operators over which the 180° pulse acts, and leaves all bilinear terms invariant. For homonuclear (spin-$\frac{1}{2}$) spins, the various terms contributing to the spectra of oriented molecules are

$$\hat{\mathcal{H}} = \hat{\mathcal{H}}_{\mathrm{Z}} + \hat{\mathcal{H}}_{\mathrm{J}} + \hat{\mathcal{H}}_{\mathrm{D}} \tag{1}$$

where $\hat{\mathcal{H}}_{\mathrm{Z}}$ involves chemical shift terms linear in spin operators, and $\hat{\mathcal{H}}_{\mathrm{J}}$ and $\hat{\mathcal{H}}_{\mathrm{D}}$ are the indirect spin–spin and direct dipole–dipole couplings, respectively, which are both bilinear in spin operators. The 180° pulse reverses the sign of $\hat{\mathcal{H}}_{\mathrm{Z}}$ and leaves $\hat{\mathcal{H}}_{\mathrm{J}}$ and $\hat{\mathcal{H}}_{\mathrm{D}}$ invariant. If all the terms commute, as happens only in weakly coupled isotropic cases where $\hat{\mathcal{H}}_{\mathrm{D}}$ is absent and $\hat{\mathcal{H}}_{\mathrm{Z}} \gg \hat{\mathcal{H}}_{\mathrm{J}}$, then $\hat{\mathcal{H}}_{\mathrm{Z}}$ refocuses, and the effective Hamiltonian is simply $\hat{\mathcal{H}}_{\mathrm{J}}$. In such cases, the 2D spin echo spectrum consists of a simple separation of chemical shifts and couplings, with the multiplets of each chemical site appearing along a 45° line from the $\omega_1 = 0$ axis[11,12] (see ***Two-Dimensional J-Resolved Spectroscopy***). When the various terms in equation (1) do not commute, the 180° pulse causes coherence transfer between various transitions, and calculations performed for strongly coupled spins show that the line intensities and frequencies along the ω_1 direction are modified and that there are additional lines in the 2D spectra.[13,14]

The first application of this experiment in oriented systems was on an AB spin system formed by the protons of 1-thio-3-selenole-2-thione oriented in MBBA.[15] The 1D spectrum of the two spins consists of four lines symmetrically displaced from the average chemical shift. The difference between the outer and inner lines is the sum $|J_{\mathrm{AB}} + 2D_{\mathrm{AB}}|$. To assign the lines, one needs additional information, which can be provided by conventional double resonance experiments or by the above 2D resolved experiment. The 2D resolved experiment has eight lines, two of which appear with negative intensity (Figure 1). There are four lines of equal intensity along the ω_1 dimension, uniquely identifying the parameter $|J_{\mathrm{AB}} + 2D_{\mathrm{AB}}|$.[15]

Another 2D spin echo study has been carried out on the AB_2 spin system of 1-bromo-2,6-dinitrobenzene oriented in the room temperature nematic, Merck Phase V.[16] Significant rf inhomogeneity gave rise to artifacts in the spectra, which were simulated as errors in the refocusing 180° pulse. Errors in the 180° pulse cause additional coherence transfer pathways of the type obtained in spin echo correlated spectroscopy (SECSY),[17] and such spectra thus have features of resolved spectroscopy and SECSY, both affected by strong couplings.

Accurate values for homonuclear dipolar couplings have been extracted from 1D spin echo spectroscopy of oriented

Figure 1 Phase-sensitive spin echo 2D resolved spectrum of two strongly coupled protons of 1-thio-3-selenole-2-thione oriented in MBBA [obtained using the pulse sequence (90°, $\frac{1}{2}t_1$, 180°, $\frac{1}{2}t_1$, t_2)], recorded at 270 MHz. While the 1D spectrum consists of four lines, the 2D spectrum has eight, two of which appear with negative intensity. (Reproduced by permission of Academic Press from Khetrapal et al.[15])

molecules containing AA′BB′-type spin systems, formed by the protons in *para*-substituted pyridines, which are coupled to an increasingly complex group of heteronuclei and to fluorines in tetrafluorinated benzenes.[18] All the echo spectra were analyzed with a modified LAOCOON-type computer program.[16,19] The echo spectra differed from the normal spectra principally in the presence of extra lines, which were interpreted as being due to $\boldsymbol{B}_1$ inhomogeneity and analyzed iteratively assuming a refocusing pulse of angle 160° ± 10°.[18]

3 TWO-DIMENSIONAL CORRELATION SPECTROSCOPY

3.1 Single Quantum Correlation (COSY)

Two-dimensional COSY utilizes a pulse sequence (90°, t_1, 90°, t_2), and gives cross peaks between transitions that are coupled to each other in a coupled network. The first application of COSY for the spectra of oriented molecules was to the AA′BB′ spin system formed by the protons of benzoselenodiazole oriented in the liquid crystal EBBA.[20] The COSY spectrum separated the symmetric and antisymmetric transitions by the absence of cross peaks between them. This separation further facilitated complete identification and analysis of the antisymmetric part of the spectrum, virtually by inspection. A more detailed analysis of the intensities of the cross peaks, by changing the flip angle of the coherence transfer pulse (the second pulse of COSY), further facilitated identification of connected transitions and the assignment of resonances.[20]

The absence of cross peaks between symmetric and antisymmetric domains in COSY has been exploited further for systems with higher symmetry. The proton spectra of oriented acetone and oriented benzene have been studied.[21] Acetone has two rotating methyl groups, each having C_{3v} symmetry, yielding a spin system of the type A_3A_3'. The eigenstates of the Hamiltonian can be grouped into four irreducible representations, namely, A_g, A_u, G_1, and G_{2g}, with analytical expressions available for the energies. The 2D technique separated the spectrum into four parts, with cross peaks within each group and no cross peaks between the groups. This yielded a complete symmetry filtering of all the transitions, with straightforward identification of each group and the values of the dipolar couplings. Benzene has D_{6h} symmetry, and the spin states are divided into six irreducible representations (A_1, A_2, B_1, B_2, E_1, and E_2). The A_2 representation has only one spin state and no transition. The remaining five representations are filtered by COSY (Figure 2) in a straightforward manner, and separate iteration of each of the domains using a modified LACOONOR program yielded all the parameters in an efficient manner.[21]

Flip-angle-dependent COSY (COSY-30; 90°, t_1, 30°, t_2) experiments have also been performed on the protons of *p*-dimethoxy[$^2H_6$]benzene oriented in the liquid crystal PCH 1132, yielding information on the directly connected transitions.[8] This system of four ring protons coupled to six methyl deuteriums forms one of the largest spin systems giving a well-resolved spectrum. The $^1H-^2H$ dipolar couplings were focused by a spin echo experiment yielding a 10-line spectrum typical of an AA′A″A‴ spin system. The connectivity information allowed a complete analysis of this spectrum, and yielded the various spectral parameters.[8] The 2D COSY spectrum of ethyl iodide oriented in a nematic phase has also been reported.[22]

3.2 Multiple Quantum Correlation

In the previous section, the use of experiments that correlate single quantum coherences with each other were described. In this section, the use of the correlation of multiple quantum coherences to single quantum coherences by 2D spectroscopy (MQ spectroscopy) and simplification of COSY spectra by multiple quantum filtering is discussed.

3.2.1 MQ Spectroscopy

Two-dimensional multiple quantum spectra are obtained by the use of the pulse sequence (90°, τ, 90°, t_1, 90°, t_2), where the (90°, τ, 90°) pulse sandwich excites all orders. These multiple quantum coherences cannot be detected directly, and therefore are monitored indirectly by the use of 2D NMR. These coherences, allowed to evolve during the period t_1, are frequency-labeled, and at the end of t_1, a 90° pulse is used to transform them into single quantum (SQ) coherences, which are detected during the period t_2. Thus, the 2D spectrum contains MQ frequencies in the ω_1 dimension correlated with various SQ frequencies in the ω_2 dimension.[12,23,24] There is no net transfer of magnetization from one order to another, but only a differential transfer; therefore, many correlations appear with negative intensity. The projection of the absolute mode of the 2D spectrum on the ω_1 axis yields a 1D MQ spectrum, which can also be obtained by single point detection of the signal in t_2.[22,25–40] While most of the applications have been demonstrated using such one-dimensional spectra, 2D spectra have also been recorded (see ***Multiple Quantum Spectroscopy of Liquid Samples***). Figure 3 shows the 2D MQ spectrum of oriented benzene.[22,39] The spectrum becomes progressively simpler as one goes to higher multiple quantum orders, there being seven four-quantum frequencies, two five-quantum frequencies, and one six-quantum frequency present in the six-proton system of oriented benzene.

The various multiple quantum orders in Figure 3 have been separated by offsetting the carrier from the middle of the single quantum spectrum. If $\Delta\omega$ is the offset parameter then various orders are separated out by $n\ \Delta\omega$. The magnetic field inhomogeneity contribution to the linewidth increases

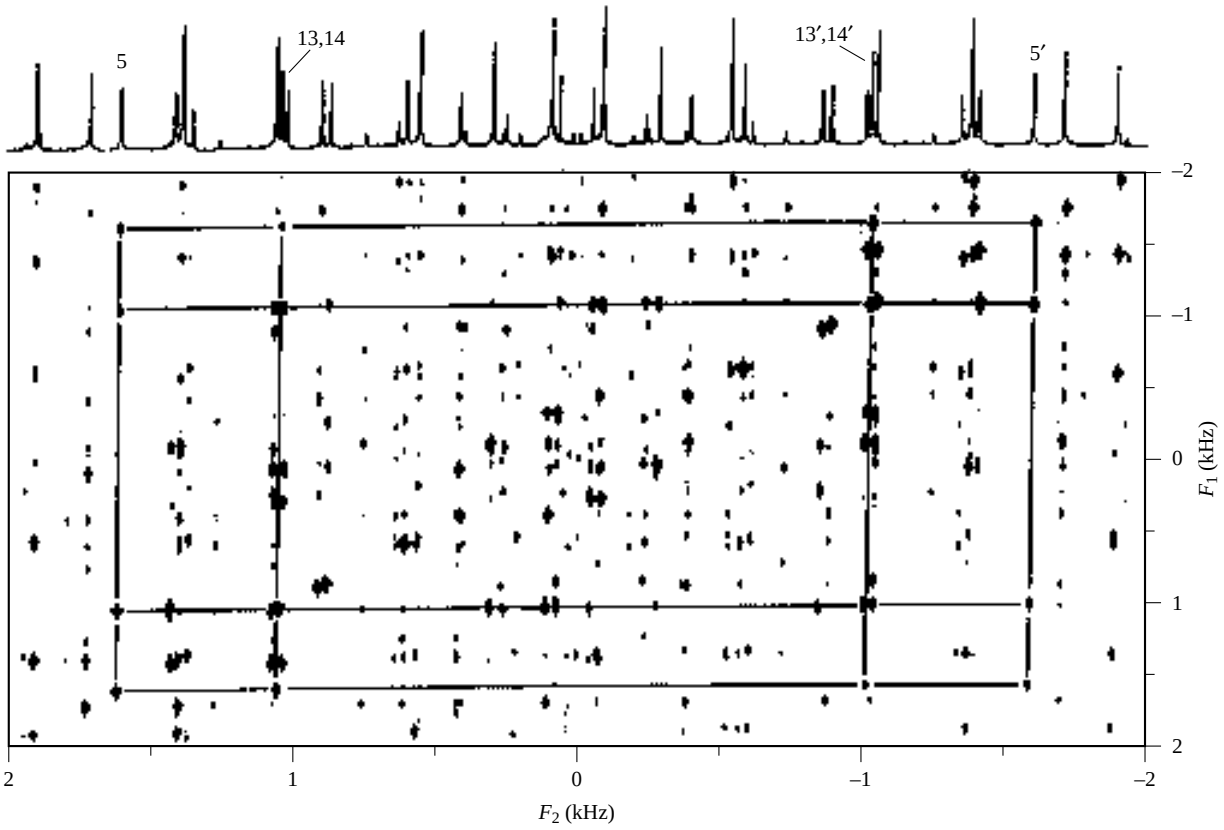

Figure 2 COSY spectrum of benzene oriented in ZLI-1167, recorded at 270 MHz. The connectivity in the B_1 symmetry domain containing lines 5, 13, 14, 14′, 13′, and 5′ is marked in the spectrum. (Reproduced by permission of Elsevier Science Publishers BV from Rukmani and Kumar[21])

proportionally for various MQ orders. In order to focus the field inhomogeneity, a 180° pulse has been introduced in the middle of the period t_1, which also focuses the offset dependence of various MQ orders. The various MQ orders in such cases are separated out by the use of time proportional phase incrementation (TPPI),[25] in which the phases of all the pulses in the excitation sequence are incremented in sequential t_1 experiments as $\phi = \Delta\omega\ t_1$. This results in a separation of various MQ orders by an effective offset parameter of $n\ \Delta\omega$. The 180° pulse in the middle of the period t_1 leaves all homonuclear couplings invariant, and, if there are no chemical shifts, yields an undistorted MQ spectrum, for example, in benzene.[25,26,32] However, if there are chemical shifts present along with dipolar and/or J couplings and the spectra are strongly coupled then the 180° pulse causes coherence transfer within each order, giving rise to new transitions and changed frequencies.[13,41,42]

Using the above pulse sequences, the 1D MQ spectrum has been obtained for the partially deuterated nematic liquid crystal 4-cyano-4′-(*n*-pentyl-d_{11})biphenyl (5CB-d_{11}), which has eight ring protons coupled to each other and yields a rather broad deuterium-decoupled single-quantum spectrum, but well-resolved five-, six-, and seven-quantum spectra (Figure 4).[33] Detailed analyses of these spectra have been carried out to obtain the dipolar couplings between various protons. The two biphenyl rings were either considered equivalent (D_4 symmetry) or inequivalent (D_2 symmetry). While an unequivocal fit was not obtained for either model, the D_4 symmetry resulted in the most physically reasonable molecular parameters. However, several splittings could not be explained by either of these models or by the effect of strong couplings, and it was suggested that rf inhomogeneity might provide an explanation for the extra splittings not predicted by the D_4 symmetry.[33]

3.2.2 Selectivity of Excitation and Detection

Attempts have been made to excite/retain only a few selected orders instead of all orders of MQ, thereby increasing the intensity of the particular order and the resolution of the detected order. Retaining a particular order is rather straightforward by phase cycling the detection pulse (the third 90° pulse) and the receiver or the excitation sequence and the receiver, in a concerted manner.[12] An example is shown in Figure 5.[34] The selection of a particular MQ order can also be achieved by using the technique of coherence transfer echo filtering (CTEF). A field gradient pulse of length τ in the MQ evolution period followed by a field gradient pulse of length $n\tau$ during the detection period refocuses only the nth order. This has been demonstrated on hexachloroethane oriented in EBBA.[43]

A large amount of effort has been made by Pines and coworkers in attempting to excite selectively all the transitions of a particular order using dipolar refocusing.[26,29,38–40] The introduction of a 180° pulse in the middle of the excitation sequence, along with appropriate phases of the two 90° pulses, yields an even- or odd-order excitation sequence for weakly coupled spins.[12] However, for dipolar-coupled spins,

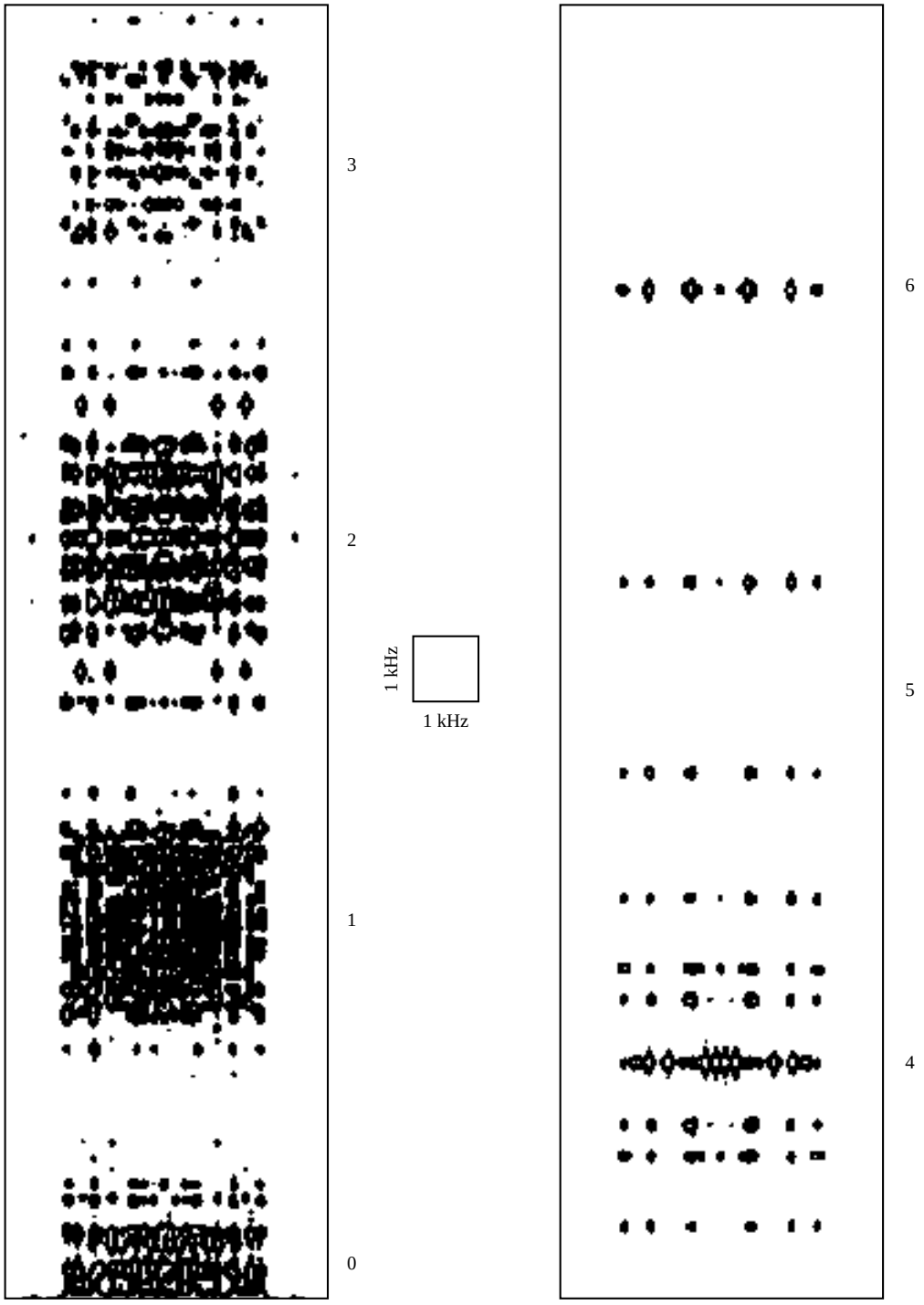

Figure 3 Two-dimensional multiple quantum spectrum of oriented benzene obtained using the pulse sequence (90°, τ, 90°, t_1, 90°, t_2), recorded at 200 MHz with a spectral offset of 6 kHz. (Reproduced by permission of Elsevier Science Publishers BV from Drobny[22])

it is possible to reverse the sign of the effective dipolar Hamiltonian by using multiple pulses, allowing one to design pulse sequences for exciting a particular order. The basic building block of the pulse sequence is shown in Figure 6. This block replaces the nonselective excitation sequence $90^\circ - \tau - 90^\circ$. Each sub-block consists of three parts. The first has a sequence of 90° pulses with interval τ, yielding a first-order average Hamiltonian $\hat{\mathcal{H}}_p$, and is applied for a time T. The second part consists of a delay $\Delta\tau_p$, and the third consists of a sequence of 90° pulses with delays of τ and 2τ, having an average Hamiltonian $-\hat{\mathcal{H}}_p'$ applied for a time T' such that $\hat{\mathcal{H}}_p T = \hat{\mathcal{H}}_p' T'$. Together, these yield the first sub-block, having an average Hamiltonian $\hat{\mathcal{H}}_0$, where the subscript refers to the phase of this sub-block. These sub-blocks are repeated n times, where n is the order to be selected, and the phase is

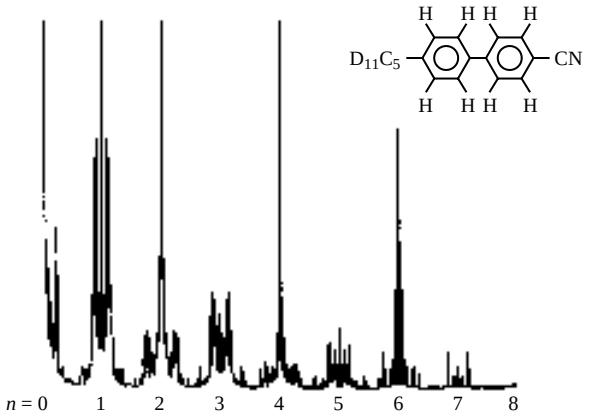

Figure 4 Multiple quantum proton spectrum of 5CB-d_{11} obtained using the pulse sequence (90°, τ, 90°, $\frac{1}{2}t_1$, 180°, $\frac{1}{2}t_1$, 90°, τ), at 182 MHz. The various multiple quantum orders are separated by TPPI, and the spectrum is the sum of magnitude mode spectra recorded for several values of τ ranging from 0.4 to 1.4 ms. (Reproduced by permission of Elsevier Science Publishers BV from Sinton and Pines[27])

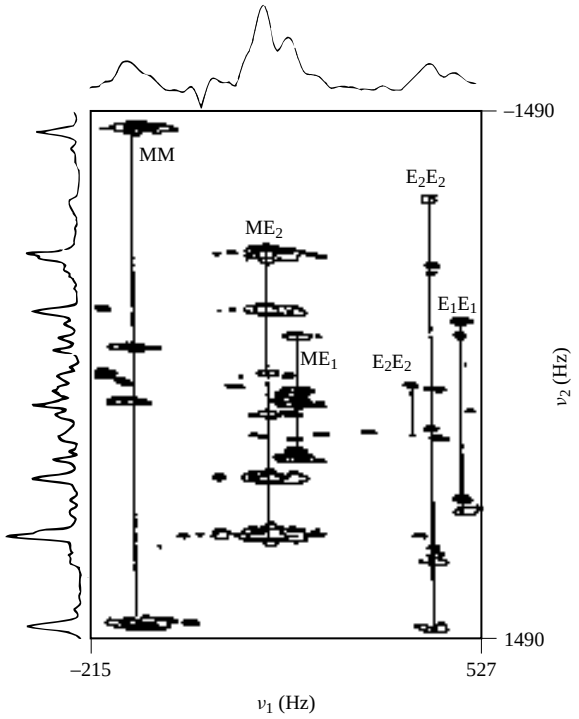

Figure 5 Double quantum versus single quantum correlation proton spectrum of 81% randomly deuterated *n*-hexane recorded by the sequence (90°$_\phi$, $\frac{1}{2}\tau_1$, 180°$_\phi$, $\frac{1}{2}\tau_1$, 90°$_\phi$, t_1, 90°$_\alpha$, $\frac{1}{2}\tau_2$, 180°$_\alpha$, $\frac{1}{2}\tau_2$, t_2), recorded at 360 MHz, under deuterium decoupling. The phase ϕ was incremented by 90° while the receiver phase was incremented by 180°. This retains double quantum coherences. Six vertical lines have been drawn at ν_1 frequencies corresponding to double quantum frequencies $2\nu_M$, $\nu_M+\nu_E$, $\nu_M+\nu_E$, $2\nu_E$, $2\nu_E$, and $\nu_E+\nu_E$. (Reproduced by permission of the American Chemical Society from Gochin et al.[34])

incremented each time for the entire subcycle by $\phi = 2\pi/n$. For better selectivity, the whole sequence may be repeated N times, where N may be 4 or 5. The results of such selective excitation are shown in Figure 7. More details about such

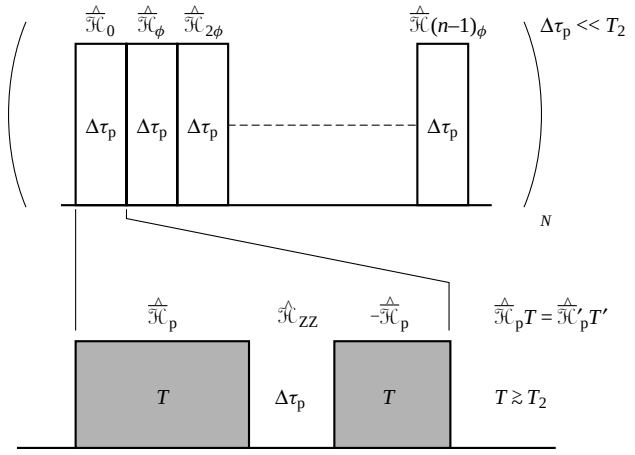

Figure 6 Pulse scheme for selective excitation of the *n*-quantum spectrum of dipolar-coupled spins. The order n is selected by incrementing ϕ in steps of $2\pi/n$. (Reproduced by permission of the American Physical Society from Warren et al.[26])

excitations are given by Warren et al.[26,29] and Drobny et al.[40] The highest order spectrum of N coupled spins $\frac{1}{2}$ is always a single line, whose position is determined by the sum of the chemical shifts of the coupled spins and is independent of spin−spin and dipolar couplings. Pines and co-workers have demonstrated that the $(N-1)$th- and $(N-2)$th-order spectra contain enough information to allow a spectral fit by iteration on the dipolar couplings, if there are no chemical shift differences, and, in general, it is possible to derive all the information from high-order MQ spectra that have a finite number of lines to be iterated upon.[25,28,30,35–40]

Most of the spectra using the above experimental procedures have been recorded using 2D pulse sequences, but recorded in a 1D manner using a single point detection in t_2. We shall restrict further discussion to 2D spectra.

3.2.3 Simplification of Spectra by Specific and Random Deuteration

As the number of dipolar-coupled spins increases beyond six or seven, the spectra become too complex for analysis by conventional procedures. Specific deuteration, coupled with deuterium decoupling—a straightforward technique for reducing the number of coupled protons—has been used in several cases. The main studies have been carried out on *n*-hexane-d_6, deuterated at methyl positions, and on 4-cyano-4′-(*n*-pentyl-d_{11})biphenyl (5CB-d_{11}), in which all the aliphatic protons have been deuterated, reducing both to systems of eight coupled protons.[27,33,35,39] The six- and seven-quantum 2D MQ spectra of *n*-hexane-d_6 (Figure 8) have been used to obtain the various dipolar couplings and their signs to estimate the dynamic molecular structure in the form of conformational probabilities.[35,39]

Another method of reducing the size of the spin system, but retaining information on dipolar couplings between all the protons of a molecule, is the technique of random deuteration combined with multiple quantum 2D spectroscopy or multiple quantum filtered COSY.[24,36,44,45] For example, an 81% random deuteration of *n*-hexane, which has 14 protons, yields approximately 6%, 18%, 25%, 25%, 14%, 5%, 3%, 2%,

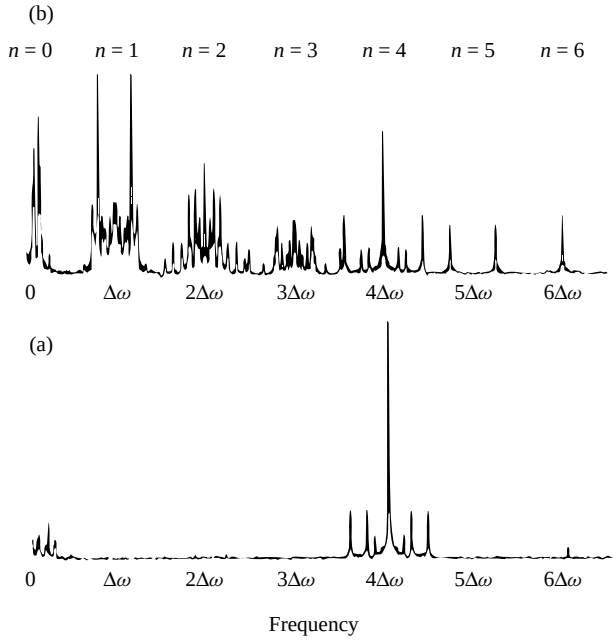

Figure 7 Four-quantum selective (a) and nonselective (b) MQ spectra of oriented benzene. (Reproduced by permission of the American Institute of Physics from Warren et al.[29])

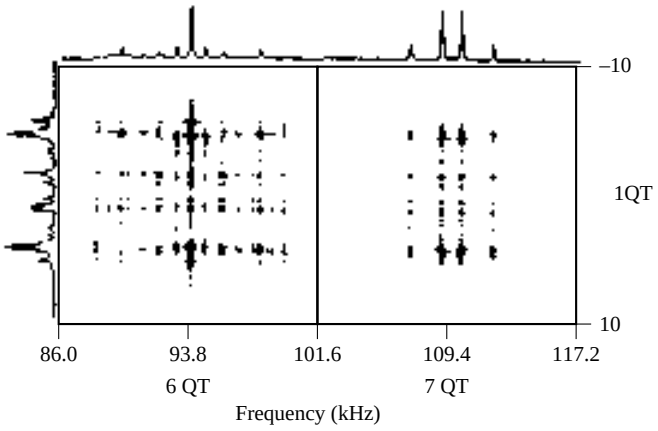

Figure 8 Absolute value six- and seven-quantum versus single-quantum correlation 2D spectrum of *n*-hexane-d_6 deuterated at methyl positions obtained by using the same pulse sequence as in Figure 5. The various orders were separated by TPPI using $\Delta\phi = 22.5°$. (Reproduced by permission of Elsevier Science Publishers BV from Gochin et al.35)

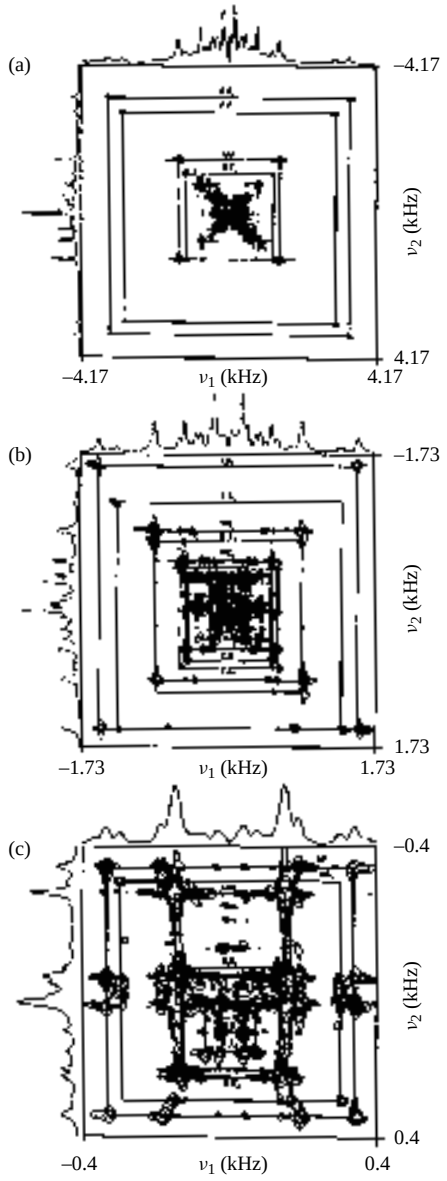

Figure 9 Double quantum filtered COSY (DQFC) spectrum of 81% randomly deuterated *n*-hexane-$d_{0.81}$ obtained using the pulse sequence ($90°_{\phi}$, $\frac{1}{2}t_1$, $180°_{\phi}$, $\frac{1}{2}t_1$, $90°_{\phi}$, $\frac{1}{2}\tau_1$, $180°_{x}$, $\frac{1}{2}\tau_1$, $90°_{x}$, $\frac{1}{2}\tau_2$, $180°$, $\frac{1}{2}\tau_2$, t_2), with phase cycling to retain double quantum coherence during the period τ_1. (a), (b), and (c) show successively expanded regions of the spectrum. The various two-spin systems are identified with square patterns. (Reproduced by permission of Taylor and Francis Ltd. from Gochin et al.[44])

and 1% molecules having 0, 1, 2, 3, 4, 5, 6, 7, and 8 protons, respectively.[36] Of these, only the one-, two-, and three-proton cases give significant intensity. The one-proton spectra can be easily filtered out using double quantum spectroscopy/filtering. The three- and high-spin spectra are quite low in intensity owing to the large number of lines and large number of possible spin systems. The double quantum filtered COSY (DQFC) spectrum thus contains prominently only the spectra of two coupled spins, and yields square patterns for each of the spin systems.[34,36] Numbering the carbons as M, E_1, E_2, E_2', E_1', and M′ in *n*-hexane, the various two-spin systems will be of the A_2 type for the protons in MM, E_1E_1, E_2E_2, E_2E_2'(*cis*), E_2E_2'(*trans*), E_1E_1'(*cis*), E_1E_1'(*trans*), and MM′ positions, and of AB type for ME_1, ME_2, ME_1', E_1E_2(*cis*), E_1E_2(*trans*), E_1E_2'(*cis*), and E_1E_2'(*trans*) positions. All such spin systems have been readily identified in the DQFC spectrum of 81% deuterated *n*-hexane recorded under deuterium decoupling (Figure 9), and several in the double-quantum 2D spectrum (Figure 5).[34,36] This yields all the dipolar couplings in *n*-hexane. Detailed analysis of the measured dipolar couplings has been carried out in terms of conformation and orientations of *n*-hexane in the liquid crystal solvent.

Recently, this idea has been extended to a series of *n*-alkanes, from hexane to decane (random deuteration level

of 80–90%), oriented in a nematic liquid crystal.[44] The DQFC spectrum in each case yields a large number of square patterns, each of which belongs to a two-spin system, yielding the totality of dipolar couplings between pairwise protons in the above molecules. The interpretation of the measured dipolar couplings is complicated, since they are averaged over molecular conformations and orientations sampled by the molecules. Nevertheless, they provide constraints on the time-averaged conformations and orientations of the molecules, which in turn allow an examination of various possible models for the solute–liquid crystal interactions.[44]

DQFC spectroscopy has also been utilized for a study of 78.7% randomly deuterated benzene oriented in a nematic phase.[36] Subspectra of three diprotonated and three triprotonated species could be identified in the spectrum. The subspectra were compared with the simulated spectra for various assignments, and the spectral parameters were obtained. A five-quantum versus single-quantum correlation 2D spectrum was also recorded for 34% randomly deuterated benzene. The five-quantum spectrum can be obtained either from fully protonated species or singly deuterated species. The singly deuterated species has only one five-quantum transition, while the fully protonated species has two five-quantum transitions, the correlation of which with various single quantum transitions yields various spectral parameters.[36]

3.2.4 Application to Chemically Exchanging Systems

Multiple quantum 2D spectroscopy has also been applied to chemically rearranging systems of oriented *s*-trioxane, which undergoes ring inversion, and oriented cyclooctatetracene, which undergoes a bond shift rearrangement.[46] Two-dimensional MQ–SQ correlation spectra were recorded at various temperatures, from which projected MQ spectra were obtained. The high-order (four and six) MQ spectra are much simpler than the single-quantum spectra, and exhibit characteristic exchange broadening and narrowing effects very similar to the single-quantum spectra. It is much easier to compare the high-order MQ spectra with the simulated spectra, calculated using exact as well as approximate expressions for the dynamic lineshapes, which then yield information on the rates of the dynamic processes. The uses, advantages, and limitations of the technique have been discussed in detail.[46]

4 EXPERIMENTS UTILIZING LONGITUDINAL SPIN ORDER

4.1 Effect of Strong Coupling in NOESY

It is known that each cross-section of the NOESY experiment using the (90°, t_1, 90°, τ_m, 90°, t_2) sequence is equivalent to a 1D difference NOE experiment in which the spin corresponding to the diagonal peak is selectively inverted at $\tau_m = 0$. It has been shown recently that this equivalence breaks down for strongly coupled spins, resulting in cross peaks in NOESY experiments, even without relaxation.[47,48] Explicit theoretical calculations have been carried out for an AB spin system, and the results are given in Figure 10.

Calculations have also been carried out for an ABX spin system, showing the existence of cross peaks between

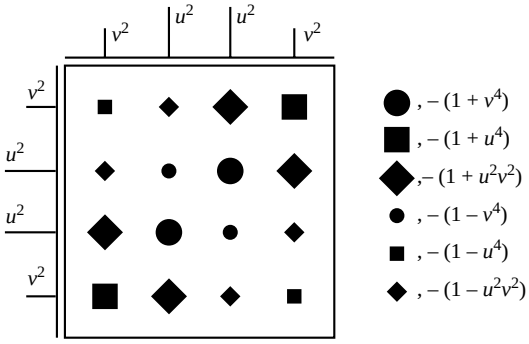

Figure 10 Schematic spectrum of an AB spin system calculated for the NOESY experiment (90°, t_1, 90°, τ_m, 90°, t_2), with phase cycling to retain longitudinal magnetization during the short period τ_m. The intensities of the 2D peaks are obtained by multiplying the symbols with the 1D intensities indicated on the ω_1 and ω_2 axes. For example, the intensity of the bottom left diagonal peak is given by $-v^4(1 + u^4)$, where $u = \cos\theta + \sin\theta$, $v = \cos\theta - \sin\theta$, and $\tan 2\theta = J_{AB}/(\nu_A - \nu_B)$. All cross peaks disappear for weakly coupled spins ($\theta = 0$, $u = v = 1$). (Reproduced by permission of the *Bulletin of Magnetic Resonance* from Christy Rani Grace and Kumar[48])

all X and AB transitions, even when X is only weakly coupled to AB.[48] The existence of such cross peaks has been experimentally demonstrated in oriented acetone (Figure 11), where a quantitative fit to the experimental cross sections, after removal of zero quantum interference, has been demonstrated by detailed calculations.[47] These cross peaks arise owing to the combined effect of strong coupling and the nonlinearity of the rf pulses. In order to examine whether the cross peaks are due to nonlinearity of the second or the third pulse in the NOESY experiment, calculations for the ABX spin system have been carried out for a small-angle second or third pulse. In an ABX spin system, there are two X transitions between pure states. In the experiments with the second pulse being of small angle and the third being 90°, there are no cross peaks from these X transitions to the AB transitions. Similarly, in the experiment in which the second pulse is 90° and the third is of small angle, there are no cross peaks from AB transitions to these X transitions. These observations indicate that the nonlinearity of a pulse is restricted to transitions within a spin or within groups of strongly coupled spins.[48]

4.2 Construction of Energy Level Diagrams

4.2.1 Using NOESY-α,β

In the linear regime, the NOESY-α,β experiment corresponds to the sequence (90°, t_1, α, τ_m, β, t_2), where α is a small-angle pulse and only longitudinal magnetization is retained during the period τ_m. It has been shown recently that, irrespective of the strength of coupling, each cross section of this experiment is equivalent to a 1D difference experiment in which the peak corresponding to the diagonal is selectively inverted at $\tau_m = 0$ and the state of spin system is monitored by the β pulse. If β is also a small-angle pulse then the state of the spin system is measured faithfully. In a coupled spin system, selective inversion of a transition gives rise to a direct population effect on all the transitions that share energy levels with the inverted transition. The transitions that increase or

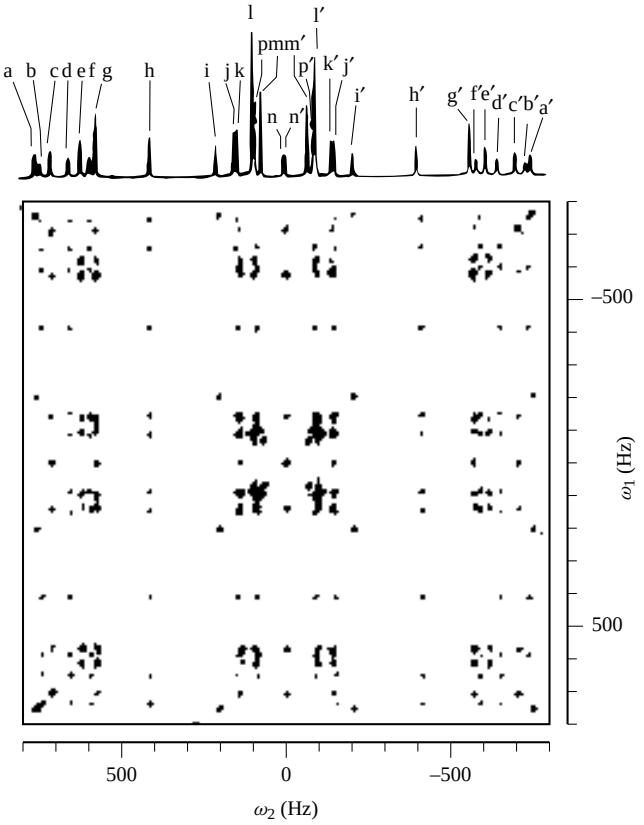

Figure 11 Phase-sensitive NOESY spectrum of oriented acetone obtained using the pulse sequence (90°, t_1, 90°, τ_m, 90°, t_2), with phase cycling to retain longitudinal magnetization during the short period τ_m (= 20 μs). Filled contours represent negative intensity. The various cross peaks here arise mainly owing to the strong coupling effect. (Reproduced by permission of Academic Press from Christy Rani Grace and Kumar[47])

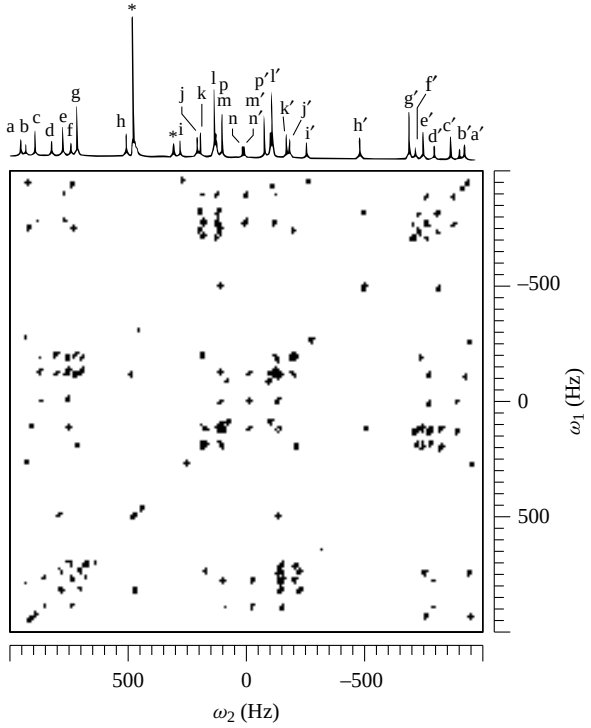

Figure 12 Phase-sensitive small-flip-angle NOESY (NOESY-α,β) spectrum of oriented acetone for α=β = 14° and τ_m = 20 μs, using the sequence (90°, t_1, α, τ_m, β, t_2) while retaining only the longitudinal magnetization during the short interval τ_m. Each diagonal peak has cross peaks only to directly connected transitions within the irreducible representation. Filled contours represent negative intensity. (Reproduced by permission of Academic Press from Christy Rani Grace and Kumar[49])

decrease in intensity are called progressively or regressively connected to the inverted transition, respectively. Use has been made of this information, without bringing in relaxation (for small values of τ_m), to construct energy level diagrams of oriented molecules.[49] This experiment is similar to a Z-COSY experiment,[50] as well as to a large number of difference 1D experiments in which one peak is selectively inverted at a time.

Figure 12 shows the 2D spectrum of oriented acetone recorded using NOESY-α,β for τ_m = 10 μs and α = β = 14°. As in COSY-β, the cross peaks here are also only between directly connected transitions within each irreducible representation, with the advantage that the 2D spectrum has pure absorptive lines.[49] From various cross sections of such spectra, a connectivity matrix is built up by entering (+1), (−1), and 0 for progressively, regressively, and unconnected transitions, respectively. This connectivity matrix is supposed to be symmetric, and its systematic analysis leads to a complete identification of the connected network of transitions, and in turn the complete energy level of a given symmetry.[49] The well-known problems of zero quantum coherences, which are not cancelled by NOESY phase cycling, also interfere in this experiment, and therefore have to be removed by known procedures.[12] The connectivity information has also been utilized for the analysis of the spectrum of *cis*,*cis*-mucanonitrile oriented in ZL1-1167, a four-spin system having C_{2h} symmetry.[51]

4.2.2 Using Z-COSY

Similar experiments (Z-COSY: 90°, t_1, α, τ_m, α) have also been performed on oriented methanol (an A_3B type of spin system) and oriented 1,3-dichlorobenzene (A_2BC). By systematically reducing the flip angle α, the direct progressive and regressive connectivities were identified. Patterns of connectivity were identified with the help of such spectra, which were then utilized for the construction of energy level diagrams. This information was in turn utilized for iteratively obtaining the complete Hamiltonian and its parameters.[50]

5 OTHER STUDIES

There has been an interesting application of near-magic-angle sample spinning combined with 2D NMR (COSY and 2D *J*-resolved experiments) of substituted benzenes dissolved in lyotropic liquid crystals. The normal spectra of these molecules were too complex to be analyzed. The near-magic-angle spinning simplified the spectrum considerably, and, in addition, the 2D *J*-resolved spectrum showed well-resolved multiplet patterns for various protons, while COSY helped in identifying the peaks of these protons.[52]

Another interesting study has been a 2D correlation of the liquid crystal spectrum with the isotropic spectrum by the use of a temperature jump during the mixing period. This allows a straightforward separation of the liquid crystal spectrum into various chemical sites.[53] There are several detailed and informative 2D NMR studies of both the spin echo and the correlated type of $I \geq 1$ spins in oriented systems, as well as many 2D NMR studies of liquid crystal molecules with and without magic angle sample spinning. Further, there have been several studies of zero field NMR of molecules oriented in liquid crystal matrices. These studies are discussed in other articles in this Encyclopedia.

6 RELATED ARTICLES

Analysis of High-Resolution Solution State Spectra; Analysis of Spectra: Automatic Methods; COSY Spectra: Quantitative Analysis; COSY Two-Dimensional Experiments; Deuterium NMR in Solids; INADEQUATE Experiment; Liquid Crystalline Samples: Carbon-13 NMR; Liquid Crystalline Samples: Deuterium NMR; Liquid Crystalline Samples: Diffusion; Liquid Crystalline Samples: Relaxation Mechanisms; Liquid Crystalline Samples: Spectral Analysis; Liquid Crystalline Samples: Structure of Nonrigid Molecules; Multidimensional Spectroscopy: Concepts; Multiple Quantum NMR in Solids; NOESY; Spin Echo Spectroscopy of Liquid Samples; Spinning Liquid Crystalline Samples; Two-Dimensional J-Resolved Spectroscopy; Zero Field NMR.

7 REFERENCES

1. A. Saupe and G. Englert, *Phys. Rev. Lett.*, 1963, **11**, 462.
2. A. D. Buckingham and K. A. McLauchlan, in *Progress in Nuclear Magnetic Resonance Spectroscopy*, ed. J. W. Emsley, J. Feeney, and L. H. Sutcliffe, Pergamon Press, Oxford, 1967, Vol. 2, p. 63.
3. P. Diehl and C. L. Khetrapal in *NMR Basic Principles and Progress*, ed. P. Diehl, E. Fluck, and R. Kosfeld, Springer-Verlag, Berlin, 1969, Vol. 1, p. 1.
4. P. Diehl, C. L. Khetrapal, and H. P. Kellerhals, *Mol. Phys.*, 1968, **15**, 333.
5. J. W. Emsley and J. C. Lindon, *NMR Spectroscopy Using Liquid Crystal Solvents*, Pergamon Press, Oxford, 1975.
6. S. Castellano and A. A. Bothner-By, *J. Chem. Phys.*, 1964, **41**, 3863.
7. P. Diehl, H. P. Kellerhals, and W. Niederberger, *J. Magn. Reson.*, 1971, **4**, 352.
8. J. W. Emsley, D. L. Turner, A. M. Giroud, and M. Longeri, *J. Chem. Soc., Faraday Trans. 2*, 1985, **81**, 603.
9. A. Kumar, *Current Sci.*, 1988, **57**, 109.
10. C. L. Khetrapal and K. V. Ramanathan, in *Specialist Periodical Reports on NMR*, ed. G. A. Webb, The Royal Society of Chemistry, London, 1994, Vol. 23, p. 439 and references therein.
11. W. P. Aue, J. Karhan, and R. R. Ernst, *J. Chem. Phys.*, 1976, **64**, 4226.
12. R. R. Ernst, G. Bodenhausen, and A. Wokaun, *Principles of Nuclear Magnetic Resonance in One and Two Dimensions*, Clarendon Press, Oxford, 1987.
13. A. Kumar, *J. Magn. Reson.*, 1978, **30**, 227 (erratum, 1980, **40**, 413).
14. A. Kumar and C. L. Khetrapal, *J. Magn. Reson.*, 1978, **30**, 137.
15. C. L. Khetrapal, A. Kumar, A. C. Kunwar, P. C. Mathias, and K. V. Ramanathan, *J. Magn. Reson.*, 1980, **37**, 349.
16. D. L. Turner, *J. Magn. Reson.*, 1982, **46**, 213.
17. K. Nagayama, A. Kumar, K. Wüthrich, and R. R. Ernst, *J. Magn. Reson.*, 1980, **40**, 321.
18. A. G. Avent, J. W. Emsley, and D. L. Turner, *J. Magn. Reson.*, 1983, **52**, 57.
19. J. W. Emsley and D. L. Turner, *J. Chem. Soc., Faraday Trans. 2*, 1981, **77**, 1493.
20. M. Albert Thomas, K. V. Ramanathan, and A. Kumar, *J. Magn. Reson.*, 1983, **55**, 386.
21. K. Rukmani and A. Kumar, *Chem. Phys. Lett.*, 1987, **133**, 485.
22. G. Drobny, *Chem. Phys. Lett.*, 1984, **109**, 132.
23. W. P. Aue, E. Bartholdi, and R. R. Ernst, *J. Chem. Phys.*, 1976, **64**, 2229.
24. A. Wokaun and R. R. Ernst, *Chem. Phys. Lett.*, 1977, **52**, 407.
25. G. Drobny, A. Pines, S. Sinton, D. P. Weitekamp, and D. Wemmer, *Faraday Symp. Chem. Soc.*, 1978, **13**, 49.
26. W. S. Warren, S. Sinton, D. P. Weitekamp, and A. Pines, *Phys. Rev. Lett.*, 1979, **43**, 1791.
27. S. Sinton and A. Pines, *Chem. Phys. Lett.*, 1980, **76**, 263.
28. J. Tang and A. Pines, *J. Chem. Phys.*, 1980, **72**, 3290; 1980, **73**, 2512.
29. W. S. Warren, D. P. Weitekamp, and A. Pines, *J. Chem. Phys.*, 1980, **73**, 2084.
30. W. S. Warren and A. Pines, *J. Chem. Phys.*, 1981, **74**, 2808; *J. Am. Chem. Soc.*, 1981, **103**, 1613.
31. D. P. Weitekamp, J. R. Garbow, and A. Pines, *J. Magn. Reson.*, 1982, **46**, 529; *J. Chem. Phys.*, 1982, **77**, 2870.
32. J. B. Murdoch, W. S. Warren, D. P. Weitekamp, and A. Pines, *J. Magn. Reson.*, 1984, **60**, 205.
33. S. W. Sinton, D. B. Zax, J. B. Murdoch, and A. Pines, *Mol. Phys.*, 1984, **53**, 333.
34. M. Gochin, K. V. Schenker, H. Zimmermann, and A. Pines, *J. Am. Chem. Soc.*, 1986, **108**, 6813.
35. M. Gochin, H. Zimmermann, and A. Pines, *Chem. Phys. Lett.*, 1987, **137**, 51.
36. M. Gochin, D. Hugi-Cleary, H. Zimmermann, and A. Pines, *Mol. Phys.*, 1987, **60**, 205.
37. M. Munowitz and A. Pines, *Science (Washington, DC)*, 1986, **233**, 525.
38. W. S. Warren, J. B. Murdoch, and A. Pines, *J. Magn. Reson.*, 1984, **60**, 236.
39. G. P. Drobny, *Annu. Rev. Phys. Chem.*, 1985, **36**, 451.
40. G. P. Drobny, A. Pines, S. W. Sinton, W. S. Warren, and D. P. Weitekamp, *Phil. Trans. R. Soc. Lond., Ser. A*, 1981, **299**, 585.
41. M. Albert Thomas and A. Kumar, *J. Magn. Reson.*, 1982, **47**, 535.
42. M. Albert Thomas and A. Kumar, *J. Magn. Reson.*, 1984, **56**, 479.
43. H. Fujiwara, N. Shimizu, T. Takagi, Y. Sasaki, and K. Takahashi *J. Magn. Reson.*, 1985, **64**, 325.
44. M. Gochin, A. Pines, M. E. Rosen, S. P. Rucker, and C. Schmidt, *Mol. Phys.*, 1990, **69**, 671.
45. M. E. Rosen, S. P. Rucker, C. Schmidt, and A. Pines, *J. Phys. Chem.*, 1993, **97**, 3858.
46. D. Gamliel, A. Maliniak, Z. Luz, R. Poupko, and A. J. Vega, *J. Chem. Phys.*, 1990, **93**, 5379.
47. R. Christy Rani Grace and A. Kumar, *J. Magn. Reson.*, 1992, **97**, 184.
48. R. Christy Rani Grace and A. Kumar, *Bull. Magn. Reson.*, 1992, **14**, 42.

49. R. Christy Rani Grace and A. Kumar, *J. Magn. Reson.*, 1992, **99**, 81.
50. P. Pfländler and G. Bodenhausen, *J. Magn. Reson.*, 1991, **91**, 65.
51. R. Christy Rani Grace, N. Suryaprakash, A. Kumar and C. L. Khetrapal, *J. Magn. Reson., Ser. A*, 1994, **106**, 79.
52. H. Fujiwara, in *Proceedings of 11th Conference of the International Society of Magnetic Resonance, Vancouver, 1992*, Abstract 0–69, p. 114; in *Proceedings of 32nd Annual NMR Symposium, Japan, 1993*, L35 p. 141.
53. K. Akasaka, A. Naito, and M. Kimura, in *Proceedings of 11th Symposium of the International Society of Magnetic Resonance, Vancouver, 1992*, Abstract 0–36, p. 81; A. Naito, M. Imanari, and K. Akasaka, *J. Magn. Reson.*, 1991, **92**, 85; K. Akasaka, A. Naito, and M. Imanari, *J. Am. Chem. Soc.*, 1991, **113**, 4688.

Biographical Sketch

Anil Kumar. *b* 1941. M.Sc., 1961, Agra, Ph.D., 1969, Indian Institute of Technology, Kanpur (supervisor, B. D. N. Rao). Postdoctoral research at Georgia Tech., Atlanta, GA (Sidney Gordon) 1969–70, University of North Carolina, Chapel Hill, NC (Charles Johnson) 1970–72, and E.T.H. Zürich, Switzerland (Richard Ernst) 1973–76. Faculty of Physics, Indian Institute of Science, Bangalore, 1977–present. Sabbatical leave at E.T.H. Zürich with Kurt Wüthrich, 1979–80. Approx 100 publications. Research interests: methodology of NMR, two-dimensional techniques, relaxation studies, applications to structure determination of biomolecules and characterization of molecular motions.

Accurate Determination of Nuclear Quadrupole Coupling Constants and other NMR Parameters in Liquids from the Combination of Molecular Dynamics Simulations and ab initio Calculations

Debra J. Searles

Griffith University, Brisbane, Australia

&

Hanspeter Huber

Institut für Physikalische Chemie der Universität Basel, Basel, Switzerland

1	Introduction	1
2	Tools for Calculation of Properties of Fluids	2
3	Results	5
4	Conclusions	10
5	References	10

1 INTRODUCTION

Quantum chemical studies are usually carried out on gases and solids where reasonable approximations can be invoked to yield accurate results. This is despite the fact that most important reactions occur in the liquid phase where both dynamics and intermolecular interactions are important. Molecular dynamics simulations are a well established technique for the study of liquids and provide a means of determining structural and dynamic properties as well as understanding the structure of the fluid and dynamics in fluids on a molecular level. Furthermore, the conditions of the system can be precisely controlled, and are not affected by experimental measurement. By combining molecular dynamics simulation with ab initio quantum chemical calculation, the range of liquid properties that can be determined is expanded. There are still limitations to the size of the system that can be studied and the timescale over which it can be investigated; however with advances in computational power these limitations will continue to be reduced.

The complexity of the structure and dynamics of liquids also presents difficulties to the experimentalist. The experimentalist must invoke various approximations to interpret the measurements made on these systems. Often it is difficult to test the accuracy of these approximations using experimental methods. Theoretical investigations using simulation and quantum chemical calculations can thus be used to obtain reliable interpretations of the experimental data.

The difference between the gas phase value and the liquid value is the 'solvent effect'. Most explanations of chemical reactions and processes are on the molecular level, without a solvent, and any unexpected behavior is often referred to as a solvent effect. A sound knowledge of the solvent effect on various properties is therefore necessary in understanding and predicting chemical behavior. Often the effects of solvents are identified by looking at trends observed in given properties and through development of models. However, because simulations are carried out at molecular level, a real understanding of the influences of the solvent can be obtained using simulations.

In this review we discuss the combined use of simulation and quantum chemical methods to determine the nuclear quadrupole coupling constants, nuclear magnetic resonance (NMR) relaxation times, chemical shifts and J-couplings in liquids. A chapter discussing nuclear quadrupole coupling constants and NMR relaxation in liquids was recently published in Volume 7 of Theoretical and Computational Chemistry.[1]

The quadrupole coupling energy is the interaction energy between the nuclear electric quadrupole moment and the electric field gradient (EFG) at the site of the nucleus that exists due to the rest of the molecule and its surroundings. The EFG is a traceless tensor, V, and in its principal axes system (α, β, γ) can be represented by two quantities, e.g., equation (1)

$$eq = V_{\alpha\alpha}$$
$$\eta = \left(\frac{V_{\beta\beta} - V_{\gamma\gamma}}{V_{\alpha\alpha}}\right) \tag{1}$$

The axes are chosen such that the components of the EFG tensor have the order $|V_{\alpha\alpha}| > |V_{\beta\beta}| > |V_{\gamma\gamma}|$. η is called the 'asymmetry parameter' and $\chi = e^2qQ/h$ is known as the nuclear quadrupole coupling constant (NQCC) where Q is the nuclear quadrupole moment. The nuclear quadrupole moment is a property of the nucleus itself. Since the EFG depends on the electric field around the nucleus, the EFG, NQCC and asymmetry parameter are sensitive to the environment of the nucleus.

Quantum mechanical calculations allow calculation of the EFG at a nucleus and therefore calculation of the NQCC and asymmetry parameter at the nucleus of a molecule is straightforward. However, since quantum mechanical calculations become more expensive in computer-time as the system size increases, the size of the molecule for which these properties can be calculated is limited. For liquid systems, this means that only the effects of a limited number of neighboring molecules (a cluster or supermolecule) can be considered or that the solvent must be treated in an approximate way. Furthermore, in the liquid state the environment of a nucleus is continually changing, and therefore an ensemble of clusters of molecules must be considered. The calculation of the NQCC for liquids using ab initio methods is discussed below.

Under extreme narrowing conditions, the spin-lattice relaxation time is given by equation (2)

$$\frac{1}{T_1} = \frac{3}{8}\frac{2I+3}{I^2(2I-1)}\left(\frac{2\pi eQ}{h}\right)^2 \int_0^\infty \mathrm{d}t \langle V_{zz}(0)V_{zz}(t)\rangle \tag{2}$$

where I is the nuclear spin, h is Planck's constant and $\langle V_{zz}(0)V_{zz}(t)\rangle$ is the correlation function of the field gradient in the laboratory coordinate system. Defining an effective correlation time, transforming to a principal axis system and using the definitions for the NQCC and asymmetry parameters above, the spin-lattice relaxation time can be expressed as equation (3)

$$\frac{1}{T_1} = \frac{3}{40}\frac{2I+3}{I^2(2I-1)}(2\pi\chi)^2\tau_{\text{eff}}\left(1+\frac{\eta^2}{3}\right) \tag{3}$$

Using this relationship, experimental values for the NQCC are often obtained from the measured T_1 and an indirect measurement or estimate of τ_{eff}. Since the value of τ_{eff} is not directly available from experiment, it is often assumed that the rotation is isotropic so that a correlation time can be estimated from the rotational correlation time along a bond or the dipole-dipole relaxation time. The asymmetry parameter cannot generally be determined directly from experiment if the NQCC is unknown, and therefore it is often assumed to be zero or is estimated from experimental or calculated gas phase or solid state values. In many cases these approximations are not justified and need to be tested. It should be noted that, in order to aid comparison between the experimental and computed NQCCs, the ensemble average NQCCs are often computed as roots of the mean square values. Calculation of various relaxation times and their equivalence is discussed in the Results section below, and compared with experimental results where available.

Recently, a new experimental method of determining the liquid state NQCC has been used by Farrar and co-workers who observed a high degree of correlation between the NQCC of a nucleus and its chemical shift.[2–4] These experimental results have been found to be in good agreement with the simulated values.

To make it feasible to carry out calculations of liquid properties and local properties of liquids, like chemical shifts, without using any empirical information some preconditions had to be fulfilled. Computers had to become fast enough for extensive simulations and quantum chemical calculations and methods had (and still have) to be developed for the calculation of these properties with the necessary accuracy. Knowledge in quantum chemistry and in simulations was developed in different groups and had to be exchanged before a combination of the two fields could occur. On the simulation side the tools were available and the computers fast enough for reasonable computations around 1980. Although quite accurate quantum chemical calculations could be performed for molecules at that time, intermolecular interactions, which are of crucial importance for liquids, could not yet be obtained with the necessary accuracy for reasonably large systems. For this purpose quite huge basis sets are usually needed with many polarization functions as well as diffuse functions, but also electron correlation has to be included on a high level in most cases. This is not only true for the interaction energy, but also for electronic properties like electric field gradients (EFGs). It was only at the end of the eighties that quantum chemistry could fulfill these preconditions. For more details on this development see Ref.[5] Some of the techniques developed are described in the next section.

2 TOOLS FOR CALCULATION OF PROPERTIES OF FLUIDS

Here we consider the tools available for calculation of solvent effects. The methods used can be grouped into three broad categories:

(1) *Macroscopic treatment of the solvent*: In this approach, the solvent is treated using continuum models or reaction fields. This is the method that is commonly incorporated in quantum chemical packages.
(2) *Microscopic cluster methods*: In these studies, the solvent molecules are explicitly treated when determining the molecular property of interest (for details see below and Figure 1). The necessary cluster size varies with the property considered as does the way in which the solvent molecule is treated. In some cases the main influence of the solvent molecules on the molecular property being determined is due to electrostatic interactions and therefore the solvent is modeled as a distribution of charges (electrostatic model), however in general the full electronic effects of the solvent should be considered.[6]
(3) *Car-Parrinello simulations*: In this case the periodic bulk fluid and its dynamics are modeled using quantum chemical calculations on the fly. Various techniques are introduced to account for the periodicity.

We will focus on microscopic cluster methods for the following reasons. Firstly we doubt that studies using the first approach can reach predictive accuracy without including increasingly more microscopic features (so that this approach becomes more like the second category; see e.g., the polarizable continuum model (PCM) by Tomasi and co-workers.[7,8]) The first approach also needs at least one empirical parameter and therefore will never be able to provide completely theoretical predictions. However, it should be noted that it is currently the only method that can be applied routinely by most scientists, and uses little additional computer time to that required for single molecule (gas phase) calculations. The third category is still very computer time intensive, and few examples of calculations of NMR related properties in liquids exist in the literature at this time. Moreover, in certain cases the density functional theory (DFT) method inherent to it might not yield the required accuracy.

2.1 Cluster Method

The cluster method involves the generation of clusters of molecules, and the treatment of each cluster as a supermolecule for which the required property of the central molecule is calculated using quantum chemistry. The fluid property is then determined from the ensemble average of its value for each of the clusters.

Liquid clusters are obtained using Monte Carlo (MC) simulations or from single configurations ('snapshots') of a classical simulation trajectory formed using molecular dynamics (MD) simulations.[9] A molecule is randomly selected from the molecules in the MC or MD liquid snapshot, and the configuration of molecules nearby the central molecule is used to form the cluster. This is illustrated in Figure 1. Periodic boundary conditions are generally used to model the bulk fluid. In MC simulations, the liquid configurations are determined by random sampling with the statistics of the ensemble required. MD

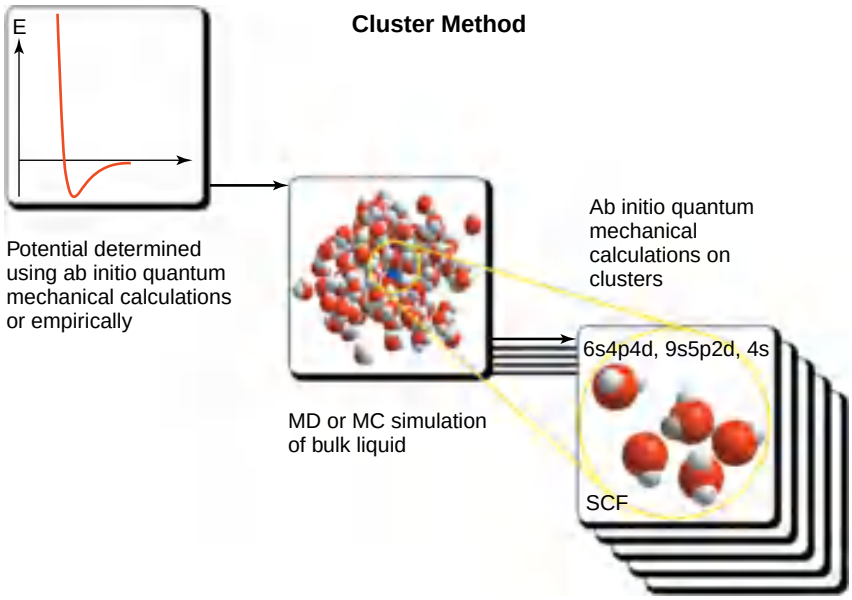

Figure 1 A schematic diagram demonstrating how the cluster method is used to determine properties in liquids. Firstly a potential energy hypersurface is determined empirically or using ab initio methods. This is then used in MD or MC calculations of the bulk liquid. Finally, 'snapshots' of the liquid are taken and clusters of molecules are used in ab initio quantum mechanical calculations to determine values for the property of interest. Averaging over many snapshots and clusters results in the liquid state value

simulations involve solution of Newton's equations of motion for each particle in the simulation box and the configurations obtained are representative of the microcanonical ensemble. Modifications to the equations of motion allow other ensembles to be sampled using MD simulations. Both MC and MD simulation techniques are thoroughly described in Allen and Tildesley.[9]

Once clusters have been generated from the snapshots, the properties of the central molecule are determined using the liquid cluster (or supermolecule) as the input structure to a quantum chemical calculation. For example, the deuterium NQCC for an atom in the central molecule is calculated quantum chemically with the cluster input as the structure for the quantum chemical calculation. This is repeated for many clusters sampled from the MC or MD simulation, and averaged to obtain the liquid state property.

Questions that must be addressed when using the cluster method are: how many snapshots of the fluid are required; how many molecules should be included in the supermolecule; how the molecules to be included in the supermolecule should be selected; and for clusters obtained from MD simulations, the time required between snapshots should be considered. Optimization of the number of surrounding molecules to be included in the cluster and the selection criteria are determined by sample calculations, and require a balance between the time taken and the accuracy required. For the properties of interest for this review, it is necessary to carry out a quantum chemical calculation to determine the property of the molecule in the liquid state cluster. The quantum chemical calculations are generally more computer time intensive than the MC or MD simulations, and therefore the number of clusters and their size are restricted. It is also important to optimize the time between snapshots so that convergence to the ensemble average property of the liquid is obtained using the minimum number of calculations.

The cluster method has been used to determine various liquid state properties. Algorithms have been developed to calculate properties including vibrations,[10] NQCCs,[11] chemical shifts,[12] J-couplings,[13] electronic spectra,[14] and EPR (electron paramagnetic resonance) hyperfine couplings.[15] In the last case the solvent is treated only in an electrostatic approximation. These algorithms have been applied extensively since these early papers and extended to study a wide range of liquids.

An approach that is related to the cluster method is the Quantum Cluster Equilibrium (QCE) method. This method has been applied to the calculation of NQCCs in fluids by Ludwig, Weinhold, Farrar and co-workers.[16–29] The QCE approach uses standard quantum statistical thermodynamics to consider the chemical equilibria existing between the clusters and thus determines the probabilities of observing clusters in the liquid state at the required temperature, pressure and composition of the fluid.[27] In contrast to the conventional cluster method discussed above, in this approach all possible clusters that might be expected to be present in the liquid are generated, and the structures of these clusters are optimized using quantum chemical calculations. A canonical ensemble is assumed, and for each cluster the energies, harmonic vibrational frequencies and moments of inertia of the cluster at its equilibrium structure are calculated using quantum mechanics. Hence partition functions for each cluster and the total partition function can be determined. The cluster populations obtained are then used to determine expectation value of the property of interest, such as the NQCC. The NQCC of nuclei in the liquid state of water,[19] formamide,[16] N-methylformamide,[17] N-methylacetamide,[18] ammonia[24] and ethanol[26] have been determined in this way. Thermodynamic and structural properties, vibrational frequencies and chemical shifts have also been calculated using the QCE method.[16,18,20,22–26,28,29] Limitations of the QCE method are discussed by Ludwig et al.[19] and include the treatment of the low-frequency intermolecular vibrational modes by a harmonic approximation, approximation of the

molecular volume, the possibility of excluding significant clusters in the ensemble and the use of a mean-field approximation to treat residual cluster-cluster interactions which requires an empirical parameter. Advantages over the cluster method where clusters are selected from a molecular dynamics simulation, are that the accuracy does not depend on the accuracy of a model potential energy function and generation of the clusters takes negligible time.

2.2 Dynamic Properties

The above cluster method is very general and can be applied to calculate most static properties at any phase point. Similarly the QCE method is very general, although it may be difficult to extend it to non-hydrogen bonded systems and some problems exist with higher order temperature derivatives.[28] However, both methods are only able to calculate static properties. This is true even if the cluster method is combined with molecular dynamics (MD) simulations, because the simulation is only used to obtain the static clusters. Hence, for relaxation times or other dynamic properties other techniques are needed.

'Mechanical' dynamic properties like transport properties can be obtained by integration of the underlying time correlation function in equilibrium simulations (Green-Kubo integrals). Relaxation times are obtained similarly (see equation (2)), the only problem is the need of additional electronic properties like field gradients (for quadrupolar relaxation, which we take as an example in the following) at each step of the simulation. The required field gradient can in principle be calculated quantum chemically at any position of the simulation cell and at each time step. However, this is not practical today. Even if one reduced the ensemble to a cluster by use of a cutoff radius, the high accuracy needed in the quantum chemical calculation would make it unfeasible to perform such a calculation at each step. The same problem would occur if one desired a quantum chemical calculation of the intermolecular potential (i.e., the forces) at each step. The usual approximation invoked in this case is to calculate pair potentials only and to assume pair additivity for the simulation. The same approximation is possible for the electronic property of interest. That means that for quadrupolar relaxation, for example, a pair EFG hypersurface is calculated firstly, e.g., in the case of Neon a one-dimensional curve of the EFG at one Neon nucleus induced by the other Neon atom as a function of the distance. This pair function, obtained pointwise from quantum chemical calculations, is fitted to an analytical function and implemented in the simulation program to obtain the property at each step of the simulation (for details see Refs.[30–32]). Another possibility would be to use Car-Parrinello types of methods[33] and to calculate the electrical property on the fly with the same density functional theory (DFT) procedure as used for the potential. To our knowledge this has not yet been done.

There are several levels of difficulty in obtaining the EFG in a liquid. The first calculations in the eighties were all for atomic ions[30–32,34] or a rare gas[35] in aqueous solutions. In these cases the EFG is completely intermolecular and can be obtained with relatively crude approximations like Hartree-Fock (HF) calculations with small basis sets or even classical electrostatic models [35]as the solvent is very polar. The next step was the treatment of the relaxation of ^{21}Ne in liquid Neon.[36] Here the solvent is also very simple, but one already needs very high-level quantum chemical calculations as we are dealing with a pure dispersion interaction. A step further leads us to molecular systems. To our knowledge the quadrupolar relaxation of a molecular nucleus has not yet been studied computationally. In our groups we are currently doing this for the system D_2O/DMSO, but with an empirical force field. For this polar system with deuterium as the nucleus of interest, a HF calculation yields a sufficiently accurate EFG. The only calculated relaxation time for a molecular system using quantum chemistry we are aware of is a dipolar relaxation, which was calculated in a slightly different manner and will be discussed in the Results section.[37]

2.3 Quantum Chemical Tools

If one is interested in obtaining completely non-empirical predictions, the interatomic potential has to be calculated quantum chemically. Except for very polar systems, dispersion energy always has a major contribution to the potential energy. This means that one has to include electron correlation on a reasonably high level and use quite large basis sets. If this is not possible one might use an empirical potential. The importance of inclusion of electron correlation for the calculation of the electric property applies equally when using a pair surface and using clusters. However, recourse to empirical approximations is usually not possible. This is the main reason why such calculations only became possible in the last decade. In the Results section we will show how improvements of the quantum chemical calculations influence the results for the example of the quadrupolar ^{21}Ne relaxation. In the cluster method one typically needs 50 to 100 quantum chemical calculations for clusters that typically consist of 5 to 15 monomers. For an electric property surface one typically needs several hundred pair calculations. This is currently only possible for reasonably small monomers, but even then it would barely be possible with the methods available two decades ago. There were two developments in the eighties that assisted these calculations greatly. One was the improvement of DFT by the introduction of the generalized gradient approximation and some additional developments, and the other was the development of special basis sets to calculate local properties in a molecule or cluster.

The latter method is based on the idea that a local property like an EFG or a chemical shift needs a very accurate basis set close to the location of interest, smaller basis sets in the next neighborhood and only small basis sets far away (note that this is a similar philosophy to that which has been applied in the so called QM/MM methods, where distant molecular parts are only treated by molecular mechanics). We developed this strategy under the name Basis sets of high local quality in the early eighties for EFG calculations and showed in many papers that it works excellently for deuterium,[38–43] but also reasonably well for other nuclei like N,[44,45] Li,[46] O[47] and S.[48,49] Chesnut et al. applied the same concept under the name Locally dense basis sets to chemical shifts,[12,50–54] whereas Hinton et al.[55] call it Attenuated basis sets. Other groups have also applied it to chemical shifts.[37,56] DiLabio et al.[57–61] and Pratt et al.[62] showed recently that the concept also works well for bond and dissociation energies, whereas Chesnut and Byrd[63] use it to get correlation energies in an additive scheme.

The DFT method, although much older, improved in the mid-eighties with the introduction of the generalized

gradient approximations and it started a triumphant advance in chemistry. Due to its lower scaling it is particularly suited to large systems such as the clusters in the cluster method. Bailey has shown recently in several papers,[64–68] that it yields excellent EFGs for nuclei like D, B, O, N, S and Ge. This new finding has not yet been applied to liquid calculations. As shown by Schwerdtfeger et al.,[69] its suitability needs to be checked for each nucleus. The sum-over-states density functional perturbation theory method is an important method for the calculation of magnetic properties that was developed by Malkin et al.[70,71] in the last decade.

3 RESULTS

3.1 Nuclear Quadrupole Coupling Constants

Some early studies of monatomic ions and atoms have been carried out with the goal of investigating quadrupole relaxation, and in these cases the NQCC was calculated assuming pair additivity (see below).

In the mid-1980s the first ab initio calculations of the NQCC and asymmetry parameter of deuterium (^{2}H or D) and oxygen (^{17}O) nuclei in water were carried out. The electric field about the isolated water molecule is not symmetric, therefore the EFG at each nucleus is non-zero and changes in the structure of the water molecule will influence the EFG. In addition, the strong intermolecular interactions in hydrogen bonded liquid water mean that the influence of neighboring molecules in the cluster will be important. Hence, liquid water is an interesting candidate for study. The first ab initio predictions of the NQCCs of liquid water did not use a cluster approach, but assumed that the water molecule was hydrogen bonded 75% of the time.[72,73] In the early 1990s the cluster approach was used to determine the D and ^{17}O NQCC and asymmetry parameters in liquid water.[11,74,75] A number of potential models were used in MD simulations to generate clusters, including the ab initio MCYL potential energy surface of Lie and Clementi.[76] The NQCC was determined at the HF level, i.e., NQCCs for liquid water were determined by purely computational methods with no empirical parameters. Furthermore, a model for the dependence of the deuterium NQCC on the structure of the water cluster was developed[11] and has been used to identify a slight temperature dependence of the deuterium NQCC43, consistent with experimental results. The HF ab initio calculations of the deuterium NQCC in single molecules indicate that a systematic error of 3% is expected due to limitations of the ab initio method used,[41] therefore the best estimate of the NQCC should be corrected by this factor. In Figure 2 the temperature dependence of the experimentally determined NQCC is compared with that obtained using the model developed in Ref.[11] and corrected by the error due to the ab initio calculations. The recent experimental results are in good agreement with the calculated values.[43,75] When the calculated value of the NQCC of ^{17}O, $\chi = 8.9 \pm 0.3$ MHz, was published in 1993 the value was somewhat higher than the best experimental results at that time. However, as is shown in Figure 3, the most recent experimental result that we are now aware of[4] is in excellent agreement with the calculated value. Rather than determine the NQCC directly from relaxation times, Ropp et al.[4] use the observed correlation between the chemical shift and the NQCC ($R^2 = 0.99$ for deuterium and $R^2 = 0.96$ for ^{17}O) for its determination and therefore do not rely on the assumptions necessary in the earlier works. For a review of the early calculations of NQCCs in the liquid state see.[43]

Alternative approaches for the computational determination of the deuterium and ^{17}O NQCC and asymmetry parameter in

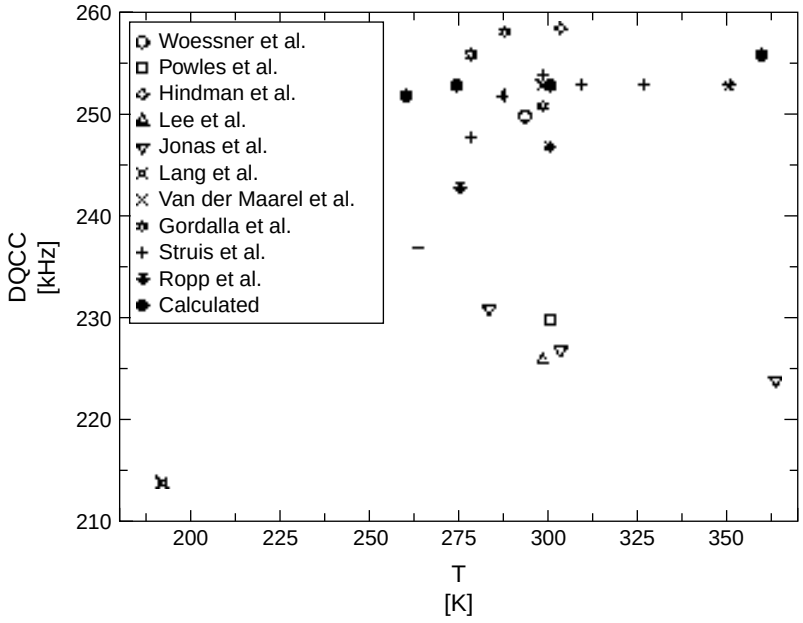

Figure 2 Experimental and calculated deuterium NQCCs. The results before 1980 have open symbols, whereas the more recent ones have crosses or star symbols. The symbol key for the experimental values is ordered by the year of publication. The calculated values are from Eggenberger et al.[11] The simulations were performed with the MCYL ab initio potential. The values were obtained from a model (see Ref.[11]) which lead to statistical errors <1 kHz and they were empirically corrected, i.e., reduced by 3% such that the gas phase value is in agreement with experiment

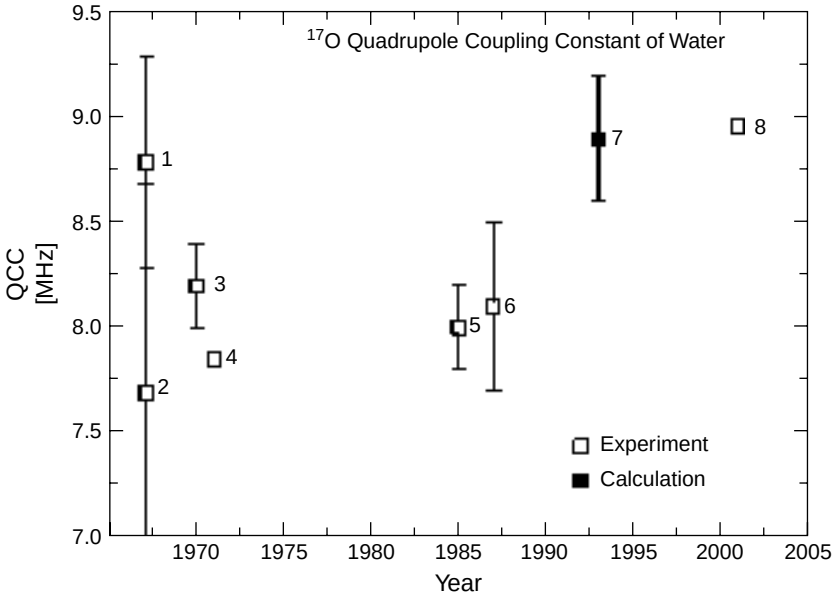

Figure 3 Experimental and calculated NQCCs for ^{17}O in water versus the year of publication. All but one result (black square) were determined experimentally (open squares). The early results of Glasel[106] (labelled 1) were criticized by later authors, although it is in good agreement with the calculated value of Eggenberger et al.[74] (labelled 7) and the newest experimental value,[4] labelled 8. The other experimental results are from the following references: 2 is from Ref.[107], 3 is from Ref.[108], 4 is from Ref.[109], 5 is from Ref.[110] and 6 is from Ref.[111]

liquid water have been taken by Moriarty et al.[77] and Ludwig et al.[19] Moriarty et al. used HF theory to treat the central water molecule within a statistical mechanical bath of water molecules. The configurations of the liquid water cluster were generated using MC simulations. Their best results include configuration interaction and a zero point energy correction, and for deuterium $\chi = 228.2\,\text{kHz}$ and $\eta = 0.1605$. For ^{17}O, $\chi = 11.04\,\text{MHz}$ and $\eta = 0.8237$. Ludwig et al.[19] used the QCE approach and for deuterium in liquid water obtained $\chi =$ 264 kHz and $\eta = 0.134$. For ^{17}O, $\chi = 8.4\,\text{MHz}$ and $\eta = 0.855$.

Experimental studies have shown an interesting and surprising behavior for the deuterium NQCC of water in a mixture of water and DMSO.[78] Recently, we have shown that this behavior is not reproduced in computational studies using the cluster approach.[79] Experimental determinations of liquid state NQCCs are not straightforward and various approximations must be employed in interpretation of the experimental results. The disagreement between experiment and computation suggests that one of these approximations is not valid, but also may be due to deficiencies in the simulations. Studies are underway to clarify the current situation.

The cluster approach has also been used to calculate ^{17}O NQCC in liquid CO_2.[80] The results were in excellent agreement with experiment and it was found that the NQCC is constant over a wide range of densities and temperatures between 298 K and 325 K, in the liquid and supercritical phase. The asymmetry parameter has a negligible contribution in equation (3). The same approach was used by Laaksonen and Wasylishen[81] to determine the ^{14}N and deuterium NQCC of liquid ammonia and their temperature dependence. The ab initio calculations of the NQCC were carried out at the MP2 level with a 6-31 G** basis set and at this level of theory the gas phase deuterium NQCC is overestimated by approximately 10% and the ^{14}N NQCC by approximately 4%. For liquid ammonia, the calculated ^{14}N NQCC at 271 K was $\chi = -3.67\,\text{MHz}$ and at 197 K $\chi = -3.43\,\text{MHz}$. For the deuterium nucleus, $\chi = 264\,\text{kHz}$ at 271 K, $\chi = 255\,\text{kHz}$ at 197 K and the asymmetry parameter is insensitive to temperature with $\eta = 0.13 \pm 0.01$ over the range of temperature studied. These values are approximately 13% higher than recent experimental results for the deuterium NQCC in liquid ammonia of Hardy and Zeidler[82] who obtained $\chi = 232\,\text{kHz}$ at 273 K. However, accounting for the 10% error due to limitations of the ab initio calculations results in excellent agreement between the computational and theoretical values. Furthermore an increase in the deuterium NQCC with temperature at a rate of $0.1\,\text{kHz}\,\text{K}^{-1}$ was observed in both the experimental and computational results. Merkling et al.[83] have calculated the deuterium NQCC of the hydroxy-deuterium of methanol in carbontetrachloride at various compositions. Experimental studies show that the NQCC decreases with an increase in the methanol mole fraction of 0.1 after a maximum at that point. Although the computed values also show a decrease with increase in the methanol mole fraction, no maximum is observed. Furthermore, the computed NQCC values are 2–20% higher than the experimental results.

Ludwig, Farrar and Weinhold have carried out QCE calculations of NQCCs for a range of liquids. As discussed above, the QCE algorithm was used to determine the deuterium and ^{17}O NQCC and asymmetry parameter in liquid water with results that are in fair agreement with experiment. Ludwig, Farrar and Weinhold use a Calibrated quadrupole moment to correct the cluster results against the single molecule value, so no correction due to inadequacies of the ab initio calculation are necessary.[19] The temperature dependencies of the NQCC and asymmetry parameter of the carbonyl deuterium, oxygen, amide trans deuterium and nitrogen nuclei in liquid formamide were also determined by Ludwig, Farrar and Weinhold.[16] The trends in the temperature dependencies are found to be in good agreement with experimental results,[3,16,84] however there are

significant discrepancies between the absolute values of the NQCCs (up to approximately 10%). The more recent experimental results for the carbonyl deuteron and the trans amide deuteron[3] show deviations of 3% from the theoretical results, while deviations of up to 13% are observed between these experimental results and the earlier results of Ludwig et al.[16,84] This indicates that the early experimental results may contain systematic errors. The new experimental results[3] are determined using the correlation between the chemical shift and NQCC whereas the earlier experimental results used relaxation data.[16,84] The differences between the two sets of experimental values highlight the difficulties in interpretation of the experimental data for determination of liquid state NQCCs. Studies on the temperature dependence of the NQCC and asymmetry parameter of nuclei in N-methylformamide[17] and N-methylacetamide[18] have also been carried out. Again, the temperature dependence of the ^{14}N and deuterium NQCC are in good agreement with the qualitative behavior of the experimental results, however the absolute values differ. NQCCs in ammonia have also been determined using the QCE method,[24] however deviations from experiment suggest that the clusters selected in the study may not be an accurate representation of the liquid.[82] Recently the QCE method has been used to determine the NQCCs of liquid ethanol[26] in the temperature range 250–350 K. The results obtained are in good agreement with experiment. In general, the temperature dependence of the NQCC that is observed in experiment can be reproduced using the QCE method. However, the absolute values of the NQCCs often differ considerably suggesting a systematic error in the experimental results or the computations. The necessity of invoking approximations in the experimental interpretations, and the variations in experimental results suggest that some of the experimental determinations are in error.

Using the cluster method accurate predictions for the NQCC of various nuclei and liquids have been obtained. The NQCC generally needs to be adjusted due to errors in the ab initio calculations of the gas phase NQCC,[43] or equivalently a Calibrated quadrupole moment needs to be used.[19] These errors can often be quantified due to the availability of accurate experimental values of the NQCC for single molecules, but suggest that improvement of the ab initio cluster calculations is an important step in obtaining NQCCs using purely computational methods. The use of DFT may alleviate these difficulties due to its ability to determine accurate values of the NQCC in an efficient manner. Bailey and co-workers have recently used DFT to calculate NQCCs of gas phase molecules with considerable success[64–68] however these are yet to be used in liquid state calculations as far as we are aware.

3.2 Relaxation Times

The history of a combined application of simulations and quantum chemical calculations for a better understanding of relaxation phenomena started just 20 years ago with an investigation on quadrupolar relaxation. In 1981 Engström and Jönsson[30] published a paper on the EFG fluctuation at the nucleus of a lithium ion in dilute aqueous solution. The results were obtained from Monte Carlo simulations on clusters of different sizes and used an EFG curve obtained from self consistent field (SCF) calculations. They used a pair approximation for the EFG, as is usually done for the potential and estimated the error due to this approximation to be smaller than 5 to 10%. The estimate was based on calculations for $Li^+ + 2H_2O$ configurations. They found interesting information that contributed to the detailed understanding of the relaxation mechanism, e.g., that the first solvation shell is the main contributor, that the lateral motion of the water molecules in this shell is much more important than the rotational motion, and that an electrostatic approximation for Li^+ is not satisfactory due to the close neighbourhood of this shell to the central ion. Although they analysed the time scale of the fluctuations, they were not yet able to calculate the relaxation time itself, as they used the static MC method rather than the dynamic MD method. This work was extended a year later to the Na^+ and Cl^- ions and for the latter case it was found that rotational motion of the water molecules has a similar influence to the translational motion.[31] In 1984 the work was further extended to MD simulations yielding, for the first time, relaxation times from first principles.[32] The dynamics clearly showed that the decay of the EFG time correlation function is not mono-exponential, and the simulated relaxation rate (experimental values in parenthesis) for Li^+ was $0.007\,s^{-1}$ ($0.027\,s^{-1}$), for Na^+ was $22\,s^{-1}$ ($16.6\,s^{-1}$) and for Cl^- was $41\,s^{-1}$ ($25\,s^{-1}$), i.e., in good agreement with the exception of Li^+. This work was recently extended by Odelius and Kowalewski.[85] They studied the dipole-dipole relaxation for Li^+ and were able to reproduce the experiment quite accurately, whereas the temperature behaviour of the quadrupolar relaxation with the EFG surface from Engström et al. showed a similar deviation as before with the deviation being a factor of 3 to 4 of the experimental value. The same system was also studied by Baumert et al.[86] by MD with an electrostatic approximation for the EFG, but in addition these authors compared the quadrupole couplings obtained from this approach and the ab initio cluster approach, finding a deviation up to a factor two and indirectly confirming the failure of the electrostatic approach for this system.

At approximately the same time that the early work of Engström et al. was performed, Schnitker and Geiger[35] used similar techniques in an MD study of the quadrupolar relaxation of ^{131}Xe in water (published for the first time in a diploma work in 1982), although they applied an empirical potential and an electrostatic approximation for the EFG. The technique applied differs from that of Engström et al. insofar as the simple electrostatic model permits calculation of the EFG 'on the fly', i.e., in each step of the simulation, rather than requiring calculation of a pair EFG surface before the simulation and use pair additivity. In many respects they came to similar conclusions, e.g., that the decay is not mono-exponential and that the first hydration shell is mainly responsible for the relaxation. In contrast to simpler theories they found agreement between simulated and experimental relaxation rates roughly within the experimental uncertainty.

With a similar method Luhmer et al.[87,88] calculated the quadrupole relaxation of ^{131}Xe dissolved in benzene. They found that no complex formation was necessary to explain the relaxation as assumed by some authors previously, but that the molecular rotation of the quadrupole of benzene around a C_2 axis can reproduce the experimental relaxation nearly quantitatively. The influence of the cross-correlation was found to be negligible and the relaxation rates between 100 and $150\,s^{-1}$ were in good agreement with experiments ($190–230\,s^{-1}$). These results are compared in a study of the dipolar relaxation of ^{129}Xe in benzene in a later paper[89]

where, in contrast to the quadrupolar relaxation, it is found that the translational motion is more important than the rotation. Additional results of similar quality were obtained with the same approach for ^{131}Xe in 1,3- and 1,4-dioxane,[90] in tetrachloride, acetonitrile, and methanol,[91,92] and in acetonitrile also for ^{21}Ne and ^{83}Kr.[93]

The only study of a relaxation time in pure water we are aware of is by Lippens et al.[94] They studied the dipolar proton relaxation of liquid water in an empirical approach with the SPC and a polarizable SPC model. The relaxation time is 75% larger than the experimental value, a detailed analysis shows however, that the intermolecular part is quite accurate.

All the simulations discussed up to now are in agreement with experiment to within approximately a factor of two. The authors of these studies usually accept this as a good agreement. There are several problems with approximations (like the difficulty in obtaining a good estimate for the Sternheimer shielding), which make it difficult to get more accurate values in this approach. Linse and Halle[34] argue that continuum-solvent theories cannot give good results. In a study of noble gases in organic solvents Vaara et al.[6] conclude that a pure electrostatic model is not good enough. These conclusions could be one reason to turn to methods that calculate the relaxation time from first principles, as performed first by Engström et al.[32] with an EFG obtained from SCF calculations. Although for more accurate values one should include electron correlation.

The quadrupolar relaxation in liquid ^{21}Ne has been treated from first principles in three papers,[36,95,96] which show the progress of the methods within a few years. This system is more difficult to handle because the EFG is completely intermolecular, but no electrostatic interaction occurs and hence electrostatic models are not possible. In addition the interaction is purely dispersive, i.e., the potential as well as the EFG has to be calculated with high-level correlation methods. In 1993 Eggenberger et al.[36] obtained values with deviations less than 20% from experiment. Although the authors discuss different error sources which might lead to fortuitous cancellations, the good agreement with experiment seduced them to assume that the error was not more than 10%, not including the error due to quantum effects at the temperatures below 33 K. Improved work in 1998 by Kirchner et al.[95] showed that the property is much more sensitive to changes in both the EFG and the potential than assumed. A better potential reduced the relaxation times by one third, whereas improving the EFG in addition increased the values by approximately 50% bringing them back close to the original results. In contrast, three-body and quantum effects were shown to induce changes of only 5 to 10% each. As a result the authors assumed that the results had, by far, not yet converged. Two years later Halkier et al.[96] were able to reach convergence (not including many-body and quantum effects) with coupled cluster calculations on the CCSD(T) level and huge basis sets for the EFG as well as for the potential. At 41 K a best estimate including quantum effects by a perturbational method is approximately 15% lower than the experimental value. Additional insights were gained by Kirchner et al.[95] from a detailed study of the self- and cross-correlation functions and a semi-quantitative model of the mechanism. There are two main effects that induce the relaxation. First an exchange between first shell and outer shell atoms with a correlation time of 5 to 0.5 ps for temperatures between 25 to 300 K and a fast process, where an outer shell atom hits a first shell atom towards the central atom with a correlation time of 200 to 50 fs for the same temperature range. The first process is a random walk process showing a linear relation with the inverse temperature, whereas the second is a linear movement (vibration), inversely proportional to the square root of the temperature.

From the experience with the quadrupolar relaxation of liquid neon, the present authors believe that most of the work on spherical symmetric systems, where the EFG is completely intermolecular, probably profited from error cancellations. For the Li^+ ions the cancellation was perhaps just not as effective as for other systems.

The most complicated system investigated by similar microscopic techniques to those discussed here was published by Scheurer et al.[37] in 1999. They studied the shielding anisotropy, dipolar relaxation and nuclear Overhauser effect values in the protein ubiquitin. MD simulations for the protein molecule in water were performed with a molecular mechanics force field. 625 snapshots of the trajectory were taken to obtain dynamic information of the magnetic properties from SOS-DFPT (sum-over-states density functional perturbation theory) calculations. Model groups or simple charges replaced part of the molecule, whereas the quantum chemical part was treated using basis sets of high local quality. They were able to reproduce experimental relaxation times and nuclear Overhauser effect values to within 10 to 20%. In our group we are currently working on the deuterium quadrupolar relaxation of the water/DMSO system, where we previously obtained the NQCC (see above).

3.3 Chemical Shieldings

Whereas in most previous sections a comparison between different results was difficult, we are here in the fortunate situation that most work on chemical shieldings up to now was performed on water at ambient conditions. A collection of results, all published between the years 1994 and 2000, is presented in Figure 4 for protons and in Figure 5 for ^{17}O. The range of the results is as large or even larger than the solvent effect itself. We will discuss the different methods here. In this section we use shift for the difference between the liquid and gas isotropic chemical shielding, i.e., no absolute shieldings are discussed here.

Method 1 is the reference interaction site model combined with self consistent field calculations (RISM-SCF approach) by Hirata and co-workers.[97] The method is in principle non-empirical and treats the solvent and the solution on an atomic level. However this first application is based on an empirical potential (TIP3P-like). The authors discuss ways to improve the method, which evidently is not yet predictive.

Method 2 is a continuum method where the water molecule is immersed in a dielectric medium. The result is again unsatisfactory with the wrong sign for the ^{17}O gas-liquid shift as above. This work by Mikkelsen et al.[98] is cited because they extended this model (Method 3) by taking a cluster with a first solvation shell which as a whole was immersed in a dielectric medium. The results improved greatly with the protons yielding a nearly perfect agreement with experiment, but for the oxygen the solvent effect is only approximately half the experimental value. The authors suggested that their somewhat accidental result (using just one fixed first solvation shell) could be improved by selection

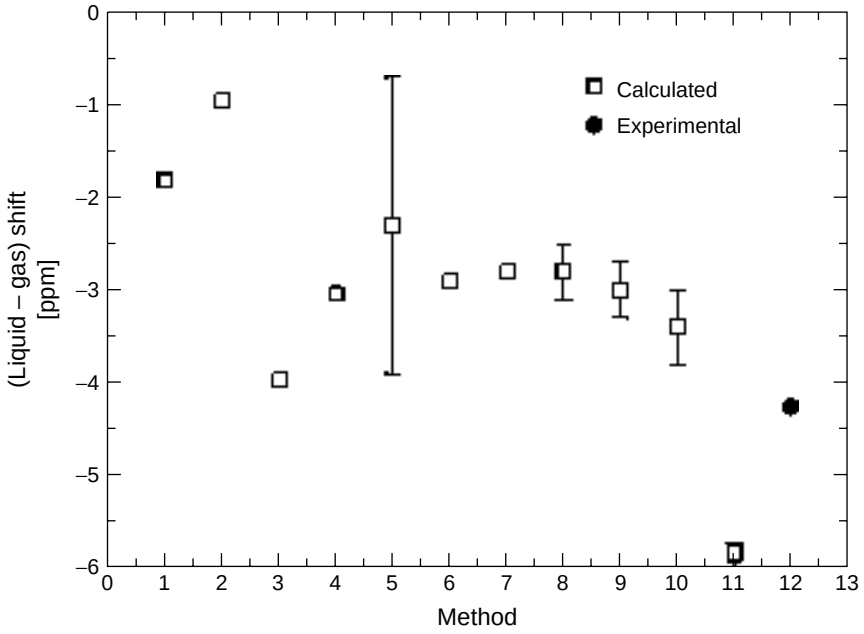

Figure 4 The solvent effect of water on the proton shift in water calculated with different methods (see text)

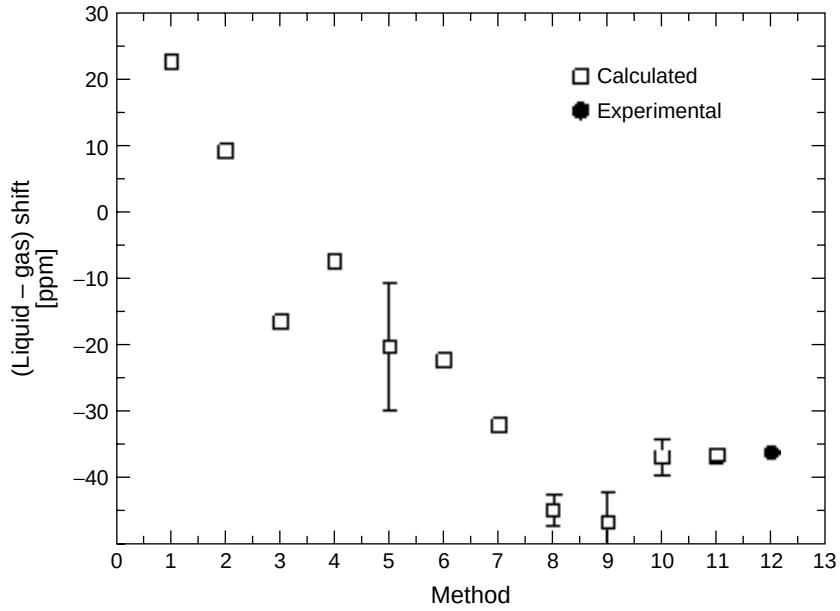

Figure 5 The solvent effect of water on the ^{17}O shift in water calculated with different methods (see text)

of clusters from simulations. This was indeed done by other authors, who also showed that the range of shifts obtained from different clusters is huge, making the method by Mikkelsen et al. not very reliable. The same authors published similar work on H_2S and HCN.[99] Method 4 by Nymand and Åstrand is a perturbational method that again does not yet give satisfying results.

Method 5 is the first work applying the cluster method. Chesnut and Rusiloski[12] used the CFF-91 force field for the simulation and the gauge including atomic orbital (GIAO) coupled HF method for the shift calculations applying locally dense basis sets. Their statistical error bars are quite large. The solvent shifts are roughly half the experimental shifts. One reason for the inadequacy of the results might be the general force field applied here in contrast to most other work where potentials calibrated for water were used. It is hard to judge whether the quality of the quantum chemical method is adequate for the intermolecular contributions.

In method 6 by Cui and Karplus[100] a QM/MM method was applied to this problem for the first time. The flexible TIP3P model by Dang and Pettitt[101] was applied in the MD simulations. DFT calculations on the B3LYP/6-311G(d,p) level were performed for 100 clusters. Their results include only the intermolecular component, which however are responsible for 90%

and 80% of the shift for protons and oxygen, respectively.[102] The results given as method 7 were obtained with a larger basis set, but for 10 clusters only.

The next three methods are by Malkin et al.[102] and apply the cluster method with different potentials. The quantum chemical method for the shift calculation is in all cases the SOS-DFPT with an IGLO-III basis set.[103] Method 8 uses the Dang and Pettitt potentials, as do methods 6 and 7. Method 9 corresponds to the potential by Bopp et al.[104] and method 10 to the MYCL potential of Lie and Clementi[76] obtained from ab initio quantum chemical calculations. Hence method 10 is the first one that uses no empirical information (with the exception of a very general empirical parameter in the SOS-DFPT method). The values presented in the figures were obtained from 10 clusters consisting of 9 water molecules. Test calculations showed that the absolute values of these shifts would increase by approximately 0.2 ppm and 1.2 ppm for H and ^{17}O, respectively, if the cluster size was increased to 13 water molecules. The small number of clusters leads to relatively large statistical errors (the bars in the figures are standard errors). In fact all three values are identical within two standard errors and two of them for oxygen and one for hydrogen, respectively, also agree with the experimental shift within two standard errors. Due to the small number of clusters it could be that the configurations do not represent the distribution of configurations in the liquid well enough. The shifts are in fair agreement with the experimental value for oxygen, the agreement is worse for protons. It would be interesting to repeat this work with today's computer power for more clusters to give a better insight into the role of the potential.

Finally, method 11 is the recent work of Pfrommer et al.[105] This is probably the first application of Car-Parrinello simulations to the calculation of magnetic properties of liquids. Their calculation of chemical shieldings with the BLYP functional is not limited to clusters of a certain size, but is performed for the ensemble consisting of 32 molecules with periodic boundary conditions. The result for oxygen is in excellent agreement with experiment, but the absolute value of the proton shift is approximately 1.6 ppm too large. The statistical errors are very small, approximately the size of the rectangle in Figure 4 and only half that size in Figure 5.

Cammi et al.[7] tested the newly developed PCM-GIAO method on the ^{13}C, ^{15}N and ^{17}O shifts for the molecules CH_3CN and CH_3NO_2 in water with good success and gave a critical evaluation of the method. Ludwig et al.[18] applied the QCE method to liquid N-methylacetamide and obtained excellent agreement with experiment for the temperature dependence of the chemical shifts of H, ^{17}O and ^{14}N and fair agreement of the shifts themselves for H and ^{17}O.

We would like to make a few concluding remarks on this comparison of calculated with experimental shifts and between different methods. The experimental error is not known, but could be sizeable. The calculations do not include rovibrational corrections in an adequate manner, but it is assumed that their classical treatment is sufficient as it will almost cancel when the difference between liquid and gas value is calculated. There are still quite a few different error sources which might cancel, like the limited quality of the potential applied in the simulation, the limited basis set and the limited treatment of correlation in the calculation of the chemical shielding, limited representation of configuration space and limited cluster size. Nevertheless the results show a great improvement in the last decade and it can be expected that such calculations will reach predictive quality in the coming decade.

3.4 J-Couplings

We are aware of only two recent papers on calculations of J-couplings in the liquid. Mikkelsen et al.[99] use a model where the solvent is represented by a dielectric medium, to study its influence on the HH^- and HS^- coupling in H_2S and the HC^-, NC^- and NH^- coupling in HCN. They find dielectric effects of more than 10% and stress the importance of geometry relaxation as they may enhance as well as oppose the direct dielectric effect. Case et al.[13] study dipeptides and ubiquitin. For the latter they apply the cluster method already applied to calculate the relaxation time of the same system[37] (see above). Their results show a reasonable scatter around an empirical Karplus curve.

4 CONCLUSIONS

Before 1990 only very few papers on the simulation of NMR properties in the liquid phase appeared. All of them were about relaxation processes for simple systems (atomic ions and rare gas atoms in polar solvents). One reason was that the computer speed and some quantum chemical tools were not yet available, but perhaps another was that simulations and quantum chemistry were completely different fields with only few people having the necessary knowledge in both fields. In the last decade the number of groups working on the subject has grown and approximately 50 papers are now available. The field is still in an experimental state, i.e., we need much more experience on the reliability of the methods. What influences do the potentials, the pair approximation in the MD cluster method or the harmonic approximations in the quantum cluster equilibrium theory have? However it has been shown that calculations of liquid properties and solvent effects have become feasible and we can see a new great area of computational chemistry evolving.

5 REFERENCES

1. M. Odelius and A. Laaksonen, in 'Molecular Dynamics. From Classical to Quantum Methods', eds P. B. Balbuena and J. M. Seminario, Amsterdam, 1999.
2. M. A. Wendt and T. C. Farrar, *Mol. Phys.*, 1998, **95**, 1077.
3. M. J. Hansen, M. A. Wendt, and T. C. Farrar, *J. Phys. Chem. A*, 2000, **104**, 5328.
4. J. A. Ropp, C. Lawrence, T. C. Farrar, and J. L. Skinner, *J. Am. Chem. Soc.*, 2001, submitted.
5. H. Huber, A. J. Dyson, and B. Kirchner, *Chem. Soc. Rev.*, 1999, **28**, 121.
6. J. Vaara, J. Jokisaari, T. T. Rantala, and J. Lounila, *Mol. Phys.*, 1994, **82**, 13.
7. R. Cammi, B. Mennucci, and J. Tomasi, *J. Chem. Phys.*, 1999, **110**, 7627.
8. C. Amovilli, V. Barone, R. Cammi, E. Cances, M. Cossi, B. Mennucci, C. S. Pomelli, and J. Tomasi, *Adv. Quant. Chem.*, 1999, **32**, 227.
9. M. P. Allen and D. J. Tildesley, in 'Computer Simulation of Liquids', Clarendon Press: Oxford, 1987.

10. K. Hermansson, S. Knuts, and J. Lindgren, *J. Chem. Phys.*, 1991, **95**, 7486.
11. R. Eggenberger, S. Gerber, H. Huber, D. Searles, and M. Welker, *J. Chem. Phys.*, 1992, **97**, 5898.
12. D. B. Chesnut and B. E. Rusiloski, *J. Mol. Struct. (Theochem)*, 1994, **314**, 19.
13. D. A. Case, C. Scheurer, and R. Brüschweiler, *J. Am. Chem. Soc.*, 2000, **122**, 10 390.
14. K. Coutinho and S. Canuto, *J. Mol. Struct. (Theochem)*, 1993, **106**, 99.
15. H. Takase and O. Kikuchi, *Chem. Phys.*, 1994, **181**, 57.
16. R. Ludwig, F. Weinhold, and T. C. Farrar, *J. Chem. Phys.*, 1995, **103**, 3636.
17. R. Ludwig, F. Weinhold, and T. C. Farrar, *J. Chem. Phys.*, 1997, **107**, 499.
18. R. Ludwig, F. Weinhod, and T. C. Farrar, *J. Phys. Chem. A*, 1997, **101**, 8861.
19. R. Ludwig, F. Weinhold, and T. C. Farrar, *J. Chem. Phys.*, 1995, **103**, 6941.
20. R. Ludwig and F. Weinhold, *J. Chem. Phys.*, 1999, **110**, 508.
21. R. Ludwig, F. Weinhold, and T. C. Farrar, *J. Chem. Phys.*, 1996, **105**, 8223.
22. R. Ludwig, O. Reis, R. Winter, F. Weinhold, and T. C. Farrar, *J. Phys. Chem. B*, 1998, **102**, 9312.
23. R. Ludwig, F. Weinhold, and T. C. Farrar, *Ber. Bunsenges. Phys. Chem.*, 1998, **102**, 197.
24. R. Ludwig, F. Weinhold, and T. C. Farrar, *Ber. Bunsenges. Phys. Chem.*, 1998, **102**, 205.
25. R. Ludwig, F. Weinhold, and T. C. Farrar, *Mol. Phys.*, 1999, **97**, 479.
26. R. Ludwig, F. Weinhold, and T. C. Farrar, *Mol. Phys.*, 1999, **97**, 465.
27. F. Weinhold, *J. Chem. Phys.*, 1998, **109**, 367.
28. F. Weinhold, *J. Chem. Phys.*, 1998, **109**, 373.
29. M. A. Wendt, F. Weinhold, and T. C. Farrar, *J. Chem. Phys.*, 1998, **109**, 5945.
30. S. Engström and B. Jönsson, *Mol. Phys.*, 1981, **43**, 1235.
31. S. Engström, B. Jönsson, and B. Jönsson, *J. Magn. Reson.*, 1982, **50**, 1.
32. S. Engström, B. Jönsson, and R. W. Impey, *J. Chem. Phys.*, 1984, **80**, 5481.
33. R. Car and M. Parrinello, *Phys. Rev. Lett.*, 1985, **55**, 2471.
34. P. Linse and B. Halle, *Mol. Phys.*, 1989, **67**, 537.
35. J. Schnitker and A. Geiger, *Z. Phys. Chem. NF*, 1987, **155**, 29.
36. R. Eggenberger, S. Gerber, H. Huber, and M. Welker, *Chem. Phys.*, 1993, **177**, 91.
37. C. Scheurer, N. R. Skrynnikov, S. F. Lienin, S. K. Straus, R. Brüschweiler, and R. R. Ernst, *J. Am. Chem. Soc.*, 1999, **121**, 4242.
38. H. Huber, *Chem. Phys. Lett.*, 1984, **112**, 133.
39. H. Huber, *J. Mol. Struct. (Theochem)*, 1985, **121**, 207.
40. H. Huber, *J. Chem. Phys.*, 1985, **83**, 4591.
41. S. Gerber and H. Huber, *J. Mol. Spectrosc.*, 1989, **134**, 168.
42. E. Fliege, H. Dreizler, S. Gerber, and H. Huber, *J. Mol. Spectrosc.*, 1989, **137**, 24.
43. H. Huber, *Z. Naturforsch.*, 1994, **49a**, 103.
44. S. Gerber and H. Huber, *Z. Naturforsch.*, 1987, **42a**, 753.
45. S. Gerber and H. Huber, *Chem. Phys.*, 1989, **134**, 279.
46. S. Gerber and H. Huber, *J. Phys. Chem.*, 1989, **93**, 545.
47. R. Eggenberger, S. Gerber, H. Huber, D. Searles, and M. Welker, *J. Mol. Spectrosc.*, 1992, **151**, 474.
48. B. Kirchner, H. Huber, G. Steinebrunner, H. Dreizler, J.-U. Grabow, and I. Merke, *Z. Naturforsch.*, 1997, **52a**, 297.
49. D. L. Fiacco, B. Kirchner, W. A. Burns, and K. R. Leopold, *J. Mol. Spectrosc.*, 1998, **191**, 389.
50. D. B. Chesnut and K. D. Moore, *J. Comp. Chem.*, 1989, **10**, 648.
51. D. B. Chesnut and C. G. Phung, *Chem. Phys. Lett.*, 1991, **183**, 505.
52. D. B. Chesnut, B. E. Rusiloski, K. D. Moore, and D. A. Egolf, *J. Comp. Chem.*, 1993, **14**, 1364.
53. D. B. Chesnut and E. F. C. Byrd, *Chem. Phys.*, 1996, **213**, 153.
54. D. B. Chesnut, *Chem. Phys.*, 1997, **214**, 73.
55. J. F. Hinton, P. Guthrie, P. Pulay, and K. Wolinski, *J. Am. Chem. Soc.*, 1992, **114**, 1604.
56. R. A. Kirby and A. E. Hansen, *Int. J. Quantum Chem.*, 1996, **57**, 199.
57. G. A. DiLabio and J. S. Wright, *Chem. Phys. Lett.*, 1998, **297**, 181.
58. G. A. DiLabio, *J. Phys. Chem. A*, 1999, **103**, 11 414.
59. G. A. DiLabio, D. A. Pratt, A. D. LoFaro, and J. S. Wright, *J. Phys. Chem. A*, 1999, **103**, 1653.
60. G. A. DiLabio, D. A. Pratt, and J. S. Wright, *Chem. Phys. Lett.*, 1999, **311**, 215.
61. G. A. DiLabio and D. A. Pratt, *J. Phys. Chem. A*, 2000, **104**, 1938.
62. D. A. Pratt, J. S. Wright, and K. U. Ingold, *J. Am. Chem. Soc.*, 1999, **121**, 4877.
63. D. B. Chesnut and E. F. C. Byrd, *J. Comp. Chem.*, 1996, **17**, 1431.
64. W. C. Bailey, *J. Mol. Spectrosc.*, 1997, **185**, 403.
65. W. C. Bailey, *J. Mol. Spectrosc.*, 1998, **190**, 318.
66. W. C. Bailey, *Chem. Phys. Lett.*, 1998, **292**, 71.
67. W. C. Bailey, *Chem. Phys.*, 2000, **252**, 57.
68. W. C. Bailey, F. M. Gonzalez, and J. Castiglione, *Chem. Phys.*, 2000, **260**, 327.
69. P. Schwerdtfeger, M. Pernpointner, and J. K. Laerdal, *J. Chem. Phys.*, 1999, **111**, 3357.
70. V. G. Malkin, O. L. Malkina, M. E. Casida, and D. R. Salahub, *J. Am. Chem. Soc.*, 1994, **116**, 5898.
71. V. G. Malkin, O. L. Malkina, L. A. Eriksson, and D. R. Salahub, in 'Modern Density Functional Theory: A Tool for Chemistry', eds J. M. Seminario and P. Politzer, Amsterdam, 1995.
72. P. L. Cummins, G. B. Bacskay, N. S. Hush, B. Halle, and S. Engström, *J. Chem. Phys.*, 1985, **82**, 2002.
73. P. L. Cummins, G. B. Bacskay, and N. S. Hush, *Mol. Phys.*, 1987, **61**, 795.
74. R. Eggenberger, S. Gerber, H. Huber, D. Searles, and M. Welker, *Mol. Phys.*, 1993, **80**, 1177.
75. R. Eggenberger, S. Gerber, H. Huber, D. Searles, and M. Welker, *J. Comp. Chem.*, 1993, **14**, 1553.
76. G. C. Lie and E. Clementi, *Phys. Rev. A*, 1986, **33**, 2679.
77. N. W. Moriarty and G. Karlström, *Chem. Phys. Lett.*, 1997, **279**, 372.
78. B. C. Gordalla and M. D. Zeidler, *Mol. Phys.*, 1986, **59**, 817.
79. B. Kirchner, D. J. Searles, A. J. Dyson, P. S. Vogt, and H. Huber, *J. Am. Chem. Soc.*, 2000, **122**, 5379.
80. M. Holz, R. Haselmeier, A. J. Dyson, and H. Huber, *Phys. Chem. Chem. Phys.*, 2000, **2**, 1717.
81. A. Laaksonen and R. E. Wasylishen, *Z. Naturforsch.*, 1995, **50a**, 137.
82. E. H. Hardy and M. D. Zeidler, *Phys. Chem. Chem. Phys.*, 2000, **2**, 1645.
83. P. J. Merkling, M. D. Zeidler, and P. A. Bopp, *J. Mol. Liq.*, 2000, **85**, 57.
84. R. Ludwig, J. Bohmann, and T. C. Farrar, *J. Phys. Chem.*, 1995, **99**, 9681.
85. M. Odelius and J. Kowalewski, *J. Chem. Soc. Faraday Trans.*, 1995, **91**, 215.
86. R. Baumert, R. Ludwig, and A. Geiger, *J. Mol. Model.*, 1996, **2**, 379.
87. A. Dejaegere, M. Luhmer, M.-L. Stien, and J. Reisse, *J. Magn. Reson.*, 1991, **91**, 362.
88. M. Luhmer, D. van Belle, J. Reisse, M. Odelius, J. Kowalewski, and A. Laaksonen, *J. Chem. Phys.*, 1993, **98**, 1566.
89. M. Luhmer, A. Moschos, and J. Reisse, *J. Magn. Reson. A*, 1995, **113**, 164.
90. M. Luhmer and J. Reisse, *J. Magn. Reson. A*, 1995, **115**, 197.

91. M. Odelius and A. Laaksonen, *Mol. Phys.*, 1994, **82**, 487.
92. M. Odelius, *J. Phys. Chem.*, 1994, **98**, 12 108.
93. M. Odelius, M. Holz, and A. Laaksonen, *J. Phys. Chem. A*, 1997, **101**, 9537.
94. G. Lippens, D. Van Belle, S. J. Wodak, and J. Jeener, *Mol. Phys.*, 1993, **80**, 1469.
95. B. Kirchner, E. Ermakova, G. Steinebrunner, A. J. Dyson, and H. Huber, *Mol. Phys.*, 1998, **94**, 257.
96. A. Halkier, B. Kirchner, H. Huber, and M. Jaszunski, *Chem. Phys.*, 2000, **253**, 183.
97. T. Yamazaki, H. Sato, and F. Hirata, *Chem. Phys. Lett.*, 2000, **325**, 668.
98. K. V. Mikkelsen, K. Ruud, and T. Helgaker, *Chem. Phys. Lett.*, 1996, **253**, 443.
99. K. V. Mikkelsen, K. Ruud, and T. Helgaker, *J. Comp. Chem.*, 1999, **20**, 1281.
100. Q. Cui and M. Karplus, *J. Phys. Chem. B*, 2000, **104**, 3721.
101. L. X. Dang and B. M. Pettitt, *J. Phys. Chem.*, 1987, **91**, 3349.
102. V. G. Malkin, O. L. Malkina, G. Steinebrunner, and H. Huber, *Chem. Eur. J.*, 1996, **2**, 452.
103. W. Kutzelnigg, U. Fleischer, and M. Schindler, in 'Deuterium and Shift Calculation', ed P. Diehl, E. Fluck, H. Günther, R. Kosfeld, and J. Seelig, Heidelberg, 1990.
104. P. Bopp, G. Jancsó, and K. Heinzinger, *Chem. Phys. Lett.*, 1983, **98**, 129.
105. B. G. Pfrommer, F. Mauri, and S. G. Louie, *J. Am. Chem. Soc.*, 2000, **122**, 123.
106. J. A. Glasel, *Proc. Natl. Acad. Sci. USA*, 1967, **58**, 27.
107. B. B. Garrett, A. B. Denison, and S. W. Rabideau, *J. Phys. Chem.*, 1967, **71**, 2606.
108. J. C. Hindman, A. Svirmickas, and M. Wood, *J. Phys. Chem.*, 1970, **74**, 1266.
109. J. C. Hindman, A. J. Zielen, A. Svirmickas, and M. Wood, *J. Chem. Phys.*, 1971, **54**, 621.
110. J. R. C. van der Maarel, D. Lankhorst, J. de Bleijser, and J. C. Leyte, *Chem. Phys. Lett.*, 1985, **122**, 541.
111. R. P. W. J. Struis, J. de Bleijser, and J. C. Leyte, *J. Phys. Chem.*, 1987, **91**, 1639.

Acknowledgements

This work is part of the project 2000-058881.99 of the Schweizerischer Nationalfonds zur Förderung der Wissenschaften. We thank the Australian Research Council for support of this work. We thank B. Kirchner and E. Hardy for reading the manuscript. We also thank those whose important contributions to the field we missed, but who are not angry with us! Our apologies – we are not perfect.

Biographical Sketches

Hanspeter Huber, *b* 1944. Diplom, 1968, ETH Zurich, Doktor, 1972, University of Basel. Postdoctoral studies with J. D. Roberts, Pasadena, (NMR) and R. Zahradnik, Prague, (quantum chemistry). Currently University Professor of Chemistry. Approx. 100 papers. Research interest: Combination of quantum chemistry and simulations to obtain bulk properties of liquids and solvent effects (mainly of NMR related properties).

Debra J. Searles, *b* 1965. BSc Hons, 1987 and PhD, 1991, University of Newcastle, Australia (quantum chemistry). Postdoctoral studies with Hanspeter Huber (bulk properties of liquids using computational chemistry) and Denis J. Evans, ANU, Australia (theoretical and computational studies of nonequilibrium liquids). Currently Chemistry Lecturer, Griffith University, Australia. Approx. 50 papers. Research interests: properties of equilibrium and nonequilibrium fluids from molecular dynamics simulations and statistical mechanics.

Coupling Constants Determined by ECOSY

Harald Schwalbe, P. Schmidt and Christian Griesinger
Universität Frankfurt, Germany

1 Introduction 1
2 The ECOSY Principle 1
3 *S* Filtered Homonuclear Correlation to Measure $^nJ(I_2, S)$ Couplings in an I_1–S–·–I_2 Spin System 1
4 Heteronuclear Long-Range Correlation to Measure $^nJ(I_1, I_2)$ Couplings in an I_1–S–·–I_2 Spin System 2
5 The SOFT-COSY Experiment to Measure Homonuclear $^nJ(I_1, I_3)$ Couplings in an I_1–I_2–I_2 Spin System and Heteronuclear $^nJ(S_2, I_1)$ Couplings in a S_2–S_1–·–I_1 Spin System 2
6 BIRD Pulses for Spin Topology Filtering: Measuring Homonuclear $^nJ(I_1, I_2)$ Couplings in an I_1–S–T–I_2 or I_1–S–·–I_2 Spin System 10
7 The ECOSY Experiment for the Measurement of Homonuclear $^nJ(I_1, I_1)$ Couplings in an I_1–I_2–I_3 Spin System and $^nJ(I_1, I_2)$ Couplings in an I_1–S_1–·–I_2 Spin System 13
8 References 16

1 INTRODUCTION

Exclusive correlation spectroscopy (ECOSY)[1–3] is one of the most powerful methods for determining homonuclear, J(H,H) and J(C,C), as well as heteronuclear coupling constants, such as J(C,H), J(N,H), J(P,H), and J(P,C), in proteins and nucleic acids. Applications to other heteronuclear systems, especially in metalloorganic chemistry, have been successfully performed to measure, for example, metal–phosphorus, metal–carbon and metal–proton coupling constants. Due to the inherent features of the experiment, precise coupling constants can be determined even if the linewidth of the involved nuclei is large (macromolecules) or the coupling constant to be determined is small. This article presents the basic principle (Section 2) and different experimental implementations (Sections 3–7) of the ECOSY experiment, together with examples. Relaxation effects that introduce systematic errors in the coupling constant determination will not be discussed here; the interested reader is referred to the literature cited.[4–8]

2 THE ECOSY PRINCIPLE

If in a three spin system consisting of spins ABC with nonvanishing couplings J(A,C) and J(B,C), A (in ω_1) is correlated with B (in ω_2) without mixing the spin states of a third spin C (Figure 1), the two-dimensional correlation spectrum can be constructed from two subspectra with spin C either in the α or in the β state (Figure 1, left and right, respectively). Since spin A and spin B have a 'chemical shift' of $\omega_1 = \Omega_A + \pi J$(A,C) and $\omega_2 = \Omega_B + \pi J$(B,C) for C in the α state, and of $\omega_1 = \Omega_A - \pi J$(A,C) and $\omega_2 = \Omega_B - \pi J$(B,C) for C in the β state, a spectrum that correlates spin A with spin B without touching C during t_1, the mixing, and t_2 will show just two cross peaks, one at $(\omega_1,\omega_2) = [\Omega_A + \pi J$(A,C), $\Omega_B + \pi J$(B,C)] and the other at $(\omega_1,\omega_2) = [\Omega_A - \pi J$(A,C), $\Omega_B - \pi J$(B,C)]. The displacement vector $\boldsymbol{J}_C$ (where the subscript C indicates the passive spin in both dimensions) has the components J(A,C) and J(B,C) in ω_1 and ω_2, respectively. As can be derived from Figure 1, a small coupling J(B,C) can be determined, irrespective of its size, provided the so-called *associated coupling* J(A,C) is larger than the linewidth and the resolution in ω_1. The sensitivity of the experiment depends upon the transfer efficiency of the correlation between A and B, rather than on the size of the coupling of interest. The precision of the coupling constant determination depends on the precision with which the position of a peak maximum can be determined for a given digital resolution of the FID and digitization of the spectrum, and on the invariance of the submultiplets in the two slices displaced in ω_2. The direction of the displacement vector indicates the relative sign of the two couplings J(A,C) and J(B,C): it points to the upper right or lower left if the signs of the two couplings are the same; and it points to the upper left or lower right if the signs are different.

Depending on the spin systems under study (e.g. whether the molecule has the isotopes in natural abundance or the nuclei have been enriched with or depleted of the magnetically active isotope, the molecular weight of the compound under investigation, and the linewidth of the resonances), there are currently four different implementations of an ECOSY-type correlation (see Sections 3–7). Rather than giving a chronological overview, the experiments are ordered according to their theoretical complexity. In the explanatory Figures given in each section, a representative pulse sequence, the spin system (with I_n, where I designates the ^{1}H spins, and n the numbers within them; S_n, where S designates the first heteronuclear spins, and n the numbers within them; and T for a second heteronuclear spin), the so-called ECOSY *triangle* and the resulting spectrum is shown. A dot in the spin system represents one or more non-NMR-active nuclei. The three essential spins A, B, and C are on the corners of the ECOSY triangle, the first active spin A (left) sharing a large, structurally uninteresting coupling with the passive spin C (top) which is used as an associated coupling to resolve the coupling of interest J(B,C) to spin B (right) which is the second active spin. In most of the proposed sequences, B is the detected spin. The sides of the triangle represent the associated coupling, the coupling of interest, and the mixing process between A and B. A and B need not be directly scalar coupled. The ECOSY triangle may serve as a graphical aid in designing new experiments to measure coupling constants.

3 *S* FILTERED HOMONUCLEAR CORRELATION TO MEASURE $^nJ(I_2,S)$ COUPLINGS IN AN I_1–S–·–I_2 SPIN SYSTEM

In a three spin system I_1–S–·–I_2 with I_1 bound to S, the ECOSY pattern will be observed in any correlation between

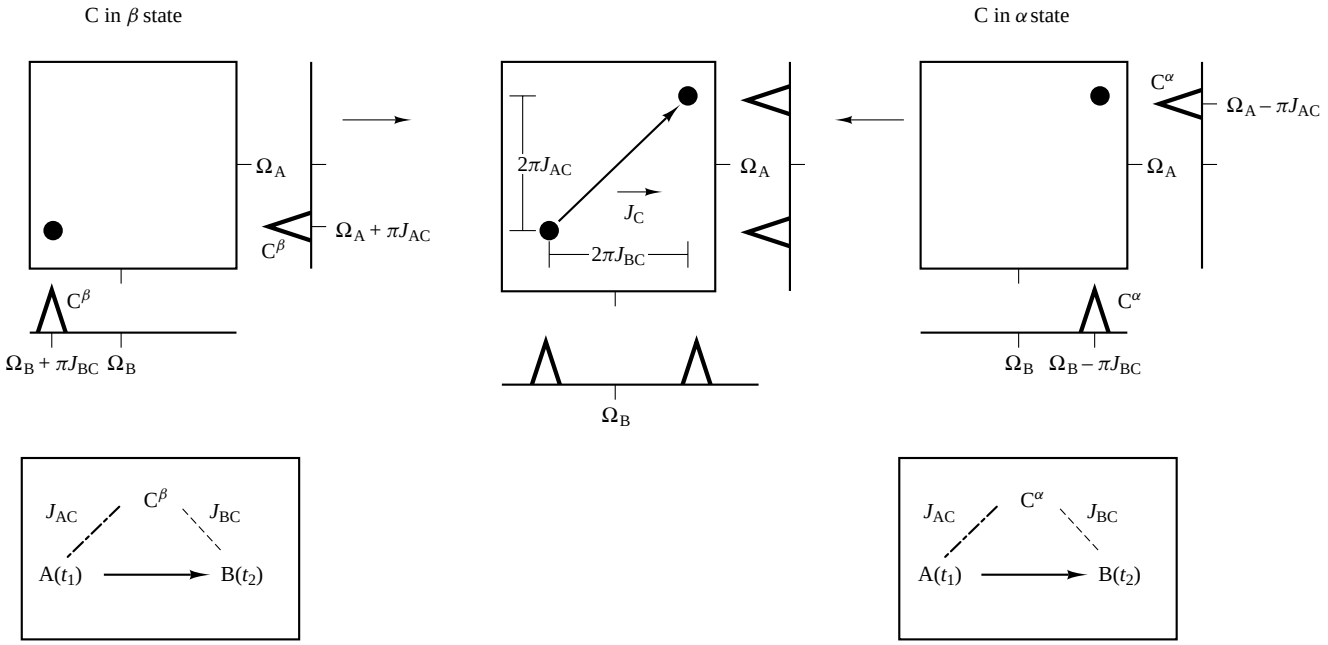

Figure 1 The ECOSY principle. In a three spin system the associated coupling J(A,C) is used to resolve the two components $\Omega_B \pm \pi J$(B,C) in ω_1. The two theoretical subspectra originate from spin C either in the α or in the β state

I_1 and I_2 obtained with an arbitrary homonuclear mixing sequence (e.g. TOCSY, NOESY, ROESY) because S remains untouched during the whole experiment (Figure 2(a)). S filtering can be inserted at the beginning of the pulse sequence to select for the NMR-active fraction of S nuclei. This classical Montelione–Wagner experiment[9,10] has been applied in a number of different applications for the measurement of J(C,H),[11–22] J(N,H),[23] J(P,H),[24] J(^{113}Cd,H),[25] J(F,H),[26] and J(F,C),[26] and is probably the best way to obtain coupling constant information for I_1–S–·–I_2 spin systems. It has been applied to the measurement of ^3J(N,H$_\beta$), ^3J(N$_i$,H$_{\alpha i-1}$), and ^3J(C,H) coupling constants. It fails, however, if the homonuclear mixing process is not efficient enough, as for example in α-helical regions of a protein where a NOESY transfer between H_i^N and H$_{\alpha i-1}$ is used for the measurement of the ^3J(N$_i$,H$_{\alpha i-1}$) coupling constant, with N as the passive spin. The NOESY transfer between H_i^N and H$_{\alpha i-1}$ is insensitive in α-helical regions due to the large distance between these protons. In proteins, labeling of the heterospin S, especially that of ^{15}N, is indispensable for sensitivity reasons. Measuring long-range J(C,H) couplings with this approach in uniformly ^{13}C labeled proteins is difficult due to multiple carbon coupling partners. Selective decoupling schemes have been designed to avoid this problem.[27–32]

Figure 3 shows an application of the S filtered experiment.[18] The diastereotopic δ-methyl groups in leucines can be stereochemically assigned by measuring heteronuclear ^3J(C$_{\delta1}$,H$_{\beta1}$) and ^3J(C$_{\delta2}$,H$_{\beta1}$), or ^3J(C$_{\delta1}$,H$_{\beta2}$) and ^3J(C$_{\delta2}$,H$_{\beta2}$) couplings, respectively, provided the β-protons are stereochemically assigned. χ_2 of Leu$_8$ in cyclolinopeptide A assumes a position of 180°. This can be derived from the known stereochemical assignment H$_{\beta1}$ = *pro-S* and H$_{\beta2}$ = *pro-R*.

4 HETERONUCLEAR LONG-RANGE CORRELATION TO MEASURE $^nJ(I_1,I_2)$ COUPLINGS IN AN I_1–S–·–I_2 SPIN SYSTEM

Choosing I_2 (B) and S (A) as the two active spins and I_1 (C) as the passive spin, $^nJ(I_1,I_2)$ coupling constants can be measured provided I_1 is not touched between t_1 and detection. A heteronuclear multiple bond correlation (HMBC)-type sequence [Figure 2(b)][33] that correlates I_1 with S via the $^{n-1}J(I_1,S)$ coupling meets this requirement. The low efficiency of the mixing process due to the usually small heteronuclear $^{n-1}J(I_1,S)$ coupling and the short proton T_2 values are the limiting factors of the method.

5 THE SOFT-COSY EXPERIMENT TO MEASURE HOMONUCLEAR $^nJ(I_1,I_3)$ COUPLINGS IN AN I_1–I_2–I_2 SPIN SYSTEM AND HETERONUCLEAR $^nJ(S_2,I_1)$ COUPLINGS IN A S_2–S_1–·–I_1 SPIN SYSTEM

By application of selective pulses, a subset of spins of a certain isotope (e.g. H$_\alpha$ or C′) can be used as passive spins while using spins of another subset of the same isotope (e.g. H$_\beta$ or C$_\alpha$) as active spins. In proton correlation[34–37] spectroscopy [Figure 4(a)], this idea has not gained widespread application in peptide or protein spectroscopy, because there are no well separated subsets of proton spins that sustain at the same time interesting coupling constants. For example, in the case of ^3J(H$_\alpha$,H$_\beta$) coupling constants, when H$_\alpha$ is used as a passive spin and the two H$_\beta$ are used as active spins the two subsets of passive and active spins are well separated; however, the associated coupling constant is a vicinal coupling, which can be very small. If, on the other hand, one of the H$_\beta$

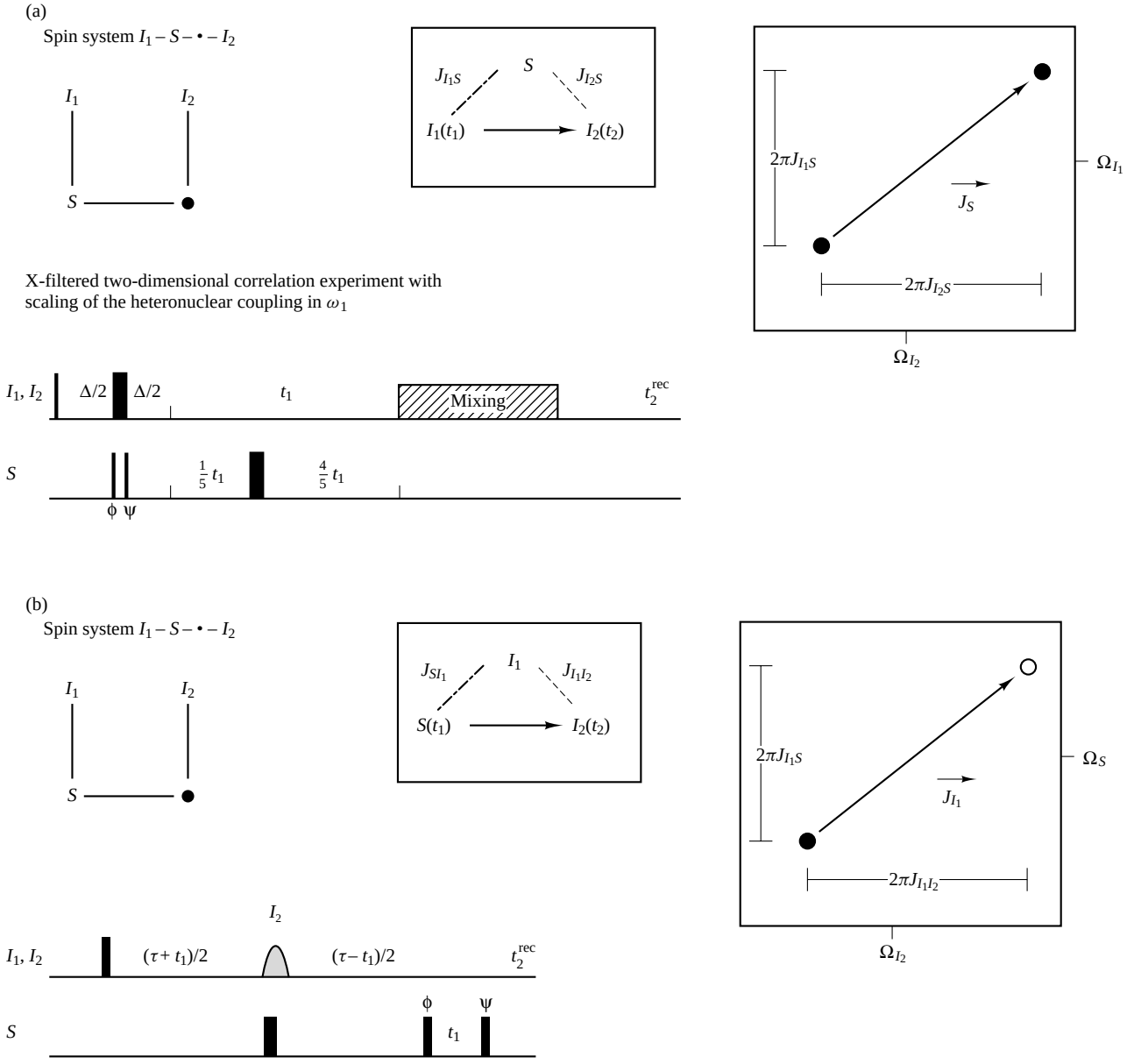

Figure 2 (a) The Montelione–Wagner experiment. In a heteronuclear I_1–S_1–•–I_2 spin system, I_1 and I_2 are correlated by an arbitrary homonuclear mixing process. The heterospin S is not touched and, therefore, remains passive during the entire experiment. Scaling of the associated coupling can be implemented to overcome problems due to overlap. The heteronuclear ${}^nJ(I_2,S)$ coupling is measured in t_2. The associated coupling ${}^1J(I_1,S)$ is scaled to 3/5 in t_1 in the example given. Typical parameters are: $\Delta = [J(I_1,S)]^{-1}$; $\phi = x, -x$; $\psi = x, x, -x, -x$; rec. = $x, -x, -x, x$. (b) The heteronuclear long-range experiment. In a heteronuclear I_1–S_1–•–I_2 spin system, S and I_2 are correlated; I_1 is untouched in the experiment. A homonuclear ${}^nJ(I_1,I_2)$ coupling is measured in t_2. The application of an I_2-selective refocusing pulse ensures pure phase lineshapes in t_2. The signal is modulated by long-range ${}^nJ(I,S)$ couplings in t_1 which are usually not resolved in t_1. Typical parameters are: $\tau \sim [2^{n-1}J(I_2,S)]^{-1}$; $\phi = x, -x$; $\psi = x, x, -x, -x$; rec. = $x, -x, -x, x$

protons is used as a passive spin and the H_α and the other H_β proton as active spins, the associated coupling is a geminal coupling ${}^2J(H'_\beta/H''_\beta)$, but the spectral displacement between the two H_β protons is small.

For carbon, however, the spectrum is composed of well separated regions. Carbonyl and aliphatic carbon resonances have a large frequency difference compared with the chemical shift dispersion of aliphatic carbon atoms. Therefore selective pulses like the Gaussian cascades G3 and G4[38,39] or IBURP and REBURP pulses[40] effectively excite, for example, an aliphatic carbon spin S_1 while leaving the carbonyl spin S_2 passive. The ${}^1J(C',C_\alpha)$ coupling is, fortunately, large in proteins and can therefore be used as an associated coupling to measure ${}^2J(C',H_\alpha)$ in SOFT-HSQC,[41] or the structurally important ${}^3J(C',H_\beta)$ couplings in SOFT-HCCH-COSY[27] (Figure 5) and the ${}^3J(C',H^N)$ couplings in the SOFT-HNCA-COSY.[42,43] A heteronuclear detected experiment for the opposite situation, in which S_1 and S_2 are protons, and I is a heteronucleus, has been published by Kessler et al.[44]

Figure 5 and Figure 6 show the application of this concept to measure ${}^3J(C',H_\beta)$ couplings in proteins. The constituent

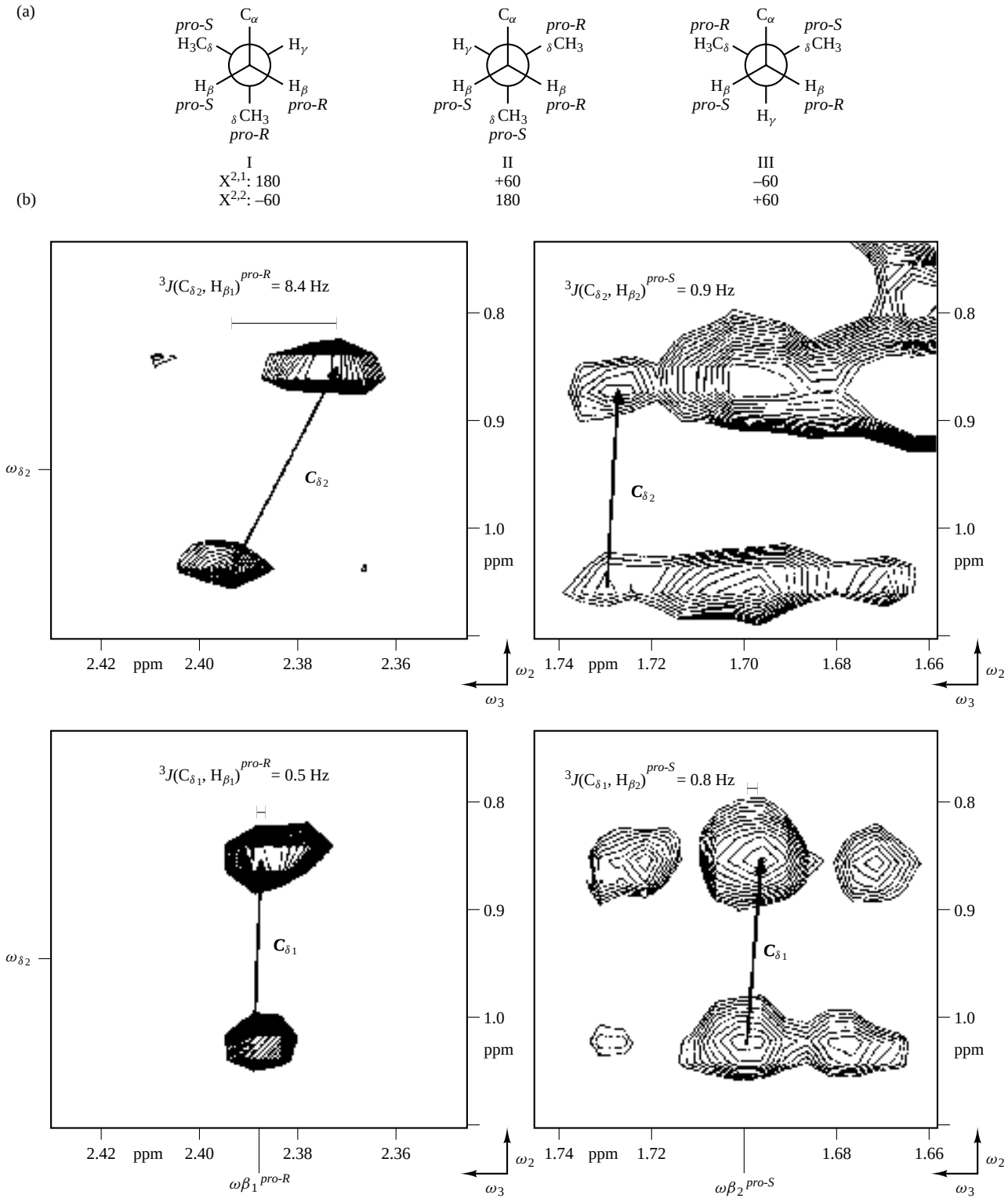

Figure 3 (a) Staggered rotamers around the $C_\beta - C_\gamma$ bond of leucine. (b) Slices through the three-dimensional HSQC-TOCSY showing the four C_δ,H_δ,H_β cross peaks with the displacement vectors due to C_δ. The lower traces are taken at $\omega_1 = \delta(C_{\delta 1}) = 23.6$ ppm and the two upper traces at $\omega_1 = \delta(C_{\delta 2}) = 20.2$ ppm

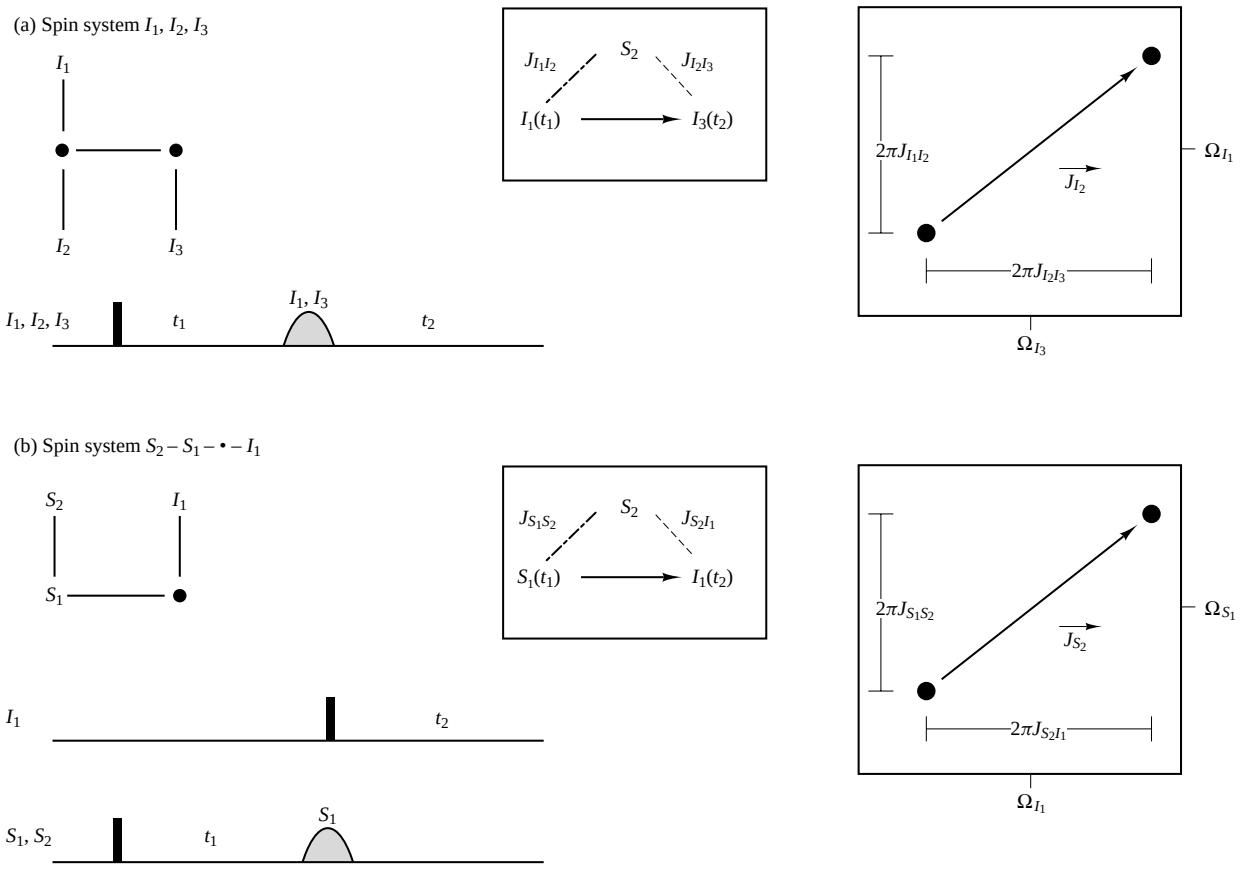

Figure 4 (a) The SOFT-COSY experiment. In a homonuclear three spin system, I_1 and I_3 are correlated by an I_1,I_3-selective mixing pulse. In the example given, the geminal $^2J(I_1,I_2)$ coupling is used as associated coupling in t_1. (b) The SOFT-hetero-COSY experiment. In the heteronuclear S_2–S_1–·–I_2 spin system S_1-selective pulses leave the S_2 spin untouched. The homonuclear $^1J(S_1,S_2)$ coupling serves as an associated coupling in t_1

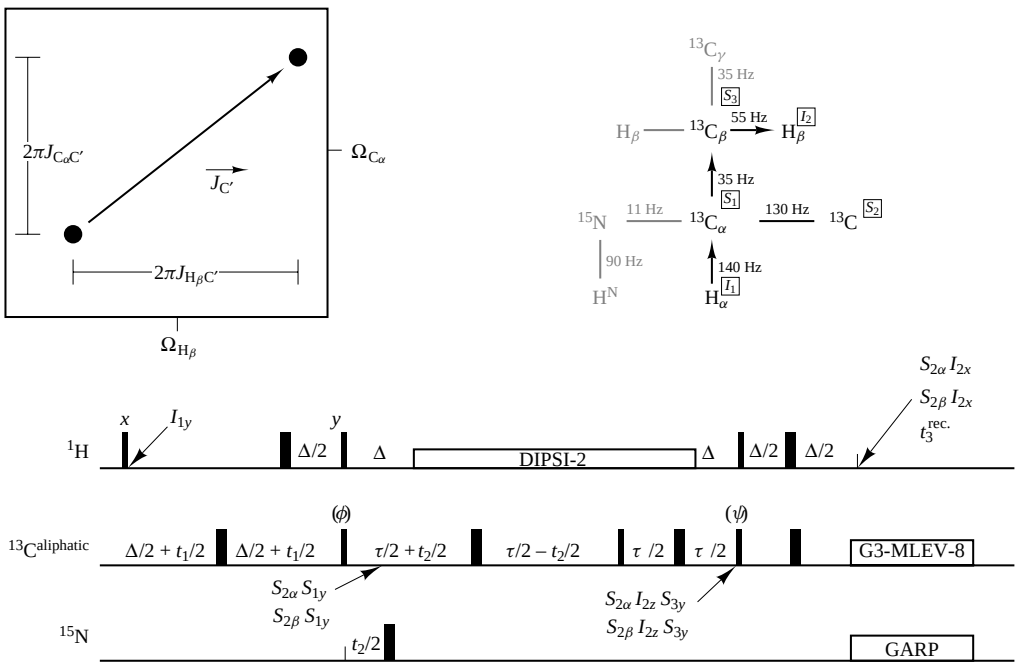

Figure 5 Pulse sequence for the SOFT-HCCH-COSY experiment. In the application to proteins, typical parameters are: $\Delta = [2^1J(C_\alpha,H_\alpha)]^{-1}$; $\tau =]2^1J(C_\alpha,C_\beta)]^{-1}$; $\tau' = [4^1J(C_\alpha,C_\beta)]^{-1}$; $\Delta' = [4^1J(C_\beta,H_\beta)]^{-1}$; $\phi = x, -x$; $\psi = x, x, -x, -x$; rec. = $x, -x, -x, x$

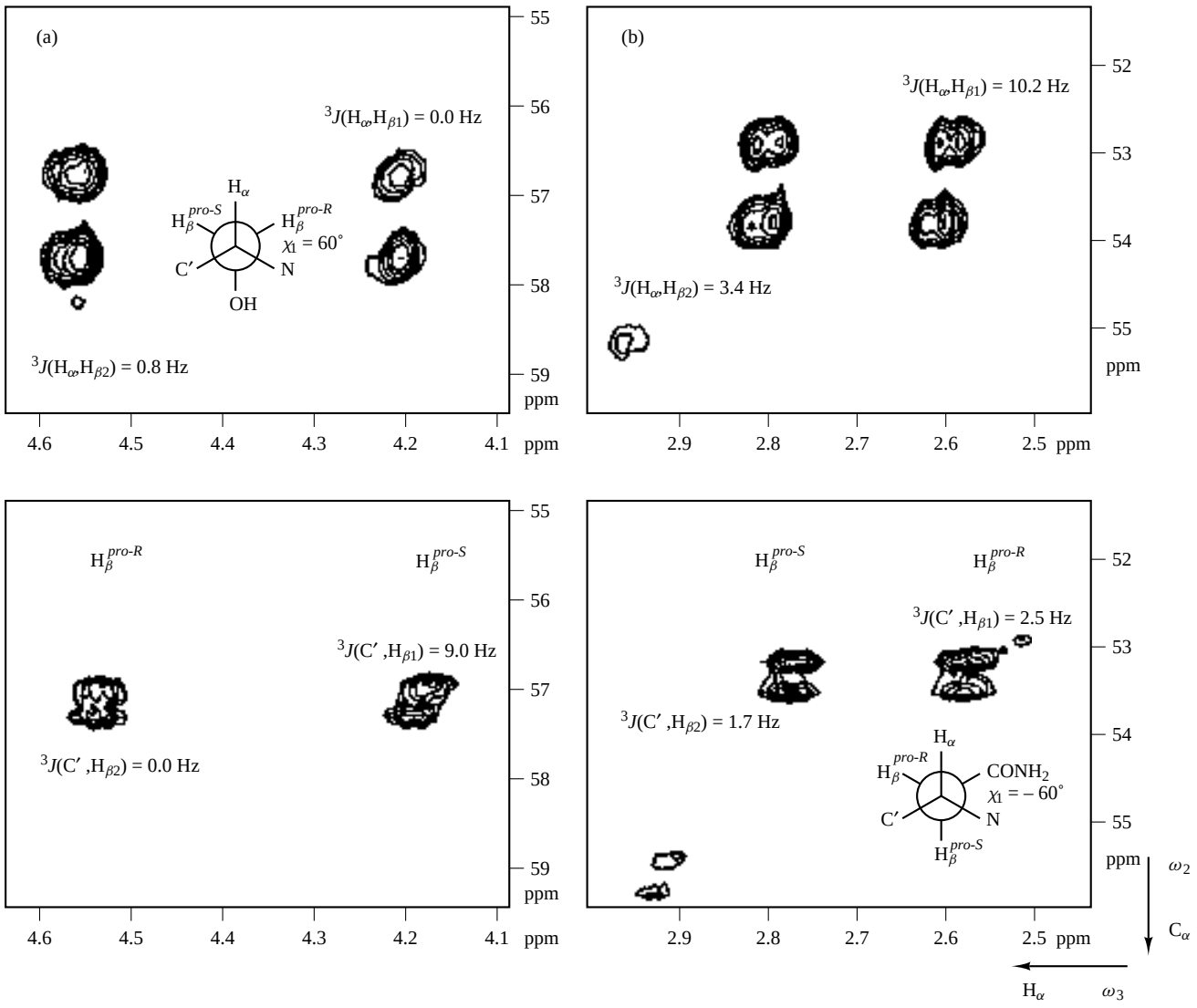

Figure 6 (a) and (b)

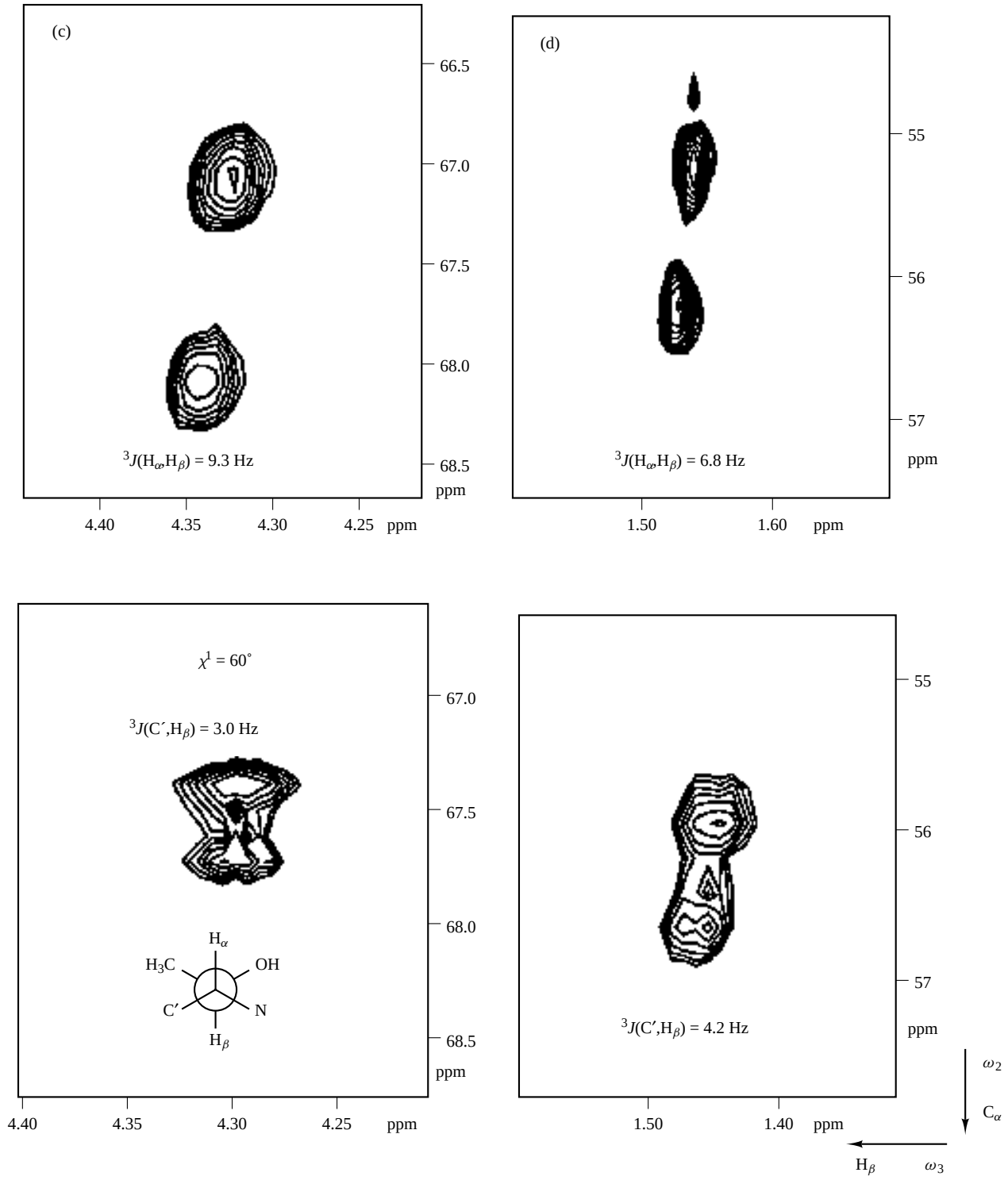

Figure 6 Cross peaks for: (a) Ser_{12}; (b) Asn_{98}; (c) Thr_{18}; (d) Ala_{21}. Upper and lower traces show the C_α,H_β cross peaks from the SOFT-HCCH-ECOSY and the SOFT-HCCH-COSY experiments, respectively. (a) Ser_{12} has two small $^3J(H_\alpha,H_\beta)$ couplings and one large $^3J(H_\beta,C')$ coupling. The predominant rotamer around χ_1 is therefore when $\chi_1 = 60^\circ$, and the higher frequency $H_{\beta 1}$ is $H_\beta{}^{pro\text{-}R}$. (b) From the two small $^3J(H_\beta,C')$ couplings and the large $^3J(H_\alpha,H_{\beta 1})$ coupling of Asn_{98}, it follows that the predominant rotamer is at $\chi_1 = -60^\circ$ and the higher frequency $H_{\beta 1}$ is $H_\beta{}^{pro\text{-}S}$. (c) Thr_{18} has a large $^3J(H_\alpha,H_{\beta 1})$ coupling of 9.3 Hz and a small $^3J(C',H_\beta)$ coupling of 3.0 Hz; χ_1 is therefore -60°. (d) The two cross peaks of Ala_{21} exhibit average $^3J(H_\alpha,H_{\beta 1})$ and $^3J(C',H_\beta)$ coupling constants of 6.8 and 4.2 Hz, respectively

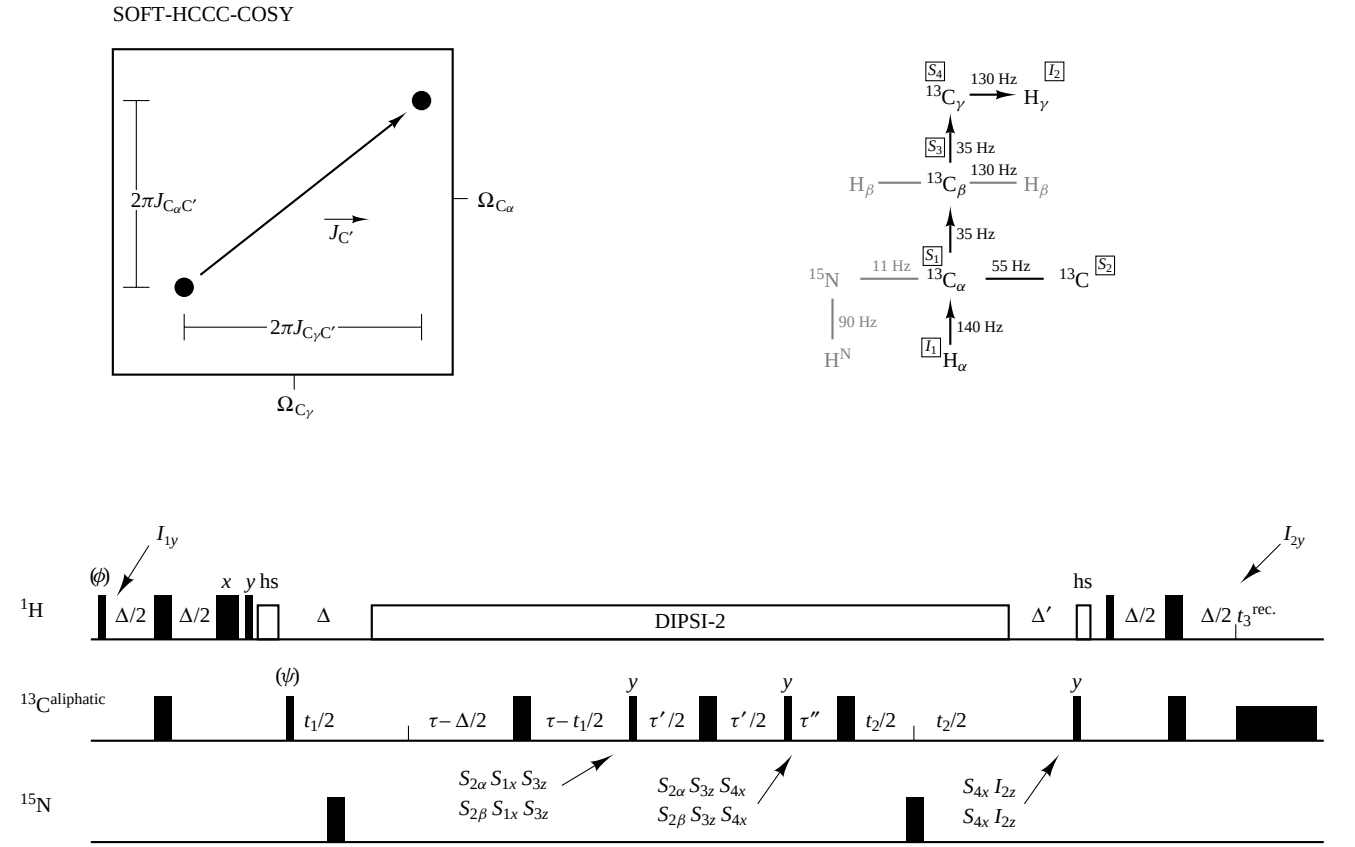

Figure 7 Pulse sequence for the SOFT-HCCC-COSY experiment. In the $S_2{-}S_1{-}\cdot{-}S_4$ spin system S_1,S_4 selective pulses leave S_2 untouched. The coupling of interest is measured in the ω_1,ω_2 cross peak of the three-dimensional experiment. In the application to proteins, typical parameters are: $\Delta = [2^1J(C_\alpha,H_\alpha)]^{-1}$; $\tau = [2^1J(C_\alpha,C_\beta)]^{-1}$; $\tau' = [(54/90)^1J(C,C)]^{-1}$; $\Delta' = [6^1J(C_\gamma,H_\gamma)]^{-1}$; $\phi = x, -x$; $\psi = x, x, -x, -x$; rec. $= x, -x, -x, x\tau''\Delta^1 + t_2(0) + \tau_p$

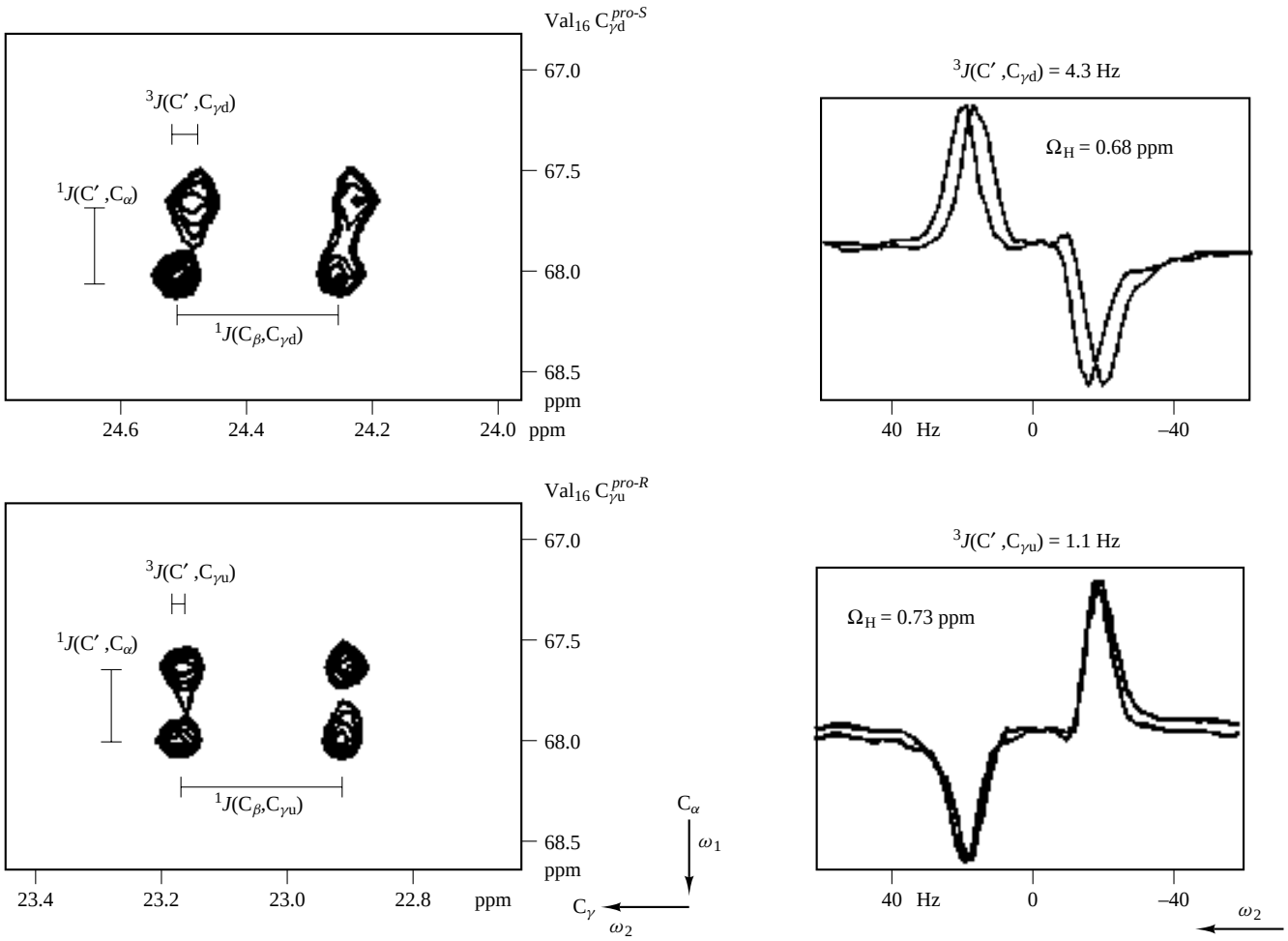

Figure 8 One-dimensional rows and two-dimensional slices from the SOFT HCCC-COSY on ribonuclease T_1. The C_β,H_β cross peaks are displaced due to C′. The antiphase splitting observed is the $^1J(C_\beta,C_\gamma)$ coupling of around 37 Hz

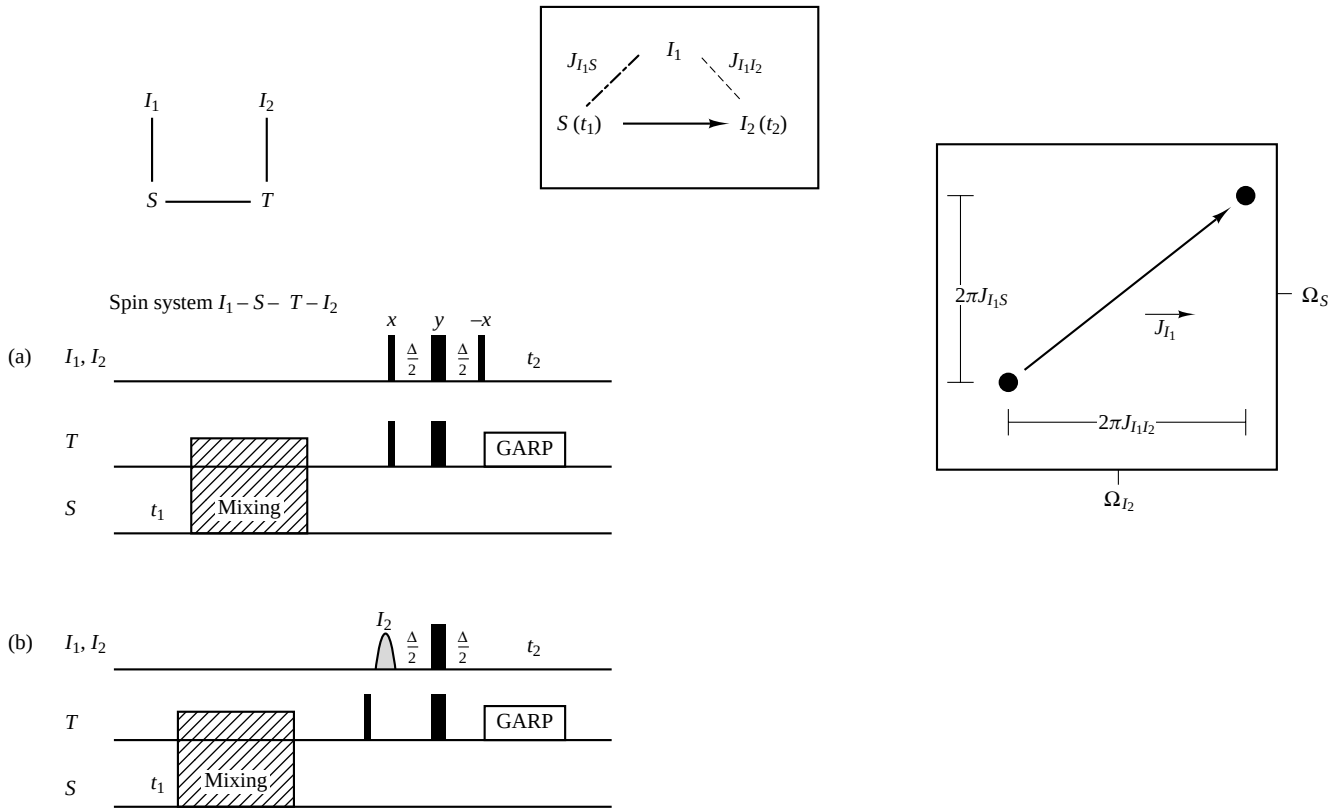

Figure 9 (a) Selection between homonuclear spins bound to different heterospins with BIRD pulses. In the $I_1{-}S{-}T{-}I_2$ spin system, I_2 bound to T evolves heteronuclear $J(I_2,T)$ coupling in the final BIRD refocusing period, whereas the spin states of I_1 bound to S remain unaltered. I_1 serves as passive spin, the ${}^nJ(I_1,I_2)$ coupling can be measured. For typical parameters see Figure 10. (b) Instead of using BIRD spin-topology-filtering techniques, I_2-selective pulses can be used in certain cases to distinguish between I_1 and I_2

experiment is a SOFT-HCCH-COSY, in which C_α (A) is correlated with H_β (B). In the constant time period $\tau = [2J(C_\alpha,C_\beta)]^{-1}$, the ${}^1J(C',C_\alpha)$ coupling, used as the associated coupling in t_1, has evolved a phase of 142°. Mirror image linear prediction[27,45,46] has to be applied to enhance the resolution in ω_1. From inspection of the ${}^3J(C',H_\beta)$ and the ${}^3J(H_\alpha,H_\beta)$ couplings (see Section 5) the conformation around χ_1 and the stereochemical assignments of the H_β protons can be derived. Four representative C_α,H_β cross peaks of the SOFT-HCCH-COSY and the SOFT-HCCH-ECOSY experiments (discussed in Section 6) measured on ribonuclease T_1 are shown. In each case, the unique pattern of large and small couplings provide the assignment to one of the three staggered rotamers. As shown in Figure 6, the predominant rotamer around χ_1 is $\chi_1 = -60°$ for Asn_{98}, since both ${}^3J(C',H_\beta)$ couplings are small and one ${}^3J(H_\alpha,H_\beta)$ coupling is large. The lower frequency H_β can be assigned as *pro-R* since it shows a large coupling with H_α. The preferred conformation and the stereochemical assignment of the other residues are indicated on the figure.

Using the same basic experiment, homonuclear ${}^3J(C',C_\gamma)$ couplings can be determined for the stereochemical assignment of valine methyl groups in the SOFT-HCCC-COSY experiments[47] by correlating C_α (A) and C_γ (B), and leaving C' as the passive spin C. Figure 7 shows the pulse sequence for the SOFT-HCCC-COSY experiment, and Figure 8 shows the two C_α,C_γ cross peaks for Val_{16} in ribonuclease T_1. The large ${}^3J(H_\alpha,H_\beta)$ coupling of 12.4 ± 0.9 Hz and the small ${}^3J(C',H_\beta)$ coupling of 0.53 ± 0.4 Hz indicate a $\chi_1 = 180°$ (not shown). Thus the low-frequency C_γ is the *pro-R* carbon atom, and the high-frequency C_γ is the *pro-S* carbon atom.

6 BIRD PULSES FOR SPIN TOPOLOGY FILTERING: MEASURING HOMONUCLEAR ${}^nJ(I_1,I_2)$ COUPLINGS IN AN $I_1{-}S{-}T{-}I_2$ OR $I_1{-}S{-}\cdot{-}I_2$ SPIN SYSTEM

If one of the active spins (e.g. B) and the passive spin C have the same spin isotope (e.g. I) nonselective pulses cannot be used for polarization transfer from A to B, because C would be touched. However, spin topology filtering using the different transformation properties of two spins of the same isotope that are bound to different heteronuclei (e.g. ${}^1H{-}{}^{13}C$ and ${}^1H{-}{}^{15}N$) under bilinear rotation[48,49] can be used such that B is sensitive for the I pulses and C is not. Effective polarization transfer to B leaving C untouched is then possible. In the following, the different transformation properties of the I_2 spin (e.g. H_α)

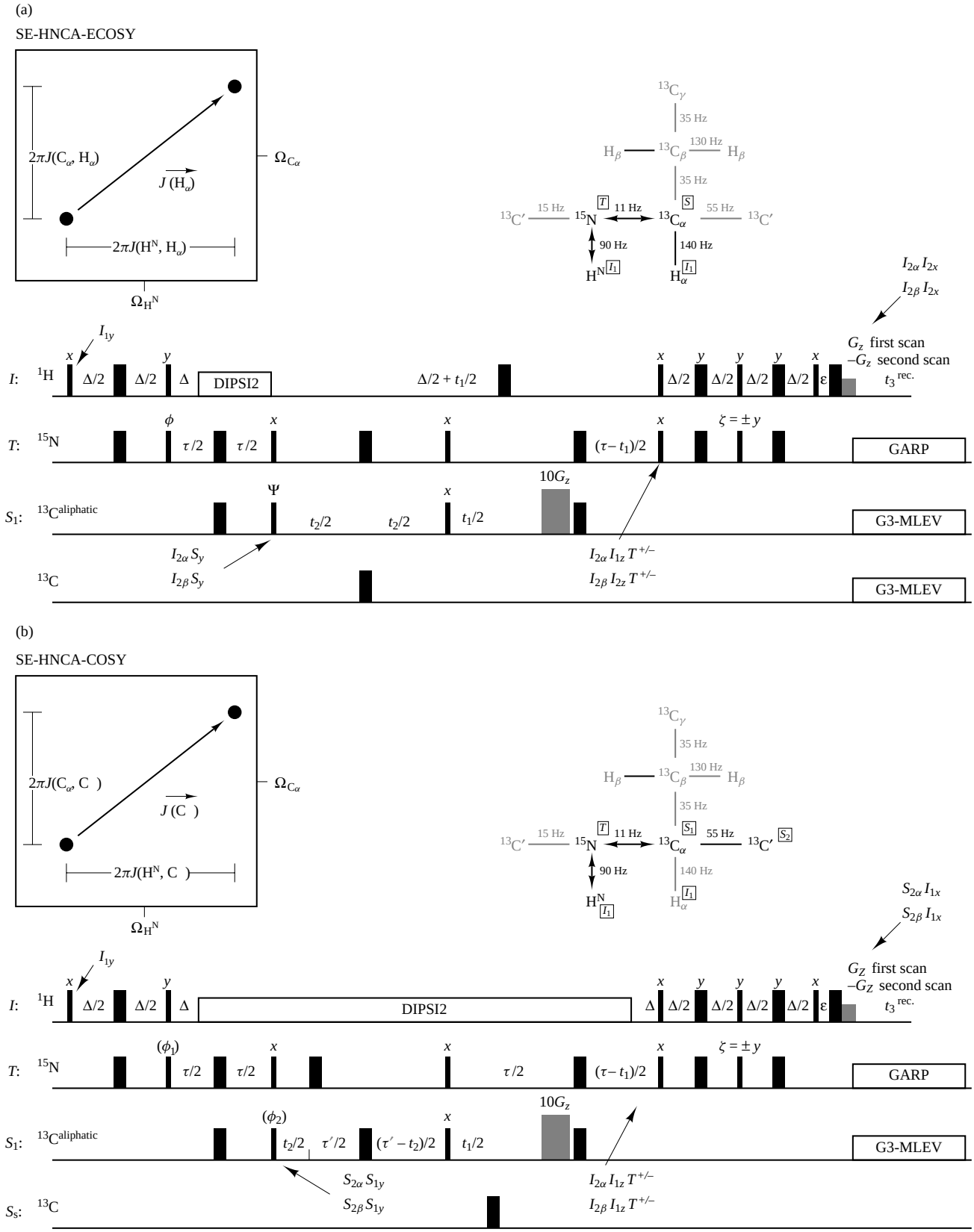

Figure 10 (a) HNCA-ECOSY with sensitivity enhancement and using a heteronuclear gradient echo to measure $^3J(H^N,H_\alpha)$ couplings. The parameters are: $\Delta = [2J(H^N,H_\alpha)]^{-1}$; $\tau = [2J(C_\alpha,N)]^{-1}$; $\tau' = [J(C_\alpha,C_\beta)]^{-1}$; $\epsilon = \tau_g$; $\phi = x, -x$; $\psi = x, x, -x, -x$; rec. = $x, -x, -x, x$. The coupling of interest is measured in the (ω_2,ω_3) plane of the three-dimensional experiment in cross peaks correlating C_α and H^N. The $^1J(C_\alpha,H_\alpha)$ coupling of 145 Hz serves as an associated coupling in ω_2. (b) SOFT-HNCA-COSY with sensitivity enhancement and using a heteronuclear gradient echo to measure $^3J(C',H^N)$ couplings. The parameters are the same as those in (a). The $^1J(C',C_\alpha)$ coupling of 55 Hz serves as an associated coupling in ω_2

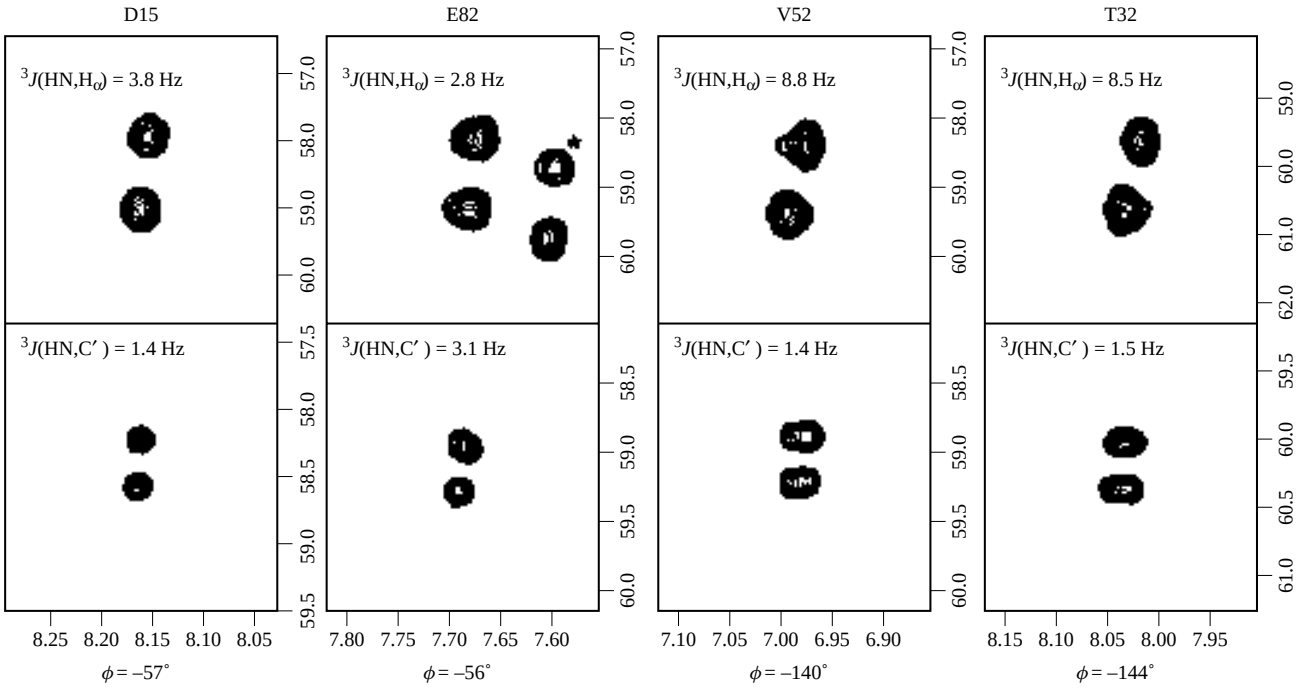

Figure 11 Cross peaks for Asp$_{15}$, Glu$_{82}$, Val$_{52}$, and Thr$_{32}$. Upper and lower traces show the C$_\alpha$,H^N cross peaks from the SOFT-HNCA-ECOSY and the SOFT gradient enhanced HNCA-COSY. The ^3J(H^N,H$_\alpha$) and ^3J(C′,H^N) coupling constants derived from the ω_3 splittings and the derived ϕ angles are indicated

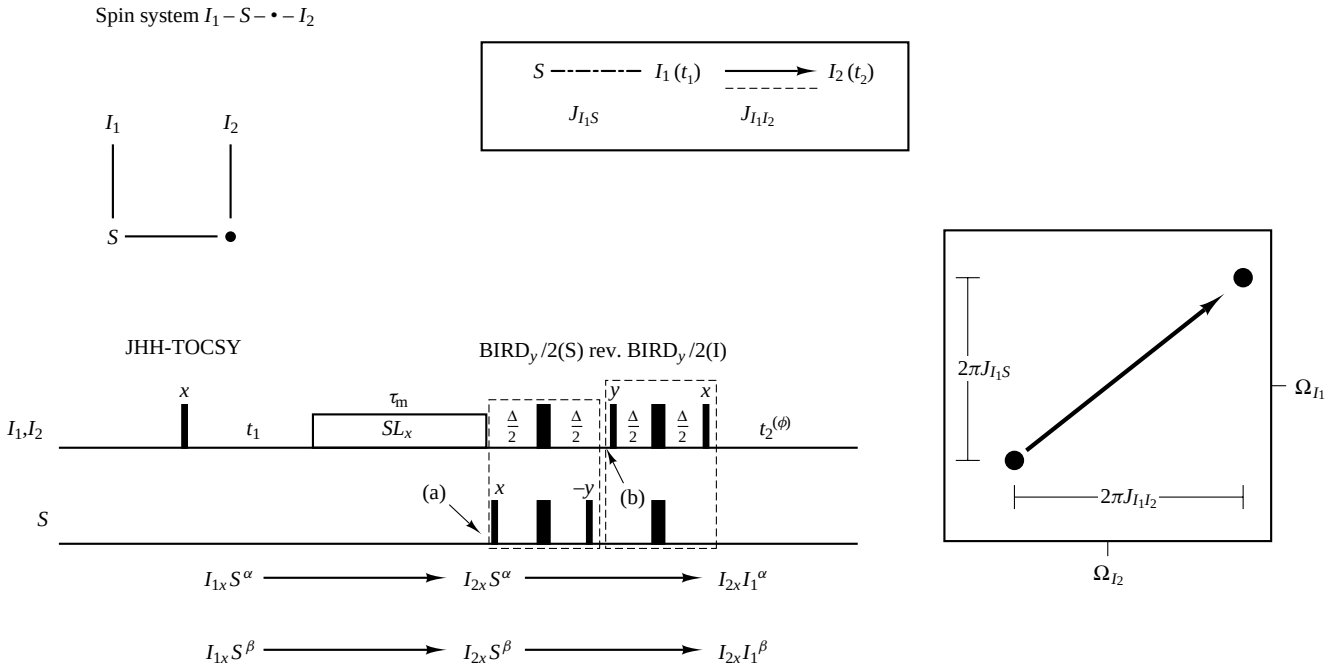

Figure 12 JHH-TOCSY for measuring $^nJ(I_1,I_2)$ couplings in a $I_1 - S - \cdot - I_2$ spin system. The spin state of S in t_1 is transferred to the spin state of spin I_1 in t_1. Selection of a coherence transfer pathway by gradients,[17] although yielding a loss of a factor of $\sqrt{2}$ in signal-to-noise ratio compared with conventional HSQC experiments, is advantageous when measuring ^3J(H^N,H$_\alpha$) couplings in proteins, since the coupling is measured on the H$_\alpha$ resonance. Typical parameters are: $\Delta = [J(I_1,S)]^{-1}$; $\phi = x, -x$; rec. = $x, -x$. Scaling of the heteronuclear coupling could be implemented [see Figure 2(a)]

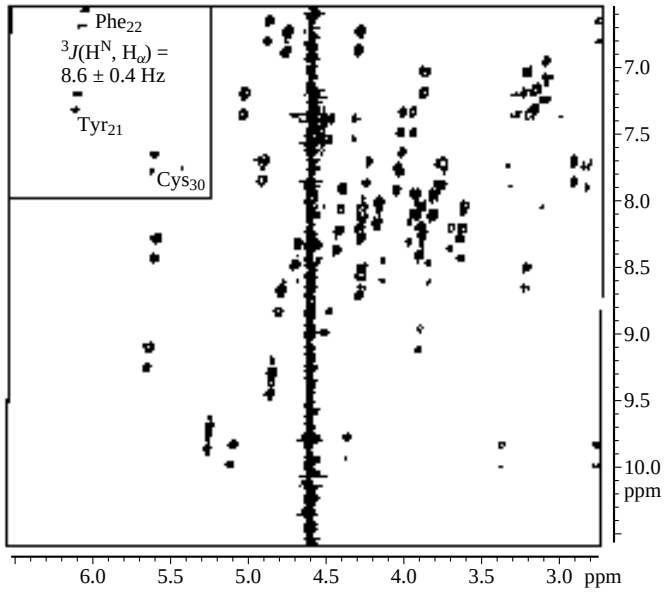

Figure 13 Two-dimensional plot of JHH-TOCSY applied to ^{15}N-enriched BPTI mutant[26] showing the excellent water suppression and the high sensitivity of the experiment

bound to the heteronucleus S ($^{13}C_\alpha$) and the I_1 spin (e.g. H^N) bound to T (^{15}N) under the BIRD sequence shown in Figure 9(a) will be discussed. Using the pulse scheme

$$90^\circ_x(I) - \Delta/2 - 180^\circ_y(I, T) - \Delta/2 - 90^\circ_{-x}(I) \qquad (1)$$

a $2I_{1z}T_z$ operator that can be prepared after the evolution period of an HSQC-type experiment is transferred to detectable proton magnetization I_{1x}, whereas for spin I_2 which is not coupled to spin T the pulses can be concatenated to a $0^\circ(I)$ pulse. Thus I_2 is not affected during the polarization transfer from spin T to I_1.[42,43,50,51]

This principle has been applied in SOFT-HNCA-ECOSY experiments correlating $^{13}C_\alpha$ (A) with H^N (B). H_α is the passive spin C. N,H^N antiphase coherence is transferred to H^N magnetization without touching H_α. From this experiment $^3J(H^N,H_\alpha)$ couplings defining the backbone angle ϕ become available.[42,43,49–54] The BIRD-filtering concept is also compatible with the use of gradient sensitivity enhanced correlation,[42] yielding excellent water suppression and optimal sensitivity. Figure 10 shows the pulse sequences SOFT-HNCA-ECOSY and SOFT-HNCA-COSY (see Section 3) obtained using gradient sensitivity enhanced correlation for the measuring of $^3J(H^N,H_\alpha)$ and $^3J(C',H^N)$ coupling constants, respectively. The resulting cross peaks are shown for four different cross peaks in ribonuclease T_1 in Figure 11. The combined analysis of these couplings leads to an unambiguous assignment of the ϕ-angle rotamer whenever only one rotamer around ϕ is populated.

Another implementation of the BIRD-filtering concept is the JHH-TOCSY developed by Willker and Leibfritz[55] (Figure 12). This experiment can be implemented in a spin system I_1–S–·–·–I_2 with one kind of heterospin. The idea of this experiment is to use S as the passive spin during t_1. This encodes a frequency shift of $\pm\pi J(I_1,S)$ onto the I_1 multiplet for S^α and S^β, respectively. After the mixing (transfer from I_1 to I_2) the polarization of the S spin is completely transferred to polarization of the I_1 spin ($S^\alpha \rightarrow I_1^\alpha$; $S^\beta \rightarrow I_1^\beta$). Then, during t_2, a frequency shift of $\pm\pi J(I_1,I_2)$ is encoded for the two submultiplets that were displaced in ω_1 by $\pm\pi J(I_1,S)$. This transfer can be achieved by the sequence (Figure 12)

$$\begin{aligned} &\text{(a)} \qquad\qquad \text{(b)} \\ I_{2x}(1/2 \pm S_z) &\rightarrow I_{2x}(1/2 \pm 2I_{1z}S_z) \rightarrow I_{2y}(1/2 \pm I_{1z}) \\ &= I_{2y}(1/2 \pm I_1^{\alpha/\beta}) \end{aligned} \qquad (2)$$

Interestingly, this is the only experiment in this section that cannot be classified according an ECOSY triangle, since two different spins serve as passive spins in t_1 and t_2. The application of this experiment on a ^{15}N-enriched sample of a BPTI mutant using gradient coherence selection ensuring excellent water suppression is shown in Figure 13.[56] A $^3J(H^N,H_\alpha)$ coupling constant of 8.6 ± 0.4 Hz is found for Phe_{22}.

7 THE ECOSY EXPERIMENT FOR THE MEASUREMENT OF HOMONUCLEAR $^nJ(I_1,I_1)$ COUPLINGS IN AN I_1–I_2–I_3 SPIN SYSTEM AND $^nJ(I_1,I_2)$ COUPLINGS IN AN I_1–S_1–·–·–I_2 SPIN SYSTEM

All the above mentioned methods impose special conditions on the spin system under study. The transfer between active spins, while not touching the passive spin, can be performed in homonuclear spin systems I_1–I_2–I_3 by a combination of experiments with different carefully chosen flip angle pulses in the ECOSY experiment (Figure 14).[1–3] An approximation to this procedure is the application of a small flip angle pulse in the P-ECOSY[2,57,58] experiment.

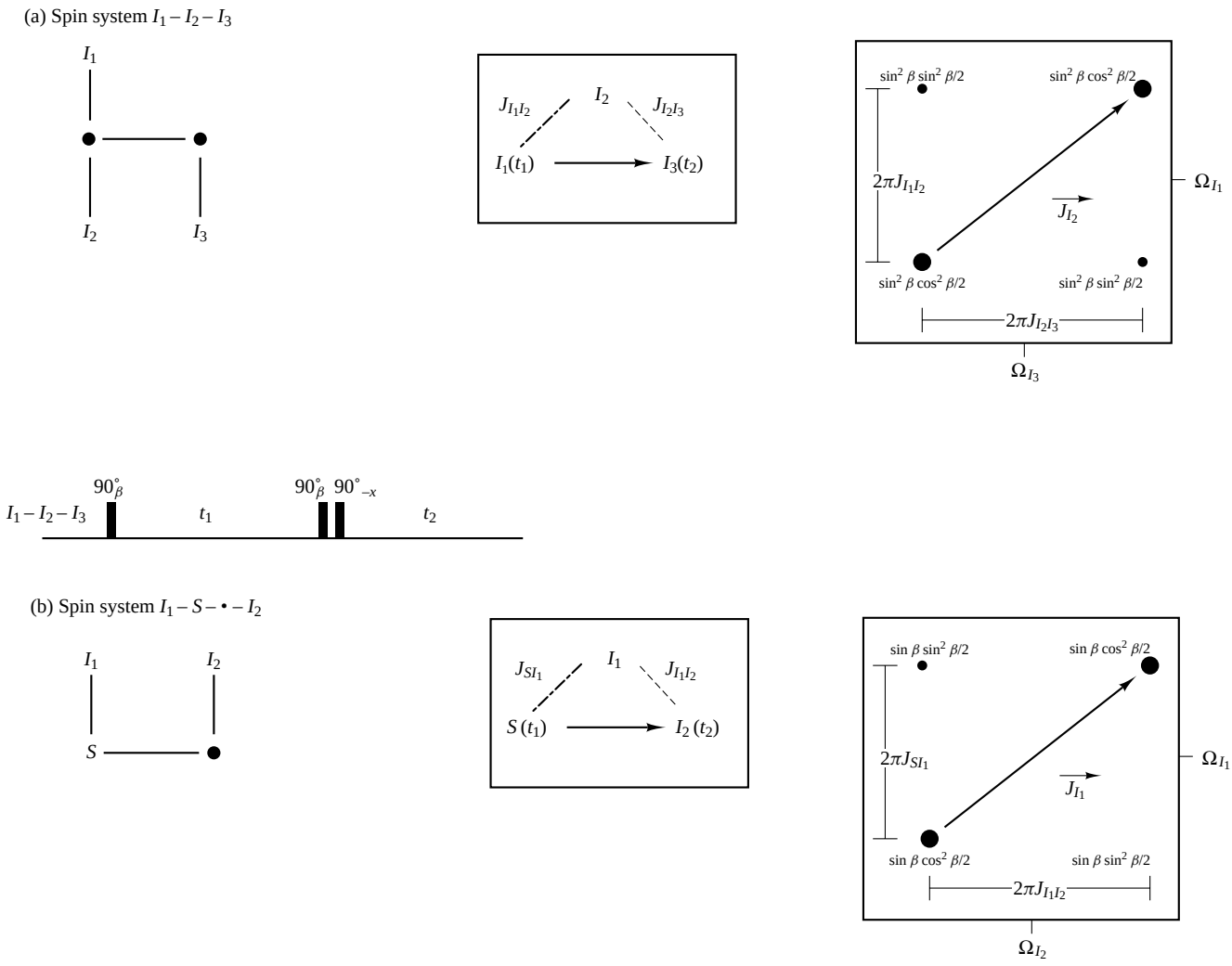

Figure 14 (a) The ECOSY experiment. In a homonuclear three-spin system, I_1 and I_3 are correlated by a $\beta \neq 90°$ mixing pulse. The cross-peak intensities of connected and nonconnected transitions of I_2, depending on the mixing pulse β, are indicated. Preferentially, geminal $^2J(I_1,I_2)$ couplings serve as associated couplings in t_1. (b) The HCCH-ECOSY experiment. In a heteronuclear $I_1{-}S_1{-}\cdot{-}I_2$ spin system, S and I_2 are correlated by a $\beta_y(I) \neq 90°$ mixing pulse implemented with phases according to the expansion: $\beta_y = 90°_x\beta_z\ 90°_{-x} = \beta_z\ 90°_\beta\ 90°_{-x}$. The cross-peak intensities of connected and nonconnected transitions of I_1, depending on the mixing pulse β, are indicated. The $^1J(S,I_1)$ coupling serves as the associated coupling in t_1. In the application to proteins, the $^1J(C',C_\alpha)$ coupling should be refocused in t_1, as should long-range $^3J(C',H_\beta)$ coupling in t_1. The parameters are: $\Delta = [2J(C_\alpha,H_\alpha)]^{-1}$; $\tau = [2J(C_\alpha,C_\beta)]^{-1}$; $\tau' = [4J(C_\alpha,C_\beta)]^{-1}$; $\Delta' = [2J(C_\alpha,H_\alpha)]^{-1}$; $\phi = x, -x$; $\psi = x, x, -x, -x$; rec. $= x, -x, -x, x$. The same pulse sequence can be used to measure J(C,H) couplings in oligonucleotides when replacing P for C′. A source of systematically smaller couplings is the evolution of chemical shift of the two rows displaced in ω_2 by $J(I_1,I_2)$. The acquired phase difference $\Delta\phi$ depends on the size of the coupling constants of interest and is given for a refocusing delay Δ: $\Delta\phi = J(\text{H,H}) \cdot \Delta \cdot 360°$. This phase difference can easily be corrected for by different phasing of the two extracted rows

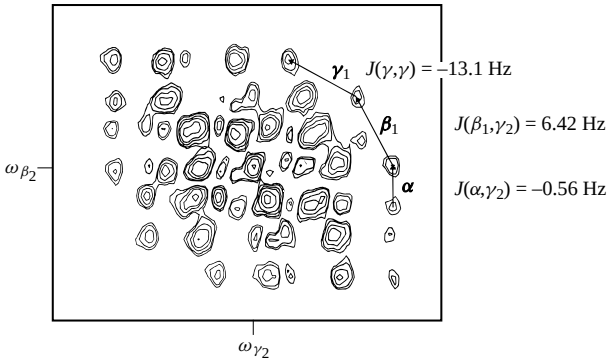

Figure 15 $H_{\beta 2} \rightarrow H_{\gamma 2}$ cross peak multiplet of Pro_8 in the 300 MHz ^1H spectrum of antamanide. The displacement vectors due to the three passive spins H_α, $H_{\beta 1}$, and $H_{\gamma 1}$ are clearly visible. All three vectors point from lower right to upper left. Assuming a negative sign for the aliphatic $^2J(H,H)$ coupling constants, the vicinal coupling $J(H_{\beta 1},H_{\gamma 2})$ is found to be positive and, due to the positive coupling constant between H_α and $H_{\beta 2}$ found in another cross peak, the $^4J(\alpha_1,\gamma_2)$ coupling is found to be negative.[3]

Thus choosing $\beta = 36^\circ$ gives a ratio for the undesired ($I_3^\alpha \rightarrow I_3^\beta$ and $I_3^\beta \rightarrow I_3^\alpha$) to the desired ($I_3^\alpha \rightarrow I_3^\alpha$ and $I_3^\beta \rightarrow I_3^\beta$) transfer of $\sin^2(\beta/2)/\cos^2(\beta/2) = \tan^2(\beta/2)$, which is about 10%. At the same time, polarization transfer between I_1 and I_2 ($2I_{1x}I_{2z} \rightarrow 2I_{1z}I_{2x}$) is achieved with a $\sin^2\beta = 35\%$ efficiency compared with the value obtained for $\beta = 90^\circ$. Transfer between a heteronucleus S to I_1 is achieved with $\sin\beta = 59\%$ compared with $\beta = 90^\circ$. Due to the incomplete suppression of the nonconnected transitions, asymmetrical signal components that systematically shift the submultiplets together and lead to systematically smaller coupling constants are introduced. Dispersive diagonal peak contributions can be suppressed in the P-ECOSY experiment by subtraction of a second experiment with $\beta = 0^\circ$.

The ECOSY procedure relies on a linear combination of different flip angles β that are chosen so as to suppress completely the undesired nonconnected transitions. The deduction of flip angles and weights depends upon the spin system under study. For more details, the interested reader is referred to the paper by Griesinger et al.[2]

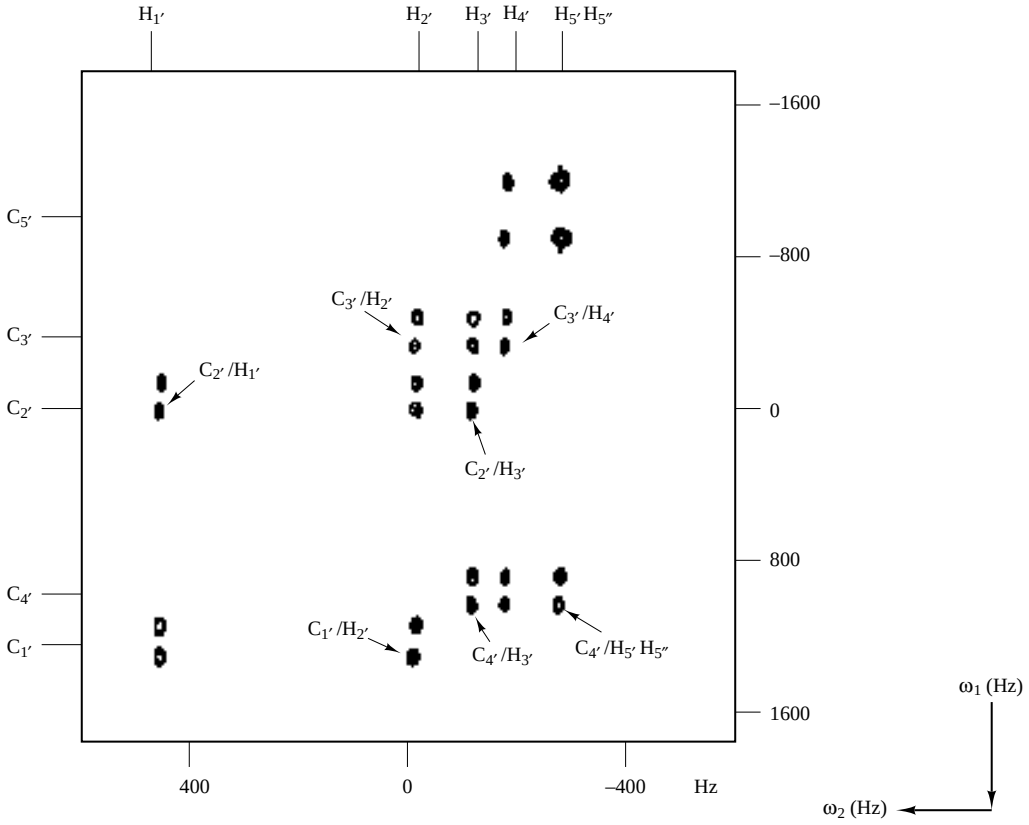

Figure 16 A 400 MHz HCCH-ECOSY spectrum with flip angle β for ^{13}C,^{15}N labeled 5′-GMP. The doublet structure in the two frequency dimensions is clearly visible

The transfer amplitudes of a polarization operator I_3^α or I_3^β are given by

$$I_3^\alpha \rightarrow I_3^\alpha \cos^2(\beta/2) + I_3^\beta \sin^2(\beta/2) \qquad (3a)$$

$$I_3^\beta \rightarrow I_3^\beta \cos^2(\beta/2) + I_3^\alpha \sin^2(\beta/2) \qquad (3b)$$

Figure 15 shows the Pro_8 β_2/γ_2 cross peak in antamanide, and the corresponding displacement vectors in this CH_2-CH_2 fragment.[3] ECOSY and P-ECOSY sequences have been successfully applied to peptides and proteins and to oligonucleotides[116–127] to obtain local conformational information. For completeness, a gradient selected ECOSY experiment based on the linear combination of multiple quantum filtered COSY spectra has been published.[128] The sensitivity

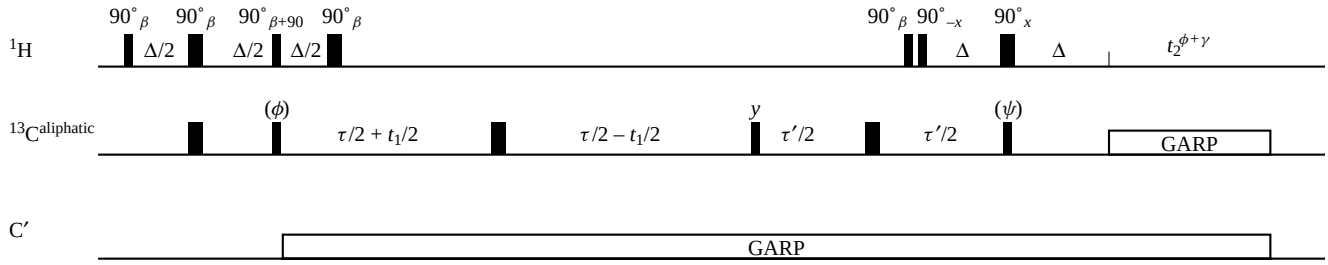

Figure 17 HCCH-ECOSY with a final 'DEPT' C7 → H transfer. The flip angle β is chosen such that the nonconnected transitions are suppressed. Alternatively, two experiments with β = 44.4 and 135.6 and weights of 6 and 1, respectively, are combined, as described for the 'INEPT' version

Table 1 Sensitivity Gain Provided by a 'DEPT Transfer'

	^{13}CH	$^{13}CH_2$	$^{13}CH_3$
S(DEPT)/S(INEPT)[a]	$1/\sin \pi J(C,H)\Delta'$	$\cos\theta/[\sin \pi J(C,H)\Delta' \cos \pi J(C,H)\Delta']$	$\cos^2\theta/[\sin \pi J(C,H)\Delta' \cos^2 \pi J(C,H)\Delta']$
$\Delta' = 1/2J(CH)$	1	–	–
$\Delta' = 1/4J(CH)$	1.41	1.62	1.85
$\Delta' = 0/2J(CH)$	1.7	1.7	1.7

[a] Δ' refers to the refocusing delay of the 'INEPT' version.

of such an experiment is, however, considerably reduced compared with the 'nongradient' versions of ECOSY or P-ECOSY.

For ^{13}C-labeled proteins the HCCH-ECOSY experiment [Figure 14(b)] can be applied to obtain proton–proton coupling constants in $H^{13}C-^{13}CH_m$ fragments (where m is the number of protons attached to the carbon atom). In this case only small flip angle pulses[27,129] or selective pulses[130] can be applied in order to fulfill the ECOSY condition, leaving one of the protons untouched in the final C → H transfer. Other implementations using TOCSY for the C → C transfer have been proposed by Emerson and Montelione.[131,132] The determination of H,H coupling constants in $H_k{}^{13}C-{}^{13}CH_m$ moieties is described in the paper by Eggenberger et al.[27]

The number of relevant spins for the C → H spin transfer is either two ($I_1-S_1-\cdot-\cdot-I_2$) or three ($I_1,I_1'-S_1-\cdot-\cdot-I_2$). Coupling constants to protons of methyl groups ($I_1,I_1',I_1''-S_1-\cdot-\cdot-I_2$) are normally not of great interest, due to conformational averaging. The transfer amplitude for a C → H INEPT-type transfer is thus given by sin β cos^2 (β/2) for the $I_1-S_1-\cdot-\cdot-I_2$ spin system and sin β cos β cos^2 (β/2) for the $I_1,I_1'-S_1-\cdot-\cdot-I_2$ spin system. For β_1 = 44.4 with a weight of 6 and β_2 = 135.6 with a weight of 1 for the $I_1-S_1-\cdot-\cdot-I_2$ and −1 for the $I_1,I_1'-S_1-\cdot-\cdot-I_2$ spin systems, the undesired components vanish completely.[133]

The application of such an HCCH-ECOSY sequence applied to ^{13}C-labeled 5′-GMP (guanosine 5′-monophosphate)[133] is shown in Figure 16. The conformational analysis reveals an N/S-conformer equilibrium of 70:30.

A further sensitivity improvement of the HCCH-ECOSY experiment[134] is provided by a 'DEPT transfer' for the last C → H transfer, as demonstrated in Figure 17. If only CH groups are detected, no gain is obtained. The gain in sensitivity of the 'DEPT' version compared with the 'INEPT' [Figure 14(b)] version for CH, CH_2, and CH_3 groups, provided the same flip angle β is used for the proton pulse in each case, is given in Table 1.

8 REFERENCES

1. C. Griesinger, O. W. Sørensen, and R. R. Ernst, *J. Am. Chem. Soc.*, 1985, **107**, 6394.
2. C. Griesinger, O. W. Sørensen, and R. R. Ernst, *J. Chem. Phys.*, 1986, **85**, 6837.
3. C. Griesinger, O. W. Sørensen, and R. R. Ernst, *J. Magn. Reson.*, 1987, **75**, 474.
4. G. S. Harbison, *J. Am. Chem. Soc.*, 1993, **115**, 3026.
5. T. J. Norwood, *J. Magn. Reson., Ser. A*, 1993, **101**, 109.
6. T. J. Norwood and K. Jones, *J. Magn. Reson., Ser. A*, 1993, **104**, 106.
7. R. E. London, *J. Magn. Reson.*, 1990, **86**, 410.
8. P. Schmidt, H. Schwalbe, and C. Griesinger, unpublished results.
9. G. Montelione and G. Wagner, *J. Am. Chem. Soc.*, 1989, **111**, 5474.
10. G. Montelione and G. Wagner, *J. Magn. Reson.*, 1990, **87**, 183.
11. A. Bax and R. Freeman, *J. Magn. Reson.*, 1981, **45**, 177.
12. M. Kurz, P. Schmieder, and H. Kessler, *Angew. Chem.*, 1991, **103**, 1341.
13. P. Schmieder, M. Kurz, and H. Kessler, *J. Biomol. NMR*, 1991, **1**, 403.
14. A. S. Edison, W. M. Westler, and J. L. Markley, *J. Magn. Reson.*, 1991, **92**, 434.
15. E. R. P. Zuiderweg and S. W. Fesik, *J. Magn. Reson.*, 1991, **93**, 653.
16. D. F. Mierke, P. Schmieder, P. Karuso, and H. Kessler, *Helv. Chim. Acta*, 1991, **74**, 1027.
17. P. Schmieder and H. Kessler, *Biopolymers*, 1992, **32**, 435.
18. M. Sattler, H. Schwalbe, and C. Griesinger, *J. Am. Chem. Soc.*, 1992, **114**, 1126.
19. J. Schleucher, B. Schwörer, C. Zirngibl, U. Koch, W. Weber, E. Egert, R. K. Thauer, and C. Griesinger, *FEBS Lett.*, 1992, **314**, 440.

20. L. Poppe, W. S. York, and H. van Halbeek, *J. Biomol. NMR*, 1993, **3**, 81.
21. J. V. Hines, G. Varani, S. M. Landry, and I. Tinoco, *J. Am. Chem. Soc.*, 1993, **115**, 11 002.
22. U. Wollborn, W. Willker, and D. Leibfritz, *J. Magn. Reson., Ser. A*, 1993, **103**, 86.
23. G. T. Montelione, M. E. Winkler, P. Rauenbühler, and G. Wagner, *J. Magn. Reson.*, 1989, **82**, 198.
24. P. Schmieder, J. H. Ippel, H. van den Elst, G. H. van der Marel, J. H. van Boom, C. Altona, and H. Kessler, *Nucleic Acids Res.*, 1992, **20**, 4747.
25. E. Worgötter, G. Wagner, M. Vasak, J. H. R. Kagi, and K. Wüthrich, *J. Am. Chem. Soc.*, 1988, **110**, 2388.
26. I. D. Rae, J. A. Weigold, R. H. Contreras, and G. Yamamoto, *Magn. Reson. Chem.*, 1992, **30**, 1047.
27. U. Eggenberger, Y. Karimi-Nejad, H. Thüring, H. Rüterjans, and C. Griesinger, *J. Biomol. NMR*, 1992, **2**, 583.
28. M. McCoy and L. Müller, *J. Am. Chem. Soc.*, 1992, **114**, 2108.
29. M. McCoy and L. Müller, *J. Magn. Reson.*, 1992, **98**, 674.
30. M. McCoy and L. Müller, *J. Magn. Reson.*, 1992, **99**, 18.
31. U. Eggenberger, P. Schmidt, M. Sattler, S. J. Glaser, and C. Griesinger, *J. Magn. Reson.*, 1992, **100**, 604.
32. M. McCoy and L. Müller, *J. Magn. Reson., Ser. A*, 1993, **101**, 122.
33. M. D. Sørensen, S. M. Kristensen, J. J. Led, and O. W. Sørensen, *J. Magn. Reson. Ser. A*, 1993, **103**, 364.
34. R. Brüschweiler, J. C. Madsen, C. Griesinger, O. W. Sørensen, and R. R. Ernst, *J. Magn. Reson.*, 1987, **73**, 380.
35. P. Berthault, H. Desvaux, and B. Perly, *Magn. Reson. Chem.*, 1993, **31**, 259.
36. L. Emsley, T. J. Dwyer, H. P. Spielmann, and D. E. Wemmer, *J. Am. Chem. Soc.*, 1993, **115**, 7765.
37. R. Konrat, G. Zieger, and H. Sterk, *Chem. Phys. Lett.*, 1993, **212**, 78.
38. L. Emsley and G. Bodenhausen, *J. Magn. Reson.*, 1989, **82**, 211.
39. L. Emsley and G. Bodenhausen, *Chem. Phys. Lett.*, 1990, **165**, 469.
40. H. Geen and R. Freeman, *J. Magn. Reson.*, 1991, **93**, 93.
41. G. W. Vuister and A. Bax, *J. Biomol. NMR*, 1992, **2**, 401.
42. R. Weisemann, H. Rüterjans, H. Schwalbe, J. Schleucher, W. Bermel, and C. Griesinger, *J. Biomol. NMR*, 1994, **4**, 231.
43. S. Seip, J. Balbach, and H. Kessler, *J. Magn. Reson.*, 1994, **B104**, 172.
44. H. Kessler, U. Anders, and G. Gemmecker, *J. Magn. Reson.*, 1988, **78**, 382.
45. G. Zhu and A. Bax, *J. Magn. Reson.*, 1992, **98**, 192.
46. G. Zhu and A. Bax, *J. Magn. Reson.*, 1990, **90**, 405.
47. H. Schwalbe, A. Rexroth, U. Eggenberger, T. Geppert, and C. Griesinger, *J. Am. Chem. Soc.*, 1993, **114**, 7878.
48. J. R. Garbow, D. P. Weitekamp, and A. Pines, *Chem. Phys. Lett.*, 1982, **93**, 504.
49. O. W. Sørensen, *J. Magn. Reson.*, 1990, **90**, 433.
50. J. C. Madsen, O. W. Sørensen, P. Sørensen, and F. M. Poulsen, *J. Biomol. NMR*, 1993, **3**, 239.
51. S. Seip, J. Balbach, and H. Kessler, *Angew. Chem., Int. Ed. Engl.*, 1992, **31**, 1609.
52. G. Wagner, P. Schmieder, and V. Thanabal, *J. Magn. Reson.*, 1991, **93**, 436.
53. S. D. Emerson and G. T. Montelione, *J. Magn. Reson.*, 1992, **99**, 413.
54. M. Gorlach, M. Wittekind, B. T. Farmer, L. E. Kay, and L. Müller, *J. Magn. Reson., Ser. B*, 1993, **101**, 194.
55. W. Willker and D. Leibfritz, *J. Magn. Reson.*, 1992, **99**, 421.
56. H. Schwalbe, H. Oschkinat, W. Bermel, P. Schmitt, and C. Griesinger, unpublished data.
57. L. Müller, *J. Magn. Reson.*, 1987, **72**, 191.
58. A. Bax and D. Marion, *J. Magn. Reson.*, 1988, **80**, 528.
59. H. Kessler, G. Gemmecker, A. Haupt, M. Klein, K. Wagner, and M. Will, *Tetrahedron*, 1988, **44**, 745.
60. P. C. Driscoll, G. M. Clore, and G. M. Gronenborn, *FEBS Lett.*, 1989, **243**, 223.
61. P. C. Driscoll, G. M. Clore, L. Beress, and G. M. Gronenborn, *Biochemistry*, 1989, **28**, 2178.
62. H. Kessler, A. Müller, and K. H. Pook, *Liebigs Ann. Chem.*, 1989, **9**, 903.
63. H. Kessler, J. W. Bats, K. Wagner, and M. Will, *Biopolymers*, 1989, **28**, 385.
64. P. J. M. Folkers, G. M. Clore, P. C. Driscoll, J. Dodt, S. Kohler, and A. M. Gronenborn, *Biochemistry*, 1989, **28**, 2601.
65. H. Kessler, M. Will, J. Antel, H. Beck, and G. M. Sheldrick, *Helv. Chim. Acta*, 1989, **72**, 530.
66. H. Haruyama, Y. Q. Qian, and K. Wüthrich, *Biochemistry*, 1989, **28**, **4301**, 4312.
67. C. Redfield and C. M. Dobson, *Biochemistry*, 1990, **29**, 7201.
68. H. Kessler, S. Mronga, M. Will, and U. Schmidt, *Helv. Chim. Acta*, 1990, **73**, 25.
69. M. Billeter, Y. Qian, G. Otting, M. Müller, W. J. Gehring, and K. Wüthrich, *J. Mol. Biol.*, 1990, **214**, 183.
70. H. Kessler, U. Anders, and M. Schudok, *J. Am. Chem. Soc.*, 1990, **112**, 5908.
71. B. A. Messerle, A. Schaffer, M. Vasak, J. H. R. Kagi, and K. Wüthrich, *J. Mol. Biol.*, 1990, **214**, 765.
72. P. Karuso, H. Kessler, and D. F. Mierke, *J. Am. Chem. Soc.*, 1990, **112**, 9434.
73. Y. M. Kim and J. H. Prestegard, *Proteins Struct. Func. Genet.*, 1990, **8**, 377.
74. J. Habazettl, C. Cieslar, H. Oschkinat, and T. A. Holak, *FEBS Lett.*, 1990, **268**, 141.
75. L. J. Smith, M. J. Sutcliffe, C. Redfield, and C. M. Dobson, *Biochemistry*, 1991, **30**, 986.
76. J. M. Moore, C. A. Lepre, G. P. Gippert, W. J. Chazin, D. A. Case, and P. E. Wright, *J. Mol. Biol.*, 1991, **221**, 533.
77. J. M. Schmidt, O. Ohlenschläger, H. Rüterjans, Z. Grzanka, E. Kojro, I. Pavo, and F. Fahrenholz, *Eur. J. Biochem.*, 1991, **201**, 355.
78. H. Kessler, S. Mronga, G. Müller, L. Moroder, and R. Huber, *Biopolymers*, 1991, **31**, 1189.
79. A. L. Breeze, T. S. Harvey, R. Bazzo, and I. D. Campbell, *Biochemistry*, 1991, **30**, 575.
80. H. Kessler, H. Matter, G. Gemmecker, A. Kling, and M. Kottenhahn, *J. Am. Chem. Soc.*, 1991, **113**, 7550.
81. K. H. Ott, S. Becker, R. D. Gordon, and H. Rüterjans, *FEBS Lett.*, 1991, **278**, 160.
82. C. Abeygunawardana, C. A. Bush, and J. O. Cisar, *Biochemistry*, 1991, **30**, 8568.
83. P. Sodano, T. H. Xia, J. H. Bushweller, O. Bjornberg, A. Holmgren, M. Billeter, and K. Wüthrich, *J. Mol. Biol.*, 1991, **221**, 1311.
84. D. Seebach, S. Y. Ko, H. Kessler, M. Köck, M. Reggelin, P. Schmieder, M. D. Walkinshaw, J. J. Bölsterli, and D. Bevec, *Helv. Chim. Acta*, 1991, **74**, 1953.

85. X. Li, M. J. Sutcliffe, T. W. Schwartz, and C. M. Dobson, *Biochemistry*, 1992, **31**, 1245.
86. U. Hommel, T. S. Harvey, P. C. Driscoll, and I. D. Campbell, *J. Mol. Biol.*, 1992, **227**, 271.
87. J. Freund, A. Kapurniotu, T. A. Holak, M. Lenfant, and W. Voelter, *Z. Naturforsch., B*, 1992, **47**, 1324.
88. D. Neri, M. Billeter, and K. Wüthrich, *J. Mol. Biol.*, 1992, **223**, 743.
89. H. Kessler, H. Matter, G. Gemmecker, M. Kottenhahn, and J. W. Bats, *J. Am. Chem. Soc.*, 1992, **114**, 4805.
90. G. T. Montelione, K. Wüthrich, A. W. Burgess, E. C. Nice, G. Wagner, K. D. Gibson, and H. A. Scheraga, *Biochemistry*, 1992, **31**, 236.
91. M. Köck, H. Kessler, D. Seebach, and A. Thaler, *J. Am. Chem. Soc.*, 1992, **114**, 2676.
92. P. J. Kraulis, A. R. C. Raine, P. L. Gadhavi, and E. D. Laue, *Nature*, 1992, **356**, 448.
93. M. Reggelin, H. Hoffmann, M. Köck, and D. F. Mierke, *J. Am. Chem. Soc.*, 1992, **114**, 3272.
94. T. H. Xia, J. H. Bushweller, P. Sodano, M. Billeter, O. Bjornberg, A. Holmgren, and K. Wüthrich, *Protein Sci.*, 1992, **1**, 310.
95. B. A. Messerle, A. Schaffer, M. Vasak, J. H. R. Kagi, and K. Wüthrich, *J. Mol. Biol.*, 1992, **225**, 433.
96. J. Saulitis, D. F. Mierke, G. Byk, C. Gilon, and H. Kessler, *J. Am. Chem. Soc.*, 1992, **114**, 4818.
97. H. Kessler, A. Geyer, H. Matter, and M. Köck, *Int. J. Pept. Protein Res.*, 1992, **40**, 25.
98. K. D. Berndt, P. Guntert, L. P. M. Orbons, and K. Wüthrich, *J. Mol. Biol.*, 1992, **227**, 757.
99. K. Wakamatsu, D. Kohda, H. Hatanaka, J. M. Lancelin, Y. Ishida, M. Oya, H. Nakamura, F. Inagaki, and K. Sato, *Biochemistry*, 1992, **31**, 12. 577.
100. T. Szyperski, P. Guntert, S. R. Stone, and K. Wüthrich, *J. Mol. Biol.*, 1992, **228**, 1193.
101. M. Gurrath, G. Müller, H. Kessler, M. Aumailley, and R. Timpl, *Eur. J. Biochem.*, 1992, **210**, 911.
102. N. Fusetani, K. Shimoda, and S. Matsunaga, *J. Am. Chem. Soc.*, 1993, **115**, 3977.
103. A. Schnuchel, R. Wiltschek, M. Czisch, M. Herrler, G. Willimsky, P. Graumann, M. A. Marahiel, and T. A. Holak, *Nature*, 1993, **364**, 169.
104. R. K. Konat, D. F. Mierke, H. Kessler, B. Kutscher, M. Bernd, and R. Voegeli, *Helv. Chim. Acta*, 1993, **76**, 1649.
105. S. Mronga, G. Müller, J. Fischer, and F. Riddell, *J. Am. Chem. Soc.*, 1993, **115**, 8414.
106. J. Kordel, N. J. Skelton, M. Arke, and W. J. Chazin, *J. Mol. Biol.*, 1993, **231**, 711.
107. L. R. Brown, S. Mronga, R. A. Bradshaw, C. Ortenzi, P. Luporini, and K. Wüthrich, *J. Mol. Biol.*, 1993, **231**, 800.
108. Y. Blancuzzi, A. Padilla, J. Parello, and A. Cave, *Biochemistry*, 1993, **32**, 1302.
109. H. Kessler, R. Haessner, and W. Schuler, *Helv. Chim. Acta*, 1993, **76**, 117.
110. Y. N. Kalia, S. M. Brocklehurst, D. S. Hipps, E. Appella, K. Sakaguchi, and R. N. Perham, *J. Mol. Biol.*, 1993, **230**, 323.
111. W. Antuch, K. D. Berndt, M. A. Chavez, J. Delfin, and K. Wüthrich, *Eur. J. Biochem.*, 1993, **212**, 675.
112. J. F. OConnell, P. E. Bougis, and K. Wüthrich, *Eur. J. Biochem.*, 1993, **213**, 891.
113. J. H. Davis, E. K. Bradley, G. P. Miljanich, L. Nadasdi, J. Ramachandran, and V. J. Basus, *Biochemistry*, 1993, **32**, 7396.
114. K. Bartik, C. M. Dobson, and C. Redfield, *Eur. J. Biochem.*, 1993, **215**, 255.
115. K. D. Berndt, P. Guntert, and K. Wüthrich, *J. Mol. Biol.*, 1993, **234**, 735.
116. A. Bax and L. Lerner, *J. Magn. Reson.*, 1988, **79**, 429.
117. U. Schmitz, G. Zon, and T. L. James, *Biochemistry*, 1990, **29**, 2357.
118. A. Foldesi, P. Agback, C. Glemarec, and J. Chattopadhyaya, *Tetrahedron*, 1991, **47**, 7135.
119. W. J. Chazin, M. Rance, A. Chollet, and W. Leupin, *Nucleic Acids Res.*, 1991, **19**, 5507.
120. S. M. Chen, W. Leupin, and W. J. Chazin, *Int. J. Biol. Macromol.*, 1992, **14**, 57.
121. S. M. Chen, W. Leupin, M. Rance, and W. J. Chazin, *Biochemistry*, 1992, **31**, 4406.
122. J. W. Cheng, S. H. Chou, M. Salazar, and B. R. Reid, *J. Mol. Biol.*, 1992, **228**, 118.
123. S. H. Chou, J. W. Cheng, and B. R. Reid, *J. Mol. Biol.*, 1992, **228**, 138.
124. S. G. Kim, L. J. Lin, and B. R. Reid, *Biochemistry*, 1992, **31**, 3564.
125. S. G. Kim and B. R. Reid, *Biochemistry*, 1992, **31**, 12. 103.
126. M. Salazar, J. J. Champoux, and B. R. Reid, *Biochemistry*, 1993, **32**, 739.
127. M. Salazar, O. Y. Fedoroff, J. M. Miller, N. S. Ribeiro, and B. R. Reid, *Biochemistry*, 1993, **32**, 4207.
128. W. Willker, D. Leibfritz, R. Kerssebaum, and J. Lohman, *J. Magn. Reson., Ser. A*, 1993, **102**, 348.
129. C. Griesinger and U. Eggenberger, *J. Magn. Reson.*, 1992, **97**, 426.
130. G. Gemmecker and S. W. Fesik, *J. Magn. Reson.*, 1991, **95**, 208.
131. S. D. Emerson and G. T. Montelione, *J. Magn. Reson.*, 1992, **99**, 413.
132. S. D. Emerson and G. T. Montelione, *J. Am. Chem. Soc.*, 1992, **114**, 354.
133. H. Schwalbe, G. C. King, R. Wechselberger, W. Bermel, and C. Griesinger, *J. Biomol. NMR*, 1994, **4**, 631.
134. H. B. Olsen, S. Ludvigsen, and O. W. Sørensen, *J. Magn. Reson., Ser. A*, 1993, **104**, 226.

Acknowledgments

We would like to thank the co-workers that contributed to the work presented in this review: Y. Karimi-Nejad, R. Weisemann and H. Rüterjans from University of Frankfurt/M, W. Bermel at Bruker/Karlsruhe, H. Oschkinat at EMBL/Heidelberg, G. King at the University of South Wales/Australia as well as A. Rexroth, U. Eggenberger, M. Sattler, J. Marino, T. Gepport, R. Wechselberger, S. Glaser and J. Schleucher.

Biographical Sketches

H. J. Schwalbe. *b* 1966. Diploma, 1990, Ph.D., 1993, Frankfurt. Postdoctorate (with Prof. C. Dobson, Oxford, 1993–present). Introduced to NMR by C. Griesinger. Research interest in development of new methods in the field of high-resolution NMR for coupling constant determination in proteins and oligonucleotides, chemical synthesis of ^{13}C-labeled RNA and DNA.

P. A. Schmidt. *b* 1966. Diploma, 1990, Ph.D., 1993, Frankfurt. Introduced to NMR by C. Griesinger, S. Glaser and G. Wagner. Research

interest in theoretical prediction and optimisations of homo- and heteronuclear mixing sequences and their applications to biomolecular NMR spectroscopy.

C. Griesinger. *b* 1960. Diploma, 1984, Ph.D., 1986, Frankfurt. Postdoctorate ETH Zürich, 1986–89. Full Professor of Organic Chemistry at the University of Frankfurt, 1990–present. Introduced to NMR by Horst Kessler, Richard R. Ernst, and O. W. Sørensen. Research interest in development of new methods in the field of high-resolution NMR, especially multidimensional NMR spectroscopy, rotating frame spectroscopy, coupling constant determination, and conformational analysis of biomacromolecules including proteins, DNA and RNA.

Decoupling Methods

A. J. Shaka
University of California, Irvine, CA, USA

1	Introduction	1
2	Theory of Broadband Decoupling	1
3	Popular Decoupling Sequences	3
4	Summary	6
5	Related Articles	6
6	References	6

1 INTRODUCTION

The purpose of spin decoupling in NMR spectroscopy of liquids is to simplify the NMR spectrum of one set of nuclear spins S by removing from their spectrum the splittings caused by scalar coupling to another set of spins I. Usually I and S are different nuclides, the most common example being protons and carbon−13. However, in some cases the same type of nuclide is involved, as in selective spin decoupling of proton spin multiplets, or in semiselective decoupling of carbonyl carbons from other carbon-13 spins in multidimensional NMR of uniformly carbon-13 enriched macromolecules. In the heteronuclear case one speaks of *broadband spin decoupling*, while in the homonuclear case the usual parlance is *selective decoupling*. Throughout this article, the focus will be on decoupling methods based on the application of rf pulses to the I spins. Decoupling based on other methods like multiple quantum techniques,[1,2] bilinear rotation decoupling (BIRD),[3] apparent decoupling in multidimensional NMR spectra by imposing a constant evolution time,[4] and other such methods will not be covered here. Space limitations, likewise, preclude a historical approach to the subject, but some of the highlights of the development of the subject are outlined in a recent review.[5]

Mathematically, spin coupling adds terms of the form $J_{IS}\hat{\boldsymbol{I}} \cdot \hat{\boldsymbol{S}}$ to the spin Hamiltonian, where J_{IS} is the coupling constant, typically 10 Hz for proton−proton coupling and 150 Hz for direct proton−carbon coupling. For the purposes of spectral simplification, it makes sense to regard complete decoupling as the condition of reducing the apparent splittings to zero, or at least to a value that is small compared with the instrumental linewidth. The success of a decoupling method can then be assessed by inspecting the S spin spectrum after a 90° pulse and looking for broadening or splitting of the resonances. However, in more complicated pulse sequences it may be necessary to adopt a slightly different definition: complete decoupling is achieved when the S spins evolve in time, at least stroboscopically, as if $J_{IS} = 0$. The difference is only important when other pulse sequences are being applied to S while the I spins are being decoupled. Depending on the type of experiment, what appears to be complete decoupling based on the absence of splittings in a conventional single pulse acquisition can actually turn into an unexpected nightmare of complicated effects when a multiple pulse sequence is applied to the S spins as well. Many of these effects remain largely unexplored up to this time.

Modern decoupling methods are best considered as a contiguous sequence of rf pulses. The purpose of the sequence is to make it appear that $J_{IS} \approx 0$ over a specified range of I spin chemical shifts with the minimum time-average expenditure of rf power. In cases where amplitude modulation of the rf pulses is used, the peak power must also be within acceptable bounds. The main reason why the rf power needs to be minimized is to minimize dielectric heating of the liquid sample. High-field spectrometers aggravate the decoupling problem, as both the spread of chemically shifted resonances and the dielectric loss are increasing functions of frequency. Likewise, the decoupling of low γ spins like nitrogen-15, or spins with very large chemical shift ranges like carbon-13, can pose special problems that tax the capability of the decoupling sequence.

2 THEORY OF BROADBAND DECOUPLING

The most successful framework for analyzing decoupling performance was first suggested by Waugh in a clear and elegant paper.[6] This theory superseded earlier progress[7–10] made using the coherent averaging approach[11] and was motivated by the promising experimental results of Levitt and Freeman.[7] Although the theory cannot be 'inverted' to suggest any new decoupling methods directly, it makes it very simple to analyze the performance of any proposed method.

To clarify the discussion, a number of simplifying assumptions need to be made: (1) the model spin system is an isolated ensemble of two coupled spin-$\frac{1}{2}$ nuclei, I and S; (2) I and S have widely separated Larmor frequencies, so that the weak coupling approximation $J_{IS}\hat{\boldsymbol{I}} \cdot \hat{\boldsymbol{S}} \rightarrow J_{IS}\hat{I}_z\hat{S}_z$ is valid and the irradiation has no direct effect on S; (3) no rf pulses are applied to S except perhaps an initial 90° pulse at the time the decoupling sequence is initiated; (4) relaxation of both I and S are neglected; (5) the decoupling sequence is periodic over some time t_S; and (6) the S-spin signal is sampled synchronously at the end of each period. The first assumption means that $I–I$ and $S–S$ couplings are neglected while the second is appropriate for heteronuclear decoupling, the most common application. The third assumption is quite crucial in simplyfing the analysis, as it allows the clean separation of the S-spin time evolution into two parts, one from S spin up and the other from S spin down. The last two assumptions allow the S-spin free induction decay (FID) to be extracted from an integration of the motion over one period, which represents both a conceptual and computational simplification. It is important to realize that in any experimental situation in which the above assumptions do not hold, the following analysis will have to be modified. Usually the results carry over quite closely (e.g. in the case of nonsynchronous sampling or additional small homonuclear couplings), but it is important to be aware of possible complications.

The time-dependent irradiation applied to the I spins is represented as a sequence of states: $\hat{\mathcal{H}}(t) = \hat{\mathcal{H}}_1, \hat{\mathcal{H}}_2, \ldots, \hat{\mathcal{H}}_n$. During each state k the Hamiltonian $\hat{\mathcal{H}}_k$ is assumed to be constant, that is a decoupler pulse of known phase, duration, amplitude, and frequency is applied. Continuous modulation is treated as a finely divided sequence of pulses. In a doubly

rotating frame at exact resonance for S and in synchronism with the decoupling field ω_2 the Hamiltonian during the first state becomes

$$\hat{\mathcal{H}}_1 = -\omega\hat{I}_z - \gamma \boldsymbol{B}_2\{\hat{I}_x \cos\phi_1 + \hat{I}_y \sin\phi_1\} + J_{IS}\hat{I}_z\hat{S}_z \quad (1)$$

reflecting a decoupler pulse of resonance offset ω from exact I- spin resonance, angular amplitude $\gamma \boldsymbol{B}_2$ and phase ϕ_1, and a coupling measured (for convenience) in angular frequency units. Defining the S-spin projectors by

$$\hat{P}_\pm = |\pm\rangle\langle\pm| \quad (2)$$

where

$$\hat{S}_z|\pm\rangle = \pm\tfrac{1}{2}|\pm\rangle \quad (3)$$

we can rewrite equation (1) in the form

$$\hat{\mathcal{H}}_1 = -\boldsymbol{\omega}\cdot\hat{\boldsymbol{I}}(\hat{P}_+ + \hat{P}_-) + \tfrac{1}{2}J_{IS}\hat{I}_z(\hat{P}_+ - \hat{P}_-) \quad (4)$$

where $\omega = (\gamma \boldsymbol{B}_2 \cos\phi_1,\ \gamma \boldsymbol{B}_2 \sin\phi_1,\ \omega)$ describes the vector field felt by I. By regrouping equation (4) as

$$\begin{aligned}\hat{\mathcal{H}}_1 &= \left(-\boldsymbol{\omega}\cdot\hat{\boldsymbol{I}} + \frac{J_{IS}}{2}\right)\hat{P}_+ + \left(-\boldsymbol{\omega}\cdot\hat{\boldsymbol{I}} - \frac{J_{IS}}{2}\right)\hat{P}_- \\ &= (-\boldsymbol{\omega}_+\cdot\hat{\boldsymbol{I}})\hat{P}_+ + (-\boldsymbol{\omega}_-\cdot\hat{\boldsymbol{I}})\hat{P}_- = \hat{\mathcal{H}}_+ + \hat{\mathcal{H}}_-\end{aligned} \quad (5)$$

and noting that $\hat{P}_+\hat{P}_- = \hat{P}_-\hat{P}_+ = 0$, the Hamiltonian separates into a sum of commuting terms according whether the S spin is up or down. The time evolution operator for the first state is thus

$$\begin{aligned}\hat{U}(t_1, 0) &= \exp(-\mathrm{i}\hat{\mathcal{H}}_1 t_1) = \exp(-\mathrm{i}\mathcal{H}_+ t_1)\exp(-\mathrm{i}\hat{\mathcal{H}}_- t_1) \\ &= \hat{P}_+\hat{R}_+^{(1)} + \hat{P}_-\hat{R}_-^{(1)}\end{aligned} \quad (6)$$

where

$$\hat{R}_\pm^{(1)} = \exp(-\mathrm{i}\boldsymbol{\omega}_\pm\cdot\hat{\boldsymbol{I}}t_1) = \exp(-\mathrm{i}\beta_\pm^{(1)}\boldsymbol{n}_\pm^{(1)}\cdot\hat{\boldsymbol{I}}) \quad (7)$$

are pure rotation operators describing a rotation of each of the I-spin lines by angles $\beta_\pm$ around unit axes $\boldsymbol{n}_\pm$. To compute the time evolution over the entire period t_s of the decoupling sequence we need to compute the time evolution operator according to

$$\begin{aligned}\hat{U}(t_n, 0) &= \hat{U}(t_n, t_{n-1})\hat{U}(t_{n-1}, t_{n-2})\cdots\hat{U}(t_1, 0) \\ &= (\hat{P}_+\hat{R}_+^{(n)} + \hat{P}_-\hat{R}_-^{(n)})(\hat{P}_+\hat{R}_+^{(n-1)} + \hat{P}_-\hat{R}_-^{(n-1)}) \\ &\quad \cdots(\hat{P}_+\hat{R}_+^{(1)} + \hat{P}_-\hat{R}_-^{(1)})\end{aligned} \quad (8)$$

which, on account of the properties of the projectors (and the initial assumption that no pulses are applied to S during the sequence) simplifies to

$$\hat{U}(t_n, 0) = \hat{P}_+\hat{R}_+ + \hat{P}_-\hat{R}_- \quad (9)$$

where $R_\pm$ are the net rotation operators produced by the sequence of pulses, computed by composing the rotations over the individual states, in the order in which they occurred. The nonlinearity of the decoupling problem is buried in the dependence of the *overall* rotation operators on the operators during each of the individual states. This dependence is intricate and complex, making it difficult to guess in advance how well a particular sequence may perform.

If we prepare the S spins in the state S_x at $t = 0$, then the ideal response would be a pure dc signal, corresponding to the complete collapse of the doublet into a singlet at the chemical shift of S, which is our rotating frame. The actual normalized first point of the FID can be calculated as:

$$M_x(t_s) = 4\mathrm{Tr}\{\hat{S}_x\hat{U}\hat{S}_x\hat{U}^{-1}\} = \tfrac{1}{8}\mathrm{Tr}\{\hat{R}_+\hat{R}_-^{-1} + \hat{R}_-\hat{R}_+^{-1}\} \quad (10)$$

This equation contains an important insight: if the rotations $\hat{R}_\pm$ are *identical* then $M_x(t_s) = M_x(0) = 1$, i.e. the FID is unmodulated by the coupling. One idea is thus to find an irradiation strategy that treats the two I-spin transitions identically by the end of the period.

The assumption of periodic, synchronous sampling now allows the entire FID to be computed with no further work. Performing the trace indicated in equation (10) gives

$$\begin{aligned}M_x(t_s) &= \cos\frac{\beta_+}{2}\cos\frac{\beta_-}{2} + \boldsymbol{n}_+\cdot\boldsymbol{n}_-\sin\frac{\beta_+}{2}\sin\frac{\beta_-}{2} \\ &\equiv \tfrac{1}{2}(1 + \boldsymbol{n}_+\cdot\boldsymbol{n}_-)\cos\left(\frac{\beta_+ - \beta_-}{2}\right) \\ &\quad + \tfrac{1}{2}(1 - \boldsymbol{n}_+\cdot\boldsymbol{n}_-)\cos\left(\frac{\beta_+ + \beta_-}{2}\right)\end{aligned} \quad (11)$$

and the group property of rotations tells us that the kth sampled point of the FID can be computed by using equation (11) with the substitution $\beta_\pm \to k\beta_\pm$. Accordingly, we get the compact result

$$\begin{aligned}M_x(kt_s) &= \tfrac{1}{2}(1 + \boldsymbol{n}_+\cdot\boldsymbol{n}_-)\cos(k\Omega_- t_s) \\ &\quad + \tfrac{1}{2}(1 - \boldsymbol{n}_+\cdot\boldsymbol{n}_-)\cos(k\Omega_+ t_s)\end{aligned} \quad (12)$$

where $\Omega_\pm$ are fictitious angular frequencies given by

$$\Omega_\pm = \frac{\beta_+ \pm \beta_-}{2t_s} \quad (13)$$

By inspection, the spectrum contains two pairs of transitions symmetrically disposed about the chemical shift of S with splittings $\Omega_\pm$, and intensities $I_\pm$ given by the coefficients of each cosine term in equation (12). In the limit that the rf field $\boldsymbol{B}_2$ is reasonably strong compared with J_{IS} the axes are nearly identical, and the outer lines have small intensity. In this regime the most useful concept is that of the scaling factor, λ defined by

$$\lambda = \frac{J_-}{J} = \frac{1}{t_s}\frac{\beta(\omega + J/2) - \beta(\omega - J/2)}{J} \approx \frac{1}{t_s}\frac{\partial\beta}{\partial\omega} \quad (14)$$

The splittings are scaled down by the gradient of the offset-dependent net rotation angle produced by the decoupling sequence, and this offset-dependent angle can be computed as

if there were no coupling at all, as it arises from the composition of pure rotations. Equation (14), first derived by Waugh,[6] allows the systematic investigation of decoupling methods by computer simulation. The rotation matrices are multiplied, and the net rotation angle computed numerically over the offset range of interest. Careful numerical differentiation gives λ. Comparing λJ with the expected instrumental linewidth will then predict the effectiveness of the decoupling. The most common strategy for practical methods is to try to find a sequence that is nearly cyclic, i.e. $\beta \approx 0$ over the offset range, the idea being that the difference of two small terms must be small itself.

3 POPULAR DECOUPLING SEQUENCES

3.1 The MLEV Sequences

The starting point for the MLEV sequences is some group of pulses, called a composite pulse, and denoted R, that will approximately invert z magnetization over a wide offset range:

$$R^{-1}\hat{I}_z R \approx -\hat{I}_z \tag{15}$$

For example, $R_1 = 90^\circ_x 240^\circ_y 90^\circ_x$ and $R_2 = 90^\circ_x 180^\circ_y 90^\circ_x$. The inversion property guarantees two things: (1) the net rotation angle $\beta \approx 180^\circ$; and (2) the axis is somewhere in the xy plane, $n_z \approx 0$. The sequence $C = RR$ is approximately cyclic, as it is an approximate 360° rotation over the same range that R is an approximate 180° rotation. It follows that the decoupling C gives is pretty good: β is small and roughly constant, and so λ is small. However, the rotation $\bar{C}$ obtained by phase shifting all the constituent pulses in C by 180° is approximately the inverse rotation, $\bar{C} \approx C^{-1}$. Hence $C^{(2)} = C\bar{C}$ gives a much smaller net rotation angle than C alone. This follows from the relationship

$$\exp(-\mathrm{i}\beta \boldsymbol{n}_1 \cdot \hat{\boldsymbol{I}}) \exp(-\mathrm{i}\beta \boldsymbol{n}_2 \cdot \hat{\boldsymbol{I}}) \approx \exp\left\{ -\mathrm{i}\left[\beta(\boldsymbol{n}_1 + \boldsymbol{n}_2)\cdot \hat{\boldsymbol{I}} + \frac{\beta^2}{2}(\boldsymbol{n}_1 \times \boldsymbol{n}_2)\cdot \hat{\boldsymbol{I}}\right]\right\} \tag{16}$$

which, because β is small, has very small quadratic terms in the exponential. Thus, to the extent that $\boldsymbol{n}_2 = -\boldsymbol{n}_1$ the net rotation angle is greatly reduced, and the decoupling is greatly improved. The primitive sequence is thus

$$\text{MLEV-4} = RR\bar{R}\bar{R} \tag{17}$$

The important discovery by Levitt et al.[10] was that this process of improving the decoupling could be made systematic by employing, in turn, 180° phase shifts to cancel out the transverse components of $\boldsymbol{n}$ and using cyclic permutations to cancel out the z component. The cyclic permutation of a single composite pulse R results in the transformation $RRR\bar{R} \rightarrow RR\bar{R}R$, which is equivalent to the unitary transformation $R\{RRR\bar{R}\}R^{-1}$, and hence, as R inverts $\hat{I}_z$, it inverts the z component of $\boldsymbol{n}$. One application of each trick leads to MLEV-16:

$$\text{MLEV-16} = RR\bar{R}\bar{R}\,R\bar{R}R\bar{R}\,\bar{R}R\bar{R}R\,\bar{R}\bar{R}\bar{R}\bar{R} \tag{18}$$

The process can be repeated, taking MLEV-16 as the input cycle, to generate MLEV-64, etc.[10] As the iterative procedure continues, the net rotation angle converges geometrically to zero over a wide bandwidth, and so $\lambda \rightarrow 0$. However, the period t_s increases as well, and finally the periodic sampling constraint cannot be met. Sampling before the end of the cycle leads to modulation sidebands in the S-spin spectrum. These 'cycling sidebands' are not serious for practical sequences like MLEV-64 but will become increasingly bad with very high order sequences, which may contain long stretches like *RRRRRRRR* or *RRRRRRRR* that give poor performance locally. In the final limit that t_s itself exceeds the acquisition time, the decoupling sequence is never actually completed, and extrapolations of fantastic performance based on calculations of λ fail to materialize.

3.2 The WALTZ Sequences

If the decoupling sequence is of the form $RR\bar{R}\bar{R}$ it is possible to show that the transverse components of $\boldsymbol{n}$ are small, so that the net rotation axis is mostly along the z axis. In this case, the operations of cyclic permutation and phase inversion can be combined into a single step.[12] First permute a 90° pulse to transform $\boldsymbol{n}$ so that it has a small z component, and then combine the permuted sequence with a copy in which all pulses are phase shifted by 180°. A 90° pulse is quite good at destroying n_z over a large bandwidth, so the iterative scheme described here converges more rapidly. The key is then to locate a suitable starting pulse R that begins with a 90° pulse. The inversion pulse $R_3 = 90^\circ_x 180^\circ_{-x} 270^\circ_x \equiv 1\bar{2}3$ (adopting a shorthand notation) fits the bill, and led to the WALTZ sequences[13,14]

$$\text{WALTZ-4} = 1\bar{2}3\,1\bar{2}3\,\bar{1}2\bar{3}\,\bar{1}2\bar{3} \tag{19}$$

$$\text{WALTZ-8} = \bar{2}4\bar{2}3\bar{1}\,2\bar{4}2\bar{3}1\,2\bar{4}2\bar{3}1\,\bar{2}4\bar{2}3\bar{1} \tag{20}$$

$$\text{WALTZ-16} = \bar{3}4\bar{2}3\bar{1}2\bar{4}2\bar{3}\,3\bar{4}2\bar{3}1\bar{2}4\bar{2}3\,3\bar{4}2\bar{3}1\bar{2}4\bar{2}3\,\bar{3}4\bar{2}3\bar{1}2\bar{4}2\bar{3} \tag{21}$$

Of these, WALTZ-16 is the most popular, having a very small scaling factor over a bandwidth $\pm\gamma B_2/2\pi$ allowing, for example, broadband proton decoupling over the 10 ppm proton range at 750 MHz using a 4 kHz rf field strength. Plots of the scaling factor versus normalized resonance offset ω/ω_2 are shown in Figure 1 for MLEV-16 (using $90^\circ_x 180^\circ_y 90^\circ_x$) and WALTZ-16. A scaling factor of 0.001 predicts a residual splitting of only 0.15 Hz for a 150 Hz proton–carbon coupling.

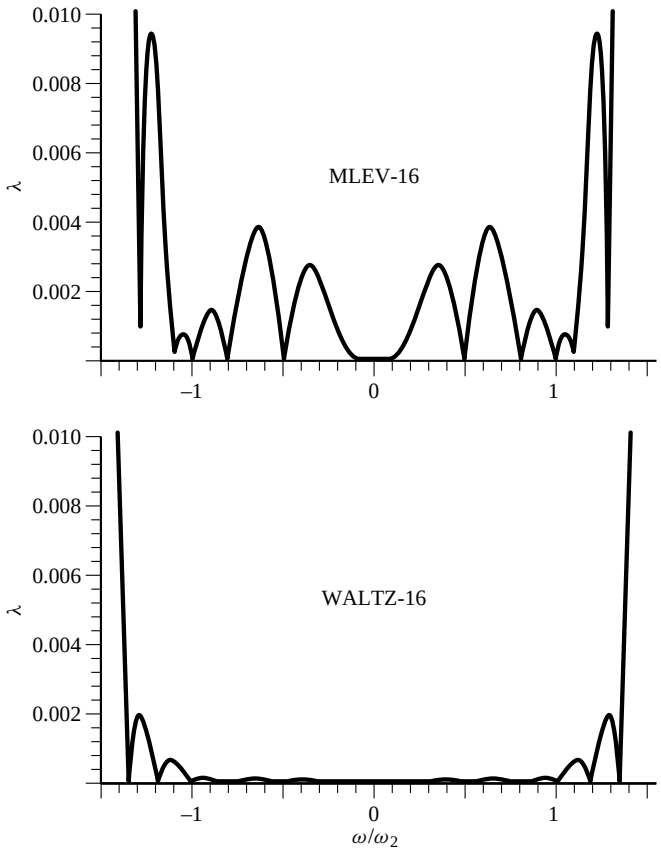

Figure 1 Scaling factors for MLEV-16, using the inversion pulse R_2 = $90°_x180°_y90°_x$, and WALTZ-16. Both decoupling sequences give symmetrical performance with respect to the sign of the decoupler resonance offset. For 2 Hz carbon-13 linewidths, these plots show that both sequences are comparable. WALTZ-16 is expected to perform much better than MLEV-16 at linewidths of 0.25 Hz, however, as it maintains $\lambda < 5 \times 10^{-4}$ over the normalized offset range ω/ω_2 = ± 1.0, so that residual splittings are kept below 0.1 Hz even for J(CH) = 200 Hz

3.3 GARP

Every decoupling sequence based on a least common multiple like a 90° pulse has a well-defined resonance offset at which it will fail, either where the initial inversion pulse fails entirely, or where the effective field results in a net 360° rotation rather than a 90° rotation. A cyclic permutation of a 90° pulse will not affect the net rotation axis of the sequence at such offsets, so no systematic improvement is obtained. For the WALTZ sequences, this offset is $\omega/\omega_2 = \sqrt{3}$, where the effective field results in flip angles a factor of 2 too large and the composite pulse $1\bar{2}3$ becomes an identity operator rather than an inversion pulse. It made sense to ask whether a larger bandwidth could be obtained by allowing flip angles of varying amounts.

A larger bandwidth can be obtained, although the scaling factor is not quite as small. The procedure used to generate the most popular of these sequences, called GARP-1,[15] was to use a composite 90° pulse with a bigger bandwidth and use computer optimization to locate a suitable starting sequence beginning with the composite 90° pulse.

The sequence is (using units of degrees) GARP-1 = $RR\bar{R}\bar{R}$, where

$$\begin{aligned} R = {} & 30.5\,\bar{5}\bar{5}.\bar{2}\,257.8\,\bar{2}\bar{6}\bar{8}.\bar{3}\,69.3\,\bar{6}\bar{2}.\bar{2}\,85.0\,\bar{9}\bar{1}.\bar{8}\,134.5 \\ & \bar{2}\bar{5}\bar{6}.\bar{1}\,66.4\,\bar{4}\bar{5}.\bar{9}\,25.5\,\bar{7}\bar{2}.\bar{7}\,119.5\,\bar{1}\bar{3}\bar{8}.\bar{2}\,258.4 \\ & \bar{6}\bar{4}.\bar{9}\,70.9\,\bar{7}\bar{7}.\bar{2}\,98.2\,\bar{1}\bar{3}\bar{3}.\bar{6}\,255.9\,\bar{6}\bar{5}.\bar{5}\,53.4 \end{aligned} \qquad (22)$$

and the corresponding scaling factor is shown in Figure 2. Acceptable performance over an offset range ω/ω_2 = ± 2.4 is indicated. This very large bandwidth, and the relative ease of its implementation, has made GARP-1 useful when decoupling nitrogen-15 from protons, as the small gyromagnetic ratio of nitrogen makes it very hard to generate a decoupling field of more than 1 or 2 kHz without strong sample heating. While λ is quite reasonable for GARP-1, the extended length of the sequence and the slow averaging action at very large offsets can lead to larger modulation sidebands in the decoupled spectrum. These sidebands can set a lower limit to the acceptable rf field strength of the decoupler channel.

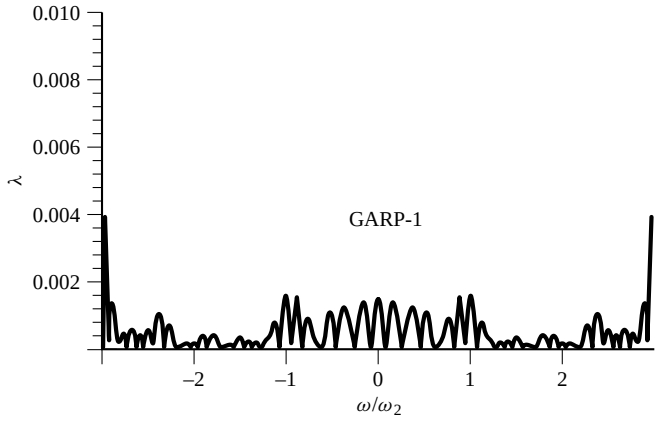

Figure 2 Scaling factor for the GARP-1 sequence. An approximate bandwidth of ω/ω_2 = ± 2.4 is obtained over which $\lambda < 2 \times 10^{-3}$, so that if residual splittings of 0.2–0.4 Hz are acceptable, GARP-1 can be useful

3.4 The MPF*n* Sequences

Another way to try to achieve a larger bandwidth is to frequency-modulate the decoupler. For example, a frequency sweep can form the starting inversion pulse, which can then be used in the MLEV scheme. Even more efficient is a frequency hopping, in which the frequency is stepped in large increments over the desired offset range. A straightforward strategy, based on the observation that a simple 180° pulse becomes a 360° rotation at offsets $\omega/\omega_2 = \pm\sqrt{3}$, is to hop the frequency by approximately this amount, applying a 180° pulse at each offset. The separate inversion pulses then become approximately independent, and so a very broadband inversion pulse is obtained. This inversion pulse R can then be turned into a decoupling sequence $RR\bar{R}\bar{R}$.

The actual procedure used for the MPF*n* sequences is essentially as described, with the addition of two refinements: (1) the flip angles and frequency hops are adjusted slightly, using

computer optimization; and (2) the resulting frequency-hopped inversion pulse is concatenated into a larger composite pulse by a symmetric phase-shifting scheme $R_{60}R_{150}R_0R_{150}R_{60}$ to improve its performance at the 'in between' offsets and with respect to rf inhomogeneity.[16]

The distinct advantage of these composite inversion pulses is that one can simply 'add on' an extra inversion pulse at the beginning and end of the MPF$_n$ − 2 sequence, which one has in hand from the last optimization, to find a composite pulse with an even bigger bandwidth. This is apparent, for example, when examining the F7 and F9 composite pulses:

$$\begin{aligned}\text{F7} = {} & 168(-4.27)\,190(-2.71)\,192(-1.37)\\ & 174(0.0)\,192(1.37)\,190(2.71)\,168(4.27)\end{aligned} \tag{23}$$

$$\begin{aligned}\text{F9} = {} & 174(-5.69)\,191(-4.19)\,185(-2.79)\\ & 177(-1.41)\,188(0.0)\,177(1.41)\,185(2.79)\\ & 191(4.19)\,174(5.69)\end{aligned} \tag{24}$$

in which the flip angles are in degrees, and the numerals in parentheses refer to the normalized resonance offset for the carrier frequency of the pulse. These composite pulses operate over the enormous bandwidths $\omega/\omega_2 = \pm 4.6$ and ± 6.0, respectively. The decoupling action is also effective over similar bandwidths, if a 3 Hz linewidth can be tolerated ($\lambda \approx 0.01$).

The ultimate limitation of the MPF*n* sequences arises mostly from the appearance of nonnegligible cycling sidebands at very low rf levels. For example, during $\frac{8}{9}$ of the F9 pulse a spin near the edge of the bandwidth will be 'marking time' as it undergoes a series of 360° rotations about strongly tilted fields. During this time the S spins experience the heteronuclear coupling, scaled by only a small amount, and the FID can depart markedly from the ideal dc signal. The MPF*n* sequences are thus most useful when the decoupling bandwidth is much greater than a representative coupling constant, for under these conditions the bandwidth requirement will dictate a reasonably fast cycling rate, leading to acceptable sideband intensity. Finally, the MPF*n* sequences require a fast frequency-agile decoupler channel, a luxury that many routine high-field spectrometers are unfortunately missing.

3.5 The DIPSI Sequences

The simplified theory presented in Section **2** is no longer strictly correct when there are several coupled protons present, as in a typical organic molecule. The theory can, however, be generalized quite easily[16] and the case of interest becomes that of two coupled protons, one of which is coupled to, for example, carbon-13. The time evolution operator once again separates into commuting terms $\hat{U}_+(t_s) = \exp(-i\hat{\mathcal{H}}_+ t_s)$ and $\hat{U}_-(t_s) = \exp(-i\hat{\mathcal{H}}_- t_s)$ with the only difference being that these 4 × 4 matrices are not pure rotation operators. The S-spin signal can be calculated as before, giving

$$\begin{aligned}\langle \hat{S}^-(t_s)\rangle &= \text{Tr}\{(\hat{S}_x - \text{i}\hat{S}_y)U(t_s)\hat{S}_x\hat{U}^{-1}(t_s)\}\\ &= \text{Tr}\{\hat{U}_+(t_s)\hat{U}_-^{-1}(t_s)\}\end{aligned} \tag{25}$$

In the regime of interest, the eigenvectors of $\hat{U}_\pm$ and hence $\hat{\mathcal{H}}_\pm$ are nearly coincident, and the difference of the energy eigenvalues determines the S-spin signal:

$$\langle \hat{S}^-(t_s)\rangle = \sum_{j=1}^{4} \exp[\text{i}t_s(\Omega_{j+} - \Omega_{j-})] \tag{26}$$

The energy eigenvalues differ only in the apparent chemical shift of the I spin coupled to S, and so can be approximated by the derivative once again:

$$\Omega_{j+} - \Omega_{j-} \approx J_{IS}\frac{\partial\Omega_j}{\partial\omega} \equiv J_{IS}\lambda_j \tag{27}$$

The set of four scaling factors determines the relative positions of the four S-spin lines. It is necessary to consider each transition separately, as the symmetry of the isolated I–S pair, in which pure amplitude modulation of the S magnetization is the only possibility, is absent here.

Examining the set of scaling factors for typical conditions used for carbon-13, J(C,H) = 200 Hz, J(H,H) = 10 Hz, $\gamma B_2/2\pi$ = 2 kHz, showed that the proton–proton coupling could be the limiting factor in obtaining very narrow carbon-13 lines, and led to a search for improved sequences in this regard. The best sequences average away all terms of the effective Hamiltonians $\hat{\mathcal{H}}_\pm$ except for the I–I coupling, which becomes slightly offset dependent.

The sequences DIPSI-2 and DIPSI-3 resulted from an optimization including the I–I coupling. DIPSI-2 in particular, can be viewed as a WALTZ-16 sequence in which the pulse widths have been altered. The alteration leads to a smaller bandwidth in the absence of I–I coupling, but improved performance when I–I coupling is the major factor limiting resolution. Both sequences conform to the *RRRR* pattern, with the following composite pulses R (with flip angles in degrees):

$$\text{DIPSI-2}: 320\,\bar{4}\bar{1}\bar{0}\,290\,\bar{2}\bar{8}\bar{5}\,30\,\bar{2}\bar{4}\bar{5}\,275\,\bar{2}\bar{6}\bar{5}\,\bar{3}\bar{7}\bar{0} \tag{28}$$

$$\begin{aligned}\text{DIPSI-3}: {} & \bar{2}\bar{4}\bar{5}\,395\,\bar{2}\bar{5}\bar{0}\,275\,\bar{3}\bar{0}\,230\,\bar{3}\bar{6}\bar{0}\,245\,\bar{3}\bar{7}\bar{0}\,340\,\bar{3}\bar{5}\bar{0}\\ & 260\,\bar{2}\bar{7}\bar{0}\,30\bar{2}\bar{2}\bar{5}\,365\,\bar{2}\bar{5}\bar{5}\,395\end{aligned} \tag{29}$$

The approximate bandwidths of these sequences are $\omega/\omega_2 = \pm 0.6$ and ± 0.8, respectively. While these bandwidths are less than MLEV, WALTZ, or GARP, the DIPSI sequences result in significant line narrowing at low B_2 levels, where the other sequences produced narrowly spaced distorted multiplets rather than a sharp singlet.[17] An example is shown in Figure 3.

It should be noted that S–S coupling, if it is not first order, can also affect the decoupling performance, although this aspect of decoupling has not yet been investigated quantitatively. It could be of some importance in multidimensional NMR of 100% ^{13}C-labeled biomolecules, as then the S-spin network can be extensive. A clear account of the extension of the theory of this section to any network of coupled heteronuclei, and including dipolar and quadrupolar interactions, is available for those wishing to pursue this area.[18]

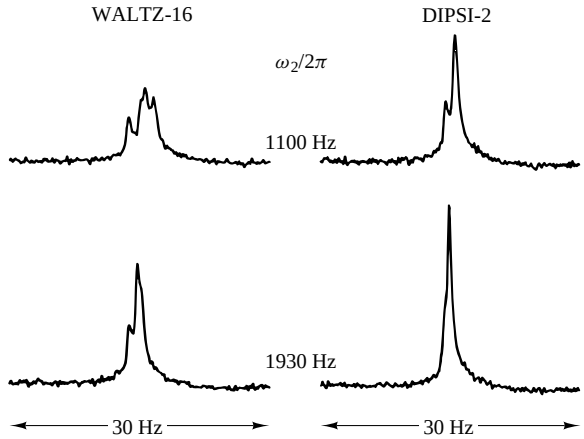

Figure 3 Comparison of DIPSI-2 with WALTZ-16 to show the influence of proton–proton couplings on the decoupling of protons from carbon-13. The low-field carbon-13 resonance of *trans*-cinnamic acid is shown for decoupler field strengths of 1100 Hz and 1930 Hz for each of the sequences. The 1100 Hz level, which is weaker than would normally be used, shows a broad multiplet with four resolved transitions with WALTZ-16, and even at the higher level there is still discernible structure and a loss of peak height. DIPSI-2 narrows the resonance more effectively, giving almost a factor of 2 gain in sensitivity. (Reproduced by permission of Academic Press from A. J. Shaka, C. J. Lee, and A. Pines, *J. Magn. Reson.*, 1988, **77**, 274)

3.6 The SEDUCE Sequences

An even more demanding decoupling application is to decouple spins within one bandwidth selectively, leaving the coupling to spins outside the bandwidth unperturbed. That is, $\lambda \rightarrow 0$ over a specified band while $\lambda \rightarrow 1$ elsewhere. WALTZ-16 is good at the first task, but certainly not the second. Outside of the effective bandwidth, the starting composite pulse is not even approximately a 180° rotation around an axis predominantly in the transverse plane, and the iterative procedure fails to converge, much as Newton's method can fail to converge if one makes an unfortunate starting guess. In these applications the entire decoupling sequence becomes analogous to a selective pulse tailored to achieve excitation or inversion only over a specified bandwidth.

It has been shown[19] recently that the straightforward approach of shaping the rectangular 180° pulses into smoothly varying functions like Gaussians, and then employing an *RRRR* pattern, works pretty well. In particular, the shaped inversion pulse

$$\omega_2(t) = \omega_{2p}\{1.0 - 7.05t - 0.225t^2 + 11.0t^3\}[\exp(-t^2)] \quad (30)$$

where the parameter $|t| \leq \sqrt{10}$ and the peak amplitude is adjusted to give a 180° flip angle, has been shown to be very effective, forming the basis of the SEDUCE-3 sequence.[19]

4 SUMMARY

The keen observation, made only a little over a decade ago, that heteronuclear spin decoupling could be vastly improved by using 180° pulses arranged in well-defined patterns[7] has led to a revolution in the area. Indeed, the progress seems to have been perfectly timed to the introduction of high-field magnets that produce spectral widths requiring the new methods. A clear, sound theoretical framework[6] allows the efficient exploration of new spin decoupling methods by computer simulation, and most of the experiments are relatively easy to perform once a candidate sequence has been found. While WALTZ-16, which requires no amplitude or frequency modulation, and which is tolerant of common instrumental imperfections, is likely to remain the routine decoupling sequence of choice for protons, progress since WALTZ-16, either to other spin systems or to very wide bandwidths (sacrificing some quality for quantity), shows that the field is still alive, and that there could be some further improvements in the future. Indeed, as the theory apparently cannot be inverted to specify the optimum decoupling sequence, it will always be tempting to try a few new sequences now and then, just to see if the envelope can be pushed a little farther out.

5 RELATED ARTICLES

Average Hamiltonian Theory; Composite Pulses; Double Resonance; Proton Decoupling in Whole Body Carbon-13 MRS; Selective Excitation in MRI and MR Spectroscopy; Shaped Pulses.

6 REFERENCES

1. R. C. Hewitt, S. Meiboom, and L. C. Snyder, *J. Chem. Phys.*, 1973, **58**, 5089.
2. A. Pines, D. J. Ruben, S. Vega, and M. Mehring, *Phys. Rev. Lett.*, 1976, **36**, 110.
3. J. R. Garbow, D. P. Weitekamp, and A. Pines, *Chem. Phys. Lett.*, 1982, **93**, 504.
4. A. Bax and R. Freeman, *J. Magn. Reson.*, 1981, **44**, 542.
5. A. J. Shaka and J. Keeler, *Prog. NMR Spectrosc.*, 1987, **19**, 47.
6. J. S. Waugh, *J. Magn. Reson.*, 1982, **50**, 30.
7. M. H. Levitt and R. Freeman, *J. Magn. Reson.*, 1981, **43**, 502.
8. M. H. Levitt, R. Freeman, and T. Frenkiel, *J. Magn. Reson.*, 1982, **47**, 328.
9. M. H. Levitt, R. Freeman, and T. Frenkiel, *J. Magn. Reson.*, 1982, **50**, 157.
10. M. H. Levitt, R. Freeman, and T. Frenkiel, *Adv. Magn. Res.*, 1983, **11**, 47.
11. U. Haeberlen and J. S. Waugh, *Phys. Rev.*, 1968, **175**, 453.
12. J. S. Waugh, *J. Magn. Reson.*, 1982, **49**, 517.
13. A. J. Shaka, J. Keeler, T. Frenkiel, and R. Freeman, *J. Magn. Reson.*, 1983, **52**, 335.
14. A. J. Shaka, J. Keeler, and R. Freeman, *J. Magn. Reson.*, 1983, **53**, 313.
15. A. J. Shaka, P. B. Barker, and R. Freeman, *J. Magn. Reson.*, 1985, **64**, 547.
16. T. Fujiwara, T. Anai, N. Kurihara, and K. Nagayama, *J. Magn. Reson., Ser. A*, 1993, **104**, 103.
17. A. J. Shaka, C. J. Lee, and A. Pines, *J. Magn. Reson.*, 1988, **77**, 274.
18. D. Suter, K. V. Schenker, and A. Pines, *J. Magn. Reson.*, 1987, **73**, 90.
19. M. A. McCoy and L. Mueller, *J. Magn. Reson., Ser. A*, 1993, **101**, 122.

Biographical Sketch

A. J. Shaka, *b* 1958. B.S., Harvey Mudd College, 1980; Ph.D., Oxford University (with Ray Freeman)., 1984. Junior research fellow, St John's College, Oxford, 1984–86. Postdoc (with Alex Pines), University of California, Berkeley, 1986–88. Currently, Associate Professor of Chemistry, University of California, Irvine. Approx. 45 publications. Current research specialty: multiple pulse NMR techniques in liquids.

Double Resonance

Ray Freeman

Cambridge University, Cambridge, UK

1	Introduction	1
2	Hole Burning	1
3	Spin Tickling	1
4	Selective Decoupling	2
5	Slow Chemical Exchange	3
6	Cross Relaxation	3
7	Cross Polarization	5
8	Broadband Decoupling in Liquids	6
9	Composite-Pulse Decoupling	7
10	Decoupling Dipolar Interactions in Solids	9
11	Related Articles	9
12	References	9

1 INTRODUCTION

An NMR spectrum has the unusual property that it is not a single entity, fixed once and for all; it can be manipulated in various ways to extract different kinds of information. One important type of modification is *double resonance*, the application of a second irradiation field ($\boldsymbol{B}_2$) at the same time as the observing field ($\boldsymbol{B}_1$). This definition of double resonance may be broadened somewhat to accommodate pulse excited NMR experiments where two different radiofrequency fields are employed but are not necessarily present simultaneously. Double resonance experiments probe *interactions* between nuclear spins—the dipolar coupling, the scalar spin–spin coupling, chemical exchange, or the nuclear Overhauser effect. Many analogs of these double resonance experiments are treated under the heading multidimensional NMR spectroscopy.

It is useful to make a distinction between double resonance experiments that rely on spin population effects (changes in longitudinal magnetization), for example hole burning, saturation transfer, and cross relaxation, and those that involve coherence effects (changes in transverse magnetization), such as spin tickling and spin decoupling. A good test to distinguish the two is to see whether the double resonance phenomenon persists after the perturbing field $\boldsymbol{B}_2$ has been extinguished; if so, then the mechanism probably involves a population disturbance which is only dissipated in a time of the order of the spin–lattice relaxation time.

Double resonance experiments may be classified according to the degree of selectivity in the frequency domain The key quantity is the intensity of the perturbing radiofrequency field expressed in frequency units ($\gamma B_2/2\pi$) compared with the linewidth, the scalar spin–spin coupling, the dipolar interaction, or the chemical shift range of a nuclear species under investigation. In general the perturbing field is effective over a frequency band of the order of $\gamma B_2/2\pi$ (Hz). It is convenient to treat the various double resonance experiments in order of increasing intensity of $\boldsymbol{B}_2$.

2 HOLE BURNING

If an NMR line is inhomogeneously broadened, for example by the spatial inhomogeneity of the magnet, it is possible to saturate one localized region of the sample volume while leaving the remainder essentially unperturbed. This is called 'burning a hole in the line'.[1] For such an experiment, the intensity of the saturating field ($\boldsymbol{B}_2$) should satisfy the conditions

$$\Delta\nu^* > \gamma B_2/2\pi > \Delta\nu \qquad (1)$$

where $\Delta\nu^*$ is the inhomogeneous linewidth and $\Delta\nu$ is the natural linewidth, both expressed in hertz. In principle the hole may be much narrower than $\Delta\nu^*$ provided that diffusion effects can be neglected.

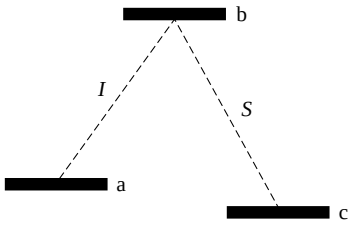

Figure 1 Energy level diagram for the hole-burning experiment

Consider a system of two coupled spins (I and S) where two transitions I_{ab} and S_{bc} share an energy level b, and have the regressive configuration (Figure 1). Saturation of transition I_{ab} equalises the spin populations on levels a and b and therefore reduces the intensity of transition S_{bc}. If the perturbing field $\boldsymbol{B}_2$ burns a hole in line I_{ab}, a corresponding hole appears in line S_{bc}. Since the coupled spins I and S are in the same molecule, they are impervious to the inhomogeneous broadening by magnet field inhomogeneity, apart from a small frequency shift. Consequently the hole in line S_{bc} is in exactly the same part of the line profile as the hole in I_{ab}. This may be used as a very accurate method for measuring the frequency of a resonance line (I_{ab}). The perturbing field $\boldsymbol{B}_2$ is applied to line I_{ab} and carefully adjusted in frequency until the hole in line S_{bc} is exactly centered on the line profile.[2] This gives the center frequency of I_{ab} with an accuracy of the order ± 0.001 Hz.

3 SPIN TICKLING

Whereas the hole-burning technique does not strictly require that the perturbing field $\boldsymbol{B}_2$ be coherent, the spin tickling[3] experiment does. In a high-resolution spectrum, if a transition I_{ab} is irradiated at exact resonance with a perturbing field that satisfies the condition

$$\gamma B_2/2\pi \sim \Delta\nu* \qquad (2)$$

where $\Delta\nu^*$ is the instrumental linewidth, then any connected transitions S_{bc} and S_{ad} become symmetrical doublets of splitting $\gamma B_2/2\pi$ (Hz). Connected transitions are those which share an energy level with the perturbed transition; they have one of two possible configurations, 'regressive' and

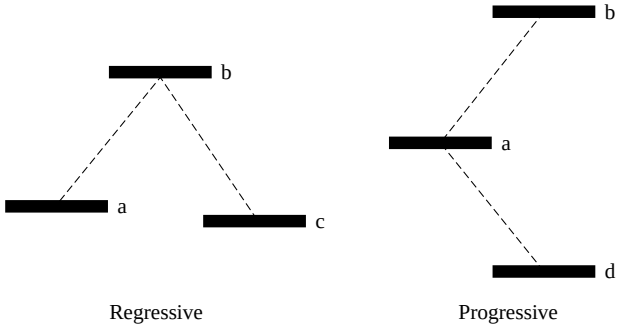

Figure 2 Two transitions that share an energy level may have the regressive or progressive configuration

'progressive' (Figure 2). The doubling of the observed resonance arises from quantum mechanical mixing with a previously forbidden transition, similar to the phenomenon of Fermi resonance in infrared spectroscopy. In the regressive case it is the zero quantum transition ZQ_{ac} that is involved, while in the progressive case it is the double quantum transition DQ_{bd}. If the perturbing field is gradually moved away from exact resonance, the intensities of the observed doublet become more and more asymmetric (Figure 3), reverting to the strong allowed transition and a weak forbidden transition which eventually disappears.

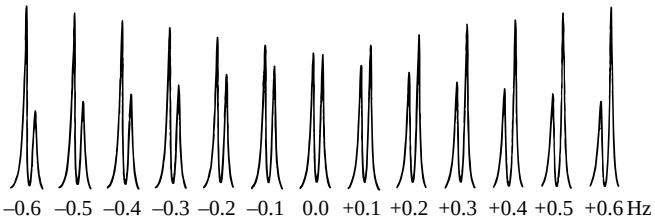

Figure 3 Experimental spin tickling spectra recorded as a function of the offset of the second radiofrequency field from exact resonance. Reproduced from 'A Handbook of Nuclear Magnetic Resonance', Longman, Harlow, 1988, with permission

Magnet field inhomogeneity has an unexpected effect on the doublets observed during a spin tickling experiment. For the regressive configuration the doublet is abnormally well resolved since (for homonuclear systems) it has 50% zero quantum character, and zero quantum transitions are themselves insensitive to variations of the applied magnetic field. For the progressive case the behavior is reversed, the doublets are less well resolved than expected since they have 50% double quantum character, and double quantum transitions are twice as sensitive to field variations as single quantum transitions. Spin tickling in heteronuclear coupled spin systems follows analogous rules except that the degree of zero or double quantum character now involves the ratio of the magnetogyric ratios, γ_I/γ_S.

4 SELECTIVE DECOUPLING

The high-resolution NMR spectra of liquid samples can be quite complex, and it is usually necessary to make an assignment of the various resonances, either on chemical shift grounds, or by *correlation*—determining which groups are related by scalar spin–spin coupling. If two spins I and S are coupled, then irradiation of the I spin at exact resonance with a perturbing field $\boldsymbol{B}_2$ such that

$$\gamma B_2/2\pi \sim J_{IS} \tag{3}$$

removes the splitting J_{IS} from the S-spin resonance, which therefore becomes a singlet. This can be thought of as a 'stirring' of the spin states of the I spin at a rate comparable with the coupling constant J_{IS} so that the S spin only 'sees' the mean value of the local field due to spin coupling. If the $\boldsymbol{B}_2$ field is gradually moved away from exact resonance, a scaled-down version of the spin multiplet structure is observed, which gradually expands until it approaches the form observed in the absence of the perturbing field $\boldsymbol{B}_2$. Figure 4 illustrates this for the ^{13}C resonance of the methyl group in methyl iodide as a function of the offset Δ of the perturbing field from exact resonance for the protons.[4] At relatively low levels of the perturbing field, some weak satellite signals may be observed symmetrically flanking the decoupled multiplet. They involve multiple quantum transitions where one or more quanta are contributed by the perturbing field $\boldsymbol{B}_2$.

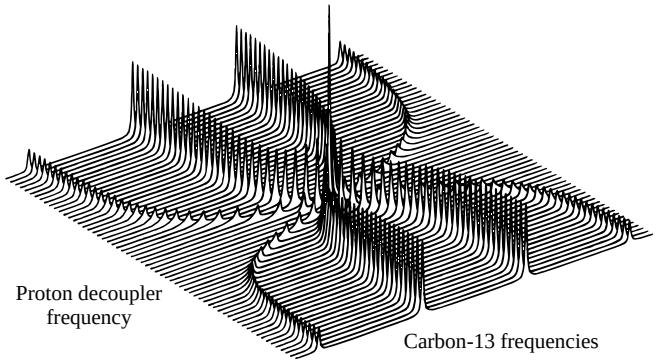

Figure 4 Simulated ^{13}C spectra for a methyl group when the proton resonance is decoupled with a coherent radiofrequency field $\boldsymbol{B}_2$. Reproduced from Freeman et al.[4] by permission of the American Chemical Society

For most assignment problems in high-resolution spectroscopy, the setting of the level of $\boldsymbol{B}_2$ is a compromise; it should be high enough to collapse the multiplet structure effectively but not so high as to begin to decouple adjacent resonances. The frequency of the perturbing field is varied until the observed S- spin multiplet coalesces to a singlet; this frequency is then taken as the chemical shift of the I spin. For homonuclear systems there is a small correction; the optimum frequency for decoupling is slightly shifted towards the S-spin resonance by an amount $(\gamma B_2/2\pi)^2/\ (\delta_I - \delta_S)$ (Hz).

Selective decoupling is a quick and direct method to test whether two groups of spins are coupled by a scalar interaction. However, this diagnostic is now more commonly performed by two-dimensional correlation spectroscopy.

4.1 Signs of Coupling Constants

Selective decoupling offers a method for determining the relative signs of spin coupling constants. The *absolute* sign of a given coupling cannot be obtained by these techniques. We require a set of three coupled spins (I–R–S), where R acts as a 'passive' spin, not directly involved in the double-resonance experiment. All three coupling constants, J_{IS}, J_{IR}, and J_{RS}, must give resolvable splittings. The passive spin R creates effective chemical shifts $\delta_I \pm \frac{1}{2}J_{IR}$ and $\delta_S \pm \frac{1}{2}J_{RS}$ instead of the actual shift δ_I and δ_S. There are therefore two subspectra, one with chemical shifts $\delta_I + \frac{1}{2}J_{IR}$ and $\delta_S + \frac{1}{2}J_{RS}$, and the other with the shifts $\delta_I - \frac{1}{2}J_{IR}$ and $\delta_S - \frac{1}{2}J_{RS}$. If we perform a selective decoupling experiment in one of these subspectra without appreciably perturbing the other, then the form of the decoupled spectrum tells us the relative signs of J_{IR} and J_{RS}. In two-dimensional correlation spectroscopy, a passive spin has an analogous effect, creating effective chemical shifts and changing the structure of a cross peak according to the relative signs of the couplings to the passive spin.

5 SLOW CHEMICAL EXCHANGE

Double resonance provides an innocuous label that makes it possible to tag a particular spin as it moves between two molecules (or between two conformations of the same molecule). The marker may be saturation or spin inversion, the latter having the advantage that it is quicker to implement. Slow chemical exchange may be monitored[5] by saturating or inverting the I spins and then following the evolution of S-spin intensity as saturated or inverted spins are carried from site I to site S.

For the simple case of equal populations at the two sites, the forward and backward transfer rates are equal, represented by a rate constant $1/\tau$. For simplicity, consider the case where the spin–lattice relaxation times at the two sites are equal (T_1). Let M_Z (S) and M_Z (I) represent the longitudinal magnetizations at some time t after the perturbation, while $\boldsymbol{M}_0(S)$ and $\boldsymbol{M}_0(I)$ are the corresponding initial (equilibrium) magnetizations. These will later be converted into observable signal intensities by a monitoring pulse. Suppose that the initial perturbation is a population inversion at site I. The time evolution may be written

$$\boldsymbol{M}_0(S) - M_Z(S) = \boldsymbol{M}_0(S)[\exp(-t/T_1) - \exp(-t/T_1 - 2t/\tau)] \quad (4)$$

$$\boldsymbol{M}_0(I) - M_Z(I) = \boldsymbol{M}_0(I)[\exp(-t/T_1) + \exp(-t/T_1 - 2t/\tau)] \quad (5)$$

If there is no chemical exchange ($\tau = \infty$) then the S-spin intensity remains unperturbed throughout, while the I-spin intensity recovers from the population inversion exponentially with time constant T_1 [Figure 5(a)]. If there is a finite rate of exchange but negligible spin–lattice relaxation ($T_1 = \infty$) the S resonance decays exponentially to zero with a time constant $\tau/2$ while the inverted I resonance returns to zero with the same time constant [Figure 5(b)]. The factor of 2 arises since each exchange event involves replacing a polarized spin with an inverted spin (or vice versa). When both exchange and relaxation effects are comparable, the inverted I spin signal recovers by spin–lattice relaxation aided by the influx of polarized S spins. The S-spin signal, initially unperturbed, diminishes in intensity through the influx of inverted I spins but then increases again as the normal spin–lattice relaxation takes over [Figure 5(c)]. Most practical cases are much more complicated than this, involving several chemical sites with different populations and different relaxation times, but by the appropriate analysis of the time development, the exchange rates (and relaxation times) can be determined.

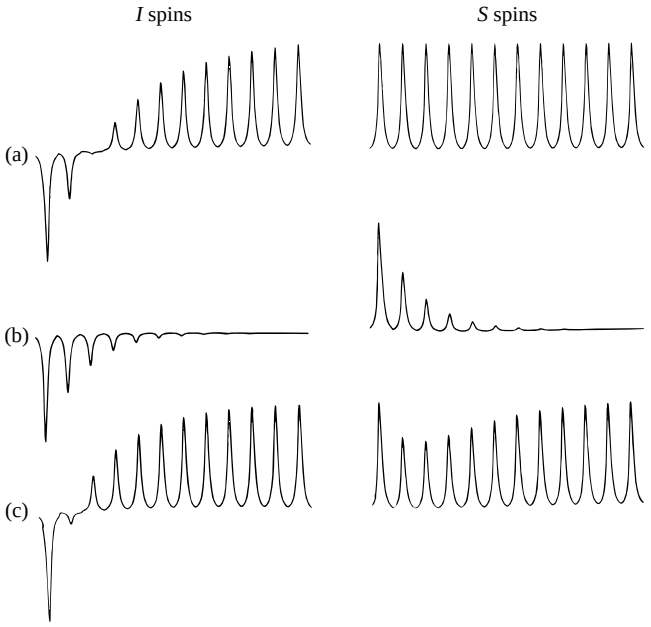

Figure 5 Simulated spectra after inverting the I spins in the presence of slow chemical exchange. (a) Negligible exchange. (b) Negligible relaxation. (c) Exchange and relaxation. Reproduced from 'A Handbook of Nuclear Magnetic Resonance', Longman, Harlow, 1988, with permission

Slow chemical exchange may also be investigated by two-dimensional NMR spectroscopy.[6] The evolution period is used to label the frequencies, and then all magnetizations are returned to the z axis for a fixed period during which chemical exchange takes place; a final pulse monitors any transfer of magnetization between the different chemical sites. This appears as a cross peak in the two-dimensional spectrum.

6 CROSS RELAXATION

6.1 The Nuclear Overhauser Effect

If two spins I and S are coupled by a dipolar interaction, saturation of the I spins causes an increase in the intensity of the S-spin signal. This is a *cross relaxation* effect, that is to say, it occurs only if S-spin relaxation is effected by the dipolar coupling to the I spins. The experiment was first proposed by Overhauser[7] for the case that the I spins were electrons and the S spins were metal nuclei. The corresponding *nuclear*

Overhauser effect has become important in two different applications—the enhancement of signals from low-sensitivity nuclei such as ^{13}C and ^{15}N when the proton resonance is saturated, and the assignment of distance constraints between protons in biochemical macromolecules, based on the r^{-3} dependence of the dipolar interaction.

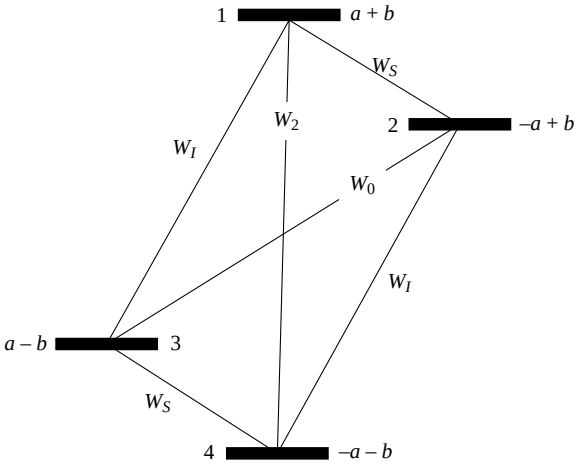

Figure 6 Energy level diagram for the nuclear Overhauser effect, showing the relaxation transition probabilities W_2, W_0, W_I and W_S. Spin populations are depicted by the numbers a and b

The nuclear Overhauser enhancement depends on the redistribution of spin populations by relaxation (predominantly by the double quantum transition probability) under conditions of continuous saturation of the I-spin resonance. The situation is succinctly described by the Solomon equations.[8] Consider the high-resolution spectrum of the IS system where the I and S doublets are resolved, although the same results apply to the case where only the overall S-spin magnetization can be detected. The energy level diagram is shown in Figure 6. The relaxation transition probabilities are represented by W_2, W_0, W_I, and W_S. The double quantum transition probability W_2 corresponds to the I and S spins flipping together in the same sense, whereas the zero-quantum probability W_0 corresponds to I and S flipping simultaneously in opposite senses. For simplicity of notation the spin populations are represented by the parameters a and b, defined by

$$2a = S_Z - S_0 \tag{6}$$

$$2b = I_Z - I_0 \tag{7}$$

where S_0 and I_0 are the populations at Boltzmann equilibrium, related by $I_0/S_0 = \gamma_I/\gamma_S$. The quantity of interest is the observable signal, which is proportional to S_Z, compared with the Boltzmann equilibrium signal, proportional to S_0. When spin populations are perturbed, spin–lattice relaxation causes a flux of spins in such a direction as to return the system toward equilibrium. This flux is proportional to the product of the appropriate population differences and the relaxation transition probabilities. The rate equations for levels 1 and 2 are

$$\frac{dn_1}{dt} = 2aW_S + 2bW_I + 2(a+b)W_2 \tag{8}$$

$$\frac{dn_2}{dt} = -2aW_S + 2bW_I - 2(a-b)W_0 \tag{9}$$

Consequently,

$$\frac{d(n_1 - n_2)}{dt} = 2a(2W_S + W_2 + W_0) + 2b(W_2 - W_0) \tag{10}$$

For a steady-state condition this derivative is zero, hence

$$\frac{-a}{b} = \frac{W_2 - W_0}{2W_S + W_2 + W_0} \tag{11}$$

This is a general expression into which is substituted the condition that the I spins are saturated ($I_Z = 0$) giving $2b = -I_0$. Recall that $I_0/S_0 = \gamma_I/\gamma_S$. Then

$$\eta = \frac{S_Z - S_0}{S_0} = \frac{W_2 - W_0}{2W_S + W_2 + W_0}\frac{\gamma_I}{\gamma_S} \tag{12}$$

The parameter η is called the nuclear Overhauser enhancement factor. In practice the observable quantity of interest is $S_Z/S_0 = 1 + \eta$.

If the relaxation is purely dipolar in origin and if the molecular reorientation is sufficiently fast compared with the Larmor frequency (the extreme narrowing condition, $\omega\tau_c \gg 1$) then the relative importance of the relaxation transition probabilities is[9]

$$W_2 : W_S : W_0 :: 12 : 3 : 2 \tag{13}$$

These may be substituted to give

$$1 + \eta = 1 + \frac{1}{2}\frac{\gamma_I}{\gamma_S} \tag{14}$$

This implies that there is a threefold enhancement of ^{13}C spectra upon saturation of the attached protons but only a 50% enhancement in homonuclear experiments. These are the maximum enhancements, only achieved if all other relaxation mechanisms are negligible. Relaxation by anything other than the dipolar mechanism is usually represented as an additional contribution to W_S, and called 'leakage'.

This analysis indicates that there is a *transient* nuclear Overhauser effect as well as the steady-state enhancement represented by equation (14). This transient enhancement is extensively used in proton NMR of biological molecules to infer distance constraints. Under the approximation that leakage mechanisms are broadly similar for all protons and that the rotational correlation times are roughly equal throughout the molecule, then the Overhauser enhancement is approximately proportional to the square of the dipolar field intensity and hence to the inverse sixth power of the interproton distance. These measurements are usually carried out by two-dimensional spectroscopy (NOESY), and there are so many nuclear Overhauser interactions in a typical biochemical molecule that the problem is vastly overdetermined, rendering the assumptions made above rather unimportant. A nuclear Overhauser effect gives rise to a cross peak in the two-dimensional spectrum, and this is taken as evidence that these two protons are separated by no more than about 0.6 nm, a 'distance constraint' which is often sufficient to allow important conclusions to be drawn about the structure of proteins.

6.2 The Rotating Frame Overhauser Effect

For many biological molecules the reorientation rate cannot be assumed to be high in comparison with the Larmor precession frequency, and the extreme narrowing condition ($\omega\tau_c \gg 1$) is not satisfied. Under these conditions the cross-relaxation rate falls off and actually passes through zero for $\omega\tau_c = 1.12$. The remedy is to study cross relaxation of *transverse* magnetization that is spin locked along a strong radiofrequency field. This method was originally called Camelspin,[10] but later became known as ROESY.[11] Cross peaks in two-dimensional ROESY spectra are always positive even though the extreme narrowing condition is violated.

7 CROSS POLARIZATION

7.1 The Hartmann–Hahn Effect in Solids

In 1962, Hartmann and Hahn[12] proposed an ingenious double-resonance method for improving the sensitivity of a low-abundance spin species S by measuring its influence on a neighboring abundant spin species I that has a strong NMR signal. In the general case the I and S spins have different Larmor precession frequencies and cannot 'talk' to each other directly. The Hartmann–Hahn experiment prepares the two spin systems in such a way that they have a frequency in common and can therefore communicate, provided there is a suitable I–S interaction. In the solid state this is the dipolar interaction D_{IS}, and in the liquid state the scalar spin–spin interaction J_{IS}.

Consider first the solid state case. The abundant I spins are spin locked along a strong radiofrequency field $\boldsymbol{B}_1$ applied along the y axis of the rotating reference frame. If it is assumed that the I spins are tightly coupled among themselves by dipolar interaction, they can be considered to constitute a thermal reservoir with its own spin temperature. The I spins are in fact very *cold* since they possess a magnetization proportional to the intense external magnetic field $\boldsymbol{B}_0$ but in the rotating frame they experience the very much weaker field $\boldsymbol{B}_1$. If the temperature in the laboratory is T_0, the spin temperature would be $T_0 B_1/B_0$. The dipolar interaction between I and S comes into play if a second radiofrequency field $\boldsymbol{B}_2$ is applied to the S spins. This second field must satisfy the Hartmann–Hahn matching condition

$$\gamma_I B_1 = \gamma_S B_2 \tag{15}$$

The local field at the I spins due to dipolar coupling to the S spins now oscillates at the frequency $\gamma_S B_2$ rad s^{-1}, and this is at just the right frequency to cause NMR transitions of the I spins. There is cross polarization; since mutual spin flips of I and S conserve energy, the 'hot' (saturated) S spins warm up (depolarize) the cold I spins. The effect is quite small because there are so few S spins, but it can be enhanced by repeatedly destroying or rapidly inverting the new magnetization of the S spins while maintaining the Hartmann–Hahn contact. If the dipolar interaction between the I spins is insufficient to maintain a uniform spin temperature, then any continued polarization transfer relies on diffusion of the heated I spins away from the locality of the S spins.

Initially the Hartmann–Hahn experiment focused on the loss of I-spin signal caused by cross polarization by the low-abundance S spins, but later extensions exploited the increased S-spin polarization after multiple contacts with the highly polarized I spins, and this has become a standard sensitivity enhancement technique for solid state NMR studies of ^{13}C nuclei, usually combined with magic angle spinning ('CP MAS').

7.2 The Hartmann–Hahn Effect in Liquids

For liquid state samples the Hartmann–Hahn effect operates through the scalar spin–spin coupling. One may no longer talk of a thermal reservoir of the abundant spins nor of a spin temperature. Suppose there is an isolated pair of spins I and S coupled by an interaction J_{IS}. Radiofrequency fields $\boldsymbol{B}_1$ and $\boldsymbol{B}_2$ are applied at the I- and S-sites simultaneously, satisfying the Hartmann–Hahn matching condition. The phase of the initial excitation pulses may be chosen so that the S nuclei are spin locked along the $-y$ axis while the I nuclei are locked along the $+y$ axis. Mutual spin flips cause the spin populations to exchange back and forth in a sinusoidal fashion with a frequency J_{IS} Hz. The total spin population is conserved. Figure 7 shows the first full cycle of this interchange of coherence between the two proton sites of uracil. Eventually these signals decay through spin–spin relaxation during the spin lock period.

This effect is exploited in liquid phase two-dimensional spectroscopy as a correlation technique,[13] operating with spin lock durations of the order of $1/J_{IS}$. This has been called 'total correlation spectroscopy' (TOCSY) or, alternatively, the 'homonuclear Hartmann–Hahn' (HOHAHA) experiment. It has the advantage that the observed signals are all in the positive absorption mode.

As an alternative to two-dimensional correlation spectroscopy, several consecutive Hartmann–Hahn coherence transfers can be strung together to give a multistage transfer experiment. If the proton spins under investigation are coupled together in a chain in the right sequence, an absorption mode signal is detected at the end of the chain. If any of the couplings are vanishingly small, no signal is detected. This can be useful for deciding between alternative molecular structures.

7.3 Polarization Transfer (INEPT)

Although high-resolution liquid phase spectra of ^{13}C and ^{15}N can be enhanced in sensitivity by the nuclear Overhauser effect, better results can be obtained by direct polarization transfer from protons.[14] This is partly because of the faster spin–lattice relaxation of protons, and partly because the population advantage is γ_I/γ_S whereas the nuclear Overhauser enhancement factor is only $1 + \frac{1}{2}\gamma_I/\gamma_S$. Fast spin–lattice relaxation allows the polarization transfer steps to be repeated more rapidly without waiting for the ^{13}C or ^{15}N spins to reach thermal equilibrium. (Indeed, even polarization transfer from the low frequency deuterium nucleus provides some enhancement by virtue of the much faster deuterium relaxation.)

The mechanism depends on a manipulation of the proton magnetization vectors that is closely related to techniques

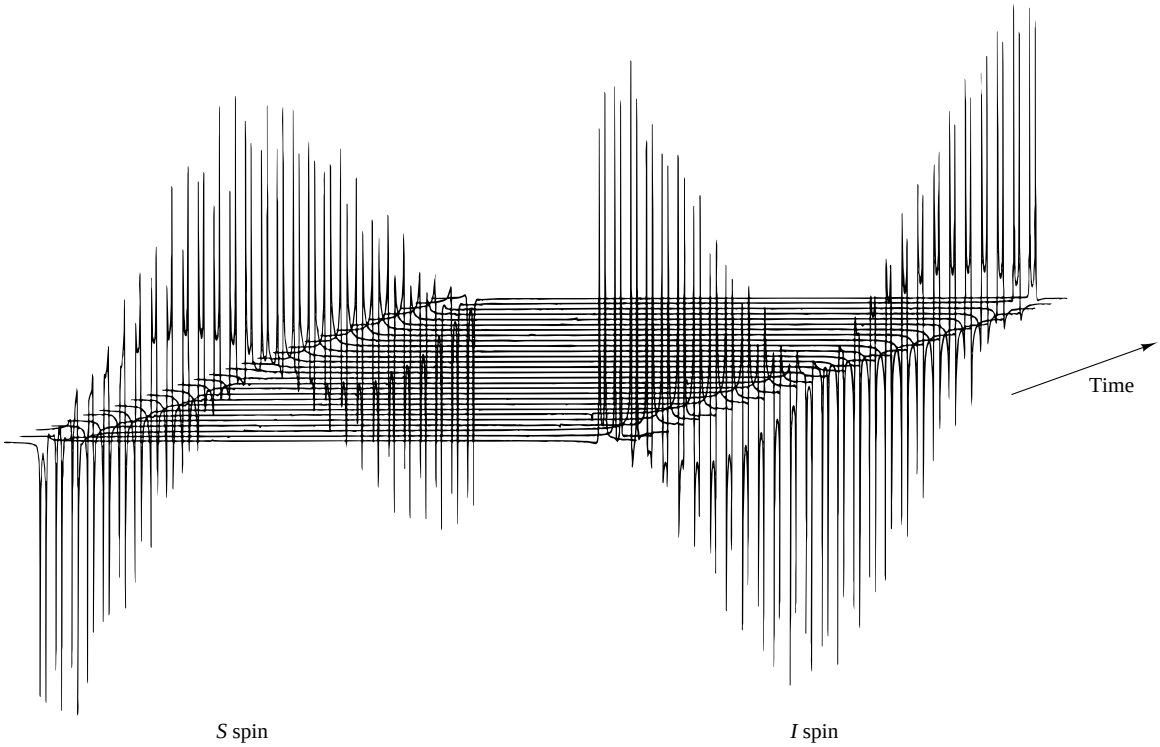

Figure 7 The Hartmann–Hahn effect in a liquid. The S-spin magnetization was aligned along the $-y$ axis and the I-spin magnetization along the $+y$ axis. During spin locking, coherence swings back and forth between the two sites. One full cycle is shown; eventually, spin–spin relaxation damps both signals. Reproduced from Kupče and Freeman, *J. Magn. Reson., Ser.A*, 1993, **105**, 234, by permission of Academic Press, Inc.

employed in two-dimensional spectroscopy. Let the two proton satellites be represented by magnetization vectors labelled α and β according to the two allowed spin states of ^{13}C. (Exactly analogous arguments apply to ^{15}N.) The spin physics can be followed with the aid of a vector diagram (Figure 8). After a $90^\circ(x)$ pulse the proton vectors are aligned along the y axis of the rotating frame [Figure 8(a)], and they precess as a result of chemical shift and spin–spin coupling effects. The duration of this precession (τ) is chosen to satisfy the condition $\tau J(\mathrm{C,H}) = 0.25$ so that the α and β vectors are just 90° apart [Figure 8(b)]. Then a $180^\circ(x)$ pulse is applied to the protons to refocus the chemical shift evolution [Figure 8(c)] while a simultaneous 180° pulse is applied to ^{13}C to flip the ^{13}C spin states and interchange the α and β proton labels [Figure 8(d)]. Free precession for a further period τ brings the proton vectors into the antiphase alignment [Figure 8(e)]. A proton $90^\circ(y)$ pulse is then applied, swinging the antiphase vectors into the $\pm z$ axis (Figure 8(f)). This corresponds to a situation where one of the two ^{13}C satellite lines has a population inversion while the other is unaffected. Consideration of the energy level diagram appropriate to the condition $\gamma_I/\gamma_S = 4$ shows that one ^{13}C line becomes five times stronger while the other becomes three times stronger but inverted (Figure 9). Since the original lines had unit intensity, the changes due to polarization transfer from protons are +4 and −4. The sensitivity of ^{13}C has been enhanced by the ratio γ_I/γ_S, although the process has introduced an 'up–down' pattern in the intensities. If necessary a further refocusing stage can be appended to correct this alternation so that proton decoupling can be used. For ^{15}N the enhancement is $\gamma_I/\gamma_S = 10$. Fast repetition of the polarization transfer gives a further improvement in sensitivity compared with direct excitation of ^{13}C or ^{15}N. Later elaborations of this technique return the enhanced polarization of ^{13}C or ^{15}N back to protons for detection so as to exploit the higher magnetic moment of the proton.[15]

8 BROADBAND DECOUPLING IN LIQUIDS

Carbon and hydrogen are the two atoms of most interest to the organic chemist. While the ^{13}C nucleus boasts a much wider range of chemical shifts, the intrinsic sensitivity is low and ^{13}C spectra can be complicated by the spin–spin coupling to protons. For these reasons, these spectra are commonly run under decoupled conditions. Not only does this afford a considerable simplification by eliminating the CH splittings but it also improves sensitivity through the nuclear Overhauser effect and by collecting all the lines of the multiplets into a single resonance at the carbon chemical shift.

The application of the perturbing field $\boldsymbol{B}_2$ often causes a saturation effect as well as coherent decoupling; indeed, in ^{13}C spectroscopy with proton decoupling both effects are useful. It is, however, important not to confuse the two. When one effect is required without the other, 'gated decoupling' may be used. For example, decoupled ^{13}C spectra can be obtained without any nuclear Overhauser effect by switching on the proton decoupler only while acquiring the ^{13}C signal. This mode of operation is sometimes forced on the operator by the need to minimize the radiofrequency heating of the sample. By contrast, the nuclear Overhauser effect can be obtained without proton decoupling by saturating the proton system during an extended preparation period and then extinguishing the decoupler just prior to signal acquisition. This highlights

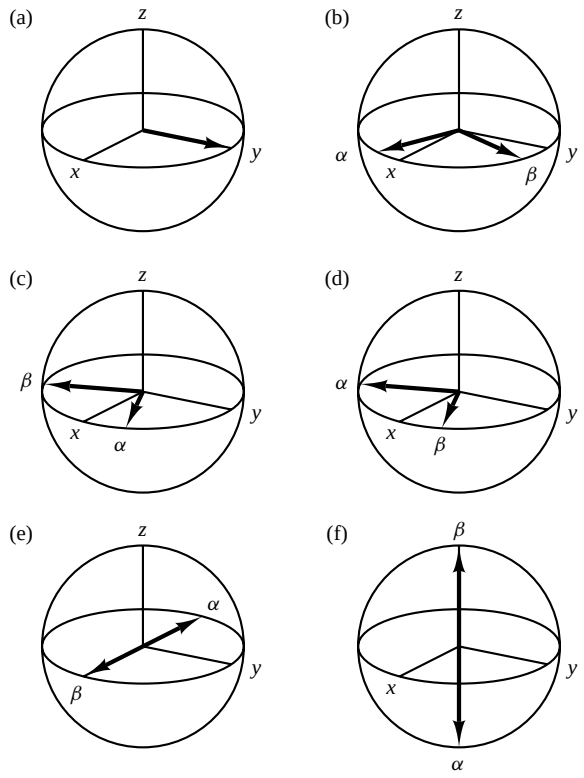

Figure 8 The INEPT experiment to transfer polarization from protons to ^{13}C. (a) A 90° pulse aligns the two proton vectors along the $+y$ axis. (b) Vectors precess until they make an angle of 90°. (c) Vectors are flipped 180° about the $+x$. (d) The α and β labels are interchanged by a 180° pulse on the ^{13}C spins. (e) Further precession for the same period and in the same sense. (f) A 90° pulse about the $+y$ axis

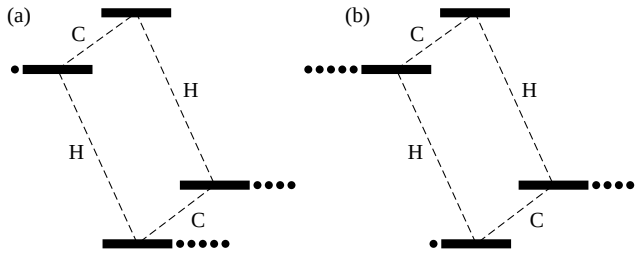

Figure 9 Spin populations in the INEPT experiment. (a) At Boltzmann equilibrium the population differences across proton transitions are four times greater than across carbon transitions. (b) After inversion of populations across one proton transition, one carbon resonance becomes five times stronger whereas the other becomes three times stronger but inverted

the distinction, made in the introduction, between population and coherence effects.

Ideally the decoupling should be effective whatever the proton chemical shift, that is to say, it should cover a bandwidth as broad as the entire range of proton shifts. The first experiments in broadband decoupling employed a pseudorandom phase alternation of the decoupler radiofrequency, the so-called noise decoupling technique.[16] This was surprisingly effective. Although in principle some incoherence may be transmitted from protons to the ^{13}C spins through the C–H coupling, in practice this is reduced to a negligible level if the decoupler power is sufficiently high. However, as magnet fields were increased in intensity and the proton shift range expanded in proportion, it became apparent that noise decoupling was not quite efficient enough, and undue sample heating could occur in high-field spectrometers. The effect is particularly severe for ionic solutions.

9 COMPOSITE-PULSE DECOUPLING

The requirement for decoupling is that the protons should be repeatedly inverted at a rate fast compared with J(C,H). This is why a continuous wave monochromatic source gives good decoupling at exact resonance. One may also use a repetitive train of 180° pulses, but if they are sufficiently intense to cover the requisite bandwidth, the radiofrequency power deposition in the sample becomes excessive. The situation is improved by using composite 180° pulses, for example $90^\circ(x)\ 180^\circ(y)\ 90^\circ(x)$, which has the property of compensating for radiofrequency offset effects.[17] However, in a long train of repeated pulses, even small pulse imperfections can build up to unacceptable levels unless a self-compensating scheme can be found. Levitt[18] showed how this could be achieved by assembling the composite 180° pulse $\bar{\text{R}}$ and its phase-inverted counterpart R into a magic cycle $\text{R}\bar{\text{R}}\text{R}\bar{\text{R}}$ or, better still, into a supercycle of the type

$$\text{MLEV-16} = \text{R}\bar{\text{R}}\bar{\text{R}}\text{R} \quad \bar{\text{R}}\text{R}\bar{\text{R}}\text{R} \quad \bar{\text{R}}\bar{\text{R}}\text{R}\bar{\text{R}} \quad \text{R}\bar{\text{R}}\bar{\text{R}}\text{R} \qquad (16)$$

It can be seen that the expansion procedure involves phase inversion and cyclic permutation of the elements of the basic cycle.

While MLEV-16 or MLEV-64 decoupling schemes offer a great improvement over noise decoupling, they nevertheless exhibit some disturbing complications when examined in detail. Incomplete decoupling first becomes apparent as a very small residual splitting of the ^{13}C resonance at certain decoupler offsets. Under most experimental conditions these splittings would be masked by the instrumental linewidth, but they may still affect the height of the decoupled ^{13}C line. For MLEV-16 decoupling these slight imperfections appeared to depend on the accuracy of the 90° phase shift used in the composite 180° pulse and, even more surprisingly, the optimum phase shift seemed to be very slightly different from 90°.

9.1 Theory of Decoupling

The initial theoretical treatment of the new broadband decoupling sequences made use of an approximate method—average Hamiltonian theory, but a later exact theory proposed by Waugh[19] makes the picture much clearer and incidentally explains the bizarre behavior of the MLEV sequences with respect to very slight variations of the 90° phase shift. These decoupling sequences are periodic and perform best when they are also closely *cyclic*. That is to say, they take the proton magnetization vectors back to the same position once every cycle. Consider the simple two-spin case ^{13}CH. Attention is focused on the two ^{13}C satellites of the main proton resonance $\boldsymbol{H}(+)$ and $\boldsymbol{H}(-)$, corresponding to the two possible spin states of the ^{13}C spin and represented by two vectors at different

offsets from the radiofrequency field $\boldsymbol{B}_2$. During one complete period of the decoupling sequence, $\boldsymbol{H}(+)$ and $\boldsymbol{H}(-)$ perform a sequence of pure rotations, one for each decoupler pulse. These can be thought of as a series of linked arcs on the surface of a sphere, and the resultant (the overall rotation) is also a short arc on the same sphere.

If the motions of $\boldsymbol{H}(+)$ and $\boldsymbol{H}(-)$ had had the same resultants, decoupling would be perfect. In practice, poor calibration, spatial inhomogeneity of the $\boldsymbol{B}_2$ field, and the inevitable difference in decoupler offset all conspire to introduce a slight difference in the two overall rotations, which may be written as

$$\mathrm{R}(+) = \exp[-\mathrm{i}\beta(+)\boldsymbol{n}(+)\cdot\ \boldsymbol{I}] \tag{17}$$

$$\mathrm{R}(-) = \exp[-\mathrm{i}\beta(-)\boldsymbol{n}(-)\cdot\boldsymbol{I}] \tag{18}$$

where $\boldsymbol{n}(+)$ and $\boldsymbol{n}(-)$ are unit vectors defining the overall rotation axes and $\beta(+)$ and $\beta(-)$ are the resultant angles through which the vectors $\boldsymbol{H}(+)$ and $\boldsymbol{H}(-)$ rotate. If attention is confined to these resultant rotations ('stroboscopic observation'), stringing several together gives rise to a uniform rotation, just as in coherent decoupling with a continuous monochromatic frequency, and the equations are analogous:

$$\begin{aligned} S(t) = {} & 0.5[1 + \boldsymbol{n}(+)\cdot\boldsymbol{n}(-)]\cos[\Omega(-)t] \\ & +0.5[1 - \boldsymbol{n}(+)\cdot\boldsymbol{n}(-)]\cos[\Omega(+)t] \end{aligned} \tag{19}$$

This indicates that the ^{13}C free induction signal is amplitude modulated at the frequencies $\Omega(+)$ and $\Omega(-)$. After Fourier transformation the ^{13}C signal is a symmetric four-line pattern consisting of a doublet with splitting $\Omega(-)/\pi$ (Hz) and intensity $I(-)$:

$$\begin{aligned} \Omega(-) &= [\beta(+) - \beta(-)]/2t, \\ I(-) &= 0.5[1 + \boldsymbol{n}(+)\cdot\boldsymbol{n}(-)] \end{aligned} \tag{20}$$

and another doublet of splitting $\Omega(+)/\pi$ (Hz) and intensity $I(+)$.

$$\begin{aligned} \Omega(+) &= [\beta(+) + \beta(-)]/2t, \\ I(+) &= 0.5[1 - \boldsymbol{n}(+)\cdot\boldsymbol{n}(-)] \end{aligned} \tag{21}$$

The $\Omega(-)$ frequency is of particular interest, since for good decoupling $\boldsymbol{H}(+)$ and $\boldsymbol{H}(-)$ experience very similar rotations, and the axis $\boldsymbol{n}(+)$ is nearly parallel to $\boldsymbol{n}(-)$. Almost all of the intensity is concentrated in this main doublet, which has a very small residual splitting $\Omega(-)/\pi$ (Hz). The other splitting gives rise to the very weak satellite lines which can be neglected for our purposes. Decoupling thus reduces the spin–spin splitting J(C,H) (Hz) to a residual splitting $\Omega(-)/\pi$ (Hz).

The aim of an efficient broadband decoupler is therefore to maintain a small residual splitting $\Omega(-)/\pi$ for all offsets within the effective bandwidth.[19] The brute force method would be to use such an intense field $\boldsymbol{B}_2$ that $\beta(+) - \beta(-)$ is always small and the axes $\boldsymbol{n}(+)$ and $\boldsymbol{n}(-)$ are closely collinear. In fact the new sequences are designed to be as nearly as possible *cyclic* so that $\beta(+)$ and $\beta(-)$ are always very small. Then it is of little importance how the rotation axes $\boldsymbol{n}(+)$ and $\boldsymbol{n}(-)$ are oriented. Good cyclicity is achieved by combining the elements R and $\bar{\mathrm{R}}$ in a suitable manner. For example, if R is close to a 180° pulse, then RR and $\mathrm{R}\bar{\mathrm{R}}$ are nearly cyclic, and their residual rotations tend to cancel.

These sequences have two very important properties. The performance is unaffected by phase inversion, so that $\mathrm{RR}\bar{\mathrm{R}}\bar{\mathrm{R}}$ has the same efficiency as $\bar{\mathrm{R}}\mathrm{RRR}$. It is also unaffected by cyclic permutation of some part of the sequence, for example $\mathrm{RR}\bar{\mathrm{R}}\mathrm{R}$ is equivalent to $\bar{\mathrm{R}}\mathrm{RR}\bar{\mathrm{R}}$. However, the nature of the residual imperfections does change with phase inversion or cyclic permutation. Cyclic permutation of a 180° pulse flips the residual rotation axis through 180°. Consequently, $\mathrm{RR}\bar{\mathrm{R}}\mathrm{R}$, which has a residual rotation axis near $+z$, is compensated by $\bar{\mathrm{R}}\mathrm{RR}\bar{\mathrm{R}}$, which has a residual rotation of about the same amplitude about an axis near to $-z$. This is therefore the first step in assembling a supercycle. It turns out that the combination $\mathrm{RR}\bar{\mathrm{R}}\bar{\mathrm{R}}\ \bar{\mathrm{R}}\mathrm{RR}\bar{\mathrm{R}}$ has a small residual rotation about an axis in the *xy* plane that can be largely cancelled by combining with the phase-inverted counterpart. The result is the MLEV-16 sequence shown in equation (16).

9.2 WALTZ Decoupling

The rule about cyclic permutation can be more generally expressed[19]—if an element (or combination of elements) representing a rotation θ about the x axis is cyclically permuted, then the axis of residual rotation of the sequence is itself rotated about the x axis through an angle θ. This implies that the permuted element itself should be well behaved as a function of proton resonance offset, otherwise the compensation will deteriorate at large offsets. One of the best elements in this respect is a 90° pulse since it is known to be largely self-compensating with respect to resonance offset.

This is the basis for the 'WALTZ' family[20] of decoupling sequences, which start with the composite inversion pulse:

$$\mathrm{R} = 90^\circ(+x)\,180^\circ(-x)\,270^\circ(+x). \tag{22}$$

No 90° phase shifts are involved, and this avoids the problem encountered with the MLEV sequences which were very sensitive to small errors in the 90° phase shifts. In a convenient shorthand notation this may be written $\mathrm{R} = 1\bar{2}3$ (hence the name). The first magic cycle is constructed as before:

$$\text{WALTZ-4} = 1\bar{2}3\quad 1\bar{2}3\quad \bar{1}2\bar{3}\quad \bar{1}2\bar{3} \tag{23}$$

The residual rotation of WALTZ-4 is about an axis near $+z$. If a 90° pulse is permuted from left to right, this shifts the residual rotation axis into the *xy* plane. It can then be compensated by combination with the phase-inverted counterpart which also has its residual rotation axis in the *xy* plane, but with its direction reversed. This gives the next supercycle:

$$\text{WALTZ-8} = \bar{2}4\bar{2}3\bar{1}\quad \bar{2}4\bar{2}3\bar{1}\quad 2\bar{4}2\bar{3}1\quad 2\bar{4}2\bar{3}1 \tag{24}$$

Similar considerations lead to the construction of an efficient and widely used supercycle:

$$\begin{aligned} \text{WALTZ-16} = {} & \bar{3}4\bar{2}3\bar{1}2\bar{4}2\bar{3}\quad 3\bar{4}2\bar{3}1\bar{2}4\bar{2}3\quad 3\bar{4}2\bar{3}1\bar{2}4\bar{2}3 \\ & \bar{3}4\bar{2}3\bar{1}2\bar{4}2\bar{3} \end{aligned} \tag{25}$$

This has an effective decoupling bandwidth equal to about $2\gamma B_2/2\pi$ (Hz), where B_2 is the intensity of the decoupler field. For experiments that demand even wider bandwidths (for example to decouple ^{13}C and observe protons), several later schemes have been devised, for example GARP[21] or sequences where the decoupler frequency is also cycled.[22]

10 DECOUPLING DIPOLAR INTERACTIONS IN SOLIDS

10.1 Homonuclear Interactions

For many years it was the perceived wisdom that high-resolution experiments could only be effective in the liquid phase because in the solid state the interesting interactions (such as chemical shift anisotropy and scalar spin–spin coupling) were obscured by the much stronger dipolar broadening. This view had to be drastically revised when several experimental innovations were made, principally magic angle spinning,[23,24] multipulse experiments,[25] and cross polarization.[12] Today, high-resolution solid state NMR is a thriving area of study.

In the liquid phase, the static dipole–dipole interaction is averaged by rapid random molecular reorientation; at the same time the anisotropies of the chemical shielding and of the spin–spin coupling are also removed. That these effects are obtained without any effort on the part of the spectroscopist accounts for the popularity of liquid phase high-resolution work. To achieve a similar averaging in the solid state requires much more sophistication. One method is rapid sample spinning[23,24] about an axis that subtends an angle of 54.74° to the magnetic field (the magic angle), or even the simultaneous spinning about two different magic angles.[26] This puts severe demands on spinner turbine technology, since the spinning rate should ideally exceed the dipolar broadening expressed in frequency units. The periphery of the rotor can reach supersonic speeds, and there is a real danger of disintegration. Helium may be used as the propelling gas rather than air.

The alternative is to perform the averaging in spin space by applying a suitable radiofrequency pulse sequence. Triggered by the surprising discovery[27] that long trains of spin echoes could be excited in the solid state, Waugh and co-workers[28] invented sophisticated pulse sequences that could remove the dipolar broadening, leaving a spectrum dominated by the chemical shift and the spin–spin coupling.

10.2 Heteronuclear Interactions

Solid state spectroscopy of nuclei such as ^{13}C and ^{15}N was neglected for many years because of the low magnetic moments, low natural abundance, and long spin–lattice relaxation times. These sensitivity problems are now circumvented by a combination of experimental techniques. Cross polarization from protons through the Hartmann–Hahn effect[12] bestows on the ^{13}C and ^{15}N species some of the useful properties of protons (high polarization and short relaxation times). Decoupling the protons (with a very intense radiofrequency field $\boldsymbol{B}_2$) simplifies the observed spectra and concentrates the intensity into fewer resonances. This technique is called proton-enhanced nuclear induction spectroscopy.[28] A later refinement[29] (CP MAS) incorporates magic angle spinning to average the chemical shift anisotropy, giving spectra from solids that approached the detail and resolution of liquid phase NMR.

11 RELATED ARTICLES

Chemical Exchange Effects on Spectra; Composite Pulses; Cross Polarization in Solids; Decoupling Methods; Double Rotation; Electron–Nuclear Multiple Resonance Spectroscopy; INEPT; Magic Angle Spinning; NOESY; Nuclear Overhauser Effect; Phosphorus-31 Magnetization Transfer Studies In Vivo; Polarization Transfer Experiments via Scalar Coupling in Liquids; Proton Decoupling During In Vivo Whole Body Phosphorus MRS; Proton Decoupling in Whole Body Carbon-13 MRS; REDOR and TEDOR; ROESY; Selective Hartmann–Hahn Transfer in Liquids; Selective NOESY; Three- and Four-Dimensional Heteronuclear Magnetic Resonance; Ultrasonic Irradiation and NMR.

12 REFERENCES

1. N. Bloembergen, E. M. Purcell, and R. V. Pound, *Phys. Rev.*, 1948, **73**, 679.
2. R. Freeman and B. Gestblom, *J. Chem. Phys.*, 1968, **48**, 5008.
3. R. Freeman and W. A. Anderson, *J. Chem. Phys.*, 1962, **37**, 2053.
4. R. Freeman, J. B. Grutzner, G. A. Morris, and D. L. Turner, *J. Am. Chem. Soc.*, 1978, **100**, 5637.
5. S. Forsén and R. A. Hoffman, *J. Chem. Phys.*, 1963, **39**, 2892.
6. J. Jeener, B. H. Meier, P. Bachmann, and R. R. Ernst, *J. Chem. Phys.*, 1979, **71**, 4546.
7. A. W. Overhauser, *Phys. Rev.*, 1953, **92**, 411.
8. I. Solomon, *Phys. Rev.*, 1955, **99**, 559.
9. A. Abragam, *The Principles of Nuclear Magnetism*, Clarendon Press, Oxford, 1961.
10. A. A. Bothner-By, R. L. Stephens, J. M. Lee, C. D. Warren, and R. W. Jeanloz, *J. Am. Chem. Soc.*, 1984, **106**, 811.
11. A. Bax and D. G. Davis, *J. Magn. Reson.*, 1985, **63**, 207.
12. S. R. Hartmann and E. L. Hahn, *Phys. Rev.*, 1962, **128**, 2042.
13. L. Braunschweiler and R. R. Ernst, *J. Magn. Reson.*, 1983, **53**, 521.
14. G. A. Morris and R. Freeman, *J. Am. Chem. Soc.*, 1979, **101**, 760.
15. P. H. Bolton and G. Bodenhausen, *Chem. Phys. Lett.*, 1982, **89**, 139.
16. R. R. Ernst, *J. Chem. Phys.*, 1966, **45**, 3845.
17. M. H. Levitt and R. Freeman, *J. Magn. Reson.*, 1979, **33**, 473.
18. M. H. Levitt, R. Freeman, and T. Frenkiel, *J. Magn. Reson.*, 1982, **47**, 328.
19. J. S. Waugh, *J. Magn. Reson.*, 1982, **50**, 30.
20. A. J. Shaka, J. Keeler, and R. Freeman, *J. Magn. Reson.*, 1983, **53**, 313.
21. A. J. Shaka, P. B. Barker, and R. Freeman, *J. Magn. Reson.*, 1985, **64**, 547.

22. T. Fujiwara, T. Anai, N. Kurihara, and K. Nagayama, *J. Magn. Reson. A*, 1993, **104**, 103.
23. E. R. Andrew, A. Bradbury, and R. G. Eades, *Nature*, 1958, **182**, 1659.
24. I. J. Lowe, *Phys. Rev. Lett.*, 1959, **2**, 285.
25. A. Pines, M. G. Gibby, and J. S. Waugh, *J. Chem. Phys.*, 1972, **56**, 1776.
26. A. Samoson, B. Q. Sun, and A. Pines, *Pulsed Magnetic Resonance: NMR, ESR and Optics*. A Recognition of E. L. Hahn, ed. D. M. S. Bagguley, Clarendon Press, Oxford, 1992, Chap. 3
27. E. D. Ostroff and J. S. Waugh, *Phys. Rev. Lett.*, 1966, **16**, 1097.
28. J. S. Waugh, L. M. Huber, and U. Haeberlen, *Phys. Rev. Lett.*, 1968, **20**, 180.
29. E. O. Stejskal, J. Schaefer, and R. A. McKay, *J. Magn. Reson.*, 1977, **25**, 569.

Biographical Sketch

Ray Freeman. *b* 1932. M.A., D. Phil., 1958, Chemistry, Oxford University, (supervisor Rex Richards). Postdoctoral research with Robert Pound and A. Abragam at the Centre d'Etudes Nucléaires de Saclay, France 1957–59. Senior scientific officer, National Physical Laboratory, England, 1959–63. Instrument Division Research, Varian Associates, Palo Alto, CA, 1963–73. University lecturer, Oxford University, 1973–87. D.Sc. Oxford University, 1975. Fellow of the Royal Society. Currently Professor of Magnetic Resonance, Cambridge University. President, International Society of Magnetic Resonance, 1989–92. Approx. 240 publications. Research specialties: NMR double resonance, relaxation times, coupling constants, spin echoes, coherence transfer, multidimensional spectroscopy, multiple quantum spectroscopy, selective excitation.

Heteronuclear Assignment Techniques

Christopher J. Turner

Massachusetts Institute of Technology, Cambridge, MA, USA

1	Introduction	1
2	Multiplicity Determination	1
3	Heteronuclear Chemical Shift Correlation	3
4	Related Articles	8
5	References	8

1 INTRODUCTION

These days the acquisition of a proton decoupled carbon-13 spectrum is relatively straightforward; however, the interpretation of the spectrum is often much more challenging. Fortunately, there are a variety of heteronuclear assignment techniques which are available to help with this task. Aside from deductions based upon chemical shifts and relaxation properties, the most common assignment technique involves the transfer of magnetization between nuclei via spin coupling, a process often referred to as coherence transfer.

There are basically two methods of transferring magnetization between nuclei, either free precession or forced precession. In both these processes, a time (τ) is chosen which is related to the reciprocal of a coupling constant. In the former method, pulses are applied separated by a delay τ during which the transmitter is turned off. In the latter method, pulses are applied for a total time τ. Thus, the difference between the two techniques is whether the transmitter is left on, or turned off for the time τ. In the past, heteronuclear assignment techniques relied almost exclusively on the former method, i.e. combinations of pulses and delays. However, the latter method, coherence transfer in the rotating frame via multiple pulse based heteronuclear J cross polarization, also known as hetero-TOCSY, has become increasingly popular.

2 MULTIPLICITY DETERMINATION

Most heteronuclear spectra are acquired with broadband proton decoupling. Despite this, it is often desirable to determine the multiplicity, or number of directly attached protons. In theory, this information could be obtained from a proton coupled spectrum; however, in practice, this is often inconvenient because of spectral overlap and low sensitivity. Therefore, experiments have been developed which encode multiplicity information into broadband decoupled spectra. This process is often referred to as spectral editing.

2.1 APT

The attached proton test (APT) interrupts the decoupling for a time (τ) between excitation and detection. The delay τ is related to the reciprocal of an appropriate heteronuclear coupling constant, usually ^1J(C,H). During the period τ the different components of the proton coupled multiplets precess at their individual frequencies, which are governed by their heteronuclear J coupling. The recombination of these components, when the decoupler is turned back on, produces a constructive or destructive interference. The signals from methine and methyl carbons appear inverted with respect to those from quaternary and methylene carbons. However, the use of this simple sequence leads to a severe frequency dependent phase shift across the spectrum, which is normally unacceptable. This phase shift can be removed by the use of a spin echo. The echoes can be modulated by either gating the decoupler,[1–3] or by use of a 180° proton pulse synchronized with the 180° carbon pulse.[4] The two methods, shown in Figure 1, are referred to as the gated decoupler and proton flip techniques by analogy to heteronuclear two-dimensional J spectroscopy.[5] The gated decoupler method is normally used; however, the proton flip method is more interesting because it can be seen, conceptually, as a step toward the SEMUT (subspectral editing using a multiple quantum trap) experiment.

Semiclassical vector models are often used to explain echo sequences.[6] However, it is necessary to use the product operator formalism here, because of the importance of techniques based upon the generation of multiple quantum coherence. The product operator approach uses a form of shorthand algebra to follow the spin gymnastics.[7,8] Let us start with a step-by-step analysis of the product operator transformations associated with the proton flip version of the attached proton test shown in Figure 1(b), for a ^{13}C,^{1}H spin system. For simplicity only terms that contribute to the final spectrum are shown. The first step is a 90° excitation pulse acting on the z magnetization of the carbons; thus equation (1) contains an operator representing the state of the magnetization (in this case, the carbon magnetization at thermal equilibrium; $\hat{C}_z$) which is acted upon by a rotation operator (in this case, a

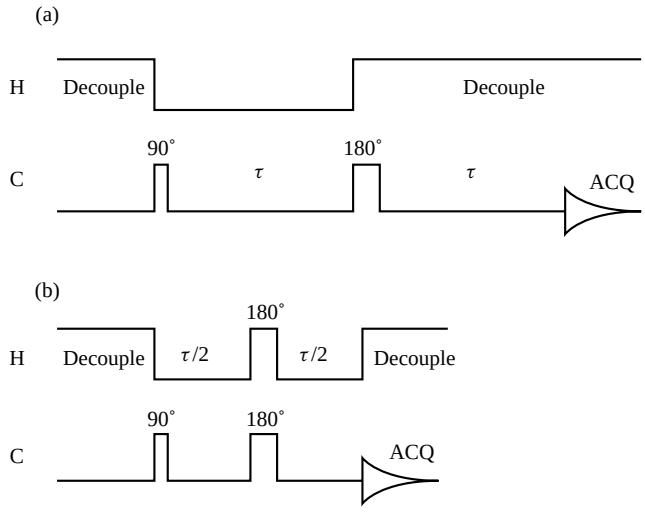

Figure 1 Basic echo sequences for heteronuclear multiplicity selection (APT). (a) Gated decoupler method; (b) spin flip method. τ is set to $1/J$ for an even/odd subspectrum. In this, and subsequent, diagrams the phase of all 180° pulses is of no practical importance, apart from the necessity of inverting the receiver reference phase if the phase of a 180° pulse is changed by 90°

rotation of the carbon magnetization about the x axis; $\hat{C}_x$):

$$\hat{C}_z \xrightarrow{(\pi/2)\hat{C}_x} -\hat{C}_y \quad (1)$$

Heteronuclear spin coupling evolves during the subsequent delay τ. The operator for spin–spin coupling is represented by $2\hat{C}_z\hat{H}_z$, that is, a rotation about the z axis for both nuclei, leading to the following:

$$-\hat{C}_y \xrightarrow{(\pi J_{CH}\tau)2\hat{C}_z\hat{H}_z} -\hat{C}_y \cos(\pi J_{CH}\tau) + 2\hat{C}_x\hat{H}_z \sin(\pi J_{CH}\tau) \quad (2)$$

If the interval τ is chosen such that $\tau = 1/(2J_{CH})$ then the cosine term becomes zero and we are left with:

$$-\hat{C}_y \xrightarrow{(\pi/2)2\hat{C}_z\hat{H}_z} +2\hat{C}_x\hat{H}_z \quad (3)$$

that is to say, two carbon magnetization vectors aligned in opposition along the $\pm x$ axes. We can ignore the simultaneous 180° pulses on both spins because they have the same effect as a single 180° pulse in a homonuclear spin system, i.e. they refocus the chemical shift while having no effect upon either homo- or heteronuclear coupling. After a further delay $\tau = 1/(2J_{CH})$ we find the two vectors are realigned again, but along the $+y$ rather than the $-y$ axis:

$$+2\hat{C}_x\hat{H}_z \xrightarrow{(\pi/2)2\hat{C}_z\hat{H}_z} \hat{C}_y \quad (4)$$

For an odd multiplicity (e.g. CH and CH_3) we can summarize this whole process as

$$\hat{C}_z \xrightarrow{(\pi/2)\hat{C}_x} -\hat{C}_y \xrightarrow{(\pi/2)2\hat{C}_z\hat{H}_z} 2\hat{C}_x\hat{H}_z \xrightarrow{(\pi/2)2\hat{C}_z\hat{H}_z} \hat{C}_y \quad (5)$$

Whereas for an even multiplicity (e.g. CH_2) these transformations become

$$\hat{C}_z \xrightarrow{(\pi/2)\hat{C}_x} -\hat{C}_y \xrightarrow{(\pi/2)2\hat{C}_z\hat{H}_z} 2\hat{C}_y\hat{H}_z \xrightarrow{(\pi/2)2\hat{C}_z\hat{H}_z} -\hat{C}_y \quad (6)$$

Notice that in the second case the magnetization passes through a magnetization state represented by the operator $2\hat{C}_y\hat{H}_z$ rather than $2\hat{C}_x\hat{H}_z$. This leads to a pairwise separation of multiplicities. Improved J compensated APT experiments have been proposed, which reduce the problems of cross-talk between the spectra due to the inevitable spread in the values of the coupling constants.[9]

2.2 SEMUT

The major disadvantage with APT is that the spectra are sorted only on the basis of even or odd multiplicity; thus, methine and methyl carbons are indistinguishable. In practice, it is more convenient to produce subspectra containing each multiplicity separately. The SEMUT pulse sequence, which is set out in Figure 2, is superior to APT in these regards.[10]

Let us follow the product operator transformations which take place during SEMUT. They take the following form when

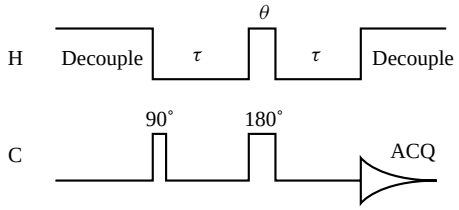

Figure 2 SEMUT pulse sequence; τ is set to $1/(2J)$

the multiplicity (n) is odd (e.g. CH_3 and CH), $\tau = 1/(2J_{CH})$ and the flip angle of the proton pulse is θ:

$$\hat{C}_z \xrightarrow{(\pi/2)\hat{C}_x} -\hat{C}_y \xrightarrow{(\pi/2)2\hat{C}_z\hat{H}_z} 2\hat{C}_x\hat{H}_z \xrightarrow{(\theta/2\pi)\hat{H}_x,(\pi)\hat{C}_x} 2\hat{C}_x\hat{H}_z \cos^n\theta \xrightarrow{(\pi/2)2\hat{C}_z\hat{H}_z} \hat{C}_y \cos^n\theta \quad (7)$$

When n is even, the product operator takes the same form at the end of the sequence, despite the fact that the magnetization passes through a state of $2\hat{C}_y\hat{H}_z$. In both cases, the spectra are edited as a function of $\cos^n\theta$. That is, the flip angle dependence for the individual CH_n intensities, $I(CH_n)$, may be written as

$$I(C) = 1 \quad (8)$$

$$I(CH) = \cos\theta \quad (9)$$

$$I(CH_2) = \cos^2\theta \quad (10)$$

$$I(CH_3) = \cos^3\theta \quad (11)$$

In practice, four different spectra are acquired with different flip angles θ, e.g. $\theta = 0°$, $\theta = 60°$, $\theta = 120°$, and $\theta = 180°$. These are combined in various proportions to produce the final C, CH, CH_2, and CH_3 subspectra. The precision of the editing procedure has been improved in the SEMUT GL sequence[11] by the introduction of a purging sandwich ($90°-\tau/2-180°-\tau/2-90°$). A further modification is that the various delays need not be equal.

2.3 INEPT

The INEPT (see ***INEPT***) was originally designed to improve the sensitivity of proton coupled heteronuclear spectra.[12] However, a modification of INEPT was later shown to be capable of multiplicity selection.[13] The pulse sequence for INEPT is set out in Figure 3. The first pulse, a 90° proton pulse about the $+x$ axis, generates transverse proton magnetization. During the following period $1/4J-180°(H,C)-1/4J$, the heteronuclear coupling (J_{CH}) evolves, while the chemical shifts of both nuclei are refocused. This produces two proton magnetization vectors aligned in opposition along the $\pm x$ axes. If a 90° pulse is applied to the protons about the $+y$ axis, longitudinal two-spin order is created, often represented by proton spin vectors aligned along the $\pm z$ axes. These population disturbances affect the carbon magnetization because

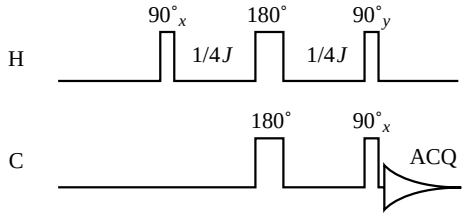

Figure 3 INEPT pulse sequence. To eliminate undesired contributions from the native ^{13}C spin magnetization, the second ^{1}H 90° should be alternately applied along the $+y$ and $-y$ axes, combined with inversion of the receiver reference phase

of their common energy levels and can be studied by a 90° pulse applied to the carbons. This process can be summarized as

$$\hat{H}_z \xrightarrow{(\pi/2)\hat{H}_x} -\hat{H}_y \xrightarrow{(\pi/2)2\hat{H}_z\hat{C}_z} 2\hat{H}_x\hat{C}_z \xrightarrow{(\pi/2)\hat{H}_y} -2\hat{H}_z\hat{C}_z \xrightarrow{(\pi/2)\hat{C}_x} 2\hat{H}_z\hat{C}_y \tag{12}$$

Proton-coupled spectra are obtained, but multiplets do not display the normal intensity distribution, because the magnetization is detected in the form $2\hat{H}_z\hat{C}_y$; thus doublets appear as +1, −1, triplets +1, 0, −1, and quartets +1, +1, −1, −1.

In order to decouple such multiplets, a delay must be added in order to allow the various components of the multiplet to interfere constructively. The length of this delay is related to both J and the multiplicity. At the center of the delay, 180° pulses are applied to both nuclei, to minimize off-resonant effects.[13] This sequence, shown in Figure 4, has been called refocused INEPT. If only a single proton is attached to each carbon then the condition for optimum signal strength is $\tau_2 = 1/4J$. However, when signals with varying multiplicities are present, a compromise value of $\tau_2 = 1/6J$ can be used which treats all multiplicities approximately equally. Alternatively, three separate spectra can be acquired with different values of τ_2, such as $\tau_2 = 1/8J$, $\tau_2 = 1/4J$, and $\tau_2 = 3/8J$, which can be used to disentangle the various multiplicities.

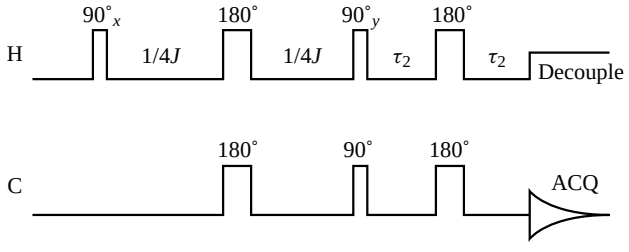

Figure 4 Refocused INEPT pulse sequence; τ_2 varies with the multiplicity of the signal to be decoupled. See text for details

Refocused INEPT has been modified to yield INEPT$^+$.[14] This improvement concerns the addition of a $90°_x$ purging pulse immediately before data acquisition so that multiplets with the normal binomial distribution pattern are obtained if the spectra are not decoupled. The INEPT$^+$ sequence is shown in Figure 5.

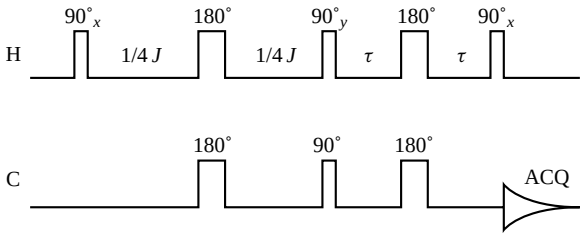

Figure 5 INEPT$^+$ pulse sequence; τ_2 is set as in refocused INEPT

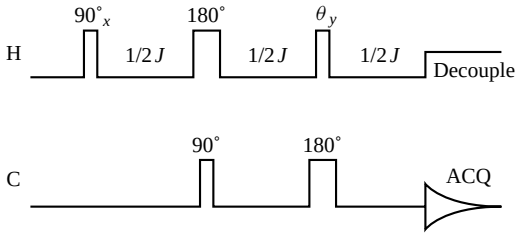

Figure 6 DEPT pulse sequence

2.4 DEPT

The DEPT experiment[15] resembles an early heteronuclear multiple quantum coherence experiment.[16] It has been widely adopted as a method of multiplicity selection because it is much less sensitive to J cross-talk than refocused INEPT. However, as a method of sensitivity enhancement it has the disadvantage that it takes three times longer than the basic INEPT sequence. The pulse sequence is set out in Figure 6.

Let us analyze the DEPT sequence for a CH group. Since the two 180° pulses serve only to refocus the chemical shift, we can ignore them in the following discussion, as well as the evolution of the chemical shift:

$$\hat{H}_z \xrightarrow{(\pi/2)\hat{H}_x} -\hat{H}_y \xrightarrow{(\pi/2)2\hat{H}_z\hat{C}_z} 2\hat{H}_x\hat{C}_z \xrightarrow{(\pi/2)\hat{C}_x} -2\hat{H}_x\hat{C}_y \xrightarrow{(\pi/2)2\hat{H}_z\hat{C}_z} -2\hat{H}_x\hat{C}_y \xrightarrow{(\theta/2\pi)\hat{H}_y} 2\hat{H}_z\hat{C}_y \sin\theta \xrightarrow{(\pi/2)2\hat{H}_z\hat{C}_z} -\hat{C}_x \sin\theta \tag{13}$$

The editing function is, to a first approximation, dependent only upon the flip angle θ, i.e. it does not depend upon J, which accounts for the superiority of DEPT over refocused INEPT as a method of multiplicity determination. Further improvements in spectral editing can be obtained with the DEPT-GL sequence.[11]

In general, multiplicity selection, or spectral editing, can be thought of as a kind of building block, which can be added to other techniques. For example, multiplicity selection has been applied to HMQC,[17] HSQC,[18] and hetero-TOCSY[19] experiments.

3 HETERONUCLEAR CHEMICAL SHIFT CORRELATION

Heteronuclear chemical shift correlation can involve either direct or indirect detection of the heteronucleus. Indirect

detection offers a sensitivity advantage of $\gamma^{3/2}$ compared with direct heteronuclear correlation. This means a sensitivity advantage of a factor of eight per transient in a ^{1}H detected ^{13}C correlation experiment, or 30 for ^{1}H detected ^{15}N correlation. For historical reasons, we start by discussing direct detection.

3.1 2D INEPT and 2D DEPT

It is useful to think of INEPT and DEPT as precursors of 2D heteronuclear chemical shift correlation experiments, despite the fact that this reverses the true chronology. The corresponding 2D experiments are formed by the introduction of an evolution period after the initial 90° pulse. Removing the heteronuclear coupling in F_1 is accomplished by the addition of a 180° pulse on the heteronucleus at the middle of the evolution time. The expansion of INEPT into a 2D experiment is shown in Figure 7.[20,21]

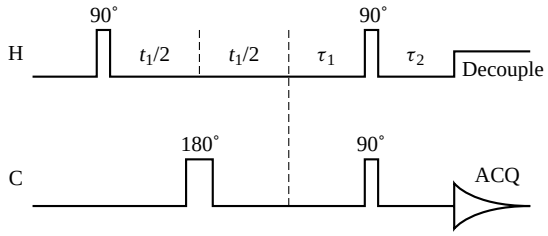

Figure 7 2D INEPT pulse sequence for heteronuclear chemical shift correlation; τ_1 is set to $1/(2J)$ while τ_2 is often set to a compromise value of $1/(3J)$. The spectra are normally displayed in the magnitude mode to avoid the problems of phase correction

Figure 8 shows the corresponding 2D DEPT experiment.[22] The 2D DEPT experiment is fully refocused, and therefore requires less frequency dependent phase correction. It also allows multiplicity determination because the correlations from CH and CH_3 moieties appear with the opposite phase to those from CH_2 moieties. Both these factors mean that 2D DEPT is probably preferable to 2D INEPT for phase sensitive work with small molecules, despite the fact that 2D DEPT is 50% longer.[23]

3.2 COLOC

2D INEPT or 2D DEPT was designed to utilize the large direct (one bond) coupling constant for the heteronuclear coherence transfer. While it is possible to use these sequences

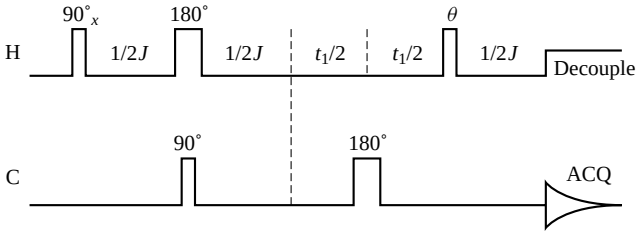

Figure 8 2D DEPT pulse sequence. Phase sensitive displays are often used which enable even/odd multiplicity determination

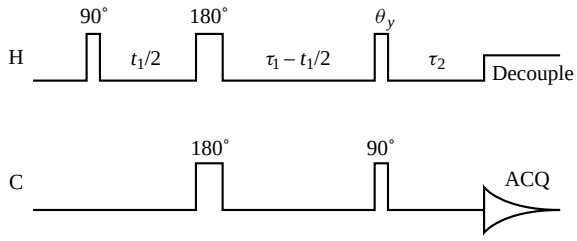

Figure 9 COLOC pulse sequence for heteronuclear chemical shift correlation through multiple bonds

for the study of long-range (multiple bond) heteronuclear correlation, it is preferable to use a sequence designed to incorporate a constant value of the evolution time,[24] because there is considerable loss of magnetization due to proton relaxation during t_1 and the delay τ_1, as well as carbon relaxation during the delay τ_2. In so-called 'constant time' experiments the evolution time is placed inside the τ_1 delay, as shown in Figure 9. This reduces the total time during which proton transverse relaxation takes place. The most popular technique is called COLOC,[25] although a variety of other sequences have been proposed.[26,27]

3.3 Relay

If a homonuclear correlation step is inserted into a heteronuclear correlation experiment we arrive at the sequence shown in Figure 10 which can be described as a proton relayed heteronuclear correlation experiment.[28] Additional signals, so-called 'relayed' peaks, appear in the spectrum which provide indirect information on connectivity of the heteronuclei. The 2D spectrum has the heteronuclear chemical shift on one axis, with signals from the directly bonded protons and protons to which they are coupled, for example their ^{3}J(HCCH) neighbors, along the other axis. Thus, the relay experiment provides complementary data to a long-range heteronuclear correlation experiment.

After proton evolution with heterodecoupling, a homonuclear transfer takes place from one proton to other protons which are spin coupled to it. The evolution of the proton chemical shift is refocused during this transfer by the first proton 180° pulse. It is also desirable to refocus the proton chemical shift during the subsequent heteronuclear transfer. This leads to a sequence with two adjacent 180° proton pulses, as shown in Figure 10. However, this can be simplified because it is

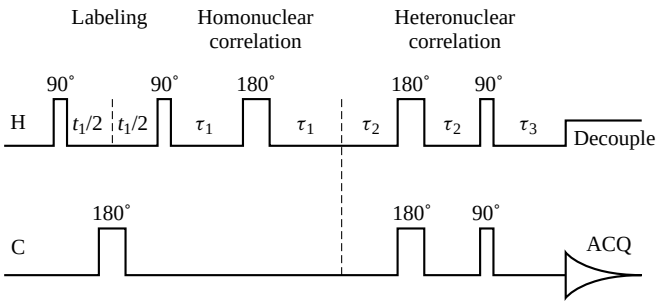

Figure 10 Proton relayed heteronuclear chemical shift correlation sequence

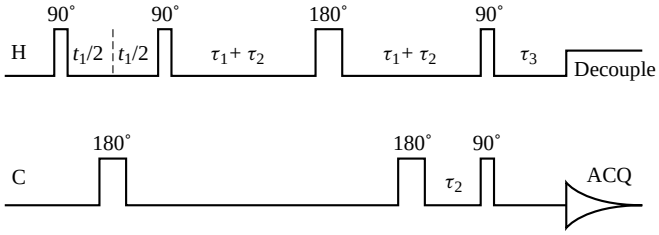

Figure 11 Optimized proton relayed heteronuclear chemical shift correlation sequence

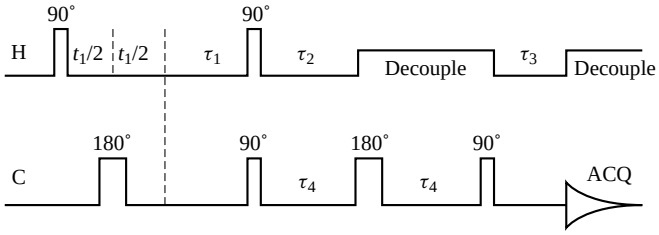

Figure 12 Carbon relayed heteronuclear chemical shift correlation sequence

often possible to concatenate 180° pulses; thus the two adjacent proton 180° pulses can be replaced by a single one in the middle of the delays $2\tau_1$ and $2\tau_2$ without changing the net effect,[29–31] as shown in Figure 11. The reverse experiment is also possible, that is, to relay the magnetization via the heteronucleus, as shown in Figure 12.[32]

3.4 Indirect Detection

Indirect detection has become the standard method of performing heteronuclear correlation. Both single or multiple quantum correlation techniques are in use. The heteronuclear multiple quantum experiments are derivatives of experiments originally proposed by Müller.[16] Most of the heteronuclear single quantum experiments are variations of a double INEPT experiment first proposed by Bodenhausen and Ruben.[33] It can be shown, both theoretically and practically, that experiments involving single quantum correlation have several advantages.[34,35]

3.5 HMQC

Heteronuclear multiple quantum correlation (HMQC) was initially very popular as a method of performing indirect detection experiments.[36] The HMQC pulse sequence is shown in Figure 13. For a heteronuclear H–C system, the experiment can be described as

$$\hat{H}_z \xrightarrow{(\pi/2)\hat{H}_x} -\hat{H}_y \xrightarrow{(\pi/2)2\hat{H}_z\hat{C}_z} -2\hat{H}_x\hat{C}_z \xrightarrow{(\pi/2)\hat{C}_x} -2\hat{H}_x\hat{C}_y$$
$$\xrightarrow{t_1} -2\hat{H}_x\hat{C}_y\cos\Omega_c t_1 \xrightarrow{(\pi/2)\hat{C}_x} -2\hat{H}_x\hat{C}_z\cos\Omega_c t_1 \qquad (14)$$

where Ω_c denotes the angular offset frequency of the carbon spin. The above expression predicts that the detected in-phase ^{1}H signal (H_y) is modulated in amplitude by Ω_c, giving

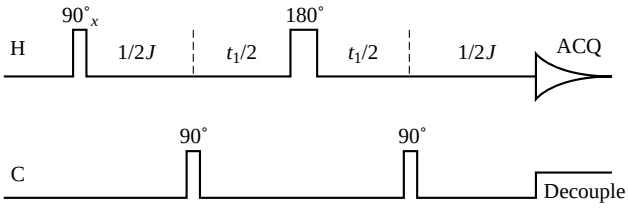

Figure 13 HMQC pulse sequence for ^{1}H detected heteronuclear chemical shift correlation utilizing heteronuclear multiple quantum coherence during the evolution period

rise to a single absorptive correlation in the 2D spectrum. Unfortunately this is not the whole story. Additional protons have an important effect. Consider an I–K–S spin system (where both I, K = ^{1}H, S = ^{13}C or ^{15}N), that is, the effect of a second proton K. The relatively small homonuclear coupling J_{IK} can safely be neglected during the delay τ. However, it cannot be neglected during the evolution time. Consequently the magnetization at the beginning of the detection period can be summarized as

$$-\hat{I}_y\cos\pi J_{IK}t_1\cos\Omega_s t_1 + 2\hat{I}_x\hat{K}_z\sin\pi J_{IK}t_1\cos\Omega_s t_1 \qquad (15)$$

The multiplet pattern resembles that of a 2D J spectrum, in that it is phase modulated in t_1. Thus, it is impossible to obtain pure phases. Another disadvantage of HMQC is that the spectrum will display homonuclear J coupling in the F_1 dimension. There is yet another problem with the resolving power of HMQC, in that the linewidth in the F_1 dimension is determined by the relaxation rate of the multiple quantum coherence $\hat{H}_x\hat{C}_y$. This often leads to broadening, since multiple quanta usually relax faster than single quanta.[34,35]

Quite a few modifications to the basic HMQC sequence have been proposed.[37–40] For example, it is often desirable to perform heteronuclear correlation without presaturation of the water signal. One method of achieving this is to replace the 90° and 180° ^{1}H pulses with jump-and-return pulses as shown in Figure 14.[41]

The suppression of spurious signals which originate from protons not bonded to the heteronucleus can be improved in a variety of ways. The most common of these is to precede HMQC by a so-called BIRD (bilinear rotational decoupling) sequence as shown in Figure 15.[42] The BIRD sequence inverts the z magnetization of protons attached to ^{12}C while leaving the magnetization of the protons attached to ^{13}C unaffected. A relaxation delay is added between the BIRD and the start of the HMQC sequence, in a manner reminiscent of WEFT.[43] The idea is to use differential relaxation as a method of improving the suppression of the unwanted signals from ^{12}C. Since ^{13}C has a spin, protons attached to ^{13}C will relax faster than those attached to ^{12}C. Thus, it may be possible to choose a delay

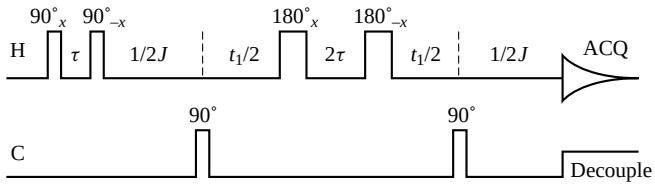

Figure 14 HMQC correlation in H_2O without presaturation

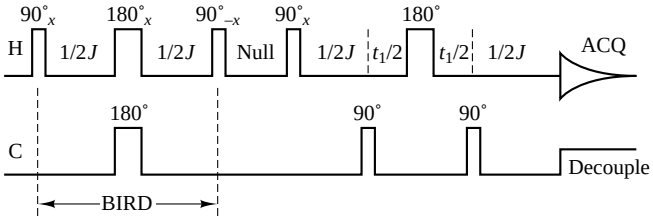

Figure 15 HMQC pulse sequence with BIRD presaturation of protons coupled to ^{12}C

such that the signal from all the protons attached to ^{12}C are approximately nulled, while all the protons attached to ^{13}C have relaxed. However, this method is unattractive for large molecules because they often exhibit a negative NOE, in which case, cross relaxation between the inverted protons attached to ^{12}C and the noninverted protons attached to ^{13}C will decrease the signal intensity.

3.6 Flip-back

An alternative approach, which avoids the problem of sensitivity loss by cross relaxation, is to refocus the magnetization of the protons attached to ^{12}C prior to the evolution period.[16] The in-phase magnetization from the protons attached to ^{12}C can then be flipped back to the $+z$ axis while the heteronuclear antiphase magnetization is unaffected. The sequence is shown in Figure 16. The sequence starts with $90^\circ_x(^1\text{H})-1/(4J)-180^\circ(^1\text{H},^{13}\text{C})-1/(4J)-$, where the simultaneous 180° pulses refocus chemical shift evolution. At the end of this period, all protons coupled to the heteronucleus are antiphase ($\hat{I}_x\hat{S}_z$) with respect to the heteronuclear coupling. Since the proton homonuclear coupling constants J(H, H) are usually much smaller than ^1J(C,H), all protons attached to ^{12}C still have essentially only in-phase magnetization (I_y). This allows a separation of protons attached to ^{12}C and ^{13}C by the action of a $90^\circ_x(^1\text{H})$ pulse at the end of the preparation period. The $90^\circ_x(^1\text{H})$ pulse flips the in-phase ^{1}H magnetization I_y of the protons attached to ^{12}C to the $-z$ axis while the antiphase I_xS_z remains unaffected. However, at the same time the $90^\circ_x(^{13}\text{C})$ converts the antiphase magnetization, I_xS_z, into heteronuclear two-spin coherence I_xS_y, which evolves during t_1. The 180° pulse at the midpoint of the evolution time interchanges the zero and double quantum frequencies. Not only does this eliminate the ^{1}H chemical shift component from the multiple quantum frequency, as in HMQC, but it also it flips the protons attached to ^{12}C back to the $+z$ axis. Cross relaxation then causes the rapid recovery of the longitudinal magnetization of the protons attached to ^{13}C.

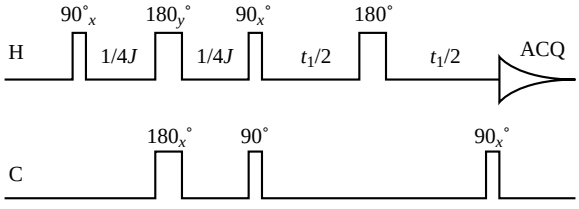

Figure 16 Flip-back chemical shift correlation

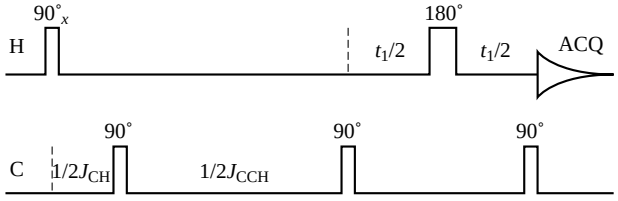

Figure 17 HMBC pulse sequence for ^{1}H detected heteronuclear multiple bond correlation utilizing heteronuclear multiple quantum coherence during the evolution period. The first ^{13}C 90° serves as a low-pass J filter. The spectra are normally displayed in the magnitude mode to avoid the problems of phase correction

Unfortunately, this modification is unsuitable if ^{13}C decoupling is desired during data acquisition, because the ^{1}H chemical shifts are in-phase at the end of the evolution period, whereas the decoupling should be started at a time $1/(2J_{\text{CH}})$ later.

3.7 HMBC

A simple extension of the HMQC experiment can be used to determine long range (two and three bond) correlations. It is convenient to add a low-pass J filter, to suppress the direct one bond correlations.[44] The resulting HMBC sequence is shown in Figure 17.[45]

Many applications of indirect detection focus on nuclei such as ^{13}C and ^{15}N; however, other interesting applications of long-range heteronuclear correlation techniques concern the indirect detection of phosphorus. In these cases, where the T_1 of the heteronucleus is shorter than the T_1 of the protons but its T_2 is longer than that of the protons, a different approach may be preferable.[46]

3.8 HSQC

The heteronuclear single quantum correlation experiment has become increasingly popular in recent years.[33] The pulse sequence is set out in Figure 18. This experiment employs an INEPT sequence[12] to transfer proton z magnetization into antiphase nitrogen magnetization. Proton decoupling during the evolution time is accomplished with a 180° proton pulse at the midpoint of the evolution time. A subsequent reverse INEPT transfer reconverts the transverse ^{13}C magnetization into observable ^{1}H magnetization. This can be summarized as

$$\hat{H}_z \xrightarrow{\text{INEPT}} -2\hat{H}_z\hat{C}_y \xrightarrow{t_1} -2\hat{H}_z\hat{C}_y\cos\Omega_c t_1 \xrightarrow{\text{reverseINEPT}} -\hat{H}_x\cos\Omega_c t_1 \qquad (16)$$

The 2D spectrum displays neither ^{1}H–^{1}H nor ^{1}H–^{13}C spin coupling in the F_1 dimension. However, ^{13}C–^{13}C spin coupling is active in the F_1 dimension, but this will normally only be visible in isotopically enriched samples. The transverse relaxation rate of $\hat{H}_z\hat{C}_y$ corresponds to the sum of the relaxation rate of $\hat{C}_y$, i.e. the reciprocal of the ^{13}C T_2, and the longitudinal relaxation rate of $\hat{H}_z$. This latter contribution is often described as scalar relaxation of the

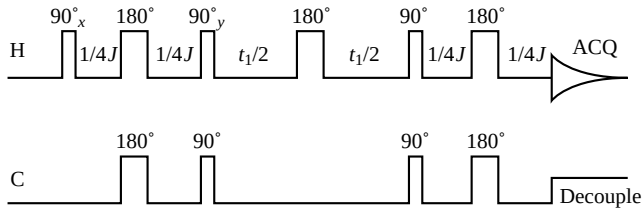

Figure 18 HSQC pulse sequence (sometimes known as the Overbodenhausen correlation experiment) utilizing heteronuclear single quantum coherence during the evolution time, and a 180° ^{1}H pulse to remove the net effect of heteronuclear coupling

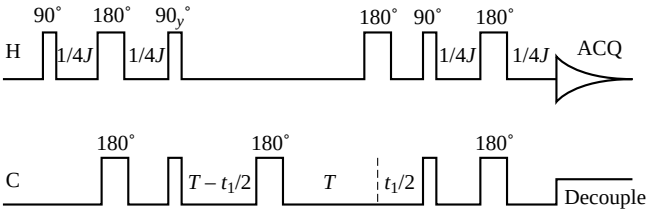

Figure 19 Constant time HSQC pulse sequence for heteronuclear correlation of isotopically enriched species

second kind.[47] Whenever H_z changes its spin state, the ^{13}C doublet component changes its frequency by J(C, H), therefore the F_1 linewidth corresponds to the ^{13}C linewidth in a ^{1}H coupled ^{13}C spectrum.

There are two major modifications to the HSQC experiment. They both pertain to resolution enhancement. Firstly, the constant time HSQC experiment shown in Figure 19 removes the effects of ^{13}C–^{13}C coupling in the F_1 dimension.[48–50] Secondly, much narrower lines can be obtained by decoupling during the evolution time as shown in Figure 20.[35]

3.9 Inverse Relay

Since relay experiments involve a combination of a heteronuclear and a homonuclear correlation step, i.e. a combination of two separate 2D experiments, they are particularly suitable for the application of 3D spectroscopy. In the past, the relay step was performed by pulsed methods; however, it is now more common to use TOCSY for this purpose. We examine two examples here, that of 2D HMQC–TOCSY[51] and 3D TOCSY–HMQC.[52] The 2D HMQC–TOCSY sequence is shown in Figure 21. The sequence combines HMQC and TOCSY in a straightforward manner. At the beginning of the TOCSY mixing step, the ^{1}H magnetization is aligned along the y axis and modulated in

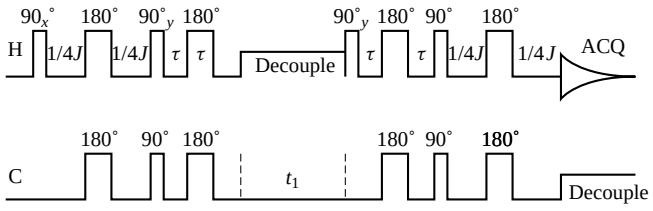

Figure 20 Decoupled HSQC pulse sequence utilizing a composite pulse decoupling scheme preceded by a refocusing interval

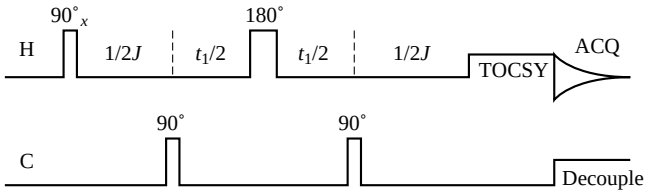

Figure 21 2D HMQC–TOCSY pulse sequence

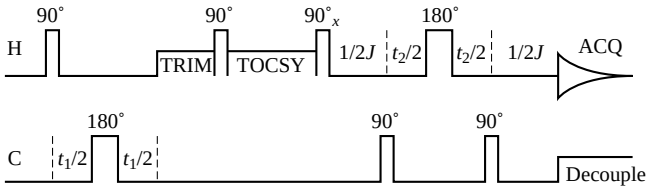

Figure 22 3D TOCSY–HMQC pulse sequence

amplitude by the heteronuclear chemical shift. The TOCSY mixing scheme then redistributes the magnetization of the heteronuclear coupled proton over all its coupling partners. So, in the final 2D spectrum, all coupled protons will be modulated by the frequency of the heteronucleus. A 3D version of the opposite combination is shown in Figure 22.

3D ^{1}H–^{15}N TOCSY–HMQC spectra can be used to identify spin systems in macromolecules, such as proteins.[53] The idea is to correlate the NH ^{1}H and ^{15}N chemical shifts of each amino acid residue with the corresponding C-αH ^{1}H chemical shifts. The first step of this process is to allow the aliphatic ^{1}H chemical shifts to evolve during the period t_1. The magnetization of the aliphatic protons is transferred by TOCSY to the corresponding intraresidue NH protons. Subsequently the NH ^{1}H magnetization is transferred to the directly bonded ^{15}N spins by HMQC. A 3D ^{1}H–^{15}N TOCSY–HMQC spectrum has the appearance of a regular 2D TOCSY spectrum apart from the fact that the signals are spread out over a series of slices edited by the ^{15}N chemical shifts.

3.10 Hetero-TOCSY

Since its first description by Hartmann and Hahn,[54] coherence transfer in the rotating frame has found wide application as a method of improving the repetition rate in solid state experiments. Although the possibility of using heteronuclear cross polarization as a method of chemical shift correlation in liquids was recognized and demonstrated long ago,[55,56] technical problems have prevented its widespread use. The solution to many of these problems has appeared as a byproduct of the interest generated by homonuclear cross polarization, otherwise known as TOCSY.[57]

Cross polarization experiments are normally carried out by applying a 90° pulse to one of the spins, followed by simultaneously spin locking both nuclei. When these spin lock fields are larger than the chemical shift, the Hamiltonian reduces to the spin–spin interaction terms, which are dipolar in origin for solids and scalar for isotropic liquids. Cross polarization occurs when the effective secondary nutation frequency of both rotating frames is the same. This is referred to as the Hartmann–Hahn condition, and has to be matched

better than the interaction frequency between the spins.[58] This is easy in solids where the large dipolar fields constitute the interaction between the spins. However, in isotropic liquids, the interaction is spin–spin coupling, giving rise to the name *J* cross polarization. The one bond coupling between ^{13}C and ^{1}H is about 140 Hz, while rf fields of the order of 10 kHz are necessary to excite the nuclei evenly. Thus, in liquids the rf amplitudes need to be matched to better than 1%, which renders the experiment technically very demanding. However, the simultaneous use of multiple pulse mixing schemes on both channels has alleviated this problem.[59–62]

The advantages of hetero-TOCSY become most apparent when long range correlation experiments are considered; for example, hetero-TOCSY has been shown to be extremely useful for ^{1}H detected ^{31}P correlation spectroscopy of nucleic acids.[63,64]

4 RELATED ARTICLES

Composite Pulses; COSY Two-Dimensional Experiments; Half-Filter Experiments: Proton–Carbon-13; Heteronuclear Shift Correlation Spectroscopy; INADEQUATE Experiment; INEPT; Multidimensional Spectroscopy: Concepts; Multiple Quantum Spectroscopy of Liquid Samples; NOESY; Phase Cycling; Relayed Coherence Transfer Experiments; ROESY; Two-Dimensional J-Resolved Spectroscopy; Water Signal Suppression in NMR of Biomolecules.

5 REFERENCES

1. C. Le Cocq and J.-Y. Lallemand, *J. Chem. Soc., Chem. Commun.*, 1981, 150.
2. D. W. Brown, T. T. Nakashima, and D. L. Rabenstein, *J. Magn. Reson.*, 1981, **45**, 302.
3. S. L. Patt and J. N. Shoolery, *J. Magn. Reson.*, 1982, **46**, 535.
4. F.-K. Pei and R. Freeman, *J. Magn. Reson.*, 1982, **48**, 318.
5. G. Bodenhausen, R. Freeman, and D. L. Turner, *J. Chem. Phys.*, 1976, **65**, 839; G. Bodenhausen, R. Freeman, R. Niedermeyer, and D. L. Turner, *J. Magn. Reson.*, 1977, **26**, 133.
6. C. J. Turner, *Progr. Nucl. Magn. Reson. Spectrosc.*, 1984, **16**, 311.
7. O. W. Sørensen, G. W. Eich, M. H. Levitt, G. Bodenhausen, and R. R. Ernst, *Progr. Nucl. Magn. Reson. Spectrosc.*, 1983, **16**, 163.
8. H. Kessler, M. Gehrke, and C. Griesinger, *Angew. Chem., Int. Ed. Engl.*, 1988, **27**, 490.
9. A. M. Torres, T. T. Nakashima, and R. E. D. McClung, *J. Magn. Reson., Ser. A*, 1993, **101**, 285.
10. H. Bildsoe, S. Donstrup, H. J. Jakobsen, and O. W. Sørensen, *J. Magn. Reson.*, 1983, **53**, 154.
11. O. W. Sørensen, S. Donstrup, H. Bildsoe, and H. J. Jakobsen, *J. Magn. Reson.*, 1983, **55**, 347.
12. G. A. Morris and R. Freeman, *J. Am. Chem. Soc.*, 1979, **101**, 760.
13. D. P. Burum and R. R. Ernst, *J. Magn. Reson.*, 1980, **39**, 163.
14. O. W. Sørensen and R. R. Ernst, *J. Magn. Reson.*, 1983, **51**, 477.
15. D. M. Doddrell, D. T. Pegg, and M. R. Bendall, *J. Magn. Reson.*, 1982, **48**, 323.
16. L. Müller, *J. Am. Chem. Soc.*, 1979, **101**, 4481.
17. L. E. Kay and A. Bax, *J. Magn. Reson.*, 1989, **84**, 598.
18. D. G. Davis, *J. Magn. Reson.*, 1991, **91**, 665.
19. T. Domke and L. McIntyre, *J. Magn. Reson.*, 1992, **96**, 143.
20. R. Freeman and G. A. Morris, *J. Chem. Soc., Chem. Commun.*, 1978, 684.
21. M. W. Edwards and A. Bax, *J. Am. Chem. Soc.*, 1986, **108**, 918.
22. M. R. Bendall and D. T. Pegg, *J. Magn. Reson.*, 1983, **53**, 144.
23. H. Kessler, C. Griesinger, and G. Zimmermann, *Magn. Reson. Chem.*, 1987, **25**, 579.
24. A. Bax and R. Freeman, *J. Magn. Reson.*, 1981, **44**, 542.
25. H. Kessler, C. Griesinger, J. Zarbock, and H. R. Loosli, *J. Magn. Reson.*, 1984, **57**, 331.
26. G. E. Martin and A. S. Zektzer, *Magn. Reson. Chem.*, 1988, **26**, 631.
27. W. F. Reynolds, S. McLean, M. Perpick-Dumont, and R. G. Enriquez, *Magn. Reson. Chem.*, 1989, **27**, 162.
28. P. H. Bolton and G. Bodenhausen, *Chem. Phys. Lett.*, 1982, **89**, 139.
29. A. Bax, *J. Magn. Reson.*, 1983, **53**, 149.
30. P. H. Bolton, *J. Magn. Reson.*, 1983, **54**, 333.
31. H. Kessler, M. Bernd, H. Kogler, J. Zarbock, O. W. Sørensen, G. Bodenhausen, and R. R. Ernst, *J. Am. Chem. Soc.*, 1983, **105**, 6944.
32. H. Kessler, W. Bermel, and C. Griesinger, *J. Magn. Reson.*, 1985, **62**, 573.
33. G. Bodenhausen and D. J. Ruben, *Chem. Phys. Lett.*, 1980, **69**, 185.
34. T. J. Norwood, J. Boyd, J. E. Heritage, N. Soffe, and I. D. Campbell, *J. Magn. Reson.*, 1990, **87**, 488.
35. A. Bax, M. Ikura, L. E. Kay, D. A. Torchia, and R. Tschudin, *J. Magn. Reson.*, 1990, **86**, 304.
36. A. Bax, R. H. Griffey, and B. L. Hawkins, *J. Am. Chem. Soc.*, 1983, **105**, 7188.
37. A. G. Redfield, *Chem. Phys. Lett.*, 1983, **96**, 537.
38. D. Brühwiler and G. Wagner, *J. Magn. Reson.*, 1986, **69**, 546.
39. G. Otting and K. Wüthrich, *J. Magn. Reson.*, 1988, **76**, 569.
40. E. R. P. Zuiderweg, *J. Magn. Reson.*, 1990, **86**, 346.
41. S. Roy, M. Z. Papastavros, V. Sanchez, and A. G. Redfield, *Biochemistry*, 1984, **23**, 4395.
42. A. Bax and S. Subramanian, *J. Magn. Reson.*, 1986, **67**, 565.
43. S. L. Patt and B. D. Sykes, *J. Chem. Phys.*, 1972, **56**, 3182.
44. H. Kogler, O. W. Sørensen, G. Bodenhausen, and R. R. Ernst, *J. Magn. Reson.*, 1983, **55**, 157.
45. A. Bax and M. F. Summers, *J. Am. Chem. Soc.*, 1986, **108**, 2093.
46. V. Sklenar, H. Miyashiro, G. Zon, H. T. Miles, and A. Bax, *FEBS Lett.*, 1986, **208**, 94.
47. A. Abragam, *The Principles of Nuclear Magnetism*, Clarendon Press, Oxford, 1961.
48. J. Santoro and G. C. King, *J. Magn. Reson.*, 1992, **97**, 202.
49. F. J. M. Van de Ven and M. E. P. Philippens, *J. Magn. Reson.*, 1992, **97**, 637.
50. G. W. Vuister and A. Bax, *J. Magn. Reson*, 1992, **98**, 428.
51. L. Lerner and A. Bax, *J. Magn. Reson.*, 1986, **69**, 375.
52. D. Marion, P. C. Driscoll, L. E. Kay, P. T. Wingfield, A. Bax, A. M. Gronenborn, and G. M. Clore, *Biochemistry*, 1989, **28**, 6150.
53. G. M. Clore, A. Bax, P. C. Driscoll, P. T. Wingfield, and A. M. Gronenborn, *Biochemistry*, 1990, **29**, 8172.
54. S. R. Hartmann and E. L. Hahn, *Phys. Rev.*, 1962, **128**, 2042.
55. A. A. Maudsley, L. Müller, and R. R. Ernst, *J. Magn. Reson.*, 1977, **28**, 463.
56. L. Müller and R. R. Ernst, *Mol. Phys.*, 1979, **38**, 963.

57. L. Braunschweiler and R. R. Ernst, *J. Magn. Reson.*, 1983, **53**, 521.
58. G. C. Chingas, A. N. Garroway, R. D. Bertrand, and W. B. Moniz, *J. Chem. Phys.*, 1981, **74**, 127.
59. D. W. Bearden and L. R. Brown, *Chem. Phys. Lett.*, 1989, **163**, 432.
60. E. R. P. Zuiderweg, *J. Magn. Reson.*, 1990, **89**, 533.
61. D. Y. Artemov, *J. Magn. Reson.*, 1991, **91**, 405.
62. G. A. Morris, *Magn. Reson. Chem.*, 1991, **29**, 83.
63. G. W. Kellogg, A. A. Szewczak, and P. B. Moore, *J. Am. Chem. Soc.*, 1992, **114**, 2727.
64. K. Y. Wang, I. Goljer, and P. H. Bolton, *J. Magn. Reson., Ser. B*, 1994, **103**, 192.

Biographical Sketch

Christopher J. Turner. *b* 1945. B.Sc., 1967, Ph.D., 1972, Chemistry, University of London, UK. Postdoctoral work, City of London Polytechnic, 1972–75, Queen Elizabeth College, 1975–77. NMR applications chemist, Varian, 1977–82. Manager of the NMR Facility, Department of Chemistry, Columbia University, New York, 1982–92. NMR spectroscopist, Francis Bitter National Magnet Laboratory, Massachusetts Institute of Technology, 1992–present. Approx. 50 publications. Research specialties: steady state effects in multidimensional data acquisition.

Indirect Coupling: Intermolecular and Solvent Effects

Isao Ando

Tokyo Institute of Technology, Tokyo, Japan

1	Introduction	1
2	The Effect of Nonbonded Interactions on J Couplings	1
3	Effect of Pressure on J Couplings	4
4	Related Articles	4
5	References	4

1 INTRODUCTION

In general, J couplings (spin–spin couplings) are solvent dependent. This arises from subtle electronic changes which occur in the solute molecule as a result of intermolecular solute–solvent interactions. Therefore, a study of medium effects on J couplings is potentially able to provide intimate information on solute–solvent interactions.

Generally, there are a number of nonbonded and bonded solute–solvent interactions that may influence NMR parameters.[1] Clearly, the relative importance of these various interactions needs to be elucidated prior to any detailed investigation. The nonbonded interactions arise from electric field influences. These appear to operate by means of some type of electrostatic interaction between the solute and solvent molecules. Consequently, a model containing an account of the charge distribution in the interacting molecules would appear to be reasonable for the nonbonded interactions. A number of specific solute–solvent bonded interactions may also occur. Examples of these are weak molecular association, hydrogen bonding, ionic interactions and intramolecular change. From a knowledge of the chemistry of the solute and solvent concerned it is often possible to estimate the extent of any bonded interactions present. Such influences should be removed from consideration before turning to the effects of the nonbonded interactions.

A satisfactory model for quantitatively understanding solvent effects will inevitably include a realistic description of the charge distribution of the solute molecule. However, the solvent molecules need not be treated so specifically. The simplest approach is to consider the solvent as a continuum surrounding the solute molecule. Several different models of this type have been proposed to understand nonbonded solute–solvent effects on J coupling. Inevitably, the polarity of the solvent medium enters into their formulation. The main purpose of this section is to provide a substantial elucidation of the nature of solute–solvent interactions in J coupling through theoretical and experimental estimates of J coupling.

2 THE EFFECT OF NONBONDED INTERACTIONS ON J COUPLINGS

The three major contributions to J coupling arise from the contact, orbital, and dipolar interactions.[2] The J coupling involving hydrogen nuclei is predominantly governed by only the contact interaction. However, the J coupling between non-hydrogen nuclei is governed by all three interactions. Within the self-consistent perturbation framework these contributions to J(A,B), the spin–spin coupling interaction between nuclei A and B, are given by equations (1)–(3).

The contact contribution, J_c, can be defined as

$$J_c(\mathrm{A,B}) = (32/9)h\pi\mu_0\mu_B^2\gamma_A\gamma_B S_A^2(0)S_B^2(0)P^{\alpha}_{S_B S_B} \quad (1)$$

where μ_0 is the permeability of a vacuum, μ_B is the Bohr magneton, $[\gamma]$ is the nuclear magnetogyric ratio divided by 2π, $S^2(0)$ is the s electron density at the nucleus concerned and $P^{\alpha}_{S_B S_B}$ refers to a diagonal element of the charge density, bond order matrix for s electron spin orbitals on nucleus B with α spin.

The orbital term, J_O, is given by

$$J_O(\mathrm{A,B}) = (2\mu_0\mu_B^2 h\gamma_A\gamma_B/3\pi)\langle r_A^{-3}\rangle_p\langle r_B^{-3}\rangle_p \times(P_{x_B y_B} + P_{z_B y_B} + P_{x_B z_B}) \quad (2)$$

where $\langle r^{-3}\rangle_p$ refers to the expectation value of the inverse cube of the separation between the nucleus concerned and its p electrons and $P_{x_B y_B}$ is the charge density, bond order matrix element for the p_x and p_y orbitals on atom B.

Finally, the dipolar expression, J_D, is

$$J_D(\mathrm{A,B}) = (\mu_0\mu_B^2 h^3\gamma_A\gamma_B/20\pi^3)\langle r_A^{-3}\rangle_p\langle r_B^{-3}\rangle_p \times(2P^{\alpha\alpha}_{z_B z_B} - P^{\alpha\alpha}_{x_B x_B} - P^{\alpha\alpha}_{y_B y_B} + 3P^{\alpha\beta}_{x_B z_B} - 3Q^{\alpha\beta}_{y_B y_B}) \quad (3)$$

where Q refers to the imaginary part of the charge density, bond order matrix.

As shown by equations (2) and (3), the orbital and dipolar contributions arise for nuclei with p valence electrons whereas equation (1) reveals that the presence of s electrons is necessary for the contact interaction.

In the absence of specific association effects the solvent dependence of coupling interactions is related to the polarity of the medium. This dependence has been studied theoretically by means of the reaction field model, a cubic closest packed cluster model and solvation model (see Section 2.2 below).

2.1 Reaction-Field Type Solvent Effect

This provides the simplest theoretical description of the interactions occurring between polar solute and polar solvent molecules.[3–5] The model treats the solute as a polarizable point dipole centered in a spherical cavity within the dielectric continuum formed by the solvent molecules. It is assumed that the solute point dipole polarizes the surrounding medium, thus creating a reaction field which is parallel to its dipole moment. By taking the direction of the dipole moment vector,

μ, to be from the positive to negative charge on the solute, the reaction field, R, lies in the same direction as μ. The relationship between R and μ is given by equation (4).

$$R = 2\mu(\epsilon - 1)(n^2 - 1)/3\alpha(2\epsilon + n^2) \tag{4}$$

where n is the refractive index of the solute, α is its polarizability, μ refers to the solute point dipole and ϵ is the dielectric constant of the solvent. Linear relationships have been reported between J coupling interactions and the reaction field parameter.

Since ^{1}H and ^{19}F nuclei are often on the surface of the solute molecule they are more directly exposed to solvent molecules than are skeletal nuclei such as ^{13}C, ^{15}N or ^{31}P. Consequently, equation (4) may need to be modified to include local effects due to polar groupings on neighboring solvent molecules when considering J couplings between peripheral nuclei.

In calculations of the effects of the reaction field on J couplings both magnetic and electric reaction fields have been considered. The inclusion of reasonable numbers in the expression obtained in the magnetic field case results in solvent effects of about 1 Hz, which is much smaller than those observed for a number of J couplings. Thus, only electrostatic interactions between the solute and solvent molecules have been extensively considered in the reaction field. A simplified sum-over-states perturbation theory was applied to the study of the electrostatic interaction. In this approach the contact contribution to the J coupling is given by[6]

$$J_c(\mathrm{A,B}) = \pi h \mu_0 \mu_B^2 \gamma_A \gamma_B S_A^2(0) S_B^2(0) \pi_{AB} \tag{5}$$

where the mutual atom–atom polarizability, π_{AB}, is expressed as

$$\pi_{AB} = 4 \sum_{j}^{\mathrm{occ}} \sum_{k}^{\mathrm{unocc}} (\epsilon_j - \epsilon_k)^{-1} C_{j,S_A} C_{k,S_A} C_{j,S_B} C_{k,S_B} \tag{6}$$

where ϵ_j and ϵ_k refer to the energies of the j occupied and k unoccupied molecular orbitals, respectively, and the C terms are the coefficients for the s orbitals on atoms A and B in these molecular orbitals. The value of π_{AB} is related to the empirical resonance and Coulomb integrals. The electric field dependence of π_{AB} is introduced by means of these empirical parameters to obtain an estimate of the solvent dependence of J_c(A,B). However, the formulation employed for the electric field effects on these parameters has been criticized. Additionally, it is claimed that the reported results are fortuitous since the transfer of electron density out of the C–H bonding region is not considered. The inclusion of this electron transfer produces satisfactory agreement between the calculated and observed solvent effects on ^2J(H,H) when Intermediate Neglect of Differential Overlap (INDO) parameters are employed.

More comprehensive calculations of J couplings, within the reaction field framework, have included a term describing the interaction between the solute molecule and neighboring electrostatic fields in the Hamiltonian governing the J coupling interaction. The solvent effects on the J couplings, ΔJ(A,B), are calculated from[7]

$$\Delta J(\mathrm{A,B}) = 10^{-5}(|R| - |R_0|)[\Delta J(\mathrm{A,B})_E] \tag{7}$$

where $|R|$ and $|R_0|$ are the magnitudes of the reaction field, given by equation (4), in the solvent of interest and in cyclohexane, respectively. ΔJ(A,B) is the difference in the J coupling constant calculated for the isolated molecule, ϵ = 1, and that due to the addition of an electric field of 10^5 esu cm^{-2}. The use of equation (8) is apparently justified by the linearity of changes in the calculated J coupling constants as a function of the reaction field for values of the latter as large as 3×10^5 esu cm^{-2}. The calculation explains well the experimental data.

2.2 Solvation Type Solvent Effect

Some attempts to perform direct quantum chemical calculations on a solvated molecule have been reported.[8] Treatments of solvent effects on nuclear shielding[9,10] and the J coupling constant[11–14] by means of the solvaton theory in conjunction with MO methods have been published. This procedure has been used to compute the wavefunctions of molecules under the influence of the solvent considered as a perturbation.

According to the solvaton model, it is assumed that the solvent molecule induces a number of charges, the solvatons, in a solvent of dielectric constant ϵ: one solvaton is associated with each atom of the solute, and its charge is equal in magnitude but opposite in sign to the net charge of the atom to which it is attached. There are no interactions between the solvatons. On the basis of this model, the Hamiltonian, $\hat{\mathcal{H}}$, of a particular molecule with M electrons and N nuclei consists of the inherent term, $\hat{\mathcal{H}}_{\mathrm{inh}}$, and the solute–solvent interaction term, $\hat{\mathcal{H}}_{\mathrm{solv}}$, and is given, in atomic units, by equations (8)–(10).[9]

$$\hat{\mathcal{H}} = \hat{\mathcal{H}}_{\mathrm{inh}} + \hat{\mathcal{H}}_{\mathrm{solv}} \tag{8}$$

$$\hat{\mathcal{H}}_{\mathrm{inh}} = \sum_{i=1}^{M} \left(-\nabla_i^2 - \sum_{n=1}^{N} \frac{Z_n}{r_{ni}} \right) + \frac{1}{2} \sum_{i}^{M} \sum_{j}^{M} \frac{1}{r_{ij}} + \frac{1}{2} \sum_{k}^{N} \sum_{l}^{N} \frac{Z_k Z_l}{r_{kl}} \tag{9}$$

$$\hat{\mathcal{H}}_{\mathrm{solv}} = \frac{\epsilon - 1}{2\epsilon} \left(\sum_{i}^{M} \sum_{s}^{N} \frac{Q_s}{r_{si}} - \sum_{r}^{M} \sum_{k}^{N} \frac{Q_s Z_k}{r_{sk}} \right) \tag{10}$$

where Q_s is the induced solvaton charge, r_{si} and r_{sk} are the solvaton–electron and solvaton–nucleus separations, respectively, and Z is the nuclear charge. The Born equation is used to approximate the solvent–solute interactions. If the atomic orbitals (AOs) and solvaton are associated with the same center, the solvaton–electron distance, r_{si}, is approximated by the van der Waals radius of the particular type of atom. If the AOs and solvaton are associated with different atomic centers, the solvaton is assumed to be centered on the atom associated with it and then r_{si} is evaluated accordingly.

This model has been employed within the Finite Perturbation Theory (FPT) formalism, in an attempt to understand the effects of solvents on ^1J(C,H), ^3J(H,H) and ^3J(C,H) couplings. The approach adopted considered only the contact interaction and the spin-unrestricted self-consistent field

equations of the Fock matrices, $F_{\mu\nu}{}^{\alpha}$ and $F_{\mu\nu}{}^{\beta}$, for α and β electron spins become[10]

$$F^{\alpha}_{\mu\nu} = H^{\text{core}}_{\mu\nu} + \sum_{\lambda\sigma}[P_{\lambda\sigma}(\mu\nu \mid \lambda\sigma) - P^{\alpha}_{\lambda\sigma}(\mu\sigma \mid \lambda\sigma)] + \frac{\epsilon - 1}{\epsilon} \times \int \phi_{\mu}\left(\sum_{s}^{N} \frac{Q^{\alpha}_{s}}{r_{sl}}\right)\phi_{\nu}\,\mathrm{d}\tau + \tfrac{8}{3}\pi\beta_{\mu}\int \phi_{\mu}\delta(r_{\mathrm{B}})\phi_{\nu}\,\mathrm{d}r \quad (11)$$

$$F^{\beta}_{\mu\nu} = H^{\text{core}}_{\mu\nu} + \sum_{\lambda\sigma}[P_{\lambda\sigma}(\mu\nu \mid \lambda\sigma) - P^{\beta}_{\lambda\sigma}(\mu\sigma \mid \lambda\nu)] - \frac{\epsilon - 1}{\epsilon} \times \int \phi_{\mu}\left(\sum_{s}^{N} \frac{Q^{\beta}_{s}}{r_{sl}}\right)\phi_{\nu}\,\mathrm{d}\tau - \tfrac{8}{3}\pi\beta_{\mu}\int \phi_{\mu}\delta(r_{\mathrm{B}})\phi_{\nu}\,\mathrm{d}r \quad (12)$$

where the fourth terms in equations (11) and (12) represent the contact interaction and $\delta(r_{\mathrm{B}})$ is the Dirac delta function which describes the contact between electrons and nucleus B; the other symbols have their usual meaning. The charges $Q_s{}^{\alpha}$ and $Q_s{}^{\beta}$ for the α and β spins, respectively, on the solvaton are assumed to be equal in magnitude but opposite in sign to those on the atom to which it is attached. The J coupling is calculated by means of the FPT method incorporating the Fock matrices given by equations (11) and (12).

The effects of solvents on the directly bonded ^{13}C–H couplings of acrylonitrile, dichloromethane, chloroform, difluoromethane and trifluoromethane have been estimated by this procedure. The tendency for the calculated values to increase with increasing ϵ agrees qualitatively with the observed tendency, except in the case of ^{1}J(C-1,H–B) + ^{1}J(C-1,H–C) for acrylonitrile.[11,12]

The values of ^{1}J(C,H) produced by the solvaton model can be fit approximately by equation (13).

$$^{1}J(\mathrm{C,H}) = a(\epsilon - 1)/\epsilon + b((\epsilon - 1)/\epsilon)^2 + c \quad (13)$$

The observed values of ^{1}J(C,H) fall approximately on a straight line when plotted against $(\epsilon - 1)/\epsilon$. Consequently the second term in equation (13) can be neglected. By plotting ^{1}J(C,H) against $(\epsilon - 1)/\epsilon$, the values of a and c are obtained: in acetonitrile the ^{1}J(C-2,H–A) data give a = 3.9 Hz and c = 176.1 Hz; in dichloromethane a = 28.0 Hz and C = 153.0 Hz; in chloroform a = 36.0 Hz and c = 182.0 Hz; in difluoromethane a = 7.7 Hz and c = 178.0 Hz; in trifluoromethane a = 22.5 Hz and c = 225.0 Hz.[11,12] By comparing various substituted methanes the values of a are found to be larger for chlorine-substituted than fluorine-substituted molecules, and those for trisubstituted methanes are larger than for disubstituted methanes. The magnitude of a provides a measure of the solvent effect on ^{1}J(C,H); thus an increase in the number of halogen-substituted atoms in methane leads to an increase in the solvent effect. In general, it seems that the solvaton model is able to reproduce the gross experimental trends of the effects of solvation on the J couplings considered.

2.3 Solvent Effects on the J Couplings of Flexible Molecules

The molecules mentioned above are considered to be rigid. However, there is another category of solvent effects of J couplings, namely, those on the coupling constants of molecules that can adopt two or more conformations. For these molecules, the observed J coupling $\langle J\rangle_{\mathrm{obs}}$ is given by

$$\langle J\rangle_{\mathrm{obs}} = \sum_{i} X_i J_i \quad (14)$$

where X_i and J_i are the molar fraction and J coupling, respectively, of conformer i. It is shown that the solvent-induced changes of ^{1}J(C,H) are very large when compared with temperature-induced changes and the greater change is proof of the larger contribution of the solvent-induced electronic changes in the solute molecules to the solvent effects of ^{1}J(C,H) than of the contribution arising from changes in the relative populations of the conformers.

Since Karplus's prediction of a strong conformational dependence of vicinal proton–proton J couplings of ethane derivatives, peptide systems and various other molecules have received the attention of many investigators. They have considered the dihedral angle, ϕ, dependence of vicinal J couplings in an isolated molecule in a similar manner to that given by the Karplus relationship.[15]

$$^{3}J(\mathrm{H,H}) = A + B\cos\phi + C\cos 2\phi \quad (15)$$

where A, B and C are coefficients to be determined for the system under consideration. In order to provide a more exact insight into the relationship between the magnitude of the vicinal coupling and the conformation, solvent effects must be taken into account. Ando and co-workers have provided a theoretical prediction of solvent effects on vicinal proton–proton and proton–carbon J couplings.[12,16–18]

The values of the coefficients A, B and C for ethane, $CHCl_2CHCl_2$ and *trans*-*N*-methylformamide, have been calculated as a function of ϵ by means of the FPT-INDO and FPT-Complete Neglect of Differential Overlap/2 approximations within the solvaton model.[12] For the H–C–N–H J couplings the values of the coefficients are smaller than those appropriate to the H–C–C–H and H–C–N–H couplings. The value of B in the former is somewhat larger than in the latter case. The calculated absolute values of the coefficients A, B and C show an increase with increasing ϵ except for the case of the coefficient C for ^{3}J(C,H) in *trans*-*N*-methylformamide obtained from INDO calculations. The values of A, B and C show the following dependence on ϵ:

$$A, B \text{ or } C = a'(\epsilon - 1)/\epsilon + b' \quad (16)$$

where a' is a measure of the strength of the dielectric solvent effect on the A, B and C coefficients and b' is the value of A, B or C at ϵ = 1. From these results, the calculated solvent dependence may be represented by

$$J = b(\epsilon - 1)/\epsilon + c \quad (17)$$

where b is a measure of the strength of the dielectric solvent effect on the vicinal J coupling constants, and c represents the

J coupling values of the *trans* and *gauche* conformers for an isolated molecule (at $\epsilon = 1$).

An oriented clustering of the polar solvent molecules around the polar solute molecule is assumed for solvent effects of J couplings.[19] The solute molecule has its dipole moment parallel to the z axis and the directions of the solvent dipoles are as indicated. Such a model may be reasonably expected to be more satisfactory than the simple reaction field model for peripheral solute nuclei which are more exposed to the influences of individual solvent molecules. In this approach the solvent and solute molecules are recognized as belonging to distinct groups with the assumption of strong orthogonality between them. The interactions between these groups are described by including attraction terms between the electrons of the solute and the nuclei of the solvents as well as intermolecular Coulomb repulsion integrals in the Hamiltonian accounting for the spin−spin interaction. In comparison with the reaction field results, it is noteworthy that those presented for formaldehyde show the correct sign and magnitude for the solvent effect on ^2J(H,H) in acetonitrile as solvent.

3 EFFECT OF PRESSURE ON J COUPLINGS

The application of pressure to pure liquids and solutions leads to a decrease of intermolecular distance.[20] Such an intermolecular change is reflected in a variation of the electronic distribution within a given molecule. This will, inevitably, be revealed by changes in the J coupling.

The pressure dependence of the directly bonded ^{13}C−H couplings for the methyl groups of ^{13}C-enriched acetaldehyde and methanol have been reported.[21,22] The value of ^1J(C,H) is found to increase linearly with increasing pressure. The experimental data have been clarified by the solvaton theory. As mentioned above, an increase in pressure usually results in a decrease in intermolecular distance and in an increase in the value of the dielectric constant for acetaldehyde and methanol. Thus, the pressure dependence of ^1J(C,H) contains the pressure effect on the intermolecular distance and on the dielectric constant. The solvaton−nucleus distance r_{sk} in equation (10) corresponds to the intermolecular distance. In the calculation, it is assumed that a variation in r_{sk} mimics the effect of changing the external pressure of the experimental system. Calculations containing such an interaction show that the pressure dependence of the J coupling arises predominantly from a change in the intermolecular distances, and is not due to the simultaneous change in the dielectric constant.

4 RELATED ARTICLES

Coupling Through Space in Organic Chemistry; Dipolar and Indirect Coupling Tensors in Solids; Indirect Coupling: Semiempirical Calculations; Indirect Coupling: Theory and Applications in Organic Chemistry.

5 REFERENCES

1. I. Ando and G. A. Webb, *Org. Magn. Reson.*, 1981, **15**, 111.
2. I. Ando and G. A. Webb, *Theory of NMR Parameters*, Academic Press, New York, 1983.
3. L. Onsager, *J. Am. Chem. Soc.*, 1936, **58**, 1486.
4. A. D. Buckingham, *Can. J. Chem.*, 1960, **38**, 300.
5. W. T. Raynes, *Mol. Phys.*, 1968, **15**, 435.
6. J. A. Pople and D. P. Santry, *Mol. Phys.*, 1964, **8**, 1.
7. M. D. Johnston and M. Barfield, *J. Chem. Phys.*, 1971, **54**, 3083.
8. G. Klopman, *Chem. Phys. Lett.*, 1967, **1**, 200.
9. I. Ando, A. Nishioka, and M. Kondo, *J. Magn. Reson.*, 1976, **21**, 429.
10. I. Ando, Y. Kato, M. Kondo, and A. Nishioka, *Makromol. Chem.*, 1977, **178**, 803.
11. M. Kondo, S. Watanabe, and I. Ando, *Mol. Phys.* 1979, **37**, 1521.
12. S. Watanabe and I. Ando, *Bull. Chem. Soc. Jpn.*, 1980, **53**, 1257.
13. K. A. K. Eraheem, S. N. Shargi, and S. A. Kadnm, *Monatsh. Chem.*, 1989, **120**, 923.
14. H. Fukui (G. A. Webb (ed.)), *Nucl. Magn. Reson.*, 1992, **21**, 106.
15. M. Karplus, *J. Chem. Phys.*, 1959, **30**, 11.
16. I. Ando, T. Asakura, and S. Watanabe, *J. Mol. Struct. (Theochem)*, 1981, **76**, 93.
17. S. Watanabe and I. Ando, *J. Mol. Struct.*, 1982, **84**, 77.
18. S. Watanabe and I. Ando, *J. Mol. Struct.*, 1983, **104**, 155.
19. M. D. Johnston and M. Barfield, *J. Chem. Phys.*, 1971, **55**, 3483.
20. I. Ando and G. A. Webb, *Magn. Reson. Chem.*, 1986, **24**, 557.
21. I. Ando, Y. Inoue, S. Watanabe, Y. Sakamoto, and G. A. Webb, *J. Mol. Liq.*, 1984, **27**, 179.
22. I. Ando, T. Sanefuji, T. Yamanobe, S. Watanabe, and G. A. Webb, *J. Mol. Liq.*, 1985, **31**, 31.

Biographical Sketch

Isao Ando. *b* 1941. Ph.D., 1972, (supervisor Atsuo Nishioka), Polymer Chemistry, Tokyo Institute of Technology. Postdoctoral work at University of Illinois, Urbana (with Herb Gutowsky). Successively research associate, Associate Professor and Professor, Tokyo Institute of Technology. Approx. 250 publications. Research specialties: structures and electronic states of solid polymers and biopolymers, solid state NMR and nuclear shielding.

Lanthanide Induced Shifts (LIS) in Structural and Conformational Analysis

Raymond J. Abraham

The University of Liverpool, Liverpool, UK

&

Fernando Sancassan

Università di Genova, Genova, Italy

1	Introduction	1
2	Theory	2
3	LIS in Structural and Conformational Analysis	3
4	Applications of the LIS Method	5
5	References	10

1 INTRODUCTION

In 1969 Hinckley[1] showed that the addition of a tris (dipivaloylmethanato) europium complex containing two molecules of pyridine [Eu $(dpm)_3$. $(pyr)_2$] could be used to produce selective shifts in the ^1H spectrum of cholesterol in chloroform without excessive line broadening. Sanders and Williams[2] then showed that the pyridine adducts were not necessary and that the Eu $(dpm)_3$ complex gave similar effects. These pioneering studies initiated the field of lanthanide induced shifts (LIS), the subject of this review and produced an explosion of investigations in this area including a book[3] and a number of reviews.[4] Since then a number of lanthanide complexes have been developed as LIS reagents. The two common reagents used are the dpm and the heptafluoro-dimethyloctanedionato (fod) complexes

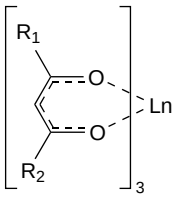

$M(dpm)_3$: $R_1 = R_2 =$ t-Bu

$M(fod)_3$: $R_1 =$ t-Bu, $R_2 = n\text{-}C_3F_7$

and a number of lanthanide atoms (Eu, Yb, Pr etc.) may be used. These reagents are soluble in $CDCl_3$ and complex with most Lewis bases in inert organic solvents. A combination of the shift reagent with Ag $(fod)_3$ can be used as a shift reagent for aromatic compounds and other weak Lewis bases.[3] Chiral shift reagents have been prepared and extensively used to determine the proportions of enantiomers.[3]

The reagent is added directly to the solution being observed and the resulting changes in the observed chemical shifts are termed LIS. The europium and ytterbium complexes give mainly lowfield (increased frequency) shifts whilst the praseodynium complexes give upfield (low frequency) shifts. Figure 1 shows the ^1H spectrum of n-hexanol in $CDCl_3$ solution and the spectra observed with the addition of Eu $(fod)_3$ and Pr$(fod)_3$. The increased dispersion of spectra resulting in the resolution of all the separate ^1H signals is dramatic. Note the tert-butyl proton signal of the shift reagents at ca. 0.42 δ for Eu$(fod)_3$ and 1.28 for Pr$(fod)_3$.

The lanthanide series of metals are unusual in their chemical behaviour in that they are able to bind with a variety of ligands and adopt a large range of coordination numbers, LnX to LnX_{12} due to the presence of large and diffuse $4f$ orbitals. As a direct result of this, a stable lanthanide complex may expand its coordination number by binding to additional ligands – these additional ligands being the functional groups in the Lewis-base substrates.

The shift reagents of Figure 1 complex reversibly with the n-hexanol substrate. On the simplest model of a 1:1 complex we may write

$$L + S = LS, \quad K = \frac{[LS]}{[L][S]} \tag{1}$$

where S is substrate and L the lanthanide reagent. The equilibrium is fast on the NMR time scale thus a time-averaged spectrum is observed in which the alcohol chemical shifts are the weighted average of the shifts of the free substrate and the lanthanide complex. As increasing amounts of shift reagent are added the equilibrium of equation (1) is shifted to the right and the substrate chemical shifts for small ratios of shift reagent to substrate (ρ) are directly proportional to the molar ratios of shift reagent and substrate. As more shift reagent is added equation (1) predicts a limiting value in which the substrate shift is independent of the added reagent (Figure 2).

The initial slope of this plot is defined as ΔM (see equation (2)). This corresponds to the shift of a given nucleus for a 1 : 1 mole ratio of the substrate to shift reagent.

$$\Delta M = \delta(LS) - \delta(S) \tag{2}$$

A more sophisticated analysis including LS_2 complexes has been given by Reubens[4a] and a critique of these methods by Raber.[4c,6] However the determination of the exact coordination of the LS complex is not a prerequisite for the use of LIS in structural analysis.

The ability of many functional groups to coordinate with these shift reagents makes them of considerable use in NMR spectroscopy. The strength of the interaction depends on the ability of the substrate to act as a Lewis base and Table 1 shows typical relative ΔM values for the methylene protons of some common functional groups using Eu $(fod)_3$.

Although LIS have been used extensively to simplify complex ^1H and ^{13}C spectra, we shall restrict this review to the quantitative application of LIS in determining solute structures and conformations.

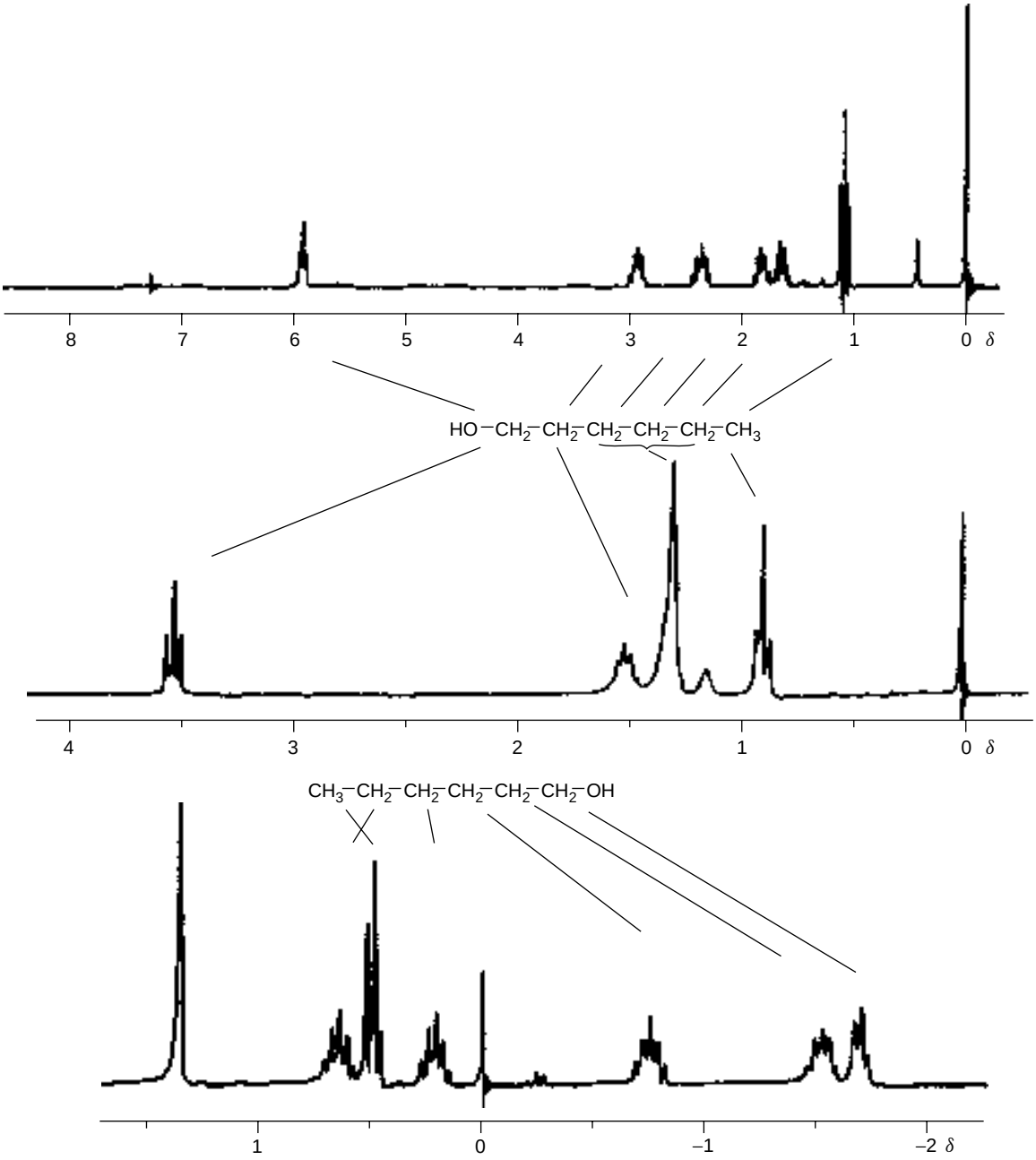

Figure 1 The 220 MHz ^{1}H Spectrum of 25 ml (0.2×10^{-3} M) of n-hexanol in 0.5 ml $CDCl_3$ (middle) and on the addition of 14 mg (1.3×10^{-5} M) of Eu(fod)$_3$ (upper) and 30 mg (2.9×10^{-5} M) of Pr(fod)$_3$ (lower). (from Ref.[5])

2 THEORY

The experimental LIS on the ith nucleus (ΔM_i) is made up of three individual components. These are the Fermi-contact shift (ΔM_i^C), the pseudo-contact shift (ΔM_i^{PC}) and the complexation (or diamagnetic) shift (ΔD_i):

$$\Delta M_i = \Delta M_i^C + \Delta M_i^{PC} + \Delta D_i \quad (3)$$

2.1 Contact Shift

The contact shift arises from the delocalization of the unpaired electron on the shift reagent to the substrate atoms. The magnitude of this shift is therefore directly proportional to the value of the unpaired electron spin density at the nucleus concerned and it will be very different for different nuclei. It is roughly proportional to the isotropic coupling constant between the atomic nucleus considered and an unpaired electron in an s-orbital and on this basis the relative values of the contact term for ^{1}H, ^{13}C, ^{19}F and ^{31}P were estimated as 1.00, 8.76, 35.90 and 17.84.[4] Although the electron delocalization can occur via both single and double bonds, in saturated systems only nuclei one or two bonds from the shift reagent appear to be affected. In contrast in conjugated and aromatic systems extensive delocalization can occur giving extensive contact shifts.

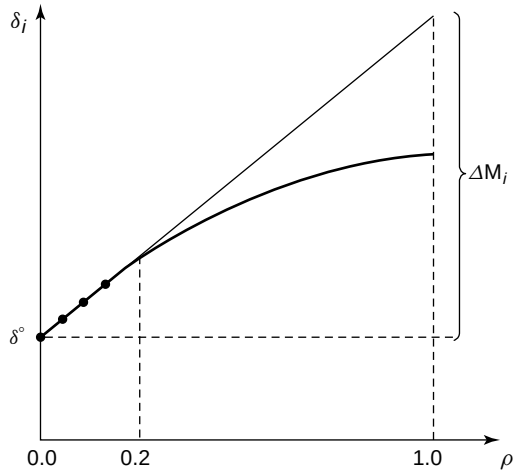

Figure 2 Graphical Illustration of δ vs ρ plot

Table 1 LIS, ΔM (Eu) values for R.CH_2X Protons (from Ref.[5])

X	NH_2	OH	CO.R	CHO	OCH_2R	CO_2Me	CN	NO_2
ΔM(Eu)	35	25	15	11	10	7	5	<1

2.2 Pseudo-contact Shift

This is also known as the dipolar term and is due to the direct magnetic field of the unpaired electrons on the shift reagent at the substrate nuclei. A number of equations of varying complexity were proposed to account for this effect.[4a,d] If the paramagnetism of the lanthanide atom is treated as a point dipole with an axially symmetric magnetic field centred along the Ln-Substrate bond, then the pseudo-contact shift at the i-th nucleus of the substrate is given by equation (4),

$$\Delta M_i^{PC} = \frac{\mu(3\cos^2\theta_i - 1)}{r_i^3} \qquad (4)$$

where μ is the paramagnetic moment of the lanthanide, r_i the distance of the i-th nucleus from the lanthanide and θ_i the angle between the Ln-Substrate bond and r_i (Figure 3).

Note that the magnetic field produced at nucleus M by the lanthanide atom is independent of the nature of M. Thus if the M nucleus were ^1H or ^{13}C the same shift would be obtained. This means that the same equation may be used to calculate the pseudo-contact shifts of all the nuclei in the substrate molecule.

2.3 Complexation Shift

The third component of the observed Lanthanide Induced Shift is the complexation shift[4d] which is due to the actual formation of the lanthanide-substrate complex. The chemical shifts of the substrate nuclei in the complex may differ from those of the free substrate. The complexation shift (ΔD) may be obtained by observing the LIS shifts of a similar lanthanide complex in which the lanthanide atom is a diamagnetic lanthanide. The diamagnetic complexes of lanthanum or lutetium, $La(fod)_3$ and $Lu(fod)_3$ are commonly used.

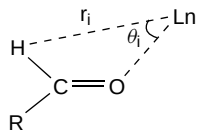

Figure 3 Geometric parameters for pseudo-contact shifts in a Ln-alcohol complex

3 LIS IN STRUCTURAL AND CONFORMATIONAL ANALYSIS

Indeed it was claimed by some investigators that LIS could be used in a similar manner to X-ray crystallography to determine molecular structures in solution. This belief was somewhat optimistic in that the LIS experiment gives only one measured quantity for each NMR active nucleus in the molecule, whereas three measurements for each atom are necessary to fully define the molecular geometry. However important information can be obtained from this technique as will be shown later. The importance of these shift reagents lies not only in their ability to resolve complex spectra but also in the possibility of using the geometrically dependent pseudo contact term of equation (4) in reverse to obtain from the LIS the geometry of the substrate molecule.

In any determination of the substrate structure it is the pseudo-contact term which is required, thus the other terms need to be either deduced or removed. The problem of separating these contributions is that sufficient experimental data is required to determine the molecular parameters of the complex before the dipolar term can be calculated. Three parameters are required to determine the coordinates of the lanthanum atom with respect to the substrate molecule. Also the effective magnetic moment of the complex [μ of equation (3)] needs to be known. Thus *four* ΔM values are required merely to define the lanthanide position and magnetic moment even when there is no contact contribution. Thus in order to determine the presence or absence of the contact contribution, the substrate should be a rigid molecule and the number of ΔM values determined must greatly exceed *four*.

In aromatic compounds such as quinoline significant contact shifts would be expected. Chalmers et al.[8] determined the contact shifts in this molecule by measuring the LIS using different lanthanide shift reagents. The relative dipolar shifts will only be a function of the geometry of the complex and therefore will be constant for the different shift reagents. In this way they determined the contact and pseudo-contact shifts at every atom in the molecule. These are given for Eu $(dpm)_3$ in Table 2.

Table 2 Contact (c) and Dipolar (d) Contributions to the ΔEu Shifts for Quinoline-Eu $(dpm)_3$ (from Ref.[8])

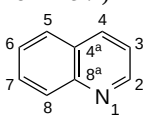

Atom	2	3	4	5	6	7	8	8a	4a
^{13}C (c)	39.8	−17.6	1.4	−4.0	−1.7	4.4	15.9	0.8	−23.5
(d)	44.7	21.6	17.4	11.9	9.1	11.0	30.6	43.4	21.4
1H (c)	−13.3	−6.4	−3.8	−3.0	0.0	1.6	−8.3		
(d)	36.9	13.6	11.0	8.3	5.3	3.9	34.8		

It can be seen that the contact shifts are significant at almost every atom in the molecule and in some cases comparable to the dipolar shifts. Thus this technique with these shift reagents could not be used to determine geometries and structures of quinoline and similar compounds.

In saturated compounds and aromatic compounds in which the complexing group is not part of the aromatic system the contact term would be expected to be less significant. An example of a systematic study of a saturated system is that by Hawkes et al.[9] They determined the ΔM values of all the ^{1}H and ^{13}C atoms in *exo*-norbornylamine and showed using the dipole equation (3) that the contact shifts of Eu(fod)$_3$ and Pr(fod)$_3$ at all these atoms were negligible except for C_1, C_2 and the NH protons. Later Abraham et al. in a series of investigations[7,10–16] demonstrated that the contact shifts for Yb(fod)$_3$ for all the ^{1}H and ^{13}C nuclei of a range of substrates including aldehydes, ketones, esters,[10] epoxides,[11] sulfoxides[12] and sulphones[13] could be ignored. These and similar investigations showed that the LIS can be used in a quantitative manner to determine molecular structures and conformations in solution provided certain conditions are met.

It is useful to summarise here the basic procedure involved in obtaining conformational information by the LIS method and the underlying assumptions made before detailing the applications of this method. This is taken from the procedure of Abraham et al.[10] which is typical of this approach.

3.1 Procedure and Assumptions

The procedure adopted and the corresponding assumptions are as follows.

1. A plot of δ (substrate) vs ρ the [L]/[S] ratio (Figure 2) is obtained. The limiting slope at $\rho > 0$ gives the ΔM values.
   (a) If the δ vs ρ plot is accurately linear one lanthanide complex is predominant and the *relative* complexation shifts will be exactly proportional to the *actual* complexation shifts.
2. Yb(fod)$_3$ is used to minimise the contact shifts.
   (a) Assumes the contact shifts are negligible for the ^{1}H and ^{13}C atoms of aliphatic and non-conjugated aromatic compounds.
3. La(fod)$_3$ or preferably Lu(fod)$_3$ is used to obtain the diamagnetic shifts (ΔD).
   (a) The pseudo-contact term $= \Delta M - \Delta D$.
4. Simultaneously determine ^{1}H and ^{13}C ΔM values.
   (a) Provides maximum degree of over-determination in the deduction of *both* the lanthanide position *and* the substrate molecular geometry.
5. Calculate ΔM for each nucleus using the dipolar equation (equation (3)).
   (a) Assumes effective axial symmetry along the Ln-substrate coordinating bond.
6. Compare the calculated and observed ΔM values by means of the crystallographic agreement factor Rx,

$$Rx = \left[\frac{\sum_i (\Delta M_{i,obs} - f\Delta M_{i,calc})^2}{\sum_i (\Delta M_{i,obs})^2} \right]^{0.5} \quad (5)$$

$$f = \frac{\sum_i \Delta M_{i,obs} \times \Delta M_{i,calc}}{\sum_i (\Delta M_{i,calc})^2}$$

   where f is the normalization factor.
   (a) This removes the use of any normalizing atom. The function f is defined as that function which gives the best agreement factor for each calculation.
7. Scan the Yb ion position over the atomic coordinates (r, ϕ, ψ) using the appropriate complexing model.
   (a) This assumes chemically reasonable binding models (see below).
8. Scan over selected variables defining the substrate molecular geometry.
   (a) Only one or two molecular parameters (e.g., a torsional angle or conformer ratio) may be varied if an over determined solution is to be obtained. Also this assumes that the complexation of the Lanthanide shift reagent to the substrate molecule does not alter the molecule's conformation in solution. This is a perennial source of contention. However despite numerous investigations there has not been a case of a non-sterically hindered mono-functional substrate molecule whose conformational profile has been affected by complexation with these lanthanide shift reagents. This is not the case for di and multifunctional molecules (e.g., 1,2-diols) where complexation with a lanthanide can significantly alter the conformation of the substrate.[3]

3.2 The Complexation Model

Due to the necessity to obtain an over-determined solution, the complexation model is a compromise between the minimum number of parameters required to define the lanthanide-substrate complex and chemically reasonable binding models. Although a number of possible lanthanide-substrate complexes were initially considered the LIRAS (Lanthanide Induced Relaxations and Shifts) suite of complexation models has been described[7,10,12] and applied to a number of different substrates and will be described here. There are three different variations of this computer model, LIRAS3, LIRAS4 and HARDER. The complexation parameters for LIRAS3 and LIRAS4 are shown in Figure 4.

The LIRAS3 coordination model was designed originally for the very common case of carbonyl complexation.[7] In the two-site model, the lanthanide is assumed to complex along the C=O lone pairs and the complexation coordinates are given by r, ϕ, ψ (Figure 4a). In order to take account of the two C=O lone pairs without doubling the number of parameters the lanthanide position is reflected in the xz plane (Figure 4a) but the populations of the two sites may be varied from 0 to

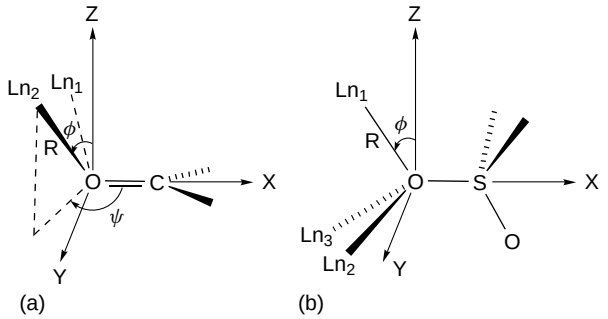

Figure 4 The LIRAS3 (a) and LIRAS4 (b) Lanthanide Coordination Models

100%. Thus four parameters are required to fix the lanthanide coordinates and populations. Note that the two-site model becomes a one-site model when the lanthanide populations are 0 or 100%. In the more diffuse 4-site model the lanthanide position is reflected about both the xz and xy planes. The population of the two sites reflected about the xz plane may be varied as in the two-site model but the population of the sites reflected about the xy plane is kept constant at 50 : 50. These options thus provide a range of possible coordination geometries for the lanthanide-substrate complex. For a planar substrate molecule these two models are identical.

The LIRAS4 model of Figure 4(b) was constructed to take account of the very different coordination geometry when a lanthanide complexes to a sulphone[12] or sulphoxide[13] group. The S–O bond is more appropriately considered as a single bond rather than as a double bond and the complexation model was modified accordingly. In this model there are three possible coordination sites reflecting the three lone pairs on the sp^3 hybridized oxygen atom. These are separated by 120° dihedral angles but may be rotated about the S–O bond. Also each of their populations may be varied from 0 to 100%. This coordination model has the same number of variable parameters as LIRAS3. This model may be applied to any sp^3 hybridized coordinating group such as alcohols (R.OH) and primary amines (RNH_2).

The HARDER model is an extension of the LIRAS model and was developed for the case of a coordinating carbonyl function in which the environment of both the coordinating sites is so different that the LIRAS3 model is inappropriate. Here both the coordination sites are considered separately thus their coordinates are varied independently. As before the populations of the two sites may be varied thus this model requires seven parameters to determine merely the lanthanide coordination. As in LIRAS3 a four site model is an option in which the lanthanide coordinates are reflected about the xy plane (Figure 4) and again the population of the sites reflected about the xy plane is kept constant at 50 : 50. An example of the use of this model was the LIS of norbornanone. Here neither of the LIRAS3 or LIRAS4 models are appropriate but the HARDER model gave a good description of the LIS.[14]

4 APPLICATIONS OF THE LIS METHOD

Many investigations have demonstrated the importance and utility of the LIS method in determining the structures and conformations of molecules in solution.[3,4] In the space allowed for this brief review we shall give merely three illustrative examples of the use of the LIS method in structural and conformational analysis. These are the determination of the solution conformation of bicyclohexan-3-one;[15] an illustration of the greater degree of precision obtained when the diamagnetic complexation shifts are measured using $Lu(fod)_3$ instead of $La(fod)_3$[16] and the use of LIS in determining the molecular geometries of some aromatic aldehydes, ketones and esters and their 2,6-dimethyl and 2,6-difluoro derivatives.[10]

4.1 The Solution Conformation of Bicyclo [3.1.0] Hexan-3-one[15]

The bicyclo [3.1.0] hexane skeleton[15]

occurs widely in nature in a number of monoterpenes of the thujane series. The conformation of the six-membered ring of this strained system can be either chair, envelope or boat. These conformations are all defined by the angle of pucker (α) of the C2 C3 C4 flap (Figure 5) and thus this is a one-dimensional problem. The LIS of the nine different ^1H and ^{13}C atoms in the molecule were determined. The normalization of the shifts plus the possible contact contribution of the carbonyl carbon atom meant that there were only seven independent LIS available to use in the analysis. The lanthanide position is defined by three coordinates and the geometry of the ketone is defined uniquely by the angle of pucker α, given that the

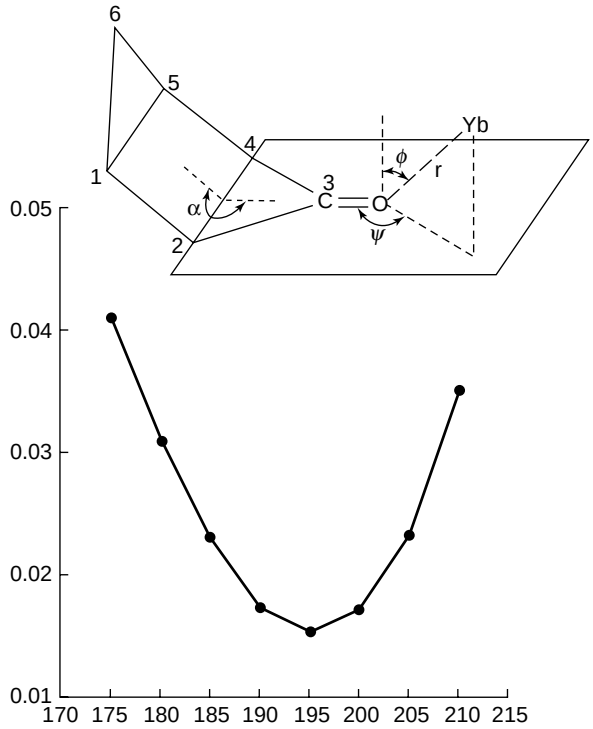

Figure 5 The agreement factor (Rx) of the best solutions vs the angle of pucker (α)

bond lengths and bond angles in the remainder of the molecule are well known. Thus the LIRAS3 programme was used to search for the best agreement of the observed vs calculated LIS varying the lanthanide position and the angle of pucker. The resulting graph of the agreement factor (Rx) vs the angle of pucker is shown in Figure 5. The best solution is for a value of α equal 195.0° which corresponds to a flattened boat conformation. This conclusion was further supported by both ab initio calculations and by a microwave study of this molecule. This is a good example of the use of the LIS method. Note the limitation to one variable molecular parameter, which results in an over-determined solution and good definition of the unknown parameter.

4.2 Lutetium vs Lanthanum in Probing Diamagnetic Complexation Shifts

A significant advance in the application of LIS in conformational analysis was made by Sancassan et al.[16] in their use of $Lu(fod)_3$ instead of $La(fod)_3$ to obtain the diamagnetic shifts of equation (3). The diamagnetic shifts (ΔD) are a significant part of the total LIS shifts and any systematic errors will affect the derived results. Lutetium is diamagnetic like lanthanum and is much more similar to ytterbium in electronic configuration and ionic radius (the trivalent ionic radii for La, Yb and Lu are 1.061, 0.858 and 0.848, respectively). The authors tested the two alternative procedures on a compound of known structure, 9-fluorenone (**1**) and then in conformational studies of acetophenone (**2**) 2,6-dimethyl-4-nitroacetophenone (**3**), 2-acetylnaphthalene (**4**), 3-methoxyacetophenone (**5**), and 2-methylacetophenone (**6**). The results of a LIS experiment on **2** including a direct comparison of the diamagnetic shifts (ΔD_{Lu} or ΔD_{La}), evaluated by use of either $Lu(fod)_3$ or $La(fod)_3$ is given in Table 3 and the results of the LIS analysis on compounds 1–6 in Table 4.

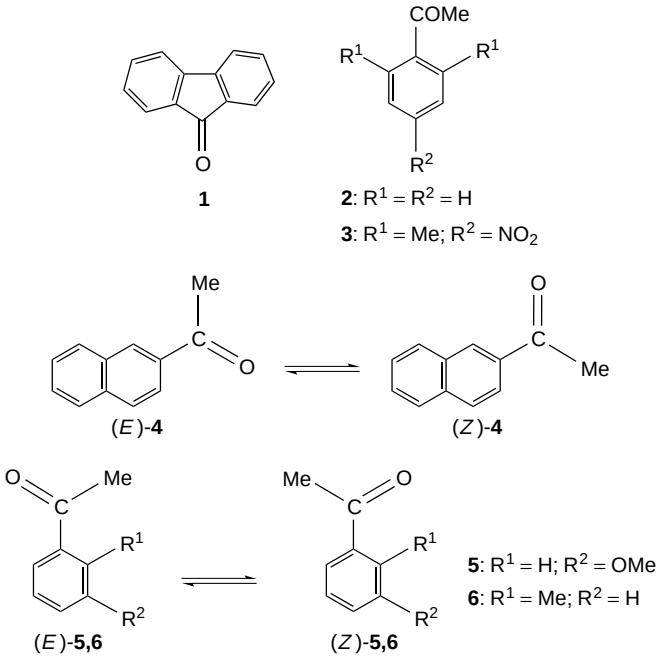

The results in Table 3 which are typical of these compounds show that the La and Lu ΔD values are qualitatively similar. They reflect predominantly π-electron transmission. The carbonyl carbon and the ortho and para carbons are deshielded while C1 is shielded and the meta and methyl carbons and the protons are unaffected. It has been suggested that these ΔD values may be used as a probe of π-electron delocalization.[17]

The results in Table 4 compare the effects of using the La vs Lu ΔD values in the analysis. For the less activated substrates (**1**) and (**3**) the use of either $La(fod)_3$ or $Lu(fod)_3$ yielded very similar sets of data, indicating in (**3**) an ca. 90° torsion angle between the acetyl and the ring. More interestingly, in the case of (**2**), (**4**), (**5**) and (**6**) the use of $Lu(fod)_3$ gave a markedly improved definition of essentially the same solutions. These are a planar conformation for (**2**), a prevalence (ca. 68%) of the E conformer for (**4**) and of the Z conformer for (**5**) and (**6**) (ca. 63% and 90% respectively). In the case of (**6**) the geometries of the two conformers were obtained through an ab-initio RHF 6-31G* optimization with GAUSSIAN92[18] indicating a planar structure for the Z and a 35°-rotated structure for the E conformer. It can be clearly seen from the results in Table 4 that the analysis using $Lu(fod)_3$, while supporting the results obtained with its lanthanum analogue, better reproduces the diamagnetic contribution to the LIS in strongly coordinating substrates. With the unhindered substrates **2**–**4**, where very reliable starting geometries were found, solutions obtained through the use of $Lu(fod)_3$ have been particularly good (Rx 0.2–0.4%). Thus pseudo-contact shifts ranging up to 130–150 p.p.m. could be reproduced with an average absolute error of $\pm$0.1 p.p.m. This demonstrates both the accuracy of the LIS method and of the theoretical background in these investigations.

4.3 The Evaluation of Molecular Geometries by the LIS Technique

A longstanding objective of the LIS technique has been the determination of molecular geometries in solution. As we noted previously this aim has to be curtailed as the LIS only provide one measured quantity for each atom whereas three are required to fully define its position. Nevertheless LIS can be used to check and refine molecular geometries and this aspect is covered in the example given here. The essential conditions necessary for successful LIS studies have been considered in section 3.1. Amongst these are the determination of only one or two molecular parameters (e.g., a torsional angle or conformer ratio) and both the quality and the comprehensiveness of the experimental data. The importance of obtaining as many pseudo-contact shifts as can be measured has also been emphasized, and all quantitative LIS studies should include all the ^{1}H and ^{13}C nuclei in the molecule. The examples in section 4.2 show that diamagnetic shifts measured using $Lu(fod)_3$ give consistently better results when used with the LIS for $Yb(fod)_3$ than the $La(fod)_3$ shifts.

This technique thus provides a means of obtaining accurate and comprehensive LIS data. It is therefore of some interest to determine whether such a data set could be used to test molecular geometries, either calculated or experimental. For this to be achieved the molecules to be examined must satisfy certain criteria.

1. They must exist in only one conformation in solution. The additional complexities involved in averaging between two

Table 3 Observed chemical shifts (δ), LIS, Yb(fod)$_3$ (ΔM), Lu(fod)$_3$ (ΔD_{Lu}), La(fod)$_3$ (ΔD_{La}), and pseudo-contact shifts (ΔM-ΔD_{Lu} and ΔM-ΔD_{La}) in ppm for acetophenone 2

Nucleus	δ[a]	ΔM[b]	ΔD_{Lu}[c]	ΔD_{La}[d]	ΔM-ΔD_{Lu}	ΔM-ΔD_{La}
C=O	198.09	166.85	9.02	13.88	157.83	152.97
$COCH_3$	26.60	70.58	−0.80	−1.30	71.38	71.88
C-1	137.15	66.66	−1.17	−2.42	67.83	69.08
C-2,6	128.31	42.41	1.80	2.86	40.61	39.55
C-3,5	128.57	19.37	0.45	0.18	18.92	19.19
C-4	133.09	17.71	2.52	3.34	15.19	14.37
$COCH_3$	2.60	46.07	0.16	–	45.91	46.07
H-2,6	7.96	43.04	–	–	43.04	43.04
H-3,5	7.46	11.52	–	–	11.52	11.52
H-4	7.57	9.60	–	–	9.60	9.60

[a]$[S]_o = 0.5\,\text{mol dm}^{-3}$ in $CDCl_3$.
[b]three additions of Yb(fod)$_3$, $\rho \cdot 10^2 = 2.87$, 9.52 and 13.49. All correlation coefficients $\geq$0.9993.
[c]From three additions of Lu(fod)$_3$, $\rho \cdot 10^2 = 3.56$, 8.06 and 11.05.
[d]From three additions of La(fod)$_3$, $\rho \cdot 10^2 = 3.13$, 6.54 and 10.15.

Table 4 LIS analysis using Lu(fod)$_3$ or La(fod)$_3$: resulting torsion angle (ω) between the acetyl and the aryl moiety, best Rx value obtained and the lanthanide position (polar coordinates and % population on the methyl side of the π-electron plane of the carbonyl)

		Result	Rx (%)	r(A)	φ(°)	Ψ(°)	Pop(%)[a]
1	Lu	–	0.9	2.75	65	155	50
	La	–	0.8	2.75	65	155	50
2	Lu	$\omega = 0°$	0.2	2.92	55	141	90
	La	$\omega = 0°$	1.2	2.96	62	140	86
3	Lu	$\omega = 90°$	0.7	2.65	70	145	100
	La	$\omega = 90°$	0.8	2.65	70	145	100
4	Lu	E% = 68	0.4	2.98	60	136	91
	La	E% = 68	1.6	3.01	65	136	90
5	Lu	Z% = 63	0.3	2.94	52	141	95
	La	Z% = 63	1.2	2.97	57	140	92
6	Lu	Z% = 92	0.8	2.68	66	144	98
	La	Z% = 92	1.5	2.69	70	145	98

or more rapidly interconverting conformers of unknown populations would undermine the direct testing of the molecular geometries.
2. There must be only one complexing atom for the lanthanide ion. Again averaging between different complexing sites would introduce too many uncertainties in the analysis.
3. The LIS complexation model used must be reliable and well characterized.

Molecules which satisfy all these criteria are aromatic carbonyl compounds and Abraham et al.[10] applied this technique to a series of substituted aromatic aldehydes, ketones and esters. The 4-methyl derivatives of benzaldehyde, acetophenone and methyl benzoate, in which steric effects are minimal were first examined and then the effects of 2,6 dimethyl and 2,6 difluoro substitution were considered. Thus the competing effects of steric repulsion versus conjugation and the theoretically important F···O interaction may be examined by this technique. The 4-methyl derivatives have the advantage over the parent compounds of an additional LIS centre plus a simpler aromatic proton spectrum, making the experimental data more definitive without introducing any extra perturbations in the molecules.

The modeling and theoretical programs used were the commercial programs PCMODEL,[19] NEMESIS[20] and GAUSSIAN92.[18] The PCMODEL program is "loosely derived" from the MM2 and MM2P force fields[21] and the NEMESIS program uses the simpler COSMIC force field.[22] The ab-initio GAUSSIAN92 program was used with the RHF/6-31G* basis set. In addition "experimental" geometries were used when available with the important caveat that crystal packing forces can affect the molecular geometry, particularly the torsional angles.

The pseudo-contact shifts were used to directly test the accuracy of the calculated molecular geometries obtained from these programs using the LIRAS3 and LIRAS4 programs. Also included for comparison are experimental or standard geometries. The authors regarded a Rx value of <1% as acceptable agreement with the observed LIS. Figure 6 and Tables 5 and 6 give the most important geometrical parameters.

The calculated geometries of **7** and **9** were found to be all planar, as expected. The bond lengths and angles for the formyl group are very similar (Table 5) and all the geometries

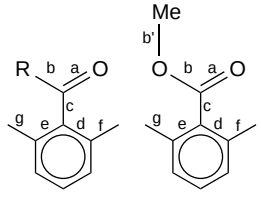

Figure 6 Explanation of symbols used in Tables 5 and 6

Table 5 Geometries and LIS Agreement Factors (Rx) for 4-Methylbenzaldehyde (**7**), 4-Methylacetophenone (**8**), methyl 4-methylbenzoate (**9**) and Mesitaldehyde[1] (**10**)

(**7**)	a	b	c	ab	ac	cd	ce	Rx(%)	
EXPTL	1.216	1.10	1.480	118.6	123.9	120.0	120.0	0.33	
GAUSS	1.191	1.095	1.481	120.4	124.7	120.6	120.1	0.33	
PCMOD	1.210	1.115	1.482	119.8	126.5	120.9	120.4	0.48	
NEM	1.228	1.089	1.444	117.5	124.0	120.7	120.8	0.59	
(**8**)									
EXPTL	1.216	1.499	1.494	121.0	120.0	122.1	117.9	0.79	
GAUSS	1.196	1.514	1.498	120.3	120.6	118.5	122.9	0.79	
PCMOD[2]	1.212	1.520	1.486	120.0	122.6	121.7	119.7	1.34	
NEM	1.227	1.502	1.449	115.4	122.6	118.6	123.6	0.64	
(**9**)	a	b	c	b′	ab	ac	bb′	Rx(%)	
EXPTL	1.199	1.343	1.484	1.445	123.4	125.0	117.2	0.76	
GAUSS	1.192	1.325	1.488	1.416	122.9	124.0	116.8	0.98	
PCMOD	1.213	1.352	1.490	1.414	121.2	123.6	123.2	1.24	
NEM	1.237	1.353	1.453	1.417	118.7	122.2	117.4	0.89	
(**10**)	a	b	c	ab	ac	cd	ce	df/ge	Rx(%)
EXPTL	1.216	1.10	1.480	118.6	123.9	120.0	120.0	124.0	0.75
GAUSS	1.194	1.090	1.483	118.6	126.1	121.4	118.7	123.0	0.75
PCMOD[3]	1.209	1.115	1.479	120.4	126.1	120.0	119.8	121.5	1.42
NEM	1.228	1.088	1.452	115.8	125.5	121.2	120.2	122.2	0.96

[1]Distances in A and angles in degrees.
[2]Torsional angle of 30.3° (see text).
[3]Torsional angle of 48.3° (see text).

Table 6 Geometries and LIS Agreement Factors (Rx) for 2,6 Di-Ortho Substituted Compounds[1]

2,6 Dimethyl Acetophenone (11)										
	c	d/e	f/g	ab	ac	cd	df/ge	Ψ^2	Rx(%)	
EXPTL	1.494	1.397	1.510	121.0	120.0	120.0	120.0	90.0	0.74	
GAUSS	1.514	1.395	1.515	121.6	121.4	119.8	121.7	84.7	0.87	
PCMOD	1.480	1.405	1.508	121.5	122.7	119.4	120.8	74.9	0.28	
NEM	1.454	1.416	1.510	113.3	123.2	119.6	121.8	28.7	1.06	
2,6 Difluoroacetophenone (12)										
EXPTL	1.494	1.397	1.354	121.0	120.0	120.0	120.0	20.0	0.82	
GAUSS	1.513	1.387	1.322	122.4	120.0	120.9	118.6	57.1	1.84	
PCMOD	1.477	1.399	1.351	121.1	122.4	120.5	120.3	59.5	2.23	
NEM	1.444	1.413	1.330	114.3	123.0	119.9	120.9	0.2	0.84	
Methyl Mesitoate (13)										
	c	d/e	f/g	ab	ac	bb′	cd/ce	df/eg	Ψ^2	AF(%)
EXPTL	1.484	1.397	1.510	123.4	125.0	120.0	120.0	120.0	65.0	0.38
GAUSS	1.497	1.400	1.515	122.3	124.7	116.9	121.2	123.2	46.6	1.58
PCMOD	1.480	1.406	1.509	122.9	123.6	123.0	120.1	121.5	60.9	0.71
NEM	1.463	1.415	1.511	117.5	123.0	118.0	120.5	122.4	9.4	3.10
Methyl 2,6 Difluorobenzoate (14)										
EXPTL	1.484	1.397	1.354	123.4	125.0	120.0	120.0	120.0	0.0	0.49
GAUSS	1.498	1.387	1.320	124.1	123.8	116.8	122.8	119.1	46.4	2.00
PCMOD	1.476	1.400	1.351	122.8	123.6	123.1	120.3	120.6	50.8	1.71
NEM	1.448	1.408	1.330	118.0	122.7	117.6	121.0	120.7	0.0	1.82

[1]Distances in A and angles in degrees.
[2]CO–Ring torsional angle.

of **7** gave good agreement factors Rx (Table 5). This was also the case for **9** except for the PCMODEL geometry. The PCMODEL geometry gives an unacceptable value of Rx = 1.24. Inspection of the geometries shows that the C.O.C angle in the PCMODEL geometry (bb′ in Table 5) is much larger than all the others (123.2° vs ca 117.0°). It was therefore of interest to determine whether this was the reason for the poor agreement and indeed optimising this angle gave Rx = 0.81 for a value of 120°. Optimising this angle with the other geometries gave values of ca 119°, thus the LIS indicate that the value of this angle is ca 120° in solution.

The molecular geometries calculated for the acetyl group of **8** (Table 5) show surprisingly large variations. All the geometries are planar except for the PCMODEL geometry, in which the angle of twist of the acetyl group from the benzene ring is 30.3°. This geometry also gave an unacceptable Rx of 1.34 and this was clearly due to the dihedral angle as rotating it to zero with the same geometry decreases Rx to 0.67, in

good agreement with the other geometries. Thus here the LIS measurements unequivocally confirm the planar geometry.

Another point of interest in these geometries are the bond angles the acetyl group makes with the benzene ring (cd and ce in Table 5). The calculated geometries oscillate between cd > ce and vice versa. Optimising this angle using LIRAS3 for both the experimental and GAUSSIAN geometries gave a value of 120° and Rx = 0.67 (experimental geometry) and 0.77 (GAUSSIAN). Whilst these changes are too small to be definitive, they support the view that the acetyl group is symmetric with respect to the benzene ring. Finally note that although the NEMESIS geometry differs somewhat from the other geometries, it does give an acceptable agreement factor.

4.4 The Non-Planar Geometries

The remaining molecules to be considered are di-ortho substituted molecules, and in consequence the C-1 substituent group and the benzene ring are often no longer coplanar. This has two important consequences. The actual value of the torsional angle Ψ is a very sensitive function of the steric interactions and the C-1 substituent torsional potential and therefore much larger differences between the calculated geometries are found than for the planar molecules considered previously. Furthermore due to the molecular symmetry the conformation at 90° torsional angle will be either a maximum or minimum on the molecular energy profile. Thus for molecules in which the minimum energy conformation is predicted to have a torsional angle of ca 80° or greater the barrier to rotation about the 90° transition state will be very small indeed, probably less than the zero-point energy of the molecule. In solution the molecules will be interconverting rapidly between the two identical conformations about 90°, thus the LIS measurements will be the average of the molecular vibrations around 90°. However even with this caveat the LIS measurements do provide a critical test of the calculated geometries investigated.

The standard geometry used for **10** was derived from that of **7** with the addition of standard methyl groups. This gave the best agreement for a planar geometry but with Rx = 1.08. Relaxing the ortho methyl C.C.C angles to 124° gave Rx = 0.75 (Table 5). The GAUSSIAN and NEMESIS geometries are planar and have the ortho methyl C.C.C angles relaxed to 123° and 122° and they give Rx = 0.78 and 0.96 respectively. In contrast the PCMODEL geometry has Ψ = 48° and gave poor agreement with the LIS (Rx = 1.42, Table 5). Merely altering Ψ to 0° gave a much better agreement (Rx = 0.87), confirming that this was the reason for the poor agreement with the LIS. These results unequivocally confirm that **10** is planar in solution with the steric strain relieved mainly by a relaxation of the ortho methyl C.C.C angles.

The experimental geometry initially used for **11** was from the Xray structure of 4-tert butyl-2,6 dimethyl acetophenone. This gave very poor agreement thus this geometry was rejected and the geometry of acetophenone used plus standard methyl groups. This gave Rx = 0.74 for Ψ = 90° (Table 6). The three calculated geometries have the same C.CO and C.C=O bond lengths as **8** (Table 5) and are not given in Table 6. The parameter which does change appreciably is Ψ the acetyl torsional angle, which varies from 85° in GAUSSIAN to 75° in PCMODEL to 29° in NEMESIS and Rx varies from a barely acceptable value in GAUSSIAN (0.87) to an excellent value in PCMODEL (0.28) to an unacceptable value in NEMESIS (1.06). Inspection of the geometries in Table 6 shows that the NEMESIS geometry has an unusually small Me.C.O angle of 113.3° compared to ca 121° for all the other geometries. To test the above variations the Me.C.O angle was changed to 121° in the NEMESIS geometry and Ψ varied for the best fit. This procedure gave Rx = 0.66 for Ψ = 55°. In contrast varying Ψ with the GAUSSIAN geometry did not affect the Rx value. These results show that both experimental and calculated geometries can be directly tested with the LIS data. They also confirm the too small value of the Me.C=O angle in the NEMESIS force field and show that Ψ in **11** in solution is ca 80°. Thus from the discussion above, in solution the acetyl group will be effectively orthogonal to the benzene ring.

The experimental geometry for **13** was that used previously for the ester group (Table 2) with the addition of standard methyl groups. Varying the ester torsional angle Ψ gave Rx = 0.73 for Ψ = 65°. Inspection of the calculated shifts showed that both the ester carbon and protons had large errors (ca 1.0 ppm) compared with the observed values whereas the remaining shifts were very well reproduced. This suggested that, as in the 4-methylbenzoate the C.O.Me angle was too small and increasing this to 120° gave an excellent value of Rx = 0.38 and this with the optimized geometry is given in Table 6.

In contrast the calculated geometries show considerable variation and in consequence large changes in the Rx values. The PCMODEL geometry, in which Ψ = 61° gave a Rx = 0.71 and reducing the C.O.C angle to 120° (see above) improved this to 0.54. In contrast both the GAUSSIAN and NEMESIS geometries gave smaller values of Ψ (46° and 9° res.) and also poor agreement with the LIS. Varying Ψ made this only slightly better. Rx for the GAUSSIAN geometry decreased to 1.48 for Ψ = 60°, whilst that for the NEMESIS geometry decreased to 1.96 for Ψ = 50°. These are still unacceptably high values of Rx.

Inspection of the geometries showed that the GAUSSIAN geometry was reasonably consistent with the other geometries except for the C.O.C angle (bb′ in Table 6) which at 116.9° seems too small. Indeed merely altering this angle to 120° as above for the experimental geometry gave an acceptable Rx = 0.83 for Ψ = 70°. The NEMESIS geometry however shows large differences from the other geometries of Table 6 and it was not considered feasible to vary all the parameters to search for the best agreement.

In conclusion the LIS measurements of this molecule taken together with the molecular geometries give Ψ = 65–70° in solution, and also suggest that the C.O.C angle in this molecule is somewhat larger than the value calculated by the 6-31G* basis set. Interestingly the 6-31G basis set gives a value for this angle of 119.4°, which is very close to the one suggested by the LIS measurements (and in consequence the 6-31G geometry gives better agreement than the 6-31G* geometry).

Fluorine poses considerable problems in both quantum mechanics and molecular modelling, thus it was of some interest to see how the programs coped with the difluoro compounds studied. The standard geometry used for **12** was obtained by adding fluorine atoms to the acetophenone geometry and then rotating the acetyl group for the best agreement. This gave Rx = 0.82 for Ψ = 20° (Table 6). In

contrast the calculated geometries all gave poorer agreement and also very different values of Ψ. Rx = 0.84 for the NEMESIS geometry with $\Psi = 0°$ but the agreement for the PCMODEL and GAUSSIAN geometries both with Ψ ca. 60°, is poor. Ψ was then optimized in both cases. For both geometries the search gave much better values (Rx = 0.64 and 1.10 for the GAUSSIAN and PCMODEL for $\Psi = 25°$ and 30° respectively). In the case of the NEMESIS geometry the 0° dihedral angle gave the best fit. Changing the value of the Me.C.O angle to the experimental value and varying Ψ gave Rx = 0.93 for $\Psi = 25°$. The conclusion from these results is that the acetyl torsional angle Ψ in this molecule in solution is 25−30°. This is quite different from the value predicted by all of the programs used, even the 6-31G* basis set.

The experimental geometry used for **14** was that used previously for methyl benzoate, with the C.O.C angle of 120° and the addition of standard fluorine atoms. Rotating the ester group for the best agreement gave a very good Rx = 0.49 for a planar molecule. In contrast, in exactly analogous manner to **12** the GAUSSIAN and PCMODEL geometries gave non-planar geometries and very poor agreement with the LIS data, ($\Psi = 46°$ and 51° and Rx = 2.0 and 1.7). Varying Ψ gave values of 0° and 10° with Rx = 0.75 and 0.47 respectively. In contrast the NEMESIS geometry is planar but gives poor agreement (Rx = 1.82). Varying Ψ with the C.O.Me angle of 120° gives a better solution (Rx = 1.11) for $\Psi = 10°$ but this is still poor agreement. The results for this molecule again demonstrate that all the calculated geometries give very poor agreement with the LIS measurements and this is largely due, in the case of the GAUSSIAN and PCMODEL geometries, to the value of Ψ the torsional angle. The LIS data clearly support a planar geometry for this molecule in solution.

The LIS studies confirm the calculated planar geometries for the 4-methyl compounds and also the essentially orthogonal geometry of **11**, but predict quite different conformations for **13** and particularly for the 2,6 difluoro derivatives than those obtained by either ab-initio or molecular mechanics calculations.

The results given above show clearly that LIS can be used to directly test molecular geometries. For the molecules considered and in particular the non-planar molecules it is shown very clearly that the calculated geometries often fail to reproduce the observed LIS. This is particularly the case for the 2,6 difluoro compounds where the calculated values of the torsional angles between the substituents and the benzene ring are very different from those obtained from the LIS. This demonstrates very clearly the need for caution in obtaining molecular torsional angles in such molecules even with sophisticated ab-initio calculations. The LIS can also be used to refine other parameters in a given geometry and to differentiate between different experimental geometries. For the molecules considered here any geometry giving an AF > 1.0 would be considered as unacceptable.

It is important however to stress that the converse of this statement does not hold. Due to the reasons mentioned at the beginning of this section good agreement does not necessarily mean a correct geometry. The LIS would need to be augmented by additional data (e.g., broadening data) to become more definitive. Also the problems of an underdetermined data set mean that caution must be exercised in obtaining bond and torsional angles from LIS data. Only one, or at most two molecular parameters can be optimized in this way.

5 REFERENCES

1. C. C. Hinckley, *J. Am. Chem. Soc.*, 1969, **91**, 5160.
2. J. K. M. Sanders and D. H. Williams, *J. Chem. Soc. Chem. Comm.*, 1970, 422.
3. T. J. Wenzel, 'NMR Shift Reagents', CRC Press: Boca Raton, FL, 1987.
4. (a) J. A. Peters, J. Huskens, and D. J. Raber, *Prog. NMR Spectrosc.*, 1996, **28**, 283; (b) O. Hofer, *Topics Stereochem.*, 1976, **9**, 111; (c) J. Reuben, *Prog. NMR Spectrosc.*, 1973, **9**, 1; (d) F. Inagaki and T. Miyazawa, *Prog. NMR Spectrosc.*, 1981, **14**, 67.
5. R. J. Abraham, J. Fisher, and P. Loftus, 'Introduction to NMR Spectroscopy', Wiley: Chichester, 1988.
6. D. J. Raber, M. D. Johnston, C. M. Campbell, C. M. Janks, and P. Sutton, *Org. Mag. Reson.*, 1978, **11**, 323.
7. R. J. Abraham, D. J. Chadwick, and F. Sancassan, *Tetrahedron*, 1982, **38**, 1485 & 3245.
8. A. A. Chalmers and K. G. R. Pachler, *J. Chem. Soc. Perkin Trans. 2*, 1974, 748.
9. G. E. Hawkes, D. Leibfritz, D. W. Roberts, and J. D. Roberts, *J. Am. Chem. Soc.*, 1973, **95**, 1659 and 1661.
10. R. J. Abraham, S. Angiolini, M. Edgar, and F. Sancassan, *J. Chem. Soc. Perkin Trans 2*, 1995, 1973.
11. R. J. Abraham, I. Castellazzi, F. Sancassan, and T. A. D. Smith, *J. Chem. Soc. Perkin Trans 2*, 1999, 99.
12. R. J. Abraham and I. S. Haworth, *Magn. Reson. Chem.*, 1988, **26**, 252.
13. R. J. Abraham, L. Pollock, and F. Sancassan, *J. Chem. Soc. Perkin Trans 2*, 1994, 2329.
14. R. J. Abraham, D. J. Chadwick, P. E. Smith, and F. Sancassan, *J. Chem. Soc. Perkin Trans 2*, 1989, 1377.
15. (a) R. J. Abraham, D. J. Chadwick, and F. Sancassan, *Tetrahedron Lett.*, 1979, 265; (b) R. J. Abraham, D. J. Chadwick, and F. Sancassan, *Tetrahedron*, 1981, 1081.
16. F. Sancassan, G. Petrillo, and R. J. Abraham, *J. Chem. Soc. Perkin Trans 2*, 1995, 1965.
17. R. J. Abraham, H. A. Bergen, D. J. Chadwick, and F. Sancassan, *J. Chem. Soc. Chem. Commun.*, 1982, 998.
18. Gaussian-92, Revision F.4; M. J. Frisch, G. W. Trucks, M. Head-Gordon, P. M. W. Gill, M. W. Wong, J. B. Foresman, B. G. Johnson, H. B. Schlegel, M. A. Robb, E. S. Replogle, R. Gomperts, J. L. Andres, K. Raghavachari, J. S. Binkley, C. Gonzalez, R. L. Martin, D. J. Fox, D. J. Defrees, J. Baker, J. J. P. Stewart, and J. A. Pople, Gaussian, Inc., Pittsburgh PA, 1992.
19. PCMODEL. Serena Software, PO box 3076 Bloomington.
20. NEMESIS. Oxford Molecular Ltd., The Magdalen Centre, Oxford Science Park, Stanford upon Thames, Oxford, OX4 4GA.
21. U. Burkert and N. L. Allinger, 'Molecular Mechanics', American Chemical Society: Washington, DC, 1982.
22. S. D. Morley, R. J. Abraham, I. S. Haworth, D. E. Jackson, M. R. Saunders, and J. G. Vinter, *J. Comp.-Aided Mol. Des.*, 1991, **5**, 475.

Acknowledgements

This review is based on investigations carried out in our research groups over many years and we acknowledge the contributions of Drs. D. J. Chadwick, L. Griffiths, G. Petrillo and numerous research students to this project. We also acknowledge financial support from the British Council, The Royal Society, Erasmus and the SERC/EPSRC.

Biographical Sketches

Raymond J. Abraham, *b* 1933, B.Sc. 1954, Ph.D. 1957, D.Sc. 1973, University of Birmingham, UK. NRC of Canada, National Physical Lab., Professor of Organic Chemistry at the University of Liverpool, UK. Approx. 280 publications. Current research interests, NMR, conformational isomerism and molecular modelling.

Fernando Sancassan, *b* 1947. Laurea, 1972, Genova, Italy. Professor in Organic Chemistry at the University of Genova. Involved in NMR research from 1972. British Council fellow 1977/8 at the University of Liverpool. Main fields of interest: (i) lanthanide shift reagents and conformational analysis and (ii) ^{13}C NMR studies of π-electron distribution in aromatic and heterocyclic compounds and Meisenheimer adducts. Approx. 60 papers.

Magnetic Susceptibility and High Resolution NMR of Liquids and Solids

David L. Vander Hart
National Institute of Standards and Technology, Gaithersburg, MD, USA

1	Introduction	1
2	Physical Origins of Susceptibility, Definitions, and Equations	1
3	Magnetic Susceptibility Effects in the High-Resolution NMR of Liquids	2
4	Magnetic Susceptibility Effects in Solid State NMR	4
5	Miscellaneous Considerations	7
6	Related Articles	8
7	References	8

1 INTRODUCTION

The principal aspects of high-resolution (HR) NMR which are influenced by magnetic susceptibility (MS) effects in nonconducting materials are spectral resolution and the accurate measurement of chemical shift. Also, with the wide application of NMR to imaging, particularly the imaging of heterogeneously structured materials, MS effects can influence the quality and interpretation of the images obtained. It is also possible to obtain MS information about materials using high-resolution NMR techniques. In this presentation, the physical origins of susceptibility in nonconducting materials are sketched, a few basic equations are given, the tensorial nature of susceptibility is pointed out, and a number of practical considerations are offered including the influence of sample spinning, particularly at the magic angle. Only diamagnetic and paramagnetic susceptibility are considered; ferromagnetism and antiferromagnetism are not discussed. Finally, a few comments are included regarding the use of high-resolution NMR to measure MS values, both molecular MS and the MS of condensed phases.

2 PHYSICAL ORIGINS OF SUSCEPTIBILITY, DEFINITIONS, AND EQUATIONS

In classical electromagnetism, the magnetic induction $\boldsymbol{B}$ and the magnetic field strength $\boldsymbol{H}$ inside a medium, are related by the equation

$$\boldsymbol{B} = \mu_0(\boldsymbol{H} + \boldsymbol{M}) \tag{1}$$

where $\boldsymbol{M}$ is the magnetization or magnetic moment per unit volume. Quantities appearing in equation (1) are in rationalized SI units where $\boldsymbol{H}$ and $\boldsymbol{M}$ are expressed in A m^{-1} and $\boldsymbol{B}$ has the units of tesla. Quantities given in bold-face type are either vectors or tensors. The permeability of free space, μ_0, takes the value $4\pi \times 10^{-7}$ T m A^{-1} (Bennett et al. have published a useful reference paper[1] delineating appropriate conversions from cgs to SI units for quantities related to magnetism.) For isotropic nonferromagnetic materials,

$$\boldsymbol{M} = \kappa \boldsymbol{H} = (d/M)\kappa_{\mathrm{M}}\boldsymbol{H} \tag{2}$$

where κ and κ_{M} are respectively called the rationalized volume and molar magnetic susceptibilities, d is the density in kg m^{-3} and M is the molar mass in kg mol^{-1}. (κ is equivalent to the quantity $4\pi\chi_{\mathrm{v}}$ in the cgs system, where χ_{v} is the volume MS; κ and χ_{v} are both dimensionless. The relationship between κ_{mole}, having units of m^3 mol^{-1}, and χ_{M} in the cgs system, having units of cm^3 mol^{-1}, is that numerically $4\pi\chi_{\mathrm{M}} = 10^6\,\kappa_{\mathrm{mole}}$.) MS is a bulk property of materials. Thus, MS is associated with an ensemble of molecules and is not intended to describe the details of the response to an external field over molecular distances. At the same time, individual molecules possess molecular susceptibility tensors.[2,3] Moreover, for nonconducting materials, the uniformity of κ_{M} for solid, liquid, and gaseous forms of the same material implies that bulk MS values probably derive from summed molecular magnetic susceptibilities.[3,4] Indeed, the molecular theory of diamagnetism is described in terms of molecular wavefunctions.

2.1 Diamagnetic and Paramagnetic Susceptibility

The two kinds of MS considered are diamagnetic and paramagnetic. Diamagnetic susceptibility is a generalized response to the magnetic field of the orbiting paired electrons in a sample.[2] This response is most often negative in sign and usually weak,[5] i.e. $\kappa \approx -10^{-5}$. Owing to the fact that the diamagnetic susceptibility arises from the reaction of electrons in their orbitals to the presence of the magnetic field, this quantity is usually quite independent of temperature. There are generally two terms contributing to the diamagnetic susceptibility,[2]

$$\kappa_{\mathrm{mole}} = -\frac{Ne^2\mu_0}{4m}\sum_i \overline{x_i^2 + y_i^2} + \frac{Ne^2\mu_0}{2m^2}\sum_{n(\neq 0)}\frac{|(0|\hat{L}_z|n)|^2}{E_n - E_0} \tag{3}$$

where N is Avogadro's number, e is the charge on the electron in coulombs, m is the mass of the electron in kg, i is an index over all electrons in the molecule, and n is an index over all excited electronic states of corresponding energies E_n (in joules) in the molecule. The first term is an average over all of the electrons in the ground state, where the z direction lies along $\boldsymbol{H}$. The size of this term is usually associated with the ability of the electrons, especially the outer electrons, to circulate freely in planes perpendicular to $\boldsymbol{H}$. The second term involves the mixing of ground and excited electron states by the angular momentum operator $\hat{L}_z$. The first term is negative and the second term is positive but usually smaller than the first; hence the sum is usually negative.

Paramagnetic susceptibility most often arises from unpaired electrons whose net polarizations in the magnetic field yield an MS which is positive in sign and somewhat larger than

the diamagnetic contribution. The latter is still there but is usually masked by the paramagnetic contribution. The electronic polarization which gives rise to the paramagnetic contribution is temperature-dependent and the paramagnetic susceptibility reflects that. For example, suppose a molecule of molar mass M has unpaired electrons, then, according to Langevin,[6]

$$\kappa_{\text{mole}} = N\mu^2\mu_0/3kT \tag{4}$$

where μ is the magnetic moment of the unpaired spins on the molecule; μ, in J T^{-1}, is given by

$$\mu = 2\beta[S(S+1)]^{1/2} \tag{5}$$

where S is the total spin which is equal to half the number of unpaired spins and β is the Bohr magneton in units of J T^{-1}. Substituting equation (5) into equation (3) gives

$$\begin{aligned}\kappa_{\text{mole}} &= 4N\mu_0\beta^2 S(S+1)/3kT \\ &= [6.286 \times 10^{-6} S(S+1)/T]\,\text{m}^3\,\text{mol}^{-1}\end{aligned} \tag{6}$$

Paramagnetic susceptibilities are usually larger than diamagnetic susceptibilities; ratios of 10 to 100 are not uncommon. Molecular oxygen has unpaired electrons and a relatively small molar mass; its presence in dissolved form can be a measurable perturbation on the measurement of diamagnetic susceptibility.[7]

2.2 Tensorial Character of Magnetic Susceptibility

In principle, the molecular MS and the bulk MS in solids is anisotropic,[2,3,8] giving rise to a *tensorial* interaction, i.e. the general definition of $\boldsymbol{M}$ in equation (2) is

$$\boldsymbol{M} = \boldsymbol{\kappa}\cdot\boldsymbol{H} \tag{7}$$

where $\boldsymbol{\kappa}$ is a tensor. Thus, $\boldsymbol{M}$ may, in principle, depart from the direction of $\boldsymbol{H}$. Anisotropic bulk MS (ABMS) is most often associated with the crystalline state of matter in contrast with the glassy or liquid states of matter where isotropic bulk MS (IBMS) is most commonly found. For diamagnetic crystals, ABMS can arise because both the magnetic susceptibility of each molecule is anisotropic and the molecules in the unit cell preserve a net orientation of their different susceptibility axes. A common molecular source of ABMS in organic compounds is the aromatic ring.[3,8,9] Ring currents, which are induced by the magnetic field when there is some projection of the normal to the ring along the magnetic field, offer a significant contribution to the MS tensor. If an aromatic compound has a crystal habit where the ring normals have a net projection along some axis, then there is a high probability that such a crystal will display ABMS. Graphite, as an extreme example, has a very large anisotropy[10] because of its dense planar fused-ring structure.

For paramagnetic materials, the existence of an anisotropic electron $\boldsymbol{g}$ tensor, for example, can give rise to ABMS since net electron polarization then becomes a function of orientation. The $\boldsymbol{g}$ tensor can become very anisotropic, particularly for certain transition metal compounds where crystal field splittings and electron spin–orbit couplings both play a role in determining the anisotropy of $\boldsymbol{g}$.[11] For example, the electrons in high-spin iron in the heme group have $g_{\parallel}$ close to the free-electron value of 2, whereas $g_{\perp}$ is about 6. As will be seen, there is considerable difference in the NMR resolution one obtains with magic angle spinning (MAS) if ABMS, rather than IBMS, is present.

2.3 Relationship Between Sample Shape and Uniform Internal Fields

For many NMR experiments, a uniform internal magnetic field is desired (uniform on a scale significantly larger than the molecular scale) so that interactions on the molecular scale can be exposed. In principle, one can make the external field very homogeneous, but the introduction of a material with finite MS into this homogeneous field generally modifies the field, both outside and inside the material. Thus, one is interested in how sample shape influences the field internal to the material and what shapes will give rise to a uniform internal field when the body is placed in a uniform external field.

For a body described by a single MS tensor, the general ellipsoid is the only finite body shape which, in the presence of a uniform external field, gives rise to a uniform internal field.[12] Cylinders of infinite length and spheres are ellipsoids of rotation; high-resolution NMR samples often approximate these shapes. It is possible, in principle, that if an ellipsoid, probably a single crystal, has an ABMS tensor whose principal axes do not coincide with the axes of the ellipsoid, that the direction of the uniform internal field will not coincide with the direction of the external field. However, for diamagnetic and paramagnetic materials, deviations from the external field direction will be negligible.

At this point we will separately consider MS effects in high-resolution liquid NMR and in solid state NMR. In liquid state NMR the measurement of chemical shifts can often be made very accurately; moreover, resolution is of primary importance. Also, most materials associated with the high-resolution experiment, including the sample, possess IBMS. In contrast, for solid state NMR, the so-called 'high-resolution' techniques generally achieve resolution which is, at best, an order of magnitude worse than in the liquid state and, more typically, two or more orders of magnitude worse. Thus, for solids, one is less concerned with the influence of MS on accurate chemical shift measurements. At the same time, in the solid state, MS effects can influence the measurement of chemical shifts in ways that do not happen for liquids. Of probably greater interest is the role which MS plays in determining resolution in the solid state. The added possibility that samples have ABMS also increases the complexity of dealing with MS, since strategies for reducing IBMS broadening only work partially when ABMS is present.

3 MAGNETIC SUSCEPTIBILITY EFFECTS IN THE HIGH-RESOLUTION NMR OF LIQUIDS

3.1 Resolution

For spectroscopic NMR applications, one generally desires the best resolution possible. MS considerations have dictated

several items in the standard practice of high-resolution NMR. Usually, sample tubes are cylindrical and are ideally filled with liquid which extends both above and below the rf coil so as to approximate an ellipsoid, thereby promoting internal field uniformity in the region of the coil. When sample volume is limited, one often uses a spherical sample tube, again approximating an ellipsoid, although the stem attached to the sphere is a significant perturbation on the uniformity of the field inside the sphere.

Sample spinning is a second way of dealing with MS effects to improve resolution, although a primary motivation for sample spinning is that it averages out inhomogeneities in the static field perpendicular to the spinning axis. Variations in the wall thickness of the NMR tube and/or a lack of concentricity cause the magnetic field to be warped in the sample region since the magnetic susceptibility of the glass is usually different from the liquid. Spinning about the tube axis helps to average these effects to smaller values. This averaging is more effective in the iron magnet geometry, where $\boldsymbol{H} \perp \boldsymbol{s}$ ($\boldsymbol{s}$ is the unit vector in the spinning-axis direction), than it is in the usual superconducting-magnet geometry where $\boldsymbol{H} \parallel \boldsymbol{s}$. This difference comes about because only in the former case does the orientation of $\boldsymbol{H}$, with respect to the vectors connecting the liquid and the tube imperfections, become modulated by spinning.

Discontinuities of MS within the sample also degrade resolution. Air bubbles, precipitates, etc. in a sample are all undesirable. Even a spherical air bubble creates a large perturbation since, in general, an ellipsoid of one susceptibility inside of an ellipsoid of a different susceptibility will result in nonuniform fields inside of both ellipsoids, even though the external field was originally uniform.

Finally, MS effects dictate certain things about probe construction. Aside from electromagnetic interferences, the asymmetric disposition of the probe elements (electronic components, mechanical supports, etc.) perturb the field lines on a distance scale comparable with the size of the object. The strategies for minimizing degradation of resolution include (a) maintaining sufficient distance between the elements and the sample so that the perturbations at the sample change slowly enough, spatially, that shim-coil compensation is possible, (b) distributing perturbing elements symmetrically, and (c) attempting to match the MS of the probe elements to that of air. The method for achieving the latter is usually to combine some paramagnetic character with the diamagnetic character of a material. For example, a substantial improvement in resolution has been demonstrated[13] by replacing a copper rf coil with one having an MS much closer to that of air. A minor drawback to this approach of MS matching is that the paramagnetic contribution will be temperature-dependent.

3.2 Chemical Shift Measurements

The NMR resonance frequency observed in a liquid for a magnetic nucleus at a given chemical site on a molecule is often a very well-defined frequency, especially for a spin-$\frac{1}{2}$ nucleus. In general, one uses measured frequencies to deduce something about the molecule, about a chemical site in the molecule, or about how a site is influenced by its immediate intermolecular interactions (e.g. hydrogen bonding, solvation shells, etc.) Of less interest are those influences on the chemical shift which derive from mean fields averaged over many molecules. The MS effects fall into this latter category. The resonance frequency ω_0 ($= 2\pi\nu_0$) for a given nucleus, ignoring spin couplings, is given by the Larmor relationship,

$$\omega_0 = \gamma \mu_0 H_{\mathrm{n}} \tag{8}$$

where H_{n} is the magnetic field strength seen by the nucleus and γ is the gyromagnetic ratio of the observed nucleus in units of rad T^{-1}. Zimmerman and Foster[12] took the approach that $\boldsymbol{H}_{\mathrm{n}}$ is the vector sum of five parallel vector fields,

$$\boldsymbol{H}_n = \boldsymbol{H}_0 + \boldsymbol{h}_1 + \boldsymbol{h}_2 + \boldsymbol{h}_3 + \boldsymbol{h}_4 \tag{9}$$

where $\boldsymbol{H}_0$ is the applied external field, $\boldsymbol{h}_1$ is the demagnetizing field, proportional to the susceptibility, arising from the shape of the sample, $\boldsymbol{h}_2$ is the contribution due to magnetization external to the Lorentz sphere,[14,15] $\boldsymbol{h}_3$ is the field associated with local intermolecular interactions, e.g. hydrogen bonding, and $\boldsymbol{h}_4$ is the field arising from intramolecular contributions, e.g. the response to the magnetic field of electrons, particularly those surrounding the nucleus observed, plus the influence of molecular conformation, etc. It is the quantity ($\boldsymbol{h}_3$ + $\boldsymbol{h}_4$) which one seeks to measure and interpret via the chemical shift measurements. For liquid samples of IBMS, having overall ellipsoidal shapes and placed into a uniform field $\boldsymbol{H}_0$,

$$\boldsymbol{h}_1 = -\alpha\kappa \boldsymbol{H}_0 \tag{10}$$

where α is the demagnetizing factor tabulated for the general ellipsoid by Osborne.[16] This factor depends on the axis ratios of the ellipsoid and the direction of the magnetic field with respect to these axes. Values of α for certain ellipsoids are as follows: 0 for $\boldsymbol{H}_0$ parallel to the axis of a long cylinder and $\frac{1}{2}$ perpendicular to the same cylinder, $\frac{1}{3}$ for a sphere, and 1 for $\boldsymbol{H}_0$ perpendicular to the plane of a thin disk. The field ($\boldsymbol{H}_0$ + $\boldsymbol{h}_1$) is considered to be the average magnetic field internal to the liquid. It is thus, perhaps, not so obvious why the field $\boldsymbol{h}_2$ must be added to this mean internal field in order to take proper account of the mean internal field seen at the nucleus.[14,15] The quantity $\boldsymbol{h}_2$ arises, in a sense, from the consideration that the mean internal field ($\boldsymbol{H}_0$ + $\boldsymbol{h}_1$) is the mean field *after* the liquid has been magnetized. Since the molecule containing the nucleus in question is also in an induced-magnetism state, it is fair to ask whether the mean effective field which magnetized a given volume is not slightly different from the final mean field. The suggestion then is that the mean field seen by the nucleus is this slightly different field. To address this problem, one considers the fictitious removal of a very small sphere of magnetized liquid surrounding a molecule. Removal is especially fictitious because one 'freezes' in the field lines prior to the removal of the sphere so that the sphere is uniformly magnetized and the magnetic field lines in the liquid near the hole are also unperturbed.[15] When one considers this problem in this so-called Lorentz sphere, one finds that the compensating field $\boldsymbol{h}_2$ is given by

$$\boldsymbol{h}_2 = (1/3)\boldsymbol{M} = (1/3)\kappa \boldsymbol{H}_0 \tag{11}$$

Therefore, the MS-corrected field $\boldsymbol{H}_{\mathrm{c}}$ seen by the molecule in its average local environment is[12]

$$\boldsymbol{H}_c = \boldsymbol{H}_0 + \boldsymbol{h}_1 + \boldsymbol{h}_2 = \boldsymbol{H}_0\{1 + [(1/3) - \alpha]\kappa\} \tag{12}$$

For a spherical liquid sample, $\boldsymbol{H}_c$ is $\boldsymbol{H}_0$; for long cylindrical spinning samples,[12,17]

$$\boldsymbol{H}_c = \boldsymbol{H}_0[1 + (1/6)(3\cos^2\beta - 1)\kappa] \tag{13}$$

where β is the angle between $\boldsymbol{H}_0$ and the spinning axis vector, $\boldsymbol{s}$. equation (13) indicates that the susceptibility corrections are very different for $\boldsymbol{H}_0$ perpendicular or parallel to $\boldsymbol{s}$; moreover, if $\boldsymbol{s}$ assumes the magic angle, β_M = arccos $(3^{-1/2})$, then the susceptibility term vanishes[17] and $\boldsymbol{H}_c = \boldsymbol{H}_0$.

A usual method of making a referenced chemical shift measurement in high-resolution NMR is to mix an internal chemical shift standard with a test liquid. This works quite well in that both kinds of molecules experience the same perturbations from MS, assuming the mixture to be a true solution. On occasion, however, chemicals are not compatible or contamination is an important issue. Then one often uses a concentric tube arrangement with one liquid in the central tube and the other in the annular space. It does not matter, from the point of view of the MS corrections to be applied, which of the spaces is occupied by the reference so long as tubes are spun. (Static concentric tubes with $\boldsymbol{H}_0$ perpendicular to the tube axis, generate a substantial distribution of internal fields over the two sample regions.[12]) Moreover, equation (13) is used to determine $\boldsymbol{H}_c$ in both liquid regions.

Recognize that the convention for chemical shift, δ, is that shifts to higher resonance frequency imply more *positive* δ values. (Note that this sign convention is also consistent with Knight shifts[18] as well as the more conventionally used chemical shift scales for protons, ^{13}C nuclei, etc.) If one measures the apparent chemical shift difference $\Delta\delta_{obs}$ (= $\delta - \delta_{ref}$) between two resonances originating from each of the sample regions, then for the iron-core magnet geometry with $\boldsymbol{H}_0 \perp \boldsymbol{s}$, the susceptibility-corrected shift $\Delta\delta_{corr}$ is given by

$$\Delta\delta_{corr} = \Delta\delta_{obs} - (1/6)(\kappa^{ref} - \kappa) \tag{14}$$

and for the superconducting geometry with $\boldsymbol{H}_0 \parallel \boldsymbol{s}$

$$\Delta\delta_{corr} = \Delta\delta_{obs} + (1/3)(\kappa^{ref} - \kappa) \tag{15}$$

where κ^{ref} is the MS of the reference liquid and κ is the MS of the test-sample liquid.

Application of equations (14) and (15) is not always convenient when one of the MS values is not known. This situation arises often for mixtures as well as neat liquids. It is possible to estimate κ, if one knows the composition and density of a material, using Pascal's constants.[3,8,19,20] This method assumes additivity relationships for the contributions from the various atoms. Corrections which depend on the nature of the bonding are also included. For known mixtures whose individual κ values are known, a molar-volume additivity assumption works quite well[21] for estimating κ for the mixture:

$$\kappa_{mixt} = \phi_1\kappa_1 + \phi_2\kappa_2 \tag{16}$$

where ϕ_1 and ϕ_2 are respectively the volume fractions of components 1 and 2.

4 MAGNETIC SUSCEPTIBILITY EFFECTS IN SOLID STATE NMR

4.1 Influence on Resolution

Solid particles come in all shapes and sizes. Particles can be crystalline, semicrystalline (e.g. polymers), amorphous or glassy materials, or even rubbery liquid-like materials. Generally, solid particles do not naturally occur as ellipsoids with ideal shape factors. This section offers a framework for estimating the spread of internal magnetic fields inside of an arbitrary particle; also an estimate of broadening in a powder sample is given. In addition, the question is raised as to what can be done, if anything, to reduce the susceptibility broadening in an NMR spectrum. The short answer is that magic angle sample spinning (MAS) will fully average to zero broadening from IBMS for particles of any shape, but when ABMS is present, MAS will result in incomplete averaging. In general, one must use single crystals of an ellipsoidal shape to eliminate ABMS broadening.

Given a particle, characterized by a single MS tensor and of a general shape, introduced into a uniform magnetic field, one can calculate the distribution of internal magnetic fields due to particle shape in the following way.[17] About any given point in the particle, where one wishes to calculate the internal field, define a primary sphere which is the largest sphere that remains within the particle. Subdivide the remaining regions of the particle into i spherical volumes, V_i, choosing the spheres of different sizes so as to account for all of the remaining particle volume. According to equation (7), the magnetic field induces a magnetic moment per unit volume in the particle; thus, each of these spheres represents a magnetic moment $\boldsymbol{\mu_i}$ given by

$$\boldsymbol{\mu}_i = V_i\boldsymbol{\kappa}\cdot\boldsymbol{H} \tag{17}$$

and the projection along $\boldsymbol{H}$ of the dipolar field $\boldsymbol{h}_i$ due to $\boldsymbol{\mu}_i$, evaluated at the center of the primary spheres will be

$$h_i = (\mu_i/r_i^3)(3\cos^2\theta_i - 1) \tag{18}$$

where, in polar coordinates centered at the origin of the primary sphere, r_i is the distance to the center of V_i and θ_i is the angle between the field direction and the line connecting the centers of the primary and the ith spheres. The sample-shape-dependent contribution to the field dispersion at the center of the primary sphere is the sum of the h_i values since the contribution from the first sphere does not contribute to the dispersion. A similar calculation can be performed at all points in the particle in order to obtain the distribution of internal fields for an arbitrary particle shape. We begin by discussing broadening for particles possessing IBMS.

4.1.1 Samples with Isotropic Magnetic Susceptibility

Drain[22] estimated the MS broadening of NMR lines in powder samples having IBMS by considering the broadening due to the shape of each particle and due to the packing of the particles. The contribution from shape was calculated by assuming that the particles were isolated prolate or oblate ellipsoids with axial ratios of 2 or 0.5, respectively. A

uniform distribution of ellipsoid orientations in the field [leading to a distribution of α values in equation (10)] gives rise to lineshapes which are asymmetric, resembling powder lineshapes for axially symmetric chemical shift tensors.[23] Drain estimated the interparticle contribution to MS broadening by using the dipole approximation to calculate the distribution within a spherical particle due to spherical cubic-close-packed arrays of neighboring particles. The result was that comparable broadening arose from sample shape and from neighbor distributions. The full width, in Hz, of the resulting resonance was about $\kappa\nu_0/4$, where it is assumed that either air or vacuum surrounds each particle. This corresponds to about 2 ppm for the typical organic material. Obviously, a significant improvement in resolution could be obtained if a liquid with a matching susceptibility were introduced into the sample chamber.[24] Then, MS broadening would be reduced to about $\Delta\kappa\nu_0/4$ where $\Delta\kappa$ is the difference in κ between the particles and the liquid. Note that Drain's estimate of line broadening assumes that the overall shape of the powder sample does not deviate strongly from an ellipsoid; if it does, there is an additional MS broadening due to overall sample shape. Another way to eliminate MS broadening in solid materials with IBMS is to melt-cast or melt-crystallize them into ellipsoidal shapes. In the absence of voids, MS broadening then ought to be very small.

One can also average to zero the broadening from IBMS effects by using MAS.[17] The dipolar form of equation (18) suggests that the angular averages of all $\boldsymbol{h}_i$ will vanish with MAS. Hence, the average dispersion will also vanish. The efficacy of MAS has also been demonstrated for samples containing liquids together with solids, such as glass beads.[17] These authors reported linewidths for the liquid-component nuclei consistent with expectations involving the rotational averages of equation (18), namely, that spinning samples with $\boldsymbol{s} \perp \boldsymbol{H}$ simply reduced the static-sample linewidth by a factor of two, whereas MAS eliminated the MS broadening when the diffusion length of the molecules in the liquid over a rotor period was small in comparison to the bead diameter. The success of eliminating MS broadening from solid state spectra is very vividly seen in the MAS ^{13}C spectrum of a cubic material such as adamantane where, in the presence of MAS, broadening due to other sources is also minimal and observed linewidths approach those expected from the inhomogeneities of the applied field.[25]

4.1.2 Samples with Anisotropic Bulk Magnetic Susceptibility

We turn now to the more complicated case of ABMS where κ is a tensor, rather than a scalar, and this tensor has principal values κ_1, κ_2, and κ_3, given in order of decreasing magnitude. In the sense that the ABMS tensor can formally be separated into an isotropic part, characterized by the mean of the principal values, and an anisotropic part, characterized by deviations from the mean, the behavior of the isotropic part will be the same as discussed above. It is only the anisotropic part which will require further consideration.

As an example of ABMS, let us consider the aromatic ring which is the most common source of diamagnetic ABMS in organic systems. Aromatic molecules typically have anisotropic molecular magnetic susceptibilities;[3] thus, their crystalline counterparts often possess ABMS as well. It is useful to think of the aromatic ring itself as an analog of ABMS in solids since, in liquid state NMR, the aromatic ring gives rise to the familiar ring current shifts.[26] These shifts are illustrated in Figure 1 where an aromatic ring is drawn and atoms A1 and A2 are placed outside of the ring, A1 along the hexad axis and A2 in the plane of the ring. If there is isotropic tumbling in a liquid containing an aromatic ring, and if the atoms A1 and A2 maintain their position with respect to this ring, then the resonance of A1 will shift to higher field and the resonance of A2 will shift to lower field. Even though the influence of the ring current on the atoms A1 and A2, at any fixed orientation, can be described as a dipolar interaction, isotropic reorientation does not average this interaction to zero because the *strength of the dipole moment is a function of orientation*. Only for a dipole moment of *fixed* magnitude, will the average dipolar field at all surrounding points vanish upon isotropic tumbling. The sign of the ring current shift at a given point in space usually takes the sign of the dipolar field when the induced moment on the ring is strongest, i.e. when $\boldsymbol{H}$ is parallel to the hexad axis.

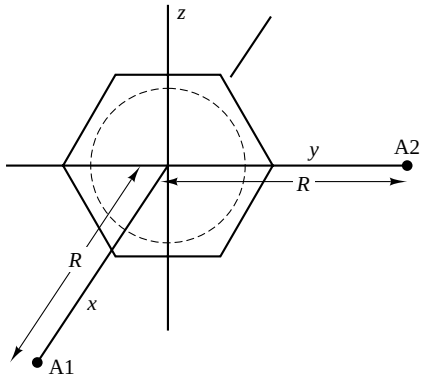

Figure 1 Geometry illustrating, at atoms A1 and A2, ring current shifts arising from the induced circulation of electrons in the π orbitals of the benzene ring. The C_6 axis of the ring, i.e. the direction of the maximum induced dipole, lies along x, and A1 is situated on x. Atom A2 lies along y. If, during isotropic tumbling or MAS, atoms A1 and A2 maintain their orientation with respect to the benzene ring, then A1 will experience an average reduction in its local field. This change in field is opposite in sign and twice the magnitude seen at A2. The interaction between the ring and the atoms is a dipolar interaction, but shifts arise because of the orientation dependence of the induced dipole. In glassy materials, aromatic rings give rise to a spread of frequencies for nearby atoms. In the presence of MAS, crystals possessing ABMS produce analogous shifts. Replace the benzene ring by a crystal with an axially symmetric κ tensor oriented along x. Similar shifts will occur for atoms in surrounding regions over distances comparable to the crystal size

For ABMS in solids, one might think of replacing the aromatic ring in Figure 1 with, say, a spherical single crystal which possesses ABMS. At some distance outside of this sphere, a change in the orientation of $\boldsymbol{H}$ with respect to the ABMS tensor of the sphere will create a change in the strength of the induced magnetic moment of the spherical crystal. This change will alter the strength of the dipolar fields emanating from this sphere. Hence, the isotropic average of the sphere's dipolar field at all external points will not, in general, vanish.

From the foregoing discussion we may draw qualitative conclusions about ABMS line broadening *in the presence of MAS*, given that MAS was effective in eliminating line broadening when only IBMS is present:

1. An isolated ellipsoidal single crystal will have no ABMS broadening since the field inside of the ellipsoid is uniform for all orientations.
2. A spherical hole inside of a sphere with ABMS will cause broadening.
3. A nonellipsoidally shaped single crystal with ABMS will cause ABMS broadening unless κ is axially symmetric and its unique axis lies along the spinning axis.
4. In a powder sample where each particle is a single crystal, ABMS broadening arises from both particle shape and from interparticle perturbations.
5. Densification via, say, melt crystallization, of a polycrystalline sample possessing ABMS increases ABMS broadening.
6. Dilution of ABMS crystallites with a material having IBMS reduces the interparticle contribution to ABMS broadening for resonances associated with these crystallites but creates ABMS broadening for resonances in the material with IBMS. The efficacy of such dilution depends rather strongly on having ABMS particles which are themselves single crystals, i.e. diluting polycrystalline ABMS particles is not very effective.

An empirical estimate of ABMS line broadening is based on MAS linewidth data[27] for hexamethylbenzene, a substance having an axially symmetric MS tensor. In a melt crystallized (densely polycrystalline) sample, ABMS line broadening yielded a full width at a halfheight of 0.93 ppm which, for hexamethylbenzene is a linewidth, in Hz, of $0.18\Delta\kappa\nu_0$ where $\Delta\kappa = \kappa_{\parallel} - \kappa_{\perp}$. In the work just referred to, points 3, 5, and 6 listed above were also demonstrated and a very crude calculation of interparticle broadening was attempted.

In the absence of MAS, ABMS line broadening is, of course, also eliminated for a *static* single crystal in the form of an ellipsoid.

4.2 Influence of Magnetic Susceptibility on Chemical Shift Measurements

4.2.1 Referencing the Anisotropic Chemical Shift

In the discussion which follows, the assumption is made that one wishes to determine the isotropic or anisotropic chemical shift values, relative to some reference material, *to a precision exceeding the magnitude of potential susceptibility corrections*. In many cases, the precision of the determination is such that one cannot justify a preoccupation with MS corrections. For example, MS issues are important in the measurement of chemical shifts for protons in organic materials because of the usually small range (8–10 ppm) of proton chemical shifts. In comparison, MS corrections for ^{13}C shifts are less important; yet MS effects can be seen because of the relatively high resolution achievable on observing dilute spin-$\frac{1}{2}$ nuclei such as ^{13}C. In paramagnetic materials or certain inorganic materials with larger susceptibilities, a consideration of the impact of MS on chemical shift is also in order.

One way to measure a chemical shift tensor is to rotate a single crystal in a magnetic field about orthogonal axes. This allows one to map the chemical shift and, by correlating these shifts with other measurements, e.g. X-ray, one can relate these shifts to directions in the molecules. Since each determination of a resonance position is undertaken using a static sample, shape effects for the crystal come into play. Obviously, the narrowest lines will be for ellipsoids. If one does not wish to make shape-dependent MS corrections at each orientation, then a sphere should be employed. If the spherical crystal has IBMS, then the chemical shift anisotropy measured will be correct. If the crystal has ABMS, then one knows that $\boldsymbol{M}$ in equation (7) has a magnitude that is a function of orientation. Yet, according to the foregoing discussion on susceptibility corrections in liquids, where equation (9) was used, if the contribution from the Lorentz sphere is included, then $(\boldsymbol{h}_1 + \boldsymbol{h}_2) = 0$ for a sphere, i.e. there should be no correction term which depends on κ at any orientation. Yet, Spiess et al.,[28] in a very careful study of ferrocene, observed small deviations from an axially symmetric shielding tensor for the protons of ferrocene in a spherical single crystal. They attributed these deviations to ABMS effects, arguing that motional averaging of the ferrocene rings and crystal symmetry combine to predict an axially symmetric shift tensor. If ABMS effects persist in a single-crystal sphere, then the appropriateness of the Lorentz correction $\boldsymbol{h}_2$ is questioned. Since the observed deviations were small, there may be alternative explanations. Nevertheless, it still seems that when the magnitude of the potential susceptibility corrections is a significant fraction of the apparent chemical shift anisotropy, the most reasonable recipe for determining true chemical shift anisotropies in materials with ABMS is to use a spherical single crystal and make no MS corrections.

4.2.2 Referencing the Isotropic Chemical Shift

The question arises as to effective strategies for referencing *isotropic* chemical shifts in solids. For solids with IBMS, an effective approach is to utilize MAS with a sample geometry such that an unknown material surrounds a central glass capillary containing a primary liquid reference, such as tetramethylsilane (TMS) for ^{13}C or ^{1}H nuclei. It does not matter whether the walls of the glass have uneven thickness or whether the spinning creates bubbles in the liquid. The main precaution, related to $\boldsymbol{B}_0$ homogeneity, is to distribute the liquid over the same axial range of the rotor that the sample occupies. The chemical shift measured between reference and solid needs no correction for MS, although there can be some other solid state contributions to the apparent chemical shift, e.g. from second-order dipolar effects.[29,30] Once the chemical shift of a suitable solid is measured in the way outlined above, that solid can be used as a secondary shift standard. For materials with IBMS, unknown and standard can be mixed in any fashion, utilizing MAS, and the measured shift differences will need no further MS correction.

The geometry for referencing the chemical shift in samples with ABMS is a more complicated problem. An approximate method is to employ MAS on a sample in which a liquid reference in a capillary is surrounded by a powder sample of the ABMS material, where the grain size of the powder is much smaller than the wall thickness of the capillary, and the particles in the powder have no preferred orientation. In this case the signal from the powder will have substantial ABMS broadening; yet, to the liquid in the capillary, the powder will look like a material with IBMS. Therefore, within the approximation that ABMS broadening in the powder is symmetric, one will get a chemical shift difference which is correct. Symmetric broadening is not necessarily

expected since broadening arises from effective dipolar interactions which typically have asymmetric, powder-average field distributions associated with them. Also, in contrast to the IBMS case, for arbitrary powder samples having ABMS, it is not required that the mean resonance position, i.e. that position about which the first moment of the resonance intensity vanishes, is without influence from ABMS. Qualitatively, one expects ABMS-induced powder-average shifts to be closely related to the existence of regular and highly asymmetric shapes for the individual powder particles.

This author is unaware of any geometry for a sample, whereby an unknown material with ABMS, *in the form of a single crystal of some shape*, can be combined with a chemical shift reference material possessing IBMS in such a way that differences in the isotropic values of unknown and reference chemical shifts can be measured reliably without a prior knowledge of the orientation of the ABMS tensor in that material. The complicated nature of chemical shift referencing has been demonstrated for a polymer film possessing ABMS.[25] In the presence of MAS, variations in shifts of about 1.5 ppm were observed between ^{13}C nuclei in TMS, contained in a central capillary tube, and ^{13}C nuclei in the oriented polymer film. These differences arose when the orientation of the unique axis of the ABMS tensor was changed from parallel to the rotor axis to perpendicular to the cylindrical walls of the rotor.

If one presumes that the Lorentz sphere correction applies to all diamagnetic and paramagnetic solids, then for a spherical single crystal possessing ABMS as well as for a spherical liquid sample, the field seen by the nucleus is just the external field $\boldsymbol{H}_0$. Hence, a true chemical shift difference, in the absence of ABMS broadening, could be measured by sequential substitution of such samples. Of course, the use of MAS for the single crystal or the employment of rotation patterns would be required in order to identify the isotropic chemical shift; moreover, for the liquid sample, the influence of the container wall will be present and this is also most easily dispensed with using MAS.

5 MISCELLANEOUS CONSIDERATIONS

5.1 Influence on Multidimensional NMR

The development of 'high-resolution' techniques in solids has enabled spectroscopists to design multidimensional NMR strategies for solids. When the chemical shifts of one nucleus form the basis for one of the NMR dimensions, then it is possible that MS effects can appear. The author has seen such effects using proton multiple pulse techniques combined with MAS. The dipolar fields arising from either IBMS or ABMS in a glassy or semicrystalline solid can be distributed in a way which is not highly correlated with the anisotropic chemical shift tensors on the molecules. The net influence of MS is to create a distribution of effective chemical shift tensors. For a given chemical site, effective tensors throughout the sample have dispersions of principal values but the same isotropic average for IBMS. For ABMS, a dispersion of isotropic shifts also exists. Thus, in a proton 2D experiment, for example, where MS effects can be a modest fraction of the chemical shift range or of chemical shift anisotropies, one tends to create spatially based as well as chemically based correlations of polarization as one increments the time for chemical shift evolution. As usual in NMR, this can be a nuisance as well as a source of information.

5.2 Use of NMR to Measure Unknown Magnetic Susceptibilities

From the foregoing discussions, it is clear that if one has two liquids in the concentric-tube geometry and utilizes MAS, any chemical shift difference associated with the two liquids will need no MS correction. A second measurement with either $\boldsymbol{s} \perp \boldsymbol{H}_0$ or $\boldsymbol{s} \parallel \boldsymbol{H}_0$ will yield the susceptibility difference between two liquids [equations (14) and (15)]. Provided the MS is known for one of the liquids, this measurement will yield the MS of the unknown liquid. One could forego the magic angle measurement above and simply use chemical shift data employing internal standards. However, any contribution to the shift arising, for example, from a change in intermolecular associations would produce an error in the susceptibility determination. Another approach[31] to measuring diamagnetic susceptibilities in liquids involves measuring a chemical shift difference from sequential experiments for some nucleus belonging to a liquid for which κ is desired. First the measurement is made for the neat liquid; then the measurement is repeated for that liquid suspended as a separate phase, in spherical droplets, in another immiscible liquid for which κ is known. This method gave reported κ values to within a few per cent of literature values.

It is also possible to estimate paramagnetic susceptibilities using NMR signals. Feher and Knight[32] in 1955 used two capillaries, filled with water, and oriented them inside of a tube filled with Mn_2O_3 powder. One capillary was parallel and one perpendicular to $\boldsymbol{B}_0$. The tube axis was in the remaining orthogonal direction. The difference in resonance frequency between the two tubes of water allowed them to estimate κ to within 6% of the listed value. Other variants of this experiment using different geometries have also been employed. For example, Li et al. measured the shift of the proton resonance in a sphere of water when that sphere was sequentially placed in a powder of an unknown and then in a powder of a reference material.[33] It is also possible to estimate the MS of a paramagnetic substance by simultaneously measuring, using concentric-tube geometry, the shift difference for a nucleus in a reference material in two solutions. One solution is the reference dissolved in a pure solvent; the other solution is the same but augmented by a known amount of paramagnetic material.[34,35]

5.3 Measurement of Anisotropic Molecular Magnetic Susceptibilities

A molecule possessing anisotropic molecular magnetic susceptibility experiences a weak alignment in a magnetic field. Its order parameter is proportional[36,37] to $\Delta\kappa H^2/kT$, where $\Delta\kappa$ is the anisotropy in the molecular magnetic susceptibility tensor. The first evidence for this alignment[36] was observed at 9.3 T in solutions of multiring aromatic compounds where deuteron resonances were split by less than 1 Hz. Subsequently, several halomethanes were examined[37] at

14.35 T, again revealing deuteron splittings of a few tenths of a Hz. The precision of these measurements is not high, but clearly the precision ought to improve rapidly as one moves to higher fields. Deuterons are ideal nuclei for observing this alignment since their natural linewidths in low viscosity liquids are quite narrow; yet, the quadrupolar interaction responsible for the splitting is conveniently large. A significant increase in the quadrupolar interaction would make the linewidths unacceptably broad for detecting small splittings.

5.4 A Basic Strategy for Suppressing MS Effects in Magnetic Resonance Imaging

One often wishes to image the density of a liquid, like water, in the vicinity of solid (e.g. bones) or rarified (e.g. as occurs for lungs[38]) phases (see ***Lung and Mediastinum: A Discussion of the Relevant NMR Physics***.). Corresponding abrupt changes in MS have the effect of modifying resonance frequencies in a local manner.[39] To the extent that the resonance frequency of a nucleus determines its spatial position in an imaging application, where field gradients are applied, the MS shift will create an undesirable apparent 'spatial shift'. A strategy[40,41] for minimizing such shifts involves creating imaging sequences where chemical shifts and MS-induced shifts are refocused but gradient pulses are applied during the dephasing and rephasing times in such a way that the resonance offsets due to these external gradients do not refocus. The result is that the 'spatial shifts' arising from MS effects get scaled approximately by the ratio of the local gradient field strength to the static field strength; hence the spatial shift becomes negligible in most materials.

6 RELATED ARTICLES

Chemical Shift Tensor Measurement in Solids; Chemical Shift Tensors in Single Crystals; Diffusion in Porous Media; Lung and Mediastinum MRI; Magnetic Field Induced Alignment of Molecules; Oil Reservoir Rocks Examined by MRI; Probe Design and Construction; Probes for High Resolution; Susceptibility and Diffusion Effects in NMR Microscopy; Susceptibility Effects in Whole Body Experiments.

7 REFERENCES

1. L. H. Bennett, C. H. Page, and L. J. Swartzendruber, *J. Res. Nat. Bur. Stand.*, 1978, **83**, 9.
2. J. H. Van Vleck, *Electric and Magnetic Susceptibilities*, Oxford University Press, Oxford, UK, 1932.
3. W. H. Flygare, *Chem. Rev.*, 1974, **74**, 653.
4. R. K. Reber and G. F. Boeker, *J. Chem. Phys.*, 1947, **15**, 508.
5. *Handbook of Chemistry and Physics*, 73rd edn., ed. D. R. Lide, CRC Press, Boca Raton, FL, 1992, Sect. 9.
6. P. Langevin, *Ann. Chim. Phys.*, 1905, **5**, 70; *J. Phys.*, 1905, **4**, 678.
7. B. C. Eggleston, D. F. Evans, and R. E. Richards, *J. Chem. Soc.*, 1954, 941.
8. J. A. Pople, W. G. Schneider, and H. J. Bernstein, *High Resolution Nuclear Magnetic Resonance*, McGraw-Hill, New York, 1959, Chaps. 2 and 4.
9. L. Pauling, *J. Chem. Phys.*, 1936, **4**, 673.
10. K. S. Krishnan, *Nature (London)*, 1934, **133**, 174.
11. J. E. Wertz and J. R. Bolton, *Electron Spin Resonance, Elementary Theory and Applications*, McGraw-Hill, New York, 1972.
12. J. R. Zimmerman and M. R. Foster, *J. Phys. Chem.*, 1957, **61**, 282.
13. L. F. Fuks, F. S. C. Huang, C. M. Carter, W. A. Edelstein, and P. B. Roemer, *J. Magn. Reson.*, 1992, **100**, 229.
14. M. A. Lorentz, *The Theory of Electrons*, Dover, New York, 1952.
15. R. P. Feynman, R. B. Leighton, and M. Sands, *The Feynman Lectures on Physics*, Addison-Wesley, Reading, MA, 1964, Vol. II, Chaps. 10, 11, 34.
16. J. A. Osborne, *Phys. Rev.*, 1945, **67**, 351.
17. D. Doskočilová, D. D. Tao, and B. Schneider, *Czech. J. Phys. B*, 1975, **25**, 202.
18. C. P. Slichter, *Principles of Magnetic Resonance*, Springer-Verlag, Berlin, 1978, Chap. 4
19. P. Pascal, *Chemie generale*, Masson et Cie, Paris, 1949.
20. C. K. Ingold, *Structure and Mechanism in Organic Chemistry*, Cornell University Press, Ithaca, NY, 1953.
21. W. R. Angus and D. V. Tilston, *Trans. Faraday Soc.*, 1947, **43**, 221.
22. L. E. Drain, *Proc. Phys. Soc.*, 1962, **80**, 1380.
23. N. Bloembergen and J. A. Rowland, *Acta Metall.*, 1953, **1**, 731.
24. M. E. Stoll and T. J. Majors, *J. Magn. Reson.*, 1982, **46**, 283.
25. W. L. Earl and D. L. VanderHart, *J. Magn. Reson.*, 1982, **48**, 35.
26. J. S. Waugh and R. W. Fessenden, *J. Am. Chem. Soc.*, 1957, **79**, 846.
27. D. L. VanderHart, W. L. Earl, and A. N. Garroway, *J. Magn. Reson.*, 1981, **44**, 361.
28. H. W. Spiess, H. Zimmermann, and U. Haeberlen, *Chem. Phys.*, 1976, **12**, 123.
29. D. L. VanderHart, *J. Chem. Phys.*, 1986, **84**, 1196.
30. M. P. Augustine, K. W. Zilm, and D. B. Zax, *J. Chem. Phys.*, 1993, **98**, 9432.
31. J. Homer and H. K. Al-Daffaee, *J. Chem. Soc., Faraday Trans. 2*, 1985, **81**, 803.
32. G. Feher and W. D. Knight, *Rev. Sci. Instrum.*, 1955, **26**, 293.
33. J. Li, M. E. Lashier, G. L. Schrader, and B. C. Gerstein, *Appl. Catal.*, 1991, **73**, 83.
34. D. F. Evans, *J. Chem. Soc.*, 1959, 2003.
35. S. K. Sur, *J. Magn. Reson.*, 1989, **82**, 169.
36. J. A. B. Lohman and C. MacLean, *Chem. Phys.*, 1978, **35**, 269.
37. A. A. Bothner-By, J. Dadok, P. K. Mishra, and P. C. M. Van Zijl, *J. Am. Chem. Soc.*, 1987, **109**, 4180.
38. D. C. Ailion, T. A. Case, D. D. Blatter, A. H. Morris, A. G. Cutillo, C. H. Durney, and S. A. Johnson, *Bull. Magn. Reson.*, 1984, **6**, 130.
39. T. A. Case, C. H. Durney, D. C. Ailion, A. G. Cutillo, and A. H. Morris, *J. Magn. Reson.*, 1987, **73**, 304.
40. P. Bendel, *IEEE Trans. Med. Imag.*, 1985, **MI-4**, 114.
41. J. B. Miller and A. N. Garroway, *J. Magn. Reson.*, 1986, **67**, 575.

Acknowledgments

The author wishes to acknowledge the assistance of L. H. Bennett, L. J. Swartzendruber, J. F. Douglas, A. N. Garroway, G. Eaton, J. Carolan, and A. Vega in the preparation of this manuscript.

Biographical Sketch

David L. VanderHart. *b* 1941. B.A., 1963, Ph.D., 1968, Physical Chemistry, University of Illinois, supervisor, H. S. Gutowsky. Postdoctoral work with W. H. Flygare (molecular Zeeman effect), 1968–69. Polymers Division, National Institute of Standards and Technology, Gaithersburg, MD, USA, 1969–present. Approx. 70 publications. Current research specialty: solid state NMR of polymers with an emphasis on obtaining morphological information.

Paramagnetic Relaxation in Solution

Jozef Kowalewski
Stockholm University, Sweden

1	Introduction	1
2	Theory	1
3	Experimental Methods	4
4	Related Articles	6
5	References	6

1 INTRODUCTION

Paramagnetic systems are materials with positive magnetic susceptibility, normally associated with unpaired electrons. Chemically, paramagnetic systems of relevance for this article are dilute aqueous or organic solutions of free radicals and transition metal ions or their complexes, including metalloproteins. The presence of unpaired electron spins has a profound influence on the NMR spectra of such solutions. The origin of the effects is to be found in the large value of the electronic magnetic moment, about 650 times that of the proton.

The influence of the paramagnetic species on NMR spectra of liquids may be two-fold. First, the nuclear spin relaxation rates are enhanced. The paramagnetic relaxation enhancement (PRE) is caused by random variation of the electron spin–nuclear spin interactions, which opens new pathways for longitudinal as well as transverse relaxation. The PRE is most often studied for $I = \frac{1}{2}$ nuclei, but oxygen-17 applications are not uncommon. Second, the NMR signals may be shifted, provided the relevant electron spin–nuclear spin interaction has a nonzero average. Paramagnetic complexes in solution often contain exchangeable ligands, and the exchange phenomena (see***Chemical Exchange Effects in Biological Macromolecules***), together with the intrinsic relaxation rates and shifts, contribute to the observed lineshapes and line positions. The paramagnetic effects have been used for several decades by chemists and biochemists as a source of structural, thermodynamic, and dynamic information. Applications of this type have been described in numerous books, recently by Bertini and Luchinat[1] and by Banci et al.[2] A more recent application of PRE is the use of paramagnetic compounds as contrast agents in MRI (see ***Contrast Agents in Whole Body Magnetic Resonance: An Overview*** and ***Contrast Agents in Magnetic Resonance: Operating Mechanisms***).

2 THEORY

The theory of nuclear relaxation in paramagnetic systems contains many intricate points, described some years ago in a review article.[3] Here, we concentrate on the most important issues and begin by formulating the relationships between the measured macroscopic PRE and the microscopic quantities. We then proceed with the theory for relaxation times for nuclei residing in the ligands in paramagnetic complexes and conclude the theory section by a brief discussion of intermolecular relaxation.

2.1 The Macroscopic and Microscopic Quantities

The PRE experiments are often performed with a considerable excess of a ligand (e.g. solvent) over the paramagnetic centers (e.g. transition metal ions). The type of information obtainable from PRE measurements in solution depends on the relative magnitudes of the exchange rates, the intrinsic relaxation rates, and shifts. The set of equations relating the relaxation, shift, and lifetime properties of the nuclei in paramagnetic complexes to the observables of the NMR experiments has been derived by Swift and Connick[4] and by Luz and Meiboom:[5]

$$T_{1\mathrm{P}}^{-1} = \frac{P_\mathrm{M}}{\tau_\mathrm{M} + T_{1\mathrm{M}}} \tag{1}$$

$$T_{2\mathrm{P}}^{-1} = \frac{P_\mathrm{M}}{\tau_\mathrm{M}} \left[\frac{T_{2\mathrm{M}}^{-2} + (T_{2\mathrm{M}}\tau_\mathrm{M})^{-1} + \Delta\omega_\mathrm{M}^2}{(T_{2\mathrm{M}}^{-1} + \tau_\mathrm{M}^{-1})^2 + \Delta\omega_\mathrm{M}^2} \right] \tag{2}$$

$$\Delta\omega_\mathrm{P} = \frac{P_\mathrm{M}\Delta\omega_\mathrm{M}}{(\tau_\mathrm{M}/T_{2\mathrm{M}} + 1)^2 + \tau_\mathrm{M}^2\Delta\omega_\mathrm{M}^2} \tag{3}$$

$T_{1\mathrm{P}}{}^{-1}$, $T_{2\mathrm{P}}{}^{-1}$, and $\Delta\omega_\mathrm{P}$ are the excess (see Section 3) spin–lattice relaxation rate, spin–spin relaxation rate and shift measured for the ligand in solution, while the properties with index M refer to the ligand in the paramagnetic complex. τ_M is the lifetime of the ligand in the complex and P_M is the mole fraction of ligand nuclei in bound positions.

2.2 The Modified Solomon–Bloembergen Equations

The nuclear spin relaxation in a paramagnetic complex arises through the electron–nucleus hyperfine interaction (see ***Electron-Nuclear Interactions***) between the nuclear spin I and the electron spin S. The hyperfine interaction consists of two parts. The first term is the dipole–dipole interaction between the nuclear magnetic moment and the electron spin of the electron outside of the nucleus; the second term is the scalar interaction or Fermi contact coupling between the nuclear magnetic moment and the spin of s electrons at the site of the nucleus. Each of these terms can be modulated by random processes and can contribute to the nuclear relaxation rates. The dipole–dipole part of the hyperfine interaction is modulated by reorientation of the spin–spin axis, by changes in the orientation of the electron spin (electron spin relaxation) and by ligand exchange. The scalar interaction part remains unaffected by reorientation of the molecule and is only modulated by electron relaxation and ligand exchange.

These qualitative ideas are reflected in the set of equations for nuclear relaxation rates in paramagnetic complexes, known as the ‘modified Solomon–Bloembergen equations’:

$$T_{1M}^{-1} = (T_{1M}^{SC})^{-1} + (T_{1M}^{DD})^{-1}$$
$$= \frac{2}{3}\left(\frac{A}{\hbar}\right)^2 S(S+1)\frac{\tau_{e2}}{1+(\omega_S-\omega_I)^2\tau_{e2}^2}$$
$$+\frac{2}{15}\left(\frac{\mu_0}{4\pi}\right)^2 S(S+1)\hbar^2\gamma_I^2\gamma_S^2 R^{-6}$$
$$\times\left[\frac{\tau_{c2}}{1+(\omega_S-\omega_I)^2\tau_{c2}^2}+\frac{3\tau_{c1}}{1+\omega_I^2\tau_{c1}^2}\right.$$
$$\left.+\frac{6\tau_{c2}}{1+(\omega_S+\omega_I)^2\tau_{c2}^2}\right] \quad (4)$$

and

$$T_{2M}^{-1} = (T_{2M}^{SC})^{-1} + (T_{2M}^{DD})^{-1} = \frac{1}{3}\left(\frac{A}{\hbar}\right)^2 S(S+1)$$
$$\times\left(\tau_{e1}+\frac{\tau_{e2}}{1+(\omega_S-\omega_I)^2\tau_{e2}^2}\right)$$
$$+\frac{1}{15}\left(\frac{\mu_0}{4\pi}\right)^2 S(S+1)\hbar^2\gamma_I^2\gamma_S^2 R^{-6}$$
$$\times\left[4\tau_{c1}+\frac{3\tau_{c1}}{1+\omega_I^2\tau_{c1}^2}+\frac{\tau_{c2}}{1+(\omega_S-\omega_I)^2\tau_{c2}^2}\right.$$
$$\left.+\frac{6\tau_{c2}}{1+\omega_S^2\tau_{c2}^2}+\frac{6\tau_{c2}}{1+(\omega_S+\omega_I)^2\tau_{c2}^2}\right] \quad (5)$$

where

$$\tau_{ci}^{-1} = \tau_R^{-1} + \tau_M^{-1} + T_{ie}^{-1} \quad (i = 1, 2) \quad (6)$$

$$\tau_{ei}^{-1} = \tau_M^{-1} + T_{ie}^{-1} \quad (7)$$

τ_R is an isotropic rotational correlation time of the complex, T_{ie} (i = 1 or 2) is the electron spin relaxation time, and S is the electron spin quantum number, $A/\hbar$ is the isotropic scalar coupling constant, μ_0 is the permeability of vacuum, R is the distance between the nuclear spin and the electron spin (considered as a point dipole), and γ_S equals $g_{eff}\beta/\hbar$, where g_{eff} is the effective g factor of the electron in the complex under consideration and β is the Bohr magneton. ω_S and ω_I are the electronic and nuclear Larmor frequencies. The electronic Larmor frequency is so much larger than the nuclear Larmor frequency that the latter can be neglected in the terms involving the sum and difference frequencies, and some of the terms in the dipole–dipole parts of equations (4) and (5) can be brought together. Note the peculiar dual role that the exchange can play in the PRE: in equations (4)–(7) the τ_M acts as a correlation time, while its role in equations (1)–(3) is that of a relaxation time.

The modified Solomon–Bloembergen equations were first presented in the papers by Connick and Fiat[6] and by Reuben et al.[7] The formal derivation of the equations is fairly complicated and was in fact published much later.[8] It is based on the Redfield relaxation theory for the nuclear spin and involves two critical assumptions. The first one is that the electron relaxation (which is a motion in the electron spin space) is uncorrelated with molecular reorientation (which is a spatial motion influencing the dipole coupling). The second assumption is concerned with the description of the dynamics in the electron spin space. It is assumed that the electron spin system is dominated by the electronic Zeeman interaction. Other interactions lead to relaxation, which can be described in terms of the longitudinal and transverse relaxation times T_{1e} and T_{2e}. This point is elaborated on in Section 2.3. In this sense, one can call the modified Solomon–Bloembergen equations a 'Zeeman-limit theory'. If the second assumption is fulfilled, then the scalar interaction parts in equations (4) and (5) become analogous to the equations describing scalar relaxation originating from the modulation of the nuclear spin–spin coupling, with the hyperfine coupling constant $A/\hbar$ replacing the J coupling constant. The first assumption does not directly influence the scalar interaction term, but the failure to fulfil it will lead to an additional interference (cross correlation) term between the dipole–dipole and the scalar interactions. The validity of both the above assumptions is questionable in many cases of practical importance.

Apart from these two main assumptions, equations (4) and (5) contain several additional approximations, the most important of which are the following:

1. The electron spin is assumed to be a point dipole centered at the metal ion. The validity of this assumption can be tested by ab initio quantum-chemical calculations, which indicate that it is reasonable for protons but may cause errors for heavier nuclei, in particular if the atoms where they reside are involved in bonding with the paramagnetic metal center.[9]
2. The electron g tensor is assumed to be isotropic. The effects of deviations from this assumption were first investigated by Sternlicht.[10]
3. It is assumed that the reorientation of the nuclear–electron spin vector can be described by a single correlation time, τ_R. This amounts to neglecting the effects of internal motion and anisotropic reorientation.
4. It is assumed that chemical exchange is uncorrelated with the remaining motions in the lattice. This assumption seems to be easy to fulfil. We return to the exchange effects in Section 3.1.

2.3 The Bloembergen–Morgan Theory for Electron Spin Relaxation

As one can see in equations (4) and (5), the magnitude of the PRE for the ligand nuclei depends on the energy level splittings and the relaxation behavior of the electron spin system of the transition metal ion in the magnetic field. For discussing the splittings, the spin Hamiltonian formalism, developed originally for the interpretation of ESR spectra,[11] normally constitutes an appropriate framework. The spin Hamiltonian is an operator involving only nuclear and electron spin operators and parameters characterizing the spin system under consideration. Neglecting the terms containing only nuclear spins and the hyperfine coupling to the ligand nuclei, the spin Hamiltonian can be written:

$$\hat{\mathcal{H}}_S = \hat{\boldsymbol{S}}\cdot\boldsymbol{g}\cdot\hat{\boldsymbol{B}}_0\cdot + \hat{\boldsymbol{S}}\cdot\boldsymbol{D}\cdot\hat{\boldsymbol{S}} + \hat{\boldsymbol{S}}\cdot\boldsymbol{A}\cdot\hat{\boldsymbol{I}}_M \quad (8)$$

$\hat{\boldsymbol{S}}$ is the electron spin operator. The first term describes the electron Zeeman interaction and the second the zero-field splitting (ZFS) interaction, which only has to be considered for systems with electron spin quantum number $S \geq 1$. The last term corresponds to the hyperfine interaction with the metal nucleus, if it has nonzero spin ($\hat{\boldsymbol{I}}_{\mathrm{M}}$ is the nuclear spin operator for the metal). The molecular parameters are the three second-rank tensors: the g tensor $\boldsymbol{g}$, the ZFS tensor $\boldsymbol{D}$ and the hyperfine coupling tensor $\boldsymbol{A}$. The combined effect of the electrostatic interactions and spin–orbit coupling renders the Zeeman interaction anisotropic and makes the average effective g value (equal to one-third of the trace of the g tensor) different from the free electron value of 2.0023. The effect of the g tensor on ESR spectra is similar to the effect of the shielding tensor in NMR.

The zero-field splitting tensor also has its origin in the intermingling of the electrostatic and spin–orbit interactions. In addition, the dipolar coupling between the electron spins can contribute to the ZFS, but this contribution is believed to be minor for transition metal complexes.[12] The ZFS tensor is traceless and can be characterized, in its principal axis system, by two constants:

$$D = D_{zz} - \tfrac{1}{2}(D_{xx} + D_{yy}) \tag{9a}$$

$$E = \tfrac{1}{2}(D_{xx} - D_{yy}) \tag{9b}$$

The ZFS interaction has a form similar to the quadrupolar interaction in NMR.

The modulation of various terms in equation (8) by random processes in liquids leads to electron spin relaxation. The rotational modulation of the anisotropies of the g and hyperfine tensors are important sources of electron relaxation for $S = \frac{1}{2}$ systems. Still another relaxation mechanism for $S = \frac{1}{2}$ systems, in analogy with the case of nuclear relaxation, is the spin–rotation coupling. The electron relaxation in $S = \frac{1}{2}$ systems is discussed at length in the book by Muus and Atkins[13] and is summarized in the book by Banci et al.[2]

For systems with $S \geq 1$, the electron spin relaxation is usually so fast (often on the picosecond timescale) that it competes effectively with complex reorientation as the main modulation mechanism for the dipole–dipole part of the modified Solomon–Bloembergen equations, even in small complexes. Bloembergen and Morgan[14] presented, as early as the early 1960s, a Redfield-type theory (see ***Relaxation Theory: Density Matrix Formulation***) where they related this efficient electronic relaxation in hexaaquo complexes of transition metal ions to the modulation of the ZFS by the distortion of the hydration shell. The Bloembergen–Morgan equations for $T_{1\mathrm{e}}$ and $T_{2\mathrm{e}}$ are often written as

$$T_{1\mathrm{e}}^{-1} = \frac{\Delta^2}{25}[4S(S+1) - 3]\left(\frac{\tau_v}{1 + \tau_v^2\omega_S^2} + \frac{4\tau_v}{1 + 4\tau_v^2\omega_S^2}\right) \tag{10}$$

$$T_{2\mathrm{e}}^{-1} = \frac{\Delta^2}{50}[4S(S+1) - 3] \times \left(3\tau_v + \frac{5\tau_v}{1 + \tau_v^2\omega_S^2} + \frac{2\tau_v}{1 + 4\tau_v^2\omega_S^2}\right) \tag{11}$$

where τ_v is the correlation time for the collision-related modulation of the ZFS, and Δ^2 is the trace of the square of the transient ZFS tensor:

$$\Delta^2 = D_{xx}^2 + D_{yy}^2 + D_{zz}^2 = \tfrac{2}{3}D^2 + 2E^2 \tag{12}$$

The combination of the modified Solomon–Bloembergen equations with the Bloembergen and Morgan theory for electron spin relaxation rates provides a complete theory for the magnetic field dependence of the PRE, known in the literature as the Solomon–Bloembergen–Morgan (SBM) theory.

The Bloembergen–Morgan theory has rather severe validity conditions, very clearly stated in the original paper. The most important limitation is the validity requirement for the Redfield-type or perturbative approach, which can generally be formulated as $\tau_v{}^2\Delta^2 \ll 1$. It is unfortunately rather common in the literature to use equations (10) and (11) uncritically, also beyond the limits of their validity. Analogous equations have also been derived for the case of rotational modulation of a static ZFS.[15] This case should be handled with care in the context of PRE, because it violates the requirement of no correlation between rotation and electron relaxation. An improvement of the SBM theory, within the same general framework and with the same validity limits, has been proposed by Rubinstein et al.[16] They noted that for systems with $S \geq \frac{3}{2}$ one may have more than one electronic T_1 or T_2, and they elegantly described the collision modulation of the ZFS as a pseudorotation process.

The issue of the electron spin relaxation for $S \geq 1$ in solution is not really settled, on the fundamental level of the applicability of the spin Hamiltonian formalism. An interesting line of thought, which still awaits a quantitative formulation, is that the electronic relaxation in liquids might in fact be similar to that in solids, where one talks about mechanisms involving interactions between the electron spin and phonons, mediated by the spin–orbit coupling.[2]

2.4 Beyond the Solomon–Bloembergen–Morgan Theory

During the last decade, significant effort has been invested into moving the paramagnetic relaxation theory beyond the limitations of the SBM theory. Two main approaches can be discerned. One of them can be referred to as 'low-field theories'. These are designed to handle cases when the electron Zeeman interaction does not dominate the energy level structure, either because the slow reorientation does not average out the anisotropic term in equation (8) or because another interaction (in the first place the ZFS interaction) simply is stronger and determines the quantization direction of the electron spin. This approach was originally proposed by Lindner[17] and was subsequently developed by Bertini and co-workers[1,2] and by Sharp.[18] The form of the resulting equation for $T_{1\mathrm{M}}{}^{-1}$ is similar to equation (4), in the sense that it consists of a sum of terms containing spectral density functions at the transition frequencies in the combined nuclear spin–electron spin system. The coefficients of the various spectral densities depend on the angle between the two molecule–fixed axis systems: the dipole–dipole axis and the principal axis of the anisotropic interaction. The electron spin relaxation enters the theories of this type in the simple form of 'electron relaxation

time', $\tau_S = T_{1e} = T_{2e}$, i.e. the electron spin is assumed to be in the Redfield limit. In addition, a frequency dependence of τ_S, similar to that given by the Bloembergen–Morgan theory, is sometimes used.

The other approach tries to solve the problem using more general, and more cumbersome, methods[3,8,19,20] based on the stochastic Liouville equation (see ***Liouville Equation of Motion***).[13] This formulation is often referred to as the 'slow-motion approach'. The nuclear spin is considered to be weakly coupled (in the sense that the Redfield formalism is valid) to a composite lattice, containing the electron spin degree of freedom as well as rotations and possibly other classical degrees of freedom. The electron spin and the classical degrees of freedom are coupled through the ZFS interaction of arbitary strength. The dynamics in the composite lattice can be described in terms of a spectral density function, and the nuclear T_1 is determined by the value of the spectral density at the nuclear Larmor frequency, while the nuclear T_2 depends on the spectral density at the nuclear Larmor frequency and at zero frequency. There is no need to invoke the concept of electronic relaxation time, even though the result of numerical calculations becomes identical to the SBM theory under appropriate limiting conditions. The disadvantage of the approach is its complexity: the composite lattice spectral density is obtained by the inversion of a complex matrix, in principle of infinite dimensions.

The magnetic field dependences of the nuclear spin–lattice relaxation rate, calculated using the methods of Bertini et al.[2] and of Benetis et al.,[8] have been compared with each other, imposing on the latter model the additional assumption of exponential electron spin relaxation.[2] For the case of large ZFS, the results of the two methods are identical and very different from the predictions of the SBM theory (Figure 1).

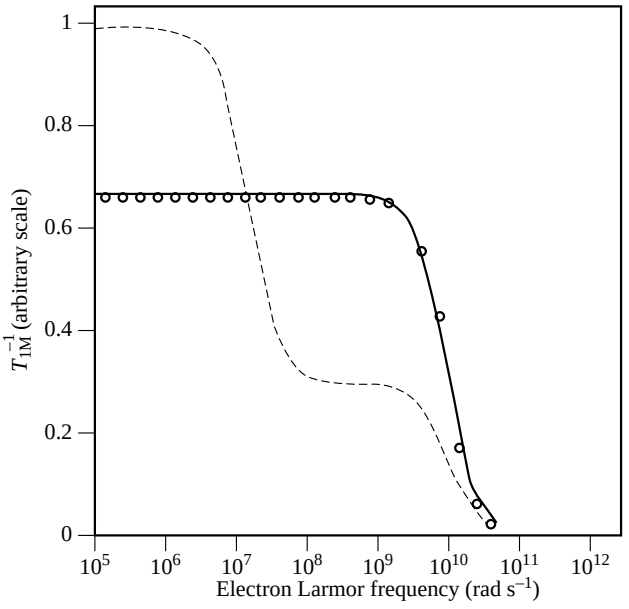

Figure 1 Calculated magnetic field dependence of proton $T_{1M}{}^{-1}$ in an $S = 1$ system according to the modified Solomon–Bloembergen equations (----), a low-field theory (—), and the slow-motion approach (○). (Reproduced by permission of VCH from L. Banci, I. Bertini, and C. Luchinat, 'Nuclear and Electron Relaxation', Weinheim, 1991)

2.5 The Curie Spin Relaxation

Gueron, Fiat, and Vega[21] have proposed an additional mechanism for the PRE, due to dipolar coupling of the nuclear spin with the thermally averaged electron magnetic moment. This average 'Curie spin' is aligned along the external magnetic field and is proportional to its magnitude. The interaction between the nuclear spin and the Curie spin is modulated by reorientation and exchange, but not by the electron spin relaxation. If the electron relaxation is much faster than the reorientation and exchange, and if the magnetic field is high, the Curie spin relaxation can become important (in particular for T_{2M}) in spite of the fact that the average electronic magnetic moment is of course much smaller than the real, rapidly oscillating one.

2.6 Intermolecular Relaxation

The above-mentioned theories of intramolecular nuclear spin relaxation due to dipole–dipole interaction assume that the distance R between the I and S spins is constant. The chemical exchange can be thought of as an extremely crude way of incorporating possible intermolecular effects or modulation of the dipole–dipole interaction by the variation of the interspin distance; it is allowed to be given a value of either R or infinity. For many transition metal complexes, this essentially intramolecular approach is sufficient. For other systems, where the paramagnetic centers in solution are either transition metal complexes with a nonlabile coordination sphere, or stable organic radicals, the relaxation of the solvent nuclei is predominantly intermolecular in nature (the concept of outer sphere relaxation is also used), and a more refined approach to the modulation of the spin–spin distance by translational diffusion is required. The problem can be solved at different levels of sophistication. The earlier development has been reviewed by Kowalewski et al.[3] Among more recent contributions, one should mention the work of Bayburt and Sharp[22] dealing with the limiting case of ZFS dominating over the electron Zeeman interaction.

3 EXPERIMENTAL METHODS

Most experimental work on PRE is technically very simple. Basically, one measures the nuclear spin–lattice or spin–spin relaxation rate (the latter is commonly estimated from the linewidth) for ligand nuclei in the presence and in the absence of the paramagnetic reagent, and one obtains the PRE by subtraction. The experiments are often performed to yield the result as a function of concentration of the paramagnetic species, temperature, pressure, or magnetic field. Variable concentration work can provide information on complexation equilibria. Variable temperature measurements can be used to clarify the relationships between the relaxation and exchange processes. Variable pressure experiments provide mechanistic information on the exchange processes (see ***Kinetics at High Pressure***). Variable field measurements are PRE experiments *par excellence*, if one is interested in verifying theoretical models. The variable temperature and variable field measurements are discussed in the following two sections, and the experimental section is concluded by a brief presentation of

the paramagnetic relaxation effects in certain two-dimensional experiments.

3.1 Variable Temperature: Fast and Slow Exchange

As can be seen from equations (1)–(3), the relationship between relaxation and exchange is simplest for the spin–lattice relaxation, where one can easily define two limiting conditions: fast exchange, $\tau_M \ll T_{1M}$; and slow exchange, $\tau_M \gg T_{1M}$. Assume a simple case of a small complex in low viscosity solution, with T_{1M} dominated by the dipole–dipole interaction and with the reorientation of the complex determining τ_{c1} and τ_{c2}. For such a case, we are likely to have $(\tau_{c1}\ \omega_I)^2 \ll 1$ and $[\tau_{c2}\ (\omega_S \pm \omega_I)]^2 \ll 1$ and, as the rate of reorientation increases with increasing temperature, the nuclear relaxation rate decreases. The opposite is true for the ligand exchange—the rate is going to increase with increasing temperature. The measurements of the PRE in the slow exchange regime give directly the exchange lifetime and its temperature dependence/activation parameters. Measurements in the fast exchange limit provide the relaxation rate in the paramagnetic complex which, given a suitable theoretical model, can yield information on structural as well as dynamic parameters. The slow and fast exchange conditions can also be formulated for paramagnetic line broadening, a quantity commonly measured in variable temperature studies. An example of variable temperature ^{17}O line-broadening data, taken from the work of Hugi et al.,[23] is shown in Figure 2.

3.2 Variable Field: Physics of Relaxation

When one wishes to reach a deeper understanding of the details of the relaxation mechanism, a variable field [nuclear magnetic relaxation dispersion (NMRD)] study is a very powerful tool. Changing the magnetic field provides a direct way of measuring the frequency dependence of the relevant spectral densities.

Figure 2 gives an example of a variable field T_2 study. More commonly, the variable field studies are concentrated on T_1 measurements. Besides performing the regular inversion–recovery experiments at as many high-field spectrometers as possible, it is useful to apply field cycling experiments (see ***Field Cycling Experiments***) to obtain the PRE also at very low magnetic fields. An illustrative example of the use of NMRD over a very wide range of magnetic fields is provided by the water proton relaxation in an aqueous solution of Mn(II) ions. The first field cycling experiments for this system were reported as early as the 1960s.[24] More recent data, as a function of solution viscosity varied by means of adding glycerol, are shown in Figure 3, taken from Bertini et al.[25] The Mn(II) ion is characterized by very small ZFS and slow electron spin relaxation; the data in Figure 3 can be interpreted successfully using the SBM theory. The scalar relaxation is observed at low field, because the electron relaxation is slow. In pure water, the scalar contribution disperses at ω_I of about 0.1 MHz, where $(T_{2e}\omega_S)^2$ becomes larger than unity. At higher fields, the dipolar relaxation dominates, and the second dispersion at ω_I of about 10 MHz corresponds to the condition $\omega_S\tau_R = 1$. Upon increasing the glycerol content, the viscosity increases, and both τ_R and τ_v increase with it, which changes the NMRD profiles.

A different case is presented by the PRE of water protons in an aqueous solution of another divalent first-row transition metal ion, Ni(II). An NMRD curve for this system, taken from work by Kowalewski et al.,[26] is shown in Figure 4. Here, the field dependence of the PRE is much weaker. The origin of this different behavior is to be sought in the electron relaxation in Ni(II), much faster than in the case of Mn(II). In fact, the nuclear and electron relaxation in aqueous Ni(II) is beyond the validity region of the SBM theory, and the details of the analysis of the data in Figure 4 are still not

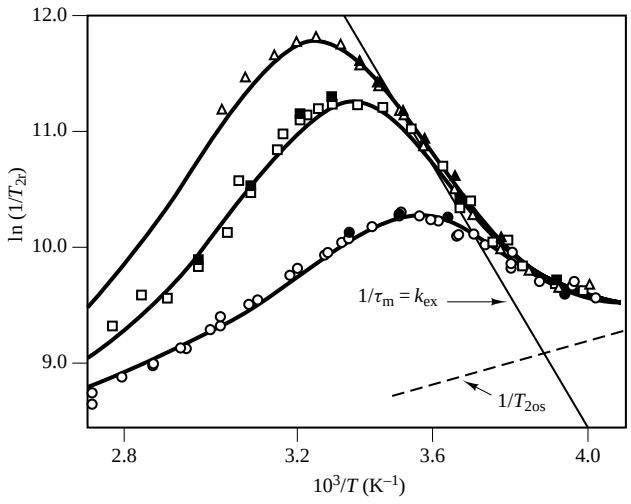

Figure 2 Oxygen-17 T_{2r}^{-1} in aqueous solution of a Ti(III) salt as a function of reciprocal temperature. Measurements were made at: (△, ▲) 8.4 T, (□, ■) 4.7 T, and (○, ●) 1.4 T. Open and filled symbols refer to different pH values. (Reproduced by permission of the American Chemical Society from A. D. Hugi, L. Helm, and A. E. Merbach, *Inorg. Chem.*, 1987, **26**, 1763)

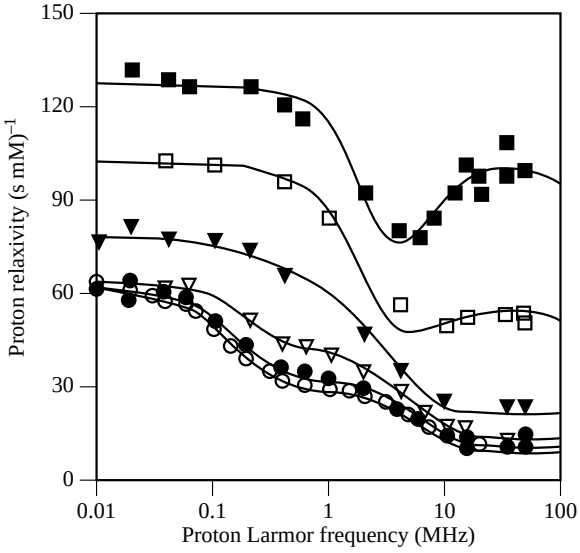

Figure 3 Water ^1H NMRD profiles of Mn(II) solutions in pure water (○) and with increasing amounts of deuterated glycerol [(●) 10%, (▼) 20%, (▼) 35%, (□) 55%, (■) 65%]. (Reproduced by permission of Academic Press from I. Bertini, F. Briganti, Z. C. Xia, and C. Luchinat, *J. Magn. Reson., Ser. A*, 1993, **101**, 198)

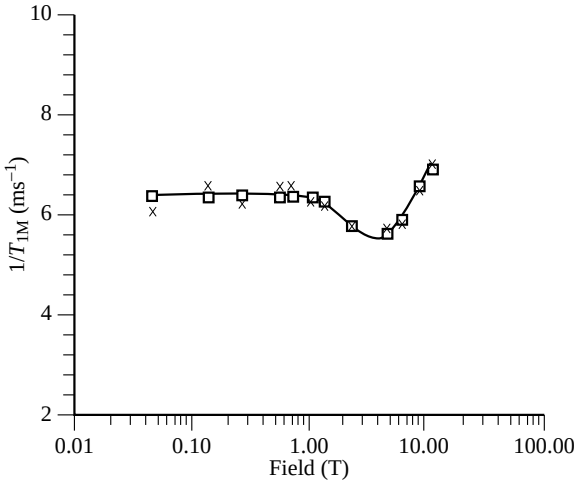

Figure 4 Water ^{1}H NMRD profile in aqueous Ni(II) solution [(×) experimental points, (□) slow-motion calculations, (—) SBM theory]. (Reproduced by permission of Academic Press from J. Kowalewski, T. Larsson, and P.-O. Westlund, *J. Magn. Reson.*, 1987, **74**, 56)

completely settled.[18,20,26] The flatness of the NMRD curve is caused by the rapid electron relaxation, which makes the scalar contribution negligible and reduces the efficiency of the dipole–dipole contribution. The weak increase of PRE at high field can be related to the onset of the dispersion of the electron relaxation.

The NMRD measurements are by no means limited to low-molecular-weight paramagnetic systems. A large number of data for metalloproteins in solutions can be found in the book by Banci et al.[2] and in a review by Koenig and Brown.[27]

3.3 Novel Experiments

The last few decades have seen a tremendous growth in the number of available NMR experiments. In many of these experiments the paramagnetic relaxation effects are a nuisance, and are carefully avoided by removing oxygen and paramagnetic impurities from the samples. In some cases, however, paramagnetic systems can be studied, and special features introduced into common two-dimensional techniques (NOESY and COSY) by the paramagnetic relaxation are worth mentioning.

The NOESY experiment suffers from the PRE in the sense that the cross-relaxation rates involving nuclei close to paramagnetic centers become much smaller than the leakage rates, which reduces the intensity of the cross peaks. As demonstrated, by Emerson and La Mar[28] among others, it is nevertheless possible to perform NOESY studies of the active site regions of fairly large paramagnetic proteins. The COSY experiments suffer from the PRE because of rapid relaxation and excessive signal cancellation when the linewidth is much larger than the J coupling. COSY cross peaks have nevertheless been reported in paramagnetic proteins. The results may, however, require a reevaluation in the light of the recent work by Bertini et al.,[29] who have demonstrated that the cross peaks may actually arise through relaxation-allowed coherence transfer, originating from cross correlation of the dipole–dipole and Curie relaxation mechanisms, rather than through J couplings.

4 RELATED ARTICLES

Chemical Exchange Effects on Spectra; Cobalt(II)- and Nickel(II)-Substituted Proteins; Contrast Agents in Whole Body Magnetic Resonance: An Overview; Contrast Agents in Magnetic Resonance: Operating Mechanisms; Copper Proteins; Electron–Nuclear Hyperfine Interactions; Electron–Nuclear Multiple Resonance Spectroscopy; Field Cycling Experiments; Iron—Sulfur Proteins; Kinetics at High Pressure; Liouville Equation of Motion; Myoglobin; Nonheme Iron Proteins; Relaxation Theory: Density Matrix Formulation; Transferrins.

5 REFERENCES

1. I. Bertini and C. Luchinat, *NMR of Paramagnetic Molecules in Biological Systems*, Benjamin/Cummings, Menlo Park, 1986.
2. L. Banci, I. Bertini, and C. Luchinat, *Nuclear and Electron Relaxation*, VCH, Weinheim, 1991.
3. J. Kowalewski, L. Nordenskiöld, N. Benetis, and P.-O. Westlund, *Progr. NMR Spectrosc.*, 1985, **17**, 141.
4. T. J. Swift and R. E. Connick, *J. Chem. Phys.*, 1962, **37**, 307.
5. Z. Luz and S. Meiboom, *J. Chem. Phys.*, 1964, **40**, 2686.
6. R. E. Connick and D. Fiat, *J. Chem. Phys.*, 1966, **44**, 4103.
7. J. Reuben, G. H. Reed, and M. Cohn, *J. Chem. Phys.*, 1970, **52**, 1617.
8. N. Benetis, J. Kowalewski, L. Nordenskiöld, H. Wennerström, and P.-O. Westlund, *Mol. Phys.*, 1983, **48**, 329.
9. D. Waysbort and G. Navon, *J. Chem. Phys.*, 1975, **62**, 1021; L. Nordenskiöld, A. Laaksonen, and J. Kowalewski, *J. Am. Chem. Soc.*, 1982, **104**, 379; N. Sahoo and T. P. Das, *J. Chem. Phys.*, 1989, **91**, 7740.
10. H. Sternlicht, *J. Chem. Phys.*, 1965, **42**, 2250.
11. A. Abragam and B. Bleaney, *Electron Paramagnetic Resonance of Transition Ions*, Clarendon, Oxford, 1970.
12. J. S. Griffith, *The Theory of Transition-Metal Ions*, Cambridge University, Cambridge, 1961.
13. L. T. Muus and P. W. Atkins (eds), *Electron Spin Relaxation in Liquids*, Plenum, New York, 1972.
14. N. Bloembergen and L. O. Morgan, *J. Chem. Phys.*, 1961, **34**, 842.
15. A. Carrington and G. R. Luckhurst, *Mol. Phys.*, 1964, **8**, 125; A. D. McLachlan, *Proc. R. Soc. London, Ser. A*, 1964, **280**, 271.
16. M. Rubinstein, A. Baram, and Z. Luz, *Mol. Phys.*, 1971, **20**, 67.
17. U. Lindner, *Ann. Phys. (Leipzig)*, 1965, **16**, 319 (Chem. Abstr., **64**: 14973c).
18. R. R. Sharp, *J. Chem. Phys.*, 1993, **98**, 912.
19. L.-P. Hwang and C.-Y. Ju, *J. Chem. Phys.*, 1985, **83**, 3775.
20. P.-O. Westlund, T. P. Larsson, and O. Teleman, *Mol. Phys.*, 1993, **78**, 1365.
21. M. Gueron, *J. Magn. Reson.*, 1975, **19**, 58; A. J. Vega and D. Fiat, *Mol. Phys.*, 1976, **31**, 347.
22. T. Bayburt and R. R. Sharp, *J. Chem. Phys.*, 1990, **92**, 5892.
23. A. D. Hugi, L. Helm, and A. E. Merbach, *Inorg. Chem.*, 1987, **26**, 1763.
24. R. Hausser and F. Noack, *Z. Phys.*, 1964, **182**, 93.
25. I. Bertini, F. Briganti, Z. C. Xia, and C. Luchinat, *J. Magn. Reson., Ser. A.*, 1993, **101**, 198.
26. J. Kowalewski, T. Larsson, and P.-O. Westlund, *J. Magn. Reson.*, 1987, **74**, 56.

27. S. H. Koenig and R. D. Brown, *Progr. NMR Spectrosc.*, 1990, **22**, 487.
28. S. D. Emerson and G. N. La Mar, *Biochemistry*, 1990, **29**, 1545.
29. I. Bertini, C. Luchinat, and D. Tarchi, *Chem. Phys. Lett.*, 1993, **203**, 445.

Biographical Sketch

Jozef Kowalewski. *b* 1947. B.Sc., 1969, Ph.D. (supervisors Ragnar Vestin and Björn Roos), 1975, Stockholm University. Postdoctoral work, Florida State University (with George Levy). Faculty, Stockholm University, 1977–present; Professor of Physical Chemistry, 1986–present. Approx. 100 publications. Research specialties: spin relaxation and molecular dynamics, cross-correlation effects, and paramagnetic systems.

Quadrupolar Nuclei in Solids

Alexander J. Vega
DuPont, Wilmington, DE, USA

1	Introduction	1
2	Basic Spin Properties	1
3	Interaction with Radiofrequency Fields	7
4	Experimental Methods	10
5	Theory	14
6	Related Articles	20
7	References	20

1 INTRODUCTION

Nuclei with spin quantum number $I \geq 1$ have an electric quadrupole moment that couples with the inhomogeneous internal electric fields existing in molecules and solids. Since this quadrupolar interaction is usually stronger than other interactions such as chemical shift and dipole–dipole couplings, it dominates the NMR spectra of quadrupolar nuclei in solid materials. Liquid state NMR spectra of quadrupolar nuclei are not affected to a comparable extent, because the fast isotropic tumbling of the molecules greatly diminishes the impact of the quadrupolar interaction. While the NMR signals of quadrupolar nuclei in solids are split into multiplets that at times broaden the lineshapes of powder samples over many megahertz, the quadrupolar interaction does not split the NMR lines of liquid samples. Instead, it has a pronounced effect on the T_1 and T_2 relaxation times of nuclei in liquids (see ***Relaxation of Quadrupolar Nuclei Measured via Multiple Quantum Filtration*** and ***Relaxation Theory for Quadrupolar Nuclei***). The NMR spectra of quadrupolar nuclei in liquid crystals, where the quadrupolar splitting is partially reduced, provide a wealth of information concerning molecular orientation and dynamics (see ***Deuteron Relaxation Rates in Liquid Crystalline Samples: Experimental Methods*** and ***Liquid Crystalline Samples: Deuterium NMR***).

This article is devoted to the solid state aspects of the quadrupolar interaction. Since many subtopics from this area of NMR are discussed elsewhere in the Encyclopedia, the aim of this article is to provide a general overview rather than comprehensive discussions of each specific method. The first two sections following this introduction summarize the quantum mechanical properties of quadrupolar spins and their response to radiofrequency pulses. This survey is given without theoretical derivations and with only a few mathematical formulas. The important experimental approaches are catalogued in Section 4. Some of the fundamental theoretical concepts underlying quadrupolar spin properties are presented in Section 5.

Quadrupolar effects in NMR of solids were first reported and analyzed in 1950 by Pound.[1] Introductions to NMR of quadrupolar nuclei are provided in the classic 1957 review article by Cohen and Reif[2] and in the textbooks by Abragam[3] and Slichter.[4] Kanert and Mehring also covered the basics of quadrupole NMR in their 1971 review of quadrupole NMR of disordered cubic solids.[5] Nuclei with half-integer spins have distinctive quantum mechanical properties that have led to the development of special methods for their detection. Progress in this area was summarized in a 1993 review article by Freude and Haase.[6] NMR of integer spin nuclei is almost exclusively limited to ^{2}H and ^{14}N. Although both are $I = 1$ spins, the disparate orders of magnitude of their quadrupolar interaction energies necessitate different methodologies for their study in the solid state. Deuterium NMR spectroscopy was reviewed by Spiess[7] in 1985.

2 BASIC SPIN PROPERTIES

2.1 Nuclear Electric Quadrupolar Interaction

The nuclear quadrupolar interaction is the coupling of the electric quadrupole of the nucleus with the gradient of the electric field generated by the other charges in the system. The quadrupole moment is usually denoted by eQ and the magnitude of the electric field gradient (EFG) by eq, where e is the elementary charge. Since it is impractical to produce NMR-detectable EFGs by means of external charged conductors, the gradients are exclusively generated by the electrons and nuclei of molecules and crystals. Thus, the size of the quadrupolar interaction experienced by a particular nucleus is a constant that is characteristic of the molecular or crystalline environment. Its value in frequency units, e^2qQ/h, is called the nuclear quadrupolar coupling constant (NQCC). In this Encyclopedia, we use the letter χ as shorthand notation for e^2qQ/h. A variety of different symbols (C_q, C_Q, C_{qcc}, $\aleph_{zz}$, ...) are found in other publications (see also ***Quadrupolar Interactions***).

Closely related to the NQCC is the so-called quadrupolar frequency ν_Q (in Hz) or ω_Q (in rad s^{-1}), in this article defined as

$$\nu_Q = \frac{\omega_Q}{2\pi} = \frac{3\chi}{2I(2I-1)} \qquad (1)$$

The use of ν_Q is often preferred over that of χ, because it simplifies equations. Moreover, the quadrupolar frequency describes the actual strength of the quadrupolar interaction more closely than does the NQCC. It should be noted that equation (1) is not a universally accepted definition of ν_Q, although in literature dealing with half-integer spins it is often (but not always) found in this form. However, in the case of $I = 1$ authors usually prefer $\nu_Q = \frac{3}{4}\chi$ over the $\nu_Q = \frac{3}{2}\chi$ that follows from equation (1). For the sake of uniformity, we shall adhere to equation (1) for all values of I throughout this article.

The EFG is a three-dimensional entity with the properties of a tensor. To describe it fully, we need to specify its size, shape, and orientation. The quantity eq was introduced above as a parameter of the size. The shape is characterized by the asymmetry parameter η, which is a measure of the deviation of the EFG from axial symmetry. η can have any value between 0 and 1, with $\eta = 0$ corresponding to axial symmetry. The orientation of the EFG with respect to the molecular or crystalline structure is defined by three Euler angles. The

tensor properties are more fully defined in Section 5.1. In the literature, quadrupolar interactions are commonly reported by specification of their NQCC and η. The angular parameters are not usually provided unless orientational information is of special interest.

The quadrupolar interaction vanishes in three general cases.

1. No quadrupolar interaction is ever associated with an $I = \frac{1}{2}$ nucleus, because eQ vanishes for all subatomic particles with spin quantum number $I = 0$ or $\frac{1}{2}$.
2. The NQCC is zero when a quadrupolar nucleus is positioned at a cubic (octahedral or tetrahedral) site, because then $eq = 0$ by symmetry.
3. The quadrupolar interaction of a nucleus belonging to a molecule in an isotropic liquid or a gas is averaged to zero by the rapid tumbling motion of the molecule.

2.2 NQR and NMR Spectra of Quadrupolar Nuclei

The nature of magnetic resonance spectra of quadrupolar nuclei in solids depends to a large extent on the size of the electric quadrupolar interaction relative to that of the Zeeman interaction with the externally applied magnetic field B_0. The strength of this magnetic interaction is given by the Larmor frequency $\omega_0 = 2\pi\nu_0 = \gamma B_0$, where γ is the gyromagnetic ratio. In this subsection, we review the general features of magnetic resonance spectra for the various magnitude ranges of the ratio ν_0/ν_Q.

We begin with the case where no magnetic field is applied at all ($\nu_0 = 0$). The quadrupolar interaction then splits the magnetic energy levels of the nuclear spins into patterns like those shown in Figure 1. The energy levels are associated with particular orientations of the nuclear spin axis with respect to the EFG axes, and can thus be identified by magnetic quantum numbers m. The spectroscopic transitions among these magnetic states can be detected with the regular radiofrequency methods of magnetic resonance. This branch of spectroscopy is known as nuclear quadrupole resonance (NQR). Its first spectrum was observed by Dehmelt and Krüger in 1949.[8] Unlike the extremely broad high-field NMR spectra of quadrupolar nuclei in randomly oriented powder samples (see below), the NQR resonances are sharp. In fact, they provide the most precise measurements of the quadrupolar frequency and the NQCC. Although NQR employs the radiofrequency methods of magnetic resonance, it is not an NMR technique in the proper sense, since NMR is defined as a spectroscopy associated with a Zeeman field. NQR is therefore outside the scope of this Encyclopedia, although some aspects of it are discussed in the articles on ***SQUIDs*** and ***Zero Field NMR***. For further literature on the subject, the reader is referred to the classic monograph by Das and Hahn,[9] several other books and tabulations,[10–12] and the review articles in the series 'Advances in Nuclear Quadrupole Resonance'.[13]

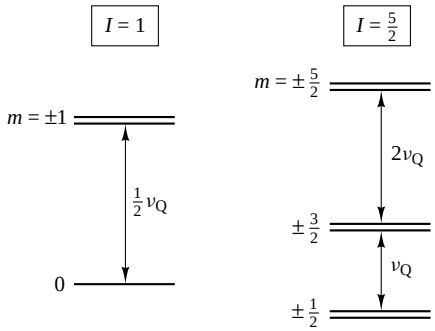

Figure 1 Quadrupolar energy levels in zero magnetic field. These two examples are for axial symmetry of the EFG. If the EFG is not axially symmetric, the transition frequencies are more complicated functions of the quadrupolar frequency ν_Q and the asymmetry parameter η, while the eigenstates are linear combinations of m states. Furthermore, the $m = \pm 1$ degeneracy of the $I = 1$ states is lifted when $\eta \neq 0$. However, the eigenstates of half-integer spins remain degenerate in pairs for any value of η

A weak magnetic field, corresponding to a Larmor frequency ν_0 smaller than ν_Q, shifts and splits the NQR lines. The frequency shifts of this so-called Zeeman effect of NQR are functions of the orientation of the magnetic field with respect to the crystal axes. Consequently, in randomly oriented powder samples, the effect is observed as a broadening of the peaks.

When ν_0 is much larger than ν_Q, we are in the regime of NMR. In the extreme limit of vanishing ν_Q, the energy levels are the $2I + 1$ Zeeman levels, $E_m = m\omega_0$, giving rise to $2I$ coinciding transitions of frequency ν_0. A relatively small quadrupolar interaction, $\nu_Q \ll \nu_0$, shifts the eigenvalues of the Zeeman levels and splits the NMR spectrum into $2I$ peaks. Examples for spins $I = 1$ and $\frac{5}{2}$ are shown schematically in Figure 2. For the theoretical description of these effects, we follow the methods of perturbation theory and express the quadrupolar corrections to the energy levels as the sums of first-order terms of order ω_Q and second-order terms of order $\omega_Q{}^2/\omega_0$ (see Section 5.3). Third- and higher-order terms do not need to be considered.

The main features of quadrupolar NMR spectra are governed by the equation describing the orientation dependence of the first-order energy corrections $\Delta E_m{}^{(1)}$ of the Zeeman levels m:

$$\Delta E_m^{(1)} = \tfrac{1}{2}\Delta\omega_Q(\theta,\phi)[m^2 - \tfrac{1}{3}I(I+1)] \qquad (2)$$

where $\Delta\omega_Q$ is a fraction of ω_Q and is a function of the polar angles θ and ϕ which relate the Zeeman field direction to the EFG principal axes system (see Section 5.1 and Figure 11):

$$\begin{aligned}\Delta\omega_Q(\theta,\phi) &= 2\pi\,\Delta\nu_Q(\theta,\phi)\\ &= \tfrac{1}{2}\omega_Q[3\cos^2\theta - 1 - \eta\sin^2\theta\cos 2\phi] \qquad (3)\end{aligned}$$

$\Delta\nu_Q$ (or $\Delta\omega_Q$) is called the quadrupolar splitting because the $2I$ lines in the spectrum are, to first order, equally spaced by $\Delta\nu_Q$. This follows from equation (2), which predicts that the first-order frequency shifts $\Delta\nu_{m\leftrightarrow m+1}^{(1)}$ of the allowed transitions $m \leftrightarrow m + 1$ are given by

$$\Delta\nu_{m\leftrightarrow m+1}^{(1)} = \Delta\nu_Q(\theta,\phi)(m+\tfrac{1}{2}) \qquad (4)$$

In powder samples, the orientation dependence of $\Delta\nu_Q$ broadens the individual transitions and causes them to overlap. However, the $-\frac{1}{2} \leftrightarrow \frac{1}{2}$ transition of noninteger spins ($I = \frac{3}{2}, \frac{5}{2}, \frac{7}{2}, \frac{9}{2}$) does not experience a first-order broadening [$m = -\frac{1}{2}$ in equation (4)]. Consequently, this 'central transition' stands out as a relatively sharp peak at the center of the 'satellite transitions'. It is clear from equation (4) that there

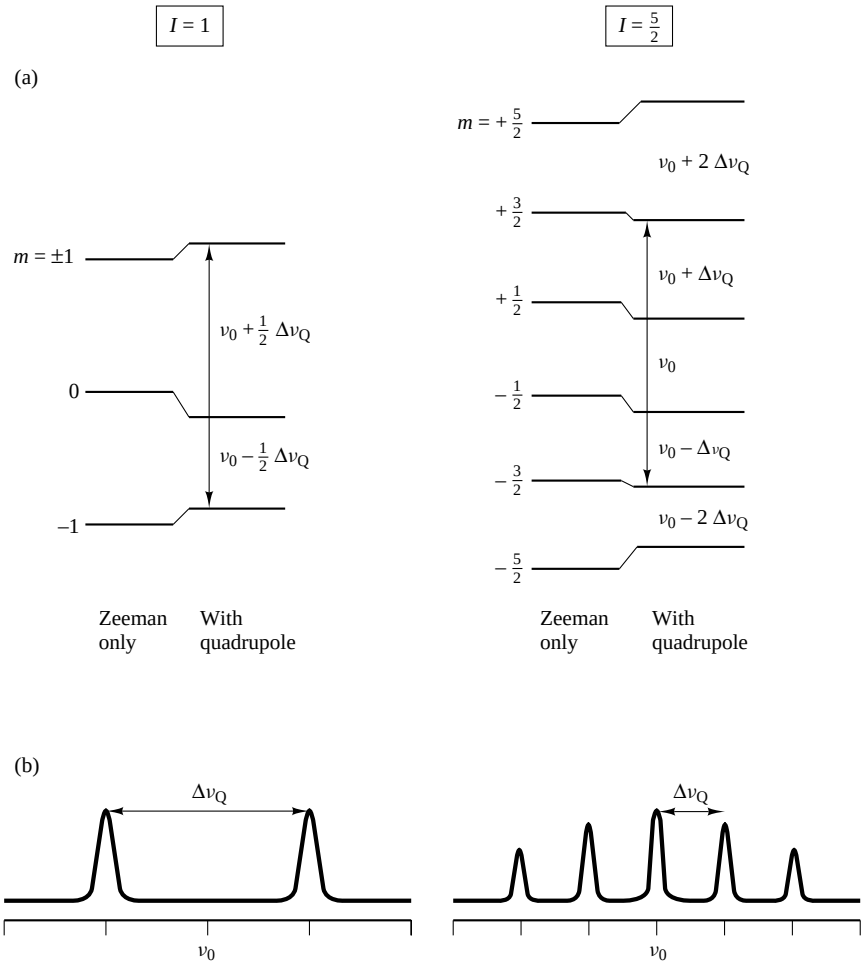

Figure 2 (a) Energy levels of spins $I = 1$ and $\frac{5}{2}$ in a Zeeman field, in the absence and in the presence of a quadrupolar interaction. The frequencies of the allowed ($\Delta m = 1$) transitions are indicated with first-order quadrupolar corrections. The arrows mark forbidden ($\Delta m = 2, 3$) transitions. (b) The corresponding quadrupole-split NMR spectra. $\omega_0 = 2\pi\nu_0$ is the Larmor frequency and $\Delta\omega_Q = 2\pi\ \Delta\nu_Q$ is the quadrupolar splitting

is no central transition associated with integer-spin nuclei. The dependence of $\Delta\nu_Q(\theta, \phi)$ on the orientation is similar to that of the anisotropic chemical shift. However, unlike the chemical shift, the first-order quadrupolar effect has no isotropic contribution, implying that the centers of gravity of the spectral distributions are not shifted. Thus, each satellite transition has a powder lineshape characteristic of the value of η, and is centered around the Larmor frequency. Figure 3 shows a few simulated examples for $I = 1$ and $\frac{5}{2}$.

The broadening of the satellites is often too large to be captured within the bandwidth of the NMR spectrometer. In such a case, we only observe the central transition, the lineshape of which is dominated by second-order quadrupolar shifts. The orientation dependence of this shift is of a different nature to that of the first-order satellite shift. A consequence of this is that it contributes to an isotropic shift of the order of $\nu_Q{}^2/\nu_0$ (see equation (15) in Section 4.3).

Equation (2) shows further that levels m and $-m$ have identical first-order energy shifts. Therefore, in addition to the central transition, there are forbidden transitions $\Delta m = 2, 3, \ldots$ (indicated in Figure 2 by arrows) with transition frequencies that are not affected to first order by the quadrupolar interaction. The experimental methods of double quantum excitation and overtone spectroscopy of $I = 1$ nuclei take advantage of this special property (see Section 4).

The energy-level diagrams of Figure 4 illustrate the transition from the NQR limit to the NMR limit. The figure shows the variation of the energy levels of a spin-$\frac{3}{2}$ when the ratio ν_0/ν_Q changes gradually from 0 to ∞. This is shown for two cases, both with an axially symmetric EFG—one with the EFG symmetry axis $\boldsymbol{q}$ parallel to the field $\boldsymbol{B}_0$, and one with $\boldsymbol{q}$ perpendicular to $\boldsymbol{B}_0$. The difference between the two sets of energy curves demonstrates the strong dependence of the transition frequencies on the relative orientations of the EFG and $\boldsymbol{B}_0$. When ν_0 is of the order of ν_Q, the powder spectra are sufficiently broad, that detection of magnetic resonance becomes impractical within the limitations of bandwidth and sensitivity of equipment currently in use.

Figure 4 also indicates the spin states in the limiting cases. Note that these eigenstates are quantized along the symmetry direction of the prevailing field, as is indicated by the Q and Z subscripts on the quantum numbers m. In general, these states are not identical. In fact, they are linear combinations of each other. A certain amount of mixing of the pure Zeeman states occurs even when the quadrupolar interaction is small in comparison with the Zeeman interaction. We say that the spins are then 'no longer quantized along the Zeeman direction'

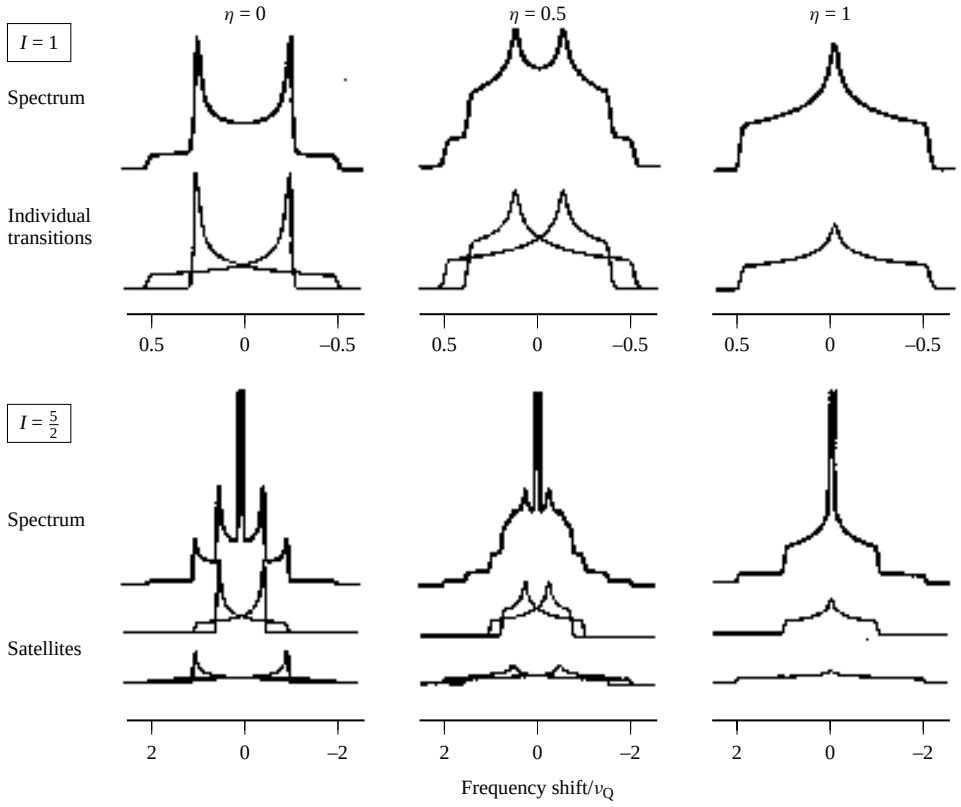

Figure 3 First-order quadrupolar spectra of powder samples simulated for $I = 1$ and $\frac{5}{2}$ and for three values of the asymmetry parameter η. The lineshapes of individual transitions are drawn below the spectra. The central transition peaks of $I = \frac{5}{2}$ are off scale. The frequency scale is in units of the quadrupolar frequency ν_Q as defined in equation (1). The Larmor frequency is at the center of the spectra

(see Section 5.3). This mixing controls a number of the NMR phenomena reviewed below, including overtone NMR, heteronuclear dipolar splittings, and zero field NMR.

2.3 Level Populations

Since $I > \frac{1}{2}$ spins have more than two Zeeman levels, it is necessary to use two or more independent parameters for the description of their relative populations. In thermal equilibrium, the high-field population pattern is as illustrated in Figure 5(a) for $I = 1$ or Figure 5(c) for $I = \frac{3}{2}$. The populations of the levels m are then given by $(1 - m\hbar\omega_0/kT)/(2I + 1)$, which is the Boltzmann distribution in the high-temperature approximation. This is called Zeeman order, because the populations are determined by the Zeeman interaction. It is characterized by uniform population increments between adjacent levels. The application of rf pulses causes deviations from the Boltzmann distribution. When these deviations are such that the Zeeman pattern is retained, we can introduce a meaningful 'spin temperature' replacing T in the distribution expression above. The distribution pattern can also be of the type depicted in Figure 5(b) and (d). This is called quadrupolar order, because the deviations from the average population follow the $m^2 - \frac{1}{3}I(I + 1)$ dependence associated with the quadrupolar interaction [equation (2)]. In general, the population distribution of spins $I = 1$ is a combination of the two. Unlike Zeeman order, quadrupolar order does not contribute to the z magnetization. In thermal equilibrium, quadrupolar order is negligible, because the population differences associated with it are ν_0/ν_Q times smaller than those of equilibrium Zeeman order.

For spins with $I \geq \frac{3}{2}$, more types of population distribution need to be considered. An important example is the $I = \frac{3}{2}$ configuration illustrated in Figure 5(e). This arrangement can be viewed as Zeeman order in which the $m = \pm\frac{1}{2}$ populations are equilibrated and do not contribute to the z magnetization (e.g., as a result of selective saturation of the central transition), whereas the equilibrium population difference of the $m = \pm\frac{3}{2}$ levels and their contribution to the z magnetization is retained. For later reference, we call this 'triple quantum order'.

2.4 Relaxation

Spin relaxation is caused by randomly fluctuating interactions (see also ***Relaxation: An Introduction*** and ***Relaxation Theory for Quadrupolar Nuclei***). In the case of quadrupolar nuclei, the fluctuations can be electric (due to a time-dependent size or orientation of the EFG) or magnetic (due to fluctuating chemical shifts, dipole–dipole interactions, or interactions with unpaired electrons). When caused by random molecular motions or lattice vibrations, the electric fluctuations usually dominate, since in most cases the quadrupolar interaction is stronger than the magnetic dipolar interactions and chemical shifts.[6] On the other hand, a magnetic relaxation mechanism mostly prevails in the presence of conduction electrons[14] or in structures containing paramagnetic centers

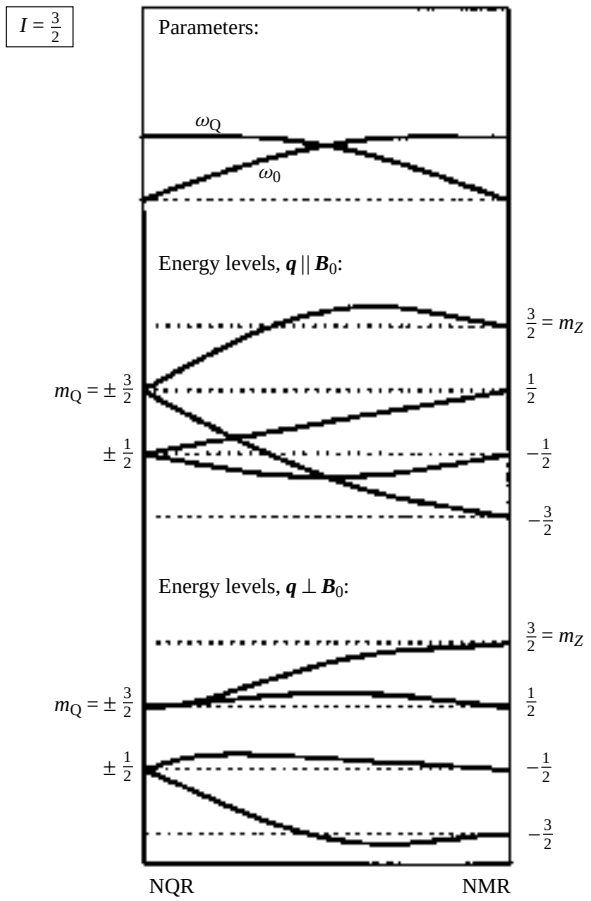

Figure 4 Energy levels of a spin $I = \frac{3}{2}$ in a coexisting electric field gradient and a magnetic Zeeman field, calculated for varying Larmor frequency ω_0 and quadrupolar frequency ω_Q. The gradual change of these parameters, from the NQR limit ($\omega_0 = 0$) on the left to the NMR limit ($\omega_Q = 0$) on the right, is shown in the curves at the top. The EFG is assumed to be axially symmetric. The corresponding energies of the spin states are shown for two relative orientations of the symmetry axis $\boldsymbol{q}$ of the EFG and the Zeeman field $\boldsymbol{B}_0$. The magnetic quantum numbers are indicated for the NQR and NMR limits (m_Q is quantized along $\boldsymbol{q}$; m_Z is quantized along $\boldsymbol{B}_0$)

such as superconducting oxide materials (see ***High Temperature Superconductors***).

Longitudinal spin–lattice relaxation is the process by which nonequilibrium level populations (see Figure 5) revert to thermal equilibrium. Unlike relaxation of spin-$\frac{1}{2}$ nuclei, which involves a single transition probability between two energy levels, relaxation of quadrupolar nuclei is generally characterized by several transition rates. Hence, the relaxation decay is multi-exponential, and cannot be quantified by a single T_1. For instance, the quadrupole-induced spin–lattice relaxation of a spin $I = 1$ has two principal spin–lattice relaxation times: the conventional T_1 for the return of Zeeman order to the equilibrium populations, and a different time T_{1Q} for the decay of quadrupolar order (see Section 2.3). Spin–lattice relaxation patterns of higher spins are more complex. Provided the initial population distribution has the form of Zeeman order, spin–lattice relaxation has one decay constant for $I = 1$, two for $I = \frac{3}{2}$ or 2, three for $I = \frac{5}{2}$ or 3, etc.[15] In powders, the complexity is compounded with

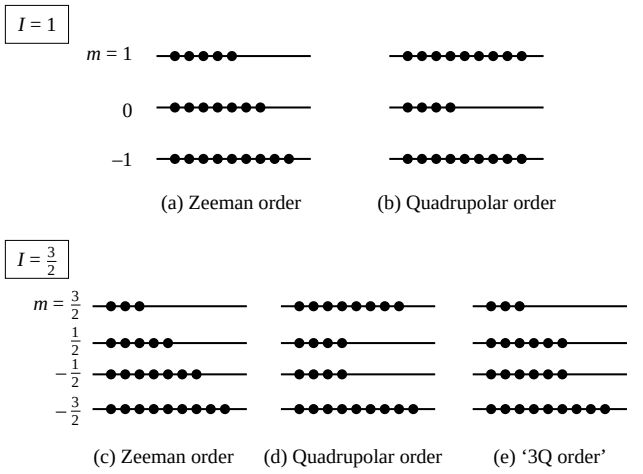

Figure 5 Level population patterns of spins 1 and $\frac{3}{2}$ according to Zeeman order, quadrupolar order, and 'triple quantum order'

a dependence of the relaxation time on the orientation of the EFG with respect to the Zeeman field. However, the transition rates are mostly of comparable magnitude, such that an approximate assessment of a global T_1 is not unwarranted. The dependence of T_1 on the correlation time τ_c of the motion follows the general Bloembergen–Purcell–Pound (BPP) or Redfield behavior (see ***Relaxation: An Introduction***) given by

$$\frac{1}{T_1} = \omega_Q^2 \left(\frac{a\tau_c}{1+\omega_0^2\tau_c^2} + \frac{b\tau_c}{1+4\omega_0^2\tau_c^2} \right) \qquad (5)$$

where the numerical coefficients a and b reflect the amplitudes of the EFG fluctuations, the geometric details of the motion, a dependence on I, and the multiexponential character of the decay. A log–log plot of T_1 versus τ_c has the familiar shape shown in Figure 6, with its minimum around ${\omega_0}^{-1}$. For relaxation due to lattice vibrations, the equation is cast in different forms reflecting the thermal behavior of the phonons.[6] A similar expression, with a hyperfine coupling constant instead of ω_Q, holds for magnetically induced relaxation.

As is usually done in BPP-type discussions of the transverse relaxation time, we define T_2 as a measure of the inverse linewidth of the spectrum. (The signal decay in echo experiments, albeit important in deuterium NMR, is outside the scope of this article.) In the slow motion limit, the powder spectra have widths and shapes like those of the examples shown in Figure 3. Hence, $1/T_2$ is approximately equal to ω_Q, except for the central transition of half-integer spins, which has $1/T_2$ of the order of ${\omega_Q}^2/\omega_0$. In the fast motion limit, the spectra are reduced to motionally narrowed Lorentzian lines having full linewidth at half-maximum equal to $1/\pi T_2$. The majority of the spectral components follow the familiar BPP pattern schematically drawn as the T_2(other) curve in Figure 6. If the relaxation mechanism is quadrupolar, the condition for motional narrowing is $\tau_c \ll {\omega_Q}^{-1}$, and the T_2 of the narrowed spectrum varies with the correlation time according to

$$\frac{1}{T_2} = c\omega_Q^2\tau_c \qquad (6)$$

where the numerical coefficient c depends on the motional model.

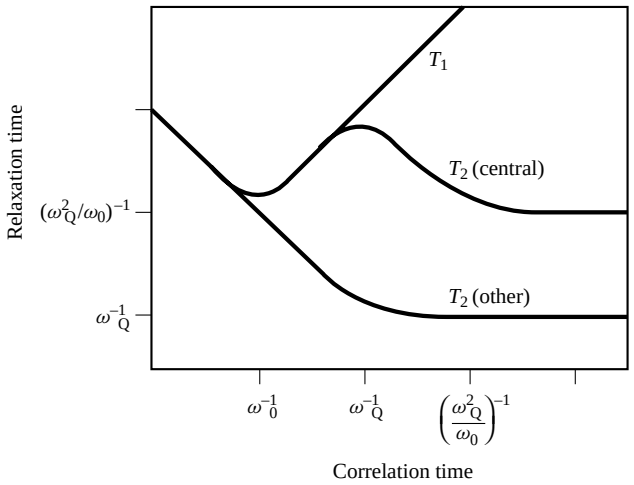

Figure 6 Idealized log–log plot of T_1 and T_2 relaxation times versus the correlation time of the motion for a model where the spin relaxation is caused by large-scale fluctuations of the EFG. T_2(central) is the inverse halfwidth of the central transition spectra of half-integer spins; T_2(other) is that of satellite transitions or transitions of integer spins

The effect of quadrupolar relaxation on T_2 of the central transition is markedly different,[16,17] as is indicated by T_2(central) in Figure 6. A gradual increase in the motional rate (decreasing correlation time) begins to narrow the rigid limit spectrum when τ_c becomes smaller than the reciprocal linewidth ($\tau_c < (\omega_Q{}^2/\omega_0)^{-1}$), but for shorter τ_c, the line broadens again, and T_2 passes through a minimum when $\tau_c \approx \omega_0{}^{-1}$. This T_2 behavior was observed for ^{23}Na in amorphous polymer electrolytes above the glass transition temperature.[18] The T_2 minimum is associated with a dynamic frequency shift[16,17] (see ***Dynamic Frequency Shift*** and ***Relaxation of Quadrupolar Nuclei Measured via Multiple Quantum Filtration***). Transverse relaxation of the central transition due to unpaired electrons does not differ substantially from the relaxation of the other transitions.

2.5 Typical Values of the Nuclear Quadrupolar Coupling Constant

Table 1 lists typical values of the NQCC (χ), the quadrupolar frequency [ν_Q as defined in equation (1)], and the Larmor frequency (ν_0 in the magnetic field of a 300 MHz spectrometer) for selected nuclei. The data were gathered from various sources in the literature. Unless the quadrupole interaction is drastically reduced by cubic symmetry, the actual NQCCs for a particular nucleus do not usually differ by more than a factor two or three from the quoted value. The multiplication factors in parentheses indicate the ratios between the NQCC of isotopes of the same element. These ratios are fixed by the ratios of their eQ values. The relative magnitudes of ν_Q and

Table 1 Typical Values of Nuclear Quadrupole Coupling Constants (NQCC), Quadrupole Frequencies (ν_Q), and Larmor Frequencies (ν_0)

Nucleus	I	Natural abundance (%)	Typical NQCC (MHz)	Typical ν_Q (MHz)	ν_0 at 7.05 T (MHz)
Integer spin:					
^{2}H	1	0.015	0.16	0.24	46.1
^{6}Li	1	7.4	0.001	0.0015	44.2
^{10}B	3	19.6	1	0.1	32.2
^{14}N	1	99.6	4	6	21.7
Half-integer spin:					
^{7}Li	3/2	92.6	0.05	0.025	116.6
^{9}Be	3/2	100	0.4	0.2	42.2
^{11}B	3/2	80.4	2	1.5	96.3
^{17}O	5/2	0.037	7	1	40.7
^{23}Na	3/2	100	2	1	79.4
^{27}Al	5/2	100	1–20	0.15–3	78.2
^{35}Cl	3/2	75.5	60	30	29.4
^{37}Cl	3/2	24.5	(× 0.788)	(× 0.788)	24.5
^{39}K	3/2	93.1	4	2	14.0
^{45}Sc	7/2	100	3	0.2	73.0
^{51}V	7/2	99.8	3	0.2	78.9
^{55}Mn	5/2	100	60	9	74.0
^{63}Cu	3/2	69.1	60	30	79.5
^{65}Cu	3/2	30.9	(× 0.925)	(× 0.925)	85.2
^{71}Ga	3/2	39.6	150	75	91.5
^{75}As	3/2	100	160	80	51.4
^{87}Rb	3/2	27.8	20	10	98.2
^{79}Br	3/2	50.5	400	200	75.2
^{81}Br	3/2	49.5	(× 0.835)	(× 0.835)	81.0
^{91}Zr	5/2	11.2	20	3	28.0
^{93}Nb	9/2	100	50	2	73.6
^{96}Mo	5/2	15.7	2	0.3	19.6
^{133}Cs	7/2	100	0.7	0.02	39.4
^{121}Sb	5/2	57.2	500	70	71.8
^{127}I	5/2	100	2000	300	60.0
^{209}Bi	9/2	100	500	20	48.2

ν_0 serve as a guide for determining whether a nucleus is better studied by NQR or by NMR.

3 INTERACTION WITH RADIOFREQUENCY FIELDS

The manner in which radiofrequency (rf) pulses affect quadrupolar spins in a high magnetic field depends strongly on the relative magnitudes (in frequency units) of three parameters. One is the rf amplitude $\omega_1 = 2\pi\nu_1 = \gamma B_1$, where B_1 is the strength of the rotating magnetic component of the rf field. The other two are the first-order quadrupolar splitting $\Delta\omega_Q = 2\pi\ \Delta\nu_Q$ and the difference $\Delta\omega_0 = 2\pi\ \Delta\nu_0$ between the resonance frequency of the spins and the carrier frequency of the rf pulse. Here, the resonance frequency is the combination of Larmor frequency, chemical shift, and second-order quadrupolar shift. While there are no other ways in which second-order quadrupolar effects impact the performance of rf pulses to a noticeable extent, first-order splittings make a large difference. Consequently, the orientation dependence of $\Delta\nu_Q$ can cause a wide range of responses to a uniform rf pulse when it is applied to a powder sample. To avoid this complication, we limit the discussion in this section to samples with a uniform $\Delta\nu_Q$ as in a single crystal. The distinct experimental conditions and their respective effects on quadrupolar spins are categorized below. The summary is descriptive in nature and is presented without theoretical explanations. For the latter, see Section 5.5. See also ***Radiofrequency Pulses: Response of Nuclear Spins***.

3.1 Nonquadrupolar Nuclei

To introduce the rf-related concepts of nutation, spin locking, and population transfer, we first consider the simple example of a vanishing NQCC ($\nu_Q = 0$). In the rotating frame (the axes system that rotates with the frequency of the rf carrier), the rf field is represented by a constant vector $\boldsymbol{\nu}_1$ of length $\boldsymbol{\nu}_1$ along x, while the Zeeman field is effectively reduced to an offset vector $\Delta\boldsymbol{\nu}_0$ of length $\Delta\nu_0$ along z (see the axis diagram in the top portion of Figure 7). The magnetization precesses about the 'effective field', which is represented by the vector $\boldsymbol{\nu}_{\text{eff}}$. We distinguish the two limiting cases of (a) irradiation close to resonance, $\Delta\nu_0 \ll \nu_1$, and (b) irradiation far off resonance, $\Delta\boldsymbol{\nu}_0 \gg \nu_1$. These cases are also represented in the more schematic illustration in the lower part of Figure 7, where the effective range of the rf field is represented in the frequency domain by a shaded rectangle of width of order ν_1 centered at the carrier frequency. In NMR terminology, the precession induced by a pulse of type (a) is referred to as 'nutation'. In general, this term relates to precessions caused by rf irradiation and that begin with the spins in thermal equilibrium. In case (a), the nutation is in the (y, z) plane, and takes place with a nutation frequency equal to the rf amplitude, $\nu_{\text{nut}} = \nu_1$. If before the application of the pulse the spins have been prepared so that they point in the x direction of the rotating frame, they will be spin locked by a pulse of type (a).

No nutation or excitation is induced by a far-off-resonance pulse, but we can speak of spin locking in its presence. Namely, the direction of the effective field $\boldsymbol{\nu}_{\text{eff}}$, which is nearly parallel to z in case (b), can be viewed formally as a spin locking field for z magnetization. This notion is a

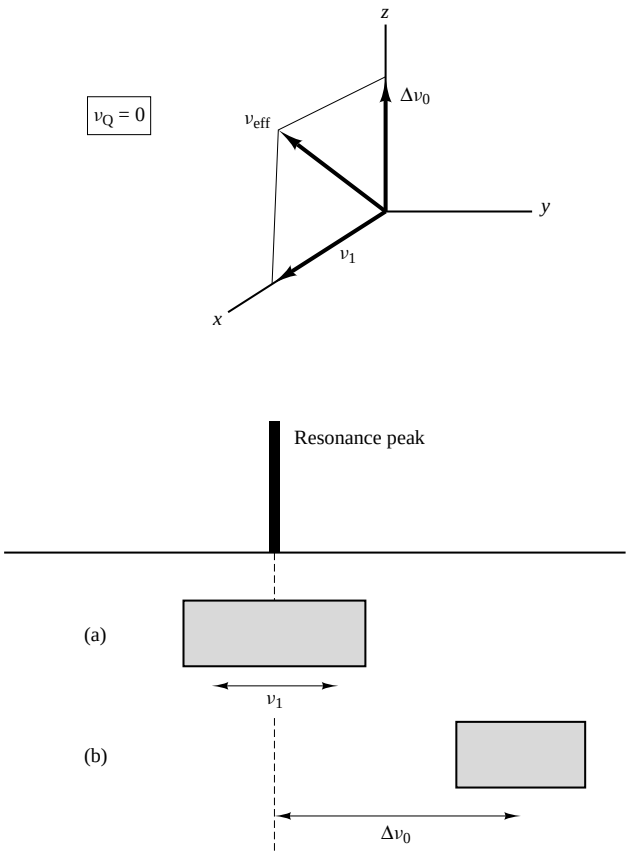

Figure 7 Top: Rotating frame representation of an rf field of ampitude ν_1 (in frequency units) and a resonance offset $\Delta\nu_0$. This representation is adequate for a nonquadrupolar spin system, either $I = \frac{1}{2}$ or $I > \frac{1}{2}$. Bottom: Schematic frequency domain representation of rf irradiation of nonquadrupolar spins. The rf excitation profile is indicated by a shaded rectangle centered at the rf carrier frequency and extending over the approximate excitation range of the rf field. The limiting cases are (a) on-resonance rf ($\Delta\nu_0 \ll \nu_1$) and (b) off-resonance rf ($\Delta\nu_0 \gg \nu_1$)

useful starting point for the description of an adiabatic passage that occurs when $\Delta\nu_0$ is slowly changed from one side of resonance to the other. During an adiabatic passage, the spins remain spin locked along $\boldsymbol{\nu}_{\text{eff}}$ and rotate together with it from z through x to $-z$. Eventually, this results in population inversion of the Zeeman levels. In the case of $I = \frac{1}{2}$ the passage transfers the population of the $\frac{1}{2}$ level to the $-\frac{1}{2}$ level and vice versa. The criterion for adiabaticity is that the parameter

$$\alpha = \frac{\omega_{\text{nut}}^2}{\mathrm{d}\Delta\omega_0/\mathrm{d}t} \tag{7}$$

must be larger than 1. If the passage is sudden ($\alpha \ll 1$), the magnetization remains in the original direction and no populations are transferred. If it is intermediate ($\alpha \approx 1$), the magnetization ends up in a direction that is not spin locked.

3.2 Spin-1 Nuclei

For the visualization of rf fields in the presence of quadrupolar interactions, we can no longer resort to a simple three-dimensional vector picture. Instead, we shall review the

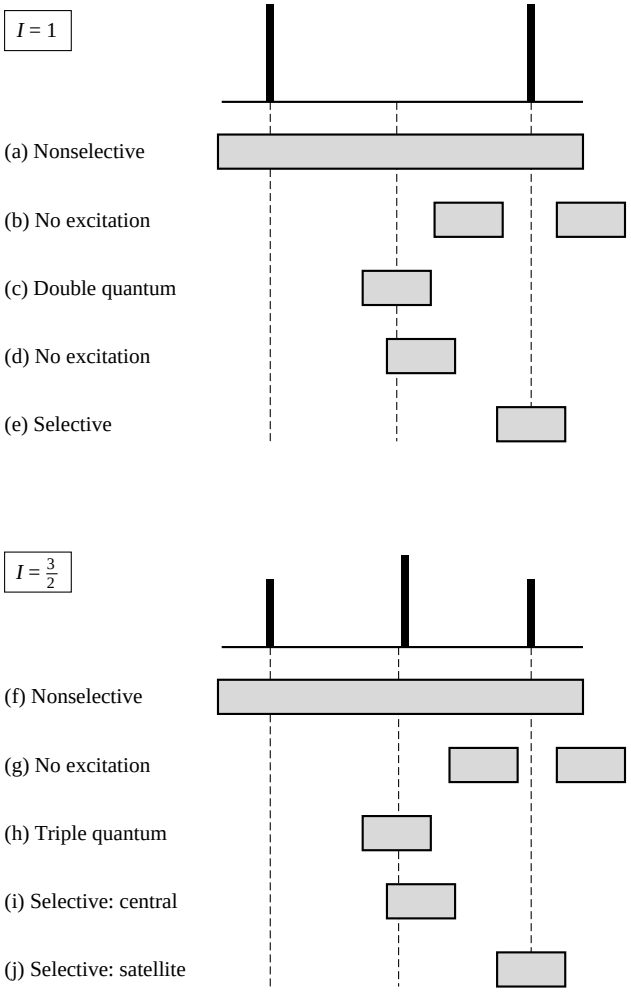

Figure 8 Schematic frequency domain representation of rf irradiation of quadrupolar spins $I = 1$ and $\frac{3}{2}$. The rf ranges are indicated as in Figure 7. The response of the spins to the irradiation depends on the position of the carrier frequency and on the width of the excitation range with respect to the quadrupole-split NMR peaks shown at the top

various aspects of rf irradiation with the help of the illustrations in the frequency domain shown in Figure 8.

3.2.1 Nutation

When $I = 1$, we distinguish five special cases denoted (a)–(e):

3.2.1.1 Case (a). The excitation is nonselective when ν_1 is larger than both $\Delta\nu_Q$ and $\Delta\nu_0$. The two allowed transitions (see the $I = 1$ portion of Figure 2) are then simultaneously excited. As in the $\nu_Q = 0$ case (Figure 7), the nonselective pulse induces nutation with frequency $\nu_{nut} = \nu_1$. However, following the pulse, the spin system will not continue to behave like a nonquadrupolar nucleus. Excitation by two or more pulses, with quadrupolar interactions acting in the intervals, can create as many as eight distinct spin state configurations, of which polarizations along x, y, and z are only three examples.

Two other kinds of spin states are of particular interest. These are 'quadrupolar order', which was discussed in the previous section (see Figure 5), and 'double quantum coherence', which is a quantum mechanical state that can be thought of as a linear combination of $m = +1$ and -1 states. Although double quantum coherence is not observable in the form of nuclear magnetization, it has some similarity to regular transverse magnetization ('single quantum coherence') in that it has x and y components that undergo precession under frequency offset. Unlike single quantum coherence, the double quantum precession frequency is twice the offset frequency. For density matrix representations of these coherences, see Section 5.4.

The most prominent nonselective pulse sequence is the quadrupolar echo sequence, also called solid echo sequence. It consists of two out-of-phase 90° pulses separated by an interval τ: $90°_x - \tau - 90°_y$. The spin dephasing due to first-order quadrupolar effects is refocused by the second pulse, and an echo is formed at time τ following the second pulse.

3.2.1.2 Case (b). When ν_1 is small ($\nu_1 \ll \Delta\nu_Q$) and the rf profile does not overlap with any of the transitions [Figure 8(b) shows two examples], the spins are not excited, except in case (c) below.

3.2.1.3 Case (c). A weak rf field ($\nu_1 \ll \Delta\nu_Q$) applied at the exact midpoint between the two spectral lines ($\Delta\nu_0 = 0$) induces $\Delta m = 2$ transitions directly between the $m = +1$ and -1 states, while leaving the $m = 0$ state unaffected. This effect was indicated in Figure 2 as the forbidden double quantum transition. It can be understood in terms of a second-order perturbation of the first-order quadrupolar interaction by the rf interaction (see Section 5.5). It results in a double quantum nutation frequency given by[19]

$$\nu_{2Q} = 2\nu_1^2/\Delta\nu_Q \tag{8}$$

A pulse of duration $\tau_p = 1/4\nu_{2Q}$ is a double quantum 90° pulse. It transforms Zeeman order into a state of double quantum coherence. A double quantum 180° pulse inverts the populations.

3.2.1.4 Case (d). When the rf carrier is slightly off resonance, no double quantum excitation occurs, despite the fact that the offset may be less than the rf amplitude ($\nu_{2Q} \ll \Delta\nu_0 < \nu_1 \ll \Delta\nu_Q$).

3.2.1.5 Case (e). Selective excitation of one of the allowed transitions ($-1 \leftrightarrow 0$ or $0 \leftrightarrow +1$) is caused by a weak rf field applied at its resonance frequency. The corresponding nutation frequency is given by $\nu_{nut} = \nu_1\sqrt{2}$.

3.2.2 Spin Locking

Each of these five forms of rf irradiation is associated with one or more spin locked spin configurations. If the rf field is applied along x in the rotating frame, the following spin states are spin locked under the various conditions: nonselective irradiation (a) spin locks transverse spin polarization along x; off-resonance irradiation (b) and (d) spin lock Zeeman and quadrupolar order; double quantum irradiation (c) spin locks double quantum coherence of type x; and selective irradiation of an allowed transition (e) spin locks the corresponding single quantum coherence.

3.2.3 Population Transfer

Adiabatic passages, similar to the population inversion described in Section 3.1, can occur for quadrupolar spins

I = 1 when the rf profile crosses over from one side of a transition to the other. For instance, a slow passage between the two situations drawn for case (b) in Figure 8 causes population exchange between the levels m = 0 and −1, and thus transforms pure Zeeman order to a combination of Zeeman and quadrupolar order. Such a passage is materialized by a slow sweep of $\Delta\nu_0$, which can in turn be done by sweeping of the carrier frequency or of the magnetic field. Another possibility is the sweeping of $\Delta\nu_Q$. Because of its orientation dependence, the quadrupolar splitting can easily be varied by simply turning the sample. The passage is adiabatic if the change in $\Delta\nu_Q$ is sufficiently slow for the condition $\alpha > 1$ to be satisfied, with the adiabaticity parameter defined as $\alpha = \omega_{nut}{}^2/(d\Delta\omega_Q/dt)$. Magic angle spinning (MAS) is a particularly effective method for $\Delta\nu_Q$ sweeping, since $\Delta\nu_Q$ of any crystallite experiences two or four zero-crossings per rotation cycle. (This is consistent with the $\Delta\nu_Q$ averaging to zero by MAS.) If the spinning rate is denoted by ν_R, the adiabaticity parameter is roughly equal to

$$\alpha \approx \frac{\nu_1^2}{\nu_R \nu_Q} \tag{9}$$

3.3 Nuclei with Half-Integer Spin

3.3.1 Nutation ($I = \frac{3}{2}$)

The response of a spin $I = \frac{3}{2}$ to the application of rf pulses is in many respects similar to that of I = 1, but there are a few differences to be pointed out. We again distinguish among five special cases illustrated in the bottom half of Figure 8.

3.3.1.1 Case (f). When ν_1 covers the entire spectrum, the excitation is nonselective and the nutation frequency is $\nu_{nut} = \nu_1$. The spin dynamics of sequences with more than one pulse is even richer than for I = 1 nuclei, since there are 15 independent spin states for $I = \frac{3}{2}$ (see Section 5.4). The nonselective solid echo sequence $90^\circ{}_x - \tau - 90^\circ{}_y$ refocuses first-order quadrupolar dephasing as in the case of I = 1.

3.3.1.2 Case (g). There is no excitation when the rf profile does not overlap with any transition (but see Section 5.5).

3.3.1.3 Case (h). A weak rf pulse applied at the exact midpoint between the satellite transitions induces a triple quantum excitation[20,21] between $m = -\frac{3}{2}$ and $\frac{3}{2}$ with a nutation frequency given by $\nu_{3Q} = \frac{3}{2}\nu_1^3/\Delta\nu_Q^2$. The resonance conditions for triple quantum transition and for the allowed central transition do not coincide exactly, because the two transitions have different second-order shifts. The triple quantum excitation is quenched when the carrier frequency is slightly off resonance ($\Delta\nu_0 > \nu_{3Q}$), but when $\Delta\nu_Q$ is not much larger than ν_1, the excitation is effective for $\Delta\nu_0 \lesssim \nu_1$.

3.3.1.4 Case (i). A weak pulse ($\nu_1 < \Delta\nu_Q$) with an rf profile that overlaps with the central transition induces selective excitation of the latter. The nutation frequency for this transition is $\nu_{nut} = 2\nu_1$.

3.3.1.5 Case (j). Selective excitation of the satellites occurs with a nutation frequency $\nu_{nut} = \nu_1\sqrt{3}$. Note that, unlike selective excitation of the narrow central transition, selective excitation of satellite transitions cannot be achieved simultaneously for all crystallites in a powder sample.

3.3.2 Spin Locking ($I = \frac{3}{2}$)

The spin states of $I = \frac{3}{2}$ nuclei that are spin locked under the various modes of rf irradiation follow a pattern similar to that of I = 1, and do not need to be discussed in detail. However, the case of selective irradiation of the central transition [case (i)] deserves some special attention. During an rf pulse of this type, two spin state configurations can be spin locked. One is the population difference of the $m = \pm\frac{3}{2}$ levels illustrated as 'triple quantum order' in Figure 5(e). For convenience, we give it the shorthand notation T_z to indicate that it is associated with the triple quantum transition and that it contributes to z magnetization. The other is single quantum coherence of the central transition, denoted by C_x, which is a linear combination of states $m = \frac{1}{2}$ and $-\frac{1}{2}$ contributing to x magnetization. Density matrix representations of T_z and C_x are given in Section 5.5. When a type (i) pulse is applied to spins $I = \frac{3}{2}$ that are initially in thermal equilibrium, two things happen simultaneously: the T_z portion of the spin state is spin locked while the central transition portion undergoes nutation. However, if the central transition portion is prepared in the C_x state by appropriately chosen preparatory pulses, simultaneous spin locking of T_z and C_x can be achieved.

3.3.3 Population Transfer ($I = \frac{3}{2}$)

An adiabatic passage caused by zero-crossing of $\Delta\nu_Q$ in a slowly rotating sample transfers a spin locked T_z state to C_x, and vice versa. As mentioned above for I = 1, magic angle spinning is an efficient method for inducing these passages. The criterion for adiabaticity is again $\alpha > 1$, with α as defined as in equation (9).[22] The populations of the $\pm\frac{3}{2}$ states can also be transferred to the $\pm\frac{1}{2}$ states by adiabatic sweeping of $\Delta\omega_0$.[23]

3.3.4 Central Transition ($I \geq \frac{3}{2}$)

Similar concepts can be applied to half-integer spins with $I > \frac{3}{2}$, but, other than the general case of central transition excitation, they will not be discussed further. The frequency of nutation of the central transition induced by nonselective irradiation, as exemplified by case (f) in Figure 8, is given by $\nu_{nut} = \nu_1$. On the other hand, when the excitation is selective as in case (i), the general formula for the nutation frequency is

$$\nu_{nut} = (I + \tfrac{1}{2})\nu_1 \tag{10}$$

This effective enhancement of the rf amplitude has obvious consequences for the choice of pulse length for obtaining optimum signal intensity in a selective single pulse excitation experiment. For $I = \frac{3}{2}$ the apparent 90° pulse is a nominal 45° pulse. Likewise, for $I = \frac{5}{2}$, it is 30°, and so on. An additional result of selective excitation is that it reduces the intensity of the resulting central transition signal. If the signal (not including the satellites) following a nonselective pulse of length τ_p can be described by

$$S(\tau_p) = S_0 \sin \omega_1 \tau_p \tag{11}$$

then the signal following a selective pulse is

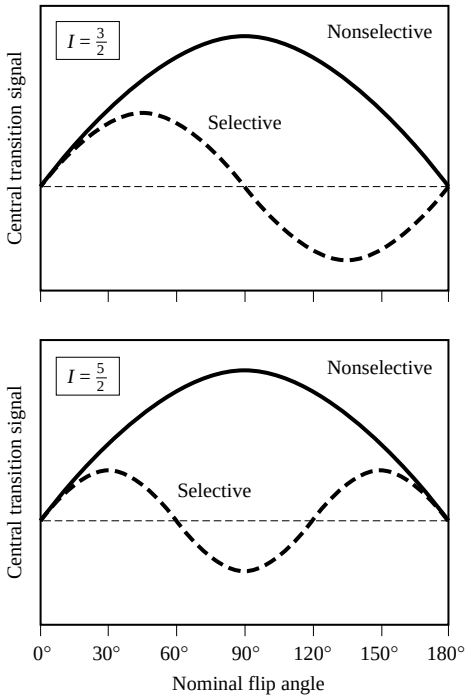

Figure 9 Central transition signal intensity following excitation by a single rf pulse of nominal flip angle $\omega_1\tau_p$, where τ_p is the duration of the pulse, plotted for the limits of nonselective ($\omega_1 \gg \Delta\omega_Q$) and selective ($\omega_1 \ll \Delta\omega_Q$) irradiation

$$S(\tau_p) = \frac{S_0}{I + \frac{1}{2}} \sin[(I + \tfrac{1}{2})\omega_1\tau_p] \qquad (12)$$

The flip angle dependence according to equations (11) and (12) is plotted in Figure 9 for $I = \frac{3}{2}$ and $\frac{5}{2}$.

So far, we have avoided discussion of rf amplitudes that are intermediate between selective and nonselective excitation ($\nu_1 \approx \nu_Q$). However, this situation is often encountered in practice. The response of the spin system to intermediate rf amplitudes is more complex than in the limiting cases. For details see ***Nutation Spectroscopy of Quadrupolar Nuclei***. A significant feature is that for relatively small flip angles ($\omega_{nut}\tau_p < \pi$), the intermediate $S(\tau_p)$ functions fall between the limits of selective and nonselective pulses. Hence, since the initial slopes of the functions of equations (10) and (11) are identical, the signal intensity following very short pulses is independent of the size of the quadrupolar interaction. This result has important implications for the quantitative interpretation of NMR signal intensities.

4 EXPERIMENTAL METHODS

Methods for NMR detection of quadrupolar nuclei in solids are surveyed in this section. The emphasis is not on the achievements of the applications of these techniques, but rather on the underlying spectroscopic principles and their interrelations. Consequently, this section frequently refers to the basic spin properties introduced in the previous sections. The survey is divided in subsections on deuterium, ^{14}N, and half-integer spins, reflecting the fact that in practical applications the choice of a workable NMR method is usually dictated by the size of the NQCC and by the presence or absence of a central transition. The section concludes with a brief introduction to zero field NMR.

4.1 Deuterium

Detailed theoretical and experimental aspects of solid state NMR of deuterium are covered in the articles ***Deuterium NMR in Solids***; ***Liquid Crystalline Samples: Deuterium NMR***; ***Liquid Crystalline Samples: Relaxation Mechanisms***; ***Membranes: Deuterium NMR***, and ***Polymer Dynamics and Order from Multidimensional Solid State NMR***. Applications to polymers were reviewed by Spiess in 1985.[7] Key references to the literature can also be found in these articles.

4.1.1 First-Order Spectra

The most intensively studied first-order quadrupolar spectra are those of deuterium. This is partially due to the chemical importance of the hydrogen atom and the advantages of selective deuteration, but there is also a fortuitous combination of spectroscopic conditions. Deuterium is among the few quadrupolar nuclei for which the total width of the spectra is never much larger than 200 kHz. This ensures that the deuterium spectrum of any chemical structure can be detected within a practical bandwidth and the spins can be excited with essentially nonselective pulses. In addition, the spectra are not appreciably affected by second-order quadrupolar shifts, dipolar broadenings, or chemical shifts, because in the case of deuterium all these contributions are at least two orders of magnitude smaller than ν_Q. Another advantage is that the powder lineshapes of the first-order spectra of spin-1 nuclei are composed of only two spectral transitions, and are thus less complex than those of higher-spin nuclei (see Figure 2 and 3). These circumstances allow the observation of the sometimes subtle lineshape changes caused by nonrandom distributions of molecular orientation (as in liquid crystalline materials) or by rapid random reorientations of the EFG tensor. In fact, the bulk of solid state deuterium NMR work is focused on the elucidation of molecular motions, particularly in polymers, liquid crystals, and adsorbed molecules. In combination with a judicious use of relaxation times and the application of two-dimensional methods (see below), motions with correlation times from nanoseconds to seconds can be characterized.

4.1.2 Zeeman Order and Quadrupolar Order

In the so-called spin-alignment experiment,[7] the spins are prepared in a state of quadrupolar order (see Section 2.3), where they can be held for a time as long as T_{1Q} permits. During that time, chemical exchange can modify the level populations. Two-dimensional methods use this and a similar Zeeman-order scheme for characterization of slow molecular dynamics.

4.1.3 Pulse Sequences

Although deuterium spins can be excited with a nonselective pulse, the FID following a single 90° excitation pulse is short and largely undetectable because of the receiver dead time.

Therefore, the signals need to be created with the solid echo sequence, $90^\circ_x - \tau - 90^\circ_y$, where the second half of the echo serves as the FID for further data processing. The dependence of the signal on τ provides an extra experimental parameter for the study of motions. Quadrupolar order is created with the Jeener–Broekaert sequence, $90^\circ_x - \tau - 45^\circ_y$,[24] and detected with a 45° read-out pulse.

4.1.4 Double Quantum Transitions

Since the double quantum transition frequency is not shifted by the quadrupolar interaction, it is useful for measurements of the chemical shift tensor[25] or, in conjunction with MAS, the isotropic chemical shift,[26] and also for achieving high resolution in imaging.[27] In fact, the double quantum coherence precesses in the rotating frame with twice the offset frequency, and thus has an enhanced sensitivity to small changes in the resonance frequency. Because double quantum coherences are not directly observable, their time dependence has to be measured in a 2D-type experiment where the spins are allowed to evolve for a stepwise incremented time t_1, at the end of which they are detected with a nonselective read-out pulse that transfers double quantum coherence to observable signals. The double quantum state can be prepared by a variety of methods:[28] a double quantum excitation pulse [Figure 8(c)], double quantum cross polarization (a method where Hartmann–Hahn contact between, say, protons and deuterons is established by adjusting ν_1 of the protons to be equal to ν_{2Q} given by equation (8)),[29] two nonselective pulses,[26] or three nonselective pulses.[27]

4.1.5 Double Quantum Decoupling

Effective dipolar decoupling of deuterium from other nuclei by nonselective irradiation of the allowed transitions requires a very high rf intensity, which is difficult to produce in practice. However, decoupling can also be achieved through stirring of the $m = +1$ and -1 states by double quantum excitation.[19] It does not matter that this method does not stir the $m = 0$ state, because the latter is magnetically 'neutral' and does not contribute to dipolar broadening. The provision that the irradiation must be close to the double quantum resonance frequency (see Section 3.2.1.4) presents no practical problem, since the resonance condition is only affected by chemical shifts and second-order quadrupolar shifts.

4.1.6 Magic Angle Spinning

The similarity between the orientational dependence of the first-order quadrupolar splitting and that of CSA implies that MAS removes quadrupolar broadening in deuterium spectra of powders in the same way in which it narrows CSA broadening. However, since rotation speeds are much smaller than the width of the spectrum, the centerband of the MAS spectrum is always accompanied by a large number of sidebands, the envelope of which resembles the static lineshape.[30,31] Owing to the absence of an isotropic first-order shift, the position of the centerband is entirely determined by isotropic chemical shifts and second-order quadrupolar shifts.

4.2 Nitrogen-14

With the exception of chemical structures where near-cubic site symmetry reduces the NQCC to small values,[32] first-order ^{14}N spectra of powders are too broad for detection by NMR. Consequently, direct measurement of ν_Q and η of most compounds is feasible only by NQR spectroscopy. The spin-$\frac{1}{2}$ isotope ^{15}N is usually preferred for solid state NMR studies, despite its low natural abundance (0.365%). (See also ***Nitrogen NMR***.) Nevertheless, ^{14}N nuclei can be detected by several indirect NMR methods that circumvent the bandwidth problems related to the first-order broadening.

4.2.1 Double Quantum Transitions

The absence of first-order quadrupolar effects on double quantum resonance frequencies reduces the spectral width to within practical detection limits. However, double quantum spectroscopy of ^{14}N is much more difficult to perform than the corresponding deuterium experiments (see above). For instance, the method of detection of double quantum coherence by way of coherence transfer to the allowed transitions is not applicable to ^{14}N, because the allowed transitions are inaccessible. Instead, double quantum coherence can be observed indirectly via cross polarization to neigboring protons.[33]

4.2.2 Overtone NMR

As was mentioned in connection with Figure 4 in Section 2.2, a strong quadrupolar interaction causes the admixture of, e.g., some $m = 0$ character in the $m = 1$ and -1 states. As a result, the nominally forbidden $\Delta m = 2$ transition between the $m = -1$ and 1 levels acquires some degree of $\Delta m = 1$ character and becomes weakly allowed. Overtone NMR is the direct excitation and observation of this transition. It is performed at twice the Larmor frequency, $2\nu_0$, which is the frequency corresponding to the energy difference between the $m = \pm 1$ levels (see Figure 2). Although both overtone excitation and double quantum excitation (Section 2.3) induce forbidden transitions between the $m = \pm 1$ levels, they are based on entirely different principles: overtone NMR makes use of the second-order quadrupolar perturbation of Zeeman levels, but is otherwise a direct detection method. On the other hand, double quantum NMR does not rely on mixing of the Zeeman levels, but rather on a second-order rf perturbation of the quadrupole energy levels (see Section 5.5). The practical incentive for overtone NMR is obviously that the resonance frequencies are not shifted by first-order quadrupolar effects, an advantage shared with double quantum NMR. For further details, see ***Overtone Spectroscopy of Quadrupolar Nuclei***.

4.2.3 Heteronuclear Dipolar Splitting

The single crystal NMR spectrum of, say, a ^{13}C nucleus coupled by dipolar interaction to a nearby ^{14}N nucleus is split into three lines corresponding to the magnetic states $m = -1$, 0, 1 of the $I = 1$ spin. In first approximation, the magnetic moments associated with these ^{14}N states are aligned with the Zeeman field and have values proportional to m. This has two consequences: the ^{13}C triplet is symmetric,

and the dependence of their spectral positions on the crystal orientation is such that MAS removes the dipolar broadening in powders. However, in the presence of a large NQCC, the ^{14}N spins are no longer quantized along the Zeeman field, as was pointed out in our discussion of Figure 4. This changes the directions and magnitudes of the magnetic moments of the three eigenstates, and, hence, the symmetry of the triplet and the orientation dependence of its peak positions. These effects were first observed in a single crystal.[34] The modified orientation dependence also prevents complete narrowing of the dipolar broadening by MAS.[35] Provided ν_Q is sufficiently small in comparison to the ^{14}N Larmor frequency ν_0, the residual splitting of the ^{13}C MAS peak can be evaluated by perturbation theory. It was shown to be of the order $\nu_D\nu_Q/\nu_0$, where ν_D is the magnitude of the dipolar interaction. The literature dealing with these phenomena is summarized in a review article by Harris and Olivieri.[36] (See ***Magic Angle Spinning Carbon-13 Lineshapes: Effect of Nitrogen-14***.)

4.2.4 Population Transfer

Slow MAS rotation under continuous rf irradiation of ^{14}N nuclei induces spin flips through adiabatic transformations among the m states (see Section 3.2). This effect has found application in a REDOR-type method for ^{13}C–^{14}N distance determination.[37] The principle of regular REDOR experiments as applied to $I = S = \frac{1}{2}$ spin pairs is as follows. The FID signal of the S spins decays as a result of the dipolar interaction between I and S, but MAS refocuses the dipolar dephasing and creates a rotational echo at the end of a full rotor period. The refocusing is undone if a 180° pulse is applied to the I spins, flipping them from one m state to another at some time during the rotor cycle. This causes a rotational echo signal reduction of S, which can be analyzed to determine the I–S atomic distance (see ***REDOR and TEDOR***). The REDOR experiment cannot be applied in this form when the I spins are ^{14}N, because the 180° pulse must be nonselective to be effective. Instead, one can bring about the desired m flips by population transfer under adiabatic sample spinning conditions (transfer of populations in double resonance or TRAPDOR).[37]

4.3 Nuclei of Half-Integer Spin

Detailed theoretical and experimental aspects of solid state NMR of half-integer spins are covered in the articles ***Double Rotation***; ***Dynamic Angle Spinning***; ***High Speed MAS of Half-Integer Quadrupolar Nuclei in Solids***; ***High Temperature Superconductors***; ***Nutation Spectroscopy of Quadrupolar Nuclei***; ***Quadrupolar Nuclei in Glasses***, and ***Variable Angle Sample Spinning***. The literature on this subject before 1993 is summarized in an extensive review article by Freude and Haase.[6] Key references to the literature can also be found in these articles.

4.3.1 Static First-Order Spectra

Examples of simulated first-order quadrupolar lineshapes of half-integer nuclei in static samples were shown in Figure 3. Experimental spectra are, however, rarely reported. Their detection necessitates excitation by more than one pulse, since the receiver deadtime renders the FID following a single pulse largely undetectable. If nonselective pulses are feasible, a quadrupolar echo sequence identical to that described above for deuterium can be applied to refocus the signal and to allow 'zero-time resolution'. This has been demonstrated for $I = \frac{3}{2}$[38] and $\frac{5}{2}$.[39] Another approach is the so-called two-pulse free induction decay.[6] It is a 2D experiment consisting of two nonselective pulses. The first creates coherences of Δm = 1 transitions that evolve with frequencies equal to multiples of $\Delta\nu_Q$. After a time t_1, the second pulse is applied to transfer the coherences to the central transition, which can easily be detected. Central transition coherences during t_1 are suppressed by phase cycling, and the 2D spectra of spins $\frac{5}{2}$ are simplified in that they are dominated by the first satellite as a result of less effective coherence transfer from the second satellites.

4.3.2 MAS of First-Order Spectra

The orientational dependence of $\Delta\nu_Q$ is such that it allows narrowing of first-order powder spectra by MAS. Compared with deuterium, this experiment is more demanding in terms of spinning stability, because the spectra are generally broader. Jakobsen and co-workers (see ***High Speed MAS of Half-Integer Quadrupolar Nuclei in Solids***) have succeeded in obtaining highly resolved sideband patterns with ν_Q as large as 1 MHz for $I = \frac{3}{2}$ and 0.5 MHz for $I = \frac{5}{2}$. Fine structure of the sidebands due to second-order shifts and sideband envelopes can be analyzed to obtain detailed information on the spin system.

4.3.3 Multiple Quantum Coherence

Triple quantum coherence can be excited with an on-resonance selective pulse,[20] as indicated in Figure 8(h). The method of pulsed multiple quantum NMR (much-practised in one- and multidimensional NMR[28]) was first demonstrated in 1975 by Hatanaka et al.,[40] who created ^{27}Al ($I = \frac{5}{2}$) double quantum coherence in a single crystal by application of two consecutive selective pulses at different allowed transition frequencies.

4.3.4 Echoes and Multiple Pulse Experiments

Numerous combinations of nonselective and selective, on- and off-resonance pulses have been reported for the excitation, refocusing, coherence transfer, or selective detection of single and multiple quantum coherences. This diverse subfield of quadrupolar NMR has been reviewed by Sanctuary and Halstead[41] and by Freude and Haase.[6]

4.3.5 Spin Counting

In NMR, the signal intensity is proportional to the number of spins that give rise to it (see ***Quantitative Measurements***). It can thus be used for quantitative analysis, provided the signals of the unknown sample and a reference sample are excited and detected under comparable conditions. In the case of NMR of half-integer spins, three complicating factors need to be considered.

1. When only the central transition is observed, the signal is reduced by a factor reflecting the relative intensities of the

central and satellite transitions. For a given spin I these are given by

$$S_{m\leftrightarrow m+1} \propto I(I+1) - m(m+1) \tag{13}$$

The relative intensities and the percentages of the total intensity represented in the central transition are listed in Table 2. The appropriate reduction factor needs to be accounted for when signal intensities of solids are compared with a liquid reference sample, because in liquids all the transitions are observed. A corresponding signal reduction is also observed when defects are introduced in cubic crystals: at perfectly cubic sites the full signal is detected because ν_Q vanishes, but defects lower the symmetry, increase ν_Q, and wipe out the satellites.[5]

2. The NQCC can be so large that even the second-order effects broaden the central transition beyond the detection limit. Aluminum-27 NMR is particularly susceptible to this effect, since minor chemical modifications can drastically enhance the NQCC (Table 1). A classic example is the disappearance of ^{27}Al signal due to atoms near the surface of high-surface-area alumina, resulting in an inverse correlation between the signal intensity and the specific surface area.[42] In studies of disordered systems, it is always good practice to supplement ^{27}Al NMR spectra with a quantitative assessment of the percentage of nuclei that are represented in the spectrum. Sometimes, more useful information on the nature of a sample is revealed by a determination of the amount of 'NMR-invisible' Al than by the interpretation of an observed but nonrepresentative lineshape.
3. For quantitative comparison between different signals, it is imperative to work with excitation pulses of sufficiently small flip angle to ensure that the signal intensity does not depend on $\Delta\nu_Q$ (compare Figure 9). The largest deviation is between purely selective and nonselective excitations. To keep it under 5%, the nominal flip angle (i.e., the nutation angle if the pulse were applied to a liquid sample) must be smaller than 18°, 11°, and 8° for $I = \frac{3}{2}, \frac{5}{2}$, and $\frac{7}{2}$, respectively. For deviations less than 10%, the flip angles must be limited to 25°, 15°, and 11°, respectively.

4.3.6 Nutation Spectroscopy

Nutation spectroscopy in its simplest form is the study of the signal intensity following a single pulse, measured as a function of the length of the pulse. Fourier transformation in 2D fashion yields a nutation spectrum that reflects the distribution of nutation frequencies ν_{nut} of the spins during the pulse. Nutation spectroscopy applied to the central transition provides indirect information on the first-order quadrupolar parameters: when $\nu_1 \gg \nu_Q$, the nutation spectrum has a peak at ν_1; when $\nu_1 \ll \Delta\nu_Q$ the peak is at $(I + \frac{1}{2})\nu_1$ [see equation (12) and Figure 9]. Nutation spectra of powders obtained with intermediate rf amplitudes ($\nu_1 \approx \nu_Q$) feature characteristic powder lineshapes that are sensitive to the ratio ν_Q/ν_1 and to η. For further details, see ***Nutation Spectroscopy of Quadrupolar Nuclei***.

Table 2 Relative Intensities of the Transitions of Half-Integer Quadrupolar Nuclei

I	Relative intensities	Central transition (%)
3/2	3 : 4 : 3	40
5/2	5 : 8 : 9 : 8 : 5	25.7
7/2	7 : 12 : 15 : 16 : 15 : 12 : 7	19.0
9/2	9 : 16 : 21 : 24 : 25 : 24 : 21 : 16 : 9	15.2

4.3.7 Second-Order Spectra: Static, MAS, and VAS

The central transition spectra of powder samples have received a great deal of attention. Figure 10 shows the spectral lineshapes for various values of η, without and with MAS. The shapes of the spectra do not depend on I, but their widths do. For that reason, the lineshapes in Figure 10 are plotted on a universal frequency scale, where one unit represents a frequency increment of

$$A = \tfrac{1}{9}[I(I+1) - \tfrac{3}{4}]\frac{\nu_Q^2}{\nu_0} \tag{14}$$

The symmetry of the orientation dependence of the second-order shift differs from that of first-order effects such as CSA, dipolar interaction, and first-order quadrupolar splitting. Consequently, complete line narrowing is not achieved with MAS, as may be seen in Figure 10. Nevertheless, MAS spectra are still preferable to static spectra, not only because the quadrupolar pattern is three to four times narrower, but also because CSA and dipolar broadenings are removed. Chemical shift resolution of MAS spectra improves dramatically when the magnetic field is increased. Since second-order broadening and chemical shift are proportional to $1/\nu_0$ and ν_0, respectively, the resolution scales as ${\nu_0}^2$. High spinning speeds also improve

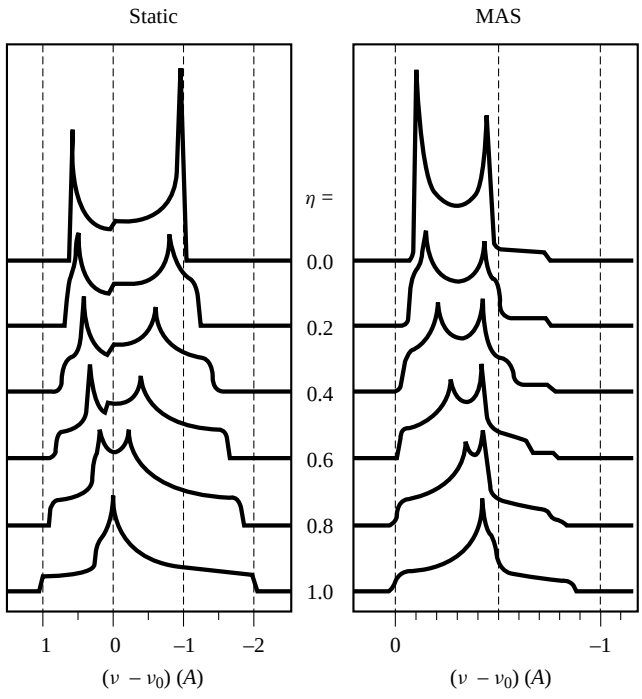

Figure 10 Central transition lineshapes of half-integer spins broadened by the second-order quadrupolar effect, calculated for static and fast MAS conditions. The frequency scale is in units of A, which is defined in equation (14)

resolution, because they prevent overlap of sidebands. Another approach is the technique of variable angle spinning (VAS), in which the samples are rotated about an axis that does not necessarily make the magic angle with the Zeeman field. Certain angles give narrower second-order spectra, but complete narrowing is not obtained. For more details, see ***Variable Angle Sample Spinning***.

4.3.8 Narrowing of Second-Order Broadening

The search for methods to remove the second-order quadrupolar broadening culminated in the inventions of two composite sample rotation techniques: DAS[43] and DOR.[44] Both methods succeed in narrowing the lines by making use of the particular orientational symmetry of the shift. For details, see ***Double Rotation*** and ***Dynamic Angle Spinning***. It should be noted that sample rotation does not change the center of gravity of the spectra. Consequently, the spectral position of the narrowed peak is the combination of a chemical shift and an isotropic second-order quadrupolar shift, where the latter is given by

$$\Delta\nu_{\mathrm{iso}}^{(2)} = -\tfrac{1}{30}[I(I+1) - \tfrac{3}{4}]\frac{\nu_{\mathrm{Q}}^2}{\nu_0}(1 + \tfrac{1}{3}\eta^2) \qquad (15)$$

More recently, line narrowing has also been achieved in a 2D multiple quantum MAS experiment which does not require composite sample rotation. In this MQMAS method the spins are first excited to a triple quantum coherence state (see Section 3.3.1.3) and are subsequently transferred to central-transition coherence where second-order dephasing is refocused.[45] See also ***Line Narrowing Methods in Solids***.

4.3.9 Heteronuclear Dipolar Splitting

Modifications of dipolar splitting patterns similar to those of nuclei coupled to ^{14}N (see Section 4.2), are also observed when the neighboring nucleus is of half-integer spin and has a large NQCC. Examples of coupling to ^{63}Cu/^{65}Cu, ^{35}Cl/^{37}Cl, and other nuclei have been documented.[36]

4.3.10 Relaxation

Spin–lattice relaxation does not usually follow a single exponential behavior for the reasons outlined in Section 2.4. Additional complications arise when the T_1 of a central transition is measured by monitoring the signal following saturation. The results depend on whether a single selective saturation pulse or a long saturation comb is applied, and on whether the measurements are done under MAS or static conditions. The apparent T_1 can vary by more than an order of magnitude, depending on the measurement method.[46] The differences are caused by variations in initial population distributions of the energy levels [compare Figure 5(c) and (e)] and by variability of the effectiveness of spin diffusion between the central transition and satellite transitions of a neighboring nucleus.[46]

4.3.11 Spin Locking and Population Transfer

The x magnetization formed by application of a selective y pulse to the central transition corresponds to the spin state C_{x} (see Section 3.3). When spin locked by rf irradiation in the x direction, it decays with the relaxation time $T_{1\rho}$. However, under MAS at slow rates [$\alpha > 1$ with α defined as in equation (9)], the relaxation decay is interrupted by adiabatic population transfer from C_{x} to T_{z} (see Section 3.3). As a result, the x magnetization of every nucleus in the sample disappears at the first zero-crossing of its oscillating quadrupolar splitting $\Delta\nu_{\mathrm{Q}}$ and then reappears again at the next zero-crossing. Since different nuclei have their zero-crossings at different times, the total signal decays gradually, but because every nucleus has an even number of zero-crossings per rotor cycle (two or four), the signal grows back toward the end of the first rotor cycle. This pattern is repeated for successive rotor cycles until $T_{1\rho}$ relaxation causes the signal to decay. However, when the rotation rate is so fast that $\alpha \ll 1$, there is no population transfer, and the signal does not decay other than by relaxation. Under rotation at intermediate rates ($\alpha \approx 1$), the passages transform C_{x} to spin states that are not spin locked, resulting in an irreversible signal decay.[22] Another method of population transfer is slow sweeping of the rf carrier frequency. For instance, it can be applied to static $I = \frac{5}{2}$ nuclei for transfer of the populations of the $m = \pm\frac{5}{2}$ states to the $m = \pm\frac{1}{2}$ states in order to obtain a fivefold increase of central transition signal intensity.[23]

4.3.12 Cross Polarization

Cross polarization (CP) is the transfer of spin locked polarization (magnetization) from nuclei S to neighboring nuclei I by simultaneous rf irradiation of the two spin systems under matched conditions of the two rf amplitudes ν_{1S} and ν_{1I}. When both I and S are spins $\frac{1}{2}$, the matching requirement is the familiar Hartmann–Hahn condition, $\nu_{1S} = \nu_{1I}$. However, if one or both are quadrupolar nuclei, the appropriate matching condition is that the two nutation frequencies be equal, $\nu_{\mathrm{nut},S} = \nu_{\mathrm{nut},I}$. Thus, for CP of the central transition of half-integer spins I from protons with spin $S = \frac{1}{2}$, the condition is $\nu_{1\mathrm{S}} = (I + \frac{1}{2})\nu_{1I}$ (see Section 3.3). The resulting I polarization has the spin locked spin configuration C_{x}. If the cross polarization is done under MAS conditions (CP MAS), complications arise as a result of the zero-crossings of $\Delta\nu_{\mathrm{Q}}$. The same rf irradiation that establishes the CP matching also serves as a spin lock field for the newly formed central transition polarization. Hence, if the adiabaticity parameter α is in the intermediate range, the signal enhancement is frustrated by the irreversible decay of C_{x} caused by the nonadiabatic passages (see the preceding paragraph). This can be a reason for poor performance of CP MAS of the central transition.[47]

4.4 Zero Field NMR

The technique of zero field NMR makes use of the connectivity, illustrated in Figure 4, between the spin states at zero Zeeman field (the NQR limit) and at high field (the NMR limit). A sample is mechanically shuttled back and forth between a position where the field is strong and another position where the field vanishes. In this way, the NQR spectrum can be indirectly detected as an NMR signal, with the combined advantages of the higher sensitivity of NMR and the higher spectroscopic resolution of NQR (see Section 2.2). For details, see ***Zero Field NMR***.

5 THEORY

5.1 Electric Field Gradient

The nuclear quadrupole interacts with an electric field gradient (EFG). This is the gradient of the electric field created by the charges other than the nucleus under consideration. The isotropic portion of the EFG, i.e., the part that originates from the s electrons, which have a nonvanishing charge density at the site of the nucleus, has no relevance to NMR, because the energy of its interaction with the nuclear charge distribution does not change when the nuclear spin axis changes orientation.[4] To be sure, the isotropic EFG contributes to isotope shifts in atomic spectra in the form of a 'volume effect' or 'field effect'.[48,49] However, in the context of NMR, it is customary to ignore its existence. The remaining EFG tensor $\boldsymbol{V}$ is thus purely anisotropic. It has three principal tensor components, V_{XX}, V_{YY}, and V_{ZZ}, which are associated with a principal axis system (PAS) X, Y, Z (in the present notation, we reserve capital indices for the PAS and let the lower case x, y, z stand for a general axis system). The off-diagonal elements V_{XY}, V_{XZ}, etc., are zero in the PAS. The diagonal elements satisfy the Laplace equation

$$V_{XX} + V_{YY} + V_{ZZ} = 0 \tag{16}$$

reflecting the fact that we ignore the isotropic component. Following the convention

$$|V_{ZZ}| \geq |V_{XX}| \geq |V_{YY}| \tag{17}$$

for the assignment of the three PAS directions, we define the quantity

$$eq = V_{ZZ} \tag{18}$$

and the asymmetry parameter

$$\eta = (V_{YY} - V_{XX})/V_{ZZ} \tag{19}$$

The convention ensures that $0 \leq \eta \leq 1$. When $\eta = 0$, the EFG tensor is axially symmetric about the Z axis: $V_{XX} = V_{YY} = -\frac{1}{2}V_{ZZ}$. For arbitrary η, equations (18) and (19) are solved to give

$$V_{XX} = -\tfrac{1}{2}(1 + \eta)eq \tag{20}$$

$$V_{YY} = -\tfrac{1}{2}(1 - \eta)eq \tag{21}$$

One should be aware that many authors prefer the convention $|V_{ZZ}| \geq |V_{YY}| \geq |V_{XX}|$ instead of equation (17) for the assignment of the X and Y axes. The appropriate definition of η is then $(V_{XX} - V_{YY})/V_{ZZ}$, and the signs of η-containing terms in formulas such as equations (3), (20), (21), and (22)–(27) are reversed.

Two kinds of local symmetry at the site of the nucleus dictate the symmetry of the EFG tensor.

1. Cubic point symmetry (including eightfold cubic, sixfold octahedral, and fourfold tetrahedral coordinations) results in $V_{XX} = V_{YY} = V_{ZZ}$, and, hence, by the Laplace equation, $eq = 0$.
2. Axial point symmetry (including structures where the nucleus lies on a threefold, fourfold, fivefold, or sixfold symmetry axis) results in $\eta = 0$.

In ionic crystals, the EFG tensor can be calculated from the known positions and charges of the surrounding ions. However, the actual EFGs experienced by the nucleus are many times larger than the calculated values as a result of distortions of the local electron cloud. The Sternheimer antishielding factor accounts for this correction (see ***Quadrupolar Interactions***).

Below are formulas for the components of the EFG tensor in a more general axis system x, y, z. To be completely general, we ought to specify three Euler angles for the orientation of x, y, z with respect to X, Y, Z. However, in most NMR experiments, we do not need to know more about the laboratory frame than the direction of the z axis specifying the $\boldsymbol{B}_0$ field orientation. In such bases, it is sufficient to define the two polar angles θ and ϕ of z with respect to the PAS. In fact, the polar angles represent two of the Euler angles, as is demonstrated in Figure 11, where the directions of x, y, and z are seen to be obtained from X, Y, and Z by rotating the system first about Z over angle ϕ and then about the new y over angle θ. The third Eulerian rotation (about z) is not executed. The transformation depicted in Figure 11 leads to

$$V_{xx} = \tfrac{1}{2}eq(3\sin^2\theta - 1 - \eta\cos^2\theta\cos 2\phi) \tag{22}$$

$$V_{yy} = \tfrac{1}{2}eq(-1 + \eta\cos 2\phi) \tag{23}$$

$$V_{zz} = \tfrac{1}{2}eq(3\cos^2\theta - 1 - \eta\sin^2\theta\cos 2\phi) \tag{24}$$

$$V_{xy} = V_{yx} = \tfrac{1}{2}eq\eta\cos\theta\sin 2\phi \tag{25}$$

$$V_{xz} = V_{zx} = -\tfrac{1}{2}eq\sin\theta\cos\theta(3 + \eta\cos 2\phi) \tag{26}$$

$$V_{yz} = V_{zy} = \tfrac{1}{2}eq\eta\sin\theta\sin 2\phi \tag{27}$$

There are, however, situations where three parameters must be specified to define the relative orientations of the PAS and

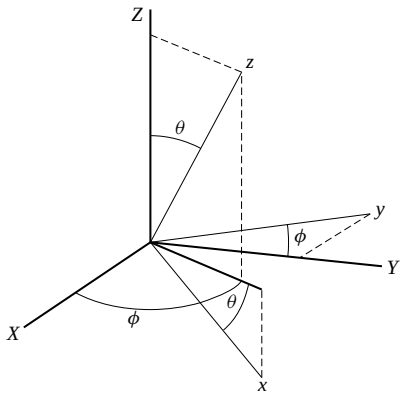

Figure 11 Transformation from a principal axis system X, Y, Z to a more general axis system x, y, z. The transformation is accomplished by a rotation through ϕ about Z followed by a rotation through θ about y. θ and ϕ are the polar and azimuthal angles of z with respect to X, Y, Z

the laboratory frame. For instance, when the EFG changes direction during the NMR experiment because of molecular motions or sample spinning, the full information concerning relative orientations at different times is generally needed for analysis of spin dynamics and relaxation rates.

5.2 Hamiltonian

The nuclear quadrupolar Hamiltonian is introduced in ***Internal Spin Interactions and Rotations in Solids*** and in ***Quadrupolar Interactions***. In the Cartesian coordinates of an arbitrary axes system, it is

$$\begin{aligned}\hat{\mathcal{H}}_{\mathrm{Q}} = \frac{eQ}{4I(2I-1)\hbar}\{&V_{zz}[3\hat{I}_z^2 - I(I+1)] \\ &+(V_{xx}-V_{yy})(\hat{I}_x^2-\hat{I}_y^2)+2V_{xy}(\hat{I}_x\hat{I}_y+\hat{I}_y\hat{I}_x) \\ &+2V_{xz}(\hat{I}_x\hat{I}_z+\hat{I}_z\hat{I}_x)+2V_{yz}(\hat{I}_y\hat{I}_z+\hat{I}_z\hat{I}_y)\}\end{aligned} \tag{28}$$

This formula contains the tensor elements of $\boldsymbol{V}$, which depend on the orientation of the axes with respect to the PAS, as was pointed out above. Another representation of the Hamiltonian is in terms of irreducible tensor operators:

$$\hat{\mathcal{H}}_{\mathrm{Q}} = \frac{1}{2\hbar}\sum_{k=-2}^{2}(-1)^k\hat{Q}_k V_{-k} \tag{29}$$

where

$$\left.\begin{aligned}\hat{Q}_0 &= \frac{eQ}{2I(2I-1)}\frac{1}{\sqrt{6}}[\hat{I}_z^2 - I(I+1)] \\ \hat{Q}_{\pm1} &= \mp\frac{eQ}{2I(2I-1)}(\hat{I}_z\hat{I}_\pm+\hat{I}_\pm\hat{I}_z) \\ \hat{Q}_{\pm2} &= \frac{eQ}{2I(2I-1)}\hat{I}_\pm^2 \\ \hat{I}_\pm &= \hat{I}_x \pm \mathrm{i}\hat{I}_y\end{aligned}\right\} \tag{30}$$

and

$$\left.\begin{aligned}V_0 &= \sqrt{\tfrac{3}{2}}V_{zz} \\ V_{\pm1} &= \mp V_{xz} - \mathrm{i}V_{yz} \\ V_{\pm2} &= \tfrac{1}{2}(V_{xx}-V_{yy}) \pm \mathrm{i}V_{xy}\end{aligned}\right\} \tag{31}$$

The transformation properties of the irreducible tensors make this form of the Hamiltonian particularly useful for description of rotations of the coordinate system. The notation of equation (29) is also helpful for writing out the Hamiltonian in matrix form.

5.3 Hamiltonian in Matrix Form

Since many aspects of the spin dynamics of quadrupolar nuclei can readily be explained by inspection of the structures of the matrices of the various contributions to the total Hamiltonian, we give here a few representative examples. The matrices are given in the standard representation of spin I, i.e., the matrix elements are $\langle m'|\hat{\mathcal{H}}_{\mathrm{Q}}|m\rangle$, where $|m\rangle$ are the $2I+1$ eigenstates of $\hat{I}_z$: $|I\rangle$, $|I-1\rangle$, ... , $|-I+1\rangle$, $|-I\rangle$. The spin operator properties of the $\hat{Q}_k$ components in equation (29) place the coefficient V_0 in the diagonal elements, $V_{\pm1}$ in elements one position removed from the diagonal, and $V_{\pm2}$ two positions removed. As two examples, we give the matrices for $I = 1$,

$$\hat{\mathcal{H}}_{\mathrm{Q}} = \frac{3eQ}{2I(2I-1)\hbar}\begin{pmatrix} \frac{1}{6}V_{zz} & \sqrt{\frac{1}{2}}V_{-1} & V_{-2} \\ -\sqrt{\frac{1}{2}}V_{+1} & -\frac{1}{3}V_{zz} & -\sqrt{\frac{1}{2}}V_{-1} \\ V_{+2} & \sqrt{\frac{1}{2}}V_{+1} & \frac{1}{6}V_{zz}\end{pmatrix} \tag{32}$$

and for $I = \frac{3}{2}$,

$$\hat{\mathcal{H}}_{\mathrm{Q}} = \frac{3eQ}{2I(2I-1)\hbar} \times \begin{pmatrix} \frac{1}{2}V_{zz} & \sqrt{\frac{1}{3}}V_{-1} & \sqrt{\frac{1}{3}}V_{-2} & 0 \\ -\sqrt{\frac{1}{3}}V_{+1} & -\frac{1}{2}V_{zz} & 0 & \sqrt{\frac{1}{3}}V_{-2} \\ \sqrt{\frac{1}{3}}V_{+2} & 0 & -\frac{1}{2}V_{zz} & -\sqrt{\frac{1}{3}}V_{-1} \\ 0 & \sqrt{\frac{1}{3}}V_{+2} & \sqrt{\frac{1}{3}}V_{+1} & \frac{1}{2}V_{zz}\end{pmatrix} \tag{33}$$

In high-field NMR, the quadrupolar Hamiltonian is considered to be a perturbation of the Zeeman Hamiltonian $\hat{\mathcal{H}}_{\mathrm{Z}} = \omega_0\hat{I}_z$. The first-order perturbation is determined by the secular part of $\hat{\mathcal{H}}_{\mathrm{Q}}$, i.e., the portion $\hat{\mathcal{H}}_{\mathrm{Q}}{}^{(1)}$ of $\hat{\mathcal{H}}_{\mathrm{Q}}$ that commutes with $\hat{\mathcal{H}}_{\mathrm{Z}}$. Since the latter is represented by a diagonal matrix with nondegenerate eigenvalues, $\hat{\mathcal{H}}_{\mathrm{Q}}{}^{(1)}$ retains only the diagonal elements of equations (32) and (33), 'truncating' $\hat{\mathcal{H}}_{\mathrm{Q}}$ to

$$\hat{\mathcal{H}}_{\mathrm{Q}}^{(1)} = \tfrac{1}{2}\Delta\omega_{\mathrm{Q}}[\hat{I}_z^2 - \tfrac{1}{3}I(I+1)] \tag{34}$$

$\hat{\mathcal{H}}_{\mathrm{Q}}{}^{(1)}$ determines the first-order energy level corrections $E_{\mathrm{m}}{}^{(1)}$ given in equation (2). The second-order corrections $E_{\mathrm{m}}{}^{(2)}$ of the eigenvalues involve double products of the off-diagonal elements of $\hat{\mathcal{H}}_{\mathrm{Q}}$ divided by differences between Zeeman energies:

$$\begin{aligned}E_m^{(2)} = -\frac{\omega_{\mathrm{Q}}^2}{9\omega_0}m\Bigg\{&2[I(I+1)-2m^2-\tfrac{1}{4}]\left(\frac{|V_1|}{eq}\right)^2 \\ &-[I(I+1)-m^2-\tfrac{1}{2}]\left(\frac{|V_2|}{eq}\right)^2\Bigg\}\end{aligned} \tag{35}$$

These eigenvalue equations are used to calculate first- and second-order quadrupolar shifts of transition frequencies. The expressions $(|V_1|/eq)^2$ and $(|V_2|/eq)^2$ in equation (35) are functions of the orientation of the Zeeman field with respect to the EFG principal axes and of η [see equations (31) and (22)–(27)]. For instance, the second-order shift of the central transition is

$$\begin{aligned}\Delta\omega_{-1/2\leftrightarrow1/2}^{(2)} = -\frac{\omega_{\mathrm{Q}}^2}{9\omega_0}&[I(I+1)-\tfrac{3}{4}] \\ &\times\left[2\left(\frac{|V_1|}{eq}\right)^2-\left(\frac{|V_2|}{eq}\right)^2\right]\end{aligned} \tag{36}$$

which for $\eta = 0$ reduces to

$$\Delta\omega^{(2)}_{-1/2\leftrightarrow 1/2} = -\frac{\omega_Q^2}{16\omega_0}[I(I+1) - \tfrac{3}{4}] \times(1-\cos^2\theta)(9\cos^2\theta - 1) \qquad (37)$$

The eigenfunctions of the Hamiltonian are also perturbed. In other words, the vectors representing them in wavefunction space are slightly tilted. The general formula for these tilted states is

$$|m\rangle \rightarrow |m\rangle + \sum_{m'\neq m} \frac{\langle m'|\hat{\mathcal{H}}_Q|m\rangle}{(m-m')\omega_0}|m'\rangle \qquad (38)$$

which can be used to evaluate the Zeeman state mixing that determines the detectability of overtone spectra and the dipolar splittings in spectra of neighboring nuclei. The correction terms have the forms $(\omega_Q/\omega_0)(V_{\pm 1}/eq)|m \pm 1\rangle$ and $(\omega_Q/\omega_0)(V_{\pm 2}/eq)|m \pm 2\rangle$ multiplied by numerical coefficients. Because the corrections involve off-diagonal elements of $\hat{\mathcal{H}}_Q$ divided by ω_0, they are considered to be second-order perturbations.

5.4 Density Matrix

The state of an ensemble of mutually noninteracting nuclei of spin I is described by a density matrix $\hat{\rho}$ having $2I + 1$ rows and columns. Since this is a Hermitian matrix, it has in addition to a unit-matrix term, $(2I + 1)^2 - 1$ independent traceless components (3 when $I = \frac{1}{2}$; 8 when $I = 1$; 15 when $I = \frac{3}{2}$; etc.). It is convenient to choose a basis set of mutually independent matrices or operators for the description of the density matrices. In the case of spin-$\frac{1}{2}$, the three operators $\hat{I}_x$, $\hat{I}_y$, and $\hat{I}_z$ are the natural selection for that purpose, but for higher spin numbers the choices are not so obvious. A number of formalisms exist. Some are based on the use of irreducible tensor operators [i.e., variations of equation (30)].[41,50,51] Others employ fictitious spin-$\frac{1}{2}$ operators[21,52] or specially adapted operators.[54] Since the spin dynamics are determined by the Liouville–von Neumann equation

$$\frac{d\hat{\rho}}{dt} = i[\hat{\rho}, \hat{\mathcal{H}}] \qquad (39)$$

the preferred formalism depends on the nature of the Hamiltonian to be analyzed, and is often the one that offers the simplest set of commutation relations. Not infrequently, however, other considerations such as ease of visualization, relaxation properties, or personal taste of the theoretician determine the choice of formalism.

Below, we give the traceless parts of the density matrices corresponding to the special spin states that were mentioned in Sections 2.3, 3.2, and 3.3. Rather than referring to a particular basis set, we reproduce here the full matrices in the standard representation. (Complete operator basis sets may be found in the respective references.)[21,41,52,53] For $I = 1$, we have mentioned Zeeman order $\hat{I}_z$ and quadrupolar order $\hat{Q}_z$,

$$\hat{I}_z = \begin{pmatrix} 1 & 0 & 0 \\ 0 & 0 & 0 \\ 0 & 0 & -1 \end{pmatrix}, \quad \hat{Q}_z = \frac{1}{\sqrt{3}}\begin{pmatrix} 1 & 0 & 0 \\ 0 & -2 & 0 \\ 0 & 0 & 1 \end{pmatrix} \qquad (40)$$

single quantum coherences $\hat{I}_x$ and $\hat{I}_y$ corresponding to x and y magnetization,

$$\hat{I}_x = \frac{1}{\sqrt{2}}\begin{pmatrix} 0 & 1 & 0 \\ 1 & 0 & 1 \\ 0 & 1 & 0 \end{pmatrix}, \quad \hat{I}_y = \frac{1}{\sqrt{2}}\begin{pmatrix} 0 & -i & 0 \\ i & 0 & -i \\ 0 & i & 0 \end{pmatrix} \qquad (41)$$

single quantum coherences $\hat{S}_x$ and $\hat{S}_y$ associated with selective excitation of the $(0, -1)$ transition,

$$\hat{S}_x = \begin{pmatrix} 0 & 0 & 0 \\ 0 & 0 & 1 \\ 0 & 1 & 0 \end{pmatrix}, \quad \hat{S}_y = \begin{pmatrix} 0 & 0 & 0 \\ 0 & 0 & -i \\ 0 & i & 0 \end{pmatrix} \qquad (42)$$

and double quantum coherences with x and y phases,

$$\hat{D}_x = \begin{pmatrix} 0 & 0 & 1 \\ 0 & 0 & 0 \\ 1 & 0 & 0 \end{pmatrix}, \quad \hat{D}_y = \begin{pmatrix} 0 & 0 & -i \\ 0 & 0 & 0 \\ i & 0 & 0 \end{pmatrix} \qquad (43)$$

The $I = \frac{3}{2}$ spin states relevant to the discussions in this article are Zeeman order $\hat{I}_z$ and quadrupolar order $\hat{Q}_z$,

$$\hat{I}_z = \frac{1}{2}\begin{pmatrix} 3 & 0 & 0 & 0 \\ 0 & 1 & 0 & 0 \\ 0 & 0 & -1 & 0 \\ 0 & 0 & 0 & -3 \end{pmatrix}, \quad \hat{Q}_z = \frac{1}{2}\begin{pmatrix} 1 & 0 & 0 & 0 \\ 0 & -1 & 0 & 0 \\ 0 & 0 & -1 & 0 \\ 0 & 0 & 0 & 1 \end{pmatrix} \qquad (44)$$

three coherences associated with the central transition,

$$\hat{C}_x = \frac{1}{2}\begin{pmatrix} 0 & 0 & 0 & 0 \\ 0 & 0 & 1 & 0 \\ 0 & 1 & 0 & 0 \\ 0 & 0 & 0 & 0 \end{pmatrix}, \quad \hat{C}_y = \frac{1}{2}\begin{pmatrix} 0 & 0 & 0 & 0 \\ 0 & 0 & -i & 0 \\ 0 & i & 0 & 0 \\ 0 & 0 & 0 & 0 \end{pmatrix}$$
$$\hat{C}_z = \frac{1}{2}\begin{pmatrix} 0 & 0 & 0 & 0 \\ 0 & 1 & 0 & 0 \\ 0 & 0 & -1 & 0 \\ 0 & 0 & 0 & 0 \end{pmatrix} \qquad (45)$$

and three coherences associated with the triple quantum transition,

$$\hat{T}_x = \frac{1}{2}\begin{pmatrix} 0 & 0 & 0 & 1 \\ 0 & 0 & 0 & 0 \\ 0 & 0 & 0 & 0 \\ 1 & 0 & 0 & 0 \end{pmatrix}, \quad \hat{T}_y = \frac{1}{2}\begin{pmatrix} 0 & 0 & 0 & -i \\ 0 & 0 & 0 & 0 \\ 0 & 0 & 0 & 0 \\ i & 0 & 0 & 0 \end{pmatrix}$$
$$\hat{T}_z = \frac{1}{2}\begin{pmatrix} 1 & 0 & 0 & 0 \\ 0 & 0 & 0 & 0 \\ 0 & 0 & 0 & 0 \\ 0 & 0 & 0 & -1 \end{pmatrix} \qquad (46)$$

Note that $\hat{T}_z$ is equivalent to the 'triple quantum order' represented in Figure 5. The nonvanishing matrix elements in equations (42), (43), (45), and (46) form 2×2 submatrices. They are examples of fictitious spin-$\frac{1}{2}$ operators.

5.5 Hamiltonian in Rotating Frame

An rf field of amplitude ω_1 and carrier frequency ω is best described in the axis frame that rotates with frequency ω with respect to the laboratory frame. The corresponding rotating-frame Hamiltonian is

$$\hat{\mathcal{H}}_{\mathrm{rf}} = \omega_1 \hat{I}_x \tag{47}$$

whose matrix elements are proportional to those of $\hat{I}_{\mathrm{x}}$:

$$\langle m|\hat{I}_x|m \pm 1\rangle = \tfrac{1}{2}\sqrt{I(I+1) - m(m \pm 1)} \tag{48}$$

In the same rotating frame, the Zeeman Hamiltonian is reduced to the resonance-offset Hamiltonian

$$\hat{\mathcal{H}}_{\mathrm{os}} = (\omega_0 - \omega)\hat{I}_z = \Delta\omega_0 \hat{I}_z \tag{49}$$

The matrix elements of the quadrupolar Hamiltonian in the rotating frame are transformed to oscillating functions obtained by replacing V_{k} in equations (29), (32), and (33) with $V_{\mathrm{k}} \exp(-\mathrm{i}k\omega t)$. In the presence of rf fields, it is usually permissible to neglect the rapidly oscillating terms. This reduces $\hat{\mathcal{H}}_{\mathrm{Q}}$ in the rotating frame to $\hat{\mathcal{H}}_{\mathrm{Q}}{}^{(1)}$ of equation (34). In summary, we consider a rotating-frame Hamiltonian consisting of three terms:

$$\hat{\mathcal{H}}_{\mathrm{R}} = \hat{\mathcal{H}}_{\mathrm{Q}}^{(1)} + \hat{\mathcal{H}}_{\mathrm{os}} + \hat{\mathcal{H}}_{\mathrm{rf}} \tag{50}$$

In matrix form, it is for $I = 1$,

$$\hat{\mathcal{H}}_{\mathrm{R}} = \frac{1}{2}\begin{pmatrix} \frac{1}{3}\Delta\omega_{\mathrm{Q}} + 2\Delta\omega_0 & \omega_1\sqrt{2} & 0 \\ \omega_1\sqrt{2} & -\frac{2}{3}\Delta\omega_{\mathrm{Q}} & \omega_1\sqrt{2} \\ 0 & \omega_1\sqrt{2} & \frac{1}{3}\Delta\omega_{\mathrm{Q}} - 2\Delta\omega_0 \end{pmatrix} \tag{51}$$

and for $I = \frac{3}{2}$,

$$\hat{\mathcal{H}}_{\mathrm{R}} = \frac{1}{2}\begin{pmatrix} \Delta\omega_{\mathrm{Q}}+3\Delta\omega_0 & \omega_1\sqrt{3} & 0 & 0 \\ \omega_1\sqrt{3} & -\Delta\omega_{\mathrm{Q}}+\Delta\omega_0 & 2\omega_1 & 0 \\ 0 & 2\omega_1 & -\Delta\omega_{\mathrm{Q}}-\Delta\omega_0 & \omega_1\sqrt{3} \\ 0 & 0 & \omega_1\sqrt{3} & \Delta\omega_{\mathrm{Q}}-3\Delta\omega_0 \end{pmatrix} \tag{52}$$

The corresponding matrices for higher values of I can be evaluated similarly. Here, we only mention that when m and $m \pm 1$ equal $-\frac{1}{2}$ and $\frac{1}{2}$, the square root in equation (48) reduces to $I + \frac{1}{2}$, resulting in

$$\langle -\tfrac{1}{2}|\hat{\mathcal{H}}_{\mathrm{rf}}|\tfrac{1}{2}\rangle = \langle \tfrac{1}{2}|\hat{\mathcal{H}}_{\mathrm{rf}}|-\tfrac{1}{2}\rangle = \tfrac{1}{2}\omega_1(I + \tfrac{1}{2}) \tag{53}$$

The nutation frequencies of selective central transition nutation, equation (10), are determined by these matrix elements.

The various ways in which rf pulses affect a quadrupolar spin system were reviewed in Section 3. In an effort to keep that presentation succinct, a quantum mechanical explanation of the effects was not given. The following discussion is intended to show how the effects are related to the Hamiltonian in the rotating frame, equation (50). As in Section 3, we begin with an example of a nonquadrupolar spin to introduce the concepts of nutation, spin locking, and population transfer. Taking $I = \frac{1}{2}$ for simplicity, we have the Hamiltonian matrix

$$\hat{\mathcal{H}}_{\mathrm{R}} = \frac{1}{2}\begin{pmatrix} \Delta\omega_0 & \omega_1 \\ \omega_1 & -\Delta\omega_0 \end{pmatrix} \tag{54}$$

If the rf field vanishes, the dependence of its eigenvalues on the offset is represented by two straight lines crossing at zero offset, as indicated by the broken lines in the top diagram of Figure 12. The associated eigenstates are $|\frac{1}{2}\rangle$ and $|-\frac{1}{2}\rangle$. Introduction of the rf term changes the eigenvalues and eigenstates provided ω_1 [occupying the off-diagonal elements in equation (54)] is not much smaller than $\Delta\omega_0$ (the difference between the diagonal elements). This leads to an avoided level crossing in the eigenvalue diagram, with a residual level splitting of ω_1 at the center. This result follows immediately from the solution of the eigenvalue equation of the matrix of equation (54) with vanishing diagonal elements. When $\Delta\omega_0 = 0$, the eigenstates of $\hat{\mathcal{H}}_{\mathrm{R}}$ are the linear combinations

$$|\mathrm{c}+\rangle = (|+\tfrac{1}{2}\rangle + |-\tfrac{1}{2}\rangle)/\sqrt{2} \tag{55}$$

$$|\mathrm{c}-\rangle = (|+\tfrac{1}{2}\rangle - |-\tfrac{1}{2}\rangle)/\sqrt{2} \tag{56}$$

Zeeman order corresponds to populations of the untilted $|\pm\frac{1}{2}\rangle$ wavefunctions. Since these are eigenstates of the Hamiltonian when $\Delta\omega_0 \gg \omega_1$, Zeeman order is spin locked far off resonance. Another way of expressing this is by saying that the density matrix $\hat{I}_{\mathrm{z}}$, which represents Zeeman order, commutes with the Hamiltonian far off resonance. On resonance, the spin locked density matrix is $\hat{I}_{\mathrm{x}}$, which corresponds to populations of the eigenstates $|\mathrm{c}\pm\rangle$. Since $\hat{I}_{\mathrm{z}}$ does not commute with the Hamiltonian on resonance, a spin system in thermal equilibrium is not spin locked on resonance, but rather undergoes nutation in the rf field with a frequency ω_{nut} equal to the level splitting, which in this case is ω_1. Population transfer occurs when $\Delta\omega_0$ is swept slowly from above to below resonance. If the passage is sufficiently slow that the adiabatic condition of equation (7) is satisfied, an eigenstate of the Hamiltonian is changed into the state that is connected to it by continuity in the level diagram. The top diagram in Figure 12 shows that, when going from above to below resonance, the $|+\frac{1}{2}\rangle$ state connects via $|\mathrm{c}+\rangle$ to $|-\frac{1}{2}\rangle$. (Compare the $z \rightarrow x \rightarrow -z$ trajectory of the magnetization vector in the axis system of Figure 7.) In this way, the density matrix is converted from $\hat{I}_{\mathrm{z}}$ to $-\hat{I}_{\mathrm{z}}$, and the populations of the Zeeman levels are exchanged.

These concepts are readily extended to quadrupolar spins. Examples of offset-dependent eigenvalues are plotted in the $I = 1$ and $I = \frac{3}{2}$ diagrams in Figure 12. They were calculated by numerical diagonalization of the matrices of equations (51) and (52) for selective rf excitation conditions ($\omega_1 < \Delta\omega_{\mathrm{Q}}$). Avoided level crossings are indicated by the circles in the figure. They occur at values of $\Delta\omega_0$ for which two diagonal elements of the Hamiltonian are equal. The numbers above the circles mark the differences Δm of the m values of the crossing states. The residual level splittings are the nutation frequencies ω_{nut} of the corresponding excitations. For single quantum crossings ($\Delta m = 1$), they are determined by the respective off-diagonal elements in the Hamiltonian. For multiple quantum transitions, the residual splittings are to be calculated by higher-order perturbation theory, resulting in the general expression

$$\omega_{\mathrm{nut}}(m' \leftrightarrow m) = M_{m' \leftrightarrow m}\omega_1 \left(\frac{\omega_1}{\Delta\omega_{\mathrm{Q}}}\right)^{\Delta m - 1} \tag{57}$$

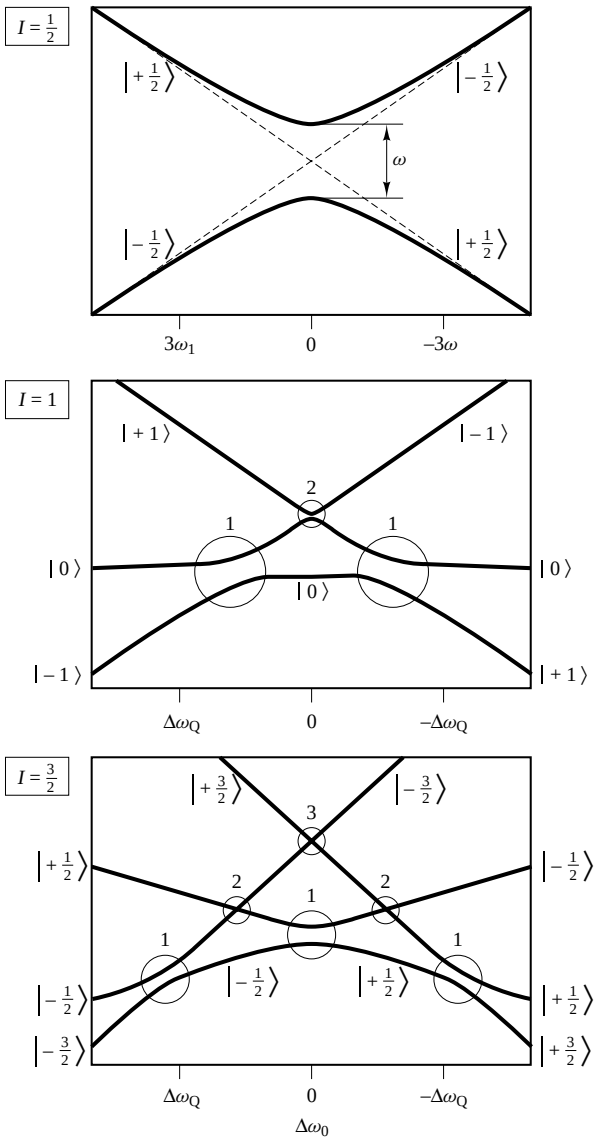

Figure 12 Eigenstate diagrams of a rotating frame Hamiltonian consisting of a first-order quadrupolar term, a frequency offset term, and an rf term. The eigenvalues are plotted versus the offset $\Delta\omega_0$. The $I = \frac{1}{2}$ diagram is representative of the case of a nonquadrupolar nucleus ($\Delta\omega_Q = 0$). The $I = 1$ and $I = \frac{3}{2}$ diagrams represent cases of weak irradiation ($\omega_1 < \Delta\omega_Q$). The actual $\Delta\omega_Q/\omega_1$ ratios used in the simulations were 5 and 10 for $I = 1$ and $\frac{3}{2}$, respectively. Eigenfuctions $|m\rangle$ outside the circled regions are indicated. The numbered circles mark regions of avoided level crossings and the respective values of Δm

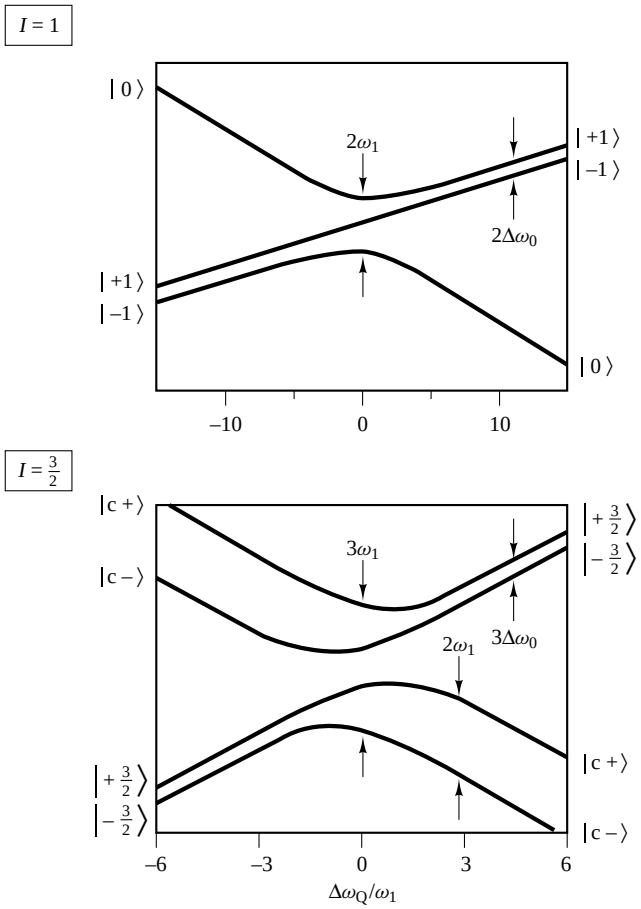

Figure 13 Eigenstate diagrams of a rotating frame Hamiltonian consisting of a first-order quadrupole term, a frequency offset term, and an rf term. The eigenvalues are plotted versus the quadrupole splitting $\Delta\omega_Q$. The diagrams represent cases of small frequency offsets ($\Delta\omega_0 < \omega_1$). The actual $\Delta\omega_0/\omega_1$ ratios used in the simulations were 0.25 and 0.15 for $I = 1$ and $\frac{3}{2}$, respectively. The eigenvalue levels for vanishing $\Delta\omega_Q$ are equally spaced by ω_1. The eigenfuctions are indicated for large $\Delta\omega_Q$. $|c\pm\rangle$ are linear combinations of $|\pm\frac{1}{2}\rangle$ (see text)

Examples of the coefficients are, for $I = 1$, $M_{0\leftrightarrow+1} = \sqrt{2}$, $M_{-1\leftrightarrow+1} = 2$; for $I = \frac{3}{2}$, $M_{-\frac{1}{2}\leftrightarrow+\frac{1}{2}} = 2$, $M_{+\frac{1}{2}\leftrightarrow+\frac{3}{2}} = \sqrt{3}$, $M_{-\frac{1}{2}\leftrightarrow+\frac{3}{2}} = 2\sqrt{3}$, $M_{-\frac{3}{2}\leftrightarrow+\frac{3}{2}} = \frac{3}{2}$. Furthermore, $M_{m'\leftrightarrow m} = M_{m\leftrightarrow m'} = M_{-m'\leftrightarrow-m}$. The coefficients for $I = \frac{5}{2}$ are tabulated elsewhere.[23] The various excitation conditions listed in Figure 8 are easily located in Figure 12. Note that the double quantum transition of $I = \frac{3}{2}$ at $\Delta\omega_0 = \frac{1}{2}\Delta\omega_Q$ was omitted in Figure 8. In the areas outside the circles, i.e. when the irradiation is off-resonance, the eigenstates are essentially pure Zeeman states $|m\rangle$. The corresponding spin locked spin configurations are populated states $|m\rangle$ (see Figure 5), which are represented by diagonal density matrices (e.g., $\hat{I}_z$, $\hat{Q}_z$, $\hat{C}_z$, and $\hat{T}_z$). An adiabatic sweep of $\Delta\omega_0$ interchanges the diagonal matrix elements by population transfer at the avoided level crossings.

Finally, examples of the dependence of the eigenvalues on $\Delta\omega_Q$ are shown in Figure 13. They were calculated for a relatively small resonance offset ($\omega_1 > \Delta\omega_0$). The case of nonselective excitation [Figure 8(a) and (f)] is represented at the centers of the diagrams ($\Delta\omega_Q \ll \omega_1$), where adjacent levels are split by ω_1. A nonselective pulse affects the entire spin system, with a nutation frequency $\omega_{nut} = \omega_1$. At large quadrupolar splittings ($\Delta\omega_Q \geq \omega_1$) all the ω_1-containing off-diagonal elements of equations (51) and (52) are nonsecular, except the central transition elements of $I = \frac{3}{2}$, which connect essentially degenerate states. Thus, the nutation frequency for the central transition is $(I + \frac{1}{2})\omega_1$, even when the quadrupolar splitting is large. The spin locked states of a spin 1 are seen to be made up of populations of Zeeman states, which can be adiabatically transferred into each other by slow sweeping of $\Delta\omega_Q$ from positive to negative values, or vice versa. In the case of half-integer spins, the situation is slightly different.

The eigenstates associated with the central transition are now the sum and difference of the Zeeman states [equations (55) and (56)] population of these eigenstates corresponds to the density matrix $\hat{C}_x$. Figure 13 further shows that an adiabatic zero-crossing of $\Delta\omega_Q$ transfers the $|c\pm\rangle$ states to the $|\pm\frac{3}{2}\rangle$ states, i.e., it transfers $\hat{C}_x$ to $\hat{T}_z$.

6 RELATED ARTICLES

Cross Polarization in Solids; Double Rotation; Dynamic Angle Spinning; Echoes in Solids; High Speed MAS of Half-Integer Quadrupolar Nuclei in Solids; Internal Spin Interactions and Rotations in Solids; Line Narrowing Methods in Solids; Liquid Crystalline Samples: Deuterium NMR; Magic Angle Spinning Carbon-13 Lineshapes: Effect of Nitrogen-14; Magic Angle Spinning: Effects of Quadrupolar Nuclei on Spin-1/2 Spectra; Membranes: Deuterium NMR; Nutation Spectroscopy of Quadrupolar Nuclei; Overtone Spectroscopy of Quadrupolar Nuclei; Quadrupolar Interactions; Quadrupolar Nuclei in Glasses; Quadrupolar Nuclei in Liquid Samples; Quadrupolar Transition Metal and Lanthanide Nuclei; Radiofrequency Pulses: Response of Nuclear Spins; Relaxation of Quadrupolar Nuclei Measured via Multiple Quantum Filtration; Relaxation Theory for Quadrupolar Nuclei; Rotating Solids; SQUIDs; Variable Angle Sample Spinning; Zero Field NMR.

7 REFERENCES

1. R. V. Pound, *Phys. Rev.*, 1950, **79**, 685.
2. M. H. Cohen and F. Reif, in *Solid State Physics*, eds. F. Seitz and D. Turnbull, Academic Press, New York, 1958, Vol. 5, p. 321.
3. A. Abragam, *Principles of Nuclear Magnetism*, Clarendon Press, Oxford, 1961, Chaps. 6 and 7.
4. C. P. Slichter, *Principles of Magnetic Resonance*, 3nd edn., Springer-Verlag, Berlin, 1990, Chap. 10
5. O. Kanert and M. Mehring, in *NMR Basic Principles and Progress*, eds. P. Diehl, E. Fluck, and R. Kosfeld, Springer-Verlag, Berlin, 1971, Vol. 3, p. 1.
6. D. Freude and J. Haase, in *NMR Basic Principles and Progress*, eds. P. Diehl, E. Fluck, and R. Kosfeld, Springer-Verlag, Berlin, 1993, Vol. 29, p. 1.
7. H. W. Spiess, *Adv. Polym. Sci.*, 1985, **66**, 23.
8. H.-G. Dehmelt and H. Krüger, *Naturwissenschaften*, 1950, **37**, 111.
9. T. P. Das and E. L. Hahn, in *Solid State Physics*, eds. F. Seitz and D. Turnbull, Academic Press, New York, 1958, Suppl. 1.
10. E. A. C. Lucken, *Nuclear Quadrupole Coupling Constants*, Academic Press, London, 1969.
11. I. P. Biriukov, M. G. Voronkov, and I. A. Safin, *Tables of Nuclear Quadrupole Resonance Frequencies*, Israel Program for Scientific Translations, Jerusalem, 1971.
12. G. K. Semin, T. A. Babushkina, and G. G. Iakobson, *Nuclear Quadrupole Resonance in Chemistry*, Wiley, New York, 1975.
13. J. A. S. Smith, ed., *Advances in Nuclear Quadrupole Resonance*, Heyden, London, 1974–1983, Vols. 1–5.
14. C. P. Slichter, *Principles of Magnetic Resonance*, 3nd edn., Springer-Verlag, Berlin, 1990, p. 157.
15. P. S. Hubbard, *J. Chem. Phys.*, 1970, **53**, 985.
16. A. Baram, Z. Luz, and S. Alexander, *J. Chem. Phys.*, 1973, **58**, 4558.
17. L. G. G. Werbelow, *J. Chem. Phys*, 1979, **70**, 5381.
18. S. G. Greenbaum, Y. S. Pak, K. J. Adamic, M. C. Wintersgill, and J. J. Fontanella, in *Solid State Ionics II*, eds. G.-A. Nazri et al., Materials Research Society Symposium Proceedings, 1991, Vol. 210, p. 237.
19. A. Pines, D. J. Ruben, S. Vega, and M. Mehring, *Phys. Rev. Lett.*, 1976, **36**, 110.
20. S. Vega, *Phys. Rev. A*, 1981, **23**, 3152.
21. A. Wokaun and R. R. Ernst, *J. Chem. Phys.*, 1977, **67**, 1752.
22. A. J. Vega, *J. Magn. Reson.*, 1992, **96**, 50.
23. J. Haase and M. Conradi, *Chem. Phys. Lett.*, 1993, **209**, 287; J. Haase, M. Conradi, C. P. Grey, and A. J. Vega, *J. Magn. Reson.*, 1994, **109**, 90.
24. J. Jeener and P. Broekaert, *Phys. Rev.*, 1967, **157**, 232.
25. S. Vega, T. W. Shattuck, and A. Pines, *Phys. Rev. Lett.*, 1976, **37**, 43.
26. R. Eckman, L. Müller, and A. Pines, *Chem. Phys. Lett.*, 1980, **74**, 376.
27. E. Günther, B. Blümich, and H. W. Spiess, *Mol. Phys.*, 1990, **71**, 477.
28. R. R. Ernst, G. Bodenhausen, and A. Wokaun, *Principles of Nuclear Magnetic Resonance in One and Two Dimensions*, Clarendon Press, Oxford, 1987, Chap. 5
29. S. Vega, T. W. Shattuck, and A. Pines, *Phys. Rev. A*, 1980, **22**, 638.
30. J. L. Ackerman, R. Eckman, and A. Pines, *Chem. Phys.*, 1979, **42**, 423.
31. J. H. Kristensen, H. Bildsøe, H. J. Jakobsen, and N. C. Nielsen, *J. Magn. Reson.*, 1991, **92**, 443.
32. J. Mason, ed., *Multinuclear NMR*, Plenum Press, New York, 1987, p. 339.
33. M. Reinhold, P. Brunner, and R. R. Ernst, *J. Chem. Phys.*, 1981, **74**, 184.
34. D. L. VanderHart, H.S. Gutowsky, and T. C. Farrar, *J. Am. Chem. Soc.*, 1967, **89**, 5056; M. E. Stoll, R. W. Vaughan, R. B. Saillant, and T. Cole, *J. Chem. Phys.*, 1974, **61**, 2896.
35. E. Lipmaa, M. Alla, H. Roude, R. Teeaar, I. Heinmaa, and E. Kundla, in *Magnetic Resonance and Related Phenomena, Proceedings of the 20th Congrès Ampère, 1979*, p. 87; S. J. Opella, M. H. Frey, and T. H. Cross, *J. Am. Chem. Soc.*, 1979, **101**, 5856.
36. R. K. Harris and A. C. Olivieri, in *Progress in Nuclear Magnetic Resonance Spectroscopy*, eds. J. W. Emsley, J. Feeney, and L. H. Sutcliffe, Pergamon Press, Oxford, 1992, Vol. 24, p. 435.
37. C. P. Grey and W. S. Veeman, *Chem. Phys. Lett.*, 1992, **192**, 379; C. P. Grey, A. J. Vega, and W. S. Veeman, *J. Chem. Phys.*, 1993, **98**, 7711.
38. K. R. Jeffrey, *J. Chem. Phys.*, 1977, **66**, 4677.
39. E. Oldfield, H. K. C. Timken, B. Montez, and R. Ramachandran, *Nature (London)*, 1985, **318**, 163.
40. H. Hatanaka, T. Terao, and T. Hashi, *J. Phys. Soc. Jpn.*, 1975, **39**, 835.
41. B. C. Sanctuary and T. K. Halstead, *Adv. Magn. Opt. Reson.*, 1990, **15**, 79.
42. D. E. O'Reilly, *Adv. Catal.*, 1960, **12**, 31.
43. A. Llor and J. Virlet, *Chem. Phys. Lett.*, 1988, **152**, 248; B. F. Chmelka, K. T. Mueller, A. Pines, J. Stebbins, Y. Wu, and J. W. Zwanziger, *Nature (London)*, 1989, **339**, 42.
44. A. Samoson, E. Lippmaa, and A. Pines, *Mol. Phys.*, 1988, **65**, 1013.

45. L. Frydman and J. S. Harwood, *J. Am. Chem. Soc.*, 1995, **117**, 5367.
46. D. E. Woessner and H. K. C. Timken, *J. Magn. Reson.*, 1990, **90**, 411.
47. A. J. Vega, *Solid State NMR*, 1993, **1**, 17.
48. H. G. Kuhns, *Atomic Spectra*, Academic Press, New York, 1962, pp. 368–380.
49. W. H. King, *Isotope Shifts in Atomic Spectra*, Plenum Press, New York, 1984.
50. H. W. Spiess, *NMR Basic Principles and Progress*, eds. P. Diehla, E. Fluck, and R. Kosfeld, Springer-Verlag, Berlin, 1987, Vol. 15, p. 55.
51. H. W. Spiess, *J. Chem. Phys.*, 1980, **72**, 6755.
52. S. Vega and A. Pines, *J. Chem. Phys.*, 1977, **66**, 5624.
53. A. J. Vega and Z. Luz, *J. Chem. Phys.*, 1987, **86**, 180.

Acknowledgments

The author wishes to thank Dr. D. Schaefer and Professor C. P Grey for helpful comments, and Dr. J. Haase and Professor B. C. Gerstein for critical reading of the manuscript.

Biographical Sketch

Alexander J. Vega. *b* 1938. B.S. (kandidaat), 1961, M.S. (doctorandus), 1967, University of Amsterdam, The Netherlands; Ph.D. (supervisor Daniel Fiat), 1974, Weizmann Institute of Science, Israel. Postdoctoral work at California Institute of Technology (with Robert W. Vaughan) 1975–77. DuPont CR&D, 1977–present. Approx. 60 publications. Research interests: solid state NMR for applications in materials research.

Recording One-Dimensional High Resolution Spectra

Oliver W. Howarth
University of Warwick, Coventry, UK

1	Introduction	1
2	The NMR Sample	1
3	Resolution	3
4	Selecting the Spectrum	3
5	Variable Temperature (VT) Measurements	4
6	Acquiring the Data	5
7	The Spectrum	5
8	Mixtures and Subtraction Spectra	10
9	Related Articles	10
10	References	10

1 INTRODUCTION

This article is intended for the near-beginner in practical NMR spectroscopy. It covers questions about sample preparation and experimental technique that are so basic that the seasoned practitioner of NMR rarely spells out their answers. If I am given access to a standard, reasonably modern, high-resolution instrument, what can I do with it, and what measurements remain inaccessible?

The core purpose of high-resolution NMR is to determine the structures of mobile molecules. However, its versatility is such that it can also answer an astonishing variety of supplementary questions. It can determine the rates of both overall and internal molecular motion, via relaxation times; the rates of kinetic processes, especially those of chemical exchange; and electron distributions, via the detailed analysis of chemical shifts and of coupling constants, as outlined below. It can quantitate the composition of mixtures and the distribution of isotopic labels. So it is not surprising that high-resolution NMR spectrometry is an essential activity for any general chemical laboratory, and that it is described in many excellent introductory[1–3] and near-introductory[4–6] texts.

However, one must also be aware at the outset of its limitations. For although NMR can usually extract some information from almost any diamagnetic material, and from many paramagnetic ones too, some types of sample demand special techniques, which lie outside the scope of this article, and also usually require nonstandard spectrometers. If they are treated naively, as if they were typical solutions for analysis, most of these samples will generate resonances that are very broad by the standards of those that arise from small, dissolved molecules. They include solid samples, near-solids such as gels and polymers below their softening temperature, heterogeneous samples where the interest lies in the surface-bound species, similar biological samples, and liquid crystalline samples. All these are discussed in other articles, along with the decoupling and rapid spinning techniques that have been developed to overcome the problems of large linewidth. Another range of techniques discussed elsewhere but not here, is that which combines imaging methods with spectroscopy, in order to generate localized measurements from within large objects. These are of particular value in noninvasive medicine.

It follows that most high-resolution NMR is concerned solely with the diamagnetic, liquid phase, in which typical linewidths are of the order of 1 Hz from nuclei with nuclear spin quantum number $I = \frac{1}{2}$. Undissolved gases are also accessible to NMR, but if they are molecular gases at normal pressures, then their spectra will usually have considerably broader resonances than at high pressure or in solution. This fact, along with the implicit diluteness of the sample, makes them unsuited for nonspecialized measurements. The broadness arises from highly efficient energy transfer, i.e. spin–lattice relaxation, in the rapidly rotating molecules, especially when the collision rate is not much greater than the NMR frequency, as in gases at lower pressures. Nevertheless, one should be aware of the possibility of such gas and vapor resonances. A supposedly empty NMR tube may show a noticeable proton signal from human breath, with a width at half height of about 100 Hz.

One other limitation should be noted. NMR is generally not a suitable technique when very rapid, irreversible changes occur in the sample, because the spins need both to reach thermal equilibrium in the magnet, and also to be given sufficient time within the detector coil to register their response to radiofrequency stimulation. Nonetheless, flow and stopped-flow NMR experiments are possible, and are discussed in the ***Flow NMR*** article.

2 THE NMR SAMPLE

The molar amount of the molecule of interest needed for an NMR measurement depends strongly on the nucleus one wishes to observe, and to a lesser extent on the nature of the sample. Proton and ^{19}F are the best known nuclei for high-sensitivity NMR. Any modern spectrometer should require at most a few milligrams of dissolved sample, of average molecular mass, for an adequate ^{1}H or ^{19}F spectrum. In extreme cases, the detection of submicrogram quantities is feasible. However, the detection limits will be raised if the resonances have many splittings, or marked broadenings or if other very strong resonances are also present, even in other regions of the spectrum. Other nuclei demand more sample. See ***Nuclear Spin Properties and Notation*** for the sensitivity of each nucleus relative to that of the proton, although these figures must be adjusted by consideration of factors such as the likely linewidth of the resonance, the simplifications that may arise from decoupling, the possible nuclear Overhauser enhancement, and any limitations imposed by spin–lattice relaxation, as described below. Some typical sample quantities for routine nonproton NMR, with samples of medium molecular mass, are 1–5 mg for ^{31}P NMR, 5–20 mg for ^{13}C, and 100–300 mg for ^{15}N, the latter two being without isotopic enrichment. At the other extreme, concentrated solutions should be avoided where possible, especially in ^{1}H NMR, because their spectra are likely to depend somewhat upon concentration, and may also suffer from broadenings due to, for example, H-bonded oligomers or to the intermolecular transfer of energy. They may also give resonances so strong that they partially detune the coil

that detects them. This process, called radiation damping, is discussed in another article, ***Concentrated Solution Effects***.

Some variation of NMR technique will usually be necessary for certain samples. If measurements are required involving less common nuclei, such as ^{14}N, ^{17}O, and many metals, then the articles on either quadrupolar ($I > \frac{1}{2}$) or transition metal $I = \frac{1}{2}$ nuclei should be studied first, along with standard texts.[7,8] $I > \frac{1}{2}$ nuclei often give problems of excessive linewidth, arising from the interaction of their nuclear electric quadrupole moments with the electric field gradients of the bonds near to them. Similar broadening can arise from dipolar relaxation in very viscous solutions or with macromolecules, because of very slow molecular tumbling. Excessive linewidth brings several problems. It reduces resolution, and hence the discrimination of distinct shifts and couplings. It reduces sensitivity, because the strength of the NMR response of a nucleus is proportional to the area of its resonance, so that any extra peak width is gained only at the expense of lost peak height. Also, resonances wider than about 10 kHz are likely to be lost, or at least severely distorted, in spectrometers which do not have especially rapid digitization of the NMR signal, for such signals will have decayed before they can be electronically captured. Conversely, nuclei with $I = \frac{1}{2}$ and also with small magnetic moments (i.e. relatively low NMR frequencies) will usually have their already low detection sensitivity further reduced by long spin–lattice relaxation times, T_1.

Anyone planning an NMR experiment must always bear in mind that all the nuclei of the chosen type will usually contribute to the resulting spectrum, unless special selective measures are possible. It may well be that the resonances of interest are small in comparison with the unwanted resonances from e.g. buffer or water. Every preparative opportunity must be taken to design the experiment so as to reduce these unwanted resonances. They not only tend to overlay the desired resonances, but also to reduce the overall sensitivity of the measurement, by introducing peak-like artifacts, rolling baselines, and digital-rounding noise. These problems can be reduced to some extent by the use of sophisticated electronics, and by such techniques as water suppression and oversampling, but it is always wise to remove them at source whenever possible by using e.g. deuterated solvents and inorganic buffers. Indeed, with the very weakest of samples, it is also necessary to take especial care to ensure the removal of all likely impurities, such as water in commercial solvents, grease from glass joints, and plasticizer leached from e.g. polypropylene vials by organic solvents. One should also remain awake to the likely presence of N_2 and O_2. N_2 usually shows, at about -70 ppm, in a ^{14}N spectrum, because its low concentration is offset by its relative narrowness. O_2 may in fact be beneficial as a modest paramagnetic relaxation agent, to reduce the longest spin–lattice relaxation times and thus facilitate more rapid acquisition of data. It may be removed, e.g. for accurate relaxation measurements, by bubbling N_2 through the solution, and both gases may be removed if necessary by repeated freezing, vacuum pumping, and thawing of the solution.

Unwanted resonances may also arise from the probe itself. Probe glass and ceramic commonly gives broad ^{29}Si and ^{27}Al resonances, poly(tetrafluoroethylene) (PTFE) can give a broad ^{19}F resonance, and probe wiring and solder can give signals from ^{63}Cu and ^{95}Mo. Also the radiofrequency pulse will commonly generate mechanical vibrations in the probe, particularly at frequencies below 50 MHz, which masquerade as weak NMR signals. They lead to severely rolling baselines and to spurious broad signal-like artifacts. Some pulse sequences exist for reducing this 'probe ringing', but none is completely satisfactory. Fortunately, probe ringing is usually brief, and so it may simply be excised from the beginning of the FID signal (see below) if the desired resonance is narrow and hence long-lasting.

Extraneous solid matter will generally degrade the NMR spectrum arising from the surrounding liquid, because its different diamagnetic susceptibility will bend the magnetic lines of force nearby. It is therefore usual to filter such a sample before it is introduced to the NMR tube. However, small amounts of solid may well settle out or spin to the tube walls, and thus have little effect on the spectrum. If more serious distortions arise, e.g. from the unavoidable presence of biological cells, large emulsion micelles, or heterogeneous interfaces essential to the experiment, then it may be possible to reduce the deleterious effects of differing magnetic susceptibility simply by altering the susceptibility of the solvent by adding e.g. an iodide. In any case, usable information may still be obtainable, especially in ^{13}C and ^{31}P NMR, where resolution is less critical. Informative NMR spectra have been acquired from such unlikely samples as seed kernels, plastic tubing, and beating rat hearts. Also, special pulse sequences can be designed to reduce the effects of local field inhomogeneities. However, these invariably exact a price, for example by reducing the reliability of the resulting peak integrals.

The worst susceptibility distortions arise from metal particles and from gas bubbles. A very high concentration of ions, especially H^+, will also degrade the radiofrequency tuning. It may even render proton decoupling from other nuclei impossible, and should therefore be avoided. Gas bubbles in heterogeneous samples, such as leaf stomata, are best removed in advance by a vacuum cycle. Bubbles and flaws are particularly problematic in near-solid polymer samples, where they are best reduced by careful casting or machining of a cylindrical sample to fit the NMR tube.

2.1 Sample Tubes

Samples are most commonly contained in 5 mm o.d. glass tubes. These are machined so as to permit slow, smooth spinning of the tube about its long axis. Such spinning, typically at 25 Hz, improves the linewidth by averaging minor variations in the field, and of the temperature, across the width of the sample. However, the residual modulation of the magnetic field is approximately equivalent to a frequency modulation, so that it can create sideband signals, spaced either side of the desired signal by the spinning frequency, or even a multiple thereof in the case of a severely irregular cross-tube gradient. These spinning sidebands will have the same phase as the central signal. Also, spinning sidebands with different phases can arise from inhomogeneities in the radiofrequency field. For this reason, spinning is not always desirable, particularly in two-dimensional (2D) and subtraction experiments, where clarity is more important than homogeneity. With a magnet of good quality, the use of spinning may only reduce the linewidth by a fraction of a hertz.

Tubes of larger diameter can be used in appropriate probes, so as to increase the resulting signal. The sensitivity gain is, however, somewhat less than the increase in sample mass, because the detection coil necessarily also has a larger diameter. Extra care must also be taken with larger tubes, to avoid vortexing when one spins the sample, and also excessive heating of the sample upon decoupling. The former may necessitate insertion of a vortex plug, especially if the sample is short. The latter may necessitate pulsed or gated decoupling.

Microtubes are also available, to maximize the signal from minimal samples and reduce those from the solvent. They are not always easy to handle or to shim, and some of the gain in using a receiver coil of reduced diameter is lost because a substantial proportion of the volume within this coil is now occupied by glass. However, the capillary type of microtube is also a useful way of introducing a reference or a lock solvent, when there are chemical reasons why this should not come into contact with the sample. It is also fairly easy to modify standard tubes so as to add a simple gas control septum cap. High-pressure NMR, however, typically requires sapphire tubes and special handling precautions. Other specialist tubes include flow-through cells, e.g. for chromatographic detection, and quartz tubes for efficient uv irradiation. Figure 1 shows a few typical specialty tubes.

Most NMR probes only detect resonances from a portion of the sample, known as the sensitive region. The rest of the sample only serves to improve the homogeneity of the magnetic field, by removing the major interfaces from this sensitive region, and also possibly unwanted traces of solid.

2.2 The Solvent

For the reasons given above, the solvent must not itself contribute an unacceptable signal. This is most commonly acheived in both proton and carbon NMR by using a deuterated solvent. Deuteration not only removes protons, but also makes any associated carbon resonance much less prominent, by removing the NOE (see below), facilitating differential saturation, and introducing splittings. It also permits locking of the magnetic field to the master spectrometer frequency, via the deuterium resonance. This resonance can be detected continuously by a separate radiofrequency channel, because it does not usually interfere with the main signal. The result is to permit long accumulations of data, with exact superimposition, and also to enable both initial and continuous adjustment of the field gradient correction (shim) coils so as to minimize the linewidths. Locking to external ^{2}H or ^{19}F is also possible, but this removes the shimming advantage, because the lock material no longer has either the same shape or the same position in the field as the sample.

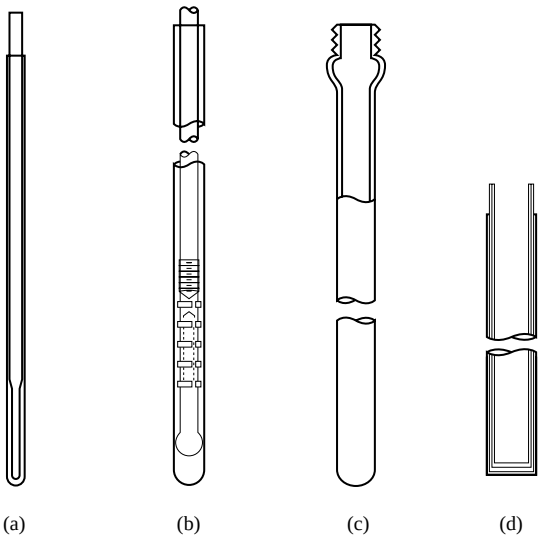

Figure 1 Specialty sample tubes for high-resolution NMR (not mutually to scale): (a) 5 mm o.d. tube with capillary insert for e.g. shift standard or sample in nonlock solvent; (b) near-spherical, sealable microinsert for very small amounts of sample, with support/extractor; (c) 10 mm o.d. tube with screw fitting for septum cap, to provide gas-protected access; (d) 10 mm o.d. tube with 8 mm parallel insert, permitting lock solvent in the annulus. (Reproduced by permission and kindly supplied by Wilmad Glass Co)

3 RESOLUTION

The resolution of a standard NMR spectrum is usually estimated in practical terms from the width at halfheight of an inherently narrow resonance, such as that of the solvent. Most NMR experiments do not require the highest possible resolution. A 1 Hz resolution is often adequate, and may in any case be imposed by the natural linewidth of the sample resonance if its molecular mass is not small. It may also be imposed by the limited digital resolution of the spectrum. If exceptional resolution is necessary, for example to study small resonances very close to large ones, then unusual care must be taken to control the sample temperature, to deoxygenate the solvent, and to shim using more correction coils than are standard. One may also routinely achieve a useful gain in resolution, without loss of signal, by the digital process of resolution enhancement. In principle, an almost infinite gain may be achieved by maximum entropy processing, although this family of methods must be used with caution. Related methods also exist for removing (strictly, deconvoluting) a fixed and undesired lineshape from the spectrum so as to reveal the interesting data in more detail (see ***Data Processing***). However, these methods are time-consuming, and should not be used simply to avoid the basic disciplines of careful sample preparation, shimming, and ensuring that the temperature, lock electronics, and physical state of the sample are stable.

4 SELECTING THE SPECTRUM

The first selection to be made in any NMR study is which nucleus to observe. The frequency range of possible resonances from any one nuclear isotope is in almost all cases much smaller than the frequency jump to any other isotope. Indeed, major hardware switching is usually necessary to change the nucleus under observation, although this switch may be concealed by clever instrument design when it is between the most commonly observed nuclei. (See ***Spectrometers: A General Overview***)

Any one nucleus may exist in a wide range of chemical environments. Each environment will either deshield or shield the nucleus from the external magnetic field, and hence will add or subtract a small fraction to the resonance frequency

of this nucleus. These fractions are normally reported in the field-independent units of chemical shift, δ, which are defined further in the section on referencing, below. Although many NMR spectra can be run using standard conditions, which detect all the likely resonances, in other cases it is necessary to decide in advance what one expects to observe, and to set the spectrometer accordingly. This is because there are physical limitations on what may be detected in any one experiment. Firstly, the maximum sweep, or spectrum width, measured in Hz, is the reciprocal of the minimum digitization interval available on the instrument. If a maximum frequency of x Hz from the spectrum center must be digitally captured, then there must be at least two digital captures per cycle, i.e. per $1/x$ seconds. Any frequency higher than this will appear folded. This means that if its true frequency is y Hz, then it will appear instead at $2x - y$ Hz. When $y \gg x$ then the folded peak can normally be removed by electronic filtering. However, if the spectrum width, $2x$, is set only slightly too small, then the folded peak will be substantial, although usually recognizable by its having an unusual phase. [This means that some peak components will be below the baseline, and not integrable, when the rest of the spectrum is entirely above it. See Figure 2(d)]. It follows that one must take care in setting the spectrum width, and that one cannot eliminate large resonances simply by setting the width to select only a portion of the spectrum, unless this portion is separated from the others by several times its width. This limitation can be removed by advanced digital electronics, if available. If ample computer power is at hand, then there are advantages in deliberately setting the spectrum width to at least four times that necessary. This 'oversampling' technique usefully reduces digital noise arising from very large signals, as well as avoiding all possibility of folding. It may also reduce unwanted rolling of the baseline.

The second limitation on the spectrum width is the normal requirement that the radiofrequency pulses stimulate the spins evenly, within this width. Although a pulse is constructed from a single frequency, its brevity gives it a frequency spread about this value. Thus a pulse lasting z μs has a width at half intensity of about $10^6/\pi z$ Hz, and over about one-fifth of this frequency spread its intensity will be acceptably uniform. If the desired spectrum width is large, then this may require unacceptably short pulses, and will also preclude any experiment requiring e.g. precise π pulses. In such cases one cannot avoid gathering the data for one nucleus in several separate experiments. These problems do not usually occur in ^{1}H, ^{13}C, and ^{31}P NMR, but they can be serious in e.g. ^{59}Co or ^{195}Pt NMR, especially with high-field instruments.

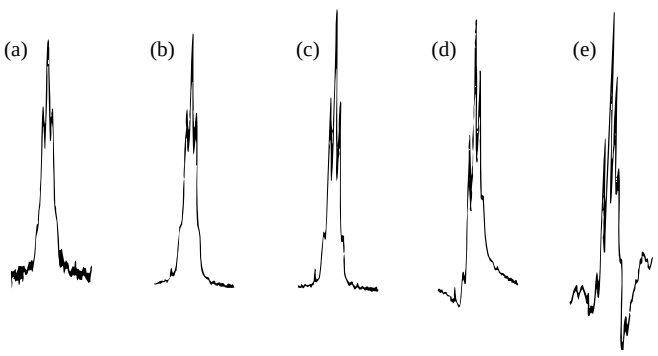

Figure 2 The same ^{1}H NMR multiplet observed under varying conditions (a) single transient, no adjustments to FID; (b) as (a), but with 16 transients accumulated. Note the $\times 4$ gain in signal-to-noise ratio; (c) as (b), but with digital resolution enhancement; (d) as (b), but with incorrect phasing; (e) as (b), but with overloaded digitizer, because the receiver gain was set too high

One may note here that it is only possible to work outwards from a frequency which has been set at the spectrum center, if the spectrometer can distinguish positive frequency changes from negative ones. This is achieved by a phase-based process called quadrature detection. In its absence, the frequency must be set to one side of all the resonances, so as to prevent peak folding. In this case the above limitations on spectrum width become twice as severe, and there is also a loss of $\sqrt{2}$ in signal-to-noise ratio, because of folded noise from the uninteresting but unavoidable half of the detected frequency range. The NMR operator should, however, be aware that any missetting of the quadrature detection system will result in unwanted peaks, which are weak 'reflections' of true resonances, about the spectrum center.

Certain, more specialized experiments generate almost the opposite requirement, namely for selective excitation of one resonance, or of a narrow group of resonances, within a crowded spectrum. This can be achieved by careful pulse shaping, if the hardware is available.

5 VARIABLE TEMPERATURE (VT) MEASUREMENTS

If possible, NMR experiments should be conducted at room temperature. Indeed, air conditioning is almost mandatory to achieve the highest stability from high-field instruments, because even minor expansion or contraction of the spectrometer materials affects both the magnetic field homogeneity and also the radiofrequency tuning. For these reasons, spectra obtained at other temperatures will usually be of reduced quality. It is also particularly difficult to eliminate temperature gradients along the sample in VT measurements. They are notably troublesome with NMR of the heavier nuclei, whose shifts depend markedly on temperature (e.g. 2 ppm $^{\circ}C^{-1}$ for aqueous Cs^{+}) and with samples locked to $^{2}H_2O$ or to an $-O^{2}H$ resonance, for the same reason.

However, there are many circumstances where the sample temperature must be varied, and most spectrometers have a control unit which allows this. Probes can also be constructed that are jacketed by a circulating liquid in place of the usual air or N_2, when the above problems are especially acute. Further problems arise for high-resolution NMR at extremes of temperature. Although toluene, methanol, acetone, and dichloromethane are convenient solvents for measurements down to about $-95\,^{\circ}C$, any work below this requires either a mixed solvent or one which vaporizes at room temperature. Similarly, the normal NMR probe is likely to be damaged at temperatures above about $120\,^{\circ}C$. Higher temperatures require special probes. Even red-hot liquid samples of silicates have been observed in furnace probes.

An approximate calibration of sample temperature is provided with standard VT units. However, this only measures the temperature of the surrounding gas, and so will have an error that depends on the rate of gas flow. More accurate measurements require either a thermocouple inserted into the sample, in the absence of any radiofrequency irradiation, or

the presence of a substance such as liquid methanol whose chemical shifts have a known dependence upon temperature.

6 ACQUIRING THE DATA

The sample is normally supported in a proprietary collar, or 'spinner', when it is introduced into the spectrometer, to facilitate both location and slow spinning. Upon introduction, it acquires a net spin polarization in the field direction, according to Boltzmann's Law. This polarization builds up over an interval of about $5T_1$, which is fast enough in most cases, but may necessitate prepolarization of samples with extremely long T_1, such as pure silica. Next, it will normally be locked and shimmed (see above) via its solvent's deuterium resonance, and the appropriate experimental parameters will be set.

A straightforward measurement will then be initiated by a radiofrequency pulse. A detailed description of the resulting resonance processes is given in several other articles at varying levels of sophistication. Very briefly, the above magnetic polarization of the appropriate nuclei in the sample may be considered to behave as a classical, magnetic gyroscope, which points initially along the direction of the magnetic field. The radiofrequency pulse then provides a torque so as to tip this net magnet. As a result, it will induce its precession in the field, at the appropriate Larmor frequency. This precession will in turn generate an alternating voltage in the tuned probe coil at the same frequency. The optimally detectable precession involves motion at right angles to the field direction, and the shortest pulse that will induce this is called a 90° or $\pi/2$ pulse. If several chemical environments of the nucleus are present, then several frequencies will be thus excited, because of the frequency spread inherent in the pulse. At this stage the probe coil will normally have been switched to its receive mode, and the signal it detects will be carefully amplified and reduced to a much lower frequency, digitizable signal by the spectrometer. This signal will typically decay over a few seconds in high-resolution NMR. It is commonly called the free induction decay, or FID, although this term strictly describes the nuclear motion.

The FID will then be digitized within the spectrometer, subject to the limitations mentioned above. One adjusts the receiver gain to ensure that the resulting digits are not too large for the memory [see Figure 2(e) for what happens if this is not done]. At this stage it is normal for the above measurement cycle to be repeated, and the resulting digitized signals added. A sequence of n repetitions increases the signal by $\times n$, whereas the random noise only increases by $\times\sqrt{n}$, because of partial cancellations. This gives a net gain in signal-to-noise ratio of $\times\sqrt{n}$, and also reduces other radiofrequency artifacts by at least this amount [see Figures 2(a) and (b)]. However, the repetition rate should ideally not exceed $1/(5T_1)$. Faster pulsing will lead to reductions in signal, called 'saturation', because Boltzmann equilibrium will not be reached. If the resulting measurement takes too long, then it may be shortened somewhat by the use of shorter pulses, typically 30°, and a delay of only about T_1. In this case, the resulting distortions of signal intensity will usually not be serious.

The FID will then commonly undergo various processes of data manipulation, culminating in Fourier transformation. These are described in detail in the articles on ***Data Processing***, and on ***Fourier Transform Spectroscopy***. Their effect is to reduce unwanted features, and to improve resolution [see Figure 2(c)]. The Fourier transformation turns the FID into a spectrum by detecting which frequencies are contained within it, and also their phases, i.e. their relative sine and cosine characters.

The first processing stage for the resulting spectrum is almost always one of 'phasing' [see Figure 2(d)]. The above process of Fourier transformation separately detects both the sine waves and the cosine waves in the FID. Both will normally be present, but only the cosine waves will give an acceptable 'absorption mode' spectrum, in which all the resonances lie above the baseline, and have symmetrical lineshapes. Only the resonances of absorption mode spectra can be quantitated directly by integration. The phasing process multiplies the sine and cosine transforms so as to produce this result across the entire spectrum. It may be automated, provided the spectrum is of good quality, with well-separated peak groups. Figure 2 illustrates several of the above features of preparing an NMR spectrum.

7 THE SPECTRUM

Figure 3 shows the essential features of a straightforward ^{1}H NMR spectrum obtained at 400 MHz, that of aspirin. The horizontal axis is generated from the frequencies of the various resonances, but is presented and calibrated in the more useful units of chemical shift, as described below. The vertical dimension records the relative contribution from the signal at each of these frequencies, above the baseline zero. Its units are entirely arbitrary, as the exact response of any sample depends markedly upon the spectrometer, the quality of the probe tuning, and upon the way in which the experiment is conducted. Only in unusually favorable circumstances is it possible to compare peak heights between different but similar samples, without the use of a common, added standard substance.

The spectrum in Figure 3 includes an expansion of the left-hand region, and also an integral of each group of resonances. The integral is simply the running sum of all the digitized peak elements, above the baseline zero. It is a more fundamental property than peak height, because in most cases it is proportional to the number of protons that give

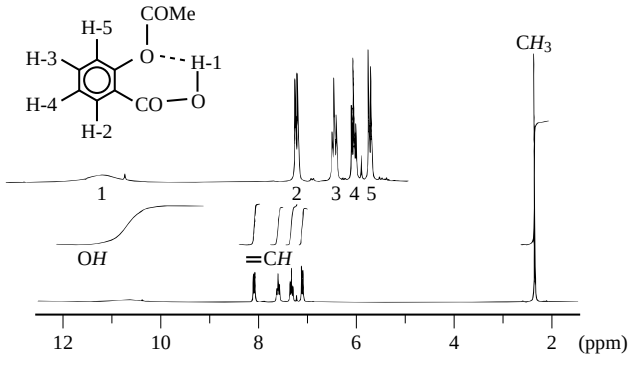

Figure 3 Proton NMR spectrum of slightly impure aspirin, dissolved in $CDCl_3$, with added integral traces and expansion of aromatic proton resonances

rise to it, whereas the peak height depends on linewidth and on splittings. Thus it permits the use of NMR as a tool for quantitation (see ***Quantitative Measurements***). One can also immediately see from the Figure that all the integral steps are equal for the aspirin molecule, except for the right-hand one, which is three times as large. This alone provides invaluable chemical information. It also enables one to distinguish the true aspirin resonances from the minor impurities present in this commercial sample, and indeed to estimate the sample's purity. Integrals can be measured either manually, as step heights, after allowing for possible baseline faults, or else digitally, e.g. as small figures below the peak groups. Their relative values are typically reliable to within a few percent, if the sample is pure and its resonances are strong, narrow, and well separated, and the baseline is carefully corrected for the distortions common to Fourier transform spectroscopy.

The ^{1}H NMR spectrum itself consists of a series of either single peaks or peak groups, called 'multiplets'. A multiplet is a group of peaks whose absolute spacing, in hertz, is independent of the spectrometer field, and which arises from a single chemical type of proton. The position of the center of each multiplet is the chemical shift of this proton type (see below). It depends slightly upon solvent, but is nevertheless an invaluable indicator of the electronic and steric environment of the relevant protons, as described in several subsequent articles. Note that it is incorrect to speak of the chemical shift of any individual peak within a multiplet, even though a computer listing may appear to do so for reasons of brevity. (Strictly speaking, the chemical shift of an atom is in fact the trace of a tensor which gives the variation of shift with the molecule's orientation in the field. The isotropic molecular tumbling in the solution state averages the components of this tensor, provided that the molecule is not significantly oriented by, for example, the field.)

Because the units of chemical shift are in parts per million (ppm), they conceal the actual frequency units from which they are derived. However, the splittings with a multiplet arise from the energies of mutual interaction, or J couplings of neighboring protons, and hence they have constant values in Hz. Therefore the spectrum of a given compound will vary in appearance when measured on spectrometers with different fields. High fields will appear to shrink the multiplets, within a given shift range. In ^{1}H NMR, each proton's resonance will in principle be split into almost equal halves by each other proton p in the molecule, by an amount J_p Hz, where $J_p/2h$ is the energy change of the one proton when the other one is inverted in the field. These successive splittings together produce the multiplet. However, in practice, most of the splittings from more distant protons will be too small to measure. Also, the splitting process is completely suppressed when the two protons have identical chemical shifts, and it gives rise to 'second-order' splittings and height distortions when the relevant multiplet separations are not large compared with J_p. Even so, the multiplets yield to thorough analysis, and the underlying coupling constants, J_p, are invaluable indicators of molecular structure and stereochemistry.

Using the above information, it is possible to extract a considerable amount of information from this spectrum. Firstly, the integrals show the presence of one group of three identical protons, i.e. a methyl group, plus five other single protons, each different from each other. (This conclusion is not altogether unchallengeable, because the molecule under study might be, for example, a fully symmetrical dimer. However, this possibility can usually be proved or disproved by the study of other NMR spectra, or by a mass spectrum.) One may note here that the integral is a particularly useful way of detecting the very broad resonance on the left of the spectrum, which might otherwise be lost under noise.

The second major source of information is the horizontal shift scale. The methyl resonance is characteristic of a methyl group attached directly to carbonyl, by reason of its shift of 2.4 ppm on this scale. The four multiplets between 7.0 and 8.2 ppm have shifts typical of aromatic protons on single rings. Their detailed positions may be approximately predicted in several ways, and these are outlined in the articles on shielding and in many practical texts.[9,10] They in fact depend strongly on the electron density at the carbon atom of attachment; the higher the density, the lower the shift. Thus the lowest shift is observed for the ring proton three bonds away from the acetyl oxygen. However, steric effects, and the proximity of other rings and multiple bonds, are also important. The final resonance is the very broad one at about 10.8 ppm. There are several ways in which this can be identified as a hydroxyl resonance. One simple way might be to shake the sample with a drop of ^2H_2O. The deuterons in the sample will then equilibrate between this and the hydroxyl group, so as to lower the intensity of its resonance to near zero, if the sample is not initially too concentrated. If the ^2H_2O is also fully soluble in the solvent of choice, e.g. dimethyl sulfoxide, then its own resonance, usually sharp, will show the presence of the protons it has thus acquired. This can be a useful technique for estimating the exchangeable proton content of a complex sample with otherwise broad resonances from exchangeable protons. However, this method is subverted if allowance is not made for ^1H_2O initially present as an impurity in the ^2H_2O.

The actual shift of a hydroxyl resonance depends very markedly on the strength of the H-bonds it forms. The strongest bonds give the highest shift values. For this reason, their shifts are less useful for structural predictions than those of CH protons. They will often depend strongly upon temperature and solvent. Their resonances are also often broad, because the protons do not move infinitely rapidly between the various inter- and intramolecular configurations available to them. The reasons for this broadening are given in ***Chemical Exchange Effects on Spectra***. The hydroxyl resonance in the above aspirin spectrum has a relatively large chemical shift, which shows that it experiences substantial H-bonding. It is also in fact less sensitive than average to changes of temperature, showing that its H-bonding is largely intramolecular. However, its marked width also shows that more than one mode of H-bonding is available to it.

Yet further information can be gained from the third major feature of the spectrum, namely the splittings within each multiplet. Even the absence of resolved splittings in the methyl 'singlet' resonance gives useful confirmation that the carbon attached to the methyl group has no attached protons. If it did, e.g. as in acetaldehyde, then the methyl resonance would be split into two equal halves by the aldehydic proton. The same principles apply to the four aromatic proton resonances, 2–5. These protons lie next to each other on the ring, so that each has at least one splitting. The outer two protons in the group give rise to the two 1:1 doublets, 2 and 5. Their splittings arise respectively from H-4 and H-3. Conversely, these inner two protons are split by their outer neighbors

H-2 and H-5. However, they also split each other. In all cases, the splittings measure the sensitivity of each proton to its neighbor's orientation in the magnetic field. All these interactions have approximately the same energy in the present case, and so all the splittings are approximately 8 Hz in magnitude. The effect of this on the inner proton pair is to turn their resonances into 1:2:1 triplets.

Protons more than three bonds apart can split each other's resonances detectably, but rarely by more than 2 Hz. Thus a brief inspection of the major splittings in a straightforward ^{1}H NMR spectrum will often reveal which protons are neighbors to which. Any ambiguities can usually be resolved by the careful matching of couplings because, as explained above, they should occur in pairs, for they are each the result of a mutual interaction.

However, this analysis will usually break down in more complex cases. A splitting may be obscured by some other broadening mechanism, as in resonance 1 above, or it may simply be lost in a multiplicity of other splittings, or it may match more than one other splitting. It may even be very small, if the stereochemistry of the molecule in the relevant region gives a fixed dihedral angle between the two C–H bonds of approximately 90°. In such cases the interpretation of the spectrum can usually be clarified by homonuclear proton decoupling. In this additional experiment, one arranges to irradiate at the frequency of any chosen multiplet, continuously, and independently of the other processes involved in obtaining the spectrum. If the strength of irradiation is correctly chosen, the result will be to remove all the splittings originating from the proton which gives rise to the irradiated multiplet, and thus to simplify the spectrum. This process may then be repeated at other multiplet positions. It is described fully in the article on ***Decoupling Methods***.

In very crowded spectra, such as those from proteins, even decoupling may not be sufficient for a full assignment, for the resonances may be highly overlapped, and also the process of decoupling distorts nearby resonances rather severely. The solution in this case is to resort to 2D or even multidimensional NMR, and to apply shift correlation methods such as COSY.

Decoupling alone will also fail to define a structure if insufficient couplings are present in the first place. An example might be a highly methylated molecule. However, other methods also exist which can determine the proximity of nuclei, especially protons, by detecting their through-space dipolar interaction. The most important method is to detect the internuclear Overhauser effect, or NOE (see ***Nuclear Overhauser Effect***). It can be implemented in either a one-dimensional or a multidimensional fashion; the former is best for smallish molecules, and the latter for large ones. The combination of all these methods will usually yield a complete molecular strucure, especially in combination with the ^{13}C resonance measurements to be discussed in the next section.

Some of the less prominent features of Figure 3 also merit comment. The linewidths of each multiplet component, except for peak 1, conceal information about the motional behavior of the molecule, in the form of the 'spin–spin relaxation time', or T_2. The observed linewidth at halfheight, after subtraction of any contributions from field inhomogeneities, equals $1/\pi T_2$. This value is only a fraction of the linewidth in most ^{1}H NMR spectra of smallish molecules in mobile solvents. However, it dominates the linewidths of large molecules, such as proteins, and indeed it makes these so large as to obscure spin couplings, when the molecular mass exceeds about 20 000 amu.

Mention has already been made of the impurity peaks. NMR often permits both their quantification and their identification. One almost unavoidable impurity peak is that of residual protons in the solvent. In the present case this means the small $CHCl_3$ singlet at about 7.2 ppm. Table 1 gives a list of common deuterated solvents, and their associated residual proton peaks, which will be multiplets when H–D couplings are present. Another common extra peak is that of any added shift standard (see below).

Finally, one may note the two tiny resonances symmetrically placed near 65 Hz either side of the methyl singlet. Similar 'carbon-13 sidebands' are in fact present around every CH_n resonance. These arise from the 1.1% of ^{13}C naturally present at every carbon site in the molecule. The ^{13}C nucleus also has $I = \frac{1}{2}$, and therefore it splits attached proton resonances into doublets of 0.55% of the main peak height and separated by 125–200 Hz. It also produces much smaller splittings, below 12 Hz, at protons two or more bonds away. These are not normally resolved, but they can be detected by e.g. the 2D COLOC (correlated spectroscopy for long-range coupling) experiment, and they are very useful in the identification of connectivities spanning unprotonated carbons.

7.1 Carbon-13 NMR Spectra

Figure 4 shows a simple ^{13}C NMR spectrum, in fact of the same aspirin sample, recorded at 100.6 MHz. Its most obvious new feature is the increased noise. Carbon-13 NMR is about 1000 times less sensitive than ^{1}H NMR, both because of the merely 1.1% natural abundance of the ^{13}C isotope and also because of its lower magnetic moment; about $\frac{1}{4}$ of the proton's. A second evident feature is the 20-fold increase in the shift scale. Shift ranges generally increase with atomic number, and also toward the right of the Periodic Table, because they depend on the density and polarizability of the surrounding electron cloud. This makes carbon shifts more useful for structural prediction than proton shifts.[11] They are more spread out, and also less influenced by distant parts of the molecule. Hence empirical shift predictions for carbon nuclei are of great value. For rather complex reasons, carbon shifts fall into a similar pattern to proton shifts, where they may be compared. Single-bonded C atoms generally give resonances in the right half of the spectrum, and double-bonded C atoms in the left half. Also, the attachment of an electron withdrawing group increases the shift. This pattern is evident in Figure 4, with the methyl carbon atom giving the peak at 21 ppm and the two carbonyl carbon atoms almost coincident at 170 ppm.

All the peaks apart from that for C^2HCl_3 are singlets, because the spectrum is in fact a $^{13}C\{^1H\}$ spectrum, i.e. obtained with broadband ^{1}H decoupling. In practical terms, this means that the entire range of ^{1}H resonances has been quite strongly irradiated, using a separate, concentric coil and frequency channel, throughout the process of obtaining the ^{13}C spectrum. Thus only the deuteron couplings remain visible. Because ^{2}H has $I = 1$, it has three possible orientations in the magnetic field. The result is a 1:1:1 triplet for the deuterochloroform carbon atom. However, other couplings are invisibly present, and the interpreter of NMR spectra needs to be aware of the circumstances in which they might

Table 1 Resonances of Common Deuterated Solvents

Solvent ($-d_n$)	δ_H for residual proton at 298 K[a]	HD_{n-1} multiplet	δ_C for perdeuterated solvent	D_n multiplet
Acetone-d_6	2.05	1:2:3:2:1	206.0, 29.8	br[b], 1:3:6:8:6:3:1
Acetonitrile-d_3	1.95	1:2:3:2:1	118.2, 1.3	br[b], 1:3:6:8:6:3:1
Benzene-d_6	7.20	br[b]	128.0	1:1:1
Chloroform-d	7.24	1	76.9	1:1:1
Cyclohexane-d_{12}	1.38	br[b]	26.1	1:2:3:2:1
Dichloromethane-d_2	5.35	1:1:1	53.6	1:2:3:2:1
Dimethylformamide-d_7	8.05, 2.94, 2.76	br[b] 1:2:3:2:1 × 2	162.7, 35.2, 30.1	2
Dimethyl sulfoxide-d_6	2.50	1:2:3:2:1	39.6	1:3:6:8:6:3:1
Methanol-d_4	4.84, 3.35	1, 1:2:3:2:1	49.0	1:3:6:8:6:3:1
Nitromethane-d_3	4.18	1:2:3:2:1	62.8	1:3:6:8:6:3:1
Pyridine-d_5	8.74, 7.54, 7.22	br[b]	149.9, 135.5, 123.5	1:1:1 × 3
Tetrahydrofuran-d_8	3.60, 1.75	br[b]	68.6, 26.7	1:2:3:2:1 × 2
Toluene-d_8	7.09, 7.00, 6.98, 2.09	br[b] ×3 1:2:3:2:1	137.5, 128.9, 128.0, 125.2, 20.4	1, 1:1:1 × 3 1:3:6:8:6:3:1
Water-d_2	4.75	1	–	–

[a]Approximate. Depends on, e.g., solute concentration.
[b]Broad peak with normally unresolved couplings.

become visible. Couplings from the ^{35}Cl and the ^{37}Cl nuclei are present, but they do not produce visible splittings, even though these nuclei each have $I = \frac{3}{2}$, because they decouple themselves by quadrupolar relaxation as noted above. They are sometimes just detectable as line broadenings. Such couplings may, however, cause considerable complication of a spectrum if they arise from relatively abundant $I = \frac{1}{2}$ nuclei, such as ^{117}Sn and ^{119}Sn, because these do not usually relax fast enough to decouple themselves. ^{13}C–^{13}C couplings are also present, but the resulting 0.55% sidebands lie well below the noise level in Figure 4. They can be exploited to reveal ^{13}C–^{13}C connectivities in favorable cases, where the signal-to-noise ratio is very high. However, the necessary INADEQUATE experiments are difficult to perform because of the need to minimize the influence of the much larger central $^{13}C-^{12}$C resonances. Although nuclei such as ^{117}Sn can in principle be decoupled from ^{13}C or ^{1}H, such 'heteronuclear' decoupling requires nonstandard equipment, and so is not commonly performed.

Finally, splittings of a different kind can arise from the variety of, for example, C^2HCl_3 molecules, or 'isotopomers', having different combinations of chlorine isotopes. Isotopic substitution produces tiny changes in the chemical shift of attached atoms (see ***Isotope Effects on Chemical Shifts and Coupling Constants*** and ***Isotope Effects in Carbocation Chemistry***). These are not resolved in Figure 4, but are visible in e.g. the ^{19}F spectra of fluorochlorocarbons. They also explain why the small residual ^{13}C peaks from protonated solvent molecules generally have a slightly higher shift than the main, deuterated solvent resonances.

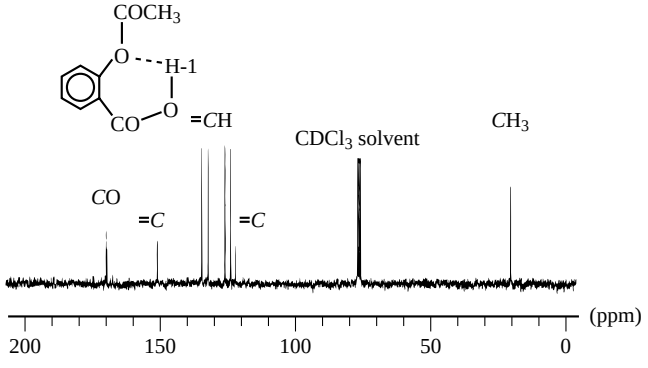

Figure 4 Carbon-13 NMR spectrum of the same aspirin sample as in Figure 3

No integrals are shown in Figure 4, because they are less reliable for quantitating carbons than their proton equivalents. Carbon spin–lattice relaxation times can be quite long in small, mobile molecules, especially if the C atom is unprotonated. Thus partial saturation is commonplace. This helps to explain why the C atom resonances in Figure 4 are less intense than the CH resonances. CH_3 resonances are also vulnerable because of rapid internal rotation of the methyl moiety, especially when this is attached to an sp^2 carbon atom. Also, the peak intensities are increased to different extents in a proton-decoupled spectrum, by the NOE mentioned previously. The gain is typically ×3 for protonated carbons and ×2 for unprotonated ones, and it arises because the spins are no longer at thermal equilibrium, owing to the input of energy to the protons. Nevertheless, carbon integrals remain informative when the signals are of adequate strength, and they can be rendered quantitative if care is taken to eliminate the NOE and to avoid saturation. One can, for example, gate the ^{1}H decoupling so as to apply it only during the relatively short data acquisition time, and not during the intervening delays that one allows for spin relaxation. Added paramagnetic relaxation agents are useful here to kill any residual NOE (see ***Quantitative Measurements***) and it is also important to ensure that the electronic switching is 100% efficient, because even very weak ^{1}H irradiation, well below that required for decoupling, can give rise to a significant NOE. It is especially important to control or remove the NOE when decoupling protons from nuclei with negative magnetic moments, such as ^{15}N and ^{29}Si, or from ^{19}F in macromolecules, because in these cases the NOE is negative, and so the signal can disappear altogether upon ^{1}H decoupling. If the NOE exceeds

$\times -1$, then the spectrum should properly be plotted to show negative-going resonances.

This gating technique has a further advantage, in that it reduces heating of the sample by the rather strong electric field of the radiofrequency. Such heating can easily exceed 10 °C with 10 mm o.d. NMR tubes, and in most cases one should use the more efficient pulse decoupling methods (see ***Decoupling Methods***) in preference to the older broadband decoupling technique, in order to minimize it. If one wants minimal heating, but also the full NOE, then one can arrange for low-power ^{1}H irradiation to continue during the relaxation delay, along with the full power for the actual decoupling, as before, because the NOE is generated via ^{1}H saturation rather than by decoupling. Conversely, one can set the power to zero during acquisition, in this experiment, in order to obtain a spectrum with no decoupling, but with full NOE.

7.2 Spectra of $I > \frac{1}{2}$ Nuclei

Although quadrupolar nuclei are discussed in other articles, a preliminary example of a typical solution state spectrum is given in Figure 5. This is an ^{17}O NMR spectrum of an aqueous solution of the heptamolybdate anion, obtained at 54.2 MHz and 280 K, with modest isotopic enrichment. All but one of the resonances are moderately broad, mainly because of quadrupolar relaxation. Note that decoupling is irrelevant for this spectrum, because any hydroxyl protons are in rapid exchange, and also because their J coupling and their dipolar interactions with the ^{17}O nucleus are much weaker than the quadrupolar interactions of ^{17}O. The narrow resonance arises from $[MoO_4]^{2-}$, also present at this pH. It is narrow because the symmetrical, monomeric anion tumbles relatively rapidly. The very large solvent water resonance at 0 ppm is not shown. The resonances of the nine chemically different types of heptamolybdate oxygen atom are only partially resolved. They resolve better at higher temperatures, but then three of them broaden into invisibility because of an internal exchange process. Such processes can give a confusing simplicity to any NMR spectrum, and so one must always be aware of their possibility. However, they are of intrinsic interest. The oxygen atom integrals in Figure 5 are reliable, and are useful for assignment when symmetry is present. They are often best estimated by careful computerized deconvolution. The shifts lie on a scale slightly larger than for carbon NMR. They relate fairly simply to the distances from the O atom in question to the nearest Mo atom, with the shortest lengths giving the largest shifts.

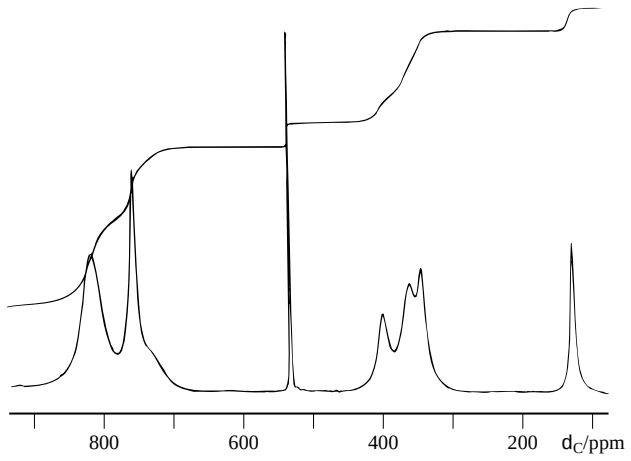

Figure 5 Oxygen-17 NMR spectrum of the heptamolybdate anion, $[Mo_7O_{24}]^{6-}$, dissolved in water at 298 K, with modest ^{17}O isotopic enrichment. The large solvent resonance at 0 ppm is not shown

7.3 Chemical Shift Scales

The shift scales in all of the above spectra were obtained by dividing the actual resonance frequencies by one-millionth of the frequency at which the spectrometer pulse was centered. Their units are therefore ppm. Thus they are independent of the measurement frequency, and even of the isotope used for the measurement if a choice is available. Instead, they measure the fractional magnetic shielding of the nucleus in question by its surrounding electrons. Ideally, one might wish to use the resonance frequency of the bare nucleus as the zero for this scale of chemical shift. As this is not available, one instead employs an added substance as a shift standard. Such a standard is best dissolved along with the sample, so that it lies in exactly the same field. If this is not possible, then corrections should be made, as outlined below. It should also be minimally influenced by different solvents, should be chemically inert, and should have a single resonance which lies conveniently away from most other likely resonances. Real shift standards all come short of this ideal, but tetramethylsilane (TMS) comes close, for use in nonhydroxylic solvents, and is therefore the primary shift standard for $^{1-3}$H, ^{13}C, and ^{29}Si NMR spectra. For other accepted standards which define shift zeroes, see ***Nuclear Spin Properties and Notation***.

A problem arises with the precise definition of chemical shift when the shift range is exceptionally large, as with ^{59}Co, whose shifts extend over 13 000 ppm. In such cases it becomes necessary to calculate shifts by dividing by the observation frequency of the standard substance, $[Co(CN)_6]^{3-}$, rather than that used for observing the actual Co-containing sample, in order to avoid possible shift errors of up to 1%, or 100 ppm. Fortunately this problem becomes negligible with more normal shift ranges. In fact, because chemical shift varies somewhat with temperature and solvent in any case, one does not usually need to measure it with extremely high accuracy. Indeed, in most cases it is not even necessary to add TMS to a dilute sample for ^{1}H or ^{13}C NMR, because the residual solvent resonance will provide an adequate secondary reference.

However, if one is forced to use an external standard, typically in a sealed capillary tube inserted coaxially into the sample, then further precautions are necessary to ensure reproducible shifts. Each volume element of the solution surrounding any one molecule of analyte alters the main magnetic field according to its magnetic susceptibility. It thus becomes a tiny induced magnet μ, aligned with the field. The analyte is thus surrounded by these magnets. If their distance is r and the angle between the field direction and the analyte molecule/volume element axis is θ, then each element contributes a field $(3\cos^2\theta - 1)\mu/r^3$ at the analyte molecule. If the sample were spherical, then these contributions would integrate to zero. However, the more remote parts of a normal cylindrical sample will create a residual shift of one or more ppm, whose direction will depend in both magnitude and

sign on the orientation of the tube with respect to the main field, although not greatly upon its length. This is a large error, particularly in ^{1}H NMR. Shifts obtained in this way should always be reported referring to an external reference of specified composition. They can be approximately corrected if the relevant diamagnetic susceptibilities are known, and indeed they offer a useful means of measuring such susceptibilities.

If a recognized standard does not exist, for example in measurements involving a very uncommon nucleus, then one normally reports the absolute frequency that the resonance would have in a field in which a TMS proton would resonate at exactly 100 MHz. Such frequencies are denoted by the Greek symbol Xi, Ξ.

8 MIXTURES AND SUBTRACTION SPECTRA

Because chemical shifts vary significantly with both solvent and temperature, in comparison with linewidths, it is difficult in NMR spectroscopy to implement computerized methods for the recognition of spectra, or for the subtraction of the contributions from known components. The problem is particularly severe for ^{1}H spectra, where the protons generally lie on the molecular periphery, and are only weakly shielded by their own electrons. Indeed, one can often resolve inconvenient peak overlaps in such spectra, simply by changing the solvent significantly.

Methods have nevertheless been developed for the NMR analysis of complex mixtures. An NMR spectrometer can be coupled to chromatography (see ***Flow NMR***). The scattered resonances from a single component can be identified via 2D shift correlation experiments. One may select for or against resonances involved in chemical exchange, such as hydroxylic protons, by the methods of saturation transfer, or by selective labeling, e.g. by ^{2}H. Components with markedly different molecular mobility can be suppressed by exploiting their different relaxation times, or by their different linear diffusion rates in a pulsed field gradient (see ***Field Gradients and Their Application***). This latter technique is especially valuable for water suppression. Finally, one may resort to computerized pattern analysis, e.g. for the automated clinical analysis of spectra from body fluids (see ***Body Fluids***).

Despite the problems of precise reproducibility, it is advisable to preserve well-characterized NMR spectra in a suitable mass storage medium, in view of the ever-increasing availability and sophistication of methods for data analysis.

9 RELATED ARTICLES

Body Fluids; Chemical Exchange Effects on Spectra; Concentrated Solution Effects; Data Processing; Decoupling Methods; Flow NMR; Fourier Transform Spectroscopy; Isotope Effects in Carbocation Chemistry; Isotope Effects on Chemical Shifts and Coupling Constants; Nuclear Overhauser Effect; Nuclear Spin Properties and Notation; Quantitative Measurements; Shielding: Overview of Theoretical Methods; Spectrometers: A General Overview.

10 REFERENCES

1. R. J Abraham, J. Fisher, and P. Loftus, *Introduction to NMR Spectroscopy*, Wiley, Chichester, 1988.
2. R. K. Harris, *NMR Spectroscopy*, Longman, London, 1986.
3. H. Friebolin, *Basic One- and Two-Dimensional NMR Spectroscopy*, VCH, New York, 1991.
4. J. K. M. Sanders and B. K. Hunter, *Modern NMR Spectroscopy*, 2nd edn., Oxford University Press, Oxford, 1992.
5. A. E. Derome, *Modern NMR Techniques for Chemistry Research*, Pergamon, Oxford, 1987.
6. E. Breitmaier, *Structure Elucidation by NMR in Organic Chemistry*, Wiley, Chichester, 1993.
7. eds. R. K. Harris and B. E. Mann, *NMR and the Periodic Table*, Academic Press, London, 1978.
8. J. Mason, ed., *Multinuclear NMR*, Plenum, New York, 1987.
9. D. H. Williams and I. Fleming, *Spectroscopic Methods in Organic Chemistry*, 5th edn., McGraw-Hill, London, 1995.
10. R. M. Silverstein, G. C. Bassler, and T. G. Morrill, *Spectrometric Identification of Organic Compounds*, 5th edn., Wiley, New York, 1991.
11. E. Breitmaier and W. Voelter, *Carbon-13 NMR Spectroscopy*, 3rd edn., revised, VCH, New York, 1989.

Biographical Sketch

Oliver W. Howarth. *b* 1941. M.A., 1963; D.Phil., 1965, Oxford University, with Sir Rex Richards. Department of Chemistry (earlier Molecular Sciences), University of Warwick, from 1967–present, subsequently also Director, Centre for NMR, and Manager of SERC High-Field NMR Service, to 1994. Approx. 140 publications. Research interests wide, but especially NMR of polyoxoanions.

Spin Echo Spectroscopy of Liquid Samples

Anthony G. Avent
University of Sussex, Brighton, UK

1	Introduction	1
2	The Spin Echo in Liquids	1
3	Calculation of Spin Echoes	4
4	Spin Echo Spectroscopy in Liquid Crystals	5
5	Related Articles	6
6	References	6

1 INTRODUCTION

The first use of an intense rf pulse to stimulate a transient response in NMR was reported by Erwin Hahn in 1950,[1] just a few years after the first NMR signals had been observed.[2,3] And it was Hahn again who, shortly afterwards, investigated the effect of applying two rf pulses separated by a period of free precession, and thereby demonstrated the generation of the spin echo.[4] This was the first multipulse NMR experiment and hence may be regarded as the precursor of the myriad of such experiments that are in current use in NMR spectroscopy.

The significance of the experiment lay in the discovery that the different interactions that determine the NMR spectrum responded to the two pulse sequence in different ways. As a result, spin echo spectroscopy can be used to distinguish, for example, field inhomogeneity and molecular diffusion effects from spin–spin relaxation, and chemical shifts, and heteronuclear couplings from homonuclear couplings. Indeed it was this experiment that first demonstrated to NMR spectroscopists that they did not have to accept meekly the NMR spectrum that nature provides, but rather they may intervene actively to mould the spectrum to their own requirements. This intervention may involve, as here, multipulse sequences, or it may involve the use of decoupling fields or the physical rotation of the sample. In all cases, however, the object is the same, to suppress effects that are of no interest or which are obscuring the effects that are of interest, in order to maximize the useful information content of the spectrum. These techniques have been vital to the establishment of NMR in its present preeminent position and all may be traced back to Hahn's original 1950 experiment with two rf pulses.

Any experiment in transient NMR that uses more than one rf pulse will generate a spin echo, and as such echoes are near ubiquitous in modern NMR. They have found applications in the NMR of gases, liquids, liquid crystals, solids, heterogeneous systems, biological systems and, latterly, in MRI. In this article we are concerned only with the liquid and liquid crystalline phases, but even here there are a vast number of multipulse experiments in use, all of which generate spin echoes; this article is then further restricted to those experiments in which the spin echo is studied for itself rather than those in which the echo is generated incidentally or as a means to some other end such as polarization transfer or multiple quantum coherence generation.

2 THE SPIN ECHO IN LIQUIDS

In 1950, Hahn demonstrated that the dephasing of the coherent magnetization which arises from field inhomogeneity is reversible.[4] He showed that a second pulse, applied a time τ after the first, produced a rephasing of the coherence a further period τ later. This refocused packet of magnetization was called a 'spin echo'.

The generation of a spin echo from the magnetization of a single site in a molecule is illustrated in Figure 1(a). Though in Hahn's original work the second pulse was of 90°, we consider here a second pulse of 180°, as this is conceptually simpler. This modification was first proposed by Carr and Purcell.[5] The first pulse produces a rotation of 90° about the x axis of the off-resonance rotating frame that converts the equilibrium z magnetization into a coherence along the y axis. This then precesses about the z axis at a frequency determined by its chemical shift offset, which is directly proportional to the static field $\boldsymbol{B}_0$. If the field is inhomogeneous there is a spread of $\boldsymbol{B}_0$ values which produces a corresponding spread in precession frequencies. This variation is represented in Figure 1(a) by two vectors labeled ***f*** and ***s***; the first represents magnetization from nuclei in regions of high magnetic field which precesses faster than the norm, and the second nuclei in regions of low field whose magnetization precesses slower. After a time τ a second pulse is applied which rotates the vectors through 180° about the y axis. If the nuclei do not move out of their original regions of field strength, then the fast and slow vectors will come together a time τ later along the y axis.

If this sequence is repeated for different values of τ and the magnetization sampled only at 2τ, then it will appear to be permanently fixed along the y axis. Any decrease in the intensity of the signal is then due solely to the entropy driven spin–spin relaxation processes characterized by the time constant T_2, upon which this sequence has no effect. Note also that the effect of chemical shift has been removed by the echo.

Figure 1(b) shows the effect of the echo sequence on the magnetization from the A spins of an AX spin system, where X is a nonresonant, usually heteronuclear, spin. The A magnetization is split into two components during precession, depending upon the state, α or β, of the X spin. The second pulse rotates these vectors into positions such that a further time τ later they refocus along the y axis, so that observations made at 2τ will not detect the effect of the heteronuclear coupling. That is, the X spins will appear to have been decoupled from the A spins.

Figure 1(c) shows the fate of the A magnetization in an AX spin system where X is a resonant, homonuclear spin. This splits during the first period of precession, as in the heteronuclear case, and the second pulse rotates the vectors as before but, in addition, because the X spin is also resonant, it flips the state of the spin and the vectors are interchanged. They now no longer refocus at 2τ; indeed, the splitting continues to develop as if the second pulse had not been applied. The effects of chemical shift and field inhomogeneity continue to refocus and observations made at 2τ will show a signal that is modulated only by the homonuclear coupling.

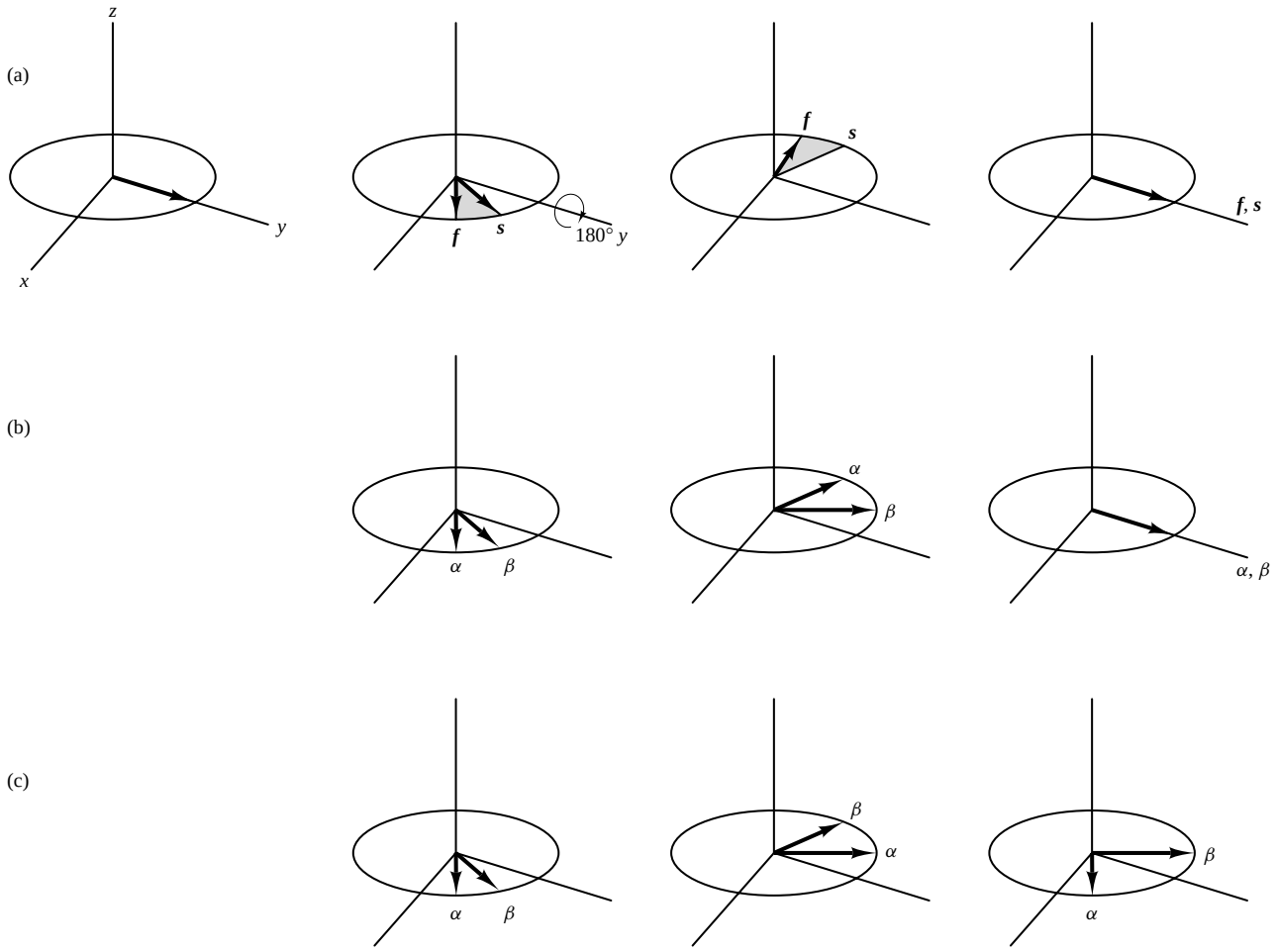

Figure 1 The effect of the 90 °−τ−180 °−τ sequence on (a) field inhomogeneity, (b) the A spins of a heteronuclear AX spin system, and (c) the A spins of a homonuclear AX spin system

To summarize, the spin echo removes the effects of field inhomogeneity but not spin–spin relaxation, and removes the effects of chemical shift and heteronuclear couplings but not homonuclear couplings; almost all applications of the spin echo in liquids exploit these differentiations.

So far the systems considered have been first order, if there is any significant second-order character to the system then this simple vector picture breaks down and to predict the echo amplitudes a full density matrix treatment is required. This is considered below.

In the early days of NMR, before magnets achieved their present level of homogeneity, the principal value of the spin echo technique was its ability to remove the effects of field inhomogeneity. This, combined with the effect of spin–spin coupling on the echo led to the discovery of J couplings, by Hahn, as a modulation in an echo experiment.[4] The molecule involved was ethanol, and a contemporary state of the art CW spectrum of the same molecule showed only three broad resonances corresponding to the three chemical environments of the protons.

The original Hahn echo experiment involved performing the pulse sequence for one value of τ, allowing the system to relax (a period that should be $>5T_1$) and repeating with a different value of τ until sufficient data had been accumulated. This is time consuming, and in experiments to measure T_2 was found to give incorrectly short values, especially where T_2 was long. This is because of molecular diffusion which means that molecules which, for example, start out in regions of relatively high magnetic field can diffuse during the course of the echo sequence into regions of low field, with the result that the effect of field inhomogeneity is not completely removed and contributes to the observed T_2.

A method that avoids this problem, and also speeds up the accumulation of data was put forward by Carr and Purcell[5] who, in addition to suggesting the use of 180° refocusing pulses, proposed the 'echo train'. This is a sequence of the kind:

$$90^\circ - [\tau - 180^\circ - \tau - \text{Sample}-]_n$$

If τ is short compared to the rate of molecular diffusion, then its effects on the observed magnetization are negligible. However, having solved one problem, Carr and Purcell were confronted with another, in that any imperfections in the 180° pulses have a cumulative effect along the echo train and lead to serious degradation of the signal.

The sources of pulse imperfections include jitter in their timing and, probably most serious, inhomogeneity in the rf field $\boldsymbol{B}_1$. This variation in $\boldsymbol{B}_1$ across the sample leads to variations in the angles of rotation produced by the refocusing pulse, which in turn leads to a distribution of magnetization

around the axis onto which it should be accurately refocused, and hence to a shortening of the apparent T_2. In systems without homonuclear coupling this problem can be overcome by phase shifting the refocusing pulses by 90° with respect to the initial pulse. This was first proposed by Meiboom and Gill[6] who showed that in this case the imperfection of the second refocusing pulse cancelled out that of the first, so that if the echo is sampled at alternate maxima a reliable result is achieved. The sequence used is then:

$$90^\circ_x - [[\tau - 180^\circ_y - \tau]_2 - \text{Sample}]_n$$

Where there is modulation by homonuclear coupling, the best solution is to improve the accuracy of each individual 180° pulse by using a composite pulse, which ensures a high quality refocusing at each echo maximum[7] (see ***Composite Pulses***).

The Carr–Purcell–Meiboom–Gill (CPMG) sequence has become established as the standard method for investigating spin–spin relaxation and related phenomena such as molecular diffusion and chemical exchange.[8]

The CPMG sequence as given above can only be used for systems that only contain, or are dominated by, a single peak, such as the protons of benzene or chloroform, or biological systems dominated by water. For multicomponent systems, such as for example, the ^{13}C nuclei of a complex organic molecule, the technique used is to apply the echo train and then sample an entire FID from the top of the final echo. This is repeated for echo trains of different lengths and the Fourier transformation of the resulting set of FIDs reveals the rate of decay of each component in the system. For systems involving homonuclear coupling the problem of echo modulation has also to be addressed. As we shall see below, one method is to pulse rapidly, but a more satisfactory method is to proceed as for multicomponent systems but with the accumulation of the whole of the final echo. That is, acquisition of data begins immediately after the final 180° pulse rather than from the top of the final echo. Fourier transformation of this whole echo combined with an absolute value mode of display then serves to eliminate the effect of modulation.[9]

In the case of molecular diffusion, the decay in the amplitude of the echo $E(2\tau)$ is given by:

$$E(2\tau) \propto \exp[-(2\tau/T_2) - 2\gamma^2 G^2 D\tau^3/3] \quad (1)$$

where τ is the echo spacing, D is the diffusion constant, G is the spatial magnetic field gradient, and γ is the magnetogyric ratio.

Note the τ^3 dependence, which explains the rapidly increasing effect diffusion has on long T_2 times. For a spectrometer in its normal mode of operation, G may be regarded as a measure of the inhomogeneity of the magnetic field, but where the echo technique is used to measure diffusion the experimenter can introduce a field gradient of known size across the sample and, by observing the effect this has on the echo amplitude, measure D[10] (see ***Diffusion Measurements by Magnetic Field Gradient Methods***).

Another source of broadening in NMR is chemical exchange, and this has also been studied by means of the spin echo technique. The echo does not remove the broadening, which is analogous to diffusion where spins move between regions of different local field strength, thus preventing the echo from refocusing properly. Here, the spins move between chemical sites of different precession frequencies, with the same result. When a system is close to either the fast or slow exchange limits, the amount of broadening caused by the exchange is small, and the spin echo can distinguish such small effects from those of field inhomogeneity better than the conventional spectrum. It can also allow the effects of small couplings to be observed at temperatures at which otherwise they are lost in the broadening linewidths.[11] Nonetheless, it must be said that the additional information produced by the echo technique is marginal when compared to the vast amount that is available from bandshape analysis and magnetization transfer experiments (see ***Chemical Exchange Effects on Spectra*** and ***Relaxation Effects of Chemical Exchange***).

As we have seen, homonuclear couplings were first observed in an echo experiment and, even at a time when CW spectrometers were well able to resolve proton–proton couplings, the echo method continued to be used. A study by Hahn and Maxwell[12] of the fluorine atoms in 1-fluoro-1,2,2-trichloroethane and 1,1-difluoro-2,2-dichloroethane was notable for providing the first example of echo modulation arising from strong coupling from nonresonant spins. Theoretical calculations of the response of various simple spin systems to the echo train were also made; these are considered in the next section. The principal difficulty with the technique lay in having to analyze complex modulations without the benefit of computerized Fourier transformation. When this became available with the advent of the computer driven spectrometer, it was first applied to the spin echo by Freeman and Hill.[13]

Their elegant experiment performed the same function as the original Hahn experiment, i.e. the removal of the effect of field inhomogeneity so as to reveal couplings otherwise obscured. Of course, given the improvements in magnet homogeneity in the intervening years, the couplings so revealed were very much smaller. The example given was of the molecule 2-bromothiophene-4-aldehyde. The Carr–Purcell echo train was used and tailored to excite selectively the aldehyde proton; the resulting echo envelope was Fourier transformed to give a 'J spectrum' consisting of a doublet of doublets showing the four- and five-bond couplings to the two ring protons (1.36 and 0.05 Hz, respectively). In addition, the linewidths of the J spectrum, in this case 0.03 Hz, provide an accurate measure of the spin–spin relaxation time of the nucleus. Selective excitation was used because, with the effect of chemical shifts removed, all the multiplets are crowded around the transmitter frequency and for systems of any size the resulting overlaps make analysis unrewarding. However, selective excitation cannot be used if the multiplets are too close together or if there are second-order effects. These drawbacks greatly restricted the use of the technique until the arrival of two-dimensional spectroscopy, which solved the overlap problem by spreading the signals into a second dimension (see ***Two-Dimensional J-Resolved Spectroscopy***).

Returning to one dimension and the echo train, a further problem or, in some cases, opportunity, arising from the experiment is that the echo amplitudes can be affected by the repetition rate of pulsing within the train, with fast repetition rates 'pulsing out' some phenomena. One example of this that has already been discussed is the removal of molecular diffusion effects; it has also been shown that chemical exchange effects are influenced by pulse rate. Furthermore, it has been shown that the modulation of the echo by

homonuclear couplings can be removed, for both first- and second-order spin systems, if the pulse rate is fast with respect to both the couplings and the chemical shift offsets of the system. For example, Freeman and Hill[8] have shown that for the molecule 1,1,2-trichloroethane, the spectrum of which consists of a triplet and a doublet (J = 7 Hz) separated by a shift difference of about 200 Hz, a pulse repetition rate such that 2τ = 2 ms is sufficient to eliminate any modulation from the echo. This effect arises because, if the repetition rate is fast compared to the offsets of the magnetization vectors from the transmitter frequency, then they are unable to precess far from the y axis onto which they were deposited by the initial 90°_x pulse, before being rotated round by a 180° pulse. Indeed, the effective field experienced by the vectors is along the y rather than z axis. The vectors are then locked onto the y axis so that phase differences are unable to build up. Such spin echo trains have a close relationship with the spin locking experiment, and it should be noted that any transverse relaxation times measured in these experiments are not true T_2 times, but rather are related to the $T_{1\rho}$ relaxation time (see ***Rotating Frame Spin–Lattice Relaxation Off-Resonance***).

3 CALCULATION OF SPIN ECHOES

For first-order spin systems the effect of the spin echo sequence can be calculated simply in terms of vector diagrams such as that shown for the AX case in Figure 1(c). Here it is clear that, with the effect of chemical shift removed but with that of homonuclear coupling left unchanged, the amplitude of the echo will be modulated as a function of τ by $\cos 2\pi J\tau$. Other first-order systems can be considered in the same way, though the results will be more complex. If the system is not first order, however, then a more rigorous approach using the density matrix formalism is required.

Before embarking on this, and to give the reader a feel for what the calculation entails, I shall begin by simply quoting the result for the simplest second-order spin system AB. An analytical equation for the echo amplitude $E(\tau)$ is possible and has been given by Abragam:[14]

$$E(2\tau) = (\delta^2/\Delta^2)\cos 2\pi J\tau + (J^2/\Delta^2)\cos 2\pi\Delta\tau\cos 2\pi J\tau + (J/\Delta)\sin 2\pi\Delta\tau\sin 2\pi J\tau \quad (2)$$

where δ is the shift difference between A and B (in hertz) and $\Delta = (J^2 + \delta^2)^{\frac{1}{2}}$.

Note that where $J \ll \delta$, equation (2) tends to $\cos 2\pi J\tau$, as in the AX case, but generally, and notwithstanding all that has been said above, the echo amplitude does now depend on chemical shifts. To see why this should be the case, consider first the AX spin system, the response of the A spins of which to the echo sequence is shown in Figure 1(c). The spectrum consists of four peaks at (1) $\nu_A + \frac{1}{2}J$, (2) $\nu_A - \frac{1}{2}J$, (3) $\nu_X + \frac{1}{2}J$, and (4) $\nu_X - \frac{1}{2}J$, and we can say that the two peaks around ν_A involve the flipping of the A spin and the two around ν_X the flipping of the X spin. Furthermore, when the system is subjected to the second pulse of the spin echo sequence, the magnetization associated with transition (1) is carried cleanly and completely into transition (2), and vice versa, and the same is true for transitions (3) and (4); this is implicit in Figure 1(c). The modulation of the echo then arises from the frequency difference between (1) and (2) and between (3) and (4), which is J. Moving on to the AB case, the situation is more complex because the stationary states of the system can no longer be described by the simple product basis set ($\alpha\alpha$, $\alpha\beta$, $\beta\alpha$, $\beta\beta$), the two central energy levels being now described by states that are linear combinations of $\alpha\beta$ and $\beta\alpha$. In turn, this means that the four transitions observed can no longer be regarded as corresponding to the flip of either the A or the X spin, but as a combination of both. So, though the transitions may still be regarded as 'A like' or 'X like', they carry an admixture of the character of the other spin. When the second pulse of the echo sequence is applied, there is now no longer a simple transfer of magnetization between well defined pairs of transitions, but rather there is a nonzero probability of transfer of magnetization from 'A like' to 'X like' transitions. It is this magnetization that gives rise to the chemical shift terms in equation (2).

We can now see that our task in calculating the response of a complex spin system to the echo sequence is firstly to calculate the frequencies and intensities of all the transitions, just as in the analysis of conventional spectra (see ***Analysis of High-Resolution Solution State Spectra***), but then we must calculate for each pair of transitions the efficiency with which they are mixed by the second and subsequent pulses.

The density matrix describes a system in the sense that the expectation value of any experimentally observable property of the system can be found by multiplying the density matrix by the matrix operator of the observable and taking the trace of the product. In this case we are interested in the magnetization in the y direction, so:

$$\langle \hat{I}_y \rangle = \mathrm{Tr}(\rho \hat{I}_y) \quad (3)$$

We now calculate the density matrix at the end of the echo sequence, $90^\circ_x - \tau - 180^\circ_y - \tau$, following the treatment of Allerhand.[15] For this we start with the time dependent form of the Schrödinger equation:

$$\mathrm{d}\hat{\rho}/\mathrm{d}t = \mathrm{i}[\hat{\rho}, \hat{\mathcal{H}}] \quad (4)$$

For a system of N spins, the static Hamiltonian $\hat{\mathcal{H}}$ is represented by a $2^N \times 2^N$ matrix which is constructed originally in the simple product basis set but is then diagonalized to give a matrix whose elements give the energies of the 2^N states of the system.

In isotropic liquids the Hamiltonian has chemical shift and J coupling terms; for liquid crystalline systems, these are supplemented by dipolar and, where appropriate, quadrupolar coupling terms. If relaxation effects are ignored, $\hat{\mathcal{H}}$ is time independent and the solution of equation (4) is

$$\rho(t) = \exp(-\mathrm{i}\hat{\mathcal{H}}t)\rho(0)\exp(2\mathrm{i}\hat{\mathcal{H}}t) \quad (5)$$

These operators can be easily derived from $\hat{\mathcal{H}}$, as the exponential of a diagonal matrix is a matrix containing the exponentials of each element.

If the rf field that provides the pulses is intense, their effect may be represented by simple rotation operators.[16] Thus the density matrix immediately after the initial 90°_x pulse, $\rho(+)$, is given by

$$\rho(+) = \exp(-\tfrac{1}{2}\mathrm{i}\pi\hat{I}_x)\rho(\mathrm{eq})\exp(\tfrac{1}{2}\mathrm{i}\pi\hat{I}_x) \quad (6)$$

The matrices representing $\hat{I}_x$, $\hat{I}_y$, and these exponential operators are constructed by taking tensor products of the

single spin operators N times, and then performing the same transformation that was required to diagonalize $\hat{\mathcal{H}}$, so as to bring them into the stationary state basis set.

Here $\rho(\text{eq})$ is the density matrix at equilibrium, which in the high-field and high-temperature approximations is proportional to $\hat{I}_z$ + Constant. Applying the rotation of equation (6) then gives:

$$\rho(+) \propto \text{Constant} + \hat{I}_y \tag{7}$$

If we now apply equation (5) for the first period of the echo, followed by an appropriate version of equation (6) for the 180°_y pulse and then equation (5) again for the second half of the echo, we have for the density matrix at the top of the echo $\rho(2\tau)$:

$$\rho(2\tau) \propto \exp(-\mathrm{i}\hat{\mathcal{H}}\tau)\exp(-\mathrm{i}\pi\hat{I}_y)\exp(-\mathrm{i}\hat{\mathcal{H}}\tau)\rho(+)\exp(\mathrm{i}\hat{\mathcal{H}}\tau) \times \exp(\pi\hat{I}_y)\exp(\mathrm{i}\hat{\mathcal{H}}\tau) \tag{8}$$

Inserting equation (8) into equation (3) and multiplying out gives the following expression for the observable magnetization at the top of the echo:

$$\langle\hat{I}_y\rangle \propto \sum_{k<l,m>n} \hat{I}_{ynm}\hat{I}_{xkl}R^{-1}_{ymk}R_{yln}\exp(\mathrm{i}2\omega_{klmn}\tau) \tag{9}$$

where

$$R_y = \exp(-\mathrm{i}\pi\hat{I}_y) \tag{10}$$

and where k, l, m, and n represent the 2^N states of the system and the sum is over all these states, ω_{klmn} represents a packet of magnetization that in the first half of the echo forms a coherence between the k and l states and which is then carried over by the second pulse to the transition between the m and n states.

On Fourier transformation, this gives a sum of δ functions at frequencies given by $[(E_l - E_k) - (E_m - E_n)]/2$, where E_l is the energy of state l, etc., with intensities given by the appropriate elements of $\hat{I}_x$, $\hat{I}_y$, ${R_y}^{-1}$, and R_y, which give a 'supertransition probability' which combines the normal transition probability of each coherence with the efficiency with which they are mixed by the rotation operator. A computer program for performing these calculations has been written by Turner;[17] its greatest challenge is to tackle the immensely complex results generated by spin echo spectroscopy of liquid crystalline phases.

4 SPIN ECHO SPECTROSCOPY IN LIQUID CRYSTALS

The unique features of the NMR spectroscopy of liquid crystalline phases are dealt elsewhere (see ***Liquid Crystals: General Considerations***). For our purposes here, the following summary is sufficient. The liquid crystalline state is characterized by long-range orientational order and by rapid relative translational motion of molecules. The orientational order gives rise to the crystalline character, and the rapid motion gives rise to the liquid like character. Molecules that form liquid crystals tend to be either long rod-like molecules or flat plate-like ones. At the local level the molecules align themselves with rods or plates parallel. This direction of preferred alignment is called the 'mesophase director' and, in the absence of any external restraint, such directors are isotropically distributed within the sample. In the presence of a magnetic field, however, the interaction between the field and the anisotropy of the bulk diamagnetic susceptibility of the system causes the local directors to become aligned with the field, thus amplifying local order into macroscopic order.

The consequences for the NMR of these systems is that anisotropic interactions such as the dipolar coupling and, for spins $>\frac{1}{2}$, quadrupolar coupling, which in ordinary liquids average to zero, are now averaged to a single, generally nonzero, value. The rapid motions of molecules within the sample ensure that resolution is still high and that any intermolecular interactions are averaged to zero. Dipolar couplings are much larger than J couplings (ranging up to a few thousand hertz), so almost all spectra are highly second order and there are significant couplings between widely separated nuclei. In addition, couplings are observed between magnetically equivalent spins so that, for example, the spectrum of water in a liquid crystalline phase is a doublet. These factors taken together mean that the spectra obtained are far more complex than those from isotropic media, to the point where the difficulty of analysis becomes a limiting factor in the use of this spectroscopy (see ***Liquid Crystalline Samples: Spectral Analysis***). It is nonetheless worth going to considerable lengths to achieve a full analysis, because of the simple relationship between dipolar couplings and internuclear distances, and hence molecular structure[18] (see ***Structure of Rigid Molecules Dissolved in Liquid Crystalline Solvents***).

One method for simplifying the problem is to deuterate the molecule partially and then observe both proton and deuteron spectra from which the effect of the heteronuclei has been removed. As we have seen in connection with Figure 1(b), the spin echo removes heteronuclear couplings and so may be regarded as a decoupling technique. The fact that it also removes the chemical shifts is no great disadvantage in liquid crystal NMR where the spectral widths are mainly determined by the large dipolar or quadrupolar couplings.

The first application of the spin echo to liquid crystalline systems was by Vold and Chan[19] who demonstrated for dichloromethane dissolved in a liquid crystalline medium that dipolar couplings produce a modulation of the echo amplitude just as J couplings do.

The echo has been investigated as a decoupling technique for various combinations of heteronuclei and for both liquid crystals and small molecules dissolved in liquid crystals.[20] Because the systems are strongly second order, the effects of heteronuclear couplings are not expected to be removed completely, just as chemical shifts are not removed from the echo spectrum of the AB system. However, calculations show that, if the heteronuclear couplings are small compared with the homonuclear ones, the decoupling effect is essentially complete and the homonuclei may be analyzed alone. An example is a study of ethylbenzene dissolved in a liquid crystalline phase. The spectrum of the fully protonated species was so complex as to defy analysis, so to simplify the system the ring protons were replaced with deuterons; the proton spectrum of this species was broad and largely featureless due the heteronuclear couplings between protons and deuterons. In contrast, the spin echo spectrum, which is shown in Figure 2(a), is a well-resolved and detailed spectrum which

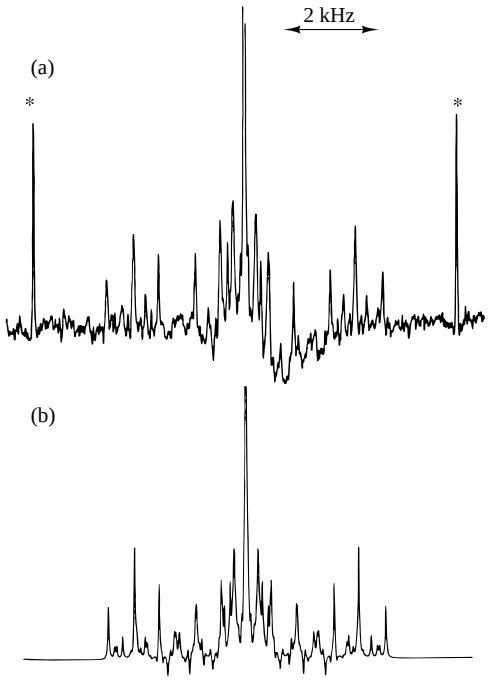

Figure 2 The experimental (a) and calculated (b) proton spin echo spectra of $C_6D_5CH_2CH_3$ dissolved in the liquid crystalline phase ZLI 1167. The peaks marked with asterisks are from water. (Reproduced by permission of the Royal Society of Chemistry from A. G. Avent, J. W. Emsley, Soon Ng, and S. M. Venables, *J. Chem. Soc., Perkin Trans. II*, 1984, 1855)

can be analyzed to give the dipolar couplings amongst the five protons of the ethyl group. The experiment used a single 180° pulse rather than an echo train in order to avoid heating the sample and pulse repetition effects. Figure 2(b) shows a computer simulation of the echo calculated using the program by Turner,[17] in which only the protons were considered. The best fit was obtained when the refocusing pulse was assumed to be 150°, which in effect allows for imperfections in the $\boldsymbol{B}_1$ field.

5 RELATED ARTICLES

Analysis of High-Resolution Solution State Spectra; Chemical Exchange Effects on Spectra; Composite Pulses; Diffusion Measurements by Magnetic Field Gradient Methods; Liquid Crystalline Samples: Spectral Analysis; Liquid Crystalline Samples: Structure of Nonrigid Molecules; Liquid Crystals: General Considerations; Relaxation Effects of Chemical Exchange; Rotating Frame Spin–Lattice Relaxation Off-Resonance; Structure of Rigid Molecules Dissolved in Liquid Crystalline Solvents; Two-Dimensional J-Resolved Spectroscopy.

6 REFERENCES

1. E. L. Hahn, *Phys. Rev.*, 1950, **77**, 297.
2. F. Bloch, W. W. Hansen, and M. Packard, *Phys. Rev.*, 1946, **70**, 474.
3. E. M. Purcell, H. C. Torrey, and R. V. Pound, *Phys. Rev.*, 1946, **69**, 37.
4. E. L. Hahn, *Phys. Rev.*, 1950, **80**, 580.
5. H. Y. Carr and E. M. Purcell, *Phys. Rev.*, 1954, **94**, 630.
6. S. Meiboom and D. Gill, *Rev. Sci. Instrum.*, 1958, **29**, 688.
7. M. H. Levitt and R. Freeman, *J. Magn. Reson.*, 1981, **43**, 65.
8. R. Freeman and H. D. W. Hill, in *Dynamic Nuclear Magnetic Resonance Spectroscopy*, ed. L. M. Jackman and F. A. Cotton, Academic, New York, 1975.
9. A. Bax, A. E. Mehlkopf, and J. Smidt, *J. Magn. Reson.*, 1979, **35**, 373.
10. P. Stilbs, *Progr. NMR Spectrosc.*, 1987, **19**, 1.
11. J. G. Powles and J. H. Strange, *Mol. Phys.*, 1964, **8**, 169.
12. E. L. Hahn and D. E. Maxwell, *Phys. Rev.*, 1952, **88**, 1070.
13. R. Freeman and H. D. W. Hill, *J. Chem. Phys.*, 1971, **54**, 301.
14. A. Abragam, *Principles of Nuclear Magnetism*, Oxford University, Oxford, 1961, p. 500.
15. A. Allerhand, *J. Chem. Phys.*, 1966, **44**, 1.
16. S. Schäublin, A. Höhener, and R. R. Ernst, *J. Magn. Reson.*, 1974, **13**, 196.
17. D. L. Turner, *J. Magn. Reson.*, 1982, **46**, 213.
18. J. W. Emsley and J. C. Lindon, *Nuclear Magnetic Resonance Spectroscopy Using Liquid Crystal Solvents*, Pergamon, Oxford, 1975.
19. R. L. Vold and S. O. Chan, *J. Chem. Phys.*, 1970, **53**, 449.
20. A. G. Avent, J. W. Emsley, Soon Ng, and S. M. Venables, *J. Chem. Soc., Perkin Trans. II*, 1984, 1855 and references therein.

Biographical Sketch

Anthony G. Avent. *b* 1956. B.A., Oxford, 1979; D.Phil., Southampton, 1983. Introduced to NMR by R. Freeman and J. W. Emsley. Manager of the NMR service at Sussex, 1983–present. Research interests: application of NMR to a wide range of organic, inorganic and organometallic chemistry, with particular recent interest in the fullerenes.

Supercritical Fluids

Craig M. V. Taylor and Gunilla B. Jacobson

Los Alamos National Laboratory, Los Alamos, NM, USA

1 Introduction to Supercritical Fluids 1
2 Supercritical Fluids 1
3 Instrument Requirements for High-Pressure NMR 7
4 Supercritical Fluid Applications 8
5 References 9

1 INTRODUCTION TO SUPERCRITICAL FLUIDS

While the existence of the supercritical 'phase' has been known for over 150 years it has been only in the last 20 years that the value of supercritical fluids (SCFs) as a medium for extraction, cleaning and synthesis has been recognized. It is now clear that SCF processes are often constrained to very narrow regions of economic feasibility due to the phase behavior of the solute-solvent system. As a result, there needs to be very tight controls over any industrial process employing SCFs. If the process parameters must be more exact, then so does the information required to generate the design parameters, which includes experimental measurements, theories, and the correlations that result in predictability in a given system. In an effort to expand the current understanding of SCFs and their applications, intensive studies are ongoing using nuclear magnetic resonance (NMR). In an effort to further explain the physical chemistry inherent to possible applications of SCFs, a brief introduction is given to this odd and often ignored 'phase' of substances. Following that is an introduction to NMR as it pertains to the study of SCF applications.

2 SUPERCRITICAL FLUIDS

2.1 General Properties

The supercritical state is defined by the critical pressure (P_c) and critical temperature (T_c). One of the most common phenomenological definitions describes critical pressure as the pressure above which, regardless of the applied temperature, a liquid cannot be made to boil. In a similar way, the critical temperature can be thought of as the temperature above which, regardless of the applied pressure, a gas cannot be converted into a liquid. Hence, above the critical point there is no longer a phase boundary between the liquid and the vapor. A liquid/vapor phase boundary represents a coexistence line so that material crossing it requires the expenditure of the latent heat of vaporization.

The concept of the supercritical state can be illustrated by a physical example. Consider a closed container of constant volume. Inside the container we start with some amount of pure liquid. The space above this pure liquid will be filled with pure vapor at the liquid's equilibrium vapor pressure. Now assume that we begin to heat up this container slowly and uniformly. The density of the liquid will begin to decrease through normal thermal expansion. Meanwhile, the density of the vapor phase begins to increase since more molecules are leaving the liquid to enter the vapor phase. Continued heating results in a further decrease of the liquid density and an increase in the vapor density. Eventually, at some temperature, T_c (and resulting, uniform pressure, P_c), the density of the liquid and vapor phases reach the same value, and the vapor and liquid 'phases' have identical compositions and identical densities.

Is this supercritical fluid phase to be considered a liquid or a gas? The answer is that a supercritical fluid reflects properties of both. Table 1 shows relative values of the density, diffusion coefficient, and viscosity for a typical liquid, gas, and supercritical fluid. These values indicate the mass transport properties (i.e., diffusivity) are similar to a gas, while the mechanical properties (viscosity and density) are similar to those of a liquid. This unique combination of properties makes supercritical fluids attractive for use as solvents. The high diffusivity and low viscosity allows the fluid to penetrate easily into matrices which are in the form of loose powders, compacted powders, or even fully cemented pre-forms. Further, the ability of a solvent to dissolve other liquids is, to a first approximation, related to the density of the solvent. The relatively high density of supercritical fluids, relative to gases, increases the useful levels of solubility that may be attained.

2.2 Supercritical CO_2

As a result of the law of corresponding states the physical properties of supercritical CO_2 apply to all fluids in the supercritical state. The critical values of temperature and pressure are unique for each gas/liquid and are determined by the type of intermolecular interactions occurring between

Table 1 Comparison of physico-chemical properties of a typical organic fluid in the liquid, gas, and supercritical fluid state

	Liquid	Supercritical fluid	Gas
Density ($g\,cm^{-3}$)	1	0.1–1	10^{-3}
Viscosity (Pa·s)	10^{-3}	10^{-4}–10^{-5}	10^{-5}
Diffusivity ($cm^2\,s^{-1}$)	10^{-5}	10^{-3}	10^{-1}

Table 2 Critical temperature, T_c, and Pressure, P_c, for some common fluids

Fluid	T_c (°C)	P_c (psi)
Neon, Ne	−229	400
Nitrogen, N_2	−147	492
Argon, Ar	−122	706
Xenon, Xe	17	858
Carbon dioxide, CO_2	31	1072
Sulfur hexafluoride, SF_6	46	545
Propane, C_3H_8	97	617
Ammonia, NH_3	133	1654
Water, H_2O	374	3209

the individual molecules. Table 2 gives the critical temperature and pressure of some common fluids. For example, the critical temperature and pressure required to transform water (H_2O) into a supercritical fluid are 374 °C and 218 atmospheres. These values are much higher than those for CO_2 because the water molecules exert an attractive force on each other, making the solid and liquid phases particularly stable. CO_2 molecules, on the other hand, have much weaker intermolecular attractive forces. It is important to note that, in the SCF region, attractive forces between molecules are minimized.

In the solid form CO_2 has a high density and a very high viscosity. Similarly, the liquid has a high density and a reasonably high viscosity, and the gas has a low density and low viscosity. Conversely, the supercritical fluid phase has a high density but a relatively low viscosity. The density of supercritical CO_2 can vary over a wide range from gas values, around 0.1 g cm^{-3}, to liquid values of about 2.0 g cm^{-3}. In other words, the density of supercritical CO_2 can be changed by over 2000% simply by varying the temperature and pressure within the supercritical region. A supercritical fluid is by definition both liquid and gas-like, and hence it is compressible. Thus, relatively small changes in temperature and/or pressure can significantly affect the density, as seen in Figure 1.

As the density of the CO_2 becomes more liquid-like, so do the solvent properties of the fluid. To a first approximation, the ability of a supercritical fluid to dissolve other fluids can be related to its density in the supercritical region. When operating in the supercritical region, therefore, both temperature and pressure can be used to vary the density, and therefore, the dissolving power of the fluid. It is this ability to alter the solvent power that makes supercritical CO_2 such an attractive solvent. To make the potential for SCFs even more promising, small additions of other components, called co-solvents or entrainers, often modify the observed phase equilibria dramatically. Again this special property affords the chemist the opportunity to *tailor* solvents to achieve a variety of goals, either in separations or reactions.

The viscosity of carbon dioxide is observed to change rapidly in the critical region, as is the case also for diffusivity. Even at high pressures of 300–400 atm it is still only about 0.09 centipoise, an order of magnitude below typical organic solvents. Because of these density and viscosity properties, supercritical CO_2 possesses certain other characteristics, which enhance its attractiveness as a solvent. In addition to possessing liquid-like densities over much of the temperature and pressure range of interest to industry, it exhibits the gas-like property of diffusivity with a zero value for the surface tension. These features alter the transport to allow for easy penetration of SCFs into nano-dimensional spaces.

The self-diffusion coefficient for carbon dioxide (which is approximately the same for similar sized molecules diffusing through carbon dioxide) is about one to two orders of magnitude higher than the diffusivities of comparable solutes in typical organic liquids.

2.3 NMR of Supercritical Fluids

The interactions of a nuclear moment with other nuclei and the electrons surrounding it provide a very sensitive site specific probe into the structure and dynamics in the solid, liquid, and gas phase. This work will concern itself with NMR in the supercritical fluid state of carbon dioxide. As mentioned above, these states exhibit properties of both the liquid and the gas phases. Thus, techniques and theory from work in both phases combine in these unique applications. Thorough reviews have been published on the unique information which can be obtained in the gas phase.[1,2] Other reviews have been published on experimental techniques and applications of high pressure NMR.[3,4] These reviews were published on or before

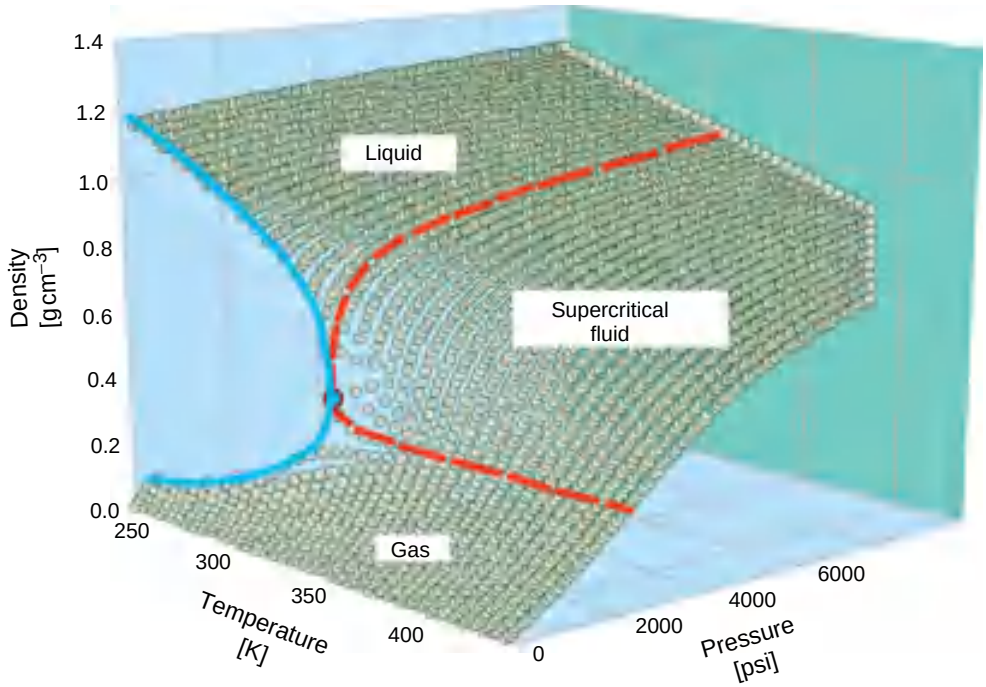

Figure 1 Pressure–temperature–density surface of pure CO_2

1991. We will discuss primarily studies published later, with information as it relates specifically to NMR determination of the dynamics and structure in the SCF state.

Although the application of high pressure NMR to simple fluids leads to some interesting additional complications, the information gained from the technique more than justifies its use. The pressure axis provides an additional dimension to the experimental matrix. For a liquid it is commonly known that temperature changes at constant pressure will effect the molecular motion via kinetic energy and molecular average volume collisional arguments. One can separate the effects of density and temperature on the molecular motion only if both the temperature and pressure are controlled variables in the NMR experiment. Increased pressure also allows for the experimental range to expand well above the normal boiling point and into the compressible supercritical fluid regime. Some examples of the usefulness of high pressure NMR will be given.

2.4 Introduction to the Basics of High-pressure NMR

The motions of molecules in liquids is accessible only through a large number of various models that depend upon phenomenological parameters such as the coefficient of rotational diffusion, the frequency of collisions, the time between jumps, etc. Three such theories: the random walk theory of Torrey,[5] the rotational diffusion theory of Abragam,[6] and the rotational Brownian motion of McConnell[7] form the basis upon which most NMR relaxation models in liquids are based. Other methods of studying molecular motion (optical, dielectric, neutron scattering, etc.) can in principal give additional detailed information. However, as a consequence of the many-particle effects present in these methods, the interpretation of the experimental results for liquids is often ambiguous. In NMR, the weak coupling of the spin system with the lattice allows one to focus better on isolated molecular motions to describe relaxation in liquids.[8] Information on the rotational motion of molecules in liquids of low viscosity, given by NMR, is obtained in the form of the integrals of the time correlation functions, i.e., the correlation times. This section will discuss the effects of dense gas and supercritical fluid states on the correlation times, and what this means to the NMR spectroscopist.

2.5 The Origin of Nuclear Spin Relaxation

Direct time dependant interactions have been shown to cause spin relaxation. However any static interaction can simply be treated as part of the normal spin Hamiltonian, altering the positions and intensities of the spectral lines. For example, a nuclear spin may experience a local magnetic field from the spins of other nuclei moving in its vicinity, from an unpaired electron, or from a variety of other mechanisms, such as the spin–rotation interaction in which the rotation of the molecular electrons generates a magnetic field at the nucleus. In general, rotational and diffusional motions are important sources of relaxation in fluids. Some mechanisms that make contributions to spin–lattice relaxation will be discussed.

2.5.1 Nuclear Spin Relaxation Mechanisms

There are a number of processes that provide the basis for nuclear spin relaxation. These include the nuclear magnetic dipole–dipole interactions (DD), the spin–rotation interactions (SR), the quadrupolar interactions (Q), and the chemical shift interactions, (CSA). The overall relaxation rate can be expressed as a sum of contributions from each mechanism.

2.5.2 Dipole–Dipole Interaction

The magnetic nuclei in molecules provide magnetic dipole fields that are proportional to the magnetic moments of the nuclei. These fields fluctuate in magnitude and direction as the molecule tumbles through space. When these random oscillating fields have magnetic field components at the Larmour frequency, the nuclear spin relaxes. This interaction depends upon the correlation time of the tumbling molecule as well as the distance between the interacting nuclei. The dipole interactions can be divided into intramolecular and intermolecular interactions. For both of these types of interactions there is a homo, and hetero-nuclear sub-interaction. These are reflected in the following equations

$$\text{For intra-homo:} \quad \frac{1}{T_1^{\mathrm{DD}}} = \frac{3\gamma_A^4\hbar^2\tau_c}{2r^6}$$

$$\text{For intra-hetero:} \quad \frac{1}{T_1^{\mathrm{DD}}} = \frac{\gamma_A^2\gamma_X^2\hbar^2\tau_c}{r^6} \tag{1}$$

$$\text{For inter-hetero:} \quad \frac{1}{T_1^{\mathrm{DD}}} = \frac{2N_x\gamma_A^2\gamma_X^2\hbar^2}{Da}$$

where r is the distance between the interacting nuclei, D is a mutual translational self-diffusion coefficient for the molecules containing A and X, and a is the distance of closest approach between A and X. τ_c is a rotational diffusion correlation time for molecular tumbling. This corresponds to the average time it takes for a molecule to rotate through one radian.

2.5.3 The Spin–Rotation (SR) Interaction

Spin–rotation relaxation of the nuclear magnetization in molecules is due to the intramolecular coupling of the individual nuclear spins to the molecular angular momentum. A fluctuating local magnetic field, which relaxes the nuclear spins, is the result of the collisional reorientation of the molecular rotational angular momentum. For linear molecules such as CO_2, the spin–rotation contribution to the total spin–lattice relaxation can be expressed as

$$\frac{1}{T_1^{\mathrm{SR}}} = \frac{4C_\perp^2 IkT\tau_j}{3\hbar^2} \tag{2}$$

$C_\perp$ is the spin–rotation constant and I is the moment of inertia. For a spherical top molecule, the relaxation rate has the form

$$\frac{1}{T_1^{\mathrm{SR}}} = \frac{2C_{\mathrm{eff}}^2 IkT\tau_j}{\hbar^2} \tag{3}$$

C_{eff} is the effective spin–rotation tensor. The τ_j is the correlation time for angular momentum transfer and therefore is closely related to the average time between collisions. The higher the temperature the faster the molecule reorients in accordance with the kT term. The result is that the spin–rotation contribution to the total spin–lattice relaxation

increases with temperature. This is quite the opposite in all other mechanisms examined in this work.

2.5.4 Quadrupolar Relaxation

Quadrupolar occurs when the nuclear electric quadrupole moment, interacts with electric field gradients to provide a very efficient nuclear relaxation process. The equation for these interactions is similar in form to that of the dipole interaction. The electric quadrupolar interaction between spin I and an electric field gradient can be written in the form given in equation (4).

$$\frac{1}{T_1^{\mathrm{Q}}} = \frac{3\pi^2(2I+3)\chi^2\tau_{\mathrm{c}}}{10[I^2(2I-1)]} \tag{4}$$

where χ is known as the nuclear quadrupolar coupling constant and is in units of frequency. The τ_{c} here is the rotational diffusion correlation time as it appeared in the dipolar equation. Because of its relative efficiency the quadrupolar interaction nearly dominates when quadrupolar nuclei are present.

2.5.5 Chemical Shift Anisotropy

Anisotropic shielding at the nucleus changes with the orientation of the molecule in a static field. Therefore the molecular tumbling modulates the local magnetic field resulting in relaxation. The spin–lattice relaxation rate due to this interaction is proportional to the square of the magnetic field:

$$\frac{1}{T_1^{\mathrm{CSA}}} = \frac{2}{15}\gamma_A^2 B^2 \Delta\sigma^2 \tau_{\mathrm{c}} \tag{5}$$

where Δ is the chemical shielding anisotropy of the nucleus and τ_{c} has the same meaning as before.

The spin–lattice relaxation can be measured and contributions from each of the mechanisms decoupled to yield dynamic and structural information pertaining to the species of interest. Each of the following sections will contain specific observation techniques and theoretical treatments used to provide insight into the often strange and unpredictable world of supercritical fluids.

Extensive studies have been performed on nuclear magnetic spin lattice relaxation and its dependence on molecular structure and dynamics. This is the subject of several review articles.[9–12] Decoupling techniques are often used to enhance the signal and to simplify the resulting spectrum. Such decoupling studies also yield the nuclear Overhauser enhancement (NOE), which allows the unique separation of the dipolar interaction from other relaxation interactions. However, decoupling also eliminates multiplet splittings from scalar couplings, thereby preventing direct measurement of some of the spectral features that are required to completely describe the relaxation of coupled nuclear spin systems.

Spin-coherent double-resonance experiments, which avoid this loss of information, and a general numerical method for analyzing the data obtained in relaxation studies of this type may be used.[13,14] Relaxation processes, described by a system of coupled linear differential equations, determine a variety of time-independent relaxation parameters that contain information on the molecular structure, and dynamic features of the motion. The relaxation parameters in the equations of motion can then be extracted from the experimental data using standard least squares methods.[13,14]

For polyatomic gases, nuclear spin relaxation proceeds primarily from the collisional modulation of the molecular rotational angular momentum coupled to the angular momentum of the nuclear spins. Reorientations of molecular angular momentum by collision then give rise to fluctuating internal magnetic fields, that effect the nuclear spins through intramolecular spin–rotation couplings. In addition to the spin–rotation mechanism molecular motional modulation of the chemical shift anisotropy, dipole-dipole and quadrupolar couplings also affect the relaxation rates.

In low-viscosity liquids and gases, spin–lattice relaxation may be treated as a temporal modulation associated with the thermal reorientation of the molecule. The study of spin lattice relaxation contributes to an understanding of molecular dynamics.[15] In dilute gaseous samples of small molecules where the interactions mediating spin relaxation are primarily intermolecular,[16,17] and the various interaction parameters are known accurately,[18–21] the study of relaxation reveals features of collisional processes responsible for reorientation of the molecules.[22–24]

2.6 Line Narrowing

All polyatomic gases possess more than one intramolecular relaxation mechanism. Even the molecule H_2, for instance, has two competing mechanisms: the spin–rotation and the direct dipole–dipole interaction. In condensed phase molecular hydrogen the contribution of the dipole–dipole mechanism is comparable to that of spin rotation because the distance between the protons is short enough for the dipole–dipole relaxation to be appreciable. In a gaseous system, however, spin rotation is normally the dominant relaxation mechanism. In such experiments high density carbon dioxide can be added to hydrogen isotopomers such as hydrogen deuteride, as suggested by Johnson and Waugh,[23] to shorten the rotational correlation times and thereby lengthen the spin–rotation relaxation time and narrow the resonances in the high-resolution spectra. The H_2 system is difficult to study because of the indistinguishability of the two particles. Thus research on the lower HD symmetry[18,19,21–23,25–28] provides more information from both the proton and deuteron resonances arising from indirect spin-spin couplings.

Supercritical fluids generally have viscosities 10–100 times lower than that of the normal liquid phase and self diffusion coefficients 10–100 times greater. To the NMR spectroscopist, these properties are of significant benefit in studying quadrupolar nuclei, since the quadrupolar linewidth is proportional to the rotational correlation time. The utility of NMR to study many quadrupolar nuclei has been somewhat limited. Quadrupolar relaxation can be very efficient, leading to broad lines and low sensitivities. In the extreme narrowing limit, the linewidth of these nuclei,$(1/\pi T_2)$ can be written as

$$\frac{1}{\pi T_2} = \frac{3}{8}\left(\frac{e^2qQ}{h}\right)^2\left(1+\frac{\eta^2}{3}\right)\tau \tag{6}$$

where e^2qQ/h is the quadrupolar coupling constant, τ is the rotational correlation time for the molecular motion, and η is the asymmetry parameter of the electric field gradient

tensor. Various studies have demonstrated the validity of the Stokes–Einstein–Debye equation.[29]

$$\tau = \frac{A\eta}{T + \tau_0} \tag{7}$$

in which τ is the rotational correlation time, η is the solvent viscosity, T is the temperature and τ_0 is the high temperature intercept. This equation predicts a linear relation between τ and η/T to a limiting value τ_0 attained in the limit as $\eta/T \rightarrow 0$. Comparisons with above equation show that NMR line widths should decrease with decreasing viscosity to a limiting value expected to be related to the free rotor correlation time given by

$$\tau_{\mathrm{FR}} = \left(\frac{2\pi I}{9kT}\right)^{1/2} \tag{8}$$

where I is the moment of inertia about the rotational axis.

2.7 NMR Determination of Structural Dynamics in High-Pressure Fluids

There have been direct spectroscopic probes of the local solvent structure around solutes in supercritical fluids. These include using the solvatochromic scales as in the ultraviolet-visible (UV) absorption of phenol blue in ethylene[30] and the fluorescence spectroscopy of pyrene in carbon dioxide.[31] The use of spectroscopic methods to study the local environment surrounding solute molecules in dilute supercritical fluid mixtures has been reviewed.[32] However the use of NMR to determine the local structure within supercritical fluids has thus far been sparse in the literature.

2.7.1 High Pressure NMR Studies of Hydrogen Bonded Liquids

An understanding of molecular interactions between solute and solvent molecules in supercritical fluids (SCF) is essential to an explanation of clustering phenomena, considered responsible for the unique SCF solvating characteristics compared to gases.[33–35] Although both theoretical[36–38] and experimental efforts[39–46] have been made to increase the understanding of these phenomena, a complete picture of clustering in SCFs is still evolving. The accumulation of experimental NMR relaxation data is expected to improve our physical picture of solvent clustering in SCF. Because the nuclear spin–lattice relaxation rates depend on the fluctuating molecular reorientation and molecular collision frequency, their measurement proves to be an effective method for studying such molecular interactions and dynamics in fluids.[47] One of the advantages of utilizing NMR relaxation data is that they provide not only information, similar to optical methods, on overall molecular motions but also site-specific information on intramolecular motions. The ^{13}C spin–lattice relaxation processes in CO_2 are dominated by spin–rotation interactions.[48–50] Nuclear spin–lattice relaxation rates have been measured under SCF conditions by Lamb et al.[51] and Etesse et al.[52–54] for various SCF mixtures. NMR chemical shift measurements[55] were also used to relate ^{129}Xe chemical shift data to the local solvent structures of SCF Xe. SCF fluid structures in pure methanol,[56] CO_2–methane,[39] CO_2–methanol,[40] and CO_2–decanol[40] mixtures have recently been made. The function of the hydroxyl group in solute-induced solvent clustering in SCF CO_2 appears to be especially important. Earlier developments in high pressure NMR studies of hydrogen bonded liquids may be found in a review article by Lang and Ludemann.[57]

Information on the nature and average rate of molecular motions may be obtained by determining the nuclear spin–lattice relaxation rates of nuclei in the molecules under investigation. The nuclear spin relaxation rate, $1/T_1$, depends on fluctuations in molecular reorientations as a consequence of molecular collisions, where T_1 is the time constant defining the exponential return of a perturbed nuclear spin to its equilibrium state. Many nuclear spin interaction mechanisms affect T_1 values. Among them, spin–rotation, quadrupolar and dipolar interactions are the most important ones at sub- and supercritical densities. Detailed descriptions of spin–rotation, quadrupolar and dipolar interactions may be found in the review articles by Grant et al.[58] and Jameson.[59] Briefly, determination of NMR nuclear relaxation rates provides the angular momentum[59] and rotational reorientation correlation times[58] from the spin–rotation and quadrupolar/dipolar interactions, respectively. Spin–rotation interactions are directly related to molecular collision frequencies and depend on macroscopic properties such as fluid density and temperature. Dipolar and quadrupolar interactions, however, are often related to fluid viscosity and temperature. Since the fluid viscosity may be treated as a function of local density in the compressible regions of CO_2, both correlation times may be considered as functions of local densities. Therefore, clustering phenomena in SCF resulting in fluctuations of local density may in principle be observed by NMR relaxation measurements.

The magnitude of the NOE effect is given by[60]

$$\mathrm{NOE}(A\{X\}) = \frac{I_A^*}{I_A^0} \tag{9}$$

where I_A^* is the integrated intensity of a decoupled spectrum with saturation of the nucleus X, and I_A^0 is the equilibrium intensity of A in the coupled spectrum. The maximum possible NOE of ^{13}C{^{1}H} occurs when ^{13}C and ^{1}H relax only by the dipolar mechanism given by[60] and is given by

$$\mathrm{NOE(max)} = 1 + \left(\frac{\gamma_{\mathrm{H}}}{2\gamma_{\mathrm{C}}}\right) = 2.988 \tag{10}$$

where γ_{H} and γ_{C} are the magnetogyric ratios for ^{1}H and ^{13}C, respectively. The NOE effect may be determined as a ratio of spectral intensities with proton decoupling to that of gated proton decoupling. Since the ^{13}C in CO_2 does not exhibit an NOE, its signal intensity may be used as a fiducial reference.

2.8 Significant Mechanism in Spin–Lattice Relaxation: Overall Rotational Motion

In general, the overall rotational motions of solute molecules depend on the intermolecular frictional forces between the solute and solvent molecules and, therefore, are dependent upon the solvent viscosity. The solvent viscoelastic response, in turn, is also dependent on various relaxation mechanisms of solvent molecules. Internal rotational motions including various local isomerization movements are driven by torsional forces.[61]

The rotational reorientation correlation time, τ_c, may be extracted from NMR spin–lattice relaxation time measurements, within the *extreme narrowing* limit, using the following expression[60]

$$T_{1,\mathrm{DD}}^{-1}(^{13}\mathrm{C}) = \frac{\upsilon\gamma_C^2\gamma_H^2\hbar^2\tau_c}{r^6} \tag{11}$$

where r is the bond distance between ^{1}H and ^{13}C (measured as 1.085 Å), and υ is the number of protons directly attached to the ^{13}C nucleus. The dipole–dipole relaxation rate, may be obtained from the standard relationship between the overall T_1 and NOE measurements:[60]

$$\mathrm{NOE} = 1 + \frac{\gamma_H}{2\gamma_C}\frac{T_{1,\mathrm{DD}}^{-1}(^{13}\mathrm{C})}{T_{1,\mathrm{Tot}}^{-1}(^{13}\mathrm{C})} \tag{12}$$

The reorientation correlation time obtained in this manner is an average assuming isotropic reorientation. This correlation time may be related to a rotational diffusion coefficient by assuming that each nuclear environment is roughly spherical and rotates randomly.[62]

$$\tau_c = \frac{1}{6D} \tag{13}$$

From the temperature dependence of rotational diffusion coefficients at fixed viscosity, one can determine effective rotational activation energies.

2.9 CO_2 Clustering

The rotational reorientation correlation time, τ_c, can be expressed by a modified Stokes–Einstein–Debye (SED) equation[63]

$$\tau_c = \frac{\eta V_p}{kT} f_{\mathrm{stick}} C + \tau_0 \tag{14}$$

where η is the fluid viscosity, V_p is the volume of solute molecule, f_{stick} is a well-defined shape parameter dependent only on the structure of solute molecules,[64] C is a boundary parameter dependent on the nature of the solute and solvent and upon their concentration, and finally τ_0 is the free-rotor correlation time. The success of this model strongly depends on the selection of parameters C and f_{stick}. Recently, Roy et al.[64] noted that the Dote, Kivelson, and Schwartz (DKS) model[63] is the best model for predicting reorientational correlation times for solutes with radii up to about 4.5 Å. Anderson and Kauffman[65] further modified the calculation of the smallest volume of free space per solvent molecule, ΔV, in the DKS model, and more recently, these two workers[66] related fluid viscosity and the parameter C in the SED model to the local density by introducing a radial distribution function into the hydrodynamic model. These modifications[65,66] by Anderson and Kauffman are referred to as the AK model.

In the AK model, the viscosity for a fluid is expressed as a function of local density ρ_{12}^1 by equation 4.7 described by Jossi et al.[67]

$$[(\eta - \eta_0)\xi_T^y + 1]^{1/4} = 1.023 + 0.23364\rho_r + 0.58533\rho_r^2 - 0.40758\rho_r^3 + 0.09324\rho_r^4 \tag{15}$$

where $\rho_r = \rho_{12}^1/\rho_c$ and $\xi_T = (T_c/M^3P_c^4)^{1/6}$. ρ_c, T_c, and P_c represent the critical density, temperature, and pressure, respectively. M is the molecular weight in the unit of g mol^{-1}. The local density of is related to the bulk density ρ by a radial distribution formalism

$$\rho_{12}^1 = \rho\{1 + F[g_{12}(r)]\} \tag{16}$$

where $F[g_{12}(r)]$ is an integral equation in the pair distribution function, $g_{12}(r)$, over the spatial coordinates and r is the distance between solvent and solute molecules. $F[g_{12}(r)]$ is a measure of the excess solvent density near the solute molecule and is treated as an adjustable parameter in the AK model. When $F[g_{12}(r)] = 0$, the local density equals the bulk density, and when $F[g_{12}(r)] = 1.0$, the local density is twice the bulk density.

In the AK model, the parameter $C(\rho_{12}^1)$ equivalent to C in the SED model, is also treated as a function of local density. According to the DKS model

$$C(\rho_{12}^1) = \frac{f_{\mathrm{slip}}V_p}{f_{\mathrm{slip}}V_p + \gamma V_p} \tag{17}$$

where f_{slip} is a factor for the slip boundary condition whose value estimated from f_{stick} by the method reported by Hu and Zwanzig[68] and γ is defined as

$$\gamma = \left(\frac{\Delta V}{V_p}\right)\left[4\left(\frac{V_p}{V_s}\right)^{\frac{2}{3}} + 1\right] \tag{18}$$

In equation (18), V_s is the solute molecular volume and ΔV is the free space volume for a solvent molecule. For supercritical fluids in their compressible regions, a large variation in the free space is expected, and ΔV is given by equation (19) relating molecular weight (MW) and local density:

$$\Delta V = \frac{\mathrm{MW}}{\rho_{12}^1} - V_s \tag{19}$$

Therefore, the parameter $C(\rho_{12}^1)$ is expressed as a function of local density ρ_{12}^1 though the free space volume ΔV.

Combining equations (18) and (19), the AK version of the SED equation may be expressed as[66]

$$\tau_c \equiv \frac{\eta(\rho_{12}^1)V_p}{kT} f_{\mathrm{stick}} C(\rho_{12}^1) + \tau_0 \tag{20}$$

Equation (20) relates the reorientation correlation time, τ_c, to the solvent local density at a given temperature. By performing a comparison experiment on *trans*,*trans*-1,4-diphenylbutadiene (DPB) solute in CO_2, Anderson and Kauffman[66] also observed that CO_2 solvent clustering only occurs in the vicinity of *trans*-4-(hydroxymethyl)stilbene (HMS) molecules. Because the extended π-electron systems existing in DPB and HMS are similar, Anderson and Kauffman concluded that the OH group in HMS is responsible for the association between the solute and solvent molecules. The one-to-one association between solute and solvent molecules may initiate further CO_2 clustering whenever strong many-body interactions affect the solvent structure in supercritical

fluids in the compressible density region. The CO_2 clustering gradients observed along the aliphatic chain of l-decanol molecules in the Bai et al.[39] study appear to support the observations by Anderson and Kauffman.

To verify further the importance of alcohol enhanced clustering, the same procedure was applied to a CO_2–methanol mixture,[69] where a specific association between CO_2 and CH_3OH has been observed also by the IR studies.[42] Such solvent-solute interactions may initiate CO_2 solvent clustering.[66] The low-pressure limit free-rotor correlation time can be calculated using the following expression[70]

$$\tau_0 = \frac{2\pi}{9}\left(\frac{I_\perp}{kT}\right)^{1/2} \tag{21}$$

where is the perpendicular component of the moment of inertia for methanol molecules. The calculated τ_0 from equation (21) is 0.20 ps, which agrees well with the 0.17 ps from fitting the low-density data.

2.10 More Evidence for the Formation of CO_2 Clusters in the Vicinity of Methanol

As stated above, NOE measurements allow the separation of the dipole–dipole contributions to spin–lattice relaxation rates from other mechanistic contributions. For methanol, the remaining relaxation contributions result essentially from the spin–rotation mechanisms described previously.[69] These spin–rotation relaxation rates allow one to calculate an angular momentum exchange correlation time, τ_J, which is strongly dependent on the fluid density. Methanol is a quasi-symmetric top molecule, but the relation between ρ, and spin–rotation relaxation rates for symmetric top molecules may be used as a good approximation for T_1^{SR}. The expression[71] is

$$\frac{1}{T_1^{SR}} = \frac{2\pi^2}{\alpha} C_{\text{eff}}{}^2 \tau_J \tag{22}$$

where pull down $\alpha = \hbar^2/(2kTI_\perp)$ and $I_\perp$ is the perpendicular part of the moment of inertia for methanol. The effective spin–rotation, C_{eff}, may be expressed as

$$C_{\text{eff}}{}^2 = k_1 C_a^2 + k_2 C_a C_d + k_3 C_d^2 \tag{23}$$

In equation (23), the structure parameters, k_i, only depend on molecular structure. C_a and C_d are the isotropic and anisotropic components of the spin–rotation tensor. Therefore, in principle, an experimental angular momentum correlation time, τ_J, may be estimated using equation (22). Since τ_J is linearly related to the time between molecular collisions, τ_{BC}, one may calculate τ_J using a gas kinetic theory. The slope of this linear relationship, called an effective collision number and referred to as Z,[72] provides the average number of collisions needed for an effective molecular angular momentum exchange. This number is found to be between 1.4 and 3.4 for many collision pairs (cf. Table 3 in Ref.[72]). In the use of a hard-sphere model (HSM) for calculating cross sections, choosing the effective collision number of two appeared to be a good approximation in the work of Maryott, Malmberg, and Gillen,[72] and therefore, this value is used in the following discussion. The expression for computing τ_J is given by[73]

$$\tau_J = \frac{Z}{\rho \overline{v} \sigma_K} \tag{24}$$

where ρ is fluid density, $\overline{v}$ is the average velocity of molecules, and ρ_K is the kinetic collisional cross section between solute and solvent molecules. Both $\overline{v}$ and σ_K may be estimated from molecular properties of the solute and solvent. If the density term, ρ, in equation (24) is replaced by a local density [cf. equation (16)], the estimated τ_J becomes a function of the excess solvent density parameter, $F[g_{12}(r)]$. In this case, equation (24) becomes

$$\tau_J = \frac{Z}{\rho\{1 + F[g_{12}(r)]\}\overline{v}\sigma_K} \tag{25}$$

There is good agreement between theoretical and experimental data when an increase in local density is employed in the predictions of τ_J. This provides additional evidence for the formation of SCF solvent clustering in the vicinity of hydrogen bonding solute molecules. Supposedly, these interactions are induced by the hydroxyl functional group present in alcohol molecules.

2.11 NMR Determination of Self-diffusion Coefficients in High-pressure Fluids

Many methods exist for measuring the diffusion coefficients of fluids. However, the experimental accuracy of many of these is quite limited.[74,75] Furthermore, methods that give reliable results in the low pressure regime are not always suitable at high pressures because the inverse dependence of the diffusion coefficient on pressure makes for experiments that take an inordinately long time. The most widely reported method for the measurement of diffusion coefficients in the SCF state is a gas chromatographic method based on Taylor dispersion, which has proven unreliable at lower pressures.[76–78]

The only other methods that can be utilized for this measurement in SCFs are photon correlation spectroscopy[79,80] and NMR.[81,82] They are not widely used at this time because the equipment is very expensive and their application to industrially important SCF's is still in its infancy. The use of the NMR technique has been confined to the measurement of self diffusion coefficients.[81,82]

3 INSTRUMENT REQUIREMENTS FOR HIGH-PRESSURE NMR

In order to perform NMR experiments under high pressure, it is necessary to devise a convenient means to control the pressure, temperature and sample concentration while it is inside the magnet. Two basic approaches to the design of high pressure NMR experiments have been reported: (1) construction of a probe which is capable of achieving the necessary pressures, referred to as the *high pressure probe technique*,[83] or (2) fabrication of a high pressure cell which can be used in a standard commercial NMR probe, referred to as the *high pressure cell technique*.

The very first high pressure NMR experiment was performed in 1954 by Benedek and Purcell.[84] They used a

hydrostatic high pressure probe capable of holding pressures up to 10 000 atm. For deformable samples the high pressure probe technique requires a sealed sample cell which incorporates a volume change mechanism such as bellows or a mercury column.[85] The cell is surrounded by a RF coil and is located inside a pressure vessel small enough to fit inside the NMR magnet. The high pressure probe technique usually offers higher sensitivity because of a better filling factor for the receiver coil. It also allows for higher pressures and is usually safer to work with. The disadvantages are that they require a more elaborate and expensive design and are therefore not suitable for a routine NMR laboratory. The approach to a high pressure probe has continually been developed by Jonas et al.[86] with improvements to pressure vessel design and electrical feed-throughs. The most recent advances to the probe design for studying supercritical fluids include the toroidal coil[87] and cavity[88] design by Rathke et al.

The high pressure cell technique allows the experiments to be performed in a commercial NMR probehead, thereby eliminating the need to alter the basic probe design. The earlier versions of high pressure cells experienced lower sensitivity and reduced working pressures. Yonker et al. designed a simple and safe method by coiling a fused silica capillary tube inside a commercial 5-mm NMR tube.[89] Newer cell designs have improved these limitations providing a more convenient and cost-effective means of carrying out high pressure NMR experiments. Roe et al.[90] designed the first cell made of single crystal sapphire and Horvath et al. later improved this design.[91,92] Pressure control while the cell is in the magnet is a major issue in the cell design. The previously reported designs of the sapphire NMR cells were unable to independently control both the sample temperature and pressure. In the Bai et al. design[93] a movable piston is used to control the sample pressure (see Figure 2). With this design it is possible to control temperature and pressure independently over a wide range of conditions while keeping the relative molar concentration ratios of the sample mixture intact. The sample volume must be restricted to the active coil in order to eliminate errors introduced through molecular diffusion between polarized and nonpolarized volume elements within the cell. Recently a high pressure cell constructed of high-performance polymers, such as poly(etherether ketone) (PEEK), was developed by Wallen et al.[94] with the purpose of simplifying the cell design to allow for more routine experiments on supercritical fluids.

The very first high pressure probe was made of a beryllium copper alloy (Berylco 25). This alloy was used due its strength and nonmagnetic properties, but does require special heat treatment and can have significant variations in the level of paramagnetic impurities. Berylco 25 is stable up to 10 000 atm and permits a temperature range of $-10\,^{\circ}\mathrm{C}$–$80\,^{\circ}\mathrm{C}$. Titanium alloys (IMI-680) are now more commonly used as they require no special heat treatment during machining and retain their strength up to 400 °C and 5000 atm. For even higher pressures, up to 100 kbar, the diamond anvil method can be used.[95] This method can only be used with very small samples so most studies concern sensitive nuclei, although a study on ^{13}C has been reported.

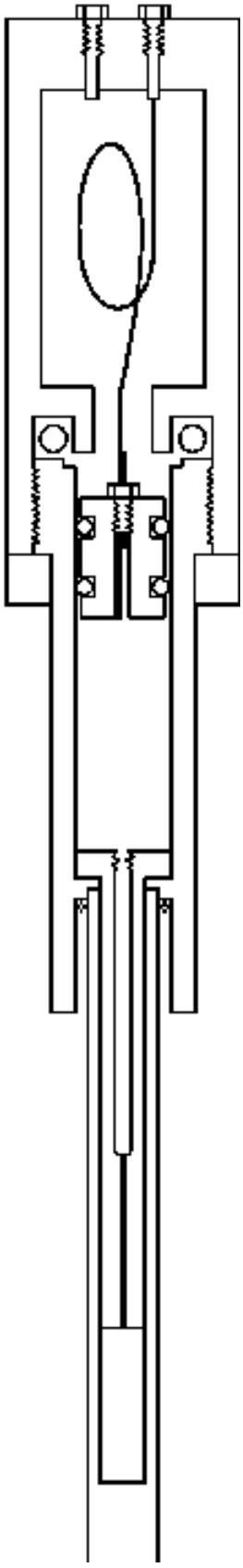

Figure 2 Schematic diagram of the high pressure piston NMR cell capable of independently controlling temperature, pressure and sample concentration

4 SUPERCRITICAL FLUID APPLICATIONS

Most of the high pressure NMR studies of supercritical fluids have involved measuring chemical shifts, such as ^{1}H,[96]

of both polar and nonpolar solute molecules in the dense phase fluid. Increased reaction rates of certain reactions in supercritical fluids has been attributed to specific solvent-solute and solute–solute interactions. By studying these specific interactions by NMR further insight into the variation of the surroundings of the solute molecules with the density of the supercritical fluid is obtained and can be compared to other experimental techniques, such as UV and vibrational spectroscopy.

Using a fused silica capillary cell an in situ photolysis study of organometallics in supercritical fluids was performed where the ligand exchange with the metal center was directly observed.[97] High pressure NMR was also used to determine the fundamental dynamic and electronic properties of the organometallic complexes in the SCF through the investigation of the spin–lattice relaxation times, T_1, and NMR magnetic shielding constants, σ.

Another interesting application of supercritical fluids is to use them as solvents for comprehensive NMR studies of large proteins. In conventional solvents large proteins (over 30 kDa) tumble too slowly and correspondingly the spin–spin relaxation times (T_2) become shorter, making some standard experiments unreliable. By encapsulating the protein in a reverse micelle dispersed in a low viscosity fluid, such as a supercritical fluid, the tumbling correlation time (τ_m) of the protein is reduced thereby increasing T_2.[98] This results in narrower lines in the spectrum.

High pressure NMR has also been used to investigate phase behavior of binary solvent systems in order to obtain vapor–liquid equilibrium (VLE) values. Usually VLE values of supercritical fluid solutions are obtained using variable volume view cells and off-line analysis techniques. By using NMR, this process can be simplified and made more efficient for numerous solvent systems. This technique is especially suitable for hydrocarbon containing solvent molecules as detection of solvent protons in both the liquid and vapor phase can be detected simultaneously.[99]

An advantage of using supercritical fluids as reaction media for chemical reactions is that gaseous reagents are completely miscible with the solvent. In catalytic reactions such as hydrogenations and hydroformylations where H_2 and CO are reactants this can have a significant impact on both the yield and selectivity of the desired products. Since only one phase is present in the supercritical system, stirring to achieve gas–liquid mixing is unnecessary. By studying these reactions in situ by NMR valuable information regarding the mechanism can be obtained.[100] In situ NMR was used to optimize the iridium catalyzed enantioselective hydrogenation of imines in supercritical CO_2. By studying the specific interactions between substrates and products with CO_2 conclusions about the different reactivities of structurally similar substrates were obtained.[101]

5 REFERENCES

1. C. J. Jameson, *Chem. Rev.*, 1991, **91**, 1375–1395.
2. R. L. Armstrong, *Magn. Reson. Rev.*, 1987, **12**, 91.
3. J. Jonas, ed, 'NMR Basic Principles and Progress', Springer Verlag: Berlin, 1991, Vol. 24 of High Pressure NMR.
4. I. T. Horvath and J. M. Millar, *Chem. Rev.*, 1991, **91**, 1339–1351.
5. H. C. Torrey, *Phys. Rev.*, 1953, **92**, 962.
6. A. Abragam, 'The Principals of Nuclear Magnetism', The Clarendon Press: Oxford, 1961.
7. J. McConnell, 'Rotational Brownian Motion and Dielectric Theory', Academic Press: London, 1980.
8. J. McConnell, 'The Theory of Nuclear Magnetic Resonance Relaxation in Liquids', Cambridge University Press: Cambridge, 1987.
9. S. W. Collins, T. D. Alger, D. M. Grant, K. F. Kuhlman, and J. C. Smith, *J. Phys. Chem.*, 1975, **79**, 2031.
10. C. L. Mayne, D. W. Alderman, and D. M. Grant, *J. Chem. Phys.*, 1975, **63**, 2514.
11. G. A. Gray and S. E. Cremer, *J. Magn. Reson.*, 1973, **12**, 5.
12. D. M. Grant, R. J. Pugmire, E. P. Black, and K. A. Christensen, *J. Phys. Chem.*, 1973, **95**, 8465.
13. D. M. Grant, C. L. Mayne, F. Liu, and T.-X. Xiang, *Chem. Rev.*, 1991, **91**, 1591–1624.
14. D. Canet, *Prog. NMR Spectrosc.*, 1989, **21**, 237.
15. D. M. Grant, C. L. Mayne, F. Liu, and T.-X. Xiang, *Chem. Rev.*, 1991, **91**, l591–1624.
16. N. Bloembergen, E. M. Purcell, and R. V. Pound, *Phys. Rev.*, 1948, **73**, 679.
17. A. Abragam, 'Principles of Nuclear Magnetism', Clarendon Press: Oxford, 1961, p. 1581.
18. N. F. Ramsey and H. R. Lewis, *Phys. Rev.*, 1957, **108**, 1246.
19. N. J. Harrick, R. G. Barnes, P. J. Bray, and N. F. Ramsey, *Phys. Rev.*, 1953, **90**, 260.
20. N. F. Ramsey, 'Molecular Beams', Clarendon Press: Oxford, 1956, p. 1454.
21. W. E. Quinn, J. M. Baker, J. T. LaTourrette, and N. F. Ramsey, *Phys. Rev.*, 1958, **112**, 1929.
22. J. R. Gains, P. C. Souers, E. M. Fearon, J. D. Sater, and E. R. Mapoles, *Phys. Rev. B*, 1989, **39**, 3943.
23. C. S. Johnson, Jr. and J. S. Waugh, *J. Chem. Phys.*, 1962, **36**, 2266.
24. P. R. McCourt, in 'NMR Basic Principles and Progress', eds P. Diehl, B. Fluck, and R. Kosfeld, Springer Verlag: Berlin, 1976, p. 56.
25. B. D. Nageswara Rao and L. R. Anders, *Phys. Rev.*, 1967, **140**, A112.
26. P. C. Souers, E. M. Fearon, J. D. Sater, E. R. Mapoles, J. R. Gaines, and P. A. Fedders, *J. Voc. Sci. Tec. A.*, 1991, **9**, 232.
27. R. S. Wagner, R. L. Armstrong, E. C. Bissonette, and F. R. W. McCourt, *J. Chem. Phys.*, 1990, **92**, 5907.
28. J. M. Deutch and I. Oppenheim, in 'Advances in Magnetic Resonance', ed J. S. Waugh, Academic Press: New York, 1966, p. 225.
29. R. B. Bird, W. E. Stewart, and L. N. Lightfoot, 'Transport Phenomena', Wiley: New York, 1960, Chapter 16.
30. S. Kim and K. P. Johnston, *Ind. Eng. Chem. Res.*, 1987, **26**, 1206.
31. J. F. Brennecke and C. A. Eckert, in *Proceedings of the International Symposium on Supercritical Fluids*, Nice, October, 1988.
32. K. P. Johnston, S. Kim, and J. Coombes, in 'Supercritical Fluid Science and Technology', eds K. P. Johnston and J. Penninger, ACS Symposium Series No. 406, American Chemical Society: Washington, DC, 1989.
33. P. G. Jessop, T. Ikariya, and R. Noyori, *Science*, 1995, **269**, 1065–1069.
34. T. J. Bruno and J. F. Ely, eds, 'Supercritical Fluid Technology – Reviews in Modern Theory and Applications', CRC Press: Boca Raton, FL, 1991.
35. E. Klesper, *Angew. Chem. Int. Ed. Engl.*, 1978, **17**, 738–746.
36. (a) J. W. Tom and P. G. Debenedetti, *Ind. Eng. Chem. Res.*, 1993, **32**, 2118–2128; (b) P. G. Debenedetti, *Chem. Eng. Sci.*, 1987, **42**, 2203–2212.
37. S. Kim and K. P. Johnston, *Ind. Eng. Chem. Res.*, 1987, **26**, 1206–1213.

38. (a) H. D. Cochran and L. L. Lee, in 'Supercritical Fluid Science and Technology – Reviews in Modern Theory and Applications', eds T. J. Bruno and J. F. Ely, CRC Press: Boca Raton, FL, 1991; (b) K. P. Johnston and J. Penninger, eds, 'Supercritical Fluid Science and Technology', ACS Symposium Series No. 406, American Chemical Society: Washington, DC, 1989, Chapter 3.
39. S. Bai, C. M. V. Taylor, F. Liu, C. L. Mayne, R. J. Pugmire, and D. M. Grant, *J. Phys. Chem. B*, 1997, **101**, 2923–2928.
40. C. M. V. Taylor, S. Bai, C. L. Mayne, and D. M. Grant, *J. Phys. Chem. B*, 1997, **101**, 5652–5658.
41. J. P. Blitz, C. R. Yonker, and R. D. Smith, *J. Phys. Chem.*, 1989, **93**, 6661–6665.
42. J. L. Fulton, G. G. Yee, and R. D. Smith, *J. Am. Chem. Soc.*, 1991, **113**, 8327–8334.
43. C. R. Yonker, S. L. Frye, D. R. Kalkwarf, and R. D. Smith, *J. Phys. Chem.*, 1986, **90**, 3022–3026.
44. C. R. Yonker and R. D. Smith, *J. Phys. Chem.*, 1988, **92**, 2374–2378.
45. J. Zagrobelny and F. V. Bright, *J. Am. Chem. Soc.*, 1993, **115**, 701–707.
46. T. A. Betts, J. Zagrobelny, and F. V. Bright, *J. Am. Chem. Soc.*, 1992, **114**, 8163–8171.
47. D. M. Grant, C. L. Mayne, F. Liu, and T. X. Xiang, *Chem. Rev.*, 1991, **91**, 1591–1624.
48. P. Etesse, J. A. Zega, and R. Kobayashi, *J. Chem. Phys.*, 1992, **97**, 2022–2029.
49. S. Bai, C. L. Mayne, R. J. Pugmire, and D. M. Grant, *J. Chem. Phys.*, 1997, **101**, 2923–2928.
50. C. J. Jameson, A. K. Jameson, N. C. Smith, and K. Jackowski, *J. Chem. Phys.*, 1987, **86**, 2717–2722.
51. D. M. Lamb, S. T. Adamy, K. W. Woo, and J. Jonas, *J. Phys. Chem.*, 1989, **93**, 5002–5005.
52. P. Etesse, J. A. Zega, and R. Kobayashi, *J. Chem. Phys.*, 1992, **97**, 2022–2029.
53. P. Etesse, A. M. Ward, and R. Kobayashi, *Physica B*, 1993, **183**, 45–52.
54. P. Etesse, W. G. Chapman, and R. Kobayashi, *Mol. Phys.*, 1993, **80**, 1145–1164.
55. D. M. Pfund, T. S. Zemanian, J. C. Linehan, J. L. Fulton, and C. R. Yonker, *J. Phys. Chem.*, 1994, **98**, 11 846–11 857.
56. S. Bai and C. R. Yonker, *J. Phys. Chem. A*, 1998, **102**, 8641–8647.
57. E. W. Lang and H. D. Ludemann, *Prog. NMR Spectrosc.*, 1993, **25**, 507.
58. D. M. Grant, C. L. Mayne, F. Liu, and T. X. Xiang, *Chem. Rev.*, 1991, **91**, 1591–1624.
59. C. J. Jameson, *Chem. Rev.*, 1991, **91**, 1375–1395.
60. R. K. Harris, 'Nuclear Magnetic Resonance Spectroscopy', The Bath Press: Avon, UK, 1986, Chapter 4.
61. F. Liu, W. J. Horton, C. L. Mayne, T. X. Xiang, and D. M. Grant, *J. Am. Chem. Soc.*, 1992, **114**, 5281–5294.
62. Y. J. Kim and J. Jonas, *J. Phys. Chem.*, 1995, **99**, 6777–6788.
63. J. L. Dote, D. Kivelson, and R. N. Schwartz, *J. Phys. Chem.*, 1981, **85**, 2169–2180.
64. M. Roy and S. Doraiswamy, *J. Chem. Phys.*, 1993, **98**, 3213–3223.
65. R. M. Anderson and J. F. Kauffman, *J. Phys. Chem.*, 1994, **98**, 12 117–12 124.
66. R. M. Anderson and J. F. Kauffman, *J. Phys. Chem.*, 1995, **99**, 13 759–13 762.
67. J. A. Jossi, L. I. Stiel, and G. Thodos, *AIChE J.*, 1961, **7**, 625.
68. C.-M. Hu and R. Zwanzig, *J. Chem. Phys.*, 1974, **60**, 4354–4357.
69. S. Bai, C. M. V. Taylor, F. Liu, C. L. Mayne, R. J. Pugmire, and D. M. Grant, *J. Phys. Chem. B.*, 1997, **101**, 2923–2928; C. M. V. Taylor, S. Bai, C. L. Mayne, and D. M. Grant, *J. Phys. Chem. B*, 1997, **101**, 5652–5658.
70. D. Ben-Amotz and T. W. Scott, *J. Chem. Phys.*, 1987, **87**, 3739.
71. B. L. Armstrong and J. Courtney, *Can. J. Phys.*, 1972, **50**, 1262–1272.
72. A. A. Maryott, M. S. Malmberg, and K. T. Gillen, *Chem. Phys. Lett.*, 1974, **25**, 169–174.
73. P. Etesse, J. A. Zega, and R. Kobayashi, *J. Chem. Phys.*, 1992, **97**, 2022–2029.
74. J. Kestin and W. A. Wakeham, in 'Transport Properties of Fluids: Thermal Conductivity, Viscosity and Diffusion Coefficients', CINDAS Data Series Material Properties, ed C. Y. Ho, Hemisphere Publishing: New York, 1988, Vol. 1.
75. T. R. Marrero and E. A. Mason, *J. Phys. Chem. Ref. Data*, 1972, **1**, 1.
76. I. Swaid and G. M. Schneider, *Ber. Bunsenges. Phys. Chem.*, 1979, **83**, 969.
77. R. Feist and G. M. Schneider, *Sep. Sci. Technol.*, 1980, **17**, 261.
78. Z. Balenovic, M. Myers, and J. C. Giddings, *J. Chem. Phys.*, 1970, **52**, 915.
79. H. Saad and E. Gulari, *Ber. Bunsenges. Phys. Chem.*, 1984, **88**, 834.
80. H. Saad and E. Gulari, *J. Phys. Chem.*, 1984, **88**, 136.
81. J. Jonas and D. M. Lamb, in 'ACS Symposium Series No. 329', eds T. G. Squires and M. E. Paulaitis, American Chemical Society: Washington, DC, 1987.
82. W. J. Lamb, G. A. Hoffmann, and J. Jonas, *J. Chem. Phys.*, 1981, **74**, 6875.
83. I. T. Horváth and J. M. Millar, *Chem. Rev.*, 1991, **91**, 1339–1351.
84. G. B. Benedek and E. M. Purcell, *J. Chem. Phys.*, 1954, **22**, 2003.
85. M. E. Smith and J. H. Strange, *Meas. Sci. Technol.*, 1997, **7**, 449–475.
86. B. Lance and J. Jonas, *Annu. Rep. NMR Spectrosc.*, 1997, **33**, 115–150.
87. J. W. Rathke, *J. Magn. Reson.*, 1989, **85**, 150–155.
88. K. Woelk, R. W. Rathke, and R. J. Klinger, *J. Magn. Reson. A*, 1994, **109**, 137–146.
89. C. R. Yonker, T. S. Zemanian, S. L. Wallen, J. C. Linehan, and J. A. Franz, *J. Magn. Reson. A*, 1995, **113**, 102.
90. D. C. Roe, *J. Magn. Reson.*, 1985, **63**, 388.
91. I. T. Horvath and E. C. Ponce, *Rev. Sci. Instrum.*, 1991, **62**, 1104.
92. I. T. Horvath and J. M. Millar, *Chem. Rev.*, 1991, **91**, 1339.
93. S. Bai, C. M. Taylor, C. L. Mayne, R. J. Pugmire, and D. M. Grant, *Rev. Sci. Instrum.*, 1996, **76**, 240–243.
94. S. L. Wallen, L. K. Schoenbachler, E. D. Dawson, and M. A. Blatchford, *Anal. Chem.*, 2000, **72**, 4230–4234.
95. R. Bertani, M. Mali, J. Roos, and D. Brinkmann, *Rev. Sci. Instrum.*, 1992, **63**, 3303.
96. M. Kanakubo, T. Aizawa, T. Kawakami, O. Sato, Y. Ikushima, K. Hatakeda, and N. Saito, *J. Phys. Chem. B*, 2000, **104**, 2749–2758.
97. J. C. Linehan, S. L. Wallen, C. R. Yonker, T. E. Bitterwolf, and J. T. Bays, *J. Am. Chem. Soc.*, 1997, **119**, 10 170–10 177.
98. M. R. Ehrhardt, P. F. Flynn, and A. J. Wand, *J. Biomol. NMR*, 1999, **14**, 75–78.
99. C. R. Yonker, J. C. Linehan, and J. L. Fulton, *J. Supercrit. Fluids*, 1998, **14**, 9–16.
100. J. W. Rathke, R. J. Klinger, R. E. Gerald II, K. W. Kramarz, and K. Woelk, *Prog. NMR Spectrosc.*, 1997, **30**, 209.
101. S. Kainz, A. Brinkmann, W. Leitner, and A. Pfalz, *J. Am. Chem. Soc.*, 1999, **121**, 6421–6429.

Biographical Sketches

Gunilla B. Jacobson, *b* 1969. Ph.D. 1996, Organic Chemistry, University of Uppsala, Sweden. Postdoctoral Research Associate with Keith P. Johnston, Univ. of Texas, Austin, 1997–1998. Research

Associate with William Tumas, Los Alamos National Laboratory, 1998–1999. Technical Staff Member, Los Alamos National Laboratory, 2000–present. Approx 30 publications. Current research interests: reactions, separations, and materials modifications using supercritical fluid technology.

Craig M. V. Taylor, *b* 1962. M.S., 1987 Organometallic Chemistry, New Mexico Institute of Mining and Technology, Ph.D. 1999, Physical Chemistry, University of Utah (supervisor David M. Grant) 1985–87 Research Associate on Supercritical Fluid Tertiary Oil Recovery, Petroleum Recovery Research Center Socorro New Mexico. 1987–94 Scientist Los Alamos National Laboratory (LANL). 1994–98 Principal Investigator Supercritical Fluids Facility, LANL. Leader of Applied Chemical Technologies Group, Chemistry Division, LANL 1998–present. Approx 25 publications. Current research interests: Supercritical Fluids Applications.

COSY Spectra: Quantitative Analysis

Alex D. Bain

McMaster University, Hamilton, Ontario, Canada

1	Introduction	1
2	COSY on a Two-Spin System	1
3	Larger Spin Systems	7
4	Fast Pulsing Artifacts	7
5	Conclusions	7
6	Related Articles	7
7	References	7

1 INTRODUCTION

The COSY[1] experiment (Figure 1) is probably the single most important two-dimensional NMR experiment. The experiment provides a homonuclear chemical shift correlation: if two spins are connected by a scalar coupling, then the COSY spectrum will show a pair of symmetrical cross peaks between the diagonal peaks of two spins (see ***COSY Two-Dimensional Experiments***). Although the SECSY experiment was often used for homonuclear correlation,[2,3] COSY is the one that has survived. It is the simplest pulse sequence, requires no prior knowledge of the spin parameters, is the easiest to analyze theoretically, provides some of the most useful structural information, and is probably the most widely used 2D experiment. For these reasons, there are several variations on the basic experiment. To begin with, a 2D experiment is not just a pulse sequence but also the associated phase cycling sequence, so that must be considered. COSY has also been the subject of many theoretical investigations. The information that it provides is often simply qualitative (on what is coupled to what), but it is important to understand the quantitative basis of COSY as well.

A quantitative analysis of COSY is needed to understand the conditions under which the experiment will work. Many spin systems have a variety of coupling constants ranging from large geminal couplings of 15 Hz or more, through typical vicinal couplings of a few Hz, down to long-range couplings of a fraction of a Hz. Under what circumstances will these couplings show up as cross peaks in a COSY? In a complex system, a multiplet will consist of several splittings corresponding to couplings to several different spins. What are the intensity ratios within a multiplet? Do any new frequencies appear in f_1? In a COSY cross peak connecting two spins, how does the active coupling (the one between the two spins in question) appear relative to the passive couplings to the other spins in the system? What happens if the flip angles or the phase cycling sequence is changed? What happens if the spin system does not reach equilibrium between pulse sequences? What is the role of phase cycling and quadrature detection? These are just some of the questions that arise from a detailed examination of the COSY experiment.

Understanding the COSY experiment is relatively easy since it is such a simple experiment. The manipulations are straightforward matrix operations and no more difficult than simple spectral analysis. COSY can also serve as a prototype for all multidimensional experiments, since it illustrates many of the principles seen in more complex techniques. In this article, we discuss a simple COSY experiment on a two-spin system in detail. This will cover many of the points raised in the previous paragraphs and serve as a basis for a discussion of more complex systems.

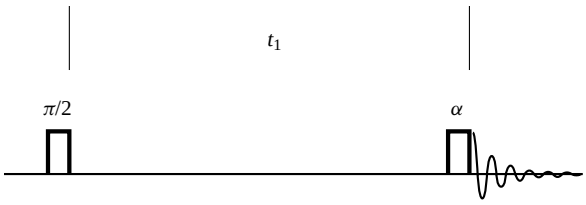

Figure 1 COSY pulse sequence. The initial $\pi/2$ pulse excites the spin system which evolves during the regularly-incremented delay t_1. The second pulse is called the mixing pulse and may have any flip angle, α. For many applications, $\alpha = \pi/2$ or $\alpha = \pi/4$

2 COSY ON A TWO-SPIN SYSTEM

The simplest system has two spins $\frac{1}{2}$, labeled A and B, with Larmor frequencies of ν_A and ν_B. These spins are scalar-coupled with a coupling constant of J, so the spectrum consists of two doublets. Figure 2 shows the energy levels and the allowed transitions. We assume the coupling is weak, so that all four lines in the spectrum have the same intensity. These four lines in the spectrum correspond to density matrix elements which oscillate at these four frequencies. The four lines will all mix with each other in a COSY, so there will be 16 lines in the two-dimensional spectrum. We can study the frequencies, intensities, and phases of these 16 lines by following the modulation of the basic spectrum in the 2D experiment.

2.1 Basic Theory

For any line in a spectrum at frequency ν(in the rotating frame of reference), there are two associated oscillating density matrix elements. These can be thought of as the x and the

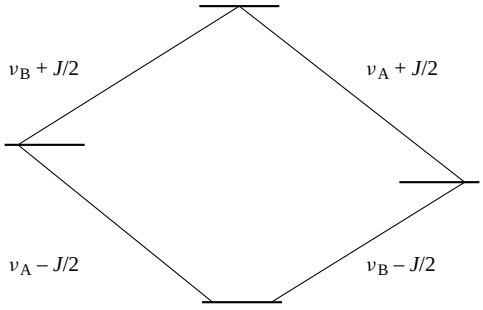

Figure 2 The energy levels of a two spin-$\frac{1}{2}$ system and the allowed single quantum transitions. The two spins, labeled A and B, have Larmor frequencies ν_A and ν_B, and are scalar coupling with a coupling constant of J

y magnetization, or as two counter-rotating magnetizations rotating at the appropriate frequency. We choose the latter picture, and denote the two density matrix elements as $|+\nu)$ and $|-\nu)$. Any coherence associated with the density matrix element $|+\nu)$ will evolve during a delay time, t, as $e^{+i\nu t}$. The terms positive and negative, strictly speaking, refer to the coherence level, a quantum number associated with each coherence. Of course, the frequencies may themselves be either positive or negative with respect to the carrier frequency, and coupling constants may have either sign. This provides the mathematical description of the rotating magnetization.

2.2 Excitation and Evolution

The COSY experiment consists of an excitation pulse, an evolution time t_1, a mixing pulse, and then detection. We will assume that the spin system is in equilibrium at the start of the sequence. The $\pi/2$ excitation pulse in Figure 1 creates coherence corresponding to the four lines in the spectrum, which we will allow to have unit intensity, for simplicity. There will be four positively-rotating elements and four negative ones. These will evolve during the evolution time, so that at the end of t_1 the positively-rotating density matrix elements are given by equation (1).

$$\left.\begin{aligned} |\nu_A + J/2) &= e^{+i(\nu_A + J/2)t_1} \\ |\nu_A - J/2) &= e^{+i(\nu_A - J/2)t_1} \\ |\nu_B + J/2) &= e^{+i(\nu_B + J/2)t_1} \\ |\nu_B - J/2) &= e^{+i(\nu_B - J/2)t_1} \end{aligned}\right\} \quad (1)$$

Similarly, the elements at negative frequency are given by equation (2).

$$\left.\begin{aligned} |-\nu_A - J/2) &= e^{-i(\nu_A + J/2)t_1} \\ |-\nu_A + J/2) &= e^{-i(\nu_A - J/2)t_1} \\ |-\nu_B - J/2) &= e^{-i(\nu_B + J/2)t_1} \\ |-\nu_B + J/2) &= e^{-i(\nu_B - J/2)t_1} \end{aligned}\right\} \quad (2)$$

The mixing pulse in the COSY experiment ends the evolution. The effect of this pulse is the key to the experiment, determining what frequencies will appear in f_1 and with which intensities and phases. In general, the calculation of the effect of a pulse with general flip angle and phase on a general spin system is quite complex and beyond the scope of this article. The simple evolution during a delay, as above, is relatively easy to picture, but the effect of a pulse is the subject of several theoretical descriptions for pulse NMR.[4,5]

2.3 Frequencies in a COSY Spectrum

The mixing pulse should not introduce any new frequencies into the spectrum, so that any frequency that appears in f_1 in a COSY spectrum should also be there in the simple 1D spectrum. The 1D spectrum may be quite complex (see ***Analysis of High-Resolution Solution State Spectra***), but regardless of how complicated the spectrum is no new frequencies will be present in f_1. The principal assumption behind this sweeping statement is that the spin system should be in equilibrium before the pulse sequence starts. This assumption is seldom true in routine practice of COSY. Artifacts[6] are quite common in COSY spectra, but these artifacts are usually simple multiples of the genuine f_1 frequencies. A more detailed discussion of these artifacts and strategies to suppress them is given later.

The reason that no new frequencies are introduced is that only single quantum transitions are excited and detected. A nonselective pulse acting on any spin system in equilibrium will produce only single quantum transitions: the normal equilibrium spectrum. If we ignore relaxation effects, the single quantum transitions will evolve only amongst themselves during the delay. Even though the mixing pulse may create all orders of multiple quantum coherence, only single quantum coherence can be detected directly. In fact, quadrature detection implies that only one of the two senses of precession will be detected, so that only one of the two sets, equation (1) or equation (2), will be observed. Hence, a two-pulse experiment like COSY acting on a spin system in equilibrium will only involve single quantum transitions.

The fact that frequencies in f_2 become frequencies in f_1 means that there is a symmetry to the COSY spectrum.[7] Cross peaks should always occur as symmetrically placed pairs about the main diagonal. This is a very powerful result. It can help us in sorting out genuine cross peaks from artifacts, since artifacts are very seldom symmetrical.

2.4 The Mixing Pulse

In the COSY experiment, where we are dealing only with single quantum coherence, the effect of the pulse is relatively simple. For a weakly coupled spin system subjected to pulses whose flip angles and phases are multiples of $\pi/2$, product operator methods are the most popular approach. In this article, we will take a more general approach in order to see what happens when we go beyond the simple systems. The possible frequencies of lines in f_1 are defined by the one-dimensional spectrum for all types of spin systems and flip angles/phases of the mixing pulse. We must calculate the intensities and phases of the lines under these circumstances.

The effect of a pulse is best handled by using the angular momentum properties of the spin system. A pulse is equivalent to a rotation of the frame of reference (see ***Radiofrequency Pulses: Response of Nuclear Spins***) and angular momentum functions, or spherical tensors, provide a natural basis for describing what happens during a rotation. For any spin system we can convert to a spherical tensor basis, and then the effect of a pulse is simply given by a Wigner matrix element, independent of the details of the spin system.

Among the single quantum transitions, the pulse can take a positive frequency and mix it with the other positive frequencies; it can take a positive frequency, reverse its sense of precession and mix it with the negative frequencies; or it can put a rotating magnetization back up on the z axis. We will ignore the magnetization put back along z and then treat each of the two other cases separately.

The matrix that takes the positive frequencies into the negative frequencies is given by equation (3). Equation (4) gives the matrix which takes the positive frequencies into themselves.

$$\begin{bmatrix} \frac{1}{2}\sin^2\frac{\alpha}{2}(1+\cos\alpha) & \frac{1}{2}\sin^2\frac{\alpha}{2}(1-\cos\alpha) & \frac{\sin^2\alpha}{4} & \frac{-\sin^2\alpha}{4} \\ \frac{1}{2}\sin^2\frac{\alpha}{2}(1-\cos\alpha) & \frac{1}{2}\sin^2\frac{\alpha}{2}(1+\cos\alpha) & \frac{-\sin^2\alpha}{4} & \frac{\sin^2\alpha}{4} \\ \frac{\sin^2\alpha}{4} & \frac{-\sin^2\alpha}{4} & \frac{1}{2}\sin^2\frac{\alpha}{2}(1+\cos\alpha) & \frac{1}{2}\sin^2\frac{\alpha}{2}(1-\cos\alpha) \\ \frac{-\sin^2\alpha}{4} & \frac{\sin^2\alpha}{4} & \frac{1}{2}\sin^2\frac{\alpha}{2}(1-\cos\alpha) & \frac{1}{2}\sin^2\frac{\alpha}{2}(1+\cos\alpha) \end{bmatrix} \tag{3}$$

$$\begin{bmatrix} \frac{1}{2}\cos^2\frac{\alpha}{2}(1+\cos\alpha) & \frac{1}{2}\cos^2\frac{\alpha}{2}(1-\cos\alpha) & \frac{-\sin^2\alpha}{4} & \frac{\sin^2\alpha}{4} \\ \frac{1}{2}\cos^2\frac{\alpha}{2}(1-\cos\alpha) & \frac{1}{2}\cos^2\frac{\alpha}{2}(1+\cos\alpha) & \frac{\sin^2\alpha}{4} & \frac{-\sin^2\alpha}{4} \\ \frac{-\sin^2\alpha}{4} & \frac{\sin^2\alpha}{4} & \frac{1}{2}\cos^2\frac{\alpha}{2}(1+\cos\alpha) & \frac{1}{2}\cos^2\frac{\alpha}{2}(1-\cos\alpha) \\ \frac{\sin^2\alpha}{4} & \frac{-\sin^2\alpha}{4} & \frac{1}{2}\cos^2\frac{\alpha}{2}(1-\cos\alpha) & \frac{1}{2}\cos^2\frac{\alpha}{2}(1+\cos\alpha) \end{bmatrix} \tag{4}$$

These equations are valid for any flip angle, α, of the mixing pulse applied to a weakly coupled spin system. For $\alpha = \pi$, note that the matrix in equation (4) vanishes completely and the only elements in equation (3) that survive are the ones that connect the two lines in each doublet together: elements (1,2), (2,1), (3,4), and (4,3). This is the mixing in the multiplets that gives rise to J-modulation in spin echoes (see ***Two-Dimensional J-Resolved Spectroscopy***).

The simple COSY experiment involves a $\pi/2$ mixing pulse, so we must include the effects of both matrices. Since we detect only one sense of precession, say the positive one, we need only calculate the coherences that contribute to that set. Therefore, to describe what the mixing pulse does, we multiply the coherences in equation (2) by the matrix in equation (3) — these are the coherences with a negative coherence level going into the positives. The result of this is given in equation (5).

$$\begin{aligned}
|\nu_A + J/2) &= \tfrac{1}{4}[+e^{-i(\nu_A+J/2)t_1} \\
&\quad +e^{-i(\nu_A-J/2)t_1} + e^{-i(\nu_B+J/2)t_1} - e^{-i(\nu_B-J/2)t_1}] \\
|\nu_A - J/2) &= \tfrac{1}{4}[+e^{-i(\nu_A+J/2)t_1} \\
&\quad +e^{-i(\nu_A-J/2)t_1} - e^{-i(\nu_B+J/2)t_1} + e^{-i(\nu_B-J/2)t_1}] \\
|\nu_B + J/2) &= \tfrac{1}{4}[+e^{-i(\nu_A+J/2)t_1} \\
&\quad -e^{-i(\nu_A-J/2)t_1} + e^{-i(\nu_B+J/2)t_1} + e^{-i(\nu_B-J/2)t_1}] \\
|\nu_B - J/2) &= \tfrac{1}{4}[-e^{-i(\nu_A+J/2)t_1} \\
&\quad +e^{-i(\nu_A-J/2)t_1} + e^{-i(\nu_B+J/2)t_1} + e^{-i(\nu_B-J/2)t_1}]
\end{aligned} \tag{5}$$

Added to this is the result of applying the matrix in equation (4) to the coherences in equation (1). The contribution of the positive coherences is given by equation (6).

$$\begin{aligned}
|\nu_A + J/2) &= \tfrac{1}{4}[+e^{+i(\nu_A+J/2)t_1} \\
&\quad +e^{+i(\nu_A-J/2)t_1} - e^{+i(\nu_B+J/2)t_1} + e^{+i(\nu_B-J/2)t_1}] \\
|\nu_A - J/2) &= \tfrac{1}{4}[+e^{+i(\nu_A+J/2)t_1} \\
&\quad +e^{+i(\nu_A-J/2)t_1} + e^{+i(\nu_B+J/2)t_1} - e^{+i(\nu_B-J/2)t_1}] \\
|\nu_B + J/2) &= \tfrac{1}{4}[-e^{+i(\nu_A+J/2)t_1} \\
&\quad +e^{+i(\nu_A-J/2)t_1} + e^{+i(\nu_B+J/2)t_1} + e^{+i(\nu_B-J/2)t_1}] \\
|\nu_B - J/2) &= \tfrac{1}{4}[+e^{+i(\nu_A+J/2)t_1} \\
&\quad -e^{+i(\nu_A-J/2)t_1} + e^{+i(\nu_B+J/2)t_1} + e^{+i(\nu_B-J/2)t_1}]
\end{aligned} \tag{6}$$

The final result is the sum of equations (5) and (6), to give the expressions in equation (7).

$$\begin{aligned}
|\nu_A + J/2) &= \tfrac{1}{4}[+\cos(\nu_A + J/2)t_1 + \cos(\nu_A - J/2)t_1 \\
&\quad -\sin(\nu_B + J/2)t_1 + \sin(\nu_B - J/2)t_1] \\
|\nu_A - J/2) &= \tfrac{1}{4}[+\cos(\nu_A + J/2)t_1 + \cos(\nu_A - J/2)t_1 \\
&\quad +\sin(\nu_B + J/2)t_1 - \sin(\nu_B - J/2)t_1] \\
|\nu_B + J/2) &= \tfrac{1}{4}[-\sin(\nu_A + J/2)t_1 + \sin(\nu_A - J/2)t_1 \\
&\quad +\cos(\nu_B + J/2)t_1 + \cos(\nu_B - J/2)t_1] \\
|\nu_B - J/2) &= \tfrac{1}{4}[+\sin(\nu_A + J/2)t_1 - \sin(\nu_A - J/2)t_1 \\
&\quad +\cos(\nu_B + J/2)t_1 + \cos(\nu_B - J/2)t_1]
\end{aligned} \tag{7}$$

This is the modulation of the lines resulting from the simple pulse sequence in Figure 1. The modulation is a cosine modulation, with the diagonal peaks (the peaks due to mixing within a multiplet) $\pi/2$ out of phase with the cross peaks, and the two cross peaks of opposite sign. Since this is a cosine modulation, a real Fourier transform (as distinct from a complex one) will extract the data. Depending on the phase correction used, the diagonal peaks will be dispersion in both dimensions and the cross peaks will be absorption in both f_1 and f_2. This is the basic COSY experiment (note that no phase cycling was done), but there are problems with it and many variations have been developed.

2.5 Different Types of COSY

The different types of COSY experiment generally do not change the basic pulse sequence in Figure 1, but rather vary the associated phase cycling scheme and the way that the data are transformed. One of the problems is that the cosine modulation in equation (7) cannot distinguish between positive and negative frequencies, so quadrature detection in f_1 is not possible. In itself this is not too much of a problem, since quadrature detection in f_1 does not give any signal to noise ratio advantage.[8] However, the lack of quadrature detection in f_1 in a homonuclear experiment prevents its use in f_2 where there is an advantage to its use.

Historically, the first solution to the problem was to use a complex FT, that is to use $e^{i\omega t}$ in the transform rather than $\cos(\omega t)$. When applied to the data in equation (7), this gives peaks at both positive and negative frequencies, since $\cos(\omega t) = 1/2(e^{i\omega t} + e^{-i\omega t})$. These peaks were called P-type and N-type peaks.[2] One or other of these can be removed by phase cycling — repeating the same pulse sequence, but with different phases in the pulses[9,10] (see ***Phase Cycling***). This removes (usually) the positive-to-positive transfer given by equation (6), so that the data have a complex modulation

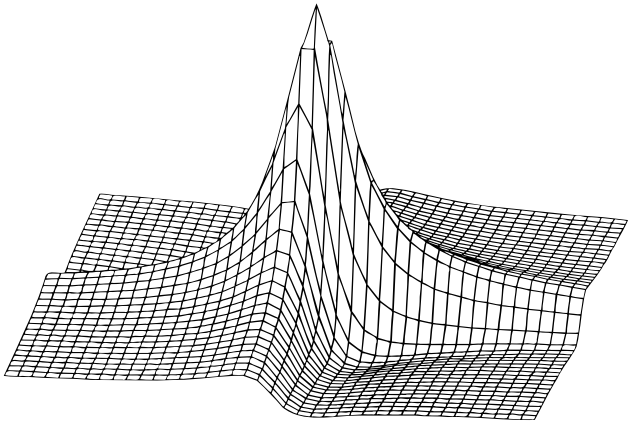

Figure 3 The so-called 'phase twist' lineshape often encountered in COSY spectra. In the center of the line the lineshape is pure absorption, but in the wings in each dimension it becomes more dispersion-like

given by equation (5). The disadvantage of this method is that the lineshapes no longer have a pure phase, but rather a so-called phase twist in which the phase in one dimension changes as one moves across the other dimension. Figure 3 shows the phase twist lineshape. This phase problem can be circumvented by the use of pseudoecho, or sine-bell type apodization functions, and a magnitude calculation rather than a phase correction after the 2D FT. This form of the COSY experiment is very popular and very simple to set up and process.

Figures 4, 5, 6, 7, and 8 show typical results from such an experiment on the molecule serine. Serine is a convenient sample for experimenting with 2D NMR since the chemical shifts of the protons can be easily manipulated by changing the pH of the solution.

Two other solutions to the quadrature detection problem keep the pure phase lineshapes. One is effectively to move $f_1 = 0$ through the use of the time proportional phase increment (TPPI) and still use a real FT.[11] The other method is to collect a parallel data set that is phase-shifted, so that there is true complex data in both dimensions. In this case, a complex FT can be used in both domains.[12] Both methods are widely used and except for some minor details in the baseline the two are essentially equivalent.[13]

The final problem is to make all of the lines, both cross peaks and diagonal peaks, the same phase. If we use a double quantum filter in the mixing pulse,[14,15] this achieves the goal of a homonuclear correlation with pure absorption lines.

For the analysis of the fine structure within a multiplet, the COSY experiment with phase sensitive transforms and double quantum filtering is the method of choice. For quick, qualitative experiments to determine a rough connectivity network, the magnitude calculation COSY is quicker to set up and process (in fact it can easily be set up automatically by the spectrometer). Depending on what sort of information is required, one of these two experiments is used in most cases.

2.6 Intensities of Cross Peaks and Digitization Effects

The fact that the two elements in the cross peak in equations (5) and (6), are of opposite sign is a general one: the cross peaks always have zero net intensity if the acquisition begins

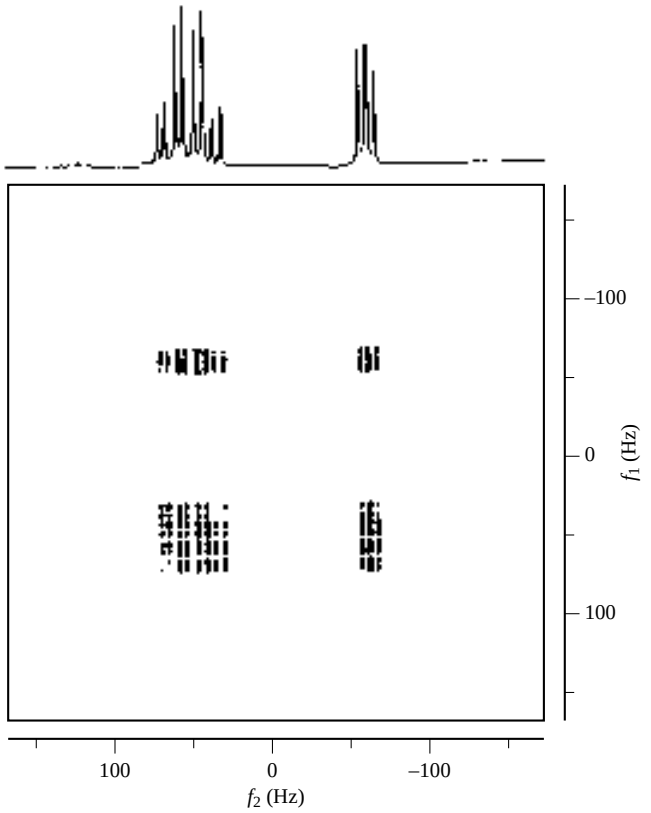

Figure 4 Magnitude calculation COSY on serine, $NH_2CH(CH_2OH)(COOH)$, in D_2O at pH 10 at a spectrometer frequency of 300 MHz. The mixing pulse had a flip angle of $\pi/2$. The raw data consisted of 256 FIDs of 1 k data points, which were Fourier-transformed using an unshifted sine-bell squared apodization in both dimensions. The spectral width in both dimensions was 338 Hz, giving a digital resolution of 0.66 Hz per point. The α proton in serine is at low frequency and the two β protons, β and β', are 0.339 and 0.410 ppm to high frequency at this pH. The measured coupling constants are $J_{\alpha\beta} = 5.9$ Hz, $J_{\alpha\beta'} = 4.3$ Hz, and $J_{\beta\beta'} = -11.2$ Hz

immediately after the mixing pulse. For a weakly coupled AX system as above, the ratio of the peaks is 1: − 1. For more complex multiplets, the relative intensities can be built up from the AX case as for 1D spectra. For equivalent spins, Pascal's triangle can be used so that for the cross peak in an AX_2 system the ratios of the peaks are 1:0: − 1 and the peaks in an AX_3 system are in the proportion of 1:1: − 1: − 1. These ratios will be evident in a phase sensitive COSY, but a magnitude calculation COSY will mask the signs of the peaks.

In a more complex spin system, the distinction between active and passive couplings becomes important. Within a given set of cross peaks, representing the correlation between spin A and spin X, the J_{AX} is the active coupling. This coupling will appear as an antiphase arrangement, as above, but all the other couplings will appear as normal. The splitting due to coupling from A to another spin, M, will appear in phase within the AX cross-peak group. Of course, in the cross-peak group joining A and M, then J_{AM} will be the active coupling.

As the coupling approaches zero the cross peak should vanish, so the net cross-peak intensity must be zero. However, adding a delay after the mixing pulse before the start of the acquisition will enhance cross peaks due to long-range coupling. This delay should be some fraction of the coupling,

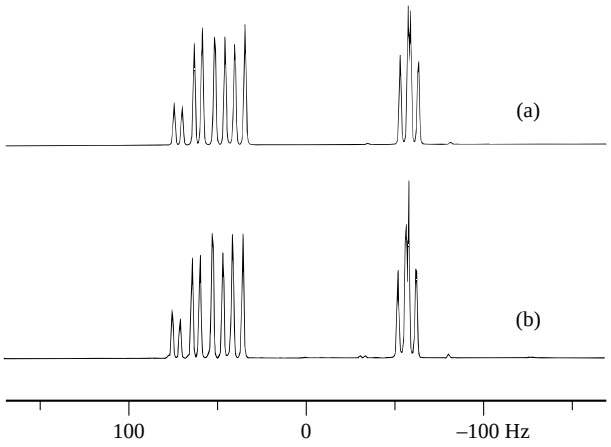

Figure 5 Plot of a row from the data matrix in Figure 4 (trace b) and a simulation of the same data (trace a). The row corresponds to the row of peaks at the bottom of the spectrum (highest frequency in f_1). The spectrum was simulated using the SIMPLTN program which provides an exact density matrix calculation

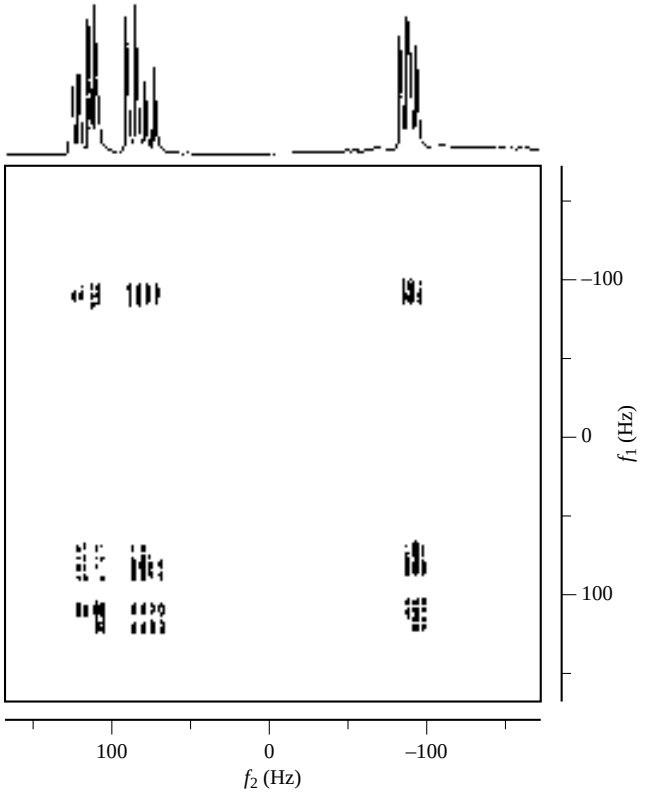

Figure 6 Magnitude calculation COSY on the same serine sample as in Figure 4, also with a mixing pulse of $\pi/2$ but at 500 MHz. The spectral width and the number of experiments is the same as in Figure 4

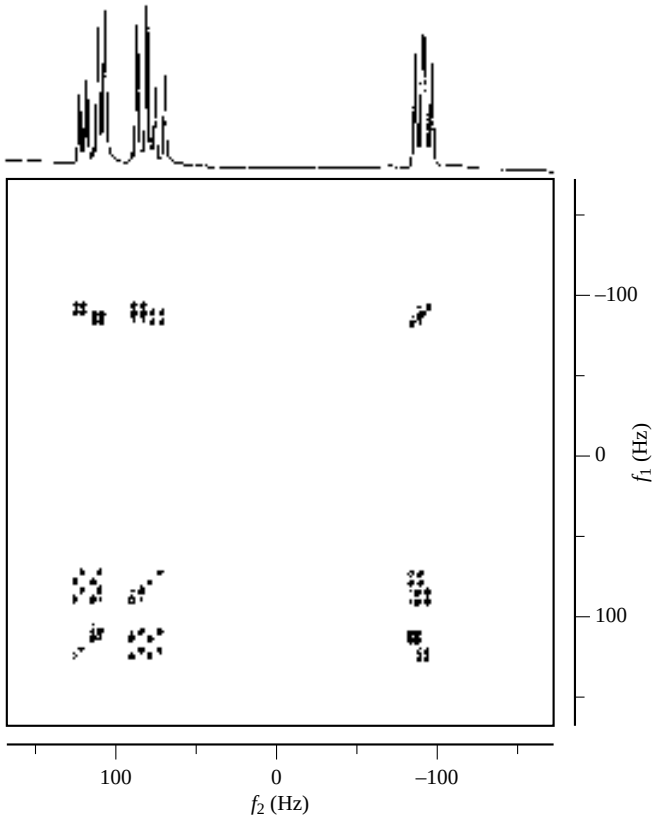

Figure 7 Magnitude calculation COSY on serine at 500 MHz, but with a mixing pulse of $\pi/4$. All other parameters are as in Figures 4 and 6

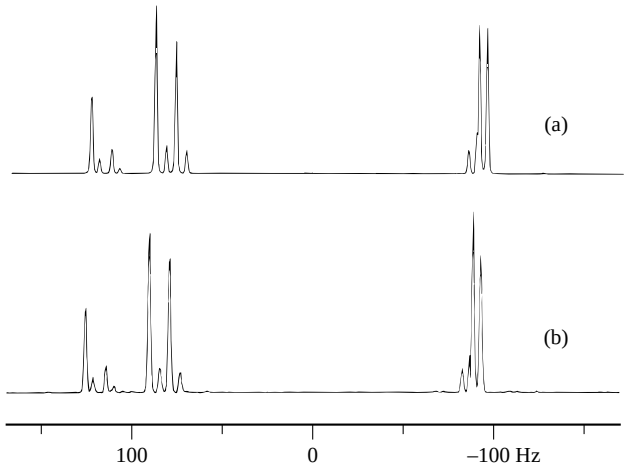

Figure 8 Plot of the row of peaks at the bottom (highest f_1 frequency) of the 2D spectrum in Figure 7[trace (b)]. Trace (a) represents a SIMPLTN simulation of the data

so that the peaks that are exactly out of phase after the mixing pulse have some time to approach being in phase. Similarly, a delay before the mixing pulse will allow multiplets time to get out of phase and enhance polarization transfer. If these delays are present, then the cross peak will acquire some net intensity and cross peaks due to quite small couplings will be evident in the 2D spectrum.[16]

Similarly, poor digitization should cause cross peaks to disappear. If the digitization is such that a single point in two dimensions represents an entire set of cross peaks due to two multiplets, that point should have zero intensity. Very good digitization should give accurate intensities. In between these extremes, however, the behavior is somewhat unusual. When the digitization (in Hz per point) approaches the value of the

coupling constant J (in Hz), simulations show that the apparent intensity of the cross peak rises rather than falls. The apparent intensity reaches a maximum at a ratio of J/digitization of approximately 1, and there is still significant intensity when the coupling is only 0.2 of the digitization.[17] This effect, combined with the possible use of fixed delays around the mixing pulse, permits us to use quite small data matrices and still see useful correlations.

Provided digital resolution is not a problem, the cross peak between an A spin and an X spin will be as follows. If it is the peak in f_1 which corresponds to the A frequency in f_2, then the rows will resemble the A spectrum and the columns the X spectrum, as shown in Figure 4. Similarly, the other cross peak will resemble the X spectrum along the f_2 rows and the A spectrum in f_1. The only difference will be that the splittings due to the A–X coupling will appear as an antiphase, 1: − 1, orientation, but all other couplings will be normal.

2.7 Flip Angle Effects

If we use the simple trigonometric identity given in equation (8), we can see from equation (3) that three of the lines in the simple two-spin COSY behave identically with respect to the flip angle of the mixing pulse. The odd line is the off-diagonal member of the diagonal group of peaks—the peak due to mixing of one line with the other line in the doublet. In Figure 2, we can observe that these are the only pairs of transitions that do not share at least one energy level. All other peaks in the 2D spectrum come from pairs of 'connected' transitions.

$$\sin^2\alpha = 2\sin^2\frac{\alpha}{2}(1+\cos\alpha) \tag{8}$$

Equation (3) predicts that this peak from 'unconnected' transitions will decrease in intensity relative to the others as the flip angle of the mixing pulse is decreased. For a flip angle of $\pi/4$, this peak is approximately 17% of the others. Judicious choice of a contour level in the plot of a 2D spectrum will make this peak disappear, so the diagonal region of the spectrum is much cleaner. This is shown by comparing Figures 6 and 7. As Figure 8 shows, the peaks do not disappear.

Another consequence of this shows up in the cross peaks of bigger spin systems. Here also there are peaks due to pairs of unconnected transitions. Depending on the relative signs of couplings, this gives a characteristic 'tilt' to the cross peak. This can be used to assign the relative signs of couplings. In an AMX spin system, the tilt of the cross peak between A and M will indicate the relative signs of J_{AX} versus J_{MX}. Figures 6 and 7 show this effect for serine. The cross peak between the two β protons at the high-frequency side of the spectrum tilts one way, since the couplings to the third (α) proton are both vicinal and of the same sign. However the α–β cross peaks tilt the other way because of the opposite signs of the vicinal and geminal couplings.

The use of a different flip angle for the mixing pulse will decrease the intensity of these peaks but it will not eliminate them, as shown in Figures 7 and 8. If the peaks are to be eliminated, then another variation of the simple experiment, ECOSY, should be used.[18] This is more complex to set up, but it will give more reliable and useful intensities. This will be useful, for example, in the automatic interpretation of COSY spectra.

2.8 Strong Coupling Effects

Most homonuclear spin systems show some signs of strong coupling. This is more evident in the intensities of the lines rather than in the line positions. This is because the intensities of the lines are determined by the xy magnetizations of the spin system, which are perturbed to first order by strong coupling. The line positions depend on the energy levels and z magnetizations, which are perturbed only to second order. The general rule that no new frequencies will appear in f_1 in COSY still holds. However, since the COSY experiment involves the mixing of xy magnetizations it is clear that intensities will be greatly affected by strong coupling.

As an example, let us consider a magnitude calculation COSY on a simple AB spin system. In such a system, we need only consider the negative frequency coherences, as in equation (2), and how much is transferred to the positives for detection, as in equation (5). For such a system, it is convenient to define the frequencies of the four lines in the spectrum in the following way. Let ν_0 be the average of the A and B Larmor frequencies, and let δ be the difference of the Larmor frequencies in Hz. If J is the scalar coupling constant between A and B, then we can define $C = (J^2 + \delta^2)^{1/2}$ and an angle, θ, by the relationship $\sin(2\theta) = J/C$. For simplicity of notation, let $c = \cos(\theta)$ and $s = \sin(\theta)$. For simplicity, let us number the frequencies as in equation (9).

$$\left.\begin{aligned}\nu_1 &= \nu_0 + C/2 + J/2\\ \nu_2 &= \nu_0 + C/2 - J/2\\ \nu_3 &= \nu_0 - C/2 + J/2\\ \nu_4 &= \nu_0 - C/2 - J/2\end{aligned}\right\} \tag{9}$$

With these definitions, we can calculate the evolution of the negative frequencies up to the mixing pulse, as in equation (2), to give equation (10).

$$\left.\begin{aligned}|-\nu_1) &= (c-s)\mathrm{e}^{-\mathrm{i}(\nu_0+C/2+J/2)t_1}\\ |-\nu_2) &= (c+s)\mathrm{e}^{-\mathrm{i}(\nu_0+C/2-J/2)t_1}\\ |-\nu_3) &= (c+s)\mathrm{e}^{-\mathrm{i}(\nu_0-C/2+J/2)t_1}\\ |-\nu_4) &= (c-s)\mathrm{e}^{-\mathrm{i}(\nu_0-C/2-J/2)t_1}\end{aligned}\right\} \tag{10}$$

Note that the coherences do not have equal intensity as was the case in the weakly coupled spin system.

Let us only consider the case of a flip angle of the mixing pulse of $\pi/2$, in order to simplify the calculation somewhat. Using published methods,[19,20] it is relatively easy to show that the effect of the mixing pulse on the coherences in equation (10) is given by the matrix in equation (11). This is the strong-coupling equivalent of equation (3) for a flip angle of $\pi/2$.

$$1/4\begin{bmatrix}(c-s)^2 & c^2-s^2 & c^2-s^2 & -(c+s)^2\\ c^2-s^2 & (c+s)^2 & -(c-s)^2 & c^2-s^2\\ c^2-s^2 & -(c-s)^2 & (c+s)^2 & c^2-s^2\\ -(c+s)^2 & c^2-s^2 & c^2-s^2 & (c-s)^2\end{bmatrix} \tag{11}$$

Finally, strong coupling also implies that not all lines are detected with equal intensity. This means that the final intensities are the result of multiplying the coherences in

equation (10) by the matrix in equation (11) and then multiplying by the detection efficiency, as in equation (12).

$$\left.\begin{aligned}
|\nu_1) = {} & \tfrac{1}{4}(c-s)[+(c-s)^2(c-s)\mathrm{e}^{-\mathrm{i}\nu_1 t_1} + (c^2-s^2)(c+s)\mathrm{e}^{-\mathrm{i}\nu_2 t_1} \\
& +(c^2-s^2)(c+s)\mathrm{e}^{-\mathrm{i}\nu_3 t_1} - (c+s)^2(c-s)\mathrm{e}^{-\mathrm{i}\nu_4 t_1}] \\
|\nu_2) = {} & \tfrac{1}{4}(c+s)[+(c^2-s^2)(c-s)\mathrm{e}^{-\mathrm{i}\nu_1 t_1} + (c+s)^2(c+s)\mathrm{e}^{-\mathrm{i}\nu_2 t_1} \\
& -(c-s)^2(c+s)\mathrm{e}^{-\mathrm{i}\nu_3 t_1} + (c^2-s^2)(c-s)\mathrm{e}^{-\mathrm{i}\nu_4 t_1}] \\
|\nu_3) = {} & \tfrac{1}{4}(c+s)[+(c^2-s^2)(c-s)\mathrm{e}^{-\mathrm{i}\nu_1 t_1} - (c-s)^2(c+s)\mathrm{e}^{-\mathrm{i}\nu_2 t_1} \\
& +(c+s)^2(c+s)\mathrm{e}^{-\mathrm{i}\nu_3 t_1} + (c^2-s^2)(c-s)\mathrm{e}^{-\mathrm{i}\nu_4 t_1}] \\
|\nu_4) = {} & \tfrac{1}{4}(c-s)[-(c+s)^2(c-s)\mathrm{e}^{-\mathrm{i}\nu_1 t_1} + (c^2-s^2)(c+s)\mathrm{e}^{-\mathrm{i}\nu_2 t_1} \\
& +(c^2-s^2)(c+s)\mathrm{e}^{-\mathrm{i}\nu_3 t_1} + (c-s)^2(c-s)\mathrm{e}^{-\mathrm{i}\nu_4 t_1}]
\end{aligned}\right\} \quad (12)$$

Equation (12) shows the intensities of all the lines in a COSY spectrum of an AB spin system. If we apply the trigonometric identities in equation (13), we can further simplify the expressions.

$$\left.\begin{aligned}
&\cos^2\theta - \sin^2\theta = \cos 2\theta \\
&(\cos\theta + \sin\theta)^2 = (1 + \sin 2\theta) \\
&(\cos\theta - \sin\theta)^2 = (1 - \sin 2\theta)
\end{aligned}\right\} \quad (13)$$

The final expressions for the COSY on an AB system are given in equation (14).

$$\left.\begin{aligned}
|\nu_1) = {} & \tfrac{1}{4}[+(1-\sin 2\theta)^2\mathrm{e}^{-\mathrm{i}\nu_1 t_1} + \cos^2 2\theta\mathrm{e}^{-\mathrm{i}\nu_2 t_1} \\
& +\cos^2 2\theta\mathrm{e}^{-\mathrm{i}\nu_3 t_1} - \cos^2 2\theta\mathrm{e}^{-\mathrm{i}\nu_4 t_1}] \\
|\nu_2) = {} & \tfrac{1}{4}[+\cos^2 2\theta\mathrm{e}^{-\mathrm{i}\nu_1 t_1} + (1+\sin 2\theta)^2\mathrm{e}^{-\mathrm{i}\nu_2 t_1} \\
& -\cos^2 2\theta\mathrm{e}^{-\mathrm{i}\nu_3 t_1} + \cos^2 2\theta\mathrm{e}^{-\mathrm{i}\nu_4 t_1}] \\
|\nu_3) = {} & \tfrac{1}{4}[+\cos^2 2\theta\mathrm{e}^{-\mathrm{i}\nu_1 t_1} - \cos^2 2\theta\mathrm{e}^{-\mathrm{i}\nu_2 t_1} \\
& +(1+\sin 2\theta)^2\mathrm{e}^{-\mathrm{i}\nu_3 t_1} + \cos^2 2\theta\mathrm{e}^{-\mathrm{i}\nu_4 t_1}] \\
|\nu_4) = {} & \tfrac{1}{4}[-\cos^2 2\theta\mathrm{e}^{-\mathrm{i}\nu_1 t_1} + \cos^2 2\theta\mathrm{e}^{-\mathrm{i}\nu_2 t_1} \\
& +\cos^2 2\theta\mathrm{e}^{-\mathrm{i}\nu_3 t_1} + (1-\sin 2\theta)^2\mathrm{e}^{-\mathrm{i}\nu_4 t_1}]
\end{aligned}\right\} \quad (14)$$

The true diagonal peaks show the expected behavior: the result of mixing a line with itself gives the square of the intensity in the 1D spectrum. However, all the other peaks show the same intensity, even as a result of mixing one low-intensity outer peak with the other outer peak. This is somewhat unexpected, but is shown experimentally in the spectra of serine in Figures 4 and 5.

3 LARGER SPIN SYSTEMS

Larger spin systems can be treated as simple combinations of two-spin systems in most cases. The cross peaks will reflect the structures of the f_1 and f_2 spectra as above, with the proviso about the active coupling being in antiphase. Provided the system is in equilibrium, there will be no new frequencies appearing in f_1. In strongly coupled systems, the intensities of some individual peaks may be such that they are missing from a contour plot, but a cross peak will still be visible. Some spin systems, such as the ABX system, can be analyzed algebraically, but the calculations can get quite complex even for a simple experiment like COSY. For these systems, computer simulations provide a very useful tool.[21–25] With modern computers, exact density matrix calculations can be done in a few minutes on systems of four or five strongly coupled spins. For example, the simulations for Figures 5 and 8 were undertaken in under 30 s on a 1992 model UNIX workstation. For systems with several spins, a combination of the basic rules for two spins and some simulations and experience will faithfully predict the quantitative nature of the COSY spectrum.

4 FAST PULSING ARTIFACTS

The statement that no new frequencies appear in a COSY rests on the assumption that the spins relax completely between pulse sequences, and this is almost never true in practice. Under normal circumstances, artifacts that are derived from the f_2 frequencies will appear in the spectrum. Usually these appear as peaks at $f_1 = 0$, small P-type peaks which have not been totally suppressed or peaks at multiples of the f_2 frequency. These are especially evident for strong singlets due to methyl groups, which often have long relaxation times. These artifact peaks can be minimized by doing dummy scans before the actual acquisition, in order to get the spin system into a steady state. Also, careful attention to the phase cycling sequence and how one experiment interacts with the next can be very helpful.[26,27] Also, the use of magnetic field gradients, rather than phase cycling, to select coherence pathways is very effective in reducing the artifacts due to incomplete relaxation.

5 CONCLUSIONS

The COSY experiment serves as the best example of two-dimensional NMR spectroscopy. In its many forms it is an extraordinarily useful experiment, and yet it is quite simple to analyze and understand. The two-spin systems described here illustrate almost all the important features of the experiment. A few pages suffice to describe these systems completely and quantitatively, so it is well within the reach of all NMR spectroscopists. This combination of simplicity and power makes the COSY experiment stand out.

6 RELATED ARTICLES

Analysis of High-Resolution Solution State Spectra; COSY Two-Dimensional Experiments; Phase Cycling; Radiofrequency Pulses: Response of Nuclear Spins; Two-Dimensional J-Resolved Spectroscopy

7 REFERENCES

1. W. P. Aue, E. Bartholdi, and R. R. Ernst, *J. Chem. Phys.*, 1976, **64**, 2229.
2. K. Nagayama, K. Wüthrich, and R. R. Ernst, *Biochem. Biophys. Res. Commun.*, 1979, **90**, 305.
3. A. D. Bain, R. A. Bell, J. R. Everett, and D. W. Hughes, *J. Chem. Soc., Chem. Commun.*, **1980**, 256.
4. O. W. Sørensen, G. W. Eich, M. H. Levitt, G. Bodenhausen, and R. R. Ernst, *Prog. Nucl. Magn. Reson. Spectrosc.*, 1983, **16**, 163.
5. A. D. Bain, *Prog. Nucl. Magn. Reson. Spectrosc.*, 1988, **20**, 295.
6. A. D. Bain, I. W. Burton, and W. F. Reynolds, *Prog. Nucl. Magn. Reson. Spectrosc.*, 1994, **26**, 59.

7. S. Boentges, B. U. Meier, C. Griesinger, and R. R. Ernst, *J. Magn. Reson.*, 1989, **85**, 337.
8. A. D. Bain, *J. Magn. Reson.*, 1988, **77**, 125.
9. A. D. Bain, *J. Magn. Reson.*, 1984, **56**, 418.
10. G. Bodenhausen, H. Kogler, and R. R. Ernst, *J. Magn. Reson.*, 1984, **58**, 370.
11. D. Marion and K. Wüthrich, *Biochem. Biophys. Res. Commun.*, 1983, **113**, 967.
12. D. J. States, R. A. Haberkorn, and D. J. Ruben, *J. Magn. Reson.*, 1982, **48**, 286.
13. J. Keeler and D. Neuhaus, *J. Magn. Reson.*, 1985, **63**, 454.
14. U. Piantini, O. W. Sørensen, and R. R. Ernst, *J. Am. Chem. Soc.*, 1982, **104**, 6800.
15. A. J. Shaka and R. Freeman, *J. Magn. Reson.*, 1983, **51**, 169.
16. A. Bax and R. Freeman, *J. Magn. Reson.*, 1981, **44**, 542.
17. T. Allman and A. D. Bain, *J. Magn. Reson.*, 1986, **68**, 533.
18. C. Griesinger, O. W. Sørensen, and R. R. Ernst, *J. Chem. Phys.*, 1986, **85**, 6837.
19. A. D. Bain, *Chem. Phys. Lett.*, 1978, **57**, 281.
20. L. E. Kay and R. E. D. McClung, *J. Magn. Reson.*, 1988, **77**, 258.
21. P. Meakin and J. P. Jesson, *J. Magn. Reson.*, 1975, **18**, 411.
22. B. K. John and R. E. D. McClung, *J. Magn. Reson.*, 1984, **58**, 47.
23. H. Widmer and K. Wüthrich, *J. Magn. Reson.*, 1986, **70**, 270.
24. W. Studer, *J. Magn. Reson.*, 1988, **77**, 424.
25. A. Majumdar and R. V. Hosur, *Prog. Nucl. Magn. Reson. Spectrosc.*, 1992, **24**, 109.
26. C. J. Turner and S. L. Patt, *J. Magn. Reson.*, 1989, **85**, 492.
27. C. J. Turner and W. C. Hutton, *J. Magn. Reson.*, 1992, **100**, 469.

Biographical Sketch

Alex D. Bain. *b* 1948. B.Sc., 1970, Toronto, M.Sc., 1972, U.B.C., Ph.D., 1975, Cambridge, (Ph.D. supervisor, Ruth Lynden-Bell, who introduced him to NMR). After postdoctoral work, was employed as Applications Spectroscopist by Bruker-Spectrospin Canada for six years. Since 1986 has been Professor of Chemistry, McMaster University. Approx. 50 publications. Research interests: spin dynamics, relaxation, chemical exchange.

COSY Two-Dimensional Experiments

David M. Doddrell
Centre for Magnetic Resonance, University of Queensland, 4072 Australia

1 Introduction 1
2 The COSY Experiment 1
3 Simplifications and Extensions of the Basic Experiment 2
4 Other Nuances of the Experiment 3
5 References 4

1 INTRODUCTION

Although conceivably the simplest two-dimensional (2D) experiment possible, the physics underpinning the COSY (homonuclear correlated spectroscopy) experiment[1] are often the most difficult for the non-NMR specialist to grasp. The reason for this difficulty is undoubtedly the reluctance of many NMR users to grapple with the basics of product-operator algebra.[2] It is a fact that although some features of NMR experiments (for example, signal generation, the formation of a spin echo, and so on) can be understood using vector arguments, these arguments do not translate simply to 2D spectroscopy. With this statement in mind, it is assumed that the interested reader of this article is familiar with product operator algebra before any attempt is made to understand the nuances of the COSY experiment (see ***Polarization Transfer Experiments via Scalar Coupling in Liquids***).

Before proceeding further, there is one important fact to note concerning the detection of NMR signals in general. Quadrature detection is employed in NMR spectroscopy to distinguish between resonances whose frequencies are either positive or negative relative to the reference frequency, usually the same frequency at which the rf pulses are applied. The reference frequency defines the rotating frame frequency. Thus, in this frame of reference, any precession of the spins that resonate at the reference frequency (the on-resonance condition) is zero and their decay as measured by the receiver is that of a pure exponential with a decay time T^*_2. The signal acquired by the U channel of the receiver is proportional to $I_x \cos \Delta\omega t_2$, where $\Delta\omega$ is the offset frequency from the reference and the signal has been acquired for a time t_2. Because $\cos x = \cos(-x)$, positive and negative frequencies are not distinguished by single channel reception. If a second channel, the V channel, is used to receive signals but its reference frequency is phase shifted by 90°, the signal acquired is proportional to $I_y \sin \Delta\omega t_2$. If the signals from the two channels are combined, the combined signal is proportional to $I_x \cos \Delta\omega t_2 + I_y \sin \Delta\omega t_2$. This can be written as $I_x \exp(-\mathrm{i}\Delta\omega t_2)$ using the Liouville space transformation between I_x and I_y; $I_y = -\mathrm{i}I_x$. The term $I_x \exp(-\mathrm{i}\Delta\omega t_2)$ thus represents a single resonance appearing at $-\Delta\omega$.

2 THE COSY EXPERIMENT

2.1 Product Operator Algebra for the Basic Pulse Sequence

The basic COSY pulse sequence is

$$\frac{\pi}{2}(i),\ t_1,\ \frac{\pi}{2}(j),\ \text{acquire for time } t_2 \qquad (1)$$

where i and j are the phases of the applied rf pulses. Consider the application of this pulse sequence to a homonuclear spin-coupled system, IS. Assume that the weak coupling approximation — $(\Delta\omega_I - \Delta\omega_S)$ — $\gg 2\pi J$ is valid, where J is the scalar I–S coupling constant and $\Delta\omega_I$ and $\Delta\omega_S$ are the frequency offsets of the I and S spins in the rotating frame, respectively (see ***Polarization Transfer Experiments via Scalar Coupling in Liquids***).

Using the ideas introduced elsewhere, the initial spin coherences prior to the application of the pulse sequence are $I_z U^{\mathrm{S}}$ and $U^{\mathrm{I}} S_z$, respectively. The first pulse with phase $i = x$ induces the following changes; $I_z U^{\mathrm{S}} \rightarrow I_y U^{\mathrm{S}}$ and $U^{\mathrm{I}} S_z \rightarrow U^{\mathrm{I}} S_y$. During the time t_1, which is incremented as $n\Delta t_1$, $n = 1, 2, 3, \ldots$, $I_y U^{\mathrm{S}}$ and $U^{\mathrm{I}} S_y$ are modified because of evolution from the combined effects of chemical shift offset and scalar coupling. The effect of each can be calculated separately by noting that for the chemical shift offset S_y evolves as follows:

$$S_y(t_1) = S_y \cos(\Delta\omega_S t_1) + S_x \sin(\Delta\omega_S t_1) \qquad (2)$$

and U^{I} evolves under the influence of the scalar coupling as

$$U^I(t_1) \rightarrow U^I \cos(\pi J t_1) - \mathrm{i} I_z \sin(\pi J t_1) \qquad (3)$$

(remember, each component of the doublet is precessing by a differential of $\pm\pi J$ rad^{-1} relative to the chemical shift offset frequency). Considering the two precessional effects acting upon $U^{\mathrm{I}} S_y$, the changes induced are as follows:

$$U^I S_y \overset{t_1, \Delta\omega_S}{\longrightarrow} U^I S_y \cos(\Delta\omega_S t_1) + U^I S_x \sin(\Delta\omega_S t_1) \qquad (4)$$

$$\overset{t_1, J}{\longrightarrow} U^I S_y \cos(\Delta\omega_S t_1)\cos(\pi J t_1) - I_z S_x \cos(\Delta\omega_S t_1)\sin(\pi J t_1)$$
$$(A) \qquad (B)$$
$$+ U^I S_x \sin(\Delta\omega_S t_1)\cos(\pi J t_1) + I_z S_y \sin(\Delta\omega_S t_1)\sin(\pi J t_1) \qquad (5)$$
$$(C) \qquad (D)$$

The precession arising from a combination of chemical shift offset and scalar coupling has evolved $U^{\mathrm{I}} S_y$ into four terms A, B, C, and D. Now the action of the second $\pi/2(j)$ pulse can be considered. (Note there will be, correspondingly, four terms generated from $I_y U^{\mathrm{S}}$.) If the phase of the final $\pi/2$ pulse is set as $j = x$, each term whose origin was S_z is changed as follows:

$$\left.\begin{aligned} A &\rightarrow -U^I S_z \cos(\Delta\omega_S t_1)\cos(\pi J t_1),\ A'_x \\ B &\rightarrow -I_y S_x \cos(\Delta\omega_S t_1)\sin(\pi J t_1),\ B'_x \\ C &\rightarrow +U^I S_x \sin(\Delta\omega_S t_1)\cos(\pi J t_1),\ C'_x \\ D &\rightarrow -I_y S_z \sin(\Delta\omega_S t_1)\sin(\pi J t_1),\ D'_x \end{aligned}\right\} \qquad (6)$$

Terms A'_x and B'_x do not represent observable signal; one term is purely z magnetization while the other is a mixture of zero and double quantum coherence and is consequently unobservable. If the phase of the second pulse is set as $j = y$, the observable terms arise from

$$\left.\begin{array}{l} U^I S_y \cos(\Delta\omega_S t_1)\cos(\pi J t_1),\ A'_y \\ \text{and} \\ I_x S_z \cos(\Delta\omega_S t_1)\sin(\pi J t_1),\ B'_y \end{array}\right\} \quad (7)$$

The significance of these terms will become apparent later.

2.2 COSY as a Two-Dimensional Experiment

One-dimensional NMR spectroscopy is well understood and can be explained using simple vectors. $U^{\mathrm{I}}S_z$ receives a $\pi/2(x)$ pulse generating $U^{\mathrm{I}}S_y \equiv (\alpha^{\mathrm{I}} + \beta^{\mathrm{I}})S_y$ and this magnetization, because of precession in the laboratory frame, generates signals the frequency of which are separated by J Hz. The signals are sampled for a time $t_2 = m\Delta t_2$, $m = 1, 2, 3, \ldots$, yielding an observable spectral width $F_2 = 1/2\Delta t_2$ assuming quadrature detection. In 2D spectroscopy, a second time period is introduced during which the magnetization is modified advantageously for extra chemical structural information to be encoded. The spectral width in the second dimension F_1 is given by $1/2\Delta t_1$, again assuming quadrature detection. The values of m and n define the spectral resolution in the F_2 and F_1 dimensions, respectively. Double Fourier transformation of the data set yield peaks at coordinates (F_1, F_2) in frequency space.

For the COSY experiment with $i = j = x$, two signal groupings arise, one from C'_x and the other from D'_x. Consider firstly the signals arising from C'_x. Assuming that quadrature detection in F_2 is employed, the signals will be centered at $\Delta\omega_S/2\pi$ in the F_2 direction because they arise from the spin coherence $U^{\mathrm{I}}S_x \equiv (\alpha^{\mathrm{I}} + \beta^{\mathrm{I}})S_x$. The COSY signal will be 90° phase shifted compared with that arising from the standard pulse-and-collect experiment which is associated with the spin coherence $U^{\mathrm{I}}S_y$ for an x-phased excitation pulse. In the F_1 direction, the behavior is complex but can be readily calculated using the trigonometric identities $\cos x = (\frac{1}{2})[\exp(\mathrm{i}x) + \exp(-\mathrm{i}x)]$ and $\sin x = (1/2\mathrm{i})[\exp(\mathrm{i}x) - \exp(-\mathrm{i}x)]$. For that component of the S doublet arising from the I eigenstate α^{I}, there will be two doublets either side of $F_1 = 0$, centered at $\pm\Delta\omega_S/2\pi$ in F_1. These arise from Fourier transformation of $\sin(\Delta\omega_S t_1)\cos(\pi J t_1)$ with respect to t_1. In F_1 the peaks occur at $(\Delta\omega_S/2\pi + J/2)$, $(\Delta\omega_S/2\pi - J/2)$ and $(-\Delta\omega_S/2\pi + J/2)$, $(-\Delta\omega_S/2\pi - J/2)$. There will be, as well, four corresponding peaks arising from the I eigenstate β^{I} yielding in total eight peaks. Note, no mention has been made concerning two-dimensional lineshapes. If the (F_1, F_2) plane (a contour map) were viewed from above, the eight peaks would appear as 'dots'.

The signals arising from D'_x are far more interesting. In the F_2 dimension they are centered at $\Delta\omega_I/2\pi$ and are generated by a signal arising from $-I_y S_z \equiv I_y(-\alpha^{\mathrm{S}} + \beta^{\mathrm{S}})$ by its evolution during t_2. (At $m = 0$, $-I_y S_z$ yields zero net signal, but during the t_2 evolution period $S_z \rightarrow [S_z \cos(\pi J t_2) - \mathrm{i}U^{\mathrm{S}} \sin(\pi J t_2)]$ giving rise to detectable magnetization.) Because the signals arise from correlated S_z magnetization, $S_z = (-\alpha^{\mathrm{S}} + \beta^{\mathrm{S}})$, they must be antiphase following the Fourier transformation. That is, the signals corresponding to α^{S} will be 180° phase shifted compared with those arising from β^{S}. Importantly, however, the signals are centered at $\pm\Delta\omega_S/2\pi$ in F_1, and specifically at $(\Delta\omega_S/2\pi + J/2)$, $(\Delta\omega_S/2\pi + J/2)$ and $(-\Delta\omega_S/2\pi + J/2)$, $(-\Delta\omega_S/2\pi - J/2)$. The salient features of this experiment are summarized in Figure 1.

The importance of this pulse sequence for structural chemistry should be now apparent. If there is J coupling between two spins I and S there is a cross peak in the 2D spectrum arising from the spin coherence represented by the term D'_x centered at frequency coordinates in absolute units at $(\Delta\omega_S/2\pi, \Delta\omega_I/2\pi)$ in the (F_1, F_2) plane. There is of course a cross peak (not shown in Figure 1) at $(\Delta\omega_I/2\pi, \Delta\omega_S/2\pi)$ as well. In total, the basic COSY experiment, $i = j = x$, yields 32 peaks in the 2D spectrum when applied to an I–S spin system. The two families of peaks are denoted as N-type or P-type.

The designation N and P is derived from the differences in the direction of precession during the t_1 and t_2 time periods. N means the direction is reversed or one the negative of the other. P means they are both of the same sign: positive. As the coherence transfer echo is usually detected (magnetic field inhomogeneity is refocused for this family of peaks), one axis of the 2D plot has frequency increasing left to right (F_2 direction) and decreasing bottom to top (F_1 direction). Thus, for the N-type peaks, the diagonal runs from left to right with a slope of 45° (see Figure 1). However, by software, one axis is usually reversed for visual display in order that chemical shifts decrease left to right and from bottom to top for display of the N-type peaks.

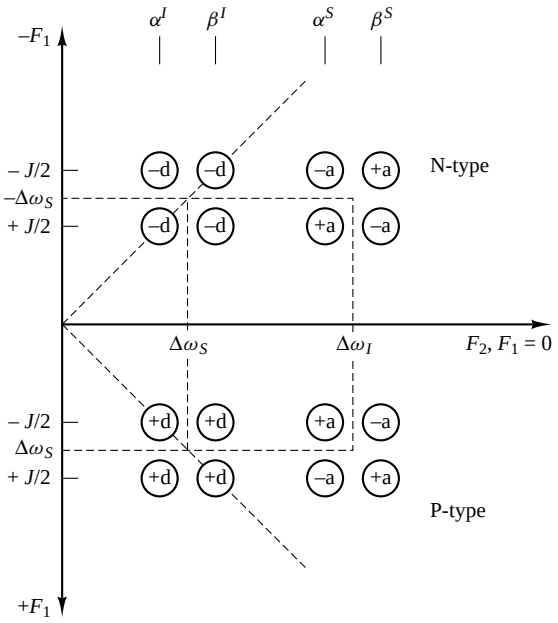

Figure 1 Theoretical COSY spectrum for two weakly coupled spins. The phases are illustrated by + or −, while the lineshapes are designated d (dispersion) and a (absorption). Only the peaks arising from spin S are shown; there are, as well, 16 peaks from spin I

3 SIMPLIFICATIONS AND EXTENSIONS OF THE BASIC EXPERIMENT

3.1 Coherence Selection by Phase Cycling

Quadrature detection in the F_1 dimension is used to eliminate either the N- or P-type peaks. For N-type selection, the simplest phase cycle is to set $i = x$ and to generate data sets for $j = x$ and $j = y$. The data sets are subtracted during the complex Fourier transformation to yield quadrature detection[3] in F_1. This is simply understood by realizing that the complex data set when transformed generates the diagonal peaks arising now from the spin coherence:

$$\begin{aligned} C'_x - A'_x &= U^I S_x \sin(\Delta\omega_S t_1)\cos(\pi J t_1) \\ &\quad -U^I S_y \cos(\Delta\omega t_1)\cos(\pi J t_1) \\ &= U^I \cos(\pi J t_1)[S_x \sin(\Delta\omega_S t_1) - S_y \cos(\Delta\omega_S t_1)] \\ &= -U^I \cos(\pi J t_1)[S_y \cos(\Delta\omega_S t_1) - \mathrm{i}S_y \sin(\Delta\omega_S t_1)] \\ &= -U^I S_y \cos(\pi J t_1)\exp(-\mathrm{i}\Delta\omega_S t_1) \end{aligned} \tag{8}$$

A similar analysis for the cross peaks yields

$$D'_x - B'_y = -S_z I_x \sin(\pi J t_1)\exp(-\mathrm{i}\Delta\omega_S t_1) \tag{9}$$

If P-type selection is desired, the data sets generated from $j = x$ and $j = y$ are added during the transform. Usually, for even modern NMR spectrometers, if N-type peaks are to be selected, the simple phase cycle above, because of pulse imperfections, does not induce accurate suppression of the P-type family. The phase cycle needs to be extended to $i = x; j = x, -x, y, -y$ and the receiver +,+, −,−. Here, note that $C'_x = C'_{-x}$ and $D'_x = D'_{-x}$.

3.2 Coherence Selection using Pulsed Field Gradients

The modification to the COSY pulse sequence incorporating pulsed field gradients[4] is shown in Figure 2. The effect of the field gradient can be rationalized as follows.[5] A field gradient varies the angular precession of the I and S spins according to their spatial position. Consider the simplest type of spatial dependence arising from the application of a linear field gradient, for example, G_z. All spins in the plane defined by a z coordinate z_i have their Larmor frequency modified by an amount $(\Delta\omega_I + \Delta\omega)$ and $(\Delta\omega_S + \Delta\omega)$, respectively; $\Delta\omega = \gamma z_i G_z$. The gradient is applied for a short time τ_D on either side of the final $\pi/2$ pulse. The first gradient pulse modifies the spin coherence that gives rise to the diagonal peaks following the final $\pi/2$ pulse, $j = x$ to

$$\begin{aligned} &U^I S_x \cos(\pi J t_1)\sin(\Delta\omega_S t_1 + \Delta\omega\tau_D) \\ &= \frac{1}{2\mathrm{i}} U^I S_x \cos(\pi J t_1)[\exp\{\mathrm{i}(\Delta\omega_S t_1 + \Delta\omega\tau_D)\} \\ &\quad - \exp\{-\mathrm{i}(\omega_S t_1 + \Delta\omega\tau_D)\}] \end{aligned} \tag{10}$$

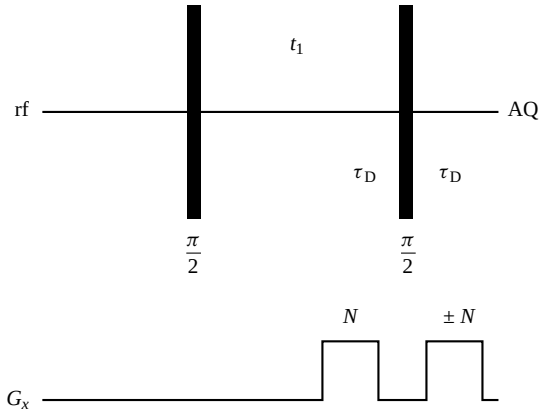

Figure 2 COSY pulse sequence incorporating field gradients for coherence selection

Application of a second equal gradient pulse having the same time integral as the first immediately before data acquisition yields evolution as:

$$\begin{aligned} &\frac{1}{4\mathrm{i}} U^I \cos(\pi J t_1)[S_+ \exp(\mathrm{i}\Delta\omega\tau_D) + S_- \exp(-\mathrm{i}\Delta\omega\tau_D)] \\ &\quad \times[\exp\{\mathrm{i}(\Delta\omega_S t_1 + \Delta\omega\tau_D)\} - \exp\{-\mathrm{i}(\Delta\omega_S t_1 + \Delta\omega\tau_D)\}] \end{aligned} \tag{11}$$

The terms in which $\Delta\omega$, the gradient-induced offset, remains represent dephased magnetization. (Their linewidth will be such that they will yield unobservable signal provided G_z is sufficiently strong.) Thus, the detected signal is given by

$$\frac{1}{4\mathrm{i}} U^I \cos(\pi J t_1)[-S_+ \exp(-\mathrm{i}\omega\Delta_S t_1) + S_- \exp(\mathrm{i}\Delta\omega_S t_1)] \tag{12}$$

which reduces to

$$-\tfrac{1}{2} U^I S_y \cos(\pi J t_1)\exp(-\Delta\omega_S t_1) \tag{13}$$

This again represents quadrature detection of S_y with respect to t_1 and again corresponds to N-type selection. Inverting the sign of the second gradient allows P-type selection. Single acquisition COSY, N-type selected and P-type selected using pulse field gradients are shown in Figure 3 and Figure 4, respectively.

4 OTHER NUANCES OF THE EXPERIMENT

The original experiment as proposed by Jeener has been explained above. Various facets and modifications, however, to this experiment have been published. Some are mentioned here to provide the interested reader with the references to probe further.

Note, that for N-type selection the sense of precession during t_1 is opposite to that for P-type selection. Thus, by analogy with the gradient selected COSY experiment, it is clear that for this peak family magnetic field inhomogeneity effects are refocused during t_2. The N-type peaks are called the coherence transfer echo; the P-type peaks the anti echo.[6]

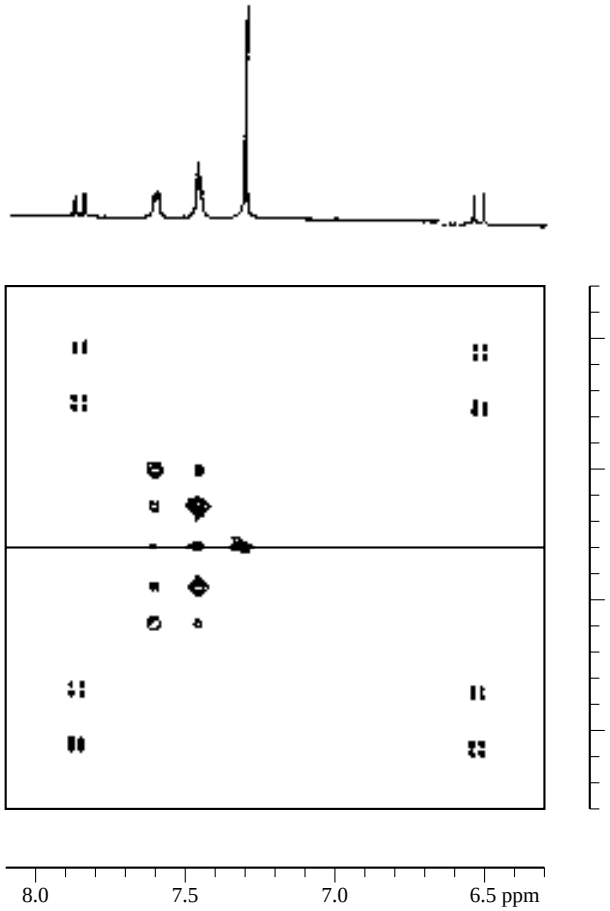

Figure 3 Contour plot of a normal COSY spectrum of 20 mM cinnamic acid in $CDCl_3$ obtained with one acquisition per t_1 increment. (No phase cycling has been employed.) A 512 × 2k data matrix with a spectral width of 1000 Hz in ω_1 and 2000 Hz in ω_2 was collected and zero filled once in ω_1 prior to 2D Fourier transformation. A simple pulse and acquire spectrum is plotted above the contour plot (see Ref. 5)

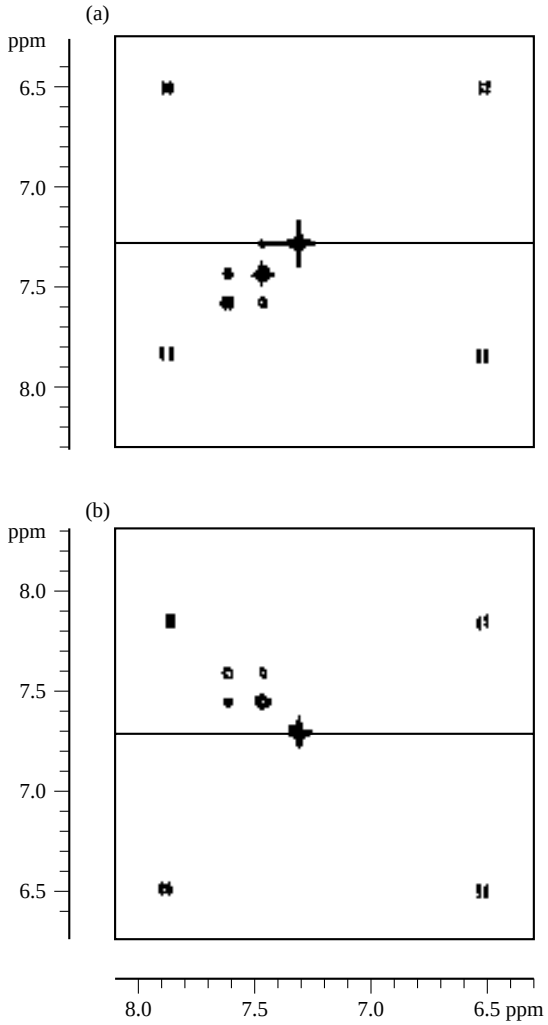

Figure 4 Contour plots of COSY spectra obtained using gradient pulses of the same sign and opposite sign, respectively. Note, the selection of the N- or P-type families of peaks. A single acquisition per t_1 increment was collected and data processed under conditions identical to those described in Figure 3 (see Ref. 5)

Because of finite linewidths in F_2, the lineshapes in the (F_1, F_2) plane are of interest. The lineshapes that will arise from the simple analysis (equation (6)) discussed above are 'phase-twisted'. More complex data analysis and phase cycling are required to remove the 2D spectral distortions that arise.[7]

The basic COSY pulse sequence has been modified to use double quantum filtering to increase the 2D spectral resolution.[1,8] Other modifications, at the expense of increasing the pulse sequence length, have been introduced to remove the antiphase character of the cross peaks.[9]

Attempts to introduce localization to the basic experiment have been published whereby the two COSY pulses have been made slice selective.[10] Only recently have gradient selective localized COSY experiments been demonstrated in vivo.[11]

5 REFERENCES

1. J. Jeener, AMPERE Summer School, Basko, Polje, Yugoslavia, 1971; W. P. Aue, E. Bartholdi, and R. R. Ernst, *J. Chem. Phys.*, 1976, **64**, 2229. For a good discussion also see H. Kessler, M. Gehnke, and C. Griesinger, *Angew. Chem., Int. Ed. Engl.*, 1988, **27**, 490.
2. Various constructions of product-operator algebra have been published, see R. R. Ernst, G. Bodenhausen, and A. Wokaun, *Principles of Nuclear Magnetic Resonance in One and Two Dimensions*, Clarendon Press, Oxford, 1987; F. J. M. van de Var and C. W. Hilbers, *J. Magn. Reson.*, 1983, **54**, 512; K. J. Packer and K. M. Wright, *Mol. Phys.*, 1983, **50**, 797; R. M. Lynden-Bell, J. M. Bulsing, and D. M. Doddrell, *J. Magn. Reson.*, 1983, **55**, 128.
3. D. J. States, R. A. Haberkorn, and D. J. Ruben, *J. Magn. Reson.*, 1982, **48** 286; D. Marion and K. Wüthrich, *Biochem. Biophys. Res. Commun.*, 1983, **113**, 967.
4. P. Barker and R. Freeman, *J. Magn. Reson.*, 1985, **64**, 334.
5. I. M. Brereton, S. Crozier, J. Field, and D. M. Doddrell, *J. Magn. Reson.*, 1991, **93**, 54.
6. K. Nagayama, K. Wüthrich, and R. R. Ernst, *Biochem. Biophys. Res. Commun.*, 1979, **90**, 305.
7. J. Keeler and D. Neuhaus, *J. Magn. Reson.*, 1985, **63**, 454.
8. A. A. Maudsley, A. Wokaun, and R. R. Ernst, *Chem. Phys. Lett.*, 1979, **55**, 9; A. Bax, P. De Jong, A. F. Mehlkopf, and J. Smidt, *Chem. Phys. Lett.*, 1980, **69**, 567.

9. A. Kumar, R. V. Hosur, and K. Chandrasekhar, *J. Magn. Reson.*, 1984, **60**, 143; S. Talluri and H. A. Scherager, *J. Magn. Reson.*, 1990, **86**, 1.
10. S. J. Blackband, K. A. McGovern, and I. J. McLennan, *J. Magn. Reson.*, 1988, **79**, 184. See also, Y. Cohen, L.-H. Chang, L. Litt, and T. L. James, *J. Magn. Reson.*, 1989, **85**, 203; G. C. McKinnon and P. Bosiger, *Magn. Reson. Med.*, 1988, **6**, 334.
11. I. M. Brereton, G. J. Galloway, S. E. Rose, and D. M. Doddrell, *Magn. Reson. Med.*, 1994 **32**, 251.

Biographical Sketch

David M. Doddrell. *b* 1944. B.Sc., 1966, University of Queensland, Ph.D., 1969, Indiana University, D.Sc., 1977, Griffith University, introduced to NMR by A. Clouse, E. Wenkert, and A. Allerhand. Faculty positions at Griffith University 1974–86, University of Queensland 1986–present. Approximately 220 publications. Research interests: multipulse NMR liquid state applications, in vivo NMR spectroscopy, magnetic resonance imaging, and hardware developments.

Coupling Constants Determined by ECOSY

Harald Schwalbe, P. Schmidt and Christian Griesinger
Universität Frankfurt, Germany

1 Introduction 1
2 The ECOSY Principle 1
3 *S* Filtered Homonuclear Correlation to Measure $^nJ(I_2, S)$ Couplings in an I_1–S–·–I_2 Spin System 1
4 Heteronuclear Long-Range Correlation to Measure $^nJ(I_1, I_2)$ Couplings in an I_1–S–·–I_2 Spin System 2
5 The SOFT-COSY Experiment to Measure Homonuclear $^nJ(I_1, I_3)$ Couplings in an I_1–I_2–I_2 Spin System and Heteronuclear $^nJ(S_2, I_1)$ Couplings in a S_2–S_1–·–I_1 Spin System 2
6 BIRD Pulses for Spin Topology Filtering: Measuring Homonuclear $^nJ(I_1, I_2)$ Couplings in an I_1–S–T–I_2 or I_1–S–·–I_2 Spin System 10
7 The ECOSY Experiment for the Measurement of Homonuclear $^nJ(I_1, I_1)$ Couplings in an I_1–I_2–I_3 Spin System and $^nJ(I_1, I_2)$ Couplings in an I_1–S_1–·–I_2 Spin System 13
8 References 16

1 INTRODUCTION

Exclusive correlation spectroscopy (ECOSY)[1–3] is one of the most powerful methods for determining homonuclear, J(H,H) and J(C,C), as well as heteronuclear coupling constants, such as J(C,H), J(N,H), J(P,H), and J(P,C), in proteins and nucleic acids. Applications to other heteronuclear systems, especially in metalloorganic chemistry, have been successfully performed to measure, for example, metal–phosphorus, metal–carbon and metal–proton coupling constants. Due to the inherent features of the experiment, precise coupling constants can be determined even if the linewidth of the involved nuclei is large (macromolecules) or the coupling constant to be determined is small. This article presents the basic principle (Section 2) and different experimental implementations (Sections 3–7) of the ECOSY experiment, together with examples. Relaxation effects that introduce systematic errors in the coupling constant determination will not be discussed here; the interested reader is referred to the literature cited.[4–8]

2 THE ECOSY PRINCIPLE

If in a three spin system consisting of spins ABC with nonvanishing couplings J(A,C) and J(B,C), A (in ω_1) is correlated with B (in ω_2) without mixing the spin states of a third spin C (Figure 1), the two-dimensional correlation spectrum can be constructed from two subspectra with spin C either in the α or in the β state (Figure 1, left and right, respectively). Since spin A and spin B have a 'chemical shift' of $\omega_1 = \Omega_A + \pi J$(A,C) and $\omega_2 = \Omega_B + \pi J$(B,C) for C in the α state, and of $\omega_1 = \Omega_A - \pi J$(A,C) and $\omega_2 = \Omega_B - \pi J$(B,C) for C in the β state, a spectrum that correlates spin A with spin B without touching C during t_1, the mixing, and t_2 will show just two cross peaks, one at $(\omega_1,\omega_2) = [\Omega_A + \pi J$(A,C), $\Omega_B + \pi J$(B,C)] and the other at $(\omega_1,\omega_2) = [\Omega_A - \pi J$(A,C), $\Omega_B - \pi J$(B,C)]. The displacement vector $\boldsymbol{J}_C$ (where the subscript C indicates the passive spin in both dimensions) has the components J(A,C) and J(B,C) in ω_1 and ω_2, respectively. As can be derived from Figure 1, a small coupling J(B,C) can be determined, irrespective of its size, provided the so-called *associated coupling* J(A,C) is larger than the linewidth and the resolution in ω_1. The sensitivity of the experiment depends upon the transfer efficiency of the correlation between A and B, rather than on the size of the coupling of interest. The precision of the coupling constant determination depends on the precision with which the position of a peak maximum can be determined for a given digital resolution of the FID and digitization of the spectrum, and on the invariance of the submultiplets in the two slices displaced in ω_2. The direction of the displacement vector indicates the relative sign of the two couplings J(A,C) and J(B,C): it points to the upper right or lower left if the signs of the two couplings are the same; and it points to the upper left or lower right if the signs are different.

Depending on the spin systems under study (e.g. whether the molecule has the isotopes in natural abundance or the nuclei have been enriched with or depleted of the magnetically active isotope, the molecular weight of the compound under investigation, and the linewidth of the resonances), there are currently four different implementations of an ECOSY-type correlation (see Sections 3–7). Rather than giving a chronological overview, the experiments are ordered according to their theoretical complexity. In the explanatory Figures given in each section, a representative pulse sequence, the spin system (with I_n, where I designates the ^{1}H spins, and n the numbers within them; S_n, where S designates the first heteronuclear spins, and n the numbers within them; and T for a second heteronuclear spin), the so-called ECOSY *triangle* and the resulting spectrum is shown. A dot in the spin system represents one or more non-NMR-active nuclei. The three essential spins A, B, and C are on the corners of the ECOSY triangle, the first active spin A (left) sharing a large, structurally uninteresting coupling with the passive spin C (top) which is used as an associated coupling to resolve the coupling of interest J(B,C) to spin B (right) which is the second active spin. In most of the proposed sequences, B is the detected spin. The sides of the triangle represent the associated coupling, the coupling of interest, and the mixing process between A and B. A and B need not be directly scalar coupled. The ECOSY triangle may serve as a graphical aid in designing new experiments to measure coupling constants.

3 *S* FILTERED HOMONUCLEAR CORRELATION TO MEASURE $^nJ(I_2,S)$ COUPLINGS IN AN I_1–S–·–I_2 SPIN SYSTEM

In a three spin system I_1–S–·–I_2 with I_1 bound to S, the ECOSY pattern will be observed in any correlation between

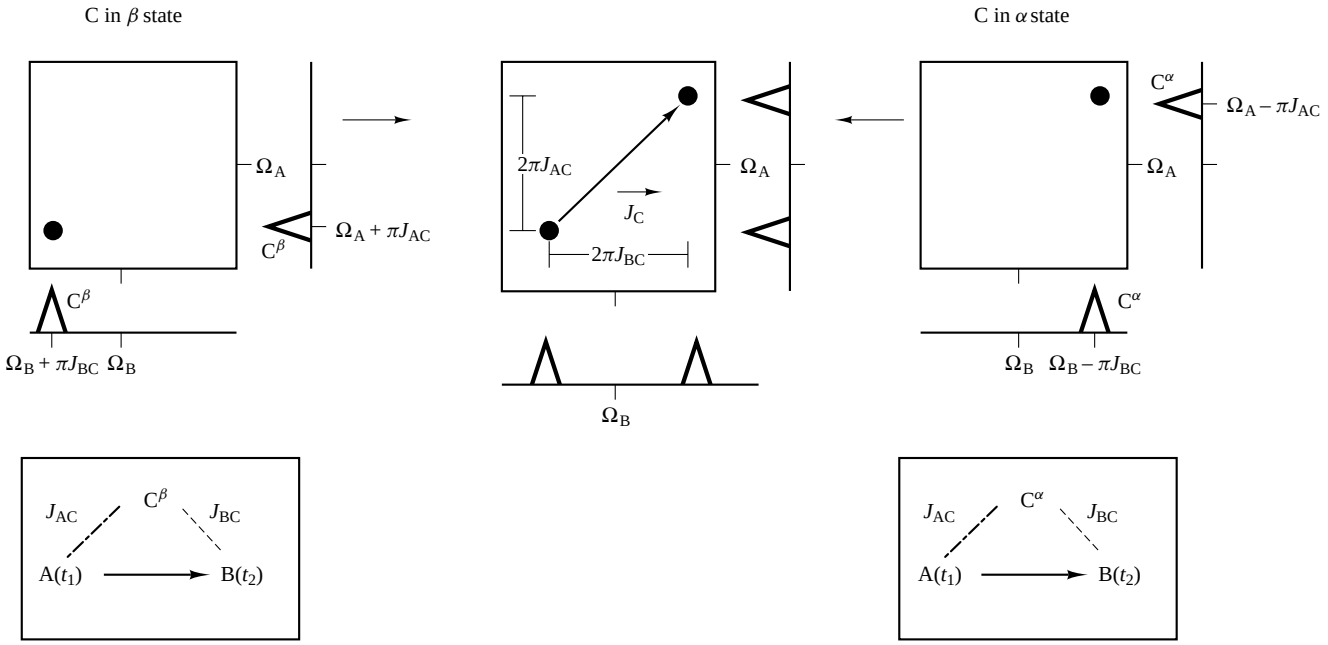

Figure 1 The ECOSY principle. In a three spin system the associated coupling J(A,C) is used to resolve the two components $\Omega_B \pm \pi J$(B,C) in ω_1. The two theoretical subspectra originate from spin C either in the α or in the β state

I_1 and I_2 obtained with an arbitrary homonuclear mixing sequence (e.g. TOCSY, NOESY, ROESY) because S remains untouched during the whole experiment (Figure 2(a)). S filtering can be inserted at the beginning of the pulse sequence to select for the NMR-active fraction of S nuclei. This classical Montelione–Wagner experiment[9,10] has been applied in a number of different applications for the measurement of J(C,H),[11–22] J(N,H),[23] J(P,H),[24] J(^{113}Cd,H),[25] J(F,H),[26] and J(F,C),[26] and is probably the best way to obtain coupling constant information for I_1–S–·–I_2 spin systems. It has been applied to the measurement of ^3J(N,H$_\beta$), ^3J(N$_i$,H$_{\alpha i-1}$), and ^3J(C,H) coupling constants. It fails, however, if the homonuclear mixing process is not efficient enough, as for example in α-helical regions of a protein where a NOESY transfer between H_i^N and H$_{\alpha i-1}$ is used for the measurement of the ^3J(N$_i$,H$_{\alpha i-1}$) coupling constant, with N as the passive spin. The NOESY transfer between H_i^N and H$_{\alpha i-1}$ is insensitive in α-helical regions due to the large distance between these protons. In proteins, labeling of the heterospin S, especially that of ^{15}N, is indispensable for sensitivity reasons. Measuring long-range J(C,H) couplings with this approach in uniformly ^{13}C labeled proteins is difficult due to multiple carbon coupling partners. Selective decoupling schemes have been designed to avoid this problem.[27–32]

Figure 3 shows an application of the S filtered experiment.[18] The diastereotopic δ-methyl groups in leucines can be stereochemically assigned by measuring heteronuclear ^3J(C$_{\delta1}$,H$_{\beta1}$) and ^3J(C$_{\delta2}$,H$_{\beta1}$), or ^3J(C$_{\delta1}$,H$_{\beta2}$) and ^3J(C$_{\delta2}$,H$_{\beta2}$) couplings, respectively, provided the β-protons are stereochemically assigned. χ_2 of Leu$_8$ in cyclolinopeptide A assumes a position of 180°. This can be derived from the known stereochemical assignment H$_{\beta1}$ = *pro-S* and H$_{\beta2}$ = *pro-R*.

4 HETERONUCLEAR LONG-RANGE CORRELATION TO MEASURE $^nJ(I_1,I_2)$ COUPLINGS IN AN I_1–S–·–I_2 SPIN SYSTEM

Choosing I_2 (B) and S (A) as the two active spins and I_1 (C) as the passive spin, $^nJ(I_1,I_2)$ coupling constants can be measured provided I_1 is not touched between t_1 and detection. A heteronuclear multiple bond correlation (HMBC)-type sequence [Figure 2(b)][33] that correlates I_1 with S via the $^{n-1}J(I_1,S)$ coupling meets this requirement. The low efficiency of the mixing process due to the usually small heteronuclear $^{n-1}J(I_1,S)$ coupling and the short proton T_2 values are the limiting factors of the method.

5 THE SOFT-COSY EXPERIMENT TO MEASURE HOMONUCLEAR $^nJ(I_1,I_3)$ COUPLINGS IN AN I_1–I_2–I_2 SPIN SYSTEM AND HETERONUCLEAR $^nJ(S_2,I_1)$ COUPLINGS IN A S_2–S_1–·–I_1 SPIN SYSTEM

By application of selective pulses, a subset of spins of a certain isotope (e.g. H$_\alpha$ or C′) can be used as passive spins while using spins of another subset of the same isotope (e.g. H$_\beta$ or C$_\alpha$) as active spins. In proton correlation[34–37] spectroscopy [Figure 4(a)], this idea has not gained widespread application in peptide or protein spectroscopy, because there are no well separated subsets of proton spins that sustain at the same time interesting coupling constants. For example, in the case of ^3J(H$_\alpha$,H$_\beta$) coupling constants, when H$_\alpha$ is used as a passive spin and the two H$_\beta$ are used as active spins the two subsets of passive and active spins are well separated; however, the associated coupling constant is a vicinal coupling, which can be very small. If, on the other hand, one of the H$_\beta$

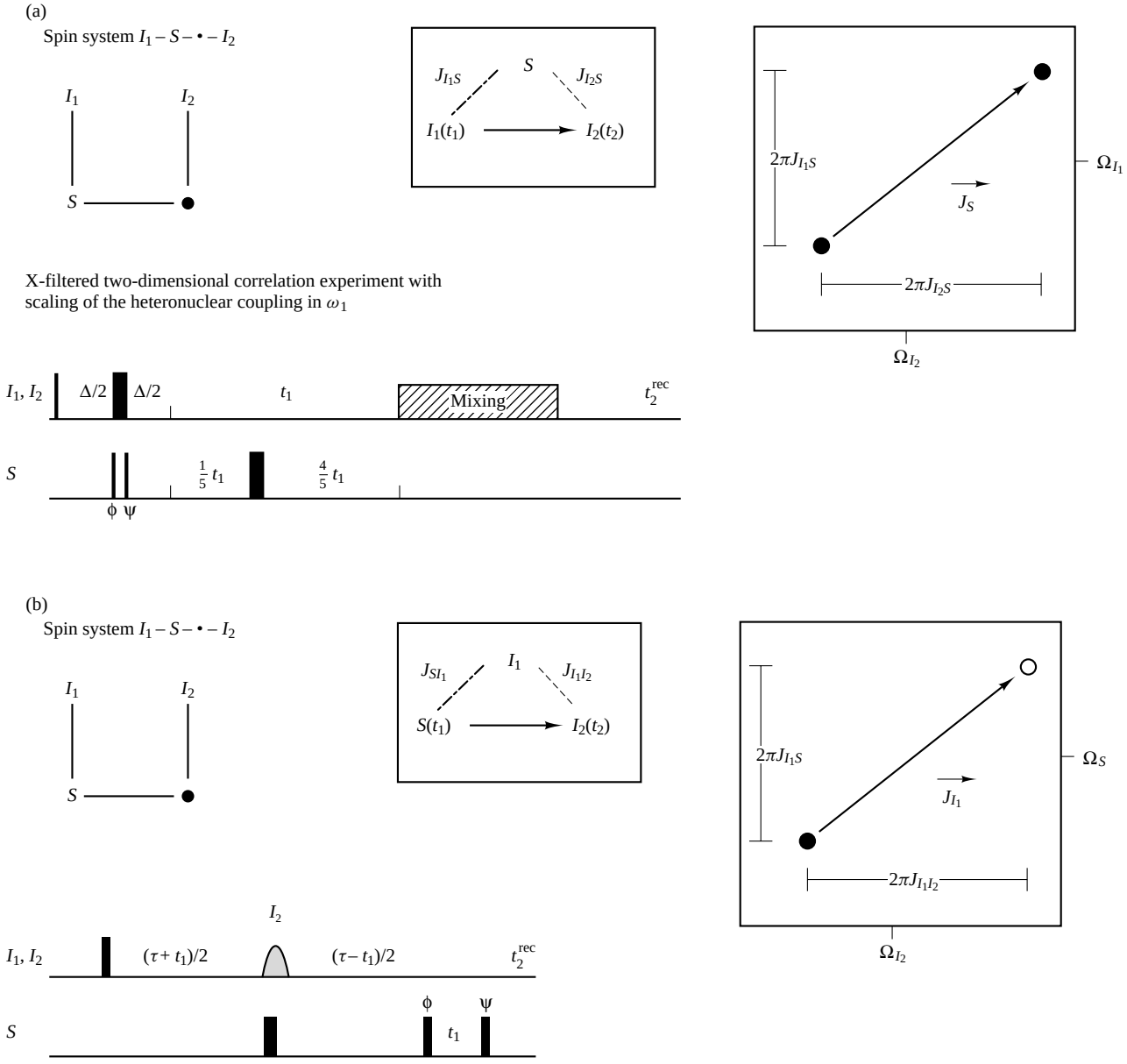

Figure 2 (a) The Montelione–Wagner experiment. In a heteronuclear I_1–S_1–•–I_2 spin system, I_1 and I_2 are correlated by an arbitrary homonuclear mixing process. The heterospin S is not touched and, therefore, remains passive during the entire experiment. Scaling of the associated coupling can be implemented to overcome problems due to overlap. The heteronuclear ${}^nJ(I_2,S)$ coupling is measured in t_2. The associated coupling ${}^1J(I_1,S)$ is scaled to 3/5 in t_1 in the example given. Typical parameters are: $\Delta = [J(I_1,S)]^{-1}$; $\phi = x, -x$; $\psi = x, x, -x, -x$; rec. = $x, -x, -x, x$. (b) The heteronuclear long-range experiment. In a heteronuclear I_1–S_1–•–I_2 spin system, S and I_2 are correlated; I_1 is untouched in the experiment. A homonuclear ${}^nJ(I_1,I_2)$ coupling is measured in t_2. The application of an I_2-selective refocusing pulse ensures pure phase lineshapes in t_2. The signal is modulated by long-range ${}^nJ(I,S)$ couplings in t_1 which are usually not resolved in t_1. Typical parameters are: $\tau \sim [2^{n-1}J(I_2,S)]^{-1}$; $\phi = x, -x$; $\psi = x, x, -x, -x$; rec. = $x, -x, -x, x$

protons is used as a passive spin and the H_α and the other H_β proton as active spins, the associated coupling is a geminal coupling ${}^2J(H'_\beta/H''_\beta)$, but the spectral displacement between the two H_β protons is small.

For carbon, however, the spectrum is composed of well separated regions. Carbonyl and aliphatic carbon resonances have a large frequency difference compared with the chemical shift dispersion of aliphatic carbon atoms. Therefore selective pulses like the Gaussian cascades G3 and G4[38,39] or IBURP and REBURP pulses[40] effectively excite, for example, an aliphatic carbon spin S_1 while leaving the carbonyl spin S_2 passive. The ${}^1J(C',C_\alpha)$ coupling is, fortunately, large in proteins and can therefore be used as an associated coupling to measure ${}^2J(C',H_\alpha)$ in SOFT-HSQC,[41] or the structurally important ${}^3J(C',H_\beta)$ couplings in SOFT-HCCH-COSY[27] (Figure 5) and the ${}^3J(C',H^N)$ couplings in the SOFT-HNCA-COSY.[42,43] A heteronuclear detected experiment for the opposite situation, in which S_1 and S_2 are protons, and I is a heteronucleus, has been published by Kessler et al.[44]

Figure 5 and Figure 6 show the application of this concept to measure ${}^3J(C',H_\beta)$ couplings in proteins. The constituent

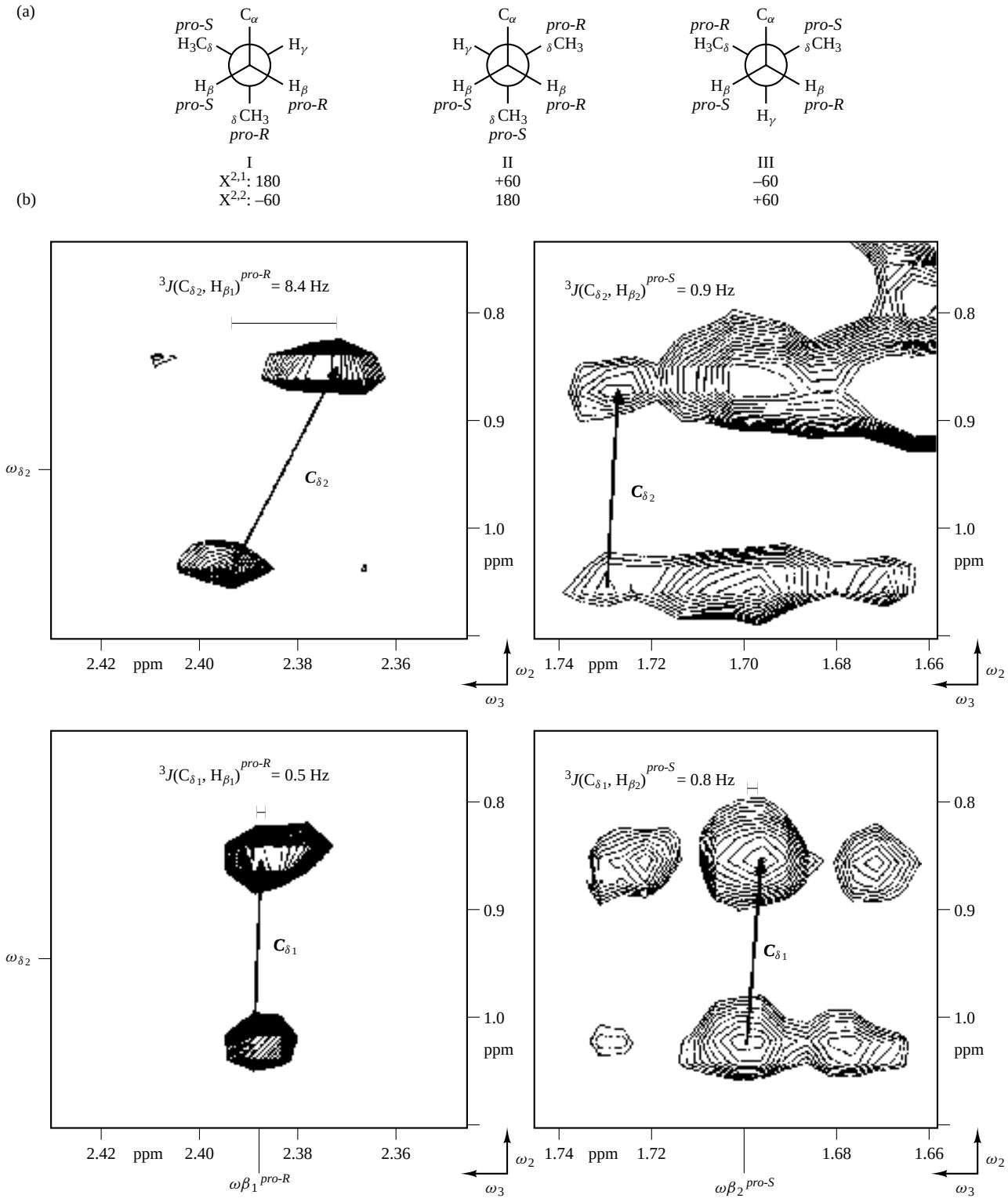

Figure 3 (a) Staggered rotamers around the $C_\beta - C_\gamma$ bond of leucine. (b) Slices through the three-dimensional HSQC-TOCSY showing the four C_δ,H_δ,H_β cross peaks with the displacement vectors due to C_δ. The lower traces are taken at $\omega_1 = \delta(C_{\delta 1}) = 23.6$ ppm and the two upper traces at $\omega_1 = \delta(C_{\delta 2}) = 20.2$ ppm

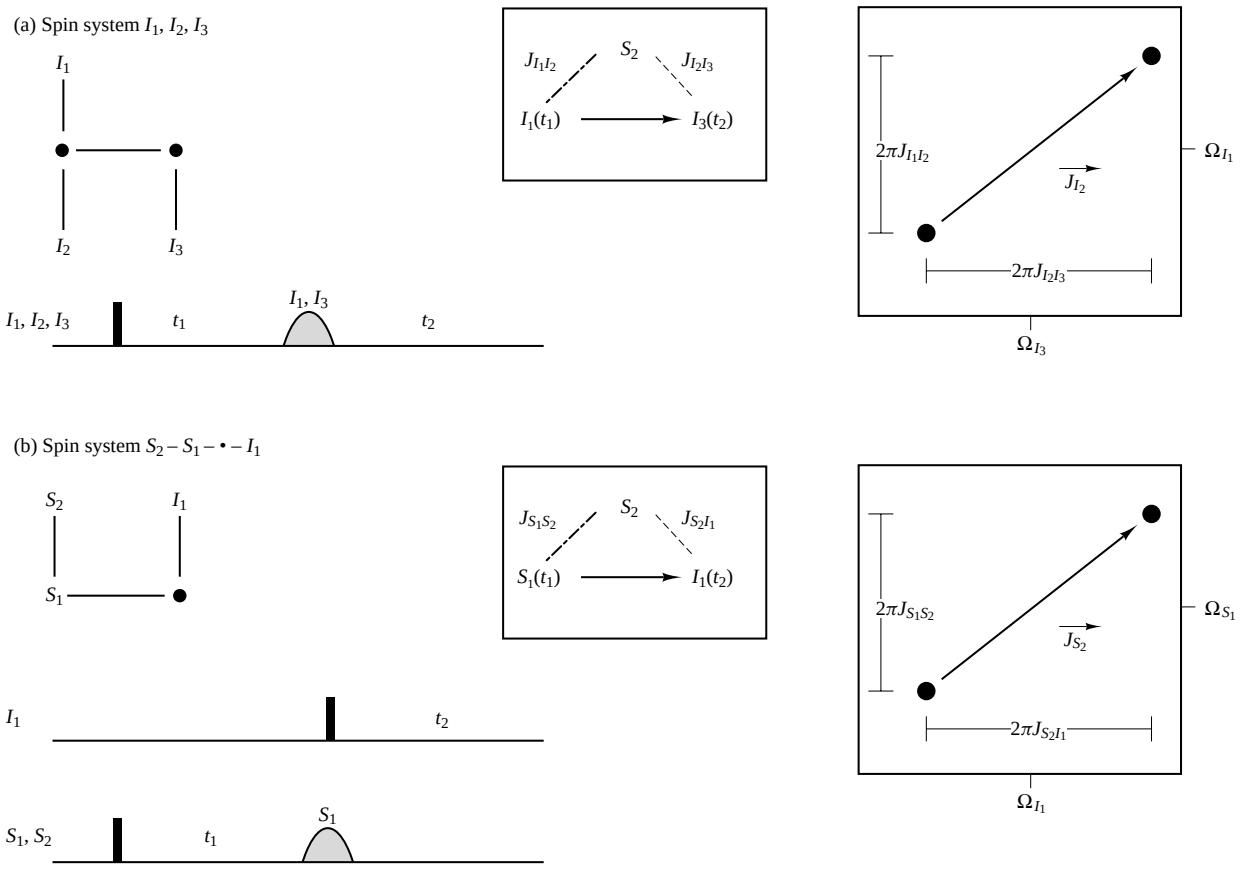

Figure 4 (a) The SOFT-COSY experiment. In a homonuclear three spin system, I_1 and I_3 are correlated by an I_1,I_3-selective mixing pulse. In the example given, the geminal $^2J(I_1,I_2)$ coupling is used as associated coupling in t_1. (b) The SOFT-hetero-COSY experiment. In the heteronuclear S_2–S_1–·–I_2 spin system S_1-selective pulses leave the S_2 spin untouched. The homonuclear $^1J(S_1,S_2)$ coupling serves as an associated coupling in t_1

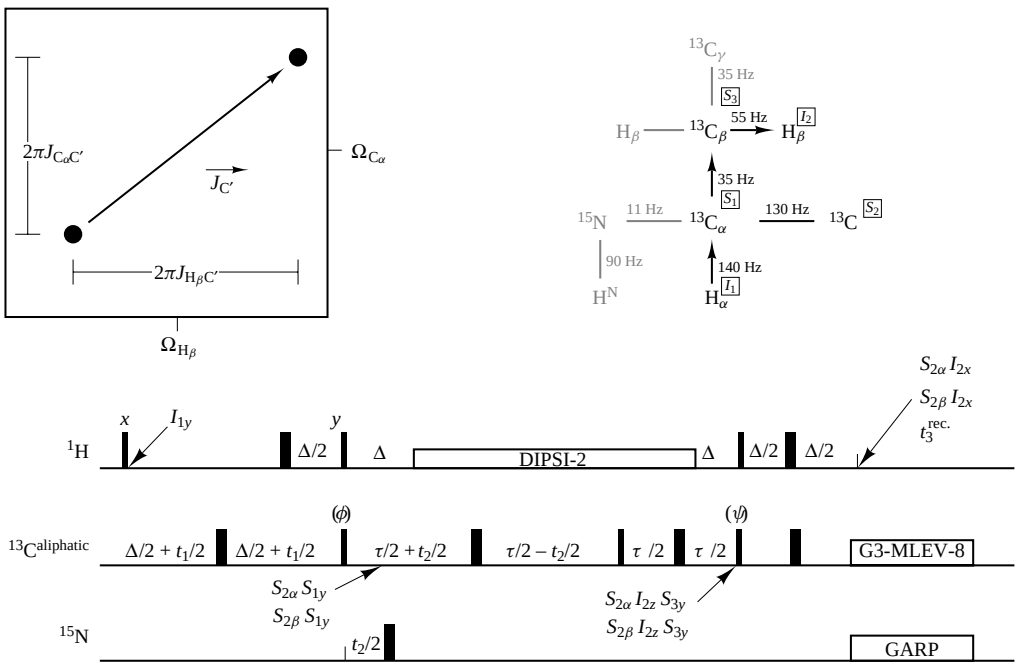

Figure 5 Pulse sequence for the SOFT-HCCH-COSY experiment. In the application to proteins, typical parameters are: $\Delta = [2^1J(C_\alpha,H_\alpha)]^{-1}$; $\tau =]2^1J(C_\alpha,C_\beta)]^{-1}$; $\tau' = [4^1J(C_\alpha,C_\beta)]^{-1}$; $\Delta' = [4^1J(C_\beta,H_\beta)]^{-1}$; $\phi = x, -x$; $\psi = x, x, -x, -x$; rec. = $x, -x, -x, x$

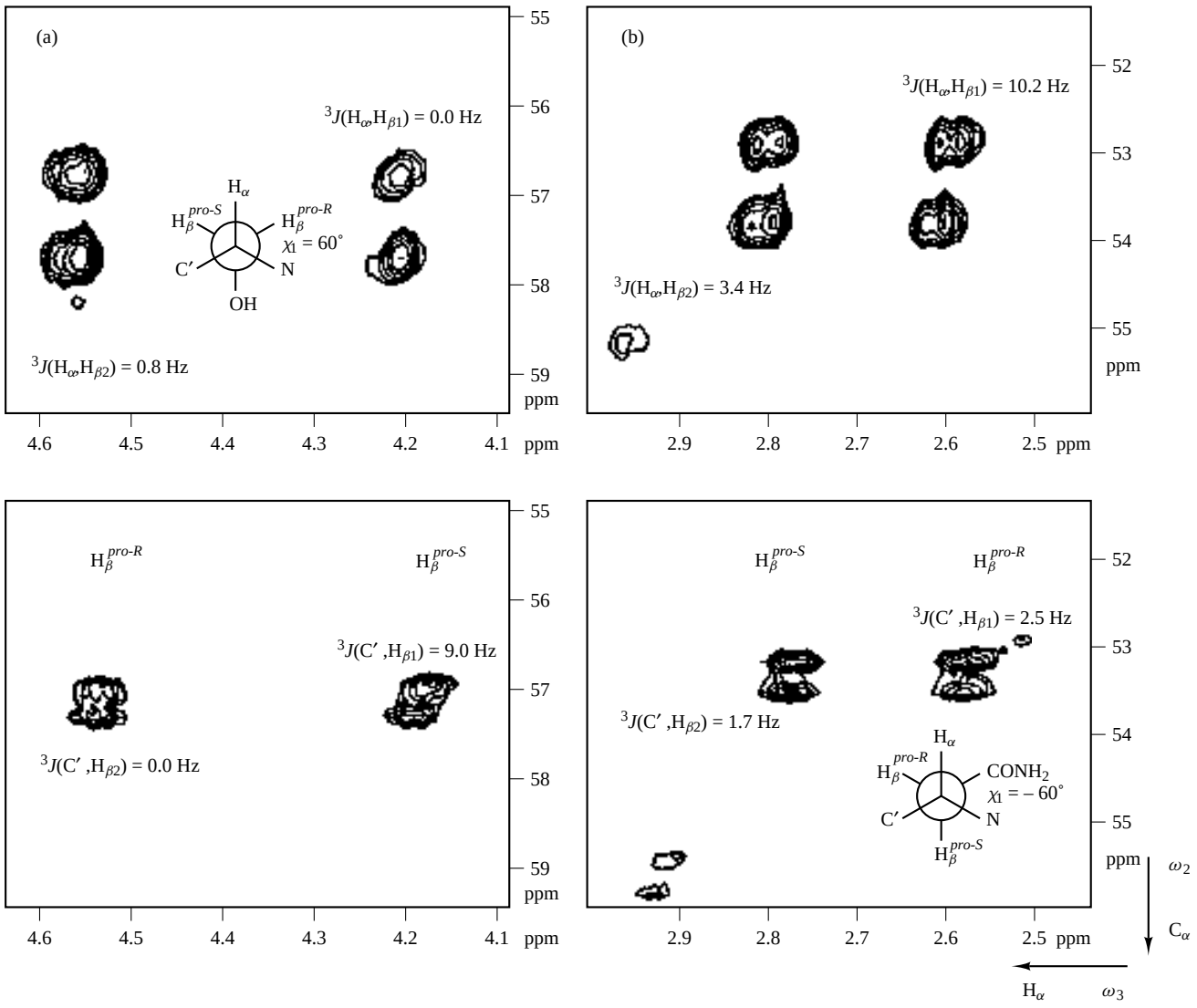

Figure 6 (a) and (b)

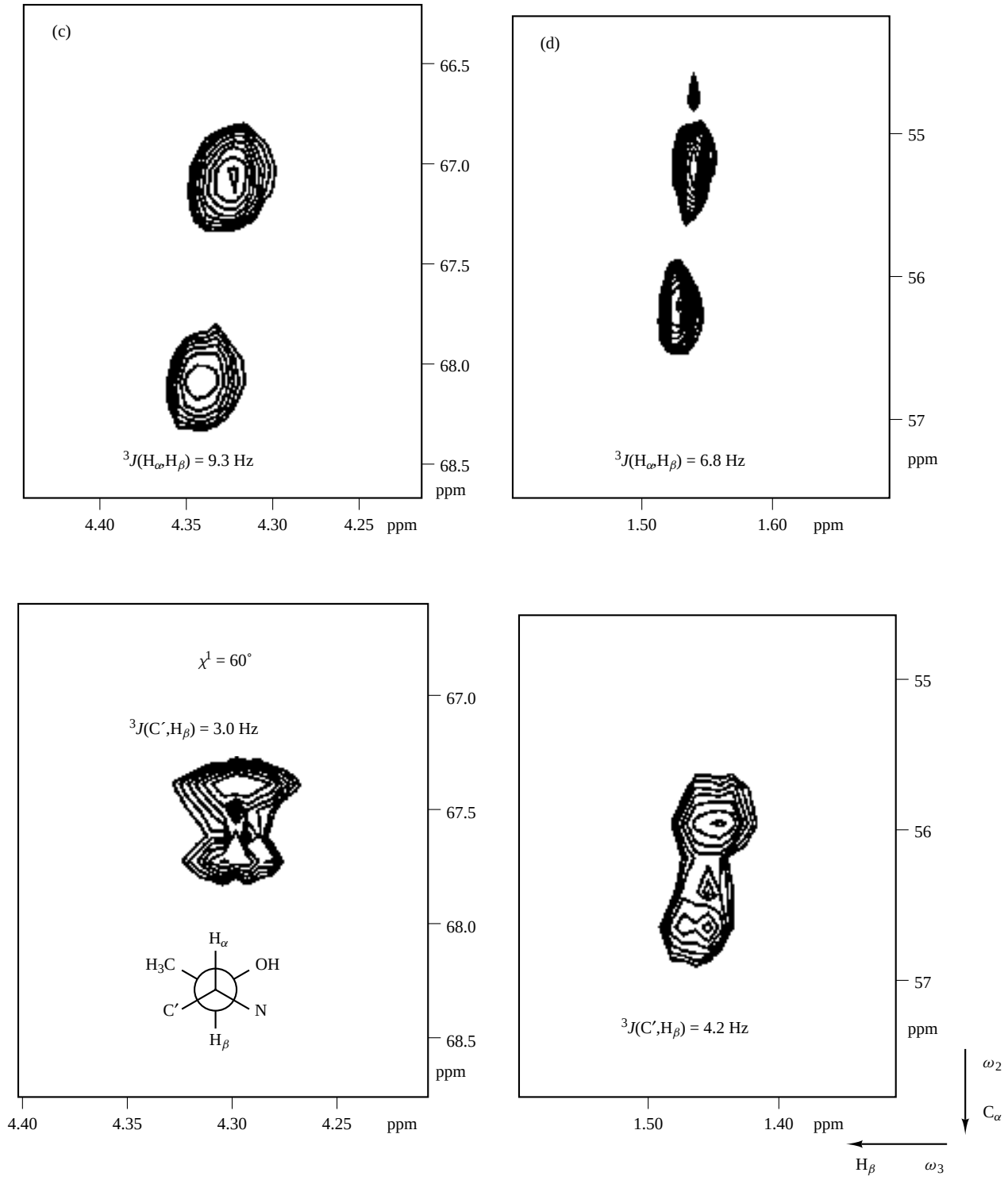

Figure 6 Cross peaks for: (a) Ser_{12}; (b) Asn_{98}; (c) Thr_{18}; (d) Ala_{21}. Upper and lower traces show the C_α,H_β cross peaks from the SOFT-HCCH-ECOSY and the SOFT-HCCH-COSY experiments, respectively. (a) Ser_{12} has two small $^3J(H_\alpha,H_\beta)$ couplings and one large $^3J(H_\beta,C')$ coupling. The predominant rotamer around χ_1 is therefore when $\chi_1 = 60^\circ$, and the higher frequency $H_{\beta 1}$ is $H_\beta{}^{pro\text{-}R}$. (b) From the two small $^3J(H_\beta,C')$ couplings and the large $^3J(H_\alpha,H_{\beta 1})$ coupling of Asn_{98}, it follows that the predominant rotamer is at $\chi_1 = -60^\circ$ and the higher frequency $H_{\beta 1}$ is $H_\beta{}^{pro\text{-}S}$. (c) Thr_{18} has a large $^3J(H_\alpha,H_{\beta 1})$ coupling of 9.3 Hz and a small $^3J(C',H_\beta)$ coupling of 3.0 Hz; χ_1 is therefore -60°. (d) The two cross peaks of Ala_{21} exhibit average $^3J(H_\alpha,H_{\beta 1})$ and $^3J(C',H_\beta)$ coupling constants of 6.8 and 4.2 Hz, respectively

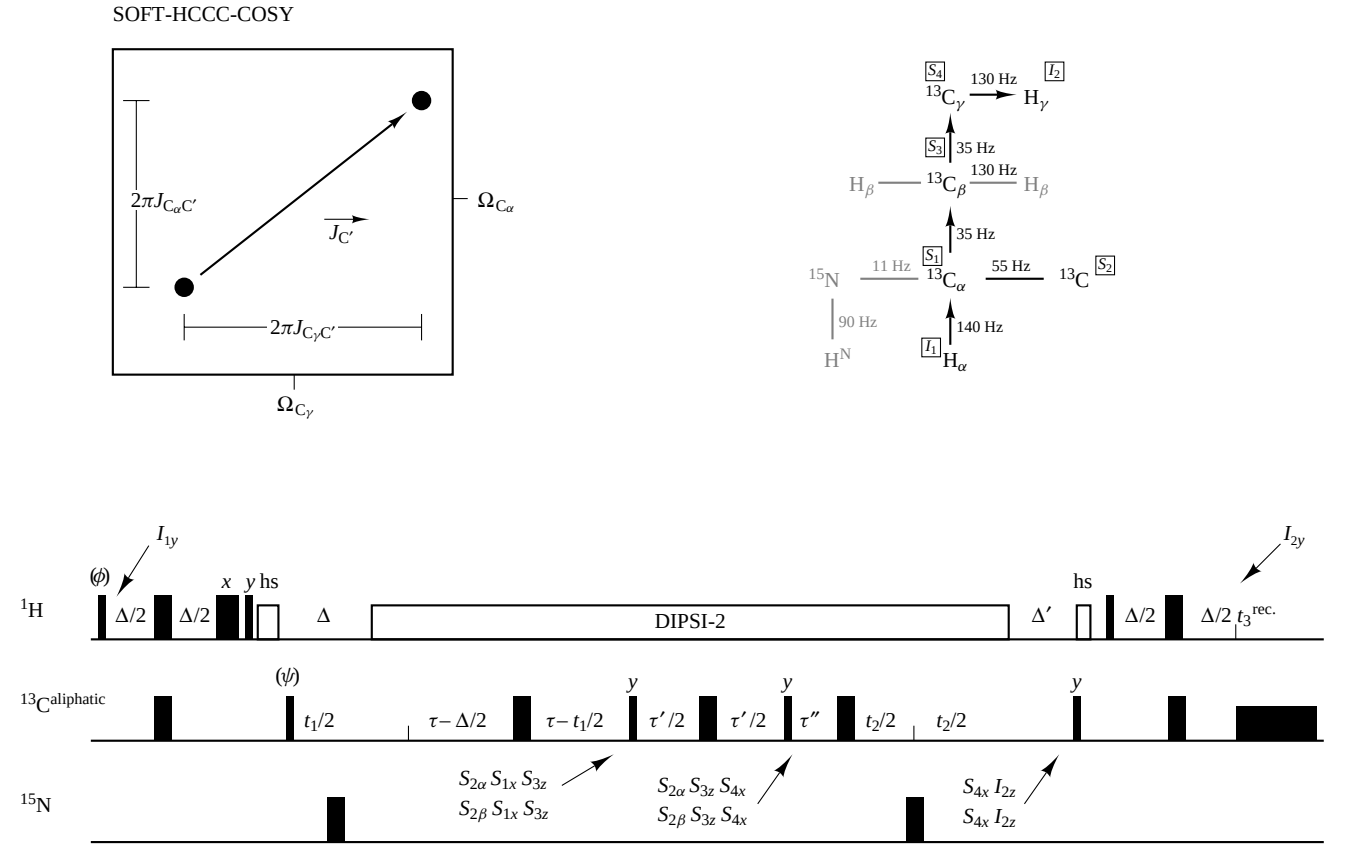

Figure 7 Pulse sequence for the SOFT-HCCC-COSY experiment. In the $S_2{-}S_1{-}\cdot{-}S_4$ spin system S_1,S_4 selective pulses leave S_2 untouched. The coupling of interest is measured in the ω_1,ω_2 cross peak of the three-dimensional experiment. In the application to proteins, typical parameters are: $\Delta = [2^1J(C_\alpha,H_\alpha)]^{-1}$; $\tau = [2^1J(C_\alpha,C_\beta)]^{-1}$; $\tau' = [(54/90)^1J(C,C)]^{-1}$; $\Delta' = [6^1J(C_\gamma,H_\gamma)]^{-1}$; $\phi = x, -x$; $\psi = x, x, -x, -x$; rec. $= x, -x, -x, x\tau''\Delta^1 + t_2(0) + \tau_p$

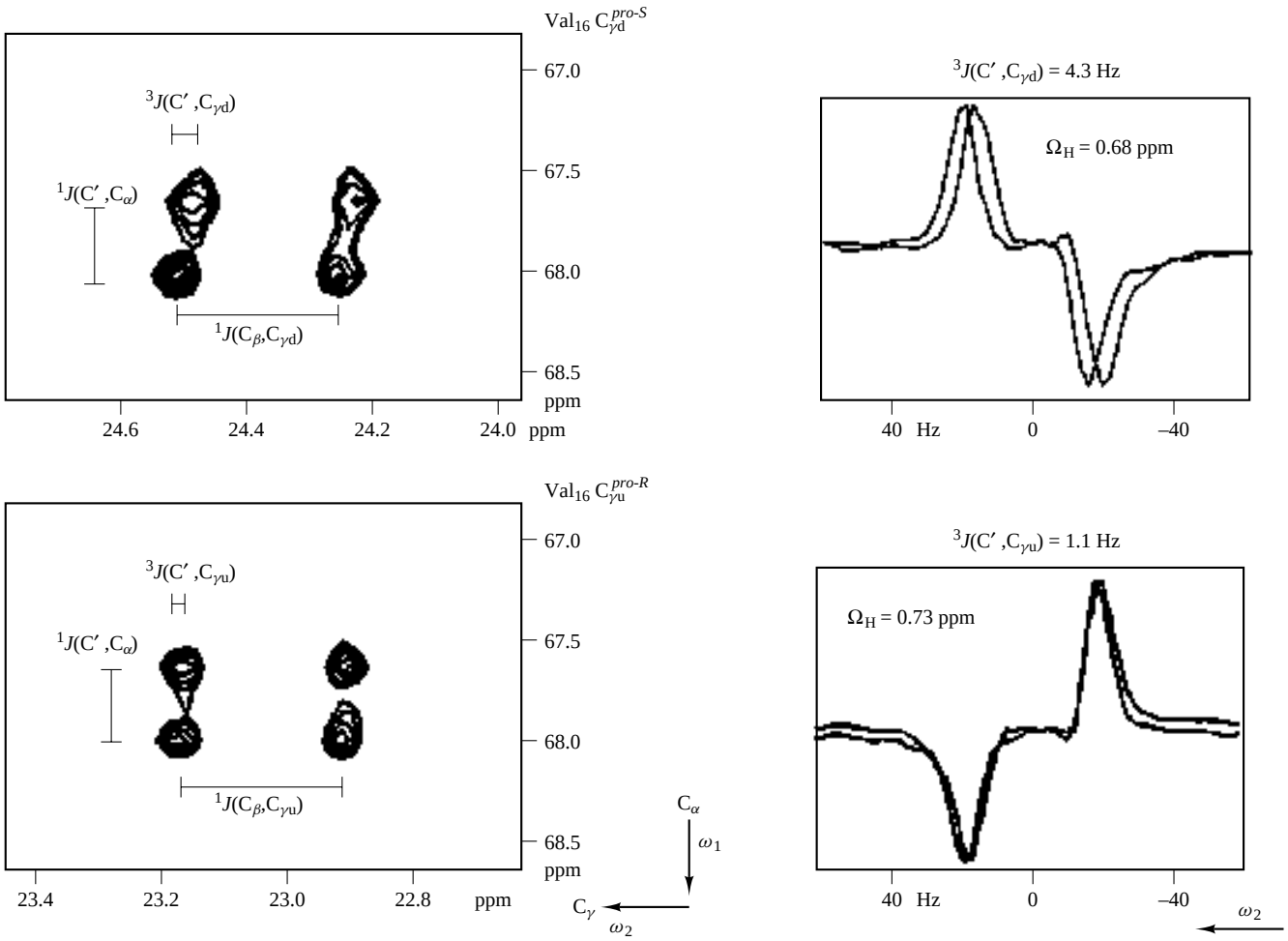

Figure 8 One-dimensional rows and two-dimensional slices from the SOFT HCCC-COSY on ribonuclease T_1. The C_β,H_β cross peaks are displaced due to C′. The antiphase splitting observed is the $^1J(C_\beta,C_\gamma)$ coupling of around 37 Hz

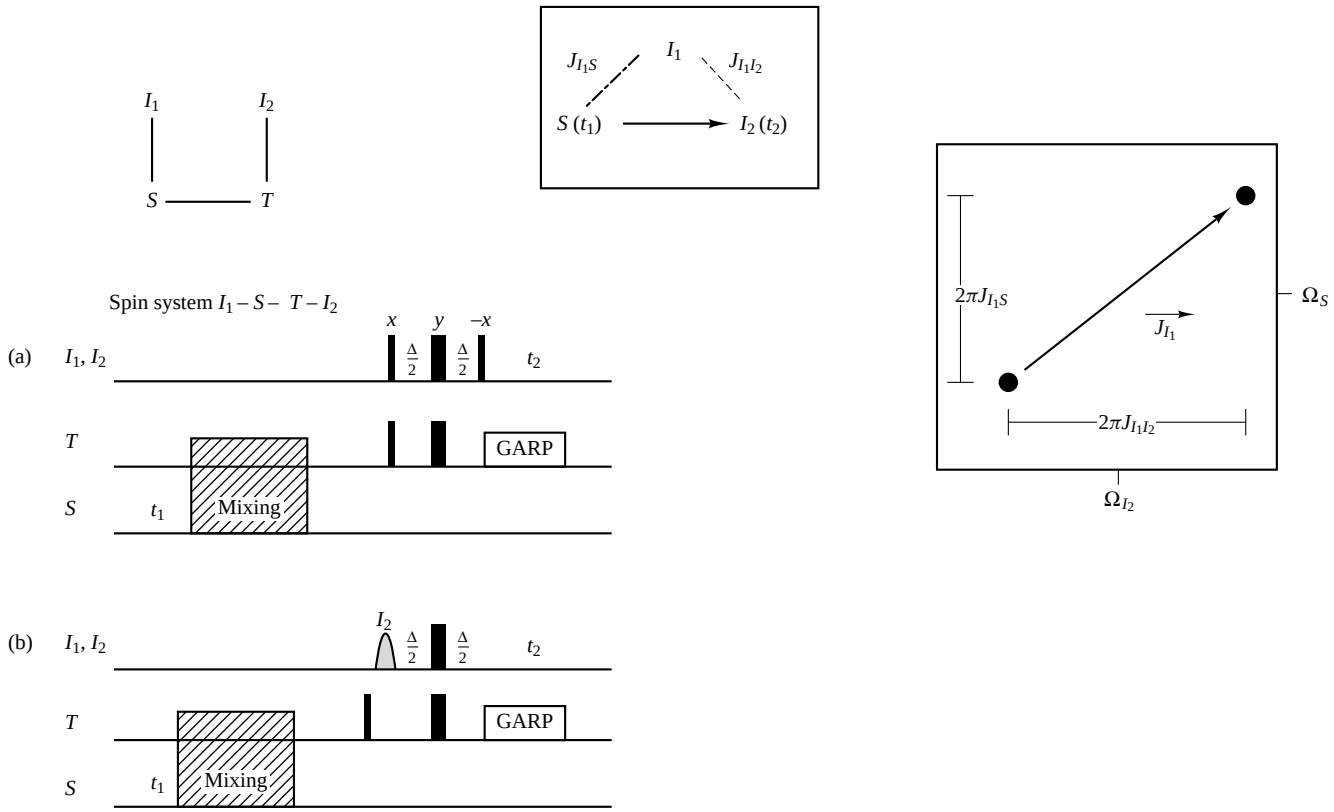

Figure 9 (a) Selection between homonuclear spins bound to different heterospins with BIRD pulses. In the $I_1{-}S{-}T{-}I_2$ spin system, I_2 bound to T evolves heteronuclear $J(I_2,T)$ coupling in the final BIRD refocusing period, whereas the spin states of I_1 bound to S remain unaltered. I_1 serves as passive spin, the ${}^nJ(I_1,I_2)$ coupling can be measured. For typical parameters see Figure 10. (b) Instead of using BIRD spin-topology-filtering techniques, I_2-selective pulses can be used in certain cases to distinguish between I_1 and I_2

experiment is a SOFT-HCCH-COSY, in which C_α (A) is correlated with H_β (B). In the constant time period $\tau = [2J(C_\alpha,C_\beta)]^{-1}$, the ${}^1J(C',C_\alpha)$ coupling, used as the associated coupling in t_1, has evolved a phase of 142°. Mirror image linear prediction[27,45,46] has to be applied to enhance the resolution in ω_1. From inspection of the ${}^3J(C',H_\beta)$ and the ${}^3J(H_\alpha,H_\beta)$ couplings (see Section 5) the conformation around χ_1 and the stereochemical assignments of the H_β protons can be derived. Four representative C_α,H_β cross peaks of the SOFT-HCCH-COSY and the SOFT-HCCH-ECOSY experiments (discussed in Section 6) measured on ribonuclease T_1 are shown. In each case, the unique pattern of large and small couplings provide the assignment to one of the three staggered rotamers. As shown in Figure 6, the predominant rotamer around χ_1 is $\chi_1 = -60°$ for Asn_{98}, since both ${}^3J(C',H_\beta)$ couplings are small and one ${}^3J(H_\alpha,H_\beta)$ coupling is large. The lower frequency H_β can be assigned as *pro-R* since it shows a large coupling with H_α. The preferred conformation and the stereochemical assignment of the other residues are indicated on the figure.

Using the same basic experiment, homonuclear ${}^3J(C',C_\gamma)$ couplings can be determined for the stereochemical assignment of valine methyl groups in the SOFT-HCCC-COSY experiments[47] by correlating C_α (A) and C_γ (B), and leaving C' as the passive spin C. Figure 7 shows the pulse sequence for the SOFT-HCCC-COSY experiment, and Figure 8 shows the two C_α,C_γ cross peaks for Val_{16} in ribonuclease T_1. The large ${}^3J(H_\alpha,H_\beta)$ coupling of 12.4 ± 0.9 Hz and the small ${}^3J(C',H_\beta)$ coupling of 0.53 ± 0.4 Hz indicate a $\chi_1 = 180°$ (not shown). Thus the low-frequency C_γ is the *pro-R* carbon atom, and the high-frequency C_γ is the *pro-S* carbon atom.

6 BIRD PULSES FOR SPIN TOPOLOGY FILTERING: MEASURING HOMONUCLEAR ${}^nJ(I_1,I_2)$ COUPLINGS IN AN $I_1{-}S{-}T{-}I_2$ OR $I_1{-}S{-}\cdot{-}I_2$ SPIN SYSTEM

If one of the active spins (e.g. B) and the passive spin C have the same spin isotope (e.g. I) nonselective pulses cannot be used for polarization transfer from A to B, because C would be touched. However, spin topology filtering using the different transformation properties of two spins of the same isotope that are bound to different heteronuclei (e.g. ${}^1H{-}{}^{13}C$ and ${}^1H{-}{}^{15}N$) under bilinear rotation[48,49] can be used such that B is sensitive for the I pulses and C is not. Effective polarization transfer to B leaving C untouched is then possible. In the following, the different transformation properties of the I_2 spin (e.g. H_α)

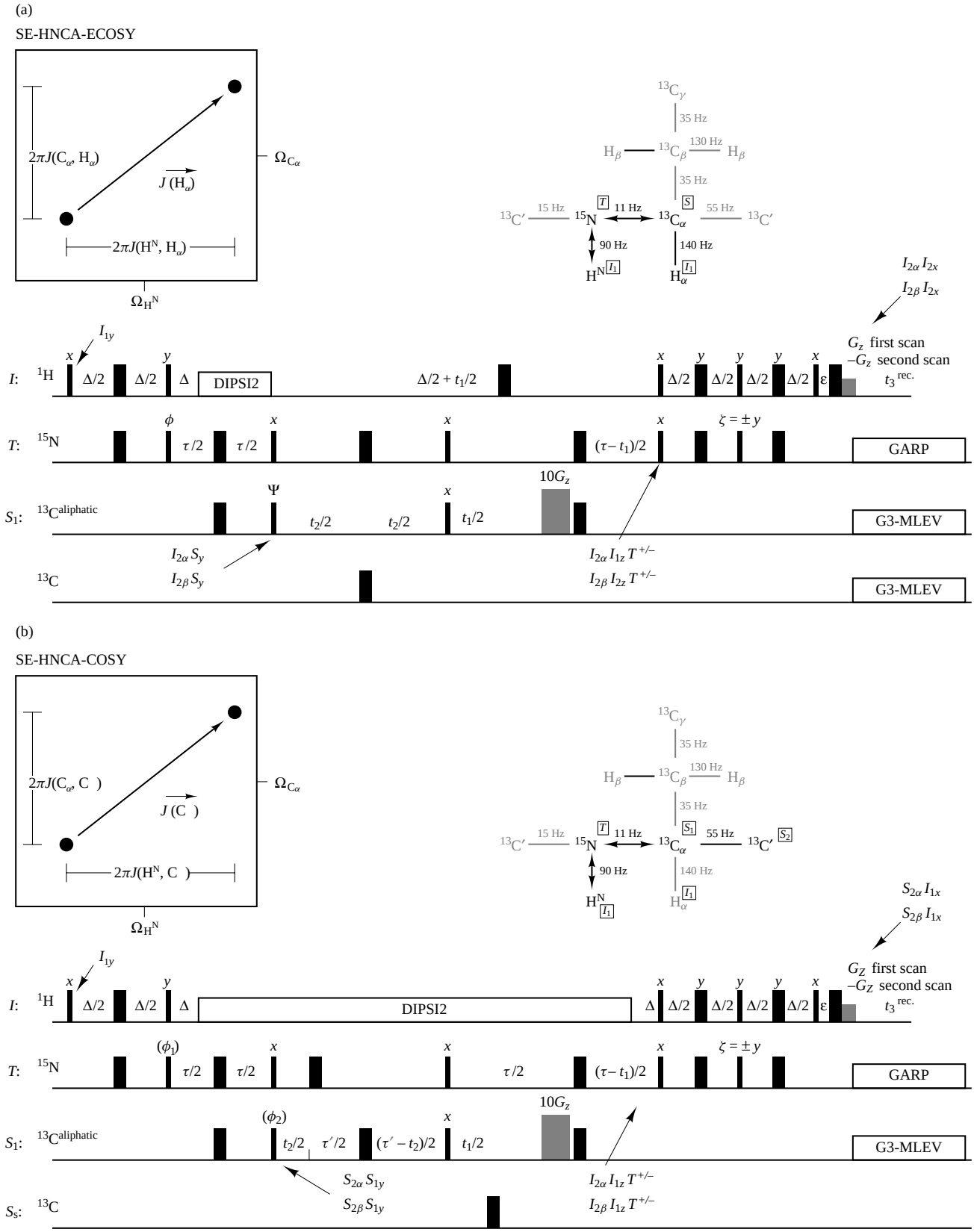

Figure 10 (a) HNCA-ECOSY with sensitivity enhancement and using a heteronuclear gradient echo to measure $^3J(H^N,H_\alpha)$ couplings. The parameters are: $\Delta = [2J(H^N,H_\alpha)]^{-1}$; $\tau = [2J(C_\alpha,N)]^{-1}$; $\tau' = [J(C_\alpha,C_\beta)]^{-1}$; $\epsilon = \tau_g$; $\phi = x, -x$; $\psi = x, x, -x, -x$; rec. = $x, -x, -x, x$. The coupling of interest is measured in the (ω_2,ω_3) plane of the three-dimensional experiment in cross peaks correlating C_α and H^N. The $^1J(C_\alpha,H_\alpha)$ coupling of 145 Hz serves as an associated coupling in ω_2. (b) SOFT-HNCA-COSY with sensitivity enhancement and using a heteronuclear gradient echo to measure $^3J(C',H^N)$ couplings. The parameters are the same as those in (a). The $^1J(C',C_\alpha)$ coupling of 55 Hz serves as an associated coupling in ω_2

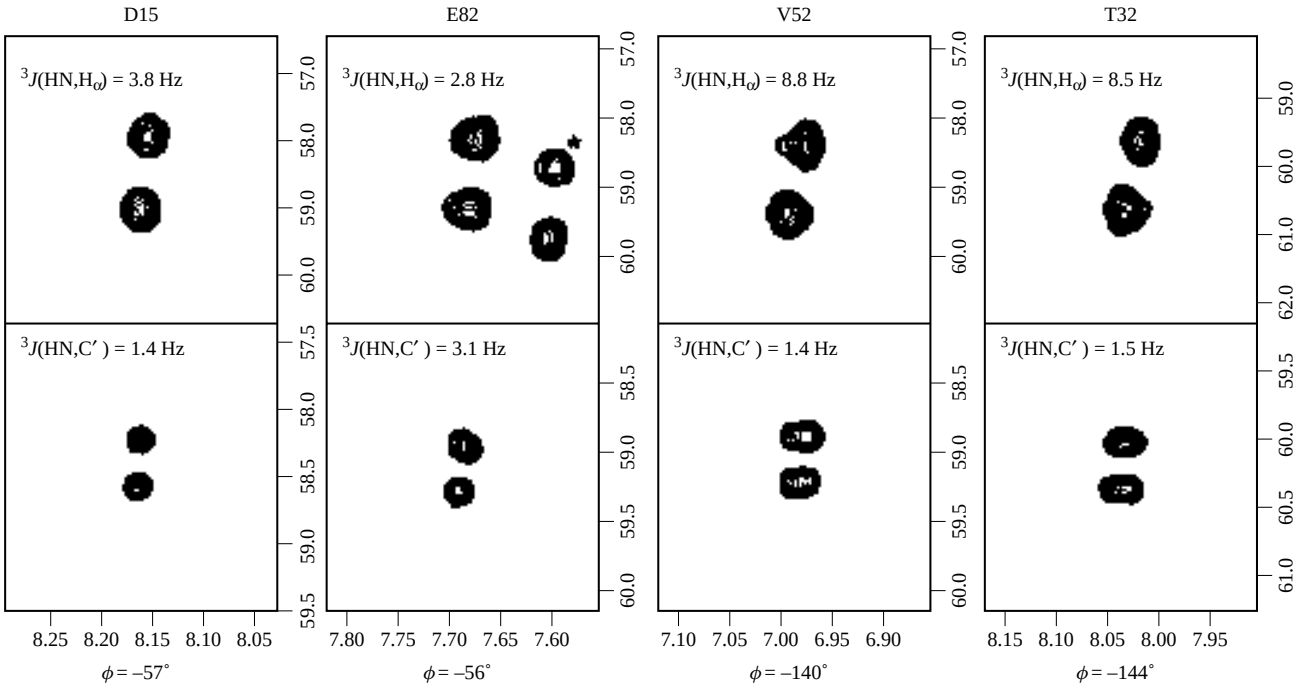

Figure 11 Cross peaks for Asp$_{15}$, Glu$_{82}$, Val$_{52}$, and Thr$_{32}$. Upper and lower traces show the C$_\alpha$,H^N cross peaks from the SOFT-HNCA-ECOSY and the SOFT gradient enhanced HNCA-COSY. The ^3J(H^N,H$_\alpha$) and ^3J(C′,H^N) coupling constants derived from the ω_3 splittings and the derived ϕ angles are indicated

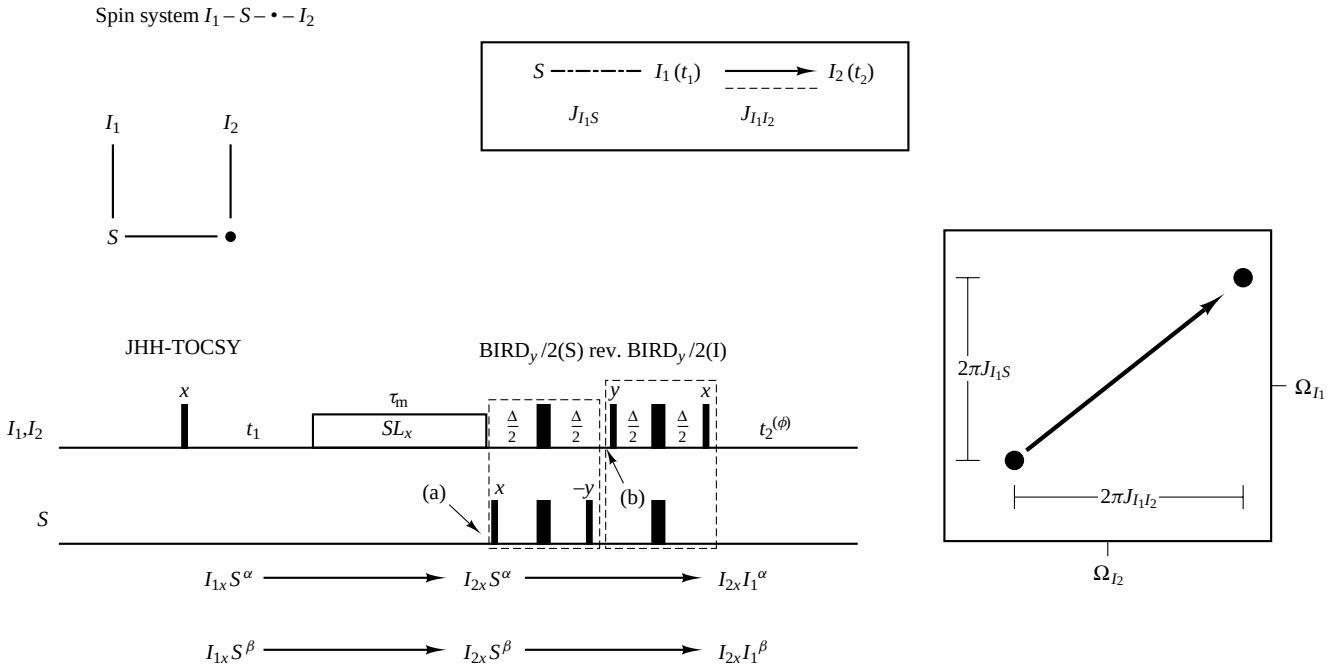

Figure 12 JHH-TOCSY for measuring $^nJ(I_1,I_2)$ couplings in a $I_1 - S - \cdot - I_2$ spin system. The spin state of S in t_1 is transferred to the spin state of spin I_1 in t_1. Selection of a coherence transfer pathway by gradients,[17] although yielding a loss of a factor of $\sqrt{2}$ in signal-to-noise ratio compared with conventional HSQC experiments, is advantageous when measuring ^3J(H^N,H$_\alpha$) couplings in proteins, since the coupling is measured on the H$_\alpha$ resonance. Typical parameters are: $\Delta = [J(I_1,S)]^{-1}$; $\phi = x, -x$; rec. = $x, -x$. Scaling of the heteronuclear coupling could be implemented [see Figure 2(a)]

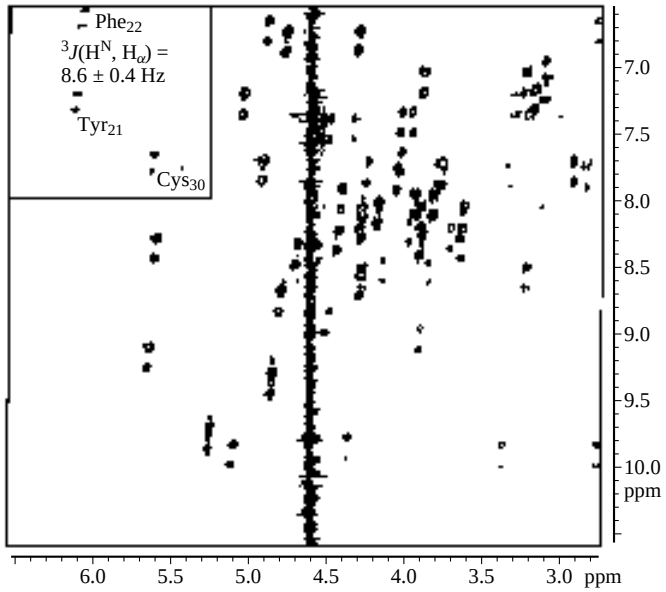

Figure 13 Two-dimensional plot of JHH-TOCSY applied to ^{15}N-enriched BPTI mutant[26] showing the excellent water suppression and the high sensitivity of the experiment

bound to the heteronucleus S ($^{13}C_\alpha$) and the I_1 spin (e.g. H^N) bound to T (^{15}N) under the BIRD sequence shown in Figure 9(a) will be discussed. Using the pulse scheme

$$90^\circ_x(I) - \Delta/2 - 180^\circ_y(I, T) - \Delta/2 - 90^\circ_{-x}(I) \qquad (1)$$

a $2I_{1z}T_z$ operator that can be prepared after the evolution period of an HSQC-type experiment is transferred to detectable proton magnetization I_{1x}, whereas for spin I_2 which is not coupled to spin T the pulses can be concatenated to a $0^\circ(I)$ pulse. Thus I_2 is not affected during the polarization transfer from spin T to I_1.[42,43,50,51]

This principle has been applied in SOFT-HNCA-ECOSY experiments correlating $^{13}C_\alpha$ (A) with H^N (B). H_α is the passive spin C. N,H^N antiphase coherence is transferred to H^N magnetization without touching H_α. From this experiment $^3J(H^N,H_\alpha)$ couplings defining the backbone angle ϕ become available.[42,43,49–54] The BIRD-filtering concept is also compatible with the use of gradient sensitivity enhanced correlation,[42] yielding excellent water suppression and optimal sensitivity. Figure 10 shows the pulse sequences SOFT-HNCA-ECOSY and SOFT-HNCA-COSY (see Section 3) obtained using gradient sensitivity enhanced correlation for the measuring of $^3J(H^N,H_\alpha)$ and $^3J(C',H^N)$ coupling constants, respectively. The resulting cross peaks are shown for four different cross peaks in ribonuclease T_1 in Figure 11. The combined analysis of these couplings leads to an unambiguous assignment of the ϕ-angle rotamer whenever only one rotamer around ϕ is populated.

Another implementation of the BIRD-filtering concept is the JHH-TOCSY developed by Willker and Leibfritz[55] (Figure 12). This experiment can be implemented in a spin system I_1–S–·–·–I_2 with one kind of heterospin. The idea of this experiment is to use S as the passive spin during t_1. This encodes a frequency shift of $\pm\pi J(I_1,S)$ onto the I_1 multiplet for S^α and S^β, respectively. After the mixing (transfer from I_1 to I_2) the polarization of the S spin is completely transferred to polarization of the I_1 spin ($S^\alpha \rightarrow I_1^\alpha$; $S^\beta \rightarrow I_1^\beta$). Then, during t_2, a frequency shift of $\pm\pi J(I_1,I_2)$ is encoded for the two submultiplets that were displaced in ω_1 by $\pm\pi J(I_1,S)$. This transfer can be achieved by the sequence (Figure 12)

$$\begin{aligned} &\text{(a)} \qquad\qquad \text{(b)} \\ I_{2x}(1/2 \pm S_z) &\rightarrow I_{2x}(1/2 \pm 2I_{1z}S_z) \rightarrow I_{2y}(1/2 \pm I_{1z}) \\ &= I_{2y}(1/2 \pm I_1^{\alpha/\beta}) \end{aligned} \qquad (2)$$

Interestingly, this is the only experiment in this section that cannot be classified according an ECOSY triangle, since two different spins serve as passive spins in t_1 and t_2. The application of this experiment on a ^{15}N-enriched sample of a BPTI mutant using gradient coherence selection ensuring excellent water suppression is shown in Figure 13.[56] A $^3J(H^N,H_\alpha)$ coupling constant of 8.6 ± 0.4 Hz is found for Phe_{22}.

7 THE ECOSY EXPERIMENT FOR THE MEASUREMENT OF HOMONUCLEAR $^nJ(I_1,I_1)$ COUPLINGS IN AN I_1–I_2–I_3 SPIN SYSTEM AND $^nJ(I_1,I_2)$ COUPLINGS IN AN I_1–S_1–·–·–I_2 SPIN SYSTEM

All the above mentioned methods impose special conditions on the spin system under study. The transfer between active spins, while not touching the passive spin, can be performed in homonuclear spin systems I_1–I_2–I_3 by a combination of experiments with different carefully chosen flip angle pulses in the ECOSY experiment (Figure 14).[1–3] An approximation to this procedure is the application of a small flip angle pulse in the P-ECOSY[2,57,58] experiment.

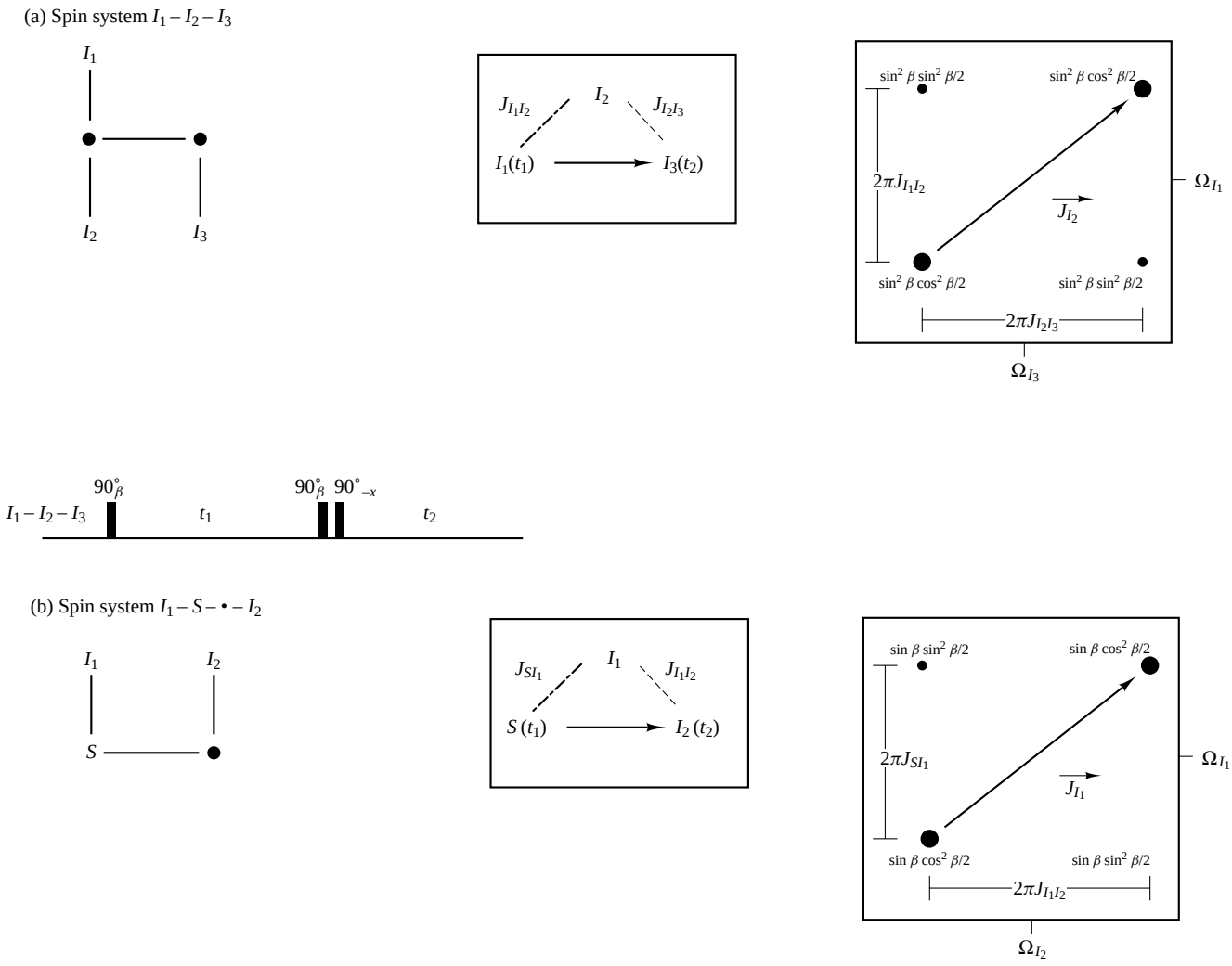

Figure 14 (a) The ECOSY experiment. In a homonuclear three-spin system, I_1 and I_3 are correlated by a $\beta \neq 90°$ mixing pulse. The cross-peak intensities of connected and nonconnected transitions of I_2, depending on the mixing pulse β, are indicated. Preferentially, geminal $^2J(I_1,I_2)$ couplings serve as associated couplings in t_1. (b) The HCCH-ECOSY experiment. In a heteronuclear $I_1{-}S_1{-}\cdot{-}I_2$ spin system, S and I_2 are correlated by a $\beta_y(I) \neq 90°$ mixing pulse implemented with phases according to the expansion: $\beta_y = 90°_x\beta_z\ 90°_{-x} = \beta_z\ 90°_\beta\ 90°_{-x}$. The cross-peak intensities of connected and nonconnected transitions of I_1, depending on the mixing pulse β, are indicated. The $^1J(S,I_1)$ coupling serves as the associated coupling in t_1. In the application to proteins, the $^1J(C',C_\alpha)$ coupling should be refocused in t_1, as should long-range $^3J(C',H_\beta)$ coupling in t_1. The parameters are: $\Delta = [2J(C_\alpha,H_\alpha)]^{-1}$; $\tau = [2J(C_\alpha,C_\beta)]^{-1}$; $\tau' = [4J(C_\alpha,C_\beta)]^{-1}$; $\Delta' = [2J(C_\alpha,H_\alpha)]^{-1}$; $\phi = x, -x$; $\psi = x, x, -x, -x$; rec. $= x, -x, -x, x$. The same pulse sequence can be used to measure J(C,H) couplings in oligonucleotides when replacing P for C′. A source of systematically smaller couplings is the evolution of chemical shift of the two rows displaced in ω_2 by $J(I_1,I_2)$. The acquired phase difference $\Delta\phi$ depends on the size of the coupling constants of interest and is given for a refocusing delay Δ: $\Delta\phi = J(H,H) \cdot \Delta \cdot 360°$. This phase difference can easily be corrected for by different phasing of the two extracted rows

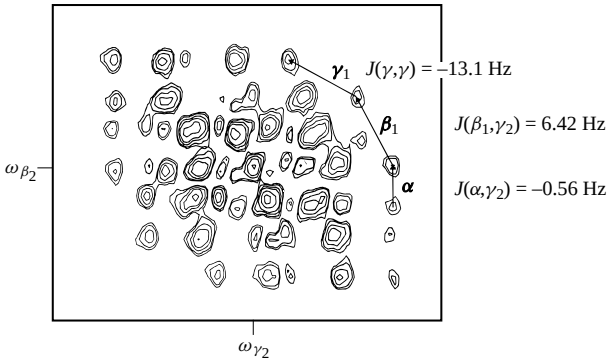

Figure 15 $H_{\beta 2} \rightarrow H_{\gamma 2}$ cross peak multiplet of Pro_8 in the 300 MHz ^1H spectrum of antamanide. The displacement vectors due to the three passive spins H_α, $H_{\beta 1}$, and $H_{\gamma 1}$ are clearly visible. All three vectors point from lower right to upper left. Assuming a negative sign for the aliphatic $^2J(H,H)$ coupling constants, the vicinal coupling $J(H_{\beta 1},H_{\gamma 2})$ is found to be positive and, due to the positive coupling constant between H_α and $H_{\beta 2}$ found in another cross peak, the $^4J(\alpha_1,\gamma_2)$ coupling is found to be negative.[3]

Thus choosing $\beta = 36^\circ$ gives a ratio for the undesired ($I_3^\alpha \rightarrow I_3^\beta$ and $I_3^\beta \rightarrow I_3^\alpha$) to the desired ($I_3^\alpha \rightarrow I_3^\alpha$ and $I_3^\beta \rightarrow I_3^\beta$) transfer of $\sin^2(\beta/2)/\cos^2(\beta/2) = \tan^2(\beta/2)$, which is about 10%. At the same time, polarization transfer between I_1 and I_2 ($2I_{1x}I_{2z} \rightarrow 2I_{1z}I_{2x}$) is achieved with a $\sin^2\beta = 35\%$ efficiency compared with the value obtained for $\beta = 90^\circ$. Transfer between a heteronucleus S to I_1 is achieved with $\sin\beta = 59\%$ compared with $\beta = 90^\circ$. Due to the incomplete suppression of the nonconnected transitions, asymmetrical signal components that systematically shift the submultiplets together and lead to systematically smaller coupling constants are introduced. Dispersive diagonal peak contributions can be suppressed in the P-ECOSY experiment by subtraction of a second experiment with $\beta = 0^\circ$.

The ECOSY procedure relies on a linear combination of different flip angles β that are chosen so as to suppress completely the undesired nonconnected transitions. The deduction of flip angles and weights depends upon the spin system under study. For more details, the interested reader is referred to the paper by Griesinger et al.[2]

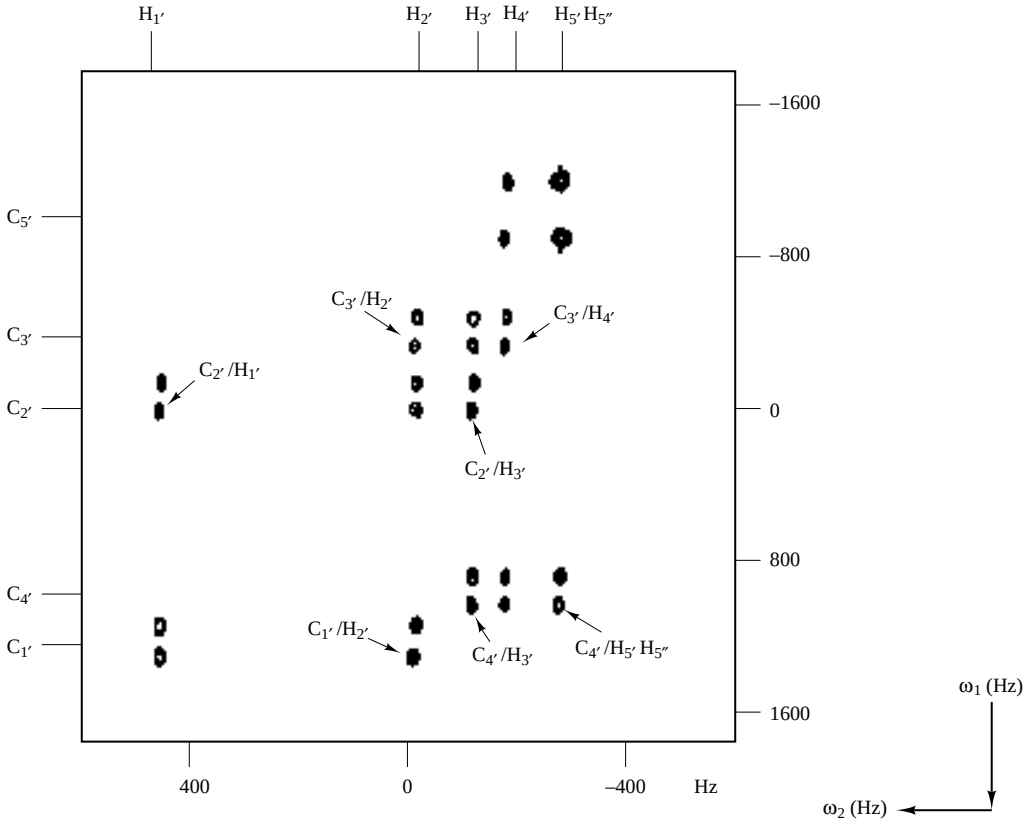

Figure 16 A 400 MHz HCCH-ECOSY spectrum with flip angle β for ^{13}C,^{15}N labeled 5′-GMP. The doublet structure in the two frequency dimensions is clearly visible

The transfer amplitudes of a polarization operator I_3^α or I_3^β are given by

$$I_3^\alpha \rightarrow I_3^\alpha \cos^2(\beta/2) + I_3^\beta \sin^2(\beta/2) \qquad (3a)$$

$$I_3^\beta \rightarrow I_3^\beta \cos^2(\beta/2) + I_3^\alpha \sin^2(\beta/2) \qquad (3b)$$

Figure 15 shows the Pro_8 β_2/γ_2 cross peak in antamanide, and the corresponding displacement vectors in this CH_2-CH_2 fragment.[3] ECOSY and P-ECOSY sequences have been successfully applied to peptides and proteins and to oligonucleotides[116–127] to obtain local conformational information. For completeness, a gradient selected ECOSY experiment based on the linear combination of multiple quantum filtered COSY spectra has been published.[128] The sensitivity

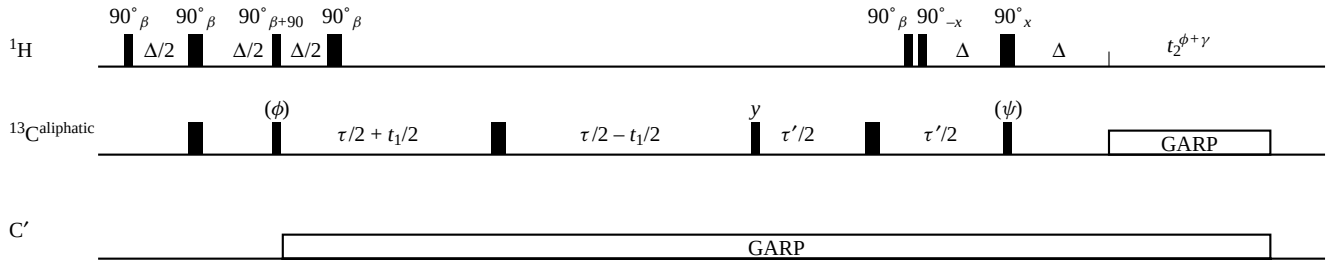

Figure 17 HCCH-ECOSY with a final 'DEPT' C7 → H transfer. The flip angle β is chosen such that the nonconnected transitions are suppressed. Alternatively, two experiments with β = 44.4 and 135.6 and weights of 6 and 1, respectively, are combined, as described for the 'INEPT' version

Table 1 Sensitivity Gain Provided by a 'DEPT Transfer'

	^{13}CH	$^{13}CH_2$	$^{13}CH_3$
S(DEPT)/S(INEPT)[a]	$1/\sin \pi J(C,H)\Delta'$	$\cos\theta/[\sin \pi J(C,H)\Delta' \cos \pi J(C,H)\Delta']$	$\cos^2\theta/[\sin \pi J(C,H)\Delta' \cos^2 \pi J(C,H)\Delta']$
$\Delta' = 1/2J(CH)$	1	–	–
$\Delta' = 1/4J(CH)$	1.41	1.62	1.85
$\Delta' = 0/2J(CH)$	1.7	1.7	1.7

[a] Δ' refers to the refocusing delay of the 'INEPT' version.

of such an experiment is, however, considerably reduced compared with the 'nongradient' versions of ECOSY or P-ECOSY.

For ^{13}C-labeled proteins the HCCH-ECOSY experiment [Figure 14(b)] can be applied to obtain proton–proton coupling constants in $H^{13}C-^{13}CH_m$ fragments (where m is the number of protons attached to the carbon atom). In this case only small flip angle pulses[27,129] or selective pulses[130] can be applied in order to fulfill the ECOSY condition, leaving one of the protons untouched in the final C → H transfer. Other implementations using TOCSY for the C → C transfer have been proposed by Emerson and Montelione.[131,132] The determination of H,H coupling constants in $H_k{}^{13}C-{}^{13}CH_m$ moieties is described in the paper by Eggenberger et al.[27]

The number of relevant spins for the C → H spin transfer is either two ($I_1-S_1-\cdot-\cdot-I_2$) or three ($I_1,I_1'-S_1-\cdot-\cdot-I_2$). Coupling constants to protons of methyl groups ($I_1,I_1',I_1''-S_1-\cdot-\cdot-I_2$) are normally not of great interest, due to conformational averaging. The transfer amplitude for a C → H INEPT-type transfer is thus given by sin β cos^2 (β/2) for the $I_1-S_1-\cdot-\cdot-I_2$ spin system and sin β cos β cos^2 (β/2) for the $I_1,I_1'-S_1-\cdot-\cdot-I_2$ spin system. For β_1 = 44.4 with a weight of 6 and β_2 = 135.6 with a weight of 1 for the $I_1-S_1-\cdot-\cdot-I_2$ and −1 for the $I_1,I_1'-S_1-\cdot-\cdot-I_2$ spin systems, the undesired components vanish completely.[133]

The application of such an HCCH-ECOSY sequence applied to ^{13}C-labeled 5′-GMP (guanosine 5′-monophosphate)[133] is shown in Figure 16. The conformational analysis reveals an N/S-conformer equilibrium of 70:30.

A further sensitivity improvement of the HCCH-ECOSY experiment[134] is provided by a 'DEPT transfer' for the last C → H transfer, as demonstrated in Figure 17. If only CH groups are detected, no gain is obtained. The gain in sensitivity of the 'DEPT' version compared with the 'INEPT' [Figure 14(b)] version for CH, CH_2, and CH_3 groups, provided the same flip angle β is used for the proton pulse in each case, is given in Table 1.

8 REFERENCES

1. C. Griesinger, O. W. Sørensen, and R. R. Ernst, *J. Am. Chem. Soc.*, 1985, **107**, 6394.
2. C. Griesinger, O. W. Sørensen, and R. R. Ernst, *J. Chem. Phys.*, 1986, **85**, 6837.
3. C. Griesinger, O. W. Sørensen, and R. R. Ernst, *J. Magn. Reson.*, 1987, **75**, 474.
4. G. S. Harbison, *J. Am. Chem. Soc.*, 1993, **115**, 3026.
5. T. J. Norwood, *J. Magn. Reson., Ser. A*, 1993, **101**, 109.
6. T. J. Norwood and K. Jones, *J. Magn. Reson., Ser. A*, 1993, **104**, 106.
7. R. E. London, *J. Magn. Reson.*, 1990, **86**, 410.
8. P. Schmidt, H. Schwalbe, and C. Griesinger, unpublished results.
9. G. Montelione and G. Wagner, *J. Am. Chem. Soc.*, 1989, **111**, 5474.
10. G. Montelione and G. Wagner, *J. Magn. Reson.*, 1990, **87**, 183.
11. A. Bax and R. Freeman, *J. Magn. Reson.*, 1981, **45**, 177.
12. M. Kurz, P. Schmieder, and H. Kessler, *Angew. Chem.*, 1991, **103**, 1341.
13. P. Schmieder, M. Kurz, and H. Kessler, *J. Biomol. NMR*, 1991, **1**, 403.
14. A. S. Edison, W. M. Westler, and J. L. Markley, *J. Magn. Reson.*, 1991, **92**, 434.
15. E. R. P. Zuiderweg and S. W. Fesik, *J. Magn. Reson.*, 1991, **93**, 653.
16. D. F. Mierke, P. Schmieder, P. Karuso, and H. Kessler, *Helv. Chim. Acta*, 1991, **74**, 1027.
17. P. Schmieder and H. Kessler, *Biopolymers*, 1992, **32**, 435.
18. M. Sattler, H. Schwalbe, and C. Griesinger, *J. Am. Chem. Soc.*, 1992, **114**, 1126.
19. J. Schleucher, B. Schwörer, C. Zirngibl, U. Koch, W. Weber, E. Egert, R. K. Thauer, and C. Griesinger, *FEBS Lett.*, 1992, **314**, 440.

20. L. Poppe, W. S. York, and H. van Halbeek, *J. Biomol. NMR*, 1993, **3**, 81.
21. J. V. Hines, G. Varani, S. M. Landry, and I. Tinoco, *J. Am. Chem. Soc.*, 1993, **115**, 11 002.
22. U. Wollborn, W. Willker, and D. Leibfritz, *J. Magn. Reson., Ser. A*, 1993, **103**, 86.
23. G. T. Montelione, M. E. Winkler, P. Rauenbühler, and G. Wagner, *J. Magn. Reson.*, 1989, **82**, 198.
24. P. Schmieder, J. H. Ippel, H. van den Elst, G. H. van der Marel, J. H. van Boom, C. Altona, and H. Kessler, *Nucleic Acids Res.*, 1992, **20**, 4747.
25. E. Worgötter, G. Wagner, M. Vasak, J. H. R. Kagi, and K. Wüthrich, *J. Am. Chem. Soc.*, 1988, **110**, 2388.
26. I. D. Rae, J. A. Weigold, R. H. Contreras, and G. Yamamoto, *Magn. Reson. Chem.*, 1992, **30**, 1047.
27. U. Eggenberger, Y. Karimi-Nejad, H. Thüring, H. Rüterjans, and C. Griesinger, *J. Biomol. NMR*, 1992, **2**, 583.
28. M. McCoy and L. Müller, *J. Am. Chem. Soc.*, 1992, **114**, 2108.
29. M. McCoy and L. Müller, *J. Magn. Reson.*, 1992, **98**, 674.
30. M. McCoy and L. Müller, *J. Magn. Reson.*, 1992, **99**, 18.
31. U. Eggenberger, P. Schmidt, M. Sattler, S. J. Glaser, and C. Griesinger, *J. Magn. Reson.*, 1992, **100**, 604.
32. M. McCoy and L. Müller, *J. Magn. Reson., Ser. A*, 1993, **101**, 122.
33. M. D. Sørensen, S. M. Kristensen, J. J. Led, and O. W. Sørensen, *J. Magn. Reson. Ser. A*, 1993, **103**, 364.
34. R. Brüschweiler, J. C. Madsen, C. Griesinger, O. W. Sørensen, and R. R. Ernst, *J. Magn. Reson.*, 1987, **73**, 380.
35. P. Berthault, H. Desvaux, and B. Perly, *Magn. Reson. Chem.*, 1993, **31**, 259.
36. L. Emsley, T. J. Dwyer, H. P. Spielmann, and D. E. Wemmer, *J. Am. Chem. Soc.*, 1993, **115**, 7765.
37. R. Konrat, G. Zieger, and H. Sterk, *Chem. Phys. Lett.*, 1993, **212**, 78.
38. L. Emsley and G. Bodenhausen, *J. Magn. Reson.*, 1989, **82**, 211.
39. L. Emsley and G. Bodenhausen, *Chem. Phys. Lett.*, 1990, **165**, 469.
40. H. Geen and R. Freeman, *J. Magn. Reson.*, 1991, **93**, 93.
41. G. W. Vuister and A. Bax, *J. Biomol. NMR*, 1992, **2**, 401.
42. R. Weisemann, H. Rüterjans, H. Schwalbe, J. Schleucher, W. Bermel, and C. Griesinger, *J. Biomol. NMR*, 1994, **4**, 231.
43. S. Seip, J. Balbach, and H. Kessler, *J. Magn. Reson.*, 1994, **B104**, 172.
44. H. Kessler, U. Anders, and G. Gemmecker, *J. Magn. Reson.*, 1988, **78**, 382.
45. G. Zhu and A. Bax, *J. Magn. Reson.*, 1992, **98**, 192.
46. G. Zhu and A. Bax, *J. Magn. Reson.*, 1990, **90**, 405.
47. H. Schwalbe, A. Rexroth, U. Eggenberger, T. Geppert, and C. Griesinger, *J. Am. Chem. Soc.*, 1993, **114**, 7878.
48. J. R. Garbow, D. P. Weitekamp, and A. Pines, *Chem. Phys. Lett.*, 1982, **93**, 504.
49. O. W. Sørensen, *J. Magn. Reson.*, 1990, **90**, 433.
50. J. C. Madsen, O. W. Sørensen, P. Sørensen, and F. M. Poulsen, *J. Biomol. NMR*, 1993, **3**, 239.
51. S. Seip, J. Balbach, and H. Kessler, *Angew. Chem., Int. Ed. Engl.*, 1992, **31**, 1609.
52. G. Wagner, P. Schmieder, and V. Thanabal, *J. Magn. Reson.*, 1991, **93**, 436.
53. S. D. Emerson and G. T. Montelione, *J. Magn. Reson.*, 1992, **99**, 413.
54. M. Gorlach, M. Wittekind, B. T. Farmer, L. E. Kay, and L. Müller, *J. Magn. Reson., Ser. B*, 1993, **101**, 194.
55. W. Willker and D. Leibfritz, *J. Magn. Reson.*, 1992, **99**, 421.
56. H. Schwalbe, H. Oschkinat, W. Bermel, P. Schmitt, and C. Griesinger, unpublished data.
57. L. Müller, *J. Magn. Reson.*, 1987, **72**, 191.
58. A. Bax and D. Marion, *J. Magn. Reson.*, 1988, **80**, 528.
59. H. Kessler, G. Gemmecker, A. Haupt, M. Klein, K. Wagner, and M. Will, *Tetrahedron*, 1988, **44**, 745.
60. P. C. Driscoll, G. M. Clore, and G. M. Gronenborn, *FEBS Lett.*, 1989, **243**, 223.
61. P. C. Driscoll, G. M. Clore, L. Beress, and G. M. Gronenborn, *Biochemistry*, 1989, **28**, 2178.
62. H. Kessler, A. Müller, and K. H. Pook, *Liebigs Ann. Chem.*, 1989, **9**, 903.
63. H. Kessler, J. W. Bats, K. Wagner, and M. Will, *Biopolymers*, 1989, **28**, 385.
64. P. J. M. Folkers, G. M. Clore, P. C. Driscoll, J. Dodt, S. Kohler, and A. M. Gronenborn, *Biochemistry*, 1989, **28**, 2601.
65. H. Kessler, M. Will, J. Antel, H. Beck, and G. M. Sheldrick, *Helv. Chim. Acta*, 1989, **72**, 530.
66. H. Haruyama, Y. Q. Qian, and K. Wüthrich, *Biochemistry*, 1989, **28**, **4301**, 4312.
67. C. Redfield and C. M. Dobson, *Biochemistry*, 1990, **29**, 7201.
68. H. Kessler, S. Mronga, M. Will, and U. Schmidt, *Helv. Chim. Acta*, 1990, **73**, 25.
69. M. Billeter, Y. Qian, G. Otting, M. Müller, W. J. Gehring, and K. Wüthrich, *J. Mol. Biol.*, 1990, **214**, 183.
70. H. Kessler, U. Anders, and M. Schudok, *J. Am. Chem. Soc.*, 1990, **112**, 5908.
71. B. A. Messerle, A. Schaffer, M. Vasak, J. H. R. Kagi, and K. Wüthrich, *J. Mol. Biol.*, 1990, **214**, 765.
72. P. Karuso, H. Kessler, and D. F. Mierke, *J. Am. Chem. Soc.*, 1990, **112**, 9434.
73. Y. M. Kim and J. H. Prestegard, *Proteins Struct. Func. Genet.*, 1990, **8**, 377.
74. J. Habazettl, C. Cieslar, H. Oschkinat, and T. A. Holak, *FEBS Lett.*, 1990, **268**, 141.
75. L. J. Smith, M. J. Sutcliffe, C. Redfield, and C. M. Dobson, *Biochemistry*, 1991, **30**, 986.
76. J. M. Moore, C. A. Lepre, G. P. Gippert, W. J. Chazin, D. A. Case, and P. E. Wright, *J. Mol. Biol.*, 1991, **221**, 533.
77. J. M. Schmidt, O. Ohlenschläger, H. Rüterjans, Z. Grzanka, E. Kojro, I. Pavo, and F. Fahrenholz, *Eur. J. Biochem.*, 1991, **201**, 355.
78. H. Kessler, S. Mronga, G. Müller, L. Moroder, and R. Huber, *Biopolymers*, 1991, **31**, 1189.
79. A. L. Breeze, T. S. Harvey, R. Bazzo, and I. D. Campbell, *Biochemistry*, 1991, **30**, 575.
80. H. Kessler, H. Matter, G. Gemmecker, A. Kling, and M. Kottenhahn, *J. Am. Chem. Soc.*, 1991, **113**, 7550.
81. K. H. Ott, S. Becker, R. D. Gordon, and H. Rüterjans, *FEBS Lett.*, 1991, **278**, 160.
82. C. Abeygunawardana, C. A. Bush, and J. O. Cisar, *Biochemistry*, 1991, **30**, 8568.
83. P. Sodano, T. H. Xia, J. H. Bushweller, O. Bjornberg, A. Holmgren, M. Billeter, and K. Wüthrich, *J. Mol. Biol.*, 1991, **221**, 1311.
84. D. Seebach, S. Y. Ko, H. Kessler, M. Köck, M. Reggelin, P. Schmieder, M. D. Walkinshaw, J. J. Bölsterli, and D. Bevec, *Helv. Chim. Acta*, 1991, **74**, 1953.

85. X. Li, M. J. Sutcliffe, T. W. Schwartz, and C. M. Dobson, *Biochemistry*, 1992, **31**, 1245.
86. U. Hommel, T. S. Harvey, P. C. Driscoll, and I. D. Campbell, *J. Mol. Biol.*, 1992, **227**, 271.
87. J. Freund, A. Kapurniotu, T. A. Holak, M. Lenfant, and W. Voelter, *Z. Naturforsch., B*, 1992, **47**, 1324.
88. D. Neri, M. Billeter, and K. Wüthrich, *J. Mol. Biol.*, 1992, **223**, 743.
89. H. Kessler, H. Matter, G. Gemmecker, M. Kottenhahn, and J. W. Bats, *J. Am. Chem. Soc.*, 1992, **114**, 4805.
90. G. T. Montelione, K. Wüthrich, A. W. Burgess, E. C. Nice, G. Wagner, K. D. Gibson, and H. A. Scheraga, *Biochemistry*, 1992, **31**, 236.
91. M. Köck, H. Kessler, D. Seebach, and A. Thaler, *J. Am. Chem. Soc.*, 1992, **114**, 2676.
92. P. J. Kraulis, A. R. C. Raine, P. L. Gadhavi, and E. D. Laue, *Nature*, 1992, **356**, 448.
93. M. Reggelin, H. Hoffmann, M. Köck, and D. F. Mierke, *J. Am. Chem. Soc.*, 1992, **114**, 3272.
94. T. H. Xia, J. H. Bushweller, P. Sodano, M. Billeter, O. Bjornberg, A. Holmgren, and K. Wüthrich, *Protein Sci.*, 1992, **1**, 310.
95. B. A. Messerle, A. Schaffer, M. Vasak, J. H. R. Kagi, and K. Wüthrich, *J. Mol. Biol.*, 1992, **225**, 433.
96. J. Saulitis, D. F. Mierke, G. Byk, C. Gilon, and H. Kessler, *J. Am. Chem. Soc.*, 1992, **114**, 4818.
97. H. Kessler, A. Geyer, H. Matter, and M. Köck, *Int. J. Pept. Protein Res.*, 1992, **40**, 25.
98. K. D. Berndt, P. Guntert, L. P. M. Orbons, and K. Wüthrich, *J. Mol. Biol.*, 1992, **227**, 757.
99. K. Wakamatsu, D. Kohda, H. Hatanaka, J. M. Lancelin, Y. Ishida, M. Oya, H. Nakamura, F. Inagaki, and K. Sato, *Biochemistry*, 1992, **31**, 12. 577.
100. T. Szyperski, P. Guntert, S. R. Stone, and K. Wüthrich, *J. Mol. Biol.*, 1992, **228**, 1193.
101. M. Gurrath, G. Müller, H. Kessler, M. Aumailley, and R. Timpl, *Eur. J. Biochem.*, 1992, **210**, 911.
102. N. Fusetani, K. Shimoda, and S. Matsunaga, *J. Am. Chem. Soc.*, 1993, **115**, 3977.
103. A. Schnuchel, R. Wiltschek, M. Czisch, M. Herrler, G. Willimsky, P. Graumann, M. A. Marahiel, and T. A. Holak, *Nature*, 1993, **364**, 169.
104. R. K. Konat, D. F. Mierke, H. Kessler, B. Kutscher, M. Bernd, and R. Voegeli, *Helv. Chim. Acta*, 1993, **76**, 1649.
105. S. Mronga, G. Müller, J. Fischer, and F. Riddell, *J. Am. Chem. Soc.*, 1993, **115**, 8414.
106. J. Kordel, N. J. Skelton, M. Arke, and W. J. Chazin, *J. Mol. Biol.*, 1993, **231**, 711.
107. L. R. Brown, S. Mronga, R. A. Bradshaw, C. Ortenzi, P. Luporini, and K. Wüthrich, *J. Mol. Biol.*, 1993, **231**, 800.
108. Y. Blancuzzi, A. Padilla, J. Parello, and A. Cave, *Biochemistry*, 1993, **32**, 1302.
109. H. Kessler, R. Haessner, and W. Schuler, *Helv. Chim. Acta*, 1993, **76**, 117.
110. Y. N. Kalia, S. M. Brocklehurst, D. S. Hipps, E. Appella, K. Sakaguchi, and R. N. Perham, *J. Mol. Biol.*, 1993, **230**, 323.
111. W. Antuch, K. D. Berndt, M. A. Chavez, J. Delfin, and K. Wüthrich, *Eur. J. Biochem.*, 1993, **212**, 675.
112. J. F. OConnell, P. E. Bougis, and K. Wüthrich, *Eur. J. Biochem.*, 1993, **213**, 891.
113. J. H. Davis, E. K. Bradley, G. P. Miljanich, L. Nadasdi, J. Ramachandran, and V. J. Basus, *Biochemistry*, 1993, **32**, 7396.
114. K. Bartik, C. M. Dobson, and C. Redfield, *Eur. J. Biochem.*, 1993, **215**, 255.
115. K. D. Berndt, P. Guntert, and K. Wüthrich, *J. Mol. Biol.*, 1993, **234**, 735.
116. A. Bax and L. Lerner, *J. Magn. Reson.*, 1988, **79**, 429.
117. U. Schmitz, G. Zon, and T. L. James, *Biochemistry*, 1990, **29**, 2357.
118. A. Foldesi, P. Agback, C. Glemarec, and J. Chattopadhyaya, *Tetrahedron*, 1991, **47**, 7135.
119. W. J. Chazin, M. Rance, A. Chollet, and W. Leupin, *Nucleic Acids Res.*, 1991, **19**, 5507.
120. S. M. Chen, W. Leupin, and W. J. Chazin, *Int. J. Biol. Macromol.*, 1992, **14**, 57.
121. S. M. Chen, W. Leupin, M. Rance, and W. J. Chazin, *Biochemistry*, 1992, **31**, 4406.
122. J. W. Cheng, S. H. Chou, M. Salazar, and B. R. Reid, *J. Mol. Biol.*, 1992, **228**, 118.
123. S. H. Chou, J. W. Cheng, and B. R. Reid, *J. Mol. Biol.*, 1992, **228**, 138.
124. S. G. Kim, L. J. Lin, and B. R. Reid, *Biochemistry*, 1992, **31**, 3564.
125. S. G. Kim and B. R. Reid, *Biochemistry*, 1992, **31**, 12. 103.
126. M. Salazar, J. J. Champoux, and B. R. Reid, *Biochemistry*, 1993, **32**, 739.
127. M. Salazar, O. Y. Fedoroff, J. M. Miller, N. S. Ribeiro, and B. R. Reid, *Biochemistry*, 1993, **32**, 4207.
128. W. Willker, D. Leibfritz, R. Kerssebaum, and J. Lohman, *J. Magn. Reson., Ser. A*, 1993, **102**, 348.
129. C. Griesinger and U. Eggenberger, *J. Magn. Reson.*, 1992, **97**, 426.
130. G. Gemmecker and S. W. Fesik, *J. Magn. Reson.*, 1991, **95**, 208.
131. S. D. Emerson and G. T. Montelione, *J. Magn. Reson.*, 1992, **99**, 413.
132. S. D. Emerson and G. T. Montelione, *J. Am. Chem. Soc.*, 1992, **114**, 354.
133. H. Schwalbe, G. C. King, R. Wechselberger, W. Bermel, and C. Griesinger, *J. Biomol. NMR*, 1994, **4**, 631.
134. H. B. Olsen, S. Ludvigsen, and O. W. Sørensen, *J. Magn. Reson., Ser. A*, 1993, **104**, 226.

Acknowledgments

We would like to thank the co-workers that contributed to the work presented in this review: Y. Karimi-Nejad, R. Weisemann and H. Rüterjans from University of Frankfurt/M, W. Bermel at Bruker/Karlsruhe, H. Oschkinat at EMBL/Heidelberg, G. King at the University of South Wales/Australia as well as A. Rexroth, U. Eggenberger, M. Sattler, J. Marino, T. Gepport, R. Wechselberger, S. Glaser and J. Schleucher.

Biographical Sketches

H. J. Schwalbe. *b* 1966. Diploma, 1990, Ph.D., 1993, Frankfurt. Postdoctorate (with Prof. C. Dobson, Oxford, 1993–present). Introduced to NMR by C. Griesinger. Research interest in development of new methods in the field of high-resolution NMR for coupling constant determination in proteins and oligonucleotides, chemical synthesis of ^{13}C-labeled RNA and DNA.

P. A. Schmidt. *b* 1966. Diploma, 1990, Ph.D., 1993, Frankfurt. Introduced to NMR by C. Griesinger, S. Glaser and G. Wagner. Research

interest in theoretical prediction and optimisations of homo- and heteronuclear mixing sequences and their applications to biomolecular NMR spectroscopy.

C. Griesinger. *b* 1960. Diploma, 1984, Ph.D., 1986, Frankfurt. Postdoctorate ETH Zürich, 1986–89. Full Professor of Organic Chemistry at the University of Frankfurt, 1990–present. Introduced to NMR by Horst Kessler, Richard R. Ernst, and O. W. Sørensen. Research interest in development of new methods in the field of high-resolution NMR, especially multidimensional NMR spectroscopy, rotating frame spectroscopy, coupling constant determination, and conformational analysis of biomacromolecules including proteins, DNA and RNA.

HETCOR in Organic Solids

Douglas P. Burum

Bruker Instruments, Inc., Billerica, MA, USA

1	Introduction	1
2	Methods for Obtaining Heteronuclear Correlation in Solids	1
3	Theory of Solids HETCOR	2
4	Experimental Considerations	4
5	Typical Results	5
6	Modified Versions of Solids HETCOR	5
7	Conclusions	6
8	Related Articles	6
9	References	6

1 INTRODUCTION

During the past few years, multidimensional experiments — 2D, 3D, etc.—have come into widespread use in high-resolution (liquid state) NMR (see ***Multidimensional Spectroscopy: Concepts***). Perhaps the most obvious advantage of this class of experiments is the possibility of correlating various spectral features. For example, COSY can be used to correlate chemically shifted peaks on the basis of *J* couplings (see ***COSY Two-Dimensional Experiments*** and ***COSY Spectra: Quantitative Analysis***), NOESY on the basis of the NOE effect (see ***NOESY***) and HETCOR on the basis of heteronuclear *J* couplings (see ***Heteronuclear Shift Correlation Spectroscopy***). A second important advantage is the ability to deconvolute overlapping resonance peaks by spreading them out in several dimensions. This can be of tremendous importance when studying very large molecules such as proteins.

A smaller number of multidimensional experiments—almost all of them 2D—have been introduced for the analysis of rigid solids. Examples include separated local field,[1] 2D chemical exchange,[2] and wideline separation spectroscopy (WISE).[3] In this article, solids HETCOR[4] is discussed. Solids HETCOR provides *het*eronuclear *cor*relations based on direct, 'through-space' interactions (dipole-dipole coupling; see ***Internal Spin Interactions and Rotations in Solids***). Since it can remove the overlap between adjacent resonances, solids HETCOR is also possibly the most powerful method available for accurate determination of proton chemical shifts in organic solids.

In addition, solids HETCOR is not especially difficult to implement. Generally speaking, almost any spectrometer capable of performing CP MAS (see ***Cross Polarization in Solids***, ***Magic Angle Spinning***, ***Rotating Solids*** and ***Cross Polarization in Rotating Solids: Spin-1/2 Nuclei***), 2D NMR and CRAMPS (see ***CRAMPS***) can be readily configured to perform solids HETCOR. In general, solids HETCOR can be applied to the correlation of any two nuclear species, so long as it is possible to transfer magnetization from one species to the other. In order to simplify the discussion, however, HETCOR will be discussed in this article in reference to the correlation of ^{1}H and ^{13}C chemical shifts.

2 METHODS FOR OBTAINING HETERONUCLEAR CORRELATION IN SOLIDS

As with any 2D experiment, solids HETCOR is composed of four basic parts—preparation, evolution, mixing and detection. Proton magnetization is created during the preparation period, and then the ^{1}H spins are allowed to precess at a rate determined by their chemical shifts. This is followed by a mixing period, during which polarization is transferred from the ^{1}H spins to nearby ^{13}C spins, and finally a detection period during which the ^{13}C FID is recorded. Typically, the sample is rotated at the magic angle throughout the entire experiment (see ***Magic Angle Spinning***; ***Rotating Solids***).

The preparation and detection parts of the HETCOR experiment are straightforward. The preparation consists of a single 90° pulse on the protons, and the detection part consists of ^{13}C signal detection during CW ^{1}H decoupling, exactly as in a standard CP MAS experiment. On the other hand, the evolution and mixing periods tend to be somewhat complicated, due to the need to suppress ^{1}H–^{1}H homonuclear dipolar coupling and ^{1}H–^{13}C heteronuclear dipolar coupling.

One approach is to spin the sample very rapidly at the magic angle, so that all dipolar coupling is suppressed.[5] If this can be accomplished, pulse sequences typical of high resolution 2D NMR can then be applied. Unfortunately, this is only practical for highly mobile solids, such as lipids, membranes and suspensions. Nevertheless, it can be a very powerful technique for these classes of materials.

In the so-called WISE experiment,[3] the ^{1}H–^{1}H dipolar coupling is allowed to be active during the evolution period. The WISE evolution period is just a time incremented delay immediately following the preparation 90° ^{1}H pulse, and the result is a 2D spectrum that correlates ^{13}C chemical shifts with ^{1}H–^{1}H dipolar broadened powder patterns. An example of a WISE spectrum is given in Figure 1.

In order to correlate ^{1}H chemical shifts with ^{13}C chemical shifts in rigid solids, some sort of multiple pulse technique must be employed to suppress dipole interactions during the evolution and mixing periods. During the ^{1}H evolution, both the ^{1}H–^{1}H homonuclear dipolar interaction and the ^{1}H–^{13}C heteronuclear dipolar interaction must be suppressed. The most commonly suggested methods include 'windowed' CRAMPS pulse sequences such as MREV-8 with simultaneous CW decoupling of the ^{13}C spins[6,7] and windowless multiple pulse sequences applied to both the ^{1}H and ^{13}C spins simultaneously.[8] Of these, the most successful method appears to be the simultaneous application of BB-24 to the ^{1}H spins and BLEW-24 to the ^{13}C spins.[4] It is interesting to note that a 48 pulse version of this pulse sequence, based on BLEW-48, has been tried, but without any improvement of the resulting spectrum.[9]

During the mixing time, the ^{1}H–^{1}H homonuclear dipolar coupling must be suppressed in order to avoid loss of correlation specificity due to homonuclear spin diffusion. However, the ^{1}H–^{13}C heteronuclear dipolar coupling must be retained to allow cross polarization (see ***Cross Polarization in Solids***). A number of methods have been suggested to accomplish this, including Hartmann–Hahn cross polarization applied with a very brief cross-polarization time,[6,7] Hartmann–Hahn cross polarization using CRAMPS line-narrowing sequences such as MREV-8 applied simultaneously to the ^{1}H and ^{13}C spins,[7] transfer of magnetization via multiple quantum states

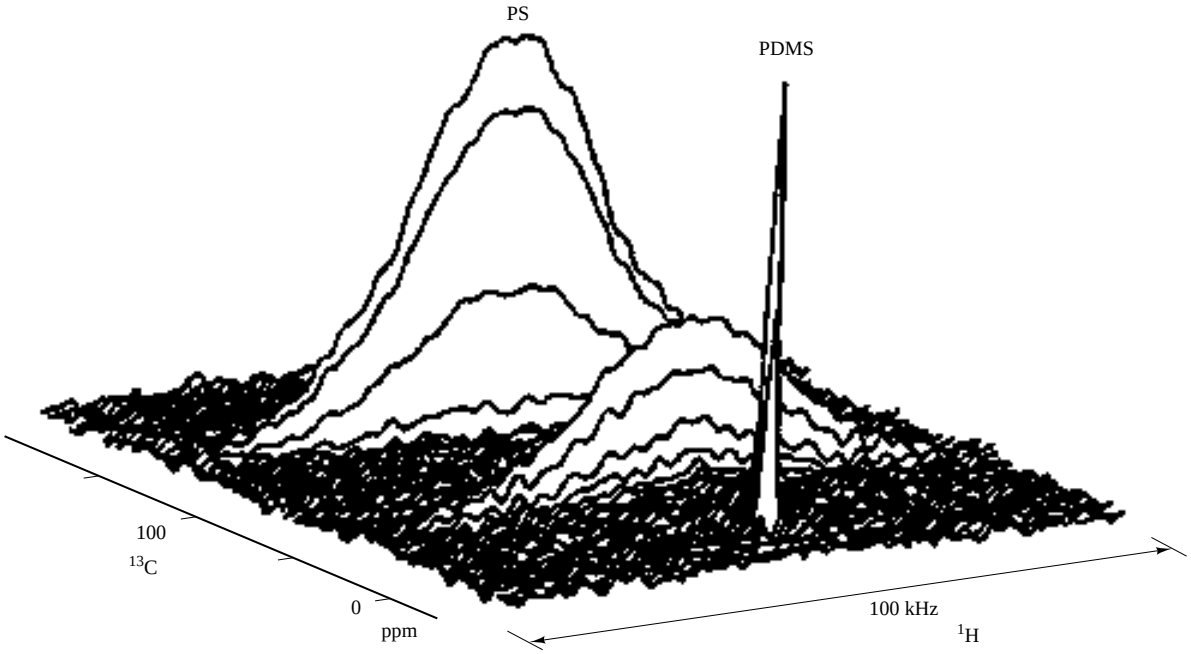

Figure 1 WISE spectrum of polystyrene block copolymer with poly(dimethylsiloxane) (PS-b-PDMS) (50:50 mol%). The reduced linewidth in the ^{1}H dimension indicates the much higher mobility of the PDMS, which does not induce significant mobility in the PS. (Reproduced by permission of Schmidt-Rohr et al.[3])

using ^{1}H CRAMPS followed by simultaneous ^{1}H and ^{13}C 90° pulses[7] and Hartmann–Hahn cross polarization using frequency switched Lee–Goldberg irradiation.[4] The most successful method appears to be cross polarization by simultaneous application of the windowless isotropic mixing (WIM) pulse sequence to the ^{1}H and ^{13}C spins[8].

3 THEORY OF SOLIDS HETCOR

The basic solids HETCOR pulse sequence is shown in its most common form in Figure 2. In order to understand the effectiveness of the BLEW-24/BB-24 combination in suppressing the heteronuclear dipolar interaction, it is useful to apply average Hamiltonian theory (see ***Average Hamiltonian Theory***), and to consider the effect on the average Hamiltonian when 90° rf pulses are applied simultaneously to both the proton and carbon spins. The secular part of the heteronuclear dipolar Hamiltonian can be expressed as

$$\hat{\mathcal{H}}_{\mathrm{D}}^{(Z)} = \sum_{i,j} A_{i,j} \hat{I}_{i,z} \hat{S}_{j,z} \tag{1}$$

If the rf amplitudes are adjusted such that the Hartmann–Hahn condition is satisfied, the proton and carbon 90° pulse

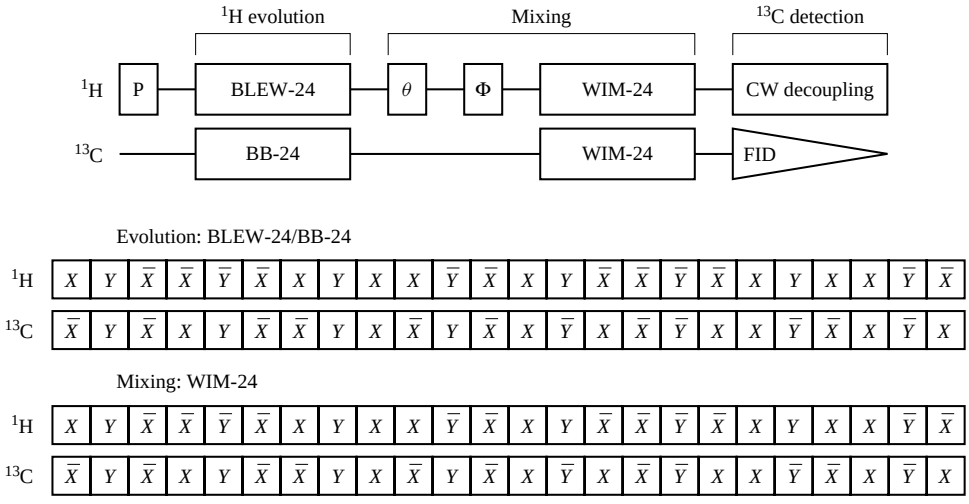

Figure 2 Basic solids HETCOR pulse sequence. In its most common form, the fully windowless BLEW-24 sequence is applied to the ^{1}H spins and the fully windowless BB-24 sequence is applied to the ^{13}C spins during the evolution period, and the fully windowless WIM-24 sequence is applied simultaneously to both spin systems during the mixing period

widths will be equal. During the simultaneous pulse, the dipolar Hamiltonian in the toggling reference frame becomes time dependent. Assuming that the rf phases for both protons and carbons lie along the Y axes in the doubly rotating frame, this time-dependent Hamiltonian can be expressed as

$$\hat{\tilde{\mathcal{H}}}_{\mathrm{D}}^{(Z)}(t) = \hat{\mathcal{H}}_{\mathrm{D}}^{(Z)} \cos^2 \Omega + \hat{\mathcal{H}}_{\mathrm{D}}^{(X)} \sin^2 \Omega + \hat{\mathcal{H}}_{\mathrm{D}}^{(ZX)} \sin 2\Omega \quad (2)$$

where Ω varies from zero to 90° during the pulse, and the cross term may be written

$$\hat{\mathcal{H}}_{\mathrm{D}}^{(ZX)} = \sum_{i,j} \tfrac{1}{2} A_{i,j} (\hat{I}_Z \hat{S}_X + \hat{I}_X \hat{S}_Z) \quad (3)$$

By simple integration on time, the zeroth-order average heteronuclear dipolar Hamiltonian for this individual, simultaneous pulse is then given by

$$\hat{\tilde{\mathcal{H}}}_{\mathrm{D}}^{(0)} = \tfrac{1}{2}\hat{\mathcal{H}}_{\mathrm{D}}^{(Z)} + \tfrac{1}{2}\hat{\mathcal{H}}_{\mathrm{D}}^{(X)} + \frac{2}{\pi}\hat{\mathcal{H}}_{\mathrm{D}}^{(ZX)} \quad (4)$$

Table 1 Phase Cycling During the Heteronuclear Correlation Experiment[a,b,c,d]

Scan	1	2	3	4	5	6	7	8
P	X	−X	X	−X	X	−X	X	−X
^{13}C WIM-24[e]	X	X	−Y	−Y	−X	−X	Y	Y
Receiver	X	−X	−Y	Y	−X	X	Y	−Y

[a]For all scans, θ = X, ϕ = 63°(−Y).
[b]All pulses except ϕ are 90° pulses.
[c]The overall ^{1}H phase of the initial pulse P, the BLEW-24 evolution period and the first mixing pulse θ are incremented by 90° after each experiment in order to obtain phase sensitive spectra by the TPPI method.
[d]Reprinted by permission of Burum et al.[4]
[e]^{13}C WIM-24 refers to the overall phase shift of the WIM-24 sequence applied to the ^{13}C nuclei.

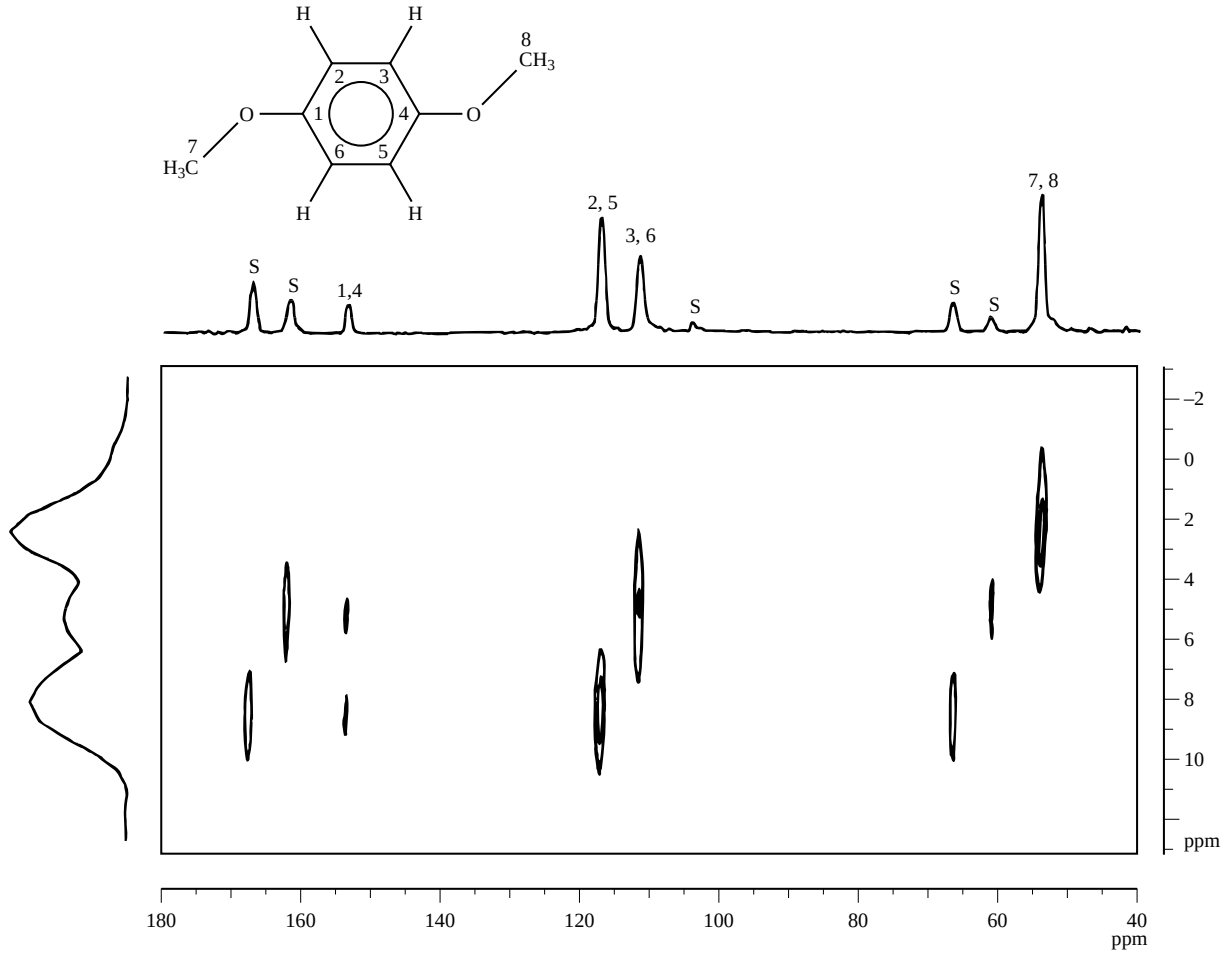

Figure 3 Solids HETCOR spectrum of *p*-dimethoxybenzene. The spectra shown above and to the left are projections of the 2D data, and are similar to what could be expected from 1D CRAMPS (^{1}H) and CP MAS (^{13}C). (Reproduced by permission of Burum et al.[4])

The BLEW-24/BB-24 sequence is entirely composed of simultaneous pulses of this type. Therefore, the zeroth-order average Hamiltonian for the sequence as a whole is simply a sum of terms of the form given in equation (4). If the terms are listed in order, one finds that the 'pure' terms cancel for each 6-pulse group, and the 'mixed' terms cancel over each 12-pulse group. The first 12 pulses of BB-24 therefore form a unit for which all zeroth-order dipolar terms vanish. By reflecting this subcycle to form BB-24, all the first-order terms are caused to vanish as well due to symmetry.

A similar analysis can be applied to WIM-24, with the result that the chemical shifts and homonuclear dipolar couplings of both the ^{1}H and ^{13}C spins vanish, and the zeroth-order average Hamiltonian for the heteronuclear dipolar coupling is given by the isotropic expression

$$\tilde{\hat{\mathcal{H}}}_{\mathrm{D}}^{(0)} = \tfrac{1}{3}[\hat{\mathcal{H}}_{\mathrm{D}}^{(X)} + \hat{\mathcal{H}}_{\mathrm{D}}^{(Y)} + \hat{\mathcal{H}}_{\mathrm{D}}^{(Z)}] \qquad (5)$$

4 EXPERIMENTAL CONSIDERATIONS

Phase cycling according to the scheme given in Table 1 is typically added to the basic experiment shown in Figure 2 to suppress potential artifacts. The 180° phase alternation of the initial $\pi/2$ pulse P is an implementation of the well-known 'spin temperature alternation' method for eliminating receiver dead time effects. The cycling of the overall ^{13}C WIM-24 phase is used to eliminate any quadrature images which might otherwise result from an improperly balanced receiver.

In order to obtain purely absorptive, phase sensitive 2D spectra, time proportional phase incrementation (TPPI)[10] can be introduced. For example, the overall ^{1}H phase of the first half of the experiment, including the first pulse, the entire evolution period and the first mixing pulse, may be advanced by 90° after each experiment.

Typical experimental conditions for solids HETCOR include a MAS spinning speed of approximately 4000 Hz, rf levels adjusted to obtain a 90° pulse on both the ^{1}H and ^{13}C channels of between 4.0 and 4.5 μs, and cross polarization using 1 or 2 WIM cycles. Optimum experimental performance may be obtained by carefully adjusting both the ^{1}H and ^{13}C rf channels of the spectrometer according to standard CRAMPS tune-up procedures[11,12] for perfect phase and flip angle and minimum phase transient. However, this is often not necessary in order to obtain good quality spectra, since the result of nonideal tuning is primarily seen in artifacts that lie either on the axes or along the center line in the ^{1}H dimension.

In order to avoid center line artifacts without degrading ^{13}C resolution, it is useful to switch the ^{1}H rf frequency during the pulse sequence, such that it lies to one side of the ^{1}H

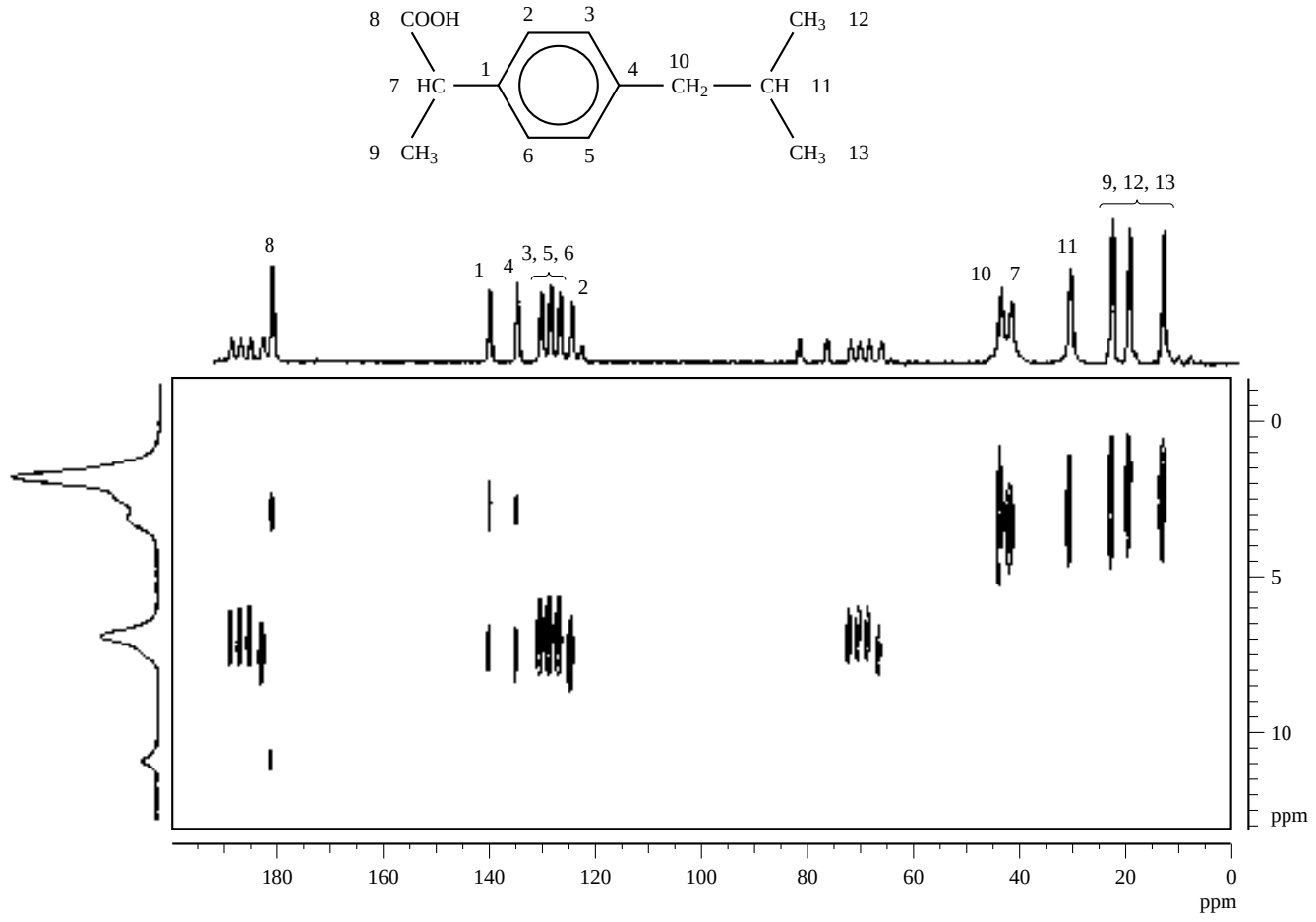

Figure 4 Solids HETCOR spectrum of ibuprofen. Note the long-range coupling information provided for nonprotonated carbons. Note also the precise proton chemical shift information available, due to the deconvolution of resonance overlaps in the carbon dimension. The 1D spectra above and to the left of the 2D spectrum are the ^{13}C CP MAS spectrum and the ^{1}H BR-24 CRAMPS spectrum of the same compound

spectrum during the preparation and evolution periods, but then is switched to the center of the ^{1}H spectrum during the mixing and detection periods.

5 TYPICAL RESULTS

A typical solids HETCOR spectrum of a small organic molecule, *p*-dimethoxybenzene, is shown in Figure 3. Not only do correlations from directly bonded $^{1}H–^{13}C$ pairs appear, but also couplings between nonprotonated carbons and more distant protons. This type of long-range correlation is also present in the solids HETCOR spectrum of ibuprofen shown in Figure 4. Both spectra illustrate the very powerful resolving power for ^{1}H chemical shifts using this method, where separate ^{1}H chemical shift values can be obtained for each line in the spectrum. In this figure, a standard ^{13}C CP MAS spectrum and a BR-24 CRAMPS spectrum have been presented in place of the usual projections. It is clear from the BR-24 ^{1}H spectrum that full deconvolution of the lines within the aromatic and aliphatic regions is not possible using CRAMPS alone.

A typical solids HETCOR spectrum of a polymer, PPO [poly(2,6-dimethyl-*p*-phenylene oxide)], is shown in Figure 5. Long range couplings between nonprotonated carbon spins and their nearest-neighbor protons have been used in this case to reveal information about the polymer chain conformation.[13] In general, useful solids HETCOR spectra can be obtained from most organic solids for which a well resolved ^{13}C CP MAS spectrum can be measured.

As a general rule, correlation peaks for directly bonded $^{13}C–^{1}H$ pairs are always visible in solids HETCOR experiments, and peaks for nonprotonated ^{13}C spins separated by two bonds from one or more ^{1}H spins are also normally present. Although the interaction is 'through space', not 'through bond', the two bond rule for long range correlations seems to be a good general guideline. When a ^{13}C spin is directly bonded to a proton, there is an interference effect that greatly reduces the interaction between that carbon and other, more distant protons. Therefore, only one strong peak is normally obtained from protonated carbons. Nonprotonated carbons, on the other hand, are often coupled to more than one proton with roughly equal strengths, in which case more than one peak can be obtained for the same carbon. Thus, nonprotonated carbons often provide some of the best structural information from solids HETCOR.

6 MODIFIED VERSIONS OF SOLIDS HETCOR

The BLEW-24/BB-24 version of solids HETCOR was introduced in 1991. Since then, a few modifications have been proposed for specific applications. In one modification,

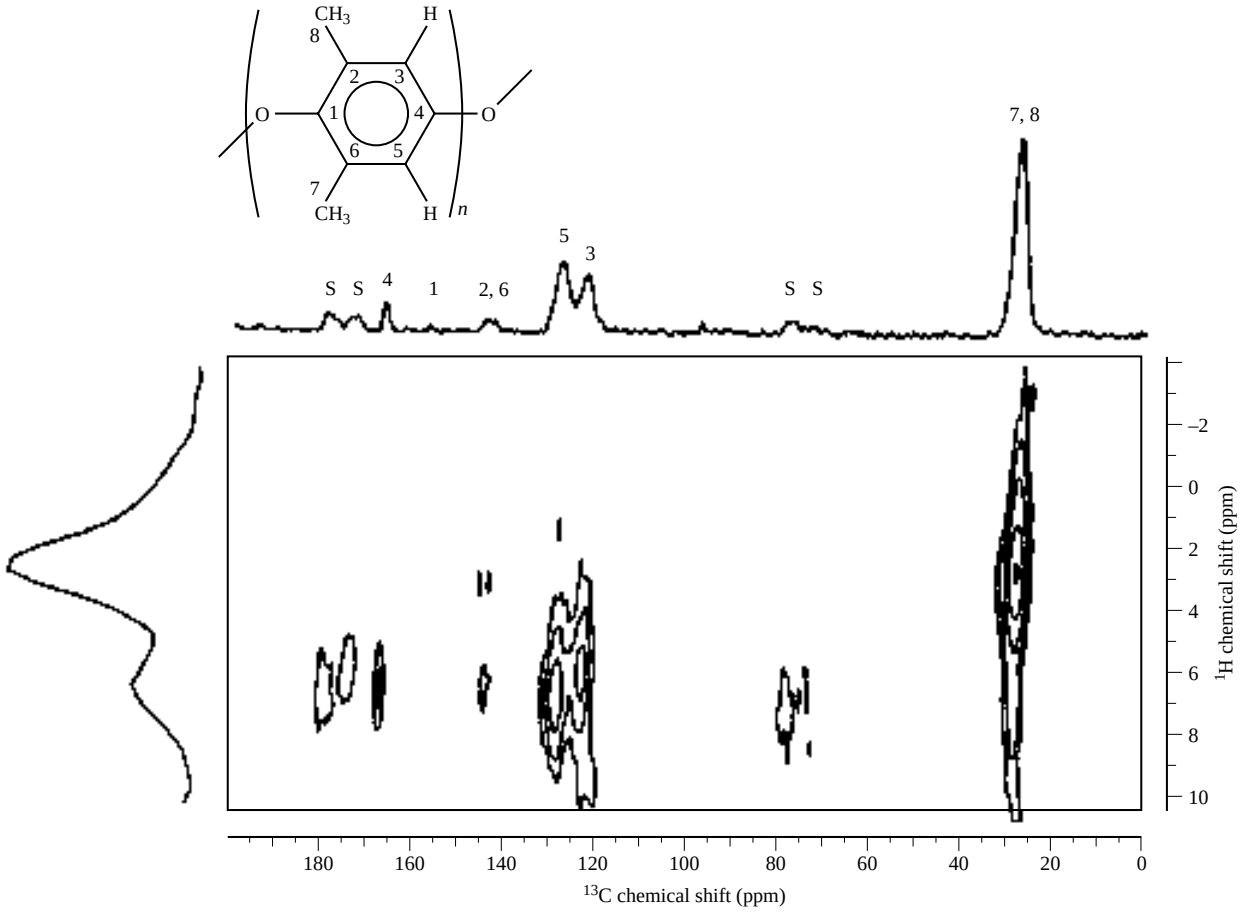

Figure 5 Solids HETCOR spectrum of poly(2,6-dimethyl-*p*-phenylene oxide) (PPO). Long range couplings from this spectrum have been used to reveal information about the polymer chain conformation. (Reprinted by permission of Burum et al.[4])

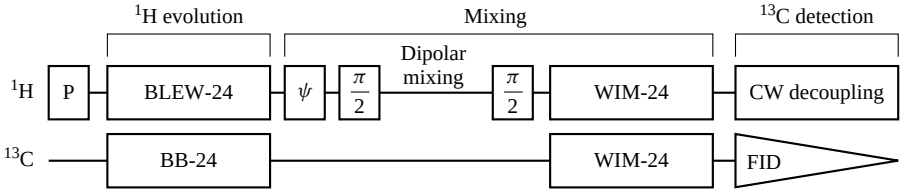

Figure 6 Solids HETCOR pulse sequence with additional ^{1}H spin diffusion mixing time

introduced by Li et al.,[14] a short delay is added between the evolution and mixing times as shown in Figure 6 to allow limited nuclear spin diffusion among the protons. This approach can be used to bypass the interference effect mentioned above and obtain correlations between protonated carbons and more distant protons. Using this technique, Li et al. were able to obtain evidence of polymer blending.

In another modified version of solids HETCOR proposed by Bronnimann et al.,[15] the mixing time is extended to enhance signals from weak, long range couplings. Normally, the mixing time in solids HETCOR is limited to a fraction of a rotor period because the cross-polarization process during WIM is reversed by the magic angle spinning. In the experiment suggested by Bronnimann et al., one or two simultaneous ^{1}H and ^{13}C WIM cycles are applied during the first portion of the rotor period, and then the ^{13}C magnetization is stored along the Z axis while WIM is applied only to the ^{1}H spins for the remainder of the rotor period. The sequence is then repeated for several additional rotor cycles, giving an effective cross-polarization period that is much longer than normal. This technique tends to be limited to samples with weakly coupled protons, since magnetization from protons with strong homonuclear dipolar coupling is difficult to maintain for long times during WIM irradiation. Nevertheless, Bronnimann et al. were able to obtain interesting results for ^{1}H–^{31}P correlation in bone using this method.

7 CONCLUSIONS

The BLEW-24/BB-24 version of solids HETCOR is relatively easy to implement, and can provide useful data for a wide variety of experimental samples. Typically, any sample for which well resolved ^{13}C CP MAS spectra can be obtained will be a good candidate for solids HETCOR. Heteronuclear correlations, obtained primarily from nonprotonated carbons, can provide useful information for structure determination and peak assignments. Deconvolution of the ^{1}H resonances in the carbon dimension allows ^{1}H chemical shifts to be determined to an accuracy unequalled by any other technique. Modified experiments have been proposed that can extend the method to detect longer range correlations, and it can be expected that more enhancements, including 3D techniques, will be forthcoming in the future.

8 RELATED ARTICLES

CRAMPS; Cross Polarization in Solids; Dipolar and Indirect Coupling Tensors in Solids; Heteronuclear Shift Correlation Spectroscopy; Internal Spin Interactions and Rotations in Solids; Magic Angle Spinning; Multidimensional Spectroscopy: Concepts.

9 REFERENCES

1. A. C. Kolbert, M. H. Levitt, and R. G. Griffin, *J. Magn. Reson.*, 1989, **85**, 42.
2. H. W. Spiess, *Chem. Rev.*, 1991, **91**, 1321.
3. K. Schmidt-Rohr, J. Clauss, and H. W. Spiess, *Macromolecules*, 1992, **25**, 3273.
4. D. P. Burum and A. Bielecki, *J. Magn. Reson.*, 1991, **94**, 645.
5. C. W. B. Lee and R. G. Griffin, *Biophys. J.*, 1989, **55**, 355.
6. P. Caravatti, G. Bodenhausen, and R. R. Ernst, *Chem. Phys. Lett.*, 1982, **89**, 363.
7. E. Roberts, S. Vega, and R. Griffin, *J. Am. Chem. Soc.*, 1984, **106**, 2506.
8. P. Caravatti, L. Braunschweiler, and R. R. Ernst, *Chem. Phys. Lett.*, 1983, **100**, 305.
9. C. E. Bronnimann, C. F. Ridenour, D. R. Kinney, and G. E. Maciel, *J. Magn. Reson.*, 1992, **97**, 522.
10. R. R. Ernst, G. Bodenhausen, and A. Wokaun, *Principles of Nuclear Magnetic Resonance in One and Two Dimensions*, Clarendon Press, Oxford, 1987, p. 340.
11. U. Haubenreisser and B. Schnabel, *J. Magn. Reson.*, 1979, **35**, 175.
12. D. P. Burum, M. Linder, and R. R. Ernst, *J. Magn. Reson.*, 1981, **43**, 463.
13. A. Bielecki, D. P. Burum, D. M. Rice, and F. E. Karasz, *Macromolecules*, 1991, **24**, 4820.
14. S. Li, D. M. Rice, and F. E. Karasz, *Macromolecules*, 1994, **27**, 2211.
15. C. E. Bronnimann, private communication.

Biographical Sketch

D. P. Burum. *b* 1952. B. S., Harvey Mudd College, 1974; Ph.D., California Institute of Technology (advisor R. W. Vaughan), 1979. Postdoctoral Assistant under R. R. Ernst 1979–80. Joined Bruker Instruments as an applications specialist in solid state NMR in 1982. Currently Bruker USA national product manager for analytical NMR. Approx. 25 publications. Research interests center around development of coherent averaging pulse techniques, including CRAMPS, two-dimensional HETCOR, spectral editing, etc.

Heteronuclear Shift Correlation Spectroscopy

Thomas T. Nakashima and R. E. D. McClung
University of Alberta, Edmonton, Alberta, Canada

1	Introduction	1
2	Basic Principles	1
3	Advancements in Heteronuclear Shift Correlation and Related Experiments	7
4	Related Articles	11
5	References	11

1 INTRODUCTION

Heteronuclear shift correlation spectroscopy is the name given to a class of two-dimensional NMR experiments (see ***Multidimensional Spectroscopy: Concepts***) that generate contour maps in which the chemical shifts of two distinct types of nuclei (hence the designation 'hetero') are correlated.[1–8] Acronyms for heteronuclear shift correlation spectroscopy include HETCOR, HSC, Hetero-COSY, H-C COSY, and H-X COSY. Although the examples described below involve $^{1}H-^{13}C$ heteronuclear shift correlation, heteronuclear shift correlation maps may be obtained for any pair of nuclei which are connected by scalar spin–spin coupling.[2] (See also ***COSY Two-Dimensional Experiments***; ***Heteronuclear Assignment Techniques***; ***Two-Dimensional Carbon–Heteroelement Correlation***.)

The most fundamental problem in the application of NMR spectroscopy to the elucidation of molecular structures is the assignment of the observed resonances in the NMR spectra to the specific atoms in the molecule (see ***Organic Chemistry Applications***). An essential component of the assignment process for ^{13}C spectra is the determination of the number of protons that are directly bonded to a given carbon atom (i.e., finding out whether a particular carbon resonance corresponds to a CH, CH_2, CH_3, or quaternary carbon). The task of assigning the peaks in NMR spectra, particularly in ^{13}C spectra, has been simplified by a number of developments over the past 30 years. The simple natural abundance ^{13}C spectrum of a molecule will show a single resonance line for each quaternary carbon atom, a 1:1 doublet for each CH carbon, a 1:2:1 triplet for each CH_2, and a 1:3:3:1 quartet for each CH_3 carbon atom, with separations of about 120–180 Hz between the various multiplet lines. The spacing here is equal to the carbon–proton coupling constant, $^{1}J_{CH}$. This simple spectrum has inherent low sensitivity, and the large spacing between multiplet lines results in considerable overlapping of the resonances from different carbon atoms. The ^{13}C spectrum obtained with broadband ^{1}H decoupling has much higher sensitivity, but contains no multiplet structure to aid in the assignment process. The introduction of selective frequency off-resonance proton decoupling (SFORD) retained the multiplet structure of the simple ^{13}C spectrum (but with considerably smaller multiplet line separations) and much of the sensitivity of the ^{1}H-decoupled spectrum, but the overlapping of peaks in crowded regions of the SFORD spectrum often prevented unambiguous assignment of the peaks.[9] (See ***Decoupling Methods***.)

With the development of FT NMR spectrometers allowing facile control of rf pulse lengths and phases on both observe and decoupler channels (see ***Spectrometers: A General Overview***), a number of experiments were developed to determine the number of protons attached to a particular carbon atom. The INEPT and DEPT sequences involve the transfer of proton magnetization to carbon.[10–12] One obtains increased sensitivity with INEPT and DEPT, and these sequences (with a refocusing period after the magnetization transfer step) yield proton-decoupled carbon spectra with distinguishable responses from CH, CH_2, and CH_3 carbons, but no responses from quaternary carbons. Another very important tool for assigning the number of protons attached to each carbon in the molecule is the APT experiment, which gives $^{13}C\{^{1}H\}$ spectra in which all quaternary and CH_2 carbons give peaks with positive phase, and all CH and CH_3 carbons give peaks with negative phase.[10–12] The INEPT, DEPT, and APT experiments are excellent analytical tools for determining the number of protons attached to a particular carbon atom, but do not connect the peaks in the ^{13}C and ^{1}H spectra to give confirmed assignments of resonances. (See ***INEPT***; ***Polarization Transfer Experiments via Scalar Coupling in Liquids***.)

Selective ^{1}H-decoupled experiments were developed to identify the carbon atom to which a particular proton is attached. The identification of carbon and hydrogen atoms that are directly bonded to each other is invaluable in making unambiguous assignments of all resonance lines in both ^{13}C and ^{1}H spectra. In selective ^{1}H decoupling, the resonance of a particular proton is selectively irradiated during the acquisition of the ^{13}C spectrum, and one observes a single sharp line for the carbon atom to which the irradiated protons are directly bonded. Selective ^{1}H-decoupling experiments are of limited utility when the region to be decoupled in the proton spectrum is crowded, or when there are nonequivalent methylene protons which cannot be decoupled simultaneously. The $^{1}H-^{13}C$ heteronuclear shift correlation experiment has revolutionized the ease with which one can correlate the ^{13}C resonance for each carbon atom in the molecule to the ^{1}H resonances of the protons that are directly attached to that carbon atom. Furthermore, since heteronuclear correlation involves the transfer of proton magnetization to carbon, the recycling times between accumulations are determined by proton relaxation times which are usually shorter than those for carbon (see ***Carbon-13 Relaxation Measurements: Organic Chemistry Applications***), and one obtains enhanced signal intensity due to the larger proton magnetization which is transferred to carbon. Both of these features lead to a sensitivity enhancement relative to normal ^{13}C spectroscopy.[1–8]

In this article, we shall describe the basic principles involved in heteronuclear shift correlation experiments, the important features that have been developed to simplify the correlation maps, and modifications that have been introduced to improve the sensitivity and expand the utility of heteronuclear shift correlation.

2 BASIC PRINCIPLES

As a typical example, the $^{1}H-^{13}C$ shift correlation map for sucrose is shown in Figure 1. The proton chemical shifts are identified in the ^{1}H spectrum along the vertical axis (often referred to as the f_1 dimension), and the carbon chemical shifts in the ^{13}C spectrum along the horizontal axis (the f_2 dimension), and the peaks in the contour map identify all directly bonded H and C atoms in the sucrose molecule. There is considerable congestion in the ^{1}H NMR spectrum (six proton resonances within the interval 3.6–4.0 ppm), but the peaks in the ^{13}C spectrum are well separated. Hence, the peaks in the 2D shift correlation map are all well resolved, so that, if the assignments of the carbon resonances are known then the assignments of the proton spectrum follow directly.

2.1 The Basic Heteronuclear Correlation Experiment

The basic principles involved in heteronuclear shift correlation experiments[1,2] are best understood by considering the pulse sequence shown in Figure 2(a). For completeness, the product operator transformations for the CH spin system during each of the steps are also included in the following description.[13] (See ***Radiofrequency Pulses: Response of Nuclear Spins***.) Proton and carbon nuclear spins are designated I and S, respectively. Heteronuclear correlation spectroscopy involves the following basic elements.

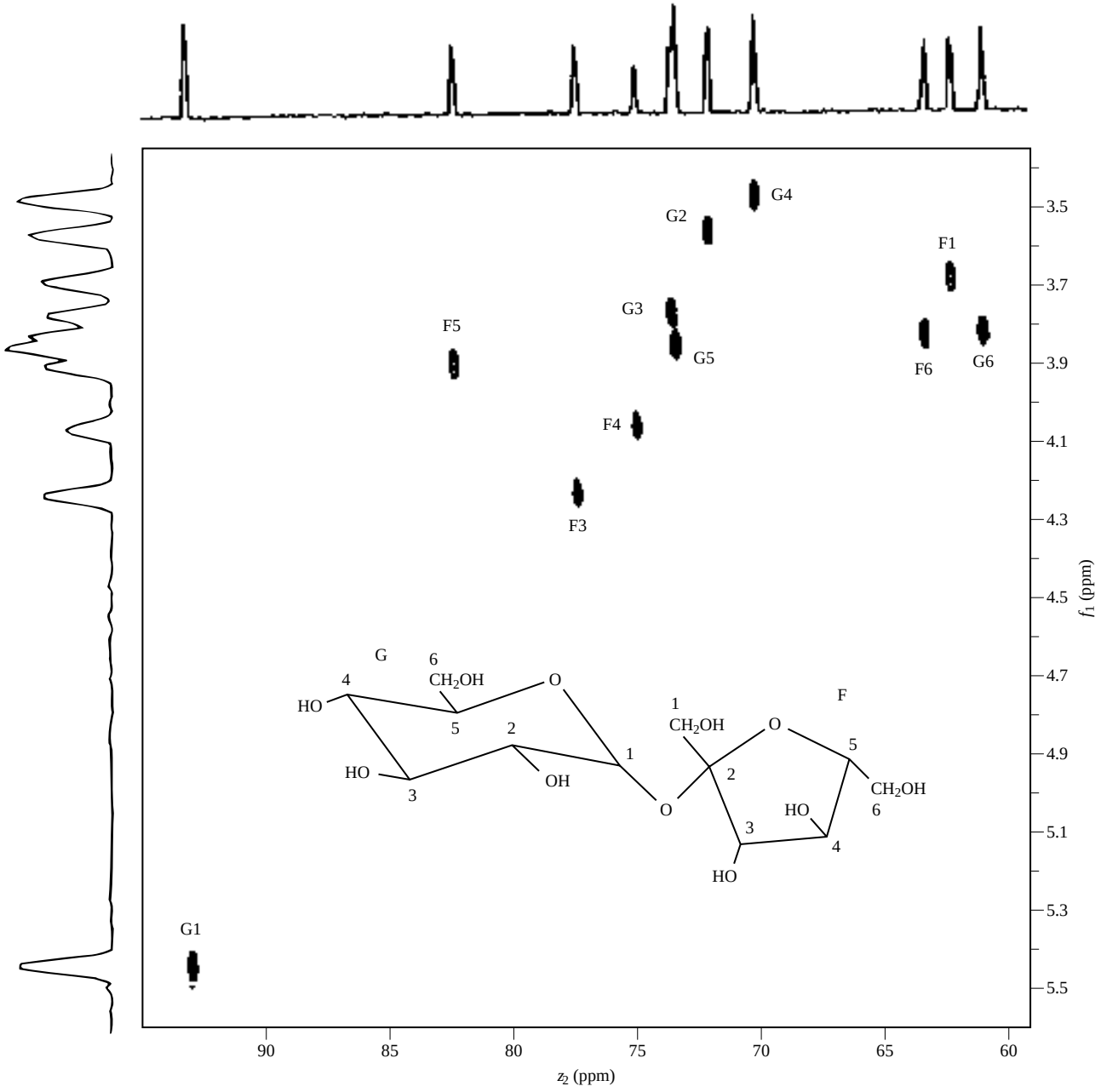

Figure 1 Conventional heteronuclear shift correlation map for sucrose in D_2O (10 mg in ≈ 0.5 mL) at 500 MHz obtained with the pulse sequence in Figure 2(d) ($^{13}C-^{1}H$ and $^{1}H-^{1}H$ decoupled in f_1, $^{13}C-^{1}H$ decoupled in f_2)

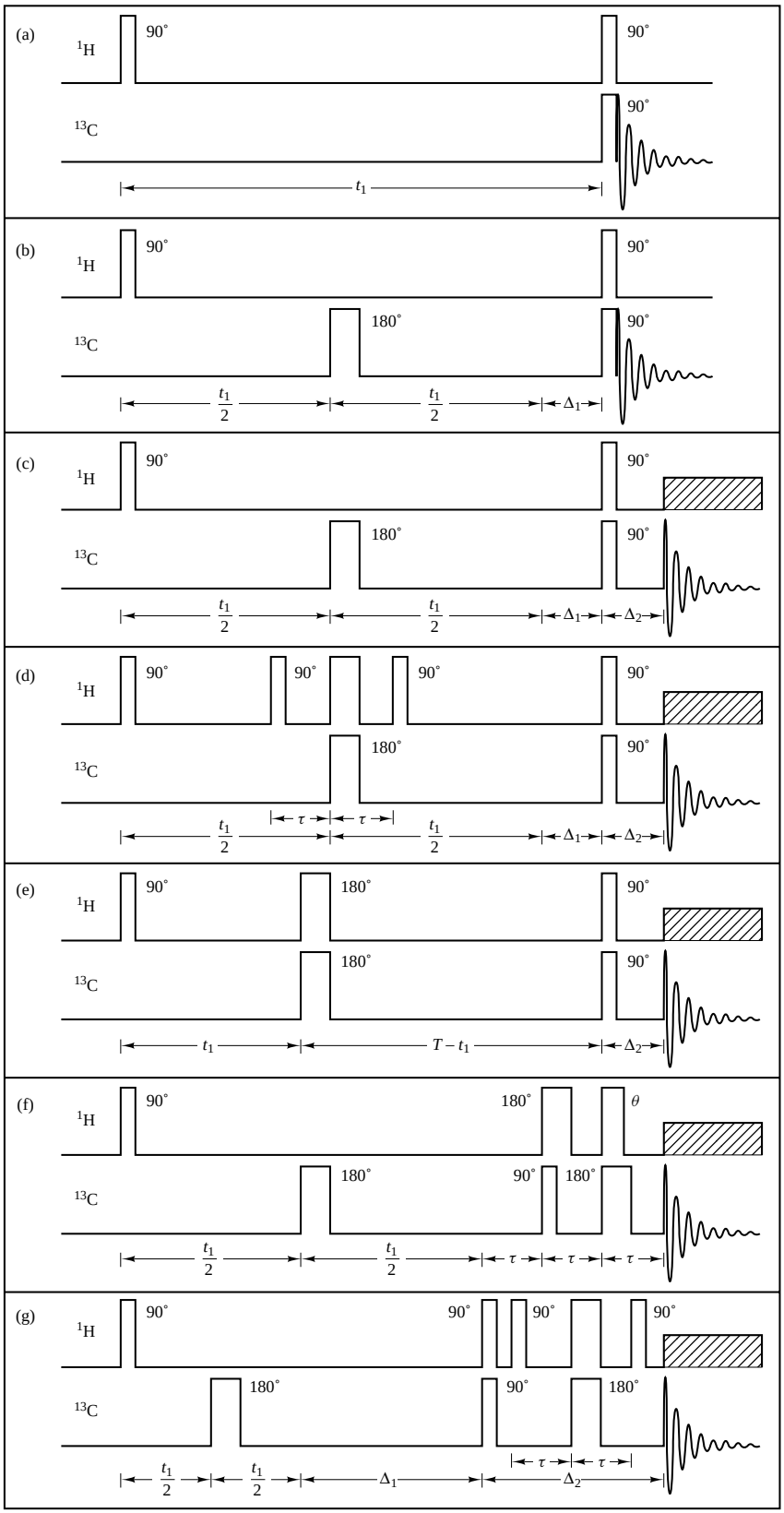

Figure 2 Heteronuclear shift correlation pulse sequences: (a) basic sequence with no decoupling; (b) sequence with ^{13}C–^{1}H decoupling in f_1; (c) sequence with ^{13}C–^{1}H decoupling in f_1 and f_2; (d) sequence with ^{13}C–^{1}H decoupling in f_1 and in f_2 and ^{1}H–^{1}H decoupling in f_1; (e) sequence using constant evolution time T; (f) sequence with DEPT magnetization transfer for multiplet selective editing; (g) sequence for detection of long range correlations. In sequences (c)–(e), $\Delta_1 = 1/(2\ ^1J_{CH})$ and $\Delta_2 \approx 1/(3\ ^1J_{CH})$. In sequence (g), $\Delta_1 = 1/(2J_{CH}^{\text{long range}})$ and $\Delta_2 \approx 1/(3J_{CH}^{\text{long range}})$. $\tau = 1/(2\ ^1J_{CH})$ in sequences (d), (f), and (g)

1. A broadband 90° ^{1}H pulse rotates the proton z magnetizations into the transverse plane (in product operator terms, $\hat{I}_z \rightarrow \hat{I}_y$).
2. The transverse proton magnetizations precess and become 'labeled' with their chemical shift frequencies (ν_H) during a precession period of incremented length t_1. The protons interact with the ^{13}C nuclei via scalar spin–spin coupling during this labeling period, and antiphase proton magnetizations are generated by these interactions. [$\hat{I}_y \rightarrow 2\hat{I}_x\hat{S}_z$ cos ($2\pi\nu_H t_1$) sin ($\pi\ ^1J_{CH}t_1$).]
3. The application of simultaneous broadband 90° pulses to both ^{13}C and ^{1}H nuclei converts the antiphase proton magnetizations into antiphase carbon magnetizations. [$2\hat{I}_x\hat{S}_z$ cos ($2\pi\nu_H t_1$) sin ($\pi\ ^1J_{CH}t_1$) $\rightarrow 2\hat{I}_z\hat{S}_y$ cos ($2\pi\nu_H t_1$) sin ($\pi\ ^1J_{CH}t_1$).]
4. These antiphase carbon magnetizations precess, are labeled with their chemical shift frequencies (ν_C), and ^{13}C–^{1}H spin–spin interactions produce in-phase carbon magnetizations, which are sampled at times t_2 during the detection period. [$2\hat{I}_z\hat{S}_y$ cos ($2\pi\nu_H t_1$) sin ($\pi\ ^1J_{CH}t_1$) $\rightarrow -\hat{S}_x$ cos ($2\pi\nu_C t_2$) sin ($\pi\ ^1J_{CH}t_2$) cos ($2\pi\nu_H t_1$) sin ($\pi\ ^1J_{CH}t_1$).]
5. Fourier transformation of the magnetization data (see ***Fourier Transform Spectroscopy***) yields a contour map that contains peaks connecting the chemical shift (ν_H) of each proton to the chemical shift (ν_C) of the carbon to which it is directly bonded.

The heteronuclear shift correlation map for sucrose shown in Figure 3 was generated using this basic pulse sequence given in Figure 2(a), and differs in two important respects from the map shown in Figure 1 obtained with the sequence in Figure 2(d)—the correlation map in Figure 3 shows ^{13}C–^{1}H spin–spin multiplets in both the f_1 (proton) and f_2 (carbon) dimensions, while ^{13}C–^{1}H couplings are absent in both dimensions and ^{1}H–^{1}H couplings are absent in the f_1 dimension of the map shown in Figure 1. A CH_3 group gives a correlation profile consisting of eight peaks (two quartets with intensities 1:1:−1:−1 in the carbon dimension at proton frequencies $\nu_H \pm \frac{1}{2}\ ^1J_{CH}$), a CH_2 group gives four peaks (two 1:0:−1 triplets), and a CH group gives four peaks (two 1:−1 doublets). The antiphase nature of the multiplets in the carbon dimension is very undesirable, since it does not permit proton decoupling during acquisition, and the presence of ^{13}C–^{1}H splitting of the profiles in both proton and carbon dimensions is undesirable, since the primary interest here is in chemical shifts, not in spin–spin couplings. Modification of this basic experiment allows decoupling in both dimensions as described below. (See ***Decoupling Methods***.)

2.2 Carbon-13 Decoupling in f_1

The ^{13}C–^{1}H couplings can be removed from the f_1 (proton) dimension of the heteronuclear shift correlation map by inserting a 180° carbon pulse in the center of the t_1 labeling period,[2] and adding a delay of length $\Delta_1 = 1/(2\ ^1J_{CH})$ before the proton and carbon 90° pulses are applied as shown in Figure 2(b). The effect of the 180° carbon pulse is to remove the effects of ^{13}C–^{1}H coupling during the labeling period [$\hat{I}_y \rightarrow \hat{I}_y$ cos ($2\pi\nu_H t_1$) − $\hat{I}_x$ sin ($2\pi\nu_H t_1$], and the delay Δ_1 must be added to allow spin–spin coupling to transform the in-phase proton magnetization into antiphase magnetization ($\hat{I}_y$ cos ($2\pi\nu_H t_1$) $\rightarrow -2\hat{I}_x\hat{S}_z$ cos [$2\pi\nu_H(t_1 + \Delta_1)$] and $\hat{I}_x$ sin ($2\pi\nu_H t_1$) $\rightarrow 2\hat{I}_y\hat{S}_z$ sin [$2\pi\nu_H(t_1 + \Delta_1)$]) so that it may be converted to antiphase carbon magnetization by the 90° pulses. The addition of the Δ_1 delay introduces phase differences between the final signals from the different proton–carbon moieties in the molecule, so phase-sensitive correlation maps are not obtained.

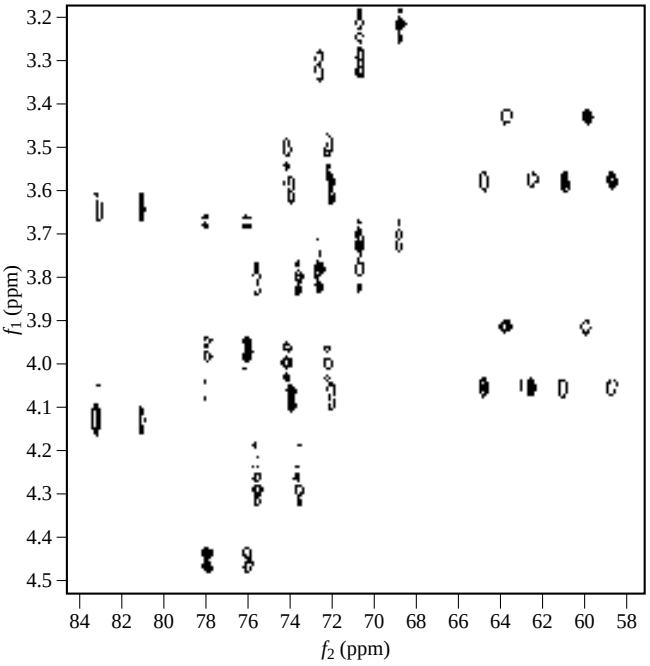

Figure 3 A portion of the heteronuclear shift correlation map for a concentrated solution of sucrose in D_2O at 300 MHz (^{1}H), with no decoupling in either dimension. Obtained with pulse sequence in Figure 2(a). Multiple contours represent positive peaks, single contours are negative peaks

2.3 ^{1}H Decoupling in f_1

The 90° carbon and proton pulses in all heteronuclear shift correlation pulse sequences convert *antiphase* proton magnetization ($\hat{I}_x\hat{S}_z$ or $\hat{I}_y\hat{S}_z$) into *antiphase* carbon magnetization ($\hat{I}_z\hat{S}_y$ or $\hat{I}_z\hat{S}_x$). If one turns on the proton decoupler immediately after these pulses, no signals will be acquired, since only *in-phase* carbon magnetization is detected. Hence, in order to effect proton decoupling during the t_2 acquisition period, one must introduce a delay of length Δ_2 between the 90° pulses and the acquisition to allow ^{13}C–^{1}H coupling to convert *antiphase* into *in-phase* magnetization ($\hat{I}_z\hat{S}_y \rightarrow -[\hat{S}_x$ cos ($\nu_C\Delta_2$) + $\hat{S}_y$ sin ($\nu_C\Delta_2$)] sin ($\pi\ ^1J_{CH}\Delta_2$)), as shown in the pulse sequence in Figure 2(c) (see ***INEPT***). When the decoupler is turned on at the end of Δ_2, a proton-decoupled carbon spectrum will be acquired and displayed in the f_2 dimension of the heteronuclear shift correlation map.[2] The relative magnitudes of the detected signals for CH, CH_2, and CH_3 groups are proportional to sin ($\pi\ ^1J_{CH}\Delta_2$), sin ($2\pi\ ^1J_{CH}\Delta_2$), and sin ($\pi\ ^1J_{CH}\Delta_2$) + sin ($3\pi\ ^1J_{CH}\Delta_2$), respectively. This dependence on the magnitude of Δ_2 implies that no single value of Δ_2 will give maximum signal amplitudes for all CH_n moieties. Instead, one should use a value $\Delta_2 \approx 1/(3\ ^1J_{CH})$ in order to obtain carbon signals of approximately equal magnitude for all spin systems.

2.4 Elimination of ^{1}H–^{1}H Couplings in f_1

The presence of ^{1}H–^{1}H couplings in the f_1 dimension of the heteronuclear shift correlation map needlessly complicates and lowers the overall intensity of the correlation peaks. These couplings arise from spin–spin interactions between the proton(s) in a ^{13}C–^{1}H$_n$ fragment ('directly bonded' protons) and the protons in neighboring ^{12}C–^{1}H$_{n'}$ fragments ('remote' protons). (The 1.1% natural abundance of ^{13}C nuclei means that the neighboring carbon atoms in the molecular skeleton will be ^{12}C in over 98% of the molecules.) These couplings can be removed by selectively inverting the magnetizations of the remote protons in the center of the t_1 labeling period without inverting the magnetizations of the directly bonded protons.[2] This selective manipulation of the remote protons can be effected using bilinear rotational decoupling (BIRD), which consists of the following sequence:[2,6–8]

$$90^\circ_{x^1\mathrm{H}} - 1/(2\,{}^1J_{\mathrm{CH}}) - 180^\circ_{^{13}\mathrm{C}},\ 180^\circ_{y^1\mathrm{H}} \\ -1/(2\,{}^1J_{\mathrm{CH}}) - 90^\circ_{x^1\mathrm{H}} \qquad (1)$$

as shown in the heteronuclear shift correlation sequence in Figure 2(d). This sequence gives heteronuclear shift correlation maps with ^{1}H–^{1}H decoupling in f_1, and is the sequence used to obtain the heteronuclear shift correlation map for sucrose given in Figure 1.

The operation of this BIRD sequence is easily understood by following the evolution of the magnetization components of the directly bonded and remote protons as shown in Figure 4. The y components of the magnetizations of both directly bonded and remote protons are converted to z magnetizations by the $90^\circ_{x^1\mathrm{H}}$ pulse, are then inverted by the $180^\circ_{y^1\mathrm{H}}$ pulse, and are finally rotated by the final $90^\circ_{x^1\mathrm{H}}$ pulse so that they again lie along the y axis. The x components of the magnetizations of remote and directly bonded protons are not affected by the $90^\circ_{x^1\mathrm{H}}$ pulse, but behave differently during the precession periods since only the directly bonded protons experience C–H coupling during these periods. The precession of the x components of the magnetizations of remote protons due to their different chemical shifts during the first $1/(2\,{}^1J_{\mathrm{CH}})$ delay period is reversed during the delay following the $180^\circ_{y^1\mathrm{H}}$ pulse, so that the magnetizations are refocused along the negative x axis just before the final $90^\circ_{x^1\mathrm{H}}$ pulse is applied. Thus, the effect of the BIRD element on the transverse magnetization of remote protons [see Figure 4(b)] is equivalent to that of a 180°_y pulse ($M_y \rightarrow M_y$ and $M_x \rightarrow -M_x$). On the other hand, C–H coupling causes the x magnetizations of directly bonded protons to precess as two separate components (one component precessing at frequency $\nu_{\mathrm{H}} + \frac{1}{2}\,{}^1J_{\mathrm{CH}}$ and one at $\nu_{\mathrm{H}} - \frac{1}{2}\,{}^1J_{\mathrm{CH}}$). The $180^\circ_{^{13}\mathrm{C}}$ and $180^\circ_{y^1\mathrm{H}}$ pulses cause the chemical shift precession during the first delay period to be reversed during the second $1/(2\,{}^1J_{\mathrm{CH}})$ delay period, and the two components of the magnetization ultimately come together and lie along the positive x direction when the final $90^\circ_{x^1\mathrm{H}}$ pulse is applied. Hence, as shown in Figure 4(a), the BIRD element has no net effect on the magnetizations of directly bonded protons ($M_y \rightarrow M_y$ and $M_x \rightarrow M_x$). The 'extra' 180° rotation that the magnetizations of directly bonded protons experience is, in fact, a result of the *bilinear* rotation due to ^{1}H–^{13}C coupling during the two $1/(2\,{}^1J_{\mathrm{CH}})$ delay periods of the BIRD sequence.

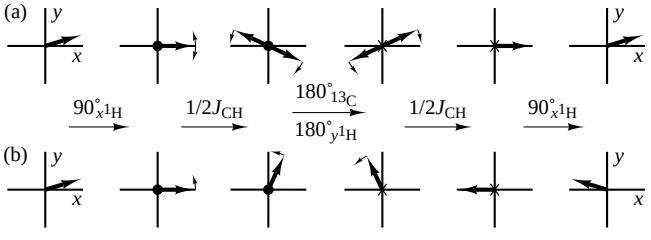

Figure 4 Behavior of transverse magnetization components for directly bonded (a) and remote (b) protons during BIRD. Symbols • and × at the origin of coordinates indicate positive and negative z components, respectively

An alternate approach to removing ^{1}H–^{1}H couplings in f_1 is directly analogous to that employed in decoupled COSY, and uses a pulse sequence with a constant evolution time T as shown in Figure 2(e)[3,6] (see ***COSY Two-Dimensional Experiments***). In this sequence, the time at which simultaneous $180^\circ_{^1\mathrm{H}} - 180^\circ_{^{13}\mathrm{C}}$ pulses are applied is 'stepped across' the evolution period from time 0 to time T in increments of T/n_1 for successive values of t_1. Here, n_1 is the total number of t_1 values. This sequence has serious drawbacks, since T must be an odd multiple of $1/(2\,{}^1J_{\mathrm{CH}})$ for maximum polarization transfer to carbon and maximum sensitivity. If T is long, small variations in $^1J_{\mathrm{CH}}$ among the various CH$_n$ fragments in the molecule lead to variations of unacceptable magnitude in the intensities of peaks in the heteronuclear shift correlation map. It has been suggested that T be set equal to 0.02 s, but this restricts the resolution in f_1 to 50 Hz point^{-1}.

2.5 Practical Considerations

In order to obtain heteronuclear correlation maps free of instrumental artifacts, one must use rf pulses whose lengths have been carefully calibrated, and cycle the phases of the pulses in an appropriate fashion as detailed in the following sections.

2.5.1 Pulse Width Calibration

One must calibrate the lengths of the pulses on both 'observe' (carbon) and 'decoupler' (proton) rf channels (see ***Radiofrequency Pulses: Response of Nuclear Spins***). One should use a sample with a short carbon relaxation time T_1, and a sufficiently strong ^{13}C signal that a single transient produces a spectrum of high signal-to-noise ratio [an approx. 60:40 $CHCl_3$:$CDCl_3$ mixture doped with tris(acetylacetonato)chromium(III) is suitable].

Calibration of pulse lengths for the 'observe' channel is straightforward: set the transmitter frequency close to the exact resonance for the sample in order to avoid off-resonance effects; and generate a series of 'one pulse' proton-decoupled carbon spectra with the carbon pulse length increased by a small amount in successive spectra (being sure to use a relaxation delay $\geq 3T_1$ between the experiments). The spectrum with lowest signal amplitude (the 'null') corresponds to a 180° pulse, and the 90° pulse length is half of this value. If a poor null is obtained, the probe has significant $\boldsymbol{B}_1$ inhomogeneity. If the signal amplitude varies in a sinusoidal

fashion with pulse length, but is skewed toward the shorter pulse lengths, the sequence of experiments should be repeated with a longer relaxation delay (see also ***Spectrometers: A General Overview***).

Calibration of pulse lengths for the decoupler channel is more complicated, since the effects of proton pulses must be observed indirectly (see ***Polarization Transfer Experiments via Scalar Coupling in Liquids***). One method for determining the 90° pulse length for protons is to perform a series of experiments using the pulse sequence

$$90^\circ_{^{13}\mathrm{C}} - 1/(2\,{}^1J_{\mathrm{CH}}) - 180_{^{13}\mathrm{C}},\ \theta_{^1\mathrm{H}} - 1/(2\,{}^1J_{\mathrm{CH}}) - \text{acquire } {}^{13}\mathrm{C} \text{ with } {}^1\mathrm{H} \text{ decoupling} \quad (2)$$

with the length of the proton θ pulse increased by a small increment in successive experiments.[5] In these experiments, it is important to set the transmitter frequencies close to exact resonance. The spectrum with minimum signal corresponds to $\theta = 90^\circ$.

2.5.2 Phase Cycling and Coherence Pathway Selection

In order to avoid the appearance of instrumental artifacts and other undesirable features in heteronuclear shift correlation maps, it is important to cycle the phases of the pulses and the detector in an appropriate manner[14] (see ***Phase Cycling***). The principles of phase cycling are deeply rooted in the concepts of coherence levels and the coherence pathways that the magnetization of the spin system follows from excitation to detection. In simple terms, one can classify time-coherent properties of a spin system by the Zeeman frequencies with which they rotate about the applied magnetic field $\boldsymbol{B}_0$. For example, in the $^{13}\mathrm{C}$–$^1\mathrm{H}$ spin system, the longitudinal magnetizations (product operators $\hat{I}_z$ and $\hat{S}_z$) do not rotate about $\boldsymbol{B}_0$, and are therefore coherences of level 0; transverse magnetizations ($\hat{I}_x \pm \mathrm{i}\hat{I}_y$ and $\hat{S}_x \pm \mathrm{i}\hat{S}_y$) rotate at frequencies $\pm\nu_{\mathrm{C}}$ or $\pm\nu_{\mathrm{H}}$ about $\boldsymbol{B}_0$, and belong to coherence levels +1 and −1; zero quantum coherences ($2\hat{I}_x\hat{S}_x + 2\hat{I}_y\hat{S}_y$ and $2\hat{I}_x\hat{S}_y - 2\hat{I}_y\hat{S}_x$) rotate at frequencies $\pm(\nu_{\mathrm{H}} - \nu_{\mathrm{C}})$, and belong to coherence level 0; while double quantum coherences ($2\hat{I}_x\hat{S}_x - 2\hat{I}_y\hat{S}_y$ and $2\hat{I}_x\hat{S}_y + 2\hat{I}_y\hat{S}_x$) rotate at frequencies $\pm(\nu_{\mathrm{H}} + \nu_{\mathrm{C}})$, and are coherences of level +2 and −2. In all FT NMR experiments, the spin system begins with longitudinal magnetization in coherence level 0 and ends with the sampling of in-phase transverse magnetization in the −1 coherence level. The trajectory that the magnetization follows during the course of the experiment defines a coherence pathway.

The coherence level of a spin system can be changed by the application of an rf pulse, but does not change during a period of free precession. When a pulse with phase angle ϕ with respect to the x axis of the rotating frame causes a change from coherence level p_1 to coherence level p_2, a phase factor $\exp[-\mathrm{i}(p_2 - p_1)\phi]$ becomes incorporated into the resulting coherence. For example, the application of a 90° proton pulse with phase ϕ to longitudinal proton magnetization (coherence level 0) produces a +1 coherence ($\hat{I}_x + \mathrm{i}\hat{I}_y$) with phase factor $\exp(-\mathrm{i}\phi)$, and a −1 coherence ($\hat{I}_x - \mathrm{i}\hat{I}_y$) with phase factor $\exp(\mathrm{i}\phi)$. If the proton signal were acquired at this point, a receiver phase factor of $\exp(\mathrm{i}\phi)$ would be applied to the detected − 1 coherence during acquisition so that the final signal is independent of ϕ. In heteronuclear shift correlation experiments where there are many pulses whose phases may vary during spectral accumulation, the phases of the pulses and detector must be varied in concert in order to select only signals derived from coherences that have followed the desired coherence pathway(s), and suppress undesirable features.

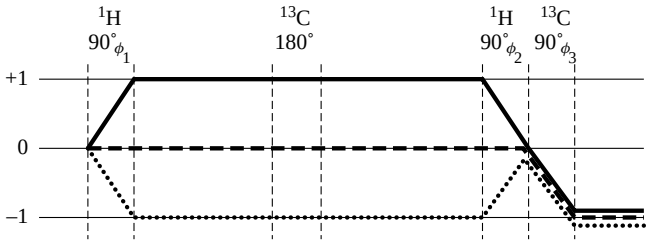

Figure 5 Coherence pathways involved in the basic heteronuclear shift correlation experiment. Pathways followed by desired signals (. . .), 'quad' images (—), and carbon magnetization (- -) are shown

Three possible coherence pathways for signals that can be observed in the heteronuclear shift correlation experiment are shown in Figure 5. The signals associated with these pathways have phase factors $\exp[\mathrm{i}(-\phi_1 + \phi_2 + \phi_3)]$ (solid line), $\exp(\mathrm{i}\phi_3)$ (dashed line), and $\exp[\mathrm{i}(\phi_1 - \phi_2 + \phi_3)]$ (dotted line). The solid pathway is followed by proton magnetization ($\hat{I}_z$), which is converted into coherence of level +1 [$(\hat{I}_x + \mathrm{i}\hat{I}_y)\exp(-\mathrm{i}\phi_1)$] by the proton $90^\circ_{\phi_1}$ pulse, and is frequency-labeled during the t_1 evolution [a factor $\exp(-2\mathrm{i}\pi\nu_{\mathrm{H}}t_1)$ is incorporated into the coherence]; the +1 coherence passes to coherence level 0 when the proton $90^\circ_{\phi_3}$ pulse is applied, is converted to antiphase transverse carbon magnetization of coherence level −1 by the carbon $90^\circ_{\phi_3}$ pulse, and ultimately gives peaks at $(-\nu_{\mathrm{H}}, \nu_{\mathrm{C}})$ on the 2D contour map. The dotted pathway is followed by proton magnetization ($\hat{I}_z$), which is converted into coherence of level −1 [$(\hat{I}_x - \mathrm{i}\hat{I}_y)\exp(\mathrm{i}\phi_1)$] by the proton $90^\circ_{\phi_1}$ pulse, and is frequency-labeled during the t_1 evolution [a factor $\exp(2\mathrm{i}\pi\nu_{\mathrm{H}}t_1)$ is incorporated]; this −1 coherence passes through the zero coherence level when the proton $90^\circ_{\phi_1}$ pulse is applied, is converted to antiphase transverse carbon magnetization of coherence level −1 by the carbon $90^\circ_{\phi_3}$ pulse, and gives peaks at $(\nu_{\mathrm{H}}, \nu_{\mathrm{C}})$. The dashed pathway is followed by carbon magnetization ($\hat{S}_z$), which is not affected by the proton pulses, is converted into observable transverse magnetization [$(\hat{S}_x - \mathrm{i}\hat{S}_y)\exp(\mathrm{i}\phi_3)$] by the carbon $90^\circ_{\phi_3}$ pulse, and gives peaks at $(0, \nu_{\mathrm{C}})$. By setting the phase angle, ϕ_{R}, of the detector equal to $\phi_1 - \phi_2 + \phi_3$, appending the phase factor $\exp(-\mathrm{i}\phi_{\mathrm{R}})$ to each of the signals as they are accumulated, and cycling the phases ϕ_1, ϕ_2, and ϕ_3 independently through values 0°–90°–180°–270°, the final spectrum will be that for spins that have followed the dotted pathway shown in Figure 5. This phase cycling suppresses signals arising from spins that have traversed the solid and dashed coherence pathways. This cycling of the phases of pulses and detector is very important, since it removes 'zero-frequency' artifacts (dashed coherence pathway) from the heteronuclear shift correlation map, and allows one to place the proton transmitter frequency at the center of the spectrum and achieve quadrature detection in f_1, since the 'quad image' peaks (solid coherence pathway) at $(-\nu_{\mathrm{H}}, \nu_{\mathrm{C}})$ are suppressed.

3 ADVANCEMENTS IN HETERONUCLEAR SHIFT CORRELATION AND RELATED EXPERIMENTS

There have been a number of advances and extensions of heteronuclear shift correlation that afford spectral editing,[3] selection of long-range rather than directly bonded correlations,[3,5–7,15] increased sensitivity, and solvent suppression using inverse detection and multiple quantum filtering techniques.[1,3,16–19] A summary of the important features of these advances is given in the following sections.

3.1 Spectral Editing

In order to remove ambiguities from congested heteronuclear shift correlation maps, it is sometimes useful to display selectively only the correlations for CH, CH_2, or CH_3 fragments.[3] In principle, this might be done by taking linear combinations of a set of correlation maps generated with the pulse sequence in Figure 2(c) or (d) using a set of suitably chosen values of Δ_2. It is, however, more efficient to use the 2D DEPT sequence shown in Figure 2(f), because the editing capability of this sequence is less sensitive to variations in $^1J_{CH}$. The evolution part of the heteronuclear shift correlation sequence is unchanged, but the transfer of magnetization from proton to carbon is now based on DEPT rather than INEPT (see ***Polarization Transfer Experiments via Scalar Coupling in Liquids***), and involves zero and double quantum coherences.[11] The editing of heteronuclear shift correlation maps according to the number of attached protons is based on the variation of the intensities of the carbon signals with the flip angle θ for the final proton pulse in the DEPT transfer:

$$I_{CH} = \sin\theta \tag{3}$$

$$I_{CH_2} = \sin 2\theta \tag{4}$$

$$I_{CH_3} = \sin\theta + \sin 3\theta \tag{5}$$

One collects FIDs for three values of θ—FID(θ_1), FID(θ_2), and FID(θ_3)—and constructs linear combinations of these FIDs that selectively enhance each of the CH_n moieties:

$$\begin{aligned} \theta_1 = 45^\circ, \quad \theta_2 = 90^\circ, \quad \theta_3 = 135^\circ \\ \mathrm{FID_{CH}} = \mathrm{FID}(90^\circ), \\ \mathrm{FID_{CH_2}} = \mathrm{FID}(45^\circ) - \mathrm{FID}(135^\circ), \\ \mathrm{FID_{CH_3}} = \mathrm{FID}(45^\circ) + \mathrm{FID}(135^\circ) - 0.707\,\mathrm{FID}(90^\circ), \end{aligned}$$

$$\left.\begin{aligned} \theta_1 = 30^\circ, \quad \theta_2 = 90^\circ, \quad \theta_3 = 150^\circ \\ \mathrm{FID_{CH}} = \mathrm{FID}(90^\circ) \\ \mathrm{FID_{CH_2}} = \mathrm{FID}(30^\circ) - \mathrm{FID}(150^\circ) \\ \mathrm{FID_{CH_3}} = \mathrm{FID}(30^\circ) + \mathrm{FID}(150^\circ) - \mathrm{FID}(90^\circ) \end{aligned}\right\} \tag{6}$$

An example of the editing effectiveness of 2D DEPT is shown in Figure 6, where the CH and CH_2 maps for cholesterol are compared with the heteronuclear shift correlation map containing peaks from all CH_n fragments. The unedited map [Figure 6(a)] shows four strong methyl resonances which are suppressed in the edited maps shown in Figures 6(b) and (c). The region near δ_C = 35 ppm in the unedited map shows several overlapping peaks, which are resolved into two CH_2 correlations and one CH correlation in the edited maps.

3.2 Heteronuclear Correlations Based on Long-Range ^1H–^{13}C Couplings

One of the most important NMR methods used in structural elucidation of complex organic molecules is the C–H correlation experiment, which is optimized for long-range magnetization transfer.[3,5–7] The 2D maps obtained with this technique are very useful in establishing the C–C connectivities in the molecule, since they show correlations between ^{13}C and protons that are separated by two or three bonds. The most obvious approach is to use the pulse sequence in Figures 2(c), (d), or (e), and set the lengths of the delays Δ_1 and Δ_2 so that maximum signals would be obtained for carbon–proton spin–spin couplings, $J_{CH}^{\text{long range}}$, of 4–10 Hz. This approach (the COLOC sequence) works well only for isolated spin systems where the carbon atom experiences only long range couplings.[3] In all other cases, the long range correlation peak intensities are modulated by factors $\cos^n(\pi\ ^1J_{CH}\Delta_2)$, where n is the number of protons directly bonded to a particular carbon atom. This modulation arises from spin–spin interactions between the ^{13}C nucleus and its directly bonded protons during Δ_2. This deficiency can be rectified by inserting a BIRD element at the center of the Δ_2 delay to decouple the directly bonded protons as shown in the pulse sequence in Figure 2(g).[3] With this sequence, there is no anomalous modulation of the long-range peaks by directly bonded C–H couplings during Δ_2. The long-range heteronuclear shift correlation map of norharmane shown in Figure 7 contains a multitude of correlations over three bonds (e.g., C_{4a}–H_1), and a few two-bond correlations (e.g., C_4–H_3). Analysis of these correlations, together with the ^1H spectrum and the normal heteronuclear correlation map, allows one to establish the structure of the norharmane molecule unambiguously. (See also ***Natural Products***.)

It is desirable to suppress all directly bonded correlations from long-range heteronuclear correlation maps as effectively as possible. The BIRD element in the center of Δ_2 significantly decreases the intensities of directly bonded correlations, but the suppression is often incomplete, particularly for compounds with a wide range of $^1J_{CH}$. A number of approaches have been used to improve the suppression efficiency. Satisfactory suppression is obtained by inserting a two step J-filter element, $-1/(2^1J_{CH}) - 90^\circ_{^{13}C} - 1/(2^1J_{CH}) - 90^\circ_{^{13}C}$–, directly after the initial $90^\circ_{^1H}$ pulse in the long range heteronuclear correlation sequence given in Figure 2(g) (the BIRDTRAP sequence).[15] An alternate approach to suppression of directly bonded correlations and improved sensitivity in long-range heteronuclear correlation spectroscopy is embodied in the FLOCK sequence, in which the $180^\circ_{^{13}C}$ pulse at the center of the t_1 labeling period is replaced by a BIRD element to effect ^1H–^1H decoupling during t_1, and a third BIRD element is placed at the center of the Δ_1 period.[3] The presence of such a large number of pulses in FLOCK makes it more sensitive to the effects of rf inhomogeneity and offset than the sequence in Figure 2(g).

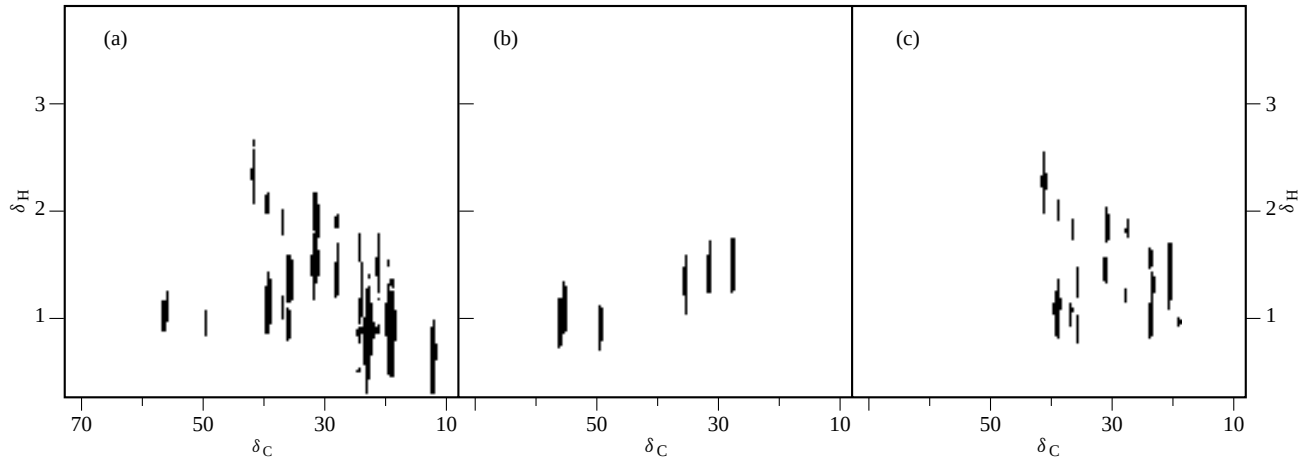

Figure 6 Heteronuclear shift correlation maps for cholesterol in $CDCl_3$ at 300 MHz (^1H) obtained with the pulse sequence in Figure 2(f): (a) transform of FID(30°) showing correlations for CH, CH_2, and CH_3 groups; (b) transform of FID(90°) showing correlations for CH fragments; (c) transform of FID(150°) − FID(30°) containing correlations for CH_2 fragments

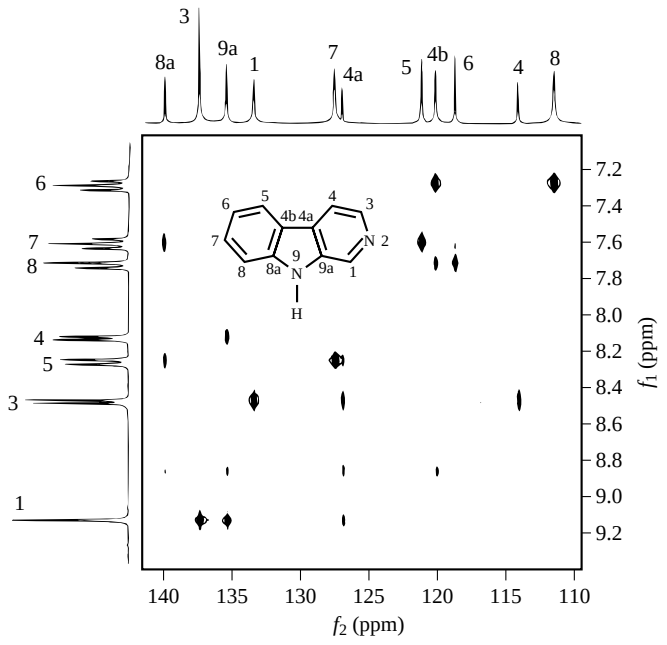

Figure 7 Long-range heteronuclear shift correlation map for norharmane in DMSO-d_6 at 300 MHz (^1H) obtained with the BIRDTRAP sequence,[15] a version of the pulse sequence in Figure 2(g) that contains a two-step J filter after the initial proton pulse

3.3 Inverse Detection: HSQC and HMQC

In the preceding sections, we have described only heteronuclear shift correlation experiments in which proton magnetization is excited and transferred to carbon for detection. The overall sensitivity of a 2D NMR experiment is proportional to $\gamma_e\gamma_d^{3/2}$, where γ_e is the magnetogyric ratio for the nucleus excited by the initial pulse and γ_d is the magnetogyric ratio of the nucleus whose magnetization is detected. Since $\gamma_{^1H} \approx 4\gamma_{^{13}C}$, the conventional ^1H–^{13}C heteronuclear shift correlation experiment is about 8 times less sensitive than 2D experiments in which proton magnetization is excited and detected.[1] This implies that the overall sensitivity of heteronuclear shift correlation spectroscopy could be improved by a factor of eight if the pulse sequence were modified so that 'inverse' (i.e. proton rather than carbon) detection could be employed.

There are a number of *technical* problems associated with the design of heteronuclear shift correlation experiments in which proton magnetization is detected:

1. The spectrometer, probe and control software must have full multichannel rf capabilities so that one can pulse ^1H and ^{13}C, and detect ^1H magnetization while performing ^{13}C decoupling. Until recently, the rf hardware in most spectrometers was designed to perform ^{13}C spectroscopy by applying ^{13}C pulses and detecting ^{13}C signals through a 'transmitter' coil, and applying ^1H pulses through a 'decoupler' coil. Modern spectrometers now provide capabilities for pulsing, decoupling, and/or observing on each of two or more independent rf channels, and the control software implements 'inverse' detection with ease. A further improvement in sensitivity is achieved by using an 'inverse' probe, which is designed with the ^1H coil wound closest to the sample for maximum detected ^1H signal. (See also ***Spectrometers: A General Overview***.)
2. One must be able to decouple ^{13}C efficiently while sampling the ^1H magnetization. This is a very demanding requirement, since the ^{13}C spectral bandwidth is much larger than the ^1H bandwidth, so that ^{13}C decoupling using conventional methods requires much higher decoupler power levels than those used in ^1H decoupling. The recent development of GARP[16] now affords very effective ^{13}C decoupling over wide bandwidths at much lower power levels than conventional methods.
3. One must selectively detect signals associated with protons in $^{13}CH_n$ fragments, while suppressing the ^1H signals associated with protons in $^{12}CH_n$ fragments. This can be very difficult, since the natural abundance of ^{13}C is only 1.1%, so one must suppress signals that may be 100 times more intense than the desired signals. One encounters severe dynamic range problems if one attempts to use a simple difference technique to eliminate the large signals from the $^{12}CH_n$ protons. The dynamic range problem

has been overcome, and excellent selectivity has been achieved by the development of suitable pulse sequences to achieve the necessary signal suppression.[17] The sensitivity of 'inverse' heteronuclear shift correlation experiments has also been improved dramatically by the use of pulsed field gradients. (See ***Field Gradients and Their Application***.)

In addition to these technical problems, the realization of a heteronuclear shift correlation experiment with ^{1}H detection required the development of robust pulse sequences to manipulate the proton magnetization in order to obtain the necessary labeling of the magnetization with ^{13}C{^{1}H} frequencies during t_1 and ultimately acquire a ^{1}H{^{13}C} FID.[17] The most straightforward approach is to use INEPT to convert proton magnetization to carbon,[11] allow it to precess and become labeled with carbon frequencies during t_1 (applying a 180° proton pulse at the center of t_1 to remove ^{13}C–^{1}H coupling), then convert the carbon magnetization back to proton magnetization (reverse INEPT) for detection, and finally collect the proton FID while applying GARP carbon decoupling.[16] This heteronuclear single quantum correlation (HSQC) sequence is shown in Figure 8(a).[17]

In order to suppress the magnetization from protons in $^{12}CH_n$ fragments, it is important to precede the proton excitation pulse by a BIRD suppression sequence[7]

$$90^\circ_{x\,^1\mathrm{H}} - 1/(2\,{}^1J_{\mathrm{CH}}) - 180^\circ_{^{13}\mathrm{C}}, 180^\circ_{x\,^1\mathrm{H}} - 1/(2\,{}^1J_{\mathrm{CH}}) - 90^\circ_{-x\,^1\mathrm{H}} - \Delta \qquad (7)$$

This BIRD element inverts the longitudinal magnetization from protons in $^{12}CH_n$ fragments, but the magnetization from protons in $^{13}CH_n$ groups is not inverted. The $^{12}CH_n$ proton z magnetization is then allowed to relax to zero during the delay period Δ so that it gives no transverse magnetization when the following 90° proton pulse is applied, thereby avoiding any potential dynamic range problems. For macromolecules that exhibit negative NOEs, this approach to selective saturation should be avoided, because cross relaxation between the inverted magnetization of the remote protons and the noninverted magnetization of the directly bonded protons during the Δ delay leads to decreased signals from the directly bonded protons.[17]

A different approach for obtaining heteronuclear shift correlation maps using inverse detection involves the creation of multiple quantum coherences (^{1}H–^{13}C zero and double quantum coherences) and the manipulation of these coherences during the evolution period so that they become labeled with carbon frequencies (see also ***Multiple Quantum Spectroscopy of Liquid Samples***). This heteronuclear multiple quantum coherence (HMQC) technique requires far fewer pulses than HSQC, as shown in the pulse sequence in Figure 8(b).[17] As in HSQC, selective saturation of $^{12}CH_n$ proton magnetization is used to suppress the large signals from the $^{12}CH_n$ protons. The proton 90° pulse following the BIRD sequence creates transverse magnetization derived only from protons in $^{13}CH_n$ groups, which is converted to antiphase magnetization during the τ delay period, then transformed into zero quantum coherence (ZQC) and double quantum coherence (DQC) by

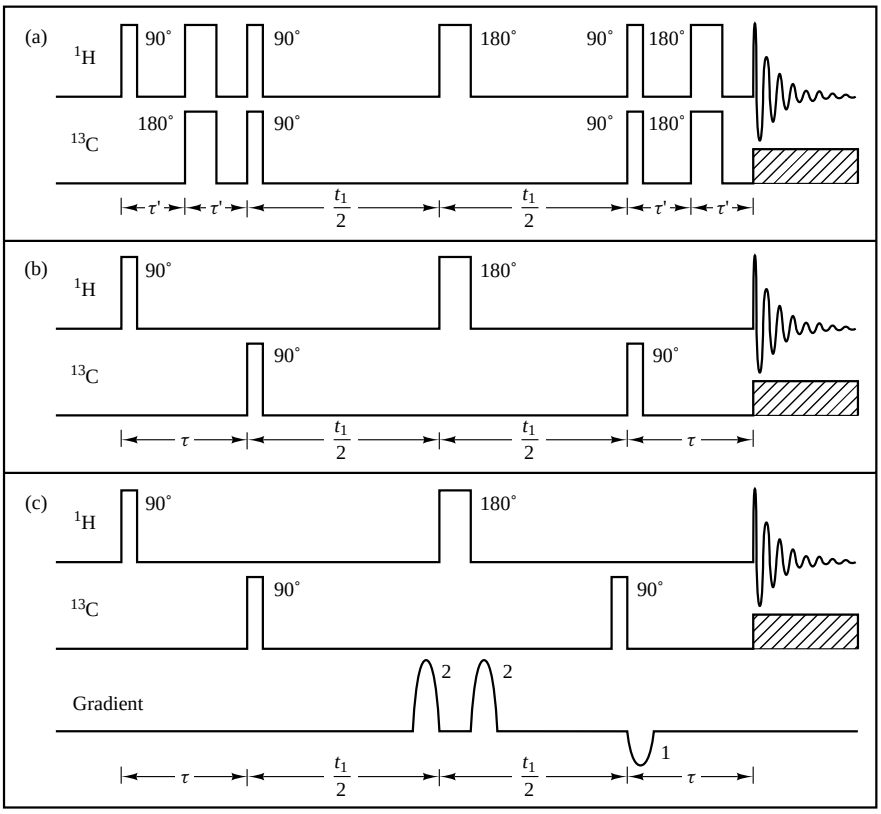

Figure 8 Pulse sequences for 'inverse' heteronuclear shift correlation experiments: (a) HSQC, (b) HMQC, and (c) PFG–HMQC. In sequence (a), $\tau' = 1/(4\,{}^1J_{\mathrm{CH}})$. In sequences (b) and (c), $\tau = 1/(2\,{}^1J_{\mathrm{CH}})$. In implementing sequences (a) and (b), a BIRD selective presaturation sequence should precede the first proton pulse

the 90° carbon pulse. The ZQC precesses at frequency $\nu_C - \nu_H$ and the DQC precesses at frequency $\nu_C + \nu_H$ during the evolution period. The proton 180° pulse at the center of the evolution period interchanges the ZQC and DQC, so that the coherence that had precessed at frequency $\nu_C + \nu_H$ during the first half of the evolution period now evolves at frequency $\nu_C - \nu_H$ and vice versa, so that, at the end of the evolution period, both multiple quantum coherences will be labeled with phase factor exp ($i\nu_C t_1$). The labeled multiple quantum coherences are transformed into antiphase proton magnetization by the 90° carbon pulse. This antiphase magnetization is converted to in-phase magnetization by $^{13}C-^{1}H$ coupling during the delay τ so that GARP carbon decoupling can be applied while the proton FID is acquired.[16] Long range $^{1}H-^{13}C$ correlations can also be observed using inverse detection (heteronuclear multiple bond correlation or HMBC).[17]

It should be noted that $^{1}H-^{1}H$ coupling is present in HMQC maps, but not in HSQC maps. This implies that HSQC should have superior sensitivity and resolution. On the other hand, HSQC has many more rf pulses, and is therefore much more susceptible to pulse imperfections than HMQC. Increased sensitivity and resolution may be obtained by combining the HSQC and HMQC sequences into the HSMQC sequence.[17]

3.4 Pulsed Field Gradients: PFG–HMQC

HMQC and HSQC experiments provide excellent heteronuclear shift correlation maps in most cases, but they require the use of phase cycling to suppress signals from protons attached to ^{12}C, and dynamic range problems in analog-to-digital signal conversion can degrade the overall sensitivity. The application of pulsed field gradients at appropriate points in the HMQC or HSQC pulse sequence gives very effective suppression of the signals from protons attached to ^{12}C and those from solvent molecules (see ***Field Gradients and Their Application***). Furthermore, the acquisition of only a single transient for each value of t_1 is often sufficient to produce a heteronuclear shift correlation map of high quality, since the applied gradients divert the unwanted signals so that they never reach the detector and need not be canceled by phase cycling. An HMQC pulse sequence employing pulsed field gradients (PFG–HMQC) is shown in Figure 8(c). In the PFG–HMQC sequence,[18] field gradients of the same phase and length are applied immediately before and after the proton 180° pulse at the center of the evolution period, and a gradient of smaller magnitude and opposite phase is applied immediately after the final carbon 90° pulse. The first field gradient pulse attaches a phase factor exp [$i(\gamma_C - \gamma_H)zG_1\tau_1$] to the ZQC and a phase factor exp [$i(\gamma_C + \gamma_H)z\,G_1\tau_1$] to the DQC. Here z is the vertical position of the molecule in the sample, G_1 is the intensity of the field gradient, and τ_1 is the duration of the field gradient pulse. The coherences in different parts of the sample now have different phases. When the proton 180° pulse is applied, the ZQC and DQC are interchanged, so that the application of the second field gradient pulse (which has the same intensity and duration as the first gradient pulse) results in phase factors of exp ($2i\gamma_C zG_1\tau_1$) being attached to both ZQC and DQC. When these multiple quantum coherences are converted to antiphase proton magnetization by the final carbon pulse, this magnetization is labeled with the gradient phase factor exp ($2i\gamma_C zG_1\tau_1$), and protons in molecules at different points in the sample have different phases. The refocusing of the disperse magnetization elements is achieved by applying a field gradient pulse of intensity G_2 and duration τ_2, which attaches a phase factor exp ($2i\gamma_H zG_2\tau_2$) to the antiphase proton magnetization. By choosing $G_2\tau_2 = -2G_1\tau_1\gamma_C/\gamma_H \approx -\frac{1}{2}G_1\tau_1$, the net effects of the pulsed field gradients on the desired

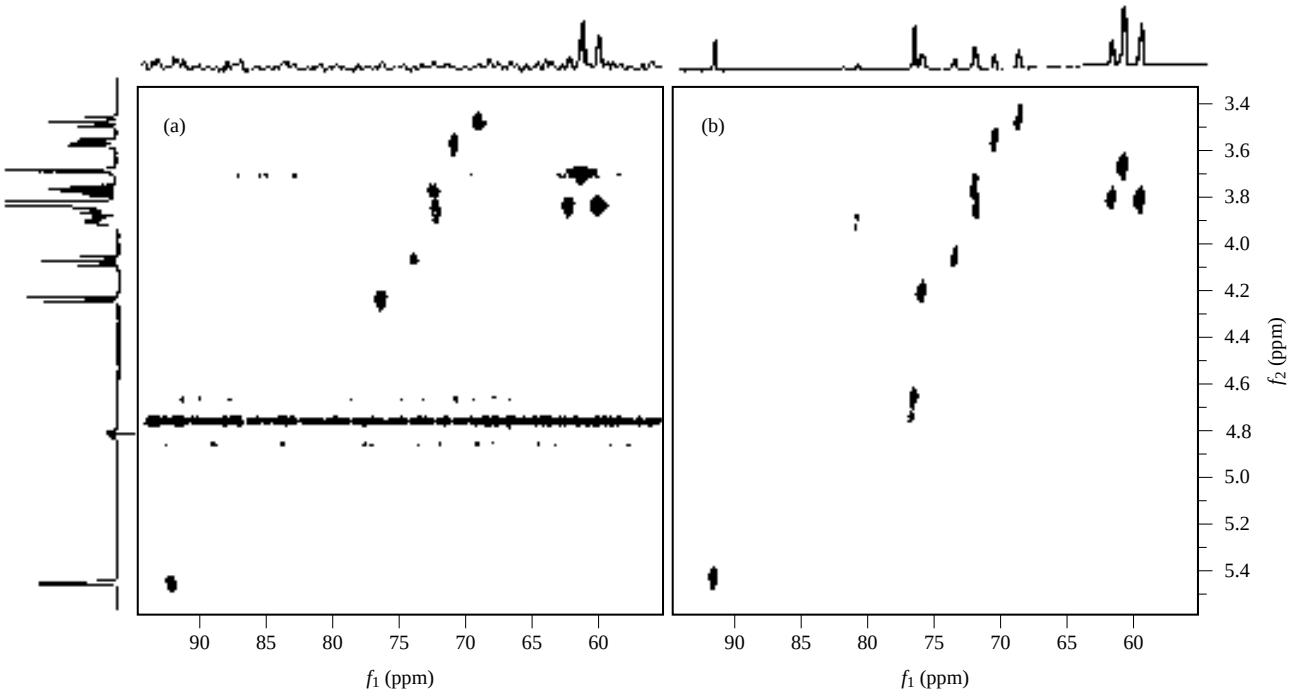

Figure 9 HMQC (a) and PFG–HMQC (b) heteronuclear correlation maps for sucrose in D_2O (10 mg in ≈0.5 mL) at 500 MHz (^{1}H). Four FIDs were accumulated per t_1 value in (a), but only a single FID per t_1 value was acquired in (b)

magnetizations will be removed, and the antiphase proton magnetizations in all parts of the sample will have the same phase. The magnetizations from the solvent protons and from protons in $^{12}CH_n$ fragments are completely dephased by the gradient pulses.

The heteronuclear shift correlation map for sucrose obtained using the HMQC sequence with a minimum four-step phase cycle is compared in Figure 9 with the corresponding PFG–HMQC map obtained by acquiring only a single FID for each t_1. The HMQC map contains a relatively intense water 'stripe' due to the incomplete subtraction of the large water signals in alternate FIDs. The projection of the HMQC map onto the ^{13}C axis is virtually useless, since it is totally dominated by the t_1 ridge of the water signal, but the individual carbon slices are useful. Because of the coherence pathway selection afforded by the pulsed field gradients, the water signal never reaches the receiver in the PFG–HMQC experiment, so the PFG–HMQC map has no water ridge. Furthermore, since one can use higher receiver gain in PFG–HMQC and achieve full digitization of the small signals of interest, the sensitivity of PFG–HMQC is higher, as evidenced by the observation of the weak C–H correlation peak for the F5 center of sucrose in the PFG–HMQC map, but not in the HMQC map. Thus, PFG–HMQC is faster and more sensitive than HMQC. Note that, because only one transient is acquired per t_1 value, any mismatch in the quadrature detectors may produce a transmitter glitch at the center of f_2, as shown in Figure 9(b). Acquisition of more than a single transient for each t_1 will suppress this artifact. Further improvements in sensitivity and resolution can be achieved with phase-sensitive versions of PFG–HMQC and PFG–HSQC.[19]

4 RELATED ARTICLES

COSY Two-Dimensional Experiments; Heteronuclear Assignment Techniques; Inorganic Nuclei: Low Sensitivity Transition Metals; Multidimensional Spectroscopy: Concepts; Phase Cycling; Polarization Transfer Experiments via Scalar Coupling in Liquids; Relayed Coherence Transfer Experiments; Three-Dimensional HMQC-NOESY, NOESY-HMQC, and NOESY-HSQC; Two-Dimensional Carbon–Heteroelement Correlation.

5 REFERENCES

1. R. R. Ernst, G. Bodenhausen, and A. Wokaun, *Principles of Nuclear Magnetic Resonance in One and Two Dimensions*, Oxford University Press, Oxford, 1987, Chap. 8
2. A. E. Derome, *Modern NMR Techniques for Chemistry Research*, Pergamon Press, Oxford, 1987, Chap. 9
3. G. E. Martin and A. S. Zektzer, *Two-Dimensional NMR Methods for Establishing Molecular Connectivity: A Chemist's Guide to Experiment Selection, Performance and Interpretation*, VCH, New York, 1988, Chap. 3
4. A. Bax, *Two-Dimensional Nuclear Magnetic Resonance in Liquids*, Delft University Press/Reidel, Dordrecht, 1982, Chap. 2
5. W. S. Brey, in *Pulse Methods in 1D and 2D Liquid-Phase NMR*, ed. W. S. Brey, Academic Press, San Diego, 1988, Chap. 1
6. G. A. Gray, in *Pulse Methods in 1D and 2D Liquid-Phase NMR*, ed. W. S. Brey, Academic Press, San Diego, 1988, Chap. 5
7. W. E. Hull, in *Two-Dimensional NMR Spectroscopy: Applications for Chemists and Biochemists*, eds. W. R. Croasmun and R. M. K. Carlson, VCH, New York, 2nd edn., 1994, Chap. 2
8. J. K. M. Sanders and B. K. Hunter, *Modern NMR Spectroscopy. A Guide for Chemists*, Oxford University Press, Oxford, 1987, Chap. 4
9. H-O. Kalinowski, S. Berger, and S. Braun, *Carbon-13 NMR Spectroscopy*, Wiley, Chichester, 1988, Chap. 2
10. R. R. Ernst, G. Bodenhausen, and A. Wokaun, *Principles of Nuclear Magnetic Resonance in One and Two Dimensions*, Oxford University Press, Oxford, 1987, Chap. 4
11. A. E. Derome, *Modern NMR Techniques for Chemistry Research*, Pergamon Press, Oxford, 1987, Chap. 6
12. O. W. Sørensen and H. J. Jakobsen, in *Pulse Methods in 1D and 2D Liquid-Phase NMR*, ed. W. S. Brey, Academic Press, San Diego, 1988, Chap. 3
13. R. R. Ernst, G. Bodenhausen, and A. Wokaun, *Principles of Nuclear Magnetic Resonance in One and Two Dimensions*, Oxford University Press, Oxford, 1987, Chap. 2
14. R. R. Ernst, G. Bodenhausen, and A. Wokaun, *Principles of Nuclear Magnetic Resonance in One and Two Dimensions*, Oxford University Press, Oxford, 1987, Chap. 6
15. A. M. Torres, T. T. Nakashima, and R. E. D. McClung, *J. Magn. Reson.*, 1992, **96**, 103.
16. A. J. Shaka, P. B. Barker, and R. Freeman, *J. Magn. Reson.*, 1985, **64**, 547.
17. G. E. Martin and R. C. Crouch, *J. Nat. Prod.*, 1991, **54**, 1.
18. R. E. Hurd and B. K. John, *J. Magn. Reson.*, 1991, **91**, 648.
19. G. Wider and K. Wüthrich, *J. Magn. Reson., Ser. B*, 1993, **102**, 239. L. E. Kay, P. Keifer, and T. Saarinen, *J. Am. Chem. Soc.*, 1992, **114**, 10 663. Y-C. Li and G. T. Montelione, *J. Magn. Reson., Ser. B*, 1993, **101**, 315.

Biographical Sketches

Thomas T. Nakashima. *b* 1942. Ph.D. (supervisor Professor Gary E. Maciel), 1972, Chemistry, University of California, Davis, USA. Currently supervisor NMR Facilities, Department of Chemistry, University of Alberta, Edmonton, Alberta, Canada. Approximately 60 publications. Research interests: application of NMR to chemical problems.

R. E. D. (Ted) McClung. *b* 1941. B.Sc., 1963, Ph.D. (supervisor Daniel Kivelson), 1967, Chemistry, University of California, Los Angeles, USA. Postdoctoral work at University of Leeds, Leeds, UK (with Peter B. Ayscough). Currently Professor of Chemistry, Department of Chemistry, University of Alberta, Edmonton, Alberta, Canada. Approximately 70 publications. Research interests: chemical exchange, multisite magnetization transfer, infrared bandshapes, molecular motion in liquids.

Homonuclear Three-Dimensional NMR of Biomolecules

Rolf Boelens and Robert Kaptein

Utrecht University, Utrecht, The Netherlands

1	Introduction	1
2	Why Higher Dimensions?	1
3	Classification of Multidimensional NMR Experiments	2
4	The Design of Multidimensional Homonuclear Experiments	2
5	Selective and Nonselective Homonuclear 3D NMR	3
6	Principles of Homonuclear 3D Spectroscopy	3
7	Practical Aspects	5
8	Applications	7
9	Prospects for 3D NMR Spectroscopy	12
10	Related Articles	13
11	References	13

1 INTRODUCTION

High-resolution NMR can be used for determining structures of small biomolecules in solution.[1] Such studies are based upon the measurement of interactions between protons. The NOE, the origin of which is dipolar cross relaxation between protons, is especially crucial since it can be used to determine distances between closely spaced protons. The other proton–proton interaction is the J coupling, which is used to identify spin systems during the resonance assignment stage but which can also give information on torsion angles and, in this way, leads to more accurate structures. For small biomolecules these proton–proton interactions are most conveniently measured by 2D NMR techniques.[2] Thus, the J coupling manifests itself as cross peaks in COSY and TOCSY (or 2D HOHAHA) spectra and the NOE as cross peaks in NOESY (or 2D NOE) spectra.

Except for some favorable cases, however, 2D NMR studies have been limited to small biomolecules with molecular masses of less than 12 kDa. Several problems arise with larger molecules. Both the number of proton resonances and the resonance linewidth increase with size. This leads to overlap of resonances, which prohibits the unambiguous assignment of 2D cross peaks to specific proton pairs. The spectral resolution can be increased by adding a third[3–8] or even a fourth frequency domain.[9,10] In this way, overlapping protons can be characterized with the additional frequency of an associated nucleus that will help in establishing the interpretation of cross peaks. An extra complication is, however, that due to the increase in linewidth for large biomolecules, it becomes more difficult to observe small proton–proton J couplings and that magnetization transfer in 3D spectra based on such J couplings becomes weak. This disadvantage may be overcome in homonuclear 3D NOESY–NOESY spectroscopy,[11] but the complexity of the 3D NOESY–NOESY spectra can be high and their sensitivity low. More recently, a number of heteronuclear 3D experiments have been developed, such as 3D NOESY–HMQC, 3D TOCSY–HQMC[12–15] and 3D triple resonance techniques for (^{13}C, ^{15}N) doubly labeled molecules.[16,17]

These heteronuclear techniques overcome the aforementioned problems, because they rely on strong heteronuclear J coupling constants and because the magnetization transfer is unique in many cases. The sensitivity of heteronuclear 3D and 4D experiments can be high and the spectral complexity low, and there is no doubt that for large biomolecules such methods are preferable to the homonuclear ones. However, the heteronuclear techniques have one clear disadvantage. They require that the biomolecular material is enriched in ^{13}C, ^{15}N or both isotopes, which is problematic if the material can only be obtained in low yields or if the biomolecule cannot be isolated from cell cultures. This applies to a large group of very interesting biomolecules, including glycoproteins, oligosaccharides, and oligonucleotides.

Several reviews on multidimensional NMR techniques have appeared, and a thorough account of various theoretical and practical aspects of 3D NMR has been given by Griesinger et al.[18] Triple resonance techniques for studies on (^{13}C, ^{15}N) doubly labeled proteins have been reviewed thoroughly by Clore and Gronenborn[19] and by Bax and Grzesiek.[20] A recent survey was provided by Oschkinat et al.[21] Our main focus will be homonuclear 3D NMR of biomolecules (see ***Three- and Four-Dimensional Heteronuclear Magnetic Resonance*** and ***Three-Dimensional HMQC-NOESY, NOESY-HMQC, and NOESY-HSQC***).

2 WHY HIGHER DIMENSIONS?

Most interactions in NMR spectroscopy are pairwise by nature. In principle, two frequency domains and, thus, 2D NMR should suffice to establish such pair interactions between magnetic nuclei.[22] Certainly for large biomolecules, however, there is a high chance of overlap for resonances of different nuclei. In that case 2D relayed experiments have been proposed, where the magnetization is transferred from the second overlapping nucleus to a third one via an additional mixing step.[23,24] Both homonuclear and heteronuclear coherence transfer steps can be used to resolve ambiguous NOEs in a new frequency domain.[25–28] For small biomolecules the comparison of resonances in the direct domain of the original 2D experiment and the indirect domain of the 2D relay experiment is in many cases sufficient to resolve most ambiguities.[29] However, for large molecules it is likely that a new overlap exists in this indirect domain. This overlap may then be resolved by a simultaneous registration of the direct and the relayed frequencies. In this way a 3D spectrum is created where overlap for the receiving nuclei can be resolved (Figure 1). If overlap exists for the originating nuclei, the magnetization in their domain may also be relayed. Modulation at both the direct and the relayed frequencies for the originating and the receiving nuclei would lead to a 4D spectrum. Higher dimensionality is probably not practical.[20,22]

In multidimensional NMR one can distinguish between the interactions of interest and those that are suitable for relaying the information to other frequency domains. The structure

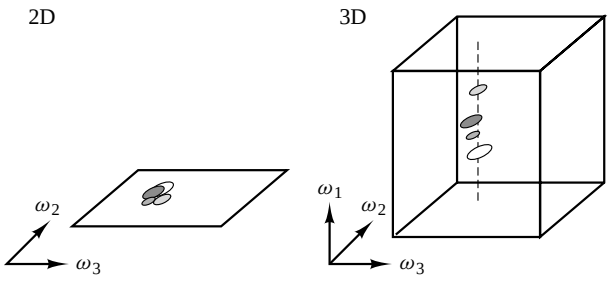

Figure 1 Illustration of the increase in resolution due to the increase in dimensionality. In the 2D spectrum four cross peaks overlap. By correlation with a third resonance frequency each cross peak achieves a different position along a line in the 3D spectrum, thus resolving the overlap problem

determination of biomolecules is mainly based on the interpretation of proton–proton NOEs, while for the prerequisite assignment of proton resonances considerable use is made of J coupling data. Therefore, it is of great importance to establish the absence and presence of these interactions unambiguously. Optimally, the frequencies connected by the relayed transfer are not linearly correlated, the relayed nuclei involved are abundant, the transfer will be very efficient introducing only low signal losses, all proton resonances can be relayed, and the relay interaction can be interpreted uniquely. In practice this is not the case, but the requirements are best met by combinations of various heteronuclear 3D and 4D experiments on (^{13}C, ^{15}N) doubly labeled compounds. When isotope labeling is not possible, however, homonuclear 3D methods may be preferable, but the analysis of the resulting spectra can be complex. A large part of this review will summarize methods for analyzing such homonuclear spectra.

3 CLASSIFICATION OF MULTIDIMENSIONAL NMR EXPERIMENTS

Over the years many pulse sequences have been proposed to establish homonuclear and heteronuclear interactions between pairs of nuclei.[2] Of course, all these pair transfers can be used as building blocks of multidimensional NMR experiments. The interactions in high-resolution ^{1}H NMR can have a coherent or an incoherent nature. Incoherent sources for interaction are kinetic exchange and dipolar cross relaxation, while the homonuclear and heteronuclear J couplings have a coherent nature. Two types of 2D experiments can be discriminated by which these processes can be measured: the large COSY family for identifying J interactions within spin systems[2,30] and the 2D exchange or NOE category for the analysis of kinetic equilibria,[31] NOESY,[32,33] and ROESY[34,35] effects. Most 2D experiments involve magnetization transfer due to a single type of interaction and thus will fall in one of these two categories. Most 3D experiments (but also relayed 2D experiments) should then belong to combinations of these two. The basic categories for double transfer will be J–J, J–NOE, NOE–J, and NOE–NOE. Of these, the J–NOE and NOE–J type experiments will contain the same information and can be brought into one category. It is obvious that one can classify 3D COSY–COSY,[5,6] 3D COSY–NOESY,[6] 3D NOESY–TOCSY experiments,[7,8] or 3D NOESY–ROESY in one of these groups. Of course, with 4D spectroscopy, or better triple transfer techniques, eight (but only six unique) classes can then already be defined, and for quadruple transfer experiments even 16. In general it can be anticipated that the J–J and J–J–J type experiments should be useful for assignment purposes, while triple transfer J–NOE–J type experiments can be helpful for identifying NOEs.

It is clear that by combination of the 'building blocks' used in 2D spectroscopy a countless number of different types of experiments can be constructed.

4 THE DESIGN OF MULTIDIMENSIONAL HOMONUCLEAR EXPERIMENTS

Each multidimensional experiment will start with a preparation period. Generally, this is a delay to bring the spin system to Boltzmann equilibrium followed by a 90° rf pulse. This will be followed by one or more evolution periods and a detection period, all separated by magnetization transfer steps similar to those in two-dimensional NMR. The experiments can be designed by the appropiate combination of two 2D NMR pulse schemes. A 3D NMR experiment can be regarded as the combination of two 2D experiments, in which the detection period of the first experiment has been replaced by the evolution, mixing, and detection periods of the second.[5] For example, a NOESY and TOCSY experiment can combine to form a 3D NOESY–TOCSY experiment.[7,8] As shown in Figure 2, the FID in the time domain t_3 is then recorded as a function of two variable times t_1 and t_2, which are independently incremented. After Fourier transformation in the three dimensions a 3D NMR spectrum is obtained with three independent frequency axes. A cross peak in the 3D spectrum arises when magnetization of one proton is transferred during the first (NOE) mixing period to a second proton and then during the second (TOCSY or HOHAHA) mixing period to a third one. Figure 3 shows a number of 3D pulse schemes and their division into preparation, evolution, and mixing periods, but basically the same principles apply to all experiments.

In 3D experiments using TOCSY, NOESY, and ROESY mixing periods the magnetization is transferred not to one but to a number of other spins. Therefore, the J or NOE interactions can be observed at a number of 3D cross

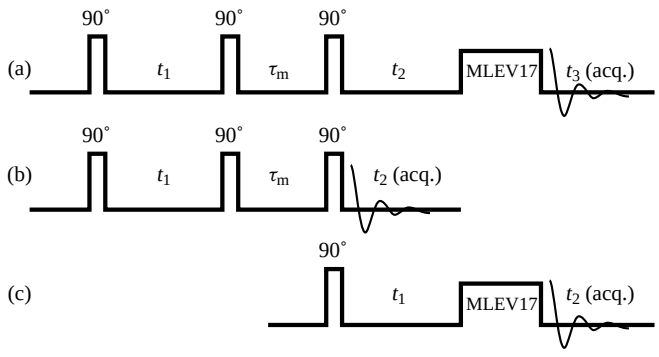

Figure 2 (a) Pulse sequence for a 3D NOESY–TOCSY experiment, constructed from (b) a 2D NOE experiment, and (c) a TOCSY experiment with a MLEV-17 mixing sequence

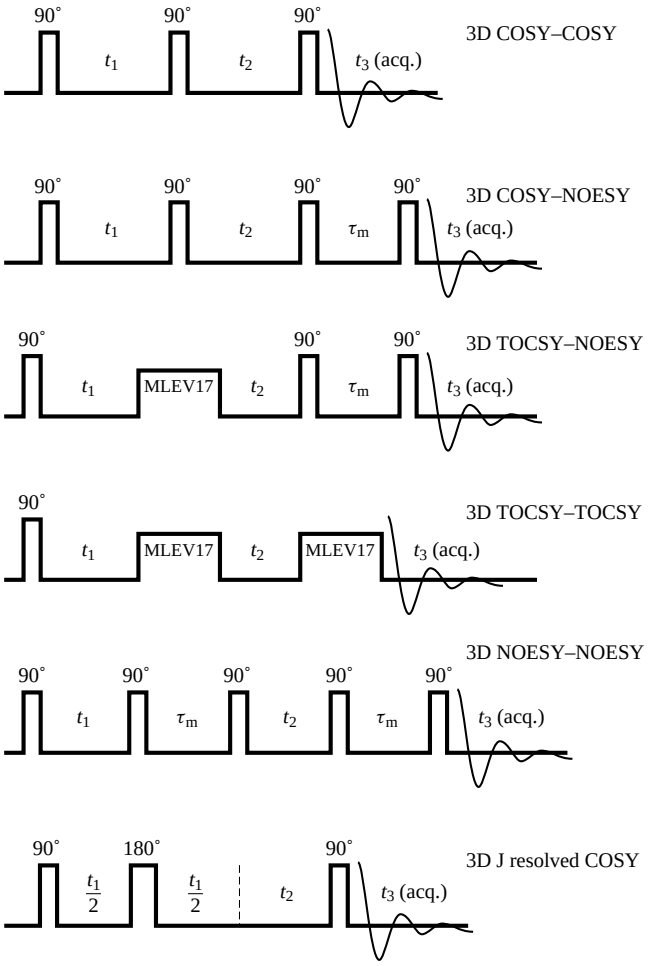

Figure 3 Pulse sequences for homonuclear 3D experiments

peaks. A coincidental overlap at one 3D cross peak can then be overcome by another nonoverlapping one. However, the disadvantages of such an approach are an increase in complexity of the 3D spectra and a reduction of signal intensity by dilution. 3D spectra which use COSY-like relays, where magnetization is transferred to one other nucleus only, lead to spectra which are much more amenable for analysis. However, for protons the ^3J(H, H) coupling, which forms the basis for the COSY magnetization transfer, is relatively weak, and the necessary development of antiphase magnetization during the evolution and acquisition periods can take a long time compared with the T_2 relaxation time. This makes 3D experiments involving a proton–proton COSY transfer insensitive for biomolecules with a short T_2, and the long sampling of the t_1 or t_2 evolution periods may create excessively long recording times. The favorable J magnetization transfer induced by the HOHAHA effect is much more suitable for homonuclear 3D experiments of biomolecules. For large (>20 kDa) biomolecules the HOHAHA transfer can also become weak. In order to avoid complex analysis the selectivity of a relayed HOHAHA or a relayed NOE transfer may be optimized by choosing a relatively short mixing time. Other suitable building blocks for homonuclear 3D experiments of biomolecules are NOESY (or EXSY) and ROESY mixing periods.

5 SELECTIVE AND NONSELECTIVE HOMONUCLEAR 3D NMR

Since both the t_1 and t_2 domains of a 3D experiment (see Figure 2) have to be incremented independently, a large number of FIDs are recorded in order to obtain a sufficiently high resolution for these two domains. In principle, this could lead to long measuring times and to practical problems in handling large data sets.

Reduction of measuring time, the amount of collected data or a need for high digitization in a selected spectral area may require that the frequency sampling in the t_1 and t_2 domains is limited by means of using semiselective rf pulses which excite only a small portion of the NMR spectrum.[5–7] In this way one zooms in, as it were, onto a part of the complete 3D spectrum. Most of the early examples of homonuclear 3D experiments were semiselective: the semiselective COSY–COSY,[5,6] the semiselective NOESY–COSY,[6] and the semiselective NOESY–TOCSY.[7,36,37] The 3D J-resolved experiments[3,4] fall in a slightly different category, since they do not correlate chemical shifts across all mixing periods, but here also the recording time is relatively short. As in 2D J-resolved spectroscopy the aim of such experiments is the separation of chemical shifts and scalar (or dipolar) interactions, which may require a very different digitization.

In the nonselective 3D NMR experiments,[8] only hard pulses are used for the t_1 and t_2 domain, which allows for a complete sampling of all frequencies in the three dimensions. Although prolonged measuring times can be anticipated, some gain is obtained through the relative simplicity of the rf pulse sequences which makes short phase cycling schemes possible. In fact, most of the nonselective homonuclear 3D NMR experiments can be carried out within 2–5 days.

In terms of analysis, however, the semiselective and nonselective 3D NMR techniques are similar.

6 PRINCIPLES OF HOMONUCLEAR 3D SPECTROSCOPY

The 3D NOESY–TOCSY spectrum recorded with the pulse scheme of Figure 2 and obtained after 3D Fourier transformation of the FIDs can be schematically presented as a cube with three frequency axes, f_1, f_2, and f_3. In a 3D spectrum obtained in this way, a body diagonal ($f_1 = f_2 = f_3$) can be identified, which contains magnetization that was not transferred during any of the mixing periods. Additionally, intensity accumulates on the three cross-diagonal planes, which is shown in Figure 4. In the case of the 3D NOESY–TOCSY experiment, the plane $f_2 = f_3$ (NOE plane) contains magnetization transferred only during the first (NOE) mixing period, whereas the plane $f_1 = f_2$ (TOCSY or HOHAHA plane) contains magnetization transferred during the second (HOHAHA) mixing period. Finally, the plane $f_1 = f_3$ (back-transfer plane) contains magnetization that was transferred during the first (NOE) mixing period from proton a to proton b and then back to proton a during the second (HOHAHA) mixing period. For the analysis of 3D NMR spectra, cross sections perpendicular to one of the frequency axes can be used. Figure 5 shows an f_1–f_2 plane (which is perpendicular to the f_3 axis). The three diagonal planes of

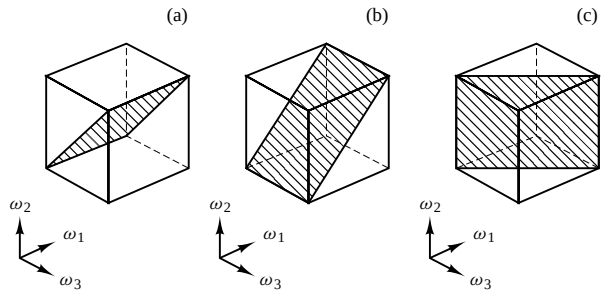

Figure 4 Cross-diagonal planes in a 3D NOESY–TOCSY spectrum: (a) NOE plane, (b) HOHAHA or TOCSY plane, and (c) back-transfer plane

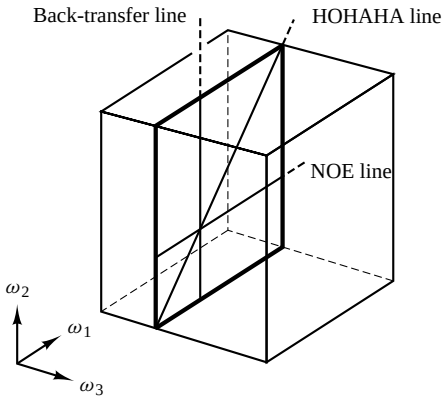

Figure 5 Schematic representation of an f_1–f_2 plane, perpendicular to the f_3 axis. The NOE, HOHAHA and back-transfer lines constitute the intersection with the three planes indicated in Figure 4

Figure 4 intersect this plane at the three lines indicated as NOE (or N), HOHAHA (or H) and back-transfer (or B) lines. These lines all share one point on the body diagonal of the spectrum.

Cross peaks that are present on the NOE and HOHAHA lines in the cross section taken at $f_3 = f_a$ represent single step magnetization transfer (by NOE and HOHAHA, respectively) to a proton a. Hence, the 3D NOESY–TOCSY spectrum contains the information that is present in traditional 2D NOESY and TOCSY spectra as a subset. All cross peaks outside the NOE and HOHAHA planes are due to double magnetization transfer. The double magnetization transfer that gives rise to peaks in the back-transfer plane is unique for homonuclear 3D experiments, since both mixing periods cover the same spectral frequencies. The closest 2D analogues of 3D NOESY–TOCSY experiments are relayed NOESY experiments[25,26] 2D TOCSY–NOESY,[27] and 2D ROESY–TOCSY and TOCSY–ROESY.[29] The information content of such spectra is present in the 3D spectrum as a projection onto the f_1–f_3 groundplane. However, since the cross peaks are labeled by three different frequencies, fewer ambiguities will arise in a 3D spectrum.

Figure 6 shows the nonselective 3D NOESY–TOCSY spectrum of a 109 residue protein, parvalbumin, in ^1H_2O. The spectrum contains a large number of cross peaks. Most of the intensity accumulates on the body diagonal and the NOE

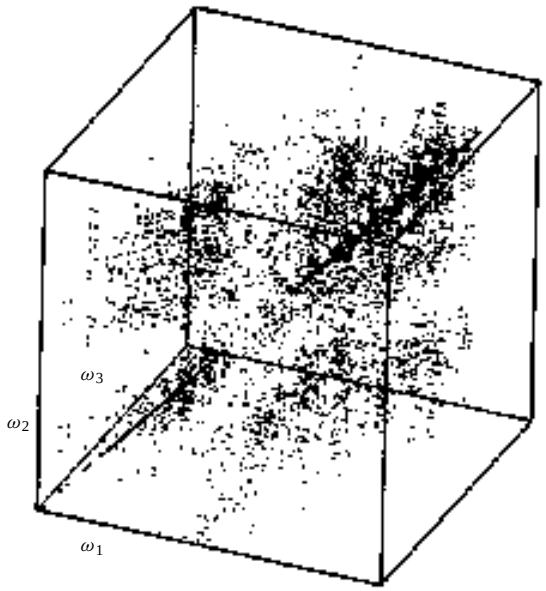

Figure 6 3D NOESY–TOCSY spectrum of a 109-residue protein in ^1H_2O. The spectrum shows local intensity maxima for most cross peaks. The data set was recorded in 171 h at 500 MHz using an eight-scan phase cycle, as described by Vuister et al.[8] The NOE mixing time was 150 ms and the HOHAHA mixing time was 47 ms. The data were processed to a resolution of 256 × 256 × 256. The sample contained 8.7 mM pike parvalbumin at pH = 4.1, 315 K, 10% D_2O.[8] (Reproduced by permission from Vuister et al.[8])

and HOHAHA planes. Less intensity accumulates on the back-transfer plane, because the associated magnetization must have gone through a double transfer. Intensities at positions ($f_1 \neq f_2 \neq f_3$), i.e. not on the three diagonal planes, correspond to magnetization which was transferred during both mixing periods. Figure 7 shows a contour plot of the NOE plane of the same 3D spectrum. This plot is very similar to a contour plot of the NOESY spectrum of this protein and indicates the need to increase the resolution for proteins of this size by using a third domain. Similarly, the HOHAHA plane resembles a TOCSY spectrum.

The analysis of 3D spectra can be accomplished in planes perpendicular to any axis of the 3D spectrum. In Figure 8(a) the flow of magnetization is sketched as observed in an f_1–f_2 plane of a 3D NOESY–TOCSY experiment. A cross peak at (f_a, f_b, f_c) indicates that magnetization started on a nucleus with frequency f_a was transferred by NOE to a nucleus with frequency f_b and was then transferred by isotropic mixing to a nucleus at f_c on the diagonal. Figure 8(b) shows the same flow in an f_2–f_3 plane, but now the magnetization originates from the diagonal. Finally Figure 8(c) shows this flow in an f_1–f_3 plane. The flow in a TOCSY–NOESY spectrum goes in the opposite direction, and the same planes can be constructed for the equivalent cross peak (f_c, f_b, f_a). Figure 8(d), 8(e) and 8(f) show the equivalence of the f_2–f_3, f_1–f_2, and f_1–f_3 planes of a 3D TOCSY–NOESY spectrum with that of the f_1–f_2, f_2–f_3, and f_3–f_1 planes of a 3D NOESY–TOCSY spectrum, respectively. Only the flow, as indicated by the arrows, is inverted, while the appearance of the spectrum is the same.

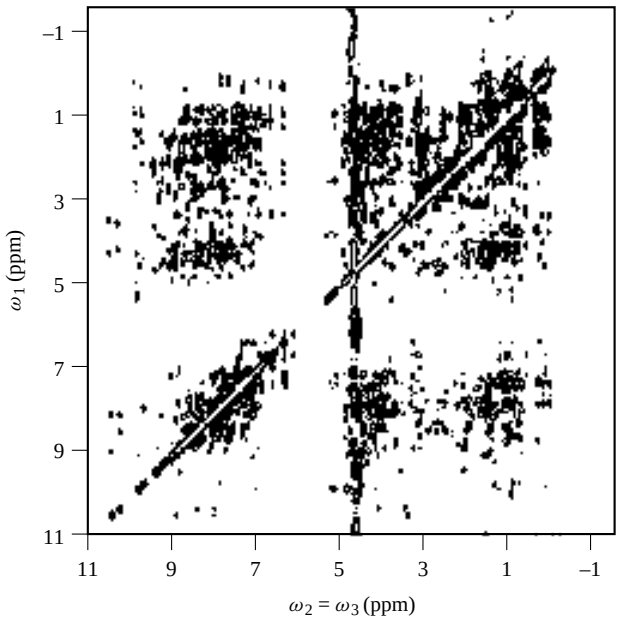

Figure 7 NOE plane of a 3D NOESY–TOCSY spectrum of the 109-residue protein of Figure 6. (Reproduced by permission from Vuister et al.[8])

The cross peaks in 3D spectra reflect connectivities between the spins. To describe the connectivities the C notation can be used: $C[M_1, M_2]_{abc}$ (i, j, k) or shorthand C_{abc} (i, j, k) means that magnetization of proton a in residue i is interacting via mixing step M_1 with proton b of residue i and next via mixing step M_2 to proton c of residue k. Thus, 3D NOESY–TOCSY and 3D TOCSY–NOESY spectra contain the same connectivity information: a $C[NOE, J]_{abc}$ (i, j, j) pathway is equivalent to a $C[J, NOE]_{cba}$ (j, j, i) pathway. Both represent the same combination of interactions. Experimentally, however, differences in t_1 and t_2 noise and in domain resolution make it quite different, whether a $C_{NN\alpha}$ $(i + 1, i, i)$ connectivity is observed in an f_1–f_2 plane at f_3 of the α proton (such as in 3D NOESY–TOCSY) or at f_3 of the NH proton (as in 3D TOCSY–NOESY).

7 PRACTICAL ASPECTS

7.1 Sensitivity

For 3D spectra a better signal-to-noise ratio is required than that of the 2D analogs, since the aim of 3D experiments is the observation of weak double magnetization transfers. Therefore, 3D techniques should only be applied in case of overlap in optimally recorded 2D spectra.

The sensitivity of a 3D experiment is determined by the efficiency of magnetization transfer in the mixing periods, by T_2 relaxation during the evolution and acquisition periods, and the method of selecting the evolved magnetization. As in 2D spectroscopy most mixing periods select only the x or y component of the magnetization from the previous evolution period, and by phase cycling the other term is removed. This leads to the loss of half of the magnetization and half of the noise power. Therefore, as pointed out by Bax and Grzesiek,[20] each addition of dimensionality may lead to a signal-to-noise reduction by $1/\sqrt{2}$. This loss in the signal-to-noise ratio can, however, be avoided by retaining both orthogonal magnetization components across the mixing periods (see Cavanagh and Rance[38] for a review). This method has been applied to 3D NOESY–TOCSY.[39] A drawback may be, however, an increase in experiment time due to additional phase cycling in order to obtain phase-sensitive spectra.

In 3D spectrocopy the signal accumulates independently in all domains. By minimizing the length of the evolution periods, loss of sensitivity due to T_2 relaxation can be avoided. The length of the evolution periods should be only so long that overlap of cross peaks is avoided, or as required for the further analysis of the 3D spectra. Since there is a lower chance of overlap in 3D than in 2D spectra the evolution periods can clearly be shorter in 3D spectra. With the crowded spectra of biomolecules, however, it is difficult to predict which resolution is finally needed until the analysis is completed. As a guideline it is noted that sampling with the evolution periods beyond $0.9T_2$ is only to increase resolution, while sampling below $0.9T_2$ will add signal to the multidimensional cross peaks. The sensitivity of the NOE and HOHAHA planes of an optimally recorded 3D NOESY–TOCSY spectrum will be similar to that of the two 2D counterparts recorded together in the same total time. However, the aim of a 3D experiment is clearly the observation of double magnetization transfer, and the corresponding cross peaks will be much weaker.

For good sensitivity of multidimensional experiments it is extremely important to optimize the transfer efficiencies of the mixing periods. For TOCSY, various improvements have been published, compensating relaxation by 'clean' TOCSY pulse sequences[40] or increasing sensitivity by orthogonal magnetization transfer, as discussed above. For ROESY, potential J transfer should be minimized.[35] For NOESY no fundamental optimizations are possible, but accurate and homogeneous 90° rf pulses will enhance the transfer. In all cases the transfer efficiencies may be optimized by adapting the length of the mixing period. Since the cross-peak intensity in 3D spectroscopy is proportional to the product of the constituent 2D transfer efficiencies, an optimal 2D mixing time will also be the optimum for three dimensions.

Another important factor for sensitivity is the number of rf pulses in combination with pulse imperfections, i.e. inaccurate flip angles or B_1 inhomogeneities. Generally, phase cycles of 2D and 3D experiments are set up so that only coherences are selected which pass the sequence assuming ideal 90° and 180° pulses and that coherences created by the imperfections are suppressed. Since most homonuclear 3D sequences contain only a few rf pulses or a self-compensated isotropic mixing period, only a small amount of magnetization is lost in this way.

However, in many cases the actual sensitivity is less favorable due to t_1 and t_2 noise caused by instrument instabilities. Such instabilities are present in 2D spectroscopy as well, but the 3D technique may sample additional instabilities due to the length of the experiment and the wish to minimize recording time. On some NMR instruments undefined delays may be introduced between the FIDs. A constant steady state magnetization may be maintained by a buffered acquisition method or by steady state pulses.

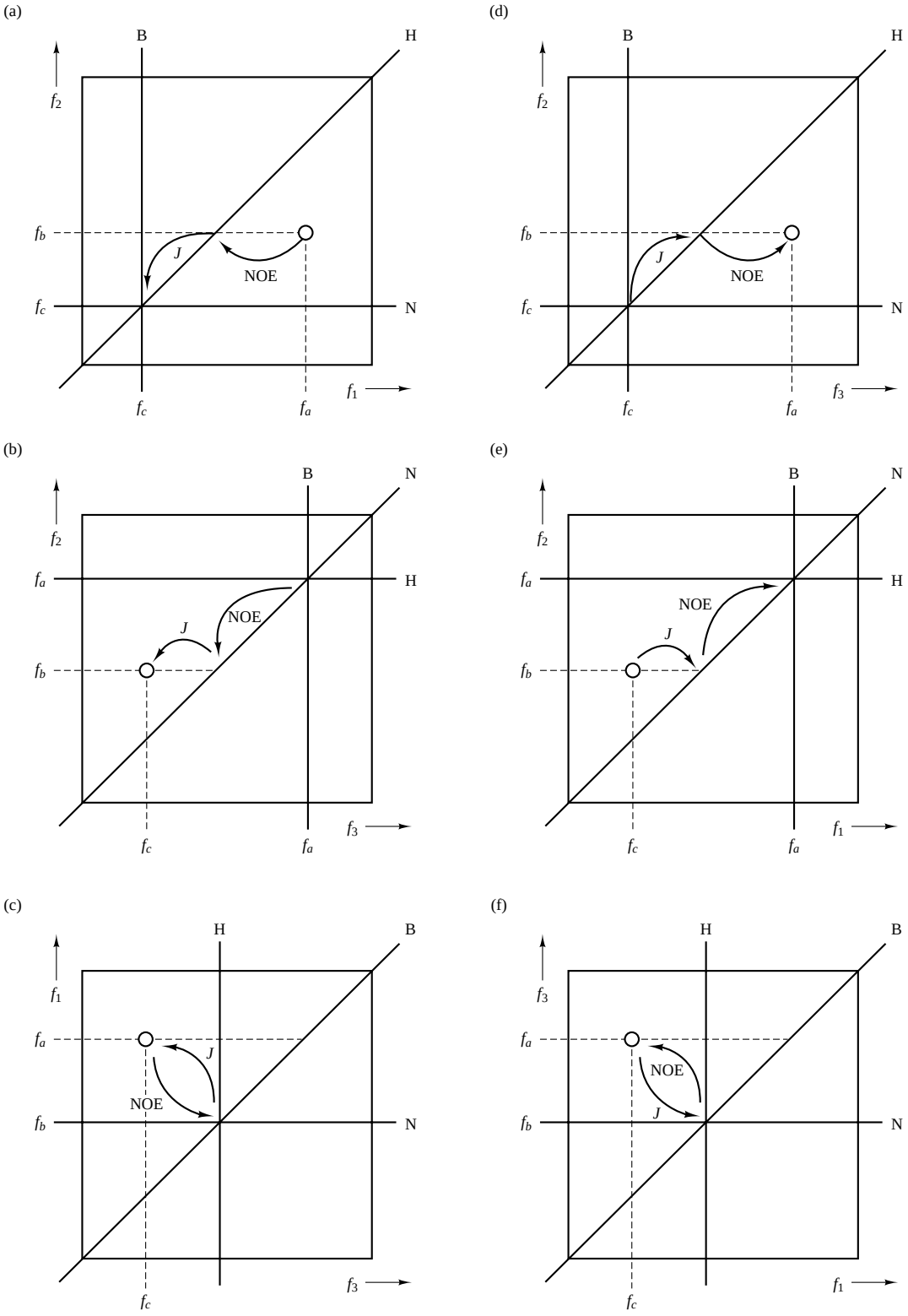

Figure 8 Flow of magnetization for a cross peak (f_a, f_b, f_c) in a 3D NOESY–TOCSY spectrum and the equivalent cross peak (f_c, f_b, f_a) in a 3D TOCSY–NOESY spectrum. (a)–(c) The f_1–f_2, f_2–f_3, and the f_1–f_3 planes of a 3D NOESY–TOCSY spectrum. (d)–(f) The f_2–f_3, f_1–f_2, and the f_1–f_3 planes of a 3D TOCSY–NOESY spectrum. The lines indicated by N, H, and B are the cross-diagonal NOE, HOHAHA (or TOCSY), and back-transfer lines, respectively. Only the flow of magnetization in the two spectra reverses; the appearance of both spectra is the same

Fluctuations in the extent of sample heating due to the pulse sequence are more difficult to avoid.

7.2 Phase Cycling and Recording Time

Both phase cycling or field gradients can be used for selecting the coherence transfer pathway in 3D experiments. Since the gradients do the selection in single experiments, use of gradients is preferable for 3D spectroscopy. Thus, the NOE effect can be selected by a single gradient pulse in the NOE mixing period.[31] However, the number of phase cycling steps can also be minimized in 3D spectroscopy. For large biomolecules the phase cycling to select NOE mixing can be short, since most undesirable coherences have decayed at the end of the NOE mixing time. Suppression of single quantum coherences is normally sufficient and can be accomplished by two phase steps. The HOHAHA mixing requires no selection of coherence level at all, if a 'clean' MLEV sequence is used.[40] Axial peaks due to T_1 relaxation can be suppressed by inversion of the first 90° rf pulse, which will double the phase cycle. Inaccurate 90° or 180° rf pulses may lead, however, to an axial plane at the f_1–f_3 ground plane of a 3D spectrum, which can be removed by inverting all pulses before the t_2 period. In order to separate positive and negative frequencies in the t_1 and t_2 domains, either a time proportional phase increment (TPPI) or a States–TPPI sampling scheme should be used, which will put potential axial peaks at the sides of the 3D cube. Homonuclear 3D spectroscopy with minimal phase cycling has been demonstrated for 3D NOESY–NOESY[41] and for 3D TOCSY–NOESY.[42] In practice, 3D TOCSY–TOCSY and gradient enhanced 3D TOCSY–NOESY with axial peak suppression in t_1 will have a minimal two-step phase cycle inverting only the very first rf pulse. Without gradients the minimal phase cycling for 3D TOCSY–NOESY becomes four and for 3D NOESY–NOESY already eight, while inclusion of axial plane correction brings this to eight and 16, respectively.

NMR receiver imperfections may require additional phase cycling in order to remove dc bias and quad-image artifacts, but they can be mixed into the phase cycle for coherence selection. Thus, depending on the level of artifact suppression needed, phase cycles of 1–6 scans can be used. Typically, 128–256 independent t_1 and t_2 increments are used to sample the corresponding domains, with an acquisition size of 512–1024 words. In order to reduce measuring time, the relaxation delay between each scan is set to a value close to the T_1 relaxation time of the biomolecule, which results in some saturation. In this fashion, the repetition rate per scan is about 1 s, and a typical 160 × 256 × 1024 3D TOCSY–NOESY experiment takes between 46 h for a four-scan and 182 h for a 16-scan version and will create 42 Mwords of data.

7.3 Processing

The heavily truncated interferograms in the t_1 and t_2 periods of 3D datasets are in principle not suitable for frequency analysis by fast Fourier transforms. Apodization functions such as the Hamming or Kaiser windows vastly decrease the amount of 'ripple' (cf. Ernst et al.[2]). A better approach is frequency analysis by parametric methods based on linear prediction[43–45] and by the maximum entropy or Bayesian methods,[46] but these methods can be computationally expensive. A more modest but practical approach is the extension of the experimental data set by linear prediction, followed by window multiplication and a fast Fourier transform.[47] Phasing parameters for the evolution periods can either be calculated from initial delay values and rf pulse widths[48] or estimated by visual inspection of the data. After the Fourier transform the 3D spectrum can be baseline corrected in all domains by a variety of methods.[49,50] Offsets and baseline distortions in the f_1 and f_2 domains can, however, already be minimized by data sampling techniques.[51,52]

For the manual analysis of 3D spectra, contour plots can be produced for all cross sections that contain cross peaks. This approach may be sufficient for settling overlap in crowded 2D spectra. Since bookkeeping of all peaks in a 3D spectrum can be cumbersome, analysis with a workstation is to be preferred. Programs have been developed that can assist the manual analysis of such spectra.[53–56] A step further is the automatic or semiautomatic analysis of patterns of correlated cross peaks, e.g. for assigning 3D proton spectra.[54,57,58] The input of such programs may require further processing of the spectra, e.g. searches of local maxima and peak boundaries, peak decomposition, and determination of intensities.

8 APPLICATIONS

8.1 3D *J*-Resolved Spectroscopy

The 3D *J*-resolved experiment can be visualized as a 2D *J*-resolved experiment in which the acquisition period has been replaced by the evolution period, mixing period, and acquisition period of a second 2D experiment. Both COSY[3,4,59] and NOESY[60] have been suggested for this second experiment. Such 3D *J*-resolved spectra can become useful when overlap interferes with the analysis of multiplet patterns in a 2D *J*-resolved spectrum. A drawback of *J*-resolved spectroscopy for measuring *J* couplings as compared with ECOSY techniques[61] is that the multiplet pattern is not simplified, but remains at full complexity. This explains the limited application of the method for high-resolution studies of biomolecules. Related 3D experiments in solid state NMR for separating chemical shift and dipolar interactions have found more extensive use.[62,63] The 3D *J*-resolved method demonstrated, however, the feasibility of 3D NMR and started the development of a large number of other 3D techniques.

8.2 3D TOCSY–NOESY and 3D NOESY–TOCSY Spectroscopy

For most biomolecular studies both the *J* coupling and the NOE interaction must be measured. Such interactions can be obtained by separate NOESY and COSY or TOCSY experiments, but it is logical to combine both into one 3D experiment in which one mixing period contains the NOE effect and the other the *J* coupling. Two types of homonuclear experiments can be envisaged: 3D NOE–*J* and 3D *J*–NOE. The first implementation was shown by Griesinger et al.[6] in a semiselective 3D NOESY–COSY experiment. However, for larger biomolecules the *J* effect is transferred much more efficiently by a HOHAHA mixing period, as was demonstrated

by Oschkinat et al.[7] in a semiselective 3D NOESY–TOCSY experiment of a 46-residue protein. Shortly after, it was shown that complete nonselective 3D NOESY–TOCSY experiments of proteins can also be executed in a reasonable time.[8] Later improvements used 'clean' MLEV sequences[37,64,65] and orthogonal isotropic mixing[39] to enhance the amount of transferred magnetization.

8.3 Observation of Sequential NOEs in Proteins

The combined observation of J couplings and NOE interactions in 3D NOESY–TOCSY spectra makes it possible to assign the proton resonances in the protein spectrum by a similar sequential assignment strategy as developed by Wüthrich and his co-workers[1] for 2D spectra. In the 2D approach, the spin systems of the protons belonging to one amino acid residue are identified by exhaustively analyzing the through-bond proton–proton connectivities in COSY and TOCSY spectra. The sequentially neighboring amino acid spin systems are then identified by observation of the sequential d_{NN}, $d_{\alpha N}$ and $d_{\beta N}$ connectivities in 2D NOE spectra. Starting at a unique spin system or by matching unique di- and tripeptide sequences on the complete protein sequence, the spin systems can be assigned to specific amino acids. In a simplified view, the spin system analysis can be reduced to observing αN connectivities between the J-coupled α and NH protons of each amino acid residue, while the sequential assignment is based (among others) on αN connectivities between neighbors. In 3D NOESY–TOCSY and 3D TOCSY–NOESY experiments, we can measure both types of connectivity simultaneously in one $C[NOE,J]_{N\alpha N}(i + 1, i, i)$ connectivity. In fact, two types of NαN connectivities exist: sequential $C_{N\alpha N}(i + 1, i, i)$ and intraresidue $C_{N\alpha N}(i, i, i)$ connectivities. Both connectivities can be observed in the scheme shown in Figure 9. The intraresidue $C_{N\alpha N}(i, i, i)$ connectivity of residue i will be found on the back-transfer line of an f_1–f_2 plane, whereas the sequential $C_{N\alpha N}(i + 1, i, i)$ connectivity to residue $(i - 1)$ will be found on a line parallel to the NOE line through the intraresidue $C_{N\alpha N}(i, i, i)$ connectivity. This then defines the NH f_3 frequency for the next f_1–f_2 plane, where we can repeat the search for both connectivities. An example of such a sequential assignment is given in Figure 10 for the 3D NOESY–TOCSY spectrum of pike parvalbumin from Asp92 to Ile97.

Complete descriptions of the sequential assignment strategy using 3D NOESY–TOCSY or 3D TOCSY–NOESY spectra were given by Vuister et al.[66] and by Oschkinat et al.[67] A full analysis of all possible 3D sequential connectivities in proteins was given, and estimates of the relative intensities of cross peaks corresponding to such connectivities for α-helical and β-sheet conformations, as summarized in Table 1 (for α- and N-protons only). Thus, by searching the 3D spectrum for such connectivities it is possible to analyze the secondary structure of the protein.

The method has been applied to the 109 amino acid residue protein parvalbumin. Most of the sequential backbone cross peaks of this protein were observed[68] in a single 3D TOCSY–NOESY spectrum of parvalbumin. The assignment based on these 3D data corresponds completely with a previous one using extensive 2D data. Even some novel NOEs, hidden due to overlap in the 2D spectra of parvalbumin,

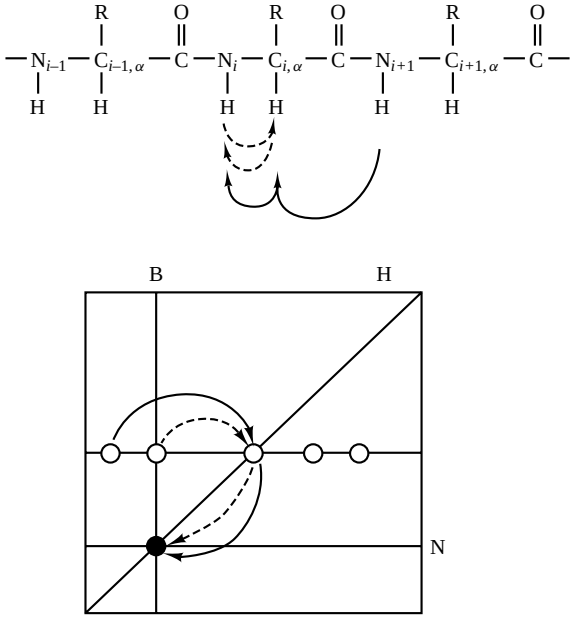

Figure 9 Sequential and intraresidue $C_{N\alpha N}$ connectivities in an f_1–f_2 plane of a 3D NOESY–TOCSY spectrum. The lines indicated by N, H, and B are the cross diagonal NOE, HOHAHA (or TOCSY), and back-transfer lines, respectively. The two dotted arrows starting at a back-transfer cross peak indicate the intraresidue $C_{N\alpha N}(i, i, i)$ connectivity, where the first arrow represents the NOE transfer from N to α and the second one the J transfer from α back to N. The two solid arrows show the interresidue $C_{N\alpha N}(i + 1, i, i)$ connectivity

could be identified. Similar results have been obtained for α-purothionin,[37] bovine pancreas trypsin inhibitor (BPTI),[67] the 113-residue protein aponeocarzinostatin,[69] a 90-residue phospholipid transfer protein,[70] a 137-residue flavodoxin,[65] the 128-residue blue copper protein azurin,[71] the 153-residue interleukin-4,[21] and the monomeric 143-residue heme protein leghemoglobin.[72] In most cases the analysis of the homonuclear 3D data led to additions or corrections in previously established assignments. The assignment for one residue was corrected for α-purothionin. Parvalbumin was shown to contain one amino acid residue more than expected on the basis of the amino acid sequence. For flavodoxin, 15 additional residues were identified from the 3D spectra. For neocarzinostatin it was possible to correct inconsistent assignments from three previous publications.

It is clear that the combination of NOE transfer and isotropic mixing in one 3D experiment is very useful in sequential assignment procedures of protein NMR spectra. Since the information is contained in one data set, these procedures may be better suited for automation than methods which rely on matching two different NOESY and TOCSY spectra. Furthermore, the increased resolution and the presence of the two-step connectivities will reduce overlap in spectra of larger biomolecules. Semiautomated approaches for analyzing 3D NOESY–TOCSY spectra of proteins have been demonstrated by Oschkinat et al.[57,58] and Kleywegt et al.[54] In this latter procedure, sets of J-coupled resonances are obtained from a peak list of the 3D spectrum. These sets are then ranked as possible spin systems using chemical shift rules and the sets are ordered using sequential 3D connectivities. By matching long stretches of such sequentially linked spin systems versus

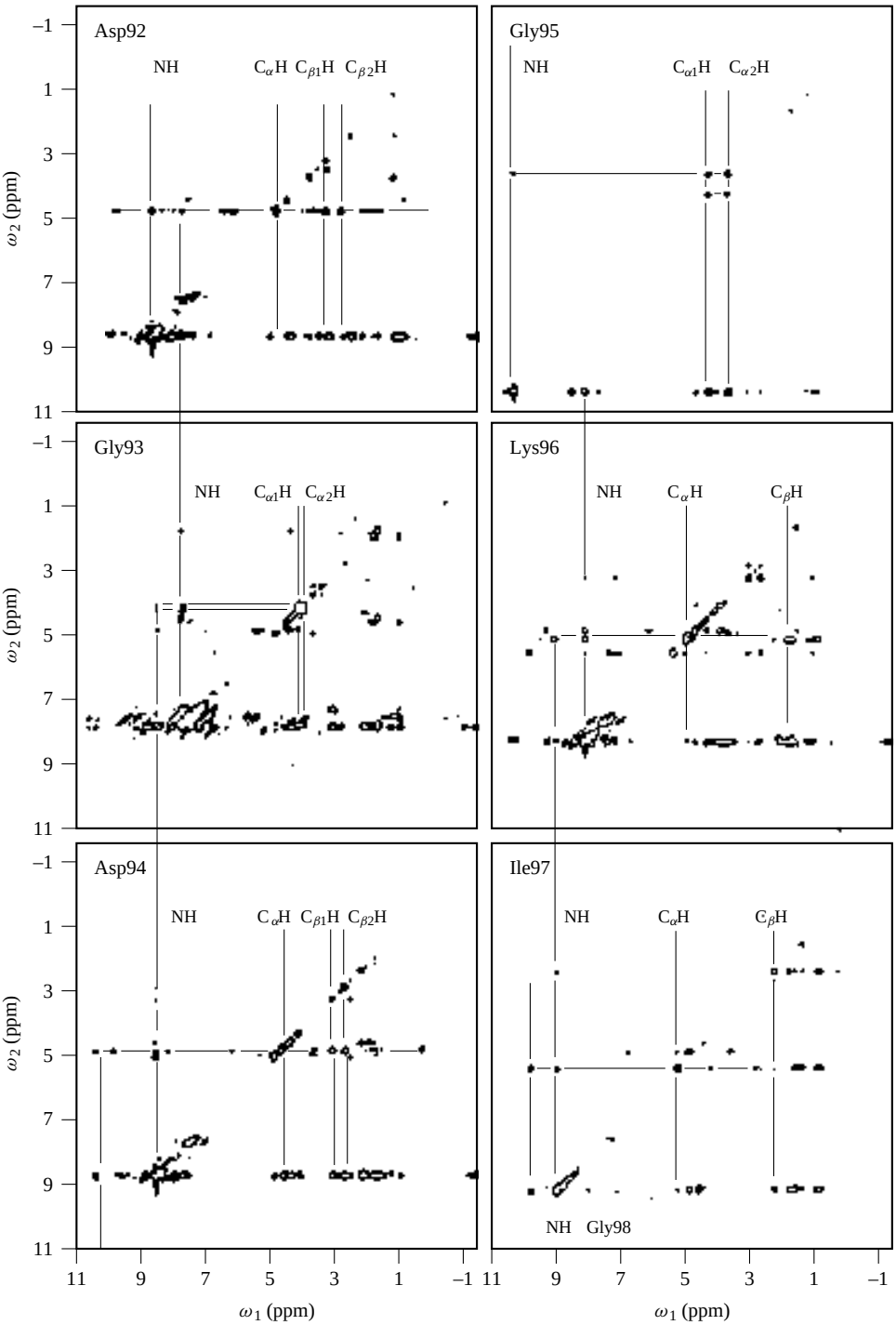

Figure 10 Sequential walk through f_1–f_2 planes in the NH region of the 3D NOESY–TOCSY spectrum of parvalbumin for f_3 frequencies of NH(Asp92) to NH(Ile97), taken from Vuister et al.[8] The spin system is indicated by vertical lines for each plane. The NOEs with the C-α atom can be found on the horizontal line parallel to the NOE line at the C-α resonance frequency. A back-transfer peak, $C_{N\alpha N}(i, i, i)$, is found at the crossing with the vertical NH line. The other cross peaks on this horizontal line in the NH region represent potential sequential cross peaks $C_{N\alpha N}(i + 1, i, i)$. The vertical line connecting to the next f_1–f_2 plane defines the NH frequency of the neighboring residue. The number of choices for sequential connectivities is significantly reduced compared with that observed in 2D spectra. Note that at Gly95 the sequential $C_{N\alpha N}(i + 1, i, i)$ connectivity is lacking, but that in this case use has been made of the single-step d_{NN} connectivity on the NOE line. (Reproduced by permission from Vuister et al.[8])

Table 1 Sequential Connectivities in 2D and 3D NMR[a]

	α-helix	β-sheet
2D NOE or NOE plane		
$d_{\alpha N}$	w	s
d_{NN}	m	a
3D NOESY–TOCSY		
$d_{\alpha N}$ $C_{N\alpha N}(i+1,i,i)$	a–w	s
$C_{\alpha N\alpha}(i-1,i,i)$	a–w	s
d_{NN} $C_{NN\alpha}(i+1,i,i)$	m	a–w
$C_{NN\alpha}(i-1,i,i)$	m	a–w

[a]Cross peak intensities: s, strong; m, medium; w, weak or a, absent. The estimates for the intensities in the 2D NOE spectra are taken from Wüthrich,[1] those for the 3D NOESY–TOCSY spectra are calculated as described by Vuister et al.[66]

the amino acid sequence it is possible to assign almost all residues of parvalbumin.[54]

In a semiautomatic procedure the analysis of 3D spectra can take place in f_1–f_2, f_2–f_3, or f_1–f_3 planes: the relationships among the cross peaks in different planes are established by the rules within the program. In an interactive analysis, especially on paper, patterns are more easily recognized in a single plot. The analysis of 3D TOCSY–NOESY and 3D NOESY–TOCSY spectra in f_1–f_3 planes has been found to be convenient, since the pattern of HOHAHA related cross peaks and the NOE relationship of this pattern with other resonances can be observed in one plane. Such planes are useful for identifying amino acid spin systems and a sequential assignment strategy mainly using f_1–f_3 planes has been outlined.[42,65]

Of course, it is not necessary to use just one 3D TOCSY–NOESY spectrum for assigning the resonances. A pragmatic approach uses 2D TOCSY and NOESY spectra for identifying the interactions between nonoverlapping resonances, whereas ambiguities are sorted out using the 3D spectra. Such procedures have been used for neocarzinostatin,[69] leghemoglobin,[72] procolipase,[73] the DNA binding domains of LexA repressor,[74] and the transcription elongation factor TFIIS.[75] Also for interleukin-4[21] and for azurin,[71] 3D TOCSY–NOESY and 3D NOESY–(^{15}N, ^{1}H)–HMQC were used together to resolve ambiguities in the assignments.

8.4 Identification of Spin Systems using 3D TOCSY–TOCSY Spectroscopy

An essential step for the sequential analysis of protein NMR spectra is the identification of spin systems. It has been demonstrated that 3D TOCSY–TOCSY spectroscopy can be of great help for deciphering spin systems.[76] The analysis of a 3D TOCSY–TOCSY spectrum is more straightforward than that of a 3D TOCSY–NOESY spectrum, since each 3D cross peak already defines three frequencies of the spin system. Similarly as in 3D TOCSY–NOESY spectra, it is relatively easy to recognize in the f_1–f_3 planes the 3D cross peaks belonging to one spin system, even in the case of overlap at the f_2 frequency. Oschkinat et al.[58] have proposed a strategy for automated assignment of proteins, where the spin systems would be identified using a 3D TOCSY–TOCSY spectrum and the sequential connectivities between the spin systems are obtained from a 3D TOCSY–NOESY spectrum. 3D TOCSY–TOCSY spectra can be very useful in those cases where strong overlap prohibits the analysis of spin systems but where efficient HOHAHA transfer is still present.

8.5 Analysis of 3D NOESY–NOESY Spectra

For larger proteins it becomes more difficult to establish the proton–proton J coupling via COSY and HOHAHA transfer steps. A 3D technique, where both mixing periods are due to cross relaxation, is in principle not limited by molecular weight. Suitable mixing periods are NOE or ROE. Thus, 3D NOESY–NOESY spectroscopy was proposed, where a NOE is now relayed by NOE to another nucleus.[11] However, since the relay can be to any neighboring nucleus, the analysis of 3D NOESY–NOESY spectra can be complex. Furthermore, since in general the NOE is weak and the relay can be to several other nuclei, a relatively low sensitivity for the 3D NOESY–NOESY could be expected. Nevertheless, 3D NOESY–NOESY spectra of good quality have been presented.[41,77–79] For proteins it has been demonstrated that the amide protons show connectivity patterns very similar to 3D NOESY–TOCSY spectra.[77] A statistical analysis of expected connectivities in 3D NOESY–NOESY spectra for 28 crystal protein structures shows that patterns of highly correlated cross peaks exist, suggesting that assignments for proteins could be based largely on NOE data.[80] A very complete analysis of sequential and medium range connectivities has been made for the 3D NOESY–NOESY spectrum of parvalbumin.[41,78] For the 109-residue parvalbumin the HOHAHA transfer is generally more efficient than the NOE transfer, thus the number of sequential and medium range connectivities in the 3D NOESY–NOESY spectrum is slightly less than that of a 3D TOCSY–NOESY spectrum. For proteins with a less efficient HOHAHA transfer, however, 3D NOESY–NOESY may perform better.

8.6 Structural Studies of Proteins

Stretches of sequential and medium range 3D connectivities can be used as indicators for α-helical, β-sheet, or turn-like structures. Thus, for the proteins parvalbumin[68] and aponeocarzinostatin[69] it was demonstrated that most of the secondary structure assignments found in 2D NOE spectra can be obtained from a 3D TOCSY–NOESY spectrum, but with fewer ambiguities. The secondary structures of a phospholipid transfer protein[70] and of leghemoglobin[72] are based on a combination of homonuclear 2D and 3D data. For ferrocytochrome c_{553} several crucial long range NOEs could be established from 3D TOCSY–NOESY spectra.[81] Similarly, many NOE restraints used for the structure determinations of procolipase[73] and the DNA binding domain of LexA repressor[74] were obtained with help from 3D TOCSY–NOESY data.

Long-range NOEs can also be observed by 3D NOESY–NOESY. Thus, 3D NOESY–NOESY data resolved crucial long range connectivities for the structure determination of the DNA binding domain of LexA repressor.[74] The analysis of 3D NOESY–NOESY spectra is complex, since a large number of cross peaks can be expected and the magnetization transfer is not limited to spin systems. The analysis improves by

comparing patterns of 3D cross peaks. For example, if for spin B a characteristic pattern of cross peaks {(A, B, P), (A, B, Q), and (A, B, R)} has been observed, the 3D NOESY–NOESY spectrum can be searched systematically for the patterns {(C, B, P), (C, B, Q), and (C, B, R)} and {(P, B, C), (Q, B, C), and (R, B, C)}. If the pattern at the row defined by (f_1, f_2) = (A, B) was observed virtually without overlap, this search is effectively a convolution of the 3D spectrum with this row. Visually, this pattern can be easily recognized in an f_1–f_3 plane. Next, one has to analyze the pattern at (f_1, f_2) = (B, C) in order to establish the nature of nucleus C. In this way the pattern of relayed intensities, which was unfavorable for an optimal signal-to-noise ratio of the 3D spectrum, turns out to be beneficial for pattern recognition. Once the 3D cross peaks have all been assigned, the intensities of the 3D cross peaks can be converted into constraints for structure refinement.

8.7 Distance Constraints from 3D Data

For structure refinement it is important to obtain as many distance constraints as possible.[1] For this, 3D spectra can be very useful, since they may resolve many ambiguities in the spectral interpretation of NOE data, and therefore lead to more restraints.[82] It is, however, also possible to use the 3D spectra directly for obtaining distance constraints. The 3D cross-peak intensity is proportional to the product of the two transfer efficiencies of the two mixing periods of a 3D experiment:

$$I_{ijk} \propto T_{ij} T_{jk} \tag{1}$$

Several approaches have been described for interpreting the 3D intensity. The ratio of the intensity of the cross peak C(A,B,C) of a 3D TOCSY–NOESY, or a 3D NOESY–NOESY spectrum and the intensity of the cross-diagonal cross peak C(A,B,B) defines the transfer efficiency T_{bc}:

$$I\{\mathrm{C(A,B,C)}\}/I\{\mathrm{C(A,B,B)}\} = T_{bc}/(1 - T_{bc}) \tag{2}$$

From this NOE transfer efficiency, T_{bc} distances can be obtained in a similar way as from regular 2D data. The relationship between NOE transfer efficiency and cross relaxation rates is

$$\mathbf{T} = \exp(-\tau_{\mathrm{m}}\mathbf{R}) \tag{3}$$

where **T** and **R** are the NOE transfer and cross-relaxation matrices, respectively, and τ_{m} the NOE mixing period. Generally, transfer efficiencies are compared with those of protons at known distances and the approximate relationship

$$T_{bc}/T_{de} = (r_{de}/r_{bc})^6 \tag{4}$$

is used. In the case of overlap at the cross-diagonal planes it is still possible to obtain the ratio of the cross peaks C(A,B,C) and C(A,B,F) which defines the ratio T_{bc}/T_{bf} and thus the ratio of the distances r_{bc}/r_{bf}.[83] If the distance r_{bf} is known, the distance r_{bc} can be derived.

A more quantitative approach uses the cross-peak intensities of a 3D NOESY–NOESY spectrum. The relationship between NOE and distance is only an approximate one, due to spin diffusion at longer NOE mixing times. Approximating this multiple-step NOE transfer to second order, the NOE intensity is equal to

$$T_{ij} = -R_{ij}\tau_{\mathrm{m}} + \sum R_{ik}R_{kj}\tau_{\mathrm{m}}^2 \ldots \tag{5}$$

The second term in equation (5) describes spin diffusion via other spins. The intensity of a cross peak in a 3D NOESY–NOESY spectrum is to a first approximation equal to

$$T_{ikj} = R_{ik}R_{kj}\tau_{\mathrm{m}}^2 \ldots \tag{6}$$

Thus the cross peaks in a 3D NOESY–NOESY spectrum define the contributions of the several spin diffusion paths via other nuclei.[11] Therefore the 3D NOESY–NOESY intensities can be used to obtain more accurate cross-relaxation rates between proton pairs, as has been shown by Kessler et al.[84] and Habazettl et al.[85]

The 3D NOESY–NOESY intensities can also be used as direct constraints for a structure refinement. This requires the calculation of the gradients of the 3D intensities with respect to the coordinates of the protons in a molecule. The gradient of a 3D NOESY–NOESY peak with a net transfer T_{ijk} can be written[86] as the sum of two terms containing the separate gradients of T_{ij} and T_{jk}:

$$\nabla T_{ijk} = T_{ij}\nabla T_{jk} + \nabla T_{ij} T_{jk} \tag{7}$$

The transfer efficiencies T_{ij} and T_{jk} can be obtained from relaxation matrix methods (cf. Bonvin et al.[87]), while the derivatives of the 2D efficiencies can be solved exactly[88] or be approximated.[89] equation (7) has been used to obtain 3D NOE restraining potentials for use in restrained molecular dynamics calculations:[86,90,91]

$$V_{\mathrm{3D\,NOE}} \sim \sum_{ijk} (T_{ijk} - T_{ijk}^{\mathrm{obs}})^2 \tag{8}$$

where T_{ijk} and $T_{ijk}{}^{\mathrm{obs}}$ are the calculated and observed transfer efficiencies, respectively. The minimization of the 3D NOE potential requires the calculation of $\nabla V_{\mathrm{3DNOE}}$. This can be accomplished by combining equations (7) and (8) as

$$\nabla V_{\mathrm{3D\,NOE}} \sim \sum_{ijk} 2(T_{ijk} - T_{ijk}^{\mathrm{obs}})(T_{ij} \cdot \nabla T_{jk} + \nabla T_{ij} \cdot T_{jk}) \tag{9}$$

It has been shown that the use of the 3D cross-peak intensities can lead to a better definition of the structures of proteins than the use of only 2D NOE data.

8.8 Protein Hydration Studies

Cross peaks in a NOESY spectrum at a line corresponding to the f_1 frequency of water can identify protons with a close proximity to water.[92] The overlap of proton signals on this line can be removed by transferring the magnetization in a second magnetization transfer step to a third nucleus. Thus, Otting et al.[93] have demonstrated the use of 3D NOESY–TOCSY and 3D ROESY–TOCSY for studies of protein hydration,

whereas Holak et al.[94] have used 3D NOESY–NOESY. In contrast to 2D methods, where the NOEs with water protons are all observed on a single frequency axis, the f_2–f_3 planes of 3D spectra at the f_1 frequency of water reveal the protons interacting with water via cross peaks in a two-dimensional map. This reduces overlap and helps to assign the protons involved. The comparison of the sign and intensities of the cross peaks in the f_2–f_3 planes of the 3D NOESY–TOCSY and 3D ROESY–TOCSY spectra distinguishes NOE and exchange effects.

8.9 Homonuclear 3D NMR of Oligosaccharides

The small chemical shift dispersion of the sugar-skeleton protons of oligosaccharides poses a major problem for structural studies. It is often still possible to obtain assignments on the basis of 2D HOHAHA experiments by exploiting the chemical shift dispersion of the anomeric protons. However, the unique identification of NOEs involving protons in the bulk region between 3 and 4 ppm is very difficult. The resolution in the bulk region can be increased by the application of 3D NOESY–TOCSY techniques, which relay the magnetization from the bulk protons to the anomeric signals.[83,95]

An example is given in Figure 11, which shows the f_1–f_2 plane at the f_3 frequency of the Man-4 H-2 anomeric signal of a biantennary asparagine-linked oligosaccharide at 4.19 ppm. An interesting 3D cross peak is observed at the f_1 frequency of Man-3 H-2, which shows the presence of an NOE between Man-4 H-5 and Man-3 H-2. The existence of this NOE was the subject of considerable discussion in the literature, although it was settled later by deuteration studies (see Vuister et al.[95] for a discussion). This NOE effect is found directly in the 3D NOESY–TOCSY spectrum.

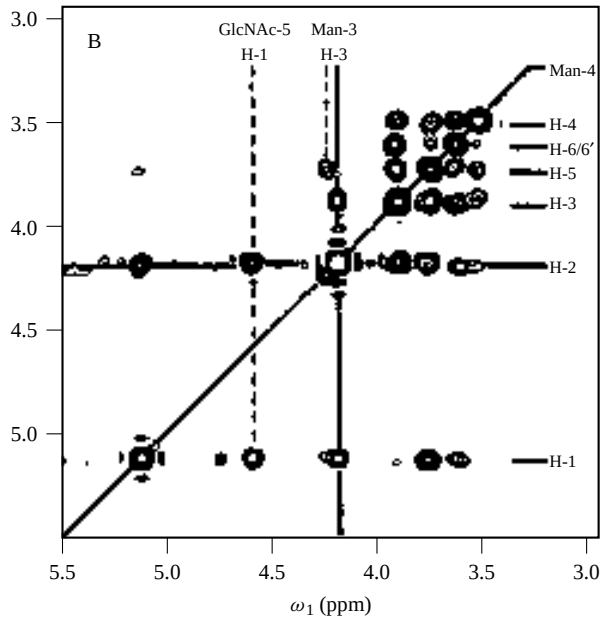

Figure 11 f_1–f_2 plane of the 3D NOESY–TOCSY spectrum of 20 mM biantennary oligosaccharide in D_2O at 304 K and pH = 7. The cross section shown is at the f_3 resonance position of Man-4 H-2 (4.19 ppm). The 144 × 144 × 1024 data set was recorded at 500 MHz in 63 h using eight scans. The NOE mixing time was 350 ms and the HOHAHA mixing time 94 ms. The spectrum was processed to a resolution of 256 × 256 × 512. (Adapted by permission from Vuister et al.[95])

8.10 Homonuclear 3D NMR of DNA and RNA Fragments

For the sequential assignment of DNA and RNA fragments it is necessary to correlate the NOEs of the aromatic protons of the nucleic acid bases with their own sugar protons and those of their neighbor. 3D TOCSY–NOESY spectra can be used for this purpose.[96,97] It turns out that even the very crowded 4′,5′,5″ region of DNA fragments now becomes accessible for analysis. Thus, 3D TOCSY–NOESY was used for a 15-residue DNA hairpin,[96] and 3D NOESY–TOCSY for a 31-residue pyrimidine–purine–pyrimidine DNA triplex.[97] Homonuclear 3D methods are very useful for RNA fragments, where considerable overlap exists for most sugar protons. Thus, most proton assignments can be obtained from a single 3D TOCSY–NOESY spectrum, as demonstrated for a 12-mer RNA duplex.[98]

Structural studies of DNA fragments can use 3D NOESY–TOCSY methods for resolving ambiguities in the assignment of cross peaks in 2D NOE spectra. Such methods have been applied for the analysis of the NOEs of a 12-mer DNA duplex containing a GG mismatch[99] and for analysis of a modified 12-mer DNA duplex.[100] In both cases the 3D spectra clarified unusual NOEs, with important consequences for the geometry.

For larger DNA and RNA fragments the HOHAHA transfer could turn out to be inefficient. In this situation 3D NOESY–NOESY is an alternative, since it is not based on a possibly weak homonuclear J coupling, and cross relaxation becomes increasingly efficient at higher molecular weights. It has been demonstrated that 3D NOESY–NOESY spectra of good quality can be recorded for a 22-mer duplex.[11] Similarly, 3D NOESY–NOESY has been applied to a 40-base three-stranded DNA junction,[101] where it allowed the completion of the proton assignments and confirmed the unusual geometry at the junction, and to a hybrid DNA–RNA dodecamer duplex,[102] where it resolved superimposed cross peaks of the RNA strand.

9 PROSPECTS FOR 3D NMR SPECTROSCOPY

The NOE effect and the J coupling can be combined in three different ways in homonuclear 3D NMR experiments. 3D experiments with a simple magnetization transfer such as in 3D COSY–COSY are most amenable for analysis. However, the linewidth of larger biomolecules is of a similar magnitude to the ^3J(H, H) coupling, which leads to weak 3D cross-peak intensities. Magnetization transfer by HOHAHA is less sensitive to line broadening, and is therefore preferable for most applications. Thus, spin systems of biomolecules with molecular masses below 20 kDa can be analyzed using 3D TOCSY–TOCSY and 3D NOESY–TOCSY spectra. Furthermore, these latter spectra turn out to be useful in assigning resonances and analyzing the secondary and even the tertiary structure of proteins. For biomolecules of greater mass than 20 kDa or with a large linewidth, mixing periods based on J(H, H) couplings may not be efficient. In this case 3D NOESY–NOESY or 3D ROESY–ROESY experiments can

be used for resolving the overlap of cross peaks in NOESY and ROESY spectra.

The analysis of many multidimensional NMR spectra may benefit from the development of programs which allow the graphical and interactive bookkeeping of the spectra on workstations. This is particularly true for the homonuclear 3D spectra of biomolecules, where the large number of interactions and the fact that the relay is to many other nuclei often leads to many cross peaks. Since the analysis of such spectra can be complex, a practical approach where the 3D spectra assist the analysis of 2D TOCSY and NOESY spectra seems to be the most fruitful. A further improvement for all multidimensional techniques is the application of field gradient methods using shielded gradient coils. This may allow a reduction in the phase cycling for coherence selection and artifact suppression, so that spectra can be obtained with a significant higher resolution per domain. This is particularly important for the automated analysis of multidimensional spectra, where a large tolerance in the coordinates of a cross peak due to low resolution may result in a large number of possible assignments.

Another class of 3D NMR experiments, not discussed in detail in the present overview, is formed by the heteronuclear 3D NMR experiments, such as 3D TOCSY–HMQC and 3D NOESY–HMQC. These methods also use a third dimension to increase the resolution. Compared with the homonuclear proton methods they have the advantage of an efficient J transfer due to the large $^{15}N-^{1}H$ and $^{13}C-^{1}H$ coupling constants. For sufficient sensitivity, it is generally necessary to obtain isotopically enriched biological material. For doubly (^{13}C, ^{15}N) labeled proteins and ^{13}C labeled oligonucleotides straightforward and powerful methods have been developed both for assigning resonances and for structural studies (see Clore and Gronenborn[19] and Oschkinat et al.[21] for reviews). In many cases, however, labeling may be impossible to realize, and then homonuclear 3D methods are still possible. In other cases only ^{15}N labeling may feasible. It is then possible to record 3D TOCSY–NOESY–(^{15}N, ^{1}H)–HSQC spectra[103,104] or 4D TOCSY–NOESY–(^{15}N, ^{1}H)–HSQC spectra[105] to resolve ambiguities in 3D NOESY–(^{15}N, ^{1}H)–HSQC spectra. It turns out that the analysis of such spectra is very similar to that of the homonuclear 3D TOCSY–NOESY spectra.

During the past few years many homonuclear and heteronuclear 3D NMR experiments have been developed. These methods can complement each other and should be explored to their limits for studying larger and more complex biomolecular systems.

10 RELATED ARTICLES

Three-Dimensional HMQC-NOESY, NOESY-HMQC, and NOESY-HSQC; Three- and Four-Dimensional Heteronuclear Magnetic Resonance; Multidimensional Spectroscopy: Concepts; Protein Hydration; Relayed Coherence Transfer Experiments.

11 REFERENCES

1. K. Wüthrich, *NMR of Proteins and Nucleic Acids*, Wiley, New York, 1986.
2. R. R. Ernst, G. Bodenhausen, and A. Wokaun, *Principles of Nuclear Magnetic Resonance in One and Two Dimensions*, Clarendon Press, Oxford, 1987.
3. H. D. Plant, T. H. Mareci, M. D. Cockman, and W. S. Brey, *27th Experimental NMR Conference, Baltimore, Maryland, April 13–17, 1986*.
4. G. W. Vuister and R. Boelens, *J. Magn. Reson.*, 1987, **73**, 328.
5. C. Griesinger, O. W. Sørensen, and R. R. Ernst, *J. Magn. Reson.*, 1987, **73**, 574.
6. C. Griesinger, O. W. Sørensen, and R. R. Ernst, *J. Am. Chem. Soc.*, 1987, **109**, 7227.
7. H. Oschkinat, C. Griesinger, P. J. Kraulis, O. W. Sørensen, R. R. Ernst, A. M. Gronenborn, and G. M. Clore, *Nature*, 1988, **332**, 374.
8. G. W. Vuister, R. Boelens, and R. Kaptein, *J. Magn. Reson.*, 1988, **80**, 176.
9. L. E. Kay, G. M. Clore, A. Bax, and A. M. Gronenborn, *Science*, 1990, **249**, 411.
10. G. M. Clore, L. E. Kay, A. Bax, and A. M. Gronenborn, *Biochemistry*, 1991, **30**, 12.
11. R. Boelens, G. W. Vuister, T. M. G. Koning, and R. Kaptein, *J. Am. Chem. Soc.*, 1989, **111**, 8525.
12. S. W. Fesik and E. R. P. Zuiderweg, *J. Magn. Reson.*, 1988, **78**, 588.
13. E. R. P. Zuiderweg and S. W. Fesik, *Biochemistry*, 1989, **28**, 2387.
14. D. Marion, L. E. Kay, S. W. Sparks, D. A. Torchia, and A. Bax, *J. Am. Chem. Soc.*, 1989, **111**, 1515.
15. D. Marion, P. C. Driscoll, L. E. Kay, P. T. Wingfield, A. Bax, A. M. Gronenborn, and G. M. Clore, *Biochemistry*, 1989, **28**, 6150.
16. G. T. Montelione and G. Wagner, *J. Magn. Reson.*, 1990, **87**, 183.
17. M. Ikura, L. E. Kay, and A. Bax, *Biochemistry*, 1990, **29**, 4659.
18. C. Griesinger, O. W. Sørensen, and R. R. Ernst, *J. Magn. Reson.*, 1989, **84**, 14.
19. G. M. Clore and A. M. Gronenborn, *Prog. Nucl. Magn. Reson. Spectrosc.*, 1991, **23**, 43.
20. A. Bax and S. Grzesiek, *Acc. Chem. Res.*, 1993, **26**, 131.
21. H. Oschkinat, T. Müller, and T. Dieckmann, *Angew. Chem., Int. Ed. Engl.*, 1994, **33**, 277.
22. O. W. Sørensen, *J. Magn. Reson.*, 1990, **89**, 210.
23. G. W. Eich, G. Bodenhausen, and R. R. Ernst, *J. Am. Chem. Soc.*, 1982, **104**, 3731.
24. P. H. Bolton and G. Bodenhausen, *Chem. Phys. Lett.*, 1982, **89**, 139.
25. G. Wagner, *J. Magn. Reson.*, 1984, **57**, 497.
26. F. J. M. Van der Ven, C. A. G. Haasnoot, and C. W. Hilbers, *J. Magn. Reson.*, 1985, **61**, 181.
27. H. Kessler, G. Gemmecker, and S. Steuernagel, *Angew. Chem., Int. Ed. Engl.*, 1988, **100**, 600.
28. P. De Waard, R. Boelens, G. W. Vuister, and J. F. G. Vliegenthart, *J. Am. Chem. Soc.*, 1990, **112**, 3232.
29. H. Kessler, G. Gemmecker, and B. Haase, *J. Magn. Reson.*, 1988, **77**, 401.
30. W. P. Aue, E. Bartholdi, and R. R. Ernst, *J. Chem. Phys.*, 1976, **64**, 2229.
31. J. Jeener, B. H. Meier, P. Bachmann, and R. R. Ernst, *J. Chem. Phys.*, 1979, **71**, 4546.
32. S. Macura and R. R. Ernst, *Mol. Phys.*, 1980, **41**, 95.
33. A. Kumar, G. Wagner, R. R. Ernst, and K. Wüthrich, *J. Am. Chem. Soc.*, 1981, **103**, 3654.

34. A. A. Bothner-By, R. L. Stephens, J. Lee, C. D. Warren, and R. W. Jeanloz, *J. Am. Chem. Soc.*, 1984, **106**, 811.
35. A. Bax and D. G. Davies, *J. Magn. Reson.*, 1985, **65**, 355.
36. H. Oschkinat, C. Cieslar, A. M. Gronenborn, and G. M. Clore, *J. Magn. Reson.*, 1989, **81**, 212.
37. H. Oschkinat, C. Cieslar, T. A. Holak, G. M. Clore, and A. M. Gronenborn, *J. Magn. Reson.*, 1989, **83**, 450.
38. J. Cavanagh and M. Rance, *Prog. Nucl. Magn. Reson. Spectrosc.*, 1993, **27**, 1.
39. F. Ni, *J. Magn. Reson.*, 1992, **100**, 391.
40. C. Griesinger, G. Otting, K. Wüthrich, and R. R. Ernst, *J. Am. Chem. Soc.*, 1988, **110**, 7870.
41. R. Boelens, C. Griesinger, L. E. Kay, D. Marion, and E. R. P. Zuiderweg, *Nato ASI Ser., Ser. A*, 1991, **A225**, 127.
42. J.-P. Simorre and D. Marion, *J. Magn. Reson.*, 1991, **94**, 426.
43. H. Barkhuizen, R. deBeer, W. M. M. J. Bovee, and D. van Ormondt, *J. Magn. Reson.*, 1985, **61**, 465.
44. H. Gesmar, J. J. Led, and F. Abildgaard, *Prog. Nucl. Magn. Reson. Spectrosc.*, 1990, **22**, 255.
45. G. Zhu and A. Bax, *J. Magn. Reson.*, 1990, **90**, 405.
46. M. Robin, M.-A. Delsuc, E. Guitet, and J.-Y. Lallemand, *J. Magn. Reson.*, 1991, **92**, 645.
47. E. T. Olejniczak and H. L. Eaton, *J. Magn. Reson.*, 1990, **87**, 628.
48. D. Marion and A. Bax, *J. Magn. Reson.*, 1989, **83**, 205.
49. R. Saffrich, W. Beneicke, K.-P. Neidig, and H. R. Kalbitzer, *J. Magn. Reson. B*, 1993, **101**, 304.
50. L. Mitschang, C. Cieslar, T. A. Holak, and H. Oschkinat, *J. Magn. Reson.*, 1991, **92**, 208.
51. G. Otting, H. Widmer, G. Wagner, and K. Wüthrich, *J. Magn. Reson.*, 1986, **66**, 187.
52. D. Marion and A. Bax, *J. Magn. Reson.*, 1988, **79**, 352.
53. P. J. Kraulis, *J. Magn. Reson.*, 1989, **84**, 627.
54. G. J. Kleywegt, G. W. Vuister, A. Padilla, R. M. A. Knegtel, R. Boelens, and R. Kaptein, *J. Magn. Reson.*, 1993, **102**, 166.
55. M. Kjaer, K. V. Andersen, S. Ludvigsen, H. Shen, P. Windekinde, B. Sørensen, and F. M. Poulson, *Nato ASI Ser., Ser. A*, 1991, **A225**, 291.
56. K.-P. Neidig, R. Saffrich, M. Lorenz, and H. R. Kalbitzer, *J. Magn. Reson.*, 1990, **89**, 543.
57. C. Cieslar, T. A. Holak, and H. Oschkinat, *J. Magn. Reson.*, 1990, **87**, 400.
58. H. Oschkinat, T. A. Holak, and C. Cieslar, *Biopolymers*, 1991, **31**, 699.
59. R. E. Hoffman and D. B. Davies, *J. Magn. Reson.*, 1988, **80**, 337.
60. P. A. Mirau, S. A. Heffner, and F. A. Bovey, *J. Magn. Reson.*, 1990, **89**, 572.
61. C. Griesinger, O. W. Sørensen, and R. R. Ernst, *J. Chem. Phys.*, 1986, **85**, 6387.
62. Y. Yang, A. Hagemeyer, K. Zemke, and H. W. Spiess, *J. Chem. Phys.*, 1990, **93**, 7740.
63. B. S. Arun Kumar and S. J. Opella, *J. Magn. Reson.*, 1993, **101**, 333.
64. G. W. Vuister, Ph.D. Thesis, Utrecht University, 1990.
65. S. S. Wijmenga and C. P. M. van Mierlo, *Eur. J. Biochem.*, 1991, **195**, 807.
66. G. W. Vuister, R. Boelens, A. Padilla, G. J. Kleywegt, and R. Kaptein, *Biochemistry*, 1990, **29**, 1829.
67. H. Oschkinat, C. Cieslar, and C. Griesinger, *J. Magn. Reson.*, 1990, **86**, 453.
68. A. Padilla, G. W. Vuister, R. Boelens, G. J. Kleywegt, A. Cavé, J. Parello, and R. Kaptein, *J. Am. Chem. Soc.*, 1990, **112**, 5024.
69. X. Gao and W. Burkhart, *Biochemistry*, 1991, **30**, 7730.
70. J.-P. Simorre, A. Caille, D. Marion, D. Marion, and M. Ptak, *Biochemistry*, 1991, **30**, 11 600.
71. M. van de Kamp, G. W. Canters, S. S. Wijmenga, A. Lommen, C. W. Hilbers, H. Nar, A. Messerschmidt, and R. Huber, *Biochemistry*, 1992, **31**, 10 194.
72. D. Morikis, C. A. Lepre, and P. E. Wright, *Eur. J. Biochem.*, 1994, **219**, 611.
73. J. N. Breg, L. Sarda, P. J. Cozzone, R. Boelens, and R. Kaptein, *Biochemistry*, 1994, in press.
74. R. Fogh, G. Ottleben, H. Rüterjans, M. Schnarr, R. Boelens, and R. Kaptein, *EMBO J.*, 1994, **13**, 3936.
75. X. Qian, S. N. Gozani, H. S. Yoon, C. J. Jeon, K. Agarwal, and M. A. Weiss, *Biochemistry*, 1993, **32**, 9944.
76. C. Cieslar, T. A. Holak, and H. Oschkinat, *J. Magn. Reson.*, 1990, **87**, 184.
77. J. N. Breg, R. Boelens, G. W. Vuister, and R. Kaptein, *J. Magn. Reson.*, 1990, **87**, 646.
78. A. Padilla, *Cahiers IMABIO CNRS (Paris)*, 1992, **3**, 19.
79. A. Ross, J. Freund, C. Cieslar, H. Oschkinat, M. Schleicher, and T. A. Holak, *J. Magn. Reson.*, 1991, **95**, 567.
80. G. W. Vuister, R. Boelens, A. Padilla, and R. Kaptein, *J. Biomol. NMR*, 1991, **1**, 421.
81. D. Marion and F. Guerlesquin, *Biochemistry*, 1992, **31**, 8171.
82. T. A. Holak, J. Habazettl, H. Oschkinat, and J. Otlewski, *J. Am. Chem. Soc.*, 1991, **113**, 3196.
83. P. de Waard, B. R. Leeflang, J. F. G. Vliegenthart, R. Boelens, G. W. Vuister, and R. Kaptein, *J. Biomol. NMR*, 1992, **2**, 211.
84. H. Kessler, S. Seip, and J. Saulitis, *J. Biomol. NMR*, 1991, **1**, 83.
85. J. Habazettl, A. Ross, H. Oschkinat, and T. A. Holak, *J. Magn. Reson.*, 1992, **97**, 511.
86. A. M. J. J. Bonvin, R. Boelens, and R. Kaptein, *J. Magn. Reson.*, 1991, **95**, 626.
87. A. M. J. J. Bonvin, R. Boelens, and R. Kaptein, in *Computer Simulation of Biomolecular Systems*, eds. W. F. van Gunsteren, P. K. Weiner, and A. J. Wilkinson, Escom, Leiden, 1993, Vol. 2, p. 403.
88. P. Yip and D. A. Case, *J. Magn. Reson.*, 1989, **83**, 643.
89. A. M. J. J. Bonvin, R. Boelens, and R. Kaptein, *J. Biol. NMR*, 1991, **1**, 305.
90. J. Habazettl, M. Schleicher, J. Otlewski, and T. A. Holak, *J. Mol. Biol.*, 1992, **228**, 156.
91. R. Bernstein, A. Ross, C. Cieslar, and T. A. Holak, *J. Magn. Reson.*, 1993, **101**, 185.
92. G. Otting and K. Wüthrich, *J. Am. Chem. Soc.*, 1989, **111**, 1871.
93. G. Otting, E. Liepinsh, B. T. Farmer II, and K. Wüthrich, *J. Biomol. NMR*, 1991, **1**, 209.
94. T. A. Holak, R. Witscheck, and A. Ross, *J. Magn. Reson.*, 1992, **97**, 632.
95. G. W. Vuister, P. de Waard, R. Boelens, J. F. G. Vliegenthart, and R. Kaptein, *J. Am. Chem. Soc.*, 1989, **111**, 772.
96. M. M. W. Mooren, C. W. Hilbers, G. A. van der Marel, J. H. van Boom, and S. S. Wijmenga, *J. Magn. Reson.*, 1991, **94**, 101.
97. I. Radhakrishnan, D. J. Patel, and X. Gao, *Biochemistry*, 1992, **31**, 2514.

98. S. S. Wijmenga, H. A. Heus, B. Werten, G. A. van der Marel, J. H. van Boom, and C. W. Hilbers, *J. Magn. Reson.*, 1994, **103**, 134.
99. M. E. Piotto and D. G. Gorenstein, *J. Am. Chem. Soc*., 1991, **113**, 1438.
100. X. Gao and P. W. Jeffs, *J. Biomol. NMR*, 1994, **4**, 17.
101. M. A. Rosen and D. J. Patel, *Biochemistry*, 1993, **32**, 6563.
102. X. Gao and P. W. Jeffs, *J. Biomol. NMR*, 1994, **4**, 367.
103. L. Mueller, S. Campbell-Burk, and P. Domaille, *J. Magn. Reson.*, 1992, **96**, 408.
104. S. Boentges, J. M. Schmidt, T. Levante, and R. R. Ernst, *15th International Conference on Magnetic Resonance in Biological Systems, Jeruzalem, Israel, August 1992*.
105. R. Boelens, *Cahiers IMABIO CNRS (Paris)*, 1992, **3**, 33.

Biographical Sketches

Rolf Boelens. *b* 1951. M.S., 1977, University of Groningen, Ph.D., 1984, University of Amsterdam. Postdoctoral associate with R. Kaptein, Groningen. Associate professor at Utrecht University, 1987–present. Over 130 publications. Research specialties: NMR method development, structure determination of biomolecules by NMR and studies on protein–DNA interaction.

Robert Kaptein. *b* 1941. M.S., 1965, Ph.D., Leiden, 1971; postdoctoral fellow with Ray Freeman, Varian 1971–1972; Shell Research Laboratory, Amsterdam, 1972–1975; Groningen University, 1975–1987; Utrecht University, Professor of Chemistry 1987–present. Research interests: biomolecular structure determination, NMR methodology, protein–DNA interactions.

Multidimensional Spectroscopy: Concepts

Richard R. Ernst
Laboratorium für Physikalische Chemie, Eidgenössische Technische Hochschule, 8092 Zürich, Switzerland

1	Introduction	1
2	Spectroscopy	1
3	Two-Dimensional and Multidimensional Spectroscopy	2
4	Coherence Transfer Pathway Selection	3
5	Building Blocks for Multidimensional NMR Experiments	5
6	Example of a Multidimensional NMR Experiment: ^{15}N–^{15}N Chemical Shift Correlation for the Sequential Assignment in Proteins	7
7	Outlook	10
8	Related Articles	10
9	References	10

1 INTRODUCTION

Two-dimensional and multidimensional spectroscopy are more than just another minor variant of the well-known, and old-fashioned, one-dimensional spectroscopy. Two-dimensional spectroscopy reveals a new general concept of experimental design which has opened up access to an astoundingly rich world of novel pulse experiments.[1–4] The principles of two-dimensional spectroscopy are in no way limited to NMR, and apply to all combinations of spectroscopic domains. However, they are most easily exemplified in NMR and have there found their most fruitful playground.

A large number of inventive and ingenious physicists and chemists have paved the way towards two-dimensional spectroscopy. Already the basic Hahn spin echo experiment bears the germ for 2D spectroscopy.[5] But, unquestionably, the most significant contribution has been made by Jean Jeener who is the actual creator of 2D spectroscopy.[6]

This brief article cannot be exhaustive and cannot do justice to all meritorious contributors who are responsible for the discovery and development of this new world of spectroscopy. Rather, the aim is to illuminate some general concepts underlying multidimensional spectroscopy which have revolutionized NMR, as an introduction to further, more specialized sections in this Encyclopedia.

2 SPECTROSCOPY

The ultimate goal of spectroscopy is the exploration of (black box) systems by means of input/output relationships, as shown in Figure 1.[1] In its most elementary form, it provides the frequency response or transfer function $H(\omega)$ that measures the (complex) transfer characteristics of a linear time-invariant

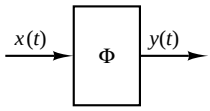

Figure 1 Input/output relationship for a system Φ with the input function $x(t)$ and the output function $y(t)$

system Φ when perturbed by the variable frequency ω or, more exactly, by its exponential function exp (iωt):

$$\hat{\Phi} \exp(\mathrm{i}\omega t) = H(\omega) \exp(\mathrm{i}\omega t) \tag{1}$$

This equation implies that the exponential functions exp (iωt) are eigenfunctions of all linear and time-invariant systems or system operators $\hat{\Phi}$. The continuous sequence of 'eigenvalues' represents the transfer function or the complex spectrum $H(\omega)$.

This immediately leads to the general spectroscopic recipe: apply a sinusoidal perturbation of frequency ω to the linear time-invariant system, measure the amplitude $H(\omega)$ of the sinusoidal response, vary the frequency, and plot $H(\omega)$ (or its real and imaginary parts) as a function of the frequency ω to obtain a spectrum.

In some cases, spectroscopy is used for the measurement of the emission characteristics of a source of spontaneous radiation, in the absence of an external perturbation. Then a frequency-selective (dispersive) element is required in the detector, and the frequency dependence is introduced by varying this dispersive element. This type of emission spectroscopy is common in astronomy, in optical flame spectroscopy, and in NMR spin-noise measurements.[7,8] It is not considered further in this article, which is restricted to measurements of input/output relationships.

In a generalized version of spectroscopy, several simultaneous sinusoidal perturbations of different frequencies and several simultaneous detectors tuned to these frequencies are conceivable. (see ***Early NMR Experiences and Experiments***) This leads either to the multiple channel spectroscopy experiment (Figure 2), in which the linear response character of the system is maintained,

$$\hat{\Phi}\left[\sum_k \exp(\mathrm{i}\omega_k t)\right] = \sum_k H(\omega_k) \exp(\mathrm{i}\omega_k t) \tag{2}$$

or to double or multiple resonance (Figure 3) when interference between the different frequencies becomes essential in a nonlinear response system, as is typical for magnetic resonance of coupled spins.[9–11]

Another form of generalized spectroscopy is the measurement of the impulse response $h(t)$, which is the response to a

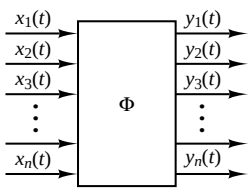

Figure 2 Multiple channel spectroscopy. For a linear system Φ, several simultaneous perturbations may be applied, and their response detected without mutual interference

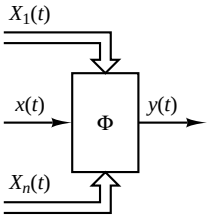

Figure 3 Multiple resonance experiment. The nonlinear system Φ is perturbed by several strong perturbations $X_1(t) \ldots X_n(t)$ while the response of a weak perturbation $x(t)$ is observed

delta-function perturbation:

$$\hat{\Phi}[\delta(t)] = h(t) \tag{3}$$

The delta function $\delta(t)$ represents an equally weighted superposition of all frequencies:

$$\delta(t) = \frac{1}{2\pi} \lim_{\Omega\to\infty} \int_{-\Omega}^{\Omega} \exp(\mathrm{i}\omega t)\, \mathrm{d}\omega \tag{4}$$

and the impulse-response measurement is the ultimate form of multiple channel spectroscopy. For a linear time-invariant system, the important FT relationships

$$H(\omega) = \int_{-\infty}^{\infty} h(t) \exp(-\mathrm{i}\omega t)\, \mathrm{d}t \tag{5}$$

and

$$h(t) = \frac{1}{2\pi} \int_{-\Omega}^{\Omega} H(\omega) \exp(\mathrm{i}\omega t)\, \mathrm{d}\omega \tag{6}$$

hold, and it is possible to compute from the measured impulse response or FID, $h(t)$, the frequency response function or the complex spectrum, $H(\omega)$. This leads to pulse FT spectroscopy.[12–15] The inherent sensitivity advantage of this most important multiple channel experiment is obvious and has been well documented.

In frequency domain spectroscopy, the excitation, the evolution of the system to be investigated, and the detection, occur simultaneously [Figure 4(a)]. This limits the degrees of freedom of experimental design and the number of possible spectroscopic experiments. In pulse FT spectroscopy, the excitation process has been detached and the evolution occurs in the absence of any perturbation [Figure 4(b)]. This has great inherent advantages. First, the excitation can take arbitrary forms such as variable flip angle pulses, $(\pi - \tau - 2/\pi)$ inversion–recovery excitation, $(2/\pi - 2/\tau - \pi - 2/\tau)$ spin echo excitation, excitation by heteronuclear polarization transfer, and many more. Second, the free evolution in the absence of a rf field leads to the most faithful representation of the spectral properties of the system investigated.

3 TWO-DIMENSIONAL AND MULTIDIMENSIONAL SPECTROSCOPY

Multidimensional spectroscopy carries to the extreme the separation of the independent units of a spectroscopic experiment as shown in Figure 4(c). The three parts–excitation, evolution, and detection–are the basic building blocks of any multidimensional spectroscopy experiment.[1,16] All three parts are indispensable. The excitation process is required for the creation of a nonequilibrium state with a density operator that does not commute with the Hamiltonian and, consequently, evolves over time. The evolution period is necessary for putting into evidence the spectral features of the investigated system. Without the detection process, the experiment would remain unnoticed. The separation of evolution and detection also allows the observation of features which are not detectable directly, such as the evolution of multiple quantum coherences.

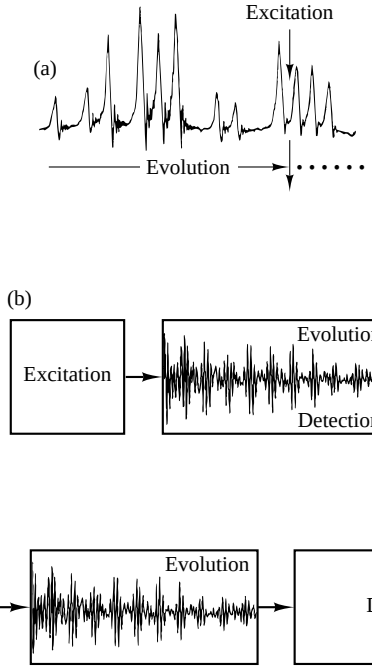

Figure 4 Three stages of sequential experimental design. (a) Simultaneous excitation, evolution, and detection in CW spectroscopy. (b) Simultaneous evolution and detection after an initial excitation in pulse FT spectroscopy. (c) Sequentially separated excitation, evolution, and detection provide the germ for multidimensional experiments

Having separated the basic building blocks, they can be tailored individually and then combined to give arbitrarily complex experiment sequences. In the following we distinguish between just two general types of building blocks: evolution blocks E, and transfer blocks T (Figure 5).

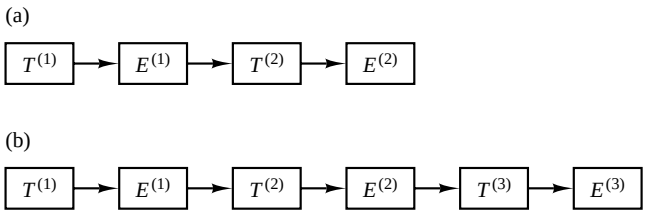

Figure 5 Prototype two- (a) and three-dimensional (b) experiments consisting of an alternating sequence of transfer and evolution blocks. Each evolution block provides a time variable that leads, after FT, to a frequency dimension in the multidimensional spectrum

3.1 The Evolution Blocks *E*

During an evolution period $E^{(r)}$, the density operator evolves under the guidance of a system Hamiltonian $\hat{\mathcal{H}}$, which may represent the unperturbed Hamiltonian $\hat{\mathcal{H}}_0$ of the system, $\hat{\mathcal{H}}_0 = \hat{\mathcal{H}}_\mathrm{I} + \hat{\mathcal{H}}_\mathrm{II} = \Sigma_k \Omega_k \hat{I}_{kz} + \Sigma_{k<l} \Sigma\, 2\pi J_{kl} \hat{I}_k \hat{I}_l$ (we address, for simplicity, only isotropic liquids). This can also be a Hamiltonian modified by a static perturbation, such as by an additional static or rf magnetic or electric field, or by a periodic or aperiodic perturbation, leading to an average Hamiltonian $\hat{\bar{\mathcal{H}}}_r$ that governs the overall time evolution of the density operator during the interval t_r:

$$\hat{\sigma}(t_r) = \exp(-\mathrm{i}\hat{\bar{\mathcal{H}}}_r t_r)\, \hat{\sigma}(t_r = 0) \exp(\mathrm{i}\hat{\bar{\mathcal{H}}}_r t_r) \tag{7}$$

Each evolution period introduces an additional time parameter t_r which can be varied systematically for putting into evidence the spectral features of the Hamiltonian $\hat{\bar{\mathcal{H}}}_r$. For simplicity, relaxation is disregarded in equation (7).

The evolution blocks provide, in general, spectral information, either in the sense of standard spectroscopy, to characterize the spectral response properties of the investigated system, or for the state identification before and after a coherence transfer step by 'frequency labeling'. The visualization of the spectral features during the period $E^{(r)}$ requires a FT of the detected response $h(\ldots, t_r, \ldots)$ as a function of t_r, thereby introducing an additional frequency variable ω_r in the spectrum $H(\ldots, \omega_r, \ldots)$. Obviously, the number of evolution periods with adjoint FT determines the dimension of the resulting multidimensional spectrum.

The last evolution period serves for detection. Usually, but not necessarily, it also provides additional spectral information in the sense of conventional FT spectroscopy. Sometimes, only a single sample value is taken during the last 'evolution' period as a measure of the preceding evolutions and transformations.

3.2 The Transfer Blocks *T*

A transfer block $T^{(r)}$ serves for the (virtually instantaneous or extended-time) transformation of the density operator, either by a unitary process

$$\hat{\sigma}'' = \hat{T}_r \hat{\sigma}' \hat{T}_r^{-1} \tag{8}$$

with the unitary transformation operator or propagator $\hat{T}_r$, or by a dissipative relaxation or chemical exchange process

$$\hat{\sigma}(\tau_r) = \hat{\sigma}(0) - \exp(-\hat{\bar{\Gamma}}_r \tau_r)\, [\hat{\sigma}(0) - \hat{\sigma}_0] \tag{9}$$

with the relaxation or chemical exchange superoperator $\hat{\bar{\Gamma}}_r$. Often, both unitary and dissipative processes occur at the same time during a transfer period $T^{(r)}$.

The transfer time τ_r of a mixing period r is usually kept constant in order to obtain a determined transfer behavior. In special situations, τ_r may be incremented in accordance with an evolution time t_s, such as in the accordion experiment.[17] In other cases, τ_r may be varied within a set of experiments, for example to visualize the build-up of transferred spin order in a cross relaxation or chemical exchange study.

A general multidimensional experiment can be conceived of as a sequence of specific T and E building blocks. Prototype two- and three-dimensional experiments are shown in Figure 5. Each multidimensional experiment starts with a T block that creates the required initial nonequilibrium state and ends with an E block for detection of the response signal. In between, an arbitrary sequence of E and T blocks can be arranged. The immediate succession of two E blocks, E_k and E_l, makes sense only when the two (average) Hamiltonians $\hat{\bar{\mathcal{H}}}_k$ and $\hat{\bar{\mathcal{H}}}_l$ are unequal. Immediately adjacent T blocks make sense only when they are distinct, effecting two different kinds of transfer or transformation or when they are subjected to unequal phase cycling procedures. Otherwise, no restrictions are imposed upon the sequence of building blocks. Two fairly complex examples, shown in Figure 10, are discussed later in this article.

4 COHERENCE TRANSFER PATHWAY SELECTION

The proper selection of coherence transfer pathways in multidimensional spectroscopy is at least as important as the proper sequence of building blocks.[1,18,19] Coherence is defined in the present context as a linear superposition of two eigenfunctions $|\phi_k\rangle$ and $|\phi_l\rangle$ of the system Hamiltonian $\hat{H}$ with the corresponding eigenvalues E_k and E_l:

$$\Psi_{kl}(t) = c_k|\phi_k\rangle \exp(\mathrm{i}E_k t/\hbar) + c_l|\phi_l\rangle \exp(\mathrm{i}E_l t/\hbar) \tag{10}$$

Coherence is reflected in the density matrix, written in the eigenbasis of the Hamiltonian, by the presence of the off-diagonal elements σ_{kl} and σ_{lk}. The contribution of coherence between states $|\phi_k\rangle$ and $|\phi_l\rangle$ to the density operator $\hat{\sigma}$ can also be written in the form

$$|k\rangle\langle l|(t) = |\phi_k\rangle\langle\phi_l| \exp[-\mathrm{i}(E_k - E_l)t/\hbar] \tag{11}$$

Coherence signifies a 'transition in progress' or the 'precession of transverse spin order' which possibly leads to transverse magnetization precessing, with the difference frequency $\omega_{kl} = (E_k - E_l)/\hbar$.

During the course of an E block, a coherence component (in the basis of the momentary Hamiltonian) retains its identity. However, the transfer blocks T transfer coherence between different components. They are therefore responsible for the coherence transfer and for the coherence-transfer pathways. Based on equation (8), for example, one can express the coherence component σ_{pq}'' after transfer in terms of the coherence components σ_{kl}' before transfer:

$$\sigma''_{pq} = \sum_{kl} (T_{pk} T_{lq}^{-1}) \sigma'_{kl} \tag{12}$$

assuming equal Hamiltonians before and after the transfer.

Most magnetic resonance experiments are performed under high magnetic field conditions where the magnetic quantum number M_k, defined as an eigenvalue of $\hat{F}_z$, is a good quantum number:

$$[\hat{\mathcal{H}}_0, \hat{F}_z] = 0 \tag{13}$$

and

$$\hat{F}_z|k\rangle = M_k|k\rangle \tag{14}$$

with $\hat{F}_z = \Sigma_p \hat{I}_{pz}$ where the summation p extends over all spins I_p of the system. Often, the average Hamiltonians $\hat{\bar{\mathcal{H}}}_k$ of the various evolution periods E_k also commute with $\hat{F}_z$,

$$[\hat{\bar{\mathcal{H}}}_k, \hat{F}_z] = 0 \tag{15}$$

and the corresponding coherences $|k\rangle\langle l|$ can be characterized by 'good' magnetic quantum numbers p_{kl}:

$$[|k\rangle\langle l|, \hat{F}_z] = p_{kl}|k\rangle\langle l| \tag{16}$$

with

$$p_{kl} = M_k - M_l \tag{17}$$

Based on the quantum number p_{kl}, coherences are classified in coherence orders with zero quantum coherences ($p_{kl} = 0$), ± 1 quantum coherences ($p_{kl} = \pm 1$), ± 2 quantum coherences ($p_{kl} = \pm 2$), etc.

The sequence of coherence orders that appears over the course of time is characteristic of the behavior of a multidimensional spectroscopy experiment. Several experiments involve the same pulse sequence and differ only in the sequence of appearance of the coherence orders. For example, relayed COSY, multiple quantum filtered COSY, and NOESY all use a sequence of three $\pi/2$ pulses, but select different coherence transfer pathways. It is thus necessary to provide a means for selecting coherence transfer pathways during the course of a pulse experiment.

Two general procedures are known for the selection of coherence orders. The first one is based on the transformation properties of coherences under z rotations.[20] With equation (16), one finds that a z rotation by the angle ϕ multiplies a coherence $|k\rangle\langle l|$ by a phase factor:

$$\exp(-\mathrm{i}\phi\hat{F}_z)\,|k\rangle\langle l|\exp(\mathrm{i}\phi\hat{F}_z) = \exp(-\mathrm{i}p_{kl}\phi)\,|k\rangle\langle l| \tag{18}$$

Let us assume that a transfer block T in an experiment is phase shifted by incrementing the phase of the involved rf pulses by ϕ. The new propagator $\hat{T}_\phi$ can then be expressed as

$$\hat{T}_\phi = \exp(-\mathrm{i}\phi\hat{F}_z)\,\hat{T}\exp(\mathrm{i}\phi\hat{F}_z) \tag{19}$$

i.e. by two phase-shifting operations bracketing the original propagator.

We assume a general coherence transfer

$$\hat{T}|k\rangle\langle l|\hat{T}^{-1} = \sum_{m,n} a_{mn}|m\rangle\langle n| \tag{20}$$

and apply the phase shift ϕ:

$$\hat{T}_\phi|k\rangle\langle l|\hat{T}_\phi^{-1} = \sum_{m,n} a_{mn}|m\rangle\langle n|\exp[-\mathrm{i}(p_{mn} - p_{kl})\phi] \tag{21}$$

In order to select the transfers with a specific change Δp in coherence order, it is possible to take advantage of the orthogonality of the Fourier series and to perform a series of N experiments with the phases

$$\phi_j = j2\pi/N \tag{22}$$

and to form a weighted linear combination of the results:

$$\begin{aligned}\sum_{j=0}^{N-1}\exp(\mathrm{i}\Delta p\phi_j)\,\hat{T}_{\phi_j}|k\rangle\langle l|\hat{T}_{\phi_j}^{-1} &= \sum_{m,n} a_{mn}|m\rangle\langle n|\sum_{j=0}^{N-1}\exp \\ &\quad\times[-\mathrm{i}(p_{mn} - p_{kl} - \Delta p)\phi_j] \\ &= \sum_{m,n} a_{mn}|m\rangle\langle n|N\sum_{q=-\infty}^{\infty} \\ &\quad\times\delta_{p_{mn}-p_{kl},\Delta p+qN}\end{aligned} \tag{23}$$

The sum over q represents the usual aliasing problem of Fourier series which renders indistinguishable coherences that differ in their order by qN. If N is selected to be sufficiently large, the aliased higher coherence orders can be disregarded, and equation (23) then expresses a unique selection of coherence transfer with $p_{mn} - p_{kl} = \Delta p$, as desired.

Equation (23) is the foundation of phase cycling procedures where the linear combination of N experiments selects a predetermined value Δp. Provided that the initial coherence order p_{kl} is known, it is also possible in this manner to select a definite final value p_{mn}. The most convenient procedure for selecting the coherence order at a particular instant in a pulse experiment is to apply a phase cycle to all preceding pulses, knowing that the initial state of the spin system had coherence order $p_{kl} = 0$. Often, several independent phase cycles applied to different pulses or pulse sequences are required to select the desired coherence transfer pathway in a particular experimental situation.[1,19] The pathways for a triple quantum filtered COSY experiment, shown in Figure 6, serve as an example.

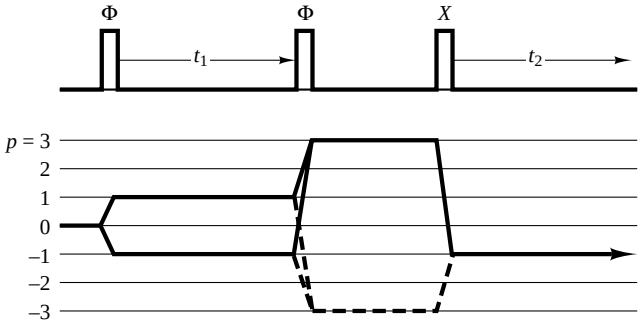

Figure 6 Coherence transfer pathways in three quantum filtered COSY. A six-step phase cycle ($\phi = k\pi/3$, $k = 0, \ldots, 5$) of the first two pulses selects a triple quantum coherence which is converted by the third pulse to a $p = -1$ coherence that is selected and measured by quadrature phase detection. To obtain pure phase peak shapes, it is necessary to retain the $p = \pm 1$ coherence during the evolution period t_1. To distinguish between positive and negative ω_1 frequencies, four-step time proportional phase incrementation (TPPI)[21] is applied to all three pulses

A second procedure for coherence transfer pathway selection (often called 'gradient-enhanced spectroscopy') exploits the different sensitivity of coherence orders to magnetic field inhomogeneity pulses.[22–24] A spatially inhomogeneous magnetic field with the gradient $\boldsymbol{g}_r$ and the local Zeeman frequency deviation at coordinate $\boldsymbol{x}$,

$$\Delta\omega_r(\boldsymbol{x}) = \boldsymbol{g}_r \cdot \boldsymbol{x} \tag{24}$$

applied for a time τ_j to a coherence $|k\rangle\langle l|$, leads to a phase distribution according to

$$\begin{aligned}&\exp(-\mathrm{i}\boldsymbol{g}_r \cdot \boldsymbol{x}\hat{F}_z\tau_r)\,|k\rangle\langle l|\exp(\mathrm{i}\boldsymbol{g}_r \cdot \boldsymbol{x}\hat{F}_z\tau_r)\\ &\quad = |k\rangle\langle l|\exp(-\mathrm{i}p_{kl}\boldsymbol{g}_r \cdot \boldsymbol{x}\tau_r)\end{aligned} \tag{25}$$

Obviously the phase dispersion is weighted by the coherence order p_{kl}. The higher the order of the coherence, the larger is the resulting spread in the phase distribution (Figure 7).

A cumulative dephasing $\phi(\boldsymbol{x})$ occurs during the course of a sequence of coherence transfers with the coherence orders $\{p_r\}$ (p_r standing for p_{kl}) when a sequence of field gradient pulses with the gradients $\boldsymbol{g}_r$ is applied for the time periods τ_r:

$$\phi(\boldsymbol{x}) = \sum_r p_r \boldsymbol{g}_r \cdot \boldsymbol{x}\tau_r \tag{26}$$

Whenever $\phi(\boldsymbol{x}) \equiv 0$, the dephasing will be fully refocused and a coherence transfer echo occurs.

In gradient-enhanced spectroscopy, a sequence of gradient pulses is selected such that only for the chosen coherence transfer pathway $\{p_1, p_2, \ldots, p_n\}$ does an echo occur at the instant of measurement. This requires that

$$\sum_{r=1}^{n} p_r \boldsymbol{g}_r \tau_r = 0 \tag{27}$$

while for all other sequences of coherence orders this expression should remain different from zero. If such a sequence of values $\{\boldsymbol{g}_r\tau_r\}$ is found, the goal has been reached and the coherence transfer pathway $\{p_1, p_2, \ldots, p_n\}$ has been uniquely selected.

Three quantum filtered COSY can serve again as an example (Figure 7). The selection of coherence order is made before and after the third pulse. The $p = 3$ quantum defocusing during the first gradient pulse of duration τ_g occurs three times as fast as for the $p = 1$ quantum coherence. The refocusing time of a coherence $p = -1$ is proportional to the degree of previous dephasing. Only the initial three quantum coherence is without phase dispersion after the second gradient pulse of duration $3\tau_g$.

Pure-phase peak shapes are obtained with the experiment shown in Figure 7, as both coherence orders ($p = \pm 1$) during the evolution period are retained. For the distinction of positive and negative ω_2 frequencies quadrature phase detection is needed, while time proportional phase incrementation (TPPI)[21] allows the distinction between positive and negative ω_1 frequencies. This gradient-enhanced experiment leads to a reduction in the sensitivity by a factor 2 compared with an experiment with coherence order selection by phase cycling, because only half of the pathways allowed in Figure 6 are retained in Figure 7.

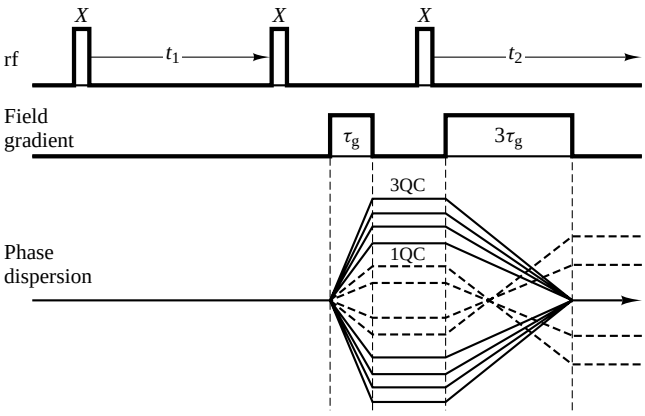

Figure 7 Coherence transfer pathway selection in three quantum filtered COSY by magnetic field gradient pulses (gradient-enhanced spectroscopy). The phase dispersion initiated by the first gradient pulse of duration τ_g is shown for $p = +1$ (----) and $p = +3$ quantum coherence (—). The refocusing time for the observed $p = -1$ quantum coherence depends on the amount of phase dispersion acquired. The former three quantum coherence components fully refocus at the end of the second gradient pulse of duration $3\tau_g$. Only the pathway $p = +3 \rightarrow p = -1$ is selected (solid lines in Figure 6), while the pathway $p = -3 \rightarrow p = -1$ (broken lines in Figure 6) is suppressed. A TPPI phase cycle on all pulses is required for the distinction of positive and negative ω_1 frequencies

5 BUILDING BLOCKS FOR MULTIDIMENSIONAL NMR EXPERIMENTS

The building blocks consist of composites of free precession periods and periods with applied rf fields. In special cases, switched dc magnetic or electric fields, temperature and pressure jumps, optical irradiation, and variable angle sample spinning may also be involved. Often, the time dependence introduced by sample spinning has to be taken explicitly into account, and then synchronization of the rf pulses and of the sampling process with the sample rotation has to be considered.

It is usually possible to concentrate, at first, on the pulse sequence, irrespective of whether the selection of the coherence transfer pathways is achieved by phase cycling or by field gradient pulses. Sometimes, however, the coherence transfer pathway selection scheme is an integral part of the building blocks, and affects the pulse sequence design directly.

Both the E (evolution) and T (transfer) blocks can be characterized by an average Hamiltonian $\hat{\mathcal{H}}_r$ and a corresponding relaxation or chemical exchange superoperator $\hat{\hat{\gamma}}_r$ which together determine the development of the density operator of the spin system within the building blocks. The only important difference between the E and T blocks is that the time parameter t_r in an $E^{(r)}$ block is used as a time variable which is incremented from experiment to experiment within a multidimensional experiment sequence, while the time parameter τ_r in a $T^{(r)}$ block is kept constant over the entire

experiment. There are also cases where even this distinction breaks down and where within a $T^{(r)}$ block a variable time parameter is used, for example for the suppression of undesired terms, such as zero quantum coherence in cross relaxation periods.[25,26] In the following, some simple building blocks are briefly discussed.

5.1 Rotations $\hat{T}^{(r)} = \exp\{-i\beta\hat{F}_q\}$

The index q indicates the rotation axis which may be $q = x, y, z$ or may represent an arbitrarily inclined axis. Rotations are the most frequently used transfer-block elements. The first transfer block $\hat{T}^{(1)}$ in a sequence, serving as a 'preparation period', often uses just a single $\pi/2$ pulse for the creation of coherence. In correlation experiments,[1,6,16] the 'mixing period' consists of a transfer block with one or several rf pulses. Usually, the pulses are considered to act instantaneously, so that relaxation can be neglected. Often the pulses are 'nonselective', in the sense that they affect all (homonuclear) spins equally.

In special cases, rf pulses with amplitude ω_1 and a variable rotation angle $\beta = \omega_1 t_r$ may also represent an $E^{(r)}$ block, for example in an experiment for measuring the spatial rf field distribution, such as in rotating frame imaging.[27]

5.2 Unperturbed Hamiltonian $\hat{\tilde{\mathcal{H}}}_r = \mathcal{H}_0$

In many basic multidimensional experiments, all $E^{(r)}$ blocks use $\hat{\tilde{\mathcal{H}}}_r = \mathcal{H}_0$. The frequency spread is then determined in all dimensions by the natural NMR spectrum, and the cross peaks map the transfer matrices of the T blocks in the eigenbasis of the Hamiltonian superoperator $\hat{\hat{\mathcal{H}}}_0$, the eigenvalues of which are the corresponding transition frequencies. Multidimensional spectra possess specific symmetry properties,[28,29] but these are lost when the average Hamiltonians of the different $E^{(r)}$ blocks are unequal.

5.3 Spin Coupling Hamiltonian $\hat{\tilde{\mathcal{H}}}_r = \mathcal{H}_{\mathrm{II}}$

In some experiments, it is desirable to suppress the Zeeman interaction and to retain exclusively the scalar spin–spin coupling. In the case of weak coupling, this can be achieved by a π refocusing pulse applied in the center of the building block (Figure 8), which leads to

$$\hat{\tilde{\mathcal{H}}}_r = \hat{\mathcal{H}}_{\mathrm{II}} = \sum_{k,l} 2\pi J_{kl} \hat{I}_{kz} \hat{I}_{lz} \tag{28}$$

It should be noted that the effect of the π pulse on the density operator remains, and that the following equivalence holds:

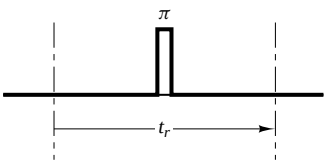

Figure 8 A building block with refocused chemical shift evolution obtained by the application of a nonselective π pulse in the center

$$\xrightarrow{\hat{\mathcal{H}}_0 t_r/2} \xrightarrow{(\pi)_x} \xrightarrow{\hat{\mathcal{H}}_0 t_r/2} \equiv \xrightarrow{\hat{\mathcal{H}}_{\mathrm{II}} t_r} \xrightarrow{(\pi)_x} \tag{29}$$

Here and in the following we use the arrow notation introduced by Sørensen et al.[30] The term on top of the arrow indicates the phase operator in the exponent of a propagator, e.g. $\xrightarrow{\hat{\mathcal{H}}_0 t_r/2}$ is equivalent to the propagator $\exp\{-i\hat{\mathcal{H}}_0 t_r/2\}$, and $\longrightarrow^{(\pi)_x}$ is equivalent to $\exp\{-i\pi\hat{F}_x\}$. Obviously, the effects of the $(\pi)_x$ pulse in equation (29) can be compensated for by appending another $(\pi)_x$ pulse at the end of the building block. Often this is irrelevant. The building block shown in Figure 8 is used as the evolution block in J-resolved spectroscopy.[31] It is also used in relayed coherence transfer,[32] and in multiple quantum spectroscopy.[33] In the latter two cases, the precession period is sandwiched between two $(\pi/2)_x$ pulses, which gives rise to the average Hamiltonian:

$$\hat{\tilde{\mathcal{H}}}_r = \sum_{k<l} 2\pi J_{kl} \hat{I}_{ky} \hat{I}_{ly} \tag{30}$$

Here, the three pulses compensate each other fully, adding up to 2π, and a pure bilinear rotation Hamiltonian remains.

5.4 Zeeman Hamiltonian $\hat{\tilde{\mathcal{H}}}_r = \mathcal{H}_{\mathrm{I}}$

With the simplicity of tailoring a pure spin-coupling Hamiltonian $\hat{\tilde{\mathcal{H}}}_r = \mathcal{H}_{\mathrm{II}}$ in mind, it appears to be equally easy to obtain a pure Zeeman Hamiltonian $\hat{\tilde{\mathcal{H}}}_r = \mathcal{H}_{\mathrm{I}}$. However, in general, this is a difficult if not impossible task, as it requires the selective suppression of $\hat{\mathcal{H}}_{\mathrm{II}}$. The latter is, however, as a scalar interaction, invariant under any rotation in the three-dimensional space, and nonselective pulses or rf fields cannot be used to manipulate $\hat{\mathcal{H}}_{\mathrm{II}}$. This is equivalent to the statement that homonuclear broadband decoupling is not feasible by a direct tailoring of the average Hamiltonian $\hat{\tilde{\mathcal{H}}}_r$. Other, less direct means have to be used to obtain $\hat{\tilde{\mathcal{H}}}_r = \mathcal{H}_{\mathrm{I}}$.

A first possibility is to use isotopic dilution, retaining in the average only one spin of a particular kind per molecule. This eliminates the homonuclear spin interactions, and the heteronuclear couplings can be rendered ineffective by standard CW or pulsed heteronuclear spin decoupling.[34,35] It is also possible to eliminate homonuclear couplings by a homonuclear decoupling scheme that uses selective irradiation of the coupling partners.

Another possible way to eliminate heteronuclear spin splittings is to apply an isotope-selective π pulse to the coupling partners at the center of an evolution interval $E^{(r)}$.[36,37] This interchanges coherence components within the multiplets and initiates refocusing of the heteronuclear multiplet evolution. Obviously this procedure cannot be applied during the detection period, because for each sampling point the π pulse would have to be positioned differently.

Sometimes, 'constant time evolution' is applied for homonuclear spin decoupling,[38] as illustrated in Figure 9. Keeping the evolution time T_r constant and varying in a systematic manner the position t_r' of a nonselective π pulse positioned within this interval, it is possible to define the variable $t_r = T_r - 2t_r'$ which governs exclusively the chemical shift evolution:

$$\hat{\sigma}(t=0) \xrightarrow{\hat{\mathcal{H}}_{\mathrm{II}} T_r} \xrightarrow{\pi_x} \xrightarrow{\hat{\mathcal{H}}_{\mathrm{I}} t_r} \hat{\sigma}(t_r, T_r) \tag{31}$$

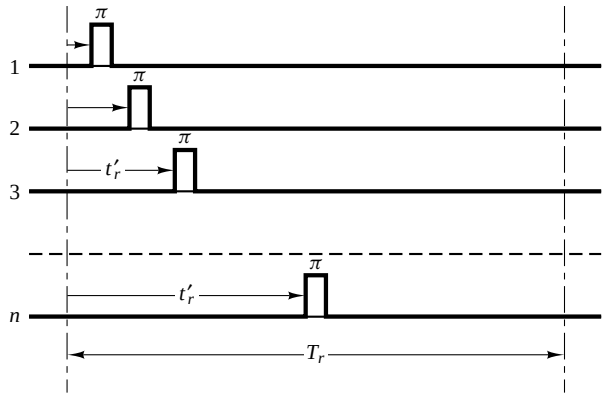

Figure 9 Constant time experiment for homonuclear spin decoupling. Instead of varying the length of an evolution period t_r, the total evolution time T_r is kept constant while a π pulse is shifted from $t_r' = 0$ to $t_r' = T_r/2$. The time variable t_r is then defined by $t_r = T_r - 2t_r'$

Obviously, the effect of $\hat{\mathcal{H}}_{\mathrm{II}}$ is not fully eliminated, although it no longer influences the time evolution in t_r. However, it contributes a T_r-dependent transformation that leads to J coupling-dependent phase shifts. The occurrence of these phase shifts usually requires the plotting of magnitude spectra.

In solids where the scalar spin–spin interaction is negligible in comparison to the much stronger magnetic dipolar interaction, homonuclear decoupling is more straightforward. Due to the second rank tensor character of the dipolar interaction, it is possible to achieve homonuclear spin decoupling by means of multiple pulse sequences[39–41] and by high speed magic angle sample spinning.[42] Multiple pulse sequences normally simultaneously reduce the chemical shift spread by scaling,[39–41] while magic angle sample spinning also eliminates the chemical shielding anisotropy.[43,44]

There is a considerable number of further other building blocks in the arsenal of the advanced NMR spectroscopist. Among others, these include evolution blocks for scaling interactions,[45,46] transfer blocks for cross polarization,[47,48] blocks for various types of coherence transfer,[49–51] and transfer blocks for the creation of multiple quantum coherence.[16,32,33] It is not the purpose of this article to describe these blocks here. Rather, we discuss below a specific example of a reasonably complex three-dimensional experiment.

6 EXAMPLE OF A MULTIDIMENSIONAL NMR EXPERIMENT: ^{15}N–^{15}N CHEMICAL SHIFT CORRELATION FOR THE SEQUENTIAL ASSIGNMENT IN PROTEINS

(Co-authors: Serge Boentges and Jürgen M. Schmidt)

The features of multidimensional NMR are here exemplified by a novel experiment[52] designed for the assignment of backbone resonances in proteins.[53] A prerequisite is a ^{15}N-labeled protein sample. The three-dimensional experiments described here, called XTONOX and XNOTOX, generate a map correlating ^{15}N resonances in sequentially adjacent or spatially neighboring amino acid residues. The two-dimensional map is spread in a third dimension by the resonances of directly bonded NH protons which also serve for high sensitivity detection.

The coherence transfer from $^{15}\mathrm{N}_i$ to $^{15}\mathrm{N}_k$ is established via a proton–proton TOCSY–NOESY (in the XTONOX experiment) or a NOESY–TOCSY relay step (in the XNOTOX experiment) bracketed by two INEPT transfers.[49] The two-step transfers are effective for typical β-sheet secondary structural elements, while in α-helices a direct proton–proton NOE transfer is more efficient. This leads to the following sequences of transfers for XTONOX:

$$^{15}\mathrm{N}_i \xrightarrow{\text{INEPT}} \mathrm{NH}_i \xrightarrow{\text{TOCSY}} \mathrm{C}_\alpha\mathrm{H}_i \xrightarrow{\text{NOESY}} \mathrm{NH}_{i+1} \xrightarrow{\text{INEPT}} {}^{15}\mathrm{N}_{i+1} \text{ for } \beta\text{-sheets}$$

and

$$^{15}\mathrm{N}_i \xrightarrow{\text{INEPT}} \mathrm{NH}_i \xrightarrow{\text{NOESY}} \mathrm{NH}_{i\pm1} \xrightarrow{\text{INEPT}} {}^{15}\mathrm{N}_{i\pm1} \text{ for } \alpha\text{-helices}$$

For XNOTOX the transfer pathways are:

$$^{15}\mathrm{N}_i \xrightarrow{\text{INEPT}} \mathrm{NH}_i \xrightarrow{\text{NOESY}} \mathrm{C}_\alpha\mathrm{H}_{i-1} \xrightarrow{\text{TOCSY}} \mathrm{NH}_{i-1} \xrightarrow{\text{INEPT}} {}^{15}\mathrm{N}_{i-1} \text{ for } \beta\text{-sheets}$$

and

$$^{15}\mathrm{N}_i \xrightarrow{\text{INEPT}} \mathrm{NH}_i \xrightarrow{\text{NOESY}} \mathrm{NH}_{i\pm1} \xrightarrow{\text{INEPT}} {}^{15}\mathrm{N}_{i\pm1} \text{ for } \alpha\text{-helices}$$

Both experiments start and end with an additional INEPT transfer to allow the usage and detection of proton magnetization for sensitivity enhancement. The two resulting pulse sequences are shown in Figure 10.

We will now analyze the XTONOX sequence in more detail. As can be seen from Figure 10, the sequence consists of seven transfer periods $T^{(1)}, \ldots, T^{(7)}$ and three evolution periods $E^{(1)}$, $E^{(2)}$, and $E^{(3)}$. The initial transfer period $T^{(1)}$ incorporates a selective saturation sequence applied to the water resonance for reducing the intensity of the disturbing water signal. For the other protons, transverse magnetization is created by a $(\pi/2)_y^I$ pulse. We concentrate here on the ^{15}NH subsystem and use I for the proton spin and S for the ^{15}N spin. Then

$$\hat{I}_z \xrightarrow{T^{(1)}} \hat{I}_x \tag{32}$$

The transfer period $T^{(2)}$ consists of a standard INEPT[49] transfer from ^{1}H to ^{15}N, for enhancing the magnetization of the latter spin. The sequence of operations can be written in the form

$$\hat{\sigma}' \xrightarrow{2\pi J_{IS}\hat{I}_z\hat{S}_z\Delta} \xrightarrow{(\pi/2)_x^{I+S}} \hat{\sigma}'' \tag{33}$$

The pair of π pulses in the center of $T^{(2)}$ refocuses the chemical shift effects, as described before. The remaining phase inversion effect, which is apparent in equation (29), has been integrated into the phase of the $(\pi/2)_x^{I+S}$ pulse pair

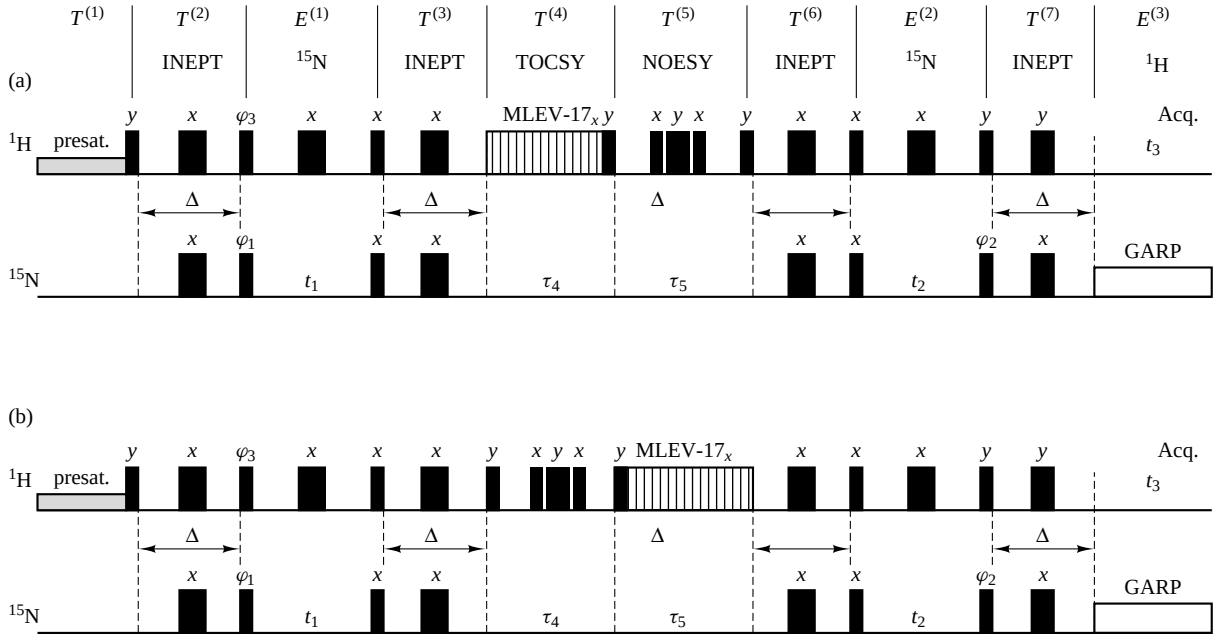

Figure 10 Pulse sequences for the XTONOX (a) and XNOTOX (b) experiments. The eight-step phase cycle used x phases with the signs (φ_1, φ_2, φ_3, acquisition): (+ + + +), (− + + −), (+ − + −), (− − + −), (+ + − +), (− + − +), (+ − − +), and (− − − −).[52] In addition, TPPI is applied to φ_1 and φ_2 to allow the distinction of positive and negative frequencies in ω_1 and ω_2

in equation (33). The transformation of equation (33) can be rewritten as

$$\hat{\sigma}'(\xrightarrow{(\pi/2)_x^{I+S}}) \xrightarrow{2\pi J_{IS}\hat{I}_y\hat{S}_y\Delta} \hat{\sigma}'' \tag{34}$$

Applying this to the result of the transfer $T^{(1)}$ [equation (32)], it is obvious that the $(\pi/2)_x^{I+S}$ pulse pair in equation (34) has no effect, and can be disregarded. The effect of $T^{(2)}$ is thus a bilinear rotation:

$$\hat{I}_x \xrightarrow{T^{(2)}} \hat{I}_x \cos(\pi J_{IS}\Delta) - 2\hat{I}_z\hat{S}_y \sin(\pi J_{IS}\Delta) \tag{35}$$

and the maximum antiphase S spin coherence $2\hat{I}_z\hat{S}_y$ is obtained for $\Delta = 1/(2J_{IS})$.

The I-spin π pulse applied in the middle of the first evolution period $E^{(1)}$ refocuses I-spin chemical shift effects, as described above, but, more importantly, also refocuses the heteronuclear J coupling effects. For the ^{15}N evolution, a pure chemical shift average Hamiltonian remains,

$$\hat{\tilde{\mathcal{H}}}^{(1)} = \Omega_S\hat{S}_z \tag{36}$$

and the ^{15}N antiphase coherence evolves as

$$2\hat{I}_z\hat{S}_y \xrightarrow{\hat{\tilde{\mathcal{H}}}^{(1)}t_1} 2\hat{I}_z(\hat{S}_y\cos\Omega_S t_1 - \hat{S}_x\sin\Omega_S t_1) \tag{37}$$

This is responsible for the frequency spread along the ω_1 axis in the three-dimensional XTONOX spectrum, and characterizes the origin spin $^{15}\mathrm{N}_i$.

The coherence transfer to spin $^{15}\mathrm{N}_{i\pm1}$ (see above) proceeds by the four transfer steps $T^{(3)}$, $T^{(4)}$, $T^{(5)}$, and $T^{(6)}$. The two INEPT steps $T^{(3)}$ and $T^{(6)}$ are fully analogous to the transfer $T^{(2)}$. The crucial processes are $T^{(4)}$ and $T^{(5)}$. The application of a CW or pulsed (e.g MLEV-17) rf field during the TOCSY period $T^{(4)}$ of duration τ_4 causes a suppression of the proton chemical shift and heteronuclear J coupling effects.[54,55] The Hamiltonian relevant for the evolution of the proton magnetization is then (expressed in a frame rotating with the rf frequency ω_{rf})

$$\hat{\tilde{\mathcal{H}}}^{(4)} = \sum_{kl} 2\pi J_{kl}\hat{\boldsymbol{I}}_k\cdot\hat{\boldsymbol{I}}_l + \omega_1\sum\hat{I}_{kx} \tag{38}$$

The first term causes isotropic mixing and a transfer of spin order between the different proton spins within one amino acid residue, while the second term with the rf amplitude ω_1 functions as a phase selection operator which selects the x phase. The most relevant transfer effected by the Hamiltonian of equation (38) is[54]

$$\begin{aligned}\hat{I}_{\mathrm{NH},x} \xrightarrow{T^{(4)}} & \tfrac{1}{2}\hat{I}_{\mathrm{NH},x}[1+\cos(2\pi J_{\mathrm{NH,C_\alpha H}}\tau_4)] \\ & +\tfrac{1}{2}\hat{I}_{\mathrm{C_\alpha H},x}[1-\cos(2\pi J_{\mathrm{NH,C_\alpha H}}\tau_4)] \\ & +(\hat{I}_{\mathrm{NH},y}\hat{I}_{\mathrm{C_\alpha H},z} - \hat{I}_{\mathrm{NH},z}\hat{I}_{\mathrm{C_\alpha H},y})\sin(2\pi J_{\mathrm{NH,C_\alpha H}}\tau_4)\end{aligned} \tag{39}$$

This leads to a transfer of the NH proton magnetization to $\mathrm{C_\alpha H}$ proton magnetization. At the same time, transfers of magnetization to the side-chain protons are also taking place.

The transfer block $T^{(5)}$ consists of a cross-relaxation period, bracketed by two $(\pi/2)_y$ pulses that convert transverse x magnetization into longitudinal z magnetization, and vice versa. During the time τ_5, the relaxation superoperator $\hat{\hat{\Gamma}}$ is acting and $T^{(5)}$ causes, among other things, a transfer

$$\begin{aligned}\hat{I}_{\mathrm{C_\alpha H}_i,x} \xrightarrow{T^{(5)}} & \hat{I}_{\mathrm{C_\alpha H}_i,x}\tfrac{1}{2}[1+\exp(-\Gamma_{\mathrm{i+1},i}\tau_5)] + \hat{I}_{\mathrm{NH}_{i+1},x} \\ & \times\tfrac{1}{2}[1-\exp(-\Gamma_{i+1,i}\tau_5)]\end{aligned} \tag{40}$$

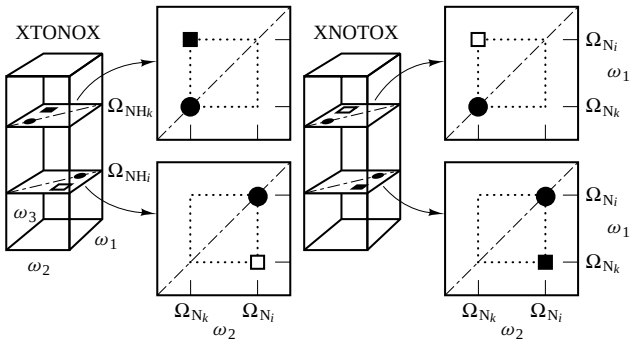

Figure 11 Schematic representation of the diagonal and cross-peak pattern in XTONOX and XNOTOX three-dimensional spectra. The 3D spectra and two representative ω_3 sections with constant Ω_{NH} frequency are shown. For β-sheet structural elements, $k = i + 1$ holds and only the black diagonal and cross peaks appear because the TOCSY–NOESY and NOESY–TOCSY transfers are unidirectional. For α-helical structural elements, $k = i \pm 1$ and all the indicated peaks can appear because here there is a one-step NOESY transfer which has no directionality. The same is true for long-range cross peaks

to a sequentially (or spatially) neighboring amino acid residue. The central composite π pulse is beneficial for the minimization of the water signal: by inversion, a recovery of the water magnetization during τ_5 is prevented.[56] The following steps ($E^{(2)}$, $T^{(7)}$, and $E^{(3)}$) proceed analogously, and do not require further comment.

A decisive advantage of the XTONOX and XNOTOX experiments for backbone assignment is the correlation of single ^{15}N resonances for each amino acid residue (except for some additional side-chain N^{15} resonances). This leads to simple, often well resolved spectra that are amenable to automated computer analysis. The additional three-dimensional spread by the NH resonances provides further enhanced resolution. The resulting three-dimensional spectrum has a characteristic appearance that is sketched in Figure 11. If we consider a particular pair $^{15}N_i$ and $^{15}N_k$, each of the planes defined by $\omega_3 = \Omega_{NH_i}$ and $\omega_3 = \Omega_{NH_k}$ contains a diagonal peak at $\omega_1 = \omega_2 = \Omega_{N_i}$ or Ω_{N_k}, respectively. For the β-sheet neighborhood and the XTONOX experiment, only the plane $\omega_3 = \Omega_{NH_k}$ contains a cross peak at $\omega_1 = \Omega_{N_i}$, $\omega_2 = \Omega_{N_k}$ when $k = i + 1$. No corresponding cross peak is found in the plane $\omega_3 = \Omega_{NH_i}$. However, the cross peak $\omega_1 = \Omega_{N_k}$, $\omega_2 = \Omega_{N_i}$ is found in the plane $\omega_1 = \Omega_{N_k}$, $\omega_2 = \Omega_{N_i}$ in the XNOTOX spectrum. For an α-helix neighborhood, each of the $\omega_3 = \Omega_{NH_k}$ planes for $k = i \pm 1$ contains a cross peak. This allows the distinction of secondary structural elements.

The XTONOX/XNOTOX experiment has been applied to ^{15}N-labeled human ubiquitin (Figure 12). A sizable fraction of the amino acid sequence could be determined without problems by using a computer analysis procedure.[52] Two

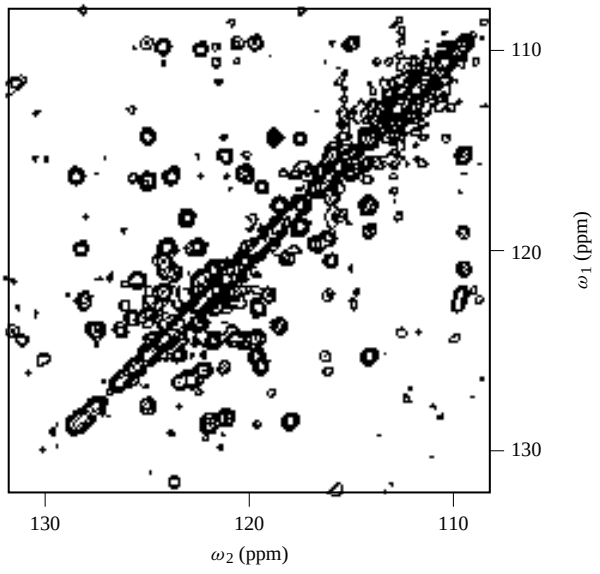

Figure 12 Skyline projection along ω_3 of a 500 MHz XNOTOX three-dimensional spectrum of a 2.65 mM solution of 99% ^{15}N-labeled human ubiquitin in 95% H_2O, 5% D_2O.[51] The spectrum shows the ^{15}N–^{15}N connectivities essential for the sequential assignment given in Figure 13

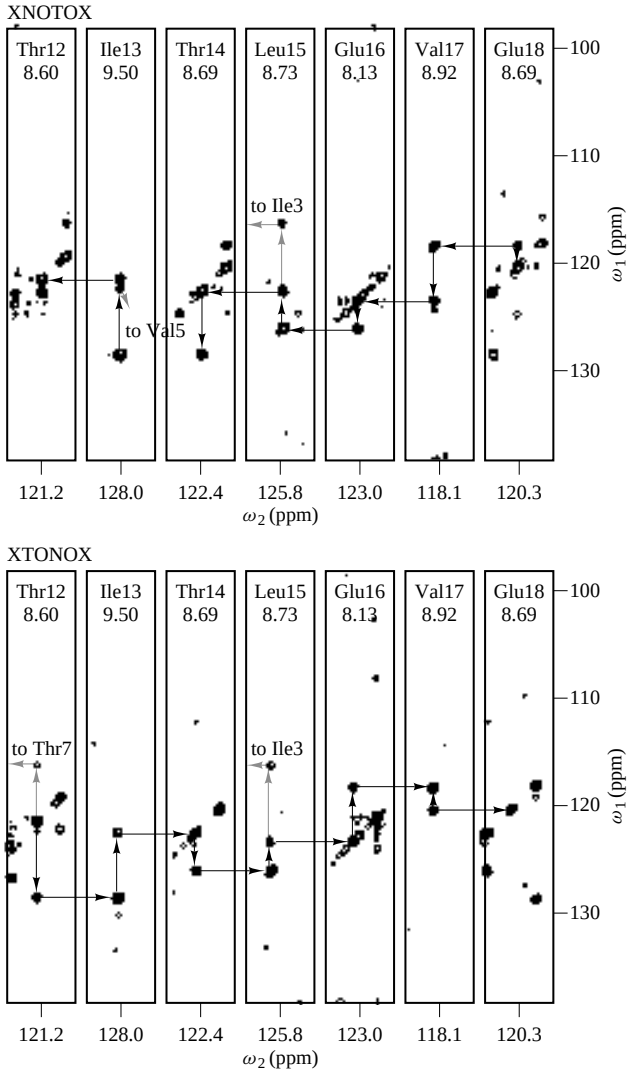

Figure 13 Sequential assignment in ^{15}N-labeled human ubiquitin based on (ω_1, ω_2) sections from 500 MHz three-dimensional XTONOX and XNOTOX ^{15}N spectra. Assignments are indicated for the second strand of the β-sheet region between Thr12 and Glu18. Additional long-range cross peaks appear for Leu15–Ile3, Ile–Val5, and Thr12–Thr7 which are due to NOE transfer only, and confirm the spatial vicinity of a further β-strand with the residues 1–7[57]

equivalent stretches of assignment steps based on two-dimensional sections from XTONOX and XNOTOX spectra are shown in Figure 13.

Naturally, the sequential assignment is interrupted by proline residues which lack the NH proton required for observation, and ambiguities occur when unidentified long-range correlations between sequentially remote but spatially neighboring residues appear. In these cases, it is necessary to make recourse to a standard primary sequence determination and to an identification of the $^{15}N_k$ and NH_k resonances by the characteristic side-chain resonances. Due to the TOCSY step in the two experiments, the required cross peaks to the side chains are also contained in the XTONOX and XNOTOX spectra.

7 OUTLOOK

Multidimensional spectroscopy is more than just a powerful assignment technique. It opens up a new world of experimental design. It is not so much the display of multidimensional maps but rather the type of underlying time domain experiments which is novel. The possibility of introducing several time variables in a complex experimental procedure provides a multitude of approaches that can be adapted to almost any conceivable practical situation.

Other articles in this Encyclopedia should be consulted in order to obtain a proper survey of the pulse sequences and multidimensional experiments available today.

8 RELATED ARTICLES

COSY Spectra: Quantitative Analysis; COSY Two-Dimensional Experiments; Double Quantum Coherence; Fourier Transform Spectroscopy; Homonuclear Three-Dimensional NMR of Biomolecules; Liouville Equation of Motion; Multiple Quantum Coherence Imaging; NOESY; Nuclear Overhauser Effect; Polarization Transfer Experiments via Scalar Coupling in Liquids; Relayed Coherence Transfer Experiments; ROESY; Selective NOESY; Stochastic Excitation; Three-Dimensional HMQC-NOESY, NOESY-HMQC, and NOESY-HSQC; Three- and Four-Dimensional Heteronuclear Magnetic Resonance; Two-Dimensional Carbon–Heteroelement Correlation; Two-Dimensional J-Resolved Spectroscopy; Two-Dimensional Methods of Monitoring Exchange; Two-Dimensional NMR of Molecules Oriented in Liquid Crystalline Phases; Two-Dimensional Powder Correlation Methods.

9 REFERENCES

1. R. R. Ernst, G. Bodenhausen, and A. Wokaun, *Principles of Nuclear Magnetic Resonance in One and Two Dimensions*, Clarendon, Oxford, 1987.
2. A. Bax, *Two-Dimensional NMR in Liquids*, Delft University/Reidel, Dortrecht, 1982.
3. Attur-ur Rahman, *Nuclear Magnetic Resonance, Basic Principles*, Springer, New York, 1986; N. Chandrakumar and S. Subramanian, *Modern Techniques in High Resolution FT-NMR*, Springer, New York, 1987; H. Friebolin, *Ein-und zweidimensionale NMR-Spektroskopie*, VCH, Weinheim, 1988; *Basic One- and Two-Dimensional NMR*, VCH, Weinheim, 1991; G. E. Martin and A. S. Zekter, *Two-Dimensional NMR Methods for Establishing Molecular Connectivity*, VCH, Weinheim, 1988; J. Schraml and J. M. Bellama, *Two-Dimensional NMR Spectroscopy*, Wiley Interscience, New York, 1988; W. S. Brey (ed.), *Pulse Methods in 1D and 2D Liquid-Phase NMR*, Academic, New York, 1988.
4. M. Goldman, *Quantum Description of High-Resolution NMR in Liquids*, Clarendon, Oxford, 1988; G. D. Mateescu and A. Valeriu, *2D NMR, Density Matrix and Product Operator Treatment*, PTR/Prentice Hall, Englewood Cliffs, NJ, 1993.
5. E. L. Hahn, *Phys. Rev.*, 1950, **80**, 580.
6. J. Jeener, *Ampère Summer School*, Basko Polje, Yugoslavia, 1971, unpublished.
7. T. Sleator, E. L. Hahn, C. Hilbert, and J. Clarke, *Phys. Rev. Lett.*, 1985, **55**, 1742; *Phys. Rev., B*, 1987, **36**, 1969.
8. M. A. McCoy and R. R. Ernst, *Chem. Phys. Lett.*, 1989, **159**, 587.
9. W. A. Anderson and R. Freeman, *J. Chem. Phys.*, 1962, **37**, 85.
10. R. Freeman and W. A. Anderson, *J. Chem. Phys.*, 1962, **37**, 2053.
11. R. A. Hoffman and S. Forsén, *Prog. NMR Spectrosc.*, 1966, **1**, 15.
12. R. R. Ernst and W. A. Anderson, *Rev. Sci. Instrum.*, 1966, **37**, 93.
13. R. R. Ernst, *Adv. Magn. Reson.*, 1966, **2**, 1.
14. T. C. Farrar and E. D. Becker, *Pulse and Fourier Transform NMR*, Academic, New York, 1971.
15. D. Shaw, *Fourier Transform NMR Spectroscopy*, 2nd edn, Elsevier, Amsterdam, 1984.
16. W. P. Aue, E. Bartholdi, and R. R. Ernst, *J. Chem. Phys.*, 1976, **64**, 2229.
17. G. Bodenhausen and R. R. Ernst, *J. Magn. Reson.*, 1981, **45**, 367.
18. A. Bain, *J. Magn. Reson.*, 1984, **56**, 418.
19. G. Bodenhausen, H. Kogler, and R. R. Ernst, *J. Magn. Reson.*, 1984, **58**, 370.
20. A. Wokaun and R. R. Ernst, *Chem. Phys. Lett.*, 1977, **52**, 407.
21. G. Drobny, A. Pines, S. Sinton, D. Weitekamp, and D. Wemmer, *Faraday Div. Chem. Soc. Symp.*, 1979, **13**, 49; G. Bodenhausen, R. L. Vold, and R. R. Vold, *J. Magn. Reson.*, 1980, **37**, 93.
22. A. A. Maudsley, A. Wokaun, and R. R. Ernst, *Chem. Phys. Lett.*, 1978, **55**, 9.
23. R. E. Hurd, *J. Magn. Reson.*, 1990, **87**, 422.
24. J. Ruiz-Cabello, G. W. Vuister, C. T. W. Moonen, P. Van Gelderen, J. S. Cohen, and P. C. M. Van Zijl, *J. Magn. Reson.*, 1992, **100**, 282.
25. S. Macura, Y. Huang, D. Suter, and R. R. Ernst, *J. Magn. Reson.*, 1981, **43**, 259.
26. S. Macura, K. Wüthrich, and R. R. Ernst, *J. Magn. Reson.*, 1982, **46**, 269.
27. D. I. Hoult, *J. Magn. Reson.*, 1979, **33**, 183.
28. C. Griesinger, C. Gemperle, O. W. Sørensen, and R. R. Ernst, *Mol. Phys.*, 1987, **62**, 295.
29. S. Boentges, B. U. Meier, C. Griesinger, and R. R. Ernst, *J. Magn. Reson.*, 1989, **85**, 337.
30. O. W. Sørensen, G. W. Eich, M. H. Levitt, G. Bodenhausen, and R. R. Ernst, *Progr. NMR Spectrosc.*, 1983, **16**, 163.
31. W. P. Aue, J. Karhan, and R. R. Ernst, *J. Chem. Phys.*, 1976, **64**, 4226.
32. G. Eich, G. Bodenhausen, and R. R. Ernst, *J. Am. Chem. Soc.*, 1982, **104**, 3731.

33. S. Vega, T. W. Shattuck, and A. Pines, *Phys. Rev. Lett.*, 1976, **37**, 43; L. Braunschweiler, G. Bodenhausen, and R. R. Ernst, *Mol. Phys.*, 1983, **48**, 535.
34. R. R. Ernst, *J. Chem. Phys.*, 1966, **45**, 3845.
35. M. H. Levitt, R. Freeman, and T. Frenkiel, *Adv. Magn. Reson.*, 1983, **11**, 47.
36. A. Kumar and R. R. Ernst, *J. Magn. Reson.*, 1976, **24**, 425.
37. L. Müller, A. Kumar, and R. R. Ernst, *J. Magn. Reson.*, 1977, **25**, 383.
38. A. Bax and R. Freeman, *J. Magn. Reson.*, 1981, **44**, 542.
39. J. S. Waugh, L. M. Huber, and U. Haeberlen, *Phys. Rev. Lett.*, 1968, **20**, 180.
40. U. Haeberlen, *High-Resolution NMR in Solids* (*Adv. Magn. Reson.*, Suppl. 1), Academic Press, New York, 1976.
41. M. Mehring, *High Resolution NMR Spectroscopy in Solids*, 2nd edn., Springer, Berlin, 1983.
42. E. R. Andrew, *Progr. NMR Spectrosc.*, 1971, **8**, 1.
43. C. A. Fyfe, *Solid State NMR for Chemists*, CFC, Guelph, Ontario, 1983.
44. B. C. Gerstein and C. R. Dybowski, *Transient Techniques in NMR of Solids*, Academic, New York, 1985.
45. J. D. Ellett and J. S. Waugh, *J. Chem. Phys.*, 1969, **51**, 2851.
46. W. P. Aue and R. R. Ernst, *J. Magn. Reson.*, 1978, **31**, 533.
47. S. R. Hartmann and E. L. Hahn, *Phys. Rev.*, 1962, **128**, 2042.
48. A. Pines, M. G. Gibby, and J. S. Waugh, *J. Chem. Phys.*, 1973, **59**, 569.
49. G. A. Morris and R. Freeman, *J. Am. Chem. Soc.*, 1979, **101**, 760.
50. D. P. Burum and R. R. Ernst, *J. Magn. Reson.*, 1980, **39**, 163.
51. D. M. Doddrell, D. T. Pegg, and M. R. Bendall, *J. Magn. Reson.*, 1982, **48**, 323.
52. S. Boentges, Dissertation, ETH, Zürich, Switzerland, 1994.
53. K. Wüthrich, *NMR of Proteins and Nucleic Acids*, Wiley, New York, 1986.
54. L. Braunschweiler and R. R. Ernst, *J. Magn. Reson.*, 1983, **53**, 521.
55. D. G. Davis and A. Bax, *J. Am. Chem. Soc.*, 1985, **107**, 2820.
56. L. Müller, S. Campbell-Burk, and P. Domaille, *J. Magn. Reson.*, 1992, **96**, 408.
57. S. Vijay-Kumar, C. Brugg, and W. J. Cook, *J. Mol. Biol.*, 1987, **194**, 531.

Acknowledgments

The section on XTONOX and XNOTOX was co-authored by Dr Serge Boentges and Dr Jürgen Schmidt. The underlying research was funded by the Swiss National Science Foundation, the Kommission zur Förderung der Wissenschaftlichen Forschung, and Spectrospin AG, Fällanden. The manuscript was processed by Mrs. Irène Müller.

Biographical Sketches

Richard R. Ernst. *b* 1933. Dipl. Ing. Chem., 1956, Ph.D., 1962, Chemistry, ETH Zürich, Switzerland. Scientific co-worker, Varian Associates, Palo Alto, CA, USA, 1963–68. Currently Professor of Physical Chemistry, ETH Zürich. Wolf Prize, Horwitz Prize, Nobel Prize in Chemistry, 1991. Research activities: methodological developments in liquid and solid state NMR, intramolecular dynamics.

Serge Boentges. *b* 1963. Dipl. Chem., 1988, Ph.D. (Chemistry), 1994, ETH Zürich, Switzerland. NMR application specialist, Spectrospin AG, Fällanden, Switzerland, 1994–present. Research activities: NMR data processing and automated computer analysis.

Jürgen M. Schmidt. *b* 1961. Dipl. Chem., 1986, Ph.D. (Biophysical Chemistry), 1990, University Frankfurt, Germany. Scientific co-worker, ETH Zürich, Switzerland, 1990–1992. Scientific assistant, University Frankfurt, 1992–present. Research activities: protein structure and dynamics.

Multiple Quantum Spectroscopy of Liquid Samples

Timothy J. Norwood
Leicester University, UK

1	Introduction	1
2	Correlation Experiments	1
3	Multiple Quantum Editing Experiments	3
4	Determination of the Sign of Scalar Coupling Constants	7
5	Correlation of External Random Magnetic Fields	7
6	Related Articles	8
7	References	8

1 INTRODUCTION

Multiple quantum coherence[1–3] is widely used in the spectroscopy of liquid samples. Its main uses can, broadly speaking, be grouped into two categories: the encoding of chemical shift in multidimensional correlation experiments, and the editing of both one-dimensional and multidimensional spectra. Multiple quantum coherence also has several less widely used applications, including scalar coupling constant sign determination and the investigation of the extent of correlation between external random magnetic fields. Herein will be described the properties of multiple quantum coherence, the construction of experiments, and its applications for liquid samples.

Multiple quantum coherences are those coherences for which $\Delta m_{\mathrm{T}} \neq \pm 1$. Unlike single quantum coherence, multiple quantum coherence cannot either be excited directly by the application of a single nonselective rf pulse to the equilibrium magnetization of a spin system, nor detected directly since it has no net magnetization associated with it. Both excitation and detection must therefore be achieved indirectly using a sequence of rf pulses. Despite these drawbacks, multiple quantum coherences play an important role in the spectroscopy of liquid samples because their properties are both different from and complementary to those of single quantum coherence. The chemical shift of a multiple quantum coherence is a linear combination of those of its active spins k:

$$\omega_{\mathrm{MQC}} = \sum\nolimits_k \omega_k \Delta m_k \tag{1}$$

Multiple quantum coherences do not exhibit scalar couplings between their active spins. The scalar coupling of a MQC to a passive spin l is the linear combination of the scalar couplings of the individual active spins to the passive spin:

$$J_{\mathrm{MQC}} = \sum \Delta m_k J_{kl} \tag{2}$$

The relaxation properties of multiple quantum coherences are also distinct from those of the single quantum coherences of their active spins.[1,3] However, individual expressions depend on the number of interacting spins considered.

In high-resolution spectroscopy of liquids, multiple quantum coherence is most commonly excited with a sequence of two nonselective pulses separated by a delay, which may contain a refocusing pulse. A commonly used excitation sequence is[3]

$$90^\circ_x - \frac{\tau}{2} - 180^\circ_y - \frac{\tau}{2} - 90^\circ_\phi$$

where $\phi = x$ to excite even orders of coherence, and $\phi = y$ to excite odd orders. Typically, $\tau < 1/(2J)$; the exact value used depends on the application. The effect of this pulse sequence, when $\phi = x$ and $\tau = 1/(2J)$, on the magnetization of a spin k coupled to a spin l is sketched below in the product operator formalism:[4]

$$I_{kz} \overset{90^\circ_x}{\rightarrow} -I_{ky} \overset{\tau}{\rightarrow} 2I_{kx}I_{lz} \overset{90^\circ_x}{\rightarrow} -2I_{kx}I_{ly}$$

where $2I_{kx}I_{ly}$ is a linear combination of zero quantum and double-quantum coherence with active spins k and l. The components of pure zero quantum coherence (ZQC) and double quantum (DQC) are given by linear combinations of two-spin product operators:

$$(\mathrm{ZQC})_x = \tfrac{1}{2}(2I_{kx}I_{lx} + 2I_{ky}I_{ly}) \tag{3}$$

$$(\mathrm{ZQC})_y = \tfrac{1}{2}(2I_{kx}I_{ly} - 2I_{ky}I_{lx}) \tag{4}$$

$$(\mathrm{DQC})_x = \tfrac{1}{2}[2I_{kx}\{I_{lx} - 2\{I_{ky}\{I_{ly}] \tag{5}$$

$$(\mathrm{DQC})_y = \tfrac{1}{2}(2\{I_{kx}\{I_{ly} + 2\{I_{ky}\{I_{lx}) \tag{6}$$

Detection is, in essence, the reverse of excitation; a single 90° pulse will usually convert a component of multiple quantum coherence into antiphase single quantum coherence. This can be allowed to become in-phase prior to acquisition, if desired, by the subsequent incorporation of a spin echo into the pulse sequence. As with single quantum experiments, the desired coherence transfer pathways in a multiple quantum experiment can readily be selected using either phase cycling (see ***Phase Cycling***) or magnetic field gradient pulses.[3]

2 CORRELATION EXPERIMENTS

Multiple quantum coherence correlation experiments can be categorized according to whether they are homonuclear or heteronuclear. This distinction is important because the motivation for using the two types of experiment is usually quite different.

In homonuclear correlation experiments multiple quantum coherence is used for one or more of three reasons:

1. Multiple quantum coherences provide alternative spectral dispersions to those of single quantum coherence. Peaks that overlap in a 'conventional' correlation spectrum such as COSY may be resolved in a multiple quantum correlation spectrum. In addition, high-order multiple quantum correlation spectra contain relatively few peaks.

2. Spectra may contain peaks that provide relay-type information, i.e. peaks which correlate pairs of spins which, while not coupled to each other, are both coupled to a common third spin.
3. Spectra of orders greater than 2 do not contain autocorrelation peaks. Autocorrelation peaks often hide cross correlations between spins with similar chemical shifts, and which consequently occur close to the diagonal of the COSY spectrum. This problem can be particularly severe in spectra of nuclei with low natural abundance, where autocorrelation peaks may be several orders of magnitude more intense than cross-correlation peaks.

Multiple quantum coherence has found widespread use in heteronuclear correlation spectroscopy. Although it is not used to encode a multiple quantum frequency, it is used as a tool of convenience for encoding the single quantum chemical shift of one of the active spins. For reasons of sensitivity, in heteronuclear correlation experiments the nucleus with the highest magnetogyric ratio is usually both excited and detected; this is known as 'inverse detection'. A typical purely single quantum pulse sequence for inversely detected heteronuclear correlation spectroscopy requires 10 pulses, while its multiple quantum analogue contains only four. By minimizing the number of pulses in a sequence, one minimizes both the amount of single lost due to pulse imperfections, and the length of the phase cycle that must be used to obtain a clean spectrum.

2.1 Homonuclear Correlation Experiments

Although many homonuclear multiple quantum correlation experiments have been proposed, very few of these have found widespread use. One of the earliest of these, and perhaps the most successful is two-dimensional INADEQUATE[3,5] [Figure 1(a)] applied to natural abundance ^{13}C. The experiment produces spectra that correlate pairs of coupled ^{13}C nuclei, while removing the singlets from uncoupled ^{13}C spins that would otherwise dominate the spectrum (see ***INADEQUATE Experiment***). In this instance double quantum excitation is particularly efficient, since homonuclear single bond ^{13}C coupling constants are both uniform and relatively large (typically 120 Hz). Furthermore, due to low natural abundance, each double quantum coherence can be considered as arising from an AX spin system.

Excitation is achieved through the process

$$(I_{Az} + I_{Xz}) \overset{90^\circ_x}{\rightarrow} -(I_{Ay} + I_{Xy}) \overset{\tau}{\rightarrow} (2I_{Ax}I_{Xz} + 2I_{Xx}I_{Az}) \overset{90^\circ_x}{\rightarrow} -(2I_{Ax}I_{Xy} + 2I_{Xx}I_{Ay})$$

When $\tau = 1/(2J_{cc})$, pure double quantum coherence [equation (6)] is excited with maximum efficiency. The delay t_1 is systematically incremented in successive experiments to encode the double quantum evolution in the second dimension of the data set. The 90° pulse following the subsequent multiple quantum evolution period t_1 reconverts the double quantum coherence into antiphase single quantum coherence which is detected as it becomes in-phase. Orthogonal components of double quantum coherence can be detected by shifting the phase of the last pulse or, alternantly, all the pulses of the excitation sequence by 45°; this enables absorptive phase sensitive spectra to be acquired.

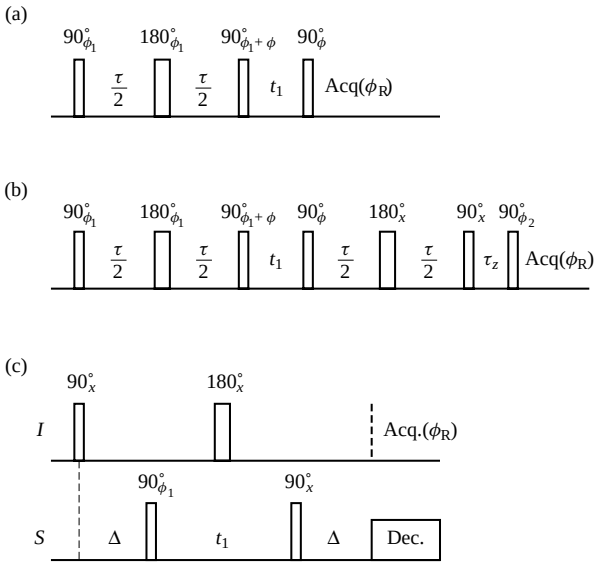

Figure 1 Pulse sequences for (a) INADEQUATE, (b) a one-dimensional multiple quantum filter producing in-phase spectra, and (c) HMQC. For (b), data must be averaged over several values of τ_z. Phase cycling for p quantum filtration for (a) and (b) where applicable: $\phi = x$ for even and y for odd orders; $\phi_1 = k\pi/p$, where $k = 0, 1, 2, \ldots, (2p - 1)$; $\phi_2 = 2p(x, y, -x, -y)$. For (a), $\phi_R = (x, -x)$, for (b) $\phi_R = (x, -x) + 2p(x, y, -x, -y)$. For (c), $\phi_1 = (x, -x)$; $\phi_R = (x, -x)$. The number before each bracketed phase cycle indicates the number of consecutive transients that are acquired with each step. Where a phase cycle is a linear combination of bracketed cycles, the phases calculated from each one are added together to obtain the phase to be used

An example of an INADEQUATE spectrum is given in Figure 2. In the spectrum each pair of coupled ^{13}C spins is correlated by a pair of peaks that occur at their single quantum frequencies in F_2 and at the sum of their rotating frame frequencies (their mutual double quantum frequency) in F_1. Consequently, all pairs of correlation peaks are symmetrically disposed about the $\omega_1 = 2\omega_2$ skew diagonal. Peaks of this sort are sometimes referred to as 'direct' correlation peaks.

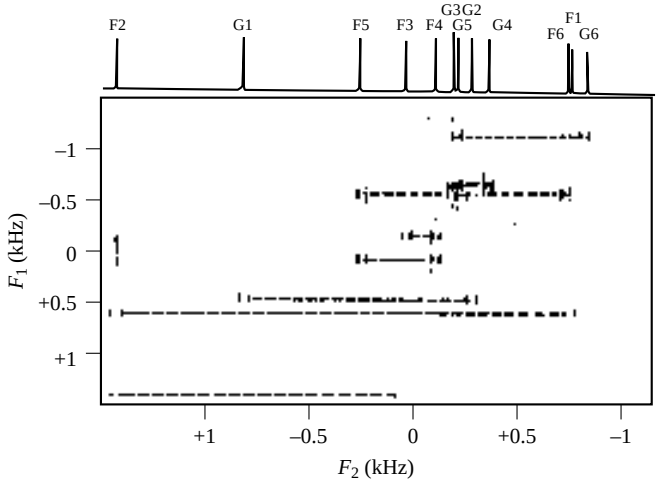

Figure 2 ^{13}C INADEQUATE spectrum of sucrose. (Reproduced by permission of Academic Press from A. Bax, R. Freeman, T. A. Frenkiel, and M. H. Levitt, *J. Magn. Reson.*, 1981, **43**, 478)

When abundant nuclei such as ^{1}H are under study, a wide range of both coupling constants and spin systems are usually encountered. The optimum value of τ will now be $1/(4J)$ where J is the average value of a coupling constant. However, to avoid the excitation of components of antiphase double quantum coherence, which would result in the introduction of dispersive components into peaks in the spectrum, a shorter value of τ must be used,[3] typically $<1/(6J)$. This has the side effect of reducing peak intensity. The spectra so produced contain remote correlation peaks in addition to the direct ones described above. Remote peaks occur at the double quantum frequency of the pair of spins active in the double quantum coherence in F_1 and the single quantum frequency of a passive spin to which both active spins are coupled in F_2.

A number of variations of the basic INADEQUATE pulse sequence have been introduced. Notable among these is a pair of experiments designed to produce spectra amenable to automated analysis.[6,7] This is achieved by reducing the number of components present in the multiplet structure of the correlation peaks.

Of the other orders of coherence, both zero and triple quantum coherence have seen limited use. Zero quantum coherence is not amenable to the conventional method of achieving phase sensitive detection in the F_1 dimension, since it is insensitive to phase shifts, and consequently separate pulse sequences must be used.[3] Furthermore, zero quantum spectra often contain intense peaks at $F_1 = 0$ arising from both coupled and uncoupled spins that cannot be removed by phase cycling. With triple and higher orders of coherence the major problems are reduced excitation efficiency and difficulty in exciting the single component of coherence necessary for producing absorptive spectra.

2.2 Heteronuclear Correlation Experiments

The most widely used heteronuclear multiple quantum correlation experiment is HMQC[3,8] (heteronuclear multiple quantum coherence) [Figure 1(c)]. This experiment produces absorptive phase sensitive spectra correlating the single quantum chemical shifts of pairs of coupled heteronuclei I and S, typically ^{15}N–^{1}H and ^{13}C–^{1}H. The experiment and its derivatives are widely used to study ^{15}N and ^{13}C labeled proteins. The first two pulses excite heteronuclear zero and double quantum coherence:

$$I_z \overset{90^\circ_x(I)}{\rightarrow} -I_y \overset{\Delta}{\rightarrow} [I_x \cos(\omega_I \Delta) + I_y \sin(\omega_I \Delta)]2S_z$$
$$\overset{90^\circ_x(S)}{\rightarrow} -[I_x \cos(\omega_I \Delta) + I_y \sin(\omega_I \Delta)]2S_y$$

where $\Delta = 1/(2J_{IS})$. Reconversion of the multiple quantum into in-phase single quantum coherence, which is accomplished by the last $90^\circ(S)$ pulse and the subsequent delay, is the reverse of excitation. The $180^\circ(I)$ pulse at the center of the evolution period interconverts components of heteronuclear zero and double quantum coherence and reverses the effects of I spin chemical shift evolution during both Δ and t_1 intervals. This ensures that only S spin chemical shift is encoded by the IS zero quantum and double quantum coherence present during t_1, and that when $t_1 = 0$ there is no offset-dependent phase shift of the observed magnetization.

Although multiple quantum coherence is used in this experiment to encode a single quantum chemical shift, it is usually preferred over purely single quantum alternatives because it requires only four pulses to do so, whereas the single quantum alternative would require 10. This means that HMQC requires less phase cycling and the smaller number of proton pulses makes solvent suppression easier.

The HMQC pulse sequence minus the first pulse is most widely used as a 'module' that can be inserted into heteronuclear two-, three-, and four-dimensional experiments (see ***Three-Dimensional HMQC-NOESY, NOESY-HMQC, and NOESY-HSQC***) to encode a heteronuclear chemical shift with the maximum efficiency and the minimum of phase cycling[3] (often an important consideration). Many of these experiments have become central to the study of the solution structure of proteins by NMR.[8]

3 MULTIPLE QUANTUM EDITING EXPERIMENTS

Experiments that use multiple quantum coherence to produce spectra that are edited in some way can be grouped into two broad categories: multiple quantum filters that edit the spectrum solely on the basis of the orders of coherence that a spin can participate in and experiments that also use multiple quantum chemical shift, scalar couplings and spin coupling topologies as a basis for editing. In the former category, multiple quantum filtered COSY and its derivative ECOSY have entered general usage, while of the latter the DEPT experiment is most widely used.

3.1 Homonuclear One-dimensional Multiple Quantum Filtration

Any experiment that uses phase cycling or magnetic field gradient pulses to select a particular order of coherence can be regarded as a multiple quantum filter. The first purpose-designed multiple quantum filter is the one-dimensional INADEQUATE[9] experiment (Figure 2). Excitation and detection occur in the same way as for the two-dimensional INADEQUATE experiment described above, and the same considerations apply (see ***INADEQUATE Experiment***). However, unlike the two-dimensional experiment, the length of the evolution period t_1 is fixed at zero. This experiment produces double quantum filtered ^{13}C–^{13}C satellite spectra from which the relatively intense peaks arising from uncoupled ^{13}C nuclei, beneath which satellite spectra are often undiscernible in the conventional single quantum spectrum, have been removed. It produces absorption spectra containing pairs of antiphase doublets that are easy to interpret.

However, problems arise when the technique is applied to ^{13}C enriched samples or to abundant nuclei such as ^{1}H. These are in many respects similar to the problems encountered in homonuclear multiple quantum correlation spectroscopy of abundant nuclei. As a consequence of the greater diversity of scalar coupling constants and spin systems, excitation becomes both less uniform and less efficient. Furthermore, filtered spectra produced with the INADEQUATE pulse sequence can be difficult to interpret since they may contain a superimposed mixture of absorptive and dispersive components that are antiphase with respect to different numbers of spins.

Relatively uniform excitation can be achieved, at the expense of efficiency, across coherences of a given order and across the different orders by setting $\tau = 1/(4J)$, where J is the average scalar coupling constant. Alternatively, the uniformity of excitation can be improved by combining spectra obtained with several different values of τ. However, to produce absorptive spectra it is necessary to modify the pulse sequence. The pulse sequence given in Figure 1(b) produces multiple quantum filtered spectra that are both absorptive and in-phase.[3] After the two central 90° pulses which comprise the multiple quantum filter, antiphase single quantum coherence will be present. In the INADEQUATE experiment the magnetization is observed at this point, and consequently the peaks in the observed spectra will be antiphase. By contrast, in the modified pulse sequence a spin echo is introduced at this point to allow this antiphase magnetization to become in-phase again. The two 90° pulses at the end of the pulse sequence comprise a z filter[1] which serves to eliminate any remaining antiphase magnetization. Consequently, since only in-phase magnetization will be present at the start of acquisition, the spectrum will also be in-phase.

When abundant nuclei are under study, nuclear magnetization can be filtered through other orders of coherence besides double quantum coherence; for nuclei of low natural abundance, sensitivity usually makes filtration through orders of coherence requiring more than two active spins impractical.

3.2 Multiple Quantum Filtered COSY

Multiple quantum filtered COSY[10,11] is one of the most widely used multiple quantum experiments. Unlike one-dimensional filters it does not suffer from the problems of uniformity of excitation or mixing of absorptive and dispersive components in the observed spectrum; indeed, the phase properties are superior to those of the conventional COSY experiment (see ***COSY Two-Dimensional Experiments***). While filtration can, in principle, be through any order of coherence greater than one, in practice it is usually restricted to double quantum, and occasionally triple quantum, coherence since sensitivity declines as coherence order increases. The main motivation for using the experiment are a reduction in the intensity of diagonal peaks relative to off-diagonal peaks and the improvement in phase properties over conventional COSY referred to above.

Multiple quantum filtered COSY differs from its precursor in that the single 90° mixing pulse of the latter is replaced by a pair of pulses (Figure 3).

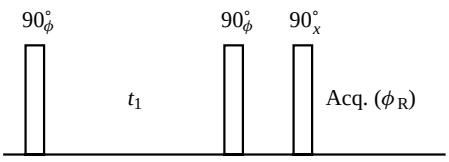

Figure 3 Pulse sequence for multiple quantum filtered COSY and ECOSY. For p quantum filtration $\phi = k\pi/p$, where $k = 0, 1, 2, \ldots, (2p - 1)$; $\phi_R = (x, -x)$. An ECOSY spectrum can be generated by taking the linear combination of two quantum and three quantum filtered spectra: {ECOSY} = {2 quantum filtered COSY} + $\frac{4}{3}${3 quantum filtered COSY}. In practice, ECOSY is acquired as a single experiment

In the conventional COSY experiment a cross-correlation peak is generated between two spins k and l through coherence transfer between components of antiphase magnetization:

$$I_{kz} \overset{90^\circ_x}{\rightarrow} -I_{ky} \overset{t_1}{\rightarrow} 2I_{kx}I_{lz} \overset{90^\circ_y}{\rightarrow} -2I_{kz}I_{lx}$$

while autocorrelation peaks arise from components of magnetization that are in-phase when the mixing pulse is applied:

$$I_{kz} \overset{90^\circ_x}{\rightarrow} -I_{ky} \overset{t_1}{\rightarrow} -I_{ky} \overset{90^\circ_y}{\rightarrow} -I_{ky}$$

Clearly, since magnetization following the two pathways differ in phase by 90°, if one is phased to be absorptive than the other must inevitably be dispersive. If cross-correlation peaks are phased to be absorptive, as is usually the case, then the diagonal peaks will be dispersive. The dispersive tails of diagonal peaks often obscure adjacent cross-correlation peaks. In a multiple quantum filtered COSY experiment, all observed magnetization must pass through multiple quantum coherence of the selected order between the two mixing pulse. For example, in the case of double quantum filtered COSY,

$$I_{kz} \overset{90^\circ_x}{\rightarrow} -I_{ky} \overset{t_1}{\rightarrow} 2I_{kx}I_{lz} \overset{90^\circ_x}{\rightarrow} \tfrac{1}{2}(2I_{kx}I_{ly} + 2I_{ky}I_{lx})$$
$$\overset{90^\circ_x}{\rightarrow} \tfrac{1}{2}(2I_{kx}I_{lz} + 2I_{kz}I_{lx})$$

where only the selected components of coherence are shown. The second 90° pulse of the sequence actually creates $2I_{kx}I_{ly}$, which consists of a linear combination of zero quantum and double quantum coherence [equations (4) and (6)]; the linear combination of product operators given above corresponds to the pure double quantum coherence selected by the phase cycle. The two components of antiphase magnetization present after the mixing period give rise to the k spin autcorrelation peak (first term) and a $k - l$ cross-correlation peak (second term). Since both components have the same phase, both diagonal and off-diagonal peaks can be phased to be absorptive simultaneously, resulting in a spectrum consisting solely of absorption peaks. The main motivation for using double quantum filtration has, until recently, been to produce pure absorption COSY spectra with low intensity diagonal peaks. While double quantum filtration might, in principle, be used to remove the signal arising from water or other uncoupled-spin solvent peaks, in practice dynamic range problems and the limited efficiency of phase cycling has precluded this. However, the recent advent of actively shielded magnetic field gradients as a means of coherence transfer pathway selection has now made solvent suppression practical as well. An example of a four quantum filtered COSY spectrum illustrating the technique's ability to produce edited spectra is given in Figure 4.

The structure of double quantum filtered COSY cross-correlation peaks is the same as in conventional COSY: they are antiphase with respect to the mutual coupling of the correlated spins in both dimensions. However, if filtration through higher orders of coherence is used, this will not be the case. In general, an n quantum filtered COSY cross-correlation peak will be antiphase with respect to $(n - 2)$ couplings in both dimensions of the spectrum in addition to the mutual coupling of the correlated spins. This is because the magnetization of a

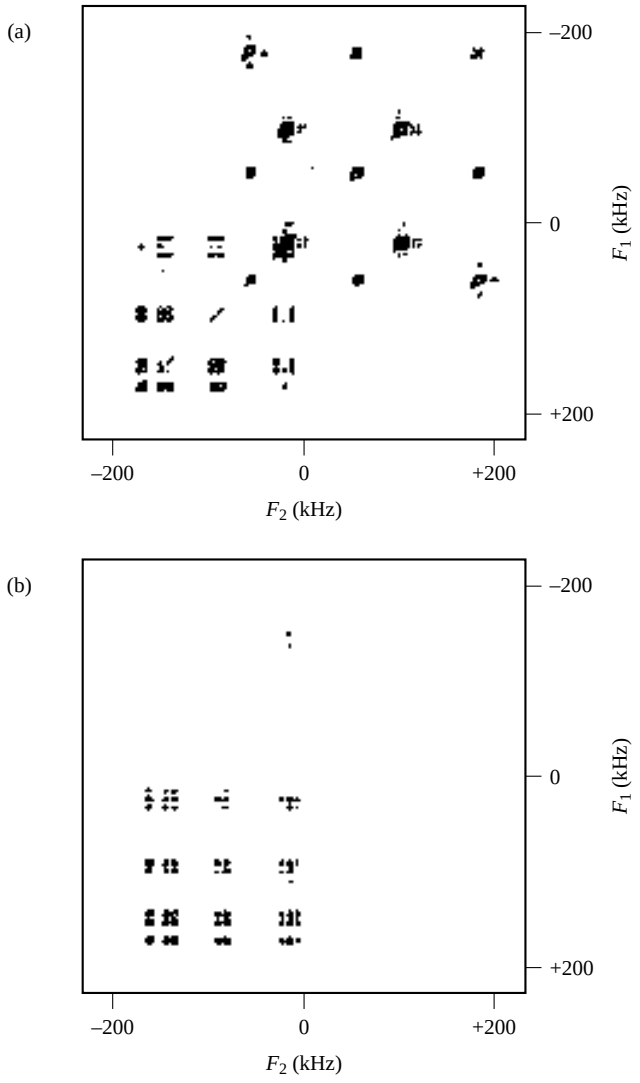

Figure 4 (a) COSY and (b) four quantum filtered COSY spectra of a mixture of 2,3-dibromothiophene, 2-furoic acid and 1-bromo-3-nitrobenzene in acetone-d_6. Only the signals from 1-bromo-3-nitrobenzene are allowed to pass by the four quantum filter. (Reproduced by permission of Academic Press from A. J. Shaka and R. Freeman, *J. Magn. Reson.*, 1983, **51**, 169)

spin and n quantum coherence can only be interconverted by a nonselective pulse if the former is antiphase with respect to $(n - 1)$ other spins.

3.3 ECOSY

The overlap present in the one-dimensional spectra of all but the smallest molecules often makes the measurement of scalar coupling constants difficult. In principle, scalar coupling constants can be measured from the cross-correlation peaks of COSY spectra. However, in practice the limited digital resolution of two-dimensional experiments and the wide lines of larger molecules can both lead to the overlap of multiplet components, making analysis difficult. The ECOSY[12] experiment alleviates this problem by taking advantage of the fact that much of the information present in cross-correlation peaks is redundant. A cross-correlation peak arising from a set of N mutually coupled spins will contain 2^{2N-1} components. ECOSY reduces this number to 2^N by restricting coherence transfer to transitions directly connected in the energy level diagram. A scalar coupling constant can be extracted from ECOSY spectra simply by measuring the distance between a pair of peaks without the need for any fitting procedure (see ***Coupling Constants Determined by ECOSY***). ECOSY uses the same pulse sequence as multiple quantum filtered COSY, but with a different phase cycle. It effectively combines two, three, and sometimes four quantum filtered COSY spectra in the ratio 1:2:4. As noted in the previous section, the antiphase structure of a COSY cross-correlation peak will vary depending on the order of coherence that it is filtered through. Consequently, if different orders of multiple quantum filtered COSY spectra are combined in the appropriate ratios, some components will cancel out. ECOSY combines multiple quantum filtered COSY spectra in such a way that components which are not the result of coherence transfer between directly connected transitions cancel out. This is represented diagramatically in Figure 5.

The ECOSY cross-peak structure is based on a series of displaced squares. A cross-correlation peak between two spins k and l at (ω_k, ω_l) will consist of a square antiphase with respect to the mutual coupling of the two spins in both dimensions. Each additional spin m to which both k and l are coupled will cause this square to be duplicated and displaced by (J_{km},J_{lm}). To determine J_{km} and J_{lm} it is only necessary to measure the displacement of the two squares in F_1 and F_2, respectively (Figure 5). It has recently been shown that differential relaxation between components of in-phase and antiphase magnetization can give rise to substantial errors in the values of poorly resolved scalar coupling constants measured from ECOSY spectra.[13]

3.4 *n*-Spin Filtration

An n quantum filter passes magnetization from spin systems containing n or more spins. An n-spin filter[3,14] is an n quantum filter modified so that it only passes magnetization from spin systems which contain exactly n spins. It consists of a multiple quantum filter with a multiplicity filter inserted into the multiple quantum evolution period. An n quantum coherence arising from a system of more than n spins will

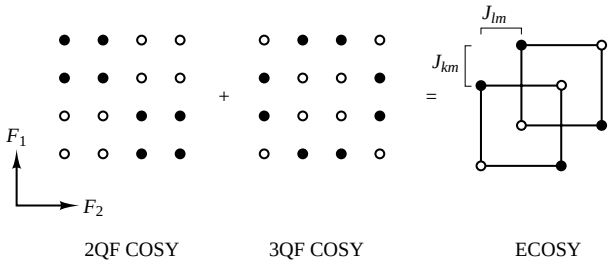

Figure 5 Representation of the generation of an ECOSY cross-correlation peak from a linear combination of two quantum (2QF) and three quantum filtered (3QF) COSY cross-correlation peaks. The correlation is from a spin k to a spin l. Both spins are also coupled to a third spin m. J_{km} and J_{lm} can be measured as the displacement of the two squares in F_1 and F_2, respectively

not be a singlet and consequently will be rejected by the multiplicity filter. The multiplicity filter consists of a spin echo of variable length. Data acquired with a number of echo times are coadded: the signals from singlets will not evolve during the echo and will therefore constructively interfere when combined, while nonsinglets will evolve due to their scalar couplings and will therefore destructively interfere. For complete cancellation of nonsinglets to occur, a wide range of echo times must be used. In practice, cancellation may be incomplete if there is a transition at the center of the multiplet, which will not evolve during the echo, or two transitions closely spaced about the center.

3.5 Spin Topology Filtration

The most sophisticated type of homonuclear ^{1}H editing experiment yet developed is the spin topology filter.[15] Filters of this type pass the magnetization of a single type of spin system. In essence, spin topology filters function by passing a particular order of coherence arising from a specific spin system. To achieve specificity it is often necessary to use a sophisticated multiple stage excitation sequence. These typically consist of a series of spin echoes sandwiched between 90° pulses. Selectivity is typically determined by the phases of the 90° pulses and the lengths of the spin echoes. The former restricts the coherence transfer process that can occur, while the latter allows manipulation of the scalar coupling evolution of intermediate coherences. The pulse sequence for AX_3 spin filtered COSY is given in Figure 6, and an experimental example is given in Figure 7.

In practice, spin topology filters can be difficult to implement and are very sensitive to variations in scalar coupling constants. This latter fact manifests itself in the presence of several peaks arising from the non-AX_3 spin systems in the example. Furthermore, long phase cycles are often required, and relaxation during the filter may result in a substantial reduction in signal intensity, precluding application to many biomolecules.

3.6 Heteronuclear Editing Experiments

Most heteronuclear multiple quantum editing experiments are designed to edit ^{13}C spectra on the basis of the number of attached protons. All make use of the relative uniformity of one bond carbon–proton couplings and the scalar coupling properties of multiple quantum filters. Multiple quantum filtration is also used in some experiments.

The earliest and most widely used of the heteronuclear multiple quantum editing technique is the DEPT[16] experiment

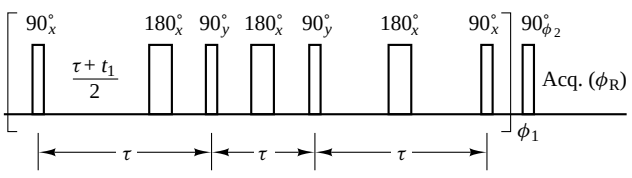

Figure 6 Pulse sequence for AX_3 spin filtered COSY.[15] $\tau = 1/(2J)$ and $\tau' = 1/(6J)$. The phases ϕ, ϕ_1, and ϕ_R are cycled to select ±4 quantum coherence between the last two pulses

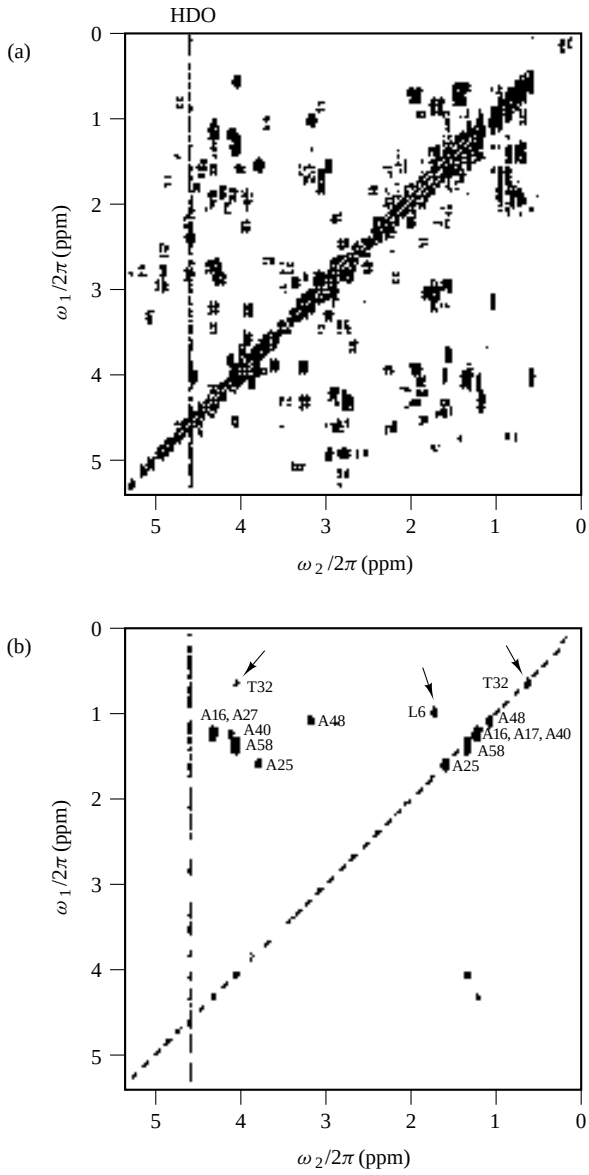

Figure 7 ^{1}H spectra of bovine trypsin inhibitor: (a) double quantum filtered COSY spectrum; (b) AX_3 spin filtered COSY spectrum. The peaks in (b) are predominantly due to alanines which have AX_3 spin systems.[15] (Reproduced by permission of the American Institute of Physics from M. H. Levitt and R. R. Ernst, *J. Chem. Phys.*, 1985, **83**, 3297)

(Figure 8). This experiment edits the response from different $^{13}CH_n$ groups into separate subspectra. Its effect is sketched in the product operator formalism:

$$H_z \xrightarrow{90^\circ_x(H)} -H_y \xrightarrow{[1/(2^1J_{CH})]} 2H_xC_z \xrightarrow{90^\circ_y(C)} 2H_xC_x \xrightarrow{[1/(2^1J_{CH})]}$$

$$\begin{array}{ll} CH: 2H_xC_x & \xrightarrow{\theta^\circ_y(H)} -2H_zC_x \sin\theta \\ CH_2: 4H_xC_yH_z & \xrightarrow{\theta^\circ_y(H)} -4H_zC_yH_z \sin\theta\cos\theta \\ CH_3: 8H_xC_xH_zH_z & \xrightarrow{\theta^\circ_y(H)} 8H_zC_xH_zH_z \sin\theta\cos^2\theta \end{array}$$

The 180° pulses serve to reverse chemical shift evolution during the pulse sequence. After the first two pulses, heteronuclear zero and double quantum coherence between attached ^{1}H and ^{13}C nuclei is created from ^{1}H magnetization.

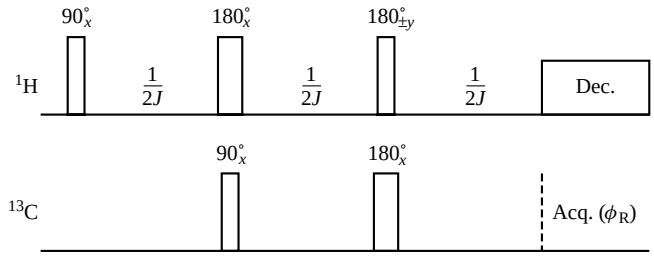

Figure 8 Pulse sequence for the DEPT experiment.[16] Edited $^{13}CH_n$ subspectra can be obtained by combining data acquired with different three values of θ: $\theta_1 = 45^\circ$, $\theta_2 = 90^\circ$, and $\theta_3 = 135^\circ$. Subspectra are generated by taking the following linear combinations: CH, θ_2; CH_2, $0.5(\theta_1 - \theta_3)$; CH_3, $0.5[0.5(\theta_1 + \theta_3) - 0.71\theta_2]$

Since scalar couplings between active spins are ineffective, the multiple quantum coherence evolves during the subsequent period solely due to its scalar couplings to passive spins, becoming (ideally) completely antiphase with respect to the remaining passive protons attached to the active carbon atom. This is then converted into ^{13}C magnetization antiphase with respect to all of its attached protons by the $\theta_y{}^\circ$(H) pulse, and is observed in the presence of proton decoupling once it has become in-phase. The efficiency of the last coherence transfer process is dependent upon both the angle θ and the type of $^{13}CH_n$ group. Consequently, by combining data acquired with three different values of θ it is possible to produce separate subspectra of CH, CH_2, and CH_3 groups. DEPT is susceptible to errors if the values of θ are mis-set. This problem is circumvented in a variation of DEPT known as POMMIE[17] in which $^{13}CH_n$ group selection is achieved with a multiple quantum filter instead of a flip angle filter.

The type of editing used in DEPT is taken a step further in two families of experiments known as SEMINA and SLAP.[18] While DEPT edits for $^{13}CH_n$ groups, these experiments produce subspectra which are edited according to the type of $^{13}CH_m$ $^{13}CH_n$ group to which the ^{13}C nuclei belong. Like DEPT, these experiments rely on the generation of intermediate multiple quantum coherence and use flip angle filters to achieve editing. Spectra can be edited either according to the individual values of m and n, or, more usually, according to the parities of $(m + n)$ and m or n.

4 DETERMINATION OF THE SIGN OF SCALAR COUPLING CONSTANTS

The properties of multiple quantum coherence provide several opportunities for determining the relative signs of scalar coupling constants. While it might be expected that this information would be accessible from their scalar coupling properties, it is perhaps more surprising that in some circumstances their relaxation rates can also be used.

It can be seen from equation (2) that the scalar couplings exhibited by multiple quantum coherences are sensitive to the signs of scalar coupling constants. For example, a zero quantum coherence with active spins k and l will exhibit a scalar coupling of $(J_{km} - J_{lm})$ to a passive spin m. Consequently, if the zero quantum coupling is equal to the difference in magnitudes of the two scalar coupling constants their signs must be the same; otherwise, the converse must be true. For the corresponding double quantum coherence this situation is reversed.[3]

When a pair of spin-$\frac{1}{2}$ nuclei are scalar coupled to a common quadrupolar nucleus, the relative signs of these two coupling constants can be determined from the scalar contribution to the relaxation of the zero and double quantum coherences in which the two spin-$\frac{1}{2}$ nuclei are active.[19] If the spin-$\frac{1}{2}$ nuclei are k and l, and the quadrupolar nucleus is S, then

$$1/T_2(\mathrm{DQC/ZQC}) = 1/T_1(k) + 1/T_1(l) + \tfrac{4}{5}N_S\pi^2 S(S+1) \times (J_{kS} \pm J_{lS})^2 T_1(S) \qquad (7)$$

where N_S is the number of S spins and $T_1(k)$ is the T_1 value of the k spin. Clearly, if the zero quantum coherence relaxes more quickly than the double quantum coherence, the scalar coupling constants must have the same sign, while if the reverse is true they must have opposite signs. It should be noted that this expression is an approximation; it is assumed that the dipolar relaxation of k and l makes a relatively small contribution to the overall relaxation rate.

5 CORRELATION OF EXTERNAL RANDOM MAGNETIC FIELDS

The interaction of molecules with each other is of great chemical and biochemical interest. When one molecule is paramagnetic it may induce random magnetic fields at the nuclei in the other, contributing to their relaxation. By measuring the transverse relaxation times of zero and double quantum coherence it is possible to determine the extent to which the random magnetic fields induced in this way are correlated for the active spins, and consequently to investigate the interaction between the two molecules.[20]

If two weakly coupled spin-$\frac{1}{2}$ nuclei k and l are considered to relax solely with external random magnetic fields, their single quantum transverse relaxation rates will be

$$1/T_2(k) = \gamma^2\tau_c[\overline{B_{lx}^2} + \overline{B_{kx}^2} + \overline{B_{kz}^2}] \qquad (8)$$

$$1/T_2(l) = \gamma^2\tau_c[\overline{B_{kx}^2} + \overline{B_{lx}^2} + \overline{B_{lz}^2}] \qquad (9)$$

where B_{ij} corresponds to the j component of the external field experienced by the nucleus i. While the relaxation rates of both coherences are sensitive to the external random fields experienced by both nuclei, they are not sensitive to any correlation between them. The corresponding relaxation rates for the zero and double quantum coherences in which these spins are active are

$$1/T_2(\mathrm{ZQC}) = \gamma^2\tau_c[\overline{B_{kx}^2} + \overline{B_{lx}^2} + \overline{B_{kz}^2} + \overline{B_{lz}^2} - 2C_{kl}(\overline{B_{kz}^2 B_{lz}^2})^{0.5}] \qquad (10)$$

$$1/T_2(\mathrm{DQC}) = \gamma^2\tau_c[\overline{B_{kx}^2} + \overline{B_{lx}^2} + \overline{B_{kz}^2} + \overline{B_{lz}^2} + 2C_{kl}(\overline{B_{kz}^2 B_{lz}^2})^{0.5}] \qquad (11)$$

where C_{kl} is a correlation coefficient. Clearly, both these coherences are sensitive to any correlation in the external random magnetic fields experienced by the two nuclei through the term $2C_{kl}(\overline{B_{kz}^2 B_{lz}^2})^{0.5}$. Since it reduces the rate of zero quantum relaxation and increases that of double quantum coherence, any correlation will manifest itself as a difference between the two rates. From this difference the extent of correlation can be determined.

6 RELATED ARTICLES

COSY Two-Dimensional Experiments; Double Quantum Coherence; Heteronuclear Shift Correlation Spectroscopy; Multiple Quantum Coherence Imaging; Multiple Quantum Coherence in Spin-1/2 Dipolar Coupled Solids; Multiple Quantum Coherences in Extended Dipolar Coupled Spin Networks; Multiple Quantum NMR in Solids; Multiple Quantum Spectroscopy in Liquid Crystalline Solvents.

7 REFERENCES

1. R. R. Ernst, G. Bodenhausen, and A. Wokaun, *Principles of Nuclear Magnetic Resonance in One and Two Dimensions*, Clarendon, Oxford, 1987.
2. M. Munowitz, *Coherence and NMR*, Wiley, New York, 1988.
3. T. J. Norwood, *Progr. NMR Spectrosc.*, 1992, **24**, 295.
4. O. W. Sørensen, G. W. Eich, M. H. Levitt, G. Bodenhausen, and R. R. Ernst, *Progr. NMR Spectrosc.*, 1983, **16**, 163.
5. A. Bax, R. Freeman, and T. A. Frenkiel, *J. Am. Chem. Soc.*, 1981, **103**, 2102.
6. S. Wimperis, *J. Magn. Reson.*, 1990, **87**, 174.
7. M. Novic, H. Oschkinat, P. Pfaendler, and G. Bodenhausen, *J. Magn. Reson.*, 1987, **73**, 493.
8. G. M. Clore and A. M. Gronenborn, *Progr. NMR Spectrosc.*, 1991, **23**, 43.
9. A. Bax, R. Freeman, and S. P. Kempsell, *J. Am. Chem. Soc.*, 1980, **102**, 4849.
10. U. Piantini, O. W. Sørensen, and R. R. Ernst, *J. Am. Chem. Soc.*, 1982, **104**, 6800.
11. A. J. Shaka and R. Freeman, *J. Magn. Reson.*, 1983, **51**, 169.
12. C. Griesinger, O. W. Sørensen, and R. R. Ernst, *J. Am. Chem. Soc.*, 1985, **107**, 6394.
13. T. J. Norwood and K. Jones, *J. Magn. Reson., Ser. A*, 1993, **104**, 106.
14. D. S. Williamson, D. L. Nagel, R. S. Markin, and S. M. Cohen, *J. Magn. Reson.*, 1987, **71**, 163.
15. M. H. Levitt and R. R. Ernst, *J. Chem. Phys.*, 1985, **83**, 3297.
16. D. M. Doddrell, D. T. Pegg, and M. R. Bendall, *J. Magn. Reson.*, 1982, **48**, 323.
17. J. M. Bulsing and D. M. Doddrell, *J. Magn. Reson.*, 1985, **61**, 197.
18. N. C. Nielsen, H. Bildsoe, H. J. Jackobsen, and O. W. Sørensen, *J. Magn. Reson.*, 1988, **78**, 223.
19. V. Mlynarik, *Chem. Phys. Lett.*, 1989, **160**, 25.
20. A. Wokaun and R. R. Ernst, *Mol. Phys.*, 1978, **36**, 317.

Biographical Sketch

Timothy J. Norwood. *b* 1962. B.Sc. (Hons), 1983, King's College, University of London; M.Sc., 1985, University of British Columbia (where introduced to NMR by Laurie Hall), Ph.D., 1989, Cambridge University. Research interests: the development and application of NMR techniques for addressing biological problems in vitro and in vivo.

Multiple-Resonance Multi-Dimensional Solid-State NMR of Proteins

Stanley J. Opella

Department of Chemistry and Biochemistry, University of California, San Diego, La Jolla, CA, USA

1	Introduction	1
2	Local Field	1
3	Separation of Local Fields	3
4	Multidimensional Solid-State NMR Correlation Spectroscopy	4
5	PISA Wheels	5
6	Calculations for Protein Structure Determination from Solid-State NMR Data	6
7	Application to the Three-Dimensional Structure of the Acetylcholine M2 Peptide in Lipid Bilayers	7
8	Summary	8
9	References	9

1 INTRODUCTION

Solid-state NMR spectroscopy is much more than a method for obtaining high resolution NMR spectra of materials that are crystalline, polymeric, aggregated, or otherwise ill-suited for more generally applicable and available solution NMR methods. It is a method for determining the structures of molecules, including those as large and complex as proteins, under the most appropriate conditions, including those where the molecular correlation times are slow. Advances in selective averaging and the measurement of local fields resulting from heteronuclear dipolar couplings were needed to transform this branch of spectroscopy into a full-blown method for structure determination. The local field, which results from the interactions of two or more proximate nuclei, provides a particularly direct source of structural information. Other nuclear spin interactions, especially the chemical shift, also provide valuable structural information, although, their interpretation is generally more complicated and somewhat less firmly grounded. Taken together, the structural constraints resulting from measurements of spectral parameters from several spin-interactions, where at least one of them is a local field, are more than sufficient to determine the three-dimensional structures of complex molecules including proteins.

The experimental demonstration of the local field by Pake in 1948 means that solid-state NMR spectroscopy has been recognized as a method for determining molecular structures for more than 50 years;[1] however, it took until the mid-1970s to develop the methods and instrumentation for structure determination of small organic molecules[2,3] and simple polymers.[4] And only recently has it become feasible to determine the structures of proteins by solid-state NMR spectroscopy. This article discusses the crucial roles of the local field in structural studies of systems that range in complexity from waters of hydration in gypsum[1] and crystalline trichloroacetate[5] to uniformly isotopically labeled membrane proteins in lipid bilayers.[6] The combination of heteronuclear dipolar coupling and chemical shift frequencies is shown to be sufficient for characterizing the structures of membrane proteins as a qualitative index[7,8] as well as through direct calculations of structures from the NMR data.[9] The approach is illustrated with an example of structure determination of a polypeptide corresponding to a transmembrane helix of the acetylcholine receptor that functions in membrane bilayers as an ion channel.[10]

2 LOCAL FIELD

"The interaction between two nuclear spins depends on the magnitude and orientation of their magnetic moments and also the length and orientation of the vector describing their relative positions."[11] As shown in Figure 1, the local magnetic field resulting from the interactions between two nuclear spins is described in a strikingly simple way. With its explicit dependence on a distance and an angle, it provides access to geometrical parameters that can be directly translated into molecular structures. It is also important for experimental spectroscopy, and many of the developments in solid-state NMR spectroscopy have been concerned with the selective averaging of dipolar couplings so that the chemical shift and other spectroscopic parameters can be observed.[12–16]

The attenuation of dipolar couplings is essential because solid-state NMR spectra are typically very broad and overlapped as a consequence of the cumulative effect of the many different local fields. Only in exceptional cases does the material of interest provide sufficient isolation among pairs of spins so that the effects of a single local field can be observed. A doublet with properties described in Figure 1 from the waters of hydration in samples of gypsum was observed by Pake.[1] While the Pake doublet from a polycrystalline sample shown in Figure 2 can be used to determine the internuclear distance between the two hydrogens, the rotation patterns from single crystals enabled the angular dependence to be confirmed and, indeed, for the distance to be measured with greater precision.

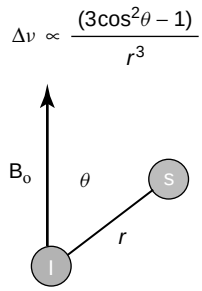

Figure 1 The principal factors that affect the splittings observed in solid-state NMR spectra from the dipole–dipole interaction between two nuclei. θ is the angle between the internuclear vector and the direction of the applied magnetic field and r is the distance between the two nuclei

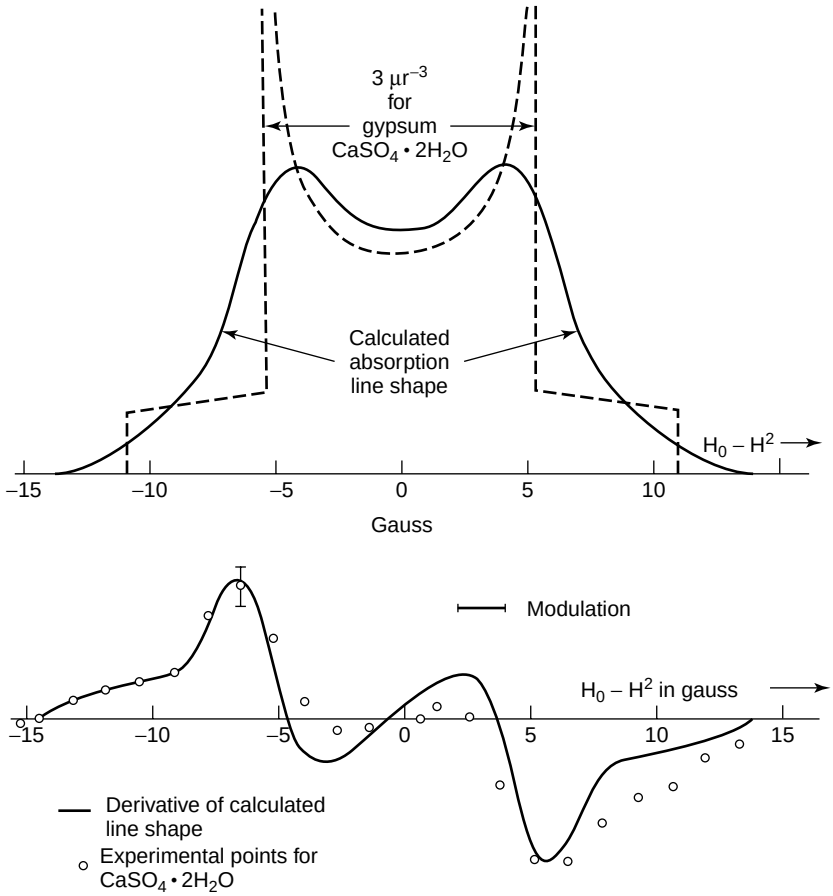

Figure 2 This is Figure 8 from the paper by Pake.[1] The broken line in the upper curve shows the calculated distribution of component line centers for the proton resonance in powdered $CaSO_4 \cdot H_2O$. The continuous line on the same plot is the calculated line shape obtained by superposing Gaussians of width 1.54 gauss according to this distribution function. The lower plot contains experimental points for powdered $CaSO_4 \cdot H_2O$, and a curve which is the derivative of the calculated line shape

Other important topics discussed in this seminal contribution on the local field include the effects of motional averaging and the dominance of homo-nuclear over hetero-nuclear couplings.

Twenty-years after Pake[1] showed that solid-state NMR spectra from samples with chemically isolated pairs of spins could be used to determine molecular structures and Van Vleck[17] discussed the consequences of truncation in NMR experiments, Waugh et al.[15] demonstrated that the severe line-broadening present in chemical samples with normally abundant collections of spins could be selectively averaged with multiple-pulse sequences that could be analyzed in terms of coherent averaging theory.[18] In particular, a pulse sequence was employed that removed the effects of homo-nuclear dipolar couplings while largely preserving the chemical shift effects. Significant parallel developments involved the application of magic angle sample spinning[12,13] and the demonstration of line narrowing by irradiation arranged by choice of amplitude and frequency-offset to place the magnetization at the magic angle with respect to the magnet field.[14,19] Thorough analysis of multiple-pulse and other line-narrowing procedures led to a thorough understanding in terms of coherent averaging theory as well as improvements in the sequences themselves.[18,20–24] Multiple-pulse sequences offer the important advantage of being able to sample the magnetization in the windows between the pulses. The high duty cycle of the Lee-Goldburg procedures, especially when implemented with phase- and frequency-alternation[25–27] has led to its use in many multi-dimensional hetero-nuclear experiments where the signals from the dilute rather than the abundant spins are observed.[28]

The development of double-resonance cross-polarization methods[16,29] enabled solid-state NMR spectroscopy to shift its emphasis to the "dilute" spins, such as ^{13}C and ^{15}N. Heteronuclear decoupling is easier to implement experimentally and can be accomplished without the scaling (reduction) of chemical shift frequencies that accompanies multiple-pulse line narrowing of ^{1}H resonances. It is possible to study polycrystalline samples with the use of magic angle sample spinning.[30] However, there is a second way to obtain high resolution chemical shift spectra of solid samples that involves the use of single crystals where the molecules have only one or a few orientations relative to each other and the applied magnetic field. Fortunately, it is not necessary to have a single crystal sample. One direction of molecular orientation is sufficient, as long as it is parallel to the magnetic field, to give all of the spectroscopic benefits of sample orientation.[4] Typically, it is much easier to prepare uniaxially oriented samples of many materials, including proteins in biological supramolecular structures like membrane bilayers, than single crystals for X-ray diffraction or even rapidly reorienting solutions for NMR spectroscopy.

The samples can take the form of drawn fibers, magnetically oriented liquid crystals, or phospholipid bilayers mechanically oriented between glass plates. In uniaxially oriented samples, each site on one molecule can be transformed into the identical site on another molecule through a combination of translation, inversion, and rotation operations about an axis parallel to the direction of the applied magnetic field. Just as observed for single crystals, the spectra of oriented protein samples are characterized by narrow single line resonances rather than powder patterns. The resonance frequencies reflect the orientations of the individual groups, and the geometrical dependencies of the chemical shift, heteronuclear dipolar, and quadrupolar interactions are well characterized. As a result, the solid-state NMR spectra of oriented samples are a rich source of structural information.

3 SEPARATION OF LOCAL FIELDS

The spectroscopic separation of effects from the chemical shift and heteronuclear dipolar interactions are manifested in several different ways in solid-state NMR experiments. This can be appreciated by considering that both the build-up of signal intensity through cross-polarization and the observation of decoupled signals depend on quite different manipulations of the heteronuclear dipolar couplings. There are additional opportunities to observe the effects of heteronuclear dipolar couplings in more complex experiments.

Transient oscillations are observed in the rates of build-up of the intensities of the dilute spin signals as they are developed through spin-lock cross-polarization.[31] These oscillations have characteristic frequencies that reflect the magnitude of the heteronuclear dipolar coupling that provides the mechanism for transfer of magnetization from the abundant ^{1}H spin to the dilute ^{13}C or ^{15}N spin.[32] Since the dilute spin signals are detected under high-resolution conditions, the signals from individual molecular sites are resolved. This is most obvious in the spectra of single crystal samples. However, it is also the case for polycrystalline samples where the chemical shift powder pattern discriminates among spins with different orientations with respect to the applied magnetic field, consistent with the representation in Figure 1. Vaughan and coworkers[5] utilized the modulation of chemical shift spectra by the effects of heteronuclear dipolar interactions of polycrystalline solids.

While most attention has been paid to heteronuclear couplings, as described above, there are situations when the homonuclear couplings are of interest. This is the case for both abundant and dilute spins, and their definitions can overlap with the use of uniformly ^{13}C and ^{15}N labeled proteins. The original work of Pake demonstrated the value of the homonuclear dipolar coupling and that it was spectroscopically accessible with a chemically dilute sample. Stoll et al.[5] demonstrated a multiple pulse experiment that incorporated two separate time incrementations. This experiment is quite interesting in that it is basically the reverse of what would be used in many subsequent multi-dimensional experiment involving heteronuclear dipolar couplings. Here the first interval is used for the evolution of the homonuclear dipolar interaction, and then the multiple-pulse sequence is applied and data acquired in the usual way in the windows. In this study, the dipolar modulated chemical shift powder patterns were analyzed by comparison to calculations based on the established properties of the molecule. As suggested by the one-dimensional ^{1}H NMR spectrum with great similarity to the Pake doublet in Figure 2, the Fourier transformation of signals in both time dimensions was about to have its enormous impact on all types of spectra, including those that separate the homonuclear dipolar Pake doublet from the chemical shift powder pattern in polycrystalline samples. Since both the chemical shift and dipolar coupling frequencies depend on orientation, hydrogens with different chemical shifts have different dipolar couplings. The first use of the Fourier transform to analyze the frequencies of the dipolar oscillations during cross-polarization

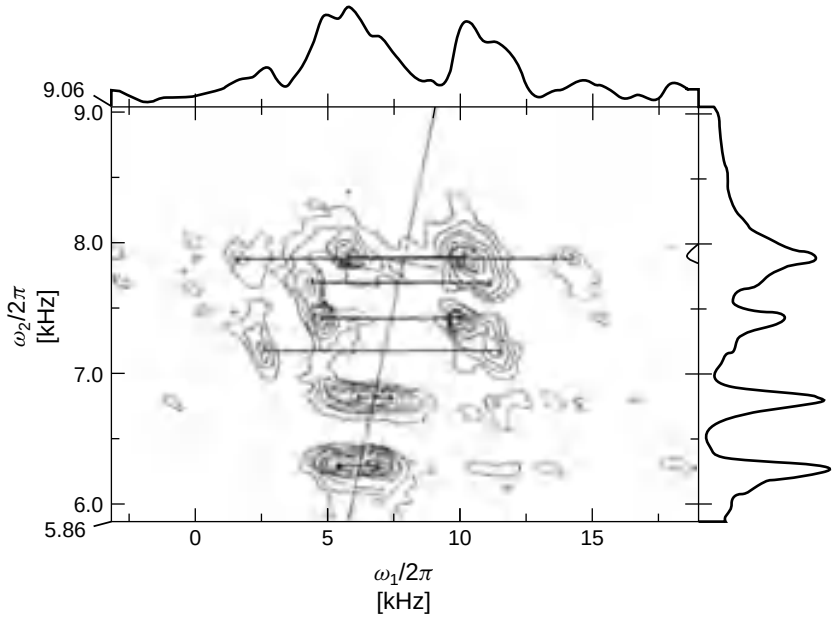

Figure 3 This is Figure 2 from the paper by Hester et al.[2] Contour plot of function f(ω1, ω2). Dipolar splittings for each of the observed seven lines are indicated by the heavy lines. The line bisecting the splittings is the locus $\omega 1 = \omega 2 = \Delta$n

was demonstrated by Hester et al.[32] However, this experiment was soon replaced by separated local field spectroscopy, which yielded direct measurements of dipolar coupling and chemical shift frequencies.[2,33]

As proposed[33] and demonstrated[2] by Waugh and coworkers, the separate lines of spectroscopic development described above could be consolidated within the domain of two-dimensional spectroscopy.[34] Separated-local-field spectroscopy elegantly incorporates radio frequency irradiations in the form of multiple-pulse sequences to average out homonuclear dipole–dipole couplings and double-resonance procedures to average out heteronuclear dipole–dipole couplings. The chemical-shift dimension in separated-local-field spectra has intrinsically high resolution because continuous on-resonance ^{1}H irradiation decouples the heteronuclear dipolar interactions during the t_2 interval when data are acquired; however, even with the use of homonuclear multiple-pulse decoupling, the doublets (or multiplets) in the dipolar frequency dimension are generally quite broad due to the rapid decay of the *S*-spin signals from incomplete decoupling of the homonuclear dipole–dipole interactions, short T_2 and cumulative effects of longer-range heteronuclear dipole–dipole interactions. The two-dimensional separated local field spectrum in Figure 3 illustrates the ability of this approach to associate a single dipolar coupling with each resolved dilute spin resonance.[2]

PISEMA (polarization inversion spin-exchange at the magic angle)[28] is a high-resolution version of separated local field spectroscopy. By combining polarization inversion with flip–flop Lee–Goldburg homonuclear decoupling on the abundant *I* spins following spin-lock cross polarization to the dilute *S* spin during the t_1 interval of the pulse sequence, very high resolution two-dimension heteronuclear $I-S$ dipolar spectra of solid samples can be obtained. Line widths in the dipolar dimension are reduced by more than an order of magnitude compared to a conventional separated local field spectrum obtained without homonuclear decoupling during the t_1 interval. The combination of narrow lines and favorable scaling factor has such a dramatic effect on the appearance of the spectra that it is now feasible to formulate solid-state NMR experiments where heteronuclear dipolar coupling frequencies provide a mechanism for resolution among similar chemical sites. Even more interestingly, dipolar coupling and chemical shift frequencies can be used in a number of complementary ways to enhance resolution in reduced or maximum dimensional experiments, and to provide qualitative and quantitative indications of molecular structure. Two-dimensional ^{1}H/^{15}N and ^{1}H/^{13}C PISEMA spectra have narrow line widths in both the heteronuclear dipolar coupling and chemical shift frequency dimensions, enabling dipolar couplings to complement chemical shifts as a mechanism for spectroscopic resolution as well as the measurement of readily interpretable orientationally dependent frequencies for individual molecular sites.

4 MULTIDIMENSIONAL SOLID-STATE NMR CORRELATION SPECTROSCOPY

The two-dimensional PISEMA experiment provides a fundamental building-block for multidimensional solid-state NMR experiments on proteins in oriented samples. The pulse sequence for three-dimensional ^{1}H shift/^{1}H–^{15}N dipolar coupling/^{15}N shift correlation spectroscopy shown in Figure 4[35] enabled the first fully resolved spectra of uniformly ^{15}N labeled proteins to be obtained for membrane proteins in lipid bilayers.[6,10,36] Further, many individual resonances could be resolved in a membrane protein with 190 residues,[37] and it is clear that with further development substantially larger membrane proteins can be studied.

The ^{1}H chemical shift, ^{1}H–^{15}N dipolar coupling, and ^{15}N chemical shift interactions at amide sites are of particular interest because of their important roles in both solution and solid-state NMR studies of ^{15}N-labeled proteins. The three-dimensional powder pattern in Figure 5(A)[35] encompasses all frequencies available to the three spin interactions present in a ^{15}N labeled amide group of a peptide. Since the $I-S$ dipolar interaction is symmetric about zero, the unique spectral information from the ^{1}H–^{15}N couplings is contained in the positive frequencies. When the spectrum in Figure 5(A)

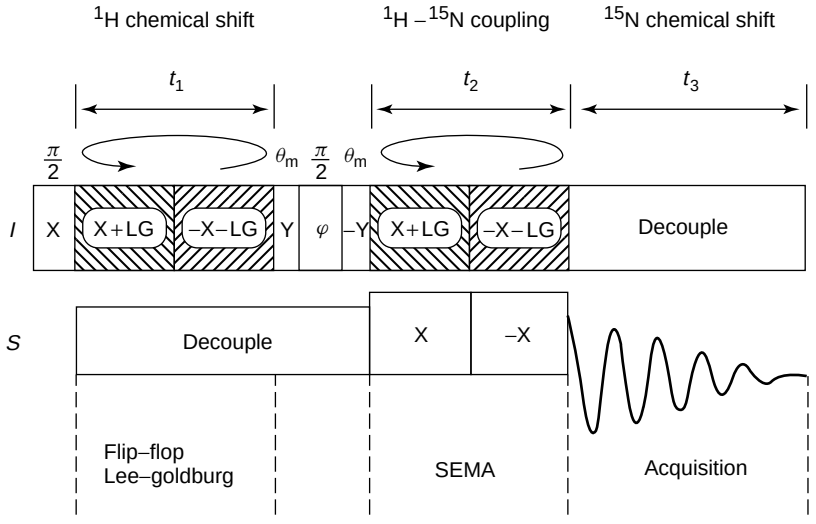

Figure 4 This is Figure 1 from the paper by Ramamoorthy et al.[35] Pulse sequence for three-dimensional $I-$spin chemical shift, $I-S$ dipolar coupling, and *S*-spin chemical-shift correlation spectroscopy

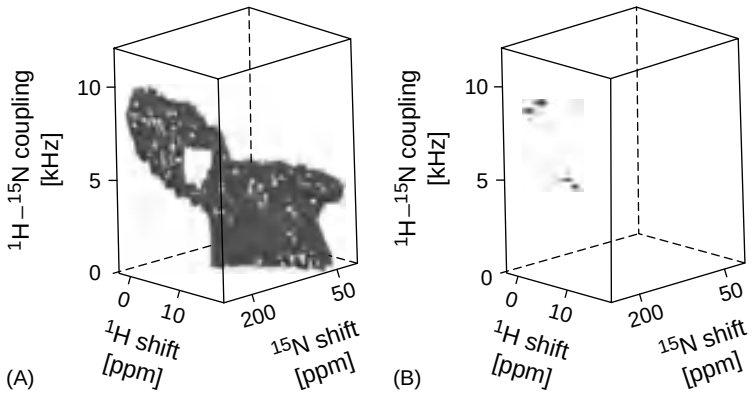

Figure 5 This is Figure 2 from the paper by Ramamoorthy et al.[35] Experimental three-dimensional ^{1}H chemical shift/^{15}N–^{1}H heteronuclear dipolar coupling/^{15}N chemical-shift correlation spectra of ^{15}N-acetyl-leucine. (A) Polycrystalline sample. (B) Single-crystal sample

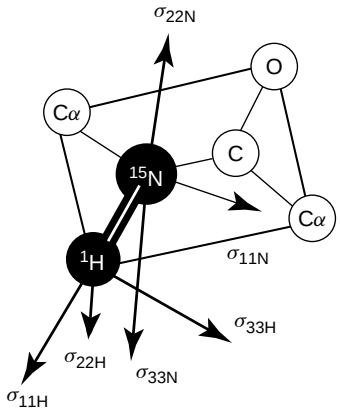

Figure 6 This is Figure 3 from the paper by Wu et al.[28] Orientation of the principal axes of the amide 1H chemical shift, ^{1}H–^{15}N dipolar, and ^{15}N chemical shift interaction tensors in a peptide bond

is viewed from the ^{15}N chemical shift/^{1}H–^{15}N dipolar coupling plane it has a characteristic low-intensity "hole" that is a consequence of the marked noncolinarity of the ^{15}N chemical-shift tensor and the N–H bond axis, as shown in Figure 6.[28]

The resolution available by applying the three-dimensional pulse sequence diagrammed in Figure 4 to the most crowded spectral regions of a protein is illustrated in Figure 7.[36] The sample is uniformly ^{15}N labeled fd coat protein in oriented lipid bilayers. This polypeptide has two major classes of resonances because it has a *trans*-membrane helix and a shorter in-plane helix that resolute in the vast majority of residues having similar backbone orientations with their N–H bonds either parallel or perpendicular to the field. However, the ^{1}H chemical shift separated two-dimensional ^{1}H–^{15}N dipolar coupling/^{15}N chemical shift planes display excellent resolution.

5 PISA WHEELS

On the path toward three-dimensional structure determination, the secondary structure and topology of membrane proteins can be described by inspection of the two-dimensional ^{1}H/^{15}N PISEMA spectra of uniformly ^{15}N-labeled samples in oriented bilayers. The characteristic 'wheel-like' patterns of resonances observed in these spectra reflect helical wheel projection of residues in both transmembrane and in-plane helices and hence provide direct indices of secondary structure and topology of membrane proteins in phospholipid bilayers. We refer to these patterns as PISA (polarity index slant angle) wheels.[7,8] The resonance frequencies in PISEMA spectra of oriented samples or membrane proteins depend on helix orientation, as well as on the backbone dihedral angles, the magnitudes and orientations of the principal elements of the amide ^{15}N chemical shift tensor, and the NH bond length. Therefore, it is possible to calculate solid-state NMR spectra for specific structural models of proteins, as shown in Figure 8.

When the helix axis is parallel to the bilayer normal all of the amide sites have an identical orientation relative to the direction of the applied magnetic field, and therefore all of the resonances overlap with the same dipolar coupling and chemical shift frequencies. Tilting the helix away from the membrane normal breaks the symmetry, introducing variations in the orientations of the amide NH bond vectors relative to the field. This is manifest in the spectra as dispersions of both the ^{1}H–^{15}N dipolar coupling and the ^{15}N chemical shift frequencies. Since a modest helix tilt of about 10° aligns the NH bond form one amide site and the σ_{33} amide ^{15}N chemical shift tensor element of another amide site with the magnetic field, the maximum values of both of these frequencies are observed in the spectrum, albeit from different amide resonances because σ_{33} of the shift tensor is rotated approximately 17° from the NH bond vector, as shown by the low-intensity region of the spectrum in Figure 6. Nearly all transmembrane helices are tilted with respect to the bilayer normal, and it is the combination of the tilt and the 17° difference between the direction of σ_{33} and the NH bond vector that makes it possible to resolve many resonances from residues in otherwise uniform helices and is responsible for the 'wheel-like' pattern in PISEMA spectra. For all helix orientations other than parallel to the field (0°), the spectra have 'wheel-like' patterns whose frequency breadths, especially in the dipolar coupling dimension, reflect the extent of helix tilt. For helices with tilts greater than 40° some amide NH bonds adopt orientations near the magic angle (55°) with respect to the direction of the magnetic field and have resonances with dipolar couplings of close to 0 kHz. Other

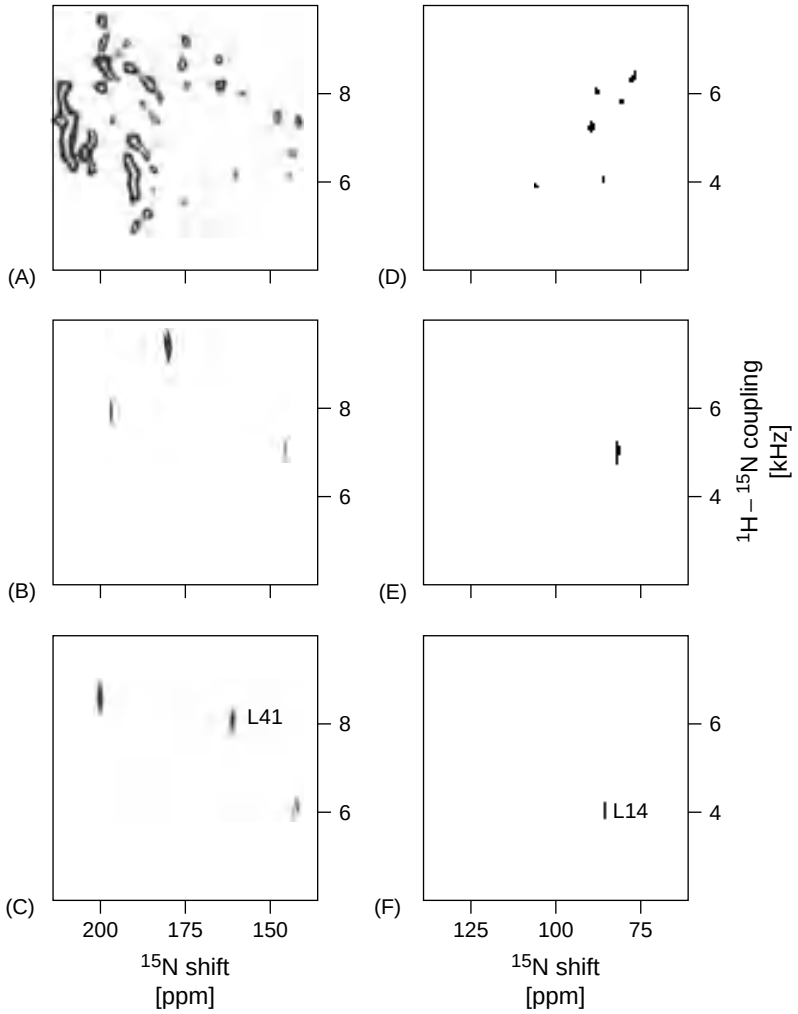

Figure 7 This is Figure 3 from the paper by Marassi et al.[6] Two-dimensional ^{1}H–^{15}N heteronuclear dipolar coupling/^{15}N chemical shift spectral planes from spectra of an oriented sample of uniformly ^{15}N-labeled fd coat protein in phospholipid bilayers. (A. and D.) expansion of the complete two-dimensional PISEMA spectrum of the protein. A is the trans-membrane helix region and D is the in-plane helix region. (B) Plane extracted from the three-dimensional correlation spectrum at ^{1}H chemical shift 7.4 ppm. (C) Plane extracted from a three-dimensional correlation spectrum at ^{1}H chemical shift 11.0 ppm; the resonance assigned to Leu-41 is marked. (E) Plane extracted from a three-dimensional correlation spectrum at ^{1}H chemical shift 12.5 ppm. (F) Plane extracted from a three-dimensional correlation spectrum at ^{1}H chemical shift 11.6 ppm; the resonance assigned to Leu-14 in the amphipathic in-plane helix is marked

amide NH bonds are oriented with angle greater than 55° and have resonances with dipolar couplings of opposite sign, which results in a portion of the 'wheel-like' PISEMA spectrum being reflected through the 0 kHz axis. Figure 8 shows that helices oriented parallel to the membrane surface have their amide NH bonds and σ_{33} of the ^{15}N chemical shift tensor nearly orthogonal to the field and give highly overlapped spectra with all of the resonance frequencies around 5 kHz and 75 ppm. The spectra in Figure 8 demonstrate that it is possible to determine the tilt of a helix in lipid bilayers without resonance assignments.

In the experimental PISEMA spectrum of AchR M2 shown in Figure 9(B), the order of resonances in the 'wheel-like' pattern follows that of the helical wheel projection shown in Figure 9(A). The helical wheel is arranged so that the residues align with their corresponding amide resonances, as predicted by the simulated spectrum in Figure 9(C). The polarity of the ordering of resonances in the 'wheel-like' pattern in a PISEMA spectrum provides a direct measure of the angle of helix rotation (polarity index) about its long axis within the membrane. In principle, only a single assignment is needed to determine the polarity of a helix in the membrane. This example is based on an ideal helix. Deviations from ideal Ramachandran angles that result in local kinks or long-range bends can be readily accommodated within this framework.

6 CALCULATIONS FOR PROTEIN STRUCTURE DETERMINATION FROM SOLID-STATE NMR DATA

In principle, a single three-dimensional correlation spectrum of an oriented sample of a uniformly ^{15}N labeled protein provides sufficient information for complete structure determination. The three frequencies, ^{1}H chemical shift, ^{15}N chemical

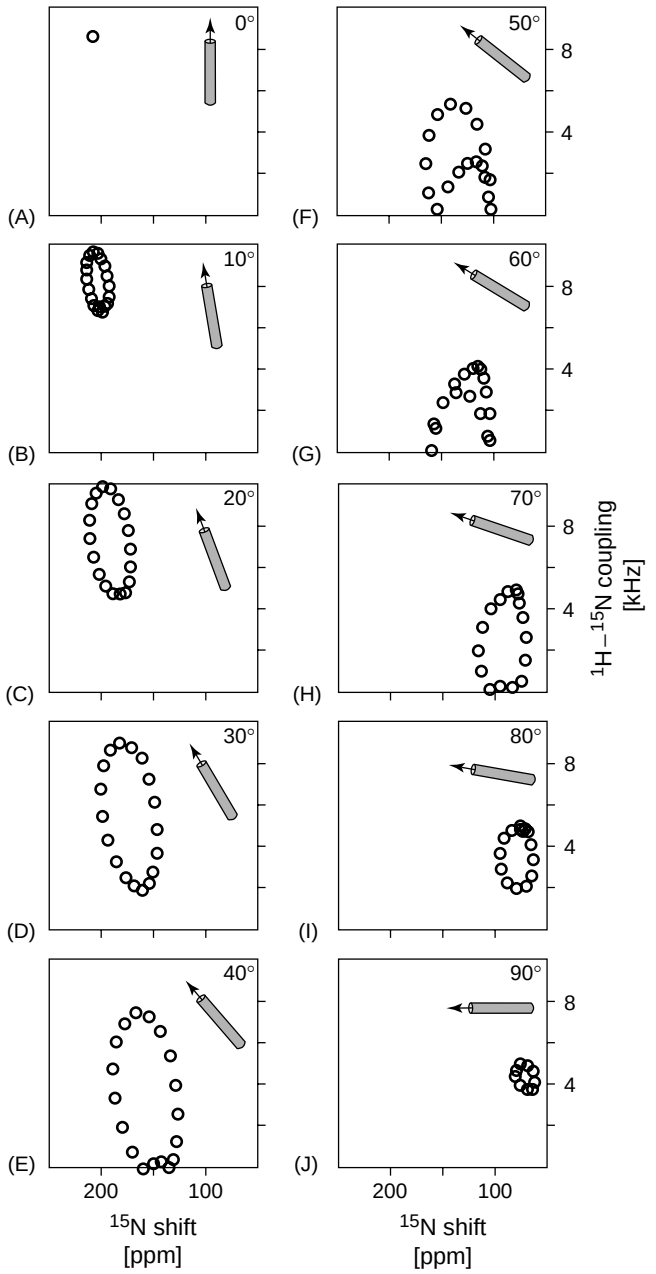

Figure 8 This is Figure 1 from the paper by Marassi and Opella.[7] PISEMA spectra calculated for a 19-residue α-helix with 3.6 residues per turn and uniform dihedral angles ($\phi = -65°$, $\psi = -40°$) at various helix tilt angles relative to the bilayer normal

shift, and ^{1}H/^{15}N dipolar coupling, measured for each resonance depend on the magnitudes and orientations of the principal elements of the spin-interaction tensors in the molecule, and on the orientation of the molecular site with respect to the direction of the applied magnetic field. Because the orientation of the bilayer is fixed by the method of sample preparation, each frequency reflects the orientation of a specific site in the protein with respect to the bilayer. Structures are calculated using the angular constraints extracted from the measured spectral frequencies. Using this approach determined the three-dimensional structure of the M2 transmembrane segment from the acetylcholine receptor, as described below.[10] The ^{13}C chemical shift and the ^{2}H quadrupolar coupling frequencies, measured from selectively or specifically labeled samples in separate experiments, also provide valuable structural information, and have been used together with the ^{15}N chemical shift and the ^{1}H/^{15}N dipolar coupling, to determine the structure of the gramicidin channel at high resolution.[38]

The backbone structure of a protein is defined by the planes formed by the individual rigid peptide bonds and their directly bonded atoms. This is equivalent to the conventional description by vectors representing bonds between non-hydrogen atoms. A standard planar peptide geometry serves as the building block for the structure assembly process. The orientation of a peptide plane consistent with the measured NMR frequencies is defined in terms of polar angles relative to the magnetic field. The inputs to the computer program are the NMR frequencies measured from a three-dimensional correlation spectrum, and the values of the amide ^{15}N and ^{1}H chemical shift tensors. Once the orientations of all the peptide planes in the protein are calculated, neighboring planes of fixed orientation are connected through their common α-carbon atom, with the only constraint of a fixed tetrahedral angle of 110°. Another program calculates the phi and psi dihedral angles for the two contiguous peptide plane combinations that satisfy tetrahedral angle geometry at the α-carbon. The advantage of this direct mathematical analysis is that it is possible to determine the standard deviations in phi and psi based on uncertainties in the experimentally determined angles. Another important advantage of the method is that is results in the 'piece-wise' assembly of structures. Different parts of the protein structure can be determined independently of the rest. This is not possible in methods where distance constraints between different regions of the protein must be established for three-dimensional structure determination. Because the orientation of individual peptide planes is determined relative to a unique external reference the corresponding errors are not cumulative.

7 APPLICATION TO THE THREE-DIMENSIONAL STRUCTURE OF THE ACETYLCHOLINE M2 PEPTIDE IN LIPID BILAYERS

The three-dimensional structures of functional peptides corresponding to the M2 segments from the α-subunit of the Acetylcholine receptor (AchR) and the NR1 subunit of the NMDA subtype glutamate receptors were determined by solution and solid-state NMR spectroscopy in membrane environments.[10] The relatively large quantities of isotopically labeled M2 peptides required for NMR spectroscopy were prepared by expression of recombinant peptides in *E. coli*, for selective or uniform isotopic labeling, and by solid-phase synthesis, for specifically labeled samples.

The incorporation of the M2 peptides into lipid bilayers reconstitutes functional, cation-selective channels. The single channel currents recorded from AchR M2 in lipid bilayers, under voltage clamp conditions have heterogeneous conductances and lifetimes, as expected for monomeric peptides that self-assemble into conductive oligomers of discrete yet variable size, and display a linear current-voltage relationship. The channels that occur most frequently exhibit a single-channel conductance of about 38 pS in both NaCl and KCl. Significantly, the channel properties of peptides prepared by solid-phase synthesis and by expression in bacteria are nearly

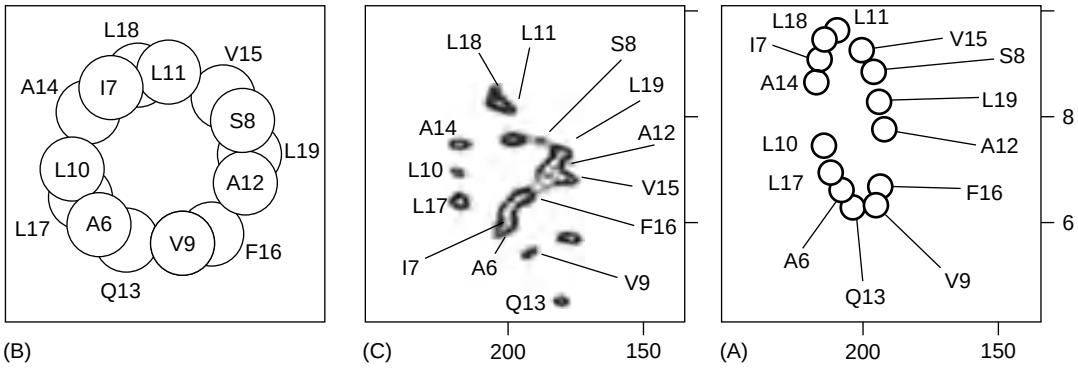

Figure 9 This is taken from Figure 2 from the paper by Marassi and Opella.[7] Helical wheel projection and two-dimensional PISEMA spectra of the uniformly ^{15}N-labeled acetylcholine receptor M2 polypeptide in oriented lipid bilayers. (A) Helical wheel projection of the amide N atoms of the polypeptide. (B) Experimental PISEMA wheel spectrum of the polypeptide, which provided most of the orientational constraints used for structure determination. (C) Spectrum calculated for an a-helix with 3.6 residues per turn, identical dihedral angles (phi $= -65\,°$, psi $= -40\,°$), and a tilt of 12° relative to the membrane normal

identical. Furthermore, peptides with the same amino acid composition as the M2 but with scrambled sequences do not form channels, nor do peptides patterned after the sequences of the predicted M1, M3 or M4 helices. Taken together, these results indicate that both the recombinant and synthetic M2 peptides used in the NMR experiments are functional, and form sequence-specific, discrete ion-channels in lipid bilayers.

The two-dimensional solid-state ^{1}H/^{15}N PISEMA spectrum of the peptide in oriented bilayers (Figure 9B) has excellent resolution, with each amide resonance characterized by ^{15}N chemical shift and ^{1}H$-^{15}$N dipolar coupling frequencies. The ^{15}N chemical shift and ^{1}H$-^{15}$N dipolar coupling frequencies provide orientational constraints for structure determination of ^{15}N labeled peptides in lipid bilayer membranes, and can be measured directly from the two-dimensional PISEMA spectrum shown in Figure 7(B) for AchR M2. The backbone structure of AchR M2, determined from ^{15}N chemical shift, ^{1}H$-^{15}$N dipolar coupling, and some ^{1}H chemical shift constraints, is shown in Figure 10. Solid-state NMR on oriented lipid bilayer samples is unique in determining the complete topology, including three-dimensional structure and orientation, of the peptide in the membrane, at high resolution. This is a crucial element of membrane protein structure, and in the case of AchR M2, sheds light on the details of supramolecular channel architecture. The AchR M2 peptide is a transmembrane α-helix with its long helix axis tilted 12° relative to the lipid bilayer normal (88° from the lipid bilayer plane).

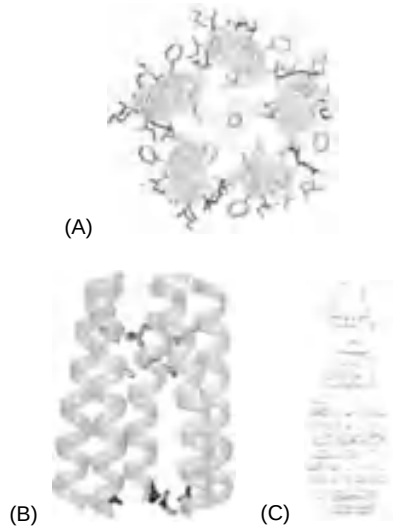

Figure 10 This is taken from Figure 5 from the paper by Opella et al.[10] Top (A) and side (B, C) views of a model of the acetylcholine receptor M2 funnel-like pentameric bundle. The channel architecture was calculated using the three-dimensional coordinates of the M2 helix in the lipid bilayer determined by solid-state NMR spectroscopy, and by imposing a symmetric pentameric organization. (C) is the pore profile

Figure 10 shows a model of the AchR channel pore. It was constructed from the three-dimensional structure of the AchR M2 helix derived from solid-state NMR data and the pentameric organization of the channel in lipid bilayers. The optimized pentameric bundle has a right-handed, inter-helical twist with an orientation angle of 12°. A central narrow pore has a diameter ranging from about 3.0 Å to 8.6 Å. Nonpolar residues are predominantly on the exterior of the bundle, while polar residues line the pore. The residues exposed to the pore lumen are Glu-1, Ser-4, Ser-8, Val-15, Leu-18 and Gln-22, which is in agreement with evidence collected from mutagenesis, affinity labeling and cysteine accessibility measurements. A side view shows a funnel-shaped bundle, 33 Å in length, with the wide mouth at the N-terminus. A dotted contour depicting the profile of the ion-conduction pore calculated from the structure is shown. The channel lining hydroxyl residues are in agreement with the expectations of a water-filled pore, and the constrictions are compatible with the permeation of both Na and K ions.

8 SUMMARY

The structure of the polypeptide shown in Figure 10 was determined using solid-state NMR methods that were direct descendents of the initial observations of doublets due to local fields in 1948. The advances required to transform solid-state NMR from a spectroscopic technique to a generally applicable method for determining molecular structures included

multiple-pulse sequences, double-resonance methods, and separated local field spectroscopy. It also required improvements in instrumentation, especially the use of high-field magnets. The pace of development is accelerating, and the local field is being utilized in an increasing number of ways in spectroscopic investigations of molecular structure and dynamics.

9 REFERENCES

1. G. E. Pake, *J. Chem. Phys.*, 1948, **16**, 327.
2. R. K. Hester, J. L. Ackerman, B. L. Neff, and J. S. Waugh, *Phys. Rev. Lett.*, 1976, **36**, 1081.
3. E. F. Rybaczewski, B. L. Neff, J. S. Waugh, and J. S. Sheerfinski, *J. Chem. Phys.*, 1976, **67**, 1232.
4. S. J. Opella and J. S. Waugh, *J. Chem. Phys.*, 1977, **66**, 4919.
5. M. E. Stull, A. J. Vega, and R. W. Vaughan, *J. Chem. Phys.*, 1978, **69**, 5458.
6. F. M. Marassi, A. Ramamoorthy, and S. J. Opella, *Proc. Natl. Acad. Sci. USA*, 1997, **94**, 8551.
7. F. M. Marassi and S. J. Opella, *J. Magn. Reson.*, 2000, **144**, 150.
8. J. Wang, J. Denny, C. Tian, S. Kim, Y. Mo, F. Kovacs, Z. Song, K. Nishimura, Z. Gan, R. Fu, J. R. Quine, and T. A. Cross, *J. Mag. Reson.*, 2000, **144**, 162.
9. S. J. Opella, P. L. Stewart, and K. G. Valentine, *Q. Rev. Biophys.*, 1987, **19**, 7.
10. S. J. Opella, F. M. Marassi, J. J. Gesell, A. P. Valente, Y. Kim, M. Oblatt-Montal, and M. Montal, *Nature Struct. Biol.*, 1999, **6**, 374.
11. A. Abragam, 'The Principles of Nuclear Magnetism', Clarendon Press: Oxford, 1961.
12. E. R. Andrew, A. Bradbury, and R. G. Eades, *Arch. Sci.*, 1958, **11**, 223.
13. I. J. Lowe, *Phys. Rev. Lett.*, 1959, **2**, 28.
14. W. J. Goldburg and M. Lee, *Phys. Rev. Lett.*, 1963, **11**, 255.
15. J. S. Waugh, L. M. Huber, and U. Haeberlen, *Phys. Rev. Lett.*, 1968, **20**, 180.
16. A. Pines, M. G. Gibby, and J. S. Waugh, *J. Chem. Phys.*, 1972, **56**, 1776.
17. J. H. VanVleck, *Phys. Rev.*, 1948, **74**, 1168.
18. U. Haeberlen and J. S. Waugh, *Phys. Rev. Lett.*, 1968, **175**, 453.
19. M. Lee and W. J. Goldburg, *Phys. Rev.*, 1965, **140**, A1261.
20. P. Mansfield, *Phys. Lett.*, 1970, **A32**, 485.
21. W.-K. Rhim, D. D. Elleman, and R. W. Vaughan, *J. Chem. Phys.*, 1973, **58**, 1772.
22. W.-K. Rhim, D. D. Elleman, and R. W. Vaughan, *J. Chem. Phys.*, 1973, **59**, 3740.
23. W.-K. Rhim, D. D. Elleman, L. B. Schreiber, and R. W. Vaughan, *J. Chem. Phys.*, 1974, **60**, 4595.
24. U. Haeberlen, 'High Resolution NMR in Solids', Academic Press: New York, 1976.
25. M. Mehring and J. S. Waugh, *Phys. Rev. B*, 1972, **5**, 3459.
26. A. Bielecki, A. C. Kolbert, and M. H. Levitt, *Chem. Phys. Lett.*, 1989, **155**, 341.
27. A. Bielecki, A. C. Kolbert, H. J. M. de Groot, R. G. Griffin, and M. H. Levitt, *Adv. Mag. Reson.*, 1990, **14**, 111.
28. C. H. Wu, A. Ramamoorthy, and S. J. Opella, *J. Mag. Reson.*, 1994, **A109**, 270.
29. A. Pines, M. G. Gibby, and J. S. Waugh, *J. Chem. Phys.*, 1973, **59**, 569.
30. J. Schaefer and E. O. Stejskal, *J. Am. Chem. Soc.*, 1976, **98**, 1031.
31. L. Muller, A. Kumar, T. Baumann, and R. R. Ernst, *Phys. Rev. Lett.*, 1974, **32**, 1402.
32. R. K. Hester, J. L. Ackerman, V. R. Cross, and J. S. Waugh, *Phys. Rev. Lett.*, 1975, **34**, 993.
33. J. S. Waugh, *Proc. Nat. Acad. Sci. USA*, 1976, **73**, 1394.
34. W. P. Ave, E. Bartholdi, and R. R. Ernst, *J. Chem. Phys.*, 1976, **64**, 2229.
35. A. Ramamoorthy, C. H. Wu, and S. J. Opella, *J. Mag. Reson.*, 1995, **B107**, 88.
36. F. M. Marassi, C. Ma, J. J. Gesell, and S. J. Opella, *J. Magn. Reson.*, 2000, **144**, 156.
37. Y. Kim, K. Valentine, S. J. Opella, S. L. Schendel, and W. A. Cramer, *Protein Sci.*, 1998, **7**, 342.
38. R. R. Ketchem, W. Hu, and T. A. Cross, *Science*, 1993, **261**, 1457.

Acknowledgements

The research on solid-state NMR of proteins was supported by grants R37GM24266, RO1GM29754, and PO1GM56538 from the National Institute of General Medical Sciences and utilized the Resource for Solid-State NMR of Proteins supported by grant P41RR09731 from the Biomedical Research Technology Program, National Center for Research Resources.

Biographical Sketch

Stanley Joseph Opella, *b* 1947. Ph.D. 1974 Physical Chemistry, Stanford University. Postdoctoral fellow, M.I.T., 1975–76; Professor of Chemistry at the University of Pennsylvania, 1976–2000. Professor of Chemistry and Biochemistry at the University of California, San Diego, 2000-present. Approx. 200 publications. Current research interests: development and application of NMR for the study of proteins.

NOESY

Michael P. Williamson
University of Sheffield, Sheffield, UK

1	Introduction	1
2	The NOESY Experiment: Theory	1
3	The NOESY Experiment: Practice	4
4	Applications of NOESY	7
5	Variations on the NOESY Experiment	8
6	Related Articles	8
7	References	8

1 INTRODUCTION

The Nuclear Overhauser Effect or NOE is a relaxation phenomenon which is used very widely in solution state NMR because it gives direct and readily interpretable information on short internuclear distances which can then be used to derive structural details (see ***Nuclear Overhauser Effect***).[1,2] A wide variety of experiments have been developed to measure NOEs. One of the most commonly used experiments is the two-dimensional NOE experiment, generally known by the acronym NOESY (two-dimensional Nuclear Overhauser Effect SpectroscopY), which was introduced by the inventors of the experiment, Richard Ernst and his colleagues.[3] The NOESY experiment is most commonly applied to the assignment and structure determination of biological macromolecules.[4]

NOESY experiments are simple to set up, and simple to interpret in a qualitative way, namely that a NOESY cross peak connecting two signals implies a short distance between them. However, a more quantitative approach is full of pitfalls for the unwary.

1.1 Interpretation of NOESY Spectra

NOESY spectra are simple to acquire, process, and interpret, which explains their widespread use. In common with most other two-dimensional experiments, NOESY spectra are normally presented as square plots containing a line of diagonal peaks and symmetrically placed cross peaks (Figure 1) (see ***Multidimensional Spectroscopy: Concepts***). The spectra are normally presented as contour plots for ease of analysis. Although the spectra are in principle symmetrical about the diagonal, in practice they are not completely symmetrical because of different digital resolution and processing parameters in the two dimensions, relaxation effects and experimental artifacts. The two dimensions are therefore distinguished by the labels F_1, F_2 (or sometimes Ω_1, Ω_2; ω_1, ω_2; ν_1, ν_2; or even the incorrect t_1, t_2), where 1 and 2 refer respectively to the indirectly and directly detected dimensions (see below). There is no convention as to which dimension is drawn as the y axis, but more normally the F_1 axis would be vertical.

Cross peaks with nonzero net intensity originate from cross relaxation between the two nuclei at the frequencies of the cross peak. Cross relaxation only occurs between nuclei that are close together, and hence a cross peak is readily interpreted as a close distance between the two nuclei at the chemical shifts of the cross peak. The meaning of 'close' obviously depends upon the molecule under investigation and the sensitivity of the experiment, but it may generally be taken to mean about 5 Å, except in cases of severe spin diffusion where a longer distance is appropriate. The relationship between distance and cross-peak intensity is discussed below and is not straightforward, but in many cases a very crude measure of intensity is sufficient to provide the required structural information.

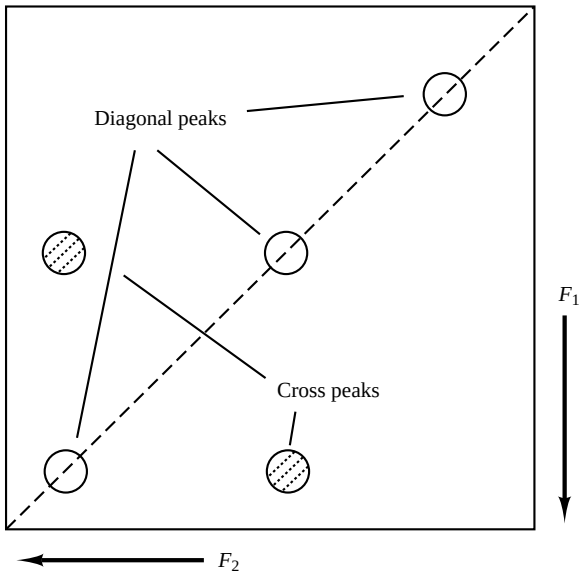

Figure 1 The basic elements of a NOESY spectrum

NOESY spectra may contain other artifactual peaks. These could include axial peaks (along the line $F_1 = 0$), quadrature images (in either dimension, but more commonly in F_1), t_1 noise, t_2 noise, and antiphase cross peaks deriving from coherent magnetization transfer. Apart possibly from the antiphase peaks, these signals contain no useful information and are minimized by suitable experimental design, as discussed below.

NOESY is a method of measuring magnetization transfer between pairs of nuclei. It is therefore equally good at measuring chemical exchange as it is at measuring NOEs, and the same experiment is used for both measurements (see ***Two-Dimensional Methods of Monitoring Exchange***).[5] This implies that it is difficult to distinguish exchange from NOEs. In practice the two effects are usually obviously distinguishable, from the chemistry of the molecule or from the different rates of the two processes, but in ambiguous cases a distinction can be made based on the effect of temperature or by using ROESY (see below).

2 THE NOESY EXPERIMENT: THEORY

2.1 The Pulse Sequence

The NOESY pulse sequence is shown in Figure 2. It consists simply of three pulses, each of 90°. The simplest

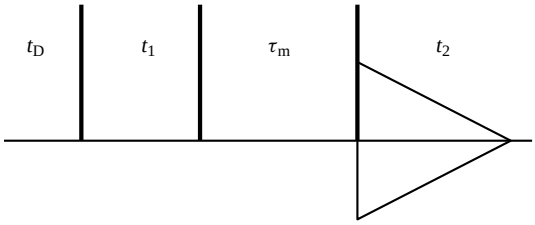

Figure 2 The NOESY pulse sequence. The vertical bars represent 90° pulses

system required to understand the pulse sequence is a system of two protons which are not spin–spin coupled. The first pulse converts longitudinal z magnetization into transverse magnetization. During the subsequent period t_1, the magnetization precesses around the z axis, so that at the end of t_1 each nucleus has precessed through an angle ωt_1, where ω is the angular frequency of the nucleus compared with the reference frequency, or in other words its chemical shift difference from the carrier, which in a quadrature detection experiment is in the center of the spectrum. The second pulse rotates this magnetization around the pulse axis, so that an x pulse would produce magnetization in the xz plane. The phases of the pulses are cycled in subsequent pulse sequences so that any residual transverse magnetization following the second pulse is canceled out. Thus, the only magnetization that is added constructively as a result of the complete phase cycle is that resulting from the magnetization that is along the z axis after the second pulse. This magnetization has the magnitude $-\cos(\omega t_1)$. The first two pulses have therefore achieved a *frequency labeling* of magnetization, in which each magnetization vector now has an intensity modulated both by t_1 and by its frequency.[6]

The period between the second and third pulses is the mixing period τ_m during which the NOE develops, as described in the next section. By the end of this period, z magnetization has become modified by cross relaxation. The z magnetization is read by the final pulse, which converts it to transverse magnetization. As in all 2D experiments, the experiment is repeated for a series of regularly incremented t_1 values and stored as a matrix of points $S(t_1, t_2)$. Finally, the relaxation delay t_D allows magnetization to relax back towards equilibrium before the start of the next pulse sequence. Ideally, $t_D + t_2$ should be at least three-times T_1 for the slowest relaxing species. In practice, this is usually not possible if the experiment is to be acquired within a reasonable length of time. For biological macromolecules, t_D is often set at 0.7–1.5 s, which allows most signals to relax back to within 95% of their equilibrium values.

2.2 NOE Buildup During τ_m

A nucleus I in the presence of other nuclei S will relax at a rate[7]

$$dI_z/dt = -R_I(I_z - I_z^0) - \sum_S (S_z - S_z^0)\sigma_{IS} \qquad (1)$$

where R_I is the longitudinal relaxation rate for spin I, I_z^0 is the equilibrium value of I_z, S_z^0 is the equilibrium value of S_z, and σ_{IS} is the cross-relaxation rate between I and S, which is given by

$$\sigma_{IS} = (1/10)K^2\left[\frac{6\tau_c}{1+\{\omega_I+\omega_S\}^2\tau_c^2} - \frac{\tau_c}{1+\{\omega_I-\omega_S\}^2\tau_c^2}\right] \qquad (2)$$

where

$$K = (\mu_0/4\pi)\hbar\gamma_I\gamma_S r_{IS}^{-3} \qquad (3)$$

In these equations, ω_I and ω_S are the Larmor frequencies for nuclei I and S respectively in rad s^{-1}, which are a factor of 2π greater than the spectrometer frequencies in Hz, and τ_c is the correlation time of the molecule, which is a measure of the time it takes to reorient. The quantities γ_I and γ_S are the magnetogyric ratios of the two nuclei, and r_{IS} is the distance between I and S. The equations are only valid for an isotropically tumbling rigid molecule, and the subsequent discussion assumes a homonuclear NOE, in particular between two protons.

These equations mean that if S_z is not at its equilibrium value, it will cause the intensity of I_z to change at a rate proportional to r_{IS}^{-6}. The basis of the NOESY experiment is that the first two pulses result in a nonequilibrium z magnetization for each nucleus, and that during the mixing period τ_m this produces cross relaxation to other neighboring nuclei. This is detected as a change in the intensity of the signal of nucleus I that is dependent on $\omega_S t_1$, and that therefore appears at $[\omega_2 = \omega_I, \omega_1 = \omega_S]$ in the 2D spectrum. The nonequilibrium magnetization of I also causes changes in the intensity of S, and produces symmetry-related cross peaks at $[\omega_2 = \omega_S, \omega_1 = \omega_I]$.

Equation (1) describes a set of coupled differential equations. This is conveniently written as a matrix equation

$$d\mathbf{M}/d\tau_m = -\mathbf{R}\mathbf{M} \qquad (4)$$

where $\mathbf{M}$ is a column matrix of nonequilibrium magnetizations $M_z - M_z^0$, and $\mathbf{R}$ is the relaxation matrix:

$$\mathbf{R} = \begin{bmatrix} R_1 & \sigma_{12} & \sigma_{13} & \dots & \sigma_{1N} \\ \sigma_{21} & R_2 & \sigma_{23} & \dots & \sigma_{2N} \\ \sigma_{31} & \sigma_{32} & R_3 & \dots & \sigma_{3N} \\ \dots & \dots & \dots & \dots & \dots \\ \sigma_{N1} & \sigma_{N2} & \sigma_{N3} & \dots & R_N \end{bmatrix}$$

The solution of this equation is

$$\mathbf{M}(\tau_m) = \exp(-\mathbf{R}\tau_m)\,\mathbf{M}(0) \qquad (5)$$

where the $\mathbf{M}(0)$ are normalization factors to allow for equivalent groups of nuclei such as methyl protons, and the matrix $\exp(-\mathbf{R}\tau_m)$ is a matrix of mixing coefficients which is directly proportional to the 2D peak intensities $\mathbf{a}(\tau_m)$. This matrix can be calculated using the equality

$$\exp(-\mathbf{R}\tau_m) = \mathbf{T}\exp(-\mathbf{D}\tau_m)\,\mathbf{T}^{-1} \qquad (6)$$

where $\mathbf{D}$ is the diagonal matrix comprised of the eigenvalues of $\mathbf{R}$ and $\mathbf{T}$ is the matrix comprised of the eigenvectors of $\mathbf{R}$.[8]

At short τ_m, the matrix can be approximated using the expansion for $\exp(-x)$

$$\exp(-x) = 1 - x + x^2/2 - \ldots \quad (7)$$

to give

$$\exp(-\mathbf{R}\tau_m) \approx \mathbf{1} - \mathbf{R}\tau_m \quad (8)$$

where **1** is the identity matrix. This shows that at short τ_m, cross-peak intensities a_{IS} [the off-diagonal elements of $\exp(-\mathbf{R}\tau_m)$] have intensities directly proportional to $\sigma_{IS}\tau_m$. However, at longer τ_m, cross-peak intensities depend on additional cross-relaxation rates also, and at long τ_m they decay towards zero, as shown in Figure 3.

Several points should be made about this result:

1. All enhancements rise rapidly and decay more slowly. The maximum enhancement is reached for different cross peaks at different times.
2. There is an 'initial rate region', as described above, in which each pair of protons can be treated as an isolated spin pair. However, this region is short and its duration is strongly dependent upon the geometry of the spins: in the example shown in Figure 3, the initial rate region is longer for the strong enhancement A–B than for the A–C enhancement, for which the indirect enhancement A–B–C rapidly dominates. Moreover, it is much longer in Figure 3(b) than in Figure 3(a), in which it lasts no more than 5 ms [see inset in Figure 3(a)].
3. During the initial rate region, the NOE cross-peak intensity is simply proportional to r^{-6}. At later times, the relationship is much more complex and depends strongly on the geometry of the nuclei.
4. The marked difference between the actual A–C cross-peak intensity (solid line) and that calculated from the isolated spin-pair approximation (dashed line) shows the importance of spin diffusion in the observed cross-peak intensity. Spin diffusion is the process whereby enhancements propagate via intermediate spins; in this example, from A to B and thence to C.[10] Spin diffusion is much more of a problem in macromolecules [Figure 3(a)], because it can be hard to distinguish a weak direct NOE from a NOE arising by spin diffusion. In theory, by observing the cross-peak intensity at very short τ_m it should be possible to distinguish the two cases, because the indirect NOE has a lag period before it starts to build up [Figure 3(a), inset]. However, in practice the signal-to-noise ratio at short τ_m is low and such observations are difficult.
5. During the later stages of cross-peak evolution, spin diffusion ensures that cross-peak intensities become increasingly similar in large molecules [Figure 3(a)].[9] Hence, the distance information that can be obtained from cross-peak intensities diminishes as τ_m increases.
6. The sign of the cross peaks relative to the diagonal peaks is opposite for large molecules [Figure 3(a)] and for small molecules [Figure 3(b)]. The sign changes when $\omega_0\tau_c = (\frac{5}{4})^{1/2} = 1.12$, where ω_0 is the Larmor precession frequency in the static applied field.[11] The molecular size corresponding to the crossover point is hard to define as τ_c can vary strongly with solvent viscosity and solute interactions, but it tends to be at the oligopeptide stage in water or rather larger in the less viscous organic solvents.

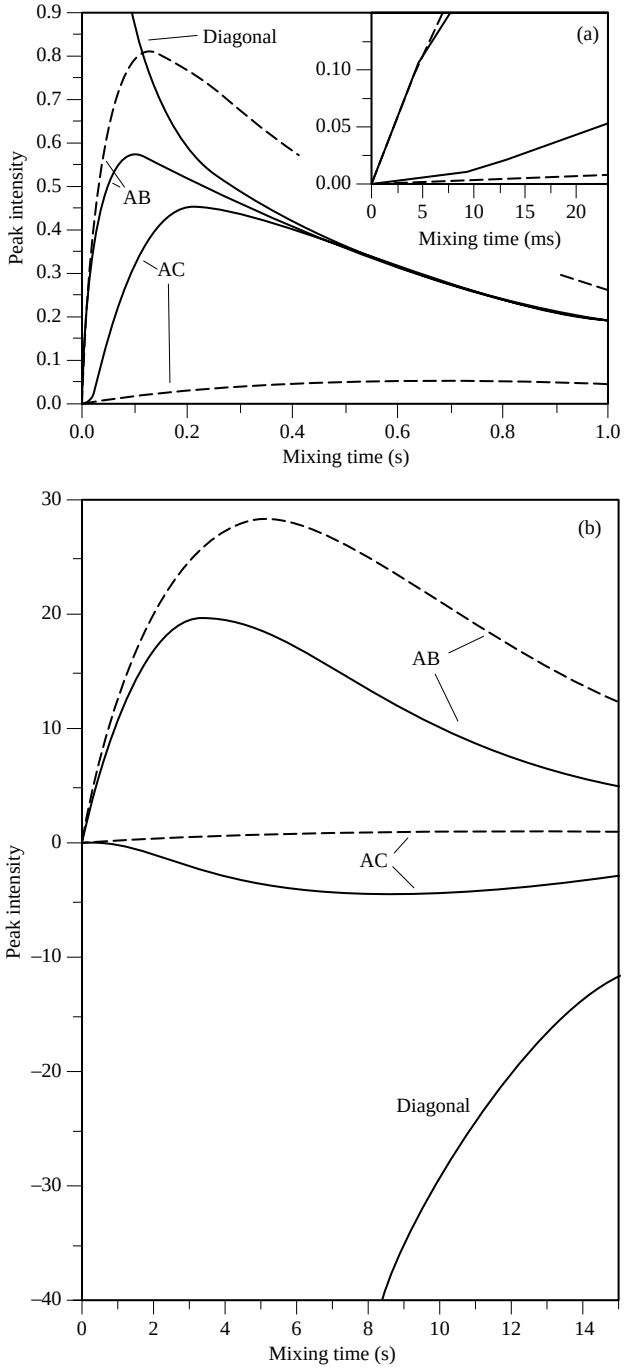

Figure 3 The dependence of cross-peak and diagonal peak intensity on τ_m in a NOESY experiment. The curves are for a three-spin system with nuclei A, B, and C which are in a straight line with $r_{AB} = r_{BC} = 2.5$ Å, and show the intensities of the A diagonal peak and the AB and AC cross peaks. The correlation time τ_c is 5×10^{-8} s in (a), as appropriate for a biological macromolecule, and 10^{-10} s in (b), as appropriate for an organic molecule in a nonviscous solvent, and the spectrometer frequency is 500 MHz [i.e. $\omega_0 = 2\pi \times 5 \times 10^8$, $\omega_0\tau_c = 157$ and 0.3 for (a) and (b), respectively]. The inset in (a) shows an expansion of the initial part of the curve. External relaxation at a rate 10% of the dipolar cross-relaxation rate is included. The curves marked by dashed lines are the equivalent curves for the two-spin systems A–B and A–C; these are the curves of the 'isolated spin pair approximation'. The diagonals have initial intensities of 2.0 and −200 in (a) and (b), respectively. Note that the absolute phases are arbitrary, and the direct AB cross peak has been presented as a positive signal in (b) merely because this is the normal presentation. Calculated using a numerical method[9]

Peak intensities in ROESY also behave as in Figure 3(b) (see below). Note also that relayed NOEs (the NOE at C, which comes largely via B) are again of the same sign as the diagonal in both large and small molecules. This is why, as noted in point 4 above, it is hard to identify spin diffusion in large molecules but easy in small molecules. Peaks in NOESY or ROESY arising from chemical exchange are always in phase with the diagonal, and therefore can be readily distinguished from NOE cross peaks in ROESY spectra where direct NOE cross peaks are of opposite phase to the diagonal.

The choice of a value for τ_m is the most difficult decision in setting up a NOESY experiment. To obtain optimum sensitivity, a value should be chosen such that cross peaks are at their maximum intensity. This time will be different for each pair of protons, and it varies strongly with the correlation time of the molecule. It is of the same order as the T_1 relaxation time, and for a small globular monomeric protein in water is roughly 250 ms. For a large protein or long DNA molecule, it can be 20 ms or less, while for small molecules in organic solvents it can be well over 1 s [as in Figure 3(b)].

However, the main concern in NOESY experiments is usually not sensitivity but structural information. The points outlined above imply that any direct relationship between cross-peak intensity and internuclear distance is only obtained for short τ_m values, and even here it is not normally feasible to relate cross-peak intensity directly to distance.

Two approaches have been taken to this problem. The first is to choose τ_m values as short as possible, and use an empirical calibration to relate intensity to distance.[12] Thus, the sequential distance HN–HN in a protein is normally about 2.8 Å in an α-helix. If sequential HN–HN NOESY cross peaks in helical regions are found to have intensities (in arbitrary units) ranging from 100 to 300, then one can make the conservative estimate that cross peaks with intensities of 100 or greater correspond to a distance of 2.9 Å or less. Further empirical calibrations are made using other predictable internuclear distances.

The second approach uses the exact solution of equation (5). The difficulty with this approach is that one can only apply the equation if all internuclear distances are known, and it is exactly this information that one is trying to derive. The typical approach is therefore to iterate towards a solution.[8,13] Using the isolated spin pair approximation, initial values are obtained for cross-relaxation rates and hence internuclear distances. These values are used to produce a structure from which relaxation rates are calculated. These derived rates are combined with experimentally determined rates to produce a hybrid relaxation matrix, and the process is iterated until it converges, which typically occurs after only one or two iterations.

3 THE NOESY EXPERIMENT: PRACTICE

3.1 Experimental Artifacts

An artifact is an unwanted signal. It may arise from a defect in the spectrometer or be inherent in the physics of the experiment, but it can be minimized by appropriate experimental design. The major artifacts are considered in turn and illustrated in Figure 4.

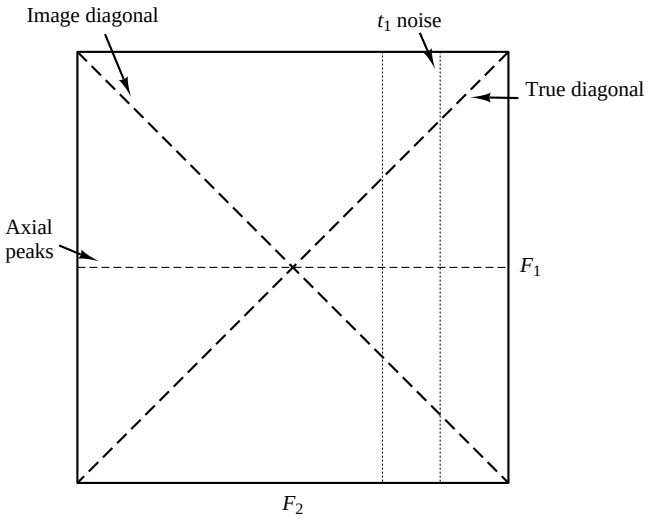

Figure 4 The position of artifacts in a NOESY spectrum acquired using the hypercomplex method. The image diagonal is an F_1 quadrature image. The spectrum also contains t_1 noise (vertical stripes) and axial peaks (horizontal line)

3.1.1 t_1 Noise

The raw data from a NOESY experiment consists of a series of FIDs acquired with different t_1 values, $S(t_1, t_2)$. The FIDs are processed by Fourier transformation in t_2 to give a series of one-dimensional spectra $S(t_1, F_2)$; this matrix of points is then transposed to give an interferogram consisting effectively of FIDs in t_1, $S(F_2, t_1)$, which are then transformed again to give the complete two-dimensional spectrum, $S(F_1, F_2)$. Any instability in signal phase, intensity, or frequency during the acquisition of a NOESY spectrum causes a random variation in peak heights in the intermediate 1D spectra, which translates to an increase in noise in the interferograms, and thence to stripes of noise parallel to the F_1 axis. This is known as t_1 noise. This explanation makes it clear that t_1 noise is only present where there are signals, and that t_1 noise is most intense for very intense, sharp peaks such as methyl groups.[14]

There is no single major source of instability. In some spectrometers the major source is pulse phase, length, or amplitude, while in others it is temperature instability. In many spectrometers the receiver circuitry is temperature-dependent, so that a change in the temperature of the room will affect the apparent phase or amplitude of the incoming signal.

Spectrometer design has improved enormously over the last few years, largely as a response to the requirements of multidimensional NMR. This means that t_1 noise is not as great a problem as it was. Nevertheless, it makes sense to reduce variability as much as possible. The obvious steps to take are to air condition the room (both magnet and console should be at constant temperature), to use enough dummy scans at the start of the experiment that the sample has had time to settle down to a constant temperature, and to run all experiments without sample spinning. Finally, careful planning of the phase cycling can be useful. As described below, the phase cycles act as difference experiments and it makes sense to juxtapose the most crucial subtractions.

Simple experiments have been described for analyzing the amount and source of spectrometer instability.[15] Simple modifications to the receiver circuitry can make a large

difference. Sometimes, installation of vibration dampers has a major impact on spectral quality.

There are three other features often seen in NOESY spectra that are not strictly t_1 noise, but can be treated under the same heading. Many spectrometers produce 2D spectra containing lines of noise parallel to the F_1 axis that do not coincide with sharp signals. These are typically regularly spaced, for example at 1000 Hz intervals either side of the carrier frequency. They presumably originate from stray rf signals picked up by the receiver circuitry, and are not easy to treat. Secondly, temperature variability (and poor shimming) can produce bands of noise running parallel to the diagonal. Thirdly, t_1 ridges are often found. These are similar in appearance to t_1 noise but contain a constant offset, either positive or negative. In some cases they can be cured by a small modification of the t_1 FT in which the first time point is multiplied by a factor of about 0.5 before the FT.[16] Otherwise, they can often be cured by suitable baseline correction of the final spectrum.

3.1.2 J Peaks

So far we have ignored much of the magnetization created by the NOESY pulse sequence. This can be calculated using the product operator formalism as follows.[17]

For the pulse sequence 90°_x, t_1, 90°_x, τ_m, 90°_x, acquire, operating on a system containing two protons I and S, dipolar coupled and spin–spin coupled with a coupling constant J, the first pulse has the effect $\hat{I}_z \rightarrow -\hat{I}_y$, and similarly on S: $\hat{S}_z \rightarrow -\hat{S}_y$.

During t_1, the spins evolve under the influence of chemical shift and J coupling to give

$$\begin{aligned}
-\hat{I}_y \rightarrow\ & (-\hat{I}_y \cos\omega_I t_1 + \hat{I}_x \sin\omega_I t_1)\cos\pi J t_1 \\
& + (2\hat{I}_x\hat{S}_z \cos\omega_I t_1 + 2\hat{I}_y\hat{S}_z \sin\omega_I t_1)\sin\pi J t_1 \\
-\hat{S}_y \rightarrow\ & (-\hat{S}_y \cos\omega_S t_1 + \hat{S}_x \sin\omega_S t_1)\cos\pi J t_1 \\
& + (2\hat{S}_x\hat{I}_z \cos\omega_S t_1 + 2\hat{S}_y\hat{I}_z \sin\omega_S t_1)\sin\pi J t_1
\end{aligned}$$

The second 90° pulse rotates all these components about the x axis, giving a total magnetization of

$$\begin{aligned}
& (-\hat{I}_z \cos\omega_I t_1 + \hat{I}_x \sin\omega_I t_1)\cos\pi J t_1 \\
& + (-2\hat{I}_x\hat{S}_y \cos\omega_I t_1 - 2\hat{I}_z\hat{S}_y \sin\omega_I t_1)\sin\pi J t_1 \\
& + (-\hat{S}_z \cos\omega_S t_1 + \hat{S}_x \sin\omega_S t_1)\cos\pi J t_1 \\
& + (-2\hat{S}_x\hat{I}_y \cos\omega_S t_1 - 2\hat{S}_z\hat{I}_y \sin\omega_S t_1)\sin\pi J t_1
\end{aligned}$$

The only components required for the NOE observation are those in $\hat{S}_z$ and $\hat{I}_z$; these are the components that exchange magnetization by cross relaxation during τ_m and are observed as single quantum magnetization after the final pulse. All the other components give rise to various undesirable signals in the NOESY spectrum and should be removed.

The single quantum in-phase and antiphase components, $\hat{I}_x \sin\omega_I t_1 \cos\pi J t_1 - 2\hat{I}_z\hat{S}_y \sin\omega_I t_1 \sin\pi J t_1 + \hat{S}_x \sin\omega_S t_1 \cos\pi J t_1 - 2\hat{S}_z\hat{I}_y \sin\omega_S t_1 \sin\pi J t_1$, continue to evolve during τ_m and are converted by the final pulse to various in-phase and antiphase signals (including in-phase cross peaks) as well as other unobservable components. These would produce diagonal and cross peaks in the same positions as found in COSY and relayed COSY spectra. They are easily removed by phase cycling (see ***Phase Cycling***). For example, the pulse sequence 90°_{-x}, t_1, 90°_{-x}, τ_m, 90°_x, which we write in shorthand as $(-x, -x, x)$, can be easily shown to produce the same z magnetization during τ_m but inverted single quantum magnetization. Thus, coaddition of the results from these two pulse sequences will remove all signals resulting from magnetization that was single quantum during τ_m.

The other unwanted contributions are the terms $-2\hat{I}_x\hat{S}_y \cos\omega_I t_1 \sin\pi J t_1 - 2\hat{S}_x\hat{I}_y \cos\omega_S t_1 \sin\pi J t_1$, which describe a mixture of double- and zero-quantum coherence, and are partially converted back to antiphase single quantum coherence by the third pulse. They both survive the phase cycle described above. The double quantum coherence can be removed by the phase cycle $(x, x, x) + (y, y, x)$: this is readily understood by comparison with the previous phase cycle, because double quantum magnetization is twice as sensitive to pulse phase changes as is single quantum magnetization, and therefore only requires a 90° phase change of the first two pulses.[18]

The zero quantum magnetization cannot be removed by a phase cycle, because it is affected by phase cycling in an identical manner to the desired z magnetization. It can, however, be removed by making use of the fact that zero quantum magnetization precesses during τ_m. Therefore, coaddition of several suitably chosen experiments with different τ_m will lead to (partial) cancellation of such terms, while those arising from z magnetization will be unaffected except that slightly different amounts of cross relaxation will have occurred. On many spectrometers this is accomplished by a random variation of τ_m by about 20 ms. Note that the random variation should only occur between iterations of a phase cycle and not during it; if τ_m is altered during a phase cycle the zero quantum contribution and the other J peaks are smeared out in F_1 rather than being neatly removed.

One final type of J peak can arise if the pulses are not 90°. In this case, magnetization of the type $\hat{I}_z\hat{S}_z$ can be produced and partially converted back to single quantum antiphase magnetization by the final pulse. This again produces COSY-type antiphase peaks for J coupled protons, which are most simply avoided by calibrating the pulse length carefully or if necessary using a composite pulse (see ***Composite Pulses***). Relaxation of $\hat{I}_z\hat{S}_z$ magnetization, also known as longitudinal two-spin order, is of interest in its own right (see ***Relaxation Processes in Coupled-Spin Systems***), but the NOESY experiment is not an efficient experiment for its study. Rather, experiments using low flip angles or selective pulses (see, for example, ***Selective NOESY***) are preferable.

3.1.3 Axial Peaks

An axial peak is an artifact along the line $F_1 = 0$, and arises from magnetization resulting from longitudinal relaxation after the first pulse. Any such magnetization is not frequency-labeled and consequently has zero frequency in F_1. For reasons elaborated below, the $F_1 = 0$ line is either in the center of the spectrum or at one edge. Axial peaks are easily removed by phase cycling, for example from the difference $(x, x, x) - (-x, x, x)$ or the sum $(x, x, x) + (-x, x, -x)$, which combines suppression of most axial peaks with removal of single quantum magnetization during τ_m and therefore shortens the total phase cycle required by a factor of two.

3.1.4 Quadrature Detection

In the usual situation where the reference frequency (carrier) is in the center of the spectrum, some method is required for distinguishing positive from negative frequencies. If the two cannot be distinguished, the spectrum is reflected about its center; if quadrature detection is applied but is imperfect, a low-intensity image of the spectrum (a quadrature image) is present, reflected around the center. In two dimensions, quadrature images can arise from reflection about either the F_1 or the F_2 axis. In practice, quadrature detection in F_2 is almost always better and the more troublesome 2D quadrature images arise from reflection in F_1.

Very similar methods for quadrature detection are used in 1D and 2D spectra. The obvious method is to collect data simultaneously from two channels in quadrature (i.e. 90° apart: an x and a y channel). Each data point is therefore complex and a complex FT is required to obtain the spectrum. In the t_1 dimension, this means that a pair of FIDs is required for each value of t_1. If the same method is used in both dimensions, the data are complex in both dimensions and a hypercomplex 2D FT is required.

The alternative method is to acquire real data but to alter the phase of the detector by 90° for each successive point. The effect of this trick (sometimes called the Redfield trick, after its originator)[19] is to make it appear that each data point is shifted from its true frequency by an amount such that it has precessed exactly an extra 90° from one point to the next. By the Nyquist equation for real data:

$$\text{Dwell time} = 1/(2 \times \text{spectral width}) \tag{9}$$

(where the dwell time is the time interval between one point and the next), this corresponds to an apparent shift of each point by half the spectral width. In other words, the carrier is now (apparently) at the edge of the spectrum rather than in the center, so that no additional 'quadrature' detection is required. This method produces real data and a real FT is required to generate a spectrum. Note that the dwell time between data points is only half as large for this latter method as for the former, but that because only one data point is collected at each time point rather than two, the overall *rate* of data acquisition is the same. When this method of quadrature detection is used in t_1 it is usually known as time proportional phase incrementation or TPPI.[20] It is possible to combine a complex acquisition in t_2 with TPPI in t_1, implying that a complex FT is needed in t_2 but a real FT in t_1.

One consequence of the methods described above is that with complex acquisition the carrier is at the center of the spectrum, but with real acquisition it behaves as if it were at one edge. In 2D, this means that axial peaks are at the center of the spectrum with complex acquisition (also known as States–Haberkorn–Ruben acquisition),[21] but at the edge with TPPI. Clearly, it is preferable to have the axial peaks at the edge. A neat method for achieving this aim is to invert the phase of the first pulse and receiver for every other pair of complex points (the States–TPPI method).[22] This has no effect on real signals, but inverts the magnetization that arises from relaxation during t_1 and τ_m and produces axial peaks. By the Nyquist equation for complex data:

$$\text{Dwell time} = 1/(\text{spectral width}) \tag{10}$$

this again corresponds to an apparent shift of each point by half the spectral width and therefore puts the axial peaks at the edge of the spectrum.

There is yet another means of obtaining quadrature detection in t_1, which consists of combining the two halves of the complex data point to produce a single phase-modulated value. This was the original method used for quadrature detection in NOESY, but it suffers from the severe disadvantage that the resultant spectra are 'phase twisted' and inherently unphaseable. They must therefore be presented in absolute value mode, which results in greatly degraded resolution.[21]

It was pointed out many years ago that quadrature images result from inaccurate 90° phase shifts or unequal quadrature channel amplitudes, and that these faults can be remedied by a phase cycle known as CYCLOPS which involves simultaneously cycling the pulse sequence and receiver through the sequence x, y, $-x$, $-y$.[23] In NOESY, it is only necessary to cycle the last pulse and receiver. When this cycle is combined with the cycles for removal of other artifacts, it produces the 16-step cycle indicated in Table 1. Note that the cycle is designed so that the artifacts likely to be most troublesome, single quantum coherence and axial peaks, are removed by adjacent steps. It will be seen that this phase cycle does nothing to reduce F_1 quadrature images. If these images are troublesome, they are most simply reduced by careful adjustments of the phase shifts of the receiver (if possible) and the amplitudes of the two channels.

Table 1 Phase Cycle for the Suppression of Artifacts in NOESY

Step[a]	90°	90°	90°	Acquisition
1	x	x	x	x
2	$-x$	x	$-x$	x
3	y	y	x	x
4	$-y$	y	$-x$	x
5	x	x	y	y
6	$-x$	x	$-y$	y
7	y	y	y	y
8	$-y$	y	$-y$	y
9	x	x	$-x$	$-x$
10	$-x$	x	x	$-x$
11	y	y	$-x$	$-x$
12	$-y$	y	x	$-x$
13	x	x	$-y$	$-y$
14	$-x$	x	y	$-y$
15	y	y	$-y$	$-y$
16	$-y$	y	y	$-y$

[a]Steps 1 to 2, 3 to 4, etc. remove axial peaks resulting from longitudinal relaxation during τ_m and magnetization that is transverse during τ_m. Steps 1 to 3, 2 to 4, etc. remove magnetization that is double quantum during τ_m. Steps 1, 5, 9, 11, etc. remove quadrature images in t_2.

Use of a 16-step phase cycle implies that the number of scans per t_1 increment (or for each of a pair of t_1 increments, if a complex quadrature detection is used in t_1) must be a multiple of 16. However, because the most essential elements of this phase cycle are contained in the first group of four steps, use of a phase cycle that is a multiple of four rather than 16 steps will only lead to increased F_2 quadrature images, and will not hinder the workings of the rest of the phase cycle.

3.1.5 Residual Solvent

Many NOESY spectra of biological molecules are run in H_2O (containing a small quantity of D_2O for the field/frequency lock). Because this signal is so intense, it causes a range of problems in NOESY spectra. This topic is discussed more generally elsewhere (see ***Water Signal Suppression in NMR of Biomolecules***), but a few words are appropriate here.

The most obvious problem is that to digitize such an intense signal, the receiver gain must be turned down so low that the signal from the sample is not adequately digitized. Many spectrometers now incorporate 16-bit digitizers which reduce the problem, but some method of reducing the solvent signal entering the receiver is necessary. This is done either by presaturation of the solvent or by the use of a composite pulse sequence prior to detection, often assisted by field gradients.

In many cases, the carrier frequency is set to coincide with the solvent signal. This allows solvent saturation/pulsing to be coherent with the other pulses, which improves solvent suppression markedly.[24]

The residual solvent signal tends to cause baseplane problems in NOESY. In particular, there are stripes parallel to the F_2 axis tailing out from the solvent signal. Many methods have been proposed to deal with this, but a combination of spin echo acquisition and time domain filtering appears to offer the best solution.[25]

3.2 The Setting of Experimental Parameters

Most experimental parameters for NOESY are very easy to set. All pulse widths should be 90°. The delay τ_m has been discussed above and the choice of a suitable value depends on whether sensitivity or precise distance information is preferred. The delay t_D should be long enough that most signals have relaxed close to equilibrium: in practice a value of at least 0.7 s is often adequate for macromolecules.

The number of points in t_2 is limited only by disk space and the required resolution: with present data storage devices, 4k complex points is not unreasonably large. With larger molecules, the signal may well have decayed to zero long before this, in which case fewer points are necessary. By contrast, it is not generally feasible to collect so many points in t_1, and this value is always a compromise between sensitivity and time pressure (which require fewer points) and resolution (which requires more points). Again, with larger molecules, the signal decays more rapidly and fewer t_1 points will be used. Typically 300–512 complex points are acquired. If too few t_1 points are acquired, the interferogram will be severely truncated (i.e. it will be cut off before it has decayed to zero). Fourier transformation of truncated FIDs produces 'sinc wiggles' around each peak [Figure 5(a)], which can be reduced but not eliminated by a suitable window function (see ***Data Processing***). Such wiggles are particularly evident in 2D spectra around the diagonal peak of sharp intense resonances such as methyl groups, which have signals that decay slowly in t_1 [Figure 5(b)].

The increments in both dimensions depend on the spectral widths and also on whether complex or real data are being acquired, as indicated in equations (9) and (10). In t_1, there is no point in acquiring over a spectral width wider than that defined by the signals of the sample. Greater resolution is obtained by using a spectral width smaller than the entire range, but unless selective pulses are used this strategy runs the risk of severe complications from the folding in of signals from outside the spectral width, since no filter is applied to such signals. In t_2, there may be a benefit in 'oversampling' (using a spectral width wider than that of the sample) to achieve a flatter baseplane,[25,26] and it is in any case advisable to use a spectral width at least 5% larger than the width of the signals to avoid distortion of the extreme signals by the audio filter.

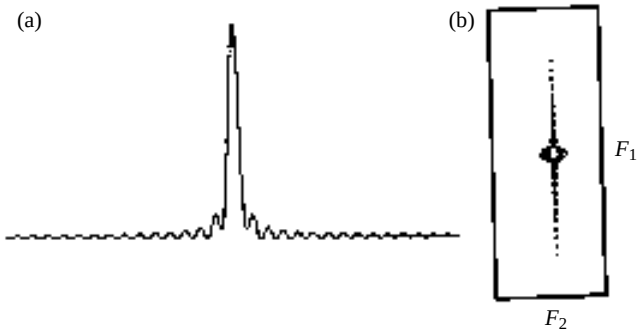

Figure 5 The effect of truncation is to give sinc wiggles. (a) Sinc wiggles in 1D. (b) Sinc wiggles in the F_1 dimension resulting from truncation in t_1

3.3 Data Processing

This topic is discussed more generally elsewhere (see ***Data Processing***). In NOESY, data processing is simple and consists largely of finding the best filters for the data, phasing the spectrum, and flattening the baseplane. The data are not greatly sensitive to the filters used and sine-bell or sine-squared-bell filters are often suitable. Phasing is independent in the two dimensions.[27] Normally, phasing in t_2 can be determined by phasing the first FID of the 2D file, while the appropriate phase in t_1 can be worked out from the initial delay between the first two pulses.

4 APPLICATIONS OF NOESY

4.1 When Should NOESY be Used?

The NOE is the most widely used structural parameter in organic and biological NMR. Although many experiments have been proposed for measuring NOEs, only three are commonly used: one-dimensional pseudo-steady-state NOE difference, NOESY, and the rotating frame NOE experiment known as ROESY or CAMELSPIN.[28] The choice of which experiment to use is essentially dictated by the size and correlation time of the molecule.

In small molecules, cross relaxation is slow. NOEs therefore build up slowly and external relaxation competes favorably with the NOE. NOEs are therefore often small. NOESY is therefore often very insensitive and takes a long time because of the long relaxation delays required [e.g. Figure 3(b)]. By comparison, 1D methods are usually more sensitive because the NOE can be driven to a steady state. In addition, in

small molecules there is usually no difficulty in achieving the specific irradiation required because there are fewer signals present. It is therefore generally preferable to use 1D difference methods. However, in cases where there are many irradiation targets, it can be more time-efficient to use NOESY or ROESY experiments.

As the size of the molecule under investigation increases, and therefore the correlation time τ_c of the molecule increases, the maximum homonuclear NOE goes from +50% to −100%, going through zero at $\omega_0\tau_c = 1.12$. As the NOE approaches zero, both the 1D NOE and the NOESY experiments become insensitive. However, cross relaxation in the rotating frame is still very significant and so ROEs can still be observed. This is therefore the only experiment useful in the region around $\omega_0\tau_c = 1.12$.

Above this point, NOESY is usually more sensitive, easier to set up, and produces fewer artifacts, and is therefore generally preferred over ROESY. However, the problem of spin diffusion is less severe in ROESY than in NOESY. This is because in ROESY, as in all cases where $\omega_0\tau_c < 1.12$, a relayed or spin diffusion NOE has the opposite sign to a direct NOE and therefore can be easily distinguished. There are therefore good reasons for using ROESY even for very large molecules. Further discussion of these points may be found elsewhere (see ***Nuclear Overhauser Effect*** and ***ROESY***).

4.2 Studies of Macromolecules

NOESY is the most widely used technique for measuring NOEs in large molecules such as proteins and nucleic acids. It is used for spectral assignment (e.g. sequential assignment) and for obtaining structural parameters. Many examples may be found elsewhere (see ***Biological Macromolecules: Structure Determination in Solution***; ***Carbohydrates and Glycoconjugates***; ***Nucleic Acid Structures in Solution: Sequence Dependence***; ***Structures of Larger Proteins, Protein-Ligand, and Protein-DNA Complexes by Multi-Dimensional Heteronuclear NMR***). NOESY is an excellent tool for obtaining qualitative information about internuclear distance, but is less good at providing quantitative information. In part, this is because the most reliable quantitative information is obtained at very short mixing times where the sensitivity is lowest and artifacts are most prominent, and also because it is not easy to integrate the volume of NOESY cross peaks accurately, particularly in crowded spectra. However, for the most part, the limitations are inherent in the systems under study. NOEs can only be interpreted quantitatively when the dynamics of the system are well characterized, and in almost all cases not enough is known about the internal dynamics of macromolecules in solution to allow the full precision of the data to be used. Nevertheless, many studies have shown that the number of structural constraints is more critical than their precision. Recently, stereospecific assignments in proteins have allowed a large increase in the number of NOE constraints, and thereby provided much better definition in the structures calculated from them. There is currently much new development in the use of heteronuclear relaxation parameters to characterize molecular dynamics, and it may be that this information can be combined with information from NOEs to allow more precise NOE constraints to be used.

5 VARIATIONS ON THE NOESY EXPERIMENT

Many variations of NOESY experiments have been proposed. Some of these are aimed at achieving flatter baseplanes, better solvent suppression, smaller diagonals, etc., and some are new pulse sequences designed to prize out more structural information from intractable data. Of these, the most useful are the three- and four-dimensional experiments described elsewhere in this Encyclopedia, which add on extra pulses and delays to separate a crowded two-dimensional spectrum into a series of subspectra.[29] Alternatively, simplification can be provided by the use of selective pulses, also described elsewhere. Crowded spectra can be made tractable by 'relaying' cross peaks to empty regions of the spectrum, which is done by combining the NOESY pulse sequence with a double quantum, TOCSY, or COSY experiment.

A variety of heteronuclear NOESY experiments, involving saturation of protons and observation of the heteronucleus, have been proposed. The only generally useful application of heteronuclear NOEs is as a method of signal enhancement, for example in broadband decoupled ^{13}C NMR. Observation of specific heteronuclear NOEs has found little application. Heteronuclear 2D NOE experiments[30] in particular are of limited application, partly because they are not an efficient way of observing NOEs, and partly because the heteronuclear NOE is inherently small in almost all the cases where a two-dimensional experiment would be of most applicability, i.e. for large molecules. For example, the maximum NOE to ^{13}C from irradiation of ^{1}H in a slowly tumbling molecule is only 15%.

There are a few NOESY variations that are designed to provide additional information to the normal experiment. For example, use of the pulse sequence 90°, t_1, 90°, kt_1, 90° (with k in the range 10–100), the so-called Accordion experiment, generates a dataset in which the t_1 decay envelopes depend on processes occurring in both t_1 and τ_m.[31] The lineshapes in F_1 therefore contain information on the rates of exchange processes occurring during the mixing period, which can be obtained by curve fitting or reverse Fourier transformation. The experiment can be suited to the range of exchange rates by an appropriate choice of k. This method is only applicable to relatively simple spectra, because of the difficulty of fitting overlapped lineshapes.

6 RELATED ARTICLES

Biological Macromolecules: Structure Determination in Solution; Carbohydrates and Glycoconjugates; Multidimensional Spectroscopy: Concepts; Nuclear Overhauser Effect; Nucleic Acid Structures in Solution: Sequence Dependence; Phase Cycling; ROESY; Selective NOESY; Structures of Larger Proteins, Protein-Ligand, and Protein-DNA Complexes by Multi-Dimensional Heteronuclear NMR; Three-Dimensional HMQC-NOESY, NOESY-HMQC, and NOESY-HSQC; Two-Dimensional Methods of Monitoring Exchange.

7 REFERENCES

1. J. H. Noggle and R. E. Schirmer, *The Nuclear Overhauser Effect; Chemical Applications*, Academic Press, New York, 1971.

2. D. Neuhaus and M. P. Williamson, *The Nuclear Overhauser Effect in Structural and Conformational Analysis*, VCH, New York, 1989.
3. S. Macura and R. R. Ernst, *Mol. Phys.*, 1980, **41**, 95.
4. K. Wüthrich, *NMR of Proteins and Nucleic Acids*, Wiley, New York, 1986.
5. J. Jeener, B. H. Meier, P. Bachmann, and R. R. Ernst, *J. Chem. Phys.*, 1979, **71**, 4546.
6. R. R. Ernst, G. Bodenhausen, and A. Wokaun, *Principles of Nuclear Magnetic Resonance in One and Two Dimensions*, Clarendon Press, Oxford, UK, 1987.
7. Ref. 2, pp. 40 and 67.
8. B. A. Borgias, M. Gochini, D. J. Kerwood, and T. L. James, *Prog. Nucl. Magn. Reson. Spectrosc.*, 1990, **22**, 83.
9. M. P. Williamson, *Magn. Reson. Chem.*, 1987, **25**, 356.
10. A. Abragam, *The Principles of Nuclear Magnetism*, Clarendon Press, Oxford, UK, 1961, p. 138.
11. Ref. 2, p. 37.
12. M. J. Sutcliffe, in *NMR of Macromolecules*, ed. G. C. K. Roberts, IRL Press, Oxford, UK, 1993, Chap. 11
13. R. Boelens, T. M. G. Koning, G. A. van der Marel, J. H. van Boom, and R. Kaptein, *J. Magn. Reson.*, 1989, **82**, 290.
14. A. F. Mehlkopf, D. Korbee, T. A. Tiggelman, and R. Freeman, *J. Magn. Reson.*, 1984, **58**, 315.
15. G. A. Morris, *J. Magn. Reson.*, 1992, **100**, 316.
16. G. Otting, H. Widmer, G. Wagner, and K. Wüthrich, *J. Magn. Reson.*, 1986, **66**, 187.
17. O. W. Sørensen, G. W. Eich, M. H. Levitt, G. Bodenhausen, and R. R. Ernst, *Prog. Nucl. Magn. Reson. Spectrosc.*, 1983, **16**, 163.
18. A. Wokaun and R. R. Ernst, *Chem. Phys. Lett.*, 1977, **52**, 407.
19. A. G. Redfield and S. D. Kunz, *J. Magn. Reson.*, 1975, **19**, 250.
20. G. Bodenhausen, R. L. Vold, and R. R. Vold, *J. Magn. Reson.*, 1980, **37**, 93.
21. D. J. States, R. A. Haberkorn, and D. J. Ruben, *J. Magn. Reson.*, 1982, **48**, 286.
22. D. Marion, M. Ikura, R. Tschudin, and A. Bax, *J. Magn. Reson.*, 1989, **85**, 393.
23. D. I. Hoult and R. E. Richards, *Proc. R. Soc. London, Ser. A*, 1975, **344**, 311.
24. E. R. P. Zuiderweg, K. Hallenga, and E. T. Olejniczak, *J. Magn. Reson.*, 1986, **70**, 336.
25. J. P. Waltho and J. Cavanagh, *J. Magn. Reson., Ser. A*, 1993, **103**, 338.
26. M. A. Delsuc and J. Y. Lallemand, *J. Magn. Reson.*, 1986, **69**, 504.
27. J. Keeler and D. Neuhaus, *J. Magn. Reson.*, 1985, **63**, 454.
28. A. A. Bothner-By, R. L. Stephens, J-M. Lee, C. D. Warren, and R. W. Jeanloz, *J. Am. Chem. Soc.*, 1984, **106**, 811.
29. G. M. Clore and A. M. Gronenborn, *Annu. Rev. Biophys. Biophys. Chem.*, 1991, **20**, 29.
30. P. L. Rinaldi, *J. Am. Chem. Soc.*, 1983, **105**, 5167.
31. G. Bodenhausen and R. R. Ernst, *J. Am. Chem. Soc.*, 1982, **104**, 1304.

Biographical Sketch

Michael P. Williamson. *b* 1957. B.A., 1978, Ph.D., 1981, University of Cambridge, supervised by Dr. Dudley Williams. Research fellow at Churchill College, Cambridge, 1981–84. NATO/SERC Overseas Research fellow with Prof. Wüthrich at ETH, Zürich, 1982–83. Team leader in Bio-NMR at Roche, UK, 1984–90. Currently reader at the University of Sheffield. Approx. 70 publications. Research interests: structure, dynamics, and interactions of peptides and proteins in solution.

Polymer Dynamics and Order from Multidimensional Solid State NMR

Hans Wolfgang Spiess

Max-Planck-Institut für Polymerforschung, Mainz, Germany

1	Introduction	1
2	Solid State NMR	1
3	Applications	4
4	Conclusions	13
5	Related Articles	14
6	References	14

1 INTRODUCTION

One of the key goals of materials science is the establishment of structure–property relationships in order to improve known and design new materials. This holds in particular for synthetic polymers, whose properties depend on both the molecular structure and the organization of the macromolecules in the solid state: their phase structure, morphology, molecular order and molecular dynamics.[1,2] Macroscopic as well as microscopic parameters are influenced by processing that follows the chemical synthesis. This calls for powerful analytical tools that can probe these aspects in the material as it is used, predominantly in the solid state. The structural aspects are studied mostly by scattering techniques or by microscopy. Information about dynamic aspects are deduced mainly from scattering or relaxation experiments.[3] Among these, nuclear magnetic resonance[4,5] is well established in structural characterization of liquids or compounds in solution; however, this is much less the case for solids.[6,7] Moreover, NMR offers numerous ways to study dynamic aspects over a large range of characteristic rates. The main advantage of NMR is its unprecedented selectivity. Thus, it is desirable to exploit this technique for studying the structure and dynamics of solid polymers.[7,8] However, owing to the presence of angular-dependent anisotropic interactions, the spectral resolution of solid state NMR spectra is orders of magnitude lower than that of high-resolution NMR in liquids. Important improvements were achieved in the 1970s by combining high-speed mechanical rotation of the sample with ingenious manipulations of the nuclear spins, such as multiple pulse irradiation, high-power decoupling and cross polarization.[9] Moreover, two- and higher-dimensional NMR techniques have been introduced that offer fundamental advantages.[10] First, as in liquids, the introduction of a new frequency dimension provides a means to increase the spectral resolution. Even more importantly, multidimensional spectroscopy also provides routes to new information, unavailable from 1D spectra even in the limit of high resolution. Experiments can be designed that correlate different spin interactions providing different structural information, or relate various states taken up by the molecular unit during different time periods by exchange, and in this way they can probe dynamic processes in real time.

Progress in multidimensional solid state NMR has been hampered by experimental and conceptual difficulties, which have now been overcome.[11–14] This article briefly outlines some of the main concepts and illustrates the information available from multidimensional solid state NMR spectra about polymer structure and dynamics through selected experimental examples, mainly from the author's laboratory.

Polymer dynamics is of central interest in our studies. Of the great variety of molecular motions possible in polymers (e.g., translations, rotations, and vibrations), rotations have the most pronounced effects on NMR lineshapes and relaxation parameters. Thus, multidimensional NMR provides, in particular, unique information about rotational motions. Their timescales are followed in real time over many orders of magnitude, covering in particular the regime of slow motions, which govern the mechanical properties of polymers. Moreover, the higher-order correlation functions provided by multidimensional NMR yield previously inaccessible model-independent information about the geometry of rotational motions, the orientational memory of molecular units involved in complex dynamics, and the nature of nonexponential relaxation in disordered systems. This information collected for a variety of polymers should eventually lead to a better understanding of their mechanical and rheological behavior, which is of interest not only for conventional but also for new advanced polymeric materials.

Two other aspects are particularly important for establishing structure–property relationships for polymer materials, namely, chain alignment in partially ordered systems and domain sizes in heterogeneous polymer materials. The orientation of macromolecular units is used to improve the properties of polymers for such different applications as high-tensile-strength fibres and nonlinear optical materials for information technology. Advanced polymer materials almost inevitably consist of more than one component, which often leads to phase separation. Careful design of the molar ratios as well as the size, composition, and morphology of the different phases offers a means to control the mechanical, electrical, and optical properties. Small domains that extend over only a few nanometers, as well as interfacial regions between the different phases, are particularly difficult to characterize. Major advances have been achieved in these areas by introducing the concepts of multidimensional spectroscopy. The new solid state NMR techniques nicely supplement well-established scattering and microscopic methods, as demonstrated by various experimental examples and by explicit comparison.

2 SOLID STATE NMR

The various aspects of solid state NMR are treated in detail in other articles in this Encyclopedia. Therefore, only a brief outline of the techniques used in the applications described below are given here. A full treatment is also available in our extended monograph on solid state NMR and polymers.[14]

2.1 One-Dimensional NMR

Solid state NMR exploits anisotropic, angular-dependent interactions of nuclear spins with their surroundings,[4,5] in particular magnetic dipole–dipole coupling of nuclei among themselves. This leads to broad NMR lines covering approximately 50 kHz for ^{1}H–^{1}H homonuclear coupling and approximately 25 kHz for ^{1}H–^{13}C heteronuclear coupling. The anisotropy of the chemical shift results in powder patterns covering approximately 15 kHz at a field strength of 7 T. In addition to these magnetic interactions, nuclei with spin $I > \frac{1}{2}$ can also have electric quadrupole moments and are subject to quadrupole coupling to the electric field gradient at the nuclear site. For ^{2}H ($I = 1$) in C–^{2}H bonds, it leads to spectral splittings of about 250 kHz. Since C–H bonds are common in polymers, ^{2}H labeling is particularly useful.

If one of the above mentioned couplings dominates, either because of its strength or because the others have been suppressed by decoupling, the angular dependence of the NMR frequency in high magnetic fields is alike for all couplings, and is given by

$$\omega = \omega_{\mathrm{L}} + \tfrac{1}{2}\Delta(3\cos^2\theta - 1 - \eta\sin^2\theta\cos 2\phi) \qquad (1)$$

Here ω_{L} is the Larmor frequency, Δ describes the strength of the anisotropic coupling (i.e., the anisotropic chemical shift or ^{13}C–^{1}H dipole–dipole coupling for ^{13}C or the quadrupole coupling for ^{2}H), and η is the asymmetry parameter describing the deviation of the anisotropic coupling from axial symmetry ($0 \leq \eta \leq 1$). The angles θ and ϕ are the polar angles of the magnetic field $\boldsymbol{B}_0$ in the principal axis system of the coupling tensor. This in turn is often simply related to the molecular geometry, with the unique axis lying along a bond direction (e.g., for dipole–dipole coupling along the ^{13}C–^{1}H bond, and for quadrupole coupling along the C–^{2}H bond), or perpendicular to an sp^2 plane as for ^{13}C chemical shift tensors in aromatic rings, etc. Depending on the total spin involved, signals described by equation (1) and their mirror images with respect to ω_{L} may be superimposed, and in powder samples spectra for all orientations are added to yield the powder lineshape (e.g., the Pake pattern for ^{2}H with spin $I = 1$).

These anisotropic interactions can be removed under rapid magic angle spinning (MAS), yielding liquid-like spectra if the spinning frequency ω_{R} is significantly larger than the width of the anisotropic powder pattern ($\omega_{\mathrm{R}} \gg \Delta$). In the slow-spinning regime, $\omega_{\mathrm{R}} < \Delta$, the centerband at the isotropic chemical shift is flanked by sidebands at multiples of ω_{R}, thus retaining information about the anisotropic coupling.

A few examples of 1D NMR spectra are collected in Figure 1, displaying single ^{13}C lines at the isotropic chemical shifts [Figure 1(a)], a chemical shift powder pattern for ^{13}C in a carboxyl group and its relation to the molecular geometry [Figure 1(b)], a ^{13}C MAS sideband pattern [Figure 1(c)], and ^{2}H NMR lineshapes for an isotropic powder [Pake pattern, Figure 1(d)], a uniaxially drawn fiber [Figure 1(e)], and a phenyl ring with motional averaging due to flipping about the axis shown [Figure 1(f)].

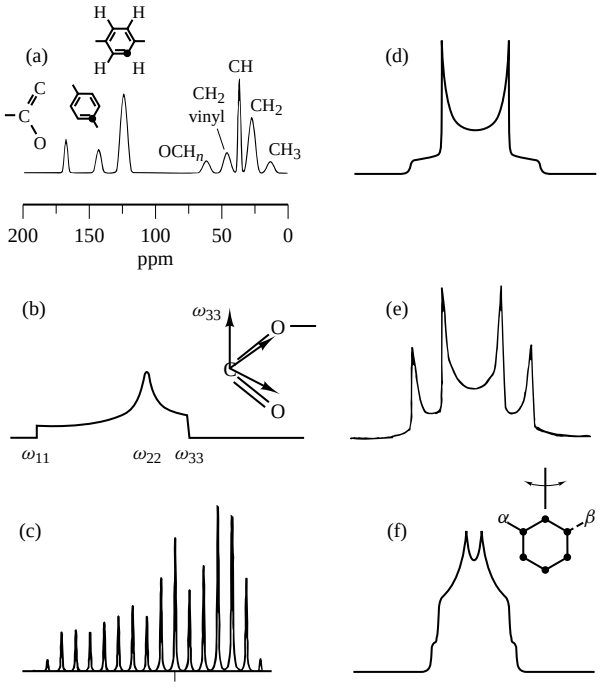

Figure 1 Examples of solid state NMR spectra: (a) ^{13}C CP MAS spectrum displaying isotropic chemical shifts of different functional groups; (b) ^{13}C powder pattern for carboxyl group, governed by chemical shift anisotropy and relationship of the principal axes system of the shielding tensor to the molecular framework; (c) ^{13}C sidebands due to anisotropic chemical shift and slow MAS; (d) ^{2}H NMR lineshape for rigid isotropic powder (Pake pattern); (e) ^{2}H NMR lineshape for a uniaxial fiber; (f) ^{2}H NMR lineshape for flipping phenyl rings

2.2 Two-Dimensional NMR

A 2D NMR spectrum is generated by recording a two-dimensional data set following pulsed irradiation as a function of two time variables, as shown schematically in Figure 2(a), and subsequent double Fourier transformation. The development of the nuclear spin system in the evolution period with incremented time t_1 at the beginning of the pulse sequence provides the basis for the first frequency dimension ω_1. The NMR signal is detected in the detection period with time t_2 at the end of the pulse sequence, providing the basis for the second frequency dimension ω_2. In the exchange experiments described here, a variable mixing period of duration t_{m}, during which dynamic processes can take place, is inserted between evolution and detection. In this way, slow molecular dynamics are probed in real time. The concept of 2D spectroscopy is readily extended to three and higher dimensions by inserting additional evolution and mixing times.

The most important aspects of 2D NMR are exemplified in Figure 2(b)–(d). First, 2D NMR is often used to increase the spectral resolution of solid state NMR spectra by separating different interactions. As an example, consider 1D sideband patterns. These are often hampered by a severe loss of spectral resolution due to overlapping sidebands of ^{13}C with different isotropic chemical shifts. This loss of resolution is circumvented at the expense of a new frequency dimension, as demonstrated in Figure 2(b), where the sideband patterns for the different sites experiencing different isotropic chemical shifts are separated from each other.

Other 2D NMR techniques aim at obtaining new information by correlating different interactions. As a specific example, Figure 2(c) displays a 2D NMR spectrum correlating a ^{13}C chemical shift with a ^{13}C–^{1}H dipolar powder

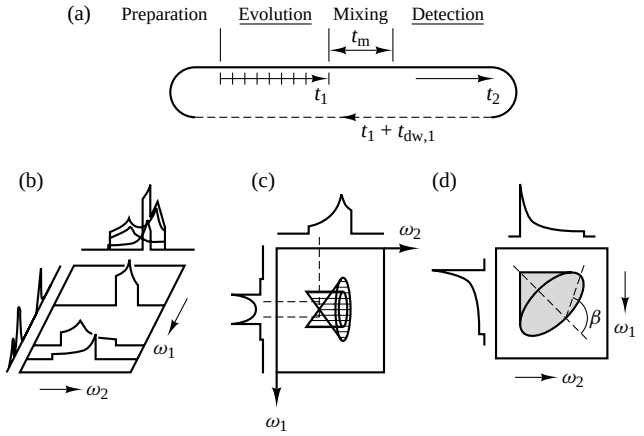

Figure 2 Principles of 2D NMR spectroscopy: (a) basic pulse sequence; (b) separation of isotropic and anisotropic chemical shifts; (c) correlation of anisotropic chemical shift and dipolar interaction; (d) 2D exchange spectrum reflecting the reorientation about the angle β through an elliptical exchange ridge

pattern. Since the dipole–dipole coupling is well understood in terms of bond lengths and angles, such spectra provide valuable information about the orientation of the principal axes of the chemical shift tensor in relation to structural units such as CH_2– groups etc.

As far as applications to polymers are concerned, 2D exchange NMR has proved to be particularly valuable. First of all, by varying the mixing time t_m, slow dynamic processes in the range of milliseconds to seconds can be followed in real time. Moreover, 2D exchange NMR spectra yield unique and model-independent information about the geometry of rotational motions. In fact, for axially symmetric tensors, ubiquitous in ^{2}H NMR of polymers, the 2D exchange spectrum yields elliptical ridge patterns from which the angle about which the molecules have rotated can be read off with a ruler [Figure 2(d)].

2.3 Multidimensional NMR

The concepts of 2D NMR are readily extended to higher dimensions. By combining the different schemes of 2D NMR, a large variety of three-dimensional experiments can be designed, as discussed, for example, for liquid state NMR by Griesinger et al.[15] In liquid state NMR, 3D techniques are mainly used to increase the spectral resolution. Although this is also an important aspect in solid state NMR (see below), 3D exchange NMR as shown schematically in Figure 3 offers fundamentally new information about higher-order correlation functions of complex motions in the solid state. Since the orientation of a given molecule is probed three times, different pathways taken by the molecule from the beginning to the end lead to different exchange signals. Thus, different motional mechanisms may be distinguished. Such information is inaccessible from 2D NMR, where the orientation of the molecule is measured only twice, and therefore no information is available about the trajectory a molecule follows when rotating from one orientation to another. Specific examples of applying three- and higher-dimensional NMR techniques to polymers are discussed below.

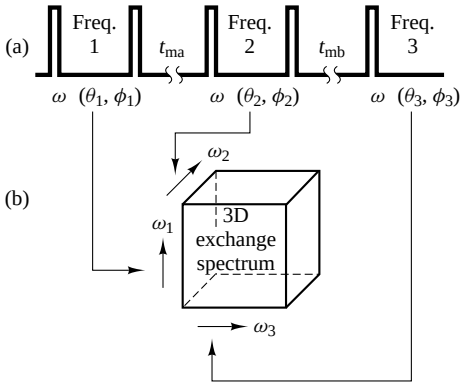

Figure 3 Principle of 3D exchange NMR: (a) pulse sequence; (b) corresponding spectral cube

2.4 Spin Diffusion

Solid state NMR can also provide information about intermolecular distances and domain sizes in heterogeneous polymers by means of spin diffusion, i.e., the diffusion of nuclear magnetization through the sample without transport of material. It is mediated by dipolar couplings, and therefore is most efficient among protons.[4] Figure 4 demonstrates schematically the connection between the spatial distribution of proton magnetization within the sample and the solid state NMR spectra for a two-phase system with spatially constant proton density. In equilibrium, the proton polarization is spatially constant, and the relative signal intensities in an NMR spectrum reflect the integral chemical composition of the sample. Differences in the chemical structure or in local molecular mobility can be used to select the proton magnetization in one component (A) and suppress it in the other (B) [Figure 4(a)]. The subsequent redistribution of magnetization by ^{1}H spin diffusion is monitored by NMR spectroscopy [Figure 4(b)]. For short times, the mean-square distance $\langle x^2 \rangle$ that the magnetization moves within time t is given by $\langle x^2 \rangle = aDt$, where D is the spin diffusion constant of the system under study. The factor a depends on the geometry of the packing (e.g., lamellar, cylindrical, or spherical). The spin diffusion constant D is related to the strength of the dipolar coupling as reflected in the width of the ^{1}H NMR

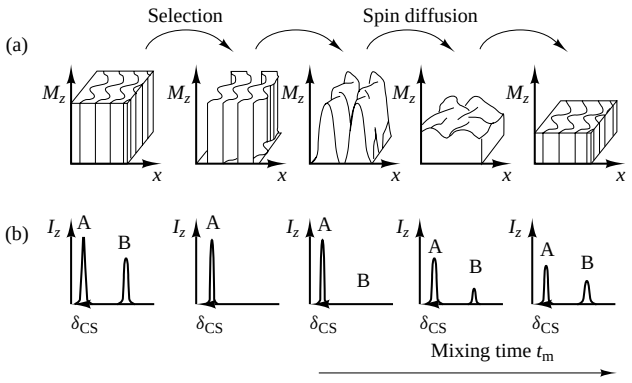

Figure 4 Schematic representation of ^{1}H spin diffusion in a two-phase system (A,B) with spatially constant proton density: (a) spatial distribution of ^{1}H magnetization; (b) NMR spectra for different mixing times t_m

spectrum, and has been calibrated for polymers of different molecular mobility by comparing spin diffusion data with direct measurements of domain sizes by X-ray scattering and electron microscopy.[16,17]

3 APPLICATIONS

3.1 Conformational Structure

The packing behavior of polymers depends strongly on their chain microstructure.[18] In particular, it is well known that only stereoregular macromolecules can crystallize. A schematic representation of the carbon backbone of an amorphous polymer is depicted in Figure 5(a). In order to specify the conformation of such a segment, one must know the bond length l, the valence angle Θ and the rotational angles Φ_i. The rotational potential $E(\Phi_i)$ around the central C–C bond in n-butane is plotted in Figure 5(b). The minima for the *gauche* conformers are higher than that of the *trans* by about 3.5 kJ mol^{-1}. Since this energy difference is comparable to the thermal energy at ambient temperatures, a large number of conformations is normally present in an amorphous polymer. Therefore, experimental techniques are needed that can check the conformational statistics.

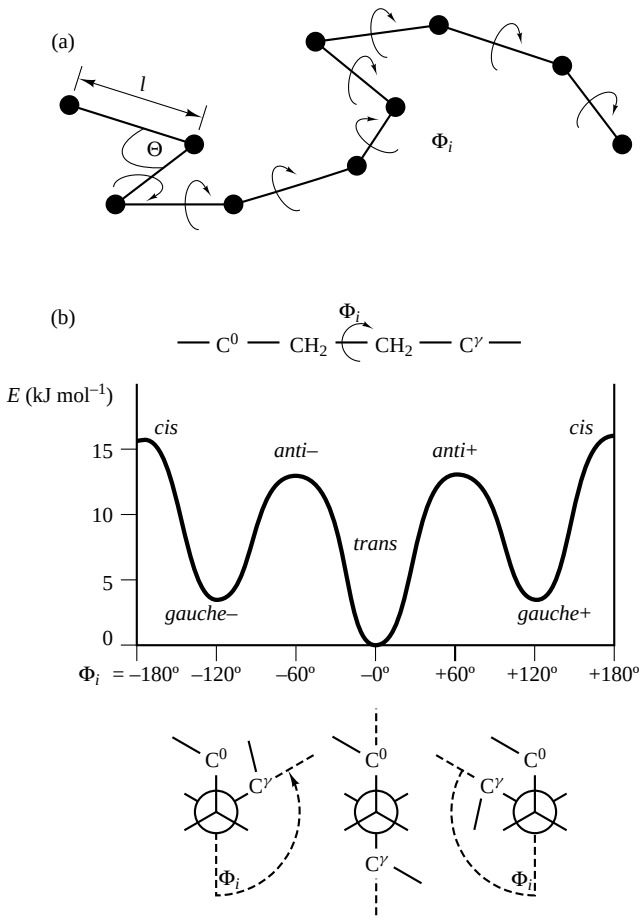

Figure 5 (a) Schematic representation of a carbon-backbone polymer chain in the amorphous state. (b) The potential energy E for rotation about the central carbon of a butane unit in a polymer chain together with Newman projections illustrating the different interactions between the atom C^0 and its γ-*gauche* substituent $C\gamma$ for the conformations *gauche*− ($g-$), *trans* (t) and *gauche*+ ($g+$)

NMR of polymers in solution is well established for determining the chain microstructure.[6,19] Glassy solid state amorphous polymers typically display broad ^{13}C *c*ross *p*olarization *m*agic *a*ngle *s*pinning (CP MAS) NMR lines due to an inhomogenous superposition of contributions from different conformations. These conformational effects on ^{13}C chemical shift have traditionally been attributed to the shielding of a reference carbon C^0 by the γ-substituent C^γ [see Figure 5(b)] in a semiempirical fashion ('the γ-*gauche* effect').[6,8,19] It has been shown that these shifts can be calculated quantitatively on the ab initio level[20] by exploiting the high computing power of modern workstations and advanced schemes for calculating NMR chemical shifts, such as *i*ndividual *g*auge for *l*ocalized *o*rbitals (IGLO).[21] Thus, it is hoped that eventually the spread in chemical ^{13}C shifts in amorphous polymers can be analyzed to provide structural information, in particular because profound correlations of the chemical shift with specific geometrical aspects such as C–C bond lengths and dihedral angles emerge.

As a specific example, Figure 6(a) displays the ^{13}C CP MAS spectrum of atactic polypropylene (aPP), with the assignment of the two partially resolved peaks and the shoulder corresponding to specific conformations of a tetrameric unit depicted in Figure 6(b). The assignment is readily made by comparison with the chemically shifted peak positions of the solid state ^{13}C NMR spectra of crystalline isotactic[22] and syndiotactic polypropylene.[23] In the glassy state, the peaks are broadened owing to differences in the geometry[20] and to the fact that numerous configurations contribute to the three main conformations, as discussed in detail elsewhere.[24]

3.2 Molecular Order

Structural characterization of polymers often requires the determination of the alignment of macromolecular chains.[25] Orientation in polymers is often induced by the production process, and has strong effects on product properties. Through the angular-dependent NMR interactions, orientation is amenable to NMR experiments. As opposed to most classical techniques, the order of both crystalline and amorphous components can be studied. For ^{2}H- or ^{13}C-enriched samples, one-dimensional experiments are sufficient to obtain orientation distributions in terms of a single angle.[26] In order to reconstruct two-dimensional orientation distributions, or to resolve overlapping patterns in natural abundance ^{13}C spectra, multidimensional spectra are required. Two examples are discussed here. Both involve 3D spectra of ^{13}C in natural abundance.

3.2.1 Chain Alignment in Drawn Poly(ethylene terephthalate)

In the case of a biaxially drawn film of poly(ethylene terephthalate) (PET) from an industrial process line, the orientational distribution was mapped out in the 3D exchange NMR spectrum by flipping the sample between different orientations with respect to the magnetic field (*d*irection *e*xchange with *c*orrelation for *o*rientation *d*istribution *e*valuation and *r*econstruction, DECODER).[27] The NMR signals of the different structural units of PET are completely resolved in the

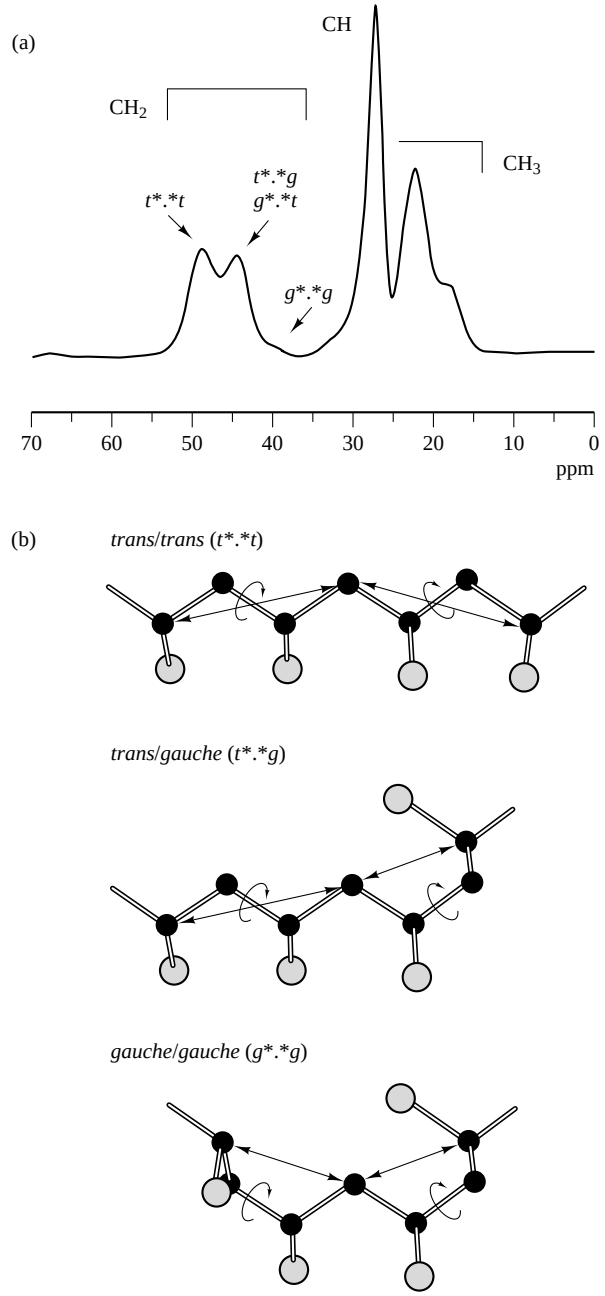

Figure 6 (a) ^{13}C CP MAS NMR spectrum of an amorphous polypropylene at T = 252 K (T_g − 6 K).[24] Note that the observed splitting is due to conformational effects. (b) Schematic representation of the conformations of a tetrameric unit in polypropylene relevant for the γ-*gauche* effect of the methylene group C^0H_2. One particular configuration, the mrr tetrad, is selected, here. The abbreviation *t**.**g* stands for a conformational unit around a carbon center denoted by '.' with undefined conformations of the neighboring bonds and *t* and *g* conformations of the next-neighboring bonds

3D cube, and their orientation distributions thus separately determined.[28] As depicted in Figure 7(b), the chain axes are confined to the film plane (full-width at half-maximum, fwhm, of 15°), while the in-plane distribution is much broader (fwhm ≈90°). The planes containing the phenylene rings and the carboxyl group are oriented preferentially parallel to the plane of the film (fwhm = 55°).

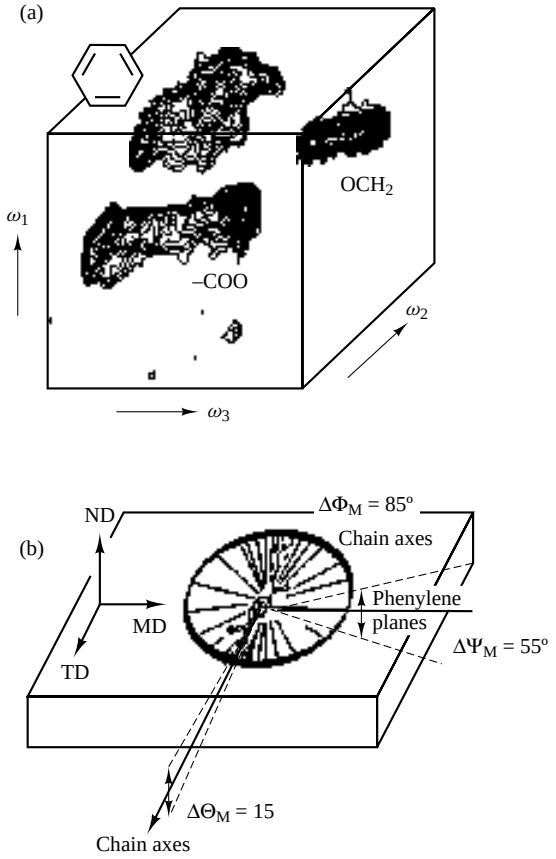

Figure 7 (a) ^{13}C 3D DECODER NMR spectrum of an industrial biaxially drawn film of poly(ethylene terephthalate), (PET).[28] (b) Schematic representation of orientation distribution derived from it

3.2.2 Molecular Order in Liquid Crystalline Polymers

New polymeric materials often contain mesogenic groups that are able to form liquid crystalline phases.[29,30] The interest in such liquid crystalline polymers (LCPs) comes from the fact that in the liquid crystalline phase, they can be macroscopically oriented not only by electric or magnetic fields but also by mechanical forces. The order thus generated in the mesophase can subsequently be retained in the solid material. This offers interesting applications, ranging from high-tensile-strength fibers to nonlinear optics and optoelectronics. In order to relate the material properties of LCPs to molecular structure, the degree of alignment as well as the mobility of the different structural units must be determined. This calls for highly selective analytical tools like NMR. In fact, pulsed ^2H NMR of selectively deuterated systems[31,32] as well as multidimensional NMR[33] have provided already a wealth of information about the structure and dynamics of these systems.

As a specific example, let us consider a side group LCP as depicted in Figure 8(a). The development of such materials has been stimulated by the concept that the mesogens with their tendency to form ordered structures can be decoupled from the polymer chain with its tendency to form a random coil by inserting a flexible spacer. By advanced 3D MAS NMR of ^{13}C in natural abundance, involving rotor-synchronized detection of molecular order with sideband separation,[34] the alignment of all structural units can be studied simultaneously. Figure 8(b) displays a 3D MAS spectrum of the frozen smectic

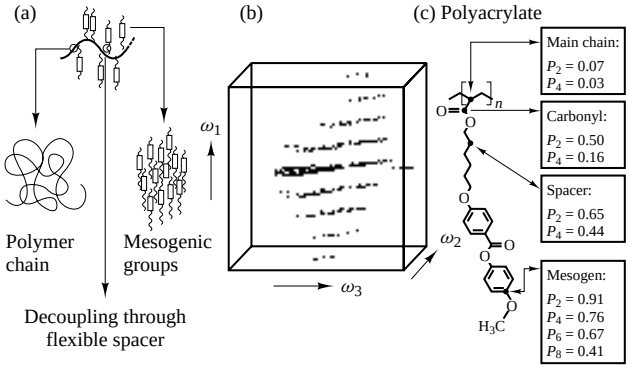

Figure 8 Molecular order in calamitic liquid crystalline side group polymers: (a) spacer model; (b) 3D CP MAS NMR spectrum of ^{13}C in natural abundance; (c) order parameters of different functional groups derived from it. For details see Titman et al.[34]

LCP aligned in the liquid crystalline phase in the magnetic field. Each dot in the spectrum corresponds to a single spinning sideband of a single resolvable carbon in the repeat unit, from which the degree of alignment of the corresponding unit can be retrieved. The results of the analysis in terms of order parameters $\langle P_2\rangle$, ... ,$\langle P_8\rangle$ are displayed in Figure 8(c). This not only reveals a pronounced order gradient from the aligned mesogen to the disordered chain, it also shows that the acrylic carbonyl group exhibits much higher order than the hydrocarbon units of the main chain. Because of its selectivity, high-resolution solid state NMR is able to reveal that the carbon–carbon bond that links the acrylic carbonyl to the main chain plays a crucial role in the decoupling of the ordered side groups from the disordered polymer chain. This information is needed to understand the differences in chain order for different backbones,[31] and the rheological behavior[35] as well as the ordering behavior of mechanically deformed LC elastomers.[36]

3.3 Molecular Dynamics

The molecular dynamics of polymer chains depend first of all on their phase structure. Most synthetic polymers are amorphous, forming a coiled shape as indicated in Figure 9(a). Stereoregular polymers can crystallize. However, owing to the enormous loss of conformational degrees of freedom, crystallization is incomplete and leads to semicrystalline materials that typically form lamellar structures, as depicted in Figure 9(b). Different aspects of the molecular dynamics are important in amorphous and semicrystalline systems, and the application of multidimensional solid state NMR has recently provided detailed information about chain dynamics for both cases.[14]

3.3.1 Rotational Motions in Crystalline Regions

Two-dimensional exchange NMR provides detailed information about the geometry of rotational motions. This was demonstrated, among other ways, by ^2H 2D exchange NMR of poly(vinylidene fluoride) (PVF_2).[37] This polymer is of particular interest because of its electrical properties.[38] The 2D spectrum for the crystalline α phase at 370 K, shown in

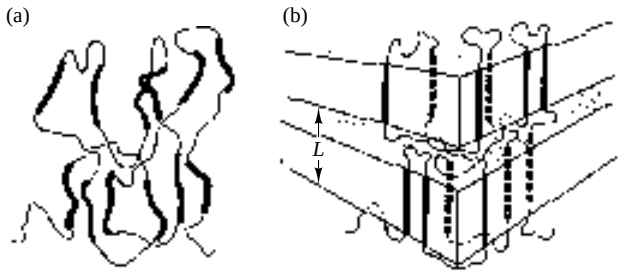

Figure 9 Schematic representation of (a) amorphous and (b) semicrystalline polymers

Figure 10(a), in addition to a well-defined powder spectrum (Pake pattern) along the diagonal, displays well-developed elliptical exchange ridges. The latter indicates jump motions of the PVF_2 chains through the crystal lattice, which interchange C–^{2}H bond directions differing by 113°, in agreement with the refined crystal structure. Altogether, 16 conformational defects had previously been proposed to be responsible for the chain dynamics in this polymer. Together with knowledge of the change in dipole moment generated by the motion, a specific conformational change $tg\bar{t}\bar{g} \leftrightarrow \bar{g}tgt$ of a chain defect

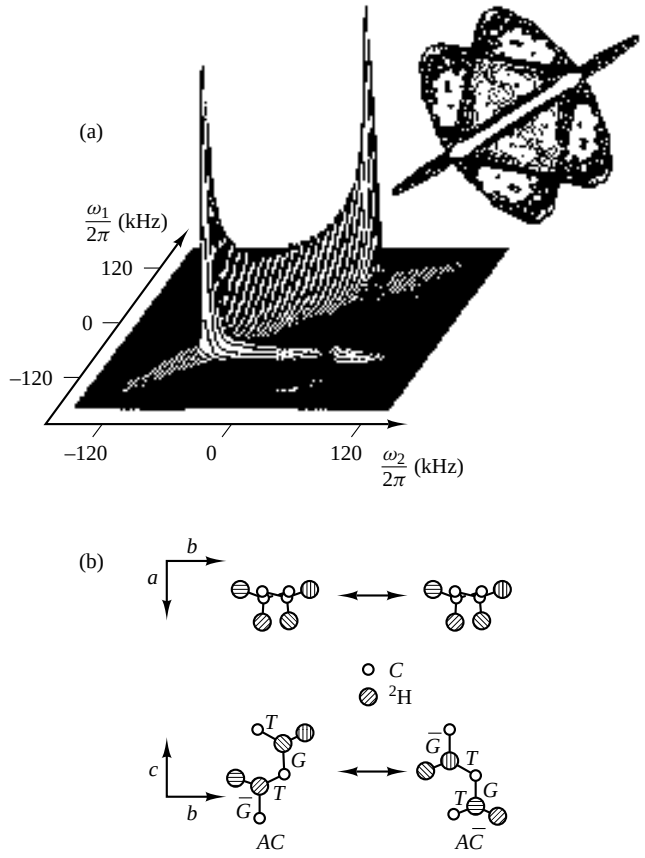

Figure 10 Chain motion in the crystalline α phase of poly(vinylidene fluoride), (PVF_2).[37] (a) Experimental ^2H 2D exchange NMR spectrum at T = 370 K, mixing time t_m = 200 ms. (b) Geometry of the conformational jumps, T and G refer to *trans* and *gauche* conformations of the respective bonds, while A and C describe the direction of the dipole moment with respect to the a and c crystal axes

[Figure 10(b)] was identified as being responsible for the mechanical and dielectric relaxation in the crystalline regions of this polymer.[37]

In other semicrystalline polymers like polypropylene, poly(oxymethylene), and poly(ethylene oxide), slow chain motions in the crystalline regions have been detected, and 2D exchange NMR of ^{2}H and ^{13}C has identified these motions as being due to helical jumps.[12–14,39]

3.3.2 Chain Diffusion between Crystalline and Amorphous Regions

Not only can two-dimensional exchange NMR detect molecular dynamics via the resulting rotations of individual groups of the monomer unit, but it is also able to detect chain diffusion from crystalline to amorphous regions in semicrystalline polymers.[40] Although occasionally postulated,[41] this process has not been accepted as a general concept, most likely because of lack of experimental evidence.

Our 2D experiment makes use of the fact that, under MAS, the all-*trans* conformation in the crystalline regions of polyethylene (PE) has an isotropic chemical shift that differs by approximately 2 ppm from that of the *gauche*-containing conformers in the amorphous regions. In the sketch of polyethylene (PE) chains in a crystallite near the interface with an amorphous region shown in Figure 11(a), carbons 1 and 2 would contribute to the "amorphous" signal [marked *a* in Figure 11(b)] and the carbons 9 and 10 would contribute to the "crystalline signal" (marked *c*). The exchange intensity between the ^{13}C signals for CH_2 groups in the crystalline and amorphous regions is clearly visible in Figure 11(b). This directly proves chain diffusion taking CH_2 groups from the crystalline into the amorphous regions and vice versa. This translational diffusion in the solid state results from the well-known α process, assigned to 180° jumps of the chain stems in the crystallites,[41] accompanied by a translation by one CH_2 unit. The quantitative analysis of our 2D NMR and relaxation data yields jump rates in complete agreement with previously reported values (activation energy E_a = 105 kJ mol^{-1}). It shows that the root-mean-square displacement of individual CH_2 groups amounts to more than 100 nm within 100 s near 360 K, corresponding to a translational diffusion constant of 10^{-14} cm^2 s^{-1}. In commercial materials, chain diffusion, as detected here, is suppressed by branching, since it leads to deterioration of the long-term mechanical properties owing to creep.

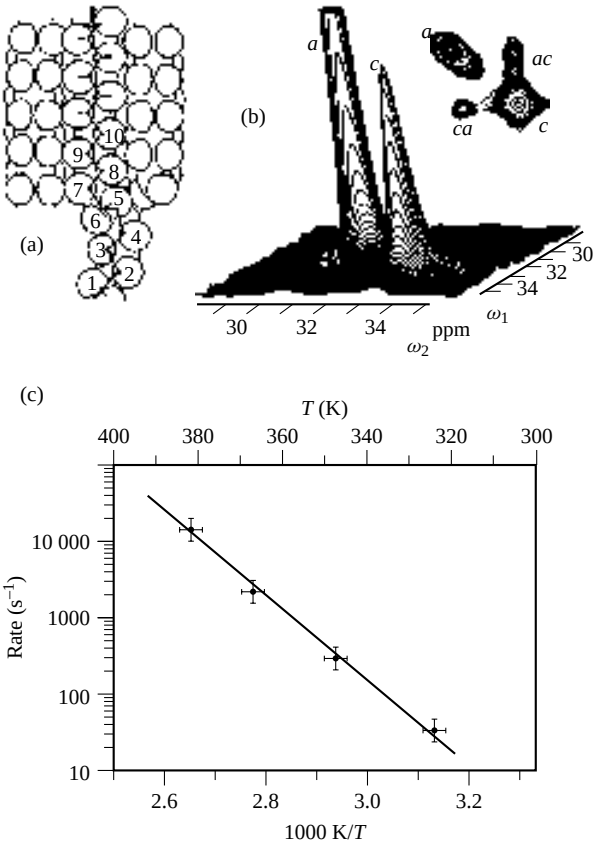

Figure 11 Chain diffusion in solid polyethylene, (PE).[40] (a) Sketch of PE chains in a crystallite, near the interface with an amorphous region. (b) ^{13}C 2D MAS NMR spectrum at T = 363 K; signal of the crystalline regions suppressed through single pulse irradiation. (c) Arrhenius plot of jump rates for the primary step of chain diffusion in PE

3.3.3 Chain Motions of Amorphous Polymers at the Glass Transition

As an amorphous polymer is heated above its glass transition temperature T_g, its mechanical properties change significantly within a temperature range of typically 20–30 K where the material transforms from a glassy solid to a highly viscous melt.[1–3,42] (An excellent overview of dynamic phenomena at the glass transition is given in special issues of the *Journal of Non-Crystalline Solids*.[43]) However, the dynamic processes on a molecular level, responsible for these changes in the macroscopic behavior, are not sufficiently well characterized. Multidimensional exchange NMR has now provided information about the chain dynamics at the glass transition in unprecedented detail.[14]

Conformational (*trans*–*gauche*) transitions are usually considered as an important aspect of polymer chain dynamics in the melt and in solution.[44] Slow conformational transitions at temperatures slightly above T_g have indeed been observed in various polymers.[24,45] This is demonstrated for aPP in Figure 12. The ^{13}C 2D exchange NMR spectrum was recorded under rapid MAS, such that isotropic lines were obtained. The conformational exchange clearly manifests itself by pronounced cross peaks between the lines corresponding to the *t**.**t* and the *t**.**g* conformers discussed earlier (see Figures 5 and 6).

However, as pointed out, for example, by Helfand et al.,[46] such motions need not be strictly local processes described by kink[47] or three-bond motions on a diamond lattice,[48] involving rotations by well-defined angles about spatially fixed C–C axes. Conformational transitions may also arise from relaxation processes involving longer chain units, leading to translational and angular displacements of different amplitudes of the corresponding monomer units. Indeed, ^{2}H 2D exchange NMR of aPP of the chain dynamics does not show any sign of preferred rotational angles.[49] As demonstrated in Figure 12(b), the ^{2}H spectra could be fitted adequately on the basis of an isotropic rotational diffusion model involving small angular steps.

The correlation times of the conformational dynamics agree remarkably well with those of the rotational motions. This is

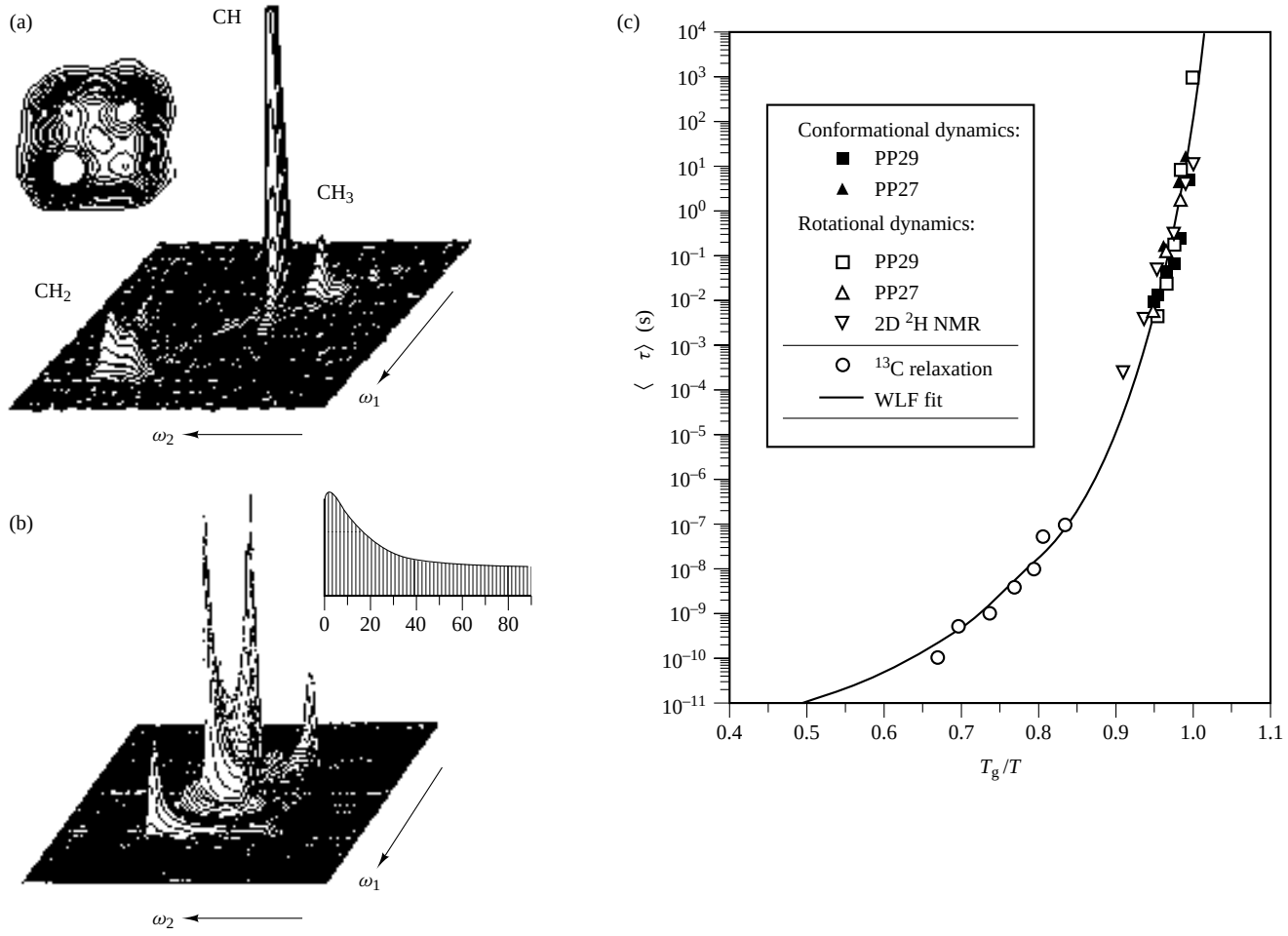

Figure 12 Chain motion of atactic polypropylene, (aPP), at the glass transition. (a) ^{13}C 2D CP MAS spectrum at T = 250 K (T_g + 12 K) and mixing time t_m = 500 ms. The cross peaks indicate conformational transitions.[45] (b) ^{2}H 2D exchange NMR spectrum at T = 270 K (T_g + 17 K) and mixing time t_m = 50 ms. The broad exchange features indicate rotational motions, which can be fitted by small-angle step rotational diffusion;[49] see also the reorientational angle distribution obtained from a quantitative fit of the spectrum. (c) Mean correlation times for the various aspects of the chain dynamics in different polypropylene samples plotted versus reduced temperature from ^{13}C and ^{2}H NMR; for details see Zemke et al.,[24] Schaefer et al.,[49] and Dekmezian et al.[50]

demonstrated in Figure 12(c), where mean correlation times determined by various techniques on different amorphous PP samples are shown.[24] Also included are values determined earlier through ^{13}C spin–lattice relaxation times by Mandelkern and co-workers[50] at elevated temperatures. All these correlation times can be fitted by the Williams–Landel–Ferry (WLF) equation[42] describing mechanical relaxation over more than 12 orders of magnitude. Thus, as noted before,[45,48,51] the timescales of the chain dynamics as probed for individual CH_2 units by 2D NMR are in excellent agreement with those of the collective processes responsible for the strong temperature dependence of the α process at the glass transition.[3,42,43]

3.3.4 Geometry of Chain Motion in Amorphous Polymers

As noted in the preceding section, conformational transitions in a vitrifying melt need not be strictly local processes involving rotations by well-defined angles in a potential that is static with respect to an external reference frame. If conformational transitions do indeed arise from relaxation processes of larger chain units[46] involving translational and angular displacements of different amplitude along such a unit then the rotational potential around a given C–C bond, which with respect to an internal frame would still look like that plotted in Figure 5(b), can be displaced by large angles after a conformational transition has occurred around that bond. Such displacements are difficult to prove experimentally. In fact, we are unaware of techniques or attempts in other groups that tackle this question. Yet it is of profound importance in order to understand the coupling of molecular dynamics and macroscopic properties such as viscosity or dynamic mechanical relaxation. Indeed, there are several ways in which such angular displacements manifest themselves in multidimensional NMR experiments.[14] A particularly direct way of proving their existence is provided by 3D exchange NMR. There the orientation of a selected group is measured at three distinct points in time through their frequencies ω_1, ω_2, ω_3, displaced by two mixing times t_{ma} and t_{mb} [Figure 3(a)]. If the conformational transitions occurred in a potential that was static on average, at least on the timescale of several jumps,

the groups under study should exhibit long-term orientational memory,[14] which should manifest itself by jumps back to the starting orientation. These can directly be probed by 3D exchange NMR, where return jumps lead to ridges with $\omega_1 = \omega_3$.

Poly(vinyl acetate) (PVAc) provides a means to check such long-term orientational memory by 3D exchange NMR. This is due to the fact that, even in the ^{13}C NMR spectrum of a nonrotating sample, the powder pattern of the carbonyl carbon is completely separated from the signals of the aliphatic carbons. Thus it was possible to record a complete 3D exchange spectrum for that position.[14] In Figure 13, it is compared with a 3D exchange NMR spectrum of poly(ethylene oxide), (PEO), a highly disordered semicrystalline polymer.[52] In both cases, the mixing times t_{ma} and t_{mb} were set equal. The ridge in the diagonal plane $\omega_1 = \omega_3$ due to return jumps indicating long-term orientational memory is a prominent feature of the PEO spectrum [Figure 13(b)], but is absent from the PVAc spectrum [Figure 13(a)]. Thus, the disordered 7_2 helix of PEO has a finite probability to return to the start position even after numerous helical jumps,[14] whereas the repeat unit of PVAc apparently loses its orientational memory at each large-angle jump. This proves that in a semicrystalline polymer the chain moves in a potential that, on average, is static, whereas no such average static potential can be associated with the chain motion of an amorphous polymer above T_g. This also means that a tight coupling of molecular and cooperative dynamics must exist in amorphous polymers.

3.3.5 *Nature of Nonexponential Relaxation above T_g*

The time dependence of relaxation processes in amorphous polymers above T_g cannot be described by single exponentials. This is inferred from nonexponential correlation functions measured by conventional relaxation techniques,[42,43] and also shows up in 2D exchange NMR.[14,49,51] This is illustrated in Figure 14 for poly(vinyl acetate), where again the carboxyl carbon only is considered.[53] From the ratio of diagonal and off-diagonal intensity of 2D exchange spectra as a function of t_m, the correlation function $\langle\omega(0)\,\omega(t_m)\rangle$ is obtained and is plotted in Figure 14(a). The nonexponential decay is consistent with a stretched exponential Kohlrausch–Williams–Watts function

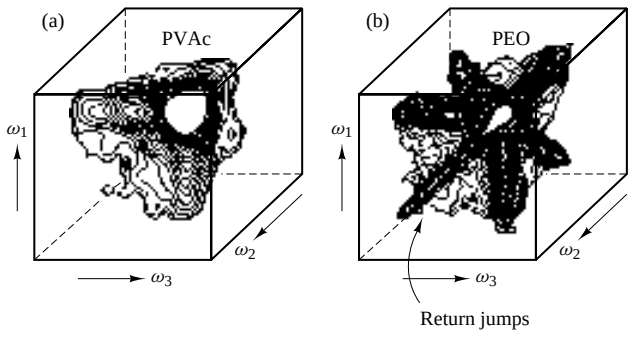

Figure 13 ^{13}C 3D exchange CP NMR spectra without MAS, comparing the chain motion in an amorphous and in a crystalline polymer: (a) poly(vinyl acetate), (PVAc), at T = 311 K (T_g + 10 K) and mixing times $t_{ma} = t_{mb}$ = 500 ms; only the carbonyl region of the spectrum is shown; (b) poly(ethylene oxide), (PEO), at T = 225 K and $t_{ma} = t_{mb}$ = 1 s; frequency scales in (a) and (b) are different for better comparison[14]

exp $[-(t/\tau_0)^{\beta}]$[54,55] with a mean correlation time τ_0 = 20 ms and β = 0.3, which translates into an asymmetric distribution of correlation times with a width of approximately three decades, as plotted in Figure 14(b).

The nature of such observations has been a matter of dispute for a long time. Two conflicting views offer explanations in terms of (i) a spatially heterogeneous distribution of correlation times (parallel processes, nonergodic) or (ii) an intrinsically nonexponential loss of correlation in a homogeneous system (a serial process, ergodic). Experimental techniques that are able to distinguish these views on a timescale relevant for the glass process, i.e., a second or so, were lacking. This distinction can be achieved by multidimensional exchange NMR, where the orientation of the same molecule can be measured by three or more subsequent points in time. In the reduced 4D exchange experiment [Figure 14(c)], we keep the first two evolution times t_1 and t_2 constant and equal. Units for which $\omega(\theta_1) = \omega(\theta_2)$, i.e., that have the same orientation before and after t_{ma}, generate a stimulated echo. The magnetization generated by the 'slow molecules' is then stored by a 90° pulse, and a 2D exchange spectrum of that selected subensemble of slow molecular units is recorded at later times, after t_{mb}, constituting a reduced 4D exchange spectrum.

In Figure 14(d)–(f), two reduced 4D exchange spectra are compared with a reference 2D NMR spectrum. The mixing times t_{ma} and t_{mc} were kept equal and comparable to τ_0. Whereas the 2D spectrum for that mixing time [Figure 14(d)] is a superposition of a diagonal ridge and broad exchange features, the reduced 4D spectrum for $t_{mb} = t_{ma} = t_{mc}$ exhibits the diagonal ridge only [Figure 14(e)]. This proves directly that the system is heterogeneous (nonergodic) on the timescale of the mean correlation time τ_0, since the spectrum of the selected subensemble is entirely different from that of the total ensemble. However, on lengthening t_{mb} by two orders of magnitude (point V in Figure 14(b)), considerable off-diagonal intensity is observed [Figure 14(e)]. This means that a significant number of units that were slow initially ($\tau \gg \tau_0$) have changed their correlation time to $\tau < \tau_0$. Thus, in the vitrifying melt, fluctuations are detected that change the reorientational dynamics of chain units. Markedly, these fluctuations causing the system to become homogeneous (ergodic) occur on timescales within the "long-time tail" of the distribution of correlation times. These experiments clearly show that, during the glass transition, the molecular units undergo non-Markovian motion with time-dependent correlation times, though not on the timescale of the mean correlation time but rather in a process limiting the longest correlation time.

3.3.6 *Local Motions in the Glassy State and Their Relation to Mechanical Properties*

The favorable mechanical properties of glassy polymers stem from relaxation processes that are possible even in the solid state.[2,3,42] However, little is known about the geometry of molecular dynamics responsible for such processes. Mechanical measurements[56,57] and ^2H 1D NMR[58] have previously established a connection between the low-temperature γ relaxation and phenylene ring motions in polycarbonate (PC), a polymer with especially favorable mechanical properties. The ring motion was identified as a flip by 180° [Figure 1(f)]. This was subsequently verified by ^{13}C NMR.[59,60] However,

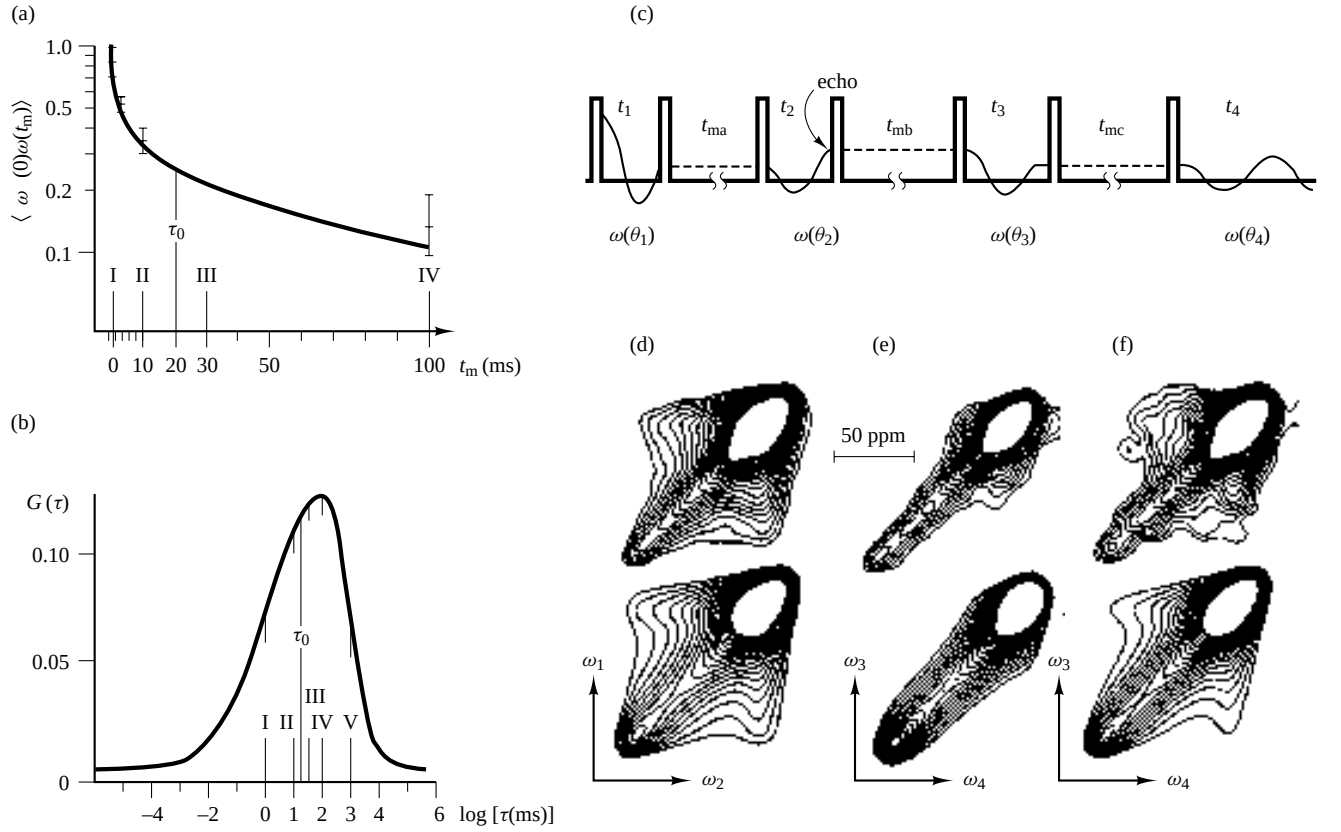

Figure 14 Nature of nonexponential loss of correlation above the glass transition.[53] (a) Nonexponential decay of correlation function with experimental points for poly(vinyl acetate), (PVAc). (b) Distribution of correlation times $G(\tau)$ derived from it. (c) Pulse sequence for reduced 4D exchange NMR. (d) Experimental and simulated ^{13}C 2D exchange NMR spectrum at T = 320 K (T_g + 20 K) and mixing time t_m = 10 ms. (e) Experimental and simulated ^{13}C reduced 4D exchange NMR spectrum at the same temperature and mixing times $t_{ma} = t_{mb} = t_{mc}$ = 10 ms. (f) Similar to (e), but with t_{mb} = 1 s and $t_{ma} = t_{mc}$ = 10 ms

the NMR lineshapes are unable to provide information about the detailed geometry of the phenylene motion at low temperatures, where it occurs on a timescale of hundreds of milliseconds, which can be probed directly by mechanical relaxation experiments. Again, such slow molecular dynamics can be detected by 2D exchange NMR, as demonstrated in Figure 15. The ^{2}H 2D exchange NMR spectrum of a sample selectively deuterated at the phenylene rings, PC-d_4, exhibits somewhat broadened elliptical ridges [Figure 15(a)],[61] which confirm the geometry of the phenylene motion as rotations around the *para* axis as indicated. However, the flip typically does not involve a rotation by exactly 180°, but by angles that can differ substantially from this mean value [Figure 15(b)]. This means that, after a rotation, the phenylene group finds itself in a slightly different environment, which readily explains the connection between this molecular dynamic process and the mechanical relaxation. Indeed, when the 2D spectrum is recorded under tensile stress, such that the sample is stretched up to the nonlinear region, yet below the yield point, the angular uncertainty in the flip angle increases further[61] [Figure 15(b)]. This is consistent with the reported increase in the strength of the mechanical relaxation under such conditions.[62] The timescale of the phenylene flips is not uniform but displays a broad distribution of correlation times[63] reflecting different activation energies in different regions of the sample.

3.3.7 Geometry of Side Group Motion in the Glassy State

The β relaxation observed in poly(methyl methacrylate), (PMMA), by means of both dielectric and dynamic–mechanical relaxation,[3] is often considered as the archetype of a localized (β) relaxation in polymers. Since this relaxation is very prominent in dielectric relaxation, it has traditionally been attributed to the carboxyl side group with its large dipole moment [Figure 16(a)]. However, quantitative analysis of relaxation strengths in both techniques is virtually impossible. Thus, neither was the geometry of the side group motion known, nor whether all or only a fraction of the groups are participating in the motion in the glassy state. A study involving both ^{13}C and ^{2}H multidimensional exchange NMR gave answers to these questions.[64] In fact, the geometry of the side group motion turned out to be more complex than originally anticipated. It involves ill-defined flips by 180° ± 20° about the C–C bond linking the carboxyl side group to the polymer backbone. This flip motion is coupled to a "rocking" motion about the local chain axis [Figure 16(a)], with a 20° root-mean-square amplitude. This motion can be detected in both ^{13}C and ^{2}H NMR, whereas the flip shows up only in the ^{13}C spectra. In the latter, the two coupled motional processes manifest themselves in the unstructured exchange intensity covering most of the 2D plane [Figure 16(b)], whereas the angular more restricted "rocking" motion leads to the exchange intensity in the ^{2}H spectrum being restricted to the vicinity of the diagonal[64] [Figure 16(c)].

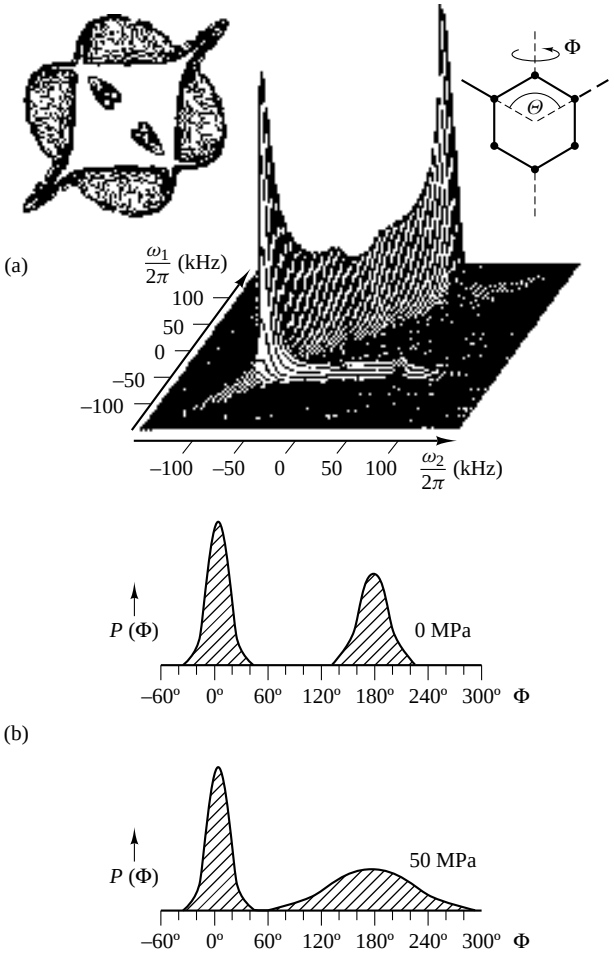

Figure 15 Phenylene motion and mechanical behavior in bisphenol-A-polycarbonate, (PC)[61]. (a) ^{2}H 2D exchange NMR spectrum of phenylene deuterated sample at T = 223 K, mixing time t_m = 500 ms. The elliptical figures (see inset) correspond to $\Phi = 180^\circ \pm 25^\circ$ phenylene flips with reorientational angle distributions shown in (b). (c) After application of 50 MPa stress, a significant broader distribution of flip angles around the same mean 180° is observed

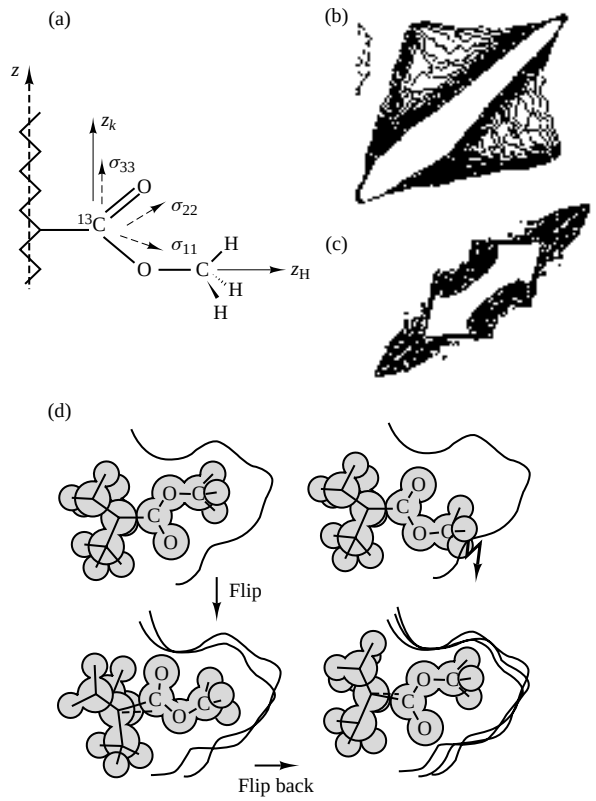

Figure 16 Side group motion in poly(methyl methacrylate), (PMMA).[64] (a) Sketch of the PMMA geometry and the principal axes for ^{13}C (carboxyl group) and ^{2}H (*O*-methyl group) NMR. (b) ^{13}C 2D exchange NMR spectrum at T = 333 K and mixing time t_m = 50 ms. (c) ^{2}H 2D exchange NMR spectrum at T = 355 K and mixing time t_m = 500 ms. (d) Sketch of the dynamics of an asymmetric side group in its correspondingly asymmetric environment, indicating that in order to fit the asymmetric side group into the volume that it had occupied before the flip, a twist around the local chain axis ("rocking" motion) is required

These findings are ascribed to the fact that the asymmetric side group, after the flip, does not fit into its original environment as depicted in Figure 16(d). Remarkably, the side group exhibits long-term orientational memory. As checked by ^{13}C 3D exchange NMR, despite the featureless exchange intensity in the 2D spectrum, the reorientation of each segment involves only two, relatively well-defined, potential energy minima. Thus, after two subsequent flips, the carboxyl group is back to almost the initial orientation [Figure 16(d)]. It is also important to realize that in the glassy state of PMMA, only about 50% of the side groups can undergo this motion. Since the side group flip requires the "rocking" motion around a locally extended chain axis, this was related to the fraction of syndiotactic triads in this polymer, which indeed favor extended conformations.[64]

This example demonstrates how complex a seemingly simple side group motion in a glassy polymer can be. The complex geometry of the side group dynamics stems from its asymmetry, since the packing apparently does provide enough free volume for a methyl group, in which it could fit after a flip. Obviously, this finding should be of interest not only for the understanding of the relation between molecular dynamics and the mechanical properties of amorphous polymers, but also in biophysics, where motions of asymmetric side groups are common dynamic processes, e.g., in proteins.[65]

3.4 Heterogeneous Polymers

In heterogeneous polymers, i.e., polymer blends or block copolymers,[1,2] domain sizes, or structures on the scale from a few to some tens of nanometers, can be be investigated by NMR spin diffusion experiments. Thus, NMR is particularly suited for characterizing small domains, nanoheterogeneities, or concentration fluctuations on lengthscales of a few nanometers, where other methods often fail owing to limitations in resolution or contrast. Thus, spin diffusion measurements are well established in solid state NMR of polymers.[8] Moreover, several advanced approaches exploiting ^{1}H spin diffusion with highly selective ^{13}C detection have been introduced.[14]

3.4.1 Wideline Separation Experiments on Polymer Blends

Spin diffusion experiments require that the different components contained in the sample be distinguished in their

NMR parameters. This is particularly straightforward if the components differ in their mobility. In fact, a long-standing method for a qualitative characterization of molecular mobility is ^{1}H wideline NMR spectroscopy.[8] There, rapid large-amplitude motions are detected through the reduction of dipolar linewidths. However, 1D proton lineshapes leave many questions open, since they typically represent superpositions of broad and narrow lines, and their relation to different structural units is often not obvious. In a straightforward combination of ^{1}H wideline NMR, cross polarization and ^{13}C MAS spectroscopy in a 2D experiment,[66] it is possible to separate the dipolar patterns for the different structural units (*wi*deline *se*paration, WISE).

The power of this technique is demonstrated in Figure 17, where data on a 50:50 wt% blend of polystyrene, (PS), and poly(vinyl methyl ether), (PVME), cast from toluene, are presented. This blend appears homogeneous by most classical techniques. The ^{1}H wideline spectrum [Figure 17(a)] consists of a rather featureless superposition of components with different dipolar linewidths, which are nicely separated in the second frequency dimension [Figure 17(b)] and related to their ^{13}C chemical shifts. Substantial motional heterogeneities, PVME being more mobile than PS, are detected despite the fact that the spectrum is recorded about 60 K above the caloric glass transition of the blend. By introducing a mixing time[66] to allow for spin diffusion, the ^{1}H lineshapes equilibrate after only 5 ms [Figure 17(c)]. From this, the domain sizes for the regions of different mobility were estimated to be 3.5 ± 1.5 nm. Thus, these advanced NMR techniques reveal substantial motional differences in different regions of this blend, which rather than homogeneous should better be described as nanoheterogeneous.

3.4.2 Domain Sizes from Spin Diffusion Experiments

Another advanced approach towards quantitative use of spin diffusion experiments exploits ^{1}H spin diffusion after high-resolution ^{1}H solid state NMR by *c*ombined *r*otation *a*nd *m*ultiple-*p*ulse *s*pectroscopy (CRAMPS), with high-resolution ^{13}C MAS detection.[14,16] In a particularly clear-cut case, this technique has been applied to a series of symmetric diblock copolymers of PS and PMMA.[16] In Figure 18(a), the increase

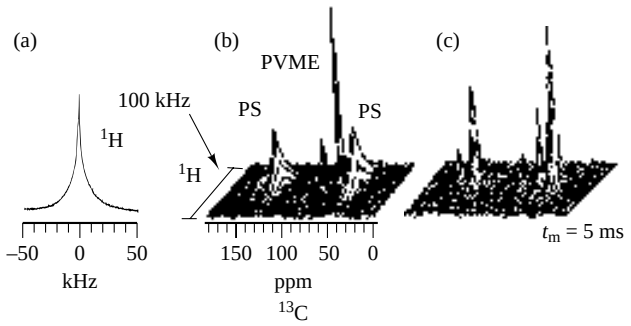

Figure 17 2D WISE NMR separating ^{1}H wideline spectra for different structural units according to their ^{13}C chemical shifts. (a) Conventional ^{1}H wideline spectrum of a blend of polystyrene, (PS), and poly(vinyl methyl ether), (PVME). (b) 2D ^{1}H ^{13}C WISE NMR spectrum at T = 320 K, note the different ^{1}H linewidths for PS and PVME. (c) Similar to (b), but with spin diffusion over a time t_m = 5 ms; note that now all lines have equal ^{1}H linewidths

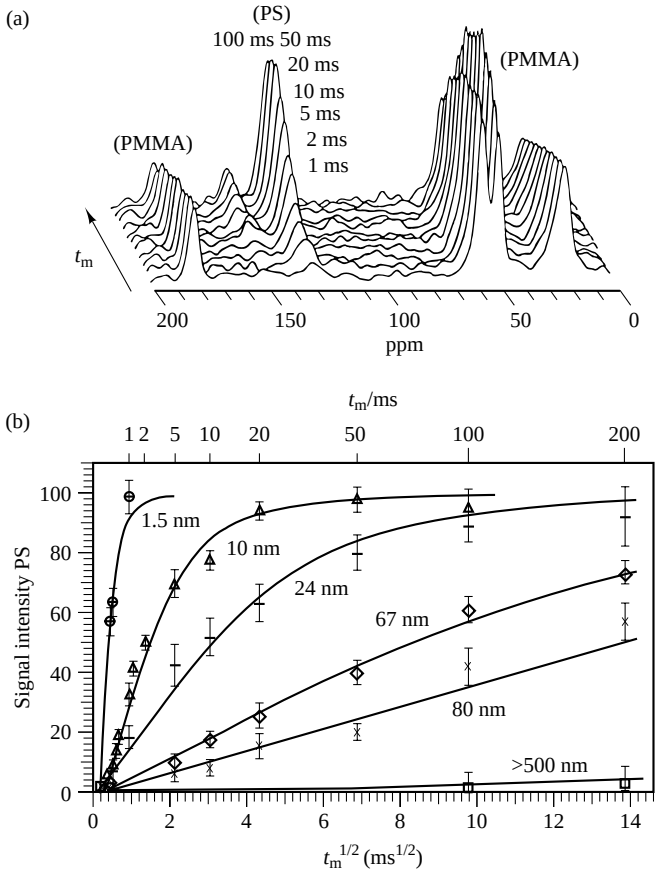

Figure 18 Spin diffusion as a tool for determining domain sizes in heterogeneous polymers.[16] (a) ^{13}C MAS spectra of the symmetric diblock copolymer PS-*b*-PMMA as a function of the diffusion time t_m after selection of proton magnetization of the methoxy group in PMMA. (b) Signal intensity of the phenyl carbons in PS as a function of t_m for different molecular weights. The numbers indicate the domain sizes obtained from the respective fits

in the carbon signal of the phenyl ring in the PS block after selection of the PMMA block is plotted against the spin diffusion time t_m for various block lengths. The equal lengths of both blocks in the symmetric copolymer ensures a lamellar structure, which makes quantitative analysis of the data easy. PMMA and PS are known to be immiscible. The spin diffusion data yield domain sizes that are consistent with the scaling law $M_n^{0.66}$, where M_n denotes the molar mass of the block, as predicted theoretically.[2] For comparison, a statistical copolymer, in which no phase separation is possible, and a blend of both homopolymers were included in the data set. The close agreement between experimental intensities and the time dependence calculated from the diffusion equation is apparent in Figure 18(b), and demonstrates that domain sizes between 0.5 and 100 nm can be determined quantitatively.

3.4.3 Packing and Mobility in Rigid Rod Systems

Advanced solid state NMR has also been applied to study the structure and dynamics of advanced polymer materials.[33] As a specific example, consider rigid rod systems consisting of *para*-substituted aromatics as stiff macromolecules, such as polyesters, polyamides and polyimides. These have attracted

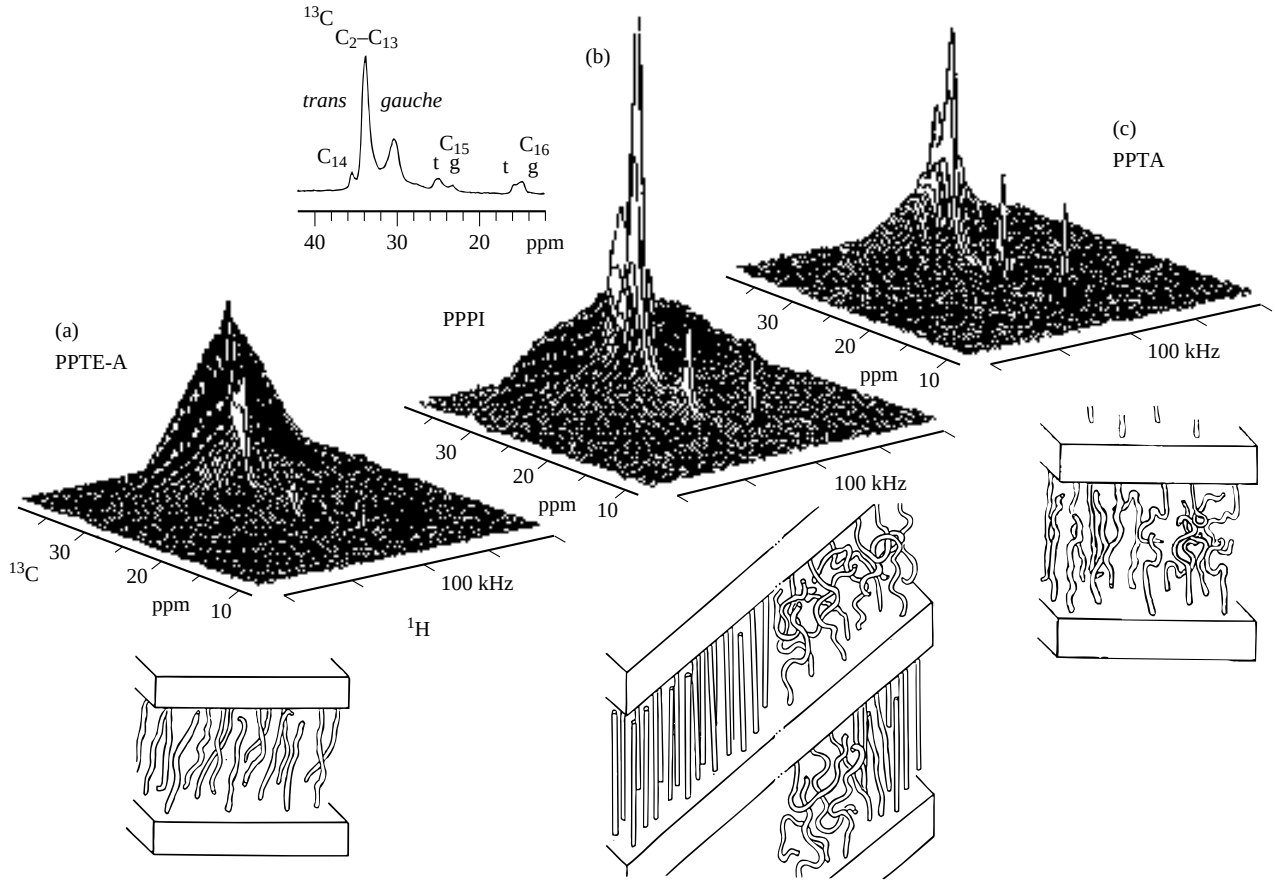

Figure 19 2D WISE NMR spectra of aliphatic side chains of various rigid rod macromolecules and structural models derived from them and spin diffusion measurements:[69] (a) polyester, A-form, PPTE-A; (b) polyimide PPPI; (c) polyamide, PPTA

considerable interest because of their unusual mechanical properties.[67] When processed from a nematic mesophase, the parallel packing of the stiff macromolecules results in high-modulus fibers. In order to increase the processability of such materials, flexible side chains are attached. However, owing to the inherent incompatibility of stiff backbone and flexible side chains, layer structures are formed where these different building elements are separated[68] (see Figure 19). Depending on the packing requirements of the stiff macromolecules, highly crystalline [form B, Figure 19(b)] or disordered amorphous [form A, Figure 19(a) and (c)] structures are formed. This imposes packing restrictions on the side chains, favoring crystallization or preventing it. Whereas X-ray scattering has been invaluable in establishing the basic features of the packing, it is difficult to provide clear-cut information about the details of the molecular organization in such complex systems.

Here, advanced 2D solid state NMR methods offer interesting alternatives. Figure 19 displays the results of 2D WISE NMR and spin diffusion experiments[69] on the side chains of a polyester (PPTE-A), a polyimide (PPPI), and a polyamide (PPTA). A high-resolution ^{13}C CP MAS spectrum of the polyimide is also displayed as an insert. The ^{1}H wideline spectra reflect the molecular dynamics of the different methylene groups. They are superpositions of broad and narrow components, even at the chain end (C_{16}). The different side-chain packings of the three systems—almost homogeneous with rather extended chain in the polyester PPTE-A, separated crystalline regions with all-*trans* chains and amorphous regions with disordered chains in the polyimide PPPI, and separated regions with extended and disordered chains in the polyamide PPTA—are nicely reflected in the different WISE NMR spectra.[69]

The delicate balance between the organization of the incompatible rigid main chains and flexible side chains in their respective layers thus leads to a considerable variety in the packing. Advanced NMR techniques yield specific information supplementing computer-aided X-ray studies, because NMR is sensitive to conformation, mobility, and spatial proximity of different structural elements.

4 CONCLUSIONS

High-resolution NMR in liquids is an indispensable analytical tool for structural characterization in chemistry, including the stereochemistry of polymers. Particularly in biochemical applications, the necessary spectral resolution can only be achieved, however, by two- and higher-dimensional spectroscopy. An analogous situation is encountered in solid polymers. Unless isotopic labeling is employed, the different anisotropic spin interactions can be separated only via multidimensional techniques. Besides providing highly selective structural information, advanced solid state NMR

offers unique possibilities for characterizing slow molecular dynamics and relating it to macroscopic material behavior.

5 RELATED ARTICLES

Brownian Motion and Correlation Times; Chemical Shift Tensors; CRAMPS; Cross Polarization in Solids; Deuterium NMR in Solids; Diffusion in Solids; Dipolar and Indirect Coupling Tensors in Solids; Dynamic Angle Spinning; HETCOR in Organic Solids; Internal Spin Interactions and Rotations in Solids; Line Narrowing Methods in Solids; Liquid Crystalline Samples: Deuterium NMR; Liquid Crystals: General Considerations; Magic Angle Spinning; Multidimensional Spectroscopy: Concepts; Polymer Blends: Miscibility Studies; Polymer MRI; Polymer Physics; Polymers: Regio-Irregular Structure; Polymers: Relaxation and Dynamics of Synthetic Polymers in Solution; Protein Dynamics from Solid State NMR; Quadrupolar Nuclei in Solids; Rotating Solids; Shielding Calculations: IGLO Method; Sideband Analysis in Magic Angle Spinning NMR of Solids; Slow and Ultraslow Motions in Biology; Sodium-23 Magnetic Resonance of Human Subjects; Two-Dimensional Methods of Monitoring Exchange; Two-Dimensional Powder Correlation Methods; Ultraslow Motions in Solids.

6 REFERENCES

1. P. J. Flory, *Principles of Polymer Chemistry*, Cornell University Press, Ithaca, NY, 1953.
2. J. I. Kroschwith (ed.), *Concise Encyclopedia of Polymer Science and Technology*, Wiley, New York, 1990.
3. N. G. McCrum, B. E. Read, and G. Williams, *Anelastic and Dielectric Effects in Polymeric Solids*, J. Wiley, New York, 1967.
4. A. Abragam, *The Principles of Nuclear Magnetism*, Oxford University Press, London, 1961.
5. C. P. Slichter, *Principles of Magnetic Resonance*, Springer-Verlag, Berlin, 1980.
6. F. A. Bovey, *Chain Structure and Conformation of Macromolecules*, Academic Press, New York, 1982.
7. R. A. Komoroski (ed.), *High Resolution NMR of Synthetic Polymers in Bulk*, VCH, Deerfield Beach, FL, 1986.
8. V. J. McBrierty, and K. J. Packer, *Nuclear Magnetic Resonance of Solid Polymers*, Cambridge University Press, Cambridge, 1993.
9. M. Mehring, *High Resolution NMR in Solids*, Springer-Verlag, Berlin, 1983.
10. R. R. Ernst, G. Bodenhausen, and A. Wokaun, *Principles of Nuclear Magnetic Resonance in One and Two Dimensions*, Oxford University Press, Oxford, 1987.
11. B. Blümich and H. W. Spiess, *Angew. Chem., Int. Ed. Engl.*, 1988, **27**, 1655.
12. A. Hagemeyer, K. Schmidt-Rohr, and H. W. Spiess, *Adv. Magn. Reson.*, 1989, **13**, 85.
13. H. W. Spiess, *Chem. Rev.*, 1991, **91**, 1321.
14. K. Schmidt-Rohr and H. W. Spiess, *Multidimensional Solid-State NMR and Polymers*, Academic Press, London, 1994.
15. C. Griesinger, O. W. Sørensen, and R. R. Ernst, *J. Magn. Reson.*, 1989, **84**, 14.
16. J. Clauss, K. Schmidt-Rohr, and H. W. Spiess, *Acta Polym.*, 1993, **44**, 1.
17. S. Spiegel, K. Schmidt-Rohr, C. Boeffel, and H. W. Spiess, *Polymer*, 1993, **34**, 4566.
18. P. J. Flory, *Statistical Mechanics of Chain Molecules*, Wiley-Interscience, New York, 1969.
19. A. E. Tonelli, *NMR Spectroscopy and Polymer Microstructure: The Conformational Connection*, VCH, New York, 1989.
20. R. Born, H. W. Spiess, W. Kutzelnigg, U. Fleischer, and M. Schindler, *Macromolecules*, 1994, **27**, 1500.
21. W. Kutzelnigg, U. Fleischer, and M. Schindler, in *NMR, Basic Principles and Progress*, ed. P. Diehl, E. Fluck, H. Günther, R. Kosfeld, and J. Seelig, Springer-Verlag, New York, 1991, Vol. 23, p. 165.
22. A. Bunn, M. E.A. Cudby, R. K. Harris, K. J. Packer, and B. J. Say, *Polymer*, 1982, **23**, 694.
23. A. Bunn, M. E.A. Cudby, R. K. Harris, K. J. Packer, and B. J. Say, *J. Chem. Soc., Chem. Commun.*, 1981, 15.
24. K. Zemke, K. Schmidt-Rohr, and H. W. Spiess, *Acta Polym.*, 1994, **45**, 148.
25. I. M. Ward (ed.), *Structure and Properties of Oriented Polymers*, Applied Science, London, 1975.
26. H. W. Spiess, in *Developments in Oriented Polymers*, ed. I. M. Ward, Applied Science, London, 1987, Vol. 1, p. 44.
27. K. Schmidt-Rohr, M. Hehn, D. Schaefer, and H. W. Spiess, *J. Chem. Phys.*, 1992, **97**, 2247.
28. B. F. Chmelka, K. Schmidt-Rohr, and H. W. Spiess, *Macromolecules*, 1993, **26**, 2282.
29. A. Ciferri (ed.), *Liquid Crystallinity in Polymers: Principles and Fundamental Properties*, VCH, Weinheim, 1991.
30. C. B. McArdle (ed.), *Liquid-Crystalline Side Group Polymers*, Blackie, Glasgow, 1988.
31. C. Boeffel and H. W. Spiess, in *Liquid-Crystalline Side Group Polymers*, ed. C. B. McArdle, Blackie, Glasgow, 1988, p. 224.
32. K. Müller, P. Meier, and G. Kothe, in *Progress in NMR Spectroscopy*, eds. J. Emsley, J. Feeney, and L. Suttcliffe, Pergamon Press, Oxford, 1985, Vol. 17, p. 211.
33. H. W. Spiess, *Ber. Bunsenges. Phys. Chem.*, 1993, **97**, 1294.
34. J. J. Titman, S. Féaux de Lacroix, and H. W. Spiess, *J. Chem. Phys.*, 1993, **98**, 3816.
35. R. M. Kannan, J. A. Kornfield, N. Schwenk, and C. Boeffel, *Macromolecules*, 1993, **26**, 2050.
36. W. Gleim and H. Finkelmann, in *Liquid Crystalline Side Group Polymers*, ed. C. B. McArdle, Blackie, Glasgow, p. 287.
37. J. Hirschinger, D. Schaefer, H. W. Spiess, and A. J. Lovinger, *Macromolecules*, 1991, **24**, 2428.
38. A. J. Lovinger, in *Developments in Crystalline Polymers*, ed. C. D. Bassett, Applied Science, London, 1981, Vol. 1, p. 195.
39. A. P. M. Kentgens, A. F. de Jong, E. de Boer, and W. S. Veeman, *Macromolecules*, 1985, **18**, 1045.
40. K. Schmidt-Rohr and H. W. Spiess, *Macromolecules*, 1991, **24**, 5288.
41. M. Mansfield and R. H. Boyd, *J. Polym. Sci., Polym. Phys. Ed.*, 1978, **16**, 1227.
42. J. D. Ferry, *Viscoelastic Properties of Polymers*, 3rd edn., Wiley, New York, 1980.
43. *J. Non-Crystal. Solids*, 1991, **131–133**; *J. Non-Crystal. Solids*, 1994, **172–174**.
44. L. Monnerie, *Makromol. Chem., Makromol. Symp.*, 1991, **48/49**, 125.
45. K. Zemke, B. F. Chmelka, K. Schmidt-Rohr, and H. W. Spiess, *Macromolecules*, 1991, **24**, 6874.
46. E. Helfand, Z. R. Wassermann, T. A. Weber, J. Skolnick, and J. H. Runnels, *J. Chem. Phys.*, 1981, **75**, 4441.

47. W. Pechold and S. Blasenbrey, *Kolloid Z.*, 1967, **216/217**, 235.
48. F. Gény and L. Monnerie, *J. Polym. Sci., Polym. Phys. Ed.*, 1979, **17**, 131, 147.
49. D. Schaefer, H. W. Spiess, U. W. Suter, and W. W. Fleming, *Macromolecules*, 1990, **23**, 3431.
50. A. Dekmezian, D. E. Axelson, J. J. Dechter, B. Bohra, and L. Mandelkern, *J. Polym. Sci., Polym. Phys. Ed.*, 1985, **23**, 367.
51. U. Pschorn, E. Rössler, H. Sillescu, S. Kaufmann, D. Schaefer, and H. W. Spiess, *Macromolecules*, 1991, **24**, 398.
52. Y. Tagahashi and H. Tadoroko, *Macromolecules*, 1973, **6**, 672.
53. K. Schmidt-Rohr and H. W. Spiess, *Phys. Rev. Lett.*, 1991, **66**, 3020.
54. R. Kohlrausch, *Pogg. Ann. Phys.*, 1854, **4**(17), 56.
55. G. Williams and D. C. Watts, *Trans. Faraday Soc.*, 1970, **66**, 80.
56. A. F. Yee and S. A. Smith, *Macromolecules*, 1981, **14**, 54.
57. E. W. Fischer, G. P. Hellmann, H. W. Spiess, F. J. Hörth, U. Ecarius, and M. Wehrle, *Macromol. Chem. Suppl.*, 1985, **12**, 189.
58. H. W. Spiess, *Colloid. Polym. Sci.*, 1983, **261**, 193.
59. P. T. Inglefield, R. M. Amici, J. F. O'Gara, C.-C. Hung, and A. A. Jones, *Macromolecules*, 1983, **16**, 1552.
60. J. Schaefer, E. O. Stejskal, R. A. McKay, and W. T. Dixon, *Macromolecules*, 1984, **17**, 1479.
61. M. T. Hansen, B. Blümich., C. Boeffel, H. W. Spiess, L. Morbitzer, and A. Zembrod, *Macromolecules*, 1992, **25**, 5542.
62. M. H. Litt and S. J. Torp, *Appl. Phys.*, 1973, **44**, 4282.
63. M. Wehrle, G. P. Hellmann, and H. W. Spiess, *Colloid. Polym. Sci.*, 1987, **265**, 815.
64. K. Schmidt-Rohr, A. S. Kulik, H. W. Beckham, A. Ohlemacher, U. Pawelzik, C. Boeffel, and H. W. Spiess, *Macromolecules*, 1994, **27**, 4733.
65. E. Clementi and S. Chin (eds), *Structure and Dynamics of Nucleic Acids, Proteins, and Membranes*, Plenum, New York, 1986.
66. K. Schmidt-Rohr, J. Clauss, and H. W. Spiess, *Macromolecules*, 1992, **25**, 3273.
67. W. J. Jackson, Jr., *Br. Polym. J.*, 1980, **12**, 147.
68. M. Ballauff, *Angew. Chem.*, 1989, **101**, 261.
69. J. Clauss, K. Schmidt-Rohr, A. Adam, C. Boeffel, and H. W. Spiess, *Macromolecules*, 1992, **25**, 5208.

Biographical Sketch

Hans Wolfgang Spiess. *b* 1942. Ph. D. 1968, Physical Chemistry, University of Frankfurt, Germany. Research associate, Florida State University, 1968–70; Max-Planck-Institute, Heidelberg with K. H. Hausser, 1970–75; University of Mainz, 1975–78. Professor at University of Mainz, 1978–80, University of Münster, 1981–82, University of Bayreuth, 1983–84. Director, Max-Planck-Institut for Polymer Research, Mainz since 1984. Approx. 250 publications. Current research interests: solid state NMR and its applications in polymer science.

ROESY

Ad Bax and Stephan Grzesiek

National Institutes of Health, Bethesda, MD, USA

1	Introduction	1
2	Principles of Rotating Frame Overhauser Spectroscopy	1
3	Comparison With Laboratory Frame NOE	2
4	Experimental Realization	4
5	Minimization of J Contributions	5
6	Examples of ROESY Applications	7
7	Different Areas of Application	7
8	Related Articles	10
9	References	10

1 INTRODUCTION

Molecular motion in liquids results in a time dependence of the dipolar coupling between two spins, which gives rise to transitions between the nuclear spin states. These transitions constitute the basis of the nuclear Overhauser enhancement (NOE) effect, which has long been one of the NMR cornerstones for the study of molecular structure.[1] As discussed in ***NOESY***, the transition rates are determined by the square of the dipolar coupling, i.e., by r^{-6}, where r is the internuclear distance, by the angular Larmor frequency ω_0, and by the decay constant τ_c of the autocorrelation function of the time-dependent dipolar coupling $D(t)$. In conventional homonuclear NOE experiments, the change in z magnetization of a spin B is monitored after the z magnetization of a spin A in its immediate vicinity has been perturbed. Provided τ_c is known, the rate at which the longitudinal magnetization of spin B changes after perturbing the z magnetization of A provides a measure of r. For $\omega_0\tau_c < 1.12$, the z magnetization of spin B will increase to a value higher than its Boltzmann equilibrium value when saturating the resonance of A (positive NOE), whereas the opposite holds for $\omega_0\tau_c > 1.12$. For many interesting molecules of intermediate size (500–2000 Da), the product $\omega_0\tau_c$ is frequently found to be close to 1, resulting in very small NOE effects.

As outlined above and described in detail elsewhere,[1–4] the NOE is a cross-relaxation effect between longitudinal components of nuclear spin magnetization. In 1983, Bothner-By and co-workers developed a different type of NOE experiment, which measures cross relaxation between magnetization components that are perpendicular to the static magnetic field.[5] The original name of this experiment is *c*ross relaxation *a*ppropriate for *m*inimolecules *e*mulated by *l*ocked *s*pins, or CAMELSPIN, but it is more commonly known as ROESY, for *r*otating-frame *O*verhauser *e*nhancement *s*pectroscopy. As implied in the original acronym of this experiment, the transverse cross relaxation is positive for all values of the rotational correlation time, i.e., it is the same as that found for small molecules in the NOESY experiment. The original motivation for this experiment was to study the structure of intermediate size molecules, which have near-zero longitudinal NOE effects. However, as pointed out in the original report,[5] the positive sign of the ROE effect also allows one immediately to distinguish cross relaxation from chemical exchange effects, which are always negative. This latter application has proven critical, for example, in studying hydration of proteins.[6,7] Other important applications lie in the area of macromolecular structure determination, where the rotating frame Overhauser enhancement, owing to its positive sign, tends to be far less susceptible to spin diffusion effects than its longitudinal counterpart.[8,9] Although for macromolecules, the inherent sensitivity of the ROESY experiment is less than for NOESY, numerous useful applications to proteins and nucleic acids have been reported. In addition to the nonselective ROESY experiment, a number of very interesting selective variants have been developed that can selectively probe small subsets of the Redfield cross-relaxation matrix. These elegant ROESY variants are particularly powerful for probing cross correlation,[10–12] and they have been treated and reviewed in great detail by Bull.[13] The discussion below is restricted to the more commonly used nonselective ROESY experiments and their various applications.

2 PRINCIPLES OF ROTATING FRAME OVERHAUSER SPECTROSCOPY

The state of a spin system is most conveniently described by the density matrix $\hat{\rho}$. For a system of two spin-$\frac{1}{2}$ nuclei, A and X, $\hat{\rho}$ is a simple 4×4 matrix. Its diagonal elements, ρ_{11}, ρ_{22}, ρ_{33}, and ρ_{44} correspond to the populations of energy levels 1, ... , 4. An off-diagonal element such as ρ_{12} represents the coherence or transition between levels 1 and 2, etc. In order to describe relaxation phenomena, the Hamiltonian is usually split into a spin-dependent part $\hat{\mathcal{H}}_S$ and a spin–lattice coupling $\hat{\mathcal{H}}_{SL}$. The spin-dependent component $\hat{\mathcal{H}}_S$ consists of the Zeeman coupling to the main external magnetic field ($\hat{\mathcal{H}}_0$) plus other, much smaller, purely spin-dependent components ($\hat{\mathcal{H}}_1$) such as chemical shift, J coupling, and coupling of the spins to radiofrequency (rf) fields. The spin–lattice part $\hat{\mathcal{H}}_{SL}$ describes the coupling of the spins to the external heat bath, which is a stochastic process. Transformation into the interaction frame makes the Zeeman term $\hat{\mathcal{H}}_0$ disappear in explicit form from the Hamiltonian, and hides it as a time dependence of the operators and the density matrix. In this interaction frame and under a number of approximations, the time dependence of the density matrix $\hat{\rho}$ is then described by

$$\frac{\mathrm{d}\hat{\rho}(t)}{\mathrm{d}t} = -\mathrm{i}[\hat{\mathcal{H}}_1, \hat{\rho}] - \hat{R}\hat{\rho} \qquad (1)$$

$\hat{R}$ is the Redfield relaxation matrix, which describes the return to equilibrium of the spin system. The relation between its elements and the spectral densities is described in detail in ***Relaxation Theory: Density Matrix Formulation***. A product $R_{1213}\rho_{13}$, for example, describes the loss per unit time of the density matrix element ρ_{12} caused by the matrix element ρ_{13}. It is important to realize, however, that relaxation is usually a slow process relative to evolution under the static Hamiltonian. Consequently, cross relaxation can only occur if the off-diagonal elements ρ_{12} and ρ_{13} oscillate at nearly the same frequencies in the laboratory frame, i.e., if the corresponding resonances overlap. In this case, the

cross relaxation between the 1–2 and the 1–3 transitions is termed a secular process. If their frequencies are different, the exchange of magnetization is a nonsecular process, and can be neglected. ROESY and its selective variants all rely on modifying the spin Hamiltonian $\hat{\mathcal{H}}_1$ in such a manner that cross relaxation can be probed between transitions that would differ in frequency in the absence of radiofrequency irradiation. In the standard ROESY experiment, this is accomplished simply by the application of a strong monochromatic rf field, which locks all magnetization that is parallel to it and dephases any perpendicular components. Neglecting off-resonance effects, the cross-relaxation rate for magnetization components locked along the rf field is therefore identical to the cross relaxation between the transverse magnetization components of two exactly overlapping resonances (identical spins).

Following Bothner-By et al.,[5] the time dependence of the spin locked magnetization components m_A and m_B of two homonuclear spins A and B is described by

$$\frac{dm_A(t)}{dt} = -R_{2A}m_A(t) - R_{AB}m_B(t) \quad (2a)$$

$$\frac{dm_B(t)}{dt} = -R_{AB}m_A(t) - R_{2B}m_B(t) \quad (2b)$$

where R_{AB} is the cross-relaxation rate of interest, and R_{2A} and R_{2B} are the autorelaxation rates, describing the loss of magnetization, which also includes processes other than cross relaxation between spins A and B. For convenience, we assume below that $R_{2A} = R_{2B} = R_2$, which results in a particularly simple solution of equations (2a) and (2b). If two experiments are done, one with $m_A(0) = m_B(0) = 1$ and one with $m_A(0) = -m_B(0) = 1$ (for example, by selectively inverting the magnetization of spin B immediately prior to a nonselective 90°_x pulse, which is followed by a y-axis spin lock), the time dependence of $m_A(t)$ and $m_B(t)$ in these two cases is given by

$$m_A(t) = m_B(t) = \exp[-(R_2 + R_{AB})t] \quad (3a)$$

$$m_A(t) = -m_B(t) = \exp[-(R_2 - R_{AB})t] \quad (3b)$$

The difference between equations (3a) and (3b) represents the ROE, which has a maximum value for

$$t = \frac{1}{2R_{AB}}\ln\frac{R_2 + R_{AB}}{R_2 - R_{AB}} \quad (4)$$

In the isolated spin pair approximation, R_2 and R_{AB} are given by

$$R_2 = \frac{\gamma^4 h^2(\mu_0/4\pi)^2}{80\pi^2 r^6}[5J(0) + 9J(\omega_0) + 6J(2\omega_0)] \quad (5)$$

$$R_{AB} = \frac{\gamma^4 h^2(\mu_0/4\pi)^2}{80\pi^2 r^6}[4J(0) + 6J(\omega_0)] \quad (6)$$

where r is the internuclear distance and, for protons, $\gamma^4 h^2(\mu_0/4\pi)^2/80\pi^2 = 2.84 \times 10^{10}\,\mathrm{s}^{-2}\,\text{Å}^6$. The reduced spectral density function $J(\omega)$ for isotropically reorienting molecules is defined as

$$J(\omega) = \frac{\tau_c}{1 + \omega^2\tau_c^2} \quad (7)$$

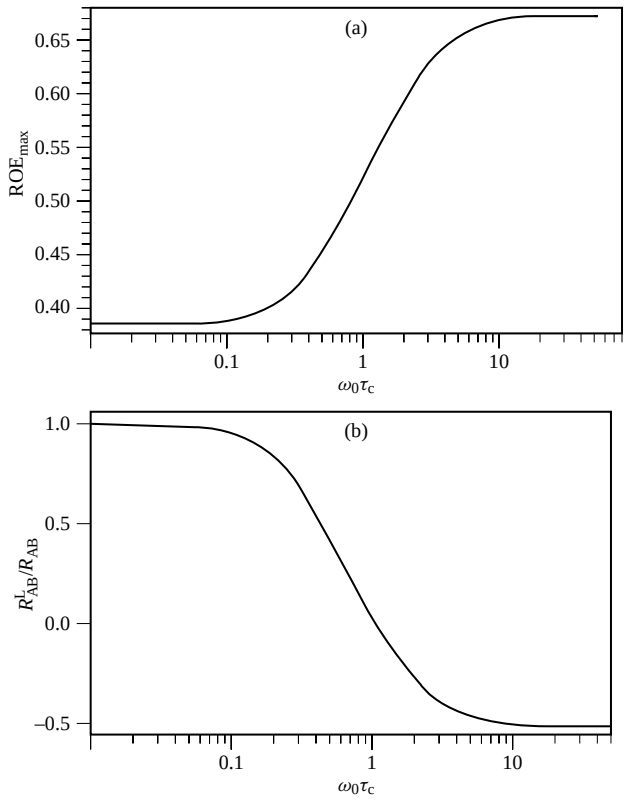

Figure 1 (a) Maximum obtainable ROE enhancement ROE_{max} in the isolated two-spin pair approximation, assuming that the spins are relaxed exclusively by homonuclear dipolar interactions. (b) The ratios of the cross relaxation rates in the laboratory frame, R^L_{AB}, and in the rotating frame, R_{AB}, as functions of $\omega_0\tau_c$

The maximum Overhauser enhancement obtainable for this isolated two-spin pair, using the ROE mixing time of equation (4), is shown graphically in Figure 1(a). In practice, the isolated spin pair approximation is usually not valid, and frequently R_2 is much larger than R_{AB}. In this case, it follows from equation (4) that the maximum ROE effect is obtained for

$$t \approx 1/R_2 \quad (8)$$

which means that the highest sensitivity is obtained for a mixing period on the order of the transverse relaxation time T_2, as measured, for example, by a selective spin echo experiment.

3 COMPARISON WITH LABORATORY FRAME NOE

In the isolated spin pair approximation and assuming rigid body motion, comparison of the ROE and NOE results is straightforward. The ROE build-up rate follows directly from equation (6), and the analogous cross-relaxation rate in the laboratory frame is given by

$$R^L_{AB} = \frac{\gamma^4 h^2(\mu_0/4\pi)^2}{40\pi^2 r^6}[6J(2\omega_0) - J(0)] \quad (9)$$

Figure 1(b) shows the ratio of the cross-relaxation rates in the laboratory and rotating frames as a function of $\omega_0\tau_c$. For

$\omega_0\tau_c \ll 1$, the build-up rates are nearly identical, whereas in the slow motion limit ($\omega_0\tau_c \gg 1$) R_{AB} approaches $-2R^L_{AB}$. Because of the dependence of R^L_{AB}/R_{AB} on $\omega_0\tau_c$, this ratio in principle can be used directly to determine the rotational correlation time τ_c, allowing one to derive absolute interproton distances from either R^L_{AB} or R_{AB}.[14] In practice, the use of this approach is limited to the region $0.3 < \omega_0\tau_c < 3$, where the ratio R^L_{AB}/R_{AB} has its steepest dependence on τ_c. A second potential problem with this approach is caused by rapid internal motion, such as methyl group rotation, which also affects R^L_{AB}/R_{AB}.[15]

3.1 Sensitivity Considerations

Although the cross-relaxation rate in the rotating frame is always higher than in the laboratory frame, this does not mean that the sensitivity of the ROESY experiment is always greater than for NOESY. The relative sensitivity of the two experiments can be derived by calculating the spectra obtained for mixing times that maximize the cross-peak intensity. As seen from equation (4), for the ROESY experiment this optimum mixing time depends on the transverse magnetization leakage rate R_2, and for the NOESY experiment it depends on the longitudinal leakage rate R_1. Neglecting the effect of the different NOESY and ROESY mixing times on the total duration of each experiment, the sensitivity ratio ξ of the NOESY versus the ROESY experiment has been calculated by Farmer et al.[15,16] for two different external relaxation rates R_{ext}, and is shown in Figure 2. This figure suggests that the ROESY experiment is expected to yield higher sensitivity

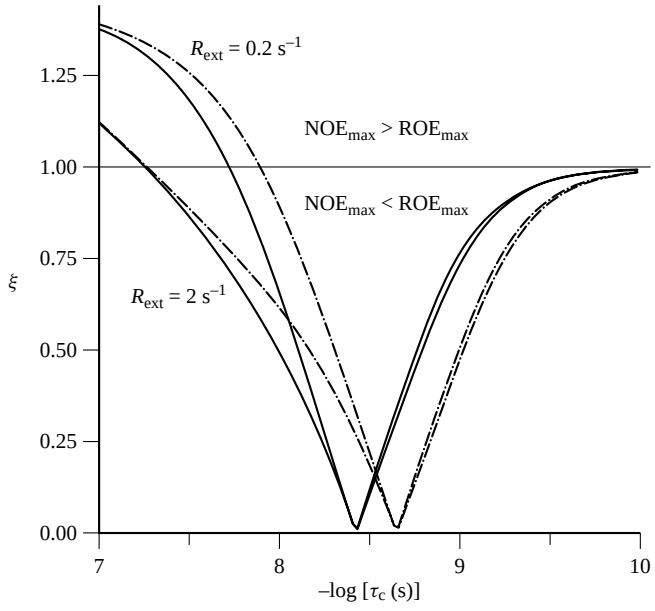

Figure 2 The ratio of the maximum cross-peak magnitude for NOESY compared with ROESY, ξ, as a function of the rotational correlation time τ_c for an AX spin system with interatomic distance r_{AX} = 0.3 nm. Plots are shown for Larmor frequencies of 300 MHz (–) and 500 MHz (-···-) and for two different external relaxation rates R_{ext}. R_{ext} represents contributions to the leakage rate from sources other than homonuclear dipolar interactions. R_{ext} was assumed to be independent of τ_c, and identical for NOESY and ROESY. Reproduced, with permission, from Farmer et al.[15]

than the NOESY experiment over a wide range of rotational correlation times. There are several practical reasons that reduce the sensitivity advantage of ROESY over NOESY, however. For example, off-resonance effects reduce the cross-relaxation rate in the ROESY experiment,[10,14–17] and so do spurious coherent Hartmann–Hahn magnetization transfer processes,[18] both discussed in some more detail below. Also, Figure 2 assumes that the external relaxation contribution R_{ext}, which represents the leakage rate from mechanisms other than homonuclear dipolar interactions, is identical for R_1 and R_2. For macromolecules, this approximation may not be valid, since proton chemical shift anisotropy and heteronuclear dipolar coupling have far larger effects on R_2 than on R_1. For $\omega\tau_c > 1.12$, there also is a third reason: because of the negative sign of the NOE, indirect contributions to the NOE cross peak increase its intensity. The opposite holds for the ROESY experiment, where the positive sign of the ROE causes the indirect contribution, relayed via one spin, to be opposite in sign to the direct contribution (the so-called three-spin effect). Indirect contributions therefore attenuate the cross-peak intensity in the ROESY spectrum and, for $\omega_0\tau_c > 1.12$, they increase the cross-peak intensity in NOESY.

3.2 The Effect of Internal Motion

In both the NOESY and ROESY experiments, cross-relaxation and leakage rates are strongly influenced by rapid internal motions. These internal motions change the shape of the spectral density function and constitute a major obstacle when attempting to derive accurate internuclear distances from the cross relaxation rates. In the model-free approach for rapid internal motion,[19,20] the spectral density function $J(\omega)$ becomes

$$J(\omega) = \frac{S^2\tau_c}{1+\omega^2\tau_c^2} + \frac{(1-S^2)\tau}{1+\omega^2\tau^2} \qquad (10)$$

where S^2 is the generalized order parameter, τ_c is again the molecular rotational correlation time, and $1/\tau = 1/\tau_e + 1/\tau_c$, with τ_e the effective correlation time of any internal motions. If S^2 and τ_e are known, equation (10) can be substituted directly into equation (6). In practice, however, detailed knowledge of S^2 and τ_e is rarely available. Note that S^2 would need to be known for every proton pair; assuming 'rigid' protons A and X and a third proton M, subject to restricted internal mobility, the order parameters for A–M and M–X interactions are likely to have different values. However, it is clear from equations (6) and (10) that rapid internal motion ($\omega_0\tau_e \ll 1$) reduces the rotating frame cross-relaxation rate. When using only a single mixing time for estimating the ROE cross-relaxation rate, the error in the linear build-up approximation also reduces the rotating frame cross-relaxation rate. Provided τ_c is known, measurement of R_{AB} therefore yields an upper limit distance constraint that is at least as large as the true interproton distance, and the errors merely weaken the constraint that is being used. In contrast, indirect NOE effects (spin diffusion) can be a major problem when using NOESY to study macromolecular conformation, since they can result in a very significant underestimate of the upper limit for the interproton distance. Such an underestimate can actually result in distorted structures.

Because of the positive sign of the ROE, indirect ROE effects generally result in a reduction in cross-peak intensity, or even in a sign change (three-spin effect), which does not result in too tight a distance constraint. As a rule of thumb, interproton distances larger than 0.35 nm rarely give rise to observable ROE cross peaks. This can, of course, also be considered to be a disadvantage, since it results in a much smaller set of interproton distance constraints. It has been suggested that for protein structure determination, the number of constraints is more important than their precise values.[21]

3.3 Equivalent Spins

Farmer et al.[15] provide a detailed discussion of the effect of equivalent spins on NOE and ROE cross-relaxation and leakage rates. For methyl groups, for example, they show that the very rapid cross relaxation among the equivalent methyl protons can lead to a dramatic increase in the leakage rate, which adversely affects the maximum obtainable ROESY cross-peak intensity. Note that intramethyl group cross relaxation does not contribute to the leakage term in the NOESY experiment. In the absence of rapid methyl group rotation and for long τ_c values (>30 ns), the maximum obtainable ROESY intensity becomes more than an order of magnitude less sensitive than for NOESY. Rapid methyl group rotation ($\tau_e < 1$ ns) quenches the intramethyl group cross relaxation, however, and NOESY and ROESY are then again of comparable sensitivity.[15] In contrast to methyl groups, methylenes are not usually subject to extensive internal dynamics, resulting in a high leakage rate in the slow tumbling limit. Cross peaks reach a maximum intensity for short mixing times, and the sensitivity of the ROESY experiment is reduced.

4 EXPERIMENTAL REALIZATION

A variety of different experimental schemes have been proposed for recording ROESY spectra. Some of the more popular ones are sketched in Figure 3, and these are briefly discussed below. The pulse schemes of Figure 3(a) and (b) are the original 1D and 2D methods for recording CAMELSPIN/ROESY spectra.[5] In (a), a selective 180° pulse inverts the z magnetization of a preselected resonance on alternate scans. After a subsequent $90°_x$ pulse, a strong monochrome radiofrequency field (SL_y) locks the spins along the y axis, and cross relaxation takes place. Subtracting odd- from even-numbered transients, recorded with and without selective inversion of the preselected resonance, yields the 1D difference spectrum, which shows intensity for spins that cross relax with the inverted spin. Figure 3(b) is the simple 2D analog of the 1D experiment, where frequency labeling is accomplished by a 90° pulse followed by the variable evolution period t_1, instead of the selective pulse.

As discussed below, for minimizing homonuclear Hartmann–Hahn transfer during the application of the spin lock field, it is necessary that the effective spin lock field for J coupled spins be different.[18] This can be accomplished either by using a relatively weak rf field strength or by positioning the rf carrier at one side of the spectrum. In this case, the effective field makes an angle θ with the z axis, and only a fraction $\sin\theta \cos \omega_A t_1$ of the A-spin magnetization is locked along the

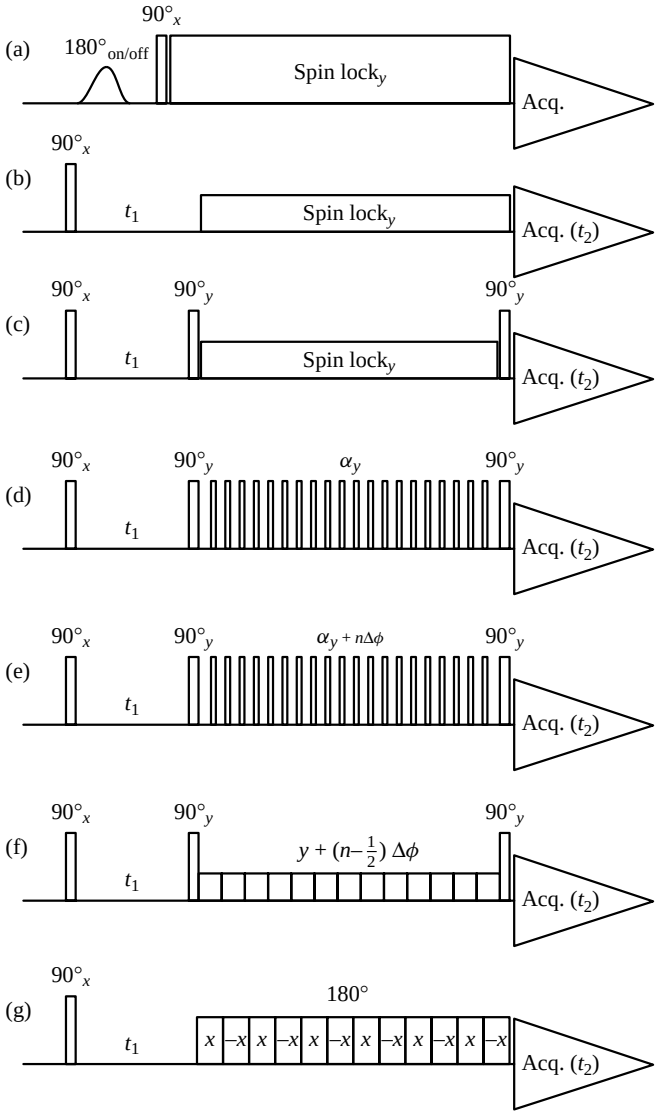

Figure 3 Experimental schemes for recording ROESY spectra. (a) One-dimensional scheme. (b) Original two-dimensional scheme. (c) Scheme with $90°_y$ pulses bracketing the y axis spin lock, to avoid signal loss caused by off-resonance spin locking. (d) Spin lock with small-angle ($\alpha \approx 30°$) pulses, separated by short delays, and bracketing pulses. (e) Spin lock with phase ramping of the α pulses. If $N\ \Delta\phi = 2\pi$, the total number of α pulses needs to be an integral multiple of N. The delay between the $90°_y$ and the first α pulse, and between the last α pulse and the following $90°_y$ pulse, needs to be half the duration of the α pulse spacing τ_d. Phase ramping merely serves to obtain the same effect as moving the carrier by $\Delta\phi/(\tau_p + \tau_d)$, where τ_p is the duration of the α pulse, from its actual position during the spin lock, without introducing problems related to phase continuity. (f) Same as (e), but using a continuous spin lock. (g) Transverse spin lock, where the spins are 'locked' along an axis perpendicular to the axis (x) along which the pulses are applied. For minimizing homonuclear Hartmann–Hahn contributions, the carrier position and rf amplitude need to be adjusted for schemes (a)–(d), and the phase-ramp-generated offset needs to be adjusted for schemes (e) and (f). To avoid excessive sample heating, the power used during the mixing period in schemes (e)–(g) may also need to be reduced. For the 2D schemes (b)–(g), quadrature in F_1 is obtained by changing the phase of the first pulse in the standard States,[22] TPPI,[23] or States–TPPI[24] manner

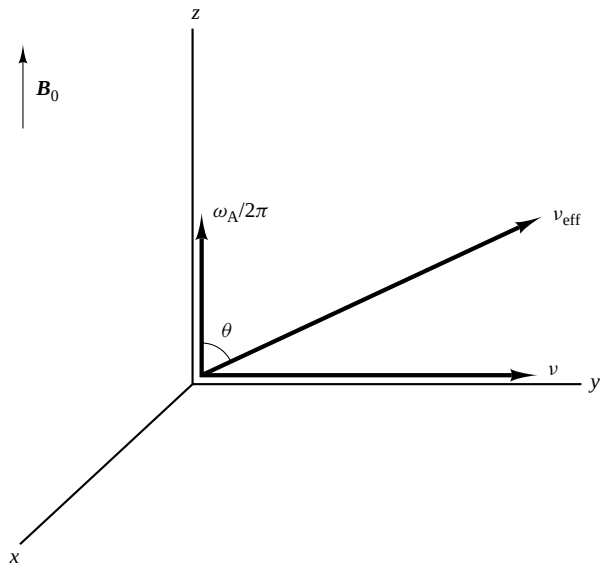

Figure 4 Definition of the effective field direction ν_{eff} for spin A at resonance offset $\omega_A/2\pi$, during irradiation with an rf field of strength ν along the y axis. Before the spin lock field is turned on, the transverse magnetization of A, $\boldsymbol{M}_A$, is in the (x,y) plane

effective field (Figure 4), where ω_A is the angular resonance frequency of spin A. After the spin lock field is turned off, only a fraction $\sin\theta$ of the spin locked magnetization is present in the transverse plane, and the sensitivity of the experiment is effectively reduced by $\sin^2\theta$. This off-resonance loss can be avoided if the weaker spin lock field is bracketed by nonselective 90°_y pulses (Figure 3c).[25] In this case, a fraction $\sin(\omega_A t_1 + \theta)$ of the transverse A-spin magnetization will be spin locked along the effective field. At the end of the ROESY mixing period, all spin locked magnetization is returned to the transverse plane by the final 90°_{-y} pulse. The loss in signal by a factor $\sin^2\theta$, as applies to the scheme in Figure 3(b), is now transferred into a phase error θ in both the F_1 and F_2 dimensions of the spectrum. To a good approximation, the phase error θ depends linearly on the resonance offset, and a first-order frequency-dependent phase correction can be used to compensate for it. Note that no phase cycling of the 90°_y pulses relative to the y axis spin lock should be used, since inverting the phase of this pulse to 90°_{-y} would also invert the phase error. Co-adding the spectra would then remove the phase error and reintroduce the amplitude loss.

The use of a low-power spin lock mixing period requires the capability to rapidly change the rf power level, which may constitute a problem on older spectrometers. This problem can be avoided by replacing the continuous spin lock by a series of closely spaced high-power pulses (Figure 3d), each of a small flip angle ($\sim 30^\circ$).[26] If the flip angle of the short pulse is α, and M pulses are applied per second, this irradiation is equivalent to spin locking with a continuous rf field of $M\alpha/2\pi$ (in Hz), provided that M (in Hz) $\gg \delta_{max}$, where δ_{max} is the maximum offset of a resonance of interest from the rf carrier frequency. Relative to a continuous rf field of equivalent field strength, the use of small flip angle pulses does not reduce the amount of undesirable homonuclear Hartmann-Hahn cross polarization[17]. If the pulse spacing is τ_d and the pulse duration is τ_p, the pulsed spin lock increases the average power used during spin lock by $(\tau_d + \tau_p)/\tau_p$ over a continuous spin lock of the same effective field strength. In some situations, this can lead to undesirable sample heating effects. The $\sin^2\theta$ signal loss that occurs in the scheme of Figure 3(b) also applies to a series of small flip angle α pulses, and this problem can again be corrected by the application of two 90°_y bracketing pulses (Figure 4d).

5 MINIMIZATION OF *J* CONTRIBUTIONS

Coherent magnetization transfer, primarily via zero quantum coherence, has been a major nuisance in NOESY spectra, where it gives rise to antiphase cross peaks of zero integrated intensity.[2,3,27] A similar problem exists in ROESY, where there are actually two distinct mechanisms for coherent transfer of magnetization between J-coupled spins: COSY and HOHAHA.

5.1 COSY Artifacts in ROESY

Considering the simplest 2D scheme of Figure 3(b), the experiment can also be considered as a COSY experiment[28] with a very long mixing pulse. During the evolution period t_1, A-spin magnetization becomes antiphase with respect to its coupling partner, X, and is subsequently transferred by the spin lock pulse, of total flip angle β, into antiphase X spin magnetization. In product operator terms,

$$\begin{aligned}\hat{A}_y &\longrightarrow^{t_1} \cos(\pi J_{AX} t_1)\hat{A}_y - 2\sin(\pi J_{AX} t_1)\hat{A}_x\hat{X}_z \\ &\longrightarrow^{\beta_y} +2\sin^2\beta\sin(\pi J_{AX} t_1)\hat{A}_z\hat{X}_x + \ldots \end{aligned} \quad (11)$$

Even though β varies spatially over the sample owing to rf inhomogeneity, $\sin^2\beta$ does not average to zero. However, with neither spin A nor X on resonance, the effective rf fields experienced by the two spins, ν_{effA} and ν_{effX}, will always be stronger than the nominal rf field strength ν:

$$\begin{aligned}\nu_{effA} &= \nu\left(1 + \frac{\delta_A^2}{\nu^2}\right)^{1/2} \approx \nu + \frac{\delta_A^2}{2\nu} \\ \nu_{effX} &= \nu\left(1 + \frac{\delta_X^2}{\nu^2}\right)^{1/2} \approx \nu + \frac{\delta_X^2}{2\nu}\end{aligned} \quad (12)$$

where δ_A and δ_X are the offsets of spins A and X. The effective flip angles β_A and β_X experienced by each of the two spins will therefore differ, and the term $\sin^2\beta$ must be rewritten as $\sin\beta_A \sin\beta_X$, and this product averages to zero when $(\delta_A{}^2 - \delta_X{}^2)\tau/2\nu$ varies rapidly over the sample volume, where τ is the duration of the spin lock period. COSY-type artifacts in ROESY spectra can therefore be minimized by

1. selecting the carrier position judiciously, to maximize $\delta_A^2 - \delta_X^2$,
2. using a relatively weak spin lock field strength ν, and
3. using a long mixing time τ.

There are limits on how weak a spin lock field strength can be used, however, since the effective fields of the two locked spins will increasingly tilt out of the transverse plane with decreasing ν. If the effective fields for spins A and B make angles of θ_A and θ_B with the z axis, chosen parallel to the static magnetic field, the cross-relaxation rate becomes:[10,14]

$$R'_{AB} = \sin\theta_A \sin\theta_B R_{AB} + \cos\theta_A \cos\theta_B R^L_{AB} \qquad (13)$$

where R_{AB} and R^L_{AB} are the transverse and longitudinal A–B cross-relaxation rates [cf. equations (6) and (9)]. Quantitative analysis of ROE cross-peak intensities should therefore account for the offsets and θ angles of the two spins involved. For molecules in the slow motion limit, R^L_{AB} and R_{AB} are of opposite sign, and θ values smaller than about 60° will seriously degrade sensitivity. In fact, if the offset and rf field strength are chosen such that the spins are aligned close to the magic angle ($\theta \approx 35°$), the direct cross relaxation R'_{AB} will be zero in the slow tumbling limit, facilitating the study of correlated cross relaxation.[10–13]

5.2 HOHAHA Artifacts in ROESY

COSY artifacts of the type discussed above are easily recognized, since they yield the characteristic antiphase multiplet pattern with zero integrated intensity. A second type of magnetization transfer can occur among J-coupled spins, and yields in-phase multiplet patterns that are of the same sign as the diagonal resonances, i.e., the artifacts are of opposite sign to the true ROESY cross peaks. This so-called homonuclear Hartmann–Hahn effect (HOHAHA) occurs when the difference in effective spin lock fields, $\nu_A - \nu_B$, is not much larger than the J coupling between A and B. This effect is fully analogous to the heteronuclear Hartmann–Hahn effect, which is commonly used for cross polarization of low-γ nuclei in solids[29,30] and liquids.[31,32]

For an isolated A–B spin pair, starting with A-spin magnetization locked along the effective spin lock field, the time dependence of the HOHAHA magnetization transfer, in the absence of an ROE effect, is given by

$$\hat{A}_z \rightarrow (1 + c^2 + s^2 \cos 2qt)\hat{A}_z + s^2(1 - \cos 2qt)\hat{B}_z + \text{antiphase terms} \qquad (14a)$$

with

$$\left.\begin{aligned} &c = \cos 2\phi, \quad s = \sin 2\phi, \quad \tan 2\phi = \frac{(1+\cos\alpha)J_{AB}}{2(\nu_A - \nu_B)} \\ &\alpha = \theta_A - \theta_B \quad 2q = 2\pi[(\nu_A - \nu_B)^2 + \tfrac{1}{4}(1+\cos\alpha)^2 J^2_{AB}]^{1/2} \end{aligned}\right\} \qquad (14b)$$

In equation (14a), the z axes have been chosen parallel to the effective field directions of the two spins, and $\hat{A}_z$ and $\hat{B}_z$ represent the in-phase A and B spin magnetization components along their respective effective fields. The angle between the two effective fields is α. Equation (14) illustrates the oscillatory behavior of the HOHAHA magnetization transfer as a function of mixing time duration. Provided $|\nu_A - \nu_B| \gg J_{AB}$, the angle 2ϕ becomes very small, resulting in a vanishingly small amount of net magnetization transfer. For reliable ROESY cross-relaxation measurements involving J-coupled spins, it is therefore essential to ensure Hartmann–Hahn mismatching for J-coupled spin pairs. When the J-coupled spins A and B are very close in chemical shift and adequate Hartmann–Hahn mismatching is not possible because of the constraints imposed by equation (14), cross relaxation between A and a third spin X will also give rise to a spurious Hartmann–Hahn relayed ROESY cross peak between B and X.[17,33] equation (14), strictly speaking, only applies for an isolated pair of coupled spins. The presence of other protons, coupled to either A or B, has the effect of making the Hartmann–Hahn match condition less sharp, and requires a larger difference $|\nu_A - \nu_B|$ to ensure minimal HOHAHA contributions.[17] In practice, a reasonable compromise between minimizing the Hartmann–Hahn effects and maximizing the transverse cross relaxation is to use a spin lock rf field strength γB_2 that is at least twice as large as the width of the spectral region of interest and to position the carrier frequency on one side of the spectrum, well outside the region of interest, such that the effective field in the center of the spectrum makes an angle of about 70° with the static magnetic field. This results in an effective mismatch $|\nu_A - \nu_B| = 0.34\ |\delta_A - \delta_B|$, whereas, according to equation (13), the rate of cross relaxation is reduced by less than about 25 %. To avoid the need to use very large spectral windows and associated large data matrix sizes, the effective position of the rf carrier may be shifted just during the spin lock duration by 'phase ramping' the spin lock pulse (Figure 3e,f). For example, if the phase of the spin lock field is increased by 10° every m μs, this has the effect of shifting the effective spin lock field by $10/(360m)$ MHz upfield or downfield from its original position.[10,34]

A detailed description of HOHAHA effects in ROESY has also been presented by Elbayed and Canet.[35]

5.3 Transverse ROESY With Minimal HOHAHA

Hwang and Shaka[36] have proposed an interesting variant of the ROESY experiment that is aimed at minimizing HOHAHA contributions. This experiment, which they refer to as transverse ROESY or T-ROESY, should not be confused with the tilted-frame T-ROESY experiment of Brüschweiler et al.,[10] which is aimed at measuring cross-correlation effects. In the transverse T-ROESY experiment, the mixing period consists of phase-alternated 180° pulses, applied preferably with no time between the pulses (Figure 3g). Near resonance, a $180°_x 180°_{-x}$ pulse pair has the net effect of a $4 \times (90° - \theta)$ rotation about the y axis, where θ is again the angle between the effective field and the field $\boldsymbol{B}_0$. Thus, a series of $180°_x 180°_{-x}$ pulse pairs has the net effect of 'spin locking' along the y axis with a spin lock field that varies approximately linearly with the resonance offset frequency δ, as $2\delta/\pi$. The strong offset dependence of the Zeeman part of the Hamiltonian minimizes strong coupling effects during the mixing period, and thereby minimizes Hartmann–Hahn effects. The trajectories of the 'locked' spins during the mixing period are the same as in a rotary echo $T_{2\rho}$ experiment,[37] and the spins, on average, are aligned for equal durations along the y and z axes. As a consequence, the effective cross-relaxation rate R_{AB}(T-ROESY) is the average of the transverse cross-relaxation rate R_{AB}, equation (6), and the longitudinal cross-relaxation rate R^L_{AB}, equation (9). For macromolecules, the opposite signs of R_{AB} and R^L_{AB} result in as much

as a fourfold reduction in cross relaxation rate compared with the standard ROESY experiment, making this type of transverse ROESY experiment less effective. However, for smaller compounds, this disadvantage is less serious, and the reduction in HOHAHA effects frequently outweighs the decrease in cross relaxation rates.[38] Mixing schemes that are more elaborate than the above-mentioned $180^\circ_x 180^\circ_{-x}$ pulse pair combination have also been suggested by Hwang and Shaka,[36] but, in practice, the simpler sequence appears to yield the most reliable results.

6 EXAMPLES OF ROESY APPLICATIONS

A few practical examples of ROESY applications are discussed below. Figure 5 shows an application of the original 1D CAMELSPIN scheme to a linear tetrasaccharide. The bottom trace is the reference spectrum, obtained after a 90°_x pulse followed by a 250 ms spin lock pulse applied along the y axis. The middle spectrum represents the same experiment, preceded by a selective 180° inversion of the highest frequency (most downfield) anomeric proton at 5.1 ppm. The top spectrum shows the difference, which exhibits significant ROEs between H-1 of one sugar unit and the H-2 and H-3 protons across the interglycosidic linkage, in addition to an intraresidue ROE to its vicinal H-2 proton.

Figure 6 shows the application of the 2D ROESY experiment to a cyclic hexapeptide, recorded at 270 MHz ^{1}H frequency with the pulse scheme of Figure 3(b). In order to emphasize how serious a problem the HOHAHA may constitute, a strong (5 kHz) spin lock field was used during the mixing period and the carrier was positioned in the center of the aliphatic region, at 3.1 ppm. Only positive contour levels, of the same sign as the diagonal resonances, are shown in this figure, and all of these cross peaks are caused by spurious magnetization transfer via the HOHAHA effect. Strong HOHAHA cross peaks are seen between the H^α and methyl protons of both the D- and the L-Ala residues, and among all the proline protons. However, true ROE contributions are also abundant in this spectrum, as illustrated by the two insets, which represent cross sections taken at the diagonal positions of the L-Ala H^N and H^α resonances. The L-Ala H^N resonance, for example, shows ROE interactions with its intraresidue methyl protons, with D-Ala H^N, and with all of the proline protons. By shifting the carrier to a higher frequency position (5.1 ppm) and reducing the strength of the spin lock field to 2 kHz, the HOHAHA contributions are greatly diminished, and only two of the proline protons (H^δ and the H^α shifted most to high frequency) exhibit significant ROEs to L-Ala H^N.[18] ROE interactions to the remaining proline protons are spurious, and are relayed via HOHAHA from Pro H^α and Pro H^δ to the other ring protons.

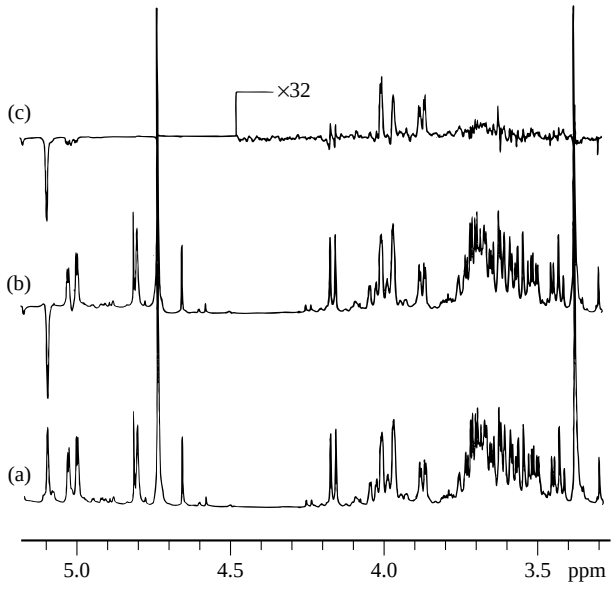

Figure 5 Spectra recorded with the scheme of Figure 3(a) for a tetrasaccharide. (a) Without selective inversion prior to the $90^\circ_x - SL_y$ sequence. (b) with selective inversion of the highest frequency (most downfield) anomeric proton. (c) The difference spectrum. Positive resonances in (c) result from ROE interactions. Reprinted from Bothner-by et al.[5]

Figure 7 illustrates the application of ROESY to basic pancreatic trypsin inhibitor, a 58-residue protein. This experiment was carried out in H_2O without solvent presaturation, using a water-flip-back scheme.[39,40] The figure compares F_1 cross-sections, taken at the F_2 frequency of Tyr-21 H^N, through the 2D ROESY (a) and NOESY (b) spectra. To compensate for the difference in longitudinal and transverse cross-relaxation rates, the NOESY mixing time (120 ms) was twice as long as for the ROESY experiment. Besides a slightly higher signal-to-noise ratio in the NOESY spectrum, the two cross sections exhibit some interesting differences. For example, the cross peak to Phe-45 H^N is relatively weak in the ROESY spectrum compared with the other cross peaks. This is due, in part, to the substantial tilt ($\theta \approx 68^\circ$) of the two spin lock fields [cf. equation (13)], which accounts for a loss of about 20% in the ROE build-up rate. Second, because no 90° bracketing pulses of the type shown in Figure 3(c) were used in this scheme, another loss of about 14% occurs (see above). Another interesting difference is seen for the Arg-20 H^β protons. Both NOESY and ROESY spectra show strong cross relaxation to the highest frequency proton of the two H^β protons, but for the low frequency H^β, the ROE cross peak is opposite in sign to the direct ROE cross peaks, indicating that it results from an indirect interaction, presumably via its geminal proton. Therefore, the NOE cross peak observed for the low frequency Arg-20 H^β proton in Figure 7(b) must also be caused largely by spin diffusion. The same is probably true for the other weak cross peaks observed in the NOESY cross-section, but absent in the ROESY spectrum. Finally, the backbone amide proton of Tyr-21 shows a NOE interaction to Tyr-21 H^δ, with only a very weak cross peak at the adjacent H^ϵ resonance, which is presumably due to spin diffusion. In the ROESY spectrum, the cross peaks to H^δ and H^ε are of comparable intensity, however, because the H^δ ROE cross-peak intensity is relayed efficiently to H^ϵ owing to the small $H^\delta - H^\varepsilon$ chemical shift difference and the large $H^\delta - H^\varepsilon$ J coupling.

7 DIFFERENT AREAS OF APPLICATION

7.1 Molecular Structure

Most applications of ROESY published to date deal with determination of either the primary structure, the

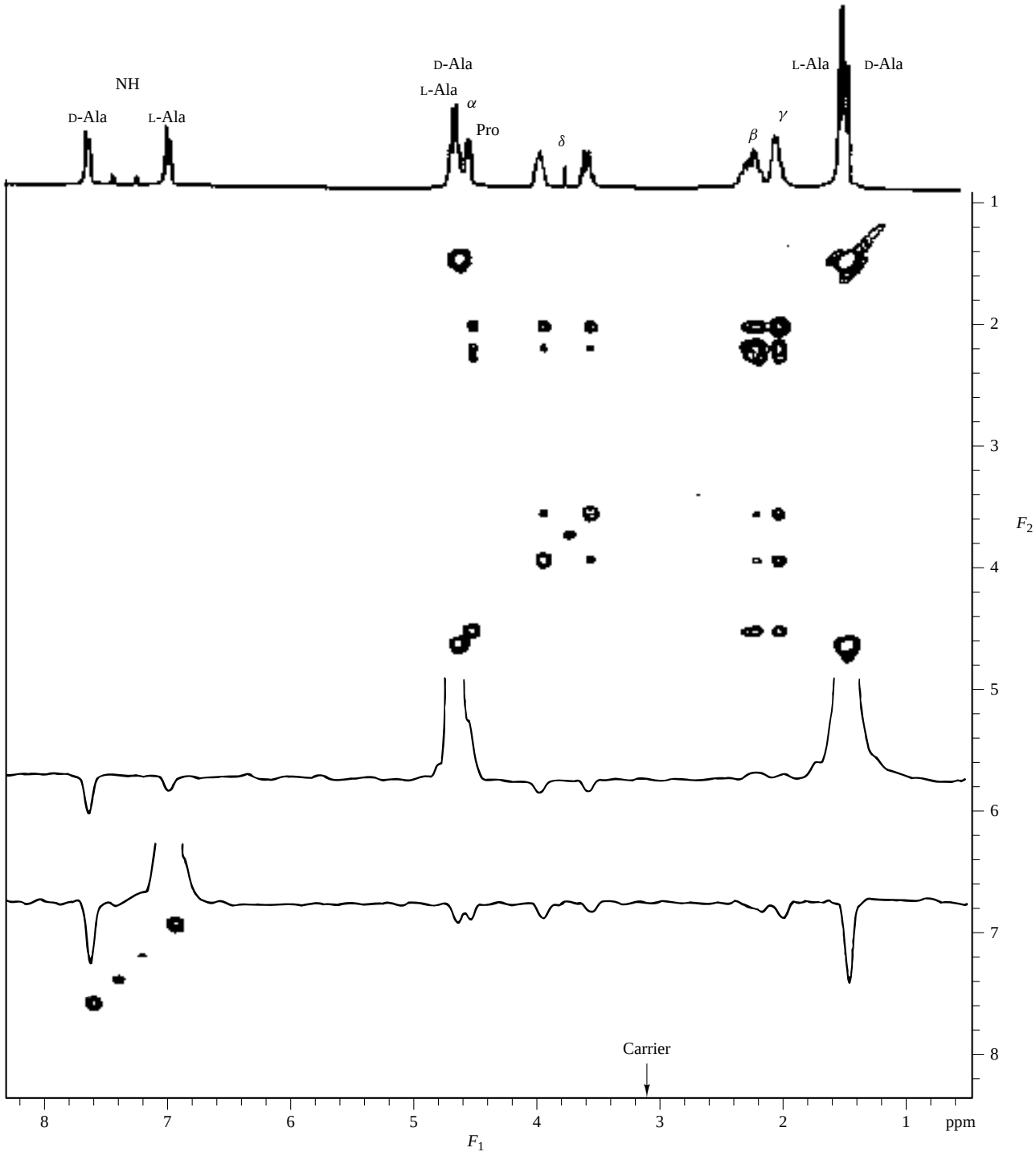

Figure 6 270 MHz 2D ROESY spectrum of a cyclic hexapeptide, (D-Ala,L-Pro,L-Ala)$_2$. Only positive contour levels (for peaks with the same sign as the diagonal) are shown. The spectrum has deliberately been recorded to maximize HOHAHA contributions by positioning the carrier at 3.1 ppm and using a strong rf field strength (γB_1 = 5 kHz) during the 200 ms spin lock. All contoured cross peaks are caused by HOHAHA transfer. The two F_1 cross sections, shown as insets, illustrate the presence of ROE cross peaks in this spectrum

stereochemistry, or the conformation of intermediate size molecules that show vanishingly weak laboratory frame NOEs. Because of the generally good ^{1}H resonance dispersion in peptides, HOHAHA effects are usually not a serious problem, and numerous applications of ROESY to the study of peptide conformation have appeared in the recent literature. Applications to the study of carbohydrate structure are also widespread, although the lack of resonance dispersion found in this class of molecules requires very careful interpretation to avoid the pitfalls of HOHAHA-relayed false ROE cross peaks. By far the largest number of literature reports on ROESY applications relates to determination of the primary structures and/or absolute configurations of natural products such as alkaloids, carotenoids, antibiotics, and other complex

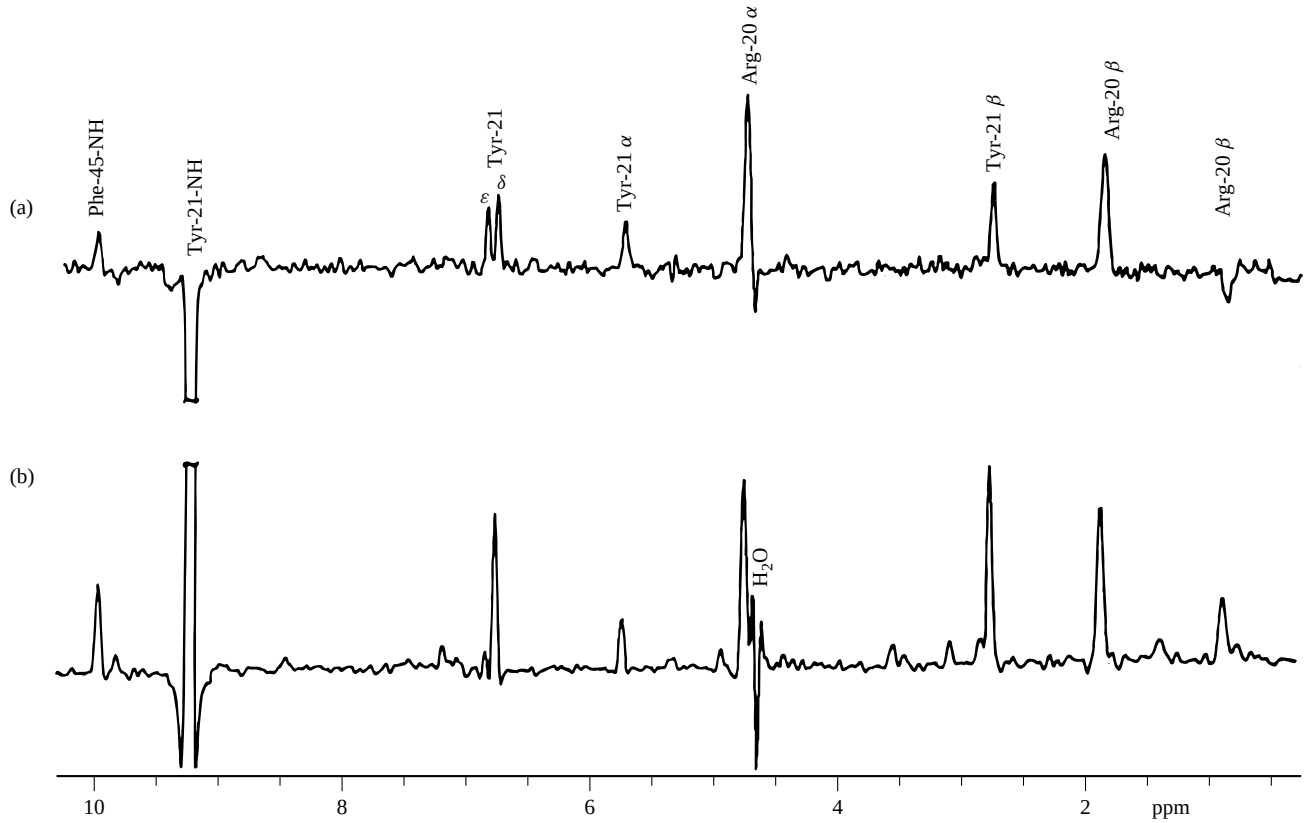

Figure 7 Comparison of F_1 cross sections through (a) the ROESY and (b) the NOESY spectra of BPTI, taken at the F_2 frequency of the Tyr-21 NH resonance. Both spectra were recorded at 500 MHz ^{1}H frequency under similar conditions, except for the mixing times (ROESY, 60 ms; NOESY, 120 ms). The ROESY carrier position was at 4.65 ppm and a 6.3 kHz spin lock field was used. From Bax.[17]

hydrocarbons. Interesting applications have also been reported for the study of the structure of inclusion complexes and other intermolecular interactions.

7.2 Macromolecular Structure

Bauer et al.[8] demonstrated by both computer simulation and experiment that spin diffusion effects in DNA generally pose less of a problem in ROESY spectra than in the corresponding NOESY spectra. They demonstrate, for example, that in regular B-form DNA, the ROE cross peak between the base H-6/H-8 proton and the H-1′ sugar proton of the preceding nucleotide never reaches a measurable value before it changes sign owing to the indirect three-spin effect via the vicinal H-2″ proton. Although the sequential base-to-H-1′ NOE cross peak frequently plays a key role in obtaining the sequential resonance assignments in DNA, the ROE experiment proves that it is almost entirely caused by spin diffusion, even at short mixing times, and it therefore has little value in structure calculations. Because of the absence of long-range NOE constraints in most regular types of DNA and RNA structure, it has been argued that it is essential to determine in a very precise manner the limited number of distances that can be measured, and the ROESY experiment can play an important role in this process.

In proteins, the emphasis has been on determining as many NOE interactions as possible,[21] and the value of using very precise interproton distances, or upper limits thereof, has not yet been convincingly demonstrated. Nevertheless, there are numerous situations where the ROESY experiment can provide important distance information in a sensitive manner, which can be critical for stereospecific assignment of H^β methylene protons, for example.[41] In the NOESY spectrum, the H^α protons of residues with a C^β methylene site invariably show NOE cross peaks to both H^β protons. If one of the H^β protons shows a weaker NOE to H^α than does its geminal partner, this could either be caused by the *gauche* and *trans* difference in $H^\alpha - H^{\beta 2}$ and $H^\alpha - H^{\beta 3}$ distances for a χ_1 rotamer of -60° or 180°, or by a small twist of a $\chi_1 = 60^\circ$ rotamer. In the ROESY spectrum, a *trans* ROE to a H^β methylene is never observed, since this interaction is again dominated by the three-spin effect via the *gauche* H^β proton. If H^α shows positive ROEs to both H^β methylene protons, this indicates a χ_1 torsion angle of $+60^\circ$, provided that HOHAHA relay via the large geminal $^1H - ^1H$ J coupling can be excluded.

7.3 Identification of Exchange Processes

As pointed out by Bothner-By et al.[5] in their original report,[5] the ROESY experiment is ideally suited for identifying chemical exchange processes that are sufficiently slow to show separate resonances for a single proton, in two or more different chemical environments, but sufficiently fast to measure magnetization transfer. The sign of the cross peak immediately discriminates between cross relaxation and chemical exchange types of magnetization transfer. In proteins and nucleic acids,

cross relaxation and chemical exchange frequently occur on similar timescales, and ROESY spectra have been used extensively to identify a variety of slow exchange processes, such as aromatic ring flipping in proteins,[42,43] monomer-duplex equilibria in DNA,[44] and conformational rearrangement in a paramagnetic model heme.[45]

7.4 Protein Hydration

A very important application for distinguishing chemical exchange from cross-correlation effects is found in the study of protein hydration. NOE interactions between labile amide protons in a protein and the bulk water resonance are indistinguishable from hydrogen exchange. In ROESY spectra, these two effects can be conveniently distinguished by the sign of the corresponding cross peak, however.[6,7] More details are given in ***Protein Hydration***

8 RELATED ARTICLES

Biological Macromolecules: Structure Determination in Solution; Biological Macromolecules: NMR Parameters; Multidimensional Spectroscopy: Concepts; NOESY; Peptides and Polypeptides; Polysaccharides and Complex Oligosaccharides; Protein Hydration; Relaxation Theory: Density Matrix Formulation; TOCSY in ROESY and ROESY in TOCSY.

9 REFERENCES

1. J. H. Noggle and R. E. Schirmer, *The Nuclear Overhauser Effect*, Academic Press, New York, 1971.
2. J. Jeener, B. H. Meier, P. Bachmann, and R. R. Ernst, *J. Chem. Phys.*, 1979, **71**, 4546.
3. S. Macura and R. R. Ernst, *Mol. Phys.*, 1980, **41**, 95.
4. D. Neuhaus and M. Williamson, *The Nuclear Overhauser Effect in Structural and Conformational Analysis*, VCH, New York, 1989.
5. A. A. Bothner-By, R. L. Stephens, J. M. Lee, C. D. Warren, and R. W. Jeanloz, *J. Am. Chem. Soc.*, 1984, **106**, 811.
6. G. Otting and K. Wüthrich, *J. Am. Chem. Soc.*, 1989, **111**, 1871.
7. G. M. Clore, A. Bax, P. T. Wingfield, and A. M. Gronenborn, *Biochemistry*, 1990, **29**, 5671.
8. C. J. Bauer, T. A. Frenkiel, and A. N. Lane, *J. Magn. Reson.*, 1990, **87**, 144.
9. A. Bax, V. Sklenar, and M. F. Summers, *J. Magn. Reson.*, 1986, **70**, 327.
10. R. Brüschweiler, C. Griesinger, and R. R. Ernst, *J. Am. Chem. Soc.*, 1989, **111**, 8034.
11. R. Brüschweiler and R. R. Ernst, *J. Chem. Phys.*, 1992, **96**, 1758.
12. T. E. Bull, *J. Magn. Reson.*, 1987, **72**, 397.
13. T. E. Bull, in *Progress in Nuclear Magnetic Resonance Spectroscopy*, eds. J. W. Emsley, J. Feeney, and L. H. Sutcliffe, Pergamon Press, Oxford, 1992, Vol. 24, p. 377.
14. D. G. Davis, *J. Am. Chem. Soc.*, 1987, **109**, 3471.
15. B. T. Farmer II, S. Macura, L. R. Brown, *J. Magn. Reson.*, 1988, **80**, 1.
16. L. R. Brown and B. T. Farmer II, in *Methods in Enzymology*, eds. T. L. James and N. Oppenheimer, Academic Press, New York, 1989, Vol. 176, p. 199.
17. A. Bax, *J. Magn. Reson.*, 1988, **77**, 134.
18. A. Bax and D. G. Davis, *J. Magn. Reson.*, 1985, **63**, 207.
19. G. Lipari and A. Szabo, *J. Am. Chem. Soc.*, 1982, **104**, 4546.
20. G. Lipari and A. Szabo, *J. Am. Chem. Soc.*, 1982, **104**, 4559.
21. G. M. Clore, M. A. Robien, and A. M. Gronenborn, *J. Mol. Biol.*, 1993, **231**, 82.
22. D. J. States, R. A. Haberkorn, and D. J. Ruben, *J. Magn. Reson.*, 1982, **48**, 286.
23. D. Marion and K. Wüthrich, *Biochem. Biophys. Res. Commun.*, 1983, **113**, 967.
24. D. Marion, M. Ikura, R. Tschudin, and A. Bax, *J. Magn. Reson.*, 1989, **85**, 393.
25. C. Griesinger and R. R. Ernst, *J. Magn. Reson.*, 1987, **75**, 261.
26. H. Kessler, C. Griesinger, R. Kerssebaum, K. Wagner, and R. R. Ernst, *J. Am. Chem. Soc.* 1987, **109**, 607.
27. M. Rance, O. W. Sørensen, W. Leupin, H. Kogler, K. Wüthrich, and R. R. Ernst, *J. Magn. Reson.*, 1985, **61**, 67.
28. W. P. Aue, E. Bartholdi, and R. R. Ernst, *J. Chem. Phys.*, 1976, **64**, 2229.
29. S. R. Hartmann and E. L. Hahn, *Phys. Rev.*, 1962, **128**, 2042.
30. A. Pines, M. G. Gibby, and J. S. Waugh, *J. Chem. Phys.*, 1973, **59**, 569.
31. R. D. Bertrand, W. B. Moniz, A. N. Garroway, and G. C. Chingas, *J. Am. Chem. Soc.*, 1978, **100**, 5227.
32. L. Müller and R. R. Ernst, *Mol. Phys.*, 1979, **38**, 963.
33. B. T. Farmer, S. Macura, and L. R. Brown, *J. Magn. Reson.*, 1987, **72**, 347.
34. L. E. Kay, M. Ikura, R. Tschudin, and A. Bax, *J. Magn. Reson.*, 1990, **89**, 496.
35. K. Elbayed and D. Canet, *Mol. Phys.*, 1990, **71**, 979.
36. T.-L. Hwang and A. J. Shaka, *J. Am. Chem. Soc.*, 1992, **114**, 3157.
37. I. Solomon, *Phys. Rev. Lett.*, 1951, **2**, 301.
38. H. P. Wessel, B. Mayer, and G. Englert., *Carbohydr. Res.*, 1993, **242**, 141.
39. A. Bax, V. Sklenar, A. M. Gronenborn, and G. M. Clore, *J. Am. Chem. Soc.*, 1987, **109**, 6511.
40. S. Grzesiek and A. Bax, *J. Am. Chem. Soc.*, 1993, **115**, 12 593.
41. G. M. Clore, A. Bax, and A. M. Gronenborn, *J. Biomol. NMR*, 1991, **1**, 13.
42. D. G. Davis and A. Bax, *J. Magn. Reson.*, 1985, **64**, 533.
43. J. Fejzo, W. M. Westler, S. Macura, and J. L. Markley, *J. Am. Chem. Soc.*, 1990, **112**, 2574.
44. U. Schmitz, I. Sethson, W. M. Egan, and T. L. James, *J. Mol. Biol.*, 1992, **227**, 510.
45. U. Simonis, J. L. Dallas, and F. A. Walker, *Inorg. Chem.*, 1992, **31**, 5349.

Biographical Sketches

Ad Bax. *b* 1956. Ph.D., 1981, Delft University of Technology, The Netherlands (on development of two-dimensional NMR methods). Postdoctoral solid state NMR work at Colorado State University, 1982–83. National Institutes of Health, Bethesda, MD, 1983–present. Currently Chief of the Section on Biophysical NMR Spectroscopy.

Stephan Grzesiek. *b* 1959. Ph.D., 1988, Free University of Berlin, Germany (on optical studies of proton release in bacteriorhodopsin). Roche Research Foundation Fellowship for NMR studies of pharamaceutically relevant biomolecules, 1989–92. National Institutes of Health, Bethesda, MD, 1992–present. Currently visiting scientist in the Section on Biophysical NMR Spectroscopy.

Selective NOESY

Geoffrey Bodenhausen
Université de Lausanne, , Switzerland/Florida State University and National High Magnetic Field Laboratory, Tallahassee, FL, USA

1	Introduction	1
2	Measurement of Cross Relaxation	1
3	Quenching of Spin Diffusion	1
4	Related Articles	4
5	References	4

1 INTRODUCTION

The meaning of the expression 'Overhauser effect' has considerably evolved over the years, and the breadth of applications could hardly have been foreseen from the original work.[1] The modern sense of the expression can be traced back to the work of Ionel Solomon.[2] In essence, the Overhauser–Solomon effect is due to a migration of populations between eigenstates which is induced by dipole–dipole interactions that are modulated by rotational diffusion of the molecule, usually in isotropic solution.[3,4] In today's terminology, the effect can be rationalized in terms of a partial interconversion of the expectation values of the longitudinal components of angular momentum, e.g. in terms of transformations of the type $\langle I_z{}^{\mathrm{A}}\rangle \rightsquigarrow \langle I_z{}^{\mathrm{X}}\rangle$. The rate of this transformation, which is known as the cross-relaxation rate, and which is usually represented in Solomon's notation by the symbol σ_{AX}, is proportional to the inverse sixth power of the distance r_{AX} between the nuclei A and X. The measurement of σ_{AX} may therefore give very accurate information about the distance r_{AX}. Such measurements are widely used both to study the conformations of small molecules and to investigate the structure of macromolecules such as proteins and nucleic acids, as well as supramolecular assemblies ranging from enzyme/substrate systems to protein/DNA complexes.

2 MEASUREMENT OF CROSS RELAXATION

It might be argued that all methods designed to observe Overhauser effects are by necessity selective. Indeed, if one wishes to monitor a process of the type $\langle I_z{}^{\mathrm{A}}\rangle \rightsquigarrow \langle I_z{}^{\mathrm{X}}\rangle$, one must initially perturb thermal equilibrium in a selective manner. If the system were in equilibrium, so that the density operator of a two-spin system would have the form $\sigma^{\mathrm{eq}} = I_z{}^{\mathrm{A}} + I_z{}^{\mathrm{X}}$, the flow of Zeeman order from one spin to the other would remain invisible. On the other hand, if one saturates one of the spins, or if one of the spins is inverted (e.g. $\langle I_z{}^{\mathrm{A}}\rangle \rightarrow -\langle I_z{}^{\mathrm{A}}\rangle$), either selectively[5] or in the course of a two-dimensional experiment,[6–8] it becomes possible to observe the migration of Zeeman order. In a selective one-dimensional experiment, we shall refer to the spin A that is inverted initially as 'source' spin. In practice, one normally considers a difference spectrum by subtracting the signals of a perturbed system from the signals excited by applying a simple monitoring pulse to a system in thermal equilibrium. In the absence of cross relaxation, only the source spin A gives rise to a signal in the difference spectrum. As the system recovers after the initial perturbation during a relaxation or mixing interval τ_{m}, the signal of the source spin A decreases, while the signal of the 'target' spin X builds up if a cross-relaxation process $\langle I_z{}^{\mathrm{A}}\rangle \rightsquigarrow \langle I_z{}^{\mathrm{X}}\rangle$ occurs. Ultimately, all signals in the difference spectrum vanish because of longitudinal spin–lattice relaxation.

A very similar behavior is observed in two-dimensional Nuclear Overhauser Effect SpectroscopY (NOESY).[6–8] The τ_{m}-dependence of the amplitude of a diagonal peak a_{AA} centered at $\omega_1 = \omega_2 = \Omega_{\mathrm{A}}$ is the same as the τ_{m} dependence of the signal of the source spin A in a one-dimensional difference spectrum. Likewise, the build-up of a cross peak a_{AX} centered at $\omega_1 = \Omega_{\mathrm{A}}$ and $\omega_2 = \Omega_{\mathrm{X}}$ follows the same pattern as the τ_{m}-dependence of the signal of a target spin X in a difference spectrum. This analogy is by no means fortuitous, for it may be argued that the two-dimensional NOESY method is equivalent to a series of one-dimensional experiments employing selective inversion at the frequencies of different source spins. The main difference lies in the fact that selective pulses required to invert the source magnetization $I_z{}^{\mathrm{A}}$ have a finite duration, so that one may have to consider cross-relaxation effects that build up *during* these selective pulses. By contrast, the nonequilibrium $I_z{}^{\mathrm{A}}$ components that begin their migration at the beginning of the mixing time τ_{m} of a two-dimensional NOESY experiment are created almost instantaneously, typically within the length of a nonselective 90° pulse. It is this feature which makes the nonselective, two-dimensional form of NOESY so attractive for studying systems with broad lines, such as macromolecules in isotropic solution or crystalline and amorphous powders. Yet if the linewidths are sufficiently narrow to make selective manipulations possible, i.e. if inhomogeneous broadening is not too pronounced and if the transverse relaxation time T_2 is not too short compared with the duration of selective pulses, one may gain in efficiency and speed by resorting to selective one-dimensional variants of NOESY. The relative merits depend on the situation: if the spectra are very crowded, it may be necessary to invert very narrow regions which would require very long pulses (typically about 100 ms to invert a region of about 30 Hz by a Gaussian Q^3 cascade[9]). In macromolecules, one would expect severe losses of magnetization due to T_2 relaxation during such long pulses, and one would have to consider the build up of cross-relaxation effects during such pulses. If, on the other hand, the spectral dispersion is sufficient, as one might expect at high fields for molecules of medium size (say, proteins with about 60 residues), it is not necessary to be too selective, and one might use for example a Gaussian Q^3 cascade of 10 ms to invert a region of 300 Hz (0.5 ppm at 600 MHz). Under such conditions, the signal intensities in selective experiments would not suffer too much from T_2 relaxation, cross relaxation during the pulses can be safely neglected, and, in terms of the information obtained per unit time, selective variants of NOESY will tend to be more efficient than nonselective two-dimensional NOESY experiments.

3 QUENCHING OF SPIN DIFFUSION

Since a review of all methods would clearly be beyond the scope of this article, we shall narrow down the definition of 'selective NOESY' to a particular class of experiments, where one focuses attention on cross relaxation processes involving two selected source and target nuclei A and X that belong to a larger network which comprises a number of perturbing spins K, K′, ... (sometimes referred to as 'clandestine' spins). Selectivity is required in the sense that these perturbing spins should not be allowed to participate in cross relaxation. A variety of methods are in development at the time of writing, and it would be premature to make a judgment as to their relative merits.

The simplest approach to this problem[10] consists of *decoupling* all perturbing spins K, K′, ... by continuous irradiation or saturation during the τ_m interval in which the migration $\langle I_z^A\rangle \rightsquigarrow \langle I_z^X\rangle$ is allowed to occur. Decoupling implies that two-step spin diffusion processes via perturbing spins K, such as $\langle I_z^A\rangle \rightsquigarrow \langle I_z^K\rangle \rightsquigarrow \langle I_z^X\rangle$, are effectively suppressed.[10] On the other hand, steady-state Overhauser effects will be induced by irradiating K, and these may lead to an enhancement (or to an attenuation, depending on the correlation time τ_c) of the Zeeman polarization of the source and target spins A and X, and this may render the interpretation of the conversion $\langle I_z^A\rangle \rightsquigarrow \langle I_z^X\rangle$ difficult. A more sophisticated approach uses a selective inversion of the magnetization of the perturbing spin $\langle I_z^K\rangle \rightarrow -\langle I_z^K\rangle$ in the middle of the relaxation or mixing interval τ_m. This may be referred to as 'editing' of the relaxation matrix.[11,12] This approach is quite effective provided that the resonance frequency of spin K is known, but is difficult to generalize[13] to systems containing several perturbing spins K, K′, ...

In nonselective two-dimensional experiments, second-order spin-diffusion effects can be identified as such by comparing cross-peak amplitudes in NOESY and in ROESY,[14] since the cross-relaxation rates in the rotating (rot) frame are opposite in sign and are twice as large as those observed in the laboratory (lab) frame ($\sigma_{AX}^{rot} = -2\sigma_{AX}^{lab}$). By combining suitable intervals of laboratory and rotating frame cross relaxation in one and the same experiment, it is possible to cancel out cross relaxation altogether.[15] It can be reintroduced by semiselective inversion of a selected group of spins, so that one can measure cross relaxation between spins belonging to this group and all other spins in the neighborhood.[16]

It is perhaps easier to focus on cross-relaxation processes between two selected spins A and X in one-dimensional spectroscopy. In the so-called synchronous nutation method,[17,18] the magnetization vectors of the two spins of interest are forced to nutate about two weak radiofrequency fields applied at the two chemical shifts. Rotary echoes are used to combat the effects of radiofrequency inhomogeneneity. The rates of the decay of the magnetization depend on the initial conditions, i.e. in macromolecules the decay rate is faster if the initial density operator is of the form $\hat{\sigma}(0) = \hat{I}_z^A + \hat{I}_z^X$ than if one starts with $\hat{\sigma}(0) = \hat{I}_z^A - \hat{I}_z^X$. The difference of the decay rates allows one to determine the cross-relaxation rate σ_{AX}. In practice, synchronous nutation experiments tend to be rather demanding from an instrumental point of view, and suffer from complications in the presence of scalar couplings.[18]

A less demanding one-dimensional experiment has become known under the acronym QUIET-NOESY, which stands for

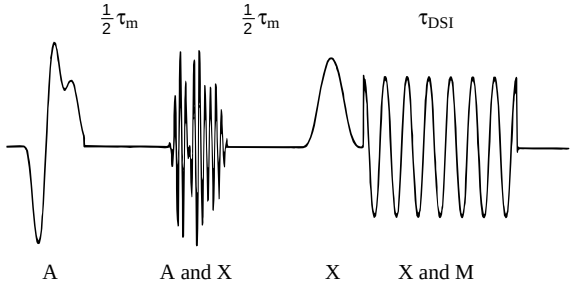

Figure 1 Sequence for the measurement of transient Overhauser effects with suppression of spin diffusion (QUIET-NOESY). The longitudinal magnetization of a selected source spin A is inverted by a Q^3 Gaussian cascade. In the middle of the relaxation or mixing interval τ_m, both the source spin A and the target spin X are inverted by an audio-modulated Q^3 Gaussian cascade. At the end of the τ_m interval, the longitudinal component $\langle I_z^X\rangle$ is converted into transverse $\langle I_x^X\rangle$ magnetization by a 270° Gaussian G^1 pulse, and transferred for observation to a scalar coupled partner $\langle I_x^X\rangle \rightarrow \langle I_x^M\rangle$ through a homonuclear Hartmann–Hahn effect during a doubly selective irradiation period τ_{DSI}. A difference spectrum is obtained by subtracting a signal recorded without initial inversion of the A spin. (Reproduced by permission of the American Chemical Society from Zwahlen et al.[19])

*q*uenching *u*ndesirable *i*ndirect *e*xternal *t*rouble in *n*uclear *O*verhauser *e*ffect *s*pectroscopy,[19] and which allows one to measure the time dependence of selected transient Overhauser effects without being affected by spin diffusion. The sequence shown in Figure 1 bears analogies to QUICK-NOESY (*q*uantitative *u*nravelling of *i*ntensities for *c*orroborating *k*nowledge in *n*uclear *O*verhauser *e*ffect *s*pectroscopy).[20] The sequence begins with the inversion of the longitudinal magnetization, $\langle I_z^A\rangle \rightarrow -\langle I_z^A\rangle$, of a selected source spin A. The initial inversion is omitted in complementary experiments, so that the signals can be subtracted in the manner of difference spectroscopy. The longitudinal magnetization (or, more accurately, its deviation from thermal equilibrium) is allowed to migrate freely under the effect of cross relaxation during the first half of the mixing interval τ_m. In the middle of this relaxation time, a fraction of the magnetization has migrated from the spin A, not only to a target spin, $\langle I_z^A\rangle \rightsquigarrow \langle I_z^X\rangle$, but also to various other clandestine spins, $\langle I_z^A\rangle \rightsquigarrow \langle I_z^K\rangle$, $\langle I_z^A\rangle \rightsquigarrow \langle I_z^{K'}\rangle$, ... , in as far as the cross-relaxation rates $\sigma_{AK}, \sigma_{AK'}, \ldots$ do not vanish. The longitudinal magnetization components of both source and target spins are then inverted simultaneously, $\langle I_z^A\rangle \rightarrow -\langle I_z^A\rangle$ and $\langle I_z^X\rangle \rightarrow -\langle I_z^X\rangle$. This can be achieved by an audiomodulated Q^3 Gaussian cascade.[21] The $\langle I_z^X\rangle$ component that remains at the end of the τ_m interval is almost entirely due to the direct conversion $\langle I_z^A\rangle \rightsquigarrow \langle I_z^X\rangle$, and not to spin diffusion. In principle, it should be possible to observe this $\langle I_z^X\rangle$ magnetization directly, but in practice we convert the longitudinal component $\langle I_z^X\rangle$ into $\langle I_x^X\rangle$ by a selective 270° Gaussian G^1 pulse.[22] The coherence $\langle I_x^X\rangle$ is then transferred to a scalar-coupled 'spy' nucleus, $\langle I_x^X\rangle \rightarrow \langle I_x^M\rangle$, through a homonuclear Hartmann–Hahn effect[23,24] during a *d*oubly *s*elective *i*rradiation (DSI) period t_{DSI}.

The mechanism of the experiment of Figure 1 may be explained by simulating the time dependence of the relevant expectation values of a system with three spins A, K, and X, as in Figure 2. The population dynamics are governed by the

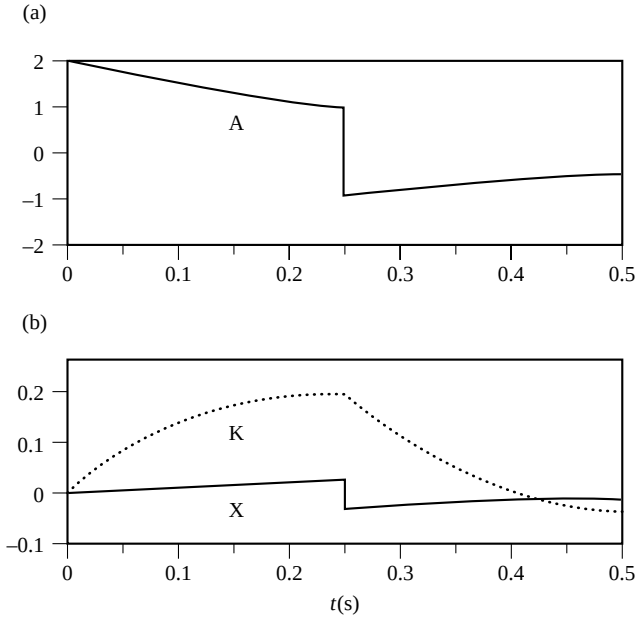

Figure 2 Simulations of the time dependence of the polarizations $\langle I_z{}^A\rangle$, $\langle I_z{}^K\rangle$, and $\langle I_z{}^X\rangle$ in the course of the relaxation interval τ_m when $\langle I_z{}^A\rangle$ and $\langle I_z{}^X\rangle$ are inverted in the middle. The parameters of the relaxation matrix are given in the text. Note the buildup of both $\langle I_z{}^K\rangle$ and $\langle I_z{}^X\rangle$ in the first half of τ_m, which is followed by a decay in the second half of τ_m. (Reproduced by permission of the American Chemical Society from Zwahlen et al.[19])

master equation:

$$\frac{\mathrm{d}}{\mathrm{d}t}\begin{pmatrix}\langle I_z^A\rangle\\ \langle I_z^K\rangle\\ \langle I_z^X\rangle\end{pmatrix} = -\begin{pmatrix}\rho_A & \sigma_{AK} & \sigma_{AX}\\ \sigma_{AK} & \rho_K & \sigma_{KX}\\ \sigma_{AX} & \sigma_{KX} & \rho_X\end{pmatrix}\begin{pmatrix}\langle I_z^A\rangle - \langle I_z^A\rangle^{eq}\\ \langle I_z^K\rangle - \langle I_z^K\rangle^{eq}\\ \langle I_z^X\rangle - \langle I_z^X\rangle^{eq}\end{pmatrix} \quad (1)$$

Since the signals are obtained from the difference between two experiments, the equilibrium terms in this equation may be dropped.

Figure 2 shows the time dependence of $\langle I_z{}^A\rangle$, $\langle I_z{}^K\rangle$, and $\langle I_z{}^X\rangle$ as a function of time within a mixing interval of fixed duration $\tau_m = 0.5\,s$. We have chosen $\rho_A = \rho_X = 3.02\,s^{-1}$, $\rho_K = 5\,s^{-1}$, $\sigma_{AK} = \sigma_{KX} = -1\,s^{-1}$, and $\sigma_{AX} = -0.02\,s^{-1}$. This is consistent with a system where $r_{AK} = r_{KX} < r_{AX}$ with dipolar relaxation in the slow tumbling limit (where $\rho_i = -\sum_j \sigma_{ij}$), with additional contributions to the diagonal elements due to chemical shift anisotropy and external random fields. In the first half of the τ_m period, one observes a typical (triexponential) decay of $\langle I_z{}^A\rangle$, which corresponds to the τ_m-dependence of the diagonal peak amplitude in NOESY. Besides the rapid buildup of $\langle I_z{}^K\rangle$ in Figure 2(b), one observes a much slower buildup of $\langle I_z{}^X\rangle$ which is mostly due to a two-step process in this example, since $\sigma_{AX}\tau_m$ is much smaller than $\frac{1}{2}\sigma_{AK}\sigma_{KX}\tau_m{}^2$. In the middle of the mixing period in Figure 2, the signs of $\langle I_z{}^A\rangle$ and $\langle I_z{}^X\rangle$ are reversed, while $\langle I_z{}^K\rangle$ remains unaffected. For clarity, this sign reversal is assumed to occur instantaneously, although in practice the audiomodulated Q^3 cascade must have a finite duration. In the second half of the mixing period, the $\langle I_z{}^K\rangle$ term decays: instead of receiving more polarization from the $\langle I_z{}^A\rangle$ bath, $\langle I_z{}^K\rangle$ now loses part of its order because the flow occurs in the reverse direction. The magnitude of the $\langle I_z{}^X\rangle$ term (deviation from zero) also decays, again because the flow of polarization, which went from K to X in the first half of τ_m, is reversed in the second half. At the end of τ_m, the polarization $\langle I_z{}^X\rangle$ that remains is mostly due to the direct transfer A $\rightsquigarrow$ X and not to the two-step process A $\rightsquigarrow$ K $\rightsquigarrow$ X.

Figure 3 shows an application to the self-complementary palindromic DNA dodecamer d(CGCGAATTCGCG)$_2$ (where d = deoxy, C = cytidine, G = guanosine, A = adenosine, and T = thymine) known as 'Dickerson's dodecamer'.[25,26] Figures 3(a) and 3(c) were recorded with the QUICK-NOESY scheme,[20] i.e. without quenching spin diffusion, and show cross-relaxation processes from two deoxyribose protons H-2′ and H-2″ of the cytosine-9 residue to the aromatic H-6 proton of the same residue. Figures 3(b) and 3(d) show the results obtained using the QUIET-NOESY sequence of Figure 1 to quench spin diffusion. Note that the C9−H-2′ $\rightsquigarrow$ C9−H-6 transfer is not dramatically affected by the quenching process, whereas the C9−H-2″ $\rightsquigarrow$ C9−H-6 transfer is almost entirely eliminated. This proves at a glance that the former process

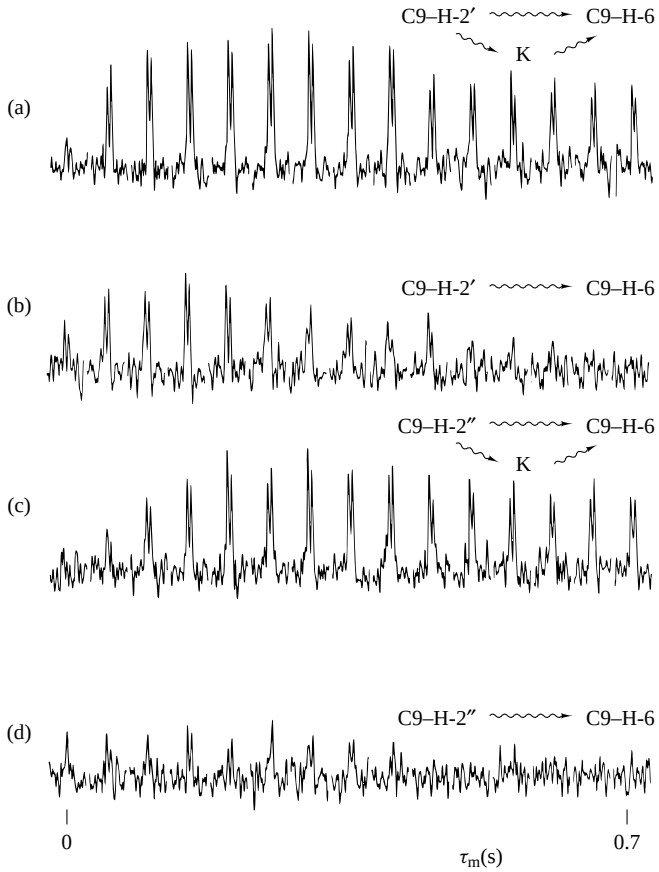

Figure 3 Selective measurements of transient Overhauser effects in the duplex d(CGCGAATTCGCG)$_2$ in D_2O at 303 K. (a) and (b): Cross relaxation from the cytosine-9 deoxyribose proton C9−H-2′ to the aromatic proton C9−H-6. (c) and (d): Cross relaxation from C9−H-2″ to C9−H-6. The magnetization was transferred from the target spin C9−H-6 to the spy spin C9−H-5 through a homonuclear Hartmann−Hahn effect. (a) and (c): Buildup curves obtained with spin diffusion, recorded with the QUICK-NOESY method (i.e. by dropping the modulated Q^3 cascade from the sequence of Figure 1). (b) and (d): Buildup curves obtained without spin diffusion, i.e. with the QUIET-NOESY method of Figure 1. (Reproduced by permission of the American Chemical Society from Zwahlen et al.[19])

corresponds to a 'true' Overhauser effect, while the latter merely results from spin diffusion. In the latter case, it appears that the C9−H-2′ proton acts as clandestine K proton that relays the information, i.e. the overall pathway would be H-2″ ⇝ H-2′ ⇝ H-6.

Selective NOESY schemes such as the experiment of Figure 1 allow one to obtain more accurate measurements of cross-relaxation rates σ_{AX}, and hence more reliable estimates of internuclear distances r_{AX}.

4 RELATED ARTICLES

NOESY; Nuclear Overhauser Effect; Selective Hartmann–Hahn Transfer in Liquids.

5 REFERENCES

1. A. W. Overhauser, *Phys. Rev.*, 1953, **92**, 411.
2. I. Solomon, *Phys. Rev.*, 1955, **99**, 559.
3. J. H. Noggle and R. E. Shirmer, *The Nuclear Overhauser Effect, Chemical Applications*, Academic Press, New York, 1971.
4. D. Neuhaus and M. P. Williamson, *The Nuclear Overhauser Effect in Structural and Conformational Analysis*, VCH, Berlin, 1989.
5. B. Boulat and G. Bodenhausen, *J. Chem. Phys.*, 1992, **97**, 6040.
6. J. Jeener, B. H. Meier, P. Bachmann, and R. R. Ernst, *J. Chem. Phys.*, 1979, **11**, 4546.
7. Anil Kumar, R. R. Ernst, and K. Wüthrich, *Biochem. Biophys. Res. Commun.*, 1980, **95**, 1.
8. S. Macura and R. R. Ernst, *Mol. Phys.*, 1980, **41**, 95.
9. L. Emsley and G. Bodenhausen, *J. Magn. Reson.*, 1992, **97**, 135.
10. W. Massefski, Jr. and A. G. Redfield, *J. Magn. Reson.*, 1988, **78**, 150.
11. J. Fejzo, W. M. Westler, S. Macura, and J. L. Markley, *J. Magn. Reson.*, 1991, **92**, 195.
12. C. G. Hoogstraten, W. M. Westler, S. Macura, and J. L. Markley, *J. Magn. Reson., Ser. B*, 1993, **102**, 232.
13. J. Fejzo, W. M. Westler, S. Macura, and J. L. Markley, *J. Magn. Reson.*, 1991, **92**, 20.
14. J. Fejzo, A. M. Krezel, W. M. Westler, S. Macura, and J. L. Markley, *J. Magn. Reson.*, 1991, **92**, 651.
15. J. Fejzo, W. M. Westler, S. Macura, and J. L. Markley, *J. Am. Chem. Soc.*, 1990, **112**, 2574.
16. J. Fejzo, W. M. Westler, J. L. Markley, and S. Macura, *J. Am. Chem. Soc.*, 1992, **114**, 1523.
17. B. Boulat, I. Burghardt, and G. Bodenhausen, *J. Am. Chem. Soc.*, 1992, **114**, 10 679.
18. I. Burghardt, R. Konrat, B. Boulat, S. J. F. Vincent, and G. Bodenhausen, *J. Chem. Phys.*, 1993, **98**, 1721.
19. C. Zwahlen, S. J. F. Vincent, L. Di Bari, M. H. Levitt, and G. Bodenhausen, *J. Am. Chem. Soc.*, 1994, **116**, 362.
20. S. J. F. Vincent, C. Zwahlen, and G. Bodenhausen, *Angew. Chem., Int. Ed. Engl.*, 1994, **33**, 343.
21. L. Emsley, I. Burghardt, and G. Bodenhausen, *J. Magn. Reson.*, 1990, **90**, 214; 1991, **94**, 448.
22. L. Emsley and G. Bodenhausen, *J. Magn. Reson.*, 1989, **82**, 211.
23. R. Konrat, I. Burghardt, and G. Bodenhausen, *J. Am. Chem. Soc.*, 1991, **113**, 9135.
24. C. Zwahlen, S. J. F. Vincent, and G. Bodenhausen, in Proceedings of the International School of Physics *Enrico Fermi*, *Course CXXIII, Nuclear Magnetic Double Resonance*, ed. B. Maraviglia, North-Holland Publishers, Amsterdam, 1993.
25. D. R. Hare, D. E. Wemmer, S.-H. Chou, G. P. Drobny, and B. R. Reid, *J. Mol. Biol.*, 1983, **171**, 319.
26. J. M. Withka, S. Swaminathan, D. L. Beveridge, and P. H. Bolton, *J. Am. Chem. Soc.*, 1991, **113**, 5041.

Biographical Sketch

Geoffrey Bodenhausen. *b* 1951. Diploma in Chemistry, ETH Zürich, Switzerland, 1974; D.Phil. with Ray Freeman, Oxford, 1977; worked with Robert and Regitze Vold at the University of California, San Diego, 1978; with Robert Griffin at the Francis Bitter National Magnet Laboratory at MIT (1979–1980); with Richard Ernst at ETH Zürich (1980–1985); associate professor at the University of Lausanne, Switzerland (1985–1994); professor at Florida State University and NMR Program Director at the National High Magnetic Field Laboratory, Tallahassee, FL (1994–present).

Three- and Four-Dimensional Heteronuclear Magnetic Resonance

G. Marius Clore and Angela M. Gronenborn
National Institutes of Health, Bethesda, MD, USA

1 Why are Three- (3D) and Four-Dimensional (4D) Experiments Required? 1
2 The Design and Implementation of 3D and 4D Experiments 1
3 Heteronuclear Editing of ^{1}H–^{1}H Experiments 1
4 Comparison of 2D, 3D, and 4D Experiments 2
5 Conclusion 6
6 Related Articles 7
7 References 7

1 WHY ARE THREE- (3D) AND FOUR-DIMENSIONAL (4D) EXPERIMENTS REQUIRED?

The principal source of geometric information used to solve 3D structures of macromolecules by NMR resides in short (<5 Å), approximate, interproton distance restraints derived from nuclear Overhauser enhancement (NOE) measurements.[1–7] In order to extract this information it is essential first to completely assign the ^{1}H spectrum of the macromolecule in question and then to assign as many structurally useful NOE interactions as possible. The larger the number of NOE restraints, the higher the precision and accuracy of the resulting structures.[7–9] Indeed, with current state-of-the-art methodology it is now possible to obtain NMR structures of proteins at a precision and accuracy comparable to 2 Å resolution crystal structures.[8–12]

For proteins of 100 residues or less, conventional homonuclear two-dimensional (2D) NMR methods can be applied with a considerable degree of success.[1–7,13,14] As the number of residues and molecular weight increases beyond 100 kDa and 12 kDa, respectively, two main obstacles present themselves, which has made it necessary to extend the 2D NMR techniques to higher dimensions and to develop new approaches. First, the increased spectral complexity arising from the presence of a larger number of protons results in extensive chemical shift overlap and degeneracy, rendering the 2D spectra uninterpretable. Second, the rotational correlation time increases with molecular weight resulting in large ^{1}H linewidths and a concomitant severe decrease in the sensitivity of correlation experiments based on intrinsically small three-bond ^{1}H–^{1}H couplings. These obstacles can be overcome by increasing the dimensionality of the spectra to resolve problems associated with spectral overlap and by simultaneously making use of heteronuclear couplings that are larger than the linewidths to circumvent limitations in sensitivity.[8,9] This approach necessitates uniform ^{15}N and/or ^{13}C labeling of the macromolecule under consideration.

The concept of increasing spectral dimensionality to extract information can perhaps most easily be understood by analogy.[8] Consider for example this Encyclopedia. In a one-dimensional (1D) representation, all the information (i.e. words and sentences arranged in a particular set order) present in the Encyclopedia would be condensed into a single line. If this line were expanded to two dimensions in the form of a page, the odd word may be resolved but the vast majority would still be superimposed on each other. When this page is expanded into a book (i.e. three dimensions) comprising a set number of lines and words per page, as well as a fixed number of pages, some pages may become intelligible, but many words will still lie on top of each other. The final expansion to the multivolume book (i.e. four dimensions) then makes it possible to extract in full all the information present in the individual entries of the encyclopedia.

2 THE DESIGN AND IMPLEMENTATION OF 3D AND 4D EXPERIMENTS

The design and implementation of higher dimensionality NMR experiments can be carried out by the appropriate combination of 2D NMR experiments, as illustrated schematically in Figure 1. A 3D experiment is constructed from two 2D pulse schemes by leaving out the detection period of the first experiment and the preparation pulse of the second.[15] This results in a pulse train comprising two independently incremented evolution periods t_1 and t_2, two corresponding mixing periods M_1 and M_2, and a detection period t_3. Similarly, a 4D experiment is obtained by combining three 2D experiments in an analogous fashion. Thus, conceptually n-dimensional NMR can be conceived as a straightforward extension of 2D NMR. The real challenge, however, of 3D and 4D NMR is twofold: first, to ascertain which 2D experiments should be combined to best advantage; and second, to design the pulse sequences in such a way that undesired artifacts, which may severely interfere with the interpretation of the spectra, are removed. This task is far from trivial.

Heteronuclear 3D and 4D NMR experiments exploit a series of large one-bond heteronuclear couplings for magnetization transfer through bonds which are summarized in Figure 2. This, together with the fact that the ^{1}H nucleus is always detected, renders these experiments very sensitive. Indeed, high-quality 3D and 4D heteronuclear-edited spectra can easily be obtained on samples of 1–2 mM uniformly labeled protein in a timeframe that is limited solely by the number of increments that have to be collected for appropriate digitization and the number of phase cycling steps that have to be used to reduce artifacts to an acceptably low level. Typical measurement times are 1–3 days for 3D experiments and 2.5–5 days for 4D ones. A detailed technical review of heteronuclear multidimensional NMR has been provided by Clore and Gronenborn.[16]

3 HETERONUCLEAR EDITING OF ^{1}H–^{1}H EXPERIMENTS

Many of the 3D and 4D experiments are based on heteronuclear editing of ^{1}H–^{1}H experiments so that the general

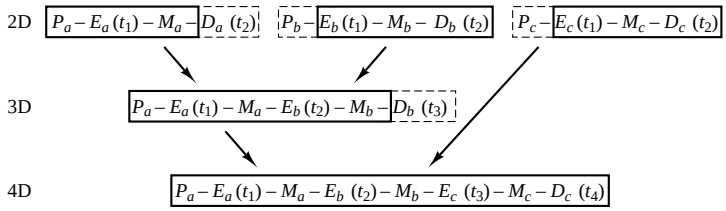

Figure 1 General representation of pulse sequences used in multidimensional NMR illustrating the relationship between the basic schemes used to record 2D, 3D, and 4D NMR spectra. Note how 3D and 4D experiments are constructed by the appropriate linear combination of 2D ones. Abbreviations: P, preparation; E, evolution; M, mixing; and D, detection. In 3D and 4D NMR, the evolution periods are incremented independently

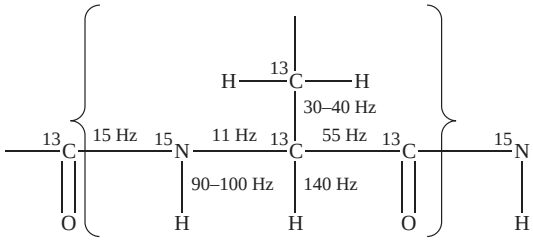

Figure 2 Summary of the one-bond heteronuclear couplings along the polypeptide chain utilized in 3D and 4D NMR experiments

appearance of conventional 2D experiments is preserved and the total number of cross peaks present is the same as that in the 2D equivalents.[8,9,16–24] The progression from a 2D spectrum to 3D and 4D heteronuclear-edited spectra is depicted schematically in Figure 3. Consider, for example the cross peaks involving a particular ^{1}H frequency in a 2D NOESY spectrum, a 3D ^{15}N or ^{13}C-edited NOESY spectrum, and finally a 4D ^{15}N/^{13}C or ^{13}C/^{13}C-edited NOESY spectrum. In the 2D spectrum a series of cross peaks will be seen from the originating proton frequencies in the F_1 dimension to the single destination ^{1}H frequency along the F_2 dimension. From the 2D experiment it is impossible to ascertain whether these NOEs involve only a single destination proton or several destination protons with identical chemical shifts. By spreading the spectrum into a third dimension according to the chemical shift of the heteronucleus attached to the destination proton(s), NOEs involving different destination protons will appear in distinct ^{1}H–^{1}H planes of the 3D spectrum. Thus each interaction is simultaneously labeled by three chemical shift coordinates along three orthogonal axes of the spectrum. The projection of all these planes onto a single plane yields the corresponding 2D spectrum. For the purposes of sequential assignment, heteronuclear-edited 3D spectra are often sufficient for analysis. However, when the goal of the analysis is to assign NOEs between protons far apart in the sequence, a 3D ^{15}N- or ^{13}C-edited NOESY spectrum will often prove inadequate. This is because the originating protons are only specified by their ^{1}H chemical shifts, and more often than not, there are several protons that resonate at the same frequencies. For example, in the case of the 153-residue protein interleukin-1β, there are about 60 protons that resonate in a 0.4 ppm interval between 0.8 and 1.2 ppm. Such ambiguities can then be resolved by spreading out the 3D spectrum still further into a fourth dimension according to the chemical shift of the heteronucleus attached to the originating protons, so that each NOE interaction is simultaneously labeled by four chemical shift coordinates along four orthogonal axes, namely those of the originating and destination protons and those of the corresponding heteronuclei directly bonded to these protons.[25–27] The result is a 4D spectrum in which each plane of the 3D spectrum constitutes a cube in the 4D spectrum.

4 COMPARISON OF 2D, 3D, AND 4D EXPERIMENTS

For illustration purposes it is also useful to compare the type of information that can be extracted from a very simple system using 2D, 3D, and 4D NMR. Consider a molecule with only two NH and two aliphatic protons in which only one NH proton is close to an aliphatic proton. In addition, the chemical shifts of the NH protons are degenerate, as are those of the aliphatic protons, so that only two resonances are seen in the 1D spectrum. In the 2D NOESY spectrum, an NOE will be observed between the resonance position of the NH protons and the resonance position of the aliphatic protons, but it will be impossible to ascertain which one of the four possible NH–aliphatic-proton combinations gives rise to the NOE. By spreading the spectrum into a third dimension, for example by the chemical shift of the ^{15}N atoms attached to the NH protons, the number of possibilities will be reduced to two, provided, of course, that the chemical shifts of the two nitrogen atoms are different. Finally, when the fourth dimension corresponding to the chemical shift of the ^{13}C atoms attached to the aliphatic protons is introduced, a unique assignment of the NH–aliphatic-proton pair giving rise to the NOE can be made.

Figure 4(a) presents a portion of the 2D ^{15}N-edited NOESY spectrum of interleukin-1β (153 residues) illustrating NOE interactions between the NH protons along the F_2 axis and the C-α,H protons along the F_1 dimension.[19] Despite the fact that a large number of cross peaks can be resolved, it can be seen that many of the cross peaks have identical chemical shifts in one or other dimensions. For example, there are 15 cross peaks involving NH protons at an $F_2(^1\text{H})$ chemical shift of $\sim$9.2 ppm. A single $^1\text{H}(F_1)$–$^1\text{H}(F_3)$ plane of the 3D ^{15}N-edited NOESY spectrum of interleukin-1β at $\delta^{15}\text{N}(F_2)$ = 123.7 ppm is shown in Figure 4(b). Not only is the number of cross peaks in this slice small, but also at $\delta^1\text{H}(F_3) \sim$ 9.2 ppm there is only a single cross peak involving one NH proton. The correlations observed in the ^{15}N-edited NOESY spectrum are through-space ones. Intraresidue correlations from the NH protons to the C-α,H and C-β,H protons can similarly be resolved using a 3D ^{15}N-edited HOHAHA spectrum in which efficient isotropic mixing sequences are used to transfer magnetization between protons via three-bond ^{1}H–^{1}H couplings.

The 3D ^{15}N-edited NOESY and HOHAHA spectra constitute only one of several versions of a 3D heteronuclear-edited

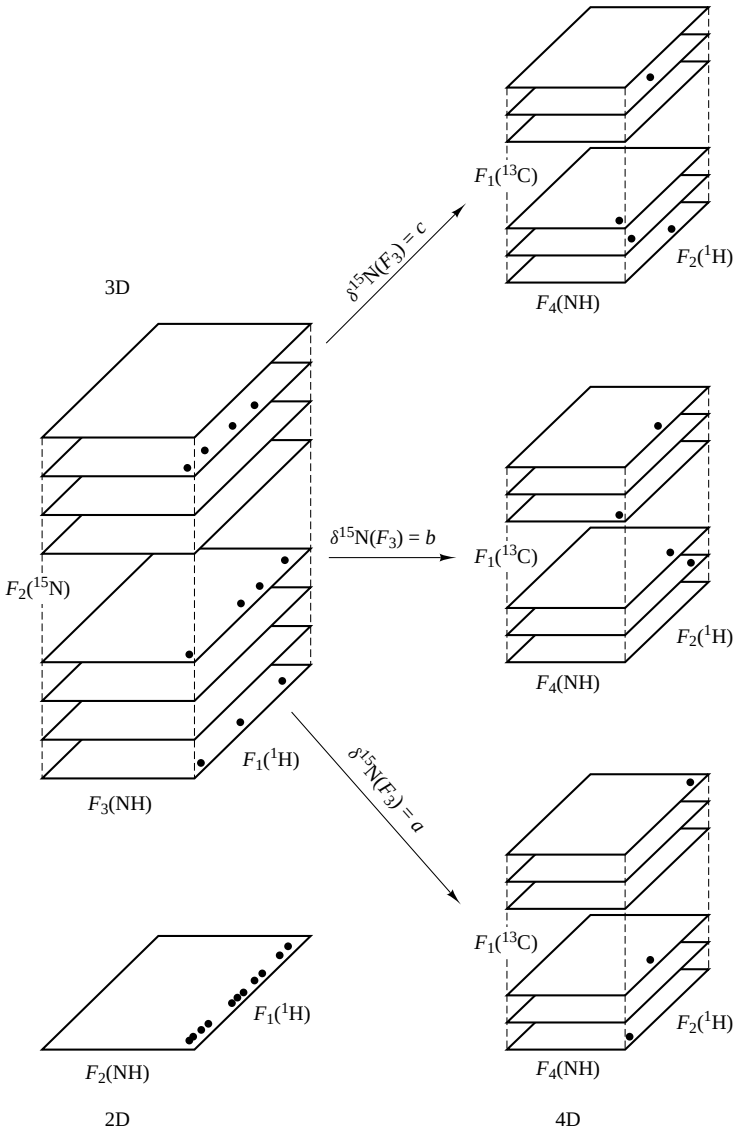

Figure 3 Schematic illustration of the progression and relationship between 2D, 3D, and 4D heteronuclear NMR experiments. The solid circles represent NOE cross peaks. In the example shown there are 11 NOEs originating from 11 different protons in the F_1 dimension to a single-frequency position in the F_2 dimension. In the 2D spectrum, it is impossible to ascertain whether there is only one destination proton or several in the F_2 dimension. By spreading the spectrum into a third dimension (labeled F_2), according to the chemical shift of the heteronucleus attached to the destination proton, it can be seen that the NOEs now lie in three distinct $^1H(F_1)-^1H(F_3)$ planes, indicating that three different destination protons are involved. However, the ^1H chemical shifts still provide the only means of identifying the originating protons. Hence the problem of spectral overlap still prevents the unambiguous assignment of these NOEs. By extending the spectrum to 4D, each NOE interaction is labeled by four chemical shifts along four orthogonal axes. Thus, the NOEs in each plane of the 3D spectrum are now spread over a cube in the 4D spectrum according to the chemical shift of the heteronucleus directly attached to the originating protons. (Reproduced by permission from Kay et al.[25])

spectrum. Many alternative through-bond pathways can be utilized to great effect. Consider, for example, the delineation of amino acid spin systems which involves grouping those resonances which belong to the same residue. In 2D NMR, correlation experiments are used to delineate either direct or relayed connectivities via small three-bond $^1H-^1H$ couplings. Even for proteins of 50–60 residues, it can be difficult to delineate long-chain amino acids such as lysine (Lys) and arginine (Arg) in this manner. In heteronuclear 3D NMR an alternative pathway can be employed which involves transferring magnetization first from a proton to its directly attached carbon atom via the large ^1J(C,H) coupling (~130 Hz), followed by either direct or relayed transfer of magnetization along the carbon chain via the ^1J(C,C) couplings (~30–40 Hz), before transferring the magnetization back to protons.[28,29,38] An example of such a spectrum is the so-called HCCH-TOCSY shown in Figure 4(c). The $^1H(F_1)-^1H(F_3)$ plane at $\delta^{13}C(F_2)$ = 59 ppm illustrates both direct and relayed connectivities along various side chains originating from C-α,H protons. As expected, the resolution of the spectrum is excellent and there is no spectral overlap. Just as importantly, however, the sensitivity of the experiment is extremely high and complete spin systems are readily identified in interleukin-1β even for long side chains, such as those of two Lys residues shown in the Figure. Indeed, analyzing spectra of this kind, it was possible

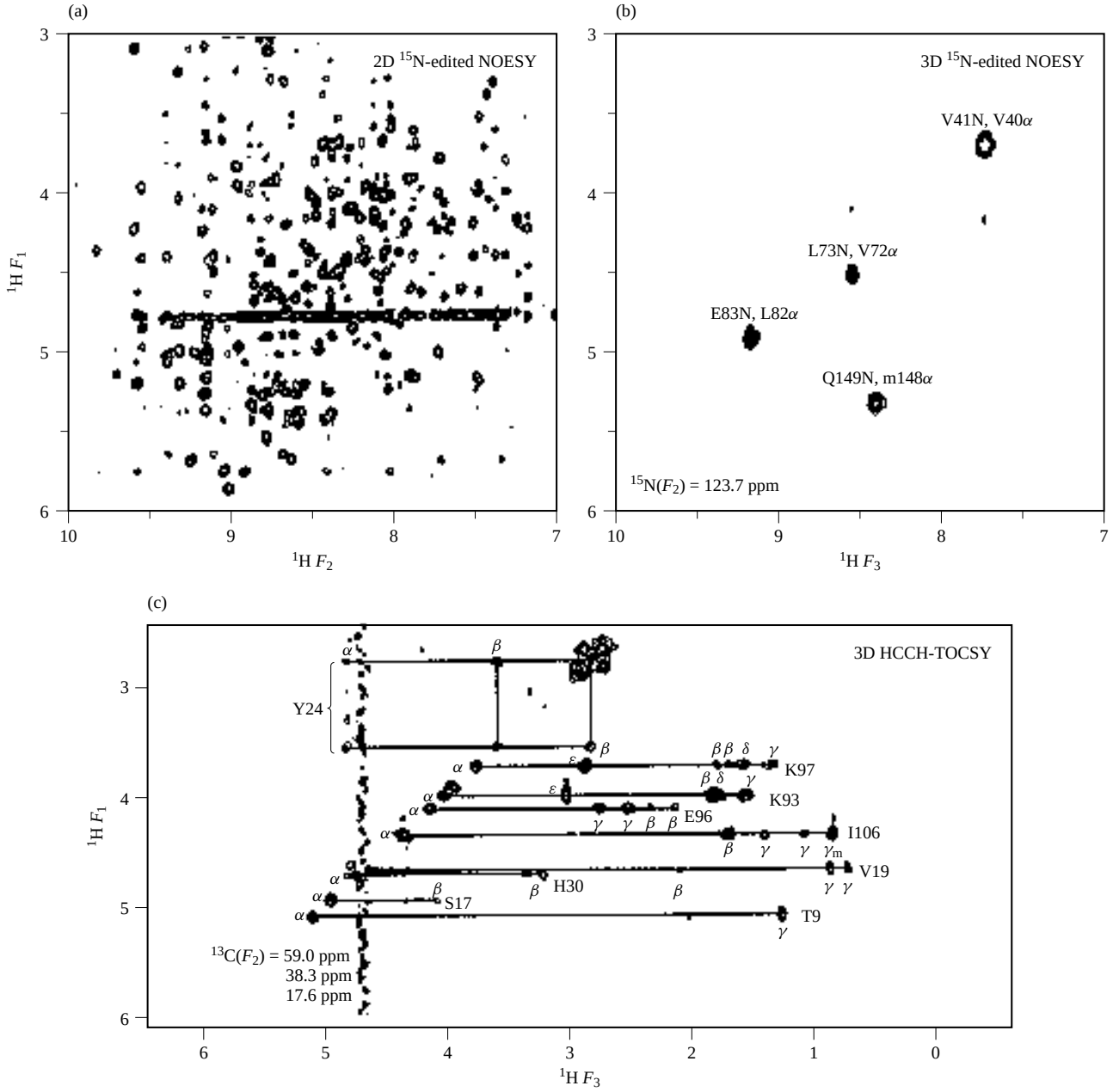

Figure 4 Example of 2D and 3D spectra of interleukin-1β recorded at 600 MHz.[19,30,48,49] The 2D spectrum in (a) shows the NH(F_2 axis)–C-α,H(F_1 axis) region of a 2D ^{15}N-edited NOESY spectrum. The same region of a single NH(F_3)–^{1}H(F_1) plane of the 3D ^{15}N-edited NOESY at δ^{15}N(F_2) = 123.7 ppm is shown in (b). The actual 3D spectrum comprises 64 such planes and projection of these on a single plane would yield the same spectrum as in (a). Part (c) shows a single ^{1}H(F_3)–^{1}H(F_1) plane of the 3D HCCH-TOCSY spectrum at δ^{13}C(F_2) = 38.3 $\pm$ nSW (where SW is the spectral width of 20.71 ppm in the ^{13}C dimension) illustrating both direct and relayed connectivities originating from the C-α,H protons. Note how easy it is to delineate complete spin systems of long side chains such as Lys (i.e. cross peaks to the C-β,H, C-γ,H, C-δ,H, and C-ϵ,H protons are observed) owing to the fact that magnetization along the side chain is transferred via large ^1J(C,C) couplings. Several features of the HCCH-TOCSY spectrum should be pointed out. First, extensive folding is employed which does not obscure analysis as ^{13}C chemical shifts for different carbon types are located in characteristic regions of the ^{13}C spectrum with little overlap. Second, the spectrum is edited according to the chemical shift of the heteronucleus attached to the originating proton rather than the destination one. Third, multiple cross checks on the assignments are readily made by looking for the symmetry-related peaks in the planes corresponding to the ^{13}C chemical shifts of the destination protons in the original slice

to obtain complete ^{1}H and ^{13}C assignments for the side chains of interleukin-1β.[30]

Three-dimensional NMR also permits one to devise experiments for sequential assignment which are based solely on through-bond connectivities via heteronuclear couplings[16,31,32] and thus do not rely on the NOESY experiment. This becomes increasingly important for larger proteins, as the types of connectivites observed in these correlation experiments are entirely predictable, whereas in the NOESY spectrum, which relies solely on close proximity of protons, it

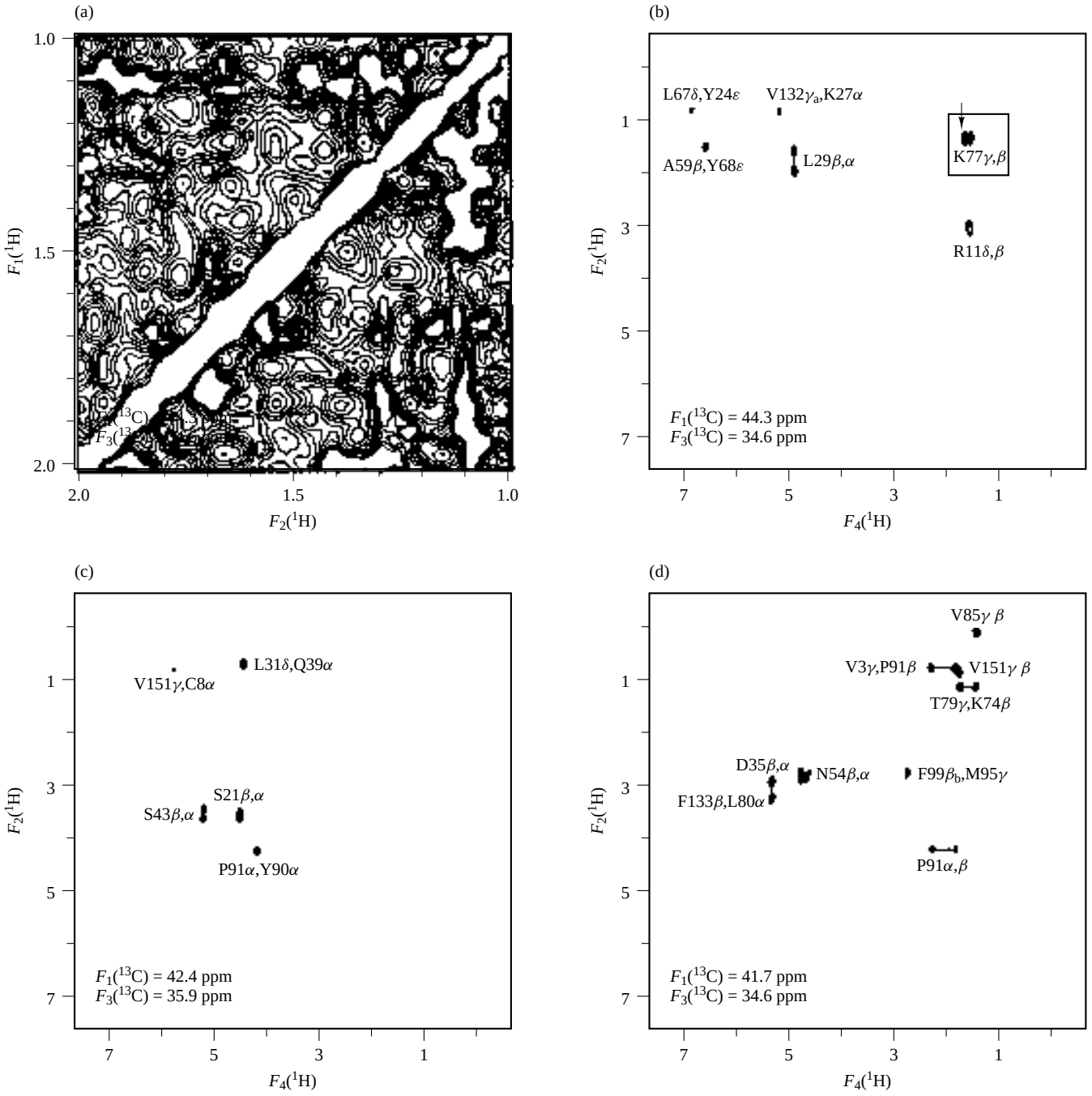

Figure 5

may be possible to confuse sequential connectivities with long-range ones. These 3D heteronuclear correlation experiments are of the triple resonance variety and make use of one-bond $^{13}CO(i-1)$–$^{15}N(i)$, $^{15}N(i)$–$^{13}C\text{-}\alpha(i)$, $^{13}C(i)$–$^{13}C(i)$, and $^{13}C\text{-}\alpha(i)$–$^{13}CO(i)$ couplings, as well as two-bond $^{13}C\text{-}\alpha(i-1)$–$^{15}N(i)$ couplings. In this manner multiple, independent pathways for linking the resonances of one residue with those of its adjacent neighbor are available, thereby avoiding ambiguities in the sequential assignment (see Table 1).

In practice, only a limited number of 3D triple and double resonance experiments need to be performed to obtain complete assignments. In our experience, the following eight 3D experiments not only provide all the information required, but are also characterized by high sensitivity and can be recorded in as little as 2 weeks of measuring time. Specifically, the 3D CBCA(CO)NH and HBHA(CBCACO)NH experiments[33,34] are used to correlate the chemical shifts of C-α/C-$\beta(i-1)$ and H-α)/H-$\beta(i-1)$, respectively, of residue $i-1$ with the $^{15}N(i)$/NH(i) chemical shifts of residue i; and the complementary 3D C(CO)NH and H(CCO)NH experiments[35] are used to correlate the chemical shifts of the aliphatic side chain ^{13}C and ^1H resonances, respectively, of residue $i-1$ with the $^{15}N(i)$/NH(i) chemical shifts of residue i. In the first two experiments, magnetization originating on C-β is transferred

Figure 5 Comparison of 2D and 4D NMR spectra of interleukin-1β recorded at 600 MHz.[26] The region between 1 and 2 ppm of the 2D NOESY spectrum is shown in (a). $^1H(F_2)$–$^1H(F_4)$ planes at several $^{13}C(F_1)$ and $^{13}C(F_3)$ frequencies of the 4D $^{13}C/^{13}C$ NOESY spectrum are shown in (b) to (d). No individual cross peaks can be observed in the 2D spectrum and the letter X has ^1H coordinates of 1.39 and 1.67 ppm. In contrast, only two cross peaks are observed in the boxed region in (b) between 1 and 2 ppm, one of which (indicated by an arrow) has the same ^1H coordinates as the letter X. Further analysis of the complete 4D spectrum reveals the presence of seven NOE cross peaks superimposed at the ^1H coordinates of the letter X. This can be ascertained by looking at the $^{13}C(F_1)$–$^{13}C(F_3)$ plane taken at the ^1H coordinates of X. True diagonal peaks corresponding to magnetization that has not been transferred from one proton to another, as well as intense NOE peaks involving protons attached to the same carbon atom (i.e. methylene protons), appear in only a single $^1H(F_2)$–$^1H(F_4)$ plane of each $^{13}C(F_1)$, $^1H(F_2)$, $^1H(F_4)$ cube at the carbon frequency where the originating and destination carbon atoms coincide (i.e. at $F_1 = F_3$). Thus, these intense resonances no longer obscure NOEs between protons with similar or degenerate chemical shifts. Two examples of such NOEs can be seen in (c), between the C-α,H protons of Pro-91 and Tyr-90, and (d), between one of the C-β,H protons of Phe-77 and the methyl protons of Met-95. These various planes of the 4D spectrum also illustrate another key aspect of 3D and 4D NMR, namely the importance of designing the pulse scheme optimally to remove undesired artifacts which may severely interfere with the interpretation of the spectra. Thus, while the 4D $^{13}C/^{13}C$-edited NOESY experiment is conceptually analogous to that of a 4D $^{13}C/^{15}N$-edited one, the design of a suitable pulse scheme is actually much more complex in the $^{13}C/^{13}C$ case. This is due to the fact that there are a large number of spurious magnetization transfer pathways that can lead to observable signals in the homonuclear $^{13}C/^{13}C$ case. For example, in the 4D $^{15}N/^{13}C$-edited case there are no 'diagonal peaks' which would correspond to magnetization that has not been transferred from one hydrogen atom to one another, as the double heteronuclear filtering (i.e. ^{13}C and ^{15}N) is extremely efficient at completely removing these normally very intense and uninformative resonances. Such a double filter is not available in the $^{13}C/^{13}C$ case so that both additional pulses and phase cycling are required to suppress magnetization transfer through these pathways. This task is far from trivial as the number of phase cycling steps in 4D experiments is severely limited by the need to keep the measurement time down to practical levels (i.e. less than 1 week). The most efficient way of obtaining artifact-free spectra is through the incorporation of pulse field gradients to suppress undesired coherence transfer pathways.[50] Indeed, inclusion of six pulse field gradients into the original pulse scheme of Clore et al.[26] reduces the phase cycle from eight to two steps.[51] The results of such care in pulse design can be clearly appreciated from the artifact-free planes shown in (b)–(d). However, when a 4D $^{13}C/^{13}C$-edited NOESY spectrum is recorded with the same pulse scheme as that used in the 4D $^{15}N/^{13}C$ experiment (with the obvious replacement of ^{15}N pulses by ^{13}C pulses), a large number of spurious peaks are observed along a pseudodiagonal at $\delta^1H(F_2) = \delta^1H(F_4)$ in planes where the carbon frequencies of the originating and destination protons do not coincide. As a result, it becomes virtually impossible under these circumstances to distinguish artifacts from NOEs between protons with the same ^1H chemical shifts, as was possible with complete confidence in (c) and (d)

to C-α by a COSY mixing pulse, while in the second pair of experiments, magnetization is transferred from a side-chain C atom along the carbon chain to C-α via isotropic mixing. Intraresidue correlations to the NH group can be obtained from the 3D CBCANH[36] and ^{15}N-edited HOHAHA[37] experiments. The 3D CBCANH experiment correlates the chemical shifts of C-$\alpha(i)$/C-$\beta(i)$ [as well as those of C-$\alpha(i-1)$/C-$\beta(i-1)$, which invariably give rise to weaker cross peaks], with the $^{15}N(i)$/NH(i) chemical shifts of residue i; the 3D ^{15}N-separated HOHAHA experiment correlates the chemical shifts of the side-chain protons of residue i with the $^{15}N(i)$/NH(i) chemical shifts of residue i. Finally, the 3D HCCH-COSY and HCCH-TOCSY experiments[28,38] can be used to confirm and obtain complete ^1H and ^{13}C assignments of the side chains.

The power of 4D heteronuclear NMR spectroscopy for unraveling interactions that would not have been possible in lower dimensional spectra is illustrated in Figure 5 by the $^{13}C/^{13}C$-edited NOESY spectrum of interleukin-1β.[26] Figure 5(a) shows a small portion of the aliphatic region between 1 and 2 ppm of a conventional 2D NOESY spectrum of interleukin-1β. The overlap is so great that no single, individual cross peak can be resolved. One might therefore wonder just how many NOE interactions are actually superimposed, for example, at the ^1H chemical shift coordinates of the letter X at 1.39 (F_1) and 1.67 (F_2) ppm. A $^1H(F_2)$–$^1H(F_4)$ plane of the 4D spectrum at $\delta^{13}C(F_1)$, $\delta^{13}C(F_3)$ = 44.3 ppm, 34.6 ppm is shown in Figure 5(b) and the square box at the top right-hand side of this panel encloses the region between 1 and 2 ppm. Only two cross peaks are present in this region, and the arrow points to a single NOE between the C-γ,H and C-β,H protons of Lys-77 with the same ^1H chemical shift coordinates as the letter X in panel A. All the other NOE interactions at the same ^1H chemical shift coordinates can be determined by inspection of a single $^{13}C(F_1)$–$^{13}C(F_3)$ plane taken at $\delta^1H(F_2)$, $\delta^1H(F_4)$ = 1.39 ppm, 1.67 ppm. This reveals a total of seven NOE interactions superimposed at the ^1H chemical shift coordinates of the letter X. Another feature of the 4D spectrum is illustrated by the two $^1H(F_2)$–$^1H(F_4)$ planes at different F_1 and F_3 ^{13}C frequencies shown in Figure 5(c) and (b). In both cases, there are cross peaks involving protons with identical or near-identical chemical shifts, namely that between proline (Pro)-91(C-α,H) and tyrosine (Tyr)-90(C-α,H), diagnostic of a *cis*-Pro, in Figure 5(c), and between phenylalanine (Phe)-99(C-βb,H) and methionine (Met)-95(C-γ,H) in Figure 5(d). These interactions could not be resolved in either a 2D spectrum or a 3D ^{13}C-edited spectrum as they would lie on the spectral diagonal (i.e. the region of the spectrum corresponding to magnetization that has not been transferred from one proton to another). In the 4D spectrum, however, they are easy to observe, provided, of course, that the ^{13}C chemical shifts of the directly bonded ^{13}C nuclei are different.

Because the number of NOE interactions present in each $^1H(F_4)$–$^1H(F_2)$ plane of 4D $^{13}C/^{15}N$ or $^{13}C/^{13}C$-edited NOESY spectra is so small, the inherent resolution in a 4D spectrum is extremely high, despite the low level of digitization. Indeed, spectra with equivalent resolution can be recorded at magnetic field strengths considerably lower than 600 MHz, although this would obviously lead to a reduction in sensitivity. Further, it can be calculated that 4D spectra with virtual lack of resonance overlap and good sensitivity can be obtained on proteins with as many as 400 residues. Thus, once complete ^1H, ^{15}N, and ^{13}C assignments are obtained, analysis of 4D spectra should permit the automated assignment of almost all NOE interactions.

5 CONCLUSION

In this article we have summarized the recent developments in heteronuclear 3D and 4D NMR which have been designed

Figure 6 Summary of Correlations Observed in the 3D Double and Triple Resonance Experiments used for Sequential and Side-Chain Assignments

Experiment	Correlation	J coupling
^{15}N-edited HOHAHA	C-α,H(i)–^{15}N(i)–NH(i)	^{3}J(H,N-α) (≈3–11 Hz)
	C-β,H(i)–^{15}N(i)–NH(i)	^{3}J(H,N-α) (≈3–11 Hz) and ^{3}J(α,β) (≈3–11 Hz)
H(CA)NH	C-α,H(i)–^{15}N(i)–NH(i)	^{1}J(N,C-α) (≈9–13 Hz)
	C-α,H($i-1$)–^{15}N(i)–NH(i)	^{2}J(N,C-α) (≈5–10 Hz)
HN(CO)HB	C-α,H($i-1$)–^{15}N(i)–NH(i)	^{2}J(CO,H-α) (≈4–7 Hz)
	C-β,H($i-1$)–^{15}N(i)–NH(i)	^{3}J(CO,H-β) (≈8 Hz for *trans* coupling)
HNHB	C-β,H(i)–^{15}N(i)–NH(i)	^{3}J(N,H-β) (≈5 Hz for *trans* coupling)
HNCA	^{13}C-α(i)–^{15}N(i)–NH(i)	^{1}J(N,C-α) (≈9–13 Hz)
	^{13}C-α($i-1$)–^{15}N(i)–NH(i)	^{2}J(N,C-α) (≈5–10 Hz)
CBCANH	^{13}C-β/C-α(i)–^{15}N(i)–NH(i)	^{1}J(C,C) (≈30–40 Hz), ^{1}J(N,C-α) (≈9–13 Hz)
	^{13}C-β/C-α($i-1$)–^{15}N(i)–NH(i)	^{1}J(C,C) (≈30–40 Hz), ^{2}J(N,C-α) (≈5–10 Hz)
HN(CO)CA	^{13}C-α($i-1$)–^{15}N(i)–NH(i)	^{1}J(N,CO) (≈15 Hz) and ^{1}J(C-α,CO) (≈55 Hz)
CBCA(CO)NH	^{13}C-β/C-α($i-1$)–^{15}N(i)–NH(i)	^{1}J(C,C) (≈30–40 Hz), ^{1}J(N,CO) (≈15 Hz), and ^{1}J(C-α,CO) (≈55 Hz)
HBHA(CO)NH	C-β,H/C-α,H($i-1$)–^{15}N(i)–NH(i)	^{1}J(C,C) (≈30–40 Hz), ^{1}J(N,CO) (≈15 Hz), and ^{1}J(C-α,CO) (≈55 Hz)
C(CO)NH	^{13}C-x,($i-1$)–^{15}N(i)–NH(i)	^{1}J(C,C) (≈30–40 Hz), ^{1}J(N,CO) (≈15 Hz), and ^{1}J(C-α,CO) (≈55 Hz)
H(CCO)NH	C-x,H($i-1$)–^{15}N(i)–NH(i)	^{1}J(C,C) (≈30–40 Hz), ^{1}J(N,CO) (≈15 Hz), and ^{1}J(C-α,CO) (≈55 Hz)
HNCO	^{13}CO($i-1$)–^{15}N(i)–NH(i)	^{1}J(N,CO) (≈15 Hz)

to extend the NMR methodology to medium-sized proteins in the 15–30 kDa range.[8] The underlying principle of this approach consists of extending the dimensionality of the spectra to obtain dramatic improvements in spectral resolution while simultaneously exploiting large heteronuclear couplings to circumvent problems associated with larger linewidths. A key feature of all these experiments is that they do not result in any increase in the number of observed cross peaks relative to their 2D counterparts. Hence, the improvement in resolution is achieved without raising the spectral complexity, rendering data interpretation straightforward. Thus, for example, in 4D heteronuclear-edited NOESY spectra, the NOE interactions between proton pairs are labeled not only by the ^{1}H chemical shifts but also by the corresponding chemical shifts of their directly bonded heteronuclei in four orthogonal axes of the spectrum. Also important in terms of practical applications is the high sensitivity of these experiments, which makes it feasible to obtain high-quality spectra in a relatively short time frame on 1–2 mM protein samples uniformly labeled with ^{15}N and/or ^{13}C.

Just as 2D NMR opened the application of NMR to the structure determination of small proteins of less than about 100 residues, 3D and 4D heteronuclear NMR provide the means of extending the methodology to medium-sized proteins in the 150–300 residue range. Indeed, the determination in 1991 of the first high-resolution structure of a protein in the 15–20 kDa range, namely the cytokine interleukin-1β (153 residues and 18 kDa), using 3D and 4D heteronuclear NMR[39] demonstrated beyond doubt that the technology is now available for obtaining the structures of such medium-sized proteins at a level of accuracy and precision that is comparable to the best results attainable for small proteins. Subsequently, a number of other medium-sized protein structures have been determined using these methods, including interleukin-4,[40–42] glucose permease IIA,[43] a complex of calmodulin with a target peptide,[44] a complex of cyclophilin and cyclosporin A,[45] and specific complexes of the transcription factor GATA-1[46] and the Antennapedia homeodomain[47] with their DNA target sites.

6 RELATED ARTICLES

Homonuclear Three-Dimensional NMR of Biomolecules; Multidimensional Spectroscopy: Concepts; Three-Dimensional HMQC-NOESY, NOESY-HMQC, and NOESY-HSQC; TOCSY in ROESY and ROESY in TOCSY.

7 REFERENCES

1. K. Wüthrich, *NMR of Proteins*, Wiley, New York, 1986.
2. G. M. Clore and A. M. Gronenborn, *Protein Eng.*, 1987, **1**, 275.
3. G. M. Clore and A. M. Gronenborn, *CRC Crit. Rev. Biochem. Mol. Biol.*, 1989, **24**, 479.
4. A. Bax, *Annu. Rev. Biochem.*, 1989, **58**, 223.
5. J. Markley, *Methods Enzymol.*, 1989, **176**, 12.
6. K. Wüthrich, *J. Biol. Chem.*, 1990, **265**, 22 059.
7. A. M. Gronenborn and G. M. Clore, *Anal. Chem.*, 1990, **62**, 2.
8. G. M. Clore and A. M. Gronenborn, *Science*, 1991, **252**, 1390.
9. G. M. Clore and A. M. Gronenborn, *Annu. Rev. Biophys. Biophys. Chem.* 1991, **20**, 29.
10. G. M. Clore, M. A. Robien and A. M. Gronenborn, *J. Mol. Biol.*, 1993, **231**, 82.
11. G. M. Clore and A. M. Gronenborn, *J. Mol. Biol.*, 1991, **221**, 47.
12. B. Shaanan, A. M. Gronenborn, G. H. Cohen, G. L. Gilliland, B. Veerapandian, D. R. Davies and G. M. Clore, *Science*, 1992, **257**, 961.
13. H. J. Dyson, G. P. Gippert, D. A. Case, A. Holmgren and P. E. Wright, *Biochemistry*, 1990, **29**, 4129.
14. J. D. Forman-Kay, G. M. Clore, P. T. Wingfield and A. M. Gronenborn, *Biochemistry*, 1991, **30**, 2685.
15. H. Oschkinat, C. Griesinger, P. J. Kraulis, O. W. Sørensen, R. R. Ernst, A. M. Gronenborn and G. M. Clore, *Nature (London)*, 1988, **332**, 374.
16. G. M. Clore and A. M. Gronenborn, *Prog. Nucl. Magn. Reson. Spectrosc.*, 1991, **23**, 43.
17. S. W. Fesik and E. R. P. Zuiderweg, *J. Magn. Reson.*, 1988, **78**, 588.
18. D. Marion, L. E. Kay, S. W. Sparks, D. A. Torchia and A. Bax, *J. Am. Chem. Soc.*, 1989, **111**, 1515.

19. D. Marion, P. C. Driscoll, L. E. Kay, P. T. Wingfield, A. Bax, A. M. Gronenborn and G. M. Clore, *Biochemistry*, 1989, **29**, 6150.
20. L. E. Kay, D. Marion and A. Bax, *J. Magn. Reson.*, 1989, **84**, 72.
21. M. Ikura, A. Bax, G. M. Clore and A. M. Gronenborn, *J. Am. Chem. Soc.*, 1990, **112**, 9020.
22. G. M. Clore, A. Bax, P. T. Wingfield and A. M. Gronenborn, *Biochemistry*, 1990, **29**, 5671.
23. M. Ikura, L. E. Kay, R. Tschudin and A. Bax, *J. Magn. Reson.*, 1990, **86**, 204.
24. E. R. P. Zuiderweg, L. P. McIntosh, F. W. Dahlquist and S. W. Fesik, *J. Magn. Reson.*, 1990, **86**, 210.
25. L. E. Kay, G. M. Clore, A. Bax and A. M. Gronenborn, *Science*, 1990, **249**, 411.
26. G. M. Clore, L. E. Kay, A. Bax and A. M. Gronenborn, *Biochemistry*, 1991, **30**, 12.
27. E. R. P. Zuiderweg, A. M. Petros, S. W. Fesik and E. T. Olejniczak, *J. Am. Chem. Soc.*, 1991, **113**, 370.
28. A. Bax, G. M. Clore, P. C. Driscoll, A. M. Gronenborn, M. Ikura and L. E. Kay, *J. Magn. Reson.*, 1990, **87**, 620.
29. S. W. Fesik, H. L. Eaton, E. T. Olejniczak, E. R. P. Zuiderweg, L. P. McIntosh and F. W. Dahlquist, *J. Am. Chem. Soc.*, 1990, **112**, 886.
30. G. M. Clore, A. Bax, P. C. Driscoll, P. T. Wingfield and A. M. Gronenborn, *Biochemistry*, 1990, **29**, 8172.
31. M. Ikura, L. E. Kay and A. Bax, *Biochemistry*, 1990, **29**, 4659.
32. R. Powers, A. M. Gronenborn, G. M. Clore and A. Bax, *J. Magn. Reson.*, 1991, **94**, 209.
33. S. Grzesiek and A. Bax, *J. Am. Chem. Soc.*, 1992, **114**, 6291.
34. S. Grzesiek and A. Bax, *J. Biomol. NMR*, 1993, **3**, 185.
35. S. Grzesiek, J. Anglister and A. Bax, *J. Magn. Reson., Ser. B*, 1993, **101**, 114.
36. S. Grzesiek and A. Bax, *J. Magn. Reson.*, 1992, **99**, 201.
37. G. M. Clore, A. Bax and A. M. Gronenborn, *J. Biomol. NMR*, 1991, **11**, 13.
38. A. Bax, G. M. Clore and A. M. Gronenborn, *J. Magn. Reson.*, 1990, **88**, 425.
39. G. M. Clore, P. T. Wingfield and A. M. Gronenborn, *Biochemistry*, 1991, **30**, 2315.
40. R. Power, D. S. Garrett, C. J. March, E. A. Frieden, A. M. Gronenborn and G. M. Clore, *Science*, 1992, **256**, 1673.
41. L. J. Smith, C. Redfield, J. Boyd, G. M. P. Lawrence, R. G. Edwards, R. A. G. Smith and C. M. Dobson, *J. Mol. Biol.*, 1992, **224**, 899.
42. R. Power, D. S. Garrett, C. J. March, E. A. Frieden, A. M. Gronenborn and G. M. Clore, *Biochemistry*, 1993, **32**, 6744.
43. W. J. Fairbrother, G. P. Gippert, J. Reizer, M. J. Saier and P. E. Wright, *FEBS Lett.*, 1992, **296**, 148.
44. M. Ikura, G. M. Clore, A. M. Gronenborn, G. Zhu, C. B. Klee and A. Bax, *Science*, 1992, **256**, 632.
45. Y. Theriault, T. M. Logan, R. Meadows, L. Yu, E. T. Olejniczak, T. F. Holzman, R. L. Simmer and S. W. Fesik, *Nature (London)*, 1993, **361**, 88.
46. J. G. Omichinski, G. M. Clore, O. Schaad, G. Felsenfeld, C. Trainor, E. Appella, S. J. Stahl and A. M. Gronenborn, *Science*, 1993, **261**, 438.
47. M. Billeter, Y. Q. Qian, G. Otting, M. Müller, W. Gehring and K. Wüthrich, *J. Mol. Biol.*, 1993, **234**, 1084.
48. P. C. Driscoll, G. M. Clore, D. Marion, P. T. Wingfield and A. M. Gronenborn, *Biochemistry*, 1990, **29**, 3542.
49. P. C. Driscoll, A. M. Gronenborn, P. T. Wingfield and G. M. Clore, *Biochemistry*, 1990, **29**, 4468.
50. A. Bax and S. S. Pochapsky, *J. Magn. Reson.*, 1992, **99**, 638.
51. G. W. Vuister, G. M. Clore, A. M. Gronenborn, R. Powers, D. S. Garrett, R. Tschudin and A. Bax, *J. Magn. Reson., Ser. B*, 1993, **101**, 210.

Acknowledgments

We thank Ad Bax for many stimulating discussions. This work was supported in part by the AIDS Targeted Anti-Viral Program of the Office of the Director of the National Institutes of Health. This article has been previously published in G. M. Clore and A. M. Gronenborn, *Methods Enzymol.*, 1994, **239**, 349, which itself was adapted and updated from G. M. Clore and A. M. Gronenborn, *Science*, 1991, **252**, 1390.

Biographical Sketches

G. Marius Clore. *b* 1955. B.Sc. University College London, 1976; MD, University College Hospital Medical School, London, 1979; Ph.D., National Institute for Medical Research, London, 1982. Scientific staff, National Institute for Medical Research, London, 1980–1984; Joint Head, Biological NMR Group, Max-Planck Institute for Biochemistry, Martinsried, West Germany 1984–1988; Chief, Section of Protein NMR, Laboratory of Chemical Physics, National Institutes of Health 1988–present. Approx. 260 publications, and with A. M. Gronenborn the book 'NMR of Proteins'. Research interests include biological NMR spectroscopy and structural biology.

Angela M. Gronenborn. *b* 1950. Dipl. Chem., 1975; Ph.D., 1978, University of Cologne; Scientific staff, National Institute for Medical Research, London, 1979–1984; Joint Head, Biological NMR Group, Max-Planck Institute for Biochemistry, Martinsried, West Germany, 1984–1988; Chief, Section of Structural Biology, Laboratory of Chemical Physics, National Institutes of Health, 1988–present. Approx. 250 publications, and with G. M. Clore the book 'NMR of Proteins'. Research interests include biological NMR spectroscopy and structural biology.

Three-Dimensional HMQC-NOESY, NOESY-HMQC, and NOESY-HSQC

Ranjith Muhandiram and Lewis E. Kay
University of Toronto, Toronto, ON, Canada

1	Introduction	1
2	HMQC(HSQC)–NOESY and NOESY–HMQC (HSQC) Experiments	1
3	Pulsed Field Gradient Methods	4
4	Sensitivity-Enhanced Versions of 3D Heteronuclear-Edited NOESY Experiments	8
5	Concluding Remarks	10
6	Related Articles	10
7	References	11

1 INTRODUCTION

The widespread application of NMR in the study of macromolecular structure is to a large extent the result of the ^{1}H–^{1}H nuclear Overhauser effect (NOE), whereby it is possible to obtain distance information relating spatially proximate protons (see ***Nuclear Overhauser Effect***). For reasonably small molecules (for example, proteins consisting of ∼100 or fewer residues) this information is readily available from two dimensional (2D) homonuclear NOESY spectra which consist of cross peaks, with intensities related to the distance between the participating spins[1] (see also ***NOESY*** and ***Biological Macromolecules: Structure Determination in Solution***). Because NOE peaks between a particular proton and all other protons within a radius of approximately 0.5 nm can, in principle be observed, the number of potential NOE cross peaks increases rapidly with molecular weight. This gives rise to considerable overlap in 2D NOE spectra of large molecules (>10 kDa), making it difficult to assign cross peaks and to obtain accurate distance information. An elegant approach to removing cross-peak overlap in 2D NOE spectra is to resolve the 2D spectrum along a third frequency dimension, the ^{15}N or ^{13}C chemical shift of the heteronucleus directly attached to one of the protons participating in the NOE transfer[2,3] (see also ***Three- and Four-Dimensional Heteronuclear Magnetic Resonance***). Such three-dimensional heteronuclear chemical shift correlated-NOESY spectra contain the same numbers of cross peaks as in a regular 2D NOESY spectrum, but the information content of these spectra (i.e., the cross peaks) is dispersed over the chemical shift range of the heteronucleus. Because of the low natural abundance of ^{15}N and ^{13}C, isotopic enrichment is necessary in order to obtain spectra with high sensitivity.[2,4]

Figure 1 illustrates the resolving power of ^{15}N-edited 3D heteronuclear NOE spectroscopy. In (a), a region from the regular 2D NOESY spectrum of the protein staphylococcal nuclease (18 kDa) is illustrated. In (b), the corresponding region is shown illustrating NOEs to NH protons attached to ^{15}N nuclei resonating at 122.3 ppm. The simplification is clearly evident.

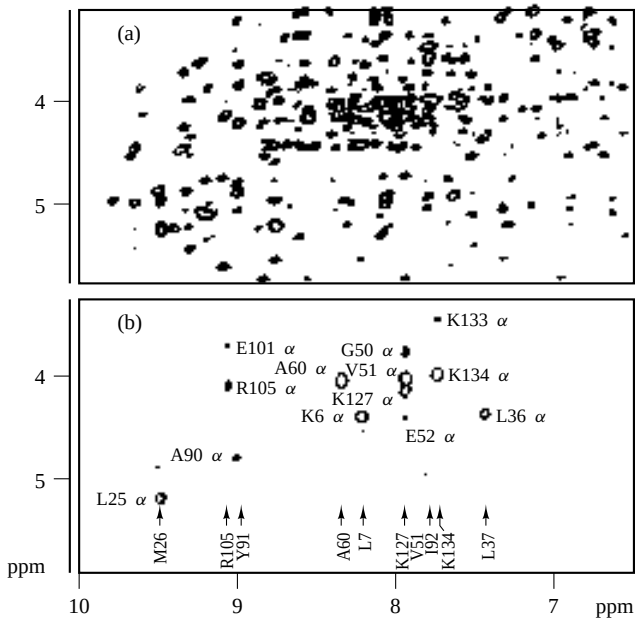

Figure 1 Comparison of NH, C_αH cross peak regions from 2D NOESY and 3D NOESY–HMQC experiments recorded at 500 MHz on a 1.5 mM sample of ^{15}N-labeled staphylococcal nuclease in 90% H_2O using a 125 ms NOE mixing time. (a) Regular 2D NOESY spectrum; (b) Corresponding region in a slice from the 3D NMR spectrum, where (^{1}H,NH) cross peaks are separated according to the ^{15}N chemical shift of the amide nitrogen one-bond-coupled to the NH proton. The section displays NH, C_αH correlations only for those amides that have an ^{15}N chemical shift of 122.3 ± 0.3 ppm. The 3D data set was collected as a 128 × 32 × 256 complex matrix (t_1, t_2, t_3). Sixteen transients were accumulated for each FID, and the total experimental time was about 64 h. Data were zero filled prior to Fourier transformation to yield a 256 × 64 × 512 data matrix (F_1, F_2, F_3) for the absorptive part of the spectrum. (Source: A. Bax, *Annu. Rev. Biochem.*, 1989, **58**, 223)

The simplification of a crowded NOESY spectrum as a result of the resolving power of the heteronuclear chemical shift enables the unambiguous assignment of many of the cross peaks, facilitates the use of automated peak picking and assignment methods, and significantly increases the effective molecular weight limitations of NMR. The method has been used for the structure elucidation of proteins having molecular weights as large as ∼25 kDa,[5,6] RNA,[7] and oligosacharides.[8] In the following sections, descriptions of many of the pulse sequences currently in use are given, with emphasis on the 3D NOESY—HMQC sequence and improved versions of NOESY—HSQC with pulsed field gradients. In addition, protein applications of these experiments are highlighted.

2 HMQC(HSQC)–NOESY AND NOESY–HMQC (HSQC) EXPERIMENTS

The heteronuclear correlated 3D NOESY experiment consists of elements of (i) the regular 2D ^{1}H–^{1}H NOESY

experiment and (ii) the proton-detected heteronuclear chemical shift correlation experiment. The latter element can be of the HMQC (heteronuclear multiple quantum correlation)[9] or HSQC (heteronuclear single quantum correlation)[10] variety, giving rise to 3D NOESY—HMQC, 3D HMQC—NOESY or 3D NOESY—HSQC, 3D HSQC—NOESY experiments, respectively. In these heteronuclear three-dimensional experiments, the flow of magnetization is controlled by the editing effect of the heteronucleus. In what follows, a brief discussion of the HMQC—NOESY[11] experiment will be provided, followed by a more detailed examination of the NOESY—HMQC[12] scheme. In subsequent sections, some HSQC versions of the experiments will be described.

2.1 3D HMQC–NOESY

Figure 2(a) illustrates one version of the HMQC—NOESY pulse scheme.[11] In order to ensure maximum sensitivity, magnetization originates on the sensitive proton spin, and proton magnetization is also detected during acquisition (t_3). Proton magnetization is recorded during t_1, with the effects of the large one-bond ^{1}H–X scalar coupling refocused through the action of the 180° X pulse applied in the middle of the t_1 evolution period. Subsequently, antiphase magnetization is generated during the τ ($\leq[2J_{HX}]^{-1}$) delay and converted into ^{1}H–X double and zero quantum coherence by the application of the first 90° X pulse. The chemical shift of the heteronucleus is recorded during the t_2 delay. The ^{1}H 180° pulse applied in the center of the t_2 evolution delay interconverts zero and double quantum coherences, so that effectively only X chemical shift is allowed to evolve during this period. Subsequently, antiphase proton magnetization is regenerated with the application of the second 90° X pulse, and refocusing due to the ^{1}H–X scalar coupling is allowed to occur during the second τ delay. Because of the phase cycle on the first 90° X pulse, only magnetization originating from proton spins directly coupled to X spins is retained. During the mixing time, magnetization on X-nucleus attached proton spins is transferred to all protons in close proximity. Therefore, during the acquisition time t_3, protons that resonate in the entire proton chemical shift range may be detected. Thus, for an ^{15}N-labeled protein (X = ^{15}N) dissolved in H_2O, the acquisition dimension is similar to the acquisition dimension of a regular 2D NOESY experiment. The final 3D spectrum consists of a set of 2D ^{1}H–^{1}H (F_1/F_3) NOESY maps separated according to the amide ^{15}N chemical shift along the third frequency dimension (F_2). In contrast to the indirectly detected dimension of a regular 2D NOESY map, the F_1 dimension of each F_1/F_3 plane consists of signals originating only from protons attached to ^{15}N, owing to the editing effect of the HMQC part of the sequence. Despite the spectral simplification attainable with ^{15}N chemical shift separation in the third dimension, protein NH, C_αH cross peaks can be obscured if the C_αH resonates close to the water resonance. Therefore, applications of this experiment have primarily been for samples dissolved in D_2O with X = ^{13}C, and the reverse version, the NOESY—HMQC experiment, where the crucial NH, C_αH cross peaks are easily observed, has been the preferred choice for ^{15}N-labeled protein samples dissolved in H_2O.

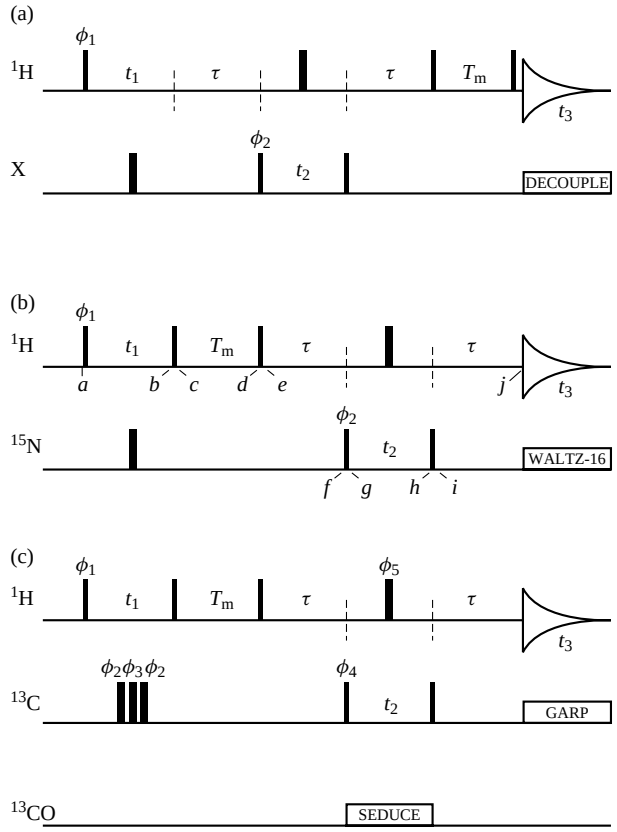

Figure 2 Pulse sequences for (a) 3D HMQC–NOESY, and (b), (c) 3D NOESY–HMQC experiments. Narrow (wide) pulses are applied with a flip angle of 90° (180°). Unless otherwise indicated all pulses are applied along the x axis. All ^{1}H and ^{13}C pulses are applied at the highest field possible (about 20 kHz), while typical ^{15}N pulses are applied with a field of about 5–6 kHz. The delay τ is set to slightly less than $[2J(X, H)]^{-1}$ to minimize relaxation losses. Quadrature in t_1 and t_2 is achieved via States–TPPI[13] of ϕ_1 and ϕ_2, respectively [sequences (a) and (b)], and ϕ_1 and ϕ_4, respectively [sequence (c)]. In (b), τ = 4.5 ms, and ^{15}N decoupling is achieved with a 1 kHz WALTZ-16[14] decoupling field. In (c), τ = 3.3 ms. During t_3, ^{13}C decoupling is achieved with a GARP[15] sequence using a 3.5–4.0 kHz field, and ^{13}CO decoupling during t_2 is achieved with a SEDUCE-1[16] field (about 1.5 kHz at peak height) centered at 175 ppm. The ^{13}C 180° pulse in the center of t_1 is of the composite variety. The phase cycling employed in (a) is ϕ_1 = $2(x),2(-x)$; $\phi_2 = x,-x$; Rec. = $x,2(-x),x$; the phase of the last ^{1}H pulse is incremented by 90° with the receiver phase after every four transients. That in (b) is $\phi_1 = x,-x$; $\phi_2 = 2(x),2(-x)$; Rec. = $x,2(-x),x$. That in (c) is $\phi_1 = x,-x$; $\phi_2 = 2(x),2(-x)$; $\phi_3 = 2(y),2(-y)$; $\phi_4 = 8(x),8(-x)$; $\phi_5 = 4(x),4(-x)$; Rec. = $4(x,-x),4(-x,x)$. [Adapted from (a) Fesik and Zuiderweg;[11] (b) Marion et al.,[12] and (c) Ikura et al.[17]]

2.2 3D ^{15}N-Edited NOESY–HMQC

Figure 2(b) illustrates the pulse scheme used to record 3D ^{15}N-edited NOESY—HMQC spectra of ^{15}N-labeled molecules.[12] The flow of magnetization during the course of the pulse sequence is conveniently described using the product operator formalism.[18] A simplified description of the magnetization transfer events is presented here. Let $\hat{I}_a$ and $\hat{I}_b$ be spin operators for two protons in close proximity, with only spin b coupled to an ^{15}N spin, denoted by the operator $\hat{N}$. The effects of relaxation during all delays, with the exception of the mixing time, are neglected. At point a in the pulse scheme of Figure 2(b), the equilibrium density operator is given by

$\hat{I}_{az}$ and $\hat{I}_{bz}$ for spins a and b respectively. The behavior of magnetization from point a to the beginning of the mixing period T_m (point c) is described by

$$\begin{array}{llll} \hat{I}_{az} & \{a\} & \xrightarrow{90^\circ \mathrm{H}} & -\hat{I}_{ay} \xrightarrow{t_1} -\hat{I}_{ay}\cos(\omega_a t_1) + \hat{I}_{ax}\sin(\omega_a t_1) \quad \{b\} \\ \hat{I}_{bz} & \{a\} & & -\hat{I}_{by} \quad\;\; -\hat{I}_{by}\cos(\omega_b t_1) + \hat{I}_{bx}\sin(\omega_b t_1) \quad \{b\} \\ & & & \xrightarrow{90^\circ \mathrm{H}} -\hat{I}_{az}\cos(\omega_a t_1) \quad \{c\} \\ & & & \qquad\qquad -\hat{I}_{bz}\cos(\omega_b t_1) \quad \{c\} \end{array} \tag{1}$$

where the letters in curly brackets { } denote the positions in the sequence where the appropriate density operators apply and ω_i is the resonance frequency of spin i (a,b). Note that the effects of ^{1}H–^{15}N scalar coupling are refocused by the end of the t_1 period due to the application of the ^{15}N 180° pulse in the center of this delay. Depending on the relative phases of the first two ^{1}H 90° pulses, either the cosine- or the sine-modulated component of magnetization is stored along the z axis at point c. One approach to obtaining quadrature in F_1 is to store both components in separate memory locations and subsequently combine them by the method of States et al.[19] In what follows, only the first line of the phase cycle that appears in the legend to Figure 2(b) is assumed (i.e., $\phi_1 = \phi_2 = x$). In the case of macromolecular applications, the transverse components of magnetization [e.g., $\hat{I}_{ax}$ sin ($\omega_a t_1$) and $\hat{I}_{bx}$ sin ($\omega_b t_1$)] that are present at the beginning of the mixing period decay rapidly as a result of short transverse relaxation times, and have therefore been omitted from equation (1). The use of a pulsed field gradient during this delay and/or the appropriate phase cycling can eliminate signals arising from such terms.

During the mixing period T_m, magnetization is transferred between proximate protons:

$$\begin{array}{llll} -\hat{I}_{az}\cos(\omega_a t_1) & \{c\} & \xrightarrow{T_m} & -A\hat{I}_{az}\cos(\omega_a t_1) - A'\hat{I}_{bz}\cos(\omega_a t_1) \quad \{d\} \\ -\hat{I}_{bz}\cos(\omega_b t_1) & \{c\} & & -B\hat{I}_{bz}\cos(\omega_b t_1) - B'\hat{I}_{az}\cos(\omega_b t_1) \quad \{d\} \end{array} \tag{2}$$

where A, A', B, and B' are constants that depend on the mixing time, the inverse sixth power of the distance between spins a and b and the motional properties of the internuclear vector connecting spins a and b. The values of A, A', B, and B' are easily obtained by solving the set of coupled differential equations that describe cross relaxation between spins a and b. Details can be found in the text by Noggle and Schirmer,[20] and will not be repeated here. In general, $A' = B'$. Since only proton b is attached to a nitrogen spin N, the only terms of the density operator that give rise to observable magnetization after the HMQC portion of the sequence (with the appropriate phase cycling of ϕ_2) are those proportional to $\hat{I}_{bz}$. Following the conversion into transverse proton magnetization by the proton 90° pulse at point d in the sequence, these terms evolve into proton magnetization that is antiphase with respect to spin N during the first τ period:

$$\begin{array}{llll} -A'\hat{I}_{bz}\cos(\omega_a t_1) & \{d\} & \xrightarrow{90^\circ \mathrm{H}} & A'\hat{I}_{by}\cos(\omega_a t_1) \quad \{e\} \\ -B\hat{I}_{bz}\cos(\omega_b t_1) & \{d\} & & B\hat{I}_{by}\cos(\omega_b t_1) \quad \{e\} \\ & & & \xrightarrow{\tau} -A'2\hat{I}_{bx}\hat{N}_z\cos(\omega_a t_1) \quad \{f\} \\ & & & \qquad\qquad -B2\hat{I}_{bx}\hat{N}_z\cos(\omega_b t_1) \quad \{f\} \end{array} \tag{3}$$

In the derivation of equation (3) the delay τ has been set equal to $[2J(\mathrm{N,H})]^{-1}$. In addition, ^{1}H chemical shift evolution during τ has been neglected, since the ^{1}H 180° pulse applied in the center of the t_2 evolution period refocuses the effect of proton chemical shifts. The 90° ^{15}N pulse at point f creates zero and double quantum terms, which subsequently evolve in t_2 to give N-spin chemical shift labeling:

$$\begin{array}{llll} -A'2\hat{I}_{bx}\hat{N}_z\cos(\omega_a t_1) & \{f\} & \xrightarrow{90^\circ \mathrm{N}} & A'2\hat{I}_{bx}\hat{N}_y\cos(\omega_a t_1) \quad \{g\} \\ -B2\hat{I}_{bx}\hat{N}_z\cos(\omega_b t_1) & \{f\} & & B2\hat{I}_{bx}\hat{N}_y\cos(\omega_b t_1) \quad \{g\} \\ & & & \xrightarrow{\frac{1}{2}t_2 180^\circ \mathrm{H} \frac{1}{2}t_2} A'2\hat{I}_{bx}\hat{N}_y\cos(\omega_a t_1)\cos(\omega_N t_2) \quad \{h\} \\ & & & \qquad\qquad B2\hat{I}_{bx}\hat{N}_y\cos(\omega_b t_1)\cos(\omega_N t_2) \quad \{h\} \end{array} \tag{4}$$

where the $\sin(\omega_N t_2)$ terms have been neglected, since for $\phi_2 = x$ these terms do not contribute to the observed signal.

After the second 90° N pulse, the double and zero quantum terms are converted into antiphase proton magnetization, which is allowed to refocus into observable proton magnetization during the second τ delay. Evolution during the acquisition time t_3 then yields

$$\begin{array}{l} A'\hat{I}_{by}\cos(\omega_a t_1)\cos(\omega_N t_2) \quad \{j\} \\ B\hat{I}_{by}\cos(\omega_b t_1)\cos(\omega_N t_2) \quad \{j\} \\ \qquad \xrightarrow{t_3} A'\hat{I}_{by}\cos(\omega_a t_1)\cos(\omega_N t_2)\cos(\omega_b t_3)(\text{cross peak}) \\ \qquad\qquad B\hat{I}_{by}\cos(\omega_b t_1)\cos(\omega_N t_2)\cos(\omega_b t_3)(\text{diagonal peak}) \end{array} \tag{5}$$

for the y component of magnetization. Similar relations hold for the x component of magnetization.

Fourier transformation of the resultant signal gives rise to cross peaks at (ω_a,ω_b) located in a slice through the 3D data set with ^{15}N frequency ω_N. In addition, a diagonal peak at (ω_b,ω_b) in the same slice is also observed. That is, a NOE cross peak at the chemical shift of the proton from which magnetization originated (F_1), the chemical shift of the destination NH proton (F_3), and the shift of the ^{15}N nucleus directly coupled to the NH spin (F_2) are obtained. Unlike 2D ^{1}H–^{1}H NOESY maps, which are symmetrical, ^{15}N-edited maps are asymmetrical, since the ^{15}N editing that occurs during the course of the pulse scheme ensures that only the transfer of magnetization to an NH proton is observed. Note that the crucial (C_αH, NH) NOE connectivities occur as (F_1,F_3) cross peaks, and can be detected in a straightforward manner without interference from the residual water signal, as shown in Figure 1.

2.2.1 *Practical Aspects of 3D Heteronuclear-Edited NOESY Pulse Schemes*

2.2.1.1 Water Suppression. Because ^{15}N-edited NOESY experiments provide crucial information linking NH protons to neighboring proton spins, these experiments must be performed on protein samples dissolved in H_2O. Water suppression schemes must therefore be employed to minimize the dynamic range problem that the use of this solvent presents. Suppression of the intense water signal is often achieved through the use of a weak coherent presaturation field (≤30 Hz) applied during the relaxation delay prior to the first 90° excitation pulse. In addition, saturation of the water resonance can proceed during the mixing time. In an early implementation of the experiment. Kay et al.[21] described the use of an off-resonance DANTE[22] sequence to suppress the water, with the carrier positioned in the center of the NH region. In addition, an off-resonance jump and return sequence of the type, $45^\circ_x - \tau - 45^\circ_x$, where τ is set according to the relation $\tau = (2 \times \text{offset of } H_2O)^{-1}$ and where the carrier is centered in the NH region, was inserted in place of the 90° ^{1}H pulse applied immediately after the mixing period.

The use of presaturation has been shown significantly to decrease the intensity of cross peaks originating from labile

protons. This can lead to a significant overall decrease in the intensity of the protein envelope due to the effect of saturation transfer. We have recently shown in applications involving the cellulose binding domain of a cellulase from *Cellulomonas fimi* (CBD, a dimer of monomers of molecular weight 11 kDa) that the use of a presaturation field (30 Hz) applied for 1 s prior to the start of the experiment can decrease the protein envelope by as much as 40%.[23] Montelione and co-workers have recently compared a number of different water suppression schemes as a function of sample pH, showing that presaturation gives the largest decrease in signal.[24] Grzesiek and Bax have also emphasized the importance of not saturating the water resonance,[25] and have suggested a strategy involving the use of pulsed field gradients and selective pulses on the water to ensure the placement of water magnetization on the +*z* axis prior to the start of the detection period in each transient. Pulse schemes incorporating field gradients are discussed in Section 3.

2.2.1.2 Phasing in the Indirectly Detected Dimensions (F_1, F_2). After Fourier transformation, the indirectly detected dimensions can be phased using calculated phase parameters. The approach of choice is to set the initial values of t_1 and t_2 [$t_1(0)$, $t_2(0)$] prior to running the experiment in order to obtain spectra having first-order phase corrections of either 0° or 180°. This ensures that flat baselines are obtained.[26] It is straightforward to calculate the appropriate values for $t_1(0)$ and $t_2(0)$ for a given pulse sequence, and in what follows we consider the ^{15}N NOESY—HMQC sequence of Figure 2(b). Noting that, to a good first approximation, a 90° pulse can be replaced by a delta function pulse followed by a delay of $(2/\pi)\tau_{90}$, where τ_{90} is the 90° pulse width.[27] the sampling delay in the t_1 dimension (NOESY portion of the sequence) is given by

$$sd(t_1) = \frac{4}{\pi}\tau_{90}(\mathrm{H}) + \tau_{180}(\mathrm{N}) + t_1(0) \tag{6}$$

where τ_{90}(H) is the ^{1}H 90° pulse width and τ_{180}(N) is the ^{15}N 180° pulse width. The sampling delay in the t_2 dimension (the HMQC portion of the sequence) is given by

$$sd(t_2) = \frac{4}{\pi}\tau_{90}(\mathrm{N}) + \tau_{180}(\mathrm{H}) + t_2(0) \tag{7}$$

where τ_{180}(H) is the duration of the ^{1}H 180° pulse in the middle of t_2.[21]

If the data are acquired in the States format, the linear phase correction that must be applied in F_i (i = 1,2) is given by $sd(t_i) \times 360/\Delta t_i$, where Δt_i is the dwell time in the t_ith dimension.[26] In order to ensure that no net phase correction is applied in the center of the spectrum, a zeroth-order phase correction of $-0.5sd(t_i) \times 360/\Delta t_i$ must be applied as well. It should be clear that if the sampling is delayed by exactly $\frac{1}{2}\ \Delta t_i$, a linear phase correction of 180° is required across the spectrum. In this case, aliased peaks will be of opposite sign relative to peaks that are not aliased.

2.3 Application to Uniformly ^{13}C-Enriched Molecules

The ^{13}C NOESY—HMQC and HMQC—NOESY experiments provide valuable distance information linking two carbon-bound protons. For reasons of sensitivity, these experiments, like the ^{15}N versions discussed previously, are performed on highly enriched, uniformly labeled samples. The use of highly enriched ^{13}C molecules results in a significant increase in the linewidths of the attached proton(s). The heteronuclear dipolar coupling between a directly coupled ^{13}C–^{1}H pair is approximately a factor of two larger than the coupling from an ^{15}N—^{1}H spin pair. A second complication associated with the use of uniform labeling is the introduction of homonuclear carbon—carbon scalar couplings, varying from approximately 60 Hz for $^{13}C_\alpha$–^{13}CO couplings to approximately 35 Hz for aliphatic carbons. These couplings can significantly degrade the resolution available in spectra. Fortunately, the large chemical shift difference between carbonyl spins and the aliphatic spins allows for the efficient decoupling of the $^{13}C_\alpha$–^{13}CO scalar interaction using selective shaped decoupling schemes such as SEDUCE-1.[16] In order to minimize the effects of the aliphatic couplings, maximum acquisition times $t_{\max} \approx 10$ ms are chosen in the carbon dimension, where $t_{\max} < [2J(\mathrm{C,C})]^{-1}$ and J(C,C) is the aliphatic scalar coupling constant. While this does limit resolution in the carbon dimension, it must be kept in mind that in many protein applications, the ^{13}C T_2 values are on the order of only 10–20 ms.

Figure 2(c) illustrates a pulse scheme for the ^{13}C NOESY—HMQC sequence.[17] The flow of magnetization is essentially identical to that discussed in connection with the ^{15}N-edited version of the experiment, and will therefore only be summarized as follows:

$$^1\mathrm{H}_i(t_1) \xrightarrow{\mathrm{NOE}} {}^1\mathrm{H}_j \xrightarrow{\mathrm{J(C,H)}} {}^{13}\mathrm{C}_j(t_2) \xrightarrow{\mathrm{J(C,H)}} {}^1\mathrm{H}_j(t_3) \tag{8}$$

with chemical shift evolution recorded during t_1, t_2, and t_3. Note that the reverse pathway, where magnetization originates on spin j and is transferred via the NOE to spin i, is also possible (providing that both proton spins i and j are bound to ^{13}C nuclei), so that symmetry related cross peaks are observed at (H_i, C_j, H_j) and (H_j, C_i, H_i). For the case of distinct carbons C_i and C_j, the symmetry related cross peaks will appear on different slices in the 3D data set. These symmetry related pairs are extremely helpful in the unambiguous assignment of NOE cross peaks.

Because of the large carbon chemical shift range, extending from approximately 10 ppm for methyl carbons to 140 ppm for aromatic carbons, many of the cross peaks in the 3D ^{13}C-edited NOESY spectra are aliased in the carbon dimension. Typically, a carbon spectral width of 3–4 kHz is employed with the carbon carrier positioned at about 65 ppm. The sampling delay in the carbon dimension is adjusted so that a 180° first-order phase correction is required. In this way, cross peaks that have been aliased an odd number of times are 180° out of phase relative to peaks that are not aliased or have been aliased an even number of times.

Figure 3 illustrates the power of the 3D ^{13}C NOESY–HMQC experiment in removing the overlap in the crowded aliphatic region of the regular NOESY spectrum. A comparison of a slice from the 3D data set recorded on the protein calmodulin (MW = 16.7 kDa) with the same region of a 2D spectrum clearly shows the resolving power in increasing the dimensionality from two to three.[17]

Up to this point in our discussion, we have focused on a number of the basic NOESY–HMQC and HMQC–NOESY pulse sequences, as they appeared in the literature, prior to the development of pulsed field gradient methods. It is generally the case that these experiments can be significantly improved

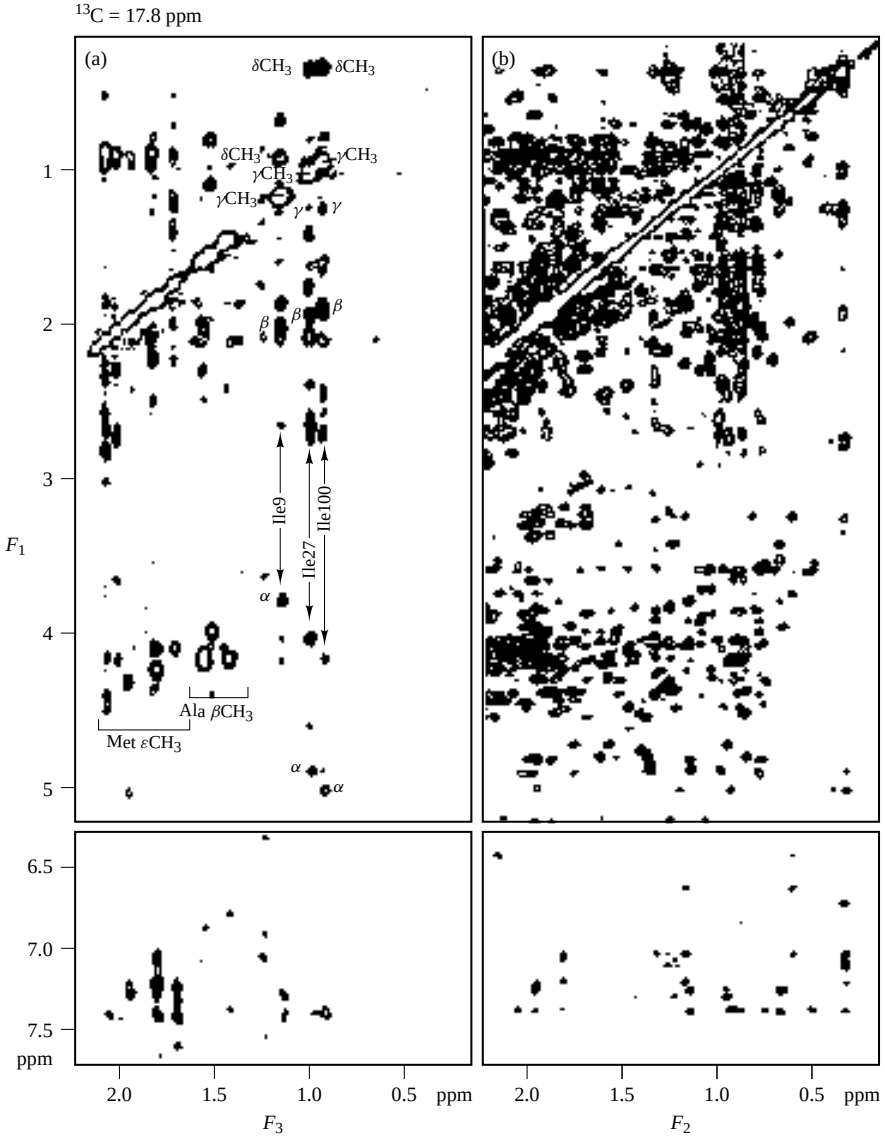

Figure 3 Comparison of (a) a section of an (F_1, F_3) slice taken at F_2 = 17.8 ppm from the 500 MHz 3D ^{13}C NOESY–HMQC spectrum of a 1.5 mM 95% ^{13}C-labeled sample of calmodulin, 6.2 mM Ca^{2+} and (b) the same region of the 600 MHz regular 2D NOESY spectrum of a 1.5 mM unlabeled calmodulin sample, 6.2 mM Ca^{2+}, using mixing times of 120 ms. The 3D data set was collected as a matrix of 128* × 64* × 512 points (t_1, t_2, t_3) in about 60 h (* denotes complex points). (Reproduced by permission of Academic Press from M. Ikura, L. E. Kay, R. Tschudin, and A. Bax, *J. Magn. Reson.*, 1990, **86**, 204)

with the incorporation of field gradients, and the use of this novel technology in such applications is discussed in the next section.

3 PULSED FIELD GRADIENT METHODS

Recent developments in pulsed field gradient technology have led to many useful applications in high-resolution NMR spectroscopy (see ***Field Gradients and Their Application***). The use of gradients allows for the efficient removal of the intense water signal in the case of samples dissolved in H_2O,[28] the elimination of undesired coherences that produce artifacts,[29] a decrease in the number of phase cycling steps, thereby reducing the overall data collection time for sufficiently concentrated samples,[30] and the selection of particular coherence transfer pathways.[31] By incorporating field gradient pulses into many of the experiments discussed earlier, data sets with improved suppression of solvent and artifacts can be obtained. A brief discussion of two heteronuclear-edited gradient NOESY experiments is presented; an ^{15}N-edited NOESY–HMQC experiment developed by Vuister et al.[30] that can be recorded using only a single transient for each ^{15}N data point, and a simultaneous ^{15}N-, ^{13}C-edited NOESY–HSQC experiment.[32]

3.1 Gradient 3D NOESY–HMQC

A pulse scheme for the gradient-enhanced 3D NOESY–HMQC experiment developed by Vuister and co-workers is shown in Figure 4(a).[30] In this experiment, the coherence

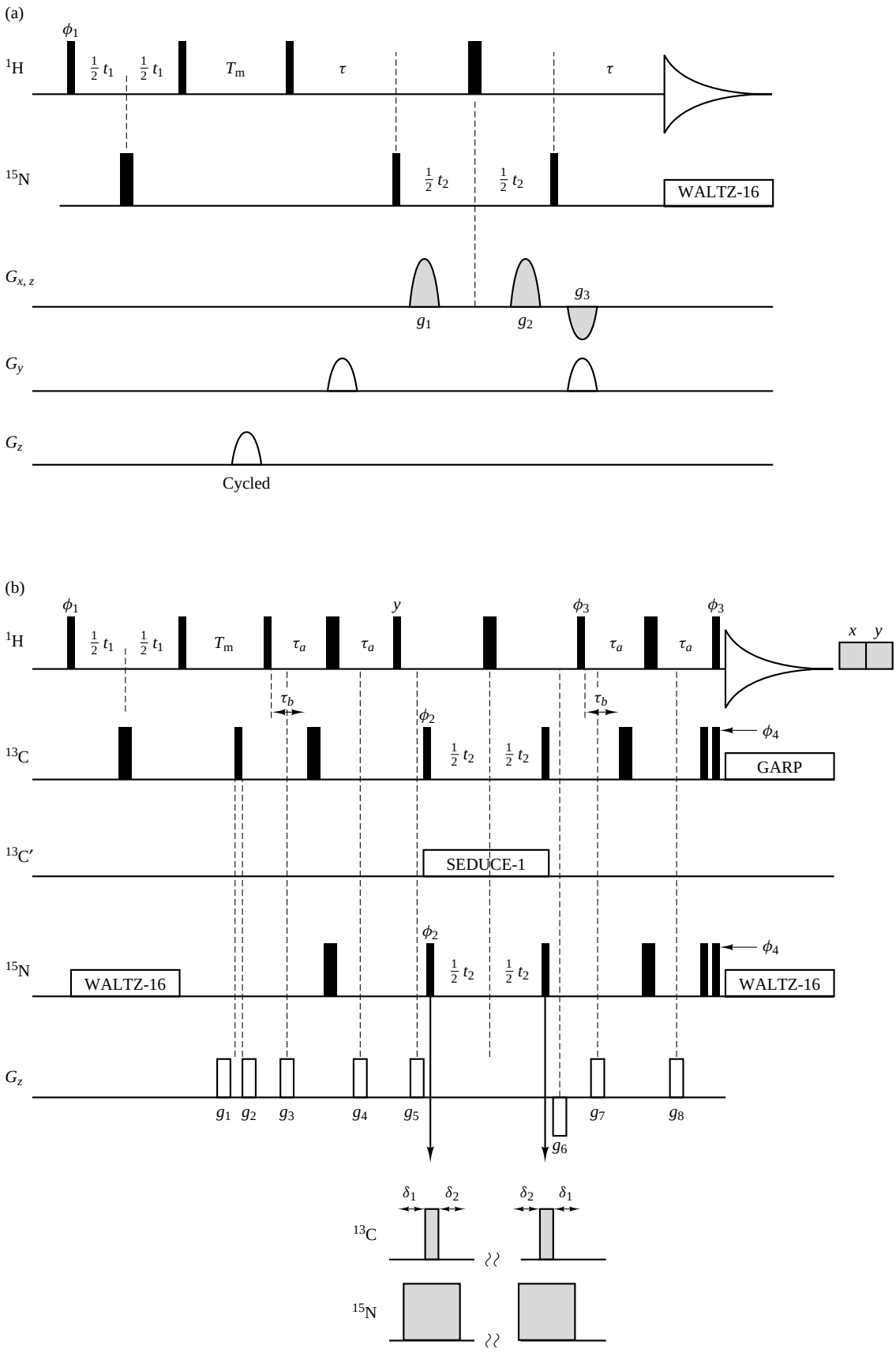
(a)
ϕ_1
^{1}H
$\frac{1}{2}t_1$
$\frac{1}{2}t_1$
T_m
τ
τ
^{15}N
$\frac{1}{2}t_2$
$\frac{1}{2}t_2$
WALTZ-16
$G_{x,z}$
g_1
g_2
g_3
G_y
G_z
Cycled
(b)
ϕ_1
y
ϕ_3
ϕ_3
^{1}H
τ_a
τ_a
τ_a
τ_a
x y
τ_b
τ_b
ϕ_2
ϕ_4
^{13}C
GARP
^{13}C′
SEDUCE-1
^{15}N
WALTZ-16
WALTZ-16
G_z
g_1 g_2 g_3 g_4 g_5 g_6 g_7 g_8
δ_1 δ_2 δ_2 δ_1
^{13}C
^{15}N

Figure 4

Figure 4 Pulse sequences for (a) the gradient NOESY–HMQC and (b) the gradient CN NOESY–HSQC experiments. Narrow (wide) pulses are applied with a flip angle of 90° (180°). Unless otherwise indicated, all pulses are applied along the x axis. All ^{1}H and ^{13}C pulses are applied at the highest field possible (about 20 kHz), while typical ^{15}N pulses are applied with a field of about 5–6 kHz. In (a), quadrature in t_1 is achieved via States–TPPI[13] of ϕ_1; τ = 4.5 ms. Gradients are of 0.8 ms in duration and are sine-bell in shape. Gradient strengths are $g_{1x} = g_{2x} = 63.7\,\mathrm{mT\,m^{-1}}$, $g_{3x} = -12.9\,\mathrm{mT\,m^{-1}}$, $g_{1z} = g_{2z} = 20.5\,\mathrm{mT\,m^{-1}}$, $g_{3z} = -4.2\,\mathrm{mT\,m^{-1}}$, and $G_y = 19.7\,\mathrm{mT\,m^{-1}}$. The G_z gradient in T_m is applied for 0.4 ms and cycled through 7, 21, 35, and 49 $\mathrm{mT\,m^{-1}}$ in successive transients. In (b), the x, y ^{1}H purge pulses immediately after the acquisition are applied for 8 and 5 ms respectively, with a 10 kHz field. The ^{13}C pulses are centered at 67 ppm. The first 180° ^{13}C pulse is a composite $90°_x180°_y90°_x$ pulse. The GARP decoupling is preceded by high-power ^{15}N and ^{13}C pulse pairs as described by Bax et al.[33] The delays τ_a and τ_b were both set to 1.7 ms. Quadrature in t_1 and t_2 is achieved via States–TPPI[13] of ϕ_1 and ϕ_2, respectively. The diagram at the bottom of the figure illustrates the adjustment of timing delays in order to obtain a 180° first-order phase correction in F_2 for both ^{15}N- and ^{13}C-modulated data. The first ^{13}C pulse, of duration pwc, commences at $\delta_1 = [(\pi - 2)/\pi]$(pwn − pwc) after the start of the ^{15}N ϕ_2 pulse of duration pwn, while the ^{13}C pulse immediately after the t_2 evolution period begins $\delta_2 = (2/\pi)$(pwn − pwc) after the start of the corresponding ^{15}N pulse (pwc < pwn). By setting the initial t_2 value, $t_2(0) = (2\mathrm{SW}_2)^{-1} - [(4/\pi)\mathrm{pwn} + 2\mathrm{pw}]$, where SW_2 is the spectral width in the ^{13}C and ^{15}N dimensions and pw is the ^{1}H 90° pulse width, a 180° first-order phase correction in F_2 is obtained. The following phase cycle is employed: $\phi_1 = 4(x),4(-x)$; $\phi_2 = 8(x),8(-x)$; $\phi_3 = (x,y,-x,-y)$; $\phi_4 = 4(x),4(-x)$; rec. = $(x,-y,-x,y,-x,y,x,-y,-x,y,x,-y,x,-y,-x,y)$. The durations and strengths of the gradients are g_1 = (3 ms, 150 $\mathrm{mT\,m^{-1}}$), g_2 = (1 ms, 200 $\mathrm{mT\,m^{-1}}$), $g_3 = g_4$ = (1 ms, 80 $\mathrm{mT\,m^{-1}}$), g_5 = (4 ms, 300 $\mathrm{mT\,m^{-1}}$), g_6 = (3 ms, −180 $\mathrm{mT\,m^{-1}}$), and $g_7 = g_8$ = (1 ms, 80 $\mathrm{mT\,m^{-1}}$). A delay of at least 50 μs between the application of a gradient pulse and the subsequent application of an rf pulse is employed. All gradient pulses are rectangular in shape. (Adapted from (a) Vuister et al.[30] and (b) Pascal et al.[32])

transfer pathway whereby magnetization passes through nitrogen is selected with the use of the appropriate pulsed field gradients. Because it is not possible for water magnetization to traverse this pathway, excellent levels of water suppression can be achieved. The gradients g_1–g_3 are employed for coherence transfer selection by adjusting their strengths according to the ratio g_1:g_2:g_3 = 4.94:4.94:1.0 ($\gamma_H/\gamma_N = -9.88$), while the gradient pair (G_y) applied on opposite sides of the ^{1}H 180° pulse in the middle of the t_2 period ensures that any artifacts that could be created owing to imperfections in this pulse are eliminated.[29] In this experiment, pure amplitude-modulated data are recorded in the t_1 dimension in the normal fashion. However, the use of gradients g_1–g_3 results in the generation of phase-modulated data in the t_2 dimension, and therefore spectra must be presented in the absolute value mode after processing. Note that phase cycling is not necessary in the present application. Thus, it is possible to obtain spectra in short periods of measuring time, assuming that the sample is sufficiently concentrated so that the signal-to-noise ratio is not limiting. For this reason, this experiment is useful for kinetic studies and for studies of molecules that are stable for only short periods of time. The requisite absolute value representation of the data, however, does result in a considerable loss in resolution, which is especially critical in macromolecular applications.

3.2 Simultaneous ^{15}N-, ^{13}C-Edited NOESY

An advantage associated with the development of pulsed field gradient technology is the potential of recording all spectra necessary for a protein structure determination using only a single ^{15}N-, ^{13}C-labeled sample dissolved in H_2O. In addition to minimizing the number of samples necessary for a structure determination, the use of just a single sample also ensures that ambiguities arising from a comparison of data recorded on a number of different samples prepared with slight differences can be minimized. This is important in order to maximize the efficiency of automated or semi-automated assignment and structure determination approaches.

The CN NOESY–HSQC experiment illustrated in Figure 4(b) provides NOEs between any two proximate protons in ^{15}N-, ^{13}C-labeled proteins separated by the chemical shift of the heteroatom to which the destination proton is attached.[32] Because spectra are recorded on samples dissolved in H_2O, valuable NOEs involving NH protons are also observed.

Pulsed field gradients are used in this experiment to aid in the removal of artifacts as well as to assist in water suppression. A detailed description of the utility of each gradient is found elsewhere.[32] Gradients g_5 and g_6 are particularly important for water suppression, since, during the time of their application, the magnetization of interest is of the form $\hat{I}_z\hat{X}_z$, where $\hat{I}_z$ and $\hat{X}_z$ are the z components of ^{1}H and ^{15}N or ^{13}C magnetizations, respectively, while water magnetization is present in the transverse plane and hence is dephased by the combined action of the gradient pair (g_5, g_6). For this reason, an HSQC-type transfer of magnetization from ^{1}H to X must be employed rather than an HMQC transfer.[34,35] Figure 5 illustrates the quality of water suppression obtained with the present sequence with the ^{15}N pulses set to zero (i.e., ^{13}C NOESY–HSQC) for a 1.5 mM sample of the cellulose binding domain CBD. The noise from the residual water obscures a region of approximately ±0.2 ppm around the water line (4.8 ppm) in F_3.

The basic flow of magnetization transfer in this experiment can be described by the following two independent pathways:

$$^1\mathrm{H}(t_1) \xrightarrow{\mathrm{NOE}} \mathrm{NH} \xrightarrow{\mathrm{J(N,H)}} {}^{15}\mathrm{N}(t_2) \xrightarrow{\mathrm{J(N,H)}} \mathrm{NH}(t_3) \tag{9}$$

$$^1\mathrm{H}(t_1) \xrightarrow{\mathrm{NOE}} \mathrm{CH} \xrightarrow{\mathrm{J(N,H)}} {}^{13}\mathrm{C}(t_2) \xrightarrow{\mathrm{J(N,H)}} \mathrm{CH}(t_3) \tag{10}$$

with chemical shifts recorded during t_1, t_2, and t_3. Note that each (F_1, F_3) slice of the data set is labeled with either the ^{15}N or ^{13}C chemical shift of the heteroatom to which the destination proton is attached. For proteins, ^{13}C- and ^{15}N-bound protons generally have quite distinct chemical shifts, and therefore, with the possible exception of a few backbone or side-chain amide and aromatic protons, the extra information in these spectra relative to single ^{15}N- or ^{13}C-edited data sets does not create ambiguities in interpretation.

A particularly important feature of the CN NOESY–HSQC data set is that, for each NOE cross peak between a carbon-bound proton and a nitrogen-bound proton at position (CH,N,NH), it is possible to find a symmetry-related cross peak at (NH,C,CH). The experiment also provides NOEs

between exclusively carbon-bound or nitrogen-bound protons. Figure 6 shows a number of slices from a 150 ms CN NOESY–HSQC data set obtained on a 1.5 mM sample of the C-terminal SH2 domain from phospholipase-Cγ1 complexed with a 12-residue phosphotyrosine-containing peptide.

4 SENSITIVITY-ENHANCED VERSIONS OF 3D HETERONUCLEAR-EDITED NOESY EXPERIMENTS

In the past several years, a family of elegant pulse schemes has been developed by Cavanagh, Palmer, and Rance that offers significant improvements in sensitivity for certain classes of experiments.[36,37] In the case of a two-dimensional experiment, for example, sensitivity gains are recognized because both the cosine- and the sine-modulated t_1 components are refocused into observable magnetization prior to detection. In this section, a description of a nongradient, sensitivity-enhanced ^{15}N-edited NOESY–HMQC experiment[37] is presented, followed by a discussion of a sensitivity-enhanced ^{15}N-edited NOESY–HSQC gradient experiment.[38] In the latter experiment, saturation of water is minimized as well by employing selective pulses on water to restore magnetization to the +z axis prior to detection.

4.1 Sensitivity-Enhanced 3D ^{15}N-Edited NOESY–HMQC

Figure 7(a) illustrates the pulse scheme used to record ^{15}N-edited NOESY–HMQC spectra with increased sensitivity.[37] Although the sequence is slightly more complicated than the unenhanced version illustrated in Figure 2(b), the flow of magnetization throughout the experiment is easily understood with the use of the product operator formalism.[18] Immediately prior to detection, the magnetization that originates on spin a and is transferred to spin b is described by

$$\hat{\rho}(\phi_2 = x) = A[-\hat{I}_{bx}\cos(\omega_N t_2) - \delta_{1,M}\hat{I}_{by}\sin(\omega_N t_2)]\cos(\omega_a t_1) \qquad (11)$$

$$\hat{\rho}(\phi_2 = -x) = A[\hat{I}_{bx}\cos(\omega_N t_2) - \delta_{1,M}\hat{I}_{by}\sin(\omega_N t_2)]\cos(\omega_a t_1) \qquad (12)$$

where $\hat{\rho}$ is the density operator, M is the number of protons (spins I) attached to the heterospin (spin N), A is a factor that depends, among other things, on the efficiency of transfer of I-spin magnetization from spin a to spin b, and $\delta_{1,M}$ = 1 if M = 1 and zero otherwise. Note that separate data sets are recorded for $\phi_2 = x$ and $\phi_2 = -x$. Using the present approach, phase-modulated data are generated in the t_2 dimension, as equations (11) and (12) suggest.

In order to generate pure absorptive lineshapes, the data can be recombined by taking the sum and the difference of the data sets obtained for $\phi_2 = \pm x$ for a given value of t_2 to generate a new data set of the form

$$(11) + (12)\hat{\rho} = -\delta_{1,M}2A\hat{I}_{by}\cos(\omega_a t_1)\sin(\omega_N t_2)(\text{SUM}) \qquad (13)$$

$$(11) - (12)\hat{\rho} = -2A\hat{I}_{bx}\cos(\omega_a t_1)\cos(\omega_N t_2)(\text{DIFFERENCE}) \qquad (14)$$

Note that the SUM signal is proportional to $\hat{I}_y$, while the DIFFERENCE signal is proportional to $\hat{I}_x$. For this reason, a

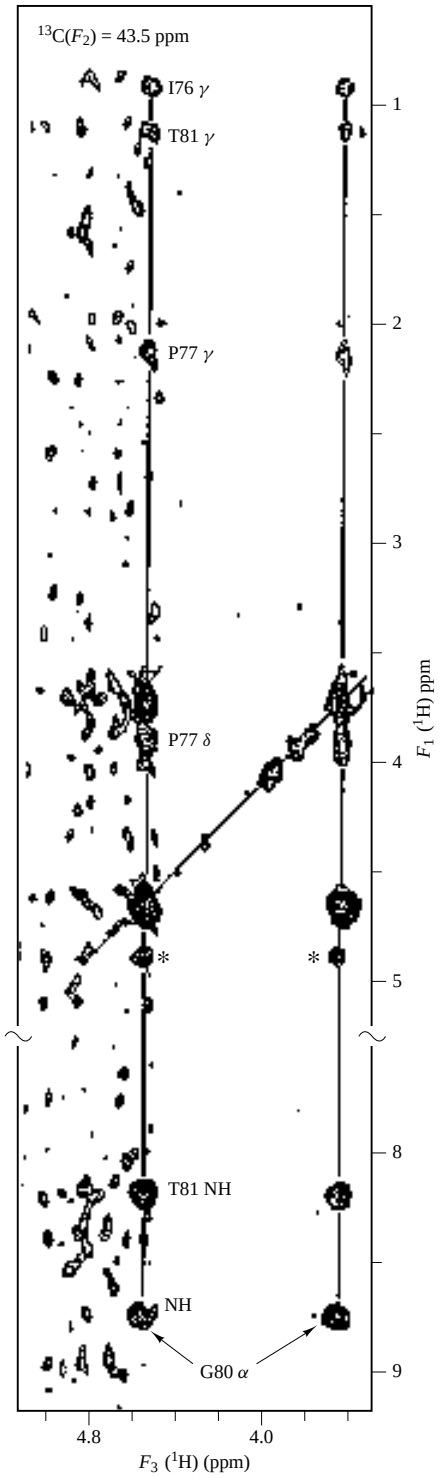

Figure 5 Section of an (F_1, F_3) slice from the 3D gradient ^{13}C NOESY–HSQC spectrum recorded at 500 MHz on a 1.5 mM sample of ^{15}N-, ^{13}C-labeled CBD, pH 7.0, 90% H_2O/10% D_2O at 30 °C, displaying a region close to the water resonance. The mixing time was 150 ms and the data set was acquired as a 128 × 32 × 416 complex matrix (t_1, t_2, t_3), in about 90 h. The data were processed to give absorptive spectra consisting of 256 × 64 × 1024 points in each of (F_1, F_2, F_3). Residual water not eliminated by the gradients was removed using a postacquisition time domain deconvolution procedure.[35] Cross peaks due to either NOEs to water or exchange with labile groups are indicated with asterisks. Interresidue NOEs are labeled with the residue name. (Adapted from Muhandiram et al.[35])

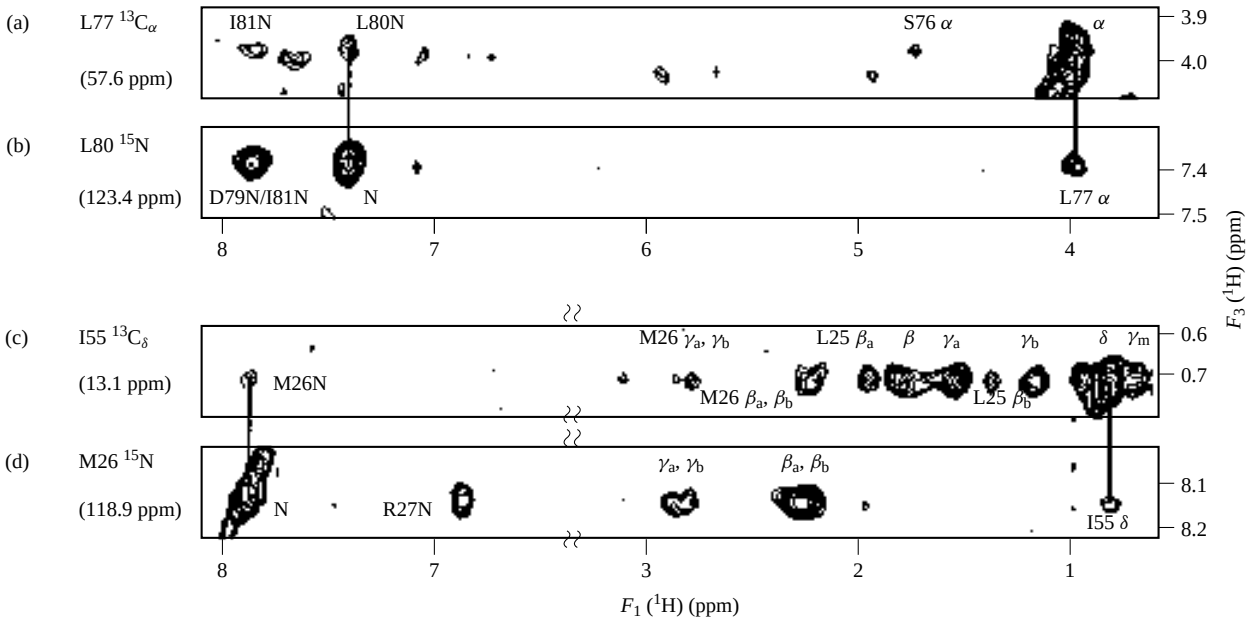

Figure 6 Slices from a CN NOESY-HSQC data set recorded at 500 MHz on a 1.5 mM sample of the protein–peptide complex PLCγ1 SH2-pY1021, showing pairs of 'symmetry-related' cross peaks for NOEs between L80NH and L77C$_\alpha$H (a, b) and M26NH and 155C$_\delta$H (c, d). The cross peaks are observed on planes with the appropriate F_2 chemical shift being either that of ^{15}N or ^{13}C, depending on whether the destination proton is an amide or aliphatic proton. The cross peak of interest from each slice is connected to the diagonal on the corresponding slice by a vertical line. Peaks are labeled with the atom name, and interresidue NOEs are additionally labeled with the residue name. The NOE mixing time was 150 ms, and the data set was acquired as a 128 × 32 × 416 complex matrix (t_1, t_2, t_3), in about 90 h. The data set was processed to give absorptive spectra consisting of 256 × 128 × 1024 points in each of (F_1, F_2, F_3). In order to optimize the resolution of the ^{15}N lines, linear prediction was employed in t_2. The intensity of the residual water signal was minimized through the time domain deconvolution procedure discussed by Muhandiram et al.[35] (Reproduced by permission of Academic Press from S. M. Pascal, D. R. Muhandiram, T. Yamazaki, J. D. Forman-Kay, and L. E. Kay, *J. Magn. Reson., Ser B*, 1994, **103**, 197)

90° zeroth-order phase correction is applied to either the SUM or the DIFFERENCE data (not both) in the time domain. After these simple time-domain manipulations have been performed, a data set is obtained that contains peaks that are purely absorptive after processing using the States recipe.[19] For the case where M = 1 (i.e., an AX ^{15}N,NH heteronuclear spin system) the process of taking the sum and the difference of the signals described by equations (11) and (12) increases the signal intensity by a factor of two relative to signals in spectra recorded using an unenhanced sequence. The noise floor increases by a factor of $\sqrt{2}$ during this process, so that the net increase in signal-to-noise ratio is a factor of $\sqrt{2}$. Of course, this theoretical sensitivity gain does not include potential losses that can occur owing to the increased number of pulses and delays in the sequence relative to the unenhanced version. For protein applications considered to date, appreciable increases in sensitivity have been obtained. Figure 8 compares the F_1 traces from regular and sensitivity-enhanced NOESY–HMQC spectra of ^{15}N-labeled calbindin D9k (75 amino acids) in 90% H_2O/10% D_2O, with sensitivity enhancements close to the theoretical maximum of $\sqrt{2}$ realized.

4.2 Sensitivity-Enhanced Gradient 3D NOESY–HSQC

Figure 7(b) illustrates the sensitivity-enhanced 3D ^{15}N-edited NOESY–HSQC sequence with gradients used to suppress artifacts, to aid in the suppression of the intense solvent signal and to select for ^{15}N magnetization during the nitrogen evolution time t_2. In the selection of ^{15}N magnetization using gradients, a sensitivity enhancement approach is taken based on the nongradient sensitivity-enhanced method discussed above.[23] Sensitivity in the experiment is increased further by restoring the water signal to the $+z$ axis prior to detection[25] in order to minimize the saturation of water during the course of the experiment. The detailed mechanism of the experiment is reported elsewhere.[38] It can easily be understood how the water is stored along the $+z$ axis after each transient by noting that for mixing times T_m in excess of about 50 ms, the effect of radiation damping is such that water magnetization is restored to the $+z$ axis at point a in the pulse scheme in a manner independent of the phase ϕ_1 of the first ^{1}H 90° pulse. In order to facilitate radiation damping, ϕ_1 is phase-cycled 45°, 225° as opposed to 0°, 180° (x, $-x$). Immediately after the first ^{1}H 90°$_y$ pulse (point b in the sequence), the water magnetization is along the y axis, while the signal of interest is of the form $\hat{I}_z\hat{N}_z$, where $\hat{I}_z$ and $\hat{N}_z$ are the z components of the NH and ^{15}N magnetizations, respectively. The water-selective pulse applied at this point rotates the (on-resonance) water magnetization to the $-z$ axis without perturbing the signal of interest. Application of the gradient g_5 immediately after the selective pulse ensures that any residual water magnetization in the transverse plane is completely dephased, thereby eliminating radiation damping at this point. It is straightforward to show that the effect of the remaining proton pulses on the water is such that water magnetization resides along the $+z$ axis at the start of the acquisition period t_3.

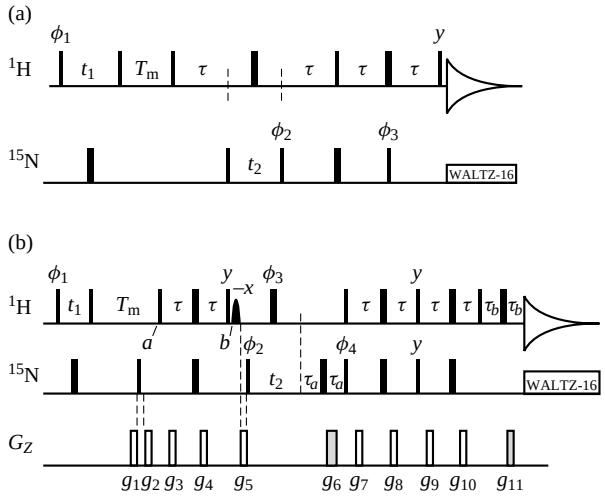

Figure 7 Pulse sequences for (a) sensitivity-enhanced 3D NOESY–HMQC and (b) sensitivity-enhanced gradient 3D NOESY–HSQC experiments. Unless otherwise stated, all parameters are as in Figure **2**. In both experiments, quadrature in t_1 is achieved by States–TPPI of ϕ_1. (a) The phase cycle is $\phi_1 = x,-x$; $\phi_2 = 2(x),2(-x)$; $\phi_3 = 2(y),2(-y)$; Rec. = $x,2(-x),x$. The phase of ϕ_2 is inverted after four transients, and the data are stored separately. Quadrature in t_2 is achieved using the method of States.[19] (b) The shaped pulse on ^{1}H is a 'water'-selective 90° pulse. This pulse is either a 2 ms rectangular pulse (125 Hz field) or a 2 ms shaped pulse (270 Hz field at peak height) having the profile of a 90° SEDUCE-1 element.[16] The phase cycle is $\phi_1 = x,-x$; $\phi_2 = 4(x),4(-x)$; $\phi_3 = 2(x),2(-x)$; $\phi_4 = x$; Rec. = $2(x,-x),2(-x,x)$. For each t_2 increment, the phase ϕ_2 and the receiver phase are inverted. For each t_2 value, two FIDs are recorded and stored separately, with the phase ϕ_4 and the amplitude of the gradient pulse g_{11} inverted for the second FID. The delays τ, τ_a and τ_b are set to 2.4 ms ($<[4J(\mathrm{N,H})]^{-1}$), 1.5 ms and 0.5 ms respectively. The durations and strengths of the gradients are g_1 = (2 ms, 100 mT m^{-1}), g_2 = (0.5 ms, 80 mT m^{-1}), $g_3 = g_4$ = (0.75 ms, 50 mT m^{-1}), g_5 = (2 ms, −150 mT m^{-1}), g_6 = (1.25 ms, 300 mT m^{-1}), $g_7 = g_8$ = (0.5 ms, 80 mT m^{-1}), $g_9 = g_{10}$ = (0.5 ms, 50 mT m^{-1}), and g_{11} = (0.125 ms, 278 mT m^{-1}). The strength of g_{11} is optimized by maximizing the signal. (Adapted from (a) Palmer et al.[37] and (b) Zhang et al.[38])

A product operator description similar to that given above shows that, immediately prior to acquisition, the magnetization associated with an NH proton is given by

$$\hat{\rho}(\phi_4 = \pm x) = A\cos(\omega_a t_1)[\pm\hat{I}_{by}\cos\theta_1 + \hat{I}_{bx}\sin\theta_1] \qquad (15)$$

where $\hat{I}_{bx}$ and $\hat{I}_{by}$ are the x and y components of NH magnetization, and all other symbols defined as above. The value of θ_1 is given by $\theta_1 = \omega_N t_2 + \gamma_N B_1(z)\tau_1 \pm \gamma_H B_2(z)\tau_2$ for $\phi_4 = \pm x$, where ω_N is the ^{15}N Larmor frequency, γ_i is the gyromagnetic ratio of spin i, and τ_i (i = 1, 2) is the duration of the z gradient pulse generating a magnetic field of magnitude B_i at position z in the sample. Assuming that

1. the gradients used to select for ^{15}N magnetization (g_6, g_{11}) are sufficiently strong that they cause complete dephasing of magnetization, and
2. for $\phi_4 = \pm x$, the gradients are adjusted so that $\gamma_N B_1(z)\tau_1 = \mp\gamma_H B_2(z)\tau_2$,

Equation (15) reduces to

$$\hat{\rho}(\phi_4 = \pm x) = A\cos(\omega_a t_1)[\pm\hat{I}_{by}\cos(\omega_N t_2) + \hat{I}_{bx}\sin(\omega_N t_2)] \qquad (16)$$

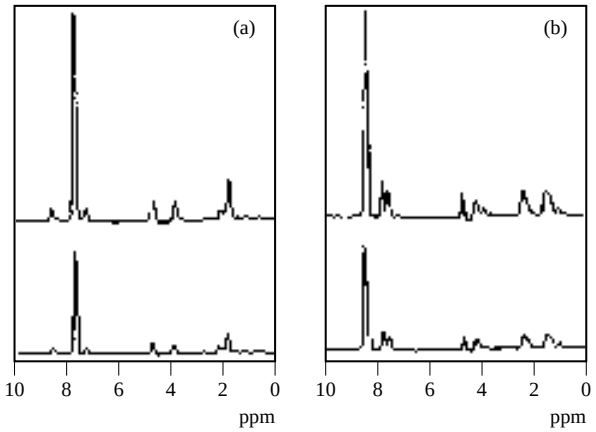

Figure 8 Comparison of conventional (bottom trace) and sensitivity-enhanced NOESY–HMQC (top trace) spectra of the protein calbindin recorded at 500 MHz. Both experiments were acquired in the same overall time as 100 × 32 × 1024 complex data sets with 16 transients per FID. The NOE mixing time was 150 ms. The figure shows F_1 cross sections for (a) Lys12 and (b) Glu35 taken at F_2, F_3 frequencies of the backbone amide ^{15}N and proton resonances, respectively. The increase in the RMS baseplane noise for the enhanced spectrum, compared with the conventional one, agrees with the theoretical value of $\sqrt{2}$. The average S/N improvements between the enhanced and conventional spectra are (a) 1.41 and (b) 1.39. (Reproduced by permission of Academic Press from A. G. Palmer, J. Cavanagh, R. A. Byrd, and M. Rance, *J. Magn. Reson.*, 1992, **96**, 416)

For each value of t_2, data sets are recorded with $\phi_4 = x$, $\gamma_N B_1(z)\tau_1 = -\gamma_H B_2(z)\tau_2$, and $\phi_4 = -x$, $\gamma_N B_1(z)\tau_1 = \gamma_H B_2(z)\tau_2$, and stored in separate memory locations. The data are subsequently manipulated in the time domain, as described in connection with the enhanced NOESY–HMQC experiment above, to yield a purely absorptive spectrum after Fourier transformation. Enhancements in signal-to-noise ratio by a factor of as much as $\sqrt{2}$ relative to unenhanced experiments can be obtained using this approach.

5 CONCLUDING REMARKS

The development of heteronuclear, multidimensional, multinuclear MR spectroscopy has facilitated large numbers of structural studies of macromolecules, and has significantly increased the size of molecules that can be studied. The heteronuclear-edited NOESY experiment provides the crucial distance information necessary for these structure determinations. Presently, the interpretation of NOESY data sets is the time-consuming step in the structure determination process. Current efforts are focusing on ways of providing a more automated approach to the assignment of NOE cross peaks and the calculation of structures.

6 RELATED ARTICLES

Biological Macromolecules: Structure Determination in Solution; Field Gradients and Their Application; Heteronuclear Shift Correlation Spectroscopy; Multidimensional Spectroscopy: Concepts; NOESY; Nuclear Overhauser Effect; Structures of Larger Proteins, Protein-Ligand,

and Protein-DNA Complexes by Multi-Dimensional Heteronuclear NMR; Three- and Four-Dimensional Heteronuclear Magnetic Resonance.

7 REFERENCES

1. J. Jeener, B. H. Meier, P. Bachmann, and R. R. Ernst, *J. Chem. Phys.*, 1979, **71**, 4546.
2. S. W. Fesik and E. R. P. Zuiderweg, *Quart. Rev. Biophys.*, 1990, **23**, 97.
3. A. Bax and S. Grzesiek, *Acc. Chem. Res.*, 1993, **26**, 131.
4. L. P. McIntosh and F. W. Dahlquist, *Quart. Rev. Biophys.*, 1990, **23**, 1.
5. G. M. Clore and A. M. Gronenborn, in *Progress in Nuclear Magnetic Resonance Spectroscopy*, eds. J. W. Emsley, J. Feeney, and L. H. Sutcliffe, Pergamon Press, Oxford, 1991, Vol. 23, p. 43.
6. G. Wagner, *J. Biomol, NMR*, 1993, **3**, 375.
7. E. P. Nikonowicz and A. Pardi, *Nature (London)*, 1992, **355**, 184.
8. P. de Waard, B. R. Leeflang, J. F. G. Vliegenthart, R. Boelens, G. W. Vuister, and R. Kaptein, *J. Biomol. NMR*, 1992, **2**, 211.
9. A. Bax, R. H. Griffey, and B. L. Hawkins, *J. Magn. Reson.*, 1983, **55**, 301.
10. G. Bodenhausen and D. J. Ruben, *Chem. Phys. Lett.*, 1980, **69**, 185.
11. S. W. Fesik and E. R. P. Zuiderweg, *J. Magn. Reson.*, 1988, **78**, 588.
12. D. Marion, L. E. Kay, S. W. Sparks, D. A. Torchia, and A. Bax, *J. Am. Chem. Soc.*, 1989, **111**, 1515.
13. D. Marion, M. Ikura, R. Tschudin, and A. Bax, *J. Magn. Reson.*, 1989, **85**, 393.
14. A. J. Shaka, J. Keeler, T. Frenkiel, and R. Freeman, *J. Magn. Reson.*, 1983, **52**, 335.
15. A. J. Shaka, P. B. Barker, and R. Freeman, *J. Magn. Reson.*, 1985, **64**, 547.
16. M. A. McCoy and L. Mueller, *J. Am. Chem. Soc.*, 1992, **114**, 2108.
17. M. Ikura, L. E. Kay, R. Tschudin, and A. Bax, *J. Magn. Reson.*, 1990, **86**, 204.
18. O. W. Sørensen, G. W. Eich, M. H. Levitt, G. Bodenhausen, and R. R. Ernst, in *Progress in Nuclear Magnetic Resonance Spectroscopy*, eds. J. W. Emsley, J. Feeney, and L. H. Sutcliffe, Pergamon Press, Oxford, 1983, Vol. 16, p. 163.
19. D. J. States, R. A. Haberkorn, and D. J. Ruben, *J. Magn. Reson.*, 1982, **48**, 286.
20. J. H. Noggle and R. E. Schirmer, *The Nuclear Overhauser Effect*, Academic Press, New York, 1971.
21. L. E. Kay, D. Marion, and A. Bax, *J. Magn. Reson.*, 1989, **84**, 72.
22. G. A. Morris and R. Freeman, *J. Magn. Reson.*, 1978, **29**, 433.
23. L. E. Kay, P. Keifer, and T. Saarinen, *J. Am. Chem. Soc.*, 1992, **114**, 10 663.
24. Y. C. Li and G. T. Montelione, *J. Magn. Reson., Ser. B*, 1993, **101**, 315.
25. S. Grzesiek and A. Bax, *J. Am. Chem. Soc.*, 1993, **115**, 12 593.
26. A. Bax, M. Ikura, L. E. Kay, and G. Zhu, *J. Magn. Reson.*, 1991, **91**, 174.
27. D. Marion and A. Bax, *J. Magn. Reson.*, 1989, **83**, 205.
28. B. K. John, D. Plant, P. Webb, and R. E. Hurd, *J. Magn. Reson.*, 1992, **98**, 200.
29. A. Bax and S. S. Pochapsky, *J. Magn. Reson.*, 1992, **99**, 638.
30. G. W. Vuister, R. Boelens, R. Kaptein, M. Burgering, and P. C. M. van Zijl, *J. Biomol. NMR*, 1992, **2**, 301.
31. R. E. Hurd and B. K. John, *J. Magn. Reson.*, 1991, **91**, 648.
32. S. M. Pascal, D. R. Muhandiram, T. Yamazaki, J. D. Forman-Kay, and L. E. Kay, *J. Magn. Reson., Ser. B*, 1994, **103**, 197.
33. A. Bax, G. M. Clore, P. C. Driscoll, A. M. Gronenborn, M. Ikura, and L. E. Kay, *J. Magn. Reson.*, 1990, **87**, 620.
34. A. Majumdar and E. R. P. Zuiderweg, *J. Magn. Reson., Ser. B*, 1993, **102**, 242.
35. D. R. Muhandiram, N. A. Farrow, G. Y. Xu, S. H. Smallcombe, and L. E. Kay, *J. Magn. Reson., Ser. B*, 1993, **102**, 317.
36. A. G. Palmer, J. Cavanagh, P. E. Wright, and M. Rance, *J. Magn. Reson.*, 1991, **93**, 151.
37. A. G. Palmer, J. Cavanagh, R. A. Byrd, and M. Rance, *J. Magn. Reson.*, 1992, **96**, 416.
38. O. Zhang, L. E. Kay, J. P. Olivier, and J. D. Forman-Kay, *J. Biomol, NMR*, 1994, **4**, 845.

Biographical Sketches

Lewis E. Kay. *b* 1961. B.Sc., 1983, University of Alberta, Canada; Ph.D., 1987, Yale University, USA. Postdoctoral work at the National Institutes of Health, USA (with Ad Bax), 1987–92. Professor, Departments of Medical Genetics, Biochemistry and Chemistry at the University of Toronto, 1992–present. Current research interests: development of multinuclear, multidimensional NMR methods for the study of structure and dynamics of proteins.

Ranjith Muhandiram. *b* 1956. B.Sc., 1979, University of Colombo, Sri Lanka; Ph.D., 1987, University of Alberta, Canada (supervisor R. E. D. McClung). Postdoctoral work at the University of Alberta (with R. E. D. McClung), 1987–89. Research associate at the National Research Council, Canada, 1989–92. Research associate with Professor Kay, 1992–present.

TOCSY in ROESY and ROESY in TOCSY

J. Schleucher, J. Quant, S. J. Glaser and C. Griesinger
Universität Frankfurt, Frankfurt, Germany

1	Introduction	1
2	Theory	3
3	Separation of Hartmann–Hahn Transfer and Cross Relaxation	7
4	References	15

1 INTRODUCTION

Homonuclear TOCSY[1] and ROESY[2] experiments are essential tools for the identification of spin systems and for the measurement of internuclear distances, respectively. (ROESY has been reviewed by Bull;[3] see also ***ROESY*** in this Encyclopedia.) TOCSY experiments rely on the transfer of polarization via J coupling, ROESY experiments rely on dipolar relaxation. Cross peaks due to slow chemical exchange are present in both experiments. The success of TOCSY and ROESY depends critically on the performance of the mixing sequence used to accomplish polarization transfer via the desired interaction. It will be shown that because of the complicated mixing sequences used, cross relaxation and J transfer cannot easily be separated. In fact, longitudinal and transverse cross relaxation and J transfer are intimately connected, and it is the aim of this article to describe handy tools to estimate the contribution of either of these interactions for a given pulse sequence. Unwanted interactions must be suppressed, since they lead to artifacts that can hamper the interpretation of the spectra. For example, transfer via J couplings alters the intensity of cross peaks in ROESY, and cross relaxation interferes with weak cross peaks in TOCSY. The offset dependence of TOCSY transfer and the offset dependence of the weight of transverse and longitudinal cross-relaxation rates in CW ROESY is illustrated in Figure 1. Hartmann–Hahn transfer along the diagonal cannot be avoided in any ROESY experiment. Hartmann–Hahn transfer along the antidiagonal is a more serious drawback, which can be overcome in more sophisticated ROESY experiments. The offset dependence of the net cross-relaxation rate σ_{net} requires offset corrections to be applied if quantitative information is to be extracted from ROESY spectra.

Therefore, separation of coherent J transfer (TOCSY) and transfer via cross relaxation is an important goal in the development of multiple pulse sequences used in these experiments. In this article, we give a summary of theoretical tools used to analyze the performance of multiple pulse sequences in this respect. We discuss approaches to obtain cross-relaxation-free TOCSY spectra and suppression of coherent transfer and longitudinal cross relaxation in ROESY spectra. Relations between J transfer, cross relaxation, and chemical exchange for molecules of different sizes are collected in Table 1 (since cross-relaxation rates are strongly

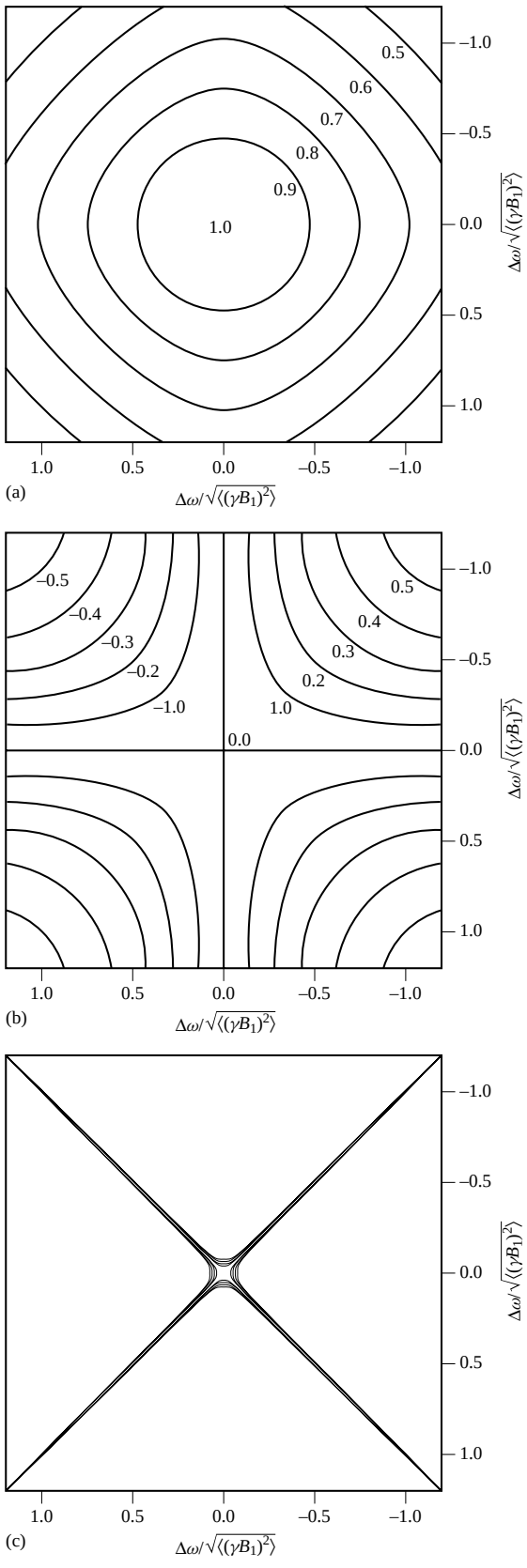

Figure 1 Simulation of the offset dependences of the weights of transverse (a) and longitudinal (b) cross relaxation and Hartmann–Hahn transfer (c) in CW ROESY.[11] In (c) the largest possible Hartmann–Hahn transfer is shown as a contour plot

Table 1 Relations between J Transfer, Cross Relaxation, and Chemical Exchange

	TOCSY	NOESY	ROESY	HSQC
(a) Large Molecules ($\omega\tau_c \gg 1$)				
J transfer		Zero for weakly coupled spins, optimally suppressed for strongly coupled spins	Suppression of J transfer and of longitudinal cross relaxation are conflicting goals	Good suppression of J transfer and both types of cross relaxation necessary and possible
Cross relaxation	Zero (clean TOCSY)	Pure		
Exchange	Fully operative	Fully operative	Fully operative	
(b) Medium-Sized Molecules ($\omega\tau_c \approx 1$)				
J transfer		Zero for weakly coupled spins, optimally suppressed for strongly coupled spins	Suppression of J transfer and maximization of transverse cross relaxation are conflicting goals	Application of NOESY yields complete suppression of cross relaxation and J transfer
Cross relaxation	Reduced (transverse cross relaxation cannot be suppressed)	Not applicable, since $\tau_{mix} = 0$		
Exchange	Fully operative	Fully operative	Fully operative	
(c) Small Molecules ($\omega\tau_c \ll 1$)				
J transfer		Zero for weakly coupled spins, optimally suppressed for strongly coupled spins	Suppression of J transfer as nearly equal longitudinal and transverse cross relaxation have the same sign	Application of NOESY suppresses J transfer in weakly coupled spin systems; cross relaxation cannot be suppressed
Cross relaxation	Small (cross relaxation rates do not compete with chemical shift differences)	Pure		
Exchange	Fully operative	Fully operative	Fully operative	

dependent on molecular weight, the possibility of separating cross relaxation from the other interactions is considered separately for small, medium sized, and large molecules). It is obvious from this table that for molecules of any size, longitudinal cross relaxation (NOE) can be observed without contributions from ROE or J transfer. Suppression of cross relaxation in TOCSY spectra is a problem for large molecules only. Suppression of TOCSY in ROESY spectra is necessary for molecules of any size. Chemical exchange cannot be suppressed in any experiment, but can be identified by its sign in ROESY spectra.

2 THEORY

2.1 Average Hamiltonian Theory

An arbitrary multiple pulse sequence can be represented formally by a time-dependent Hamiltonian $\hat{\mathcal{H}}(t)$. $\hat{\mathcal{H}}(t)$ can generally be represented by a series of constant Hamiltonians that act for finite intervals of time. Each Hamiltonian introduces a unitary transformation of the density matrix that is given by its propagator, and the overall effect of the multiple pulse sequence is given by the product of these propagators. Since the product of unitary transformations is again a unitary tranformation, the product of propagators can always be written as a single propagator. The Hamiltonian corresponding to this propagator is called the effective Hamiltonian $\hat{\mathcal{H}}_{\text{eff}}$ of the multiple pulse sequence. Average Hamiltonian theory[4–6] yields criteria indicating whether the effective Hamiltonian can be expressed as an 'average Hamiltonian' and whether the effective and the average Hamiltonian are the same. It also shows how the average Hamiltonian for a given $\hat{\mathcal{H}}(t)$ can be obtained. Average Hamiltonian theory is most useful if $\hat{\mathcal{H}}(t)$ fulfills two conditions:

1. $\hat{\mathcal{H}}(t)$ is periodic with a cycle time τ_{cyc}, i.e., $\hat{\mathcal{H}}(t + n\tau_{\text{cyc}}) = \hat{\mathcal{H}}(t)$;
2. the state of the spin system is only sampled at times $n\tau_{\text{cyc}}$.

These conditions are generally fulfilled for multiple pulse sequences used for TOCSY and ROESY. $\hat{\mathcal{H}}(t)$ is time-dependent during each cycle of the multiple pulse sequence, and the state of the spin system is interrogated only at multiples of the cycle times, i.e., at the end of the mixing time.

To apply average Hamiltonian theory to an arbitrary multiple pulse sequence, we first note that $\hat{\mathcal{H}}(t)$ can be decomposed into a constant part $\hat{\mathcal{H}}^0$, the Hamiltonian of the spin system in the absence of any rf irradiation, and a time-dependent part $\hat{\mathcal{H}}^1(t)$, which describes the action of the multiple pulse sequence:

$$\hat{\mathcal{H}}(t) = \hat{\mathcal{H}}^0 + \hat{\mathcal{H}}^1(t), \quad \hat{U}(t) = T \exp\left\{ -\mathrm{i} \int_0^t [\hat{\mathcal{H}}^0 + \hat{\mathcal{H}}^1(t')]\, \mathrm{d}t' \right\} \quad (1)$$

The propagator $\hat{U}(t)$ has been expressed as a time integral, as a generalization of the product of two propagators. The Dyson time-ordering operator[7,8] T formally expresses the fact that in the operator product, factors with different time arguments must be arranged in order of decreasing time from left to right. The propagator $\hat{U}^1(t)$ of $\hat{\mathcal{H}}^1(t)$ takes the form

$$\hat{U}^1(t) = T \exp\left[-\mathrm{i} \int_0^t \hat{\mathcal{H}}^1(t')\, \mathrm{d}t' \right] \tag{2}$$

Multiple pulse sequences with the property $\hat{U}^1(t) = 1$ for multiples of the cycle time ($t = n\tau_{\mathrm{cyc}}$) are called cyclic sequences. By definition, such sequences leave the state of the spin system unchanged after completion of a cycle. For such sequences and times $t = n\tau_{\mathrm{cyc}}$, it is a good approach to try to split $\hat{U}(t)$ into a product of two terms:

$$\hat{U}(\tau_{\mathrm{cyc}}) = \hat{U}^1(\tau_{\mathrm{cyc}})\hat{\tilde{U}}(\tau_{\mathrm{cyc}}) \tag{3}$$

By definition of cyclic sequences ($\hat{U}^1(\tau_{\mathrm{cyc}}) = 1$), $\hat{\tilde{U}}(\tau_{\mathrm{cyc}})$ alone describes the time evolution of the spin system for times $t = n\tau_{\mathrm{cyc}}$. $\hat{\tilde{U}}(\tau_{\mathrm{cyc}})$ is the propagator of the toggling-frame Hamiltonian $\hat{\tilde{\mathcal{H}}}^0(t)$, which is defined by transforming $\hat{\mathcal{H}}^0$ into the time-dependent coordinate system defined by the action of $\hat{\mathcal{H}}^1(t)$:

$$\hat{\tilde{\mathcal{H}}}^0(t) = [\hat{U}^1(t)^{-1}]\hat{\mathcal{H}}^0\hat{U}^1(t) \tag{4}$$

Looking at the time evolution of a density matrix $\hat{\sigma}(t)$, we see that this definition of $\hat{\tilde{\mathcal{H}}}^0(t)$ indeed yields a simplified description.[5] $\hat{\sigma}(t)$ can be expressed as

$$\hat{\sigma}(t) = \hat{U}^1(t)\hat{\tilde{\sigma}}(t)[\hat{U}^1(t)]^{-1} \tag{5}$$

Differentiation yields [note equation (2) and $\dot{\hat{U}}^1(t) = -\mathrm{i}\hat{\mathcal{H}}^1(t)\hat{U}^1(t)$]:

$$\begin{aligned}
&= \dot{\hat{U}}^1(t)\hat{\tilde{\sigma}}(t)[\hat{U}^1(t)]^{-1} + \hat{U}^1(t)\dot{\hat{\tilde{\sigma}}}(t)[\hat{U}^1(t)]^{-1} \\
&\quad + \hat{U}^1(t)\hat{\tilde{\sigma}}(t)\{[\hat{U}^1(t)]^{-1}\}^{\cdot} \\
&= -\mathrm{i}\hat{\mathcal{H}}^1(t)\hat{U}^1(t)\hat{\tilde{\sigma}}(t)[\hat{U}^1(t)]^{-1} + \hat{U}^1(t)\dot{\hat{\tilde{\sigma}}}(t)[\hat{U}^1(t)]^{-1} \\
&\quad + \mathrm{i}\hat{U}^1(t)\hat{\tilde{\sigma}}(t)[\hat{U}^1(t)]^{-1}\hat{\mathcal{H}}^1(t) \\
&= -\mathrm{i}[\hat{\mathcal{H}}^1(t), \hat{U}^1(t)\hat{\tilde{\sigma}}(t)[\hat{U}(t)]^{-1}] + \hat{U}^1(t)\dot{\hat{\tilde{\sigma}}}(t)[\hat{U}^1(t)]^{-1}
\end{aligned} \tag{6}$$

Inserting the definition of $\hat{\mathcal{H}}(t)$ [equation (1)] and equation (5) into the Liouville–von Neumann equation, we obtain for $\dot{\hat{\sigma}}(t)$

$$\dot{\hat{\sigma}} = -\mathrm{i}[\hat{\mathcal{H}}^0 + \hat{\mathcal{H}}^1(t), \hat{U}^1(t)\hat{\tilde{\sigma}}(t)[\hat{U}^1(t)]^{-1}] \tag{7}$$

Equating equation (6) and equation (7), the commutators involving $\hat{\mathcal{H}}^1(t)$ cancel, and we obtain,

$$\hat{U}^1(t)\dot{\hat{\tilde{\sigma}}}(t)[\hat{U}^1(t)]^{-1} = -\mathrm{i}[\hat{\mathcal{H}}^0, \hat{U}^1(t)\hat{\tilde{\sigma}}(t)[\hat{U}^1(t)]^{-1}] \tag{8}$$

Multiplying this equation by $[(\hat{U}^1(t)]^{-1}$ from the left and by $\hat{U}^1(t)$ from the right yields

$$\begin{aligned}
\dot{\hat{\tilde{\sigma}}}(t) &= -\mathrm{i}\{[\hat{U}^1(t)]^{-1}\hat{\mathcal{H}}^0\hat{U}^1(t)\hat{\tilde{\sigma}}(t) - \hat{\tilde{\sigma}}(t)[\hat{U}^1(t)]^{-1}\hat{\mathcal{H}}^0\hat{U}^1(t)\} \\
&= -\mathrm{i}[[\hat{U}^1(t)]^{-1}\hat{\mathcal{H}}^0\hat{U}^1(t), \hat{\tilde{\sigma}}(t)] = -\mathrm{i}[\hat{\tilde{\mathcal{H}}}^0(t), \hat{\tilde{\sigma}}(t)]
\end{aligned} \tag{9}$$

The formal solution of this equation is [note that $\hat{\tilde{\sigma}}(0) = \hat{\sigma}(0)$]

$$\hat{\tilde{\sigma}}(t) = \hat{\tilde{U}}(t)\hat{\tilde{\sigma}}(0)[\hat{\tilde{U}}(t)]^{-1} = \hat{\tilde{U}}(t)\hat{\sigma}(0)[\hat{\tilde{U}}(t)]^{-1} \tag{10}$$

where

$$\hat{\tilde{U}}(t) = T \exp\left[-\mathrm{i} \int_0^t \hat{\tilde{\mathcal{H}}}^0(t')\, \mathrm{d}t' \right] = \exp(-\mathrm{i}\hat{\mathcal{H}}_{\mathrm{eff}}t) \tag{11}$$

Inserting equation (10) into equation (5), we see that the propagator given in equation (3) is a valid decomposition of $\hat{U}(t)$.

As has been mentioned, $\hat{\tilde{U}}(\tau_{\mathrm{cyc}})$ yields a complete description of the time evolution of the spin system under cyclic sequences. $\hat{\mathcal{H}}_{\mathrm{eff}}$ is the effective Hamiltonian. In general, the effective Hamiltonian has the form

$$\hat{\mathcal{H}}_{\mathrm{eff}} = \hat{\mathcal{H}}_{\mathrm{eff}}^{\mathrm{lin}} + \hat{\mathcal{H}}_{\mathrm{eff}}^{\mathrm{bil}} + \hat{O}(\geq 3) \tag{12}$$

The terms that are linear in spin operators are collected in $\hat{\mathcal{H}}_{\mathrm{eff}}^{\mathrm{lin}}$.

$$\hat{\mathcal{H}}_{\mathrm{eff}}^{\mathrm{lin}} = \sum_k \sum_\mu c_{k\mu}\hat{I}_{k\mu} \tag{13}$$

with $\mu = x$, y, or z. With the help of the coefficients $c_{k\mu}$, the effective offset of spin k may be defined as

$$\Omega_k^{\mathrm{eff}} = \sqrt{\sum_\mu |c_{k\mu}|^2} \tag{14}$$

Terms that are bilinear in spin operators are summarized in $\hat{\mathcal{H}}_{\mathrm{eff}}^{\mathrm{bil}}$, which may be used to define effective coupling constants J_{kl}^{eff}. All terms that contain products of three or more spin operators are represented in Equation (12) by $\hat{O}(\geq 3)$.

$\hat{\mathcal{H}}_{\mathrm{eff}}$ can be expanded with the help of the Magnus expansion.[5,9] The zeroth-order term in the Magnus expansion is the average Hamiltonian $\hat{\mathcal{H}}$, which is given by

$$\hat{\bar{H}} = \frac{1}{\tau_{\mathrm{cyc}}} \int_0^{\tau_{\mathrm{cyc}}} \hat{\tilde{\mathcal{H}}}^0(t')\, \mathrm{d}t' \tag{15}$$

2.2 Hartmann–Hahn Transfer

Let us consider a system of two coupled spins $\frac{1}{2}$. The Hamiltonian for this system can be written as a sum of the Zeeman part $\hat{\mathcal{H}}_{\mathrm{Z}}$ and a coupling part $\hat{\mathcal{H}}_J$:

$$\hat{\mathcal{H}}_0 = \hat{\mathcal{H}}_Z + \hat{\mathcal{H}}_J$$
$$= \Omega_1 \hat{I}_{1z} + \Omega_2 \hat{I}_{2z} + 2\pi J(\hat{I}_{1x}\hat{I}_{2x} + \hat{I}_{1y}\hat{I}_{2y} + \hat{I}_{1z}\hat{I}_{2z}) \quad (16)$$

Assuming the spin system to be prepared at $t = 0$ with spin 1 polarized along z and spin 2 saturated, the initial density operator can be represented as $\hat{\rho}(0) = \hat{I}_{1z}$. For the analysis of Hartmann–Hahn transfer, it is more convenient to decompose $\hat{\mathcal{H}}_0$ into the terms $\hat{\mathcal{H}}_0'$ and $\hat{\mathcal{H}}_0''$:

$$\hat{\mathcal{H}}_0' = (\Omega_1 - \Omega_2)\frac{\hat{I}_{1z} - \hat{I}_{2z}}{2} + 2\pi J(\hat{I}_{1x}\hat{I}_{2x} + \hat{I}_{1y}\hat{I}_{2y}) \quad (17a)$$

$$\hat{\mathcal{H}}_0'' = (\Omega_1 + \Omega_2)\frac{\hat{I}_{1z} + \hat{I}_{2z}}{2} + 2\pi J\hat{I}_{1z}\hat{I}_{2z} \quad (17b)$$

$\hat{\mathcal{H}}_0''$ does not influence the time evolution of the density operator, and can be ignored, since it commutes with both $\hat{\mathcal{H}}_0'$ and $\hat{\rho}(0) = \hat{I}_{1z}$.

The evolution of $\hat{\rho}(t)$ due to the remaining operator $\hat{\mathcal{H}}_0'$ is strongly dependent on the ratio of the coupling constant J with the difference $\Delta\Omega = (\Omega_1 - \Omega_2)$. The evolution of $\hat{\rho}(t)$ is presented in Figure 2 with numerical simulations for the cases $|\Delta\Omega| \gg |2\pi J_{12}|$ [(a): weak coupling limit], $|\Delta\Omega| \approx |2\pi J_{12}|$ [(b): strong coupling], and $|\Delta\Omega| \ll |2\pi J_{12}|$ [(c): Hartmann–Hahn limit].

In the weak coupling limit (Figure 2a), the density operator of the spin system does not evolve, so the polarization of spin 1 is invariant.

In the case of strong coupling (Figure 2b), the density operator evolves in an oscillatory manner. Starting from $\hat{\rho}(0) = \hat{I}_{1z}$, terms $\hat{I}_{2z}$ as well as $\hat{I}_{1y}\hat{I}_{2x} - \hat{I}_{1x}\hat{I}_{2y}$ and $\hat{I}_{1x}\hat{I}_{2x} + \hat{I}_{1y}\hat{I}_{2y}$ are created periodically. Thus, a part of the initial polarization of spin 1 ($\hat{I}_{1z}$) is periodically transferred to spin 2 ($\hat{I}_{2z}$).

In the Hartmann–Hahn limit (Figure 2c), only the terms $\hat{I}_{2z}$ and $\hat{I}_{1y}\hat{I}_{2x} - \hat{I}_{1x}\hat{I}_{2y}$ are formed, starting from $\hat{\rho}(0) = \hat{I}_{1z}$. The characteristic property of this limiting case is the complete transfer of polarization between the coupled spins after a time $1/2J$.

In the general case, the rate and maximum efficiency of transfer via scalar coupling in multiple pulse sequences is a complicated function of the exact sequence.[10,11] Such cases can be described using effective offsets $\Omega_{\text{eff},1}$ and $\Omega_{\text{eff},2}$ as well as an effective coupling constant J_{12}^{eff} (cf. equations (12)–(14)). Fulfillment of the Hartmann–Hahn condition $|\Delta\Omega| \ll |2\pi J_{12}|$ is a necessary condition for the occurrence of Hartmann–Hahn transfer between two spins. Under the influence of a multiple pulse sequence, the Hartmann–Hahn condition takes the form $|\Delta\Omega_{\text{eff}}| \ll |2\pi J_{12}^{\text{eff}}|$. For spins that have similar chemical shift, corresponding to cross peaks along the diagonal of a 2D spectrum, $\Delta\Omega_{\text{eff}}$ can be expressed as $\Delta\Omega_{\text{eff}} = (\Delta\Omega_{\text{eff}}/\Delta\Omega)\,\Delta\Omega \approx (\partial\Omega_{\text{eff}}/\partial\Omega)\,\Delta\Omega = \lambda\,\Delta\Omega$. Thus, the slope λ of Ω_{eff} as a function of Ω gives a measure for the occurrence of Hartmann–Hahn transfer near the diagonal. λ is identical to the scaling factor introduced by Waugh[12] in the context of heteronuclear decoupling.

2.3 Invariant Trajectory Approach

Consider an uncoupled spin k subject to the action of an arbitrary multiple pulse sequence consisting of a

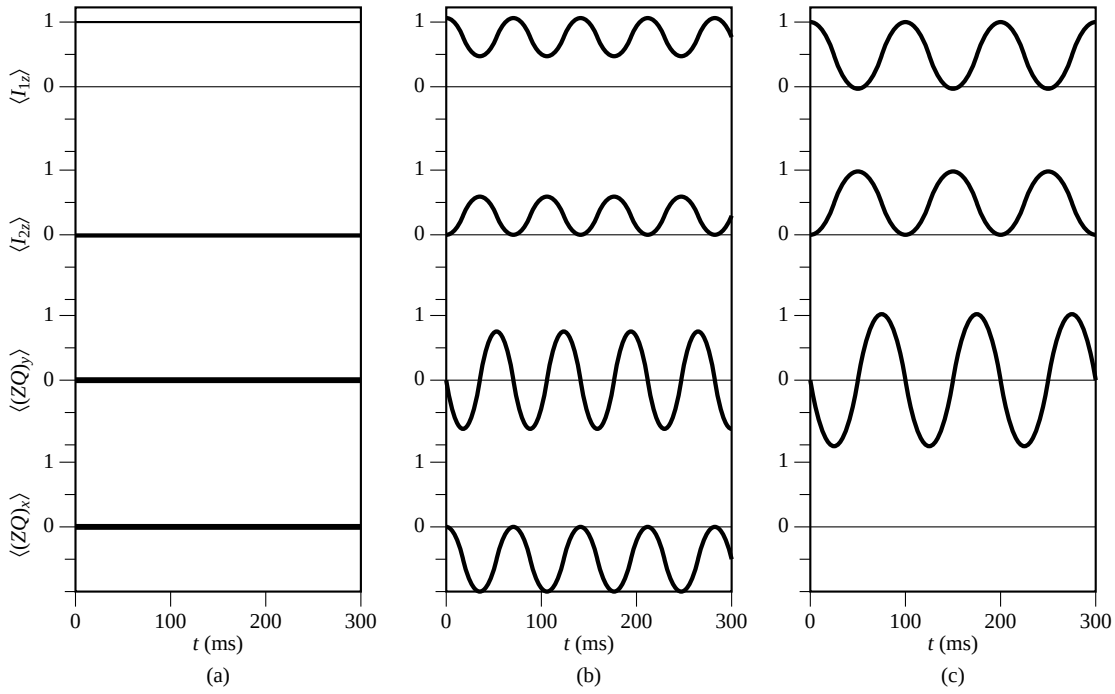

Figure 2 Time evolution of the initial density operator $\hat{\rho}(0) = \hat{I}_{1z}$ in a two-spin system with a coupling of 10 Hz under the influence of the Hamiltonian $\hat{\mathcal{H}}_0$. Curves from top to bottom show the expectation values of $\hat{I}_{1z}$, $\hat{I}_{2z}$, $\hat{I}_{1y}\hat{I}_{2x} - \hat{I}_{1x}\hat{I}_{2y} = (\text{ZQ})_y$ and $\hat{I}_{1x}\hat{I}_{2x} + \hat{I}_{1y}\hat{I}_{2y} = (\text{ZQ})_x$. (a) In the weak coupling limit ($|\Delta\nu| = 1000\,\text{Hz} \gg |J_{12}|$), the polarization of $\hat{I}_{1z}$ is invariant. (b) In the case of strong coupling ($|\Delta\nu| = 10\,\text{Hz} = |J_{12}|$), the polarization $\hat{I}_{1z}$ is partly transferred to $\hat{I}_{2z}$. (c) In the Hartmann–Hahn limit ($|\Delta\nu| = 0\,\text{Hz} \ll |J_{12}|$), transfer of $\hat{I}_{1z}$ to $\hat{I}_{2z}$ is complete for odd multiples of $1/2J$

basic sequence that is repeated during the mixing time of an experiment. The trajectory followed by a magnetization vector during the basic sequence is called invariant[13] if the orientations of the vector at the beginning and end of the basic sequence are the same. By definition, magnetization that moves on this trajectory does not experience a net rotation during a complete basic sequence. All other magnetization components experience a net rotation after each basic sequence, and are dephased by rf inhomogeneity during the repetitions of the basic sequence. The extent of dephasing depends on the effective field produced by the multiple pulse sequence, the mixing time, and the rf inhomogeneity of the probe. In this case, only the behavior of magnetization moving on the invariant trajectory need be considered in order to understand the properties of the multiple pulse sequence. The method of invariant trajectories allows an easy calculation of the effective cross relaxation rate σ_{eff} that is active during a multiple pulse sequence. For a pair of spins with identical offsets, σ_{eff} is given by

$$\sigma_{\mathrm{eff}} = w_{\mathrm{l}}\sigma_{\mathrm{NOE}} + w_{\mathrm{t}}\sigma_{\mathrm{ROE}} \tag{18}$$

where the weights w_{l} and w_{t} of longitudinal and transverse cross relaxation are given by the average squared longitudinal and transverse components of the invariant trajectory:[13]

$$w_{\mathrm{l}} = \frac{1}{\tau_{\mathrm{cyc}}}\int_0^{\tau_{\mathrm{cyc}}} n_{0,z}^2(t)\,\mathrm{d}t = \langle n_{0,z}^2\rangle$$
$$w_{\mathrm{t}} = \frac{1}{\tau_{\mathrm{cyc}}}\int_0^{\tau_{\mathrm{cyc}}} (n_{0,x}+n_{0,y})^2(t)\,\mathrm{d}t = \langle n_{0,(x,y)}^2\rangle \tag{19}$$

Thus, the effective cross relaxation during a multiple pulse sequence is a linear combination of the longitudinal and transverse cross relaxation rates σ_{NOE} and σ_{ROE}, which are properties of the sample, with the weights $w_{\mathrm{l}}(\Omega)$ and $w_{\mathrm{t}}(\Omega)$, which are properties of the sequence. As an example, invariant trajectories of the phase-alternating ROESY sequence $(\pi_x\pi_{-x})_n$ for two offsets are shown in Figure 3. From the x, y, and z components of the invariant trajectories of this sequence (top of Figure 3), the weights of longitudinal and transverse cross relaxation can be obtained (bottom).

2.4 Connection between the Invariant Trajectory Approach and AHT

For basic sequences that create a nonzero effective field $B_{\mathrm{eff},k}$ (spin lock sequences), the orientation of the invariant trajectory is given by the orientation of $B_{\mathrm{eff},k}$.

However, there is also a more fundamental connection between invariant trajectories and effective fields. In the following discussion, we shall show that for any multiple pulse sequence, there is a relationship between the time-averaged z component of the invariant trajectory $\langle n_{0,z}\rangle$ and the slope λ of the effective field as a function of the offset.[14] This result is central to the development of ROESY sequences, since the weight of longitudinal cross relaxation is proportional to $\langle n_{0,z}^2\rangle$, while λ is a measure for the occurrence of Hartmann–Hahn transfer along the diagonal of the 2D spectrum.

In order to calculate $\lambda = \partial\Omega_{\mathrm{eff}}/\partial\Omega$ as the limit $\lim_{\Delta\Omega\to 0} \Delta\Omega_{\mathrm{eff}}/\Delta\Omega = \lim_{\Delta\Omega\to 0} (\Omega_{\mathrm{eff}} - \Omega'_{\mathrm{eff}})/\Delta\Omega$, the effective propagator $\hat{U}(\tau_{\mathrm{cyc}})$ after one cycle of duration τ_{cyc} of a repetitive multiple pulse sequence is calculated:

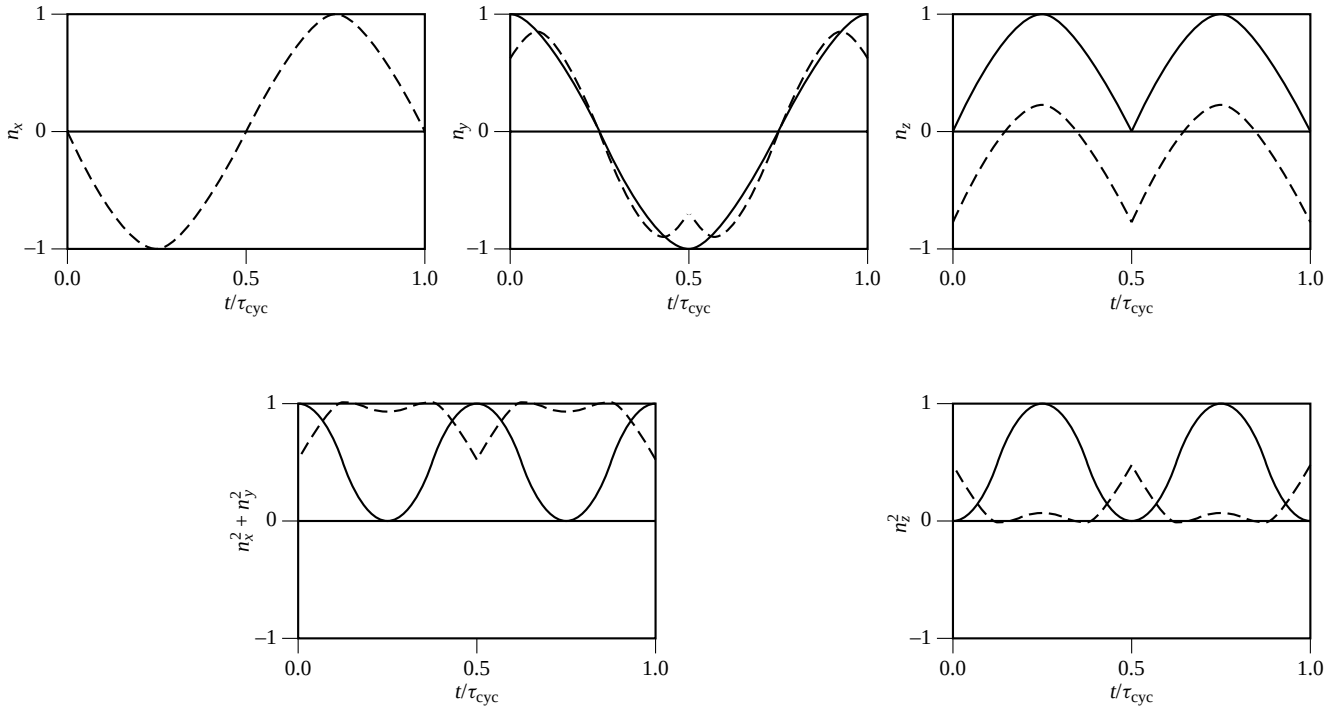

Figure 3 Invariant trajectories for the sequence $(\pi_x\pi_{-x})_n$ for an on-resonant spin (solid lines) and for an off-resonant spin with offset $\Omega{=}\gamma B_1$ (dashed lines). The x, y, and z components, together with the squares of the longitudinal and transverse components, are shown. For off-resonant spins, the sequence locks in the (y,z) plane. The weights w_{t} and w_{l} of transverse and longitudinal cross relaxation are calculated as the average square transverse and average square longitudinal components of the invariant trajectories. For the on-resonant spin, $\langle n_x^2 + n_y^2\rangle = \langle n_z^2\rangle = 0.5$, and for the off-resonant spin, $w_t = \langle n_x^2 + n_y^2\rangle = 0.88$ and $w_l = \langle n_z^2\rangle = 0.12$

$$\hat{U}(\tau_{cyc}) = \prod_j \hat{U}_j = \prod_j \exp(-i\hat{\mathcal{H}}_j\tau_j) = \exp(-i\hat{\mathcal{H}}_{eff}\tau_{cyc})$$
$$= \exp[-i\Omega_{eff}\tau_{cyc}\hat{I}_0(0)] \quad (20)$$

$\hat{U}(\tau_{cyc})$ is given by the time-ordered product of individual pulse propagators $\hat{U}_j$, which represent the propagators for individual pulses of duration τ_j and Hamiltonian $\hat{\mathcal{H}}_j$. $\hat{\mathcal{H}}_{eff}$ is the effective Hamiltonian for one cycle. For a system consisting of a single spin-$\frac{1}{2}$, the effective Hamiltonian $\hat{\mathcal{H}}_{eff}$ may be written as $\Omega_{eff}\hat{I}_0(0)$, where Ω_{eff} is the effective chemical shift and $\hat{I}_0(0)$ defines the invariant trajectory[13] at time $t = 0$:

$$\hat{\mathcal{H}}_{eff} = \Omega_{eff}\hat{I}_0(0) \quad (21)$$

To calculate the effective chemical shift Ω'_{eff} at the offset $\Omega' = \Omega + \Delta\Omega$, the $\hat{\mathcal{H}}_j$ are modified by $\hat{\mathcal{H}}_1 = \Delta\Omega\hat{I}_z : \hat{\mathcal{H}}'_j = \hat{\mathcal{H}}_j + \hat{\mathcal{H}}_1 = \hat{\mathcal{H}}_j + \Delta\Omega\hat{I}_z$. The resulting propagator,

$$\hat{U}'(\tau_{cyc}) = \exp(-i\hat{\mathcal{H}}'_{eff}\tau_{cyc}) = \exp[-i\Omega'_{eff}\tau_{cyc}\hat{I}'_0(0)] \quad (22)$$

may be divided into two factors:[4,5]

$$\hat{U}'(\tau_{cyc}) = \hat{U}(\tau_{cyc})\hat{U}_1(\tau_{cyc}) \quad (23)$$

with

$$\hat{U}_1(\tau_{cyc}) = \exp(-i\hat{\mathcal{H}}_{1,eff}\tau_{cyc}) = T\exp\left\{-i\left[\int_0^{\tau_{cyc}} \tilde{\hat{\mathcal{H}}}_1(t)\,dt\right]\right\} \quad (24)$$

where the toggling frame Hamiltonian is given by $\tilde{\hat{\mathcal{H}}}_1(t) = \hat{U}^{-1}(t)\Delta\Omega\hat{I}_z\hat{U}(t)$. In zeroth-order average Hamiltonian theory, equation (24) simplifies to

$$\hat{U}_1(\tau_{cyc}) = \exp(-i\hat{\mathcal{H}}_{eff,1}\tau_{cyc}) = \exp\left\{-i\left[\int_0^{\tau_{cyc}} \tilde{\hat{\mathcal{H}}}_1(t)\,dt\right]\right\} \quad (25)$$

This simplification is justified in the limit $\Delta\Omega \to 0$. Expansion of $\hat{U}'(\tau_{cyc})$, equation (23), according to the Baker–Campbell–Haussdorff formula to first order yields

$$\hat{U}'(\tau_{cyc}) = \exp\{-i(\hat{\mathcal{H}}_{eff}\tau_{cyc} + \hat{\mathcal{H}}_{eff,1}\tau_{cyc}) - \tfrac{1}{2}[\hat{\mathcal{H}}_{eff}, \hat{\mathcal{H}}_{eff,1}]\tau_{cyc}^2\} \quad (26)$$

Comparing equations (22) and (26), we find

$$\hat{\mathcal{H}}'_{eff} = \Omega'_{eff}\hat{I}'_0(0) = (\hat{\mathcal{H}}_{eff} + \hat{\mathcal{H}}_{eff,1}) - \tfrac{1}{2}i[\hat{\mathcal{H}}_{eff}, \hat{\mathcal{H}}_{eff,1}]\tau_{cyc} \quad (27a)$$
$$= \Omega_{eff}\hat{I}_0(0) + \Omega_{eff,1}\hat{I}_1(0)$$
$$-\tfrac{1}{2}i\Omega_{eff}\Omega_{eff,1}[\hat{I}_0(0), \hat{I}_1(0)]\tau_{cyc} \quad (27b)$$

where $\hat{I}_1(0)$ is defined as $\hat{\mathcal{H}}_{eff,1}/\Omega_{eff,1}$

For $\Delta\Omega \ll \Omega_{eff}$ and $\Delta\Omega\ \tau_{cyc} \ll 1$, only terms parallel to $\hat{I}_0(0)$ contribute to the magnitude of the effective field Ω'_{eff} at offset Ω'. Since the commutator $[\hat{I}_0(0),\hat{I}_1(0)]$ is perpendicular to $\hat{I}_0(0)$, the last term in equation (27b) may be neglected. To find the contribution of the second term of equation (27b), we calculate the projection of $\Omega_{eff,1}\hat{I}_1(0)$ onto the direction of $\hat{I}_0(0)$. This is given by $\Omega_{eff,1}$ Tr $\{\hat{I}_0(0)\hat{I}_1(0)\}$. Thus, the magnitude of the effective field Ω'_{eff} at offset Ω' is given by

$$\Omega'_{eff} = \Omega_{eff} + \Omega_{eff,1}\mathrm{Tr}\{\hat{I}_0(0)\hat{I}_1(0)\} \quad (28)$$

For $\Delta\Omega \to 0$, the slope λ can be expressed as

$$\lambda = \frac{\Omega'_{eff} - \Omega_{eff}}{\Delta\Omega} = \frac{\Omega_{eff,1}}{\Delta\Omega}\mathrm{Tr}\{\hat{I}_0(0)\hat{I}_1(0)\} \quad (29)$$

According to equation (25), $\Omega_{eff,1}\hat{I}_1(0) = \hat{\mathcal{H}}_{eff,1}$ is given by

$$\Omega_{eff,1}\hat{I}_1(0) = \frac{1}{\tau_{cyc}}\int_0^{\tau_{cyc}} \tilde{\hat{\mathcal{H}}}_1(t)\,dt$$
$$= \frac{1}{\tau_{cyc}}\int_0^{\tau_{cyc}} \hat{U}^{-1}(t)\Delta\Omega\hat{I}_z\hat{U}(t)\,dt \quad (30)$$

Inserting equation (30) into equation (29), we find

$$\lambda = \frac{1}{\tau_{cyc}}\mathrm{Tr}\left\{\hat{I}_0(0)\int_0^{\tau_{cyc}} \hat{U}^{-1}(t)\hat{I}_z\hat{U}(t)\,dt\right\}$$
$$= \frac{1}{\tau_{cyc}}\int_0^{\tau_{cyc}} \mathrm{Tr}\{\hat{I}_0(0)\hat{U}^{-1}(t)\hat{I}_z\hat{U}(t)\}\,dt$$
$$= \frac{1}{\tau_{cyc}}\int_0^{\tau_{cyc}} \mathrm{Tr}\{\hat{U}(t)\hat{I}_0(0)\hat{U}^{-1}(t)\hat{I}_z\}\,dt$$
$$= \frac{1}{\tau_{cyc}}\int_0^{\tau_{cyc}} \mathrm{Tr}\{\hat{I}_0(t)\hat{I}_z\}\,dt$$
$$= \frac{1}{\tau_{cyc}}\int_0^{\tau_{cyc}} n_{0,z}(t)\,dt = \langle n_{0,z}\rangle \quad (31)$$

where $n_{0,z}(t)$ is the z component of the invariant trajectory $\hat{I}_0(t)$. The general result of equation (31) can be stated as follows: the slope of Ω_{eff} with respect to Ω is identical to the average z component of the invariant trajectory. Equation (28) relates the parameter λ central to the theory of spin decoupling to the invariant trajectory approach. We shall return to this result in Section 3.2.

3 SEPARATION OF HARTMANN–HAHN TRANSFER AND CROSS RELAXATION

3.1 Cross-Relaxation Compensated TOCSY Experiments

The TOCSY experiment is used to achieve transfer among spins in scalar-coupled spin systems. To achieve efficient TOCSY transfer, the effective fields experienced by the spins must be matched over the offset range of interest ($\lambda \ll 1$). Several multiple pulse sequences have been proposed to achieve this goal.[1,11,15–18] During these multiple pulse sequences, longitudinal and transverse cross-relaxation rates σ_{NOE} and σ_{ROE} are active and contribute to the effective cross relaxation rate σ_{eff} with the weights w_l and w_t [equation (18)]. Since σ_{NOE} and σ_{ROE} have the same sign for small molecules, it follows that cross-relaxation contributions cannot be suppressed near the diagonal of TOCSY spectra of small molecules, since, whatever w_t and w_l might be, the terms in equation (18) will always add to yield a nonvanishing σ_{eff}. Fortunately, cross-relaxation rates of such molecules are small, so that artifacts due to cross relaxation are rarely observed in the relatively short mixing times used.

As shown in Figure 4(a), y magnetization of on-resonant spins entering the $90°_x180°_y90°_x$ composite pulse of a MLEV sequence spends equal amounts of time along longitudinal and transverse directions; therefore, $w_t = w_l = \frac{1}{2}$. Since

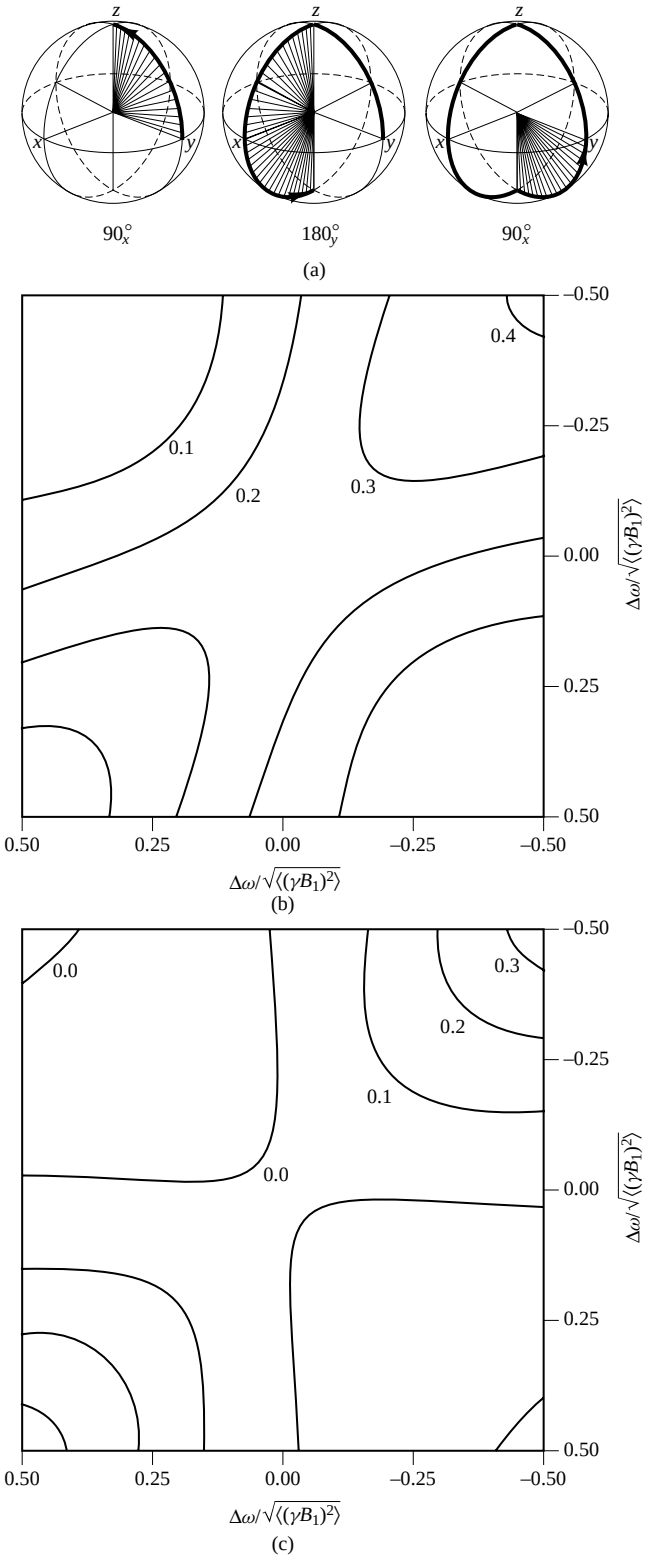

Figure 4 (a) Invariant trajectory starting from y magnetization for the $90^\circ_x 180^\circ_y 90^\circ_x$ composite pulse of the MLEV sequence for on-resonant irradiation. In (b) and (c), the offset dependence of the effective cross-relaxation rate σ_{eff} is shown in units of σ_{eff} in the spin diffusion limit. On-resonance, longitudinal and transverse cross relaxation have equal weights ($w_l = w_t = \frac{1}{2}$). Therefore, a net cross-relaxation rate of $\frac{1}{4}\sigma_{\text{ROE}}$ is observed for two on-resonant spins during this sequence for a molecule in the spin diffusion limit (b). Introduction of delays of length $\Delta = \tau_{90}$ in CLEAN MLEV,[19] $90^\circ_x \Delta 180^\circ_y \Delta 90^\circ_x$, results in suppression of cross relaxation on-resonance (c)

$\sigma_{NOE} = 0$ for medium sized molecules, a cross relaxation contribution $\frac{1}{2}\sigma_{ROE}$ results for TOCSY spectra obtained with this mixing sequence. This contribution cannot be suppressed, since this would require $w_t = 0$, which cannot be realized for any multiple pulse sequence. In the case of large molecules ($\sigma_{ROE}/\sigma_{NOE} = -2$), cross-relaxation rates are large, and cross relaxation can therefore compete with TOCSY transfer, leading to artifacts. It follows from equation (19) that for $w_t \approx w_l$, the contribution $w_t\sigma_{ROE}$ of transverse cross relaxation outweighs $w_l\sigma_{NOE}$, and a residual ROE contribution is therefore observed in TOCSY spectra of large molecules. The net cross-relaxation rate of this sequence for molecules in the spin diffusion limit is displayed in Figure 4(b) in units of σ_{ROE}. On resonance, ROESY cross peaks of one-quarter maximum intensity are expected to appear. From the invariant trajectory of the $90^\circ_x 180^\circ_y 90^\circ_x$ composite pulse (Figure 4a), there follows a straightforward way to eliminate this contribution for large molecules. If delays of appropriate duration ($\Delta = \tau_{90}$ for $\sigma_{ROE}/\sigma_{NOE} = -2$) are introduced into the MLEV scheme at positions where the magnetization is longitudinal, w_t and w_l can be modified such that ROE and NOE contributions cancel each other. Figure 4(c) shows the offset dependence of the cross-relaxation rate in the so-called CLEAN TOCSY experiment[19] obtained in this way. Cross relaxation is completely suppressed on-resonance in this experiment, while residual ROE contributions remain along the diagonal of the 2D spectrum.

While the introduction of delays is the most straightforward approach to suppress cross relaxation, and has been used frequently,[19,20] it suffers from an increase in the rf power dissipated in the sample (at constant average field strength γB_1), since the introduction of delays into any multiple pulse sequence lowers the duty ratio. This undesired effect is alleviated in more modern approaches to obtain cross relaxation compensated TOCSY mixing sequences. These approaches make use of crafted pulses to achieve a proper weighting of NOE and ROE during the multiple pulse sequence. Either the individual pulses of an existing TOCSY sequence are replaced by shaped pulses,[21] or TOCSY mixing sequences are optimized from scratch with the required weighting of NOE and ROE as a constraint,[22–24] resulting in sequences such as CITY[22] and TOWNY.[23] An example of a cross-relaxation compensated TOCSY spectrum, obtained using a MLEV mixing sequence consisting of shaped 90° pulses, is displayed in Figure 5.

An alternative approach to separate Hartmann–Hahn transfer and ROE was suggested by Ravikumar and Bothner-By.[25] It relies on the characteristic time evolution of coherent and incoherent magnetization transfer. However, the separation remains incomplete, since cross relaxation and coherent transfer both contain zero-frequency contributions.

3.2 Suppression of Hartmann–Hahn Transfer in ROESY Experiments

Using equation (31), which relates λ to $\langle n_{0,z}\rangle$, a relation between λ and the weight of longitudinal cross relaxation $w_l = \langle n_{0,z}^2\rangle$ can be derived for cross peaks near the diagonal. As the inequality $\langle n_{0,z}^2\rangle \geq \langle n_{0,z}\rangle^2$ always holds, it follows immediately that

$$w_l \geq \lambda^2 \tag{32}$$

This inequality shows that the suppression of longitudinal cross relaxation (w_l = min.!) and of TOCSY transfer (λ = max.!) are conflicting goals. Suppression of longitudinal cross relaxation can be achieved only if TOCSY transfer is allowed, and vice versa—or, there is no ROESY without NOESY and without TOCSY. The best a sequence can do is.

$$w_l = \lambda^2 \tag{33}$$

This is only possible if $n_{0,z}(t)$ is constant during τ_{cyc}, as is the case in CW ROESY.[2,26,27] The latter can be described analytically in the following way. The invariant trajectory is static and has the orientation

$$\boldsymbol{n}_0 = \cos\theta \boldsymbol{e}_z + \sin\theta \boldsymbol{e}_x, \quad \text{with } \tan\theta = \frac{\gamma B_1}{\Omega - \Omega_{rf}} \tag{34}$$

where γB_1 is the spin lock field strength, θ is the lock angle as measured off the z axis, and Ω_{rf} is an offset frequency of the CW irradiation. The weights for longitudinal (w_l) and transverse (w_t) cross relaxation along the diagonal are

$$w_l = \cos^2\theta, \quad w_t = \sin^2\theta \tag{35}$$

The effective chemical shift Ω_{eff} is given by

$$\Omega_{eff} = \sqrt{(\gamma B_1)^2 + (\Omega - \Omega_{rf})^2} \tag{36}$$

and the scaling $\lambda_{CW} = \partial\Omega_{eff}/\partial\Omega$ of the chemical shift of this sequence is

$$\lambda_{CW} = \frac{\partial\Omega_{eff}}{\partial\Omega} = \frac{\Omega - \Omega_{rf}}{\sqrt{(\gamma B_1)^2 + (\Omega - \Omega_{rf})^2}} = \cos\theta = \sqrt{w_l} \tag{37}$$

Thus, CW ROESY has the best properties with respect to the simultaneous suppression of NOE and TOCSY that are possible, since equation (33) is fulfilled. For any w_t, there is no better ROESY sequence with respect to the goal of suppressing longitudinal cross relaxation and TOCSY simultaneously. In practice, a compromise must be made between the efficiency of ROESY transfer (minimization of w_l) and the degree of suppression of coherent transfer (maximization of λ). The large variation in w_l and w_t over the spectral range in CW ROESY is a strong drawback of this sequence. From an experimental point of view, an additional requirement is that w_t be uniform over the spectral width and λ not be scaled beyond a certain degree over the spectral width. A number of approaches have been proposed to address this goal.

3.2.1 Sequences Composed of CW Irradiations

The application of a very strong spin lock field in a ROESY experiment yields a very smooth offset dependence in CW ROESY, as displayed in Figure 6(a) (left). However, the application of such strong fields is prohibitive because of serious Hartmann–Hahn transfer (Figure 6(a), right). Therefore, judicious choice of the spin lock field strength is important, as shown in Figure 6(b).[26] Furthermore, coherent transfer is much more dependent on the position of the rf irradiation frequency than cross relaxation. Therefore, coherent transfer can be reduced by judicious placement of the irradiation position (Figure 6c).[26,28] However, optimal placement of the transmitter offset requires prior knowledge of the coupling networks that can lead to TOCSY transfer.

Without such prior knowledge, the transmitter offset has to be placed outside the spectral region according to equation (37) in order to avoid Hartmann–Hahn matching between any two spins. However, this results in a strong dependence of the net cross-relaxation rate on Ω, which renders the interpretation of the spectra difficult. Still, the optimal behavior of CW irradiation with respect to TOCSY suppression renders sequences employing stretches of CW irradiation attractive.

Two related approaches have been developed to deal with the stated problem. In the first, proposed by Cavanagh and Keeler,[29] the transmitter offset is swept through the offset range of the spectrum as depicted in Figure 7(a). This method avoids continuous irradiation at any one frequency, and therefore avoids extended periods of Hartmann–Hahn matching. However, the offset dependence of the cross-relaxation rate of this sequence has not been published, and only qualitative interpretations of such spectra appear feasible at this time. Furthermore, the programming of the frequency sweep is rather demanding from an experimental point of view.

The second approach to modify CW ROESY to obtain ROESY spectra with suppression of TOCSY transfer—the use of JS ROESY ('jump symmetrized') sequences—makes use of

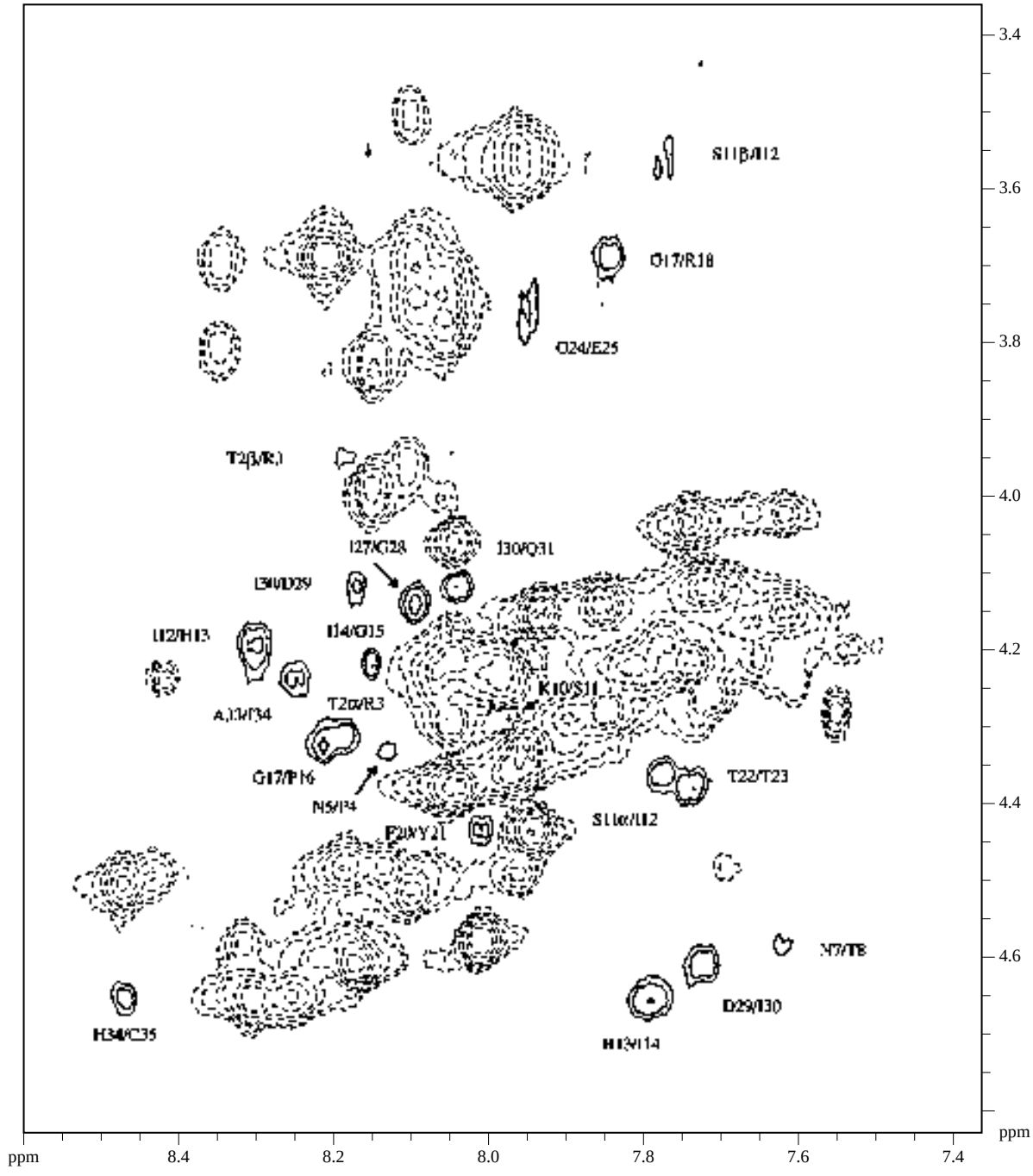

(a)

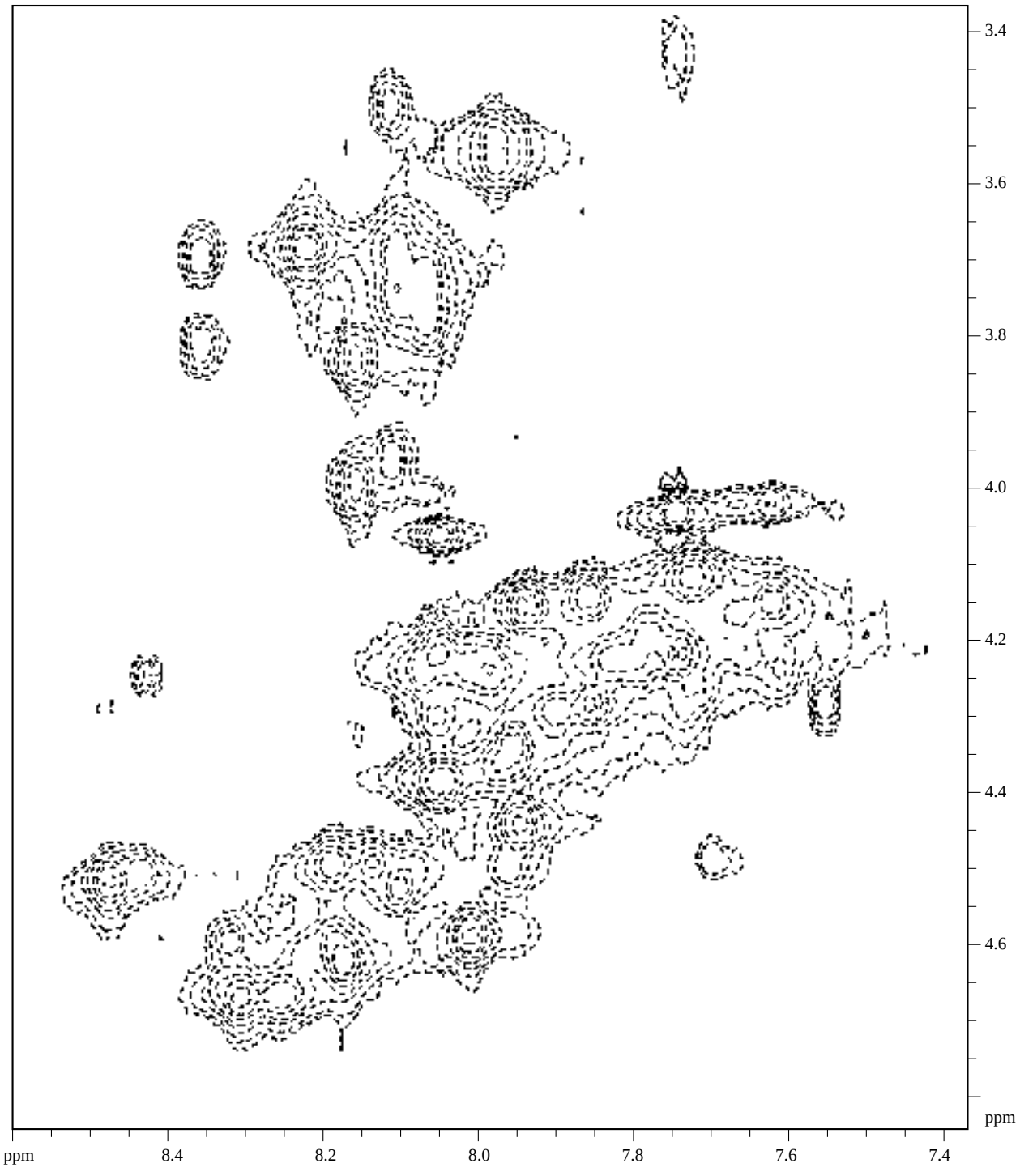

(b)

Figure 5 MLEV-17 spectra of the oxidized form of the peptide CTRPNNNTRKSIHIGPGRAFYTTGEIIGDIRQAHC in DMSO at 24 °C, recorded using a mean rf field strength $\gamma B_1/2\pi$ = 6.79 kHz at 600 MHz. Cross peaks with the same sign as the diagonal peaks (coherent transfer) are plotted as dashed lines. Cross peaks with opposite sign (incoherent transfer) are plotted as solid lines. Only the cross-relaxation peaks are assigned. (a) In the uncompensated TOCSY experiment, strong cross peaks occur owing to cross relaxation. (b) In the TOCSY spectrum recorded using an MLEV-17 expansion of an optimized shaped 90° pulse,[21] the cross-relaxation peaks have disappeared

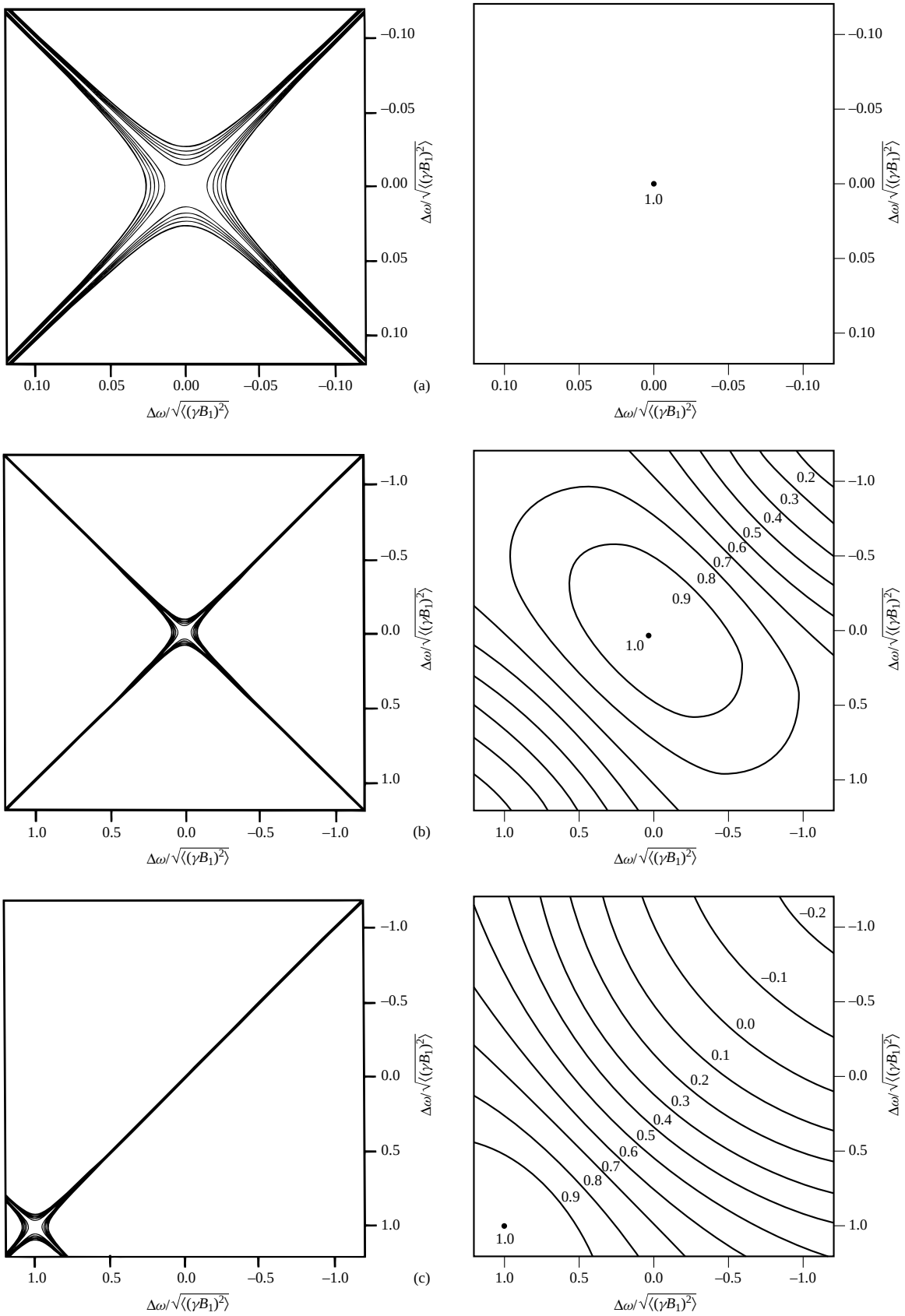
(a)
(b)
(c)
1.0
0.2
0.3
0.4
0.5
0.6
0.7
0.8
0.9
–0.2
–0.1
0.0
0.1
0.2
0.3
0.4
0.5
0.6
0.7
0.8
0.9
$\Delta\omega/\sqrt{\langle(\gamma B_1)^2\rangle}$

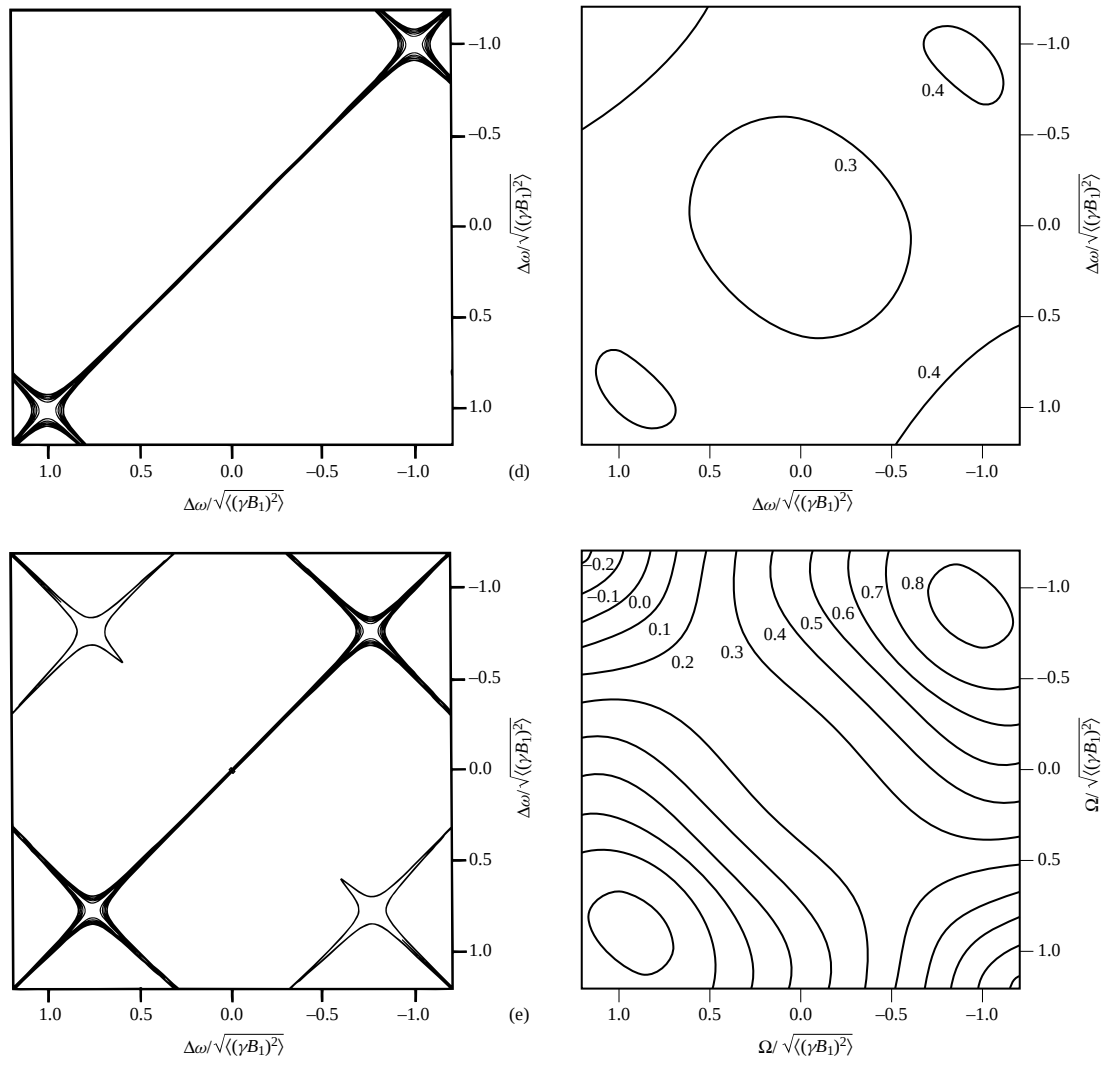

Figure 6 Simulations of Hartmann–Hahn transfer (left) and net cross-relaxation rate σ_{net} (right) for a molecule in the spin diffusion limit in ROESY sequences. Application of a very strong spin lock field (a) would result in a maximal σ_{net}, but complete Hartmann–Hahn matching would make such spectra useless. Reducing the spin lock field strength (b) strongly attenuates TOCSY at the expense of a relatively moderate offset dependence of σ_{net}. TOCSY transfer along the antidiagonal, as observed in (b), is suppressed by off-resonant irradiation of the spin lock field (c). However, the offset dependence of σ_{net} is much more pronounced in this case. Alternating application of two spin lock fields at opposite ends of the spectrum in JS ROESY (b) results in very smooth offset behavior, with TOCSY still being suppressed (d). Phase-alternating ROESY sequences (Figure 7a) show similar offset behavior for cross relaxation and coherent transfer (e). It is obvious that maximal transverse cross relaxation is achieved on-resonance at the cost of complete Hartmann–Hahn matching. Simulations of TOCSY show contour plots of the largest possible Hartmann–Hahn transfer amplitude in a two-spin system. The lowest level corresponds to a transfer amplitude of 0.1; the level spacing is 0.2

only two irradiation positions placed outside the low- and high-field edges of the spectrum [Figure 7(b)]. Since the directions of the spin lock axes differ for the high-field and the low-field spin lock for all offsets (except for $\Omega = 0$), a compensating pulse has to be applied that rotates the magnetization into the new lock direction for every offset. In the pulse sequence of JS ROESY shown in Figure 7(b), this is achieved by the pair of 180° pulses between the two off-resonant spin locks. The field strength of these pulses is related to the spin lock field strength and to the on-resonance lock angle θ.[14] The averaging of the offset dependences of the two stretches of CW irradiation results in a very smooth offset behavior and good suppression of Hartmann–Hahn transfer, as shown in Figure 6(d). Close to on-resonance, this sequence achieves optimal suppression of TOCSY, since λ does not differ from the optimum value [given by equation (37)] at any time. Further off-resonance, the performance of the sequence is reduced, since the λ value for a given offset may differ grossly for high-field and low-field CW irradiation, and must not be averaged between the extended stretches of CW irradiation. The smaller of the two λ values (of the low- and high-field irradiations) gives a measure of the occurrence of TOCSY.

3.2.2 $\pi_x\pi_{-x}$ ROESY

A second approach to obtain ROESY spectra with suppression of TOCSY transfer is the use of multiple pulse sequences optimized for this goal. Only one group of sequences has so far been proposed.[30,31] These consist of a series of phase-alternating 180° pulses $(\pi_x\pi_{-x})_n$ (Figure 8), where

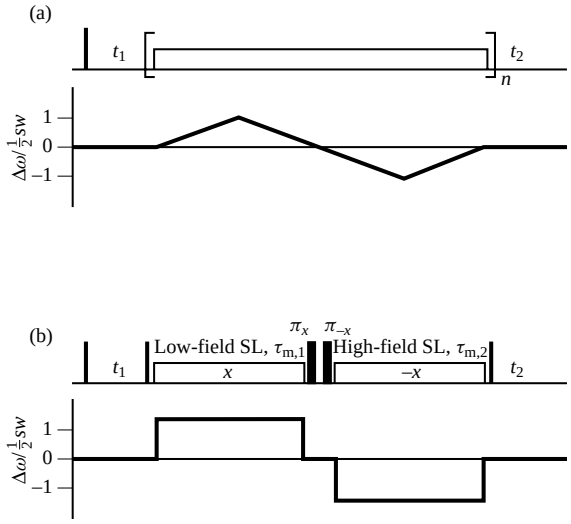

Figure 7 CW ROESY sequences with off-resonant irradiation spin locks. For each experiment, the pulse sequence (upper trace) and the position of the spin lock irradiation (lower trace) are given. (a) In the frequency swept variant,[29] the irradiation frequency is moved from the middle of the spectral region to the low-field edge, to the high-field edge, and back to the middle. (b) In the JS ROESY experiment, the mixing time consists of periods of low-field and high-field irradiation with a pair of 180° pulses mediating between the spin locks. The offset of the spin locks is generated by superimposing a phase gradient over a CW spin lock

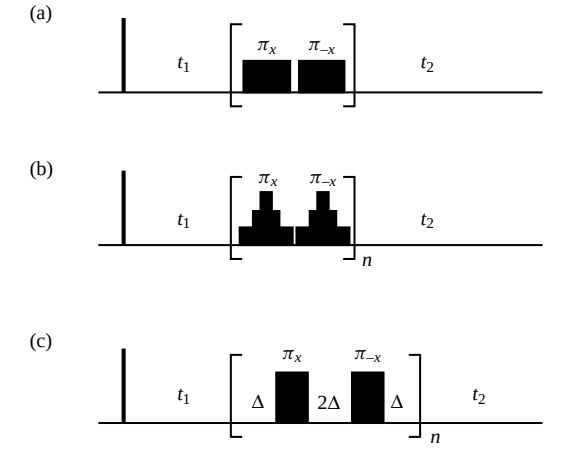

Figure 8 ROESY sequences employing spin locks consisting of phase-alternating pulses.[30,31]. The original sequence (a) can be modified by the use of shaped pulses (b) or by the introduction of delays (c) to increase the weight of transverse cross relaxation

Figure 9 Simulations of the offset behavior of cross relaxation of JS ROESY and a ROESY employing a phase-alternating spin lock $(\pi_x^{3L}\pi_{-x}^{3L})_n$,[31] with parameters chosen to yield a net cross-relaxation rate of $0.476\sigma_{ROE}$ on-resonance. For JS ROESY (a), an on-resonance lock angle $\theta_0 = 53.77°$ was used. The phase-modulating sequence (b) yields the same net cross-relaxation rate using the shaped pulse described by Hwang et al.[31] The offset dependence of cross relaxation is less pronounced in JS ROESY, making direct use of intensities feasible for distance calculations. (c) Simulations of λ as a function of Ω in the offset range $\pm 1.2\sqrt{\langle(\gamma B_1)^2\rangle}$. Near on-resonance, JS ROESY suppresses TOCSY better, while the phase-alternating sequence performs better towards the edges of the spectrum

each individual 180° pulse can be rectangular (which might include delays) or shaped. Sequences using pulses with flip angles other than 180° can also be used, and have been

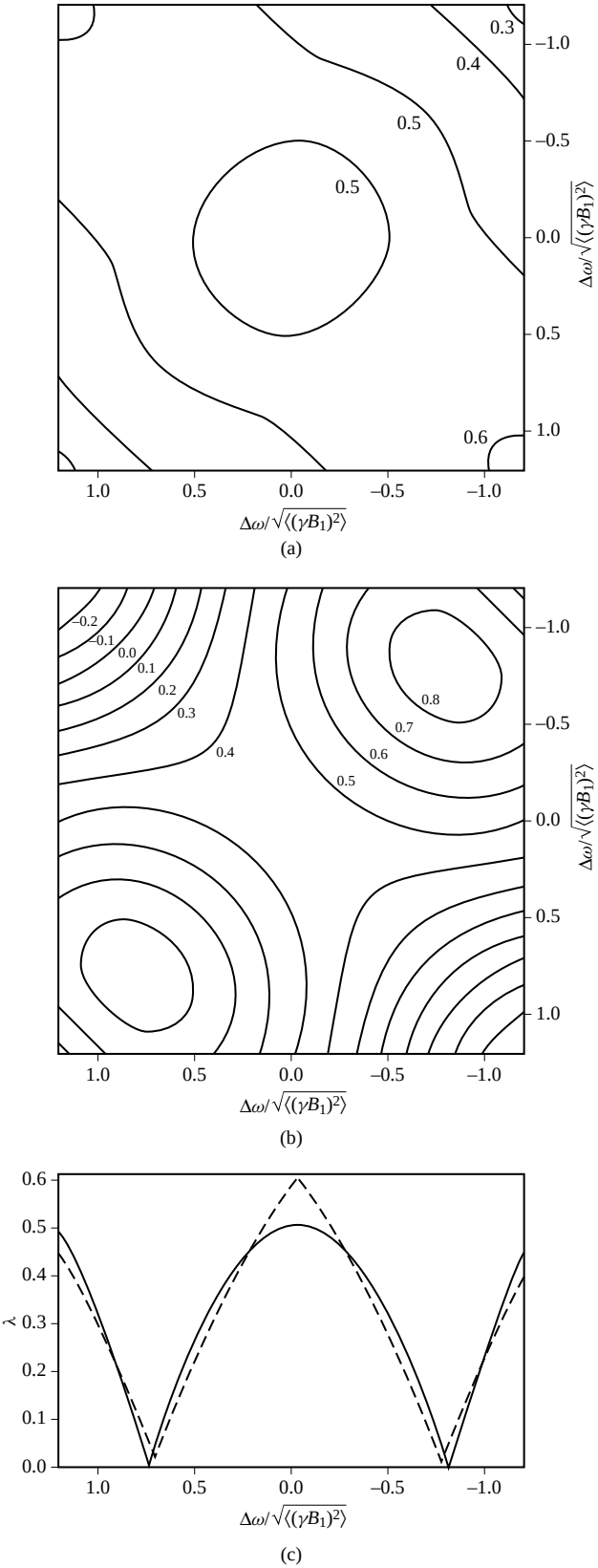

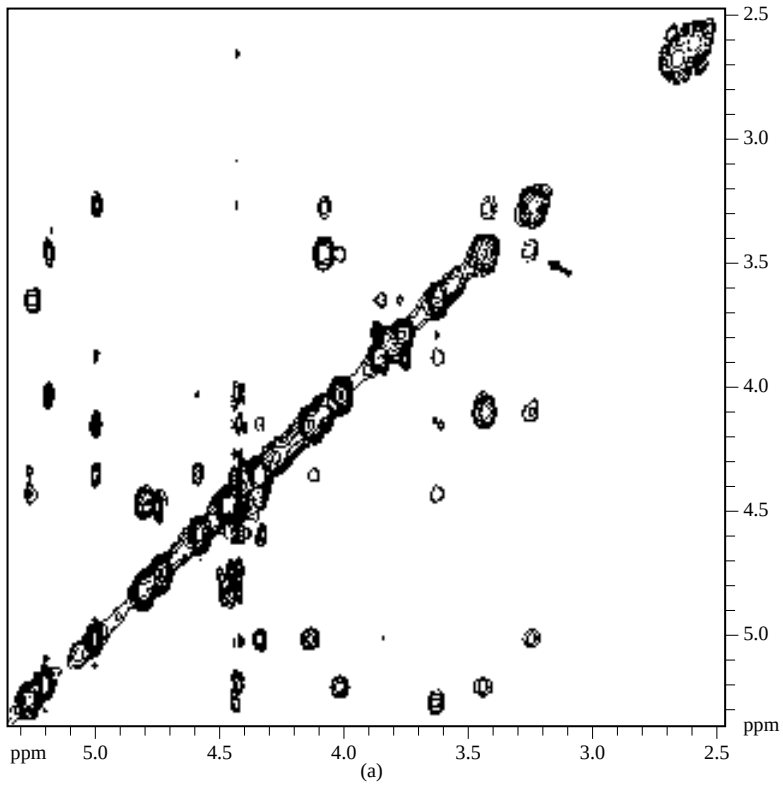

Figure 10 ROESY spectra of a disaccharide obtained with the ROESY sequences of Figures 7(b) (a) and Figure 8(b) (b). Positive (negative) levels are plotted as dashed (solid) lines. Both pulse sequences show similar ROE cross-peak intensities (solid contour lines). An artifact due to Hartmann–Hahn transfer between geminal protons is visible in both spectra (marked with an arrow). In contrast, no TOCSY transfer is observed between the geminal protons at 2.6 and 2.7 ppm, although they are even more strongly coupled than the protons mentioned above. This is probably due to the oscillatory behavior of TOCSY transfer, which vanishes for the chosen mixing time for the pair of geminal protons at 2.6 and 2.7 ppm. The example shows that a careful analysis of ROESY spectra is mandatory for signals close to the diagonal

exploited to suppress cross relaxation in exchange spectra of macromolecules.[32] For large ($\omega\tau_c \gg 1$) or intermediate sited ($\omega\tau_c \approx 1$) molecules, the unmodified mixing scheme $(\pi_x\pi_{-x})_n$ yields a net ROE rate of only $\frac{1}{4}\sigma_{ROE}$ or $\frac{1}{2}\sigma_{ROE}$ on resonance,[30] since $w_l = w_t = \frac{1}{2}$. It is therefore of interest to increase the weight of transverse cross relaxation. This can be achieved using shaped pulses (Figure 8b), or by the introduction of delays into the sequence (Figure 8c).

In the following, ROESY sequences will be compared that yield equal net cross-relaxation rates on-resonance and that dissipate the same power in a sample. Figure 9 shows the offset behavior of cross relaxation of JS ROESY [(a): $\theta = 53.77°$] and of a phase-alternating ROESY employing a shaped 180° pulse to increase w_t. (b):[31]

The offset dependence of the cross relaxation of the JS ROESY sequence is somewhat less pronounced than that of the phase-alternating sequence.

In Figure 9(c), the scaling λ is plotted as a function of the offset for both sequences. The minimal λ of the two spin locks is plotted for JS ROESY, since λ may not be averaged in the case of extended stretches of CW irradiation. On-resonance, λ is larger for JS ROESY than for the phase-alternating sequence. This result is a direct consequence of the fact that the scaling of λ in CW sequences is minimal at given w_t. For larger offsets, the phase-alternating sequence yields a somewhat better suppression of TOCSY (larger λ). Although λ can serve as a measure of TOCSY transfer along the diagonal only, this reasoning shows that it appears to be worthwhile to search for optimized ROESY sequences that minimize the loss in λ on-resonance while achieving maximum λ off-resonance.

Figure 10 shows a comparison of JS ROESY and the phase-alternating ROESY sequence. The spectra differ only marginally. Coherent transfer is well suppressed, except for the two strongly coupled geminal protons H-6′, H-6″. For more details, see the figure legend.

4 REFERENCES

1. L. Braunschweiler and R. R. Ernst, *J. Magn. Reson.*, 1983, **53**, 521.
2. A. A. Bothner-By, R. L. Stephens, J. M. Lee, C. D. Warren, and R. W. Jeanloz, *J. Am. Chem. Soc.*, 1984, **106**, 811.
3. T. E. Bull, *J. Magn. Reson.*, 1988, **80**, 470; T. E. Bull, in *Progress in Nuclear Magnetic Resonance Spectroscopy*, eds. J. W. Emsley, J. Feeney, and L. H. Sutcliffe, Pergamon Press, Oxford, 1992, Vol. 24, p. 377.
4. U. Haeberlen and J. S. Waugh, *Phys. Rev.*, 1968, **175**, 453.
5. Haeberlen, U. *High Resolution NMR in Solids*, Academic Press, New York, 1976, pp. 47–69.
6. R. R. Ernst, G. Bodenhausen, and A. Wokaun, *Principles of Nuclear Magnetic Resonance in One and Two Dimensions*, Oxford University Press, Oxford, 1987.
7. F. J. Dyson, *Phys. Rev.*, 1949, **75**, 486, 1736.
8. R. P. Feynman, *Phys. Rev.*, 1951, **84**, 108.
9. W. Magnus, *Commun. Pure Appl. Math.*, 1954, **7**, 649.
10. J. S. Waugh *J. Magn. Reson.*, 1986, **68**, 189.
11. S. J. Glaser and G. P. Drobny, in *Advances in Magnetic Resonance*, ed. W. S. Warren, Academic Press, New York, 1990, Vol. 14, p. 35.
12. J. S. Waugh, *J. Magn. Reson.*, 1982, **50**, 30.
13. C. Griesinger and R. R. Ernst, *Chem. Phys. Lett.*, 1988, **152**, 239.
14. J. Schleucher, J. Quant, S. J. Glaser, and C. Griesinger, submitted.
15. A. Bax and D. G. Davis, *J. Magn. Reson.*, 1985, **65**, 355.
16. A. J. Shaka, J. Keeler, and R. Freeman, *J. Magn. Reson.*, 1983, **53**, 313.
17. S. P. Rucker and A. J. Shaka, *Mol. Phys.*, 1989, **68**, 509.
18. M. Kadkhodaie, O. Rivas, M. Tan, A. Mohebbi, and A. J. Shaka *J. Magn. Reson.*, 1991, **91**, 437.
19. C. Griesinger, G. Otting, K. Wüthrich, and R. R. Ernst, *J. Am. Chem. Soc.*, 1988, **110**, 7870.
20. J. Cavanagh and M. Rance, *J. Magn. Reson.*, 1992, **96**, 670.
21. U. Kerssebaum, R. Markert, J. Quant, W. Bermel, S. J. Glaser, and C. Griesinger, *J. Magn. Reson.*, 1992, **99**, 184.
22. J. Briand and R. R. Ernst, *Chem. Phys. Lett.*, 1991. **185**, 276.
23. M. Kadkodaei, T.-L. Hwang, J. Tang, and A. J. Shaka, *J. Magn. Reson., Ser. A*, 1993, **105**, 104.
24. J. Quant, Diploma Thesis, University of Frankfurt, 1992.
25. M. Ravikumar and A. A. Bothner-By, *J. Am. Chem. Soc.*, 1993, **115**, 7537.
26. A. Bax and D. G. Davis, *J. Magn. Reson.*, 1985, **63**, 207.
27. C. Griesinger and R. R. Ernst, *J. Magn. Reson.*, 1987, **75**, 261.
28. D. Neuhaus and J. Keeler, *J. Magn. Reson.*, 1986, **68**, 568.
29. J. Cavanagh and J. Keeler, *J. Magn. Reson.*, 1988, **80**, 186.
30. T.-L. Hwang and A. J. Shaka, *J. Am. Chem. Soc.*, 1992, **114**, 3157.
31. T.-L. Hwang, M. Kadkhodaei, A. Mohebbi, and A. J. Shaka, *Magn. Reson. Chem.*, 1992, **30**, 24.
32. J. Fejzo, W. M. Westler, S. Macura, and J. L. Markley, *J. Magn. Reson.*, 1991, **92**, 20.

Acknowledgments

This work was supported by the Fonds der Chemischen Industrie. J.S. and J.Q. thank the Graduiertenkolleg Chemische und Biologische Synthese von Wirkstoffen at the Institute for Organic Chemistry (Gk Eg 53/3-3) for support. J.Q. gratefully acknowledges a scholarship of the Fonds der Chemischen Industries. S.G. thanks the DFG (Gl 203/1-1, Gl 203/1-2) and the Dr. Otto Röhm Stiftung for support. The sample of TFPI-2 was a gift from Novo Nordisk A/S. We thank Dr T. Keller, Dr W. Bermel, and Dr R. Kerssebaum, BRUKER Analytische Meßtechnik, for continuous support.

Two-Dimensional Carbon–Heteroelement Correlation

Stefan Berger

Philipps University Marburg, Marburg, Germany

1	Introduction	1
2	Selection of Nuclei	1
3	Hardware Considerations	2
4	Selection of Pulse Methods	2
5	Chemical Applications	2
6	Conclusions	5
7	Related Articles	5
8	References	5

1 INTRODUCTION

Two-dimensional correlation spectroscopy, originally proposed by Jeener[1] in 1971, was developed by Ernst et al.[2] and abbreviated with the term COSY. Since then, this method has played the most important role in the structure elucidation of organic compounds. In 1978, Freeman and Morris[3] created the polarization transfer experiment to correlate chemical shifts of carbons and protons. This type of H,C COSY experiment dominated the following decade because it could be easily implemented on FT spectrometers which were constructed for proton-decoupled carbon NMR measurements. Although the more attractive 'inverse' (i.e. proton) detection was invented in the early 1980s,[4] these new methods struggled because the existing spectrometer generation did not support the necessary phase coherence between the proton decoupler and the receiver. Since 1989, inverse detection has been a standard feature of modern commercial instruments. For the inverse H,C COSY experiment, two pulse sequences were used: HMQC[5] and HSQC.[6] The main difference between them is the order of the coherence which is relevant to the information transfer between the nuclei. The abbreviations HMQC and HSQC refer to Heteronuclear *Multiple* and *Single* Quantum Coherence, respectively.

Heteronuclear correlation spectroscopy is not restricted to the spin pair ^{1}H,^{13}C. ^{1}H,^{n}X correlations are also used for structure elucidation, e.g. ^{1}H,^{31}P for organophosphorus compounds. In fact, the inverse experiments were introduced for the spin pair ^{1}H,^{15}N. Today, indirect detection is the method of choice for rare nuclei.

The molecular skeleton, however, is usually made from carbon. In organometallic, bioorganic, and heterocyclic chemistry we find, in addition, one or more heteroelements embedded in the carbon framework, whereas the protons only cover the outer surface of the molecule. It is therefore straightforward to create 2D NMR methods to detect directly the connectivity between the carbon atoms and magnetically active heteroelements. In this article we review the hardware requirements needed for this purpose, discuss a variety of pulse methods used, and discuss the chemical applications achieved so far with these techniques.

2 SELECTION OF NUCLEI

Possible correlation partners of ^{13}C are all spin $\frac{1}{2}$ nuclei, such as ^{19}F, ^{15}N, ^{31}P, ^{29}Si, ^{77}Se, ^{119}Sn, ^{125}Te, ^{195}Pt, ^{199}Hg, or ^{207}Pb. For special applications quadrupolar nuclei such as ^{2}H, ^{6}Li, or ^{11}B may also be of interest. Of course, the relative importance of these correlations is dictated by the chemistry of these classes of compounds. In a ^{13}C,^{n}X correlation one is faced with the question of which nucleus one should detect and which should develop chemical shift during t_1. There are complex arguments based on the pulse sequences used, the T_1 and T_2 relaxation times of the two nuclear species involved, the spectral width required in both the F_1 and F_2 dimensions, and many more. At first sight, perhaps surprisingly, the natural abundance of a nucleus gives no direct argument, since for correlation NMR it is always the product of both natural abundances that is decisive. There is, however, a practical reason why the relative natural abundances have to be considered. In the case of, for example, a ^{13}C,^{31}P correlation, each rare ^{13}C spin 'sees' a phosphorus, whereas only 1% of the phosphorus atoms 'see' a ^{13}C spin. The suppression of unwanted signals must therefore be rather efficient if one is to detect the nucleus with the higher abundance.

Next, one should consider the linewidth of the 1D spectra of both nuclei. The detected nucleus should be the one with the smaller linewidth, since a short T_2 leads to signal losses during the pulse sequence. In the case of ^{13}C,^{n}X correlations (^{n}X = ^{77}Se, ^{125}Te, ^{195}Pt, ^{199}Hg, and ^{207}Pb), carbon has the smaller linewidth. Because of the chemical shift anisotropy and the temperature dependence of the chemical shift of heavy nuclei, the measurement of ^{13}C would therefore be favored in these cases.

For carbon detection, in addition, the large NOE enhancement caused by proton irradiation has to be taken into account. Heteronuclei usually have no directly bound proton, their NOE factors are therefore usually less than the maximum value. To facilitate further discussion, the γ values and the natural abundances of the nuclei used for ^{13}C,^{n}X correlation are given in Table 1.

Table 1 Gyromagnetic Ratios and Natural Abundances of Selected Nuclei

Nucleus	γ (10^7rad T^{-1}s^{-1})	Natural abundance
^{2}H	4.106	0.015
^{6}Li	3.937	7.42
^{11}B	8.583	80.42
^{13}C	6.726	1.108
^{15}N	−2.711	0.37
^{19}F	25.166	100
^{29}Si	−5.314	4.7
^{31}P	10.829	100
^{77}Se	5.101	7.58
^{119}Sn	−9.971	8.58
^{125}Te	−8.452	6.99
^{195}Pt	5.75	33.8
^{199}Hg	4.769	16.84
^{207}Pb	5.597	22.6

By inspection of Table 1, it is possible to group the possible correlation partners of carbon into three classes. One group has lower γ values (^{2}H, ^{6}Li, ^{15}N), one group quite comparable γ values (^{29}Si, ^{195}Pt, ^{199}Hg, ^{207}Pb), and a third group definitively higher γ values (^{11}B, ^{19}F, ^{31}P, ^{119}Sn, ^{125}Te). For this last group, therefore, using the HMQC method, ^{n}X detection should be preferable if arguments based on γ values were the only factors. However, even in this group polarization transfer with carbon detection might be competitive, since the higher γ value of the X nucleus is transferred to the carbon signal, and this itself is enhanced by NOE.

The repetition time of these experiments is governed by the T_1 relaxation of nucleus 1 in HMQC and HSQC, but of nucleus 2 in the polarization transfer experiment. At high magnetic fields, heteronuclei relax not only by dipolar but also, to a considerable extent, by other relaxation mechanisms such as chemical shift anisotropy. Hence, the relaxation times of metal nuclei are very often in the range of 1 s. This again would favor the HMQC method with ^{n}X detection or the polarization transfer method with ^{13}C detection.

A final argument stems from the required spectral width in both dimensions. It is very inconvenient to have a large spectral width in F_1 because this would be very time-consuming; furthermore, signal folding in F_1 cannot be filtered out. Thus, it is often better to detect the nucleus with the larger spectral width. In addition, this can be more easily separated into different parts if the spectral width is too large to allow reasonably uniform 180° pulses.

3 HARDWARE CONSIDERATIONS

The experiments described in this article are usually performed under complete proton decoupling. Thus, in addition to the ^{1}H coil and the standard ^{2}H lock signal, one needs two more frequencies to be delivered to the sample. The simplest approach would be a fixed probehead, with an additional coil double-tuned to, for example, ^{13}C and ^{15}N. This is very popular in protein research, because proteins doubly labeled with ^{13}C and ^{15}N are now fairly readily available. The drawback of such a probehead is obvious; it is restricted to the special spin triple ^{1}H,^{13}C,^{15}N, and no other experiment is possible. A second approach would be to have one multinuclear tuneable coil, and double tune the second X nucleus to the ^{1}H coil. One has to decide which X nucleus to choose. For the experiments described here, ^{13}C was chosen since in organoelement chemistry carbon is the common denominator. The spectrometer needs an independent third radiofrequency channel, which can deliver its pulses to the appropiate coil of the probehead. Such a third radiofrequency channel usually requires a second frequency synthesizer, some gating electronics, and a power amplifier. The feature of a third radiofrequency channel is standard in research instruments built later than 1990; however, it has been adapted in many NMR laboratories to older instruments.

4 SELECTION OF PULSE METHODS

The basic pulse sequences known from ^{13}C,^{1}H correlation have all been adapted for ^{13}X,^{n}X correlation under proton decoupling. In Figure 1 the three common pulse sequences are shown.

In the HMQC technique [Figure 1(a)], transverse magnetization of nucleus 1 is first generated. Antiphase magnetization which evolves during the first delay is transferred to nucleus 2 which evolves under the chemical shift during t_1. This is transferred back to nucleus 1. During the final acquisition time, t_2, the chemical shift of nucleus 1 and heteronuclear coupling to nucleus 2 evolve; thus, at the end of this pulse sequence we measure the magnetization which originates from the equilibrium magnetization of the detected nucleus. Neglecting, at this stage, relaxation arguments, the overall sensitivity[7] of the HMQC sequence is then proportional to $\gamma_1{}^{5/2}$. Thus, for a ^{13}C,^{n}X correlation with this technique, theory strongly suggests the choice of the nucleus with the higher γ value as the detected nucleus.

The HSQC sequence [Figure 1(b)] consists of two INEPT sandwiches, which are separated by the evolution time t_1. Here we again start with the equilibrium magnetization of nucleus 1. If we compare the magnetization transfer ways with the HMQC method, we realize that in both experiments the same equilibrium magnetization is finally used for detection; hence, the sensitivity arguments stay the same. For the application discussed here, homonuclear spin couplings can be neglected and thus the HSQC method should yield comparable results to HMQC. The HMQC experiment, however, does need more than double the number of radiofrequency pulses. For practical reasons of error propagation, it might therefore be less favorable. Another point of discussion would be the different relaxation properties of single- and multiple-quantum coherences which, in the case of heteronuclear correlation, are not predominant.

In contrast to the HMQC and the HSQC experiment, transverse magnetization of nucleus 2, which is **not** detected later, will be created in the beginning of the polarization transfer experiment [Figure 1(c)]. In the following evolution time this magnetization is modulated with the chemical shift of nucleus 2. Since nucleus 1 is detected, the overall sensitivity in this experiment[7] is related to the factors $\gamma_1{}^{3/2}\gamma_2$; hence, the choice of the detected nucleus is not as obvious as in the two former pulse sequences. There is a further point to be considered in a comparison of the three pulse sequences. In both HMQC and HSQC magnetization is transferred twice, forwards and backwards, between the two nuclei. In the polarization transfer method this occurs only once. If this transfer is not optimal due to a range of different spin coupling constants, there are inevitable losses of signal in each transfer; thus, the method with only one transfer might be favored. Modifications of the above pulse sequences employ an INEPT transfer from protons to one heteronucleus prior to the start of the actual correlation.[8,9]

5 CHEMICAL APPLICATIONS

5.1 ^{13}C,^{31}P Correlation

Most of the published work has been performed on the spin pair ^{13}C,^{31}P; hence, it seems appropriate to review this nucleus first. Martin and co-workers[10] showed the feasibility of this technique with a homebuilt probe and the HMQC

method. They used triphenylphosphane oxide as an example. Since the spectrometer used did not have three rf channels, proton decoupling could not be employed. Of course, 2D correlation on this simple compound does not give new chemical insights, it merely served as a model compound. A more systematic study compared the three pulse methods taking triphenylphosphane as an example using ^{31}P and ^{13}C detection.[11] The merits of the different methods were discussed and it was found that for ^{31}P detection the polarization transfer method was the most suitable; for ^{13}C detection the HMQC method was the most suitable. As a first real example, the ^{13}C,^{31}P correlation of nicotinamide adenine dinucleotide (NAD^+) was measured. This example is given in Figure 2 and shows very nicely the ease of assignment with such methods. Further examples given by Bast et al.[11] were a mixture of mononucleotides.

Examples from the chemistry of phosphonates have been published by Grossmann and co-workers.[12] For a mixture of stereoisomeric diphosphonates they could, with the help of ^{13}C,^{31}P correlation, assign the three different sets of signals and determine the P,P′ spin coupling constant in these compounds. Other examples from the same group include bis(dialkoxythiophosphoryl) sulfides and their polysulfides.[13] An example from the field of ligands used in organometallic chemistry is provided by the molecule prophos (see Figure 3) in which we find all the phenyl groups to be inequivalent due to chirality, and one might question the relative assignments of these carbon atoms.[14] The ^{31}P NMR spectrum is easily assigned via H,P correlation. Phosphorus A ($\delta = -25$ ppm) couples with all aliphatic protons while phosphorus B ($\delta = -4.7$ ppm) only couples with the methylene and methine group. The phosphorus-substituted *ipso*-carbon atoms of the four phenyl rings are particularly difficult to assign by any other method. In Figure 3 the extension of a 2D ^{13}C,^{31}P correlation is shown, which immediately relates the connectivity of the pairs of diastereotopic *ipso*-carbon atoms with their corresponding phosphorus atoms. Close inspection of Figure 3 reveals, from the slant of the cross peaks, that the signs of the ^1J(P,C) and ^3J(P,P) spin coupling constants are the same; ^1J(P,C) spin coupling constants for threefold coordinated phosphorus are known to be negative.[15] The possibility of evaluating the relative sign of coupling constants can be viewed as a further asset of ^{13}C,^{n}X correlations.

Very recently, ^{19}F,^{13}C correlations have been published.[27–29]

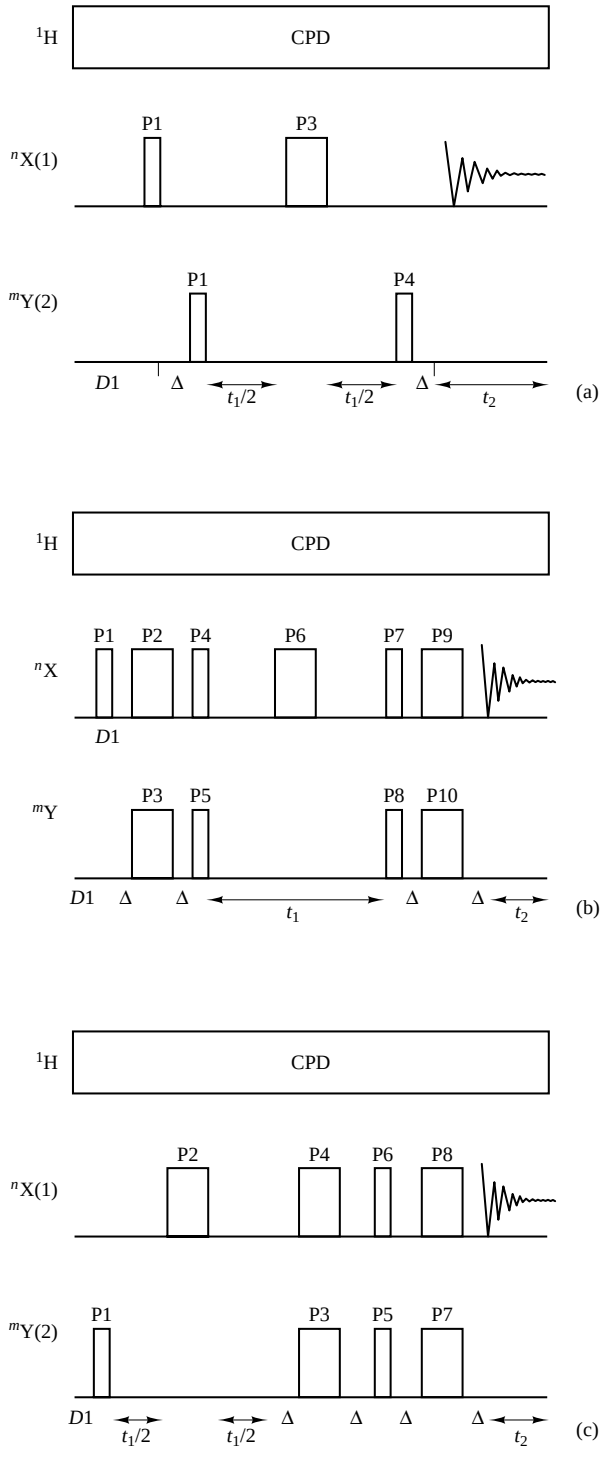

Figure 1 Pulse sequences for X,Y correlation under proton decoupling. (a) HMQC pulse sequence adapted for X,Y correlation; P1, P2, and P4 represent 90° pulses, P3 a 180° pulse, $D1$ = relaxation delay, $\Delta = \frac{1}{2}J$(X,Y). The pulse and receiver phases are: P1, P3: x, P2: x, $-x$, incremented by time proportional phase incrementation (TPPI), P4: x, x, $-x$, $-x$, rec: x, $-x$, $-x$, x. (b) HSQC pulse sequence adapted for X,Y correlation under ^{1}H decoupling; P1, P4, P5, P7, and P8 represent 90° pulses, P2, P3, P6, P9, and P10 180° pulses, $D1$ = relaxation delay, $\Delta = \frac{1}{4}J$(X,Y). The pulse and receiver phases are: P1, P2, P6, P9: x, P3, P10: $(x)_4$, $(-x)_4$, P4, P7: y, P5: x, $-x$, incremented by TPPI, P8: x, x, $-x$, $-x$, rec: x, $-x$, $-x$, x. (c) Polarization transfer sequence adapted for X,Y correlation under ^{1}H decoupling; P1, P5, and P6 represent 90° pulses, P2, P3, P4, P7, and P8 180° pulses, $D1$ = relaxation delay, $\Delta = \frac{1}{4}J$(X,Y). The pulse and receiver phases are: P1: x, P2, P3, P4, P7: x, x, $-x$, $-x$, P5: y, $-y$, incremented by TPPI, P6: $(x)_4$, $(y)_4$, $(-x)_4$, $(-y)_4$, P8: $(x)_2$, $(-x)_2$, $(y)_2$, $(-y)_2$, rec: $(x, -x)_2$, $(y, -y)_2$, $(-x, x)_2$, $(-y, y)_2$

5.2 ^{13}C,^{15}N Correlation

The ^{13}C,^{15}N correlation is especially important in the protein field and was therefore, up to now, only applied in this class of compounds. Doubly-labeled material has to be used, but this is readily available by biological methods. Using the HMQC method, the first paper in this field[16] correlated the signals of

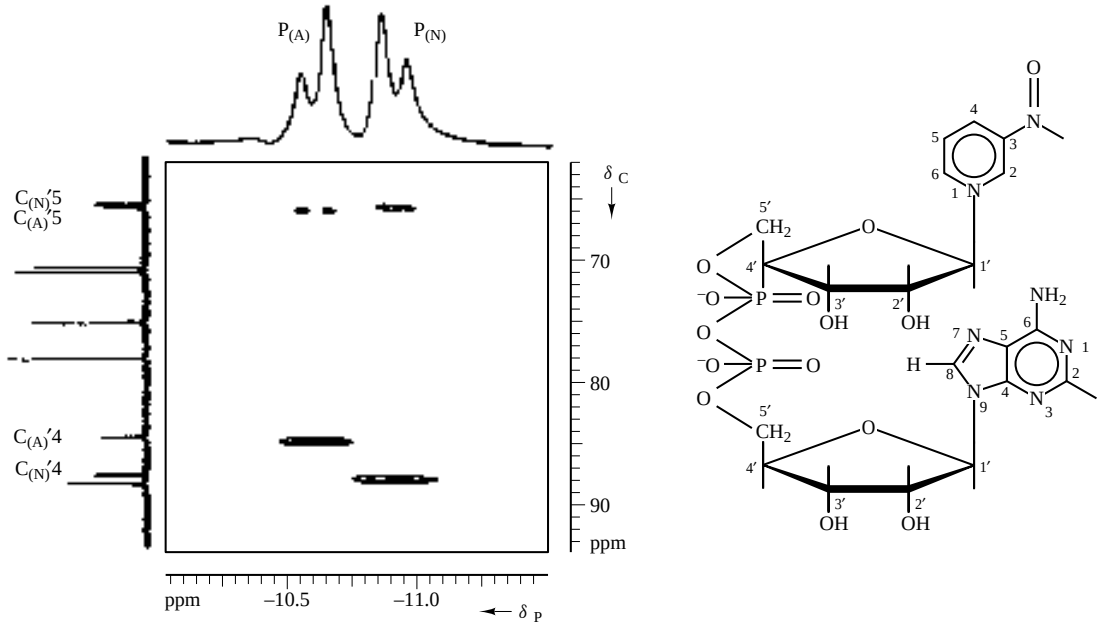

Figure 2 2D $^{13}C,^{31}P$ correlation of NAD^+ using ^{31}P detection (taken from Bast et al.[11])

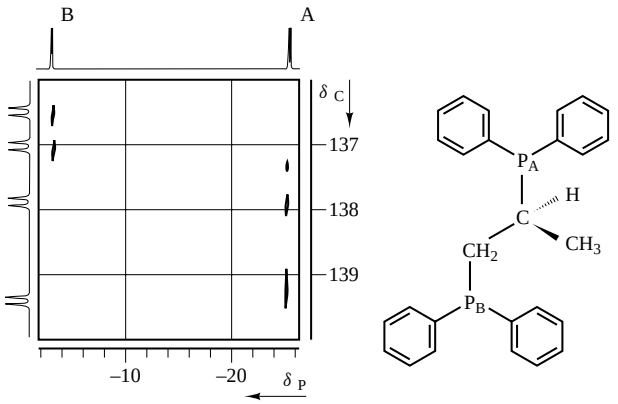

Figure 3 2D $^{13}C,^{31}P$ correlation of the chiral ligand prophos using ^{31}P detection and the HMQC method with extension for the *ipso*-carbon atoms being shown

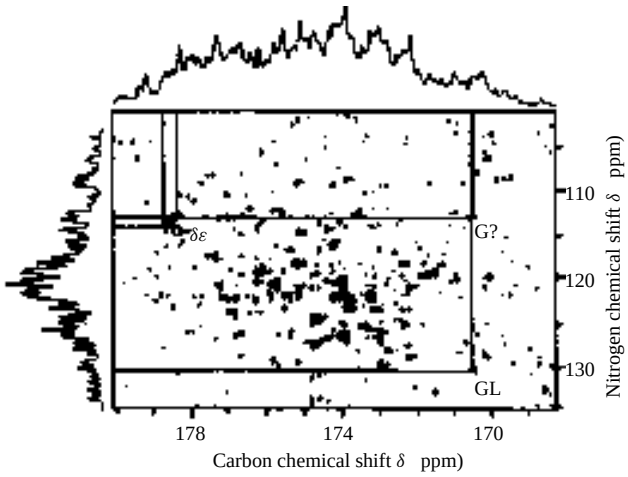

Figure 4 2D $^{13}C,^{15}N$ correlation of ^{13}C and ^{15}N labeled flavodoxin from *Anabaena* 7120 (taken from Westler et al.[16])

a protein of molecular weight of 20 000 Da (see Figure 4). A huge number of cross peaks describing the amide links of the protein can be seen. After methodical research on labeled acetamide[8] to find the best possible pulse sequence, another group used this method to elucidate the structure of a cyclic decapeptide.[17]

5.3 Correlation with Metal Nuclei

This application of correlation spectroscopy is very recent. For ^{29}Si, a new pulse sequence, a combination of INEPT and HMQC, was proposed and applied to decamethyltetrasiloxane as a model compound and to a polymer silicon oil as an example.[9] This technique has also been used in organoselenium chemistry, where, for example, a full assignment of the ^{13}C and ^{77}Se chemical shifts could be achieved for olefins bearing two different phenylseleno groups. Furthermore, incorrect literature structures could be corrected.[18] Another olefin with two different trimethyltin groups served as the first example for $^{13}C,^{119}Sn$ correlation.[19] It was shown that long range coupling constants can also be used to correlate carbon and tin chemical shifts. Conformational assignment can therefore be made by these means. Recently, two examples from organomercury[20] and organolead[21] chemistry have been tested.

5.4 Correlation with Quadrupolar Nuclei

Although, at first sight, 2D correlation spectroscopy of ^{13}C with quadrupolar nuclei does not seems feasible due to relaxation problems, there are two nuclei where, due to the relatively small quadrupolar moment, such a correlation has been performed, i.e. the ^{2}H and the ^{6}Li nuclei. Günther and co-workers were the first to employ these methods for both nuclei. For ^{2}H they chose 2,4,5,6-pyridine-d_4 as an example

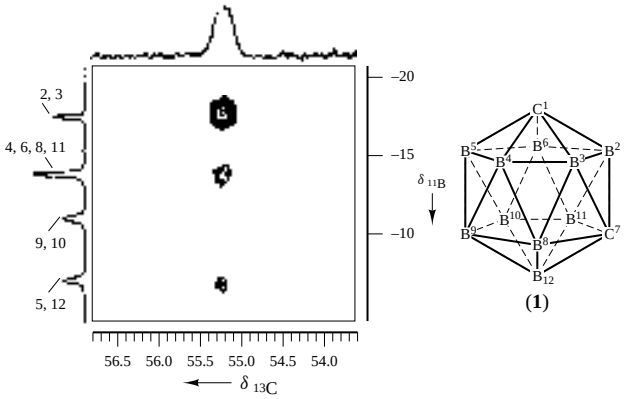

Figure 5 2D $^{13}C,^{11}B$ correlation of 1,7-dicarba-*closo*-dodecaborane(12) (taken from Fäcke and Berger[26])

to test the correlation technique[22] and, later on, applied this to the analysis of isotopomeric mixtures of bicyclic compounds in which the deuterium label was distributed during a chemical reaction.[23] By means of the $^{13}C,^{2}H$ correlation the signals in this mixture could be easily assigned. For this technique, the usual ^{2}H lock of modern instruments cannot be used and must be replaced by a ^{19}F lock system. In organolithium compounds one is often faced with dynamic equilibria between aggregates of different sizes, depending on temperature and solvent. The structures obtained by X-ray crystallography do not necessarily correspond to those predominant in solution. In two reports[24,25] it was shown that a 2D $^{13}C,^{6}Li$ correlation can contribute to the analysis of organolithium compounds. Carboranes and metallacarboranes provide a large class of compounds where sometimes, due to symmetry reasons, the ^{11}B signals display reasonably small linewidths on the order of the $^{13}C,^{11}B$ spin coupling constant. A $^{13}C,^{11}B$ correlation was therefore attempted for selected carboranes. In Figure 5 the result for the *meta*-dodecaborane (**1**) is shown,[26] displaying nicely the different connections within this cage compound.

6 CONCLUSIONS

We have shown in this article the feasibility and possibilities of 2D $^{13}C,^{n}X$ correlation, and demonstrated that this technique often provides a very direct and straightforward signal assignment. The further development and application of these techniques will certainly give new possibilities in structural elucidation in the field of organoelement chemistry.

7 RELATED ARTICLES

COSY Two-Dimensional Experiments; Heteronuclear Assignment Techniques; Heteronuclear Shift Correlation Spectroscopy; Organometallic Compounds.

8 REFERENCES

1. J. Jeener, lecture given at *AMPÈRE International Summer School*, Basko Polje, Yugoslavia, 1971.
2. W. P. Aue, E. Bartholdi, and R. R. Ernst, *J. Chem. Phys.*, 1976, **64**, 2229.
3. R. Freeman and G. A. Morris, *J. Chem. Soc., Chem. Commun.*, 1978, 684.
4. L. Müller, *J. Am. Chem. Soc.*, 1979, **101**, 4481.
5. A. Bax, R. H. Griffey, and B. L. Hawkins, *J. Magn. Reson.*, 1983, **55**, 301.
6. G. Bodenhausen and D. J. Ruben, *Chem. Phys. Lett.*, 1980, **69**, 185.
7. R. R. Ernst, G. Bodenhausen, and A. Wokaun, *Principles of Nuclear Magnetic Resonance in One and Two Dimensions*, Clarendon Press, Oxford, 1987, p. 468.
8. W. P. Niemczura, G. L. Helms, A. S. Chesnick, R. E. Moore, and V. Bornemann, *J. Magn. Reson.*, 1989, **81**, 635.
9. S. Berger, *J. Magn. Reson., Ser. A*, 1993, **101**, 329.
10. L. D. Sims, L. R. Soltero, and G. E. Martin, *Magn. Reson. Chem.* 1989, **27**, 599.
11. P. Bast, S. Berger, and H. Günther, *Magn. Reson. Chem.*, 1992, **30**, 587.
12. H. Beckmann, G. Grossmann, and G. Ohms, *Magn. Reson. Chem.*, 1992, **30**, 860.
13. G. Grossmann and H. Komber, *Phosphorus, Sulfur, Silicon, Relat. Elem.*, 1991, **61**, 269.
14. T. Fäcke, R. Wagner, and S. Berger, *Concepts Magn. Reson.*, 1994, **6**, 293.
15. S. Berger, S. Braun, and H. O. Kalinowski, *NMR-Spektroskopie von Nichtmetallen*, Thieme Verlag, Stuttgart, 1993, Vol. 3, p. 135.
16. W. M. Westler, B. J. Stockman, and J. L. Markley, *J. Am. Chem. Soc.*, 1988, **110**, 6256.
17. R. E. Moore, V. Bornemann, W. P. Niemczura, J. M. Gregson, J. L. Chen, T. R. Norton, G. M. L. Patterson, and G. L. Helms, *J. Am. Chem. Soc.*, 1989, **111**, 6128.
18. T. Fäcke, R. Wagner, and S. Berger, *J. Org. Chem.*, 1993, **58**, 5475.
19. S. Berger and T. N. Mitchell, *Organometallics*, 1992, **11**, 3481.
20. T. Fäcke and S. Berger, *J. Organomet. Chem.*, in press.
21. T. Fäcke and S. Berger, *Main Group Metal Chem.*, 1994, **17**, 463.
22. J. R. Wesener, P. Schmitt, and H. Günther, *Magn. Reson. Chem.*, 1984, **22**, 468.
23. J. R. Wesener and H. Günther, *J. Am. Chem. Soc.*, 1985, **107**, 1537.
24. D. Moskau, F. Brauers, H. Günther, and A. Maercker, *J. Am. Chem. Soc.*, 1987, **109**, 5532.
25. H. J. Gais, J. Vollhardt, H. Günther, D. Moskau, H. J. Lindner, and S. Braun, *J. Am. Chem. Soc*, 1988, **110**, 978.
26. T. Fäcke and S. Berger, *Magn. Reson. Chem.*, 1994, **32**, 436.
27. A. A. Ribeiro and M. J. Geen, *J. Magn. Reson., Ser. A*, 1994, **107**, 158.
28. S. Berger, *J. Fluorine Chem.*, 1995, **72**, 117.
29. R. Eujeu and A. Putorru, *J. Organomet. Chem.*, 1992, **438**, 57.

Biographical Sketch

Stefan Berger. *b* 1946. Ph.D., 1973, University Tübingen, under supervision of Prof. Dr. A. Rieker 1973. Introduced to NMR by H. Suhr and A. Rieker. Postdoctoral fellow with Prof. J. D. Roberts, California Institute of Technology, 1973–74. Habilitation, 1981. Faculty, University Marburg, 1974–present. Approx. 100 publications. Current research interests: development of selective pulse methods and applications of NMR in the field of organometallic and bioorganic chemistry.

Two-Dimensional *J*-Resolved Spectroscopy

Gareth A. Morris

University of Manchester, Manchester, UK

1	Introduction	1
2	Historical Review	1
3	Theory	2
4	Applications	4
5	Related Articles	5
6	References	5

1 INTRODUCTION

J-resolved 2D spectroscopy (also commonly known as 2D *J* spectroscopy) is a class of two-dimensional NMR methods that separate chemical shifts from multiplet structure. In pulse sequences for *J*-resolved 2D spectroscopy, a 180° pulse is applied at the centre of the evolution period t_1, generating a spin echo. The modulation of spin echoes by scalar coupling causes signals to be dispersed in the f_1 domain of the resultant 2D spectrum according to their position within scalar coupling multiplets. This allows the separation of multiplet structure from chemical shifts, improving the resolution of individual signals in spectra with overlapping multiplets. There is a further gain in resolution in the f_1 domain of the 2D spectrum, because the spin echo suppresses the effects of $\boldsymbol{B}_0$ inhomogeneity, giving f_1 linewidths approaching the natural limit $1/\pi T_2$. *J*-resolved 2D spectroscopy is now much less widely used than correlated 2D methods, but still finds application, for example in the analysis of complex spin systems and in the separation of homonuclear from heteronuclear coupling structure.

Both homonuclear and heteronuclear multiplet structure can be investigated by *J*-resolved spectroscopy. Since broadband suppression of homonuclear couplings during measurement of the free induction decay is not possible, homonuclear *J*-resolved 2D spectroscopy[1] produces spectra with multiplet structure in f_1, and both multiplet structure and chemical shifts in f_2. In heteronuclear *J*-resolved 2D spectroscopy,[2,3] on the other hand, it is normal to apply broadband decoupling during data acquisition, so that multiplet structure is suppressed in f_2 and a complete separation is achieved between multiplet structure in f_1 and chemical shifts in f_2. For weakly coupled spin systems, a similar separation can be achieved in homonuclear *J*-resolved 2D spectroscopy by 'shearing' or 'tilting' the 2D data matrix[1] to give a 45° tilt in frequency space:

$$S(f_1, f_2') = S(f_1, f_2 - f_1) \tag{1}$$

A further difference between homonuclear and heteronuclear methods lies in the origin of the echo modulation. In the homonuclear experiment, the modulation arises naturally from the action of the 180° pulse used to generate the spin echo, since it affects both the partners in any scalar coupling. In the heteronuclear experiment, couplings to weakly coupled heteronuclei do not give rise to any modulation of the spin echo unless a suitable perturbation is applied to the heteronuclei.

The simplest form of *J*-resolved spectroscopy is the homonuclear experiment of the following sequence, in which the basic Carr–Purcell method A spin echo sequence[4] forms the evolution period of a 2D experiment:

$$90^\circ \qquad \tfrac{1}{2}t_1 \qquad 180^\circ \qquad \tfrac{1}{2}t_1 \qquad \text{Acquire} \tag{2}$$

This experiment is normally used in proton NMR, but is applicable to any nuclei with homonuclear couplings. Because the resulting signals are phase-modulated with respect to t_1, it is not normally practicable to use phase-sensitive display. In order to secure acceptable absolute value mode lineshapes, it is usual to apply either pseudoecho[5] or sine-bell[6] weighting in both frequency dimensions, despite the signal-to-noise ratio penalty. This forces the time domain signals into an approximately symmetric envelope, so that dispersion-mode contributions (which have odd symmetry) are absent from the resultant frequency domain lineshapes.

Sequence (2) will not normally generate any echo modulation as a result of heteronuclear couplings; this is the basis of the use of homonuclear *J*-resolved spectroscopy to distinguish between homonuclear and heteronuclear multiplet structure. (Echo modulation due to heteronuclear couplings can arise, however, if there is coupling to a group of heteronuclei that are strongly coupled amongst themselves.[7]) For simplicity, it will be assumed here that the nucleus being observed is ^{13}C and that the coupled nuclei are protons. Although the great majority of experimental applications of heteronuclear *J*-resolved spectroscopy are to this pair of nuclei, there are of course many other possibilities.

Two methods are commonly used to ensure that heteronuclear couplings generate echo modulation. In the 'gated decoupler' method,[2,3,8,9] broadband decoupling is applied during one half only of the evolution period t_1; decoupling is normally also used during the preparation period (to provide the NOE) and during measurement of the free induction decay (to remove multiplet structure from f_2):

$$\begin{array}{lccccc} ^1\text{H} & \leftarrow \text{ Decouple } & & \rightarrow & & \leftarrow \text{ Decouple } \rightarrow \\ ^{13}\text{C} & 90^\circ & \tfrac{1}{2}t_1 & 180^\circ & \tfrac{1}{2}t_1 & \text{Acquire} \end{array} \tag{3}$$

This gives a 2D spectrum in which the multiplet structure is scaled down to half its normal width in f_1, but otherwise faithfully reflects the conventional spectrum, even where there is strong proton–proton coupling.

The second, 'proton flip', technique[3,8,10] uses a 180° pulse to invert the coupled heteronuclei at the midpoint of the evolution period; again, decoupling is normally used during the preparation and detection periods:

$$\begin{array}{lcccccc} ^1\text{H} & \leftarrow \text{ Decouple } \rightarrow & & & 180^\circ & & \leftarrow \text{ Decouple } \rightarrow \\ ^{13}\text{C} & 90^\circ & \tfrac{1}{2}t_1 & 180^\circ & \tfrac{1}{2}t_1 & \text{Acquire} \end{array} \tag{4}$$

Here the multiplet structure appears without any scaling, but only matches that in the 1D spectrum if the heteronuclei (here protons) are weakly coupled. The analysis of strongly coupled proton flip *J*-resolved spectra is discussed in Section 3.2, and closely parallels the analysis for the homonuclear case.

2 HISTORICAL REVIEW

The earliest use of Fourier transformation of the dependence of echo amplitude on the spin echo delay t_1 was the

'*J* spectroscopy' experiment of Freeman and Hill.[11] This involved measuring the amplitude of the signal at the peak of the echo for a series of equally spaced values of t_1, and Fourier transformation with respect to t_1 to generate a '*J* spectrum' in which chemical shifts and line broadening due to field inhomogeneity were suppressed. This experiment was of little practical utility, because all the multiplets in a spectrum were superimposed, so that only the simplest of spin systems could be studied. The effect of measuring just the single data point at the maximum of the echo is equivalent to carrying out an integral projection of a 2D *J*-resolved spectrum onto the f_1 axis.

The first two-dimensional experiments to use spin echoes were reported in Aue, Bartholdi, and Ernst's classic introductory paper[12] on 2D NMR; these were effectively COSY experiments with 180° mixing pulses. Homonuclear *J*-resolved spectroscopy proper was introduced a few months later,[1] in a communication that pointed out the possibility of obtaining a 'decoupled' proton spectrum from a 45° projection. The first heteronuclear experiments were proposed independently by Freeman and co-workers shortly afterwards.[2] Heteronuclear *J*-resolved spectroscopy proved a useful vehicle for the technical development of 2D NMR,[13] since it required only modest data storage.

The observation of artifacts caused by imperfect 180° pulses prompted the development of EXORCYCLE,[14] one of the first and most widely used phase cycling techniques; the acronym derived from the use of the terms 'ghost' and 'phantom' for the spurious signals. The differences in multiplet structure between gated decoupler and proton flip heteronuclear *J*-resolved spectra seen in the presence of strong proton–proton coupling[8–10] led to the development of analytical solutions and numerical software for calculating strongly coupled homonuclear and proton flip heteronuclear *J*-resolved spectra.[10,15,16] Heteronuclear *J*-resolved spectroscopy was also the vehicle for early investigations of the problem of lineshapes in phase-sensitive 2D spectra. Phase modulation leads to 'phasetwist' lineshapes, which are an inseparable mixture of 2D absorption and dispersion mode lineshapes.[13] This problem can be cured in heteronuclear *J*-resolved spectra by combining results from two experiments that have opposite senses of precession in t_1; the apparent sense of precession can be reversed either by adding a second 180° pulse at the end of the evolution period[17] or, in the gated decoupler experiment, by changing from decoupling during one half of t_1 to decoupling in the other.[18] Such expedients are actually seldom used, since in f_2-decoupled heteronuclear *J*-resolved spectroscopy, phase-sensitive f_1 cross-sections (which can be phased to absorption mode, since they pass through the midpoints of the phasetwisted lineshapes) can usually be obtained free of overlap from neighboring signals in f_2.

With the introduction of better spectrometer computers, *J*-resolved spectroscopy was quickly eclipsed by the more powerful and general class of correlated 2D experiments such as COSY and NOESY, but, nevertheless, a number of useful extensions have been demonstrated. Making the 180° proton pulse of sequence (4) selective restricts the modulation of the spin echo to couplings to protons with a particular chemical shift.[19] If the carbon and proton 180° pulses of a proton flip experiment are replaced by a BIRD (bilinear rotation decoupling) sequence,[20] the refocusing can be made selective for either long-range or one-bond heteronuclear couplings. This is known as semiselective *J* spectroscopy,[21] giving *J*-resolved spectra in which, depending on the relative phases of the pulses in the BIRD sequence, either the one-bond or the longer range couplings are removed from the f_1 dimension, simplifying analysis. Again, strong proton–proton coupling can complicate spectra very considerably, but numerical simulations can be performed;[22] the large number of lines produced can actually be an advantage, because it increases the accuracy with which spin system parameters may be derived.

Another extension is known as indirect *J* spectroscopy;[23,24] this adds a polarization transfer step to a proton spin echo, transferring the proton *J* modulation to ^{13}C signals. This works well where the ^{13}C satellites in the proton spectrum are weakly coupled, allowing clean resolution of individual proton multiplets, even in systems where the proton spectrum is completely unresolved. It has been little used, however, and for most purposes a high-f_2-resolution HMQC experiment[25] is preferable; this does not give any proton linewidth improvement, but is quicker, and doubles the chances of avoiding strong coupling if run without ^{13}C decoupling in t_2.

3 THEORY

3.1 Weak Coupling

Consider first a weakly coupled homonuclear system of two spins $\frac{1}{2}$, *I* and *S*; the energy level diagram and spectrum are shown in Figure 1. There are two *I* transitions: one for the half of the spin systems in which *S* is in the α state and one for those in which it is β, and a similar pair of *S* transitions. Initially, the magnetizations for the four transitions will be at equilibrium; the state of the spin system may represented in the product operator formalism[26] as $\hat{I}_z + \hat{S}_z$, and the four magnetizations will point along the *z* direction in the rotating frame of reference. The initial 90° pulse of sequence (2) will rotate the four magnetizations down to the $-y$ axis of the rotating frame to give $-\hat{I}_y - \hat{S}_y$; the *I*-spin magnetizations are shown diagrammatically in Figure 2(a). During the first half of the evolution period, the chemical shifts of spins *I* and *S* will cause the magnetizations to precess through angles $\phi_I = \pi\delta_I t_1$ and $\phi_S = \pi\delta_S t_1$ (in rad), respectively, where δ_I and δ_S are the offsets from resonance (in Hz) of the two spins. The scalar coupling J_{IS} will cause the two components of each multiplet to diverge by an angle $\theta_1 = \pi J_{IS} t_1$, giving the state

$$\begin{aligned} -\hat{I}_y \cos = {} & \phi_I \cos \tfrac{1}{2}\theta_1 + \hat{I}_x \sin\phi_I \cos \tfrac{1}{2}\theta_1 + 2\hat{I}_x\hat{S}_z \cos\phi_I \sin \tfrac{1}{2}\theta_1 \\ & + 2\hat{I}_y\hat{S}_z \sin\phi_I \sin \tfrac{1}{2}\theta_1 - \hat{S}_y \cos\phi_S \cos \tfrac{1}{2}\theta_1 + \hat{S}_x \sin\phi_S \cos \tfrac{1}{2}\theta_1 \\ & + 2\hat{S}_x\hat{I}_z \cos\phi_S \sin \tfrac{1}{2}\theta_1 + 2\hat{S}_y\hat{I}_z \sin\phi_S \sin \tfrac{1}{2}\theta_1 \end{aligned} \quad (5)$$

for which the *I* magnetizations are shown in Figure 2(b); for the time being, relaxation will be neglected. The 180° pulse,

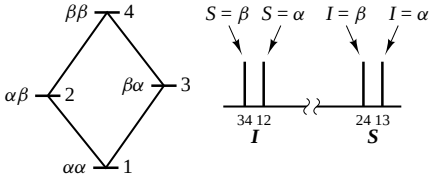

Figure 1 Energy level diagram and spectrum for a weakly coupled *IS* system of two spins $\frac{1}{2}$

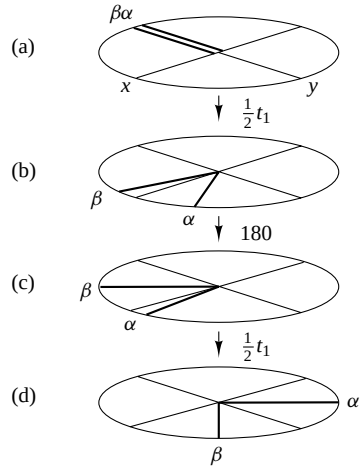

Figure 2 Motion of the two I magnetizations in a weakly coupled IS system of two spins $\frac{1}{2}$ during sequence (2)

applied about the x axis in the rotating frame, will have two effects. It will change the signs of all the terms in $\hat{I}_y$ and $\hat{S}_y$, reflecting the corresponding magnetization vectors about the (x,z) plane of the rotating frame. It will also invert all terms in $\hat{I}_z$ and $\hat{S}_z$; this corresponds to interchanging α and β spins, so that, for example, the I magnetization associated with transition 12 before the 180° pulse (for which S is in the α state) is transferred to transition 34 ($S = \beta$), giving the situation shown in Figure 2(c).

During the second half of the evolution period, the I and S magnetizations will again precess through angles ϕ_I and ϕ_S respectively, and the two components of the I and S pairs will again diverge by $\frac{1}{2}\theta_1$ radians. The effect of the chemical shift precession during the second half of t_1 exactly matches the shift precession during the first half, so that in the absence of any coupling J_{IS}, all four magnetizations would refocus along the $\hat{I}_y$ axis. In the presence of a coupling, the two components of the I and S multiplets end up disposed symmetrically either side of the $\hat{I}_y$ axis, an angle θ apart (Figure 2d), giving the state $+\hat{I}_y \cos\theta_1 - 2\hat{I}_x\hat{S}_z \sin\theta_1 + \hat{S}_y \cos\theta_1 - 2\hat{S}_x\hat{I}_z \sin\theta_1$. The signal at time t_1 is thus unaffected by chemical shifts (or inhomogeneity of the static magnetic field): a spin echo is produced, which is modulated only by the scalar coupling J_{IS}. Each multiplet is a mixture of in-phase absorption mode signals ($\hat{I}_y$) and antiphase dispersion signals ($2\hat{I}_x\hat{S}_z$); the net effect of the modulated spin echo is to multiply one multiplet component by a phase factor $e^{-i\pi J_{IS}t_1}$ and the other by $e^{i\pi J_{IS}t_1}$.

At time t_1, the second half of the modulated echo is recorded as a free induction decay $S(t_2)$. Neglecting relaxation, the complex signal $S(t_1,t_2) = M_y - iM_x$ recorded can then be written as

$$S(t_1,t_2) = \tfrac{1}{2}(e^{i\pi J_{IS}t_1}e^{i(2\pi\delta_I+\pi J_{IS})t_2} + e^{-i\pi J_{IS}t_1}e^{i(2\pi\delta_I-\pi J_{IS})t_2} + e^{i\pi J_{IS}t_1}e^{i(2\pi\delta_S+\pi J_{IS})t_2} + e^{-i\pi J_{IS}t_1}e^{i(2\pi\delta_S-\pi J_{IS})t_2}) \quad (6)$$

which consists of four signals with frequency coordinates (f_1,f_2) of $(\frac{1}{2}J_{IS}, \delta_I + \frac{1}{2}J_{IS})$, $(-\frac{1}{2}J_{IS}, \delta_I - \frac{1}{2}J_{IS})$, $(\frac{1}{2}J_{IS}, \delta_S + \frac{1}{2}J_{IS})$ and $(-\frac{1}{2}J_{IS}, \delta_S - \frac{1}{2}J_{IS})$: the signals are dispersed according to their normal frequencies $\delta \pm \frac{1}{2}J_{IS}$ in f_2, and with just their multiplet structure $\pm\frac{1}{2}J_{IS}$ in f_1. The extension to larger spin systems is straightforward.

The same logic can be applied to heteronuclear J-resolved experiments. The analysis of the proton flip method parallels that for the homonuclear case, except that the initial 90° pulse affects only (say) spin I, so that all terms in $\hat{S}_x$ and $\hat{S}_y$ disappear. In the gated decoupler method, the use of broadband S-spin decoupling during the first half of the evolution period suppresses the effects of J_{IS} in the first half of t_1, so that the frequencies in f_1 are halved to $\pm\frac{1}{4}J_{IS}$. In both methods, broadband decoupling is normally used during t_2 to remove multiplet structure from f_2.

3.2 Strong Coupling

In the presence of strong coupling, the simple analysis given in Section 3.1 breaks down, and it is generally necessary to use density matrix theory. Although analytical results have been presented for some simple spin systems,[16] it is usual to employ numerical methods; a modified version of the 1D spin simulation program LAOCN3,[27] SONOFLAOCOON,[10] may be used both for simulation and for iterative analysis of strongly coupled J-resolved spectra.

Consider a system containing two weakly coupled groups of spins I and S, either of which may be strongly coupled, where only the spins I are to be observed. In the heteronuclear case [sequence (4)], group I will generally contain a single ^{13}C spin and S the coupled protons; in the homonuclear case [sequence(2)], all the spins will belong to group I. If the matrix representation of the q component of spin angular momentum for group I is denoted by $\mathbf{I}^q$, the initial reduced density matrix $\boldsymbol{\rho}_0^I$ for group I will be equal to some constant m_0 times $\mathbf{I}^z$, and the effect of the 90° I pulse will be to rotate $\boldsymbol{\rho}_0$ into $-m_0\mathbf{I}^y$. If calculations are performed in the eigenbasis, the ijth element of $\boldsymbol{\rho}^I$ at time $\frac{1}{2}t_1$ will be $-m_0 \exp[i\pi t_1(\nu_i - \nu_j)]\, I^y_{ij}$, where ν_i is the ith energy eigenvalue of the spin system (in Hz). If the matrix representation for 180° rotation of spins I and S is $\mathbf{T}^{IS}$ then the effect of the 180° I and S pulses will be to transfer coherences ρ_{ij} into other coherences ρ_{kl}:

$$\rho_{kl} = \sum_i \sum_j \rho_{ij} T^{IS*}_{ik} T^{IS}_{jl} \quad (7)$$

Thus, at the end of the evolution period, the total y signal will be

$$S = -m_0 \sum_i \sum_j \sum_k \sum_l I^y_{ij} T^{IS*}_{ik} T^{IS}_{jl} I^y_{lk} \times \exp[i\pi t_1(\nu_i - \nu_j + \nu_l - \nu_k)] \quad (8)$$

The 2D J-resolved spectrum thus consists of a series of responses S_{ijkl} of f_1 frequencies $\frac{1}{2}(\nu_i - \nu_j + \nu_l - \nu_k)$, with intensities given by the preexponential terms in equation (8). Only when all spins are weakly coupled are the f_1 frequencies determined solely by coupling constants; where there is strong coupling, they will also contain terms in chemical shifts (often leading to folding in f_1), and the signals may have negative intensity.

The calculation of a 2D J-resolved spectrum thus reduces to the diagonalization of the nuclear spin Hamiltonian, as in conventional spin simulation programs such as LAOCN3,[27] followed by construction of the eigenbasis matrix representations of the y component of angular momentum and of the 180° rotation operator. By suitable choice of the groups of spins I and S, the same program may be used to calculate

Table 1 Phase Cycling for Sequences (2)–(4); Phase Shifts are Indicated as Multiples of 90° for the 90° Pulse (ϕ_1), 180° Pulse (ϕ_2), and Receiver (ϕ_R); the Phase of the Proton 180° Pulse in Sequence (4) is Immaterial

ϕ_1	0321	1032	2103	3210
ϕ_2	0000	1111	2222	3333
ϕ_R	0123	1230	2301	3012

both homonuclear and proton flip heteronuclear *J*-resolved spectra. More complex experiments such as semiselective *J* spectroscopy[21,22] can be simulated by replacing $\mathbf{T}^{IS}$ with the matrix representation of a BIRD operator.[20]

4 APPLICATIONS

4.1 Practical Implementation

J-resolved spectroscopy is one of the easiest 2D methods to implement. Sequences (2) and (3) require only the usual calibration of the 90° observe pulse width, which is not critical; if α is the actual flip angle of a nominal 90° pulse, the signal obtained is proportional to $\sin\alpha\cos 2\alpha$. Calibration of the proton 180° pulse in sequence (3) can be carried out by setting t_1 equal to $1/^1J$(C,H) and varying the proton pulse width; the signal is nulled when the flip angle is 90°, and inverted when it is 180°. For all three basic sequences the phases of the 90° pulse, 180° refocusing pulse, and receiver should follow a scheme such as that in Table 1, which combines EXORCYCLE[14] and CYCLOPS.[28]

The two principal advantages of *J*-resolved spectroscopy are the decrease in f_1 linewidth afforded by suppressing $\boldsymbol{B}_0$ inhomogeneity effects, and the improved ability to distinguish signals that results from separating multiplet structure from chemical shifts. The former advantage is generally restricted to small molecules with long T_2s, and is most commonly exploited in ^{1}H–^{13}C heteronuclear *J*-resolved spectroscopy, while the latter is most useful in ^{1}H homonuclear *J*-resolved spectroscopy.

4.2 Homonuclear *J*-Resolved 2D spectroscopy

Figure 3 shows the sugar ring region of the 300 MHz proton spectra of a solution of sucrose octaacetate in deuterochloroform. At the right is the normal 1D spectrum, together with a contour plot of the *J*-resolved spectrum. Pseudoecho weighting was used, with absolute value display; good results are also achievable with sine-bell weighting. Strong coupling signals are visible, for example in the region around 5.4 ppm, in addition to the expected multiplets. The effects of 'tilting' the data matrix at 45° in frequency space

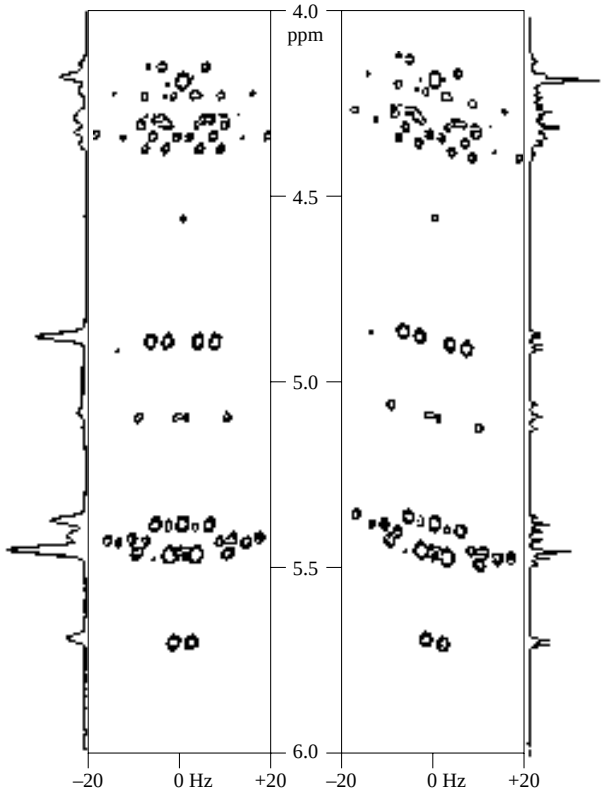

Figure 3 300 MHz proton spectra of sucrose octaacetate. From right to left: normal 1D spectrum; *J*-resolved spectrum; tilted *J*-resolved spectrum; and f_2 projection of the tilted *J*-resolved spectrum

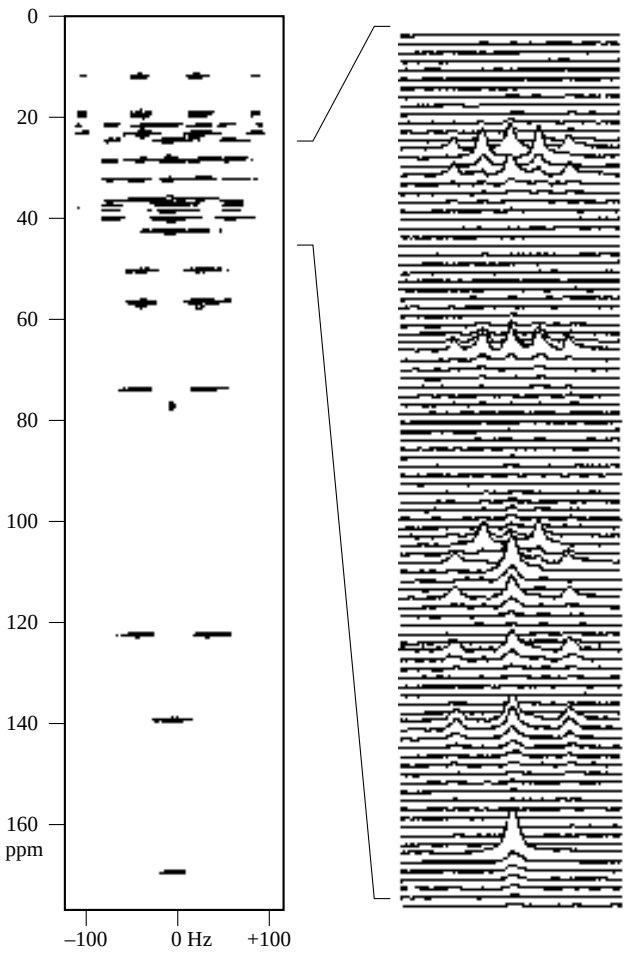

Figure 4 Gated decoupler heteronuclear *J*-resolved ^{13}C spectrum of cholesteryl acetate, showing a stacked trace plot of an expanded region

are illustrated in the left-hand contour plot of Figure 3, which shows the *J*-resolved spectrum after applying equation (1). At the far left of Figure 3, the results of integrating or 'projecting' the tilted spectrum along the f_1 direction to give a 'proton-decoupled proton' spectrum are shown; again, strong coupling artifacts are visible, for example around 5.4 ppm.

4.3 Heteronuclear *J*-Resolved 2D Spectroscopy

The two classical uses of heteronuclear *J*-resolved spectroscopy are with low f_1 resolution for the determination of multiplicity, and with high f_1 resolution for the measurement of long-range $^1H-^{13}C$ couplings in small molecules. DEPT is now generally preferred for multiplicity determination, but *J*-resolved spectroscopy remains the method of choice for high-resolution measurements of ^nJ(C,H). One advantage of heteronuclear *J*-resolved spectroscopy for multiplicity determination is that it gives clear results in the presence of ^{13}C shift degeneracy: Figure 4 shows a contour plot of a gated decoupler spectrum of a solution of cholesteryl acetate in deuterochloroform, together with an expanded stacked trace plot of an overlapping region, showing the coincidence of a methine and a methylene signal at about 29 ppm.

4.4 Semiselective *J*-Resolved 2D Spectroscopy

Figure 5 shows experimental and theoretical cross sections through a high-resolution heteronuclear semiselective 2D *J* spectrum of thiophene in acetone-d_6. One-bond couplings have been suppressed by choosing phases 0, 0, and 180° for the three successive proton pulses of the BIRD sequence.[20] The cross sections illustrate both the high resolution achievable and the complexity of the spectra that can result even from relatively small strongly coupled spin systems. The theoretical trace was calculated using the approach outlined in Section 3.2;[22] the delays during the BIRD sequence allow some of the strong coupling responses to appear in dispersion mode.

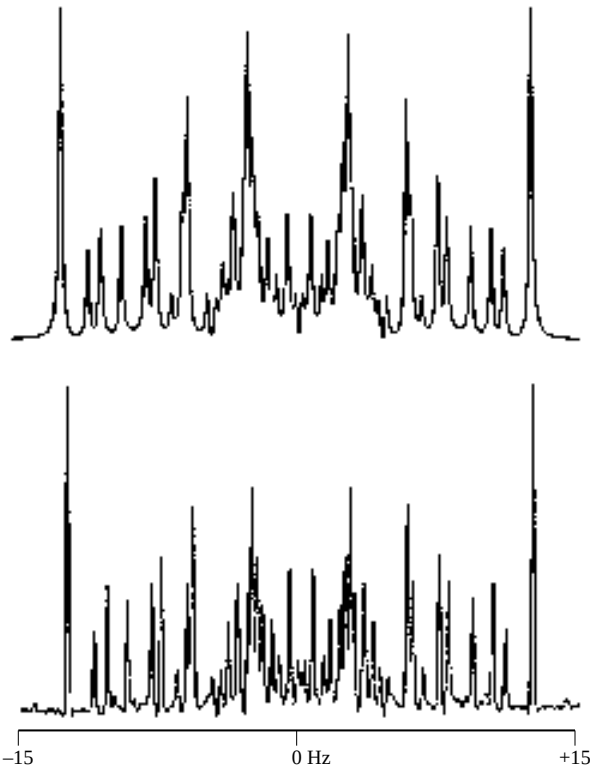

Figure 5 Semiselective one-bond suppressed heteronuclear *J*-resolved ^{13}C spectra for C-2 of thiophene (60% v/v solution in deuteroacetone): (top) calculated and (bottom) experimental. The sequence of Bax[21] was used, on a 400 MHz spectrometer

5 RELATED ARTICLES

Analysis of High-Resolution Solution State Spectra; Indirect Coupling: Theory and Applications in Organic Chemistry; Liouville Equation of Motion; Multidimensional Spectroscopy: Concepts; Phase Cycling; Spin Echo Spectroscopy of Liquid Samples; Two-Dimensional NMR of Molecules Oriented in Liquid Crystalline Phases.

6 REFERENCES

1. W. P. Aue, J. Karhan, and R. R. Ernst, *J. Chem. Phys.*, 1976, **64**, 4226.
2. G. Bodenhausen, R. Freeman, and D. L. Turner, *J. Chem. Phys.*, 1976, **65**, 839.
3. L. Müller, A. Kumar, and R. R. Ernst, *J. Magn. Reson.*, 1977, **25**, 383.
4. H. Y. Carr and E. M. Purcell, *Phys. Rev.*, 1954, **94**, 630.
5. A. Bax, R. Freeman, and G. A. Morris, *J. Magn. Reson.*, 1981, **43**, 333.
6. J. C. Lindon and A. G. Ferrige, in *Progress in Nuclear Magnetic Resonance Spectroscopy*, ed. J. W. Emsley, J. Feeney, and L. H. Sutcliffe, Pergamon Press, Oxford, 1980, Vol. 14, p. 27.
7. A. Kumar and R. R. Ernst, *Chem. Phys. Lett.*, 1976, **37**, 162.
8. G. Bodenhausen, R. Freeman, R. Niedermeyer, and D. L. Turner, *J. Magn. Reson.*, 1976, **24**, 291.
9. R. Freeman, G. A. Morris, and D. L. Turner, *J. Magn. Reson.*, 1977, **26**, 373.
10. G. Bodenhausen, R. Freeman, G. A. Morris, and D. L. Turner, *J. Magn. Reson.*, 1977, **28**, 17.
11. R. Freeman and H. D. W. Hill, *J. Chem. Phys.*, 1971, **54**, 301.
12. W. P. Aue, E. Bartholdi, and R. R. Ernst, *J. Chem. Phys.*, 1976, **64**, 2229.
13. G. Bodenhausen, R. Freeman, R. Niedermayer, and D. L. Turner, *J. Magn. Reson.*, 1977, **26**, 133.
14. G. Bodenhausen, R. Freeman, and D. L. Turner, *J. Magn. Reson.*, 1977, **27**, 511.
15. A. Kumar, *J. Magn. Reson.*, 1978, **30**, 227; *J. Magn. Reson.*, 1980, **40**, 413.
16. G. Bodenhausen, R. Freeman, G. A. Morris, and D. L. Turner, *J. Magn. Reson.*, 1978, **31**, 75.
17. P. Bachmann, W. P. Aue, L. Müller, and R. R. Ernst, *J. Magn. Reson.*, 1977, **28**, 29.
18. R. Freeman, S. P. Kempsell, and M. H. Levitt, *J. Magn. Reson.*, 1979, **34**, 663.
19. A. Bax and R. Freeman, *J. Am. Chem. Soc.*, 1982, **104**, 1099.
20. J. R. Garbow, D. P. Weitekamp, and A. Pines, *Chem. Phys. Lett.*, 1982, **93**, 504.
21. A. Bax, *J. Magn. Reson.*, 1983, **52**, 330.

22. P. Sándor, G. A. Morris, and A. Gibbs, *J. Magn. Reson.*, 1989, **81**, 255.
23. G. A. Morris, *J. Magn. Reson.*, 1981, **44**, 277.
24. V. Rutar, *J. Magn. Reson.*, 1984, **56**, 413.
25. A. Bax, and S. Subramaniam, *J. Magn. Reson.*, 1986, **67**, 565.
26. O. W. Sørensen, G. W. Eich, M. H. Levitt, G. Bodenhausen, and R. R. Ernst, in *Progress in Nuclear Magnetic Resonance Spectroscopy*, ed. J. W. Emsley, J. Feeney, and L. H. Sutcliffe, Pergamon Press, Oxford, 1983, Vol. 16, p. 163.
27. A. A. Bothner-By and S. M. Castellano, in *Computer Programs for Chemistry*, ed. D. F. DeTar, Benjamin, New York, 1968, Vol. 1.
28. D. I. Hoult and R. E. Richards, *Proc. R. Soc. Lond. Ser. A*, 1975, **344**, 311.

Biographical Sketch

Gareth A. Morris. *b* 1954. M.A. (Nat.Sci.), Ph.D., 1978, (supervisor Ray Freeman) Oxford University, UK. Fellow by Examination, Magdalen College, Oxford, 1978–81; Izaak Walton Killam Postdoctoral fellow, University of British Columbia (with Laurie Hall) 1978–79. Lecturer (1982–89) and Reader (1989 to date) in Chemistry, University of Manchester. Approx. 100 publications. Current research interests: development and application of novel NMR techniques to problems in chemistry, biochemistry, and medicine.

Two-Dimensional Powder Correlation Methods

Craig D. Hughes
Los Alamos National Laboratory, Los Alamos, NM, USA

1	Introduction	1
2	Experimental	1
3	Results	2
4	Simulations	4
5	Discussion	6
6	Related Articles	7
7	References	7

1 INTRODUCTION

There are two general motivations to measure the ^{13}C chemical shift tensor in a solid. The first is that it is sensitive to the electronic structure of the molecule in the vicinity of the nucleus, and therefore provides useful experimental data for testing theoretical models of molecular electronic structure. The second, more practical, motivation is analytic in nature; the chemical shift tensor is a sensitive and often unique tool for characterizing heterogeneous materials, and its orientational dependence can be exploited to help characterize partially oriented materials.

The measurement of the ^{13}C chemical shift tensor's principal values and its orientation with respect to the molecular coordinate system is often difficult. A common method is to rotate a single crystal of the sample in a magnetic field and map the relationship between the field direction and the resonance frequency for each magnetically equivalent carbon nucleus in the sample.[1] As the number of magnetically unique carbon nuclei in the crystal increases, correlated 2D exchange NMR spectroscopy is a powerful tool in resolving and correlating the peaks resulting from similar chemical shift tensors.[1,2]

When a good single crystal of the sample is not available, powder techniques must be used. In simple cases, the principal values may be measured from the breakpoints of a 1D powder pattern. The powder spectrum is then simulated with a chemical shift powder pattern for each unique carbon in the sample in order to measure the principal values. This technique is limited to relatively simple spectra, owing to the complexity of fitting multiple, overlapping 1D powder patterns. There are a number of alternate experimental approaches to solving this problem, many of which are reviewed elsewhere in this Encyclopedia.

A relatively simple 2D technique for measuring principal values of overlapping ^{13}C chemical shift tensor patterns in powders is the chemical shift–chemical shift correlation experiment developed for single crystal measurements.[2–4] The sample is rotated relative to the external magnetic field during the mixing time of a 2D exchange experiment, which correlates the powder patterns in the two different orientations. The resulting 2D powder patterns have a characteristic shape that depends on the angle of the rotation and the principal values of the chemical shift tensors in the sample. This method utilizes the additional resolution available in 2D spectroscopy, and is especially useful for sorting the principal values of chemical shift tensors in badly overlapped 1D powder patterns.

2 EXPERIMENTAL

The probe appropriate for the 2D powder correlation experiment is a double tuned, large-sample-volume system designed to allow ^{1}H decoupling and rapid 90° rotation of the sample about an axis perpendicular to the external magnetic field, as shown in Figure 1. The results reported here were obtained using a Bruker CXP-200 NMR spectrometer, with a resonance frequency of 50.3 MHz for ^{13}C.

The pulse sequence used in the experiment is shown in Figure 2. The first part of the pulse sequence is the common cross-polarization technique with Hartmann–Hahn matching and spin locking between the ^{1}H and ^{13}C spins. The remainder of the sequence is a chemical exchange experiment that correlates two different ^{13}C chemical shift evolutions. Here, v and w are the phases of the ^{1}H rf pulses, and x and Φ_i those of the ^{13}C pulses. In this experiment, the measured chemical shift is determined solely by the orientation of the crystallite in the magnetic field. The sample is rotated by 90° during the mixing time, so each crystallite in the powdered sample 'sees' two different magnetic field directions during t_1 and t_2, which results in two different evolution frequencies ω_1 and ω_2. The resulting 2D powder patterns contain information about all of the ^{13}C chemical shift tensors in the sample, and are characteristic of the 90° sample rotation.

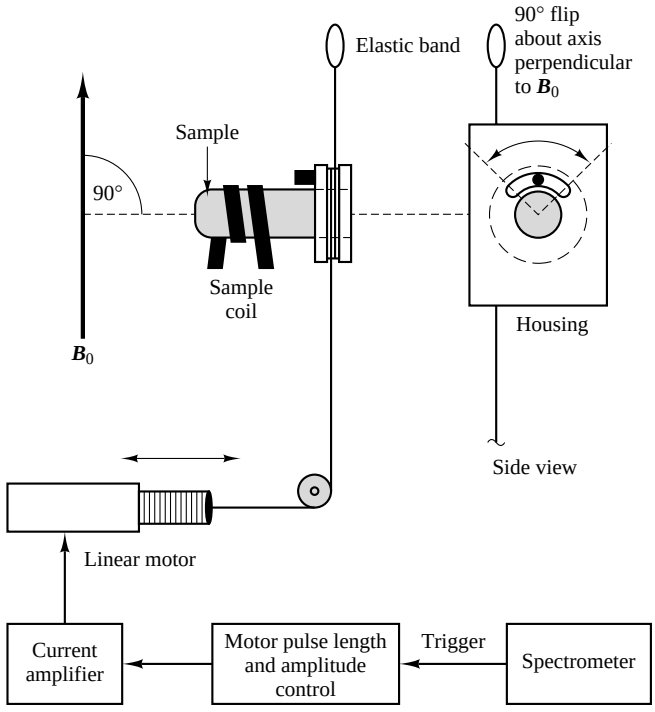

Figure 1 90° sample reorientation apparatus. The powdered sample is placed in a shortened 12 mm NMR tube, which is then epoxied into the sample pulley. The pulley is rotated inside a circular recess in the housing by pulling the attached string

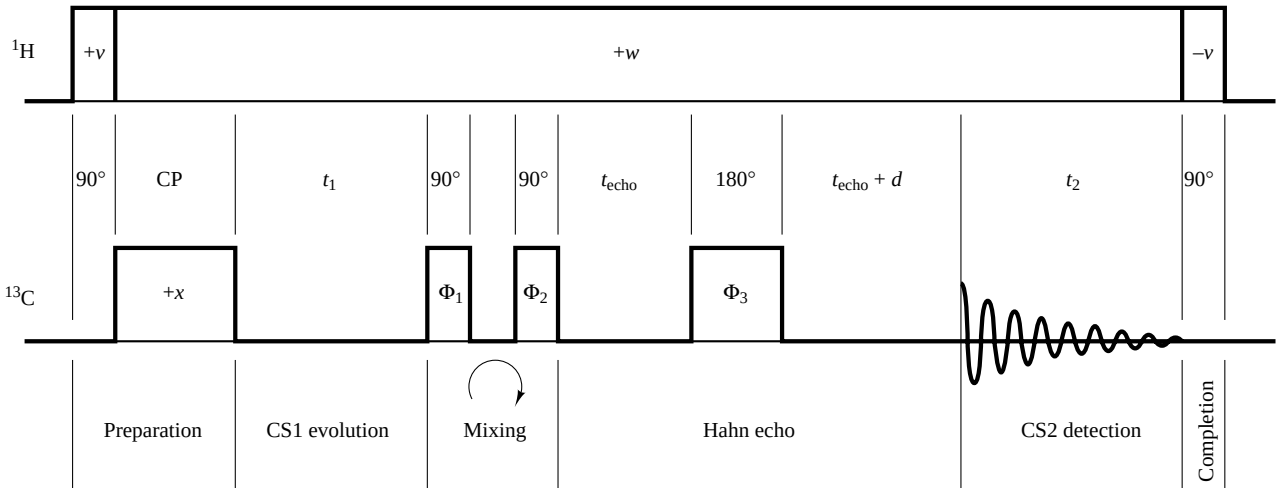

Figure 2 Chemical shift–chemical shift correlation pulse sequence. Phase cycling corrects for artifacts resulting from ^{13}C T_1 relaxation during the mixing time and cross polarization during the 180° echo pulse, and allows for quadrature detection during the evolution dimension. The mixing period is 35 ms long

The 2D data are gathered according to the prescription of States, Haberkorn, and Ruben,[5] which gives amplitude-modulated hypercomplex multidimensional data sets.

3 RESULTS

The spectrum in Figure 3 is a contour plot of the 2D chemical shift correlation spectrum of ferrocene, with the more familiar 1D projections of the spectrum shown at the sides. Ferrocene has an axially symmetric ^{13}C chemical shift tensor whose orientation is determined by its motion about the molecular rotational axis; $\delta_{\parallel}$ is the principal value of the chemical shift tensor when the field is parallel to ferrocene's rotational axis, and $\delta_{\perp}$ is the degenerate principal value when the field lies parallel to the ring plane. An axially symmetric 2D powder pattern has three large peaks connected by ridges forming a right isosceles triangular pattern with a deep basin in its interior. Comparing the features of the 2D spectrum with its 1D projections indicates that the peaks or cusps define the principal values of the chemical shift tensor.

The ferrocene spectrum is a simple example of a 2D chemical shift correlation pattern. The principal values could have been obtained equally well from a 1D powder spectrum. The 2D technique is significantly more useful when multiple overlapping bands in a 1D powder spectrum leave unresolvable ambiguities. The spectrum of coronene shown in Figure 4 illustrates how powerful the 2D correlation technique is. Coronene has three sets of unique carbons, and the molecule rapidly rotates about an axis perpendicular to its plane, averaging all of its chemical shift tensors to axial symmetry. The foremost challenge in measuring the principal values of the three coronene tensors from the 1D powder spectrum was to determine which pairs of the six breakpoints are grouped together as the principal values for each of the three different ^{13}C nuclei in the molecule. The spectrum in Figure 4 exhibits how these groupings were readily determined with the 2D chemical shift correlation experiment. The correlative properties of the powder pattern allows immediate connection of principal value pairs from each chemically distinct nucleus.

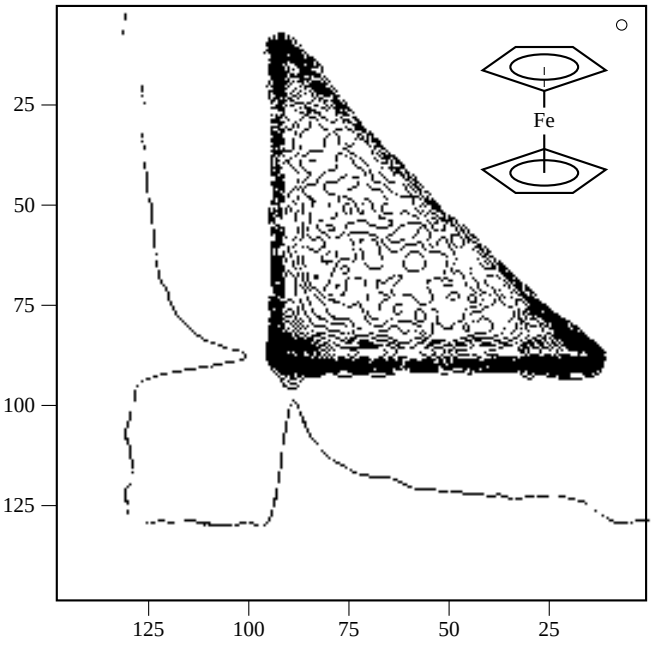

Figure 3 Equal-amplitude contour plot of the 2D ^{13}C chemical shift–chemical shift correlation experimental spectrum of ferrocene (dicyclopentadienyliron). The scales are in ppm from liquid TMS (positive values are to high frequency). ω_1 is the vertical dimension and ω_2 is the horizontal dimension. The diameter of the small circle plotted in the upper right-hand corner is the full width at halfheight of the Gaussian broadening ($\Delta\omega_G$) function that is convolved with the data. In this figure, $\Delta\omega_G$ = 3 ppm. The 1D powder projections are plotted on the vertical and horizontal axes

The 2D chemical shift correlation spectrum of isotactic polypropylene is shown in Figure 5. This spectrum indicates that the added correlation and resolution of two dimensions resolves three different chemical shift tensor patterns in a situation where the 1D powder pattern is intractable.

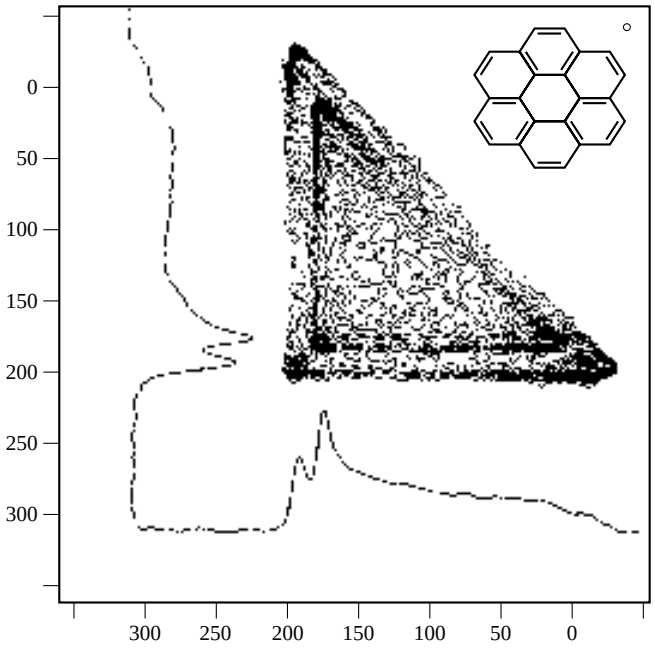

Figure 4 Contour plot of the spectrum of coronene (hexabenzobenzene). The Gaussian broadening in this figure is 3 ppm

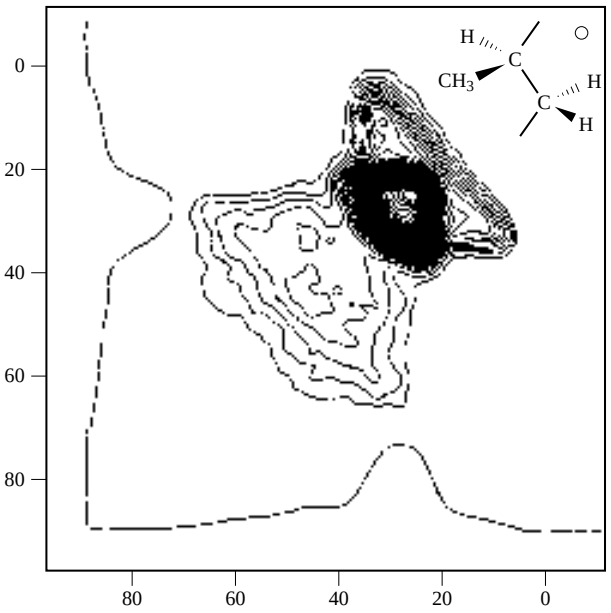

Figure 5 Contour plot of the spectrum of isotactic polypropylene. The Gaussian broadening in this figure is approximately 2.5 ppm

In an effort to determine the limits of resolution of this technique, a spectrum of methyl α-D-glucopyranoside was acquired (Figure 6). Methyl α-D-glucopyranoside has seven carbon types, whose severely overlapped ^{13}C chemical shift tensors have been measured in a single crystal, and therefore is an excellent candidate for comparison of techniques. The 1D powder spectrum is severely overlapped, with almost no distinguishable features to facilitate conventional fitting techniques. However, the 2D powder pattern does show a considerable improvement in resolution. At least four distinct powder patterns may be immediately recognized by the

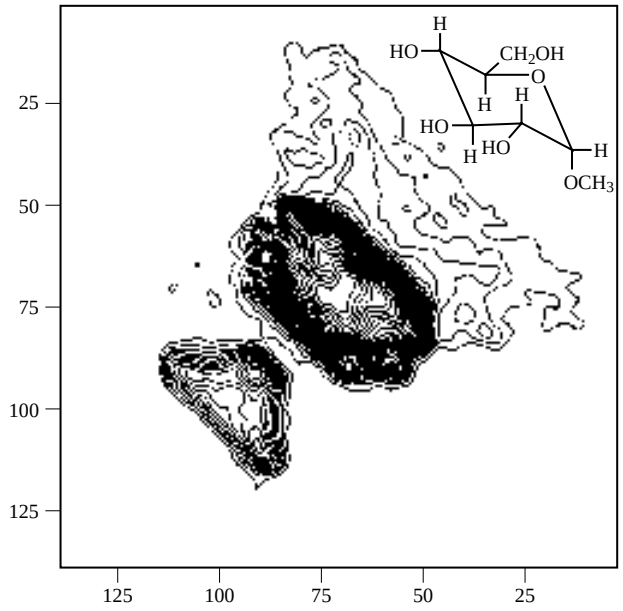

Figure 6 Contour plot of the spectrum of methyl α-D-glucopyranoside

outlines of the cliff-like features that form the boundaries of the patterns. This spectrum was simulated by successively subtracting out simulated components from the pattern and finding new component patterns in the residual spectrum. Prior knowledge of the tensor principal values was not used. The results of this fitting agree well with previous results,[6] as shown in Figure 7. Although this fitting technique left two possible shift tensors unresolved, one of the simulated component patterns has roughly twice the integrated amplitude of the remaining five patterns, indicating that the two unresolved tensor patterns have very similar principal values, which could not be reliably distinguished with this analysis technique.

The measurement of six of the seven ^{13}C chemical shift tensor principal values in methyl α-D-glucopyranoside represents a remarkable increase in resolution over 1D powder spectroscopy, and perhaps an upper limit on the number of overlapping powder patterns that can be successfully resolved with the 2D chemical shift correlation technique. The agreement between the single crystal data and the powder fitting data is very good.

The increased resolving power of the chemical shift correlation experiment has been applied to complex samples such as coals in order to measure the aromaticity of the sample. Figure 8 shows the spectrum of the Argonne premium coal, Pocahontas #3. This spectrum has a clear segregation of amplitude between two different regions. The small volume in the upper right-hand corner of the spectrum has a relatively narrow chemical shift anisotropy and an average chemical shift of approximately 25 ppm. These chemical shifts fall into a range expected from aliphatic carbon nuclei; therefore, this volume represents the aliphatic fraction of the sample. The triangular shaped volume in the lower left-hand corner of this spectrum has a broader chemical shift anisotropy, and an average chemical shift of approximately 130 ppm, and represents the aromatic fraction of the sample. The ratio of these two volumes gives an estimate of the sample's aromaticity:

$$\%\ \text{Aromaticity} = \frac{\text{Volume}_{\text{aromatic}}}{\text{Volume}_{\text{aromatic}} + \text{Volume}_{\text{aliphatic}}} \times 100\% \qquad (1)$$

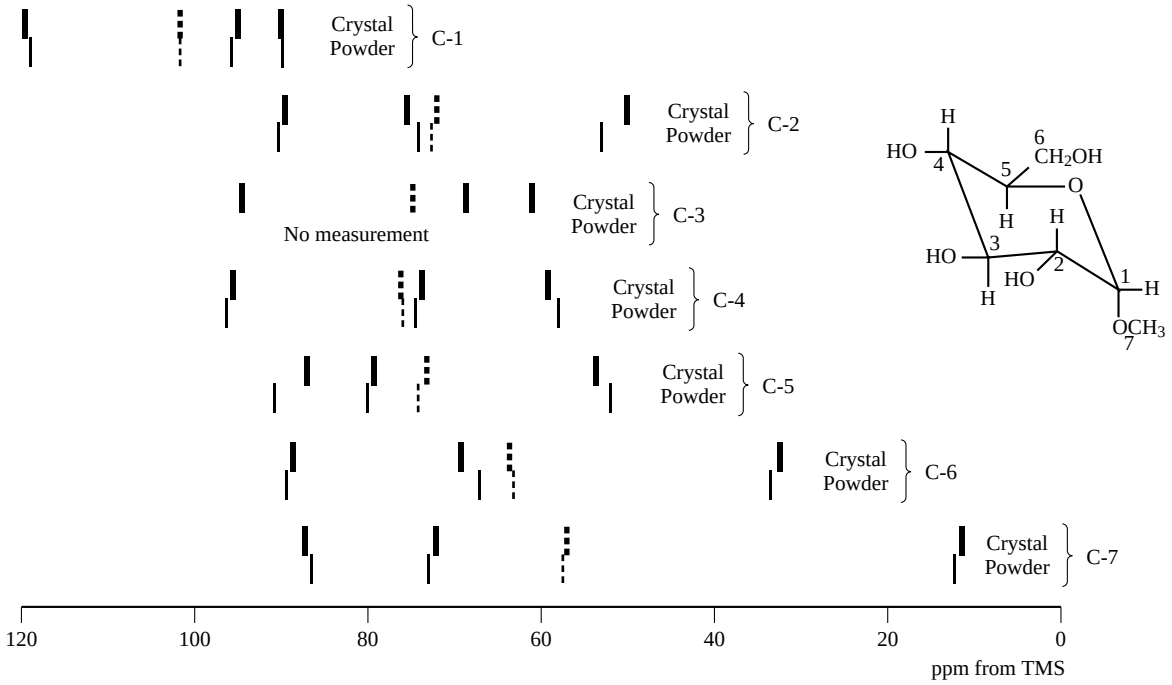

Figure 7 Chemical shift tensor principal values of methyl α-D-glucopyranoside. The bold lines indicate values measured in a single crystal experiment.[6] The lighter faced lines indicate values measured from fitting the 2D powder spectrum. The dashed lines indicate the values of the average chemical shift, i.e., $\delta_{\text{average}} = \frac{1}{3}(\delta_{11} + \delta_{22} + \delta_{33})$

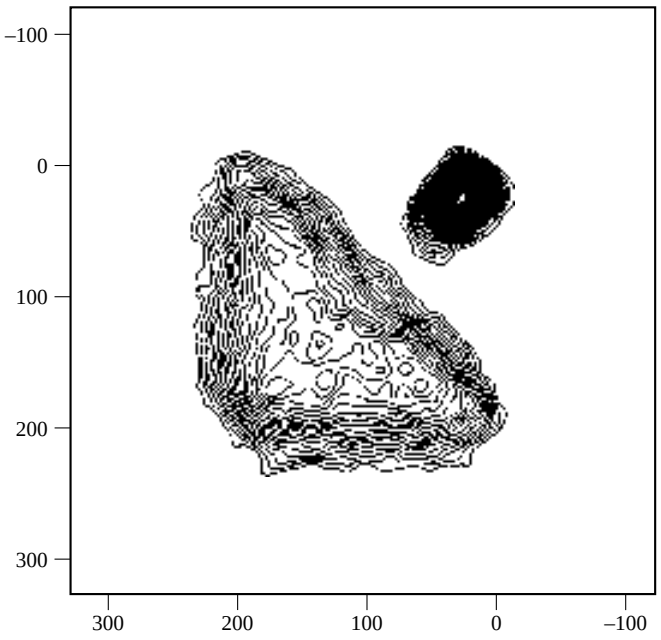

Figure 8 Contour plot of the spectrum of the Argonne premium coal, Pocahontas #3. The Gaussian broadening in this figure is approximately 20 ppm

This quantity has been measured from the spectrum in Figure 8, and the result is 87%. There is good agreement between the aromaticity measured from these data and the more conventional CP MAS result of 86%. An advantage of the chemical shift correlation technique is that it is less sensitive to the Hartmann–Hahn matching condition than is the CP MAS technique. This data also has the potential for testing theoretical models that attempt to correlate the components of the chemical structure of coals and related materials with the distributions of chemical shift anisotropy.

4 SIMULATIONS

In order briefly to establish the correspondence between the principal values of the chemical shift tensor and the features of 2D chemical shift correlation spectra, a series of computer simulations for the 90° sample rotation experiment representing the different classes of chemical shift tensors are shown in Figure 9. The general triangular or hexagonal shape of the simulations is a characteristic of the 90° sample rotation experiment. These simulations show the relationships between the ridges and peaks of this new type of 2D spectrum and the breakpoints in the 1D powder spectra, which are plotted as projections below the 2D simulations.

Often, the measurement of principal values from 1D powder patterns is seriously hindered by nonideal distribution of amplitude across the spectrum, especially when cross-polarization techniques are used. The ability to simulate this amplitude distortion in a 2D powder pattern would increase the accuracy of the measurement of principal values. The frequency and amplitude of the NMR signal from a particular nucleus in a given crystallite in a powdered sample is determined by the principal values of its chemical shift tensor and by that crystallite's orientation relative to the external magnetic field. Therefore, the simulation model is parameterized in terms of chemical shift tensor principal values and the three Euler orientation angles α, β, and γ that describe the relative orientation of the nuclear environment with the external magnetic field in a randomly oriented powder.

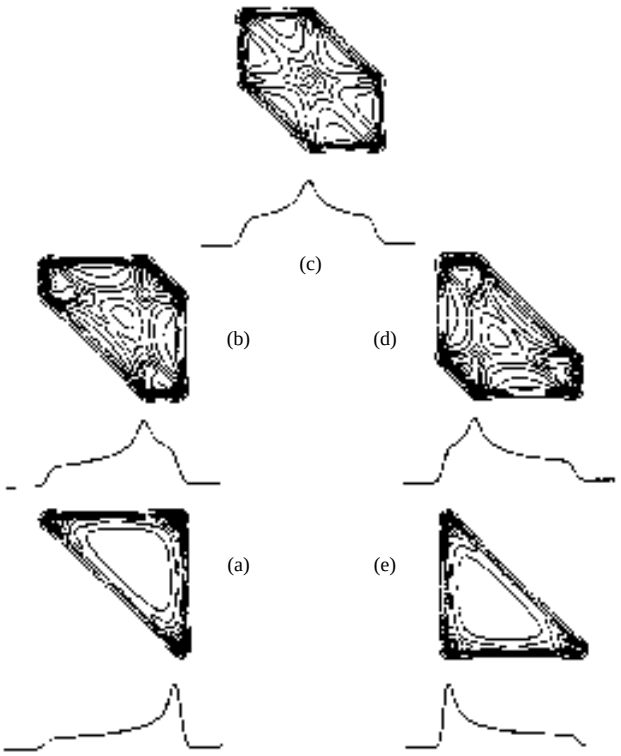

Figure 9 Contour plots of 2D 90° sample rotation simulations resulting from five different chemical shift tensors, showing the correspondence between the features in the 2D powder patterns and conventional 1D powder patterns: (a) axially symmetric chemical shift tensor with low-frequency (upfield) degenerate principal values; (b) general chemical shift tensor with $\delta_{11} - \delta_{22} = 3(\delta_{22} - \delta_{33})$; (c) general chemical shift tensor with $\delta_{11} - \delta_{22}=\delta_{22} - \delta_{33}$; (d) general chemical shift tensor with $3(\delta_{11} - \delta_{22}) = \delta_{22} - \delta_{33}$; (e) axially symmetric chemical shift tensor with high-frequency degenerate principal values

In this experiment, each nucleus in the sample has two resonance frequencies, which correspond to the two different orientations that the nucleus may have with the external field during t_1 and t_2. Assuming a random distribution of crystallite orientations, the simulated hypercomplex 2D FID from a single nucleus in an experiment where the external field is along the x sample axis during t_1 and along the y sample axis during t_2 can be written as

$$\begin{aligned} s_{\text{sim}}(t_1, t_2) = \frac{1}{8\pi^2} \int \mathrm{d}\alpha \sin\beta \, \mathrm{d}\beta \, \mathrm{d}\gamma \, A(\alpha, \beta, \gamma) \\ \times \left[\exp\{\mathrm{i}_1[\omega_x(\alpha, \beta, \gamma) - \omega_0]t_1\} \exp\left(-\frac{t_1^2 \Delta\omega_{\text{G1}}^2}{G^2}\right)\right] \\ \times \left[\exp\{\mathrm{i}_2[\omega_y(\alpha, \beta, \gamma) - \omega_0]t_2\} \exp\left(-\frac{t_2^2 \Delta\omega_{\text{G2}}^2}{G^2}\right)\right] \end{aligned} \quad (2)$$

where $A(\alpha, \beta, \gamma)$ is an amplitude weighting function that depends upon the crystallite orientation in the field. The frequency ω_0 is the spectrometer carrier frequency, and $\Delta\omega_{\text{G1}}$ and $\Delta\omega_{\text{G2}}$ are Gaussian broadenings in the t_1 and t_2 dimensions, respectively. G^2 is a constant equal to $4 \ln (2)/\pi^2$. The imaginary units i_1 and i_2 (with $\mathrm{i}_1^2 = \mathrm{i}_2^2 = -1$) distinguish the independent imaginary parts of the hypercomplex t_1 and t_2 data.[7] The resonance frequencies for the x and y field directions of a given crystallite with an α, β, γ orientation relative to the principal axis frame of the tensor are given by the matrix products

$$\left.\begin{aligned} \omega_x(\alpha, \beta, \gamma) = \boldsymbol{x}^{-1}\mathbf{R}^{-1}(\alpha, \beta, \gamma)\boldsymbol{\delta}\mathbf{R}(\alpha, \beta, \gamma)\boldsymbol{x} \\ \omega_y(\alpha, \beta, \gamma) = \boldsymbol{y}^{-1}\mathbf{R}^{-1}(\alpha, \beta, \gamma)\boldsymbol{\delta}\mathbf{R}(\alpha, \beta, \gamma)\boldsymbol{y} \end{aligned}\right\} \quad (3)$$

where $\boldsymbol{x}$ and $\boldsymbol{y}$ are unit column vectors in the x and y sample frame directions, respectively. The unitary rotation matrix $\mathbf{R}(\alpha, \beta, \gamma)$ rotates the chemical shift tensor $\boldsymbol{\delta}$ from its principal axis frame to the sample frame, and this tensor in the principal axis frame is

$$\boldsymbol{\delta} = \begin{bmatrix} \delta_{11} & 0 & 0 \\ 0 & \delta_{22} & 0 \\ 0 & 0 & \delta_{33} \end{bmatrix} \quad (4)$$

Nonideal amplitude distributions in powder spectra are primarily artifacts resulting from the orientational dependence of both cross polarization and spin relaxation. Functions of orientation described by the Euler angles α, β, and γ are conveniently expanded in the Wigner rotation matrices $\mathcal{D}^{(j)}_{m',m}(\alpha, \beta, \gamma)$, which form a complete, orthonormal basis set.[8,9] The three-dimensional amplitude weighting function that accounts for the polarization efficiency can be expanded as

$$A(\alpha, \beta, \gamma) = \sum_{j,m',m} a^{(j)}_{m',m} \mathcal{D}^{(j)}_{m',m}(\alpha, \beta, \gamma) \quad (5)$$

where the j sum is from 0 to ∞ and the m and m' sums run from $-j$ to $+j$. The expansion coefficients $a^{(j)}_{m',m}$ thus provide a complete description of the different amplitudes resulting from all possible crystallite orientations. The mathematical construct of Equation (5) can also be used to characterize ordering in partially oriented samples.

It can be shown that the simulated 2D FID may be expanded in a complete set of Wigner 2D subFIDs, where the linear coefficients $a^{(j)}_{m',m}$ are the weighting factors for each of the orthonormal Wigner subFIDs $s^{(j)}_{m',m}(t_1, t_2)$ in the basis set

$$s_{\text{sim}}(t_1, t_2) = \sum_{j,m',m} a^{(j)}_{m'm} s^{(j)}_{m',m}(t_1, t_2) \quad (6)$$

These functions can be used to determine any general amplitude distribution in the spectrum using standard linear fitting techniques.

Although all of the fitting is done in the time domain, the 2D Fourier transform of the 2D FID produces the more familiar simulated 2D spectra:[7]

$$\begin{aligned} S(\omega_1, \omega_2) = \int_{-\infty}^{+\infty} \mathrm{d}t_1 \exp(-\mathrm{i}_1\omega t_1) \\ \times \int_{-\infty}^{+\infty} \mathrm{d}t_2 \exp(-\mathrm{i}_2\omega t_2) s(t_1, t_2) \end{aligned} \quad (7)$$

Likewise, the Fourier transforms of the subFIDs give the subspectra:[10]

$$\begin{aligned} S^{(j)}_{m',m}(\omega_1, \omega_2) = \int_{-\infty}^{+\infty} \mathrm{d}t_1 \exp(-\mathrm{i}_1\omega t_1) \\ \times \int_{-\infty}^{+\infty} \mathrm{d}t_2 \exp(-\mathrm{i}_2\omega t_2) s^{(j)}_{m',m}(t_1, t_2) \end{aligned} \quad (8)$$

The first subspectrum in the series, $S^0_{0,0}$, is the 'ideal' powder spectrum. This subspectrum represents the case where each

spin in the sample contributes the same amplitude to the spectrum, and where every crystallite orientation is equally probable. This term is also the only member of the expansion whose integrated spectrum has a nonzero volume. The higher order subspectra in the series are positive in some areas and negative in others, so that they integrate to zero volume over the domain of the spectrum. These higher order subFIDs or subspectra describe modifications in the spectral amplitude that deviate from the 'ideal' powder response, and may be used to characterize the orientational dependence of the amplitude that results either from experimental artifacts or from macroscopically ordered samples. It has been found for most powder spectra that the number of terms necessary to simulate effectively all of the deficiencies in the spectrum is relatively small, indicating that $A(\alpha, \beta, \gamma)$ is a fairly smooth function in α, β, and γ. It has also been found for the 2D powder spectra presented here that the coefficient $a^0_{0,0}$ is much larger than the higher order coefficients, supporting the general observation that the amplitude distribution across a powder pattern is nearly ideal, with only relatively small nonideal contributions.

5 DISCUSSION

The chemical shift tensor principal values reported here result from fitting simulations calculated from Equation (6) to the data. The fitting is done in the time domain, where the fractional residual is taken as the figure of merit for any given simulation, and is minimized to find the 'best fit'. The fractional residual is defined as

$$\text{fractional residual} = \frac{\sum_{t_1,t_2} |s_{\text{data}}(t_1, t_2) - k s_{\text{sim}}(t_1, t_2)|^2}{\sum_{t_1,t_2} |s_{\text{data}}(t_1, t_2)|^2} \quad (9)$$

where $s_{\text{data}}(t_1, t_2)$ is the 2D hypercomplex data FID, and k is a scaling constant that adjusts for experimental factors in the acquisition and processing of the data.

The 'best fit' results for ferrocene, coronene, polyethylene, and polypropylene given in Table 1 are in excellent agreement with previous results.[11–14] The chemical shift principal values differ by 3 ppm or less from the values measured with other techniques, while the average chemical shifts i.e., $\delta_{\text{average}} = \frac{1}{3}(\delta_{11} + \delta_{22} + \delta_{33})$ differ from published CP MAS isotropic chemical shifts by 1 ppm or less.

This 2D technique has some distinct advantages over other methods for measuring ^{13}C shift tensor principal values in complex powdered solids. The inherent correlation and resolution advantage of 2D powder spectroscopy over conventional 1D techniques is evident in the spectra of coronene, polypropylene, methyl α-D-glucopyranoside, and coal. Powder patterns that overlap severely in 1D spectra can often be untangled with this 2D spectroscopy. Another powerful advantage of the technique is that the data can be simulated and fit with a high degree of fidelity using a straightforward physical model.

Another significant advantage of the technique is its simplicity. The sample does not spin at high speeds at the

Table 1 Chemical Shift Tensor Principal Values from Fits (ppm from External Liquid TMS)

	$\delta_\perp$		$\delta_\parallel$	δ_{average}	δ_{liquid}
Ferrocene:					
This work	94		17	68	
Previous results[11]	94		18	69	69.4
	$\delta_\perp$		$\delta_\parallel$	δ_{average}	δ_{CPMAS}
Coronene:					
(Protonated)					
This work	178		15	124	
Previous results[12]	175		15	122	123.5
(Bridging)					
This work	197		−15	126	
Previous results[12]	196		−16	125	126.0
(Inner)					
This work	193		−26	120	
Previous results[12]	191		−26	119	119.8
	δ_{11}	δ_{22}	δ_{33}	δ_{average}	δ_{CPMAS}
Polypropylene:					
(Methine)					
This work	37	22	22	27	26.5
Previous results	38[14]	21[14]	21[14]	27[14]	26.5[13]
(Methylene)					
This work	65	45	25	45	44.5
Previous results	65[14]	44[14]	26[14]	45[14]	44.5[13]
(Methyl)					
This work	32	32	5	23	22.5
Previous results	32[14]	32[14]	3[14]	22[14]	22.5[13]

magic angle; therefore, the probe can be designed to accept a larger volume sample inside a transverse solenoidal coil in order to optimize sensitivity. The 90° rotation of the sample is not difficult to accomplish accurately, both in terms of constructing and driving the mechanism. The sample is stationary during the cross-polarization time, which results in more effective Hartmann–Hahn matching. The principal values of the chemical shift are represented in frequencies measured from the spectrum, not from information encoded in spinning sideband amplitudes, as in slow spinning techniques. Furthermore, the frequencies of the principal values of the chemical shift tensors are measured directly from the spectra; there is no scaling factor relating the frequencies measured in the spectrum to the principal values of the chemical shift tensor.

6 RELATED ARTICLES

Chemical Shift Tensor Measurement in Solids; Chemical Shift Tensors; Chemical Shift Tensors in Single Crystals; Coal Structure from Solid State NMR; Double Resonance; Fossil Fuels; Magic Angle Turning and Hopping; Multidimensional Spectroscopy: Concepts; Polymer Dynamics and Order from Multidimensional Solid State NMR; Polymer Physics; Sideband Analysis in Magic Angle Spinning NMR of Solids; Variable Angle Sample Spinning.

7 REFERENCES

1. J. Jeener, B. H. Meier, P. Bachmann, and R. R. Ernst, *J. Chem Phys.*, 1979, **71**, 4546.
2. C. M. Carter, D. W. Alderman, and D. M. Grant, *J. Magn. Reson.*, 1985, **65**, 183.
3. P. M. Henrichs, *Macromolecules*, 1987, **20**, 2099.
4. C. D. Hughes, M. H. Sherwood, D. W. Alderman, and D. M. Grant, *J. Magn. Reson., Ser. A*, 1993, **102**, 58.
5. D. J. States, R. A. Haberkorn, and D. J. Ruben, *J. Magn. Reson.*, 1982, **36**, 286.
6. D. L. Sastry, K. Takegoshi, and C. A. McDowell, *Carbohydr. Res.*, 1987, **165**, 161.
7. R. R. Ernst, G. Bodenhausen, and A. Wokaun *Principles of Nuclear Magnetic Resonance in One and Two Dimensions*, Clarendon Press, Oxford, 1987, Chap. 6
8. A. R. Edmonds, *Angular Momentum in Quantum Mechanics*, Princeton University Press, Princeton, NJ, 1960, Chaps. 1 and 4.
9. M. E. Rose, *Elementary Theory of Angular Momentum*, Wiley, New York, 1957.
10. R. Hentschel, J. Schlitter, H. Sillescu, and H. W. Spiess, *J. Chem. Phys.*, 1978, **68**, 56.
11. D. E. Wemmer and A. Pines, *J. Am. Chem. Soc.*, 1980, **103**, 34.
12. H. A. Resing and D. L. VanderHart, *Z. Phys. Chem.*, 1987, **151**, 137.
13. A. Bunn, M. E. A. Cudby, R. K. Harris, K. J. Packer, and B. J. Say, *J. Chem. Soc., Chem. Commun.*, **1981**, 15.
14. T. Nakai, J. Ashida and T. Terao, *Magn. Reson. Chem.*, 1989, **27**, 666.

Biographical Sketch

Craig D. Hughes. *b* 1963. B.S., 1985, New Mexico Institute of Mining and Technology; Ph.D., University of Utah, 1992. Introduced to NMR by L. G. Werbelow and D. M. Grant. Research specialties; characterization of powdered, heterogeneous and oriented materials, catalytic zeolites, and imaging.

Force Detection and Imaging in Magnetic Resonance

Costantino S. Yannoni
Almaden Research Center, San Jose, CA, USA
and
Othmar Züger
University of Washington, Seattle, WA, USA

1 Introduction 1
2 Principles of Magnetic Resonance Force Microscopy 1
3 Experimental Results 2
4 Detecting the NMR of a Single Proton 7
5 Summary and Conclusions 7

1 INTRODUCTION

NMR is not only the most detailed probe of molecular structure and dynamics with the highest spectral resolution, it is also the basis for MRI. Nonetheless, an ever-present drawback of NMR, due to the low transition frequency, is a requirement for large amounts of sample, containing at least 10^{15}–10^{16} spins. Therefore, the suggestion by Sidles[1] that it might be possible to use force to detect and image the nuclear resonance of a single proton was remarkable. His idea was to effect three-way resonant coupling among (1) a precessing proton mounted on (2) a vibrating substrate and (3) a mechanical oscillator holding a magnetic particle which produces both a dc field and a strong magnetic field gradient. The proton exerts a force on the mechanical oscillator through interaction with the magnetic field gradient generated by the particle. Energy transfer into the oscillator, mediated via the magnetic force between the proton and oscillator, is sufficient that single-proton detection is possible by sensing excitation of the mechanical oscillator.

Sidles also carried out a quantum mechanical analysis of his proposal,[2] showing the resemblance to a Stern–Gerlach experiment[3] in the sense that the linear trajectory of the spins in the latter becomes folded into the cyclic phase-space trajectory of the oscillator on which the gradient source is mounted. Sidles et al.[4] have comprehensively discussed the physics of oscillator-coupled imaging, while Sidles and Rugar[5] have compared the sensitivity of force and inductive methods of detection and have concluded that the former is a viable alternative to the latter as size is reduced to dimensions of the order of tens of nanometers. The first experimental force detection of magnetic resonance was achieved by Rugar et al.,[6] who used a modified magnetic force microscope[7] to detect electron spin resonance (ESR). A key feature of their approach was to modulate the ESR condition at low frequency in order to overcome the gap between the Larmor frequency of electron spins, normally in the gigahertz range, and the kilohertz frequencies of mechanical cantilevers used for atomic or magnetic force microscopy. Subsequently, Züger and Rugar[8,9] were able to obtain ESR images demonstrating spatial resolution of about $1\,\mu$m. Most recently, Rugar et al. made the first successful force detection of NMR with subfemtonewton force sensitivity.[10] Based on these results and the near-theoretical performance of their force probe, they estimated that it should be possible to detect a single proton at temperatures of about 1 K.

Sidles and Garbini[11] have reviewed the current status of magnetic resonance force microscopy, and have concluded that the use of a submicrometer size gradient source, coupled with interferometric detection methods,[12,13] make single-spin detection with a magnetic resonance force microscope (MRFM) a realistic possibility. Bloom[14] has analyzed Sidles's proposed single-spin-imaging idea in the light of Stern–Gerlach phenomenology,[15] and more recently, Leskowitz and Weitekamp[16] have suggested a method for doing force-detected NMR spectroscopy using rf gradients. In the present article the principles underlying magnetic resonance force detection and microscopy, as well as the ESR and NMR experiments are reviewed.[16a] A brief discussion of the feasibility of imaging a single proton is also given.

The appeal of single-spin NMR is compelling. Single-nucleus magnetic resonance with subangstrom spatial resolution would revolutionize the determination of molecular structure, and myriad significant applications could lead to breakthroughs in materials science as well as in the biological sciences. Even at much lower levels of spatial resolution (of the order of tens to hundreds of angstroms), MRFM would signify a quantum leap in the imaging power of magnetic resonance microscopy.

2 PRINCIPLES OF MAGNETIC RESONANCE FORCE MICROSCOPY

The force detected in MRFM is given by

$$\boldsymbol{F} = (\boldsymbol{m} \cdot \nabla)\boldsymbol{B} \tag{1}$$

where $\boldsymbol{m}$ is a magnetic moment due to electron or nuclear spins, and $\boldsymbol{B}$ is an inhomogeneous magnetic field. The spin magnetic moment is $\boldsymbol{m} = \boldsymbol{M}V$, where $\boldsymbol{M}$ is the Curie spin magnetization and V is the sample volume. $\boldsymbol{M}$ is given by[17]

$$\boldsymbol{M} = N\gamma^2\hbar^2 I(I+1)\boldsymbol{B}/3k_{\mathrm{B}}T \tag{2}$$

where N is the number of spins per unit volume, γ is the spin magnetogyric ratio, I is the nuclear spin quantum number, and k_{B} is Boltzmann's constant. A sketch of a probe for doing force-detected magnetic resonance is shown in Figure 1.

The apparatus resembles a magnetic force microscope[7] with the addition of a millimeter-size rf coil mounted close to the sample. The coil provides an oscillating field to excite magnetic resonance. In the absence of rf excitation, the force on the spin magnetization of the sample, mounted on the cantilever, in the field gradient generated by the nearby magnetic particle

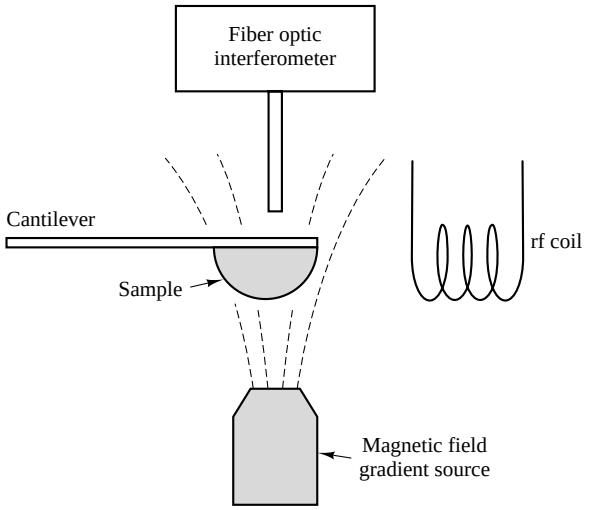

Figure 1 Basic configuration of a magnetic resonance force microscope. The force on the sample magnetization in the gradient of a proximate magnetic field source causes a deflection of the cantilever which is sensed optically. The rf coil is used to excite spin resonance

causes a deflection of the cantilever which is sensed by a fiber-optic interferometer.[12,13] If the spin magnetization is changed, then the force and corresponding cantilever deflection will be changed and sensed. Magnetic resonance techniques can be used to manipulate the spin magnetization by applying an rf field. The device sensitivity can be increased considerably by changing the sample magnetization at the same frequency as the mechanical resonance frequency of the cantilever.[4] The cantilever deflection amplitude is then enhanced by the quality factor of the cantilever, and the resulting vibration amplitude is

$$A = Q(F/k) \tag{3}$$

where Q is the quality factor, and k the spring constant of the cantilever. The deflection signal is synchronously detected at the cantilever frequency using a lock-in amplifier and experiments are carried out in modest vacuum (about 0.133–0.0133 Pa) in order to avoid air damping of the cantilever motion which would result in a low Q. Typical Q values of cantilevers used for atomic force microscopy (AFM)[18] in vacuo are 10^3 to 10^5. The kilohertz resonance frequency and high Q result in time constants of the order of seconds. Since this corresponds to the time it takes to build up to the cantilever amplitude given by equation (3), the low-frequency spin motion required to change the spin magnetization at the cantilever frequency should be sustained for a correspondingly long time. In existing devices, sensitivity of the MRFM is limited mainly by thermal noise, manifested as a fluctuating force acting on the cantilever:[4,19,20]

$$F_{\min} = (4kk_{\mathrm{B}}T\,\Delta\nu/Q\omega_{\mathrm{c}})^{1/2} \tag{4}$$

where ω_{c} is the cantilever frequency and $\Delta\nu$ is the detection bandwidth in hertz. The minimum detectable magnetic moment in the presence of thermal noise is therefore given by:

$$m_{\min} = F_{\min}/|\nabla B| \tag{5}$$

This moment sets a lower limit on the number of spins that can be detected.

3 EXPERIMENTAL RESULTS

3.1 Electron Spin Resonance

The first successful force detection of magnetic resonance was carried out on a sample containing unpaired electron spins.[5] A micrometer-size sample of diphenylpicrylhydrazyl (DPPH) was mounted on a silicon nitride cantilever of the type commonly used for atomic force microscopy.[21] The cantilever was 200 μm long and 0.7 μm thick, with a force constant k = 0.1 N m^{-1} The frequency of the loaded cantilever was 8 kHz and Q was 2000. The experiment was done at room temperature in a vacuum of about 0.133 Pa. The gradient source, which generated a field gradient of 10 T m^{-1} at the sample, was a cylindrical NdFeB permanent magnet, 3 mm long and 3 mm diameter. A continuous wave 220 MHz rf field was applied to the spins via a millimeter-size coil positioned about 1 mm from the sample. A small electromagnet was used to scan and modulate the dc field.

3.1.1 Cyclic Saturation

As noted above, detection sensitivity is enhanced if the spin magnetization is made to oscillate at the resonance frequency of the cantilever. This was accomplished by means of a cyclic saturation technique,[22] which is illustrated in Figure 2. To understand the technique, it is useful to consider the behavior of the longitudinal magnetization when the sample is subjected to an rf field $\boldsymbol{B}_1$, which is linearly polarized in a direction perpendicular to the dc field B_z. This case has been investigated theoretically.[23] Figure 2(a) shows M_z as a function of

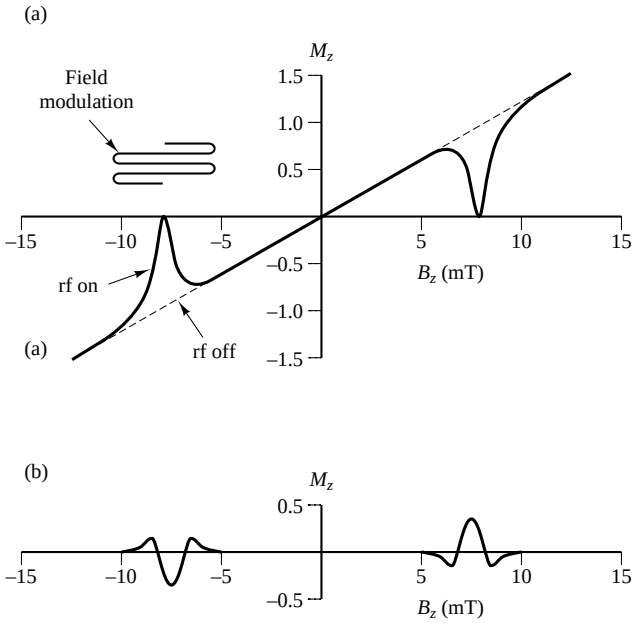

Figure 2 (a) The behavior of longitudinal magnetization (M_z) under the influence of an rf field in the presence of relaxation. The field modulation shown is used to change the resonance condition at the cantilever frequency and to excite the cantilever. M_z is suppressed when the resonance condition is met. (b) The second harmonic response resulting from modulation of the resonance condition effected by field modulation

an externally applied field, the resultant of the field from the electromagnet and proximate NdFeB magnet. The effect of the 220 MHz rf field is to saturate the spin levels at resonance, $B_z = \pm 7.9$ mT, driving M_z to zero. The low-frequency force modulation necessary to enhance deflection of the cantilever [equation (3)] can thus be achieved by cyclic saturation, i.e. by modulating the amplitude of the electron spin magnetization. This was accomplished by modulating the dc field in and out of resonance. When the modulation amplitude is zero, the field is on resonance and $M_z = 0$, due to saturation by the rf field, while off resonance, M_z will recover if the electron spin–lattice relaxation time T_{1e} is sufficiently short. Since T_{1e} in DPPH[22] is 6.2×10^{-8} s and the modulation period is much longer (2.5×10^{-4} s for a 4 kHz modulation frequency), M_z recovers fully when the modulation moves the field off resonance. Furthermore, M_z goes to zero twice during each modulation cycle, resulting in the second harmonic response (M_2) shown in Figure 2(b). Therefore, modulation of B_z at 4 kHz excites the cantilever at its resonance frequency (8 kHz), thus minimizing on-resonance feed-through problems that arise when the modulation frequency is 8 kHz. This process can be continued indefinitely due to the short electron spin T_{1e}, thus giving the cantilever ample time to build up a large deflection amplitude.

3.1.2 Force Detection of ESR

Figure 3(a) shows the vibration amplitude of the cantilever on which the DPPH sample was mounted as the dc field was scanned and modulated at 4 kHz. The peaks in the cantilever oscillation amplitude occurred when the ESR condition was met. The 0.28 nm cantilever vibration corresponds to an oscillatory driving force of only 10^{-14} N. Figure 3(b) shows a calculation of the second harmonic response, M_2, using known experimental parameters. The modulation field used was 1 mT (zero to peak), and the rf field strength, obtained from the simulation, was 3.4 mT. The change in cantilever frequency due to sample loading indicated that approximately 15 ng of DPPH, corresponding to 2×10^{13} electron spins, contributed to the signal. The good agreement between experiment and theory is evident in Figure 3.

The gradient used to obtain the data shown in Figure 3(a) was 10 T m^{-1}. When this was increased to 60 T m^{-1} by using a smaller magnetic particle, two resonance lines spaced 1.1 mT apart were resolved, suggesting that there may be two spatially separated DPPH particles, an idea confirmed upon inspection with an optical microscope. This spectral separation corresponded to a distance of 19 μm. The fact that such high spatial resolution was obtained in the first force detection experiment illustrates the imaging potential of force detection of magnetic resonance.

3.1.3 Force-Detected ESR Microscopy

The first MRFM images were obtained by Züger and Rugar[8,9] on micrometer-size particles of DPPH. An optical micrograph of critical components of the probe, similar to that used for the ESR experiment, is shown in Figure 4. The spring constant of the silicon nitride cantilever.[24] was $k = 0.05$ N m^{-1} and the rf coil (0.7 mm diameter, 2.5 turns), located 0.5 mm from the sample, was tunable from 800 to 1610 MHz. The magnetic field gradient source, a conical NdFeB permanent

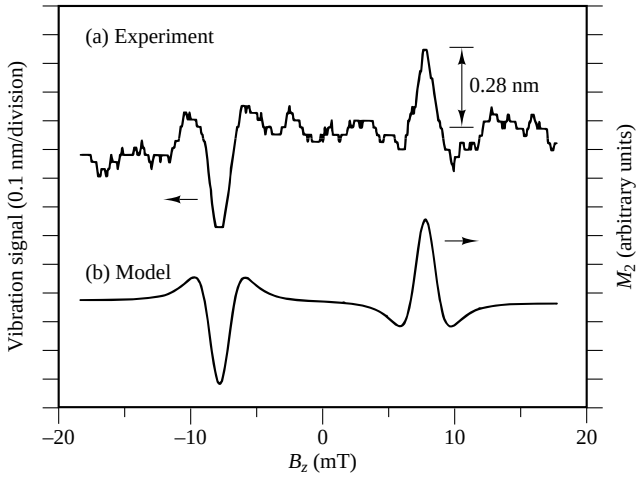

Figure 3 (a) Amplitude of cantilever vibration as the polarizing field is scanned through the ESR condition for DPPH. The field was modulated at 4 kHz with a zero-to-peak amplitude of 1 mT. The data shown are the average of 54 sweeps, each lasting 20 s. The time constant of the lock-in amplifier was 0.3 s. (b) Calculation of the second-harmonic response of the magnetization induced by modulation of the ESR of DPPH. The only parameter that was not known was the strength of the rf field, chosen to be 3.4 mT on the basis of the best fit with the data in (a)

magnet (0.5 mm diameter, 1 mm long) was mounted on a piezoelectric translator to allow mechanical scanning in any of three dimensions relative to the sample (mounted on the cantilever). Figure 5(a) shows a surface of constant (resonance) field $\boldsymbol{B}_t(x,y,z) = \boldsymbol{B}_0$ generated by such a tip. The imaging behavior of the MRFM can be understood by moving a point sample in the xy plane perpendicular to the symmetry axis z of the tip. Since the $\boldsymbol{B}_0$ surface approximates a paraboloid the apex of which is located along the axis of the tip, intersection of the sample with such a surface results in force mapping of a circle of resonance responses. The diameter of the circle depends on the distance from the tip to the sample along the symmetry axis of the tip (z coordinate). This behavior,

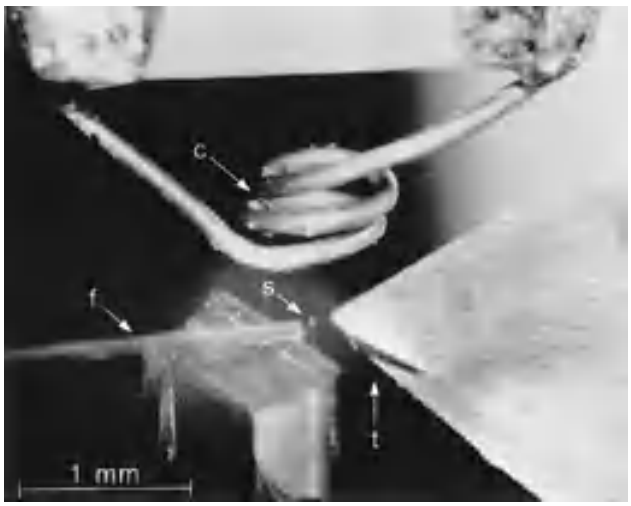

Figure 4 Optical micrograph of key components of the force probe developed by Züger and Rugar[8,9] for ESR imaging. f, Optical fiber of the interferometer; c, rf coil; t, permanent magnet tip (dark region); s, DPPH sample glued on the cantilever

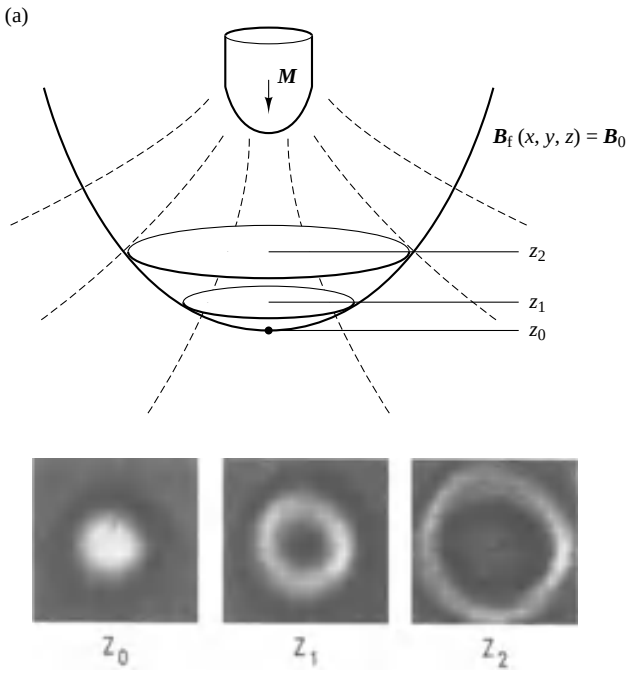

Figure 5 (a) Dashed lines, showing the magnetic field lines from a conical-shaped magnetic tip used for ESR force imaging. The surface of constant field strength is a paraboloid near the axis of the tip, and the circles indicate where the magnetic resonance condition is met on the surface $\boldsymbol{B} = \boldsymbol{B}_0$ as the tip is scanned in the xy plane at a fixed sample distance z from the tip. (b) Measured force maps for a small DPPH particle scanned in the xy plane at three different distances from the tip: $z_0 \approx 200\,\mu$m, $z_1 = z_0 - 3\,\mu$m, and $z_2 = z_0 - 8\,\mu$m. The gray scale represents cantilever vibration amplitude, with white representing maximum amplitude. The image size is $200\,\mu\text{m} \times 200\,\mu\text{m}$

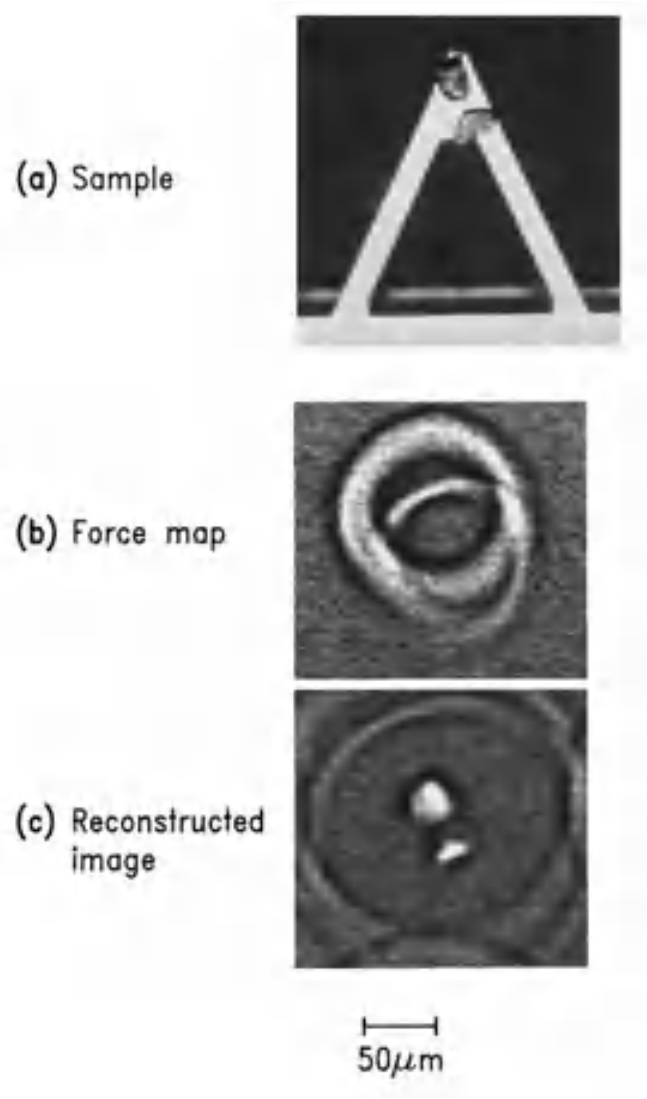

Figure 6 (a) Optical micrograph showing two DPPH particles (about $20\,\mu$m wide) attached to a silicon nitride cantilever. The distance between particles is about $35\,\mu$m. (b) Magnetic resonance force map of the sample measured at a distance of $z = z_0 - 6 \approx 124\,\mu$m. The data shown consist of a 128×128 pixel array which was acquired during a 90-min scan. (c) Reconstructed spin density image obtained by deconvolving the data in (b) using a Wiener filter. The two bright features correspond to the two DPPH particles. The large rings slightly visible in the image are artifacts of the deconvolution procedure

sketched in Figure 5(a) for three different values of z, has been confirmed experimentally, as shown in Figure 5(b). If the tip is at z_0, resonance only occurs at the apex of the paraboloid, resulting in a single-point response, while at distances closer to the tip force mapping traces out circles of resonance which get larger as the tip is approached. These results permitted a quantitative characterization of the tip field, from which a point-response function, the oscillatory force per spin as a function of position, can be determined. This function can then be used to reconstruct the spatial distribution of spin density from the force map of a three-dimensional sample.

The success of this approach is illustrated in Figure 6, which shows the results of a two-dimensional ESR force mapping of the unpaired electron spin density in two micrometer-size particles of DPPH. An optical micrograph of the sample mounted on the cantilever [Figure 6(a)] shows that the particles are about $20\,\mu$m wide and are separated by $35\,\mu$m. An ESR force map of this sample, taken at a distance from the tip of about $124\,\mu$m, is shown in Figure 6(b). Two resonance circles with slightly different diameter and radial thickness were obtained. The diameter difference is due to a small difference in the z position of the particles, while a difference in lateral particle size accounts for the difference in circle thickness. An image-reconstruction technique using inverse filtering resulted in the spin density image shown in Figure 6(c). The ESR image shows two spin density maxima $35\,\mu$m apart, in agreement with the optical micrograph. Even the triangular shape of the lower particle in Figure 5(a) is reproduced in the reconstructed image. The extension of this method to three dimensions using a set of force maps measured at different values of z is straightforward.

An estimate of the resolution of the MRFM used in this experiment was obtained from a knowledge of the ESR linewidth and the axial and lateral gradients characterizing the magnetic tip. The spatial resolution in the z direction was determined to be about $1\,\mu$m, a factor of at least 5 greater than the resolution achieved using conventional ESR imaging methods.[25,26] The resolution in the lateral xy direction was estimated to be $5.3\,\mu$m. An analysis of the signal-to-noise ratio indicated that 10^9 electron spins could be detected. Thus, even in these early experiments, force detection was quite sensitive, being comparable to 140 GHz high-field ESR.[27]

3.2 NMR

3.2.1 Challenges

Force detection of NMR, which was recently reported,[10] presented a greater challenge than ESR for two reasons: (1) the magnetic moment of, and corresponding force exerted by, any nucleus is about 10^3 times less than for electron spins (657 times less for protons); and (2) nuclear spin–lattice relaxation times are typically 10^6 times longer than the electron spin T_{1e}, and thus the cyclic saturation method used in the ESR experiment will not work. In order to meet these challenges, three steps were taken: (1) ultrathin cantilevers which yielded subfemtonewton force sensitivity were fabricated;[20] (2) the experiment was carried out at higher magnetic field (2.4 T) to increase the nuclear magnetization which interacts with the gradient source; and (3) the required low-frequency force modulation was produced by means of cyclic adiabatic inversion, a method which can be used periodically to invert the direction of the nuclear magnetic moment.[28]

3.2.2 Custom-Fabricated Cantilevers

A micrograph of the silicon nitride cantilever which was custom-fabricated by Hoen et al.[20] is shown in Figure 7. This cantilever, which is considerably smaller than the one used for the ESR experiment,[6] has a stem 50 μm long and 5 μm wide which supports a 30 μm × 30 μm paddle. The proton-containing sample, 14 ng of ammonium nitrate, was mounted on this paddle using UV-curable epoxy glue. The cantilever is only 90 nm thick, resulting in a spring constant of 10^{-3} N m^{-1}, at least 30 times smaller than for typical AFM cantilevers. The force sensitivity, to our knowledge the highest reported to date, was found[20] to be 5×10^{-16} N. The frequency of the loaded cantilever was 1.4 kHz with an intrinsic Q value of 3000.

3.2.3 Cyclic Adiabatic Inversion

Cyclic adiabatic inversion is a CW NMR method which works well with nuclei that have long spin–lattice relaxation times.[28] Since nuclear magnetization is not only conserved but reversed in sign during an adiabatic passage, the force created between the magnetization and a gradient source will oscillate sinusoidally. Therefore, subjecting the nuclear spins to a prolonged sequence of cyclic adiabatic reversals will generate the low-frequency spin motion required to enhance the cantilever deflection amplitude. The inversion was accomplished by using the frequency modulation scheme shown in Figure 8(a).

Before the rf field is turned on, the rf frequency is set 500 kHz (several linewidths) below resonance, as shown in Figure 8(a). After allowing time for the nuclei to polarize (dashed lines), the rf amplitude is turned up, creating an effective field in the rotating frame.[29]

$$\boldsymbol{B}_{\text{eff}} = \boldsymbol{B}_1\hat{\boldsymbol{x}} + (B_z - \omega/\gamma)\hat{\boldsymbol{z}} \tag{6}$$

where ω is the radiofrequency. Since the frequency is far below resonance, the proton magnetization $\boldsymbol{M}_0$ becomes locked along an effective field[30] parallel to $\boldsymbol{B}_0$ so that the longitudinal component M_z has a maximum positive value [Figure 8(b)].

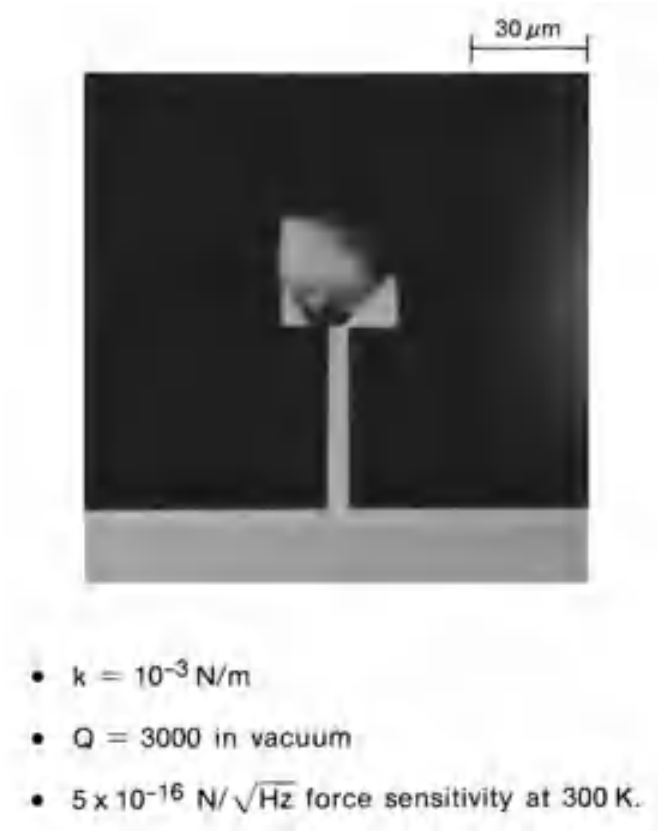

Figure 7 Optical micrograph of the 90 nm thick silicon nitride cantilever. A small grain of the sample (ammonium nitrate) is visible on the upper portion of the paddle-shaped cantilever. The narrow stem of the cantilever is 50 μm long and 5 μm wide. The cantilever was fabricated by S. Hoen, IBM Almaden Research Center

$\boldsymbol{M}_z$ is of interest since the deflection of the cantilever is along the z direction, i.e. the relevant force is

$$F_z = M_z V(\partial B_z/\partial z) \tag{7}$$

where V is the sample volume. The frequency is then slewed onto resonance sufficiently slowly that the adiabatic condition is satisfied:[31]

$$|\mathrm{d}\boldsymbol{B}_{\text{eff}}/\mathrm{d}t| \ll \gamma_{\text{H}}\boldsymbol{B}_1^2 \tag{8}$$

where γ_{H} is the proton magnetogyric ratio. The direction of $\boldsymbol{M}_0$ follows the direction of the effective field[29] and M_z decreases to zero as the rf approaches the resonance value. As the frequency sweep is continued through resonance, M_z becomes negative. At the most positive frequency excursion, M_z reaches a maximum negative value. The modulation is then continued as shown in Figure 8(a) and the resulting time-dependent longitudinal magnetization (Figure 8(b)) makes the force on the sample cyclic and causes the cantilever to vibrate at its resonance frequency. This process is continued as long as the amplitude of the magnetization does not decay so much that the oscillating force becomes too small for the cantilever to be excited. The proton magnetization decays in two ways: (1) violation of the adiabatic condition, and (2) a short relaxation time in the rotating frame ($T_{1\rho}$).[30] The adiabatic condition can

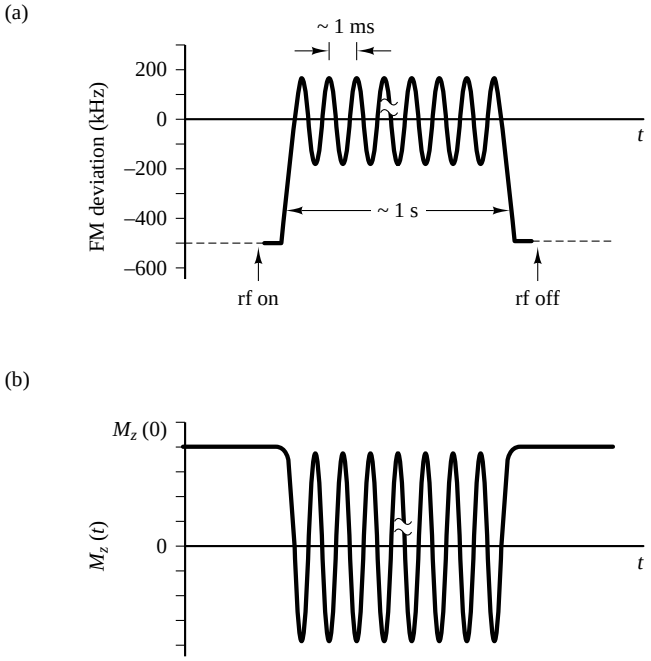

Figure 8 (a) Frequency modulation pattern used for cyclic adiabatic inversion. The dashed lines indicate time (>4 s) that is used to allow the nuclei to polarize with the rf field off. A single modulation cycle lasts about 1 ms, and in the actual experiment is repeated several thousand times. (b) Time dependence of M_z resulting from the frequency modulation shown in (a)

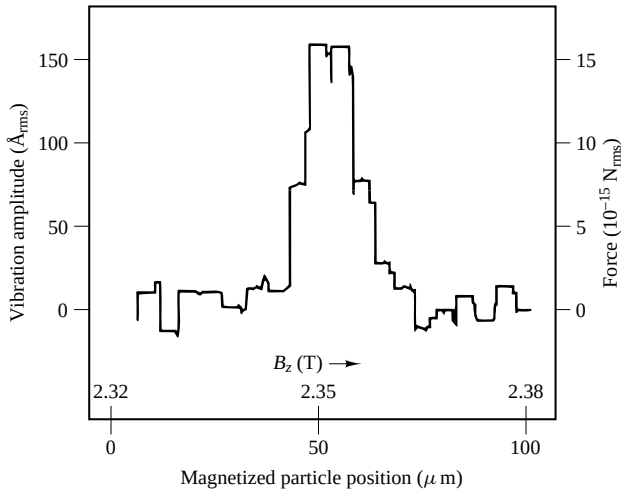

Figure 9 Amplitude of the cantilever vibration as the magnetized particle is moved relative to the ammonium nitrate sample, scanning the field through the ^{1}H resonance. At each discrete position of the particle, indicated by the plateaus, the modulation sequence shown in Figure 8(a) is applied to the sample and the peak cantilever vibration amplitude was measured. The rms force noise is about 5×10^{-16} N

be satisfied readily since the rf and modulation field strengths can be varied independently (the modulation frequency is fixed at the cantilever frequency). Decay due to rotating-frame relaxation depends primarily upon the presence of low-frequency lattice motions,[32] and in this respect ammonium nitrate is a favorable material since the protons have a long $T_{1\rho}$ (about 2 s) at room temperature.[33,34] Since this was a first attempt at force detection of NMR, a comprehensive study of the spin dynamics in bulk ammonium nitrate was carried out[34] to ensure that the proton magnetization would (1) follow the behavior sketched in Figure 8(b) and (2) not decay too quickly while subject to the irradiation shown in Figure 8(a). The parameters used to achieve cyclic adiabatic reversal in the force experiment were guided by the results of this study.

3.2.4 Force Detection and Imaging of NMR

The gradient source in this experiment was a magnetizable iron cylinder (1.5 mm diameter, 4 mm long) mounted on a piezoelectric translator. In an external field of 1.95 T, the iron cylinder produced an additional field of 0.4 T when positioned 700 μm from the sample, resulting in a total field of 2.35 T and a proton resonance frequency of 100 MHz. The gradient at the sample was 600 T m^{-1}. The experiment was carried out at room temperature in a vacuum of about 0.0133 Pa.

In order to locate the resonance, the dc field was scanned by moving the gradient source relative to the sample/cantilever. Each time the position of the source was changed, the sample was allowed to polarize for about 4 s before the rf was turned on and the frequency modulated as shown. The rf field (1.5 mT at 100 MHz) was generated in a coil 800 μm in diameter positioned 700 μm from the sample and was frequency modulated with a deviation of 170 kHz (4 mT) at the cantilever frequency (1.4 kHz). The angstrom-scale motion of the cantilever was monitored optically[12,13] and the signal synchronously detected using a lock-in amplifier. The result of a 60 mT (100 μm) scan is shown in Figure 9, in which the vibration amplitude of the cantilever is plotted as a function of the position of the gradient source. The plateaus along the horizontal represent discrete positions of the gradient source, corresponding to discrete values of the field at the sample. The cantilever deflection amplitude reached a maximum of 160 Å (16 nm) at the field strength where the proton resonance condition was met with a single-scan root-mean-square (rms) signal-to-noise ratio of 22. Since the sample contained 3.6×10^{14} protons, the minimum detectable number of protons (a signal-to-noise ratio of unity) was 1.6×10^{13}. The response was confirmed as arising from NMR by changing the rf frequency and locating the maximum in the cantilever response at different positions of the gradient source. The magnetic field gradient of 600 T m^{-1} was also measured using this procedure.

The imaging capability of the MRFM was characterized by performing rapid (5 s) scans of the modulated carrier frequency. The result is shown in Figure 10. The gradient source was fixed, so that different z slices of the sample experienced different dc fields and came into resonance as the rf field swept through the Larmor frequency corresponding to those slices. The plot of cantilever amplitude (force) is thus a plot of proton spin density in the z direction perpendicular to the plane of the paddle (see Figure 7). The strength of the rf and modulation fields was decreased in order to achieve the highest possible spatial resolution. Furthermore, the cantilever was damped to shorten the response time,[35] resulting in an effective Q of 800. The frequency range over which the cantilever responded was 240 kHz, corresponding to a sample thickness of about 9 μm. The width between the 10% and 90% amplitude points at the steepest part of the response (the back side of the sample mounted to the cantilever) was Δf = 67 kHz, corresponding to a spatial resolution of $\Delta z = 2\pi\Delta f$

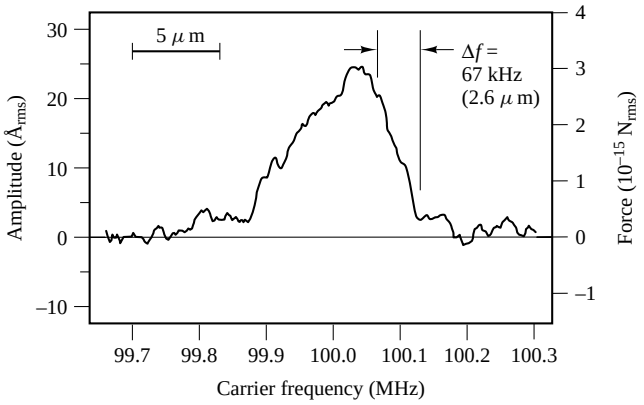

Figure 10 One-dimensional image of proton density in a 12-ng sample of ammonium nitrate, obtained by measuring the cantilever vibration amplitude as a function of the carrier frequency. The 640 kHz frequency range was scanned in 5 s with the rf field on continuously and frequency modulated. The signal-to-noise ratio was improved by averaging 120 scans. The length of the 5 μm bar is based on the 600 T m^{-1} gradient over the sample. The 2.6-μm spatial resolution was estimated from the width of 67 kHz between the 10% and 90% amplitude points on the right-hand edge of the spin density profile. The measurement conditions were: $\boldsymbol{B}_1$ = 0.83 mT, modulation deviation (zero-to-peak) = 25 kHz, and effective cantilever Q = 800

$(\gamma \partial B_z/\partial z)$ = 2.6 μm. This resolution is roughly an order of magnitude greater than has been achieved using conventional NMR microscopy on nonmetallic solid samples.[36]

4 DETECTING THE NMR OF A SINGLE PROTON

The remarkable sensitivity of force detection in the experiments performed to date[6,8,10] coupled with the good agreement between the calculated and experimental performance of the force detection apparatus, permits a realistic quantitative assessment of the possibility of detecting a single proton using force methods. One approach for judging the feasibility of doing this is to note that it was possible to detect the force on 1.6×10^{13} proton magnetic moments in a gradient of 600 T m^{-1}. The actual moment interacting with the gradient is not given by the total number of protons in the sample, but by the excess number in the state with lower Zeeman energy:

$$N = N_{\mathrm{H}}(\hbar\gamma_{\mathrm{H}}\boldsymbol{B}_0/2k_{\mathrm{B}}T) \tag{9}$$

where N_{H} is the total number of protons, and the Boltzmann factor (in parentheses) is about 10^{-5} for a 2.5 T field at ambient temperature. Therefore, only 10^8 proton moments interacted with the gradient and provided the force in the NMR experiment. Thus, the improvement in sensitivity that is required for single-proton detection is 10^8 rather than 10^{13}. Another way of looking at this is to recognize that a single proton is always fully 'polarized', while ensembles of protons are subject to the cancellation of moments inherent in a Boltzmann population of spin states of opposite polarity. The factor of 10^8 improvement in sensitivity can be gained by a combination of higher field gradients, lower temperatures, and improved cantilevers.

A factor of 10^5 in signal strength/spin can be obtained by using a much stronger gradient source. Magnetic tips with a radius of curvature of 30 nm have been fabricated[37] and would generate gradients of 10^8 T m^{-1}. This is 10^5 times greater than the gradient used in the first NMR force-detection experiment,[10] yielding a force/spin and concomitant signal 5 orders of magnitude larger.

Another order of magnitude in sensitivity can be gained by operating at 1 K, resulting in a 10-fold reduction in the force noise due to thermal fluctuations [equation (4)]. Further reduction in force noise can be realized if softer, higher Q cantilevers can be fabricated. For example, it should be feasible to make a silicon nitride cantilever 50 μm long, 2 μm wide and 20 nm thick. The force constant for such a 'diving board' structure would be 5×10^{-6} N m^{-1} with a resonance frequency of 10 kHz and a Q of 10^4. These characteristics lead to another 2 orders of magnitude increase in force sensitivity. Hoen et al.[20] have already shown that it is possible to fabricate ultrathin cantilevers with these dimensions. Compounding these improvements leads to an overall increase in sensitivity of 10^8, making single-proton imaging realistic.

5 SUMMARY AND CONCLUSIONS

The idea of using force to detect magnetic resonance[1] has been realized experimentally for NMR[10] and ESR,[6] with exceptional sensitivity in both instances. Furthermore, the first ESR images from a magnetic resonance force microscope have been obtained with high spatial resolution.[8,9] The theoretical basis for force-detected single-spin imaging has also been investigated, without evidence for violation of any fundamental physical principles.[2,4,14] The ultimate goal of this work is to develop an instrument that can detect NMR from individual atoms within a sample with three-dimensional subangstrom spatial resolution. Such a capability would allow visualization of the three-dimensional structure of molecules and would represent a revolutionary advance in magnetic resonance imaging. Furthermore, because of its subsurface imaging potential and elemental specificity, MRFM would take a major step beyond the capabilities of present-day scanning tunneling and atomic force microscopies. The availability of an atomic MRFM would have broad implications in molecular biology, materials and polymer science, surface science, and nanotechnology.

Achieving the ultimate goal of three-dimensional atomic-scale imaging will be challenging and technically demanding, and will require considerable innovation in a number of areas, especially improved sensors to detect extremely small forces and new methods for manipulating nuclear spins. Despite the enormity of the challenge, the practical applications of single-spin MRFM imaging are sufficiently important, and the results to date sufficiently encouraging, that a serious and sustained MRFM development effort is justified.

6 REFERENCES

1. J. Sidles, *Appl. Phys. Lett.*, 1991, **58**, 2854.
2. J. Sidles, *Phys. Rev. Lett.*, 1992, **68**, 1124.
3. N. F. Ramsey, *Molecular Beams*, Clarendon, Oxford, 1956.
4. J. Sidles, J. Garbini, and G. Drobny, *Rev. Sci. Instrum.*, 1992, **63**, 3881.
5. J. Sidles and D. Rugar, *Phys. Rev. Lett.*, 1993, **70**, 3506.

6. D. Rugar, C. Yannoni, and J. Sidles, *Nature*, 1992, **360**, 563.
7. P. Grütter, H. Mamin, and D. Rugar, in *Scanning Tunneling Microscopy*, ed. R. Wiesendanger and H.-J. Güntherodt, Springer, Berlin, 1992, Vol. 2, pp. 151–207.
8. O. Züger and D. Rugar, *Appl. Phys. Lett.*, 1993, **63**, 2496.
9. O. Züger and D. Rugar, *J. Appl. Phys.*, 1994, **75**, 6211.
10. D. Rugar, O. Züger, S. Hoen, C. S. Yannoni, H. Vieth, and R. D. Kendrick, *Science*, 1994, **264**, 1560.
11. J. A. Sidles and J. L. Garbini, *Proceedings of the MRS Fall Meeting: Symposium on Nanoscale Properties, 1993*.
12. D. Rugar, H. J. Mamin, and P. Guethner, *Appl. Phys. Lett.*, 1989, **55**, 2588.
13. T. Albrecht, P. Grütter, and D. Rugar, *Ultramicroscopy*, 1992, **42–44**, 1638.
14. M. Bloom, in *Nuclear Magnetic Double Resonance. Proceedings of the International School of Physics Enrico Fermi*, ed. B. Maraviglia, 1993, p. 473.
15. M. Bloom and K. Erdman, *Can. J. Phys.*, 1962, **40**, 179.
16. G. M. Leskowitz and D. P. Weitekamp, *'Abstracts of the 35th Experimental NMR Conference, Asilomar, California', 11–15 April 1994*.
17. J. A. Sidles, J. L. Garbini, K. L. Broland, D. Rugar, O. Züger, S. Hoen, and G. S. Yannoni, *Rev. Mod. Phys.*, 1995, **67**, 249.
18. A. Abragam, *The Principles of Nuclear Magnetism*, Oxford University Press, London, 1961, p. 2.
19. T. Albrecht, P. Grütter, D. Horne, and D. Rugar, *J. Appl. Phys.*, 1991, **69**, 668.
20. U. Dürig, O. Züger, and A. Stalder, *J. Appl. Phys.*, 1992, **72**, 1778.
21. S. Hoen, O. Züger, C. S. Yannoni, H. J. Mamin, K. Wago, and D. Rugar, 'Technical Digest of the 1994 Solid-State Sensor and Actuator Workshop, Hilton Head, SC', Transducers Research Foundation, Catalog no. 94TRF-0001, pp. 209–212.
22. T. Albrecht, S. Akamine, T. Carver, and C. Quate, *J. Vac. Sci. Technol. A*, 1990, **8**, 3386.
23. G. Whitfield and A. G. Redfield, *Phys. Rev.*, 1957, **106**, 918.
24. M. Garstens and J. Kaplan, *Phys. Rev.*, 1955, **99**, 459.
25. The cantilevers are commercially available from Park Scientific Instruments, Sunnyvale, CA, or Digital Instruments Inc., Santa Barbara, CA, USA.
26. A. Smirnov, O. Poluectov, and Y. Lebedev, *J. Magn. Reson.*, 1992, **97**, 1.
27. M. Ikeya, in *Magnetic Resonance Microscopy*, ed. B. Blümich and W. Kuhn, Plenum, Weinheim, 1992, pp. 133–149.
28. Y. S. Lebedev, in *Modern Pulsed and Continuous-Wave Electron Spin Resonance*, ed. L. Kevan and M. K. Bowman, Wiley Interscience, New York, 1990.
29. A. Abragam, *The Principles of Nuclear Magnetism*, Oxford University Press, London, 1961, pp. 86, 545–550.
30. C. Slichter, *Principles of Magnetic Resonance*, Springer, Berlin, 1990, p. 12.
31. A. G. Redfield, *Phys. Rev. Sci.*, 1955, **98**, 1787.
32. A. Abragam, *The Principles of Nuclear Magnetism*, Oxford University Press, London, 1961, p. 66.
33. G. P. Jones, *Phys. Rev.*, 1966, **148**, 332.
34. M. Riggin, R. Knispel, and M. Pintar, *J. Chem. Phys.*, 1972, **56**, 2911.
35. H.-M. Vieth, R. D. Kendrick, D. Rugar, O. Züger, S. Hoen, and C. S. Yannoni, to be published.
36. J. Mertz, O. Marti, and J. Mlynek, *Appl. Phys. Lett.*, 1993, **62**, 2344.
37. D. G. Cory, *Ann. Rep. NMR Spectrosc.*, 1992, **24**, 87.
38. D. Rugar, H. J. Mamin, P. Guethner, S. Lambert, J. Stern, I. McFadyen, and T. Yogi, *J. Appl. Phys.*, 1990, **68**, 1169.

Acknowledgments

The authors thank S. Hoen, H.-M. Vieth, J. L. Garbini, T. R. Albrecht, R. D. Kendrick, K. Wago, and M. Bloom for stimulating discussions and for their contributions to the results described here.

Biographical Sketches

Costantino S. Yannoni. *b* 1935. B.A., 1957, Harvard College, M.A., 1960, Ph.D. 1966, Chemistry, Columbia University, USA. Staff member, Union Carbide Research Institute, Tarrytown, New York. Research Staff member, IBM Research Division, T.J. Watson Research Center, Yorktown Heights, NY, USA, 1967–71; Almaden Research Center, San Jose CA, USA, 1971–present. Approx. 100 publications. Research specialties/interests: development and application of solid state NMR methods for solving problems involving structure and dynamics in materials, especially organic reactive intermediates; and magnetic resonance analogues of coherent optical phenomena; current interest is force detection of magnetic resonance for ultra-high-resolution imaging.

Othmar Züger. *b* 1961. Diploma, 1987, Ph.D., 1992, Physics, Swiss Federal Institute of Technology (ETH), Switzerland. Predoctoral researcher, IBM Zürich Research Laboratory, 1987–92. Visiting scientist, IBM Research Division, Almaden Research Center, San Jose, CA, USA, 1992–present. Approx. 20 publications. Current research specialties: magnetic resonance force microscopy, scanning tunneling microscopy, and novel applications of scanning probe techniques.

Daniel Rugar. *b* 1953. B.A. (physics), 1975, Pomona College, USA. Ph.D. (applied physics), 1982, Stanford University. F.V. Hunt Postdoctoral research fellow of the Acoustical Society of America, and Research Associate, Stanford University, 1982–84. Research staff member, IBM Research Division, Almaden Research Center, San Jose, CA, USA 1984–88. Manager of Exploratory Storage Studies, 1988–present. Approx. 60 publications. Current research specialties: magnetic resonance force microscopy, scanning probe microscopy, detection of ultrasmall forces, and novel data storage techniques.

John A. Sidles. *b* 1952. B.S., 1974, Ph.D., (physics; particle theory), 1982, University of Washington, USA. Research scientist, Dynamics Technology Corporation, 1980–83. Began doing medical research in 1983. Volunteer and hourly employee in 1983. Research assistant in 1984. Research Assistant Professor, 1984–86. Assistant Professor, 1986–92. Associate Professor, Department of Orthopaedics, School of Medicine, University of Washington, 1992–present. Approx. 25 publications, coauthor of *Practical Evaluation and Management of the Shoulder*. Research interests: the surgical biomechanics of knee, shoulder, and ankle reconstruction; avocational interest in magnetic resonance as a means to image biomolecular structure directly.

Optically Enhanced Magnetic Resonance

Dieter Suter
Universität Dortmund, Germany

1	Introduction	1
2	Physical Background	1
3	Applications	5
4	Related Articles	9
5	References	9

1 INTRODUCTION

1.1 Motivation

The physical mechanism of nuclear magnetic resonance spectroscopy, the excitation of transitions between nuclear spin states, was explored in the years after World War II, and is by now well characterized. Today's interest in the field is based largely on the immense potential for applications: spins can serve as probes for their environment because they are weakly coupled to other degrees of freedom. In most magnetic resonance experiments, these couplings are used to monitor the environment of the nuclei, like spatial structures or molecular dynamics. While the direct excitation of nuclear spin transitions requires irradiation with a radiofrequency field, many systems offer the alternative possibility of using light for polarizing the spin system or for observing its dynamics. This possibility arises from the coupling between the spins and the electronic degrees of freedom: optical photons excite transitions between states that differ both in electronic excitation energy as well as in their angular momentum states.

The light can serve three different purposes: it can polarize the spin system, thereby creating the 'raw material' for spectroscopic experiments; it can measure the spin polarization, serving as a detector; and it can influence the dynamics of the system. Some motivations for using light in magnetic resonance experiments include the following:

Sensitivity. In many cases, the possible sensitivity gains are the primary reason for using optical methods. Compared to conventional NMR, sensitivity gains of more than 10 orders of magnitude are possible. Thus so far, two groups have demonstrated the magnetic resonance of individual molecules,[1,2] while a typical NMR sample contains of the order of 10^{20} spins.

Selectivity. Using lasers, it is possible to observe selectively signals from certain regions in space, such as surfaces. Alternatively, a laser pulse may define the time of an observation with a resolution of 10^{-14} s or select a particular chemical environment like the chromophore of a molecule or a quantum well in a semiconductor. Crystal imperfections can change the optical properties of an atomic or molecular site in such a way that optical excitation can distinguish those sites against a background that is orders of magnitude larger.

Speed. Conventional magnetic resonance requires the presence of population differences between spin states to excite transitions between them. In most cases, thermal relaxation establishes these population differences. At low temperatures, this coupling process may be too slow for magnetic resonance experiments. In the case of optical excitation, a polarizing laser beam creates the population differences. The time required for polarization of the system then depends only on the laser intensity and can be instantaneous on the timescale of the magnetic resonance experiment, independent of temperature.

Experiments in electronically excited states. If information about an electronically excited state that is not populated in thermal equilibrium is desired, it may be necessary to use light to populate this state. It is then certainly advantageous to populate the different spin states unequally to obtain at the same time the polarization differences that are needed to excite and observe spin transitions.

1.2 Laser Spectroscopy

Apart from magnetic resonance, the interaction of matter with laser light is the second most important ingredient for the experiments that will be discussed below. In laser spectroscopy, light induces transitions between different electronic states. Many of the differences between laser spectroscopy and magnetic resonance arise from the different frequency scales: optical frequencies are more than six orders of magnitude higher than rf frequencies. An important consequence is that laser spectroscopy is much more sensitive as a technique: optical experiments on individual atoms[3,4] and molecules[5,6] have become routine in the last few years. While the first experiments of this type used atomic ions in ultrahigh vacuum, they can now also be performed in condensed matter, like solutions[5] or solid matrices.[6]

Another attractive feature of laser spectroscopy is the high time resolution, which is of course also intimately linked to the high frequencies of optical radiation. Technical limits to the time resolution are now of the order of a few femtoseconds, corresponding to only a few optical cycles. In chemistry, this resolution allows 'real time' monitoring of chemical reactions, e.g. by measuring the intermolecular potential as a function of time during the reaction. Also in solid state physics, laser spectroscopy allows the monitoring of fast processes, such as the excitation and recombination of electrons and holes in semiconductors.

In the field of high-resolution spectroscopy, it is also possible to achieve very high frequency resolution: some systems can now reach resolutions of better than 1 Hz, corresponding to a relative frequency stability of some 10^{15}. This high-frequency resolution is especially attractive for metrology, where many groups are trying to build new, more precise frequency standards based on optical transitions. These properties of laser spectroscopy, high-frequency resolution and high temporal resolution open attractive possibilities for applications in optically enhanced magnetic resonance experiments.

The next section discusses the most important physical phenomena that permit the use of laser radiation in magnetic resonance experiments. Examples of applications to specific systems are discussed in the third section.

2 PHYSICAL BACKGROUND

2.1 Angular Momentum

The possibility of using optical radiation for exciting and detecting spin polarization can be traced to the angular momentum of the photon. Photons as carriers of the electromagnetic interaction carry one unit ($\hbar$) of angular momentum, which is oriented parallel or antiparallel to the direction of light propagation. Since angular momentum is a conserved quantity, the total angular momentum of the system (radiation and matter) remains constant during absorption and emission of radiation. When an atom or molecule absorbs a photon, it must incorporate not only the photon energy but also its angular momentum (see Figure 1). The resulting angular momentum of the atom is the vector sum of its initial angular momentum plus the angular momentum of the absorbed photon.

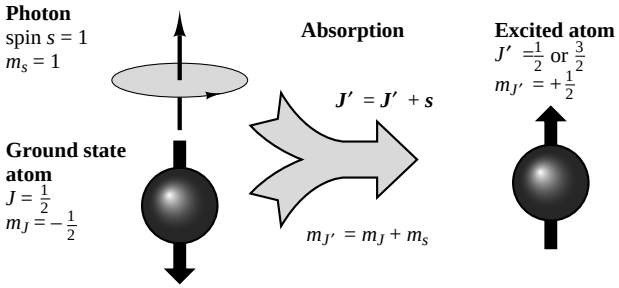

Figure 1 Conservation of angular momentum during absorption of a photon

Magnetic resonance spectroscopy requires a spin polarization inside the medium. In conventional magnetic resonance experiments, thermal contact of the spins with the lattice establishes this polarization. This process is relatively slow, especially at low temperatures where relaxation times can be many hours. The polarizations are limited by the Boltzmann factor, which is typically less than 10^{-5}. Photon angular momentum, in contrast, can be created in arbitrary quantities with a polarization that can be arbitrarily close to unity. If it is possible to transfer this polarization to nuclear or electronic spins, their polarization can reach the same values.

2.2 Optical Pumping

This possibility was first suggested by Kastler.[7,8] Figure 2 illustrates the principle of operation. The model atomic system consists of two electronic states, labelled $|g\rangle$ for ground state and $|e\rangle$ for excited state. We assume that both have an angular momentum $J = \frac{1}{2}$; their angular momentum substates are labeled as $J_Z = +\frac{1}{2}$ and $J_Z = -\frac{1}{2}$ in the figure. If the system is irradiated by circularly polarized light, the photons have a spin quantum number $m_s = +1$. Since the absorption of a photon is possible only if both the energy and the angular momentum of the system are conserved, only those ground state atoms that are initially in the $J_Z = -\frac{1}{2}$ state can absorb photons. If an atom is initially in the state $J_Z = +\frac{1}{2}$, the resulting excited

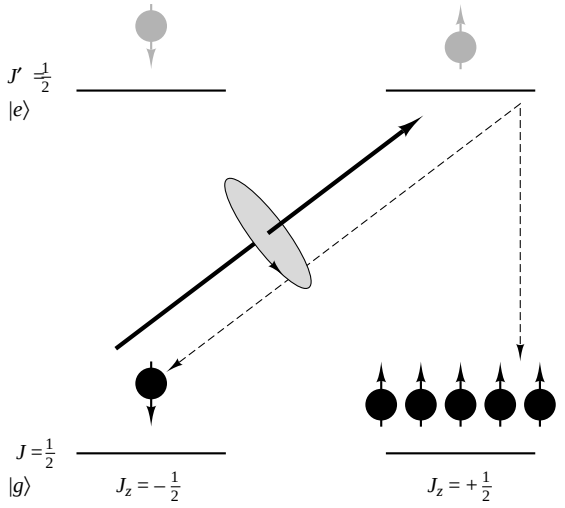

Figure 2 Principle of optical pumping illustrated for a simple atomic system

state would have to be a $J_Z = +\frac{3}{2}$ state, which does not exist in the atom of our model system.

An atom that has absorbed a photon will re-emit one after the excited state lifetime. Spontaneous emission can occur in an arbitrary direction in space and is therefore not subject to the same selection rules as the excitation process with a laser beam of definite direction of propagation. The spontaneously emitted photons carry away angular momentum with different orientations and the atom can therefore end up in either of the two ground states. If it ends up in the original state, it can absorb another photon and repeat the cycle; if it ends up in the other state, it no longer couples to the laser field and remains in this state indefinitely. The net effect of the absorption and emission processes is therefore a transfer of population from one spin state to the other and thereby a polarization of the atomic system.

2.3 Dynamics

As in conventional magnetic resonance, the spin polarization undergoes Larmor precession in an external magnetic field. If we use light to drive the spin system, it also affects the spin dynamics: if the laser couples to a particular transition, it appears to shift the energy of the levels to which it couples.[9,10] Shifts of energy levels always affect the dynamics of the corresponding system. In this case, the energy level shift has exactly the same effect as a magnetic field parallel to the direction of the laser beam. The light shift effects are therefore often analyzed in terms of virtual magnetic fields. The strength of this virtual magnetic field depends on the detuning of the laser from the electronic transition frequency. Besides these level shifts, the laser light also causes a damping of the spin polarization. In contrast to the light shift effect, which has a dispersive dependence on the laser detuning, the damping effect has an absorptive behavior, i.e. its maximum occurs when the laser frequency is exactly resonant with the optical transition frequency. Light shift and damping are the main contributors to laser-induced dynamics in atomic spin systems.[11]

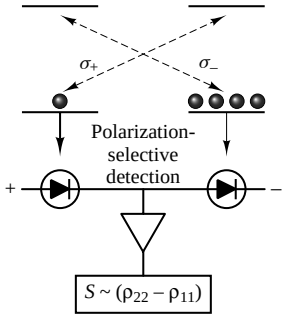

Figure 3 Principle of observation of spin polarization by optical radiation

2.4 Observation

The last requirement for optically enhanced magnetic resonance is a method for observing the spin polarization. An early suggestion that magnetic resonance transitions should be observable in optical experiments is due to Bitter.[12] The physical process used in such experiments is the complement of optical pumping: it transfers spin angular momentum to the photons and polarization-selective detection measures the photon angular momentum. Figure 3 illustrates this for the same model system that we considered for optical pumping. Light with a given circular polarization interacts only with one of the ground state sublevels. Since the absorption of the medium is directly proportional to the number of atoms that interact with the light, a comparison of the absorption of the medium for the two opposite circular polarizations yields the population difference between the two spin states directly. This population difference is directly proportional to the component of the magnetization parallel to the laser beam. This analysis of the transmitted light allows the observation of spin polarization in the electronic ground state. Another possibility is the analysis of the fluorescence light: angular momentum conservation imposes correlations between the direction and polarization of the spontaneously emitted photons, which depend on the angular momentum state of the excited atom.

As shown schematically in Figure 4, the difference between the atomic angular momentum of the excited and ground states determines the angular momentum $\boldsymbol{J}_\nu$ of the spontaneously emitted photon. This condition determines the polarization of the emitted radiation for a given direction. In the first experiments on optical pumping, observation of the fluorescence allowed not only the measurement of the excited state polarization, but also the ground state polarization to be inferred.[13]

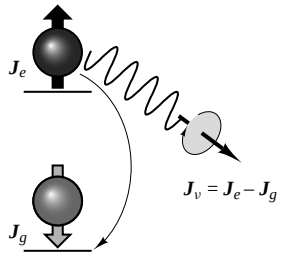

Figure 4 Polarization of the fluorescence depends on the spin state of the excited atoms

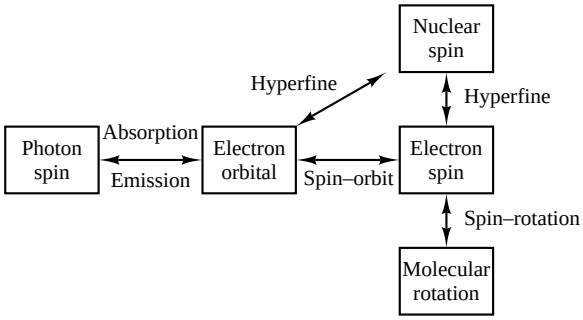

Figure 5 Summary of the most important reservoirs of angular momentum

2.5 Angular Momentum Reservoirs

Atoms and molecules may contain different types of angular momentum. The most important reservoirs include the rotational motion of molecules, the orbital angular momentum of electrons, and the spin angular momentum of electrons and nuclei. Not all these types of angular momentum couple directly to the radiation field: in free atoms, only the orbital angular momentum of the electrons is directly coupled to the optical transitions. However, various interactions couple the different types of angular momentum to each other and allow the polarization to flow from the photon spin reservoir through the electron orbital to all the other reservoirs, as shown schematically in Figure 5. This is, of course, of spatial interest for nuclear magnetic resonance, since there is no direct transfer to nuclear spins. However, the coupling between electronic and nuclear angular momentum is usually strong enough to provide an efficient transfer mechanism. This even allows the polarization of nuclear spin systems in diamagnetic ground states.

In the example of Figure 6, the electronic ground state is diamagnetic and has a nuclear spin $I = \frac{1}{2}$. Since the nuclear spin does not affect the absorption of light, both spin states interact with a circularly polarized laser beam. Angular momentum conservation requires that optical excitation populates only the states with an electronic angular momentum of $m_J = 1$. If electronic and nuclear spin are parallel in the excited state ($m_J = 1$, $m_I = \frac{1}{2}$, dashed line in Figure 6), the resulting state does not evolve until it reemits a photon and decays into the state from which it was excited. If, however, the nuclear spin is oriented antiparallel to the electronic angular momentum ($m_J = 1$, $m_I = -\frac{1}{2}$), the hyperfine interaction can induce simultaneous spin flips that conserve the total angular momentum and transfer the atom into the ($m_J = 0$, $m_I = \frac{1}{2}$) state. Spontaneous decay from this state again leaves the nuclear spin unchanged and thus brings the

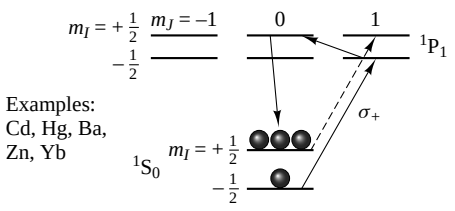

Figure 6 Polarization of nuclear spin reservoirs in diamagnetic ground states

atom into the $m_I = +\frac{1}{2}$ ground state. The net effect of the absorption–hyperfine–emission cycle is therefore the transfer of an atom from the $-\frac{1}{2}$ to the $+\frac{1}{2}$ nuclear spin state. A sequence of such cycles polarizes the nuclear spin system in complete analogy to the case of electronic spin polarization.

Spin polarization can be transferred between different reservoirs, not only within one atomic species but also between different particles. This was first demonstrated by Dehmelt who used transfer to free electrons to polarize them.[14] Another frequently used transfer process includes optical pumping of alkali atoms, in particular Rb and Cs, and the transfer of their spin polarization to noble gas atoms like Xe. This method was pioneered by Happer et al.[15] and applied to the study of surfaces in systems with high surface to volume ratios like graphitized carbon[16] or to the construction of NMR gyroscopes.[17,18] The transfer from alkali to noble gas atoms is relatively efficient because they form van der Waals complexes. During the lifetime of this quasi-molecule, the dipole–dipole interaction between the two spins induces simultaneous flips of the two spin species, which transfer polarization from the Rb atoms to the Xe nuclear spin. Typical cross-polarization times are on the order of minutes, but the long lifetime of the Xe polarization permits reaching polarizations close to unity. The spin polarization survives freezing[19] and can be transferred to other spins by thermal mixing.[20]

At low magnetic fields, the coupling between the reservoirs can exceed the Zeeman interaction between the individual spins and the magnetic field. This implies that the spins do not evolve independently, but as a collective entity that may include electronic as well as nuclear spins. Under these conditions, the traditional distinction between ESR and NMR loses its meaning: electronic and nuclear spins undergo simultaneous transitions. Nevertheless, it may be possible to extract the different physical parameters for the various interactions. Figure 7 shows an example: in Na atoms, the hyperfine interaction couples the electron ($S = \frac{1}{2}$) and nuclear spins ($I = \frac{3}{2}$) with a coupling constant of 1.8 GHz. In fields less than 0.1 T, the hyperfine interaction is therefore significantly stronger than the Zeeman interaction. For the spectrum shown here, the atoms were placed in a field of 0.7 mT. At these field strengths the two spins remain strongly coupled but, as shown in the spectrum, the electron Zeeman interaction can be determined as 5 MHz and the nuclear Zeeman interaction as 19 kHz.

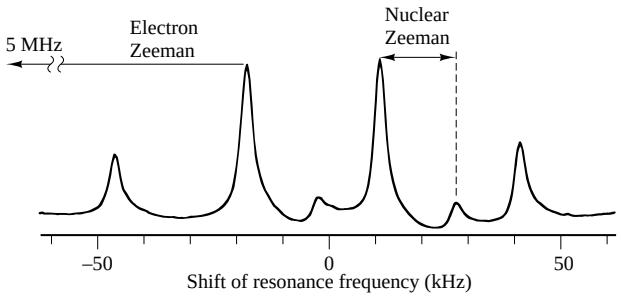

Figure 7 Example of an optically detected magnetic resonance spectrum in a strongly coupled system

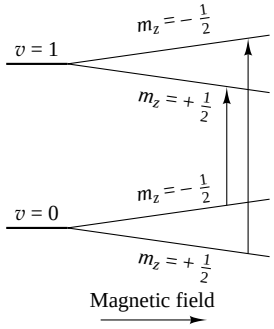

Figure 8 Principle of laser magnetic resonance

2.6 Laser Magnetic Resonance

A method for the optical detection of magnetic resonance transitions that does not directly rely on the conservation of angular momentum is laser magnetic resonance. It uses transitions between states that differ both in their electronic or vibrational and angular momentum quantum numbers. Transitions between such states depend on magnetic interactions but fall into the optical frequency range. The population difference between the two states is thus close to unity and the detection of the radiation is highly efficient.

Figure 8 illustrates the principle of the method: a magnetic field lifts the degeneracy of both the ground and excited states. For the figure, only a single spin $I = \frac{1}{2}$ was assumed. If the laser induces transitions that change both the vibrational and the spin quantum number, such as the transitions indicated by arrows in Figure 8, the resonance frequency depends clearly on the magnetic field strength. The resulting spectra contain the information about the magnetic interactions in both the excited and the ground state. Experiments of this type were performed in molecular gases[21] as well as in semiconductor materials, where the process is known as spin-flip Raman scattering.[22,23]

While this method allows high sensitivity, its resolution is lower than with direct detection. In most experimental settings, the laser linewidth limits the resolution. Optical rf double resonance methods[24] or a modification of the basic Raman experiment that is known as coherent Raman scattering can overcome this limitation.

2.7 Coherent Raman Processes

Raman processes can be considered as an interaction between two optical photons and a material excitation, as shown schematically in Figure 9. The arrows labeled ω_1, ω_2 represent two optical fields that couple to two allowed optical transitions that share the energy level $|3\rangle$. If two laser fields with these frequencies are incident on the three-level system, they excite coherences in all three transitions of the three-level system, in particular also the coherence labeled ω_{12} in the transition that is not directly coupled to the laser fields. If, conversely, the coherence in transition $|1\rangle \leftrightarrow |2\rangle$ is already present in the material, and a single laser field at frequency ω_1 is incident on the system, it excites a Raman field at frequency $\omega_2 = \omega_1 + \omega_{12}$. This Raman field propagates with the incident laser field and the frequency ω_{12} can be measured as the difference between the two optical frequencies. If the laser frequency drifts, the frequency of the incident field as well

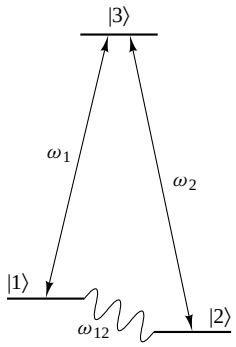

Figure 9 Raman processes couple two electromagnetic fields (ω_1, ω_2) with a material excitation

as that of the Raman field changes by the same amount. As a result, the difference frequency is unchanged and the resolution of the measurement is not affected by laser frequency jitter or broad optical resonance lines.[25] Coherent Raman processes therefore provide a combination of high resolution with high sensitivity.

The implementation of coherent Raman scattering must somehow create the coherent excitation of the material. This can be achieved either with optical fields[26–28] or with radiofrequency irradiation.[29]

2.8 Sensitivity

Several mechanisms contribute to the increase in sensitivity by optical methods. The first is the spin polarization that can be achieved. If thermal relaxation establishes the spin polarization, it cannot exceed the Boltzmann factor which is at most on the order of 10^{-5}. Optically, it is possible to polarize the spins completely and thereby gain some five orders of magnitude.[30] In addition, the optical detection process occurs at much higher energies: optical photons have energies some seven orders of magnitude higher than that of rf photons. Detecting a small number of optical photons is therefore significantly easier than detection of rf photons. At the same time, thermal noise is almost negligible at optical frequencies. A third reason for the increased sensitivity is that laser irradiation can polarize the spins much faster: depending primarily on the laser intensity, complete polarization of the spin system may require less than 1 μs.[31]

Since optical detection directly measures the magnetization, in contrast to pick-up coils that measure its time-derivative, the detection sensitivity is independent of the resonance frequency. It is therefore possible to perform experiments at low or vanishing fields with the same detection efficiency as at high fields. This is of particular interest in cases where one wants to measure small effects like rotational velocities, which cannot be seen in high fields.[32]

2.9 Information Content

Apart from the advantage of sensitivity, optically enhanced magnetic resonance is sometimes capable of providing information which conventional methods cannot provide. We illustrate this with the measurement of the sign of the nuclear

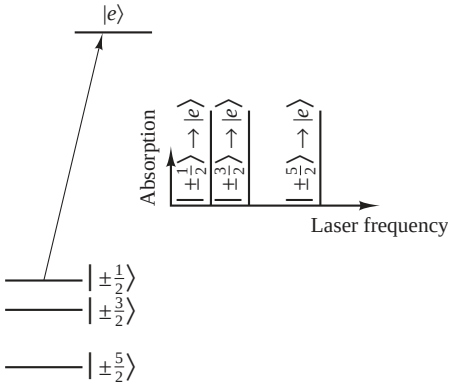

Figure 10 Principle of the measurement of nuclear quadrupole interaction by laser spectroscopy

quadrupole interaction. The nonspherical part of the charge distribution of atomic nuclei with spin $I > \frac{1}{2}$ is a sensitive probe of the electric field at the site of the nucleus. Measurements of the interaction between the nuclear quadrupole moment and the electric field gradient (EFG) tensor can provide information about the electronic and structural environment of the nuclei, as well as about motional processes. Many experiments in magnetic resonance are therefore performed to measure quadrupole couplings.[33] However, conventional magnetic resonance experiments cannot provide the sign of the coupling.[34]

In the simplest case of axial symmetry, the Hamiltonian $\hat{\mathcal{H}}_Q$ of the nuclear quadrupole interaction is given by a coupling constant D multiplied by the square of the nuclear spin operator $\hat{I}_Z$, $\hat{\mathcal{H}}_Q = D\hat{I}_Z^2$. The coupling constant D is determined by the size of the nuclear quadrupole moment and the electric field gradient. It can be measured either without a magnetic field, which corresponds to the case of pure quadrupole coupling, or in a high magnetic field, which corresponds to the case of high-field NMR. In both cases, the spectra are identical for positive and negative sign of the coupling constant D.

Figure 10 schematically shows how laser spectroscopy can be used to measure the nuclear quadrupole interaction with the sign information. In the model system considered here, the spin is $\frac{5}{2}$ and a measurement is performed in zero magnetic field. In the electronic ground state, the system then has three sets of doubly degenerate states. If we can neglect the quadrupole splitting in the excited state, as assumed in Figure 10, the absorption spectrum directly provides the splittings between the levels. Reversal of the sign of the quadrupole splitting leads to a reversal of the line positions in the spectrum (Figure 11). In actual systems, the inhomogeneous broadening of the optical resonance lines complicates the procedure. Closely analogous measurements are nevertheless possible and have allowed the measurement of the quadrupole coupling constant of Pr^{3+} in the host material $YAlO_3$ as shown in Figure 11.[35]

3 APPLICATIONS

It is of course impossible to give a complete summary of the large number of applications that have used optically enhanced magnetic resonance techniques in various systems. The present selection tries to demonstrate the wide range of systems for

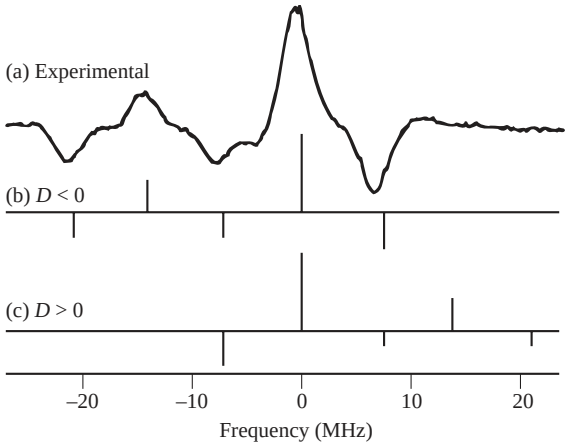

Figure 11 Comparison of the experimental spectrum (top) with theoretical stick spectra for negative and positive quadrupole coupling

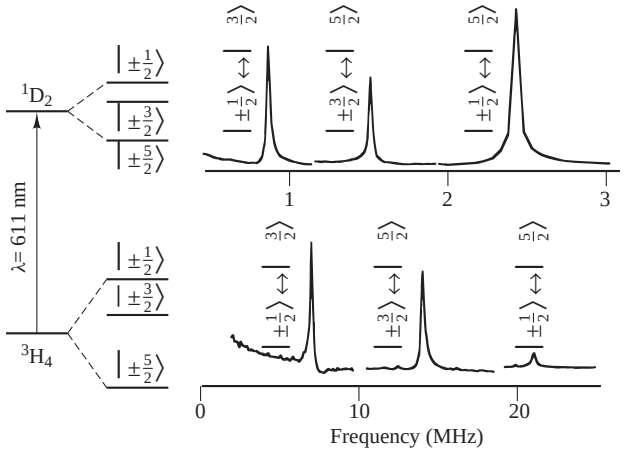

Figure 12 Example of NQR spectra obtained by purely optical excitation and detection of nuclear spin coherence. Both spectra were combined from three partial spectra which were recorded with different modulation frequencies in order to reduce distortion due to finite excitation range

which optical methods can be used, but also in addition the various ways in which optical radiation can enhance magnetic resonance spectroscopy.

3.1 Dielectric Solids

Optical pumping and optical detection of magnetic resonance transitions were first demonstrated in atomic vapors[8,13] but soon afterwards also in ionic solids.[36,37] Ruby (Cr^{3+}:Al_2O_3) proved an ideal test material, as it has relatively narrow optical absorption lines and allows different methods of optical pumping. Most experiments reported to date have been performed with inorganic ionic solids, in particular rare earth and transition metal compounds. The experimental techniques used for these studies include purely optical methods such as photon echo modulation[38,39] and coherent Raman beats,[40] as well as double resonance methods such as Raman heterodyne spectroscopy.[41]

We start the discussion with an example for a purely optical method that combines several attractive features: while its sensitivity is that of an optical method, its resolution is not limited by laser jitter or optical dephasing, but only by the natural linewidth. Furthermore, it yields magnetic resonance spectra from an electronically excited as well as from the ground state. The material system that we consider here consists of the rare earth ion $^{141}Pr^{3+}$ with a nuclear spin $I = \frac{5}{2}$. The ions are substituted into the host material of $YAlO_3$, where they occupy the Y sites with a doping concentration of 0.1%. In zero magnetic field, the interaction between the nuclear quadrupole moment and the electric field gradient (EFG) tensor lifts the degeneracy of the nuclear spin states of ^{141}Pr; the interaction with the quenched electronic spin enhances the quadrupole coupling as well as the nuclear Zeeman interaction.

The experimental scheme uses Raman processes for exciting the nuclear spin transitions as well as for observing the spin precession. A laser pulse that couples to two optical transitions sharing a common energy level excites a coherence in the third transition of the three-level system, as explained above. The excitation pulse should not be longer than the spontaneous lifetime of the electronic state. For the $^1D_2$ state of Pr^{3+}, this limits the duration of the laser pulses to $\tau_P < 100\,\mu s$. After the pulse, the coherence is allowed to precess freely and a second, weaker laser beam is used to observe the precession, again using a Raman process. The condition for efficient excitation of the sublevel coherence is that the difference between the two frequency components of the exciting laser pulse is close to the sublevel transition frequency.[28] For the observation process, the laser frequency must be close to one of the two optical transition frequencies. The signal that is observed after the optical pulse can be Fourier-transformed to recover the usual NMR/NQR spectrum.

Figure 12 shows two examples of spectra that were measured with this method. They represent nuclear spin transitions of the electronic ground state and an electronically excited state of Pr^{3+}:$YAlO_3$. For both states, not only the magnetic dipole allowed transitions ($\pm\frac{1}{2} \leftrightarrow \pm\frac{3}{2}, \pm\frac{3}{2} \leftrightarrow \pm\frac{5}{2}$) are visible, but also the double quantum transition ($\pm\frac{1}{2} \leftrightarrow \pm\frac{5}{2}$), indicating that the selection rules of conventional magnetic resonance do not apply to Raman-detected magnetic resonance. The quadrupole interaction strength differs significantly for excited and ground state (0.9 MHz versus 7 MHz). As with magnetically excited spectra, the bandwidth of the excitation process is limited. In this case, the transition strength is quite low. With a laser power of 20 mW, it was possible to excite subspectra with a width of approximately 1 MHz. To reduce the distortions associated with the excitation of considerably wider spectra, we therefore combined three subspectra containing one resonance line each. The width of the resonance lines is determined by spin-diffusion of the dipole–dipole interaction with the neighboring Al nuclei.

Excitation of magnetic resonance transitions with radiofrequency irradiation relies on the conversion of longitudinal into transverse magnetization; an experiment can therefore start only after thermal relaxation has established population differences by coupling to the lattice. At low temperatures, this process can be very slow in rigid solids. Optical excitation, in contrast, converts population differences between different electronic states into transverse magnetization. Spontaneous emission establishes these population differences on a very short timescale (nanoseconds to femtoseconds), independent of temperature. As a result, purely optical experiments do not require long relaxation delays and allow fast repetition rates.

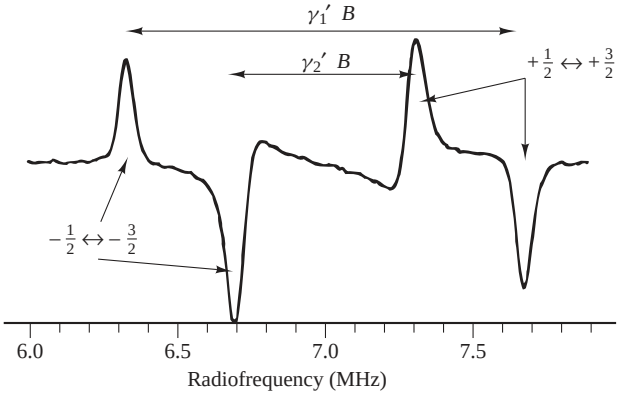

Figure 13 Raman heterodyne spectrum of Pr^{3+}:$YAlO_3$ in a weak magnetic field

Raman experiments do not have to use only optical techniques. Double resonance techniques that include optical as well as rf irradiation have been used successfully. The rf field establishes a coherence in a magnetic resonance transition, and the same Raman process that we discussed above detects it. In such an experiment, the laser beam serves a threefold purpose: it establishes a population difference, which the rf field converts into transverse magnetization. The same[41] or a second[35] laser beam partially converts the precessing magnetization into optical polarization by a coherent Raman process, and as a third function, the laser beam serves as the local oscillator for the detection of the Raman field. This technique was first used to observe NMR transitions in rare earth compounds[29,41] and later also to ESR[42] and ENDOR.[43,44]

Figure 13 shows the Raman heterodyne signal, again from Pr^{3+}:$YAlO_3$, as a function of the frequency of the rf field. For this spectrum we applied a small magnetic field of a few gauss, so that the transitions between the $+\frac{1}{2}$ and $+\frac{3}{2}$ states were no longer degenerate with the transition from the $-\frac{1}{2}$ to the $-\frac{3}{2}$ state. In addition, the crystal has two nonequivalent sites, resulting in a total of four lines which are assigned in the figure. Again, the width of these resonance lines is independent of the laser linewidth and only due to the properties of the crystal.

In these experiments, the laser beam interacts directly with the atom whose nuclear spin transitions are the subject of interest. In other cases, spin–spin couplings exchange polarizations with neighboring spins. It is then possible to polarize optically those spins and detect their NMR transitions optically.[45,46] In other cases, the interaction between two neighboring atoms manifests itself more strongly in the optical transition. The position of the optical resonance within the inhomogeneously broadened resonance line allowed the assignment of the magnetic resonance spectrum to a pair of neighboring spins.[47] While most experiments of this type were performed in ionic materials, color centers in diamond have also been studied.[43]

3.2 Semiconductors

Semiconductors have become a very active area for applications of optically enhanced magnetic resonance. The first demonstrations of the technique were performed in GaAs.[48] For the optical excitation, one usually chooses a photon energy at the exciton resonance or just above the band gap, thereby creating holes at the top of the valence band and electrons at the bottom of the conduction band. Under these conditions, the system behaves to some degree like free atoms. Figure 14 shows the relevant band structure for the technically important case of a III–V semiconductor with tetrahedral symmetry.

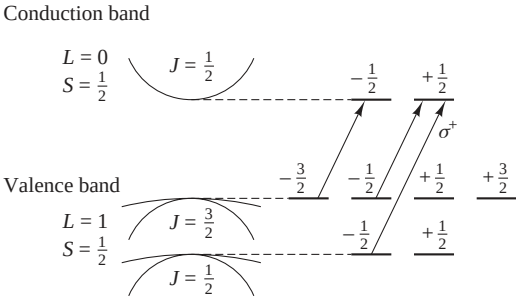

Figure 14 Optical pumping in semiconductors: level scheme for a III–V compound with tetrahedral symmetry

In these compounds, the valence band consists of p type orbitals ($L = 1$). Spin–orbit coupling splits the band into a $J = \frac{1}{2}$ and a $J = \frac{3}{2}$ subband. The conduction band consists of s type orbitals and the total electronic angular momentum of the excited electrons is therefore $J = \frac{1}{2}$. Absorption of a circularly polarized photon by an electron in the $J = \frac{1}{2}$ valence band then creates a hole and a conduction band electron, both with $J_Z = +\frac{1}{2}$. In the valence band as well as in the conduction band the electron spin system becomes polarized to some degree that depends on the thermalization times of the hole and the electron. As in the case of free atoms, the spin polarization reflects itself in the polarization of the luminescence.

The hyperfine interaction between electrons and nuclear spins can transfer spin polarization from the electrons to nuclei. If resonant rf irradiation perturbs the nuclear spin reservoir, it also affects the electron spin polarization and the polarization of the luminescence. By observing the luminescence and scanning the radiofrequency in a constant magnetic field, it is thus possible to record magnetic resonance spectra.[48,49] Figure 15 shows an example of such a spectrum from GaAs, reproduced from Krapf et al.[49] Two different isotopes of Ga are clearly visible, as well as the As resonance. The positions of the resonance lines depend on the polarization of the electron spins, as shown in the lower left part of the spectrum. Such experiments may well become an interesting addition to the analytical tools of the semiconductor industry. Most experiments performed up to now have used GaAs, but Si, Ge,[50] and InSb[51] have also been investigated.

Apart from the polarization and intensity of the light, NMR transitions can also be observed indirectly through changes in the ESR resonance position:[52] the coupling between the electronic and nuclear spins shifts the ESR transition frequency. By applying pulsed or CW radiofrequency fields to the nuclear spins, it is possible to change their polarization and thereby the ESR frequency. If the number of spins is large enough, it is even possible to observe the NMR spectrum directly in a conventional spectrometer modified for optical pumping.[53]

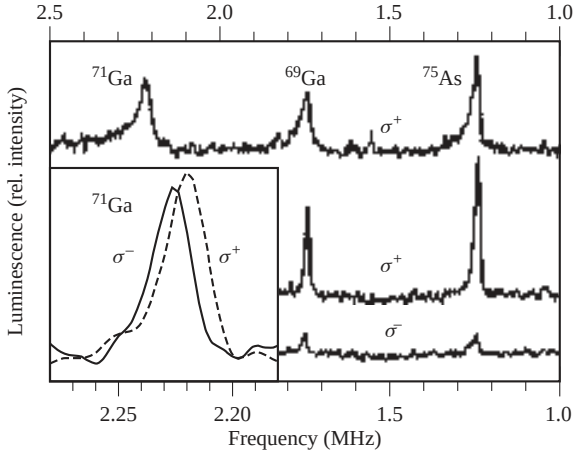

Figure 15 Example of optically detected NMR spectrum of GaAs. The signal was recorded by scanning the radiofrequency and observing the luminescence in a constant magnetic field of 0.17 T

The high sensitivity of optical techniques is a very attractive feature for studying the thin films used in integrated circuits. The optical techniques could become even more attractive for studying quantum confined structures.[54] Confinement of the conduction electrons to small regions, like quantum wells, quantum wires, or quantum dots, modifies the optical absorption spectra considerably. It is then possible to selectively excite only those areas where the electrons are confined and to measure magnetic resonance spectra specifically from those areas. Such experiments therefore require not only high sensitivity for measuring signals from small parts of the sample, but also good selectivity to extract this signal from the large background of the entire sample.

3.3 Surfaces

Quasi two-dimensional systems have always proved difficult to investigate by conventional NMR, since the number of spins in these systems is quite small.[55,56] Increasing the spin polarization by optical pumping has significantly improved the sensitivity of this type of experiment. In particular, the transfer of spin polarization from optically pumped alkali atoms to Xe nuclear spins[15] has allowed the study of the effect of surfaces on the magnetic resonance spectrum.[57,58] In the fast exchange regime, the distribution of spins between the surface adsorbate and vapor phase determines the averaged magnetic resonance spectrum. For oriented surfaces, where most spins are in the vapor phase, the splittings and shifts are then in the mHz range, requiring highly sensitive detection methods. Other work has therefore concentrated on systems with a large surface-to-volume ratio like zeolites[59] where most of the atoms are close to the interface.

For experiments with oriented surfaces, apart from the sensitivity advantages, the use of light for optical pumping as well as for detection also brings the possibility of selecting signal contributions that originate from atoms which are close to the surface. For this purpose, changes in the penetration depth of light with wavelength[60] have been used, but more frequently the selection is achieved by reflecting a laser beam from the interface being investigated. The reflection coefficient for the laser beam depends on the refractive indexes on both

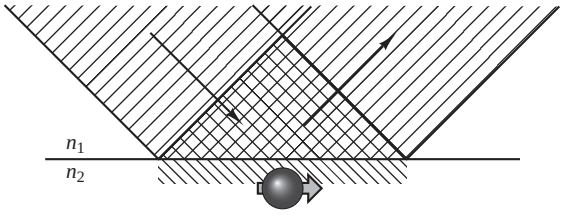

Figure 16 Principle of optical detection of magnetic resonance close to a surface. The refractive indices on both sides of the interface are denoted as n_1 and n_2

sides of the interface and is therefore affected by atoms close to the interface that are resonant with the laser light (see Figure 16). The changes in the reflection coefficient, which can be measured through changes of the amplitude and polarization of the reflected beam, therefore contain information on the atoms close to the interface. The combination of optical pumping with this type of optical detection provides sufficient sensitivity such that it is no longer necessary to use samples with high surface-to-volume ratios and permits the study of oriented surfaces.

One method that relies on such a technique allowed the study of the nuclear quadrupole resonances of Pr^{3+} in LaF_3.[61] In this case, the beam was reflected from an optically dense material. The reverse is also possible: if the laser beam undergoes total internal reflection at an interface to an optically less dense medium, an evanescent wave penetrates into the thinner medium by a distance of the order of the optical wavelength. Atoms in this evanescent wave can thus modify the reflected laser beam by absorbing light from it and by their effect on the reflection coefficient.[62]

3.4 Molecules

Conventional magnetic resonance has been applied most successfully to molecular systems. These systems can also be investigated with optical methods. Aromatic organic molecules are particularly suitable because their chromophores make optical spectroscopy particularly attractive. Experiments with these systems typically use optical excitation from the ground state to an excited singlet state with a pulsed UV laser. From the excited singlet state, intersystem crossing (ISC) can populate a nearby triplet state (see Figure 17). The intersystem crossing populates the different levels of the triplet state unequally. In addition, the triplet substates have in general different lifetimes. The polarization and intensity of the

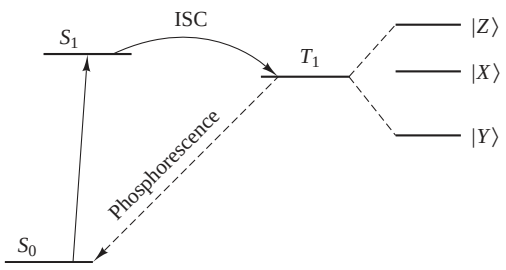

Figure 17 Principle of optically detected magnetic resonance in excited triplet states

phosphorescence depend on the population of the individual states and allow an assessment of the population differences. By applying rf fields to the system, it is possible to induce transitions between the different triplet states; these transitions can be observed in the phosphorescence. Similar experiments have been performed on many other systems. Two groups demonstrated the high sensitivity of the method very strikingly by measuring the magnetic resonance of individual pentacene molecules in *p*-terphenyl hosts.[1,2] Work is now in progress to extend these experiments to NMR transitions.

4 RELATED ARTICLES

Polarization of Noble Gas Nuclei with Optically Pumped Alkali Metal Vapors; Quantum Optics: Concepts of NMR; Ruby NMR Laser.

5 REFERENCES

1. J. Köhler, J. A. J. M. Disselhorst, M. C. J. M. Donckers, E. J. J. Groenen, J. Schmidt, and W. E. Moerner, *Nature (London)*, 1993, **363**, 242.
2. J. Wrachtrup, C. Borczyskowski, J. Bernard, M. Orrit, and R. Brown, *Nature (London)*, 1993, **363**, 244.
3. G. S. Hurst, M. G. Payne, S. D. Kramer, and J. P. Young, *Rev. Mod. Phys.*, 1979, **51**, 767.
4. H. Dehmelt, *Rev. Mod. Phys.*, 1990, **62**, 525.
5. D. C. Nguyen, R. A. Keller, and M. Trkula, *J. Opt. Soc. Am., Ser. B*, 1987, **4**, 138.
6. W. E. Moerner and L. Kador, *Phys. Rev. Lett.*, 1989, **62**, 2535.
7. A. Kastler, *J. Phys. Radium*, 1950, **11**, 255.
8. A. Kastler, *Science*, 1967, **158**, 214.
9. J. P. Barrat and C. Cohen-Tannoudji, *J. Phys. Radium*, 1961, **22**, 443.
10. A. Kastler, *J. Opt. Soc. Am.*, 1963, **53**, 902.
11. D. Suter and J. Mlynek, in *Advances in Magnetic and Optical Resonance*, ed. W. S. Warren, Academic Press, San Diego, CA, 1991.
12. F. Bitter, *Phys. Rev.*, 1949, **76**, 833.
13. J. Brossel, A. Kastler, and J. Winter, *J. Phys. Radium*, 1952, **13**, 668.
14. H. G. Dehmelt, *Phys. Rev.*, 1958, **109**, 381.
15. W. Happer, E. Miron, S. Schaefer, D. Schreiber, W. A. v. Wijngaarden, and X. Zeng, *Phys. Rev. A*, 1984, **29**, 3092.
16. D. Raftery, H. Long, T. Meersmann, P. J. Grandinetti, L. Reven, and A. Pines, *Phys. Rev. Lett.*, 1991, **66**, 584.
17. B. C. Grover, E. Kanegsberg, J. G. Mark, and R. L. Meyer, Nuclear Magnetic Resonance Gyro, US Patent 4157495, June 1979.
18. M. Mehring, S. Appelt, B. Menke, and P. Scheufler, in *High Precision Navigation*, eds. K. Linkwitz and U. Hangleiter, Springer-Verlag, Berlin, 1988.
19. G. D. Cates, D. R. Benton, M. Gatzke, W. Happer, K. C. Hasson, and N. R. Newbury, *Phys. Rev. Lett.*, 1990, **65**, 2591.
20. C. R. Bowers, H. W. Long, T. Pietrass, H. C. Gaede, and A. Pines, *Chem. Phys. Lett.*, 1993, **205**, 168.
21. T. J. Sears, P. R. Bunker, A. R. W. McKellar, K. M. Evenson, D. A. Jennings, and J. M. Brown, *J. Chem. Phys.*, 1982, **77**, 5348.
22. R. E. Slusher, C. K. N. Patel, and P. A. Fleury, *Phys. Rev. Lett.*, 1967, **18**, 77.
23. S. R. J. Brueck and A. Mooradian, *Opt. Commun.*, 1973, **8**, 263.
24. W. Hofmann, H. Pascher, and G. Denninger, *J. Magn. Reson.*, 1992, **98**, 157.
25. Y. S. Bai and R. Kachru, *Phys. Rev. Lett.*, 1991, **67**, 1859.
26. R. M. Shelby, A. C. Tropper, R. T. Harley, and R. M. Macfarlane, *Opt. Lett.*, 1983, **8**, 304.
27. R. M. Shelby and R. M. MacFarlane, *J. Luminesc.*, 1984, **31**, 839.
28. T. Blasberg and D. Suter, *Opt. Commun.*, 1994, **109**, 133.
29. J. Mlynek, N. C. Wong, R. G. DeVoe, E. S. Kintzer, and R. G. Brewer, *Phys. Rev. Lett.*, 1983, **50**, 993.
30. D. Suter, *J. Magn. Reson.*, 1992, **99**, 495.
31. D. Suter, M. Rosatzin, and J. Mlynek, *Phys. Rev. A*, 1990, **41**, 1634.
32. P. Härle, G. Wäckerle, and M. Mehring, *Appl. Magn. Reson.*, 1993, **5**, 207.
33. M. H. Cohen and F. Reif, *Solid State Phys.*, 1957, **5**, 321.
34. A. Abragam, *The Principles of Nuclear Magnetism*, Oxford University Press, Oxford, UK, 1961.
35. T. Blasberg and D. Suter, *Phys. Rev. B*, 1993, **48**, 9524.
36. I. Wieder, *Phys. Rev. Lett.*, 1959, **3**, 468.
37. S. Geschwind, R. J. Collins, and A. L. Schawlow, *Phys. Rev. Lett.*, 1959, **3**, 545.
38. Y. C. Chen, K. Chiang, and S. R. Hartmann, *Phys. Rev. B*, 1980, **21**, 40.
39. A. Szabo, *J. Opt. Soc. Am., Ser. B*, 1986, **3**, 514.
40. R. G. Brewer and E. L. Hahn, *Phys. Rev. A*, 1973, **8**, 464.
41. N. C. Wong, E. S. Kintzer, J. Mlynek, R. G. DeVoe, and R. G. Brewer, *Phys. Rev. B*, 1983, **28**, 4993.
42. K. Holliday, X. F. He, P. T. Fisk, and N. B. Manson, *Opt. Lett.*, 1990, **15**, 983.
43. N. B. Manson, X. F. He, and P. T. H. Fisk, *Opt. Lett.*, 1990, **15**, 1094.
44. N. B. Manson, P. T. H. Fisk, and X. F. He, *Appl. Magn. Reson.*, 1992, **3**, 999.
45. A. Szabo, T. Muramoto, and R. Kaarli, *Phys. Rev. B*, 1990, **42**, 7769.
46. L. E. Erickson, *Phys. Rev. B*, 1993, **47**, 8734.
47. M. Lukac and E. L. Hahn, *Opt. Commun.*, 1989, **70**, 195.
48. D. Paget, *Phys. Rev. B*, 1981, **24**, 3776.
49. M. Krapf, G. Denninger, H. Pascher, G. Weimann, and W. Schlapp, *Solid State Commun.*, 1991, **78**, 459.
50. E. Glaser, J. M. Trombetta, T. A. Kennedy, S. M. Prokes, O. J. Glembocki, K. L. Wang, and C. H. Chern, *Phys. Rev. Lett.*, 1990, **65**, 1247.
51. W. Hofmann, H. Pascher, and G. Denninger, *Semicond. Sci. Technol.*, 1993, **8**, S309.
52. W. Hofmann, G. Denninger, and H. Pascher, *Phys. Rev. B*, 1993, **48**, 17035.
53. S. E. Barrett, R. Tycko, L. N. Pfeiffer, and K. W. West, *Phys. Rev. Lett.*, 1994, **72**, 1369.
54. T. Uenoyama and L. J. Sham, *Phys. Rev. Lett.*, 1990, **64**, 3070.
55. C. P. Slichter, *Annu. Rev. Phys. Chem.*, 1986, **37**, 25.
56. T. M. Duncan and C. Dybowski, *Surf. Sci. Rep.*, 1981, **1**, 157.
57. Z. Wu, W. Happer, M. Kitano, and J. Daniels, *Phys. Rev. A*, 1990, **42**, 2774.
58. R. Butscher, G. Wäckerle, and M. Mehring, *J. Chem. Phys.*, 1994, submitted
59. B. F. Chmelka, D. Raftery, A. V. McCormick, L. C. DeMenorval, R. D. Levine, and A. Pines, *Phys. Rev. Lett.*, 1991, **66**, 580.
60. D. J. Lepine, *Phys. Rev. B*, 1972, **6**, 436.

61. M. Lukac and E. L. Hahn, *J. Luminesc.*, 1988, **42**, 257.
62. D. Suter, J. Aebersold, and J. Mlynek, *Opt. Commun.*, 1991, **84**, 269.

Biographical Sketch

Dieter Suter. *b* 1956. Diploma in Chemistry, 1979, Ph.D., 1985, ETH Zürich (with Richard Ernst). Postdoctoral research, University of California, Berkeley (with Alex Pines), 1986–88. Postdoctoral research, ETH Zürich (with Jürgen Mlynek and Peter Günter), 1988–92. Lecturer in Physics, ETH Zürich, 1992–95. Professor, University of Dortmund, 1995–present. Approx. 70 publications. Research specialties: dynamics of radiatively coupled atomic multilevel systems, optically enhanced magnetic resonance.

Adiabatic Polarization-Transfer Methods in MAS Spectroscopy

Matthias Ernst and Beat H. Meier

ETH Zürich, Physical Chemistry, ETH-Hönggerberg, Zürich, Switzerland

1	Introduction	1
2	Theory	3
3	Methods of Heteronuclear Polarization Transfer	5
4	Methods of Homonuclear Polarization Transfer	7
5	Related Articles in this Volume	9
6	Related Articles in Volumes 1–8	10
7	References	10

1 INTRODUCTION

Transfer of spin order is of great importance in magnetic resonance and plays a crucial role in two-dimensional correlation spectroscopy, two-dimensional exchange spectroscopy, and for the sensitivity enhancement of low-γ nuclei. Well-known examples are Hartmann–Hahn cross polarization,[1,2] spin diffusion,[3] INEPT,[4] and NOESY[5] experiments.

All experiments mentioned above are 'sudden' experiments in the sense that they start with the preparation of an initial state characterized by a density operator which corresponds to a non-equilibrium state. Such a non-equilibrium state evolves under the transfer Hamiltonian. The time-evolution of the density operator leads to a transfer of spin order. In an adiabatic experiment, on the other hand, one starts with a density operator that does not evolve under the initial Hamiltonian. The time evolution is initiated by 'slowly' and continuously changing the Hamiltonian in the course of the spin-order transfer such that the density operator follows the Hamiltonian.

A simple example to illustrate the differences between sudden and adiabatic experiments is the inversion of the z-magnetization of a single spin 1/2. The 'sudden' version is a π-pulse applied on-resonance with a pulse duration of $\tau = \pi/\omega_1$. The behavior of the magnetization during the pulse is illustrated in Figure 1(a,c). Critical settings for obtaining perfect inversion are the resonance frequency (which must be 'on-resonance', i.e., $\omega_{\mathrm{rf}} \approx \omega_0$) and the product of pulse length τ and rf-field strength ω_1. The well-known oscillatory behavior of M_z as a function of the pulse length (Figure 1c) is typical for 'sudden' experiments. The adiabatic counterpart of such an inversion pulse is an adiabatic passage through resonance realized by a frequency sweep of the rf-irradiation frequency $\omega_{\mathrm{rf}}(t)$. The behavior is illustrated in Figure 1(b,d). The inversion starts by irradiating the spin system with an irradiation frequency $\omega_{\mathrm{rf}}(0)$ much lower than the resonance frequency ω_0 and ends with a frequency $\omega_{\mathrm{rf}}(\tau)$ much higher than ω_0. The precise shape of the frequency sweep $\omega_{\mathrm{rf}}(t)$ is only important if one is interested in minimizing the pulse length at a certain 'degree of adiabaticity'. The Hamiltonian in the rotating frame (rotating with frequency ω_0 about the static magnetic field) is given by

$$\mathcal{H} = \chi(t) I_z + \omega_1 I_x \tag{1}$$

where $\chi(t) = \omega_{\mathrm{rf}}(t) - \omega_0$ is the off-resonance term. As a function of the time t, the Hamiltonian is rotated from being parallel with I_z to being antiparallel with I_z. As long as the frequency sweep $\omega_{\mathrm{rf}}(t)$ is slow enough (see below) and the sweep range is large enough ($|\omega_{\mathrm{rf}}(0) - \omega_0| \gg |\omega_1|$ and $|\omega_{\mathrm{rf}}(\tau) - \omega_0| \gg |\omega_1|$), the magnetization is inverted irrespective of the exact values of the resonance frequency ω_0, the sweep length τ, and the rf-field strength ω_1. It will become clear in the following, that the polarization transfer experiments of interest are also fully described, for two spin systems, by the simple picture of Figure 1. The polarization transfer will take place in a fictitious spin-1/2 subspace. The only difference to the inversion of z-magnetization will be the labelling of the axes.

In the absence of relaxation, the time evolution of a spin system always conserves the entropy and the total spin order. It is, therefore, in principle reversible and 'adiabatic' in a thermodynamical sense. This is obvious for the simple example of Figure 1 but has also been shown for polarization transfer processes in multi-spin systems for the case of spin diffusion[6,7] and cross polarization.[8,9] In the present context, we use the term adiabatic in a more restricted sense, namely for processes where in addition to the conservation of spin order, the density operator and the instantaneous Hamiltonian commute at all times,[10] i.e.,

$$[\sigma(t), \mathcal{H}(t)] = 0 \tag{2}$$

In this chapter, we will treat the transfer of polarization or longitudinal magnetization between two spins. We start with z-magnetization on a source spin (spin 1) as described by a density operator of the form $\sigma(0) = cI_{1z}$ and measure the amount of polarization on the destination spin (spin 2) after the transfer. The final density operator is of the form $\sigma(\tau) = c'(\tau) I_{2z} + Z(\tau)$ and we can abbreviate the transfer as $I_{1z} \rightarrow I_{2z}$. Here $Z(\tau)$ describes the part of the density operator orthogonal to I_{2z}. We define the polarization P_k of spin k as the expectation value of the operator I_{kz}. The polarization is related to the longitudinal magnetization by $M_{kz} = N_k \hbar \gamma_k P_k$. In general, neither the magnetization nor the polarization of the entire spin system are conserved quantities,[11] but there is an important class of experiments where the sum polarization $\sum_k P_k$ is conserved. Therefore, we will discuss the experiments always in terms of polarization.

Polarization transfer is a special form of the more general term spin-order transfer. Other examples of spin-order transfer include coherence transfer, e.g., $I_{1x} \rightarrow I_{2x}$, and transfer of coherences to two-spin order terms, e.g., $I_{1x} \rightarrow 2I_{1y}I_{2z}$. The distinction between polarization and coherence depends on the frame of reference and is not always unique.

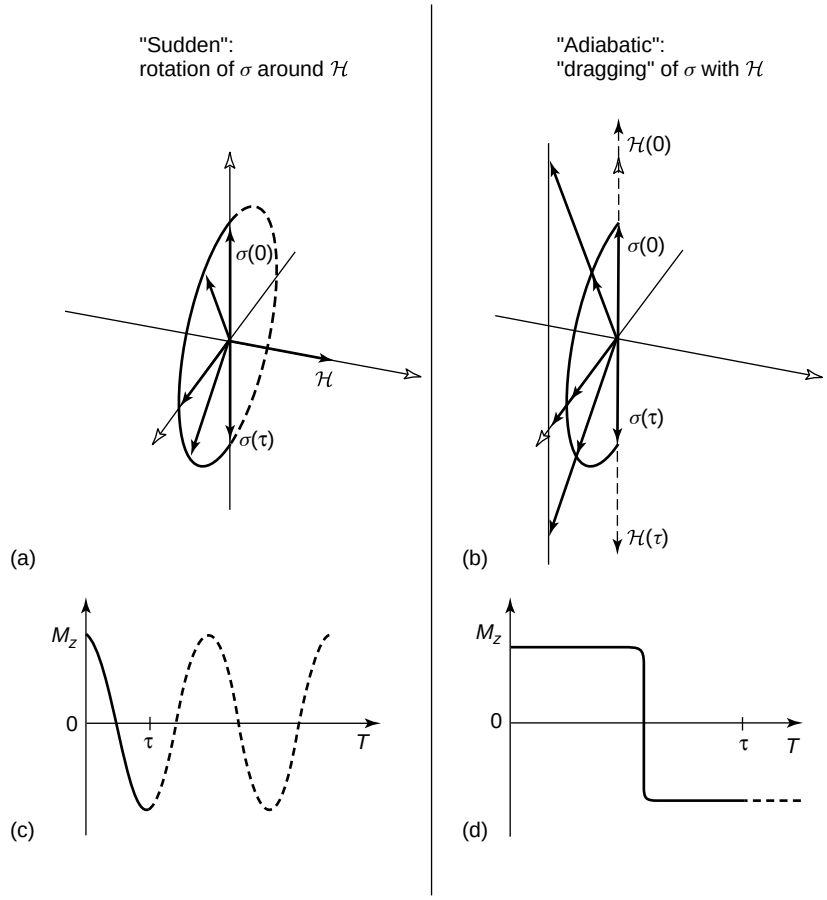

Figure 1 Schematic comparison of (a) sudden and (b) adiabatic inversion of the z-component of the magnetization vector. In the sudden case a π pulse is applied while in the adiabatic case a frequency sweep is shown. The time evolution of the z-magnetization as a function of the pulse duration τ is shown in (c) and (d) for sudden and adiabatic schemes, respectively. For the sudden experiment, the precise choice of τ is crucial to obtain efficient inversion; for adiabatic experiments a variation within rather wide limits does not lead to significant changes in inversion efficiency

Polarization transfer between two spins can often be described by a fictitious spin-1/2 system.[12,13] This is a consequence of the structure of the dipolar-coupling interaction, which has a matrix representation in the product base $|\alpha\alpha\rangle, |\alpha\beta\rangle, |\beta\alpha\rangle, |\beta\beta\rangle$ of the form

$$\frac{1}{2}\begin{bmatrix} \xi^{\Sigma} & 0 & 0 & d^{\Sigma} \\ 0 & \xi^{\Delta} & d^{\Delta} & 0 \\ 0 & d^{\Delta} & \xi^{\Delta} & 0 \\ d^{\Sigma} & 0 & 0 & \xi^{\Sigma} \end{bmatrix} \tag{3}$$

There are no coupling elements between the sum-polarization subspace spanned by $|\alpha\alpha\rangle, |\beta\beta\rangle$ and the difference polarization subspace spanned by $|\alpha\beta\rangle, |\beta\alpha\rangle$. The scalar J-coupling Hamiltonian has the same basic structure. If, besides the dipolar interaction, only a 'Zeeman-type' interaction of the form

$$\frac{1}{2}\begin{bmatrix} \chi^{\Sigma} & 0 & 0 & 0 \\ 0 & \chi^{\Delta} & 0 & 0 \\ 0 & 0 & -\chi^{\Delta} & 0 \\ 0 & 0 & 0 & -\chi^{\Sigma} \end{bmatrix} \tag{4}$$

is present, the total Hamiltonian can be written as the sum of two fictitious spin-1/2 Hamiltonians

$$\mathcal{H} = \mathcal{H}^{\Sigma} \oplus \mathcal{H}^{\Delta} \tag{5}$$

with

$$\mathcal{H}^{\kappa} = \chi^{\kappa} \cdot S_z^{\kappa} + d^{\kappa} \cdot S_x^{\kappa} + \frac{1}{2}\xi^{\kappa} \cdot 1I^{\kappa} \tag{6}$$

where κ stands for either Σ (the double-quantum subspace) or Δ (the zero-quantum subspace) and $1I^{\kappa}$ is the identity operator in the considered subspace. The symbol '$\oplus$' emphasizes that we take the direct sum of the two subspaces of dimension 2×2. Not considering the term proportional to the identity operator which does not influence the evolution of the density operator in the subspace κ, the Hamiltonian

$$\mathcal{H}^{\kappa} = \chi^{\kappa} \cdot S_z^{\kappa} + d^{\kappa} \cdot S_x^{\kappa} \tag{7}$$

has the same form as the one of equation (1) with the dipolar amplitude coupling element d^{κ} taking the role of the rf field in equation (1). The separation into a sum and difference subspace can also be applied to the density operator σ, given that $\sigma(0)$ can be divided according to

$$\sigma = \sigma^{\Sigma} \oplus \sigma^{\Delta} \tag{8}$$

If the density operator contains only terms proportional to I_z, such a separation is always possible according to

$$\sigma = p_1 I_{1z} + p_2 I_{2z} = p^{\Sigma} I_z^{\Sigma} + p^{\Delta} I_z^{\Delta} \tag{9}$$

with $p^{\Sigma} = p_1 + p_2$, $p^{\Delta} = p_1 - p_2$, $I_z^{\Sigma} = 1/2(I_{1z} + I_{2z})$, and $I_z^{\Delta} = 1/2(I_{1z} - I_{2z})$. Obviously, the inversion of the difference polarization $I_z^{\Delta} \rightarrow -I_z^{\Delta}$ is equivalent to a complete polarization transfer, i.e., $I_{1z} \rightarrow I_{2z}$ while the inversion of the sum magnetization $I_z^{\Sigma} \rightarrow -I_z^{\Sigma}$ leads to the polarization transfer $I_{1z} \rightarrow -I_{2z}$.

In polarization transfer schemes based on the dipolar coupling, the value of the effective dipolar coupling constant d^{κ} depends on one or two of the three Euler angles which describe the orientation of the crystallite in the rotor-fixed frame. For a powder sample, the resulting distribution of effective dipolar coupling frequencies does not allow a complete polarization inversion by the equivalent of a 180° pulse with $\tau \cdot d^{\kappa} = \pi$. An optimum choice of the pulse length τ leads to a maximum transfer efficiency for such a 'sudden' experiment of 73% and to an equilibrium value of 50% in an isolated two-spin system. For adiabatic methods, the maximum transfer efficiency is still 100% even in a powder sample. It will be shown below, that adiabatic polarization transfer schemes show a greatly reduced sensitivity to rf-field inhomogeneities compared to their sudden equivalent.

If the adiabaticity is violated during the sweep, the density operator and the Hamiltonian do not commute at all times during the polarization-transfer process ($[\mathcal{H}(t), \sigma(t)] \neq 0$). Under this condition, the density operator starts to precess around the Hamiltonian. Such a precession will be damped by relaxation and possibly rf-field inhomogeneities and lead to a reduction in transfer efficiency.

A number of adiabatic heteronuclear polarization transfer methods have been introduced starting with the ADRF-ARRF scheme for static samples[2,14,15] and the static adiabatic passage through the Hartmann–Hahn matching condition.[16] Adiabatic passage Hartmann–Hahn cross polarization (APHH CP) can also be applied under MAS.[17–21] In these experiments, the amplitude difference of the two applied rf-fields $\omega_{1I}(t) - \omega_{1S}(t)$ is the parameter $\chi(t)$ which is varied in an adiabatic fashion around the Hartmann–Hahn matching condition, i.e., $\chi(t) = \omega_{1I}(t) - \omega_{1S}(t) - f \cdot \omega_r$ with $f = \pm 1, \pm 2$. The variation can also take place around the original Hartmann–Hahn condition with $f = 0$ if the adiabatic transfer is combined with multiple-pulse irradiation.[22]

There is also a number of homonuclear adiabatic polarization transfer schemes under MAS. In adiabatic passage rotational resonance (APRR)[23] the spinning frequency of the MAS rotor $\omega_r(t)$ is varied to obtain a sweep through the rotational resonance condition[24–26] $\Omega_1 - \Omega_2 = n\omega_r$ with $n = \pm 1, \pm 2$ and Ω_k being the isotropic chemical shift of spin k. This leads to the definition $\chi(t) = \Omega_1 - \Omega_2 - n\omega_r(t)$. Adiabatic passage RR was also applied to the central transition of half-integer quadrupolar spins where conventional RR cannot be applied due to the broadening of the resonances by second-order quadrupolar terms.[27] A variation of APRR is the rotational resonance tickling experiment[28–30] where the RR experiment is carried out in a tilted rotating frame and the sweep is accomplished at constant MAS frequency by changing the amplitude of the applied rf-field.

In the adiabatic version of the homonuclear rotary-resonance (HORROR) experiment[31] called dipolar recoupling enhancement through amplitude modulation (DREAM)[32,33] the amplitude of the applied rf-field $\omega_1(t)$ is varied as a function of time to obtain an adiabatic sweep through the HORROR recoupling condition $n \cdot \omega_1 = \omega_r$ with $n = \pm 1, \pm 2$ leading to $\chi(t) = \omega_r - n \cdot \omega_1(t)$. Recently a rf-field-driven dipolar recoupling scheme for half-integer quadrupolar nuclei was introduced[34] which can also be implemented in an adiabatic fashion.

2 THEORY

A spin system which is subject to magic-angle sample spinning (MAS) and to a slow variation of a parameter due to an adiabatic process can be described by a time-dependent Hamiltonian $\mathcal{H}(t, T)$. In this notation, the time-variable t characterizes the fast time dependence due to the MAS and the time-variable T describes the slow time dependence due to the adiabatic variation of a spin-system variable. If we assume that the changes due to T can be neglected over a time period $\tau_r = 2\pi/\omega_r$ then we can define a t-time averaged Hamiltonian

$$\mathcal{H}(T) = \langle \mathcal{H}(T) \rangle_{\tau_r} \tag{10}$$

which no longer depends on the time-variable t and is, therefore, independent of the MAS rotation. There are several ways of carrying out the averaging. The most common descriptions use average Hamiltonian and Floquet theory. The details of this averaging process depend on the specific polarization transfer process under discussion. Different approaches have been used and can be found in the original literature (see below).

For a pair of spins 1/2, the relevant process of the adiabatic polarization transfer can always be described in a subspace κ of the Hamiltonian which is defined by a fictitious spin-1/2 system.[12,13] The T-time dependent system Hamiltonian in this subspace is given by

$$\mathcal{H}^{\kappa}(T) = \chi^{\kappa}(T) \cdot S_z^{\kappa} + |d_{\text{eff}}^{\kappa}| \cdot (\cos(\varphi) S_x^{\kappa} + \sin(\varphi) S_y^{\kappa}) \tag{11}$$

Equation (11) is a trivial generalization of equation (7) caused by the fact that the effective dipolar coupling d_{eff}^{κ} appearing in the context of recoupling experiments is a complex number with absolute value $|d_{\text{eff}}^{\kappa}|$ and the phase $\arg(d_{\text{eff}}^{\kappa}) = \varphi$. The size of $|d_{\text{eff}}^{\kappa}|$ depends on the two Euler angles α and β which describe the rotation from the principal-axis system of the dipolar interaction tensor to the rotor-fixed coordinate system. The third Euler angle γ determines the phase φ but does not influence the magnitude of the coupling, $|d_{\text{eff}}^{\kappa}|$. The phase is simply an integer multiple of γ where the integer depends on the matching condition employed. In a powder sample each crystallite has a different Euler angle γ and, therefore, a different phase φ. The Hamiltonian for each crystallite lies in a different plane spanned by the operators S_z^{κ} and $\cos(\varphi) S_x^{\kappa} + \sin(\varphi) S_y^{\kappa}$. To simplify the theoretical description we can rotate the Hamiltonian by the crystallite-dependent angle φ about $-S_z^{\kappa}$ and recover the simple form of equation (7):

$$\mathcal{H}^{\kappa}(T) = \chi^{\kappa}(T) \cdot S_z^{\kappa} + |d_{\text{eff}}^{\kappa}| \cdot S_x^{\kappa} \tag{12}$$

In the course of the adiabatic polarization transfer the effective chemical-shift term is changed from $\chi(0) = \chi_i$ to $\chi(\tau) = \chi_f$ (where χ_i and χ_f have a different sign) in such a way that the adiabaticity condition

$$a(T) = \frac{\sqrt{\chi^{\kappa}(T)^2 + |d_{\text{eff}}^{\kappa}|^2}}{|\mathrm{d}\Theta^{\kappa}(T)/\mathrm{d}T|} \gg 1 \tag{13}$$

is fulfilled for all times T. Note that the adiabaticity parameter is T-time dependent. Here, the angle $\Theta^\kappa(T) = \arctan(|d^\kappa_{\text{eff}}|/\chi^\kappa(T))$ describes the time-dependent angle between the Hamiltonian and the z-axis. We start at time $T = 0$ with an initial density operator $\sigma^\kappa(0^-) = p^\kappa \cdot S^\kappa_z \approx c \cdot \mathcal{H}^\kappa(0)$ along the z-axis of the subspace κ. If the Hamiltonian $\mathcal{H}^\kappa(0)$ is not parallel with the z-axis, e.g., if the initial offset is not large enough, only the part of the initial density operator that is parallel to the Hamiltonian $\mathcal{H}^\kappa(0)$ has to be taken into account for the further course of the experiment. We denote the density operator just before a projection step at time t by $\sigma^\kappa(t^-)$ and just after the projection step by $\sigma^\kappa(t^+)$. Each projection decreases the spin order because the orthogonal components are assumed to decay irreversibly. After the projection we obtain

$$\sigma^\kappa(0^+) = p^\kappa \cdot \cos(\Theta(0)) S^\kappa_{\text{eff}}(0) \tag{14}$$

where the cosine of the angle $\Theta(0) = \arctan(|d_{\text{eff}}|/\chi^\kappa_i)$ determines the initial loss of polarization due to the projection on the operator $S^\kappa_{\text{eff}}(0)$. This projection is schematically illustrated in Figure 2. The operator

$$S^\kappa_{\text{eff}}(T) = \cos(\Theta(T)) S^\kappa_z + \sin(\Theta(T)) S^\kappa_x \tag{15}$$

stays always parallel to the Hamiltonian. Ideally, the sweep is applied such that $\Theta(0) \approx 0$ and

$$\sigma^\kappa(0^+) \approx p^\kappa \cdot S^\kappa_z \tag{16}$$

If the effective coupling $|d^\kappa_{\text{eff}}|$ is non-zero and equation (13) is fulfilled, the density operator always stays parallel to the Hamiltonian (i.e., along $S^\kappa_{\text{eff}}(T)$) and follows the movement of the Hamiltonian and describes an arc in the plane spanned by S^κ_z and $\cos(\varphi)S^\kappa_z + \sin(\varphi)S^\kappa_y$. For $\varphi = 0$, one obtains the following expression for the density operator during the adiabatic sweep:

$$\sigma^\kappa(T) = p^\kappa \cdot \cos(\Theta_i) S^\kappa_{\text{eff}}(T) \tag{17}$$

Figure 2 shows the trajectory followed by the density operator for a single arbitrary crystallite in the plane spanned by S^κ_z and $\cos(\varphi)S^\kappa_z + \sin(\varphi)S^\kappa_y$ as a function of the time-variable T. For a powder each crystallite follows such a trajectory but due to the variation in the phase φ for the different crystallites the planes are different. At time $T = 0$ the magnetization of all crystallites are aligned along S^κ_z. At the center of the sweep at $\chi^\kappa(T = \tau/2) = 0$ the magnetization is distributed over the plane spanned by S^κ_x and S^κ_y depending on the value of φ. At the end of the sweep at $T = \tau$ the magnetization of all different crystallites is again aligned but now along $-S^\kappa_z$.

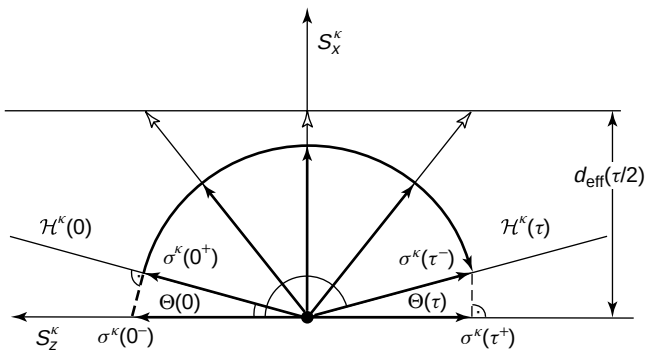

Figure 2 Schematic representation of the adiabatic polarization transfer for a single crystallite orientation in the subspace spanned by S^κ_z and S^κ_x. The initial projection with $\Theta(0)$ the subsequent rotation imposed by the rotation of the Hamiltonian, and the final projection with $\Theta(\tau)$ of the density operator is shown

The density operator at the end of the sweep at $\chi^\kappa(\tau) = \chi^\kappa_f$ is then given by

$$\sigma^\kappa(\tau^-) = p^\kappa \cdot \cos(\Theta(0)) \cdot [\cos(\Theta(\tau)) S^\kappa_z + \sin(\Theta(\tau)) S^\kappa_x] \tag{18}$$

where the angle $\Theta(\tau) = \pi + \arctan(|d^\kappa_{\text{eff}}|/\chi^\kappa_f)$. We have to project the density operator at the end of the sweep onto the z-axis of the subspace κ and obtain the final density operator

$$\sigma^\kappa(\tau^+) = p^\kappa \cdot \cos(\Theta(0)) \cos(\Theta(\tau)) S^\kappa_z \tag{19}$$

For a well-designed experiment, we require that $\Theta(0) \approx 0$ and $\Theta(\tau) \approx \pi$ leading to

$$\sigma^\kappa(\tau^+) \approx -p^\kappa \cdot S^\kappa_z \tag{20}$$

The loss of polarization caused by the two projections at the beginning and the end of the sweep are expressed by the factors $\cos(\Theta(0))$ and $\cos(\Theta(\tau))$ in equation (19), respectively, and can be minimized by starting and ending the adiabatic sweep with initial and final values of the effective chemical shift largely exceeding the value of the effective coupling frequency $|d^\kappa_{\text{eff}}|$.

If the effective coupling $|d^\kappa_{\text{eff}}|$ is zero, the density operator is unchanged by the sweep and we obtain a final density operator $\sigma^\kappa(\tau) \approx \sigma^\kappa(0) = p^\kappa \cdot S^\kappa_z$, assuming that $\Theta(0) \approx 0$ and $\Theta(\tau) \approx \pi$.

In principle, any continuous shape for $\chi^\kappa(T)$ can be used which fulfills equation (13), but to minimize relaxation effects it is advantageous to use a sweep which is as short as possible while still maintaining adiabaticity at all times T. The best shape with respect to adiabaticity is a shape where the angular velocity $\alpha(T) = \mathrm{d}\Theta(T)/\mathrm{d}T$ is proportional to the effective field $\omega_{\text{eff}}(T) = \sqrt{|d^\kappa_{\text{eff}}| + \chi^\kappa(T)^2}$. This requirement is fulfilled for a sweep rate of[35,36]

$$\frac{\mathrm{d}}{\mathrm{d}T}\chi^\kappa(T) \propto \frac{(|d^\kappa_{\text{eff}}|^2 + \chi^\kappa(T)^2)^{3/2}}{|d^\kappa_{\text{eff}}|} \tag{21}$$

Such a function leads to a fast change of $\chi^\kappa(T)$ far from the center of the sweep and a slow change close to the center. To design such a sweep, the sweep has to fulfill the condition $\chi^\kappa(\tau/2) = 0$ which is not possible for all spins in the presence of chemical-shift offsets or rf-field inhomogeneity. A linear sweep of

$$\chi^\kappa(T) = \chi^\kappa_i - \left(\frac{\chi^\kappa_i - \chi^\kappa_f}{\tau} \cdot T\right) \tag{22}$$

is the shape which shows the smallest sensitivity to the value of the system parameters but requires the longest sweep time to remain adiabatic during the entire sweep. In practice, a good compromise is to maintain constant angular velocity during the

sweep for a 'typical' value of the dipolar coupling constant d_{est} which can be implemented by the function

$$\alpha(T) = \frac{\mathrm{d}\Theta(T)}{\mathrm{d}T} = \frac{2}{\tau} \cdot \arctan\left(\frac{\chi_i}{|d_{\text{est}}|}\right) \tag{23}$$

Such a solution leads to the functional form

$$\chi^{\kappa}(T) = |d_{\text{est}}| \cdot \tan\left(\alpha \cdot \left[\frac{\tau}{2} - T\right]\right) \tag{24}$$

for $0 \leq T \leq \tau$ which is more tolerant than the one described by equation (21) to an imprecise estimation of the parameters for the center of the sweep and to the variation of $d_{\text{eff}}(\alpha, \beta, \gamma)$ as a function of the crystallite orientation.

In principle, one can achieve 100% polarization transfer using adiabatic methods compared to a maximum of 73% efficiency using 'sudden' methods. This requires of course, that the polarization transfer process is in the adiabatic limit ($a(T) \gg 1$) for all orientation-dependent effective coupling frequencies $d_{\text{eff}}(\alpha, \beta, \gamma)$. This increased efficiency is due to the fact that the transfer speed of the adiabatic polarization transfer is independent of the Euler angles and of the orientation-dependent size of the effective coupling constant. As was shown earlier, the Euler angle γ only influences the phase in the $S_x^{\kappa} - S_y^{\kappa}$-plane where the trajectory crosses but all trajectories reach the final point at the same point in time (Figure 2b).

3 METHODS OF HETERONUCLEAR POLARIZATION TRANSFER

3.1 Hartmann–Hahn Cross Polarization by Adiabatic Passage

Adiabatic Passage Hartmann–Hahn cross polarization (APHH)[16–21] was designed to combine the advantages of Hartmann–Hahn cross polarization, namely the conservation of the sum polarization, with the advantages of ADRF-ARFF which has a higher transfer efficiency and no critical matching condition. In this experiment the amplitude of one or both of the rf-fields is changed in an adiabatic fashion during the cross-polarization time period (Figure 3) in order to obtain a sweep through the sideband f of the Hartmann–Hahn matching condition $\omega_{1I} - \omega_{1S} = f \cdot \omega_r$.

In the APHH experiment, the sum polarization and σ^{Σ} are constants of the motion and the relevant subspace of the heteronuclear two-spin Hamiltonian is the zero-quantum subspace $\kappa = \Delta$. The Hamiltonian in this subspace has exactly the form of equation (7)

$$\mathcal{H}^{\Delta}(T) = \chi^{\Delta}(T) \cdot S_z^{\Delta} + |d_{f,\text{eff}}| \cdot S_x^{\Delta} \tag{25}$$

with $\chi^{\Delta}(T) = \omega_{1I}(T) - \omega_{1S}(T) - f\omega_r$ where $\omega_{1I}(T)$ and $\omega_{1S}(T)$ are the time-dependent amplitudes of the applied rf fields. The parameter $f = \pm 1, \pm 2$ denotes the sideband of the Hartmann–Hahn matching condition under MAS[37–39] and $d_{f,\text{eff}}$ is the Fourier coefficient of order f of the heteronuclear dipolar coupling. In APHH CP the initial and final value of the amplitude sweep $\chi_i^{\Delta} = \omega_{1I}(0) - \omega_{1S}(0) - f\omega_r$ and $\chi_f^{\Delta} = \omega_{1I}(\tau) - \omega_{1S}(\tau) - f\omega_r$ are limited to about $\pm 1/2\omega_r$

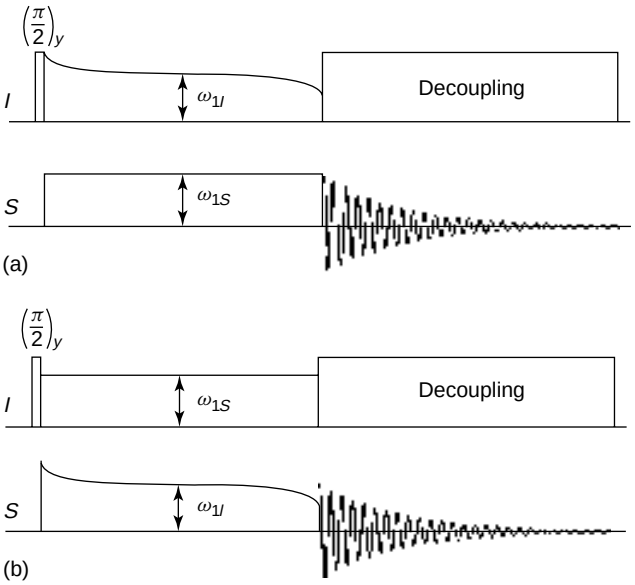

Figure 3 Pulse sequence used for adiabatic cross polarization. The amplitude modulation during the cross-polarization time can be applied either to the proton (a) or to the carbon (b) channel. Cross polarization uses of phase X

in order not to touch one of the other sideband matching conditions. The fictitious spin-1/2 operators in the zero-quantum subspace are defined as $S_z^{\Delta} = 1/2 \cdot (I_z - S_z)$, $S_x^{\Delta} = 1/2 \cdot (S^+I^- + S^-I^+)$, and $S_y^{\Delta} = i/2 \cdot (S^+I^- - S^-I^+)$, where the z-axis (defining I_z and S_z) is chosen along the effective field direction in the rotating frame.[40] Rotating the density operator in the zero-quantum subspace from S_z^{Δ} to $-S_z^{\Delta}$ leads to a complete transfer of magnetization from I_z to S_z because the double-quantum subspace density operator does not evolve during the APHH period of the experiment.

The above description assumes the ideal case of an isolated dipolar-coupled two-spin system where both spins are on-resonance. In the presence of chemical-shift offsets the amplitudes of the rf-fields have to be replaced by the effective fields $\omega_{I,\text{eff}} = \sqrt{(\omega_{1I}(T))^2 + \Omega_I^2}$ and $\omega_{S,\text{eff}} = \sqrt{(\omega_{1S}(T))^2 + \Omega_S^2}$, respectively.[40] In addition, the effective dipolar-coupling frequency $d_{f,\text{eff}}$ becomes weakly time dependent with T.

Adiabatic cross polarization can also be done using the J coupling as a transfer mechanism in liquid[41,42] and solid[43] samples. If we consider the isotropic J-coupling in addition to the dipolar coupling, we can get polarization transfer under MAS for the $f = 0$ matching condition[43] with $d_{0,\text{eff}} = J$. If the system is not isolated but has homonuclear dipolar couplings we can also get polarization transfer for the $f = 0$ and for the $|f| > 2$ matching conditions and the coupling strength of the $f = \pm 1, \pm 2$ matching conditions is modified.

The experimental results of Figure 4 show that adiabatic-passage Hartmann–Hahn cross polarization yields an S-spin signal that is always equal to or larger than the one obtained using Hartmann–Hahn cross polarization with the same contact time. At longer contact times where the transient oscillations[44] are dying out (in the example of Figure 4 for $\tau > 0.4$ ms) a gain of a factor of two in signal is

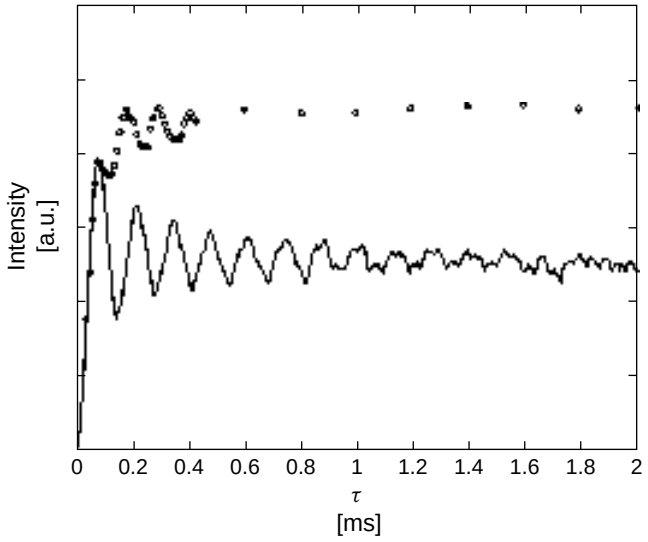

Figure 4 Comparison of the cross-polarized magnetization in Hartmann–Hahn cross polarization (solid line) and adiabatic passage Hartmann–Hahn cross polarization (open circles) measured on a sample of 10% 2-^{13}C-3,3,3-^{2}H-alanine diluted in perdeuterated alanine. The Hartmann–Hahn cross polarization shows the transient oscillations of the one-bond heteronuclear carbon–proton dipolar coupling as a function of the cross-polarization time τ. The adiabatic passage cross polarization is also shown as a function of the total sweep length and leads to a signal which is larger by a factor of almost two. The experiments were carried out at a spinning speed of $\omega_r/2\pi = 22\,\text{kHz}$ using the $f-1$ matching condition and a proton field strength of $\omega_{1I}/2\pi = 108\,\text{kHz}$. (Figure courtesy of René Verel)

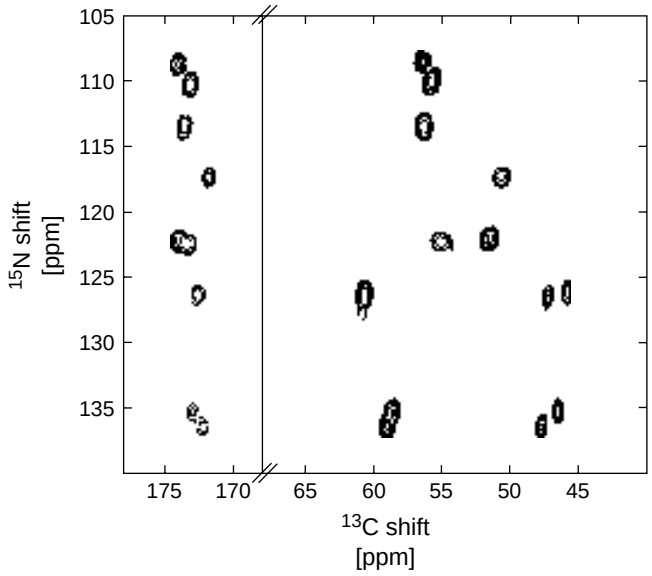

Figure 5 Chemical shift correlation spectrum for a fully ^{13}C, ^{15}N-labelled sample of the cyclic decapeptide antamanide using adiabatic passage Hartmann–Hahn cross polarization. The resulting spectrum correlates each amide nitrogen N_κ with the directly attached carbons: C_α^κ in the same residue and $C'_{\kappa-1}$ in the previous residue. (Figure courtesy of Dr. Andreas Detken)

observed caused by an improved polarization transfer. The theoretical gain of the APHH CP compared to the conventional cross polarization experiment in larger spin systems (IS_n) have been investigated.[21] It was found that APHH CP should always outperforms CP by a factor close to two. For a large system with $n \to \infty$, the theoretical gain is again two[21] although experimentally much lower gains have been found.[17]

A further benefit of the APHH CP experiment is the insensitivity to the matching condition. For small dipolar couplings and fast spinning, the Hartmann–Hahn match is very narrow. It can become quite difficult to match the rf amplitudes and to keep the rf amplitude stable enough over the course of signal accumulation.[45] An example for such a difficult system is ^{13}C–^{15}N cross polarization. For the APHH experiments,[20] these difficulties are greatly reduced because the precise matching condition will be fulfilled at some time during the sweep. The exact position does not play a significant role. Figure 5 shows an example of a heteronuclear ^{13}C–^{15}N correlation experiment where APHH cross polarization between ^{13}C and ^{15}N was used to establish the chemical-shift correlation.[20]

An additional gain in signal intensity can be realized due to the relative insensitivity of APHH cross polarization to rf-field inhomogeneities. Only part of the sample is exactly at the Hartmann–Hahn match of the rf-fields in normal cross polarization. This problem is overcome by APHH cross polarization where all spins go through the matching condition but at different times during the sweep. A similar approach can also be used in 'sudden' experiments by ramping the amplitude

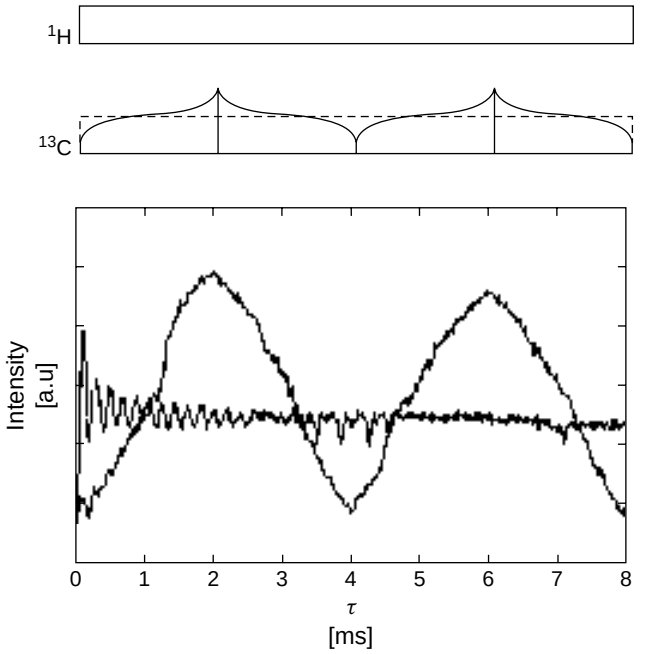

Figure 6 Multiple adiabatic sweeps through the Hartmann–Hahn matching condition allow the reversible transfer of magnetization between protons and carbons. The experiments were carried out using a sample of 10% 2-^{13}C-3,3,3-^{2}H-alanine diluted in perdeuterated alanine. The spinning speed was $\omega_r/(2\pi) = 22\,\text{kHz}$. The $f = -1$ matching condition and a proton field strength of $\omega_{1I}/(2\pi) = 108\,\text{kHz}$ were used. Each of the four adiabatic sweeps had a length of 2 ms. For comparison we also show the intensity of the magnetization which was obtained in the corresponding Hartmann–Hahn cross-polarization experiment as a function of the cross-polarization time. (Figure courtesy of René Verel)

in a CP experiment.[46,47] The ramp CP experiment leads to an equilibrium polarization of ca. 50% in two-spin systems even in the presence of rf-field inhomogeneity but the adiabatic gain of an additional factor of two can only be obtained if the design principles for an adiabatic transfer are employed.

The adiabatic gain can be experimentally verified by an experiment where several adiabatic sweeps are performed sequentially as shown in Figure 6. The behavior during the first sweep is completely equivalent to the one in Figure 5. During the second sweep ($2\,\text{ms} \leq \tau \leq 4\,\text{ms}$) the polarization is transferred back from the ^{13}C spins to the source spin(s), in this case the protons. The whole cycle can be repeated again without noticeable loss of polarization. The polarization in the adiabatic experiments flows back and forth approximately symmetrically around the equilibrium value obtained in a normal CP experiment. The initial jump in the magnetization at $\tau < 1\,\text{ms}$ is due to the initial projection of equation (15).

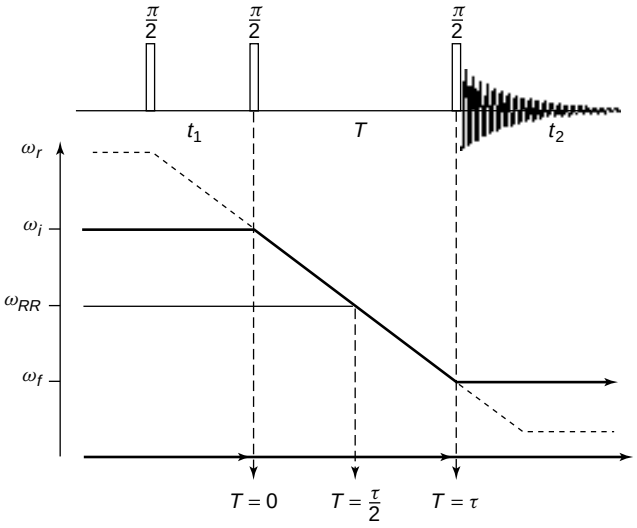

Figure 7 Pulse scheme of the APRR experiment. The pulse scheme follows the basic principle of two-dimensional exchange spectroscopy. The variation of the spinning rate was obtained by using a home-built setup consisting of a parallel arrangement of an air line with a needle valve to control the flow and an air line with a TTL-operated air-valve. This arrangement was placed in parallel with the spinning-speed controller. Upward and downwards spinning-speed ramps were produced by opening or closing the air valve using a user-defined TTL gate from the pulse programmer. Using a 4 mm rotor, a maximum slope of $6000\,\text{s}^{-2}$ was obtained. For higher spinning speeds (>5000 Hz) downward ramps perform better, for low spinning speed upward ramps should be used. If a stable spinning frequency during the t_1 and t_2 periods is not required the linear ramp can be extended (dashed line) to include these time periods. (Figure adapted from Ref.[23])

4 METHODS OF HOMONUCLEAR POLARIZATION TRANSFER

4.1 Adiabatic Passage Rotational Resonance

In the adiabatic passage, rotational-resonance experiment (APRR)[23] the frequency of the rotor is changed during the course of the experiment such that the rotor frequency is swept through the rotational-resonance (RR) condition[24–26] $\Omega_1 - \Omega_2 = n \cdot \omega_r$ in an adiabatic fashion (Figure 7). Such a spinning-frequency sweep can be achieved by suddenly increasing (decreasing) the air pressure on the drive air of the MAS rotor. This can be implemented either by changing

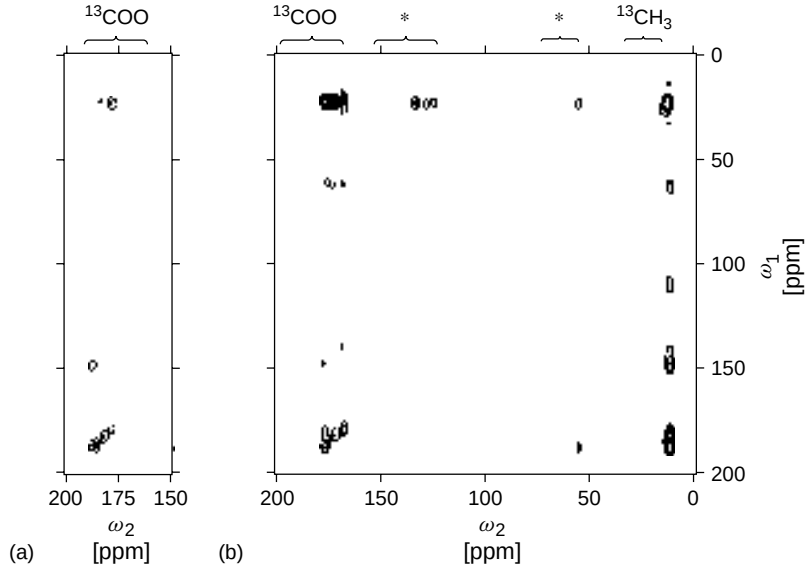

Figure 8 (a) Two-dimensional ^{13}C chemical-shift correlation spectrum of uniformly ^{13}C labelled calcium-acetate monohydrate using RR as a mixing sequence. The strip from the 2D spectrum shows the carboxylic diagonal peaks and the cross peaks to the methyl group region for an experiment recorded at a constant spinning frequency matching the rotational resonance for the spin pair involving the most shielded carboxylic resonance. (b) Two-dimensional ^{13}C chemical-shift correlation spectrum of uniformly ^{13}C labelled calcium-acetate monohydrate using APRR as the mixing sequence. During the mixing time of 40 ms, the spinning frequency was ramped from 1.70 kHz to 1.88 kHz. The APHH passage covered all the $n = 4$ resonances between methyl and carboxylic spins. Four transients were co-added for each of the 256 t_1 increments recorded. The assignment of the resonance lines is given on top of the figure, the chemical shifts are referenced to TMS. Spinning sidebands are denoted by *. (Figure adapted from Ref.[23])

the setting of the spinning-speed controller from the pulse programmer or by using a magnetic valve which opens a bypass high-pressure line.

As the APHH CP experiment, the APRR experiment is a zero-quantum polarization-transfer experiment and the relevant Hamiltonian is the same as for APHH

$$\mathcal{H}^{\Delta}(T) = \chi^{\Delta}(T) \cdot S_z^{\Delta} + |d_{n,\mathrm{eff}}| \cdot S_x^{\Delta} \tag{26}$$

except that $\chi^{\Delta}(T) = \Omega_1 - \Omega_2 - n\omega_r(T)$ where Ω_1 and Ω_2 are the isotropic chemical shifts of the two spins. The effective coupling $d_{n,\mathrm{eff}}$ is given by the Fourier component $n = \pm 1, \pm 2$ of the homonuclear dipolar coupling. Again, a rotation of the density operator from S_z^{Δ} to $-S_z^{\Delta}$ induced by a variation of the MAS frequency, leads to a full transfer of magnetization from spin 1 to spin 2 as the double-quantum subspace is untouched.

In the presence of a non-vanishing chemical-shielding difference tensor the effective coupling frequencies are somewhat modified and higher-order matching conditions with $|n| > 2$ become allowed.

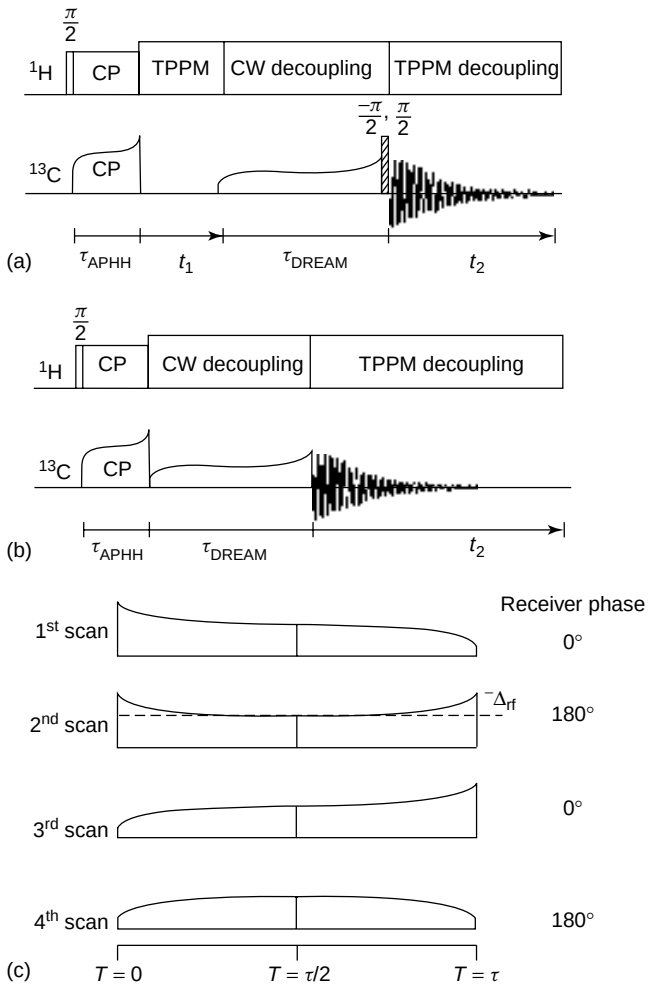

Figure 9 Pulse sequence for (a) the two-dimensional DREAM correlation experiment and (b) the DREAM spin-pair selective experiments. (c) Four different amplitude shapes which can be used in the spin-pair filter experiment and appropriate modification of the receiver phase. (Figure adapted from Ref.[33])

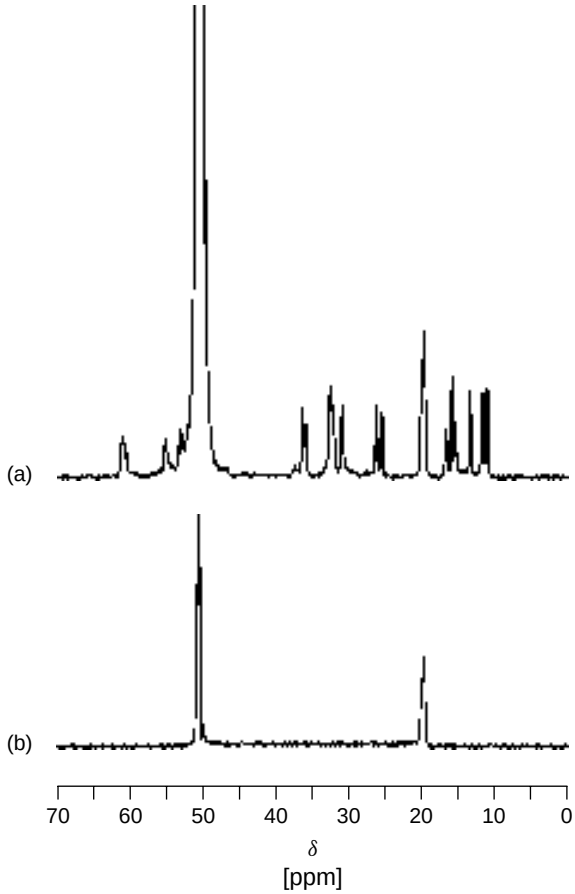

Figure 10 Cross polarization (a) and DREAM SPS (b) spectra of a mixture of 1-$^{13}C_1$-alanine, natural abundance methionine and natural abundance *iso*-leucine. The three substances were mixed in approximately equal weight parts and the sample restricted to the central region of the rotor with a total length of about 3 mm. A total of 3072 scans was co-added for each of the spectra. The spinning frequency was set to $\omega_r/2\pi = 28$ kHz and stabilized within 25 Hz with a spinning speed controller. (Figure adapted from Ref.[32])

One can perform the rotational-resonance experiment also in a tilted frame of reference where the chemical shifts of spins 1 and 2 have to be replaced by the effective fields $\omega_{1,\mathrm{eff}} = \sqrt{(\omega_1(T))^2 + \Omega_1^2}$ and $\omega_{2,\mathrm{eff}} = \sqrt{(\omega_1(T))^2 + \Omega_2^2}$, respectively.[28–30] Instead of a sweep of the spinning frequency ω_r one can change the effective fields as a function of T. The experiment is almost completely equivalent to the spinning-frequency ramp except that the variation of $\chi^{\Delta}(T)$ is now caused by rf-field amplitude changes in full analogy to the APHH experiment.

Figure 8 shows a comparison of a standard RR experiment (Figure 8a) and an APRR experiment (Figure 8b) on a sample of uniformly labelled calcium acetate. The three different resonance lines in the carboxyl region of the spectrum are due to packing effects. The four crystallographically non-equivalent carbonyl carbons give rise to three resolved resonances. The APRR experiment is more broadband and covers all three resolved $^{13}CH_3-{}^{13}COO$ spin pairs while the RR experiment (Figure 8a) leads to transfer for one of these pairs only. Furthermore, APRR shows much higher cross peak intensity. For a fully adiabatic transfer we would expect all intensity to

be in the cross peaks with no intensity left in the diagonal peaks.

Rotational-resonance experiments on the central transition of a pair of dipolar-coupled half-integer quadrupolar spins can be described in full analogy to the rotational resonance experiments in spin-1/2 nuclei if at least one of the two quadrupolar nuclei has a large quadrupolar coupling constant. In half-integer quadrupolar nuclei the central transition is broadened by the second-order quadrupolar shift. Therefore, the conventional rotational-resonance experiment will only allow polarization transfer for a small number of spins which have an averaged chemical-shift difference close to the selected MAS rotation frequency. If we use a sweep through the rotational-resonance condition of all crystallites, then we are able to achieve recoupling for the whole second-order broadened powder pattern and we obtain polarization transfer independent of the crystallite orientation.[27]

4.2 DREAM

In the DREAM experiment[32,33] (Figure 9) a sweep of the rf-field amplitude through the HORROR recoupling condition[31] $2 \cdot \omega_1 = \omega_r$ is used to transfer polarization between homonuclear dipolar-coupled spin pairs. The relevant subspace of the homonuclear dipolar-coupling Hamiltonian is the double-quantum subspace $\kappa = \Sigma$. The Hamiltonian in this subspace is again of the 'standard form' and is given by

$$\mathcal{H}^{\Sigma}(T) = \chi^{\Sigma}(T) S_z^{\Sigma} + |d_{1,\mathrm{eff}}| S_x^{\Sigma} \tag{27}$$

with $\chi^{\Sigma}(T) = 2 \cdot \omega_1(T) - \omega_r$ where $\omega_1(T)$ is the time-dependent rf-field amplitude and $d_{1,\mathrm{eff}}$ is the $f = 1$ Fourier component of the homonuclear dipolar-coupling constant. The fictitious spin-1/2 operators are defined as $S_z^{\Sigma} = (1/2) \cdot (S_{1z} + S_{2z})$, $S_x^{\Sigma} = (1/2) \cdot (S_1^+ S_2^+ + S_1^- S_2^-)$, and $S_y^{\Sigma} = (i/2) \cdot (S_1^+ S_2^+ - S_1^- S_2^-)$ where the z-axis (defining S_{1z} and S_{2z}) is along the applied rf-field. A rotation of the density operator from S_z^{Σ} to $-S_z^{\Sigma}$ leads to a full transfer of polarization from spin 1 to spin 2 assuming that no zero-quantum transitions take place.

The DREAM recoupling sequence has been used as the mixing scheme in two-dimensional correlation experiments (Figure 9a) and in the context of an efficient homonuclear spin-pair filter (Figure 9b) by combining different shapes for the adiabatic sweep. Such a filter is more efficient than a 'sudden' double-quantum filter since not all crystallites need to go through the double-quantum state $S_x^{\Sigma} \cos(\varphi) + S_y^{\Sigma} \sin(\varphi)$ at the same point in time. The different amplitude shapes and their corresponding receiver phase are shown in Figure 9c.

Figure 10 shows an application of the DREAM spin-pair filter to the suppression of natural abundance background signals in a mixture of the amino acids alanine, methionine, and *iso*-leucine. The C_α position of alanine was ^{13}C labelled, all other carbon atoms had natural isotopic abundance. The filtered spectrum (Figure 10b) shows only the alanine C_α,C_β spin-pair resonances, all other resonance are attenuated below the noise level. The efficiency of the selection of the adiabatic spin-pair filter is measured to be 61% from the intensity of the CH_3 resonance. The higher intensity of the (100% labeled) C_α resonance compared to the C_β resonance can be explained by intermolecular $C_\alpha - C_\alpha$ couplings that allow additional spin pairs to pass partially through the filter and is not due to incomplete suppression of isolated spins.

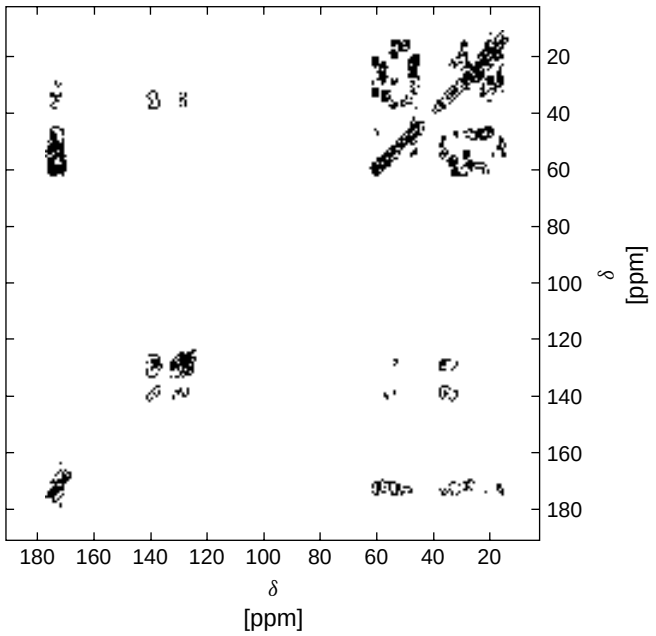

Figure 11 Two-dimensional ^{13}C chemical shift correlation spectrum of the cyclic decapeptide Antamanide using adiabatic DREAM mixing. The spectrum was recorded at a spinning frequency of $\omega_r(2\pi) = 40$ kHz at a proton Larmor frequency of 500 MHz. (Figure courtesy of Aswin Verhoeven)

Figure 11 shows the application of the DREAM sequence as the correlation mechanism in a two-dimensional chemical-shift correlation spectrum. Due to the fact that it is a double-quantum mixing scheme the cross peaks show alternating negative and positive intensities. The spectrum was taken at a MAS frequency of $\omega_r/(2\pi) = 40$ kHz using an rf-field strength at the center of the sweep of $\omega_1/(2\pi) = 20$ kHz. Many dipolar recoupling sequences suffer from the fact that they are more difficult to apply at higher spinning frequencies since the rf-field has to be an integer multiple of the spinning frequency. For DREAM the required rf-field strength is only 1/2 of the spinning frequency which makes the DREAM method very well suited for application at high MAS frequencies. In fact, the method becomes more useful at higher MAS frequencies because the broadbandedness of the DREAM mixing with respect to chemical-shift offsets increases linearly with ω_r. As a rule of thumb, the bandwidth of the sequence is approximately equal to $\pm\omega_r/4$. To cover an entire ^{13}C spectrum on a spectrometer with 400 MHz proton resonance frequency, a spinning frequency of about 35 kHz is required.

5 RELATED ARTICLES IN THIS VOLUME

Three-dimensional Molecular Structures in Uniformly Labelled Solids Determined Using Rotational Resonance in the Tilted Rotating Frame; Magic-angle Spinning Extensions.

6 RELATED ARTICLES IN VOLUMES 1–8

Average Hamiltonian Theory, Volume 2; Cross Polarization in Rotating Solids: Spin-1/2 Nuclei, Volume 3; Cross Polarization in Solids, Volume 3; Floquet Theory, Volume 3; Homonuclear Recoupling Schemes in MAS NMR, Volume 4; Magic Angle Spinning, Volume 5; Rotating Solids, Volume 7.

7 REFERENCES

1. S. R. Hartmann and E. L. Hahn, *Phys. Rev.*, 1962, **128**, 2042.
2. A. Pines, M. G. Gibby, and J. S. Waugh, *J. Chem. Phys.*, 1972, **56**, 1776.
3. N. Bloembergen, *Physica*, 1949, **15**, 386.
4. G. A. Morris and R. Freeman, *J. Am. Chem. Soc.*, 1979, **101**, 760.
5. J. Jeener, B. H. Meier, P. Bachmann, and R. R. Ernst, *J. Chem. Phys.*, 1979, **71**, 4546.
6. S. Zhang, B. H. Meier, and R. R. Ernst, *Phys. Rev. Lett.*, 1992, **69**, 2149.
7. S. M. De Paul, M. Tomaselli, A. Pines, M. Ernst, and B. H. Meier, *J. Chem. Phys.*, 1998, **108**, 826.
8. M. Ernst, B. H. Meier, M. Tomaselli, and A. Pines, *J. Chem. Phys.*, 1998, **108**, 9611.
9. M. Ernst, B. H. Meier, M. Tomaselli, and A. Pines, *Mol. Phys.*, 1998, **95**, 849.
10. A. Abragam, 'The Principles of Nuclear Magnetism', Clarendon Press: Oxford, 1961.
11. S. Zhang, P. Xu, O. W. Sorensen, and R. R. Ernst, *Concepts Magn. Reson.*, 1994, **6**, 275.
12. A. Wokaun and R. R. Ernst, *J. Chem. Phys.*, 1977, **67**, 1752.
13. S. Vega, *J. Chem. Phys.*, 1978, **68**, 5518.
14. A. Pines, in 'First Specialized Colloque Ampere', Krakow: Poland, 1973.
15. M. Mehring, 'Principles of High Resolution NMR in Solids', 2nd edn., Springer: Berlin, 1983.
16. S. Hediger, B. H. Meier, N. D. Kurur, G. Bodenhausen, and R. R. Ernst, *Chem. Phys. Lett.*, 1994, **223**, 283.
17. S. Hediger, B. H. Meier, and R. R. Ernst, *Chem. Phys. Lett.*, 1995, **240**, 449.
18. S. Zhang, C. L. Czekay, and W. T. Ford, *J. Magn. Reson. Ser. A*, 1994, **111**, 87.
19. S. Zhang, *J. Magn. Reson. Ser. A*, 1994, **110**, 73.
20. M. Baldus, D. G. Geurts, S. Hediger, and B. H. Meier, *J. Magn. Reson. Ser. A*, 1996, **118**, 140.
21. P. Hodgkinson and A. Pines, *J. Chem. Phys.*, 1997, **107**, 8742.
22. S. Hediger, P. Signer, M. Tomaselli, R. R. Ernst, and B. H. Meier, *J. Magn. Reson.*, 1997, **125**, 291.
23. R. Verel, M. Baldus, M. Nijman, J. W. M. van Os, and B. H. Meier, *Chem. Phys. Lett.*, 1997, **280**, 31.
24. D. P. Raleigh, A. C. Kolbert, T. G. Oas, M. H. Levitt, and R. G. Griffin, *J. Chem. Soc., Faraday Trans.*, 1988, **84**, 3691.
25. M. G. Colombo, B. H. Meier, and R. R. Ernst, *Chem. Phys. Lett.*, 1988, **146**, 189.
26. M. H. Levitt, D. P. Raleigh, F. Creuzet, and R. G. Griffin, *J. Chem. Phys.*, 1990, **92**, 6347.
27. M. Nijman, M. Ernst, A. P. M. Kentgens, and B. H. Meier, *Mol. Phys.*, 2000, **98**, 161.
28. K. Takegoshi, K. Nomura, and T. Terao, *Chem. Phys. Lett.*, 1995, **232**, 424.
29. K. Takegoshi, K. Nomura, and T. Terao, *J. Magn. Reson.*, 1997, **127**, 206.
30. P. R. Costa, B. Q. Sun, and R. G. Griffin, *J. Am. Chem. Soc.*, 1997, **119**, 10 821.
31. N. C. Nielsen, H. Bildsoe, H. J. Jakobsen, and M. H. Levitt, *J. Chem. Phys.*, 1994, **101**, 1805.
32. R. Verel, M. Baldus, M. Ernst, and B. H. Meier, *Chem. Phys. Lett.*, 1998, **287**, 421.
33. R. Verel, M. Ernst, and B. H. Meier, *J. Magn. Reson.*, 2001, **150**, 81.
34. M. Baldus, D. Rovnyak, and R. G. Griffin, *J. Chem. Phys.*, 2000, **112**, 5902.
35. J. Baum, M. Munowitz, A. N. Garroway, and A. Pines, *J. Chem. Phys.*, 1985, **83**, 2015.
36. C. J. Hardy, W. A. Edelstein, and D. Vatis, *J. Magn. Reson.*, 1986, **66**, 470.
37. R. A. Wind, S. F. Dec, H. Lock, and G. E. Maciel, *J. Magn. Reson.*, 1988, **79**, 136.
38. M. Sardashti and G. E. Maciel, *J. Magn. Reson.*, 1987, **72**, 467.
39. B. H. Meier, *Chem. Phys. Lett.*, 1992, **188**, 201.
40. M. H. Levitt, D. Suter, and R. R. Ernst, *J. Chem. Phys.*, 1986, **84**, 4243.
41. R. D. Bertrand, W. B. Moniz, A. N. Garroway, and G. C. Chingas, *J. Am. Chem. Soc.*, 1978, **100**, 5227.
42. G. C. Chingas, A. N. Garroway, W. B. Monitz, and R. D. Bertrand, *J. Am. Chem. Soc.*, 1980, **102**, 2526.
43. A. Verhoeven, R. Verel, and B. H. Meier, *Chem. Phys. Lett.*, 1997, **266**, 465.
44. L. Muller, A. Kumar, T. Baumann, and R. R. Ernst, *Phys. Rev. Lett.*, 1974, **32**, 1402.
45. E. W. Hagaman, P. C. Ho, L. L. Brown, F. M. Schell, and M. C. Woody, *J. Am. Chem. Soc.*, 1990, **112**, 7445.
46. G. Metz, Xiaoling-Wu, and S. O. Smith, *J. Magn. Reson. Ser. A*, 1994, **110**, 219.
47. G. Metz, M. Ziliox, and S. O. Smith, *Solid State NMR*, 1996, **7**, 155.

Biographical Sketches

Matthias Ernst, *b* 1964. Dipl. Chem., 1988; Dr. sc. nat., 1993, ETH Zürich, Switzerland, with Prof. Richard R. Ernst. Postdoctoral Fellow, University of California at Berkeley, USA, with Prof. Alexander Pines, 1994–1996; Research scientist, University of Nijmegen, The Netherlands, 1996–1998; Research Scientist, ETH Zürich, Switzerland, 1998–present. Research interests include development of new methods for high-resolution solid-state NMR and application of these techniques to materials and biological systems.

Beat H. Meier, *b* 1954. Dipl. Chem., 1978; Dr. sc. nat., 1984, ETH Zürich, Switzerland, with Prof. Richard R. Ernst. Postdoctoral Fellow, 1985–1986, Los Alamos National Laboratory, USA, with Dr. William Earl; Research scientist, 1987–1994, ETH Zürich, Switzerland. Professor of Chemistry, University of Nijmegen, The Netherlands, 1994–1998; Professor of Chemistry, ETH Zürich, Switzerland, 1998–present. Research interests include development of new methods for high-resolution solid-state NMR and application of these techniques to materials and biological systems.

Chemically Induced Dynamic Nuclear Polarization

Heinz D. Roth

Rutgers University, New Brunswick, NJ, USA

1	Introduction	1
2	Mechanism of CIDNP Generation	1
3	Experimental Techniques	6
4	Applications of CIDNP in Chemistry	6
5	Perspective	12
6	Related Articles	13
7	References	13

1 INTRODUCTION

At its most elementary level, nuclear magnetic resonance has three characteristic features that make it uniquely suitable for the identification of materials or compounds in chemistry, biology, and medicine, *chemical shift*, *spin–spin coupling* and *signal intensity*. In the typical NMR experiment, the signal intensity is proportional to the relative abundance of the nuclei represented. However, products generated by radical pair reactions may show dramatically perturbed signal intensities shortly after their formation. Such products show transient signals with anomalous intensities in either absorption (A) or emission (E).[1,2] These effects are induced as a result of magnetic interactions in radical or radical ion pairs on the nanosecond timescale. They are known as 'chemically induced dynamic nuclear polarization' (CIDNP).[3–8] The CIDNP effects (and similar anomalies for electron paramagnetic resonance spectra)[9] are closely interconnected with *magnetic field* and *isotope effects*, which cause the dependence of radical reaction kinetics and yields on the strength of the hyperfine coupling between a nucleus and an electron.[10] These phenomena arise as manifestations of closely related physical mechanisms. They are brought about by the existence of two radicals or radical ions in close proximity to each other (in a 'cage') so that they constitute a 'pair'. CIDNP, as well as magnetic isotope effects, are 'induced' by singlet–triplet transitions occurring within the 'cage' during the radical pair lifetime.

2 MECHANISM OF CIDNP GENERATION

Nuclear spin polarization effects can be induced by a variety of mechanisms, including magnetic interactions in radical pairs or biradicals, electron–nuclear cross relaxation in free radicals, or reactions with *para*-hydrogen. The following brief overview includes some aspects of radical pairs and their interactions in magnetic fields.

2.1 The Radical Pair Mechanism

The radical pair mechanism explains the generation of CIDNP effects on the basis of two principles: the rates of radical pair reactions depend on the electron spin multiplicity of the pair; and the intersystem crossing in a radical pair can be influenced by the spin states of nuclei interacting with the electron spin(s).[6,11–14] Combined, these selection principles cause a 'sorting' of nuclear spin states into different products and result in characteristic nonequilibrium populations in the nuclear spin levels of geminate reaction products and in complementary nonequilibrium populations in the spin levels of free radical ('escape') products.

Radical pairs in solution can be characterized by geometric parameters such as distance or orientation, or by electronic and magnetic parameters such as electron spin multiplicity or exchange interaction. Concerning the electronic spin state, radical pairs (RPs) can be either correlated or uncorrelated; radical pairs generated by a single, well-defined event (geminate RPs) are correlated, whereas radical pairs formed by the diffusion of two independently generated radicals are uncorrelated. Pairs having antiparallel electron spins have singlet spin multiplicity (S), whereas pairs with parallel spins are triplet (T). In an external magnetic field, the energy level of a triplet radical pair is split by the Zeeman interaction into three sublevels, T_+, T_0, and T_- (Figure 1). The magnitude of the splitting is field ($\boldsymbol{B}_0$) dependent; it equals $g\beta B_0$ (g is the electron g factor; β is the Bohr magneton). Because of the exchange interaction, $2J$, singlet and triplet radical pairs have slightly different energies; however, $2J$ falls off rapidly upon separation and can be neglected at distances greater than 1 nm, i.e., greater than a few molecular diameters.

Chemical reactions carried out under controlled conditions give rise to correlated (geminate) radical pairs. Thermal reactions typically produce S pairs, whereas photochemical reactions generate S or T pairs, depending on the spin multiplicity of the precursor state. Once generated, the radical pairs can recombine (couple) or disproportionate to give diamagnetic products (Scheme 1). This, however, depends critically on the spin multiplicity; coupling is allowed for singlet pairs but is, in almost all cases, spin forbidden for triplet pairs. Competing with these reactions is separation by diffusion, leading to solvent separated pairs; this process is accompanied by intersystem crossing. Solvent separated pairs have a finite probability to diffuse together again and to react with each other. Alternatively, they may separate and react with the solvent or another substrate to give radical transfer products. The lifetime of geminate pairs is 10^{-12}–10^{-11} s,

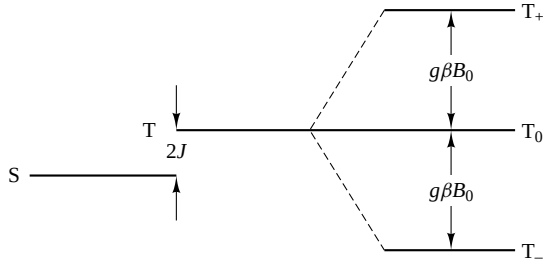

Figure 1 Radical pair energy level diagram in a magnetic field

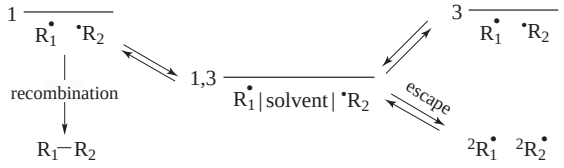

Scheme 1

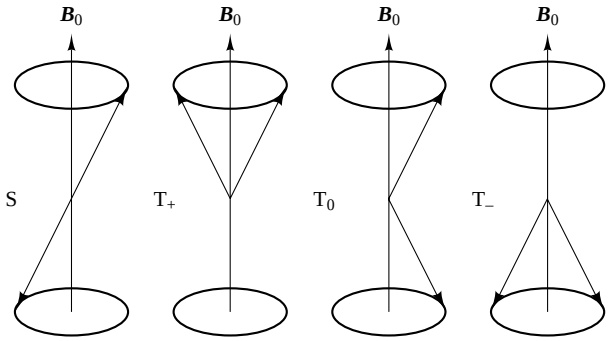

Figure 2 Vector model of radical pair spin states

whereas that of solvent separated pairs is 10^{-9}–10^{-8} s; free radicals may live as long as 10^{-4} s.

Because of the key role of spin multiplicity in determining radical pair reactions, intersystem crossing is of paramount importance. This transition can occur by several mechanisms; of these, loss of electron spin orientation by relaxation results in irreversible losses. In contrast, dephasing induced by differences in the electron Larmor precession (Δg mechanism), or because of hyperfine interactions between the unpaired electrons and nearby nuclei (hf mechanism), have the character of quantum mechanical oscillations; these mechanisms cause reversible dephasing. Intersystem crossing resulting from these interactions can be illustrated by a vector model describing the relative orientation of the electron spins in the magnetic field, $\boldsymbol{B}_0$ (Figure 2).[7] The electron spins precess with Larmor frequency [equation (1)]

$$\omega = g\beta B_0/h \tag{1}$$

The unpaired spins of a singlet pair precess with a phase difference of 180°; their vector sum is zero (Figure 2). The total spin of a triplet equals unity; the vector sum of their projection onto the external field direction can have three values, +1, 0, or − 1, corresponding to the T_+, T_0, and T_- levels (Figure 2). The vector model illustrates that simple dephasing of the spin precessions can cause transitions between the S and T_0 states. For example, the electron spins of two radicals, $R_1\cdot$ and $R_2\cdot$, with different g factors, $g_1 \neq g_2$, will precess at different rates; the difference, $\Delta\omega_{ST0}$, is dictated by the difference, Δg, between the g factors [equation (2)].

$$\Delta\omega_{ST0} = \omega_1 - \omega_2 = (g_1 - g_2)\beta B_0/h = \Delta g\beta B_0/h \tag{2}$$

The hyperfine-dependent mechanism also contributes to intersystem crossing. Magnetic nuclei in one or both radicals also precess around the magnetic field axis, generating local magnetic fields. The electron precession frequency, ω, is dictated primarily by $\boldsymbol{B}_0$, but the local fields due to nearby nuclei make small contributions. Since the nuclei are oriented parallel or antiparallel to the external field, they can increase or decrease ω, causing different degrees of dephasing for different nuclear spin states. Thus, $\Delta\omega_{ST0}$ will be changed by a value of $\pm a/2$ [equation (3)]

$$\Delta\omega_{ST0} = (g_1 - g_2)\beta B_0/h \pm \tfrac{1}{2}a_n \tag{3}$$

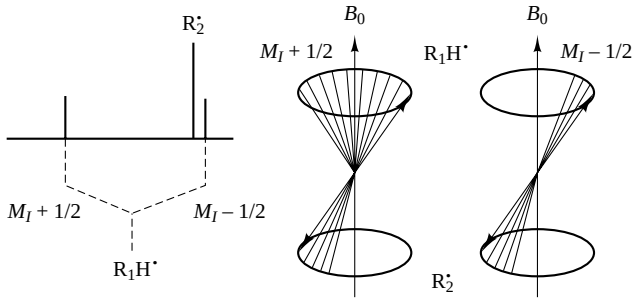

Figure 3 ESR spectra (left) and precession of electron spins of a radical pair, $R_1H\cdot$ and $R_2\cdot$, in a magnetic field ($g_1 > g_2$; $a_H > 0$; singlet precursor). The different orientations of the nuclear spin create two types of radical pairs with precession frequencies $\omega_1{}^+ > \omega_2$ ($M_I = +\frac{1}{2}$; left), causing rapid loss of singlet character, or $\omega_1{}^- \approx \omega_2$ ($M_I = -\frac{1}{2}$; right), causing the pair to maintain its singlet character

The vector model for a radical pair, with g factors $g_1 > g_2$, with one magnetic nucleus (^{1}H in $R_1H^{\cdot}$; $a_H > 0$), and generated from a singlet precursor, is illustrated in Figure 3.[7] The different orientations of the nuclear spin result in the existence of two types of radical pairs. One type has substantially different precession frequencies, $\omega_1{}^+ > \omega_2$ ($M_I = +\frac{1}{2}$; left), leading to rapid loss of singlet character. For the second type of pairs the precession frequencies are similar, $\omega_1{}^- \approx \omega_2$ ($M_I = -\frac{1}{2}$; right); these pairs maintain their singlet character longer.

Upon reencounter, pairs which have conserved singlet character can recombine, leading to a product, R_1H–R_2, in which the nuclear level $M_I = -\frac{1}{2}$ is overpopulated (Figure 4). On the other hand, pairs that have undergone intersystem crossing can only diffuse apart, forming free radical reaction products, R_1H–X, in which the nuclear level $M_I = +\frac{1}{2}$ is overpopulated (Figure 4).[7] NMR transitions in the newly formed products occur in the direction towards restoring the equilibrium (Boltzmann) populations; the intensities will depend on the deviation from equilibrium. This model illustrates that products generated by different mechanisms will have opposite polarization. Similarly, a change in the sign of Δg or a, or a change in the initial spin multiplicity, will invert the signal direction.

The above effects are *net* effects; these are typically observed when the two radicals of the pair have sufficiently different g factors. When Δg is small or equal to zero, the so-called *multiplet* effect is observed, where signals representing a nucleus (or a group of magnetically equivalent nuclei) show both A and E. A population diagram illustrating this effect is shown in Figure 5.[7] The pair consists of two radicals, $R_1H_1H_2\cdot$ and $R_2\cdot$, generated from a triplet precursor and with identical g factors, $g_1 = g_2$; one of the radicals has two nonequivalent protons ($a_{H_1}, a_{H_2} > 0$).

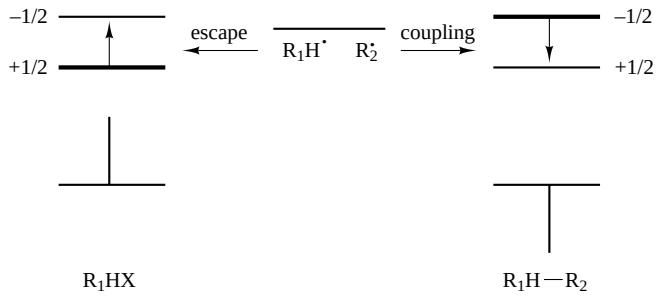

Figure 4 Recombination of and escape from the pair, $R_1H\cdot$ and $R_2\cdot$. The CIDNP effects, emission for $R_1H{-}R_2$, enhanced absorption for R_1HX, arise because the nuclear spin levels of the products are populated at different rates

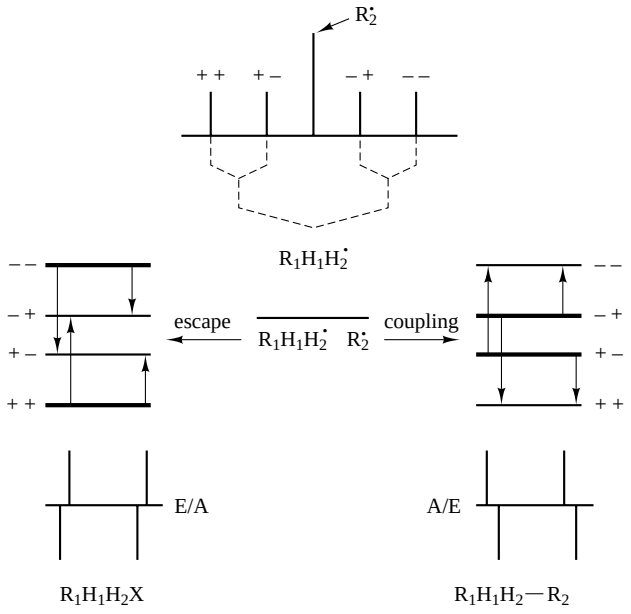

Figure 5 Two-spin energy levels and NMR spectra of escape and recombination products of a radical pair $R_1H_1H_2\cdot + R_2\cdot$. A schematic EPR spectrum of the two radicals is shown above the pair

The quantitative theory of CIDNP is developed to a state where the intensity ratios and absolute enhancement factors of CIDNP spectra can be computed on the basis of diffusion, reaction, and relaxation rates, and with characteristic parameters of the radical pair (initial spin multiplicity, μ), the individual radicals (electron g factors, hyperfine coupling constants, a), and the products (spin–spin coupling constants, J).[7,11–14] The observed effects are optimal for radical pairs with lifetimes in the nanosecond range; on a shorter timescale, hyperfine-induced intersystem crossing is inefficient, whereas on longer timescales the polarization decays due to spin–lattice relaxation in the radicals.

CIDNP patterns induced via the radical pair mechanism may be more complicated than discussed above, because (1) they may reflect the magnetic parameters of more than one radical pair; (2) the polarization may be influenced by nearby, strongly coupled nuclei; or (3) the effects may be 'distorted' by relaxation or cross-relaxation phenomena. The involvement of two or more consecutive pairs has been delineated in several

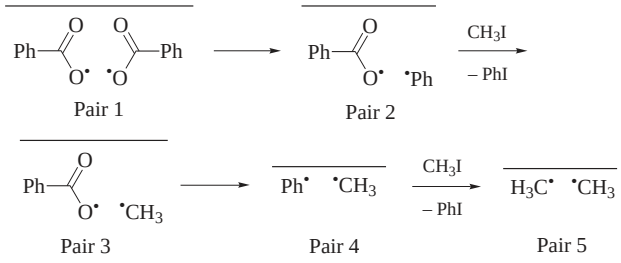

Scheme 2

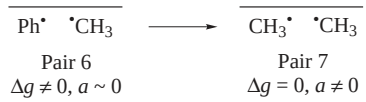

Scheme 3

specific cases. For example, one radical of a geminate pair may undergo a rapid radical transfer reaction, generating a new pair with conservation of spin multiplicity. This 'pair substitution' can transfer *net* effects induced in a nonsymmetrical pair to a symmetrical pair and to a coupling product. The resulting polarization is known as a 'memory effect'. In an extreme case, the decomposition of benzoyl peroxide in the presence of methyl iodide leads to net emission for methyl benzoate, toluene, and ethane, all owing to the involvement of the (singlet) benzoyl–methyl pair and formed by four consecutive pair substitution processes (Pair 1–Pair 5 in Scheme 2).[7]

In some cases CIDNP effects can be induced in consecutive pairs, although neither pair by itself is expected to generate polarization. The thermal decomposition of acetyl benzoyl peroxide gives rise to net emission for both the methyl and phenyl signals of toluene; this effect is incompatible with the benzoyloxy–methyl pair (Pair 6 in Scheme 3) because the phenyl protons have no hyperfine interaction, as well as with the phenyl–methyl pair (Pair 7 in Scheme 3) because it has no Δg. The observed effects can be explained as 'cooperative effects'; they can be reproduced accurately, if one considers the $S{-}T_0$ evolution as a continuous process throughout the lifetime of both radical pairs.[15]

Other deviations from the CIDNP effects expected from the examination of Δg and a_H may be caused by the presence of nuclei with strong hyperfine coupling constants (hfcs), particularly ^{13}C nuclei whose hfcs may exceed 100 G. The ^1H enhancement factors induced in radical pairs generated by α-cleavage of $^{13}C{=}O$ labeled ketones may be enhanced or depressed relative to the analogous $^{12}C{=}O$ labeled ketones. The magnitude of the deviation depends on factors such as Δg, $\boldsymbol{B}_0$, and the hfcs, a_H and a_C, of the two nuclei under consideration. The quantitative theory accounts correctly for the observed effects.[16]

Finally, any comparison of enhancement factors induced in magnetically distinct nuclei must take into account the differences in spin–lattice relaxation times, as well as considering distortions due to cross relaxation. Cross-relaxation processes can be viewed as 'CIDNP pumped NOE effects'; they induce polarization in nuclei which have no hyperfine interaction with the unpaired electron spin. Both scalar and dipolar cross-relaxation mechanisms have been established, generating in secondary nuclei either polarization of the same phase as that of the primary nucleus or the opposite phase.[17,18]

These distortions impose important limitations on the interpretation of CIDNP results, particularly in attempts to delineate the electronic structures of reactive intermediates based on the polarization patterns of their reaction products (Section 4.5). All distortions due to relaxation phenomena can be eliminated by time-resolved experiments.[19]

2.2 CIDNP Effects at Low Magnetic Fields

Although CIDNP effects are studied most conveniently at the magnetic field of the spectrometer, effects induced at lower fields are interesting and have provided relevant information.[7,20] At low fields, the Zeeman interaction becomes sufficiently small that S can mix with all three T levels. The polarization induced under these conditions differs from the high-field polarization. The Δg term is no longer pertinent; recombination and radical transfer products show the same polarization phase. On the other hand, S and T precursors still give opposite polarization, as do hfcs of opposite sign.

Interestingly, the polarization phase can change direction several times as a function of field strength. Photolysis of diisopropyl ketone in CCl_4 gives rise to polarized $CHCl_3$, apparently by disproportionation of an isopropyl–$CCl_3\cdot$ pair (Pair 8 in Scheme 4); the most likely pathway involves pair substitution. Between 0.5 and 80 G $CHCl_3$ shows A; the polarization changes to E between 80 and 450 G, and again to A for $B > 450$ G. Another notable feature of low field CIDNP are '$n-1$ multiplets'. The multiplets of two groups of magnetically nonequivalent nuclei each show one line of zero intensity. For example, ethyl bromide generated by decomposition of propionyl peroxide in the presence of CCl_3Br at 0.5 G shows three lines at 3.2 ppm and two lines at 1.6 ppm. At fields above 20 G the 'missing' signals begin to appear.[7,20] Low-field CIDNP effects have played an important role in the development of the CIDNP theory since they afford a stringent test for the dynamic models used, but have provided little information about reaction mechanisms.

2.3 Biradical Polarization

The interactions of two correlated electron spins may also lead to CIDNP effects when the two spins are linked by a chain, as in a biradical. Depending on the chain length, two different polarization types are possible. For sufficiently long chains, the exchange integral, J, is of comparable magnitude as A; in such a biradical $S-T_0$ mixing can induce CIDNP effects when a reaction channel other than recombination is available. The resulting CIDNP effects follow the rules for nonlinked pairs. Examples include the multiplet polarization induced in a decamethylene biradical or the net effects induced in a 1-acyl-12-benzyl biradical. The 1,10-biradical is generated in a complex reaction sequence by thermolysis of cyclohexane diperoxide; it gives rise to cyclodecane and decene.[7] The 1,12-biradical (**1**) is formed by photolysis of 2-phenylcyclododecanone-1,2-$^{13}C_2$; it can regenerate the starting material or couple in the *para*-position, forming a ring-expanded ketone (**2**). This example is particularly illustrative as it generates CIDNP effects only in the presence of radical scavengers. In CCl_4, for example, chlorine abstraction by the acyl radical prevents the longer-lived biradicals from intersystem crossing and coupling.[16]

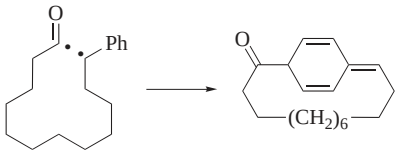

(1) **(2)**

For biradicals with shorter chains, a different mechanism involving $S-T_-$ mixing has been established. In a biradical with $2J \cong g\beta B_0$, the hyperfine interaction, a, can induce transitions satisfying the selection rules, $\Delta M_S = +1$ and $\Delta M_I = -1$.[7,20] When the biradical is generated from a T precursor and forms products from the S state, pure net emission will result. The magnetic field dependence of the CIDNP effects observed for a series of biradicals reflects their average singlet–triplet splitting as well as the biradical lifetimes (Figure 6). The underlying photoreaction will be discussed in more detail in Section 4.4. The diradicals in which the radical centers are separated by tethers of five or more CH_2 groups are best documented; however, smaller diradicals have been detected by CIDNP, for example a 1,5-diradical is formed in the photolysis of camphor and cyclopentane-1,3-diyl is obtained from a bicyclic azo precursor.[7,20]

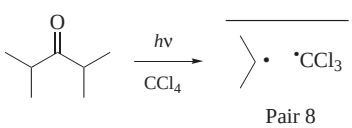

Pair 8

Scheme 4

2.4 The Triplet Overhauser Mechanism

A limited number of CIDNP phenomena have been ascribed to an alternative process, the triplet Overhauser mechanism. This mechanism requires the precise timing of four consecutive steps: (1) generation of an electron spin polarized triplet by preferential intersystem crossing from an excited singlet state to one triplet sublevel; (2) rapid transfer of the electron polarization to a radical or radical ion; (3) electron–nuclear cross relaxation during the lifetime of the radical intermediate; and (4) transfer of the resulting nuclear spin polarization to a diamagnetic species.[21,22] The first two steps are unexceptional; they are the basis for many chemically induced dynamic electron polarization (CIDEP) effects.[23,24] Although the electron relaxation of polarized triplet states occurs with half-lives $^3T_{1e} \approx 10^{-9}$ s, electron-transfer quenching reactions ($k_e \approx 2 \times 10^{10}$ M^{-1} s^{-1}) at sufficiently high quencher concentrations ([Q] $\geq 10^{-1}$ M) can compete with this process. Hydrogen-abstraction reactions ($10^7 > k_H > 5 \times 10^5$ M^{-1} s^{-1}), on the other hand, are usually too slow; thus, cross relaxation was specifically eliminated in photoreactions of benzophenone and diphenylmethylene with benzylic hydrogen donors.[25]

The two crucial steps in this mechanism are the electron–nuclear cross relaxation and the transfer of nuclear polarization from the radical (ion) to the product. The rotational tumbling of a radical changes the orientation of the

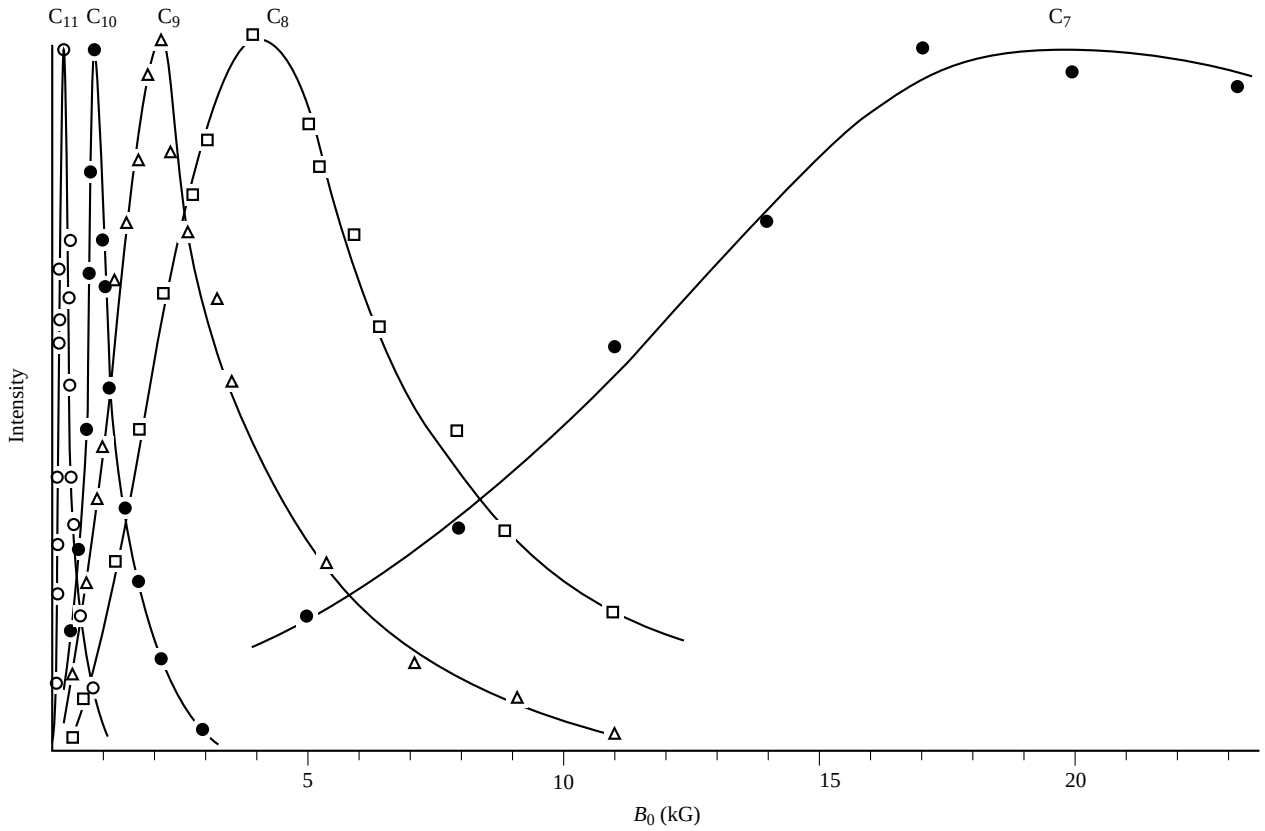

Figure 6 Normalized intensity versus field curves of aldehyde proton signals obtained upon photolysis of the C_7–C_{11} cycloalkanones; all signals are in emission. (Adapted from data of Closs[20])

electron and the nuclear spin relative to the magnetic field, modulating the anisotropic hyperfine interaction. This process causes mainly dipolar transitions (W_2, net change in spin quantum number: 2) and, to a lesser extent, electron and nuclear spin–lattice relaxation (W_e and W_n, respectively) and scalar cross relaxation (W_0, net change in spin quantum number: 0). The efficiency of these processes is proportional to the square of the anisotropic hyperfine tensor, ${B_z}^2$, and is a complex function of the rotational correlation time, τ_r [equation (4)].[26]

$$W_2 \propto B_z^2 \tau_r / (1 + \omega^2 \tau_r^2) \tag{4}$$

Scalar cross relaxation can be induced more efficiently by rapid degenerate exchange or by an internal motion such as the rotation of a CH_3 or CF_3 group. Here, the efficiency is proportional to the mean square variation of the isotropic hyperfine coupling and the rotational correlation time of the methyl group [equation (5)].

$$W_0 \propto (\delta a)^2 \tau_r \tag{5}$$

The final step, degenerate electron transfer, is uniquely suited for an efficient transfer of nuclear polarization from the radical (ion) to the product; it allows rapid transfer of nuclear polarization while conserving the electron polarization of the radical ion. Because of the square dependence upon B_z or δa, the signal direction induced by this mechanism is independent of the sign of the hyperfine coupling, but is determined by the predominant mechanism of cross relaxation.

Because of the short lifetime of polarized triplet states ($^3T_{1e} \sim 10^{-9}$ s), only a narrow range of quencher concentrations is suitable for this mechanism. This is illustrated by the CIDNP effects observed during the electron transfer quenching of *p*-fluorotrifluoroacetophenone by dimethoxybenzene (Figure 7). The ^{19}F signals of the aromatic F and of the CF_3 group show opposite signal directions due to predominantly dipolar (Ar–F) and scalar cross relaxation (CF_3), respectively.[22]

2.5 *para*-Hydrogen-Induced Polarization

The third polarization mechanism is unrelated to those previously described. These effects are observed during homogeneous hydrogenation reactions, in which the atoms of *para*-hydrogen are added pairwise to alkynes or alkenes. These reactions do not involve radicals and occur without loss of spin correlation. Therefore, a separate acronym has been adopted to designate the phenomenon, *para*-hydrogen-induced polarization (PHIP).[27]

The underlying mechanism is based on the fact that molecular hydrogen has four magnetic states: α,α; β,β; $\alpha\beta + \beta\alpha$ (*ortho*-hydrogen); and $\alpha\beta - \beta\alpha$ (*para*-hydrogen). At room temperature the four levels are populated virtually identically, but at lower temperatures *para*-hydrogen becomes more favorable. Appropriate catalysts can establish different equilibrium concentrations; at ~80 K, the *ortho*/*para* equilibrium reaches

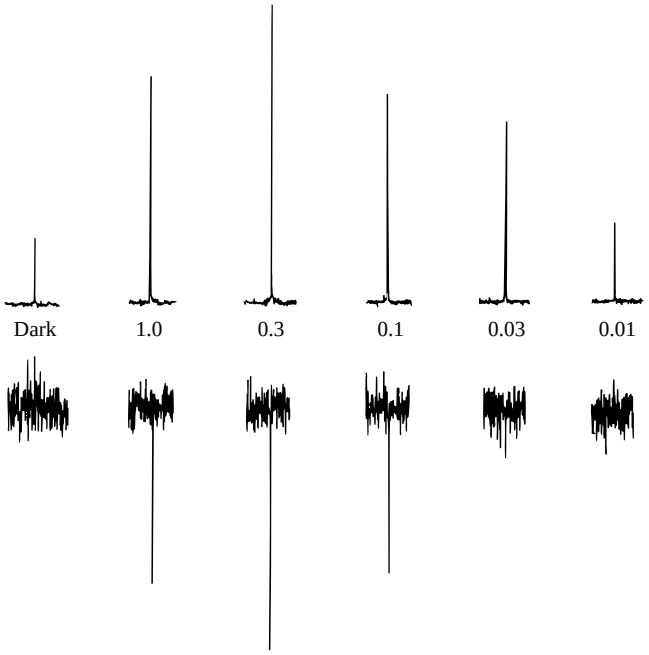

Figure 7 Quencher concentration dependence of CIDNP effects observed during the electron transfer reaction between photoexcited *p*-fluorotrifluoroacetophenone (0.03 M) by dimethoxybenzene (reproduced by permission of Verlag Chemie from H. D. Roth, R. S. Hutton, and M. L. Schilling, *Rev. Chem. Intermed.*, 1979, **3**, 169)

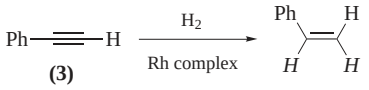

(3)

Scheme 5

~1:1. When *para*-enriched molecular hydrogen is transferred pairwise to a substrate and yields a product in which the two nuclei are magnetically distinct, two of the resulting nuclear spin levels can be significantly overpopulated at the expense of the others.[28] The NMR spectra of the hydrogenation products will show polarization similar to the multiplet effects discussed in Section 2.1 though induced by an entirely different mechanism (cf., Figure 5).

PHIP effects were discovered when samples containing platinum group hydride complexes (e.g. Rh) and phenylacetylene (**3**), which had been stored at liquid nitrogen temperature under hydrogen, were thawed and introduced into an NMR probe to follow the ensuing reaction (Scheme 5).[27] Interestingly, a complementary experiment can be carried out with *ortho*-hydrogen that has been separated by low-temperature chromatography. The resulting PHIP effects are expected to show polarization of the opposite phase as observed for *para*-hydrogen, and they do indeed.[29]

3 EXPERIMENTAL TECHNIQUES

The CIDNP method requires acquisition of an NMR spectrum during, or within a few seconds of, the generation of radical or radical ion pairs. The technique is applied mostly in solution, typically at ambient temperatures, mainly under steady-state conditions. However, a few experiments have been carried out in the gas phase,[10] at low temperatures,[30] and with modest time resolution.[19,31]

Simple thermally-induced CIDNP experiments can be carried out without modification of the spectrometer. Thermal decomposition or rearrangement reactions are initiated by placing a sample in the preheated probe. The reaction can then be followed by scanning the appropriate region repeatedly. For best results, the temperature should be adjusted so that the reaction proceeds with a half-life of a few minutes. In special cases, when the nuclei under investigation have long spin–lattice relaxation times, longer half-lives also can be accommodated.

The photochemical generation of radical pairs offers definite advantages over thermal CIDNP experiments, but poses the problem of how to introduce the light into the probe. In some cases, quartz light guides have been immersed into the sample tube; however, irradiation perpendicular to the long axis of the tube appears to be more efficient. The superconducting magnets of high-field spectrometers can be modified for irradiation by a light guide along the insert. Appropriate light sources include mercury arcs (200–1000 W), xenon arcs, or assorted lasers. Typically, the light beam is collimated and guided by quartz lenses or light pipes into the probe. Use of a quartz insert significantly expands the range of the optical spectrum accessible for excitation and of substrates suitable for study.

The Fourier transform (FT) technique offers significant advantages, because it makes it possible to follow the time evolution of all affected signals at high resolution.[19] With appropriate modifications, the FT method also allows microsecond and even submicrosecond resolution. Flash photolysis with CIDNP detection combines the advantages of time-resolved laser spectroscopy with the structural information content unique to CIDNP.[19,31] The basis for the success of the time-resolved method is the fact that geminate processes are complete in a fraction of a microsecond, while combination of free ions and/or exchange reactions may take tens or hundreds of microseconds depending on concentration. An example is discussed in Section 4.4

On the other hand, the application of FT spectroscopy to CIDNP presents some problems because many spin systems respond in a nonlinear fashion to a series of strong rf pulses. Most significantly, pure multiplet effects vanish completely at a flip angle $\alpha = 90^\circ$. Therefore, considerably weaker pulses ($\alpha = 15^\circ$) have to be applied, diminishing the sensitivity of the experiment somewhat.[19]

When measuring low-field effects, the experiment is carried out in a secondary magnet and the sample transferred to a conventional spectrometer. This experiment has two principal problems: the reaction has to be interrupted reproducibly before the sample is transferred; and the transfer has to be rapid and reproducible because the polarization decays with typical spin–lattice relaxation times, T_1.[7,20] Photochemical reactions induced either by a pulsed laser or a conventional light source with a reliable shutter allow the reaction to be interrupted reproducibly. Use of either a flow system with an efficient mixing chamber or a falling-tube system ensures reproducible transfer times.[32,33]

4 APPLICATIONS OF CIDNP IN CHEMISTRY

The CIDNP technique has found various applications in chemistry and has provided valuable information that was or is not available by any other technique. Typical applications include: (a) determining the mechanism of a reaction, i.e., establishing the involvement of a free radical process; (b) demonstrating the involvement of short-lived reaction products (enols, cyclononatetraene); (c) probing the nature of the reactive intermediate generating the radical pair, e.g., determining the spin multiplicity or the reactivity pattern of photoexcited ketones or carbenes; or (d) characterizing the spin density distribution of an intermediate. The patterns of signal directions and intensities observed for different nuclei of a reaction product can be interpreted in terms of the hyperfine coupling constants of the same nuclei in the radical cation intermediate.

4.1 Qualitative Sign Rules

The application of CIDNP as a mechanistic tool has been aided immeasurably by the development of two simple qualitative sign rules that allow the prediction of CIDNP net [equation (6)] or multiplet effects [equation (7)] from the knowledge of four or six parameters, respectively.[34] Alternatively, experimental CIDNP results can be used to derive one of the polarization determining parameters. The application of these rules requires a basic understanding of the underlying reaction and polarization mechanism.

$$\Gamma_{\mathrm{ne}} = \mu \times \epsilon \times a_i \times \Delta g \tag{6}$$

$$\Gamma_{\mathrm{me}} = \mu \times \epsilon \times a_i \times a_j \times J_{i,\,j} \times \sigma_{i,\,j} \tag{7}$$

The following convention is used for the signs of the individual parameters:

μ + the pair is formed from a triplet precursor (**T**) or by an encounter of free radicals (**F**)
− the pair is formed from a singlet (**S**) precursor

ϵ + for products formed by coupling or disproportionation ('in-cage')
− for products formed by cage-escape reactions

$a_{i,j}$ + if the nucleus under consideration has a positive coupling constant
− if the nucleus under consideration has a negative coupling constant

Δg + for the radical with the higher g factor
− for the radical with the lower g factor

$J_{i,j}$ + if nuclei i and j have a positive spin–spin coupling constant
− if nuclei i and j have a negative spin–spin coupling constant

$\sigma_{i,j}$ + when nuclei i and j belong to the same radical
− when nuclei i and j belong to different radicals

Γ_{ne} + enhanced absorption, **A**
− emission, **E**

Γ_{me} + the low field signal(s) of a multiplet shows E, whereas the high-field signal(s) shows A (**E/A**)
− the low-field signal(s) of a multiplet shows A, whereas the high-field signal(s) shows E (**A/E**)

The definition of the parameter ϵ requires comment. The key to this parameter lies in the electron spin dependence of the product forming reactions. Originally formulated to distinguish 'in-cage' from 'escape' products, it is clear that it differentiates between products formed in reactions with electron spin restriction (only singlet pairs can couple or disproportionate; $\epsilon > 0$) and those formed without spin restriction (typically radical transfer products; $\epsilon < 0$). In radical ion pair reactions, on the other hand, both singlet and triplet pairs can undergo reverse electron transfer in the geminate cage (Section 4.5). In this case, singlet coupling corresponds to $\epsilon > 0$, whereas $\epsilon < 0$ denotes triplet coupling. Yet another spin sorting mechanism has been documented for acyl–benzyl radical pairs in micelles. Here, recombination can be faster than decarbonylation for some pairs, whereas it is slower for others. Pairs that undergo intersystem crossing rapidly regenerate the starting material ($\epsilon > 0$); the other pairs also react by coupling but after decarbonylation, giving rise to a different product ($\epsilon < 0$). Clearly, the assignment of ϵ requires an understanding of the spin sorting process. As a general rule, early reactions of singlet pairs correspond to $\epsilon > 0$; delayed singlet or triplet coupling correspond to $\epsilon < 0$, even in the geminate cage.

4.2 CIDNP in Rearrangement Reactions

Many mechanistic applications of CIDNP deal with different rearrangement types, including molecular rearrangements proceeding via radical pairs, structural rearrangements of radicals, or rearrangements involving consecutive intermediates. In general, a molecular rearrangement is a conversion of the type shown in equation (7). M is a migrating group, whereas Q and T, charged or neutral, are the original and terminal centers between which the migration occurs.[35] The rearrangements proceed with varying degrees of retention of configuration at the migrating carbon and display varying CIDNP intensities. The polarization observed in these reorganizations constitute the most elementary application of the technique, where CIDNP is used as an indicator for radical intermediates.

$$\mathrm{M-Q^{(+)}-T^{(-)} \rightarrow Q-T-M} \tag{8}$$

The course of the (Stevens) rearrangement of ammonium ylides (e.g., **4**) has been studied in detail (Scheme 6); different substrates or reaction conditions result in varying degrees of retention in the rearranged product (**5**). The reaction is induced by the addition of a strong base, converting the ammonium precursor to the ylide which undergoes a thermal rearrangement; the product shows CIDNP effects of intermediate intensity. The results are compatible either with a radical pair mechanism with exceptionally fast pair recombination, or with concurrent pathways involving radical pairs as well as a concerted process. The second possibility appears to be more likely because quantitative CIDNP measurements showed that the experimental enhancement factors are only $\leq$25% of the value expected for a reaction proceeding exclusively by the free radical pathway.[36]

The photolysis of aromatic esters and ethers may result in intramolecular rearrangements generating substituted phenols. CIDNP studies suggest that the rearrangement of aromatic esters (photo-Fries) and the reorganization of phenyl ethers

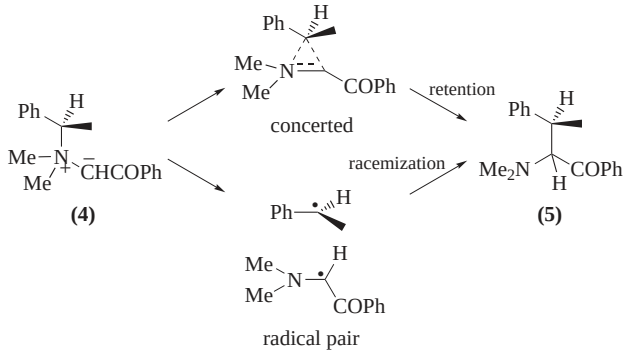

Scheme 6

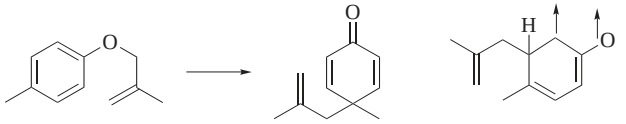

Scheme 7

(photo-Claisen) proceed via radical pairs generated from the excited singlet state.[37] Of special interest are results observed for the rearrangement of *p*-cresyl methallyl ether (**6**) (Scheme 7). The major product, a cyclohexadienone (**7**) is formed by coupling in the *para* position; the observed CIDNP effects support this assignment. A minor product formed by coupling in the *meta* position (**8**) showed the opposite signal direction; this was explained by coupling of triplet pairs followed by intersystem crossing and hydrogen migration, one of the rare examples of triplet recombination in neutral radical pairs.

When the aromatic group does not have a *para* substituent, the initially formed cyclohexadienones undergo rapid hydrogen shifts to yield the phenol isomers. However, under appropriate conditions, intermediates such as benzylcyclohexadienone have lifetimes in the range of several seconds, allowing the observation of their enhanced spectra. The identification of short-lived intermediates is an attractive application of the CIDNP method.

Several carbon radicals undergo skeletal rearrangements which can be followed by CIDNP. The thermal decomposition of cyclopropylacetyl peroxide in hexachloroacetone produces 4-chloro-1-butene, among other products. This conversion proceeds via cleavage of the peroxide bond, decarboxylation of the radicals so generated, and cyclopropylcarbinyl (**9**) to butenyl (**10**) rearrangement (Scheme 8). The vinylic CH_2 group shows the strongest enhancement, although these protons have negligible hfcs in the buten-4-yl radical. The resulting effects are good examples of cooperative effects where the polarization is determined by two consecutive pairs preceding the product.[7]

Scheme 8

In other studies, CIDNP results failed to support previously suggested rearrangements or structures. Thus, the nonclassical structure (**11**) suggested for the β-bromoethyl radical requires identical hfcs for the α- and β-protons. However, the CIDNP effects observed during photolysis of $Ph-CO_2-O_2C-CH_2CH_2-Br$ show opposite signal directions for the α- and β-protons for coupling as well as radical transfer products. This result supports a nonsymmetric radical such as (**12**) with $a_\alpha < 0$; $a_\beta > 0$.[10]

The CIDNP technique has been instrumental in documenting many additional skeletal rearrangements of radical cations. Perhaps the best known of these is the valence isomerization of quadricyclane radical cation (**13**) to that of norbornadiene (**14**).[30] The geometric isomerization of alkene radical ions will be discussed in Section 4.5

4.3 CIDNP in Carbene Reactions

Among the characteristic reactions of carbenes are additions to unsaturated bonds and 'insertions' into C–H, C–Cl, or O–H single bonds. Delineating the exact mechanism of a carbene reaction involves, inter alia, differentiating between one-step (concerted) mechanisms and alternative two-step sequences involving biradicals or radical pairs, and determining the spin multiplicity of the reacting carbene. The CIDNP technique has been applied to the abstraction–recombination reactions of many carbenes. The reaction of triplet diphenylmethylene with toluene proceeds by hydrogen abstraction and produces triphenylethane with A/E multiplet polarization. The same product is also formed by the thermolysis of triphenylazomethane. In this reaction an E/A multiplet effect is observed, because the fragmentation of the azo compound proceeds from the singlet state.

CIDNP effects observed during the reactions of the parent compound, CH_2, and several simple β,γ-unsaturated derivatives, viz., vinyl-, methoxycarbonyl-, cyano-, acetyl-, several phenylmethylenes, and cyclohexadienylidene, identified the spin multiplicity of the reacting carbene and established the reactivity pattern of both the singlet and triplet states.[6,38] For example, both $^1CH_2$ and $^3CH_2$ abstract chlorine atoms from CCl_4, but show significant selectivity in their reactions with $CHCl_3$. While $^1CH_2$ abstracts chlorine atoms preferentially, $^3CH_2$ attacks the hydrogen exclusively. The CIDNP effects observed during the reaction of monosubstituted carbenes with $CHCl_3$ are ideally suited to probe the preference for H- versus Cl-abstraction (Scheme 9). Chlorine abstraction generates 2-substituted 1,1,2-trichloroethanes (**15**), whose pairs of doublets are readily differentiated from the sharp singlet of the 2-substituted 1,1,1-trichloroethanes (**16**) formed by hydrogen

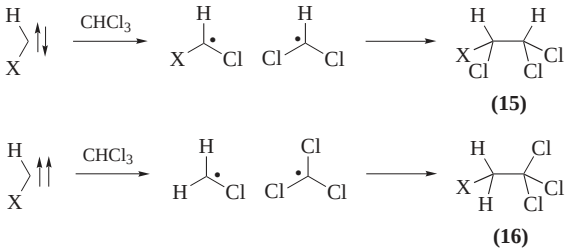

(15)

(16)

Scheme 9

abstraction. The results shown in Figure 8 were generated by benzophenone-photosensitized decomposition of methyl diazoacetate in $CHCl_3$. The singlet at 3.7 ppm is compatible with H-abstraction by triplet methoxycarbonylcarbene (^{3}CHX; X = $COOCH_3$), whereas the pair of doublets at 4.5 and 5.9 ppm is due to Cl-abstraction by the singlet carbene (^{1}CHX; X = $COOCH_3$). These results suggest that the triplet carbene undergoes intersystem crossing in competition with H-abstraction.[38]

Related experiments were carried out with the heavy carbene analogs, dimethylsilylene and dimethylgermylene.[39,40] These intermediates abstract benzylic or otherwise activated chlorine, bromine, or iodine atoms; the resulting radical pairs

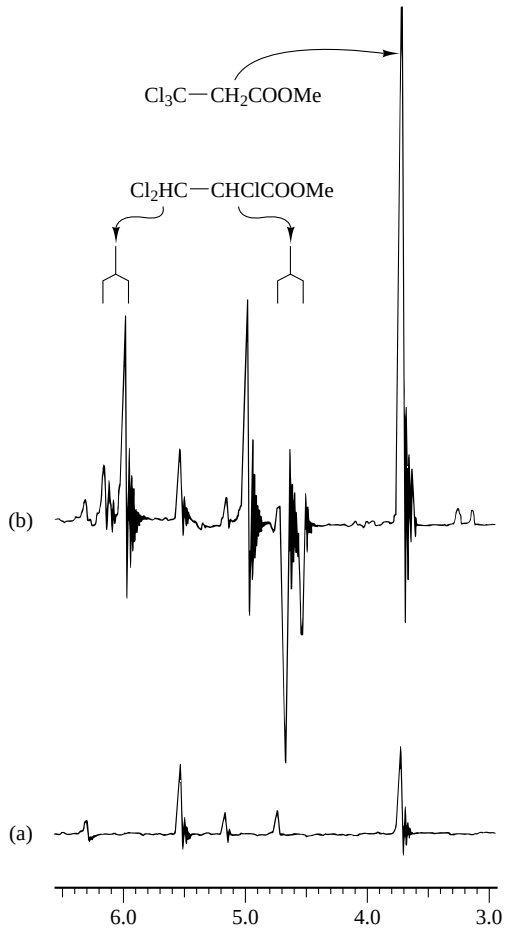

Figure 8 ^{1}H NMR spectrum of methyl diazoacetate in trichloromethane (a) and the CIDNP spectrum observed during the photosensitized decomposition of the diazo compound (b). (Adapted from H. D. Roth, *Acc. Chem. Res.*, 1987, **20**, 343)

form coupling products or diffuse apart, generating radical transfer products. CIDNP effects observed during these reactions suggest the involvement of singlet intermediates; apparently the corresponding triplet states are not accessible under the reaction conditions. CIDNP effects observed during the photolysis of tribenzylstannyl chloride in benzene were rationalized via dibenzylstannylene.[41]

4.4 CIDNP During Photoreactions of Carbonyl Compounds

Extensive studies of the photochemistry of aldehydes and ketones have revealed several general primary photochemical processes including: cleavage of a C–C bond α to the carbonyl function (Norrish type 1 cleavage); abstraction of a hydrogen atom, either intramolecular from the γ-carbon generating a 1,4-biradical, or intermolecular from a suitable donor; capture of an electron from an electron donor generating a radical ion pair; and addition to unsaturated bonds, which may also lead to 1,4-biradical formation.[25] The processes involving radical pairs can be studied by CIDNP, but those involving 1,4-biradicals are not readily amenable to this technique. Although CIDNP has been observed in reactions proceeding via biradicals, effective S–T mixing has been observed only when the electrons are separated by at least three carbons (Section 2.2).

The Norrish type 1 cleavage of ketones is a classic example of a photoinduced homolysis reaction and has been studied in great detail. CIDNP studies confirmed that the cleavage in many ketones occurs from the triplet state, although several aliphatic ketones show evidence for the involvement of singlet as well as triplet precursors.[37] The involvement of dual states is supported by nonlinear Stern–Volmer plots. Significant polarization for cross coupling products indicates a high degree of cage escape, estimated to be as high as 99%. In some cases, however, a relatively high degree of cage return is indicated. For example, the ketone polarization generated by photolysis of dibenzyl ketone, was not affected by addition of the free radical scavenger tri-*n*-butyltin hydride (Pair 9).

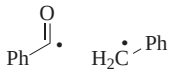

Pair 9

Products arising by geminate pair recombination can be differentiated from those formed by free radical coupling by the time-dependence of their polarization. For example, the light-induced α-cleavage of deoxybenzoin generates polarized reactant by geminate recombination (E; Figure 9; trace B) and bibenzyl as a free radical product (A; trace A). At delay times $>1\,\mu$s, both signals grow due to increasing free radical encounters. Addition of free radical scavengers, such as thiols, suppresses the free radical contribution but does not affect the in-cage polarization (trace C).[31]

The irradiation of cyclic ketones generates α-aroyl–ω-alkyl biradicals (**17**). These intermediates can recombine, regenerating the reactant, or disproportionate, generating acyclic products such as ω-unsaturated aldehydes (**18**) or ketenes (**19**) (Scheme 10). The polarization induced in these systems shows pronounced field-dependence (Figure 6). With

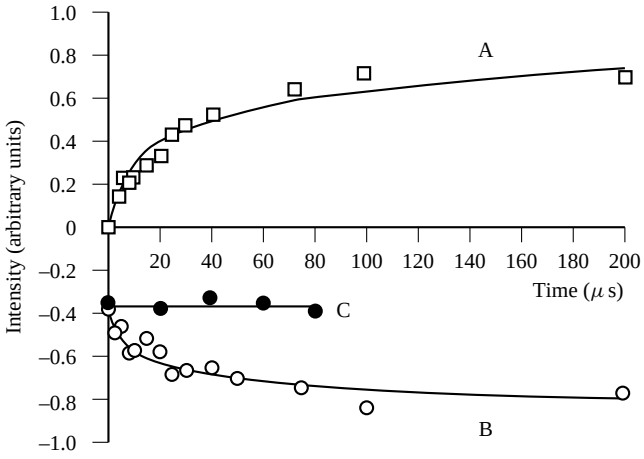

Figure 9 Normalized line intensities of bibenzyl (A) and deoxybenzoin (B) observed during the photolysis of deoxybenzoin as a function of delay time τ. The deoxybenzoin polarization in the presence of a (thiol) free radical scavenger is designated as C. (Adapted from data of G. L. Closs and R. J. Miller, *J. Am. Chem. Soc.*, 1979, **101**, 1639)

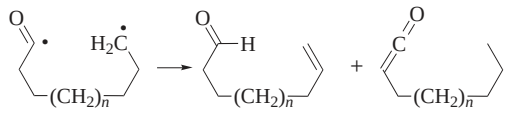

(17) **(18)** **(19)**

Scheme 10

increasing chain length, the average singlet–triplet splitting decreases and the polarization maximum is shifted to lower fields. The width of the curves reflects the lifetimes of the singlet states.

Ketones for which both α-cleavage and intramolecular hydrogen abstraction are unfavorable may react by intermolecular hydrogen abstraction. The hydrogen abstraction reaction by photoexcited benzaldehydes from diphenylmethanes was used to test the predictive power of the radical pair theory. The resulting CIDNP effects, ranging from pure multiplet to pure net effects (Figure 10), can be reproduced by Δg values ranging from 2.7×10^{-3} [Figure 10(a)] to -2.3×10^{-3} [Figure 10(e)], demonstrating elegantly the dependence of the CIDNP polarization pattern on the relative g factors (Δg) of the radical pairs.[42]

Bimolecular reactions of photoexcited ketones may lead to the formation of short-lived diamagnetic products. Thus, hydrogen abstraction by dialkyl or aryl alkyl ketones from a phenol gives rise to ketyl–phenoxyl radical pairs whose disproportionation either forms short-lived enols or regenerates the starting ketone, depending on whether the hydrogen transferred to the phenoxyl radical comes from the O–H or the C–H group.[37]

4.5 CIDNP in Radical Ion Reactions

The applications of CIDNP in photoinduced electron transfer reactions have elucidated the mechanistic details of important reactions and given insight into unusual short-lived radical cations.[30] The geometric isomerization of alkenes may be

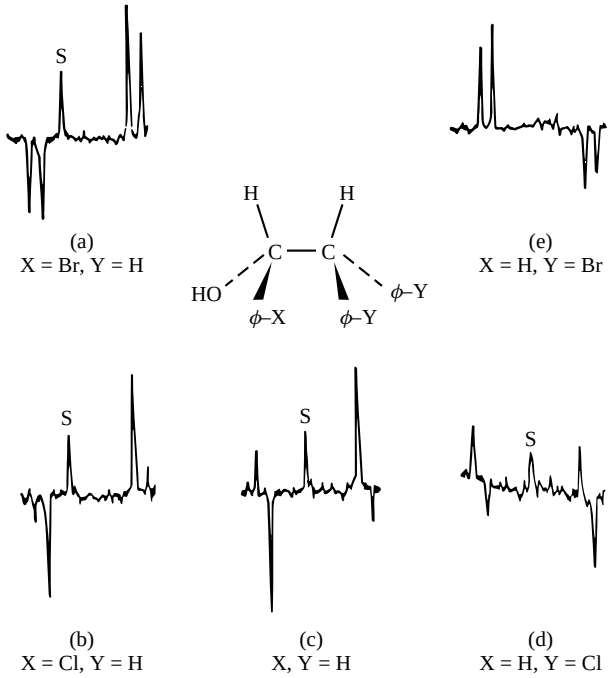

Figure 10 CIDNP spectra (benzylic protons) of coupling products generated via hydrogen abstraction by photoexcited benzaldehydes from diphenylmethanes. (Adapted from data of G. L. Closs, C. E. Doubleday, and D. R. Paulson, *J. Am. Chem. Soc.*, 1970, **92**, 2185)

(*cis*-**20**$^{+\bullet}$) (*trans*-**20**$^{+\bullet}$)

Scheme 11

initiated by an electron-transfer process and proceed via two divergent mechanisms. The isomerization of some donor olefins is illustrated by the chloranil-sensitized isomerization of *cis*- and *trans*-1-phenylpropene (Scheme 11); the polarization of the regenerated isomer is stronger than that of the rearranged alkene, and the reaction of the *cis*-isomer generates stronger effects than the reaction of the *trans*-isomer. These results support the rearrangement of the *cis*- and *trans*-radical cations (**20**) via a common (perpendicular) transition state.[30]

When strong electron donors, viz., *N*,*N*-tetramethylphenylenediamine (**21**), react with *cis*- and *trans*-**20**, the two olefins show well-balanced CIDNP effects regardless of which is the reactant (Figure 11). The results suggest a different mechanism in which **20** serves as the acceptor. Because of its high reduction potential ($E_{A-/A} \approx -2.7$ V), the free energy of the radical ion pair lies above the triplet state of **20** ($E_T \approx 2.6$ eV), allowing both singlet and triplet pairs to recombine. Singlet pairs regenerate the ground state reagents ($\epsilon > 0$), whereas triplet pairs populate the olefin triplet state ($\epsilon < 0$). This type of triplet has a minimum near a perpendicular configuration to minimize the repulsive interaction between the unpaired spins. The perpendicular triplet state can decay to either isomer and, thus, is the key intermediate in the rearrangement.[30] The recombination of **20**$^{\cdot -}$ and **21**$^{\cdot +}$ is one of several well-established cases documenting the triplet recombination of radical ion pairs.

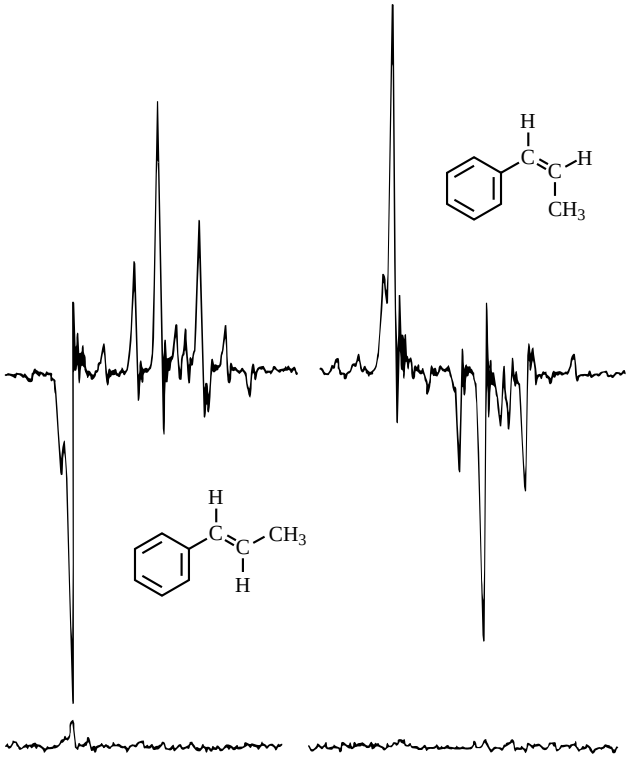

Figure 11 ^{1}H CIDNP spectra observed during the photoreaction of *N*,*N*-tetramethylphenylenediamine with *trans*- (left) and *cis*-1-phenylpropene (right). In each spectrum, the multiplet on the right represents the β proton of the *cis*-isomer whereas the multiplet on the left represents the β proton of the *trans*-isomer. (Adapted from data of H. D. Roth and M. L. M. Schilling, *J. Am. Chem. Soc.*, 1980, **102**, 4303)

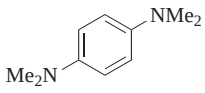

(21)

In additional applications, CIDNP signal directions and intensities are used to derive the hyperfine coupling pattern of radical ions. The ^{1}H hfcs are related to carbon spin densities either by π,σ polarization (causing negative hfcs) or due to a hyperconjugative interaction (π,σ delocalization; causing positive hfcs).[26] Therefore, the pattern of CIDNP signal directions and intensities reveal the spin density distribution and, hence, structural details of the paramagnetic intermediates. The results are often unambiguous because NMR chemical shifts are usually well understood and the identity of the coupled nuclei is, thus, clearly established.[30]

Determinations of hfc patterns are not limited to small molecules. Time-resolved CIDNP spectroscopy was applied successfully to determine the relative hfcs of radical ions derived from chlorophyll and derivatives.[43] The CIDNP effects are generated by a photoinduced electron transfer reaction; the effects observed with a 1 μs delay yield signs and relative magnitudes of hfcs in good agreement with ENDOR results.

4.6 Probing Mechanistic and Structural Aspects of Biomolecules

Charge transfer plays a key role in the mechanisms of many significant biological processes. The resulting zwitterionic biradicals or radical ion pairs are suitable targets for CIDNP studies. Various aspects of biomolecules have been probed by this method; the applications range from in vitro studies of model reactions, involving inter- or intramolecular electron transfer, to probing the three-dimensional structure of globular systems by interaction with an external reaction partner.

Among the model reactions, the electron transfer photosensitized cleavage of thymine dimers was the first to be scrutinized by CIDNP. In fact, electron transfer from *cis*,*syn*-(*N*,*N*-dimethylthymine) dimer (**22**) to anthraquinone sulfonate was the first radical ion reaction for which CIDNP effects were observed;[44] the results indicated efficient electron transfer induced cleavage of **22**. More recent studies of dimers (**23**), in which the N-1 positions are linked by a trimethylene chain, provided clear evidence for the dimer radical cation as an intermediate in the cleavage reaction.[45]

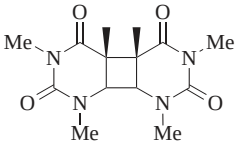

(22)

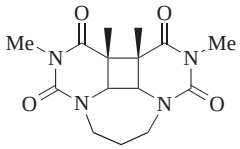

(23)

Other model studies have been carried out with the photosynthetic pigments. In these studies, the excited chlorophyll served either as an electron donor (e.g., towards a quinone) or as an acceptor.[46] All CIDNP effects observed must be ascribed to the chlorin triplet state as the reactive intermediate. Bifunctional molecules in which a tryptophan is tethered as a secondary donor to a chlorophyll molecule give rise to strong polarization for the amino acid residue.[47] However, the initial reaction clearly involves electron transfer to an external quinone, which is then followed by intramolecular electron transfer to the chlorin radical cation. Apparently the model systems have, so far, failed to reproduce the rapid charge transfer characteristic for the rigid photosynthetic reaction center.

Photoinduced hydrogen abstraction and electron transfer reactions can be applied for identifying structural features of biomolecules, such as proteins or enzymes. These macromolecules have globular structures with some amino acid residues on the surface, whereas others are contained in the bulk of the molecule. If an external acceptor, such as 3-carboxylumiflavin (**24**), is irradiated in the presence of such a biomolecule, accessible residues which can function as H- or electron donors may give rise to CIDNP effects.[48] Suitable residues include histidine (**25**), methionine, tryptophan (**26**), or tyrosine (**27**). The mechanistic aspects of the interactions between photoexcited lumiflavin and individual amino acid residues have been studied in detail and are well understood.[49] The observed effects (Figure 12) reflect the reaction parameters (μ,$\epsilon > 0$), the hfcs of the aromatic ($a > 0$) and benzylic protons ($a < 0$), and Δg (g_{Trp}, $g_{\mathrm{His}} < g_{\mathrm{F}} < g_{\mathrm{Tyr}}$). For optimal CIDNP observation, the background signals of the biomolecules were suppressed by presaturation techniques

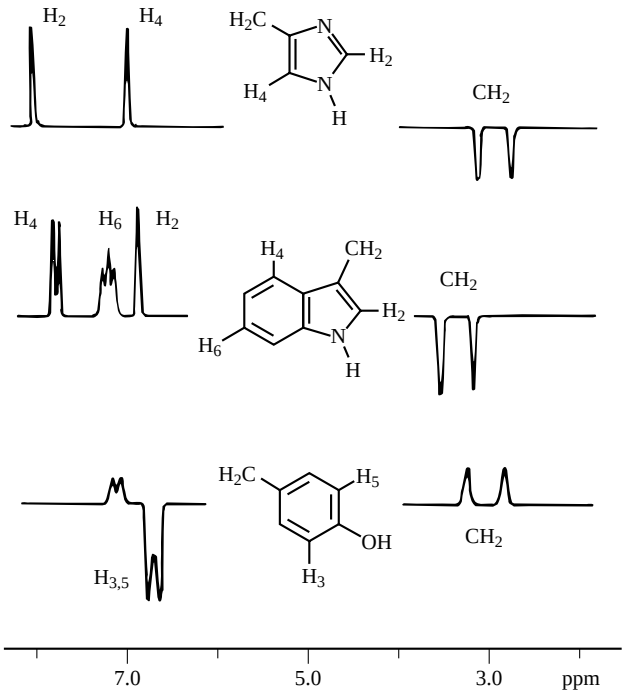

Figure 12 Schematic ^{1}H CIDNP spectra induced during the photoreaction of a lumiflavin with histidine, tryptophan, and tyrosine. (Adapated from data of S. Stob and R. Kaptein, *Photochem. Photobiol.*, 1989, **49**, 565)

and the spectra accumulated by alternating light and dark pulses.

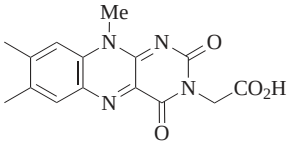

(24)

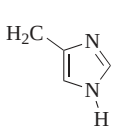

(25)

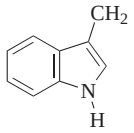

(26)

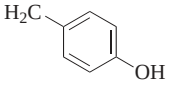

(27)

For example, bovine pancreatic ribonuclease A (13 700 Da) shows CIDNP for one histidine (His-119) and two tyrosine units (Tyr-76, -115). The His-119 function must be located in the active site of the enzyme, since the effect is suppressed by ribonuclease A inhibitor. Bovine pancreatic trypsin inhibitor (6500 Da) shows CIDNP for Tyr-10 and Tyr-21. These results show that the two Tyr residues are on the surface, in solution as in the crystal (based on X-ray studies). A weak emission line was assigned to the ϵ-CH_2 group of Lys-41. Since lysine is CIDNP inactive (though ϵ-*N*-dimethyllysine is active), the effects were ascribed to dipolar cross relaxation, implying that Lys-41 is adjacent to Tyr-10.

Photoexcitation of the coenzyme flavin adenine dinucleotide (**28**) generates a biradical by electron transfer from the adenine to the flavine moiety. The resulting CIDNP effects were studied as a function of magnetic field as well as pH. The complete absence of polarization at neutral pH was interpreted as evidence for stacking of the aromatic units. The field-dependent CIDNP curves observed at acid pH suggest the presence of at least two biradical conformers which slowly interconvert on the CIDNP timescale.[33]

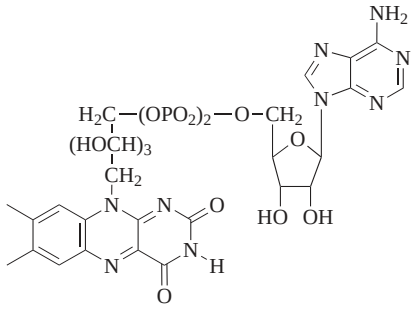

(28)

4.7 Miscellaneous Reaction Types

The preceding selection of CIDNP topics is obviously incomplete. Many reaction types giving rise to CIDNP effects could not be covered here because of space limitations. Perhaps the most notable omission is the area of organometallic reactions; we have mentioned only the PHIP phenomenon (Section 2.5).[27] Bimolecular reactions between alkyllithium compounds and organohalides have played a significant role in the discovery and development of the CIDNP effect,[2,50] and many thermal and light-induced bond homolysis reactions of organometallics also give rise to spin polarization phenomena.[51]

Studies of the early phases of polymer growth should be a natural application of the CIDNP method. In fact, the earliest case of spin polarization was observed during a polymerization initiated by the thermal decomposition of benzoyl peroxide.[1] As yet, few studies have addressed the aspect of chain growth;[52] most studies do not go beyond the primary thermal or photochemistry of the free radical initiators. Finally, we have not treated, as has been the custom, peroxide decompositions in a separate section, but have discussed the subsequent radical pairs in the context of appropriate reactions.

5 PERSPECTIVE

Chemically induced dynamic nuclear polarization is an interesting phenomenon as well as a powerful tool for a broad range of mechanistic and structural problems. Its application has brought to light a rich variety of intermediates, especially in photoinduced reactions. The characterization of short-lived intermediates utilizes the unique information inherent in NMR chemical shifts of reaction products combined with the characteristic distortion of intensities due to CIDNP. These applications remain a promising prospect. Significant additional results can be expected in photoinduced

reactions, particularly in biomolecules and in studies utilizing time-resolved techniques. Although its time resolution cannot rival that of optical spectroscopy, CIDNP has the advantage of identifying the target species unambiguously. Finally, the early phases of polymer growth are a significant target, if the chains are intercepted by rapid chain transfer reactions.

6 RELATED ARTICLES

Dynamic Nuclear Polarization and High-Resolution NMR of Solids; Electron–Nuclear Hyperfine Interactions; Nuclear Overhauser Effect; Optically Enhanced Magnetic Resonance; Ortho–Para Hydrogen at Low Temperature; Polarization Transfer Experiments via Scalar Coupling in Liquids.

7 REFERENCES

1. J. Bargon, H. Fischer, and U. Johnsen, *Z. Naturforsch., Teil A*, 1967, **22**, 1551.
2. H. R. Ward and R. G. Lawler, *J. Am. Chem. Soc.*, 1967, **89**, 5518.
3. A. R. Lepley and G. L. Closs (eds.), *Chemically Induced Magnetic Polarization*, Wiley, New York, 1973.
4. R. G. Lawler, *Prog. Nucl. Magn. Reson.*, 1973, **9**, 145.
5. H. R. Ward, in *Free Radicals*, ed. J. K. Kochi, Wiley-Interscience, New York, 1973, Vol. 1, Chap. 6
6. A. L. Buchachenko, *Chemical Polarization of Electrons and Nuclei*, Nauka, Moscow, 1974.
7. R. Kaptein, *Adv. Free-Radical Chem.*, 1975, **5**, 319.
8. L. T. Muus, P. W. Atkins, K. A. McLauchlan, and J. B. Pedersen (eds.), Chemically Induced Magnetic Polarization, *NATO Adv. Study Inst. Ser.*, C34, Reidel, Dordrecht, The Netherlands, 1977.
9. P. W. Atkins and G. T. Evans, *Adv. Chem. Phys.*, 1976, **35**, 1.
10. K. M. Salikhov, Yu. N. Molin, R. Z. Sagdeev, and A. L. Buchachenko, *Spin Polarization and Magnetic Effects in Radical Reactions*, ed. Yu. N. Molin, Elsevier, Amsterdam, 1984.
11. S. H. Glarum, in *Chemically Induced Magnetic Polarization*, ed. A. R. Lepley and G. L. Closs, Wiley, New York, 1973.
12. G. L. Closs, *Adv. Magn. Reson.*, 1974, **7**, 157.
13. J. H. Freed and J. B. Pedersen, *Adv. Magn. Reson.*, 1976, **8**, 1.
14. F. J. Adrian, *Rev. Chem. Intermed.*, 1979, **3**, 3.
15. R. Kaptein, in *Chemically Induced Magnetic Polarization*, ed. L. T. Muus, P. W. Atkins, K. A. McLauchlan, and J. B. Pedersen, *NATO Adv. Study Inst. Ser.*, C34, Reidel, Dordrecht, The Netherlands, 1977, Chap. 14
16. K. C. Hwang, N. J. Turro, H. D. Roth, and C. Doubleday, Jr., *J. Phys. Chem.*, 1991, **95**, 63.
17. G. L. Closs and M. S. Czeropski, *J. Am. Chem. Soc.*, 1977, **99**, 6127.
18. G. L. Closs and M. S. Czeropski, *Chem. Phys. Lett.*, 1977, **45**, 115.
19. S. Schäublin, A. Wokaun, and R. R. Ernst, *J. Magn. Reson.*, 1977, **27**, 273.
20. G. L. Closs, in *Chemically Induced Magnetic Polarization*, ed. L. T. Muus, P. W. Atkins, K. A. McLauchlan, and J. B. Pedersen, *NATO Adv. Study Inst. Ser.*, C34, Reidel, Dordrecht, The Netherlands, 1977, Chap. 13
21. F. J. Adrian, in *Chemically Induced Magnetic Polarization*, ed. L. T. Muus, P. W. Atkins, K. A. McLauchlan, and J. B. Pedersen, *NATO Adv. Study Inst. Ser.*, C34, Reidel, Dordrecht, The Netherlands, 1977, Chap. 21
22. H. D. Roth, R. S. Hutton, and M. L. M. Schilling, *Rev. Chem. Intermed.*, 1979, **3**, 169.
23. P. W. Atkins, in *Chemically Induced Magnetic Polarization*, ed. L. T. Muus, P. W. Atkins, K. A. McLauchlan, and J. B. Pedersen, *NATO Adv. Study Inst. Ser.*, C34, Reidel, Dordrecht, The Netherlands, 1977, Chap. 11
24. K. A. McLauchlan and D. G. Stevens, *Acc. Chem. Res.*, 1988, **21**, 54
25. N. J. Turro, *Modern Molecular Photochemistry*, Benjamin/Cummings, Menlo Park, 1978, Chap. 10
26. A. Carrington and A. D. McLachlan, *Introduction to Magnetic Resonance*, Harper & Row, New York, 1967.
27. R. Eisenberg, T. C. Eisenschmid, M. S. Chinn, and R. U. Kirss, *Adv. Chem. Ser. No. 230*, Am. Chem. Soc., Washington, DC, 1992, p. 47.
28. C. R. Bowers and D. P. Weitekamp, *J. Am. Chem. Soc.*, 1987, **109**, 5541.
29. J. Bargon, J. Kandels, and K. Woelk, *Angew. Chem., Int. Ed. Engl.*, 1990, **29**, 58.
30. H. D. Roth, *Acc. Chem. Res.*, 1987, **20**, 343.
31. G. L. Closs, R. J. Miller, and O. D. Redwine, *Acc. Chem. Res.*, 1985, **18**, 196.
32. R. O. Kühne, T. Schaffhauser, A. Wokaun, and R. R. Ernst, *J. Magn. Reson.*, 1979, **35**, 39.
33. S. Stob, J. Kemmink, and R. Kaptein, *J. Am. Chem. Soc.*, 1989, **111**, 7036.
34. R. Kaptein, *J. Chem. Soc., Chem Commun.*, 1971, 732.
35. A. R. Lepley, in *Chemically Induced Magnetic Polarization*, ed. A. R. Lepley and G. L. Closs, Wiley, New York, 1973, Chap. 8
36. U. H. Dolling, G. L. Closs, A. H. Cohen, and W. D. Ollis, *J. Chem. Soc., Chem Commun.*, 1975, 545.
37. H. D. Roth, in *Chemically Induced Magnetic Polarization*, ed. L. T. Muus, P. W. Atkins, K. A. McLauchlan, and J. B. Pedersen, *NATO Adv. Study Inst. Ser.*, C34, Reidel, Dordrecht, The Netherlands, 1977, Chap. 4
38. H. D. Roth, *Acc. Chem. Res.*, 1977, **10**, 85.
39. M. Lehnig, H. Klaukien, and F. Reininghaus, *Ber. Bunsenges. Phys. Chem.*, 1990, **94**, 1411.
40. J. Köcher, M. Lehnig, and W. P. Neumann, *Organometallics*, 1988, **7**, 1201.
41. A. Standt and H. Dreeskamp, *J. Organomet. Chem.*, 1987, **322**, 49.
42. G. L. Closs, C. E. Doubleday, and D. R. Paulson, *J. Am. Chem. Soc.*, 1970, **92**, 2185.
43. G. L. Closs and E. V. Sitzmann, *J. Am. Chem. Soc.*, 1981, **103**, 3217.
44. H. D. Roth and A. A. Lamola, *J. Am. Chem. Soc.*, 1972, **94**, 1013.
45. T. Young, R. Nieman, and S. D. Rose, *Photochem. Photobiol.*, 1990, **52**, 661.
46. A. A. Lamola, M. L. Manion, H. D. Roth, and G. Tollin, *Proc. Natl. Acad. Sci. USA*, 1975, **72**, 3265.
47. A. Osuka and K. Maruyama, *Chem. Lett.*, 1986, 1853.
48. R. Kaptein, in *Biological Magnetic Resonance*, ed. L. J. Berliner and J. Reuben, Plenum Press, New York, 1982, Vol. 4, p. 145.
49. S. Stob and R. Kaptein, *Photochem. Photobiol.*, 1989, **49**, 565.
50. R. G. Lawler, in *Chemically Induced Magnetic Polarization*, ed. L. T. Muus, P. W. Atkins, K. A. McLauchlan, and J. B.

Pedersen, *NATO Adv. Study Inst. Ser.*, C34, Reidel, Dordrecht, The Netherlands, 1977, Chap. 15

51. R. Benn, *Rev. Chem. Intermed.*, 1979, **3**, 45.
52. A. Borer, R. Kirchmayr, and G. Rist, *Helv. Chim. Acta*, 1978, **61**, 305.

Biographical Sketch

Heinz D. Roth. *b* 1936. Dipl.Chem., Dr.rer.nat. (with Emanuel Vogel), 1965, Chemistry, Universität Köln, Germany. Postdoctoral work at Yale University, New Haven (with William Doering). Member (1967–1982), Distinguished Member of Technical Staff (1982–1988), (AT&T) Bell Laboratories, Murray Hill. Currently Professor of Chemistry, Rutgers University, New Brunswick. Over 100 publications. Research specialties: structure and reactivity of short-lived intermediates, NMR, ESR.

Cross Polarization in Rotating Solids: Spin-$\frac{1}{2}$ Nuclei

Frank Engelke

Ames Laboratory, IA, USA

1	Introduction	1
2	Magnetization Transfer in the Radiofrequency Rotating Frame	1
3	Cross Polarization and Dipolar Coupling	2
4	Dipolar Couplings in Rotating Solids	3
5	Cross Polarization in Rotating Solids[28]	4
6	Modified CP Experiments and MAS	5
7	Related Articles	6
8	References	6

1 INTRODUCTION

The development of cross polarization (CP) techniques, allowing the transfer of magnetization from a system of spins I with high abundance (e.g. ^{1}H, ^{19}F, and ^{31}P) to a system of spins S with low natural abundance (e.g. ^{13}C and ^{15}N) was a major step to *enhance the sensitivity* of these rare nuclei in solid state NMR.[1–3] As the sensitivity thresholds for rare nuclear spins have been lowered, NMR has become available for extensive studies of solid materials.

A second problem peculiar to solid state NMR originates from the fact that, in solids, molecules or molecular groups are generally not subject to fast isotropic motions as they are in liquids. Consequently, NMR applied to solid samples, e.g. polycrystalline or amorphous materials, is characterized by spatially anisotropic spin interactions. The dominating interactions for spin-$\frac{1}{2}$ nuclei in solids are the direct dipole–dipole coupling between spins, and the magnetic shielding due to the electronic environment of a given nucleus, causing the chemical shift of resonance lines. The resulting spectra of polycrystalline or amorphous samples typically reveal broad lineshapes reflecting these anisotropic interactions. It was a major technical goal in NMR to invent techniques which play, at least in part, a role analogous to that of thermal motion in liquids, i.e. to average out or reduce the anisotropic contribution of the spin interactions. This averaging can take place either in spin space or in ordinary coordinate space,[4,5] depending on the interaction. To remove homonuclear dipolar couplings, averaging in spin space requires the application of multiple pulse sequences (see ***CRAMPS***). In order to eliminate broadening of resonance lines of rare S spins due to heteronuclear dipolar interactions with abundant I spins, rf irradiation near the Larmor frequency of I spins can be applied (heteronuclear high power decoupling[3]). The removal of line broadening originating from the chemical shift anisotropy (CSA) can be accomplished by averaging performed in coordinate space, i.e. by rotating the sample around a spatially fixed axis inclined by a specific angle θ_m, called the 'magic angle', relative to the direction of the external field $\boldsymbol{B}_0$. Magic angle spinning (MAS) and some descendent techniques are nowadays well established and routinely included in high-resolution solid state NMR studies, allowing the identification of chemical environments by the isotropic chemical shift.

Fast sample rotation also affects homo- and heteronuclear dipole–dipole couplings.[6,7] Because these interactions provide the physical basis on which polarization transfer between different spin systems occurs, they are here considered first in some detail (see Sections 2 and 3). Following these considerations, the influence of sample spinning on the CP process will be discussed (Sections 4 and 5). Because sample spinning may impose dramatic effects on the CP process, effects which are undesirable from an experimental point of view, the possibilities of circumventing some of these difficulties are reviewed in Section 6. Since the majority of applications are based on the spin lock, cross polarization technique, proposed by Hartmann and Hahn,[1] and Pines, Gibby, and Waugh,[2] the present article is concerned with this method.[28] For details of other techniques, such as adiabatic demagnetization in the rotating frame[1,3] and the nuclear solid effect,[8,12] the reader is referred to the literature (see also ***Cross Polarization in Solids***).

2 MAGNETIZATION TRANSFER IN THE RADIOFREQUENCY ROTATING FRAME

Figure 1 shows the basic pulse sequence used in CP experiments.[2,3] Initially, a 90° ($\pi/2$) pulse is applied at the resonance frequency ω_{0I} of the abundant I spins with magnetogyric ratio γ_I, creating transverse magnetization. In the subsequent time interval, denoted by τ_{CP}, the rf field (strength in angular frequency units $\Omega_{1I} = \gamma_I B_{1I}$) is applied parallel to the transverse I-spin magnetization, thus locking the magnetization in the direction of the $\boldsymbol{B}_{1I}$ rf field. Simultaneously, rf irradiation (strength $\Omega_{1S} = \gamma_S B_{1S}$) occurs at the resonance frequency ω_{0S} for the rare S spins with magnetogyric ratio γ_S, the initial transverse magnetization of which is zero. If the Hartmann–Hahn condition[1]

$$\gamma_I B_{1I} = \gamma_S B_{1S} \tag{1}$$

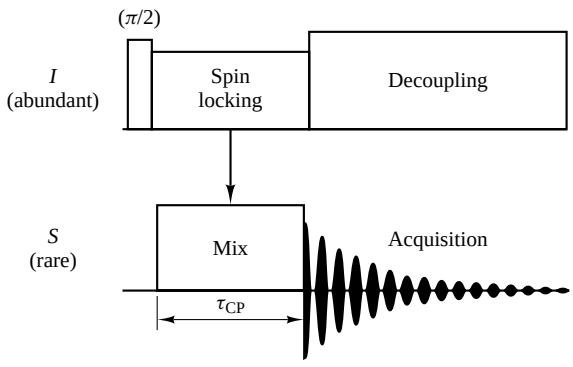

Figure 1 Pulse sequence for standard cross polarization. Radiofrequency irradiation occurs at the Larmor frequencies ω_{0I} and ω_{0S} for I and S spins simultaneously

for the rf field strengths is satisfied, transfer of magnetization from the I-spin system to the S-spin system can take place during the cross polarization mixing time τ_{CP}, resulting in a build-up of transverse S-spin magnetization, which can be observed after switching off the rf field in the S-spin channel. During this acquisition period, the rf irradiation in the I-spin channel may continue to provide decoupling of the $I-S$ dipolar interaction.[3]

The elementary process for cross polarization involves transitions of dipolar-coupled I and S spins, frequently called flip-flop transitions or mutual spin flips, because one spin is changing its state from a higher to a lower energy, while simultaneously a neighboring spin moves from a state with lower to a state with higher energy. If a solid, containing systems of spins I and S with different magnetogyric ratios γ_I and γ_S, is subjected only to the external magnetic field $\boldsymbol{B}_0$, then the energy levels for both systems are given by the Zeeman interaction in the laboratory frame. The splitting of energy levels (in angular frequency units) is different for I and S spins, and is equal to their respective Larmor frequencies ω_{0I} and ω_{0S} [Figure 2(a)]. Under these circumstances flip-flop transitions involving $I-S$ spin pairs possess a vanishingly small probability rate, because the (virtual) photon which would be emitted during an I-spin transition could not be absorbed by an S-spin transition between Zeeman energy levels. This situation changes if rf fields are present for both spin systems [Figure 2(b)]. The total Hamiltonian of the two spin systems in the laboratory frame of reference becomes oscillatory time dependent due to the presence of rf fields. It is convenient to choose a frame of reference which is rotating with the applied rf fields (doubly rotating frame), generally known in quantum mechanics as the transformation from the Heisenberg operator representation to the interaction representation.[9] In this frame the time dependence originating from the rf fields (frequencies ω_k, $k = I$ or S) vanishes[10] for $\omega_k = \omega_{0k}$ (on-resonance). Identifying the new z axis with the direction of the rf field vectors $\boldsymbol{B}_{1I}$ and $\boldsymbol{B}_{1S}$, the total spin Hamiltonian in this tilted rotating frame (TRF)[3,13] with spin components $\hat{I}_{zk}$, $\hat{I}_{xk}$ for the spins I_k, $\hat{I}_z = \Sigma_k \hat{I}_{zk}$ and the spin components $\hat{S}_z$, $\hat{S}_x$ for a single S spin is:

$$\hat{\mathcal{H}} = \hat{\mathcal{H}}_I + \hat{\mathcal{H}}_S + \hat{\mathcal{H}}_{IS}$$

$$\hat{\mathcal{H}}_I = -\Omega_{1I}\hat{I}_z + \hat{\mathcal{H}}_{II} \quad \hat{\mathcal{H}}_S = -\Omega_{1S}\hat{S}_z$$
$$\hat{\mathcal{H}}_{IS} = 2\sum_k D_k \hat{I}_{xk}\hat{S}_x \qquad (2)$$

where it has been assumed that both rf fields are in resonance with the I and S spins, respectively. $\hat{\mathcal{H}}_I$ denotes the Hamiltonian for the I-spin system, whereas $\hat{\mathcal{H}}_{II}$ and $\hat{\mathcal{H}}_{IS}$ are the $I-I$ homonuclear and $I-S$ heteronuclear dipolar Hamiltonians. The homonuclear dipolar couplings among S spins can be neglected, due to the low abundance of S spins. D_k denotes the dipolar coupling strength between spin S and spin I_k. The above Hamiltonian includes the two terms $\Omega_{1I}\hat{I}_z$ and $\Omega_{1S}\hat{S}_z$, which represent the Zeeman interaction in the TRF for I and S spins, respectively. The corresponding splitting of Zeeman energy levels in the TRF, therefore, is given by Ω_{1I} and Ω_{1S}, which are experimental parameters. Satisfying the Hartmann–Hahn matching condition $\Omega_{1I} = \Omega_{1S}$ [equation (1)] provides equal TRF–Zeeman splittings for both spin systems, such that an energy transfer can take place between I and S spins [Figure 2(b)].

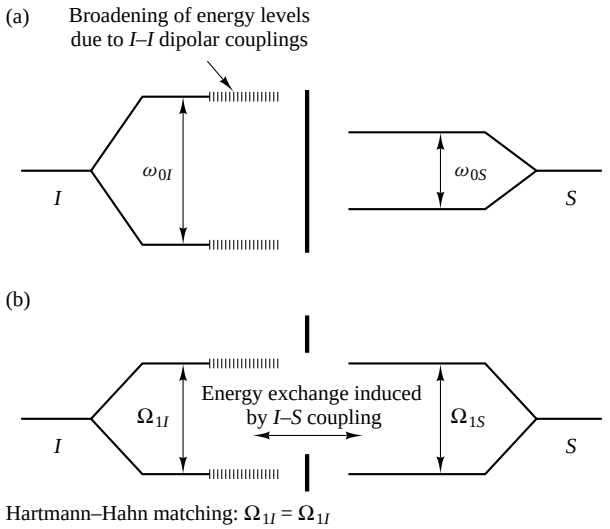

Figure 2 Energy levels of I and S spins (a) in the laboratory frame and (b) in the rf rotating frame

3 CROSS POLARIZATION AND DIPOLAR COUPLING

It is instructive to consider first a simple system, consisting of an isolated dipolar-coupled $I-S$ spin pair, providing some basic concepts necessary to show the impact which MAS has on cross polarization. The energy levels of the spin system, i.e. the possible total energies of both spins, are shown in Figure 3(a). $|++\rangle$, $|+-\rangle$, etc., denote product TRF–Zeeman spin-state vectors $|m_I,m_S\rangle$ (with magnetic quantum numbers $m_{I,S} = +\frac{1}{2}$ for the z-spin component parallel, and $m_{I,S} = -\frac{1}{2}$ for the z-spin component antiparallel to the rotating rf field). If dipolar couplings are not present and $\Delta\Omega = \Omega_{1I} - \Omega_{1S} = 0$, then Zeeman state vectors are eigenvectors of the TRF Hamiltonian. The two states with antiparallel spin orientations are degenerate (i.e. having the same energy). $\Delta\Omega \neq 0$ removes this degeneracy, the eigenstates are now $|2\rangle$ and $|3\rangle$. For small $\Delta\Omega$ the magnetic quantum numbers m_I and m_S are still 'good' quantum numbers. The presence of $\hat{\mathcal{H}}_{IS}$ leads to transitions between Zeeman states or, in general, between $|2\rangle$ and $|3\rangle$, and $|1\rangle$ and $|4\rangle$. In Figure 3(a) the probabilities of these transitions are labeled W_0 and W_2. The same holds for $\Delta\Omega = 0$ for the Zeeman states $|++\rangle$,$|+-\rangle$, $|-+\rangle$, and $|--\rangle$. The energy levels in the TRF, including the dipolar Hamiltonian $\hat{\mathcal{H}}_{IS}$ and $\Delta\Omega$ being non-zero, can be obtained from the Hamiltonian $\hat{\mathcal{H}}$ in equation (2) (with $\hat{\mathcal{H}}_{II} = 0$) by using a matrix representation with the Zeeman state vectors, and solving the eigenvalue problem for $\hat{\mathcal{H}}$. The transition probabilities W_0 and W_2 are then given as the square modulus of the corresponding matrix elements of the time evolution operator[9] $\hat{U}(t) = \exp(-i\hat{\mathcal{H}}t)$. If the sum of the two rf fields, $\Sigma = \Omega_{1I} + \Omega_{1S}$, is large compared to their difference $\Delta\Omega = \Omega_{1I} - \Omega_{1S}$, and to the dipolar coupling strength D between I and

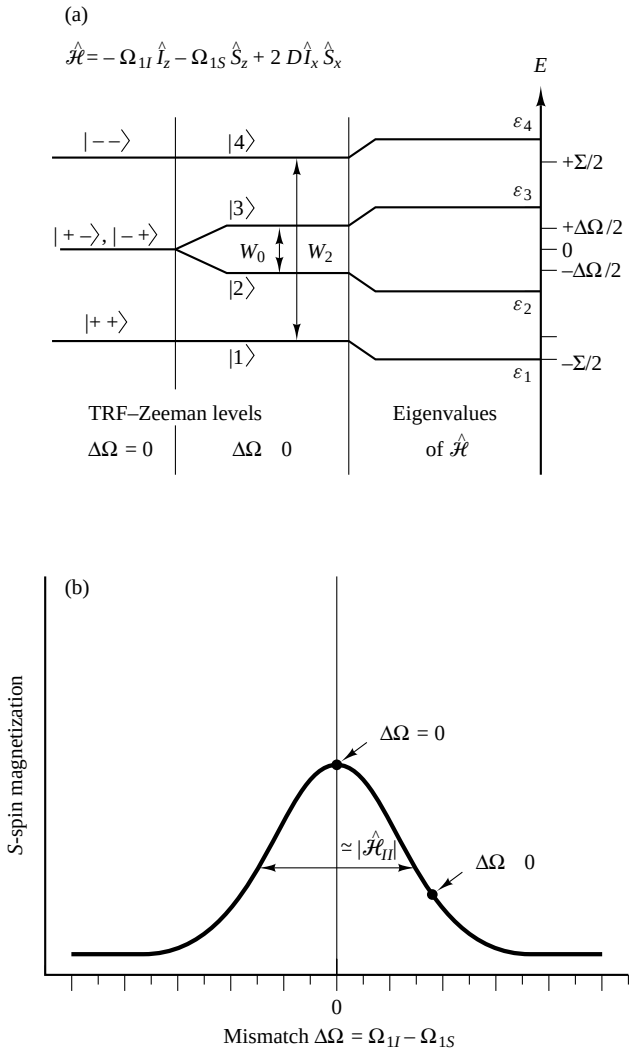

Figure 3 (a) Energy levels of an $I-S$ two-spin system in the tilted rotating frame for matching ($\delta\Omega = 0$) and mismatching ($\delta\Omega \neq 0$) the Hartmann–Hahn condition; (b) Hartmann–Hahn matching curve for a nonrotating solid

S spins, and if, in addition, the quantity $\Delta\Omega$ (referred to in the following as Hartmann–Hahn mismatch) is small compared to D, then the flip-flop transition probability W_0 dominates. W_0 depends on the coupling strength D, and is much larger than W_2:

$$W_0 \propto \frac{D^2}{D^2 + \Delta\Omega^2} \approx 1, \quad W_2 \propto \frac{D^2}{D^2 + \Sigma^2} \ll 1 \qquad (3)$$

for D, $\Delta\Omega \ll \Sigma$, and $\Delta\Omega \ll D$. In general, $I-I$ dipolar couplings are present in the solid, giving rise to a broadening of the I-spin levels.[11,12] With increasing mismatch $\Delta\Omega$, the two energy levels for the states $|\,2\rangle$ and $|\,3\rangle$ of the $I-S$ spin system shift relative to each other [Figure 3(a)], and for $\Delta\Omega > D$ [equation (3)] and $\delta\Omega$ larger than the $I-I$ dipole couplings, the transition probability W_0 decreases significantly.

An entirely isolated $I-S$ spin system would periodically exchange magnetization between I and S spin. The presence of many spins interacting with each other introduces the statistical, or thermodynamic, aspect[3,13,14] into cross polarization. Under standard CP conditions (Figure 1) the initial I-spin magnetization is transferred irreversibly to the S-spin system. However, the behavior of the elementary flip-flop transition allows one to understand, at least qualitatively, the efficiency of CP under mismatch conditions ($|\,\Delta\Omega\,| \neq 0$), as illustrated in Figure 3(b). The polarization transfer is most efficient for $\Delta\Omega = 0$. Increasing mismatch leads to a gradual decrease of S-spin magnetization as long as the levels of the spin states $|\,2\rangle$ and $|\,3\rangle$ still overlap, originating from their finite width due to $I-I$ dipolar couplings. CP becomes completely inefficient if the mismatch becomes larger than the $I-I$ dipolar coupling strengths. The plot of S-spin magnetization obtained by CP versus mismatch $\Delta\Omega$ is called the Hartmann–Hahn or CP-matching curve, and is drawn schematically in Figure 3(b). As will be shown below, the CP-matching curve, as an indicator of efficiency for $I-S$ magnetization transfer, is of utmost importance when combining CP and MAS.

The result that magnetization transfer conserving the total spin energy occurs predominantly for small mismatch $\Delta\Omega$ can be expressed by the selection rules

$$\Delta m_I + \Delta m_S = 0, \quad |\Delta\Omega| \leq D_{IS}, D_{II} \qquad (4)$$

i.e. CP takes place via flip-flop transitions (total change of the magnetic quantum numbers m_I and m_S is zero). The second condition in equation (4) includes the broadening of TRF–Zeeman levels, leading to a CP-matching curve of finite width.

4 DIPOLAR COUPLINGS IN ROTATING SOLIDS

The dipolar coupling strengths D_{jk} between two spins j and k depend on their mutual distance r_{jk} and on the orientational angle ϑ_{jk} of the internuclear vector $\boldsymbol{r}_{jk}$ relative to the static field $\boldsymbol{B}_0$ (see also ***Internal Spin Interactions and Rotations in Solids***):

$$D_{jk} = \frac{\mu_0 \gamma_j \gamma_k \hbar^2}{4\pi r_{jk}^3} \frac{1}{2}(3\cos^2\vartheta_{jk} - 1) \qquad (5)$$

Spinning of the sample around an axis tilted by the angle θ_m relative to $\boldsymbol{B}_0$ leads to a periodic time dependence of the angle ϑ_{jk} with the frequency ω_r of rotation as shown in Figure 4. The time-dependent term $\cos\vartheta_{jk}(t)$ can be expressed as a function of the angles θ_m, θ_{jk} and $\omega_r t$, and the angle-dependent part of D_{jk} then reads

$$\begin{aligned}(3\cos^2\vartheta_{jk}(t) - 1) = {} & \tfrac{1}{2}(3\cos^2\theta_m - 1)(3\cos^2\theta_{jk} - 1) \\ & + \tfrac{3}{2}\sin 2\theta_m \sin 2\theta_{jk} \cos(\omega_r t) \\ & + \tfrac{3}{2}\sin^2\theta_m \sin^2\theta_{jk} \cos(2\omega_r t) \end{aligned} \qquad (6)$$

Decomposing the time-dependent cosine terms into complex exponentials, the Fourier expansion (with Fourier coefficients $d_{jk}^{(n)}$) is obtained:

$$D_{jk}(t) = \sum_{n=-2}^{+2} d_{jk}^{(n)}[\exp(in\omega_r t)] \qquad (7)$$

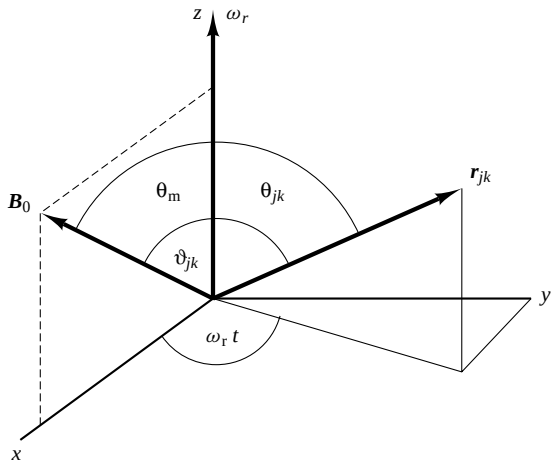

Figure 4 Coordinate frame of reference for a sample spinning around the axis ω_r, and the vector $\boldsymbol{r}_{jk}$ rotating with a polar angle $\omega_r t$

The first term on the right-hand side of equation (6) is time independent [Fourier coefficient $d_{jk}^{(0)}$ in equation (7)], and becomes equal to zero for $\theta_m = 54.7°$—this is called the 'magic angle'. The other two terms in equation (6) show that sample rotation results in a modulation of the dipolar coupling strengths D_{jk} with spinning frequencies ω_r and $2\omega_r$ and an average value equal to zero. Therefore, under sample rotation the dipolar Hamiltonians $\hat{\mathcal{H}}_{II}$ and $\hat{\mathcal{H}}_{IS}$ become periodically time-dependent with the period $2\pi/\omega_r$ of sample rotation.

5 CROSS POLARIZATION IN ROTATING SOLIDS[28]

As illustrated in Section 3, the CP rate, as a function of the transition probabilities of $I-S$ flip-flop transitions, and the form of the CP-matching curve depend on the $I-S$ and $I-I$ dipolar coupling strengths. In order to proceed with the quantum mechanical model discussed above, the resulting time periodicity of dipolar Hamiltonians originating from MAS has to be included. For an isolated $I-S$ spin system in the presence of sample spinning the problem can be solved, for example, using the Floquet formalism (see ***Floquet Theory***).[15,16] Within this theory, originally proposed as a general method for solving linear differential equations with periodic coefficients, an average Hamiltonian, called the Floquet Hamiltonian, can be derived by using the Fourier decomposition of the periodic time-dependent dipolar coupling strengths [equation (7)]. For very fast sample spinning (i.e. when the MAS frequency ω_r is comparable to or larger than the dipolar coupling coefficients $d_{jk}^{(n)}$, $n = \pm1$ or ±2), the flip-flop transitions responsible for $I-S$ magnetization transfer are subject to conditions which are more rigorous than the selection rules given in equation (4), because they now include the MAS frequency ω_r:[16]

$$\Delta m_I + \Delta m_S = 0, \quad |\Delta\Omega + n\omega_r| \leq \tfrac{1}{2} d_{jk}^{(n)}, \quad n = \pm1, \pm2 \quad (8)$$

which means, that CP is possible for mismatch values $\Delta\Omega = \pm\omega_r$ and $\pm2\omega_r$, and becomes small for $n = 0$ because of the disappearance of the zero-order Fourier coefficient $d_{jk}^{(0)}$ at the magic angle [see equations (5)–(7)]. From the conditions given in equation (8), it follows that the CP-matching curve, being rather broad and featureless for a nonrotating solid [Figure 3(b)], splits into sidebands separated by the MAS frequency ω_r, as shown in Figure 5. For very fast spinning, maximum CP does not occur at $\Delta\Omega = 0$, as in the static case, but takes place at $\Delta\Omega$ close to the first and second-order sidebands. The widths of these sidebands depend on the dipolar coupling parameters $d_{jk}^{(n)}$ ($n \neq 0$), and on ω_r as increasing spinning rates provide a more complete averaging of dipolar couplings. The CP-matching curves shown in Figure 5 are calculated by means of a statistical theory,[17] taking into account that: (1) in a solid, usually many I spins interact with each other; and (2) each S spin may be coupled to more than one I spin. The dipolar couplings are introduced as parameters, which represent average values for the I and S spin systems (so-called 'second moments'[12]), while the spin dynamics are described by statistical spin-correlation functions.

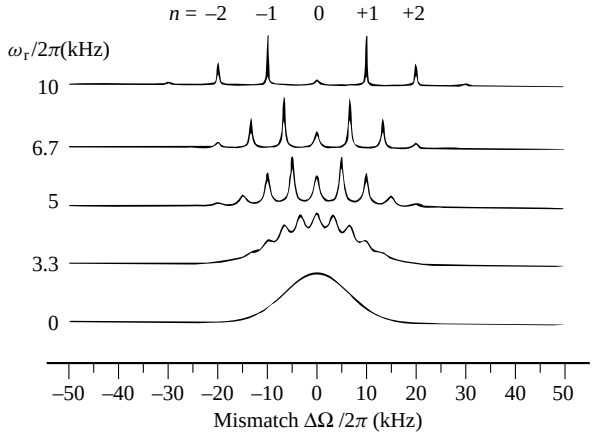

Figure 5 CP-matching curves for various spinning rates for a solid with relatively weak dipolar couplings, e.g. hexamethylbenzene

Experimental evidence for the break-up of the CP-matching curve into a sideband pattern was first provided by Stejskal et al.[18] for adamantane. Many other examples of CP-matching behavior under MAS have been found experimentally.[19–22] Figure 6 shows the $^1H-^{13}C$ CP matching curve for aromatic carbon in polycrystalline hexamethylbenzene (HMB) obtained at a spinning rate of $\omega_r/2\pi = 5$ kHz. In this experiment the

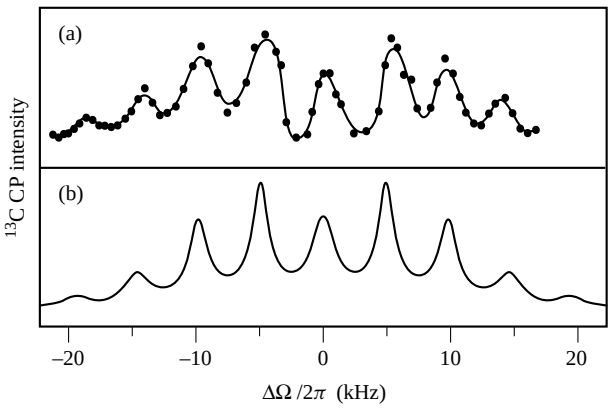

Figure 6 CP-matching curves for aromatic ^{13}C nuclei in hexamethylbenzene: (a) experimental curve obtained at $\omega_r/2\pi = 5$ kHz; (b) theoretical curve

proton rf field was fixed at $\Omega_{1I}/2\pi$ = 40 kHz and the ^{13}C rf field was varied in the range $\Omega_{1S}/2\pi$ = 18 to 57 kHz. Each experimental data point in Figure 6 represents an intensity value of the ^{13}C NMR line resonating at ca. 130 ppm (isotropic chemical shift relative to tetramethylsilane), attributed to aromatic carbon nuclei in HMB. The theoretical curve was obtained[17] using values for the $I-I$ and $I-S$ dipolar coupling parameters determined from the internuclear distances and the crystal structure of HMB.

The appearance of sharp CP-matching sidebands at high spinning rates causes various experimental difficulties. First, the maximum of S-spin magnetization is not obtained at $\Delta\Omega$ = 0, as for the static case. The mismatch has to be adjusted to one of the sidebands, the location of which depends on ω_r. Second, the sidebands become narrow at high MAS rates, requiring highly stable rf amplitudes Ω_{1I} and Ω_{1S}, and accurate spinning rates which have to remain constant over extended periods of time. Otherwise, slight deviations lead to dramatic losses of the CP enhancement for S-spin magnetization. Furthermore, the spectrum of the S spins may possess a variety of resonance lines with different resonance frequencies; for example, ^{13}C NMR spectra of organic solids very often reveal resonance frequencies over a range of 200 ppm, which leads to resonance offsets resulting in different mismatch values $\Delta\Omega$ for each resonance line. This means that some S spins are properly cross polarized, while other S spins with different $\Delta\Omega$ values due to resonance offsets are only weakly polarized. Any of the latter cases results in distortions of the relative intensities in CP MAS spectra.

6 MODIFIED CP EXPERIMENTS AND MAS

Because of the usefulness of the CP MAS technique, much effort has been made in recent years to develop methods which circumvent the experimental disadvantage originating from the Hartmann–Hahn condition under MAS. These methods can be grouped as follows:

1. Mechanical techniques, for example, off-magic angle spinning[20] and stop-and-go magic angle spinning.[21]
2. Techniques based on modifications of the standard CP rf-pulse scheme (Figure 1), including rf phase or amplitude modulation,[16,23,24] or rf amplitude variation.[25]
3. Alternative ways of magnetization transfer, for example, via the nuclear solid effect.[8,12] or dynamic nuclear polarization.[12,26]

The following brief discussion will focus on methods (1) and (2).

Off-magic angle spinning exploits the fact that the zero-order coefficients $d_{jk}^{(0)}$ of the Fourier expansion [equation (7)] become unequal to zero for spinning angles θ different from the magic angle θ_m, which should lead to an increase in the CP-matching centerband (at high spinning rates) and to a broadening of the center- and sidebands. Sardashti and Maciel[20] employed a CP technique, using the angle $\theta = 90^\circ$ during the CP period, and switching to the magic angle before starting acquisition of the NMR signal. According to equation (6), only centerbands and second-order sidebands appear in the CP-matching curve. A broadening of the center- and sidebands originating from the less severe averaging of $I-I$ dipolar couplings for $\theta \neq \theta_m$ is also observed in this experiment.

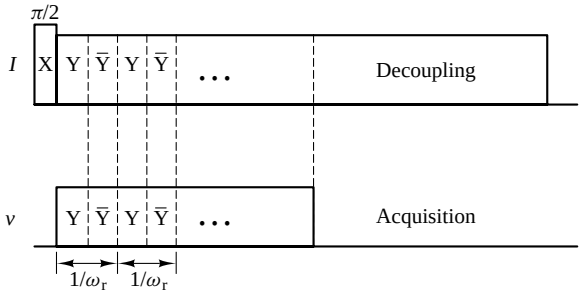

Figure 7 CP pulse sequence with simultaneous phase inversion

Stop-and-go sample spinning, proposed by Zeigler et al.,[21] is even more straightforward in its attempt to avoid CP-matching sidebands. During the CP period the sample is not spinning, or it is slowed down, while during detection MAS is turned on. Both techniques require advanced mechanical capabilities for the spinner system, either being able quickly to switch the spinner axis or to turn the spinning on and off during the CP experiment.

A general way to improve the magnetization transfer under MAS conditions is based on modifications of the CP rf-irradiation scheme.[16,23–25] One possibility[25] consists of applying stepwise rf-amplitude variations of the spin lock field [variable amplitude CP (VACP)], thus creating a whole series of slightly different Hartmann–Hahn matching conditions during one CP period. In this way an averaging over rf-amplitude mismatches is achieved, resulting in a remarkable smoothing of CP-matching curves. Another strategy, which may give an idea of the general philosophy involved, introduces an additional time dependence into the CP Hamiltonian [equation (2)] by periodically inverting the phases of the rf fields in the I and S spin channels simultaneously,[16,23,24] synchronized with sample spinning (Figure 7). The time dependence of the TRF Hamiltonian then originates from: (1) the MAS modulation of the dipolar interactions, and (2) the modulation of the rf fields. One effect of this pulse sequence, which is important from a practical point of view, consists of averaging or compensating for $\Delta\Omega$ deviations due to rf inhomogeneities.[24,27] The pulse sequence of Figure 7 has been shown to provide a significant broadening of the CP-matching curve.[16,24] Improvements have been proposed[16] leading to a whole new class of general amplitude-modulation CP (AMCP) schemes based on the study of detailed time dependences of the TRF Hamiltonian, and allowing the design of pulse sequences to restore CP-matching conditions under MAS, which are similar to those in nonrotating solids.

7 RELATED ARTICLES

CRAMPS; Cross Polarization in Solids; Dynamic Angle Spinning; Internal Spin Interactions and Rotations in Solids; Floquet Theory; Line Narrowing Methods in Solids; Magic Angle Spinning; Rotating Solids; Spectral Editing Techniques: Hydrocarbon Solids; Spin Diffusion in Solids; Variable Angle Sample Spinning

8 REFERENCES

1. S. R. Hartmann and E. L. Hahn, *Phys. Rev.*, 1962, **128**, 2042.
2. A. Pines, M. G. Gibby, and J. S. Waugh, *J. Chem. Phys.*, 1972, **56**, 1176; 1973, **59**, 569.
3. M. Mehring, *Principles of High Resolution NMR in Solids*, 2nd edn., Springer, Berlin, 1983, Chaps 2 and 4.
4. U. Haeberlen, *High Resolution NMR in Solids—Selective Averaging*, *Advances in Magnetic Resonance*, Suppl. 1, Academic, New York, 1976, Chap. IV.
5. B. C. Gerstein and C. R. Dybowski, *Transient Techniques in NMR of Solids—An Introduction to Theory and Practice*, Academic, Orlando, FL, 1985, Chaps 5 and 6.
6. E. R. Andrew, A. Bradbury, and R. G. Eades, *Nature*, 1958, **182**, 223; 1959, **183**, 1802.
7. I. J. Lowe, *Phys. Rev. Lett.*, 1959, **2**, 285.
8. R. A. Wind and C. S. Yannoni, *J. Magn. Reson.*, 1986, **68**, 373; 1987, **72**, 108.
9. M. Weissbluth, *Atoms and Molecules*, Academic, New York, 1978, Chap 9.3; S. Gasiorowicz, *Quantum Physics*, Wiley, Chichester, 1974, Chap. 14
10. This transformation can be achieved for circularly polarized rf fields only. However, a linearly polarized rf field (frequency ω_k, $k = I, S$) can be decomposed into two circular polarized fields, rotating with angular frequencies $\omega_{0k} - \omega_k$ and $\omega_{0k} + \omega_k$ in the rotating frame. If the resonance offset $\omega_{0k} - \omega_k$ is small compared with $\omega_{0k} + \omega_k$, and if the rf field amplitudes Ω_{1k} are small compared with ω_{0k}, only the circular polarized component rotating with ω_{0k}—ω_k needs to be considered; the other one has negligible influence (Bloch–Siegert effect, see Shirley,[15] Section III).
11. A. Das and A. C. Melissinos, *Quantum Mechanics*, Gordon & Breach, New York, 1986, Chap. 5
12. A. Abragam, *The Principles of Nuclear Magnetism*, Clarendon, Oxford, 1961, Chaps IV and IX.
13. D. E. Demco, J. Tegenfeldt, and J. S. Waugh, *Phys. Rev. B*, 1975, **11**, 4133.
14. D. Suter and R. R. Ernst, *Phys. Rev. B*, 1985, **32**, 5608; M. H. Levitt, D. Suter, and R. R. Ernst, *J. Chem. Phys.*, 1986, **84**, 4243.
15. J. H. Shirley, *Phys. Rev. B*, 1965, **138**, 979.
16. S. Hediger, B. H. Meier, and R. R. Ernst, *Chem. Phys. Lett.*, 1993, **213**, 627.
17. F. Engelke, T. Kind, D. Michel, M. Pruski, and B. C. Gerstein, *J. Magn. Reson.*, 1991, **95**, 286.
18. E. O. Stejskal, J. Schaefer, and J. S. Waugh, *J. Magn. Reson.*, 1977, **28**, 105.
19. E. O. Stejskal, J. Schaefer, and R. A. McKay, *J. Magn. Reson.*, 1984, **57**, 471; J. Schaefer, E. O. Stejskal, J. R. Garbow, and R. A. McKay, *J. Magn. Reson.*, 1984, **59**, 150.
20. M. Sardashti and G. E. Maciel, *J. Magn. Reson.*, 1987, **72**, 467; R. A. Wind, S. F. Dec, H. Lock, and G. E. Maciel, *J. Magn. Reson.*, 1988, **79**, 136.
21. R. C. Zeigler, R. A. Wind, and G. E. Maciel, *J. Magn. Reson.*, 1988, **79**, 299.
22. M. Pruski, L. DelaRosa, and B. C. Gerstein, *Energy Fuels*, 1990, **4**, 160.
23. T. M. Barbara and E. H. Williams, *J. Magn. Reson.*, 1992, **99**, 439.
24. X. Wu and K. W. Zilm, *J. Magn. Reson., Ser. A*, 1993, **104**, 154.
25. O. B. Peersen, X. Wu, I. Kustanovich, and S. O. Smith, *J. Magn. Reson., Ser. A*, 1993, **104**, 334.
26. R. A. Wind, F. E. Anthonio, M. J. Duijvestijn, J. Schmidt, J. Trommel, and G. M. C. DeVette, *J. Magn. Reson.*, 1983, **52**, 424.
27. X. Wu and K. W. Zilm, *J. Magn. Reson.*, 1991, **93**, 265.
28. D. Michel and F. Engelke, in *NMR Basic Principles and Progress*, Springer, Berlin, 1994, vol. 32, pp. 69–125.

Biographical Sketches

Frank Engelke. *b* 1955. M.Sc. (physics), Ph.D. (supervisor Dieter Michel), habilitation, University of Leipzig, Germany. Postdoctoral work at Saarbruecken University, Germany (with Jorn Petersson), and since 1992 at Ames Laboratory, USA (with Bernie Gerstein, Marek Pruski and Terry King). Approx. 20 publications. Current research specialties: solid state NMR in rotating solids and solid state NMR applications on metal surfaces.

Cross Polarization in Solids

Douglas P. Burum

Bruker Instruments, Inc., Billerica, MA, USA

1	Introduction	1
2	Strategies for Achieving High-Resolution NMR in Solids	1
3	Theory of Cross Polarization in Solids	2
4	Cross Polarization at High Spinning Speeds	4
5	Spectral Editing and Other Tricks Using Cross Polarization	7
6	Conclusions	7
7	Related Articles	8
8	References	8

1 INTRODUCTION

A number of techniques exist for producing well resolved NMR spectra of solid samples. Some, including very rapid rotation about the 'magic' angle[1] of 54.7° and CRAMPS (see ***CRAMPS***) multiple pulse irradiation, attempt to produce well resolved spectra of abundant nuclei such as ^{1}H or ^{19}F. However, much greater success has been achieved in obtaining high-resolution solid state spectra of 'rare' NMR isotopes such as ^{13}C and ^{15}N. Typically, three techniques are combined: cross polarization[2] to increase signal strength and measurement repetition rate, heteronuclear decoupling[3] to remove line broadening due to surrounding abundant spins, and magic angle spinning[4] to eliminate chemical shift anisotropy (CSA) effects.

This article deals primarily with cross polarization in solids. Heteronuclear decoupling and magic angle spinning are briefly mentioned, but more detailed discussions of these techniques are presented in other articles (see ***Magic Angle Spinning*** and ***Rotating Solids***).

2 STRATEGIES FOR ACHIEVING HIGH-RESOLUTION NMR IN SOLIDS

It is helpful to begin by considering the various interactions that occur in the solid state.[5] In order of their relative magnitudes, the interactions may be summarized as follows:

1. *Quadrupolar* This is an interaction involving electric field gradients that occurs only for nuclei of spin quantum number greater than $\frac{1}{2}$. Since most important NMR nuclei, including ^{1}H, have spin-$\frac{1}{2}$, they are not subject to quadrupolar effects.
2. *Dipolar* This is the effect that the nuclear dipole field generated by each nuclear spin has on its neighboring spins, and it is the dominant interaction for abundant nuclei such as ^{1}H spins in solids. Dipolar interactions are often referred to as either 'homonuclear', for interaction between nuclei of the same species (e.g. ^{1}H–^{1}H), or heteronuclear, for interaction between nuclei of different species (e.g. ^{1}H–^{13}C). Due to rapid, isotropic molecular motion, dipolar interactions are averaged to zero in liquids, but do contribute to the longitudinal relaxation parameter T_1.
3. *Chemical Shift Anisotropy (CSA)* The magnitude of the diamagnetic effect that surrounding electrons have on the nucleus usually depends on molecular orientation. The average, or isotropic, shift is observable in both liquids and solids. In addition, resonance lines for most solids exhibit an additional shift based on molecular orientation. For single crystals this is manifested as a dependence of the resonance frequency on orientation. For a powder sample, all orientations are represented simultaneously and the result is a broad CSA 'powder pattern'. These powder patterns often overlap and cause loss of resolution.
4. *Isotropic Chemical Shift* In a liquid, rapid molecular reorientation allows only the average, or isotropic chemical shift to be observed. In solids, the same result is often achieved by rapid rotation of the sample about an axis tilted away from the magnetic field by 54.7°, often referred to as the 'magic' angle. Magic angle spinning is discussed in more detail in other articles (see ***Magic Angle Spinning*** and ***Rotating Solids***).
5. *J Coupling* This is an indirect coupling of nuclei to each other, mediated by shared electrons. As such, it is a 'through-bond' coupling, and is of great importance in liquids. However, it is too weak to be observable in most spectra of solids.

Elimination of the direct dipolar interaction between nuclei is clearly the first step in achieving high-resolution NMR in solids. The dipolar interaction between a given pair of spin-$\frac{1}{2}$ nuclei, as expressed by the dipolar Hamiltonian[6] $\hat{\mathcal{H}}_{\mathrm{D}}$, can be written as

$$\hat{\mathcal{H}}_D \propto \left(\frac{1}{r^3}\right)(1 - 3\ \cos^2\theta)\ \text{spin part} \qquad (1)$$

where r is the internuclear distance, and θ is the angle that the internuclear vector makes with the magnetic field. The 'spin part' varies, depending on whether the two nuclei are of the same species (homonuclear) or different species (heteronuclear). For example, the spin part for two coupled ^{1}H spins is given by:

$$\text{Homonuclear spin part} = \{\hat{I}_1 \cdot \hat{I}_{2-3}\hat{I}_{z1}\hat{I}_{z2}\} \qquad (2)$$

where the labels 1 and 2 refer to the two ^{1}H spins. On the other hand, the spin part for dipolar coupling between a ^{1}H and a ^{13}C nucleus is given by:

$$\text{Heteronuclear spin part} = \{\hat{I}_z\hat{S}_z\} \qquad (3)$$

where I and S refer to the ^{1}H and ^{13}C nuclei, respectively.

Clearly, the dipolar interaction may be eliminated by causing any of the three terms in equation (1) to vanish. In some cases, rapid rotation of the sample about the magic angle can be used to eliminate the second term.[7] However, for most rigid solids it is usually not possible to spin fast enough for this approach to be effective in eliminating dipolar couplings. For heteronuclear coupling, the spin part can usually be eliminated by strong rf irradiation of one of the nuclear

species,[3] whereas for homonuclear coupling the spin part can sometimes be sufficiently reduced by the CRAMPS multiple rf pulse technique (see ***CRAMPS***).

The most commonly used approach is to observe a nuclear spin for which the NMR active isotope has a low abundance. For these 'rare' spins, such as ^{13}C, the homonuclear coupling is automatically eliminated since the large distances between NMR active nuclei cause the first term of equation (1) to be vanishingly small. At the same time, the heteronuclear interaction with surrounding abundant spins, usually ^{1}H nuclei, is eliminated by strong continuous rf irradiation[3] of the abundant nuclei to cause the spin part given in equation (3) to average to zero. For powder samples, magic angle spinning is also applied to eliminate CSA broadening.

There are two important disadvantages associated with NMR of rare nuclei in solids, namely low sensitivity and, in most cases, long relaxation times. The low sensitivity is an obvious result of low natural abundance.

The long relaxation times,[8] or T_1 values, are essentially due to an accident of nature. For spin-$\frac{1}{2}$ nuclei, the nuclear spin energy is coupled to the surrounding environment, or 'lattice', via locally generated time varying magnetic fields. The strength of the coupling, and therefore the rate at which the nuclear spins return to equilibrium, is governed by the magnetogyric ratio. Unfortunately, all of the spin-$\frac{1}{2}$ NMR nuclei with rare isotopic abundance have relatively low gyromagnetic ratios, and therefore long relaxation times, compared with the most commonly observed abundant NMR spins, namely ^{1}H, ^{19}F, and ^{31}P.

Low sensitivity can be improved by using a very high magnetic field, but the expense is often prohibitive and, for some nuclei, especially ^{13}C, a very high field can make it difficult or impossible to eliminate CSA effects. Another approach is to enrich isotopically the rare nucleus to a higher abundance. This approach can be very successful for improving sensitivity and for spectral editing, but it can also be very time consuming and expensive. In addition, enrichment beyond approximately 10% can cause broadening due to dipolar interactions between the 'rare' nuclei.

T_1 can sometimes be reduced by introducing paramagnetic impurities[9] into the sample, or in some cases by varying the sample temperature. However, these are inconvenient and specialized techniques.

The most commonly used method for increasing the sensitivity and experiment repetition rate when observing rare spins in solids is to transfer polarization from surrounding abundant spins, usually ^{1}H nuclei, to the rare spins. This is referred to as 'cross polarization'. Cross polarization not only enhances the signal strength of the rare spins, but also allows the experiment to be repeated at a rate governed by the T_1 of the abundant spins.

3 THEORY OF CROSS POLARIZATION IN SOLIDS

At equilibrium, the degree of nuclear polarization P_0 depends on the strength of the applied magnetic field $\boldsymbol{B}_0$, the magnetogyric ratio γ, and the 'lattice' temperature T_{L}:[2]

$$P_0 \propto \frac{\gamma B_0}{kT_L} \tag{4}$$

where k is Boltzmann's constant. The polarizations of different nuclear species will therefore be proportional to their magnetogyric ratios:

$$\frac{P_{0I}}{P_{0S}} = \frac{\gamma_I}{\gamma_S} \tag{5}$$

The key to understanding cross polarization in solids is the concept of mutual spin flips. This is a process whereby two coupled spins undergo simultaneous, opposite transitions in their spin states. Essentially, one spin makes a transition from 'spin up' to 'spin down', while the other goes from 'spin down' to 'spin up'. This process occurs spontaneously among abundant nuclei in solids. Since the total polarization is unchanged, the process conserves energy, and the spin part of the homonuclear dipolar coupling contains appropriate mutual spin flip terms. In order to show this better, equation (2) can be rewritten in terms of raising and lowering operators:

$$\text{Homonuclear spin part} = \left\{ \frac{1}{2}[\hat{I}_+\hat{S}_- + \hat{I}_-\hat{S}_+ - 2\hat{I}_z\hat{S}_z] \right\} \tag{6}$$

Because of this process of mutual spin flips, which is often referred to as nuclear 'spin diffusion', abundant spins tend to maintain a uniform degree of polarization despite localized perturbations such as paramagnetic impurities. For this reason, they are often described as a 'thermodynamic bath' of spins with an effective spin 'temperature'.

Of course, mutual spin flips do not occur between rare spins since they are not coupled to each other. Also, they do not occur spontaneously between nuclei of different species, since a mutual spin flip of this sort does not conserve energy, and the spin part given in equation (3) does not contain the necessary raising and lowering operators.

Cross polarization in solids is normally achieved by using rf irradiation to induce heteronuclear mutual spin flips. Since the abundant spins far outnumber the rare spins, this process causes the polarization of the rare spins to be made equal to that of the abundant spins. According to equation (5) this means that the polarization of the rare spins is increased by a factor equal to the ratio of their magnetogyric ratios. For coupled ^{1}H and ^{13}C spins, the ratio is approximately 4. Due to relaxation phenomena and other imperfections, a polarization enhancement factor of 3 is more typically achieved.

The basic method for inducing mutual spin flips between different nuclear species was introduced by Hartmann and Hahn, and is commonly called 'Hartmann–Hahn' cross polarization.[10] The pulse sequence is shown in Figure 1. An initial I-spin pulse places the I magnetization along the y axis in the I-spin rotating frame. This is followed by continuous irradiation along y in the I frame, together with simultaneous irradiation of the S spins. The rf power levels for the two nuclear species are adjusted such that the 'Hartmann–Hahn' condition is met:

$$\omega_{1I} \equiv \gamma_I B_{1I} = \gamma_S B_{1S} \equiv \omega_{1S} \tag{7}$$

In practical terms, this means that the length of a $\pi/2$ pulse is the same for both spin systems. During a few milliseconds of simultaneous irradiation, a substantial magnetization develops along the irradiation axis in the S-spin rotating frame. In

order to acquire a FID, it is then only necessary to turn off the rf on the S channel and observe the signal while the I-spin irradiation is continued for the purpose of heteronuclear decoupling.

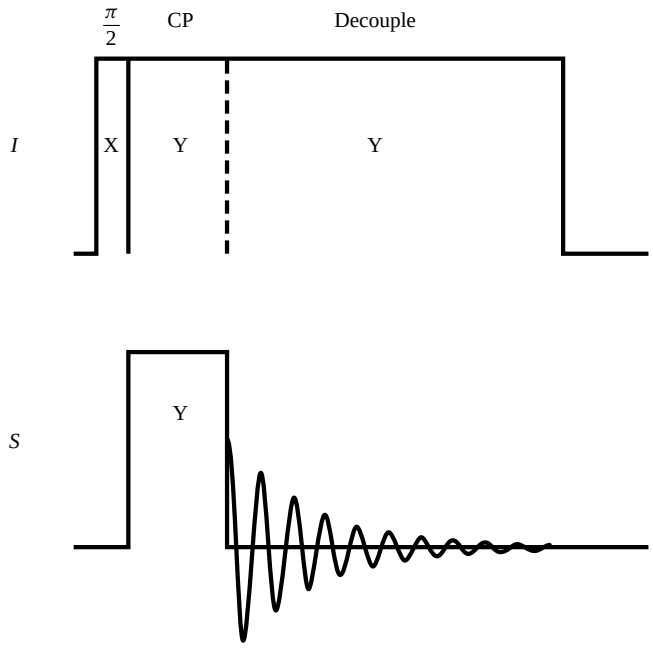

Figure 1 Basic pulse sequence for Hartmann–Hahn cross polarization

Hartmann–Hahn cross polarization can best be understood by carrying out a few simple quantum mechanical manipulations. In the doubly rotating reference frame of the Zeeman interactions for spins I and S, the Hamiltonian for the system may be written as:

$$\hat{\mathcal{H}}_{\mathrm{R}} = \omega_{1I}\hat{I}_Y + \omega_{1S}\hat{S}_Y + \beta_{IS}\hat{I}_z\hat{S}_z \tag{8}$$

where ω_1 is the rf nutation frequency, β_{IS} is a constant, and all other Hamiltonian terms such as chemical shift have been omitted for the sake of clarity. When the Hartmann–Hahn condition is matched, $\omega_{1I} = \omega_{1S}$, and equation (8) may be written as:

$$\hat{\mathcal{H}}_{\mathrm{R}} = \omega_1(\hat{I}_Y + \hat{S}_Y) + \beta_{IS}\hat{I}_z\hat{S}_z \tag{9}$$

The two terms in equation (9) do not commute, but if $\omega_1 \gg \beta_{IS}$ the situation can be further simplified by transforming to the frame of the interaction $(I_y + S_y)\omega_1$. The Hamiltonian in this frame is:

$$\hat{\mathcal{H}}^I_{\mathrm{R}} = \beta_{IS}[\hat{I}_z\cos(\omega_1 t) + \hat{I}_x\sin(\omega_1 t)] \times[\hat{S}_z\cos(\omega_1 t) + \hat{S}_x\sin(\omega_1 t)] \tag{10}$$

Keeping only the time independent, 'secular' part gives:

$$\hat{\mathcal{H}}^I_{\mathrm{R}} = \tfrac{1}{2}\beta_{IS}[\hat{I}_z\hat{S}_z + \hat{I}_x\hat{S}_x] \tag{11}$$

which is the first order average Hamiltonian, and commutes with the major interaction $\omega_1(I_y + S_y)$.

The significance of $\hat{\mathcal{H}}^I_{\mathrm{R}}$ can be better seen if both the I and S coordinate axes are tilted by 90°, such that I_z' and S_z' are parallel with the applied rf fields, i.e. they point along I_y and S_y, which is to say the axis of quantization has been changed to the direction along I_y,S_y. In this doubly tilted frame, the Hamiltonian becomes

$$\hat{\mathcal{H}}^{I'}_{\mathrm{R}} = \tfrac{1}{2}\beta_{IS}(\hat{I}_x\hat{S}_x + \hat{I}_y\hat{S}_y) \tag{12}$$

which can be rewritten in terms of raising and lowering operators as:

$$\hat{\mathcal{H}}^{I'}_{\mathrm{R}} = \tfrac{1}{4}\beta_{IS}(\hat{I}_+\hat{S}_- + \hat{I}_-\hat{S}_+) \tag{13}$$

Clearly, mutual spin flips will occur under these circumstances, but they will occur between magnetization aligned along the y axes in the I and S spin reference frames. Note that if the Hartmann–Hahn condition is not met, there is no secular part in equation (11), and the effect of simultaneous irradiation will simply be to eliminate the heteronuclear coupling.

This simple quantum mechanical treatment applies strictly to an isolated pair of spins. In such a case, the result of Hartmann–Hahn irradiation is an oscillation of magnetization between the two spins. However, in most cases the I spin is coupled to a large number of other I spins via homonuclear dipolar coupling. This coupling to a 'bath' of I spins quickly damps out any oscillation and results in a smooth buildup of S spin magnetization along the y axis.

Note that a similar quantum mechanical treatment may be used to show that application of CW irradiation to two spins coupled by homonuclear dipolar coupling yields an effective Hamiltonian that remains dipolar in form but is rotated in spin space and reduced in magnitude by a factor of 2. The result is that CW rf irradiation slows, but does not quench, spin diffusion between the I spins.

The rate of polarization buildup in the S spins will be governed by the strength of the heteronuclear coupling and by the rate of I spin diffusion. The characteristic time for this process[11] is often called T_{CH}, emphasizing the fact that the method is most commonly applied to cross polarization of ^{13}C spins coupled to ^{1}H spins. At the same time that the S spin polarization is growing, the I spin polarization will tend to decay according to the characteristic 'spin locked' or 'rotating frame' relaxation time[12] $T_{1\rho}$. The competition between these two rates will determine what level of polarization enhancement is actually achieved, how critical the cross polarization time is, and how quantitative the resulting spectrum will be.

Figure 2 presents two ^{13}C spectra of glycine, both obtained with magic angle spinning and heteronuclear decoupling and equal numbers of scans. The first spectrum shows the sensitivity obtained without cross polarization, while the second shows the spectrum obtained using Hartmann–Hahn cross polarization. It can be seen from Figure 2 that a substantial increase in signal strength is realized, although not quite the theoretical increase of 4. Also, a slight perturbation in the relative intensities of the resonance lines is evident. This is due to different values of T_{CH} and $T_{1\rho}$ for the two

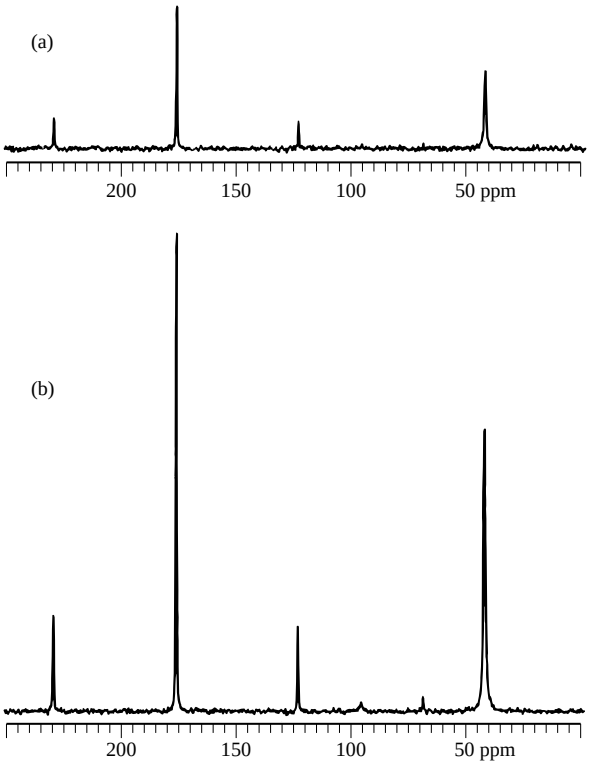

Figure 2 Comparison of ^{13}C MAS spectra for glycine obtained by (a) block decay (single pulse) with heteronuclear decoupling, and (b) Hartmann–Hahn cross polarization followed by heteronuclear decoupling

lines. When multiple scans are to be accumulated, an additional gain in sensitivity is realized due to the shorter relaxation time, or T_1, of the ^1H spins in glycine as compared with the ^{13}C spins (approximately 3 s as compared to 30 s). Figure 3 presents the 'T_{CH}' polarization curve for Hartmann–Hahn cross polarization of glycine. The effects of the competing T_{CH} and $T_{1\rho}$ time constants can easily be seen from the figure.

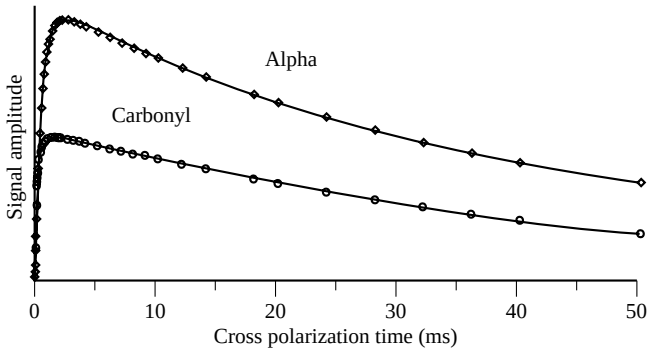

Figure 3 T_{CH} cross polarization curves for glycine

It should be pointed out that Hartmann–Hahn cross polarization can also be described in thermodynamic terms.[13] The abundant I spins are treated as a 'bath', with a 'spin' temperature determined by the degree of polarization and the energy associated with a nuclear spin state transition, i.e. spin 'flip'. Although the S spins are not in direct contact with each other, they are also treated as if they were a thermodynamic bath, and their low abundance is incorporated by assigning them a very low heat capacity. During the Hartmann–Hahn cross polarization period, the I and S spins are quantized along y, and are said to have spin temperatures determined by their polarizations and the strengths of the applied rf fields. The Hartmann–Hahn irradiation has the effect of thermally connecting the two spin baths and, since the S spins have very low heat capacity, they tend to approach the I spin temperature. As the rf fields are equal (in units of 1/second), equal temperatures imply equal degrees of polarization.

It should also be pointed out that there are other methods of cross polarization in solids. One approach uses rf irradiation with adiabatically varied amplitude to transfer magnetization via a 'dipolar' polarization state.[14,15] Another uses the 'Jener–Brockhard' pulse sequence to transfer polarization via multiple quantum states.[16] Still others transfer magnetization using nonthermodynamic techniques similar to those commonly used for liquids.[17] However, all of these alternative techniques have significant disadvantages in comparison with Hartmann–Hahn cross polarization, and none of them is widely used.

4 CROSS POLARIZATION AT HIGH SPINNING SPEEDS

As was mentioned in the introduction, cross polarization in solids is usually combined with magic angle spinning in order to eliminate chemical shift anisotropies, or CSAs. This combined experiment is often called CP MAS, and it is without doubt the most commonly used experimental method in solid state NMR.

In order completely to eliminate CSA effects, the MAS spinning rate must be faster than the width (in hertz) of the broadest CSA pattern in the spectrum. CSA magnitudes depend heavily on the nuclear species and chemical environment. For example, CSAs for ^{15}N and ^{29}Si are typically less than 20 ppm, while CSAs for ^{31}P can be as large as 300 ppm or more. For ^{13}C,

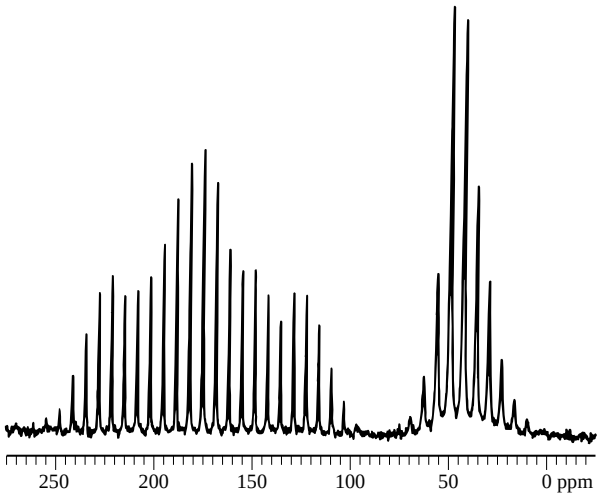

Figure 4 Glycine ^{13}C spectrum with slow spinning MAS. The spinning sidebands approximately trace out the CSA pattern

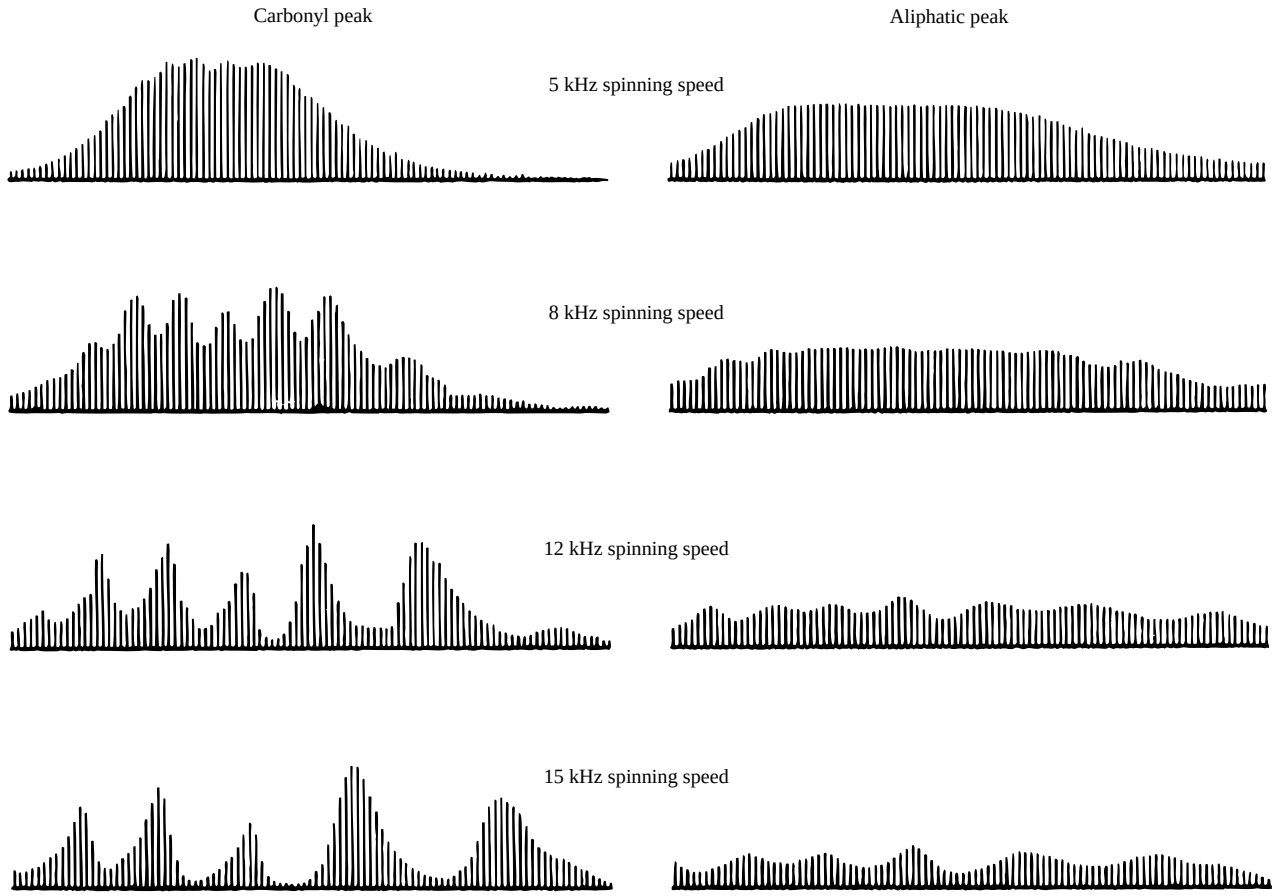

Figure 5 Glycine CP MAS signal strength as a function of Hartmann–Hahn mismatch and spinning speed. The match condition breaks into mismatch sidebands as the spinning speed is increased

CSA widths range from a few parts per million for methyl carbons atoms to 150 ppm or more for rigid aromatic carbon atoms.

If the MAS spinning rate is smaller than the CSA width, the CSA pattern breaks into 'sidebands' that are spaced at the MAS rate and approximately trace out the CSA pattern.[18] An example of this is presented in Figure 4 for glycine. A small number of sidebands can generally be tolerated, especially in highly crystalline samples like glycine that yield spectra with sharp lines. In fact, well resolved sidebands can be analyzed to extract the principal values of the CSA tensor.[18] Nevertheless, it is usually desirable to minimize the occurrence of CSA spinning sidebands by spinning rapidly. Since the CSA width is proportional to the magnetic field strength, the need for fast magic angle spinning increases at higher fields.

MAS spinning above approximately 20 kHz is a difficult mechanical and materials problem, and it also interferes with cross polarization because it tends to suppress heteronuclear dipolar coupling. Although the spinning rate is rarely fast enough completely to eliminate dipolar coupling, it is often sufficient to cause the Hartmann–Hahn match condition to become very critical and inefficient. As the spinning rate increases, additional 'match' conditions appear,[19] making it possible to cross polarize when the rf strength of one channel is mismatched from the other by either one or two times the spinning rate. At very high spinning speeds, cross polarization under these special mismatched conditions remains relatively efficient, even when almost no cross polarization is possible under normal matched conditions. An example of this high speed spinning effect for ^{13}C in glycine is shown in Figure 5.

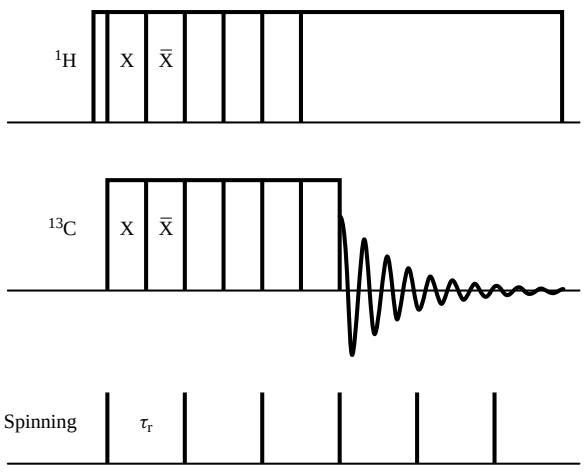

Figure 6 Pulse sequence using alternating π pulses to improve cross polarization during high speed MAS

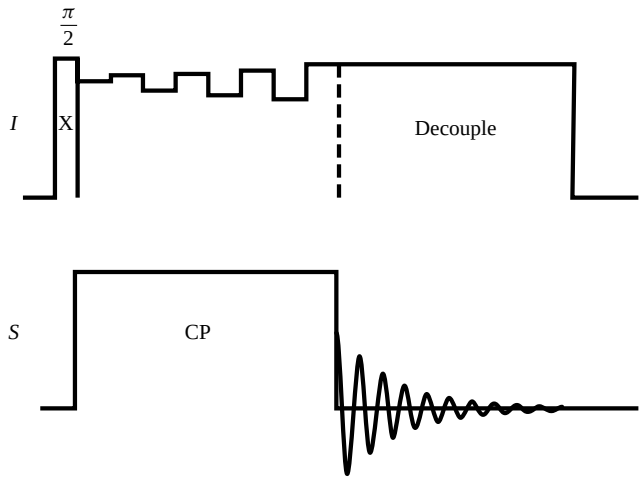

Figure 7 Variable amplitude cross polarization pulse sequence as it was originally proposed. The 'stair step' rf amplitude variation may be replaced by other functions such as a ramp or 'sawtooth'

that will provide sufficient signal intensity and yet will not overly complicate the data analysis by introducing too many spinning sidebands. Typically, CP MAS spectra of ^{13}C are measured in NMR spectrometers with ^{1}H resonance frequencies of 200–300 MHz, and are rarely attempted above 400 MHz. MAS rates are usually kept in the range 4–8 kHz, although spinning up to 15 kHz and beyond is not mechanically difficult. Even under these optimum conditions, ^{13}C CP MAS spectra of rigid solids are rarely free of CSA sidebands.

Several methods have been proposed to improve cross polarization during high speed spinning. In some, the spinning rate[20] or even the spinning angle[21] is changed between the cross polarization and signal detection phases of the experiment. Other approaches use 180° rf pulses to 'spoil' MAS dipolar suppression during the cross polarization[22] A typical pulse sequence for this method is shown in Figure 6.

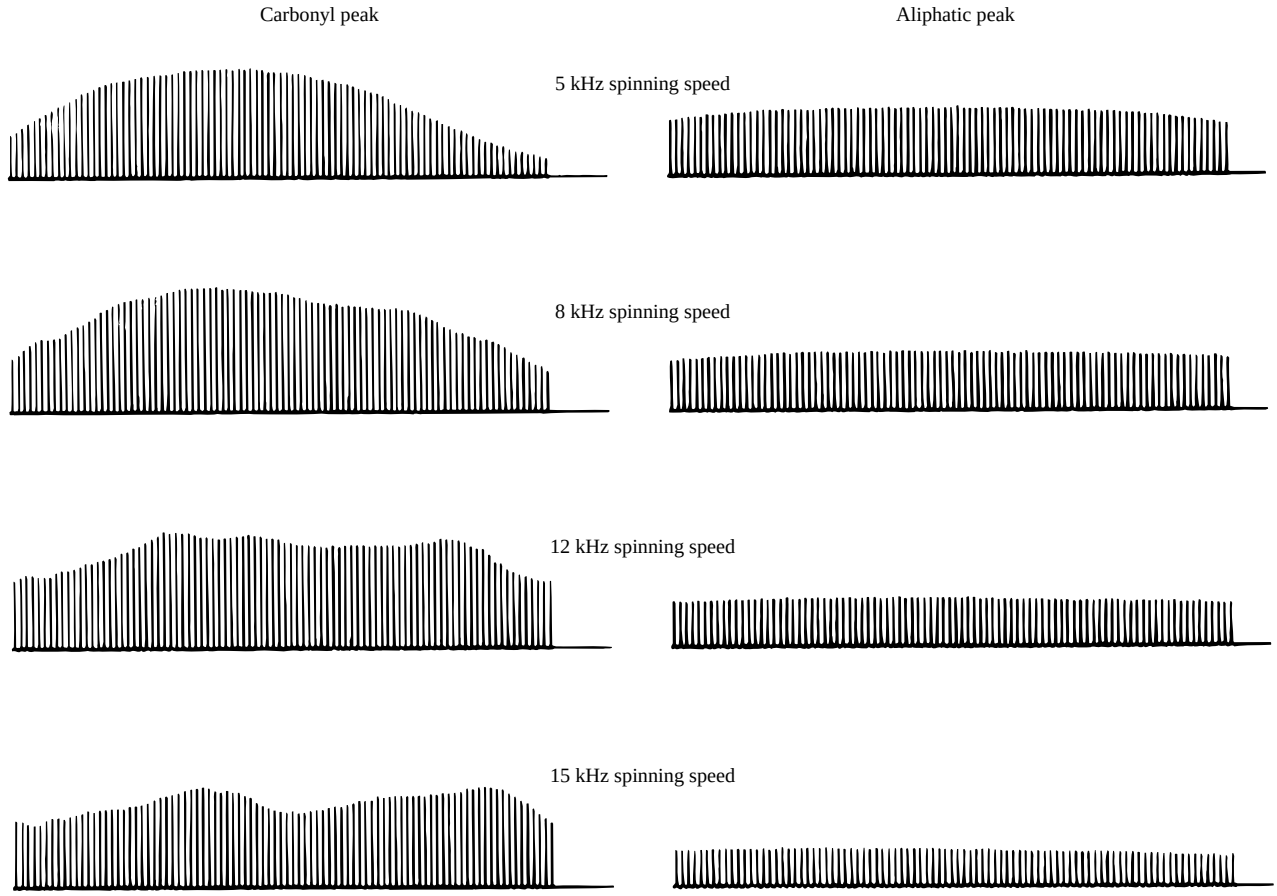

Figure 8 Glycine VACP signal strength as a function of Hartmann–Hahn mismatch and spinning speed.

Unfortunately, it is difficult to achieve stable and reproducible results using mismatched Hartmann–Hahn cross polarization, because the mismatched conditions are very critical and strongly dependent on the spinning rate.

Because of the problems associated with high speed spinning, it is often necessary to select a magnetic field strength

The technique that currently appears to offer the greatest promise for cross polarization at high spinning speeds is called 'variable amplitude cross polarization' (VACP).[23] A diagram of the experiment as it was originally introduced is shown in Figure 7. Essentially, the method depends on the fact that, in many cases, especially for ^{13}C in most

samples, the cross polarization rate T_{CH} is much faster than $T_{1\rho}$. Therefore, there is time to vary the rf levels over a range of values, essentially searching for one or more of the special mismatched Hartmann–Hahn conditions. At most rf settings, no match will occur and the I and S spins will simply remain 'spin locked'. Hopefully, however, at least one of the rf level settings will be near enough to a mismatched Hartmann–Hahn condition to result in significant cross polarization.

For many samples, VACP works very well. An example is given in Figure 8 for glycine spinning at 15 kHz. For experimental convenience, the 'stair step' approach illustrated in Figure 7 is often replaced by a simple amplitude ramp, and the range of rf levels is made large enough to extend from the exact Hartmann–Hahn match to an offset of twice the MAS frequency. Typical VACP cross polarization times are 10–20 ms, as compared to 1–5 ms for traditional Hartmann–Hahn cross polarization.

5 SPECTRAL EDITING AND OTHER TRICKS USING CROSS POLARIZATION

Experiments that serve to identify what functional group a given resonance belongs to are commonly referred to as 'spectral editing' techniques (see ***Spectral Editing Techniques: Hydrocarbon Solids***). This is because they normally cause certain lines in the spectrum to be suppressed or inverted. There are several variations of the Hartmann–Hahn cross polarization method that are useful for spectral editing. Two examples that identify CH_2 carbon resonances are reverse polarization,[24] which depends on differences in T_{CH}, and WIMSE,[25] which uses a sophisticated heteronuclear multiple pulse cross polarization technique known as 'windowless isotropic mixing' or 'WIM'.[26] Whereas most spectral editing methods depend on differences in coupling strength or polarization time, WIMSE makes use of basic differences in spin dynamics. During WIM cross polarization the I spins are isolated from each other, and a dynamic rather than thermodynamic behavior results. A diagram of the WIMSE experiment is presented in Figure 9, and WIMSE spectra of solid gelatin are presented in Figure 10.

WIM cross polarization is also very useful for heteronuclear two-dimensional spectroscopy in solids.[27] A diagram of the WIM based two-dimensional HETCOR experiment is presented in Figure 11. During the first part of this experiment, the BLEW-24 and BB-24 multiple pulse sequences are used to suppress both the homonuclear and heteronuclear dipolar couplings. As a result, the I spins evolve only under

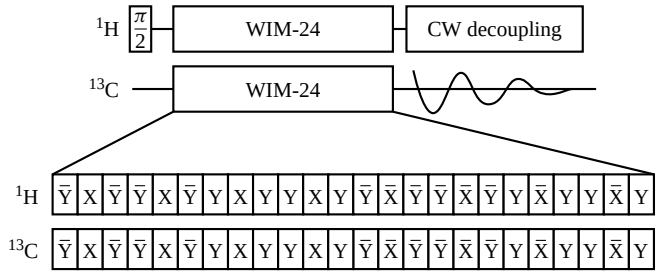

Figure 9 WIMSE spectral editing pulse sequence

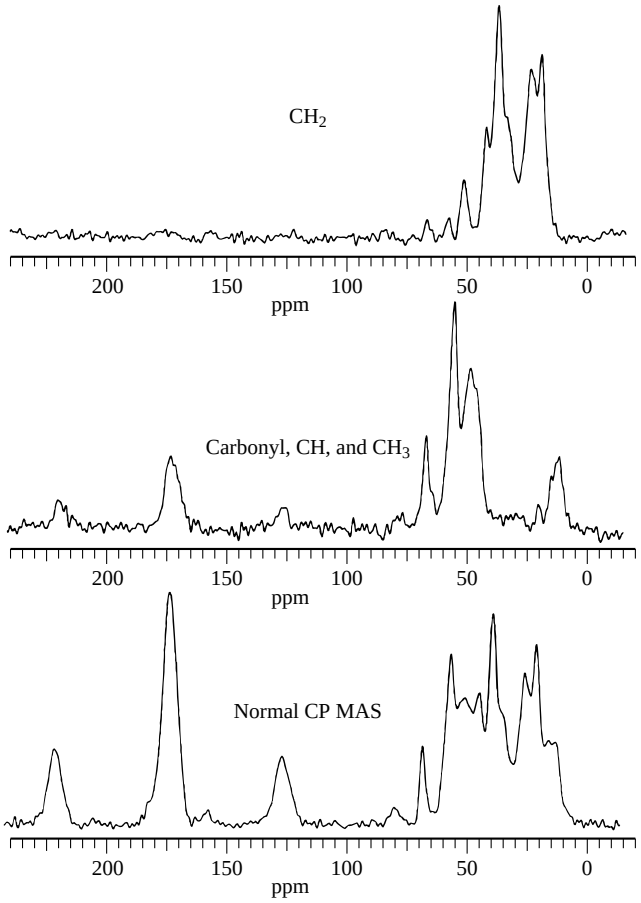

Figure 10 WISME spectra for solid gelatin showing only CH_2 resonances (top), carbonyl, CH and CH_3 resonances (middle) and all resonances (bottom)

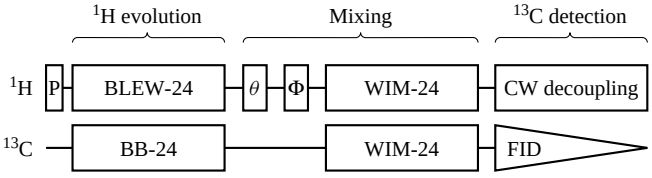

Figure 11 Two-dimensional HETCOR pulse sequence

the influence of resonance offset and chemical shift. The magnetization is then cross polarized to the S spins using WIM, and the S signal is detected. An example of two-dimensional HETCOR applied to ibuprofen is presented in Figure 12. Because WIM is used for cross polarization, peaks occur in the spectrum only at positions that correlate directly coupled ^1H–^{13}C spins. If the usual Hartmann–Hahn method were used, rapid ^1H spin diffusion would occur during the cross polarization time, and 'cross peaks' would appear for all possible combinations of ^1H and ^{13}C.

A number of other methods have been used to isolate spin groups during cross polarization, including simultaneously applied CRAMPS pulse sequences,[28] frequency switched Lee–Goldburg irradiation,[29] and very rapid Hartmann–Hahn irradiation.[30] So far, WIM appears to be the most successful of these methods.

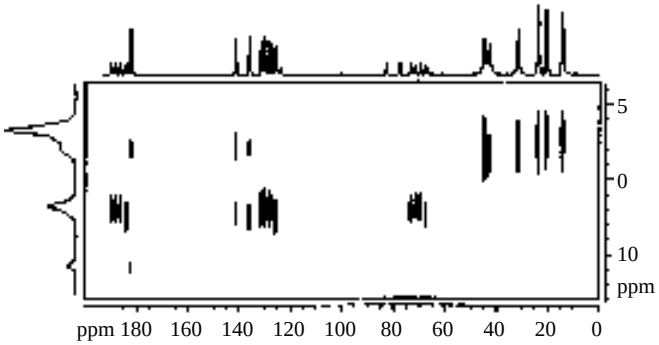

Figure 12 Two-dimensional HETCOR spectrum of ibuprofen. The one-dimensional spectra shown along the axes are a BR-24 CRAMPS spectrum (vertical) and a conventional CP MAS spectrum (horizontal) which were obtained in separate measurements

6 CONCLUSIONS

Hartmann–Hahn cross polarization is widely used to improve sensitivity and experiment repetition rate for rare spins in solids. Although some loss of quantitative information often occurs, the benefits usually far outweigh the disadvantages. At high MAS spinning speeds, cross polarization becomes problematic, but the recently introduced variable amplitude method appears to reduce greatly these difficulties in many cases. A variety of specialized techniques based on Hartmann–Hahn cross polarization have been developed, including spectral editing methods and pulse sequences that suppress spin diffusion during cross polarization.

7 RELATED ARTICLES

CRAMPS; Dipolar and Indirect Coupling Tensors in Solids; Internal Spin Interactions and Rotations in Solids; Magic Angle Spinning; Rotating Solids; Spectral Editing Techniques: Hydrocarbon Solids

8 REFERENCES

1. See for example: E. R. Andrew, W. S. Hinshaw, and R. S. Riffen, *Phys. Lett., Ser. A.*, 1973, **46**, 57.
2. M. Mehring, *Principles of High Resolution NMR in Solids*, 2nd edn, Springer, Berlin, 1983, Sections 4.2 and 4.3.
3. M. Mehring, *Principles of High Resolution NMR in Solids*, 2nd edn, Springer, Berlin, 1983, Section 4.4.
4. M. Mehring, *Principles of High Resolution NMR in Solids*, 2nd edn, Springer, Berlin, 1993, Section 2.6.
5. M. Mehring, *Principles of High Resolution NMR in Solids*, 2nd edn, Springer, Berlin, 1983, Sections 2.1 and 2.2.
6. M. Mehring, *Principles of High Resolution NMR in Solids*, 2nd edn, Springer, Berlin, 1983, p. 16.
7. (a) E. R. Andrew, and R. G. Eades, *Proc. R. Soc. London, Ser. A*, 1953, **216**, 398; (b) references given in M. Mehring, *Principles of High Resolution NMR in Solids*, 2nd edn, Springer, Berlin, 1983, Section 2.6.
8. A. Abragam, *Principles of Nuclear Magnetism*, Clarendon, Oxford, 1961, Section IX.IV.A–C.
9. A. Abragam, *Principles of Nuclear Magnetism*, Clarendon, Oxford, 1961, Section IX.II.A–B.
10. S. R. Hartmann and E. L. Hahn, *Phys. Rev.*, 1962, **128**, 2042 and A. Pines, M. G. Gibby, and J. S. Waugh, *J. Chem. Phys.*, 1973, **59**, 569.
11. M. Mehring, *Principles of High Resolution NMR in Solids*, 2nd edn, Springer, Berlin, 1983 p. 153.
12. M. Mehring, *Principles of High Resolution NMR in Solids*, 2nd edn, Springer, Berlin, 1983, p. 132.
13. M. Mehring, *Principles of High Resolution NMR in Solids*, 2nd edn, Springer, Berlin, 1983 Section 4.1.
14. R. R. Ernst, G. Bodenhausen, and A. Wokaun, *Principles of Nuclear Magnetic Resonance in One and Two Dimensions*, Clarendon, Oxford, 1987, Section 4.145.
15. R. R. Ernst, G. Bodenhausen, and A. Wokaun, *Principles of Nuclear Magnetic Resonance in One and Two Dimensions*, Clarendon, Oxford, 1987, Section 4.146.
16. R. R. Ernst, G. Bodenhausen, and A. Wokaun, *Principles of Nuclear Magnetic Resonance in One and Two Dimensions*, Clarendon, Oxford, 1987, Section 4.298.
17. A. Bax, N. M. Szeverenyi, and G. E. Maciel, *J. Magn. Reson.*, 1982, **50**, 227.
18. J. Herzfeld and A. Berger, *J. Chem. Phys.*, 1980, **73**, 6021.
19. E. O. Stejskal, J. Schaefer, and J. S. Waugh, *J. Magn. Reson.*, 1977, **28**, 105.
20. R. C. Ziegler, R. A. Wind, and G. E. Maciel, *J. Magn. Reson.*, 1988, **79**, 299.
21. M. Sardashti, and G. E. Maciel, *J. Magn. Reson.*, 1987, **72**, 467.
22. T. M. Barbara and E. H. Williams, *J. Magn. Reson.*, 1992, **99**, 439.
23. O. B. Peersen, X. Wu, I. Kustanovich, and S. O. Smith, *J. Magn. Reson., Ser. A*, 1993, **104**, 334.
24. X. Wu, and K. W. Zilm, *J. Magn. Reson., Ser. A*, 1993, **102**, 205.
25. D. P. Burum and A. Bielecki, *J. Magn. Reson.*, 1991, **95**, 184.
26. P. Caravatti, L. Braunschweiler, and R. R. Ernst, *Chem. Phys. Lett.*, 1983, **100**, 305.
27. D. P. Burum and A. Bielecki, *J. Magn. Reson.*, 1991, **94**, 645.
28. J. E. Roberts, S. Vega, and R. G. Griffin, *J. Am. Chem. Soc.*, 1984, **106**, 2506.
29. A. Bielecki, A. C. Kolbert, H. J. M. De Groot, R. G. Griffin, and M. H. Levitt, *Adv. Magn. Reson.*, 1990, **14**, 111.
30. P. Caravatti, G. Bodenhausen, and R. R. Ernst, *Chem. Phys. Lett.*, 1982, **89**, 363.

Biographical Sketch

Douglas P. Burum. *b* 1952. B.S., Harvey Mudd College, 1974; Ph.D., California Institute of Technology (advisor R. W. Vaughan), 1979. Postdoctoral Assistant under R. R. Ernst 1979–80. Joined Bruker Instruments as an applications specialist in solid state NMR in 1982. Currently Bruker USA national product manager for analytical NMR. Approx. 25 publications. Research interests center around development of coherent averaging pulse techniques, including CRAMPS, two-dimensional HETCOR, spectral editing, etc.

Dynamic Nuclear Polarization and High-Resolution NMR of Solids

Robert A. Wind

Battelle/Pacific Northwest Laboratories, Richland, WA, USA

1	Introduction	1
2	Theory	1
3	Applications of DNP NMR	4
4	Summary, Conclusions, and Perspectives	8
5	Related Articles	9
6	References	9

1 INTRODUCTION

In solids containing both magnetic nuclei and unpaired electrons, polarization transfer can be obtained between the electron and nuclear spin systems by irradiating at or near the electron Larmor frequency. The result is an enhanced nuclear polarization and, henceforth, an enhanced NMR signal. This effect is called dynamic nuclear polarization (DNP).

Several mechanisms can be responsible for the DNP phenomenon. In 1953, Overhauser predicted that in metals the NMR signal could be enlarged by saturating the resonance line of the conducting electrons: the Overhauser effect.[1] Carver and Slichter[2] showed experimentally in metallic lithium that Overhauser's revolutionary concept was correct.

Later on, Abragam and Proctor[3] and, independently, Jeffries[4] and Erb et al.[5] found the occurrence of a DNP effect in solids containing fixed, mutually more or less isolated, unpaired electrons: the solid state effect. Finally, a third DNP effect has also been observed: the thermal mixing effect, which is present when the concentration of (fixed) unpaired electrons is so high that the mutual dipolar interactions between the electrons become comparable to the other interactions between the electrons and their surroundings. Provotorov[6] showed that in that case the electron spin system can be characterized by two polarizations: one associated with the population distribution over the Zeeman levels and one associated with the population distribution over the internal local magnetic fields which the electrons are experiencing. These polarizations may change if off-resonance irradiation is applied. Abragam and Borghini[7] used the results of Provotorov and showed that when the polarization associated with the local fields is changed, the nuclear polarization changes as well, due to a coupling between these two polarizations induced by the irradiating microwave field: the indirect thermal mixing effect. Goldman[8] remarked that this coupling could be present also in the absence of microwave irradiation, and its significance for DNP was shown by Buishvili:[9] the direct thermal mixing effect. The thermal mixing effects become especially important when the nuclear Larmor frequency is comparable to or smaller than the ESR line width.

In principle large NMR signal enhancements can be obtained via DNP, maximal of the order of the ratio of the gyromagnetic ratios of the electrons and the nuclei. For example, for protons this would result in an enhancement factor of 660, and for ^{13}C nuclei this factor would be as large as 2600. In the earlier days of DNP this aspect was mainly used and applied for the production of polarized targets used in high-energy physics or to study magnetic ordering in the μK region. However, during the past 15 years new applications have emerged as well. This has been achieved by combining DNP with modern solid state NMR techniques such as cross polarization (CP), magic angle spinning (MAS), and two-dimensional NMR spectroscopy. As a result, more detailed information about structures and dynamics of materials amenable to DNP NMR could be obtained than would have been possible without DNP.

DNP NMR spectroscopy can be applied successfully in a large variety of solid materials such as those in which the unpaired electrons occur naturally, e.g., in the form of dangling bonds, materials in which bond ruptures have occurred, e.g., resulting from pyrolysis or ionizing radiation, materials containing paramagnetic impurities, and materials doped with a suitable paramagnetic agent. In this paper several applications of DNP NMR spectroscopy in solid materials research will be given following a brief description of the DNP phenomenon. Finally, some future aspects of the technique will be discussed.

2 THEORY

Extensive reviews of the different DNP effects have been given elsewhere.[10–14] Here we shall confine ourselves to a short treatment of the main features of DNP. We shall restrict ourselves to discussing only the Overhauser and the solid state effects. Hence we shall neglect the thermal mixing effects The main reasons for this omission are that in many cases the Overhauser and solid state effects dominate, and that the overall features of the thermal mixing effects are not much different from that of the solid state effect. Moreover, the thermal mixing effects require a rather lengthy derivation, which is beyond the scope of this article.

As is necessary in the description of any NMR experiment, we have to start with the Hamiltonian. For an electron–nuclear spin system the relevant Hamiltonian is given by

$$\hat{\mathcal{H}} = -\omega_e \hat{S}_z - \omega_n \hat{I}_z + \hat{\mathcal{H}}_{ee} + \hat{\mathcal{H}}_{en} + \hat{\mathcal{H}}_{nn} \qquad (1)$$

The first two terms are the Zeeman interactions of the electrons and nuclei, respectively, where $\hat{S}_z = \sum_{j=1}^{N_e} \hat{S}_z^j$ are the electron spin operators and $\hat{I}_z = \sum_{i=1}^{N_n} \hat{I}_z^i$ are the nuclear spin operators. The term N_e is the number of unpaired electrons and N_n is the number of nuclei. Furthermore, in equation (1), $\omega_e = \gamma_e B_0$ and $\omega_n = \gamma_n B_0$, where γ_e and γ_n are the magnetogyric ratios of the electrons and nuclei, respectively, and B_0 is the external magnetic field strength. Finally, $\hat{\mathcal{H}}_{ee}$, $\hat{\mathcal{H}}_{en}$, and $\hat{\mathcal{H}}_{nn}$ denote the spin–spin interactions between the electrons, between the electrons and the nuclei, and between the nuclei, respectively. For DNP, the most

important term in equation (1) is the so-called hyperfine interaction term $\hat{\mathcal{H}}_{\mathrm{en}}$. In general, this term consists of two parts, the scalar interaction term $\hat{\mathcal{H}}^{\mathrm{s}}_{\mathrm{en}}$ and the dipolar term $\hat{\mathcal{H}}^{\mathrm{d}}_{\mathrm{en}}$. The scalar interaction arises from a finite electron spin density at the nuclear sites, either directly from the unpaired electron itself or mediated by bonding electrons polarized by the unpaired electrons.

Before describing the DNP phenomenon we first consider the energy level scheme of electron–nuclear spin pairs. For simplicity we restrict ourselves to nuclear spin-$\frac{1}{2}$ systems, with positive γ_{n} values. The result is then the simple four-energy-level scheme given in Figure 1. Also given are the nuclear and electron quantum numbers, m_{n} and m_{e}, respectively (for the electrons the highest energy state corresponds to $m_{\mathrm{e}} = +\frac{1}{2}$, because γ_{e} is negative), and as usual we denote a state in which, for example, $m_{\mathrm{n}} = +\frac{1}{2}$ and $m_{\mathrm{e}} = -\frac{1}{2}$ by the notation $|+-\rangle$. Finally, the amount of nuclei in each state is denoted by $N_{\mathrm{n}1}, N_{\mathrm{n}2}$, etc. Then, defining $N_{\mathrm{n}}^{+} = N_{\mathrm{n}2} + N_{\mathrm{n}4}$ and $N_{\mathrm{n}}^{-} = N_{\mathrm{n}1} + N_{\mathrm{n}3}$ as the total amounts of nuclei in the + and − states, respectively, we can define the nuclear polarization, P_{n}, as

$$P_{\mathrm{n}} = \frac{N_{\mathrm{n}}^{+} - N_{\mathrm{n}}^{-}}{N_{\mathrm{n}}^{+} + N_{\mathrm{n}}^{-}} = \frac{N_{\mathrm{n}}^{+} - N_{\mathrm{n}}^{-}}{N_{\mathrm{n}}} = \frac{\Delta N_{12} + \Delta N_{34}}{N_{\mathrm{n}}} \qquad (2)$$

In Figure 1 the situation of thermal equilibrium is depicted, where the population distribution is governed by the Boltzmann distribution corresponding to the lattice temperature. Then P_{n} is defined as P_{n}^{0}. Similar expressions can be given for the electron polarization, P_{e}, and its thermal equilibrium value, P_{e}^{0}. It can easily be derived that in the high-temperature approximation, where $h\omega_{\mathrm{e}}/kT_{\mathrm{L}}$, $h\omega_{\mathrm{n}}/kT_{\mathrm{L}} \ll 1$, P_{n}^{0} and P_{e}^{0} are given by

$$P_{\mathrm{n}}^{0} = \frac{1}{2}\,\omega_{\mathrm{n}}\hbar(kT_{\mathrm{L}})^{-1} \quad \text{and} \quad P_{\mathrm{e}}^{0} = \frac{1}{2}\omega_{\mathrm{e}}\hbar(kT_{\mathrm{L}})^{-1} \qquad (3)$$

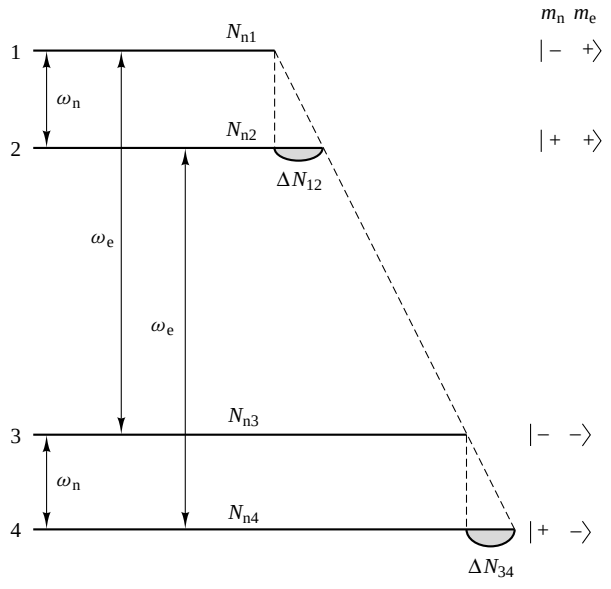

Figure 1 The Zeeman energy level scheme of electron–nuclear spin pairs. The population distribution over the energy levels depicts the thermal equilibrium situation

where T_{L} is the lattice temperature. It follows from equation (3) that the thermal equilibrium polarization of the electrons is a factor $\gamma_{\mathrm{e}}/\gamma_{\mathrm{n}}$ larger than that of the nuclei. It is this difference in polarization that is used in DNP, which we shall now consider.

2.1 The Overhauser Effect

The Overhauser effect occurs when $\hat{\mathcal{H}}_{\mathrm{en}}$ is time-dependent on a timescale of the order ω_{e}^{-1}. Then $\hat{\mathcal{H}}_{\mathrm{en}}(t)$ causes relaxation transitions between the various levels depicted in Figure 1, which, when combined with an irradiation at the electron Larmor frequency, results in a change in the nuclear polarization.

In order to illustrate this, we assume that the scalar interaction term, $\hat{\mathcal{H}}^{\mathrm{s}}_{\mathrm{en}}$, dominates. It can be shown that $\hat{\mathcal{H}}^{\mathrm{s}}_{\mathrm{en}}$ causes a relaxation transition between the $|+-\rangle$ and $|-+\rangle$ states of the electron–nuclear system, hence between the levels 1 and 4 in Figure 1. We shall call this relaxation rate W^{s}_{14}, which is given by $W^{\mathrm{s}}_{14} = \frac{1}{2}\overline{a_{ij}^{2}}\,\boldsymbol{J}(\omega_{\mathrm{e}} + \omega_{\mathrm{n}}, \tau_{\mathrm{c}})$; $\boldsymbol{J}(\omega, \tau_{\mathrm{c}})$ is the spectral density function characterizing the time dependence, $\overline{a_{ij}^{2}}$ is the time-averaged value of a_{ij}^{2}, where a_{ij} denotes the strength of the scalar interaction. As with all relaxation transitions, after some population distortion $W_{14}{}^{\mathrm{s}}$ restores the Boltzmann distribution between the energy levels connected by W^{s}_{14}, hence between levels 1 and 4. Now suppose that we are irradiating with a microwave field of amplitude B_1 and a frequency ω close to ω_{e}. This means that we are irradiating between the electron Zeeman levels 1 and 3 respectively 2 and 4 with an induced transition probability $W/2 = (\pi/2)\gamma_{\mathrm{e}}^{2}B_1^{2}g(\omega - \omega_{\mathrm{e}})$, where $g(\omega)$ is the normalized lineshape function of the ESR line.

Suppose also that W is large enough to saturate the ESR line completely. Then in the stationary situation, the population distribution over the various levels becomes as given in Figure 2. Due to the saturating irradiation the population of level 1 becomes equal to that of level 3, and the population of level 2 becomes equal to that of level 4. Due to the relaxation transition, W^{s}_{14}, the Boltzmann distribution exists between the levels 1 and 4. As a result, the population differences between the nuclear Zeeman levels 1 and 2 respectively 3 and 4 is increased: the nuclear polarization is (positively) enhanced. The enhancement curve, which is the Overhauser enhancement factor as a function of the irradiation frequency ω, reflects the (saturated) ESR line, and is symmetrical about ω_{e} for symmetrical ESR lines. The enhancement becomes maximal for $\omega = \omega_{\mathrm{e}}$. An Overhauser effect also occurs when the (time-dependent) dipolar electron–nuclear interactions, $\hat{\mathcal{H}}^{\mathrm{d}}_{\mathrm{en}}$, dominate. It can be shown that $\hat{\mathcal{H}}^{\mathrm{d}}_{\mathrm{en}}$ causes relaxation transitions between all four energy levels, so that the result becomes more complicated. However, it can be shown that often the relaxation transition between the levels 2 and 3 dominates, and the reader can easily convince himself that in this situation the nuclear polarization enhancement becomes negative.

The question arises under which circumstances we can expect to observe an Overhauser effect. As already stated above, a time-dependence in $\hat{\mathcal{H}}_{\mathrm{en}}$ is needed with a correlation time of the order of $(\omega_{\mathrm{e}} \pm \omega_{\mathrm{n}})^{-1} \simeq \omega_{\mathrm{e}}{}^{-1}$, which in practice means that τ_{c} has to be of the order 10^{-11} to 10^{-12} s. In

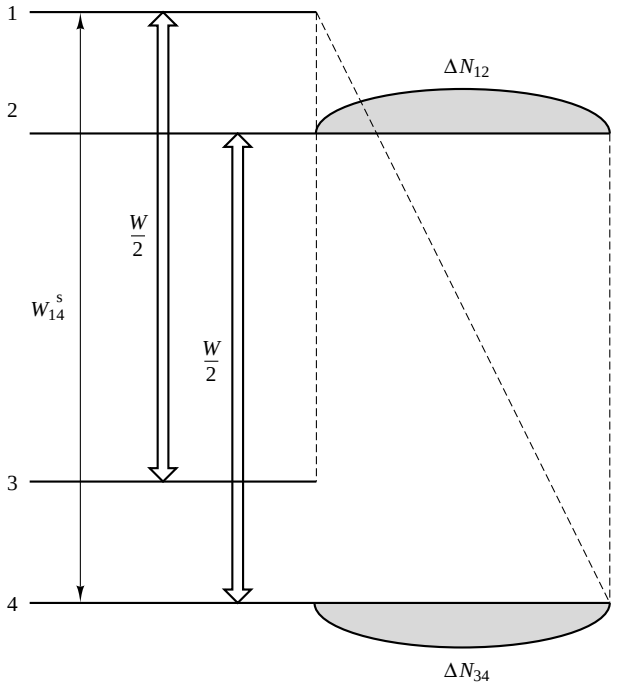

Figure 2 The Overhauser effect due to the scalar electron–nuclear interactions. The population distribution over the energy levels depicts the stationary situation

solids, the molecular motions are almost never that fast, so that an Overhauser effect due to this type of motion is highly unlikely. However, other processes may occur in solids that do provide the required time dependence: (1) in conductors or semiconductors, the conducting electrons move very rapidly through the lattice, rendering the spatial coordinates in $\hat{\mathcal{H}}_{\text{en}}$ time-dependent on a fast scale (this explains the success of observing an Overhauser effect in metals[2]); (2) in solids with large amounts of unpaired electrons and/or with electrons with a delocalized electron density distribution, strong electron–electron spin exchange interaction may occur.[15] These interactions, which arise from electrostatic Coulomb interactions, cause a time-dependence in the electron spin operator $\hat{S}$ occurring in $\hat{\mathcal{H}}_{\text{en}}$, and hence in $\hat{\mathcal{H}}_{\text{en}}$ itself. Also this time-dependence can be fast enough to fulfill the requirements for the Overhauser effect.[10] An example is the Overhauser effect observed in graphite and other solids containing large aromatic clusters.

2.2 The Solid State Effect

The solid state effect occurs in solids with fixed paramagnetic centers and with electron–nuclear interactions that are time-independent or only slowly time-dependent, with correlation times typically larger than about 10^{-5} s. The presence of $\hat{\mathcal{H}}_{\text{en}}$ means that there exist, beside the external B_0 field, static local magnetic fields in the sample, partly oriented perpendicular to B_0. It is well known from second-order perturbation theory that the result of such interactions is that the electron–nuclear states can no longer be described by the pure product functions given in Figure 1, but become mixed with other states. The admixture coefficient depends on the energy

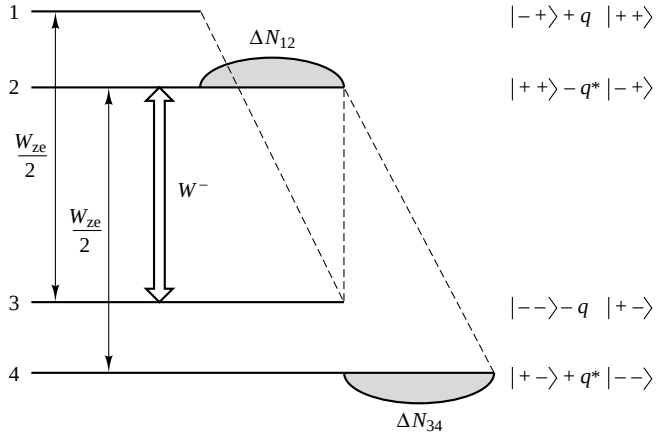

Figure 3 The solid state effect due to the forbidden transition W^-. The population distribution over the energy levels depicts the stationary situation

difference between the levels corresponding to the states and increases with decreasing energy differences. Hence, in highest order, the mixture occurs between the states corresponding to the levels 1 and 2 respectively 3 and 4. The result is given in Figure 3, where q (and its complex conjugate q^*) denotes the admixture coefficient. It should be emphasized that q is small, typically of the order 10^{-3} to 10^{-4}. Nevertheless, these small admixtures have as an important consequence that irradiation with a frequency $\omega_e - \omega_n$ or $\omega_e + \omega_n$ leads to a nonzero transition probability between the levels 2 and 3 respectively 1 and 4.

In order to understand this we consider the effect of irradiating with a frequency $\omega_e - \omega_n$. If the eigenstates were not mixed nothing would happen, because the matrix element $\langle -- |\hat{\mathcal{H}}_{\text{rf}}| ++\rangle$ is zero as the Hamiltonian $\hat{\mathcal{H}}_{\text{rf}}$ representing the rf irradiation is proportional to single spin operators. However, if the eigenstates are mixed, a small but nonzero transition probability is obtained because now nonzero matrix elements such as $-q\langle +- |\hat{\mathcal{H}}_{\text{rf}}| ++\rangle$ occur. This is called the 'forbidden' transition, W^-. Similar results are obtained for irradiation at $\omega_e + \omega_n$, giving rise to a 'forbidden' transition W^+. The quantities W^+ and W^- are given by

$$W^{\pm} = 2|q|^2 \pi \gamma_e^2 \boldsymbol{B}_1^2 g(\omega_e - \omega \pm \omega_n) \qquad (4)$$

The effect of irradiating at $\omega_e - \omega_n$ on the nuclear polarization is depicted in Figure 3. Here we have also incorporated the effect of the electron Zeeman relaxation rate, W_{Ze}. Then, in the stationary situation, W_{Ze} maintains the Boltzmann distribution between the electron Zeeman levels 1 and 3 with respect to 2 and 4, whereas W^- equalizes the populations of levels 2 and 3. The result is a positive enhancement of the nuclear polarization P_n: the solid state effect. In a similar way it can be shown that irradiation at $\omega_e + \omega_n$ leads to a negative enhancement of P_n. For symmetrical ESR lines the solid state enhancement curve, which is the enhancement factor as a function of the irradiation frequency ω, is antisymmetrical about ω_e. The enhancement becomes maximal for $\omega = \omega_e \pm \omega_n$.

In Figure 4 examples are given of enhancement curves due to the various DNP effects, including the effects of thermal mixing. As mentioned before we will not treat thermal mixing in any detail. Here we confine ourselves to remarking that,

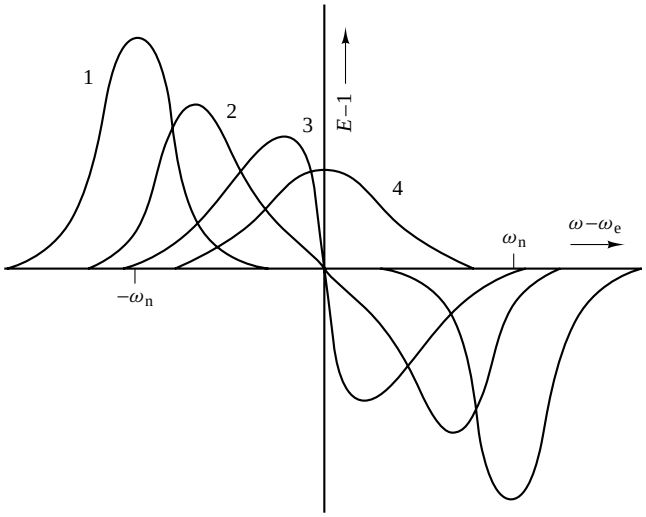

Figure 4 The enhancement curves of the various DNP effects: curve 1, solid state effect; curve 2, indirect thermal mixing effect; curve 3, direct thermal mixing effect; curve 4, Overhauser effect. Reproduced by permission of Marcel Dekker, Inc., from R. A. Wind, in 'Modern NMR Techniques and Their Application in Chemistry', eds. A. I. Popov and K. Hallenga, 1991, p. 125

like the enhancement curve due to the solid state effect, the thermal mixing enhancement curves are antisymmetrical about ω_e for symmetrical ESR lines. The direct effect of thermal mixing becomes maximal when the offset frequency, $\omega - \omega_e$, is comparable to the ESR linewidth, whereas indirect thermal mixing gives a maximal enhancement for offset frequencies between those for which the direct thermal effect and the solid state effect become maximal.

2.3 Enhancement Factors

As already mentioned in the Introduction, in theory large DNP enhancement factors can be expected, of the order of γ_e/γ_n. However, in practice, several factors can limit the magnitude of the enhancement factor which is actually obtained. We shall illustrate this for enhancements by the Overhauser and solid state DNP effects (for a more general treatment the reader is referred elsewhere[13,14,16,17]). For the Overhauser effect, we have already remarked that DNP enhancement can be positive or negative, depending on whether the scalar or the dipolar electron–nuclear interactions dominate. As a consequence, as in general both types of interactions are present, the enhancement is reduced and can become almost zero in unfavorable cases.

In the solid state effect, irradiation with a frequency ω can lead simultaneously to both forbidden transition probabilities W^- and W^+. This is especially the case when the ESR linewidth is comparable to the ω_n, see Figure 5 (in fact, as is shown in the figure, irradiation can result in both the allowed transition probability, W, and the forbidden transition probabilities W^- and W^+). As W^- and W^+ result in enhancements of opposite sign, the result is a decreased solid state enhancement, the so-called unresolved solid state effect. This can occur especially for low γ_n nuclei, for which ω_n is small. (However, it can be shown[13,14] that in these cases the enhancements due to thermal mixing increase, so that

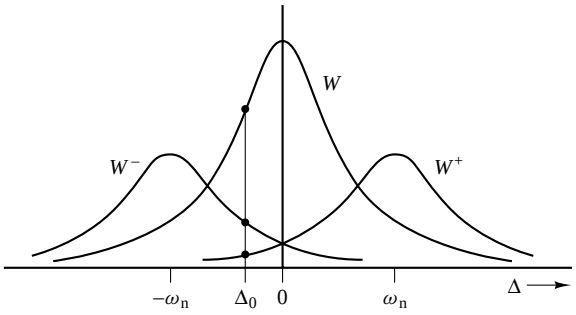

Figure 5 The allowed and forbidden transition probabilities as a function of the offset frequency $\Delta = \omega - \omega_e$. Irradiation at Δ_0 simultaneously leads to W, W^-, and W^+

the overall enhancement can still be large.) Other parameters that determine the enhancements are the amount of unpaired electrons, N_e, which has to be relatively large; the ESR linewidth, which should be small; the electron spin–lattice relaxation rate, W_{ze}, which should be large; the amplitude of the microwave field, B_1, which should be large; the external magnetic field, B_0, which should be small in order to obtain appreciable forbidden transition rates (this is only important for the solid state effect); the nuclear Zeeman relaxation rate, which should be small; and the correlation time τ_c characterizing the time dependence in $\hat{\mathcal{H}}_{en}$. As has already been mentioned, if $\tau_c \approx \omega_e \approx 10^{-11}$ to 10^{-12} s, the Overhauser effect dominates, whereas the solid state effect is observed when $\tau_c \geq 10^{-5}$ s. For τ_c values between these limits, both effects are small; if electron–nuclear interactions exist with different time constants, both effects might be present. We shall encounter this situation later.

The author and others[14,16,17] have given expressions for the different enhancement factors, from which the enhancements can be calculated if the various parameters mentioned above are known. For instance, for abundant-spin systems with large γ_n values and fixed paramagnetic centers, appreciable solid state enhancement factors (a factor 10 or more) can be expected under the following conditions: $N_e \geq 10^{24}\,m^{-3}$; ESR linewidth ≤ 1 mT; ${W_{ze}}^{-1}$ of the order of μ s; $B_1 \geq 0.03$ mT; $B_0 = 1.4$ T; nuclear Zeeman relaxation time ≥ 1 s. For rare-spin systems with small γ_n values, the enhancement factors are often at least an order of magnitude larger, which is mainly due to larger Zeeman relaxation times and an increased importance of the direct thermal mixing effect.[14]

It should be kept in mind, however, that these parameters are not independent of each other, and that large enhancements have been observed under completely different conditions. For instance, in natural diamonds a large ^{13}C enhancement factor of 200 is observed[14] despite the small value of N_e ($\simeq 10^{22}\,m^{-3}$). The reason is the large carbon Zeeman relaxation time ($\simeq 2000$ s) occurring in this material.

3 APPLICATIONS OF DNP NMR

Both the DNP enhancement curves and the DNP-enhanced NMR spectra can be used to obtain detailed and often unique information about the chemical and physical properties of solid materials, and representative illustrations of such applications will be given in this section. All experiments that will be

described have been performed in an external field of 1.4 T, corresponding to an electron Larmor frequency of 40 GHz and nuclear Larmor frequencies of 60 MHz for protons, 15 MHz for ^{13}C nuclei, and 12 MHz for ^{29}Si nuclei. Elaborate descriptions of the experimental setups, including the probes have been given.[18,19] All measurements were performed at room temperature.

3.1 The DNP Enhancement Curves

The symmetrical or antisymmetrical character of the DNP curve makes it possible to determine whether the electron–nuclear interactions are time-dependent, time-independent, or whether both types of interactions are present. This is illustrated in Figure 6, where are given the enhancement curves for ^{1}H and ^{13}C using DNP for a low-volatile bituminous coal. The ^{1}H DNP curve, Figure 6(a), contains both a symmetric and antisymmetric contribution, presumably because part of the electrons undergo rapid spin-exchange interactions whereas other electrons behave as fixed paramagnetic centers. The ^{13}C curve, Figure 6(b), is antisymmetric within experimental error, probably due to the much larger enhancements resulting from the static electron–carbon interactions, which overshadow the relatively small Overhauser enhancement. The occurrence of both the Overhauser and solid state effect in the ^{1}H DNP curves has been observed in a large variety of coals of different rank,[20] as well as in cellulose heat-treated in the temperature range 250–1000 °C.[21] It was found that for heating temperatures above 275 °C unpaired electrons were formed as a result of band ruptures and a DNP effect was observed. In the lower temperature range, up to ca. 450 °C, the solid state and thermal mixing effects dominate, whereas, between 450 °C and 700 °C, it is mainly an Overhauser effect which is observed (above 700 °C no DNP effect may be measured because the ESR line becomes very broad). However, the DNP enhancement curves indicate that an Overhauser effect also exists in the low temperature range, and that the solid state and thermal mixing effects are present for heating temperatures up to 500 °C. This is attributed to the small amounts of unpaired electrons undergoing rapid spin-exchange interactions at low temperatures, and behaving as fixed centers at the higher temperatures, respectively. In fact, it could be shown that the DNP curves could be used to detect fractions of electrons smaller than 1% either behaving as fixed centers or submitted to exchange interactions.

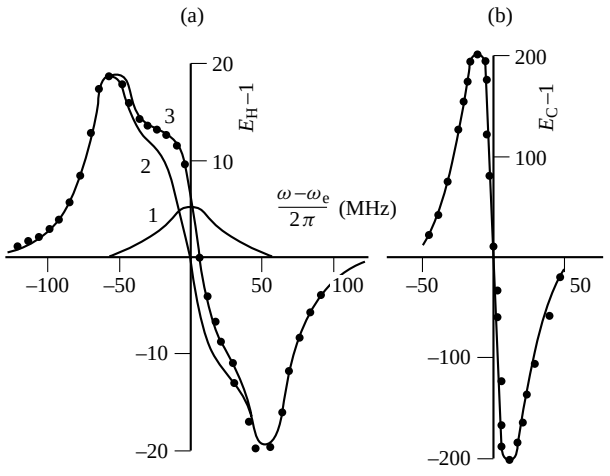

Figure 6 DNP enhancement curves obtained in a low-volatile bituminous coal. (a) ^{1}H DNP curves: curve 1, symmetric part; curve 2, antisymmetric part; curve 3, overall enhancement; dots, experimental. (b) ^{13}C DNP curve. Reproduced by permission of the American Chemical Society from R. A. Wind, R. H. Lewis, H. Lock, and G. E. Maciel, in 'Magnetic Resonance in Carbonaceous Solids', eds. R. E. Botto and Y. Sanada, ACS Ser. No. 229, 1993, p. 45

3.2 DNP and High-Resolution NMR in Solids

The increase in the NMR signal due to DNP can be used to reduce measuring times or to measure relatively small amounts of compounds. This ability is especially important for NMR spectroscopy on rare-spin species where, in the absence of DNP, long measuring times, several hours or more, are required in order to obtain an acceptable signal-to-noise ratio. In this section we shall give examples of such DNP NMR experiments.

In solids containing, besides unpaired electrons, both abundant spins and rare spins, the rare-spin polarization can be enhanced via DNP in two ways. (1) *Indirectly*, by first enhancing the abundant-spin polarization followed by a polarization exchange between the abundant and rare spins via cross polarization (CP). This is called the DNP CP (or DNP CP MAS when magic angle spinning is applied as well) experiment. In those cases where both the abundant spins and the electrons are homogeneously distributed in the sample, the spin diffusion among the abundant nuclei is generally strong enough to establish a single, average, polarization enhancement for all abundant nuclei, resulting, after CP, in an enhanced, undistorted, NMR spectrum of the rare nuclear spins. (In compounds where the electrons and/or the abundant nuclei are not homogeneously distributed, a distribution in DNP enhancements may also occur. As we shall see later, this effect can be used selectively to study interfaces and surfaces.) (2) The rare-spin polarization can also be enhanced *directly* via a polarization exchange between the electrons and the rare nuclei. This experiment, in which the rare-spin NMR signal is observed via a standard 90° rf pulse, will be called the DNP SP (MAS) experiment (SP = single pulse). Of course, in materials such as ceramics and diamonds, which do not contain abundant spins, DNP SP is the only possible technique. As the spin diffusion between rare spins is small, a distribution of enhancement factors often exists in the DNP SP experiment with larger enhancements for the nuclei in the vicinity of the unpaired electrons.[14] This has the disadvantage that distortions can occur in the DNP SP NMR spectra, but has the (potentially powerful) advantage that this experiment makes it possible selectively to probe structures and dynamics near the unpaired electrons.

It should be noted that in solids containing both rare and abundant nuclear spins, even in a DNP SP experiment the rare spin polarization can also be enhanced indirectly via a polarization exchange with the abundant spins. This has been called the three-spin effect.[22] This phenomenon is observed in cases that the rare-spin Zeeman relaxation is dominated by the interactions between the rare and abundant nuclear spins. Hence this effect is more likely to occur for rare nuclei remote from the unpaired electrons, where the electron–nuclear

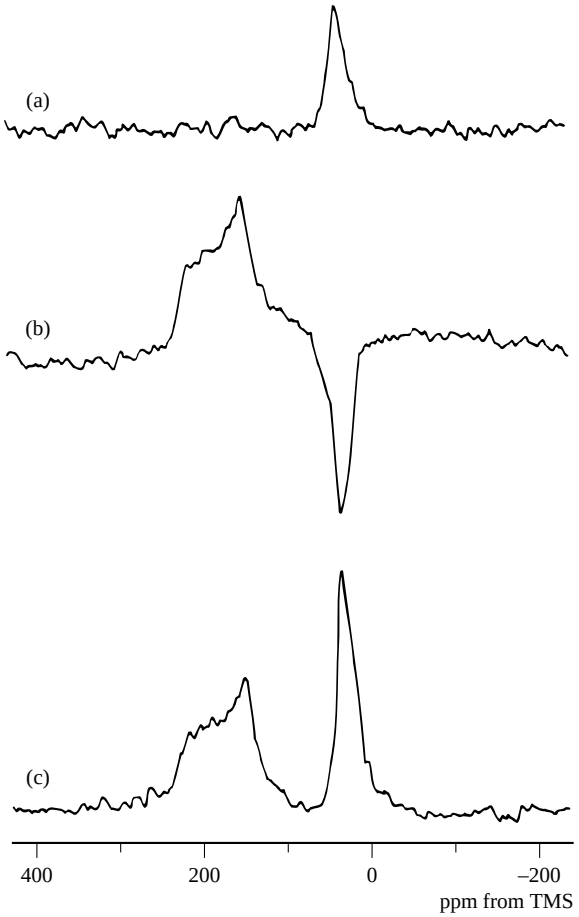

Figure 7 ^{13}C NMR spectra of a composite of *trans*-polyacetylene and polyethylene. (a): Result of an SP experiment; (b) and (c): Results of a DNP SP experiment without (b) and with (c) proton saturation. Reproduced by permission of the Academic Press from G. G. Maresch, R. D. Kendrick, C. S. Yannoni, and M. E. Galvin, *J. Magn. Reson.*, 1989, **82**, 41

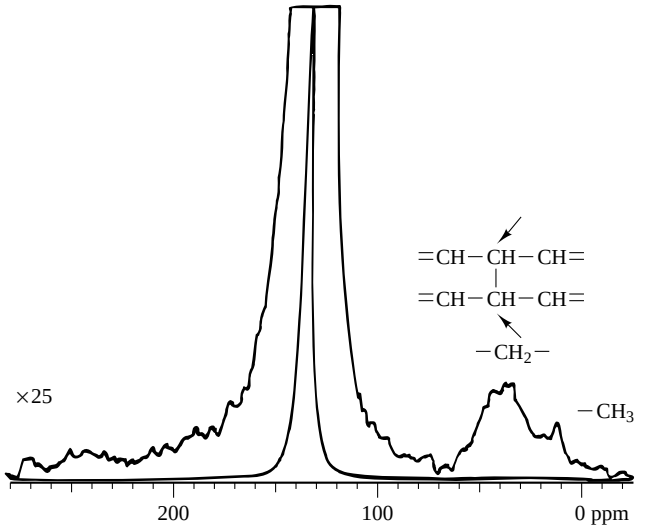

Figure 8 ^{13}C spectrum of *trans*-polyacetylene, obtained via ^{1}H–^{13}C DNP CP MAS NMR. The main line at 135 ppm is due to the ^{13}C nuclei inside the $(CH)_x$ chains; structural defects responsible for the other lines are indicated in the figure

interactions become weak. The three-spin effect arises from the nuclear Overhauser effect (NOE). This is similar to the Overhauser effect described in Section 2. The only differences are that NOE is caused by nuclear–nuclear interactions instead of electron–nuclear interactions, and that NOE is due to dipolar interactions only. It follows from Section 2 that NOE leads to a positive polarization enhancement of the rare-spin polarization if the abundant spin polarization is decreased via saturation (assuming that the gyromagnetic ratio of the nuclei is positive). However, if the abundant spin polarization is, for example, positively enlarged via DNP, the NOE enhancement of the rare spins becomes negative. Consequently, in a rare-spin DNP SP experiment, a positive direct enhancement from the electrons can be counteracted by a negative NOE enhancement. The three-spin effect is illustrated in Figure 7 where ^{13}C spectra are shown of a polymer consisting of small islands of *trans*-polyacetylene (PA) embedded in a matrix of polyethylene (PE). In *trans*-polyacetylene, $(CH)_x$, unpaired electrons (the so-called solitons) are present, presumably arising from bond-alternation domain walls.[23] These solitons move rapidly over the chains at least part of the time, giving rise to an Overhauser effect.[14,24] It follows that for the ^{13}C line around 20 ppm, which is due to the PE carbons which are for the major part remote from the solitons in the PA chains, the NOE effect leads to a negative enhancement in a DNP SP experiment without proton saturation. However, the ^{13}C line around 200 ppm is due to the carbons in the PA chains. Here the soliton–carbon interactions are so strong that the NOE effect is not observed. The three-spin effect can be avoided by partially saturating the abundant-spin polarization to such an extent that the polarization remains at its thermal equilibrium value.

We shall now consider applications of the DNP CP MAS and DNP SP MAS experiments.

3.2.1 Increase in Sensitivity

The increase in sensitivity due to DNP can result in dramatic decreases in the measuring time of an experiment. This can be used, for instance, for a fast (of the order of minutes) characterization of coal,[20] ceramics,[25] and diamonds,[14] to perform two-dimensional experiments in a relatively short time[24] (in this latter case, a two-dimensional experiment is reported for PA which would have required a measuring time of 165 years without DNP!), or to detect small amounts of molecules. An example of the latter application is shown in Figure 8 where the (natural abundance) ^{13}C DNP CP MAS spectrum of *trans*-polyacetylene is shown. Despite the fact that the amount of material was small (8 mg), the ^{1}H enhancement was so large (27-times in this experiment), that a ^{13}C spectrum with an excellent signal-to-noise ratio was obtained in a relatively short time.[26] In fact, it can be determined that the small narrow line at 13 ppm, which is due to the methyl end groups of the polyacetylene chains, represents only 0.5% of the total amount of carbons, or 3×10^{16} ^{13}C nuclei.

3.2.2 Structures and Dynamics Near the Unpaired Electrons

An example of the type of local information that can be obtained via DNP is shown in Figure 9. In this figure, ^{13}C spectra are shown of *trans*-polyacetylene obtained after a few

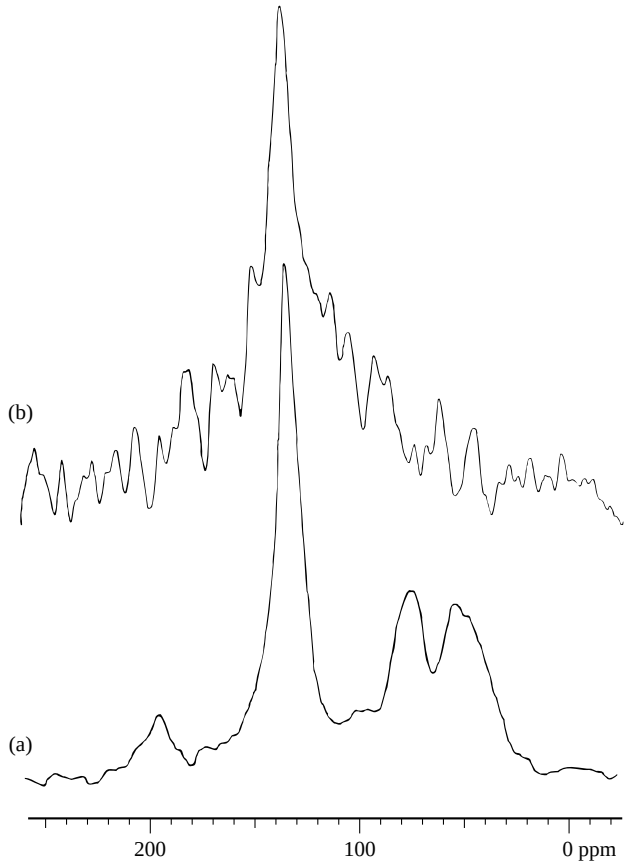

Figure 9 ^{13}C spectra of *trans*-polyacetylene, exposed to air for 4 months, obtained via (a) DNP CP MAS NMR and (b) DNP SP MAS NMR

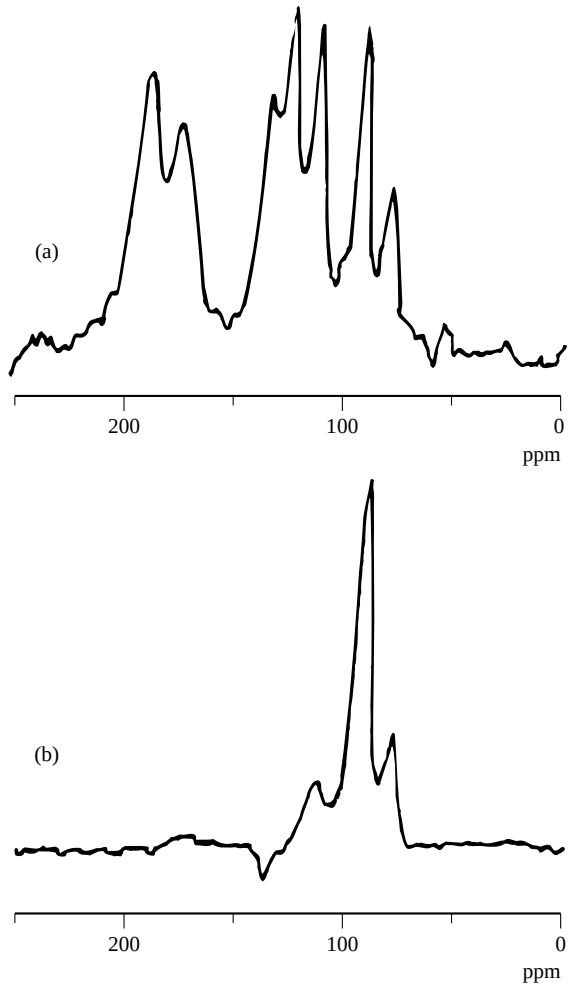

Figure 10 ^{13}C spectra of (fluoranthenyl)$_2PF_6$, obtained via (a) DNP CP MAS NMR and (b) DNP SP MAS NMR. Reproduced by permission of Marcel Dekker, Inc., from R. A. Wind, in 'Modern NMR Techniques and Their Application in Chemistry', eds. A. I. Popov and K. Hallenga, 1991, p. 125

months of exposure of the sample to air. Figure 9(a) shows the result of a DNP CP MAS experiment on ^{13}C. Compared with Figure 8, it follows that extra lines are observed due to the formation of ethene oxide groups, oxygen bridges, hydroxyl groups, and carbonyl groups.[27] Figure 9(b) shows the spectrum obtained via a ^{13}C DNP SP MAS experiment. We observe here that only the carbons in the $(CH)_x$ chains are detected. Hence in the latter experiment mainly the carbons in the chains below the surface are observed. These are not affected by exposure to the air.

Another type of local information that can be obtained via DNP SP MAS is the spin-density distribution of the unpaired electrons over the molecules.[26] An example of this possibility is the organic conductor (fluoranthenyl)$_2PF_6$. At room temperature this material behaves as a one-dimensional metal where the conduction electrons move more or less freely along paths parallel to the molecular stacks.[28] The electron mobility is so large that only an Overhauser effect is observed in this sample.[29] The average enhancement for ^1H is positive. This means that the dominating electron–proton hyperfine interaction is scalar. As a consequence, the overall enhancement of the DNP CP MAS spectrum of ^{13}C is positive as well, and Figure 10(a) shows the result of such an experiment. However, completely different results are obtained in the DNP SP MAS experiment on ^{13}C, shown in Figure 10(b). Here some lines are enhanced positively, indicative of a dominant electron–carbon scalar interaction, and one line is enhanced negatively due to a dominating electron–carbon dipolar interaction, whereas for the other lines the two DNP effects eliminate one another, resulting in a negligibly small enhancement. This phenomenon is due to the distribution of the electron density over the fluoranthenyl molecules, which is different at the different sites of the carbons, resulting in different ratios of the electron–carbon scalar and dipolar interactions. Hence, experiments utilizing DNP SP MAS can be used to determine the electron density distribution over the sites of the chemically different carbons.

Another application of DNP NMR in conductors is the determination of Knight shifts.[29] The Knight shift is proportional to the polarization of the conducting electrons. Hence, by saturating the ESR line, not only a signal enhancement due to DNP is obtained, but the Knight shift is suppressed as well. It has been shown[29] that for (fluoranthenyl)$_2PF_6$ the Knight shifts in the various carbon lines could be separated from the 'ordinary' chemical shift.

3.2.3 Interfaces and Surfaces

An example of an interfacial study with DNP NMR is an investigation of an immiscible mixture of polycarbonate

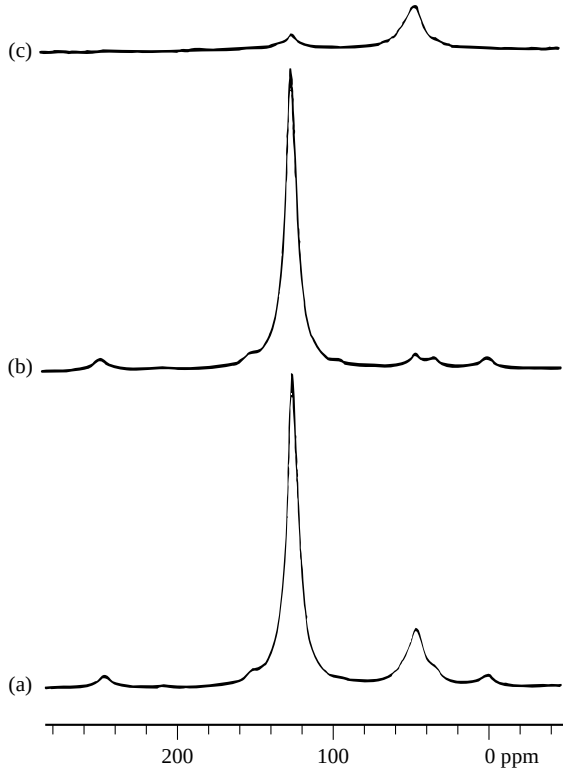

Figure 11 ^{13}C CP MAS NMR spectra of polycarbonate/polystyrene blends (a) with and (b) without ^{1}H DNP. The difference spectrum (c) has two features: the intensity around 40 ppm is due to the sp^3-hybridized carbons in PS whereas the intensity around 120 ppm arises from the carbons in the PC chains at the interface. Reproduced by permission of the American Society from M. Afeworki, R. A. McKay, and J. Schaefer, *Macromolecules*, 1992, **25**, 4084

(PC) and polystyrene (PS).[19,30] The samples consisted of thin film blends in which the polystyrene was doped with the stable radical BDPA [1,3-bis(diphenylene)-2-phenylallyl]. The interfacial region of PC could then be studied by measuring the DNP enhancement of protons via $^{1}H-^{13}C$ DNP CP MAS NMR. Figure 11 shows the results of such a measurement, carried out on a blend consisting of PC, which is labeled at the 3 and 3′ ring positions with 99 atom% ^{13}C, and PS, which is ^{13}C-depleted in all phenyl ring carbons. In this way, interferences between the NMR resonances of the aromatic carbons of the two polymers, which are partially overlapping, were avoided, and the peak observed at 120 ppm was almost exclusively due to the ^{13}C-labeled sites in PC. As the unpaired electrons in BDPA behave as fixed paramagnetic centers, the DNP enhancement of ^{1}H is mainly due to the solid state effect. Figure 11(a) and (b) show the $^{1}H-^{13}C$ CP MAS spectra obtained with and without ^{1}H DNP, respectively. It follows that the protons in PS, which are close to the unpaired electrons, are enhanced to the greatest extent (a factor of 20) and that there is also a small but noticeable enhancement for the protons in PC. This can be seen more clearly in Figure 11(c) where the differential spectrum is given. It has been shown[30a] that the proton polarization in PC is enhanced due to direct polarization transfer from these protons to the electrons, and that the signal of ^{13}C in PC observed in the differential spectrum arises from a 60 Å region from the PC/PS boundary which is 2% of the PC film thickness. Moreover, the

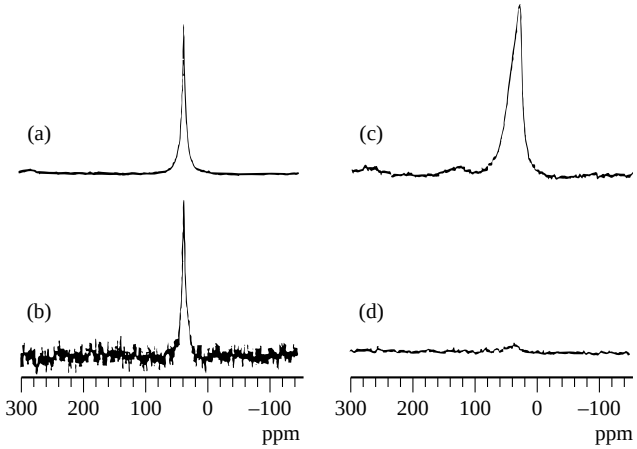

Figure 12 ^{13}C spectra of a 14% ^{13}C-enriched CVD diamond film, obtained via (a) DNP SP MAS NMR, (b) SP MAS NMR, (c) $^{1}H-^{13}C$ DNP CP MAS NMR, and (d) $^{1}H-^{13}C$ CP MAS NMR. Reproduced by permission of the American Institute of Physics from H. Lock, R. A. Wind, and G. E. Maciel, *J. Chem. Phys.*, 1993, **99**, 3363

authors were able to show that the interfacial aromatic carbons in PC have less motion than that of the bulk-PC aromatic carbons. This was attributed to restricted interchain motions resulting from a more dense packing for the PC chains near the PS barrier.

An example of a surface that can be studied via DNP NMR is provided by an investigation of chemical vapor deposited (CVD) diamond films.[31] Figure 12 shows ^{13}C spectra of a 14% ^{13}C enriched diamond film prepared by microwave-plasma-assisted CVD, using CH_4 and H_2 as feed gases.[31b] During the formation of the diamond films, unpaired electrons occur in the form of dangling bonds, which can be used for DNP measurements. Figure 12(a) and (b) show the results of ^{13}C DNP SP MAS NMR and SP MAS NMR, respectively, illustrating the increase in sensitivity due to DNP (the ^{13}C DNP enhancement factor is 50). Figure 12(c) and (d) show ^{13}C spectra obtained via $^{1}H-^{13}C$ DNP CP MAS and CP MAS NMR. A small percentage of protons (<0.1 atom %) is present at the intergrain boundaries of the diamond, and DNP can be used to enhance the proton signal (the enhancement factor is 25). It follows from Figure 12(c) that the hydrogenated diamond surfaces give rise to new resonances in the carbon spectrum (it was shown that the broad resonance at around 45 ppm actually consists of two lines), and the chemical shifts corresponding to these lines have been used to investigate the possibilities of different ‘diamondoids’, hydrogen-bearing carbon structures, occurring at the surfaces.[31b]

4 SUMMARY, CONCLUSIONS, AND PERSPECTIVES

High-resolution NMR combined with microwave-induced DNP has resulted in new areas of rare-spin NMR studies in solids. In many materials large DNP enhancement factors have been observed, which made possible NMR experiments which could not have been performed without DNP. The maximum proton enhancement that has been measured in a probe capable of MAS was 60, carbon enhancements of a few hundred were no exception, and in a ceramic fiber a silicon

enhancement factor 1000 was reported.[25] Although the DNP enhancements were not so large in some other materials, it should be kept in mind that even smaller enhancements can be very useful as they cause a reduction in the measuring time proportional to the square of the enhancement. Besides increasing the NMR sensitivity, DNP can also be used for other purposes such as the study of the structures and dynamics near the unpaired electrons, the detection of small amounts of electrons undergoing strong exchange interactions or behaving as fixed centers, the determination of the mobility and the spin-density distribution of conducting electrons, the study of surfaces and interfaces, the determination of Knight shifts, and DNP-enhanced imaging.[32] Finally, DNP NMR has been applied in a large variety of solid materials, such as doped polymers, coal, pyrolyzed materials, amorphous silica, organic conductors, semiconductors, natural and artificial diamonds, polymer composites, and ceramics.

However, it should be noted that many other possibilities for utilizing DNP NMR still remain to be explored:

1. Other types of radicals such as ions, nitroxide radicals, or radicals resulting from ionizing radiation.
2. Other materials; for example, experiments have already been started to explore the potential of DNP in zeolites, catalysts, and biomaterials.
3. High-resolution DNP NMR on quadrupolar nuclei.
4. High-resolution DNP NMR at different temperatures.
5. High-resolution DNP NMR at different pressures.
6. Combination of DNP with other high-resolution solid NMR techniques such as CRAMPS, fast MAS, DAS, DOR.
7. Combination of high-resolution NMR with different DNP techniques, which have been developed to increase the DNP enhancement factors and to improve the polarization transfer rates. Examples of these new techniques are the NOVEL (Nuclear spin Orientation Via Electron spin Locking) experiment,[33] which is an electron–nuclear analog of the CP experiment, and which provides fast polarization transfer (μs); the integrated solid effect (ISE),[34] where DNP is combined with adiabatic rapid passage through the ESR line, resulting in increased enhancement factors; DNP in the nuclear rotating frame,[35] which reduces the polarization transfer time by several orders of magnitude and which can be used to avoid distortion in the CP spectra resulting from rotating frame relaxation effects; DNP in higher external magnetic fields,[36] which might improve the resolution of the NMR spectra, and nuclear polarization enhancement using light irradiation. Examples of the latter techniques are microwave-induced optical nuclear polarization (MIONP),[37] optically polarized xenon and other rare gases, which can be used to study surfaces[38] and optical nuclear polarization (ONP).[39] Large enhancements have been obtained; for example, by applying the ISE technique in a naphthalene crystal doped with pentacene, in which the triplet state is highly polarized by photo-excitation, a DNP enhancement factor of the naphthalene protons of 5500 has been found.[40]

It can be expected that this and the other new methodologies and applications will further enhance the applicability of solid state NMR, and that many exciting new results will emerge in the near future.

5 RELATED ARTICLES

Cross Polarization in Rotating Solids: Spin-1/2 Nuclei; Cross Polarization in Solids; Electron–Nuclear Hyperfine Interactions; Electron–Nuclear Multiple Resonance Spectroscopy; Magic Angle Spinning; Nuclear Overhauser Effect; Optically Enhanced Magnetic Resonance.

6 REFERENCES

1. A. W. Overhauser, *Phys. Rev.*, 1953, **92**, 411.
2. T. R. Carver and C. P. Slichter, *Phys. Rev.*, 1953, **92**, 212.
3. A. Abragam and W. G. Proctor, *C. R. Acad. Sci.*, 1958, **246**, 2253.
4. C. D. Jeffries, *Phys. Rev.*, 1957, **106**, 164.
5. E. Erb, J. L. Motchane, and J. Uebersfeld, *C. R. Acad. Sci.*, 1958, **246**, 2121.
6. B. N. Provotorov, *Sov. Phys. JETP*, 1962, **14**, 1126.
7. A. Abragam and M. Borghini, in *Progress in Low Temperature Physics*, ed. C. J. Gorter, North-Holland Publishing Co., Amsterdam, 1964, Vol. 4, Chap. 8
8. M. Goldman, *Phys. Rev.*, 1965, **138**, A1675.
9. L. L. Buishvili, *Sov. Phys. JETP*, 1966, **22**, 1277.
10. A. Abragam, *The Principles of Nuclear Magnetism*, Clarendon Press, Oxford, 1961.
11. K. H. Hausser and D. Stehlik, in *Advances in Magnetic Resonance*, ed. J. S. Waugh, Academic Press, New York, 1968, Vol. 3, p. 79.
12. M. Goldman, *Spin Temperature and NMR in Solids*, Clarendon Press, Oxford, 1970.
13. A. Abragam and M. Goldman, *Nuclear Magnetism: Order and Disorder*, Clarendon Press, Oxford, 1982.
14. R. A. Wind, M. J. Duijvestijn, C. van der Lugt, A. Manenschijn, and J. Vriend, *Prog. NMR Spectrosc.*, 1985, **17**, 33.
15. N. W. Ashcroft and N. D. Mermin, *Solid State Physics*, Saunders College, Philadelphia, PA, 1976, Chap. 32
16. M. J. Duijvestijn, R. A. Wind, and J. Smidt, *Physica*, 1986, **138B**, 147.
17. R. A. Wind, R. H. Lewis, H. Lock, and G. E. Maciel, in *Magnetic Resonance of Carbonaceous Solids*, eds. R. E. Botto and Y. Sanada, *ACS Ser. No. 229*, 1993, 45.
18. R. A. Wind, F. E. Anthonio, M. J. Duijvestijn, J. Smidt, J. Trommel, and G. M. C. de Vette, *J. Magn. Reson.*, 1983, **52**, 424.
19. M. Afeworki, R. A. McKay, and J. Schaefer, *Macromolecules*, 1992, **25**, 4084.
20. R. A. Wind, M. J. Duijvestijn, C. van der Lugt, J. Smidt, and H. Vriend, *Fuel*, 1987, **66**, 876.
21. R. A. Wind, L. Li, G. E. Maciel, and J. B. Wooten, *Appl. Magn. Reson.*, 1993, **54**, 161.
22. G. G. Maresch, R. D. Kendrick, C. S. Yannoni, and M. E. Galvin, *J. Magn. Reson.*, 1989, **82**, 41.
23. W. P. Su, J. R. Schrieffer, and A. J. Heeger, *Phys. Rev. Lett.*, 1978, **42**, 1698.
24. M. J. Duijvestijn, A. Manenschijn, J. Smidt, and R. A. Wind, *J. Magn. Reson.*, 1985, **64**, 461.
25. R. H. Lewis, R. A. Wind, and G. E. Maciel, *J. Mater. Res.*, 1993, **8**, 649.
26. R. A. Wind, in *Modern NMR Techniques and Their Application in Chemistry*, eds. A. I. Popov and K. Hallenga, Marcel Dekker, Inc., New York, 1991, p. 125.
27. R. A. Wind, M. J. Duijvestijn, and J. Vriend, *Solid State Commun.*, 1985, **56**, 713.

28. M. Mehring and J. Spengler, *Phys Rev. Lett.*, 1984, **53**, 2441.
29. (a) W. Stocklein, C. S. Yannoni, H. Seidel, and D. Singel, *Chem. Phys. Lett.*, 1987, **141**, 277; (b) R. A. Wind, H. Lock, and M. Mehring, *Chem. Phys. Lett.*, 1987, **141**, 283.
30. (a) M. Afeworki and J. Schaefer, *Macromolecules*, 1992, **25**, 4092; (b) M. Afeworki and J. Schaefer, *Macromolecules*, 1992, **25**, 4097; (c) M. Afeworki, S. Vega, and J. Schaefer, *Macromolecules*, 1992, **25**, 4100.
31. (a) H. Lock, G. E. Maciel, and C. E. Johnson, *J. Mater. Res.*, 1992, **7**, 2791; (b) H. Lock, R. A. Wind, and G. E. Maciel, *J. Chem. Phys.*, 1993, **99**, 3363.
32. G. E. Maciel and M. F. Davis, *J. Magn. Reson.*, 1985, **64**, 356.
33. A. Henstra, P. Dirksen, J. Schmidt, and W. Th. Wenckebach, *J. Magn. Reson.*, 1988, **77**, 389.
34. A. Henstra, P. Dirksen and W. Th. Wenckebach, *Phys. Lett. A*, 1988, **134**, 134.
35. R. A. Wind and H. Lock, *Adv. Magn. and Opt. Reson.*, 1990, **15**, 51.
36. S. Un, T. Prisner, R. T. Weber, M. J. Seaman, K. W. Fishbein, A. E. Dermott, D. J. Singel, and R. G. Griffin, *Chem. Phys. Lett.*, 1992, **189**, 54.
37. (a) H. Brunner, R. H. Fritsch, and K. H. Hausser, *Z. Naturforsch.*, 1987, **42a**, 1456; (b) P. Dirksen, A. Henstra, and W. Th. Wenckebach, *J. Magn. Reson.*, 1990, **86**, 549.
38. (a) Z. Wu, W. Happer, M. Kitano, and J. Daniels, *Phys. Rev. A*, 1990, **42**, 2774; (b) D. Raftery, L. Reven, H. Long, A. Pines, P. Tang, and J. A. Reimer, *J. Phys. Chem.*, 1993, **97**, 1649.
39. (a) D. Stehlik and H.-M. Vieth, in *Pulsed Magnetic Resonance: NMR, ESR and Optics*, ed. D. M. S. Bagguley, Clarendon Press, Oxford, UK, 1992, p. 446; (b) S. K. Buratto, D. N. Shykind, and D. P. Weitekamp, *Phys. Rev. B*, 1991, **44**, 9035.
40. A. Henstra, T.-S. Lin, J. Schmidt, and W. Th. Wenckebach, *Chem. Phys. Lett.*, 1990, **165**, 6.

Biographical Sketch

R. A. Wind. *b* 1942. B.S., 1966, Ph.D., 1972, Delft, The Netherlands Introduced to NMR by J. Smidt. Faculty in Delft University of Technology, 1972–85; Senior research scientist, Colorado State University, 1985–90; Director of Research and Development, Chemagnetics/Otsuka Electronics, 1990–93; Senior staff scientist, Battelle/PNL, 1993–present. Approx. 90 publications. Current research specialties: NMR/DNP NMR and its applications in liquids and solids chemistry.

Electron–Nuclear Multiple Resonance Spectroscopy

Hans Thomann and Marcelino Bernardo

Exxon Research and Engineering Company, Annandale, NJ, USA

1	Introduction	1
2	Basic Principles	2
3	Experimental Techniques with Selected Applications	6
4	Concluding Remarks	15
5	Related Articles	15
6	References	16

1 INTRODUCTION

The term 'pulsed electron–nuclear multiple resonance' (PE NMR) spectroscopy refers to a broad range of experimental methods in which pulsed NMR techniques are combined with pulsed electron paramagnetic resonance (EPR) techniques. This combination provides the capability to measure the spectra and spin dynamics of nuclei which are magnetically coupled to unpaired electrons by the hyperfine interaction. Related experimental techniques for measuring the interactions of nuclei coupled to unpaired electrons are paramagnetically shifted NMR, dynamic nuclear polarization (DNP), electron spin resonance (ESR), the pulsed ESR technique of electron spin echo envelope modulation (ESEEM), and continuous wave (CW) electron–nuclear double resonance (ENDOR). These techniques are complementary rather than competing methods for measuring different aspects of the magnetic interactions of the coupled electron–nucleus spin system. Each technique offers certain advantages as well as certain limitations. The most appropriate experimental approach for a given problem also depends on the type of information desired.

The PE NMR techniques discussed in this article are best suited for measuring the magnetic interactions of nuclei in the local coordination structure of a paramagnetic electron. A distinguishing characteristic of nuclei which are detected in PE NMR experiments is that the NMR transition frequencies are shifted by very large values when compared with NMR spectra of diamagnetic samples. These large shifts arise from the large local magnetic fields originating from the unpaired electron spins. Consequently, the resonance frequency is described by the hyperfine coupling and is measured in units of kilohertz or megahertz as opposed to a resonance frequency shift of parts per million referenced to the nuclear Larmor frequency of a standard.

Nuclei which experience large local magnetic fields originating from unpaired electrons are encountered in a wide spectrum of research areas, including chemistry, materials science, polymer science, environmental science, and the biological sciences. Specific examples include: organic and inorganic radical molecules;[1–3] fossil fuels;[4,5] organic conductors, semiconductors and electroactive polymers; organometallic transition metal complexes;[6,7] dopants and other localized states in semiconductors;[8] surfaces such as on oxides and semiconductors; at the internal interfaces of semiconductors, superlattice structures, polymers, and composite materials; catalysis; transition metal ions in zeolites; and at the active sites for electron transfer or substrate binding in metalloproteins and metalloenzymes.[9]

If the unpaired electron spins can be treated as independent (or only weakly coupled) dipoles, their magnetic susceptibility is described by paramagnetism. Nuclei which sustain a hyperfine coupling with such electrons are therefore also referred to as paramagnetically coupled nuclei. Under certain conditions the NMR spectrum of paramagnetically coupled nuclei can be observed directly in the NMR spectrum as a paramagnetic shift. This is usually identified by the magnitude of the frequency shift and its temperature dependence. The local magnetic field originating from the unpaired electron spin shifts the NMR frequency and broadens the linewidth for those nuclei which sustain a hyperfine interaction. Both the magnitude of the frequency shift and the linewidth depend on the magnitude of the hyperfine coupling and on the details of the spin dynamics, specifically on the spin relaxation rates of the electron and nuclei. Well-resolved NMR lines can be observed if the electron spin–lattice relaxation time T_{1e}, or electron spin correlation time τ_e, which describes the time dependence of the local magnetic field, is short enough to assure that the orientation dependence of the local field is time averaged to its isotropic value. The paramagnetic shift is then determined by the isotropic hyperfine coupling arising from the unpaired spin density on the nucleus. Several texts have been written which describe the theory and applications of NMR to paramagnetic molecules including proteins and enzymes with paramagnetic transition metal ions.[10–12]

The short electron spin relaxation time required to observe paramagnetically shifted nuclei directly in NMR spectra also typically result in very broad ESR linewidths. In fact, as a rough guide, paramagnetically shifted NMR transitions are usually only observed in cases where the ESR spectrum is too broad to be observed. However, very broad ESR linewidths can also originate from inhomogeneous line broadening, even if the electron spin relaxation times are very long. In either case, if an ESR spectrum is observed, several experimental approaches are potentially applicable for the measurement of the magnetic interactions of the hyperfine coupled nuclei in these cases. These include DNP, ESR, ESEEM, ENDOR, and the extension of the latter to PE NMR.

In DNP spectroscopy the hyperfine coupling is used as a mechanism to enhance the nuclear polarization. The details of the mechanism for this enhancement and the magnitude of the enhancement depend on the details of the hyperfine interaction, particularly on the time dependence of the hyperfine coupling, and on the details of the ESR spectrum, such as the ESR linewidth and relaxation time. The theory and applications of DNP spectroscopy have been discussed in several texts and review articles.[13–18] (See ***Dynamic Nuclear Polarization and High-Resolution NMR of Solids***.) Here we discuss only those aspects of DNP spectroscopy that are relevant for comparison and contrast with the related techniques mentioned above.

In DNP spectroscopy the NMR signal is detected directly. The ESR transition is used only as a source for achieving enhanced nuclear polarization. Theoretically a maximum enhancement of the NMR signal of the order of ω_e/ω_n can be achieved, but in practice significantly lower values are

usually observed. Direct detection of the NMR signal has the advantage that the high resolution of NMR spectroscopy is maintained. At the same time, this excludes from detection those nuclei which have large hyperfine couplings. This is a result of the combination of low sensitivity and the large shift in transition frequencies. DNP spectroscopy has been applied most successfully in cases where the ESR spectrum consists of a narrow line which is easily saturated. Examples include studies of fossil fuels[19] and polymer interfaces.[20–22]

Paramagnetically coupled nuclei may be observed directly as hyperfine splittings in the ESR spectrum. Such splittings are often observed in ESR spectra of organic radical molecules in liquids (see ***Electron–Nuclear Hyperfine Interactions***). However, if the spin dynamics are not in the fast motion limit, hyperfine splittings are generally not resolved because of inhomogeneous line broadening.

Two different general approaches are available for measuring the magnetic couplings of nuclei which are not resolved in the ESR spectra. One approach is ESEEM.[23–26] In this technique both the allowed and the semiforbidden ESR transitions are coherently excited using two or more short, intense microwave pulses. The nuclear hyperfine and quadrupole interactions (in the case of nuclei with spin multiplicity $I \geq 1$) are observed as a periodic modulation of the envelope of the primary spin echo or stimulated echo intensity. Fourier transformation of this modulation pattern yields a spectrum of frequencies corresponding to the hyperfine (and quadrupolar for $I \geq 1$) frequencies.

One of the advantages of the ESEEM experiment is its high sensitivity, which is roughly comparable with that obtained in an ESR experiment. Furthermore, by selecting the appropriate microwave excitation frequency and applied magnetic field conditions, it is possible to measure the pure nuclear quadrupolar resonance frequencies for nuclei with $I \geq 1$.[27,28] This is possible despite the fact that the experiment is performed at finite magnetic field and the only spin transitions that are excited are the ESR transitions. One limitation of this type of experiment is that nuclear modulation can only be observed if the hyperfine interaction has finite anisotropic coupling components. The second criteron for modulation to be observed is that the microwave pulses must be able to excite both allowed and semiforbidden ESR transitions. This places constraints on the nature of the hyperfine interaction which will yield observable modulation. The theory, techniques, and applications of ESEEM spectroscopy have been reviewed in several texts and review articles.[23–27,29]

The second approach for measuring the magnetic couplings of nuclei which are not resolved in the ESR spectra is directly to excite both the NMR and ESR transitions with rf and microwave excitation. The first double resonance experiment of this type, known as an 'electron–nuclear double resonance', or simply ENDOR, experiment was reported by Feher in 1956.[30] The continuous wave (CW) ENDOR experiment is performed by applying a strong microwave field which is selected to irradiate continuously an EPR transition while simultaneously applying a strong rf field. The rf field is swept through the range of frequencies that encompass the NMR spectrum while continuously observing the intensity of the EPR transition. The intensity of the latter changes whenever the rf frequency matches an NMR transition frequency. The intensity of the EPR transition plotted as a function of the rf frequency generates the ENDOR spectrum. Thus, the ENDOR spectrum is a spectrum of the NMR transitions detected indirectly via the EPR transition. This is in contrast to the ESEEM experiment where the nuclear spin flip is a consequence of exciting a semiforbidden ESR transition. As a result, anisotropic hyperfine interactions are not necessary to observe hyperfine frequencies in the ENDOR experiment.

The ENDOR technique and applications have been documented in several texts and review articles.[1,8,9,31–36] In the case of one electron coupled to a spin-$\frac{1}{2}$ nucleus, and considering for simplicity that the hyperfine interaction is isotropic, the ENDOR spectrum comprises two transitions corresponding to one NMR transition for each of the two electron spin states. There exists a one-to-one correspondence between the number of coupled inequivalent nuclei and the number of ENDOR transitions observed. This can be contrasted to the number of transitions observed in the EPR spectrum where the number of transitions observed is a multiplicative function of the number of inequivalent nuclei coupled to the unpaired electron spin. The reduced number of transitions results in spectral simplification and, consequently, in enhanced spectral resolution.

While the success of the CW ENDOR experiment has been well documented, certain inherent problems in the technique have also limited its applicability. One well-documented limitation of the CW ENDOR experiment is the constraints on the relationship between NMR and ESR relaxation rates that must be satisfied in order to observe an ENDOR signal.[31,32,37–41] These constraints are changed (although not removed) with pulsed excitation techniques. This was recognized by W. B. Mims who reported the first pulsed ENDOR experiment in 1965, roughly a decade after Feher's initial report of the CW ENDOR experiment. Since then the advantages and applications of employing pulsed excitation techniques for both the ESR and NMR transitions have been demonstrated in publications from several laboratories.[37,38,41–46]

A second significant advantage of employing pulsed excitation techniques for both the ESR and NMR transitions is the potential for extending the type of experiments which can be performed. This is in many respects analogous to the extension of the experimental capabilities which become possible using pulsed excitation techniques in NMR spectroscopy. There are, however, distinct differences that must be kept in mind when using the analogy to pulsed NMR. These will be discussed in more detail in the next section. Furthermore, since multiple irradiation frequencies may be used to excite both the NMR and EPR transitions, the modern combined pulsed NMR and pulsed EPR experiments will be referred to as 'pulsed electron NMR' (PE NMR) spectroscopy. In this article, we describe the basic principles of these techniques, their implementation, including the pulse schemes and specific examples of experimental techniques, and illustrate the type of information that can be derived with examples in selected applications.

2 BASIC PRINCIPLES

In this section the magnetic interactions that determine the frequencies and amplitudes in pulsed ENDOR spectra are briefly reviewed. More comprehensive treatments can be found in several texts.[2,6,31,32,47,48] The analysis of the pulsed ENDOR spectrum provides the starting point for understanding the extensions of the basic pulsed ENDOR technique. After

the properties of the pulsed ENDOR spectrum have been presented, the general approach for the PE NMR techniques will be introduced. This is followed by specific experimental techniques with examples of applications.

2.1 Nuclear Spin Interactions and the Spectrum

2.1.1 Transition Frequencies

For spin-$\frac{1}{2}$ nuclei, the NMR spectrum of the paramagnetically coupled nuclei is dominated by the local magnetic field generated by the unpaired electron spin and by the applied magnetic field. The magnitude and orientation of this local field depends on whether the electron spin is aligned along or opposed to the direction of the external magnetic field. The effect of the combined local field and applied field on the nuclear spin is described by the nuclear spin Hamiltonian (expressed in units of frequency)

$$\hat{\mathcal{H}}_n = \sum_{i=1}^{3} (\hat{\boldsymbol{S}}' \cdot \boldsymbol{A} - g_n \beta_n B_0 b_i) \hat{I}_i \tag{1}$$

where the subscript i = 1, 2, 3 on $\hat{I}_i$ refers to the x, y, z components of the nuclear spin operator $\hat{\boldsymbol{I}}$. The prime on the electron spin operator $\hat{\boldsymbol{S}}'$ indicates that a coordinate system is selected in which the $\boldsymbol{g}$ tensor is diagonal. The b_i are the unit vectors of the applied magnetic field expressed in spherical polar coordinates:

$$(b_1, b_2, b_3) = (\cos\phi \sin\theta, \sin\phi \sin\theta, \cos\phi) \tag{2}$$

In most pulsed EPR experiments, particularly on transition metal ions, the microwave pulses excite only a small region of the spectrum centered about the magnetic field for resonance. This magnetic field position selects a subset of molecular orientations defined by the resonance condition, $h\nu = g\beta B_0$, where the orientation dependence of the electronic g factor is expressed by

$$g(\theta, \phi) = \left[\sum_{i=1}^{3} (g_i b_i)^2 \right]^{1/2} \tag{3}$$

The number of molecular orientations which contribute to the ENDOR spectrum is minimum for values of (θ,ϕ) that correspond to the principal axes of the $\boldsymbol{g}$ tensor. This phenomenon is referred to as g-factor orientation selectivity.[49] Since a lower number of molecular orientations contribute, higher spectral resolution can be observed in ENDOR spectra recorded at magnetic field values corresponding to those values of (θ,ϕ) which correspond to these principal axes.

The local field is described by the term $\hat{\boldsymbol{S}}' \cdot \boldsymbol{A}$, where $\boldsymbol{A}$ is the hyperfine interaction tensor. The magnitude of the local field depends on the distance between the electron and the nucleus and on the nature of the chemical bonding that pertains to the electron and nucleus, i.e. on the electronic state in which the electron resides. The distance separating the electron and nucleus determines a classical dipolar interaction. Since the gyromagnetic ratio of the electron is very large, this local magnetic field can be very large. The classical dipolar field will only provide a valid description of the distance between the electron and nucleus if the electron can be treated as a point dipole. Contributions to the hyperfine anisotropy also depend on the nature of the electronic wavefunction. The latter also determines whether the nucleus has a finite unpaired electron spin density at the nucleus. A finite unpaired spin density at the nucleus can only occur if the molecular orbital that describes the unpaired electron has some atomic s-orbital contribution in the wavefunction. The nonclassical contribution to the hyperfine anisotropy is sometimes referred to as 'pseudodipolar coupling'.

The orientation dependence of the local field can be expressed by an orientation-dependent hyperfine coupling $A(\theta, \phi)$. The NMR transition frequencies are then given by

$$\nu_{\pm} = \nu_n \pm \tfrac{1}{2}|A(\theta, \phi)| \tag{4a}$$

$$\nu_{\pm} = \tfrac{1}{2}|A(\theta, \phi)| \pm \nu_n \tag{4b}$$

where the first expression applies if $2\nu_n > |A|$ and the second expression applies if $2\nu_n < |A|$, while in both cases it is assumed that $I = \frac{1}{2}$.

The two limiting expressions [equations (4a) and (4b)] for the NMR frequencies are a recognition of the fact that the local magnetic field described by the hyperfine interaction can be comparable to or larger than the applied magnetic field. This is especially the case at the low applied field strengths, typically 0.35 T, at which many ENDOR and PE NMR experiments are performed. If the local field is greater than the applied field, then the local field is the dominant term that defines the nuclear quantization axis and the applied field is a perturbation. In either case, equations (4a) and (4b) indicate that for a nucleus with $I = \frac{1}{2}$, two NMR transitions will be observed in the ENDOR spectrum, with one transition originating from each of the two electron spin manifolds defined by the eigenvalue, $m_{S'}$, of $\hat{\boldsymbol{S}}'$. These NMR transitions will either be centered on the nuclear Larmor frequency if $2\nu_n > |A|$ or on one-half of the hyperfine coupling if $2\nu_n < |A|$.

In the case of organic radicals, the anisotropy of the g factor can be ignored in the first order analysis of the paramagnetically shifted NMR transitions. The NMR transition frequencies $\nu_{\pm}$ are then given by[50]

$$\begin{aligned} \nu_{\pm} = [&(S_z A_{xx} - \nu_n)^2 \sin^2\theta \cos^2\phi \\ &+ (S_z A_{yy} - \nu_n)^2 \sin^2\theta \sin^2\phi \\ &+ (S_z A_{zz} - \nu_n)^2 \cos^2\theta]^{1/2} \end{aligned} \tag{5}$$

where θ and ϕ are the spherical polar angles relating the applied static field $\boldsymbol{H}_0$ to the principal axis of the hyperfine tensor (A_{xx}, A_{yy}, A_{zz}). Equation (5) assumes that the high-field approximation is valid where the electron and nuclear spin operators $\hat{\boldsymbol{S}}$ and $\hat{\boldsymbol{I}}$ are completely decoupled from the molecular framework and quantized along the applied magnetic field direction. An energy level structure corresponding to an arbitrary selected set of (θ, ϕ) values is shown in Figure 1.

In general, the g factor for the electron will not be isotropic as assumed in the expressions described by equations (4a), (4b) and (5). Anisotropy of the electron g factor is usually

significant in ESR spectra of transition metal ions.[6,7] If the g factor is anisotropic, the NMR frequencies and lineshape will depend on the magnetic field position and microwave frequency selected.[6,48,51,52] In a noncrystalline solid, a single pair of NMR transitions will only be observed if the principal axes of the $\boldsymbol{g}$ and $\boldsymbol{A}$ matrices are collinear. Otherwise a powder pattern lineshape will be observed because of the angular dependence of the $\boldsymbol{g}$ and $\boldsymbol{A}$ matrices.

The NMR frequencies described in equation (5) do not account for the second-order frequency shifts of the ENDOR lines observed for large hyperfine couplings. Since these second-order frequency shifts are proportional to $A^2/4\nu_e$, they can usually be ignored under most experimental conditions. However, even for relatively small hyperfine coupling values, these second-order effects, arising from the spin Hamiltonian terms $\hat{S}_x\hat{I}_x$ and $\hat{S}_y\hat{I}_y$ must be included to calculate correct wave functions that reproduce the rf frequency dependence of the ENDOR amplitudes. These spin coupling terms lead to an enhancement, known as the 'hyperfine enhancement', of the rf field seen by the nucleus. Note that the enhancement can also be negative, i.e. a decrease in the rf field at the nucleus, depending on the eigenvalue m'_S of $\hat{\boldsymbol{S}}'$.

The simple four-level system with isotropic hyperfine coupling described by the spin Hamiltonian:

$$h^{-1}\hat{\mathcal{H}}_0 = \nu_e\hat{S}_z - \nu_n\hat{I}_z + aS_z\hat{I}_z \tag{6}$$

is usually adequate for describing the basic concepts for the sublevel polarization transfer experiments as well as several other PE NMR experiments described later in this article. In the high temperature limit, i.e. $g_e\beta_eB_0/kT \ll 1$, the spin eigenvalues, $h^{-1}E_0(M_S,M_I)$, are given by:

$$h^{-1}E_0(M_S, M_I) = \nu_eM_S - \nu_nM_I + aM_SM_S \tag{7}$$

The energy levels in Figure 1 also describe these eigenstates which arise from the coupling of an $S = I = \frac{1}{2}$ system with isotropic hyperfine coupling. With this level of simplification it is possible to gain considerable insight into the spin dynamics of PE NMR experiments using the spin operator formalism[42] frequently used in NMR spectroscopy.[53]

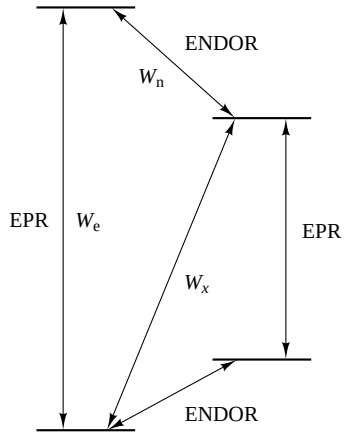

Figure 1 Energy level structure corresponding to the spin Hamiltonian of a four-level system. EPR, ENDOR, and relaxation transitions are identified

In the literature on pulsed ENDOR and PE NMR spectroscopy, the hyperfine splitting of the electron spin eigenstates are referred to as 'hyperfine sublevels' or simply as 'sublevels'. The EPR, NMR, and spin relaxation transitions relevant in the discussion of the ENDOR experiment are identified in Figure 1. The ENDOR transitions indicated in the figure are NMR transitions detected indirectly by the ESR transition. The electron and nuclear relaxation transition probabilities W_e and W_n correspond to effective T_{1e}^{-1} and T_n^{-1} rates; these are also identified in Figure 1. In the analysis of signal amplitudes in the CW ENDOR experiment, the effective rates are the intrinsic rates enhanced by the application of the microwave or rf excitation fields.

If the nuclear spin multiplicity $I \geq 1$, the quadrupolar interaction will result in additional splittings of the hyperfine sublevels. The quadrupolar interaction is described by adding the nuclear self-coupling term, $\hat{\boldsymbol{I}} \cdot \boldsymbol{P} \cdot \hat{\boldsymbol{I}}$ to the spin Hamiltonians of either equation (1) or equation (6). If the principal axes of the $\boldsymbol{g} \cdot \boldsymbol{A} \cdot \boldsymbol{P}$ are collinear and the magnetic field $\boldsymbol{B}_0$ is oriented parallel to one of these principal axes, the first-order ENDOR frequencies are given by[2,6,48]

$$\nu_{ENDOR} = \left| \frac{A_i}{2} \pm \nu_n \pm \frac{3}{2}|P_i|(2m_i + 1) \right| \tag{8}$$

where A_i and P_i denote the principal values of the $\boldsymbol{A}$ and $\boldsymbol{P}$ tensors along the i axis. The nuclear transitions in equation (8) are assumed to increase in the nuclear spin quantum number, i.e. $m_I \rightarrow m_I + 1$. It has also been assumed that ($|A| > 2\nu_n > 3|P_i|$). The principal values of the quadrupolar tensor $\boldsymbol{P}$ are defined as $|P_{zz}| > |P_{yy}| > |P_{xx}|$. These principal values are related to the magnitude of the quadrupolar coupling constant χ and asymmetry parameter η by

$$\chi = 2I(2I - 1)P_zz \tag{9a}$$

$$\eta = \frac{P_xx - P_yy}{P_zz} \tag{9b}$$

According to equation (8), four ENDOR transitions are expected for a nucleus with $I = 1$. However, not all ENDOR transitions may be observed when exciting an ESR transition at a given magnetic field value, since it is possible that each m_I state may be selectively excited. For example, a two-line ENDOR spectrum will be observed if the ESR transition connects the $m_I = 1$ to $m_I = 1$ sublevels of the $m_S = +\frac{1}{2}$ and $m_S = -\frac{1}{2}$ electron spin manifolds.

2.1.2 ENDOR Amplitudes

ENDOR signal amplitudes are proportional to the change in the EPR signal intensity, ΔE, induced by an NMR transition. Since the EPR signal intensity E is proportional to the electron spin susceptibility χ_e, a relative ENDOR susceptibility can be defined by

$$\frac{\Delta\chi_e}{\chi_e} = \frac{\Delta E}{E} \tag{10}$$

The transition frequencies and amplitudes that are described by the time-independent terms in the spin Hamiltonian are independent of the method of exciting and detecting the transitions. However, the dynamic terms of the total spin Hamiltonian that describe the spin system have different effects on the amplitudes in the CW and pulsed experiment. In the CW experiment, the ENDOR signal amplitude depends on the rate at which the ESR and NMR transitions are excited by the applied microwave and rf magnetic fields compared with the rate of intrinsic relaxation pathways that will compete to restore the spin system to thermal equilibrium. Once the spin eigenstates and relaxation rates that connect the eigenstates have been defined, coupled rate equations can be used to model the ENDOR signal amplitude. In contrast, the pulsed ENDOR or ENMR experiment is performed on a timescale which is short compared with the intrinsic spin relaxation rates. The amplitudes can therefore be analyzed without resorting to coupled rate equations.

In the CW experiment, the interplay between the transition intensity induced by the applied magnetic fields and the intrinsic spin relaxation rates is further complicated by the effect of the hyperfine enhancement on the ENDOR amplitudes.[31,32,50,54] For intense rf fields, the ENDOR amplitudes can be independent of the rf frequency. For very weak rf fields, the ENDOR amplitudes increase with the square of the rf frequency. For intermediate values, the ENDOR amplitudes can be a complex function of the transition moments and relaxation parameters, especially since both the transition moments and the relaxation rates can be orientation dependent.

In pulsed ENDOR experiments, the analysis of the hyperfine enhancement and the effects of the spin relaxation on the ENDOR amplitudes is less complex. The pulsed ENDOR experiment is usually performed on a timescale which is short compared with the electron, nuclear, and the electron–nucleus cross-relaxation rates. In this case the relaxation rates do not influence the relative ENDOR amplitudes. The loss of electron spin polarization by T_{1e} processes during the mixing period (described in Section 2.2) results in a uniform decrease in the signal amplitudes, $\Delta\chi_e/\chi_e$, across the ENDOR spectrum. The hyperfine enhancement of the NMR transition moment is then simply observed as a change in the sublevel nutation angle as a function of rf frequency. The sublevel nutation angle θ_R is given by $\theta_R = \gamma_n \epsilon B_2 t_{rf}$, where ϵ is the hyperfine enhancement factor. If the hyperfine interaction is isotropic, the hyperfine enhancement factor is given by $\epsilon = |1 + m_s a/\nu_n|$. The hyperfine enhancement can be observed directly in EPR detected sublevel transient nutation experiments.[43,55]

As described in the next section, the pulsed ENDOR experiment can be divided into pulse periods. The ENDOR amplitude is a function of the microwave pulses in the preparation period and detection period as well as of the nutation angle of the sublevel polarization in the mixing period. The latter can be expressed by

$$EA(\nu_{rf}) = \tfrac{1}{2}(1 - \cos(\theta_{R\pm})) \qquad (11)$$

In the limit of small nutation angles, the cosine term can be expanded in a power series:

$$EA(\nu_{rf}) \approx \frac{(\theta_{R\pm})^2}{4} = \frac{(m_s A)^2}{(2\nu_n)^2} = \frac{(m_s)^2}{(2\nu_n)^2}(\nu_\pm - \nu_n)^2 \qquad (12)$$

Equation (12) explicitly indicates that the Fermi golden rule result for the rf frequency dependence of the transition probability is obtained in the limit of small nutation angle. If the nutation angle is adjusted to correspond to a π pulse at each ENDOR frequency, the ENDOR amplitudes should be independent of the hyperfine enhancement factor. It is straightforward, although time consuming, to measure the sublevel nutation frequency at each ENDOR frequency in the ENDOR spectrum for a quantitative analysis of the ENDOR amplitudes. Additional contributions to the ENDOR amplitudes arise from the effect of hyperfine contrast selectivity in the preparation period and from possible electron–nucleus coherence effects in the detection period.[37,38] These effects are discussed in more detail in Section 3. Contributions originating from the hyperfine anisotropy[6,48] and g-factor orientation selectivity[6,48] will also affect the amplitudes in both the CW and pulsed ENDOR experiments.

2.2 Pulse Schemes

Many of the PE NMR experimental techniques can be understood by analogy to heteronuclear NMR experiments. However, in making this comparison between PE NMR and heteronuclear NMR experiments, some important differences must be recognized. These originate from the fundamental properties of the unpaired electron compared with a nucleus. The two most significant differences are the γ values of the electron and nucleus and the differences between the nature of the wave functions that describe the electron and the nucleus.

The larger γ for the electron compared with any nucleus has two important consequences. The first is the practical consequence for the type of instrumentation required for PE NMR experiments compared with heteronuclear NMR experiments. The heteronuclear NMR experiment requires a transmitter, probe, and receiver capable of handling two (or more) different rf frequencies. In contrast, for the double resonance experiment between the electron and nucleus, the hardware must be capable of handling both rf and microwave frequency components.

A second consequence of the larger γ of the electron is that the local magnetic field generated by the electron is much larger than is generated by any nucleus. This has several consequences on the properties of the spectra observed for nuclei that are coupled to this local field and also has implications on the types of experiments which can be performed. In most cases, PE NMR experiments must be analyzed within the so-called ‘soft pulse limit’, i.e. the bandwidth of the excitation pulses for both the ESR and NMR transitions are much smaller than the spectral bandwidth. In other words, both the ESR and NMR pulses are generally selective excitation pulses. The broad linewidths also exclude certain techniques such as cross polarization in the rotating frame and magic angle spinning which have had such an important impact on NMR of solids from being directly adapted to PE NMR experiments.

The second important difference to bear in mind when comparing PE NMR spectroscopy with pulsed heteronuclear NMR is the difference in the nature of the total wavefunction associated with the electron compared with the nucleus. The electron is generally in an eigenstate, such as an atomic or

molecular orbital, which has a much greater spatial extent than the localized eigenstate which describes the nucleus. This has the consequence that the electron spin is delocalized so that the electron is generally coupled to many more nuclei than would be the case if the electron were represented by a point dipole. The delocalization of the electron spin density in molecular orbitals that have well defined spatial extents can also contribute large anisotropic components to the local (i.e. hyperfine) field. The anisotropy of the hyperfine interaction also assures that the quantization axis for the nucleus does not point in the same direction in the two electron spin eigenstates. This anisotropy in the hyperfine interaction is therefore responsible for the broad spectral widths observed for the NMR transitions and also affects the transitions which are observed, since formally forbidden transitions become 'semiforbidden' transitions.

Another consequence of the nature of the electronic states that host the unpaired electron is that spin coupling mechanisms such as the spin–orbit coupling are effective in broadening the ESR linewidth and in enhancing the spin relaxation rate. Both the broad lines and the shorter relaxation times have implications on the types of PE NMR experiments that can be performed.

The pulse sequences employed in PE NMR experiments can be conveniently divided into pulse periods in direct analogy to NMR spectroscopy. With the above-mentioned caveats in mind, the pulse periods can be analyzed by analogy to a pulsed heteronuclear NMR solids experiment within the soft pulse limit, wherein selective excitation is considered in the analysis. The most basic experiment consists of a preparation, mixing, and detection period. The purpose of the preparation period is to create an initial state perturbed from the equilibrium spin polarization established by the conditions of the temperature and external field (as well as by the level structure of the electron–nuclear coupled spin system). In all PE NMR experiments reported to date, one or two microwave pulses are applied to excite ESR transitions in the preparation period.

Two basically different types of PE NMR experiments will be performed depending on whether the microwave preparation pulses have created sublevel nuclear spin polarization or electron spin coherence at the end of the preparation period. The former are the starting points for ESR detected sublevel polarization transfer experiments and for ESR detected nuclear coherence experiments. The latter is the starting point for coherence transfer ENDOR experiments. In this experiment, a single microwave pulse, ideally a $\pi/2$ pulse, creates electron spin coherence in the preparation period.

In the mixing period, one or more rf pulses are applied to manipulate the sublevel polarization or sublevel coherence. The nature of the perturbation determines the type of experiment performed. The mixing period may include an evolution period, again depending on the type of experiment performed. If sublevel nuclear coherence has been created and is to be indirectly observed via the ESR transition intensity, the mixing period must end with a $\pi/2$ rf pulse that converts the sublevel coherence to sublevel polarization.

In the detection period one or more microwave pulses are applied to create electron spin coherence which is detected in the PE NMR experiment. The electron spin transverse magnetization provides a readout of the electron–nucleus longitudinal order. The transverse magnetization can be detected by a primary spin echo,[56] a stimulated echo,[57] or as a free induction signal.[58] It is also possible to use CW irradiation to detect the transverse electron magnetization[42] or to detect the longitudinal electron magnetization directly.[29]

3 EXPERIMENTAL TECHNIQUES WITH SELECTED APPLICATIONS

3.1 ESR Detected Sublevel Polarization Transfer

It is possible to envisage many pulse sequences which create sublevel nuclear spin polarization. The most common methods, shown in Figure 2, are a single microwave pulse which selectively excites one ESR transition or two microwave pulses. The former was first proposed by Davies[56] and is the starting point for what has become known as the Davies ENDOR experiment. The latter was first proposed by Mims[57] and is the preparation pulse sequence for the experiment now known as Mims ENDOR.

Referring to Figure 3, the selective excitation of one of the two allowed ESR transitions converts the electron spin polarization, represented by the boxes, into electron–nucleus two-spin longitudinal order. The spin polarization from the nuclear Zeeman and hyperfine interactions is negligible compared with the electron spin polarization and can be ignored. The two spin order refers to the fact that the nuclear spins in both NMR transitions are polarized.

Two spin electron–nucleus longitudinal order can also be created using two selective microwave pulses or two nonselective microwave excitation pulses if an evolution time separates the two pulses.[42] Sublevel polarization is created from the transverse components of the magnetization that evolves following the first pulse in the local field of the hyperfine interaction. The second pulse converts the transverse magnetization to two-spin longitudinal order. This suggests that the two pulses should be $\pi/2$ pulses for maximum efficiency in creating sublevel polarization. After the second

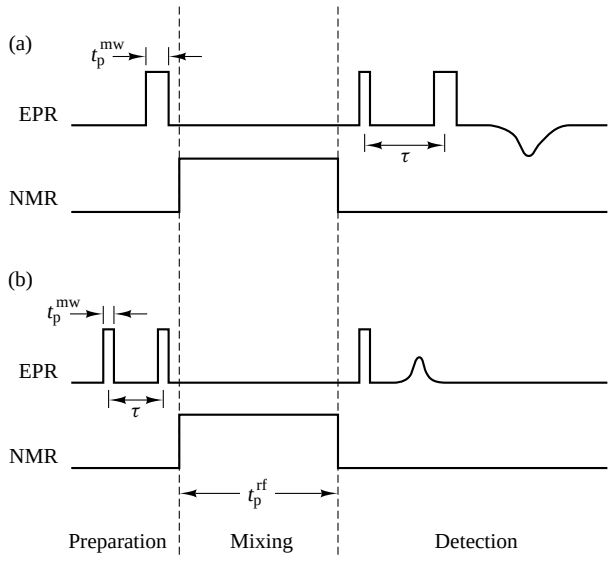

Figure 2 Davies ENDOR (a) and Mims ENDOR (b) pulse sequences

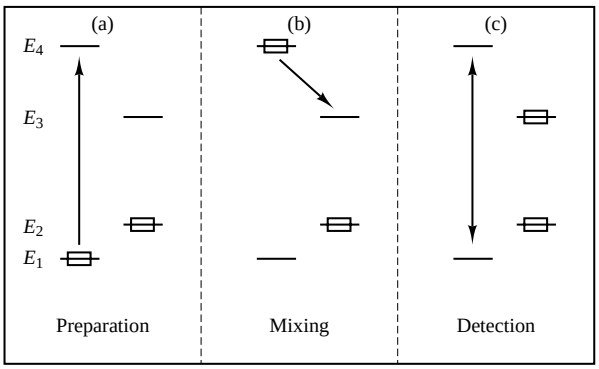

Figure 3 The transfer of spin polarization during the preparation (a), mixing (b) and detection (c) periods of the Davies ENDOR sequence for the four level system shown in Figure 1

pulse, the net sublevel polarization is approximately $\sin(a\tau/2)$ $\sin(\Omega_S\tau)$, where a is the hyperfine coupling in equation (6) and Ω_S is a resonance offset. Note that no sublevel polarization exists for values $a\tau/2 = n\pi$, where n is an integer. These are known as blind spots in the Mims ENDOR experiment.

For an ESR lineshape which is inhomogeneously broadened, the sublevel polarization created by the microwave pulses in the preparation period burn a hole into the envelope of the ESR absorption lineshape as shown in Figure 4(a). The width of the hole is determined by the excitation bandwidth of the preparation pulse. In the case of two pulse excitation, a serrated pattern of magnetization is superimposed on the hole, as shown in Figure 4(b).

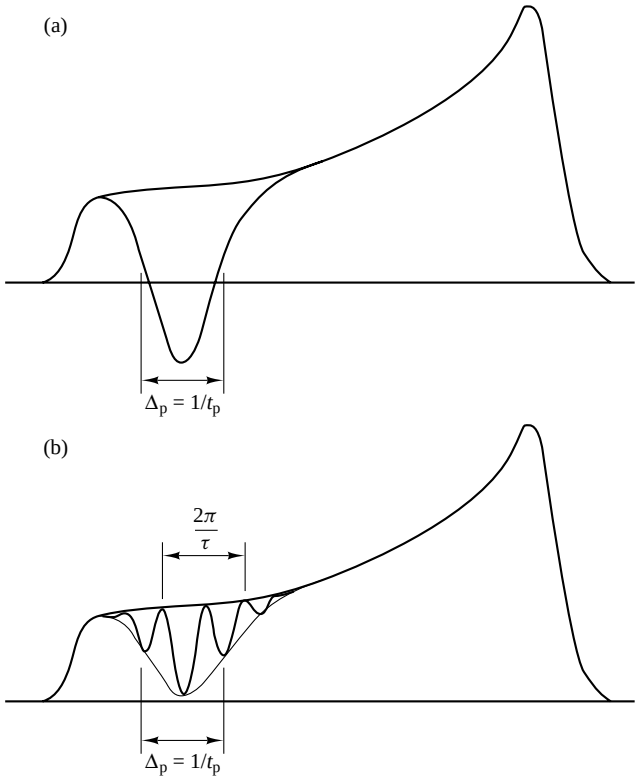

Figure 4 EPR spectra of an inhomogeneously broadened line after the preparation period in the Davies ENDOR (a) and Mims ENDOR (b) pulse sequences. (Reproduced by permission of Academic Press from H. Thomann and M. Bernardo, in 'Methods in Enzymology', eds. J. F. Riordan and B. L. Vallee, 1993, Vol. 227, Chap. 6)

3.1.1 Davies and Mims ENDOR

The pulse sequences for the two most commonly used experiments for the ESR detection of sublevel polarization transfer are shown in Figure 2. The hole-burning effect created by the preparation pulses on an inhomogeneously broadened ESR absorption envelope is shown in Figure 4. The effect of a selective ESR excitation on the electron spin polarization in a four level system described by equation (7) is shown in Figure 3(a). The electron spin polarization associated with these two energy levels will be inverted if the selective microwave pulse is a π pulse. Note that the sublevel longitudinal polarization of both the upper and lower NMR sublevels are not at equilibrium at the end of the preparation period.

In the next step of the pulse sequence, an rf pulse transfers and thereby 'mixes' the electron spin polarization between the sublevels. This is shown in Figure 3(b) for an rf pulse on resonance with the upper sublevel. In the hole-burning picture shown in Figure 4, the sublevel polarization transfer corresponds to the transfer of polarization from within the hole to a frequency offset by the value of the hyperfine coupling. This sublevel polarization transfer occurs at frequencies corresponding to the NMR frequency shifted by the hyperfine interaction (see Section 2.1.1).

The sublevel polarization transfer could, in principle, be detected directly as an NMR signal. Indeed, this would correspond to a pulsed DNP experiment. Note, however, that the sublevel polarization transfer has also changed the electron longitudinal polarization of the two ESR transitions. The sublevel polarization transfer can therefore be detected by measuring the change in the ESR transition intensity. This can be accomplished using a variety of techniques, as discussed in Section 2.2. In the Davies and Mims ENDOR pulse sequences the change in electron longitudinal polarization is detected by observing the change in intensity of a primary or stimulated spin echo. This electron spin coherence is indicated by the double arrow in Figure 3(c).

The spectrum of NMR transition frequencies shifted by the hyperfine coupling, i.e. the ENDOR spectrum, usually far exceeds the excitation bandwidth of the rf pulses. The complete spectrum must therefore be recorded by incrementing stepwise the rf frequency on successive iterations of the pulse sequences shown in Figure 2. The limit of resolution in the spectrum is determined by the excitation bandwidth of the rf pulse.

The Davies ENDOR spectrum of a single crystal of malonic acid which has been irradiated by X-rays to generate carbon π radicals[59] is shown in Figure 5. The transitions at approximately 5 and 30 MHz are the two sublevel transitions associated with the α proton of the CH fragment of the $\dot{C}H(COOH)_2$ radical molecule. The other proton lines originate from the carboxylic protons, from coupling to protons on neighboring malonic molecules, and from overlapping ESR signals from different malonic acid radical molecules.[59] The increase in spectral resolution obtained by decreasing the excitation bandwidth of the rf mixing pulse is shown in the inset of the figure.

The relative amplitudes of the ENDOR transitions are determined by the spin Hamiltonian (as discussed in

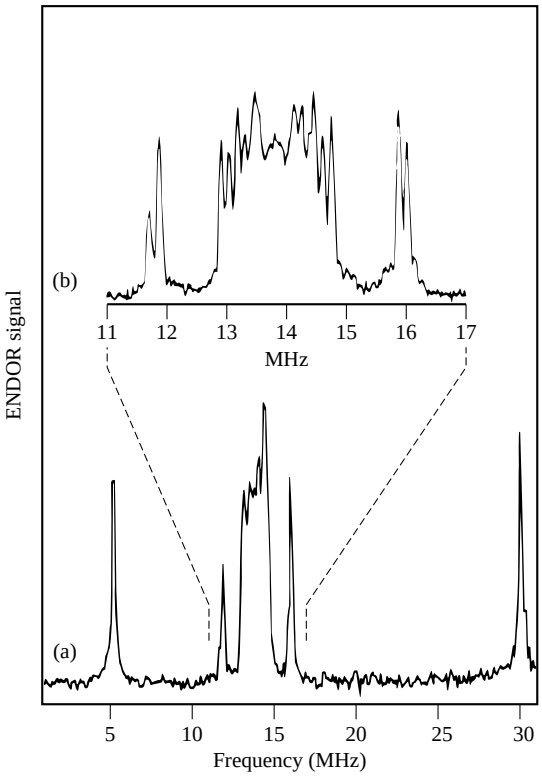

Figure 5 Davies ENDOR spectrum of an X-ray irradiated crystal of malonic acid with rf pulse widths of 5 μs (a) and 10 μs (b). (Reproduced by permission of the American Chemical Society from H. Thomann and M. Bernardo, in 'Advances in Chemistry Series 229: Magnetic Resonance of Carbonaceous Solids', eds. R. E. Botto and Y. Sanada, Washington, DC, 1993, Chap. 4)

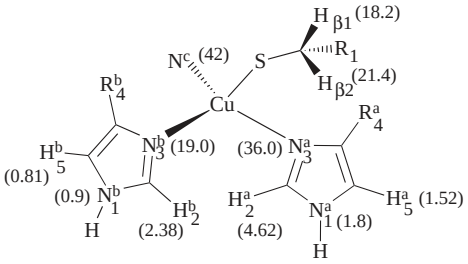

Figure 6 Spectroscopic model for the copper coordination structure in the high pH form of stellacyanin showing the hyperfine couplings (in MHz). (Reproduced by permission of Academic Press from H. Thomann and M. Bernardo, in 'Methods in Enzymology', eds. J. F. Riordan and B. L. Vallee, London, 1993, Vol. 227, Chap. 6)

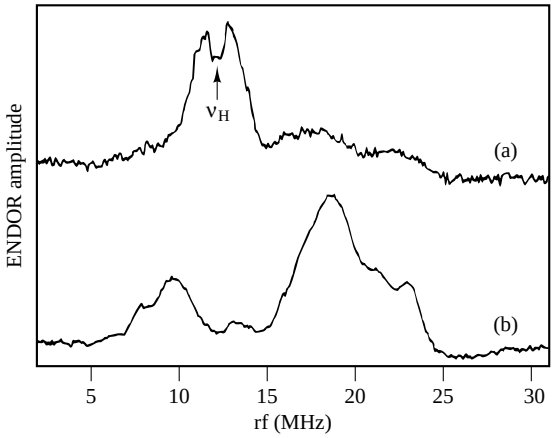

Figure 7 Davies ENDOR spectra of stellacyanin using microwave inversion and detection pulse widths t_{mw} of 0.40, 0.20, 0.40 μs (a) and 0.04, 0.02, 0.04 μs (b). (Reproduced by permission of Academic Press from H. Thomann and M. Bernardo, in 'Methods in Enzymology', eds. J. F. Riordan and B. L. Vallee, 1993, London, Vol. 227, Chap. 6)

Section 2.1.2) but also by the excitation bandwidth, Δ_p of the preparation pulse. In order for a sublevel polarization transfer signal to be detected indirectly using the Davies ENDOR pulse sequence [Figure 2(a)], the condition that $\Delta_p > a$, where a is the hyperfine coupling, must be satisfied.[56] If $\Delta_p > a$, the transfer of polarization remains within the hole burned into the absorption envelope. In this case the change in electron polarization is reduced, resulting in a weaker ENDOR signal. This relationship between Δ_p and a has been referred to as 'hyperfine contrast selectivity',[37–39] as a 'spin alignment hole',[41] and as a 'self-ELDOR effect'.[42] The relationship between Δ_p and a can be used to eliminate or reduce the overlap of ENDOR signals originating from nuclei with different hyperfine couplings.[37–39,60]

Davies ENDOR spectra on a blue copper protein, stellacyanin,[61] will serve to illustrate the application of pulsed ENDOR (and PE NMR) spectroscopy. Transition metal ions and ion clusters are found at the active site for electron transfer in metalloproteins and at the active site for substrate conversion in metalloenzymes. The electron spin echo detected ESR (ED ESR) absorption envelope recorded by plotting the intensity of the primary electron spin echo as a function of magnetic field is shown in the inset of Figure 9. A spectroscopic model for the ligand coordination structure of the Cu^{2+} ion for the high-pH form of the protein is shown in Figure 6. The hyperfine coupling frequencies for each nucleus on the copper ligands are indicated in Figure 6. The NMR transitions for nuclei in the primary ligand coordination structure of the Cu^{2+} ion would be difficult to measure by any other spectroscopic technique.

The hyperfine contrast selectivity mechanism for eliminating the overlap of ENDOR lines is illustrated in Figure 7, where two Davies ENDOR spectra of stellacyanin[61] are shown. When a preparation pulse with narrow excitation bandwidth is used [Figure 7(a)], the proton ENDOR lines which have small hyperfine coupling values that originate from protons on the two imidazole ligands overlap the nitrogen ENDOR lines, particularly the nitrogen line centered at roughly 8 MHz. When a larger excitation bandwidth is used [Figure 7(b)] the amplitudes for these proton ENDOR lines are significantly attenuated. The 1 : 2 relative intensities of the two ^{14}N ENDOR lines centered at 8 and 18 MHz in Figure 7(b) are in agreement with the expected intensity difference due to the hyperfine enhancement factor.[37,38]

The proton ENDOR signals from protons with small hyperfine couplings can also be observed using preparation pulses with large excitation bandwidths with the Mims ENDOR pulse sequence. A comparison of the Davies and Mims ENDOR spectra for the stellacyanin protein is shown in Figure 8. The arrows in the Mims ENDOR spectrum indicate the positions of the 'blind spots' where no ENDOR signal is observed. The position of these blind spots in the spectrum

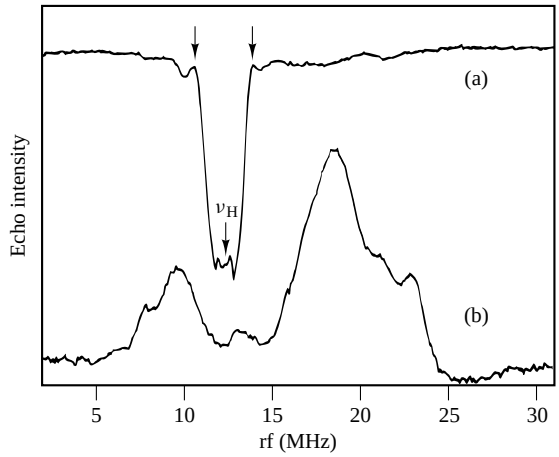

Figure 8 Comparison of the Davies and Mims ENDOR spectra for the stellacyanin protein. (Reproduced by permission of Academic Press from H. Thomann and M. Bernardo, in 'Methods in Enzymology', eds. J. F. Riordan and B. L. Vallee, London, 1993, Vol. 227, Chap. 6)

can be selected by the value of τ chosen in the Mims ENDOR pulse sequence. Note that the ENDOR signal for the protons with small hyperfine couplings is significantly enhanced in the Mims ENDOR spectrum. This is a consequence of the fact that a larger fraction of the electron magnetization can be sampled without suppressing the ENDOR signals from the nuclei with small hyperfine couplings.

An example of the advantage of the increased sensitivity achieved by the indirect detection scheme of the pulsed ENDOR experiment is shown in Figure 9, where the ENDOR signals from the central metal Cu^{2+} ion as well as those from all the (NMR active) ligand nuclei on the metal ligands are observed. The position in the ED ESR spectrum at which this Davies ENDOR spectrum was recorded is shown in the inset of the figure. Although the hyperfine splitting of the Cu^{2+} ion can be observed at the high-field end of the ESR spectrum, the hyperfine splittings are not resolved in the low-field region of the ESR spectrum. Note also that the pulsed ENDOR spectrum reveals the quadrupolar splitting of the Cu^{2+} nucleus. It is not possible to measure these quadrupolar interactions in the ESR spectrum.

3.1.2 Transient Nuclear Nutations

The sublevel nuclear transient nutations can be detected indirectly with the pulse sequences in Figure 2 by incrementing stepwise the rf pulse length on successive pulse sequence iterations. An example is shown for the malonic acid radical in Figure 10. The effect of the time dependence of the signal from the electron spin–lattice relaxation during the mixing time can be eliminated by choosing a fixed, long mixing time before detection or by subtracting the signal recorded without the rf pulse applied (or with the rf frequency set to an off-resonance position in the ENDOR spectrum). The electron spin echo amplitude in the detection period oscillates with a periodicity proportional to $\cos \theta_2$ where θ_2 is the sublevel nutation angle (see Section 2.1.2). These oscillations are sometimes referred to as Rabi oscillations. The influence of the hyperfine enhancement factor on the nutation angle is evident in Figure 10.

The sublevel nutation experiment provides a method for setting the rf mixing pulse conditions to the selected nutation angle. For ESR detected sublevel polarization transfer experiments, the optimum pulse is a π pulse. For the ESR detection of sublevel coherence, the rf mixing pulse would be set for a $\pi/2$ pulse. For samples which are not single crystals and that exhibit hyperfine anisotropy, the Rabi oscillations are rapidly damped after the first period.[37,38] Consequently, the effect on the ENDOR amplitudes due to the hyperfine enhancement can be reduced by selecting a long rf pulse length. However, this produces power broadened lines, and therefore a lower resolution in the spectrum. When two or more magnetically equivalent nuclei are coupled to the electron, harmonics may be observed in the sublevel nutation pattern.[42] An example is shown in Figure 11. Analysis of these

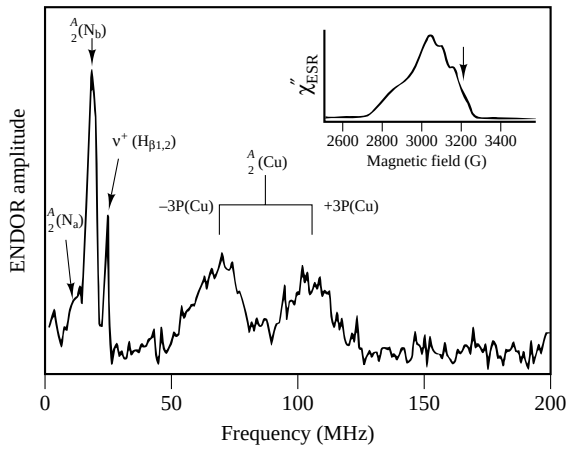

Figure 9 Davies ENDOR spectra of stellacyanin showing the Cu, N, and H resonances. Inset shows the position in the ED ESR spectra where the ENDOR spectra was recorded. (Reproduced by permission of Plenum Press from H. Thomann and M. Bernardo, in 'Biological Magnetic Resonance', eds. L. J. Berliner and J. Reuben, New York, 1993, Vol. 13, Chap. 7)

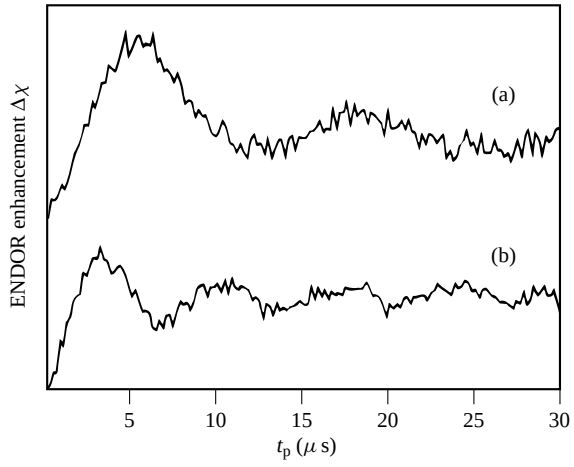

Figure 10 Sublevel nuclear transient nutations detected for the irradiated malonic acid radical at an rf of (a) 7.32 and (b) 21.29 MHz. (Reproduced by permission of the American Chemical Society from H. Thomann and M. Bernardo, in 'Advances in Chemistry Series 229: Magnetic Resonance of Carbonaceous Solids', eds. R. E. Botto and Y. Sanada, Washington, DC, 1993, Chap. 4)

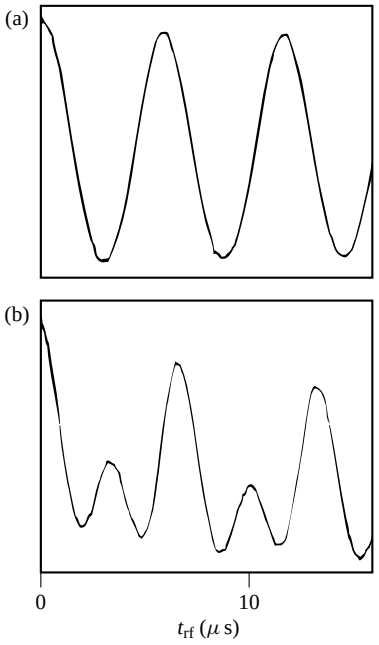

Figure 11 Sublevel nuclear transient nutation patterns of protons in VO(IV)- and Cu(II)-doped $Mg(NH_4)_2(SO_4)_2{\cdot}6H_2O$ single crystals: (a) one proton in $VO(H_2O)_5^{2+}$ and (b) two magnetically equivalent protons in $Cu(H_2O)_6^{2+}$. (Reproduced by permission of the American Chemical Society from C. Gemperle and A. Schweiger, *Chem. Rev.*, 1991, **91**, 1481)

harmonics provides a method for determining the number of equivalent nuclei coupled to the electron.

3.1.3 Optimized Davies and Mims ENDOR

The Davies or Mims ENDOR pulse sequences produce a maximum ENDOR enhancement of $\Delta\chi_e/\chi_e = 1$. A pulse scheme for theoretically increasing this efficiency to $\Delta\chi_e/\chi_e = 2$ has been proposed and demonstrated.[42] This is accomplished by inserting a microwave π pulse and a second rf π pulse following the first rf π pulse in the mixing period. This pulse sequence is the pulsed analog of the Special TRIPLE resonance technique which was also introduced to improve the efficiency in the CW ENDOR experiment.[34,62,63] In practice, the improvement in efficiency of the Davies or Mims ENDOR signal intensity is much smaller than theoretically possible, primarily because of pulse imperfections. Nevertheless, a gain in ENDOR enhancement is observed, as shown in the example given in Figure 12. Nonideal nutation angles due to pulse imperfections are particularly problematic for noncrystalline samples where the ENDOR lines are significantly overlapped.

3.1.4 Electron–Nucleus Coherence Effects

Electron–nucleus coherence effects can be observed in the Davies ENDOR experiment if the microwave pulses in the detection period excite both allowed and semiforbidden ESR transitions.[38,37] These coherence effects generate a nuclear modulation on the envelope of the primary electron spin echo in the detection period analogous to the ESEEM experiment. An example of this phenomenon is shown in Figure 13 where two Davies ENDOR spectra for the blue copper protein,

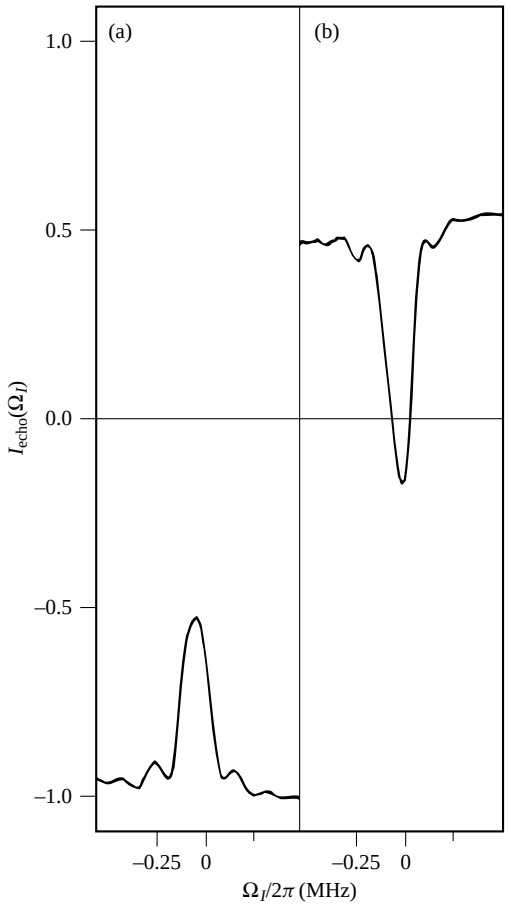

Figure 12 Mims-ENDOR spectra (a) of Cu(II)-doped TGS single crystal around the proton transition at $\omega_p/2\pi = 10.15$ MHz and the optimized spectra obtained using the pulse sequence described in the text. (Reproduced by permission of Academic Press from C. Gemperle et al., *J. Magn. Reson.*, 1990, **87**, 502)

stellacyanin, are shown recorded for two different values of the spin echo delay time τ in the detection period. The values of τ used in the detection period are indicated on the echo envelope waveform shown in the inset. These coherence effects can have important consequences for the analysis of the ENDOR spectrum. Note that the relative amplitudes of the ENDOR intensities depend on the value of τ in the detection period. This effect can be used as a spectral editing technique.[38,37]

3.1.5 Electron–Nucleus–Nucleus Triple Resonance

The Double ENDOR was originally introduced as a CW ENDOR technique to establish the connectivity of hyperfine sublevels and to determine the relative signs of the hyperfine interaction for nonequivalent nuclei.[63,64] The pulsed implementation of the Double ENDOR experiment is shown in Figure 14.[41] The experiment is analogous to the Davies ENDOR experiment, except that a second rf π pulse is inserted in the mixing period to irradiate a preselected ENDOR transition. The Double ENDOR difference spectrum, obtained from the difference between the ENDOR and Double ENDOR spectrum, identifies any changes in intensities of the ENDOR transitions induced by pumping at the second rf frequency. A peak in the Double ENDOR difference spectrum will only be

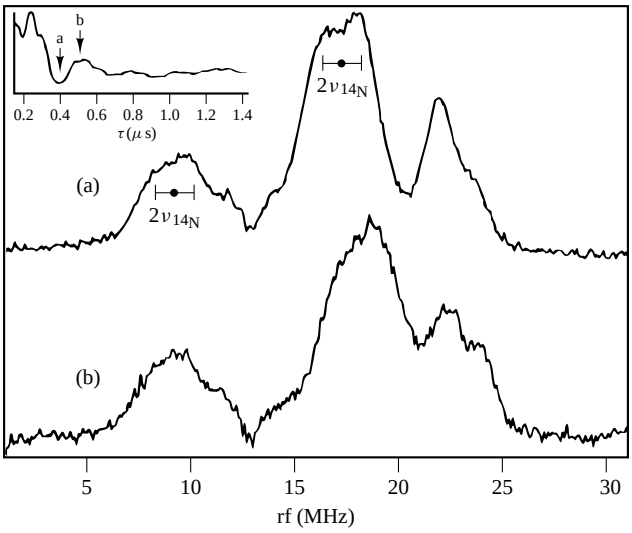

Figure 13 Davies ENDOR spectra of stellacyanin at the two pulse modulation minimum at τ = 0.40 μs (a) and at the maximum at τ = 0.51 μs (b). (Reproduced by permission of Academic Press from H. Thomann and M. Bernardo, in *Methods in Enzymology*, eds. J. F. Riordan and B. L. Vallee, London 1993, Vol. **227**, Chap. 6)

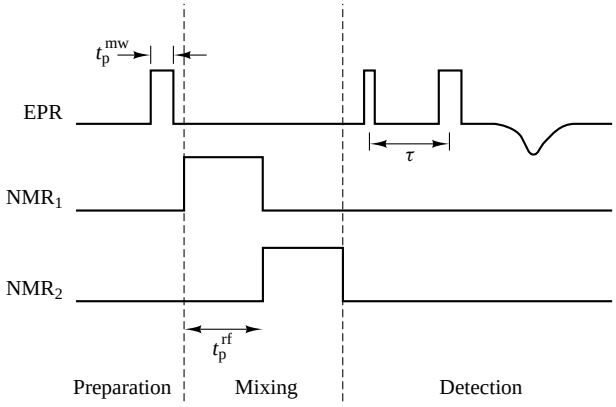

Figure 14 Pulsed implementation of double ENDOR. (Reproduced by permission of Academic Press from H. Thomann and M. Bernardo, in 'Methods in Enzymology', eds. J. F. Riordan and B. L. Vallee, London 1993, Vol. 227, Chap. 6)

observed if the two sublevels each have a level in common with the ESR transition.

An example of the pulsed Double ENDOR and Double ENDOR difference spectrum recorded for the radical in the conjugated conducting polymer, polyacetylene, is shown in Figure 15.[41] The Double ENDOR difference spectra indicate that the unpaired electron is coupled to protons with both positive and negative hyperfine interactions. In this case, similar conclusions were obtained using the CW Double ENDOR experiment and the results were used to determine an electron–electron correlation energy using a Hartree–Fock molecular orbital calculation.[65] However, the CW Double ENDOR experiment was only successful over a restricted temperature range, which is not the case for the pulsed version of the experiment. The pulsed Double ENDOR experiment has also been applied to studies of the irradiated malonic acid radical molecule[45,43] and to studies of the coordination

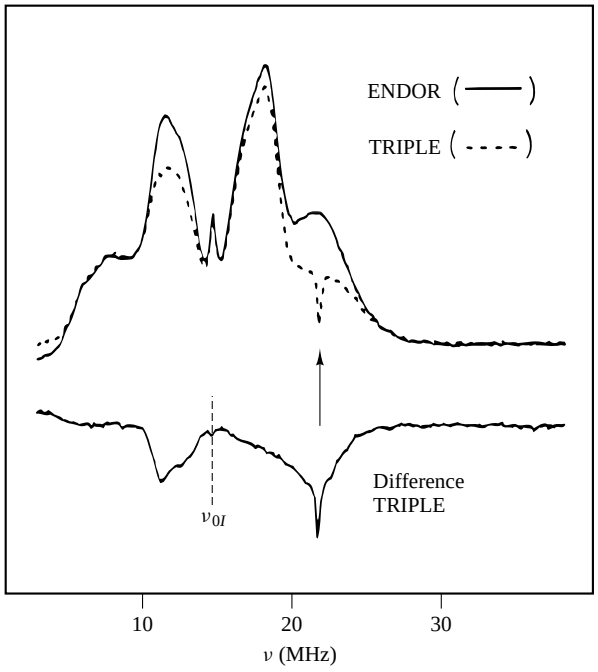

Figure 15 Pulsed Double and Double ENDOR difference spectrum of the polyacetylene radical. (Reproduced by permission of John Wiley & Sons from A. Grupp and M. Mehring in 'Modern Pulsed and Continuous Wave Electron Spin Resonance', eds. L. Kevan and M. K. Bowman, Chichester, 1979, Chap. 4)

structure of transition metal ions and metal clusters in metalloenzymes.[38]

3.1.6 Electron–Nucleus–Electron Triple Resonance

Another variation of a pulsed triple resonance experiment is shown in Figure 16.[38,37] This experiment is related to the Davies ENDOR experiment, except that the frequency of the detection pulses are offset by a frequency Δ from the frequency of the preparation pulse. This is shown schematically in Figure 17 by the magnetic positions at which the preparation, indicated by B_p, and detection, indicated by B_d, irradiation pulses are applied within the ESR absorption envelope. Sublevel polarization transfer that connects the positions B_p and B_d must originate from rf driven sublevel NMR transitions. Polarization transfer by mechanisms other than rf driven nuclear spin flips, such as by spin diffusion, are ineffective because of the short time interval between the preparation and detection period. The value of Δ therefore preselects nuclei with the hyperfine coupling $A = \Delta$. For this reason, the ENDOR spectrum generated for $\Delta = A$ is referred to as a hyperfine selective (HS) ENDOR spectrum. An HS ENDOR spectrum can also be generated by jumping the applied magnetic field.[42]

The HS ENDOR technique is illustrated in Figure 18. The Davies ENDOR spectra for the blue copper protein, stellacyanin, recorded for the native pH 7 form of the protein and for the high-pH (pH 11) perturbed blue form of the protein are shown in Figures 18(a) and 18(b), respectively. The spectra are identical except for the intensity of a transition at 21 MHz observed in the spectrum of the high-pH form. The assignment of this peak is facilitated using the HS ENDOR experiment, as

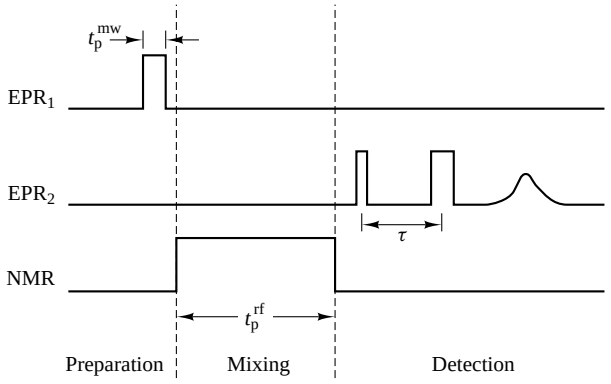

Figure 16 Pulsed electron–nucleus–electron triple resonance pulse sequence. (Reproduced by permission of Academic Press from H. Thomann and M. Bernardo, in 'Methods in Enzymology', eds. J. F. Riordan and B. L. Vallee, London 1993, Vol. 227, Chap. 6)

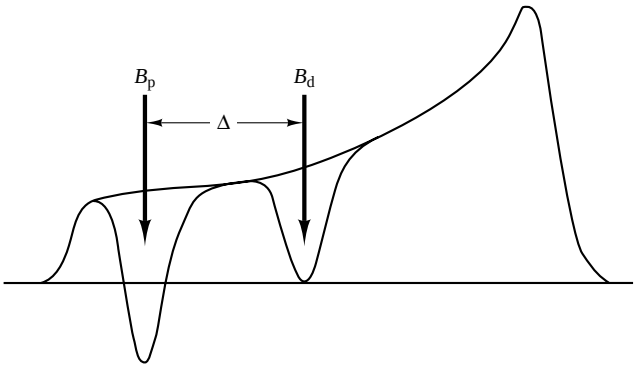

Figure 17 EPR spectra of an inhomogeneously broadened line showing the inversion 'hole' at B_p after the preparation period and the position B_d of the detection pulses. (Reproduced by permission of Academic Press from H. Thomann and M. Bernardo, in 'Methods in Enzymology', eds. J. F. Riordan and B. L. Vallee, London, 1993, Vol. 227, Chap. 6)

illustrated by the three HS ENDOR spectra recorded for values of Δ = 19, 42, and 36 MHz, which are shown in Figures 18(c), 18(d) and 18(e) respectively.

3.2 EPR Detected Sublevel Nuclear Coherence

Sublevel coherence can be created by a $\pi/2$ rf pulse applied at the end of the preparation period. Once created, this sublevel coherence can be manipulated in analogy to many other solid state NMR experiments. Specific examples of these type of experiments are described in this section.

3.2.1 Nuclear Free Induction

The evolution of the sublevel coherence under free precession in the local field can be detected indirectly using the pulse sequence shown in Figure 19.[41,43] The frequency of the rf pulses are set to excite a transition in the ENDOR spectrum. The sublevel coherence evolving during the evolution time t_1 is converted back to electron spin longitudinal polarization by a second rf $\pi/2$ pulse. The sublevel coherence signal at evolution time t_1 is then detected indirectly from the intensity

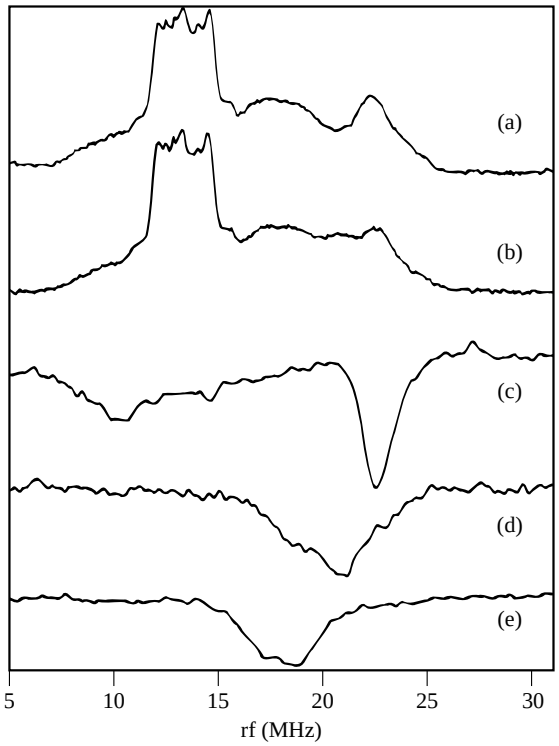

Figure 18 Davies ENDOR spectra of the native (pH 7) form (a) and the high-pH (pH 11) form (b) of stellacyanin. HS ENDOR spectra of the high pH form with Δ = 19.0 (c), 42.0 (d), and 36 (e) MHz were used to assign the feature at 21 MHz to nitrogen. (Reproduced by permission of Academic Press from H. Thomann and M. Bernardo, in 'Methods in Enzymology', eds. J. F. Riordan and B. L. Vallee, London, 1993, Vol. 227, Chap. 6)

modulation of the primary electron spin echo in the detection period. The sublevel free induction signal is then detected point by point by incrementing t_1 on successive pulse sequence iterations. Both the in-phase and phase-quadrature sublevel free precession signals can be detected by phase shifting the relative phase of the two rf pulses by $\pi/2$. Additional phase cycling by π can be used to cancel the effects of electron spin–lattice magnetization recovery during the t_1 evolution period. The rf pulse excitation bandwidth is usually much smaller than the spectral spread of the ENDOR spectrum. In order to record the entire ENDOR spectrum, the pulse sequence shown in Figure 19 must be repeated with the rf frequency incremented on successive experiments. A spectral slice of the overall ENDOR spectrum, determined by the bandwidth of the rf excitation pulse, is recorded for each selected rf. The whole ENDOR spectrum is reconstructed by adding the slices of the limited spectral regions recorded in each experiment.

The ESR detected sublevel free precession experiment is illustrated in Figure 20. These data are collected for a crystal of irradiated malonic acid. In the Davies ENDOR spectrum, a transition that shows no evidence of fine structure is observed at 14.42 MHz. The in-phase and phase-quadrature sublevel free precession signals recorded using the pulse sequence in Figure 19 and the procedure described above are shown in Figure 20(a). The complex Fourier transform of these waveforms is shown in Figure 20(b). This spectrum indicates that the ENDOR line is composed of three overlapping

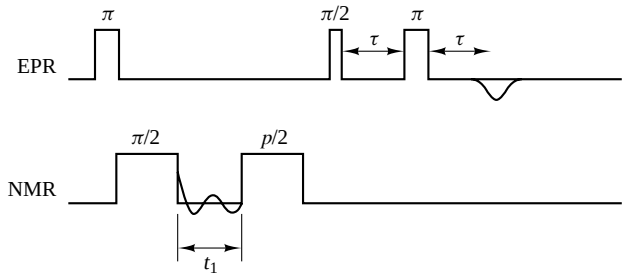

Figure 19 Pulse sequence for EPR detection of sublevel FID. (Reproduced by permission of the American Chemical Society from H. Thomann and M. Bernardo, in 'Advances in Chemistry Series 229: Magnetic Resonance of Carbonaceous Solids', eds. R. E. Botto and Y. Sanada, Washington, DC, 1993, Chap. 4)

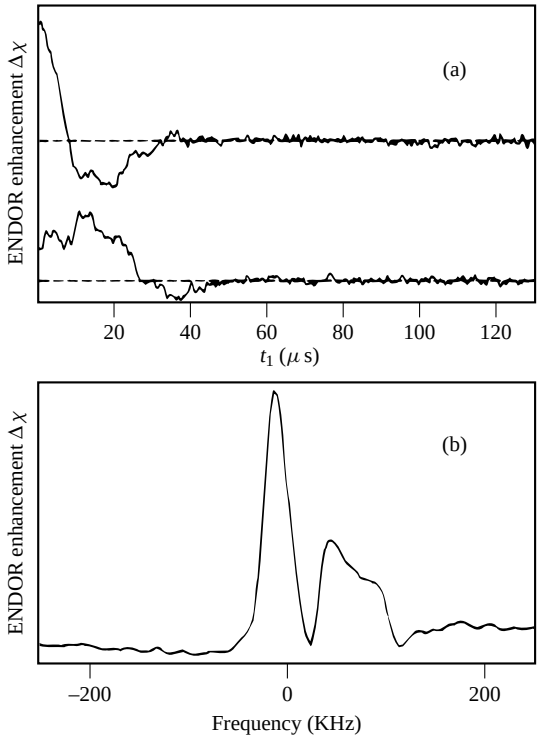

Figure 20 Quadrature sublevel FID signals of malonic acid with ν_{rf} = 14.42 MHz (a) and corresponding complex FT spectrum (b). (Reproduced by permission of the American Chemical Society from H. Thomann and M. Bernardo, in 'Advances in Chemistry Series 229: Magnetic Resonance of Carbonaceous Solids', eds. R. E. Botto and Y. Sanada, Washington, DC, 1993, Chap. 4)

transitions which are not resolved in the Davies ENDOR spectrum.

3.2.2 Multiple Quantum Electron–Nucleus Coherence

The coupling of two or more nuclei with equivalent hyperfine couplings can be detected indirectly using the pulse sequences shown in Figure 21.[41,66] The sublevel polarization can be created using either the inversion–recovery technique with primary spin echo detection (i.e. as in the Davies ENDOR pulse sequence) or by the two pulse excitation in the preparation period with a single pulse in the detection

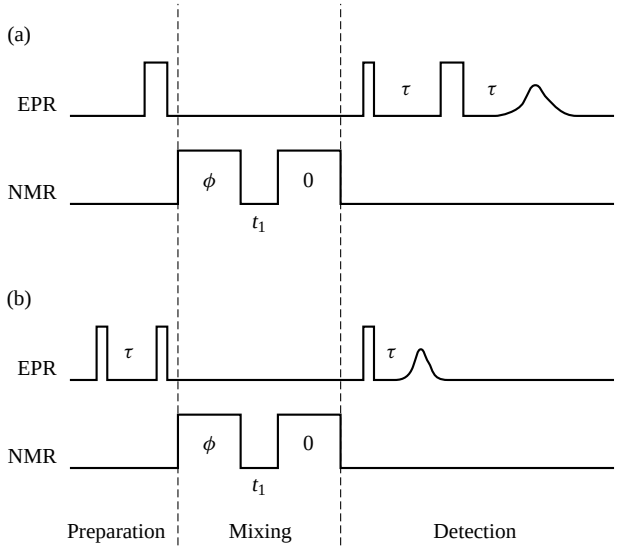

Figure 21 Multiple quantum (MQ) ENDOR pulse sequences: Davies MQ ENDOR (a) and Mims MQ ENDOR (b). (Reproduced by permission of Laser Pages Publishing from H. Thomann and M. Bernardo, *Isr. J. Chem.*, 1992, **32**, 323)

period to create a stimulated echo (i.e. as in the Mims ENDOR pulse sequence). An n-quantum sublevel coherence is detected using the phase incrementation technique in analogy to the NMR experiment.[53,67] An n-quantum coherence accumulates a phase $\theta_n = n\omega_{ENDOR}t_{evol}$ where t_{evol} is an evolution time and ω_{ENDOR} is the sublevel transition frequency.

In the present experiments the phase accumulation occurs during the nutation of the sublevel polarization so that $t_{evol} = t_p^{rf}$. This phase accumulation can be detected by incrementing the phase of the rf mixing pulse in the middle of the mixing period. Theoretically, the optimum ENDOR signal is obtained by applying two $\pi/2$ rf pulses. Each point on the plot of the phase interferogram is collected by incrementing the phase of the second rf pulse on successive pulse sequence iterations.

An example of a multiple quantum spectrum recorded using the pulse sequence in Figure 21(a) for the malonic acid radical molecule is shown in Figure 22.[66] Multiple quantum coherences up to n = 3 are observed for an ENDOR transition at 14.42 MHz recorded for the malonic acid radical molecule in a crystal at an arbitrary orientation. This is consistent with the three lines observed in the ESR detected sublevel FID spectra recorded under identical conditions [Figure 20(b)]. Multiple quantum spectra recorded for several evolution times for free precession are also shown in Figure 22. The oscillation for each order of coherence originates from the free precession of transverse sublevel magnetization in the presence of the local field.

3.2.3 Nuclear Spin Echoes

Hyperfine sublevel spin echoes can be created and detected indirectly by inserting a refocusing rf pulse in the evolution period of the mixing period for the pulse sequence shown in Figure 20. The pulse sequence for this indirect detection of sublevel spin echoes is shown in Figure 23.[40,41] The first rf pulse in the mixing period creates sublevel coherence. This coherence evolves under free precession for time τ_n and is

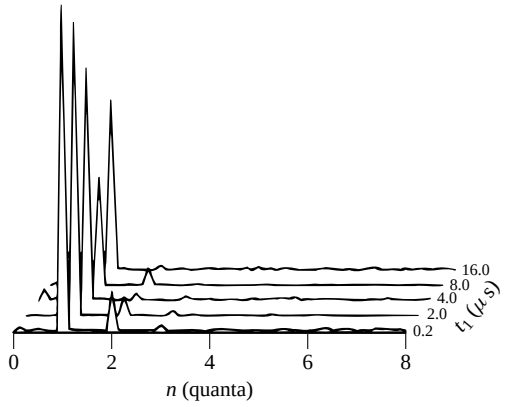

Figure 22 Davies multiple quantum ENDOR spectra of the malonic acid radical for various evolution times. (Reproduced by permission of Laser Pages Publishing from H. Thomann and M. Bernardo, *Isr. J. Chem.*, 1992, **32**, 323)

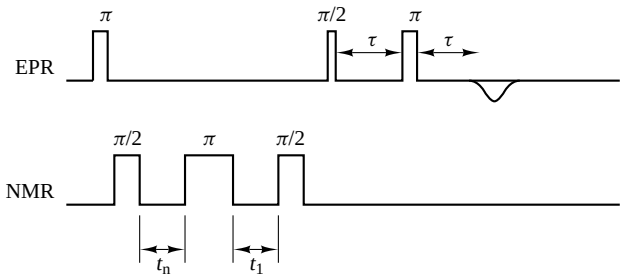

Figure 23 Pulse sequence for EPR detection of sublevel spin echo. (Reproduced by permission of the American Chemical Society from H. Thomann and M. Bernardo, in 'Advances in Chemistry Series 229: Magnetic Resonance of Carbonaceous Solids', eds. R. E. Botto and Y. Sanada, Washington, DC, 1993, Chap. 4)

then refocused by the rf π pulse. The sublevel spin echo formed at time τ_n after the refocusing pulse can be detected by incrementing the time t_1 of the third rf mixing pulse. The third rf pulse transforms the sublevel coherence into two spin electron–nucleus longitudinal order. This is transformed to electron spin coherence for detection of the electron spin polarization by the microwave pulses in the detection period.

The sublevel echo can be detected point by point by incrementing the value of t_1 from $t_1 < \tau_n$ to $t_1 > \tau_n$ on successive pulse sequence iterations. In each pulse sequence iteration the sublevel coherence is detected by the change in intensity of the electron spin echo in the detection period. An example of sublevel spin echoes detected by this procedure for an X-ray irradiated malonic acid crystal are shown in the inset of Figure 24. The two sublevel spin echoes shown were recorded for τ_n values of 5 and 20 μs.

The circles shown in the inset of Figure 24 indicate the echo envelope intensities recorded for several values of $t_1 = \tau_n$. The full sublevel spin echo decay envelope along with a fit to a single exponential and the residuals for the fit are also shown in Figure 24. These sublevel echoes and envelope decay were recorded for the ν_+ = 30.19 MHz ENDOR transition. This corresponds to the proton NMR transition for the α proton of the $\cdot CH(COOH)_2$ radical molecule which is shifted to the high-frequency side of the proton Larmor frequency. The sublevel T_{2n} decay time obtained from the single exponential fit shown

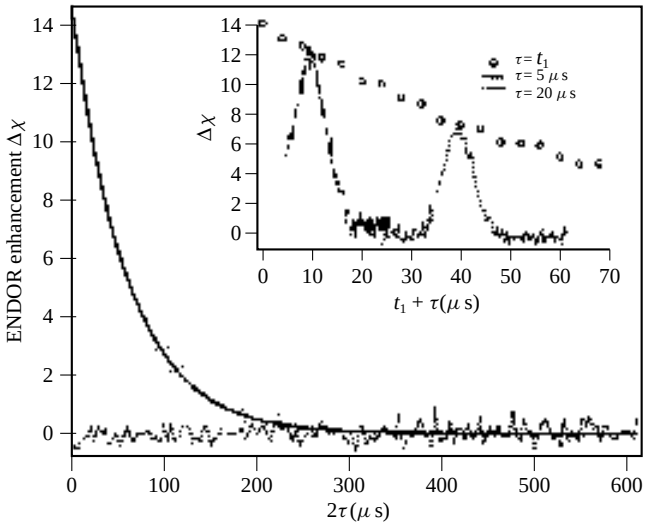

Figure 24 The sublevel spin echo decay recorded with $t_1 = \tau_n$ along with the fit to a single exponential and the residuals of the fit. (Reproduced by permission of the American Chemical Society from H. Thomann and M. Bernardo, in 'Advances in Chemistry Series 229: Magnetic Resonance of Carbonaceous Solids', eds. R. E. Botto and Y. Sanada, Washington, DC, 1993, Chap. 4)

in Figure 24 is 60 μs. The proton T_{2n} values measured for $\nu_{rf} = \nu_n$ are shorter than the values measured at frequencies shifted away from the proton Larmor frequency.

Similar results have been obtained in sublevel nuclear T_{2n} studies of protons in coal samples.[46] In these coal studies, the ESR detected sublevel T_{2n} values measured at $\nu_{rf} = \nu_n$ were similar to the value measured directly by NMR.[68] The ESR detected sublevel T_{2n} values increased for NMR transitions shifted further away from the proton Larmor frequency. Apparently the time-dependent local magnetic field from the hyperfine interaction is not an effective sublevel T_{2n} relaxation mechanism. The T_{2n} value measured directly by NMR is determined by the proton homonuclear dipolar coupling. The equivalence of the value measured in the ESR detected sublevel T_{2n} experiment for $\nu_{rf} = \nu_n$ suggests that the T_{2n} value is also determined by the proton dipolar interaction with the hyperfine coupling serving only as a mechanism for detecting the sublevel coherence signal. Quite different results can be expected if the time dependence of the local field is an effective T_{2n} mechanism. In this case the T_{2n} values would be expected to decrease as the NMR transition frequency is shifted away from the proton Larmor frequency.

3.3 Coherence Transfer ENDOR

In analogy to the coherence transfer experiments known in NMR spectroscopy, it is also possible to detect the hyperfine sublevel transitions by an electron–nuclear double resonance coherence transfer experiment.[41,43,69] Three different pulse sequences for coherence transfer ENDOR experiments are shown in Figure 25. The basic principle in all three types of experiment is similar. The rf pulses applied during the period of free precession of the electron spin coherence created by a $\pi/2$ microwave pulse interfere with the refocusing of this electron coherence following the microwave π pulse.

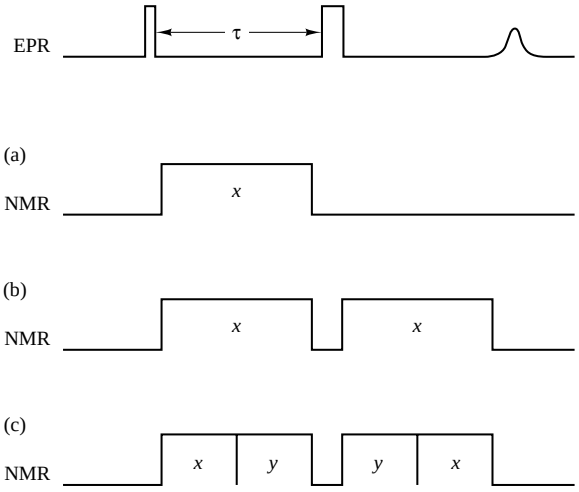

Figure 25 Pulse sequences for coherence transfer ENDOR

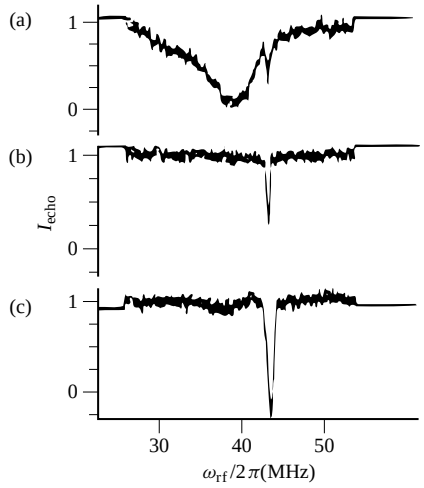

Figure 26 Coherence transfer single crystal ENDOR spectra of the malonic acid radical recorded with corresponding pulse sequences shown in Figure 25. (Reproduced by permission of the American Chemical Society from C. Gemperle and A. Schweiger, *Chem. Rev.*, 1991, **91**, 1481)

This occurs if the rf pulse is on resonance with an NMR transition that has a sublevel in common with the electron spin eigenlevel that belongs to the states from which the electron spin coherence was created. In this case, the sublevel NMR transition shifts the phase of the electron spin coherence which is detected as an attenuation of the electron spin echo. If the rf pulse is a π pulse the electron spin echo intensity is reduced to zero resulting in $\Delta\chi_e/\chi_e = 1$. If the rf pulse is a 2π pulse, the echo intensity changes sign resulting in $\Delta\chi_e/\chi_e = 2$. If a 4π pulse is applied, the electron spin echo intensity returns to its original intensity. This response of the electron spin echo intensity to the rotational symmetry of the sublevel nutation angle is called the 'spinor property' and is a property of wavefunctions for spin-$\frac{1}{2}$ particles.

The ENDOR spectrum recorded using the pulse sequence shown in Figure 25(a) is sufficient to observe the coherence transfer ENDOR effect. However, the application of a single rf pulse also produces a large Bloch–Siegert (BS) frequency shift $\omega_{BS} = -\gamma_e(B_2^2/B_0)$, which results in a phase shift of $\omega_{BS}t_p^{rf}$. Since the rf magnetic field strength is not constant as a function of frequency across the ENDOR spectrum, the Bloch–Siegert phase shift is observed as a broad feature, as shown in Figure 26(a), which can mask the ENDOR transitions. The Bloch–Siegert phase shift can be refocused by applying a second rf pulse, as shown in Figure 25(b), which is symmetrically displaced about the microwave refocusing pulse. This eliminates the broad feature in the ENDOR spectrum as shown in Figure 26(b). The maximum ENDOR effect of $\Delta\chi_e/\chi_e = 1$ is observed when the two rf pulses are π pulses. The efficiency of the ENDOR effect can theoretically be increased to $\Delta\chi_e/\chi_e = 2$ if the two rf pulses are 2π pulses but with a 90° shift introduced, as shown in Figure 25(c).[41,43] The enhancement in the ENDOR signal intensity is shown in Figure 26(c). In practice, the ENDOR efficiency is improved for this phase shifted spinor ENDOR pulse sequence, but because of technical limitations (primarily pulse imperfections) the increase in efficiency is much smaller than theoretically expected. Another limitation of coherence transfer ENDOR experiments is that the ENDOR lines are usually power broadened because of the short electron phase memory time encountered for most samples. It is rare that phase memory times are longer than a few microseconds, even at liquid helium temperatures. Nevertheless, the coherence transfer ENDOR experiment has revealed fundamentally interesting properties of the spin dynamics of the electron–nucleus spin system.

4 CONCLUDING REMARKS

ENDOR and the extension to PE NMR spectroscopy are presently tools of the specialist. They are very powerful techniques in specific cases where the spectra and/or spin dynamics for the nuclei of interest are strongly influenced by the large local magnetic fields originating from the hyperfine coupling with unpaired electron spins. In such cases the NMR transition frequencies are shifted by very large values when compared with NMR spectra of diamagnetic samples. When these circumstances do apply, ENDOR and PE NMR spectroscopy are often the only techniques which can provide the desired information. In this review we have included examples of applications in organic solids, metallobiochemistry, and organometallic chemistry. With the introduction of pulsed excitation techniques, extension to multiple irradiation frequencies, and the introduction of commercially available pulsed instrumentation, continued development of the methodology and an increasing range of applications can be expected for these techniques in the near future. Recent developments in high-frequency ESR,[70] including the extension to high-frequency ENDOR,[71] will also likely expand the range of research applications. The combination of pulsed ESR and pulsed NMR should continue to be a vibrant area of research as new technology becomes available and as new methodologies and applications are developed.

5 RELATED ARTICLES

Chemically Induced Dynamic Nuclear Polarization; Cobalt(II)- and Nickel(II)-Substituted Proteins; Contrast

Agents in MRI: Superparamagnetic Iron Oxide; Contrast Agents in Whole Body Magnetic Resonance: An Overview; Contrast Agents in Magnetic Resonance: Operating Mechanisms; Copper Proteins; Dynamic Nuclear Polarization and High-Resolution NMR of Solids; Electron–Nuclear Hyperfine Interactions; EPR and In Vivo EPR: Roles for Experimental and Clinical NMR Studies; Heme Peroxidases; Iron—Sulfur Proteins; EPR and In Vivo EPR: Roles for Experimental and Clinical NMR Studies.

6 REFERENCES

1. H. Kurreck, B. Kirste, and W. Lubtiz, *ENDOR Spectroscopy of Radicals in Solution*, VCH, New York, 1988.
2. J. E. Wertz and J. R. Bolton, *Electron Spin Resonance: Elementary Theory and Practical Applications*, Chapman & Hall, London, 1986.
3. J. A. Weil (ed.), *Electronic Magnetic Resonance of the Solid State*, Canadian Society for Chemistry, Ottawa, 1987.
4. L. Petrakis and J. R. Fraissard (eds), *Magnetic Resonance. Introduction to Advanced Topics and Applications to Fossil Energy* (*NATO ASI Series C, Vol. 124*), Reidel, Dordrecht, 1984.
5. R. E. Botto and Y. Sanada (eds), *Advances in Chemistry Series: Magnetic Resonance of Carbonaceous Solids*, American Chemical Society, Washington, DC, 1993.
6. A. Abragam and B. Bleaney, *Electron Paramagnetic Resonance of Transition Ions*, (*International Series of Monographs on Physics*), Oxford University Press, Oxford, 1970.
7. J. R. Pilbrow, *EPR of Transition Metal Ions* (*International Series of Monographs on Physics*), Clarendon, Oxford, 1991.
8. J.-M. Spaeth, J. R. Niklas, and R. H. Bartram, *Structural Analysis of Point Defects in Solids*, Springer, New York, 1992.
9. L. J. Berliner and J. Reuben (eds), *EMR of Paramagnetic Molecules* (*Biological Magnetic Resonance, Vol. 13*), Plenum, New York, 1993.
10. L. J. Berliner and J. Reuben (eds), *NMR of Paramagnetic Molecules* (*Biological Magnetic Resonance, Vol. 12*), Plenum, New York, 1993.
11. I. Bertini and C. Luchinat, *NMR of Paramagnetic Molecules in Biological Systems*, Benjamin Cummings, Menlo Park, CA, 1986.
12. G. N. LaMar (ed.), *NMR of Paramagnetic Molecules*, Academic, New York, 1973.
13. A. Abragam, *The Principles of Nuclear Magnetism* (*International Series of Monographs on Physics*), Oxford University Press, Oxford, 1961.
14. C. D. Jeffries, *Dynamic Nuclear Orientation*, Wiley, New York, 1963.
15. M. Goldman, *Spin Temperature and Nuclear Magnetism in Solids* (*International Series of Monographs on Physics*), Oxford University Press, Oxford, 1970.
16. A. Abragam and M. Goldman, *Nuclear Magnetism: Order and Disorder* (*International Series of Monographs on Physics*), Oxford University Press, Oxford, 1982.
17. R. A. Wind, M. J. Duijvestijn, C. van der Lugt, A. Manenschijn, and J. Vriend, *Prog. NMR Spectrosc.*, 1985, **17**, 33.
18. R. D. Bates, Jr, *Magn. Reson. Rev.*, 1993, **16**, 237.
19. R. A. Wind, R. Lewis, H. Lock, and G. E. Maciel, in *Advances in Chemistry Series: Magnetic Resonance of Carbonaceous Solids*, ed. R. E. Botto and Y. Sanada, American Chemical Society, Washington, DC, 1993, Vol. 229, Chap. 3, p. 45.
20. M. Afeworki, R. McKay, and J. Schaefer, *Macromolecules*, 1992, **25**, 4084.
21. G. G. Maresch, R. D. Kendrick, C. S. Yannoni, and M. E. Galvin, *J. Magn. Reson.*, 1989, **82**, 41.
22. R. A. Wind, in *Modern NMR Techniques and their Applications in Chemistry*, eds. A. I. Popov and A. I. Hallenga, Marcel Dekker, New York, 1991.
23. W. B. Mims, in *Electron Paramagnetic Resonance*, ed. S. Geschwind, Plenum, New York, 1973.
24. S. A. Dikanov and Yu. D. Tsvetkov, *Electron Spin Echo Envelope Modulation (ESEEM) Spectroscopy*, CRC, Boca Raton, FL, 1992.
25. L. Kevan and R. N. Schwartz (eds.), *Time Domain Electron Spin Resonance*, Wiley, New York, 1979.
26. L. Kevan and M. K. Bowman (eds.), *Modern Pulsed and Continuous Wave Electron Spin Resonance*, Wiley, New York, 1990.
27. W. B. Mims and J. Peisach, in *Biological Magnetic Resonance*, Plenum, New York, 1981, Vol. 3, p. 213.
28. D. J. Singel, in *Advanced EPR: Applications in Biology and Biochemistry*, ed. A. J. Hoff, Elsevier, Amsterdam, 1989.
29. A. Schweiger, *Angew. Chem., Int. Ed. Engl.*, 1991, **30**, 265.
30. G. Feher, *Phys. Rev.*, 1956, **103**, 834.
31. L. Kevan and L. D. Kispert, *Electron Spin Double Resonance Spectroscopy*, Wiley, New York, 1976.
32. M. M. Dorio and J. Freed (eds.), *Multiple Electron Resonance Spectroscopy*, Plenum, New York, 1979.
33. B. M. Hoffman, *Acc. Chem. Res.*, 1992, **24**, 164.
34. K. Moebius, M. Plato, and W. Lubitz, *Phys. Rep.*, 1982, **87**, 171.
35. A. J. Hoff (ed.), *Advanced EPR: Applications in Biology and Biochemistry*, Elsevier, Amsterdam, 1989.
36. A. Schweiger, in *Structure & Bonding*, Springer, Berlin, 1982, Vol. 51, p. 1.
37. H. Thomann and Marcelino Bernardo, in *Biological Magnetic Resonance*, eds. L. J. Berliner and J. Reuben, Plenum, New York, 1993, Vol. 13, Chap. 7, p. 275.
38. H. Thomann and M. Bernardo, in *Methods in Enzymology*, eds. J. F. Riordan and B. L. Vallee, Academic, San Diego, 1993, Vol. 227, Chap. 6, p. 118.
39. H. Thomann and W. B. Mims, in *Pulsed Magnetic Resonance: NMR, ESR, and Optics*, ed. D. M. S. Bagguley, Clarendon, Oxford, 1992, p. 362.
40. P. Hoefer, A. Grupp, and M. Mehring, in *Electronic Magnetic Resonance of the Solid State*, ed. J. A. Weil, Canadian Society for Chemistry, Ottawa, 1987.
41. A. Grupp and M. Mehring, in *Modern Pulsed and Continuous Wave Electron Spin Resonance*, eds. L. Kevan and M. K. Bowman, Wiley, New York, 1979, Chap. 4, p. 195.
42. C. Gemperle and A. Schweiger, *Chem. Rev.*, 1991, **91**, 1481.
43. M. Mehring, P. Hoefer, and A. Grupp, *Ber. Bunsenges. Phys. Chem.*, 1987, **91**, 1132.
44. W. A. J. A. van der Poel, D. J. Singel, J. Schmidt, and J. H. van der Waals, *Mol. Phys.*, 1983, **49**, 1017.
45. H. Thomann and M. Bernardo, in *Magnetic Resonance of Carbonaceous Solids* (*Advances in Chemistry Series, Vol. 229*), ed. R. E. Botto and Y. Sanada, American Chemical Society, Washington, DC, 1993, Chap. 4, p. 65.
46. H. Thomann, M. Bernardo, and B. G. Silbernagel, in *Magnetic Resonance of Carbonaceous Solids*, (*Advances in Chemistry Series, Vol. 229*), eds. R. E. Botto and Y. Sanada, American Chemical Society, Washington, DC, 1993, Chap. 30, p. 561.
47. C. P. Slichter, *Principles of Magnetic Resonance* (*Springer Series in Solid State Sciences*), 3rd edn., Springer, New York, 1990.

48. N. M. Atherton, *Principles of Electron Spin Resonance*, Ellis Horwood, Chichester, 1993.
49. G. H. Rist and J. H. Hyde, *J. Chem. Phys.*, 1970, **52**, 4633.
50. L. R. Dalton and A. L. Kwiram, *J. Chem. Phys.*, 1972, **57**, 1132.
51. G. C. Hurst, T. A. Henderson, and R. W. Kreilick, *J. Am. Chem. Soc.*, 1985, **107**, 7294.
52. B. M. Hoffman, J. Martinsen, and R. A. Venters, *J. Magn. Reson.*, 1984, **59**, 110.
53. R. R. Ernst, G. Bodenhausen, and A. Wokaun, *Principles of Nuclear Magnetic Resonance in One and Two Dimensions*, Clarendon, Oxford, 1987.
54. V. L. Hochmann, V. Ya. Zevin, and B. D. Shanina, *Sov. Phys. Solid State*, 1968, **10**, 269.
55. C. Gemperle, A. Schweiger, and R. R. Ernst, *Chem. Phys. Lett.*, 1988, **1**, 145.
56. E. R. Davies, *Phys. Lett. Ser. A*, 1974, **47**, 1.
57. W. B. Mims, *Proc. R. Soc. London*, 1965, **283**, 452.
58. T. Wacker, G. A. Sierra, and A. Schweiger, *Isr. J. Chem.*, 1992, **32**, 305.
59. R. C. McCalley and A. L. Kwiram, *J. Phys. Chem.*, 1993, **97**, 2888.
60. P. E. Doan, C. Fan, C. E. Davoust, and B. M. Hoffman, *J. Magn. Reson.*, 1991, **95**, 169.
61. J. Peisach, W. G. Levine, and W. E. Blumberg, *J. Biol. Chem.*, 1967, **242**, 2847.
62. K. Moebius, W. Lubitz, and M. Plato, in *Advanced EPR: Applications in Biology and Biochemistry*, ed. A. J. Hoff, Elsevier, Amsterdam, 1989, p. 441.
63. K. Moebius, in *Multiple Electron Resonance Spectroscopy*, eds. M. M. Dorio and J. Freed, Plenum, New York, 1979.
64. R. J. Cook and D. H. Whiffen, *Proc. R. Soc. London*, 1964, **84**, 845.
65. H. Thomann and L. R. Dalton, in *Handbook of Conducting Polymers*, ed. T. A. Skotheim, Marcel Dekker, New York, 1986, p. 1157.
66. H. Thomann and M. Bernardo, *Isr. J. Chem.*, 1992, **32**, 323.
67. J. Baum, M. Munowitz, A. N. Garroway, and A. Pines, *J. Chem. Phys.*, 1985, **83**, 2015.
68. B. C. Gerstein, C. Chow, R. G. Pembleton, and R. C. Wilson, *J. Phys. Chem.*, 1977, **81**, 565.
69. I. M. Brown, D. J. Sloop, and D. P. Ames, *Phys. Rev. Lett.*, 1969, **22**, 324.
70. S. S. Eaton and G. R. Eaton, *Magn. Reson. Rev.*, 1993, **16**, 157.
71. O. Burghaus, A. Kischkat-Toth, R. Klette, and K. Mobius, *J. Magn. Reson.*, 1988, **80**, 383.

Biographical Sketches

Hans Thomann. *b* 1954. B.S., 1976, Ph.D., 1982, Chemistry, State University of New York at Stony Brook, USA. Research interests: development of pulsed electron NMR techniques and their application to problems in catalysis, metallobiochemistry, and molecular solids; spin relaxation and molecular motion of fluids in porous media.

Marcelino Bernardo. *b* 1957. B.S., 1979, Rochester Institute of Technology, NY, USA. Research interests: development of pulsed electron NMR techniques and their application to problems in catalysis, metallobiochemistry, and molecular solids; MRI.

Enzyme-Catalyzed Exchange: Magnetization Transfer Measurements

Kevin M. Brindle

University of Cambridge, Cambridge, UK

1	Introduction	1
2	Theory and Experimental Methods	1
3	Fluxes Measured In Vivo	4
4	Concluding Remarks	6
5	Related Articles	6
6	References	6

1 INTRODUCTION

Magnetization transfer is a rapid reaction technique which can be used to measure enzyme-catalyzed fluxes with rate constants of the order of $1-10\,s^{-1}$. These measurements can be made not only in vitro but also in some cases in an intact living system, where this might be anything from microbial cells growing in culture to specific regions of the human brain. The techniques for measuring transfer of magnetization, which were discussed in detail and applied by Forsén and Hoffman,[1] were first applied to an enzyme-catalyzed reactions in vitro by Brown and Ogawa who measured exchange in the reaction catalyzed by adenylate kinase,[2] and by Brown and Cheshnovsky, who measured the rate of the reversible hydration of acetaldehyde catalyzed by carbonic anhydrase.[54] The first measurements made in vivo were also made by Brown and co-workers, who measured flux between inorganic phosphate (Pi) and adenosine triphosphage (ATP) in cells of the bacterium, *Escherichia coli*.[3] Since that time there have been numerous magnetization transfer studies of enzyme-catalyzed exchange both in vitro and in vivo. These have been discussed in a number of reviews.[4–7] I will concentrate here on applications of the technique in ^{31}P NMR measurements in vivo. Applications in whole body MR spectroscopy are also discussed elsewhere in the Encyclopedia.

2 THEORY AND EXPERIMENTAL METHODS

When the exchange rate constant is comparable to the spin–lattice relaxation rate and separate resonances are observed for the exchanging species then it is possible to determine the rate of exchange by measuring the transfer of nuclear polarization from one resonance to another. In ^{31}P NMR measurements in vivo, the spin–lattice relaxation rates are of the order of $0.1-1\,s^{-1}$.

Consider a two-site exchange system in which a nucleus exchanges between two sites, A and B.

$$\mathrm{A} \underset{k_{-1}}{\overset{k_{+1}}{\rightleftharpoons}} \mathrm{B} \qquad (1)$$

The z magnetizations of the A (M_A) and B (M_B) spins are described by the Bloch equations, which have been modified to include this exchange:

$$dM_A/dt = -\rho_A(M_A - M_0^A) - k_{+1}M_A + k_{-1}M_B \qquad (2)$$

$$dM_B/dt = -\rho_B(M_B - M_0^B) - k_{-1}M_B + k_{+1}M_A \qquad (3)$$

where $M_0{}^A$ and $M_0{}^B$ are the equilibrium z magnetizations of the A and B spins and ρ_A and ρ_B are their spin–lattice relaxation rates. The solutions of these equations are:

$$M_{A(t)} = C_1\exp(\lambda_+ t) + C_2\exp(\lambda_- t) + M_0^A \qquad (4)$$

$$M_{B(t)} = C_3\exp(\lambda_+ t) + C_4\exp(\lambda_- t) + M_0^B \qquad (5)$$

where $C_3 = C_1(\lambda_+ + \rho_A + k_{+1})/k_{-1}$ and $C_4 = C_2(\lambda_- + \rho_A + k_{+1})/k_{-1}$ and the constants C_1 and C_2 are determined by the values of M_A and M_B at $t = 0$. The quantities λ_+ and λ_- are given by:

$$\lambda_{+/-} = 1/2(-(\rho_A + k_{+1} + \rho_B + k_{-1}) + / - \{[(\rho_A + k_{+1}) - (\rho_B + k_{-1})]^2 + 4k_{+1}k_{-1}\}^{1/2}) \qquad (6)$$

Equations for exchange between three or more sites are of the same form as equations (2) and (3). Although there are no analytical solutions for systems containing more than four sites,[7] it is straightforward to solve the equations numerically.

There are several magnetization transfer experiments which can be used to measure the exchange rates in a simple two-site exchange system.[8]

2.1 Selective Inversion

If a selective 180° pulse is applied to the B spin then in general its resonance will undergo a nonexponential recovery towards its equilibrium value while the intensity of the A resonance undergoes a transient decrease in intensity. The z magnetization of the A spin at time t is given by:

$$M_{A(t)} - M_0^A = \frac{-2M_0^B k_{-1}}{\lambda_+ - \lambda_-}[\exp(\lambda_+ t) - \exp(\lambda_- t)] \qquad (7)$$

while the magnetization of the B spin is given by:

$$M_{B(t)} - M_0^B = \frac{-2M_0^B}{\lambda_+ - \lambda_-}[(\rho_A + k_{+1} + \lambda_+)\exp(\lambda_+ t) - (\rho_A + k_{+1} + \lambda_-)\exp(\lambda_- t)] \qquad (8)$$

The exchange rate constants can be obtained either by fitting the data to these solutions or initial rates can be measured to give $(\rho_B + k_{-1})$ for B and k_{+1} for A.[2,9] A selective inversion pulse can be obtained by using a relatively long, low power pulse. However for those spectrometers which lack the facility to produce low power pulses, selective inversion can also be obtained by using hard pulses in the DANTE sequence[10] or

by using a shortened one-dimensional (1D) version of the two-dimensional (2D) exchange experiment, which is described in Section 2.3. In the latter case the pulse sequence is: $\pi/2_x - t_1 - \pi/2_x$, where $t_1 = \frac{1}{2}\Delta\nu$ and $\Delta\nu$ is the difference in resonance frequencies of the A and B spins. If the transmitter frequency is set to the resonant frequency of the A spin then at the end of this sequence the A magnetization will lie along the $-z$ axis while the B magnetization is returned to the $+z$ axis.[11]

2.2 Selective Saturation

If the B spin is selectively irradiated (such that $M_B = 0$ at $t = 0$) for a time, t, then the observed intensity of the A resonance decays with a time constant $\rho_A + k_{+1}$ and reaches a new equilibrium value:

$$M^A_{(t=\infty)} = \frac{\rho_A M^A_0}{(\rho_A + k_{+1})} \tag{9}$$

Thus both ρ_A and k_{+1} can be calculated. The saturation pulse can be generated either by using a long, low power pulse or by using hard pulses in the DANTE sequence. Although instantaneous saturation is incompatible with the mechanism of saturation, it can be approximated by using a relatively large irradiating field strength.[12] The limit imposed on the amplitude of the saturating field is set by the requirement that the saturating pulse should be selective. Too large a saturating field will result in nonspecific saturation of the observed resonance leading to decreases in its steady-state magnetization ($M_\infty{}^A$) and apparent spin–lattice relaxation time.[13] Both effects will lead to an overestimation of the exchange rate. This experiment, which is sometimes referred to as the time-dependent saturation transfer experiment, has two variants which have also been used to measure enzyme-catalyzed exchange. In these experiments the steady state and equilibrium magnetizations of the nonirradiated spin ($M^A_{(t=\infty)}$ and $M_0{}^A$, respectively) are measured in order to obtain the ratio $\rho_A/(\rho_A + k_{+1})$ [see equation (9)]. The sum, $(\rho_A + k_{+1})$ is then determined in separate experiments by measuring the z magnetization of the A spin following either its inversion or saturation in the presence of saturation of the B spin. The A magnetization relaxes exponentially toward its steady-state value ($M^A_{(t=\infty)}$) with a time constant $(\rho_A + k_{+1})$. The relative accuracy of the kinetic parameters derived from these experiments in a given amount of time have been compared using simulated data.[14] The choice of which particular saturation transfer experiment to use depends on the rate constant to be measured and the T_1 of the observed resonance.

2.3 Two-Dimensional Exchange Experiments

The two-dimensional exchange experiment introduced by Jeener et al.[15] uses the following pulse sequence: $\pi/2 - t_1 - \pi/2 - t_m - \pi/2 - t_2$. The first two pulses frequency label the z magnetization. Transfer of this magnetization between the A and B spins due to cross relaxation or chemical exchange during the t_m period is then detected during the t_2 period following the third 90° pulse. These signals are recorded for regular increments of t_1 and the resulting matrix of free induction decays is then double Fourier transformed to produce a 2D spectrum. Magnetization that has exchanged between the A and B sites will appear as cross peaks while the diagonal peaks represent magnetization which has failed to migrate. Cross peaks arising from coherent magnetization transfer due to scalar coupling are eliminated by phase cycling the pulses.[16] The amplitudes of the peaks in the 2D spectrum are described by equations similar to those that describe signal intensities in the selective inversion experiment.[7] In early applications of the technique the exchange rate constants were estimated by recording 2D spectra at a series of t_m values and fitting the observed cross-peak intensities versus t_m to the appropriate exchange equation. Alternatively the rate constants can be estimated from the initial rate of cross-peak buildup, which is equal to k_{+1} (or k_{-1}). Recording a series of 2D spectra is extremely time consuming and therefore a method of analysis was developed to determine the rate constants from a single 2D exchange spectrum.

The 2D spectrum can be described by the following equation:

$$\mathbf{M} = \exp(\mathbf{R}t_m)\mathbf{M}_0 \tag{10}$$

where $\mathbf{M}$ is a matrix comprising the peak volumes in the spectrum and $\mathbf{R}$ is the matrix of exchange and relaxation rate constants. For the simple two-site exchange system described above, $\mathbf{R}$ has the form:

$$\mathbf{R} = -\begin{bmatrix} \rho_A + k_{+1} & -k_{-1} \\ -k_{+1} & \rho_B + k_{-1} \end{bmatrix} \tag{11}$$

$\mathbf{M}_0$ is a diagonal matrix representing the 2D spectrum obtained with $t_m = 0$. This is usually replaced with $\alpha\mathbf{S}_0$, where $\mathbf{S}_0$ is the diagonal matrix of mole fractions obtained from a fully relaxed 1D experiment and α is an unknown scaling factor. Replacing $\mathbf{M}_0$ with $\alpha\mathbf{S}_0$, which avoids collecting another 2D spectrum, gives rise to false values for the diagonal elements in the $\mathbf{R}$ matrix but leaves the off-diagonal elements, which specify the exchange rate constants, unaffected. This method, which has been termed 'back transformation'[17,18] and a 1D counterpart derived from it,[19] essentially involve fitting an exponential function to a data set consisting of only two time points. These are the magnetizations (signal intensities) of the exchanging species when $t_m = 0$ and when t_m is set at some other value. The value of t_m which will give the most precise estimate of the exchange rate constants, has been estimated to be equal to $1/(R + k)$, where R and k are the mean values of the relaxation and exchange rate constants, respectively.[20] The back transformation method has been used to estimate the exchange rate constants in the reactions catalyzed by adenylate kinase and phosphoglycerate mutase in vitro.[21]

Exchange rate constants can also be obtained from a single 2D exchange spectrum by using the 'accordion' experiment described by Bodenhausen and Ernst.[22] This is a modification of the 2D experiment in which the t_m period is incremented in steps of t_1 and the rate constants are obtained by analysis of the lineshapes in the resulting 2D spectrum. If, in the two-site exchange system discussed above, ρ_A and ρ_B and the concentrations of the A and B spins are equal then the diagonal peaks in the accordion spectrum will have a lineshape which is given by the sum of two Lorentzian lines with linewidths ρ and $(k_{+1} + k_{-1} + \rho)$ while the cross-peak lineshapes are given

by the difference between these two Lorentzian lines. This analysis of the accordion experiment was used to estimate the exchange rate constants in the reaction catalyzed by creatine kinase in vitro.[23] Analysis of the accordion experiment in a more typical case, where the populations of the exchanging spins are unequal and the relaxation rate constants are different has been considered by Kuchel.[7]

2.4 Comparison of 1D and 2D Methods

Two-dimensional methods have the advantage that in multisite exchange systems they can, in principle, detect all the exchanges in a single experiment. The 2D exchange experiment and its 1D counterpart also have the advantage that they use nonselective pulses and therefore avoid the problems associated with the limited selectivity of the irradiating field in the 1D experiments. All the methods described require some preliminary estimate of the exchange rate constant in order to optimize the experimental protocol, for example to choose the optimal t_m in the 2D experiments or the optimal saturation transfer protocol in the 1D experiments. For experiments in vivo, where limited sample viability precludes long data acquisition times, the 1D methods are preferred over the more time consuming 2D methods. This is reflected in the fact that although 2D exchange experiments have been performed,[24] the overwhelming majority of magnetization transfer measurements in vivo have employed 1D methods.

2.5 Effect of the Equilibrium Constant on Exchange Measurements

In the selective inversion and 2D experiments, which follow the z magnetization of the exchanging species after a transient perturbation, the amplitude of these changes depends on the mole fractions of both species. This is illustrated by equation (7) for the inversion transfer experiment. This is not the case in a saturation transfer experiment in which changes in the z magnetization of the A spin are independent of the concentration of the B spin [see equation (9)]. Thus a saturation transfer experiment may detect exchange between a metabolite present in high concentration and one present in low concentration, even if the latter is so low in concentration as to be undetectable in the NMR spectrum. This is illustrated by the saturation transfer spectra, obtained from the dog heart in vivo, shown in Figure 1. Saturation of the γ-phosphate resonance of ATP also results in saturation of the β-phosphate resonance of adenosine diphosphate (ADP), which is less than 1 ppm upfield and which is too low in concentration to be observable in these spectra. Exchange between the β-phosphate of ADP and the β-phosphate of ATP results in a decrease in the resonance intensity of the latter. The lower limit on the concentration of the metabolite to which flux can be measured is imposed by the amount of power required to achieve saturation of the nucleus in this site. For any given flux, as the concentration of the metabolite is decreased the residence time of the nucleus in this site will also decrease and the irradiating field required to achieve its saturation will increase. This was demonstrated experimentally with a study of ATP–ADP exchange catalyzed by creatine kinase in vitro.[25]

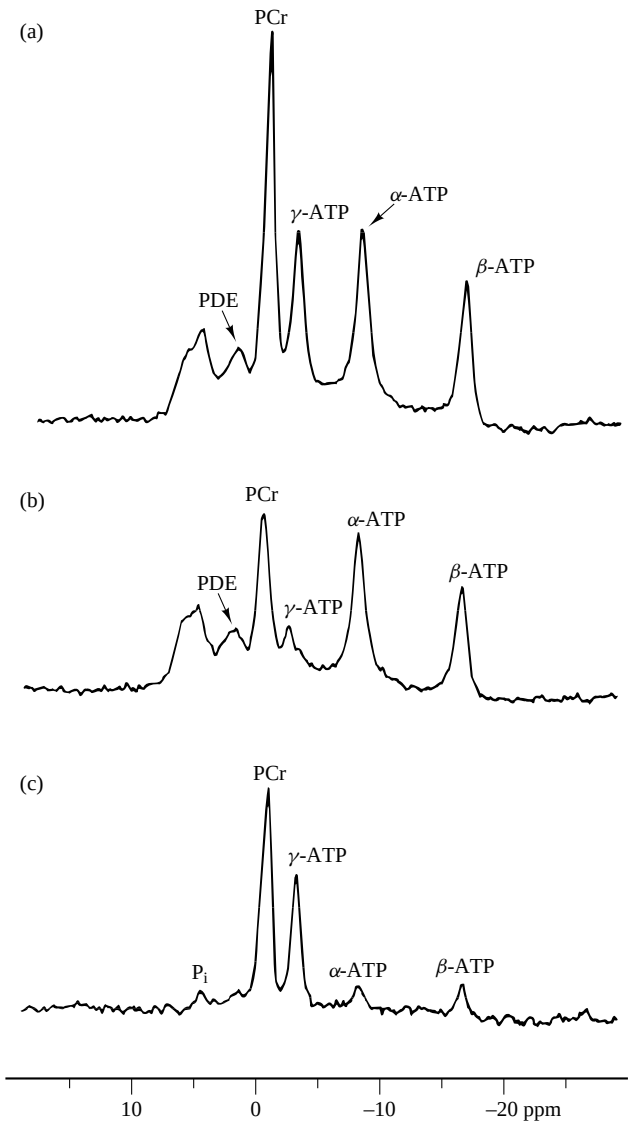

Figure 1 ^{31}P NMR saturation transfer spectra of the dog heart in vivo. The spectra were acquired using a surface coil placed over the heart. Saturation of the γ-phosphate resonance of ATP results in transfer of magnetization to the phosphocreatine and Pi resonances. This is manifest as a decrease in their resonance intensities [compare spectra (a) and (b)], which is clearly seen in the difference spectrum (c). The decrease in the β-phosphate resonance of ATP is due to exchange between ADP and ATP (see text). The decrease in the α-phosphate resonance, which has also been observed in a number of other studies and which cannot be explained by the lack of selectivity of the saturating field, is unexplained. Abbreviations: PDE, phosphodiester; PCr, phosphocreatine; γATP, γ-phosphate resonance of ATP; α-ATP, α-phosphate resonance of ATP; β-ATP, β-phosphate resonance of ATP. (Reproduced by permission of Academic Press, from K. M. Brindle, B. Rajagopalan, D. S. Williams, J. A. Detre, E. Simplaceanu, C. Ho, and G. K. Radda, *Biochem. Biophys. Res. Commun.*, 1988, **151**, 70)

2.6 Assumptions Made in Analyzing Magnetization Transfer Data

2.6.1 Two-Site Exchange

Magnetization transfer measurements of exchange between two substrates in an enzyme-catalyzed reaction are frequently

analyzed using the two-site exchange model described above. Enzyme-bound intermediates in the exchange reaction, which in general will be very low in concentration compared with the free substrates and therefore turning over very rapidly, can usually be ignored. However an intermediate could affect the measured exchange velocity if there was rapid loss of the magnetic label at this site, i.e. if the T_1 of the exchanging nucleus in this site were very short. Although modeling studies have shown that the T_1 would have to be very short,[25] and there appears to be no evidence for this from ^{31}P NMR studies of enzyme-bound substrates, there are now two independent reports that indicate that this may occur in the exchange between ATP and ADP catalyzed by creatine kinase in vitro.[25,26] These compared isotope exchange measurements with magnetization transfer measurements and showed that under some conditions the latter underestimated the exchange rate. However it should be emphasized that for the exchange most often measured in vivo, i.e. that between phosphocreatine and ATP, there was good agreement between the isotope exchange and magnetization transfer data.

2.6.2 Relationship Between Measured Exchange and Net Flux

Since the magnetization transfer experiment, like an isotope exchange experiment, only measures exchange between a pair of substrates there need be no direct relationship between this exchange flux and the metabolically relevant net flux catalyzed by the enzyme. Consider, for example, the reaction mechanism of creatine kinase, which is illustrated in Figure 2. Magnetization transfer measurements of exchange between ATP and ADP and between phosphocreatine and ATP and isotopic measurements of exchange between ATP and ADP, between PCr and ATP and between PCr and Cr have been shown to be similar under most conditions, consistent with rate-limiting interconversion of the two ternary complexes (E.MgADP.PCr and E.MgATP.Cr).[25,26] Therefore under these conditions it is valid to equate magnetization transfer measurements of PCr $\leftrightarrow$ ATP exchange with net flux in the reaction since the same step, the interconversion of the ternary complexes, is rate-limiting for all the exchanges and for the net flux catalyzed by the enzyme. However at high [PCr]/[Cr] ratios (above 2) the ATP $\leftrightarrow$ PCr exchange flux exceeds the ADP $\leftrightarrow$ ATP exchange flux, indicating that control has shifted from the interconversion of the ternary complexes to the steps of substrate–enzyme complex formation and breakdown.

Magnetization transfer measurements of steady-state ATP turnover appear to be measuring net flux. The evidence for this has come from the correspondence between P:O ratios

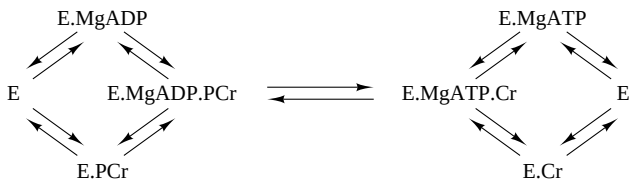

Figure 2 Reaction mechanism of creatine kinase. E represents free enzyme; PCr represents phosphocreatine and Cr represents creatine; MgADP and MgATP represent the Mg^{2+}-bound forms of ADP and ATP respectively

(moles of ATP synthesized: atoms of oxygen consumed) measured in the cell with those measured in suspensions of isolated mitochondria catalyzing net ATP synthesis (discussed in Section 3.2). However, evidence has been obtained recently that mitochondria in vivo can catalyze an ATP $\leftrightarrow$ Pi exchange reaction under some conditions.

3 FLUXES MEASURED IN VIVO

3.1 Creatine Kinase

Creatine kinase catalyses the reaction:

$$MgATP^{2-} + Cr \rightleftharpoons PCr^{2-} + MgADP^{-} + H^{+} \qquad (12)$$

The enzyme is abundant in muscle and neural tissue, where the reaction is normally near-to-equilibrium.[27] When an energy demand is placed on the tissue, the ATP concentration is maintained at the expense of phosphocreatine. Phosphocreatine thus acts as an energy store, buffering temporal changes in the ATP and ADP concentrations.

3.1.1 The Shuttle Hypothesis

A second role for the enzyme has been proposed based on the observation that the enzyme is spatially localized (reviewed by Wallimann et al.[27]). For example in muscle, concentrations of the enzyme are found at the myofibrils and at the mitochondria. In the latter case there is a distinct mitochondrial isoform which is located in the intermembrane space. According to the 'shuttle hypothesis' phosphocreatine also acts as a spatial energy buffer, shuttling energy between the sites of production, the mitochondria, to the sites of utilization, in muscle the myofibrillar Mg^{2+}-ATPase. In its simplest form phosphocreatine and creatine are thought to act as parallel diffusion pathways for the diffusion of ATP and ADP, respectively, between the mitochondria and myofibrils.[28] More elaborate models take into account the apparent functional interactions between the enzyme and other proteins in the muscle. For example there is good evidence that the mitochondrial isoform interacts directly with the adenine nucleotide translocase in the inner mitochondrial membrane, resulting in channeling of mitochondrially-generated ATP between the two proteins.[27] Inevitably ^{31}P NMR magnetization transfer measurements of creatine kinase kinetics in vivo have been used to look for evidence of the shuttle.

Studies in the perfused heart, which showed an increase in the reaction velocity with increased ATP turnover despite only small changes in the enzyme's steady state substrate concentrations, indicated a discrepancy with the solution properties of the enzyme.[29,30] A similar increase in creatine kinase flux with increased ATP turnover has also been observed in brain.[31] Measurements in neonatal rabbit hearts, at different stages of development, showed that the reaction velocity increased as the concentration of the mitochondrial isoform increased,[32] a result which is consistent with the shuttle hypothesis and with functional coupling between the mitochondrial isoform and the adenine nucleotide translocase. This study also showed, as expected from the solution properties of the enzyme, that flux increased with the increase

in creatine and phosphocreatine contents that occurred during development. These data may explain why in skeletal muscle, which contains only 2% mitochondrial creatine kinase activity, there is no increase in creatine kinase reaction velocity with increased work.[33,34] Further evidence for compartmentation of creatine kinase came from the observation that in a time-dependent saturation transfer experiment the decay of the phosphocreatine resonance was not always a single exponential. A kinetic model developed to explain these data attributed this to a nonsaturable mitochondrial pool of ATP in exchange with phosphocreatine in the reaction catalyzed by the mitochondrial isoform.[35] More recent work in the heart has shown that the presence of the mitochondrial isoform is not a prerequisite for the increase in creatine kinase flux with work. Increased flux was shown to result from changes in the enzyme's substrate concentrations. However there was, in addition, an unexplained change in the kinetic properties of the enzyme between rest and work.[36]

The role of creatine kinase in the shuttle has also been investigated by feeding animals creatine analogs which accumulate in cardiac and skeletal muscle and which inhibit the enzyme.[37,38] Magnetization transfer measurements of creatine kinase fluxes in these muscles, which were less than or comparable to the ATP turnover rates, showed that phosphocreatine could not be an obligatory intermediate in energy transduction. However it is now clear that during the long feeding periods required, skeletal muscle undergoes compensatory metabolic adaptations.[39] Furthermore in heart, it was subsequently shown that the presence of a creatine analog does in fact impair muscle function.[40]

Further information about the role of creatine kinase in muscle function will undoubtedly come from using NMR magnetization transfer techniques in conjunction with molecular genetic methods for manipulating the tissue concentrations of the enzyme. For example the role of the different isoforms in muscle function is being investigated by changing their expression in the skeletal muscle of transgenic mice.[41] Elimination of the M isozyme, using gene targeting techniques, was shown totally to eliminate magnetization transfer between phosphocreatine and ATP.[42] Remarkably the phosphocreatine levels declined normally during exercise. Presumably this was due to the residual mitochondrial creatine kinase activity present. Interestingly the muscle adapted to the absence of the M isoform and these adaptations show some similarities to those observed in muscle of analog-fed animals.

3.1.2 Differences in the Forward and Reverse Fluxes

Despite the fact that the reaction catalyzed by creatine kinase is normally near-to-equilibrium there have been numerous magnetization transfer studies which have shown that the forward and reverse fluxes are unequal. Two models have been proposed to explain this difference. One proposes that there are two pools of ATP, a large pool and a small pool which are both in exchange with phosphocreatine. Saturation of the observed γ-phosphate resonance of ATP allows measurement of flux from phosphocreatine to both pools of ATP. However the converse is not true since saturation of the phosphocreatine resonance will result in flux being measured predominantly between the large ATP pool and phosphocreatine. This model was elaborated in terms of the shuttle hypothesis, where the cytosolic ATP pool constitutes the large pool and the small pool is represented by ATP in the mitochondria and at the myofibrils.[43] In support of this proposal it was shown that the discrepancies in the forward and reverse fluxes reported in the literature increased as the rate of ATP synthesis increased. It was also pointed out that the forward and reverse fluxes measured in rat brain were equal if measured using a 2D exchange experiment but were unequal if measured using a saturation transfer experiment. As pointed out above, the saturation transfer experiment is capable of measuring exchange between metabolites present in very unequal concentrations whereas in a 2D exchange experiment, both exchanging pools need to be present at a significant concentration for the exchange to be observed. The second model considers the difference in the fluxes to be due to the fact that the γ-phosphate of ATP is in exchange with Pi as well as with phosphocreatine. Thus while exchange measurements of the flux from phosphocreatine to ATP can be analyzed using a two-site exchange model the reverse flux may be underestimated if not treated as a three-site exchange system, i.e. PCr $\leftrightarrow$ ATP $\leftrightarrow$ Pi. Much of the evidence which supports a compartmentation model is also compatible with this model (discussed by Brindle[6]). For example the difference in creatine kinase fluxes in this model would be expected to increase as the rate of ATP $\leftrightarrow$ Pi exchange increases. The elegant study of Ugurbil et al.[44] on the perfused working rat heart appeared to provide an answer as to which model was correct when it was shown that the forward and reverse fluxes were equal if the reverse flux was measured by saturating both the phosphocreatine and Pi resonances and employing a three-site exchange model for data analysis. However there are two problems with this experiment. As Ugurbil et al.[44] point out, the fractional reduction in the γ-phosphate resonance of ATP, when both the phosphocreatine and Pi resonances are saturated, should be equal to or less than the value observed when only the phosphocreatine resonance is saturated. This was not the case under one set of perfusion conditions. Another problem is that the measured ATP $\leftrightarrow$ Pi exchange is simply not fast enough to give the observed discrepancy.[45] An early study, which showed a difference in the forward and reverse fluxes despite the application of a correction factor which allowed for the observed exchange between ATP and Pi, concluded that the γ-phosphate of ATP must be in rapid exchange with other sites.[46]

There appears at present to be no completely satisfactory explanation for the discrepancy in the forward and reverse fluxes. However, in the context of compartmentation, perhaps tissue heterogeneity should also be considered. For example, in skeletal muscle measurements of enzyme levels in individual fibers have shown extreme heterogeneity, even between adjacent fibers.[47]

3.2 ATP Turnover

A significant limitation of magnetization transfer measurements in vivo is that very few enzyme-catalyzed fluxes are measurable. For example the spectra shown in Figure 1 illustrate almost all the exchanges that can be measured using ^{31}P NMR magnetization transfer measurements in vivo. However, in measuring the fluxes between Pi and ATP the technique can be used to determine arguably the most important fluxes in a living cell, ATP synthesis and hydrolysis. In early measurements of the flux between Pi and ATP it

was assumed that the flux was catalyzed solely by the mitochondrial F_1F_0 ATP synthase. However subsequent studies, in a number of systems including *E. coli*, yeast and the perfused heart, demonstrated that the coupled reaction catalyzed by the glycolytic enzymes, glyceraldehyde 3-phosphate dehydrogenase (GAPDH) and phosphoglycerate kinase (PGK) could also participate in this exchange reaction (reviewed by Brindle[6]). Elimination of this glycolytic exchange allows the Pi ↔ ATP exchange catalyzed by the mitochondria to be determined. For example, a detailed study of Pi → ATP and ATP → Pi fluxes in the perfused rat heart, in which the glycolytic exchange was inhibited, either by iodoacetate treatment or by depletion of glycolytic intermediates, showed that the P:O ratio was approximately 2.4.[48] The similarity of this value to that displayed by isolated mitochondria in vitro catalyzing net ATP synthesis suggests that the mitochondrial ATP synthase is operating unidirectionally in vivo and that the technique measures net ATP turnover. The technique can thus be used to assess the degree of mitochondrial coupling in vivo. For example measurements of P:O ratios in the postischemic perfused rat heart showed that mitochondrial uncoupling, which would lead to a decrease in the measured P:O ratio, could not be the cause of the observed postischemic depression in mechanical function.[49]

The measurements of Pi → ATP flux have also been used to examine the properties of the glycolytic enzymes. Studies of the perfused rat heart[49] and the dog heart in vivo[50] have shown that the activities of GAPDH and PGK are altered in the postischemic myocardium. Measurements of Pi → ATP flux in yeast cells, in which the concentration of PGK had been increased using molecular genetic techniques, allowed a detailed study of the kinetic properties of this enzyme in the intact cell. This showed that there were no unusual kinetic properties conferred on the enzyme by its cellular environment.[51]

Although the glycolytic exchange reaction can compromise magnetization transfer measurements of ATP turnover, particularly in the presence of glucose, this may be less of a problem in vivo. For example the glycolytic contribution to the measured Pi → ATP flux in the postischemic dog heart in vivo appeared to be much lower than that observed in postischemic glucose-perfused rat hearts.[49,50] In rat skeletal muscle in vivo, the measured Pi → ATP flux correlated well with the work performed. Although a glycolytic contribution could not be rigorously excluded the measured flux showed good agreement with ATP turnover rates estimated from oxygen consumption measurements in the perfused hind limb and the rates of phosphocreatine breakdown during a tetanus.[34]

Recent studies on yeast have shown that the measured Pi → ATP flux is increased in cells which have been genetically modified to overexpress an isoform of the mitochondrial adenine nucleotide translocase.[55] This increase in flux, which occurred in the absence of an increase in oxygen consumption, suggested that the mitochondria were catalysing predominantly an ATP ↔ Pi exchange reaction under these conditions rather than net ATP synthesis. This interpretation of the data is in accord with an earlier radioisotope study of ATP ↔ Pi exchange in isolated mammalian mitochnodria which showed that, at low rates of respiration, mitochondria can catalyze an ATP ↔ Pi exchange, but that at higher rates of respiration the Pi → ATP flux becomes unidirectional. Thus it is possible that in mammalian systems at low rates of respiration, even when the glycolytic contribution has been removed, the Pi → ATP flux measured in a magnetization transfer experiment might include some contribution from a mitochondrially catalyzed ATP ↔ Pi exchange.

4 CONCLUDING REMARKS

An interesting area, which I have not covered, is measurements of membrane transport (reviewed by Kuchel[7]). Of particular interest is a ^{19}F NMR study of 3-fluoro-3-deoxy-D-glucose transport across the red cell membrane.[52] However it is not yet clear whether this technique can be applied in other systems. Another interesting study employed the ^{31}P NMR saturation transfer experiment to measure ATP ↔ ADP exchange across the membrane of isolated mitochondria.[53] This showed that the exchange rates were more than 10 times faster than the rates previously determined using isotopic techniques and that they were almost 10 times faster than the ATP synthase (ATP ↔ Pi) exchange rates.

I have concentrated on ^{31}P NMR magnetization transfer measurements in vivo as this reflects my own interest, an interest which was initially stimulated by the potential of the technique to provide unique information on the kinetic properties of enzymes in vivo.

5 RELATED ARTICLES

Chemical Exchange Effects on Spectra; Enzymes Utilizing ATP: Kinases, ATPases and Polymerases; Peripheral Muscle Metabolism Studied by MRS; Phosphorus-31 Magnetization Transfer Studies In Vivo; Relaxation Effects of Chemical Exchange; Two-Dimensional Methods of Monitoring Exchange; Whole Body Studies: Impact of MRS.

6 REFERENCES

1. S. Forsén, and R. A. Hoffman, *J. Chem. Phys.*, 1963, **39**, 2892.
2. T. R. Brown and S. Ogawa, *Proc. Natl. Acad. Sci. U.S.A.*, 1977, **74**, 3627.
3. T. R. Brown, K. Ugurbil, and R. G. Shulman, *Proc. Natl. Acad. Sci. U.S.A.*, 1977, **74**, 5551.
4. J. R. Alger and R. G. Shulman, *Quart. Rev. Biophys.*, 1984, **17**, 83.
5. A. P. Koretsky and M. W. Weiner, in *Biomedical Magnetic Resonance*, eds. T. L. James and A. R. Margulis, Radiology Research and Education Foundation, San Francisco, 1984, p. 209.
6. K. M. Brindle, *Prog. NMR Spectrosc.*, 1988, **20**, 257.
7. P. W. Kuchel, *NMR Biomed.*, 1990, **3**, 102.
8. I. D. Campbell, C. M. Dobson, R. G. Ratcliffe, and R. J. P. Williams, *J. Magn. Reson.*, 1978, **29**, 397.
9. H. Degani, M. Laughlin, S. Campbell, and R. G. Shulman, *Biochemistry*, 1985, **24**, 5510.
10. G. A. Morris and R. Freeman, *J. Magn. Reson.*, 1978, **29**, 433.
11. G. Robinson, P. W. Kuchel, B. E. Chapman, D. M. Doddrell, and M. G. Irving, *J. Magn. Reson.*, 1985, **63**, 314.
12. C. M. Dobson, E. T. Olejniczak, F. M. Poulsen, and R. G. Ratcliffe, *J. Magn. Reson.*, 1982, **48**, 97.

13. W. Kuhn, W. Offermann, and D. Leibfritz, *J. Magn. Reson.*, 1986, **68**, 193.
14. M. Rydzy, R. Deslauriers, I. C. P. Smith, and J. K. Saunders, *Magn. Reson. Med.*, 1990, **15**, 260.
15. J. Jeener, B. H. Meier, P. Bachmann, and R. R. Ernst, *J. Chem. Phys.*, 1979, **71**, 4546.
16. S. Macura, Y. Huang, D. Suter, and R. R. Ernst, *J. Magn. Reson.*, 1981, **43**, 259.
17. C. L. Perrin and R. K. Gipe, *J. Am. Chem. Soc.*, 1984, **106**, 4036.
18. J. Bremer, G. L. Mendz, and W. J. Moore, *J. Am. Chem. Soc.*, 1984, **106**, 4691.
19. R. E. Engler, E. R. Johnston, and C. G. Wade, *J. Magn. Reson.*, 1988, **77**, 377.
20. C. L. Perrin, *J. Magn. Reson.*, 1989, **82**, 619.
21. G. L. Mendz, G. Robinson, and P. W. Kuchel, *J. Am. Chem. Soc.*, 1986, **108**, 169.
22. G. Bodenhausen and R. R. Ernst, *J. Am. Chem. Soc.*, 1982, **104**, 1304.
23. J. Boyd, K. M. Brindle, I. D. Campbell, and G. K. Radda, *J. Magn. Reson.*, 1984, **60**, 149.
24. R. S. Balaban, H. L. Kantor, and J. A. Ferretti, *J. Biol. Chem.*, 1983, **258**, 12 787.
25. K. M. Brindle, and G. K. Radda, *Biochim. Biophys. Acta*, 1985, **829**, 188.
26. V. V. Kupriyanov, R. S. Balaban, N. V. Lyulina, A. Ya. Steinschneider, and V. A. Saks, *Biochim. Biophys. Acta*, 1990, **1020**, 290.
27. T. Wallimann, M. Wyss, D. Brdiczka, K. Nicolay, and H. M. Eppenberger, *Biochem. J.*, 1992, **281**, 21.
28. R. A. Meyer, H. L. Sweeney, and M. J. Kushmerick, *Am. J. Physiol.*, 1984, **246**, C365.
29. V. V. Kupriyanov, A. Ya. Steinschneider, E. K. Ruuge, V. I. Kapel'ko, M. Ya. Zueva, V. L. Lakomkin, V. N. Smirnov, and V. A. Saks, *Biochim. Biophys. Acta*, 1984, **805**, 319.
30. J. A. Bittl and J. S. Ingwall, *J. Biol. Chem.*, 1985, **260**, 3512.
31. A. Sauter and M. Rudin, *J. Biol. Chem.*, 1993, **268**, 13 166.
32. S. B. Perry, J. McAuliffe, J. A. Balschi, P. R. Hickey, and J. S. Ingwall, *Biochemistry*, 1988, **27**, 2165.
33. R. Zahler, J. A. Bittl, and J. S. Ingwall, *Biophys. J.*, 1987, **51**, 883.
34. K. M. Brindle, M. J. Blackledge, R. A. J. Challiss, and G. K. Radda, *Biochemistry*, 1989, **28**, 4887.
35. R. Zahler and J. S. Ingwall, *Am. J. Physiol.*, 1992, **262**, H1022.
36. J. J. McAuliffe, S. B. Perry, E. E. Brooks, and J. S. Ingwall, *Biochemistry*, 1991, **30**, 2585.
37. E. A. Shoubridge, and G. K. Radda, *Biochim. Biophys. Acta*, 1984, **805**, 79.
38. E. A. Shoubridge, F. M. H. Jeffry, J. M. Keogh, G. K. Radda, and A.-M. L. Seymour, *Biochim. Biophys. Acta*, 1985, **847**, 25.
39. E. A. Shoubridge, R. A. J. Challiss, D. J. Hayes, and G. K. Radda, *Biochem. J.*, 1985, **232**, 125.
40. J. L. Zweier, W. E. Jacobus, B. Korecky, and Y. Brandejs-Barry, *J. Biol. Chem.*, 1991, **266**, 20 296.
41. M. J. Brosnan, S. P. Raman, L. Chen, and A. P. Koretsky, *Am. J. Physiol.*, 1993, **264**, C151.
42. J. van Deursen, A. Heerschap, F. Oerlemans, W. Ruitenbeek, P. Jap, H. ter Laak, and B. Weiringa, *Cell*, 1993, **74**, 621.
43. A. P. Koretsky, V. J. Basus, T. L. James, M. P. Klein, and M. W. Weiner, *Magn. Reson. Med.*, 1985, **2**, 586.
44. K. Ugurbil, M. Petein, R. Maidan, S. Michurski, and A. H. L. From, *Biochemistry*, 1986, **25**, 100.
45. K. M. Brindle and G. K. Radda, *Biochim. Biophys. Acta*, 1987, **928**, 45.
46. P. M. Matthews, J. L. Bland, D. G. Gadian, and G. K. Radda, *Biochim. Biophys. Acta*, 1982, **721**, 312.
47. C. V. Lowry, J. S. Kimmey, S. Felder, M. M.-Y. Chi, K. K. Kaiser, P. N. Passonneau, K. A. Kirk, and O. H. Lowry, *J. Biol. Chem.*, 1978, **253**, 8269.
48. P. B. Kingsley-Hickman, E. Y. Sako, P. Mohanakrishnan, P. M. L. Robitaille, A. H. L. From, J. Foker, and K. Ugurbil, *Biochemistry*, 1987, **26**, 7501.
49. E. Y. Sako, P. B. Kingsley-Hickman, A. H. L. From, J. Foker, and K. Uğurbil, *J. Biol. Chem.*, 1988, **263**, 10 600.
50. P.-M. Robitaille, H. Merkle, E. Sako, G. Lang, R. M. Clack, R. Bianco, A. H. L. From, J. Foker, and K. Uğurbil, *Magn. Reson. Med.*, 1990, **15**, 8.
51. K. M. Brindle, *Biochemistry*, 1988, **27**, 6187.
52. J. R. Potts, A. M. Hounslow, and P. W. Kuchel, *Biochem. J.*, 1990, **266**, 925.
53. P. T. Masiakos, G. D. Williams, D. A. Berkich, M. B. Smith, and K. F. LaNoue, *Biochemistry*, 1991, **30**, 8351.
54. D. Chesnnovsky and G. Navon, in *Nuclear Magnetic Resonance Spectroscopy in Molecular Biology*, ed. B. Pullman, Reidel, Dordrecht, 1978, p. 261.
55. K. Brindle, S. Fulton, J. Sheldon, and S. Williams, *Biochem. Soc. Trans.*, 1995, **23**, 374.

Biographical Sketch

Kevin M. Brindle. *b*. 1955. B.A., 1978, D.Phil., 1982, University of Oxford. He did his D.Phil. in Professor Iain Campbell's laboratory, where he worked on ^{1}H NMR studies of cells, then 4 years in Professor George Radda's laboratory before taking up a Royal Society University Research Fellowship in 1986. Lecturer at the University of Manchester, 1991, lectureship in Cambridge, 1993. Approx. 50 publications. Research interests: application of NMR techniques to study the properties of enzymes in vivo.

Low Spin Temperature NMR

Maurice Goldman
Service de Physique de l'Etat Condensé, CEA Saclay, Gif-sur-Yvette, France

1	Introduction	1
2	Methods of Production of Low Nuclear Temperatures	1
3	The Resonance Signal	2
4	Rigorous NMR Results	5
5	Nonlinear Effects in Spin Temperature	8
6	Related Articles	10
7	References	10

1 INTRODUCTION

The manipulation of nuclear spin systems by rf fields and/or the observation of the signal they induce in a pick-up coil nearly always starts from an initial state characterized by one or several temperatures for the nuclear spins. The simplest example, that of a spin system of Hamiltonian $\mathcal{H}$ and single spin temperature T, corresponds to a density matrix for the spins of the form

$$\sigma = \exp(-\mathcal{H}/kT)/\mathrm{Tr}[\exp(-\mathcal{H}/kT)] \tag{1}$$

The description of more complex cases can be found in textbooks.[1–3]

In the vast majority of the uses of NMR, the characteristic frequencies ω associated with the Hamiltonian (for instance, in the Zeeman case, the Larmor frequency) are such that we have

$$\hbar\omega \ll kT \tag{2}$$

In such a case it is permissible, for most practical purposes, to replace the exact density matrix [equation (1)] by the expansion

$$\sigma \simeq (1 - \beta\mathcal{H})/\mathrm{Tr}(1) \tag{3}$$

where $\beta = 1/kT$ is called the 'inverse temperature'. This is known as the 'high-temperature approximation', and it brings about an enormous simplification in the theoretical handling of NMR—most quantities of interest are linear in the inverse temperature β (with the exception of entropy, which is quadratic in β), so that their relative values are independent of spin temperature.

Low spin temperature NMR deals with the case when equation (2) is not valid and one has to use the full expression [equation (1)] for the density matrix. This leads to so-called 'nonlinear effects' in spin temperature, and eventually to nuclear magnetic ordering. There is an exception to the above statement; this is the case when equation (2) is valid as regards the nuclear frequencies, but when the nuclear spins are used to probe the properties of systems at low temperature, which depend strongly on temperature. Examples are electronic ferro-, antiferro-, or ferri-magnets, or superfluid helium-3. These cases are explicitly omitted from the present article.

Low nuclear spin temperatures do not occur spontaneously in nature. Indeed, their production turns out to be extremely laborious, and it can only be justified by the pursuit of a valuable end. This means that, by contrast with the quasigeneral usage in the high-temperature domain, in low spin temperature NMR the nuclear spins are not used as probes of other systems [e.g. proteins or high T_c superconductors (see ***High Temperature Superconductors***)], but they are the system whose properties are studied for their own sake: actors rather than spectators. The 'valuable' aim is essentially nuclear magnetic ordering.

After a brief description of the methods of production of low nuclear spin temperatures, we analyze some of the properties of such systems. In general, the discussion is limited to the domain of paramagnetism. Nuclear ordering, which is described elsewhere in this Encyclopedia (see ***Nuclear Ferromagnetism and Antiferromagnetism*** and ***Thermodynamics of Nuclear Magnetic Ordering***), will only occasionally be touched upon.

This article is to a large extent inspired by Chapter 5 in the book by Abragam and Goldman,[4] although here greater emphasis is put on the ideas behind and the principles of the formal calculations rather than on their detailed description.

2 METHODS OF PRODUCTION OF LOW NUCLEAR TEMPERATURES

The most obvious method is known under the delicate name of the 'brute force' method. It consists of waiting for thermal equilibrium with the lattice at a very low temperature of nuclear spins in a very high magnetic field. Let us give figures. Since both $\hbar\omega = h\nu$ and kT are energies, it is possible to express temperature in terms of frequency, and vice versa. It is useful to remember that $1\,\mathrm{K} \simeq 20.8$ GHz, or

$$1\ \mathrm{mK} \simeq 20.8\ \mathrm{MHz} \tag{4}$$

so that a 'low' Zeeman temperature would correspond to several millikelvin in a field of several tesla. The only problem involves the time required for the nuclear Zeeman interaction to reach equilibrium with the lattice, i.e. the length of the longitudinal relaxation time T_1. In insulators, where nuclear relaxation is due to paramagnetic centers, T_1 becomes extremely long at low lattice temperature and in high field may reach a few hundred hours. Even though much shorter than predicted theoretically, for reasons not yet understood, such values of T_1 deprive the 'brute force' method of its attraction. The situation is different with metals, because their relaxation by the Korringa mechanism is much faster, and the 'brute force' method has been used with success for various metals. It should be noted that at high field, when the Zeeman interaction dominates all other interactions, a low spin temperature corresponds to a high nuclear polarization, through the relationship

$$P = B_I(\hbar\omega/kT) \tag{5}$$

where B_I is the Brillouin function for a nucleus of spin I. For the simplest case, i.e spin $\frac{1}{2}$, this function is

$$B_I(x) = \tanh(x/2) \tag{6}$$

It is apparent from equation (5) that the polarization depends only on the ratio ω/T, i.e. the same physical state would be obtained with a different temperature, by varying the Larmor frequency in proportion. Therefore, the concept of temperature itself is of limited interest and for NMR in high field, 'high-polarization NMR' would be a more appropriate description than 'low spin temperature NMR'. The necessity for a low lattice temperature is a mere consequence of the practical limitations on the value of the external field.

For insulators, a successful alternative to the inefficient 'brute force' method is dynamic nuclear polarization (DNP) which results from the EPR off-resonance irradiation of paramagnetic centers introduced purposely at low concentration in the solid. The basic phenomenon is the following: if electronic spins of Larmor frequency ω_e are irradiated at a frequency $\omega \neq \omega_e$, each time a photon is absorbed the energy of the system increases by $\hbar\omega$, and an upwards electronic spin-flip is produced, resulting in an increase in the electronic Zeeman energy of $\hbar\omega_e$. The energy imbalance $\hbar(\omega_e - \omega)$ serves eventually to modify the Zeeman energy of the nuclear spins.

In its first version, corresponding to the so-called 'solid effect',[5] the irradiation frequency is the difference between or the sum of the electronic and nuclear Larmor frequencies $\omega_e \pm \omega_n$. The transitions are 'forbidden' flip-flop transitions or flip-flip transitions of an electron and a nuclear spin, which can only take place due to the dipolar interaction between these spins. Flip-flop transitions at $\omega_e - \omega_n$ yield a nuclear polarization parallel to the equilibrium value, and flip-flip transitions at $\omega_e + \omega_n$ yield a nuclear polarization of opposite sign. Under strong irradiation and in the absence of parasitic nuclear relaxation, the nuclear polarization modulus eventually becomes equal to that of the thermal equilibrium electronic polarization.

In many cases, when the EPR linewidth exceeds the nuclear Larmor frequency ω_n, the mechanism of DNP is different: off-resonance microwave irradiation produces allowed electronic transitions which lead to a cooling of the electron spin–spin reservoir. As this reservoir is in thermal contact with the nuclear Zeeman reservoir, the latter also becomes cooled, resulting in an increase in its polarization modulus. The sign is the same as for the solid effect: for $\omega < \omega_e$ it corresponds to a positive spin temperature and for $\omega > \omega_e$ to a negative spin temperature. Detailed descriptions of DNP are given by Abragam and Goldman.[4,6]

Physicists are interested not only in nuclear spins with low Zeeman temperatures, but also in spins whose low temperature affects their spin–spin interactions: dipolar, indirect (in heavy nuclei), or RKKY[1,3] (in metals). One can start from nuclei with large polarizations (low Zeeman temperatures) and perform an adiabatic demagnetization. This has been done for 'brute force' polarized nuclei[7,8] and DNP-polarized nuclei in insulators (see e.g. Abragam and Goldman,[4] Chapters 5 and 8). The adiabatic demagnetization can be done by actually reducing the field to zero, in which case the final interactions are the full spin–spin interactions. It can also be done at high field, by slowly sweeping an rf field from a frequency far off-resonance down to on-resonance. As a result of this adiabatic demagnetization in the rotating frame (ADRF),[9] it is the effective field in the rotating frame that is reduced to zero, and the remaining interactions are the so-called 'secular spin–spin interactions', consisting of that part of the spin–spin interactions which commutes with the Zeeman coupling.[1,2]

In zero field, either actual or effective, the nuclear polarization vanishes, and 'high-polarization NMR' is no longer an adequate description. One quantity that is conserved in adiabatic demagnetization is the entropy of the system. The large initial nuclear polarization corresponds to a low entropy, and the only adequate title for this article should therefore be 'low-entropy NMR'.

3 THE RESONANCE SIGNAL

It is well known from general principles (i.e. linear response theory[10]) that the CW nuclear absorption signal is the Fourier transform of the FID signal observed after an infinitely small pulse θ (see e.g. Goldman,[11] Chapter 1). It is then sufficient to analyze the signal observed after such a pulse.

We consider, for simplicity, a system with Zeeman and dipolar interactions having a density matrix of the form

$$\sigma_0 = \exp\left(-\sum_\mu \beta_\mu Z_\mu - \beta_D \mathcal{H}'_D\right) \Big/ \mathrm{Tr}\{\exp(\ldots)\} \tag{7}$$

where Z_μ is the Zeeman interaction $\omega_\mu I_z^\mu$ of the nuclear species μ, β_μ is the corresponding inverse spin temperature, $\mathcal{H}'_D$ is the secular dipolar interaction, and β_D its inverse temperature. This is transformed by a pulse θ at the Larmor frequency of species 0 into

$$\sigma(0) = \exp(-i\theta I_x^0)\,\sigma_0 \exp(i\theta I_x^0) \tag{8}$$

Its subsequent evolution is

$$\sigma(t) = \exp(-i\mathcal{H}t)\,\sigma(0)\exp(i\mathcal{H}t) \tag{9}$$

where $\mathcal{H}$ is the (supposedly static) Hamiltonian. In an appropriate rotating frame, $\mathcal{H}$ reduces to $\mathcal{H}'_D$. The expectation value of a quantity Q is

$$\langle Q\rangle(t) = \mathrm{Tr}\{Q\sigma(t)\} \tag{10}$$

When the angle θ is infinitely small, equation (8) yields, to first order (linear response)

$$\sigma(0) \simeq \sigma_0 - i\theta[I_x, \sigma_0] \tag{11}$$

and the FID signal $\langle I_+\rangle(t)$ (a transverse vector expressed in the form of a complex number) becomes

$$\langle I_+\rangle(t) = -i\theta\ \mathrm{Tr}\{I_+ \exp(-i\mathcal{H}'_D t)[I_x, \sigma_0]\exp(i\mathcal{H}'_D t)\} \tag{12}$$

or, after a few manipulations,

$$\langle I_+\rangle(t) = -i\theta\langle[I_+(t), I_x]\rangle_0 \tag{13}$$

with the notation

$$Q(t) = \exp(+i\mathcal{H}'_D t)\,Q\exp(-i\mathcal{H}'_D t) \tag{14}$$

$$\langle Q\rangle_0 = \mathrm{Tr}\{Q\sigma_0\} \tag{15}$$

3.1 Difference of the High-Temperature Case

We consider, for simplicity, a density matrix corresponding to pure Zeeman order for a system of identical spins $\frac{1}{2}$, I_i:

$$\sigma_0 = \exp\left(-\beta \sum I_z^i\right) \Big/ \mathrm{Tr}\left\{\exp\left(-\beta \sum I_z^i\right)\right\} = \prod_i (1 - t_\beta I_z^i) \tag{16}$$

where

$$t_\beta = \tanh(\tfrac{1}{2}\beta\omega_0) \tag{17}$$

This is transformed by the θ pulse [equation (8)] into

$$\sigma(0) = \prod_i [1 - t_\beta(\cos\theta\, I_z^i + \sin\theta\, I_y^i)] \tag{18}$$

The FID of spin I_i, which is representative of the total FID, is then

$$\langle I_+^i \rangle = -t_\beta \sin\theta\ \mathrm{Tr}\left\{ I_+^i(t) I_y^i \prod_{j\neq i} [1 - t_\beta(\cos\theta\, I_z^j + \sin\theta\, I_y^j)] \right\} \tag{19}$$

In the low θ limit, pertaining to the analysis of the absorption signal, this yields

$$\langle I_+^i \rangle = -t_\beta\theta\ \mathrm{Tr}\left\{ I_+^i(t) I_y^i \prod_{j\neq i} (1 - t_\beta I_z^j) \right\} \tag{20}$$

It is easily shown that this is identical to equation (13). At high temperature, $t_\beta \simeq \frac{1}{2}\beta\omega_0 \ll 1$, so that $\Pi_j(\ \ldots\ ) \simeq 1$, and one obtains

$$\langle I_+^i \rangle = -\tfrac{1}{2}\beta\omega_0\theta\ \mathrm{Tr}\{I_+^i(t) I_y^i\} \tag{21}$$

It is the fact that t is no longer negligible at low temperature which distinguishes the low-temperature case from the high-temperature one. We end this subsection by emphasizing two of the conspicuous consequences of this difference:

1. It is apparent from equation (19) that, even with one nuclear species and purely Zeeman initial order, the FID shape does depend on the pulse angle θ. This observation has had two main consequences.
   (i) A great surprise, after its experimental discovery, for a Ph.D. student of J. S. Waugh (private communication).
   (ii) A disproval, or rather a correction, of the so-called 'Lowe–Norberg theorem'[12] that the CW signal is the Fourier transform of the FID signal. This theorem stems from the fact that under the two conditions of high temperature and purely Zeeman order the FID signal following a rf pulse is proportional to sin θ, but its shape is independent of θ, as can be seen from equation (21). This fact, which was known earlier [E. M. Purcell, NMR Lectures Notes, Harvard (1953); A. Abragam, NMR Lectures Notes, Saclay (1955)], is really an extension of the validity of a general theorem that the CW signal is the Fourier transform of the FID signal following a pulse of infinitely small angle θ, a consequence of linear response theory[10] (see also Abragam and Goldman,[6] Chapter 1, and Goldman,[11] Chapter 1).
2. In the case when there are several different polarized nuclear species, and/or secular dipolar order (nonnegligible β_D) in addition to Zeeman order, the FID signal shape of *one* nuclear species depends on *all* spin temperatures. It should be noted that, in the case of Zeeman plus dipolar order, the FID signal of spins I_μ depends on both β_μ and β_D, and on the angle θ, even at high temperature.[2]

3.2 Qualitative Features of the Zeeman Signal

We refer again to the FID signal following a pulse of infinitely small angle θ, but starting from a state of pure Zeeman order [$\beta_\mathrm{D} = 0$ in equation (7)]. By contrast with the high-temperature case, the absorption signal shape is, in general, not symmetrical, and not centered on the Larmor frequency. This manifests itself by the fact that this CW signal has no vanishing odd moments. This can be shown by simple qualitative arguments that are not be given here. Furthermore, all moments, whether odd or even, depend on the polarization, i.e. the shapes of the FID signal or absorption signal depend on the polarization. There is, however, a property of the high-temperature case that remains true for low temperature: the area of the absorption signal of a given nuclear species is proportional to its polarization. (This is also the initial FID signal following a small θ pulse). This property, which is associated with the polarization dependence of the first few moments of the absorption signal (i.e. the first few derivatives of the FID at $t = 0$), makes it possible to perform an absolute calibration of the nuclear polarizations. This has still another advantage, resulting from the following properties:

1. By manipulation of equation (13) one can derive a simple relationship between the integral of the absorption signal $-\int_{-\infty}^{+\infty} \langle I_y \rangle(\omega - \omega_0) d\omega$ and the nuclear polarization. The absorption signal thus defined corresponds to a nonsaturating rf field ω_1/γ along Ox in the rotating frame.
2. The 'absorption' voltage detected is

$$V(\omega) = \xi\omega_1 \langle I_y \rangle(\omega) \tag{22}$$

where ξ is a factor depending on the coil and on the receiver amplification.

Once one has a calibration of the nuclear polarization, the experimental integral

$$\int V(\omega)\, \mathrm{d}\omega \tag{23}$$

yields a calibration of the product $\xi\omega_1$. Since, as will be seen later, ω_1 can be independently calibrated, we obtain the value of the so-called spectrometer 'gain factor' ξ, which can be used to calibrate other physical quantities of interest. This is essential in a domain where everything is highly nonlinear.

Of course, it is equivalent to use the formal expression of the initial FID $\langle I_y \rangle$ following a small-angle pulse and the initial experimentally detected voltage.

3.3 The Moments of the Zeeman Absorption Signal

This section deals only with results, and qualitative comments are made. Detailed calculations can be found in, for example, Abragam et al.[13] and Roinel and Bouffard.[14]

3.3.1 The First Moment

The first moment of the absorption signal (with respect to the Larmor frequency) characterizes the overall shift in the resonance frequency, irrespective of any change in signal shape. The Larmor frequency is determined as the low-polarization limit of the frequency with respect to which the first moment vanishes. One must distinguish between cases when there are one or several spin species.

3.3.1.1 One spin species: the $\frac{3}{2}$ effect. By this we mean nuclear spins with the same chemical shift and the same nuclear environment, e.g. ^{19}F in CaF_2. Conversely, $KMgF_3$ contains three imbricated simple cubic arrays of ^{19}F nuclei which, for a given field orientation, differ both in their secular dipolar couplings and in their chemical shifts.[15]

For a simple spin species, the first moment is not equal to the average (Weiss) field experienced by the spins of other nuclei, rather it is $\frac{3}{2}$ times larger. This can be illustrated as follows. The secular dipolar interaction experienced by a spin I_i is

$$\mathcal{H}'^{(i)}_{\mathrm{D}} = \frac{\gamma^2\hbar}{2}\sum_j \frac{1-3\cos^2\theta_{ij}}{r_{ij}^3}\{2I_z^iI_z^j - I_x^iI_x^j - I_y^iI_y^j\} \quad (24)$$

The term inside the braces can be written

$$\{\ldots\} = \{2I_z^i\langle I_z^j\rangle + 2I_z^i(I_z^j - \langle I_z^j\rangle) - I_x^iI_x^j - I_y^iI_y^j\} \quad (25)$$

It might seem that the first term on the right-hand side will contribute to the shift of the signal, whereas the remaining terms, corresponding to short-range correlations, affect only the lineshape. This argument is wrong. Indeed, we may write the term in braces in equation (24) in the form

$$\{\ldots\} = \{3I_z^iI_z^j - \boldsymbol{I}^i\cdot\boldsymbol{I}^j\} \quad (26)$$

The scalar product commutes with

$$I_+ = I_+^i + I_+^j + \sum_{k\neq i,j} I_+^k \quad (27)$$

and it does not contribute to the FID derivative at $t = 0$ (proportional to $\langle[I_+, \mathcal{H}_{\mathrm{D}}]\rangle$). The remaining term is

$$3I_z^iI_z^j = 3I_z^i\langle I_z^j\rangle + 3I_z^i(I_z^j - \langle I_z^i\rangle) \quad (28)$$

The first term on the right-hand side contributes to the first moment, and the second one to the lineshape; thus the '$\frac{3}{2}$ effect' is recovered. What was wrong with the first reasoning? This was pinpointed by Kittel.[16] We have tacitly assumed in equation (25) that only the longitudinal spin components have nonvanishing average values. In the presence of rf irradiation, the transverse components no longer vanish, and one should use

$$I_x^iI_x^j = I_x^i\langle I_x^j\rangle + I_x^i(I_x^j - \langle I_x^j\rangle) \quad (29)$$

and similarly for the I_y terms. The Weiss fields originating from these transverse components, however small, are sufficient to account for the $\frac{3}{2}$ effect.

Owing to the long range of the dipolar couplings [equation (24)], the NMR first moment depends on the sample shape. The only case for which the Weiss field is the same for all spins is when the sample is ellipsoid in shape. Otherwise, there is a distribution of Weiss fields, and hence an extra broadening of the line. The case when the first moment vanishes is that of a spherical sample of nuclear spins in cubic symmetry, such as ^{19}F in CaF_2. It is only when the first moment does not vanish that it can be used for polarization calibration.

3.3.1.2 Several spin species. We consider the case where there are only two species from different nuclear elements, e.g. LiF or LiH. We call the spins I and S. There is no '$\frac{3}{2}$ effect' between unlike spins, because they precess at different frequencies. The first moments of the two NMR signals are of the form

$$m_{1I} = \tfrac{3}{2}B_{I\to I}Ip_I + B_{S\to I}Sp_S \quad (30a)$$

$$m_{1S} = B_{I\to S}Ip_I + \tfrac{3}{2}B_{S\to S}Sp_S \quad (30b)$$

where p_I and p_S are the polarizations.

The various Weiss fields (or their average values in nonellipsoidal samples) can be calculated theoretically. The variation in the moments with the absorption signal areas then yields an absolute calibration of the polarizations. Figure 1 illustrates the use of this method for LiF. The method is easily extended to more than two species.

3.3.2 The Second Moment

Consider the case when the first moment vanishes, for instance that of ^{19}F in a sphere of CaF_2. The theoretical expression of the second moment is[13]

$$M_2 = \langle[\mathcal{H}'_{\mathrm{D}}, I_+][I_-, \mathcal{H}'_{\mathrm{D}}]\rangle_0/\langle I_+I_-\rangle_0 \quad (31)$$

For spins $\frac{1}{2}$, equation (31) yields the following dependence on the nuclear polarization p:

$$M_2(p) = M_2(0)(1-p^2) \quad (32)$$

One should then observe a linear variation of the experimental M_2 as a function of the square of the signal area.

Figure 2 shows that this is actually the case, for two spherical samples of CaF_2. The only problem is that the value of M_2 extrapolated to zero polarization is larger than its theoretical value, and different in the two samples. The origin is in the presence of paramagnetic centers at low concentration (Tm^{2+} in the present case), which produce a Lorentzian distribution of fields at the ^{19}F sites.[13] The two samples have different Tm^{2+} concentrations, and thus different

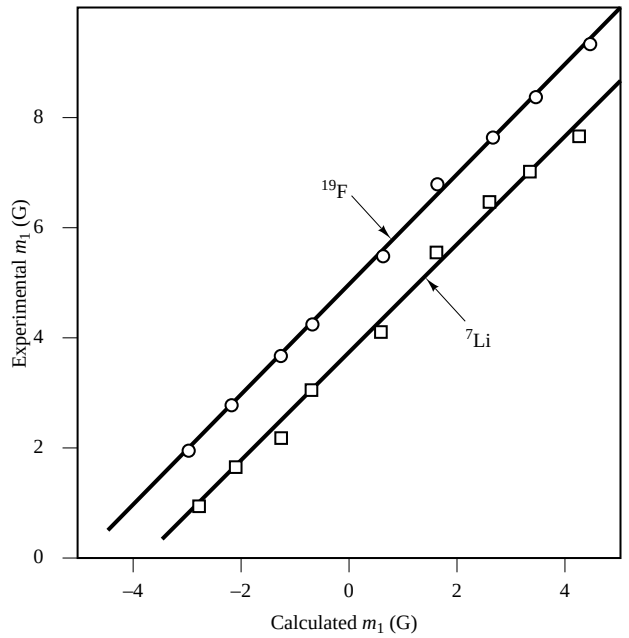

Figure 1 Experimental first moments (to within an arbitrary constant) of ^{7}Li and ^{19}F against their best-fit value in a parallelepiped of LiF. (Reproduced by permission of Oxford University Press from Abragam and Goldman[4])

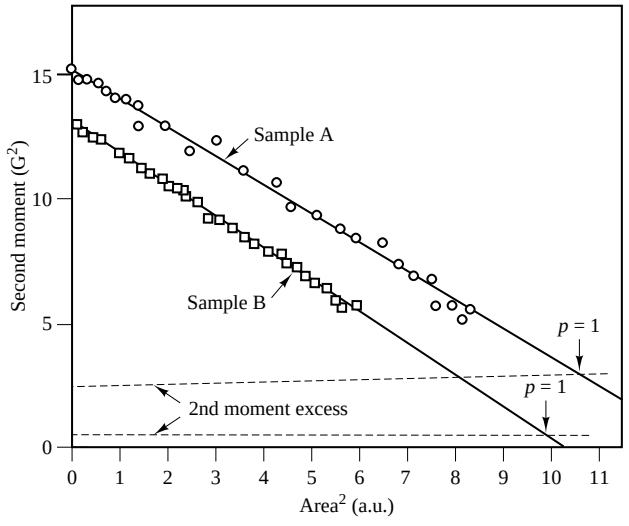

Figure 2 Second moment of the ^{19}F absorption signal against its area squared (in arbitrary units), for two spherical samples of CaF_2, with $\boldsymbol{B}_0 \| [100]$. (Reproduced with permission from Abragam et al.[13])

values of the second-moment excess. This excess depends slightly on nuclear polarization, as derived in Abragam et al.[13]

3.3.3 Higher Moments

These moments also depend on polarization, and could potentially be used for polarization calibration. In particular, for a simple cubic system of spins $\frac{1}{2}$ in a sphere, one predicts for the third moment

$$M_3 \propto p(1 - p^2) \tag{33}$$

which goes through a maximum for $p = 1/\sqrt{3}$. Experimentally, it is extremely difficult to avoid 'contamination' of the absorption signal by a small dispersion contribution, whose antisymmetric shape in the wings is sufficient to deprive experimental third moments of any significance.

4 RIGOROUS NMR RESULTS

We list below several results derived theoretically from equation (13). These results are rigorous for systems in the paramagnetic state, that is with an initial density matrix of the form given by equation (1) in an appropriate reference frame. From plausibility arguments, one is inclined to think that many remain valid even in nuclear magnetic ordered states, that is under conditions of symmetry breaking when equation (1) cannot be rigorous.

Each of these results has been implemented experimentally and used as a practical tool for the investigation of spin systems at low temperature. We cite and comment on these investigations, but no detailed calculations are given. We have already described the first investigation, which is concerned with the area of the absorption signal which, after calibration, yields both the polarization and the 'gain coefficient–rf field' product $\xi\omega_1$.

4.1 Rate of Change of the Polarization

Consider for simplicity a single-species system subjected to a small rf irradiation at a distance Δ from resonance. Its Hamiltonian in the rotating frame is

$$\mathcal{H} = \Delta I_z + \omega_1 I_x + \mathcal{H}'_{\mathrm{D}} \tag{34}$$

According to the Liouville–von Neumann evolution equation for the density matrix, the rate of change in the longitudinal spin expectation is

$$\begin{aligned} \frac{\mathrm{d}}{\mathrm{d}t}\langle I_z\rangle &= \mathrm{Tr}\left\{ I_z \frac{\mathrm{d}\sigma}{\mathrm{d}t} \right\} \\ &= \mathrm{Tr}\{-\mathrm{i} I_z[\mathcal{H}, \sigma]\} \\ &= \mathrm{Tr}\{-\mathrm{i}[I_z, \mathcal{H}]\sigma\} \\ &= \langle -\mathrm{i}[I_z, \mathcal{H}]\rangle_0 \end{aligned} \tag{35}$$

and thus, according to equation (34)

$$\frac{\mathrm{d}}{\mathrm{d}t}\langle I_z\rangle = \omega_1 \langle I_y\rangle \tag{36}$$

If one monitors the absorption signal during an irradiation process, the total change is given by

$$\delta\langle I_z\rangle = \int \omega_1 \langle I_y\rangle \, \mathrm{d}t \tag{37}$$

Use has been made of this method to measure the longitudinal susceptibility in demagnetized spin systems.[17]

The basis of the method is as follows. Starting from equilibrium after ADRF, i.e. an initial density matrix

$$\sigma_i = \exp(-\beta_i \hat{\mathcal{H}}'_{\mathrm{D}})/\mathrm{Tr}\{\dots\} \tag{38}$$

a saturating rf field is suddenly applied at a (small) distance Δ from resonance and one monitors the absorption signal over the course of the evolution of the system towards a new equilibrium of density matrix

$$\sigma_f = \exp[-\beta_f(\mathcal{H}'_{\mathrm{D}} + \Delta I_z + \omega_1 I_x)]/\mathrm{Tr}\{\dots\} \tag{39}$$

If Δ and ω_1 are much smaller than the local field, one has $\beta_f \simeq \beta_i$, and

$$\delta\langle I_z\rangle = \langle I_z\rangle_f = \omega_1 \chi_{\parallel}(\beta) \tag{40}$$

This is measured from the absorption signal using equation (37) and the calibrated value of $\xi\omega_1$.

4.2 Slightly Saturating Linear Passages

We consider a linear sweep of the field (or irradiation frequency) through resonance, with the time of sweep of the linewidth being much longer than T_2. The irradiation produces a saturation of both the polarization and the dipolar energy, which we presume to be small.

4.2.1 Saturation of the Polarization

Let $\mathrm{d}\Delta/\mathrm{d}t = \dot{\Delta}$. Equation (37) then yields

$$\delta\langle I_z\rangle = \frac{\omega_1}{\dot{\Delta}} \int_{-\infty}^{+\infty} \langle I_y\rangle(\Delta)\,\mathrm{d}\Delta \tag{41}$$

The limits can be taken equal to $-\infty$ and $+\infty$ if the sweep starts well below resonance and ends well above it. The integral of the absorption signal is precisely related to the value of $\langle I_z\rangle$, which yields

$$\frac{\delta\langle I_z\rangle}{\langle I_z\rangle} = -\epsilon = -\pi\frac{\omega_1^2}{\dot{\Delta}} \tag{42}$$

an expression which is valid for $\epsilon \ll 1$. By performing n passages, one obtains

$$\frac{\langle I_z\rangle(n)}{\langle I_z\rangle(0)} = (1-\epsilon)^n \simeq \exp(-n\epsilon) \tag{43}$$

through which one measures ϵ. If the sweep rate $\dot{\Delta}$ is known, this provides [from equation (42)] a calibration of ω_1, that is of the rf field amplitude. An experimental result for CaF_2 is shown in Figure 3. From the calibration of ω_1, one obtains a calibration of ξ.

4.2.2 Saturation of Dipolar Energy

A Hamiltonian of the form given by equation (34), at constant Δ, is time independent and the energy associated with it is conserved. If ω_1 is strong enough to ensure a single spin temperature in the rotating frame but is so small that the energy term $\omega_1\langle I_x\rangle$ is negligible, one obtains

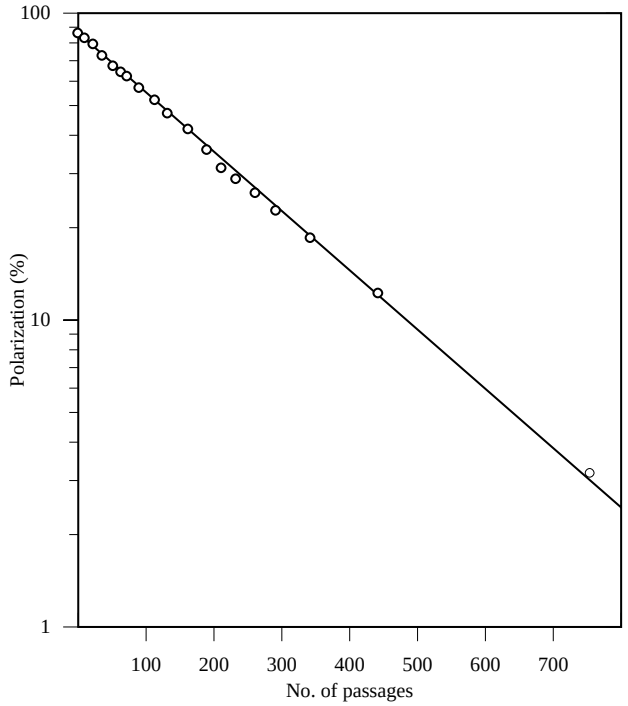

Figure 3 ^{19}F nuclear polarization in CaF_2 as a function of the number of slightly saturating passages. (Reproduced with permission from Abragam et al.[13])

$$\Delta\langle I_z\rangle + \langle\mathcal{H}'_{\mathrm{D}}\rangle = \text{constant} \tag{44}$$

or

$$\Delta\frac{\mathrm{d}}{\mathrm{d}t}\langle I_z\rangle + \frac{\mathrm{d}}{\mathrm{d}t}\langle\mathcal{H}'_{\mathrm{D}}\rangle = 0 \tag{45}$$

which, according to equation (36), gives

$$\frac{\mathrm{d}}{\mathrm{d}t}\langle\mathcal{H}'_{\mathrm{D}}\rangle = -\omega_1\Delta\langle I_y\rangle(\Delta) \tag{46}$$

Under a linear passage through resonance, with a frequency sweep rate $\dot{\Delta}$ so slow that equation (46) remains valid at all times, one obtains

$$\delta\langle\mathcal{H}'_{\mathrm{D}}\rangle = -\frac{\omega_1}{\dot{\Delta}}\int_{-\infty}^{+\infty}\Delta\langle I_y\rangle(\Delta)\,\mathrm{d}\Delta \tag{47}$$

a result which is valid only if $\langle\delta\mathcal{H}'_{\mathrm{D}}\rangle$ is small. What can be measured is the dipolar energy variation corresponding to n passages. Provided the product $\xi\omega_1$ is calibrated as explained above, the experimental results can be connected to the high-temperature linear value

$$\langle\mathcal{H}'_{\mathrm{D}}\rangle = -\beta\ \mathrm{Tr}\ \mathcal{H}'^2_{\mathrm{D}} \tag{48}$$

and thus one obtains a calibrated value of the energy. It makes use of the (nonnormalized) first moment

$$\mathcal{M}_1 = \int_{-\infty}^{+\infty} \Delta\langle I_y\rangle(\Delta)\,\mathrm{d}\Delta \tag{49}$$

and equation (47) becomes

$$\delta\langle\mathcal{H}'_{\mathrm{D}}\rangle = -\frac{\omega_1}{\dot{\Delta}}\mathcal{M}_1 \tag{50}$$

This result is independent of whether there are several spin species or not. This method has been used to calibrate the dipolar energy in LiH.[18]

4.3 First Moment of the Absorption Signal

We return to the first moment as defined by equation (49). This must not be confused with the normalized first moment described in Section 3.2.1. As the absorption signal $I_y(\Delta)$ is the Fourier transform of the (normalized) FID signal [equation (13)], then

$$\begin{aligned}\Delta\langle I_y\rangle(\Delta) &= \frac{\omega_1}{4}\int_{-\infty}^{+\infty}\langle[I_-, I_+(t)]\rangle_0\,\Delta\exp(\mathrm{i}\Delta t)\,\mathrm{d}t \\ &= -\mathrm{i}\frac{\omega_1}{4}\int_{-\infty}^{+\infty}\langle[I_-, I_+(t)]\rangle_0\frac{\mathrm{d}}{\mathrm{d}t}[\exp(\mathrm{i}\Delta t)]\,\mathrm{d}t\end{aligned} \tag{51}$$

Upon integration by parts over t, and then integration over Δ, one obtains finally[19]

$$\mathcal{M}_1 = \frac{\pi}{2}\omega_1\langle[I_-, [I_+, \mathcal{H}'_{\mathrm{D}}]]\rangle_0 \tag{52}$$

The simplest case is when the system contains only one spin species. Through the commutation relations of spin operators, and the form [equation (24)] of the homonuclear secular dipolar interactions, one obtains

$$\mathcal{M}_1 = 3\pi\omega_1\langle\mathcal{H}'_{\mathrm{D}}\rangle_0 \tag{53}$$

What is actually measured is

$$\mathcal{M}'_1 = \xi\mathcal{M}_1 = 3\pi\xi\omega_1\langle\mathcal{H}'_{\mathrm{D}}\rangle_0 \tag{54}$$

The calibration of $\xi\omega_1$ then gives access to a calibrated value of $\langle\mathcal{H}'_{\mathrm{D}}\rangle$.

Consider now the case when there are, say, two spin species I and S. Secular dipolar interactions between unlike spins do not contain flip-flop terms, and it is elementary to show that in such a case

$$\mathcal{M}_1(I) = \pi\omega_1^I\{3\langle\mathcal{H}'_{\mathrm{D}II}\rangle_0 + \langle\mathcal{H}'_{\mathrm{D}IS}\rangle_0\} \tag{55}$$

and for the spins S signal

$$\mathcal{M}_1(S) = \pi\omega_1^S\{\langle\mathcal{H}'_{\mathrm{D}IS}\rangle_0 + 3\langle\mathcal{H}'_{\mathrm{D}SS}\rangle_0\} \tag{56}$$

Together with the measurement of the total dipolar energy

$$\langle\mathcal{H}'_{\mathrm{D}II}\rangle_0 + \langle\mathcal{H}'_{\mathrm{D}IS}\rangle_0 + \langle\mathcal{H}'_{\mathrm{D}SS}\rangle_0 \tag{57}$$

by using the saturation method described in the preceding section, it is possible in principle to derive calibrated values for the three partial energies

$$\langle\mathcal{H}'_{\mathrm{D}II}\rangle_0, \quad \langle\mathcal{H}'_{\mathrm{D}IS}\rangle_0, \quad \langle\mathcal{H}'_{\mathrm{D}SS}\rangle_0 \tag{58}$$

4.4 Qualitative Shape of the Absorption Signal

When a spin system, with a single spin species I (for simplicity), is subjected to an ADRF stopped at the distance Δ_0 from resonance, its density matrix is of the form

$$\sigma = \exp[-\beta(\Delta_0 I_z + \mathcal{H}'_{\mathrm{D}})]/\mathrm{Tr}\{\exp(\dots)\}$$

We assume that $\beta > 0$. If one then looks at the absorption signal $I_y(\Delta)$ with a small, nonsaturating rf field, it can be shown (see Abragam and Goldman,[6] Chapter 5), that this absorption signal is positive for $\Delta \leq \Delta_0$, vanishes at $\Delta = \Delta_0$, and is negative for $\Delta \geq \Delta_0$. This makes it possible to determine the value of Δ_0 in equation (58), that is the effective field. In the particular case when $\Delta_0 = 0$, it can be shown that the absorption signal is antisymmetric at all spin temperatures

$$\langle I_y\rangle(-\Delta) = -\langle I_y\rangle(\Delta) \tag{59}$$

4.5 Linear Response and Transverse Susceptibility

The transverse susceptibility can be defined through two seemingly different approaches:

1. We wait for the thermal equilibrium when a small (but saturating) rf field is applied at a distance Δ_0 from resonance. This corresponds to a density matrix

$$\sigma_{\mathrm{eq}} = \exp[-\beta(\Delta_0 I_z + \omega_1 I_x + \mathcal{H}'_{\mathrm{D}})]/\mathrm{Tr}\{\dots\} \tag{60}$$

which yields a transverse spin expectation value

$$\langle I_x\rangle_{\mathrm{eq}} = \chi_\perp\omega_1 \tag{61}$$

2. Starting from a density matrix

$$\sigma_{\mathrm{eq}} = \exp[-\beta(\Delta_0 I_z + \mathcal{H}'_{\mathrm{D}})]/\mathrm{Tr}\{\dots\} \tag{62}$$

we apply a small rf field of amplitude ω_1/γ and look for the dispersion signal at frequency Δ_0

$$\langle I_x\rangle(\Delta_0) = \chi'_\perp\omega_1 \tag{63}$$

It can be shown, on the basis of linear response theory, that the two transverse susceptibilities are equal

$$\chi_\perp = \chi'_\perp \tag{64}$$

The former definition corresponds to the observation of dispersion during a fast passage (slow enough for the system to be at all times infinitely close to equilibrium, but fast enough for spin–lattice relaxation to be negligible). For the second definition, it is not necessary to look at the dispersion signal.

Instead, one can observe the absorption signal $\langle I_y\rangle(\Delta)$ and compute the dispersion $\langle I_x\rangle(\Delta_0)$ from the Kramers–Kronig relation[1]

$$\langle I_x\rangle(\Delta_0) = -\frac{1}{\pi}\mathcal{P}\int_{-\infty}^{+\infty}\frac{\langle I_y\rangle(\Delta)\,\mathrm{d}\Delta}{\Delta-\Delta_0} \tag{65}$$

Since the absorption signal is calibrated, as shown above, this method yields a calibrated value for the transverse susceptibility.

4.6 Cotanh Transform of the Absorption Signal: Measurement of the Dipolar Temperature

The cotanh transform is one form of the fluctuation–dissipation theorem,[20] as applied to the absorption signal.[18] For a system demagnetized to the distance Δ_0 from the spins I resonance, i.e. for a single spin system, when its density matrix is of the form given by equation (62), the cotanh transform (a neologism) is formally defined by

$$\mathcal{C}(\beta) = \int_{-\infty}^{+\infty}\langle I_y\rangle(\Delta)\,\coth\left[\frac{\beta}{2}(\Delta-\Delta_0)\right]\mathrm{d}\Delta \tag{66}$$

where $\langle I_y\rangle(\Delta)$ is the absorption signal.

It can be shown that

$$\mathcal{C}(\beta) = -\pi\omega_1\langle I_x^2 + I_y^2\rangle_0 \tag{67}$$

This property is valid even when there are several spin species. It can be used when, besides the abundant spins, the system also contains a spin species in low abundance (for instance ^{43}Ca in CaF_2). It is these spins that we call I. Since, for example,

$$I_x = \sum_i I_x^i \tag{68}$$

is the sum of all individual spin components, we have

$$\langle I_x^2\rangle_0 = \sum_i\langle I_x^{i2}\rangle_0 + \sum_{i\neq j}\langle I_x^i I_x^j\rangle_0 \tag{69}$$

For low-abundance spins, their relative distance is large, on average, so that

$$\langle I_x^i I_x^j\rangle_0 \simeq \langle I_x^i\rangle_0\langle I_x^j\rangle_0 \quad (i\neq j) \tag{70}$$

which vanishes when the spins I are not purposely given a transverse polarization. One is then left with

$$\langle I_x^2\rangle_0 + \langle I_y^2\rangle_0 \simeq \sum_i\langle I_x^{i2} + I_y^{i2}\rangle_0 = \sum_i[I(I+1) - \langle I_z^{i2}\rangle_0] \tag{71}$$

In the presence of N_I equivalent spins I, one then has

$$\mathcal{C}(\beta) = -N_I\pi\omega_1[I(I+1) - \langle I_z^{i2}\rangle_0] \tag{72}$$

In the case when nuclear alignment is negligible

$$\langle I_z^{i2}\rangle_0 = \tfrac{1}{3}I(I+1) \tag{73}$$

and one finally obtains

$$\mathcal{C}(\beta) \simeq -\tfrac{2}{3}N_I\pi\omega_1 I(I+1) \tag{74}$$

Using calibrated absorption signals, one adjusts by trial-and-error the value of β in equation (66) so as to satisfy equation (74). This yields a calibrated value of the spin temperature β^{-1}.

5 NONLINEAR EFFECTS IN SPIN TEMPERATURE

Consider, for simplicity, a system with only one spin species, subjected to Zeeman and dipolar interactions. At high field, there are two constants of the motion: the Zeeman energy $\omega_0 I_z$ and the secular dipolar energy $\langle\mathcal{H}'_\mathrm{D}\rangle$. Internal equilibrium corresponds to the most probable state, i.e. that which maximizes the entropy

$$S = -k_\mathrm{B}\ \mathrm{Tr}\{\sigma\ \ln\sigma\} \tag{75}$$

where σ is the spin density matrix, and is consistent with the conservation of the above-mentioned quantities. This corresponds to a density matrix of the form

$$\sigma = \exp(-\beta_\mathrm{Z}\omega_0 I_z - \beta\mathcal{H}'_\mathrm{D})/\mathrm{Tr}\{\exp(\dots)\} \tag{76}$$

where β_Z and β are the Zeeman and dipolar inverse temperatures, respectively. If we introduce the partition function

$$\mathcal{Z}(\beta_\mathrm{Z},\beta) = \mathrm{Tr}\{\exp(-\beta_\mathrm{Z}\omega_0 I_z - \beta\mathcal{H}'_\mathrm{D})\} \tag{77}$$

we have

$$\omega_0\langle I_z\rangle = \omega_0\ \mathrm{Tr}\{\sigma I_z\} = -\frac{\partial}{\partial\beta_\mathrm{Z}}\ln\mathcal{Z} \tag{78}$$

$$\langle\mathcal{H}'_\mathrm{D}\rangle = \mathrm{Tr}\{\sigma\hat{\mathcal{H}}'_\mathrm{D}\} = -\frac{\partial}{\partial\beta}\ln\mathcal{Z} \tag{79}$$

At high temperature, that is to first order with respect to the inverse spin temperature, one obtains the well-known result

$$\omega_0\langle I_z\rangle = -\beta_\mathrm{Z}\omega_0^2\ \mathrm{Tr}\{I_z^2\} \tag{80a}$$

$$\langle\mathcal{H}'_\mathrm{D}\rangle = -\beta\ \mathrm{Tr}\{\mathcal{H}'^2_\mathrm{D}\} \tag{80b}$$

At lower temperature, both $\omega_0\langle I_z\rangle$ and $\langle\mathcal{H}'_\mathrm{D}\rangle$ depend, in a complicated way, on both inverse temperatures, β_Z and β. All the problems arise from the term in $\mathcal{H}'_\mathrm{D}$. If β is zero, that is there is purely Zeeman order, it is elementary to calculate all steady-state expectation values of interest (as seen above, calculating a dynamic quantity such as the FID remains a formidable task). We describe a perturbative approach in which one calculates the physical quantities to all orders with respect

to the inverse Zeeman temperature β_Z, but in the form of a power expansion in dipolar inverse temperature β (it will be shown that, in fact, we can achieve slightly more than that). For secular dipolar interactions, and especially for spins $\frac{1}{2}$, the most convenient approach is through the diagrammatic method devised by Stinchcombe et al.[21,22] The method is not described in detail here. Suffice it to say that the diagram contains bonds, associated with dipolar interaction coefficients, and vertices, the values of which depend on the inverse Zeeman temperature. More precisely, for spins $\frac{1}{2}$, the values depend on

$$t = \tanh(-\tfrac{1}{2}\beta_Z\omega_0) \tag{81}$$

By differentiating equations (78) and (79) with respect to β and with respect to β_Z, respectively, we obtain

$$\frac{\partial}{\partial\beta}\omega_0\langle I_z\rangle = \frac{\partial}{\partial\beta_Z}\langle\mathcal{H}'_D\rangle \tag{82}$$

whence

$$\omega_0\langle I_z\rangle(\beta_Z,\beta) = \omega_0\langle I_z\rangle(\beta_Z,0 + \int_0^\beta \frac{\partial}{\partial\beta_Z}\langle\mathcal{H}'_D\rangle(\beta_Z,\lambda)\,d\lambda \tag{83}$$

This enables one to calculate $\langle I_z\rangle$ as a power expansion in β from the corresponding expansion for $\langle\mathcal{H}'_D\rangle$. One can also obtain β-expansion formulas for the entropy, free energy, etc.

There is an advantage in using this approach for systems where the spins experience a longitudinal average field, that is when, in equation (24)

$$\frac{\gamma^2\hbar}{2}\sum_j \frac{1-3\cos^2\theta_{ij}}{r_{ij}^3} = q \neq 0 \tag{84}$$

a value which is equal for all spins i.

It can be proved that, in such a case, all vertices can be 'renormalized' in such a way that:

1. one considers only diagrams with no free ends; and
2. in each vertex, the term t in equation (81) is replaced by

$$t' = \tanh(-\tfrac{1}{2}\beta_Z\omega_0 - \tfrac{1}{2}\beta q t) \tag{85}$$

For a given physical quantity, the term of zero order corresponds to the mean-field approximation, and the terms in increasing powers of β correspond to the contributions of short-range correlations of increasing order.

We present below several experimental illustrations of nonlinear effects in spin temperature, for ^{19}F spins in spherical samples of CaF_2 (q = 0), together with the theoretical predictions from expansions up to β^3.

5.1 Dipolar Energy versus Polarization in High Effective Field

The experiment consists of measuring $\langle\mathcal{H}'_D\rangle$ as a function of polarization p in a system having a density matrix

$$\sigma = \exp[-\beta(\Delta_0 I_z + \mathcal{H}'_D)]/\mathrm{Tr}\{\ldots\} \tag{86}$$

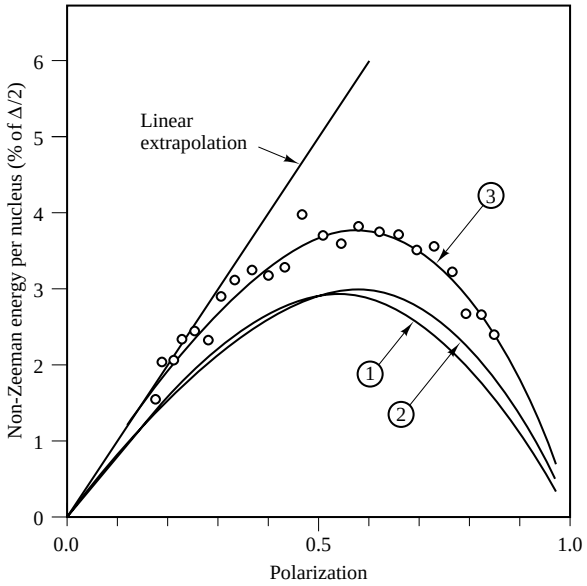

Figure 4 Non-Zeeman energy per fluorine spin as a function of nuclear polarization, in a spherical sample of CaF_2 at thermal equilibrium in the rotating frame in an effective field of 7.12 G·$\boldsymbol{B}_0$‖[100] and $T > 0$. Curves 1 and 2: first- and third-order approximations with dipolar interactions only. Curve 3: after addition of an adjusted contribution from impurities. (Reproduced with permission from Goldman et al.[23])

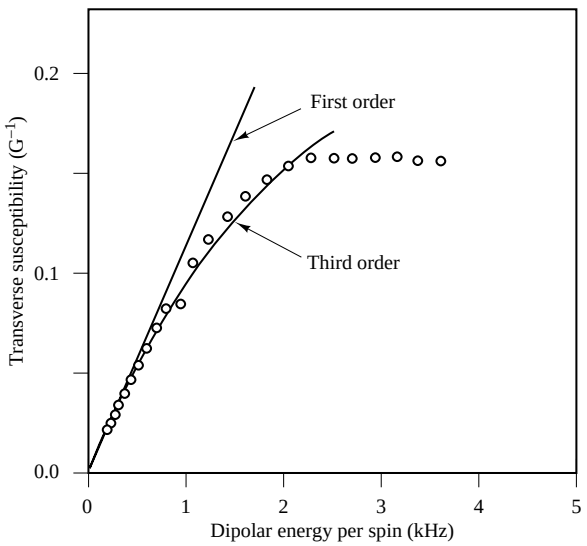

Figure 5 Transverse susceptibility of ^{19}F in a spherical sample of CaF_2 in zero effective field, against dipolar energy, together with first- and third-order approximations. Conditions: $\boldsymbol{B}_0$‖[100], $T < 0$. (Reproduced with permission from Goldman et al.[23])

in the case when Δ_0 is much larger than the local frequency D. When limited to the first order in β, the theoretical expression is

$$\langle\mathcal{H}'_D\rangle = \frac{N}{4}\frac{D^2}{\Delta_0}\ln\left(\frac{1+p}{1-p}\right) \times (1-p^2)(1-\tfrac{2}{3}p^2) \tag{87}$$

where β is expressed as a function of p.

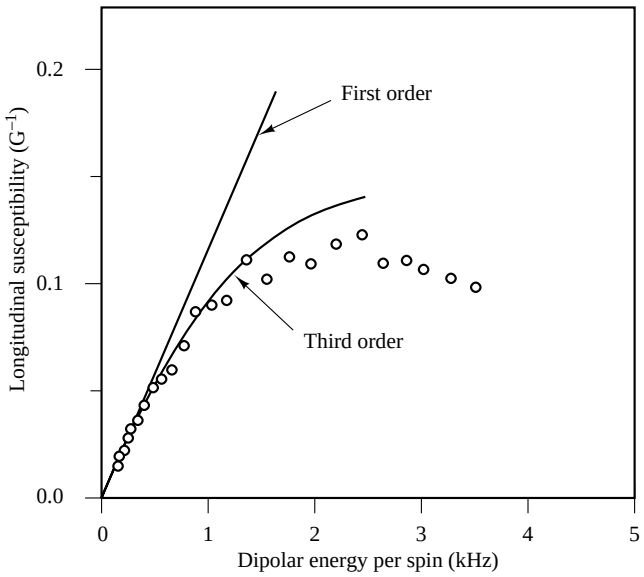

Figure 6 Longitudinal susceptibility of ^{19}F in the same sample and under the same conditions as in Figure 5. (Reproduced with permission from Goldman et al.[23])

Experimentally, one measures the loss of polarization resulting from a sudden rf irradiation at Δ_0 from resonance, starting from a state of pure Zeeman order. Figure 4 shows that agreement with theory requires the addition of an extra term to the secular dipolar reservoir.[23] The extra term has been identified as originating in the random field distribution due to the presence of paramagnetic impurities.

5.2 Transverse and Longitudinal Susceptibilities

Figures 5 and 6 show the transverse and longitudinal susceptibilities in zero effective field as a function of the dipolar energy,[23] together with the theoretical expectation from expansions up to β^3. The experimental method[23] used to obtain these two figures is rather complicated and is not described here. As can be seen in Figures 5 and 6, the results depart markedly from theory at dipolar energies per spin above about 2 kHz. This is no accident: these experiments were part of a general study of nuclear magnetic ordering and, as confirmed by other observations, the departures coincide with the onset of nuclear antiferromagnetism—but that is another story.

6 RELATED ARTICLES

Nuclear Ferromagnetism and Antiferromagnetism; Thermodynamics of Nuclear Magnetic Ordering.

7 REFERENCES

1. A. Abragam, *The Principles of Nuclear Magnetism*, Clarendon, Oxford, 1961.
2. M. Goldman, *Spin Temperature and Nuclear Magnetic Resonance in Solids*, Clarendon, Oxford, 1970.
3. C. P. Slichter, *Principles of Magnetic Resonance*, 3rd edn, Springer, Berlin, 1990.
4. A. Abragam and M. Goldman, *Nuclear Magnetism: Order and Disorder*, Clarendon, Oxford, 1982.
5. A. Abragam and W. G. Proctor, *C. R. Acad. Sci., Paris*, 1958, **246**, 2253.
6. A. Abragam and M. Goldman, *Rep. Prog. Phys.*, 1978, **41**, 395.
7. N. Kurti, F. N. H. Robinson, F. Simon, and D. A. Spohr, *Nature*, 1956, **178**, 450.
8. P. J. Hakonen and S. Yiu, *J. Low Temp. Phys.*, 1991, **85**, 25, and references therein.
9. A. G. Anderson and S. R. Hartmann, *Phys. Rev.*, 1962, **128**, 2023.
10. R. Kubo, *J. Phys. Soc. Jpn*, 1957, **12**, 570.
11. M. Goldman, *Quantum Description of High-Resolution NMR in Liquids*, Clarendon, Oxford, 1988.
12. I. J. Lowe and R. E. Norberg, *Phys. Rev.*, 1957, **107**, 46.
13. A. Abragam, M. Chapellier, J. F. Jacquinot, and M. Goldman, *J. Magn. Reson.*, 1973, **10**, 322.
14. Y. Roinel and V. Bouffard, *J. Magn. Reson.*, 1975, **18**, 304.
15. P. Bonamour, V. Bouffard, C. Fermon, M. Goldman, J. F. Jacquinot, and G. Saux, *Phys. Rev. Lett.*, 1991, **66**, 2810.
16. C. Kittel, *Phys. Rev.*, 1948, **73**, 155.
17. J. F. Jacquinot, M. Chapellier, and M. Goldman, *Phys. Lett. A*, 1974, **48**, 303.
18. M. Goldman, Y. Roinel, and V. Bouffard, *J. Magn. Reson.*, 1982, **46**, 110.
19. M. Goldman, *J. Magn. Reson.*, 1975, **17**, 393.
20. R. Brout, *Phase Transitions*, Benjamin, New York, 1965.
21. R. Stinchcombe, G. Horwitz, F. Englert, and R. Brout, *Phys. Rev.*, 1963, **130**, 155.
22. R. Brout, in *Magnetism*, eds. G. T. Rado and H. Suhl, Academic, New York, 1965, Vol. IIA, p. 43.
23. M. Goldman, J. F. Jacquinot, M. Chapellier, and Vu Hoang Chau, *J. Magn. Reson.*, 1975, **18**, 22.

Biographical Sketch

Maurice Goldman. *b* 1933. Diplôme d'Ingénieur Chimiste ESPCI, 1955, Doctorat d'Etat, 1967, University of Paris. Physicist, Commissariat à l'Energie Atomique (CEA), 1955–69. Vice-Director, College de France, 1969–83. Physicist, CEA, 1984–89. Research Director, CEA, 1989–93. Vice-President, ISMAR, 1992–present. Scientific Advisor, CEA, 1993–present. Approx. 100 publications, including three books. Research specialties: spin temperature and thermodynamics, nuclear magnetic ordering, relaxation in liquids and solids, and quantum theory of high-resolution NMR.

Optically Pumped NMR of Semiconductors and Two-Dimensional Electron Systems

Robert Tycko

National Institutes of Health, Bethesda, MD, USA

&

Sean E. Barrett

Department of Physics, Yale University, New Haven, CT, USA

1 Introduction 1
2 Directly Detected vs. Optically Detected 1
3 Mechanism of Optical Pumping 2
4 Application to Two-Dimensional Electron Systems in the Quantum Hall Regime 4
5 Concluding Remarks 7
6 Related Articles in this Volume 7
7 Related Articles in Volumes 1–8 7
8 References 7

1 INTRODUCTION

In the context of this article, the term 'optical pumping' refers to the creation of large, nonequilibrium nuclear spin polarizations by irradiation of a sample at optical wavelengths. Significant optical pumping effects have been reported in several classes of samples, including organic molecular crystals,[1] mixtures of noble gases and alkali metal vapors,[2] biological photosynthetic systems,[3–5] and inorganic semiconductors.[6,7] Optical pumping of nuclear spin polarization in a semiconductor was first described by George Lampel in 1968, for the case of crystalline Si.[6] In Lampel's original experiments, Si samples were irradiated with an arc lamp at 77 K and fields of 0.16 T or less, and ^{29}Si polarization was measured by direct NMR detection. Optical pumping was observed with both circularly polarized and unpolarized light. Lampel's observations were explained in terms of photoexcitation of conduction electrons with nonequilibrium electron spin polarization and subsequent dynamic polarization of hyperfine-coupled nuclear spins. Although the magnitude of the ^{29}Si polarizations in Lampel's experiments were only of order 10^{-5}, these experiments set the stage for later optical pumping experiments in which polarizations of order 10% have been achieved.[8,9]

Following Lampel's experiments and other optical pumping experiments on Si,[10–12] attention shifted to III–V semiconductors, principally GaAs and AlGaAs, and to optical detection of the NMR spectra.[13–17] These and other recent experiments have been performed at temperatures on the order of 10 K or lower. In optically detected NMR (ODNMR) experiments, the large nuclear spin polarization created by optical pumping exerts a strong average hyperfine field on the photoexcited electrons, which can then affect the evolution or steady-state of the photoexcited electron spin polarization. In analogy to the Hanle effect,[18,19] the optically pumped nuclear hyperfine field can be made to reduce the degree of circular polarization of the photoluminescence that accompanies electron-hole recombination when radio-frequency (rf) fields are applied near the NMR lines. The original ODNMR experiments on semiconductors[13–17] were carried out on bulk materials and with continuous wave (cw) rf irradiation (i.e., frequency domain ODNMR). Recent ODNMR experiments have focussed on semiconductor thin films and heterostructures[20–23] and on the development of time-domain variants that lead to dramatic improvements in NMR resolution.[9,24,25] Simultaneously, there has been a revival of interest in directly detected, optically pumped NMR (OPNMR).[8,26–33] OPNMR measurements with direct detection have been used to investigate the properties of quantum confined conduction electrons in two-dimensional systems at low temperatures and high fields,[34–38] a topic of considerable interest to condensed matter physicists.[39–41] Notably, OPNMR measurements have provided the first evidence for and characterization of novel electron states called skyrmions in two-dimensional electron systems (2DES).[34,35]

2 DIRECTLY DETECTED VS. OPTICALLY DETECTED

An important advantage of both time-domain and frequency-domain ODNMR methods is their extremely high sensitivity. Because of the high efficiency for detection of optical photons, it is possible in principle to detect the NMR spectrum of nuclei in the vicinity of single luminescent defect or impurity site in a semiconductor sample, comprising roughly 10^5 nuclei. In fact, ODNMR spectra of single GaAs quantum dots containing approximately this number of nuclei have been reported,[42–44] although in these experiments the NMR spectra were detected through modulation of the photoluminescence energy, rather than polarization, by manipulation of the optically pumped nuclear polarization. In ODNMR experiments in which photoluminescence polarization was monitored, NMR spectra of less than 10^{11} nuclei have been detected.[16,21]

An apparent limitation on ODNMR techniques based on photoluminescence polarization is that they can only be applied when the nuclear hyperfine field is a significant fraction of the external magnetic field. In practice, such ODNMR experiments are typically performed at magnetic field strengths below 1 T.

Advantageous features of directly detected OPNMR include: (1) compatibility with high fields (to the extent that the optical pumping effect itself occurs at high field);[31,33] (2) absence of photoluminescence requirements; (3) ability to detect NMR spectra of both the ground state and the photoexcited state of the sample; (4) ability to detect NMR spectra of sample regions that are spatially distinct from the optically absorbing regions, through nuclear spin diffusion;[34,35]

(5) full compatibility with pulsed NMR methodology, including multiple pulse line-narrowing techniques, heteronuclear decoupling, multidimensional spectroscopy, and nuclear spin relaxation measurements. Some of these advantages are shared by time-domain or time-sequenced ODNMR techniques.[9,24,25] In principle, because optical pumping can produce nuclear spin polarizations of order 10%,[8,9] the sensitivity of directly detected OPNMR is sufficient for the observation of roughly 10^{14} nuclei (with signal averaging), or the number of nuclei in a semiconductor monolayer with a surface area of approximately 0.2 cm.[2]

Examples of OPNMR spectra of bulk GaAs and InP are shown in Figures 1 and 2. Spectra of semiconductor quantum well samples are discussed in Section 4.

Very recently, all-optical NMR experiments on semiconductors, i.e., experiments in which nuclear spin transitions are detected with only optical irradiation of a sample, have been reported.[45–47] In these experiments, a near-infrared pump laser tuned near the semiconductor absorption band edge and propagating in a direction not parallel to the applied static magnetic field is pulsed[45,46] or modulated in amplitude or phase[47] at radio frequencies, but no rf irradiation or pulses are applied. A plot of the Faraday rotation of a weaker probe laser[45,46] or of photoluminescence polarization[47] versus the modulation frequency of the pump laser shows discontinuities at the NMR frequencies. Such experiments have been reported both for bulk GaAs[45,46] and for GaAs quantum wells.[46,47] Both single-quantum ($|\Delta m| = 1$) and overtone ($|\Delta m| = 2$) NMR transitions have been detected. Single-quantum transitions are attributed to modulation of electron-nucleus magnetic hyperfine couplings at the laser modulation frequency,[45–47] while overtone transitions are attributed to modulation of nuclear electric quadrupole couplings at the laser modulation frequency.[46,47] Observation of both types of NMR transitions is dependent upon optical pumping of nuclear spin polarizations away from resonance and subsequent destruction of the nuclear spin polarization at the resonant conditions. Further exploration and exploitation of all-optical NMR effects in semiconductors, and possibly other materials, is likely in the near future.

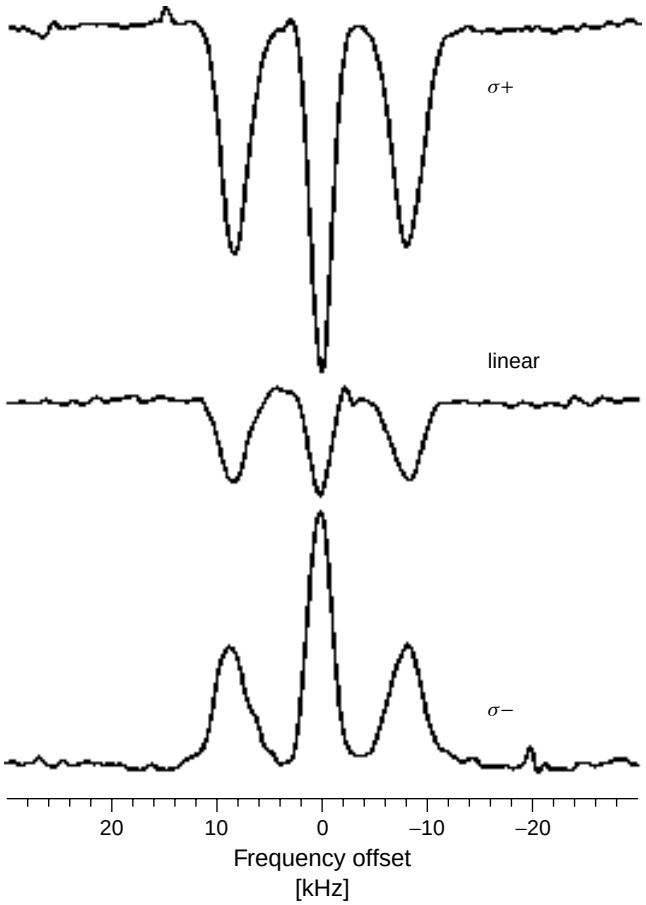

Figure 1 Optically pumped ^{71}Ga NMR spectra of a semi-insulating GaAs wafer at 4.3 K in a 9.39-T field, obtained with an optical pumping time of 10 s, a photon energy of 1.49 eV (831 nm wavelength), and the indicated light polarizations. The laser power was 240 mW in a 5-mm diameter spot. Emissive OPNMR signals are observed with linear and $\sigma+$ polarization. Under the conditions of these experiments, the optically pumped nuclear spin polarizations are of order 1%, but larger polarizations are created with longer pumping times. No NMR signals are detectable when the laser light is blocked, because of both the smaller nuclear spin polarization at equilibrium and the very long spin-lattice relaxation times in the dark ($>10^3$ s). Quadrupole splittings of the NMR lines arise from strain due to thermal contraction of the GaAs wafer, which was glued to a sapphire block in the low-temperature NMR probe

3 MECHANISM OF OPTICAL PUMPING

The general features of the physical mechanism of optical pumping in semiconductors have been described.[7] Briefly, photoexcitation of a direct-gap, ZnS-structure, bulk semiconductor at the band edge (Γ point) in zero magnetic field creates conduction electrons with spin polarization $\langle S_z \rangle = \pm(1/4)\sigma$, where the light helicity σ is $+1$ for left-circular-polarized light, -1 for right-circular-polarized light, and 0 for unpolarized light. Provided that the spin-lattice relaxation time of photoexcited electrons is not much less than the photoexcitation lifetime, a net nonequilibrium electron spin polarization is created. The electrons couple to nuclei by Fermi contact hyperfine interactions. If the hyperfine interactions fluctuate with a sufficiently short correlation time, flip–flop transitions efficiently transfer electron spin polarization to the nuclei. At steady state, the nuclear spin temperature T_n is related to the electron spin temperature T_e and lattice temperature T by the expression $(T_n^{-1} - T^{-1}) = \gamma_e/\gamma_n(T^{-1} - T_e^{-1})$, where γ_e and γ_n are the electronic and nuclear magnetogyric ratios. Since $\gamma_e/\gamma_n \sim 10^3$, a small deviation of the electron spin polarization from thermal equilibrium produces a very low (positive or negative) nuclear spin temperature, i.e., a large nuclear spin polarization.

It is commonly assumed that optical pumping is driven primarily by localized electron states (e.g., electrons trapped at defect or shallow donor sites), rather than delocalized, Bloch-function states. This is because the rate of flip–flop transitions depends on the square of the hyperfine couplings, and therefore on the square of the electron probability density at the nuclei. Because the total electron probability density (not squared) is normalized, electron states that concentrate the probability density in a smaller volume can produce a greater net flip–flop rate.

Despite this general understanding of optical pumping, nearly all details of the mechanism remain mysterious. For example:

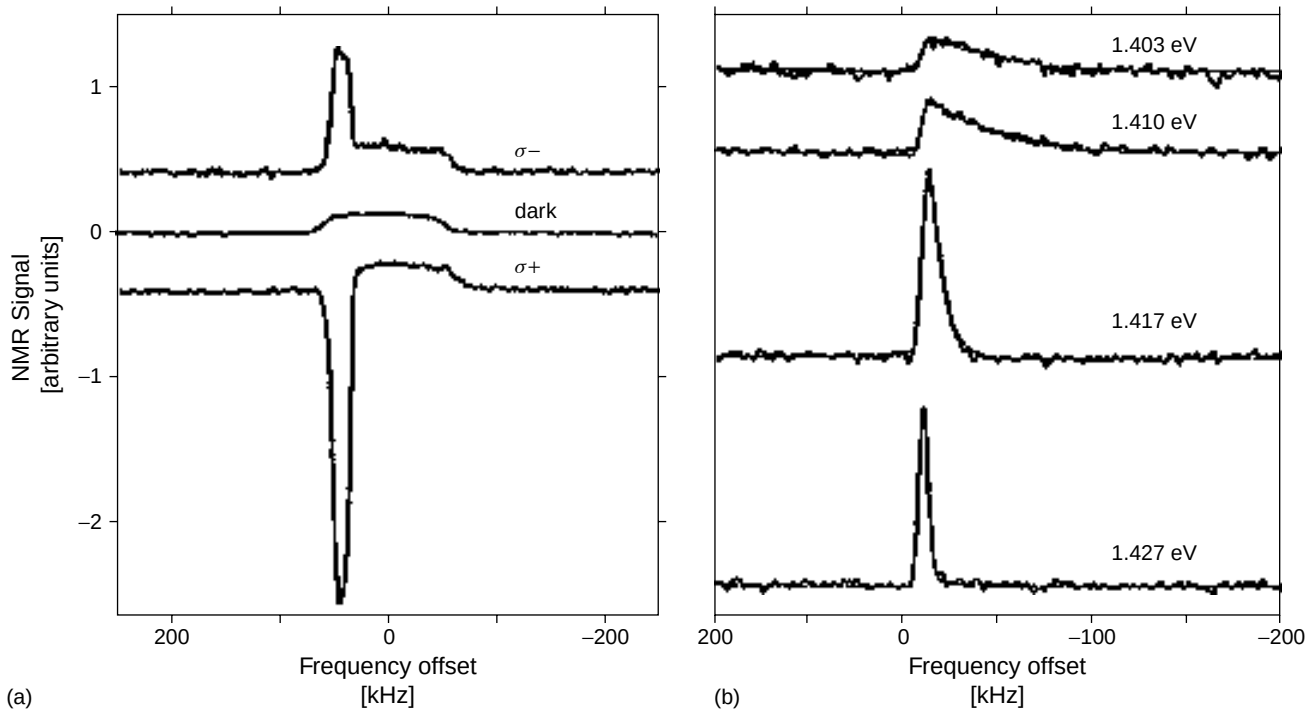

Figure 2 Optically pumped ^{13}P NMR spectra of a 348-μm thick Fe-doped semi-insulating InP wafer at 6 K, obtained in a superconducting magnet with a central field of 9.39 T. The InP wafer was located outside the homogeneous region of the magnet, producing a strong field gradient perpendicular to the surface of the wafer. The spectra then represent one-dimensional images of the nuclear spin polarization.[8] (a) Low resolution images. The InP wafer is situated in a 0.195 T/cm gradient, with an optical pumping time of 600 s at 1.412 eV, or 878 nm wavelength. Spectra were obtained with $\sigma+$ and $\sigma-$ polarized light, at a power of 200 mW in a 3.7-mm diameter spot, and in the dark. The wafer thickness corresponds to an NMR frequency range of 116 kHz. With optical pumping, ^{31}P nuclei near the laser-irradiated surface acquire either positive or negative nonequilibrium spin polarizations, depending on the direction of light polarization. (b) High resolution images. The InP wafer is situated in a 0.453 T/cm gradient, with an optical pumping time of 120 s at the indicated photon energies. Spectra were obtained with $\sigma+$ polarized light, at a power of 25 mW in a 0.45-mm diameter spot. Vertical axis is reversed relative to (a). The absorption band edge for InP at low temperatures occurs at approximately 1.427 eV, where the light penetration depth is approximately 2 μm. As the laser is tuned to lower energies, the pumping light penetrates deeper into the wafer, producing an asymmetrically broadened ^{31}P NMR lineshape. A 2-μm distance corresponds to an NMR frequency shift of 1.6 kHz. (Adapted from Ref.[8])

1. The identity of the localized states that produce optical pumping is not firmly established in any specific sample, either bulk or heterostructure.
2. The source of hyperfine fluctuations has not yet been identified conclusively. The classic Overhauser effect in a *metal* depends on hyperfine fluctuations due to translational motion of delocalized electrons near the Fermi surface. In optically pumped semiconductors, this contribution is considered negligible. Recent studies of the field dependence of optical pumping in GaAs and InP suggest that the relevant fluctuations have time scales of order 10 ps.[31,33,48]
3. Possible effects of high fields on the band structure, optical selection rules, electron-hole pairing and localization, or other aspects of the photophysics relevant to optical pumping have not been explored in theory or experiment.
4. Possible contributions to the optical pumping process from hyperfine couplings to photoexcited valence band holes and effects of spin-selective electron-hole recombination[49] on the electron spin polarization have not been analyzed in detail.
5. The signs of optically pumped ^{31}P polarizations in undoped InP[27,33] (but not Fe-doped, semi-insulating InP[8,28]) have been found to be opposite to expectations based on the simple theory outlined above, i.e., $\sigma-$ and linearly polarized light produce negative ^{31}P polarization, while $\sigma+$ light produces positive polarization. In GaAs, the signs of optically pumped nuclear spin polarizations are in accord with expectations.
6. The dependences of nuclear spin polarization on the optical photon energy in bulk GaAs and InP are not well understood. In bulk GaAs, a strong maximum in the nuclear spin polarization is observed at photon energies approximately 20 meV below the band edge, and little or no polarization is created at higher energies.[29] This observation has been attributed tentatively to direct pumping of shallow traps or excitons.[29] In bulk InP, a similar maximum has been shown by stray-field NMR imaging to be due primarily to the increased optical absorption length (i.e., greater optically pumped volume) below the band edge.[8] In bulk InP, substantial nuclear spin polarizations are generated with photon energies up to at least 60 meV above the band edge.[8,27]
7. In GaAs/AlGaAs quantum well samples at high field, optical pumping effects saturate at very low photon flux,[26] of order 60 mW cm^{-2}, while photoluminescence does not saturate up to at least 3 W cm^{-2}. This observation suggests a 'phase-space filling' phenomenon in which a rather

low density of photoexcitations is sufficient to occupy all electronic states that play a role in optical pumping.

8. Recent OPNMR experiments on bulk InP have revealed that optical pumping creates nuclear spin dipolar order in addition to the Zeeman order predicted by the simple theory outlined above.[28] Possible explanations for optical pumping of dipolar order include direct generation through electron-nuclear cross relaxation, dependent on dipolar hyperfine interactions and nuclear dipole-dipole couplings,[50] and indirect generation through diffusion of Zeeman order in the presence of spatial gradients of NMR frequencies.[28] The dominant mechanism for optical pumping of dipolar order has not been established experimentally.

Obviously, there is a great deal of room for further research into the fundamental aspects of optical pumping in semiconductors. Nonetheless, even in the absence of a detailed understanding of the mechanism, the optical pumping effect can be useful both for sensitivity enhancement and for spatial localization of NMR signals. The utility of optical pumping is exemplified by OPNMR studies of 2DES in GaAs/AlGaAs quantum wells, as described below.

4 APPLICATION TO TWO-DIMENSIONAL ELECTRON SYSTEMS IN THE QUANTUM HALL REGIME

A 2DES, cooled to extremely low temperatures in a strong magnetic field, exhibits many exotic phenomena, including the integer[51] and fractional[52] quantum Hall effects that are the subject of a large body of experimental and theoretical studies by condensed matter physicists. Transport and optical studies of the 2DES have shown that the low-energy physics in these extreme conditions is driven by the electron–electron Coulomb interaction,[53] making this 'simple' system one of the hardest to understand theoretically. OPNMR studies have contributed to the recent progress on this problem by providing important new insights into the electron spin degree of freedom, which helps to shed light on the low-lying many-body states that exist in a real 2DES.[39–41]

For these OPNMR experiments, samples typically contain multiple copies (up to forty) of a fundamental unit: a GaAs quantum well (i.e., a GaAs layer approximately 300 Å thick) doped with electrons ($n \sim 1 \times 10^{11}\,cm^{-2}$), sandwiched between $Al_{0.1}Ga_{0.9}As$ barriers (i.e., $Al_{0.1}Ga_{0.9}As$ layers approximately 1500 Å thick).[54–56] At low temperatures, all conduction electrons are confined to the quantum wells and are in the same '2D state' (i.e., the lowest electronic subband of the well). The normal component of a strong magnetic field ($B\cos\theta$, where θ is the angle between the external field **B** and the direction normal to the plane of the quantum well) quantizes the 2D motion into spin–split Landau levels.[54,55] In this regime, the many-body states and thus the physical properties of the 2DES are determined by the Landau level filling factor $\nu = (nhc/eB\cos\theta)$, where h, c, and e are Planck's constant, the velocity of light, and the electron charge. By varying n, B, or θ, ν may be tuned to reach integral[51] (e.g., $\nu = 1$) or fractional[52] (e.g., $\nu = 1/3$) quantum Hall ground states.[39–41,53] These are states in which the longitudinal resistivity ρ_{xx} of the 2DES vanishes and the transverse (or Hall) resistivity ρ_{xy} plateaus at the values $(hc/\nu e^2)$. In OPNMR experiments on 2DES in GaAs quantum wells,[34–38,57,58] ν is varied for a sample with given n by varying θ and by performing experiments at several values of B.

Figure 3 shows ^{71}Ga OPNMR spectra of a multiple quantum well sample, acquired using the timing sequence SAT – τ_L – τ_D – DET.[26,34,35,57] SAT represents an rf pulse train that saturates nuclear spin polarization. During τ_L, a near-infrared laser optically pumps the quantum well, using a photon energy above the band edge of the well and below that of the barrier. Because the laser is tuned to be absorbed only in the quantum well layers, only nuclear spins in the quantum wells, and not in the barrier, become strongly polarized. The enhanced NMR signal observed after a short illumination period (e.g., $\tau_L \sim 5$ s) is due to nuclei in the quantum wells ('W' signals in Figure 3). Eventually (e.g., as $\tau_L \to 200$ s), the optically pumped nuclear polarization spreads into the barrier regions

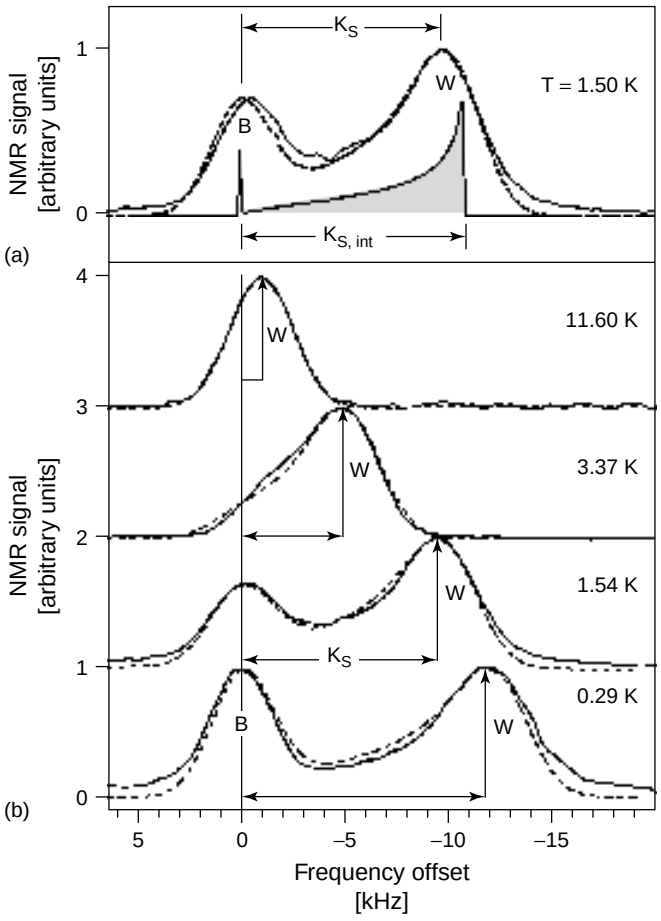

Figure 3 ^{71}Ga NMR lineshapes of an optically pumped GaAs multiple quantum well sample, obtained in a 12 T field at the indicated temperatures.[37] (a) Spectrum at Landau level filling factor $\nu = 1/3$ after approximately 60 s of optical pumping. Peak labeled W arises from nuclei in the 26-nm thick GaAs wells. Peak labeled B arises from the 312-nm thick $Al_{0.1}Ga_{0.9}As$ barriers between wells. The Knight shift K_S is defined empirically as the splitting between the peaks. The shaded lineshape is a simulation of the intrinsic Knight shift lineshape, with maximum shift $K_{S,int}$. The dashed line is a fit to the experimental lineshape obtained by convoluting the intrinsic lineshape with a Gaussian lineshape attributable to nuclear magnetic dipole-dipole couplings. (b) Temperature dependence of the optically pumped ^{71}Ga NMR lineshape at $\nu = 0.267$. (Reprinted from Ref.[37])

by nuclear spin diffusion. A second NMR signal due to nuclei in the barriers then appears ('B' signals in Figure 3). After a period τ_D in the dark ($\tau_D \geq 1$ s), nuclear free induction decay signals are recorded in the period DET. These signals probe the equilibrium properties of the 2DES as functions of ν and temperature. Nuclear spin-lattice relaxation rates R_1 at thermal equilibrium can be determined from the dependence of OPNMR signal amplitudes on τ_D[35].

The Knight shift (K_S) of quantum well signals may be defined[26,34,35] as the peak-to-peak splitting between quantum well and barrier signals (see Figure 3). K_S is due to Fermi contact hyperfine couplings between nuclei and doped (not photoexcited, because the OPNMR signals are observed in the dark after τ_D) conduction electrons confined in the quantum wells and is proportional to the spin polarization of the 2DES. The temperature dependence of K_S [Figure 3(b)] reveals the increasing spin polarization of the electrons[36] as they are cooled into a ferromagnetic ground state[59] [see Figure 4(a)]. As shown in Figure 3(a) (dashed line), a more quantitative determination of K_S[37] is achieved by fitting the experimental OPNMR lineshape to the convolution of the intrinsic hyperfine lineshape of the well and barrier [Figure 3(a), shaded] with a 3.5 kHz FWHM Gaussian lineshape due to nuclear magnetic dipole–dipole couplings. The central assumption of this model of the lineshape is that nuclei in the quantum well experience a hyperfine magnetic field that scales with the electron probability density in the direction perpendicular to the plane of the well but is uniform in the plane of the well. This model requires that any reversed electron spins [e.g., thermally excited spin waves, see Figure 4(b)] are delocalized within the plane of the quantum well, such that the electron spin polarization appears spatially homogeneous when averaged over the time scale of the NMR experiment, which is of order 40 μs. Simulated OPNMR lineshapes in this motionally-narrowed limit fit the experimental spectra at $\nu = 1/3$ and $\nu = 1$ over the observed temperature range.

The experimentally determined $K_S(T, \nu)$ represents a direct and calibrated measure[34,36] of the 2DES spin polarization $P(T, \nu) \equiv \langle S_z(T, \nu)\rangle / \max\langle S_z\rangle$. Figure 5 shows P(T, ν) measured by OPNMR at three important filling factors, $\nu = 1$,[60] $\nu = 1/3$,[36] and $\nu = 1/2$.[38] Both the $\nu = 1$ and the $\nu = 1/3$ electronic states become fully polarized in the low temperature limit [see Figure 4(a)], in agreement with theoretical predictions[59,61–63] that these integer and fractional ground states are quantum Hall ferromagnets (QHFM). P(T, ν) decreases with increasing temperature due to thermally excited spin-waves [see Figure 4(b)]. Data at $\nu = 1$ were obtained at B $\approx$ 7 T, where the electron Zeeman energy corresponds to a temperature $T_Z \approx 2.1$ K, whereas data at $\nu = 1/3$ were obtained at B $\approx$ 12 T, where $T_Z \approx 3.5$ K. The more rapid drop-off of P(T,$\nu = 1/3$) shows the dominant role that the electron–electron Coulomb interaction plays in the spectrum of excited states.[61] Specifically, the 'spin stiffness' at $\nu = 1$ is expected[64] to be much higher than at $\nu = 1/3$, which means that the number of spin waves present at low temperature is much less for $\nu = 1$, consistent with the data (Figure 5). OPNMR measurements of P(T,$\nu = 1$) have stimulated additional progress on the theoretical description of QHFM,[65–68] since the conventional assumption of dilute spin waves can not describe the experiments once the temperature exceeds T_Z.

Figure 5 also shows OPNMR measurements of P(T,$\nu = 1/2$), which appear to indicate a partially polarized 2DES state in the low-temperature limit.[38] These data also drop off more rapidly with increasing temperature than data taken in either the integral ($\nu = 1$) or the fractional ($\nu = 1/3$) quantum Hall regimes. Both observations are qualitatively consistent with the emerging picture that the $\nu = 1/2$ state is best described as a compressible (i.e., gapless) state of composite fermions.[69–77] OPNMR measurements of P(T,$\nu = 1/2$) and of the temperature dependence of the nuclear spin-lattice relaxation rate $R_1(T,\nu = 1/2)$ provide important constraints[38,78] on the theoretical description of the $\nu = 1/2$ state and shed new light on the nature of the composite fermion.[79,80]

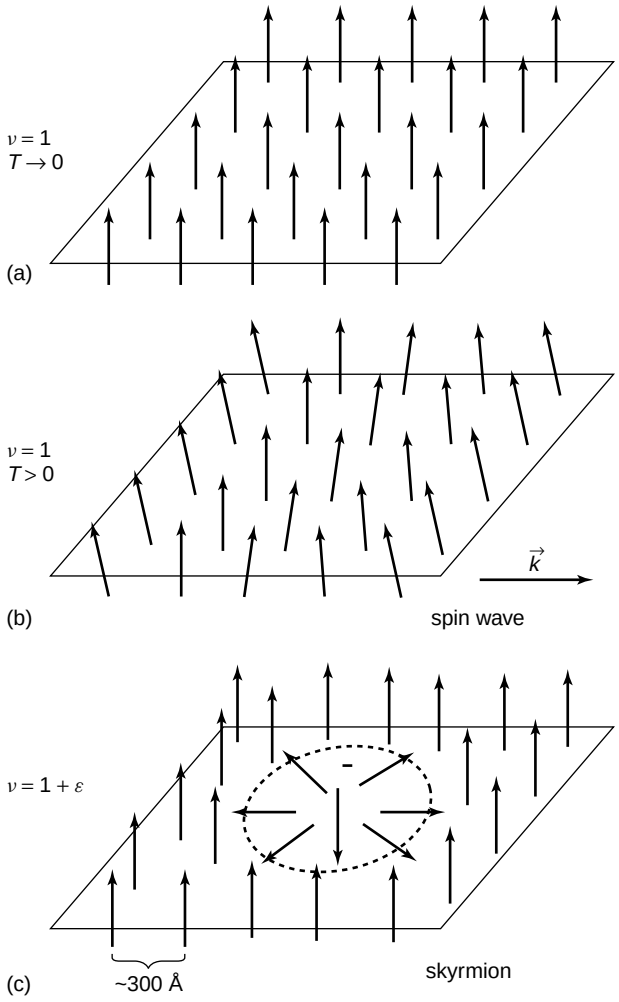

Figure 4 Illustration of electronic states in a two-dimensional system at low temperatures and high magnetic fields, as for conduction electrons in a OPNMR experiments on GaAs quantum wells. (a) At very low temperatures and Landau level filling factor $\nu = 1$, the electrons fill the lowest state of translational energy with maximum spin polarization, producing the maximum Knight shift in an OPNMR measurement. (b) At somewhat higher temperatures, thermally excited electron spin waves reduce the electron spin polarization, thereby reducing the Knight shift. (c) At very low temperatures and filling factors slightly above one, additional electrons must occupy spin-reversed states. Electron–electron interaction energies are minimized by tilting the spins of neighboring electrons, resulting in a more rapid destruction of the electron spin polarization and Knight shift than expected in the non-interacting limit. The electronic ground state contains skyrmions

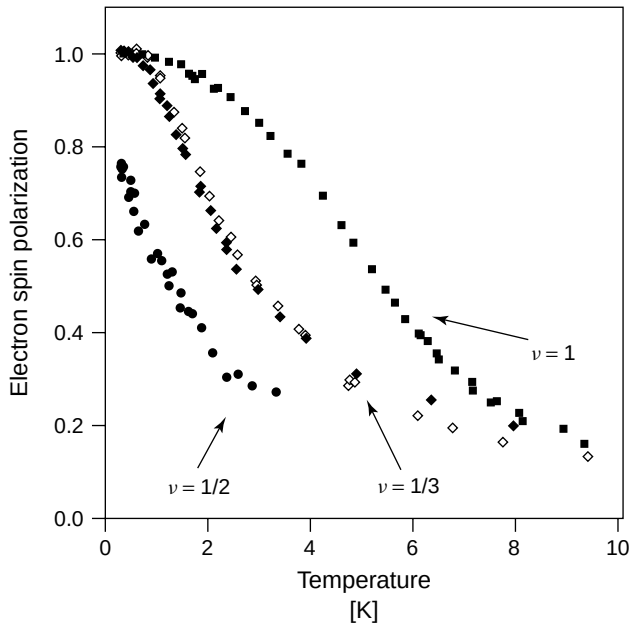

Figure 5 Temperature dependence of the electron spin polarization of a GaAs quantum well at integral ($\nu = 1$) and fractional ($\nu = 1/2$, $\nu = 1/3$) filling factors, determined from Knight shifts in OPNMR spectra. Two-dimensional electron systems at $\nu = 1$ and $\nu = 1/3$ exhibit the integer and fractional quantum Hall effects, respectively. The electronic ground state at $\nu = 1/2$ is described theoretically as a compressible (i.e., gapless) state of composite fermions

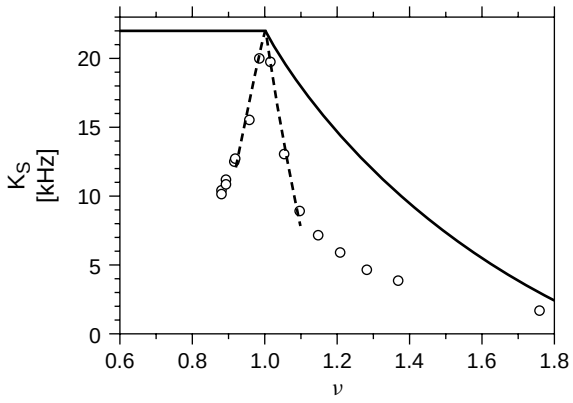

Figure 6 Dependence of the ^{71}Ga Knight shift on filling factor (open circles), obtained from OPNMR measurements on a multiple quantum well sample with 30-nm thick GaAs wells and 180-nm thick $Al_{0.1}Ga_{0.9}As$ barriers at a field of 7.05 T and 1.55 K. The filling factor was varied by tilting the sample in the field. The solid line is the theoretical curve for noninteracting electrons in a two-dimensional system. The dashed lines are fits to the data, assuming a skyrmion model in which each skyrmion carries an effective spin of 1.8, or 3.6 times the spin of a single electron. Data of this type provided the first experimental evidence for skyrmions in two-dimensional electron systems. (Reprinted from Ref.[34])

OPNMR data on GaAs quantum wells, such as the data in Figure 6, also provided the initial experimental evidence[34,35] for novel charged spin-texture excitations[62,63] called skyrmions in 2DES. To understand the meaning of a skyrmion state, consider the ground state of the QHFM at $\nu = 1$ (Figure 4(a)), and then add one electron (at fixed temperature), to move to $\nu = 1 + \varepsilon$. By the Pauli exclusion principle, the spin of the additional electron must be reversed with respect to the electron spins at $\nu = 1$. However, theory predicts a more dramatic effect: to minimize electrostatic repulsions, nearby electron spins will twist as well, making nearest neighbors more nearly parallel, until the reduction in Coulomb energy is balanced by the higher Zeeman energy of multiple reversed electron spins.[59] The resulting many-body state, a skyrmion, has one more electron but many more net reversed spins ($\sim$3 per additional electron in most experiments), relative to the $\nu = 1$ ground state. As shown in Figure 6, $K_S(\nu)$ at low temperature, and thus $P(\nu)$, drops rapidly[34] as more skyrmions (or antiskyrmions, corresponding to $\nu = 1 - \varepsilon$) are added to the system[63,81] by moving farther above or below $\nu = 1$. A similar drop has been reported[82] near $\nu = 3$. The presence of many skyrmions also leads to a strong dependence of R_1 on ν near the integral quantum Hall condition.[35] From a purely phenomenological standpoint, the effects of varying ν can be quite dramatic: at 2.1 K and 7.05 T, the spin-lattice relaxation rate of ^{71}Ga nuclei in a GaAs quantum well near $\nu = 1$ changes by a factor of 20 when the sample is rotated by only 3°! Similar effects have subsequently been observed in specific heat measurements.[83,84]

As Figure 4(c) shows, the size of the skyrmion is expected to be much less than that of spin waves [which are extended objects, Figure 4(b)], but also much greater than the internuclear spacing of roughly 3 Å. The spatial extent of the skyrmion is relatively unimportant at temperatures where skyrmions are delocalized and the OPNMR spectra are motionally narrowed[37] (i.e., the time-averaged value of $P(T,\nu)$ is invariant to translation in the plane of the quantum well).

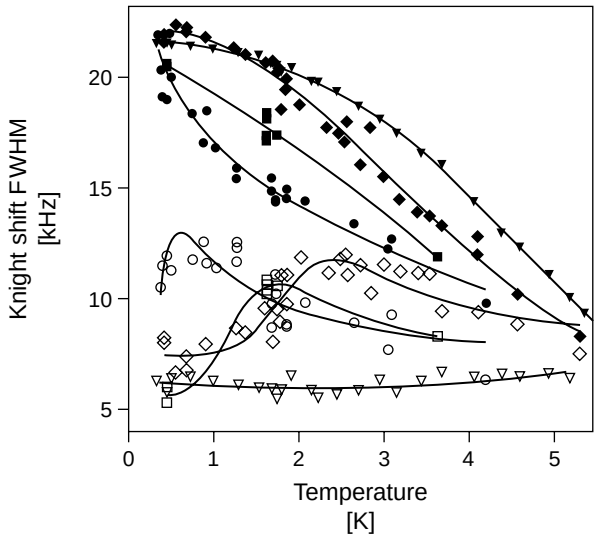

Figure 7 Dependences of the Knight shift (filled symbols) and quantum well NMR linewidth (open circles) on temperature, from ^{71}Ga OPNMR measurements on GaAs quantum wells at filling factors $\nu = 1.00$ (triangles), 0.969 (diamonds), 1.045 (squares), and 0.949 (circles). Lines are guides to the eye. The non-monotonic temperature dependence of the linewidth indicates a transition from the motionally narrowed limit at higher temperatures towards the static limit at lower temperatures, where the motion in question is translation of skyrmions in the plane of the quantum well

However, for $\nu \neq 1$, Figure 7 shows that lowering the temperature causes the width of the quantum well lineshape (open symbols) first to increase and then to decrease,[85] in stark contrast with the temperature independence of the quantum well linewidth at $\nu = 1$. Similar trends were uncovered in earlier measurements[37] near $\nu = 1/3$. The non-monotonic temperature dependence of the linewidth in Figure 7 is consistent with the evolution of the quantum well OPNMR lineshape from the motionally narrowed regime to the static regime as the temperature is lowered. Specifically, the motion at higher temperatures is that of delocalized skyrmions. As the temperature is lowered, fluctuations in local hyperfine fields freeze out as the skyrmions become localized. With spectra approaching the frozen limit, future OPNMR measurements should provide new details about the spatial distribution of skyrmions in a 2DES and the nature of the many-skyrmion ground state, which may possess unusual order.[86–92]

5 CONCLUDING REMARKS

More than three decades have passed since the first demonstration by Lampel[6] of optical pumping of nuclear spins in a semiconductor and of directly detected, optically pumped NMR. As described in this chapter, Lampel's early work has been followed by a large number of interesting methodological extensions, including the development of ODNMR techniques, time-domain ODNMR, and high-field OPNMR, and important applications, most notably the use of OPNMR as a probe of the properties of conduction electrons in two-dimensional systems in the quantum Hall regime of low temperatures and high magnetic fields. Because of the practical importance of sensitivity enhancement in all areas of NMR and the commercial and scientific importance of semiconductor devices, investigations and applications of optical pumping effects in semiconductors are certain to continue. Likely areas for future research include clarifications of the physical mechanism of optical pumping in semiconductors, investigations of optical pumping effects in other semiconductor materials and other quantum-confined structures (e.g., quantum dots), further development of all-optical NMR methods, and possibly the use of optically pumped semiconductor wafers as sources of nuclear spin polarization for sensitivity enhancement in NMR measurements on organic or biological materials deposited on the semiconductor surface.[27]

6 RELATED ARTICLES IN THIS VOLUME

Stray Field (STRAFI) NMR: Imaging in Large Field-Gradients.

7 RELATED ARTICLES IN VOLUMES 1–8

Dynamic Nuclear Polarization & High-Resolution NMR of Solids, Volume 3; Electron-Nuclear Hyperfine Interactions, Volume 3; Knight Shift, Volume 4; Optically Enhanced Magnetic Resonance, Volume 5; Quadrupolar Nuclei in Solids, Volume 6.

8 REFERENCES

1. J. Allgeier, V. Macho, D. Stehlik, H. M. Vieth, W. Auch, and J. U. Vonschutz, *Chem. Phys. Lett.*, 1982, **86**, 522.
2. T. G. Walker and W. Happer, *Rev. Mod. Phys.*, 1997, **69**, 629.
3. M. G. Zysmilich and A. McDermott, *J. Am. Chem. Soc.*, 1994, **116**, 8362.
4. M. G. Zysmilich and A. McDermott, *Proc. Natl. Acad. Sci. USA*, 1996, **93**, 6857.
5. T. Polenova and A. E. McDermott, *J. Phys. Chem. B*, 1999, **103**, 535.
6. G. Lampel, *Phys. Rev. Lett.*, 1968, **20**, 491.
7. F. Meier and B. P. Zakharchenya, 'Optical Orientation', Elsevier: Amsterdam, 1984.
8. C. A. Michal and R. Tycko, *Phys. Rev. B*, 1999, **60**, 8672.
9. J. A. Marohn, P. J. Carson, J. Y. Hwang, M. A. Miller, D. N. Shykind, and D. P. Weitekamp, *Phys. Rev. Lett.*, 1995, **75**, 1364.
10. N. T. Bagraev and L. S. Vlasenko, *Sov. Phys. Solid State*, 1979, **21**, 70.
11. N. T. Bagraev and L. S. Vlasenko, *Sov. Phys. JETP*, 1978, **48**, 878.
12. N. T. Bagraev, L. S. Vlasenko, and R. A. Zhitnikov, *Sov. Phys. Solid State*, 1977, **19**, 1467.
13. A. I. Ekimov and V. I. Safarov, *JETP Lett.*, 1972, **15**, 319.
14. D. Paget, G. Lampel, B. Sapoval, and V.I. Safarov, *Phys. Rev. B*, 1977, **15**, 5780.
15. D. Paget, *Phys. Rev. B*, 1981, **24**, 3776.
16. D. Paget, *Phys. Rev. B*, 1982, **25**, 4444.
17. D. Paget, *Phys. Rev. B*, 1984, **30**, 931.
18. W. Hanle, *Z. Phys.*, 1924, **30**, 93.
19. R. R. Parsons, *Phys. Rev. Lett.*, 1969, **23**, 1132.
20. G. P. Flinn, R. T. Harley, M. J. Snelling, A. C. Tropper, and T. M. Kerr, *Semicond. Sci. Technol.*, 1990, **5**, 533.
21. G. P. Flinn, R. T. Harley, M. J. Snelling, A. C. Tropper, and T. M. Kerr, *J. Lumines.*, 1990, **45**, 218.
22. V. K. Kalevich, V. L. Korenev, and O. M. Fedorova, *JETP Lett.*, 1990, **52**, 349.
23. M. Krapf, G. Denninger, H. Pascher, G. Weimann, and W. Schlapp, *Solid State Commun.*, 1991, **78**, 459.
24. S. K. Buratto, D. N. Shykind, and D. P. Weitekamp, *Phys. Rev. B*, 1991, **44**, 9035.
25. S. K. Buratto, D. N. Shykind, and D. P. Weitekamp, *J. Vac. Sci. Technol. B*, 1992, **10**, 1740.
26. S. E. Barrett, R. Tycko, L. N. Pfeiffer, and K. W. West, *Phys. Rev. Lett.*, 1994, **72**, 1368.
27. R. Tycko, *Solid State Nucl. Magn. Reson.*, 1998, **11**, 1.
28. C. A. Michal and R. Tycko, *Phys. Rev. Lett.*, 1998, **81**, 3988.
29. T. Pietrass, A. Bifone, T. Room, and E. L. Hahn, *Phys. Rev. B*, 1996, **53**, 4428.
30. T. Pietrass, A. Bifone, J. Kruger, and J. A. Reimer, *Phys. Rev. B*, 1997, **55**, 4050.
31. P. L. Kuhns, A. Kleinhammes, T. Schmiedel, W. G. Moulton, P. Chabrier, S. Sloan, E. Hughes, and C. R. Bowers, *Phys. Rev. B*, 1997, **55**, 7824.
32. T. Pietrass and M. Tomaselli, *Phys. Rev. B*, 1999, **59**, 1986.
33. A. Patel, O. Pasquet, J. Bharatam, E. Hughes, and C. R. Bowers, *Phys. Rev. B*, 1999, **60**, R5105.
34. S. E. Barrett, G. Dabbagh, L. N. Pfeiffer, K. W. West, and R. Tycko, *Phys. Rev. Lett.*, 1995, **74**, 5112.
35. R. Tycko, S. E. Barrett, G. Dabbagh, L. N. Pfeiffer, and K. W. West, *Science*, 1995, **268**, 1460.
36. P. Khandelwal, N. N. Kuzma, S. E. Barrett, L. N. Pfeiffer, and K. W. West, *Phys. Rev. Lett.*, 1998, **81**, 673.
37. N. N. Kuzma, P. Khandelwal, S. E. Barrett, L. N. Pfeiffer, and K. W. West, *Science*, 1998, **281**, 686.
38. A. E. Dementyev, N. N. Kuzma, P. Khandelwal, S. E. Barrett, L. N. Pfeiffer, and K. W. West, *Phys. Rev. Lett.*, 1999, **83**, 5074.
39. T. Chakraborty and P. Pietilainen, 'The Quantum Hall Effects: Integral and Fractional', 2nd edn., Springer: Berlin, 1995.

40. R. E. Prange and S. M. Girvin, 'The Quantum Hall Effect', 2nd edn., Springer: New York, 1990.
41. S. Das Sarma and A. Pinczuk, 'Perspectives in Quantum Hall Effects: Novel Quantum Liquids in Low-Dimensional Semiconductor Structures', Wiley: New York, 1997.
42. S. W. Brown, T. A. Kennedy, D. Gammon, and E. S. Snow, *Phys. Rev. B*, 1996, **54**, 17 339.
43. D. Gammon, S. W. Brown, E. S. Snow, T. A. Kennedy, D. S. Katzer, and D. Park, *Science*, 1997, **277**, 85.
44. S. W. Brown, T. A. Kennedy, and D. Gammon, *Solid State Nucl. Magn. Reson.*, 1998, **11**, 49.
45. J. M. Kikkawa and D. D. Awschalom, *Science*, 2000, **287**, 473.
46. G. Salis, D. T. Fuchs, J. M. Kikkawa, D. D. Awschalom, Y. Ohno, and H. Ohno, *Phys. Rev. Lett.*, 2001, **86**, 2677.
47. M. Eickhoff, B. Lenzman, G. Glinn, and D. Suter, *Phys. Rev. B*, in press.
48. C. R. Bowers, *Solid State Nucl. Magn. Reson.*, 1998, **11**, 11.
49. D. Mao, P. C. Taylor, and W. D. Ohlsen, *Phys. Rev. B*, 1994, **49**, 7952.
50. R. Tycko, *Mol. Phys.*, 1998, **95**, 1169.
51. K. von Klitzing, G. Dorda, and M. Pepper, *Phys. Rev. Lett.*, 1980, **45**, 494.
52. D. C. Tsui, H. L. Stormer, and A. C. Gossard, *Phys. Rev. Lett.*, 1982, **48**, 1559.
53. R. B. Laughlin, *Phys. Rev. Lett.*, 1983, **50**, 1395.
54. C. Weisbuch and B. Vinter, 'Quantum Semiconductor Structures: Fundamentals and Applications', Academic Press: San Diego, 1991.
55. D. Heiman, in 'Semiconductors and Semimetals', eds D. G. Seiler and C. L. Littler, Academic Press: London, 1992, Vol. 36.
56. L. N. Pfeiffer, K. W. West, J. P. Eisenstein, K. W. Baldwin, and P. Gammel, *Appl. Phys. Lett.*, 1992, **61**, 1211.
57. P. Khandelwal, N. N. Kuzma, S. E. Barrett, L. N. Pfeiffer, and K. W. West, *Physica B*, 1998, **256–258**, 113.
58. N. N. Kuzma, P. Khandelwal, S. E. Barrett, L. N. Pfeiffer, and K. W. West, *Physica B*, 1998, **256–258**, 121.
59. S. M. Girvin and A. H. MacDonald, in 'Perspectives in Quantum Hall Effects', eds S. Das Sarma and A. Pinczuk, Wiley: New York, 1997.
60. A. E. Dementyev, N. N. Kuzma, P. Khandelwal, S. E. Barrett, L. N. Pfeiffer, and K. W. West, submitted.
61. B. I. Halperin, *Helv. Phys. Acta*, 1983, **56**, 75.
62. S. L. Sondhi, A. Karlhede, S. A. Kivelson, and E. H. Rezayi, *Phys. Rev. B*, 1993, **47**, 16 419.
63. H. A. Fertig, L. Brey, R. Cote, and A. H. MacDonald, *Phys. Rev. B*, 1994, **50**, 11 018.
64. K. Moon, H. Mori, K. Yang, S. M. Girvin, A. H. MacDonald, L. Zheng, D. Yoshioka, and S. C. Zhang, *Phys. Rev. B*, 1995, **51**, 5138.
65. N. Read and S. Sachdev, *Phys. Rev. Lett.*, 1995, **75**, 3509.
66. M. Kasner and A. H. MacDonald, *Phys. Rev. Lett.*, 1996, **76**, 3204.
67. R. Haussmann, *Phys. Rev. B*, 1997, **56**, 9684.
68. C. Timm, S. M. Girvin, P. Henelius, and A. W. Sandvik, *Phys. Rev. B*, 1998, **58**, 1464.
69. B. I. Halperin, P. A. Lee, and N. Read, *Phys. Rev. B*, 1993, **47**, 7312.
70. R. L. Willett, K. W. West, and L. N. Pfeiffer, *Phys. Rev. Lett.*, 1995, **75**, 2988.
71. R. L. Willett, R. R. Ruel, K. W. West, and L. N. Pfeiffer, *Phys. Rev. Lett.*, 1993, **71**, 3846.
72. W. Kang, H. L. Stormer, L. N. Pfeiffer, K. W. Baldwin, and K. W. West, *Phys. Rev. Lett.*, 1993, **71**, 3850.
73. V. J. Goldman, B. Su, and J. K. Jain, *Phys. Rev. Lett.*, 1994, **72**, 2065.
74. J. H. Smet, D. Weiss, R. H. Blick, G. Lutjering, K. von Klitzing, R. Fleischmann, R. Ketzmerick, T. Geisel, and G. Weimann, *Phys. Rev. Lett.*, 1996, **77**, 2272.
75. R. R. Du, A. S. Yeh, H. L. Stormer, D. C. Tsui, L. N. Pfeiffer, and K. W. West, *Phys. Rev. Lett.*, 1995, **75**, 3926.
76. I. V. Kukushkin, K. von Klitzing, and K. Eberl, *Phys. Rev. Lett.*, 1999, **82**, 3665.
77. K. Park and J. K. Jain, *Phys. Rev. Lett.*, 1998, **80**, 4237.
78. S. Melinte, N. Freytag, M. Horvatic, C. Berthier, L. P. Levy, V. Bayot, and M. Shayegan, *Phys. Rev. Lett.*, 2000, **84**, 354.
79. R. Shankar, *Phys. Rev. Lett.*, 2000, **84**, 3946.
80. R. Shankar, *Phys. Rev. B*, 2001, **63**, 5322.
81. E. H. Aifer, B. B. Goldberg, and D. A. Broido, *Phys. Rev. Lett.*, 1996, **76**, 680.
82. Y. Q. Song, B. M. Goodson, K. Maranowski, and A. C. Gossard, *Phys. Rev. Lett.*, 1999, **82**, 2768.
83. V. Bayot, E. Grivei, S. Melinte, M. B. Santos, and M. Shayegan, *Phys. Rev. Lett.*, 1996, **76**, 4584.
84. V. Bayot, E. Grivei, J. M. Beuken, S. Melinte, and M. Shayegan, *Phys. Rev. Lett.*, 1997, **79**, 1718.
85. P. Khandelwal, A. E. Dementyev, N. N. Kuzma, S. E. Barrett, L. N. Pfeiffer, and K. W. West, *Phys. Rev. Lett.*, 2001, **86**, 5353.
86. L. Brey, H. A. Fertig, R. Cote, and A. H. MacDonald, *Phys. Rev. Lett.*, 1995, **75**, 2562.
87. A. G. Green, I. I. Kogan, and A. M. Tsvelik, *Phys. Rev. B*, 1996, **54**, 16 838.
88. R. Cote, A. H. MacDonald, L. Brey, H. A. Fertig, S. M. Girvin, and H. T. C. Stoof, *Phys. Rev. Lett.*, 1997, **78**, 4825.
89. M. Rao, S. Sengupta, and R. Shankar, *Phys. Rev. Lett.*, 1997, **79**, 3998.
90. M. Abolfath and M. R. Ejtehadi, *Phys. Rev. B*, 1998, **58**, 10 665.
91. Y. V. Nazarov and A. V. Khaetskii, *Phys. Rev. Lett.*, 1998, **80**, 576.
92. A. J. Nederveen and Y. V. Nazarov, *Phys. Rev. Lett.*, 1999, **82**, 406.

Biographical Sketches

Robert Tycko, *b* 1959. A.B., 1980, Princeton University. Ph.D., 1984, University of California at Berkeley. Began his career at AT&T Bell Laboratories, where he developed new solid state NMR methods, such as zero-field NMR in high field, and applied solid state NMR to problems in condensed matter physics. Moved to the National Institutes of Health in 1994, and now develops and applies solid state NMR methods for structural studies of biopolymers. Approx. 100 papers on all areas of magnetic resonance. Research interests: optical pumping, NMR theory and methodology, structure of proteins and amyloid fibrils.

Sean E. Barrett, *b* 1965. A.B., 1987, Princeton University. Ph.D., 1992, University of Illinois at Urbana-Champaign. Recipient of the 1995 William L. McMillan Award for outstanding contributions to condensed matter physics, in particular the development at AT&T Bell Laboratories of optically pumped NMR as a probe of two-dimensional electron systems. Approx. 25 papers on NMR in condensed matter physics. Research interests: optical pumping, two-dimensional electron systems, high-temperature superconductivity.

Parahydrogen Enhanced NMR Spectroscopic Methods: A Chemical Perspective

Simon B. Duckett and Simon A. Colebrooke

University of York, York, UK

1	Introduction	1
2	General Principles Behind the Parahydrogen Effect	1
3	The Role of H_2	2
4	Strategies for using Parahydrogen	2
5	Demonstration of the p-H_2 Effect	2
6	Applications to Inorganic Systems	3
7	Applications to Organic Systems	6
8	Kinetic Measurements	7
9	Nature of Polarization and Different Spin Systems	8
10	PHIP as a Probe of Regio and Stereoselectivity	9
11	Related Articles in this Volume	9
12	Related Articles in Volumes 1–8	9
13	References	9

1 INTRODUCTION

The study of the mechanisms of catalytic action of coordination compounds has become an important part of modern chemistry. Many different spectroscopic methods have been applied with the coupling of time-resolved laser spectroscopy, for example, where matrix isolation provides an approach that has enabled the direct detection of unsaturated intermediates and the rationalization of their subsequent reactivity. The characterization of species in solution can, however, be more accurately achieved using NMR spectroscopy and since this technique also offers the opportunity to probe stereochemistry and monitor kinetic activity, it has many advantages over methods where only a limited number of parameters can be examined. Unfortunately, the inherent low sensitivity of NMR results in the fact that the most reliably studied reactions correspond to those where high concentrations of substrate are available. Since the study of reaction mechanisms requires the detection of reaction intermediates that are present in low concentration, NMR might initially be thought to be unsuitable for this work.

One route to achieving high concentrations of reactive species is to use photochemistry to prepare them at temperatures where they are stable. Using this approach Ball recently characterized the first sigma alkane complex by NMR spectroscopy.[1] A second approach that is becoming more widely accepted involves the independent synthesis of molecules in specific spin-states. Under these conditions, the observable NMR signals have strengths that are not governed by Boltzmann statistics but rather by the efficiency of the initial spin state preparation. Parahydrogen with a lifetime of one year provides one example of where spin state synthesis has been used successfully in NMR. Bowers and Weitekamp first suggested and later proved that significantly enhanced NMR signals could be obtained from molecules that were formed by the addition of dihydrogen enriched in the *para* spin state.[2] This article is devoted to describing the chemical applications of *para*-hydrogen enhanced NMR spectroscopy that are illustrated in Scheme 1.

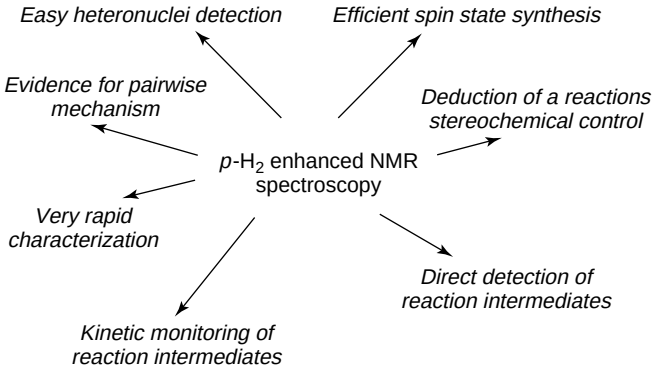

Scheme 1 Summary of chemical applications of p-H_2 enhanced NMR spectroscopy

2 GENERAL PRINCIPLES BEHIND THE PARAHYDROGEN EFFECT

The *para*-isomer of H_2 possesses the anti-symmetric spin configuration ($\alpha\beta - \beta\alpha$). Triply degenerate *ortho*-isomers with symmetric spin configurations ($\alpha\alpha$, $\beta\beta$, $\alpha\beta + \beta\alpha$) are also possible. For the synthesis of *para*-H_2 to be viable these two forms must have sufficiently long lifetimes to enable their separation. Fortunately, interconversion between *ortho*- and *para*-forms is symmetry forbidden with conversion times approaching one year under normal conditions. The difference in internal energy between the two forms of H_2 enables their separation: *para*-H_2 is restricted to even values of J, the rotational quantum number, and *ortho*-H_2 to odd values of J.

Para-hydrogen enrichment of hydrogen can be achieved by simply cooling H_2 to 77 K in a glass bulb that contains a small amount of iron oxide to catalyze the interconversion process.[3] The resulting *para*-enriched H_2 (p-H_2) can be transferred to an NMR tube with a Young's valve prior to in situ NMR monitoring. An alternative approach that generates a continuous stream of p-H_2 via passage through a U-shaped metal tube containing activated charcoal that is cooled in a bath of liquid nitrogen to 77 K has also been reported.[4] Hydrogen gas is then bled through a capillary into the NMR solution for a few seconds, the capillary removed and data acquisition started.[5] Both these methods generate a mixture of 51% *para*-hydrogen and 49% *ortho*-hydrogen via equilibration at 77 K.

The initial article by Bower's discusses the NMR aspects of the p-H_2 approach.[5] However, the resulting spectral effect can be easily understood by reference to Figure 1, which shows

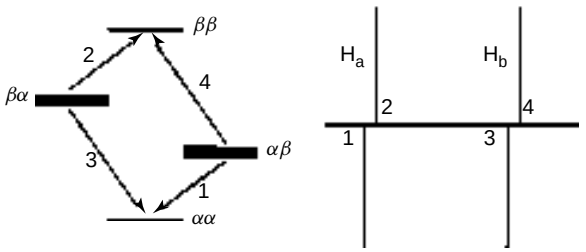

Figure 1 Energy level diagram and ^{1}H spectral features for a metal dihydride with magnetically distinct protons H_a and H_b. Population differences indicate the situation that arises when the product is formed from *p*-H_2

the situation that exists for a metal complex that contains two inequivalent hydride ligands, H_a and H_b, that are spin–spin-coupled. Since the nuclear spins of H_a and H_b can be arranged in the orientations $\alpha\alpha$, $\alpha\beta$, $\beta\alpha$, $\beta\beta$ the associated ^{1}H NMR spectrum consists of two distinct doublet resonances for protons H_a and H_b. When protons H_a and H_b originate from a *para*-hydrogen molecule and the addition process is spin correlated, the starting $(\alpha\beta - \beta\alpha)$ spin state converts into $\alpha\beta$ and $\beta\alpha$ product states. Consequently, the population differences, and hence signal intensities, for the resonances due to the metal hydride ligands show 'emission' and 'absorption' character and are enhanced over their normal levels. The results of this process have been referred to by the terms PASADENA (Parahydrogen And Synthesis Allow Dramatically Enhanced Nuclear Alignment) and PHIP (ParaHydrogen Induced Polarization) and are rigorously treated elsewhere.[6,7]

3 THE ROLE OF H_2

H_2 plays an important role in many catalytic reactions, with the addition of H_2 to a metal center often involving the formation of an intermediate containing an η^2-H_2 interaction prior to the formation of the corresponding metal dihydride. From a synthetic perspective, one of the easiest routes to prepare a metal dihydride complex therefore involves the reaction of a suitable precursor with H_2. Such reactions can be readily monitored by NMR spectroscopy since the associated hydride resonances are normally shifted to low frequency.

When metal hydride complexes play a role in a catalytic transformation such as hydrogenation, the most interesting complexes have short lifetimes and are therefore present in very low concentration. Halpern and Brown most elegantly illustrated the importance of the detection of minor species during their NMR studies of asymmetric hydrogenation. These studies involved the hydrogenation of prochiral enamides by cationic rhodium complexes containing a chiral diphosphine such as DIPAMP. Normal NMR methods revealed that the least stable enamide isomer reacted substantially faster with H_2 and was responsible for the observed enantiomeric selectivity in the corresponding hydrogenation product.[8] When reactions with *p*-H_2 are studied the detection of minor components in reactions becomes much easier.

4 STRATEGIES FOR USING PARAHYDROGEN

When *p*-H_2 adds to a substrate to generate a product with two distinct, and coupled protons, the product operator $I_z^A I_z^X$ defines the initial magnetization. In this notation the subscripts refer to the orientation of the magnetization in a Cartesian coordinate system with z along B_o, the applied magnetic field, and the superscripts refer to the nuclei A and X. Application of a radio frequency pulse of flip angle α to this starting state generates four new terms as shown in equation (1).

$$2I_z^A I_z^X \longrightarrow 2I_z^A I_z^X \cos^2\alpha + 2I_X^A I_z^X \cos\alpha \sin\alpha + 2I_z^A I_X^X \cos\alpha \sin\alpha + 2I_X^A I_X^X \sin^2\alpha \quad (1)$$

The first and last terms correspond to zero and double quantum coherence and are not directly observable. The two remaining terms are observable and correspond to magnetization that is oriented anti-phase with respect to the scalar coupling J_{AX}. The contribution of these terms is maximized with a $\pi/4$ pulse. However, the $I_z^A + I_z^X$ starting point for conventional magnetization generates maximum signal with a $\pi/2$ pulse as shown in equation (2).

$$I_z^A + I_z^X \longrightarrow I_z^A \cos\alpha + I_z^X \cos\alpha + I_X^X \sin\alpha + I_X^A \sin\alpha \quad (2)$$

Clearly, the situations with normal and *p*-H_2 based magnetization are different and consequently, great care must therefore be taken when multiple pulse experiments are used in conjunction with *p*-H_2 based magnetization. It should be noted however, that standard magnetization can be achieved via selective excitation methods or simple refocusing with respect to J_{HH}.

The ^{1}H spectrum shown in Figure 2 was collected using single a $\pi/4$ pulse on a benzene-d_6 solution of $IrCl(CO)(PPh_3)_2$ at 323 K in the presence of 3 atm of *p*-H_2. The two signals at δ −6.65 and −17.47 are due to the hydride ligands of $IrH_2Cl(CO)(PPh_3)_2$ and are split into emission and absorption components (e/a) in accordance with the generation of the $I_z^A I_X^X$ and $I_X^A I_z^X$ spin states indicated above. This result can also be understood by reference to the non-Boltzmann spin state populations shown in Figure 1 that have opposite sense for transitions separated by J_{HH}.

5 DEMONSTRATION OF THE *p*-H_2 EFFECT

The first reported experimental observations attributed to the PASADENA/PHIP effect were those of Bowers

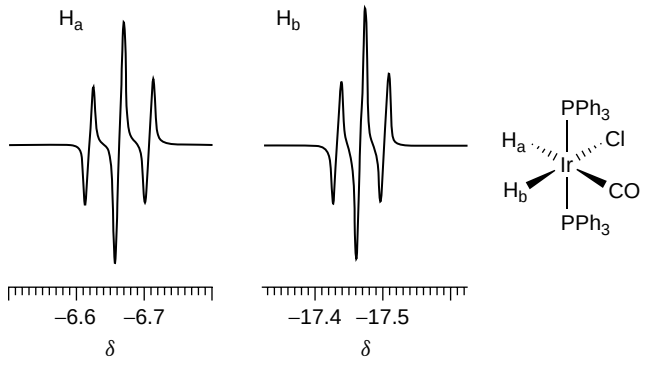

Figure 2 ^{1}H NMR spectrum (400 MHz, 295 K) showing the appearance of the hydride resonances of $IrH_2Cl(CO)(PPh_3)_2$ (structure inset) when the product is generated from a 0.1 mM solution of $IrCl(CO)(PPh_3)_2$ in benzene-d_6 under 3 atm of *p*-H_2

and Weitekamp.[6] In this study, Wilkinson's catalyst was used to convert acrylonitrile (CH_2CHCN) to propionitrile (CH_3CH_2CN) under an atmosphere of p-H_2.[9] NMR spectra revealed enhancements of between 100 and 200 fold in the ^1H resonances of propionitrile for positions corresponding to nuclei originally in p-H_2. The spectra also contained weak, and very broad, p-H_2 enhanced resonances for the hydride ligands of the dihydride complex $RhH_2Cl(PPh_3)_3$.

Since this first report the resonances of both inorganic complexes and organic substrates have been successfully probed using p-H_2. This article now focuses on helping the reader understand how p-H_2 can help them study chemical systems. A number of other articles review more clearly the chronological development of this effect.[10]

6 APPLICATIONS TO INORGANIC SYSTEMS

Since the process of oxidative addition of hydrogen proceeds to increase the electron count of a metal center by two units, 16 electron square planar d^8 complexes often feature as systems that readily add H_2. The often cited reaction of the d^8 complex $IrCl(CO)(PPh_3)_2$ with H_2 follows a concerted pathway, with addition over the OC-Ir-Cl axis selectively placing the hydrides in a mutually *cis* orientation. When this reaction was studied with p-H_2, at 295 K where the addition is irreversible, the corresponding ^1H NMR spectrum contained polarized hydride resonances for *cis-trans*-$IrH_2(CO)(PPh_3)_2Cl$ and the new product *cis–cis*-$IrH_2(CO)(PPh_3)_2Cl$. The enhanced hydride resonance associated with this minor species were only visible with p-H_2 and indicated that H_2 addition over the P-Ir-P axis of $IrCl(CO)(PPh_3)_2$ is possible. The successful observation of this new species using the p-H_2 approach provides just one illustration of the many that show it is possible to see previously unobserved complexes via this route.

The exchange of p-H_2 into $Ir(H)_2Cl(CO)(PPh_3)_2$, and the complexes $Rh(H)_2(PMe_3)_4Cl$, and $Rh(H)_2(PMe_3)_3Cl$ has been used to show that the monitoring of p-H_2 enhanced products can be achieved by 2D COSY, HMQC and NOESY methods. The observation of heteronuclei, including low sensitivity nuclei such as ^{103}Rh, the determination of heteronuclear coupling constants and the measurement of their relative signs was demonstrated (Figure 3). The dihydride addition product $Ir(H)_2Cl(CO)(PPh_3)_2$ was shown to contain a *trans* labilized carbonyl ligand, and substitution with appropriate phosphines demonstrated to bring about the formation of metal phosphine complexes with new ligand spheres. An appropriately modified NOESY experiment enabled the rapid probing of the structural arrangements of these products and the monitoring of dihydride exchange. In the case of $Ir(H)_2Cl(PPh_3)_3$, dihydride exchange proceeded mainly via the intermediate $Ir(H)_2Cl(PPh_3)_2$, which was shown to contain inequivalent hydrides.

Reactions of the d^8-rhodium complexes $RhX(CO)(PR_3)_2$ where X = Cl, Br, I and R = Ph, Me with p-H_2 have also been described.[11] However, unlike $IrCl(CO)(PPh_3)_2$, these complexes had not previously been seen to react with dihydrogen. The $RhX(CO)(PPh_3)_2$ complexes were shown to yield unexpected dinuclear products of the general formula $H_2Rh(PPh_3)_2(\mu\text{-}X)_2Rh(PPh_3)(CO)$, where the hydrides that are *trans* to the halide bridges are rendered inequivalent by the ligands on the Rh(I) center. Since the initial dihydrogen activation product $RhH_2X(CO)(PPh_3)_2$ was not detected it was suggested that facile CO loss led to the generation of

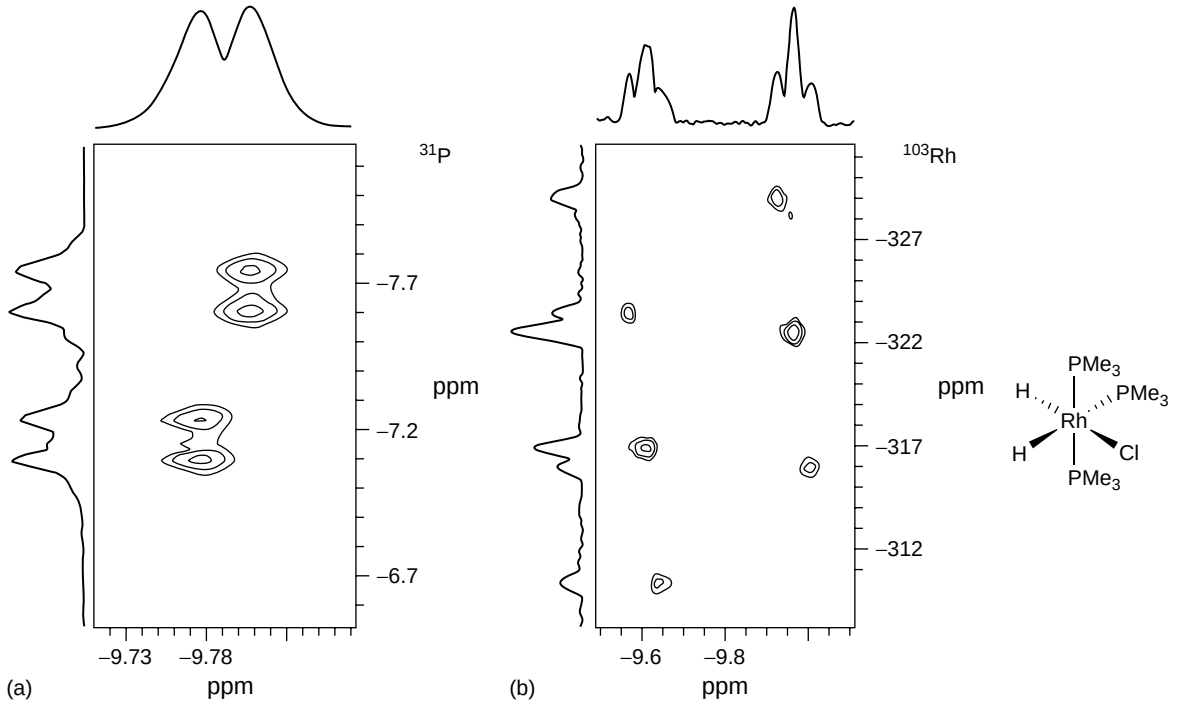

Figure 3 Selected cross peaks (positive contours) and projections from $^1H-^{31}P$ and $^1H-^{103}Rh$ correlation spectra of $Rh(H)_2(PMe_3)_3Cl$ obtained with p-H_2 in CD_2Cl_2 at 313 K. (a) ^{31}P decoupled 500 MHz $^1H-^{31}P$ correlation spectrum showing cross peaks between H and P indicated in inset structure. (b) ^{103}Rh decoupled 500 MHz $^1H-^{103}Rh$ correlation spectrum showing correlated transitions between H and Rh

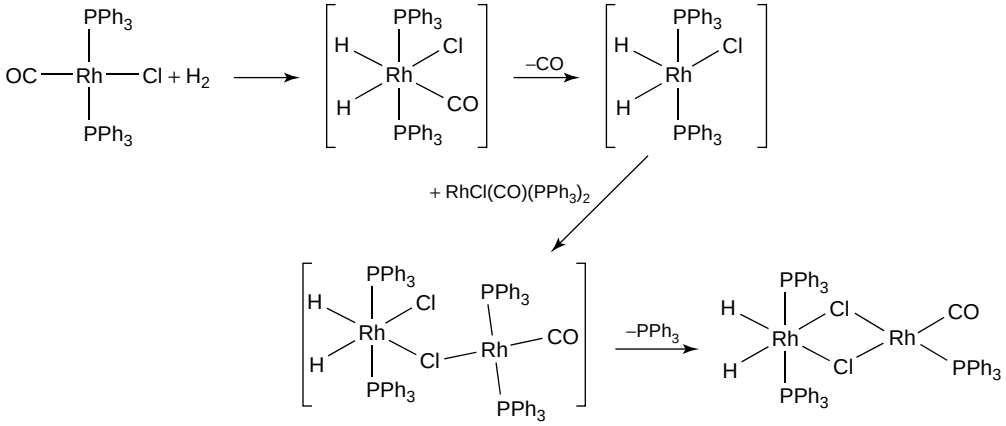

Scheme 2 Suggested route to $H_2Rh(PPh_3)_2(\mu\text{-}C1)_2Rh(PPh_3)(CO)$ as detected in the reaction of $RhCl(CO)(PPh_3)_2$ with p-H_2

the unsaturated species $RhH_2X(PPh_3)_2$. The formation of these reaction products was suggested to involve the co-ordinatively unsaturated species $RhH_2X(PPh_3)_2$ as shown in Scheme 2.

When the reaction of $RhCl(CO)(PMe_3)_2$ was monitored at 342 K under 3 atm of p-H_2, the major product corresponded to $H(Cl)Rh(PMe_3)_2(\mu\text{-}H)(\mu\text{-}Cl)Rh(PMe_3)(CO)$ with bridging and terminal hydrides. However, when $RhI(CO)(PMe_3)_2$ was monitored, NMR spectroscopy enabled the detection of five new species. At 348 K the most intense signals were shown to originate from the analogous complex $(H)(I)Rh(PMe_3)_2(\mu\text{-}H)(\mu\text{-}I)Rh(CO)(PMe_3)$ in which the hydrido-bridge is *trans* to phosphine. A minor reaction product corresponding to the isomer of $(H)(I)Rh(PMe_3)_2(\mu\text{-}H)(\mu\text{-}I)Rh(CO)(PMe_3)$ with the hydrido-bridge *trans* to carbonyl was also characterized at this temperature. The remaining products were reported to have the structures $(H)_2Rh(PMe_3)_2(\mu\text{-}I)_2Rh(CO)(PMe_3)$, $Rh(H)_2I(PMe_3)_3$ and $HRh(PMe_3)_2(\mu\text{-}H)(\mu\text{-}I)_2Rh(PMe_3)(CO)$. These reactions were shown to be consistent with results from density functional theory that predicted all four structural types correspond to reaction intermediates rather than transition states. A typical ^1H NMR spectrum produced from such a reaction is shown in Figure 4.

Significantly, when the reactions involving $RhCl(CO)(PMe_3)_2$ with p-H_2 were monitored in the presence of styrene, a dramatic increase in hydride signal enhancements was observed. This facilitated the detection of the $(H)_2Rh(PMe_3)_2(\mu\text{-}Cl)_2Rh(CO)(PMe_3)$ in addition to $HRh(PMe_3)_2(\mu\text{-}H)(\mu\text{-}Cl)_2Rh(CO)(PMe_3)$.[11] This result demonstrated that a sacrificial alkene can dramatically extend the sensitivity of the parahydrogen methods by promoting H_2 cycling.

The reactions of stable 18 electron complexes such as $RuH_2(CO)_2(PMe_3)_2$ have also been monitored with p-H_2. When a C_6D_6 solution containing <1 mg of $RuH_2(CO)_2(PMe_3)_2$ was monitored under normal-H_2, only the *tcc* isomer was observed after 10 000 scans. The detection and conclusive identification of the elusive *ccc* isomer became possible with the onset of rapid free p-H_2-RuH_2 exchange at 328 K.[12] In addition, it was reported that the introduction of a ^{13}CO label made the major *tcc* isomer p-H_2 active by virtue of the second order spin system that is created. At the time, this represented the first report of p-H_2 activity in a system containing a square planar $MH_2(CO)(^{13}CO)$ core and served to illustrate that the need for magnetically distinct hydrides could be satisfied synthetically. The reactions of a number of other dihydride complexes including $Ir(CO)(PPh_3)(Et_2dtc)$, $Pt(H)_2((dpp)_2mop)$ [where $((dpp)_2mop) = Ph_2PCH_2CH(Me)OPPh_2$] have also been explored using this approach (Figure 5).

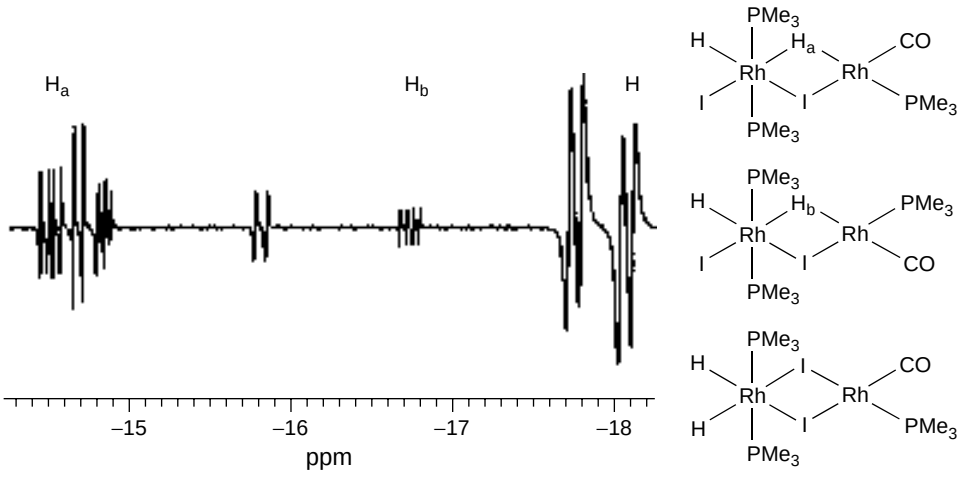

Figure 4 400 MHz $^1H\{^{31}P\}$ NMR spectrum showing the hydride region after warming a sample of $RhI(CO)(PMe_3)_2$ with p-H_2 in C_6D_6 to 348 K. Selected product resonances indicated via H_a, H_b and H with assignments according to the inset pictures

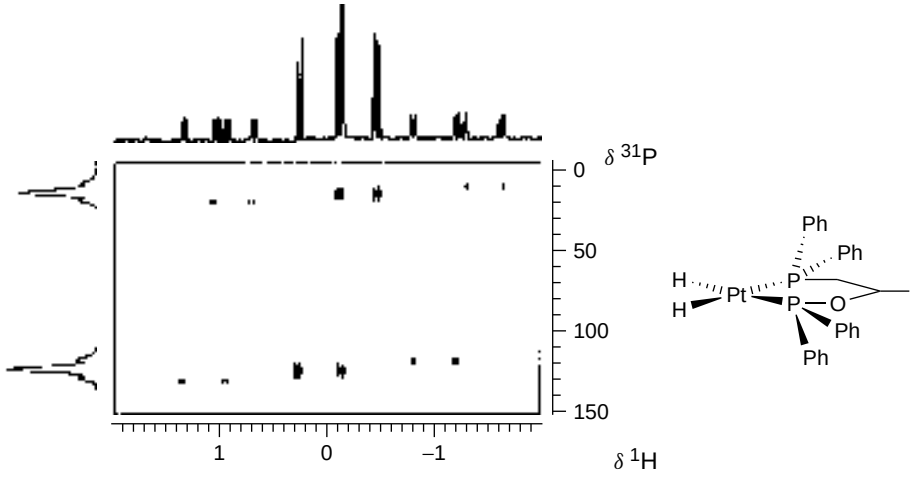

Figure 5 500 MHz ^1H–^{31}P correlation spectrum of $PtH_2(Ph_2PCH_2CH(Me)OPPh_2)$ at 298 K in toluene-d_8 under p-H_2

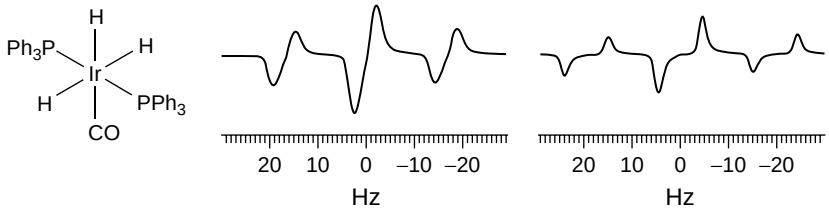

Figure 6 400 MHz ^1H NMR spectra for the inset complex obtained with p-H_2. The larger H–H splitting in the right trace is due to the hydride ligand that is *trans* to CO. It is twice the size of corresponding splitting for the left trace

It has also been shown that trihydrides such as $IrH_3(CO)_x(PR_3)_y$ [$x = 2$ and $y = 1$; $x = 1$ and $y = 2$; $PR_3 = PPh_3$, PMe_3 and $AsMe_2Ph$] can be examined with p-H_2. These studies have provided a number of interesting observations. Firstly, the ^1H NMR spectra of the isomers of $IrH_3(CO)(PPh_3)_2$, with *trans* phosphines and *mer*-hydrides and with *cis* phosphines and *fac*-hydrides, yield enhanced hydride resonances. The two polarized hydride resonances of the *mer*-isomer were expected to appear as doublets and triplets respectively in the ^{31}P decoupled spectrum with peak separations J_{HH}. However, with p-H_2, while the observed signals have relative intensities of 2 : 1 their anti-phase line separation is 4.4 and 8.8 Hz respectively. This indicates that the central feature of the triplet is no longer visible as shown in Figure 6.[13]

This observation has been explained by reference to the populations of the eight associated spin wave-functions of the trihydride (AX_2). While four wave-functions are simple products of the form $\alpha\alpha\alpha$, $\underline{\alpha\beta\beta}$, $\underline{\beta\alpha\alpha}$ and $\beta\beta\beta$, four belong to combinations of the form $\underline{\alpha(\alpha\beta - \beta\alpha)}$, $\underline{\alpha(\alpha\beta + \beta\alpha)}$, $\underline{\beta(\alpha\beta - \beta\alpha)}$ and $\underline{\beta(\alpha\beta + \beta\alpha)}$. Exchange with p-H_2 ($\alpha\beta - \beta\alpha$ spin state) involves the A and one X nucleus, with the result that the underlined states become equally populated while the $\alpha\alpha\alpha$ and $\beta\beta\beta$ states are unpopulated. Consequently, visible transitions for nucleus A, correspond to spin flips $\alpha\alpha\alpha \leftrightarrow \underline{\beta\alpha\alpha}$ and $\underline{\alpha\beta\beta} \leftrightarrow \beta\beta\beta$, and the outer lines of the triplet, separated by $\underline{2J_{AX}}$, and are seen in emission and absorption. The central line, corresponding to the transitions $\alpha(\alpha\beta - \beta\alpha) \leftrightarrow \beta(\alpha\beta - \beta\alpha)$ and $\alpha(\alpha\beta - \beta\alpha) \leftrightarrow \beta(\alpha\beta - \beta\alpha)$, vanishes because the associated levels have identical populations. Examination of the four symmetry allowed transitions for X_2 reveals that observable spin flips connect $\alpha\alpha\alpha \leftrightarrow \underline{\alpha(\alpha\beta + \beta\alpha)}$ and $\underline{\beta(\alpha\beta + \beta\alpha)} \leftrightarrow \beta\beta\beta$. These transitions, separated by $\underline{J_{AX}(J_{HH})}$, are also visible as emission and absorption signals, with twice the overall intensity seen for the signal due to H_A, the hydride that is *trans* to CO.

Eisenberg et al. have reported studies on the reaction of the benzyne-hydride complex ($Cp^*_2Ta(C_6H_4)H$) with p-H_2.[14] At 273 K, the complex reacts to form a new phenyl dihydride complex, $Cp^*_2Ta(C_6H_5)H_2$, which yields enhanced hydride resonances with p-H_2. This complex proceeds to eliminate benzene and react with H_2 to form the trihydride complex $Cp^*_2TaH_3$. The central component of the proton resonance due to the central hydride ligand is again absent under PHIP conditions.

A number of recent studies have involved the examination of clusters with p-H_2. Up to this point this article has referred to a number of straightforward examples in which the nuclei originating in parahydrogen are transported into magnetically distinct environments. One potential drawback of the parahydrogen technique is therefore the need to create a product with magnetically inequivalent hydrides. Surprisingly, a number of instances have been described in the literature where enhanced signals are observed for pairs of magnetically equivalent protons.[12,15] Aime and Canet elegantly illustrated the origin of this effect by reference to the addition of parahydrogen to $Os_3(CO)_{10}(NCCH_3)_2$.[16] This reaction first yields two isomers of $H(\mu\text{-}H)Os_3(CO)_{10}(NCCH_3)$ which react further to form $H_2Os_3(CO)_{10}$, a species in which

the two hydrogen nuclei are magnetically equivalent. They demonstrated that the observation of an enhanced hydride signal for $H_2Os_3(CO)_{10}$ necessitates the involvement of an intermediate with inequivalent hydrides, and subsequent cross-correlation between dipolar interactions and chemical shift anisotropy. These workers have also examined the reaction of $Ru_3(CO)_{11}(NCCH_3)$ with parahydrogen.[17] The observation of an enhanced emission signal for molecular hydrogen was interpreted to indicate the reversible interaction of p-H_2 via the formation of a Ru_3 cluster with inequivalent hydrides. The reactions of the cluster series $Ru_3(CO)_9(PR_3)_3$, $Ru_3(CO)_{10}(PR_3)_2$ and $Ru_3(CO)_{11}(PR_3)$ [$PR_3 = PPh_3$, PMe_2Ph and PCy_3] with p-H_2 have also been examined.[18] These studies revealed that related products such as $H(\mu\text{-}H)Ru_3(CO)_8(PPh_3)_3$ are formed, and that in the case of $PR_3 = PPh_3$, cluster fragmentation leads to the observation of signals for the meridional isomer of $Ru(CO)_3(H)_2(PPh_3)$.

Another system in which PHIP has enabled the detection of dihydride species involves rhodium complexes with tin trichloride ligands. Rhodium monohydrides such as $[HRh(SnCl_3)_5]^{3-}$ yielded dihydride complexes upon reaction with phosphines and hydrogen, the species were again detectable only because of the PHIP effect.[19] Dihydride complexes of the form $Rh(H)_2(SnCl_3)(PR_3)_3$ were later shown to be obtainable via the reaction of $[RhCl(CO)_2]_2$ with $SnCl_2$ and three equivalents of PR_3 and p-H_2.[20]

When Brown and Bargon revisited asymmetric hydrogenation with p-H_2, the detection and characterization of a rather unusual hydride complex was achieved using PHIP.[21] At $-40\,^{\circ}C$ in methanol with an enamide substrate, two polarized hydride resonances were observed at δ -1.9 and δ -18.9 at the same time as PHIP effects were detected in the signals of the hydrogenation product. The use of other substrates produced analogous hydride resonances at slightly different chemical shifts, whilst the simultaneous use of two different enamides produced two distinct species. Furthermore, when the enamide was ^{13}C labeled at the β-C position, an extra splitting of 86 Hz was observed in the higher frequency hydride resonance, whereas a ^{13}C label in the α-C position produced only a small additional splitting of 3 Hz. This experimental evidence was interpreted to indicate the detection of a species in which one hydride had been transferred to the substrate and existed as an agostic hydrogen atom, bound between the rhodium nucleus and the β-carbon. The lower frequency resonance corresponded to a signal from a hydride *trans* to the carbonyl oxygen of the chelating ligand. Support for this structure was obtained from DFT calculations, which located an agostic species as a significant energy minimum, presumably as a direct precursor of an alkyl hydride.

7 APPLICATIONS TO ORGANIC SYSTEMS

A particularly important class of reactions studied by p-H_2 corresponds to metal catalyzed hydrogenation. Since the $RhCl(PPh_3)_3$ mediated hydrogenation of acrylonitrile was described using this approach, a large body of literature has developed. One of the earliest reports showed that enhanced resonances for styrene observed during the $Rh_2(CO)_2(dppm)_2$ catalyzed hydrogenation of phenylacetylene, resulted from p-H_2 rather than Chemically Induced Dynamic Nuclear Polarization (CIDNP), as had been originally

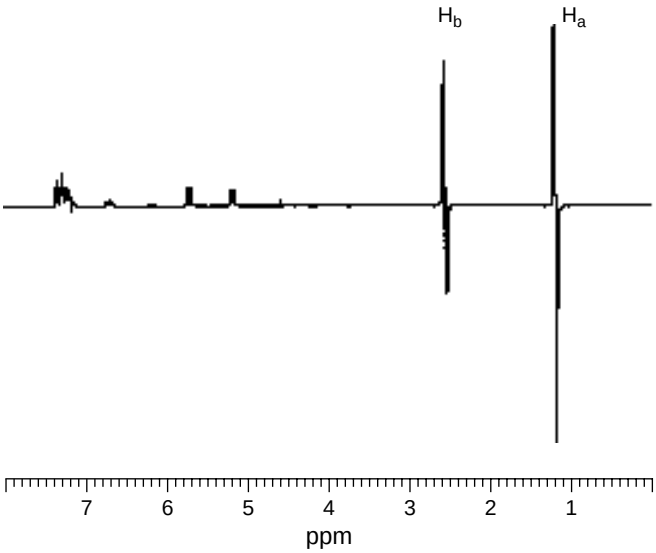

Figure 7 40 MHz ^1H NMR spectrum illustrating the effect of polarization on the signals for the resonances in ethylbenzene

suggested.[22,23] Similar polarization effects were reported when $[Rh_3Cl_2H_2(CO)_2((Ph_2PCH_2)_2\text{-}PPh)_2]^+$ catalyzed the hydrogenation of phenylacetylene. The intensely polarized resonances at δ 6.57 and δ 5.06 confirmed *cis*, pairwise transfer of H_2. Weaker polarization, via cross relaxation, was obtained for the geminal proton that did not originate from a H_2 molecule. Figure 7 illustrates a typical spectrum showing polarization in an organic product, in this case ethylbenzene.

Eisenberg then linked the occurrence of PHIP in the ^1H resonances of hydrogenation products to the mechanism of H_2 delivery to the substrate. For instance, the reaction of d^8-styrene with p-H_2 in the presence of $RuH_4(PPh_3)_3$ produced PHIP effects for protons in the alkyl chain of the product ethylbenzene.[24] This requires that protons from a single H_2 molecule transfer to the styrene. When styrene was hydrogenated with p-H_2 by $RuHCl(PPh_3)_3$, weaker PHIP signals were observed in the ^1H resonances of ethylbenzene. Hydrogenation can therefore proceed via pairwise transfer of H_2 to the alkene. By demonstrating that $RuHCl(PPh_3)_2$ could not itself be the active catalytic intermediate, the authors were able to propose that the formation of $RuH_2(PPh_3)_2$ was possible. Thus p-H_2 enhanced NMR demonstrated that one of the pathways of $RuHCl(PPh_3)_3$ catalyzed hydrogenation involves a small but active quantity of $RuH_2(PPh_3)_2$.

Eisenberg and others have also shown that information about the reversibility of H_2 addition to a catalyst precursor can be deduced from PHIP spectra of a hydrogenation product. Reaction of PhC≡CH with para-enriched hydrogen in the presence of $RhCl(PPh_3)_3$ for instance, results in weakly polarized resonances of the product styrene with the degree of polarization decaying rapidly.[25] When $Rh(COD)(dppe)^+$ was used, considerably larger enhancements were obtained which were observable for substantially longer. The extended period over which PHIP could be observed was taken to indicate that slow *ortho–para* equilibration was occurring. The authors concluded that while H_2 addition to the $RhCl(PPh_3)_3$ is reversible, irreversible addition occurs with $Rh(COD)(dppe)^+$.

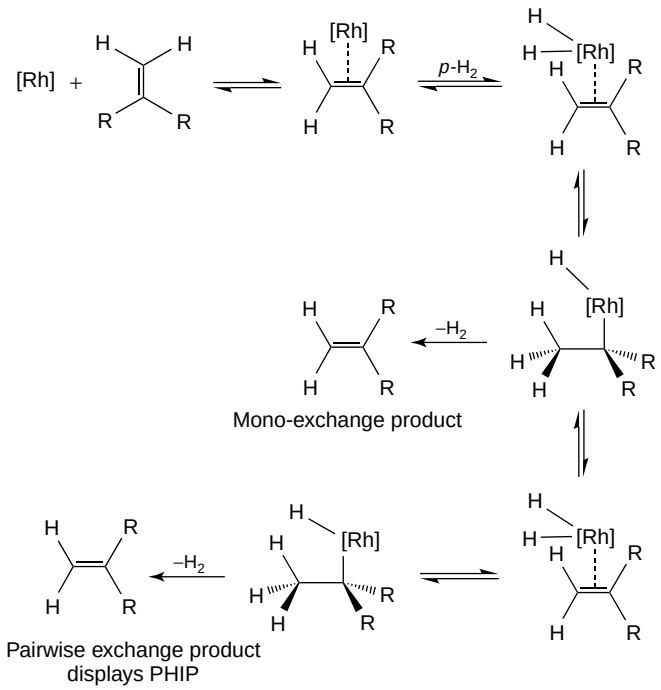

Figure 8 Mechanism of hydrogen exchange accounting for the enhancement of signals in the substrate. Competing hydrogenation pathway not shown

Using a very different catalyst system, Bargon found evidence for the reversible hydrogen transfer into the alkene substrate.[26] With methylacrylate as the substrate, polarized ^{1}H resonances were observed for both the geminal protons in the starting material indicating the pairwise exchange of parahydrogen into these positions. The mechanism proposed to account for substrate hydrogenation as well as both mono and pairwise exchange of the geminal protons is shown in Figure 8.

Similar geminal proton exchange with p-H_2 was also observed during the hydrogenation of styrene by [Rh(COD)(dppb)]BF_4.[27] Interestingly, the co-ordination of the styrene to the metal center through the π-system of the phenyl ring of the substrate was proposed to assist the pairwise exchange process. This was demonstrated via the observation of a second set of enhanced signals, with identical multiplicity and J_{HH} coupling constants to those of ethylbenzene but with different chemical shifts.[28] This second pair of resonances was attributed to recently formed ethylbenzene molecules that remained co-ordinated to the catalyst complex. The co-ordination of product ethylbenzene to the catalyst fragment $[Rh(dppb)]^+$ was later proven via a 1D NOESY experiment.[29] Selective irradiation of either of the two new protons of the bound ethylbenzene resulted in the observation of nOe connections to the ortho phenyl protons of the dppb ligand as shown in Figure 9. No nOe interactions with the catalyst were observed by irradiating either of the protons in free ethylbenzene. Equivalent results were obtained using a PHIP modified ROESY experiment.[29] The role of p-H_2 as a tool for probing hydrogenation products is therefore well established.

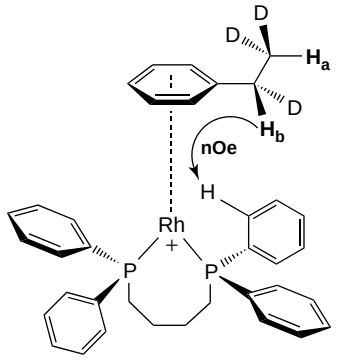

Figure 9 Intramolecular nOe connections visible during catalysis of styrene hydrogenation with $[Rh(dppb)]^+$

8 KINETIC MEASUREMENTS

The studies of catalytic systems have also resulted in the development of methods to investigate hydrogenation rates using p-H_2. With $RuH_4(PPh_3)_3$ as the catalyst for example, the nature of the polarization in the product molecules was found to be different for alkene and alkyne substrates.[24] While hydrogenation of d^8-styrene yielded ethylbenzene resonances with multiplet polarization while alkynes, including PhC≡CH and CH_2=CHO_2Me, resulted in the observation of the corresponding product alkenes with net polarization. Since multiplet polarization corresponds to hydrogenation inside the high magnetic field of the probe, while net polarization requires the reaction to proceed at weaker magnetic fields, it could be concluded that alkynes were being hydrogenated faster than the alkenes.

Rather more quantitative studies have also been performed. Eisenberg has analyzed the decay of polarization during a reaction to estimate the rate hydrogenation and developed a methodology termed ROCHESTER (Rates Of Catalytic Hydrogenation Estimated Spectroscopically Through Enhanced Resonances).[30] This was achieved via the reduction of ethyl (Z)-α-acetamidocinnamate using the chiral catalyst [Rh(NBD)(chiraphos)]BF_4. Integration of the polarized resonances and those of the acyl methyl protons revealed that the rate of polarization decay matched the rate of hydrogenation. Furthermore, increasing the overall catalyst concentration resulted in a faster rate of both hydrogenation and polarization decay. Upon analysis, the estimated rate of hydrogenation was found to be comparable to that determined by Halpern using a different method.[31] It should be noted that the catalyst was carefully chosen so that reversible addition of H_2 would not occur and lead to *ortho–para* equilibriation.

Bargon and others have provided a detailed analysis of a modified ROCHESTER experiment.[32] In this study, an automated procedure for saturating a solution with p-H_2 inside the NMR probe was presented. This had the advantage that no H_2 atmosphere remained above the solution once hydrogenation was complete and thus no diffusion between the solution and the gas phase occurred. A refined experimental method, termed DYPAS (DYnamic PASadena spectroscopy), was also outlined which allowed the determination of rates of intermediate formation and decay, as well as relaxation rates and the overall rate of hydrogenation. The pulse sequence used in this approach is illustrated in Figure 10. In principle, all processes leading to the formation and decay of a PHIP signal can be measured using this approach. The DYPAS

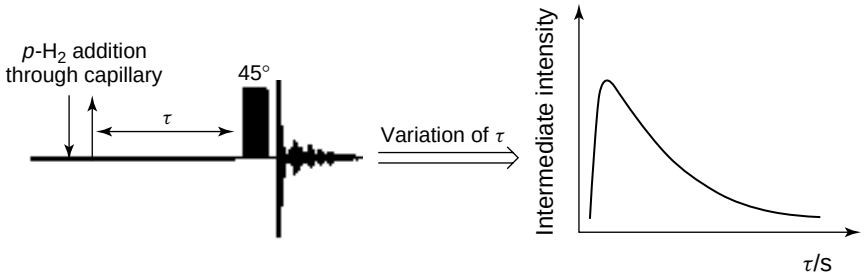

Figure 10 Pulse sequence for DYPAS experiment

method involves a variable delay between the addition of para-enriched hydrogen and a 45° read pulse, yielding a plot of signal intensity versus time (i.e., length of variable delay). Providing that a mechanistic scheme for the hydrogenation reaction exists, the decay of intensity can be described by a series of differential equations that can be solved to yield rate constants.

The potential of this method was illustrated using the $[Rh(COD)(dppb)]BF_4$ catalyst system, which, as described previously, yields product-catalyst complexes during the hydrogenation of styrene. Using a range of para-substituted styrenes, the rate constants for hydrogenation and product detachment from the catalyst were determined. The results revealed that increasing the electron donating ability of the para substituent both increased the overall rate of hydrogenation and decreased the rate of product detachment, presumably via increasing the binding potential of the arene ring to the rhodium center. The effects were sufficient for detachment to become rate limiting in the case of NH_2 substituted styrene. The more complex case of using a chiral catalyst and thus forming two diastereoisomeric product-catalyst complexes was also investigated in this way and a mechanistic scheme shown to be appropriate to the observed kinetic behavior.[23]

9 NATURE OF POLARIZATION AND DIFFERENT SPIN SYSTEMS

Bargon has also investigated hydrogenation reactions that produce more complex spin systems than those described so far. The reaction of the complex $[Rh(NBD)(PPh_3)_2]PF_6$ (NDB = 2,5-norbornadiene), with p-H_2 for example, initially produced polarized resonances attributable to 2-norbornene and at longer reaction times, norbornane resonances also displayed PHIP.[33] In the case of both products, while the added protons are chemically equivalent their magnet inequivalence activates the PHIP effect.

The presence of magnetic ^{13}C nuclei at natural abundance in hydrogenation products that are otherwise symmetrical is also sufficient to produce polarization in the ^1H spectra of product molecules. The hydrogenation of acetylene to ethene using para-enriched hydrogen for instance, yielded strongly polarized ^1H resonances corresponding to substrate molecules containing one ^{13}C nucleus, i.e., $H_2{}^{12}C{=}{}^{13}CH_2$.[34] Similar results were obtained in similar reactions with symmetrically substituted acetylenes and alkenes. Following the hydrogenation of $CH_3O_2CC{\equiv}CCO_2CH_3$, polarization was observed in the ^1H resonances of product alkene molecules that contained a ^{13}C nucleus at either the vinyl or carbonyl positions. In both cases, spin–spin coupling interactions existed between these carbon nuclei and the added protons, with the final PHIP spectrum representing resonances from two distinct hydrogenation products. Enhancements were quoted as being of the order of 10^3 fold.

Using the same substrates, Bargon demonstrated that the NMR spectra of heteronuclei can be enhanced.[35] Enhancements of over 2580 fold in the ^{13}C spectrum of $CH_3O_2CHC{=}CHCO_2CH_3$ were recorded by simply acquiring a normal ^{13}C spectrum using a single 90° pulse. The enhancement in the NMR signals of the heteronuclei was shown to be greater when the protons from parahydrogen were transferred to chemically equivalent but magnetically distinct positions. Other methods of characterizing hydrogenation products have been developed. Bargon has used a number of modified INEPT experiments to obtain ^{13}C spectra of 1,4-diphenylbut-1-en-3-yne formed via the hydrogenation of 1,4-diphenylbutadiyne, including signal enhancements of over 300 fold.[36] Optimization of the experimental parameters allowed the transfer of polarization to a large part of the carbon skeleton of the product. In addition, a PHIP modified INADEQUATE experiment has been performed, allowing the measurement of J_{CC} coupling constants in the product molecule.[37] Similar experiments with a silane compound allowed acquisition of ^{29}Si resonances.

Bargon has also published a number of studies in which analysis of the polarization patterns in the hydrogenation products reveals details of the catalytic mechanism and reaction intermediates. The $RhCl(PPh_3)_3$ catalyzed hydrogenation of two different precursors to tetrahydrofuran for instance, produced different polarization patterns in the product.[33] This indicated that the ^1H PHIP spectra of hydrogenation products contain information about the origin of the product as well as the structure of the product itself.

The nature of the polarization in the organic hydrogenation product is also influenced by the nature of the catalyst used.[38] Information about the coordination geometry and lifetime of the intermediates can be deduced from the associated spectra. In the case of $RhCl(PPh_3)_3$, the dwell time of the hydrides in the dihydride alkene intermediate was estimated as at least 1.7 ms via this approach. In contrast, the polarization pattern obtained from the $[Rh(COD)(Ph\text{-}\beta\text{-glup-OH})]BF_4$ system required that the catalytic intermediates contained hydrides in chemically equivalent positions, or, that once activated by the metal hydrogen transfer to the substrate was fast and irreversible. This latter proposal was consistent with other work performed on charged rhodium catalysts where the hydrogenation proceeds via alkene co-ordination followed by H_2 activation and rapid and irreversible hydrogen transfer. The spectral characteristics of the reaction products therefore provide

indirect information about the catalytic intermediates and the reaction mechanism.

10 PHIP AS A PROBE OF REGIO AND STEREOSELECTIVITY

PHIP spectra have also been used to investigate selectivity in hydrogenation reactions. It has for example, been shown possible to determine the position of hydrogen addition to the allene 1-methoxy-propa-1,2-diene, a process which can result in three different products after the reduction of one double bond.[39] The regioselectivities of three rhodium catalysts, $[Rh(NBD)(PPh_3)_2]PF_6$, $RhCl(PPh_3)_3$ and [Rh(COD)(Ph-β-glup-OH)]BF_4 towards this substrate were investigated via simulations of the PHIP spectra of each product. Analysis revealed considerable differences in the selectivity of the three catalysts under comparable reaction conditions. Whilst [Rh(COD)(Ph-β-glup-OH)]BF_4 does not favor the hydrogenation of either double bond, $[Rh(NBD)(PPh_3)_2]PF_6$ displays considerable selectivity for addition to the C=C bond closest to the methoxy substituent. In contrast $RhCl(PPh_3)_3$ fails to hydrogenate either bond.

11 RELATED ARTICLES IN THIS VOLUME

Sensitivity Enhancement Utilizing Parahydrogen.

12 RELATED ARTICLES IN VOLUMES 1–8

Fluxional Motion, Volume 3; Inorganic Chemistry Applications, Volume 4; Inorganic Nuclei: Low Sensitivity Transition Metals, Volume 4; Noble Gas Elements, Volume 5; Optically Enhanced Magnetic Resonance, Volume 5; Organometallic Compounds, Volume 5; Ortho-Para Hydrogen at Low Temperature, Volume 5; Selective NOESY, Volume 7.

13 REFERENCES

1. S. Geftakis and G. E. Ball, *J. Am. Chem. Soc.*, 1999, **121**, 6336.
2. C. R. Bowers and D. P. Weitekamp, *Phys. Rev. Lett.*, 1986, **57**, 2645.
3. S. B. Duckett, C. L. Newell, and R. Eisenberg, *J. Am. Chem. Soc.*, 1994, **116**, 10 548.
4. K. F. Bonhoeffer and P. Harteck, *Z. Phys. Chem.*, 1929, **B4**, 113.
5. J. Bargon, J. Kandels, and K. Woelk, *Z. Phys. Chem.*, 1993, **180**, 65.
6. C. R. Bowers and D. P. Weitekamp, *J. Am. Chem. Soc.*, 1987, **109**, 5541.
7. T. Eisenschmid, R. Kirss, P. Deutsch, S. Hommeltoft, R. Eisenberg, J. Bargon, D. G. Lawler, and A. L. Balch, *J. Am. Chem. Soc.*, 1987, **109**, 8089.
8. J. M. Brown, *Chem. Soc. Rev.*, 1993, **22**, 25.
9. J. F. Young, J. A. Osborn, F. H. Jardine, and G. W. Wilkinson, *J. Chem. Soc. Chem. Commun.*, 1965, 131.
10. (a) C. R. Bowers, D. H. Jones, N. D. Kurur, J. A. Labinger, M. G. Pravica, and D. P. Weitekamp, *Adv. Magn. Reson.*, 1990, **14**, 269; (b) J. Natterer and J. Bargon, *Prog. Nucl. Magn. Reson. Spectrosc.*, 1997, **31**, 293; (c) S. B. Duckett and C. J. Sleigh, *Prog. Nucl. Magn. Reson. Spectrosc.*, 1999, **34**, 71.
11. P. D. Morran, S. B. Duckett, P. R. Howe, J E. McGrady, S. A. Colebrooke, R. Eisenberg, M G. Partridge, and J. A. B. Lohman, *J. Chem. Soc., Dalton Trans.*, 1999, 3949.
12. S. B. Duckett, R. J. Mawby, and M. G. Partridge, *J. Chem. Soc. Chem. Commun.*, 1996, 383.
13. S. Hasnip, S. B. Duckett, D. R. Taylor, and M. J. Taylor, *J. Chem. Soc. Chem. Commun.*, 1998, 923.
14. S. P. Millar, D. L. Zubris, J. E. Bercaw, and R. Eisenberg, *J. Am. Chem. Soc.*, 1998, **120**, 5329.
15. M. Haake, J. Barkemeyer, and J. Bargon, *J. Phys. Chem.*, 1995, **99**, 17 539.
16. S. Aime, R. Gobetto, and D. Canet, *J. Am. Chem. Soc.*, 1998, **120**, 6770.
17. S. Aime, W. Dastru, R. Gobetto, A. Russo, A. Viale, and D. Canet, *J. Phys. Chem.*, 1999, **103A**, 9702.
18. C. J. Sleigh, S. B. Duckett, R. J. Mawby, and J. P. Lowe, *Chem. Commun.*, 1999, 1223.
19. C. Ulrich, A. Permin, V. Petrosyan, and J. Bargon, *Eur. J. Inorg. Chem.*, 2000, 889.
20. A. Koch, C. Ulrich, and J. Bargon, *Tetrahedron*, 2000, 3177.
21. R. Giernoth, H. Heinrich, N. J. Adams, R. J. Deeth, J. Bargon, and J. M. Brown, *J. Am. Chem. Soc.*, 2000, **122**, 12 381.
22. T. C. Eisenschmid, R. U. Kirss, P. P. Deutsch, S. I. Hommeltoft, R. Eisenberg, J. Bargon, R. G. Lawler, and A. L. Balch, *J. Am. Chem. Soc.*, 1987, **109**, 8089.
23. S. I. Hommeltoft, D. H. Berry, and R. Eisenberg, *J. Am. Chem. Soc.*, 1986, **108**, 5345.
24. R. U. Kirss, T. C. Eisenschmid, and R. Eisenberg, *J. Am. Chem. Soc.*, 1988, **110**, 8564.
25. R. U. Kirss and R. Eisenberg, *J. Organomet. Chem.*, 1989, **359**, C22.
26. A. Harthun, R. Selke, and J. Bargon, *Angew Chem, Int. Edn.*, 1996, **35**, 2505.
27. A. Harthun, R. Giernoth, C. J. Elsevier, and J. Bargon, *Chem. Commun.*, 1996, 2483.
28. R. Giernoth, P. Huebler, and J. Bargon, *Angew. Chem. Int. Edn.*, 1998, **37**, 2473.
29. P. Hubler and J. Bargon, *Angew. Chem. Int. Edn.*, 2000, **39**, 3701.
30. M. S. Chinn and R. Eisenberg, *J. Am. Chem. Soc.*, 1992, **114**, 1908.
31. A. S. C. Chan, J. J. Pluth, and J. Halpern, *J. Am. Chem. Soc.*, 1980, **102**, 5952.
32. P. Hubler, R. Giernoth, G. Kummerle, and J. Bargon, *J. Am. Chem. Soc.*, 1999, **121**, 5311.
33. J. Bargon, J. Kandels, P. Kating, A. Thomas, and K. Woelk, *Tetrahedron Lett.*, 1990, 5721.
34. M. Haake, J. Barkemeyer, and J. Bargon, *J. Phys. Chem.*, 1995, **99**, 17 539.
35. J. Barkemeyer, M. Haake, and J. Bargon, *J. Am. Chem. Soc.*, 1995, **117**, 2927.
36. M. Haake, J. Natterer, and J. Bargon, *J. Am. Chem. Soc.*, 1996, **118**, 8688.
37. J. Natterer, J. Barkemeyer, and J. Bargon, *J. Magn. Reson.*, 1996, **123**, 253.
38. P. Kating, A. Wandelt, R. Selke, and J. Bargon, *J. Phys. Chem.*, 1993, **97**, 13 313.
39. A. Harthun, J. Bargon, and R. Selke, *Tetrahedron Lett.*, 1994, 7755.

Biographical Sketches

Simon B. Duckett, *b* 1965. B.Sc., 1986, D.Phil., 1990, York. Introduced to parahydrogen by R. Eisenberg in 1991. Approx. 20 publications in this field. Research interests in using NMR to probe reaction mechanisms and developing new catalysts.

Simon A. Colebrooke, *b* 1975. B.Sc., 1997, Started work in the parahydrogen area on a project sponsored by Bruker UK in 1997. Research interests in NMR spectroscopy.

Polarization of Noble Gas Nuclei with Optically Pumped Alkali Metal Vapors

William Happer

Princeton University, Princeton, NJ, USA

1	Introduction	1
2	Optical Pumping of Alkali Vapors	1
3	Spin Exchange with Noble Gas Nuclei	2
4	Relaxation Mechanisms for the Alkali Atoms	3
5	Relaxation Mechanisms for the Noble Gas Atoms	4
6	Related Articles	5
7	References	5

1 INTRODUCTION

Recently, it has become clear that very large samples of highly polarized noble gas nuclei can be prepared by spin exchange with optically pumped alkali metal vapors. Several liter-atmospheres of gas, with nuclear polarizations of 10–90%, have already been obtained and put to good use in applications as diverse as targets for nuclear physics experiments,[1] the determination of how quarks produce the spins of protons and neutrons from high energy electron scattering on polarized ^{3}He targets,[2] the demonstration that Raman scattering of phonons through the nuclear spin–rotation interaction is responsible for the exceptionally slow relaxation of ^{129}Xe in frozen xenon,[3] setting limits on the electric dipole moments of nuclei,[4] studies of the pore structure of zeolites with highly polarized ^{129}Xe probe gas,[5] and enhanced magnetic resonance imaging of lungs with highly polarized ^{129}Xe gas.[6]

This high nuclear polarization has its origins in photons of visible light. In 1948, Albert Kastler[7] showed that it is possible to transfer much of the spin polarization of circularly polarized photons to the electron and nuclear spins of atoms. Kastler called this process *optical pumping*. Optical pumping has turned out to be practical for only a few atoms of the Periodic Table. The atomic vapors of alkali metals can be readily pumped[8] with the strong, near-infrared and visible resonance lines of lamps—and in more recent years with tunable lasers. For optically pumped alkali metal vapors, both the unpaired electron spin and the nuclear spin are polarized. Mercury and cadmium atoms can also be polarized by optical pumping with the near-ultraviolet resonance lines.[9] In the case of these diamagnetic atoms, all of the polarization is carried by the nucleus. Finally, the 2^3S state of metastable helium can be strongly polarized by optical pumping[10] with the near-infrared 1.08 μm resonance line of the triplet spectrum.[10] If ^{3}He is pumped by these methods, much of the angular momentum initially imparted by the photons to the electrons of metastable helium atoms can be efficiently transferred to the nuclei of ground state ^{3}He atoms by metastability exchange collisions.[11]

There are a few additional systems that have been polarized by optical pumping, but the great majority of work involves the alkali metal vapors, mercury vapor, or metastable helium atoms.[12] These systems have several features in common. All of the atomic species have very symmetric ground states, with spherically symmetric electron charge distributions, ^2S states for the alkali metal atoms, a ^1S state for mercury atoms, and a ^3S state for metastable helium atoms. Such electronic states are exceptionally resistant to electron or nuclear spin depolarization during collisions. Furthermore, all of these systems can be pumped with near-visible light. Some important species, like hydrogen atoms, are very similar to alkali metal atoms and can be optically pumped, but the need for vacuum ultraviolet resonance radiation (Lyman α) has made direct optical pumping impractical. The widely used systems mentioned above all have adequate atomic number densities at convenient temperatures. Containing the gases and vapors presents manageable materials problems.

The extension of optical pumping methods to include spin exchange polarization of noble gas nuclei began with the demonstration by Carver and Bouchiat[13] at Princeton University in 1960 that a substantial fraction of the electron spin angular momentum of optically pumped alkali atoms could be transferred to the nucleus of ^{3}He by spin exchange collisions. In 1978, Grover[14] and a group at Litton Industries reported the extension of the spin exchange method from ^{3}He to isotopes of xenon and krypton. Extensive studies of the physics of spin exchange between the electrons of alkali metal atoms and noble gas nuclei were subsequently carried out at Princeton University.[15]

Although Kastler began his work with a few hundred microwatts of useful resonance light from lamps, it is now straightforward to get some watts of useful laser light for optical pumping experiments. A watt of 7947 Å Rb resonance radiation is 4×10^{18} photons per second. Since one electron spin can be polarized for every photon absorbed by the Rb atoms, 4×10^{18} fully polarized electron spins can be produced per second. In favorable cases, about 10% of the electron spin polarization can be transferred by spin exchange to nuclear spin polarization of noble gases in the same container with the alkali- metal vapor. The spin can be accumulated for a time period on the order of T_1, the longitudinal spin relaxation time of the noble gases. T_1 can be hours or longer for spin-$\frac{1}{2}$ species like ^{129}Xe or ^{3}He, so some 10^{21} highly polarized spins can be produced. The polarization is independent of the magnetic field. With more powerful tunable lasers, for example the AVLIS lasers developed for isotope separation at Lawrence Livermore National Laboratory in California, it would be possible to produce many grams of solid ^{129}Xe with nearly complete nuclear polarization.

2 OPTICAL PUMPING OF ALKALI VAPORS

Although all of the alkali metals have vapors suitable for spin exchange polarization of noble gas nuclei, rubidium is often chosen since it can be readily vaporized at modest temperatures where chemical attack on the glass container is not a problem. The 7947 Å resonance line lies in a region where tunable dye lasers, titanium sapphire lasers and gallium aluminum arsenide

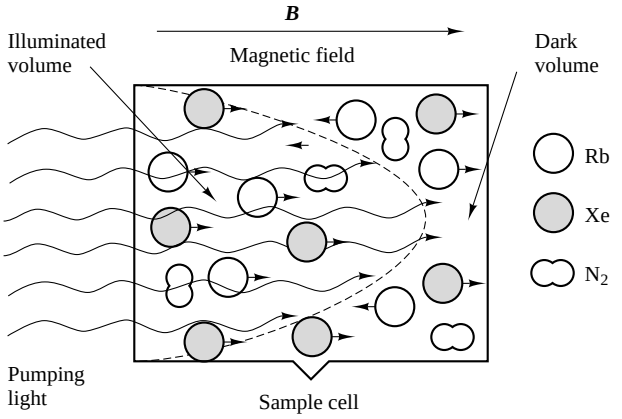

Figure 1 A typical experimental arrangement for spin exchange optical pumping to produce high nuclear spin polarization of noble gas nuclei

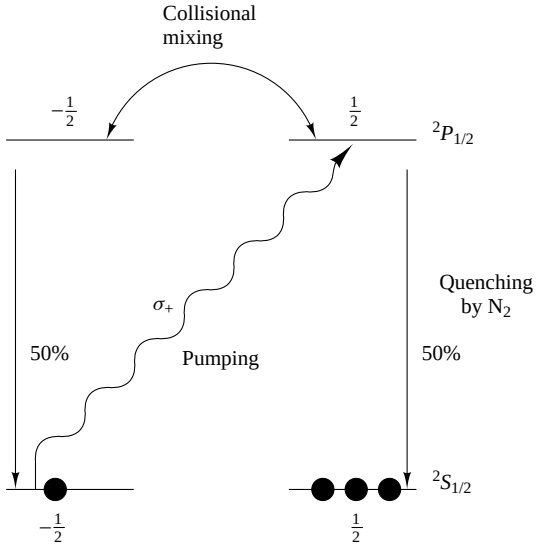

Figure 2 Optical and nonradiative transitions involved in optical pumping of an alkali metal vapor at high optical density

injection lasers can be used as intense light sources. It is also possible to use incoherent light from a resonance lamp for the optical pumping. A typical experimental arrangement is sketched in Figure 1. Not shown is the source of the static magnetic field $\boldsymbol{B}$, which is often only a few ten-thousandths of a tesla, produced by Helmholtz coils and designed to prevent the spin depolarization by stray 60 Hz fields or the ambient field of the Earth. A simple oven is used to keep the cell at a constant temperature, usually greater than 80 °C and less than 150 °C. This ensures that the saturated vapor pressure of a few droplets of Rb metal in the cell is adequate. The number density of Rb atoms is typically 10^{11}–10^{14} atoms cm^{-3}. More intense pumping light is needed to handle the higher number densities. The sample cell also contains the noble gas that is to be polarized by spin exchange and a chemically inert quenching gas, normally nitrogen, to prevent reradiation of light from the excited atoms. Since the reradiated light would be nearly unpolarized and can be absorbed by the Rb atoms, it would optically *depump* the atoms. The damage done by the reradiated photons becomes more severe at high Rb vapor densities, where the reradiated photon can be scattered several times and depolarize several atoms before escaping from the cell.

The mechanism for optical pumping is shown in Figure 2. We consider an imaginary alkali atom for which the nuclear spin is zero. All real alkali atoms have nonzero nuclear spins, but the basic mechanisms of optical pumping and spin exchange are qualitatively similar. Circularly polarized D_1 resonance light is incident on the atoms. The light can excite the atoms from the $^2S_{\frac{1}{2}}$ ground state into the $^2P_{\frac{1}{2}}$ first excited state. In both the ground state and the excited state, the electronic angular momentum of the atom can point up or down. This is represented by two Zeeman sublevels, which are split by their respective Larmor frequencies when the atom is in an external magnetic field. Since the atom must absorb both the energy and the spin angular momentum of the photon, transitions are only possible from the spin-down ground state sublevel to the spin-up excited state sublevel. The noble gas and the quenching gas collisionally transfer atoms between the sublevels of the excited state. When a quenching collision finally deexcites the atom, both ground state sublevels will be repopulated with nearly equal probability. Since the atom had $-\frac{1}{2}$ units of spin angular momentum before absorbing the photon and 0 units of spin angular momentum after being quenched from the excited state, each absorbed photon deposits $\frac{1}{2}$ a unit of spin angular momentum in the vapor.

Even though the alkali vapor is often many optical depths thick, intense circularly polarized laser light can still illuminate most of the cell,[16] as indicated in Figure 1. In the illuminated part of the cell, most of the alkali metal atoms are pumped into the nonabsorbing $+\frac{1}{2}$ sublevel of the ground state, and the spin polarization is nearly 100%. In the dark volume where no light penetrates, the alkali metal spin polarization is nearly zero, but some small spin polarization may be maintained by spin exchange with the polarized nuclei of the noble gas. Because of its long relaxation time, the spin polarization of the noble gas is nearly the same throughout the cell. The boundary between the illuminated and dark volumes of the cell is about one optical depth thick. In a well-designed system, the gas composition, the cell temperature, and the laser intensity are matched to ensure that most of the cell is illuminated.

3 SPIN EXCHANGE WITH NOBLE GAS NUCLEI

The transfer of angular momentum from the electron spin $\boldsymbol{S}$ of the alkali atom to the nuclear spin $\boldsymbol{I}$ of a noble gas atom during a collision is mediated by the Fermi contact interaction

$$\alpha \boldsymbol{S} \cdot \boldsymbol{I} \tag{1}$$

The coupling coefficient is given by the Fermi–Segré formula[17]

$$\alpha = \frac{16\pi}{3} \frac{\mu_B \mu_I}{I} |\eta \psi_0(R)|^2 \tag{2}$$

Here μ_B is the Bohr magneton, μ_I is the magnetic moment of the noble gas nucleus, and $\psi_0(R)$ is the value of the valence electron wave function of a free alkali metal atom at a distance R from the nucleus. Because the electron of the alkali atom is sucked into the attractive core of the noble gas

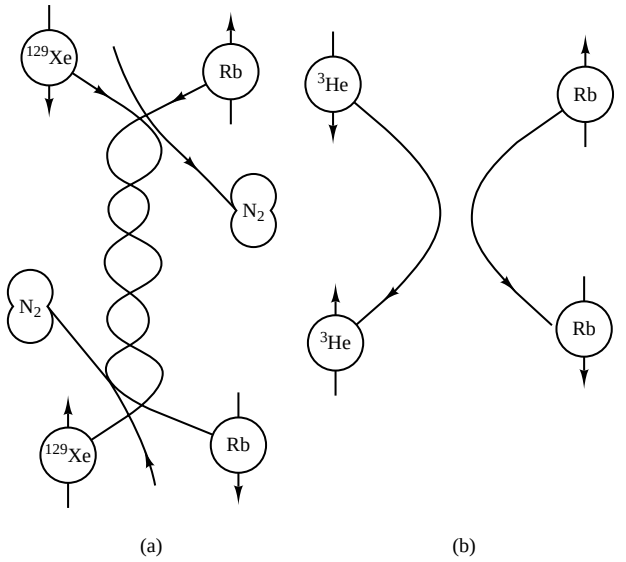

Figure 3 Spin exchange through the formation of van der Waals molecules (a) and in binary collisions (b)

atom, the valence electron wave function $\psi(R)$ is larger by an enhancement factor η than it would be if the xenon atom were not there. Approximate values for the enhancement factors for He, Ne, Ar, Kr, Xe, and Rn are[18,19] −9.5, 15, −21, 35, −50, and 63, respectively.

As indicated in Figure 3, spin exchange from the alkali metal electron to the nucleus of the noble gas can occur either in a three-body collision [Figure 3(a)], for which a third body carries away the binding energy of the van der Waals molecule that is formed, or in a simple binary collision [Figure 3(b)]. The main observable difference between the two types of collision is that the relaxation and spin transfer caused by the van der Waals molecules, while extremely efficient, can be suppressed with external magnetic fields of a few hundredths to a few tenths of a tesla. The relaxation due to binary collisions is hardly affected by magnetic fields which are readily available in the laboratory.[15] The relaxation due to van der Waals molecules also depends nonlinearly on the gas pressures in the cell.[15] The three-body collisions can account for much of the spin exchange for the heavier noble gases, namely, Kr, Xe, or Rn, but binary collisions are the dominant spin exchange mechanism for the light gases He and Ne, which have particularly weak van der Waals wells with alkali metal atoms.

Bernheim[20] first pointed out that a large fraction of the spin angular momentum $\boldsymbol{S}$ of the alkali metal atoms is lost to the rotational angular momentum $\boldsymbol{N}$ of the alkali metal atom and its collisional partner through the spin–rotation interaction

$$\gamma \boldsymbol{S} \cdot \boldsymbol{N} \tag{3}$$

In close analogy to the Fermi–Segré formula, equation (2), the coupling constant for the heavier alkali metal atoms is given by[21]

$$\gamma = \frac{mG}{MR} \frac{\mathrm{d}|\psi_0(R)|^2}{\mathrm{d}R} \tag{4}$$

where m is the electron mass and M is the reduced mass of the alkali metal atom paired with the noble gas atom. Approximate values, in units of MHz cm^5, of the spin–rotation coupling factors G are 2.4×10^{-4}, 2.8×10^{-3}, 0.25, 1.5, 6.0, and 30 for He, Ne, Ar, Kr, Xe, and Rn, respectively.[21,22]

The fraction of angular momentum that is transferred to the nucleus of the noble gas is

$$\epsilon = \frac{\alpha^2}{\frac{4}{3}(\gamma N)^2 + \alpha^2} \tag{5}$$

For example,[19] for the pair ^{129}Xe Rb, the root mean square values of the coupling coefficients are α/h = 38 MHz and $\gamma N/h$ = 121 MHz, so the efficiency of spin exchange would be about 4%; that is, $1/\eta$ = 25 photons are needed to produce each fully polarized ^{129}Xe nuclear spin.

4 RELAXATION MECHANISMS FOR THE ALKALI ATOMS

The amount of nuclear spin polarization that can be accumulated by spin exchange optical pumping is limited by the loss of spin angular momentum through relaxation mechanisms. We have already discussed the important spin–rotation interaction, equation (3), which causes a loss of electronic spin angular momentum $\boldsymbol{S}$ to rotational angular momentum $\boldsymbol{N}$ during collisions of the alkali atom with the noble gas atom or with the quenching gas molecules.

The spin exchange probability per collision is small for the lighter noble gases ^{3}He and ^{21}Ne because the enhancement factor η of equation (2) is small and because there are few sticking collisions like those of Figure 3(a). In these cases, it is advantageous to operate with as high a number density of alkali metal atoms as possible to speed up the spin exchange. At high densities, there are frequent spin exchange collisions between alkali metal atoms A and B:

$$\mathrm{A}(\uparrow) + \mathrm{B}(\downarrow) \rightarrow \mathrm{A}(\downarrow) + \mathrm{B}(\uparrow) \tag{6}$$

The up and down arrows indicate the orientations of the electron spins. The cross sections for electron–electron spin exchange collisions[12] are on the order of $10^{-14}\,\mathrm{cm}^{-2}$, so the exchange rates can be on the order of $10^4\,\mathrm{s}^{-1}$ at alkali metal atomic number densities of $10^{14}\,\mathrm{cm}^{-3}$. Electron–electron exchange is much faster than any other spin relaxation rate, but since such collisions conserve the total spin of the vapor, they do not interfere with the polarization of noble gas nuclei. Electron spin exchange does broaden the spin resonance lines of the alkali vapor, and the broadening can be used to measure the vapor density.[23]

Unfortunately, a small fraction of the collisions between alkali metal atoms transfer spin angular momentum to the translational angular momentum of the vapor. Bhaskar et al.[24] have shown that for cesium atoms A and B, spin-destroying collisions of the form

$$\mathrm{A}(\uparrow) + \mathrm{B}(\downarrow) \rightarrow \mathrm{A}(\downarrow) + \mathrm{B}(\downarrow) \tag{7}$$

occur at about 1% of the rate of spin exchange collisions, equation (6). The basic physics of the interaction, equation (7), has not been studied in detail, but it must be related in part

to the physics of the spin–rotation interaction, equation (3). Knize[25] has shown that the rate of spin-destroying collisions, equation (7), is less for the lighter alkali metal atoms Rb and K than for Cs. For the important case of ^{3}He gas, in which the electron–nucleus spin exchange interaction, equation (1), and the spin–rotation interaction, equation (2), are both very small, it is the spin-destroying collisions, equation (7), between alkali metal atoms that set the practical upper limit on the alkali metal vapor pressure and on the speed with which the ^{3}He can be polarized.[1,2]

The walls of ordinary glass or metal containers completely depolarize the spin of an alkali atom that hits them. However, alkali atoms can bounce off walls coated with paraffin or silicone[26] with little loss of angular momentum. Experimental conditions for spin exchange polarization of noble gas nuclei are usually such that losses due to the interactions, equations (3) and (7), are much larger than any losses due to wall interactions of the alkali metal atoms.

5 RELAXATION MECHANISMS FOR THE NOBLE GAS ATOMS

The spin exchange interaction, equation (1), can be an important source of relaxation for noble gas nuclei when the alkali metal atoms have a high density and are nearly unpolarized, as they are when no pumping light is present. Studies[15] of this type of relaxation have been the main experimental source of information about the magnitude of the spin exchange coupling coefficient α of equation (1) and also of the spin–rotation coupling constant γ of equation (3).

When the density of alkali metal atoms is small enough, various intrinsic mechanisms can cause the noble gas atoms to relax. The dipole–dipole interaction between the magnetic moments of ^{3}He nuclei can be a limiting relaxation mechanism in high-density helium gas,[27] one of the few practical situation where this plausible but usually ineffectual interaction actually dominates the longitudinal relaxation rates. The observed longitudinal relaxation of the spin-$\frac{1}{2}$ nuclei of ^{129}Xe in high-pressure xenon gas is much too fast to be due to the magnetic dipole–dipole interaction, and Torrey[28] showed that the relaxation is due to the nuclear spin–rotation interaction

$$\gamma \boldsymbol{I} \cdot \boldsymbol{N} \tag{8}$$

For the spin-$\frac{3}{2}$ nucleus of ^{131}Xe high-pressure gases, and presumably for other noble gas nuclei with electric quadrupole moments. Brinkmann et al.[29] have shown that the observed relaxation is due to torques on the nuclear quadrupole from field gradients induced during the collisions.

Since the noble gas atoms diffuse readily in the gas phase and the optical pumping is often done at small magnetic fields (on the order of a few ten thousandths of a tesla), residual inhomogeneities of the magnetic field can be a serious source of relaxation. At sufficiently high gas pressures, the longitudinal relaxation rate due to field inhomogeneities is[30]

$$\frac{1}{T_1} = D\frac{|\nabla B_x|^2 + |\nabla B_y|^2}{B_0^2} \tag{9}$$

where B_x and B_y are the components of the inhomogeneous field along the x and y axes, at right-angles to the mean field $\boldsymbol{B}_0$, which defines the z axis of the coordinate system. The diffusion coefficient of the noble gas in the cell is D. Cates et al.[31] have investigated relaxation of the transverse spin polarization in inhomogeneous fields and also transverse and longitudinal spin relaxation at very low pressures where motional narrowing and the dimensions and shape of the cell are important. In practice, it is not difficult to make the field inhomogeneities small enough to contribute a negligible amount to spin relaxation.

Spin depolarization at the walls is an important consideration for the nuclei of the noble gases. Fitzsimmons et al.[32] showed that very long longitudinal relaxation times T_1 can be obtained for ^{3}He in aluminosilicate glass cells, particularly Corning 1720 glass. Much shorter relaxation times are observed for borosilicate glass or quartz. The reason seems to be that the small ^{3}He atoms diffuse into the rather loose SiO_2 lattice structure of borosilicate or quartz, but are unable to penetrate the much tighter aluminosilicate network. Although most of the work of Fitzsimmons et al.[32] was done in metal-free cells, aluminosilicate glass cells that also contain droplets of alkali metal[1,2] have proven to be excellent containers for ^{3}He. Relaxation times of many hours can be obtained for well-prepared cells of this kind.

The situation is less clear for the heavier noble gases like ^{129}Xe, which cannot penetrate the SiO_2 lattice structure of borosilicate or quartz. Here most of the interactions seem to occur on the glass surface. The nature of the glass surface in sample cells exposed to the vapors of alkali metals is very poorly understood at present. Relaxation times of a minute or less are usually observed for ^{129}Xe in newly manufactured glass cells. Over a period of some days, glass cells develop longer and longer relaxation times as they 'cure'. Well-cured borosilicate glass cells have relaxation times of about one hour for ^{129}Xe. Neither quartz nor aluminosilicate cells seems to undergo 'curing'.

For noble gases like ^{21}Ne ($I = \frac{3}{2}$), ^{83}Kr ($I = \frac{9}{2}$), and ^{131}Xe ($I = \frac{3}{2}$), the wall relaxation is normally dominated by nuclear quadrupole interactions,[33,34] and is much shorter than for spin-$\frac{1}{2}$ nuclei, which have no quadrupole moment. Substantially longer spin relaxation times for noble gases with nuclear quadrupole moments are observed if a few hundred Pa of hydrogen gas are included in the cell before it is sealed off. The hydrogen slowly reacts with alkali metal on the glass wall to form alkali hydride salt crystals.

Extreme motional narrowing is often observed in cells with relatively low-pressure gas. Nuclei with quadrupole moments interact with the ensemble-averaged electric field gradient of the inner wall of asymmetric cells like that of Figure 4(a). The Zeeman degeneracy of the magnetic sublevels is lifted by the surface-averaged quadrupole interaction, as sketched in Figure 4(b). The transverse relaxation transients exhibit beats, as indicated in Figure 4(c), and the Fourier transform of the relaxation transient gives the energy intervals of the spin, as sketched in Figure 4(d).

Silicone wall coatings like 'Surfasil' from Pierce Chemical can greatly lengthen the relaxation times for the spin-$\frac{1}{2}$ nuclei of ^{129}Xe in glass cells,[35] but they speed up[36] the relaxation of the spin-$\frac{3}{2}$ nuclei of ^{131}Xe. Understanding and controlling wall interactions is the most pressing problem outstanding for artificial polarization of noble gas nuclei by spin exchange with optically pumped alkali metal atoms.

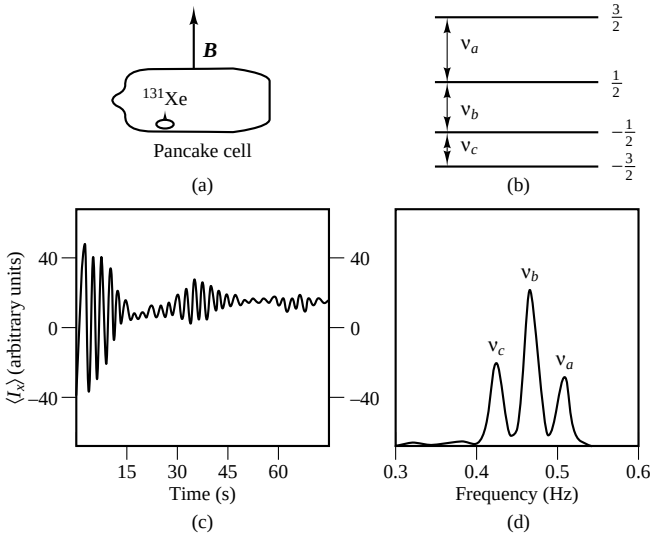

Figure 4 Beats in the free induction decay of nuclei with spins greater than $\frac{1}{2}$ due to quadrupolar interactions on the walls of an asymmetric cell

6 RELATED ARTICLES

Brownian Motion and Correlation Times; Diffusion Measurements by Magnetic Field Gradient Methods; Electron–Nuclear Hyperfine Interactions; Electron–Nuclear Multiple Resonance Spectroscopy; Gas Phase Studies of Intermolecular Interactions and Relaxation; Noble Gas Elements; Optically Enhanced Magnetic Resonance; Quadrupolar Interactions; Relaxation Theory for Quadrupolar Nuclei; Silica Surfaces: Characterization; Spin–Rotation Relaxation Theory.

7 REFERENCES

1. K. P. Coulter, A. B. McDonald, W. Happer, T. E. Chupp, and M. E. Wagshul, *Nucl. Instrum.*, 1988, **A270**, 90.
2. P. L. Anthony et al., *Phys. Rev. Lett.*, 1993, **71**, 959.
3. M. Gatzke, G. D. Cates, B. Driehuys, D. Fox, W. Happer, and B. Saam, *Phys. Rev. Lett.*, 1993, **70**, 690.
4. T. G. Vold, R. Raab, B. Heckel, and E. N. Fortson, *Phys. Rev. Lett.*, 1954, **52**, 2229.
5. B. F. Chemelka, D. Raftery, A. V. McCormick, L. C. DeMenorval, R. D. Levine, and A. Pines, *Phys. Rev. Lett.*, 1991, **66**, 580 *Phys. Rev. Lett.*, 1991, **67**, 931.
6. M. S. Albert, G. D. Cates, B. Driehuys, W. Happer, B. Saam, C. S. Springer Jr., and A. Wishnia, *Nature (London)*, 1994, **370**, 199.
7. A. Kastler, *J. Phys. Radium*, 1950, **11**, 255.
8. J. Brossel, A. Kastler, and J. Winter, *J. Phys. Radium*, 1952, **13**, 668; W. B. Hawkins and R. H. Dicke, *Phys. Rev.* 1953, **91**, 1008; J. P. Barrat, J. Brossel, and A. Kastler, *C. R. Hebd. Seances Acad. Sci.*, 1954, **239**, 1196.
9. B. Cagnac, *J. Phys. Radium*, 1958, **19**, 863.
10. P. A. Franken and F. D. Colgrove, *Phys. Rev. Lett.*, 1958, **1**, 316.
11. G. K. Walters, F. D. Colgrove, and L. D. Schearer, *Phys. Rev. Lett.*, 1962, **8**, 439.
12. W. Happer, *Rev. Mod. Phys.*, 1972, **44**, 169.
13. M. A. Bouchiat, T. R. Carver, and C. M. Varnum, *Phys. Rev. Lett.*, 1960, **5**, 373.
14. B. C. Grover, *Phys. Rev. Lett.*, 1978, **40**, 391; C. H. Volk, T. M. Kwon, and J. G. Mark, *Phys. Rev. A*, 1980, **21**, 1549.
15. N. D. Bhaskar, W. Happer, and T. McClelland, *Phys. Rev. Lett.*, 1982, **49**, 25; N. D. Bhaskar, W. Happer, M. Larsson, and X. Zeng, *Phys. Rev. Lett.*, 1983, **50**, 105; W. Happer, E. Miron, S. Schaefer, D. Schreiber, W. A. van Wijngaarden, and X. Zeng, *Phys. Rev. A*, 1984, **29**, 3092; X. Zeng, Z. Wu, T. Call, E. Miron, D. Schreiber, and W. Happer, *Phys. Rev. A*, 1985, **31**, 260; S. R. Schaefer, G. D. Cates, Ting-Ray Chien, D. Gonatas, W. Happer, and T. G. Walker, *Phys. Rev. A*, 1989, **39**, 5613.
16. A. C. Tam and W. Happer, *Phys. Rev. Lett.*, 1979, **43**, 519.
17. E. Fermi and E. Segré, *Z. Phys.*, 1933, **82**, 729.
18. R. M. Herman, *Phys. Rev.*, 1965, **137**, A1062.
19. T. G. Walker, *Phys. Rev. A*, 1989, **40**, 4959.
20. R. A. Bernheim, *J. Chem. Phys.*, 1962, **36**, 135.
21. Z. Wu, T. G. Walker, and W. Happer, *Phys. Rev. Lett.*, 1985, **54**, 1921.
22. T. G. Walker, K. Bonin, and W. Happer, *Phys. Rev. A*, 1987, **35**, 3749.
23. W. Happer and A. C. Tam, *Phys. Rev. A*, 1977, **16**, 1877; N. D. Bhaskar, J. Camparo, W. Happer, and A. Sharma, *Phys. Rev. A*, 1981, **23**, 3048.
24. N. D. Bhaskar, J. Pietras, J. Camparo, and W. Happer, *Phys. Rev. Lett.*, 1980, **44**, 930.
25. R. L. Knize, *Phys. Rev. A*, 1989, **40**, 6219.
26. M. A. Bouchiat, *J. Phys. (Orsay, Fr.)* 1963, **24**, 379; M. A. Bouchiat, *J. Phys. (Orsay, Fr.)* 1963, **24**, 611.
27. N. R. Newbury, A. S. Barton, G. D. Cates, W. Happer, and H. Middleton, *Phys. Rev. A*, 1993, **48**, 4411.
28. H. C. Torrey, *Phys. Rev.*, 1963, **130**, 2306.
29. D. Brinkmann, E. Brun, and H. H. Staub, *Helv. Phys. Acta*, 1962, **35**, 431; F. J. Adrian, *Phys. Rev.* 1965, **138**, A403.
30. R. L. Gamblin and T. R. Carver, *Phys. Rev.* 1965, **138**, A946; L. D. Schearer and G. K. Walters, *Phys. Rev.*, 1965, **139**, A1398.
31. G. D. Cates, S. R. Schaefer, and W. Happer, *Phys. Rev. A*, 1988, **37**, 2877; G. D. Cates, D. J. White, Ting-Ray Chien, S. R. Schaefera, and W. Happer, *Phys. Rev. A*, 1988, **38**, 5092; K. C. Hasson, G. D. Cates, K. Lerman, P. Bogorad, and W. Happer, *Phys. Rev. A*, 1990, **41**, 3672; S. D. Stoller, W. Happer, and F. J. Dyson, *Phys. Rev. A*, 1991, **44**, 7459.
32. W. A. Fitzsimmons, L. L. Tankersley, and G. Walters, *Phys. Rev.*, 1969, **179**, 156.
33. C. H. Volk, J. G. Mark, and B. Grover, *Phys. Rev. A*, 1979, **20**, 2381.
34. T. M. Kwon, J. G. Mark, and C. H. Volk, *Phys. Rev. A*, 1981, **24**, 1894.
35. X. Zeng, E. Miron, W. A. van Wijngaarden, D. Schreiber, and W. Happer, *Phys. Lett. A*, 1983, **96**, 191.
36. Z. Wu, W. Happer, M. Kitano, and J. Daniels, *Phys. Rev. A*, 1990, **42**, 2774; Z. Wu, S. Schaefer, G. Cates, and W. Happer, *Phys. Rev. A*, 1988, **37**, 1191.

Biographical Sketch

William Happer. *b* 1939. B.S., 1960, University of North Carolina, USA; Ph.D., 1964, Princeton University, USA. Physics Department, Columbia University, 1964–80. Physics Department, Princeton University, 1980–90. Director, Office of Energy Research, Department of Energy, Washington, DC, 1991–93. Professor, Department of Physics, Princeton University, 1993–present. Research interests include laser spectroscopy of atoms and molecules, fine and hyperfine structure of atoms and molecules, surface physics and chemistry.

Polarization Transfer Experiments via Scalar Coupling in Liquids

David M. Doddrell

University of Queensland, Australia

1	Introduction	1
2	Product Operator Algebra for IS_n Spin Systems	1
3	Polarization Transfer Process	3
4	Conclusions	9
5	References	9

1 INTRODUCTION

The sensitivity for detection of the bulk magnetization induced in a collection of nuclear spins by an externally applied magnetic field $\boldsymbol{B}_0$ is proportional to the magnetogyric ratio γ of the nuclei in question and their natural abundance. If the sensitivity is poor or the amount of material (usually a chemical compound) available for analysis is small then the signal strength recorded following a standard pulse-and-collect experiment may be insufficient relative to the thermal noise of receiver systems, rf coil, preamplifier, etc. to analyze the spectrum. Consequently, signal averaging to improve spectral quality may be necessary. The signal-to-noise (S/N) ratio will improve proportionally to $\sqrt{N}$, where N is the number of acquisitions or repetitions of the sequences of rf pulses used to generate the free induction decay (FID) from the nuclei of interest. If signal averaging is a requirement to obtain a desired S/N, the interrelationship of the repetition time of the experiment (TR) relative to the spin–lattice relaxation time T_1 of the nuclei in question becomes an important consideration. Based upon this consideration, it is possible to calculate an optimum for the flip angle (the Ernst angle) for use in a multi-acquisition single pulse experiment so as to ensure that the S/N per acquisition is maximized.

^{1}H is a nucleus of high natural abundance and large γ. In general, for organic molecules in solution, the T_1 values are of the order of a few seconds or shorter, allowing the acquisition of high quality spectra from solutions having a concentration of $\leq 10\,\mu$M in a relatively short time period, usually minutes. ^{1}H NMR spectroscopy, for these and other reasons, is one of the most important techniques for the structure determination of organic and biorganic molecules.

NMR detection of so-called heteronuclei (^{13}C, ^{15}N, ^{29}Si, ^{119}Sn, and others) was recognized in early studies using magnetic resonance methods as having great potential for chemical structure determination. ^{13}C and ^{15}N are the most important; both nuclei have low natural abundance and greatly reduced γ values relative to ^{1}H. Although T_1 values for ^{13}C are as short as those for ^{1}H, ^{15}N can have long T_1 values in many structurally interesting environments. In addition, γ for ^{15}N is negative, and thus depends on the relative values of the ^{15}N spin–lattice relaxation processes operating (^{1}H–^{15}N dipole–dipole, relaxation arising from unpaired electrons present in paramagnetic species, etc.). Therefore nuclear Overhauser enhancement (NOE) of ^{15}N signals consequent on the application of a ^{1}H decoupling field to remove ^{1}H–^{15}N scalar couplings can have a deleterious effect on the ^{15}N signal intensity. If the extreme narrowing limit is applicable, $\omega\tau \ll 1$, where ω is the resonance frequency in rad s^{-1} and τ the correlation time for the relaxation process, the maximum NOE value arising from ^{1}H dipolar coupling is $1 + \gamma_H/2\gamma_X$, where X is the heteronucleus.[1] For ^{13}C, the maximum NOE is 2.98, but for ^{15}N it is -3.93.

The central theme of this article is polarization transfer methods.[2] The discussion will be limited to liquid state studies, where the only mechanism available to induce the transfer is via the scalar interaction $J\boldsymbol{I}\cdot\boldsymbol{S}$, where $\boldsymbol{I}$ and $\boldsymbol{S}$ are the coupled spin partners having coupling constant J (in Hz: $2\pi J$ in rad s^{-1}). In the following discussion, $\boldsymbol{S}$ refers to the spin having the larger γ:$|\gamma_S| > |\gamma_I|$. (Originally, $\boldsymbol{I}$ and $\mathbf{S}$ were identified with '*i*nsensitive' and '*s*ensitive', respectively. This article has been written with this assignment in mind—other authors[3] have inverted this definition.) $\boldsymbol{S}$ is usually the ^{1}H spin. The basic idea is to transfer polarization from $\boldsymbol{S}$ to $\boldsymbol{I}$ yielding a signal intensity boost that depends upon the number of $\boldsymbol{S}$ spins scalar-coupled to $\boldsymbol{I}$ by an amount $\geq|(\gamma_S/\gamma_I)|$; an added bonus is that the experimental acquisition conditions now depend upon the $\boldsymbol{S}$-spin T_1 values. This is a particularly desirable feature for ^{15}N NMR. It should be clearly understood that the magnetization giving rise to the $\boldsymbol{I}$ polarization transfer signal is in no way related to the natural magnetization induced into the $\boldsymbol{I}$ spins in the sample by the application of $\boldsymbol{B}_0$. (Below, the symbol $\boldsymbol{K}^C$ is used to represent the natural magnetization induced into ^{13}C spins by the applied magnetic field.)

Before polarization transfer pulses sequences are discussed in detail, some simple ideas involving product operator algebra will be introduced. (Note that various constructions of product operator algebra have been published.[2,4])

2 PRODUCT OPERATOR ALGEBRA FOR IS_n SPIN SYSTEMS

In order best to summarize the ideas behind these experiments, it is useful to concentrate the discussion where appropriate on the cases $n = 1$ and $n = 2$ and allow the interested reader to investigate the general case. It is assumed that the IS_n spin system is weakly coupled. This one assumption, clearly valid for CH_n and NH_n spin systems, allows enormous simplification of the mathematical description of the effect of polarization transfer pulse trains on the available spin coherences.[4]

Fact 1. The initial spin coherence for IS_n can be represented as $I_z(U^S)^n$ and n states of the form $U^I S_z(U^S)^{n-1}$, where I_z and S_z are the z components of the $\boldsymbol{I}$ and $\boldsymbol{S}$ spin angular momenta, respectively, and U^S and U^I are unit operators for each of the remaining spins, proportional to the sum of the respective populations α and β. As opposed to other constructions of product operator algebra,[4] the unit operators are retained, since, as shown below, they readily allow the prediction of the appearance of the spectrum. For $n = 1$, the initial spin coherences are therefore I_zU^S and U^IS_z, while for $n = 2$, they are $I_z(U^S)^2$ and two states of the form $U^IS_zU^S$.

Table 1 Summary of the Effect of Pulses and Periods of Free Precession on the Operator Basis S_x,S_y,S_z[a]

$\frac{1}{2}\pi(x)$	$\frac{1}{2}\pi(y)$	$\frac{1}{2}\pi(-x)$	$\frac{1}{2}\pi(-y)$
$S_x \rightarrow S_x$ $S_y \rightarrow -S_z$ $S_z \rightarrow S_y$	$S_x \rightarrow S_z$ $S_y \rightarrow S_y$ $S_z \rightarrow -S_x$	$S_x \rightarrow S_x$ $S_y \rightarrow S_z$ $S_z \rightarrow -S_y$	$S_x \rightarrow -S_z$ $S_y \rightarrow S_y$ $S_z \rightarrow S_x$

The general case becomes, for a $\frac{1}{2}\pi(\Psi)$ pulse,
$S_x \rightarrow S_x \cos^2 \Psi + S_y \sin \Psi \cos \Psi + S_z \sin \Psi$
$S_y \rightarrow S_y \sin^2 \Psi + S_x \cos \Psi \sin \Psi - S_z \cos \Psi$
$S_z \rightarrow S_y \cos \Psi + S_x \sin \Psi$

Periods of free precession, free-precession time τ (on resonance) are analyzed using
$U^S \rightarrow U^S \cos(\pi J\tau) - \mathrm{i}S_z \sin(\pi J\tau)$
$S_z \rightarrow S_z \cos(\pi J\tau) - \mathrm{i}U^S \sin(\pi J\tau)$

Axes after evolutionary period are defined as[b]
$\mathrm{i}S_y \equiv S_x$, $-S_y \equiv \mathrm{i}S_x$, $-\mathrm{i}S_y \equiv -S_x$, $S_y \equiv -\mathrm{i}S_x$

[a] U^S is unaffected by any pulse.
[b] Following a period of free precession, the axis definitions must be made before the effect of any further pulse is considered. For example, consider $I_xU^S \rightarrow I_x[U^S \cos(\pi J\tau) - \mathrm{i}S_z \sin(\pi J\tau)]$. This must be rewritten as $I_xU^S \cos(\pi J\tau) + I_yS_z \sin(\pi J\tau)$ before the effect of any further ***I***-spin rf pulses can be determined.

Fact 2. A Cartesian basis is chosen to model pulse rotations. The effect of rotation by a $\frac{1}{2}\pi(i)$ pulse (where i is the phase of the rf pulse) on the basis set (S_x,S_y,S_z) is given in Table 1.

Fact 3. During detection, the z-eigenstate probabilities of the coupled spin partner determine the appearance of the spectrum. For example, application of a $\frac{1}{2}\pi(x)$ pulse to the ***I*** spins in an IS_2 spin system causes the change

$$I_z(U^S)^2 \rightarrow I_y(U^S)^2 \tag{1}$$

If $I_y(U^S)^2$ is now detected, a 1:2:1 multiplet is clearly observed as $I_y(U^S)^2 \equiv I_y(\alpha_S^2 + 2\alpha_S\beta_S + \beta_S^2)$. If a series of rf pulses and timing periods are applied to generate the spin coherence $I_yU^SS_z$, for example, and this is now detected, a 1:0:−1 multiplet is observed as $I_yU^SS_z \equiv I_y(\alpha_S + \beta_S)(\alpha_S - \beta_S) = I_y(\alpha_S^2 - \beta_S^2)$. (The instantaneous emf induced in the receiver coil from this spin coherence is zero, but during the acquisition time t_2, a signal is induced, and the multiple structure observed in the frequency domain is the Fourier transform of this signal.) This illustrates the advantage of retaining the unit operators in describing the effects of a pulse sequence on the spin coherences at the start of, during, and at the detection stages of the pulse train. The linkage of the spin coherences at each stage of a pulse sequence following an rf pulse or timing period is called a coherence pathway.[5]

Fact 4. To calculate the time evolutions of the Cartesian spin operators S_x and S_y, it is more convenient to treat such precessional effects using a different basis system. Define $S_x = \frac{1}{2}(S_+ + S_-)$ and $S_y = (1/2\mathrm{i})(S_+ - S_-)$. Then, with these transformations, $S_x = \mathrm{Re}\, S_+ = \mathrm{Re}\, S_-$ and $S_y = \mathrm{Im}\, S_+ = -\mathrm{Im}\, S_-$. The time evolutions of S_+ and S_- are

$$\left.\begin{aligned} S_+(\tau) &= S_+ \exp(\mathrm{i}\beta) \\ S_-(\tau) &= S_- \exp(-\mathrm{i}\beta) \end{aligned}\right\} \tag{2}$$

where β is the angle (in rad) in the rotating frame through which the transverse magnetization has precessed. It can be readily shown that if scalar coupling is the only effect operating (that is, π pulses have been inserted at the appropriate timing points during the pulse sequence in order to eliminate precessional effects arising from chemical shift offset) then U^S and S_z are modified as follows:

$$U^S \rightarrow U^S \cos(\pi J\tau) - \mathrm{i}S_z \sin(\pi J\tau) \tag{3}$$

$$S_z \rightarrow S_z \cos(\pi J\tau) - \mathrm{i}U^S \sin(\pi J\tau) \tag{4}$$

These equations are the key to understanding polarization transfer pulse sequences in liquids; consequently, it is useful to follow their derivation in some detail. Within the spirit of this article, only an *IS* spin-coupled spin system is considered.

Suppose the ***S*** spins receive a broadband $\frac{1}{2}\pi(x)$ rf pulse; the initial spin coherence U^IS_z is modified: $U^IS_z \rightarrow U^IS_y \equiv (\alpha_I + \beta_I)S_y$. Acquisition of the signal at this point yields the expected 1:1 doublet. Suppose the magnetization is allowed to precess before acquisition begins. How are the changes in the spin coherences calculated? α_IS_y and β_IS_y will both precess with a period of $1/2J$ (in s), but their angular velocity will be $\pm\pi J$ (in rad s^{-1}), respectively. Precessional effects arising owing to chemical offset are neglected. If τ is set such that α_IS_y and β_IS_y have precessed through angles of $\pm\frac{1}{2}\pi$, respectively, then α_IS_y will be changed to $-\alpha_IS_x$ and β_II_y to β_IS_x. The precessional time required to induce this change is given by $\pi J\tau = \frac{1}{2}\pi$ or $\tau = 1/2J$. These changes are shown diagrammatically in Figure 1. The effect of such a time period is thus

$$U^IS_y \equiv (\alpha_I + \beta_I)S_y \xrightarrow[1/2J]{} -\alpha_IS_x + \beta_IS_x \tag{5}$$

$(-\alpha_IS_x + \beta_IS_x)$ may be written as $-(\alpha_I - \beta_I)S_x$. Of course $(\alpha_I - \beta_I)$ is proportional to I_z, and so the effect of the $1/2J$ time period may be summarized as follows:

$$U^IS_y \xrightarrow[\frac{1}{2}\pi(S,x)]{} U^IS_y \xrightarrow[1/2J]{} -I_zS_x \tag{6}$$

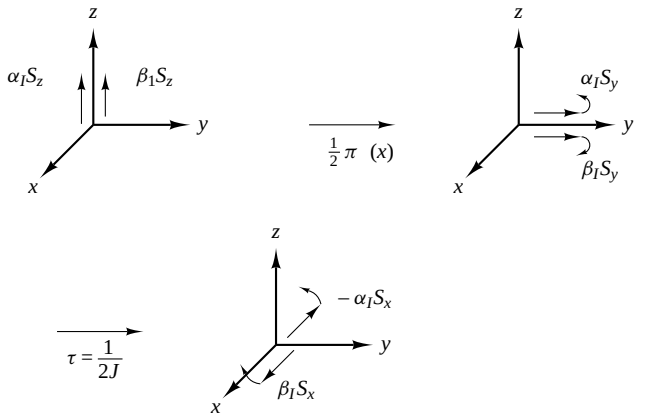

Figure 1 Vector diagrams illustrating the precessional effects following the pulse sequence $\frac{1}{2}\pi(S, x)-1/2J-$ applied to an *IS* spin system. The pulse sequence shows how magnetization is generated in a coupled spin partner via precession. This magnetization will wax and wane as the precessional effects continue in the transverse plane

Thus, following the $1/2J$ time period, magnetization is induced in the scalar-coupled spin partner, and of course I_z is observable (see below) by the application of an rf pulse to the ***I*** magnetization. Note that the magnetization induced in the sample by this process is quite independent of the bulk magnetization induced in the ***I*** spins by the static magnetic field; I_z induced by the polarization transfer process depends on the ***S*** population difference. If τ differs from $1/2J$ then the derivation of equations 3 and 4 follows easily from the fact that

$$\left.\begin{aligned} S_y(\tau) &= S_y \cos\beta + S_x \sin\beta \\ S_x(\tau) &= S_x \cos\beta - S_y \sin\beta \end{aligned}\right\} \tag{7}$$

3 POLARIZATION TRANSFER PROCESS

3.1 The SPT Experiment

The selective population transfer (SPT) experiments[6] were the forerunners of the general pulse sequence procedures used to transfer polarization nonselectively. Here 'nonselectively' implies the transfer of polarization between, for example, ^{1}H and scalar-coupled ^{13}C nuclei irrespective of the ^{1}H or ^{13}C resonance frequency relative to the frequencies of the rf pulses.

For the $^1\text{H} \rightarrow {}^{13}\text{C}$ SPI polarization transfer, the coherence pathway may be written as

$$\begin{aligned} &U^{\text{C}} S_z^{\text{H}} (U^{\text{H}})^{n-1} \propto (\alpha_{\text{C}} + \beta_{\text{C}}) S_z^{\text{H}} (U^{\text{H}})^{n-1} \\ &\xrightarrow[\text{selective}]{\pi(\text{H})_{\alpha_{\text{C}}}} (-\alpha_{\text{C}} + \beta_{\text{C}}) S_z^{\text{H}} (U^{\text{H}})^{n-1} \propto S_z^{\text{C}} S_z^{\text{H}} (U^{\text{H}})^{n-1} \end{aligned} \tag{8}$$

where now S_z^{H} and S_z^{C} represent the ^{1}H and ^{13}C magnetizations. $\pi(\text{H})_{\alpha_{\text{C}}}$ is a selective inversion pulse on the low-frequency ^{13}C satellite of a particular ^{1}H resonance. Of course, $S_z^{\text{C}} S_z^{\text{H}} (U^{\text{H}})^{n-1}$ does not give rise to any observable signal. However, if a hard non-selective $\frac{1}{2}\pi(x)$ pulse is now applied to the ^{13}C spins and ^{13}C acquisition is commenced immediately then the observed signal arises from a combination of the natural ^{13}C magnetization originating from $K_z^{\text{C}}(U^{\text{H}})^n \rightarrow K_y^{\text{C}}(U^{\text{H}})^n$ and from acquisition of $S_z^{\text{C}} S_z^{\text{H}} (U^{\text{H}})^{n-1} \rightarrow S_y^{\text{C}} S_z^{\text{H}} (U^{\text{H}})^{n-1}$. (See the comment on data acquisition above regarding how $S_y^{\text{C}} S_z^{\text{H}} (U^{\text{H}})^{n-1}$ gives rise to the observable original.) Different symbols have been used for the two different components of the ^{13}C magnetization to emphasize the fact that the total ^{13}C magnetization observed originates from two different sources; $S_y^{\text{C}}/K_y^{\text{C}} = \gamma_{\text{H}}/\gamma_{\text{C}}$.

If $n = 1$ then the observed signal originates from $K_y^{\text{C}} U^{\text{H}} + S_y^{\text{C}} S_z^{\text{H}}$. Given that $\gamma_{\text{H}}/\gamma_{\text{C}} \approx 4$, the observed signal appears as a 5:−3 or −3:5 doublet, depending upon which ^{13}C satellite is inverted in the ^{1}H spectrum. If $n = 2$ and two acquisitions are acquired, with the π(H) selective pulse being applied alternately to each ^{13}C satellite and the phase of the receiver being inverted for each acquisition, then the overall signal can be viewed as arising from the total coherence given by $[K_y^{\text{C}}(U^{\text{H}})^2 + S_y^{\text{C}} S_z^{\text{H}} U^{\text{H}}] - [K_y^{\text{C}}(U^{\text{H}})^2 - S_y^{\text{C}} S_z^{\text{H}} U^{\text{H}}] = 2 S_y^{\text{C}} S_z^{\text{H}} U^{\text{H}}$; as explained before, this yields a 1:0:−1 'triplet'. Noting that the natural magnetization is present, (here represented by a different symbol K_y^{C}) and that it can always be removed by phase cycling, in subsequent discussion any signal arising from it will be neglected.

3.2 The INEPT Pulse Sequence

The first nonselective polarization transfer technique was developed by Morris and Freeman.[7] Its application to $^1\text{H} \rightarrow {}^{13}\text{C}$ polarization transfer will be illustrated. For the double on-resonance case, the pulse sequence is

$$\frac{\pi}{2}(\text{H}, x) - \frac{1}{2J} - \frac{\pi}{2}(\text{H}, \pm y)\frac{\pi}{2}(\text{C}, x) - \text{Acquire}\ {}^{13}\text{C} \tag{9}$$

where 'Acquire ^{13}C' means to turn the ^{13}C receiver on (the form of the signal observed is governed by Fact 3 above) and $\pm y$ means that the phase of the last ^{1}H pulse is alternated (with receiver phase alternation concurrently) to remove signal arising from the natural ^{13}C magnetization. The coherence pathway may be summarized as follows:

$$\begin{aligned} &U^{\text{C}} S_z^{\text{H}} (U^{\text{H}})^{n-1} \xrightarrow[\frac{1}{2}\pi(\text{H},x)]{} U^{\text{C}} S_y^{\text{H}} (U^{\text{H}})^{n-1} \xrightarrow[1/2J]{} -S_z^{\text{C}} S_x^{\text{H}} (U^{\text{H}})^{n-1} \\ &\xrightarrow[\frac{1}{2}\pi(\text{H},y)]{} -S_z^{\text{C}} S_z^{\text{H}} (U^{\text{H}})^{n-1} \xrightarrow[\frac{1}{2}\pi(\text{C},x)]{} -S_y^{\text{C}} S_z^{\text{H}} (U^{\text{H}})^{n-1} \end{aligned} \tag{10}$$

It is clear that on data acquisition, for $n = 1$, a 1:−1 doublet will be observed; for $n = 2$, a 1:0:−1 triplet will be observed; and for $n = 3$, a 1:1:−1:−1 quartet will be observed. These multiplets will all be enhanced relative to that arising from the natural magnetization eliminated by the pulse sequence, because its phase does not depend upon the phase of the second $\frac{1}{2}\pi(\text{H}, y)$ pulse. It is also obvious why a y-phased pulse is required at this timing point, since it acts on a spin coherence of the form $-S_z^{\text{C}} S_x^{\text{H}} (U^{\text{H}})^{n-1}$. Clearly, the rules introduced above allow a simple analysis of a pulse sequence in terms of how the final spectrum appears and what the phase of each

of the rf pulses is at each point in a pulse sequence. Off-resonance effects (that is, nonselectivity) can be eliminated by breaking the $1/2J$ timing period by two π pulses as follows: $-1/4J-\pi(\mathrm{C})\pi(\mathrm{H})-1/4J-$. The application of two π pulses is required in order to remove chemical shift offset effects for ^{1}H *and* to ensure that S_z^{C} is generated by the precession. If $\pi(\mathrm{H})$ were applied without the $\pi(\mathrm{C})$ pulse (remember that during the first timing period only ^{1}H magnetization is in the transverse plane) then the transverse magnetization giving rise to the ^{13}C satellites in the ^{1}H spectrum would simply rephase (a spin echo) along the y axis after the second $1/4J$ time period. The $\pi(\mathrm{C})$ ensures that this does not occur by inverting the ^{13}C spin states.

It is clear that the detectable ^{13}C coherence following the INEPT pulse sequence remains correlated with S_z^{H}. As noted, if the ^{13}C magnetization is now detected, the individual multiplet resonances phase alternate. Consequently, if broadband proton decoupling is applied concurrently with ^{13}C data acquisition then all detectable signal is destroyed. To overcome this problem, delayed acquisition (by an amount Δ) is employed.[8] The effect of this added time (implemented as $-\frac{1}{2}\Delta-\pi(\mathrm{C})\pi(\mathrm{H})-\frac{1}{2}\Delta-$ to eliminate chemical shift offset effects) can be calculated using the results in Table 1 as follows:

$$-S_y^{\mathrm{C}}S_z^{\mathrm{H}}(U^{\mathrm{H}})^{n-1} \longrightarrow_{\Delta} S_x^{\mathrm{C}}(U^{\mathrm{H}})^n \sin(\pi J\Delta) \times \cos^{n-1}(\pi J\Delta) + \cdots \qquad (11)$$

Proton decoupling eliminates all terms except the first. For interesting values of n = 1, 2, or 3, it can be shown that the signal intensity is modulated as shown in Table 2. It is clear from this analysis how the INEPT pulse sequence can be used to distinguish the number of protons scalar-coupled to a particular carbon nucleus by observing a proton-decoupled ^{13}C spectrum. This experimental method is very valuable in structural organic chemistry, since it allows the chemist to 'count' the number of protons attached to a particular carbon center.

For n protons scalar-coupled to a nucleus $\boldsymbol{I}$, it has been shown[9] that the ^{1}H-decoupled enhancement E_{d} following the INEPT pulse sequence is given by

$$E_{\mathrm{d}} = n(\gamma_{\mathrm{H}}/\gamma_I)\sin(\pi J\Delta)\cos^{n-1}(\pi J\Delta) \qquad (12)$$

The first maximum of this function occurs at Δ_{opt}, where

$$\Delta_{\mathrm{opt}} = (\pi J)^{-1}\arcsin(1/\sqrt{n}) \qquad (13)$$

Table 2 Summary of the Effects of Selected Time Periods for Different Protonated ^{13}C Resonances Following the INEPT Pulse Sequence[8]

Group	Modulation function	Comment
^{13}CH	$\sin(\pi J\Delta)$	Maximum at $\Delta = 1/2J$
^{13}CH$_2$	$\frac{1}{2}\sin(2\pi J\Delta)$	Maximum at $\Delta = 1/4J$ Zero at $\Delta = 1/2J$ Maximum but phase-inverted at $\Delta = 3/4J$
^{13}CH$_3$	$\sin(\pi J\Delta)\cos^2(\pi J\Delta)$	Maximum at $\Delta = 0.196/J$ Zero at $\Delta = 1/2J$ No phase change at $\Delta = 3/4J$

giving the optimum decoupled enhancement factor E_{dopt}:

$$E_{\mathrm{dopt}} = \frac{\gamma_{\mathrm{H}}}{\gamma_I}\sqrt{n}\left(1-\frac{1}{n}\right)^{(n-1)/2} \qquad (14)$$

Table 3 shows that E_{dopt} increases as n increases. $E_{\mathrm{dopt}} = \gamma_{\mathrm{H}}/\gamma_I$ for n = 1, 2, but it can exceed $2\gamma_{\mathrm{H}}/\gamma_I$ for $n \geq 11$. Such behavior is significantly different from that observed for the NOE, which is independent of n, and large polarization transfer enhancements are possible for a variety of interesting systems having large n. Results obtained from ^{29}Si and ^{119}Sn NMR have confirmed the theoretical predictions noted above. Note that for ^{15}N NMR, the INEPT pulse sequence is an ideal measuring method compared with the conventional pulse-and-collect technique, since the complication of a negative NOE does not arise.

3.3 The DEPT Pulse Sequence

The basic ideas behind nonselective polarization transfer are clearly evident from analysis of the INEPT pulse sequence. However, the amount of polarization transfer depends upon J. If there are a range of J values for the same nucleus because structurally different chemical environments are present in the compound of interest then there will be a variability in the amount of polarization transfer for the different resonances using the INEPT technique. In addition, as a general guide, any multipulse sequence should use the minimum number of rf pulses to induce the desired result, thus reducing the effects of errors in rf pulse angle and phase. To reduce the J dependence (but not eliminate it) and to reduce the number of rf pulses employed to effect polarization transfer, the DEPT pulse sequence was developed.[10] This is the series of rf pulses written and analyzed as follows for $^1\mathrm{H} \rightarrow {}^{13}\mathrm{C}$ polarization transfer.

$$\frac{\pi}{2}(\mathrm{H},x) - \frac{1}{2J} - \frac{\pi}{2}(\mathrm{C},x)\pi(\mathrm{H}) - \frac{1}{2J} - \theta(\mathrm{H},y)\pi(\mathrm{C}) - \frac{1}{2J} - \text{Acquire } {}^{13}\mathrm{C} \qquad (15)$$

$\theta(\mathrm{H},y)$ is a ^{1}H pulse applied along the y axis of the rotating frame such that the nutation angle is θ. Such a pulse causes the following rotations:

$$\left.\begin{aligned} S_x^{\mathrm{H}} &\rightarrow S_z^{\mathrm{H}}\sin\theta + S_x^{\mathrm{H}}\cos\theta \\ S_y^{\mathrm{H}} &\rightarrow +S_y^{\mathrm{H}} \\ S_z^{\mathrm{H}} &\rightarrow S_z^{\mathrm{H}}\cos\theta - S_x^{\mathrm{H}}\sin\theta \end{aligned}\right\} \qquad (16)$$

Note that the pulse sequence can be broken into two overlapping halves. During the first half, only ^{1}H magnetization is in the transverse plane, thus requiring only one $\pi(\mathrm{H})$ pulse to eliminate chemical shift offset effects; during the second half only ^{13}C magnetization is in the transverse plane, and consequently only one $\pi(\mathrm{C})$ pulse is required. The number of π pulses compared with the INEPT sequence has thus been reduced by two. Also, multiplicity differences are, as shown below, differentiated by the application of different but specific values of the pulse angle θ. The timing periods are not changed, and so any variability in T_2 between different resonances is not a consideration, as would occur using the INEPT

Table 3 Values of Δ_{opt} to Give the Maximum Decoupled Enhancement E_{dopt} as a Function of the Number of Scalar-Coupled Protons[9]

n	1	2	3	4	6	8	9	12	15	18
Δ_{opt}/J^{-1}	0.50	0.25	0.196	0.167	0.134	0.115	0.108	0.093	0.083	0.076
$E_{dopt}/(\gamma_H/\gamma_I)$	1.0	1.0	1.155	1.299	1.553	1.772	1.873	2.147	2.389	2.610

pulse sequence as Δ is changed. As will become apparent, all multiples are enhanced, but since the multiplet structure arises from $S_y^C(U^H)^n$, the spectral appearance is the same as that obtained using conventional pulse-and-collect technology.

Although some appreciation of how the INEPT pulse sequence operates can be obtained using simple spin vector diagrams,[7] such an approach fails when applied to the DEPT experiment. The power of the product operator method in analyzing this pulse sequence is clearly evident. Consider first the case, $n = 1$ that is, for a CH group. The coherence pathway can be written as follows (neglecting chemical shift offset effects):

$$\begin{aligned} U^C S_z^H &\underset{\frac{1}{2}\pi(H,x)}{\longrightarrow} U^C S_y^H \underset{1/2J}{\longrightarrow} -S_z^C S_x^H \underset{\frac{1}{2}\pi(C,x)}{\longrightarrow} -S_y^C S_x^H \\ &\underset{1/2J}{\longrightarrow} -S_y^C S_x^H \underset{\theta(H,y)}{\longrightarrow} -S_y^C(S_z^H \sin\theta + S_x^H \cos\theta) \\ &\underset{1/2J}{\longrightarrow} S_x^C U^H \sin\theta - S_y^C S_x^H \cos\theta \end{aligned} \tag{17}$$

Considering the end product of the pulse sequence, the only detectable magnetization arises from $S_x^C U^H \sin\theta$. This gives rise to an enhanced 1:1 ^{13}C doublet, whose intensity is modulated as $\sin\theta$; the maximum occurs when $\theta = \frac{1}{2}\pi$. The second term, $S_y^C S_x^H \cos\theta$, can be written, neglecting the θ dependence, as $-S_y^C S_x^H \equiv -(1/4i)(S_+^C S_+^H - S_-^C S_-^H + S_+^C S_-^H - S_-^C S_+^H)$. The first two terms are known as double quantum coherence (in a z-eigenstate description, states separated by two quanta of energy, e.g. $|\alpha\alpha\rangle$ and $|\beta\beta\rangle$, can be connected) and the last two terms represent zero quantum coherence. No observable signal can result from the coherence $-S_y^C S_x^H \cos\theta$. As a general rule, observable signal arises when there is only one spin in the transverse plane.

Consider the case $n = 2$, that is, for a CH_2 group. The first $\frac{1}{2}\pi(H,x)$ pulse acts on the spin coherence $U^C S_z^H U^H$, and the resulting changes induced by the first half of the pulse sequence can be summarized as follows:

$$\begin{aligned} U^C S_z^H U^H &\underset{\frac{1}{2}\pi(H,x)}{\longrightarrow} U^C S_y^H U^H \underset{1/2J}{\longrightarrow} -S_z^C S_x^H U^H \\ &\underset{\frac{1}{2}\pi(C,x)}{\longrightarrow} -S_y^C S_x^H U^H \end{aligned} \tag{18}$$

Because the ^{13}C J coupling is of course still acting, the second $1/2J$ time period induces the following change:

$$-S_y^C S_x^H U^H \underset{1/2J}{\longrightarrow} S_x^C S_x^H S_z^H \tag{19}$$

As noted above, only single quantum terms can yield observable magnetization. Thus the only term of interest following the $\theta(H, y)$ pulse is

$$S_x^C S_x^H S_z^H \underset{\theta(H,y)}{\longrightarrow} S_x^C (S_z^H)^2 \sin\theta\cos\theta \tag{20}$$

Compared with the case, $n = 1$ the $\pi(C)$ must invert the sign of this coherence if it is applied along the y axis, $S_x^C \underset{\pi(C,y)}{\longrightarrow} -S_x^C$, or invert the sign of the coherence at the corresponding timing point for $n = 1$ if it is applied as $\pi(C, x)$. For the discussion presented here, a $\pi(C, y)$ pulse will be assumed, yielding, after the last $1/2J$ time period,

$$-S_x^C (S_z^H)^2 \sin\theta\cos\theta \rightarrow \tfrac{1}{2} S_x^C (U^H)^2 \sin 2\theta \tag{21}$$

Consequently, a 1:2:1 doublet is observed that is nulled when $\theta = \frac{1}{2}\pi$, maximized when $\theta = \frac{1}{4}\pi$, and maximized but inverted in phase when $\theta = \frac{3}{4}\pi$. Clearly, the effects of θ are the same as for $\pi J\Delta$ in the INEPT sequence; indeed, for the general case, the signal intensity is modulated as $\sin\theta\cos^{n-1}\theta$, since it arises from the spin coherence

$$S_x^C (U^H)^n \sin\theta\cos^{n-1}\theta \tag{22}$$

Figure 2 and Figure 3 illustrate the enhancements possible when the DEPT pulse sequence is employed to record ^{29}Si and ^{15}N NMR spectra. These results are consistent with the values given in Table 3, on substituting θ for $\pi J\Delta$.

The DEPT pulse sequence can be utilized to produce edited ^{13}C spectra;[10] that is, to obtain proton-decoupled ^{13}C spectra arising only from CH groups, CH_2 groups, or CH_3 groups. To edit a ^{13}C spectrum, spectra are obtained using the DEPT method for three different values of θ: $\theta_1 = \frac{1}{4}\pi$, $\theta_2 = \frac{1}{2}\pi$, and $\theta_3 = \frac{3}{4}\pi$. In order to have comparable intensities, twice as many acquisitions are taken for θ_2 as for the other θ values. For perfectly homogeneous rf pulses, the θ_2 spectrum is the CH subspectrum. The other subspectra are obtained by linear combinations of the acquired spectra:

$$\left.\begin{aligned} &CH_2 \text{ subspectrum} \rightarrow (\theta_1 - \theta_3) \text{ combination} \\ &CH_3 \text{ subspectrum} \rightarrow (\theta_1 + \theta_3 - 0.707\theta_2) \text{ combination} \end{aligned}\right\} \tag{23}$$

An example illustrating these ideas is shown in Figure 4.

Variations on the INEPT and DEPT pulse sequence have been published, but the basic ideas are the same.[11] The only significant variation is the POMMIE pulse train,[12] which for $^1H \rightarrow {}^{13}C$ polarization transfer is

$$\begin{aligned} &\frac{\pi}{2}(H, x) - \frac{1}{2J} - \frac{\pi}{2}(C, x)\pi(H) - \frac{1}{2J} - \frac{\pi}{2}(H, x) \\ &\quad \times \frac{\pi}{2}(H, \Psi)\pi(C) - \frac{1}{2J} - \text{Acquire } {}^{13}C \end{aligned} \tag{24}$$

$\frac{1}{2}\pi(H, \Psi)$ is a $\frac{1}{2}\pi$ pulse applied phase-shifted by an amount Ψ from the x axis of the rotating frame. The interested reader can, using the equations presented in Table 1, show that the observed coherence arises from

$$S_x^C (U^H)^n \sin\Psi\cos^{n-1}\Psi \tag{25}$$

for the spin grouping CH_n. Comparing the results given in equations (12), (22), and (25), the correspondence between Δ, θ, and Ψ can be seen.

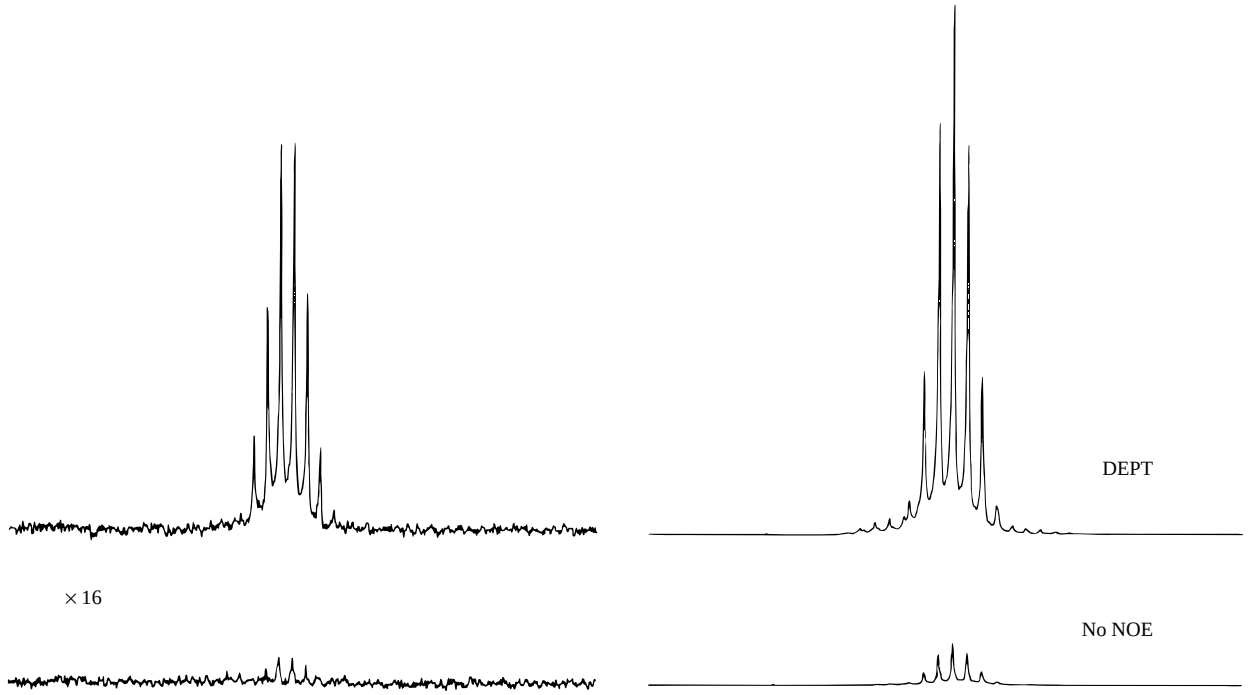

Figure 2 79.5 MHz ^{29}Si spectra of a silicone oil (50% in C_6D_6). The ^{1}H-coupled spectrum (lower) was acquired using a spectral width of 4 kHz (32 acquisitions) and without NOE. The DEPT spectrum was recorded with $\theta = 0.13\pi$. The multiplet plotted to the right corresponds to the $Si(CH_3)_2$ groups of the polymer chain. The multiplet to the left [30 ppm to high frequency (downfield)] is from $Si(CH_3)_3$ end groups. The two-bond scalar coupling used to induce the transfer was taken as 7.4 Hz. A recycle time of 7 s was used

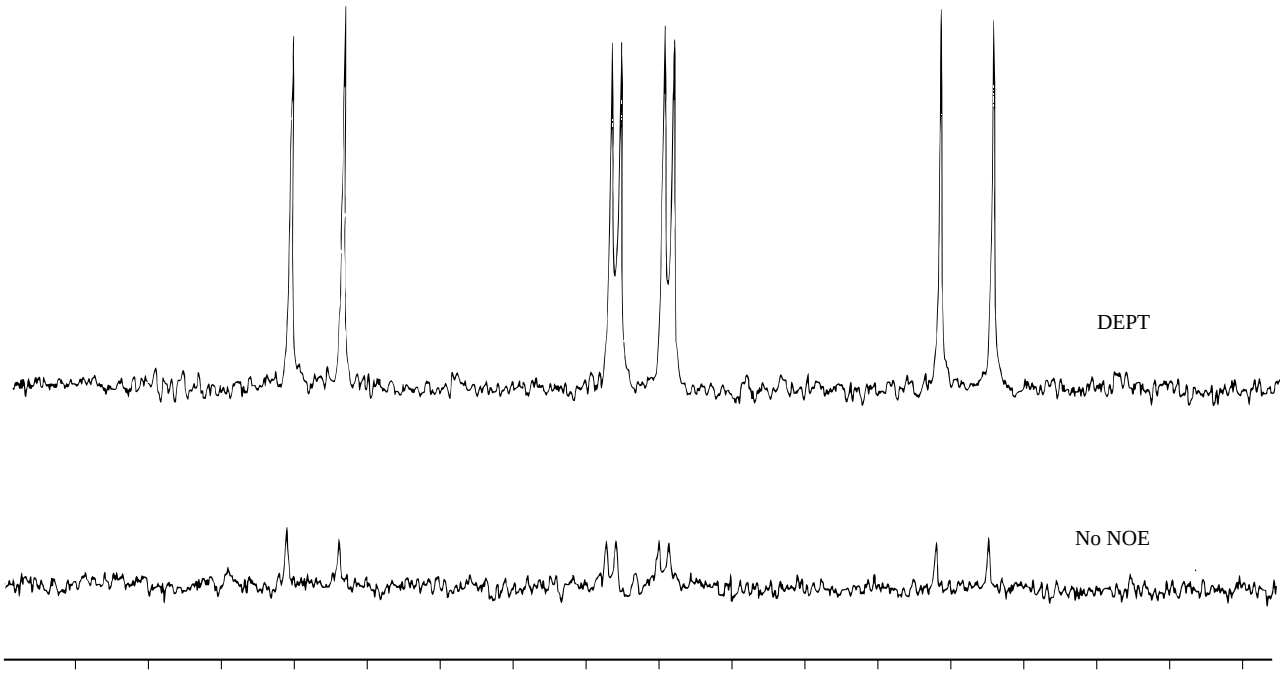

Figure 3 40.5 MHz ^{15}N spectrum of formamide (90% in DMSO-d_6, 10 mm sample). The ^{1}H-coupled spectrum (one acquisition) is compared with the DEPT spectrum acquired with $\theta = \frac{1}{4}\pi$

3.4 Inverse Polarization Transfer

It has been assumed above that $|\gamma_S| > |\gamma_I|$ and it has been illustrated how polarization transfer from more abundant large-γ spins, ^{1}H, to heteronuclei is advantageous for recording heteronuclear NMR. The situation can arise where the ^{1}H-detect $\boldsymbol{I} \rightarrow {}^1$H polarization transfer (called 'inverse,' since superficially an S/N reduction by an amount γ_I/γ_H must occur) experiment[13] may be useful. This situation arises when ^{1}H spectroscopy is to be carried out in H_2O as solvent and mainly

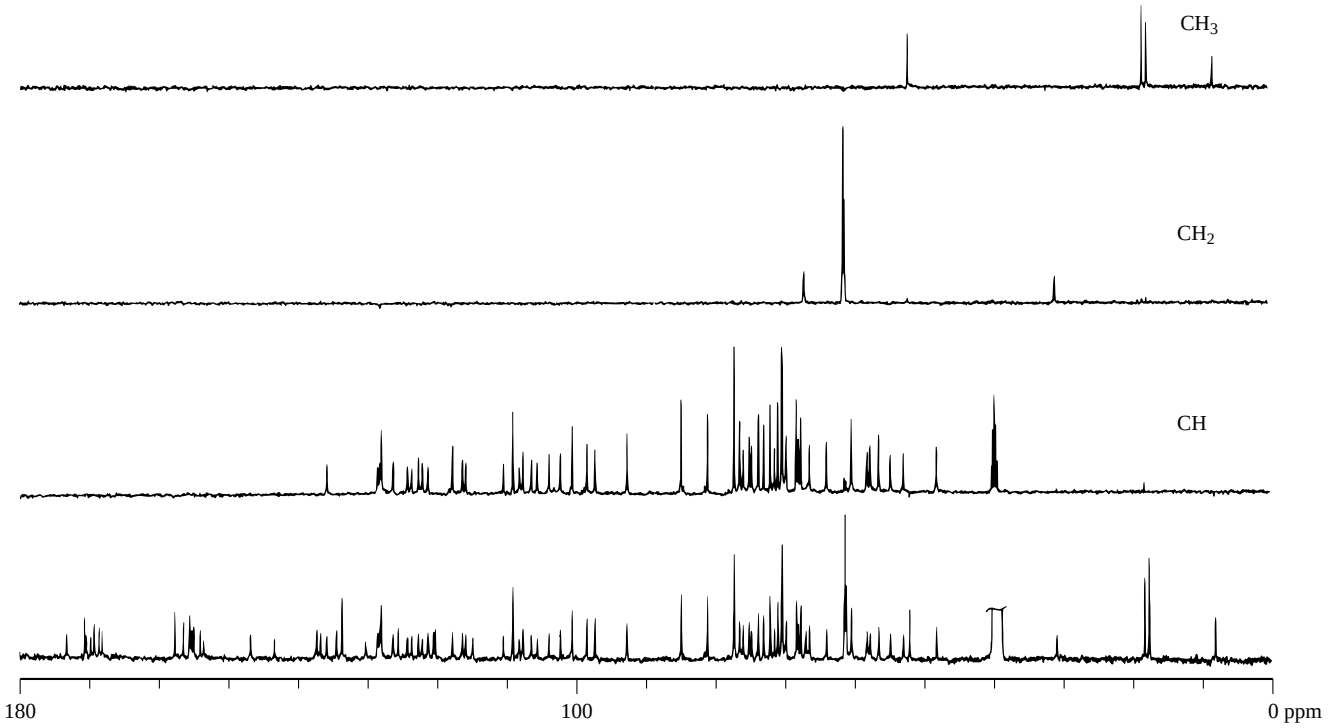

Figure 4 Edited ^{13}C spectra of ristocetin A in DMSO (120 mg ml^{-1}, 70 °C) at 100.6 MHz. The bottom spectrum is the normal ^{1}H-decoupled spectrum (400 acquisitions), showing all ^{13}C resonances. The edited spectra were acquired as per the text, and result from the combination of 800 acquisitions with $\theta = \frac{1}{4}\pi$ and $\frac{3}{4}\pi$, and 1600 acquisitions at $\theta = \frac{1}{2}\pi$

if metabolic processes are to be followed using ^{13}C-labeled precursors. In this discussion, one pulse sequence is analyzed. This is the $^{13}C \rightarrow {}^{1}H$ inverse DEPT sequence[14,15]

$$\underset{^1\mathrm{H}}{\text{randomize}} : \frac{\pi}{2}(\mathrm{C}, \pm x) - \frac{1}{2J} - \pi(\mathrm{C})\theta(\mathrm{H}, x) - \frac{1}{2J} - \frac{\pi}{2}(\mathrm{C}, y)\pi(\mathrm{H}, y) - \frac{1}{2J}\text{-Acquire}\,{}^{13}\mathrm{C} \tag{26}$$

A purging pulse, $\theta(\mathrm{H}, x)$, can be added before data acquisition.[15] Its benefits are illustrated in Figure 5. The following points should be noted.

1. The pulse sequence begins by randomizing the ^{1}H spins. An rf burst at the ^{1}H resonance frequency to cover the ^{1}H spectral width is applied. The inhomogeneity of the ^{1}H rf coil ensures that there is no net ^{1}H magnetization remaining. However, because of the $^{1}H \rightarrow {}^{13}C$ NOE, the ^{13}C magnetization is boosted by a factor of approximately 3. (Note that ^{1}H decoupling per se does not necessarily yield zero net ^{1}H magnetization at the instant the decoupling field is removed—a randomization is required.) The physics of the first step of this pulse sequence is thus complex. Because of the NOE, the observed ^{1}H signal induced by the transfer process will only be reduced by one-quarter compared with the natural ^{1}H magnetization.
2. If the randomization field is completely efficient then, prior to the application of any rf pulse, $\langle \boldsymbol{S} \rangle = 0$ from all sources of ^{1}H signal, including that from H_2O. ^{1}H magnetization from H_2O as solvent builds up during the pulse sequence, and, given that H_2O is 55 M in concentration, a significant ^{1}H signal can still be observed. However, its phase does not depend upon the phase of the first $\frac{1}{2}\pi(\mathrm{C})$ pulse. Thus, further H_2O suppression will result, with phase alternation of this pulse and concurrent phase alternation of the receiver.

The product operator analysis of this pulse sequence is presented for a CH_2 group. The initial coherence is $S_z^{\mathrm{C}}(U^{\mathrm{H}})^2$, and the following changes occur:

$$S_z^{\mathrm{C}}(U^{\mathrm{H}})^2 \underset{\frac{1}{2}\pi(\mathrm{C},x)}{\longrightarrow} S_y^{\mathrm{C}}(U^{\mathrm{H}})^2 \underset{1/2J}{\longrightarrow} -S_y^{\mathrm{C}}(S_z^{\mathrm{H}})^2 \underset{\theta(\mathrm{H},x)}{\longrightarrow} -S_y^{\mathrm{C}}S_z^{\mathrm{H}}S_y^{\mathrm{H}}\sin\theta\cos\theta \tag{27}$$

Following the $\theta(\mathrm{H}, x)$ pulse there are four terms, only one of which can yield a detectable ^{1}H signal. This term arises from $S_y^{\mathrm{C}}S_z^{\mathrm{H}}S_y^{\mathrm{H}}$, and has an angular dependence of sin 2θ. It is thus maximized at $\theta = \frac{1}{4}\pi$, zero at $\theta = \frac{1}{2}\pi$, and maximized but phase-inverted at $\theta = \frac{3}{4}\pi$. During the remaining period of the pulse sequence, the following changes occur to yield a detectable signal:

$$S_y^{\mathrm{C}}S_z^{\mathrm{H}}S_y^{\mathrm{H}} \underset{1/2J}{\longrightarrow} -S_x^{\mathrm{C}}U^{\mathrm{H}}S_y^{\mathrm{H}} \underset{\frac{1}{2}\pi(\mathrm{C},y)}{\longrightarrow} -S_z^{\mathrm{C}}U^{\mathrm{H}}S_y^{\mathrm{H}} \underset{1/2J}{\longrightarrow} U^{\mathrm{C}}U^{\mathrm{H}}S_x^{\mathrm{H}} \tag{28}$$

Any detectable H_2O signal will be phase shifted by $\frac{1}{2}\pi$ relative to $U^{\mathrm{C}}U^{\mathrm{H}}S_x{}^{\mathrm{H}}$, and can be further removed from the detection plane by application of a $\theta(\mathrm{H}, x)$ purging pulse. Results using this pulse sequence to monitor metabolism of ^{13}C-labeled glucose in a mouse liver cell extract (H_2O solvent) are shown in Figure 6. Suppression of the H_2O signal by a factor of 8×10^5 is possible using reverse polarization transfer.[15] The important point to note is that most of the signal suppression is

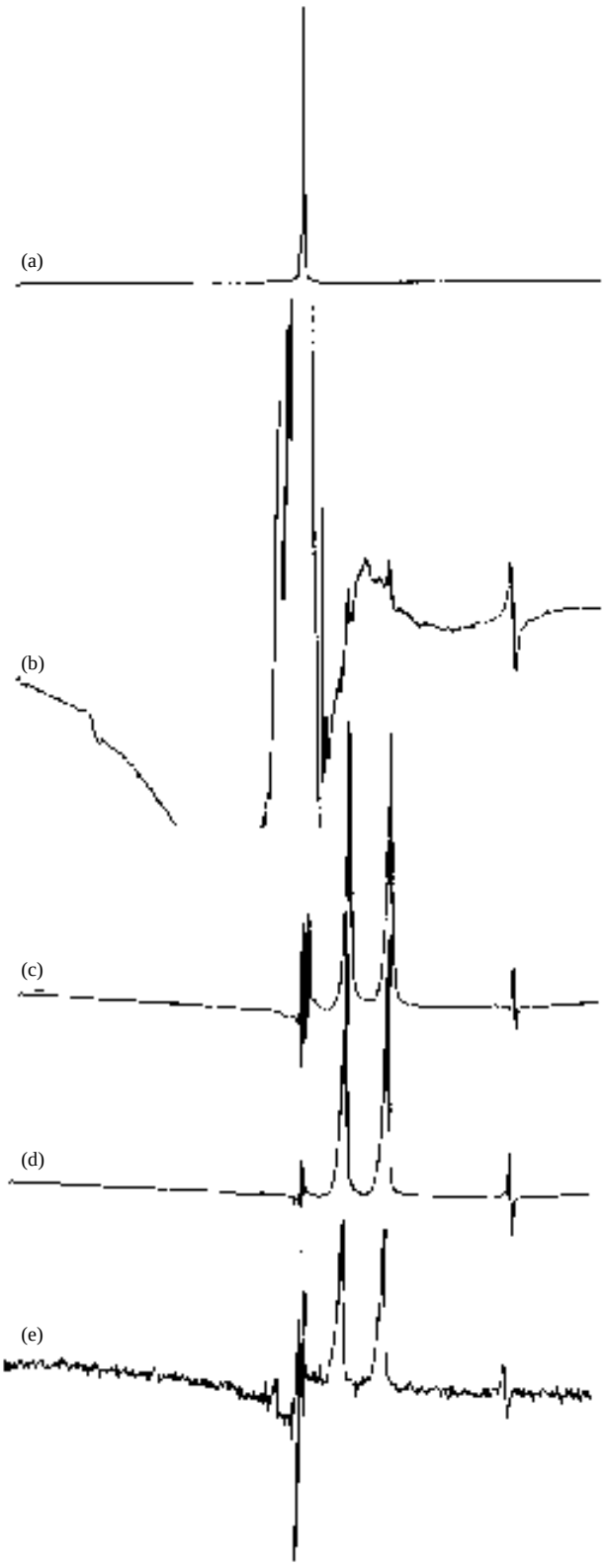

Figure 5 Application of the reverse DEPT pulse sequence to a sample of ^{13}C-labeled ethanol in neat H_2O. (a) Normal pulse-and-collect low-gain ^1H spectrum. (b) High-gain pulse-and-collect spectrum showing the ethanol CH_2 protons. (c) Reverse DEPT spectrum without the purging pulse. (d) Reverse DEPT spectrum with the purging pulse. In all cases, the sample concentration was 100 mM. (e) Reverse DEPT spectrum, sample concentration 10 mM

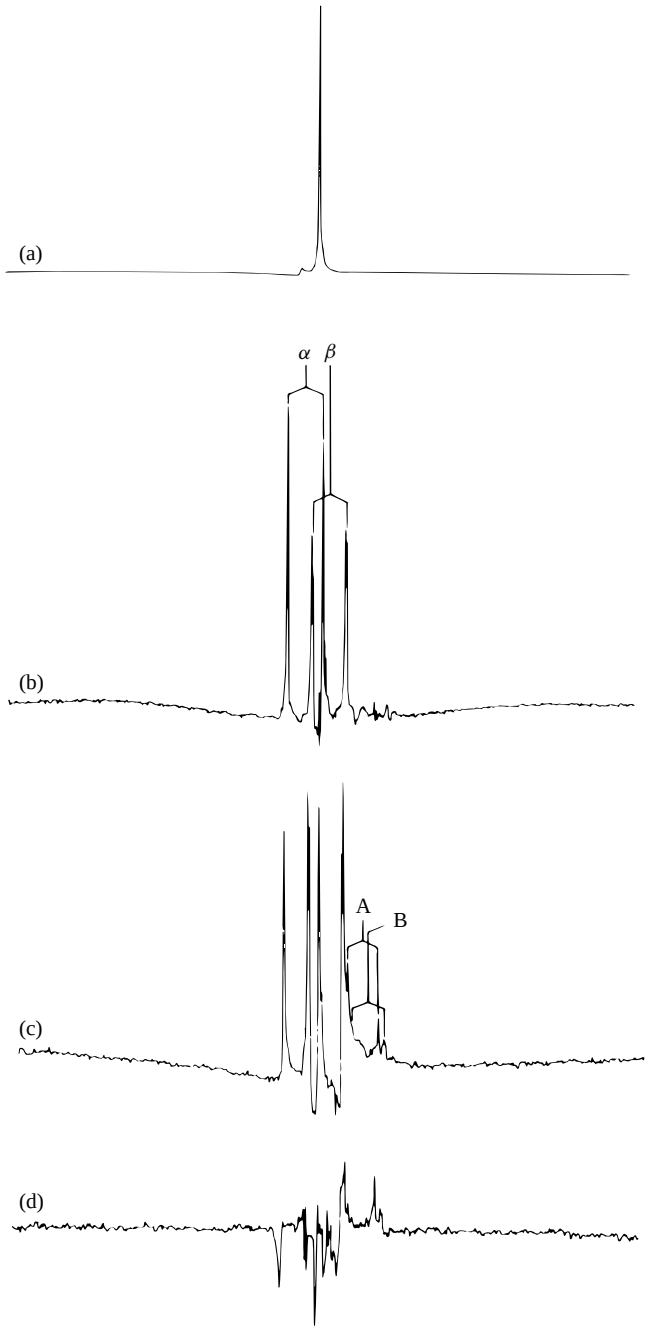

Figure 6 Application of the reverse DEPT pulse sequence to monitor metabolism of ^{13}C-labeled glucose by a mouse liver cell extract. (a) Normal pulse-and-collect spectrum in H_2O. (b) Reverse DEPT spectrum showing the α and β anomeric proton resonances. (c) After 1.5 h of metabolism, two different CH_2 proton resonances are observed: A and B. (d) An edited spectrum as per Brooks et al.,[15] confirming that the metabolic product arises from a CH_2 molecular fragment

achieved prior to the detection step, and thus the full dynamic range of the receiver can be utilized to detect weak signals.

3.5 2D Experiments

A variety of multidimensional NMR experiments are possible based upon either a modified INEPT or DEPT pulse

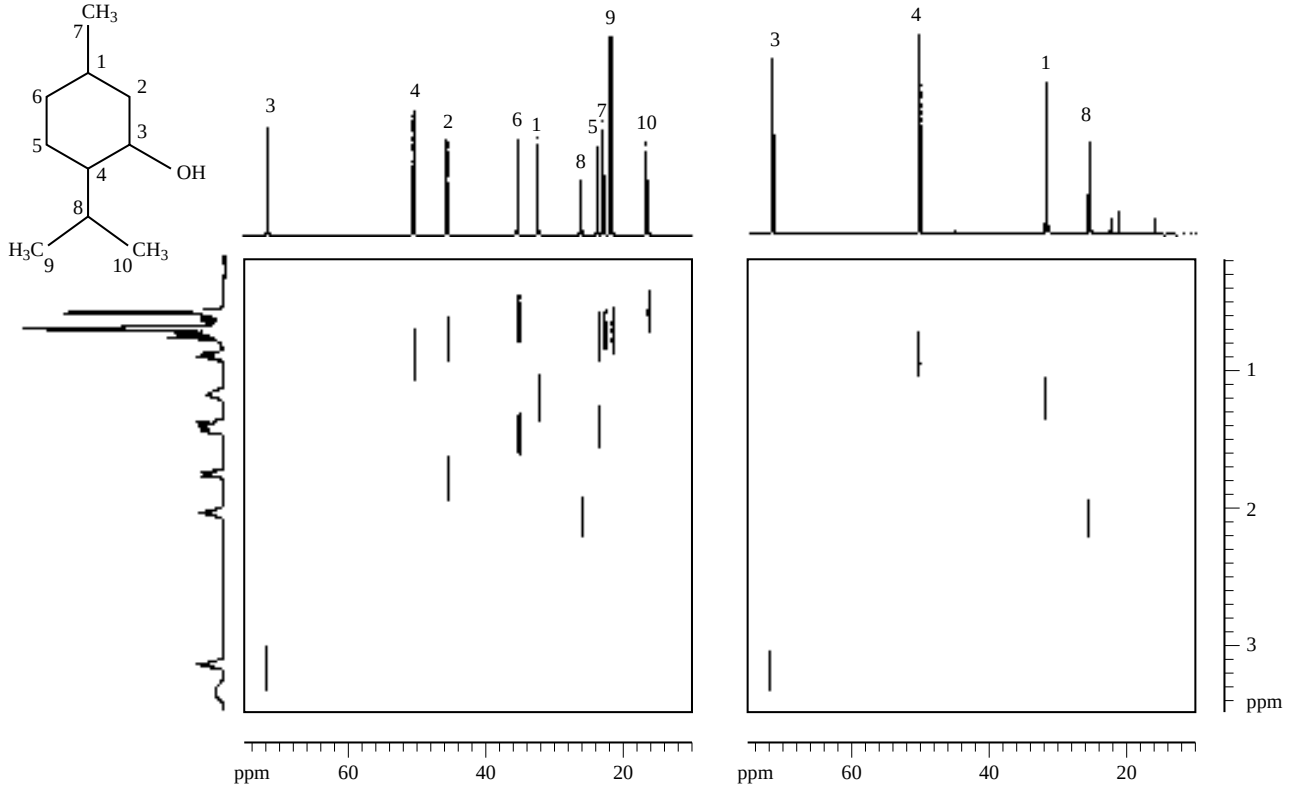

Figure 7 Edited 2D ^{13}C-observe ^{13}C–^{1}H heteronuclear cross correlation spectra obtained from a saturated solution of menthol in $CDCl_3$. Four acquisitions per t_1 increment and 512 points in the ω_1 direction were acquired. Values of θ were $\theta = \frac{1}{4}\pi$ and $\theta = \frac{1}{2}\pi$ (the CH subspectrum)

sequence or on using these pulse sequences as sources of transverse magnetization[16] (for a discussion of the possible 2D pulse sequences, see Kessler[3]). A simple example is provided by the heteronuclear chemical shift correlation experiment

$$\frac{\pi}{2}(\mathrm{H}, x) - \frac{t_1}{2} - \pi(\mathrm{C}) - \frac{t_1}{2} - \frac{1}{2J} - \pi(\mathrm{H})\frac{\pi}{2}(\mathrm{C}) - \frac{1}{2J} - \theta(\mathrm{H}, y)\pi(\mathrm{C}) - \frac{1}{2J}\text{-Acquire}\,^{13}\mathrm{C} \qquad (29)$$

During the time t_1, ^{1}H chemical shift evolution occurs; ^{13}C decoupling in the ω_1 direction is achieved by insertion of the π(C) pulse. By setting θ as noted above, it is possible to generate 2D heteronuclear chemical shift correlated subspectra. The results of such an experiment are shown in Figure 7.

4 CONCLUSIONS

As noted by Ernst,[2] polarization transfer experiments are a subclass of the general class of coherence transfer processes. Previously, the term 'population transfer' had also been used to signify the fact that the Zeeman population of the coupled spin partner was controlling the observed S/N. This article has focussed on the methodology and utility of polarization-transfer experiments, and has attempted to explain the spin physics involved without recourse to more complex quantum mechanical descriptions. (Hartmann–Hahn cross polarization[17] via scalar coupling has been neglected because of limitations of space; for details, see Doddrell et al.[18]) As has been illustrated here, these experiments have wide applicability for structural studies using magnetic resonance.

5 REFERENCES

1. K. F. Kuhlmann, D. M. Grant, and R. K. Harris, *J. Chem. Phys.*, 1970, **52**, 3439.
2. R. R. Ernst, G. Bodenhausen, and A. Wokaun, *Principles of Nuclear Magnetic Resonance in One and Two Dimensions*, Clarendon, Oxford, 1987.
3. H. Kessler, *Angew. Chem., Int. Ed. Engl.*, 1988, **27**, 490.
4. F. J. M. van de Var and C. W. Hilbers, *J. Magn. Reson.*, 1983, **54**, 512; K. J. Packer and K. M. Wright, *Mol. Phys.*, 1983, **50**, 797; R. M. Lynden-Bell, J. M. Bulsing, and D. M. Doddrell, *J. Magn. Reson.*, 1983, **55**, 128.
5. J. M. Bulsing and D. M. Doddrell, *J. Magn. Reson.*, 1985, **61**, 197.
6. K. G. R. Pachler and P. L. Wessels, *J. Magn. Reson.*, 1973, **12**, 337; S. Sørensen, R. S. Hansen, and H. L. Jakobsen, *J. Magn. Reson.*, 1974, **14**, 243; H. J. Jakobsen, S. Aa. Linde, and S. Sørensen, *J. Magn. Reson.*, 1974, **15**, 385.
7. G. A. Morris and R. Freeman, *J. Am. Chem. Soc.*, 1979, **101**, 760.
8. D. M. Doddrell and D. T. Pegg, *J. Am. Chem. Soc.*, 1980, **102**, 6388.
9. D. M. Doddrell, D. T. Pegg, W. Brooks, and M. R. Bendall, *J. Am. Chem. Soc.*, 1981, **103**, 727.
10. D. M. Doddrell, D. T. Pegg, and M. R. Bendall, *J. Magn. Reson.*, 1982, **48**, 323.

11. O. W. Sørensen and R. R. Ernst, *J. Magn. Reson.*, 1983, **51**, 477.
12. J. M. Bulsing, W. M. Brooks, J. Field, and D. M. Doddrell, *J. Magn. Reson.*, 1984, **56**, 167.
13. R. Freeman, T. H. Mareci, and G. A. Morris, *J. Magn. Reson.*, 1981, **42**, 341.
14. M. R. Bendall, D. T. Pegg, D. M. Doddrell, and J. Field, *J. Magn. Reson.*, 1983, **51**, 520.
15. W. M. Brooks, M. G. Irving, S. J. Simpson, and D. M. Doddrell, *J. Magn. Reson.*, 1984, **56**, 521. J. M. Bulsing and D. M. Doddrell, *J. Magn. Reson.*, 1986, **68**, 52.
16. M. H. Levitt, O. W. Sørensen, and R. R. Ernst, *Chem. Phys. Lett.*, 1985, **53**, 144.
17. S. R. Hartmann and E. L. Hahn, *Phys. Rev.*, 1962, **128**, 2042.
18. D. M. Doddrell, D. T. Pegg, and M. R. Bendall, *J. Magn. Reson.*, 1982, **49**, 181.

Biographical Sketch

David M. Doddrell. *b* 1944. B.Sc., 1966, University of Queensland, Ph.D., 1969, Indiana University, D.Sc., 1977, Griffith University. Introduced to NMR by A. Clouse, E. Wenkert, and A. Allerhand. Faculty positions at Griffith University 1974–86, University of Queensland 1986–present. Approximately 220 publications. Research interests: multipulse NMR liquid state applications, in vivo NMR spectroscopy, magnetic resonance imaging, and hardware developments.

Relayed Coherence Transfer Experiments

Philip H. Bolton
Wesleyan University, Middletown, CT, USA

1 Introduction 1
2 The Original Relay Transfer Experiments 1
3 The Development of Relay Transfer Experiments 4
4 Related Articles 5
5 References 5

1 INTRODUCTION

In the late 1970s and early 1980s the basic principles of two-dimensional NMR were beginning to become clear. It was also clear that the experiments being used at that time would not be sufficient to solve many interesting problems, especially those concerning nucleic acids and proteins. The experiments that were then in use included INEPT, INADEQUATE, NOESY, homonuclear and heteronuclear *J* spectroscopy, as well as variants of what has come to be known as COSY type experiments and heteronuclear correlation experiments which involved detection of the heteronucleus.

The author's interest in two-dimensional NMR began with the use of heteronuclear $^{31}P-^{1}H$ experiments to utilize the ^{31}P nucleus to 'spy' on the proton nuclei.[1] These experiments were originally aimed at obtaining proton–proton and proton–phosphorus scalar couplings and proton chemical shifts via use of experiments such as the one schematically illustrated in Figure 1. In this basic type of heteronuclear two-dimensional NMR experiment the free precession information of the protons is transferred to the heteronuclear 'spy' nucleus, in this case ^{31}P, by the simultaneous proton and heteronuclear pulses.

The proton spectrum which is detected in this type of experiment can be thought of as a difference spectrum.[1] The normal proton spectrum can be thought of as arising from the sum of the two subspectra which arise from the two possible polarizations of the heteronucleus. The proton spectrum detected in the heteronuclear experiment is the difference between these two subspectra. This principle is illustrated in Figure 2. The spectrum in (a) is the sum of the two subspectra corresponding to the two polarizations of the phosphorus nucleus and is the normal one-dimensional proton spectrum. The spectra in (b) and (c) are the two proton subspectra corresponding to the two different polarizations of the phosphorus nucleus. The spectrum in (d) is the difference spectrum between the two subspectra.

The comparison of the predicted and observed results is shown in the spectra on the right-hand side of Figure 2 along with the structure of 2′-guanosine monophosphate (2′-GMP) which was the molecule used for these experiments. There is good agreement between the predicted and observed spectra.

This single quantum experiment and various multiple quantum variations were applied to a number of nucleotides including ones which exhibit strong proton–proton scalar coupling and scalar coupling between the protons and more than one phosphate.[2–5] In addition, the flip angle dependence of the intensities of the individual lines in the heteronuclear spectra was extensively investigated.[3,4,6] These studies allowed us to analyze essentially any spectrum obtained in a heteronuclear two-dimensional chemical shift correlation experiment. These methods were even applied to nucleotides bound to an enzyme.[7]

In these heteronuclear two-dimensional experiments, the heteronucleus could report on the protons which had scalar couplings to the heteronucleus but did not report directly on any other protons. For example, in both the predicted and experimental results on 2′-GMP, no information about the chemical shift of the H-3′ proton is obtained. Thus, the results of a heteronuclear experiment on 2′-GMP do not offer complete information about the protons which are not directly coupled to the heteronucleus. As in many cases, the information which is of most interest is not necessarily the most accessible information. The nomenclature which was introduced was to call the protons directly coupled to the heteronuclear 'spy' as 'neighbor' nuclei and the protons coupled to the neighbors as 'remote' nuclei.

One way to obtain information about the remote nuclei was to apply a weak continuous wave decoupling field at the chemical shift of the remote nucleus during the evolution time.[8] When the decoupling field was on resonance then the coupling of the remote nucleus with the neighbor nucleus would be suppressed. Figure 3 illustrates the expected change in a heteronuclear two-dimensional experiment. At the time that this double resonance, two-dimensional experiment was first conceived it was not trivial to carry it out. The Varian XL-200 spectrometer that was in use at the time required *milliseconds* to carry out a change in the power level of the proton channel, since the power change was carried out by means of *mechanical* relays which could be monitored by simply listening to the spectrometer. However, application of a proton decoupling field during the evolution time of a heteronuclear two-dimensional experiment could be implemented and typical results are shown in Figure 4. As expected the double resonance, two-dimensional experiment did allow the determination of the couplings between the neighbor and remote protons. The chemical shift of the remote protons could be determined by observing the neighbor protons as a function of the frequency of the decoupling field and this was actually carried out on a nucleotide–protein complex.[7]

2 THE ORIGINAL RELAY TRANSFER EXPERIMENTS

About the time that the galley proofs on the above work were being corrected it became apparent that this was not a very clever way to obtain information about the remote protons. The basic heteronuclear two-dimensional experiment can be considered as the successor of the process of obtaining a series of one-dimensional spectra of the heteronucleus as a function of the frequency of a proton decoupling field. A better way to obtain information about the remote protons is to substitute a frequency independent procedure for the decoupling field applied during the evolution time.

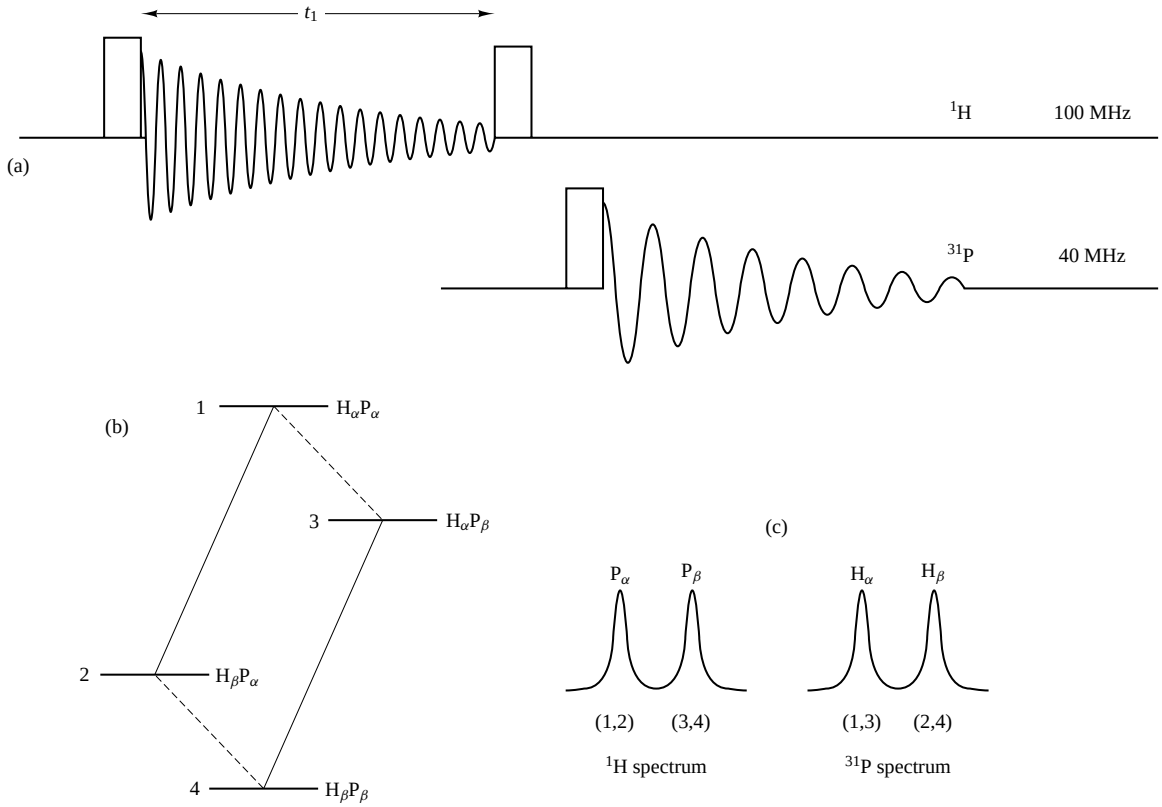

Figure 1 (a) A depiction of the basic pulse sequence used for heteronuclear chemical shift correlation spectroscopy. (b) The energy levels of a two-spin heteronuclear spin system and (c) the proton and phosphorus spectra together with labelings of the subspectra. (Adapted from Bolton and Bodenhausen[1])

This substitution could be based on the same basic idea as the heteronuclear two-dimensional NMR experiment, that is, the transfer of magnetization between nuclei which are scalar coupled by means of pulses rather than a set of experiments varying the frequency of the decoupling field. The basic procedure was to have two, successive magnetization transfers. The first magnetization transfer would be from remote to neighbor protons and the second transfer from the neighbor protons to the heteronuclear spy nucleus whose free precession would be detected.

Thus, the basic idea was simple and so obvious it was surprising no one had implemented it much earlier. The experiment was a straightforward combination of two two-dimensional experiments: a proton–proton COSY experiment and a heteronuclear two-dimensional chemical shift correlation experiment. The pulse sequence for a proton–proton COSY experiment is 90°, t_1, 90°, t_2. The pulse sequence for a heteronuclear two-dimensional experiment is that shown in Figure 1. The pulse sequence for the combined heteronuclear experiment is

$$^1\text{H: } 90^\circ,\ t_1,\ 90^\circ,\ t_m,\ 90^\circ$$

$$\text{X: } 90^\circ,\ t_2$$

The mixing time, t_m, is chosen to be long enough for the protons to become antiphase with respect to both the heteronuclear and homonuclear couplings. A typical value for a proton–phosphorus experiment is 30 ms. This experiment was named the *relayed coherence transfer* experiment as the magnetization is relayed from the remote to the neighbor to the spy.[9,10]

The first experiments were carried out on phosphothreonine[9] with typical data shown in Figure 5. The experiment succeeded in correlating both the remote and neighbor protons with the heteronuclear spy, which in this case includes all of the nonexchangeable protons of the molecule. This demonstrated that two two-dimensional experiments could be combined into a single experiment. In addition, the relay transfer experiment contains essentially all of the information present in the separate two-dimensional experiments.

While the application of the heteronuclear relay transfer experiment to molecules containing phosphorus was a success, the much more interesting application was to use ^{13}C as the spy nucleus.[10] The original pulse sequence is

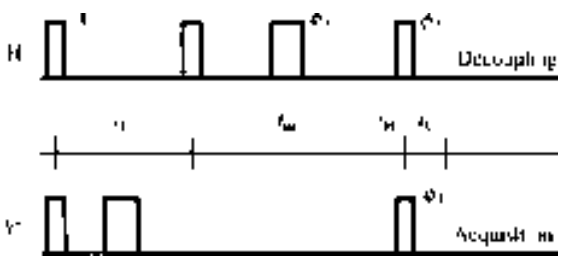

with t_H the delay time to allow the magnetization to become antiphase with respect to the heteronuclear couplings so that transfer can occur, and t_C the delay time to allow the carbon

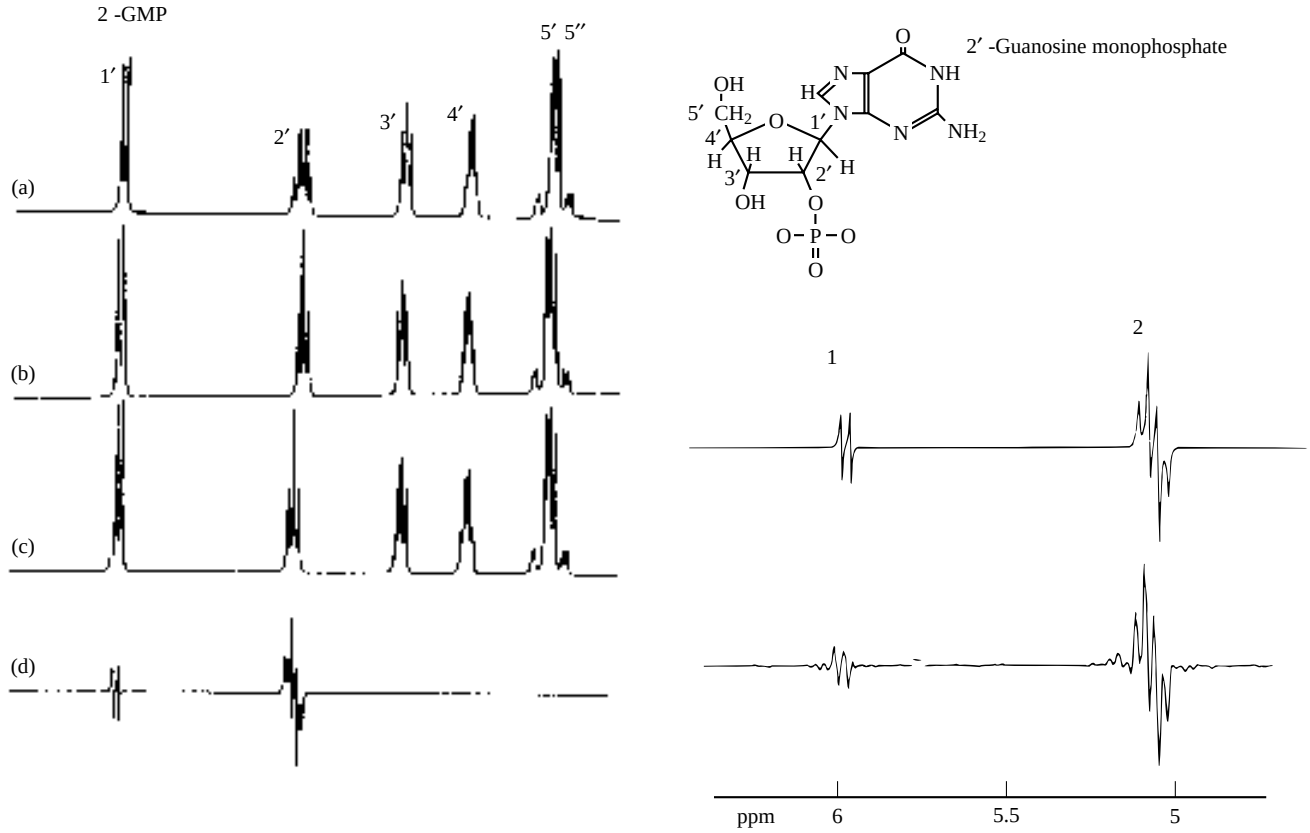

Figure 2 The left side of the figure contains the normal proton spectrum of 2′-GMP (a); the two subspectra which arise from the two polarizations of the phosphorus heteronucleus (b,c); and the predicted heteronuclear spectrum of this sample (d). The right side contains a comparison between the predicted heteronuclear spectrum (top) and the observed spectrum (bottom). (Adapted from Bolton and Bodenhausen[1])

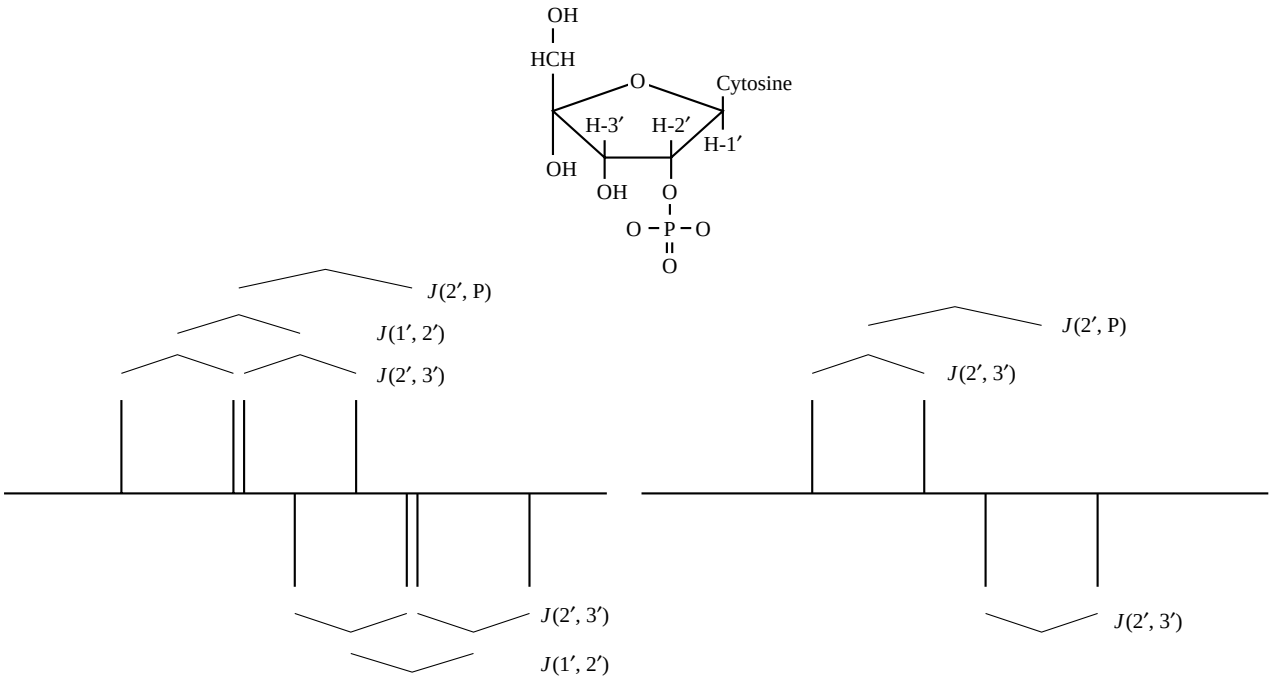

Figure 3 The predicted changes in the heteronuclear two-dimensional spectrum of cytosine 2′-monophosphate upon decoupling of the H-1′ proton are shown. The decoupling removes the H-1′–H-2′ coupling from the heteronuclear spectrum. (Adapted from Bodenhausen and Bolton[6])

Figure 4 The spectrum on the top left is the experimental heteronuclear chemical shift correlation spectrum of 2′-CMP and on the bottom left the predicted spectrum. The spectrum on the top right is the experimental heteronuclear chemical shift correlation spectrum of 2′-CMP obtained with decoupling of the H-1′ proton and on the bottom right the predicted spectrum. (Adapted from Bodenhausen and Bolton[6])

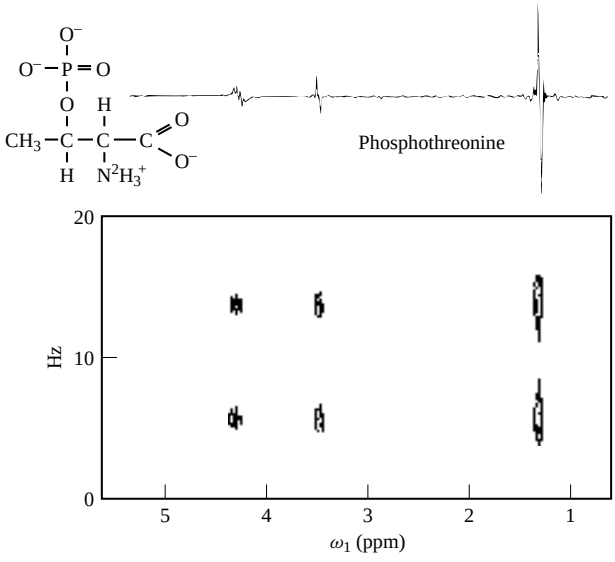

Figure 5 The two-dimensional spectrum is a relay transfer data set obtained on a sample of phosphothreonine. Along the vertical axis is the ^{31}P frequency and along the horizontal the proton frequencies. The heteronuclear coupling is present in each dimension. The trace shown at the top is in the phase sensitive mode. (Adapted from Bolton and Bodenhausen[9])

magnetization to become in-phase to allow acquisition of the data with proton decoupling.

Consider the case of 1-pentanol, which is $C_{(5)}H_3-C_{(4)}H_2-C_{(3)}H_2-C_{(2)}H_2-C_{(1)}H_2-OH$. Carbon-5 will correlate with its neighbor protons as well the remote protons attached to carbon-4. Carbon-4 will correlate with the remote protons

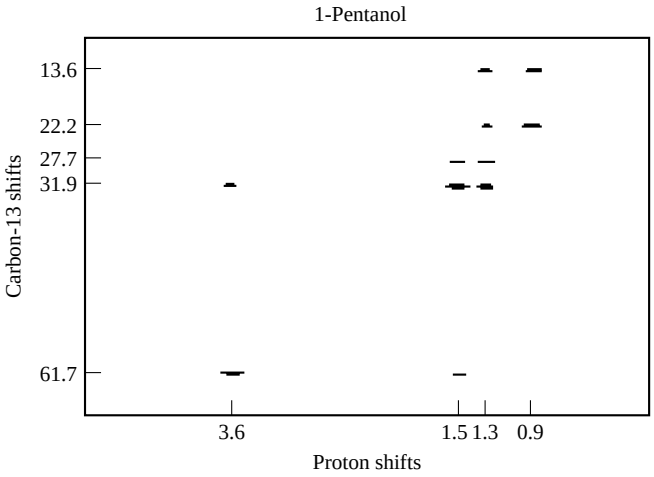

Figure 6 A two-dimensional spectrum relay transfer data set obtained on 1-pentanol. (Adapted from Eich et al.[11])

of carbon-5 and carbon-3 as well as its own neighbor protons. Thus, a single relay experiment on a molecule like pentanol can allow complete sequential assignment of both the proton and ^{13}C spectra, since each carbon will correlate not only with its neighbor protons but the remote protons on adjacent carbons. Thus, the relay data can allow the sequential assignments of the carbon and proton resonances.[10] The spectrum in Figure 6 shows that the relay transfer information does indeed allow the sequential connectivities to be made. The only additional information which is needed is to be able to assign cross peaks to the neighbor and remote categories. This can be done either by comparison with a heteronuclear two-dimensional experiment or by elimination of the neighbor signals.

Almost simultaneously with the introduction of the heteronuclear relay transfer experiments, Eich, Bodenhausen and Ernst demonstrated homonuclear relay transfer experiments.[11] These experiments were based on the same principles as the heteronuclear relay transfer experiments.

The original versions of the relay transfer experiments were modified to include improved phase cycling and methods to discriminate between neighbor and remote protons; multiple quantum versions were introduced as were constant time variations. These procedures allowed a number of systems to be investigated. The product operator description of relay transfer experiments can be found elsewhere.[9,12] The main impact of relay transfer experiments was the demonstration that two, or more, two-dimensional experiments could be combined to yield a new experiment more powerful than any combination of the results of the individual experiments.

3 THE DEVELOPMENT OF RELAY TRANSFER EXPERIMENTS

Subsequent to the original introduction of heteronuclear relay transfer experiments there have been three types of significant improvements in the experimental approach. The original experiments relied on free precession of the protons during the mixing time to obtain magnetization which contained at least some antiphase character with respect to both the proton

and heteronucleus.[9,10,13] More uniform proton–proton transfer can be obtained by the use of a homonuclear spin lock during the magnetization transfer followed by an INEPT, or analogous, heteronuclear transfer.[14,15] This procedure allows heteronuclear relay transfer experiments to be successfully carried out on a wide range of spin systems. The use of homonuclear spin locks is discussed elsewhere in this Encyclopedia.

A major improvement in the sensitivity of the heteronuclear relay transfer experiment was the conversion to proton detection.[16] In the proton detection heteronuclear relay transfer experiments, the proton magnetization is transferred to the heteronucleus which is then allowed to precess. The magnetization is then transferred back to the neighbor protons. The magnetization can then be transferred to the remote protons and, with a spin lock throughout the proton spin system, the magnetizations of both the remote and neighbor protons detected. The original proton detection relay transfer experiments were carried out without the use of spin locks[16] and the first application to a labeled protein occured in 1986.[17] The proton detection versions of heteronuclear relay transfer currently in use are heteronuclear single quantum spectroscopy (HSQC)–TOCSY, heteronuclear multiple quantum spectroscopy (HMQC)–NOESY, and so on.[18–21] Proton–phosphorus relay correlations are now being performed via three-dimensional experiments which transfer magnetization via spin locks from phosphorus to neighbor protons to remote protons on DNA at millimolar concentrations.[22]

The conversion of heteronuclear relay transfer experiments into three-dimensional experiments is accomplished by the use of an evolution time rather than a constant mixing time. This allows experiments to be performed in which the neighbor-remote proton connectivities are in two-dimensional planes resolved by the frequencies of the spy nucleus along the third frequency axis. Three-dimensional HSQC–TOCSY experiments, for example, can be thought of as the combination of two, two-dimensional experiments into a three-dimensional experiment. Extensions to four- and five-dimensional experiments have also been made. The availability of isotopically labeled biological materials has made the development and application of these types of experiments powerful tools for studying the structure and dynamics of proteins and nucleic acids.

The original version of the heteronuclear relay transfer experiment has been vastly superseded by its offspring, both in terms of sensitivity and resolution. Improvements in the sensitivity and resolution of the two-dimensional heteronuclear relay experiment continue to be developed.[23] The fundamental idea of the relay transfer experiments, which is to combine two or more magnetization transfers to obtain a new experiment which contains more information than is present in the results of both of the parent experiments, has remained a very fruitful idea.

4 RELATED ARTICLES

Double Resonance; Heteronuclear Assignment Techniques; Heteronuclear Shift Correlation Spectroscopy; Three-Dimensional HMQC-NOESY, NOESY-HMQC, and NOESY-HSQC; Three- and Four-Dimensional Heteronuclear Magnetic Resonance.

5 REFERENCES

1. P. H. Bolton and G. Bodenhausen, *J. Am. Chem. Soc.*, 1979, **101**, 1080.
2. P. H. Bolton, *J. Magn. Reson.*, 1983, **52**, 326.
3. P. H. Bolton, *J. Magn. Reson.*, 1981, **45**, 239.
4. P. H. Bolton, *J. Magn. Reson.*, 1984, **60**, 342.
5. P. H. Bolton, *J. Magn. Reson.*, 1984, **57**, 427.
6. G. Bodenhausen and P. H. Bolton, *J. Magn. Reson.*, 1980, **39**, 399.
7. P. H. Bolton, *J. Magn. Reson.*, 1982, **46**, 91.
8. P. H. Bolton and G. Bodenhausen, *J. Magn. Reson.*, 1981, **43**, 339.
9. P. H. Bolton and G. Bodenhausen, *Chem. Phys. Lett.*, 1982, **89**, 139.
10. P. H. Bolton, *J. Magn. Reson.*, 1982, **48**, 336.
11. G. W. Eich, G. Bodenhausen, and R. R. Ernst, *J. Am. Chem. Soc.*, 1982, **104**, 3731.
12. R. R. Ernst, G. Bodenhausen, and A. Wokaun, *Principles of Magnetic Resonance in One and Two Dimensions*, Oxford University Press, Oxford, 1987.
13. P. H. Bolton, *J. Magn. Reson.*, 1983, **54**, 333.
14. A. Bax, D. G. Davis, and S. K. Sarkar, *J. Magn. Reson.*, 1985, **63**, 230.
15. L. Lerner and A. Bax, *J. Magn. Reson.*, 1986, **69**, 375.
16. P. H. Bolton, *J. Magn. Reson.*, 1985, **62**, 143.
17. J. A. Wilde, P. H. Bolton, N. J. Stolowich, and J. A. Gerlt, *J. Magn. Reson.*, 1986, **68**, 168.
18. G. Otting and K. Wüthrich, *J. Magn. Reson.*, 1988, **76**, 569.
19. L. Müller, *J. Am. Chem. Soc.*, 1979, **101**, 4481.
20. T. J. Norwood, J. Boyd, J. E. Heritage, N. Soffe, and I. D. Campbell, *J. Magn. Reson.*, 1990, **87**, 488.
21. G. Bodenhausen and D. J. Ruben, *Chem. Phys. Lett.*, 1980, **69**, 185.
22. K. Y. Wang, I. Goljer, and P. H. Bolton, *J. Magn. Reson., Ser. B*, 1994, **103**, 192.
23. J. Cavanagh, A. G. Palmer, P. E. Wright, and M. Rance, *J. Magn. Reson.*, 1991, **91**, 429.

Biographical Sketch

Philip H. Bolton. *b* 1950. B.S., 1972, chemical physics, Michigan State University, Ph.D., 1976, University of California, San Diego (supervisor David R. Kearns). Postdoctoral work with David R. Kearns at University of California, San Diego, 1976–78, and with Thomas L. James at University of California, San Francisco, 1978–79. Faculty in Chemistry at Wesleyan University, 1979–present. Approximately 100 publications. Research specialties: NMR and molecular modeling of aptamer, damaged and telomere DNAs, and proteins involved in DNA repair.

Selective Hartmann–Hahn Transfer in Liquids

Geoffrey Bodenhausen
Université de Lausanne, Switzerland/Florida State University and National High Magnetic Field Laboratory, Tallahassee, FL, USA

1	Introduction	1
2	Hamiltonian and Coherence Transfer	1
3	Decoupling and Relaxation Effects	3
4	One-Dimensional Applications	3
5	Use in Selective Two-Dimensional Spectroscopy	4
6	Related Articles	5
7	References	5

1 INTRODUCTION

Of the numerous methods that have been devised for manipulating magnetization, the cross-polarization method invented by Hartmann and Hahn (see also ***Cross Polarization in Solids***) may be regarded as one of the most ingenious.[1] It is also one of the most difficult experiments to explain in simple pedagogical terms, since semiclassical vector pictures do not appear to provide adequate insight. Historically, cross polarization was first developed for use in solids, more specifically to bring about a transfer of magnetization between unlike spins such as protons and ^{13}C, henceforth referred to as species I and S. Early experiments were not so much concerned with the idea of detecting the enhanced S magnetization, but rather with monitoring the loss of I magnetization that occurs during polarization transfer. Cross polarization gained a great deal of popularity when the emphasis was shifted to the detection of enhanced S nuclei,[2] particularly in combination with magic angle spinning.

In solids, a Hartmann–Hahn transfer by cross polarization can be described in terms of spin thermodynamics, using suitably defined heat reservoirs, with heat capacities and kinetic rates to describe the flow of order from one bath to another. This type of description is not applicable to magnetic resonance in liquids, for it presupposes large ensembles of coupled spin systems which only occur in solids with extensive dipolar interactions. Besides, the thermodynamic description remained for many years unfamiliar to most specialists of liquid state NMR, so that cross polarization tended to be confined to solid state applications. It was perhaps fortunate that the thermodynamic description was not completely satisfactory to describe the behavior in solids, particularly for materials that contain reasonably isolated spin pairs I and S, such as ferrocene. Indeed, among other things, the thermodynamic description failed to account for the appearance of so-called transient oscillations in cross polarization.[3] These phenomena could however be understood by adapting to the solid state the density-operator approach which is commonly used for the description of scalar-coupled spin systems in liquids.[3]

Once it had become clear that cross polarization could be described as a coherent effect, and that the relevant (heteronuclear) coupling Hamiltonian which drives the phenomenon has the same form $\hat{I}_z\hat{S}_z$ in dipole-coupled solids as in scalar-coupled liquids, the main obstacle to cross fertilization from solids to liquids was removed. This lead to detailed studies[4,5] of heteronuclear Hartmann–Hahn effects in liquids, using simultaneous nonselective spin locking of both species I and S. That Hartmann–Hahn effects could also occur between *like* spins (e.g. between two protons I^{A} and I^{X}) was, in a sense, tacitly assumed in the early thermodynamic description, but this feature could not be exploited for any useful purpose until the advent of two-dimensional Fourier transform spectroscopy. The use of homonuclear Hartmann–Hahn effects in nonselective two-dimensional correlation spectroscopy lead to TOtal Correlation SpectroscopY (TOCSY), which is today one of the most popular tools in the arsenal of multidimensional NMR.[6] It derives its name from the fact that the magnetization is transferred between all spins belonging to a common network of scalar-coupled spins. This method is sometimes referred to as 'HOmonuclear HArtmann–HAhn' (HOHAHA) spectroscopy. The choice of nomenclature merely reflects a preference for one or the other of the schools of thought that have given birth to these abbreviations.

In this article, we focus attention on Hartmann–Hahn effects that arise under doubly-selective irradiation. Such effects cannot give rise to 'total' coherence transfer processes as encountered in TOCSY, hence the expression 'doubly-selective homonuclear Hartmann–Hahn' (DS-HOHAHA) for this type of experiment.

2 HAMILTONIAN AND COHERENCE TRANSFER

Consider for simplicity two weakly scalar-coupled spins I^{A} and I^{X} with $I = \frac{1}{2}$, such as two protons, which are subjected to two selective radiofrequency (rf) fields that are applied precisely on-resonance at the two chemical shifts ν_{A} and ν_{X}. We assume that the rf amplitudes $\nu_{1\mathrm{A}}$ and $\nu_{1\mathrm{X}}$ of these two rf fields are precisely equal. This can be easily achieved in practice by setting the rf carrier frequency half-way between the two chemical shifts, $\nu_{\mathrm{c}} = (\nu_{\mathrm{A}} + \nu_{\mathrm{X}})/2$, and by modulating the shape of the rf pulse with a cosine-wave, i.e. by multiplying the envelope with $\cos \nu_{\mathrm{a}}t$, where $\nu_{\mathrm{a}} = (\nu_{\mathrm{A}} - \nu_{\mathrm{X}})/2$, so that the rf spectrum splits into two sidebands which coincide with the two chemical shifts ν_{A} and ν_{X}. Each sideband has an amplitude $\nu_1 = \nu_{1\mathrm{A}} = \nu_{1\mathrm{X}}$. In the usual laboratory frame, the Hamiltonian is:

$$\begin{aligned}\hat{\mathcal{H}} = {} & 2\pi\nu_{\mathrm{A}}\hat{I}_z^{\mathrm{A}} + 2\pi\nu_{\mathrm{X}}\hat{I}_z^{\mathrm{X}} \\ & + 4\pi\nu_1 \cos 2\pi\nu_{\mathrm{a}}t[(\hat{I}_x^{\mathrm{A}} + \hat{I}_x^{\mathrm{X}})\cos 2\pi\nu_{\mathrm{c}}t \\ & + (\hat{I}_y^{\mathrm{A}} + \hat{I}_y^{\mathrm{X}})\sin 2\pi\nu_{\mathrm{c}}t] + \pi J_{\mathrm{AX}} 2\hat{I}_z^{\mathrm{A}}\hat{I}_z^{\mathrm{X}} \end{aligned} \quad (1)$$

This Hamiltonian can be simplified[7] by transformation into a frame rotating at the average precession frequency $\nu_{\mathrm{c}} = (\nu_{\mathrm{A}} + \nu_{\mathrm{X}})/2$, which leads to:

$$\begin{aligned}\hat{\mathcal{H}} = {} & 2\pi\nu_{\mathrm{a}}\hat{I}_z^{\mathrm{A}} - 2\pi\nu_{\mathrm{a}}\hat{I}_z^{\mathrm{X}} + 4\pi\nu_1 \cos 2\pi\nu_{\mathrm{a}}t(\hat{I}_x^{\mathrm{A}} + \hat{I}_x^{\mathrm{X}}) \\ & + \pi J_{\mathrm{AX}} 2\hat{I}_z^{\mathrm{A}}\hat{I}_z^{\mathrm{X}} \end{aligned} \quad (2)$$

A second transformation[7] into a doubly-rotating frame, also called interaction frame, leads to the removal of the first two terms, which correspond to Zeeman interactions. If we neglect time-dependent nonsecular terms, which describe the weak interaction of the rf field component rotating at ν_A with spin I^X and of the rf component at ν_X with spin I^A, one obtains the simple form:

$$\hat{\mathcal{H}} = 2\pi\nu_1(\hat{I}_x^A + \hat{I}_x^X) + \pi J_{AX} 2\hat{I}_z^A \hat{I}_z^X \tag{3}$$

The effect of this Hamiltonian on an arbitrary initial condition can be calculated analytically.[7] If we assume for simplicity that the initial density operator σ has the following form at the beginning of the Doubly-Selective Irradiation (DSI) interval τ_{DSI}:

$$\sigma(\tau_{DSI} = 0) = \hat{I}_x^A \tag{4}$$

it can be shown that this in-phase coherence is transformed into a superposition of six terms:

$$\langle \hat{I}_x^A \rangle(\tau_{DSI}) = (1/2)[\cos\omega_J\tau_{DSI} + (\omega_J/\omega_{eff})^2 \cos\omega_{eff}\tau_{DSI} + (2\omega_1/\omega_{eff})^2] \tag{5}$$

$$\langle \hat{I}_x^X \rangle(\tau_{DSI}) = (1/2)[-\cos\omega_J\tau_{DSI} + (\omega_J/\omega_{eff})^2 \cos\omega_{eff}\tau_{DSI} + (2\omega_1/\omega_{eff})^2] \tag{6}$$

$$\langle 2\hat{I}_y^A \hat{I}_z^X \rangle(\tau_{DSI}) = (1/2)[\sin\omega_J\tau_{DSI} + (\omega_J/\omega_{eff}) \sin\omega_{eff}\tau_{DSI}] \tag{7}$$

$$\langle 2\hat{I}_z^A \hat{I}_y^X \rangle(\tau_{DSI}) = (1/2)[-\sin\omega_J\tau_{DSI} + (\omega_J/\omega_{eff}) \sin\omega_{eff}\tau_{DSI}] \tag{8}$$

$$\langle 2\hat{I}_z^A \hat{I}_z^X \rangle(\tau_{DSI}) = (\omega_1\omega_J/\omega_{eff}^2)(1 - \cos\omega_{eff}\tau_{DSI}) \tag{9}$$

$$\langle 2\hat{I}_y^A \hat{I}_y^X \rangle(\tau_{DSI}) = -(\omega_1\omega_J/\omega_{eff}^2)(1 - \cos\omega_{eff}\tau_{DSI}) \tag{10}$$

where $\omega_J = \pi J$ and $\omega_{eff} = (4\omega_1^2 + \pi^2 J^2)^{\frac{1}{2}}$. The remaining 10 terms that could arise in the 16-dimensional density operator of an isolated two-spin system remain equal to zero. The expectation values of equations (5)–(10) are shown graphically in Figure 1 as a function of the doubly-selective irradiation period τ_{DSI}. It should be noted that for $\tau_{DSI} = 1/J_{AX}$, the in-phase term $\hat{I}_x^A$ is *completely* converted into in-phase magnetization $\hat{I}_x^X$. However, if τ_{DSI} is not precisely 'matched' to the inverse of the coupling constant (either because the latter is not known, or because relaxation makes it desirable to keep the transfer period as short as possible), one cannot avoid the appearance of antiphase terms $< 2\hat{I}_y\hat{I}_z^X >$ and $< 2\hat{I}_z^A\hat{I}_y^X >$,

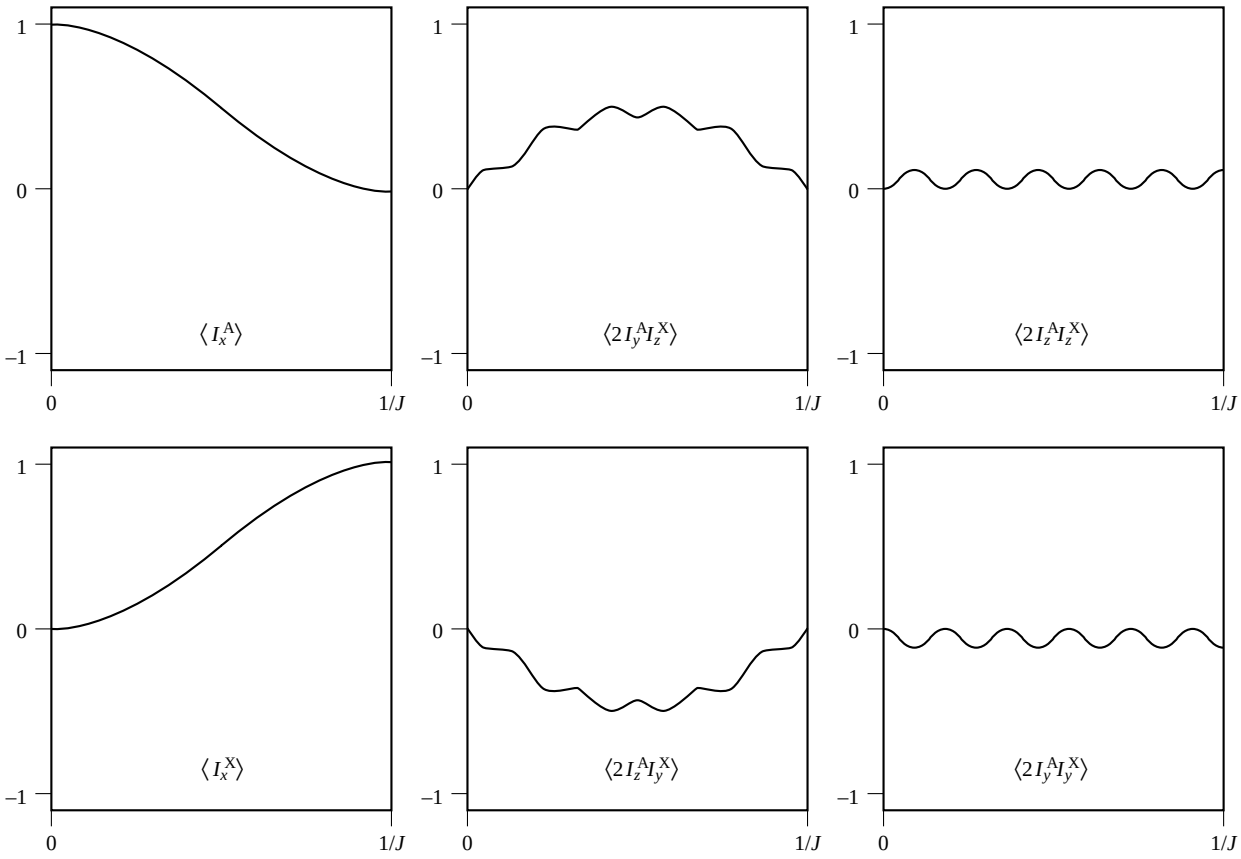

Figure 1 Expectation values of the six nonvanishing components of the density operator of a scalar-coupled two-spin system in the course of doubly-selective Hartmann–Hahn transfer, starting with in-phase magnetization of spin I^A as described by equations (5)–(10). (Reproduced by permission of North-Holland Elsevier Science Publishers from Zwahlen et al.[7])

of longitudinal two-spin order $< 2\hat{I}_z^{\mathrm{A}}\hat{I}_z^{\mathrm{X}} >$, and of the two-spin term $< 2\hat{I}_y^{\mathrm{A}}\hat{I}_y^{\mathrm{X}} >$, which corresponds to a superposition of zero- and double-quantum coherences. In some experiments, it is necessary to eliminate these undesirable terms by some combination of selective pulses, phase cycling, or gradient suppression schemes.

3 DECOUPLING AND RELAXATION EFFECTS

It is a remarkable feature of selective Hartmann–Hahn transfer in liquids that the two nuclei I^{A} and I^{X} that are irradiated selectively are in effect *decoupled* from all other spins in their environment. This can be rationalized by noting that the two selected spins are both spin locked and hence quantized in the transverse plane, while all other spins (whether of the same species, e.g. protons, or of other, 'heteronuclear' species, such as ^{13}C) are not perturbed and hence remain quantized along the longitudinal axis. This implies that the transfer of coherence is *highly directional*, i.e. that the coherence cannot propagate to any other spins in the coupling network, except if they are degenerate in chemical shift and hence also affected by one of the selective spin locking fields. This 'directional' feature may be appreciated in Figure 2, which illustrates a transfer of in-phase magnetization in a high-resolution proton spectrum of a peptide. This stands in contrast to nonselective Hartmann–Hahn transfer as it occurs in TOCSY,[6] where the coherence is 'spread out' among all coupling partners, so that the signal intensities depend on the magnitudes of all scalar coupling constants in the network.

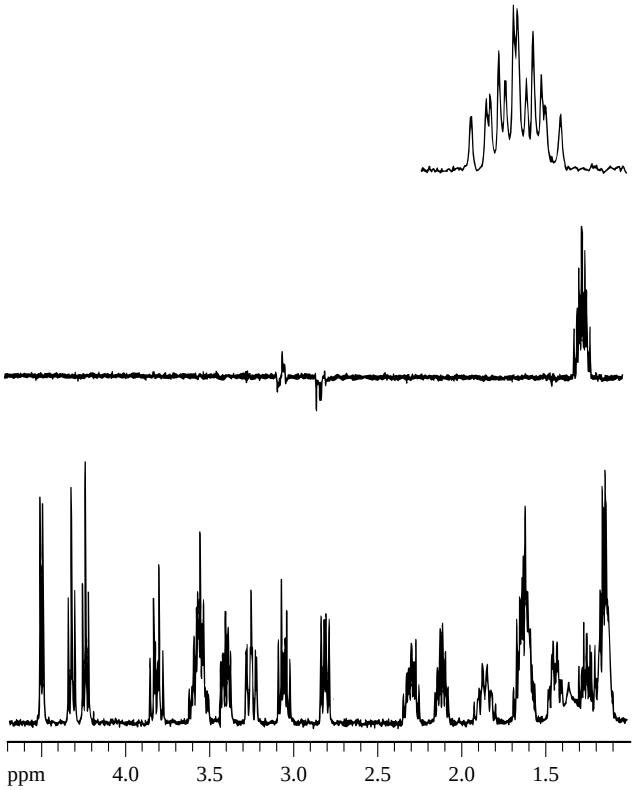

Figure 2 Doubly-selective Hartmann–Hahn transfer in a high-resolution proton spectrum of *cyclo*-triproline. Bottom: conventional one-dimensional 400 MHz proton spectrum with partly overlapping multiplets belonging to three coupling networks with seven protons each. Middle: isolated multiplet belonging to an H^{β} proton at 1.2 ppm, obtained by selective excitation of the corresponding H^{α} proton by a 270° Gaussian pulse at 2.8 ppm, followed by doubly-selective Hartmann–Hahn transfer from H^{α} to H^{β} by simultaneous irradiation at 2.8 and 1.2 ppm. Top: enlarged multiplet of H^{β} proton showing fine structure due to interactions with four coupling partners H^{α}, $H^{\beta'}$, H^{γ}, and $H^{\gamma'}$

On the other hand, the efficiency of the doubly-selective Hartmann–Hahn transfer is limited by relaxation. The Hamiltonian of equation (3) contains only one bilinear term $\pi J_{\mathrm{AX}} 2\hat{I}_z^{\mathrm{A}}\hat{I}_z^{\mathrm{X}}$ (as opposed to two terms $\pi J_{\mathrm{AX}} 2\hat{I}_z^{\mathrm{A}}\hat{I}_z^{\mathrm{X}} + \pi J_{\mathrm{AX}} 2\hat{I}_y^{\mathrm{A}}\hat{I}_y^{\mathrm{X}}$ that arise in TOCSY), so that the transfer from I^{A} to I^{X} is optimum for $\tau_{\mathrm{DSI}}{}^{\mathrm{opt}} = (J_{\mathrm{AX}})^{-1}$. This stands in contrast to $\tau_{\mathrm{DSI}}{}^{\mathrm{opt}} = (2J_{\mathrm{AX}})^{-1}$ for TOCSY and other nonselective Hartmann–Hahn experiments. Thus the signal intensity that can be obtained with the directional doubly-selective Hartmann–Hahn method may suffer from relaxation, particularly in macromolecules. It should be noted that the relevant relaxation time is $T_{1\rho}$ rather than T_2, and that, for a variety of reasons,[8] $T_{1\rho}$ can be longer than T_2 and hence more favorable.

It is also possible to achieve homonuclear Hartmann–Hahn effects with modified Hamiltonians so that the trajectories in Liouville space depend in a different manner on longitudinal and transverse relaxation. This applies to TAilored Correlation SpectroscopY (TACSY),[9] and to broadband FLOPSY methods[10] used in combination with DANTE-like intervals,[11] all of which have more favorable profiles (transfer efficiency as a function of offset) than straight doubly-selective irradiation.

4 ONE-DIMENSIONAL APPLICATIONS

The example of Figure 2 shows how a selective transfer makes it possible to separate multiplets which suffer from extensive overlap in normal one-dimensional spectra.[12] To record such multiplets, some previous knowledge about the chemical shifts is of course required. The shifts of a coupled pair of spins are normally estimated from a low-resolution two-dimensional correlation spectrum (COSY), but the scalar coupling need not be known, since the duration of the doubly-selective irradiation interval τ_{DSI} can be calibrated empirically to optimize the transfer. The digital resolution of a multiplet such as that shown in Figure 2 is normally much better than that of a multiplet extracted from a two-dimensional spectrum. The doubly-selective Hartmann–Hahn method should therefore be regarded as a complement to (rather than a competitor of) two-dimensional correlation techniques.

Figure 3 shows another application of the selective Hartmann–Hahn effect: the measurement of relaxation parameters of nuclei with overlapping resonances.[8,13] This principle can easily be extended to encompass the determination of longitudinal relaxation rates ('T_1') by selective or nonselective inversion–recovery, the measurement of $T_{1\rho}$ by selective spin locking, and of T_2 by selective refocusing.[14] It is also possible to measure cross relaxation rates in a selective manner (see ***Selective NOESY***). In most cases, the methods used for probing relaxation phenomena are not innovative by themselves, and the Hartmann–Hahn transfer is simply used as a tool which allows one to pick up the magnetization of an arbitrary spin and to transfer it to a scalar-coupled partner. If the

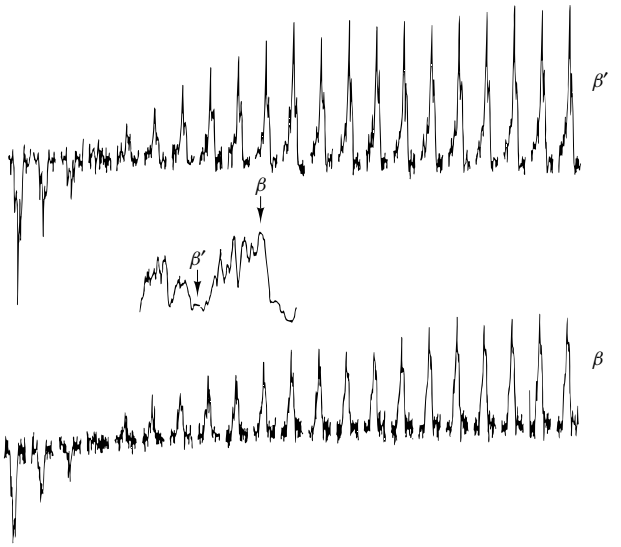

Figure 3 Measurement of longitudinal relaxation rate in cysteine-30 in basic pancreatic trypsine inhibitor. Center: expansion of the crowded H^{β} region of the one-dimensional proton spectrum at 300 MHz. Top: recovery monitored after selective inversion of $H^{\beta'}$, conversion of the partly recovered longitudinal magnetization into transverse magnetization by a Gaussian 270° pulse, and transfer by doubly-selective Hartmann–Hahn cross polarization from $H^{\beta'}$ to H^{β}. Bottom: recovery of H^{β} monitored by a doubly-selective Hartmann–Hahn transfer to $H^{\beta'}$. (Reproduced by permission of the American Chemical Society from Boulat et al.[13])

signals overlap heavily, it is possible to use several consecutive transfer steps, so that the resolving power approaches that of three- or higher-dimensional spectroscopy.[12,15,16]

5 USE IN SELECTIVE TWO-DIMENSIONAL SPECTROSCOPY

So far, the principle of doubly-selective Hartmann–Hahn transfer has found two distinct applications in the area of selective two-dimensional spectroscopy. It is possible to insert a Hartmann–Hahn transfer either in the preparation period or in the mixing interval. The first idea, which leads to a 'Separation of Patterns by Lifting the Imbroglio of Transfer' (SPLIT-COSY), is useful whenever two or more multiplets overlap in soft COSY spectra.[17] Typically, such a situation arises when an A–X cross peak belonging to a network R overlaps with an A′–X′ cross-peak arising from another network R′ because the chemical shifts of A and A′ on the one hand and of X and X′ on the other are nearly or completely degenerate. The multiplets can easily be separated provided that there exists at least one passive coupling partner K or K′ in one of the networks which does *not* suffer from overlap. In this case, selective excitation of transverse magnetization of K or K′ can be followed by one or several consecutive,[15,16] selective Hartmann–Hahn transfer steps so that one obtains in-phase magnetization of either of the nuclei A or A′. This is followed up by a normal soft COSY sequence (or, for that matter, by any other selective two-dimensional sequence), so that one can split overlapping patterns. An example is shown in Figure 4.

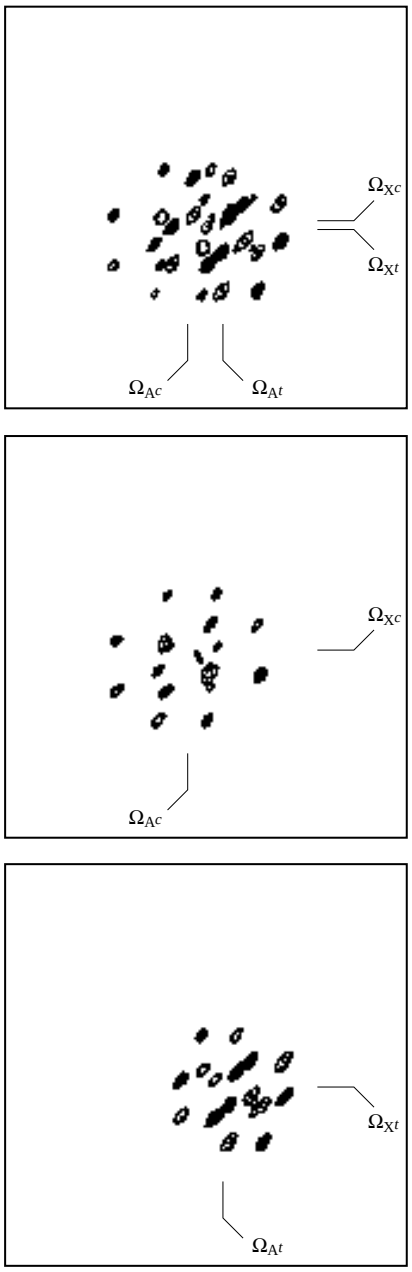

Figure 4 Separation of overlapping multiplets by SPLIT-COSY. Top: overlapping soft-COSY multiplets belonging to a mixture of *cis* (*c*)- and *trans* (*t*)-cyclopropane derivatives, due to coherence transfer from X^{cis} to A^{cis} and from X^{trans} to A^{trans}. Middle: SPLIT-COSY multiplet due to the *cis* isomer only, obtained by injecting magnetization from M^{cis} to X^{cis} in the preparation interval of the two-dimensional experiment. Bottom: SPLIT-COSY multiplet due to the *trans* isomer only, obtained by injection from M^{trans} to X^{trans} at the beginning of the evolution interval. (Reproduced by permission of Verlag Chemie from Vincent et al.[17])

A more sophisticated application of selective Hartmann–Hahn transfer to two-dimensional spectroscopy is used in Pure In-phase Correlation SpectroscopyY (PICSY), where a doubly-selective irradiation is inserted in the mixing period.[18] In this case, evolution under various scalar couplings leads to a manifold of antiphase terms at the beginning of the mixing period, some of which have to be eliminated by

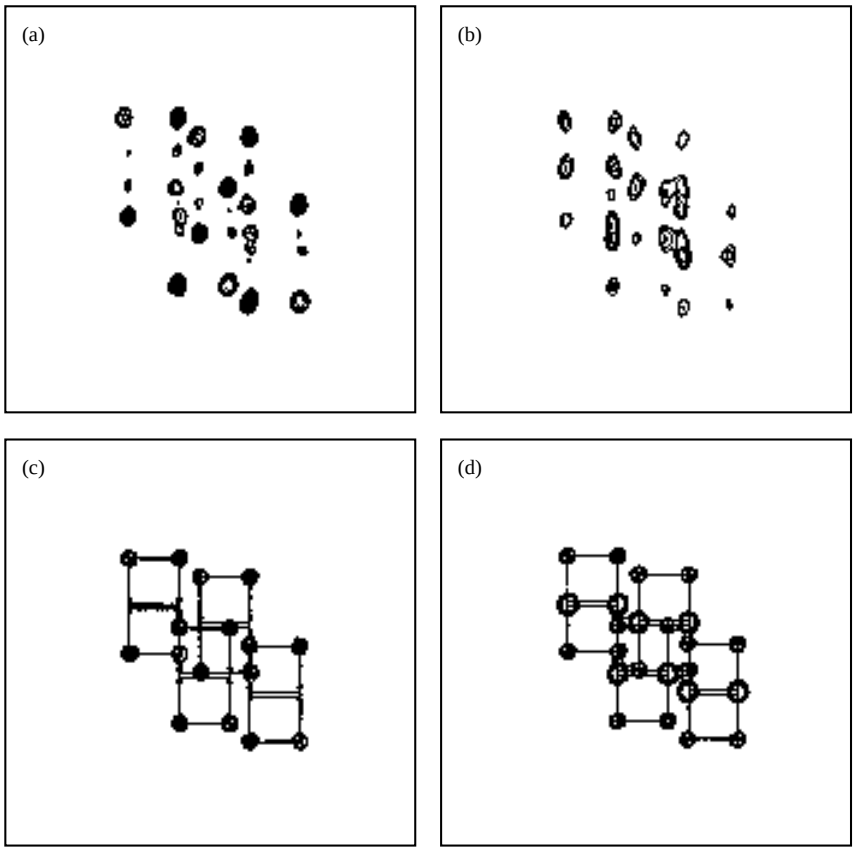

Figure 5 Multiplets correlating the γ^{cis} and δ^{cis} protons of D-proline (Pro) in *cyclo*(L-Pro-L-Pro-D-Pro). (a) Experimental soft-COSY multiplet. (b) In-phase multiplet obtained by PICSY. (c) Simulation corresponding to (a), showing the cancelation of signals with opposite signs (negative signals are filled in black). (d) Simulation corresponding to (b), showing the constructive interference of nearly-degenerate signals. (Reproduced by permission of the American Chemical Society from Vincent et al.[18])

suitable purging pulses. The resulting in-phase multiplets are particularly easy to analyze, since they do not suffer from cancelation of signals with opposite signs. The binomial rules that govern the amplitudes of multiplets are the same as in conventional one-dimensional spectra. An example is shown in Figure 5.

In conclusion, it appears that the selective transfer of magnetization by Hartmann–Hahn cross polarization in liquids opens a wide range of possibilities for the simplification of spectra and for the investigation of dynamic processes. The examples shown in the article are not intended to provide a complete overview.

6 RELATED ARTICLES

Cross Polarization in Solids; Selective NOESY.

7 REFERENCES

1. S. R. Hartmann and E. L. Hahn, *Phys. Rev.*, 1962, **128**, 2042.
2. A. Pines, M. G. Gibby, and J. S. Waugh, *J. Chem. Phys.*, 1973, **59**, 569.
3. L. Müller, Anil Kumar, T. Baumann, and R. R. Ernst, *Phys. Rev. Lett.*, 1974, **32**, 1402.
4. L. Müller and R. R. Ernst, *Mol. Phys.*, 1979, **38**, 963.
5. G. C. Chingas, A. N. Garroway, R. D. Bertrand, and W. B. Moniz, *J. Chem. Phys.*, 1981, **74**, 127.
6. L. Braunschweiler and R. R. Ernst, *J. Magn. Reson.*, 1983, **53**, 521.
7. C. Zwahlen, S. J. F. Vincent, and G. Bodenhausen, Proceedings of the International School of Physics *Enrico Fermi*, *Course CXXIII, Nuclear Magnetic Double Resonance*, ed. B. Maraviglia, North-Holland Publishers, Amsterdam, 1993.
8. B. Boulat and G. Bodenhausen, *J. Biomol. NMR*, 1993, **3**, 335.
9. S. J. Glaser, *J. Magn. Reson, Ser. A*, 1993, **104**, 283.
10. M. Kadkhodaie, O. Rivas, M. Tan, A. Mohebbi, and A. J. Shaka, *J. Magn. Reson.*, 1991, **91**, 437.
11. A. Mohebbi and A. J. Shaka, *J. Magn. Reson.*, 1991, **94**, 204.
12. R. Konrat, I. Burghardt, and G. Bodenhausen, *J. Am. Chem. Soc.*, 1991, **113**, 9135.
13. B. Boulat, R. Konrat, I. Burghardt, and G. Bodenhausen, *J. Am. Chem. Soc.*, 1992, **114**, 5412.
14. L. Emsley, J. Kowalewski and G. Bodenhausen, *Appl. Magn. Reson.*, 1990, **1**, 139.
15. E. Kupče and R. Freeman, *J. Magn. Reson.*, 1992, **100**, 208.
16. E. Kupče and R. Freeman, *J. Magn. Reson., Ser. A*, 1993, **101**, 225.
17. C. Zwahlen, S. J. F. Vincent, and G. Bodenhausen, *Angew. Chem., Int. Ed. Engl.*, 1992, **31**, 1248.
18. S. J. F. Vincent, C. Zwahlen, and G. Bodenhausen, *J. Am. Chem. Soc.*, 1993, **115**, 9202.

Biographical Sketch

Geoffrey Bodenhausen. *b* 1951. Diploma in Chemistry, ETH Zürich, Switzerland, 1974; D.Phil. with Ray Freeman, Oxford, 1977; worked with Robert and Regitze Vold at the University of California, San Diego, 1978; with Robert Griffin at the Francis Bitter National Magnet Laboratory at MIT (1979–1980); with Richard Ernst at ETH Zürich (1980–1985); associate professor at the University of Lausanne, Switzerland (1985–1994); professor at Florida State University and NMR Program Director at the National High Magnetic Field Laboratory, Tallahassee, FL (1994–present).

Sensitivity Enhancement Utilizing Parahydrogen

Clifford R. Bowers

University of Florida, Gainsville, FL, USA

1 Introduction 1
2 Nuclear Spin States of H_2 and D_2 1
3 General Theory of the PASADENA Effect 3
4 PASADENA Effect in Weakly Coupled Spin Systems 6
5 Experimental PASADENA NMR Spectroscopy in Liquids 9
6 The ALTADENA Effect 14
7 Theory of Ortho/Para D_2 Enhancement 16
8 PASADENA Effect at a Solid Surface 17
9 Conclusions 19
10 References 19

1 INTRODUCTION

In 1985, Weitekamp envisioned a phenomenon wherein the singlet state nuclear spin order associated with parahydrogen (p-H_2) could be converted into observable nuclear spin magnetization.[1] In this effect, which was given the acronym PASADENA (Parahydrogen and Synthesis Allows Dramatically Enhanced Nuclear Alignment),[2] a highly ordered nonequilibrium nuclear spin state distribution is obtained on the product of a hydrogenation reaction with H_2 enriched in the p-H_2 mole fraction. The proposal, together with the density operator theory of the PASADENA phenomenon, was published in 1986,[3] and the experimental demonstration came shortly thereafter.[4] The PASADENA enhanced proton spectrum of propionitrile resulting from the $Rh(I)(PPh_3)_3Cl$ catalyzed hydrogenation of acryolonitrile was shown to agree exactly with the density matrix simulation of the A_2X_3 proton spectrum. This was the first time a hydrogenation reaction had been knowingly conducted with the intention of converting the symmetrization order of para-enriched H_2 into enhanced NMR signals. Later that same year, Eisenshmid et al. confirmed the observation of the PASADENA effect in several other hydrogenation reactions.[5] By this time, it was also recognized that there were several previous reports of unusual NMR signal enhancements in hydrogenation reactions under conditions that, by happenstance, were ideal for the observation of PASADENA signal enhancement.[6–8] Understandably, the signals were in some cases misinterpreted as originating from a particular mechanism of chemically induced dynamic nuclear polarization (CIDNP).[9,10] An interesting historical account on these events has appeared in the literature.[11]

Since the original experimental demonstration of the PASADENA effect using Wilkinson's Catalyst, the phenomenon has been confirmed with many other hydrogenation catalysts, including $Rh_2H_2(CO)_2(dppm)_2$ (dppm = bis (diphenylphosphino) methane),[5] $[Rh_3(CO)_2Cl_2H_2((Ph_2PCH_2)_2PPh)_2]^+$,[5] $Pd_2Cl_2(dppm)_2$,[5] $Rh(diphos)^+$ (diphos = bis (dephenylphosphino)ethane),[12] $Ir(CO)(PPh)_2Cl$ (Vaska's catalyst),[3,12] and others complexes of Rh, Ir, Ru, Pt, and Os.[13] Furthermore, the basic PASADENA effect has been coupled to a variety of one and two-dimensional NMR pulse sequences.[12–14] For example, the sharing of the p-H_2 singlet spin order with other nuclei (protons, ^{13}C, ^{31}P, ^{15}N, etc.) via evolution under scalar or dipolar interactions has been demonstrated.[15] The kinetics and mechanisms of several hydrogenation reactions has been investigated in detail using p-H_2 as a spin label. In some cases, new intermediates have been made observable as a result of the signal enhancement.[12,16–18] PASADENA NMR spectroscopy has also been extended to two time dimensions for the purpose of probing chemical exchange and for mapping coupling connectivities.[12–14]

Due to space limitations, it is possible to mention only a fraction of the examples of chemical applications and pulse sequences that have been developed over the past 15 years. Fortunately, there are several other reviews describing the chemical applications and pulse sequence methodology in p-H_2 enhanced NMR spectroscopy.[13,14] The emphasis of this article is on the density operator/matrix theory of the PASADENA technique along with several demonstrative chemical applications. NMR signals are calculated for spin systems in the solution state and at a solid surface. Next, a brief review of the ALTADENA effect (Adiabatic Longitudinal Transport After Dissociation Engenders Net Alignment) will be presented. This is followed by a presentation of the theory for deuteron NMR enhancement by chemical addition of ortho-enriched D_2, where the ground rotational state corresponds to symmetric (ortho) nuclear spin states. Finally, the first experimental demonstration of proton NMR enhancement by the PASADENA effect at a surface is described.

2 NUCLEAR SPIN STATES OF H_2 AND D_2

2.1 Dihydrogen Wave Function

The total wave function of any homonuclear diatomic must be formulated in accordance with the Pauli Exclusion Principle which in essence states that the total wave function must be antisymmetric with respect to permutation of the nuclear labels in the case of half-integer nuclei, and symmetric for permutation of nuclei with integral or zero spin. For H_2 and D_2, the ground electronic state is $^1\Sigma_g^+$, a symmetric function with respect to inversion and reflection of the electronic coordinates. In the Born-Oppenheimer, rigid-rotor approximation, the overall wave function may be factored as follows:

$$\Psi_{\text{tot}} = \psi_e \psi_v \psi_r \psi_n \tag{1}$$

Consequently, the symmetries of the rotational and nuclear spin functions are correlated. In the case of H_2, the nuclear spin state must be symmetric when the molecule occupies an antisymmetric, odd J-valued rotational state. For $I = 1/2$, the nuclear spin triplet functions corresponding to the sum of

the angular momenta, $I_1 + I_2 = I = 1$, are symmetric, while the singlet spin state corresponding to $I_1 - I_2 = I = 0$ is antisymmetric. Hydrogen in the symmetric nuclear spin state is known as orthohydrogen (o-H_2), while parahydrogen (p-H_2) refers to molecules in the antisymmetric nuclear spin state:

$$|\psi_{\text{ortho}}\rangle = \begin{cases} |\beta\beta\rangle & m_1 = -1 \\ \frac{1}{\sqrt{2}}(|\alpha\beta\rangle + |\beta\alpha\rangle), & m_1 = 0 \text{ (odd } j) \\ |\alpha\alpha\rangle, & m_1 = +1 \end{cases} \quad (2)$$

$$|\psi_{\text{para}}\rangle = \frac{1}{\sqrt{2}}(|\alpha\beta\rangle - |\beta\alpha\rangle) \text{ (even } j) \quad (3)$$

These nuclear spin functions are eigenfunctions of the permutation operator $\hat{\mathcal{P}}_n$ with eigenvalues of ± 1: $\hat{\mathcal{P}}_n \psi_n = \pm \psi_n$. In addition, the two states Ψ_{tot} (1,2) and Ψ_{tot} (2,1) are exchange degenerate since the total molecular Hamiltonian $\hat{\mathcal{H}}$ is necessarily a symmetric operator. Thus, $\hat{\mathcal{H}}\hat{\mathcal{P}}\Psi_{\text{tot}} = \hat{\mathcal{P}}\hat{\mathcal{H}}\Psi_{\text{tot}}$ and the two operators commute: $[\hat{\mathcal{P}}, \hat{\mathcal{H}}] = 0$. Consequently the singlet and triplet nuclear spin states are also eigenfunctions of the nuclear spin Hamiltonian of the molecule. In its application to H_2 and D_2, the Pauli Exclusion principle is responsible for the following properties:

(1) Symmetry considerations based on symmetry lead to several remarkable features of H_2 and D_2. These gases can exist in either of two distinct quasi-stable forms: the para (antisymmetric) and ortho (symmetric) nuclear spin states. Since transitions between singlet and triplet nuclear spin states are magnetic dipole forbidden, it is possible to prepare a quasi-stable nonequilibrium ortho-para H_2 mixture. It was Dennison who first realized that the interconversion of o-H_2 to p-H_2 was extremely slow in the absence of a catalyst.[19]

(2) The degeneracy of the o-H_2 rotational levels is $3(2j + 1)$ while the degeneracy of the p-H_2 levels is $2j + 1$. As a result, the ortho : para ratio of an H_2 sample in the high temperature regime ($T \gg \theta_r$), referred to as n-H_2, approaches 3 : 1, while the ortho : para ratio of n-D_2 approaches 2 : 1.

(3) At sufficiently low temperature ($T \leq \Theta_r$ i.e., where Θ is the characteristic temperature of rotation) there will be a substantial enrichment of p-H_2 (or o-D_2). The interconversion may be catalyzed by a paramagnetic solid such as activated charcoal[20] or iron filings. Commercial catalysts such as Apachi (a nickel silica gel) have been developed.[21] The mechanism for interconversion depends on the type of catalyst. One mechanism involves chemisorption of H_2 to form atomic hydrogen. Spin-lattice relaxation, and subsequent recombination result in the thermal equilibrium mixture composition. Alternatively, the paramagnetic solid may provide field gradients on the molecular scale that break the magnetic equivalence of the protons, allowing the ortho-para transitions to become slightly allowed due to single-triplet mixing.

(4) Once enriched at low temperature, the gas can be removed from the catalyst, warmed, and stored for days without significant reconversion. A convenient temperature at which to perform the enrichment is 77 K where the equilibrium p-H_2 mole fraction is $\chi_p = 0.51$ while the equilibrium o-D_2 mole fraction is $\chi_o = 0.70$. Thus, it is the rotational constant that determines the energy separation of the $I = 0$ and $I = 1$ nuclear spin states in this strongly coupled spin system rather than differences in the nuclear Zeeman energy as is the usual case for nuclear spin systems in a molecule with symmetry number $\sigma = 1$.

The equilibrium ortho-para composition of H_2 or D_2 can be derived from the rigid rotor partition function. For H_2, the ortho-para ratio is:

$$\frac{N_{\text{ortho}}}{N_{\text{para}}} = \frac{3 \sum_{j=1,3,\ldots} (2j+1) e^{-\Theta_r j(j+1)/T}}{\sum_{j=0,2,\ldots} (2j+1) e^{-\Theta_r j(j+1)/T}} \quad (4)$$

where $\Theta_R = \hbar^2/2kA$, $A = \mu r_{12}^2$ is the moment of inertia for the internuclear separation r_{12}, and $\mu = m_1 m_2/(m_1 + m_2)$ is the reduced mass of the homonuclear diatomic molecule. The percentage composition of p-H_2 and o-H_2 is plotted in Figure 1. Since the characteristic temperature of rotation of H_2 is $\Theta_r = 85.3$ K, the low temperature regime (with respect to rotation) is relatively easy to access, and is well above the boiling point of the gas. It follows that thermal equilibration of a volume of H_2 gas at 77 K should produce an appreciable enrichment of the para spin isomer. Indeed, the percentage of molecules in the singlet nuclear spin state is 51% at this temperature (compared to approximately 25% at 300 K). One might expect a substantial enhancement of the NMR absorption signal following equilibration of the gas at 77 K. The problem is that the symmetrization order of the rotationally cooled gas in not observable by NMR because the singlet-triplet magnetic dipole transition is strictly forbidden. In fact, the only NMR signal that can be detected from the H_2 gas is due to transitions among the triplet states, but in this manifold, the Boltzmann factor is determined by the nuclear Zeeman interaction rather than the rotational splitting, yielding population differences on the order of only tens of parts per million at typical NMR fields. However, it turns out to be possible to transform the symmetrization order associated with p-H_2 into dramatic NMR signal enhancements if the molecule is deposited into a symmetry breaking magnetic environment

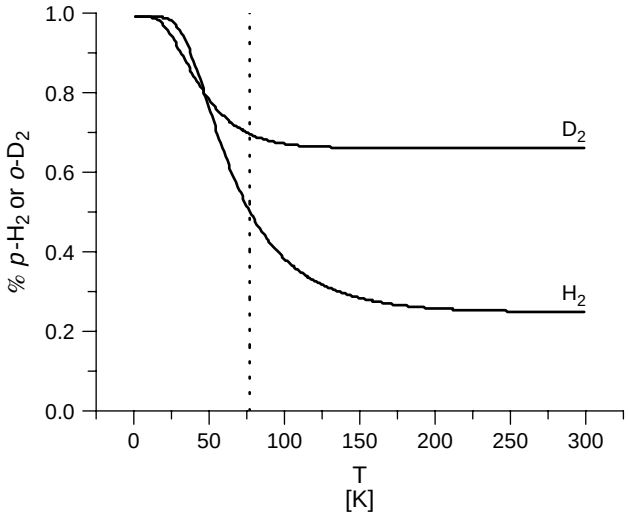

Figure 1 Percentage composition of p-H_2 or o-D_2 as a function of temperature

wherein the protons of the original H_2 molecule remain coupled. The analogous phenomenon is expected for D_2.

2.2 Nuclear Spin Density Operator of H_2

The spin dynamics and NMR signal enhancement resulting from chemical addition of ortho/para H_2 or D_2 into a symmetry breaking magnetic environment is most conveniently investigated using density matrix or density operator methods. The H_2 density matrix for a sample with arbitrary ortho/para composition is readily constructed using the singlet/triplet nuclear spin eigenstates of equations (2) and (3). From this matrix, the density operator can be obtained and subjected to varying reaction conditions. Finally, the NMR observables can be calculated from the time evolution of the density operator according to the Liouville-von Neumann equation together with the standard trace relations for the complex transverse magnetization.

For an arbitrary ortho-para mixture with mole fraction χ_p of p-H_2, the equilibrium density matrix in the singlet-triplet basis is

$$\rho = \begin{matrix} \\ \Psi_{1,1} \\ \Psi_{1,0} \\ \Psi_{1,-1} \\ \Psi_{0,0} \end{matrix} \begin{matrix} \begin{matrix} \quad\quad & \quad\quad & \quad\quad & \quad\quad \end{matrix} \\ \begin{bmatrix} (1-\chi_p)/3 & 0 & 0 & 0 \\ 0 & (1-\chi_p)/3 & 0 & 0 \\ 0 & 0 & (1-\chi_p)/3 & 0 \\ 0 & 0 & 0 & \chi_p \end{bmatrix} \end{matrix} \quad (5)$$

The equilibrium density operator for the arbitrary ortho-para mixture may be written as:

$$\hat{\rho} = \frac{1}{4}\hat{1} - f\hat{\mathbf{I}}_1 \cdot \hat{\mathbf{I}}_2 \quad (6)$$

where $\hat{\mathbf{I}}_1$ and $\hat{\mathbf{I}}_2$ are the nuclear spin operators for each nucleus and $f = (4\chi_p - 1)/3$. In most applications, H_2 will be incorporated by chemical addition into a substrate nuclear spin system that is essentially disordered. Although there will be some equilibrium Curie-Law paramagnetism, this can usually be neglected. The density operator of the unpolarized substrate spin system (labeled 3..N) is:

$$\hat{\rho}^s = \prod_{i=3,N} \frac{\hat{\mathbf{1}}}{d_i} \quad (7)$$

where $d_i = 2I_i + 1$ and the product is a tensor product. The tensor product is also used to construct the total spin system including the original H_2 and the substrate nuclei. Thus

$$\hat{\rho}^{\text{adduct}} = \hat{\rho}^{H_2} \otimes \hat{\rho}^s \quad (8)$$

The density operator resulting from H_2 addition serves as the initial condition for the ensuing spin dynamics due to radio frequency pulses and free evolution under the internal Hamiltonian.

Implicit in equation (8) is the chemically unrealistic assumption that the time of product formation is identical for all molecules in the sample. In most cases, there will be a distribution of formation times, and the form of the density matrix will depend on the details of the chemical kinetics and mechanism. To determine the response of the spin system, it is useful to transform the density matrix of the H_2 to the eigenbasis of the product spin system. These will be the eigenstates $|\psi_i\rangle$ satisfying $\hat{\mathcal{H}}_{\text{int}}|\psi_i\rangle = \varepsilon_i\hbar|\psi_i\rangle$ of the high field, rotating frame Hamiltonian $\hat{\mathcal{H}}_{\text{int}}$ consisting of chemical shifts, dipolar and J couplings. The diagonal elements of the density matrix in this basis have no time evolution, aside from spin-lattice relaxation, while the off-diagonal elements ρ_{ij} (i.e., coherences) oscillate at frequencies $(\varepsilon_j - \varepsilon_i)/\hbar$. To model a finite reaction rate, the density matrix resulting from hydrogenation must be averaged over the distribution of product formation times. If the reaction is slow such that the distribution of formation times is broad compared to the period of this oscillation, then the coherences will lose amplitude or even vanish due to destructive interference.

2.3 Nuclear Spin Density Operator of the Product Molecule

In general, the high speed spin Hamiltonian on the product molecule will consist of chemical shift, dipolar coupling and scalar coupling terms. The high-field, rotating-frame Hamiltonian for two spins-1/2 is:

$$\hat{\mathcal{H}}_{\text{int}} = \omega_{z1}\hat{I}_{z1} + \omega_{z2}\hat{I}_{z2} + D[\hat{\mathbf{I}}_1 \cdot \hat{\mathbf{I}}_2 - 3\hat{I}_{z1}\hat{I}_{z2}] + J\hat{\mathbf{I}}_1 \cdot \hat{\mathbf{I}}_2 \quad (9)$$

where ω_{z1}, ω_{z2} are the rotating frame chemical shifts of each spin, J is the scalar coupling constant, $D = (\omega_D/2)(3\cos^2\vartheta - 1)$ and $\omega_D = \gamma^2\hbar/r^3$. The eigenstates are:

$$|1\rangle = |\alpha\alpha\rangle \quad (10)$$

$$|2\rangle = c_1|\alpha\beta\rangle + c_2|\beta\alpha\rangle \quad (11)$$

$$|3\rangle = -c_2|\alpha\beta\rangle + c_1|\beta\alpha\rangle \quad (12)$$

$$|4\rangle = |\beta\beta\rangle \quad (13)$$

where $c_1 = \cos(\kappa/2)$, $c_2 = \sin(\kappa/2)$ and $\tan(\kappa) = (D + J)/\Delta\omega_z$. The parameters $\overline{\omega} = 1/2(\omega_{z1} + \omega_{z2})$ and $\Delta\omega_z = \omega_{z1} - \omega_{z2}$ are the average chemical shift and chemical shift difference, respectively. The dipolar interaction depends on the angle ϑ between the internuclear vector and the applied field. In general the chemical shifts $\omega_{zi}(\vartheta, \phi, \Omega_i)$ depend on the Euler angles $\Omega_i = \{\alpha_i, \beta_i, \gamma_i\}$ relating the principal axis system of the chemical shift to that of the dipolar interaction. The orientation dependence of the chemical shifts and dipolar coupling introduces distinct spectral features for solid or surface bound nuclei, as will be explored in Section 8. For a liquid sample, the rapid reorientation of the spin system reduces the tensorial spin interactions to their isotropic values. The angle κ specifies the strength of the coupling. For weak coupling, $\Delta\omega_z \gg \{J, D\}$, $\kappa \to 0$ and the simple product states $|\alpha\alpha\rangle$, $|\alpha\beta\rangle$, $|\beta\alpha\rangle$, and $|\beta\beta\rangle$ are recovered. The singlet-triplet states are obtained in the strong coupling limit, where $\kappa \to \pi/2$. These are the same nuclear spin states as in the original H_2 molecule.

3 GENERAL THEORY OF THE PASADENA EFFECT

3.1 The Sudden Approximation

When the protons of H_2 are deposited into magnetically inequivalent sites of the product molecule, the internal Hamiltonian of the 2-spin system suddenly changes. The given initial state $|\psi_i\rangle$ will continue to describe the quantum state of

the system even though it is not necessarily an eigenstate of the product molecule Hamiltonian. According to the sudden approximation, the transition probability from an initial state $|\psi_i\rangle$ to a final state $|\psi_f\rangle$ may be calculated from the square of the projection of $|\psi_i\rangle$ onto $|\psi_f\rangle$:

$$p_{fi} = |\langle\psi_f|\psi_i\rangle|^2. \tag{14}$$

The transition probabilities from singlet H_2, where $|\psi_i\rangle = 2^{-1/2}(|\alpha\beta\rangle - |\beta\alpha\rangle)$ to the final states, $|1\rangle$, $|2\rangle$, $|3\rangle$ and $|4\rangle$ given in equations (10)–(13), are:

$$\begin{aligned} p_1 &= \frac{1}{2}\langle 1|\alpha\beta - \beta\alpha\rangle = 0 \\ p_2 &= \frac{1}{2}\langle 2|\alpha\beta - \beta\alpha\rangle = \frac{1}{2}(1 - \sin\kappa) \\ p_3 &= \frac{1}{2}\langle 3|\alpha\beta - \beta\alpha\rangle = \frac{1}{2}(1 + \sin\kappa) \\ p_4 &= \frac{1}{2}\langle 4|\alpha\beta - \beta\alpha\rangle = 0 \end{aligned} \tag{15}$$

These transition probabilities determine the population distribution of the final states. The resultant nuclear spin density matrix summarizes the state of the ensemble of spin systems formed by the instantaneous reaction of H_2 of arbitrary ortho-para composition. In the basis set $|1\rangle$, $|2\rangle$, $|3\rangle$ and $|4\rangle$ [equations (10)–(13)], the density matrix of the adduct is

$$\rho^{\text{adduct}} \longrightarrow \begin{bmatrix} \frac{1-f}{4} & 0 & 0 & 0 \\ 0 & \frac{1+f}{4} - \frac{f}{2}\sin\kappa & \frac{f\cos\kappa}{2} & 0 \\ 0 & \frac{f\cos\kappa}{2} & \frac{1+f}{4} + \frac{f}{2}\sin\kappa & 0 \\ 0 & 0 & 0 & \frac{1-f}{4} \end{bmatrix} \tag{16}$$

There are several noteworthy features of this density matrix.

- Notice that the reaction of pure p-H_2, where $\chi_p = 1$ and $f = (4\chi_p - 1)/3 \to 1$, leads to the population of states $|2\rangle$ and $|3\rangle$ but not $|1\rangle$ and $|4\rangle$, with the branching ratio dependent upon the coupling strength parameter κ. The reaction with pure o-H_2 ($\chi_p = 0$) yields population of all four states, but with greater population of the outer states $|1\rangle$ and $|4\rangle$. The population distributions resulting from each of these two cases is illustrated in Figure 2.
- The reaction with n-H_2, where $\chi_p = 1/4$, leads to equal population of all 4 states. This case is illustrated by combining the population distribution resulting from p-H_2 and o-H_2, as is evident in Figure 2.
- Nuclear spin coherences are also created, with the amplitude depending on κ. In the weak coupling limit the coherences may be identified as pure zero quantum transitions ($|\alpha\beta\rangle \leftrightarrow |\beta\alpha\rangle$).

3.2 Time Evolution of the Adduct Density Matrix

Neglecting spin relaxation, the time evolution of the density matrix is obtained by solving the Liouville-von Neumann equation. With energies expressed in units of frequency (we take $\hbar = 1$),

$$\frac{\mathrm{d}}{\mathrm{d}t}\hat{\rho}(t) = -i[\hat{\mathcal{H}}(t), \hat{\rho}(t)] \tag{17}$$

This has the formal solution

$$\hat{\rho}(t) = \hat{U}(t)\hat{\rho}(0)\hat{U}^{\dagger}(t) \tag{18}$$

where

$$\hat{U}(t) = \hat{T}\exp\left\{-i\int_0^t \hat{\mathcal{H}}(t')\mathrm{d}t'\right\} \tag{19}$$

and $\hat{T}$ is the Dyson time-ordering operator. When $\hat{\mathcal{H}}$ is time-independent, or if the evolution can be broken down into periods which are piecewise time-independent, the propagator

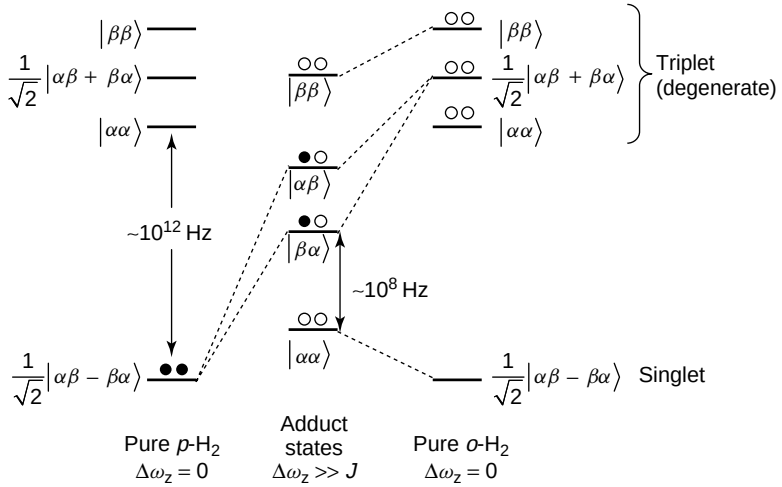

Figure 2 Correlation diagram for the nuclear spin states resulting from dihydrogen addition in the PASADENA effect. Starting with 2 moles of parahydrogen (left), the addition into weakly coupled, chemically inequivalent sites leads to 1 mole in each of the two middle states ($|\alpha\beta\rangle$ and $|\beta\alpha\rangle$). Starting with 6 moles of orthohydrogen (right), the result is 2 moles in each of the outer states and 1 mole in the middle two states. Starting with 8 moles of hydrogen initially equilibrated at high temperature, the resulting populations would be the combination of hollow and filled circles: the four states would be equally populated with two moles in each

can be factored. For example, the evolution over two periods t_1 and t_2 may be written as

$$\hat{\rho}(t_0 + t_1 + t_2) = e^{-i\hat{\mathcal{H}}_2 t_2} e^{-i\hat{\mathcal{H}}_1 t_1} \hat{\rho}(t_0) e^{-i\hat{\mathcal{H}}_1 t_1} e^{i\hat{\mathcal{H}}_2 t_2} \tag{20}$$

The time dependence of any expectation value may be calculated from the trace of the product of $\hat{\rho}(t_0 + t_1 + t_2)$ with the appropriate observable operator. For example, the observed rotating frame NMR signal is proportional to the complex transverse magnetization, which is proportional to $\langle \hat{I}_+ \rangle$:

$$\begin{aligned} S(t) &= Tr\{\hat{I}_+ e^{-i\hat{\mathcal{H}}t} \hat{\rho}(t=0) e^{i\hat{\mathcal{H}}t}\} \\ &= \sum_{m,n} \langle m|\hat{I}_+|n\rangle \langle n|e^{-i\hat{\mathcal{H}}t} \hat{\rho}(t=0) e^{i\hat{\mathcal{H}}t}|m\rangle \\ &= \sum_{m,n} \langle m|\hat{I}_+|n\rangle \langle n|\hat{\rho}(t=0)|m\rangle e^{-i\omega_{mn}t} \end{aligned} \tag{21}$$

The summation is over the basis states of the matrix representation. The ω_{mn} are the single quantum transition frequencies. For example, the $|1\rangle \rightarrow |2\rangle$ transition frequency is

$$\omega_{12} = \overline{\omega} - D + \frac{J}{2} - \frac{1}{2}(\Delta\omega_z^2 + (D+J)^2)^{1/2} \tag{22}$$

3.3 Density Matrix Averaged Over Product Formation Times

As was shown in Section 3.1, the sudden change that occurs upon H_2 addition results in a superposition of states $|2\rangle$ and $|3\rangle$ which is generally not an eigenfunction of the product molecule spin Hamiltonian. In the weak coupling limit, this superposition corresponds to a zero quantum transition, $|\alpha\beta\rangle \rightarrow |\beta\alpha\rangle$, with a Bohr frequency $\omega_{23} = [(J+D)^2 + \Delta\omega_z^2]^{1/2}$. If the distribution of product formation times is relatively long compared to $2\pi/\omega_{23}$, then the off-diagonal elements $f\cos\kappa/2$ of the density matrix (equation (16)) will vanish upon averaging over the distribution of product formation times, yielding

$$\langle \rho^{\text{adduct}} \rangle = \begin{bmatrix} \frac{1-f}{4} & 0 & 0 & 0 \\ 0 & \frac{1+f}{4} - \frac{f}{2}\sin\kappa & 0 & 0 \\ 0 & 0 & \frac{1+f}{4} + \frac{f}{2}\sin\kappa & 0 \\ 0 & 0 & 0 & \frac{1-f}{4} \end{bmatrix} \tag{23}$$

For analytical calculations of the FID, it is convenient to express this diagonal density matrix in operator form:

$$\begin{aligned} \langle \hat{\rho}^{\text{adduct}} \rangle = \frac{1}{4}\hat{1} - f \Big\{ &\frac{1}{2}\sin\kappa\cos\kappa(\hat{I}_{z1} - \hat{I}_{z2}) \\ &+ \frac{1}{3}\cos^2\kappa(3\hat{I}_{z1}\hat{I}_{z2} - \hat{\mathbf{I}}_1 \cdot \hat{\mathbf{I}}_2) \\ &+ \left[1 - \frac{2}{3}\cos^2\kappa\right]\hat{\mathbf{I}}_1 \cdot \hat{\mathbf{I}}_2 \Big\} \end{aligned} \tag{24}$$

3.4 Calculation of the NMR Signal

Having derived the two-spin density operator and density matrix following hydrogenation of a substrate, the next step is to calculate the free induction decay signal. Inspection of the density operator reveals that only the first two terms in brackets in equation (24) can lead to transverse magnetization following a single rf pulse. The third term contains the scalar operator $\hat{\mathbf{I}}_1 \cdot \hat{\mathbf{I}}_2$ that is invariant to rotations. Applying an rf pulse with tip angle θ yields the following expression for the density operator, where only single quantum coherences are retained:

$$\begin{aligned} \langle \hat{\rho} \rangle_{\text{SQ}}(\theta) = f \Big\{ &\frac{1}{2}\sin\kappa\cos\kappa\sin\theta(\hat{I}_{x2} - \hat{I}_{x1}) \\ &- \cos^2\kappa\sin\theta\cos\theta(\hat{I}_{z1}\hat{I}_{x2} + \hat{I}_{x1}\hat{I}_{z2}) \Big\} \end{aligned} \tag{25}$$

The NMR signal is calculated using the trace formula [equation (21)].

$$\begin{aligned} S(t,\kappa) = \frac{f}{4}\cos^2\kappa\sin\theta \big\{ &(-\cos\theta + \sin\kappa - \cos\theta\sin\kappa)e^{-i\omega_{12}t} \\ &+ (-\cos\theta - \sin\kappa + \cos\theta\sin\kappa)e^{-i\omega_{13}t} \\ &+ (\cos\theta - \sin\kappa + \cos\theta\sin\kappa)e^{-i\omega_{24}t} \\ &+ (\cos\theta + \sin\kappa - \cos\theta\sin\kappa)e^{-i\omega_{34}t} \big\} e^{-t/T_2} \end{aligned} \tag{26}$$

A phenomenological damping factor has been appended to account for transverse spin relaxation. Spectra corresponding to the Fourier transform of this signal expression are plotted in Figure 3 for $D = 0$ and for varying coupling strengths, as determined by the chemical shift to J-coupling ratio, $\Delta\omega_z/J$. The spectra were plotted for two different pulse angles: $\theta = \pi/2$ and $\theta = \pi/4$. For reference, the figure also includes the conventional NMR spectra derived from Zeeman order due to thermal polarization within the high temperature approximation.

3.5 NMR Enhancement Factor

To quantify the signal enhancement resulting from *p*-H_2 addition it is useful to relate the signal amplitudes to a reference. Two meaningful choices are the NMR signals arising from a hypothetical sample at 0 K and a sample at thermal equilibrium at 300 K. At 0 K only the $|\alpha\alpha\rangle$ state is populated. The two-spin density operator is a linear combination of scalar, Zeeman and dipolar order, as follows:

$$\hat{\rho}_{\text{eq}} = \frac{1}{4}\hat{1} + a\hat{\mathbf{I}}_1 \cdot \hat{\mathbf{I}}_2 + b\hat{I}_z + c(3\hat{I}_{z1}\hat{I}_{z2} - \hat{\mathbf{I}}_1 \cdot \hat{\mathbf{I}}_2) \tag{27}$$

If a $\pi/2$ pulse is applied, only the Zeeman order ($b\hat{I}_z$) produces detectable transverse magnetization, so only this term needs to be retained in the signal calculation. At any temperature, application of a $\pi/2$ pulse yields

$$\begin{aligned} S_{\text{eq}}(t,\kappa) = \frac{b(T)}{2}\{&(1+\sin\kappa)(e^{-i\omega_{12}t} + e^{-i\omega_{24}t}) + (1-\sin\kappa) \\ &\times (e^{-i\omega_{12}t} + e^{-i\omega_{24}t})\} \end{aligned} \tag{28}$$

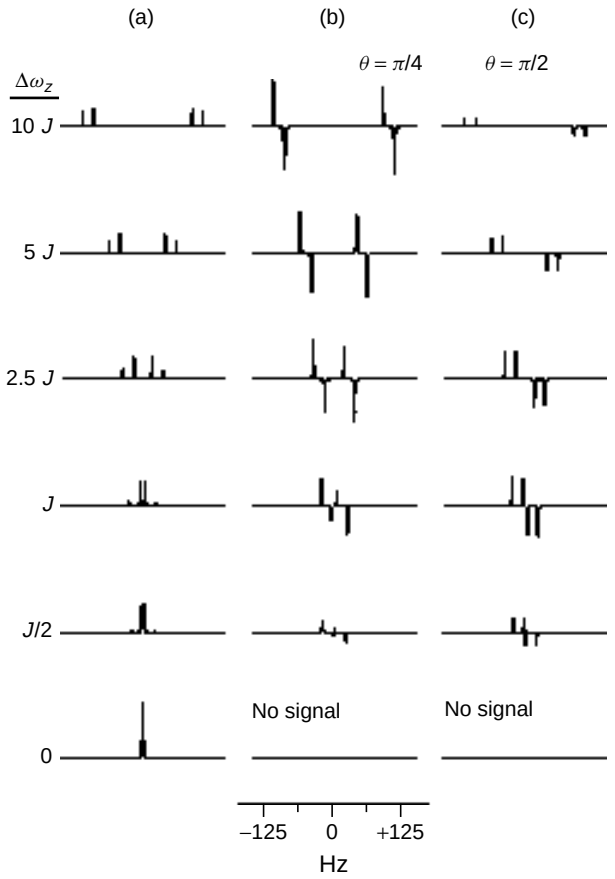

Figure 3 Two spin simulations as a function of the ratio $\Delta\omega_z/J$ using two pulse angles θ: column (b) $\theta = \pi/4$ and column (c) $\theta = \pi/2$. Column (a) is the spectrum obtained from Zeeman order pertaining to thermal polarization of the spin system in the high temperature limit

The enhancement factor is defined as the ratio of the signal intensities for a specified transition. The theoretical ratio of the amplitudes of the ω_{12} transition is

$$\frac{S_{\text{PAS}}}{S_{\text{eq}}} = \frac{f\cos^2\kappa\sin\theta[\sin\kappa - \cos\theta - \cos\theta\sin\kappa]}{2[1+\sin\kappa]b(T)} \tag{29}$$

At 0 K the coefficient $b(0\,\text{K}) = 1/2$ can be determined using the fact that at this temperature the spins are completely ordered and the density operator is simply $\hat{\rho}(0\,\text{K}) = |\alpha\alpha\rangle\langle\alpha\alpha|$.

$$Tr\{\hat{I}_z\hat{\rho}(0\,\text{K})\} = 1 = b(0\,\text{K})Tr\{\hat{I}_z^2\} = 2b(0\,\text{K}) \tag{30}$$

Substitution into equation (29) shows that the theoretical signal obtained from 100% p-H_2 with a $\theta = \pi/4$ pulse in the weak-coupling limit ($\kappa \to 0$) is exactly half the maximum possible signal obtained from the hypothetical sample at 0 K.

In the high temperature regime,

$$b(T) = \frac{\gamma\hbar H_0}{kT(2I+1)^N} \tag{31}$$

In comparison to the theoretical signal amplitude in the weak-coupling limit with $\theta = \pi/4$ at $T = 300\,\text{K}$ and $H_0 = 4.7\,\text{T}$ (200 MHz ^{1}H), the enhancement numerically evaluates to $31\,240\cdot f$.

4 PASADENA EFFECT IN WEAKLY COUPLED SPIN SYSTEMS

To extend the discussion of proton signal enhancement by p-H_2 addition to a great variety of experiments involving molecules in liquid solution, progress can be made by restricting the PASADENA theory to weakly coupled spin systems, where the Hamiltonian becomes

$$\hat{\mathcal{H}}_{\text{int}} = \sum_{i<j}^{N} J_{ij}\hat{I}_{zi}\cdot\hat{I}_{zj} + \sum_{i}^{N}\omega_{zi}\hat{I}_{zi} \tag{32}$$

Two spins are said to be weakly coupled when $\Delta\omega_z \gg J$. Thus, according to equations (10)–(13), $\kappa \to 0$, and the eigenfunctions become the direct product functions. Restriction to weak coupling permits the use of the product operator formalism[22,23] which has the advantage of preserving operator properties (and the physical meaning associated with them) throughout the calculation of the time evolution of the spin system.

4.1 Creation of Coherence from J-Order

The time averaged density operator of a weakly coupled two spin adduct formed using an arbitrary ortho-para H_2 mixture is:

$$\hat{\rho}(0) = \frac{1}{4}\hat{1} - f\hat{I}_{z1}\hat{I}_{z2} \tag{33}$$

Application of a y-phase rf pulse with tip angle θ transforms the density operator as follows:

$$\hat{\rho}(0) \xrightarrow{\theta\hat{I}_y} \frac{1}{4} - f\cos^2\theta\hat{I}_{z1}\hat{I}_{z2} - f\sin^2\theta\hat{I}_{x1}\hat{I}_{x2} - f\sin\theta\cos\theta(\hat{I}_{z1}\hat{I}_{x2} + \hat{I}_{x1}\hat{I}_{z2}) \tag{34}$$

This expression illustrates that a single rf pulse creates zero, single and double quantum coherences from the initial density operator. The last term corresponds to bilinear single quantum coherence that is optimized by a $\theta = \pi/4$ pulse. Such operators require a J-coupling and a chemical shift difference (or other form of magnetic inequivalence) to evolve into detectable signal. The $\hat{I}_{x1}\hat{I}_{x2}$ term commutes with the J-coupling interaction, and therefore, the $p = 0, \pm 2$ quantum coherences evolve only under the influence of the sum and difference of the rotating frame chemical shifts. For more than two spins, not all couplings will commute, giving rise to J-coupling structure in the $p = 0, \pm 2$ quantum transitions. While the zero and double quantum transitions are not directly observable, they can be useful in the context of 2D pulse sequences such as the chemical exchange sequence described in Section 5.2.6.

The overall time evolution of the density operator (equation (34)) under the internal Hamiltonian in equation (32) is

$$\hat{\rho}(0) \xrightarrow{\theta\hat{I}_y} \frac{1}{4} - f\cos^2\theta\hat{I}_{z1}\hat{I}_{z2} \qquad \text{populations} \tag{35}$$

$$-\frac{f}{4}\sin^2\theta\{\hat{I}_{-1}\hat{I}_{+2}\exp(2i\Delta\omega_z t) + \hat{I}_{+1}\hat{I}_{-2}\exp(-2i\Delta\omega_z t)\} \quad \text{ZQC} \tag{36}$$

$$-\frac{f}{4}\sin^2\theta\{\hat{I}_{+1}\hat{I}_{+2}\exp(2i\overline{\omega}t)+\hat{I}_{-1}\hat{I}_{-2}\exp(-2i\overline{\omega}t)\}\quad \text{DQC} \tag{37}$$

$$\begin{aligned}&-\frac{f}{2}\sin\theta\cos\theta\left\{\cos\omega_{z2}t\left[2\cos\frac{Jt}{2}\hat{I}_{z1}\hat{I}_{x2}-\sin\frac{Jt}{2}\hat{I}_{y2}\right]\right.\\&-\sin\omega_{z2}t\left[2\cos\frac{Jt}{2}\hat{I}_{z1}\hat{I}_{y2}-\sin\frac{Jt}{2}\hat{I}_{x2}\right]\quad\text{SQC}\\&+\cos\omega_{z1}t\left[2\cos\frac{Jt}{2}\hat{I}_{x1}\hat{I}_{z2}-\sin\frac{Jt}{2}\hat{I}_{y1}\right]\\&\left.-\sin\omega_{z1}t\left[2\cos\frac{Jt}{2}\hat{I}_{y1}\hat{I}_{z2}-\sin\frac{Jt}{2}\hat{I}_{x1}\right]\right\}\end{aligned} \tag{38}$$

4.2 A_2X_3 PASADENA Spectrum – Product Operator Treatment

Section 5 will present the results of PASADENA experiments involving the catalytic hydrogenation of styrene to ethylbenzene and acrylonitrile to propionitrile. Both product molecules may be described as weakly coupled A_2X_3 spin systems (including the two protons originally in the H_2 molecule, but ignoring the uninvolved aromatic group protons in the case of ethylbenzene). Therefore, the product operator description of the PASADENA effect for the A_2X_3 case will be given special consideration here.

The NMR signals resulting from either PASADENA spin order or conventional thermal spin polarization of the A_2X_3 system may be derived using the product operator treatment together with the following expansions for the trigonometric functions of spin operators for the AX_2 and AX_3 cases:

$$\begin{aligned}&\text{AX}_2\text{: Let } \hat{I}_a=\hat{I}_{a1}+\hat{I}_{a2},\ \text{where } a=x,y,\ \text{or } z\\&\quad\cos(\chi\hat{I}_a)=\cos^2\left(\frac{\chi}{2}\right)-4\hat{I}_{a1}\hat{I}_{a2}\sin^2\left(\frac{\chi}{2}\right)\\&\quad\sin(\chi\hat{I}_a)=\hat{I}_a\sin\chi\\&\text{AX}_3\text{: Let } \hat{I}_a=\hat{I}_{a1}+\hat{I}_{a2}+\hat{I}_{a3},\ \text{where } a=x,y,\ \text{or } z\\&\quad\cos(\chi\hat{I}_a)=\cos^3\left(\frac{\chi}{2}\right)-4(\hat{I}_{a1}\hat{I}_{a2}+\hat{I}_{a1}\hat{I}_{a3}+\hat{I}_{a2}\hat{I}_{a3})\\&\qquad\qquad\times\sin^2\left(\frac{\chi}{2}\right)\cos\left(\frac{\chi}{2}\right)\\&\quad\sin(\chi\hat{I}_a)=2\hat{I}_a\sin\left(\frac{\chi}{2}\right)\cos^2\left(\frac{\chi}{2}\right)-8\hat{I}_{a1}\hat{I}_{a2}\hat{I}_{a3}\sin^3\left(\frac{\chi}{2}\right)\end{aligned}$$

According to the high temperature approximation, the traceless part of the initial density operator used to compute the conventional NMR signal consists of Zeeman order; $\hat{\rho}_{\text{eq}}\propto b(\hat{I}_{za}+\hat{I}_{zb})$, where the subscripts a and b denote magnetically equivalent groups of three and two spins, respectively; $\hat{I}_{za}=\hat{I}_{z1}+\hat{I}_{z3}+\hat{I}_{z5}$ and $\hat{I}_{zb}=\hat{I}_{z2}+\hat{I}_{z4}$. The time-domain NMR signal obtained from thermal equilibrium Zeeman order in the high temperature regime is:

$$S_{\text{eq}}(t)=8b(T)\left\{3\cos^2\frac{Jt}{2}e^{i\omega_{zA}}+2\cos^3\frac{Jt}{2}e^{i\omega_{zB}}\right\} \tag{39}$$

The amplitude factor $b(0\,\text{K})$ is calculated following the same procedure used in the two-spin case (Section 3.5). The result is

$$b(0\,\text{K})=\frac{Tr(\hat{I}_z|\alpha\alpha\alpha\alpha\alpha\rangle\langle\alpha\alpha\alpha\alpha\alpha|)}{5Tr(\hat{I}_{z1}^2)}=\frac{1}{16}$$

The absolute transition amplitudes of the methyl triplet and methylene quartet at 0 K are therefore $\{3/8, 3/4, 3/8\}$ and $\{1/8, 3/8, 3/8, 1/8\}$, respectively. The relative amplitudes of the A_2X_3 PASADENA signal can be derived from the PASADENA signal calculation or else by direct extension of the two-spin theory. The methyl group yields $\{f/8,0,-f/8\}$, while the methylene protons yield $\{f/16 : f/16 : -f/16 : -f/16\}$. If the J-coupling is not fully resolved, the ideal intensity ratios may be distorted by interference effects that can lead to partial cancellation of intensity, especially for the inner lines of the multiplet transition. For this reason, the outer lines are used to compute the enhancement factor. The calculated numerical value of the enhancement factor of the PASADENA signal over the conventional signal obtained at 300 K is:

$$\frac{|S_{\text{PAS}}|}{|S_{\text{eq}}(300\,\text{K})|}=\frac{|S_{\text{PAS}}|}{|S_{\text{eq}}(0\,\text{K})|}\times\frac{|b(0\,\text{K})|}{|b(300\,\text{K})|}=20\,800\cdot f$$

The reduced enhancement relative to the 2-spin case is due to the dilution of the spin order of p-H_2 by the unpolarized protons of the substrate. The spin order of the incoming protons is shared among the nuclei of the magnetically equivalent groups due to bilinear cross polarization.

4.3 Evolution of Coherences Induced by Rapid Addition of p-H_2

When the time-scale of the chemical reaction is short compared to the period of the spin coherences initiated upon incorporation of H_2 into the substrate, the off-diagonal elements of the density operator represented by $\hat{I}_{x1}\hat{I}_{x2}+\hat{I}_{y1}\hat{I}_{y2}$ do not vanish. Since $[\hat{\mathcal{H}}_{\text{int}},\ \hat{I}_1\cdot\hat{I}_2]\neq 0$, the density operator becomes time dependent during the period before the rf read pulse.

$$\begin{aligned}\hat{\rho}(t_r)=&\frac{1}{4}-\hat{I}_{z1}\hat{I}_{z2}-(\hat{I}_{x1}\hat{I}_{x2}+\hat{I}_{y1}\hat{I}_{y2})\cos(\Delta\omega_z t_r)\\&+(\hat{I}_{x1}\hat{I}_{y2}-\hat{I}_{y1}\hat{I}_{x2})\sin(\Delta\omega_z t_r)\end{aligned} \tag{40}$$

Application of the θ angle pulse followed by further free evolution and detection gives the signal during t_2:

$$\begin{aligned}S(t_r,\theta,t_2)=-\frac{1}{8}\{&(a-ib)[\exp(i(\omega_{z1}+J/2)t_2)\\&-\exp(i(\omega_{z1}-J/2)t_2)]\\&-(a+ib)[\exp(i(\omega_{z2}+J/2)t_2)\\&-\exp(i(\omega_{z2}-J/2)t_2)]\}\end{aligned} \tag{41}$$

where $a=2\sin\theta\sin(\Delta\omega_z t_r)$ and $b=\sin 2\theta(1-\cos(\Delta\omega_z t_r))$. The amplitude of the observed response is a function of t_r. The total signal energy is proportional to the integral of the modulus squared of the free induction decay:

$$E(t_r,\theta)\propto\int_0^\infty|S(t_r,\theta,t_2)|^2\mathrm{d}t_2 \tag{42}$$

It is convenient to reference the PASADENA signal energy to the signal energy that would be obtained from a fully polarized product molecule using a 90° detection pulse. The

dimensionless ratio R for a two spin system, obtained using equation (41), is

$$R(t_r) = \frac{E(t_r)}{E_0} = \frac{1}{4}\{4\sin^2\theta\sin^2\Delta\omega_z t_r + \sin^2 2\theta[1-\cos\Delta\omega_z t_r]^2\} \quad (43)$$

This function is plotted for $N = 2$ spins in Figure 4(a). The dashed horizontal line in this plot indicates the level expected when the ensemble of product molecules is formed incoherently. The results of a numerical density matrix calculation of the ratio $R(t_r)$ for product molecules with $N = 3$ is shown in Figure 4(b). Notice that in all cases, the chemical shift difference is important in that it breaks the symmetry during t_r, allowing escape from the singlet state. However, in the weak-coupling limit, the J-coupling sets the timescale for development of signal.

4.4 Bilinear Cross Polarization

While the spin order associated with the protons originating on p-H_2 may be distributed to other magnetically equivalent nuclei in the adduct molecule due to the scalar coupling with them, a magnetically inequivalent spin may not receive polarization through this mechanism since the scalar coupling is truncated. As an example, Figure 5(a) shows a density matrix simulation of the PASADENA magnitude spectrum for bromoethylene formed by hydrogenation with p-H_2. In this simulation, the time-averaged initial density matrix, with off-diagonal elements set to zero, has been subjected to a 45° pulse. Notice that transitions involving the third proton, *cis* to Br, are absent.[3]

In many applications it will be desirable to transfer the p-H_2 spin order to other spins to enhance the signal of a larger number of site-specific resonances. The sequence shown below serves this purpose. In this sequence, **R** may represent a nutation pulse or a multiple pulse train such as a series of π pulses having the effect of averaging away the chemical shifts.[24,25]

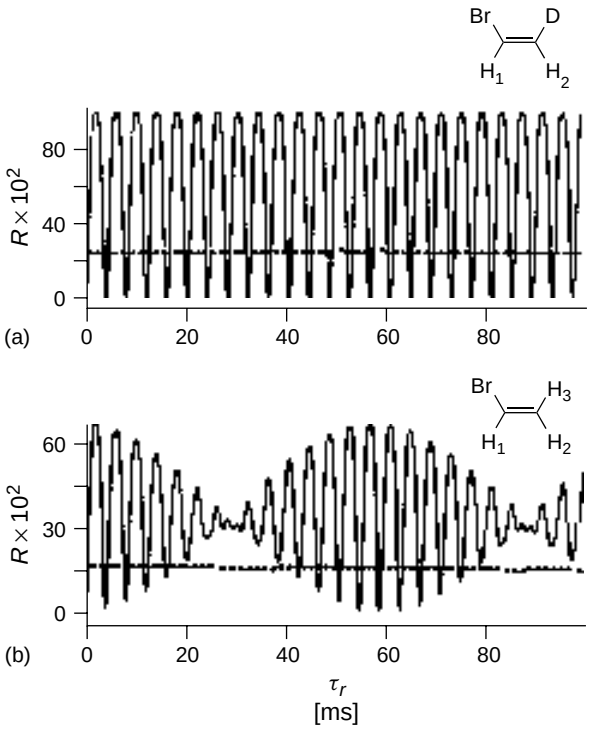

Figure 4 Calculated dependence (see equation (43)) of the signal energy on the delay between the reaction (assumed instantaneous) and a $\pi/4$ rf pulse. (a) $N = 2$, *cis*-1-deuterio-2-bromethylene ($J_{12}/2\pi = 7.2$ Hz, $\nu_{z1} = -132$ Hz, $\nu_{z2} = 112$ Hz); (b) $N = 3$, bromoethylene ($J_{12}/2\pi = 7.2$ Hz, $J_{13}/2\pi = 15.0$ Hz, $J_{23}/2\pi = -1.7$ Hz, $\nu_{z1} = 112$ Hz, $\nu_{z2} = -132$ Hz, $\nu_{z2} = -200$ Hz). The chemical shifts correspond to a proton Larmor frequency at 500 MHz. Trace (b) was calculated by a numerical density matrix simulation. The vertical scales are relative to the signal energies that would be seen for perfect nuclear paramagnetic ordering subjected to a $\pi/2$ pulse. The dashed lines indicate the level expected when the ensemble of product molecules is formed incoherently

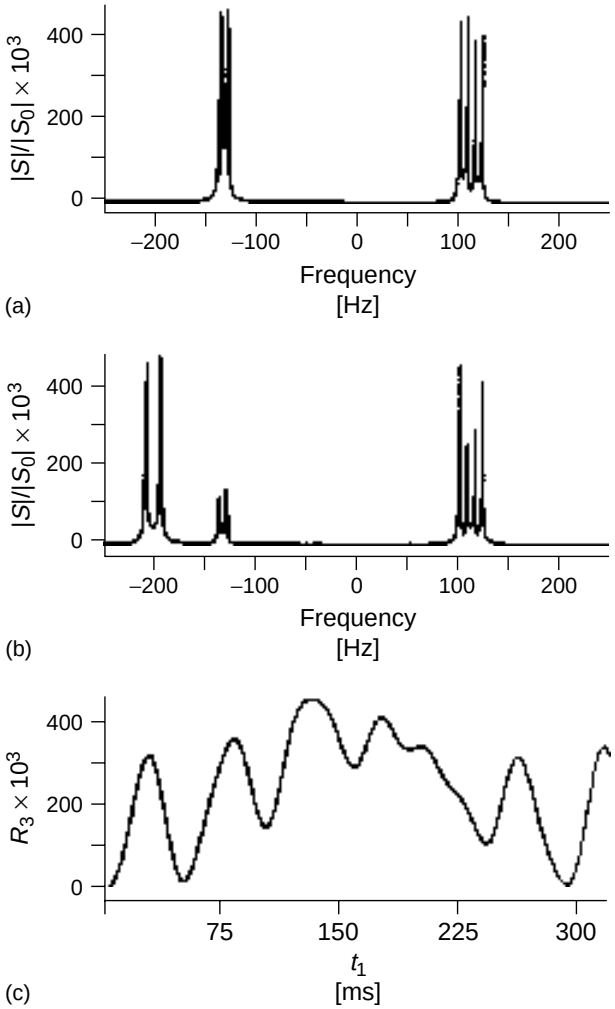

Figure 5 Bilinear cross polarization on bromoethylene. (a) The magnitude spectrum without cross polarization ($t_1 = 0$ in Figure 5c). (b) The corresponding spectrum with $t_1 = 131.2$ ms, at which time the multiplet due to H_3 (*cis* to br) has grown to a maximum at the expense of resonances due to the protons originating on p-H_2. (c) The signal energy of this H_3 multiplet as a function of t_1. The pulse sequence during t_1 consisted of repetitions of a train of 25 contiguous phase-shifted π-pulses, each pulse of length 64 ms

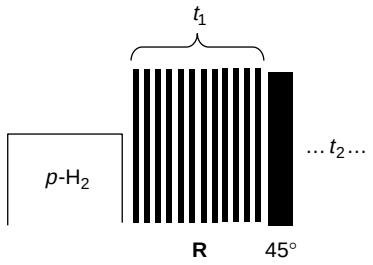

The spectrum of Figure 5(b) was obtained by simulating the application of a π pulse train for a time $t_1 = 131.2$ ms followed by a $\pi/4$ read pulse. The simulation demonstrates that the intense non-equilibrium magnetization is now shared with the third proton. The dependence of the signal energy of this new multiplet on the cross-polarization time t_1 is shown in Figure 5(c). The plotted quantity $R_3(t_1)$ is analogous to the energy ratio introduced in equation (43), but here the ratio refers to the multiplet of the third (magnetically inequivalent) proton. The sharing of spin-order occurs prior to any development of magnetization.

5 EXPERIMENTAL PASADENA NMR SPECTROSCOPY IN LIQUIDS

5.1 Experimental Apparatus

The simplest procedure for observing NMR signal enhancements by the PASADENA effect is to pressurize an NMR tube containing a premixed solution of the substrate and hydrogenation catalyst with p-H_2 gas. The hydrogenation reaction is initiated by shaking the tube followed by immediate insertion into the NMR probe to observe the enhanced signal. In the weak-coupling limit, the PASADENA signal is maximized using a $\pi/4$ pulse rather than the usual $\pi/2$ pulse. The reaction essentially stops once the dissolved H_2 has been consumed, since dissolution across the gas-liquid interface is slow. By ejecting the tube, shaking, and reinserting, additional enhanced spectra can be acquired using the same sample. However, caution be exercised in this method because net alignment of the multiplet signals may result from the adiabatic longitudinal transport of the spin order generated while the sample is at zero or low magnetic field. This is the ALTADENA effect which will be reviewed in Section 6.

An improved method providing a more controlled, repeatable and reproducible aliquot of p-H_2 employs the in-situ reaction apparatus shown in Figure 7. To produce a continuous stream of para-enriched H_2 for stopped-flow kinetic and 2D PASADENA NMR experiments, the gas is passed through a column packed with Apachi nickel silica gel catalyst.[21] Before use, the coil is purged at room temperature with a stream of H_2 for a period of about one hour. Following the purge, the glass coil is immersed in liquid nitrogen. Solenoid valves are used to gate p-H_2 gas flow. Bubbles are produced by a glass capillary inserted into the reaction solution contained in the standard 5 mm NMR tube, as shown in the figure. The apparatus shown here produced a consistent and well-defined burst of H_2 through the solution. This is a critical requirement for stopped-flow kinetics studies as well as 2D PASADENA experiments that are susceptible to T_1 noise contributions due to variations in the amount of product magnetization formed per H_2 burst. The system shown in Figure 7 has the added advantage of being closed to the external atmosphere, reducing the problem of catalyst poisoning by air. A disadvantage of this apparatus is that does not allow the tube to spin. If sample spinning to improve resolution is desired, the capillary can be inserted into an open NMR tube with no physical connection to the tube. With careful alignment of the capillary it proved possible to spin the NMR tube at 15 Hz.

5.2 Applications

When evaluating the potential applicability of PASADENA to the study of a specific hydrogenation reaction, one must keep in mind that the following two conditions need to be fulfilled in order to observe NMR signal enhancements:

(1) The reaction must be molecular, so that the two protons of the original hydrogen molecule are transferred pairwise into magnetically inequivalent sites on the product. A resolved spin-spin coupling between these nuclei is also required.
(2) The time-scale of the molecular addition should be short compared to the T_1 on the hydrogenation product. If a stepwise reaction mechanism is involved, the lifetime of any intermediate species should be short compared to the T_1 on each species.

Fortunately, there are a large variety of transition metal complexes that function as efficient hydrogenation catalysts in liquids at ambient temperature and pressure.

5.2.1 Hydrogenation of Acryolonitrile to Propionitrile by Wilkinson's Catalyst

Perhaps the best known homogeneous hydrogenation catalyst is $Rh(PPh_3)_3Cl$, Wilkinson's catalyst.[26] It was this particular catalyst that was used in the original experimental demonstration of the PASADENA effect.[4] Para-enriched H_2 was added to acrylonitrile to form propionitrile, as follows:

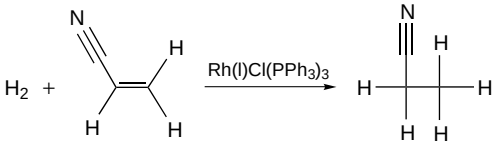

The reaction was carried out with H_2 that had been equilibrated for approximately one-half hour at 77 K in the presence of Apachi,[21] yielding 50% p-H_2. The proton NMR spectrum of the d-chloroform solution containing the acrylonitrile substrate and catalyst was recorded prior to adding any H_2, as shown in Figure 6(a). The p-H_2 was then bubbled for about 1s through the d-chloroform solution containing the substrate and catalyst. Following a delay of about 1 s to allow the solution to settle, a single hard $\pi/4$ pulse was applied. The resulting PASADENA enhanced spectrum is shown in Figure 6(b). For comparison, an exact numerical density matrix simulation of the PASADENA lineshape is presented in Figure 6(d). Excellent

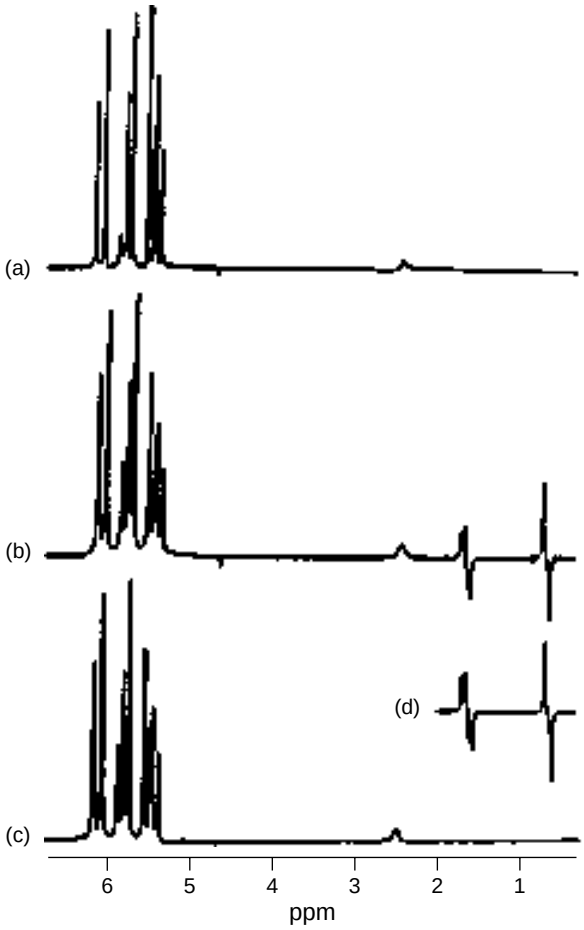

Figure 6 The first experimental demonstration of the PASADENA effect. (a) ^{1}H NMR spectrum prior to the reaction. The intense lines are due to the acrylonitrile substrate. (b) Signal acquired using a $\pi/4$ pulse immediately following a 1s burst of 50% p-H_2 gas through the solution. (c) Spectrum of the equilibrated sample (following complete spin-lattice relaxation) shows that the signal in (b) was a large transient enhancement. (d) Numerical density matrix simulation demonstrating the agreement of theory with the spectrum in (b)

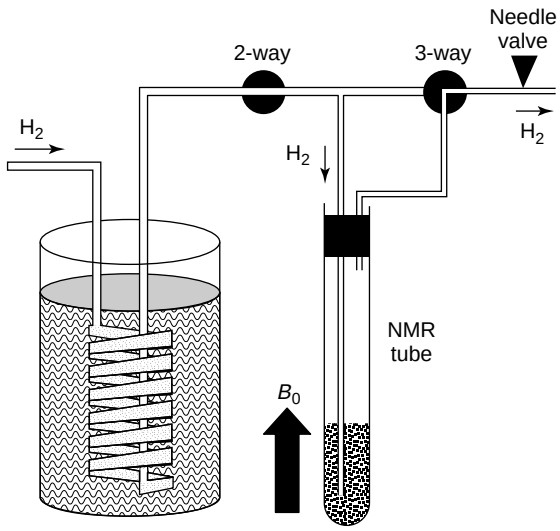

Figure 7 In-situ PASADENA hydrogenation apparatus. The volume above the liquid sample can be pressurized to 1.5−2 atm with gas enriched to $\chi_p = 0.5$, while a needle valve on the 1/8" diameter kel-F™ tubing at the gas outlet is adjusted to obtain fine bubbles from a submerged glass capillary tube. The solenoid valves are under pulse-programmer control. The column containing Apachi[21] (the ortho-para conversion catalyst) consists of a ∼15 turn, 8 mm inner diameter pyrex coil. Two separate TTL control lines from the pulse programmer were used to control the solenoid valves. This arrangement has the advantage of allowing the gas pressure on the inlet and outlet of the NMR tube to be rapidly equalized following an H_2 burst. To minimize ortho-para reconversion that may occur in the room temperature components of the gas delivery system, valves with Teflon internal surfaces were employed, and all fittings, tubing and connectors were glass, Teflon or kel-F™

agreement between the simulation and experiment is evident. The spectrum acquired immediately following the hydrogen burst exhibits antiphase multiplet signals corresponding to the NMR shifts of the conventional quartet and triplet multiplets of propionitrile (centered near 1.7 and 0.6 ppm). After waiting several minutes, the spectrum of Figure 6(d) was acquired. Here, the enhanced transitions observed in Figure 6(b) are totally absent. Spin lattice relaxation has returned the nuclear magnetization to its thermal equilibrium value.

5.2.2 PASADENA Signal Enhancement of Rh(I)(PPh)$_3$H$_2$Cl

The reaction of H_2 with $Rh(PPh_3)_3Cl$ in the absence of substrate yields $Rh(PPh_3)_3ClH_2$.[29] The proton spectrum of the dihydride in the hydride region immediately following reaction with p-H_2 is shown in Figure 8. The multiplet patterns due to both hydride protons are observed; the shift at the position trans to PPh_3 is $\delta_1 = -9.4$ ppm with $J_{PH} = 160$ Hz, and the second appears at $\delta_2 = -16.8$ ppm with an unresolved spin coupling. The multiplet patterns here exhibit the E/A antiphase pattern rather than A/E as was observed in the PASADENA

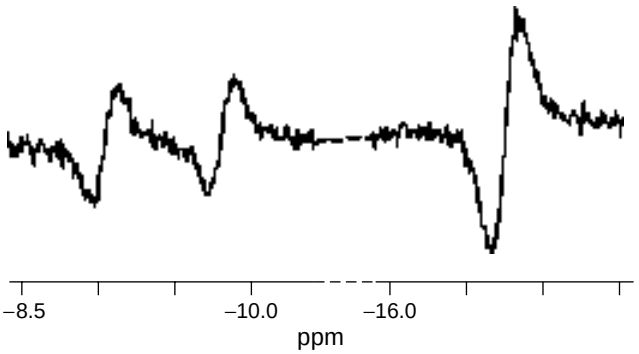

Figure 8 PASADENA enhanced ^{1}H NMR spectrum (200 MHz) of the hydride region of $RhCl(PPh_3)_2H_2$ formed from the reaction of Wilkinson's catalyst with 50% p-H_2 in deuteriobenzene solution. Due to ligand exchange, the only resolved J splitting is for the hydride proton trans to phosporous. The E/A multiplet intensity pattern indicates that the unresolved scalar coupling between the hydride protons is negative

spectrum of ethylbenzene or propionitrile. This highlights a unique aspect of the PASADENA experiment. There is usually no information on the sign of J in the weak coupling multiplet pattern, but the PASADENA enhanced multiplet reflects the absolute sign of J. This is immediately evident from the density operator calculations of equation (38) or (26), or by considering the transition intensity pattern predicted by the

two-spin energy level diagram in Figure 2. Secondly, J_{HH} between the hydride protons is not fully resolved, resulting in destructive interference and cancellation of signal amplitude. The apparent low enhancement is also due to the relatively rapid spin-relaxation of the hydride protons. The spin-lattice relaxation time of Zeeman order (T_{1z}) of the dihydride was measured to be 0.28 s.

5.2.3 *Stopped-Flow Kinetics of Styrene Hydrogenation by Rh(I)(PPh)$_3$Cl*

The kinetics and mechanism of Wilkinson's catalyst,[26] Rh(I)(PPh)$_3$Cl, structure I in scheme 1, has been extensively studied since its discovery nearly 30 years ago. The mechanism is complex, with competing pathways involving mononuclear as well as binuclear dihydride complexes, the concentrations of which are highly sensitive to temperature.[16] A key intermediate in the generally accepted *hydride route* mechanism is structure II shown in Scheme 1.[26–28] Remarkably, direct evidence for the existence of this intermediate was only recently obtained by PASADENA NMR studies.[16]

Here, the application of PASADENA NMR to probe the kinetics of styrene hydrogenation by Rh(I)(PPh)$_3$Cl, assuming the generally accepted mechanism outlined in Scheme 1, is described.[27] The catalyst and substrate were dissolved in d_6-benzene and placed into a 5mm NMR tube connected to the p-H_2 delivery system shown in Figure 7. The time dependence of the product molecule PASADENA signal was mapped by incrementing the delay between the 1.0 s p-H_2 burst and the signal acquisition, resulting in the data set shown in Figure 9(a). A simplified kinetic scheme can be constructed to model this data.

The premixed benzene solution containing Rh(PPh$_3$)$_3$Cl and styrene consists of three major species in equilibrium, but the catalyst is largely undissociated:[27]

$$\mathrm{Rh(PPh_3)_3Cl} \rightleftharpoons \mathrm{Rh(PPh_3)_2Cl} \rightleftharpoons \mathrm{Rh(PPh_3)_2Cl(styrene)}$$

The equilibrium is upset as H_2 enters the solution, as it may react with any of the three species. It is known, however, that H_2 reacts only slowly with the triphenylphosphine and olefin coordinated complexes.[29] The rate of formation of the intermediate, Rh(PPh$_3$)$_2$H$_2$Cl(styrene), is limited only by the PPh$_3$ dissociation step. At high H_2 concentration (i.e., saturation), this reaction step is effectively unimolecular, and we may write

$$\begin{aligned} -\mathrm{d[Rh(PPh_3)_3Cl]}/\mathrm{d}t &\approx +\mathrm{d[Rh(PPh_3)_2ClH_2(styrene)]}/\mathrm{d}t \\ &\approx k_F\mathrm{[Rh(PPh_3)_3Cl]} \end{aligned} \tag{44}$$

Under these conditions, the primary pathway of the styrene hydrogenation may be reduced to the following two-step process:

$$\begin{array}{ccc} \mathbf{I} & & \mathbf{II} \\ \mathrm{Rh(PPh_3)_3Cl} & \xrightarrow{k_F} & \mathrm{Rh(PPh_3)_2ClH_2(styrene)} \\ & & \mathbf{P} \\ & \xrightarrow{k_D} & \text{ethylbenzene} \end{array}$$

The NMR observable in PASADENA kinetics experiments is the total J-order (or zz-order) of each species (ZZ_I, ZZ_{II}, ZZ_P). Thus, the correspondence between the chemical kinetics and the PASADENA kinetics may be represented as follows:

$$\begin{aligned} \frac{\mathrm{d}}{\mathrm{d}t}\mathrm{[II]} = k_F h(t)\mathrm{[I]} - k_D\mathrm{[II]} &\longrightarrow \frac{\mathrm{d}}{\mathrm{d}t}\mathrm{ZZ_{II}} \\ &= k_F h(t)\mathrm{ZZ_I} - \mathrm{Z_{II}}\left(k_D + 1/T_{1ZZ}^{\mathrm{II}}\right) \end{aligned} \tag{45}$$

The function $h(t)$ is used to account for the transient presence of H_2 in the solution due to the bubbling. For the J-order on the product, P:

$$\frac{\mathrm{d}}{\mathrm{d}t}\mathrm{[P]} = k_D\mathrm{[P]} \longrightarrow \frac{\mathrm{d}}{\mathrm{d}t}\mathrm{ZZ_P} = \mathrm{ZZ_{II}}k_D - \mathrm{ZZ_P}/T_{1ZZ}^{\mathrm{P}} \tag{46}$$

It is possible to analytically solve these equations for ZZ_{II} and ZZ_P in terms of the parameters k_F, k_D, T_{1ZZ}^{II} and T_{1ZZ}^{P}. Fortunately, several of these parameters can be deduced from independent experiments. Halpern and Wong investigated the kinetics of formation of Rh(PPh$_3$)$_2$ClH$_2$ in the absence of any substrate.[29] In the presence of excess H_2, the rate law with no added PPh$_3$ yields $k_F \approx 0.34\,\mathrm{s}^{-1}$. The spin-lattice of relaxation of J-order on the product can also be measured under equilibrium conditions. This leaves k_D and T_{1ZZ}^{II} to be determined by fitting the model to PASADENA kinetics data. Implementation of this model produced the theoretical fit to the experimental data shown in Figure 9(a),

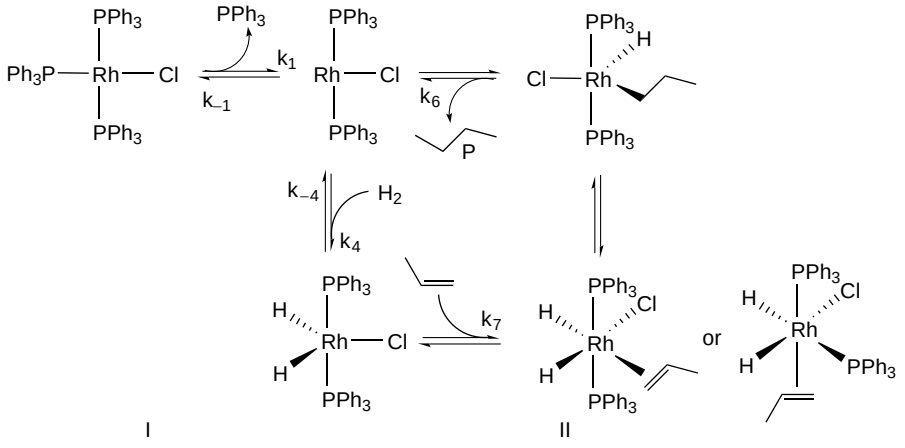

Scheme 1

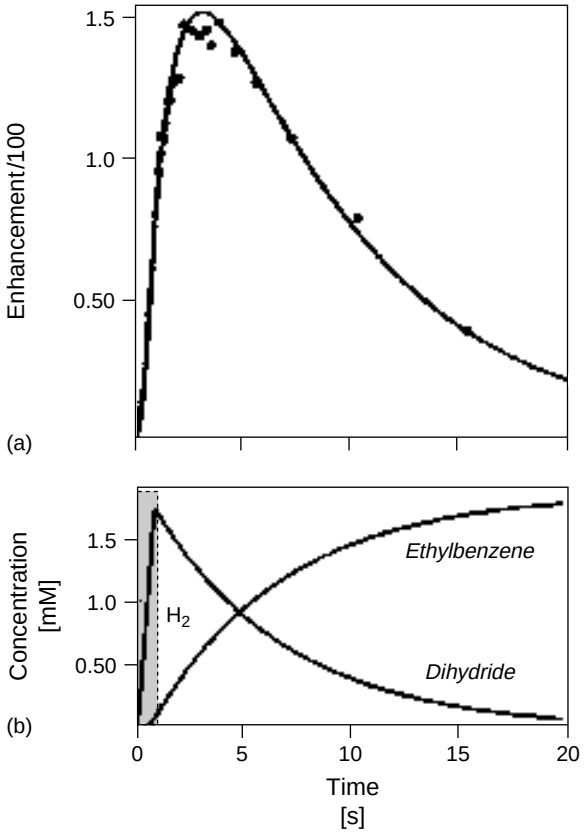

Figure 9 Stopped flow PASADENA kinetics of the formation of ethylbenzene by the $RhCl(PPh_3)_3$ catalyzed hydrogenation of styrene using 50% p-H_2. (a) PASADENA signal amplitude as a function of time between the hydrogen burst and the $\pi/4$ detection pulse. (b) Concentration time dependence of **II** and the product alkane determined by fitting the solution of equation (46) to the kinetic data. The shaded area indicates the period during which 50% p-H_2 is bubbled through the solution containing the catalyst and substrate

yielding $k_D = 0.160\,\mathrm{s}^{-1}$, $T_{1ZZ}^{\mathrm{II}} = 1.68\,\mathrm{s}$, and $T_{1ZZ}^{\mathrm{P}} = 8.15\,\mathrm{s}$.[12] The rate constants can be inserted into the conventional kinetic expressions to find the concentration time dependence of each species, as shown in Figure 9(b).

5.2.4 *Evidence for Catalyic Intermediates from PASADENA NMR*

Perhaps the most intriguing aspect of the PASADENA method is the potential to observe catalytic intermediates or other transient species in hydrogenation reactions. For example, Harthun and Bargon reported a transient rhodium-substrate-dihydrido species in the hydrogenation of itaconic acid dimethyl ester by a cationic rhodium complex.[30] The hydride region exhibited enhancements that were not observed in the absence of the substrate, but the spectrum could not be unequivocally assigned to a catalytic intermediate since the signals did not appear to be associated with a *cis* arrangement of the H_2 protons as would be expected in a catalytic hydrogenation intermediate.

The occurrence of catalytic intermediates can also be inferred from the appearance of the PASADENA enhanced multiplet patterns. Bargon et al. have noted that enhanced product spectra resulting from the p-H_2 addition to norbornadiene depended on the catalyst used. This could be explained if the rate of reaction is so rapid that the spin coherences (off-diagonal element of the density operator) are preserved, as described in Section 4.3. The density matrix representing the spin system resulting from the addition of p-H_2 to the catalyst or the product would then consist of a diagonal part, $\hat{I}_{zA}\hat{I}_{zB}$ (J-order) as well as off-diagonal terms associated with zero and double quantum coherence (see equations (35)–(38)). The density operator will reflect the spin Hamiltonian on the intermediate as well as the lifetime of this species, and this technique may therefore be used to differentiate between structural candidates for catalytic intermediates that cannot be directly observed.

5.2.5 *Elucidation of a Reaction Pathway Involving a Catalytic Intermediate*

Using a similar catalytic rhodium catalyst, $Rh(diphos)^+$, a new type of transient species was observed in the hydrogenation of styrene.[12] The reaction solutions initially contained 1 ml d_6-acetone, 0.015 g of the catalyst precursor, $[Rh(diphos)(nbd)]^+PF_6^-$, and 0.1 ml styrene in a 5 mm standard NMR tube. The catalyst was activated by bubbling p-H_2 through the solution for several seconds to release norbornane, while in the process yielding dramatic PASADENA NMR enhancement on both the norbornene and norbornane adducts. After about 20 s of H_2 bubbling, these signals subside, and in place of the norbornadiene the styrene becomes coordinated to the $Rh(diphos)^+$ with an equilibrium constant of $K_2 = 20\,\mathrm{M}^{-1}$.[31]

The accepted mechanism for the $Rh(diphos)^+$ catalyzed hydrogenation of styrene is presented in Scheme 2.[32] The rate-limiting step is the formation of the rhodium-olefin-dihydride species (**III**). PASADENA enhanced NMR studies have revealed a new type of transient species, identified as a rhodium-η_6-ethylbenzene complex identified as **V** in the scheme. The PASADENA spectrum (Figure 10) exhibits two sets of enhanced ethylbenzene alkyl group resonances. In the first set, the chemical shifts of the CH_3 and CH_2 group protons are the same as that of ethylbenzene in this solvent, and after 30–40 individual 1 s H_2 bursts, thermal equilibrium NMR signals can be detected and continue to grow in intensity as product accumulates. The other pair of enhanced multiplets occurs at lower shielding, but there is no accumulation of a thermally polarized signal at these chemical shifts. These observations lead to the hypothesis that the pair of resonances at higher shielding represent a transient *bound* alkane species, depicted as V in scheme 2. The decay rates of each pair of resonances was measured by varying the delay between the H_2 burst and the acquisition pulse. Decay times of 1.94 s and 3.35 s were obtained for the J-order of the bound and free forms of ethylbenzene, respectively. The faster decay of the bound form could be attributed to (1) the shorter rotational correlation time of the bound complex or (2) the dissociation of the bound alkane to yield free alkane.

The proposed bound $\rightarrow$ free pathway was investigated by 2D PASADENA exchange NMR.[12] Recall that cross-peaks in a 2D exchange experiment can confirm or refute the existence of an exchange event, and when cross peak/diagonal peak ratios can be measured from a series of 2D spectra in which the

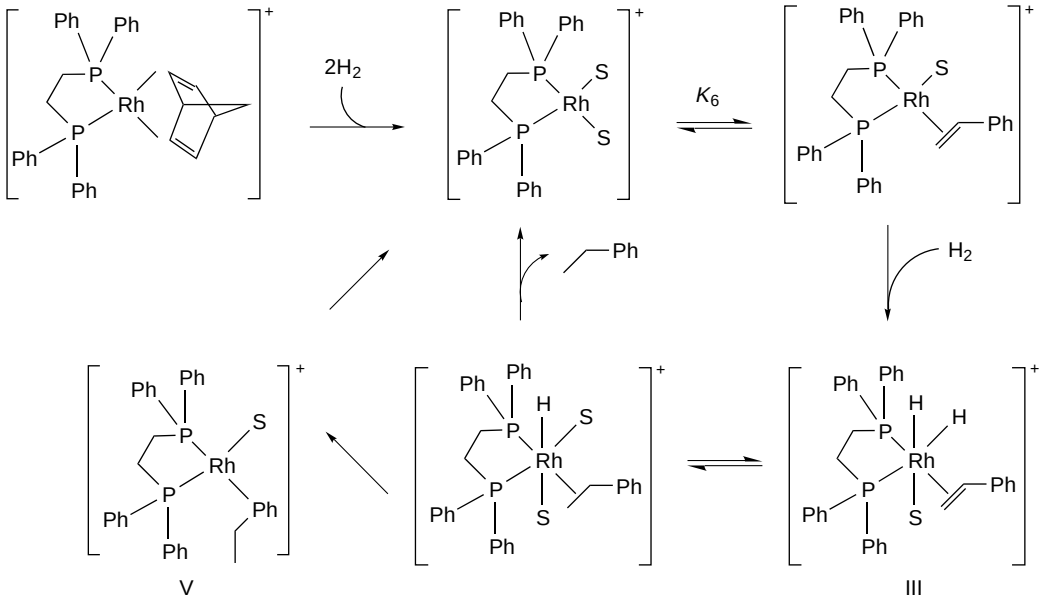

Scheme 2

exchange time is varied, the exchange rate can be determined. Section 5.2.6 describes the details of the pulse sequence development used in this investigation.

5.2.6 Two-Dimensional Exchange PASADENA NMR

This section describes some of the considerations for designing a pulse sequence for probing reaction pathways using 2D exchange PASADENA NMR. The sequence shown below was developed to investigate the rate of release of the bound form of ethylbenzene from Rh[diphos]$^+$ as described in Section 5.2.5.

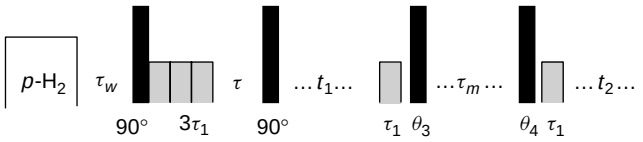

The reaction is initiated with a burst of p-H_2 followed by a delay to allow the solution to settle. Pure zero quantum coherence (ZQC) is generated in the preparation period by a $\pi/2$ pulse followed by 3 periods during which a homospoil gradient is applied. The choice of ZQC has the advantage that evolution of ZQC is independent of the receiver offset. This makes the sequence more robust and eases the task of setting the preparation time τ. Conversion into single quantum coherence is optimized by a second $\pi/2$ pulse. One only needs to consider the evolution of single quantum coherence during t_1 since the 1Q $\rightarrow$ 1Q coherence transfer echo filter removes all other coherence orders. Following the evolution of 1Q coherence during t_1, the coherence is stored as a superposition of Zeeman and J-order populations using a pulse θ_3. During the mixing period, τ_m, chemical exchange or cross-relaxation is allowed to occur. The populations are subsequently transformed back to single quantum coherences for detection with the pulse θ_4.

A two-spin product operator calculation reveals how the choice of the pulse angles θ_3 and θ_4 affects the type of spin order that is stored and the factors that impact the efficiency of its detection. The density operator following preparation, evolution, and storage is:

$$\begin{aligned}\hat{\rho}(\tau, t_1, \tau_1) = {} & \frac{1}{2}\hat{I}_{z1}\sin\theta_3\sin(\Delta\omega_z\tau)\sin\left(\frac{J}{2}t_1'\right) \\ & \times \{\sin\delta(\vec{r})\tau_1\sin\omega_{z1}t_1' - \cos\delta(\vec{r})\tau_1\cos\omega_{z1}t_1'\} \\ & - \frac{1}{2}\hat{I}_{z2}\sin\theta_3\sin(\Delta\omega_z\tau)\sin\left(\frac{J}{2}t_1'\right) \\ & \times \{\sin\delta(\vec{r})\tau_1\sin\omega_{z2}t_1' - \cos\delta(\vec{r})\tau_1\cos\omega_{z2}t_1'\} \\ & + \hat{I}_{z1}\hat{I}_{z2}\sin(\Delta\omega_z\tau)\sin\theta_3\cos\theta_3\cos\left(\frac{J}{2}t_1'\right) \\ & \times \{\sin\delta(\vec{r})\tau_1[\cos\omega_{z2}t_1' - \cos\omega_{z1}t_1'] \\ & + \cos\delta(\vec{r})\tau_1[\sin\omega_{z2}t_1' - \sin\omega_{z1}t_1']\} \end{aligned} \quad (47)$$

where $t_1' = t_1 + \tau_1$, $\delta(\vec{r})$ is the offset due to the homospoil gradient, and $\Delta\omega_z$ is the chemical shift difference. This expression is written in a form to emphasize that the population differences stored during the exchange time can be written as a linear combination of Zeeman and J-order, the weight of each type being dependent on the pulse angle θ_3. J-order is fully suppressed using $\theta_3 = \pi/2$, while Zeeman order is optimized. Also note that the t_1 dependence of the Zeeman order contains the factor $\sin J^b t_1'/2$ responsible for the A/E multiplet pattern in the frequency domain. Additional insights can be gained by following through with the signal calculation. The 2D time-domain signal associated with the cross-peak due to slow bound $\rightarrow$ free exchange is:

$$\begin{aligned} S_{b\rightarrow f} = {} & \frac{1}{4}\sin\left(\Delta_{1,2}^{b,b}\tau\right)\cos\left(\frac{J^b}{2}t_1'\right)\sin\left(\frac{J^f}{2}t_2'\right)\sin\theta_3\cos\theta_3\sin\theta_4\cos\theta_4 \\ & \times \left\{\exp\left[-i\left(\Delta_{1,1}^{b,f}\tau_1 + \omega_{z1}^b t_1 - \omega_{z1}^f t_2\right)\right]\right. \end{aligned}$$

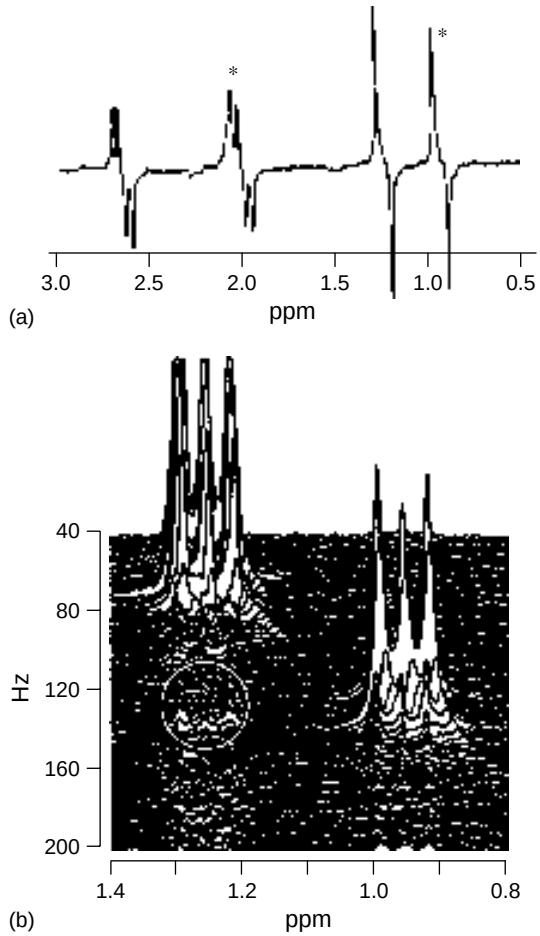

Figure 10 200 MHz PASADENA enhanced ^{1}H NMR spectrum of ethylbenzene formed by the Rh(diphos)$^+$ catalyzed hydrogenation of styrene in d_6-acetone solvent. The appearance of two pairs of methyl and methylene multiplets indicates that two distinct alkane species are formed in approximately equal amounts. The multiplets centered at 2.7 and 1.25 ppm occur at the same chemical shifts as free ethylbenzene, while the peaks marked by asterisks are attributed to an intermediate in a parallel pathway in which the nascent alkane remains or becomes bound to the Rh complex. (b) 200 MHz PASADENA 2D exchange spectrum (magnitude shown) resulting from the sequence described in the text, with $\tau_m = 2.0$ s, a 2 s 50% p-H_2 burst, and $\theta_3 = \theta_4 = \pi/2$. Single quantum transitions of the methyl region of ethylbenzene are shown in both frequency dimensions. An off-diagonal cross-peak due to the release of the bound alkane from the catalyst during tm would be observed in the region indicated by the white circle if the alkane which was "bound" prior to the first pulse of the sequence were to become free during τ_m. The diagonal multiplets centered at 0.96 and 1.25 ppm represent ethylbenzene that remained in the bound and free chemical environments throughout the entire sequence

$$
\begin{aligned}
&- \exp\left[-i\left(\Delta_{2,1}^{b,f}\tau_1 + \omega_{z2}^{b}t_1 - \omega_{z1}^{f}t_2\right)\right] \\
&+ \exp\left[-i\left(\Delta_{1,2}^{b,f}\tau_1 + \omega_{z1}^{b}t_1 - \omega_{z2}^{f}t_2\right)\right] \\
&- \exp\left[-i\left(\Delta_{2,2}^{b,f}\tau_1 + \omega_{z2}^{b}t_1 - \omega_{z2}^{f}t_2\right)\right]\Big\} \\
&+ \frac{1}{4}\sin\left(\Delta_{1,2}^{b,b}\tau\right)\sin\theta_3\sin\theta_4\sin\left(\frac{J^b}{2}t_1'\right)\cos\left(\frac{J^f}{2}t_2'\right) \\
&\times\left\{\exp\left[-i\left(\omega_{z2}^{b}t_1 - \omega_{z2}^{f}t_2\right)\right] - \exp\left[-i\left(\omega_{z1}^{b}t_1 - \omega_{z1}^{f}t_2\right)\right]\right\} \quad (48)
\end{aligned}
$$

where $\Delta_{i,j}^{x,y} = \omega_{zi}^{x} - \omega_{zj}^{y}$ and $t_2' = t_2 + \tau_1$. The diagonal bound peak signals can be derived from this expression by setting $\omega_{zi}^{f} \rightarrow \omega_{zi}^{b}$ and similarly for the "f" diagonal peaks we set $\omega_{zi}^{b} \rightarrow \omega_{zi}^{f}$. Inspection of this time-domain cross-peak signal reveals that the first term, which is optimized for the choice $\theta_3 = \theta_4 = 45°$, produces an antiphase (A/E) doublet in the ω_2 domain while yielding an absorption phase doublet in ω_1. This is significant because it implies that the spectrum of the bound species can be indirectly observed with undiminished PASADENA enhancement even if $J^b = 0$ so long as $|J^f| \gg 1/T_2^f$. Conversely, the choice $\theta_3 = \theta_4 = 90°$ will facilitate the observation of the fully enhanced transitions on the free species even if the J-coupling on this species was unresolved.

Now consider the application of the 2D exchange PASADENA NMR sequence to the particular example described in Section 5.2.5 in which two sets of enhanced ethylbenzene resonances were detected. Recall that one of these sets corresponded to ethylbenzene bound to Rh[diphos]$^+$, while the other represented free ethylbenzene. For the resolved couplings of bound and free ethylbenzene, where $J^b = J^f$, PASADENA enhanced signals are observed regardless of the choice of θ_3 and θ_4. Yet there is a potential advantage to the choice $\theta_3 = \theta_4 = 45°$ if there is a loss of catalytic activity during the course of the hydrogenation reaction. The finite lifetime of the catalyst may possibly limit the number of t_1 points that can be collected before the reaction terminates, which in turn limits the resolution of the J-coupling in this dimension.

Under the conditions used to study the Rh[diphos]$^+$ catalyzed hydrogenation of styrene, approximately 256 t_1 points could be acquired before the enhanced signal disappeared. The 2D exchange PASADENA NMR spectrum of the methyl region is presented in Figure 10b. A density matrix simulation of the zero quantum coherence formed by a $\pi/2$ pulse in the five spin system was used to choose the optimum preparation time of 409 ms. The spectrum was acquired using $\tau_w = 2$ s, $\theta_3 = \theta_4 = 90°$, and $\tau_m = 2$ s. In the case of the proposed bound $\rightarrow$ free pathway, cross-peaks are not observed in the 2D PASADENA exchange spectrum. However, from the S/N ratio of the diagonal peak magnitude signal, an upper limit of $k_6 \leq 0.05\,\text{s}^{-1}$ for the bound $\rightarrow$ free step can be established. Thus, it is concluded that this pathway is not involved in the primary catalytic hydrogenation cycle.

6 THE ALTADENA EFFECT

Recall that in the PASADENA effect the population distribution of the high field eigenstates was determined by the transition probabilities that may be calculated from projection of the singlet state (in the case of p-H_2) onto the high field eigenstates of the product molecule. This procedure relies on the validity of the sudden approximation in which the spin Hamiltonian was assumed to change instantaneously due to the rapid chemical addition to a substrate. Subsequent to product formation, there was no further change in the internal Hamiltonian before detection of the spin order by NMR.

Now consider a variation of the PASADENA effect whereby the hydrogenation product is formed at essentially zero magnetic field and then adiabatically transported to high magnetic field for NMR acquisition. Using the $Rh(PPh_3)_3Cl$

catalyzed hydrogenation of styrene, Weitekamp and Pravica[33] demonstrated that this procedure results in an initial spin state distribution that is qualitatively different from that obtained by doing the hydrogenation entirely at high field, as in PASADENA. Because the enhanced NMR spectra that result from this field cycled procedure exhibit net alignment of the mutiplets, the technique was given the acronym ALTADENA (Adiabatic Longitudinal Transport After Dissociation Engenders Net Alignment). Here, the theoretical description presented in the original paper is outlined.[33]

Upon reaction at zero field, the rotational energy splitting suddenly becomes negligible, but the singlet-triplet spin eigenstates remain the same. As the product molecule is adiabatically transported to high magnetic field, the eigenstates develop into the direct product states of the weakly coupled system. As illustrated in Figure 11, these state-to-state correlations, assuming J and $\Delta\omega_z$ have the same sign, are as follows: $|\alpha\alpha\rangle \rightarrow |\alpha\alpha\rangle$, $2^{-1/2}(|\alpha\beta\rangle + |\beta\alpha\rangle) \rightarrow |\alpha\beta\rangle$, $2^{-1/2}(-|\alpha\beta\rangle + |\beta\alpha\rangle) \rightarrow |\beta\alpha\rangle$, and $|\beta\beta\rangle \rightarrow |\beta\beta\rangle$. The high field population distribution resulting from adiabatic transport is not the same as the distribution obtained under the sudden approximation (compare to Figure 2).

Using a procedure analogous to the one used to find the density operator of H_2, the density operator corresponding to the population distribution due to hydrogenation and transport to high field is

$$\hat{\rho}_{ad} = \frac{1}{4} - f\left[\hat{I}_{z1}\hat{I}_{z2} \pm \frac{1}{2}(\hat{I}_{z1} - \hat{I}_{z2})\right] \tag{49}$$

Of course, when J and $\Delta\omega_z$ have opposite signs, the correlation of the singlet state is to the $|\alpha\beta\rangle$ state rather than to the $|\beta\alpha\rangle$ and the lower $(-)$ sign in equation (49) applies. It is evident from equation (49) that the NMR signal will be a superposition of contributions from both terms in square brackets, with the relative contribution determined by the applied pulse angle. As was shown in Section 3.4 the J-order term $\hat{I}_{z1}\hat{I}_{z2}$ yields a spectrum that is optimized for a $\theta = \pi/4$ pulse and consists of a A/E doublet at each chemical shift. The term $\hat{I}_{z1} - \hat{I}_{z2}$ yields *net alignment* of each multiplet with the relative amplitudes determined by the usual Pascal's triangle factors. The signal intensity from this term is optimized with $\theta = \pi/2$. A signal calculation yields the following relative transition amplitudes:

$$\begin{aligned}(f/2)\sin\theta(1+\cos\theta) \;:\; (f/2)\sin\theta(1-\cos\theta)\\ -(f/2)\sin\theta(1-\cos\theta) \;:\; -(f/2)\sin\theta(1+\cos\theta)\end{aligned} \tag{50}$$

Consequently, only two transitions are observed when the signal is detected with a small pulse angle. This is consistent with the expectations of the population distribution shown in Figure 11. A $\pi/2$ detection pulse elicits two doublets with relative amplitudes of $\{1:1\}$ and $\{-1:-1\}$.

The ALTADENA effect was originally demonstrated by Pravica and Weitekamp in the $Rh(I)[PPh_3]_3Cl$ catalyzed hydrogenation of styrene by bubbling 50% p-H_2 for 1s at a field of 9 mT followed by insertion of the sample into the NMR spectrometer at a field of 4.7 T.[33] The transport step was carried out in less than about 3 s. The spectrum resulting from a small tip angle pulse ($\pi/11$ rad) is shown in Figure 12(a), and the spectrum resulting from a $\pi/2$ pulse is shown in Figure 12(b). The amplitude patterns are in agreement with the predictions of theory if the density operator given in equation (49) is generalized to 5 spins:

$$\hat{\rho}_{ad} = -f\left[\hat{I}_{za}\hat{I}_{zb} \pm \frac{1}{2}(\hat{I}_{za} - \hat{I}_{zb})\right] \tag{51}$$

Here, the subscripts "a" and "b" refer to the magnetically equivalent CH_3 and CH_2 protons of ethylbenzene. The signal calculation yields the following relative line amplitudes:

For the quartet:

$$\begin{aligned}&\{\sin\theta(1+\cos\theta)/2 : \sin\theta(3+\cos\theta)/2 :\\ &\sin\theta(3-\cos\theta)/2 : \sin\theta(1-\cos\theta)/2\}\end{aligned} \tag{52}$$

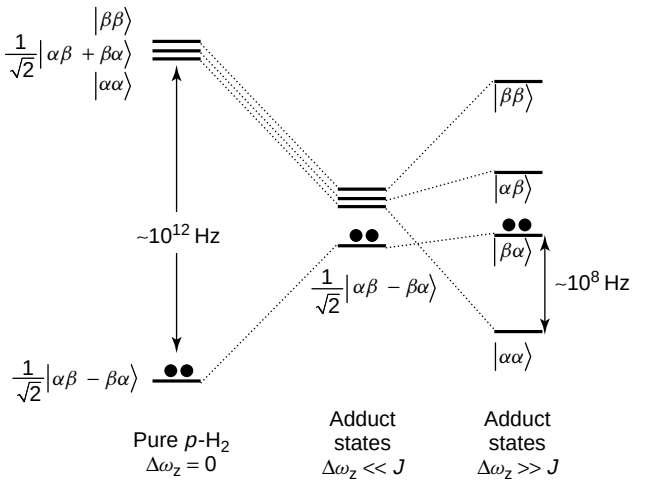

Figure 11 Energy level correlation diagram in the ALTADENA experiment

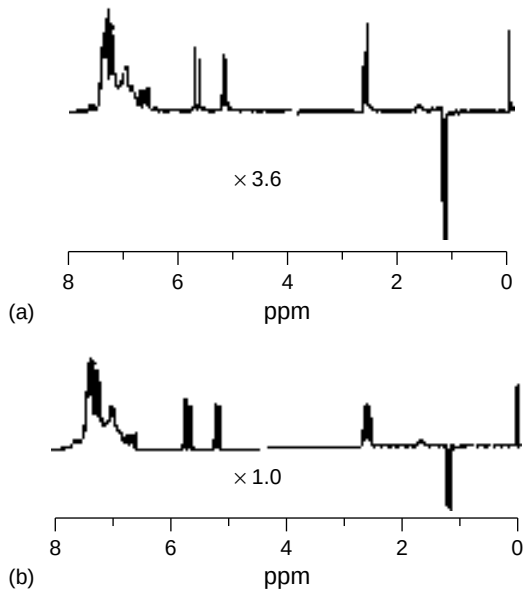

Figure 12 Experimental ALTADENA experiment (courtesy of Weitekamp and Pravica)

For the triplet:

$$\{-\sin\theta(\cos\theta-1):-2\sin\theta:-\sin\theta(1+\cos\theta)\} \tag{53}$$

By analogy with the 2-spin case, a $\pi/2$ pulse yields net alignment with relative amplitudes determined by the usual Pascal's triangle factors, while a small angle pulse leads to the ratios $\{1:2:1:0\}$ and $\{0:-2:-2\}$ in which transitions are noticeably absent from each multiplet. In conclusion, the predictions of the density operator theory for the ALTADENA effect are in striking agreement with experiment.

7 THEORY OF ORTHO/PARA D_2 ENHANCEMENT

7.1 Nuclear Spin Functions of D_2

As with H_2, the product of the rotational and nuclear spin symmetries must be correlated, but due to the fact that deuterons are bosons ($I=1$), odd j rotational states are associated with antisymmetric (para) spin states, while even valued j correspond to symmetric (ortho) spin states. Therefore, the ground rotational state is o-D_2. Here, the derivation of the density operator in the case of molecular addition of D_2 with arbitrary ortho/para composition will be presented.[12,37] The time-averaged operator required to calculate the PASADENA signal in the slow-reaction rate limit will be obtained from this result.

There are $2I+1=3$ states $|m_i\rangle$ of a deuterium nuclear spin, which shall be labeled $|1\rangle$, $|0\rangle$, $|-1\rangle$. For a deuteron pair, there are $(2I+1)^2=9$ direct product states $|m_1m_2\rangle$. These are eigenfunctions of $\hat{I}_z=\hat{I}_{z1}+\hat{I}_{z2}$, but not of $\hat{I}^2=(\hat{I}_1+\hat{I}_2)^2$. Since angular momentum must be conserved in an isolated molecule, the total angular momentum is a quantum mechanical constant of the motion, and hence $[\hat{\mathcal{H}},\hat{I}^2]=0$. It follows that $\hat{\mathcal{H}}$ and $\hat{I}^2$ have the same spin eigenstates. The eigenstates of $\hat{I}^2$ can be obtained from the appropriate unitary transformation of the direct product states, $|m_1m_2\rangle$. The appropriate linear combination can be found by evaluating the Clebsch–Gordon coefficients:[34–36]

$$C^{I_1I_2I}_{m_1m_2m}\equiv\langle I_1m_1I_2m_2|I_1I_2Im\rangle \tag{54}$$

In terms of these coefficients, the coupled states are given by

$$|I_1I_2Im\rangle=\sum_{m_1m_2}C^{I_1I_2I}_{m_1m_2m}|I_1I_2m_1m_2\rangle \tag{55}$$

where the resultant values of I are given by the Clebsch–Gordon series; $I=\{I_1+I_2,\ldots|I_1-I_2|\}$. For D_2, $I_1=I_2=1$, and $I=\{2,1,0\}$. This yields three manifolds consisting of 5, 3 and 1 state(s), respectively. The eigenstates of $\hat{I}^2$ are as follows:

$$\text{ortho-}D_2\begin{cases}|22\rangle=|\alpha\alpha\rangle\\ |21\rangle=2^{-1/2}(|\alpha0\rangle+|0\alpha\rangle)\\ |20\rangle=6^{-1/2}(|\alpha\beta\rangle+2|00\rangle+|\beta\alpha\rangle)\\ |2-1\rangle=2^{-1/2}(|\beta0\rangle+|0\beta\rangle)\\ |2-2\rangle=|\beta\beta\rangle\\ |00\rangle=3^{-1/2}(|\alpha\beta\rangle-|00\rangle+|\beta\alpha\rangle)\end{cases} \tag{56}$$

$$\text{para-}D_2\begin{cases}|11\rangle=2^{-1/2}(|0\alpha\rangle-|\alpha0\rangle)\\ |10\rangle=2^{-1/2}(|\beta\alpha\rangle-|\alpha\beta\rangle)\\ |1-1\rangle=2^{-1/2}(|\beta0\rangle-|0\beta\rangle)\end{cases} \tag{57}$$

The transformation matrix formed by these eigenvectors can be used to diagonalize the Hamiltonian. The transformation is represented as

$$\{\hat{\mathcal{H}}\}_{\text{Eigen}}=A\{\hat{\mathcal{H}}\}_{\text{prod}}A^T \tag{58}$$

7.2 Molecular Deuterium Nuclear Spin Density Matrix

The density matrix for some arbitrary mixture of ortho/para deuterium maybe written as

$$\rho=\begin{pmatrix}\chi_o/6 & & & & & & & & \\ & \chi_o/6 & & & & & & & \\ & & \chi_o/6 & & & & & & \\ & & & \chi_o/6 & & & & & \\ & & & & \chi_o/6 & & & & \\ & & & & & \chi_o/6 & & & \\ & & & & & & \chi_p/3 & & \\ & & & & & & & \chi_p/3 & \\ & & & & & & & & \chi_p/3\end{pmatrix} \tag{59}$$

While it is most convenient to specify the matrix elements in the eigenbasis, the calculations that follow are more easily carried out in the direct product basis. The required transformation of the density matrix is:

$$\{\hat{\mathcal{H}}\}_{\text{prod}}=A^T\{\hat{\mathcal{H}}\}_{\text{Eigen}}A \tag{60}$$

With the density matrix now in the direct product basis, it may be expressed as a linear combination of spin operators. In the case of H_2, this was $\hat{1}/4-f\hat{I}_1\cdot\hat{I}_2$. This operator is a scalar, i.e., it commutes with $\hat{I}$. Similarly, the density operator of D_2 should also be of a scalar form. The construction of scalar operators is achieved using irreducible tensor operators. The irreducible tensor operator (ITO) of rank k is defined as the set of $2k+1$ operators T^k_q that transform under coordinate rotations according to the relation[34–36]

$$D(\alpha,\beta,\gamma)T^k_qD^{-1}(\alpha,\beta,\gamma)=\sum_{q'}T^k_{q'}\mathcal{D}^{(k)}_{q'q}(\alpha,\beta,\gamma) \tag{61}$$

where q and q' take on integer values running from $-k$ to $+k$ and $\mathcal{D}^{(k)}_{q'q}(\alpha,\beta,\gamma)$ are elements of the Wigner rotation matrix. To form the density operator of D_2, compound irreducible tensor operators are employed. The general expression for a compound irreducible tensor operator is[34]

$$\{T^{k_1}(1)\otimes T^{k_2}(2)\}^k_q=\sum_{q_1q_2}\langle k_1q_1k_2q_2|k_1k_2kq\rangle T^{k_1}_{q_1}(1)T^{k_2}_{q_2}(2) \tag{62}$$

The coefficients in the summation are the Clebsch–Gordon coefficients. Since the D_2 density operator is expected to be a scalar, only the $k=q=0$ compound ITO needs to be evaluated. In terms of the 3-j symbol,

$$\{T^{k_1}(1)\otimes T^{k_2}(2)\}^0_0=\sum_{q_1q_2}(-1)^{k_1-k_2}\begin{pmatrix}k_1 & k_2 & 0\\ q_1 & -q_2 & 0\end{pmatrix}\times T^{k_1}_{q_1}(1)T^{k_2}_{q_2}(2) \tag{63}$$

where

$$\begin{pmatrix}k_1 & k_2 & 0\\ q_1 & -q_2 & 0\end{pmatrix}=(-1)^{k_1-m_1}(2k_1+1)^{-1/2}\delta_{k_1k_2}\delta_{m_1m_2} \tag{64}$$

The functional form requires that the rank of the individual tensors be the same (i.e., $k' = k_1 = k_2$). The resulting zero rank compound ITO becomes

$$\{T^k(1) \otimes T^k(2)\}_0^0 = \sum_q (-1)^{k-q}(2k'+1)^{-1/2} T_q^k(1) T_{-q}^k(2)$$
$$= (-1)^k (2k+1)^{-1/2} \mathcal{A}^k \quad (65)$$

where
$$\mathcal{A}^k = \sum_q (-1)^q T_q^k(1) T_{-q}^k(2) \quad (66)$$

Assume that the density operator can be decomposed as follows:

$$\begin{aligned}\hat{\rho} &= c_0\mathcal{A}_0 + c_1\mathcal{A}_1 + c_2\mathcal{A}_2 \\ &= c_0 T_0^0(1)T_0^0(2) + c_1[T_0^1(1)T_0^1(2) - T_{-1}^1(1)T_1^1(2) - T_1^1(1)T_{-1}^1(2)] \\ &\quad + c_2[T_0^2(1)T_0^2(2) - T_{-1}^2(1)T_1^2(2) - T_1^2(1)T_{-1}^2(2) \\ &\quad + T_{-2}^2(1)T_2^2(2) + T_2^2(1)T_{-2}^2(2)] \end{aligned} \quad (67)$$

In terms of the Cartesian spin operators,

$$\begin{aligned}\hat{\rho} &= c_0\hat{1} + c_1\hat{I}_1 \cdot \hat{I}_2 \\ &\quad + \frac{c_2}{4}\left\{\frac{8}{3}\hat{1} + \hat{I}_{-1}^2\hat{I}_{+2}^2 + \hat{I}_1^2\hat{I}_{-2}^2 + 6\hat{I}_{z1}^2\hat{I}_{z2}^2 - 4\hat{I}_{z1}^2 - 4\hat{I}_{z2}^2\right. \\ &\quad + (\hat{I}_{-1}\hat{I}_{+2} + \hat{I}_{+1}\hat{I}_{-2})(4\hat{I}_{z1}\hat{I}_{z2} - \hat{1}) \\ &\quad \left. +2(\hat{I}_{-1}\hat{I}_{+2} - \hat{I}_{+1}\hat{I}_{-2})(\hat{I}_{z1} - \hat{I}_{z2})\right\} \end{aligned} \quad (68)$$

The next step is to find the matrix representation of ρ so that it may be equated with the D_2 density matrix and the coefficients c_0, c_1 and c_2 determined. Equating the elements of the two different matrix formulations of ρ,

$$c_0 = \frac{1}{9} \quad c_1 = \frac{f}{2} \quad c_2 = f \quad (69)$$

where f is related to the mole fraction of p-D_2 by $f = (1/3 - \chi_p)/4$. Equation (68), along with the coefficients given in equation (69), is in agreement with expressions derived by Pravica.[37]

7.3 The Time-Averaged Initial Condition

When the D_2 addition rate is slow compared with the period of the ensuing coherence evolution, the off-diagonal elements of the density matrix (expressed in the eigenbasis of the adduct spin Hamiltonian) vanish and the time averaged density matrix becomes diagonal. The signal arising from this averaged initial condition will now be calculated, assuming the weak-coupling limit as the case may be in liquids. Dropping the off-diagonal terms,

$$\begin{aligned}\hat{\rho}_{\text{diag}} &= \sum_i \langle i|\rho|i\rangle |i\rangle\langle i| \\ &= \frac{1}{9}\hat{1} + \frac{f}{2}(\hat{I}_{z1}\hat{I}_{z2} + 3\hat{I}_{z1}^2\hat{I}_{z2}^2 - 2\hat{I}_{z1}^2 - 2\hat{I}_{z2}^2) \end{aligned} \quad (70)$$

The single-quantum operators generated from the response of $\hat{\rho}_{\text{diag}}$ to a θ_x rf pulse are:

$$\begin{aligned}\hat{\rho}_{\text{diag}} \xrightarrow{\theta\hat{I}_x} &\frac{-f}{2}\sin\theta\cos\theta\{\hat{I}_{y1}\hat{I}_{z2} + \hat{I}_{z1}\hat{I}_{y2} \\ &- 2(\hat{I}_{y1}\hat{I}_{z1} + \hat{I}_{z1}\hat{I}_{y1} + \hat{I}_{y2}\hat{I}_{z2} + \hat{I}_{z2}\hat{I}_{y2}) \\ &- 3\cos^2\theta(\hat{I}_{y1}\hat{I}_{z1}\hat{I}_{z2}^2 + \hat{I}_{z1}\hat{I}_{y1}\hat{I}_{z2}^2 \\ &+ \hat{I}_{z1}^2\hat{I}_{y2}\hat{I}_{z2} + \hat{I}_{z1}^2\hat{I}_{z2}\hat{I}_{y2})\} \end{aligned} \quad (71)$$

The FID arises from terms which evolve under $\hat{\mathcal{H}}_{\text{int}}$ to yield nonzero traces with $\hat{I}_+$. The relevant traces are

$$\begin{aligned} Tr\{\hat{I}_+\hat{I}_{x1}\hat{I}_{z2}^2\} &= Tr\{\hat{I}_+\hat{I}_{z1}^2\hat{I}_{x2}\} = 4 \\ Tr\{\hat{I}_+\hat{I}_{y1}\hat{I}_{z2}^2\} &= Tr\{\hat{I}_+\hat{I}_{z1}^2\hat{I}_{y2}\} = 4i \end{aligned} \quad (72)$$

After expanding the trigonometric functions of the $I = 1$ spin operators:

$$S(t) = 2f\sin\theta\cos\theta\sin Jt\{e^{-i\omega_{z1}t} + e^{-i\omega_{z2}t}\} \quad (73)$$

This signal closely resembles the PASADENA signal for a two-spin system of weakly coupled protons with the exception that the splitting between the two lines is now $2J$. Again, maximum signal is obtained using a $\theta = \pi/4$ pulse, and the central transition is again absent in the PASADENA spectrum in which the absolute line amplitudes are $\{-1/12, 0, +1/12\}$ for pure p-D_2. The signal amplitudes derived from equation (73) may be compared to the conventional signal derived form Zeeman order in the high temperature regime.

$$\begin{aligned}&\hat{\rho}(0) = b(T)\hat{I}_z \xrightarrow{\frac{\pi}{2}\hat{I}_y} \xrightarrow{\hat{\mathcal{H}}_{\text{int}}} \hat{\rho}(t) \\ &S(t) = Tr\{\hat{I}_+\hat{\rho}(t)\} = 2b(T)(1 + 2\cos Jt)\{e^{-i\omega_{z1}t} + e^{-i\omega_{z2}t}\} \end{aligned} \quad (74)$$

Here, the spectrum of two weakly coupled deuterons exhibits two triplets with line amplitudes $2b(T)\{1, 1, 1\}$.

8 PASADENA EFFECT AT A SOLID SURFACE

This section reviews the extension of the PASADENA effect to H_2 chemisorption at the surface of ZnO.[38] Adsorption, kinetics and infrared studies have previously characterized the active sites of the catalytic surface.[39–41] Due to the appearance of O–H and Zn–H adsorption bands in the infrared spectra,[42] it has been proposed that the following surface species is produced upon chemisorption:

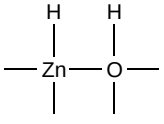

Molecular addition is a fundamental requirement to observe the PASADENA effect since randomization of the spins on

a surface would lead to immediate loss of spin order. In ZnO, isotopes studies have shown that a mixture of H_2 and D_2 added to the surface simultaneously during olefin hydrogenation yields predominantly alkane-d_2 and alkane-H_2 adducts. This is evidence that the two protons of H_2 remain in close proximity once adsorbed to the active site. Therefore, a PASADENA signal enhancement is expected at these sites, while in principle, physisorbed or binding sites that dissociate hydrogen should be discriminated against.

Adsorption experiments on powdered ZnO[43] were performed using both normal H_2 and para-enriched H_2 at room temperature and under moderate vacuum conditions. A 0.3 g sample of ZnO was packed into a modified NMR tube connected to an evacuation line and a p-H_2 delivery line with a standing pressure of 160 kPa and held in place by glass wool. The sample was first heated under vacuum to 673–723 K for >4 h. Parahydrogen was prepared by passing H_2 gas through activated Apachi[21] at 77 K. NMR was performed at 4.7 T (1H resonance at 198 MHz). For each spectrum a period of evacuation of the sample, typically several minutes, was followed by a brief burst of p-H_2, and then immediate re-evacuation. A resonant rf pulse (1.8 μs, 45° flip angle) to excite coherence was delivered at the end of the nominal burst time, followed by detection of transverse magnetization (128 points at 10 ms/point after 20 ms delay). The transients were zero-filled to 256 points before Fourier transformation without apodization. Figure 13(a) shows the spectrum obtained when a ∼50 ms burst of n-H_2 was delivered to the sample. The broad, weak resonance is due to species present before the burst. The relatively sharp (FWHM = 1 kHz) resonance was attributed to gas-phase o-H_2 (p-H_2 has no NMR signal). Figure 13(b) shows the spectrum obtained after the same procedure was repeated using para-enriched H_2. The prominent anti-phase signal is interpreted as the PASADENA NMR of hydrogen chemisorbed on ZnO. This PASADENA enhanced signal is unlike the NMR lineshape obtained with n-H_2 here or in previous NMR studies of H_2 on ZnO.[44,45] Figure 13(c) presents the pure PASADENA NMR spectrum after subtraction of the broad background signal. The resonance due to gaseous o-H_2 in the n-H_2 experiment has also been subtracted away after scaling by a factor of 2/3 to account for the ratio of the mole fraction of o-H_2 in each experiment. Larger signal amplitudes were observed with burst lengths of 100 and 200 ms, indicating that additional binding site are available for chemisorption. However, the line shapes (not shown) also changed with increasing exposure to p-H_2. This could be either due to adsorption by different types of binding sites or due to spin-diffusion to other protons in the vicinity of the binding site. The signal enhancement in these spectra was estimated to be in the neighborhood of 400–1000.

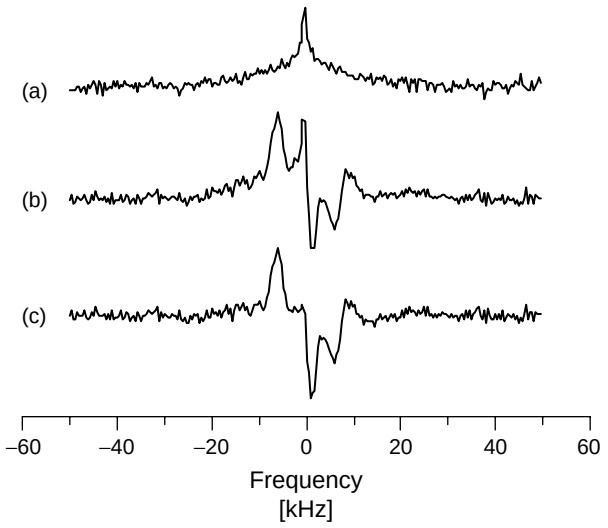

Figure 13 (a) ^{1}H NMR spectrum immediately after a ∼50 ms burst of n-H_2 delivered to polycrystalline ZnO. (b) Spectrum recorded under the same conditions as in (a) but using 50% p-H_2. (c) Pure PASADENA spectrum obtained by taking the ortho-weighted difference of (a) and (b) as described in the text

When ZnO is continuously exposed to p-H_2, the enhancement disappears over a period of tens of seconds, indicating that the adsorption sites observed by PASADENA become saturated. As the adsorption sites become occupied, the signal due to chemisorbed H_2 dies off due to spin lattice relaxation. However, the PASADENA signal following a short burst of p-H_2 was consistent and repeatable if the sample was evacuated for a few seconds in between bursts. These experiments indicate reversible binding sites consistent with Type I adsorption at room temperature.

The PASADENA line shape contains information about the electronic structure of the catalytically actives sites of ZnO. It can be quantitatively modeled if it is assumed that (1) the line shape obtained for a short (50 ms) p-H_2 burst arises from a single type of adsorption site and (2) that the product state is taken to be a static, magnetically isolated two-spin system formed by dissociative chemisorption. The high-field, rotating frame spin Hamiltonian including chemical shifts, dipolar and scalar couplings is given by equation (9). Since the ZnO is in a high surface area, polycrystalline form, the simulation of the spectrum must account for all random distribution of orientations of the binding site with respect to the magnetic field. The anisotropy of the dipolar and chemical shielding interactions can be expressed in terms of the principal components of the dipolar and chemical shielding tensors. However, care must be exercised to preserve the relative orientations of the dipolar and chemical shielding principal axis systems when computing the transition frequency. Thus, three transformations are required: the first two relate the principal axis systems of the chemical shielding tensors to the principal axis system of the dipolar tensor (defined by the internuclear vector), and the third transformation relates the internuclear vector to the magnetic field axis. Hence, the observed chemical shift $\omega_{zi}(\vartheta, \phi, \Omega_i)$ of the ith proton incorporates the set of Euler angles $\Omega_i = \{\alpha_i, \beta_i, \gamma_i\}$ relating the principal axis of the chemical shielding tensor to that of the dipolar coupling, while the polar angle ϑ and azimuthal angle ϕ relate the orientation of the internuclear vector to the magnetic field direction. The final expression for the chemical shift of the ith nucleus for an arbitrary orientation is given by[46,47]

$$\omega_{zi} = \omega_0\sigma_i + \omega_0(8\pi/15)^{1/2}\delta_i \sum_{m'} Y_{2,-m'}(\vartheta, \phi) \times \left[(3/2)^{1/2} D^2_{0m'}(\Omega_i) + \frac{\eta_i}{2}[D^2_{2m'}(\Omega_i) + D^2_{-2m'}(\Omega_i)]\right] \quad (75)$$

where $D^l_{m,m'}(\Omega)$ are elements of the Wigner rotation matrix, Y^m_l are the spherical harmonics, $\omega_0 = -\gamma_n B_0$, $\delta_i = \sigma^i_{ZZ} -$

$1/3Tr\sigma^i$ is the chemical shift anisotropy, and $\eta_i = (\sigma^i_{YY} - \sigma^i_{XX})/\delta_i$ is the asymmetry parameter.

The diagonalization of this Hamiltonian led to the eigenstates given by equations (10)–(13), and the initial density matrix describing the spins at the moment of chemisorption was previously derived (equation (16)). When the distribution of reaction times is broad compared to the period of the coherent evolution at the surface, the time-averaged density operator, with vanishing off-diagonal elements, is obtained. This is likely to be a realistic model of the dynamics in view of the decay of coherent oscillations associated with a powder distribution of proton dipolar couplings and shifts. The signal derived from the time-averaged density matrix (equation (26)), together with equation (75), is the starting point for the line shape powder averaging. Population inversion across two of the four dipole-allowed transitions results in powder patterns with antiphase character. Destructive interference between different transitions occurs due to the variation of the phase of the transitions across the powder pattern, resulting in a loss of signal intensity.

Figure 14 shows a simulation of the surface PASADENA spectrum using the following parameters: interproton distance of 0.26 nm ($\nu_D = 6$ kHz); principal components of the chemical shielding tensors, $\sigma_1 = \{5.0, 0.8, -3.8\}$ and $\sigma_2 = \{2.5, 1.0, -5.4\}$; Euler angles (in degrees) $\Omega_1 = \{0, 71, 37\}$, $\Omega_2 = \{116, 71, 21\}$. Although the chemical shift tensor information is not considered reliable in this simulation due to the large range of tensor parameters that gave a reasonable match to the spectrum, fits of the simulation to the experimental spectrum were optimized at an interproton distance of either 0.18 or 0.25 nm. A 2D NMR nutation study by Carson resulted in an optimal fit at an interproton separation of 0.25 nm.[48]

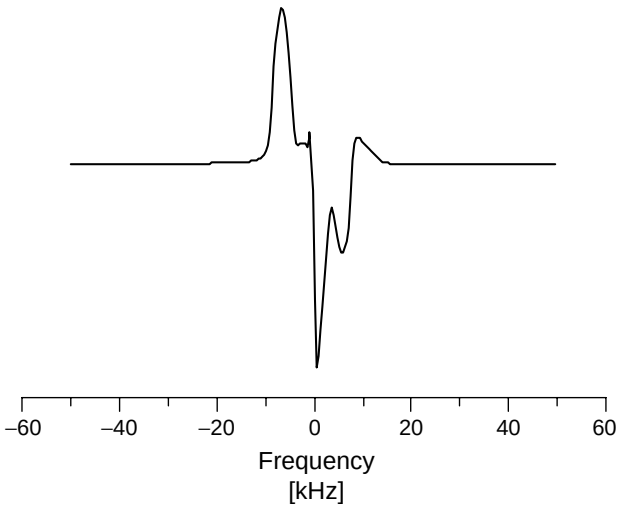

Figure 14 Simulated PASADENA lineshape in a powdered sample with an interproton distance of 2.6 Å (dipolar coupling parameter $\nu_D = 6$ kHz). The principle components of the chemical shift tensor (in kHz) are $\sigma_1 = \{5.0, 0.8, -3.8\}$ and $\sigma_2 = \{2.5, 1.0, -5.4\}$ and the Euler angles (in degrees) are $\Omega_1 = \{0, 71, 37\}$ and $\Omega_2 = \{116, 71, 21\}$. The spectrum was simulated using a $\pi/4$ detection pulse

9 CONCLUSIONS

NMR is a powerful technique for the elucidation of structure and dynamics at the molecular level, but a problem that is frequently encountered in this form of low energy spectroscopy is the issue of signal-to-noise. The search to find new methods to obtain sensitivity enhancement in NMR is ongoing, and there is currently a substantial effort by numerous research groups to improve, generalize and demonstrate the utility of existing techniques. These include optical pumping, microwave dynamic nuclear polarization, chemically induced dynamic nuclear polarization and cross-polarization. Incremental increases can be gained by further increases in magnetic field strength, but there are clear practical (and economical!) limits of this brute force approach. Decreasing the temperature can also help in certain studies, but the experimental conditions and spin-lattice relaxation considerations limit the generality of this approach. Unfortunately, there is no single method that is completely general, and the choice of which method to employ depends on the specific characteristics of the system of interest as well as the desired experimental conditions.

The PASADENA effect is an important new addition to this arsenal of NMR signal enhancement techniques, and it is the method of choice for the study of catalytic hydrogenation kinetics and mechanism. Since the original proposal and experimental demonstration using Wilkinson's catalyst, the phenomenon has been confirmed with many other hydrogenation catalysts, and there have been dozens of pulse sequence extensions and chemical applications of the basic phenomenon, a few of which have been reviewed here.

In theory, the NMR signal that can be obtained by the PASADENA effect using 100% p-H_2 approaches the value that would be obtained for a fully polarized nuclear spin system. In the variation of the PASADENA effect known as ALTADENA, theory indicates that perfect nuclear spin order is in principle obtainable. There are very few examples, if any, of NMR signal enhancement techniques that can produce such a high degree of spin order under ambient sample conditions. The signal enhancement that is available by the PASADENA effect will surely lead to many new discoveries pertaining to hydrogenation chemistry.

10 REFERENCES

1. D. P. Weitekamp, in 'Encyclopedia of NMR', eds D. M. Grant and R. K. Harris, Wiley: Chichester, 1996, p. 696.
2. Acronyms serve an indispensable role in the description of NMR experiments. The acronyms PASADENA and ALTADENA concisely identify the two types of experiment that are the subject of this review. However, the reader should be informed that certain authors prefer to use a shorter acronym, *PHIP* (ParaHydrogen Induced Polarization), to refer to both types of experiments.
3. C. R. Bowers and D. P. Weitekamp, *Phys. Rev. Lett.*, 1986, **57**, 2645.
4. C. R. Bowers and D. P. Weitekamp, *J. Am. Chem. Soc.*, 1987, **109**, 5541.
5. T. C. Eisenschmid, R. U. Kirss, P. A. Deutsch, S. I. Hommeltoft, R. Eisenberg, J. Bargon, R. G. Lawler, and A. L. Balch, *J. Am Chem. Soc.*, 1987, **109**, 8089.
6. H. E. Bryndza, Ph.D. Thesis, Berkeley, 1981.
7. P. F. Seidler, H. E. Bryndza, J. E. Frommer, L. S. Stuhl, and R. G. Bergman, *Organometallics*, 1983, **2**, 1701.

8. S. I. Hommeltoft, D. H. Berry, and R. Eisenberg, *J. Am. Chem. Soc.*, 1986, **108**, 5346.
9. R. Kaptein and L. J. Oosterhoff, *Chem. Phys. Lett.*, 1969, **195**, 214.
10. G. L. Closs, *J. Am. Chem. Soc.*, 1969, **91**, 4552.
11. R. Eisenberg, *Acc. Chem. Res.*, 1991, **24**, 110.
12. C. R. Bowers, Ph.D. Thesis, California Institute of Technology, 1990.
13. S. B. Duckett and C. J. Sleigh, *J. Prog. NMR Spectrosc.*, 1999, **34**, 71 and references therein; S. B. Duckett, in 'Encyclopedia in NMR', vol. 9, eds D. M. Grant and R. K. Harris, Wiley: Chichester, 2002.
14. J. Natterer and J. Bargon, *Prog. NMR Spectrosc.*, 1997, **31**, 293.
15. J. Barkemeyer, M. Haake, and J. Bargon, *J. Am. Chem. Soc.*, 1995, **117**, 2927.
16. S. B. Duckett, C. L. Newell, and R. Eisenberg, *J. Am. Chem. Soc.*, 1994, **116**, 10 548.
17. S. B. Duckett, C. L. Newell, and R. Eisenberg, *J. Am. Chem. Soc.*, 1997, **119**, 2048.
18. A. Harthun and J. Bargon, *Angew. Chem.*, 1997, **109**, 1155.
19. D. M. Dennison, *Proc. R. Soc.*, 1927, **A115**, 483.
20. A. Farka, 'Orthohydrogen, Parahydrogen and Heavy Hydrogen', Cambridge University Press: London, 1935.
21. Apachi^{TM} nickel silica gel catalyst, 197-CP, Houdry Division of Air Products, Inc., Philadelphia, PA.
22. O. W. Sorenson, G. W. Eich, M. H. Levitt, G. Bodenhausen, and R. R. Ernst, *Prog. NMR Spectrosc.*, 1983, **16**, 163.
23. R. R. Ernst, G. Bodenhausen, and A. Wokaun, 'Principles of Nuclear Magnetic Resonance in One and Two Dimensions', Oxford, 1987.
24. D. P. Weitekamp, J. R. Garbow, and A. Pines, *J. Chem. Phys.*, 1982, **77**, 2870; ibid, 1984, **80**, 1372.
25. L. Braunschweiler and R. R. Ernst, *J. Magn. Reson.*, 1983, **53**, 521.
26. J. A. Osborne, F. H. Jardine, J. F. Young, and G. Wilkinson, *J. Chem. Soc. A*, 1966, 1711.
27. J. Halpern, T. Okamato, and A. Zakhariev, *J. Mol. Catal.*, 1976, **2**, 65.
28. J. Halpern, *Inorg. Chim. Acta*, 1981, **50**, 11.
29. J. Halpern and C. S. Wong, *J. Chem. Soc., Chem. Commun.*, 1973, 629.
30. A. Harthun and J. Bargon, *Angew. Chem.*, 1997, **109**, 1155.
31. J. Halpern, A. S. C. Chan, D. P. Riley, and J. J. Pluth, *J. Am. Chem. Soc.*, 1977, **99**, 8055.
32. J. Halpern, *Science*, 1982, **217**, 401.
33. M. G. Pravica and D. P.Weitekamp, *Chem. Phys. Lett.*, 1988, **145**, 255.
34. B. L. Silver, 'Irreducible Tensor Methods', Academic Press: New York, 1976.
35. A. R. Edmonds, 'Angular Momentum in Quantum Mechanics', Princeton University Press: Princeton, 1957.
36. M. E. Rose, 'Elementary Theory of Angular Momentum', Wiley: New York, 1957.
37. M. G. Pravica, 1988, unpublished.
38. P. J. Carson, C. R. Bowers, and D. P. Weitekamp, submitted, 2001.
39. A. Y. Rozovskii and G. I. Lin, *Kinet. Catal.*, 1999, **40**, 773.
40. J. B. L. Martins, C. A. Taft, S. K. Lie, and E. Longo, *Theochem-J. Mol. Struct.*, 2000, **528**, 161.
41. T. Fujitani and J. Nakamura, *Appl. Catal. A-Gen.*, 2000, **191**, 111.
42. R. P. Eischens, W. A. Pliskin, and M. J. D. Low, *J. Catal.*, 1962, **1**, 180.
43. 99.8% purity, 3.5 m^2/g mean surface area, 0.31 μm mean particle size, Strem Chemicals, Inc., Newburyport, MA.
44. M. Watanabe and T. Ito, *Jpn. J. Appl. Phys.*, 1980, **19**, 1863.
45. P. R. Dennison, K. J. Packer, and M. S. Spencer, *J. Chem. Soc., Faraday Trans. 1*, 1989, **85**, 3537.
46. U. Haeberlen, 'High Resolution NMR in Solids, Selective Averaging', Academic Press: New York, 1976.
47. M. Mehring, 'Principles of High Resolution NMR in Solids', 2nd edn., Springer-Verlag: New York, 1983.
48. P. J. Carson, Ph.D. Thesis, California Institute of Technology, 1997.

Acknowledgements

C.R.B. acknowledges Daniel P. Weitekamp of the Caltech Chemistry Department for supervising his research on the PASADENA effect as a Ph.D. thesis topic. The author would also like to thank Paul J. Carson for contributing the experimental and simulated PASADENA results on zinc oxide. Michael G. Pravica is acknowledged for providing notes on the derivation of the PASADENA effect for deuterium.

Biographical Sketch

Clifford Russell Bowers, *b* 1963. Ph.D. 1990 Physical Chemistry, California Institute of Technology, Pasadena, California with Daniel P. Weitekamp; Postdoctoral Fellow, University of Stuttgart, Germany with Michael Mehring, 1990–1991; Postdoctoral Fellow, University of California, Berkeley with Alex Pines, 1992–1993; Assistant Professor, University of Florida, Gainesville, 1994–2000, Associate Professor since 2000. Approx. 30 publications. Current research interest: development of techniques for sensitivity enhancement of NMR, ESR and MRI with applications in materials science.

Composite Pulses

Malcolm H. Levitt

Stockholm University, Stockholm, /Sweden

1	Introduction	1
2	Notation	1
3	Pulse Imperfections	2
4	An Example of Error Compensation: The Composite Pulse $90_{90}180_{0}90_{90}$	3
5	Composite Pulses: Spin Couplings Ignored	5
6	Composite Pulses: Spin Couplings Included	12
7	Compensation for Coupling Variations	14
8	References	15

Turn, turn, turn. (The Byrds)

1 INTRODUCTION

A composite pulse is a small number of contiguous, or near-contiguous, rf pulses with different phase. The composite pulse emulates the effect of a simple rf pulse, but has an inbuilt compensatory mechanism which renders it less sensitive to common experimental imperfections. Composite pulses may be compensated against the inevitable spread in the amplitude of the applied rf field over a sample of finite extent; they may be rendered insensitive to the limited strength of the applied rf field compared with the interactions of the spins with each other (spin–spin couplings) or with the molecular electron clouds (chemical shifts). In some cases other common pulse imperfections such as pulse shape errors are compensated. Composite pulse sequences are useful in a wide range of experimental situations in NMR. They are particularly important when critical experiments are performed in difficult situations, such as when the sample is large compared with the rf coil, absorbs rf fields strongly, or when the attainable field is restricted because heating must be avoided.

A case of particular importance is broadband heteronuclear spin decoupling (see ***Decoupling Methods***). Here a continuous train of composite pulses is applied to one spin species while a different spin species is observed. Suitable composite pulse sequences cause the spin system to evolve as if the heteronuclear spin–spin couplings were absent. The minimization of heating effects is particularly demanding in this application since the rf field may be applied continuously over a period of seconds. Composite pulse techniques have allowed a large reduction in the usable rf power and are now almost universal in heteronuclear liquid state NMR.

Compensation of the nuclear spin dynamics is also important in solid state NMR. Controlled spin manipulations can be achieved even when the achievable rf field is comparable with magnetic dipole–dipole couplings or electric quadrupole couplings. They are used in quadrupole echo experiments, methods to determine the orientation dependence of spin–lattice relaxation times, and for heteronuclear decoupling. Composite pulses have also been designed for NMR in zero magnetic field[1] (see ***Zero Field NMR***), in nuclear quadrupole resonance (NQR) spectroscopy[2,3] and even in coherent optical experiments.[4–6]

The original idea of compensating rf pulses for imperfections has been extended in several additional directions.

1. Composite pulses have been designed with an *exaggerated* sensitivity to the rf field amplitude. The response with respect to the rf field strength may be tailored so that there is strong uniform excitation within a given range and minimal excitation otherwise. In combination with careful rf coil design, such composite pulses comprise a means of spatial localization (see ***Rotating Frame Methods for Spectroscopic Localization***) of the nuclear spin signal.
2. Composite pulses have been designed with a carefully-tailored *frequency response*, i.e. dependence of spin dynamics on chemical shifts. This can be used, for example, in the suppression of undesirable NMR signals from solvent spins (see ***Water Suppression in Proton MRS of Humans and Animals***).
3. Composite pulses may be constructed which simulate the effect of arbitrary rf phase shifts on spectrometers which are equipped only to produce 90° phase steps.
4. Many experiments in coupled spin systems require some knowledge of the typical values of spin–spin coupling constants or quadrupole couplings. In practice, there is some spread in the magnitudes of these interactions, leading to a reduced experimental efficiency or, in some cases, extra peaks in two-dimensional spectra. By making analogies with composite pulses, methods have been designed which are internally compensated against deviations of the couplings from their expected values.
5. Composite pulse sequences closely related to heteronuclear decoupling sequences are widely used for the propagation of spin coherence through extended networks of spin–spin couplings.

The variety of composite pulse sequences, and the range of associated theoretical approaches and applications, is large. The choice of topics covered here is necessarily subjective. A more detailed, and theoretical, review of the field up to 1986 is given by Levitt.[7]

2 NOTATION

Consider a spin species I with magnetogyric ratio γ_I, exposed to a strong static magnetic field $\boldsymbol{B}_0$. The Larmor frequency of the spins, neglecting for the moment chemical shifts and spin–spin couplings, is given by $\omega_0 = -\gamma_I B_0$, in units of rad s^{-1}. For example, the Larmor frequency $\omega_0/2\pi$ for protons in a field $B_0 = 11.74\,\mathrm{T}$ is approximately $-500\,\mathrm{MHz}$.

During an rf pulse, an additional oscillating magnetic field is applied. The oscillation frequency of the applied field will be denoted by ω_1 (this conforms to the notational convention used in this Encyclopedia, but the reader is warned against conflicts with much published work). Usually ω_1 is very close to the Larmor frequency of the spins ω_0.

For high-field NMR, the relevant component of the rf magnetic field is perpendicular to the static magnetic field, and rotates around $\boldsymbol{B}_0$ in the same sense as the precessional motion of the spins. The *amplitude* of the relevant component

of the oscillating rf field is denoted by B_1. This is usually written in terms of the *nutation frequency*

$$\Omega_1 = -\gamma_I B_1 \tag{1}$$

The nutation frequency $\Omega_1/2\pi$ is usually of the order of kilohertz or tens of kilohertz, and is generally assumed to be positive for convenience (for spins with positive γ_I, this implies that the field component B_1 is taken to be negative).

In general, Ω_1 is spatially inhomogeneous, i.e. differs from place to place in the sample. This will sometimes be stressed by writing $\Omega_1(\boldsymbol{r})$, where $\boldsymbol{r}$ is a spatial coordinate.

To set the pulse durations it is necessary to assume a certain 'nominal' nutation frequency Ω_1^0. This represents roughly the most probable value of Ω_1 over the sample volume, and is normally determined by some simple experimental procedure. For example, the '90° pulse length' τ_{90} can be set by finding the pulse duration giving the maximum NMR signal. The nominal nutation frequency Ω_1^0 is then defined through the relationship:

$$\Omega_1^0 \tau_{90} = \pi/2 \tag{2}$$

Other experimental procedures may give slightly different estimates. This does not matter very much. Ω_1^0 should simply be somewhere near the center of the actual $\Omega_1(\boldsymbol{r})$ distribution.

The *duration* τ_p of a single rf pulse is conveniently denoted in terms of Ω_1^0 by the 'nominal flip angle' β_p^0, defined by

$$\beta_p^0 = \Omega_1^0 \tau_p \tag{3}$$

A rectangular rf pulse can therefore be specified by using the two angles β_p^0 (for the duration) and ϕ_p (for the rf phase), and will be denoted $(\beta_p^0)_{\phi p}$, with the angles given in degrees. Otherwise, radians will be used. For example, 90_{45} denotes a rectangular rf pulse with an rf phase $\phi_p = \pi/4$ and a pulse duration $\tau_p = (\pi/2)/\Omega_1^0$.

A composite pulse is simply a sequence of single rectangular pulses. For simplicity, only *contiguous* composite pulses will be considered here, i.e. there are no spaces between the pulses. All component pulses are assumed to have the same frequency, although this is not always the case in practice.[8] The composite pulse sequence is written in chronological order from left to right. For example, $90_{45}180_0$ denotes a rectangular rf pulse with rf phase of $\pi/4$ and a duration of $\tau_p = (\pi/2)/\Omega_1^0$, immediately followed by another rectangular pulse with an rf phase of zero and a duration of $\tau_p = \pi/\Omega_1^0$.

Sometimes it is necessary to denote an overall phase shift of an entire group of pulses. This is done using square brackets, for example $[(\beta_1^0)_{\phi 1}(\beta_2^0)_{\phi 2}]_\Phi$, which is equivalent to $(\beta_1^0)_{\phi 1+\Phi}(\beta_2^0)_{\phi 2+\Phi}$.

A pulse sequence $\mathbb{S}$ with an element $\mathbb{E}$ missing at the front will be denoted by $\mathbb{E}^{-1}\mathbb{S}$. For example, if a sequence $\mathbb{S}$ is given by $\mathbb{S} = 90_{45}180_090_{180}$, then $(90_{45})^{-1}\mathbb{S}$ is given by 180_090_{180}. Similarly, $\mathbb{S}(90_{180})^{-1}$ is given by $90_{45}180_0$. The pulse sequence $\mathbb{E}^{-1}\mathbb{S}\mathbb{E}$ derived from $\mathbb{S}$ by taking the element $\mathbb{E}$ from the front to the back is a *cyclic permutation* of $\mathbb{S}$.

The chronological reverse of a pulse sequence $\mathbb{S}$ is denoted by $\mathbb{S}^{\text{rev}}$. In the example above, $\mathbb{S}^{\text{rev}}$ would be $90_{180}180_090_{45}$.

3 PULSE IMPERFECTIONS

Two common causes of imperfect pulse performance are: (i) lack of uniformity in the applied rf field, and (ii) limited amplitude of the rf field compared with the other interactions experienced by the spins.

3.1 Radiofrequency Field Inhomogeneity

The amplitude of the relevant rf field component varies from place to place in the sample. The rf field experienced by the spins is conveniently represented by the dimensionless parameter Ω_1/Ω_1^0, which is equal to 1.0 for the nominal rf field. In practice, Ω_1/Ω_1^0 deviates from unity by a few percent in a well-designed high-resolution NMR probe, but the deviations may exceed 20% for a surface coil in NMR imaging (see ***Surface Coil NMR: Detection with Inhomogeneous Radiofrequency Field Antennas***).

3.2 Limited rf Field Amplitude

The usable rf field amplitude is always limited, either because sample heating must be minimized, or because of the risk of electrical failure in the amplifiers or rf coil. Magnetic fields associated with chemical shifts or spin couplings compete with the rf field during the pulse and bring about a degradation in pulse performance.

3.2.1 Isotropic Liquids

In isotropic liquids, spin–spin couplings are small. Imperfect pulse performance at low rf fields is caused mainly by chemical shifts and field inhomogeneities which cause the Larmor frequency of the spins to differ from site to site in the sample. If the electronic shielding constant for a site is σ^j, and the applied magnetic field is B_0, the Larmor frequency $\omega_0{}^j$ of that site is given by:

$$\omega_0^j = -\gamma_I B_0(1 - \sigma^j) \tag{4}$$

The *resonance offset* $\Delta\omega^j$ of a set of chemically equivalent spins I_j is equal to the difference between the Larmor frequency and the irradiation frequency:

$$\Delta\omega^j = \omega_0^j - \omega_1 \tag{5}$$

For a sample containing only one chemical site, in a perfectly homogeneous static magnetic field, $\Delta\omega^j$ may be set to zero simply by using an rf ω_1 exactly equal to the chemically-shifted Larmor frequency ω_0^j. However, when the sample contains many different chemical sites, or when the static field is inhomogeneous, resonance offset effects are inevitable.

The seriousness of resonance offset effects may be quantified by the dimensionless parameter $\Delta\omega^j/\Omega_1^0$ which will be called the *relative resonance offset*. For high-resolution proton spectroscopy, the magnitude of the relative offset is typically less than 0.1. For decoupling experiments, and for composite pulses on nuclei with larger chemical shift ranges, relative offsets of 1.0 or more are common.

The resonance offsets $\Delta\omega^j$ may have either algebraic sign, depending on whether the Larmor frequency is higher or lower than the irradiation frequency. For a conventionally presented spectrum of nuclei with a positive magnetogyric ratio such as ^{1}H or ^{13}C, spins with positive $\Delta\omega^j$ appear on the right-hand side of the spectrum. (Remember that the Larmor frequency ω_0^j and irradiation frequency ω_1 are close to $-\gamma_I B_0$ and are therefore negative.)

3.2.2 Anisotropic Liquids and Solids

In anisotropic systems, the situation is more complicated as there are many spin interactions large enough to compete with the applied rf field. For spins $I \geq 1$, quadrupolar interactions are usually dominant. For ^{1}H spins in solids, on the other hand, through-space dipole–dipole interactions are large and produce imperfect pulse performance. For dilute spin-$\frac{1}{2}$ nuclei like ^{13}C and ^{15}N, chemical shifts often dominate and the situation is similar to that in isotropic liquids, although the magnitude of the interactions is larger.

The anisotropic case is examined in Section 6 of this article. In most of the following discussion, isotropic liquid phase is assumed and resonance offset effects quantified by the parameter $\Delta\omega^j/\Omega_1^0$.

3.3 Other Pulse Imperfections

There are a number of other common pulse imperfections, such as errors in the profile of the pulse in time, errors or instability in the rf phase, and induced fields associated with coupling of the nuclear spin magnetization to the resonant detection coil (see ***Concentrated Solution Effects***). Generally speaking these errors are left uncompensated by composite pulses, although there are exceptions. In particular, composite pulses always assume highly accurate and stable rf phases. Fortunately, digital electronic synthesis of the rf signals generally ensures precise phases in modern instruments.

4 AN EXAMPLE OF ERROR COMPENSATION: THE COMPOSITE PULSE $90_{90}180_0 90_{90}$

To introduce the concept of error compensation, consider one of the common tasks of a 180° pulse, namely the sign inversion of the z component of spin angular momentum. This corresponds to an exchange of spin state populations and is often exploited for measuring relaxation time constants (see ***Relaxation: An Introduction***).

4.1 Single Pulse Propagator

Consider a single rectangular pulse of nominal flip angle β_p^0 and phase ϕ_p. If the rf field is much larger than the spin–spin couplings, and β_p^0 is not extremely large, then the pulse duration is short on the timescale of spin–spin couplings and the individual spin states undergo a simple rotation in three-dimensional space. The quantum states $|\psi\rangle^j$ of spins I_j before and after a pulse p are related by

$$|\psi\rangle_{\text{after}}^{j} = \hat{U}_p^{\,j} |\psi\rangle_{\text{before}}^{j} \tag{6}$$

where $\hat{U}_p^j$ is the rotating frame pulse *propagator* for spins I_j, given by

$$\hat{U}_p^{\,j} = \exp\{-\mathrm{i}\xi_p^{\,j} \hat{\boldsymbol{I}}_j \cdot \boldsymbol{n}_p^{\,j}\} \tag{7}$$

ξ_p^j is the rotation angle of spins I_j during pulse p, and $\boldsymbol{n}_p^j$ is the rotation axis.

For an *ideal pulse* of nominal flip angle β_p^0 and phase ϕ_p, the rotation angle is $\xi_p^j = \beta_p^0$, and the rotation axis is $\boldsymbol{n}_p^j = \boldsymbol{e}_x \cos\phi_p + \boldsymbol{e}_y \sin\phi_p$, where $\boldsymbol{e}_x$ and $\mathbf{e}_y$ are unit vectors along the x and y axes. If there are finite resonance offset effects or rf amplitude errors, on the other hand, the rotation parameters are

$$\xi_p^{\,j} = \beta_p^0 \sqrt{\frac{(\Omega_1)^2 + (\Delta\omega^{\,j})^2}{(\Omega_1^0)^2}} \tag{8}$$

$$\boldsymbol{n}_p^{\,j} = \boldsymbol{e}_z \cos\theta^{\,j} + \boldsymbol{e}_x \sin\theta^{\,j} \cos\phi_p + \boldsymbol{e}_y \sin\theta^{\,j} \sin\phi_p \tag{9}$$

where the angle θ^j is

$$\tan\theta^{\,j} = \Omega_1/\Delta\omega^{\,j} \tag{10}$$

4.2 Single 180_0 Pulse

Consider now the specific case of a 180_0 pulse, i.e. $\beta_p^0 = \pi$ and ϕ_p = 0. For small offsets $\Delta\omega^j/\Omega_1^0$, the propagator is simply

$$\hat{U}_p^{\,j} \simeq \exp\{-\mathrm{i}\xi_p^{\,j} \hat{I}_{jx}\} \tag{11}$$

with

$$\xi_p^{\,j} = \pi\,\Omega_1/\Omega_1^0 \tag{12}$$

indicating that the spin angular momentum turns through an angle ξ_p^j about the x axis of the rotating reference frame. Depending on the rf field Ω_1, this angle can be either smaller or greater than the nominal flip angle $\beta_p^0 = \pi$.

The transformation of z angular momentum by an imperfect 180_0 pulse is readily understood geometrically. An ensemble of spins I_j with finite polarization along the z axis has a spin density operator $\hat{\sigma}_{\text{before}} = \hat{I}_{jz}$ (inessential constants being omitted). This can be represented as an angular momentum vector along the z axis of the rotating reference frame [Figure 1(a)]. After the pulse the density operator is

$$\begin{aligned}\hat{\sigma}_{\text{after}} &= \hat{U}_p^{\,j} \hat{I}_{jz} \hat{U}_p^{j\dagger} \\ &= \hat{I}_{jz} \cos\xi_p^{\,j} - \hat{I}_{jy} \sin\xi_p^{\,j}\end{aligned} \tag{13}$$

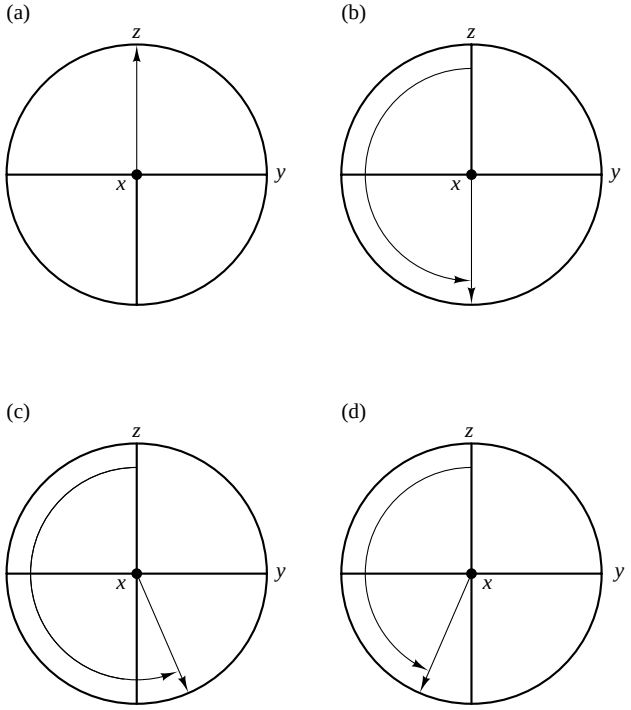

Figure 1 Effect of an imperfect rf field on a 180_0 pulse. (a) The equilibrium spin magnetization is represented as a unit vector along the z axis of the rotating reference frame. (b) For nominal rf fields ($\Omega_1 = \Omega 0/1$), the magnetization vector rotates through 180° around the x axis, ending up exactly at the $-z$ axis. (c) For rf fields stronger than the nominal, the magnetization vector overshoots the $-z$ axis. (d) For rf fields weaker than the nominal, the vector falls short of the $-z$ axis. In both cases, the z component of the final vector is larger than -1

This can be understood as a rotation of the angular momentum of the spin ensemble around the x axis through an angle ξ_p^j. For nominal rf fields, $\xi_p^j = \pi$ and the spin angular momentum is along the $-z$ axis after the pulse [Figure 1(b)]. For rf fields larger than the nominal [Figure 1(c)], the vector 'overshoots' the $-z$ axis, and for weak rf fields, the vector falls short [Figure 1(d)]. The transformed z angular momentum of spins I_j, given by the parameter

$$\begin{aligned} R_{zz}^j &= \mathrm{Tr}\{\hat{U}_p^j \hat{I}_{jz} \hat{U}_p^{j\dagger} \hat{I}_{jz}\}/\mathrm{Tr}\{\hat{I}_{jz}^2\} \\ &= \cos \xi_p^j \end{aligned} \tag{14}$$

is equal to -1 for an ideal 180_0 pulse, but is larger than -1 if the pulse is imperfect [Figure 2(a)]. For small rf field errors, the transformed z angular momentum is

$$R_{zz}^j \simeq -1 + \tfrac{1}{2}\pi^2 \left(\frac{\Omega_1 - \Omega_1^0}{\Omega_1^0} \right)^2 \tag{15}$$

i.e. it is quadratically dependent on the rf error. In practice this means that the degree of spin population inversion is spatially dependent, with detrimental experimental consequences.

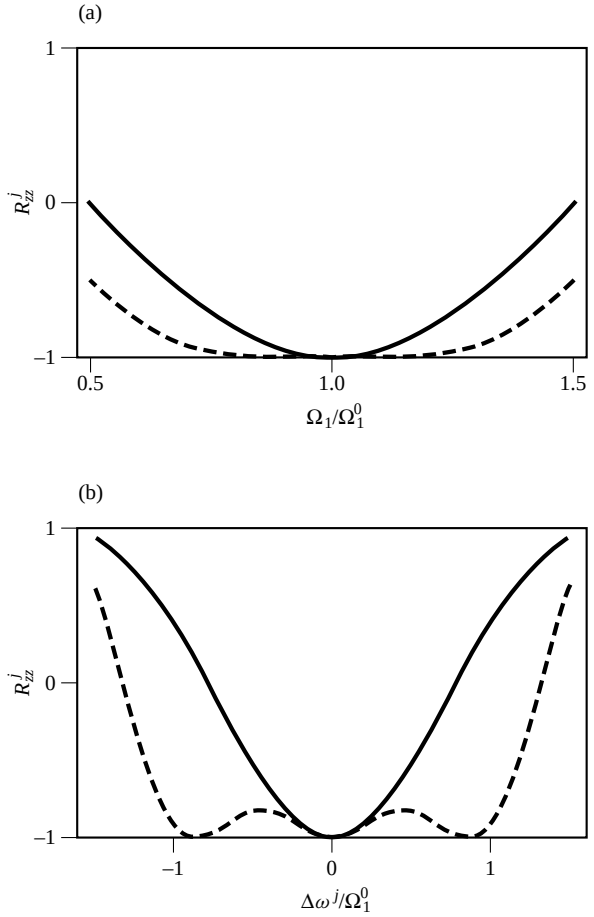

Figure 2 Transformation parameters of z angular momentum R_{zz}^j for a single 180_0 pulse (——), and a composite $90_{90}180_090_{90}$ pulse (– – –). (a) Dependence of R_{zz}^j on the rf field $\Omega_1\Omega_1^0$. (b) Dependence of R_{zz}^j on the relative resonance offset $\Delta\omega^j/\Omega_1^0$

4.3 Composite Pulse $90_{90}180_090_{90}$

The imperfect transformation of z angular momentum may be corrected[9] by using a composite pulse $90_{90}180_090_{90}$ as illustrated in Figure 3. The trajectories of the tips of a family of vectors, all starting out along the z axis, are tracked out during the pulse sequence. The vectors in the family correspond to different rf field values; to simplify the picture, all represent rf fields weaker than the nominal.

During the first 90_{90} element, all vectors rotate around the y axis, starting at the z axis and turning towards the x axis. An ideal 90_{90} pulse would take them exactly to the x axis, but, as the fields are weak, they fall short. The next 180_0 element rotates these vectors around the x axis. After this element, the vectors still lie approximately in the xz plane, but they now lie in the southern hemisphere of the unit sphere. Indeed, the tips of the vectors after the first and second pulses are related as approximate mirror images in the xy plane. The last 90_{90} element again rotates the vectors around the y axis, through exactly the same angle as the first element. The error compensation works as follows; just those vectors which lag the most after the first pulse are helped the most by the second pulse, so that they don't have as far to go during the last pulse. On the other hand, if the rf field is close to the nominal, the

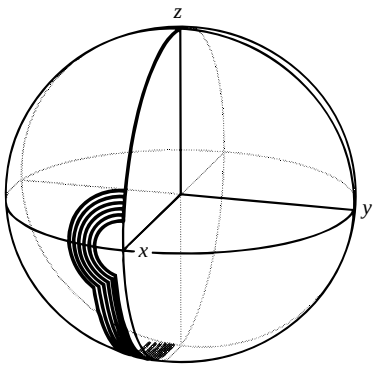

Figure 3 Geometrical mechanism of rf field compensation for the composite pulse $90_{90}180_{0}90_{90}$

vectors are already taken nearly to the x axis by the first pulse, so that they are almost unaffected by the second pulse. Again they are in the right position to be taken to the $-z$ axis by the last pulse. Hence the angular momentum vectors for spins in a range of rf fields concentrate near the $-z$ axis at the end of the sequence. A plot of R_{zz}^{j} against relative rf field Ω_1/Ω_1^0 for the composite pulse $90_{90}180_{0}90_{90}$ is shown by the dashed line in Figure 2(a).

An accurate analysis of the sequence $90_{90}180_{0}90_{90}$ shows[10] that for small resonance offsets the transformed z angular momentum is given by

$$R_{zz}^{j} = \cos\left\{2\arccos\left[\cos^2\left(\frac{\pi\Omega_1}{2\Omega_1^0}\right)\right]\right\} \tag{16}$$

For small rf field errors this can be approximated as

$$R_{zz}^{j} \simeq -1 + \tfrac{1}{8}\pi^4\left(\frac{\Omega_1 - \Omega_1^0}{\Omega_1^0}\right)^4 \tag{17}$$

The transformation of z magnetization is sensitive only to the fourth order in rf field error.

It happens that $90_{90}180_{0}90_{90}$ also gives a rather good compensation for resonance offsets, as long as the rf field intensity is close to the nominal. A simulation of R_{zz}^{j} against resonance offset $\Delta\omega^j/\Omega_1^0$, in the case of an exactly set rf field $\Omega_1 = \Omega_1^0$, is shown in Figure 2(b). The compensation of offset is not very exact, but quite broadband, giving fair inversion of z angular momentum for all offsets between $-1.0 \le \Delta\omega^j/\Omega_1^0 \le 1.0$.

A picture of what happens when both offset and rf error are introduced at the same time is given in Figure 4(b). This shows a contour plot of R_{zz}^{j} against resonance offset $\Delta\omega^j/\Omega_1^0$ (horizontal) and rf field Ω_1/Ω_1^0 (vertical). The darkest portions of the plot are regions of excellent population inversion ($R_{zz}^{j} \le -0.98$). These regions are far more extensive for $90_{90}180_{0}90_{90}$ than for a single pulse 180_0 [Figure 2(a)]. However, the sequence $90_{90}180_{0}90_{90}$ cannot strictly be said to compensate for *simultaneous* resonance offset and rf field errors. There is trouble if the rf field is weak at the same time as there is a moderate resonance offset. For truly simultaneous compensation, one must use more complicated sequences, such

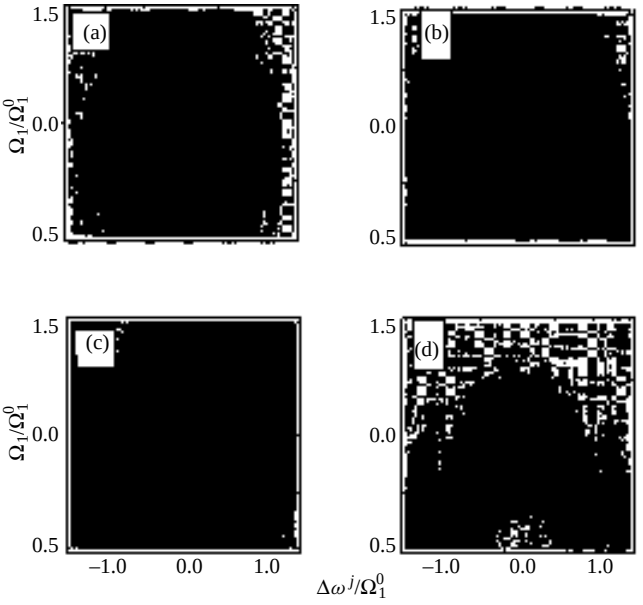

Figure 4 Contour plots of the parameter R_{zz}^{j} as a function of rf field Ω_1/Ω_1^0 and resonance offset $\Delta\omega^j/\Omega_1^0$ for four different pulse sequences. Inside the darkest region, the parameter R_{zz}^{j} is less than -0.98. Increasingly bright regions are delimited by contours at $\{-0.95, -0.9, -0.8, -0.6, -0.4, \ldots\}$. (a) Single pulse 180_0. (b) Composite pulse $90_{90}180_{0}90_{90}$. (c) Composite pulse $270_{180}360_{0}90_{90}270_{270}360_{90}90_{0}$. (d) Composite pulse $180_{30}180_{205}180_{230}180_{85}180_{0}180_{85}180_{230}180_{205}180_{30}$

as

$$270_{180}360_{0}90_{90}270_{270}360_{90}90_{0} \tag{18}$$

whose performance is illustrated in Figure 4(c).[11]

The above analysis considered only the z component of spin angular momentum. In general, other angular momentum components are also important. Figure 5 illustrates the subtleties which arise when composite pulses are applied to general states of the spin ensemble. The spin density operator is represented not as a vector but as a full three-dimensional object with low symmetry, here a simple L shape.

In Figure 5(a) the L shape is subjected to a sequence of three rotations, a 90° rotation around the y axis, followed by a 180° rotation around the x axis, and a 90° rotation around the y axis again. These three rotations may be shown to be equivalent to a single rotation, through 180° around the x axis, as shown by the final position in Figure 5(a).[12] The composite pulse $90_{90}180_{0}90_{90}$ is equivalent to a single 180_0, if all pulses are ideal.

Figure 5(b) illustrates the behavior of the composite pulse if the rf field is somewhat weaker than nominal. After the three mis-set rotations, the long arm of the L is taken almost exactly to the $-z$ axis, as expected from Figure 3. However, the L shape is also rotated around the z axis, as can be seen by comparing the final positions in Figure 5(a) and (b). In the language of nuclear spin dynamics, the compensated population inversion is accompanied by a *phase shift* of the spin coherences. Such induced *phase distortions* are a common feature of most composite pulses, and must carefully be taken into account in general applications.

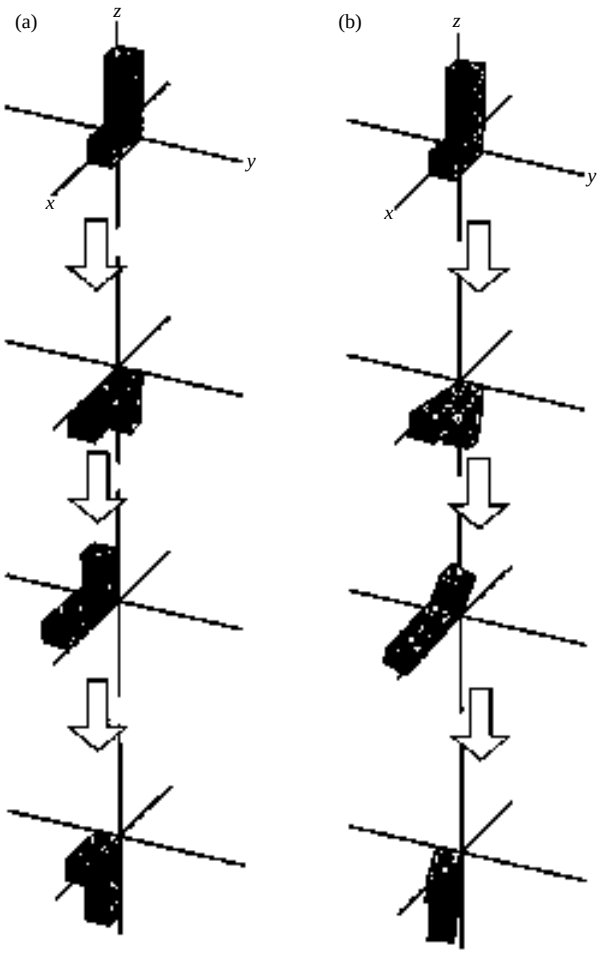

Figure 5 Transformations of a three-dimensional object by a succession of three rotations. (a) A 90° rotation about the y axis, followed by a 180° rotation about the x axis, followed by a 90° rotation about the y axis. (b) A 80° rotation about the y axis, followed by a 160° rotation about the x axis, followed by a 80° rotation about the y axis

5 COMPOSITE PULSES: SPIN COUPLINGS IGNORED

The response of a general spin system to a composite pulse raises complex issues. Fortunately, the treatment is greatly simplified if the composite pulse is very short compared with the spin–spin coupling constants. Under this approximation, all rf pulses induce simple three-dimensional rotations of the individual spin angular momenta. Such composite pulses can be considered manifestations of the three-dimensional rotation group, and are amenable to geometric representation.

This type of composite pulse only works properly if it is short compared with the timescale set by spin–spin couplings and spin relaxation. This condition is usually readily satisfied in isotropic liquids. Breakdown of this assumption eventually sets a limit on the length of usable sequences.

This restriction should not be taken to imply that such composite pulses can only be applied to systems without spin–spin couplings. The point is merely that the couplings can be ignored *during* the composite pulse. The spin–spin couplings can still be active during the much longer periods *between* the pulses.

A smaller group of composite pulses (discussed in Section 6) takes into account explicitly the spin couplings during the pulse. The dynamics of the spins cannot then be described as rotations in a three-dimensional space.

5.1 Composite Pulse Propagator

Consider a composite pulse with n pulse elements, applied to a system of N coupled spins. If the spin–spin couplings are neglected, the overall propagator $\hat{U}$ of the entire spin system can be factorized into a product of individual propagators $\hat{U}^j$, one for each spin:

$$\hat{U} \simeq \hat{U}^1 \hat{U}^2 \cdots \hat{U}^N \tag{19}$$

The individual spin propagators $\hat{U}^j$ all commute, so equation (19) can be written in any order. Each overall spin propagator $\hat{U}^j$ is, in turn, a product of spin rotations $\hat{U}_p^j$ corresponding to the individual pulses p:

$$\hat{U}^j = \hat{U}_n^j \cdots \hat{U}_2^j \hat{U}_1^j \tag{20}$$

$\hat{U}_p^j$ is given in equation (7). The operators $\hat{U}_p^j$ do not commute, so the product must be written in strict chronological order from right to left.

Since any product of rotations is another rotation, the overall composite pulse propagator for each individual spin I_j is also a rotation operator, and can be written in the form

$$\hat{U}^j = \exp\{-\mathrm{i}\bar{\xi}^j \hat{\boldsymbol{I}}_j \cdot \bar{\boldsymbol{n}}^j\} \tag{21}$$

where $\bar{\xi}^j$ is the overall rotation angle, and $\bar{\boldsymbol{n}}^j$ is the overall rotation axis.

There is another way of writing equation (21), which brings out more clearly the 'phase-distortion' properties of the composite pulse. Any rotation can be expressed as three consecutive rotations, about the z axis, the y axis, and the z axis again. The composite pulse propagator can therefore be written

$$\hat{U}^j = \exp\{-\mathrm{i}\bar{\gamma}^j \hat{I}_{jz}\} \exp\{-\mathrm{i}\bar{\beta}^j \hat{I}_{jy}\} \exp\{-\mathrm{i}\bar{\alpha}^j \hat{I}_{jz}\} \tag{22}$$

where the three angles $\{\bar{\alpha}^j, \bar{\beta}^j, \bar{\gamma}^j\}$ are called the *Euler angles* for the overall rotation.[13] In general, the Euler angles depend on the parameters Ω_1/Ω_1^0 and $\Delta\omega^j/\Omega_1^0$, and are different for each set of spins I_j.

5.2 Classification of Composite Pulses

The properties of composite pulses are defined by the dependence of the three Euler angles $\{\bar{\alpha}^j, \bar{\beta}^j, \bar{\gamma}^j\}$ on the imperfection parameters $\Delta\omega^j/\Omega_1^0$ and Ω_1/Ω_1^0.

The central angle $\bar{\beta}^j$ is the most important. If $\bar{\beta}^j$ is close to some angle Θ, the composite pulse behaves 'like' an ideal pulse of nominal flip angle Θ. The composite pulse is then called a *composite* Θ *pulse*. For example, $90_{90}180_0 90_{90}$ is a composite 180° pulse since $\bar{\beta}^j$ is close to 180° for small values of $\Delta\omega^j/\Omega_1^0$ and Ω_1/Ω_1^0.

Table 1 Variable Rotation Composite 90° Pulses[a]

Sequence	Ref.	rf field range (Ω_1/Ω_1^0)[b]	Offset range $(\Delta\omega^j/\Omega_1^0)$[c]
90_0	–	{0.89, 1.11}	{−0.92, 0.92}
$90_0 90_{90}$	18	{**0.73, 1.27**}	{*−0.10, 0.10*}
$90_0 180_{120}$	19	{**0.62, 1.37**}	{*−0.13, 0.10*}
$180_{97.2} 360_{291.5} 180_{97.2} 90_0$	15	{**0.58, 1.42**}	{*−0.88, 0.36*}
$180_0 360_{180} 180_0 270_{180} 90_{90}$	42	{**0.58, 1.42**}	{**−1.24, 1.24**}

[a]Bandwidths which are extended with respect to a single 90° pulse are in bold type. Bandwidths which are contracted with respect to a single 90° pulse are in italics.
[b]The range of rf field values for which the angle β^j is between 80° and 100°, at zero resonance offset.
[c]The range of offset values for which the angle β^j is between 80° and 100°, at nominal rf field.

5.2.1 Broadband Composite Pulses

Often, the composite pulse is designed such that $\bar{\beta}^j$ remains close to some value Θ over a range of rf field or resonance offset which is larger than for a single pulse. The composite pulse is then called a *broadband composite* Θ *pulse*.

The range of rf field or resonance offset for which $\bar{\beta}^j$ is 'close' to Θ is called the *compensation bandwidth*. The compensation bandwidths of some selected composite pulses are given in Tables 1 and 2. The tabulated figures indicate the range of $\Delta\omega^j/\Omega_1^0$ and Ω_1/Ω_1^0 within which $\bar{\beta}^j$ is within 10° of the flip angle Θ. For example, for the composite pulse $90_{90}180_0 90_{90}$, the angle $\bar{\beta}^j$ is between 170° and 190° for all values of rf field in the range $0.81 \leq \Omega_1/\Omega_1^0 \leq 1.19$, if the resonance offset is zero. Similarly, $\bar{\beta}^j$ is between 170° and 190° for all values of resonance offset in the range $-0.09 \leq \Delta\omega^j/\Omega_1^0 \leq 0.09$, providing the rf field is nominal. Parameter ranges which are extended with respect to a single rf pulse are indicated in bold type. Those which are more restricted than for a single pulse are in italics. For example, the sequence $180_{120}180_{240}180_{120}$ tolerates a wider range of rf field strengths than a single 180_0 pulse, but only if the resonance offset is kept within stringent limits.

Since R_{zz}^j is equal to $\cos\bar{\beta}^j$, the quoted bandwidths also apply to the corresponding transformations of z angular momentum. For composite 180° pulses, R_{zz}^j is less than −0.984 within the quoted bandwidths; for composite 90° pulses, R_{zz}^j is between −0.17 and +0.17 over the tabulated compensation bands.

This bandwidth definition does not yet say anything about the angles $\bar{\alpha}^j$ and $\bar{\gamma}^j$. The behavior of these angles introduces further nuances:

1. For *variable rotation composite pulses*, the Euler angles $\bar{\alpha}^j$ and $\bar{\gamma}^j$ are unconstrained, and may vary arbitarily within the compensation band.
2. For *constant rotation composite pulses*, the only variations in $\bar{\alpha}^j$ and $\bar{\gamma}^j$ over the compensation band keep the overall rotation operator $\hat{\bar{U}}^j$ close to that generated by an ideal Θ_0 pulse.[4]

In Table 3 and 4, some constant rotation composite pulses are listed, together with the ranges of $\Delta\omega^j/\Omega_1^0$ and Ω_1/Ω_1^0 for which they provide a rotation close to the ideal. The compensation range of such composite pulses is more difficult to define than for variable rotation composite pulses, since all three Euler angles are involved. The tabulated constant rotation bandwidths are based upon the values of the angle $\bar{\xi}_\Delta^j$, defined by the equation

$$\hat{\bar{U}}^j = \exp\{-i\Theta\hat{I}_{jx}\}\exp\{-i\bar{\xi}_\Delta^j \hat{\boldsymbol{I}}_j \cdot \boldsymbol{n}_\Delta^j\} \qquad (23)$$

where $\bar{U}^j$ is given by equation (21) and $\boldsymbol{n}_\Delta^j$ is a unit vector. $\bar{\xi}_\Delta^j$ can be interpreted as the 'deviation angle' between the actual

Table 2 Variable Rotation Composite 180° Pulses[a]

Sequence	Ref.	rf field range (Ω_1/Ω_1^0)[b]	Offset range $(\Delta\omega^j/\Omega_1^0)$[c]
180_0	–	{0.94, 1.06}	{−0.08, 0.08}
$90_{90}180_0 90_{90}$	9	{**0.81, 1.19**}	{−0.09, 0.09}
$90_0 360_{120} 90_0$	19	{**0.71, 1.29**}	{−0.08, 0.08}
$180_{120}180_{240}180_{120}$	33	{**0.71, 1.29**}	{*−0.05, 0.05*}
$180_{104.5}360_{313.4}180_{104.5}180_0$	15	{**0.69, 1.31**}	{−0.09, 0.09}
$90_0 225_{180} 315_0$	29	{0.94, 1.06}	{**−0.68, 0.68**}
$158_{180}171.2_0 342.8_{180}145.5_0 81.2_{180}85.3_0$	28	{0.94, 1.06}	{**−1.50, 1.50**}
$90_0 240_{90} 90_0$	18	{**0.67, 1.09**}	{**−0.52, 0.52**}
$270_{180}360_0 90_{90}270_{270}360_{90}90_0$	11	{**0.72, 1.28**}	{**−0.45, 0.50**}
$180_0180_0180_{120}180_{60}180_{120}180_0180_0180_{120}180_{60}180_{120}$ $180_{120}180_{120}180_{240}180_{180}180_{240}180_{60}180_{60}180_{180}180_{120}$ $180_{180}180_{120}180_{120}180_{240}180_{180}180_{240}$	34	{**0.68, 1.33**}	{**−0.76, 0.95**}

[a]Bandwidths which are extended with respect to a single 180° pulse are in bold type. Bandwidths which are contracted with respect to a single 180° pulse are in italics.
[b]The range of rf field values for which the angle $\bar{\beta}^j$ is between 170° and 190°, at zero resonance offset.
[c]The range of offset values for which the angle $\bar{\beta}^j$ is between 170° and 190°, at nominal rf field.

Table 3 Constant Rotation Composite 90° Pulses[a]

Sequence	Ref.	rf field range (Ω_1/Ω_1^0)[b]	Offset range $(\Delta\omega^j/\Omega_1^0)$[c]
90_0	–	{0.89, 1.11}	{−0.13, 0.13}
$385_0320_{180}25_0$	25	{0.89, 1.11}	{**−0.30, 0.30**}
$113_{180}316_0113_{180}$	27	{0.89, 1.11}	{**−0.26, 0.26**}
$24_0152_{180}346_0152_{180}24_0$	27	{0.89, 1.11}	{**−0.40, 0.40**}
$119_{180}183_0211_{180}384_0211_{180}183_0119_{180}$	27	{0.89, 1.11}	{**−0.83, 0.83**}
$180_{97.2}360_{291.5}180_{97.2}90_0$	15	{**0.59, 1.41**}	{−0.13, 0.13}

[a]Bandwidths which are extended with respect to a single 90° pulse are in bold type.
[b]The range of rf field values for which the angle $\bar{\xi}_\Delta{}^j$ is less than 10°, at zero resonance offset.
[c]The range of offset values for which the angle $\bar{\xi}_\Delta{}^j$ is less than 10°, at nominal rf field.

Table 4 Constant Rotation Composite 180° Pulses[a]

Sequence	Ref.	rf field range (Ω_1/Ω_1^0)[b]	Offset range $(\Delta\omega^j/\Omega_1^0)$[c]
180_0	–	{0.94, 1.06}	{−0.09, 0.09}
$180_{120}180_{240}180_{120}$	33	{**0.80, 1.20**}	{*−0.05, 0.05*}
$180_{104.5}360_{313.4}180_{104.5}180_0$	15	{**0.69, 1.31**}	{−0.09, 0.09}
$59_{180}298_059_{180}$	27	{0.94, 1.06}	{**−0.23, 0.23**}
$58_0140_{180}344_0140_{180}58_0$	27	{0.94, 1.06}	{**−0.39, 0.39**}
$27_099_{180}180_0211_{180}386_0211_{180}180_099_{180}27_0$	27	{0.94, 1.06}	{**−0.86, 0.86**}
$180_0180_0180_{120}180_{60}180_{120}180_0180_0180_{120}180_{60}$ $180_{120}180_{120}180_{120}180_{240}180_{180}180_{240}180_{60}180_{60}$ $180_{180}180_{120}180_{180}180_{120}180_{120}180_{240}180_{180}180_{240}$	34	{**0.88, 1.12**}	{**−0.48, 0.48**}

[a]Bandwidths which are extended with respect to a single 180° pulse are in bold type. Bandwidths which are contracted with respect to a single 180° pulse are in italics.
[b]The range of rf field values for which the angle $\bar{\xi}_\Delta{}^j$ is less than 10°, at zero resonance offset.
[c]The range of offset values for which the angle $\bar{\xi}_\Delta{}^j$ is less than 10°, at nominal rf field.

rotation $\bar{\hat{U}}^j$ and the desired ideal rotation. If the rotation is already ideal, $\bar{\xi}_\Delta^j$ is equal to zero. In terms of the Euler angles, it can be shown that $\bar{\xi}_\Delta^j$ is given by

$$\cos(\bar{\xi}_\Delta{}^j/2) = \cos(\bar{\beta}^j/2)\cos(\Theta/2)\cos\left(\frac{\bar{\alpha}^j+\bar{\gamma}^j}{2}\right) + \sin(\bar{\beta}^j/2)\sin(\Theta/2)\sin\left(\frac{\bar{\alpha}^j-\bar{\gamma}^j}{2}\right) \quad (24)$$

The tabulated constant rotation bandwidths indicate the range of $\Delta\omega^j/\Omega_1^0$ and Ω_1/Ω_1^0 for which the 'deviation angle' $\bar{\xi}_\Delta^j$ is always less than 10°. Within these parameter ranges the composite pulses may be used to replace the single pulse, independent of the experimental context.

The distinction between the different types of composite pulse is illustrated in Figure 6. This shows the dependence of the angles $\bar{\beta}^j$ and $\bar{\xi}_\Delta^j$ on the rf field Ω_1/Ω_1^0, for the variable rotation composite pulse $90_{90}180_090_{90}$ and the constant rotation sequence $180_{104.5}360_{313.4}180_{104.5}180_0$.[15] In both cases, $\bar{\beta}^j$ is kept close to 180° over a range of rf fields, but $\bar{\xi}_\Delta^j$ is kept low only for the second sequence. The sequence $180_{104.5}360_{313.4}180_{104.5}180_0$ behaves similarly to an ideal pulse 180_0 over the entire compensation band.

5.2.2 Narrowband and Band-Reject Composite Pulses

For broadband composite pulses, $\bar{\beta}^j$ is kept almost constant over a certain range of rf fields or resonance offsets. This is not the only possible mode of control of $\bar{\beta}^j$. Some other possibilities are:

1. For *narrowband composite pulses*, $\bar{\beta}^j$ is kept close to zero over a wide range of parameters, except for certain special values, where $\bar{\beta}^j$ is close to the nominal flip angle Θ of the composite pulse. Narrowband composite pulses can be used for selecting NMR signals originating in spatial regions with defined values of the rf field amplitude.
2. A *band-reject composite pulse* resembles a broadband composite pulse except for a 'hole' in the excitation around some special value of rf field or offset frequency, i.e. $\bar{\beta}^j$ is large over a wide range except in a narrow region where it approximates zero. Composite pulses with band-reject characteristics for offset $\Delta\omega^j/\Omega_1^0$ can be used for solvent peak suppression.

Most of this article concerns broadband composite pulses. The other possibilities are treated briefly in Section 5.6

5.3 Coherence Transfer Amplitudes

To appreciate the practical significance of the angles $\bar{\alpha}^j$ and $\bar{\gamma}^j$, consider the case where the composite pulse is applied to a weakly coupled system of N spins, prepared such that the density operator contains coherences σ_{rs} between two spin eigenstates $|r\rangle$ and $|s\rangle$. In general, the composite pulse sequence converts this coherence partially to another coherence σ_{tu}, between eigenstates $|t\rangle$ and $|u\rangle$. The amplitude for this particular coherence transfer process is written $Z_{rs\ tu}$.

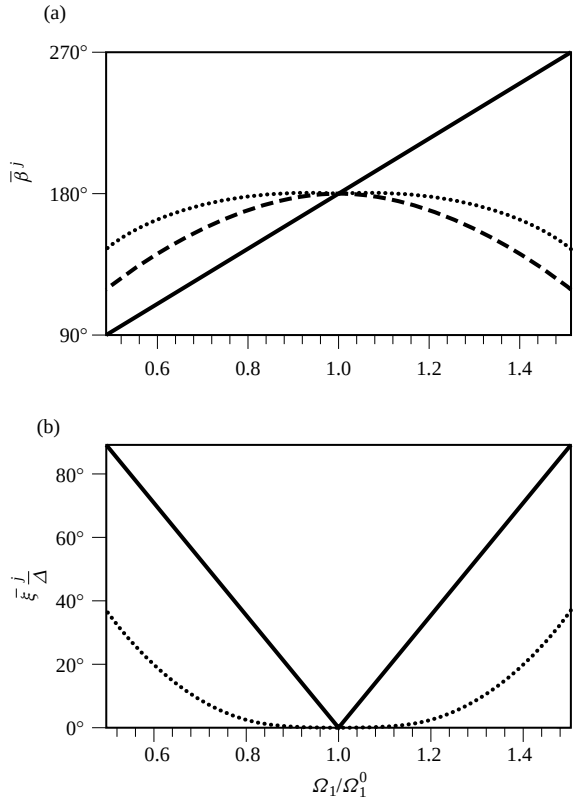

Figure 6 Performance of the single pulse 180_0 (——), composite pulse $90_{90}180_0 90_{90}$ (– – –), and composite pulse $180_{104.5}360_{313.4}180_{104.5}180_0$ (····) as a function of rf field. (a) Euler angle β^j. (b) Deviation angle ξ^j_Δ. The curves for the single 180_0 pulse and composite pulse $90_{90}180_0 90_{90}$ are superimposed in (b)

The manipulation of spin state populations may be handled by taking the case $r = s$ or $t = u$ (see ***Molecular Motions: T_1 Frequency Dispersion in Biological Systems***).

It may be shown that for a composite pulse with a propagator defined by equation (22), within its compensation band, the amplitude for the coherence transfer process is given by

$$Z_{rstu} \simeq \exp\left\{ -\mathrm{i}\sum_j [(\bar{\gamma}^j + \pi/2)p_j^{(tu)} + (\bar{\alpha}^j - \pi/2)p_j^{(rs)}]\right\} Z^0_{rs\,tu} \qquad (25)$$

where $p_j^{(tu)} = m_j^{(t)} - m_j^{(u)}$, $p_j^{(rs)} = m_j^{(r)} - m_j^{(r)}$, and $m_j^{(s)}$ is the z angular momentum of spin I_j in the eigenstate $|s\rangle$ (weak coupling is assumed). Z^0_{rstu} denotes the coherence transfer amplitude for a strong ideal pulse of flip angle β^0.

The experimental significance of the angles $\bar{\alpha}^j$ and $\bar{\gamma}^j$ depends on the quantum numbers characterizing the coherence transfer process. If only populations are involved ($p_j^{(tu)} = p_j^{(rs)} = 0$), the Euler angles $\bar{\alpha}^j$ and $\bar{\gamma}^j$ may be ignored. If coherences are involved, on the other hand, $\bar{\alpha}^j$ and $\bar{\gamma}^j$ must be taken into account.

It would therefore seem advisable to use constant rotation composite pulses whenever spin coherences are involved. However, this is not always the best strategy. Constant rotation composite pulses are often long and have small compensation bandwidths. In many circumstances, variable rotation composite pulses are to be preferred:

1. In heteronuclear experiments, composite pulses applied to one spin species do not affect the phases of coherences associated with a different spin species. For example, variable rotation composite 180° pulses such as $90_{90}180_0 90_{90}$ may be applied to the I spins in order to change the sign of density operator terms such as $\hat{I}_z\hat{S}_x$. Such manipulations are common in two-dimensional heteronuclear shift correlation experiments (see ***Heteronuclear Shift Correlation Spectroscopy***).
2. For some variable rotation composite pulses, the angles $\bar{\alpha}^j$ and $\bar{\gamma}^j$ are linearly dependent on resonant offset $\Delta\omega^j$. In simple experiments involving only one coherence transfer step, phase distortions can then be removed simply by applying a numerical frequency-dependent phase correction to the spectrum.
3. If a phase cycle is performed so as to select signals arising only from *one single coherence transfer pathway* (see ***Phase Cycling***), then the angles $\bar{\alpha}^j$ and $\bar{\gamma}^j$ only contribute to a rather harmless overall phase shift of the signal.
4. Even in arbitary experiments involving many coherence transfer steps and many coherence transfer pathways, it is usually possible to choose variable rotation composite pulses such that the phase shifts induced by one composite pulse are cancelled out by the next composite pulse.[7,16,17] A general procedure is described in Section 5.5

5.4 Construction of Broadband Composite Pulses

There is a great variety of theoretical approaches to composite pulse construction. The following summary is superficial.

5.4.1 Geometry

The first composite pulse $90_{90}180_0 90_{90}$ was discovered by the geometrical arguments outlined in Figure 3. This simple method should not be underestimated. It exploits the impressive human faculty of three-dimensional visualization. However, so far, only variable-rotation composite pulses have been derived geometrically. Apart from $90_{90}180_0 90_{90}$, geometrical reasoning has led to the useful sequences 90_0180_{120} (an rf-compensated 90° pulse with a large bandwidth) and $90_0360_{120}90_0$ (a highly rf-compensated 180° pulse).[18–20]

5.4.2 Rotation Analysis

Geometrical reasoning may be assisted by mathematical methods such as quaternion algebra[21]. One powerful result is as follows.[10] Suppose a rotation through the angle ξ_1 about the axis $\boldsymbol{n}_1$ is followed by a rotation through the angle ξ_2 about the axis $\boldsymbol{n}_2$. The two consecutive rotations are equivalent to a single rotation through the angle ξ_{12} about the axis $\boldsymbol{n}_{12}$. It is possible to show that ξ_{12} and $\boldsymbol{n}_{12}$ are given by

$$\left.\begin{aligned} c_{12} &= c_1c_2 - s_1s_2\boldsymbol{n}_1\cdot\boldsymbol{n}_2 \\ s_{12}\boldsymbol{n}_{12} &= s_1c_2\boldsymbol{n}_1 + c_1s_2\boldsymbol{n}_2 - s_1s_2\boldsymbol{n}_1\times\boldsymbol{n}_2 \end{aligned}\right\} \qquad (26)$$

where $c_p = \cos(\xi_p/2)$, $s_p = \sin(\xi_p/2)$, $c_{12} = \cos(\xi_{12}/2)$, $s_{12} = \sin(\xi_{12}/2)$.

Using such formulae, it is possible to show, for example, that the Euler angle $\bar{\beta}^j$ for the composite pulse $90_{90}180_0 90_{90}$ at resonance offset $\Delta\omega^j = 0$ is given by

$$\cos(\bar{\beta}^j/2) = \cos^2(\pi\Omega_1/2\Omega_1^0) \tag{27}$$

while for the composite pulse $90_0 360_{120} 90_0$ the corresponding Euler angle is

$$\cos(\bar{\beta}^j/2) = \cos^3(\pi\Omega_1/2\Omega_1^0) \tag{28}$$

The powers of the cosine function on the right-hand sides of these equations indicate an increasing degree of compensation.

Such results are useful for understanding the response of existing composite pulses but have not yet proved very useful for the design of original sequences.

5.4.3 Coherent Averaging Theory

Coherent averaging theory is a form of dynamic perturbation theory, frequently used in multiple pulse sequence development (see ***Average Hamiltonian Theory***; ***Line Narrowing Methods in Solids***). (In the present context, coherent averaging theory writes the 'difference rotation' of Equation (23) as a convergent series:

$$\bar{\xi}_\Delta^j \hat{\boldsymbol{I}}_j \cdot \boldsymbol{n}_\Delta^j = \bar{\xi}_\Delta^{j(0)} \hat{\boldsymbol{I}}_j \cdot \boldsymbol{n}_\Delta^{j(0)} \hat{\boldsymbol{I}}_j + \bar{\xi}_\Delta^{j(1)} \hat{\boldsymbol{I}}_j \cdot \boldsymbol{n}_\Delta^{j(1)} + \ldots \tag{29}$$

For a given type of imperfection, it is possible to develop simple algebraic equations for the terms $\bar{\xi}_\Delta^{j(k)}$ as functions of the pulse durations and phases. By solving the equations analytically or numerically, pulse sequences are derived for which as many terms $\bar{\xi}_\Delta^{j(k)}$ as possible vanish. The more terms that are removed, the higher the degree of compensation.[15,22–26]

This approach allows the construction of constant rotation composite pulses. One example is the offset-compensated composite 90° pulses $385_0 320_{180} 25_0$.[26] A continuous set of offset-compensated constant rotation composite pulses with arbitary flip angle Θ was derived by exploiting pulse sequence symmetries to reduce the number of simultaneous equations.[27] Two such constant rotation offset-compensated composite pulses are the 180° pulse $59_{180} 298_0 59_{180}$ and the 90° pulse $114.3_{180} 318.6_0 114.3_{180}$.[27]

A continuous set of rf-compensated constant rotation composite pulses has also been found.[15] An rf-compensated rotation with $\bar{\beta}^j \simeq \Theta$ is generated by the sequence $180_{\phi 1} 360_{\phi 2} 180_{\phi 1}\ \Theta_0$ where $\phi_1 = \arccos(-\Theta/4\pi)$ and $\phi_2 = 3\phi_1$. Two examples are the broadband 180° pulse $180_{104.5} 360_{313.4} 180_{104.5} 180_0$ and the broadband 90° pulse $180_{97.2} 360_{291.5} 180_{97.2} 90_0$.

5.4.4 Numerical Optimization

It is also feasible to find composite pulses by fairly straightforward numerical optimization methods. The multidimensional space of pulse durations and pulse phases is searched until a sequence with the required properties is found.[8,27–31] Efficient optimization algorithms such as simulated annealing are often helpful.[30,31] Pulse sequence symmetry may be used to reduce the number of independent variables.

Another variant is to extend the bandwidth of an existing composite pulse by adding small extra pulses and optimizing numerically. This can be repeated many times. An example is the composite 180° pulse $158.0_0\ 171.2_{180}\ 342.8_0\ 145.5_{180}\ 81.2_0\ 85.3_{180}$ which has $\bar{\beta}^j \simeq \pi$ over a wide range $-1.5 \leq \Delta\omega^j/\Omega_1^0 \leq 1.5$.[28] A different starting point is provided by analytical results for *smooth* rf waveforms (see ***Shaped Pulses***). The composite 180° pulse $64_{232}\ 122_{96}\ 310_0\ 122_{96}\ 64_{232}$ was derived this way.[32] Wide bandwidth variable rotation composite pulses may be constructed particularly rapidly by allowing the rf frequencies ω_1 of subsequent pulses to be different.[8]

5.4.5 Iterative Expansion

Highly compensated sequences require very many pulses. It is very difficult to find such sequences by theoretical techniques such as coherent averaging theory (since the number of simultaneous equations becomes very large) or by numerical optimization (which eventually resembles searching for a needle in a haystack). A complementary approach is *iterative expansion*.[23,33–39] This defines an optimization procedure which (given a suitable starting point) leads inexorably to a sequence with the desired properties. The drawback is that the process is inefficient, often producing extremely long pulse sequences with moderate bandwidths. However, they can be very accurate.

Iterative expansion starts with some pulse sequence $\mathbb{S}^{(0)}$ whose properties are close to those desired. The sequence is duplicated a small number of times Q. Each of the Q clones is subjected to a different 'mutation' which preserves its length. Two common transformations are to change the phase, or to permute an element from the beginning to the end. The Q mutations $\{\mathbb{S}_1^{(0)} \ldots \mathbb{S}_Q^{(0)}\}$ are spliced together to form a sequence $\mathbb{S}^{(1)}$ which is Q times longer than $\mathbb{S}^{(0)}$:

$$\mathbb{S}^{(1)} = \mathbb{S}_1^{(0)} \mathbb{S}_2^{(0)} \cdots \mathbb{S}_Q^{(0)} \tag{30}$$

The properties of the expansion depend on the mutations and their order. In many cases, it is possible to demonstrate that as long as $\mathbb{S}^{(0)}$ performs reasonably well, then $\mathbb{S}^{(1)}$ will perform better. Hence $\mathbb{S}^{(1)}$ can be reinserted in the machinery to derive a sequence $\mathbb{S}^{(2)}$ which performs better still:

$$\mathbb{S}^{(2)} = \mathbb{S}_1^{(1)} \mathbb{S}_2^{(1)} \cdots \mathbb{S}_Q^{(1)} \tag{31}$$

If the original sequence $\mathbb{S}^{(0)}$ has n elements, the sequence $\mathbb{S}^{(M)}$ derived by M stages of expansion has nQ^M elements. Very long sequences with very high performance are rapidly built up.

Some examples of iterative expansion procedures are:

(1) *Cycles* are composite pulses whose overall rotation angles $\{\bar{\alpha},\bar{\beta},\bar{\gamma}\}$ are all very close to zero.[40] They are used for broadband heteronuclear decoupling (see below). Cycles may be constructed by the following twofold iterative expansion.[35,36]

$$\mathbb{S}^{(m+1)} = [\mathbb{E}^{-1}\mathbb{S}^{(m)}\mathbb{E}]_{180}[\mathbb{E}^{-1}\mathbb{S}^{(m)}\mathbb{E}]_0 \tag{32}$$

where $\mathbb{E}$ is an element on the end of $\mathbb{S}^{(m)}$ with $\bar{\beta} \simeq \pi/2$, i.e. a nominal 90° pulse. This procedure consists of chaining together two cyclic permutations of the original sequence with different phases. Ideally, the sense of the cyclic permutation, and order of chaining, is reversed on alternate expansion stages, i.e.

$$\mathbb{S}^{(m+2)} = [\mathbb{E}\,\mathbb{S}^{(m+1)}\mathbb{E}^{-1}]_0[\mathbb{E}\,\mathbb{S}^{(m+1)}\mathbb{E}^{-1}]_{180} \tag{33}$$

The accurate broadband cycle WALTZ-16[41] was constructed roughly this way. It is given by

$$\begin{aligned}&270_{180}360_0180_{180}270_090_{180}180_0360_{180}180_0270_{180}-\\&270_0360_{180}180_0270_{180}90_0180_{180}360_0180_{180}270_0-\\&270_0360_{180}180_0270_{180}90_0180_{180}360_0180_{180}270_0-\\&270_{180}360_0180_{180}270_090_{180}180_0360_{180}180_0270_{180}\end{aligned} \tag{34}$$

(2) *Compensated for rf field inhomogeneity 90° pulses* can be constructed by the following twofold expansion:[42]

$$\mathbb{S}^{(m+1)} = [(\mathbb{S}^{(m)})^{\text{rev}}]_{270}[\mathbb{S}^{(m)}]_0 \tag{35}$$

The pulse sequence is written in inverse time order, shifted in phase by 270°, and placed next to the original sequence. For example, starting from $\mathbb{S}^{(0)} = 90_0$, we get $\mathbb{S}^{(1)} = 90_{270}90_0$ and $90_{270}90_{180}90_{270}90_0$, and so on. The longer the sequence, the better the rf compensation. This expansion produces variable rotation composite 90° pulses.

3. *Broadband 180° pulses* can be constructed by fivefold expansions, including[33,34]

$$\mathbb{S}^{(m+1)} = [\mathbb{S}^{(m)}]_0[\mathbb{S}^{(m)}]_0[\mathbb{S}^{(m)}]_{120}[\mathbb{S}^{(m)}]_{60}[\mathbb{S}^{(m)}]_{120} \tag{36}$$

This procedure is capable of compensating both resonance offset effects and rf inhomogeneity at the same time or, indeed, any form of pulse imperfection as long as it is reproducible and transforms properly under rf phase shifts. The highly compensated 25-element composite 180° pulse $180_0\ 180_0\ 180_{120}\ 180_{60}\ 180_{120}\ 180_0\ 180_0\ 180_{120}\ 180_{60}\ 180_{120}\ 180_{120}\ 180_{120}\ 180_{240}\ 180_{180}\ 180_{240}\ 180_{60}\ 180_{60}\ 180_{180}\ 180_{120}\ 180_{180}\ 180_{120}\ 180_{120}\ 180_{240}\ 180_{180}\ 180_{240}$ was constructed this way.[33,34] This fivefold expansion procedure gives rise to variable rotation composite 180° pulses.

There is no space here to explain how these iterative expansion schemes work. An illuminating analysis has been given using the mathematical properties of repeated maps.[34]

5.5 Global Pulse Sequence Compensation

Variable rotation composite pulses are generally shorter and have wider compensation bandwidths than constant rotation composite pulses. However, they must be used cautiously in experiments involving coherences, since they induce phase shifts according to Equation (25).

In weakly coupled spin systems, it is possible to balance the phase shift associated with one composite pulse by an equal and opposite phase shift associated with the following pulse. This requires that all pulses applied to a given spin species are replaced simultaneously by variable rotation composite pulses of compatible construction.

A general method is to replace pulses with flip angle Θ and phase ϕ by composite pulses of the form $[\mathbb{L}]_\phi\ [\mathbb{R}]_{\phi-\theta}$. Here $\mathbb{R}$ is a composite pulse with flip angle $\bar{\beta}^j \simeq \pi/2$ and $\mathbb{L}$ is a composite pulse with $\bar{\beta}^j \simeq -\pi/2$. The sequence $\mathbb{L}\mathbb{R}$ without any relative phase shift comprises a cycle. For brevity, the composite pulse pair $[\mathbb{L}]_\Phi\ [\mathbb{R}]_\Psi$ is denoted below by $\mathbb{L}_\Phi\mathbb{R}_\Psi$.

For offset compensation, suitable 'left' and 'right' sequences are

$$\left.\begin{aligned}\mathbb{L} &= 180_{180}360_0180_{180}270_0\\ \mathbb{R} &= 90_0\end{aligned}\right\} \tag{37}$$

In this case the Euler angles of the sequence $\mathbb{L}_\phi\mathbb{R}_{\phi-\theta}$ are

$$\left.\begin{aligned}\bar{\alpha}^j &\simeq \pi - \frac{\Delta\omega^j}{\Omega_1^0} - \phi\\ \bar{\beta}^j &\simeq \Theta\\ \bar{\gamma}^j &\simeq -\pi + \frac{\Delta\omega^j}{\Omega_1^0} + \phi - \Theta\end{aligned}\right\} \tag{38}$$

In weakly coupled spin systems, the 'extra' $\bar{\alpha}^j$ and $\bar{\gamma}^j$ rotations commute with the evolution in the interpulse delays. The $\bar{\gamma}^j$ rotation of one composite pulse can then be cancelled out by the $\bar{\alpha}^j$ rotation of the following composite pulse, providing the phase of the following pulse and all subsequent ones are shifted by $-\Theta$. These extra phase shifts must be accumulated iteratively throughout the sequence.

For example, a compensated version of the three-pulse sequence

$$(\Theta)_{\phi_1} - \tau - (\Xi)_{\phi_2} - \tau - (\Psi)_{\phi_3} - \ldots \tag{39}$$

is

$$\begin{aligned}&\mathbb{L}_{\phi_1}\Big[\mathbb{R}_{\phi_1} - \tau - \mathbb{L}_{\phi_2}\big[\mathbb{R}_{\phi_2} - \tau - \mathbb{L}_{\phi_3}\\ &\quad[\mathbb{R}_{\phi_3} - \ldots]_{-\Psi}\big]_{-\Xi}\Big]_{-\Theta}\end{aligned} \tag{40}$$

or, explicitly,

$$\begin{aligned}&\mathbb{L}_{\phi_1}\mathbb{R}_{\phi_1-\Theta} - \tau - \mathbb{L}_{\phi_2-\Theta}\mathbb{R}_{\phi_2-\Theta-\Xi} - \tau\\ &\quad-\mathbb{L}_{\phi_3-\Theta-\Xi}\mathbb{R}_{\phi_3-\Theta-\Xi-\Psi} - \ldots\end{aligned} \tag{41}$$

This procedure is readily extended to any number of pulses.

For compensation of rf inhomogeneity effects, the composite pulses $\mathbb{L} = 180_{300}90_{180}$ and $\mathbb{R} = 90_0180_{120}$ may be used instead.

The only defect in this scheme, apart from its complexity, is that the $\bar{\gamma}^j$ phase shift induced by the last composite pulse is left over at the end of the sequence. For resonance offset compensation this final phase shift is quite harmless. The frequency-dependent phase of the NMR signal is easily corrected by complex multiplication of the spectrum in the usual way. For rf field inhomogeneity, on the other hand, the final phase shift does lead to some signal loss by spatial dispersion of the magnetization vectors.

This type of global pulse sequence compensation has been demonstrated in multiple quantum NMR.[7,16,17]

5.6 Nonbroadband Composite Pulses

Error compensation is only one mode of control of the nonlinear spin response. Several applications of composite pulses extend this concept.

5.6.1 Radiofrequency Field Selection

It is possible to design *narrowband* pulse sequences in which $\bar{\beta}^j$ is very small except for a narrow range of rf field strengths Ω_1. Such pulse sequences do not perturb the spin populations appreciably unless the rf field is close to the nominal value Ω_1^0. It is possible to use this property as a means for *spatial selection* of the NMR signal.[43–48] The pulse sequence is transmitted through an rf excitation coil with a well-defined spatial variation of rf field amplitude $\Omega_1(\boldsymbol{r})$. Only spins located in spatial regions with $\Omega_1 \simeq \Omega_1^0$ contribute strongly to the final NMR signal.

The most widely used composite pulses of this type have $\bar{\beta}^j \simeq \pi$ over a narrow rf field range. Narrowband composite 180° pulses can be engineered by a number of methods, including the threefold iterative expansion scheme.[43]

$$\mathbb{S}^{(m+1)} = [\mathbb{S}^{(m)}]_{240}[\mathbb{S}^{(m)}]_0[\mathbb{S}^{(m)}]_{120} \qquad (42)$$

The challenge is to find a pulse sequence with narrowband rf response which is not too adversely affected by resonance offsets. The performance of the composite 180° pulse $180_{30}180_{205}180_{230}180_{85}180_0180_{85}180_{230}180_{205}180_{30}$[48] is illustrated in Figure 4(d). The narrowband selection of rf fields is maintained fairly well within the offset range $-0.3 \leq \Delta\omega^j/\Omega_1^0 \leq 0.3$.

5.6.2 Frequency-Selective Excitation

It is also possible to design pulse sequences with a tailored response with respect to the resonance offset $\Delta\omega^j$. For example, pulse sequences may be constructed with $\bar{\beta}^j$ close to 90° over a wide frequency range, except for a narrow 'hole' close to $\Delta\omega^j = 0$. These *band-reject excitation* sequences can be used in the NMR of dilute solutions. Weak off-resonance solute NMR signals may be excited while avoiding the excitation of strong near-resonant signals from abundant solvent spins.

Sequences with this type of frequency-dependent excitation characteristic were available long before the first composite pulse appeared. However, insights from composite pulse design have allowed the construction of sequences which control the *phase* of the excited solute signals, as well as the amplitude. The angles $\bar{\alpha}^j$ and $\bar{\gamma}^j$ may be kept almost constant over the excitation bandwidth. Distortions associated with spectral phase gradients may thereby be avoided.[49–53] The field is discussed further in ***Water Signal Suppression in NMR of Biomolecules***.

5.6.3 Composite z Pulses

If rf field errors and resonance offset effects are small, the *composite z pulse* $90_{270}\Theta_0 90_0$ produces an overall rotation defined by the angles $\{\bar{\alpha}^j, \bar{\beta}^j, \bar{\gamma}^j\} \simeq \{\Theta, 0, 0\}$. This represents a rotation of the spin angular momenta through an angle Θ about the z axis, as is easily verified by rotating any three-dimensional object, on the lines in Figure 5. In high magnetic field this z rotation is equivalent to a phase shift of all previous rf pulses by the same angle Θ. It is therefore possible to emulate the effect of arbitary phase shifts on instruments equipped only for phase steps in multiples of 90°.[54,55] This application was important before digital phase shifting became generally available on commercial instruments.

If the rf field is inhomogeneous in space, composite z pulses with very long nominal flip angle Θ produce a z rotation through a strongly spatially dependent angle $\bar{\alpha}(\boldsymbol{r})$. The effect is similar to a *static field gradient pulse*, except that the inhomogeneity of the rf field, rather than that of the static magnetic field, is involved. Long composite z pulses of this type have been exploited to select signals arising from defined coherence transfer processes, as an alternative to phase cycling.[56] Time can be saved, and the suppression of undesirable signals improved.

6 COMPOSITE PULSES: SPIN COUPLINGS INCLUDED

In the applications discussed below, spin couplings are active during the composite pulse, and the dynamics of the spins cannot generally be visualized in three-dimensional space.

6.1 Heteronuclear Decoupling in Liquids

One of the most important applications of composite pulses is *broadband heteronuclear decoupling* in liquids (see ***Decoupling Methods***). The NMR signals from one spin species (conventionally denoted as the S spins) is observed at the same time as a second spin species (conventionally the I spins) is irradiated with a long composite pulse sequence. Ideally the S spins evolve independent of the IS spin–spin coupling, even when there is a wide range of chemical shifts of the I spin species.

In isotropic liquids, it is usually a good approximation to ignore the *homonuclear* interactions between the irradiated I spins and take into account only the *heteronuclear* interactions, which are generally an order of magnitude larger. With this assumption, it has been shown that the problem of constructing a broadband decoupling sequence is formally equivalent to the construction of an accurate broadband *cycle* on *isolated* spins.[35,36] This result, which is far from obvious, allows composite pulse sequences obtained by ignoring spin–spin couplings to be transplanted directly to this different context.

A wide range of broadband decoupling sequences have been constructed, usually by a combination of numerical optimization and iterative expansion. The popular sequence WALTZ-16 is given in equation (34).

For the highest possible resolution, sequences have been developed which also take the homonuclear J couplings into account.[37]

6.2 Quadrupolar Compensation

In solids, spin interactions are large, and applied rf fields face serious competition. For example, quadrupole interactions of

spins $I \geq 1$ are generally much larger than achievable rf fields. Only for ^{2}H is the quadrupolar interaction sufficiently small that the concept of an 'ideal' rf pulse is at all realistic. But even in this case, the achievable rf field is generally comparable to the quadrupolar splitting. Composite pulses can then help make up for insufficient rf field strength.

6.2.1 Compensated Quadrupolar Echoes

The ^{2}H NMR signals of solid powders decay very rapidly because of the strong orientation dependence of the quadrupole splitting (see ***Quadrupolar Nuclei in Solids***; ***Deuterium NMR in Solids***). To obtain undistorted signals it is usually necessary to refocus the free induction decay by a *quadrupole echo*. This involves using two 90° pulses, 90° out of phase with each other, separated by a small delay τ_1:

$$90_0 - \tau_1 - 90_{90} - \tau_2 - \text{Observe} \qquad (43)$$

A spin echo is formed after an interval $\tau_2 \simeq \tau_1$ measured from the end of the second 90° pulse. Acquisition of NMR signals starting at the top of the spin echo gives high-fidelity ^{2}H powder spectra.

In a disordered sample, the quadrupole splitting in high field depends on the environment and molecular orientation of the nuclear site j and will be denoted here by $2\omega_Q^j$. If the rf field Ω_1 is comparable to $2\omega_Q^j$, the spin transformations induced by the 90° pulses are imperfect and the spin echo is distorted. This usually appears as weakened intensity at the edges of the ^{2}H powder peakshape. An example is the spectrum of d_5-phenylalanine shown in Figure 7(a).

To correct this effect, each 90° pulse may be replaced by a composite 90° pulse. The composite pulse must take into account the competition between the rf field and the quadrupole coupling.

Construction of such composite pulses is far from easy. In principle, the density operator for a spin $I = 1$ evolves in an eight-dimensional space. However, there is one simplifying factor. In ^{2}H NMR, the chemical shifts are small. Although the frequencies of the two allowed transitions of the spin $I = 1$ nucleus are strongly orientation dependent, the *mean* frequency of the two transitions is always the same. It is possible to show that in this case, under certain constraints, quadrupole-compensated composite 90° pulses may be constructed by taking offset-compensated 180° pulses for isolated spins $\frac{1}{2}$, and dividing all pulse lengths by two.[57] The offset-compensated spin-$\frac{1}{2}$ 180° pulses must have the following properties:

1. Only 180° phase shifts must be involved.
2. Over the compensation bandwidth, the angles $\bar{\alpha}^j$ and $\bar{\gamma}^j$ must depend linearly on resonance offset $\Delta\omega^j / \Omega_1^0$.

The broadband spin-$\frac{1}{2}$ composite pulses $90_0180_{180}270_0$ and $90_0270_{180}180_0360_{180}180_0$ fulfil these conditions satisfactorily over the offset range $-1.0 \leq \Delta\omega^j / \Omega_1^0 \leq 1.0$ (the latter sequence being more accurate). On halving the pulse durations, the compensated quadrupole echo sequences

$$45_090_{180}135_0 - \tau_1 - 45_{90}90_{270}135_{90} - \tau_2 - \text{Observe} \qquad (44)$$

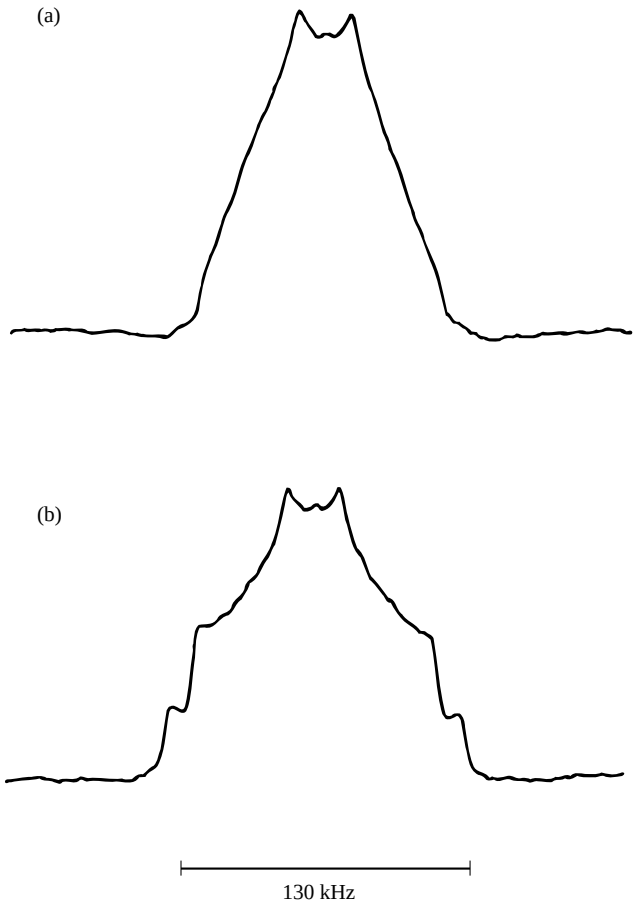

Figure 7 ^{2}H spectra of d_5-phenylalanine, obtained using (a) the simple quadrupole echo pulse sequence [equation (43)], and (b) a composite pulse quadrupole echo sequence [equation (44)]. The rf field was rather weak in both cases, the duration of a nominal 90° pulse being 6.2 μs. (Reproduced by permission of Elsevier from M. H. Levitt, *Prog. NMR Spectrosc.*, 1986, **18**, 61)

and

$$45_0135_{180}90_0180_{180}90_0 - \tau_1 - 45_{90}135_{270}90_{90}180_{270}90_{90} - \tau_2 - \text{Observe} \qquad (45)$$

are constructed. The improvement in spectral appearance produced by equation (44) is illustrated in Figure 7(b). Other sequences have also been suggested.[7,57–61]

One problem of these quadrupole echo sequences is that they are rather long. Signal is lost if the coherence dephasing time T_2 of the deuterium spins is short due to molecular motion on a suitable timescale. This case is not uncommon. Composite pulse quadrupole echo formation is examined critically in Siminovitch et al.[61]

6.2.2 Compensated Population Inversion

Anisotropic molecular motion in solids is probed by measuring the orientation dependence of the ^{2}H spin–lattice relaxation time constant T_1 in a powder sample. A 180° pulse is applied to disturb the spin populations, a variable waiting period τ_{relax} is left, and a quadrupole echo sequence applied

to measure the NMR signal. Spectra are taken for a range of values of τ_{relax}. The partially relaxed quadrupole lineshapes may be analyzed to obtain the dependence of T_1 on sample orientation.

This method requires proper performance of the first 180° pulse. However, a 180° pulse applied to spins $I = 1$ is very sensitive to the quadrupole splitting.[7] The transformed z angular momentum R^j_{zz} is below -0.8 only if the quadrupole splitting $2\omega^j_Q$ is less than around $1.2\Omega^0_1$, where Ω^0_1 is the rf field strength. To get a reasonable inversion of a 150 kHz wide ^{2}H powder pattern, the rf field must be sufficiently strong that the 90° pulse duration is less than 2 μs.

Broadband population inversion of ^{2}H spins may be achieved with much weaker rf fields by using composite 180° pulses. The sequence $45_0 90_{180} 135_0 45_{90} 90_{270} 135_{90} 45_0 90_{180} 135_0$ allows inversion of a 150 kHz quadrupole powder pattern using an rf field of only $\Omega^0_1/2\pi = 37.5$ kHz, which corresponds to a 90° pulse length of 6.5 μs.[7] Longer sequences with flatter inversion profiles have also been designed.[60] Improved performance is attainable even with the simple composite pulse $90_0 90_{90} 90_0$.[62]

6.3 Dipolar Compensation

Nuclear spin dynamics are extremely complicated in the presence of extended dipolar coupling networks, as is typical for abundant spin species in solids. Compensation of these effects is even more challenging than for quadrupole couplings.

6.3.1 Compensation of Homonuclear Dipolar Couplings

Coherent averaging theory (Section 5.4.3) provides a general framework for compensation of undesirable interactions, using only the rotational symmetry of those interactions. This has allowed the development of composite pulses such as $45_0 180_{90} 90_{180} 180_{90} 45_0$, a broadband 180° pulse compensated for dipolar or quadrupolar interactions.[25] Improved population inversion has been demonstrated for networks of coupled protons in solids as well for quadrupolar spins. Composite pulses have also been constructed for NMR imaging in solids.[63]

The theory of composite pulses in dipolar-coupled systems overlaps strongly with the theory of line-narrowing multiple-pulse sequences (see ***Line Narrowing Methods in Solids***). Indeed, many of the same pulse sequences can be used. The composite pulse $90_0 180_{90} 90_{180} 180_{90}$ is a dipolar-compensated 180° pulse as well as a segment of the line-narrowing sequence BLEW-12.[64]

6.3.2 Heteronuclear Decoupling in Anisotropic Systems

Heteronuclear decoupling in solids and liquid crystals is far more difficult than in isotropic liquids, because both homonuclear and heteronuclear interactions are generally large. Despite the theoretical difficulties, progress has been made towards the goal of low-power broadband decoupling in anisotropic systems.[65–67] One promising sequence is

$$[\mathbb{E}]_{90}[\mathbb{E}]_0[\mathbb{E}]_{90}[\mathbb{E}]_0[\mathbb{E}]_{90}[\mathbb{E}]_0[\mathbb{E}]_{270}[\mathbb{E}]_0[\mathbb{E}]_{270} \times [\mathbb{E}]_0[\mathbb{E}]_{270}[\mathbb{E}]_0 \quad (46)$$

where each element $\mathbb{E}$ is a constant rotation offset-compensated composite 90° pulse, $\mathbb{E} = 385_0 320_{180} 25_0$. Improved heteronuclear decoupling in liquid crystals and magic angle spinning solids has been demonstrated.[65–67]

6.4 Coherence Propagation through J-Coupling Networks

Another important application of composite pulse sequences is to propagate spin coherence through the J coupling networks of molecules in isotropic solution. In conjunction with two-dimensional spectroscopy, such sequences are commonly used as an aid to spectral assignment. The method is generally known under the names total coherence transfer spectroscopy (TOCSY) or homonuclear Hartmann Hahn (HOHAHA) spectroscopy. A similar application is when long composite pulse sequences are used to implement coherence transfer through transverse cross relaxation—an experiment generally known under the (misleading) name rotating frame nuclear Overhauser effect spectroscopy (ROESY) (see ***ROESY***).

The theory of composite pulse sequences in this context is challenging. In particular, analysis of the relaxation during long composite pulse trains has required theoretical innovations.[68] Some of the popular pulse sequences are discussed in ***TOCSY in ROESY and ROESY in TOCSY***.

7 COMPENSATION FOR COUPLING VARIATIONS

In the intervals between rf pulses, evolution of the spin system takes place under the influence of chemical shifts, quadrupole couplings and spin–spin coupling terms. Many pulse sequences include fixed delays which should be matched to certain coupling constants for proper operation. For example, in the NMR of isotropic liquids, pulse sequences commonly include a fixed delay $\tau_J = 1/(2J)$ to allow exchange of antiphase and in-phase coherences under the influence of the J coupling. Often 180° pulses are inserted in the middle of the delay to suppress chemical shift evolution. A typical example is the INEPT sequence (see ***INEPT***) for polarization transfer from I spins to S spins.

$$\begin{array}{lllll} I: & 90_0 - \tau_J/2 & - 180_0 - \tau_J/2 & - 90_{90} & \\ S: & & 180_0 & 90_0 \text{ (Acquire signal)} & \end{array}$$

Polarization transfer is only optimal if the heteronuclear J coupling really does correspond to the set delay τ_J. In real samples there is a spread of J values leading to a loss of polarization transfer for some sites.

This situation resembles that of a single rf pulse an inhomogeneous rf field, where the chosen pulse duration corresponds to a nominal rf field actually experienced only by a minority of spins. In that case the spread of nutation angles is compensated by making composite pulses. Similarly, the spread of J couplings in polarization transfer experiments is compensated by building composite INEPT analogs.

Several research groups have investigated this.[70,71] One general procedure is explained,[70] where the following compensated sequence is demonstrated:

$$\begin{array}{llllll} I: & 90_{0-} \tau_J/2 - 180_{0-} \tau_J/2 - 120_{90} - \tau_J/2 - 180_{0-} \tau_J/2 - 30_{90} & & & & \\ S: & & 180_0 & & 180_0 & 90_{90} \text{ (acquire)} \end{array}$$

Although far from obvious, this composite INEPT sequence is an analog of the rf-compensated composite 90° pulse 90_0180_{120}. The polarization transfer is less sensitive than ordinary INEPT to variations in the values of the J couplings. It has also been shown that in some many-spin systems, certain J-compensated INEPT sequences can induce more coherence transfer than ordinary INEPT, even when the latter is at its optimum. For example, for $^1H \rightarrow {}^{13}C$ polarization transfer in CH_3 groups, around 33% more polarization transfer is achieved by certain composite INEPT sequences compared to ordinary INEPT.[70]

This is only one example of a large range of composite pulse sequences compensated for variations in coupling constants. Some others are as follows:

1. Hartmann–Hahn cross polarization experiments in liquids have been compensated for variations in J values by making an analogy with the composite pulse $90_{90}180_090_{90}$.[72]
2. Double quantum excitation sequences in liquid crystal NMR have been compensated for a range of dipolar coupling constants.[73]
3. Bilinear rotation sandwiches have been compensated for J coupling variations in a whole palette of intriguing pulse schemes.[70,71,74–81]
4. Sequences for exciting quadrupolar order in solids and liquid crystals (Jeener–Broekaert sequences) have been compensated for a spread in quadrupolar coupling constants caused by orientational inhomogeneity.[82]
5. Excitation of spin magnetization in nuclear quadrupole resonance (NQR) (see ***Quadrupolar Interactions***) has been compensated for the spread of effective nutation fields caused by the orientational distribution in a powder sample.[2,3]

8 REFERENCES

1. A. M. Thayer and A. Pines, *J. Magn. Reson.*, 1986, **70**, 518.
2. N. Sunitha Bai, M. Ramakrishna, and R. Ramachandran, *J. Magn. Reson.* ***A***, 1993, **104**, 203.
3. G. Y. Li, Y. Jiang, and X. W. Wu, *Chem. Phys. Lett.*, 1993, **202**, 82.
4. W. S. Warren and A. H. Zewail, *J. Chem. Phys.*, 1983, **78**, 2279.
5. W. S. Warren and A. H. Zewail, *J. Chem. Phys.*, 1983, **78**, 2298.
6. W. S. Warren and A. H. Zewail, *J. Chem. Phys.*, 1983, **78**, 3583.
7. M. H. Levitt, *Prog. NMR Spectrosc.*, 1986, **18**, 61.
8. T. Fujiwara and K. Nagayama, *J. Magn. Reson.*, 1988, **77**, 53.
9. M. H. Levitt and R. Freeman, *J. Magn. Reson.*, 1979, **33**, 473.
10. C. Counsell, M. H. Levitt, and R. R. Ernst, *J. Magn. Reson.*, 1985, **63**, 133.
11. A. J. Shaka and R. Freeman, *J. Magn. Reson.*, 1983, **55**, 487.
12. M. H. Levitt and R. Freeman, *J. Magn. Reson.*, 1981, **43**, 65.
13. H. W. Spiess, in *NMR Basic Principles and Progress*, ed. P. Diehl, E. Fluck, and E. Kosfeld, Springer, Berlin, 1978.
14. There are also some composite pulses which give a fixed overall rotation over the compensation band, but for which that rotation is different from that generated by an ideal pulse. See Levitt,[7] Tycko et al.,[26] and Shaka, and Pines.[27]
15. S. Wimperis, *J. Magn. Reson.* ***A***, 1994, **109**, 221.
16. M. H. Levitt and R. R. Ernst, *Mol. Phys.*, 1983, **50**, 1109.
17. M. H. Levitt and R. R. Ernst, *J. Chem. Phys.*, 1985, **83**, 3297.
18. R. Freeman, S. P. Kempsell, and M. H. Levitt, *J. Magn. Reson.*, 1980, **38**, 453.
19. M. H. Levitt, *J. Magn. Reson.*, 1982, **48**, 234.
20. M. H. Levitt, *J. Magn. Reson.*, 1982, **50**, 95.
21. B. Blümich and H. W. Spiess, *J. Magn. Reson.*, 1985, **61**, 356.
22. M. H. Levitt and R. Freeman, *J. Magn. Reson.*, 1981, **43**, 502.
23. M. H. Levitt, R. Freeman, and T. A. Frenkiel, *Adv. Magn. Reson.*, 1983, **11**, 47.
24. R. Tycko, *Phys. Rev. Lett.*, 1983, **51**, 775.
25. R. Tycko, E. Schneider, and A. Pines, *J. Chem. Phys.*, 1984, **81**, 680.
26. R. Tycko, H. M. Cho, E. Schneider, and A. Pines, *J. Magn. Reson.*, 1985, **61**, 90.
27. A. J. Shaka and A. Pines, *J. Magn. Reson.*, 1987, **71**, 495.
28. A. J. Shaka, *Chem. Phys. Lett.*, 1985, **120**, 201.
29. Z. Starčuk and V. Sklenář, *J. Magn. Reson.*, 1985, **62**, 113.
30. C. S. Poon and R. M. Henkelman, *J. Magn. Reson.*, 1992, **99**, 45.
31. N. Sunitha Bai, M. Ramakrishna, and R. Ramachandran, *J. Magn. Reson.* ***A***, 1993, **102**, 235.
32. J. Baum, R. Tycko, and A. Pines, *J. Chem. Phys.*, 1983, **79**, 4643.
33. R. Tycko and A. Pines, *Chem. Phys. Lett.*, 1984, **111**, 462.
34. R. Tycko, A. Pines, and J. Guckenheimer, *J. Chem. Phys.*, 1985, **83**, 2775.
35. J. S. Waugh, *J. Magn. Reson.*, 1982, **50**, 30.
36. J. S. Waugh, *J. Magn. Reson.*, 1982, **49**, 517.
37. A. J. Shaka, C. J. Lee, and A. Pines, *J. Magn. Reson.*, 1988, **77**, 274.
38. M. H. Levitt, R. Freeman, and T. Frenkiel, *J. Magn. Reson.*, 1982, **47**, 328.
39. M. H. Levitt, R. Freeman, and T. Frenkiel, *J. Magn. Reson.*, 1982, **50**, 157.
40. More strictly, for a cycle, both $\bar{\beta}^j$ and $\bar{\xi}_\Delta{}^j$ are very small.
41. A. J. Shaka, J. Keeler, T. Frenkiel, and R. Freeman, *J. Magn. Reson.*, 1983, **52**, 335.
42. M. H. Levitt and R. R. Ernst, *J. Magn. Reson.*, 1983, **55**, 247.
43. R. Tycko and A. Pines, *Chem. Phys. Lett.*, 1984, **111**, 462.
44. R. Tycko and A. Pines, *J. Magn. Reson.*, 1984, **60**, 156.
45. A. J. Shaka and R. Freeman, *J. Magn. Reson.*, 1985, **64**, 145.
46. A. J. Shaka, J. Keeler, M. B. Smith, and R. Freeman, *J. Magn. Reson.*, 1985, **61**, 175.
47. A. J. Shaka and R. Freeman, *J. Magn. Reson.*, 1985, **63**, 596.
48. J. Baum, R. Tycko, and A. Pines, *Chem. Phys.*, 1986, **105**, 7.
49. M. H. Levitt and M. F. Roberts, *J. Magn. Reson.*, 1987, **71**, 576.
50. M. H. Levitt, J. L. Sudmeier, and W. W. Bachovchin, *J. Am. Chem. Soc.*, 1987, **109**, 6540.
51. M. H. Levitt, *J. Chem. Phys.*, 1988, **88**, 3481.
52. A. Bielecki and M. H. Levitt, *J. Magn. Reson.*, 1989, **82**, 562.
53. A. L. Davis and S. Wimperis, *J. Magn. Reson.*, 1989, **84**, 620.
54. R. Freeman, T. A. Frenkiel, and M. H. Levitt, *J. Magn. Reson.*, 1981, **44**, 409.
55. A. Bax, R. Freeman, T. A. Frenkiel, and M. H. Levitt, *J. Magn. Reson.*, 1981, **43**, 478.
56. C. J. R. Counsell, M. H. Levitt, and R. R. Ernst, *J. Magn. Reson.*, 1985, **64**, 470.

57. M. H. Levitt, D. Suter, and R. R. Ernst, *J. Chem. Phys.*, 1984, **80**, 3064.
58. T. Fujiwara and K. Nagayama, *J. Magn. Reson.*, 1991, **93**, 563.
59. D. Wang, G. Li, and X. Wu, *J. Magn. Reson.*, 1987, **74**, 464.
60. D. P. Raleigh, E. T. Olejniczak, and R. G. Griffin, *J. Magn. Reson.*, 1989, **81**, 455.
61. D. J. Siminovitch, D. P. Raleigh, E. T. Olejniczak, and R. G. Griffin, *J. Chem. Phys.*, 1986, **84**, 2556.
62. N. J. Heaton, R. R. Vold, and R. L. Vold, *J. Magn. Reson.*, 1988, **77**, 572.
63. J. B. Miller and A. N. Garroway, *J. Magn. Reson.*, 1989, **85**, 432.
64. D. P. Burum, M. Linder, and R. R. Ernst, *J. Magn. Reson.*, 1981, **44**, 173.
65. K. V. Schenker, D. Suter, and A. Pines, *J. Magn. Reson.*, 1987, **73**, 99.
66. D. Suter, K. V. Schenker, and A. Pines, *J. Magn. Reson.*, 1987, **73**, 90.
67. D. Suter, A. Pines, J. H. Lee, and G. Drobny, *Chem. Phys. Lett.*, 1988, **144**, 324.
68. C. Griesinger and R. R. Ernst, *Chem. Phys. Lett.*, 1988, **152**, 239.
69. G. A. Morris and R. Freeman, *J. Am. Chem. Soc.*, 1979, **101**, 760.
70. S. Wimperis and G. Bodenhausen, *J. Magn. Reson.*, 1986, **69**, 264.
71. O. W. Sørensen, J. C. Madsen, N. C. Nielsen, H. Bildsøe, and H. J. Jakobsen, *J. Magn. Reson.*, 1988, **77**, 170.
72. G. C. Chingas, A. N. Garroway, R. D. Bertrand, and W. B. Moniz, *J. Magn. Reson.*, 1979, **35**, 283.
73. T. M. Barbara, R. Tycko, and D. P. Weitekamp, *J. Magn. Reson.*, 1985, **62**, 54.
74. J. R. Garbow, D. P. Weitekamp, and A. Pines, *Chem. Phys. Lett.*, 1982, **93**, 504.
75. S. Wimperis and R. Freeman, *J. Magn. Reson.*, 1984, **58**, 348.
76. S. Wimperis and R. Freeman, *J. Magn. Reson.*, 1985, **62**, 147.
77. A. M. Torres, R. E. D. McClung, and T. T. Nakashima, *J. Magn. Reson.*, 1990, **87**, 189.
78. A. M. Torres and R. E. D. McClung, *J. Magn. Reson.*, 1991, **92**, 45.
79. A. M. Torres, T. T. Nakashima, R. E. D. McClung, and D. R. Muhandiram, *J. Magn. Reson.*, 1992, **99**, 99.
80. A. M. Torres, T. T. Nakashima, and R. E. D. McClung, *J. Magn. Reson.* ***A***, 1993, **102**, 219.
81. A. M. Torres, T. T. Nakashima, and R. E. D. McClung, *J. Magn. Reson.* ***A***, 1993, **101**, 285.
82. S. Wimperis and G. Bodenhausen, *Chem. Phys. Lett.*, 1986, **132**, 194.

Biographical Sketch

Malcolm H. Levitt. *b* 1957. B.A., 1978, D.Phil., 1981 (supervisor: Ray Freeman), Oxford University, UK. Postdoctoral work at Weizmann Institute, Israel (with Shimon Vega), 1981–82, and ETH-Zürich, (with Richard Ernst), 1982–86. Research Associate at Francis Bitter Magnet Laboratory, Massachusetts Institute of Technology, 1986–90; Royal Society Research Fellow, Interdisciplinary Research Centre for Superconductivity, Cambridge University, UK, 1990–91. Presently Lecturer in the Physical Chemistry Division, Stockholm University. Approx. 80 publications. Current research speciality: principles and methodology of NMR in both solid and liquid phases.

CRAMPS

Bernard C. Gerstein

Ames Laboratory of Iowa State University, Ames, IA, USA

1	Introduction	1
2	Rotations in Real Space	2
3	Rotations in Spin Space	3
4	Echoes and the Average Hamiltonian	4
5	CRAMPS	6
6	Caveats	7
7	Related Articles	8
8	References	8

1 INTRODUCTION

Combined rotation and multiple pulse spectroscopy (CRAMPS)[1] is one means of using transient techniques in NMR to achieve liquid-like high-resolution NMR spectra of hydrogen and fluorine in solids. Herein will be described the basic ideas leading to the achievement of this resolution. The background required is that obtained by exposure to an undergraduate physical chemistry course, with a smattering of perturbation theory included. There will necessarily be some overlap between the description below, and other articles in this Encyclopedia. Cross references to pertinent subjects are given at the end of the article.

Of all the elements encountered by medical, biological, chemical, and physical scientists, hydrogen is perhaps the most common. The NMR-active nuclide, ^{1}H, is 99.98% abundant, and the magnetic moment is exceeded in magnitude only by the nonnaturally occurring tritium, ^{3}H. ^{1}H was the first nucleus for which NMR was reported.[2,3] Because of the magnitude of its magnetic moment, and its natural abundance, hydrogen is the most easily detected nucleus commonly encountered in NMR. It is routinely used for qualitative and quantitative analysis of organic molecules in the liquid state.

Chemical shifts of hydrogen in organic molecules in solution commonly have a range of about 15 ppm of the resonance frequency. For example, protons in common organic molecules in a spectrometer operating at 500 MHz for ^{1}H will exhibit a chemical shift range of about $15 \times 500 = 7500$ Hz. Scalar couplings to other hydrogen atoms and to carbon atoms are characteristically around 100 Hz. Resolution in commercial liquid state spectrometers is of order of a few tens of hertz, so hydrogen NMR on molecules in the liquid state supplies an easily detectable, well resolved, and sensitive fingerprint for routine analysis.

It was thus initially disappointing that under a single resonant excitation such as was used on liquids, NMR spectra of hydrogen in solids such as ice, or high molecular weight proteins, are broad and featureless. The linewidths are about 15 kHz, an example being given for hydrogen in adipic acid in Figure 1(a).

Exactly those qualities which make ^{1}H such a valuable label for liquid state NMR destroy the resolution of the NMR spectrum of hydrogen in solids. The reasons are physically

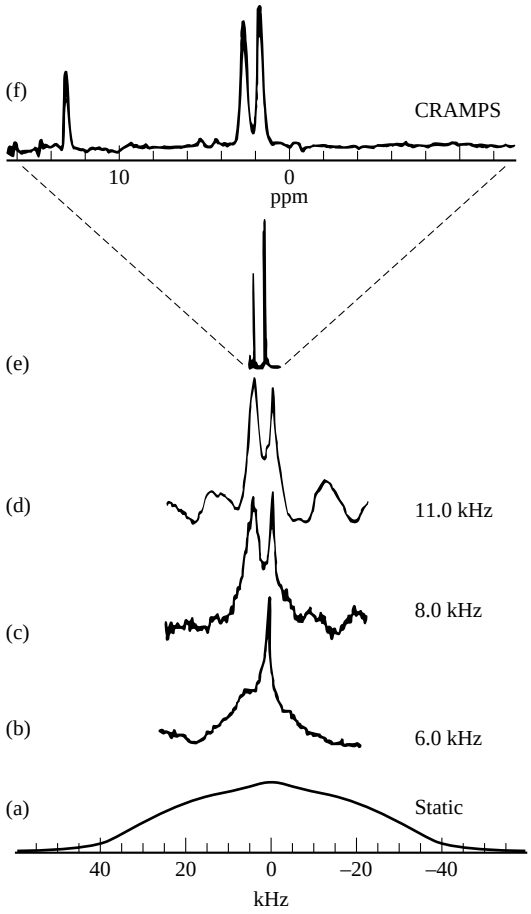

Figure 1 Comparison of NMR spectra taken under: (a) single pulse excitation; (b) MAS at 6 kHz; (c) MAS at 8 kHz; (d) MAS at 11 kHz; (e, f) CRAMPS. (Courtesy of Gary Maciel)

obvious. ^{1}H is a nucleus with relatively high abundance and large magnetic moment. In a static field it behaves as a magnet, producing a magnetic field with the familiar symmetry exhibited by iron filings aligning in the neighborhood of a bar magnet. In the solid state, each hydrogen atom will be exposed not only to the static field of the magnet used for NMR, but also to the sum of the 'dipolar' fields of all other abundantly present protons in the sample. The result is that the resonance frequency of any hydrogen atom in the sample is homogeneously broadened by the effect of the dipolar fields. In addition, there is NMR line broadening in a motionless solid due to the nonspherical symmetry of the surrounding bonding electronic cloud, i.e. due to 'shielding anisotropies'. CRAMPS was developed to attenuate these two major sources of line broadening such that liquid-like NMR spectra of ^{1}H and ^{19}F in solids are achieved in favorable cases.

CRAMPS involves manipulations common to NMR of both liquids and solids. These cause the system under observation to vary in time such that chemical shifts become more resolved. Other interactions, e.g. dc field inhomogeneities in liquids, are averaged to small values. A critical fact here is that all observables depend on variables in both real space (r, θ, ϕ), and spin space (components of spin angular momentum, $\hat{I}_k$, $k = x, y, z$) (see ***Internal Spin Interactions and Rotations in Solids***). The manipulations used selectively to attenuate

internal interactions which cause a loss of resolution therefore include the following:

1. Sample motion in the laboratory makes θ and ϕ time-dependent. For liquids, spinning rates are roughly 100 Hz. Solids are commonly spun 100 times faster.
2. Radiofrequency (rf) pulsing makes the components of the spin angular momentum operators ($\hat{I}_x$, $\hat{I}_y$, and $\hat{I}_z$) time-dependent.

Rotations in real space,[4,5] e.g. magic angle spinning, accomplish what molecular tumbling of molecules in the liquid state does for the shielding anisotropy; namely, it averages the anisotropic shielding to its isotropic, or average, value.

Radiofrequency pulses may be thought of as rotating magnetic moments in 'spin space'. We may therefore think of the combined rotation and multiple pulse technique as using rotations in both 'spin space' and in the real space of the laboratory. As understood early on[6–8] and shown below, rotations in spin space via rf pulses can be arranged to average local dipolar fields, and the resulting NMR line broadening to values smaller than differences in chemical shifts.

An example of the CRAMPS spectrum[9] of hydrogen in adipic acid, $HOOC(CH_2)_4COOH$, is shown in Figure 1(e) and (f). Figure 1(b)–(d) show spectra of the static sample under a single pulse excitation, roughly 40 kHz wide, and the spectrum of the sample under magic angle spinning (see below) at frequencies between 6 and 11 kHz. It can be seen that the resolution between the top and the bottom spectrum has increased under CRAMPS by a factor of roughly 600.

In order to illustrate how the experiment works, we first consider how the physical rotation of solid samples narrows the broadening effect of shielding anisotropies. Then we consider how sequences of rf pulses narrow dipolar broadening.

2 ROTATIONS IN REAL SPACE

The most common motion familiar to the NMR spectroscopist working in liquids is that of simply spinning the NMR tube containing the liquid sample about an axis perpendicular to the static field. This partially averages dc field inhomogeneities over the sample volume and improves resolution. Rotation of a liquid at the magic angle further narrows the lines of liquids (see ***Magnetic Susceptibility and High Resolution NMR of Liquids and Solids***). The manner in which this works might be perhaps understood by a related example. An individual enthusiastic about the game of football, but without much background in mechanics, constructs a sheet metal wind vane, cut into the shape of an American football. The dynamic balance of this particular device is such that instead of pointing to indicate wind direction, it rotates as the wind blows. For rotation too fast for the eye to follow, the football shaped device, being a thin slice the width of the metal when viewed end-on, and a football shaped object when viewed perpendicular to the surface, seems on average to become something smaller than a football, and something larger than a line. On average, it seems that a circular object is seen. Glancing at the wind vane in a high wind, the builder rapidly blinks at this dysfunction of the device. In doing so, the blinking is unwittingly done in concert with the rotation period of the wind vane, and for an instant, instead of the football shaped wind vane, a very narrow line is seen! Each time the eyes were opened, a stroboscopic observation was made of the wind vane viewed head-on.

Following the football analogy, consider the symmetry of the bonding electron cloud about an NMR active ^{13}C in a CO_2 molecule, O=C=O. Clearly this cloud is roughly football shaped. This bonding electron cloud may be thought to circulate in reaction to the imposition of a static magnetic field, producing a 'shielding field'. The details of the circulation, and thus the shielding field, described in terms of a 'shielding ellipsoid' $\boldsymbol{\sigma}$, will be different when the static field is perpendicular to the unique axis of the football than when parallel to it. In fact the shielding field produces an NMR line at $\delta = -90$, i.e. 90 ppm upfield (down frequency; shielded) with respect to ^{13}C in tetramethylsilane (TMS), when the static field is parallel to the unique axis. With the field perpendicular to the unique axis, δ is 245 ppm deshielded with respect to ^{13}C in TMS. In the liquid state, the NMR spectrum of ^{13}C in CO_2 is a narrow line 133 ppm deshielded from TMS. Sufficiently rapid isotropic (random in space) tumbling of the molecule in the liquid results in this football shaped object becoming spherical as viewed by the eye of NMR; the anisotropic shielding is averaged to its isotropic value, which is the average of the three principal axes of the shielding ellipsoid. Note that $133 = (245 + 245 - 90)/3$; the isotropic value of the chemical shift of ^{13}C in CO_2 in the liquid is the average of the values with the dc field along the x, y, and z axes of the shielding ellipsoid.

When the NMR spectrum of carbon dioxide is measured in the powdered, solid state, as dry ice, molecular tumbling is absent. In this case each crystallite contributes an NMR line between 245 ppm and −90 ppm, depending upon the orientation of the shielding ellipsoid in the crystallite to the static field. The total spectrum appears as the 'powder pattern' shown in Figure 2. The weighting of intensity on the high frequency side, corresponding to the static field in the (x, y) plane of the shielding ellipsoid, corresponds to the fact that it is more likely that a given crystallite will have the static field near the (x, y) plane of the shielding ellipsoid than uniquely along the axis of rotation.

The resonance frequency depends on the orientation of the shielding ellipsoid with respect to the static magnetic field, specified by angles θ and ϕ, as shown in Figure 3, and on the asymmetry of the ellipsoid. This asymmetry is uniquely specified by the magnitudes of its three principal axes in ppm

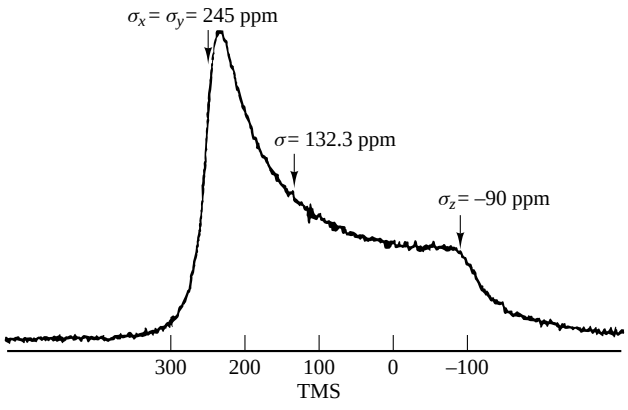

Figure 2 NMR of ^{13}C in powdered solid CO_2. Illustration of shielding anisotropy for an axially symmetric shielding environment. (Courtesy of Anita Orendt)

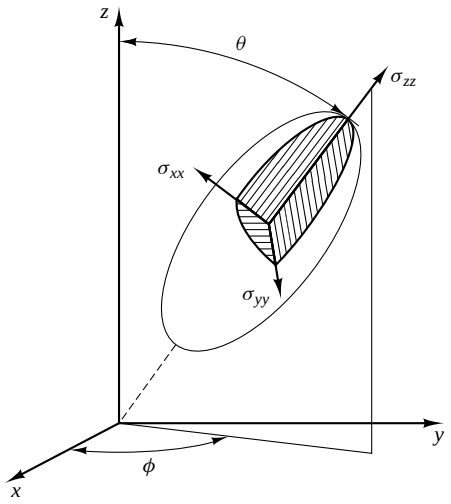

Figure 3 Relationship between the principal axes of the shielding ellipsoid and the laboratory coordinate system; definitions of θ and ϕ

of the resonance frequency, denoted by σ_{xx}, σ_{yy}, and σ_{zz}, or in terms of linear combinations of these which more clearly exhibit the symmetry properties. The combinations are

(a) the average of the magnitudes of the three principal axes, $\sigma_{\rm iso}$, the isotropic shielding, which is that quantity observed in NMR of liquids;
(b) the anisotropy ζ, equal to the difference between σ_{zz} and $\sigma_{\rm iso}$;
(c) the asymmetry η, proportional to the difference in the x and y components.

We note that a similar ellipsoid describes the anisotropy of the dipolar interaction $\boldsymbol{D}$ between two nuclei, but in this case the interaction is axially symmetric, $D_{xx} = D_{yy}$, so the asymmetry for the dipolar interaction is zero.

The resonance frequency of a shielding ellipsoid oriented at θ, ϕ with respect to $\boldsymbol{B}_0$, and with symmetry specified by $\sigma_{\rm iso}$, ζ, and η is given by

$$\omega(\theta, \phi, \sigma_{\rm iso}, \zeta, \eta) = \omega_0\{\sigma_{\rm iso} + \zeta[\tfrac{1}{2}(3\cos^2\theta - 1) + \tfrac{1}{2}\eta \sin 2\theta \cos 2\phi]\} \quad (1)$$

When the sample is set in motion, e.g. by random molecular tumbling, as would take place when the sample is heated to the liquid state, or by sonic agitation of the finely divided solid in a suitable liquid (see ***Ultrasonic Irradiation and NMR***), or by the experimenter about an axis oriented at an angle β to the static field, and at a frequency that is fast compared with the spectral width $\omega_0(\sigma_{xx} - \sigma_{zz})$, it may be shown (see ***Internal Spin Interactions and Rotations in Solids***) that the averaged frequency becomes only a function of the isotropic chemical shift $\sigma_{\rm iso}$, the anisotropy ζ, and the angle β between the spinning axis and the field. This relationship is given by

$$\omega(\omega_0, \beta, \sigma_{\rm iso}, \zeta) = \omega_0[\sigma_{\rm iso} + \tfrac{1}{2}\zeta(3\cos^2\beta - 1)] \quad (2)$$

The terms in η disappear if the sample is spun rapidly enough, or contribute to sidebands if the spinning rate is smaller than the shielding spectral width. Clearly at the 'magic' angle β = arccos $(\frac{1}{3})^{1/2}$, only the isotropic value remains; the spinning has achieved a liquid-like spectrum by averaging the anisotropic information to zero.

It was recognized early on that MAS could also average the dipolar broadening to zero. However, since all nuclei in a sample rich in protons are connected to all others via the through-space dipolar interactions, it is necessary to spin fast compared with the dipolar linewidth to achieve effective narrowing. This means spinning fast compared with 15 kHz, or fast compared with roughly 10^6 rev min^{-1}. Such spinning speeds are not easily achieved, but have been realized in homemade spectrometers with easily machineable polyimide resins,[10] and are also now available in commercial spectrometers making use of high-precision cylindrical ceramic rotors. A comparison of narrowing under ultrafast MAS and the use of CRAMPS has been made,[11] with the conclusion that one would like to have access to both techniques, depending upon the sample. Furthermore, there are spin dynamics containing added information which one may perform using CRAMPS which are not available within the expedient of high speed spinning.

We now consider how manipulating the nuclear spin system with rf pulses averages the dipolar interactions to values smaller than differences in chemical shifts. To do so, we use the background developed in the article ***Echoes in Solids***.

3 ROTATIONS IN SPIN SPACE

All spectroscopy experiments implicitly or explicitly involve solutions of the time dependent Schrödinger equation. We have implicitly invoked one such solution in discussing MAS, above. An understanding of NMR appropriate to the level of this Encyclopedia involves at least a rudimentary knowledge of the solutions of this equation in the density operator formulation. Fortunately there are texts for students at both the entry level[12,13] and advanced levels,[14–16] presenting both these pictures. As a basis for understanding the multiple pulse portion of the CRAMPS experiment, I briefly summarize the results of selective averaging theory on first the shielding interaction, and then the dipolar interaction. Let us start in the rotating frame of the Zeeman interaction, the frame in the real world in which NMR signals are detected after demodulation removes the carrier frequency from the information content of the signal. In the rotating frame, the principal effective magnetic fields which cause a proton to resonate for detection by NMR are: (a) the externally applied rf field, $\boldsymbol{B}_1$, and (b) the sample-supplied, or internal average, of the dipolar fields of all other protons, $\boldsymbol{B}_{\rm D}$. A smaller perturbation is that of the anisotropic shielding field associated with the reaction to electrons in the environment of the hydrogen nucleus of the static external field.

With each field is associated an energy, and a quantum mechanical energy operator $\hat{\mathcal{H}}$. Thus the energy operator in the rotating frame is given by

$$\hat{\mathcal{H}} = \hat{\mathcal{H}}_{\rm rf} + \hat{\mathcal{H}}_{\rm int} \quad (3)$$

where the magnitude of $\hat{\mathcal{H}}_{\rm rf}$ for purposes of solid state experiments is about 5 mT. The magnitude of $\hat{\mathcal{H}}_{\rm int}$ is never greater than a few tenths of a millitesla in the case discussed here—that of homonuclear dipolar coupling. The equation of

motion of the system is then given by the solution to the time dependent Schrödinger equation in the density matrix formulation:

$$i\frac{d\hat{\rho}}{dt} = [\hat{\mathcal{H}}, \hat{\rho}] \tag{4}$$

Here, $\hat{\mathcal{H}}$ is the sum of the rf and internal interactions, as specified in equation (3), $\hat{\rho}$ is the density operator, specified by the wavefunction $|\psi\rangle$, as $|\psi\rangle\langle\psi|$ in Dirac bracket notation. The average values of observables, e.g. $\langle\hat{I}_y(t)\rangle$, the free induction decay detected along the y phase in the rotating frame, are given by

$$\langle\hat{I}_y(t)\rangle = \mathrm{Tr}\,[\hat{\rho}(t)\hat{I}_y] \tag{5}$$

With the interactions separated in magnitude in this manner, it makes sense to treat $\hat{\mathcal{H}}_{\mathrm{int}}$ as a perturbation on $\hat{\mathcal{H}}_{\mathrm{rf}}$. Recall that the transformation to the frame of the Zeeman interaction (the rotating frame) simplifies the description of a nuclear spin in the presence of other interactions; e.g. the oscillating on-resonance rf field becomes static in the rotating frame. Similarly, transformation to the frame of the now largest interaction, the rf field, further simplifies the description of the system. The transformation to the frame of the rf field is accomplished by the relationships

$$\hat{\rho} = \hat{U}_{\mathrm{rf}}\hat{\tilde{\rho}}\hat{U}_{\mathrm{rf}}^{-1} \tag{6}$$

$$i\frac{dU_{\mathrm{rf}}}{dt} = \hat{\mathcal{H}}_{\mathrm{rf}}\hat{U}_{\mathrm{rf}} \tag{7}$$

$$\hat{U}_{\mathrm{rf}}(0,0) \equiv \hat{U}_{\mathrm{rf}}(t=0) = \hat{1} \tag{8}$$

$$\hat{\tilde{\mathcal{H}}}_{\mathrm{int}}(t) = \hat{U}_{\mathrm{rf}}^{-1}(t,0)\hat{\mathcal{H}}_{\mathrm{int}}\hat{U}_{\mathrm{rf}} \tag{9}$$

As mentioned above, the notation $\hat{U}(t, 0)$ is a formal way of saying that the propagator $\hat{U}$ drives the system from time 0 to time t. An explicit operational form of $\hat{U}$ will be given below; for now, accept it as that quantity causing the system to proceed in time, with physical origin in the time-dependent sequence of rf pulses, and the internal interactions as affected by these pulses. The result,

$$i\frac{d\hat{\tilde{\rho}}}{dt} = [\hat{\tilde{\mathcal{H}}}_{\mathrm{int}}, \hat{\tilde{\rho}}] \quad \text{(energy in units of frequency)} \tag{10}$$

is the equation of motion in the frame of the rf field. Now, in the same spirit with which we used the interaction $\hat{\mathcal{H}}$ to transform itself out of the equation of motion [this interaction does not appear in equation (10)] we use the interaction $\hat{\mathcal{H}}_{\mathrm{int}}$ to make another transformation which transforms $\hat{\mathcal{H}}_{\mathrm{int}}$ out of the equation:

$$\hat{\tilde{\rho}} = \hat{U}_{\mathrm{int}}(t,0)\hat{\tilde{\tilde{\rho}}}\hat{U}_{\mathrm{int}}^{-1}(t,0) \tag{11}$$

$$i\frac{d\hat{U}_{\mathrm{int}}}{dt} = \hat{\tilde{\mathcal{H}}}_{\mathrm{int}}\hat{U}_{\mathrm{int}} \tag{12}$$

$$\hat{U}_{\mathrm{int}}(0,0) = 1 \tag{13}$$

Thus $\hat{\rho}$ is replaced by $\hat{\tilde{\rho}}$, $\hat{\tilde{\rho}}$ is replaced by $\hat{\tilde{\tilde{\rho}}}$, $\hat{U}_{\mathrm{rf}}$ is replaced by $\hat{U}_{\mathrm{int}}$, etc. As shown by equation (14), the system in this frame is static; that is,

$$i\frac{d\hat{\tilde{\tilde{\rho}}}}{dt} = [0, \hat{\tilde{\tilde{\rho}}}] = 0 \tag{14}$$

We formally identify this static system with the system at time zero; $\hat{\tilde{\tilde{\rho}}}$ then becomes identical to $\hat{\rho}(0)$. In this perturbation picture, with $\hat{\tilde{\tilde{\mathcal{H}}}}_{\mathrm{int}}$ being a perturbation on $\hat{\mathcal{H}}_{\mathrm{rf}}$, the motion of the system, is then described by

$$\hat{\rho}(t) = \hat{U}_{\mathrm{rf}}(t,0)\hat{U}_{\mathrm{int}}(t,0)\hat{\rho}(0)\hat{U}_{\mathrm{int}}^{-1}(t,0)\hat{U}_{\mathrm{rf}}^{-1}(t,0) \tag{15}$$

4 ECHOES AND THE AVERAGE HAMILTONIAN

Before discussing the operational forms of the propagators $\hat{U}$ explicitly, let us examine equation (15) more closely. It is clear that if both $\hat{U}_{\mathrm{rf}}(t_c,0)$ and $\hat{U}_{\mathrm{int}}(t_c,0)$ are unity at some particular time t_c, then at this special time it appears that the system has simply not changed, i.e. equations (4) and (15) at time t_c tell us that the value of any observable at this time is the value of that observable's operator at time zero; at time t_c, $\hat{\rho}(t_c) = \hat{\rho}(0)$. There is therefore an enormous simplicity in the behavior of the system which the experimenter may accomplish with proper arrangements of rf pulses, since both $\hat{U}_{\mathrm{rf}}$ and $\hat{U}_{\mathrm{int}}$ depend upon $\hat{\mathcal{H}}_{\mathrm{rf}}$—the rf pulses which we supply! The fields (5 MT) generated by the rf pulses are much larger than the 'internal fields' due to dipolar and shielding interactions (<0.3 MT). Therefore, as long as $\hat{U}_{\mathrm{rf}}$ operates for times that are short compared with times in which $\hat{U}_{\mathrm{int}}$ affects the system, its motion is predominantly controlled by $\hat{U}_{\mathrm{rf}}$. Then if the sequence of rf pulses generating $\hat{U}_{\mathrm{rf}}(t_c, 0)$ returns the system to its initial state, $\hat{U}_{\mathrm{rf}}(t_c, 0)$ is formally equal to unity, a result inferred from physics rather than mathematics. Examples of such pulse sequences are easily imagined if the physics is kept clearly in mind. For example, the sequence (τ, 180°_x, 2τ, 180°_x, τ) results in a rotation by 2π about the x axis, leaving the system invariant at cycle time t_c equal to time 4τ. The sequence (τ, 90°_y, τ, 90°_x, 2τ, 90°_{-x}, τ, 90°_{-y}, τ) has phase alternated pairs of pulses which cancel against each other (the y pulse cancels against the $-y$ pulse, and similarly for x) and leaves the system invariant at a cycle time t_c of 6τ. This phase alternated sequence (for each x, a $-x$, and for each y a $-y$) is a variant of the solid echo sequence[17–19] which became famous as the WAHUHA (after John Waugh, Lee Huber, and Ulrich Haeberlen) sequence. Such sequences are said to be cyclic. If these groups of pulses are repeated periodically, they are both cyclic and periodic (see ***Average Hamiltonian Theory***). As long as $\hat{U}_{\mathrm{rf}}(nt_c, 0)$ is the dominant propagator, in the 'windows' between these groups of pulses, the system will behave as if it is not moving in time. The

situation is quite analogous to the observation of the spinning football shaped object by the blinking football fan. If the blinking is done in concert with the rotation at such a time that the object is viewed head-on, i.e. when it appears as a thin line, then only a thin line will be seen at all times *of observation*.

A closer look at equation (15), however, clearly indicates that as time progresses, $\hat{U}_{\text{int}}(nt_c,0)$ begins to affect the motion of the system. Stroboscopic observation as time progresses, in the windows nt_c, will reveal some motion due to $\hat{U}_{\text{int}}(nt_c, 0)$. Now this propagator, $\hat{U}_{\text{int}}(nt_c, 0)$, is determined by $\hat{\tilde{\mathcal{H}}}_{\text{int}}$. The interaction $\hat{\tilde{\mathcal{H}}}_{\text{int}}$ is the sum of $\hat{\tilde{\mathcal{H}}}_{\text{D}}$ and $\hat{\tilde{\mathcal{H}}}_{\text{CS}}$, the dipolar and shielding interactions as manipulated by the rf pulses. If somehow the dipolar interaction (but not the shielding interaction) can be selectively set in motion so that its time average at times nt_c is zero, the remaining information in the windows of the stroboscopic observation will be the shielding. This is exactly what multiple pulse homonuclear decoupling attempts to accomplish. To see how this works, one needs an explicitly operational form for the internal propagator $\hat{U}_{\text{int}}(nt_c, 0)$. The form is illustrated by the spin echo sequence $(\tau, 180^\circ_y, \tau, 180^\circ_y, \tau)$. In the spin echo sequence, we take the internal Hamiltonian to represent any interaction proportional to the operator $\hat{I}_z$: e.g. shielding, resonance offset, static field inhomogeneities, and scalar couplings to unlike nuclei. Homonuclear dipolar coupling, as shown below, is not proportional to $\hat{I}_z$.

When we manipulate $\hat{\tilde{\mathcal{H}}}_{\text{int}}$ by cyclic and periodic sequences of rf pulses (meaning $\hat{U}_{\text{rf}}(t_c, 0)$ is unity) the form of the propagator $\hat{U}_{\text{int}}$ becomes an exponential,[20] with the leading term in the result, stroboscopically observed at cycle times nt_c, given by

$$\begin{aligned}\hat{\rho}(nt_c) &= \hat{U}_{\text{int}}(t_c, 0)\hat{\rho}(0)\hat{U}^{-1}_{\text{int}}(t_c, 0) \\ &= \exp\,(-\mathrm{i}\hat{\bar{\mathcal{H}}}^{(0)}_{\text{int}} nt_c)\ \hat{\rho}(0) \exp\,(\hat{\bar{\mathcal{H}}}^{(0)}_{\text{int}} nt_c)\end{aligned} \tag{16}$$

Here, $\hat{\bar{\mathcal{H}}}^{(0)}_{\text{int}}$, which is equal to the integral over a cycle of the internal Hamiltonian as manipulated in time by the rf pulses,

$$\hat{\bar{\mathcal{H}}}^{(0)}_{\text{int}} = \frac{1}{t_c}\int_0^{t_c} \hat{\tilde{\mathcal{H}}}_{\text{int}}\,\mathrm{d}t \tag{17}$$

may be interpreted as the time average of this manipulated internal Hamiltonian. The manner of manipulation of $\hat{\mathcal{H}}_{\text{int}}$ is given by:

$$\hat{\tilde{\mathcal{H}}}_{\text{int}}(t) = \hat{U}^{-1}_{\text{rf}}(t, 0)\hat{\mathcal{H}}_{\text{int}}\hat{U}_{\text{rf}}(t, 0) \tag{18}$$

$\hat{\tilde{\mathcal{H}}}_{\text{int}}(t)$ is the instantaneous value of the internal Hamiltonian as determined by the rf pulses. $\hat{U}_{\text{rf}}(t, 0)$ is the propagation operator due to the rf pulses from time zero to time t. For n time intervals $\Delta1$, followed by $\Delta2$, ... , followed by Δn, $\hat{U}_{\text{rf}}$ is clearly the propagator during interval $\Delta1$, followed by the propagator over $\Delta2$, ... , as shown by

$$\hat{U}_{\text{rf}}(t, 0) = \hat{U}_{\text{rf}}(\Delta n)\cdots\hat{U}_{\text{rf}}(\Delta1) \tag{19}$$

The inverse of this product of matrix operators is given by

$$\hat{U}^{-1}_{\text{rf}}(t, 0) = \hat{U}^{-1}_{\text{rf}}(\Delta1)\cdots\hat{U}^{-1}_{\text{rf}}(\Delta n) \tag{20}$$

The physical meaning of the exponentials in equation (16) can always be expressed as a product of rotations in spin space acting on components of angular momentum operators. For example, consider the rf pulse sequence with perfect delta function pulses $(\tau, 180^\circ_y, 2\tau, 180^\circ_y, \delta)$ shown in Figure 4. This sequence is used to produce $\hat{\mathcal{H}}_{\text{rf}}$, and thus $\hat{U}_{\text{rf}}$, equal to $\exp\,(-i\int\hat{\mathcal{H}}_{\text{rf}}\,\mathrm{d}t)$, as indicated in Figure 4.

At times $0 < t < \tau$, when the rf Hamiltonian is zero, $\hat{U}_{\text{rf}}(t, 0)$ takes the form $\mathrm{e}^0 = 1$, and in this time interval the value of $\hat{I}_z$ as manipulated by the rf pulse sequence in Figure 4 is given by equation (18). We may physically identify $\hat{U}_{\text{int}}(0 < t < \tau)$ as given in equation (18) with a rotation $\hat{R}$, of unity, performed on $\hat{I}_z$, symbolized by $\hat{R}\hat{I}_z = 1\hat{I}_z$. At time $t = \tau$, the rf Hamiltonian corresponding to the delta function pulse becomes an infinitely fast 180° rotation about the y axis. $\hat{U}_{\text{rf}}(t = \tau) = \exp\,(\mathrm{i}\pi\hat{I}_y)$, and the physical result is a 180°_y rotation $\hat{R}_{180y}$, which sends the operator $\hat{I}_z$ into the operator $-\hat{I}_z$: $\hat{R}_{180y}\hat{I}_z = -\hat{I}_z$. For $\tau < t < 2\tau$ the rf again is zero, and $\hat{U}_{\text{rf}}$ is unity. At $t = 3\tau$, another 180°_y takes place. Under this sequence, therefore, with the spin portion of $\hat{\mathcal{H}}_{\text{int}}$ being proportional to $\hat{I}_z$, and keeping in mind the time ordering dictated by equations (19) and (20), we find the sequence of values of $\hat{I}_z$, the value of $\hat{I}_z$ in the frame of the rf pulses as indicated in Figure 4, and illustrated by the equations

$$0 < t < \tau: \quad \hat{I}_z = \mathrm{e}^{-\mathrm{i}0}\hat{I}_z\mathrm{e}^{\mathrm{i}0} = 1\hat{I}_z1 = 1\hat{I}_z = \hat{I}_z \tag{21a}$$

$$t = \tau: \quad \hat{I}_z = 1\hat{R}_{180y}\hat{I}_z = -\hat{I}_z \tag{21b}$$

$$\tau < t < 2\tau: \quad \hat{I}_z = 1\hat{R}_{180y}1\hat{I}_z = -\hat{I}_z \tag{21c}$$

$$t = 2\tau: \quad \hat{I}_z = 1\hat{R}_{180y}1\hat{R}_{180-y}\hat{I}_z = \hat{I}_z \tag{21d}$$

$$2\tau < t < 3\tau: \quad \hat{I}_z = 1\hat{R}_{180y}1\hat{R}_{180-y}1\hat{I}_z = \hat{I}_z \tag{21e}$$

The familiar result is that at periodic cycle times $4n\tau$, under the spin echo sequence $(\tau, 180^\circ_y, 2\tau, 180^\circ_y, \tau)n$, chemical shifts, and field inhomogeneities, with spin operators $\hat{I}_{zk}$, vanish (but other interactions, such as homonuclear dipolar coupling, do not). This is to say that at cycle times $4n\tau$, with the internal Hamiltonian being proportional to $\hat{I}_z$, $\hat{\bar{\mathcal{H}}}^{(0)}_{\text{int}}$ is zero, as explicitly shown by

$$\hat{\bar{\mathcal{H}}}^{(0)}_{\text{int}}(4n\tau) \approx \frac{1}{4\tau}\int_0^{4\tau}\hat{\mathcal{H}}_{\text{int}}\,\mathrm{d}t = \frac{1}{4\tau}\omega_{\text{CS}}[\hat{I}_z\tau + (-\hat{I}_z)\tau] = 0 \tag{22}$$

Here, ω_{CS} is a product of a constant (γB_{eff}) and the portion of the chemical shift Hamiltonian which is a function of the real space angular variables θ and ϕ considered explicitly earlier when talking about magic angle spinning. We may think of observation at periodic cycle times $t = 4n\tau = nt_c$ as observation in the frame of $\hat{\rho}$.

With the basic ideas outlined above, one may now understand how averaging is accomplished for a more complicated internal interaction than one simply proportional to $\hat{I}_z$. One creates periodic groups of cyclic sequences of

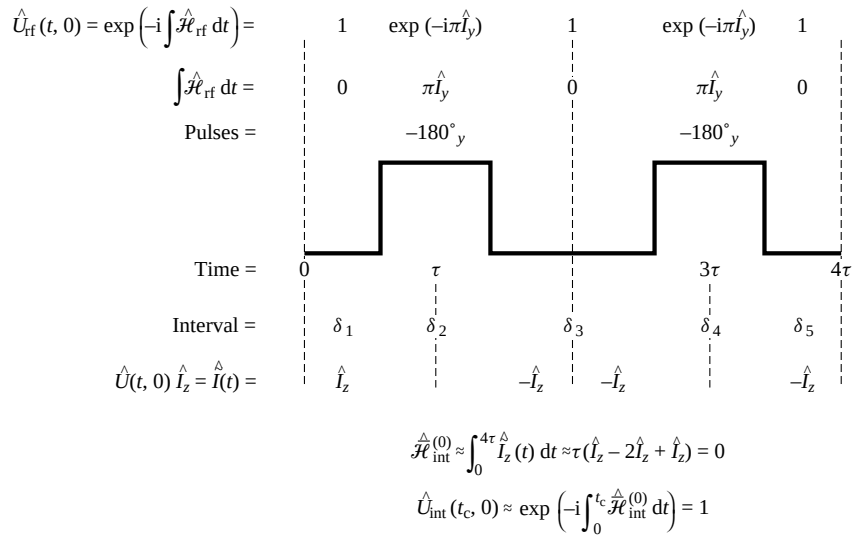

Figure 4 Spin echo sequence (τ, 180°_y, 2τ, 180°_y, τ). Cycle time $t_c = 4\tau$. Also indicated are values of $\hat{\mathcal{H}}_{rf}(t)$, $\hat{U}_{rf}(t, 0)$, $\hat{I}_z(t) = \hat{U}_{rf}{}^{-1}(t, 0)\,\hat{I}_z\hat{U}_{rf}(t, 0)$

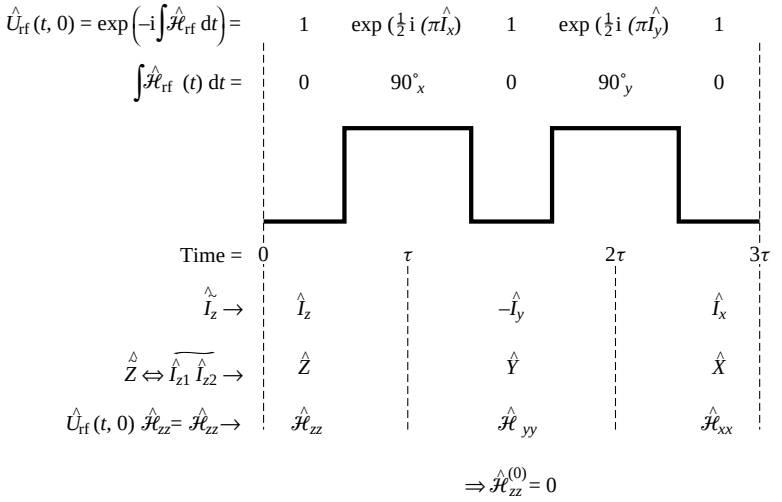

Figure 5 Dipolar echo sequence (τ, 90°_x, τ, 90°_y, τ). Cycle time $t_c = 3\tau$. Also indicated are the values of $\hat{\mathcal{H}}_{rf}(t, 0)$, $\hat{U}_{rf}(t, 0)$, $\hat{I}_z(t)$, $\hat{I}_{z1}\hat{I}_{z2}(t)$, and $\hat{\boldsymbol{I}}_1\cdot\hat{\boldsymbol{I}}_2(t)$

pulses, such that the propagator due to the rf Hamiltonian $\hat{U}_{rf}(nt_c, 0)$ is unity, and such that the internal Hamiltonian in question $\hat{\mathcal{H}}_{int}$ becomes time dependent, i.e. becomes $\hat{\mathcal{H}}_{int}(t)$, and arranges for its time average over a cycle, $(1/t_c)\oint dt\,\hat{\mathcal{H}}_{int}(t)$, to be zero. The resulting modulated echo signal in the time domain, when Fourier transformed, yields a spectrum which reflects all other internal Hamiltonians not averaged to zero by the rf pulses.

5 CRAMPS

Applied to the major broadening interaction in proton or in fluorine containing systems, where ^{1}H or ^{19}F is the only magnetically abundant spin present, the internal interaction between two protons due to dipolar coupling is given by

$$\hat{\mathcal{H}}_{DII} = \omega_D(\theta)(\hat{\boldsymbol{I}}_1 \cdot \hat{\boldsymbol{I}}_2 - 3\hat{I}_{z1}\hat{I}_{z2}) \tag{23}$$

$\omega_D(\theta)$ is the product of a constant and the real space variable θ, the angle between the internuclear vector defining the orientation of the dipole with respect to the external static field. The form need not concern us at this point, except to mention that it must be time-independent. The total dipolar interaction is the sum over all two-body interactions.

Let us denote this two-body interaction by $\hat{\mathcal{H}}_{zz}$, relating to the product of the z components of the two spins in equation (23). Since $\hat{\boldsymbol{I}}_1\cdot\hat{\boldsymbol{I}}_2$ is a scalar product invariant under rotation, pulse sequences will not affect this part of $\hat{\mathcal{H}}_{zz}$. As shown in Figure 5, a 90°_x pulse at time τ rotates the operator $\hat{I}_z$ into the operator $-\hat{I}_y$, via equation (18).

After this 90°_x pulse, therefore, $\hat{\mathcal{H}}_{zz}$ is transformed into $\hat{\mathcal{H}}_{yy}$. A further 90°_y pulse at time 2τ will be seen, using equations (18)–(20), to result in $\hat{\mathcal{H}}_{zz}$ being transformed into $\hat{\mathcal{H}}_{xx}$. Then at a time $t = 3\tau$ the average homonuclear dipolar Hamiltonian [equation (17)] becomes equal to $(\frac{1}{3}\tau)(\hat{\mathcal{H}}_{xx} + \hat{\mathcal{H}}_{yy} + \hat{\mathcal{H}}_{zz})$, which is zero, i.e. the sum $(\hat{\boldsymbol{I}}_1 \cdot \hat{\boldsymbol{I}}_2 - 3\hat{I}_{z1}\hat{I}_{z2}) + (\hat{\boldsymbol{I}}_1 \cdot \hat{\boldsymbol{I}}_2 - 3\hat{I}_{x1}\hat{I}_{x2}) + (\hat{\boldsymbol{I}}_1 \cdot \hat{\boldsymbol{I}}_2 - 3\hat{I}_{y1}\hat{I}_{y2})$ is equal to $3\hat{\boldsymbol{I}}_1 \cdot \hat{\boldsymbol{I}}_2 - 3\hat{\boldsymbol{I}}_1 \cdot \hat{\boldsymbol{I}}_2$. This basic dipolar echo sequence (τ, 90°_x, τ, 90°_y, τ) is not cyclic, since the system is not returned to its initial value at time 3τ. However, as explained above, the phase alternated sequence in which the 90°_x pulse is followed by a 90°_y pulse, then by a 90°_{-y} pulse, and then by a 90°_x pulse is cyclic, and incorporates two dipolar echo experiments. This is the WAHUHA four-pulse sequence. It was first used with stroboscopic observation, as indicated in Figure 6 (see below) to demonstrate that cyclic periodic sequences of rf pulses could lead to averaging of dipolar interactions with resultant detection of much smaller shielding anisotropies. Improved sequences have been developed to remove the loss of resolution associated with experimental artifacts. Two of the best known are the MREV-8 pulse sequence[21] and the BR-24 pulse sequence.[22]

An example of the increase in length of time decay achieved under the BR-24 pulse sequence is shown in Figure 6. Here, the time decay of the magnetization of protons in high density linear polyethylene under the BR-24 sequence, with observation in the first ten windows of the multiple pulse experiment [Figure 6(a)] and a single pulse excitation [Figure 6(b)] are compared. Since the spectral linewidth is proportional to the inverse of the length of the time decay, we see that the resolution under the homonuclear decoupling has been enormously enhanced, the time decay under the BR-24 sequence lasting more than 2 μs, and the decay under a single pulse being over in less than 20 ms. Figure 6(c) shows the Fourier transform of the time decay under the BR-24 sequence, illustrating the shielding anisotropy of protons in high density linear crystalline polyethylene. Combined rotation (MAS) and multiple pulse spectroscopy (CRAMPS) would then collapse the shielding powder pattern to its isotropic value, as shown for adipic acid in Figure 1. Thus combined rotation and multiple pulse spectroscopy, based on the above described ideas, when improved a bit by more complicated pulse sequences to remove loss of resolution due to experimental artifacts, e.g. the the MREV-8 and the BR-24 sequences, is the basic CRAMPS technique today.

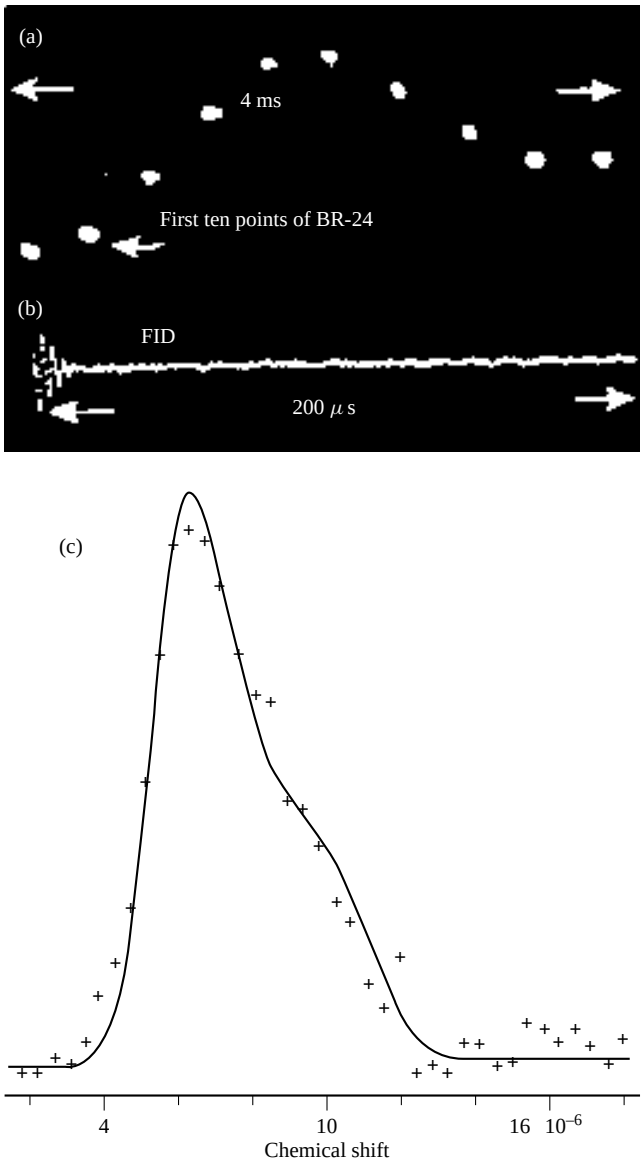

Figure 6 (a) The first ten points of the stroboscopically observed signal of protons in high density linear polyethylene under the BR-24 sequence. (b) FID under a single pulse excitation. Note that the decay under the single pulse excitation is over in roughly 20 μs, whereas the decay under the BR-24 lasts longer than 20 ms. Under MAS, the powder pattern, (c) would collapse to a single line, the isotropic value, obtained in the full CRAMPS experiment, as shown for adipic acid in Figure 1

6 CAVEATS

In the above some implicit assumptions have been made which I will make specific at this point.

1. There exist infinitely fast rf pulses which are '90°' pulses.
2. These rf pulses are in fact much larger than any effects of internal interactions.
3. It is possible to place these pulses sufficiently close together such that the times over which they operate cyclically to bring the system back to its initial state is indeed short compared with dephasing times due to internal interactions.
4. It is possible to observe stroboscopically in the windows between these high-powered pulses.
5. Rotation of the sample does not interfere with the averaging due to spin rotations by the rf pulses.
6. The selective averaging of major broadening interactions (dipolar and shielding anisotropy) does not affect the desired interaction—the isotropic chemical shift.

Each of these assumptions is violated in real experiments to a certain extent:

1. There is no infinitely fast pulse. All rf pulses have a finite width, and have transient phase impurities (the 'phase glitch') associated with them, e.g. a 90°_x pulse will have some transient y phase during the turn-on and turn-off periods. In this multiple pulse experiment with stroboscopic observation of the magnetization, errors in pulse flip angle

and pulse phase rapidly accumulate. For example, a 1° error in flip angle, repeated 1024 times, could result in a 90° pulse becoming a 1114° pulse. To achieve 90° pulses which are sufficiently uniform over the entire sample for this experiment, it is necessary to have an rf coil which is long compared with its diameter. In addition, pulses of a given phase always contain transient phase effects which must be cancelled by use of symmetry adapted pulse sequences. These impurities may be treated theoretically as additional internal interactions which may then be averaged by proper selection of rf pulse sequences.[23]

2. Radiofrequency fields of 5 mT are not infinitely large compared with dipolar fields of ca. 0.3 mT, but are indeed good enough, as shown in Figure 1.
3. With dipolar interactions causing line broadening of 20 kHz, it is necessary that the time over which the dipolar echo sequence operates is short compared with 50 ms.
4. Achieving the 3τ cycle time of the dipolar echo experiment, which is short compared with 50 ms, with a 500 W amplifier, and a receiver recovery time short enough to allow stroboscopic observation of the motion of the system in the observation window lasting 2τ s, is a result of careful engineering of solid state spectrometers; this facility is not generally available in spectrometers used for liquid state NMR, and in some commercially sold spectrometers for high-resolution solid state NMR.
5. Physical rotation of the sample can indeed interfere with the selective averaging performed by the multiple pulse sequences.[24] This interference can produce an extra peak in CRAMPS spectra which is easily recognizable. There are improved pulse sequences being developed which will help reduce this artifact.[25]
6. The multiple pulse sequences which severely attenuate dipolar broadening also generally affect the isotropic shielding by scaling shielding differences. In general, the scaling factor depends upon the sequence used, and the length of the rf pulses compared with the 3τ cycle time of the dipolar echo sequence. Under the MREV-8, sequence for example, the scaling factor is roughly $\frac{1}{2}$, so that a chemical shift difference of 10 ppm, measured at a spectrometer frequency of 100 MHz for ^{1}H, does not translate into 1000 Hz in the observed spectrum, but into 500 Hz. Thus resolution is lost. The scaling factor may be easily determined experimentally.[24]

7 RELATED ARTICLES

Average Hamiltonian Theory; Chemical Shift Tensors in Single Crystals; Echoes in Solids; Internal Spin Interactions and Rotations in Solids; Magic Angle Spinning; Rotating Frame Spin–Lattice Relaxation Off-Resonance; Rotating Solids; Rudimentary NMR: The Classical Picture; Shielding Tensor Calculations; Sideband Analysis in Magic Angle Spinning NMR of Solids; Two-Dimensional Powder Correlation Methods

8 REFERENCES

1. B. C. Gerstein, R. G. Pembleton, R. C. Wilson, and L. M. Ryan, *J. Chem. Phys.*, 1977, **66**, 361.
2. F. Bloch, W. W. Hansen, and M. Packard, *Phys. Rev.*, 1946, **70**, 474.
3. E. M. Purcell, H. C. Torrey, and R. V. Pound, *Phys. Rev.*, 1946, **69**, 37.
4. E. R. Andrew and R. G. Eades, *Proc. R. Soc. Lond., Ser. A*, 1953, **216**, 398.
5. I. Lowe, *Phys. Rev. Lett.*, 1959, **2**, 285.
6. I. J. Lowe, *Bull. Am. Phys. Soc.*, 1957, **2**, 344.
7. P. Mansfield, *Phys. Rev.*, 1965, **137**, A961.
8. J. S. Waugh, L. M. Huber, and U. Haeberlen, *Phys. Rev. Lett.*, 1968, **20**, 180.
9. S. F. Dec, C. E. Bronniman, R. A. Wind, and G. E. Maciel, *J. Magn. Reson.*, 1989, **82**, 454.
10. S. F. Dec and G. Maciel, *J. Magn. Reson.*, 1990, **87**, 153.
11. S. F. Dec, C. E. Bronniman, R. A. Wind, and G. E. Maciel, *J. Magn. Reson.*, 1989, **82**, 454.
12. T. C. Farrar *Introduction to Pulse NMR Spectroscopy*, Farragut, Madison, WI, 1989.
13. B. C. Gerstein and C. R. Dybowski, *Transient Techniques in NMR of Solids; An Introduction to the Theory and Practice*, Academic, Orlando, FL. 1985.
14. M. Mehring, *Principles of High Resolution NMR in Solids*, 2nd edn, Springer, Berlin, 1983.
15. U. Haeberlen, *High Resolution NMR in Solids; Selective Averaging*, Academic, New York, 1976.
16. R. R. Ernst, G. Bodenhausen, and A. Wokaun, *Principles of Nuclear Magnetic Resonance in One and Two Dimensions*, Clarendon, Oxford, 1987.
17. I. J. Lowe, *Bull. Am. Phys. Soc.*, 1957, **2**, 344.
18. P. Mansfield, *Phys. Rev.*, 1965, **137**, A961.
19. J. S. Waugh, L. M. Huber, and U. Haeberlen, *Phys. Rev. Lett.*, 1968, **20**, 180.
20. B. C. Gerstein and C. R. Dybowski, *Transient Techniques in NMR of Solids; An Introduction to the Theory and Practice*, Academic, Orlando, FL, 1985, Chap. 4
21. P. Mansfield, *Phil. Trans. R. Soc. Lond., Ser. A*, 1981, **299**, 479; W.-K. Rhim, D. D. Elleman, and R. W. Vaughan, *J. Chem. Phys.*, 1973, **58**, 1772.
22. D. Burum and W.-K. Rhim, *J. Chem. Phys.*, 1979, **71**, 944.
23. R. R. Ernst, G. Bodenhausen, and A. Wokaun, *Principles of Nuclear Magnetic Resonance in One and Two Dimensions*, Clarendon, Oxford, 1987, Chap. 5
24. B. C. Gerstein and C. R. Dybowski, *Transient Techniques in NMR of Solids; An Introduction to the Theory and Practice*, Academic, Orlando, FL, 1985, Chap. 5
25. J. S. Waugh, Personal communication, MIT, Cambridge, MA, May 1993.

Biographical Sketch

Bernard C. Gerstein. *b* 1932. B.S., 1953, Purdue, USA; Ph.D., 1960, Iowa State. Introduced to NMR by R.W. Vaughan. Faculty in Chemistry, Iowa State University, 1962–present. Approx. 150 publications. Research interests include the theory and practice of learning, and applications of solid state NMR to problems in the physics and chemistry of materials, fossil fuels, and heterogeneous catalysis.

Diffusion Measurements by Magnetic Field Gradient Methods

Charles S. Johnson Jr

University of North Carolina, Chapel Hill, NC, USA

1	Introduction	1
2	Effects of Translational Motion in NMR	2
3	Pulsed Field Gradient NMR	4
4	The FT-PFG-NMR Method and Diffusion Ordered Two-Dimensional NMR Spectroscopy	9
5	The Average Propagator and the Scattering Analogy	11
6	Restricted Diffusion and Diffusive Diffraction	13
7	Anisotropic Diffusion	14
8	Chemical Exchange Involving Diffusing Molecules	14
9	Large Gradients and the Measurement of Small Displacements	15
10	Data Analysis and Polydispersity	16
11	Mass and Size Distributions from NMR Diffusion Data	17
12	Literature Sources for NMR Diffusion Measurements	17
13	Related Articles	18
14	References	18

1 INTRODUCTION

Diffusion measurements by field gradient methods in this article refer to the measurement of translational diffusion. Rotational diffusion and spin diffusion by means of mutual spin flips are treated elsewhere. Measurements of translational diffusion are important in the determination of sizes and shapes of molecules and molecular aggregates, and NMR in the presence of magnetic field gradients is a uniquely powerful method for making such measurements. The NMR method also provides a means for correlating diffusion coefficients with chemical shifts, characterizing the microgeometry of porous materials, investigating anisotropy of organized phases, and determining degrees of solubilization, to list only a few applications. In this article we present the principles of NMR diffusion measurements and discuss some useful techniques. This represents only a sampling of an extensive field, and we rely on recent review articles to fill in some of the gaps. Also, recent advances that offer new insights and expand the range of applications are emphasized at the expense of some important older contributions. Although some applications appear as examples, a review of applications is not intended. Appropriate textbooks and reviews are cited in the various sections, and Section 12 is devoted to sources for background material and additional reading.

1.1 Fick's Laws

According to Fick's first law of diffusion, the particle flux $\boldsymbol{J}$ at position $\boldsymbol{r}$ is proportional to the gradient of the concentration. Thus,

$$\boldsymbol{J}(\boldsymbol{r}, t) = -D\nabla c(\boldsymbol{r}, t) \tag{1}$$

where D is the diffusion coefficient and $c(\boldsymbol{r}, t)$ is the concentration in number of particles per unit volume. The conservation of mass is assured by the equation of continuity,

$$\frac{\partial c(\boldsymbol{r}, t)}{\partial t} = -\nabla \cdot \boldsymbol{J}(\boldsymbol{r}, t) \tag{2}$$

and this equation can be combined with equation (1) to obtain Fick's second law of diffusion:[1]

$$\frac{\partial c(\boldsymbol{r}, t)}{\partial t} = D\nabla^2 c(\boldsymbol{r}, t) \tag{3}$$

It is assumed that D has at most a weak dependence on the concentration and that the concentration is low. However, equation (3) is useful over a wide range of concentrations.

In the following it is convenient to introduce the conditional probability $P(\boldsymbol{r}_0 \mid \boldsymbol{r}, t)$ that a particle initially at $\boldsymbol{r}_0$ will be at $\boldsymbol{r}$ at time t, and it is reasonable to assume that $P(\boldsymbol{r}_0 \mid \boldsymbol{r}, t)$ also obeys the diffusion equation so that:

$$\frac{\partial P(\boldsymbol{r}_0 \mid \boldsymbol{r}, t)}{\partial t} = D\nabla^2 P(\boldsymbol{r}_0 \mid \boldsymbol{r}, t) \tag{4}$$

The solution of equation (4) by standard means for unrestricted diffusion with the initial condition $P(\boldsymbol{r}_0 \mid \boldsymbol{r}, 0) = \delta(\boldsymbol{r}_0 - \boldsymbol{r})$ yields the expected Gaussian dependence on the displacement:

$$P(\boldsymbol{r}_0 \mid \boldsymbol{r}, t) = (4\pi Dt)^{-3/2} \exp[-(\boldsymbol{r} - \boldsymbol{r}_0)^2/4Dt] \tag{5}$$

The calculation of the average square displacement by means of equation (5) gives the Einstein–Smoluchowski equation:

$$\langle(\boldsymbol{r} - \boldsymbol{r}_0)^2\rangle = 6Dt \tag{6}$$

Thus, molecular displacement resulting from diffusion is simply related to the diffusion coefficient.

1.2 The Stokes–Einstein Equation and Tracer Diffusion

Much of the interest in diffusion arises because of the connection between D and molecular size. For macromolecules, at least, this connection is usually made through the Stokes–Einstein equation:[2]

$$D = k_{\mathrm{B}}T/f \tag{7}$$

where f is the friction factor. For a spherical particle with hydrodynamic radius R_{h} immersed in a fluid of viscosity η, Stokes's law gives $f = 6\pi\eta R_{\mathrm{h}}$. Analytical expressions are also available for the friction factors of oblate and prolate ellipsoids and approximate results have been reported for complex structures made of identical subunits.[3]

The diffusion coefficient of interest here is the tracer diffusion coefficient, sometimes called the self-diffusion or intra-diffusion coefficient.[2] Nuclear spin states provide perfect labels that have almost no effect on the hydrodynamic properties of molecules. The samples under study are homogeneous and the translational motion of nuclear spins can be detected directly as described below. In a mixture with $N + 1$ components (including the solvent) there are $N + 1$ distinct tracer diffusion coefficients. This must be contrasted with the situation in which there are concentration gradients, and molecular species diffuse into each other in a process called 'interdiffusion'. The diffusion coefficients measured in such systems are known as the 'mutual diffusion' or 'interdiffusion' coefficients. In the limit of infinite dilution, tracer and mutual diffusion coefficients are equal, but at higher concentrations they may be quite different. Also, mutual diffusion in mixtures invariably involves coupled flows, and in a volume fixed frame a system with $N + 1$ components has $N(N + 1)/2$ independent Onsager diffusion coefficients.

Dynamic light scattering (DLS), a method that depends on concentration fluctuations, is often used to measure mutual diffusion coefficients.[4,5] DLS is a standard method, even though the diffusion coefficients obtained are not necessarily equal to the mutual diffusion coefficients that are measured with macroscopic concentration gradients.[6] At low concentrations NMR and DLS give similar diffusion coefficients for macromolecules in solution, but the dependence on concentration is usually much stronger for tracer diffusion coefficients than for mutual diffusion coefficients. In contrast to equation (7), the mutual diffusion coefficient D_{m} for a macromolecule can be expressed as

$$D_{\mathrm{m}} = \frac{k_{\mathrm{B}}T}{f}\left(1 + \frac{\partial \ \ln \ \gamma'}{\partial \ \ln \ c}\right)(1 - \phi') \tag{8}$$

where γ' is the activity coefficient and ϕ' is the volume fraction of solute.[7,8] Primes have been used here since the same symbols are used elsewhere for different quantities. The last two factors on the right-hand side of equation (8) largely account for the difference between mutual and tracer diffusion coefficients, but in principle the friction factors for mutual and tracer diffusion are not equal.[9]

2 EFFECTS OF TRANSLATIONAL MOTION IN NMR

The ability of NMR to detect translational motion and to image spin density depends on two essential facts: (1) a nucleus at position $\boldsymbol{r}$ precesses with the frequency

$$\omega(\boldsymbol{r}) = -\gamma B(\boldsymbol{r}) \tag{9}$$

where γ is the magnetogyric ratio and $B(\boldsymbol{r})$ is the magnitude of the local magnetic field (flux density), and (2) the local fields can be manipulated through the use of magnetic field gradients so that the spatial positions of nuclei can be encoded. The spin echo experiment is the basis of NMR diffusion measurements, since this experiment involves the refocusing of magnetization in inhomogeneous magnetic fields, a process that is extremely sensitive to the translational motion of spins.

2.1 Spin Echoes and Magnetization Helices

Consider the experiment illustrated in Figure 1(a) for a sample with a single resonance line. The applied magnetic field is in the z direction and a hard 90°_x rf pulse at $t = 0$ rotates magnetization from all parts of the NMR active volume into the y direction. Here x and y refer to a reference frame rotating about the field direction at the average precession frequency ω_0 for spins in the applied field $\boldsymbol{B}_0$. The resultant magnetization in each differential volume element is described by a vector (known as an 'isochromat') that precesses in the xy plane at a frequency that depends on the local field as indicated by equation (9). The interpretation is simpler if the inhomogeneity results from a constant field gradient $\boldsymbol{g}$ applied and controlled externally. Such a gradient is described by:

$$\boldsymbol{g} = \frac{\partial B_z}{\partial x}\boldsymbol{i} + \frac{\partial B_z}{\partial y}\boldsymbol{j} + \frac{\partial B_z}{\partial z}\boldsymbol{k} \tag{10}$$

where $\boldsymbol{i}$, $\boldsymbol{j}$, and $\boldsymbol{k}$ are unit vectors in the x, y, and z directions, respectively. Thus the magnitude of the total external magnetic field at $\boldsymbol{r}$ is given by:

$$B = B_0 + \boldsymbol{g} \cdot \boldsymbol{r} \tag{11}$$

In the following we assume that only a z gradient of magnitude $g = \boldsymbol{g}\cdot\boldsymbol{k}$ is present. In the presence of this gradient, isochromats with different frequencies are associated with different values of z, and it is instructive to represent the magnetization immediately after the 90°_x pulse as a ribbon formed by the isochromats with their tails on the centerline of the sample. Initially, the resultant magnetization in the y direction is equal to M_0, the magnitude of the equilibrium magnetization prior to the rf pulse. The effect of the gradient is to give the isochromat at coordinate z a phase angle $\phi(z) = \gamma gzt$ with respect to the yz plane at time t. This is represented in Figure 1(b) by the magnetization helices with pitches given by $\Lambda = 2\pi/(\gamma gt)$.[10] The detected signal, that is proportional to the resultant magnetization in the y direction, decays to zero with increasing time as illustrated by the FID in Figure 1(a). In the absence of diffusion the interpretation of the experiment is straightforward. The 180°_y pulse at τ rotates each isochromat about the y axis and thus changes the phase angle of the isochromat at z by the amount $-2\gamma gz\tau$. Precession then continues as before since the local magnetic field is unaffected by the rf pulse. In the period between τ and 2τ the helix unwinds so that the resultant is again directed along the y axis (in the absence of directed flow) and a spin echo signal is created. Thus, the isochromats have been refocused and the only attenuation of the echo results from the intrinsic T_2 of the sample, i.e. the echo amplitude is proportional to $M_0 \exp(-t/T_2)$.

2.2 Bloch Equations including Diffusion

As emphasized in Figure 1(b), the effect of the 90°_x pulse followed by the z gradient is to create a magnetization pattern in the sample. Diffusion smears out this pattern and leads to attenuation of the spin echo. The tightly wound helices are more easily disturbed by diffusion, and analytical equations

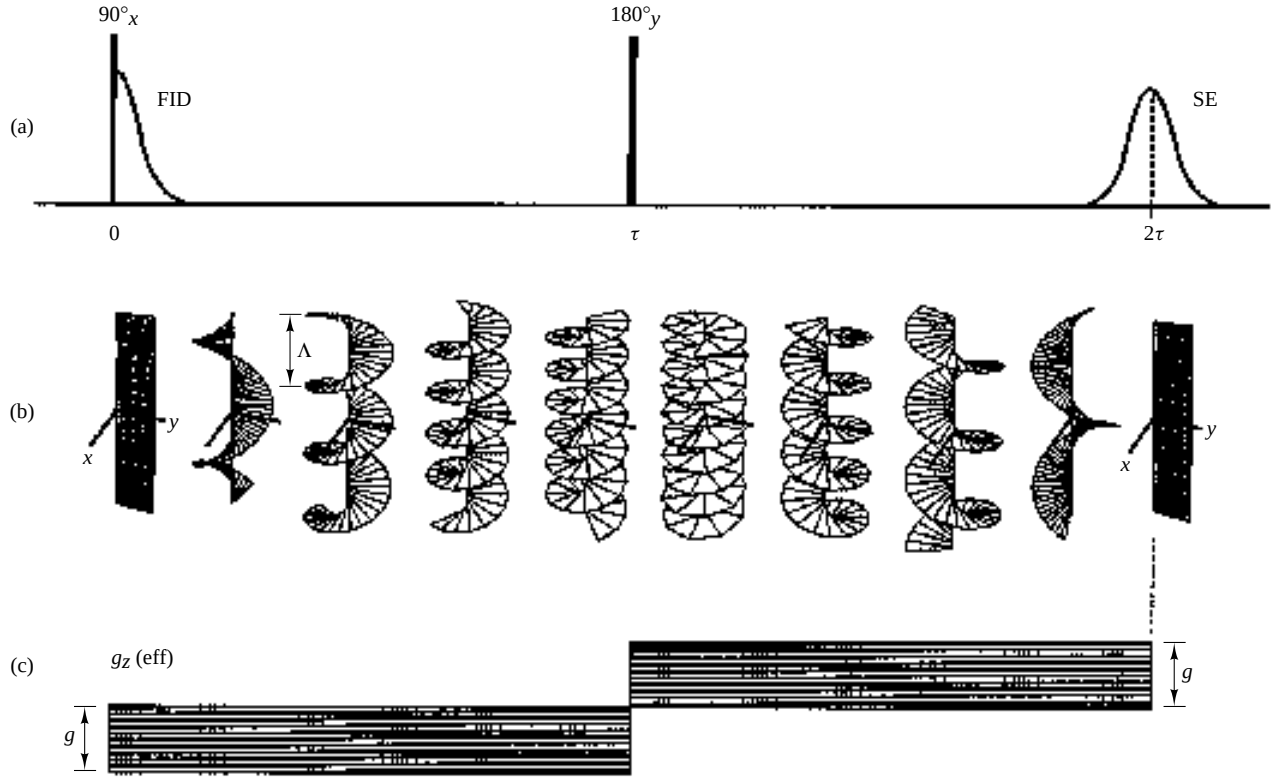

Figure 1 Spin echoes with a constant gradient: (a) the Hahn spin echo pulse sequence; (b) magnetization helices formed by isochromats; and (c) the effective gradients in the presence of a 180° rf pulse

can be derived to describe this effect. In the standard mathematical description of this experiment a term describing the rate of translational diffusion of magnetization is added to the Bloch equations to obtain a macroscopic theory of diffusion effects in NMR. Following the notation of Abragam[11] this gives,

$$\frac{\partial \boldsymbol{M}(\boldsymbol{r},t)}{\partial t} = \gamma \boldsymbol{M} \times \boldsymbol{B}(\boldsymbol{r},t) - \frac{M_x \boldsymbol{i}' + M_y \boldsymbol{j}'}{T_2} - \frac{(M_z - M_0)\boldsymbol{k}'}{T_1} + D\nabla^2 \boldsymbol{M} \qquad (12)$$

A more convenient equation for the investigation of transverse magnetization is obtained from equation (12) by defining the complex magnetization $M_+ = M_x + \mathrm{i}M_y$, setting $B_x = B_y = 0$, and denoting the magnitude of the average precession frequency in the sample by $\omega_0 = \gamma B_0$. The resulting equation is

$$\frac{\partial M_+}{\partial t} = \mathrm{i}\omega_0 M_+ - \frac{M_+}{T_2} - \mathrm{i}\gamma(\boldsymbol{g}\cdot\boldsymbol{r})M_+ + D\nabla^2 M_+ \qquad (13)$$

The uninteresting parts of the time dependence are then transformed away by means of the substitution

$$M_+ = \psi \exp(\mathrm{i}\omega_0 t - t/T_2) \qquad (14)$$

to yield the equation[12]

$$\frac{\partial \psi}{\partial t} = -\mathrm{i}\gamma g z \psi + D\nabla^2 \psi \qquad (15)$$

In the absence of diffusion equation (15) is easily solved for the magnetization in the rotating frame as a function of z and t. If the initial condition is a coherent state created by a 90° rf pulse, the magnetization pattern evolving under the influence of g is just the helix previously described. A gradient pulse with amplitude g and duration δ is said to have an area of $q = \gamma g \delta$, and the helix at the end of the pulse is described by $S(z) = m \exp(-\mathrm{i}qz)$, where m is the magnetization density per unit length in the z direction. The integral of the effective gradient areas at the time of the echo must be zero so that the pitch of the helix becomes much larger than the active volume. This can be achieved either by reversing the direction of the gradient to obtain a 'gradient echo' or by applying a $180°_y$ pulse to set back the phase to achieve a spin echo. In fact, it is convenient in mathematical derivations to replace $180°_y$ rf pulses by the inversion of previous gradient pulses.[13] The complete sequence of rf and gradient pulses can then be described by an effective $g(t)$. With this approach it has been shown that the solution of equation (15) in the presence of diffusion and a time dependent gradient can be written as

$$\ln \psi = -D\left[\int_0^t q^2(t')\,\mathrm{d}t'\right] \qquad (16)$$

where

$$q(t') = \int_0^{t'} \gamma g(t'')\,\mathrm{d}t'' \qquad (17)$$

It is important to note that gradient echoes and spin echoes have quite different properties in many experiments. The 180°

rf pulse refocuses phase dispersion resulting from background gradients, chemical shifts, susceptibility effects in heterogeneous samples, etc., while the reversed gradient pulse only refocuses phase dispersion resulting from a previously applied gradient pulse.

2.3 Diffusion Effects on Magnetization Patterns

According to Figure 1, the projection of the helix onto either the *xz* or the *yz* plane yields a simple sinusoidal grating function, e.g. Re $[S(z)] = m \cos(qz)$ for the *yz* plane. The effect of diffusion (in the direction of the gradient) on such a grating can be obtained immediately through the use of equation (5). First we integrate over the x and y coordinates to obtain

$$P(z_0 \mid z, t) = (4\pi Dt)^{-1/2} \exp[-(z - z_0)^2/4Dt] \tag{18}$$

Then $P(0 \mid z,t)$ is convoluted with $S(z)$ to obtain an expression for the time dependent gratings. The effect of diffusion is to 'smear out' the spatial gratings, and the time dependent helix is described by $S(z, t) = S(z) * P(0 \mid z, t)$, where '*' means convolution, and we can write

$$S(z, t) = \frac{m}{(4\pi D\Delta)^{1/2}} \int_{-\infty}^{\infty} \exp(-\mathrm{i}qz') \exp[(z - z')^2/4Dt]\, \mathrm{d}z' \tag{19}$$

Equation (19) can be evaluated directly or by means of the convolution theorem to obtain

$$S(z, t) = m \exp(-\mathrm{i}qz) \exp(-Dq^2 t) \tag{20}$$

This expression includes the amplitude attenuation resulting from diffusion for a helix with a constant q value, i.e. a constant pitch. The attenuation factor can also be recognized as $F(q, t)$, the spatial Fourier transform of $P(0 \mid \boldsymbol{r}, t)$:

$$F(q, t) = \int_0^{\infty} P(0 \mid \boldsymbol{r}, t) \exp(-\mathrm{i}q \cdot \boldsymbol{r})\, \mathrm{d}\boldsymbol{r} \tag{21}$$

The time evolution of $F(q, t)$ is described by the spatial Fourier transform of equation (4). This gives

$$\frac{\partial F(q, t)}{\partial t} = -Dq^2 F(q, t) \tag{22}$$

and we again find that $F(q,t) = F(q,0) \exp(-Dq^2 t)$. Note that the right-hand side of equation (21) can be interpreted as an average of the phase factor over the distribution of displacements. This viewpoint is explored in Section 5.

2.4 Echo Attenuation in a Constant Gradient

When gradients are present and q is time dependent, $S(z, t)$ in equation (20) describes the evolution of the attenuation factor at a specific time, and the cumulative attenuation is obtained by multiplying together the attenuation factors for the differential time increments. As expected, this procedure yields the diffusion factor displayed in equation (16).

As an illustration of the use of equation (16), consider the echo attenuation for the simple $90^\circ_x - \tau - 180^\circ_y - \tau$ echo experiment shown in Figure 1. In the regions 0 to τ and τ to 2τ the effective gradient amplitudes are $-g$ and g, respectively, as shown in Figure 1(c), and equation (17) gives

$$q(t) = -\int_0^t \gamma g\, \mathrm{d}t', \quad 0 < t < \tau$$
$$q(t) = -\gamma g\tau + \int_\tau^t \gamma g\, \mathrm{d}t', \quad \tau < t < 2\tau \tag{23}$$

q(t) from equation (23) is then substituted into equation (16) to obtain

$$\ln\ \psi(2\tau) = -D(\gamma g)^2 \left[\int_0^{\tau} (t')^2\, \mathrm{d}t' + \int_\tau^{2\tau} (t' - 2\tau)^2\, \mathrm{d}t' \right] \tag{24}$$

Therefore, the attenuation resulting from diffusion at the echo time 2τ is found to be

$$\ln\ \psi(2\tau) = \tfrac{1}{12} D\gamma^2 g^2 (2\tau)^3 \tag{25}$$

and the total echo amplitude $S(2\tau)$ is given by

$$S(2\tau) = M_0 \exp(-2\tau/T_2) \exp[-D\gamma^2 g^2 (2\tau)^3/12] \tag{26}$$

The well-known τ^3 dependence of the exponent in the diffusion factor is the reason why the simple spin echo experiments are usually not satisfactory for the measurement of T_2.[14,15]

3 PULSED FIELD GRADIENT NMR

The introduction of pulsed field gradients (PFGs) in place of steady gradients for diffusion measurements greatly improves the spin echo diffusion experiment and opens a wide range of applications.[12] The basic Stejskal–Tanner experiment, illustrated in Figure 2, has two major advantages over constant gradient methods. First, by confining the gradients to relatively narrow time intervals, this experiment permits gradient areas to be varied without changing the echo time, so that the attenuation resulting from relaxation can be held constant. Second, the echo can be recorded in a homogeneous magnetic field. Spectral information is, therefore, retained and frequency resolved diffusion measurements are possible. These advantages are widely acknowledged, and almost all modern NMR diffusion measurements are made with some form of pulsed gradient experiment. However, a disadvantage of pulsed experiments should be noted. The switched gradient experiments require current pulses that inevitably produce heat, mechanical forces, and eddy currents.

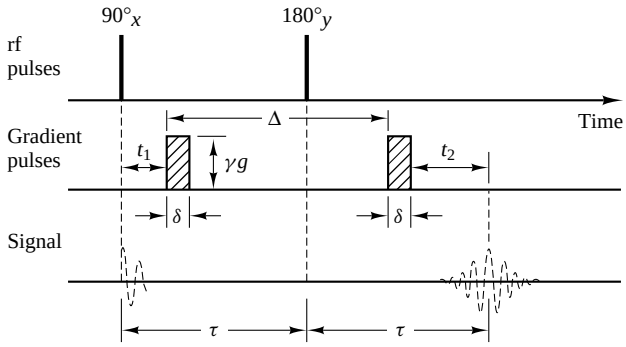

Figure 2 The Stejskal–Tanner pulsed field gradient spin echo diffusion experiment

3.1 The Spin Echo SE Diffusion Experiment

The echo attenuation resulting from diffusion with the sequence shown in Figure 2 can be obtained by direct application of equation (16). The total echo amplitude is given by[12]

$$S(2\tau) = M_0 \exp(-2\tau/T_2) \exp[-Dq^2(\Delta - \delta/3)] \qquad (27)$$

where $q = \gamma g \delta$ and the effect of transverse relaxation has been included. The attenuation factor $\psi(2\tau)$ for diffusion alone is easily isolated by taking the ratio of the echo amplitude with applied gradient switched on, $S(2\tau)$, to the amplitude with gradient switched off, $S_0(2\tau)$. Thus $\psi(2\tau) = S(2\tau)/S_0(2\tau)$. However, transverse relaxation diminishes the signal-to-noise ratio and may present a serious problem for slowly tumbling macromolecules and molecular aggregates where T_2 values tend to be short. Transverse relaxation and J modulation effects present special problems for coupled spin systems.[16,17] T_2 is often much shorter for coupled spins than expected from the rotational correlation times alone, and spin coupling in homonuclear spin systems can prevent complete refocusing of the spin echo. The latter effect arises because hard rf pulses exchange the spin states of nuclei that are coupled to the nuclei under observation. Precession frequencies change, and refocusing depends on the magnitude of the spin coupling constant J. For a coupled pair of spin-$\frac{1}{2}$ nuclei this leads to echo maxima when $\tau = n/J$ and negative echoes when $\tau = n/(2J)$, where n is an integer and J is in hertz.

Equation (27) is appropriate for the analysis of experimental data when the magnetic field $\boldsymbol{B}_0$ is homogeneous and the gradient pulses are well matched. It may be possible to approximate the effect of an inhomogeneous magnetic field by a constant background gradient $\boldsymbol{g}_0$. The effective gradient is then $\boldsymbol{g} + \boldsymbol{g}_0$ and a complete analysis gives the diffusion factor:[12]

$$\begin{aligned}\psi(t) = \exp\{-D\gamma^2[&g^2\delta^2(\Delta - \delta/3) + 2g_0^2\tau^3/3 \\ &-\boldsymbol{g}\cdot\boldsymbol{g}_0\delta(t_1^2 + t_2^2 + \delta(t_1 + t_2) \\ &+2\delta^2/3 - 2\tau^2)]\}\end{aligned} \qquad (28)$$

Gradient pulse mismatch changes the position and intensity of the echo. Some investigators have resorted to adjusting the width of the second gradient pulse to reposition the echo, but this is not a practical solution in experiments where the gradient areas are automatically ramped through a series of values and the signal is recorded starting from the center of the echo. A detailed analysis shows that sensitivity to the gradient pulse mismatch is decreased by the application of a constant gradient parallel to the gradient pulses.[18]

3.2 The Stimulated Echo Diffusion Experiment

A sequence containing three 90° rf pulses was among the first echo forming sequences studied by Erwin Hahn in his pioneering work on time dependent NMR.[14] He found that five echoes are formed in a steady gradient experiment. As shown in Figure 3(a) they are the primary echo (PE) at $2\tau_1$, the stimulated echo (STE) at $\tau_1 + \tau_2$, and three secondary echoes that are usually not of interest. The effect of diffusion on the STE has been investigated for a steady gradient[19] and for gradient pulses.[20] Both versions of the experiment are of current interest (Section 9), but this section focuses on pulsed gradients.

An intuitive understanding of the formation of the stimulated echo can be gained from the graphical representation of the isochromats shown in Figure 3(b). Here the superscripts (−) and (+) indicate 'immediately before' and 'immediately after' the rf pulse at the indicated time. The magnetization ribbon at 0^+, characterized by $q = 0$, is wound up by the action of the first gradient pulse so that at τ_1^- the pitch of the resulting helix is $\Lambda = 2\pi/q$. In the presence of the gradient pulse and a very weak background gradient, $q \approx \gamma g \delta$. The new feature here is the rf pulse at time τ_1 that rotates each isochromat through 90° about the $-x$ axis so that its y component is stored in the z direction. The resulting pattern of z magnetization is responsible for the STE. At τ_2 the third 90° rf pulse rotates the z magnetization back into the yx plane. If this pulse is directed along the x axis, the isochromats all become collinear with the y axis so that the magnetization lies in the yz plane as represented by the cos (qz) function shown in Figure 3(b). The refocusing effect necessary to form the STE results from twisting action of the second gradient on this pattern. At the time of the STE the y components of the isochromats are all positive and their resultant reaches a maximum along the y direction, even though they do not all lie in the yz plane. In fact, the projection of the tips of the isochromats onto the xy plane gives a circle tangent to the xz plane. Note that the STE results from a pattern of magnetization density in the z direction, regardless of the source of the pattern. A specially prepared sample with alternating layers having different spin densities can give an STE in an experiment with a single rf pulse.

The magnetization components remaining in the x and y directions after the second rf pulse are responsible for the primary echo and secondary echoes. These components result from the x and z components of the magnetization at τ_1^-. In the pulsed gradient experiment the PE and the secondary echoes do not refocus.

The primary advantage of the STE sequence is that the transverse evolution time for magnetization can be reduced. This is especially important when T_2 is small but, as mentioned above, can also be used to minimize the effects of J modulation. In the absence of a significant background

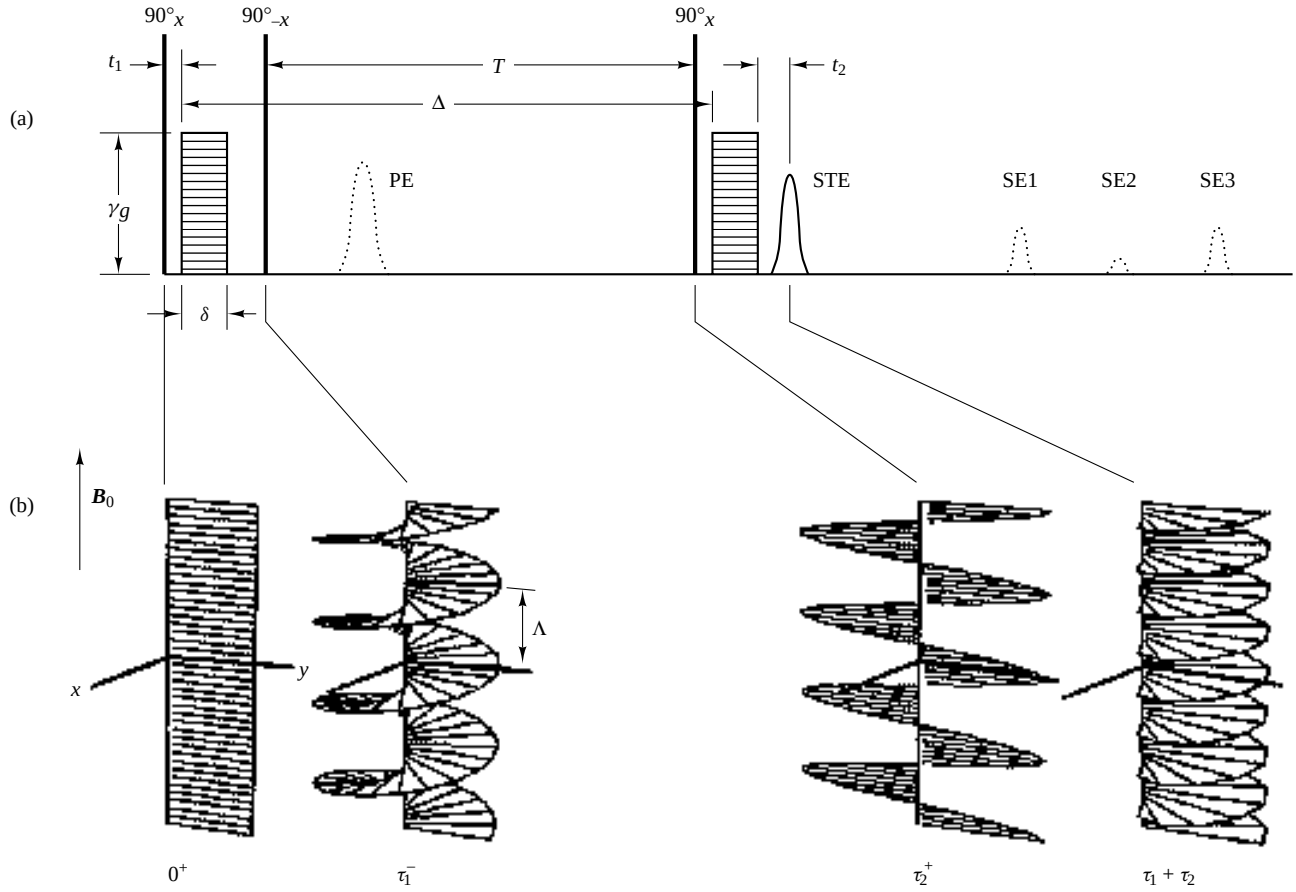

Figure 3 The pulsed field gradient stimulated echo (STE) diffusion experiment: (a) the pulse sequence and echoes; (b) evolution of the isochromats

gradient, i.e. when $g_0 \approx 0$, the total amplitude of the STE is given by

$$S(T + 2\tau_1) = (M_0/2)\exp(-2\tau_1/T_2 - T/T_1) \times \exp[-Dq^2(\Delta - \delta/3)] \quad (29)$$

Equation (29) also shows the major disadvantage of STE experiments, namely the amplitude of the echo is reduced by a factor of 2 relative to a spin echo (SE) if T_1 and T_2 are equal. The reason for this loss is obvious from Figure 3(b). The second rf pulse only stores the y components, and the second gradient only partially refocuses the magnetization for the STE. This loss may be recovered many times over depending on the ratio of T_2 to T_1 and the amount of attenuation. For example, when T_2/T_1 = 0.5 and T/T_1 = 0.1 the STE signal is 23% larger than an SE with the same echo time (TE), and when T/T_1 = 0.5 the STE is 45 times as large as the SE. It is also advantageous to keep $\tau \ll 1/J$ for spin coupled systems, in order to minimize the modulation of intensities and to make sure that all signals are positive. In general, the advantages of the STE experiment outweigh the loss of signal resulting from the factor of 0.5, and STE is becoming the standard method for diffusion measurements.

3.3 Special Sequences for Heterogeneous Samples

In some cases background gradients cannot be ignored. When the background gradients are uniform, corrections can be applied to the attenuation factor as shown in equation (28) for the spin echo experiment. However, in heterogeneous samples where the backgrounds gradients $\boldsymbol{g}_0$ have random magnitudes and directions and may be comparable in magnitude to the applied gradients, simple corrections are not possible. Fortunately, pulse sequences can be designed to minimize the corrupting effects of the background gradients. A useful principle is that a 180° rf pulse refocuses isochromats dispersed by a time independent gradient, but that refocusing of the effects of an applied gradient $\boldsymbol{g}_A$ can be avoided either by changing the polarity of the gradient or by applying the gradient pulse on one side of the 180° rf pulse. A number of sequences have been proposed to minimize the effect of the cross term $\boldsymbol{g}_0 \cdot \boldsymbol{g}_A$. Here two schemes are used as illustrations, one for SE and one for STE experiments.

The Karlicek–Lowe (KL) alternating PFG sequence is shown in Figure 4.[21] Background gradients are effectively reversed by the second 180° rf pulse, but the effective applied gradient $\boldsymbol{g}_A$ is unchanged. The third 180° pulse begins the refocusing period, since the applied gradient is not reversed this time. Note that the intervals δ_1 and δ_2 have been introduced in the pulse sequence so that the rf pulses and the gradient pulses will not overlap. The general version of this sequence has n 180° pulses and the echo occurs at $2n\tau$. The cross term $\boldsymbol{g}_0 \cdot \boldsymbol{g}_A$ is avoided by requiring that the number of positive $\boldsymbol{g}_A$ intervals equal the number of negative $\boldsymbol{g}_A$ intervals, thus restricting n to the values (5, 9, ... , $4m$ +

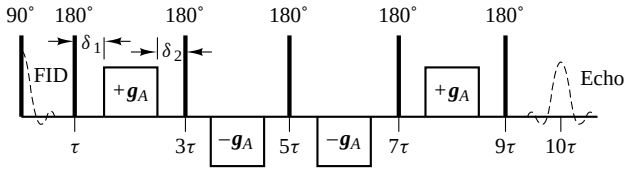

Figure 4 The Karlicek–Lowe alternating pulsed field gradient experiment for minimizing the effects of background gradients[21]

1; m = 1, 2, 3, ...). The effect of the complete sequence on the echo amplitude can be calculated by means of equation (16), with the simplifying assumption that 180° pulses can be replaced with gradient reversals. The solution for the general sequence is:

$$\ln[\psi(2n\tau)] = \frac{-2\gamma^2 D}{3}\left\{ng_0^2\tau^3 + (n-1)^3 g_A^2 \left[\tau - \frac{(\delta_1+\delta_2)}{2}\right]^2\left[\tau + \frac{(\delta_1+\delta_2)}{(n-1)^2}\right]\right\} \quad (30)$$

This sequence has been demonstrated with heterogeneous samples having g_0 values of nearly 3 kG cm^{-1}. It has also been used in imaging applications to determine the spatial distribution of diffusion coefficients.[21]

The KL sequence is effective, but is at a disadvantage for samples having T_2 much smaller than T_1. In order to deal with short transverse relaxation times Cotts et al.[22] have proposed a number of sequences based on the STE diffusion experiment. The standard STE pulsed gradient diffusion sequence in the presence of a background gradient $\boldsymbol{g}_0$ is shown in Figure 5(a) and the attenuation factor obtained by Tanner is given by[20,22]

$$\ln\ \psi[(\Delta+2\tau)] = -\gamma^2 D\left\{\delta^2\left(\Delta+\tau-\frac{\delta}{3}\right)g_A^2 + \delta\left[2\tau\Delta + 2\tau^2 - \frac{2\delta^2}{3} - \delta(\delta_1+\delta_2) - (\delta_1^2+\delta_2^2)\right]\times \boldsymbol{g}_A\cdot\boldsymbol{g}_0 + \tau^2\left(\Delta+\frac{2\tau}{3}\right)g_0^2\right\} \quad (31)$$

A sequence that eliminates the cross term $\boldsymbol{g}_0\cdot\boldsymbol{g}_A$ when $\delta_1 = \delta_2$ and reduces the effect of g_0^2 is shown in Figure 5(b). The attenuation factor calculated for this 13 interval sequence is

$$\ln[\psi(\Delta+4\tau)] = -\gamma^2 D\left[\delta^2\left(4\Delta+6\tau-\frac{2\delta}{3}\right)g_A^2 + 2\tau\delta(\delta_1-\delta_2)\boldsymbol{g}_A\cdot\boldsymbol{g}_0 + \frac{4\tau^3 g_0^2}{3}\right] \quad (32)$$

A number of more effective but also more complicated sequences have been designed. For example, a 17 interval sequence that is the STE version of the KL sequence with storage at 6τ and recovery of transverse magnetization at Δ + 6τ has the advantages of the 13 interval sequence but gives a larger coefficient for g_A^2. An extension to n pairs of gradient pulses ($n \leq 12$) has been found to be even more effective in eliminating the effects of g_0.[23]

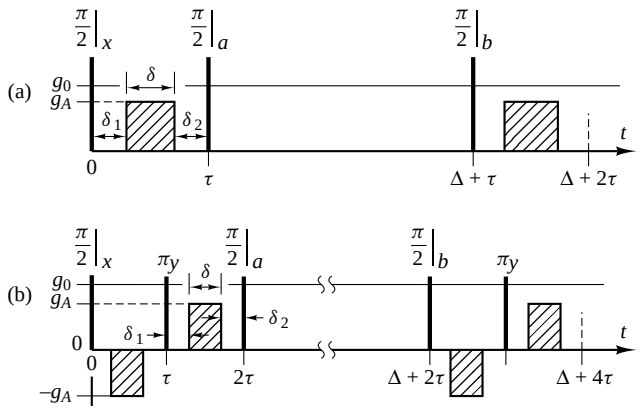

Figure 5 (a) The standard stimulated echo (STE) sequences with a background gradient. (b) A 13 interval STE sequence for minimizing the effects of background gradients[22]

3.4 Modulated Gradients

Modulated gradients, in particular gradients with sinusoidal time dependence, have been suggested as alternatives to pulsed gradients.[12,24] Modulated gradients may be easier to implement than pulsed gradients and may cause less trouble with eddy currents in metal magnet structures. These advantages have not yet attracted many users. However, modulated gradients should be of interest for another reason: they introduce flexibility into NMR studies of motion and may permit frequency-dependent diffusion coefficients to be studied that are inaccessible with conventional PFG-NMR experiments.[25,26]

In transport theory the frequency dependent self-diffusion tensor is defined as the spectrum of the velocity correlation function:

$$D_{\alpha,\beta}(\omega) = \frac{1}{2}\int_{-\infty}^{\infty} \overline{v_\alpha(0)v_\beta(t)}\exp(\mathrm{i}\omega t)\,\mathrm{d}t \quad (33)$$

where α and β represent the Cartesian coordinates x, y, z. In order to investigate the frequency dependence of $D_{\alpha\beta}(\omega)$, Stepisnik[26] has developed a general theory for the echo attenuation exponent $\alpha(t)$, defined by $\psi \propto \exp[-\alpha(t)]$, in the presence of a modulated gradient. Under certain conditions $\alpha(t)$ can be expressed as

$$\alpha(t) = \frac{1}{2\pi}\gamma^2\int_{-\infty}^{\infty} D_{zz}(\omega)S(\omega,t)\,\mathrm{d}\omega \quad (34)$$

where

$$S(\omega,t) = \frac{|\boldsymbol{g}(\omega,t)|^2}{\omega^2}, \quad \boldsymbol{g}(\omega,t) = \int_0^t \boldsymbol{g}_{\mathrm{eff}}(t')\exp(-\mathrm{i}\omega t')\,\mathrm{d}t' \quad (35)$$

Here $\boldsymbol{g}_{\mathrm{eff}}(t)$ includes inversions to account for 180° pulses, as discussed in Section 2.2. Equation (34) shows that echo

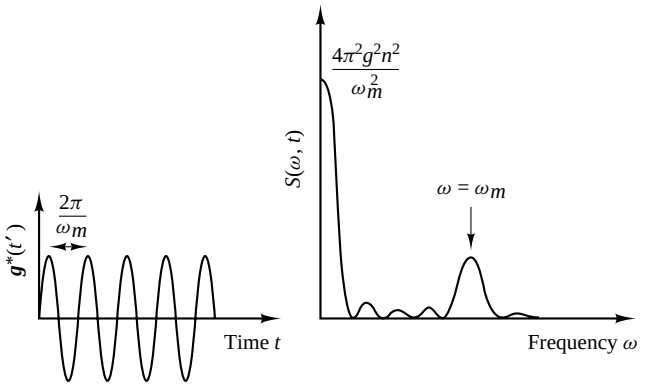

Figure 6 Sinusoidal modulation: the gradient $\boldsymbol{g}_{\text{eff}}(t)$ and its spectrum $S(\omega, t)$[25]

attenuation depends on the spectral density of molecular motion and the spectrum of the gradient.

This 'gradient spectrum' formulation is consistent with the Stejskal–Tanner result for the conventional gradient echo experiment that depends on $\boldsymbol{D}(0)$. The power of Stepisnik's method is revealed with modulated gradients that offer the possibility of probing the frequency dependence of $\boldsymbol{D}(\omega)$. For example, Figure 6 shows a sinusoidal gradient with amplitude $\boldsymbol{g}$ and its spectrum, and the application of equation (34) gives:

$$\alpha(t) = \frac{\gamma^2 \boldsymbol{g}^2}{\omega_{\text{m}}^2} t[D_{zz}(0) + \tfrac{1}{2} D_{zz}(\omega_{\text{m}})] \qquad (36)$$

Therefore, $\boldsymbol{D}(\omega)$ can be investigated by measuring $\alpha(t)$ for different modulation frequencies. It has been pointed out that this technique permits rapid motions to be investigated without reducing the evolution period.

3.5 Radiofrequency Field Gradients

The difficulties encountered in producing large pulsed gradient fields and in controlling the induced eddy currents are well known. A method that avoids these problems, albeit at some cost, is the use of rf field gradients in place of B_z gradients. This is essentially an extension of the rotary echo method to diffusion measurements.[27] A single turn rf coil around the x axis in the laboratory frame provides a $\boldsymbol{B}_1$ field gradient, $\boldsymbol{g}_1$ perpendicular to the $\boldsymbol{B}_0$ field. The result is phase encoding of x positions, so that a helix of magnetization lies along the x axis. One implementation of this method (Figure 7) uses two rf coils to produce homogeneous and inhomogeneous rf fields.[28] An inhomogeneous pulse of length δ imparts the phase angle $\gamma g_1 x \delta$ in the yz plane at x. A homogeneous (hard) 180°_y pulse reverses the sign of the phase, and the second inhomogeneous pulse unwinds the helix to refocus magnetization along the z axis. Finally, a hard 90°_x pulse rotates the magnetization into the y direction in the rotating frame so that the signal can be detected.

The effect of diffusion is to smear out the helix as in the conventional PFG-SE experiment, and the same arguments lead to the exponential attenuation factor in equation (27). However, the effect of spin relaxation is different with rf gradients. If $T_2 \gg \Delta$, the magnetization is completely recovered by the second gradient pulse in the absence of

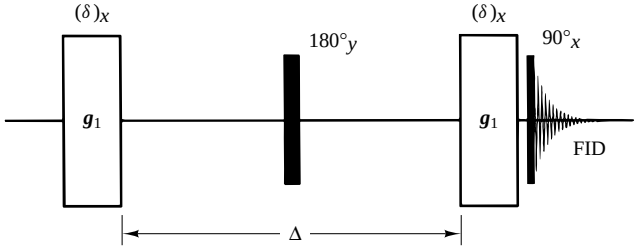

Figure 7 Sequence for rf gradient diffusion measurements with two coils: rf gradients $\boldsymbol{g}_1$ and hard 90° and 180° pulses are shown[28]

diffusion. However, with $T_2 \ll \Delta$ the isochromats are parallel to the z axis at the beginning of the second inhomogeneous pulse and refocusing only recovers half of the initial magnetization as recovered in STE experiments. Net transverse magnetization can also be removed by means of an inhomogeneous $\boldsymbol{B}_0$ field during Δ to ensure the rotary equivalent of the STE experiment. The signal at $\Delta + \delta$ is known as a 'stimulated rotary echo' (SRE).[29] There is also an echo at 2Δ that is T_2-weighted but may be useful for diffusion measurements. It turns out that the SRE experiment can be implemented with a single rf coil and without the hard 180_x and 90°_x rf pulses. As in the STE experiment the 180_x pulse is not needed, and in place of the 90°_x rf pulse the second inhomogeneous pulse can be lengthened by the amount τ that corresponds to a 90° rotation for isochromats at the center of the sample.

The rf gradient experiments are successful and provide convenient gradient switching without harmful eddy currents. Unfortunately, the gradient amplitudes are limited. The largest g_1 reported to date is 15.2 G cm^{-1}, and the measurement of small diffusion coefficients requires rf pulse lengths greater than 10 ms. Still a diffusion coefficient of 3.3×10^{-8} cm^2 s^{-1} has been measured to within 5%, and the method is promising.[29]

3.6 Multiple Quantum Diffusion Measurements

Multiquantum (MQ) NMR experiments have the following advantages for the study of molecular diffusion: (a) precession frequencies increase linearly with the order $n = \Delta m$ of the coherence; (b) MQ spectra are simplified with respect to the single quantum spectrum; and (c) for N coupled protons the N-quantum transition is free of dipolar couplings. The possible limitations are that the spectrum must show splittings from scalar, dipolar, or quadrupolar coupling; and that, except for double quantum excitations, there is a loss of sensitivity because of the inefficient transfer of magnetization.

The first two demonstrations of MQ diffusion measurements involved solutes in liquid crystal solvents where dipolar splittings are evident.[30,31] For example, benzene in a nematic phase diffusion permits measurements to be made with n = 1 to 6 by means of the pulse sequence shown in Figure 8.[31] In this sequence MQ orders are present during the diffusion period Δ and at the MQ echo. A short gradient pulse after the echo, but during the MQ evolution, and a set of n gradient pulses after recall of single quantum coherence provide the n-quantum filter. The effective gradient is increased by a factor

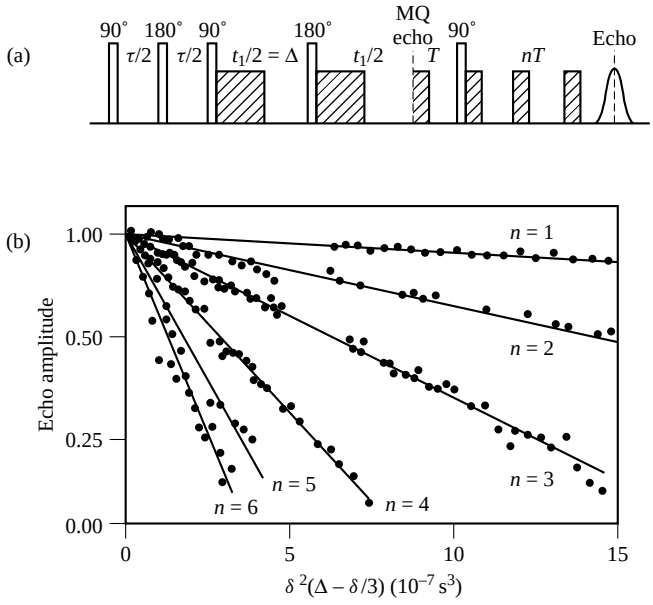

Figure 8 The multiquantum (MQ) diffusion experiment: (a) sequence for multiquantum excitation and n-quantum filtering; (b) echo intensities for coherences with n = 1 to 6 for benzene in a nematic solvent[31]

of n for the n-quantum coherence and the echo attenuation factor becomes:

$$\psi(t_1) = \exp[-n^2\gamma^2 g^2 \delta^2 D(\Delta - \delta/3)] \qquad (37)$$

This effect is elegantly illustrated by the plot of echo amplitudes for benzene shown in Figure 8(b). While this experiment may be most valuable for slow moving molecules in anisotropic environments, it can also provide enhanced gradients and MQ filtering in isotropic phases when scalar coupling is present.[32,33]

The use of zero quantum coherences in diffusion studies has been discussed in connection with the use of static gradients and the avoidance of eddy current effects.[34] However, high resolution is still obtained by switching off the gradient before data acquisition.

4 THE FT-PFG-NMR METHOD AND DIFFUSION ORDERED TWO-DIMENSIONAL NMR SPECTROSCOPY

The measurement of spin relaxation in complex systems by FT methods was suggested and demonstrated by Vold et al.[35] Their example was an inversion recovery experiment for the measurement of T_1, but frequency resolved measurements of transverse relaxation and diffusion rates were also discussed. The simultaneous measurement of diffusion coefficients for all components in a mixture was demonstrated by James and McDonald[36] with a spin echo experiment similar to that illustrated in Figure 2 except that the gradient was on almost the full time between the rf pulses. The second half of the spin echo at 2τ was Fourier transformed to obtain the complete spectrum of a mixture of dimethyl sulfoxide (DMSO) and water, and the experiment was repeated for 10 values of τ. The ratios of the peak intensities with and without the gradient pulses then gave the diffusion factor $\psi(2\tau)$ for each line. This type of experiment has been implemented on FT NMR spectrometers and applied to a variety of chemical systems.[37–39] The work of Stilbs and coworkers in particular stimulated much interest in diffusion measurements. An early example of the FT-PFG-NMR experiment for a mixture containing chloroform, benzene, dichloroethane, 1,4-dioxane, acetone, cyclopentane, cyclohexane, and tetramethylsilane is shown in Figure 9.[40] The gradient pulse amplitude was approximately 1.2 G cm^{-1} and the different values of q were obtained by varying the duration δ as shown on the right-hand side of the figure.

FT-PFG-NMR experiments demonstrate that information about diffusion and flow can be encoded into high-resolution data sets. This is very important because it addresses the shortcoming of NMR as an analytical tool. High-resolution NMR is highly selective because it reports on details of the local environments of nuclei, i.e. short range interactions. However, NMR is not sensitive to long range interactions of nuclei (>1 nm) and is only indirectly affected by the overall sizes and charges of macromolecules and molecular aggregates. Therefore, NMR is not particularly good for the analysis of complex mixtures. However, hydrodynamic properties do depend on size and charge, and FT-PFG-NMR opens the door to the utilization of this information in NMR analysis.

Diffusion ordered two-dimensional NMR (DOSY) is primarily concerned with the analysis and display of data obtained in FT-PFG-NMR experiments.[41] Plots of signal intensities versus gradient pulse lengths, or areas, are somewhat analogous to FIDs. The data sets can be analyzed to determine one or possibly more diffusion coefficients, but the results are not obvious by inspection of the decay curves. Just as FIDs are Fourier transformed to obtain 'user-friendly' frequency spectra, diffusion dependent decays can be transformed to obtain 'diffusion spectra'. DOSY experiments are designed to acquire automatically high-resolution NMR data sets for an exponentially spaced set of q values. The frequency spectra are obtained by Fourier transformations and the data sets at each chemical shift are inverted by approximate inverse Laplace transforms (ILTs) with respect to q^2 to generate two-dimensional diffusion spectra.

Signal stability is crucial in DOSY, and the following features have been incorporated: (i) the gradient pulses are matched within 10 ppm so that the echo positions do not vary as q is changed;[42] (ii) currents induced by the gradient pulses are minimized through the use of actively shielded gradient coils;[43,44] and (iii) signal distortions resulting from residual eddy currents are avoided through storage of the echo signal while the eddy currents decay. The pulse sequence chosen for this experiment is the 'longitudinal eddy delay' (LED) sequence shown in Figure 10.[45] This is a modified STE sequence with a fourth rf pulse to store the STE and a fifth rf pulse to recall the magnetization after the eddy current settling period. The gradient prepulses establish a steady state response so that the fourth and fifth gradient pulses will have equivalent effects.[46] Note that $\Delta = T + \tau$ and, in general, $\tau \ll T$, so that the evolution period for transverse magnetization between the first rf pulse and the STE is negligible. Also, phase cycling of the five rf pulses and a homospoil gradient pulse during T_e are used to eliminate the secondary echoes. With this

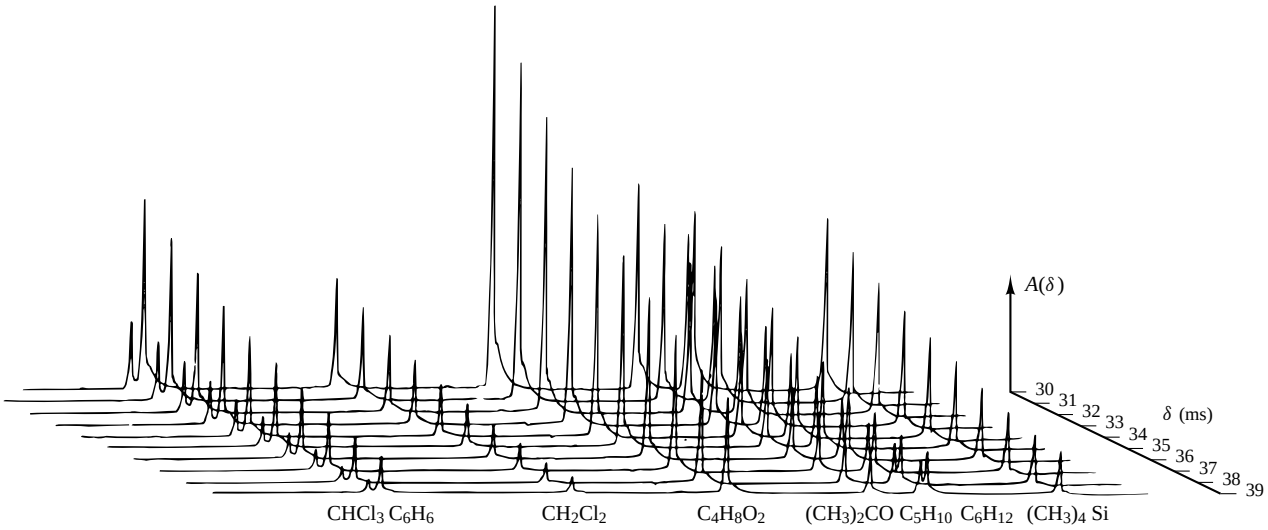

Figure 9 FT-PFG-NMR stack plot for a multicomponent mixture. The gradient pulse amplitude is constant, and the pulse duration δ increases from back to front[40]

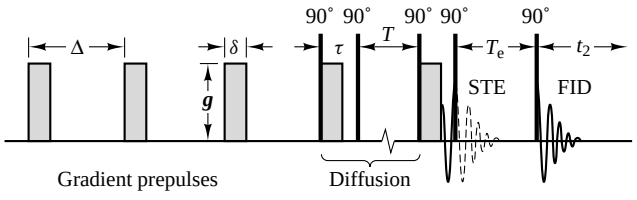

Figure 10 The LED pulse sequence. The phase cycling and homospoil pulse during T_e are not shown

system diffusion coefficients down to 10^{-10} cm^2 s^{-1} have been measured for gel stabilized samples. The lower limit for low viscosity samples is usually determined by convection currents resulting from temperature gradients.[47]

In DOSY, FIDs are acquired for 20–50 exponentially spaced q values and are Fourier transformed to obtain frequency spectra. The result is a two-dimensional data set of the form

$$f(q, \nu) = \sum_{j=1}^{N_\lambda} A_j(\nu) \exp[-D_j(\Delta - \delta/3)q^2] \qquad (38)$$

where $A_j(\nu)$ is the one-dimensional NMR spectrum of the jth diffusing species when $q = 0$ (taking into account transverse and longitudinal relaxation), D_j is the associated tracer diffusion coefficient, and N_λ is the number of components required for the fit. The aim is to analyze the data set for each frequency ν so that a set of amplitudes A_j and diffusion coefficients D_j is obtained. This set is then used to generate a diffusion spectrum with peak positions and amplitudes that correspond to the D_j and A_j values, respectively.

Unfortunately, the fitting of data (with noise) with an equation of the form of equation (38) is an ill-conditioned problem, and infinitely many sets of solutions may fit the data very well (see Section 10). Since it is not sufficient to fit the data, additional information must be introduced to aid in selecting the most likely solution for a real mixture. The first decision is whether the sample contains components with well defined (discrete) diffusion coefficients or if continuous distributions, i.e. polydispersity, must be considered. In the discrete case, data inversion programs such as DISCRETE[48,49] and SPLMOD[50,51] are appropriate for automated analysis since they do not require initial estimates of the parameters, but they must be supplemented with prior knowledge about the nature of the acceptable solutions. For example, signal amplitudes in LED experiments (with $\tau \ll \Delta$) and decay constants (diffusion coefficients) must be nonnegative. Also, the range of physically acceptable diffusion coefficients, the diffusion coefficients accessible to the PFG-NMR experiment, and the resolving power of the SPLMOD analysis are known. This knowledge combined with data analysis experience led to the following conservative set of acceptability criteria:

1. Diffusion coefficients must be feasible and experimentally accessible.
2. Standard errors in diffusion coefficients reported by SPLMOD must be less than 30%.
3. Diffusion coefficients of components at the same chemical shift must differ by a factor of more than 2.

These rules are included in a computer algorithm so that frequently occurring artifacts can be rejected.

When a solution has been found that meets the criteria at each frequency in the NMR spectrum, the DOSY display is generated with normalized Gaussians having center positions and intensities equal to the derived diffusion coefficients and amplitudes, respectively. Thus, the DOSY display has the form

$$F(D, \nu) = \sum_{j=1}^{N_\lambda} A_j(\nu) G_j(D) \qquad (39)$$

where

$$G_j = \frac{1}{\sqrt{2\pi\sigma_j^2}} \exp\left[-\frac{(D - D_j)^2}{2\sigma_j^2}\right] \qquad (40)$$

Here σ_j is derived from the error reported by the analysis program with an allowance for systematic errors. An example

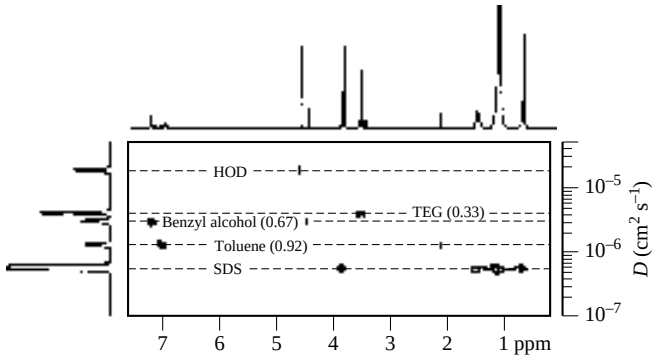

Figure 11 DOSY display processed with SPLMOD for a mixture containing toluene, benzyl alcohol, tetraethylene glycol (TEG), and SDS micelles in D_2O.[52] The degrees of solubilization p_j are given in parentheses

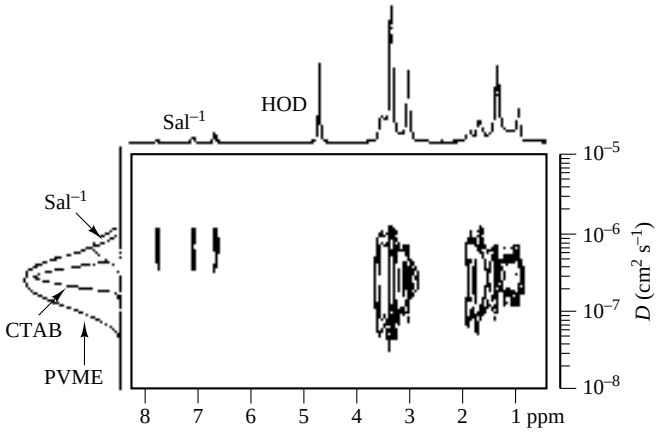

Figure 12 DOSY display precessed with CONTIN for a mixture containing CTAB, PVME, and NaSal (see text)[57]

of the application of DOSY to a discrete mixture is shown in Figure 11.[52] The various solutes are solubilized by the surfactant sodium dodecyl sulfate (SDS). The solutes exchange between SDS micelles and the bulk solution so rapidly that the PFG-NMR experiment reports only the time averaged diffusion coefficient for each species. Therefore, for the jth solute the observed diffusion coefficient D_j is given by[53,54]

$$D_j = p_j D_j^{\text{mic}} + (1 - p_j) D_j^{\text{free}} \tag{41}$$

where p_j is the degree of solubilization, and D_j^{mic} and D_j^{free} are the tracer diffusion coefficients for solubilized and free molecules, respectively. The diffusion coefficients in this example are so similar that resolution in the NMR dimension is essential for a complete analysis. High-resolution spectra were obtained in this experiment by means of a stop-and-go spinner system that permitted the sample to be stationary during the diffusion time Δ but to spin during data acquisition.[55]

Continuous distributions are encountered with many systems of interest. Examples include micelles, microemulsion droplets, vesicles, and polymers. Equation (38) can be rewritten to emphasize the continuous distribution $g(\lambda)$ of diffusion coefficients contributing to the data set at a particular frequency ν. Thus

$$G(s) = \int_0^\infty g(\lambda) \exp(-\lambda s)\, \mathrm{d}\lambda \tag{42}$$

where $\lambda = D$ and $s = q^2(\Delta - \delta/3)$. The factoring of the exponent in equation (38) is a matter of convenience, and in cases where $(\Delta - \delta/3)$ is constant one might choose $s = q^2$. The inversion of a data set $G(s)$ containing noise to obtain the diffusion spectrum $g(\lambda)$ is a long-standing problem in data analysis, and its ill-posed nature has been emphasized repeatedly. A large body of literature has been devoted to this problem (see Section 10). The ill-conditioned inverse Laplace transform ILT has been approached by a variety of methods including regularized least-squares (CONTIN) and maximum entropy (MEM). Thus far only CONTIN has been applied to DOSY analyses.[41,56] In this program the linear least-squares method is augmented with prior knowledge about the nature of the solutions and the principle of parsimony. We know that the decay constants (diffusion coefficients) are nonnegative and that the decay kernels are exponential. Also, as noted above, the LED experiment ensures that the signal amplitudes are positive. Parsimony implies that the simplest (smoothest) solution consistent with a priori information and the data is selected. This amounts to discriminating against solutions with high-frequency components (wiggles) by introducing a term to penalize such solutions. The weight given to the penalty is the regularization parameter α that is determined on the basis of the Fisher F-test or by input from the user. Therefore, CONTIN provides an automatic analysis that has some capability to handle multimodal distributions. The primary shortcoming is that enforced smoothness reduces the ability to resolve peaks in the diffusion spectrum and leads to overestimation of the widths of narrow peaks.

The generation of DOSY displays with CONTIN is straightforward. The $G(s)$ versus s data sets are analyzed at every frequency point where the signal-to-noise ratio exceeds a predetermined threshold value to obtain new data sets of intensities versus values of D. Stack plots or contour plots are then constructed without any additional data manipulation. An example of a CONTIN analysis is provided by the DOSY display in Figure 12 for a sample containing 25.0 mM hexadecyltrimethylammonium bromide (CTAB), 15.0 mM sodium salicylate (NaSal), and 7.40 g L^{-1} poly(vinyl methyl ether) (PVME) at 30 °C.[57] The projections on the left-hand side show diffusion distributions for PVME, CTAB, and NaSal. The addition of PVME to the viscoelastic CTAB/NaSal sample resulted in a marked reduction in the viscosity. It is thought that the polymer reduces the length of threadlike CTAB micelles by wrapping around the micelles. Note that the polydispersity of the polymer is consistent with the width of the distribution, but that the associated CTAB shows a much narrower distribution. The width for CTAB results primarily from regularization in the analysis, since CTAB molecules exchange rapidly between aggregates associated with different PVME molecules and exchange narrowing is expected. Figure 12 also shows the smoothing effect of CONTIN on the distribution for NaSal which is monodisperse and should have a vanishingly small width. When preliminary analysis indicates that a relatively narrow unimodal distribution of diffusion coefficients is present at a particular chemical shift, the direct cumulants analysis method may be preferable to CONTIN (see Section 10).

5 THE AVERAGE PROPAGATOR AND THE SCATTERING ANALOGY

In the short gradient pulse limit ($\delta \ll \Delta$) the equations given in Section 2 for the echo amplitude can be recast in a useful and instructive form. Consider the SE experiment illustrated in Figure 2 with gradient pulses of amplitude g in the z direction. The first gradient pulse instantaneously encodes the phase shift $-\gamma\delta g z_0$ for spins at position z_0. During the interval Δ the spins diffuse a distance Z parallel to the gradient to the position $z_0 + Z$, and finally the second gradient pulse, inverted relative to the first one or effectively inverted by a 180° rf pulse, gives the additional phase shift $\gamma\delta g(z_0 + Z)$. Thus, the net phase shift is $\gamma\delta g Z$ for spins starting at time zero. Of course, the echo arises from all of the excited spins and depends on both the initial spatial distribution of spins $\rho(z_0)$ and the conditional probability $P(z_0 \mid z_0 + Z, \Delta)$ that a spin at z_0 at time zero will be at $z_0 + Z$ at time Δ. The sum over all NMR active spins leads to the expression[58]

$$\psi = \int\int \rho(z_0) P(z_0 \mid z_0 + Z, \Delta) \exp(\mathrm{i}qZ)\, \mathrm{d}(z_0 + Z)\, \mathrm{d}z_0 \tag{43}$$

where again $q = \gamma\delta g$ and spin relaxation has been neglected.

We now define the 'average propagator'

$$\overline{P}(Z, \Delta) = \int \rho(z_0) P(z_0 \mid z_0 + Z, \Delta)\, \mathrm{d}z_0 \tag{44}$$

so that the echo amplitude can be written as

$$\psi(q) = \int \overline{P}(Z, \Delta) \exp(\mathrm{i}qZ)\, \mathrm{d}Z \tag{45}$$

This reveals the Fourier transform relationship between $\psi(q)$ and $\overline{P}(Z, \Delta)$ and indicates that $\overline{P}(Z, \Delta)$ can be obtained as the Fourier transform of the echo amplitude.[59,60] Note that for free diffusion in a homogeneous sample, the average propagator is simply the Gaussian function shown in equation (18) with Δ in place of t. Substitution of equation (18) into equation (45) gives

$$\psi(q) = 2(4\pi D\Delta)^{-1/2} \int_0^\infty \exp(-Z^2/4D\Delta) \cos(qZ)\, \mathrm{d}Z \tag{46}$$

and evaluation of equation (46) shows that the echo amplitude is just $\psi(q) = \exp(-Dq^2\Delta)$, as previously derived. In general, the shape of the propagator $\overline{P}(Z, \Delta)$ is determined by average molecular displacements in the sample under study. An example is provided by the diffusion of ethane in NaCaA zeolites;[59] for further information see ***Diffusion in Porous Media***.

It has been pointed out that the Fourier transformation of $\psi(q)$ provides an image of the propagator analogous to the image of spatial positions provided by magnetic resonance imaging (MRI). The q space introduced here is conjugate to the dynamic displacement space $\boldsymbol{R}$ or Z.

Equation (46) suggests an analogy with scattering experiments, in particular dynamic light scattering (DLS), neutron scattering, and holographic relaxation spectroscopy (HRS). In the idealized scattering experiment an incident plane wave having the wave vector $\boldsymbol{k}_\mathrm{i}$ of magnitude $2\pi/\lambda$ is scattered through an angle θ_s by suspended particles. The scattered wave is described by the wave vector $\boldsymbol{k}_\mathrm{s}$ that has a different direction but the same magnitude as the wave vector of the incident wave. In DLS we are concerned with the relative phase ϕ_j of the electric field E_s of the light scattered by the jth scatterer at the detector. This phase angle depends on the path lengths and, as illustrated in Figure 13,

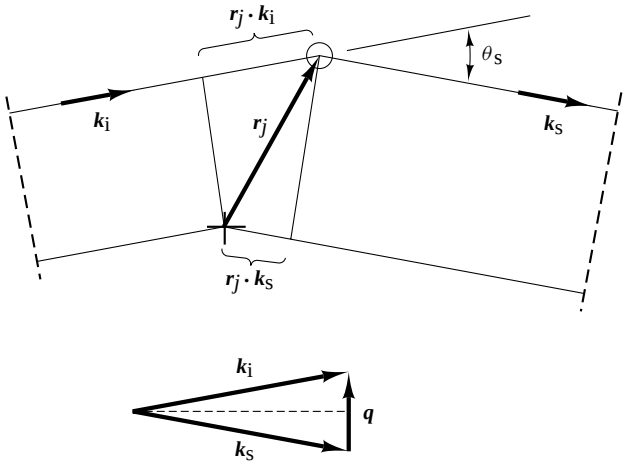

Figure 13 Scattering of a plane wave from a particle at $\boldsymbol{r}_j$ and the reference point (+)

$$\phi_j = \boldsymbol{k}_\mathrm{i} \cdot \boldsymbol{r}_j - \boldsymbol{k}_\mathrm{s} \cdot \boldsymbol{r}_j = \boldsymbol{q} \cdot \boldsymbol{r}_j \tag{47}$$

where elementary trigonometry shows that $|\, q \,| = (4\pi/\lambda) \sin(\theta_\mathrm{s}/2)$. The quantity derived from DLS data is the reduced first-order correlation function $g^{(1)}(\tau)$ defined by

$$g^{(1)}(\tau) = \frac{\langle E_\mathrm{s}^*(0) E_\mathrm{s}(\tau)\rangle}{\langle |E_\mathrm{s}(0)|^2\rangle} \tag{48}$$

If the motions of the scatterers are independent and certain other conditions are satisfied, only 'self-correlation' terms are important and equations (47) and (48) can be combined to obtain:[5,61]

$$|g^{(1)}(\tau)| = \langle \exp\{\mathrm{i}\boldsymbol{q} \cdot [\boldsymbol{r}_j(\tau) - \boldsymbol{r}_j(0)]\}\rangle \tag{49}$$

where $\langle\ \rangle$ represents an average over all scattering particles. This, of course, is equivalent to equation (43) for a uniform distribution of scatterers with τ in place of Δ. The discussion of DLS also applies to neutron inelastic scattering, except that the self-correlation function is available directly without assumptions about independent motions of scatterers from the neutron scattering function for the incoherent fraction.

In DLS the scattering angle determines the magnitude of $\boldsymbol{q}$ and $\sin(\theta_\mathrm{s}/2)$ plays a role similar to that of the gradient area in NMR. Similarly, the diffraction spot in DLS is analogous to the spin echo in NMR. This analogy can be pursued to show why DLS and PFG-NMR measure different types of diffusion coefficient. The key to the difference is the condition necessary for there to be a signal. In the case of light scattering a perfectly uniform distribution of scatterers, as for example in a perfect crystal, cannot produce a diffraction spot since light

scattered by the different scattering centers will interfere and cancel at the detector. The way to get around this problem is to arrange the scatterers so that they behave as a diffraction grating and produce intensity at the desired scattering angle. That is what actually happens in a solution or suspension of particles. Instantaneous concentration fluctuations have Fourier components that scatter light in various directions. This is why a grainy pattern of twinkling speckles is observed when light from a laser beam is scattered by a solution onto a flat surface. The important point is that the concentration of scatterers must vary with position, and time-dependent concentration changes result from mutual diffusion in the presence of concentration gradients.

In NMR it is well known that a single 90° rf pulse cannot produce a spin echo for a uniform sample. After the FID there is complete interference and the isochromats do not refocus. A close analogy with the optical case is found in the STE experiment. Here the magnetization pattern, created prior to the third 90° pulse, plays the role of a 'diffraction grating'. The 90° rf pulse rotates the isochromats into the *xy* plane where they evolve under the influence of a gradient until an echo is formed. The vector addition problem is identical to that found for the electric field in small angle light scattering. However, STE formation does not require spatial variations in the concentrations of particles but rather in the spin polarization (or phases) of the nuclei. Therefore, PFG-NMR detects tracer diffusion. It is, of course, possible to measure mutual diffusion with NMR by creating a periodic concentration pattern, as discussed in Section 3.2.

HRS provides an even more obvious analogy with the STE experiment.[10,62,63] In HRS two monochromatic laser beams are crossed at a small angle in a sample to form an interference pattern that in turn produces a volume hologram of photoproducts. In the low intensity limit the concentration of the jth photoproduct can be expressed as:

$$c_j(z,t) = \langle c_j \rangle + c_{1j} \cos(qz) \tag{50}$$

where $\langle\ \rangle$ represents an average over space and c_{1j} is the amplitude of the grating. The time evolution of the grating is monitored by a laser probe beam incident on the sample at the Bragg angle. In a heterodyne experiment where the diffracted light is mixed with a reference beam, the electric field of the diffracted light is determined and the amplitude of the grating can be mapped as a function of time. If photoexcitation changes optical properties and not hydrodynamic properties, this experiment permits tracer diffusion rates to be measured.

Analogies also appear in the spatial imaging of gratings. In the optical grating experiment a Fourier transformation of the electric field of the diffracted light with respect to the scattering angle yields an image of the diffracting grating. In the simplest case the diffraction spot is represented by a delta function at the angle θ_s and the grating is a cosine function. In the STE experiment an image of the magnetization grating can be obtained by reading out the stimulated echo in the presence of a constant gradient and Fourier transforming the signal with respect to time measured from the third 90° rf pulse. Images of transient magnetization gratings (TMGs) are useful for monitoring the spatial dependence of diffusion and flow.[10] In the medical literature this method is known as 'spatial manipulation of magnetization' (SPAMM).[64]

6 RESTRICTED DIFFUSION AND DIFFUSIVE DIFFRACTION

A significant fraction of NMR diffusion studies have been devoted to the restricted diffusion of fluids since Woessner's studies of porous materials with CW gradients.[65] PFG-NMR studies of restricted diffusion date from the pioneering work of Tanner and Stejskal.[66] Their procedure was to solve the diffusion equation with appropriate boundary conditions for $P(r \mid r', t)$ and to determine the echo amplitude by means of equation (43). Echo amplitudes have been derived for systems where diffusion is restricted by reflecting surfaces in the form of parallel planes, cubic cavities, cylinders, and spheres for steady gradients[67] and pulsed gradients.[66,68] There is much current interest in the study of porous materials by means of PFG-NMR.

The spherical cavity provides an important model for restricted motion in pores and in biological cells and vesicles. This case was treated by Neuman[67] for a steady gradient assuming a Gaussian distribution of phases at the time of the echo, and the calculation was later extended by Murday and Cotts[68] to the pulsed gradient SE experiment. The pulsed gradient solution is shown in equation (51) for a sphere of radius R:

$$\ln[\psi(q)] = -2\gamma^2 g^2 \sum_{m=1}^{\infty} \frac{1}{\alpha_m^4 D(\alpha_m^2 R^2 - 2)} \times \left(2\delta - \frac{2 + x_m^{\tau-\delta} - 2x_m^{\delta} - 2x_m^{\tau} + x_m^{\tau+\delta}}{\alpha_m^2 D}\right) \tag{51}$$

Here $x_m = \exp[-(\alpha_m{}^2 D)]$ and α_m is the mth root of the equation

$$(\alpha_m^2 R^2 - 2)\sin(\alpha_m R) + 2\alpha_m R \cos(\alpha_m R) = 0 \tag{52}$$

The parameters τ, δ, and g are defined in Figure 2, except that here $\tau = \Delta$. In the short time limit ($\Delta \ll R^2/2D$), equation (51) gives $\psi(q) = \exp(-Dq^2\Delta)$ as expected for unbounded diffusion; in the long time limit ($\Delta \gg R^2/2D$), $\psi(q) = \exp(-q^2R^2/5)$. Comparison of these results suggests that the effective diffusion coefficient in the long time limit is $D_{\text{eff}} = R^2/5\Delta$. This turns out to be precisely the mean square displacement $\langle Z^2 \rangle$ divided by 2Δ. The exact solution for $\psi(q)$ in the long time limit obtained by adapting results from the literature of heat diffusion is

$$\psi(q) = 9[qR\cos(qR) - \sin(qR)]^2/(qR)^6 \tag{53}$$

The long time limit of equation (51) agrees with exact result for small values of qR and the deviation is only 0.29% at $qR = 1$.

It is instructive to investigate the long time limit in more detail. If the fluid has the initial density distribution $\rho(z_0)$, in the limit $\Delta \to \infty$ we expect that $P(z_0 \mid z_0 + Z)$ will equal $\rho(z_0 + Z)$. Therefore, the average propagator can be written as

$$\overline{P}(Z,\infty) = \int \rho(z_0)\rho(z_0 + Z)\,\mathrm{d}z_0 \tag{54}$$

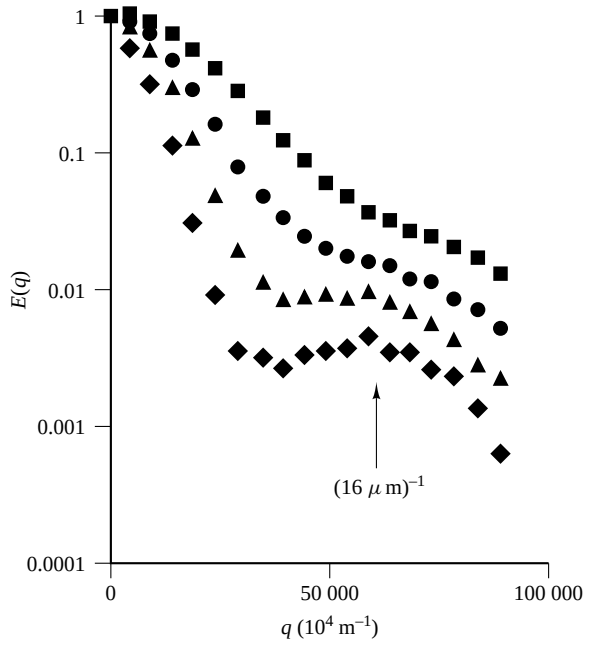

Figure 14 Echo amplitudes versus q^2 for pore glass. The data sets were obtained with Δ = 20 (■), 40 (●), 70 (▲), and 110 (♦) ms. (q in this figure is defined as $1/\Lambda$)[70]

and $\bar{P}(Z,\infty)$ is just the autocorrelation function of the molecular density or the convolution of the density with itself. It is also easy to show that equation (45) takes the form

$$\psi_\infty(q) = \left| \int \rho(z_0) \exp(-\mathrm{i}qz_0)\, \mathrm{d}z_0 \right|^2 \qquad (55)$$

Equations (45) and (54) show that the inverse Fourier transform of the echo intensity provides an image of the autocorrelation function of the density in real space.[69,70] This is the origin of diffraction-like effects in NMR diffusion studies, an idea that has led to a powerful method for the investigation of the structure of porous materials. For example, a 'pore glass' consisting of water in the presence of monodisperse spheres gives the echo intensities versus q shown in Figure 14.[70] At short times there is little indication that a water molecule samples more than one pore, while at longer times the diffraction effect resulting from neighboring pores is clearly visible. A Fourier transformation of an echo curve gives an image of the autocorrelation function. Note that this type of imaging gives resolution several orders of magnitude higher than MRI, since intensity is provided by the entire sample rather than a small voxel; but the information is limited to average features of local structure rather than positions of individual molecules in space.

Other important restricted diffusion problems include motion near an attracting center, diffusion in the presence of permeable walls and surface relaxers, inhomogeneous initial magnetization, and the effect of surface to volume ratios on the time dependence of the average propagator. These topics have been reviewed elsewhere,[25] except for the last one involving microgeometry and surface relaxation, a topic of considerable current interest in connection with the determination of pore size distributions.[71–73]

7 ANISOTROPIC DIFFUSION

Anisotropic environments are found in organized phases such as liquid crystals and zeolite crystallites. The description of diffusion in such systems requires the diffusion tensor $\boldsymbol{D}_{\alpha,\beta}$ in place of the scalar coefficient D. As a consequence, the flux defined in equation (1) depends on orientation and the right-hand side of equation (4) becomes $-\nabla \cdot \boldsymbol{D} \cdot \nabla P(\boldsymbol{r}_0|\boldsymbol{r}, t)$. The attenuation factors have the same forms as previously found except that g^2D is replaced by $\boldsymbol{g} \cdot \boldsymbol{D} \cdot \boldsymbol{g}$. Therefore, if D_x, D_y, and D_z are defined as the principal values of the diffusion tensor the attenuation factor has the form

$$\psi(\theta, \phi) = \exp[-q^2(D_x \cos^2\phi \sin^2\theta + D_y \sin^2\phi \sin^2\theta + D_z \cos^2\theta)\Delta] \qquad (56)$$

where θ and ϕ indicate the orientation of the gradient with respect to the principal axes of the diffusion tensor. For an axially symmetric diffusion tensor with $D_x = D_\perp$ and $D_z = D_\parallel$, we find that the mean square displacement in the direction of the gradient is proportional to $D_\parallel \cos^2\theta + D_\perp \sin^2\theta$. This type of treatment is appropriate for D_2O partially oriented in the lamellar phase of potassium palmitate/D_2O.[74] In this system water diffusion is relatively unrestricted parallel to the bilayers but is limited in the direction of the director.

Unfortunately, the organized systems of interest for PFG-NMR studies are likely to present problems because of severe dipolar and quadrupolar broadening. Both quadrupolar[75] and solid echoes[76] may be useful replacements for the Hahn echo in such cases. Also, a Waugh-type line-narrowing sequence, modified to permit refocusing in the presence of gradient pulses, has been used to measure the anisotropy of a diffusion tensor of liquid crystal molecules in smetic-A and smetic-C phases.[77] These and other examples of measurement of anisotropic diffusion have recently been reviewed by Callaghan.[25]

8 CHEMICAL EXCHANGE INVOLVING DIFFUSING MOLECULES

Chemical rate processes are detected by NMR when nuclei exchange between sites characterized by different spin Hamiltonians.[78] It is also possible that the sites will have similar spin Hamiltonians but will differ in hydrodynamic properties. In such cases the one-dimensional NMR spectrum is unaffected by exchange, but diffusion measurements may reveal the exchange process and permit it to be studied. Examples include: (i) association equilibria in which molecules diffuse freely or in association with larger, more slowly diffusing particles; and (ii) samples composed of subregions that are characterized by different numbers of spins and different diffusion coefficients.

Consider an FT-PFG-NMR experiment of the SE or STE type on a sample in which nuclei in various 'exchanging' sites all contribute to the same NMR line. In the slow exchange limit where exchange between sites is unlikely during the diffusion time Δ the signal amplitude can be described by a sum of exponentials as shown in equation (38). At the other extreme where many exchanges occur during Δ, a single exponential decay is found with a weighted average diffusion

coefficient. For intermediate exchange rates in the absence of strong spin coupling a simple theory of exchange, based on Bloch equations with diffusion and exchange terms, can be used to describe the evolution of longitudinal magnetization during the diffusion sensitive time interval $T = \Delta$ with $\tau, \delta \ll \Delta$. In this formulation the 'on resonance' magnetization $M_n(r, \Delta)$ for the nth species with spatial coordinates r is described by

$$\frac{\mathrm{d}M_n(r,T)}{\mathrm{d}T} = -\frac{1}{T_{1n}}M_n(r,T) - \nabla \cdot \boldsymbol{J}_n(r,T) + \sum_m K_{nm}M_m(r,T) \quad (57)$$

where the rate constants are given by $k_n = -K_{nn}$ and $k_{nm} = K_{nm}$. The flux $\boldsymbol{J}_n(r,T)$ is defined by

$$\boldsymbol{J}_n(r,T) = -D_n\nabla M_n(r,T) + M_n(r,T)v_n(r,T) \quad (58)$$

where D_n and $\boldsymbol{v}_n(r,T)$ are the diffusion coefficient and velocity for the nth species, respectively. The calculation of the signal is simplified by taking the spatial Fourier transform of equation (57) to obtain

$$\frac{\mathrm{d}M_n(q,T)}{\mathrm{d}T} = (\mathrm{i}\Omega_n - R_n)M_n(q,T) + \sum_m K_{nm}M_m(q,T) \quad (59)$$

where

$$M_n(q,T) = \int \exp(-\mathrm{i}\boldsymbol{q}\cdot\boldsymbol{r})\,M_n(r,T)\,\mathrm{d}r \quad (60)$$

Here $R_n = 1/T_{1n} + D_nq^2$ is a relaxation term, and $\Omega_n = \boldsymbol{q}\cdot\boldsymbol{v}_n$ describes the change in phase angle that results from flow, but for this discussion $1/T_{1n}$ and Ω_n are neglected. These equations and their solutions in special cases have been discussed by Kärger et al.,[60] and similar equations have been derived and studied for nuclear magnetic relaxation in multiple phase systems.[79]

Most attention has been focused on the two-site exchange case that can be solved exactly. The fast and slow exchange limits can be recovered from the solutions and useful simple equations can be derived for special cases, but in general one must resort to numerical solutions. Special problems may arise in the application of the exchange model to porous systems since the transport processes may not be adequately described by equation (59), samples may not be sufficiently uniform in properties including spin relaxation rates, and susceptibility differences may distort local magnetic fields. However, exchange in liquids is free of such complications and should be well described by equation (59).

Chemical exchange in liquid mixtures is of interest in connection with DOSY.[54] In order to simulate diffusion spectra with exchange, the ILT of $M_n(q,T)$ must be obtained. In the two-site case the inversion can be performed analytically, and whenever equations are available for $M_n(q,T)$ the Fourier transform method (q^2 replaced with $\mathrm{i}\omega$) can be used to obtain the ILT. The important quantity is the mean number of exchanges N that occur during the diffusion time T. In the slow exchange limit ($N \ll 1$) the diffusion spectrum consists of delta functions at the various diffusion coefficients, and as the exchange rate increases the spectrum evolves into a single Gaussian peak centered on the average diffusion coefficient. For example, if spins exchange between two sites (A and B) with populations p_A and p_B and diffusion coefficients D_A and D_B, respectively, the peak is centered at $\langle D\rangle = p_AD_A + p_BD_B$. The distribution of diffusion rates results from the sequences of N exchanges that occur during T and the fraction of the time that a spin occupies each site. A simple calculation for $N \gg 1$ of the number of independent sequences associated with each diffusion coefficient gives a Gaussian distribution with the square deviation $\sigma^2 = \Delta D^2 p_A(1 - p_A)/N$ where $\Delta D = D_A - D_B$. Therefore, the width of the distribution depends on the exchange rate and offers the possibility of measuring this rate.

The fast and slow exchange limits are frequently encountered and recognized, but the intermediate exchange region is difficult to identify. The amplitude of the diffusion spectrum is low in the intermediate region, and as T/N increases the linewidth decreases and becomes difficult to measure. It is also difficult to distinguish between polydispersity and exchange broadening. However, the diffusion time T can be varied, and it may be possible in some cases to determine exchange rates by means of PFG-NMR. In fact, plots of the attenuation factor Ψ versus q^2 have been used in special cases to estimate the mean lifetime in a site.[60] But it should be clear that measurements of diffusion coefficients in the slow and fast limits give no information about exchange rates.

9 LARGE GRADIENTS AND THE MEASUREMENT OF SMALL DISPLACEMENTS

The measurement of small diffusion coefficients ($D \leq 10^{-11}$ cm^2 s^{-1}) requires large values of the 'scattering vector' $\boldsymbol{q}$. Typically this is accomplished by increasing the amplitude of the gradient pulses. Modern gradient drivers for use with high-resolution spectrometers deliver 20–50 A for durations of a few milliseconds with pulse area matching to 10 ppm.[42] The gradient coils, either Maxwell pairs or quadrupolar coils, then produce gradients of a few hundred gauss per centimeter.[80,81] Much higher gradients have been reported, but usually at the cost of imperfect matching. However, even at the lower levels the pulsed gradient systems suffer from joule heating, vibrations, and pulse induced eddy currents in the metal components of the probe and neighboring magnet structures. Each of these problems can be minimized by special probe designs, but still the useful limit for stable gradient pulses appears to be approximately 10^3 G cm^{-1} in a narrow bore (5 cm) solenoid.

One way around the problem of gradient mismatch and sample motion is to accept phase variation from experiment to experiment and to correct the acquired data. A scheme to do this is called modulus addition using spatially separated echo spectroscopy (MASSEY), and the idea is as follows.[82] A phase error resulting from gradient mismatch means that the magnetization helix is not exactly unwound at the echo time. Therefore, if the echo is read out in the presence of a small read gradient g_r, a coherent superposition will occur in the vicinity of the expected echo center. One should then Fourier transform the echo with respect to $\gamma g_r t$, where t is

measured from the beginning of the read gradient, and use the modulus spectrum to measure the echo amplitude. The procedure of Fourier transformation prior to signal averaging permits displacements in the range of 1–10 nm to be measured, but does lead to a loss in the signal-to-noise ratio.

In a very different approach Kimmich et al.[83] have reported diffusion experiments in the fringe field of a superconducting magnet. Gradients of up to 42 T m^{-1} were obtained in a 4.7 T, 40 cm bore solenoid, and consistent results have been obtained in narrow bore solenoids. Thus, gradients of extremely high stability are obtained without heating, vibrations, and eddy currents. The supercon fringe field (SFF) experiment is remarkably easy to perform in any spectrometer system since one only needs the amplifier, receiver, and probe for the appropriate frequency in the fringe field. However, in its original form the SFF experiment has two major disadvantages. First, all frequency resolution is lost since the signal is acquired in the presence of the gradient. This is a serious loss, but useful information can still be obtained for specially selected systems. We note that successful experiments have been performed on polymer solutions and melts.[84] Second, the frequency gradient is approximately 2 MHz mm^{-1}, and a 1 μs rf pulse only excites a layer 0.5 mm thick. This results in very poor filling factors and small signal-to-noise ratios.

Both SE or STE diffusion experiments are easy in the fringe field, but the STE experiment is more flexible. As illustrated in Figure 3, the gradient in the STE experiment is only effective for phase encoding and decoding during the time intervals τ_1 after the first and third rf pulses, and the result is identical to a pulsed gradient experiment with pulses of duration $\delta = \tau_1$. An estimate of the lowest accessible diffusion coefficient $D_{\min}$ can be made by demanding that the attenuation caused by diffusion be equal to that resulting from relaxation. The result of this calculation is

$$D_{\min} \simeq \frac{1}{\gamma^2 g^2} \frac{1}{\delta^3(2/3 + T/\delta)} \left(\frac{T}{T_1} + \frac{2\delta}{T_2}\right) \qquad (61)$$

If τ_1 and T are of the order of T_2 and T_1, respectively, and g = 42 T m^{-1}, equation (61) gives $D_{\min} \approx 2 \times 10^{-20}/(T_1 T_2{}^2)$ in m^2 s^2. An improved STE experiment that permits the effective gradient duration to be varied without affecting relaxation is shown in Figure 15.[85] The introduction of 180° pulses in the encode and decode intervals partially refocuses the magnetization and cancels part of the effective gradient.

While the gradient amplitudes achieved in SFF are accessible with pulsed field gradients, the freedom from complications and the absence of rise and decay times for gradient pulses makes SFF a very powerful technique. The shortcomings mentioned above are already being addressed. For example, small excitation volumes can be used to advantage by exciting nonoverlapping slices without having to wait for T_1 recovery. Also, shaped rf pulses can be used to permit different pulse lengths while maintaining the same bandwidth. The loss of resolution appears to be intractable unless the sample can be moved into a homogeneous field for data acquisition. A shuttle system of the type developed for zero field spectroscopy can satisfy this requirement for samples with $T_1 > 100$ ms.

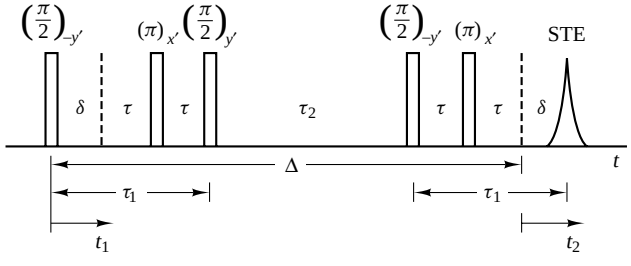

Figure 15 The five pulse STE sequence for SFF experiments. The effective gradient for encoding and decoding spatial positions has the duration δ[85]

10 DATA ANALYSIS AND POLYDISPERSITY

Data sets from PFG-NMR (SE and STE) experiments are usually in the form of a signal versus q^2 or $q^2\Delta$. For a monodisperse sample a single exponential decay as shown in equations (27) and (29) is expected. The logarithm of the signal can be fit as a linear function, but this emphasizes noise as the signal approaches zero and complicates the problem of proper weighting factors for the data points. It is better to use a nonlinear regression method to fit the exponential function directly. The Levenberg–Marquardt method is popular for this purpose.[86]

The problem may be much more difficult when more than one diffusing species contributes to the observed decay. The discrete and continuous distributions of diffusion coefficients as described by equations (38) and (42), respectively, were discussed in connection with automated analysis to obtain diffusion ordered spectra. The same analysis problem has played a major role in the development of dynamic light scattering and the extensive reviews can be found in the literature of DLS. Highly recommended sources are the analysis chapters in the monographs by Schmitz[87] and Chu[4] and the recent review by Štěpánek.[88] In general, the analysis problem is intractable. Exact answers cannot be extracted from the data and sometimes a wide variety of parameter sets fits the data within experimental error. There are, of course, some special cases where accurate answers can be determined easily or where the limited information required to characterize a distribution can be measured quite directly.

The discrete two-component decay, i.e. equation (38) with N_λ = 2, requires two decay constants, two amplitudes, and perhaps a baseline. Analysis is easy only when the decay constants differ by a large factor, the amplitudes are comparable, and the signal-to-noise ratio is high. When the answers are not obvious from a log plot, nonlinear regression procedures are sometimes used, but the latter do not provide a reliable procedure for multicomponent exponential decays, even when the number of components is known. The problem is that initial guesses of the parameters are required, and these may determine the outcome. For objective conclusions about the answers or even about the intractability of the problem, it is essential that the analysis not be biased by the user. A reasonable alternative is to use the program DISCRETE, which determines initial parameters by a Fourier method and then applies the least-squares method.[48,49] The program SPLMOD is similar but faster, and it permits the simultaneous analysis of multiple data sets.[50,51]

The continuous case requires, in principle, an ILT to determine the distribution of diffusion coefficients. There

appears to be only one simple case. If the distribution is unimodal and the distribution is narrow, a direct cumulant analysis may suffice. This method, introduced by Koppel,[89] is based on the expansion of the exponential function in equation (42) about the average decay constant $\langle\lambda\rangle$. The result is

$$G(s) = \exp\left[-\langle\lambda\rangle s + \frac{\mu_2}{2!}s^2 - \frac{\mu_3}{3!}s^3 + \frac{(\mu_4 - 3\mu_2^2)}{4!}s^4 + \ldots\right] \quad (62)$$

where

$$\langle\lambda\rangle = \int_0^\infty \lambda g(\lambda)\,\mathrm{d}\lambda, \quad \mu_n = \int_0^\infty (\lambda - \langle\lambda\rangle)^n g(\lambda)\,\mathrm{d}\lambda \quad (63)$$

A fit of equation (62) to the experimental data set, $G(s)$ versus s, by means of nonlinear regression typically yields $\langle D\rangle$ and $\mu_2 = (\langle D^2\rangle - \langle D\rangle^2)/\langle D\rangle^2$ with reasonable accuracy. The higher moments are less reliable. The ratio $\mu_2/\langle D\rangle^2$ is commonly used as an index of polydispersity; but, when this ratio exceeds 0.3, equation (62) is not justified.

When broad or multimodal distributions are expected, general ILT analyses are required. Seven schemes have recently been compared by Štěpánek.[88] The most widely used methods are constrained regularization (CONTIN), nonlinear regularization (REPES), maximum entropy (MEM), and exponential sampling. Prospective users should study the reviews to become familiar with the types of artifacts characteristic of these methods. Also, it is strongly advised that simulated data similar to the data of interest be analyzed to obtain experience with limitations of the analyses. When noise is present, the information content of the PFG-NMR data sets is simply not sufficient to provide an exact image of the distribution. One must be satisfied with a reasonable estimate rather than no solution at all.

11 MASS AND SIZE DISTRIBUTIONS FROM NMR DIFFUSION DATA

The PFG-NMR data set $G(s)$ collected at a specific chemical shift for a polydisperse sample has the form (see Section 4.1):

$$G(s) = \int_0^\infty g_\kappa(\kappa)\exp[-D(\kappa)s]\,\mathrm{d}\kappa \quad (64)$$

If $\kappa = D$ then $D(\kappa) = D$ and equations (64) and (42) are identical, but equation (64) is more general since κ may represent another molecular parameter of interest, e.g. molecular radius R or molar mass M. For example, the ILT of $G(q^2)$ gives $g_D(D)$, but $g_M(M)$ the distribution function for molar mass may be of interest. Equation (64) indicates that the normalized distribution for molar mass is given by $g_M(M) = g_D(D)\,|\mathrm{d}D/\mathrm{d}M|$.[4] For linear polymers this transformation can be carried out with the assumption that $D(M) = KM^{-\alpha}$, where K is a constant. Here α ranges from 0.6 for dilute solutions to 2.0 for melts when the 'reptation' model holds.[90] However, this treatment ignores possible spin relaxation effects that may depend on the mass. In general, the distribution functions should include a relaxation factor, e.g. $g_M(M)$ becomes $A_0(M)g_M(M)$, where $A_0(M)$ depends on T_1 and T_2. The small molecules tend to have longer relaxation times and, therefore, contribute disproportionately to the measured diffusion coefficient. Therefore, the neglect of $A_0(M)$ leads to higher apparent diffusion coefficients.

Unfortunately, equation (64) is not always appropriate. A number of experimental studies of polymer mixtures have found essentially exponential attenuation curves and, therefore, much less indication of polydispersity than predicted.[91,92] The important point is that equation (64) only holds when the diffusion rate of a polymer molecule is independent of the lengths of the neighboring polymer chains.[93] This condition is satisfied in very dilute solutions[94] and in the melts when diffusion can be described by the 'reptation' model.[90] Otherwise, little information can be obtained from $G(s)$ about $g_M(M)$. The averaging effect resulting from interactions with neighbors has been called 'microscopic' averaging.[92]

Another aim of diffusion studies is to size particles, i.e. to determine $g_R(R)$. As shown above $g_R(R)$ can be obtained from $g_D(D)$ if the relation between D and R is known. For spherical particles equation (7) with appropriate corrections for volume fraction can be assumed and $g_R(R)$ can be derived. However, this distribution is weighted by the number of nuclei contributing to the signal, i.e. the number of nuclei with diffusion coefficients in the range D to $D + \mathrm{d}D$. The number of particles in the range D to $D + \mathrm{d}D$ may be the quantity of interest, and these distributions can be related if the number of nuclei can be determined as a function of R. For example, for vesicles the number of molecules in the bilayer increases roughly with R^2 while the number of molecules entrapped in the aqueous cavity increases with R^3.[56] Therefore, the unnormalized distribution function for the number of nuclei associated with radii in the range R to $R + \mathrm{d}R$ is proportional to $R^n g_R(R)$, with $n = 2$ or 3 depending on the source of the signal. Also, the relaxation factor $A_0(R)$ is important here since T_2 is short for bilayer protons and depends on R through the rotational correlation time. The result is that the uncorrected diffusion coefficients determined from bilayer signals are much higher than those obtained with signals from molecules entrapped in the aqueous cavity. In addition, the microscopic averaging effect mentioned above may reduce the effect of polydispersity on the observed signals. All of these problems are compounded because data inversion methods often yield inaccurate estimates of $g_R(R)$.

Similarities between NMR and DLS analyses have been noted, but it should be kept in mind that different kinds of averaging processes are involved. When relaxation can be ignored NMR intensities depend on the number of nuclei involved in the resonance and this number may be proportional to the molecular weight of a molecule, the volume of an entrapped fluid, etc. In DLS the intensity is proportional to the number of scatterers, but each scatterer is weighted by the square of the number of electrons. In some cases the number of electrons is proportional to the mass and to the volume of a molecule. This is the origin of the well-known rule that scattering from a particle is proportional to the square of its volume. Therefore, in the limit of infinite dilution where tracer and mutual diffusion coefficients are equal, NMR and DLS may still give different average diffusion coefficients for polydisperse samples. Also, as a practical matter, PFG-NMR data sets usually have fewer points and lower signal-to-noise ratios than data sets obtained in DLS.

12 LITERATURE SOURCES FOR NMR DIFFUSION MEASUREMENTS

The most complete, up-to-date treatment of translational dynamics and its study by NMR is found in the book by Callaghan.[25] The experimental and theoretical aspects of diffusion in liquids are treated in the monograph by Tyrrell and Harris,[2] and Crank's book[1] is still the standard reference for the mathematics of diffusion. The principles and applications of PFG-NMR have been reviewed by Kärger et al.,[60] and Stilbs[39] has provided a detailed review of FT diffusion studies. NMR studies of diffusion in polymer systems have been reviewed by von Meerwall.[95,96] Wade[97] has reviewed lateral diffusion in lipids including NMR measurements, and Chachaty[98] has reviewed NMR relaxation and diffusion studies of micellar solutions. Molecular diffusion in NMR imaging has been reviewed by Le Bihan[99] (note that the references in this review incorrectly replace *Phys*. with *Physiol*. in several places). Multiple-quantum methods including sensitivity to gradients and use in diffusion studies have been reviewed by Norwood.[100]

13 RELATED ARTICLES

Chemical Exchange Effects on Spectra; Diffusion: Clinical Utility of MRI Studies; Diffusion and Flow in Fluids; Diffusion and Perfusion in MRI; Diffusion in Porous Media; Diffusion in Rare Gas Solids; Diffusion in Solids; Electrophoretic NMR; Field Gradients and Their Application; Flow NMR; Gradient Coil Systems; Liquid Crystalline Samples: Diffusion; NMR Microscopy: Resolution; Radiofrequency Gradient Pulses; Spin Echo Spectroscopy of Liquid Samples

14 REFERENCES

1. J. Crank, *The Mathematics of Diffusion*, 2nd edn, Oxford University Press, Oxford, 1975.
2. H. J. V. Tyrrell and K. R. Harris, *Diffusion in Liquids: A Theoretical and Experimental Study*, Butterworths, London, 1984.
3. C. R. Cantor and P. R. Schimmel, *Biophysical Chemistry, Part II: Techniques for the Study of Biological Structure and Function*, W. H. Freeman and Co., San Francisco, 1980.
4. B. Chu, *Laser Light Scattering: Basic Principles and Practice*, Academic, Boston, 1991.
5. C. S. Johnson, Jr, and D. A. Gabriel, *Laser Light Scattering*, Dover, New York, 1994.
6. D. G. Leaist and L. Hao, *J. Phys. Chem.*, 1993, **97**, 7763.
7. L. Onsager and R. M. Fuoss, *J. Phys. Chem.*, 1932, **36**, 2689.
8. J. G. Kirkwood, R. L. Baldwin, P. J. Dunlop, L. J. Gosting, and G. Kegeles, *J. Chem. Phys.*, 1960, **33**, 1505.
9. J. A. Marqusee and J. M. Deutch, *J. Chem. Phys.*, 1980, **73**, 5396.
10. T. R. Saarinen and C. S. Johnson, Jr, *J. Magn. Reson.*, 1988, **78**, 257.
11. A. Abragam, *The Principles of Nuclear Magnetism*, Oxford University Press, London, 1961.
12. E. O. Stejskal and J. E. Tanner, *J. Chem. Phys.*, 1965, **42**, 288.
13. R. F. Karlicek and I. J. Lowe, *J. Magn. Reson.*, 1980, **37**, 75.
14. E. L. Hahn, *Phys. Rev.*, 1950, **80**, 580.
15. H. Y. Carr and E. M. Purcell, *Phys. Rev.*, 1954, **94**, 630.
16. R. L. Vold and R. R. Vold, *J. Am. Chem. Soc.*, 1974, **96**, 4043.
17. R. L. Vold and R. R. Vold, *Prog. Nucl. Magn. Reson. Spectrosc.*, 1978, **12**, 79.
18. M. I. Hrovat and C. G. Wade, *J. Magn. Reson.*, 1981, **44**, 62.
19. D. E. Woessner, *J. Chem. Phys.*, 1961, **34**, 2057.
20. J. E. Tanner, *J. Chem. Phys.*, 1970, **52**, 2523.
21. J. Lian, D. S. Williams, and I. J. Lowe, *J. Magn. Reson., Ser. A*, 1994, **106**, 65.
22. R. M. Cotts, M. J. R. Hoch, T. Sun, and J. T. Marker, *J. Magn. Reson.*, 1989, **83**, 252.
23. L. L. Latour, L. Li, and C. H. Sotak, *J. Magn. Reson., Ser. B*, 1993, **101**, 72.
24. B. Gross and R. Kosfeld, *Messtechnik*, 1969, **7/8**, 171.
25. P. T. Callaghan, *Principles of Nuclear Magnetic Resonance Microscopy*, Oxford University Press, Oxford, 1991.
26. J. Stepisnik, *Prog. NMR Spectrosc.*, 1985, **17**, 187.
27. I. Solomon, *Phys. Rev. Lett.*, 1959, **2**, 301.
28. D. Canet, B. Diter, A. Belmajdoub, J. Brondeau, J. C. Boubel, and K. Elbayed, *J. Magn. Reson.*, 1989, **81**, 1.
29. R. Dupeyre, P. Devoulon, D. Bourgeois, and M. Decorps, *J. Magn. Reson.*, 1991, **95**, 589.
30. J. F. Martin, L. S. Selwyn, R. R. Vold, and R. L. Vold, *J. Chem. Phys.*, 1982, **76**, 2632.
31. D. Zax and A. Pines, *J. Chem. Phys.*, 1983, **78**, 6333.
32. L. E. Kay and J. H. Prestegard, *J. Magn. Reson.*, 1986, **67**, 103.
33. C. H. Sotak, *J. Magn. Reson.*, 1990, **90**, 198.
34. T. J. Norwood, *J. Magn. Reson.*, 1992, **99**, 208.
35. R. L. Vold, J. S. Waugh, M. P. Klein, and D. E. Phelps, *J. Chem. Phys.*, 1968, **48**, 3831.
36. T. L. James and G. G. McDonald, *J. Magn. Reson.*, 1973, **11**, 58.
37. J. Kida and H. Uedaira, *J. Magn. Reson.*, 1977, **27**, 253.
38. P. Stilbs and M. E. Moseley, *Chem. Script.*, 1979, **13**, 26.
39. P. Stilbs, *Prog. Nucl. Magn. Reson. Spectrosc.*, 1987, **19**, 1.
40. P. Stilbs and M. E. Moseley, *Chem. Script.*, 1980, **15**, 176.
41. K. F. Morris and C. S. Johnson, Jr, *J. Am. Chem. Soc.*, 1993, **115**, 4291.
42. R. M. Boerner and W. S. Woodward, *J. Magn. Reson., Ser. A*, 1994, **106**, 195.
43. P. Mansfield and B. Chapman, *J. Magn. Reson.*, 1986, **66**, 573.
44. S. J. Gibbs, K. F. Morris, and C. S. Johnson, Jr, *J. Magn. Reson.*, 1991, **94**, 165.
45. S. J. Gibbs and C. S. Johnson, Jr, *J. Magn. Reson.*, 1991, **93**, 395.
46. E. von Meerwall and M. Kamat, *J. Magn. Reson.*, 1983, **83**, 309.
47. W. J. Goux, L. A. Verkruyse, and S. J. Salter, *J. Magn. Reson.*, 1990, **88**, 609.
48. S. W. Provencher, *J. Chem. Phys.*, 1976, **64**, 2772.
49. S. W. Provencher, *Biophys. J.*, 1976, **16**, 27.
50. S. W. Provencher and R. H. Vogel, in *Numerical Treatment of Inverse Problems in Differential and Integral Equations*, eds. P. Deuflhard and E. Hairer, Birkhauser, Boston, 1983, p. 304.
51. R. H. Vogel, SPLMOD Users Manual (Technical Report DA06), European Molecular Biology Laboratory, Heidelberg, 1983.
52. K. F. Morris, P. Stilbs, and C. S. Johnson, Jr, *Anal. Chem.*, 1994, **66**, 211.

53. P. Stilbs, *J. Colloid Interface Sci.*, 1982, **87**, 385.
54. C. S. Johnson, Jr. *J. Magn. Reson., Ser. A*, 1993, **102**, 214.
55. D. Wu, W. S. Woodward, and C. S. Johnson, Jr, *J. Magn. Reson., Ser. A*, 1993, **104**, 231.
56. D. P. Hinton and C. S. Johnson, Jr, *J. Phys. Chem.*, 1993, **97**, 9064.
57. K. F. Morris, C. S. Johnson, Jr, and T. C. Wong, *J. Phys. Chem.*, 1994, **98**, 603.
58. E. O. Stejskal, *J. Chem. Phys.*, 1965, **43**, 3597.
59. J. Kärger and W. Heink, *J. Magn. Reson.*, 1983, **51**, 1.
60. J. Kärger, H. Pfeifer, and W. Heink, in *Advances in Magnetic Resonance*, ed. W. W. Warren, Academic, New York, 1988, Vol. 12, p. 1.
61. B. J. Berne and R. Pecora, *Dynamic Light Scattering*, Wiley, New York, 1976.
62. H. J. Eichler, P. Gunter, and D. W. Pohl, *Laser-induced Dynamic Gratings*, Springer, Berlin, 1986.
63. H. Hervet, W. Urbach, and F. Rondelez, *J. Chem. Phys.*, 1978, **68**, 2725.
64. L. Axel, *Radiology*, 1989, **171**, 841.
65. D. E. Woessner, *J. Phys. Chem.*, 1963, **67**, 1365.
66. J. E. Tanner and E. O. Stejskal, *J. Chem. Phys.*, 1968, **49**, 1768.
67. C. H. Neuman, *J. Chem. Phys.*, 1974, **60**, 4508.
68. J. S. Murday, and R. M. Cotts, *J. Chem. Phys.*, 1968, **48**, 4938.
69. D. G. Cory and A. N. Garroway, *Magn. Reson. Med.*, 1990, **14**, 435.
70. P. T. Callaghan, A. Coy, D. MacGowan, K. J. Packer, and F. O. Zelaya, *Nature*, 1991, **351**, 467.
71. P. P. Mitra and P. N. Sen, *Phys. Rev. B*, 1992, **45**, 143.
72. P. P. Mitra, P. N. Sen, L. M. Schwartz, and P. L. Doussal, *Phys. Rev. Lett.*, 1992, **68**, 3555.
73. J. E. M. Snaar and H. Van As, *J. Magn. Reson., Ser. A*, 1993, **102**, 318.
74. P. T. Callaghan, M. A. Le Gros, and D. N. Pinder, *J. Chem. Phys.*, 1983, **79**, 6372.
75. J. H. Davis, K. R. Jeffrey, M. Bloom, M. I. Valic, and T. P. Higgs, *Chem. Phys. Lett.*, 1976, **42**, 390.
76. G. J. Kruger, H. Spiesecke, R. von Steenwinkle, and F. Noack, *Mol. Cryst. Liq.*, 1977, **40**, 103.
77. R. Blinc, M. Burgar, M. Luzar, J. Pirs, I. Zupanzic, and S. Zumer, *Phys. Rev. Lett*. 1974, **33**, 1192.
78. C. S. Johnson, Jr, in *Advances in Magnetic Resonance*, ed. J. S. Waugh, Academic, New York, 1965, Vol. 1, p. 33.
79. J. R. Zimmerman and W. E. Brittin, *J. Phys. Chem.*, 1957, **61**, 1228.
80. J. E. Tanner, *Rev. Sci. Instrum.*, 1965, **36**, 1086.
81. D. S. Webster and K. H. Marsden, *Rev. Sci. Instrum.*, 1974, **45**, 1232.
82. P. T. Callaghan, *J. Magn. Reson.*, 1990, **88**, 493.
83. R. Kimmich, W. Unrath, G. Schnur, and E. Rommel, *J. Magn. Reson.*, 1991, **91**, 136.
84. G. Fleischer, F. Fujara, and B. Stuehn, *Macromolecules*, 1993, **26**, 2340.
85. R. Kimmich and E. Fischer, *J. Magn. Reson., Ser. A*, 1994, **106**, 229.
86. W. H. Press, S. A. Teukolsky, W. T. Vettering, and B. P. Flannery, *Numerical Recipes in FORTRAN*, Cambridge University Press, New York, 1992.
87. K. S. Schmitz, *An Introduction to Dynamic Light Scattering by Macromolecules*, Academic, Boston, 1990.
88. P. Štěpánek, in *Dynamic Light Scattering: The Method and Some Applications*, ed. W. Brown, Clarendon, Oxford, 1993, p. 177.
89. D. E. Koppel, *J. Chem. Phys.*, 1973, **57**, 4814.
90. R. Bachus and R. Kimmich, *Polymer*, 1983, **24**, 964.
91. R. Raghavan, T. L. Maver, and F. D. Blum, *Macromolecules*, 1987, **20**, 814.
92. P. T. Callaghan and D. N. Pinder, *Macromolecules*, 1985, **18**, 373.
93. G. Fleischer, *Polymer* 1985, **26**, 1677.
94. E. D. von Meerwall, *J. Magn. Reson.*, 1982, **50**, 409.
95. E. D. von Meerwall, *Adv. Polym. Sci.*, 1983, **54**, 1.
96. E. D. von Meerwall, *Rubber Chem. Technol. (Rubber Rev.)*, 1985, **58**, 527.
97. C. G. Wade, in *Structure and Properties of Cell Membranes*, ed. G. Benga, CRC Boca Raton, FL, 1985, Vol. 1, p. 51.
98. C. Chachaty, *Prog. NMR Spectrosc.*, 1987, **19**, 183.
99. D. Le Bihan, *Magn. Reson. Quart.*, 1991, **7**, 1.
100. T. J. Norwood, *Prog. NMR Spectrosc.*, 1993, **24**, 295.

Biographical Sketch

Charles S. Johnson, Jr. *b* 1936. B.S., 1958, Georgia Institute of Technology, Ph.D., 1961, Massachusetts Institute of Technology, (supervisor John Waugh). NAS-NRS Postdoctoral fellow and instructor at Illinois (with Herb Gutowsky). Faculty member Yale University 1962–67, University of North Carolina, Chapel Hill, 1967–present. Research interests include dynamic light scattering (DLS), electrophoretic NMR, diffusion-ordered 2D NMR, and applications of DLS and NMR to complex liquid mixtures.

Filter Diagonalization Methods for Time-Domain Signals

A. J. Shaka and Vladimir A. Mandelshtam

Chemistry Department, University of California at Irvine, Irvine, CA, USA

1 Introduction 1
2 Formulation of the Problems 1
3 Parameter and Spectral Estimation by 1D FDM 2
4 mD FDM 4
5 Practical Considerations 5
6 Selected Applications 6
7 Remaining Problems 7
8 References 9

1 INTRODUCTION

The *filter diagonalization method* (FDM) is a linear algebraic method of spectral analysis of time signals and, in particular, NMR signals, that is meant to compliment or replace Fourier Transform (FT) spectral analysis. One-dimensional (1D) FDM and its multi-dimensional (mD) extensions exist. Related techniques that have emerged from the FDM are the *regularized resolvent transform* (RRT) and *extended fourier transform* (XFT). Most results reported here can be found in Refs.[1–18] We attempt to present FDM critically, emphasizing both its advantages and drawbacks. FDM is not always advantageous, but for many kinds of spectra it can be. Some unsolved challenges, either conceptual or computational, associated mostly with the mD FDM, are identified. The first sections lay the mathematical underpinnings, while the latter sections show applications and highlight experimental considerations.

1.1 Important Notations

A linear operator is identified by a cap: $\widehat{A}$. In the expression $|b) = \widehat{A}|c)$ a vector $|c)$ from a linear space is mapped to a vector $|b)$ from the same space. $(c|$ defines a dual vector to $|c)$ and $(c|b) = (b|c)$, complex symmetric (i.e., no complex conjugation) inner product between the two vectors $|c)$ and $|b)$. Bold characters, as $\mathbf{A}$ or $\mathbf{C}$ are used for matrix representations of linear operators or vectors. Their elements are then defined using the following notations: $[\mathbf{A}]_{mn}$ or $[\mathbf{C}]_n$. $\mathbf{A}^{\mathrm{T}}$ is a transpose of matrix $\mathbf{A}$, while $\mathbf{A}^{\dagger}$, is its adjoint (transposed and complex conjugated) matrix. Almost all variables are *complex* numbers, including ω_k, d_k, etc., although time variables t, τ, etc., are real.

2 FORMULATION OF THE PROBLEMS

2.1 1D Spectral Analysis

Consider a finite complex valued 1D time signal $c_n := c(n\tau)$, $(n = 0, \ldots, N-1)$, that has been sampled instantaneously on an equidistant discrete set of time points. By the *Fourier spectral estimation* problem we mean estimating the infinite time discrete Fourier transformation (DFT) of c_n:

$$I(s) := \sum_{n=0^+}^{\infty} c_n z^{-n} := \sum_{n=0}^{\infty} \left(1 - \frac{\delta_{n0}}{2}\right) c_n z^{-n} \tag{1}$$

using the finite data set. Here $z = e^{-i\tau s}$; the 'shortcut' $\Sigma_{n=0^+}$, meaning that the first term in the sum is multiplied by 1/2, will be used throughout the article. The latter corrects an error due to the discretization of the half-line Fourier integral

$$I_0(s) := \int_0^{\infty} c(t) e^{its} dt = \lim_{\tau \to 0} \tau I(s) \tag{2}$$

The 1D *parameter estimation* or *harmonic inversion problem* (HIP), by contrast, corresponds to the *fitting* of the finite data set c_n by the form

$$c_n = \sum_{k=1}^{K} d_k u_k^n \tag{3}$$

with $u_k = e^{-i\tau\omega_k}$. The unknown parameters are the complex poles u_k (or, alternatively, the frequencies ω_k) and complex amplitudes d_k. It is not obvious that a linear algebraic solution of the HIP exists as at first glance it requires a nonlinear least squares fit.

Once a *line list* $\{u_k, d_k\}$ is obtained, one can construct an *ersatz spectrum*

$$I(s) = \sum_k d_k \left\{ \frac{z}{z - u_k} - \frac{1}{2} \right\} \tag{4}$$

which estimates the DFT spectrum (1). Note that, although the infinite Fourier series (1) converges only if all poles u_k satisfy $|u_k| \le 1$, a sensible and stable result can be obtained using equation (4), even when this is not the case. Moreover, the stability is maintained only if one does not exclude or modify the 'unphysical' entries with u_k far outside the unit circle. It is recommended though to flip the poles with $|u_k| > 1$ which are close to the unit circle, i.e., $|u_k| \sim 1$, using $u_k \to u_k/|u_k|^2$ before inserting into equation (4). This eliminates sign problems caused by inaccurate width estimation for very narrow peaks when using short data records.

Note also that, if the sampling theorem is satisfied, there is no significant difference in the appearance of the DFT spectrum (1) and the integral half-line FT integral (2), except for very broad lines (i.e., with line widths $|\mathrm{Im}\ \omega_k|$ comparable to the spectral width $\mathrm{SW} = 1/\tau$). The dispersion-mode wings of these lines, in particular, alias in the DFT case. Practically speaking the form (4) is significantly more stable than its integral counterpart[16]

$$I_0(s) = \sum_k \frac{i d_k}{s - \omega_k} \tag{5}$$

and is what is used in practice.

2.2 mD Spectral Analysis

Consider a general complex valued mD time signal $c_{n_1,\ldots,n_D} := c(n_1\tau_1, \ldots, n_D\tau_D)$, defined on an equidistant rectangular time grid of size $N_{\text{total}} = N_1 \times \cdots \times N_D$.

The mD Fourier spectral estimation problem then becomes that of estimating the infinite sum,

$$I(s_1, \ldots, s_D) = \sum_{n_1=0^+}^{\infty} z_1^{-n_1} \cdots \sum_{n_D=0^+}^{\infty} z_D^{-n_D} c_{n_1,\ldots,n_D} \tag{6}$$

with $z_l = e^{-i n_l \tau_l s_l}$, $(l = 1, \ldots, D)$.

One possible and, probably, most desirable formulation of the mD HIP is

$$c_{n_1,\ldots,n_D} = \sum_{k=1}^{K} d_k u_{1k}^{n_1} \cdots u_{Dk}^{n_D} \tag{7}$$

where the unknown parameters are the complex amplitudes d_k and frequencies ω_{lk} with $u_{lk} = e^{-i n_l \tau_l \omega_{lk}}$, $(l = 1, \ldots, D)$. These parameters, once computed, can be used to construct various representations of the mD spectrum, such as that defined by equation (6),

$$I(s_1, \ldots, s_D) = \sum_k d_k \prod_{l=1}^{D} \left\{ \frac{z_l}{z_l - u_{lk}} - \frac{1}{2} \right\} \tag{8}$$

or a more useful mD absorption-mode spectrum

$$A(s_1, \ldots, s_D) = \text{Re} \sum_k d_k \prod_{l=1}^{D} \text{Re} \left\{ \frac{z_l}{z_l - u_{lk}} - \frac{1}{2} \right\} \tag{9}$$

Unfortunately, the present versions of FDM can provide a sensible mD line list only when the data well approximates the form equation (7) with high signal-to-noise ratio (SNR). We will refer to such cases as the *well defined HIP*. However, for a poorly defined mD HIP various spectral representations, including absorption-mode spectra, can still be constructed in the FDM framework, but by carefully avoiding the solution of equation (7).

3 PARAMETER AND SPECTRAL ESTIMATION BY 1D FDM

The commonly used starting point in most linear algebraic approaches is the autoregression (AR) assumption, which in 1D case reads

$$c_n = \sum_{p=1}^{K} a_p c_{n-p} \tag{10}$$

This assumption is equivalent to equation (3), but requires that one solves for the auxiliary prediction coefficients a_p. These are not, however, the ultimate quantities of interest. To recast the spectral analysis problem into the linear algebraic framework in FDM one assumes the existence of an auxiliary quantum dynamical system with a complex symmetric evolution operator $\widehat{U}$ of rank K and a fictitious state Φ, so that the data may be represented in the form of the autocorrelation function[1]

$$c_n = (\Phi | \widehat{U}^n | \Phi) \tag{11}$$

It can be shown that the three assumptions (3), (10) and (11) are equivalent, although the latter leads directly to the solution of either HIP or the spectral estimation problem and is therefore more economical. For example, assuming $\widehat{U}$ is diagonalizable,

$$\widehat{U} \Upsilon_k = u_k \Upsilon_k, \quad (k = 1, \ldots, K) \tag{12}$$

we get equation (3) with

$$d_k = (\Phi | \Upsilon_k)^2 (\Upsilon_k | \Upsilon_k)^{-1} \tag{13}$$

which suggests that the HIP is equivalent to a matrix eigenvalue problem arising from equation (12). This can be shown by using $N = 2M$ and implementing the Krylov basis

$$\Phi_n := \widehat{U}^n \Phi, \quad (n = 0, \ldots, M-1)$$

We can now define the evolution operator matrix $\mathbf{U}_1$, the overlap matrix $\mathbf{U}_0$ and the signal vector $\mathbf{C}$ and evaluate them in terms of the signal points c_n utilizing the assumption (11):

$$[\mathbf{U}_p]_{nm} := (\Phi_n | \widehat{U}^p | \Phi_m) = c_{n+m+p}$$
$$[\mathbf{C}]_n := (\Phi | \Phi_n) = c_n$$

By expanding the eigenfunctions, $\Upsilon_k = \Sigma_k [\mathbf{B}_k]_n \Phi_n$, we obtain the generalized eigenvalue problem

$$\mathbf{U}_1 \mathbf{B}_k = u_k \mathbf{U}_0 \mathbf{B}_k \tag{14}$$

for the unknown eigenvalues u_k and eigenvectors $\mathbf{B}_k$. If $M \geq K$, with exact arithmetic equation (14) then yields the exact solution of the HIP (3) with

$$d_k = \left(\mathbf{C}^{\text{T}} \mathbf{B}_k\right)^2 \left(\mathbf{B}_k^{\text{T}} \mathbf{U}_0 \mathbf{B}_k\right)^{-1} \tag{15}$$

The latter result is derived from equation (13). This and similar expressions have been first derived in the FDM framework.[1,2] Note though that equation (14) was used previously[19] to estimate the parameters u_k.

Interestingly, once the data arrays $\mathbf{U}_0$, $\mathbf{U}_1$ and $\mathbf{C}$ are obtained in a suitable representation, the DFT spectrum $I(s)$ can be estimated *directly*, avoiding the use of the spectral parameters u_k and d_k and hence the solution of the generalized eigenvalue problem. This is done by first inserting equation (11) into equation (1) and evaluating the geometric series,

$$I(s) = (\Phi | \left(\frac{1 - \widehat{U}}{z} \right)^{-1} | \Phi) - \frac{c_0}{2}$$

and then using the above matrix representations

$$I(s) = \mathbf{C}^{\mathrm{T}}\mathbf{R}^{-1}\mathbf{C} - \frac{c_0}{2}, \quad \mathbf{R} = \frac{\mathbf{U}_0 - \mathbf{U}_1}{z} \tag{16}$$

In the noiseless case for $M = K$ the spectral estimate (16) is exact. For $M \geq K$ the matrix pencil $\mathbf{R}$ is singular and the evaluation of the resolvent $\mathbf{R}^{-1}$ requires a *regularization*. For example, one can implement the *singular value decomposition* (SVD) of $\mathbf{R}$ and then evaluate the inverse in the range subspace of $\mathbf{R}$. This still gives the exact result for the noiseless case. In practice $\mathbf{R}$ is never exactly singular, but could be ill-conditioned, so that regularization is most definitely required. In this case truncated SVD (as described above) is not recommended. Instead, a rather more robust regularization scheme can be implemented,[14,17] such as the Tikhonov regularization,[20] that requires solution of a Hermitian linear least squares problem at each value of frequency s:

$$I(s) \approx \mathbf{C}^{\mathrm{T}}\mathbf{X} - \frac{c_0}{2}, \quad \left(\mathbf{R}^{\dagger}\mathbf{R} + q^2\right)\mathbf{X} = \mathbf{R}^{\dagger}\mathbf{C} \tag{17}$$

where q is a real regularization parameter that controls the noise and artifact suppression. Bigger values of q lower the resolution, but lead to more uniform spectral estimates, rather like line broadening in FT analysis. The spectral estimate (17) was derived in Ref.[14] and named RRT (Regularized Resolvent Transform). In a related technique XFT the spectrum is estimated by partitioning the infinite DFT sum (1) into a finite DFT over the measured data length and a correction term, which is evaluated using an RRT-type expression.[17]

3.1 Fourier Subspace Filtering

Solution of the $M \times M$ generalized eigenvalue problem (14) or the matrix inversion in equation (17) has $\sim M^3$ numerical scaling and is thus impractical. A Fourier basis has proven to be very efficient for such problems.[1,2] A small Fourier subspace $\{\tilde{\Phi}_j\}$ of size $K_{\mathrm{win}} \ll M$ is constructed by choosing K_{win} complex numbers on the unit circle $y_j = e^{-i\tau\varphi_j}$, $(j = 1, \ldots, K_{\mathrm{win}})$ and using

$$\tilde{\Phi}_j = \sum_{n=0}^{M-1} \left(\frac{\widehat{U}}{y_j}\right)^n \Phi$$

where the tilde over vectors or matrices will denote the use of a Fourier basis. The results are not usually sensitive to the parameters of the basis as long as the points φ_j are chosen appropriately. In most cases an equidistant grid is effective, with spacing

$$\Delta\varphi = \frac{2\pi}{\aleph M \tau} \tag{18}$$

and adjustable parameter $\aleph \geq 1$ (e.g., one can use $\aleph = 1.2$). Since the basis is localized in the frequency domain, the diagonal elements of the matrices will dominate, and the off-diagonal elements will drop off as a sinc function. This allows an accurate solution of equation (14) or the spectral estimation in equation (17) in a small subspace, leading to numerically inexpensive linear algebra. A further gain may be achieved by using a multi-scale Fourier basis[11] with a non-uniform set of φ_j values, containing information about the entire spectrum rather than just the spectral window. Note that filtering the *basis* is conceptually different than e.g., digital filtering of the *signal*. That is, the true signal is used to construct matrix elements, and then this matrix, which is potentially huge, is treated in a basis which allows diagonalization to proceed in a block-diagonal fashion, so that only a relatively small numbers of matrix elements need to be computed.

The matrix elements of the $K_{\mathrm{win}} \times K_{\mathrm{win}}$ square matrices $\tilde{\mathbf{U}}_1$ and $\tilde{\mathbf{U}}_0$ can be computed using[2]

$$\begin{aligned}\left[\tilde{\mathbf{U}}_p\right]_{jj'} &:= (\tilde{\Phi}_j|\widehat{U}^p|\tilde{\Phi}_{j'}) \\ &= \widehat{S} \sum_{\sigma=0,1} \frac{(-1)^\sigma (y_j/y_{j'})^M}{1 - y_j/y_{j'}} \sum_{n=\sigma M}^{(\sigma+1)(M-1)} y_j^{-n} c(n+p)\end{aligned}$$

where $\widehat{S}$ defines symmetrization operator over the variables y_j and $y_{j'}$,

$$\widehat{S}g(y_j, y_{j'}) = g(y_j, y_{j'}) + g(y_{j'}, y_j)$$

For $j = j'$ we have

$$\left[\tilde{\mathbf{U}}_p\right]_{jj} = \sum_{n=0}^{2M-2} y_j^{-n}(M - |M - n - 1|)c(n+p)$$

The state vector Φ in the Fourier basis is a $1 \times K_{\mathrm{win}}$ column vector with elements

$$[\tilde{\mathbf{C}}]_j := (\tilde{\Phi}_j|\Phi) = \sum_{n=0}^{M-1} y_j^{-n} c_n$$

The generalized eigenvalue problem (14) in the Fourier basis now reads

$$\tilde{\mathbf{U}}_1\tilde{\mathbf{B}}_k = u_k\tilde{\mathbf{U}}_0\tilde{\mathbf{B}}_k \tag{19}$$

with the coefficients computed by

$$d_k = \left(\tilde{\mathbf{C}}^{\mathrm{T}}\tilde{\mathbf{B}}_k\right)^2 \left(\tilde{\mathbf{B}}_k^{\mathrm{T}}\tilde{\mathbf{U}}_0\tilde{\mathbf{B}}_k\right)^{-1} \tag{20}$$

Defining the $K_{\mathrm{win}} \times K_{\mathrm{win}}$ matrix-pencil $\tilde{\mathbf{R}} = \tilde{\mathbf{U}}_0 - \tilde{\mathbf{U}}_1/z$ in the Fourier basis, the RRT spectral estimate becomes

$$I(s) \approx \tilde{\mathbf{C}}^{\mathrm{T}}\tilde{\mathbf{X}} - \frac{c_0}{2}, \quad \left(\tilde{\mathbf{R}}^{\dagger}\tilde{\mathbf{R}} + q^2\right)\tilde{\mathbf{X}} = \tilde{\mathbf{R}}^{\dagger}\tilde{\mathbf{C}} \tag{21}$$

Since a small subspace, rather than the complete basis $\{\Phi_n\}$, is used, equations (19), (20) and (21) must be viewed as an approximation to equations (14), (15) and (17) with convergence parameter K_{win}. However, an acceptable convergence is usually achieved for sufficiently small sizes in the range $K_{\mathrm{win}} \sim 10{-}100$. Moreover, in the Fourier basis, the matrices are much less ill-conditioned, which makes them easier to handle numerically.

4 mD FDM

Generalizing the 1D quantum ansatz (11) the mD signal is assumed to be generated by D commuting complex symmetric evolution operators $\widehat{U}_l$, $(l = 1, \ldots, \mathrm{D})$:

$$c_{n_1,\ldots,n_\mathrm{D}} = (\Phi|\prod_{l=1}^{\mathrm{D}} \widehat{U}_l^{n_l}|\Phi) \tag{22}$$

Clearly, if all the operators $\widehat{U}_l$ have the same rank K with nondegenerate eigenvalues u_{lk} and the corresponding eigenfunctions Υ_k, equation (22) yields equation (7) with the amplitudes $d_k = (\Phi|\Upsilon_k)^2(\Upsilon_k|\Upsilon_k)^{-1}$. However, the assumption about the existence of a simultaneous basis $\{\Upsilon_k\}$ leads to numerical troubles.[8] It turns out that it can be avoided by keeping only the requirement that $\widehat{U}_l$ commute with each other. That is, we will label the eigenfunctions of $\widehat{U}_l$ by l:

$$\widehat{U}_l\Upsilon_{lk} = u_{lk}\Upsilon_{lk}, \quad (l = 1, \ldots, \mathrm{D}) \tag{23}$$

By inserting the quantum ansatz (22) into equation (6) and evaluating the product of D geometric sums, in analogy with equation (16), we get the resolvent representation of the mD DFT spectrum:

$$I(s_1, \ldots, s_\mathrm{D}) = (\Phi|\prod_{l=1}^{\mathrm{D}} \left\{\frac{z_l}{z_l - \widehat{U}_l} - \frac{1}{2}\right\}|\Phi) \tag{24}$$

Now using $2M_l = N_l$ for $l = 1, \ldots, \mathrm{D}$ and representing everything in the Krylov basis $\Phi_{n_1,\ldots,n_\mathrm{D}} := \widehat{U}_1^{n_1}, \ldots, U_\mathrm{D}^{n_\mathrm{D}}\Phi$ with total size $M_\mathrm{total} = M_1 \times \cdots \times M_\mathrm{D}$, we can replace equation (23) by generalized eigenvalue problems with known data matrices $\mathbf{U}_l$ or, alternatively, obtain an mD RRT spectral estimate. However, as in the 1D case, it is advantageous to implement a Fourier basis. For the sake of simplicity, here we consider only the $\mathrm{D} = 2$ case.

4.1 Fourier Basis: 2D Case

Let $\{\varphi_{1j}, \varphi_{2j}\}$ be a set of $K_{1\mathrm{win}} \times K_{2\mathrm{win}} = K_\mathrm{win}$ grid points in a chosen 2D frequency window with spacings, given by equation (18), in each dimension. We can now define the Fourier basis using:

$$\tilde{\Phi}_j = \sum_{n_1=0}^{M_1-1}\sum_{n_2=0}^{M_2-1}\left(\frac{\widehat{U}_1}{y_{1j}}\right)^{n_1}\left(\frac{\widehat{U}_2}{y_{2j}}\right)^{n_2}\Phi$$

with $y_{lj} = e^{-in\tau_l\varphi_{lj}}$, $(l = 1, 2)$. The square complex symmetric matrices of $\widehat{U}_1$, $\widehat{U}_2$ and the identity operator (the overlap matrix) in this basis are defined by $\tilde{\mathbf{U}}_1$, $\tilde{\mathbf{U}}_2$ and $\tilde{\mathbf{U}}_0$, accordingly. To consolidate the expressions, three new data sets are defined:

$$c^{(0)}_{n_1,n_2} := c_{n_1,n_2}; \quad c^{(1)}_{n_1,n_2} := c_{n_1+1,n_2}; \quad c^{(2)}_{n_1,n_2} := c_{n_1,n_2+1}$$

The matrix elements of the U-matrices for both $y_{1j} \neq y_{1j'}$ and $y_{2j} \neq y_{2j'}$ can be computed by[3]

$$\begin{aligned}[\mathbf{U}_l]_{jj'} = \widehat{S}_1 \sum_{\sigma_1=0,1} \frac{(-1)^{\sigma_1}(y_{1j}/y_{1j'})^{M_1}}{1 - y_{1j}/y_{1j'}} \\ \times \widehat{S}_2 \sum_{\sigma_2=0,1} \frac{(-1)^{\sigma_2}(y_{2j}/y_{2j'})^{M_2}}{1 - y_{2j}/y_{2j'}} \\ \times \sum_{n_1=\sigma_1 M_1}^{(\sigma_1+1)(M_1-1)} \sum_{n_2=\sigma_2 M_2}^{(\sigma_2+1)(M_2-1)} y_{1j}^{-n_1} y_{2j}^{-n_2} c^{(l)}_{n_1 n_2}\end{aligned}$$

where $\widehat{S}_1$ and $\widehat{S}_2$ define the symmetrization operators over the corresponding pairs of variables as, e.g.,

$$\widehat{S}_1 g(y_{1j}, y_{1j'}) = g(y_{1j}, y_{1j'}) + g(y_{1j'}, y_{1j})$$

For $y_{1j} = y_{1j'}$ and $y_{2j} \neq y_{2j'}$ we have

$$\begin{aligned}[\mathbf{U}_l]_{jj'} = \widehat{S}_2 \sum_{\sigma_2=0,1} \frac{(-1)^{\sigma_2}(y_{2j}/y_{2j'})^{M_2}}{1 - y_{2j}/y_{2j'}} \\ \times \sum_{n_1=0}^{2M_1-2} \sum_{n_2=\sigma_2 M_2}^{(\sigma_2+1)(M_2-1)} y_{1j}^{-n_1} y_{2j}^{-n_2} c^{(l)}_{n_1 n_2} \\ \times (M_1 - |M_1 - n_1 - 1|)\end{aligned}$$

which can trivially be rewritten for the symmetric case of $y_{1j} \neq y_{1j'}$ and $y_{2j} = y_{2j'}$. For the case of both $y_{1j} = y_{1j'}$ and $y_{2j} = y_{2j'}$, i.e., the diagonal elements of the U-matrices, we have

$$\begin{aligned}[\mathbf{U}_l]_{jj} = \sum_{n_1=0}^{2M_1-2} \sum_{n_2=0}^{2M_2-2} y_{1j}^{-n_1} y_{2j}^{-n_2} c^{(l)}_{n_1 n_2} \\ \times (M_1 - |M_1 - n_1 - 1|)(M_2 - |M_2 - n_2 - 1|)\end{aligned}$$

We will also need the $1 \times K_\mathrm{win}$ column vector:

$$[\tilde{\mathbf{C}}]_j = \sum_{n_1=0}^{M_1-1} \sum_{n_2=0}^{M_2-1} y_{1j}^{-n_1} y_{2j}^{-n_2} c_{n_1 n_2}$$

4.2 Regularization of the mD FDM: FDM2K

Armed with the above expressions, we can replace the eigenvalue problems for the effective evolution operators (23) by generalized eigenvalue problems with known matrices and unknown eigenvalues u_{lk} and eigenvectors $\mathbf{B}_{lk}$:

$$\tilde{\mathbf{U}}_l\tilde{\mathbf{B}}_{lk} = u_{lk}\tilde{\mathbf{U}}_0\tilde{\mathbf{B}}_{lk}, \quad (l = 1, \ldots, \mathrm{D}) \tag{25}$$

Unfortunately, unlike the 1D case, unless we are dealing with a noiseless well-defined mD HIP, a straightforward numerical solution of these equations gives meaningless results. A meaningful solution may be obtained by implementing a truncated SVD in which one defines the effective range space of $\mathbf{U}_0$, e.g., by keeping the largest P singular values, and then reevaluates the U-matrices in this subspace. However, this type of regularization, as in the RRT case, is usually quite sensitive to the choice of P and requires a lot of fiddling

around. We have discovered empirically[15] a much more robust regularization procedure, in which equation (25) is replaced by

$$\tilde{\mathbf{U}}_0^{\dagger}\tilde{\mathbf{U}}_l\tilde{\mathbf{B}}_{lk} = u_{lk}\left(\tilde{\mathbf{U}}_0^{\dagger}\tilde{\mathbf{U}}_0 + q^2\right)\tilde{\mathbf{B}}_{lk}$$

with regularization parameter q. The effect of the regularization is similar to that in RRT in that the results depend fairly smoothly on q, eliminating the need for extensive fiddling. Even though expression (20) to compute the coefficients holds, in principle, in the mD case, it is very tricky to use and is avoided here. A more correct approach is to use the eigenvalues u_{lk} and eigenvectors B_{lk} to construct the mD spectrum:[10,16]

$$I(s_1, \ldots, s_{\mathrm{D}}) = \sum_{k_1,\ldots,k_{\mathrm{D}}} d_{k_1,\ldots,k_{\mathrm{D}}} \prod_{l=1}^{\mathrm{D}} \left\{ \frac{z_l}{z_l - u_{lk_l}} - \frac{1}{2} \right\} \qquad (26)$$

with

$$d_{k_1,\ldots,k_{\mathrm{D}}} = \frac{\tilde{\mathbf{C}}^{\mathrm{T}}\tilde{\mathbf{B}}_{1k_1}\tilde{\mathbf{B}}_{1k_1}^{\mathrm{T}}}{\tilde{\mathbf{B}}_{1k_1}^{\mathrm{T}}\tilde{\mathbf{U}}_0\tilde{\mathbf{B}}_{1k_1}} \left(\prod_{l=2}^{\mathrm{D}} \frac{\tilde{\mathbf{U}}_0\tilde{\mathbf{B}}_{lk_l}\tilde{\mathbf{B}}_{lk_l}^{\mathrm{T}}}{\tilde{\mathbf{B}}_{lk_l}^{\mathrm{T}}\tilde{\mathbf{U}}_0\tilde{\mathbf{B}}_{lk_l}} \right) \mathbf{C}$$

Clearly, equation (26) has somewhat different structure from the form of equation (8) as each combination $(u_{1k_1}, \ldots, u_{\mathrm{D}k_{\mathrm{D}}})$ gives a peak with the amplitude $d_{k_1,\ldots,k_{\mathrm{D}}}$, i.e., many more than one would expect. This is the price for avoiding the use of a simultaneous eigenbasis in equation (23). Numerically, though, most cross-amplitudes $d_{k_1,\ldots,k_{\mathrm{D}}}$ will vanish. Expression (26) appears much more stable and easier to use numerically than equation (8) in the case of degenerate eigenvalues u_{lk} or low SNR.

By analogy with equation (9) an absorption-mode mD spectrum can be constructed, even from a single phase-modulated data set, by replacing the complex (phase-twist) Lorentzians by the absorption-mode lineshapes in equation (26):

$$A(s_1, \ldots, s_{\mathrm{D}}) = \mathrm{Re} \sum_{k_1,\ldots,k_{\mathrm{D}}} d_{k_1,\ldots,k_{\mathrm{D}}} \prod_{l=1}^{\mathrm{D}} \mathrm{Re}\ \left\{ \frac{z_l}{z_l - u_{lk_l}} - \frac{1}{2} \right\}$$

Of course the FT cannot construct an absorption-mode spectrum unless matched pairs of data sets are available (either N- and P- or sine and cosine) and in some cases this may save considerable instrument time, particularly with 3D or 4D spectra.

4.3 2D Spectral Estimation by RRT

As in the 1D case, the spectral estimation can be done directly by evaluating the resolvent matrix element in equation (24). For simplicity here we present only the 2D expression. Let $\tilde{\mathbf{R}}_l = \tilde{\mathbf{U}}_0 - \tilde{\mathbf{U}}_l/z_l$, $(l = 1, 2)$. The 2D RRT spectral estimate then becomes

$$I(s_1, s_2) \approx \tilde{\mathbf{X}}_1^{\mathrm{T}}\tilde{\mathbf{U}}_0\tilde{\mathbf{X}}_2 - \tilde{\mathbf{C}}^{\mathrm{T}}\frac{(\tilde{\mathbf{X}}_1 + \tilde{\mathbf{X}}_2)}{2} + \frac{c_{00}}{4} \qquad (27)$$

with the two frequency-dependent vectors $\tilde{\mathbf{X}}_l = \tilde{\mathbf{X}}_l(s_l)$, $(l = 1, 2)$, computed by solving the regularized Hermitian linear least squares problems,

$$\left(\tilde{\mathbf{R}}_l^{\dagger}\tilde{\mathbf{R}}_l + q^2\right)\tilde{\mathbf{X}}_l = \tilde{\mathbf{R}}_l^{\dagger}\tilde{\mathbf{C}} \qquad (28)$$

Note that the total number of the linear systems (28) to be solved for each 2D frequency window is equal to $N_{s_1} + N_{s_2}$, where N_{s_1} and N_{s_2} are the numbers of the frequency grid points, s_1 and s_2, to plot the spectrum in the window. In practice, RRT is very fast indeed.

When only the complex DFT spectrum (6) is of interest, RRT is, arguably, the most consistent approach. Once again, as in 1D case, using exact arithmetic for noiseless case when $N_{\mathrm{total}} \geq 4K$ (i.e., for the well defined mD HIP), the estimate (27) is essentially exact. In practice, however, there are several factors that affect the convergence; the regularization parameter q being an adjusting knob to choose between the high-resolution regime ($q \sim 0$), and noisy spectrum, and the low resolution regime (large q) with strong suppression of the artifacts.

Even though various spectral representations can be produced by RRT, unfortunately, it is difficult to compute a double-absorption spectrum by the 2D RRT using only a single purely phase modulated data set. Because a direct line list is not produced in RRT its scope is more limited. Thus FDM with its potential ability to generate a direct line list seems much more appealing.

5 PRACTICAL CONSIDERATIONS

The foregoing mathematical development, while of interest to those with training in alternative methods to the FT, will not be transparent to a typical experimentalist primarily interested in the question 'What's in it for me?'. In the following, a more pictorial and qualitative exposition will be used.

The first thing to keep in mind is that FDM is most useful when the data is likely to fit the model of discrete Lorentzian lines (7), and when the time-frequency uncertainty principle is limiting the FT resolution substantially. Very noisy data does not fit the model, as noise cannot be encapsulated by any parametric description with a limited number of parameters. Lines in solids are usually not purely Lorentzian, which may limit the application of FDM. Likewise, data that has been sampled essentially well into the noise, cannot magically be processed to extract small splittings well within the instrumental linewidth. When using FDM the key question is this: If the data could be fully sampled in all dimensions, would the spectrum look like a discrete number of Lorentzians? If it would, then the same result can be obtained by FDM with much shorter data records. But if it would not, then FDM may not be useful. The presence of t_1-noise, which is definitely non-Lorentzian, must also be kept in mind. Generally speaking, FDM is a method to use on high-quality spectra that have been recorded expertly, using the best available technology. It is not a method to clean up bad data sets.

FDM is particularly advantageous in so-called Constant Time (CT) experiments, in which a fixed time, denoted $2T$, is used for chemical shift encoding by changing the position of a 180° refocusing pulse. These experiments are often employed in the study of uniformly labeled proteins. The interferograms from CT-HSQC experiments show essentially no decay in the indirect dimension(s) and so are, by definition, transform limited. The full-width at half-maximum (FWHM) of the sinc-function, resulting from transformation of an unapodized CT signal, is $0.6034/T$. Apodization by a cosine function, $\cos(\pi t/2T)$, reduces sidelobe amplitude to less than 5% of

the main peak, but increases the FWHM to $0.8197/T$. Thus the transform-limited resolution is about 63 Hz, or 0.5 ppm at 125 MHz ^{13}C frequency, for a typical CT experiment with $2T = 26$ ms. For a hypothetical CT experiment with $2T = 4.7$ ms, lines no narrower than 348 Hz can be expected. To do better than this, some alternative to the FT must be used. Note that simply increasing $2T$ is not usually possible, as catastrophic loss of signal by transverse relaxation can ensue, especially for the important C_α resonances.

It might be tempting to assume that FDM, as it fits the lines including their widths, could give essentially infinite resolution in a CT-HSQC experiment: after all, the lines should have nearly zero width in F_1. Very narrow lines can indeed be obtained, *but only if there are not too many of them, too closely spaced*. In other words, FDM cannot give infinite resolution, but only resolution commensurate with the local density of basis functions. This resolution is, as described above, dependent roughly on the *product* of acquisition times, so that some information in the acquisition dimension can be used to improve that in the shorter dimension, provided the signal does not decay too quickly.

The situation is shown in Figure 1, with closed shapes showing hypothetical peak positions, and crosses showing the position of 2D Fourier basis functions. The top panels represent the initial matrix construction, and the lower panels are the FDM output. On the left panels, the local density of functions is four, but there are seven peaks present. Diagonalization does not change the size of the basis, so only four peaks can be used to fit seven. The result is shown in the lower panel, with three broad (and unstable) features masquerading as three sets of two lines, and one converged feature. In the right panel, the basis density is increased to eight by taking twice as many points in the vertical dimension. Now the vertical pair in the top right quadrant is resolved completely, as is the pair in the lower right quadrant, in which the F_1 frequencies are close, but not identical. However, the pair in the lower left quadrant is not resolved. The F_1 frequencies are nearly identical, so that increasing the sampling along F_1 does not help much: even though there are two basis functions in the vicinity, the two lines cannot be resolved. This kind of local convergence, in which more crowded spectral regions are the last to 'settle down', is completely different than the slow but uniform convergence familiar from FT analysis. This behavior can be rationalized within a linear algebraic context. If two lines have equal frequencies (and linewidths), e.g., along F_1 (or if both of these are very close in practical terms), then $\widehat{U}_1$ will have two degenerate eigenvalues. In order to resolve these two peaks in the F_2 dimension, one needs a basis of at least two linearly-independent vectors containing the corresponding two-dimensional eigensubspace of $\widehat{U}_1$. However, those cannot be constructed using, for example, Krylov vectors $\Phi_{n_1,n_2} = \widehat{U}_1^{n_1}\widehat{U}_2^{n_2}\Phi$ with some fixed values of n_2 and any number of different n_1 values. One needs at least two vectors Φ_{n_1,n_2} with different n_2. In practice, these considerations must be applied locally in the frequency domain, i.e., using the Fourier basis (the crosses), rather than Krylov basis, and have less obvious consequences because of several other factors. For instance, what happens to the 'unused' basis functions? They end up fitting residual noise or non-Lorentzian components in the skirts of the peaks. How far can an initial basis function 'move'? That depends on the SNR. The higher it is, the more freedom the crosses acquire to 'lock on' to a signal peak. It is thus important to emphasize that the ideal kind of spectrum for FDM analysis is one in which the features are a fixed number of randomly distributed sharp Lorentizians that are well above the noise floor. This kind of signal can always be dominated by the available basis functions as more data is acquired. High noise levels effectively rob the algorithm of basis functions by pinning down many of them to fit noise locally. Spectra like COSY, in which many lines are absolutely degenerate, and there are locally dense regions within cross peak multiplets, cannot benefit much, if at all, from FDM. That is, it will still require many increments to resolve a COSY spectrum properly and, as new weak cross peaks continuously emerge when the evolution time is incremented, convergence may never be achieved at all.

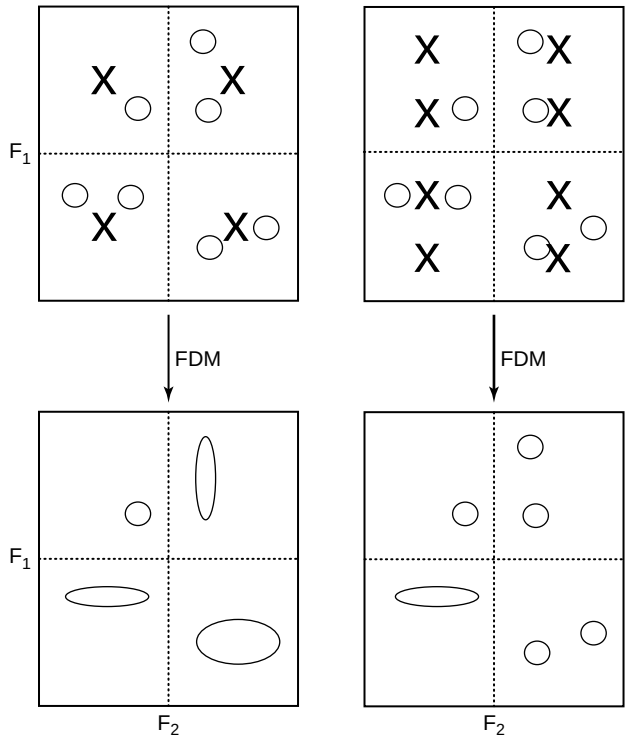

Figure 1 A schematic representation of how FDM treats a local spectral region. At the top, peaks are represented with circles and Fourier basis functions with crosses. At the bottom is the expected result after diagonalization. The left-hand panels show a situation in which four basis functions are available to try to fit the seven genuine peaks. A 'best effort' fit leaves only one line converged, with the other three pairs fit as broader singlets. In the right-hand panels, eight basis functions are available because twice as much data has been sampled in the vertical dimension. Five of the seven peaks can be resolved, but the pair in the lower left-hand quadrant cannot, because they are degenerate in the vertical dimension. (Doubling the sampling in the horizontal dimension would, of course, resolve the two peaks)

6 SELECTED APPLICATIONS

6.1 2D Constant-Time HSQC Spectra

With these cautions in mind, the results for protein NMR can be startlingly good. The three figures (Figures 2–4), show

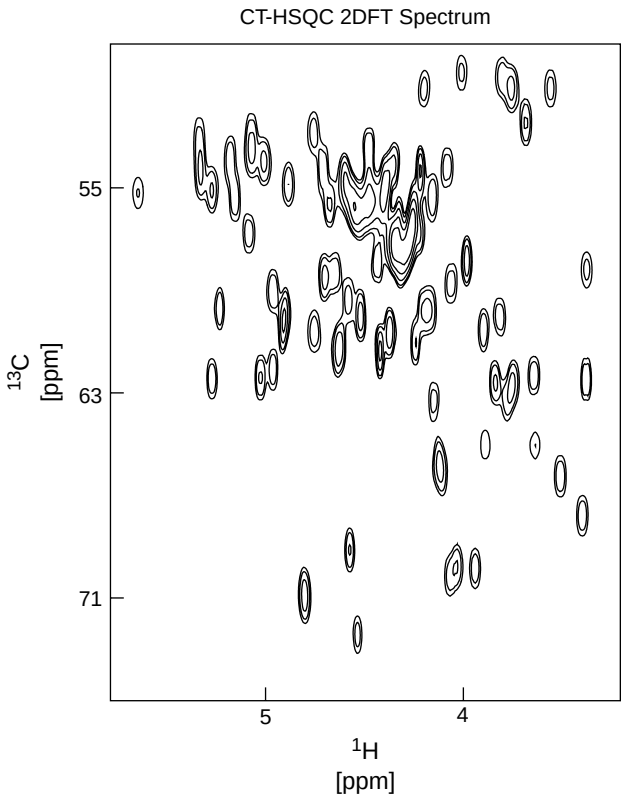

Figure 2 A small portion of the CT-HSQC spectrum of human ubiquitin (1 mM solution, 500 MHz proton frequency) obtained with a very short CT period of 4.7 ms and processed by 2DFT. The C_α–H_α region is displayed. The broadening in the vertical dimension is primarily due to the time-frequency uncertainty principle, so that, while sensitivity is quite good, resolution is sufficient to make only a small fraction of the assignments

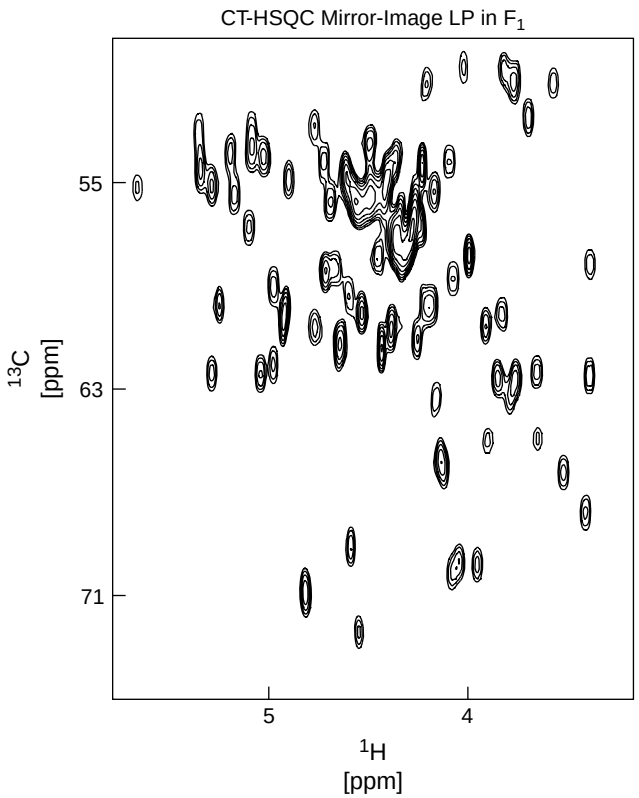

Figure 3 The same data set as in the two previous figures, using mirror-image Linear Prediction in the vertical dimension to first extend the data length by a factor of two, followed by FT processing. Resolution is better than the 2DFT, but not as good as 2D FDM, as can be clearly seen by examining the clusters of peaks in the lower part of the figures

the C_α–H_α region of a CT-HSQC spectrum of uniformly labeled human ubiquitin (1 mM, 5 mm tube, 500 MHz) using a very short 4.7 ms CT. The FT spectrum shows the expected broad peaks in F_1, in accordance with the time-frequency uncertainty principle. Using Mirror-Image Linear Prediction in F_1[18] and FT in F_2 improves matters somewhat, but the spectrum is a distant second to the FDM2K result, in which nearly every resonance is fully resolved except for the predictable non-convergence of the most congested region. The peaks are genuine, as can be verified by acquiring a much longer CT data set.[18]

6.2 45° Projections of 2D *J* Spectra

The unique ability to create a pseudo-absorption spectrum from a single phase-twist FT spectrum is quite useful when there *is* only a single data set, as in 2D *J*-spectroscopy.[5,9,10] In this case, the improved resolution can be used to construct a proton-decoupled proton spectrum by computing the phase-sensitive 45° projection. This projection vanishes in the FT spectrum because of the phase-twist line shape. Furthermore, this decoupling can be applied to other mD spectra, to condense proton multiplets into sharp singlets, thereby improving the resolution substantially. This combination of spectroscopic simplification with alternative methods of analysis is opening up new possibilities for future research. An example of a 1D 45° projection of a 2D *J* data set, with only a few increments in the *J* dimension, is shown in Figure 5. The results are quite encouraging, although more work needs to be done to make the method a turn-key experiment. Proper regularization of these projections is an area of current research.

7 REMAINING PROBLEMS

Both 1D FDM and RRT (its offspring) are essentially developed and well tested techniques that are generally as reliable as the FFT, sufficiently fast, and can often deliver resolution beyond the FT uncertainty relation if the data can be well represented by Lorentzians and is not very noisy.

FDM provides one with an effective evolution operator $\widehat{U}$ with eigenvalues and eigenvectors directly related to the spectral parameters. However, the difficulties associated with the construction of a meaningful line list for data of poor quality (i.e., not characterized by equation (3)) exist. These difficulties are not associated with the lack of a reliable algorithm for selecting the 'genuine' poles and throwing away the 'noise' poles from the full list of complex eigenvalues of $\widehat{U}$, but are rather conceptual, and caused by the intrinsic ambiguity of the line list for a general data set that, a priori, does not fit any particular parametric form.

The mD case is considerably more difficult. For example, the multidimensional spectrum cannot generally be constructed

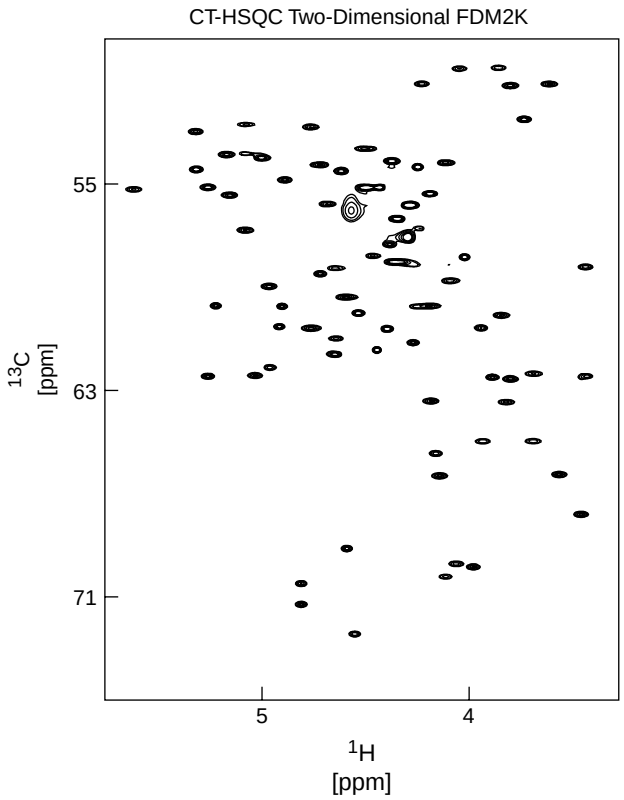

Figure 4 The same data set as in the previous figure, but processed by FDM2K. No FT was used to construct the spectrum: it came directly from the FDM2K line list. To improve the appearance of the spectrum (cosmetically) Gaussian line shapes have been substituted for the Lorentzian lines that are the natural form of the FDM spectrum. Resolution is dramatically enhanced. The spectrum is completely converged except for the most crowded region, which shows the kind of non-convergence described when more local features are present than the number of local Fourier basis functions available to FDM

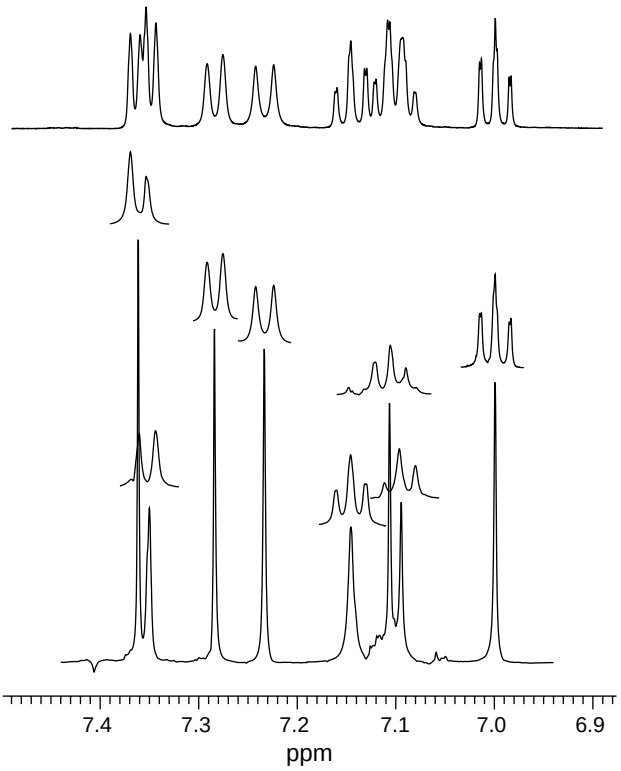

Figure 5 An example of direct calculation of a 1D 45° projection (the lowest trace) and multiplet cross sections by FDM. The upper trace corresponds to a conventional ^{1}H spectrum. The spectra were obtained using a purely phase modulated 2D-J signal of dityptophan tripeptide[9] with just $N_1 = 4$ points along the J-dimension. $N_{\mathrm{FDM}} = 20$ calculations, with different number of points along the running time dimension in the range $N_2 = 11\,000-12\,000$, were added together to obtain artifact free spectra. Only a small part of the spectrum is shown, while the two spectral widths were $SW_1 = 80$ Hz and $SW_2 = 8$ kHz

from the multidimensional line list, as the latter can be very hard to obtain. Fortunately, various spectra can be obtained by avoiding the line list construction and using the resolvent expressions. The resolvent operator formalism appears to be very convenient as it allows one to construct various types of spectra, including absorption-mode spectra (non-trivial spectral projections discussed above). The main computational problem associated with the implementation of the resolvent formulas is that one typically deals with very ill-conditioned matrices, causing the spectrum to be very unstable with respect to both the FDM parameters, and small variations of the input data. Thus, unlike the 1D case, there are major problems to be solved in the multidimensional versions of both FDM and RRT. For instance, for a typical 2D NMR data set, even with relatively high SNR, one has difficulties in constructing two adequate commuting effective evolution operators $\widehat{U}_1$ and $\widehat{U}_2$ describing the 2D signal. This, in turn, makes it difficult to construct an adequate 2D line list corresponding to equation (7). We believe that this problem is, as in the 1D case, a consequence of the ill-defined nature of equation (7), although the additional requirement that the operators $\widehat{U}_l$ commute with each other makes the problem much worse than in 1D. Clearly, the key issue in mD FDM is to find a general computationally inexpensive and robust procedure that could be applied to regularize the FDM equations. At the present stage the problem is only partially solved. For example, the regularization procedure in RRT is very efficient, but, unfortunately, it can be used only as a spectral estimator and cannot easily overcome some of the DFT limitations. Regularization of RRT is not directly extendable to FDM, although several methods have already been developed, such as truncated SVD of $\mathbf{U}_0$ or FDM averaging.[10,12,16] Unfortunately, the former is not generic, while the latter is computationally very expensive and cannot be used to construct a multidimensional line list. Currently, the most promising regularization technique seems to be that associated with FDM2K.[15] Its implementation is computationally very simple and inexpensive, although, at this stage, it is not clear how general and reliable it is for various types of NMR data.

To conclude, the main avenues for the future research seem to be the following.

(i) Given the matrix representations of the evolution operators, $\widehat{U}_1$, $\widehat{U}_2$, etc., in a non-orthonormal basis, which are possibly very ill-conditioned, find a fast and reliable method of evaluating various resolvents associated with these operators.

(ii) Given the matrix representations of the evolution operators, construct a set of commuting effective Hamiltonians $\widehat{\Omega}_1$, $\widehat{\Omega}_2$, etc., with eigenvalues and eigenvectors yielding the line list.

Both goals are associated with finding reliable and computationally inexpensive regularization techniques.

8 REFERENCES

1. M. R. Wall and D. Neuhauser, *J. Chem. Phys.*, 1995, **102**, 8011.
2. V. A. Mandelshtam and H. S. Taylor, *J. Chem. Phys.*, 1997, **107**, 6756.
3. V. A. Mandelshtam and H. S. Taylor, *J. Chem. Phys.*, 1998, **108**, 9970.
4. J. W. Pang, T. Dieckmann, J. Feigon, and D. Neuhauser, *J. Chem. Phys.*, 1998, **108**, 8360.
5. V. A. Mandelshtam, H. S. Taylor, and A. J. Shaka, *J. Magn. Reson.*, 1998, **133**, 304.
6. V. A. Mandelshtam, H. Hu, and A. J. Shaka, *Magn. Res. Chem.*, 1998, **36**, S17.
7. H. Hu, Q. N. Van, V. A. Mandelshtam, and A. J. Shaka, *J. Magn. Reson.*, 1998, **134**, 76.
8. M. R. Wall, T. Dieckmann, J. Feigon, and D. Neuhauser, *Chem. Phys. Lett.*, 1998, **291**, 465.
9. V. A. Mandelshtam, Q. N. Van, and A. J. Shaka, *J. Am. Chem. Soc.*, 1998, **120**, 12 161.
10. V. A. Mandelshtam, N. D. Taylor, H. Hu, M. Smith, and A. J. Shaka, *Chem. Phys. Lett.*, 1999, **305**, 209.
11. J. Chen and V. A. Mandelshtam, *J. Chem. Phys.*, 2000, **112**, 4429.
12. V. A. Mandelshtam, *J. Magn. Reson.*, 2000, **144**, 343–356.
13. A. A. De Angelis, H. Hu, V. A. Mandelshtam, and A. J. Shaka, *J. Magn. Reson.*, 2000, **144**, 357.
14. J. Chen, A. J. Shaka, and V. A. Mandelshtam, *J. Magn. Reson.*, 2000, **147**, 129.
15. J. Chen, V. A. Mandelshtam, and A. J. Shaka, *J. Magn. Reson.*, 2000, **146**, 363.
16. V. A. Mandelshtam, *Prog. NMR Spectosc.*, 2001, **38**, 159.
17. G. S. Armstrong and V. A. Mandelshtam, *J. Magn. Reson.*, submitted.
18. A. A. De Angelis, J. Chen, V. A. Mandelshtam, and A. J. Shaka, *J. Biomol. NMR*, submitted.
19. Y. Hua and T. K. Sarkar, *IEEE Trans. ASSP*, 1990, **38**(5), 814.
20. A. Tikhonov, *Soviet Math. Dokl.*, 1963, **4**, 1035–1038; A. Tikhonov and V. Arsenin, 'Solutions of ill-posed problems', Winston and Sons, Washington, 1977.

Acknowledgements

VAM acknowledges NSF CHE-9807229 and AJS, NSF CHE-9900422, for support. We are indebted to Ms. Anna De Angelis and Mr. Jianhan Chen for help in producing the FDM2K CT-HSQC spectra.

Biographical Sketches

A. J. Shaka, *b* 1958. B. S. Harvey Mudd College, 1980; Ph.D., Oxford University, 1984, with Ray Freeman. Junior Research Fellow, St. John's College, Oxford, 1984–1986. Post-doc, UC Berkeley, with Alex Pines, 1986–1988. Currently Professor of Chemistry, UC Irvine. Approx. 75 publications. Current research specialty: NMR techniques in liquids.

V. A. Mandelshtam, *b* 1964. M.S., Moscow Institute of Steel and Alloys, 1987; Ph.D., Institute of Spectroscopy, Academy of Sciences of the USSR, 1991. Post-doc, University of Southern California, 1991–1996. Research Assistant Professor, University of Southern California, 1996–1997. Assistant Project Scientist, UC San Diego, and Assistant Researcher, UC Irvine, 1997–1998. Currently Assistant Professor of Chemistry, UC Irvine. Approx. 65 publications. First involved with NMR in 1997. Research interests: Theoretical and Computational Chemistry.

INADEQUATE Experiment

Joachim Buddrus

Institut für Spektrochemie, Dortmund, Germany

1	Introduction	1
2	Conventional ^{13}C NMR Spectroscopy	1
3	One-Dimensional INADEQUATE ^{13}C NMR Spectroscopy	2
4	Two-Dimensional INADEQUATE ^{13}C NMR Spectroscopy	3
5	Sensitivity of the INADEQUATE	5
6	Applications: Organic and Inorganic Compounds	6
7	Outlook	8
8	Related Articles	9
9	References	9

1 INTRODUCTION

The INADEQUATE (Incredible Natural Abundance DoublE QUAntum Transfer Experiment) consists of a special pulse sequence which eliminates the NMR signals from isolated spins (spin system A) displaying signals from coupled spins (spin system AX or higher spin systems). It is of great importance when applied to molecules with skeleton elements such as carbon, silicon or tungsten, all of which contain a small percentage of spin-$\frac{1}{2}$ isotopes embedded in magnetically inactive isotopes. The large signals from the spin type A are eliminated, while the tiny signals from the rarely occurring spin types AX are well displayed. Analysis of the AX type spectra gives not only the coupling J_{AX} but also the connectivity pattern of the skeleton atoms in molecules of unknown structure. Most important is the structural determination of carbon compounds including those that cannot be analyzed by X-ray, either because the compound does not crystallize or because the crystals obtained exhibit unfavorable properties. Representative examples for the determination of connectivites by INADEQUATE are the carbon compound (**1**) and the silicon compound (**2**).

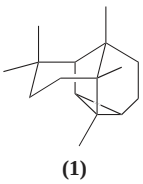

(1)

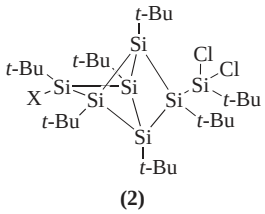

(2)

In principle, the determination of the connectivity pattern via AX coupling can also be performed by conventional NMR spectroscopy; this will be demonstrated in Section 2. However, a severe drawback is the large A type signals; therefore, one- and especially two-dimensional INADEQUATE spectra are preferred (Sections 3 and 4). Due to the low abundance of neighbored AX spins efforts to improve the sensitivity of INADEQUATEs have received much interest (section 5). Section 6 describes the application to various elements. As carbon compounds are the main objective of the INADEQUATE experiment, the principles of tracing atomic connectivities by conventional NMR or INADEQUATEs will be explained with the aid of the element carbon (for a review see Buddrus and Bauer[1]).

2 CONVENTIONAL ^{13}C NMR SPECTROSCOPY

The element carbon contains 98.9% of the isotope ^{12}C (spin quantum number $I = 0$) and 1.1% of the isotope ^{13}C ($I = \frac{1}{2}$). Almost all carbon compounds thus consist of a number of isotopomers. Thus for example even the simple three-carbon molecule 1-iodopropane exists as a mixture of the following eight isotopomers (when hydrogen is considered to be isotopically pure):

$H_3C-CH_2-CH_2-I$		
96.73%		
$H_3{}^{13}C-CH_2-CH_2-I$	$H_3C-{}^{13}CH_2-CH_2-I$	$H_3C-CH_2-{}^{13}CH_2-I$
1.08%	1.08%	1.08%
$H_3{}^{13}C-{}^{13}CH_2-CH_2-I$	$H_3{}^{13}C-CH_2-{}^{13}CH_2-I$	$H_3C-{}^{13}CH_2-{}^{13}CH_2-I$
0.01%	0.01%	0.01%
$H_3{}^{13}C-{}^{13}CH_2-{}^{13}CH_2-I$		
0.0001%		

The proportion of an isotopomer with a ^{13}C atom in a certain position is $0.011^1 \times 0.989^{n-1}$ (n is the number of carbon atoms in the molecule), that of an isotopomer with two ^{13}C atoms in defined positions (whether these are directly neighboring or not) is $0.011^2 \times 0.989^{n-2}$, and so on. This means that only one single molecule in 10 000 has two neighboring ^{13}C atoms in a certain position.

Broadband decoupling of the attached protons converts isotopomers with only a single ^{13}C nucleus to spin systems of type A, so that singlet signals are observed (this is the conventional ^{13}C NMR spectrum). Isotopomers with two ^{13}C nuclei behave just like those with only a single ^{13}C nucleus if the ^{13}C nuclei are separated by several bonds. If however the ^{13}C nuclei are separated by only a few bonds (generally one to three) they couple and, thus, unless they are isochronous, they form AB or AX spin systems whose spectra consist of two doublets. ^1J(C,C′), the coupling constant over one bond, depends on the hybridization of the carbon orbitals and on the substituent X in the fragment ^{13}C–^{13}C–X and varies between about 35 and 75 Hz. Coupling constants over two or three bonds are much smaller, typically between 0 and 5 Hz.

In ^{13}C NMR spectra with a sufficient signal-to-noise ratio (>500:1) the weak signals of the coupled nuclei can be seen on both sides of the strong singlet signals of the isolated ^{13}C nuclei (see Figure 1). The intensity ratio of the singlet to one of the four signals of the coupled nuclei is about 200:1. If the various coupling constants have different values, a comparison of the coupling constants of all ^{13}C nuclei in a molecule shows which atom is bonded to which, yielding the exact structure of the carbon skeleton. Thus the C-2 signal of (**3**) (Figure 2) is accompanied by two pairs of satellite signals, the splitting of which proves the structure of this part of the molecule.

The extraction of all ^1J values from a conventional ^{13}C spectrum is difficult, because spinning sidebands or signals due to impurities can be incorrectly identified as satellite signals

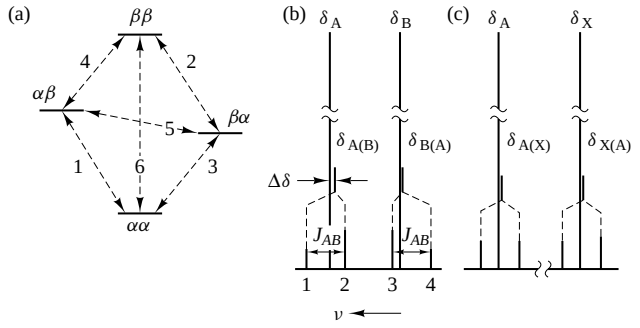

Figure 1 Term scheme and NMR spectrum of a $^{13}C-^{13}C$ fragment. (a) Term scheme: 1, 2, 3, and 4 are allowed single quantum transitions, and 5 and 6 forbidden zero- and double-quantum transitions respectively. (b) and (c) NMR spectra of an AB and an AX spin system. The chemical shifts of the coupled ^{13}C nuclei are shifted to lower frequency by between 0 and 0.03 ppm (isotope effect on the chemical shift). (Reproduced by permission, from Buddrus and Bauer[1])

or satellite signals can be hidden (by other satellite signals or by signals due to isolated ^{13}C nuclei).

Many of these difficulties can be avoided when instead of the conventional recording technique the pulse sequence INADEQUATE is used; this sequence was first suggested by Bax et al.[2] The basis for this particular pulse sequence is the method of multiquantum NMR spectroscopy developed by Aue and Wokaun et al.[3,4] (for reviews see Bodenhausen and Braunschweiler et al.[5,6]).

The influence of high frequency pulses on coupled spin systems is described by the density matrix formalism, or in a less cumbersome way by the product operator formalism (see Sørensen et al.[7]). For application of the density matrix formalism to the INADEQUATE experiment see the review by Buddrus and Bauer[1] and Bax.[8] Where necessary, the results of this treatment will be presented here either in a descriptive way or as drawings of vector models.

3 ONE-DIMENSIONAL INADEQUATE ^{13}C NMR SPECTROSCOPY

The INADEQUATE method consists of a pulse sequence which in the simplest version is executed twice (the 'two-step cycle'), whereby the phase of the last 90° pulse and of the detector data acquisition system differ in the two steps. Two FIDs are thus obtained, and the coaddition of these leads to the elimination of the strong signals due to the isolated ^{13}C nuclei.

Step 1: $90°_x - \tau - 180°_y - \tau - 90°_x - \Delta - 90°_x -$ data acquisition (x)

Step 2: $90°_x - \tau - 180°_y - \tau - 90°_x - \Delta - 90°_y -$ data acquisition ($-y$)

The effect on a C_2 fragment is shown in Figure 3. The first part of the INADEQUATE pulse sequence ($90°_x - \tau - 180°_y - \tau$) is identical to a homonuclear spin echo experiment. It produces transverse magnetization from the isolated spins A in the y direction and from the coupled AX spins in $\pm x$ direction

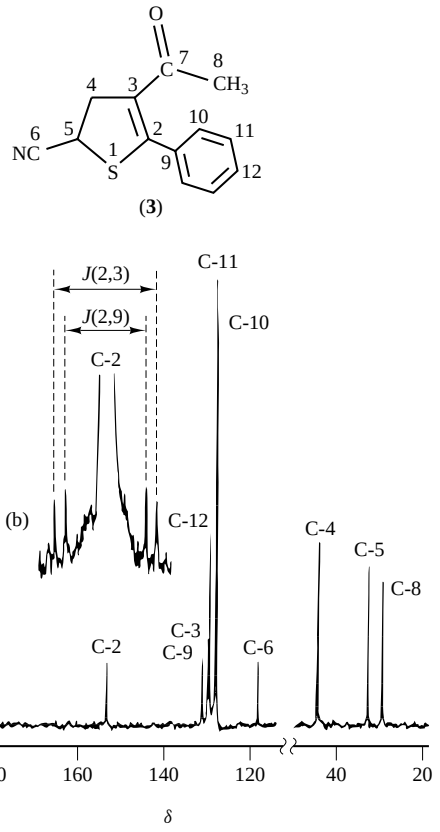

Figure 2 25 MHz $^{13}C\{^1H\}$ NMR spectrum of (**3**) (0.5 g) + $Cr(acac)_3$ (acac = acetylacetonate) (about 10 mg) (for T_1 relaxation enhancement) in $CDCl_3$ (1.5 mL). Digital resolution: 0.5 Hz per data point. (a) Single transient. (b) 60 000 transients, repetition interval 4 s (partial spectrum). $J(2,3)$ = 72.9 Hz, $J(2,9)$ = 57.7 Hz. (Reproduced from Buddrus and Bauer[1])

(antiphase magnetization). The subsequent $90°_x$ pulse shifts the magnetization of the isolated spins to the $-z$ direction, while the antiphase magnetization from the AX spins is transferred into the so-called double quantum coherence, directed along the y axis of the rotating double quantum coordinate system. The double quantum coherence does not represent observable magnetization. The last 90° pulse (the 'read pulse') comes from the x direction (first step) or from the y direction (second step); it shifts the magnetizations from the isolated spins into the $-y$ and x direction respectively, and the double quantum coherence is converted to single quantum coherence directed along the x' or y' axis respectively. The phase of the detector is then switched in such a way that it follows only magnetizations of the AX spin system. Addition of the two FIDs leads to the addition of magnetization of the AX spins, *but elimination of the large magnetization from the isolated spins.* Finally, Fourier transformation affords the frequency spectrum, which only contains the two doublets (in antiphase to each case) of the AX spin system.

A one-dimensional INADEQUATE ^{13}C NMR spectrum consists in theory only of signals from coupled nuclei: the unwanted signals due to isolated ^{13}C nuclei (whether from the main component or from impurities) as well as the spinning sidebands from these signals are not present. The power of the one-dimensional INADEQUATE method is demonstrated in Figure 4. Due to the presence of five oxygen atoms distributed

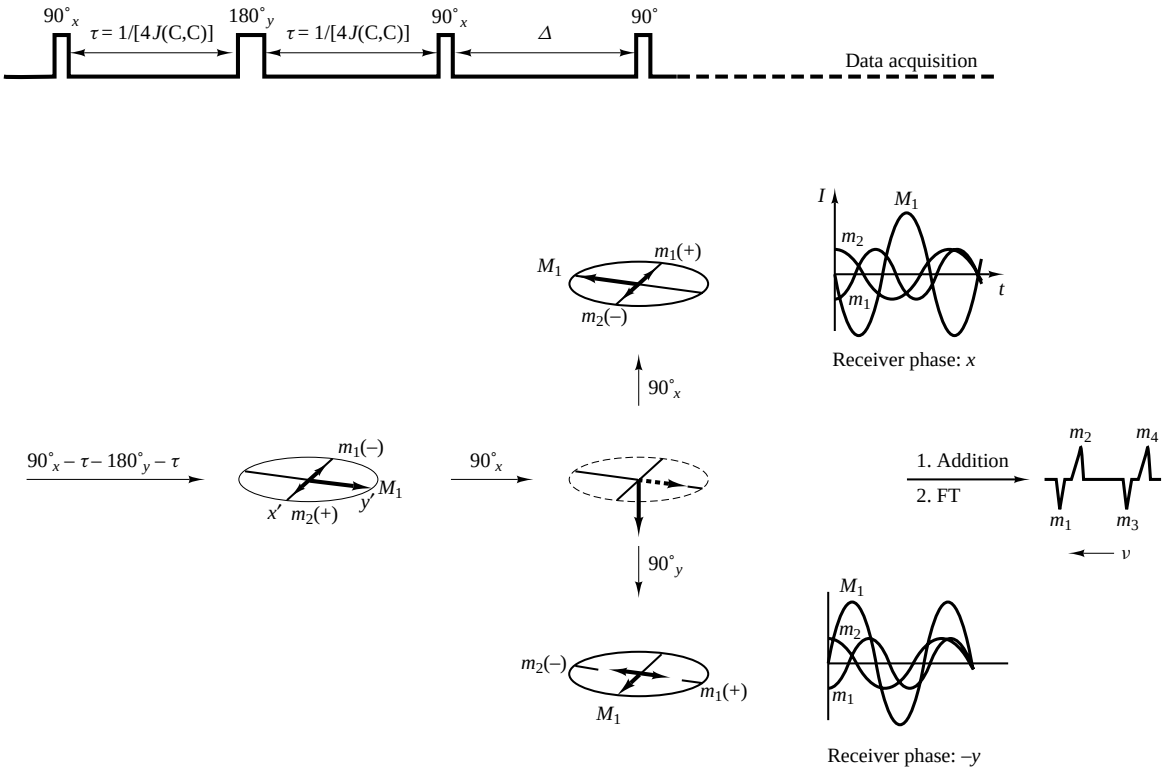

Figure 3 The INADEQUATE pulse sequence and its effect on a C_2 fragment. M_1, M_2 and m_1 to m_4 are the magnetizations of the isotopomeric fragments $^{13}C–^{12}C$, $^{12}C–^{13}C$ and $^{13}C–^{13}C$. The delay time τ and the switching time Δ (about 10 μs) are not shown to scale. M_1, $m_1(+)$, $m_2(-)$: the Larmor frequency of m_1 is larger and that of m_2 smaller than that of M_1 (this is the situation after the first 90° pulse). For clarity the fates of M_2, m_3 and m_4 have been considered only after FT. (Reproduced from Buddrus and Bauer[1])

over compound (**4**) the couplings ^1J(C,C) differ sufficiently so that all connectivities can be unequivocally traced (e.g. between C-1 and C-6a) establishing the proposed structure and excluding alternative structures.

As can be seen from Figure 4, the intensities of the satellite signals differ from one AX spin system to another; for instance, the intensity ratio at the C-4 signal is about 1:0.5:0.5. This results from different ^1J(C,C) values. If the actual coupling constant (J_a) differs from the value J used in $\tau = 1/[4 \times {}^1J(C,C)]$, the intensity I will be decreased in the AX case according to equation (1), since the magnetization is no longer directed exactly along the $\pm x$ axis (Figure 3).

$$I = I_{max} \sin(2\pi J_a \tau) \quad (1)$$

However, the results of this deviation from ideality are not serious: 50% or more of the maximum intensity I_{max} is still observed when $\frac{1}{3}J \leq J_a \leq \frac{5}{3}J$.

4 TWO-DIMENSIONAL INADEQUATE ^{13}C NMR SPECTROSCOPY

If the ^{13}C, ^{13}C coupling constants differ only slightly from one another then an overlap of satellite signals (for AX spectra) or ambiguities in recognizing the coupling partner may occur. Difficulties of this type can be avoided when the INADEQUATE sequence is made two-dimensional. The pulse sequence for the two-dimensional experiment is almost exactly the same as that in one dimension: the change is that the short switching time Δ in Figure 3 is replaced by the time t_1, which is incremented stepwise. When $t_1 = 0$, the nonobservable double quantum coherence is directed along the y' axis of the double quantum coordinate system [Figure 5(a)]. It then rotates at the double quantum frequency ν_{DQ} in the x,y plane of this coordinate system; after the evolution times $t_1 = n/(4\nu_{DQ})$, (n = 1–4), it is directed as shown in Figure 5. Conversion to single quantum coherence by means of the 90° read pulse, followed by Fourier transformation, gives the satellite signals, the intensity of which is now modulated by ν_{DQ}.

$$\nu_{DQ} = \nu_A + \nu_X - 2\nu_0 \quad (2)$$

ν_A, ν_X: resonance frequency of the nuclei A or X; ν_0: exciting frequency.

A second Fourier transformation, in this case applied to the intensity variation of the satellite signals, gives the double quantum frequency ν_{DQ} of the AX spin system. Since this frequency is equal for all four signals of an AX spin system, the satellite signals appear in the same row (f_1 = constant) of the two-dimensional spectrum, though with differing phase. The situation is analogous for each further AX spin system. The advantage over a one-dimensional spectrum is that no overlap can occur, even when ^1J(C,C) values are equal, since the double doublets of each of the different AX spin systems occur in different rows.

Figure 6 shows the two-dimensional INADEQUATE spectrum of the initially unknown compound (**5**). In order to

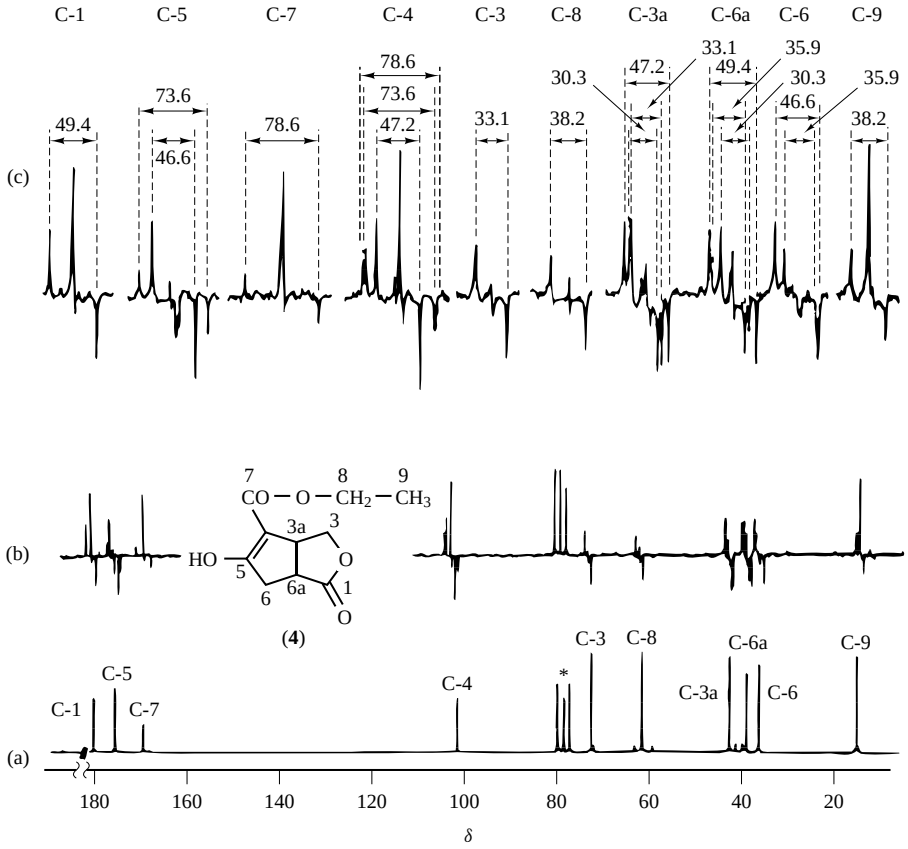

Figure 4 25 MHz $^{13}C\{^1H\}$ NMR spectrum of (**4**) (1.2 g) + $Cr(acac)_3$ (20 mg) in $CDCl_3$ (1.0 mL). (a) Conventional spectrum: 1000 transients. (b) One-dimensional INADEQUATE spectrum; $\tau = 1/(4J)$ (J = 50 Hz); 122 000 transients; repetition interval 4 s (total measuring time 135 h); digital resolution 0.5 Hz per data point. (c) Expanded INADEQUATE spectrum. *Solvent signal. (Reproduced from Buddrus and Bauer[1])

identify the carbon skeleton, the signals are numbered from left to right, the corresponding numbers are joined up as in (**5a**), and finally the numbers are replaced by the corresponding CH_n fragments, which have previously been obtained from a DEPT experiment. The result is (**5b**); after the keto group (δ = 229.5 ppm) has been added, the final structure (**5c**) [(**5**) in Figure 6] is obtained.

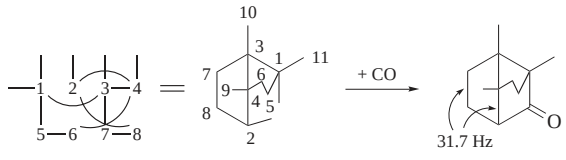

(5a) **(5b)** **(5c)**

If all the contours in a two-dimensional (2D) INADEQUATE spectrum are visible, its interpretation requires little time and can be carried out without any particular spectroscopic or chemical experience.

4.1 Phase Cycling

In practice, the two-step cycle described above affords only an incomplete elimination of the signals of isolated ^{13}C nuclei. The reasons for this are firstly the nonideal spectrometer conditions such as pulse angle errors and phase errors, and secondly differences between the two recording channels (receiver systems), each of which has its own analog–digital converter and amplifier. However, the residual signals can be reduced further by using extended phase cycles. The double quantum coherence produced by the pulse sequence $90°_x - \tau - 180°_y - \tau - 90°_x$ can be read by a $90°_{-x}$ or $90°_{-y}$ pulse as well as by a $90°_x$ or $90°_y$ pulse. This 4-step cycle[2] compensates for the inequality of the recording channels. Additional cycling through the phases of the other pulses results in a 2^n step cycle (n = 2, 3 . . . .8) ending up with 256 steps (for details see the review by Buddrus and Bauer[1]).

4.2 Quadrature Detection

As shown by Figure 5 the 90° read pulse in the two-dimensional version results in an amplitude modulation: the Fourier transformation of the FIDs gives not only the required signals (echoes) with double quantum frequency ν_{DQ}, but also the unrequired reflected signals (antiechoes) whose frequency is ν_{-DQ} [marked in Figure 5(e) by crosses]. The unrequired signals can be eliminated by quadrature detection, which is achieved by executing two measurements at each setting of t_1. The crucial step is to induce a 90° phase shift of the double quantum coherence. This can be achieved either by altering the phase of the first three pulses of the sequence by 45° or by rotating the double quantum coherence itself by a so-called

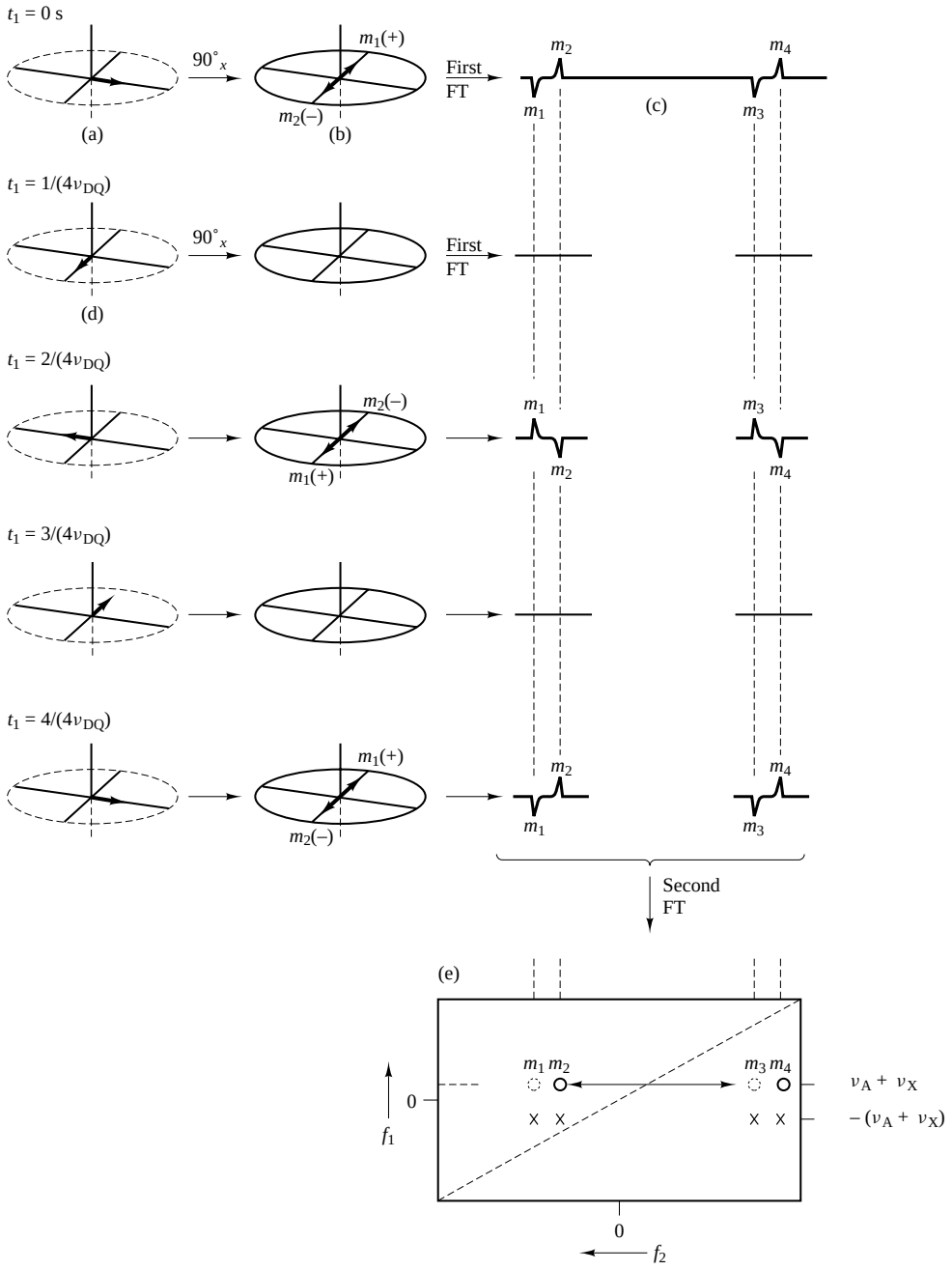

Figure 5 Influence of the evolution time t_1 (which replaces Δ in Figure 3) on the magnetization of a C_2 fragment. For clarity only the effect of the read pulse $90°_x$ (step 1 in Section 3) on the magnetizations m_1 to m_4 is shown and the notations m_3 and m_4 are omitted. One should note the general agreement between (a), (b) and (c) and Figure 3. (e) The contours (full and broken circles: above and below the plane of the paper respectively) of the four signals m_1 to m_4 of an AX spin system. The midpoints of those contours which belong together lie on the frequency diagonal $f_1 = 2f_2$ (f_1, f_2: double and single quantum frequencies respectively). The positions marked by crosses are those of the antiechoes observed in experiments without quadrature detection in f_1. (Reproduced from Buddrus and Bauer[1])

$45°_z$ pulse, which is in practice replaced by the combination $90°_{-x} - 45°_{-y} - 90°_x$.

$$90°_x - \tau - 180° - \tau - 90°_x - 45°_z - t_1 - 90°_x - \text{acquisition}$$

For further discussion and experimental details see Bax et al.[9] and Lambert et al.[10] The spectrum in Figure 6 has been obtained after quadrature detection in both dimensions.

5 SENSITIVITY OF THE INADEQUATE

The poor sensitivity of the INADEQUATE method has already been mentioned. In the case of carbon compounds 1–2 days are needed (with 0.5–1 mmol of the substance and a 9.4 T spectrometer) to get a spectrum with a sufficient signal-to-noise ratio (S//N). An increase in the sensitivity can be achieved by transfer of polarization from protons to the insensitive nuclei: INEPT–INADEQUATE and

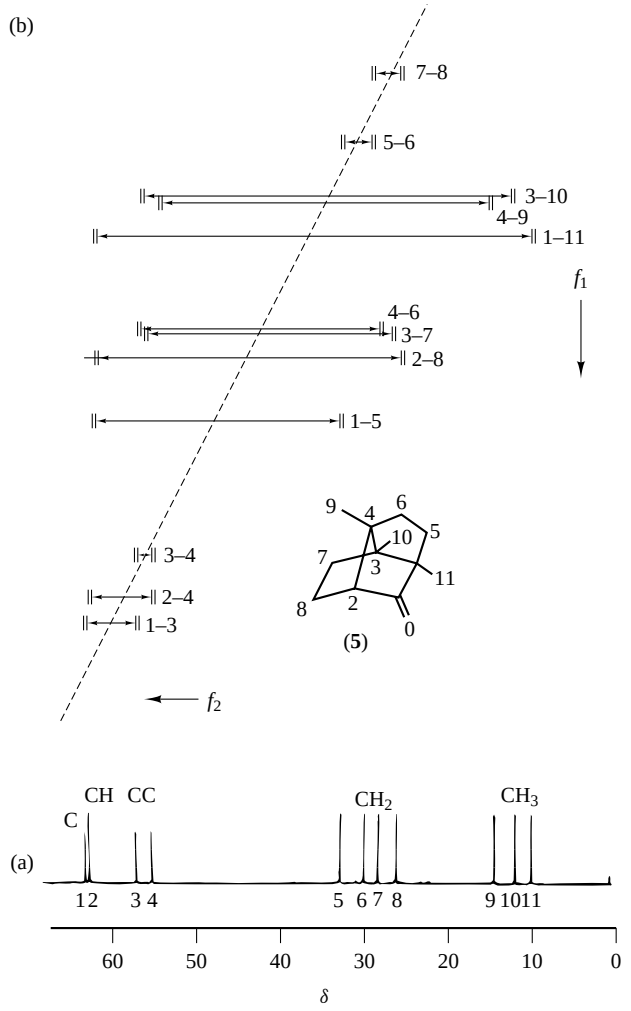

Figure 6 100 MHz $^{13}C\{^1H\}$ NMR spectrum (aliphatic part) of (**5**) (1.2 g) + $Cr(acac)_3$ (10 mg) in $CDCl_3$ (1.5 mL). (a) Conventional spectrum. (b) Two-dimensional INADEQUATE spectrum, $\tau = 1/(4J)$ (J = 35 Hz), quadrature detection in both dimensions. f_2 = 8771 Hz (8K data points), f_1 = 8771 Hz per 512 data points. 113 rows were recorded, each with 128 transients; repetition interval 4 s; measuring time 16 h. The data matrix was zero filled to 16K × 512 and Fourier transformed after Gaussian multiplication in f_1 and f_2. (Reproduced from Buddrus and Bauer[1])

DEPT–INADEQUATE. The factor of increase is small for ^{13}C ($\geq \frac{4}{3}$) and larger for ^{29}Si ($\geq \frac{5}{1.5}$); in addition the repetition interval can be decreased as long as the relaxation times T_1 of the protons are shorter than those of the insensitive nuclei ^{13}C, ^{29}Si, etc. A remarkable increase in sensitivity has been obtained by the ^1H-detected method INSIPID. The interfering signals from protons attached to ^{12}C were eliminated by field gradient pulses. See Weigelt and Otting.[11]

Due to the logic of a 2D INADEQUATE spectrum, analysis is also possible with the aid of a computer program. Contrary to manual interpretation even tiny satellite signals may be recognized and interpreted. Mutual addition of the four signals of an AX spin system of a phase sensitive 2D INADEQUATE spectrum can also be carried out by a computer. This gives a S/N improvement of two, equivalent to a reduction of measurement time by a factor of four. Figure 7 demonstrates this improvement for the weakest satellite signals (signals from the adjacent quaternary carbons) of compound (**6**).

6 APPLICATIONS: ORGANIC AND INORGANIC COMPOUNDS

6.1 Organic Compounds

6.1.1 Constitution

Most convincingly ^{13}C, ^{13}C spin–spin coupling can be used for the determination of the constitution of the following types of carbon compound, the structures of which can either not be determined or determined only with difficulty using other NMR methods (including 2D techniques):

1. Hydrocarbons or hydrocarbon-like compounds (**1**, **7**, **8**): their ^1H NMR spectra are complex, while normal ^{13}C NMR spectra do not afford much information.

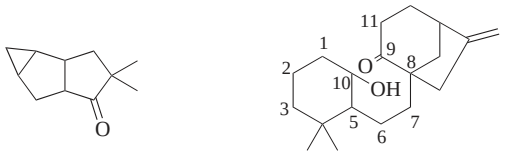

(7) **(8)**

2. Compounds in which those carbon atoms which are important for determining their constitution carry few if any hydrogens. In such cases ^1H NMR is unsuccessful because of the lack of hydrogen atoms, while normal ^{13}C spectra can often not be interpreted with certainty. Examples are highly chlorinated compounds (**9**), (**10**) or certain cycloaddition products (**11**), (**12**); the wavy lines in the formulas of the latter indicate the starting materials used and make clear the regiochemical problems, which can easily by solved by INADEQUATE.

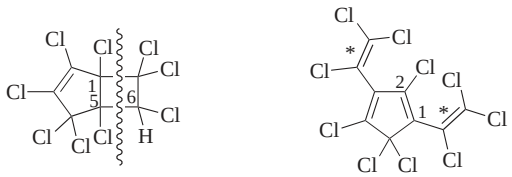

(9) **(10)**

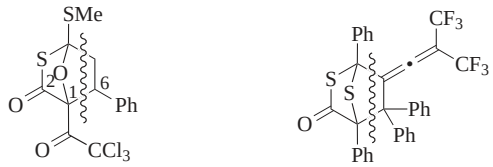

(11) **(12)**

3. Compounds with particular symmetry properties, independent of whether the carbon atoms are hydrogen-rich or hydrogen-poor. Thus, the isomers (**13**) and (**14**) (head-to-head and head-to-tail products from photodimerizations) can be distinguished simply from the ratio of the satellite pairs at the *C*H signals: 1:1 for the former and 1:2 for the latter.[1]

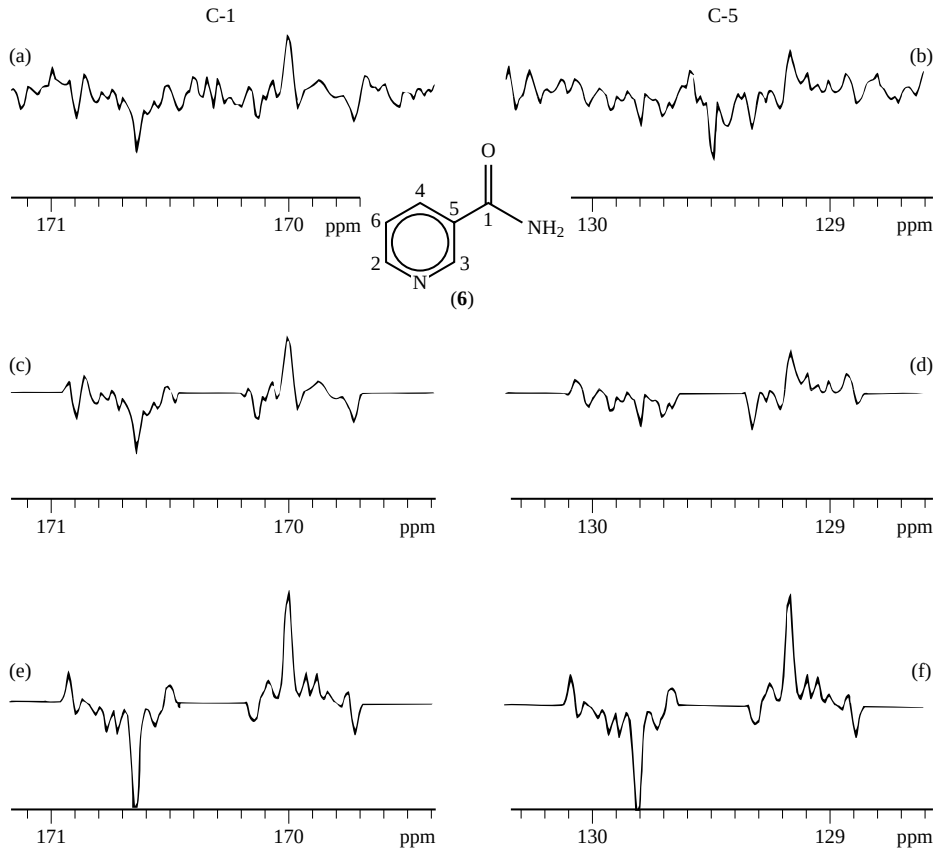

Figure 7 Cross peaks of the row $\nu_{DQ} = \nu_{C-1} + \nu_{C-5} - 2\nu_0$ from the 2D INADEQUATE spectrum of (**6**). (a,b) Untreated. (c,d) Filled with zeros at positions where no double quantum signal can occur. (e,f) Treated with mutual addition of the four satellite signals. Note the S/N improvement in (f) compared with (b). (Reproduced from Lambert and Buddrus[12])

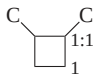

(13)

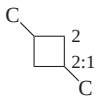

(14)

6.1.2 Assignment

The INADEQUATE method can also be applied simply to assign ^{13}C NMR signals of known compounds. The results are unequivocal, contrary to those obtained from the incremental method or from comparison with model compounds. Numerous examples for carbon (and also silicon) compounds are described in the literature.

6.1.3 Biosynthetic Studies

Carbon-13 labeled precursors have long been used in the determination of biosynthetic pathways. One important precursor is labeled sodium acetate yielding labeled polyketides. Most useful is the incorporation of two adjacent ^{13}C nuclei which give information on folding, rearrangement, etc. of polyketide chains. For a review see Floss and Beale;[13] see also Buddrus and Bauer.[1] Double labeling is achieved by adding either a 1:1 mixture of 1- and 2-^{13}C acetate or an approximately 3:1 mixture of nonlabeled and doubly labeled acetate. An isotopomeric mixture of polyketides results in the ^{13}C nuclei neighboring at C-2 and C-3 [Figure 8(g)] or neighboring at C-1 and C-2 *or* at C-3 and C-4 [Figure 8(l)]. As a result of this labeling, ^{13}C, ^{13}C satellite signals of increased intensity are observed. The increase of the satellite signals is remarkable. A 3:1 mixture (see above) gives a theoretical increase of about 2500 if no dilution by additional unlabeled acetate occurs. Therefore, amounts between 100 μg and a few mg of the polyketide are sufficient, even for molecules containing about 50 carbon atoms.

6.2 Inorganic Compounds

The INADEQUATE pulse sequence can also be used to investigate inorganic compounds containing elements with a spin-$\frac{1}{2}$ isotope of low natural abundance (<15%): examples are provided by the elements silicon (4.7% ^{29}Si), tin (7.6% ^{117}Sn, 8.6% ^{119}Sn) and tungsten (14.3% ^{183}W). The INADEQUATE spectra contain only signals from the AX spin system, from which the atomic skeleton of the molecule can be derived; beyond this, determination of the ^1J values and assignment of the NMR signals of A type nuclei is possible.

Most important is the application to silicon compounds, either as liquids or as solids. The two ^{29}Si isotopes are either directly connected (as in silanes) or separated by one oxygen atom (as in siloxanes or silicates). Therefore, the delay time τ in the INADEQUATE pulse sequence has to be adjusted to either $1/(4\ ^1J)$ or $1/(4\ ^2J)$. The values in silicon compounds

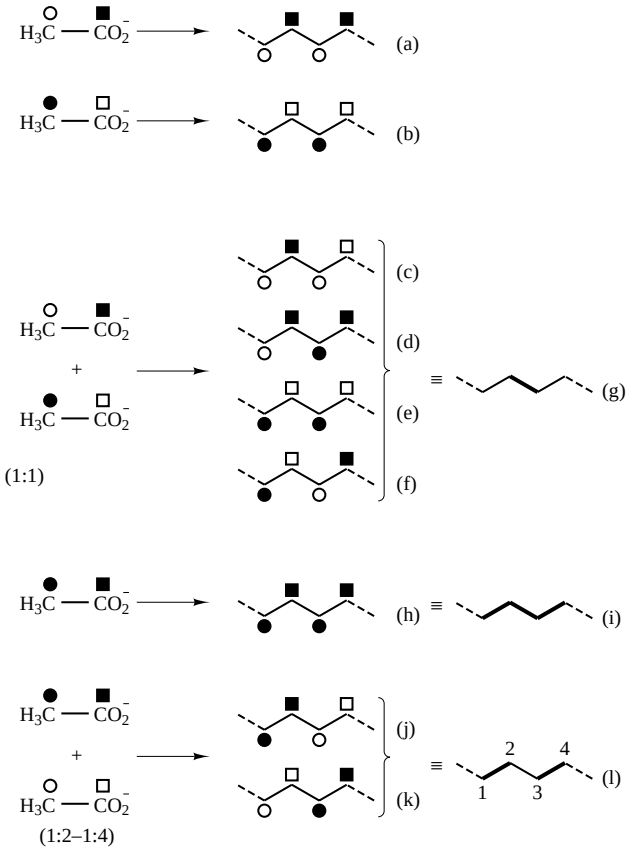

Figure 8 Distribution of ^{13}C nuclei in polyketide chains: sections of chain after incorporation of differently labeled acetates. For explanation see text. ^{12}C is denoted by ○ or □, ^{13}C by ● or ■. Isotopomers which contain neighboring ^{13}C nuclei at increased abundance are also indicated by bold lines at the appropriate positions; compare (g), (i) and (l). (Reproduced from Buddrus and Bauer[1])

are comparable to those in carbon compounds.

^{13}C–^{13}C	^{13}C–C–^{13}C	^{29}Si–^{29}Si	^{29}Si–Si–^{29}Si	^{29}Si–O–^{29}Si
$^1J \approx 50$ Hz	$^2J \approx 0$–5 Hz	$^1J \approx 50$ Hz	$^2J \approx 15$ Hz	$^2J \approx 1$–10 Hz

Figure 9 shows the 2D ^{29}Si–INEPT–INADEQUATE spectrum of the cyclosilane (**15**). The ^{29}Si–^{29}Si connectivities prove that the structure is that of (**15**) while structure (**16**) with adjacent trimethylsilyl groups can be excluded. Due to large ^2J coupling, not only connectivities through one bond are observed (horizontal lines in the spectrum) but also those through more than one bond (a–c; e–f). However, long-range coupling is easily recognized by its value, and so there is no ambiguity in establishing the structure.

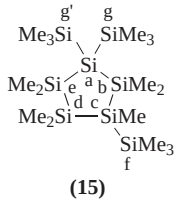

(15)

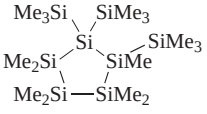

(16)

Compounds in the solid state can also be investigated by 2D techniques such as COSY or INADEQUATE, provided the MAS technique is applied; see Benn et al.[15] MAS eliminates shielding anisotropies and direct dipole–dipole coupling, leaving indirect coupling through one or more bonds (J coupling). The linewidth can be as low as 1–20 Hz (under proton decoupling conditions where necessary). With 2D MAS–INADEQUATE several zeolites have been studied. Figure 10 shows the ^{29}Si MAS and MAS–INADEQUATE spectrum of (**17**), a zeolite with seven crystallographically inequivalent tetrahedral lattice sites indicated by Si1, Si2 ... Si7.

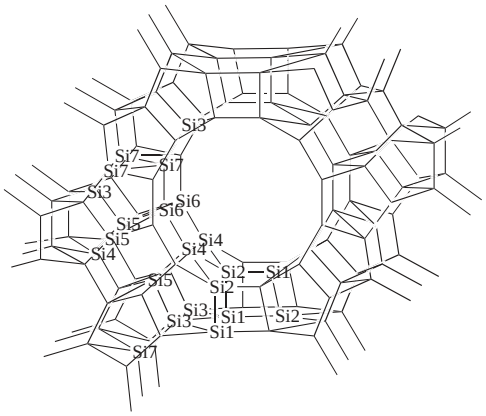

(17)

Starting from a signal with a well known assignment all other signals can be unequivocally assigned. Generally, INADEQUATE is superior to COSY, because in the latter method diagonal signals can interfere with cross peaks (compare T_4T_6).

Other nuclei, which have been investigated by INADEQUATE, either in liquids or solids, are: ^{183}W, ^{119}Sn and ^6Li. Interestingly, the 2D INADEQUATE experiment can also be applied to compounds with elements consisting mainly or entirely of only spin-$\frac{1}{2}$ isotopes (H, P or F). Such compounds are e.g. hydrogen containing organic compounds yielding multispin systems. The behavior of multispin systems (ABC; ABCD ...) toward the INADEQUATE pulse sequence is treated by Braunschweiler et al.[17] In the case of the simple three-spin system AMX a total of six double quantum coherences is possible. Several proton spin systems have been studied by INADEQUATE. The advantages and disadvantages with respect to COSY are discussed by Boyd et al.[18]

7 OUTLOOK

Two-dimensional INADEQUATE spectroscopy is a useful method for the determination of the constitution of unknown carbon and silicon and other compounds. The simplicity and logic of the spectra are fascinating. There is no ambiguity. The inherent insensitivity has been reduced to some extent in the past and will surely be further reduced. The day will come when a few mg of an unknown compound from a plant or a microorganism, measured overnight, will yield the secret of its constitution by daybreak.

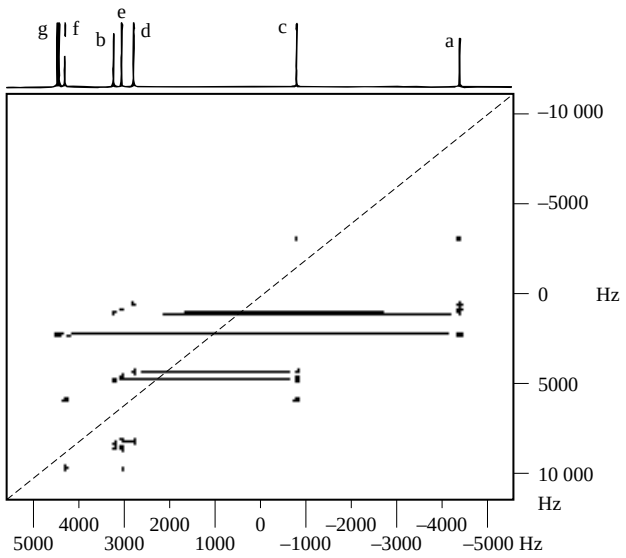

Figure 9 Two-dimensional 71.5 MHz ^{29}Si INEPT–INADEQUATE NMR spectrum of (**15**). For explanation of horizontal lines see text. (Reproduced by permission, from Maxka et al.[14])

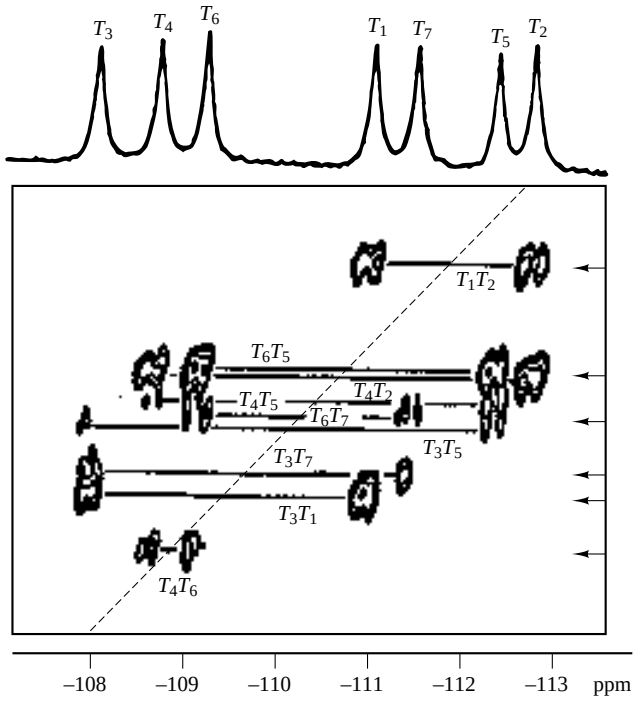

Figure 10 ^{29}Si MAS NMR spectrum of the zeolite ZSM-12 (**17**) (top) and its two-dimensional INADEQUATE version (bottom). τ set according to ^2J = 12.5 Hz. (Reproduced by permission, from Fyfe et al.[16])

8 RELATED ARTICLES

Analysis of High-Resolution Solution State Spectra; Multiple Quantum Spectroscopy of Liquid Samples.

9 REFERENCES

1. J. Buddrus and H. Bauer, *Angew. Chem., Int. Ed. Engl.*, 1987, **26**, 625.
2. A. Bax, R. Freeman, and S. P. Kempsell, *J. Am. Chem. Soc.*, 1980, **102**, 4849; A. Bax, R. Freeman, and T. A. Frenkiel, *J. Am. Chem. Soc.*, 1981, **103**, 2102.
3. W. P. Aue, E. Bartholdi, and R. R. Ernst, *J. Chem. Phys.*, 1976, **64**, 2229.
4. A. Wokaun and R. R. Ernst, *Chem. Phys. Lett.*, 1977, **52**, 407.
5. G. Bodenhausen, *Prog. Nucl. Magn. Reson. Spectrosc.*, 1981, **14**, 137.
6. L. Braunschweiler, G. Bodenhausen, and R. R. Ernst, *Mol. Phys.*, 1983, **48**, 535.
7. O. W. Sørensen, G. W. Eich, M. H. Levitt, G. Bodenhausen, and R. R. Ernst, *Prog. Nucl. Magn. Reson. Spectrosc.*, 1983, **16**, 163.
8. A. Bax, *Two-Dimensional Nuclear Magnetic Resonance in Liquids*, Reidel, Dordrecht, 1982, Appendix 1.
9. A. Bax, R. Freeman, T. A. Frenkiel, and M. H. Levitt, *J. Magn. Reson.*, 1981, **43**, 478.
10. J. Lambert, H. J. Kuhn, and J. Buddrus, *Angew. Chem., Int. Ed. Engl.*, 1989, **28**, 728.
11. J. Weigelt and G. Otting, *J. Magn. Reson., Ser. A*, 1995, **113**, 128.
12. J. Lambert and J. Buddrus, *J. Magn. Reson., Ser. A*, 1993, **101**, 307.
13. H. G. Floss and J. M. Beale, *Angew. Chem., Int. Ed. Engl.*, 1989, **28**, 146.
14. J. Maxka, B. R. Adams, and R. West, *J. Am. Chem. Soc.*, 1989, **111**, 3447.
15. R. Benn, H. Grondey, C. Brevard, and A. Pagelot, *J. Chem. Soc., Chem. Commun.*, 1988, 102.
16. C. A. Fyfe, Y. Feng, H. Gies, H. Grondey, and G. T. Kokotailo, *J. Am. Chem. Soc.*, 1990, **112**, 3264.

17. L. Braunschweiler, G. Bodenhausen, and R. R. Ernst, *Mol. Phys.*, 1983, **48**, 535.
18. J. Boyd, C. M. Dobson, and C. Redfield, *J. Magn. Reson.*, 1983, **55**, 170.

Biographical Sketch

J. Buddrus. *b* 1932. Diploma 1958, Doctor's degree 1961, Habilitation 1969, TU Berlin. Institut für Spektrochemie 1968–present. Approx. 90 publications and the textbook 'Grundlagen der Organischen Chemie' (840pp). Present research interests: application of liquid NMR to organic molecules including enantiomers and humic substances.

INEPT

Gareth A. Morris
University of Manchester, Manchester, UK

1	Introduction	1
2	Historical Review	1
3	Theory	2
4	Applications	4
5	Related Articles	5
6	References	5

1 INTRODUCTION

INEPT (insensitive nuclei enhanced by polarization transfer) is a pulse sequence used to transfer spin-state polarization from one nucleus to another. Its original use was to transfer polarization from protons to nuclei X of lower magnetogyric ratio γ, in order to enhance the signals of X: it has also been widely used to determine the multiplicities of X signals (i.e. how many protons are directly bonded to a given X). Although now partly superseded by the DEPT sequence, it is still in widespread use, and is frequently incorporated as a building block into more complex pulse sequences. The main significance of INEPT in the development of multiple pulse NMR methods was that it was one of the first sequences to use a modulated spin echo to effect a broadband (i.e. independent of chemical shift) manipulation of the spin system, a feature of many subsequent experiments. Several useful reviews have been published.[1–4]

There are two main reasons for transferring polarization between heteronuclei: to transfer information (e.g. to establish scalar coupling relationships), and to enhance signal intensity. The latter benefit arises from the dependence of the intensity of an NMR signal on (inter alia) the spin state population difference (or polarization) across the transition concerned. In the high-temperature approximation, the Boltzmann equilibrium polarization is proportional to γ. Since protons are chemically ubiquitous and enjoy a high γ and a high natural abundance, polarization transfer is usually effected from protons to X, resulting in X signals that are a factor γ_H/γ_X stronger than those obtained from equilibrium X polarization. In the discussion that follows, the starting nucleus will be assumed to be the proton, although a variety of other nuclei have been used, including ^{31}P and ^{2}D.

In its basic form,[5] the INEPT sequence consists of five pulses, and transfers polarization from protons to X (often ^{13}C) through one-bond couplings ^1J(X, H):

$$\begin{array}{lccccc} ^1H & 90^\circ & & 180^\circ & & 90^\circ_y \\ & & \tau & & \tau & \\ X & & & 180^\circ & & 90^\circ \quad \text{Acquire} \end{array}$$

where all pulses have x phase unless otherwise indicated. The delay 2τ generates a spin echo modulated by the heteronuclear coupling; if $\tau = 1/[4^1J(\text{X,H})]$, the proton and X 90° pulses transfer the resultant antiphase proton magnetization to X. This gives an X spectrum in which the multiplets are in antiphase with respect to the coupling ^1J(X,H); no proton decoupling is used, since collapsing the antiphase multiplets would destroy the enhanced signal. Where X = ^{13}C, the comparative uniformity of one-bond ^{1}H–^{13}C couplings ^1J(C,H) allows a single value of τ to be used for most types of carbon. Common chemical environments for CH_n groups give ^1J(C,H) values in the range 120–170 Hz; a compromise value $\tau \approx 1.8$ ms generally gives good results. With longer delays it is possible to transfer polarization through long-range couplings ^nJ(X, H), although the presence of multiple competing couplings can make this inefficient.

Table 1 Phase Cycling for the Refocused INEPT Sequence; Phase Shifts are Indicated as Multiples of 90°. For the Basic Sequence, ϕ_3 Follows the Cycle 0321 Throughout

ϕ_1	0202 0202 2020 2020
ϕ_2	0202 2020 1313 3131
ϕ_3	0321 2103 0321 2103
ϕ_4	0101 1212 0101 1212
Receiver	0123 0123 0123 0123

If a decoupled X spectrum is required, the antiphase X magnetization may be left to evolve for a time 2Δ into in-phase signal before decoupling is applied;[6] to avoid large frequency-dependent phase errors in the X spectrum, refocusing is generally used. This gives the seven-pulse 'refocused INEPT' sequence[7] (phase cycling is given in Table 1):

$$\begin{array}{lccccccc} ^1\text{H} & 90^\circ_{\phi_1} & & 180^\circ_{\phi_2} & & 90^\circ_y & & 180^\circ_x \quad \text{Decouple} \\ & & \tau & & \tau & & \Delta & \quad \Delta \\ \text{X} & & & 180^\circ_x & & 90^\circ_{\phi_3} & & 180^\circ_{\phi_4} \quad \text{Acquire} \end{array}$$

which is that most widely used. The X signal obtained depends on Δ and on the multiplicity of X: this is the basis of INEPT spectral editing in ^{13}C NMR.

INEPT has now been partially supplanted by DEPT[8] (distortionless enhancement by polarization transfer), which for spectral editing purposes is less affected by variations in ^1J(C,H). DEPT also yields in-phase proton coupled X multiplets with normal intensity ratios, whereas the basic INEPT sequence gives antiphase multiplets (refocused INEPT gives normal multiplet patterns if a proton 90° purging pulse is added). The pros and cons of different editing methods are discussed by Sørensen and Jakobsen.[3] DEPT is half as long again as INEPT, which makes it less suitable for systems that have short transverse relaxation times T_2. The most widespread current use of INEPT is as a building block in more complex experiments. Two-dimensional (2D) and three-dimensional (3D) NMR experiments frequently need broadband transfer of polarization between nuclei; INEPT is usually preferred to DEPT for this purpose, partly because of its lower T_2 losses. Popular examples include relayed heteronuclear shift correlation[9] and the HSQC experiment.[10]

2 HISTORICAL REVIEW

Before the introduction of pulsed methods, a number of different techniques were used for the transfer of polarization between heteronuclei. These included selective population

transfer[11] (SPT), which may be regarded as a frequency-selective precursor of INEPT and DEPT, and Hartmann–Hahn transfer.[12] SPT uses selective pulses to transfer polarization to one X nucleus at a time. The basic Hartmann–Hahn experiment, while very effective in solid state NMR, is of little practical use in liquid state NMR because it requires very accurate matching of proton and X rf fields. Although some useful progress was made in its application to liquids[13] in the 1970s, such methods did not find significant application until the recent introduction[14] of methods based on composite pulse decoupling sequences.

INEPT was first conceived as a tool for improving the sensitivity of low-γ nuclei, following the observation that the good sensitivity of the 2D heteronuclear correlation experiment arose in part from the transfer of spin state polarization from protons to ^{13}C. The first experiments used a short extra delay off resonance to achieve a proton 90° phase shift; after a phase shifter was constructed, both the five pulse and the refocused seven-pulse INEPT experiment were tried. Only the results from the five-pulse sequence were published, because the refocused sequence showed poorer signal enhancement. The acronym INEPT was chosen as a reaction against the fashion for burdening experiments with names which promised more than they could deliver; this policy continued with INADEQUATE.

Perhaps the most important contribution to the application of INEPT came from Doddrell and Pegg,[15] who showed that the 2Δ dependence of the enhanced X signal on multiplicity (see Figure 3 below), up to then simply regarded as a nuisance, which required the use of a compromise value for the final delay Δ_2 in 2D shift correlation, was the basis of an efficient means of determining ^{13}C multiplicities. Until then, multiplicities had generally been determined using coherent off-resonance decoupling, which sacrifices sensitivity and is susceptible to artifacts. The INEPT method gives a sensitivity comparable to that of conventional proton-decoupled ^{13}C NMR, and in systems with uniform one-bond couplings gives clean and unambiguous results. Where a range of J values is present, DEPT and SEMUT give cleaner results; the GL versions of these sequences are still less vulnerable to J variation.[3]

Many variations on and refinements of INEPT have been described. The concept of INEPT can be extended to transfer between groups of non-spin-$\frac{1}{2}$ nuclei.[16] INEPT can provide signal enhancement for relaxation time measurements[17] or for experiments such as INADEQUATE.[18] The antiphase nature of the intermediate state between the proton 90°_y and X 90° pulses allows INEPT to be used to probe specific heteronuclear relaxation pathways.[19] The sensitivity of INEPT to mismatch between the coupling constant J(X, H) and the delays τ and Δ can be reduced by replacing the modulated echoes of the basic sequence with composite bilinear rotations.[4,20] INEPT can be made selective for a given range of chemical shifts, for example by using soft pulses for the protons.[21]

3 THEORY

3.1 Vector Picture Description

The original INEPT experiments were developed using simple ideas based on Bloch vector pictures; the more recent introduction of product operator methods[22] has greatly simplified the rigorous description of multiple pulse NMR experiments in weakly coupled spin systems. The original description of INEPT gives a useful insight into the mechanism of the experiment, as well as an illustration of the strengths and weaknesses of the vector picture approach. For simplicity, the nuclei involved here will be assumed to be ^{13}C and protons; the arguments apply equally to any pair of spin-$\frac{1}{2}$ nuclei.

Consider a ^{1}H–^{13}C two-spin system CH, in which there is a scalar coupling J(C, H). Suppose that the spin system initially has the normal Boltzmann polarization for protons, but no polarization for ^{13}C (this could easily be achieved by saturating the ^{13}C transitions; in practice, phase cycling suppresses signals from this source). There will be a fractional population difference $P_H = \gamma_H B_0/(2kT)$ across the proton transitions, where B_0 is the static magnetic field, k is Boltzmann's constant, and T is the absolute temperature. The relative populations of the spin states are as shown on the energy level diagram in Figure 1(a). The ^{13}C and proton spectra would then be as shown in Figure 1(b): no signal for ^{13}C, and two signals (the ^{13}C satellites) for protons, one for the molecules in which the ^{13}C spin is in state α, and one for the other half in which the carbon is β.

Suppose a selective 180° pulse is applied to the 'β' satellite (transition 34). This will exchange the populations of the spin states $\beta\alpha$ and $\beta\beta$, inverting the proton β satellite, but also changing the population differences across the two carbon transitions. The effect on the carbon spectrum [Figure 1(c)] is to give two antiphase signals, again one for molecules with proton α and one for proton β. The intensities of these carbon signals are determined by the initial proton population difference P_H, and hence are four times those of normal ^{13}C signals (assuming no Overhauser enhancement). This SPT/SPI experiment serves two purposes: it shows which ^{13}C is coupled to the proton inverted, and it gives ^{13}C signals with fourfold enhanced intensity.

INEPT uses a modulated proton spin echo to give the same effect of inverting one satellite, but for all CH_n groups in a sample, irrespective of proton chemical shift. Starting once again from a state in which the spin system has Boltzmann polarization for protons but none for ^{13}C, consider the effect of the basic INEPT sequence on the two proton magnetizations, viewed in a frame of reference rotating at the proton transmitter

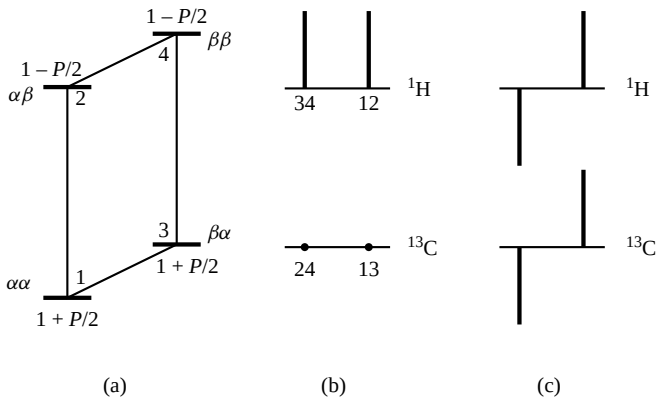

Figure 1 Energy level diagram (a) and stick spectra for a CH spin system, (b) before and (c) after application of a selective 180° pulse to transition 34

frequency (Figure 2). The first proton 90°_x pulse rotates the magnetizations from their equilibrium position pointing along the $\boldsymbol{B}_0$ (z) direction to lie along the $-y$ axis (for consistency with the product operator description that follows, a right-handed axis convention will be used here). After a time $\tau = 1/[4J(\mathrm{C,H})]$, the two vectors have precessed apart by 90° [Figure 2(b)]; their positions in the transverse plane depend on the frequency difference between the proton chemical shift and the proton transmitter. The proton 180°_x pulse reflects the positions of the α and β vectors about the xz plane, just as in a normal spin echo, but the carbon 180° pulse then interchanges the labels of the α and β satellites [Figure 2(c)], since a 180° pulse interchanges α and β spin states. The second delay τ causes the gap between the two proton magnetizations to widen to 180°, but the refocusing effect of the proton 180° pulse ensures that the two magnetizations end up aligned along the $\pm x$ axes of the proton rotating frame irrespective of the chemical shift [Figure 2(d)].

The proton 90°_y pulse then rotates the β magnetization down to the $-z$ axis, and the α magnetization back up to the $+z$ axis [Figure 2(e)]: the effect of the sequence so far is the same as that of the selective proton 180° pulse in the SPT experiment, except that the effect achieved is independent of the proton shift. The carbon 90° pulse produces two antiphase transverse carbon magnetizations, with intensities four times those of normal carbon signals. In the refocused INEPT experiment, a second modulated spin echo period $\Delta - 180^\circ_{\mathrm{H}}$, $180^\circ_{\mathrm{X}} - \Delta$ allows the two ^{13}C magnetizations to precess back into phase, aligning along the x axis of the ^{13}C rotating frame of reference at the end of the second Δ delay for $\Delta = 1/[4J(\mathrm{C,H})]$. The same logic may be applied to CH_2 and CH_3 spin systems, leading to the conclusion that the basic INEPT sequence generates ^{13}C multiplet patterns of a 1:0:$-$1 triplet for CH_2, and a 1:1:$-$1:$-$1 quartet for CH_3. The effect of the final refocusing delay in the refocused INEPT sequence depends on the multiplicity: for CH_2 groups the antiphase signals come back into phase for $\Delta = 1/[8J(\mathrm{C,H})]$, but for CH_3 there is no value of Δ for which all four magnetizations are in phase. The different behavior of CH, CH_2, and CH_3 groups as a function of Δ is explored in Section 3.2, and forms the basis of the use of INEPT for ^{13}C spectral editing.

The vector description of the action of INEPT given above is self-consistent, and predicts correctly the results of INEPT experiments in simple CH_n groups, and the dependence of those results on parameters such as delays and pulse flip angles. The limitations of the approach become clear if the order in which the proton and ^{13}C 90° pulses are applied is inverted. This has no effect on the outcome of the experiment (the two pulses may be applied in either order, or indeed simultaneously), but the effect of applying a 90° ^{13}C pulse to a CH spin system with antiphase proton magnetizations is to generate heteronuclear multiple quantum coherence, and cannot be described using simple vector pictures. The simplest rigorous way to describe pulsed experiments on weakly coupled spin systems is by using the product operator formalism.[22]

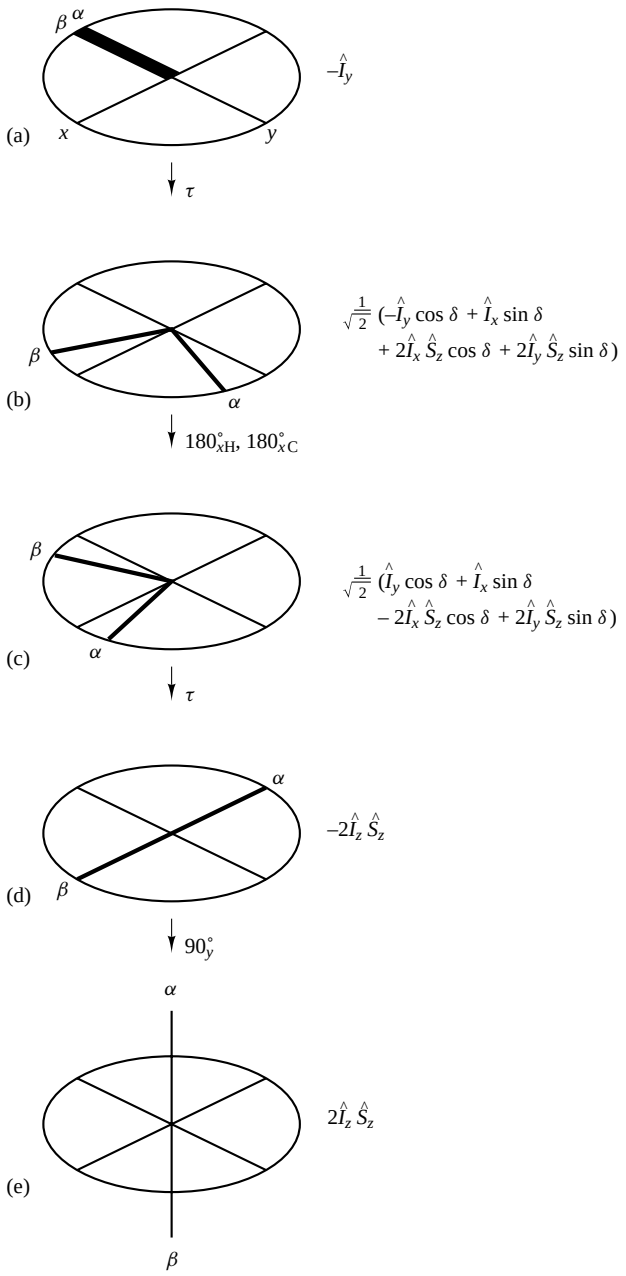

Figure 2 Vector description of the basic INEPT sequence for a CH spin system, showing the product operator representations of each state

3.2 Product Operator Description

In the product operator formalism the state of a spin system is represented as a linear combination of products of the spin operators $\hat{I}_x$, $\hat{I}_y$, and $\hat{I}_z$. For a CH group, let S denote carbon and I proton; the initial state in which only the protons are polarized is then $\hat{I}_z$. The initial polarization is once again $P_{\mathrm{H}} = (\gamma_{\mathrm{H}} B_0/2kT)$; thus if the signal were measured immediately after the 90° pulse, the proton y magnetization would be

$$M_y^{\mathrm{H}} = N\gamma_{\mathrm{H}}\ \mathrm{Tr}\{-P_{\mathrm{H}}\hat{I}_y\hat{I}_y\} = -\frac{N\gamma_{\mathrm{H}}^2 B_0}{4kT} \qquad (1)$$

where N is the number of spin systems per unit volume. In the basic INEPT sequence this proton y magnetization goes on to evolve under the proton chemical shift and the ^{1}H–^{13}C scalar coupling (the intermediate states are indicated in Figure 2), to form the modulated spin echo $-2\hat{I}_x\hat{S}_z$ at time

2τ. The proton 90°_y pulse converts this to $2\hat{I}_z\hat{S}_z$, followed by the carbon 90°_x pulse which converts the J-ordered state [Figure 2(e)] into antiphase carbon y magnetization $-2\hat{I}_z\hat{S}_y$. In contrast to the problems encountered with the vector treatment, interchanging the proton and carbon 90° pulses here does not affect the argument: the sequence of states just changes from $-2\hat{I}_x\hat{S}_z \rightarrow 2\hat{I}_z\hat{S}_z \rightarrow -2\hat{I}_z\hat{S}_y$ to $-2\hat{I}_x\hat{S}_z \rightarrow 2\hat{I}_x\hat{S}_y \rightarrow -2\hat{I}_z\hat{S}_y$, where the intermediate state is a mixture of heteronuclear zero and double quantum coherence rather than a J-ordered state. Extending the basic sequence to the refocused INEPT sequence adds a further modulated spin echo $\Delta - 180^\circ_H, 180^\circ_X - \Delta$, converting the antiphase carbon doublet $-2\hat{I}_z\hat{S}_y$ into the in-phase signal $\hat{S}_x$ when $\Delta = 1/[4J(\mathrm{C,H})]$. For an arbitrary delay Δ the final state at the end of the refocused sequence is

$$-2\hat{I}_z\hat{S}_y \cos[2\pi\Delta J(\mathrm{C,H})] + \hat{S}_x \sin[2\pi\Delta J(\mathrm{C,H})] \qquad (2)$$

When proton (I) decoupling is used during measurement of the carbon (S) free induction decay, only the second term is observed. By analogy with equation (1) above, the net ^{13}C magnetization produced is

$$M_x^{\mathrm{C}}(\Delta) = N\gamma_{\mathrm{C}}\ \mathrm{Tr}\{\hat{S}_x P_{\mathrm{H}} \hat{S}_x\} = \frac{N\gamma_{\mathrm{C}}\gamma_{\mathrm{H}}B_0}{4kT} \sin[2\pi\Delta J(\mathrm{C,H})] \qquad (3)$$

which is enhanced by a factor $\gamma_{\mathrm{H}}/\gamma_{\mathrm{C}}$ compared with the normal signal.

For CH_2 and CH_3 groups, denoting the chemically equivalent protons I_1, I_2 and I_1, I_2, I_3 respectively, the basic INEPT sequence yields the states $-2(\hat{I}_{1z} + \hat{I}_{2z})\hat{S}_y$ and $-2(\hat{I}_{1z} + \hat{I}_{2z} + \hat{I}_{3z})\hat{S}_y$. The refocused sequence for arbitrary Δ gives

$$\hat{S}_x \sin 2\theta - 2(\hat{I}_{1z} + \hat{I}_{2z})\hat{S}_y \cos 2\theta + 4\hat{I}_{1z}\hat{I}_{2z}\hat{S}_x \sin 2\theta \qquad (4)$$

for CH_2 and

$$\begin{aligned} 3\hat{S}_x \cos^2\theta \sin\theta + 2(\hat{I}_{1z} + \hat{I}_{2z} + \hat{I}_{3z})\hat{S}_y(2\sin^2\theta\cos\theta - \cos^3\theta) \\ + 4(\hat{I}_{1z}\hat{I}_{2z} + \hat{I}_{1z}\hat{I}_{3z} + \hat{I}_{2z}\hat{I}_{3z})\hat{S}_x(2\cos^2\theta\sin\theta \\ - \sin^3\theta) + 24\hat{I}_{1z}\hat{I}_{2z}\hat{I}_{3z}\hat{S}_y \sin^2\theta\cos\theta \end{aligned} \qquad (5)$$

for CH_3, where $\theta = 2\pi\Delta J(\mathrm{C,H})$. In all three cases, the effect of using an arbitrary delay τ is simply to multiply the end result by a factor $\sin[2\pi\tau J(\mathrm{C,H})]$.

The net decoupled carbon signals at the end of the refocussed INEPT sequence for CH, CH_2 and CH_3 signals are thus

$$M_x^{\mathrm{CH}}(\Delta) = S\sin\theta \qquad (6)$$

$$M_x^{\mathrm{CH_2}}(\Delta) = S\sin 2\theta \qquad (7)$$

$$M_x^{\mathrm{CH_3}}(\Delta) = 3S\cos^2\theta\sin\theta = \tfrac{3}{4}S(\sin\theta + \sin 3\theta) \qquad (8)$$

where $S = (N\gamma_{\mathrm{C}}\gamma_{\mathrm{H}}B_0/4kT)$. This dependence of the INEPT enhanced ^{13}C signal on Δ and multiplicity, illustrated in Figure 3, may be exploited for spectral editing by repeating the experiment with delays Δ of $1/[4J(\mathrm{C,H})]$, $2/[4J(\mathrm{C,H})]$, and $3/[4J(\mathrm{C,H})]$. The first gives positive signals for all protonated carbons, the second gives positive signals for CH and zero for CH_2 and CH_3, and the last gives positive signals for CH and CH_3 and negative for CH_2. The three resultant spectra S_1, S_2, and S_3 may be combined to give separate subspectra for each multiplicity:

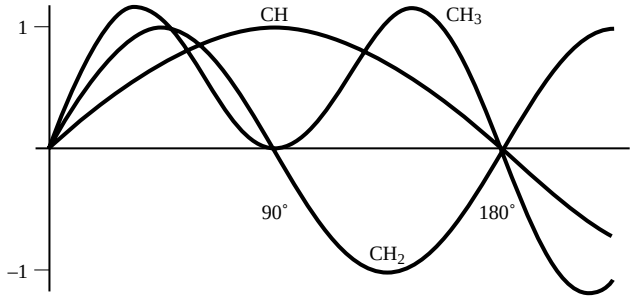

Figure 3 Dependence of the refocussed INEPT signal for CH, CH_2 and CH_3 on $\theta = 360\Delta J(\mathrm{C,H})$

$$\left.\begin{aligned} S_{\mathrm{CH}} &= S_2 \\ S_{\mathrm{CH_2}} &= (S_1 - S_3)/2 \\ S_{\mathrm{CH_3}} &= (\sqrt{2}S_1 + \sqrt{2}S_2 - 2S_3)/3 \end{aligned}\right\} \qquad (9)$$

In practice it is usual to use least-squares optimization of the coefficients of S_1, S_2, and S_3 to minimize cross-talk between the three subspectra.

Where INEPT is to be used to measure enhanced proton coupled spectra, normal multiplet intensity ratios may be restored by adding a 90° purging pulse to the refocused sequence to give the INEPT$^+$ sequence:[3]

^{1}H	90°		180°		90°_y		180°		90°
		τ		τ		Δ		Δ	
X			180°		90°		180°		Acquire

This has the effect of converting all the antiphase terms in equations (2), (4), and (5) above into heteronuclear multiple quantum coherence, leaving only the term in $\hat{S}_x$ observable. For the general case of an I_nS spin system the final observable state is simply $n\ \sin\theta\ \cos^{n-1}\theta\ \hat{S}_x$.

4 APPLICATIONS

4.1 Practical Implementation

Both the basic and refocused INEPT sequences are suitable for routine use. The two main considerations when programing these pulse sequences on a spectrometer are choice of phase cycling, and the need for care with timing of pulses and delays. The primary role of phase cycling is to ensure that only signals from polarization transfer survive time averaging; a secondary aim is to ensure smooth off-resonance behavior by using EXORCYCLE[23] on the two refocusing pulses. Table 1 shows one possible implementation. Care with timing is needed in order to ensure that exact refocusing is obtained from the first modulated echo: any imbalance between the two τ delays, between the first proton 90° pulse and the proton 180°, and between the 180° and the proton 90°_y, will be punished

by extra loss of polarization transfer efficiency off-resonance. Although it is common to apply the pairs of proton and X 90° and 180° pulses simultaneously, with normal rf field strengths this is not necessary provided that the two proton interpulse delays τ and the carbon interpulse delays Δ are kept equal. Calibration of 90° pulses for X and proton is more critical than for single pulse experiments, but 10% accuracy is generally adequate.

It is occasionally recommended that composite 180° pulses be used in experiments such as INEPT. Here it is necessary to distinguish between inversion pulses (the first X 180° and the second proton 180°) and refocusing pulses (the first proton 180° and the second X 180°). Inversion pulses may be replaced by composite 180° pulses with impunity (and with a small improvement in performance). However, if refocusing 180° pulses are replaced by composite pulses it is vital either that constant-phase pulses[24] be used, or that the phase shifts introduced by the composite pulses be compensated.[25]

4.2 Signal Enhancement

Most current applications of the basic and the refocused sequences are to the enhancement of spectra of low-γ nuclei, using polarization from either protons or ^{31}P; INEPT is especially valuable for nuclei with negative γ, which can show Overhauser 'enhancements' of less than unity. Figure 4 shows the sensitivity improvement obtainable for ^{15}N in a small cyclic peptide, gramicidin S. Polarization transfer is particularly helpful in the measurement of proton coupled X spectra, although intensity anomalies can occur in spectra with strong proton–proton coupling. Proton relaxation during acquisition provides an additional time saving; the signal-to-noise ratio gain compared with the normal single pulse X spectrum (without Overhauser enhancement) is approximately $(\gamma_H/\gamma_X)\sqrt{(T_1^X/T_1^H)}$. The choice of whether to use the basic sequence or the INEPT$^+$ sequence depends on the degree of crowding in the coupled X spectrum and on the multiplicities of the nuclei of interest; with overlapping signals or XH_2 groups it is important to have the in-phase multiplets and normal intensity ratios given by INEPT$^+$ to avoid signal cancellation, but in less crowded spectra the extra intensity of the outer components of multiplets with the basic sequence can be an advantage.

4.3 Spectral Editing

Figure 5 shows the results of INEPT measurements of the ^{13}C spectrum of menthol using the refocused sequence with a

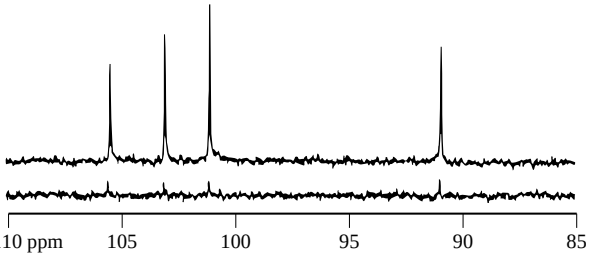

Figure 4 ^{15}N spectra obtained in 6 h at 11.75 T for a 40 mM solution of gramicidin S in dimethyl sulfoxide-d_6, obtained using (top) INEPT, and (bottom) single 90° pulses without Overhauser enhancement

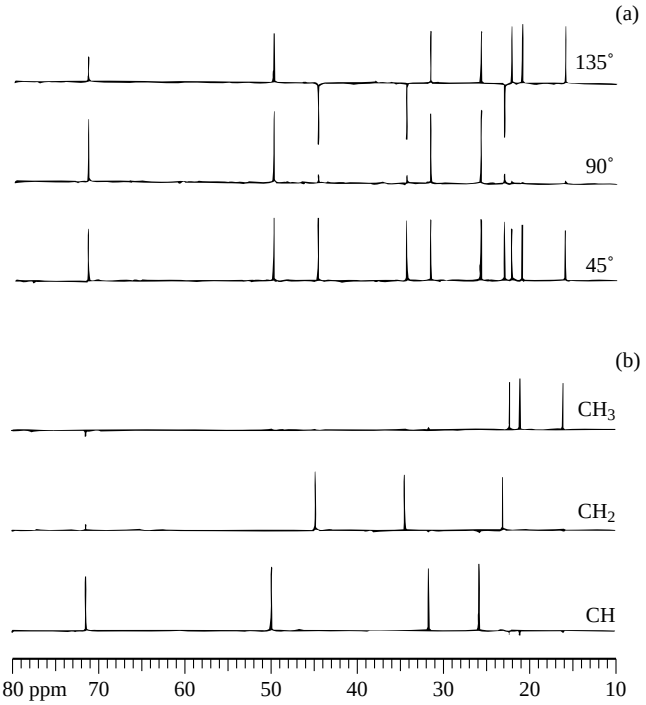

Figure 5 Refocused INEPT spectra of menthol at 7.05 T: (a) using delays Δ of 2, 4, and 6 ms; and (b) the same data combined to give CH, CH_2, and CH_3 subspectra

delay τ of 4 ms and delays Δ of 2, 4, and 6 ms, corresponding to approximate values of $\theta = 360\Delta J$(C, H) of 45°, 90°, and 135°. Combining the three experimental spectra using least-squares fitting to optimize the separation into subspectra gives the CH, CH_2, and CH_3 subspectra of Figure 5(b).

5 RELATED ARTICLES

Composite Pulses; Cross Polarization in Solids; Heteronuclear Assignment Techniques; Heteronuclear Shift Correlation Spectroscopy; Multidimensional Spectroscopy: Concepts; Multiple Quantum Spectroscopy of Liquid Samples; Phase Cycling; Polarization Transfer Experiments via Scalar Coupling in Liquids; Selective Pulses.

6 REFERENCES

1. G. A. Morris, in *Topics in Carbon-13 NMR*, ed. G. C. Levy, Wiley, New York, 1984, Vol. 4, Chap. 7
2. W. S. Brey, in *Pulse Methods in 1D and 2D Liquid-Phase NMR*, ed. W. S. Brey, Academic Press, San Diego, 1987, Chap. 1
3. O. W. Sørensen and H. J. Jakobsen, in *Pulse Methods in 1D and 2D Liquid-Phase NMR*, ed. W. S. Brey, Academic Press, San Diego, 1987, Chap. 3
4. O. W. Sørensen, *Prog. NMR Spectrosc.*, 1989, **21**, 503.
5. G. A. Morris and R. Freeman, *J. Am. Chem. Soc.*, 1979, **101**, 760.
6. G. A. Morris, *J. Am. Chem. Soc.*, 1980, **102**, 428.
7. D. P. Burum and R. R. Ernst, *J. Magn. Reson.*, 1980, **39**, 163.

8. D. M. Doddrell, D. T. Pegg, and M. R. Bendall, *J. Magn. Reson.*, 1982, **48**, 323.
9. P. H. Bolton and G. Bodenhausen, *Chem. Phys. Lett.*, 1982, **89**, 139.
10. A. Bax, M. Ikura, L. E. Kay, D. A. Torchia, and R. Tschudin, *J. Magn. Reson.*, 1990, **86**, 304.
11. K. G. R. Pachler and P. L. Wessels, *J. Magn. Reson.*, 1973, **12**, 337.
12. S. R. Hartmann and E. L. Hahn, *Phys. Rev.*, 1962, **128**, 2042.
13. R. D. Bertrand, W. B. Moniz, A. N. Garroway, and G. C. Chingas, *J. Am. Chem. Soc.*, 1978, **100**, 5227.
14. M. Ernst, C. Griesinger, R. R. Ernst, and W. Bermel, *Mol. Phys.*, 1991, **74**, 219.
15. D. M. Doddrell and D. T. Pegg, *J. Am. Chem. Soc.*, 1980, **102**, 6388.
16. M. R. Bendall, D. T. Pegg, G. M. Tyburn, and C. Brevard, *J. Magn. Reson.*, 1983, **55**, 322.
17. J. Kowalewski and G. A. Morris, *J. Magn. Reson.*, 1982, **47**, 331.
18. O. W. Sørensen, R. Freeman, T. A. Frenkiel, T. H. Mareci, and R. Schuck, *J. Magn. Reson.*, 1982, **46**, 180.
19. D. Marion, C. Garbay-Jaureguiberry, and B. P. Roques, *J. Am. Chem. Soc.*, 1982, **104**, 5573.
20. S. Wimperis and G. Bodenhausen, *J. Magn. Reson.*, 1986, **69**, 264.
21. A. Bax, *J. Magn. Reson.*, 1984, **57**, 314.
22. O. W. Sørensen, G. W. Eich, M. H. Levitt, G. Bodenhausen, and R. R. Ernst, *Prog. NMR Spectrosc.*, 1983, **16**, 163.
23. G. Bodenhausen, R. Freeman and D. L. Turner, *J. Magn. Reson.*, 1977, **27**, 511.
24. A. J. Shaka and A. Pines, *J. Magn. Reson.*, 1987, **71**, 495.
25. M. H. Levitt and R. R. Ernst, *Mol. Phys.*, 1983, **50**, 1109.

Biographical Sketch

Gareth A. Morris. *b* 1954. M.A. (Nat. Sci.), Ph.D., 1978, (supervisor Ray Freeman) Oxford University, UK. Fellow by Examination, Magdalen College, Oxford, 1978–81; Izaak Walton Killam Postdoctoral Fellow, University of British Columbia (with Laurie Hall) 1978–79. Lecturer (1982–89) and Reader (1989–present) in Chemistry, University of Manchester. Approx. 100 publications. Current research interests: development and application of novel NMR techniques to problems in chemistry, biochemistry, and medicine.

Magic-angle Turning Spectra of Solids Involving 5π-pulse Sequences

David M. Grant

University of Utah, Salt Lake City, UT, USA

1 Introduction 1
2 The Classical Banded-Matrix Secular Treatment of Slow Turning Spectra 1
3 The 5π-Pulse Experiment 7
4 TIGER Processing of Two-Dimensional NMR Spectra 9
5 The FIREMAT Variant of the 5π-PULSE Experiment 11
6 The 2D-PASS Form of a 5π-Pulse Experiment 12
7 Comparison of 5π-Pulse Type of Experiments 15
8 References 17

1 INTRODUCTION

The initial publication of the *Encyclopedia of Nuclear Magnetic Resonance* contains a description of several slow magic angle turning (MAT) experiments[1,2] that have as their antecedent the magic angle hopping (MAH) experiment of Bax, Szvereneyi and Maciel.[3] The MAT articles are based on the seminal work of Gan[4] and several subsequent developments that improve the spectral quality. Pulse breakthrough may distort MAT spectra, and the distortion can be minimized with three echo refocusing π-pulses.[5] Time reversal symmetry in the phase corrected MAT (PHORMAT) enhancement,[6] eliminates the need for computer shearing of a skewed spectrum arising from the use of combined amplitude and phase modulation in the original MAT experiment. The PHORMAT approach gives a high-quality hypercomplex 2D spectrum with the isotropic shifts along the evolution axis and tensor bands in the acquisition dimension. Unfortunately, PHORMAT suffers, as do all amplitude modulated MAT experiments, from the use of flip back pulses that are costly in the signal-to-noise (S/N) ratio. The 5π-PULSE/MAT experiment[7] directly improves this situation by leaving the magnetization totally in the *xy*-plane during the entire evolution period.

Before discussing the phase-modulated 5π-pulse experiments with emphasis on the two most popular variants, basic principles of sample rotation are discussed in Section 2 with a classical formulation of appropriate Bloch equations. A banded-matrix secular equation[8] is used for characterizing the spinning-sideband amplitudes common to magic angle rotating samples. The approach also processes rotational sideband data to yield principal-shift frequencies. This *classical* method is a numerically efficient alternative to Floquet theory[9] and/or the Bessel functions solutions used by Hertzfeld and Berger.[10] The banded matrix method, in concert with a SIMPLEX minimization procedure, converges rapidly to the principal-shift values used in fitting the time-dependent free induction decays (FID). The fit of time-dependent FID data is considerably more precise than the fit of single peak intensities.

The 5π-PULSE/MAT experiment[7] is discussed in Section 3. It provides a basis for constructing a two-dimensional FID in which the spectrum is transformed into isotropic shifts along the evolution axis and individual tensor bands along the acquisition axis. Two important variants of 5π-PULSE/MAT, i.e., the five π replicated magic angle turning (FIREMAT)[11] and the 2D phase adjusted spinning sidebands (2D-PASS),[12,13] improve the S/N and yield higher quality spectral resolution in a more time-efficient manner. In a matter of hours, either of these two methods provides 2D spectra on molecules containing 50 or more carbon atoms. The FIREMAT variant is a direct extension of the original 5π-PULSE/MAT technique, whereas the related 2D-PASS approach evolved more from the PASS sideband manipulation experiments of Dixon.[14] Otherwise, both FIREMAT and 2D-PASS share a common starting point at the zero evolution time, $t_e = 0$ and may be explained with the same theoretical machinery.

A useful development in data processing, the technique for importing greater evolution resolution[15] (TIGER) treated in Section 4, may be used to enhance MAT methods. TIGER with MAT data enhances simultaneously the resolution and S/N in the evolution dimension. In contrast to Fourier transform (FT) methods, TIGER is a convolution technique that contracts one of the dimensions of the 2D FIDs of MAT by importing resolution from an associated 1D guide spectrum. TIGER yields a 1D acquisition FID for each nuclear spin that is immediately suited for banded-matrix processing and generally increases the efficiency of data collection by reducing the number of evolution increments, especially in smaller molecules.

FIREMAT (Section 5) includes TIGER but also involves a method for replicating periodic blocks of acquisition FIDs. These replicated blocks of evolution data enhance the resolution and time efficiency of FIREMAT. The creative 2D-PASS (Section 6) approach separates, by sideband order, the magnetization in the evolution dimension. In Section 7, the results of 5π-PULSE (with and without TIGER), FIREMAT, and 2D-PASS (with both FT and fast FT) are compared, and their respective sensitivities and time efficiencies briefly discussed.

2 THE CLASSICAL BANDED-MATRIX SECULAR TREATMENT OF SLOW TURNING SPECTRA

2.1 Bloch's Equation of Motion

Bloch's equation, ignoring relaxation, is given by

$$\frac{\mathrm{d}\vec{\mu}_\nu}{\mathrm{d}t} = \vec{\mu}_\nu \times \gamma_\nu \vec{B}_0 = -\vec{\Omega}_\nu \times \vec{\mu}_\nu \qquad (2.1)$$

where $\vec{\mu}_\nu$ is the magnetic moment of the spin ν, and $\vec{\Omega}_\nu = \gamma_\nu \vec{B}_0 = -\omega_\nu(\mathrm{LAB})$ is an angular precession velocity that is

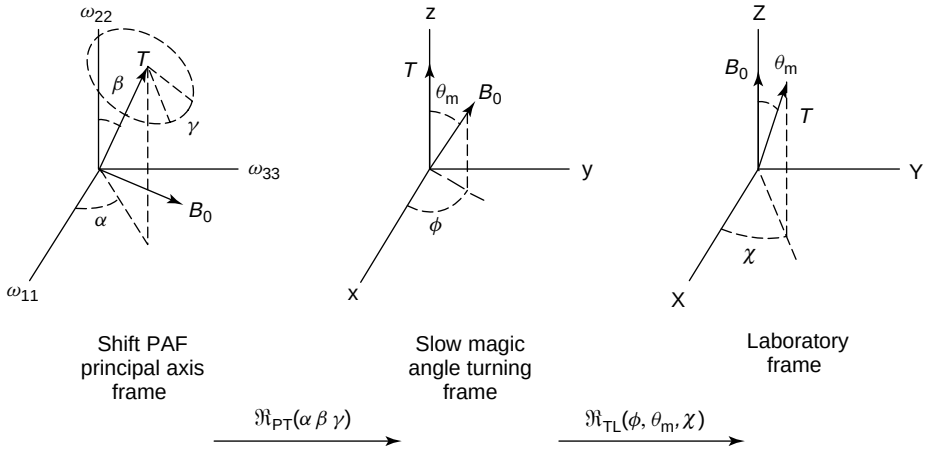

Figure 1 The principal shift axis, turning and laboratory frames for sample rotation

co-linear with $\vec{B}_0$. The Zeeman approximation locks the νth spin to the strong $\vec{B}_0$ lying along the Z-axis in the laboratory or Zeeman frame. Utilizing equation (2.1) in the detection plane yields two differential equations for the counter-rotating vectors:

$$\frac{\mathrm{d}\mu_{\nu+}}{\mathrm{d}t} = -i\omega_\nu(\mathrm{LAB})\mu_{\nu+}, \quad \frac{\mathrm{d}\mu_{\nu-}}{\mathrm{d}t} = +i\omega_\nu(\mathrm{LAB})\mu_{\nu-} \quad (2.2)$$

The irreducible representations of the magnetic moment, $\mu_{\nu\pm}$, in the xy plane are

$$\mu_{\nu\pm} = \mu_{\nu x} \pm i\mu_{\nu y} \quad (2.3)$$

In the absence of a sign for γ_ν, component $\mu_{\nu+}$ is selected arbitrarily as the preferred form for the following development. It is an equally simple matter to use $\mu_{\nu-}$.

2.2 Transformations Between Relevant Chemical Shift Frames

The three frames, given in Figure 1, are necessary to describe the spin precession in a rotating sample. They are the principal axis frames, the slow turning axis frame and the laboratory frame with the turning axis at the magic angle relative to the magnetic field.

An equation for ω_ν(LAB) in the laboratory frame may be given in terms of the zeroth and 2nd rank irreducible shift frequencies,[16] $\omega_0^{(0)}(\mathsf{LAB})$ and $\omega_0^{(2)}(\mathbf{LAB})$, respectively:

$$\omega_\nu(\mathrm{LAB}) = \frac{1}{\sqrt{3}}\omega_0^{(0)}(\mathsf{LAB}) + \sqrt{\frac{2}{3}}\omega_0^{(2)}(\mathsf{LAB}) \quad (2.4)$$

The spin label, ν, is ignored for the moment to reduce the complexity of the expressions. The zero-rank frequency, $\omega_0^{(0)}(\mathsf{LAB}) = \omega_0^{(0)}(\mathrm{PAF}) = \sqrt{3}\omega_{\mathrm{iso}}$, is rotationally invariant in all frames. Only the $m = 0$ projection, $\omega_0^{(2)}(\mathbf{LAB})$, is relevant under the Zeeman approximation for the $l = 2$ second-order irreducible spherical frequencies given in the LAB frame. The transformations between various reference frames using Wigner rotational matrix terms yield the following:

$$\begin{aligned}\omega_0^{(2)}(\mathsf{LAB}) &= \sum_{n=-2}^{+2} \mathbf{D}_{o,n}^{(2)^*}(\phi, \theta, \chi)_{\mathrm{TL}}\omega_n^{(2)}(\mathsf{TURN}) \\ &= \sum_{n=-2}^{+2}\sum_{m=-2}^{+2} \mathbf{D}_{o,n}^{(2)^*}(\phi, \theta, \chi)_{\mathrm{TL}}\mathbf{D}_{n,m}^{(2)^*}(\alpha, \beta, \gamma)_{\mathrm{PT}}\omega_m^{(2)}(\mathsf{PAF})\end{aligned} \quad (2.5)$$

where $\omega_{\pm1}^{(2)}(\mathsf{PAF}) = 0$. Typical Euler angle sets, $(\alpha\beta\gamma)$ and $(\phi\theta\chi)$, are used for the (PAF $\rightarrow$ TURN) and (TURN $\rightarrow$ LAB) transformations denoted in Figure 1 as PT and TL, respectively. Zare[17] discusses the molecular to laboratory expansion, given by equation (2.5), in terms of rotational matrix components, $\mathbf{D}_{n,m}^{(\ell)^*}(\alpha, \beta, \gamma)_{\mathrm{PT}}$. It is critical that the correct matrix be used for the forward and reverse transformations between the laboratory and molecular frames. The Wigner rotation matrix that transforms irreducible-shift frequencies from the (LAB $\rightarrow$ TURN) or (TURN $\rightarrow$ PAF) has matrix elements defined by Zare:[18]

$$\mathbf{D}_{m,n}^{(\ell)}(\alpha, \beta, \gamma)_{\mathrm{TP}} = e^{-im\alpha}d_{m,n}^{(\ell)}(\beta)e^{-in\gamma} \quad (2.6)$$

The reverse rotational transformation from the PAF, fixed in the molecular frame, to the laboratory TURN frame is accomplished with a rotation matrix that is the inverse of equation (2.6), i.e., the complex conjugate of its transpose. Hence, the $\mathbf{D}_{n,m}^{(\ell)^*}(\alpha, \beta, \gamma)_{\mathrm{PT}}$ terms in equation (2.5) are given by

$$\mathbf{D}_{n,m}^{(\ell)^*}(\alpha, \beta, \gamma)_{\mathrm{PT}} = \mathbf{D}_{m,n}^{(\ell)^{-1}}(\alpha, \beta, \gamma)_{\mathrm{TP}} = e^{in\gamma}d_{n,m}^{(\ell)}(\beta)e^{im\alpha} \quad (2.7)$$

Note in equation (2.5) the row and column indices conform and specify a matrix multiplication without violating the commutation rules of rotational operators. Differences in conventions have made this topic somewhat perplexing in the literature. Thus, for the convenience of the reader the form of the Wigner rotation matrix, $\mathbf{D}^{(2)^*}(\alpha, \beta, \gamma)_{\mathrm{PT}}$, used herein is provided as follows:

$$\mathbf{D}^{(2)^*}(\alpha,\beta,\gamma)_{\mathrm{PT}} =$$

$$\begin{bmatrix}
\frac{1}{4}e^{-2i\gamma}(1+\cos\beta)^2e^{-2i\alpha} & \frac{1}{2}e^{-2i\gamma}\sin\beta(1+\cos\beta)e^{-i\alpha} & \sqrt{\frac{3}{8}}e^{-2i\gamma}\sin^2\beta & -\frac{1}{2}e^{-2i\gamma}\sin\beta(\cos\beta-1)e^{i\alpha} & \frac{1}{4}e^{-2i\gamma}(1-\cos\beta)^2e^{2i\alpha} & -2\\
-\frac{1}{2}e^{-i\gamma}\sin\beta(1+\cos\beta)e^{-2i\alpha} & \frac{1}{2}e^{-i\gamma}(2\cos\beta-1)(1+\cos\beta)e^{-i\alpha} & \sqrt{\frac{3}{2}}e^{-i\gamma}\cos\beta\sin\beta & \frac{1}{2}e^{-i\gamma}(2\cos\beta+1)(1-\cos\beta)e^{i\alpha} & -\frac{1}{2}e^{-i\gamma}\sin\beta(\cos\beta-1)e^{2i\alpha} & -1\\
\sqrt{\frac{3}{8}}\sin^2\beta e^{-2i\alpha} & -\sqrt{\frac{3}{2}}\cos\beta\sin\beta e^{-i\alpha} & \frac{1}{2}(3\cos^2\beta-1) & \sqrt{\frac{3}{2}}\cos\beta\sin\beta e^{i\alpha} & \sqrt{\frac{3}{8}}\sin^2\beta e^{2i\alpha} & 0\\
\frac{1}{2}e^{i\gamma}\sin\beta(\cos\beta-1)e^{-2i\alpha} & \frac{1}{2}e^{i\gamma}(2\cos\beta+1)(1-\cos\beta)e^{-i\alpha} & -\sqrt{\frac{3}{2}}e^{i\gamma}\cos\beta\sin\beta & \frac{1}{2}e^{i\gamma}(2\cos\beta-1)(1+\cos\beta)e^{i\alpha} & \frac{1}{2}e^{i\gamma}\sin\beta(1+\cos\beta)e^{2i\alpha} & +1\\
\frac{1}{4}e^{2i\gamma}(1-\cos\beta)^2e^{-2i\alpha} & \frac{1}{2}e^{2i\gamma}\sin\beta(\cos\beta-1)e^{-i\alpha} & \sqrt{\frac{3}{8}}e^{2i\gamma}\sin^2\beta & -\frac{1}{2}e^{2i\gamma}\sin\beta(1+\cos\beta)e^{i\alpha} & \frac{1}{4}e^{2i\gamma}(1+\cos\beta)^2e^{2i\alpha} & +2\\
-2 & -1 & 0 & +1 & +2 & n
\end{bmatrix} \quad M \tag{2.8}$$

The combination of equations (2.4) and (2.5) gives the following frequency expression in the laboratory frame, $\omega(\mathbf{LAB})$, for the various spins,

$$\omega(\mathrm{LAB}) = \frac{1}{\sqrt{3}}\omega_0^{(0)}(\mathsf{PAF}) + \sqrt{\frac{2}{3}}\sum_{n=-2}^{+2}\sum_{m=-2}^{+2}\mathbf{D}_{o,n}^{(2)^*}(\phi,\theta,\chi)_{\mathrm{TL}}\mathbf{D}_{n,m}^{(2)^*}(\alpha,\beta,\gamma)_{\mathrm{PT}}\omega_m^{(2)}(\mathsf{PAF}) \tag{2.9}$$

The alternative, but equivalent, similarity transformations use the standard directional-cosine matrix[19]

$$\mathbf{R}(\alpha,\beta,\gamma)_{\mathrm{PT}} = \begin{bmatrix} \cos\alpha\cos\beta\cos\gamma - \sin\alpha\sin\gamma & \sin\alpha\cos\beta\cos\gamma + \cos\alpha\sin\gamma & -\sin\beta\cos\gamma \\ -\cos\alpha\cos\beta\sin\gamma - \sin\alpha\cos\gamma & -\sin\alpha\cos\beta\sin\gamma + \cos\alpha\cos\gamma & \sin\beta\sin\gamma \\ \cos\alpha\sin\beta & \sin\alpha\sin\beta & \cos\beta \end{bmatrix}$$

to convert the chemical-shift tensor from the PAF into the turning frame and subsequently to the laboratory frames as follows:

$$\begin{aligned} T_{\mathrm{TURN}} &= \mathbf{R}(\alpha,\beta,\gamma)_{\mathrm{PT}}\cdot T_{\mathrm{PAF}}\cdot\mathbf{R}^{-1}(\alpha,\beta,\gamma)_{\mathrm{PT}} \\ T_{\mathrm{LAB}} &= \mathbf{R}(\phi,\theta,\chi)_{\mathrm{TL}}\cdot T_{\mathrm{TURN}}\cdot\mathbf{R}^{-1}(\phi,\theta,\chi)_{\mathrm{TL}} \\ &= \mathbf{R}(\phi,\theta,\chi)_{\mathrm{TL}}\cdot\mathbf{R}(\alpha,\beta,\gamma)_{\mathrm{PT}}\cdot T_{\mathrm{PAF}} \\ &\quad\cdot\mathbf{R}^{-1}(\alpha,\beta,\gamma)_{\mathrm{PT}}\cdot\mathbf{R}^{-1}(\phi,\theta,\chi)_{\mathrm{TL}} \end{aligned} \tag{2.10}$$

$\mathbf{R}^{-1}(\alpha,\beta,\gamma)_{\mathrm{PT}}$ is the transpose of the unitary matrix, $\mathbf{R}(\alpha,\beta,\gamma)_{\mathrm{PT}}$. Application of equation (2.10) yields the same expression for $\omega(\mathsf{LAB})$ (i.e., the [3,3] term in T_{LAB}) as obtained for the Wigner rotation transformations given in equation (2.9) when equation (2.8) is employed.

2.3 Irreducible-Spherical Shift Frequencies and Appropriate Rotational Transformations

The definition of irreducible-spherical shift frequencies[16] in any molecular frame is as follows:

$$\begin{aligned} \omega_0^{(0)}(\mathrm{mol}) &= \frac{1}{\sqrt{3}}[\omega_{zz}+\omega_{xx}+\omega_{yy}] = \sqrt{3}\omega_{\mathrm{iso}} \\ \omega_0^{(2)}(\mathrm{mol}) &= \sqrt{\frac{2}{3}}\left[\omega_{zz}-\frac{1}{2}(\omega_{xx}+\omega_{yy})\right] = \sqrt{\frac{3}{2}}[\omega_{zz}-\omega_{\mathrm{iso}}] \\ \omega_{\pm1}^{(2)}(\mathrm{mol}) &= \frac{1}{2}[\mp(\omega_{xz}+\omega_{zx}) - i(\omega_{yz}+\omega_{zy})] \\ \omega_{\pm2}^{(2)}(\mathrm{mol}) &= \frac{1}{2}[(\omega_{xx}-\omega_{yy}) \pm i(\omega_{xy}+\omega_{yx})] \end{aligned} \tag{2.11}$$

These irreducible frequencies in radians per second express the symmetrical portion of the chemical shift tensor. Division by 2π converts equation (2.11) from radians per second to cps or Hz. In the PAF tensor only diagonal elements exist and equation (2.11) reduces to the zero-rank isotropic frequency and three ($m = -2, 0, 2$) of the five second-rank frequencies, respectively, as follows:

$$\omega_0^{(0)}(\mathsf{PAF}) = \sqrt{3}\omega_{\mathrm{iso}} \tag{2.12}$$

with the second-rank frequencies given in vector form, i.e.,

$$\overline{\omega}^{(2)} = \begin{bmatrix} \omega_{-2}^{(2)}(\mathsf{PAF}) \\ \omega_{-1}^{(2)}(\mathsf{PAF}) \\ \omega_0^{(2)}(\mathsf{PAF}) \\ \omega_1^{(2)}(\mathsf{PAF}) \\ \omega_2^{(2)}(\mathsf{PAF}) \end{bmatrix} = \begin{bmatrix} \frac{1}{2}\omega_{\mathrm{span}} \\ 0 \\ \sqrt{\frac{2}{3}}\omega_{\mathrm{acent}} \\ 0 \\ \frac{1}{2}\omega_{\mathrm{span}} \end{bmatrix} \tag{2.13}$$

where $\omega_{\mathrm{iso}} = (1/3)(\omega_{11}+\omega_{22}+\omega_{33})$, $\omega_{\mathrm{acent}} = \omega_{22} - (1/2)(\omega_{11}+\omega_{33})$ and $\omega_{\mathrm{span}} = (\omega_{11}-\omega_{33})$. The notations iso, acent, and span are used for isotropic, acentricity, and span, respectively. Note that the ω_{zz} direction is best identified with the ω_{22} principal frequency and the ω_{xx} and ω_{yy} terms with ω_{11} and ω_{33} principal frequencies, respectively. The ω_{11}, ω_{22} and ω_{33} are the principal chemical shift frequencies. In Mason's[20] convention for symmetry combination of tensor terms, iso and span are the same as used herein, but acent, equal to the product of Mason's skew times the span, is preferred in this work. These proposed simple irreducible forms are very useful with Wigner rotation matrices because they exhibit the symmetry features of irreducible tensors while skew and the traditional asymmetry parameter are ratios of irreducible forms.

It is convenient to evaluate the relevant part of the rotational matrix RTL using values of the Euler angles: $\phi, \theta = \theta_m, \chi = 0$. The selection of χ equal to zero, while arbitrary, expresses the cylindrical symmetry of the $\vec{B}_0$ magnetic field in the laboratory frame. Thus,

$$\mathbf{D}_{0,0}^{(2)^*}(\phi,\theta_m,\chi)_{\mathrm{TL}} = d_{0,0}^{(2)}(\theta_m) = \frac{1}{2}(3\cos^2\theta_m - 1) = 0$$

$$\begin{aligned}
\mathbf{D}^{(2)^*}_{0,\pm1}(\phi,\theta_m,\chi)_{\mathrm{TL}} &= d^{(2)}_{0,\pm1}(\theta_m)e^{\pm i\phi} \\
&= \pm\sqrt{\frac{3}{2}}\sin\theta_m\cos\theta_m e^{\pm i\phi} = \pm\sqrt{\frac{1}{3}}e^{\pm i\phi} \\
\mathbf{D}^{(2)^*}_{0,\pm2}(\phi,\theta_m,\chi)_{\mathrm{TL}} &= d^{(2)}_{0,\pm2}(\theta_m)e^{\pm 2i\phi} \\
&= \sqrt{\frac{3}{8}}\sin^2\theta_m e^{\pm 2i\phi} = \sqrt{\frac{1}{6}}e^{\pm 2i\phi} \qquad (2.14)
\end{aligned}$$

Here, $\cos^2\theta_m = 1/3$ and $\sin^2\theta_m = 2/3$. The transformation matrix from the TURN frame to LAB frame now is limited to the row vector,

$$\mathbf{D}^{(2)^*}_{0,n(-2,-1,0,+1,+2)}(\phi,\theta,\chi)_{\mathrm{TL}} = \left[\sqrt{\frac{1}{6}}e^{-2i\phi} \quad -\sqrt{\frac{1}{3}}e^{-i\phi} \quad 0 \quad +\sqrt{\frac{1}{3}}e^{i\phi} \quad \sqrt{\frac{1}{6}}e^{+2i\phi}\right] \qquad (2.15)$$

Note that χ drops out of equation (2.15) because of the cylindrical symmetry in the magnetic field. While the generalized $\mathbf{D}^{(2)^*}(\phi,\theta,\chi)_{\mathrm{TL}}$ Wigner rotation matrix is a 5×5 matrix, only the middle row of the matrix, $\mathbf{D}^{(2)^*}_{0,n(-2,-1,0,+1,+2)}(\phi,\theta,\chi)_{\mathrm{TL}}$, is relevant to the angular precession frequency in the Zeeman approximation. This simplification in the mathematics arises whenever $\vec{B}_0$, the static magnetic field, dominates all other interactions and defines the Z-axis as the relevant laboratory direction for the angular precession frequency, $\omega_\nu(\mathrm{LAB})$.

The summations in equation (2.9) over n and m express a $(1\times5)\cdot(5\times5)\cdot(5\times1)$ matrix multiplication of the matrices contained in equations (2.15), (2.8), and (2.13). Thus,

$$\begin{aligned}
\omega_\nu(\mathrm{LAB}) = \omega_{\mathrm{iso}} &+ \sqrt{\frac{2}{3}}\left[\sqrt{\frac{1}{6}}e^{-2i\phi} \quad -\sqrt{\frac{1}{3}}e^{-i\phi} \quad 0 \quad +\sqrt{\frac{1}{3}}e^{i\phi} \quad \sqrt{\frac{1}{6}}e^{+2i\phi}\right]\cdot \qquad (2.16)\\
&\begin{bmatrix}
\frac{1}{4}e^{-2i\gamma}(1+\cos\beta)^2e^{-2i\alpha} & (\cdots) & \sqrt{\frac{3}{8}}e^{-2i\gamma}\sin^2\beta & (\cdots) & \frac{1}{4}e^{-2i\gamma}(1-\cos\beta)^2e^{2i\alpha}\\
-\frac{1}{2}e^{-i\gamma}\sin\beta(1+\cos\beta)e^{-2i\alpha} & (\cdots) & \sqrt{\frac{3}{2}}e^{-i\gamma}\cos\beta\sin\beta & (\cdots) & -\frac{1}{2}e^{-i\gamma}\sin\beta(\cos\beta-1)e^{2i\alpha}\\
(\cdots) & (\cdots) & (\cdots) & (\cdots) & (\cdots)\\
\frac{1}{2}e^{i\gamma}\sin\beta(\cos\beta-1)e^{-2i\alpha} & (\cdots) & -\sqrt{\frac{3}{2}}e^{i\gamma}\cos\beta\sin\beta & (\cdots) & \frac{1}{2}e^{i\gamma}\sin\beta(1+\cos\beta)e^{2i\alpha}\\
\frac{1}{4}e^{2i\gamma}(1-\cos\beta)^2e^{-2i\alpha} & (\cdots) & \sqrt{\frac{3}{8}}e^{2i\gamma}\sin^2\beta & (\cdots) & \frac{1}{4}e^{2i\gamma}(1+\cos\beta)^2e^{2i\alpha}
\end{bmatrix}\cdot
\begin{bmatrix}
\frac{1}{2}\omega_{\mathrm{span}}\\ 0\\ \sqrt{\frac{2}{3}}\omega_{\mathrm{acent}}\\ 0\\ \frac{1}{2}\omega_{\mathrm{span}}
\end{bmatrix}
\end{aligned}$$

The null terms arising in the two outer vectors greatly simplifies the result of multiplying the three matrices (a vector, a square matrix, and a vector) found in equation (2.16). Thirteen of the 25 terms in the 5×5 matrix are nonvanishing, but they become irrelevant due to the null terms in the TL transformation and in the PAF irreducible principal-frequency vector.

2.4 Precession Frequency Dependency on Transformation Angles

Consideration of the first matrix multiplication in equation (2.16) makes it immediately obvious that the overall transformation depends only on the sum of $(\phi+\gamma)$. Therefore, it is possible to subsume ϕ and γ into a single angle identified with the mechanical rotation of the sample.[21] Apportioning $(\phi+\gamma)$ into pre-pulse and post-pulse periods divides the angle into useful time-independent and time-dependent components. A sudden approximation at zero-time, $t=0$, is invoked for the B_1 pulse that nutates the magnetic spin into the xy-observing plane. The $(\phi+\gamma)$ angle therefore divides into an orientational lattice angle, γ_o, and a time-dependent angular term, $\gamma_t = \omega_r t$, where the mechanical rotational frequency is given by ω_r. Thus,

$$(\phi+\gamma) = \gamma_o + \gamma_t = \gamma_o + \omega_r t \qquad (2.17)$$

The spin identity of unique nuclei now is reintroduced with the index ν. Equations (2.16) and (2.17) render $\omega_\nu(\mathrm{LAB})$ in the following compacted form,[22]

$$\omega_\nu(\mathrm{LAB}) = \sum_{n=-2}^{2} W_{\nu,n}(\alpha,\beta)e^{ni\gamma_o}e^{ni\omega_r t} \qquad (2.18)$$

The phase factor, $e^{ni\gamma_o}$, depends on the lattice angle, γ_o, and on the second-rank projection index, n. The explicit form of the $W_{\nu,n}(\alpha,\beta)$ terms, obtained from the matrix multiplications in equation (2.16), depends on the irreducible shift-frequency parameters, $(\omega_{\mathrm{iso}},\omega_{\mathrm{acent}},\omega_{\mathrm{span}})$, for each ν spin as follows:

$$\begin{aligned}
W_2(\alpha,\beta) &= \frac{1}{24}[(1+\cos\beta)^2e^{i2\alpha} + (1-\cos\beta)^2e^{-i2\alpha}]\omega_{\mathrm{span}} \\
&\quad + \frac{1}{6}[\sin^2\beta]\omega_{\mathrm{acent}} \\
W_1(\alpha,\beta) &= \frac{\sqrt{2}}{12}[\sin\beta(1+\cos\beta)e^{i2\alpha} + \sin\beta(\cos\beta-1)e^{-i2\alpha}]\omega_{\mathrm{span}} \\
&\quad - \frac{\sqrt{2}}{3}[\sin\beta\cos\beta]\omega_{\mathrm{acent}} \\
W_o &= \omega_{\mathrm{iso}} \\
W_{-1}(\alpha,\beta) &= \frac{\sqrt{2}}{12}[\sin\beta(\cos\beta-1)e^{i2\alpha} + \sin\beta(1+\cos\beta)e^{-i2\alpha}]\omega_{\mathrm{span}} \\
&\quad - \frac{\sqrt{2}}{3}[\sin\beta\cos\beta]\omega_{\mathrm{acent}} \\
W_{-2}(\alpha,\beta) &= \frac{1}{24}[(1-\cos\beta)^2e^{i2\alpha} + (1+\cos\beta)^2e^{-i2\alpha}]\omega_{\mathrm{span}} \\
&\quad + \frac{1}{6}[\sin^2\beta]\omega_{\mathrm{acent}} \qquad (2.19)
\end{aligned}$$

Note that the zero-rank shift frequency, $\omega_0^{(0)}(\mathsf{LAB})$, provides the expression for W_0, whereas $\omega_0^{(2)}(\mathsf{LAB})$ relates to W_{-2}, W_2, W_{-1} and W_1. Substituting equation (2.18) into equation (2.2) and using the μ_+ form, as indicated earlier, gives the following Bloch equation:

$$\frac{\mathrm{d}\mu_\nu(\alpha,\beta,\gamma_o|t)}{\mathrm{d}t} = -i\sum_{n=-2}^{2} W_{\nu,n}(\alpha,\beta,)e^{in\gamma_o}e^{in\omega_r t}\mu_\nu(\alpha,\beta,\gamma_o|t) \tag{2.20}$$

2.5 Powder Averaging of Bloch's Equation of Motion in MAT Experiments

The orientation of all equivalent nuclei in a single crystal, as a function of time, is represented by $(\alpha,\beta,\gamma_o|t)$. Thus, the magnetization of nuclei in microcrystalline powders with identical spatial-orientations is given by the designation $\mu(\alpha,\beta,\gamma_o|t)$. Maricq and Waugh[23] observed in single crystals, with only one molecular orientation, that phase variations appear in the spectral sidebands relative to the center-band phase. These phase variations relate to $e^{in\gamma_o}$, providing the rf observing pulses are synchronized with the angular positions of the rotating sample.

In a microcrystalline sample, the phase factor $e^{in\gamma_o}$, must be powder averaged, thereby resulting in some loss of phase specificity. When equation (2.18) is powder averaged over the γ_o angle, $\mu(\alpha,\beta,\gamma_o|t)$ is converted into an ensemble magnetization, $m_\nu(\alpha,\beta|t)$. This $m_\nu(\alpha,\beta|t)$ ensemble consists of the ν spins in those crystallites with a common turning axis, which is described by α and β in the PAF. Members of this subset distribute uniformly over the different values of γ_o. Consequently, equation (2.20) becomes

$$\frac{\mathrm{d}m_\nu(\alpha,\beta|t)}{\mathrm{d}t} = -i\sum_{n=-2}^{2} W_{\nu,n}(\alpha,\beta)\overline{e^{in\gamma_o}}e^{in\omega_r t}m_\nu(\alpha,\beta|t) \tag{2.21}$$

2.5.1 Powder Average over γ_o

Focus now turns to the average phase factor, $\overline{e^{in\gamma_o}}$, and its ensemble $m_\nu(\alpha,\beta|t)$. In an elegant proof, Levitt[24] exhibited that the phase factors for the center-band and sidebands were all equal in rotating micro-crystalline powders. Levitt's treatment assumes three constraints. (i) All spins in the $\mu_\nu(\alpha,\beta,\gamma_o|t)$ subset experience the same *average* Hamiltonian. (ii) The sample rotation takes the sub-ensemble of spins, $\mu_\nu(\alpha,\beta,\gamma_o|t)$, related to the turning axis through a periodic cycle of resonance frequencies. (iii) The orientations of these $\mu(\alpha,\beta,\gamma_o|t)$ crystallites experience a uniform distribution over γ_o. Postulate (i) defines the subset of spins belonging to the α,β turning axis. The periodic character of $e^{in\gamma_o}$ satisfies (ii). Finally, (iii) specifies an essential feature of a random powder to give uniform mathematical averaging of the phase factor around the rotational path. The uniform angular probability leads to the following expression:

$$\int_0^{2\pi} P(\gamma_o)d\gamma_o = P(\gamma_o)\int_0^{2\pi} d\gamma_o = 1 \tag{2.22}$$

hence $P(\gamma_o) = 1/2\pi$.

If one integrates $e^{in\gamma_o}$ from a to $a+2\pi$, expressions for the average phase factor are obtained as follows:

$$\begin{aligned}\overline{\exp(in\gamma_o)} &= \exp\left(inP(\gamma_o)\int_a^{a+2\pi}\gamma_o d\gamma_o\right) = \exp\left(\frac{in}{4\pi}[\gamma_o^2]_a^{a+2\pi}\right)\\ &= \exp(in(\pi+a)) = [\exp(i(\pi+a))]^n = (\pm1)^n\end{aligned} \tag{2.23}$$

The averaged factors reference the phase of the sidebands to the corresponding center-band identified with the zero rank W_o. The selection of a specific crystallite by the parameter a is totally arbitrary. Thus it is convenient to choose real values for a (e.g., $a=\pi$ or $a=0$) to give the final term in equation (2.23). For $n=+2$ or -2 the phase factor is always unity, but when $n=+1$ or -1 then the arbitrariness of odd rank projections creeps into the phase factor. Zare has treated this feature at some length.[25] The ensemble average of γ_o, given in equation (2.23), is now complete. It is easily shown below that use of either $+1$ or -1 for $\overline{e^{in\gamma_o}}$ will not alter the results of this treatment. In keeping with traditional practices,[26] the negative sign for $(\pm1)^n$ is arbitrarily selected for this development. Equation (2.18) then becomes

$$\begin{aligned}\omega_\nu(\mathrm{LAB}) &= \sum_{n=-2}^{2}(-1)^n W_{\nu,n}(\alpha,\beta)e^{in\omega_r t}\\ &\equiv \sum_{n=-2}^{2}(-1)^n W_{\nu,n}(\alpha,\beta)e^{in\gamma_t}\end{aligned} \tag{2.24}$$

and equation (2.21) yields

$$\frac{\mathrm{d}m_\nu(\alpha,\beta|t)}{\mathrm{d}t} = -i\sum_{n=-2}^{2}(-1)^n W_{\nu,n}(\alpha,\beta)e^{in\omega_r t}m_\nu(\alpha,\beta|t) \tag{2.25}$$

2.5.2 Solution of the Bloch equation for the m_ν $(\alpha,\beta|\mathrm{t})$ Subsystem of Spins

The $e^{in\omega_r t}$ term makes equation (2.25) quite intractable; consequently, an infinite Fourier expansion is used for $m_\nu(\alpha,\beta|t)$ to provide a numerical solution for equation (2.25):

$$m_\nu(\alpha,\beta|t) = A\sum_{k=-\infty}^{+\infty} a_{\nu,k}(\alpha,\beta)e^{-i(\omega_{\nu,\mathrm{iso}}+k\omega_r)t} \tag{2.26}$$

where A includes arbitrary spectral phase factors, $e^{-\rho}$, and scaling constants such as m_0. The $a_{\nu,k}(\alpha,\beta)$ are expansion coefficients for the α,β designated subsystem. Inserting equation (2.26) into equation (2.25) gives the following expressions:

$$\begin{aligned}\frac{\mathrm{d}m_\nu(\alpha,\beta|t)}{\mathrm{d}t} &= -iA\sum_{k=-\infty}^{+\infty}(\omega_{\nu,\mathrm{iso}}+k\omega_r)a_{\nu,k}(\alpha,\beta)e^{-i(\omega_{\nu,\mathrm{iso}}+k\omega_r)t}\\ &\equiv -iA\sum_{k=-\infty}^{+\infty}\sum_{n=-2}^{2}(-1)^n W_{\nu,n}(\alpha,\beta)\\ &\quad\times e^{in\omega_r t}a_{\nu,k}(\alpha,\beta)e^{-i(\omega_{\nu,\mathrm{iso}}+k\omega_r)t}\end{aligned} \tag{2.27}$$

Equation (2.27) may be simplified by dropping $dm_\nu(\alpha, \beta|t)/dt$, clearing the common factors, $-iAe^{i\omega_{\nu,\mathrm{iso}}t}$, and rearranging and collecting the remaining terms to obtain the following:

$$\sum_{k=-\infty}^{+\infty} \sum_{n=-2}^{2} \left\{ \begin{array}{c} (\omega_{\nu,\mathrm{iso}} + k\omega_r) a_{\nu,k}(\alpha, \beta) e^{-ik\omega_r t} - \\ (-1)^n W_{\nu,n}(\alpha, \beta) a_{\nu,k}(\alpha, \beta) e^{-i(k-n)\omega_r t} \end{array} \right\} = 0 \quad (2.28)$$

Equation (2.28) is multiplied by $e^{i\lambda\omega_r t}$ and integrated over time. The Kronecker delta is used to exploit the orthogonal character of the Fourier expansion terms to give

$$\sum_{k=-\infty}^{+\infty} \sum_{n=-2}^{2} \left\{ \begin{array}{c} (\omega_{\nu,\mathrm{iso}} + k\omega_r) a_{\nu,k}(\alpha, \beta) \delta_{k,\lambda} - \\ (-1)^n W_{\nu,n}(\alpha, \beta) a_{\nu,k}(\alpha, \beta) \delta_{k-n,\lambda} \end{array} \right\} = 0 \quad (2.29)$$

Equation (2.29) may be placed into a compacted expression by enforcing the various $\delta_{k,\lambda}$ terms, expanding the n index explicitly, and temporarily ignoring the α, β and ν designations to reduce complexity. This gives the following set of constrained equations:

$$\sum_{\lambda=-\infty}^{+\infty} \{W_2 a_{\lambda+2} - W_1 a_{\lambda+1} + \lambda\omega_r a_\lambda - W_{-1} a_{\lambda-1} + W_{-2} a_{\lambda-2}\} = 0 \quad (2.30)$$

Each set of five terms in $n = -2, \ldots, +2$ for a constant value of λ becomes linearly independent expressions, and a summation over λ converts equation (2.30) into the following set of simultaneous equations:

$$\begin{array}{ccccccc} & & \cdots & & \cdots & \cdots \\ W_{-2}a_{-4} & -W_{-1}a_{-3} & -2\omega_r a_{-2} & -W_1 a_{-1} & +W_2 a_0 & = 0 & \lambda = -2 \\ W_{-2}a_{-3} & -W_{-1}a_{-2} & -\omega_r a_{-1} & -W_1 a_0 & +W_2 a_1 & = 0 & \lambda = -1 \\ W_{-2}a_{-2} & -W_{-1}a_{-1} & +0 & -W_1 a_1 & +W_2 a_2 & = 0, & \text{for } \lambda = 0 \\ W_{-2}a_{-1} & -W_{-1}a_0 & +\omega_r a_1 & -W_1 a_2 & +W_2 a_3 & = 0 & \lambda = 1 \\ W_{-2}a_0 & -W_{-1}a_1 & +2\omega_r a_2 & -W_1 a_3 & +W_2 a_4 & = 0 & \lambda = 2 \\ & & \cdots & & \cdots & \cdots \end{array} \quad (2.31)$$

The compacted notation for the W_n and a_λ is used for convenience, but it must be remembered that W_n and a_λ terms both include ν and the $\alpha\beta$ axis designations. By converting equation (2.31) into a matrix product, this set of simultaneous equations gives the typical secular equation as follows:

$$\begin{bmatrix} \cdots & \cdots & \cdots & \cdots & & & & & \\ W_{-2} & -W_{-1} & -2\omega_r & -W_1 & W_2 & 0 & 0 & 0 & 0 \\ 0 & W_{-2} & -W_{-1} & -\omega_r & -W_1 & W_2 & 0 & 0 & 0 \\ 0 & 0 & W_{-2} & -W_{-1} & 0 & -W_1 & W_2 & 0 & 0 \\ 0 & 0 & 0 & W_{-2} & -W_{-1} & \omega_r & -W_1 & W_2 & 0 \\ 0 & 0 & 0 & 0 & W_{-2} & -W_{-1} & 2\omega_r & -W_1 & W_2 \\ & & & & & \cdots & \cdots & \cdots & \cdots \end{bmatrix} \times \begin{bmatrix} \cdots \\ a_{-2} \\ a_{-1} \\ a_{0^-} \\ a_1 \\ a_2 \\ \cdots \end{bmatrix} = 0 \quad (2.32)$$

Diagonalization of the banded matrix with the Gaussian elimination procedure yields values for the $a_{\nu,\lambda}(\alpha\beta)$ eigenvectors that encode the $W_{\nu,n}(\alpha, \beta)$ information for the νth spin. Recall from equation (2.19) that $W_{\nu,n}(\alpha, \beta)$ contains the acent and span irreducible spectral parameters and the α, β Euler angles that prescribe the geometric orientation α, β of the turning axis relative to the PAF. The infinite expansion in λ converges quite rapidly once λ times the interval between spinning sidebands exceeds the span of the tensor band. As k and λ are both arbitrary indices in equation (2.29), the solution for $a_{\nu,\lambda}(\alpha\beta)$ from equation (2.32) converts equation (2.26) into

$$m_\nu(\alpha, \beta|t) = A \sum_{\lambda=-\infty}^{+\infty} a_{\nu,\lambda}(\alpha, \beta) e^{-i(\omega_{\nu,\mathrm{iso}} + \lambda\omega_r)t} \quad (2.33)$$

2.5.3 *Powder Averaging over α and β*

A final powder average over the α, β turning axes still is needed to compare the results with the acquisition FID. This step is accomplished by solving equation (2.32) for each member of the complete set of spherical surface points defined by α, β. One then must sum $m_\nu(\alpha, \beta|t)$ over all α, β rotation axes to define $M_\nu(t)$, the acquisition FID, of the νth spin as follows:

$$M_\nu(t) = \sum_{\alpha\beta} w_{\alpha\beta} \cdot m_\nu(\alpha\beta|t) \quad (2.34)$$

The weighting factor, $w_{\alpha\beta}$, for the α, β mechanical turning vector prescribes the fraction of spherical surface area assigned to each α, β rotational axis. Thus, $w_{\alpha\beta}$ are essential to weight the fractional contributions of a surface summation over $a_{\nu,\lambda}(\alpha\beta)$.

The powder averaging is straightforward as long as one is moving in the forward direction, where known chemical-shift values simulate a rotational pattern. This process involves merely selecting a representative and distributed number of surface points over which the numerical mapping can faithfully convert the shift values into adequate spectral response functions. Such ensemble averaging over α, β affects only the $W_{n=\pm1,\pm2}$ terms in equation (2.32). Accordingly, the $a_{\nu,\lambda}(\alpha\beta)$ values for each subset of spins, properly weighted and designated by α, β are stored in a summation register to give the ensemble average for $M_\nu(t)$.

Among the first numerical approaches used in such problems was the POWDER method by Alderman et al.[27] This method utilizes an octahedral face embedded into one of the PAF octants prescribed by the chemical shift tensor. The equilateral triangular face is readily subdivided to yield the number of points required for convergence. These points also have a specific factor that weights the fraction of surface points subtended in the solid angle of the incremental triangular segment. A numerical method by Lebedev,[28] and used by Eden and Levitt,[29] is based on a mathematical procedure for averaging physical properties over the surface of a sphere. The machinery, involving spherical-harmonic expansions of the spherical surface, requires the utilization of defined surface points along with appropriate weighting factors. The Utah laboratory has found that the Lebedev method converges rapidly and its sophistication makes it slightly more precise than the POWDER method for the same number of α, β points. However, increasing the number of spherical surface points to achieve more precision in the Lebedev convergence can become somewhat laborious if the set is not

readily available. Conversely, altering the number of surface points is easily achieved in the POWDER method.[27] A number of other numerical schemes[28] have been used to powder-average α, β surface points, but our laboratory has had experience only with POWDER and the Lebedev approach.

A slightly more challenging problem is the extraction of chemical shift parameters from the rotational bands found for a new nuclear rotational pattern. In this reverse approach, one uses successive iterations, guided by the simplex method, to converge on the best set of tensor-shift parameters to fit the rotational patterns. Initial shift parameters are selected and used with equation (2.32) to obtain an initial set of $a_{\nu,\lambda}(\alpha\beta)$. These initial FID values are compared with the experimental FID values, and simplex fitting varies the shift parameters until satisfactory convergence is reached between the experimental and computed results. In subsequent iterations, the set of $a_{\nu,\lambda}(\alpha\beta)$ must be re-scaled by properly weighting with $w_{\alpha\beta}$. As the Gaussian elimination procedure for diagonalizing a banded matrix is efficient, this iterative numerical method for powder averaging α, β orientations achieves convergence with remarkably efficiency even with a modest PC computer.

3 THE 5π-PULSE EXPERIMENT[7]

Figure 2 presents the basic sequence for the 5π-PULSE experiment subdivided into the evolution and acquisition regimes. During the rotor period, T, five π or 180° pulses modulate the developing phases of the magnetization, Φ_j, in the evolution regime. Figure 2 summarizes the respective evolution details rendered in time variables (T, t_e), or in phase angles $(2\pi, \Phi_{j=1,\ldots,6})$.

A mixture of γ_t in radians and degrees will be used for clarity and/or compaction of the notation. This use should be clear even if slightly inconsistent. Note the phase modulation in the evolution dimension at T is only dependent on the isotropic shifts of the various nuclear spins.

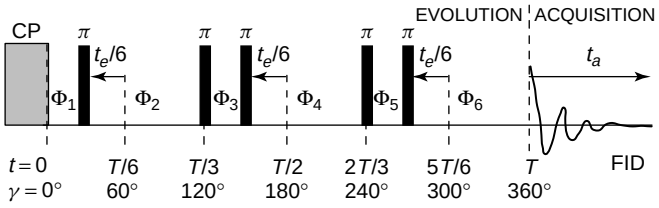

Figure 2 Carbon channel pulse sequence for the 5π-PULSE experiment. (Adapted from Ref.[7] with permission)

3.1 Magnetization in the 5π-PULSE Experiment

A standard 2D FID for a multinuclear subsystem of spins has the following general form:

$$m_\nu(t_e, t_a) = \sum_{\nu=1}^{N_\nu} m_o(\nu) \cdot g_\nu(t_e) \cdot f_\nu(t_a) \tag{3.1}$$

The sum over the index ν includes the different nuclei in the sample. $m_o(\nu)$ is the initial magnetization of the νth spin. The time-dependent function, $f_\nu(t_a)$, expresses the contribution from the νth FID. These functions are digitized and converted into frequency space using FT methods. At $t = T$ the phase accumulation during the evolution period for the νth nucleus is

$$g_\nu(t_e) = e^{-R_\nu(T)} e^{i\Phi_\nu(t_e)} \tag{3.2}$$

The term, $e^{i\Phi_\nu(t_e)}$, is a periodic phase-angle accumulation factor characterized by the angle, $\Phi_\nu(t_e)$. Equal pulse offsets, given in Figure 2 for the 1st, 3rd and 5th π pulses, are defined by the evolution time, t_e, on which $\Phi_\nu(t_e)$ depends. The five π pulses are equally spaced at $t_e = 0$, leaving the phase accumulation, for this specific evolution time, refocused and unaltered at time T. Combining equations (3.1) and (3.2) yields

$$m_\nu(t_e, t_a) = m_o(\nu) e^{-R_\nu(T)} e^{i\Phi_\nu(t_e)} f_\nu(t_a) \tag{3.3}$$

The relaxation term, $e^{-R_\nu(T)}$, in equations (3.2) and (3.3) decreases $m_o(\nu)$ to an effective magnetization value, $m_o(\nu)e^{-R_\nu(T)}$, that obtains when the acquisition FID begins. This decrease results from spin-spin relaxation with an effective rate given by

$$R_\nu(T) = l\left(\frac{T}{T_{L_\nu}}\right) + h\left(\frac{T}{T_{G_\nu}}\right)^2 \tag{3.4}$$

The relaxation constants, T_{L_ν} and T_{G_ν}, are the respective Lorentzian and Gaussian relaxation times typically used in solid-state studies, and mixing coefficients are l and h.

3.2 The Relationship between Phase Accumulation and the 5π-Pulse Scheme

An analysis of the phase angles in Figure 2 supplies the phase factors associated with the evolution dimension of the 2D spectrum. Table 1 summarizes the accumulation of angular phase due to rotation in the MAT experiment and to the π reflections on $m_\nu(\alpha, \beta|t)$ found in equation (2.33). The five π pulses are specified in Figure 2.

In this development, the B_1 field lies along the original $m_o(\nu)$ axis, but any other presumption would only produce

Table 1

jth phase	Developing phase accumulation	
	At the beginning of the jth period	At the end of the jth period
1	0	ϕ_1
2	$-\phi_1$	$\phi_2 - \phi_1$
3	$\phi_1 - \phi_2$	$(\phi_1 + \phi_3) - \phi_2$
4	$\phi_2 - (\phi_1 + \phi_3)$	$(\phi_2 + \phi_4) - (\phi_1 + \phi_3)$
5	$(\phi_1 + \phi_3) - (\phi_2 + \phi_4)$	$(\phi_1 + \phi_3 + \phi_5) - (\phi_2 + \phi_4)$
6	$(\phi_2 + \phi_4) - (\phi_1 + \phi_3 + \phi_5)$	$(\phi_2 + \phi_4 + \phi_6) - (\phi_1 + \phi_3 + \phi_5)$

an arbitrary phase shift that ultimately fails to affect the conclusions. At the end of the evolution period, i.e., $t = T$, the phase-angle accumulation becomes

$$\Phi_\nu(t_e) = (\Phi_2 + \Phi_4 + \Phi_6) - (\Phi_1 + \Phi_3 + \Phi_5) \tag{3.5}$$

The six phase periods, Φ_j, develop according to the following integrals along the γ_t path:

$$\Phi_j = \int_{t(j-1)}^{t(j)} \omega_\nu(\mathrm{LAB}|t)\,\mathrm{d}t = \frac{T}{2\pi}\int_{\gamma(j-1)}^{\gamma(j)} \omega_\nu(\mathrm{LAB}|\gamma_t)\,\mathrm{d}\gamma_t \tag{3.6}$$

where $\omega_\nu(\mathrm{LAB}|t)$ and $\omega_\nu(\mathrm{LAB}|\gamma_t)$ are the relevant t or γ_t forms of equation (2.24) for the νth spin. The two forms of integrals in equation (3.6) relate by a conformal change of variables from time to a rotational angle given by

$$\gamma_t = \omega_r t \quad \text{and} \quad \mathrm{d}t = \frac{\mathrm{d}\gamma_t}{\omega_r} = \frac{T}{2\pi}\,\mathrm{d}\gamma_t \tag{3.7}$$

The constraints imposed by equation (3.7) upon equation (3.6) and by the information and conventions in Figure 2 specify the specific phase-angle expressions as follows:

$$\begin{aligned}
\Phi_1 &= \frac{T}{2\pi}\int_0^{\frac{\pi}{3}-\frac{\pi}{3}t_e/T} \omega_\nu(\mathrm{LAB}|\gamma_t)\,\mathrm{d}\gamma_t \\
\Phi_2 &= \frac{T}{2\pi}\int_{\frac{\pi}{3}-\frac{\pi}{3}t_e/T}^{\frac{2\pi}{3}} \omega_\nu(\mathrm{LAB}|\gamma_t)\,\mathrm{d}\gamma_t \\
\Phi_3 &= \frac{T}{2\pi}\int_{\frac{2\pi}{3}}^{\pi-\frac{\pi}{3}t_e/T} \omega_\nu(\mathrm{LAB}|\gamma_t)\,\mathrm{d}\gamma_t \\
\Phi_4 &= \frac{T}{2\pi}\int_{\pi-\frac{\pi}{3}t_e/T}^{\frac{4\pi}{3}} \omega_\nu(\mathrm{LAB}|\gamma_t)\,\mathrm{d}\gamma_t \\
\Phi_5 &= \frac{T}{2\pi}\int_{\frac{4\pi}{3}}^{\frac{5\pi}{3}-\frac{\pi}{3}t_e/T} \omega_\nu(\mathrm{LAB}|\gamma_t)\,\mathrm{d}\gamma_t \\
\Phi_6 &= \frac{T}{2\pi}\int_{\frac{5\pi}{3}-\frac{\pi}{3}t_e/T}^{2\pi} \omega_\nu(\mathrm{LAB}|\gamma_t)\,\mathrm{d}\gamma_t
\end{aligned} \tag{3.8}$$

The $\omega_\nu(\mathrm{LAB}|\gamma_t)$ frequency response function in the laboratory frame, taken from equation (2.24), is modified to separate the zero-rank from the second-rank terms, as follows:

$$\begin{aligned}
\omega_\nu(\mathrm{LAB}|\gamma_t) &= \sum_{n=-2}^{2} (-1)^n W_{\nu,n}(\alpha,\beta)e^{in\gamma_t} \\
&= W_{\nu,o} + \sum_{n=\pm1,\pm2} (-1)^n W_{\nu,n}(\alpha,\beta)e^{in\gamma_t}
\end{aligned} \tag{3.9}$$

The $\omega_\nu(\mathrm{LAB}|\gamma_t)$ in equation (3.9) is divided into its two parts (i.e., the zero-rank rotationally invariant term, $W_{\nu,o}$, and four second-rank terms given by the summation of n over ±1 and ±2).

3.2.1 The Zero-Rank Term

The phase associated with the zero-rank term, $W_{\nu,o} = \omega_{\mathrm{iso}}$, of equation (3.9) when substituted into equation (3.8) and in turn into equation (3.5) yields the following:

$$\begin{aligned}
&\Phi_\nu(t_e) \\
&= \frac{T\omega_{\mathrm{iso}}}{2\pi}\left\{\begin{aligned}
&-\int_0^{\frac{\pi}{3}-\frac{\pi}{3}t_e/T}\mathrm{d}\gamma_t + \int_{\frac{\pi}{3}-\frac{\pi}{3}t_e/T}^{\frac{2\pi}{3}}\mathrm{d}\gamma_t - \int_{\frac{2\pi}{3}}^{\pi-\frac{\pi}{3}t_e/T}\mathrm{d}\gamma_t \\
&+\int_{\pi-\frac{\pi}{3}t_e/T}^{\frac{4\pi}{3}}\mathrm{d}\gamma_t - \int_{\frac{4\pi}{3}}^{\frac{5\pi}{3}-\frac{\pi}{3}t_e/T}\mathrm{d}\gamma_t + \int_{\frac{5\pi}{3}-\frac{\pi}{3}t_e/T}^{2\pi}\mathrm{d}\gamma_t
\end{aligned}\right\} \\
&= \frac{T\omega_{\mathrm{iso}}}{2\pi}\left\{2\left(-\tfrac{\pi}{3}+\tfrac{2\pi}{3}-\pi+\tfrac{4\pi}{3}-\tfrac{5\pi}{3}\right)+2\pi+2\pi\frac{t_e}{T}\right\} \\
&= \omega_{\mathrm{iso}}t_e
\end{aligned} \tag{3.10}$$

This form may now be substituted into equation (3.2) as discussed below.

3.2.2 The Second-rank Terms

Attention is now directed to the second-rank terms (i.e., $n = \pm1,\ \pm2$) of equation (3.9). These components vanish under the symmetry of equation (3.5). It is sufficient to show that any one of the generic terms is zero for all four second-rank terms to vanish. Thus, equations (3.5), (3.6) and any of the $n \neq 0$ components of equation (3.9) gives

$$\begin{aligned}
\Phi_{\nu,n}(t_e) &= \frac{T(-1)^n W_{\nu,n}(\alpha,\beta)}{2\pi} \\
&\times\left\{\begin{aligned}
&-\int_0^{\frac{\pi}{3}-\frac{\pi}{3}t_e/T} e^{in\gamma_t}\,\mathrm{d}\gamma_t + \int_{\frac{\pi}{3}-\frac{\pi}{3}t_e/T}^{\frac{2\pi}{3}} e^{in\gamma_t}\,\mathrm{d}\gamma_t \\
&-\int_{\frac{2\pi}{3}}^{\pi-\frac{\pi}{3}t_e/T} e^{in\gamma_t}\,\mathrm{d}\gamma_t + \int_{\pi-\frac{\pi}{3}t_e/T}^{\frac{4\pi}{3}} e^{in\gamma_t}\,\mathrm{d}\gamma_t \\
&-\int_{\frac{4\pi}{3}}^{\frac{5\pi}{3}-\frac{\pi}{3}t_e/T} e^{in\gamma_t}\,\mathrm{d}\gamma_t + \int_{\frac{5\pi}{3}-\frac{\pi}{3}t_e/T}^{2\pi} e^{in\gamma_t}\,\mathrm{d}\gamma_t
\end{aligned}\right\}
\end{aligned} \tag{3.11}$$

Upon integrating, one obtains

$$\begin{aligned}
\Phi_{\nu,n}(t_e) &= \frac{T(-1)^n W_{\nu,n}(\alpha,\beta)}{2\pi i n} \\
&\times\left\{\begin{aligned}
&2(+e^{in120^\circ}+e^{in240^\circ})+e^{in0^\circ}+e^{in360^\circ} \\
&+2(e^{in60^\circ}+e^{in180^\circ}+e^{in300^\circ})e^{in60^\circ t_e/T}
\end{aligned}\right\} = 0
\end{aligned} \tag{3.12}$$

Hence, the symmetry of the 5π-pulse sequence results in nullifying the four second-rank terms and in turn suppressing each of the sideband terms. This pulse scheme leaves the 2D spectrum to develop along the evolution direction under the influence of only the isotropic shifts.

3.3 The 2D FIREMAT FID Magnetization

The evolution FID for the νth nucleus is given by substituting equation (3.10) into equation (3.2),

$$g_\nu(t_e) = e^{-R_\nu(T)}e^{i\omega_{\nu,\mathrm{iso}}t_e} \tag{3.13}$$

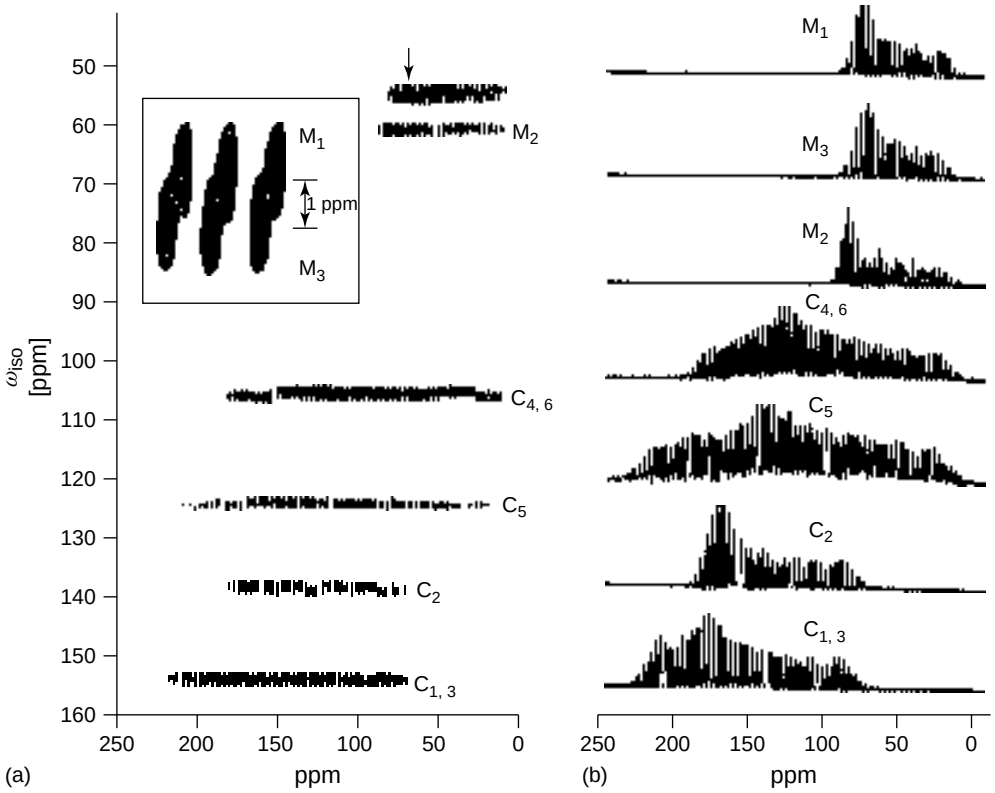

Figure 3 (a) A contour plot of the 5π-PULSE spectrum of 1,2,3-trimethoxybenzene, and (b) the corresponding ω_{iso} slices through the contour plot. The insert in (a) is a blow-up of a portion in the 1 and 3 methyl patterns to indicate the resolution between M_1 and M_3. (Reproduced from Ref.[7] with permission)

which when substituted into equation (3.1) yields an expression for the 2D FID.

$$m_\nu(t_e, t_a) = \sum_{\nu=1}^{N_\nu} m_o(\nu) e^{-R_\nu(T)} e^{i\omega_{\nu,\mathrm{iso}} \cdot t_e} f_\nu(t_a) \qquad (3.14)$$

Equation (3.14) is now in the standard mathematical form of a typical 2D FID with the acquisition FIDs separated linearly from the isotropic FID. The 2D FT of equation (3.14) yields a high-quality 2D spectrum in the frequency domain of solid 1,2,3-trimethoxybenzene (see Figure 3). Both the contour plot and corresponding slices through the different carbon-tensor bands exhibit representative data from the 5π-PULSE experiment.

3.3.1 The Individual Spin FIDs in the Acquisition Dimension

The acquisition FID, $f_\nu(t_a)$, is sampled rapidly and extends for a sufficient period for the νth nucleus to yield adequate spectral range and resolution in this dimension. In Figure 3(b) the spinning sideband patterns for the νth nucleus are separated by their isotropic shifts. A trade-off exists between decreasing the magnetization at T (i.e., $t_a = 0$) due to spin relaxation and the need for t_e to be sufficiently long to yield an evolution spectrum of adequate resolution.

4 TIGER PROCESSING OF TWO-DIMENSIONAL NMR SPECTRA

The rather significant compromises, made between S/N and resolution in solid NMR spectra, impact the accuracy of determining spectral parameters in solid NMR experiments. All Fourier methods experience such difficulties, of course, but solid spectra are particularly sensitive to this trade-off because of relatively rapid spin-spin relaxation in solids compared with liquids. Shortening the length of the evolution sampling periods minimizes loss of magnetization from such relaxation effects and increases the time efficiency of the experiment. Unfortunately, the resolution of the experiment is adversely affected. Early MAT solid-state experiments suffered from detrimental flip back pulses that significantly attenuate the magnetization in the xy plane, but the 5π-PULSE method avoids this problem of flip back pulses in the traditional MAT suite of experiments. However, as implied in Section 3 this method still requires relatively extensive evolution data-tables to achieve high resolution.

The so-called TIGER procedure[15] offers a way to extract high-resolution data from an otherwise truncated evolution data. Conversely, use of more but shorter t_e time increments increases the spectral width and thereby diminishes the incidence of aliasing in the evolution dimension. Such compromises in the t_a dimension are avoided because of the size of the acquisition FID data tables. In the process of achieving this objective with TIGER, the workers at the Utah NMR laboratory rediscovered two important papers by Manassen, Navon, and Moonen,[30,31] in which an extensive mathematical basis for TIGER is given. The minor differences between TIGER and the work of Manassen et al.[30,31] primarily reflect the different spectroscopic capabilities common in spectrometers extant at the two different publication times (separated by a decade). Specialists will want to study the complete

mathematical treatments of TIGER contained in these three relevant references.[15,30,31] TIGER is a general multidimensional method that has potential for enhancing a number of NMR applications, but the space and focus of this article precludes treatments that go beyond how TIGER works in MAT experiments.

4.1 Matrix Form of the FID Expression

Equation (3.14) may be formulated in standard matrix notation by first casting this equation in a form that reflects the digitized arrays encountered in data collection methods. This is done by expressing $t_e = (n_e - 1)\tau_e$ and $t_a = (n_a - 1)\tau_a$, where τ_e and τ_a are the incremental sampling periods in the respective evolution[32] and acquisition dimensions. The integer 1 is subtracted from digitization indices, n_e and n_a, to allow t_e and t_a to assume zero values. Thus, the digitizing indices, $n_e = 1, \ldots, N_e$ and $n_a = 1, \ldots, N_a$, are associated with N_e and N_a that are respectively the total number of evolution and acquisition increments. The νth spin index is n_ν. The digitized matrices appear as follows:

$$\mathbf{M}(n_e, n_a)_{N_e \text{ by } N_a} = \mathbf{G}(n_e, \nu)_{N_e \text{ by } N_\nu} \cdot \mathbf{F}(\nu, n_a)_{N_\nu \text{ by } N_a} \quad (4.1)$$

where

$$\mathbf{G}(n_e, \nu) = m_o(n_\nu) e^{-R_\nu(T)} e^{i(n_e-1)\omega_{\nu,\text{iso}}\tau_e} \quad (4.2)$$

$$\mathbf{F}(\nu, n_a) = f_\nu([n_a - 1]\tau_a) \quad (4.3)$$

The matrix multiplication in equation (4.1) represents the sum over ν in equation (3.14). In addition, the matrix dimensions, given in equation (4.1), assist in their physical interpretation as a row labeled by ν in $\mathbf{F}(\nu, n_a)$ contains the acquisition contribution to the FID for the νth spin. Likewise, the ν column in $\mathbf{G}(n_e, \nu)$ specifies the corresponding evolution FID component for the νth spin. While the individual $\mathbf{G}(n_e, \nu)$ and $\mathbf{F}(\nu, n_a)$ components are not directly measurable in the 5π-PULSE experiment, the 2D digitized components represented by $\mathbf{M}(n_e, n_a)$ are obtained directly in 2D 5π-PULSE experiments.

Manipulating equation (4.1) allows the extraction of $\mathbf{F}(\nu, n_a)$ from $\mathbf{M}(n_e, n_a)$. Multiplying both sides of equation (4.1) by the complex transpose, $\tilde{\mathbf{G}}^*(\nu, n_e)$, yields

$$\tilde{\mathbf{G}}^*(\nu, n_e)_{N_\nu \text{ by } N_e} \cdot \mathbf{M}(n_e, n_a)_{N_e \text{ by } N_a} = \{\tilde{\mathbf{G}}^*(\nu, n_e) \cdot \mathbf{G}(n_e, \nu)\}_{N_\nu \text{ by } N_\nu} \cdot \mathbf{F}(\nu, n_a)_{N_\nu \text{ by } N_a} \quad (4.4)$$

The inverse square matrix $\{\tilde{\mathbf{G}}^*(\nu, n_e) \cdot \mathbf{G}(n_e, \nu)\}^{-1}$, converts equation (4.4) into equation (4.5) and provides the desired $\mathbf{F}(\nu, n_a)$:

$$\mathbf{F}(\nu, n_a)_{N_\nu \text{ by } N_a} = \{\tilde{\mathbf{G}}^*(\nu, n_e) \cdot \mathbf{G}(n_e, \nu)\}^{-1}_{N_\nu \text{ by } N_\nu} \cdot \tilde{\mathbf{G}}^*(\nu, n_e)_{N_\nu \text{ by } N_e} \cdot \mathbf{M}(n_e, n_a)_{N_e \text{ by } N_a} \quad (4.5)$$

Both sides of equation (4.5) generate matrices that are of identical dimensions, N_ν by N_a. Hence, corresponding ν rows identify directly with each other. These $\mathbf{F}(\nu, n_a)$ vectors provide a separated and digitized FID for each of the νth spins. Hamilton[33] and Graybill[34] describe this matrix process as a way to perform a linear regression or a linear least-squares fit in general, and in particular for the FID of each individual spin in this application. Redundant data, when available, actually improve the mathematical analysis.

The mathematical developments linking equations (4.1) and (4.5) presumes a number of constraints on the equations to render the matrix procedures viable. It is essential that $N_e \geq N_\nu$. The index N_e is the total number of evolution increments and N_ν is the number of different nuclear spins. When $N_e < N_\nu$, the evolution data are insufficient to complete the matrix operations for all nuclear spins (i.e., $\nu = 1, \ldots, N_\nu$) and the process fails. If $N_e > N_\nu$, redundancy exists in the evolution data, and the matrix manipulations provide an even better regression or least-squares fit of the data. Should $N_e = N_\nu$, the operations yield solutions for the $\mathbf{F}$ vectors but without the statistical benefit of redundant data. Redundancy reduces the errors in a least-squares analysis. A final constraint on the mathematical manipulations requires the existence of a so-called guide spectrum expressed by $\mathbf{G}(n_e, \nu)$. Further details appear in Section 4.2.

This contraction of the 2D digitized FID data to individual nuclear 1D FIDs, is definitely not an FT procedure. Instead, the process involves more of a convolution method based on linear regression principles used in matrix least-squares computations.

4.2 Fitting the Guide Spectrum

The digitized guide spectra, contained in the $\mathbf{G}(n_e, \nu)$ matrix, starts with a typical isotropic spectrum such as obtained from a MAS high-speed spinning spectrum. Each isotropic peak is simulated and the corresponding digitized vector is placed into the νth row of the associated $\tilde{\mathbf{G}}^*(\nu, n_e)$ matrix to give

$$\tilde{\mathbf{G}}^*(\nu, N_e) = [\tilde{g}^*(\nu, 1) \cdots \tilde{g}^*(\nu, n_e) \cdots \tilde{g}^*(\nu, N_e)] \quad (4.6)$$

The individual digitized $\tilde{g}^*(\nu, n_e)$ value is the n_e element of the $\tilde{\mathbf{G}}^*(\nu, N_e)$ vector for the νth spin, and standard matrix methods give $\mathbf{G}(N_e, \nu)$ from the associated matrix, $\tilde{\mathbf{G}}^*(\nu, N_e)$.

Fitting a high-resolution isotropic spectrum (e.g., a MAS spectrum) to $\tilde{\mathbf{G}}^*(\nu, N_e)$ or $\mathbf{G}(N_e, \nu)$ becomes a crucial step in modeling FIDs such as described in equation (4.6). The fitting procedure adjusts the isotropic spectral frequencies and line shapes with a SIMPLEX algorithm until a satisfactory spectral fit is achieved. The isotropic frequencies follow directly from the independent guide spectrum and the line shapes are simulated using both Lorentzian and Gaussian relaxation processes in accordance with equation (3.4).

4.3 Illustration of the TIGER Method

The most instructive drawing in the literature[15] for the TIGER procedure uses as an example the PHORMAT spectrum (a rotational, but dense sideband spectrum) of 1,2,3-trimethoxybenzene (see Figure 4). The TIGER method is general and an additional application of TIGER will be provided as an example of a FIREMAT spectrum in Section 5. Figure 4 provides a graphic illustration on how the isotropic guide spectrum is decomposed into the individual νth columns of the $\mathbf{G}(N_e, \nu)$ matrix and then used with the 2D FID data to obtain the acquisition FIDs that exhibit the shift-tensor information. In this example, the number of evolution increments was only

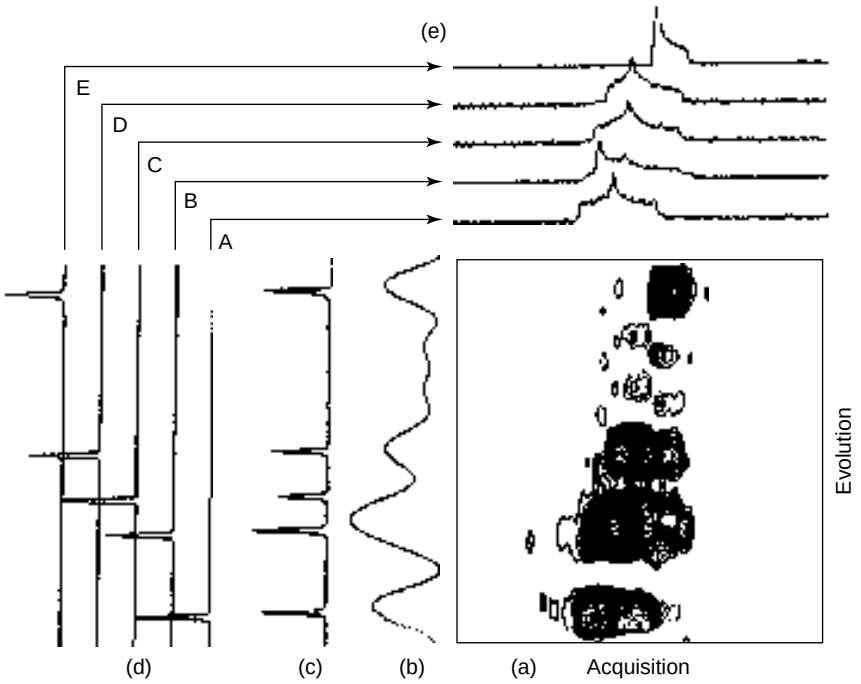

Figure 4 TIGER processing of a 2D solid spectrum of 2,6-dimethoxynaphthalene. (a) Typical 2D FT results obtained for the sparse eight evolution increments. (b) The projection of the 2D-frequency spectrum onto the evolution dimension illustrates the very broad lines in this dimension. (c) A sharp CP/MAS isotropic guide spectrum. (d) Individually simulated peaks of the CP/MAS spectrum provide the information for populating the **G** matrix. The simulated peaks involve a regression fit of both the frequency and shapes of the individual lines in the guide spectrum. (e) The de-convoluted individual ν shift-tensor bands. (Reproduced from Ref.[15] with permission)

eight, a number barely more than the six different nuclei in 2,6-dimethoxynaphthalene. This figure illustrates the unusual resolving power of the technique without a high evolution sampling rate that is costly in time. The narrow isotropic line widths imported into the evolution frequency dimension are at least an order of magnitude narrower than the corresponding line widths from a truncated FT of the 2D FID data. While the greater resolution of TIGER data is beneficial because of its discriminating abilities, the sharper line patterns also improve the S/N in the frequency domain.

Figure 4 includes one case of accidental degeneracy in peak B that is readily observable as two tensors in the B spectral band. Note importing the very narrow guide spectrum has the same effect of converting the broad peaks, shown in (b), into sharp frequency responses shown in Figure 4(c) for shift-tensor bands. This high resolution affects the accuracy with which spectral parameters can be determined. The increase in spectral definition and sensitivity is a hallmark of a TIGER processed spectrum.

5 THE FIREMAT VARIANT OF THE 5π-PULSE EXPERIMENT

The FIREMAT extension to the 5π-PULSE experiment uses the same evolution pulse scheme and TIGER processing method as the parent experiment. This new method also employs the pseudo 2D sideband suppression (P2DSS) replication strategy of Gan[35] to expand the data in the evolution dimension. By replicating information collected in the acquisition dimension and placing these data into the evolution dimension, the resolution is enhanced considerably along the isotropic shift axis. Whereas P2DSS collects data only at the rotor's echo position (i.e., 0, T, $2T$, etc.), FIREMAT replicates echoing data blocks found at all digitized increments. This allows one to decrease the number of evolution increments below the number of different nuclei that influences the TIGER method.

5.1 The P2DSS Method[35] and Replication of Refocused Spectral Data

The data replication scheme of P2DSS is given in Figure 5. The periodic features of MAT create rotational echoes in both dimensions and allow the data reorganization depicted in Figure 5. The echoes in both dimensions allow isotropic data tables to be populated solely from acquisition magnetization detected at multiples of T.

One may use the 1D string of evolution data along $t_a = 0$ to create a FID for the isotropic dimension. A Fourier transform from time to frequency space yields isotropic spectra that mimic a CP/MAS spectrum except for artifacts introduced by the discontinuous relaxation parameters, represented by the step functions along the right edge of Figure 5. Simulations indicate that sinc-type functions, resulting from these discontinuities, can introduce significant artifacts into the frequency spectrum whenever $T_2 \approx T$. Fortunately, the discontinuities smooth out when $T_2 > T$ and leave the baseline relatively unaffected as indicated in Figure 6.

5.2 The FIREMAT Method with Full Replication of Refocused Spectral Data

The FIREMAT variant[11] expands upon the P2DSS approach and digitizes throughout the whole rotor period in accordance with Figure 7. The magnetization experiences rotational

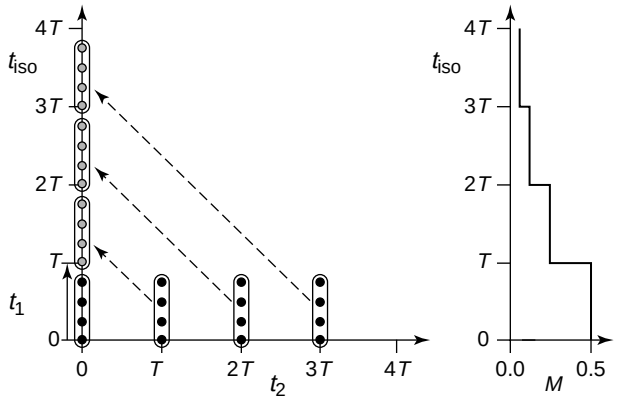

Figure 5 Graphical example of Gan's P2DSS Replication Scheme. The 2D FID is sampled in the acquisition dimension only at the echo position of the rotor. The solid circles represent the actual data. The open circles are replicated data obtained from the measured data and transported as shown in the figure. The right-hand side of the figure schematically represents the attenuation of the echo intensity due to relaxation during one rotation. (Reproduced from Ref.[11] with permission)

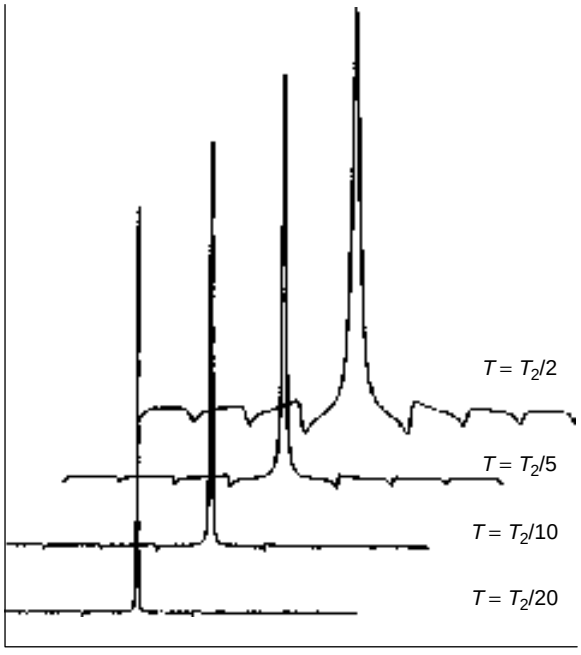

Figure 6 Sync-type artifacts are due to stepped relaxation discontinuities in the evolution data, but TIGER ameliorates this problem by minimizing the distortions. Note that, unlike true sidebands, the artifacts are dispersive and opposite in phase on each side of the spectral line. (Adapted from Ref.[11] with permission)

echoes at $t_a = T, 2T, \ldots, nT$, and, with repeated replication, a fully populated 2D evolution array may be obtained from the acquisition data-table. An $N_e \times N_a$ array bounds the size of this 2D data set, except as truncated by the replication process. The right border of Figure 7 again represents the discontinuous relaxation that may introduce spectral artifacts such as found in Figure 6.

Note the 1D string of FIREMAT data points along $t_a = 0$ constitutes the same 1D data used by Gan[35] to obtain

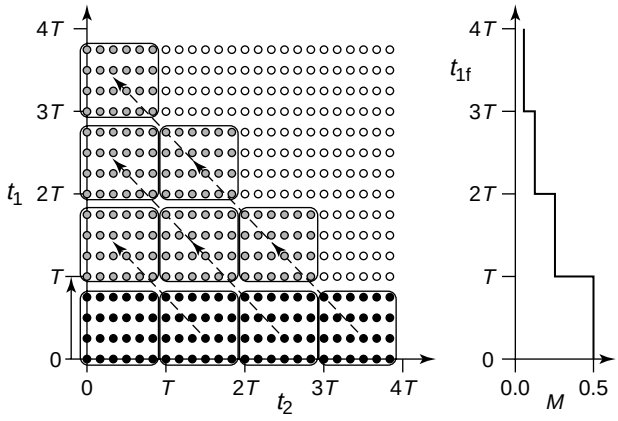

Figure 7 Graphical example of the FIREMAT replication scheme. Solid and open circles are actual and replicated data points of the type shown in Figure 5. The discontinuous relaxation intensities are again represented on the right-hand side of the figure. Data at the rotational echo positions and all intermediate positions populates a full 2D FT data table. (Reproduced from Ref.[11] with permission)

his P2DSS. While Gan's isotropic spectrum is more of an idiosyncratic construct of a CP/MAS spectrum, it becomes a special kind of 1D guide spectrum in the FIREMAT procedure. The guide, when constituted in this manner, arises directly from the 2D data and thus mitigates artifacts arising from irregularities in the replication step. The irregularities include discontinuous relaxation, correlation effects from repeated use of the same data, and possible abnormalities due to the manner in which the replicated blocks are truncated. Comparisons between single crystal and FIREMAT data fail to reveal significant replication errors.

5.3 FIREMAT Spectra of Erythromycin-A

Figure 8 illustrates the use of the FIREMAT method to obtain a spectrum on the medicinal, erythromycin-A, containing 36 different carbon atoms. The spectral quality and power of this 2D solid state technique is obvious and the time to acquire the data was only 19 h. The large numbers of carbons in erythromycin-A prevent the data from being presented conveniently in a single figure. Thus, the two remaining sp^2 carbons and a structure for erythromycin-A are given independently in Figure 8. Benefit is derived by aliasing the two sp^2 carbons into open spectral regions as the evolution timing increments can be decreased and the time-efficiency enhanced.

6 THE 2D-PASS FORM OF A 5π-PULSE EXPERIMENT

Antzutkin et al.[12] first proposed 2D-PASS by combining strategies used in PASS by Dixon[14] and in those underlying the 5π-PULSE experiment. In the evolution dimension, the 2D-PASS method separates, by spinning sideband order, the 2D FID. As the evolution dimension merely orders the sidebands by rank, this does not affect the high-resolution spectra found in the 2D-PASS approach[12] because all critical information is contained in the extensive acquisition FID. The original 1D-PASS, also a rotating solids experiment, uses only 4-π pulses

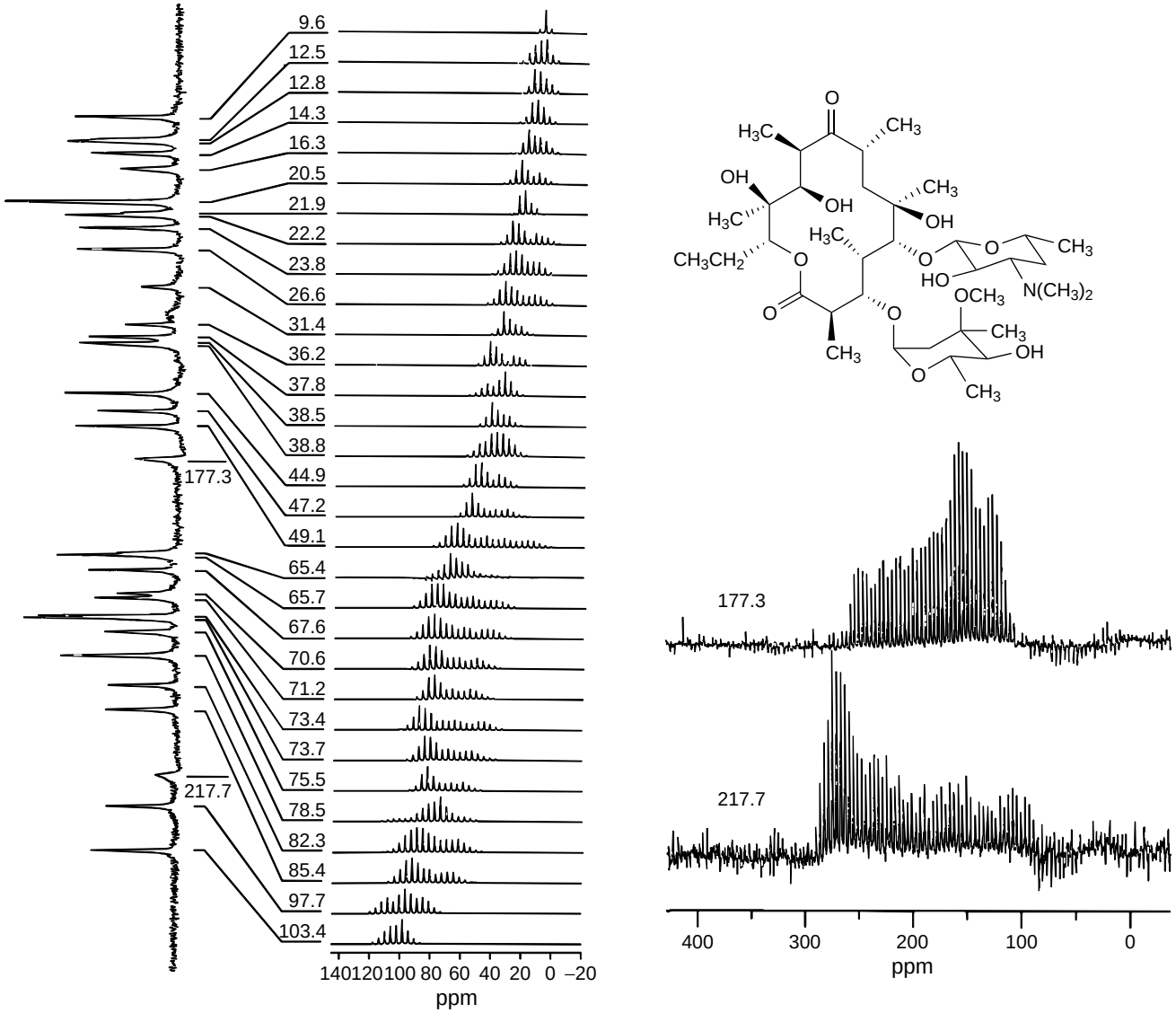

Figure 8 FIREMAT spectra of Erythromycin A Dihydrate shown from left to right for isotropic shifts and spinning sidebands of (a) sp^3 and (b) sp^2 carbons, respectively. (Reproduced from Ref.[11] with permission)

to phase adjust the spinning sidebands. However, if the original PASS approach[14] is adapted to a 2D 4π-PASS scheme, it would involve a variable-duration preparation period thereby introducing nonuniform relaxation. The fifth π-pulse included in 2D-PASS by Antzutkin et al.[12] refocuses the magnetization at a constant evolution period, T, and avoids variable spin relaxation perturbations that would otherwise deteriorate the 2D spectral quality.

6.1 The Postulated Pitch Angle

The 2D-PASS method utilizes a postulated variable pitch angle, Θ_e, or evolution time, t_e, defined in several different ways as follows:

$$\Theta_e = \omega_r t_e = 2\pi \frac{t_e}{T} = 2\pi \frac{n_e - 1}{N_e} \tag{6.1}$$

where ω_r is the slow-turning angular velocity and T is the period of the sample revolution.[36] The Θ_e and t_e have been formulated with linearly displaced evolution increments. The increment index is n_e, and the total number of evolution increments is N_e. To designate the $t_e = 0$ choice for the first increment, the integer 1 is again subtracted from n_e. Unfortunately, values for t_e are not programmed directly into the spectrometer's computer. A mathematical relation, however, relates the five π-pulses in the t_k timing sequence to the postulated Θ_e. Further, each of the five π-pulses is characterized by a time, t_k, or timing angle, θ_k, related to one another as follows: $t_k/T = \theta_k/2\pi$. This so-called pitch angle, Θ_e, is an important mathematical construct, designed to create a proper Fourier frequency conjugate that transforms the FIDs into separated rank-ordered sidebands. Hence,

$$m_v(t_e, t_a) = m_o(v)\Omega(t_e)F(t_a) \tag{6.2}$$

where the evolution phase factor, $\Omega(t_e)$ is given as

$$\Omega(t_e) = e^{-R(T)} e^{im\omega_r t_e} = e^{-R(T)} e^{im\Theta_e} \tag{6.3}$$

$F(t_a)$ is the acquisition FID separated by spinning sideband order. The formulation of Θ_e, in terms of the timing sequence of the π-pulses given by t_k, is represented graphically in Figure 9. This creative construction of Θ_e preserves the symmetry of the sideband information, while conforming to the standard 2D FID format for $m_\nu(t_e, t_a)$ given in equation (6.2).

6.2 The Relationships between the Pitch Angle and Timing Sequence

The connection between the evolution pitch angle, Θ_e, and the five timing angles, $\theta_{k=1,\ldots,5}$, follows the same mathematical machinery with slightly different notations from that used in Section 3.2. (Note $\theta_{k=0} = 0$ and $\theta_{k=6} = 2\pi$). This allows a direct comparison of the 5π-PULSE and 2D-PASS methods. It should be emphasized, however, that the expressions used herein are equivalent to the quintessential equations (28) and (29) of Antzutkin et al.[12] Using a common formalism enables one to appreciate the subtle differences and similarities between the 5π-PULSE and the 2D-PASS methods. The following equations are reproduced for convenience:

$$\Phi_\nu(t_e) = (\Phi_2 + \Phi_4 + \Phi_6) - (\Phi_1 + \Phi_3 + \Phi_5) \tag{3.5}$$

$$\Phi_j = \int_{t(j-1)}^{t(j)} \omega_\nu(\mathrm{LAB}|t)\,\mathrm{d}t = \frac{T}{2\pi}\int_{\gamma(j-1)}^{\gamma(j)} \omega_\nu(\mathrm{LAB}|\gamma_t)\,\mathrm{d}\gamma_t \tag{3.6}$$

$$\omega_\nu(\mathrm{LAB}) = \sum_{n=-2}^{2} (-1)^n W_{\nu,n}(\alpha,\beta)e^{in\gamma_t} = W_{\nu,o} + \sum_{n=\pm1,\pm2} (-1)^n W_{\nu,n}(\alpha,\beta)e^{in\gamma_t} \tag{3.9}$$

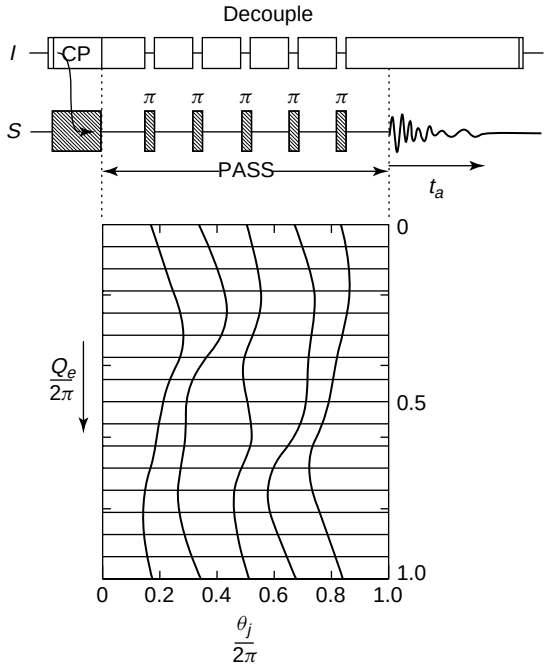

Figure 9 The pitch angle, Θ_e, plotted versues the phase displacements, $\theta_{j=1,\ldots,5}$, of the five π-pulses needed to refocus different sideband orders in the 2D PASS approach. (Adapted from Ref.[12] with permission)

The integral limits in 2D-PASS are specified by $\gamma(j) = \theta_j$. The total phase accumulation up to the time, t_e, for the nucleus ν is indicated by $\Phi_\nu(t_e)$, and the six corresponding sub-period phase accumulations by $\Phi_{j=1,\ldots,6}$ designated by the index j. These phase accumulations, illustrated explicitly in Figure 2 and implied in Figure 9, hold for each independent nucleus, ν. The zero-rank, $W_{\nu,n=o} = \omega_{\nu,\mathrm{iso}}$, and the second-rank, $W_{\nu,n=\pm1,\pm2}(\alpha,\beta)$, frequency terms are given explicitly in equation (2.19).

The imposed boundary conditions on the timing sequence differ between the 5π-PULSE and 2D-PASS experiments. In Section 3.2 it was noted that the 5π-PULSE timing sequence preserves the $\omega_{\nu,\mathrm{iso}}$ terms, but the remaining four second-rank terms, $W_{\nu,n=\pm1,\pm2}(\alpha,\beta)$, average to zero. It now is shown how 2D-PASS suppresses by design the $\omega_{\nu,\mathrm{iso}}$ terms while implementing a spectral feature based on the four $W_{\nu,n=\pm1,\pm2}(\alpha,\beta)$ terms.

6.2.1 The Zero-rank Term

By analogy to the 5π-PULSE development in Section 3.2.1, $\Phi_\nu(\Theta_e)$ may also be expressed for the zero-rank term in $\Phi_{j=1,\ldots,6}$ as follows:

$$\Phi_{\nu,n=o}(\Theta_e) = \omega_{\nu,\mathrm{iso}}\frac{T}{2\pi}\left[\left(\int_{\theta_1}^{\theta_2}\mathrm{d}\gamma_t + \int_{\theta_3}^{\theta_4}\mathrm{d}\gamma_t + \int_{\theta_5}^{2\pi}\mathrm{d}\gamma_t\right) - \left(\int_0^{\theta_1}\mathrm{d}\gamma_t + \int_{\theta_2}^{\theta_3}\mathrm{d}\gamma_t + \int_{\theta_4}^{\theta_5}\mathrm{d}\gamma_t\right)\right] \tag{6.4}$$

Integrating equation (6.4) yields the following expressions:

$$\Phi_{\nu,n=o}(\Theta_e) = \omega_{\nu,\mathrm{iso}}\frac{T}{2\pi}[-2(\theta_1 - \theta_2 + \theta_3 - \theta_4 + \theta_5) + 2\pi] = 0 \tag{6.5}$$

where $\Phi_{\nu,o}(\Theta_e)$ has been suppressed by setting it equal to zero. From equation (6.5) it becomes a simple matter to suppress the $\omega_{\nu,\mathrm{iso}}$ by forcing the linear combination of time angles to vanish. Hence, this null condition is used to form one of five constraints in the construction of Θ_e, and is expressed as

$$\pi - (\theta_1 - \theta_2 + \theta_3 - \theta_4 + \theta_5) = 0 \text{ or } t_1 - t_2 + t_3 - t_4 + t_5 = \frac{1}{2}T \tag{6.6}$$

The equivalent expression in time follows from $\theta_\kappa = 2\pi(t_\kappa/T)$.

6.2.2 The Second-rank Terms

Attention is now turned to the second-rank terms. As before, it is sufficient to integrate only one of the $n = \pm1, \pm2$ terms. Following the logic of Section 3.2.2, the n-labeled second-rank terms becomes

$$\Phi_\nu(\Theta_e) = (-1)^n W_{\nu,n}(\alpha,\beta) \times \frac{T}{2\pi}\left[\left(\int_{\theta_1}^{\theta_2} e^{in\gamma_t}\mathrm{d}\gamma_t + \int_{\theta_3}^{\theta_4} e^{in\gamma_t}\mathrm{d}\gamma_t + \int_{\theta_5}^{2\pi} e^{in\gamma_t}\mathrm{d}\gamma_t\right) - \left(\int_0^{\theta_1} e^{in\gamma_t}\mathrm{d}\gamma_t + \int_{\theta_2}^{\theta_3} e^{in\gamma_t}\mathrm{d}\gamma_t + \int_{\theta_4}^{\theta_5} e^{in\gamma_t}\mathrm{d}\gamma_t\right)\right] \tag{6.7}$$

Table 2 Timings for 2D-PASS Experiment Shown in Figure 9 (taken from Ref.[12])

Evolution increment	Pitch angle $\frac{\Theta_e}{2\pi} = \frac{n_e - 1}{N_e}$	$\frac{\theta_1}{2\pi}$	$\frac{\theta_2}{2\pi}$	$\frac{\theta_3}{2\pi}$	$\frac{\theta_4}{2\pi}$	$\frac{\theta_5}{2\pi}$
1	0.00000	0.16667	0.33333	0.50000	0.66667	0.83333
2	0.06250	0.18989	0.36501	0.52042	0.69657	0.85127
3	0.12500	0.21668	0.39542	0.53812	0.72177	0.86239
4	0.18750	0.24453	0.42002	0.54898	0.73845	0.86496
5	0.25000	0.26915	0.43011	0.54584	0.74192	0.85703
6	0.31250	0.28147	0.41078	0.52131	0.73135	0.83935
7	0.37500	0.26731	0.35926	0.49092	0.71890	0.81992
8	0.43750	0.23472	0.31159	0.48618	0.71464	0.80533
9	0.50000	0.20979	0.29022	0.50000	0.70979	0.79022
10	0.56250	0.19467	0.28536	0.51382	0.68841	0.76528
11	0.62500	0.18008	0.28110	0.50908	0.64074	0.73269
12	0.68750	0.16065	0.26865	0.47870	0.58922	0.71853
13	0.75000	0.14297	0.25808	0.45416	0.56990	0.73085
14	0.81250	0.13504	0.26155	0.45102	0.57998	0.75547
15	0.87500	0.13761	0.27823	0.46188	0.60458	0.78333
16	0.93750	0.14874	0.30343	0.47958	0.63499	0.81011

Evaluating the integrals in equation (6.7) gives the following:

$$\Phi_{\nu,n}(\Theta_e) = W_{\nu,n}(\alpha, \beta)\frac{(-1)^n T}{in2\pi} \times [e^0 + e^{2\pi} + 2(-e^{in\theta_1} + e^{in\theta_2} - e^{in\theta_3} + e^{in\theta_4} - e^{in\theta_5})] \tag{6.8}$$

Using definitions given in equations (6.3) and (3.9), the total phase accumulation, $\Phi_\nu(t_e)$, for the postulated pitch angle is given by

$$\Phi_{\nu,n}(\Theta_e) = (-1)^p W_{\nu,n}\frac{T}{2\pi}\int_0^{\Theta_e} e^{in\gamma_t}\,\mathrm{d}\gamma_t = -W_{\nu,n}\frac{T}{in2\pi}(e^{in\Theta_e} - 1) \tag{6.9}$$

Note $(-1)^p$ provides the alternating phase coherency of successive π-pulses (in this case $p = 5$).

Combining equations (6.8) and (6.9) and eliminating common factors yields

$$e^{in\Theta_e} + 1 + 2(-e^{in\theta_1} + e^{in\theta_2} - e^{in\theta_3} + e^{in\theta_4} - e^{in\theta_5}) = 0 \tag{6.10}$$

Five simultaneous equations were obtained from equations (6.6) and (6.10) from which five θ_k values are found for a given value of Θ_e. The four equations ($n = \pm 1, \pm 2$) embodied in equation (6.9) are best separated[12] into $n = 1, 2$ and into real and imaginary components to calculate values for four of the five θ_k constraints that yield each set of $\Theta_e = 2\pi(n_{e-1}/N_e)$ evolution increments. Antzutkin et al.[12] include a simultaneous equation sub-routine (Mathematica[37]) in their appendix for calculating the five $\theta_k/2\pi$ values that are used to construct Θ_e. Typical timing values are given in Table 2 for the 16 incremented pitch angles in the 2D-PASS experiment.

6.3 2D-PASS Spectra of Ampicillin

The 2D-PASS spectra (both contour and peak plots) for ampicillin[13] are presented in Figure 10. Note how the data combine in such a way that the evolution dimension contains only rank-ordered sidebands, whereas the acquisition-dimension portrays both isotropic and shift tensor information of each sideband component. Computer shearing of the 2D spectral data provides the same rotational sideband pattern for a given nucleus, as found in the FIREMAT spectrum given in Figure 8. Considerable benefits in spectral resolution derive from the larger acquisition data tables in 2D-PASS. These advantages mirror the improvements in the FIREMAT spectra due to data replication.

7 COMPARISON OF 5π-PULSE TYPE OF EXPERIMENTS

7.1 Qualitative Comparison of FIREMAT and 2D-PASS Methods

A careful comparison of Figures 2 and 9, at $t_e = 0$, indicates that 2D-PASS and FIREMAT, along with its predecessor 5π-PULSE, should all give equivalent spectral responses at $t_e = 0$. This similarity in the time-zero magnetization for FIREMAT and 2D-PASS suggests, to a first approximation, that these experiments should have comparable S/N. This conclusion has been verified when a constant number of evolution increments is used in both FIREMAT and 2D-PASS data on the same compound.[38] Further, the error propagation in the fit of principal shift values revealed no statistically significant difference, providing proper allowance is made for the greater implementation of automation in the FIREMAT data analysis.

FIREMAT includes automated subroutines for the TIGER and Banded-Matrix-SIMPLEX processing of FIDs in the time domain. Considerably more data in regression fits usually enhance the spectral quality. Hence, the extracted shift parameters are improved considerably by time domain fitting of the FIDs. The sensitivity of spectral parameters from 2D-PASS data would also probably benefit from time-domain fitting of the FIDs. The Herzfeld–Berger method[10] is often used to extract the 2D-PASS shift parameters from peak-height measurements that unfortunately fail to take advantage of the increased data found in a time domain FID.

Except for $t_e = 0$, the 2D-PASS and FIREMAT methods diverge in their treatment of the evolution dimension, and a number of differences may affect the time efficiency of the relative experiments. These differences primarily deal with the use of

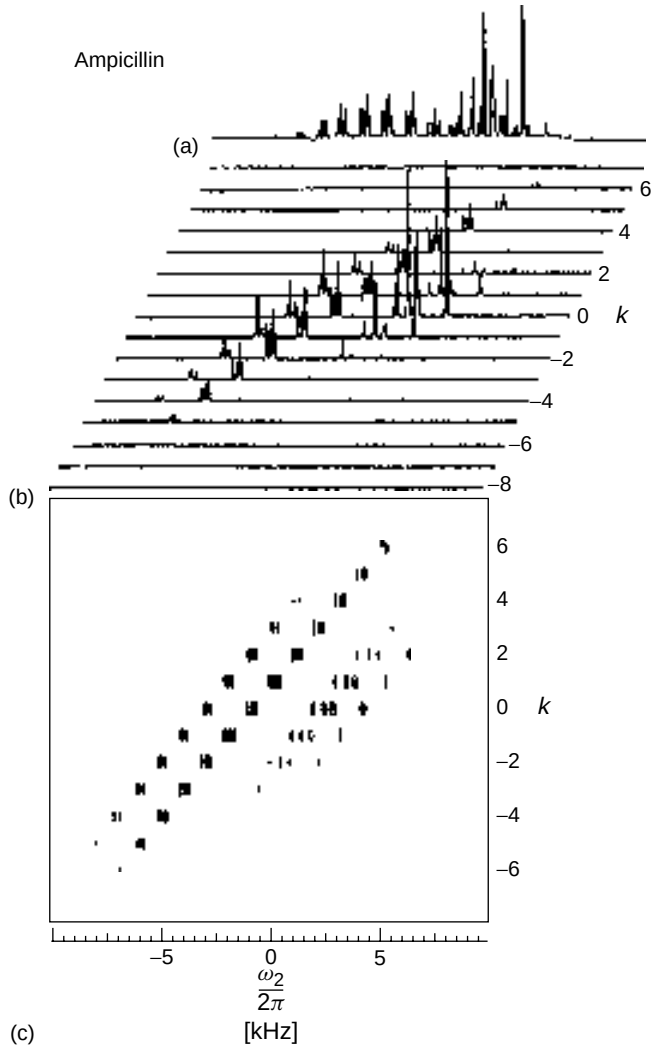

Figure 10 2D-PASS of ampicillin. (Reproduced from Ref.[13] with permission)

TIGER and with spectral aliasing in the evolution dimension that may or may not be important depending upon the molecular size and spectral complexity. The spectroscopist's control over these factors is limited to the selection of the turning frequency, $1/T$, and sampling rate, $1/\tau_e$, whether one uses an actual (FIREMAT) or an effective (2D-PASS) value for τ_e, which is the incremental sampling period. Discounting differences in aliasing and the benefits and/or disadvantages of TIGER, the two methods are otherwise essentially the same except for the visual presentation of the spectral results in frequency space.

7.2 Turning Rates, ω_r, Turning Period, T, and Minimum Span, ω_{span}, of the Shift Tensor

At least three spinning bands (the center and a minimum of two sidebands) for each unique nucleus must be collected in order to determine three principal shift-tensor frequencies and/or the corresponding three irreducible shift frequencies: ω_{iso}, ω_{acent}, and ω_{span}. When the turning rate exceeds a value somewhere between $\omega_{span}/3$ (for axially symmetric tensors) to $\omega_{span}/2$ (for centro-symmetric tensors), the number of spinning bands could be less than three. In this instance, it is impossible to determine chemical shift principal values from such a rotation pattern. ω_{span}^{min} is defined as the minimal spectral width for the narrowest tensor, which establishes the maximum rotation rate that will allow all tensors in the sample to be determined simultaneously. The situation of an axially symmetric shift tensor is more restrictive because ω_{iso} is no longer found at the mid-point of the band. In this situation the factor of 1/3 should be used to specify the maximum turning rate, ω_r^{max}, or minimum turning period, T^{min}. Under these constraints the various quantities are related by

$$\omega_r^{max} = \left(\frac{2\pi}{T^{min}}\right) \leq \left(\frac{\omega_{span}^{min}}{3}\right) \text{ or } T^{min} \geq \left(\frac{6\pi}{\omega_{span}^{min}}\right) \qquad (7.1)$$

Consider a typical methyl chemical-shift ω_{span} of 1500 Hz obtained from a 15 ppm ω_{span} in a 400 MHz proton instrument (i.e., 100 MHz for ^{13}C). This value in equation (7.1) requires that the maximum turning rate, $\omega_r^{max}/2\pi$, be 500 Hz or less in order to observe at least three sidebands. Slower turning rates further increase the number of sidebands that are beneficial to the precision of the extracted principal shift values.

7.3 Spectral Evolution Resolution, ω_{res}^{evol}, Spin-spin Relaxation, T_2, Evolution Periods, T

Standard FT relationships affecting resolution also govern in the solid state experiments encountered in this article. Thus, the evolution resolution, ω_{res}^{evol}, is limited by the spin-spin relaxation time, T_2, in accordance with

$$\omega_{res}^{evol} \cong \left(\frac{1}{T_2}\right) \geq \frac{2\pi}{T^{min}} \text{ or } T^{min} \geq 2\pi T_2 \cong \left(\frac{2\pi}{\omega_{res}^{evol}}\right) \qquad (7.2)$$

When $1/T_2$ is greater than $2\pi/T^{min}$, the relaxation broadens the rotational sidebands beyond the ω_{span}^{min} of the tensor and it becomes impossible to characterize such tensor bands. Hence, as a practical matter, ω_{span}^{min} is specified by the narrowest shift tensor whose principal values can be measured from the spinning bands. When one or more of the narrower shift tensors is not distinguishable from spherically symmetric tensors due to relaxation limitations, the anisotropic features of the tensor are lost. Careful attention must be given to this problem because both relaxation and rapid rotations that are too fast will exhibit spherical tensor properties. Relaxation in most bio-organic solids, which tend to exhibit considerable internal motion, usually does not limit the anisotropic tensor information for many bio-molecules. Turning the sample too rapidly need not be a problem as this situation is under the control of the spectroscopist.

7.4 Evolution Spectral Widths and the Sampling Rates

To monitor a spectral width in the evolution dimension and avoid aliasing, the evolution sampling-rate, $1/\tau_e$, must be greater than the evolution spectral width, ω_{SW}^{evol}, properly converted into Hz. This condition is expressed by

$$\frac{1}{\tau_e} \geq \left(\frac{\omega_{SW}^{evol}}{2\pi}\right) \qquad (7.3)$$

For the 5π-PULSE experiment, $\omega_{SW}^{evol} = \omega_{isoW}^{evol}$, the overall width of the isotropic spectrum. Aliasing or resolution in the evolution dimension for 2D-PASS is not of concern. The only issue in 2D-PASS becomes one of the total number of sidebands required to cover the largest tensor band, while maintaining at least three tensor sidebands for the narrowest tensor (see below).

7.5 The Parent 5π-PULSE Experiment

It is a simple matter to calculate a minimal number of evolution increments, $N_e = T/\tau_e$, by multiplying equations (7.1) by (7.3). The inequality is still valid providing the 5π-PULSE experiment is not limited by relaxation as indicated in equation (7.2). In this limit, the following expression is obtained:

$$N_e(5\pi\text{-Pulse}) = \frac{T^{min}}{\tau_e} \geq \left(\frac{3 \cdot \omega_{isoW}^{evol}}{\omega_{span}^{min}}\right) \tag{7.4}$$

Further, the required number of evolution increments depends on the number of nuclear spins that must be differentiated with the FID or with TIGER. This expression is given as follows:

$$N_e(5\pi\text{-Pulse}) \geq N_\nu \tag{7.5}$$

Assuming possible values of $\omega_{isoW}^{evol} \approx 150$ ppm and $\omega_{span}^{min} \approx 10$ ppm, the number of evolution increments, in the absence of relaxation constraints, would exceed 45 irrespective of the molecular size. Greater efficiency could be realized if ω_{isoW}^{evol} were smaller or if ω_{span}^{min} were to be larger. For example, the more favorable case where $\omega_{isoW}^{evol} \approx 80$ ppm and $\omega_{span}^{min} \approx 20$ ppm, would require only 12 increments. One can also escape some of the time inefficiencies if a modest amount of aliasing can be tolerated, especially in relatively small molecules where aliasing may be readily identified. Line broadening due to truncating the FID unduly will limit the S/N ratio and the effective resolution of the frequency domain.

7.6 The Parent 5π-PULSE Experiment with TIGER

The introduction of TIGER processing usually leaves the rotational lines narrower and enhances the S/N. The information from the guide spectrum can be used to optimize resolution and avoid aliasing. Sharper lines from the guide spectrum also yield higher peak intensities with a favorable impact on the S/N in the frequency domain. TIGER is especially powerful when the isotropic width and the minimum span are very similar. In this case, very narrow lines obtain with N_e barely larger than N_ν as found in Figure 4. Nonetheless, the TIGER formalism still requires that the minimum number of evolution increments be equal to or greater than the number of nuclear spins in order to obtain the matrix inverse required.[39] This situation is quite critical when molecular size increases to 50–100 carbon-13 nuclei for relevant bio-molecules, and one must conform to the expression in equation (7.5). Further, the creation of a suitable guide spectrum is much more difficult when overlapping isotropic peaks found in larger molecules introduces accidental degeneracy into the spectrum.

7.7 The FIREMAT Variant of 5π-PULSE

In the absences of a relaxation limitation, the replication provides efficiency for FIREMAT that no longer depends on number of nuclear spins. The replication scheme used in this method contains sufficient N_e to eliminate the constraint on N_ν. The evolution time sampling rate, $1/\tau_e$, still governs aliasing in the evolution dimension and the second term of equation (7.5) still obtains:

$$N_e(\text{FIREMAT}) \geq \left(\frac{3 \cdot \omega_{isoW}^{evol}}{\omega_{span}^{min}}\right) \tag{7.6}$$

7.8 The 2D-PASS Alternative to 5π-PULSE

The number of sidebands in 2D-PASS needed to span the widest tensor band determines N_e(2D-PASS). The minimal number of sidebands is readily calculated by enforcing at least three sidebands for the narrowest tensor and noting the corresponding impact on the number of sidebands in the widest tensor. Hence, the constraint for 2D-PASS yields the following:

$$N_e(\text{2D-PASS}) \geq \left(\frac{3 \cdot \omega_{SW}^{max}}{\omega_{span}^{min}}\right) \tag{7.7}$$

where ω_{SW}^{max} is the maximum width of the spectrum, including all of the rank-ordered side bands. To optimize the use of Fast-FT methods with 2D-PASS, it becomes necessary to increase the number of evolution increments to the next higher power of 2 above N_e(2D-PASS) given in equation (7.7). One of the benefits claimed for 2D-PASS is that standard 2D FT methods may be used to secure a frequency domain spectrum. TIGER, it may be argued, benefits the FIREMAT approach.

7.9 Comparison of 2D-PASS and FIREMAT

Abandoning the alleged advantages of using Fast FT methods or TIGER, equations (7.6) and (7.7) identify the factors that primarily differentiate the two methods. As ω_{SW}^{max} and ω_{isoW}^{evol} are very similar, one is left with the conclusion that the two approaches are comparable. There are instances when the maximum spectral span is larger than the spread of isotropic shifts and vice versa. Hence, the two methods are each preferred under different circumstances. The differences that the author's laboratory has found, deal primarily with the efficiencies of fitting time domain FIDs or peak heights in the frequency domain. Use of TIGER can produce enhanced S/N in the frequency domain and favors peak-height fitting. Time domain fitting of FIDs would equalize this advantage. Thus, both FIREMAT and 2D-PASS are sufficiently similar that personal experience likely becomes the dominant factor in choosing between the two approaches. However, both methods have proven sufficiently successful with moderately large biomolecules to attest to the arrival of 2D solid state methods in chemical studies.

8 REFERENCES

1. A. M. Orendt, in 'Encyclopedia of Nuclear Magnetic Resonance', eds D. M. Grant and R. K. Harris, John Wiley & Sons: Chichester, 1996, Vol. 2, p. 1282.

2. J. Zh. Hu, W. Wang, and R. J. Pugmire, in 'Encyclopedia of Nuclear Magnetic Resonance', eds D. M. Grant and R. K. Harris, John Wiley & Sons: Chichester, 1996, Vol. 5, p. 2914.
3. A. Bax, N. M. Szvereneyi, and G. E. Maciel, *J. Magn. Reson.*, 1983, **52**, 147.
4. Z. Gan, *J. Am. Chem. Soc.*, 1992, **114**, 8307.
5. J. Zh. Hu, A. M. Orendt, D. W. Alderman, R. J. Pugmire, C. Ye, and D. M. Grant, *Solid State NMR*, 1994, **3**, 181.
6. J. Zh. Hu, W. Wang, F. Liu, M. S. Solum, D. W. Alderman, R. J. Pugmire, and D. M. Grant, *J. Magn. Reson. A*, 1994, **113**, 210.
7. J. Zh. Hu, D. W. Alderman, C. Ye, R. J. Pugmire, and D. M. Grant, *J. Magn. Reson. A*, 1993, **105**, 82.
8. N. K. Sethi, D. W. Alderman, and D. M. Grant, *Mol. Phys.*, 1990, **71**, 217.
9. S. Vega, in 'Encyclopedia of Nuclear Magnetic Resonance', eds D. M. Grant and R. K. Harris, John Wiley & Sons: Chichester, 1996, Vol. 3, p. 2011.
10. J. Herzfeld and A. E. Berger, *J. Chem. Phys.*, 1980, **73**, 6021.
11. D. W. Alderman, G. McGeorge, J. Zh. Hu, R. J. Pugmire, and D. M. Grant, *Mol. Phys.*, 1998, **95**, 1113.
12. O. N. Antzutkin, S. C. Shekar, and M. H. Levitt, *J. Magn. Reson.*, 1995, **115**, 7.
13. O. N. Antzutkin, Y. K. Lee, and M. H. Levitt, *J. Magn. Reson.*, 1998, **135**, 144.
14. W. T. Dixon, *J. Magn. Reson.*, 1981, **44**, 220; *J. Chem. Phys.*, 1982, **77**, 1800.
15. G. McGeorge, J. Zh. Hu, C. L. Mayne, D. W. Alderman, R. J. Pugmire, and D. M. Grant, *J. Magn. Reson.*, 1997, **129**, 134.
16. D. M. Grant, in 'Encyclopedia of Nuclear Magnetic Resonance', eds D. M. Grant and R. K. Harris, John Wiley & Sons: Chichester, 1996, Vol. 2, p. 1305.
17. R. N. Zare, 'Angular Momentum', John Wiley & Sons: New York, 1988, pp. 177–180. Zare closes his discussion of conventions, "by considering the always vexing problem of relating spherical tensor components defined in space-fixed and molecule-fixed frames".
18. R. N. Zare, 'Angular Momentum', John Wiley & Sons: New York, 1988, p. 85.
19. R. N. Zare, 'Angular Momentum', John Wiley & Sons: New York, 1988, p. 81.
20. J. Mason, *Solid State NMR*, 1993, **2**, 285.
21. M. Mehring, 'High Resolution NMR in Solids', 2nd edition, Springer: New York, 1983. Mehring provides an equivalent transformation from frame P to L using two spherical harmonic expansions. This approach is comparable to the two Wigner rotation matrix transformations used in this work as only four variable rotational angles are needed in either formalism.
22. Maple 6, © Waterloo Maple Inc. Automatic mathematical software is used to derive the expression in equation (2.15). Agreements between the Wigner rotation matrix and the similarity transformations mutually confirm the validity of the derivations.
23. M. M. Maricq and J. S. Waugh, *J. Chem. Phys.*, 1979, **70**, 3300. These workers found experimentally that sidebands exhibit different phases relative to the center band in rotating single crystals. Conversely, it had been known for some time that spinning side bands on powder microcrystalline materials have identical phase factors.
24. M. H. Levitt, *J. Magn. Reson.*, 1989, **82**, 427.
25. R. N. Zare, 'Angular Momentum', John Wiley & Sons: New York, 1988, note 5, page 18. "In my first encounter with phase conventions I took the attitude, 'Why should I bother because after all, the phase is arbitrary?' .... This is the first of many instances where care must be exercised in the choice of phase, a most vexing aspect of angular momentum theory. Finally, a warning should be made to the uninitiated that phase conventions must be checked in going from one literature reference to another ...". The reader is referred to Zare's profundity on this subject, much of which had to be omitted.
26. E. U. Condon and G. H. Shortley, 'Theory of Atomic Spectra', Cambridge University Press, 1935; paperback 1963.
27. D. W. Alderman, M. S. Solum, and D. M. Grant, *J. Chem. Phys.*, 1986, **84**, 3717.
28. V. I. Lebedev, *Zh. Vychisl. Mat. Fiz.*, 1975, **15**, 48; 1976, **16**, 193; *Sibirsk. Mat. Zh.*, 1977, **18**, 132; *Sov. Phys.-Dokl.*, 1992, **45**, 587.
29. M. Eden and M. H. Levitt, *J. Magn. Reson.*, 1998, **132**, 220.
30. Y. Manassen, G. Navon, and C. T. W. Moonen, *J. Magn. Reson.*, 1987, **72**, 551.
31. Y. Manassen and G. Navon, *J. Magn. Reson.*, 1988, **79**, 291.
32. To be precise, the TIGER method does not require that the t_e increments be equal as required by FT methods. However, the replication scheme employed in the FIREMAT application in this article is best served with equal increments. Further information on unequal t_e intervals is treated in the literature.
33. W. C. Hamilton, 'Statistics in Physical Science', Ronald Press, New York, 1964.
34. F. A. Graybill, 'Theory and Application of the Linear Model', Wadsworth and Brooks/Cole: Pacific Grove, 1976.
35. Zh. Gan, *J. Magn. Reson. A.*, 1994, **109**, 253.
36. The development of the topic in terms of angle or time is immaterial, because the angular velocity, ω_r, is constant and converts the two quantities directly into each other.
37. S. Wolfram, 'Mathematica: A System for Doing Mathematics by Computer', Addison-Wesley: Reading, MA, 1988.
38. J. Zh. Hu, F. Guenneau, C. M. V. Taylor, D. W. Alderman, R. J. Pugmire, and D. M. Grant, 'Comparison between FIREMAT and 2D-PASS, unpublished.
39. See discussion of equations (2.41) to (4.5) in section 4.1.

Acknowledgements

Today's diverse scientific endeavors seldom allow one to point to a single overpowering contribution. The author has attempted to provide a rather extensive list of citations that underlie the anthology of this topic. All of these contributions have been significant, but many other essential sources also warrant commendation. During the preparation of this article, the author was supported by the National Institutes of Health (grant GM 08521-41) and by the Department of Energy (grant DE-FG03-94ER14452).

Biographical Sketch

David M. Grant, *b* 1931. B.S., 1954, Ph.D., 1957, Chemistry, University of Utah, USA. Positions: DuPont Instructor, University of Illinois, 1957–1958, introduced to NMR by Herb Gutowsky and Martin Karplus. Faculty in Chemistry, University of Utah since 1958, presently Distinguished Professor. Awards and Recognitions: 1969 Calif. Section Gold Medal (ACS); 1973 Utah ACS Section Award; 1973–1974; Sherman Fairchild Distinguished Scholar, Cal. Inst. Tech.; 1987 Univ. of Utah Rosenblatt Prize; 1991 ACS Award in Petroleum Chem.; 1992 Utah Governor's Medal for Science; 1995 Vaughan Prize; 1998, Treasurer, ISMAR. Current research specialties: methods and theoretical foundations of carbon-13 NMR, coupled spin relaxation and molecular motions, chemical shifts in liquids and solids with emphasis on carbon-13 shift tensors and their origins in electronic and molecular structure. About 400 Scientific Publications.

Overtone Spectroscopy of Quadrupolar Nuclei

Robert Tycko

National Institutes of Health, Bethesda, MD, USA

1	Introduction	1
2	Theory	1
3	Experiments	2
4	Conclusions	4
5	Related Articles	5
6	References	5

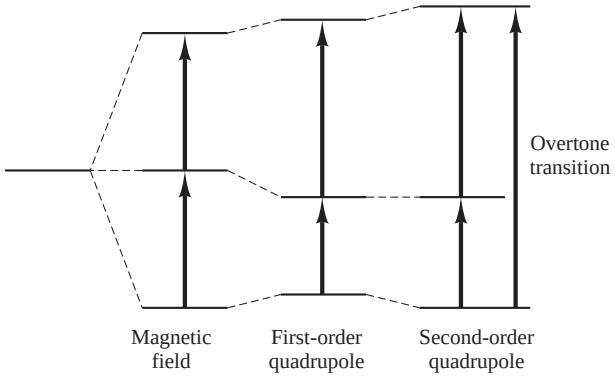

Figure 1 Spin energy levels for a spin-1 nucleus. The splitting of the energy levels due to a strong magnetic field and the first-order and second-order perturbations of the energy levels due to a quadrupole coupling are shown. (Adapted by permission of the American Chemical Society from R. Tycko and S. J. Opella, *J. Am. Chem. Soc.*, 1986, **108**, 3531)

1 INTRODUCTION

In the context of NMR, 'overtone spectroscopy' refers to the direct excitation of nuclear spin transitions and coherences and the direct detection of NMR signals at frequencies that are nearly multiples of the Larmor frequency ν_0. Overtone spectroscopy depends on the excitation and detection of 'forbidden' transitions, i.e. transitions that cannot be excited or detected directly in the limit of very strong external dc magnetic fields but that become excitable or detectable directly when the interactions of nuclear spins with the dc field are not very much stronger than the internal nuclear spin couplings. Recent interest in overtone spectroscopy grew out of the work of Bloom and LeGros,[1] who showed that overtone transitions have sufficient intensity in practice to be of experimental utility. Subsequent work[2,3] showed that overtone spectroscopy has real advantages when applied to solid state NMR measurements of integer-spin nuclei with large quadrupole couplings. Since ^{14}N is the most important nucleus of this type from the standpoint of chemistry and biochemistry, recent work has focused on ^{14}N overtone NMR.

Overtone spectroscopy should be distinguished from multiple quantum spectroscopy. In multiple quantum spectroscopy, one typically applies rf pulses with a carrier frequency close to ν_0 in order to excite nuclear spin coherences with oscillation frequencies that are nearly multiples of ν_0. The oscillation of these coherences is then detected indirectly through its effect on the single quantum signals near ν_0. In overtone spectroscopy, the rf carrier frequency is about equal to the oscillation frequency of the coherences, and the oscillation of the coherences is detected directly. Conceptually speaking, overtone spectroscopy can be thought of as a single photon spectroscopy, while multiple quantum spectroscopy can be thought of as a multiple photon spectroscopy. In some cases, the same coherences may be excited and detected either by overtone NMR or by multiple quantum NMR. As a general rule, overtone methods are probably more effective than multiple quantum methods when the nuclear quadrupole splittings exceed 1 MHz.

Figure 1 shows a spin energy level diagram for a spin-1 nucleus such as ^{14}N. A spin-1 nucleus has three possible eigenstates. In the absence of all spin interactions, the three states are degenerate. The interaction with an external dc field produces three equally spaced energy levels and two allowed, single quantum transitions at frequency ν_0. A nuclear quadrupole coupling that is weaker than the interaction with the external field perturbs the energy levels. To first order, a quadrupole coupling with coupling constant ν_Q shifts the middle ($m = 0$) level relative to the upper and lower ($m = \pm 1$) levels by an amount $\nu_Q^{(1)}$ proportional to ν_Q. This produces the first-order quadrupole splitting, with single quantum transitions at $\nu_0 \pm \nu_Q^{(1)}$. To second order, the quadrupole coupling additionally shifts the upper and lower levels by amounts $\pm\nu_Q^{(2)}$ proportional to ν_Q^2/ν_0. This is the second-order quadrupole shift. The single quantum transitions are then at $\nu_0 \pm \nu_Q^{(1)} + \nu_Q^{(2)}$. In addition, the overtone transition at frequency $2\nu_0 + 2\nu_Q^{(2)}$ becomes weakly allowed, producing signals and nutation frequencies proportional to ν_Q/ν_0 in pulsed NMR experiments. Although the overtone signals are intrinsically weaker than the allowed single quantum (or 'fundamental') signals, the fact that the overtone spectrum spans a frequency range that is narrower than the single quantum spectrum by a factor of the order of ν_Q/ν_0 makes measurement of the overtone signals substantially more tractable, especially in polycrystalline and noncrystalline solids (where the resonance lines are inhomogeneously broadened powder patterns) and in single crystals with several inequivalent sites. Thus, particularly in ^{14}N NMR, overtone spectroscopy allows NMR signals to be obtained and nuclear relaxation rates to be measured in systems where NMR experiments would otherwise be extremely difficult or impossible. Overtone spectra also contain structural information that is absent in single quantum spectroscopy, through the dependence of the overtone transition moment on the molecular or crystal orientation and on the direction of the applied rf field.

Overtone NMR spectroscopy of spin-1 nuclei is analogous to earlier 'half-field' electron paramagnetic resonance (EPR) studies of triplet states,[4,5] with the nuclear quadrupole coupling taking the place of the electronic spin–spin coupling or zero field splitting. Calculations of lineshapes and transition probabilities carried out for half-field EPR[6,7] are therefore applicable to overtone NMR of spin-1 nuclei.

2 THEORY

A detailed description of the theory and the implementation of overtone spectroscopy has been given by Tycko and Opella.[3] The essential theoretical points follow from consideration of the spin Hamiltonian $\hat{\mathcal{H}}$ for a quadrupolar nucleus with spin $\hat{S}$:

$$\hat{\mathcal{H}} = \hat{\mathcal{H}}_{\mathrm{S}} + \hat{\mathcal{H}}_{\mathrm{rf}} \tag{1}$$

$$\hat{\mathcal{H}}_{\mathrm{S}} = -h\nu_0\hat{S}_z + h\nu_{\mathrm{Q}}[3\hat{S}^2_{z'} - \hat{S}^2 + \eta(\hat{S}^2_{x'} - \hat{S}^2_{y'})] \tag{2}$$

$$\hat{\mathcal{H}}_{\mathrm{rf}} = 2\hbar\gamma_S B_1(\hat{S}_x\cos\theta + \hat{S}_z\sin\theta)\cos(2\pi\nu t + \phi) \tag{3}$$

$\hat{\mathcal{H}}_{\mathrm{S}}$ includes the interaction with the external dc field along z (the Zeeman interaction) and the quadrupole coupling. The principal axes of the quadrupole coupling tensor are $x'y'z'$. ν_{Q} is defined as $(e^2qQ)/[4S(2S-1)]$. $\hat{\mathcal{H}}_{\mathrm{rf}}$ is the interaction with an rf field with amplitude $\boldsymbol{B}_1$, frequency ν, phase ϕ, and direction in the xz plane at angle θ to x. γ_S is the nuclear gyromagnetic ratio. In the limit $\nu_0 \gg \nu_{\mathrm{Q}}$, the eigenstates of $\hat{\mathcal{H}}_{\mathrm{S}}$ are simply the eigenstates of S_z, i.e. $\{|m\rangle\}$. When this limit does not apply, but $\nu_0 > \nu_{\mathrm{Q}}$, the eigenstates are $\{|\psi_m\rangle\}$, given by

$$|\psi_m\rangle = |m\rangle + \sum_{m'\neq m} C_{mm'}|m'\rangle \tag{4}$$

If the laboratory axes (xyz) and quadrupole principal axes ($x'y'z'$) are related by Euler angles α, β, and γ, the coefficients $C_{mm'}$ are given to first order in ν_{Q}/ν_0 by

$$\begin{aligned} C_{mm'} = \frac{\nu_{\mathrm{Q}}}{2(m'-m)\nu_0}\{&-\delta_{m',\,m+1}[S(S+1) \\ &-m(m+1)]^{\frac{1}{2}}(2m+1)F(\alpha,\beta,\gamma) - \delta_{m',\,m-1} \\ &\times[S(S+1)-m(m-1)]^{\frac{1}{2}}(2m-1)F^*(\alpha,\beta,\gamma) \\ &+\delta_{m',\,m+2}\{[S(S+1)-m(m+1)][S(S+1) \\ &-(m+1)(m+2)]\}^{\frac{1}{2}}G(\alpha,\beta,\gamma) \\ &+\delta_{m',\,m-2}\{[S(S+1)-m(m-1)][S(S+1) \\ &-(m-1)(m-2)]\}^{\frac{1}{2}}G^*(\alpha,\beta,\gamma)\} \end{aligned} \tag{5a}$$

$$\begin{aligned} F(\alpha,\beta,\gamma) = e^{i\gamma}[&3\sin\beta\cos\beta - \eta(\cos 2\alpha\sin\beta\cos\beta \\ &+ i\sin 2\alpha\sin\beta)] \end{aligned} \tag{5b}$$

$$\begin{aligned} G(\alpha,\beta,\gamma) = e^{2i\gamma}\Bigg\{&\frac{3}{2}\sin^2\beta \\ &+\eta\left[\frac{1}{2}\cos 2\alpha(1+\cos^2\beta) + i\sin 2\alpha\cos\beta\right]\Bigg\} \end{aligned} \tag{5c}$$

To second order in ν_{Q}/ν_0, the energy E_m of the state $|\psi_m\rangle$ is

$$\begin{aligned} E_m = h\nu_0\Bigg\{&-m + \frac{\nu_{\mathrm{Q}}}{2\nu_0}[3m^2 - S(S+1)][(3\cos^2\beta - 1) \\ &+\eta\cos 2\alpha\sin^2\beta] + \sum_{m'\neq m}(m'-m)|C_{mm'}|^2\Bigg\} \end{aligned} \tag{6}$$

The orientation-dependent frequency of the overtone transition in a spin-1 nucleus is then

$$\nu_{1,\,-1}(\alpha,\beta,\gamma) = 2\nu_0 + \frac{\nu_{\mathrm{Q}}^2}{\nu_0}(|F(\alpha,\beta,\gamma)|^2 + |G(\alpha,\beta,\gamma)|^2) \tag{7}$$

and the orientation-dependent transition moment is

$$\begin{aligned} M_{1,\,-1}(\alpha,\beta,\gamma) &\equiv \langle\psi_1|S_x\cos\theta + S_z\sin|\psi_{-1}\rangle \\ &= \frac{\nu_{\mathrm{Q}}}{\nu_0}[\sin\theta F(\alpha,\beta,\gamma) + \cos\theta G(\alpha,\beta,\gamma)] \end{aligned} \tag{8}$$

The nutation frequency (i.e. the inverse of the 2π pulse length) for excitation of the overtone transition is given by $\gamma_S B_1|M_{1,-1}|/\pi$. The overtone signal amplitude is proportional to $|\rho_{1,-1}M_{1,-1}|$, where $|\rho_{1,-1}|$ is the amplitude of the overtone coherence excited by rf pulses. Thus, equation (8) displays the unusual features of overtone spectroscopy that the nutation frequency depends on the orientation of the quadrupole tensor principal axis system, that overtone transitions can be excited by rf fields applied parallel to the external dc field ($\theta = \pi/2$), and that signals can be detected by rf solenoid coils wound parallel to the dc field. Overtone powder pattern lineshapes in polycrystalline and noncrystalline solids are determined by the orientation-dependent overtone frequency in equation (7) weighted by an orientation-dependent function related to $M_{1,-1}$. The precise details of the weighting function depend on the excitation method. In the linear (i.e. small flip-angle pulse) regime, the weighting function is $|M_{1,-1}|^2$. Equation (8) shows that the weighting function, and hence the observed lineshape, depends on θ.

Since the coefficients $C_{mm'}$ are nonzero only for $|m - m'| = 1$ or 2, only the first ($\nu \approx 2\nu_0$) and second ($\nu \approx 3\nu_0$) overtone transitions have transition moments proportional to ν_{Q}/ν_0, and only the first overtone transition has a transition moment proportional to ν_{Q}/ν_0 when $\theta = \pi/2$. Higher overtone transitions are weaker, with transition moments proportional to higher powers of ν_{Q}/ν_0.

3 EXPERIMENTS

3.1 Detection of ^{14}N Overtone Transitions by CW NMR

Creel et al.[8] have reported the detection of the ^{14}N spectrum of hexamethylenetetramine by CW NMR methods in fields up to 2.2 T, where ν_0 = 6.6 MHz. The quadrupole coupling frequency $\nu_{\mathrm{Q}} = (e^2qQ)/4h$ is roughly 1.1 MHz in hexamethylenetetramine. Although the fields in these experiments were low by modern standards, they were high enough that the highest frequency ^{14}N signals can be considered to be overtones of the lower frequency signals.

3.2 Indirect Detection of ^{14}N Overtone Transitions

Blinc et al.[9] measured the ^{14}N NMR spectrum of triglycine sulfate by means of the Hartmann–Hahn double resonance, indirect detection technique.[10] Working in a 0.42 T field, they determined the ^{14}N resonant frequencies by observing proton NMR signals following an adiabatic demagnetization–adiabatic remagnetization cycle, with rf irradiation of the ^{14}N nuclei during a delay period between the demagnetization and remagnetization steps. In such an experiment, the proton NMR signals are destroyed or attenuated whenever the rf frequency is close to a ^{14}N resonance. In the work of Blinc et al., three resonances were observed for a single ^{14}N site, but the dc field was so low that it would be improper to call one resonance an overtone of the others. Essentially the same method was later applied to overtone spectroscopy at considerably higher fields by Tycko and Opella and by Garroway and Miller.[11] Related experiments, but involving double quantum rather than overtone excitation, were carried out by Schnur et al.[12] The indirect detection method is a comparatively simple way to locate overtone resonances in organic compounds, with high sensitivity (in favorable cases, on a single transient) but with low resolution. Figure 2 shows double resonance rf pulse sequences for the indirect detection of overtone signals.

3.3 Direct Detection of ^{14}N Overtone Signals Following Double Quantum Excitation

Bloom and LeGros[1] showed that the ^{14}N overtone signals from a single crystal of $NaNO_2$, with ν_Q = 1.4 MHz, could be detected directly with adequate sensitivity in a 5.4 T field

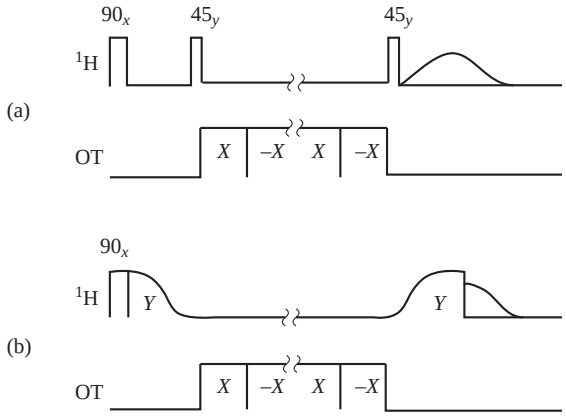

Figure 2 Sequences of rf pulses applied to proton (^{1}H) spins and to an overtone (OT) transition for the indirect detection of overtone transitions in organic solids. (a) Proton dipolar order is created by a two pulse Jeener–Broekaert sequence. A train of OT pulses, with alternating rf phases, destroys part of the dipolar order when the OT carrier frequency is close to a nuclear resonance. Proton NMR signals, proportional to the remaining dipolar order, are detected after the final proton pulse. In a typical application, one scans the OT carrier frequency and looks for a reduction in the proton signal at the OT resonance. (b) Same procedure as (a), but with dipolar order created by adiabatic demagnetization in the rotating frame (ADRF) and proton signals detected after adiabatic remagnetization in the rotating frame (ARRF). A signal enhancement by a factor of 4 over the Jeener–Broekaert method is possible

(ν_0 = 16.6 MHz). In the experiments of Bloom and LeGros, rf pulses were not applied at the overtone resonant frequency. Instead, the overtone coherence was excited by the double quantum excitation technique of Vega and Pines,[13] in which a rf pulse at frequency $\nu_0 + \nu_Q^{(2)}$, with amplitude less than ν_Q/γ_S, is applied for a time about equal to $3\pi\nu_Q/2(\gamma_S B_1)^2$. Thus, signals were detected at twice the frequency of the applied pulses. So far, this method of exciting overtone transitions has been of interest primarily from the standpoint of pure spectroscopy. Excitation near the overtone resonant frequency itself has proven to be a more practical approach.

3.4 Direct Detection and Direct Excitation of ^{14}N Overtone Transitions

Tycko and Opella[2,3] carried out a series of experiments that demonstrated the feasibility of the direct excitation and direct detection of ^{14}N overtone spectra in single crystal and polycrystalline organic solids. They showed that overtone coherences could be excited both by direct pulsed excitation of the overtone transition and by cross polarization from proton magnetization. They demonstrated the high resolution inherent in overtone spectroscopy when high-power proton decoupling is employed (overtone resonances in single crystals subject to small strains and small degrees of disorder are broadened by second-order rather than first-order quadrupole effects). They showed that quadrupole coupling constants and asymmetry parameters could be determined from overtone lineshapes of polycrystalline samples and that the powder pattern lineshapes depend on the direction of the rf coil used for excitation and detection. They also demonstrated two-dimensional overtone nutation spectroscopy, for measuring overtone nutation frequencies, and two-dimensional overtone separated-local-field spectroscopy, for measuring ^{14}N–^{1}H dipole–dipole couplings. Radiofrequency pulse sequences for the acquisition of one-dimensional ^{14}N overtone spectra of organic solids are shown in Figure 3. Examples of one-dimensional ^{14}N overtone spectra are shown in Figures 4 and 5.

Tycko and Opella[3] have discussed the comparative sensitivities of ^{14}N overtone spectroscopy and single quantum spectroscopy. Because of the reduced spectral widths and linewidths in typical overtone spectra, overtone spectroscopy has sensitivity at least comparable to that of single quantum spectroscopy despite the weakly allowed nature of overtone transitions.

Tycko and Opella[3] have also carried out preliminary experimental investigations of the effects of rapid sample spinning on ^{14}N overtone spectra of polycrystalline solids. They found that spinning about a single axis changed, but did not narrow, the overtone powder pattern lineshape. Takegoshi and Hikichi[14] performed calculations of overtone lineshapes under sample spinning that supported the experimental results. They have also discussed the use of double rotation (DOR) and dynamic angle spinning (DAS) methods as a means of narrowing the second-order quadrupole shift powder patterns observed in ^{14}N overtone spectroscopy.[14] Although this approach to line narrowing has not been demonstrated in experiments, it may turn out to be a valuable one. In principle, either the DOR or the DAS technique, or some suitable variant of these techniques, may allow one to obtain resolved ^{14}N

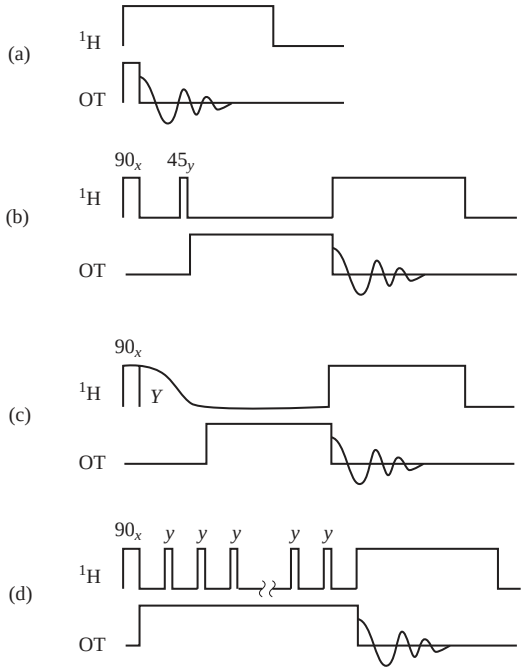

Figure 3 Pulse sequences for the direct detection of overtone spectra in organic solids. (a) Direct excitation of overtone coherences with a single OT pulse. High-power proton decoupling is applied during the acquisition of the overtone signals. (b) A Jeener–Broekaert sequence is used to create proton dipolar order. Overtone coherences are generated by cross polarization from dipolar order. (c) Adiabatic demagnetization in the rotating frame is used to create proton dipolar order. Overtone coherences are generated by cross polarization from dipolar order. (d) Overtone coherences are generated by cross polarization from transverse proton magnetization, prepared by pulsed spin locking. Pulsed, rather than continuous, spin locking reduces the effective proton rf field, allowing a Hartmann–Hahn match to be achieved despite the relatively weak effective OT rf field (due to the weakly allowed nature of the overtone transitions). (Adapted by permission of the American Institute of Physics from Tycko and Opella, *J. Chem. Phys.*, 1987, **86**, 1761)

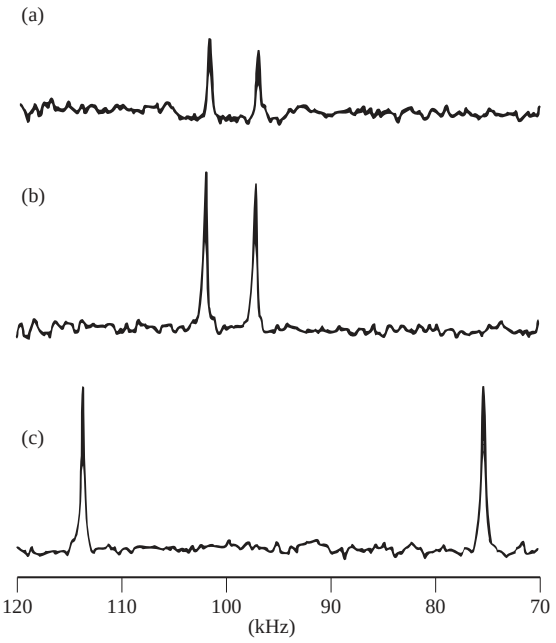

Figure 4 ^{14}N overtone NMR spectra of a 50 mg single crystal of *N*-acetyl-D,L-valine, obtained at 5.89 T ($2\nu_0$ = 36.118 MHz). The two lines result from the two magnetically inequivalent molecules in the unit cell. All spectra result from the acquisition of 1024 transients. (a) Direct excitation, using the pulse sequence in Figure 3(a). (b) Cross polarization, using the pulse sequence in Figure 3(b). (c) Cross polarization, using the pulse sequence in Figure 3(b), after an arbitrary 10° rotation of the crystal. The change in the overtone resonant frequencies is due to the orientation dependence of the second-order quadrupole shifts. (Adapted by permission of the American Chemical Society from Tycko and Opella, *J. Am. Chem. Soc.*, 1968, **108**, 3531)

overtone NMR lines from chemically inequivalent nitrogen sites in a complex polycrystalline solid (i.e. a polycrystalline peptide or oligonucleotide). The resonant frequencies in such an experiment would be determined by the isotropic parts of the chemical shift and the second-order quadrupole shift. In addition, one expects a small contribution to the overtone lineshapes from a spinning sample due to Berry's phase, as observed in pure NQR spectra of spinning samples.[15] The effects of Berry's phase, which arise because the nuclear spin eigenstates are functions of orientation when the quadrupole coupling is large, are expected to be of the order of $|C_{mm'}|^2\nu_R$, where ν_R is the sample spinning frequency, which is less than 100 Hz for typical experimental conditions.

Takegoshi and Hikichi[16] have also carried out a rotation study of a single crystal of L-alanine to determine the ^{14}N quadrupole coupling constant and asymmetry parameter in this compound. The observed angular dependences of the overtone frequency and intensity were well described by the expressions derived by perturbation theory.

Ramanathan and Opella[17] have investigated the effects of irradiation of ^{14}N overtone resonances on the ^{13}C NMR spectrum of a single crystal of *N*-acetyl-D,L-valine. The ^{13}C NMR lineshapes at 3.52 T are asymmetric triplets for carbon atoms that are coupled to ^{14}N nuclei in this crystal, with asymmetry due to the large ^{14}N quadrupole coupling (ν_Q = 0.8 MHz). Irradiation of the ^{14}N overtone resonances caused the triplet ^{13}C lineshapes to collapse into unresolved doublets. Ramanathan and Opella showed that this 'overtone decoupling' could be carried out selectively, allowing particular ^{14}N overtone resonances to be correlated with particular ^{13}C resonances. Selective overtone decoupling may be useful in the assignment of resonances in single crystal NMR studies.

4 CONCLUSIONS

Overtone spectroscopy is a useful addition to the techniques of solid state NMR. The reduced spectral widths and linewidths of ^{14}N overtone spectra compared with traditional single quantum spectra clearly make overtone spectroscopy the preferred means of applying ^{14}N NMR to the study of many classes of solids. In many cases, overtone spectroscopy is the only practical way to observe ^{14}N NMR signals. At the very least, this allows measurements of spin relaxation rates and approximate quadrupole coupling constants to be performed. Such measurements can probe the chemical, structural, dynamical, and electronic properties of solids.

Extensions of overtone spectroscopy to NMR of nuclei with spins greater than one are possible, but have not yet been

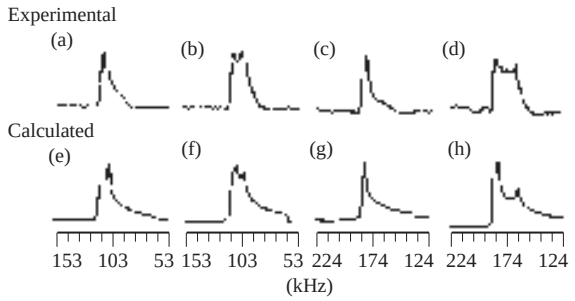

Figure 5 Experimental (a–d) and (e–h) calculated ^{14}N overtone NMR spectra of *N*-acetyl-D,L-valine powder, obtained at 5.89 T (a,b,e,f) and 3.54 T (c,d,g,h) with the pulse sequence in Figure 3(c). The rf solenoid coil used for excitation and detection of overtone signals is perpendicular to the external magnetic field in (a), (c), (e), and (g), and parallel to the external magnetic field in (b), (d), (f), and (h). Each experimental spectrum is the result of approximately 20 000 transients on a 200 mg sample. In the calculations, signal contributions from the various possible molecular orientations are weighted by $|M_{1,-1}|$ (see text), and effects of the ^{14}N chemical shift anisotropy are included. (Adapted by permission of the American Institute of Physics from Tycko and Opella, *J. Chem. Phys.*, 1987, **86**, 1761)

investigated in detail. For most quadrupolar nuclei, with non-integer spins, the 'central transition' (i.e. the $m = \frac{1}{2} \leftrightarrow m = -\frac{1}{2}$ transition) is already unaffected by first-order quadrupole splittings and is fully allowed. The arguments in favor of overtone spectroscopy are therefore less compelling. Nonetheless, one expects the observation of overtone signals in conjunction with single quantum signals to afford spectral simplification, contribute to the determination of quadrupole coupling parameters, and facilitate the assignment of resonances. The measurement of overtone relaxation rates may also add to the information available from relaxation measurements on the central transition.

5 RELATED ARTICLES

Cross Polarization in Solids; Double Rotation; Dynamic Angle Spinning; Geometric Phases; Quadrupolar Nuclei in Glasses; Quadrupolar Nuclei in Solids.

6 REFERENCES

1. M. Bloom and M. A. LeGros, *Can. J. Phys.*, 1982, **64**, 1522.
2. R. Tycko and S. J. Opella, *J. Am. Chem. Soc.*, 1986, **108**, 3531.
3. R. Tycko and S. J. Opella, *J. Chem. Phys.*, 1987, **86**, 1761.
4. J. H. van der Waals and M. S. deGroot, *Mol. Phys.*, 1959, **2**, 333.
5. M. S. deGroot and J. H. van der Waals, *Mol. Phys.*, 1960, **3**, 190.
6. P. Kottis and R. Lefebvre, *J. Chem. Phys.*, 1963, **39**, 393.
7. P. Kottis and R. Lefebvre, *J. Chem. Phys.*, 1964, **41**, 379.
8. R. B. Creel, E. D. von Meerwall, and R. G. Barnes, *Chem. Phys. Lett.*, 1977, **49**, 501.
9. R. Blinc, M. Mali, R. Osredkar, A. Prelesnik, I. Zupancic, and L. Ehrenberg, *J. Chem. Phys.*, 1971, **55**, 4843.
10. S. R. Hartmann and E. L. Hahn, *Phys. Rev.*, 1962, **128**, 2042.
11. A. N. Garroway and J. B. Miller, *J. Magn. Reson.*, 1989, **82**, 591.
12. G. Schnur, R. Kimmich, and F. Winter, *J. Magn. Reson.*, 1986, **66**, 295.
13. S. Vega and A. Pines, *J. Chem. Phys.*, 1977, **66**, 5624.
14. K. Takegoshi and K. Hikichi, *Chem. Phys. Lett.*, 1992, **194**, 359.
15. R. Tycko, *Phys. Rev. Lett.*, 1987, **58**, 2281.
16. K. Takegoshi and K. Hikichi, *Chem. Phys. Lett.*, 1993, **206**, 450.
17. K. V. Ramanathan and S. J. Opella, *J. Magn. Reson.*, 1988, **78**, 367.

Biographical Sketch

Robert Tycko. *b* 1959. A.B., 1980, Princeton University; Ph.D., 1984, University of California at Berkeley. Postdoctoral fellow, University of Pennsylvania, 1984–86. Member of the Technical Staff, AT&T Bell Laboratories, Murray Hill, NJ, 1986–94. Investigator, National Institutes of Health, Bethesda, MD, 1994–present. Approx. 50 publications on magnetic resonance. Research specialties: fundamental principles of magnetic resonance spectroscopy, development of new NMR techniques, characterization of the structural, dynamical, and electronic properties of chemical systems, materials, and biochemical systems.

Phase Cycling

David L. Turner
University of Southampton, UK

1	Introduction	1
2	Theory	1
3	Exorcycle	4
4	Multiple Quantum Selection	5
5	Heteronuclear Experiments and Selective Pulses	5
6	Pure Absorption Lineshapes	6
7	Optimum Ordering Within Cycles	7
8	Related Articles	8
9	References	8

1 INTRODUCTION

Phase cycling is a method of canceling out unwanted types of signal from NMR spectra that are generated by a sequence of two or more pulses. The principle is therefore closely related to CYCLOPS,[1] which is used to reduce quadrature images by averaging the response from imperfectly balanced receivers, and is an extension of the use of phase alternation between pulse sequences to reduce the influence of residual transverse magnetization from one FID on the next when time averaging. The essence of the method is to add together a number of FIDs generated by a pulse sequence in which the phases of the radiofrequency pulses are shifted in a specific pattern. The effect of these phase shifts depends on the order of coherence of each component of the magnetization and hence an appropriate phase cycle allows signals that result from a chosen sequence of states to coadd, while all other signals cancel.

I first became aware of the possibilities of the method as a result of a conversation with Dr. S. L. Patt, who brought phase-alternated pulse sequences[2] to my attention. We had identified nonrefocused magnetization and signals arising from longitudinal relaxation in the two-pulse experiments for COSY and J spectra as the source of artifacts in the spectra and were seeking a method of eliminating them. These signals had been given the jocular labels 'phantoms' and 'ghosts' (now more commonly referred to as axial peaks and antiecho or P-type peaks, respectively), and we developed a four-step phase cycle[3] for their removal, which was christened with the name 'Exorcycle'. Very soon after that, Maudsley and Ernst presented a two-step cycle for selecting only that magnetization which had been transferred between heteronuclei[4] and, a few months later, Wokaun and Ernst set out the general theory of phase cycling in the context of selecting multiple quantum coherences within pulse sequences.[5] The ability to select specific signals also laid the foundation for generating 'pure phase' two-dimensional spectra by combining signals that are symmetrical about the center of the spectrum in the F_1 dimension, a development which was first announced in an important note added in proof by Bachmann et al.[6] Thus by the end of 1977 the method had become established to the extent that no new pulse sequence was published without an associated phase cycle thereafter. Many of the cycles proposed turned out to be fundamentally identical to Exorcycle, prompting a series of articles that set out general principles for designing phase cycles.[7–9] Most spectroscopists now take the existence of phase cycles for granted, simply having to follow the instruction to set the number of transients for each increment in their experiment to a multiple of some magic number.

An ideal single pulse experiment has no need of phase cycling since the system at equilibrium comprises only populations of the magnetic energy levels, and the FID detected after the pulse is restricted to single quantum coherence by the selection rules. Adding a second, 'mixing', pulse of arbitrary flip angle creates two additional routes for magnetization, which may be detected in the FID. First there may be longitudinal magnetization present just before the second pulse, resulting from relaxation and from deviations from a 90° flip angle for the first pulse, and this may be turned into observable magnetization by the mixing pulse. This component is not modulated by the evolution period between the pulses in a two-dimensional experiment and hence appears on the zero frequency axis of the F_1 dimension: the 'axial' peaks. Second, part of the transverse magnetization created by the first pulse may be refocused by the mixing pulse. The refocused component is so called because it comes from that part of the magnetization which experiences a 180° phase shift and will go on to form a spin echo. In a two-dimensional spectrum, refocused magnetization appears with negative frequencies in F_1, whereas the unrefocused part leads to positive frequencies: hence 'N-type' and 'P-type' peaks. Exorcycle separates these three contributions to the FID by combining the signals from four different experiments in which the relative phase of the mixing pulse is shifted in 90° steps. Essentially all experiments benefit from cancelation of the axial peaks and, in addition, most of the early two-dimensional experiments were designed to retain the N-type peaks and discard the P-type peaks. More recent pulse sequences usually retain both the P-type and N-type peaks but separate them so that they can be recombined to produce signals with pure absorption lineshapes in both dimensions.

2 THEORY

The effect of phase shifting is described most conveniently in terms of the difference in Zeeman quantum number between the stationary states involved in each component of the magnetization. In the eigenbase of the Hamiltonian, each component of magnetization corresponds to a single element of the density matrix and the difference in quantum numbers of the basis functions is known as the 'order of the coherence'. Thus the population of an energy level represents the coherence of a wavefunction with itself and has order zero. The transverse magnetization generated from isolated spin-$\frac{1}{2}$ nuclei involves both of the wavefunctions, $m_z = +\frac{1}{2}$ and $m_z = -\frac{1}{2}$ and is associated with two elements with order +1 and −1. If, as is usual, a single coil is used for detection, then the choice of the order ascribed to the FID is arbitrary and we shall label it +1, in line with the convention used for the population differences for protons (the operator for the observable being $\hat{I}_+$). The requirement of Exorcycle was therefore to select

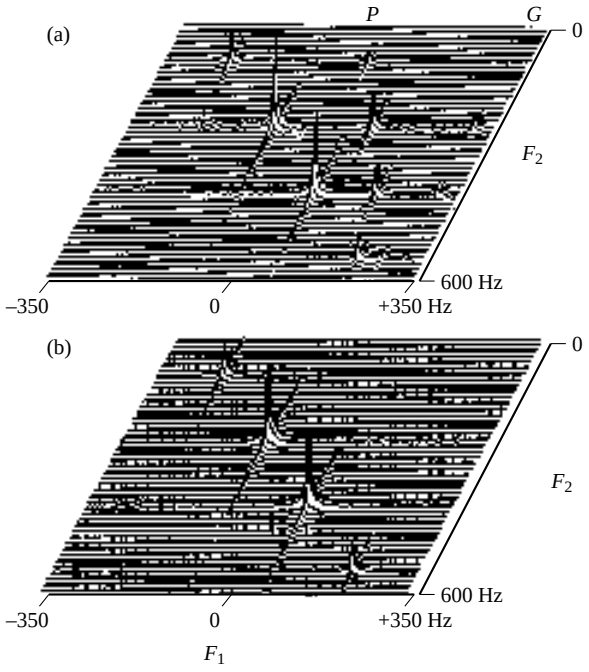

Figure 1 A heteronuclear J spectrum (a) haunted by phantoms and ghosts and (b) obtained with phase cycling. (Reproduced by permission of Academic Press from G. Bodenhausen et al.[3])

signals that originated with order 0 before the first pulse of the sequence, evolved with order -1, and were detected with order +1, while canceling all other signals.

Mathematically, the state of any system may be described by a density operator and our viewpoint corresponds to the set of basis functions chosen to represent it, usually eigenfunctions of the spin Hamiltonian. For an isolated spin-$\frac{1}{2}$ nucleus the eigenfunctions of the z component, $\hat{I}_z$, of the spin operator $\hat{\boldsymbol{I}}$ with eigenvalues $m_z = +\frac{1}{2}$ and $m_z = -\frac{1}{2}$ are labelled $|\alpha\rangle$ and $|\beta\rangle$. The angular momentum operator is $\hbar\hat{\boldsymbol{I}}$ and the operator for the nuclear magnetic moment $\gamma\hbar\hat{\boldsymbol{I}}$, so these observables and the voltages that are actually measured are simply proportional to the component of spin. The labels $|\alpha\rangle$ and $|\beta\rangle$ represent solutions of the time-independent Schrödinger equation, but NMR is concerned with coherent radiation and we cannot ignore the time-dependent phase factors of the wavefunctions,

$$\mathrm{i}\hbar\mathrm{d}|\Psi\rangle/\mathrm{d}t = \hat{\mathcal{H}}|\Psi\rangle \tag{1}$$

The time dependence is therefore generated by the operator $\exp(\mathrm{i}\gamma B_0 t\hat{I}_z)$ for a magnetic field B_0 applied along the z axis, and we note that the matrix representation of the exponential of an operator in its eigenbase is simply given by the exponentials of the diagonal elements.

The phases are random in a sample at equilibrium so there is no observable transverse magnetization, but let us consider a sample with all of the nuclei in a state $|\psi\rangle = 2^{-1/2}|\alpha\rangle + 2^{-1/2}|\beta\rangle$. This is obviously still an eigenfunction of $\hat{\boldsymbol{I}}^2$, but it is an eigenfunction of $\hat{I}_x$, since $\hat{I}_x|\psi\rangle = \frac{1}{2}|\psi\rangle$, rather than of $\hat{I}_z$. The z component of the angular momentum of each spin therefore cannot be given simply by an eigenvalue, but is determined by the ensemble average, or expectation value, $\langle\hat{I}_z\rangle = \langle\psi|\hat{I}_z|\psi\rangle = 0$. The expectation value of the transverse magnetization is no longer zero, but it is certainly time-dependent since

$$\begin{aligned}\langle\hat{I}_x\rangle &= \langle\psi|\exp(-\mathrm{i}\gamma B_0 t\hat{I}_z)\,\hat{I}_x\exp(\mathrm{i}\gamma B_0 t\hat{I}_z)|\psi\rangle \\ &= \tfrac{1}{2}\cos(\gamma B_0 t) \\ \langle\hat{I}_y\rangle &= -\tfrac{1}{2}\sin(\gamma B_0 t)\end{aligned} \tag{2}$$

so the Larmor frequency emerges from the time-dependent phases of the wavefunctions, and we note in passing that the sense of rotation of the magnetization is negative when the magnetogyric ratio of the nuclei is positive.

This also illustrates how the exponential operators derived from the components of the angular momentum operator generate rotations about the respective axes. Thus, the operator corresponding to measurement along the x' axis in a coordinate frame rotating about the z axis at a frequency ω is obtained from the time-dependent similarity transform

$$\hat{I}'_x = \exp(-\mathrm{i}\omega t\hat{I}_z)\,\hat{I}_x\exp(\mathrm{i}\omega t\hat{I}_z) \tag{3}$$

which is effectively what we observe by using a phase-sensitive detector with ω as the reference frequency. The magnetization will therefore appear constant if we measure at a frequency $\omega = -\gamma B_0$. In practice, the use of single-coil detectors means that the sense of rotation is lost and all spectra are plotted as if the frequency were positive, so we shall treat the Larmor frequency as $\Omega = |\gamma B_0|$. However, we can still distinguish signals with absolute frequencies greater or less than that of the reference frequency by means of quadrature detection. The distinction is achieved by splitting the signal into two and detecting it with respect to references that are 90° out of phase, i.e. $\cos(\omega t)$ for detector A and $\sin(\omega t)$ for detector B, and treating each pair of samples as a complex number $S = A + \mathrm{i}B$ so that the measuring operator is effectively $\hat{I}_x + \mathrm{i}\hat{I}_y = \hat{I}_+$. Simply regarding the signal as $S' = B - \mathrm{i}A$ would advance the effective phase of the reference by 90° and hence retard the phase of the resulting spectrum. We shall follow the convention of taking $\hat{I}_+$ to be the operator for magnetization detected in quadrature, regardless of the sign of the magnetogyric ratio, but if we chose to regard the signal as $S'' = A - \mathrm{i}B$ then the corresponding observable would be $\hat{I}_-$.

Using explicit matrix representations of the operators of equation (2) in the basis $(|\alpha\rangle,|\beta\rangle)$, the process of calculating the signal generated in quadrature in the rotating frame from our state $|\psi\rangle$ becomes

$$\begin{aligned}S \propto &\begin{pmatrix}\sqrt{\frac{1}{2}} & \sqrt{\frac{1}{2}}\end{pmatrix}\begin{pmatrix}\mathrm{e}^{\mathrm{i}(\Omega-\omega)t/2} & 0\\ 0 & \mathrm{e}^{-\mathrm{i}(\Omega-\omega)t/2}\end{pmatrix}\begin{pmatrix}0 & 1\\ 0 & 0\end{pmatrix} \\ &\times\begin{pmatrix}\mathrm{e}^{-\mathrm{i}(\Omega-\omega)t/2} & 0\\ 0 & \mathrm{e}^{\mathrm{i}(\Omega-\omega)t/2}\end{pmatrix}\begin{pmatrix}\sqrt{\frac{1}{2}}\\ \sqrt{\frac{1}{2}}\end{pmatrix}\end{aligned} \tag{4}$$

So far we have discussed the time-dependent phase of the wavefunctions and the phase of the signal detected in the rotating frame. This sets the scene for describing the effect of changing the phase of a radiofrequency pulse. The form of pulse operators is described elsewhere and is not essential to a discussion of phase cycling since the designer of the pulse sequence is responsible for ensuring that the proper signals

are generated and the phase cyclist merely has to ensure that the undesirable signals are canceled. The transformation of a system with all of the spins in the $|\alpha\rangle$ state to the one discussed above, in which they are all in the state $2^{-1/2}|\alpha\rangle + 2^{-1/2}|\beta\rangle$, may be achieved with a pulse with a 90° flip angle and the appropriate phase. Note that the phase of the radiofrequency pulses is properly considered as a phase difference between the applied rf field and the reference frequency, since if a pulse with the same frequency as the reference is switched on at some arbitrary point in time, then the absolute phase is also arbitrary. It is the phase of the pulse relative to the reference that is crucial, since the same reference is supplied to the phase-sensitive detector and hence defines the phase of the signals, regardless of the time at which the experiment began.

The 'phase' of a pulse will therefore be understood as its phase in a system of coordinates rotating about the axis of the static magnetic field (the rotating frame) at the frequency of the reference that is physically used by the spectrometer. Consider a children's merry-go-round at a fair: an imaginative stationary observer might believe that the children are driving, for example, toy cars around in circles. An observer standing on the platform would not be surprised to see that those cars had no moving parts. The picture is much simpler in the rotating frame and it is implicit in most descriptions of NMR experiments. To change the phase of his viewpoint in relation to the rotating frame, our observer on the platform could simply walk around the edge. Alternatively, he could step off the platform, have it rotated in the opposite sense, and step back on. The latter approach is certainly more involved, but it makes the effect of phase-shifted pulses more easy to comprehend.

In general we are concerned with complex mixtures of spin states rather than the pure state, $|\psi\rangle = 2^{-1/2}|\alpha\rangle + 2^{-1/2}|\beta\rangle$, used in the example above. It is then convenient to use a density operator and its explicit matrix representation. This contains all of the information necessary to calculate observables in the form of products of the coefficients of wavefunctions averaged across the sample. The density matrix formalism is discussed elsewhere and, as is the case with the explicit form of pulse operators, a detailed understanding is not necessary for our purposes. It is sufficient to note that the transformation from $|\alpha\rangle$ to $|\psi\rangle$ can be expressed in the density matrix formalism as

$$\tilde{\mathbf{P}}^* \begin{pmatrix} 1 & 0 \\ 0 & 0 \end{pmatrix} \mathbf{P} = \begin{pmatrix} \frac{1}{2} & \frac{1}{2} \\ \frac{1}{2} & \frac{1}{2} \end{pmatrix} \tag{5}$$

where $\mathbf{P}$ is the matrix representation of the pulse operator. The observable signal is obtained as

$$S \propto \mathrm{Tr} \begin{pmatrix} 0 & 1 \\ 0 & 0 \end{pmatrix} \begin{pmatrix} e^{-i(\Omega-\omega)t/2} & 0 \\ 0 & e^{i(\Omega-\omega)t/2} \end{pmatrix} \begin{pmatrix} \frac{1}{2} & \frac{1}{2} \\ \frac{1}{2} & \frac{1}{2} \end{pmatrix} \times \begin{pmatrix} e^{i(\Omega-\omega)t/2} & 0 \\ 0 & e^{-i(\Omega-\omega)t/2} \end{pmatrix} \tag{6}$$

in which the operator $\hat{I}_+$ has been transformed implicitly into the rotating frame and, since $|\psi\rangle$ was chosen to be a pure state, this expression corresponds simply to a cyclic permutation of the terms in equation (4). Now consider the effect of a pulse which has its phase incremented by 90°, $\hat{P}' = \hat{U}^+ \hat{P} \hat{U}$, where $\hat{U} = \exp(\frac{1}{4} i\pi \hat{I}_z)$ provides the similarity transform for a 90° rotation. The result is mathematically identical to applying a negative rotation to the system in its initial state, $\hat{\rho} \rightarrow \hat{U}\hat{\rho}\hat{U}^+$, transforming the system by applying a pulse without any phase shift, and then rotating the system forward again, $\hat{\rho}' \rightarrow \hat{U}^+\hat{\rho}'\hat{U}$. The effect of shifting the phase of pulses can therefore be understood without reference to the power, duration, frequency, shape, or any other property of the pulse itself. In this simple case, and for all systems at equilibrium, $\hat{\rho} = \hat{U}\hat{\rho}\hat{U}^+$. The only observable change is therefore the forward rotation of the system after the pulse and so the effect of the phase-shifted pulse is to rotate the observed magnetization forward through 90°, as expected.

The result is easily generalized for systems with several magnetic nuclei. The components of the spin operators are given by the direct sum of the components for each of the nuclei present. The eigenfunctions $|\Psi_i\rangle$ are characterized by their total magnetic (Zeeman) quantum number, M_z, and we shall label them accordingly. The magnetic quantum numbers of the individual nuclei are no longer appropriate since they only hold good if the nuclei are weakly coupled, that is if their individual spin operators commute with the complete spin Hamiltonian. A straightforward expansion of the operator for rotation about the z axis then shows that applying a rotation through an angle θ to the system has the effect of changing the phase of elements of the density matrix according to the prescription

$$\rho_{rs} \rightarrow \exp[i\theta(s - r)]\, \rho_{rs} \tag{7}$$

in which we note that the imaginary part of ρ_{sr} changes in the opposite sense to that of ρ_{rs}, maintaining the Hermitian property of the density matrix. The difference in M_z between the basis functions, $s - r$, is known as the order of coherence of the matrix element ρ_{rs}. This follows the opposite sign convention to that introduced by Wokaun and Ernst[5] for the 'transition order' and agrees with that of Bain,[8] who called it the 'coherence level'.

In terms of the individual density matrix elements, the example above which describes a pulse with a 90° phase shift applied to a system of isolated spin-$\frac{1}{2}$ nuclei involved first the negative rotation

$$\rho_{\alpha\alpha} \rightarrow \exp[-\tfrac{1}{2} i\pi(\tfrac{1}{2} - \tfrac{1}{2})]\, \rho_{\alpha\alpha} = \rho_{\alpha\alpha} \tag{8}$$

followed by a pulse with no phase shift, and then obtaining the signal $S \propto \rho_{\beta\alpha}$ after restoring the system to its original reference coordinates by means of the positive rotation

$$\rho_{\beta\alpha} \rightarrow \exp[\tfrac{1}{2} i\pi\{\tfrac{1}{2} - (-\tfrac{1}{2})\}]\, \rho_{\beta\alpha} = i\rho_{\beta\alpha} \tag{9}$$

so that the signal acquires the expected 90° phase shift.

Although the theory of phase cycling does not require an understanding of free precession and relaxation, it is important to note that these do not affect the order of coherence, at least not in a coherent fashion. Obviously, any state will return to equilibrium, order zero, if it is left for long enough, but this is the result of random changes in the spin states of individual nuclei so that all phase coherence is lost. A change in the order of coherence requires that the nuclei all experience the same perturbation simultaneously, i.e. the

perturbation itself must be coherent. This is taken for granted in radiofrequency spectroscopy since the technology required to generate monochromatic radiation with phase coherence throughout large samples has been available for many years. A change in the order of coherence, that is a change in spin state which occurs with phase coherence across the sample, therefore requires an applied coherent radiofrequency field, or pulse. Radiofrequency pulses transfer magnetization between elements of the density matrix, $D_{prqs}\rho_{pq} \rightarrow \rho_{rs}$, where D_{prqs} is a coefficient for the transfer of coherence which depends on the exact form of the pulse. These coefficients can remain part of a black box for our purposes, and hence, by extension of equations (8) and (9), a phase-shifted pulse generates

$$D^{\theta}_{prqs}\rho_{pq} \rightarrow \exp[\mathrm{i}\theta(p - q + s - r)]\,\rho_{rs} \qquad (10)$$

The final step of quadrature detection produces signal exclusively from elements for which $s - r = +1$, and so we are ready to analyze any phase cycle.

3 EXORCYCLE

Exorcycle was developed to select N-type peaks in a two-pulse experiment so the mixing pulse is required to generate a 180° phase shift, or inversion, of the magnetization. Since we detect ρ_{rs}, where $s - r = +1$, we are only interested in the part of the magnetization present before the pulse, ρ_{pq}, for which $q - p = -1$. That magnetization should be generated from a system at equilibrium, for which only the diagonal elements ρ_{kk} are nonzero. The signals are therefore required to follow the route 0:−1:+1, where pulses are indicated by colons and the numbers specify the orders of coherence between pulses. If the initial pulse and the mixing pulse have relative phases θ and ϕ, which were restricted to multiples of $\pi/2$ when Exorcycle was developed, then the initial pulse gives

$$D^{\theta}_{kpkq}\rho_{kk} \rightarrow \exp[\mathrm{i}\theta(k - k + q - p)]\,\rho_{pq} \qquad (11)$$

and the mixing pulse gives

$$D^{\phi}_{prqs}\rho_{pq} \rightarrow \exp[\mathrm{i}\phi(p - q + s - r)]\,\rho_{rs} \qquad (12)$$

Overall, the phase shifts cause the desired signal from the route 0:−1:+1 to change by a factor exp [i(2ϕ − θ)]. This phase shift must be constant if the signal is to add coherently with a constant receiver phase. The phase of the signals is arbitrary so long as it is constant for all steps of the phase cycle, but it is convenient to let that constant phase be zero, i.e. $2\phi - \theta = 2n\pi$. If the mixing pulse is incremented in 90° steps, 0, $\pi/2$, π, $3\pi/2$, in separate experiments then the initial pulse must have the phases 0, π, 0, π. The undesirable axial peaks arise from the route 0:0:+1, and the P-type peaks from 0:+1:+1, and Table 1 gives the phase factors for each type of signal in the four steps of the cycle.

The sum of the four experiments clearly cancels both of the undesirable signals, but the cancelation will be imperfect if any instability alters the characteristics of the spectrometer. Since axial peaks are often the most intense, it may be preferable to take the transients in the order 1, 3, 2, 4, so that any change in the spectrometer that occurs between FIDs which cancel the axial contribution when co-added is as small as possible.

Table 1 Phase Factors for Four-Step Cycle

	θ	ϕ	N-type exp [i(2ϕ − θ)]	P-type exp (iθ)	Axial exp (iϕ)
1.	0	0	+1	+1	+1
2.	π	$\pi/2$	+1	−1	+i
3.	0	π	+1	+1	−1
4.	π	$3\pi/2$	+1	−1	−i

If the experiment is of the type in which the P-type and N-type signals are of equal intensity, then the combinations of signals 1 + 2 + 3 + 4 and 1 − 2 + 3 − 4 may be stored separately for processing into pure absorption lineshapes, thereby enhancing both sensitivity and resolution.

More recent spectrometers allow phase shifts other than 90°, and the cycle may be reduced to three steps if 120° shifts are available,[9] though this may be less satisfactory since precise 120° shifts are more difficult to obtain and the cycle is not easily adapted to produce pure absorption lineshapes. The phase factors for the three-step cycle are shown in Table 2

Although these explicit phase cycles are chosen to give a zero phase shift for the desired signal, it should be noted that arbitrary constant shifts may be added to the initial pulse, and to the mixing pulse, and, since it is all relative, to the reference used in the receiver. That would only alter the phase of the desired signal in the eventual spectrum, which normally requires some correction in any case, and would not affect the cancelation of the other signals. This is true of all phase cycles, so that particular experiments may appear with phase cycles which are dressed up differently but are in principle identical.

The addition of CYCLOPS to suppress the 'quadrature images' which are produced by unbalanced detectors involves shifting the effective phase of the reference frequency by exchanging the signals from the two detectors, $B - \mathrm{i}A = \exp(-\mathrm{i}\pi/2)(A + \mathrm{i}B)$, and hence requires 90° to be added to the phase of both pulses in each step of the cycle. The operator for measuring the signal is intended to be $\hat{I}_+$ but this is distorted to give $\hat{I}_+ + \delta\hat{I}_-$ if the detectors are unbalanced. This admits detection of magnetization of order −1, which has an apparently negative Larmor frequency, $\Omega_{-1} = -\Omega_{+1}$, and so leads to the peaks known as quadrature images. As it stands, Exorcycle would not distinguish the desired route 0:−1:+1 from the mirror image, 0:+1:−1. The 90° phase shift applied to both pulses introduces a 90° phase shift of all signals arising from routes of the type 0 ... +1, and −90° for signals arising from routes of the type 0 ... −1. Advancing the effective receiver phase retards the apparent signal phase and so restores the phase of the 0 ... +1 signals to zero, but it leaves the 0 ... −1 signals shifted by 180° so that they cancel out. This refinement may not be essential since a

Table 2 Phase Factors for Three-Step Cycle

	θ	ϕ	N-type exp [i(2ϕ − θ)]	P-type exp (iθ)	Axial exp (iϕ)
1.	0	0	+1	+1	+1
2.	$2\pi/3$	$4\pi/3$	+1	$-\frac{1}{2} + \mathrm{i}(3/4)^{1/2}$	$-\frac{1}{2} - \mathrm{i}(3/4)^{1/2}$
3.	$4\pi/3$	$2\pi/3$	+1	$-\frac{1}{2} - \mathrm{i}(3/4)^{1/2}$	$-\frac{1}{2} + \mathrm{i}(3/4)^{1/2}$

properly adjusted receiver should produce images that are no more than a few percent of the 'true' signal.

4 MULTIPLE QUANTUM SELECTION

The extension to multiple quantum experiments is straightforward if the notion of a pulse is broadened slightly. Generating multiple quantum coherence requires at least two pulses which are separated by a fixed delay, or an extended composite pulse. These complex pulses are black boxes which need not be opened if the phase shift is understood to apply to all segments of the sequence. We might wish to select refocused triple quantum magnetization according to the route 0:−3:+1. Let the whole of the initial pulse or pulse sequence be given a phase shift θ, and the mixing pulse (or 'read' pulse) a shift of ϕ. The desired signal undergoes a phase shift of $\exp[i(4\phi - 3\theta)]$ and so the ability to shift the phase in steps of $\pi/6$ is convenient, allowing steps of 120° for θ and 90° for ϕ. The sum of 12 transients in which ϕ cycles through 0°, 90°, 180°, and 270° with θ fixed at 0° for the first group of four, 120° for the second, and 240° for the third, will select only magnetization which has evolved with an order of coherence $-3 \pm 12n$. The coherence transfer coefficients are unlikely to allow significant magnetization of the order of +9 or higher to be present, so the route is effectively unique. Similarly, subtracting alternate signals in this cycle will select the P-type signals from the route 0:+3:+1, which have the phase factors $\exp[i(-2\phi + 3\theta)]$.

A simple alternative description of the effect of phase shifting pulses is now apparent: if a pulse changes the order of a coherence from $Q = q - p$ to $S = s - r$ then shifting the phase of that pulse by an angle θ will change the phase of the signal through an angle $\theta(S - Q)$. Since the 'pulse' may involve any number of segments, adding 90° to both θ and ϕ in the example above, which involves magnetization beginning with order 0 and finishing with order +1 as usual, will shift the phase of the signal by 90°, and switching the output from the quadrature detectors from $A + iB$ to $B - iA$ will achieve the improvements of CYCLOPS as before.

5 HETERONUCLEAR EXPERIMENTS AND SELECTIVE PULSES

Important simplifications arise whenever the spin Hamiltonian factorizes, that is whenever the operator $\hat{F}_z^S$ for some subgroup (S) comprising one or more nuclei commutes with the complete Hamiltonian. This is true whenever spins are weakly coupled, which is often the case for a homonuclear system and is almost always the case for nuclei of different isotopes. It is then possible to classify each spin wavefunction according to the magnetic quantum numbers of the subgroups, as well as for the total, and to consider pulses which act selectively on one of the subgroups. Consider two strongly coupled protons forming an *AB* system: the total magnetic quantum number may take the values −1, 0, +1, but quantum numbers of the individual nuclei are not meaningful for the mixed wavefunctions and, for the same reason, it is not possible to produce a pulse that will affect one nucleus and not the other. If the nuclei are weakly coupled, as in an *AX* system, then the individual nuclei have good quantum numbers (the wavefunctions are simply products of the eigenfunctions of the two nuclei), and it is straightforward to perturb the transitions of one nucleus without affecting the other. Whenever this 'X-approximation' is applicable, the overall order of coherence is given by the sum of the orders of coherence of each of the subgroups which interact weakly with each other, and radiofrequency pulses may be applied selectively to the subgroups of nuclei.

All pulses are in reality selective pulses since, for example, a pulse applied at the proton frequency will have a negligible effect on ^{13}C transitions. Breaking the overall order down into the sum of the orders of the subgroups, $p_{tot} = \sum p_k$, is convenient since a pulse which affects subgroup S can only alter the order with respect to this group. Thus the discussion of Exorcycle or the selection of multiple quantum states in a system of protons, labelled I, would not be altered by the presence of heteronuclear spins, labelled S, so long as the pulses are selective for protons and the order of coherence is understood to be the proton order p_I, where $p_{tot} = p_I + p_S$. Since the orders are integral no matter what spins the individual nuclei have, and the detection of signals requires that $p_{tot} = +1$, then to observe a proton signal requires that p_I equals +1 and any heteronuclei must therefore have the same order as at equilibrium, $p_S = 0$, so they can be neglected.

The value of splitting up the overall order becomes apparent in experiments with pulses applied separately to two or more subgroups. Consider a heteronuclear experiment that concludes with the detection of a signal at the proton frequency, $p_I = +1$, $p_S = 0$, after a variety of pulses have been applied to each group of nuclei: since the experiment begins and ends with $p_S = 0$, the result must be independent of any phase shift that is applied to all of the pulses on the heteronuclei, and so the transmitter at the heteronuclear frequency does not need to be phase-locked with the proton transmitter.

Heteronuclear J spectra provide the simplest example. The nuclei to be observed, commonly ^{13}C, follow the route 0:−1:+1 which is selected by Exorcycle. The heteronuclei, usually protons in this case, are unaffected at the time of the initial pulse applied to the ^{13}C nuclei, indicated by a point, and are inverted by a pulse which is simultaneous with the ^{13}C mixing pulse, indicated by a colon, and so the protons follow the route 0:0:0. The result is clearly independent of the phase of the pulse that inverts the heteronuclei, but this means that phase cycling is incapable of eliminating magnetization in which the heteronuclei are not inverted.

Now consider the heteronuclear shift correlation experiment in which the S spins are excited, the magnetization evolves, and is then transferred to the I spins by a mixing pulse that involves separate pulses at frequencies ω_I and ω_S, and is finally detected with respect to the reference ω_I. P-type peaks arise from magnetization that has p_S following the route 0:+1:0, while p_I follows 0:0:+1. Once again, it is clear that a phase shift applied to both of the I pulses will not affect the signal since the magnetization begins and ends with $p_S = 0$, and so the relative phase of the transmitters of ω_I and ω_S at the beginning of the experiment is irrelevant. If these pulses are obtained simply by switching the amplifier on and off with a continuous input at the frequency ω_S then the phase of the second pulse relative to the reference at frequency ω_I will be shifted by an additional amount $t_1(\omega_S - \omega_I)$, where t_1 is the time delay between the two pulses. At first sight this would

appear to shift the phase of the signal by $t_1(\omega_S - \omega_I)$, and since t_1 is incremented during a two-dimensional experiment, this would introduce a frequency shift of $-(\omega_S - \omega_I)$ into the F_1 dimension. However, the actual frequency for evolution of the S spins during t_1 is given by $(\Omega_S - \omega_I)$ in the frame rotating at the reference frequency and so the signals appear at the F_1 frequency $(\Omega_S - \omega_S)$. This is exactly the same frequency that would be obtained in a normal one-dimensional experiment for observing the S spins directly with a reference at ω_S. So it turns out that considering the phase of the S spin pulses with respect to the reference at ω_I is an unnecessary complication.

A more straightforward picture emerges in a frame that rotates both at the frequency ω_I and at ω_S. This may seem complex, but, returning to the fairground, think of a more sophisticated merry-go-round complete with riding horses. Our stationary observer might believe that there is a herd of horses leaping and running in a circle, but an observer riding on the platform would see wooden horses fixed on poles that are simply moving up and down. To admire the artwork on the horses, the observer would be better placed sitting astride one of them. The transformation of the wavefunctions of an isolated spin into the rotating frame was accomplished with the operator $\hat{U} = \exp(\mathrm{i}\omega t\hat{I}_z)$ and the corresponding operator for a multispin system is $\hat{U} = \exp(\mathrm{i}\omega t\hat{F}_z)$. Now $\hat{F}_z = \hat{F}_z^I + \hat{F}_z^S$, and these operators must commute since they affect different groups of spins. Therefore

$$\begin{aligned}\hat{U} &= \exp(\mathrm{i}\omega t\hat{F}_z^I)\exp(\mathrm{i}\omega t\hat{F}_z^S)\\ &= \exp(\mathrm{i}\omega t\hat{F}_z^S)\exp(\mathrm{i}\omega t\hat{F}_z^I)\end{aligned} \tag{13}$$

and there is no reason why the frequencies of rotation for the two groups of spins should not be different. In fact most descriptions of heteronuclear experiments make implicit use of the *doubly* rotating frame generated with $\hat{U} = \exp(\mathrm{i}\omega_I t\hat{F}_z^I)\exp(\mathrm{i}\omega_S t\hat{F}_z^S)$. It is therefore convenient to extend the definition of the phase of a pulse whenever the X approximation applies such that the phase of any pulse at frequency ω_Q is understood to be relative to a reference frequency that also has frequency ω_Q.

In the heteronuclear shift correlation experiment described above, selection of the route 0:±1:0 for the S spins simply requires that the second pulse at frequency ω_S has an equal and opposite phase shift to the first, while the I spins follow the route 0:0:+1. CYCLOPS compensation may be achieved by adding 90° phase shifts to the single pulse at frequency ω_I and switching the output of the detectors. This is suitable if the spectrum is to be processed with pure absorption lineshapes, otherwise it is preferable to select the N-type peaks that have the route 0:−1:0 for p_S. Not surprisingly, the phase cycle for this is none other than Exorcycle in which the phases for pulses at frequency ω_I are defined with respect to the reference at ω_I and those of pulses at ω_S are defined with respect to the reference at ω_S.

Heteronuclear multiple quantum experiments are only slightly more complex. Selection of a refocused signal that has evolved as heteronuclear double quantum magnetization[10] requires the observed nucleus to follow the route for p_I 0:−1:+1, which can be selected by applying Exorcycle to the pulses with frequency ω_I, and the heteronuclei follow the route for p_S 0:−1:0. The pulses in this case must not be simultaneous, otherwise the coefficients for transfer to the double quantum state, $p_{\mathrm{tot}} = -1 - 1$, will be zero, but this is irrelevant to the design of a phase cycle. The relative phase of the transmitter for the heteronuclear S spins is again unimportant since p_S is unchanged by the complete sequence, beginning and ending at zero. Equal and opposite phase shifts applied to the two heteronuclear pulses will leave the signal phase unaltered, but will not distinguish magnetization that has evolved with $p_S = +1$ or -1. If an additional 90° phase shift is added to the first ω_S pulse, which changes p_S by ±1, then signals from these two routes will be shifted by 90° in opposite directions: it does not matter that the pulse generates so-called heteronuclear multiple quantum magnetization since the order of coherence of the I spins is not affected. Adding 90° to all of the pulses at ω_I and summing will therefore select $p_S = +1$ and cancel $p_S = -1$.

6 PURE ABSORPTION LINESHAPES

The principles outlined so far have concerned the selection of signals that arise from a single, unique, route of coherence transfer. Such signals are phase modulated in two (or more)-dimensional experiments and hence give rise to 'phase twisted' lineshapes in the final spectrum, that is lineshapes that are an admixture of double absorption and double dispersion. The absorption lineshape is symmetric about the line frequency and the dispersion is antisymmetric, so a pure absorption lineshape could be obtained by taking the mirror image of a line about its center and adding it to the original. This is totally impracticable in complicated spectra. Refocused and nonrefocused signals, the N-type and P-type peaks that evolved with equal and opposite orders of coherence, automatically appear at frequencies which are mirror images about $F_1 = 0$, and so taking the mirror image of one group and adding it to the other will produce pure absorption lineshapes throughout the spectrum *so long as* the intensities are equal in the two groups. The principles of separating signals that have evolved with order $\pm n$ were noted in the description of Exorcycle, and it can be seen that it costs nothing in spectrometer time to keep both signals, but brings the advantage of a $\sqrt{2}$ improvement in sensitivity when they are coadded.

Reversal and addition of these signals is straightforward once they have been separated. This recombination may be achieved by a number of fundamentally equivalent methods of data handling that need not concern us here. There are two common methods for the separation of the mirror image signals: the use of separate storage areas for the two signals, and frequency shifting. As discussed in Section 3, most phase cycles that can be used to select a route 0:−n:+1 can also be used to select the route 0:+n:+1 if half of the signals are subtracted instead of added. For example, in the table of phase shifts used in Exorcycle, the simple sum of the four signals leaves only N-type peaks, and the combination of signals 1 − 2 + 3 − 4 leaves only P-type peaks. These two combinations may be stored and processed separately.

Alternatively, P-type and N-type signals may be selected simultaneously by using only steps 1 and 3 of the cycle, in which case they must be separated by being shifted into different regions of the spectrum. The reference frequency is usually placed in the center of the spectrum and the sampling rate and size of increments in the evolution time are adjusted such that the spectral widths are just large enough to include

all of the signals. In that case the P-type and N-type signals occupy the same spectral region and cannot be separated. Separation into different spectral regions therefore requires that the spectral width be doubled and that P-type and N-type signals each be shifted by half of the original spectral width, in opposite directions. This is easily achieved in the F_1 dimension of a two-dimensional experiment since the evolving signals are not observed in real time, successive samples being taken from different increments in the experiment. If the initial pulse has its phase shifted by 90° for each increment in the evolution time, then the P-type signals, which have order +1 during the evolution period, will have their phases advanced by 90° in each increment, while the N-type signals, which evolve with order -1, have their phases retarded. This corresponds to an apparent increase in the F_1 frequencies of the P-type peaks by one-quarter of the new, doubled, spectral width and an apparent decrease in the F_1 frequencies of the N-type peaks by the same amount. Hence the two groups of signals have been shifted far enough apart to remove the overlap and the two halves of the spectrum can be combined to give pure absorption lineshapes. The same principle, sometimes called 'time proportional phase incrementation' or 'Redfield quadrature', may be applied to signals that evolve with orders $\pm n$ by applying proportionately smaller phase increments to all of the pulses in the preparation sequence.

These procedures appear to be very different, but the results are virtually identical: frequency separation requires a phase cycle which has only half as many steps as that needed to distinguish P-type and N-type peaks in order to store them separately, but doubling the spectral width in F_1 means that twice as many increments are needed to provide the same digital resolution. The two methods therefore require the same length of time and the same amount of data storage; only folded signals and artifacts that have escaped the phase cycle could tell the difference.

It is up to the designer of the pulse sequence to ensure that the coherence transfer coefficients are identical for the mirror image routes, but there are a few aspects of the requirement for equal intensities that relate to the theory of phase cycling. Preparation of the system is generally symmetric since the orders $\pm n$ are obtained from order zero at equilibrium: the breakdown of symmetry is associated with detecting order +1 and rejecting -1 with phase-sensitive detectors in quadrature, which is reinforced by CYCLOPS. The NOESY experiment, for example, involves selecting orders 0:±1:0:+1, where the second period with zero order is the fixed mixing time during which the longitudinal relaxation cross relaxes or exchanges chemically. Evolution with order +1 or -1 is therefore treated equally, regardless of the flip angle of the pulses, and so it is straightforward to obtain pure absorption lineshapes. The basic COSY experiment, however, requires a mixing pulse of exactly 90° flip angle to produce symmetric P- and N-type peaks. This requirement does not apply to heteronuclear shift correlation since the selective pulses process the coherence of the heteronuclei symmetrically through the orders 0:±1:0, while the observed nuclei follow the route 0·0:+1.

7 OPTIMUM ORDERING WITHIN CYCLES

This discussion of the principles of phase cycling has taken a constant receiver phase as its basis in order to present the minimum cycle necessary to select the chosen route for the signals. Generally, a sequence that involves x separate pulses with phase shifts in multiples of π/y will allow $2xy$ different combinations, each of which will present the desired signal with different phases, but these signals may all be coadded if the receiver phase is shifted appropriately. Exorcycle plus CYCLOPS involves two pulses and phase shifts of $\pi/2$ so that the maximum cycle has a manageable 16 steps. The example of triple quantum magnetization has a cycle which expands to 48 steps with the inclusion of CYCLOPS. The basic three-pulse NOESY experiment would require 64 steps if $\pi/2$ phase shifts are used, and so on. In an experiment that required 10 000 transients to obtain adequate sensitivity and only 1000 increments to provide sufficient digital resolution, such complete cycles would be acceptable, but if 1000 transients were sufficient for sensitivity then using a phase cycle would multiply the length of the experiment unnecessarily. It is therefore convenient to take the steps of each complete phase cycle in an order that cancels the most disturbing artifacts in the shortest loops and then goes on to cancel lesser irritants if time allows. This is also desirable in view of spectrometer instability and, as noted above, axial peaks may be canceled in just two steps. The most intrusive artifact of all is the signal from protons without heteronuclear couplings in 'reverse-mode' correlation experiments involving heteronuclei of low abundance, but this may also be dealt with in two steps along with the axial peaks. If the time available for the experiment allows only a single step for each increment, as may be the case in three- or four-dimensional experiments, then there is no room at all for phase cycling, and the use of field gradient pulses may be the only alternative. This is a crude method insofar as unwanted magnetization is only attenuated, never eliminated, and it is impossible to retain P-type peaks together with N-type peaks for producing pure absorption lineshapes and enhancing sensitivity. The use of field gradients instead of phase cycles, which was first outlined in 1977[5] and has been reinvented several times since then, has led to important technological developments. Excellent results can be obtained when the spectrometer stability is poor or the system has insufficient time to return to equilibrium and cancelation is therefore imperfect; these techniques are described elsewhere.

The question of ordering phase cycles is complicated to some extent by the fact that systems are never at equilibrium at the beginning of each pulse sequence since there may also be some coherence persisting after the previous FID. Higher order coherence decays rapidly and even single quantum coherence may be attenuated by field gradient pulses during the relaxation period, but there may be persistent unobservable zero quantum coherence or longitudinal J ordered states (also of order zero) left over from the previous pulse sequence. Although the amplitude of multiple quantum coherence after a single pulse is applied to a system at equilibrium is negligible, residual zero-order coherence may be converted into higher order coherence and the Exorcycle sequence will allow signals from the route 0:+3:+1 to add coherently. However, each step of the phase cycle increments the phase of residual zero quantum magnetization by 90° so that if the following sequence turns it into observable signal with its phase unchanged it will cancel over a four-step cycle.

A more insidious problem arises when the residual coherence is presented with a phase shift that is reversed by the next

pulse sequence. The routes 0:±1:0 leave a residual longitudinal magnetization which oscillates through the basic Exorcycle sequence, resulting in a cyclic deviation from a notional 'steady state', which replaces the true equilibrium at the start of each pulse sequence. The ordering described above causes P-type peaks to be canceled by alternate transients, effectively modulating their intensity with respect to the transient number at twice the rate of the residual longitudinal magnetization, and so its effects are canceled. However, if the sequence is reordered to provide axial peak cancelation on alternate scans then the modulation of the residue and of the P-type peaks are matched and the cancelation will be imperfect. Unfortunately, the relative magnitudes of different types of artifact in a particular type of spectrum depend upon the recycle time, the nature of the sample, and the state of the spectrometer, and so the optimum ordering for the steps of each phase cycle is a matter of trial and error.[11]

Finally, it must be stressed that phase cycling is essentially a difference method and so depends critically on the stability of the spectrometer and the accuracy of the phase shifts it provides. The stability of the phase of the radiofrequencies is of particular concern. When instrument designers are seeking to improve this, they must also bear in mind that essentially all useful phase shifts are simple *rational* numbers of circles: a phase which must be set in multiples of 1.1°, for example, cannot provide accurate shifts of π/n. For these reasons, there can be no completely general prescription for optimimum ordering within cycles and there may even be differences between spectrometers of the same model.

8 RELATED ARTICLES

Analysis of High-Resolution Solution State Spectra; Composite Pulses; COSY Two-Dimensional Experiments; Double Quantum Coherence; Field Gradients and Their Application; Fourier Transform Spectroscopy; Heteronuclear Shift Correlation Spectroscopy; Liouville Equation of Motion; Multidimensional Spectroscopy: Concepts; Radiofrequency Pulses: Response of Nuclear Spins; Relaxation: An Introduction; Spin Echo Spectroscopy of Liquid Samples.

9 REFERENCES

1. D. I. Hoult and R. E. Richards, *Proc. R. Soc. London, Ser. A*, 1975, **344**, 311.
2. D. E. Demco, P. Van Hecke, and J. S. Waugh, *J. Magn. Reson.*, 1974, **16**, 467.
3. G. Bodenhausen, R. Freeman, and D. L. Turner, *J. Magn. Reson.*, 1977, **27**, 511.
4. A. A. Maudsley and R. R. Ernst, *Chem. Phys. Lett.*, 1977, **50**, 368.
5. A. Wokaun and R. R. Ernst, *Chem. Phys. Lett.*, 1977, **52**, 407.
6. P. Bachmann, W. P. Aue, L. Müller, and R. R. Ernst, *J. Magn. Reson.*, 1977, **28**, 29.
7. H. Santos, D. L. Turner, and A. V. Xavier, *J. Magn. Reson.*, 1983, **55**, 463.
8. A. D. Bain, *J. Magn. Reson.*, 1984, **56**, 418.
9. G. Bodenhausen, H. Kogler, and R. R. Ernst, *J. Magn. Reson.*, 1984, **58**, 370.
10. L. Müller, *J. Am. Chem. Soc.*, 1979, **101**, 4481.
11. C. J. Turner and S. L. Patt, *J. Magn. Reson.*, 1989, **85**, 492.

Biographical Sketch

David L. Turner. *b* 1953. M.A., D.Phil., University of Oxford, 1977. Introduced to NMR by Alan Carrington. Postdoctoral work with Sture Forsén, Lund, Sweden; advanced research fellow, University of Southampton; lecturer, University of Leicester; senior lecturer, University of Southampton, since 1988. Approx. 100 publications. Research specialties: theory of multidimensional NMR and applications of NMR in physical and biophysical chemistry.

Radiofrequency Gradient Pulses

Daniel Canet

Université H. Poincaré, Vandoeuvre–Nancy, France

1 Introduction 1
2 Translational Diffusion and Flow Velocity Measured by Means of Radiofrequency Gradients 2
3 NMR Imaging by Radiofrequency Gradient Pulses 2
4 Purely Spectroscopic Applications of Radiofrequency Gradient Pulses 3
5 Related Articles 5
6 References 6

1 INTRODUCTION

The use of the spatial variation of the static magnetic field $\boldsymbol{B}_0$ is almost as old as NMR. The very first experiment, namely the Hahn spin echo experiment, did rely on the condition that, if $\boldsymbol{B}_0$ is not perfectly homogeneous across the sample (and can be made purposely inhomogeneous), it produces a dephasing that can be refocused by a proper spin manipulation. As everyone knows, this property has led to numerous applications, ranging from the measurement of translational diffusion coefficients to NMR imaging, including purely spectroscopic applications such as the selection of coherence pathways. Less attention has been paid to the possibility of taking advantage of the spatial variation of the other magnetic field involved in any NMR experiment, namely the radiofrequency field $\boldsymbol{B}_1$, which is necessary for inducing transitions or, in a more general way, for manipulating nuclear magnetization and especially taking it away from its equilibrium position or creating nonequilibrium spin orders.

The incentive for substituting $\boldsymbol{B}_0$ gradients by $\boldsymbol{B}_1$ gradients originates from the recognition that

1. $\boldsymbol{B}_1$ gradient pulses involve negligibly small rise and fall times because they are created via tuned circuits;
2. they do not entail any eddy currents as do $\boldsymbol{B}_0$ gradients;
3. they do not perturb the frequency/field lock channel;
4. the relevant instrumentation is relatively simple compared with that required by $\boldsymbol{B}_0$ gradients.

However, there do exist some drawbacks related to

1. the difficulties of generating strong $\boldsymbol{B}_1$ gradients;
2. creating independent $\boldsymbol{B}_1$ gradients along the three spatial dimensions.

Nevertheless, the first suggestion of using $\boldsymbol{B}_1$ gradients (combined with $\boldsymbol{B}_0$ gradients) for performing NMR imaging, dates from the end of the 1970s, and was dubbed rotating frame zeugmatography.[1] The exploitation of $\boldsymbol{B}_1$ gradients in relation with surface coil methodology[2,3] and spectroscopic imaging[4] was developed during the 1980s. However, these methods aimed at one-dimensional spatial selection, and do not rely necessarily on *uniform* gradients. On the purely spectroscopic side, $\boldsymbol{B}_1$ gradients (or rather the inevitable inhomogeneity of the $\boldsymbol{B}_1$ field delivered by the transmitter coil of a high-resolution NMR spectrometer) were used during the same period for purging purposes[5] or for selecting specific coherences.[6]

$\boldsymbol{B}_1$ gradient pulses will be discussed here, with the emphasis on their potential for

1. the measurement of self-diffusion coefficients and the study of flow;
2. two-dimensional imaging;
3. the selection of coherence pathways.

These capabilities are based on the usual defocusing and refocusing properties of gradients combined with the fact that a $\boldsymbol{B}_1$ gradient acts on nutation (rotation about the $\boldsymbol{B}_1$ axis in the rotating frame) and not on precession as does a $\boldsymbol{B}_0$ gradient. Since the $\boldsymbol{B}_1$ amplitude is several orders of magnitude smaller than the $\boldsymbol{B}_0$ amplitude, $\boldsymbol{B}_1$ gradients do not suffer from some problems encountered with $\boldsymbol{B}_0$ gradients that are directly related to factors affecting the resonance frequency, namely residual $\boldsymbol{B}_0$ inhomogeneity, magnetic susceptibility variations across the sample, and various heterogeneities that may contribute to lowering the effective transverse relaxation time T_2*. In fact, the effective relaxation rate during the application of a $\boldsymbol{B}_1$ gradient pulse is given by[7]

$$\frac{1}{T_{1,2}} = \frac{1}{2}\left(\frac{1}{T_1} + \frac{1}{T_2}\right) \tag{1}$$

In this expression, T_2* is not involved (for the reasons mentioned above), and, even in unfavorable situations where T_2 is short and much smaller than T_1, $T_{1,2}$ is seen to be twice as large as T_2. This feature may be appreciable, especially in the context of imaging experiments. The mechanism by which a $\boldsymbol{B}_1$ gradient pulse (of duration τ) acts on magnetization can be understood through the nutation angle, which depends on the location of the considered magnetization along the gradient axis X (in the following, the laboratory frame axes will be denoted by capital letters X, Y, and Z, where the Z axis coincides with the direction of $\boldsymbol{B}_0$):

$$\theta(X) = 2\pi k X \tag{2}$$

where the usual k variable has been introduced:

$$k = \frac{\gamma g_1}{2\pi}\tau \tag{3}$$

g_1 being the gradient strength. For a gradient pulse of sufficient duration and a homogeneous sample, the following averages (over the whole sample) hold:

$$\left.\begin{aligned} &\langle \sin\theta \rangle = \langle \cos\theta \rangle = \langle \sin 2\theta \rangle = \langle \cos 2\theta \rangle = 0 \\ &\langle \sin^2\theta \rangle = \langle \cos^2\theta \rangle = \tfrac{1}{2} \end{aligned}\right\} \tag{4}$$

It must be borne in mind, however, that the spatial encoding represented by equation (2), as well as the averages given above are reversible processes: refocusing can be made to occur by applying the same gradient pulse but with the radiofrequency field shifted in phase by 180°.

It should finally be mentioned that experiments based on $\boldsymbol{B}_1$ gradients can be carried out with only slight modifications of a standard high-resolution NMR spectrometer. The basic experimental set-up is shown in Figure 1;[8,9] it is essentially a high-resolution probe to which a single turn coil has been

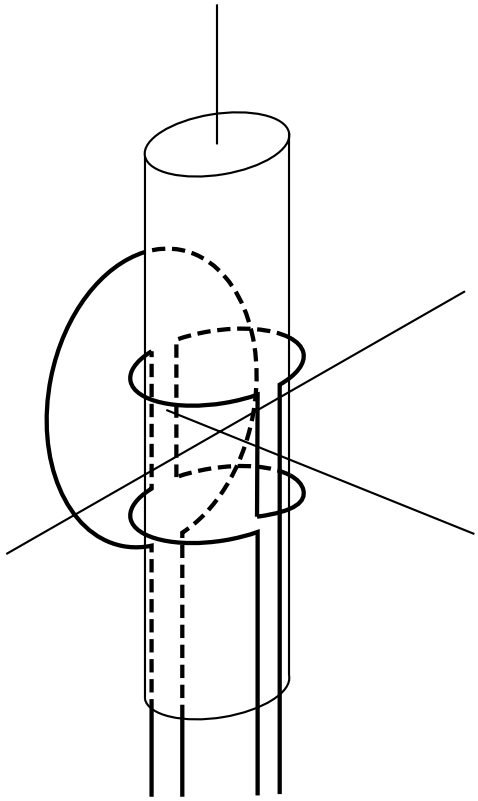

Figure 1 The design of a probe adapted to a vertical cryomagnet. The saddle coil is used for detection purpose and/or for generating homogeneous rf pulses. The $\boldsymbol{B}_1$ gradient is delivered by the simple single turn coil, appropriately located in order to make it uniform across the sample (object) under investigation.[8]

added for radiofrequency field gradient generation. These two coils can be fed by two different transmitters whose relative phases can be adjusted so that they operate in the *same* rotating frame.

2 TRANSLATIONAL DIFFUSION AND FLOW VELOCITY MEASURED BY MEANS OF RADIOFREQUENCY GRADIENTS

A straightforward sequence[9] devised for measuring self-diffusion coefficients by means of $\boldsymbol{B}_1$ gradients is a sort of replica, although somewhat simpler, of the well-known PFGSE using $\boldsymbol{B}_0$ gradients.[10] It is sketched in Figure 2. The first $\boldsymbol{B}_1$ gradient pulse produces a dephasing, depending on the location of the considered elementary magnetization [see equation (2)] which, owing to the central π pulse, would be entirely refocused along the z axis by the second gradient pulse. The last $\pi\backslash 2$ pulse would thus probe the whole longitudinal nuclear magnetization (possibly affected by relaxation). However, because molecules translate during the interval Δ, the nutation induced by the second gradient pulse is different from that produced by the first gradient pulse, and longitudinal magnetization is not entirely refocused. Along the same lines as for the PFGSE experiment, it can be shown that the longitudinal magnetization is attenuated by a factor $\exp(-\gamma^2 g_1^2 \delta^2 D\Delta)$, as long as $\Delta \gg \delta$ and provided that relaxation during Δ has been disregarded. In practice, Δ is maintained at a fixed value and the experiment is repeated for different values of δ; attenuation due to relaxation phenomena is therefore irrelevant, since they affect all experiments in the same way. At the outset, the magnetization measured by the final $\pi/2$ read pulse is plotted as a function of δ^2, yielding the diffusion coefficient D. In alternative sequences,[11,12] the central homogeneous π pulse is dropped; refocusing relies on the average $\langle \cos^2 \theta \rangle = \frac{1}{2}$ [see equation (4)], entailing a reduction of signal intensity by a factor of $\frac{1}{2}$. The simple two-step phase cycle indicated in Figure 3 removes all contributions of transverse magnetization, which would otherwise lead to the formation of stimulated echoes. An interesting feature of this sequence comes from the fact that a homogeneous $\pi/2$ read pulse is not strictly necessary, and can be delivered by the gradient coil. The corresponding flip angle is therefore not exactly the same in all parts of the sample, causing no problem, since one is interested in evaluating the diffusion coefficient for the whole sample (by varying δ).

Finally, it should be mentioned that these sequences can also be used for studying coherent motions. As a simple example, one may consider a fluid flowing with a constant and uniform velocity v along the gradient direction. If the additional nutation angle caused by this displacement is denoted by $\varphi = \gamma g_1 v \delta \Delta$, it is easily shown that the magnetization components just after the second gradient pulse in the sequence of Figure 2 are $m_x = 0$, $m_y = -m_0 \sin \varphi$ and $m_z = -m_0 \cos \varphi$. Because only m_z is converted into observable magnetization, the observed signal is modulated according to $\cos \varphi$, readily yielding the velocity v if the experiment is repeated for different values of the gradient pulse duration δ. As far as the sequence of Figure 3 is concerned, owing to the phase cycling and to the averages given by equation (4), the same result holds, with, however, a signal reduction by a factor of $\frac{1}{2}$.

3 NMR IMAGING BY RADIOFREQUENCY GRADIENT PULSES

Following Hoult's early experiment,[1] $\boldsymbol{B}_1$ gradients, as far as NMR imaging is concerned, have found an interesting field of applications since the beginning of the 1980s, essentially in the context of the so-called rotating frame spectroscopic imaging technique (for a comprehensive review of this subject, see Styles[4]). Basically, the experiment is two-dimensional in nature, one dimension being related to spatial information along the axis of the $\boldsymbol{B}_1$ gradient (X), the other dimension providing chemical shift information. The simplest sequence[13] consists of application of the $\boldsymbol{B}_1$ gradient for an incrementable time t_1, followed by the acquisition of the NMR signal, with which is associated the time variable t_2. This corresponds to an amplitude-modulated two-dimensional experiment, provided that the increment in t_1 is properly chosen to examine the whole sample size and that the dwell time in t_2 fits the chemical shift range. Owing to the form of the collected signal

$$S(t_1, t_2) = \sin(2\pi X k) \cos(2\pi \nu t_2) \tag{5}$$

here $k = \gamma g_1 t_1 / 2\pi$, and one obtains, after a double Fourier transform, the chemical shift information in ν_2 and the spatial information in ν_1. Refinements of the method, including quadrature detection and thus sensitivity improvements,

Figure 2 A pulse sequence for measuring translational diffusion coefficients, with radiofrequency field gradient pulses (g_1). The rf pulses denoted by π and $\pi/2$ are homogeneous. Subscripts indicate rf phases

Figure 3 A simplified version of the pulse sequence of Figure 1. Note the phase cycle of the second gradient pulse, which allows one to retain only contributions from longitudinal magnetization

were published later. Along the same lines, spin density profiles have been obtained through the observation of ^{23}Na resonances.[14]

NMR imaging, as it is usually understood, namely, the spatial variation of the spin density pertaining to a single chemical species, can be performed by resorting only to $\boldsymbol{B}_1$ gradients. Again the method is a sort of transportation of procedures using $\boldsymbol{B}_0$ gradients. The advantages as well as pitfalls of $\boldsymbol{B}_1$ gradients (listed above) support the conclusion that, at the present time, $\boldsymbol{B}_1$ gradients can better be used for NMR microscopy, with applications essentially in the field of materials science.[15] This basic scheme of 2D imaging by $\boldsymbol{B}_1$ gradients[16] involves at the onset a slice selection procedure. The latter is carried out by the rf gradient of the saddle coil of Figure 1. Selectivity in the Z direction is achieved by a pulse train of the DANTE type,[17] provided that the saddle coil has been purposely designed for presenting a strong $\boldsymbol{B}_1$ variation along Z. Thereafter the (X, Y) plane can be examined by means of projections along the gradient axis, collected for different orientations of the object with respect to the Z axis. To this end, the experiment, including the initial slice selection, is repeated for as many sample rotations as necessary, performed in a stepped manner around Z. The whole set of data (projections) can be treated with the help of the 'filtered back projection' (FBP) algorithm,[18] which provides the image reconstruction in the (X, Y) plane. The pulse sequence for obtaining *one* projection (defined by α, which specifies the angle by which the object has been rotated with respect to its initial position) is sketched in Figure 4. It relies on the nutation angle produced by the $\boldsymbol{B}_1$ gradient delivered by the simple single turn coil, which can be expressed as

$$2\pi k(X\cos\alpha + Y\sin\alpha + D) \tag{6}$$

where X and Y are the coordinates of the considered elementary magnetization, D is the distance between the

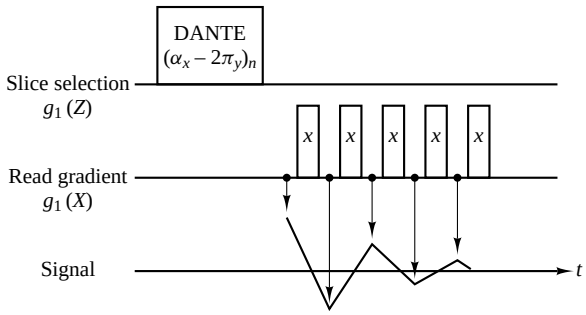

Figure 4 Sequence corresponding to 1D $\boldsymbol{B}_1$ gradient encoding (profile). The magnetization of interest is selected along the y axis of the rotating frame by means of a DANTE-like pulse train (the relevant $\boldsymbol{B}_1$ gradient is created by the vertical saddle coil, which is also employed for signal detection). The pseudo-FID (signal) is obtained by application of the read gradient [$g_1(X)$, created by the single turn coil—see Figure 1] along the x direction of the rotating frame. This pseudo-FID reflects nutation, which is spatially dependent. Dots denote data acquisition, which can be performed only when the $g_1(X)$ gradient is turned off because of residual coupling between the two coils

rotating axis and the virtual point where $\boldsymbol{B}_1$ is zero, and k is related to the time t during which the gradient has been applied ($k = \gamma g_1 t/2\pi$). The collected signal has the form

$$S(k,\alpha) = \int\int \varrho(X,Y)\cos[2\pi k(X\cos\alpha + Y\sin\alpha + D)]\,\mathrm{d}X\,\mathrm{d}Y \tag{7}$$

which lends itself to the reconstruction procedure alluded to above (FBP) for obtaining the spin density $\varrho(X, Y)$. The image of a water phantom is shown in Figure 5.

Another approach,[19] based on a nonuniform $\boldsymbol{B}_1$ gradient created by a toroidal cavity resonator, has been shown to enable spatial resolution of the order of a few micrometers.

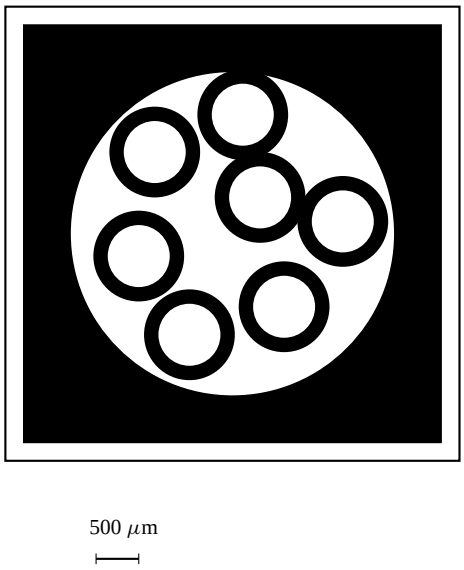

Figure 5 A phantom image obtained by $\boldsymbol{B}_1$ gradient imaging (see Figure 4). Thickness of capillary walls is about 100 μm

4 PURELY SPECTROSCOPIC APPLICATIONS OF RADIOFREQUENCY GRADIENT PULSES

The use of $\boldsymbol{B}_1$ gradients in spectroscopy seems rather promising. As for static gradients, spectral selectivity is the natural field of application. A first example is provided by solvent peak suppression, which can be simply and efficiently performed by means of a DANTE train of $\boldsymbol{B}_1$ gradient pulses.[20] It is based on the way in which a classical DANTE sequence,[17] made of homogeneous hard pulses, acts on a spin system. It can be schematized by $[(\alpha)_x - \tau]_n$. The pulse denoted by $(\alpha)_x$ flips the magnetization by a small angle α around the x axis of the rotating frame; magnetization is then allowed to precess for a time τ. Except for resonances ν' at zero frequency (coinciding with the carrier frequency) or at $\nu' = k/\tau$ (k integer), the next rf pulse will not produce the same nutation, since the corresponding magnetization is no longer in a plane perpendicular to $\boldsymbol{B}_1$. In fact, after n cycles, these magnetizations are merely restored toward the Z axis—in other words, to the equilibrium axis. Conversely, for magnetizations at k/τ (including zero frequency), no net precession occurs, and the effect of pulses is *cumulative*, leading to a total nutation angle $n\alpha$. Hence, magnetizations relevant to these frequencies are selectively taken to any location in the (y, z) plane by adjusting n and α. When using $\boldsymbol{B}_1$ gradient pulses instead of homogeneous (α) pulses, magnetizations at frequencies k/τ are progressively defocused in the course of the n cycles, whereas other magnetizations benefit from the usual behavior of a DANTE sequence, and thus remain along the Z axis. This procedure is rather simple to run, and proves to be very efficient for eliminating the solvent resonance, as shown in Figure 6. It must be emphasized that this is not a saturation process, since the total application of the $\boldsymbol{B}_1$ field (in the form of a gradient) is, in duration, largely below relaxation times.

Another interesting application of gradients in spectroscopy concerns the so-called selection of coherence pathways, which amounts to avoiding the phase cycling schemes and thus

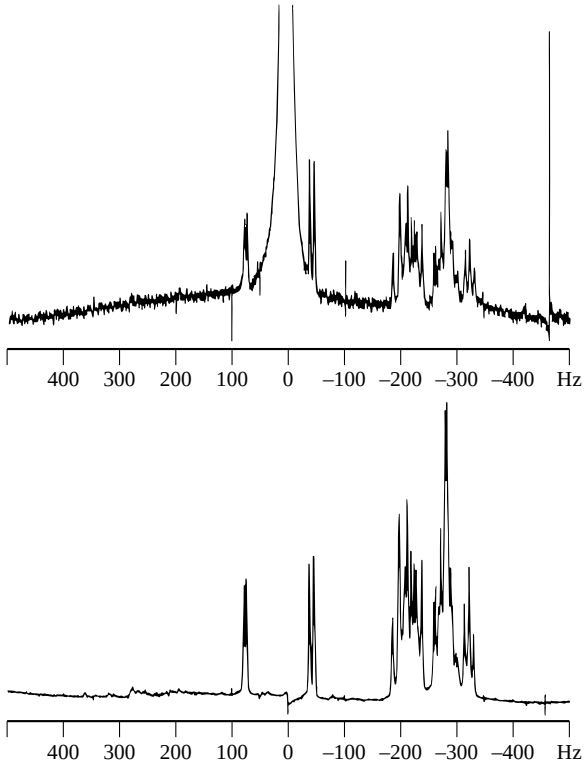

Figure 6 Solvent peak suppression obtained by applying a DANTE train of $\boldsymbol{B}_1$ gradient pulses prior to a normal read pulse (bottom). Note the increase of sensitivity with respect to the conventional spectrum (top), owing to the availability of the whole dynamic range of the analog-to-digital converter

reduces the measurement time in two-dimensional correlation experiments. The very first COSY experiment by which quadrature detection in the t_1 time domain could be obtained in a single transient per t_1 value can be schematized as follows:[21]

$$(\pi/2)_x - t_1 - (g_0) - (\pi/2)_x - (g_0) - \mathrm{Acq}(t_2) \qquad (8)$$

where $(\pi/2)$ stands for a homogeneous radiofrequency pulse and (g_0) for a static field gradient ($\boldsymbol{B}_0$) pulse of arbitrary duration. The analog of the sequence in equation (8) with $\boldsymbol{B}_1$ gradient pulses can be devised by referring to clusters involving homogeneous pulses and one $\boldsymbol{B}_1$ gradient, which have the same effect as a single $\boldsymbol{B}_0$ gradient pulse:[6]

$$(\pi/2)_x - t_1 - (\pi/2)_x - (g_1)_y - (\pi/2)_x - (g_1)_y - (\pi/2)_{-x} - \mathrm{Acq}(t_2) \qquad (9)$$

This sequence has actually been worked out in conjunction with *radial* $\boldsymbol{B}_1$ gradients[22] (such gradients, based on a quadrupolar arrangement, correspond to a spatial variation of $\boldsymbol{B}_1$ along radii intersecting at the center of the sample, by contrast with the *planar* gradient created by the simple device shown in Figure 1), which imply further clusters of homogeneous pulses for compensating purposes. An even simpler sequence,[23] using planar $\boldsymbol{B}_1$ gradients, leads exactly to the same result. It has the form

$$(\pi/2)_x - t_1 - (\pi/2)_y (g_1)_x (g_1)_y (\pi/2)_x - \mathrm{Acq}(t_2) \qquad (10)$$

It will be briefly analyzed, with the emphasis put on the inherent quadrature prevailing in the t_1 domain. For that purpose, the quantities pertaining to a two-spin-$\frac{1}{2}$ system (A, X) and that exist at the end of the evolution time t_1 will be considered. These are $\hat{I}_x$, $\hat{I}_y$ for in-phase magnetizations, and $2\hat{I}_{A,x}\hat{I}_{X,z}$, $2\hat{I}_{A,y}\hat{I}_{X,z}$ for antiphase magnetizations relative to a spin A, J-coupled to a spin X.[24] By combining, on the one hand, rotations due to homogeneous ($\pi/2$) pulses, and, on the other, averaging effects due to $\boldsymbol{B}_1$ gradient pulses [equation (4)], it turns out that these quantities under the cluster $(\pi/2)_y$ $(g_1)_x$ $(g_1)_y$ $(\pi/2)_x$, transform as

$$\hat{I}_x \rightarrow \tfrac{1}{2}\hat{I}_y \tag{11}$$

$$\hat{I}_y \rightarrow \tfrac{1}{2}\hat{I}_x \tag{12}$$

$$2\hat{I}_{A,x}\hat{I}_{X,z} \rightarrow \tfrac{1}{2}(2\hat{I}_{A,z}\hat{I}_{X,y}) \tag{13}$$

$$2\hat{I}_{A,y}\hat{I}_{X,z} \rightarrow \tfrac{1}{2}(2\hat{I}_{A,z}\hat{I}_{X,x}) \tag{14}$$

It can be seen that equations (13) and (14) indicate coherence transfers from A to X (cross peaks in the 2D map), whereas equation (11) and (12) will give rise to diagonal peaks, all with a loss of sensitivity by a factor of two. For these four quantities, it can be seen that the x component in t_1 (denoted below by x_1) transforms into a y component in t_2 (denoted below by y_2), and, conversely, that y_1 transforms into x_2. Now, disregarding a trivial phase angle affecting all magnetization components uniformly, it can be assumed that, under precession, the x component is modulated by a cosine function and the y component by a sine function [$x \propto \cos(2\pi\nu t)$ and $y \propto \sin(2\pi\nu t)$]. Because quadrature detection is physically employed in t_2, one has

$$\left.\begin{aligned} x_2 &\propto \exp(2\mathrm{i}\pi\nu_2 t_2) \\ y_2 &\propto \mathrm{i}\exp(2\mathrm{i}\pi\nu_2 t_2) \end{aligned}\right\} \tag{15}$$

Referring to the relationships $x_1 \rightarrow y_2$ and $y_1 \rightarrow x_2$, one obtains for x_1,

$$\cos(2\pi\nu_1 t_1)\,\mathrm{i}\exp(2\mathrm{i}\pi\nu_2 t_2) \tag{16}$$

and for y_1,

$$\sin(2\pi\nu_1 t_1)\exp(2\mathrm{i}\pi\nu_2 t_2) \tag{17}$$

Since x_1 and y_1 coexist at the end of the t_1 interval, as well as the relevant quantities during t_2, the total signal can be expressed as the sum of equations (16) and (17):

$$S(t_1, t_2) = \mathrm{i}\exp(-2\mathrm{i}\pi\nu_1 t_1)\exp(2\mathrm{i}\pi\nu_2 t_2) \tag{18}$$

This equation shows that quadrature in t_1 is effective with a single transient (without any phase cycling); S must, however, be subjected to a complex two-dimensional Fourier transform, with the unavoidable phase twist phenomenon and the necessity to display the final spectrum in the magnitude mode.

The next step is to devise a procedure using $\boldsymbol{B}_1$ gradients that would be the equivalent to the widely used double quantum filtered COSY experiment.[25] The latter has two major advantages:

1. attenuation (in principle elimination) of single quantum coherences, especially the one related to the solvent peak;
2. identical phases for diagonal and cross peaks, which allows the reduction of overlaps between these two types of peaks.

The objective is still to reduce the measuring time by avoiding phase cycling (a single transient per t_1 value). The interest of such an experiment was demonstrated for $\boldsymbol{B}_0$ gradients,[26] although, in that case, it proved difficult to obtain pure absorption spectra. With $\boldsymbol{B}_1$ gradients, the basic sequence[27] can be schematized as

$$(\pi/2)_x - t_1 - (g_1)_x(2g_1)_y - \mathrm{Acq}(t_2) \tag{19}$$

where $(2g_1)$ indicates a $\boldsymbol{B}_1$ gradient pulse of duration twice that of (g_1). Further discussions about the sequence in equation (19) and some of its variants can be found in the literature.[28] In order to trace the quantities that survive after the two $\boldsymbol{B}_1$ gradient pulses, it suffices to resort to the averaging of nutation angles given by equation (4) as was done to obtain the results in equations (11)–(14). This yields

$$\hat{I}_x \rightarrow 0 \tag{20}$$

$$\hat{I}_y \rightarrow 0 \tag{21}$$

$$2\hat{I}_{A,x}\hat{I}_{X,z} \rightarrow 0 \tag{22}$$

$$2\hat{I}_{A,y}\hat{I}_{X,z} \rightarrow \tfrac{1}{4}(2\hat{I}_{A,y}\hat{I}_{X,z}) + \tfrac{1}{4}(2\hat{I}_{A,z}\hat{I}_{X,y}) \tag{23}$$

As can be seen from the above results, all single quantum coherences vanish whereas one antiphase magnetization, $(2\hat{I}_{A,y}\hat{I}_{X,z})$, leads to a diagonal peak, $\frac{1}{4}(2\hat{I}_{A,y}\hat{I}_{X,z})$, and a cross peak, $\frac{1}{4}(2\hat{I}_{A,z}\hat{I}_{X,y})$, representing coherence transfer from A to X. It is perfectly clear that the same goal has been achieved as in DQF-COSY, with a single transient per t_1 value. Although quadrature detection in t_1 is no longer an inherent feature of the experiment, it can be retrieved by the time proportional phase incrementation (TPPI) procedure[29] applied to the first $\pi/2$ homogeneous pulse. As shown in Figure 7, the experiment affords especially clean spectra.

Finally, it should be mentioned that the use of $\boldsymbol{B}_1$ gradients is not limited to homonuclear systems: a $\boldsymbol{B}_1$ gradient pulse can be implemented in a variant of the heteronuclear multiple quantum correlation (HMQC) experiment.[30]

5 RELATED ARTICLES

COSY Two-Dimensional Experiments; Diffusion and Flow in Fluids; Diffusion Measurements by Magnetic Field Gradient Methods; Field Gradients and Their Application; Rotating Frame Methods for Spectroscopic Localization; NMR Microscopy: Resolution; Probe Design and Construction; Projection–Reconstruction in MRI; Radiofrequency Systems and Coils for MRI and MRS; Water Signal Suppression in NMR of Biomolecules.

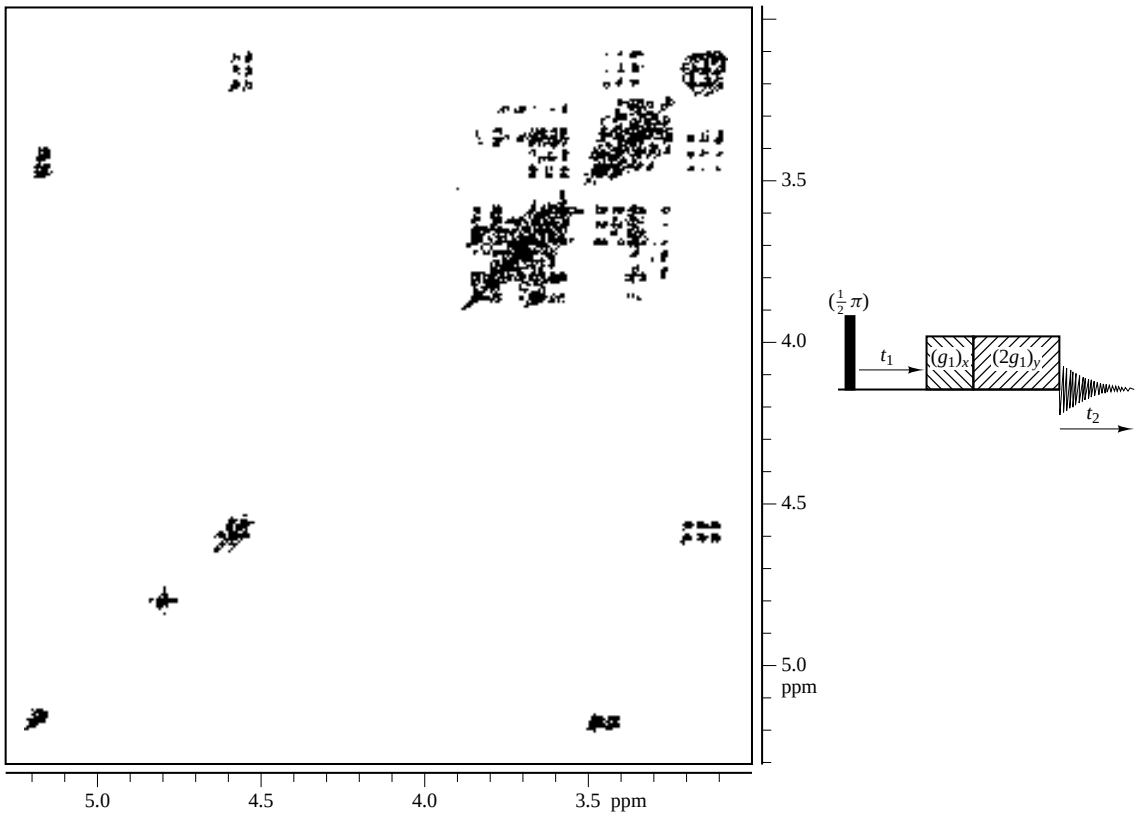

Figure 7 A typical pure absorption 2D map obtained by the sequence in equation (19) (0.9 M glucose in H_2O). The elimination of the water peak has been improved by inserting, prior to the first $\frac{1}{2}\pi$ pulse, a train of $\boldsymbol{B}_1$ gradient pulses. Dotted peaks are negative

6 REFERENCES

1. D. I. Hoult, *J. Magn. Reson.*, 1979, **33**, 183.
2. C. S. Bosch and J. J. H. Ackerman, in *NMR Basic Principles and Progress*, eds. P. Diehl, and E. Fluck, 1992, Vol. 27, p. 3.
3. P. A. Bottomley, in *NMR Basic Principles and Progress*, eds. P. Diehl, E. Fluck, and R. Kosfeld, Springer-Verlag, Berlin 1992, Vol. 27, p. 67.
4. P. Styles, in *NMR Basic Principles and Progress*, eds. P. Diehl, E. Fluck, and R. Kosfeld, Springer-Verlag, Berlin 1992, Vol. 27, p. 45.
5. G. Otting and K. Wüthrich, *J. Magn. Reson.*, 1988, **76**, 569.
6. C. J. R. Counsell, M. H. Levitt, and R. R. Ernst, *J. Magn. Reson.*, 1985, **64**, 470.
7. H. C. Torrey, *Phys. Rev.*, 1949, **76**, 1059.
8. A. J. Shaka, J. Keeler, M. B. Smith, and R. Freeman, *J. Magn. Reson.*, 1985, **61**, 175.
9. D. Canet, B. Diter, A. Belmajdoub, J. Brondeau, J. C. Boubel, and K. Elbayed, *J. Magn. Reson.*, 1989, **81**, 1.
10. E. O. Stejskal and J. E. Tanner, *J. Chem. Phys.*, 1965, **42**, 288.
11. G. S. Karczmar, D. B. Twieg, T. J. Lawry, G. B. Matson, and M. W. Weiner, *Magn. Reson. Med.*, 1988, **7**, 111.
12. R. Dupeyre, Ph. Devoulon, D. Bourgeois, and M. Décorps, *J. Magn. Reson.*, 1991, **95**, 589.
13. S. J. Cox and P. Styles, *J. Magn. Reson.*, 1980, **40**, 209.
14. J. P. Bachman, K. R. Metz, J. Mao, and R. Briggs, *Magn. Reson. Med.*, 1990, **16**, 335.
15. P. Maffei, L. Kiéné, and D. Canet, *Macromolecules*, 1992, **25**, 7114.
16. P. Maffei, P. Mutzenhardt, A. Retournard, B. Diter, R. Raulet, J. Brondeau, and D. Canet, *J. Magn. Reson., Ser. A*, 1994, **106**, 40.
17. G. A. Morris and R. Freeman, *J. Magn. Reson.*, 1978, **29**, 433.
18. P. T. Callaghan, *Principles of Nuclear Magnetic Resonance Microscopy*, Clarendon, Oxford, 1991.
19. K. Woelk, J. W. Rathke, and R. J. Klinger, *J. Magn. Reson., Ser. A*, 1993, **105**, 113.
20. D. Canet, J. Brondeau, E. Mischler, and F. Humbert, *J. Magn. Reson., Ser. A*, 1993, **105**, 239.
21. P. Barker and R. Freeman, *J. Magn. Reson.*, 1985, **64**, 334.
22. W. Maas, F. Laukien, and D. G. Cory, *J. Magn. Reson., Ser. A*, 1993, **103**, 115.
23. P. Mutzenhardt, J. Brondeau, and D. Canet, *J. Magn. Reson., Ser. A*, 1994, **108**, 110.
24. O. W. Sørensen, G. W. Eich, M. H. Levitt, G. Bodenhausen, and R. R. Ernst, in *Progress in Nuclear Magnetic Resonance Spectroscopy*, eds. J. W. Emsley, J. Feeney, and L. H. Sutcliffe, Pergamon Press, Oxford, 1983, Vol. 16, p. 163.
25. U. Piantini, O. W. Sørensen, and R. R. Ernst, *J. Am. Chem. Soc.*, 1982, **104**, 6800.
26. R. E. Hurd, *J. Magn. Reson.*, 1990, **87**, 422.
27. J. Brondeau, D. Boudot, P. Mutzenhardt, and D. Canet, *J. Magn. Reson.*, 1992, **100**, 611.
28. D. G. Cory, F. H. Laukien, and W. E. Mass, *J. Magn. Reson., Ser. A*, 1993, **105**, 223.
29. D. Marion and K. Wüthrich, *Biochem. Biophys. Res. Commun.*, 1983, **113**, 967.
30. J. M. Nuzillard, G. Gasmi, and J. M. Bernassau, *J. Magn. Reson., Ser. A*, 1993, **104**, 83.

Biographical Sketch

Daniel Canet. *b* 1944. B.S., 1966; Thesis, 1973, University of Nancy, France. Introduced to NMR by Pierre Granger. Postdoctoral work at UCSD with R. L. Vold and R. R. Vold. Faculty in Physical Chemistry, University of Nancy, 1973–present. Approx. 160 publications. Research specialties: spin relaxation, selectivity in NMR, and use of radiofrequency field gradients in NMR.

REDOR and TEDOR

Jacob Schaefer

Department of Chemistry, Washington University, St. Louis, MO, USA

1	Refocusing and Dephasing	1
2	REDOR Dephasing for Recrystallized Labeled Alanines	1
3	Long-Range Couplings and the Natural-Abundance Background	3
4	Coherence Transfer and Selectivity	5
5	Combination Experiments and Synchronous Detection	6
6	Related Articles	7
7	References	7

1 REFOCUSING AND DEPHASING

Rotational echo double resonance (REDOR) NMR is a new analytical spectroscopic technique for solids spinning at the magic angle which has been developed during the last 6 years.[1] REDOR provides a direct measure of heteronuclear dipolar coupling between isolated pairs of labeled nuclei. In a solid with a $^{13}C-^{15}N$ labeled pair, for example, the ^{13}C rotational echoes that form each rotor period following a $^{1}H-^{13}C$ cross polarization transfer can be prevented from reaching full intensity by insertion of a ^{15}N π pulse each half rotor period (Figure 1). The ^{15}N pulse in the middle of the evolution period is replaced by a ^{13}C pulse so that isotropic carbon chemical shifts are in phase at the beginning of data acquisition. The REDOR difference (the difference between a ^{13}C NMR spectrum obtained under these conditions and one obtained with no ^{15}N π pulses) has a strong dependence on the $^{13}C-^{15}N$ dipolar coupling and hence the $^{13}C-^{15}N$ internuclear distance.[2] REDOR is described as double resonance even though three radiofrequencies (typically ^{1}H, ^{13}C, and ^{15}N) are used because the protons are removed from the important evolution part of the experiment by resonant decoupling. The dephasing of magnetization in REDOR arises from a local dipolar $^{13}C-^{15}N$ field gradient and involves no polarization transfer. REDOR has no dependence on ^{13}C or ^{15}N chemical shift tensors and does not require resolution of a $^{13}C-^{15}N$ coupling in the chemical shift dimension.[2]

The evolution of observable S-spin magnetization for a single crystallite on resonance under magic angle spinning and an $I-S$ dipolar coupling is shown in Figure 2 (left). Each dot represents the result of evolution for an equal fraction of a rotor period, with a minor homogeneous decay superimposed for display purposes. At the beginning of the rotor cycle, the magnetization is the observable, $\langle\hat{S}_x\rangle$. Under sample rotation and $I-S$ dipolar coupling, the observable magnetization is transformed into nonobservable bilinear coherence, $\langle\hat{I}_z\hat{S}_y\rangle$, and then back into $\langle\hat{S}_x\rangle$. By the end of the rotor cycle the full observable magnetization has been recovered. For a collection of crystallites in a powder, individual phase accumulations (the product of resonance frequency and time) vary in size and sign depending on crystallite orientation in the magnetic field. This causes phase interference during the rotor cycle and an apparent decay of the observable signal for the powder. Nevertheless, because the magnetization from each crystallite refocuses completely, the dephasing for the powder is also refocused into a full rotational echo at the end of the rotor cycle.

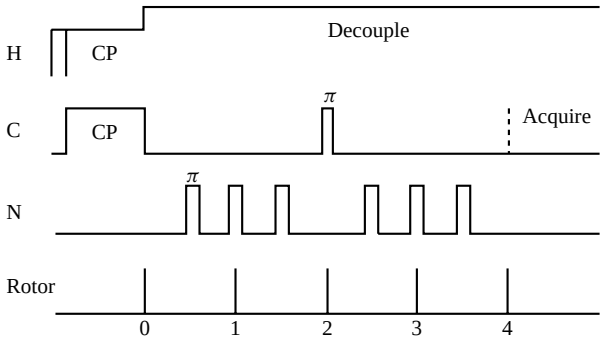

Figure 1 Pulse sequence for a version of REDOR ^{13}C NMR. Two equally spaced, ^{15}N 180° pulses per rotor period result in the dephasing of transverse carbon magnetization produced by a cross-polarization (CP) transfer from dipolar-coupled protons. Carbon–nitrogen dipolar coupling determines the extent of dephasing. A ^{13}C 180° pulse replaces the ^{15}N pulse in the middle of the dephasing period and refocuses isotropic ^{13}C chemical shift differences at the beginning of data acquisition. After the CP transfer, resonant decoupling removes the protons from the experiment. The illustration is for four rotor cycles

However, even for a single crystallite, the refocusing is incomplete in the presence of dephasing I-spin π pulses (Figure 2, right). Evolution for the crystallite is identical to that shown at the left of the figure between times '1' and '2'. The I-spin inverting π pulse, which ends at time '3', changes the sign of $\langle\hat{I}_z\hat{S}_y\rangle$. This process is repeated under the second I-spin π pulse which ends at time '5'. At the end of the rotor cycle (time '6'), the transformation of bilinear coherence created during the rotor cycle into observable magnetization is incomplete. For a powder, a rotational echo of diminished intensity is observed. The extent of the diminution depends on the $I-S$ coupling. The diminution is maximum for two dephasing pulses and is independent of their exact placement so long as the pulse spacing is one-half of the rotor period.[2]

2 REDOR DEPHASING FOR RECRYSTALLIZED LABELED ALANINES

The results of a REDOR experiment performed using the pulse sequence of Figure 1 on an equimolar, recrystallized mixture of L-[2-^{13}C,^{15}N]alanine and L-[1-^{13}C]alanine are shown in Figure 3.[3] The full echo ^{13}C NMR spectrum (S_0) after two rotor cycles with no dephasing is at the bottom of the Figure, and the REDOR difference ($\Delta S = S_0 - S$, where S is the spectrum with dephasing) as a function of the number of rotor cycles, is shown at the top of the Figure. The 900 Hz intramolecular $^{13}C-^{15}N$ coupling results in a sizeable ΔS for the methine carbon atom after only two rotor cycles; this ΔS reaches a maximum after four rotor cycles, and then oscillates in amplitude. The average 100 Hz intermolecular coupling produces a small carboxyl carbon atom ΔS after two rotor cycles, which increases monotonically with dephasing time.

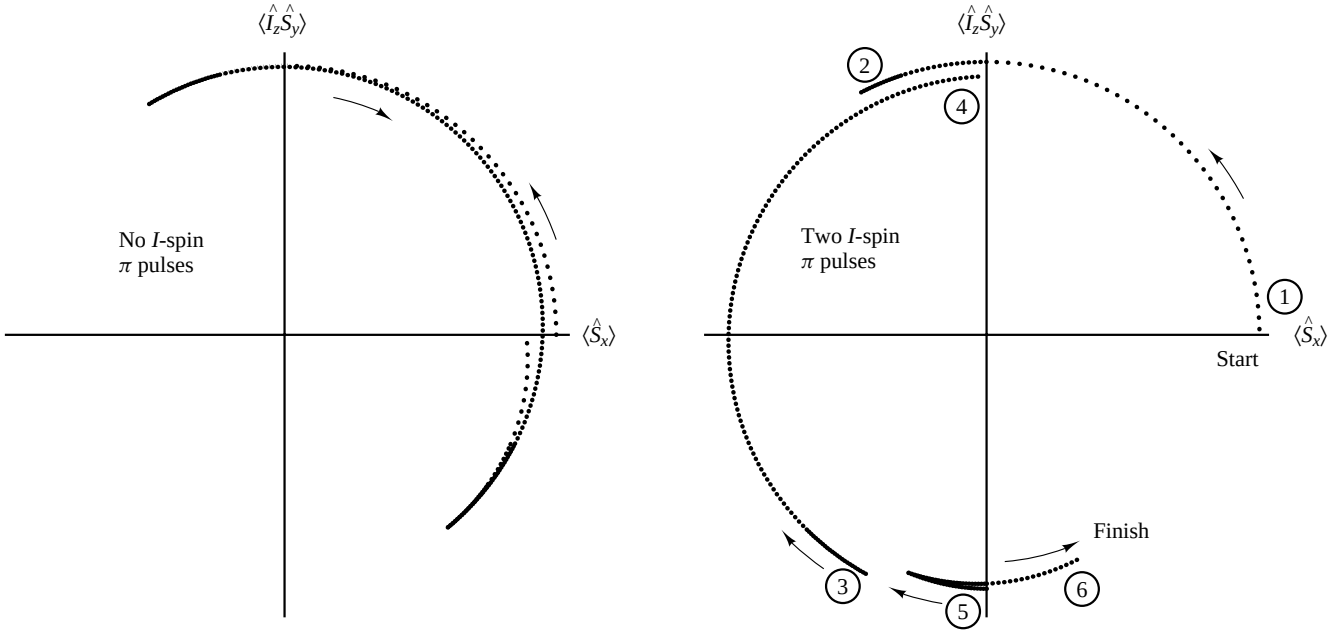

Figure 2 Schematic diagram of the evolution of the IS density matrix for a single crystal under magic angle spinning and $I-S$ dipolar coupling during a REDOR pulse sequence with no dephasing pulses (left) and with dephasing pulses (right)

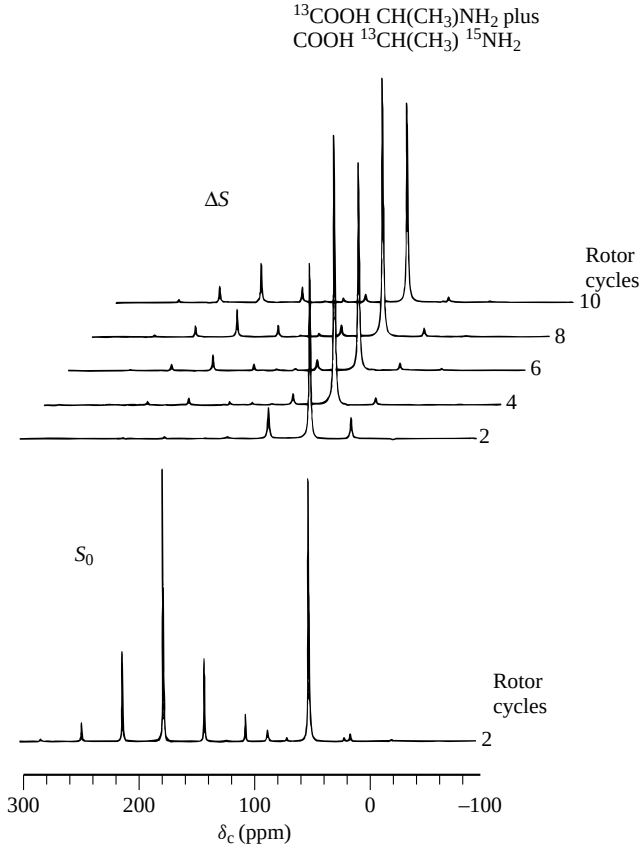

Figure 3 The 50.3-MHz REDOR ^{13}C NMR spectra of an equimolar, recrystallized mixture of L-[2-^{13}C,^{15}N]alanine and L-[1-^{13}C]alanine, as a function of the number of rotor cycles. A full echo spectrum (S_0) after two rotor cycles is shown at the bottom of the Figure and REDOR difference spectra (ΔS) at the top. Magic angle spinning was at 2702 Hz

The $\Delta S/S_0$ ratios for both carbon atoms have the same dependence on the dimensionless parameter, λ_D (Figure 4, solid circles and squares). The theoretical dependence (Figure 4, solid line) was calculated by performing an isotropic powder average over the dephasing for individual crystallites (Figure 2, right). Thus, the angular dependence of the dipolar interaction is suppressed. The resulting universal dephasing behavior needs to be calculated only once for all heteronuclear spin-1/2 pairs. (REDOR applications also include quadrupolar nuclei like ^{2}H, with either direct observation of deuterium or indirect observation through REDOR dephasing. Calculation of the theoretical $\Delta S/S_0$ behavior is slightly more complicated.)[4]

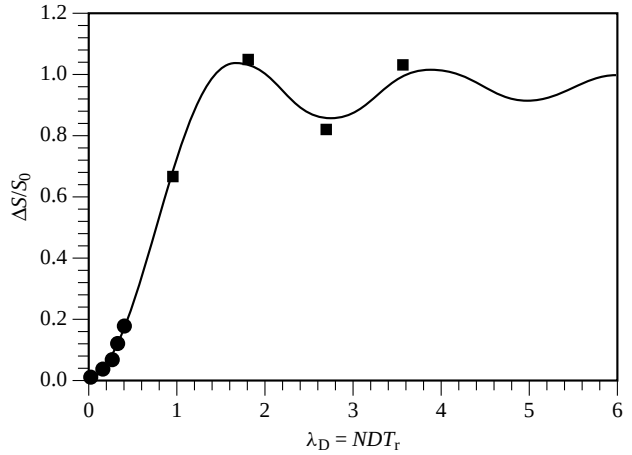

Figure 4 Observed dependence of $\Delta S/S_0$ on the universal parameter, λ_D, for the ^{13}C–^{15}N double-labeled alanine mixture of Figure 3. (N is the number of rotor cycles with dephasing, D is the dipolar coupling constant, and T_r is the rotor period)

A few experimental values of $\Delta S/S_0$ determine λ_D, which then establishes D since the total dephasing time (the product of the number of rotor cycles of dephasing and the rotor period) is known. Because $D = \gamma_I\gamma_S h/2\pi r^3_{IS}$, the observed dephasing can be translated into an internuclear distance directly. If $\Delta S/S_0$ and hence D are known experimentally to 10%, the distance is known with 2% accuracy. Weak dipolar couplings associated with large internuclear distances can be effectively amplified in REDOR by simply allowing the rotor to go around. The only practical problem is holding the echo train together. This depends on the technical difficulty of completely decoupling the protons, which may require low temperatures to suppress kHz regime molecular motions.[5] Translating dipolar couplings into distances in the presence of large-amplitude motions involves specifying a model for the motion.[6]

3 LONG-RANGE COUPLINGS AND THE NATURAL-ABUNDANCE BACKGROUND

In the early applications of REDOR to C–N distance determinations in peptides, relatively few dephasing pulses were used so that sometimes large natural-abundance corrections were necessary.[7] More recently, increased dephasing has been possible as a result of the development of phase routing schemes[8] (Figure 5) that eliminate the dependence of REDOR determinations on frequency offsets and pulse imperfections.[9]

For example, the ^{13}C signal for the label in the nine-residue emerimicin fragment, Ac-Phe-[1-^{13}C]MeA$_2$-MeA-MeA-Val-[^{15}N]Gly$_6$-Leu-MeA-MeA-*O*-Bzl, where Ac = acetyl, Phe = phenylalanine, MeA = methylalanine, Val = valine, Gly = glycine, Leu = leucine, Bzl = benzyl is not resolved from that of natural-abundance peptide carbonyl carbon atoms, which make a constant 7.7% contribution to the full echo signal, S_0. This correction can either be measured in a separate experiment on a natural-abundance sample, or calculated from the known structure.[10] In addition, the natural-abundance ^{13}C carbonyls of Val$_5$ and Gly$_6$ are, respectively, one and two bonds away from the ^{15}N label and so will make a contribution to ΔS that reaches a maximum value of 2% by about N_c = 16. The other natural-abundance carbonyl ^{13}C atoms are all farther away from the ^{15}N label than is the carbonyl label at MeA$_2$. Thus, for $N_c > 32$, the observed ΔS is dominated by the coupling of the ^{15}N–^{13}C labels and additional natural-abundance corrections are unimportant. By N_c = 96, $\Delta S/S_0$ is greater than 0.7 (Figure 6), consistent with a D value of 40 Hz, corresponding to a C–N distance of 4.2 ± 0.1 Å. The distance by X-ray analysis[11] is 4.16 Å. The natural-abundance correction to D is less than 2 Hz when N_c = 96, which means that less than a 0.05-Å correction for the C–N distance is required. The agreement between X-ray and REDOR determinations of the [1-^{13}C]MeA$_2$–[^{15}N]Gly$_6$ distance for this calibration sample for N_c = 8 to N_c = 112

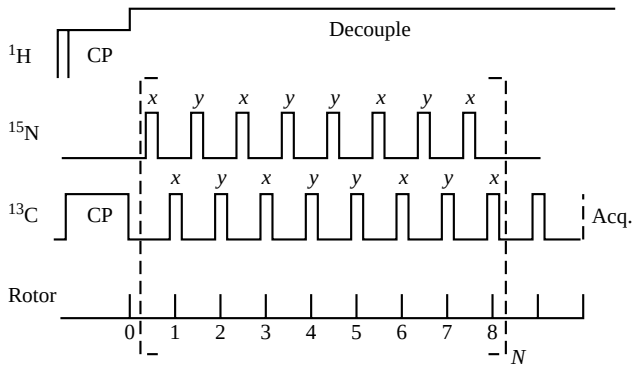

Figure 5 REDOR pulse sequence with dephasing π pulses on both the nitrogen and carbon channels. The pulses are applied using an *xy*-8 phase cycling scheme to eliminate offset effects and pulse imperfections. Signal acquisition begins two rotor cycles after the completion of a full 8*N* rotor cycles of dephasing. CP = cross polarization. Acq = acquisition

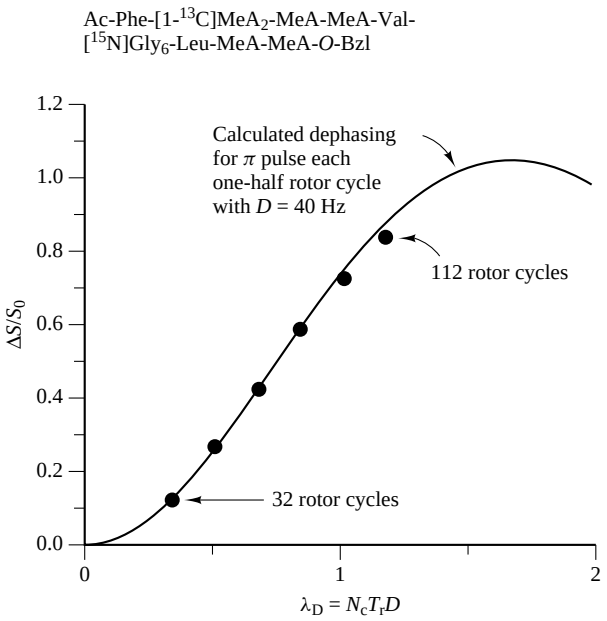

Figure 6 Observed dependence of $\Delta S/S_0$ on the universal parameter, λ_D, for a ^{13}C–^{15}N double-labeled fragment of emerimicin. The pulse sequence of Figure 5 was used. The experimental results (solid circles) are in agreement with calculation (solid line) assuming a ^{13}C–^{15}N dipolar coupling of 40 Hz corresponding to a C–N distance of 4.1 ± 0.1 Å. The natural-abundance correction to $\Delta S/S_0$ at N_c = 8 is 50% and at N_c = 100 is 4%

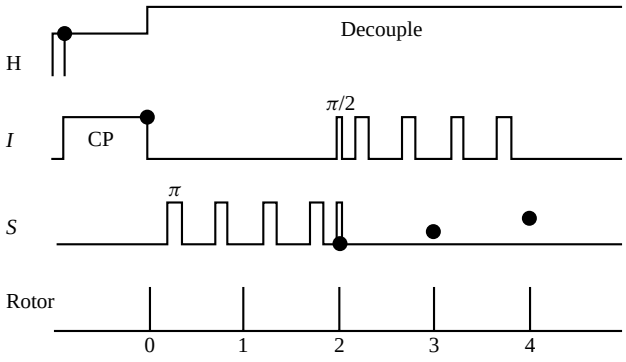

Figure 7 Pulse sequence for TEDOR *I*–*S* NMR. Following a cross-polarization (CP) transfer from abundant protons to generate initial *I*-spin magnetization, the effect of the protons is removed by resonant decoupling. The π pulses are shown separated by one-half rotor periods. The coherence transfer is achieved by simultaneous $\pi/2$ pulses in the middle of the evolution period. The solid circles represent observable magnetization

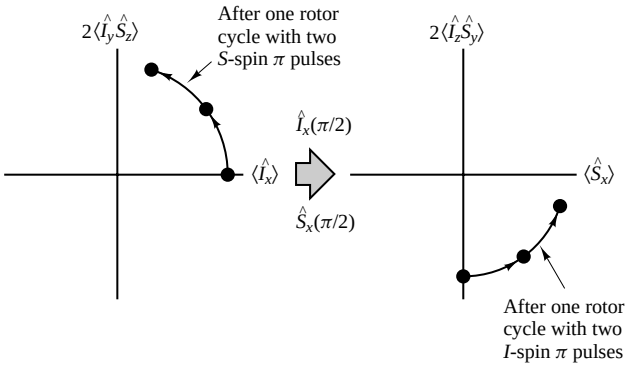

Figure 8 Schematic diagram of the evolution of the density matrix for a powder during the TEDOR pulse sequence of Figure 7 before the coherence transfer pulses (left) and after the application of the transfer pulses (right). The phase angle between $\langle\hat{I}_x\rangle$ and $\langle\hat{I}_y\hat{S}_z\rangle$ for each rotor cycle is indicated by the solid circles and is calculated using the technique illustrated in Figure 2 (right) together with a powder average. The effect of the 90° pulses is to permute I and S subscript indices

confirms that with the compensation of the *xy*-8 phase cycling scheme, hundreds of dephasing pulses can be used with no significant accumulation of error for a REDOR difference.[10] A few, accurate long range distance determinations are often sufficient to establish unambiguously the local conformation of a peptide or protein.[12]

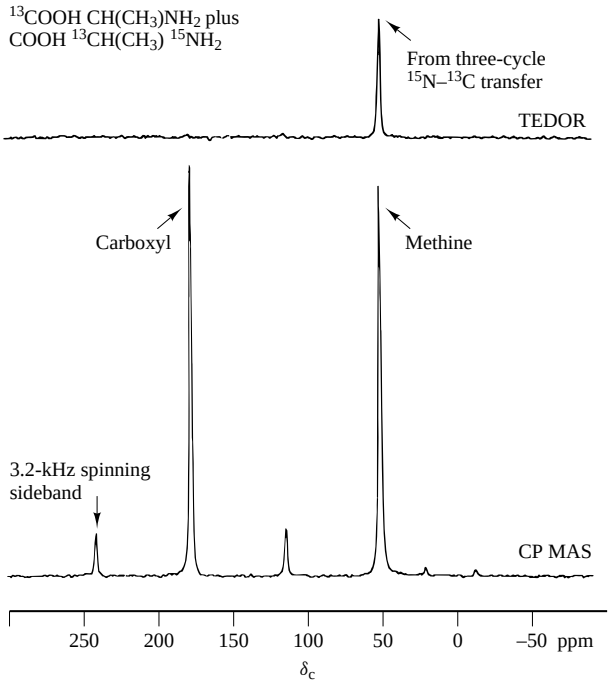

Figure 9 Transferred-echo double-resonance (top) and cross-polarization, magic angle spinning (CP MAS, bottom) ^{13}C NMR spectra of a recrystallized equimolar mixture of L-[2-^{13}C,^{15}N]alanine and L-[1-^{13}C]alanine. The TEDOR spectrum was obtained using three rotor cycles each of dephasing and refocusing. This is insufficient to generate significant carboxyl-carbon magnetization because the average intermolecular C–N dipolar coupling is weak

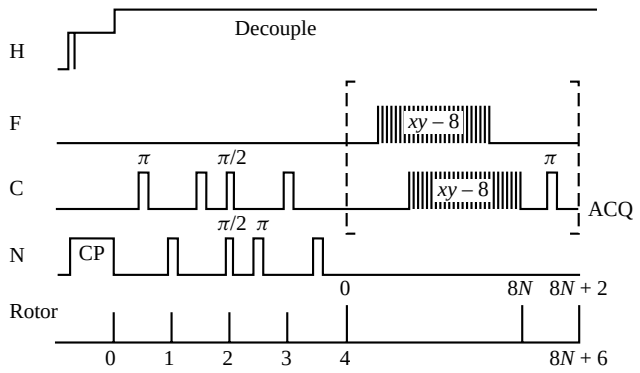

Figure 10 Pulse sequence for TEDOR combined with REDOR. The TEDOR part of the experiment (which for this illustration extends over the first four rotor cycles following the H–N cross polarization transfer) selects ^{13}C magnetization by a coherence transfer from ^{15}N. The REDOR part of the experiment (broken brackets) immediately follows the TEDOR preparation and measures dipolar coupling of the selected ^{13}C to ^{19}F. REDOR dephasing is performed using the phase-routing scheme illustrated in Figure 5. Two rotor cycles are added to the sequence so that the start of data acquisition is not coincident with a pulse

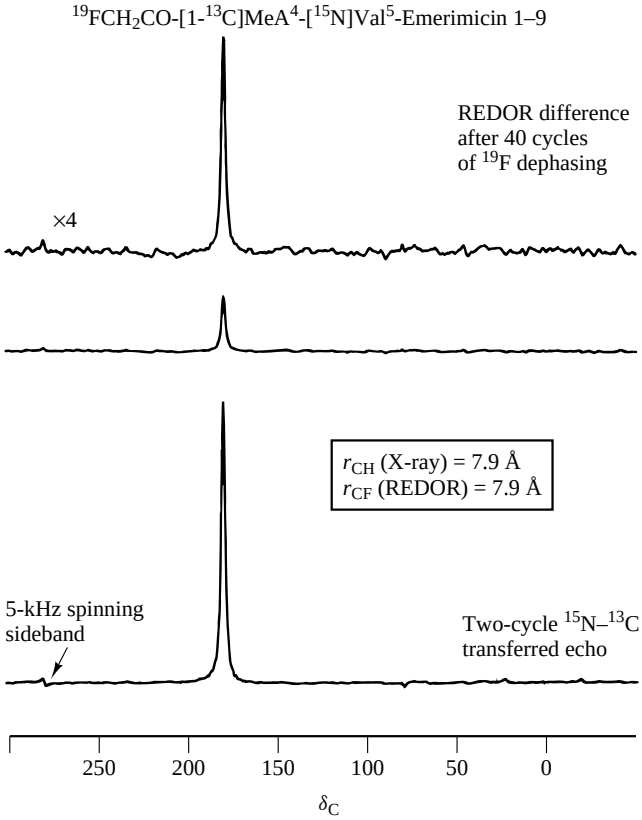

Figure 11 TEDOR–REDOR ^{13}C NMR spectra of a ^{19}F, ^{13}C, ^{15}N-labeled emerimicin (see Figure 6). The TEDOR spectrum (bottom) was obtained using an N–C coherence transfer as illustrated in Figure 7. The TEDOR–REDOR difference spectrum (the difference between TEDOR spectra with and without dephasing REDOR pulses) is shown at the top of the Figure. This spectrum was obtained by ^{19}F dephasing of the ^{15}N-TEDOR-selected ^{13}C magnetization over 40 rotor cycles

Background corrections for ^{13}C-observe ^{15}N-dephase REDOR are relatively simple to calculate because the ^{15}N natural abundance is low and γ_N is small. A measured value involves a separate sample with no ^{15}N label. The minor, observed $\Delta S/S_0$ for the single-labeled sample is then usually just subtracted from that for the double-labeled sample.[3] The correction is more involved for ^{13}C–^{31}P and ^{13}C–^{19}F pairs. For example, a ^{19}F-observe ^{13}C-dephase REDOR experiment designed to measure the dipolar coupling for a labeled ^{19}F–^{13}C pair separated by 10 Å must take into account the sizeable number of natural-abundance ^{13}C atoms within dephasing range of the ^{19}F. One way[13] to interpret the observed $\Delta S/S_0$ is to generate a model lattice with 1% randomly distributed ^{13}C. If all ^{13}C–^{13}C coupling is ignored, the ^{19}F-observed, ^{13}C-dephase REDOR ΔS can be interpreted in terms of a collection of independent, ^{19}F(label)-^{13}C(label)-^{13}C(natural abundance), three-spin clusters, whose dipolar-tensor orientations are known from the lattice parameters.

4 COHERENCE TRANSFER AND SELECTIVITY

Sometimes a natural-abundance background cannot be measured or calculated easily. In this situation, the dipolar-coupled spins can be selected from among the background of uncoupled spins by a coherence transfer from one spin of the heteronuclear pair to the other. The pulse sequence for this selection is shown in Figure 7. Transverse magnetization is first established in the I-spin system by a cross-polarization transfer from abundant protons. The dephasing of I-spin magnetization by dipolar-coupled S spins through rotor-synchronized S-spin π pulses leads to a bilinear coherence (Figure 8, left) that is transferred by an I,S pair of $\pi/2$ pulses (Figure 8, shaded arrow). These pulses occur together at the completion of a rotor cycle (Figure 7) and interchange the indices of the bilinear coherence. Finally, the transferred bilinear coherence is transformed into observable S-spin transverse magnetization by rotor-synchronized I-spin π pulses (Figure 8, right). The entire procedure is called transferred echo double resonance (TEDOR).[14] TEDOR is a rotor-synchronized solid state experiment which is based on some of the same coherence transfer principles as the INEPT solution state experiment.

The results of a TEDOR experiment using the pulse sequence of Figure 7 performed on the mixed double-labeled alanine sample discussed above are shown in Figure 9. Proton polarization is first transferred to nitrogen atoms. Then three rotor cycles are used to create bilinear ^{15}N–^{13}C coherence, and three more rotor cycles to produce observable methine carbon atom magnetization following the coherence transfer. The TEDOR theoretical transfer efficiency[14] is 50% compared with the observed 35% (Figure 9). Because TEDOR is not a difference experiment, TEDOR has the same theoretical sensitivity as REDOR. No sizeable carboxyl

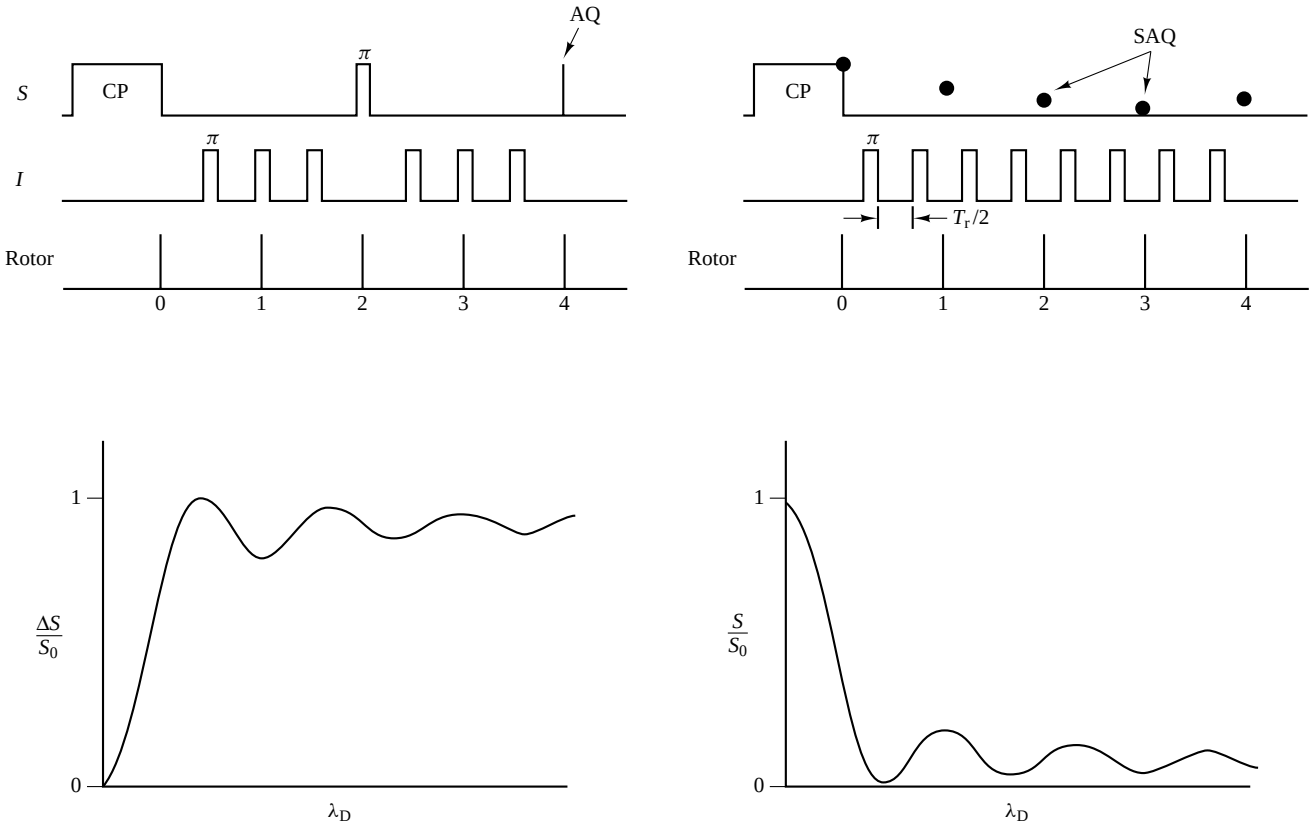

Figure 12 Two schemes for REDOR. (Left) Acquisition of a time domain signal follows evolution during which dephasing pulses diminish observable magnetization and create nonobservable $I-S$ bilinear coherence. This scheme is suitable for multiline spectra and a separate $\Delta S/S_0$ is measured for each line in the spectrum. The dependence on λ_D is determined by varying the number of rotor cycles. (Right) Synchronous detection of a time domain signal during evolution is suitable for a single-line spectrum. The observed S/S_0 is $1 - (\Delta S/S_0)$. AQ = acquisition; SAQ = synchronous acquisition

carbon magnetization is observed in Figure 9 because the short evolution time was insufficient for the weak intermolecular $^{15}N-^{13}C$ coupling to create significant bilinear coherence. If there had been a collection of nitrogen atoms all with comparable strong, couplings to carbon atoms, the TEDOR coherence transfer could still have been made selective by alternating the sign of the starting nitrogen magnetization for just one type of ^{15}N by DANTE inversion of the selected nitrogen atom signal every other scan.[15] The sign of the transferred bilinear coherence would then alternate, as would that of the observed carbon atom magnetization corresponding to the selected $^{15}N-^{13}C$ coupling. Data routing could then discriminate between carbon signals.

5 COMBINATION EXPERIMENTS AND SYNCHRONOUS DETECTION

TEDOR can be used alone or in combination to make highly selective TEDOR–TEDOR and TEDOR–REDOR experiments.[16] The pulse sequence for the latter is illustrated in Figure 10. A TEDOR sequence is tailored to select the carbonyl carbon atom signal of residue 4 of a ^{19}F, ^{13}C, ^{15}N triple-labeled emerimicin fragment (Figure 11). The $^{15}N-^{13}C$ selected magnetization is then dephased by REDOR ^{19}F π pulses resulting in the determination of a selected 8-Å C–F distance. This combination experiment involves four radiofrequencies in the same sequence which is possible using transmission-line probe technology.[17] The tuning elements in these probes are outside the magnet in a large, shielded box with isolation of all radiofrequencies, making high power on four channels practical.[18]

The observed signal in the TEDOR–REDOR experiment can be detected either as part of a two-dimensional experiment in which full S and S_0 spectra are obtained by normal acquisition starting with a rotor cycle (Figure 12, left), or synchronously with one sampling per rotor cycle (Figure 12, right). The former is used for complicated spectra with more than one resonance even after selection by TEDOR. The latter is used for the simple, one-line spectra that usually result from a TEDOR preparation. Synchronous detection[2] has the sensitivity advantage of generating the entire REDOR dephasing pattern in real time. The dipolar evolution dimension can be mapped by variation of the number of rotor cycles,[1] or variation of the position of the dephasing pulse within the rotor period.[2] The latter has a constant total dipolar evolution time which eliminates the echo-train lifetime from the analysis. In both of these two-dimensional methods, spins which contribute to the S-spin signal but have no $I-S$ coupling (a common situation for a natural-abundance background) do not interfere with the determination of the $I-S$ interaction.[16] Such spins produce a constant offset in the dipolar time domain and so a zero-frequency spike in the dipolar frequency domain. The $I-S$ coupling is determined by the width of the dipolar spectrum.[2]

Even an efficient TEDOR transfer does not result in observable magnetization associated with an isotropic powder. Thus, some crystallite orientations are discriminated against depending on the orientation of the *IS* and *SX* dipolar tensors in an $I-S-X$ three-spin TEDOR–REDOR experiment. Nevertheless, following an efficient $I-S$ TEDOR transfer, the *initial* S-observe, X-dephase REDOR behavior depends only on the size of the dipolar tensors and not on their orientation (Figure 13). Thus, interpretation of the 20% dephasing (Figure 14) in a TEDOR–REDOR experiment on the triple-labeled peptide of Figure 11 does not require knowledge of $^{15}N-^{13}C-^{19}F$ geometry in order to extract a C–F distance.[16] This will be the situation for most long-range distance determinations in general, simply because little dephasing is observed and determination of the dipolar coupling is based on the initial S/S_0 behavior. However, for systems with stronger couplings, Fourier transforms of the TEDOR–REDOR dipolar evolution offer the opportunity to establish geometry by comparisons with theoretical dipolar lineshapes (Figure 15).

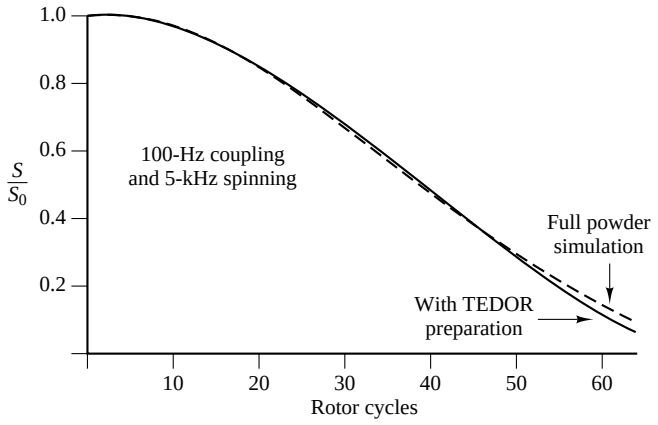

Figure 13 Simulation of X-spin REDOR dephasing of $I-S$ TEDOR-selected S-spin magnetization (solid line). The simulation assumed an $I-S$ coherence transfer after two rotor cycles of dephasing, followed by two rotor cycles of transformation of coherence into observable S-spin magnetization (see Figure 7). For $S/S_0 > 0.5$, the simulation is almost independent of orientation of $I-S$ and $S-X$ dipolar tensors (results not shown) and closely matches that for a full isotropic powder (dotted line). All simulations were performed assuming that the $I-S$ coupling was 1.2 kHz, the $S-X$ coupling was 100 Hz, and the magic angle spinning was 5 kHz

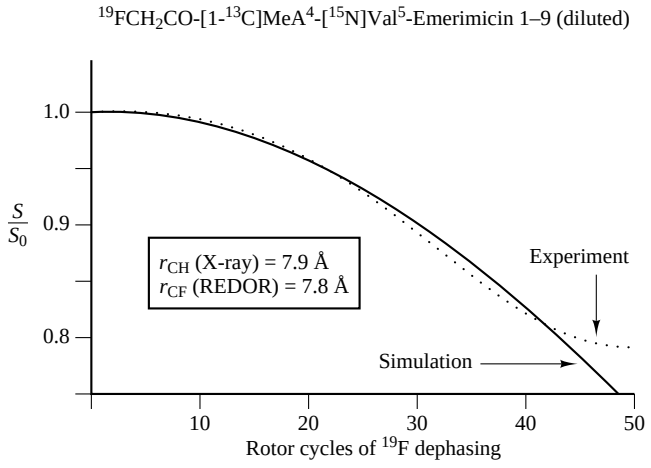

Figure 14 Synchronously sampled time domain ^{13}C signal of a ^{19}F, ^{15}N, ^{13}C-triple-labeled emerimicin diluted by natural-abundance peptide. The ^{15}N TEDOR-selected ^{13}C signal is sampled once each rotor period either with (S) or without (S_0) ^{19}F dephasing pulses. Magic angle spinning was at 5 kHz

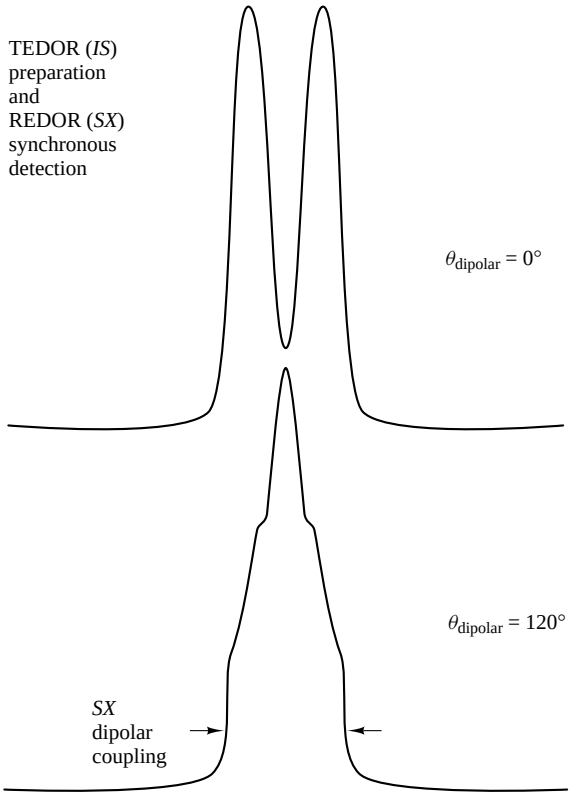

Figure 15 Dipolar spectra obtained by Fourier transforms of time domain simulations performed as described in the caption to Figure 13. The widths of both dipolar spectra are determined by the 100-Hz $S-X$ coupling. Details of the lineshape are determined by orientation of $I-S$ and $S-X$ dipolar tensors

6 RELATED ARTICLES

Cross Polarization in Solids; Electron– Nuclear Multiple Resonance Spectroscopy; INEPT; Magic Angle Spinning; Rotating Solids; Selective Excitation in MRI and MR Spectroscopy.

7 REFERENCES

1. T. Gullion and J. Schaefer, *J. Magn. Reson.*, 1989, **81**, 196.
2. T. Gullion and J. Schaefer, *Adv. Magn. Reson.*, 1989, **13**, 55.
3. Y. Pan, T. Gullion, and J. Schaefer, *J. Magn. Reson.*, 1990, **90**, 330.
4. A. Schmidt, R. A. McKay, and J. Schaefer, *J. Magn. Reson.*, 1992, **96**, 644.
5. B. A. Lewis, G. S. Harbison, J. Herzfeld, and R. G. Griffin, *Biochemistry*, 1985, **24**, 4671.
6. J. Schaefer, E. O. Stejskal, R. A. McKay, and W. T. Dixon, *Macromolecules*, 1984, **17**, 1479.
7. G. R. Marshall, D. D. Beusen, K. Kociolek, A. S. Redlinski, M. T. Leplawy, Y. Pan, and J. Schaefer, *J. Am. Chem. Soc.*, 1990, **112**, 963.
8. T. Gullion, D. B. Baker, and M. S. Conradi, *J. Magn. Reson.*, 1990, **89**, 479.
9. T. Gullion and J. Schaefer, *J. Magn. Reson.*, 1991, **92**, 439.
10. A. W. Hing, N. Tjandra, P. F. Cottam, J. Schaefer, and C. Ho, *Biochemistry*, 1994, **33**, 8651.
11. G. R. Marshall, E. E. Hodgkin, D. A. Langs, G. D. Smith, J. Zabrocki, and M. T. Leplawy, *Proc. Natl. Acad. Sci. U.S.A.*, 1990, **87**, 487.
12. A. M. Christensen and J. Schaefer, *Biochemistry*, 1993, **32**, 2868.
13. L. M. McDowell, C. A. Klug, D. D. Beusen, and J. Schaefer, *Biochemistry*, submitted.
14. A. W. Hing, S. Vega, and J. Schaefer, *J. Magn. Reson.*, 1992, **96**, 205.
15. D. D. Mueller, A. Schmidt, K. L. Papan, R. A. McKay, and J. Schaefer, 1995, **34**, 5597.
16. S. M. Holl, G. R. Marshall, D. D. Beusen, K. Kociolek, A. S. Redlinski, M. T. Leplawy, R. A. McKay, S. Vega, and J. Schaefer, *J. Am. Chem. Soc.*, 1992, **114**, 4830.
17. S. M. Holl, R. A. McKay, T. Gullion, and J. Schaefer, *J. Magn. Reson.*, 1990, **89**, 620.
18. R. A. McKay, US Patent 4446431, 1994.

Acknowledgments

This work was supported by NIH grant GM-40634.

Biographical Sketch

Jacob Schaefer, *b* 1938. B.S., 1960, Ph.D., 1964, physical chemistry, University of Minnesota, USA. Research scientist at Monsanto Company, St. Louis, 1964–1986; collaborated with E. O. Stejskal in 1976 to combine cross polarization with magic angle spinning. Faculty in Chemistry, Washington University in St. Louis, 1986–present. Approx. 200 publications. Research specialty: development of techniques for the NMR of polymeric and biological solids.

Selective Pulses

Lyndon Emsley

Ecole Normal Supérieure de Lyon, Lyon, France

1	Introduction	1
2	Excitation Pulses	3
3	Inversion Pulses	5
4	General Rotations	5
5	Other Selective Pulses	6
6	Bandwidth–Duration Products	7
7	NMR Techniques Using Soft Pulses	7
8	Conclusion	8
9	Related Articles	8
10	References	8

1 INTRODUCTION

Selective excitation first became important in the field of magnetic resonance imaging, where it is used to select slices or volumes in an object.[1] It was only with the development of DANTE sequences,[2] which allowed the implementation of amplitude modulated pulses on conventional spectrometers, and the subsequent availability of fully modulatable low-power transmitters on modern spectrometers, that shaped pulses became important in high-resolution spectroscopy. While there are many facets in common between selective excitation in imaging experiments and in high-resolution experiments, there are nevertheless some differences in what is important and what can be achieved. (The phase problem, for example, is much less crucial in imaging than in spectroscopy). This article is directed toward selective excitation techniques for high-resolution spectroscopy, and a related article by Maudsley, see ***Selective Excitation in MRI and MR Spectroscopy***., is biased toward imaging. Selective pulses are also considered in the articles by Warren, ***Shaped Pulses***, Morris, ***Complex Radiofrequency Pulses***, and Young, ***Selective Excitation Methods: Artifacts***, and techniques using selective pulses can be found in the articles by Bodenhausen, ***Selective Hartmann–Hahn Transfer in Liquids*** and ***Selective NOESY***, and Rossi, ***Selective Relaxation Techniques in Biological NMR***. Reviews covering selective pulses and their applications in high-resolution NMR include those by Warren and Silver,[3] Freeman,[4] and Emsley.[5]

The idea behind the majority of high-resolution NMR experiments that utilize selective pulses is that more information can be obtained if the spectral region affected by the pulses in the experiment is reduced. This increase in information can take two forms. Firstly, by reducing the spectral width the digital resolution of the spectrum can be increased, revealing aspects of the spectrum that were previously unresolvable. Secondly, restriction of the spectral range allows one to manipulate the spins in new ways (we are able to treat homonuclear systems in a similar way to heteronuclear systems), so that the spectra convey new information, which may have been previously unobtainable.

Nonselective excitation is usually achieved by applying a short, high-power, pulse to the spin system. Because the pulse is short, we know that its frequency response will be very broad (the bandwidth of the frequency response is proportional to the inverse pulse length).[6–9] On the other hand, a long, low-power pulse could have a very narrow bandwidth. In addition to having a narrow *bandwidth*, an ideal selective pulse should have a narrow *transition region* between the part of the response that is excited, and that which is not affected at all. In order to achieve this, we use amplitude- (and phase-) modulated pulses.

To approach the problem of selective excitation we must first be able to predict how a particular arbitrarily shaped time domain pulse affects the spin system to produce a particular frequency domain magnetization. The Fourier transform would appear to be an ideal candidate for this purpose. The Fourier transform of a function $f(t)$ is defined as[6]

$$F(\omega) = \int_{-\infty}^{+\infty} f(t) \exp\{-\mathrm{i}\omega t\} \, \mathrm{d}t \qquad (1)$$

We see from the above formula that the Fourier transform has a reciprocal property: if $F(-\omega)$ is the transform of $f(t)$, then $f(-t)$ is the transform of $F(\omega)$. It is this feature of the Fourier transform that allows us to do the inverse transform, and which makes it so attractive as a method of determining pulse shapes. For example, if a 'top hat' frequency domain response is desired, the appropriate pulse shape would be the inverse Fourier transform of a 'top hat', i.e. a sinc function as shown in Figure 1.[6,10] At the same time we can see how a normal rectangular pulse is particularly poor in terms of selectivity, since its transform is a sinc function having extensive 'wiggles' in the frequency domain. Indeed, a useful concept arises from Fourier transform theory, which is that if the first noncontinuous derivative of $f(t)$ is the ath, then $F(\omega)$ falls off as $(1/\omega)^a$ at large ω. For the square pulse the first derivative is infinite (i.e. impulsive) at the edges of the pulses, and the excitation falls off as $1/\omega$.

With this in mind we introduce the Gaussian as another useful function, since a Gaussian can be differentiated an infinite number of times. Indeed, the first use of Gaussian-shaped pulses in NMR spectroscopy was proposed by Bauer et al.[11] on the grounds of its Fourier transform properties; the transform of a Gaussian is another Gaussian (see Figure 1). The Fourier transform would thus appear to be a particularly convenient method for linking the two domains.

The shift theorem of the Fourier transform can be used to derive a very important result. The theorem states that if $f(t)$ is the transform of $F(\omega)$, then $f(t - \tau)$ has the transform $\exp\{-2\pi \mathrm{i} t\omega\}F(\omega)$. The Fourier transforms shown in Figure 1(a)–Figure 11(c), are for functions centered at $t = 0$, i.e., the first half of the pulse was applied during negative time. The shift theorem tells us that if a function is shifted by an amount τ, the Fourier components will all retain the same amplitudes, but they will have a *phase shift proportional to* ω. This situation is illustrated for a (truncated) Gaussian pulse starting at $t = 0$ in Figure 1(d). Since we cannot turn on the transmitter before the beginning of the experiment this would be the situation present in any NMR experiment using any pulse shape, in as far as can be predicted by the Fourier transform. (*Note added in proof*. It has very recently been demonstrated that this situation can in fact be avoided, and that

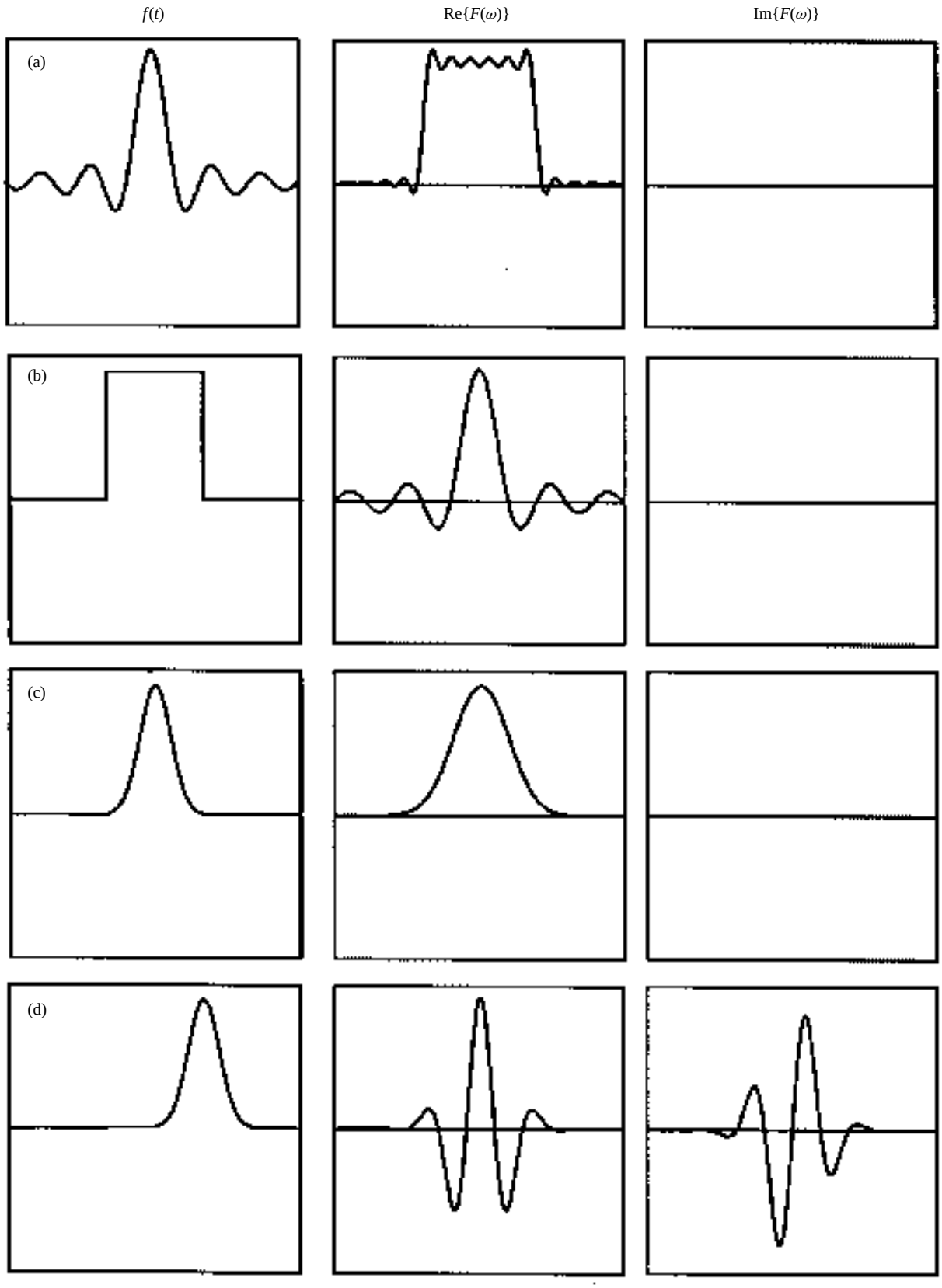

Figure 1 Fourier transforms of some common time-domain shape functions. All the pulses are on the same scales in which the time domain is 150 ms long and the frequency domain is 200 Hz wide. In (a)–(c) are shown the responses to a truncated sinc, a rectangle, and a truncated Gaussian, all centered at $t = 0$, while (d) shows the response to a Gaussian which commences at $t = 0$. The vertical scales are arbitrary. (Reproduced by permission from Emsley[65])

a pure-phase response can be obtained with pulses predicted using the Fourier transform.[79]

Fortunately, this is not the whole story, and in fact the Fourier transform is only of limited validity in predicting responses because it is only applicable in the linear response regime.[6,12] The NMR response is highly nonlinear (doubling the pulse length from 90° to 180° does not double the signal intensity). In order to obtain an exact description of the NMR response we must turn to a solution of the quantum mechanical equations of motion for a spin in an external field. For a time-independent (i.e. constant amplitude and phase) pulse, these equations can be solved analytically to yield[7–9]

$$\begin{aligned}\langle \hat{I}_z(t)\rangle &= -\langle \hat{I}_y(0)\rangle \sin\theta \sin\beta_{\text{eff}} \\ &\quad +\langle \hat{I}_x(0)\rangle (1-\cos\beta_{\text{eff}})\cos\theta\sin\theta \\ &\quad +\langle \hat{I}_z(0)\rangle (\cos\beta_{\text{eff}}\sin^2\theta+\cos^2\theta) \\ \langle \hat{I}_y(t)\rangle &= \langle \hat{I}_y(0)\rangle \cos\beta_{\text{eff}} + \langle \hat{I}_x(0)\rangle \cos\theta\sin\beta_{\text{eff}} \\ &\quad -\langle \hat{I}_z(0)\rangle \sin\theta\sin\beta_{\text{eff}} \\ \langle \hat{I}_x(t)\rangle &= \langle \hat{I}_y(0)\rangle \cos\theta\sin\beta_{\text{eff}} \\ &\quad +\langle \hat{I}_x(0)\rangle (\cos\beta_{\text{eff}}\cos^2\theta+\sin^2\theta) \\ &\quad +\langle \hat{I}_z(0)\rangle (1-\cos\beta_{\text{eff}})\cos\theta\sin\theta \end{aligned} \tag{2}$$

where the $\langle \hat{I}_k(t)\rangle$, $k = x, y, z$, correspond to the expectation values of the angular momentum operators in the rotating frame, where θ is the tilt angle of the effective field with respect to the z axis of the rotating frame, $\tan\theta = \omega_1/\Omega$, and β_{eff} is the flip angle about the effective field, $\beta_{\text{eff}} = \sqrt{(\omega_1^2+\Omega^2)}t$. ω_1 is the amplitude of the applied radiofrequency field in rad s^{-1}, and $\Omega = \omega - \omega_0$ is the frequency offset from the transmitter frequency ω_0. The magnetization precesses around the effective field $\boldsymbol{B}^{\text{eff}}$ at angular frequency $\omega^{\text{eff}} = \sqrt{(\omega_1^2+\Omega^2}$, as illustrated in Figure 2. Although they are only valid when $\boldsymbol{B}^{\text{eff}}$ is not time dependent, equation (2) forms the basis of the exact calculations for all the responses calculated in this article (and in most other articles concerned with the response of a single spin). Solutions for responses to time-dependent pulses can be obtained 'numerically' by solving the problem in a stepwise manner, i.e. by dividing the pulse into sufficiently small increments so that we may neglect the variation in amplitude during each increment, and merely consider the variation from step to step. We shall refer to this technique as 'numerical integration'. The enormous disadvantage of this technique as compared with the Fourier transform is that we cannot readily do the inverse operation. On the other hand, we can imagine that by exploiting the nonlinear response of the NMR system, we may be able to overcome the phase problem.

2 EXCITATION PULSES

The limit of the validity of the linear response is found to be to small excursions from the z axis.[3,12] Thus the response to simple pulses with small flip angles can be predicted using the Fourier transform. Even up to around 90°, the deviations from exact behavior are not too large. In this case the phase gradient

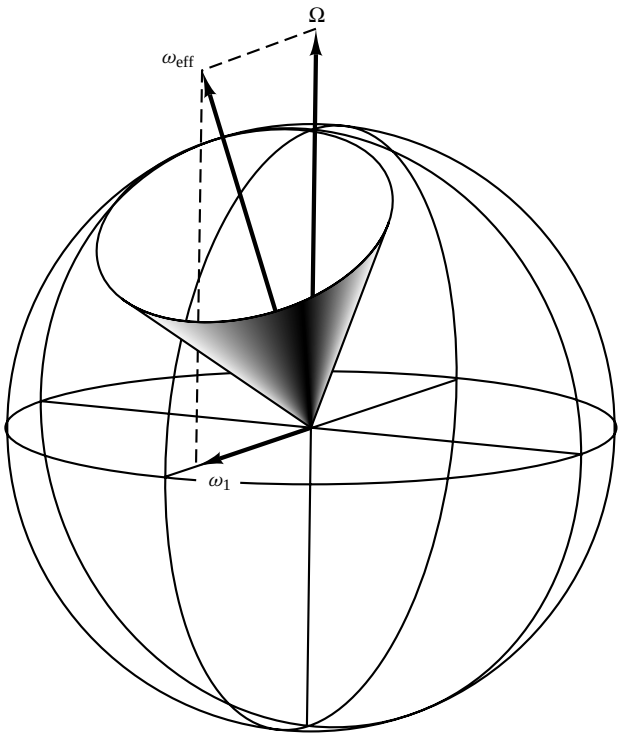

Figure 2 In the rotating frame, the magnetization precesses in a cone about a static field ω_{eff} which is the resultant of its offset from the frequency of rotation of the frame, $\Omega = (\omega - \omega_0)$, and the applied field, ω_1. (Reproduced by permission from Emsley.[65])

in the transverse magnetization after a selective pulse is linear. Therefore it is, in principle, for simple one-dimensional spectra, possible to apply a first-order phase correction, but as a result of the magnitude of the errors this is usually not possible in practice without introducing large baseline rolls into the spectra. In more advanced pulse experiments involving coherence transfer phenomena the implications are more important since the pulse will not only create in-phase magnetization, but also at least in part antiphase magnetization. In general it is therefore not sufficient merely to apply a baseline correction to the spectra.

If the pulse is used to excite a region of the spectrum containing no scalar couplings, or a spectrum in which the couplings are small compared with the region being excited, then the pulse sequence:

$$90^\circ_{\text{soft}} - 180^\circ_{\text{hard}} - \tau - \text{Acquire}$$

can be used to refocus the magnetization.[13] However the extension of the length is not welcome since it will increase losses due to relaxation. More importantly, this approach will not work at all to refocus coupled spins and will actually make the phase error worse in such cases. In contrast, if the whole pulse is soft, the coupling partners of a multiplet are not affected and the evolution of the magnetization due to couplings will be refocused in exactly the same way as if it were due to chemical shifts.

Freeman and co-workers[14,15] proposed the use of a series of pulse shapes, including the half Gaussian, as a means of eliminating the phase errors inherent in selective excitation. Although these pulses do not in themselves produce

magnetization with constant phase, spectra having constant phase can be obtained by adding together the results of two pulse sequences involving the half Gaussian with a hard 180° purging pulse on alternate scans. This has the effect of canceling out the y component of the magnetization while retaining the x component.

More straightforward solutions to the phase problem involve pulses which produce in-phase responses by exploiting the nonlinear behavior of the spin system. There now exists a fairly wide class of pulses in this category which range from the very simple to the extraordinarily complex.[16–27] We provide first an example of the simplest (and perhaps most useful) solution, and then a brief outline of some of the more complex solutions.

The simplest solution to the phase problem is to use a Gaussian-shaped pulse having an on-resonance flip angle of 270°. The response has a much improved phase behavior compared with that of the conventional 90° Gaussian pulse.[16] In Figure 3 we show the I_x and I_y responses of 90° and 270° Gaussian pulses as a function of offset, and in Figure 4 we show the effect this has on an experimental spectrum of a multiplet in 2-phenylcyclopropanecarboxylic acid methyl ester.

The 270° Gaussian pulses provide a reasonable approximation to in-phase excitation which is sufficient for the majority of applications, especially those that are multiplet selective (see Section 7). However, the improvement in phase properties is at the expense of top-hat selectivity, and there is nevertheless a residual phase dispersion. Using more complex solutions, a more demanding frequency response can be achieved. Many proposals have been made to solve this problem, which (limiting the choice to purely amplitude modulated pulses) can be broadly divided into two categories. The first relies on dividing a trial pulse into many discrete intervals, and varying the rf amplitude in each interval until the response closely approaches a target function.[17,18,28] Several degrees of sophistication can be employed toward this end, including the optimal control techniques first used by Conolly

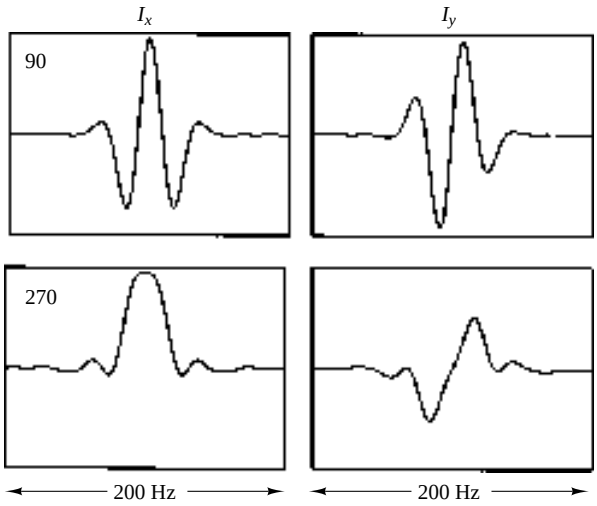

Figure 3 I_x and I_y responses of a 90° and a 270° Gaussian pulse. In both cases the pulse was 50 ms in duration and the pulses were truncated at 2.5% of the maximum value. (Reproduced by permission from Emsley[65])

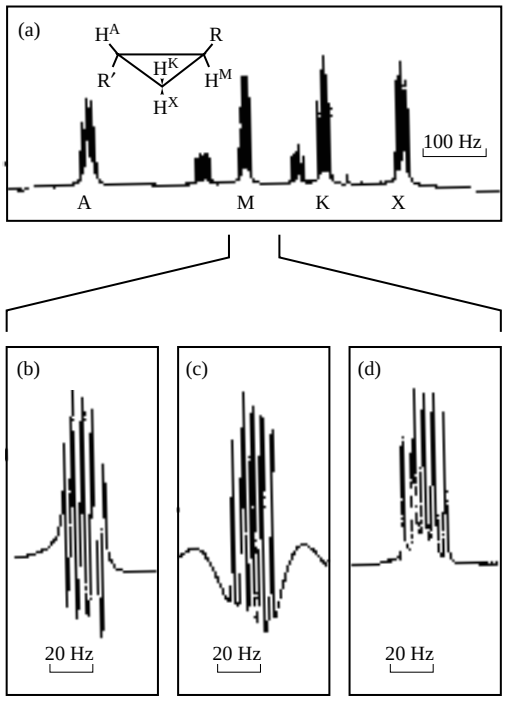

Figure 4 (a) Nonselective 400 MHz proton spectrum of a mixture of *cis*- and *trans*-2-phenylcyclopropanecarboxylic acid methyl ester recorded on a Bruker AM-400 spectrometer equipped with an Oxford Research Systems selective excitation unit. (b) Spectrum of the M multiplet (see inset) obtained with a 90° Gaussian pulse (33 ms duration) without phase correction. (c) Same spectrum in positive absorption with a large frequency dependent phase correction. (d) Multiplet excited with a 270° Gaussian pulse (33 ms duration). No frequency dependent phase correction was applied to (d). The frequency domain response outside the region shown is flat

and Macovski to obtain a magnitude response,[29] and subsequently by Smith et al.[28] to obtain an in-phase response, the conjugate gradient method first used by Murdoch et al.[78] (once again to obtain a magnitude response), and the linearization of the Bloch equations due to Ngo and Morris.[18] These methods provide excellent results, with those of Ngo and Morris approaching very closely an ideal response. However, the resulting envelopes require as many as 100 to 500 independent parameters to be defined, making their practical implementation awkward, and normally resulting in relatively long pulses to achieve a particular selectivity.

The second category of pulses includes those which are optimizations of analytical pulse forms.[19–26] The most popular of these are pulses defined by either a sum of Gaussians[22,24] or a Fourier series.[20,21,23] If the pulse is represented as a sum of Gaussians (a so-called Gaussian pulse cascade) the rf is defined by

$$\hat{\mathcal{H}}_1(t) = \omega_1(t)\hat{I}_x = \left(\sum_{n=1}^{N} A_n \exp\{-B_n(t - t_n^{\max})^2\}\right)\omega\hat{I}_x \qquad (3)$$

where ω is the rf field in radians per second. This function represents an envelope of duration t_p consisting of a superposition of N Gaussians, where for the nth Gaussian the position

Table 1 (a) Parameters for the SEEK-3 and G^4 Gaussian Pulse Cascades[5,22]

Pulse	n =	1	2	3	4
SEEK-3	$t^{\max}/t_p$	21.0	71.9	46.9	
	A	2.3	18.2	−12.7	
	$2\Delta t_{\frac{1}{2}}/t_p$	19.0	18.6	19.6	
G^4	$t^{\max}/t_p$	17.7	49.2	65.3	89.2
	A	0.62	0.72	−0.91	−0.33
	$2\Delta t_{\frac{1}{2}}/t_p$	17.2	12.9	11.9	13.9

Table 1 (b) Parameters for the E-BURP-2 Pulse[21,23]

n	A_n	B_n
0	0.26	–
1	0.91	−0.12
2	0.45	−1.79
3	−1.31	0.01
4	−0.12	0.41
5	0.03	0.08
6	0.01	0.07
7	0.06	0.01
8	0.01	−0.04
9	−0.02	−0.01
10	−0.01	0.00

of the maximum is given by $t_n^{\max}$, the peak amplitude by A_n, and the width by

$$B_n = \frac{\ln 2}{(\Delta t_{\frac{1}{2}}^n)^2} \quad (4)$$

$\Delta_{\frac{1}{2}}^n$ being the width at halfheight. Using this function pulses have been developed for inversion with $N = 3$ and for inphase excitation with $N = 4$, which are fully defined by only nine and 12 independent parameters respectively. In the case of the Fourier series pulses, introduced simultaneously by Morris et al.[20] and by Geen and co-workers,[21,23] the rf is defined by a function of the form

$$\hat{\mathcal{H}}_1(t) = \left\{A_0 + \sum_{n=1}^{N}[A_n \cos(n\omega t) + B_n \sin(n\omega t)]\right\}\omega \hat{I}_x \quad (5)$$

The Fourier coefficients A_0, A_1, ... and B_1, B_2, ... are the free parameters available for optimization. The series is usually truncated at values of $N < 10$, thereby reducing the number of variable parameters to less than 20. The parameters for both types of pulse are optimized using some sort of computer method by minimizing the deviation with respect to a target function. Some of the results of these techniques are illustrated in Figure 5 where we show the simulated performance of a range of different selective excitation pulses [the parameters describing the various shapes are given in Tables 1(a) and 1(b)]. It can be appreciated that the improvement in going from the original 90° Gaussian pulses to the more sophisticated pulses such as the G^4 Gaussian pulse cascade is really quite remarkable (Figure 5).

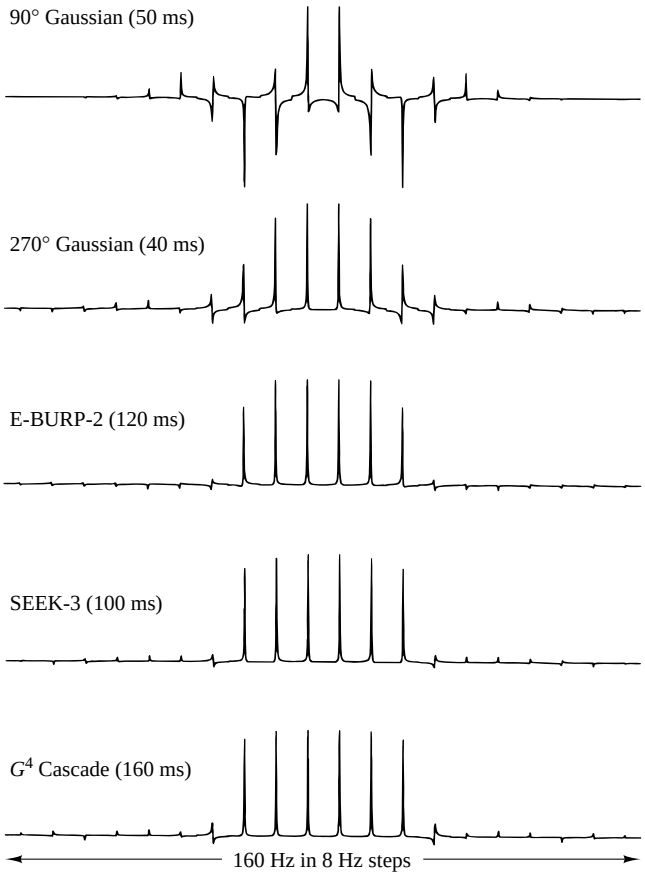

Figure 5 A comparison of the (simulated) performance of a 90° Gaussian,[11] a 270° Gaussian,[16] an E-BURP-2 Fourier series pulse,[23] a SEEK-3 Gaussian pulse cascade,[5] and a G^4 Gaussian pulse cascade.[22] Parameters for the last three pulses can be found in Table 1. The Figure shows the expected lineshape and amplitude for resonances situated in a region ±80 Hz from resonance in 8 Hz steps. (Reproduced by permission from Emsley[65])

3 INVERSION PULSES

Inversion pulses are developed in the same way as excitation pulses. It is worth noting that the optimization approaches outlined above are even more essential for inversion pulses, as the Fourier transform does not predict the existence of z magnetization, and would therefore appear to be particularly useless as a tool for predicting pulse shapes for inversion. Indeed, we see in Figure 6 how the response of a 180° sinc pulse has little relation to its Fourier transform behavior, and does not seem to be a particularly effective pulse for inversion. In contrast, using the optimization techniques mentioned previously the inversion problem becomes quite simple. It is an easier problem than in-phase excitation because we have to optimize only one component of the magnetization rather than two. Most of the references cited above for excitation also treat inversion, and Figure 6 shows a selection of responses to increasingly sophisticated inversion pulses. Note that in addition to functions that were discussed for excitation, the Hermite pulse[12] is a simple analytical shape with one variable parameter that performs well for inversion.

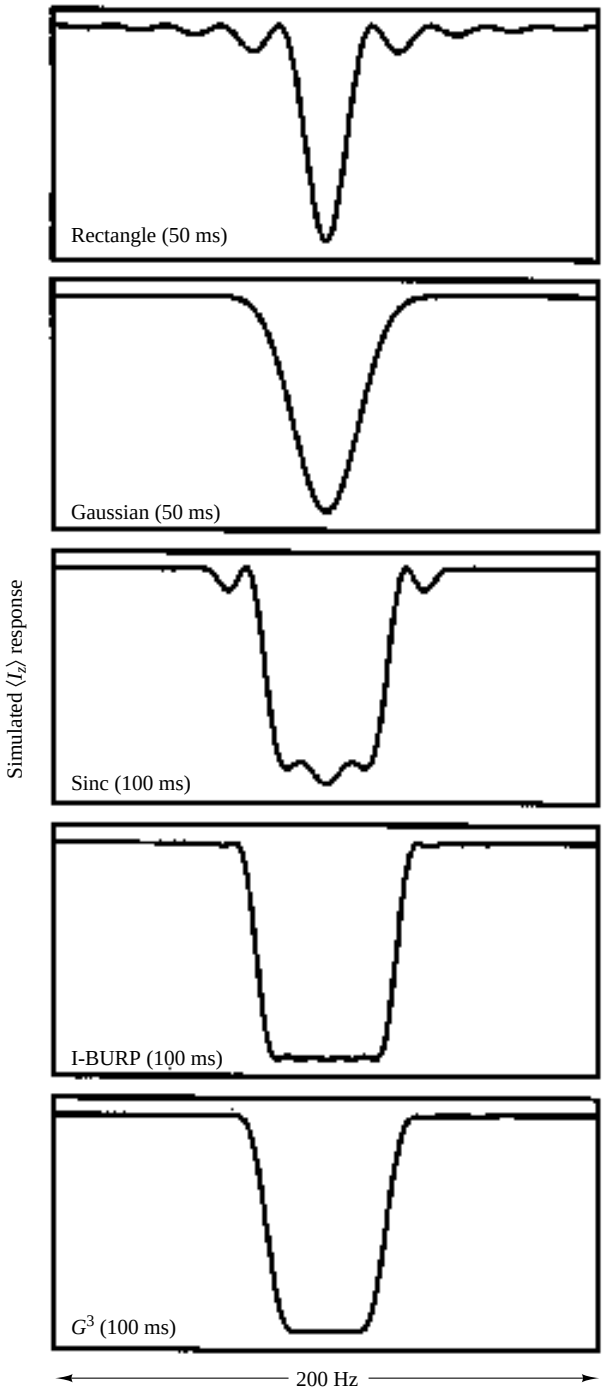

Figure 6 A comparison of the (simulated) $\langle I_z \rangle$ response (vertical axis) as a function of offset from the carrier frequency for a rectangular pulse, a 180° Gaussian, a 180° sinc, an I-BURP Fourier series pulse,[23] and a G^3 Gaussian pulse cascade.[22]

4 GENERAL ROTATIONS

The selective pulses described above were designed by optimizing the response of a spin whose initial state is proportional to $\hat{I}_z$ and is subsequently converted into a transverse operator, for example $\hat{I}_x$, or is converted into $-\hat{I}_z$. However, in many instances pulses are required to convert transverse components into longitudinal ones (for example in soft-COSY), or in the case of refocusing the pulse should produce a 180° rotation in the transverse plane. There is a subtle but important difference between a pulse that was optimized to produce a particular *transformation* and a pulse that was optimized to produce a particular *rotation*. It may be tempting to assume that a pulse that converts $\hat{I}_z$ into $\hat{I}_x$ would also necessarily convert $\hat{I}_x$ into $-\hat{I}_z$. This is not in general true, as there are an infinity of rotations that will produce the transformation. For example, either a 90° rotation around the *y* axis, or a 180° rotation about an axis inclined at 45° in the *xz* plane achieves the first transformation. A 90° rotation around the *y* axis will indeed also convert $\hat{I}_x$ into $-\hat{I}_z$, but a 180° rotation about an axis inclined at 45° in the *xz* plane achieves the opposite result, converting $\hat{I}_x$ into $+\hat{I}_z$.

In order to find a pulse which selectively achieves the pure rotation one must produce a so-called 'general rotation' or 'universal pulse'.[23,24] These are pulses which are tailored to produce a particular rotation (normally 90° or 180°) about a fixed axis (normally in the transverse plane). Two approaches have so far been adopted in the optimization of general rotation pulses. The first utilizes symmetry properties of selective pulses, as it has been shown that a time-symmetric amplitude modulated pulse with phase *y* is constrained to produce a rotation in the *yz* plane.[30,31] Thus, if a time-symmetric pulse achieves the transformation of $\hat{I}_z$ into $\hat{I}_x$ it must correspond to a rotation of 90° about the *y* axis. The same logic applies to 180° rotations. Geen and Freeman[23] have constrained Fourier series pulses to be time symmetric and produced general rotation pulses in this way. The second approach relies on an optimization of the rotation matrix, or propagator, of the pulse directly. This approach has the advantage that the pulse need not be time symmetric, and in this way Emsley and Bodenhausen[24] have produced asymmetric Gaussian pulse cascades for general rotations. The pulses were produced by optimizing the elements of a quaternion representation of the propagator,[30,32,33] which can be simply related to the rotation axis and flip angle of the pulse.[24]

5 OTHER SELECTIVE PULSES

Selective pulses which are produced for excitation and inversion of a single spin $I = \frac{1}{2}$ are by far the most common. There are, however, a few variations that have been developed for other purposes. The most common variation is undoubtedly modulation of a given inversion or excitation pulse so as to produce multiple inversions or excitation. The principle is simply that modulation of the time domain pulse by a function $\exp\{-i\omega_{mod}t\}$ shifts the region of excitation or inversion by a distance ω_{mod} away from the carrier frequency in the frequency domain (this simple result is predicted by the convolution theorem of the Fourier transform). The addition theorem of the Fourier transform tells us that if we add several time domain functions, the result in the frequency domain is the addition of the individual responses. Therefore addition of pulses with different modulation frequencies should produce excitation or inversion at those different frequencies. Although we have seen that the Fourier transform is not valid to predict nonlinear responses, the addition theorem still holds for NMR excitation, and multiply-selective manipulations are indeed possible. The condition for validity is that the frequency difference between two adjacent affected regions should be

larger than the radiofrequency field strength of the individual pulse, $\Delta\omega_{\mathrm{mod}} > \omega_1$. If this condition is not met, the field at one frequency will interfere with the effect of the field at another, and the responses will be spoiled.

Multiply-selective excitation by frequency modulation is an old idea which is commonly used in MRI experiments to select multiple slices through an object. It has only recently, however, become a popular tool in high-resolution experiments since it has been shown that it is often useful to irradiate two coupled spins simultaneously. This is simply achieved by modulation of the pulse shape with a cosine function which produces two symmetrically disposed sidebands at $\pm$ the modulation frequency. The related article by Bodenhausen, ***Selective Hartmann–Hahn Transfer in Liquids***, treats these experiments in more detail. One should note, however, that when pulses are applied simultaneously to two (or more) *coupled* spins the response is no longer the same as it would be for the individual spin case. The equation of motion governing the evolution of a two-spin system would be in a 15-dimensional basis space, instead of the three-dimensional space that governs the single spin. Indeed it has been recognized that multiply-selective irradiation can lead directly to the creation of multiple quantum coherences in coupled spin systems,[34,35] although it is then difficult to control the offset dependence of the excitation.

At the time of writing the only shaped pulses that have been developed specifically to act on both partners in a coupled spin system are those of Lee et al.[36] for refocusing of the dipole–dipole interaction. The shape is described by an expansion in terms of Legendre polynomials,[19] and the coefficients of the polynomials were optimized so that the leading error terms appear in the higher orders of an average Hamiltonian treatment (see ***Average Hamiltonian Theory***). However, the application is not selective but on the contrary is designed to be broadband, with the far off-resonance behavior being of little consequence. Nevertheless it is interesting to note that shaped pulses are shown to be more power efficient in this application than rectangular pulses.

Another interesting development using selective pulses has recently been demonstrated for selective spin decoupling.[37–39] In the approach of Eggenberger et al.[37] a selective inversion pulse (specifically a G^3 Gaussian pulse cascade[22]) is used as the building block in a recursive decoupling scheme. The resulting multiple-selective pulse sequences are shown to be very effective at decoupling within a selected region, while they have no effect outside the decoupled region. These sequences are shown to be useful in multidimensional experiments on large molecules, where it is necessary to decouple, for example, carbonyl carbons, while leaving the aliphatic carbons untouched. One should note that as long as the initial condition of the spins to be decoupled is proportional to $\hat{I}_z$, the G^3 pulse is suitable (as it is specifically an inversion pulse), but that in general one should use 180° general rotation pulses in the recursive expansion to produce an isotropic sequence to decouple any initial condition.

Finally, we note that Warren and co-workers have developed selective pulses which are insensitive to the effects of radiation damping during the pulse, or similarly to the effects of transverse relaxation on the frequency domain profile of the response. The pulses were developed simply by extending the equations of motion of equation (2) to include the desired interference effect, and subsequently optimizing the pulse over a range of different values for the interference term. (These results have been presented at conferences, but so far appear to be otherwise unpublished). Some selective pulses have been shown to be particularly sensitive to radiofrequency field inhomogeneity,[23] and it would be useful to find pulses which were less sensitive to this ever-present effect, although to date nobody appears to have done so.

6 BANDWIDTH–DURATION PRODUCTS

A selective pulse must fulfil several criteria before it can be judged 'good' or 'bad'. As we mentioned in the Introduction, the pulse should have a good 'shape selectivity', and this quality can be measured as the size of the deviation of the frequency domain response from an ideal 'top hat'. This is the quality that is used as the target function in the least-squares optimization of the pulses discussed above, and we have seen that in this respect pulses can be made nearly ideal. However, there is a price to pay for this high performance in shape selectivity, and that is in the 'time efficiency' of the pulse. A selective pulse should have a *bandwidth–duration product* that is as small as possible. It turns out that a useful way to quantify the width of a function is by the variance of the mean-squared modulus, which for a function $f(x)$ is given by[6,40]

$$\Delta x^2 = \frac{\int x^2 |f(x)|^2 \,\mathrm{d}x}{\int |f(x)|^2 \,\mathrm{d}x} - \left(\frac{\int x |f(x)|^2 \,\mathrm{d}x}{\int |f(x)|^2 \,\mathrm{d}x} \right)^2 \qquad (6)$$

where the integrals are all taken between infinite limits. While there are many possible definitions of a bandwidth–duration product, this definition has the advantage that it can be used in either domain, i.e., $x = \Omega$ or $x = t$, and that it can be shown that the product $\Delta t \Delta\Omega$ is constant. Thus for a given pulse shape we can calculate the width of the pulse and the width of the response independently of the actual duration of the pulse, and the value of $\Delta t \Delta\Omega$ for a given pulse/response combination therefore represents the time efficiency of the pulse. In Table 2 we give the bandwidth–duration products for the various pulses of Figures 1 and 5. The values are expressed in units of $1/(4\pi)$, as this is the theoretical minimum value permitted by the uncertainty condition in a linear response regime. In Figure 7 we show graphically how the change in bandwidth–duration product affects the selectivity of the pulse. Note that, in general, the better the shape selectivity, the worse the time efficiency. One of the few remaining challenges in the area of selective excitation is to find pulses that are both shape selective and time efficient.

7 NMR TECHNIQUES USING SOFT PULSES

There now exists a broad range of experiments which use selective pulses and we shall not review them in detail here. The simplest applications use selective pulses to increase resolution in multidimensional experiments so as to allow a quantitative determination of scalar coupling constants.[41–43] Alternatively, resolution remains the same and the number of increments in the indirectly recorded dimension is reduced, thereby reducing the experimental time required to obtain a spectrum.[41,42,44] In general experiments

Table 2 Bandwidth–Duration Products $\Delta t \Delta\Omega$

Pulse	90° sinc	90° Gaussian	270° Gaussian	E-BURP-2	SEEK-3	G^4
$\Delta t \Delta\Omega$	2.77	1.1	0.9	2.90	2.37	6.7

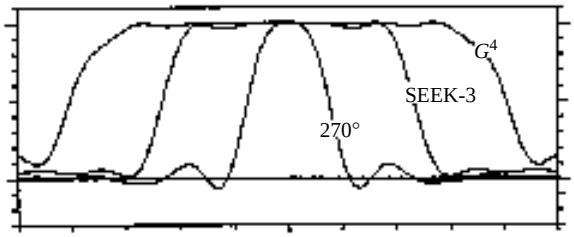

Figure 7 A comparison of the bandwidth of the $\langle I_x \rangle$ response (vertical axis) for G^4, SEEK-3, and 270° Gaussian pulses. All the pulses are 50 ms in duration. The horizontal axis spans ±100 Hz from resonance

using selective pulses can be divided into two broad classes. The first are sequences which use selective pulses (often in combination with nonselective pulses) to reduce the dimensionality of experiments.[45–56] The second contains sequences which use only selective pulses to record two-dimensional spectra,[5,16,41–43,57–62] and which have been developed for assignment based on soft-COSY methods or selective TOCSY methods. Several three-dimensional techniques using selective pulses have been proposed,[51,63–65] but until the time of writing these do not appear to have gained much popularity. Techniques based on double irradiation form a category on their own for both assignment and distance determination.[34,54–56,61,62,66–70]

Finally, there also exist several different techniques for the determination of relaxation parameters,[16,55,66,70–77] from a simple determination of transverse relaxation in coupled spin systems,[76] to a complete determination of the individual elements of the relaxation matrix.[75] (These experiments are considered in more detail in the articles ***Selective NOESY*** and ***Selective Relaxation Techniques in Biological NMR***).

8 CONCLUSION

The development of sophisticated pulses for selective excitation and inversion has triggered an explosion in the development of techniques using selective manipulations. These techniques can aid at all stages in structure determination, from assignment to the determination of coupling constants and relaxation rates. The number of experiments, and their relative efficiency, are growing rapidly and are likely to become an indispensable tool in cases where a structure does not yield to routine nonselective approaches.

9 RELATED ARTICLES

Average Hamiltonian Theory; Complex Radiofrequency Pulses; Decoupling Methods; Selective Excitation Methods: Artifacts; Selective Hartmann–Hahn Transfer in Liquids; Selective NOESY; Selective Relaxation Techniques in Biological NMR; Shaped Pulses.

10 REFERENCES

1. P. G. Morris, *Nuclear Magnetic Resonance Imaging in Medicine and Biology*, Clarendon, Oxford, 1986.
2. G. A. Morris and R. Freeman, *J. Magn. Reson.*, 1978, **29**, 433.
3. W. S. Warren and M. S. Silver, *Adv. Magn. Reson.*, 1988, **12**, 247.
4. R. Freeman, *Chem. Rev.*, 1991, **91**, 1397.
5. L. Emsley, in Nuclear Magnetic Resonance, Part C, *Methods in Enzymology*, 1994, **239**, 207.
6. R. N. Bracewell, *The Fourier Transform and its Applications*, 2nd edn., McGraw-Hill, New York, 1978.
7. A. Abragam, *Principles of Nuclear Magnetism*, Clarendon, Oxford, 1961.
8. C. P. Slichter, *Principles of Nuclear Magnetic Resonance*, 3rd edn., Springer, New York, 1990.
9. R. R. Ernst, G. Bodenhausen, and A. Wokaun, *Principles of Nuclear Magnetic Resonance in One and Two Dimensions*, Clarendon, Oxford, 1987.
10. A. J. Temps and C. F. Brewer, *J. Magn. Reson.*, 1984, **56**, 355.
11. C. Bauer, R. Freeman, T. Frenkiel, J. Keeler, and A. J. Shaka, *J. Magn. Reson.*, 1984, **58**, 442.
12. W. S. Warren, *J. Chem. Phys.*, 1984, **81**, 5437.
13. R. Brüschweiler, C. Griesinger, O. W. Sørensen, and R. R. Ernst, *J. Magn. Reson.*, 1988, **78**, 178.
14. J. Friedrich, S. Davies, and R. Freeman, *J. Magn. Reson.*, 1987, **75**, 390.
15. P. Xu, X. L. Wu, and R. Freeman, *J. Magn. Reson.*, 1992, **99**, 308.
16. L. Emsley and G. Bodenhausen, *J. Magn. Reson.*, 1989, **82**, 211.
17. F. Loazia, M. A. McCoy, S. L. Hammes, and W. S. Warren, *J. Magn. Reson.*, 1988, **77**, 175.
18. J. T. Ngo and P. G. Morris, *Magn. Reson. Med.*, 1987, **5**, 217.
19. W. S. Warren, *Science*, 1988, **242**, 878.
20. P. G. Morris, D. J. O. McIntyre, D. E. Rourke, and J. T. Ngo, *NMR Biomed.*, 1989, **2**, 257.
21. H. Geen, S. Wimperis, and R. Freeman, *J. Magn. Reson.*, 1989, **85**, 620.
22. L. Emsley and G. Bodenhausen, *Chem. Phys. Lett.*, 1990, **165**, 469.
23. H. Geen and R. Freeman, *J. Magn. Reson.*, 1991, **93**, 93.
24. L. Emsley and G. Bodenhausen, *J. Magn. Reson.*, 1992, **97**, 135.
25. D. E. Rourke and P. G. Morris, *Phys. Rev. A*, 1992, **46**, 3631.
26. D. E. Rourke and P. G. Morris, *J. Magn. Reson.*, 1992, **99**, 118.
27. J. Slotboom, J. W. Gunning, A. F. Mehlkopf, and W. M. M. J. Bovee, *J. Magn. Reson. A*, 1993, **101**, 257.
28. V. Smith, J. Kurhanewicz, and T. L. James, *J. Magn. Reson.*, 1991, **95**, 41.
29. S. Conolly and A. Macovski, in *Proceedings of the Fourth Annual Meeting of the Society of Magnetic Resonance in Medicine, London, 1985*, p. 958.
30. C. Counsell, M. H. Levitt, and R. R. Ernst, *J. Magn. Reson.*, 1985, **63**, 133.
31. J. T. Ngo and P. G. Morris, *J. Magn. Reson.*, 1987, **74**, 122.
32. W. R. Hamilton, *Proc. R. Ir. Acad.*, 1844, **2**, 424.

33. B. Blümich and H. W. Spiess, *J. Magn. Reson.*, 1985, **61**, 356.
34. L. Emsley, I. Burghardt, and G. Bodenhausen, *J. Magn. Reson.*, 1990, **90**, 214.
35. S. Nicula and G. Bodenhausen, *J. Magn. Reson. A*, 1993, **101**, 209.
36. C. J. Lee, N. Murali, and W. S. Warren, *J. Magn. Reson.*, 1989, **84**, 643.
37. U. Eggenberger, P. Schmidt, M. Sattler, S. J. Glaser, and C. Griesinger, *J. Magn. Reson.*, 1992, **100**, 604.
38. M. A. McCoy and L. Müller, *J. Am. Chem. Soc.*, 1992, **114**, 2108.
39. E. Kupce and R. Freeman, *J. Magn. Reson. A*, 1993, **102**, 364.
40. P. Borgnat, A. Lesage, S. Caldarelli, and L. Emsley, submitted.
41. R. Brüschweiler, J. C. Madsen, C. Griesinger, O. W. Sørensen, and R. R. Ernst, *J. Magn. Reson.*, 1987, **73**, 380.
42. J. Cavanagh, J. P. Waltho, and J. Keeler, *J. Magn. Reson.*, 1987, **74**, 386.
43. L. Emsley, T. J. Dwyer, H. P. Spielmann, and D. E. Wemmer, *J. Am. Chem. Soc.*, 1993, **115**, 7765.
44. B. Brutscher, J. P. Simorre, and D. Marion, *J. Magn. Reson.*, 1992, **100**, 416.
45. H. Kessler, H. Oschkinat, C. Griesinger, and W. Bermel, *J. Magn. Reson.*, 1986, **70**, 106.
46. H. Kessler, U. Anders, G. Gemmecker, and S. Steuernagel, *J. Magn. Reson.*, 1989, **85**, 1.
47. H. Kessler, S. Mronga, and G. Gemmecker, *Magn. Reson. Chem.*, 1991, **29**, 527.
48. S. Berger, *Angew. Chem., Int. Ed. Engl.*, 1988, **27**, 1196.
49. S. Davies, J. Friedrich, and R. Freeman, *J. Magn. Reson.*, 1987, **75**, 540.
50. S. Davies, J. Friedrich, and R. Freeman, *J. Magn. Reson.*, 1988, **76**, 555.
51. J. Friedrich, S. Davies and R. Freeman, *Mol. Phys.*, 1988, **64**, 691.
52. S. Davies, J. Friedrich, and R. Freeman, *J. Magn. Reson.*, 1988, **79**, 211.
53. R. Freeman, J. Friedrich, and S. Davies, *Magn. Reson. Chem.*, 1988, **26**, 903.
54. R. Konrat, I. Burghardt, and G. Bodenhausen, *J. Am. Chem. Soc.*, 1991, **113**, 9135.
55. B. Boulat, R. Konrat, I. Burghardt, and G. Bodenhausen, *J. Am. Chem. Soc.*, 1992, **114**, 5412.
56. E. Kupce and R. Freeman, *J. Magn. Reson.*, 1992, **100**, 208.
57. L. Emsley, P. Huber, and G. Bodenhausen, *Angew. Chem., Int. Ed. Engl.*, 1990, **29**, 517.
58. L. Emsley and G. Bodenhausen, *J. Am. Chem., Soc.*, 1991, **113**, 3309.
59. L. Emsley and G. Bodenhausen, in *Computational Aspects of the Study of Biological Macromolecules by Nuclear Magnetic Resonance Spectroscopy*, ed. J. C. Hoch, Plenum Press, New York, 1991.
60. N. Müller, L. DiBari, and G. Bodenhausen, *J. Magn. Reson.*, 1991, **94**, 73.
61. C. Zwahlen, S. J. F. Vincent, and G. Bodenhausen, *Angew. Chem., Int. Ed. Engl.*, 1992, **31**, 1248.
62. S. J. F. Vincent, C. Zwahlen, and G. Bodenhausen, *J. Am. Chem. Soc.*, 1993, **115**, 9202.
63. C. Griesinger, O. W. Sørensen, and R. R. Ernst, *J. Am. Chem. Soc.*, 1987, **109**, 7227.
64. C. Griesinger, O. W. Sørensen, and R. R. Ernst, *J. Magn. Reson.*, 1987, **73**, 574.
65. H. Oschkinat, C. Cieslar, T. A. Holak, G. M. Clore, and A. M. Gronenborn, *J. Magn. Reson.*, 1989, **83**, 450.
66. B. Boulat, I. Burghardt, and G. Bodenhausen, *J. Am. Chem. Soc.*, 1992, **114**, 10 679.
67. E. Kupce and R. Freeman, *J. Am. Chem. Soc.*, 1992, **114**, 10 671.
68. E. Kupce and R. Freeman, *J. Magn. Reson. A*, 1993, **105**, 234.
69. E. Kupce and R. Freeman, *J. Magn. Reson. A*, 1993, **102**, 122.
70. E. Kupce and R. Freeman, *J. Magn. Reson. A*, 1993, **101**, 225.
71. R. L. Vold, R. R. Vold, and H. E. Simon, *J. Magn. Reson.*, 1973, **11**, 283.
72. R. L. Vold and R. R. Vold, *Prog. NMR Spectrosc.*, 1978, **12**, 79.
73. H. Oschkinat and W. Bermel, *J. Magn. Reson.*, 1989, **81**, 220.
74. H. Oschkinat, D. Limat, L. Emsley, and G. Bodenhausen, *J. Magn. Reson.*, 1989, **81**, 13.
75. L. DiBari, J. Kowalewski, and G. Bodenhausen, *J. Chem. Phys.*, 1990, **93**, 7698.
76. L. Emsley, J. Kowalewski, and G. Bodenhausen, *Appl. Magn. Reson.*, 1990, **1**, 139.
77. I. Burghardt, R. Konrat, and G. Bodenhausen, *Mol. Phys.*, 1992, **75**, 467.
78. J. B. Murdoch, A. H. Lent, and M. R. Kritzer, *J. Magn. Reson.*, 1987, **74**, 226.
79. S. Caldarelli et al., *J. Magn. Reson. A*, 1995, **116**, 129.

Acknowledgments

I am grateful to Michel Bardet and the Département de la Recherche Fondamentale sur la Matière Condensée, Grenoble, for support, and for providing the stimulating environment in which this article was written.

Biographical Sketch

Lyndon Emsley, *b*. 1964. BSc. Imperial College, London, 1986, Ph.D., Université de Lausanne, Switzerland, 1991 under the direction of Geoffrey Bodenhausen. Fellow of the Miller Institute for Basic Research in Science, UC Berkeley, 1991–1993 (collaboration with Alex Pines). Foreign member of the Institut Universitaire de France, 1994. Professor of Chemistry, Ecole Normale Supérieure de Lyon 1995–present. Current research interests focus on fundamental aspects of NMR, with an emphasis on the solid state.

Shaped Pulses

Warren S. Warren and Suzanne M. Mayr
Princeton University, Princeton, NJ, USA

1	Introduction	1
2	Rectangular Pulse Effects	1
3	General Effects of Shaped Pulses	2
4	Pulse Shaping in Two-Level Systems	3
5	Pulse Shaping in Multilevel Spin Systems	6
6	Conclusions	8
7	Related Articles	8
8	References	8

1 INTRODUCTION

NMR spectroscopists have traditionally used constant amplitude ('rectangular') radiofrequency pulses, for a variety of reasons. During a rectangular pulse, the Hamiltonian remains constant in the rotating frame. For uncoupled spin systems, this permits direct integration of the Bloch equations; the pulse generates a readily predicted rotation of the magnetization, and the spin vector follows a very simple trajectory. Even when a density matrix approach is needed, it is often true that couplings can be neglected during any individual pulse, and visualizing the effect of each individual pulse as a simple rotation dramatically simplifies the theoretical description of the effects of complex sequences. There were once technological reasons for the popularity of rectangular pulses as well:rapid development of digital technology in the 1960s and 1970s made it possible to generate quite complex 'data patterns' (and hence pulse sequences where the radiofrequency gate was either 'on' or 'off'). Finally, the very small voltages characteristic of NMR signals (many orders of magnitude weaker than the irradiating pulses) demanded techniques for producing excellent isolation between transmitter and receiver, and such isolation is far easier with switches that have only two states than with devices that produce an adjustable output voltage. Thus extremely sophisticated sequences of rectangular pulses are easily implemented on most commercial spectrometers, and have obviously been used successfully in an enormous variety of applications.

Even after 50 years of this development, however, some experiments remain fundamentally difficult, and applications to more complicated systems require additional technique development. The most common example of an NMR problem that is not easily solvable by a rectangular pulse sequence is selective excitation (see ***Selective Pulses***) of a single transition or range of frequencies. Selectively exciting the spectral region of interest reduces data acquisition time and spectral complexity, especially in multidimensional experiments. Alternatively, for an experiment such as solvent suppression, one may wish to excite over a broad frequency range with the exception of a narrow frequency region or notch. As another example, the need for expensive high-power amplifiers to cover the large spectral width in solid state experiments can lead to problems such as sample heating or probe arcing.

This article will focus on the uses of shaped pulses (including amplitude modulation and either phase or frequency modulation) to address these issues and others. Any conceivable waveform with a bandwidth comparable to the width of the NMR spectrum is readily synthesized today with inexpensive commercial components. Sequences of shaped pulses have been successfully used in a wide variety of experiments. Pulse shaping has been extensively applied to ensembles of two-level systems; common applications include clean selective inversion with reduced power dissipation, self-refocused selective excitation, and solvent suppression experiments. Shaped pulses are also routinely used in magnetic resonance imaging (MRI) (see ***Magnetic Resonance Imaging: A Historical Overview***) to improve resolution and reduce power dissipation. Applications to coupled multilevel systems remain an active area of research today, but shaped pulse sequences have been used to replace complex multiple pulse sequences in applications with scalar-coupled spins, dipolar-coupled spins, and quadrupolar nuclei. This can overcome instrumental limitations and provide broader uniform excitation at reduced peak powers. In principle, it is virtually always possible to get reduced power dissipation, better resolution, or artifact reduction with non-rectangular pulses; the difficulty comes in trying to find the best pulse shape to use.

2 RECTANGULAR PULSE EFFECTS

The simplest and most straightforward method of selective excitation is to use a single, low-amplitude rectangular rf pulse of relatively long duration. Starting from z magnetization ($M_z = 1, M_x, M_y = 0$) the excitation after a rectangular pulse phased along the rotating frame x axis with peak Rabi frequency ω_1, duration T (which is much shorter than any relaxation time in the system), and resonance offset $\Delta\omega$ ($\Delta\omega = \omega_0 - \omega$, where ω_0 is the resonance frequency and ω is the carrier frequency of the rf wave) can be calculated analytically (neglecting relaxation):[1]

$$M_x(\omega_1, T, \Delta\omega) = 2M_0 \frac{\omega_1 \Delta\omega}{\Delta\omega^2 + \omega_1^2} \sin^2[\tfrac{1}{2}(\Delta\omega^2 + \omega_1^2)^{1/2} T] \quad (1)$$

$$M_y(\omega_1, T, \Delta\omega) = M_0 \frac{\omega_1}{(\Delta\omega^2 + \omega_1^2)^{1/2}} \sin[(\Delta\omega^2 + \omega_1^2)^{1/2} T] \quad (2)$$

$$M_z(\omega_1, T, \Delta\omega) = M_0\{\cos^2[\tfrac{1}{2}(\Delta\omega^2 + \omega_1^2)^{1/2} T] - \frac{\omega_1^2 - \Delta\omega^2}{\omega_1^2 + \Delta\omega^2} \sin^2[\tfrac{1}{2}(\Delta\omega^2 + \omega_1^2)^{1/2} T] \quad (3)$$

If the pulse is applied on resonance ($\Delta\omega = 0$), it generates a rotation about the x axis by an angle $\theta = \omega_1 T$, which is also universally known as the flip angle. A $\frac{1}{2}\pi$ pulse ($\theta = \frac{1}{2}\pi$) creates the maximum possible transverse magnetization; a π pulse generates complete inversion of the populations. This result is equivalent to that obtained through density matrix mechanics.

From equations (1)–(3), the excitation from a $\frac{1}{2}\pi$ or π pulse decreases substantially if $\Delta\omega \gtrsim \omega_1$. Lengthening the pulse while keeping θ constant decreases ω_1, and hence increases the selectivity—as expected from the uncertainty

principle relation $\Delta\nu\ \Delta\tau \approx 1$ (the exact value depends on the pulse shape). However, the excitation is not uniform near resonance, and some excitation persists far outside the nominal bandwidth. This is easy to understand in the linear response limit, which corresponds to a very small flip angle; in that case, the transverse magnetization [equations (1) and (2)] reduces to the Fourier transform of the rectangular pulse itself. The discontinuities at the beginning and end of the pulse produce high-frequency components in the excitation, thus introducing excitation far outside the nominal bandwidth. Solvent suppression sequences, which aim to produce a broad and uniform excitation profile with a sharp 'hole' in the middle, encounter similar difficulties.

The excitation profile from a radiofrequency pulse clearly depends critically on the pulse shape, since changing the shape changes the magnitude of the frequency components; however, predicting pulse shape effects is generally far more complicated than simply Fourier transforming the waveform. For example, Fourier transform arguments predict that a sin $(\alpha t)/t$ (sinc) pulse produces a rectangular excitation profile but this only works well if the pulse is very weak.[2] As shown in Figure 1, the excitation becomes highly distorted as the pulse area approaches π. Nonetheless, more sophisticated treatments show that Fourier arguments have their uses. For example, it is generally true that any waveform with edges will have trouble producing highly localized excitation. Thus, for example, sequences of back-to-back rectangular pulses (see ***Composite Pulses***) have been extremely successful in compensating for many of the practical limitations of rectangular pulse trains; but each added pulse introduces more discontinuities into the excitation profile, and, as a result, the performance far from resonance is generally difficult to control.

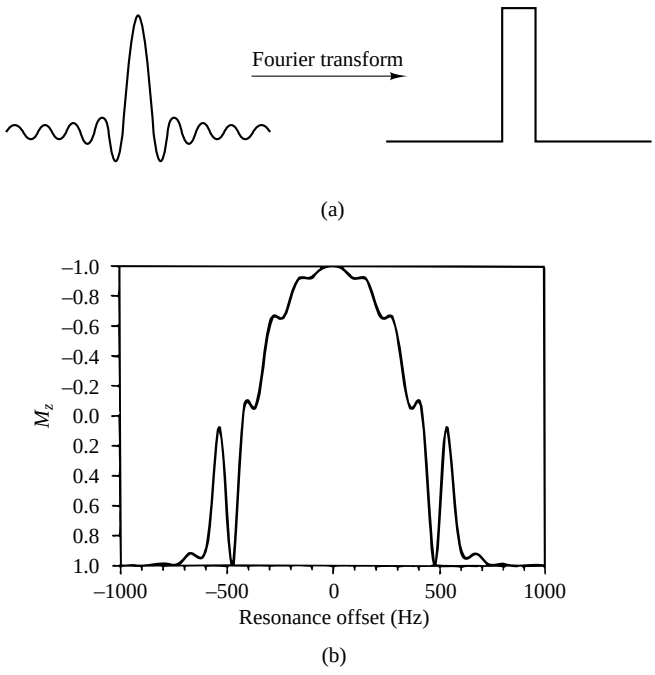

Figure 1 (a) The Fourier transform of a sin $(\alpha t)/t$, or sinc, pulse is a rectangle. This argument only works well to $\theta = 30^\circ$. (b) The inversion profile for a sinc π pulse. The deviations from linear response are quite substantial

3 GENERAL EFFECTS OF SHAPED PULSES

Pulse shaping provides a powerful means to circumvent the limitations of rectangular pulses. The effects of an arbitrarily phase- or amplitude-modulated pulse can be formally calculated by breaking up the pulse into a large number of small, nearly constant pieces and then either solving the Bloch equations or employing density matrix mechanics. For two-level systems, both methods are equivalent. In the laboratory frame, the radiofrequency pulse $\boldsymbol{B}_1(t)$ is generally produced along a single axis (which we shall call the x axis, with unit vector $\boldsymbol{i}$): $\boldsymbol{B}_1(t) = B_1(t)\boldsymbol{i}$. The Hamiltonian, which includes the effects of the static magnetic field $\boldsymbol{B}_0 = B_0\boldsymbol{k}$ (along the z axis, with unit vector $\boldsymbol{k}$) as well as this pulse, can be written as

$$\hat{\mathcal{H}}(t) = \hbar\gamma[B_0\boldsymbol{k} + B_1(t)\boldsymbol{i}] \cdot \hat{\boldsymbol{I}} = \hbar[\omega_0\hat{I}_z + \omega_1(t)\hat{I}_x] \quad (4)$$

An arbitrarily modulated pulse $\omega_1(t)$ can be described[3,4] by a time-dependent amplitude $A(t)$ and phase $\vartheta(t)$:

$$\omega_1(t) = A(t)\,\mathrm{Re}\{\exp[\mathrm{i}\vartheta(t)]\}, \quad A(t) \geq 0 \quad (5)$$

where the total phase $\vartheta(t)$ is known modulo 2π. While Equation (5) is perfectly general, it is normally the case in NMR that only a small fractional bandwidth about some fixed carrier frequency ω is needed (for example, normal ^{1}H solution NMR spectra spread over 10 ppm = 10^{-5} of the center frequency) so it is more convenient to write

$$\omega_1(t) = A(t)\,\mathrm{Re}\{\exp[\mathrm{i}[\omega t + \phi(t)]]\} \quad (6)$$

If ω is correctly chosen, $\phi(t)$ varies far more slowly than does $\vartheta(t)$. We can then write

$$\begin{aligned}\omega_1(t) &= [A(t)\cos\phi(t)]\cos\omega t - [A(t)\sin\phi(t)]\sin\omega t \\ &\equiv \omega_{1x}(t)\cos\omega t - \omega_{1y}(t)\sin\omega t \end{aligned} \quad (7)$$

with the amplitude and phase modulation of the pulse reflected in $\omega_{1x}(t)$ and $\omega_{1y}(t)$. Changing the assumed carrier frequency ω changes the functions $\phi(t)$, $\omega_{1x}(t)$, and $\omega_{1y}(t)$. Transforming to a frame rotating at the carrier frequency ω gives the following Hamiltonian:

$$\hat{\mathcal{H}}(t) = \hbar[\Delta\omega\hat{I}_z + \omega_{1x}(t)\hat{I}_x + \omega_{1y}(t)\hat{I}_y] \quad (8)$$

In a density matrix picture, this rotating frame transformation is accomplished by the unitary operator

$$\hat{U} = \exp[-\mathrm{i}\omega t\hat{I}_z] \quad (9)$$

This frame of reference is also known as the phase-modulated (PM) frame. In this frame, the instantaneous rotation generated by the pulse is about an axis in the direction $[\omega_{1x}(t), \omega_{1y}(t), \Delta\omega]$. The phase-modulated frame rotates at a constant frequency, and is thus equivalent to the usual NMR definition of rotating frame.

Alternatively, the pulse can be expressed by the time-dependent amplitude $A(t)$ and the instantaneous frequency $\omega_\mathrm{i}(t)$. It is tempting, but *incorrect*, to write $\vartheta(t) = \omega_\mathrm{i}(t)t$ and conclude that the instantaneous frequency is just the phase

divided by time. Instead, the instantaneous frequency $\omega_{\mathrm{i}}(t)$ is properly defined as the time derivative of the total phase $\dot{\vartheta}(t)$:

$$\omega_{\mathrm{i}}(t) \equiv \dot{\vartheta}(t) = \omega + \dot{\phi}(t) \tag{10}$$

This perspective leads naturally to the frequency-modulated (FM) rotating frame, which at any instant in time is synchronous with the instantaneous pulse frequency $\omega_{\mathrm{i}}(t)$. This rotating-frame transformation is accomplished by the unitary operator

$$\hat{U} = \exp\{-\mathrm{i}[\omega t + \phi(t)]\hat{I}_z\} \tag{11}$$

In this frame, the Hamiltonian becomes

$$\hat{\mathcal{H}}(t) = \hbar\{[\omega_0 - \omega_{\mathrm{i}}(t)]\hat{I}_z - A(t)\hat{I}_x\} \equiv \hbar[\Delta\omega(t)\hat{I}_z - A(t)\hat{I}_x] \tag{12}$$

where the instantaneous resonance offset $\Delta\omega(t) = \dot{\phi}(t)$ and the amplitude $A(t)$ dictate the direction of the rotation axis. Note that the y component has disappeared, at the expense of a time-varying z component; hence the PM and FM frames each have calculational advantages. At any instant in time, the PM and FM frames are related by a z axis rotation equal to the instantaneous phase $\phi(t)$ $\{\equiv\arctan[\omega_{1y}(t), \omega_{1x}(t)]\}$ that explicitly depends on the choice of carrier frequency ω.

For example, consider an amplitude- and phase-modulated Gaussian pulse envelope[5]

$$\omega_1(t) = C\exp[-(at)^2]\exp[\mathrm{i}(\omega t + bt^2)] \tag{13}$$

with carrier frequency ω, pulse amplitude $A(t) = C\exp[-(at)^2]$, and time-varying phase function $\vartheta(t) = \omega t + bt^2$. The instantaneous frequency is given by equation (10) as

$$\omega_{\mathrm{i}}(t) = \omega + 2bt \tag{14}$$

not $\omega + bt$, as would be found if $\vartheta(t) = \omega_{\mathrm{i}}(t)t$. For this pulse, $\omega_{\mathrm{i}}(t)$ varies linearly with time; the pulse is said to be 'chirped'.

Some general properties of shaped pulses are well known. A purely amplitude-modulated pulse on resonance generates a rotation determined by the flip angle of the pulse, just as for the rectangular case. Therefore, we can generate the desired rotation by adjusting either the peak amplitude or pulse duration. However, off-resonance effects cannot be generalized from rectangular pulse behavior, because the peak Rabi frequency, ω_1, is not constant. The variation in the direction of the rotation axis or size of the rotation angle with changing $\Delta\omega$ or ω_1 is not calculable analytically, except for a very few special cases.

The effects of phase-modulated or frequency-modulated pulses cannot be extrapolated from rectangular pulse solutions. The concept of flip angle is not valid for phase-modulated or frequency-modulated pulses.[6,7] One important special case of frequency modulation is adiabatic inversion: if the frequency $\omega(t)$ is swept very slowly through the spectral range of interest (from far below resonance to far above resonance), the magnetization vector will be completely inverted from M_z to $-M_z$ as long as the pulse amplitude exceeds a certain level. Even if the amplitude is increased further, the pulse is effectively a π pulse. The phase-modulated pulse envelope $\omega_1(t) = (\mathrm{sech}\ \alpha\mathrm{T})^{1+\mu\mathrm{i}}$ with $\mu = 5$ has been shown to perform such an adiabatic inversion with the added benefit of a rectangular inversion profile.[3] This pulse can also be viewed as a frequency-swept pulse with amplitude $A(t) = \mathrm{sech}\ \alpha T$, phase $\phi(t) = \mu\ \ln(\mathrm{sech}\ \alpha T)$ and instantaneous frequency $\omega_{\mathrm{i}}(t) = \mu\alpha\ \tanh(\alpha T)$. Silver et al.[8] showed that the even if the peak amplitude is increased by a factor of 10, the $(\mathrm{sech}\ \alpha T)^{1+5\mathrm{i}}$ pulse remains a π pulse, whereas the flip angle of a rectangular pulse would have increased to 10π. This means that frequency-modulated pulses can compensate for effects such as rf inhomogeneity, which presents some obvious advantages; for example, the sample can be larger than the coil volume but still be inverted uniformly. However, a frequency-modulated pulse is difficult to use as an echo pulse (see ***Spin Echo Spectroscopy of Liquid Samples***), because the apparent rotation axis changes as the amplitude increases. For this reason, purely amplitude-modulated pulses are usually the best choice to replace rectangular π pulses in existing sequences.

4 PULSE SHAPING IN TWO-LEVEL SYSTEMS

Pulse shaping theory for unrelaxed and uncoupled two-level systems has been extensively developed. The response of a spin system to any shaped pulse can always be exactly calculated by breaking the pulse into a large number of small rectangles. However, the inverse problem, determining what pulse shape to use to achieve a desired response, is the real problem of interest and is not easily solvable. Theoretical progress towards solving this problem comes from three somewhat different but complementary directions: closed form solutions for specific pulse shapes, perturbative or exact expansions for describing the effects of arbitrary pulse shape, and computerized optimization.

Closed-form solutions for specific pulse shapes are most valuable for the insight they provide. Unfortunately, the exact effects of any arbitrarily shaped pulse on the magnetization are not known analytically. In fact, analytic solutions exist for only two other waveforms besides the rectangular pulse case: a $(\mathrm{sech}\ \alpha\mathrm{T})^{1+\mu\mathrm{i}}$ pulse with arbitrary α and μ (equivalently, a sech pulse envelope with a tanh frequency sweep)[4] and an exponential envelope pulse.[9,10] Furthermore, a rectangular pulse is the only one that can be solved for all initial conditions, all resonance offsets, and all amplitudes. In practice, most of the commonly used pulse shapes were found by numerical methods.

Several different approximate approaches have been used to describe the behavior of arbitrarily shaped pulses. Approximate solutions are useful because they provide physical insight: they tell us why a particular shape behaves as it does and suggest directions for improvement. For example, the frequency response produced by a pulse can be approximated using Fourier arguments, as previously described. These predictions from linear response theory are accurate in the limit where the pulse area is small. Other treatments that give some physical insight include perturbative expansions of the magnetization and perturbative expansions of the effective Hamiltonian.[4] Formalisms such as inverse scattering[11,12] or Floquet operators[13,14] have been used to produce analytic expressions for the inversion profile from an arbitrary pulse shape. More recently, Shinnar and Leigh[15] have developed a 'direct synthesis' technique for the numerical inversion of the Bloch equations. In many of these cases, the theoretical

treatment is nearly exact in certain limits, and may be extrapolated to cover a wider range of experimental conditions. The key difference between these treatments generally has to do with the range over which they adequately approximate the exact solutions, which can always be obtained (numerically) by breaking the pulse into many rectangular pieces.

Because the number of analytic solutions is quite limited, virtually all of the truly useful waveforms have been generated by computerized optimization. Optimization starts by defining the following elements: the functional form of the pulse shape, the method of calculating the spin response for a define spectral range, and the quality factor Q for the pulse shape, which quantifies deviations from the idealized target profile (for example, the root-mean-square deviation from a profile that reflects complete inversion over some bandwidth and no effect outside that bandwidth). These parameters must be carefully defined, because, even for a simple pulse shape, it is impossible to explore the entire range of parameter space. The pulse shape is systematically varied as the quality factor is assessed, until the desired response is achieved. Optimization algorithms range from conjugate gradient routines[16] to more sophisticated schemes[17] such as evolutionary methods,[27] simulated annealing, and neural networks. Each method has its own advantages and disadvantages, depending on the need to find a local or a global minimum.

An optimized shaped pulse can easily be created for most applications involving two-level systems, ignoring the effects of relaxation, coupling, and radiation damping. Many different optimization schemes have been used to create useful shapes.[18] For example, computerized optimization in two-level systems has produced shaped pulses for clean selective inversion with reduced power dissipation;[19] self-refocused selective excitation (including compensation for phase roll),[20] and solvent suppression.[21,22] This approach allows us to calculate numerically the effects of any pulse shape. Unfortunately, it gives little insight into why a particular shape would work well. Therefore, computerized optimization is most effective when used in combination with an approximate solution.

4.1 Tradeoffs

In two-level systems, many different pulses produce the same or nearly the same inversion profile. There is no 'best' pulse shape. The best pulse for any specific application is determined by experimental details such as the need for uniform excitation versus the need for localized effect or the narrowest possible bandwidth. In general, there are tradeoffs between pulse complexity, peak power, total applied energy, and phase distortions far from resonance. The significance of these tradeoffs is different for different applications. For example, a more complicated pulse can be used for selective excitation to give sharper edges in the 'transition region' between complete inversion and no effect at the expense of increased power dissipation or pulse length. The importance of these tradeoffs is illustrated in Table 1, which examines the inversion profiles of four amplitude modulated pulses shown in Figure 2 at the same peak power.

Ideally, there would be 100% excitation over the bandwidth of interest (frequency selectivity) and no excitation outside this range (no side lobes). Rectangular pulses excite the broadest range of frequencies but only a small region is completely inverted and low amplitude side lobes lead to unwanted excitation far from resonance. Gaussian pulses[23,24] eliminate the long frequency tails produced by rectangular pulses, at the expense of somewhat increased pulse length and smaller completely inverted region. Also, Gaussian pulses produce a broad region of excitation that is too large to be neglected but does not reach 100%. These "semiselective" pulses have been used quite extensively (see, e.g., Kessler et al.[25]), perhaps because of the simplicity of the waveform, but in fact current technology allows for the generation of much more sophisticated waveforms with equal ease. A Hermite pulse[26] (a polynomial multiplying a Gaussian) has a much larger completely excited bandwidth for the same peak power. At the opposite extreme, the asymmetric pulse shape[4,27] provides a vastly larger completely excited bandwidth, but it is substantially longer. This longer pulse could present a problem if extremely narrowband excitation is desired; the pulse length could then become comparable to relaxation times.

4.2 Phase Roll

There is one important problem with many of the shaped pulses described above. Because they are relatively long, they induce a strong variation in the phase of the excited signal across the selected region. This can be described physically as a spreading out of spin isochromats that are experiencing different effective fields. In the simple example of a long

Table 1 Comparison of Amplitude-Modulated Pulse Shapes (Reproduced by Permission of John Wiley & Sons from S. McDonald and W. S. Warren, *Concepts Magn. Reson.*, 1991, **3**, 55)

Shape	Length (peak power ω_1)	Completely inverted region[a]	Bandwidth (fwhm)	Completely uninverted region[b]
Rectangular pulse [Figure 2(a)]	$1.0T$ $(= \pi/\omega_1)$	$< \pm 0.09\omega_1$	$\pm 0.8\omega_1$	$> \pm 11\omega_1$
Gaussian pulse [Figure 2(b)]	$2.0T$[c]	$< \pm 0.06\omega_1$	$\pm 0.63\omega_1$	$> \pm 1.6\omega_1$
Hermite pulse [Figure 2(c)]	$4.8T$[c]	$< \pm 0.15\omega_1$	$\pm 0.55\omega_1$	$> \pm 1.5\omega_1$
Asymmetric pulse [Figure 2(d)]	$8.0T$	$< \pm 0.45\omega_1$	$\pm 0.77\omega_1$	$> \pm 1.05\omega_1$

[a]Within this frequency range, magnetization starting at $+I_z$ ends up within 10° of $-I_z$.
[b]Outside of this frequency range, magnetization starting at $+I_z$ ends up within 10° of $+I_z$.
[c]These pulse shapes are assumed to be truncated at 5% of peak amplitude.

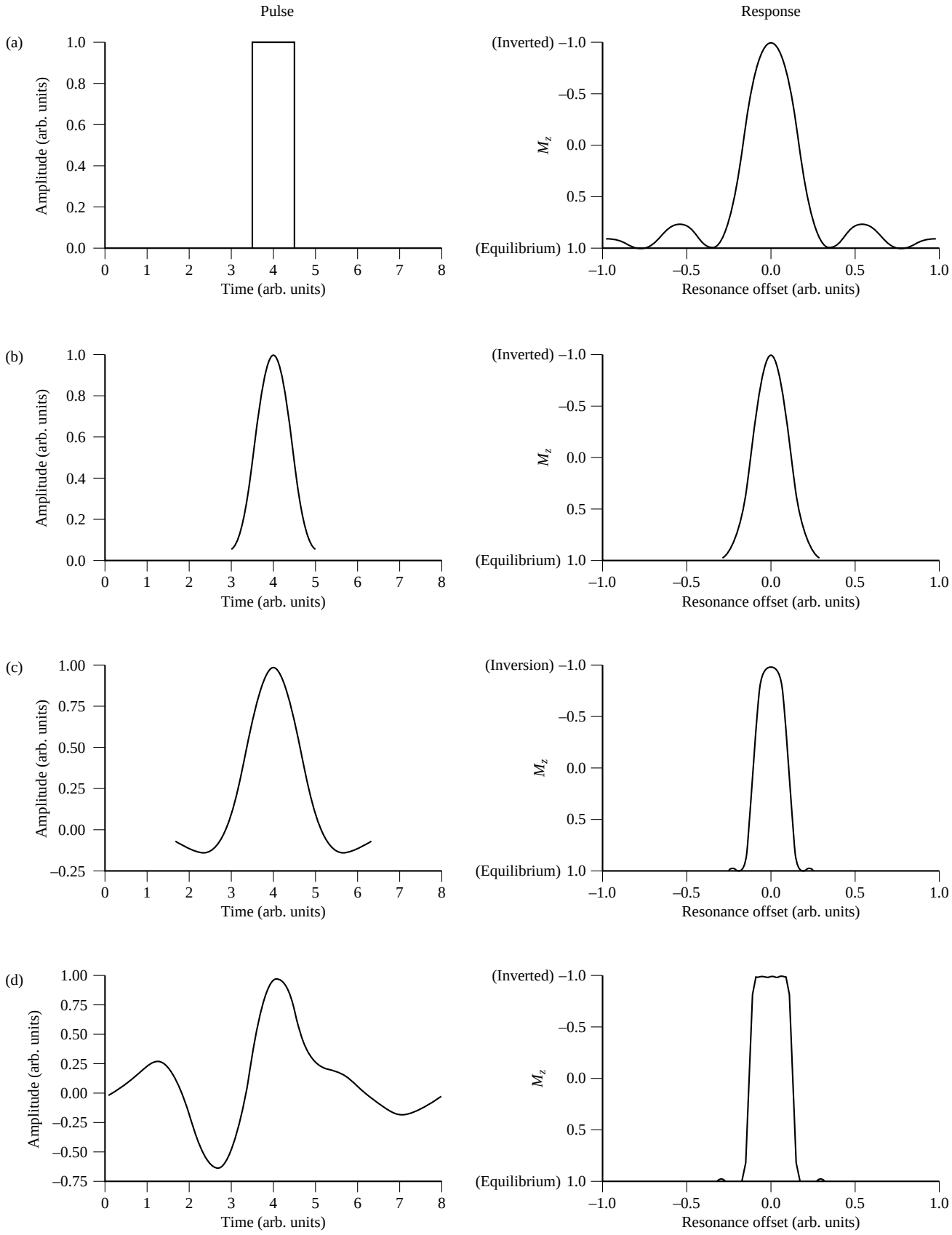

Figure 2 Various amplitude-modulated π pulses at the same peak power (left-hand plots) and the responses to them (right-hand plots): (a) square pulse; (b) Gaussian pulse; (c) Hermite pulse; (d) asymmetric pulses. (Reproduced by permission of John Wiley & Sons from S. McDonald and W. S. Warren, *Concepts Magn. Reson.*, 1991, **3**, 55)

rectangular pulse of duration T, phase roll originates from the delay of $\frac{1}{2}T$ between the pulse center (since the Fourier transform of the pulse is only real if this point is chosen as $T = 0$) and the end of the pulse when detection is possible. Phase rolls are not detected in routine spectra of liquids because the short intense $\frac{1}{2}\pi$ or π pulses making $\Delta\omega\ T$ small for the entire spectrum. If the lines are narrow and resolved, conventional NMR processing software routines can be used to correct a linear phase variation. This is much harder (and sometimes impossible) if peaks overlap; compensating for phase roll becomes a much more difficult task. In some cases, refocusing can be achieved by applying a hard π pulse after the shaped pulse, but customized shaped pulse schemes are more efficient at eliminating phase roll. This has been accomplished with amplitude-modulated $\frac{3}{2}\pi$ pulses and with phase- and amplitude-modulated pulses.[20, 28]

5 PULSE SHAPING IN MULTILEVEL SPIN SYSTEMS

Most of the advanced experiments in NMR cannot be adequately described by a distribution of uncoupled and unrelaxed two-level systems, and pulse shapes derived in this context have severe limits in their applicability. Shaped pulse sequences designed for two-level systems cannot be successfully extended to applications of multilevel spin systems when pulse lengths become comparable to the reciprocal of a typical coupling. For example, shaped pulses developed for double selective inversion experiments do not work well in the presence of scalar couplings owing to the creation of double quantum coherence.[31] Amplitude-modulated waveforms optimized for narrowband inversion of uncoupled spins encounter similar difficulties when applied to dipolar-coupled spins.[30]

Several groups have shown that is possible to devise sequences of shaped pulses that compensate for the effects of couplings, relaxation or radiation damping. This represents the frontier of the current understanding of pulse shape generation, and optimal waveforms are still evolving. Multilevel systems present the same 'inverse' problem as did two-level systems—usually the desired spin response is known, and an appropriate irradiation scheme is desired. Because the Bloch equations cannot be used to establish the effects of a shaped pulse on multilevel spin systems, density matrix mechanics must be employed. The time evolution of the density operator $\hat{\rho}(t)$ of a spin system under a time-dependent Hamiltonian $\hat{\mathcal{H}}(t)$ can be determined from the Liouville–von Neumann equation

$$\frac{\mathrm{d}\hat{\rho}(t)}{\mathrm{d}t} = -\mathrm{i}[\hat{\mathcal{H}}(t), \hat{\rho}(t)] \tag{15}$$

For a time-independent Hamiltonian, equation (15) integrates to

$$\hat{\rho}(t) = \hat{U}(t)\hat{\rho}(0)\hat{U}^{-1}(t) \tag{16}$$

where $\hat{U}(t)$ is the propagator, defined as

$$\hat{U}(t) = \exp(-\mathrm{i}\hat{\mathcal{H}}t) \tag{17}$$

The effects of any pulse on a two-level system can be completely characterized by calculating the propagator $\hat{U}(\Delta\omega)$ while scanning the single parameter of resonance offset. The situation becomes far more complicated in multilevel spin systems. N coupled spins generate a $2^N \times 2^N$ Hamiltonian, and, even in favorable cases (such as molecules dissolved in liquid crystal solvents, where only a few spins have measurable couplings), the size of these matrices guarantees that calculations will be exceedingly slow. The extent of these calculations makes brute force optimization impractical for coupled spin systems. In addition, one finds empirically that local minima in the quality factor are abundant in these problems, and it is very difficult to use gradients (changes in the quality factor from small changes in the pulse shape) to produce dramatic improvements. But if these were the only problems, supercomputers and ever-faster workstations would provide a straightforward solution. The real challenge is to find pulse shapes that will be *robust*—they have to be usable without knowing in advance every possible detail of the Hamiltonian, and they must be insensitive to rf inhomogeneity and the exact magnitude of coupling matrix elements. Building such robustness into a normal optimization is extraordinarily difficult. A two-level system has only one parameter in its internal Hamiltonian (the resonance offset), and the effects of a pulse shape might be calculated for 100 resonance offsets at each stage of the optimization. In the next simplest case (two coupled spins A and B), the Hamiltonian in general has two chemical shifts $\Delta\omega_\mathrm{a}$ and $\Delta\omega_\mathrm{b}$, plus coupling J_ab:

$$\hat{\mathcal{H}} = \Delta\omega_\mathrm{a}\hat{I}_{\mathrm{a}z} + \Delta\omega_\mathrm{b}\hat{I}_{\mathrm{b}z} + 2\pi J_\mathrm{ab}\hat{\boldsymbol{I}}_\mathrm{a} \cdot \hat{\boldsymbol{I}}_\mathrm{b} \tag{18}$$

But then an optimization with equivalent frequency resolution would require $(100)^3$ calculations at each stage, or else a new waveform would be needed for every possible molecule! Even if fewer J values were examined, the size of the calculation would still increase dramatically. For networks of coupled spins, this method is hopeless.

A more promising approach is to combine computerized optimization with other techniques to restrict the searches to a more meaningful range. For example, average Hamiltonian theory and predictions based on symmetry considerations can be used to constrain a search to sequences that are more likely to be robust and can produce simple and useful pulse shapes.

5.1 Average Hamiltonian Theory and Symmetry Considerations

Average Hamiltonian theory is an alternative approach to calculating the exact Hamiltonian during a pulse sequence (see ***Average Hamiltonian Theory***). The propagator $\hat{U}_\mathrm{int}(t)$ corresponding to the time-dependent internal Hamiltonian $\hat{\mathcal{H}}_\mathrm{int}(t)$ is defined as

$$\hat{U}_\mathrm{int}(t) = \hat{\mathcal{T}} \exp\left[-\mathrm{i} \int_0^t \hat{\mathcal{H}}_\mathrm{int}(t)\,\mathrm{d}t \right] \tag{19}$$

where $\hat{\mathcal{T}}$ is the Dyson time ordering operator. If the exponential is expanded and terms of equal order are collected, the propagator becomes

$$\hat{U}(t) = \exp(-\mathrm{i}t\ \hat{\bar{\mathcal{H}}}) \tag{20}$$

with

$$\tilde{\hat{\mathcal{H}}}(t) = \sum_{k=0}^{\infty} \tilde{\hat{\mathcal{H}}}^{k}(t) \tag{21}$$

This is known as the Magnus expansion.[32] The effective Hamiltonian is still in the time-dependent or toggling frame. If the Hamiltonian is periodic with period t_c,

$$\hat{\mathcal{H}}(t + nt_c) = \hat{\mathcal{H}}(t) \tag{22}$$

and if the system is only observed at multiples of the cycle time, then the propagator $\hat{U}(t_c)$ expressed in terms of the average Hamitonian $\tilde{\hat{\mathcal{H}}}(t)$ predicts the time evolution of the system.

Predictions can be made by symmetry considerations (based on average Hamiltonian theory), which are applicable to any spin system and help reduce the vastly increased degrees of freedom associated with optimizing sequences of shaped pulses. For example, the basic decoupling pulse sequence R should not just be repeated to perform decoupling for a long interval; it will perform better in this application if it is phase-shifted and permuted into the configuration (RR$\overline{\text{R}}\overline{\text{R}}$), where the pulse $\overline{\text{R}}$ is the mirror image of R, phase shifted by 180° (obtained by time-reversing the order of the individual pulses and rotating by π about the z axis).[29] Any rf field applied antisymmetrically in time,

$$\hat{\mathcal{H}}_{\text{rf}}(t_c - t) = -\hat{\mathcal{H}}_{\text{rf}}(t) \tag{23}$$

produces a symmetric $\tilde{\hat{\mathcal{H}}}_{\text{int}}$.[33] If $\tilde{\hat{\mathcal{H}}}_{\text{int}}$ is symmetric in time,

$$\tilde{\hat{\mathcal{H}}}_{\text{int}}(t - t_c) = \tilde{\hat{\mathcal{H}}}_{\text{int}}(t) \tag{24}$$

and all odd-order terms in the Magnus expansion vanish. This property has been used extensively for designing sequences for selective averaging of unwanted operator terms in the Hamiltonian. In general, this implies that one can either use symmetric pulse shapes in the sequence, or asymmetric pulse shapes in the first half of the sequence with their mirror images in the second half. The propagator for these backward pulses (mirror images) is closely related to the propagators for the forward pulses. Therefore, a pulse shape need not be constrained to be symmetric, and this greatly reduces computation time.

5.2 Optimization of Pulse Shapes

It does not make sense to 'start from scratch' in an optimization for a multilevel system, particularly for an experiment that has been extensively analyzed for rectangular pulses. A more productive approach is to embed the pulse shape into a pulse sequence framework that already has some desirable properties. For example, one of the first coupled spin experiments to be optimized using shaped pulses was dipolar time reversal or double quantum excitation,[34] an experiment notoriously sensitive to experimental imperfections. To simplify the optimization, Lee et al.[34] started with the simplest two-quantum sequence, the two-pulse sequence shown in Figure 3(a). In addition, this sequence consists of purely amplitude-modulated pulses, which further restricts the calculation.

A straightforward method for amplitude modulation is to divide the pulse into N points, either in the time or frequency domain, and vary each point subject to the constraints

$$|\omega_1(t)| \leq \omega_{1\text{peak}} \tag{25}$$

$$\int_0^{t_p} \omega_1(t)\, \mathrm{d}t = \theta \tag{26}$$

where θ is the total area of the pulse. For this experiment, $\theta = \frac{1}{2}\pi$. Because these optimizations can be time-consuming, it is useful to keep the number of free parameters to be varied to a minimum while exploring all reasonable pulse shapes. However, a low-resolution approximation will produce pulses with crude shapes; furthermore, because each point is still rectangular, discontinuities at the edges can erode some of the advantages of pulse shaping. One approach to overcome these limitations is to expand the pulse in terms of some basis function that can be systematically varied. This has the advantage of ensuring that the pulse envelope contains no discontinuities or steep edges at the beginning or end of the pulse. For the two-quantum dipole sequences, the pulse shape was expressed as a series of Legendre polynomials,[34] and then the coefficients of the polynomials were optimized so that the leading error terms appear in $\tilde{\hat{\mathcal{H}}}^{(2)}$. An effective shaped pulse sequence [Figure 3(b)] was generated with only three polynomials. In other applications, a finite Fourier series[35] was used as the basis for expansion. This expansion is useful, because limiting the contribution from higher-order terms in the series discourages the introduction of more convoluted shapes.

Another approach for parameterizing the pulse shape is based on spline interpolations.[36] The shaped pulse is defined by a relatively small number n of variable relative amplitudes a_i at variable relative time points t_i, and then a cubic spline interpolation is used to approximate the pulse shape as N rectangular subpulses k with amplitudes A^k and durations t_k. This procedure produces smooth shapes that can have rapid amplitude changes. Also, the number of maxima and minima in the pulse shape is limited by the n 'anchor points' (a typical value of n is 10). By comparison with the basis function parameterization, which gives rise to global changes in the shape as coefficients are varied, this method is local in the sense that the shape changes only in the region of the varied parameter.

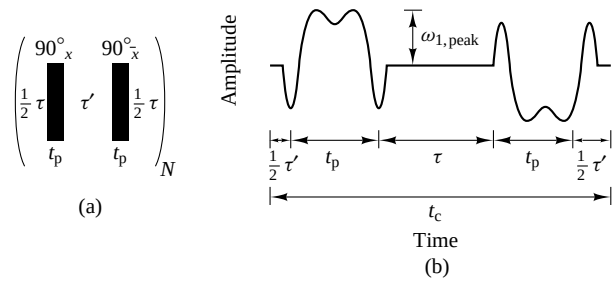

Figure 3 (a) The simplest pulse sequence for generating dipolar time reversal. (b) Amplitude-modulated shaped pulse sequence optimized to generate a two-quantum effective Hamiltonian

5.3 Applications

These principles have been used to produce shaped pulse sequences that show improved performance in applications with scalar-coupled spin systems, dipolar-coupled spin systems, and quadrupolar nuclei. Optimizations that were restricted to a system of two coupled spins produced shapes that are useful for networks of coupled spin systems. The resultant shaped pulse sequence for dipolar time reversal, as shown in Figure 3(b), has been experimentally demonstrated to work for benzene molecules in a liquid crystal with as many as 64 energy levels.[34] (The energy level structure was not included in the optimization.) The shaped pulse sequence operates well with a peak power that is more than an order of magnitude less than the rectangular pulse experiments. In another application, shaped pulses designed for narrowband inversion of dipolar-coupled spin pairs[30] show a degree of selectivity for the coupling strength that may prove useful for imaging order in liquid crystals and polymers.

In high-resolution NMR, complicated multiple pulse sequences can be replaced with shaped pulses optimized for multilevel spin systems. This has been demonstrated in homonuclear decoupling experiments. The most effective but experimentally demanding mechanism of homonuclear coherence transfer is isotropic mixing, used in total correlation spectroscopy or TOCSY (see ***TOCSY in ROESY and ROESY in TOCSY***). Isotropic mixing allows in principle for efficient coherence transfer between all spins belonging to the same coupling network, even if spins are separated by multiple bonds. This contributes significant new information by giving rise to additional cross peaks from indirectly coupled spins that can help assign long-chain amino acids in proteins and confirm ambiguous assignments made by other methods. TOCSY uses an extended mixing period during which a suitably chosen pulse sequence suppresses chemical shift terms, leaving an effective Hamitonian with only isotropic scalar coupling terms ($\tilde{\mathcal{H}}_{\mathrm{m}} = \sum_{k<l} 2\pi J_{kl} \hat{I}_k \hat{I}_l$). A good mixing sequence allows efficient coherence transfer over a wide offset range. This is limited by the amount of available rf power and by sample heating problems associated with extended mixing sequences of high-power pulses. Thus, the TOCSY experiment is a good candidate for pulse shape optimization.

An amplitude-modulated shaped pulses sequence optimized for TOCSY has been shown[37] to outperform the conventional decoupling sequences, such as MLEV-16,[38] WALTZ-16,[39] and DIPSI-2,[40] especially at low peak powers. In addition, pulse shaping forms the basis for a chemical-shift-selective version of TOCSY. In tailored correlation spectroscopy or TACSY,[41] shaped pulses can accomplish efficient coherence transfer over a range of chemical shifts (e.g., in the aliphatic region of ^{13}C) without affecting a specified region (e.g., carbonyl resonances). Current progress in the optimization of sequences for isotropic mixing involves minimizing the effects of cross relaxation, which can decrease the amplitude of desired cross peaks. The effects are suppressed by clean TOCSY sequences which have been created by modifications to existing sequences[42] and computer optimization.[43]

6 CONCLUSIONS

Pulse shaping provides an extra degree of freedom for designing pulse sequences that has been shown to be useful in a wide variety of experimental contexts. By combining exact solutions, approximate methods, and computerized optimization, it is conceivable to create an optimized shaped pulse sequence that gives the desired spin response for most applications. Sequences of shaped pulses have overcome many 'instrumental' contraints such as peak excitation power, heating effects, and bandwidth considerations. In multilevel applications, complex multipulse sequences can be profitably replaced with simple shaped pulses.

7 RELATED ARTICLES

Average Hamiltonian Theory; Composite Pulses; Magnetic Resonance Imaging: A Historical Overview; Selective Pulses; Spin Echo Spectroscopy of Liquid Samples; TOCSY in ROESY and ROESY in TOCSY.

8 REFERENCES

1. I. I. Rabi, *Phys. Rev.*, 1937, **51**, 652.
2. W. S. Warren, *J. Chem. Phys.*, 1984, **81**, 5437.
3. J. Baum, R. Tycko, and A. Pines, *Phys. Rev. A*, 1985, **32**, 3435.
4. W. S. Warren and M. S. Silver, in *Advances in Magnetic Resonance*, ed. J. S. Waugh, Academic Press, New York, 1988, Vol. 12, p. 247.
5. A. Siegman, *Lasers*, University Science Books, Mill Valley, CA, 1986, p. 331.
6. C. Zener, *Proc. R. Soc. Lond., Ser. A*, 1932, **137**, 696.
7. L. Landau, *Phys. Z. Sowjet.*, 1932, **2**, 46.
8. M. S. Silver, R. I. Joseph, and D. I. Hoult, *Phys. Rev. A*, 1985, **31**, 2753.
9. M. A. Keniry and B. C. Sanctuary, *Chem. Phys. Lett.*, 1990, **172**, 295.
10. G. Campolieti and B. C. Sanctuary, *J. Chem. Phys.*, 1989, **91**, 2108.
11. J. W. Carlson, *J. Magn. Reson.*, 1991, **94**, 376.
12. A. Hasenfeld, S. L. Hammes, W. S. Warren, *Phys. Rev. A*, 1988, **38**, 2678.
13. D. B. Zax, G. Goelman, and S. Vega, *Phys. Rev. A*, 1989, **39**, 5725.
14. D. B. Zax, G. Goelman, D. Abramovich, and S. Vega, in *Advances in Magnetic Resonance*, ed. J. S. Waugh, Academic Press, New York, 1990, Vol. 14, p. 219.
15. M. Shinnar and J. S. Leigh, *J. Chem. Phys.*, 1993, **98**, 6121.
16. S. McDonald and W. S. Warren, *Concepts Magn. Reson.*, 1991, **3**, 55.
17. R. Freeman, *Chem. Rev.*, 1991, **91**, 1397.
18. (a) S. Connolly, D. Nishimura, and A. Macovski, *IEEE Trans. Med. Imag.*, 1989, **5**, 106; (b) D. J. Lurie, *Magn. Reson. Imag.*, 1985, **3**, 193; (c) J. B. Murdoch, A. H. Lent, M. R. Kritzer, *J. Magn. Reson.*, 1987, **74**, 226; (d) M. R. Bendall, M. Garwood, K. Ugurbil, and D. T. Pegg, *Magn. Reson. Med.*, 1987, **4**, 493; (e) E. R. Andrew and L. Latanowicz, *J. Magn. Reson.*, 1986, **68**, 232; (f) H. Geen and R. Freeman, *J. Magn. Reson.*, 1990, **87**, 415.
19. M. A. McCoy and W. S. Warren, *J. Magn. Reson.*, 1985, **65**, 178.
20. F. Loaiza, M. A. McCoy, S. L. Hammes, and W. S. Warren, *J. Magn. Reson.*, 1988, **77**, 175.
21. J. H. Gutow, M. McCoy, F. Spano, and W. S. Warren, *Phys. Rev. Lett.*, 1985, **55**, 1090.

22. M. McCoy and W. S. Warren, *Chem. Phys. Lett.*, 1987, **133**, 165.
23. C. Bauer, R. Freeman, T. Frenkiel, J. Keeler, and A. J. Shaka, *J. Magn. Reson.*, 1984, **58**, 442.
24. L. Emsley and G. Bodenhausen, *Chem. Phys. Lett.*, 1990, **165**, 469.
25. H. Kessler, S. Mronga and G. Gemmecker, *Magn. Reson. Chem.*, 1991, **29**, 527.
26. M. A. McCoy and W. S. Warren, *J. Magn. Reson.*, 1985, **65**, 178.
27. F. Loaiza, K. T. Lin, W. S. Warren, M. Silver, H. Egloff, G. Laub, and B. Kiefer, *Health Care Instrum.*, 1986, **1**, 188.
28. L. Emsley and G. Bodenhausen, *J. Magn. Reson.*, 1989, **82**, 211.
29. M. H. Levitt, in *Progress in Nuclear Magnetic Resonance Spectroscopy*, eds. J. W. Emsley, J. Feeney, and L. H. Sutcliffe, Pergamon Press, Oxford, 1986, Vol. 18, p. 61.
30. B. Ewing, S. J. Glaser, and G. P. Drobny, *J. Magn. Reson.*, 1992, **98**, 381.
31. L. Emsley, I. Burghardt and G. Bodenhausen, *J. Magn. Reson.*, 1990, **90**, 214.
32. W. Magnus, *Commun. Pure Appl. Math.*, 1954, **7**, 649.
33. C. J. Lee and W. S. Warren, *J. Magn. Reson.*, 1989, **82**, 185.
34. C. J. Lee, N. Murali, and W. S. Warren, in *Advances in Magnetic Resonance*, ed. J. S. Waugh, Academic Press, New York, 1990, Vol. 16, p. 241.
35. H. Geen and R. Freeman, *J. Magn. Reson.*, 1991, **93**, 93.
36. B. Ewing, S. J. Glaser, and G. P. Drobny, *Chem. Phys.*, 1990, **147**, 121.
37. S. Mayr, Q. He, N. Murali, and W. S. Warren, in preparation.
38. M. H. Levitt, R. Freeman, and T. Frenkiel, *J. Magn. Res.*, 1983, **47**, 328.
39. A. J. Shaka, J. Keeler, and R. Freeman, *J. Magn. Res.*, 1983, **53**, 313.
40. A. J. Shaka, C. J. Lee, and A. Pines, *J. Magn. Res.*, 1988, **77**, 274.
41. P. Schmidt, H. Schwalbe, S. J. Glaser, and C. Griesinger, *J. Magn. Reson., Ser. B*, 1993, **101**, 328.
42. D. W. Bearden, S. Macura, and L. R. Brown, *J. Magn. Res.*, 1988, **80**, 534.
43. J. Briand and R. R. Ernst, *Chem. Phys. Lett.*, 1991, **185**, 276.

Biographical Sketches

Warren S. Warren. *b* 1955. A.B., 1977, Harvard University; M.S., 1979, Ph.D., 1980, University of California, Berkeley, USA. Professor of Chemistry, Princeton University, NJ, USA. Editor, *Advances in Magnetic and Optical Resonance* (Academic Press). Approx. 100 publications. Research specialties: NMR with shaped pulses, multiple quantum NMR, NMR concentrated solution effects, and coherent laser spectroscopy.

Suzanne M. Mayr. *b* 1968. B.S., 1989, M.A., 1991, Ph.D. candidate (supervisor Warren S. Warren), Princeton University, USA. Five publications. Current research: NMR with shaped pulses.

Spectral Editing Techniques: Hydrocarbon Solids

Kurt W. Zilm

Yale University, New Haven, CT, USA

1	Introduction	1
2	Background on Spectral Editing of Liquids	1
3	Challenges Posed by Solids	1
4	Experimental Considerations and Caveats	5
5	Summary	6
6	Related Articles	6
7	References	6

1 INTRODUCTION

Spectral editing techniques in NMR in general are methods that aid the spectroscopist in assigning or simplifying complex high-resolution spectra. Most approaches to spectral editing have been developed in the context of NMR of ^{13}C where the emphasis has been on separating ^{13}C resonances on the basis of their multiplicity, i.e. the number of directly attached ^{1}Hs. This type of information, when combined with the analysis of ^{13}C chemical shifts, is very often sufficient for determining the chemical structure of rather complex organic molecules. As such, spectral editing of solution NMR finds wide application in industry for the structural characterization of polymers, drugs, and petroleum based products. Development of similar methods which are applicable to solid samples has been motivated by a large number of important applications to geochemical and material science.

This article deals with spectral editing approaches developed specifically for high-resolution solid state NMR of ^{13}C. Many different strategies have been applied to this problem, and the space provided here unfortunately does not permit covering every aspect of this subfield. Most of the relevant literature is cited in two recent papers,[1,2] and the interested reader may find more extensive citations contained therein.

2 BACKGROUND ON SPECTRAL EDITING OF LIQUIDS

The high information content of ^{13}C NMR spectra of liquids is well known. It follows directly from the large dispersion of the ^{13}C chemical shift and the remarkably tight correlation of ^{13}C chemical shifts with structure. The beautiful stick-spectrum simplicity of ^{13}C spectra is made possible by ^{1}H decoupling and the low natural abundance of ^{13}C which eliminates complications from ^{13}C–^{13}C J couplings. Their information content is greatly increased if the multiplicity of the ^{13}C resonances can be determined.

Editing techniques for ^{13}C NMR of liquids rely on the fairly narrow range of values for $^{1}J(^{13}\mathrm{C},^{1}\mathrm{H})$. This permits one to devise pulse sequences in which the evolution of the ^{13}C magnetization can be made to depend principally upon the number n of directly attached ^{1}Hs in CH_n groups. The attached proton test (APT) is the simplest example. In its most basic form, a $\pi/2$, τ, π, τ, acquire echo sequence is applied to the ^{13}C with ^{1}H decoupling during acquisition. A π pulse is also applied to the ^{1}Hs after the first τ, resulting in J modulation of the ^{13}C spin echo. During the 2τ evolution period the dephasings of the ^{13}C chemical shifts are refocused, while those due to $^{1}J(^{13}\mathrm{C},^{1}\mathrm{H})$ accumulate. Setting τ to $\frac{1}{2}J$ produces a spectrum in which the CH_3 and CH_1 resonances are inverted, while the CH_2 and CH_0 resonances are absorptive.

For complex ^{13}C spectra, more powerful methods are required, but all rely upon J couplings in some manner. In editing protocols based on INEPT, J modulation is used to label the ^{1}H magnetization which is then transferred to the ^{13}C (see ***INEPT***). The various CH_n groups can be amplitude modulated in distinct ways depending upon the length of the time evolution due to J coupling. On this basis schemes can be devised in which linear combinations of a few different experiments produce CH_3-only, CH_2-only, CH_1-only, and CH_0-only spectra. Techniques utilizing DEPT provide some improvement in selectivity, as the differentiation of CH_n groups depends upon a pulse flip angle rather than a period τ of free evolution under $^{1}J(^{13}\mathrm{C},^{1}\mathrm{H})$. Especially clean separation of CH_n subspectra has been achieved using multiple quantum coherence among the J-coupled spins. This *s*ubspectral *e*diting using a *mu*ltiple-quantum *t*rap (SEMUT) has the advantage of being relatively insensitive to the value of $^{1}J(^{13}\mathrm{C},^{1}\mathrm{H})$.

3 CHALLENGES POSED BY SOLIDS

As discussed elsewhere in the Encyclopedia, obtaining high-resolution ^{13}C spectra of organic solids requires both magic angle spinning (MAS) and high-power decoupling of the protons. These techniques are usually combined with cross polarization (CP) in a CP MAS experiment. The need to remove broadening associated with chemical shift anisotropy and ^{13}C–^{1}H dipolar couplings presents a new set of problems in the design of methods for spectral editing. Over the last 20 years of development in high-resolution NMR of solids three basic strategies have been applied to this problem. The first has been to design pulse sequences which produce J-modulated signals in solids, and thereby directly adapt the techniques just discussed to solids. The others use ^{13}C–^{1}H dipolar couplings as the basis for selection of CH_n. Some of these methods use the relative strengths of dipolar couplings or rates of CP to differentiate ^{13}C signals of different multiplicities. Others rely upon the establishment of quasi-equilibrium states in the CP process and thus differentiate the ^{13}C multiplicities on the basis of the ratio of the inverse rotating frame spin temperature of the ^{13}C to that for its directly bonded protons.

3.1 *J* Modulation in Solids

Observing resolved $^{1}J(^{13}\mathrm{C},^{1}\mathrm{H})$-coupled multiplets in CP MAS ^{13}C spectra of solids is made difficult by the strong

$^1H-^1H$ and $^1H-^{13}C$ dipolar couplings. In the absence of strong on-resonance ^1H decoupling, CP MAS spectra of typical rigid samples are broad and relatively featureless. The $^1H-^{13}C$ dipolar broadening is by itself inhomogeneous, and should therefore be suppressed by MAS. However the spin-exchange mediated by the $^1H-^1H$ dipolar couplings is faster than typical rates of MAS. Therefore the spin states of ^1H can change several times during a MAS cycle, and the average of the $^1H-^{13}C$ dipolar interaction is then no longer zero. In a simplified picture one can consider this to be a lifetime broadening of the ^{13}C resonances due to the short lifetime of the spin states of the directly attached protons. Terao and co-workers[3] first demonstrated that suppression of the $^1H-^1H$ dipolar couplings could make it possible to observe $^1J(^{13}C,^1H)$-coupled multiplets in solids. In their work, ^1H decoupling at the magic angle in the rotating frame was first used. Subsequently a number of homonuclear sequences such as MREV-8 have been applied as homonuclear multiple pulse decoupling (MPD) for this purpose. For systems such as plastic crystals where molecular motion has already appreciably averaged the dipolar couplings, MPD produces CP MAS spectra with well-resolved $^1J(^{13}C,^1H)$ coupled multiplets. The couplings observed are reduced by the scaling factor appropriate to the particular MPD sequence used.

This approach has been extended to editing schemes that most resemble those used in liquids. The basic approach is to insert MPD sequences in the periods of free evolution under $^1J(^{13}C,^1H)$. APT-type spectra of motionally narrowed solids have been acquired in this fashion, but in the general case the MPD does not produce sufficient narrowing of the proton NMR spectra to permit sustained J modulation. Terao and co-workers[4] have investigated the limitations of this approach most extensively for rigid solids. One sequence they have successfully used in producing J modulation for rigid solids consists of CP followed by a J-modulated rotor synchronized echo. During the first half of the echo, magnetization of the ^{13}C nuclei evolves under proton homonuclear decoupling. This period, t_1, is adjusted to be equal to one rotor cycle. Over the course of the rotor period J modulation accumulates, but any modulation by the $^{13}C-^1H$ dipolar coupling and the ^{13}C CSA is refocused. After the π pulse, high-power dipolar decoupling is applied for another period t_1. This second interval refocuses the isotropic chemical shift and effects of any bulk susceptibility broadening that accumulated during the first t_1 period. FIDs taken as a function of t_1 then are largely only modulated by $^1J(^{13}C,^1H)$. In this manner a 2D heteronuclear J-resolved spectrum can be obtained with multiplets in the ω_1 dimension. However this approach still does not yield clean multiplets. For instance, the outer lines in quartets for CH_3 groups are very much broader than the central pair, and they are barely resolved.

At the moment, J modulation based editing techniques for solids will remain useful only for systems with significant motional narrowing. Advances in the efficiency of homonuclear decoupling, especially under conditions of MAS, are needed before such techniques can become widely applicable. Problems also remain in combining these homonuclear decoupling requirements with the typical hardware used for CP MAS NMR. While the approach has been proven in principle, development of generally applicable methods for solids along these lines remains a challenge for the future.

3.2 Dipolar Dephasing and Related Schemes

The most generally applicable editing techniques for solids take advantage of the strong dipolar couplings inherent in solids, rather than treating them as a nuisance to be eliminated. The simplest approach to spectral editing in CP MAS NMR of organic solids is the venerable technique[5] of dipolar dephasing (DD) or interrupted decoupling. After CP, the ^1H decoupler is turned off for $\sim 50\,\mu s$. This is a sufficient time for the $^{13}C-^1H$ dipolar coupling to dephase the transverse magnetization for any ^{13}C with a directly bonded ^1H, as long as the dipolar coupling is not motionally averaged. Therefore the lines for rigid CH_1 and CH_2 groups are effectively suppressed. Rapid rotation of CH_3 groups at room temperature leads to different behavior for these protonated carbons. This rotation renders the three $^{13}C-^1H$ dipolar couplings equal, and reduces them to one-third of their static value. Depending upon the spin state of the protons, the ^{13}C in a CH_3 group can experience one of two possible dipolar fields. Whenever the three protons are in the same state ($\alpha\alpha\alpha$ or $\beta\beta\beta$), the three couplings reinforce one another, and the ^{13}C experiences the field of a single full $^{13}C-^1H$ dipolar coupling. However, three-quarters of the time the ^1Hs are in a state such as $\alpha\alpha\beta$ or $\beta\beta\alpha$. In this instance the fields due to two of the couplings will exactly cancel. The net dipolar field then is usually only one-third of a single $^{13}C-^1H$ dipolar coupling, and this is similar to that often experienced through nonbonded contacts by a CH_0. Thus, in most instances, methyl groups at room temperature behave like nonprotonated carbons under dipolar dephasing. The DD spectrum then consists of slightly attenuated resonances for just the CH_0 and CH_3 groups. Comparison with a fully polarized CP MAS spectrum provides a simple qualitative method for categorizing resonances as either CH_3 + CH_0 or CH_2 + CH_1. In many instances, a simple CP MAS spectrum can be fully assigned using this approach in combination with information from linewidth or chemical shifts.

Several approaches have been taken to improve on the basic DD technique. In some instances the dephasing interval leads to an unacceptable linear phase correction due to the delayed acquisition. A π pulse may be inserted in the interrupted decoupling interval to alleviate this to some degree. However, as first pointed out by Munowitz and Griffin,[6] the π pulse should be applied only after a full rotor period to ensure that both the isotropic and anisotropic portions of the ^{13}C chemical shift are refocused. Other groups have investigated the spin dynamics of the DD experiment with the desire to separate CH_n resonances more completely or quantitatively.[7] The approach has been to fit the dephasing of the ^{13}C resonances as a function of the dephasing time, τ_D, to some type of model dephasing function. Since it can be argued the different CH_n groups may have characteristic dephasing characteristics, this approach would seem to have some validity. In this manner one can then extrapolate back in dephasing time to recover the initial intensities of the CH_3 and CH_0 resonances.

The best way to view the DD experiment is actually as a low-resolution 1D version of separated local field (SLF) spectroscopy under MAS conditions. During τ_D the ^{13}C FID is dominated by the $^{13}C-^1H$ dipolar couplings, and is damped by the $^1H-^1H$ dipolar interactions. An isolated CH_1 group then has a decay profile that is essentially a damped Pake doublet FID, that for a CH_2, i.e. a Pake 'triplet'. Since the local structure of isolated CH_n groups of a given n does not

vary appreciably in organic solids, these decays would be quite characteristic were it not for the $^1H-^1H$ dipolar couplings. This complication can be removed by applying MPD during the dephasing interval. In this manner the number of dipolar couplings is determined from a spectral pattern, i.e. sideband intensities, rather than from a less structure-specific average dephasing rate.

The first proposal for this type of MAS SLF spectroscopy was by Munowitz and Griffin[6] as a means of measuring C–H distances. Webb and the author[8] later investigated using the spinning sideband patterns characteristic of the different CH_n groups for spectral editing. The proposed 2D experiment consists of CP followed by MPD (usually MREV-8) for t_1 to produce dipolar evolution in the first frequency dimension. This is followed by a $\pi/2(\phi_i)$, τ, $\pi/2(x)$ sequence to selectively project the ^{13}C magnetization onto one axis of the rotating frame. The period, τ, is a few hundred μs and is used to dephase magnetization not placed along z by the $\pi/2(\phi_i)$ pulse. Following the $\pi/2(x)$ pulse, the normal dipolar decoupled ^{13}C FID is acquired during time period t_2. Cycling the phase ϕ_i in a time proportional phase incrementation scheme avoids the need to acquire a quadrature data set in t_1. The sideband patterns generated this way in the ω_1 dimension retain both dipolar and CSA effects. However, at low-to-moderate field strengths the patterns are so dominated by the $^{13}C-^1H$ dipolar couplings that they can still be easily deconvolved into their CH_n components. Since CH_2 groups have two dipolar couplings, they have nearly twice as many sidebands, and are readily distinguished from CH_1 groups by this technique. Decomposition of complex CP MAS spectra with many overlapping lines has been demonstrated using this approach. At higher fields the same deconvolution methods can be applied using Munowitz and Griffin's rotor-synchronized sequence to eliminate the complications due to CSA. The requirement for delaying acquisition to several rotor periods after the initial CP interval, however, can result in substantial losses in sensitivity. A further simplification has been proposed by Sethi.[9] Since the temporal evolution during t_1 in the MAS SLF experiments is well understood, only a few special times t_1 need be acquired. Using this approach Sethi has introduced 1D editing schemes that also can be used to separate CH_1 and CH_2 resonances.

3.3 Schemes Using CP Dynamics

The previous methods rely upon the relative strengths of $^{13}C-^1H$ dipolar couplings or the different numbers of dipolar couplings to discriminate between different CH_n groups. The dipolar couplings are used essentially to dephase or modulate the ^{13}C resonances in a predictable manner. Another strategy is to use the ways in which these differences in the dipolar coupling network result in differences in the CP dynamics between the CH_n groups.

The simplest description of the CP process considers the transfer as a first-order kinetic process with a time constant T_{CH}. However, it is well known that this description is only qualitatively correct, and only phenomenologically describes the long-time behavior ($t \gg T_2$). At short CP times the Hartmann–Hahn transfer is dominated by the details of the dipolar coupling network between a ^{13}C and its directly bonded ^1Hs. In single crystals, one even observes transient oscillations in the polarization transfer. For powdered samples under moderate MAS, the transient effect manifests itself as a rapid initial period of CP transfer in which the ^{13}C and its attached ^1Hs come into a quasi-equilibrium. Spin diffusion to the more distant protons transports polarization more slowly to these ^1Hs coupled to the ^{13}C. This slower process determines the rate at which the ^{13}C reaches its final fully polarized state. In the quasi-equilibrium state, the initially unpolarized ^{13}C nuclei share the polarization equally with their directly attached protons. CH_1 and CH_2 groups then polarize to one-half and two-thirds of their full intensity, respectively, on the short timescale. Because of their motionally averaged dipolar field, CH_3 groups behave similarly to nonprotonated carbons. Both the CH_0 and CH_3 groups then polarize more slowly, with the polarization bottleneck to full enhancement usually being the rate of $^1H-^1H$ spin diffusion. As long as the transfer of transient polarization among the closely coupled spins is faster than the $^1H-^1H$ spin diffusion and direct transfer from more distant protons, it can be put to good use in spectral editing schemes.

One particularly useful approach for distinguishing the signals of $CH_1 + CH_2$ from those of $CH_0 + CH_3$ based on the previous ideas is the depolarization (DEP) technique.[10] After a several ms CP interval, the spin locked ^1H magnetization is allowed to dephase by turning off the ^1H rf for several hundred μs, while keeping the ^{13}C spin locked. Turning the ^1H rf back on reestablishes the CP contact, and the ^{13}C magnetization can be used to repolarize the depolarized ^1Hs. If the phase of the ^1H rf is switched 90° every 25–50 μs over a total period of a few hundred μs, there will be no net buildup in the ^1H magnetization, only a net drain from the ^{13}C. Since only the $CH_1 + CH_2$ carbons polarize on this timescale, their signals are fully depleted after the depolarization, while the $CH_0 + CH_3$ signals are attenuated only slightly. The resulting DEP spectrum is much like a DD spectrum. However since the ^{13}C are spin locked until the depolarization is finished, there are no problems with linear phase errors as in DD.

Polarization inversion (PI) can also be used in a similar fashion.[11] In this technique the ^{13}C are first fully polarized by CP, and the phase of the rf in the ^1H channel suddenly inverted. Since the ^1H spin temperature has now been inverted, the ^{13}C will try to follow. Those ^{13}C with strong $^{13}C-^1H$ dipolar couplings first quickly depolarize, and then repolarize in the opposite direction. Since the zero crossings for CH_1 and CH_2 groups are different, they can be used in some instances to distinguish resonances. Nulling of resonances in this manner has also been referred to as cross depolarization[12] (CPD). A further variant adds a final short polarization period onto the CPD sequence.[13] The depolarization and repolarization periods in this cross-depolarization–repolarization technique (CPDR) can be adjusted so as simultaneously to null the CH_1 and CH_2 groups. This is not in general possible with the cross-depolarization interval alone.

Sangill et al.[2] have presented a thorough study of the use of CPD and CPDR in spectral editing. Their analysis focused on using optimized combinations of CPD and CPDR spectra to produce CH_n-only spectra, $n = 0–3$, while maintaining good sensitivity. By paying careful attention to the CP dynamics, they were able successfully to separate complex CP MAS spectra into their CH_n subspectral components.

Burum and Bielecki[14] have introduced a particularly clever method based on CP dynamics for selectively detecting CH_2

groups in CP MAS NMR. Their method, WIMSE (*w*indowless *i*sotropic *m*ixing for *s*pectral *e*diting), starts with a CP interval under a multiple pulse cycle which eliminates the $^1H-^1H$ dipolar couplings during the CP step while maintaining the $^{13}C-^1H$ couplings. Over a MAS rotor period under these conditions, no net polarization is transferred to ^{13}C nuclei in CH groups. Instead, whatever magnetization is transferred at the start of the rotor cycle 'echoes' back from the ^{13}C to the ^1H at the end. However, the presence of two dipolar couplings in a CH_2 group defeats this 'rotational polarization echo' effect. The resulting spectrum then consists solely of the CH_2 component in a complex CP MAS spectrum. CH_3 and CH_0 lines do not appear as their CP rates are too slow.

3.4 Techniques Using Quasi-Equilibrium States

Another successful method based on differences in CP dynamics between the different CH_n groups is the solid state attached proton test, or SSAPT method. Initially the ^{13}C are fully polarized using a 2–3 ms CP interval. Immediately following this, a short PI period is applied, typically on the order of 50 μs. At the beginning of the PI time the ^{13}C and their directly attached ^1Hs are equally polarized. Upon reversal of the phase in the ^1H spin locking rf, this equilibrium is broken, and the spins try to reequilibrate. Since the CH_3 and CH_0 groups polarize slowly, they are relatively unaffected by this short PI interval. The CH_2 and CH_1 groups, on the other hand, have sufficient time to reach a quasi-equilibrium state through a rapid transient CP transfer. In the case of the CH_1 group, the ^{13}C and the ^1H have equal but opposite polarizations at the start of the PI. During the short PI time these magnetizations cancel, and the signal for the CH_1 carbons is very effectively nulled. The ^{13}C nuclei in the CH_2 groups carry 1 unit of polarization as opposed to the -2 units in the ^1Hs at the beginning of the PI interval. This results in -1 unit of total polarization to be shared among the three spins in the quasi-equilibrium state. At the end of the PI period, the CH_2 signal is then inverted with an intensity of $-\frac{1}{3}$ of its fully polarized signal. The SSAPT spectrum then has CH_3 + CH_0 signals nearly fully polarized and positive, CH signals nulled, and CH_2 signals inverted at one-third intensity. In many instances this provides a very straightforward means of separating the contributions from the different CH_n groups to a ^{13}C CP MAS spectrum.[15,16]

This approach has been extended to a complete spectral editing protocol by Wu, Burns, and the author.[1] Since the establishment of the quasi-equilibrium state depends upon the ratio of the inverse rotating frame spin temperatures of the ^{13}C and its directly bonded ^1Hs, this technique is less sensitive to the CP rates. In this sense it is a relatively robust editing procedure.

The complete spectral editing procedure due to Wu et al. uses four basic experiments (see Figure 1). One begins by acquiring a CH_2-only spectrum. The sequence used starts with a short CP contact which polarizes the CH and CH_2 groups to their quasi-equilibrium intensities of $\frac{1}{2}$ and $\frac{2}{3}$ respectively. This is followed by a short PI interval of roughly the same length. During PI the CH signals null, as does any small CH_3 or CH_0 polarization built up during the CP step. The CH_2 ^{13}C magnetization goes to $-\frac{1}{3}$ of its initial value, resulting in a spectrum with $-\frac{2}{9}$ the intensity for these carbons. This

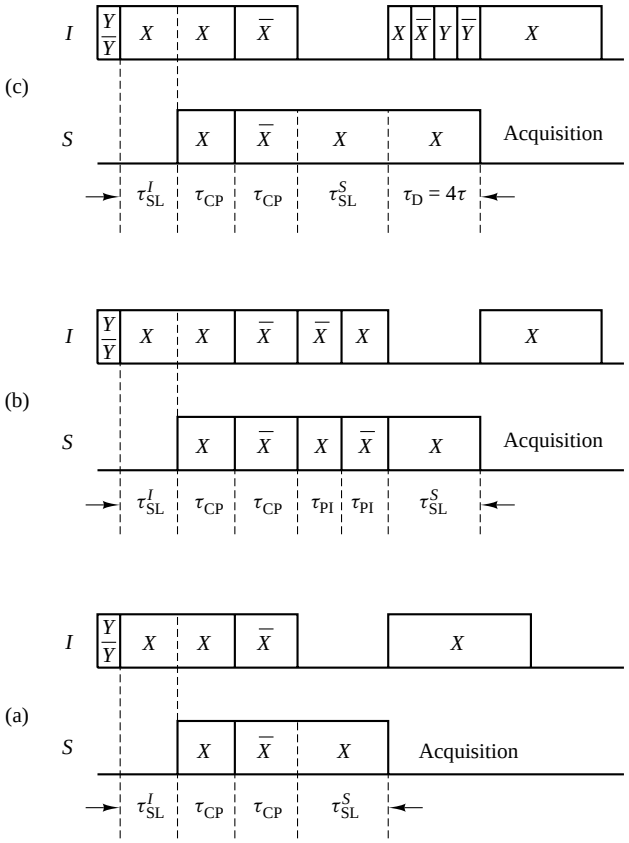

Figure 1 Sequences used in the editing protocol of Wu et al. All employ simultaneous phase inversion to alleviate problems with Hartmann–Hahn mismatches. (a) CP sequence. The additional spin locking delay τ_{SL}^S is used to make the total ^{13}C spin locking time the same in all of the sequences. (b) SCPPI sequence used to acquire CH_2-only spectra. (c) Depolarization sequence. The time τ_{SL}^I is added in these sequences mainly to minimize distortions from ^1H rotating frame relaxation

short CP polarization inversion (SCPPI) spectrum then has contributions from only the CH_2 groups.

The second experiment is a short contact CP (SCP). This will have intensity principally from the CH and CH_2 carbons. Another short CP spectrum with a depolarization interval is also acquired (SCPD). The SCPD spectrum can be used to subtract out the contamination of the SCP data from CH_3 and CH_0 groups. Unfortunately the CH_3 and CH_0 carbons have sufficiently different CP dynamics that they are differentially attenuated, and this subtraction alone is insufficient. In most instances, however, the shift ranges for CH_3 and CH_0 groups are adequately separated so that a dividing line on the ^{13}C chemical shift scale can be chosen to separate these groups. Different weighting factors can then be applied to the upfield (CH_3) and downfield (CH_0) regions for this purpose. The result of this procedure is a relatively clean CH-only spectrum.

To acquire semiquantitatively correct CH_0 and CH_3 spectra, a long CP depolarization spectrum is acquired (LCPD). This spectrum is again split into CH_0 and CH_3 regions, and each part corrected for the differential signal loss of the two types of groups in the depolarization step.

The cleanest and most quantitative results are obtained with this method if the intensity factors for spectral decomposition are determined experimentally on a known model system.

Table 1 Typical Intensities for CH_n Resonances in Pulse Sequences Used for Spectral Editing

	CH_n			
Experiment	CH_0	CH_1	CH_2	CH_3
LCP	100	100	100	100
SCP	10.5	57.5	68	22.6
SCPPI	0	0	−22	0
SCPD	7.2	0	0	10.4
LCPD	82.5	0	0	57.5

Using the set of sequences shown in Figure 1, the intensity matrix in Table 1 is found to be typical. LCP is used to denote a standard (long) CP experiment which is used as the 100% intensity reference.

As the entries demonstrate, the CH and CH_2 group intensities in the SCPPI and SCP experiments are quite close to those expected from the quasi-equilibrium description of the CP dynamics.

Figure 2 compares the four spectra acquired in the editing protocol for cholesteryl acetate to the normal CP MAS spectrum. In the solid state there are two molecules in the unit cell producing a doubling of the lines. Furthermore, changes in conformation lead to significant shifts in many resonances. Using the intensity matrix in Table 1, the CH_n, $n = 0-3$, only spectra can be reconstructed from these data. The results of this data manipulation are shown in Figure 3, clearly demonstrating the simplifications made possible by this spectral editing approach. As a check on this editing protocol, one may sum the CH_n subspectra to produce a synthetic CP MAS spectrum. This is compared with the normal CP MAS spectrum in Figure 4, along with the difference of the two. The small differences observed indicate the reliability of the approach used.

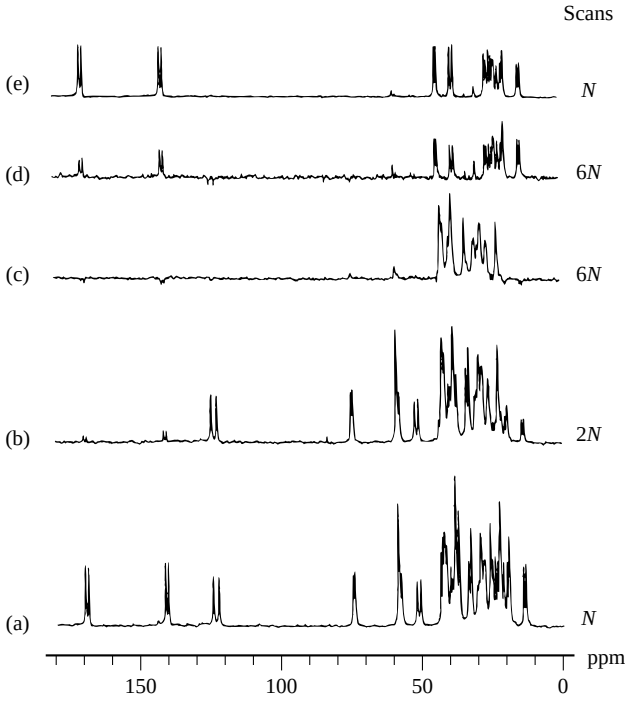

Figure 2 Data from a spectral editing experiment on cholesteryl acetate. (a) Normal CP spectrum for comparison. (b) SCP spectrum. (c) SCPPI spectrum. (d) SCPD spectrum. (e) LCPD spectrum. In practice larger numbers of scans are acquired for the lower signal-to-noise experiments as indicated in the figure

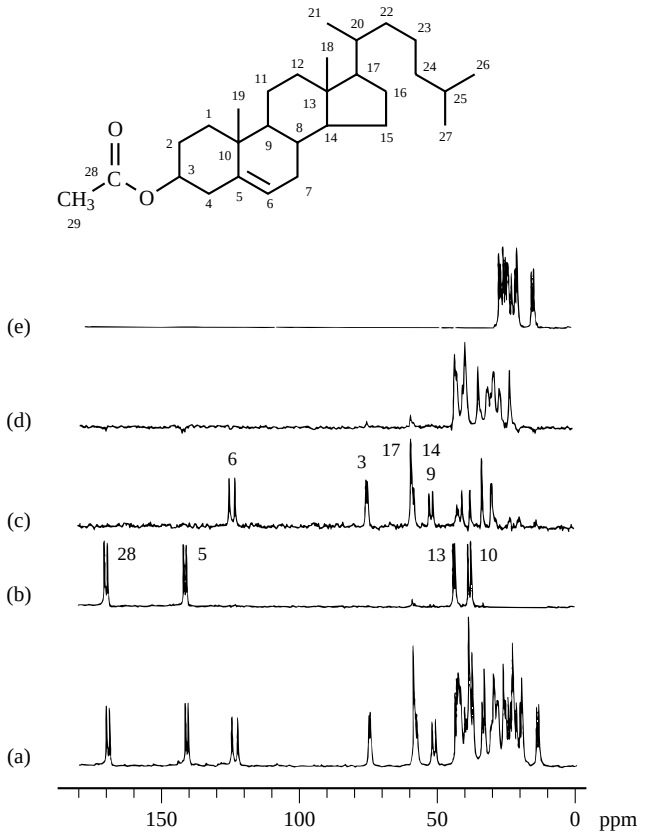

Figure 3 Subspectra constructed from the data in Figure 2. (a) Normal CP MAS spectrum again for comparison. (b) CH_0-only. (c) CH_1-only. (d) CH_2-only. (e) CH_3-only. Some of the assignments made possible by the editing technique are given in the inset

4 EXPERIMENTAL CONSIDERATIONS AND CAVEATS

Except for the simplest approaches to spectral editing in solids, one must pay some extra attention to the experimental setup. In particular, very high MAS spin rates and rf inhomogeneity can adversely affect the CP dynamics relied upon in most methods. The sharpening of the Hartmann–Hahn condition, and the need to match typically on a sideband condition, $\omega_1 = \omega_2 + \omega_r$, makes a homogeneous rf field more important than in a standard CP MAS experiment. Good experimental practice requires stable rf levels, restricting the sample to well within the rf coil, and a stable spin rate. For experiments utilizing short CP, PI, or depolarization periods, additional modifications that make the matching condition less sensitive are needed. Our group has found the simultaneous phase inversion method[1,14,15] easy to incorporate in editing schemes. The pulse sequences in Figure 1 utilize this approach to make the results much less sensitive to how well the matching condition is set and maintained throughout the experiment.

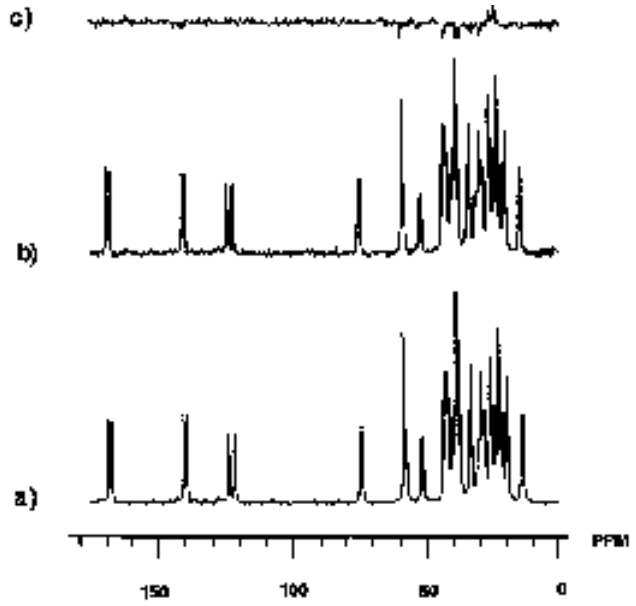

Figure 4 Comparison of the (a) normal CP MAS spectrum and (b) the synthetic one produced by direct summation of the subspectra in Figure 3(b)–(e). (c) The difference between the normal and synthetic CP MAS spectra

When spectra are to be combined in an editing procedure, it is also important to consider rf heating, droop in the rf levels, and $T_{1\rho}$ relaxation. Whenever possible, it is a good practice then to keep the rf fields on for comparable periods of time in the different experiments to be combined. The sequences in Figure 1 have been constructed to take these additional complications into account. Table 2 gives the set of delays in reference to Figure 1 that have been found to give optimal performance in editing applications on rigid solids at moderate fields and MAS rates. These parameters have been used and tested in applications to many coals and polymers as well as on model systems.

Methods which employ homonuclear decoupling sequences require additional care in spectrometer alignment. For these methods one must more carefully adjust all rf levels, and pay especial attention to rf homogeneity. In practice one must follow the same procedures as used to prepare for a ^{1}H CRAMPS experiment. Similar complications from the interaction of the MAS and the MPD also occur as found in CRAMPS.

The majority of the methods that have been discussed here rely on differences in the dipolar coupling networks found between the various CH_n groups. These are washed out when there is significant motional averaging, and as such all of these methods have limitations. On the other hand, such motional narrowing has many signatures which are easy to recognize, and provides another means of discriminating between resonances in a complex spectrum. When very fast MAS rates are employed, the spin dynamics also change.[17] Most methods presented here work best at low to moderate MAS rates (5 kHz or below). Additional complications can arise at high fields because of the CSA spinning sidebands. Since different molecular orientations with respect to the rotor contribute more intensity to some sidebands than others, the inhomogeneous nature of the CP dynamics can be accentuated. Under many editing schemes the center and sidebands can then behave differently, complicating analysis. In the light of these difficulties, most applications to complex systems have employed low field operation ($B_0 < 4$ T). Additional work is needed to delineate how high-field and high-speed MAS operation can be accommodated with the majority of these methods.

Table 2 Delay Parameters for Spectral Editing

	Delay (μs)				
Experiment	$\tau_{SL}{}^I$	$2\tau_{CP}$	$2\tau_{PI}$	$\tau_{SL}{}^S$	τ_D
LCP	140	1500	0	400	0
SCP	1600	40	0	400	0
SCPPI	1600	40	35	365	0
SCPD	1600	40	0	300	100
LCPD	140	1500	0	300	100

5 SUMMARY

At present there are many methods available for distinguishing CH_3 + CH_0 groups from CH and CH_2 centers in CP MAS spectra. A number of reliable approaches for separating CH and CH_2 groups have also appeared, and some of these have been combined in complete spectral editing protocols which separate resonances by multiplicity. These methods have many applications in organic geochemistry and polymer science. Further advances are required before most of these techniques can be combined with operation at the highest available field strengths and spin rates.

6 RELATED ARTICLES

CRAMPS; Cross Polarization in Rotating Solids: Spin-1/2 Nuclei; Cross Polarization in Solids; Fossil Fuels; Heteronuclear Assignment Techniques; INEPT; Magic Angle Spinning; Quantitative Measurements; Rotating Solids; Solid State Probe Design; Spin Echo Spectroscopy of Liquid Samples.

7 REFERENCES

1. X. Wu, S. T. Burns, and K. W. Zilm, *J. Magn. Reson. Ser. A*, 1994, **107**, in press.
2. R. Sangill, N. Rastrup-Andersen, H. Bildsøe, H. J. Jakobsen, and N. C. Neilsen, *J. Magn. Reson. Ser. A*, 1994, **107**, 67.
3. T. Terao, H. Miura, and A. Saika, *J. Chem. Phys.*, 1981, **75**, 1573.
4. H. Miura, T. Terao, and A. Saika, *J. Chem. Phys.*, 1986, **85**, 2458.
5. M. Alla and E. Lippmaa, *Chem. Phys. Lett.*, 1976, **37**, 260.
6. M. G. Munowitz and R. G. Griffin, *J. Chem. Phys.*, 1982, **76**, 2848.
7. L. B. Alemany, D. M. Grant, R. J. Pugmire, T. D. Alger, and K. W. Zilm, *J. Am. Chem. Soc.*, 1983, **105**, 2133.
8. G. W. Webb and K. W. Zilm, *J. Am. Chem. Soc.*, 1989, **111**, 2455.
9. N. K. Sethi, *J. Magn. Reson.*, 1991, **93**, 265.

10. X. Wu, S. Zhang, and X. Wu, *Chem Phys. Lett.*, 1989, **162**, 321.
11. X. Wu, S. Zhang, and X. Wu, *J. Magn. Reson.*, 1988, **77**, 343.
12. M. T. Melchior, *22nd Exp. NMR Conf., Asilomar, CA, March 1991*, poster B-29.
13. J. S. Hartman and J. A. Ripmeester, *Chem. Phys. Lett.*, 1990, **168**, 219.
14. D. P. Burum and A. Bielecki, *J. Magn. Reson.*, 1991, **95**, 184.
15. X. Wu and K. W. Zilm, *J. Magn. Reson., Ser. A*, 1993, **104**, 119.
16. X. Wu and K. W. Zilm, *J. Magn. Reson., Ser. A*, 1993, **102**, 205.
17. X. Wu and K. W. Zilm, *J. Magn. Reson., Ser. A*, 1993, **104**, 154.

Acknowledgments

I wish to acknowledge the especially important contributions of two of my colleagues in this field. The first is Dr Gretchen Webb, my first graduate student, who was instrumental in working out 2D MAS SLF methods for editing, as well as developing much of the hardware that still makes these experiments work so well in our laboratory. The second is Dr Xiaoling Wu, my long-time associate, collaborator, and friend. It is because of Xiaoling's experimental acumen and theoretical insight that our laboratory has been able to contribute so successfully to the development of spectral editing methods for solids.

Biographical Sketch

Kurt W. Zilm. *b* 1955. B.S., 1976, Ph.D., 1981, University of Utah. Introduced to NMR by D. M. Grant. Faculty in Chemistry Yale University, 1983–present. Approx. 80 publications. Research interests: theory and development of NMR techniques for solving problems of chemical interest, studies of transition metal polyhydrides, supported metal catalysts, matrix-isolated organic intermediates and metal clusters, applications of optical pumping in gas phase NMR, tunneling in NMR, dipolar demagnetizing field effects in NMR and development of new solids NMR techniques for structural studies in polymers and organic geochemistry.

Stochastic Excitation

Bernhard Blümich
Rheinisch-Westfälische Technische Hochschule Aachen, Aachen, Germany

1 Introduction 1
2 Excitation and Response 2
3 Cross Correlation 3
4 Imaging 5
5 Interference 7
6 Quo Vadis? 8
7 Related Articles 9
8 References 9

1 INTRODUCTION

Stochastic excitation is used for heteronuclear broadband decoupling in liquid state NMR and as a way to acquire spectra. This article is devoted to the second topic, which is known by the name of stochastic NMR spectroscopy.

1.1 Early History

The use of stochastic excitation in NMR has been a topic of continuous interest since the late 1950s. The idea of exploring noise in NMR goes back to two sources.

1. In Switzerland, Hans Primas was intrigued by the Wiener theory of nonlinear systems[1] and its consequences for NMR in the context of hole burning. The subsequent investigations of quantum mechanical systems with a stochastic Hamiltonian eventually led to the Habilitation work of Primas[2,3] and to the Dissertation work of Richard Ernst.[4]
2. In the USA, noise was mentioned among other forms of excitation in a patent by Russel Varian relating to ways of improving the relative frequency stability of NMR spectrometers as well as the signal-to-noise ratio of NMR spectra.[5] In 1966 stochastic excitation was put to practical use as a method for heteronuclear decoupling in high-resolution NMR.[6]

After the introduction of Fourier transform (FT) NMR in 1966,[7] methods were sought that would keep the multiplex advantage of FT NMR but in addition would allow independent adjustment of sensitivity and resolution. It was Richard Ernst who pointed out that this could be achieved by using stochastic excitation,[8] and he, as well as Reinhold Kaiser, published the first experimental stochastic NMR spectra in subsequent papers of the same issue of the *Journal of Magnetic Resonance* in 1970.[9,10]

1.2 Noise

The type of noise most suitable for excitation in NMR is still being discussed. Many variants are conceivable: binary noise, which can assume two values with equal probability quaternary noise, which can assume four values with different probabilities, and noise with a Gaussian probability distribution, to name but a few. These types of noise can be used to modulate the rf excitation in amplitude or in phase or in both parameters. Most experiments so far have used binary and quaternary white noise excitation either as pure amplitude or as four-valued phase modulation. To complicate the choice, the question of what white means can readily be answered for excitation of the linear response by the shape of the first-order autocorrelation function or its Fourier transform, the power spectral density. Ideally, the power spectral density should be a constant differing from zero and extending from minus infinity to plus infinity for white noise. But as soon as the response becomes nonlinear, higher order autocorrelation functions of the excitation need to be investigated.[11] On the other hand, the noise may deliberately be colored for selective excitation or suppression of particular frequency regions. This was demonstrated by Tomlinson and Hill in 1973.[12]

1.3 Linear Response

A particularly suitable type of noise for excitation of the linear response was investigated independently by Ziessow[13,14] and Kaiser:[15] If so-called m-sequences or maximum length binary sequences are used for excitation, the discrete power spectrum of the excitation is constant, just like that of a delta function pulse. This is remarkable insofar as the power spectrum of ordinary zero-mean white noise is again a noise signal. Only its mean value differs from zero, but its variance is as great as its mean. Increasing the length of such a noise sample will not change the variance of the power spectrum—only the spectral resolution will change.[16] This is a manifestation of the well-known fact that the Fourier transform of white noise is an inconsistent estimate of the power spectral density. Therefore, ordinary stochastic NMR spectra are always contaminated by systematic noise.[17] When m-sequences are used, this is not the case, and the NMR spectrum can be calculated by successive applications of the Hadamard transformation and the Fourier transformation. For this reason, this type of stochastic NMR is known as Hadamard NMR. In general, the linear response is processed to conventional 1D spectra, unless, in the presence of magnetic field gradients, it is processed to a projection of the object.[18]

1.4 Nonlinear Response

With the introduction of two-dimensional NMR in 1976, it was clear that similar spectra should also be obtainable with stochastic excitation. How this can be done eventually became my dissertation with Dieter Ziessow in Berlin.[19] This work has been reviewed on a number of occasions.[20–22]

The theoretical treatment of stochastic excitation was complicated by the requirement of solving stochastic differential equations,[9,23] and eventually Reinhold Kaiser and the mathematician Bill Knight succeeded in providing solutions, which showed the correct power dependence of stochastic NMR spectra.[24,25] These studies were later refined in the context of NMR imaging with stochastic excitation.[26,27]

1.5 The Use of Stochastic Excitation

Up to now, stochastic excitation has not become a widely accepted technique in magnetic resonance for various reasons. One objection is a seemingly complicated theory. We are used to the vector representation of pulsed NMR, and the use of correlation integrals requires additional training. But more severe objections are that the manifold of tailored experiments is rather limited, and that most stochastic NMR spectra are contaminated by systematic noise. The dramatic power saving that stochastic excitation provides seems to be of little interest for most NMR applications. This is not so, however, for NMR imaging at high fields[28–30] and for investigations of large objects by EPR,[31] NMR, and NQR. In addition, novel types of non-white-noise excitations such as a time-shifted sum excitation (see below) can provide improved signal-to-noise ratios at known low power levels.[31,32] Therefore, a valid interest beyond pure scientific curiosity remains. But, though the enthusiastically envisioned general applicability of the technique has not come to pass, its investigation in NMR provides detailed insight into nonlinear incoherent spectroscopy (NOISY), which has interesting potential for realizations of 2D spectroscopy in the optical frequency regime by interferometric techniques.[32]

In the following discussion, the principles of stochastic excitation will be summarized, experimental examples will be given, and topics of current research will be addressed.

2 EXCITATION AND RESPONSE

Figure 1 illustrates what typical excitation and response signals look like.[9] In this case, the excitation $x(t)$ (top) is binary noise, i.e., a signal that fluctuates at random between two values. In practice, these two values are assigned to flip angles $+\alpha$ and $-\alpha$ of a string of closely spaced rf excitation pulses. One pulse is applied at the beginning of each sampling interval, and, right before the next pulse, one value of the response $y(t)$ (bottom) is sampled. Thus, there is a one-to-one correspondence between excitation and response values. The use of pulses for excitation and the principle of time sharing between excitation and response are similar to FT NMR, but the durations of excitation and response, extending in principle from minus to plus infinity, are similar to continuous wave (CW) NMR. But, for practical reasons, time sharing is restricted to spectral widths smaller than about 100 kHz. For larger spectral widths, schemes that permit simultaneous detection of excitation and response, like the use of magnetic field modulation[10] and crossed transmitter and receiver coils must be considered.

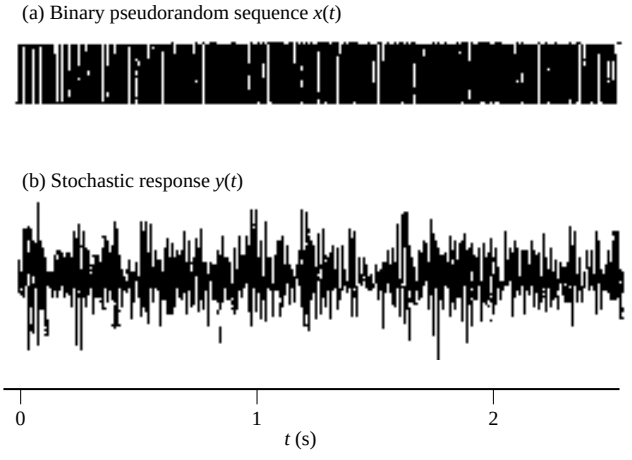

Figure 1 Binary excitation sequence $x(t)$ (a) and the corresponding stochastic response $y(t)$ (b) of the ^{19}F resonance of 40 vol% 2,4-difluorotoluene at a frequency of 56.4 MHz.[9]

The formal description of stochastic NMR is based on the Volterra and Wiener theories, which describe the relationship between excitation and response of nonlinear systems in general.[33] The system to be characterized is represented by a 'black box', which transforms an input signal into an output signal. Because the system is unknown, a perturbation expansion is followed, which applies to the general input for the Volterra approach and to Gaussian white noise for the Wiener approach. The shortcoming of the Volterra approach is the perturbative treatment, because the NMR response often is highly nonlinear [see Figure 2(a)] and the convergence of the perturbation analysis breaks down at high excitation levels.

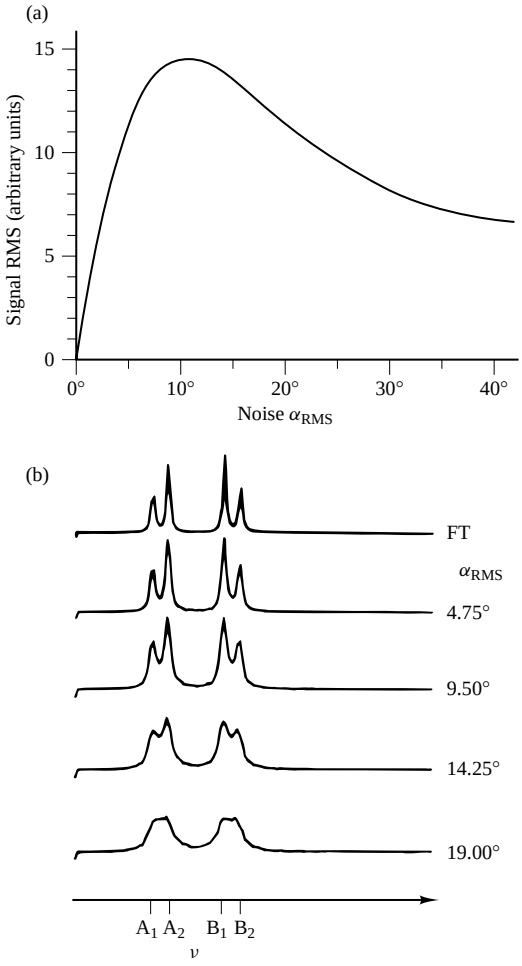

Figure 2 (a) Saturation of the transverse magnetization (signal RMS) as a function of the excitation level, demonstrating the nonlinearity of the response as a function of the excitation amplitude. (b) Simulated single pulse response spectra (FT, top) and stochastic 1D spectra for different excitation levels α_{RMS}, denoting the RMS flip angle of the excitation pulses with a white Gaussian distribution

2.1 The Volterra Series

The general system response $y(t)$ is expanded in a series of increasing powers of the excitation $x(t)$.[34] Because physical systems have memory, integrals over the memory times have to be incorporated. This results in the Volterra series

$$\begin{aligned} y(t) = k_0 &+ \int_{-\infty}^{\infty} k_1(\tau)x(t-\tau)\,\mathrm{d}\tau \\ &+ \int_{-\infty}^{\infty}\int_{-\infty}^{\infty} k_2(\tau_1,\tau_2)x(t-\tau_1)x(t-\tau_2)\,\mathrm{d}\tau_2\,\mathrm{d}\tau_1 \\ &+ \int_{-\infty}^{\infty}\int_{-\infty}^{\infty}\int_{-\infty}^{\infty} k_3(\tau_1,\tau_2,\tau_3)x(t-\tau_1)x(t-\tau_2) \\ &\times x(t-\tau_3)\,\mathrm{d}\tau_3\,\mathrm{d}\tau_2\,\mathrm{d}\tau_1 + \ldots \end{aligned} \tag{1}$$

The second term in equation (1) is a linear convolution integral, and the higher order terms are nonlinear convolution integrals of kernel functions $k_n(\tau_1, \ldots, \tau_n)$ with the nth-order product of the excitation at times $t - \tau_i$, where $1 \leq i \leq n$. These kernel functions are memory functions that correlate n events at times τ_i in the past, and they are characteristic of the system under investigation. Thus, the goal in characterizing the system is to determine these memory functions.

The first term, k_0, is just a dc (direct current) term, which can be neglected in practice. Then, for a linear system, only the second term is relevant. Here, $k_1(\tau)$ or its Fourier transform, $K_1(\omega)$, are readily determined by the familiar excitation signals from NMR. In CW NMR, the excitation $x(t) = x_0 \exp(i\omega t)$ is a continuous wave, so that $K_1(\omega)$ is measured directly. Thus, $K_1(\omega)$ is equivalent to the conventional 1D NMR spectrum. In 1D FT NMR, the excitation $x(t) = x_0\delta(t)$ is a delta function pulse, giving $k_1(t)$. Thus, $k_1(t)$ corresponds to an FID signal. Correspondingly, $k_n(\tau_1, \ldots, \tau_n)$ is the Fourier transform of an nD NMR spectrum. With respect to NMR, the odd orders of equation (1) apply to transverse magnetization and the even orders to longitudinal magnetization. Thus, in most cases, only odd-order terms need be considered—in particular, the linear and cubic terms.

2.2 The Wiener Series

The Volterra series in equation (1) was adapted by Wiener for zero-mean Gaussian white noise excitation.[1] With the original goal in mind of describing the system response with improving accuracy by incorporation of higher order terms, it is advantageous to orthogonalize the Volterra functionals. Then, neglecting even-order terms, the Wiener series can be derived from the Volterra series:

$$\begin{aligned} y(t) = &\int_{-\infty}^{\infty} h_1(\tau)x(t-\tau)\,\mathrm{d}\tau \\ &+ \int_{-\infty}^{\infty}\int_{-\infty}^{\infty}\int_{-\infty}^{\infty} h_{3s}(\tau_1,\tau_2,\tau_3)x(t-\tau_1)x(t-\tau_2) \\ &\times x(t-\tau_3)\,\mathrm{d}\tau_3\,\mathrm{d}\tau_2\,\mathrm{d}\tau_1 \\ &-3\mu_2\int_{-\infty}^{\infty}\int_{-\infty}^{\infty} h_{3s}(\tau_1,\tau_2,\tau_2)x(t-\tau_1)\,\mathrm{d}\tau_2\,\mathrm{d}\tau_1 + \ldots \end{aligned} \tag{2}$$

Here, the second moment μ_2, or the power of the noise excitation, appears.

The leading terms of the Wiener and Volterra series are similar. For the Wiener kernels, the symbol $h_{ns}(\tau_1, \ldots, \tau_n)$ has been used for discrimination from the Volterra kernels $k_n(\tau_1, \ldots, \tau_n)$, because as a result of the orthogonalization the kernels become dependent on the excitation power, and their Fourier transforms exhibit changes in linewidths and amplitude [Figure 2(b)], which are similar to saturation features observed in CW NMR, except, that they are also observed in multidimensional stochastic spectra.[19] Also, an additional index s for 'symmetric' has been attached to the Wiener kernels, because they are often taken to be invariant under permutation of time arguments. This is mathematically convenient, but it violates the principle of causality, which becomes evident when the kernels are analyzed in terms of quantum mechanics (see below).

3 CROSS CORRELATION

The way to arrive at NMR spectra in stochastic NMR is by comparison of excitation and response records. Mathematically, a comparison is achieved by cross correlation, because the amplitude of the cross-correlation function is high, whenever the cross-correlated signals are similar. Because one is dealing with nonlinear response signals, nonlinear cross-correlation functions become of interest. The cross correlation of order n produces an n-dimensional function

$$\begin{aligned} c_n(\sigma_1,\ldots,\sigma_n) &= \lim_{T\to\infty}\frac{1}{2T}\int_{-T}^{T} y(t)x^*(t-\sigma_1)\ldots x^*(t-\sigma_n)\,\mathrm{d}t \\ &= n!\mu_2^n h_n(\sigma_1,\ldots,\sigma_n) \end{aligned} \tag{3}$$

where * denotes the complex conjugate. The cross correlation function is defined in a time−displacement space, where the displacements σ_n count from the present t into the past (see Figure 3). Interestingly, as long as none of the time arguments are equal, the second equality holds, and the cross-correlation function is proportional to the Wiener kernel.[35]

For acquisition of the stochastic response in NMR, the multiplex advantage applies, similarly to pulsed FT NMR.[36] But in multidimensional pulsed FT NMR, it applies to only one dimension, because the indirectly detected dimensions are scanned in a pointwise fashion. For the nonlinear Wiener kernels and their Fourier transforms, it applies to all dimensions in principle, because complete kernels can be calculated from a single record of input and output data. What limits the practical exploitation of the multidimensional multiplex advantage is the current unavailability of a suitable algorithm to derive the higher order Wiener kernels from finite-length excitation and response records free of systematic noise.

3.1 Quantum Mechanical Interpretation

The nonlinear cross-correlation functions and, by equation (3), the Wiener kernels, have been calculated in Liouville space.[24,25] It turns out that they can be interpreted in terms of a multipulse response reminiscent of multidimensional FT NMR. This is illustrated in Figure 3 together with the Liouville space expression of c_3. Time proceeds from right to left. Instead of a thermodynamic equilibrium density matrix $\hat{\rho}_\infty$ the density matrix $\hat{\rho}'_\infty$ in equilibrium with the uninterrupted stochastic excitation appears. $\hat{\hat{B}}$ is a superoperator that is the first-order term of the pulse rotation operator. Thus, it is referred to as the pseudopulse operator. It changes the

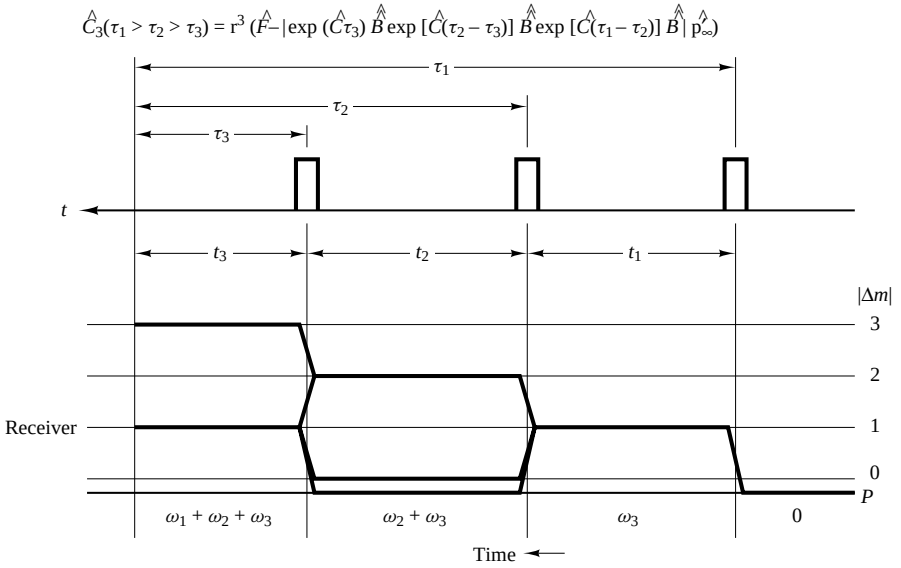

Figure 3 Liouville-space expression for the third-order correlation function (top) and graphical interpretation (middle) in terms of a 3D experiment with pseudopulse excitation. Each pseudopulse $\hat{\hat{B}}$ induces transitions by $|\Delta m| = 1$ in the density matrix, giving rise to the coherence transfer diagram depicted at the bottom. Note that time proceeds from right to left

coherences in a given response order of the density matrix by exactly $\Delta m = \pm 1$. $\hat{F}_-$ is the operator describing quadrature detection, and exp $(\hat{C}t)$ is the Liouville operator for the nuclear spin precession around the z axis with saturation effects included, which derive from the continuous presence of the excitation. For weak excitation, exp $(\hat{C}t)$ approaches the operator of the free induction decay. The remaining difference from multidimensional pulse NMR is the nomenclature for the time variables. In stochastic NMR, the natural quantities are the time displacements σ_i or τ_i from the present t to the event (pseudopulse) in the past, while in pulse NMR, the pulse separations t_i are used.[37,38]

The interpretation of the correlation function in terms of successive pairs of pseudopulse operators $\hat{\hat{B}}$ and evolution operators exp $(\hat{C}t)$ leads to an intuitive understanding of correlation functions in stochastic NMR.[36] For example, for fixed t_1 and very short t_2, the stochastic equivalent of the $90^\circ - t_1 - 180^\circ - t_3$ excitation is obtained, and an echo is observed for $t_3 = t_1$ in the respective 1D cross-section through the third-order correlation function (Figure 4).[31,39]

From the pseudopulse interpretation of correlation functions, it is clear that the time shifts σ_i and τ_i are time-ordered by causality (see Figure 3). Nevertheless, the Wiener approach is based on symmetric kernels $h_{ns}(\sigma_1, \ldots, \sigma_n)$. Here, the time order has been lifted by sweeping the delays in the cross-correlation function, equation (3), through equal ranges, independent of each other, though the complete information is already obtained in the section of 3D time–displacement space,[38] where, for instance,

$$\sigma_1 \geq \sigma_2 \geq \sigma_3 \tag{4}$$

3.2 Frequency Domain

Fourier transformation of the cross-correlation expression in equation (3) and use of the Wiener series expansion in equation (2) for the system response $y(t)$ leads to expressions by which the Fourier transforms of the kernels $h_{ns}(\sigma_1, \ldots, \sigma_n)$ can be evaluated. This is convenient in practice, because the fast Fourier transformation algorithm can be used, and higher order stochastic NMR spectra can be evaluated at the frequency regions of interest only. For practical purposes, this is particularly important for evaluation of the third order response in terms of a 3D spectrum $H_{3s}(\omega_1, \omega_2, \omega_3)$. Denoting time domain expressions by lower case letters and frequency domain expressions by capital letters, one obtains

$$H_1(\omega) = \frac{\langle Y(\omega) X^*(\omega) \rangle}{\langle |X(\omega)|^2 \rangle} \tag{5}$$

$$H_{3s}(\omega_1, \omega_2, \omega_3) = \frac{\langle Y_3(\omega_1 + \omega_2 + \omega_3) X^*(\omega_1) X^*(\omega_2) X^*(\omega_3) \rangle}{3! \langle |X(\omega_1)|^2 \rangle \langle |X(\omega_2)|^2 \rangle \langle |X(\omega_3)|^2 \rangle} \tag{6}$$

where

$$Y_3(\omega) = H_1(\omega) X(\omega) \tag{7}$$

With reference to equation (3), the second moment μ_2 of the excitation has been replaced by the mean power spectral density $\langle |X(\omega|^2 \rangle$. The angle brackets denote ensemble averages over excitation and response sample spectra, respectively, to reduce the variance of the stochastic response, which manifests itself in terms of systematic noise in stochastic NMR spectra. In fact, this systematic noise is a severe limitation on practical use of the technique. Therefore, considerable effort has been spent in devising schemes alternative to equations (5)–(7) that extract the Fourier transforms of the Wiener kernels at better ratios of signal to systematic noise.

3.3 Experimental Examples

The Wiener theory is applicable to the analysis of nonlinear systems with zero-mean Gaussian white noise excitation. The optimum excitation power is determined by the maximum

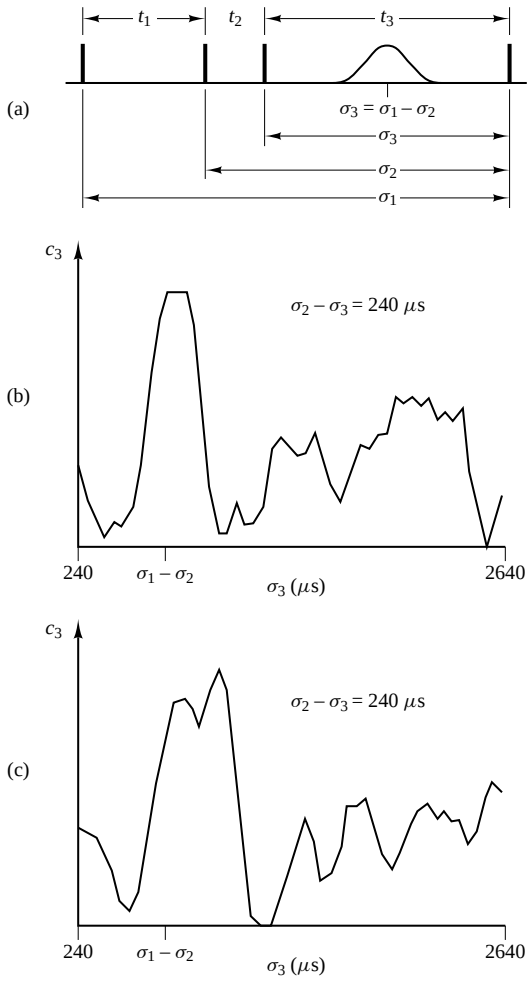

Figure 4 (a) Timing diagram for the cross correlation delays σ_i to observe an echo. (b) Stochastic echo of water doped with copper(II) sulfate in an inhomogeneous magnetic field for t_1=$\sigma_1 - \sigma_2$ = 720 μs. (c) Stochastic echo for t_1 = 960 μs

amplitude of the stochastic transverse magnetization response [see Figure 2(a)].[19] In practice, often noise with non-Gaussian probability distributions is used. For such excitation, the Wiener description of the nonlinear response can be extended.[19]

3.3.1 Liquids

Stochastic excitation is most easily applied in liquid state NMR, where transverse and longitudinal relaxation times are about equal. Here, the maximum signal response is obtained. If T_1 is much longer than T_2, the excitation power needs to be reduced to avoid complete saturation, and the response amplitude decreases accordingly. In practice, 1D and 2D stochastic NMR spectra have been calculated from equations (5) and (6), respectively, where a COSY-like 2D spectrum is obtained from equation (6) by setting $\omega_3 = -\omega_2$ (Figure 5b). Three-dimensional peaks outside of this 2D cross-section elsewhere in the 3D spectrum provide connectivities of three single quantum transitions.[38] High spectral resolution can be obtained in all dimensions of multidimensional stochastic NMR spectra, because the resolution is determined for all dimensions by the length of the sample records, which are averaged after Fourier transformation.

Figure 5 illustrates such stochastic NMR spectra with the Fourier transform $H_1(\omega)$ of the first-order Wiener kernel and the 2D cross-section $H_{3s}(\omega_1, \omega_2, -\omega_2)$ of a mixture of ethanol and acetylacetone in methanol-d_4.[40] The 2D cross-section has been evaluated only at the frequency coordinates of interest, which have been identified in the 1D spectrum. The signals in the 2D spectrum are each a sum of four contributions, because the spectrum is a cross-section through the Fourier transform of a symmetric Wiener kernel.[41] The individual contributions exhibit different lineshapes and different physical origins. They arise from connectivities of the single quantum coherences, which are plotted along the spectral axes via common energy levels (population effects), and zero and double quantum transitions. These connectivity types correspond to the coherence orders present during the evolution time t_2 in the coherence transfer diagram of Figure 3. Because there is a population path associated with an evolution time, these cross-sections are sensitive to chemical exchange and cross relaxation. However, because they are essentially derived from a 3D Fourier transform, the exchange signals are associated with the integral over all mixing times up to the length of the sample record.

3.3.2 Solids

In solids, T_1 is usually larger than T_2, and the amplitude of the response to stochastic excitation is weak. Nevertheless, spectrometers are sensitive enough for acquisition of the stochastic solid state response. Figure 6 depicts ^{1}H spectra of natural rubber for a nonspinning sample and under MAS.[42] Clearly, there are no fundamental complications with stochastic excitation and MAS in solids. In fact, even MAS imaging experiments have already been performed with noise excitation.[42]

For practical purposes, the use of noise excitation is of interest in wideline NMR of powder and partially oriented samples. Here, pulsed excitation requires the use of an echo to overcome receiver deadtime. This leads to complications in the intermediate exchange regime, where the signal decays substantially within the deadtime. With low-power stochastic excitation, the deadtime can be shortened. The equivalence in terms of sensitivity of pulsed and Hadamard excitation is demonstrated in Figures 7(a) and (b), where equal signal-to-noise ratios are obtained for the ^{2}H resonance of hexamethylbenzene-d_{18}.[43] This, however, applies only for large filter bandwidths, because the time sharing principle requires multipulse conditions in the experiment. When the echo is detected instead [Figure 7(c)], a matched filter can be used, and the signal-to-noise ratio improves. Time sharing can be discarded and matched filters can be used if crossed receiver and transmitter coils are employed, or if the excitation is realized by random magnetic field modulation.[10] In this case, even ^{14}N NMR of disordered solids may become feasible with stochastic excitation.

4 IMAGING

The most useful feature of stochastic excitation in NMR is the low power compared with pulsed excitation. The rf

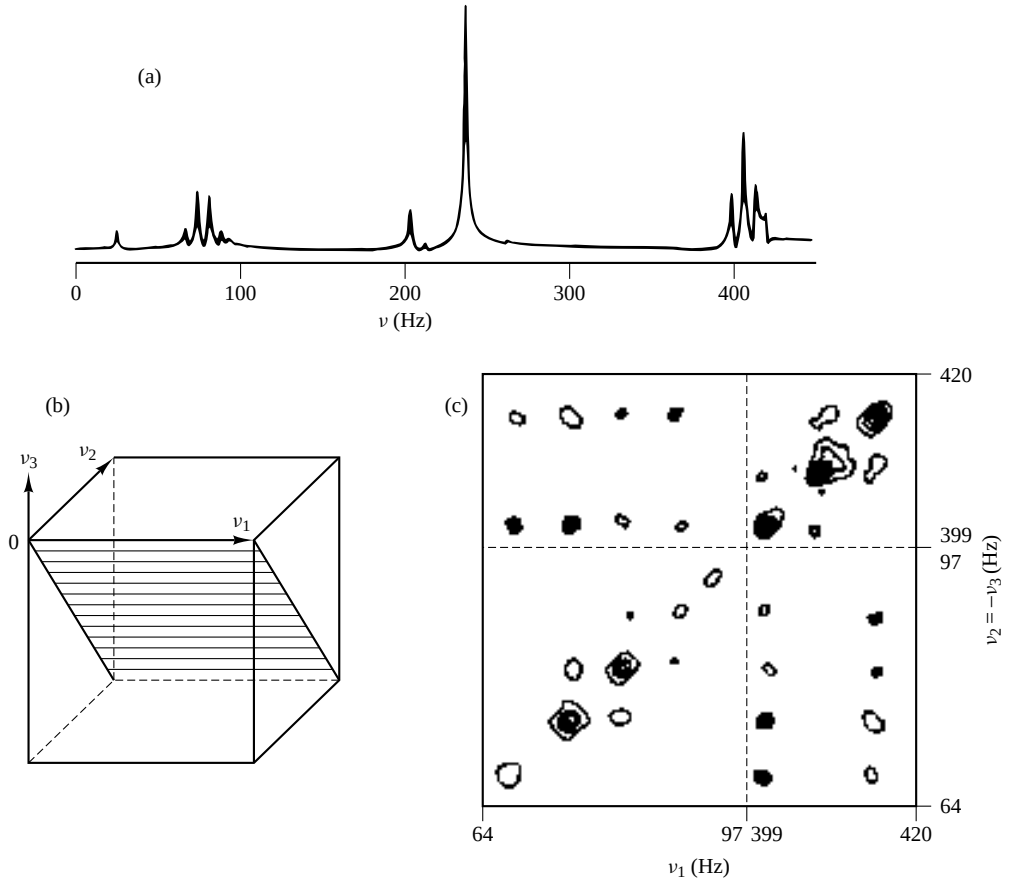

Figure 5 (a) 1D stochastic NMR spectrum or Fourier transform of the first-order Wiener kernel of a mixture of ethanol and acetylacetone in methanol-d_4. The spectrum was computed from 10^6 excitation and response data pairs using equation (5). (b) 3D frequency cube $H_{3s}(\omega_1, \omega_2, \omega_3)$ of the Fourier transform of the third-order Wiener kernel and location of the subdiagonal 2D cross section $H_{3s}(\omega_1, \omega_2, -\omega_2)$. (c) Subdiagonal 2D cross-section $H_{3s}(\omega_1, \omega_2, -\omega_2)$ of the frequency regions of interest in (a) computed from the same data as the 1D spectrum using equation (6)

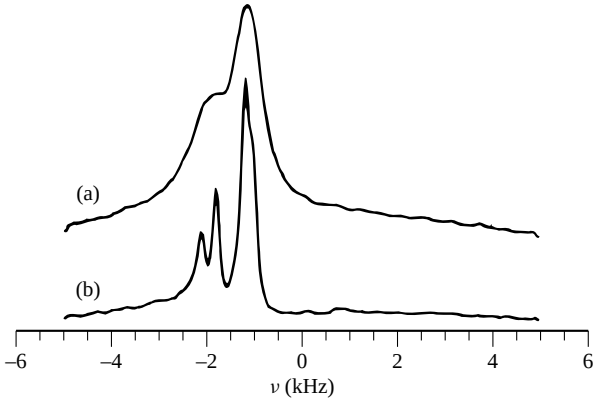

Figure 6 Stochastic ^{1}H spectra of natural rubber from 16 K complex excitation and response data pairs each. The excitation was four-phase constant-amplitude noise. (a) Spectrum of the static sample. (b) MAS spectrum

power is proportional to the square of the magnetic field amplitude. While the particular optimum excitation amplitude depends on the nuclear relaxation times, typical average flip angles in a string of stochastic rf pulses are of the order of $0.1^\circ - 10^\circ$. Thus, the rf amplitude is reduced by a factor of about 10^2 compared with pulsed NMR, so that a factor of 10^4 can be saved for the excitation power. This is of interest not only in wideline spectroscopy, but also for whole body investigations of large objects and for imaging at high magnetic fields. For this reason, stochastic excitation has been explored for medical[28–30,44] as well as materials imaging.[42,44] Two approaches are distinguished. One is based on cross correlation and time-dependent magnetic field gradients; the other is based on the back-projection technique.

4.1 Cross Correlation

In the presence of time-dependent magnetic field gradients, the nuclear spin response can be described in terms of the linear system response $y_1(t)$ to four inputs.[28] These are the rf excitation and the gradient modulations in the three space directions. If $M_0(\boldsymbol{r}, \omega)$ is the spin density, which depends on the space coordinate vector $\boldsymbol{r}$ and the chemical shift ω, then the linear response kernel $k_1(t)$ can be written for liquid systems as the integral over all FID signals for each space coordinate $\boldsymbol{r}$ and each chemical shift ω:

$$k_1(t) = \int\int M_0(\boldsymbol{r}, \omega) \exp\left[-\left(\frac{1}{T_2} - \mathrm{i}\omega\right) t\right] \mathrm{d}\omega \times \exp[\mathrm{i}\boldsymbol{k}(t, 0) \cdot \boldsymbol{r}]\, \mathrm{d}^3 r \quad (8)$$

Here $\boldsymbol{k}(t,0)$ is the Fourier conjugate of the space vector $\boldsymbol{r}$, proportional to the time integral of the gradient vector $\boldsymbol{G}$ from

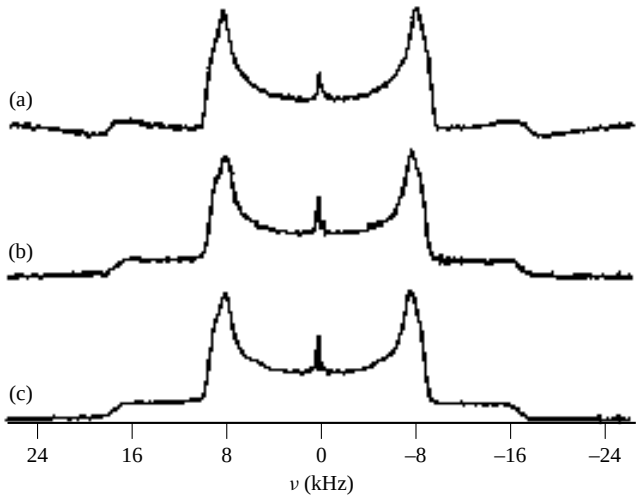

Figure 7 Comparison of solid echo and Hadamard spectra of the ^{2}H resonance of hexamethylbenzene-d_{18}. All spectra were acquired in 5 s. (a) Solid echo spectrum, 500 kHz filter bandwidth. (b) Hadamard spectrum, 500 kHz filter bandwidth. (c) Solid echo spectrum, matched filter with 30 kHz bandwidth. The power of the stochastic rf excitation was 100 mW

time zero to t. First-order cross correlation of the system response, equation (2), with the linear kernel, equation (8), according to

$$c_1(\boldsymbol{r},\sigma) = \int y(t)\exp[-\mathrm{i}\boldsymbol{k}(t,t-\sigma)\cdot\boldsymbol{r}]\,x^*(t-\sigma)\,\mathrm{d}t \qquad (9)$$

can produce the spin density as a function of $\boldsymbol{r}$ weighted with the FID as a function of σ for each position $\boldsymbol{r}$.[28] Thus, in the cross correlation in equation (9) both $\boldsymbol{r}$ and σ need to be varied. Spectroscopic images of phantoms have been obtained in this way.[29] The cross-correlation approach can, in principle, be extended to incorporate the nonlinear response for stochastic imaging with 2D spectroscopic resolution.[18] Random, oscillating, and rotating gradients have been investigated in the context of the cross-correlation approach.

4.2 Back-Projection

Experimentally, the least demanding gradients are static only. In this case, projections of the object are derived from the linear response to stochastic excitation. Both random noise[44] and Hadamard excitation[30,45] have been explored. The Hadamard technique promises to be of most interest, because the projections can be obtained free of systematic noise, so that extensive averaging is unnecessary. Thus, the method is fast. Imaging times have been estimated as 3 min for 3D images with 256^3 voxels and as 2 s for 2D images with 256^2 pixels. However, in either case, slice selection poses a problem, because the conventional theory applies to dynamic equilibrium of the response with the noise excitation. Slice selection would invariably violate this equilibrium and lead to turn-on effects, which result in noise-like signal degradations.[14,43] But, in some cases, these turn-on effects can be neglected, and a theory can be devised that inverts the linear convolution in equation (2), taking care of the fact that the noise excitation has been turned on at time $t = 0$. Figure 8 demonstrates the use of the Hadamard technique in combination with the back-projection method and slice selection by a surface-rendered 3D image of an olive reconstructed from 12 projections. To preserve the low-power advantage of stochastic excitation during slice selection, low-power presaturation needs to be employed.[46]

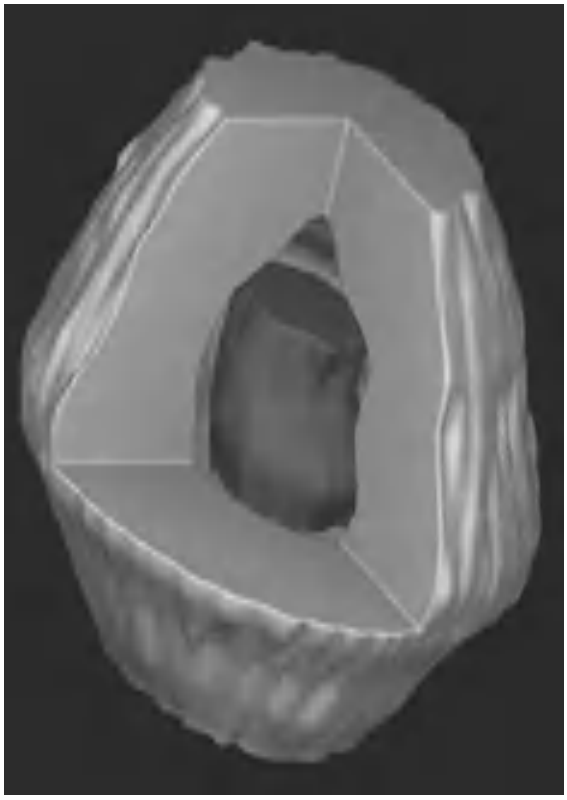

Figure 8 Surface-rendered 3D image of an olive reconstructed from 12 projections. Hadamard excitation has been used in combination with low-power slice selection. Mean excitation flip angle 1.1°; slice dimension 127 × 127 pixels calculated from 64 projections; slice thickness 1.6 mm; field-of-view 4 cm × 4 cm per slice. Signals are observed from the meat of the olive as well as from the interior of the pit

5 INTERFERENCE

The multidimensional cross correlation in equation (3) can be evaluated numerically from experimental excitation and response records or in an analog fashion during the experiment. In the latter case, only the cross-correlation function is recorded as a function of the time shifts σ_i. A one-dimensional correlator based on this principle is the Michelson interferometer.[47,48] In Figure 9, the block diagram of a first-order cross correlator with a single delay σ is compared with a modified Michelson interferometer. The white noise source is white light, the time shift is introduced by variation of the optical path length, and the formation of the product of excitation and response signals as well as the integration over time are achieved in a slow intensity detector, which detects the squared magnitude of the time-averaged sum of electromagnetic fields impinging on its surface. Such an

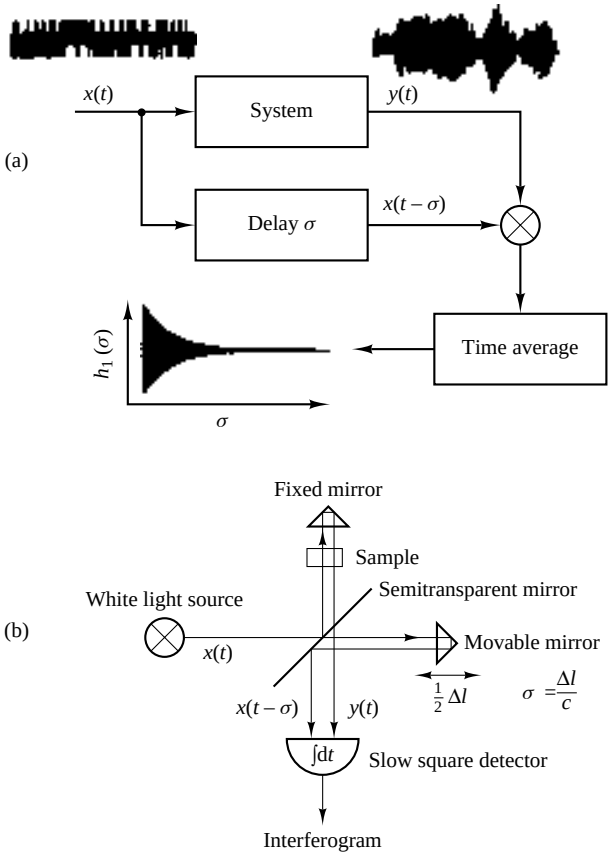

Figure 9 (a) First-order cross correlator. The time delay σ is varied to scan the cross-correlation function $h_1(\sigma)$ of excitation $x(t)$ and response $y(t)$. (b) A Michelson interferometer modified for measurement of the cross-correlation function. The time delay σ is introduced by a pathlength variation via a movable mirror

analog device is particularly suitable for measurement of cross-correlation functions of signals, which are too fast for direct sampling. The interferogram can be sampled as slowly as the delay σ is varied.

The Michelson interferometer is the heart of a Fourier infrared spectrometer. Here, the correlation function is called an interferogram. Thus, linear stochastic NMR is equivalent to Fourier spectroscopy in the optical regime.[47] Moreover, there is an equivalence between correlation and interference. Given the fact that nonlinear cross-correlation functions are defined and can be evaluated in stochastic NMR, nonlinear interference can be defined in optics as the analog realization of higher order cross correlation [cf. equation (3)].[49,50] In fact, to demonstrate this equivalence experimentally, the NMR echoes of Figure 5(b) have been recorded by scanning the time delay σ_3 in a third-order cross correlator built from electronic components.[39] Thus, the stochastic echo is an example of a nonlinear interferogram. The closeness of the Wiener series perturbation approach to nonlinear optics is further underlined by the fact that the Volterra kernels are the Fourier transforms of the nonlinear susceptibilities in optics, and that the Wiener kernels are equivalent to the Volterra kernels apart from excitation-power-dependent saturation effects.

The echo is the fundamental phenomenon that introduces two time axes into spectroscopy: one, the echo time, measures the position of the echo maximum, and the other the rise and decay of the echo itself. Thus, 2D spectra can be derived from a set of echoes that have been measured in a systematic fashion for several echo times. To overcome the low signal-to-noise ratio of the third-order cross-correlation function and the necessity of multiplying four broadband optical signals, an alternative route to stochastic echoes can be followed. Instead of a single noise source $x(t)$, a time-shifted sum excitation is used:[32]

$$x'(t) = x(t) + rx(t - \sigma_1) \tag{10}$$

where r is a scaling factor. The nonlinear response of the system to this excitation is evaluated. This has been done in optics by recording the intensity of the third-order response as a function of the time shift σ_1. The resultant autocorrelation function has been termed an incoherent echo. It has been shown to reveal information about T_1 and T_2.[51–53] However, a true echo is characterized by two time parameters. These can be introduced by evaluating the first-order cross-correlation function of the nonlinear response to the sum excitation with $x(t - \sigma_2)$. An optical device that does this in an analog fashion can readily be built by combining the Michelson interferometer with the incoherent echo experiment [Figures 10(a) and (b)].[32] By phase cycling the components of the sum excitation, 2D spectra reminiscent of COSY NMR spectra can be derived in the optical regime, which can help to unravel the energy level structure of molecules from high-resolution data obtained in the gas phase or by matrix isolation techniques. The result of a simulation in the case of NMR for a high-resolution AB system is depicted in Figure 10(c). A COSY spectrum is obtained at a remarkably good signal-to-noise ratio. The good signal-to-noise ratio results from the fact that the response probes all odd orders of Wiener functionals because the sum excitation is no longer white.

6 QUO VADIS?

Stochastic excitation in NMR started out from pure curiosity. Noise decoupling for a long time has been the superior decoupling method in liquid state NMR. The acquisition of NMR spectra with noise excitation has never become popular, because of the superior features of pulsed FT NMR for dedicated rf manipulation of nuclear spin interactions and for the possibility of designing special experiments tailored to the information required. With stochastic NMR based on the Wiener series, all the available information is acquired in a single experiment, and it is sorted out during data processing. Here, however, the problem of systematic noise enters, which prohibits a clean separation of information as a result of the statistical nature of the excitation in connection with finite-length excitation and response records. Consequently, schemes that produce spectra with better signal-to-noise ratios by sacrificing the generality of the excitation but retaining the excitation power advantage appear most promising for practical use.

Examples of such schemes are Hadamard excitation for the linear response and the time-shifted sum excitation for interrogation of the nonlinear response. The low power of the stochastic excitation reduces probe ringing, relaxes the requirements for high-power amplifiers in spectroscopy and imaging, reduces the power heating in dissipative objects, and gives access to larger spectral width. Areas where these

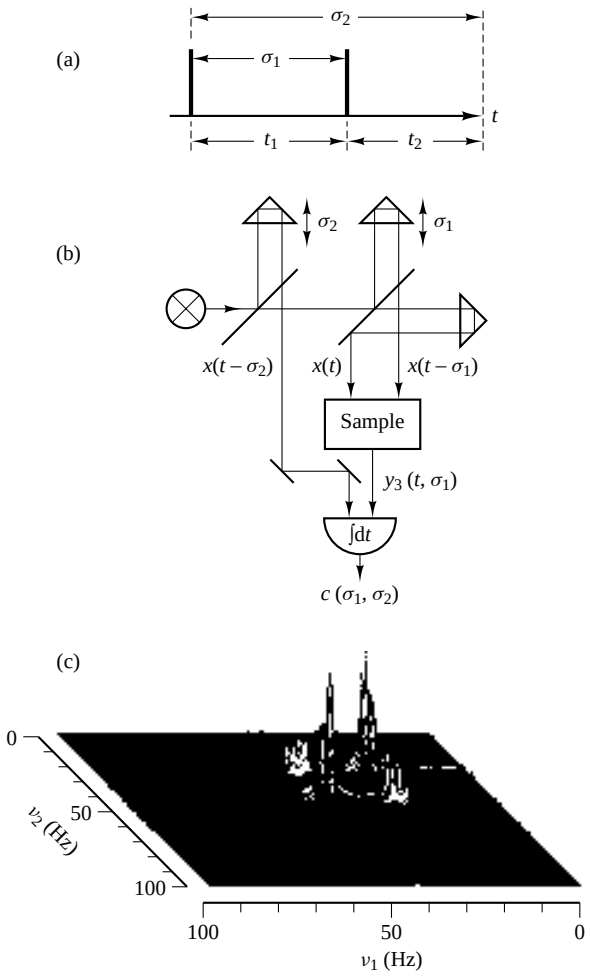

Figure 10 2D correlation spectroscopy by linear interference of the nonlinear response. (a) Timing of the pseudopulses for the cross-correlation function. (b) Schematic diagram showing the principle experimental set-up. The experiment combines the Michelson interferometer with the incoherent echo experiment. The spatial separation of optical signals from different response orders is not shown. (c) Fourier transform of a 2D interferogram simulated for an AB system in high-resolution NMR, including phase cycling of the excitation sum for elimination of unwanted terms

features are of interest are in medical and materials imaging, and in wideline spectroscopy, such as in solid state ^{2}H and ^{14}N NMR, in EPR, and in NQR spectroscopy.

The time-shifted sum excitation is particularly intriguing for several reasons.

1. The excitation power is as low as for true white-noise excitation, yet the excitation spectrum carries a sinusoidal modulation.
2. The data processing can readily be achieved in the optical regime with analog components.
3. The signal-to-noise ratio of the linear correlation function of the nonlinear response is high, because a superposition of Wiener kernel transforms from all response orders is observed.
4. Phase cycling can be used in the sum excitation for elimination of artifacts and unwanted response contributions. A most fascinating outlook is the use of such excitation for the generation of optical 2D spectra. In fact, Hadamard excitation has already been used to acquire ultrahighly resolved optical 1D spectra.[54]

The bottom line of stochastic excitation 50 years after the discovery of NMR is that its investigation has produced a thorough understanding of nonlinear incoherent spectroscopy. This is the counterpart of nonlinear coherent spectroscopy, which traditionally belongs to the optical regime, where coherent laser irradiation is standard, but the development of incoherent excitation sources of sufficient strength for excitation of the nonlinear response has been neglected.

7 RELATED ARTICLES

Deuterium NMR in Solids; Double Resonance; Fourier Transform Spectroscopy; Image Formation Methods; Multidimensional Spectroscopy: Concepts; Quantum Optics: Concepts of NMR; Rapid Scan Correlation Spectroscopy.

8 REFERENCES

1. N. Wiener, *Nonlinear Problems in Random Theory*, Wiley, New York, 1958.
2. H. Primas, *Helv. Phys. Acta*, 1961, **34**, 36.
3. R. R. Ernst and H. Primas, *Helv. Phys. Acta*, 1963, **36**, 583.
4. R. R. Ernst, *I. Kernresonanzspektroskopie mit stochastischen Hochfrequenzfeldern. II. Zur Konstruktion eines optimalen Kernresonanz-Messkopfes*, Dissertation 3300, ETH Zürich, 1962.
5. R. H. Varian, 'Gyromagnetic resonance methods and apparatus', US patent 3 287 629, Nov. 22, 1966.
6. R. R. Ernst, *J. Chem. Phys.* 1966, **45**, 3845.
7. R. R. Ernst and W. A. Anderson, *Rev. Sci. Instrum.* 1966, **37**, 93.
8. R. R. Ernst, in *Protokoll Tagung über Hochfrequenzspektroskopie, Karl-Marx-Universität Leipzig, 1969*, Physikalischen Gesellschaft DDR, Berlin, 1969, p. 31.
9. R. R. Ernst, *J. Magn. Reson.*, 1970, **3**, 10.
10. R. Kaiser, *J. Magn. Reson.*, 1970, **3**, 28.
11. H. Armitage, U. Blömer, I. Genge, A. Khuen, E. E. Wille, and D. Ziessow, *Ber. Bunsenges. Phys. Chem.*, 1987, **91**, 1115.
12. B. L. Tomlinson and H. D. W. Hill, *J. Chem. Phys.*, 1973, **59**, 1775.
13. D. Ziessow, *On-line Rechner in der Chemie*, Walter de Gruyter, Berlin, 1973.
14. D. Ziessow and B. Blümich, *Ber. Bunsenges. Phys. Chem.*, 1974, **78**, 1168.
15. R. Kaiser, *J. Magn. Reson.*, 1974, **15**, 44.
16. J. S. Bendat and A. G. Piersol, *Random Data Analysis and Measurement Procedures*, Wiley, New York, 1971.
17. J. Paff, R. Freeman, and B. Blümich, *J. Magn. Reson., Ser. A*, 1993, **102**, 332.
18. B. Blümich, *J. Magn. Reson.*, 1990, **90**, 535.
19. B. Blümich and D. Ziessow, *J. Chem. Phys.* 1983, **78**, 1059.
20. B. Blümich, *Bull. Magn. Reson.*, 1987, **7**, 5.
21. B. Blümich, in *Progress in Nuclear Magnetic Resonance Spectroscopy*, eds. J. W. Emsley, J. Feeney, and L. H. Sutcliffe, Pergamon Press, Oxford, 1987, Vol. 19, p. 331.
22. R. R. Ernst, G. Bodenhausen, and A. Wokaun, *Principles of Nuclear Magnetic Resonance in One and Two Dimensions*, Clarendon Press, Oxford, 1987.

23. E. Bartholdi, A. Wokaun, and R. R. Ernst, *Chem. Phys.*, 1976, **18**, 57.
24. E. R. Knight and R. Kaiser, *J. Magn. Reson.*, 1982, **48**, 293.
25. R. Kaiser and W. R. Knight, *J. Magn. Reson.*, 1982, **50**, 467.
26. S. T. S. Wong, M. S. Roos, and R. D. Newmark, *J. Magn. Reson.*, 1990, **87**, 242.
27. S. T. S. Wong, M. S. Roos, and R. D. Newmark, *J. Magn. Reson.*, 1990, **87**, 265.
28. B. Blümich, *J. Magn. Reson.*, 1984, **60**, 37.
29. M. S. Roos and S. T. S. Wong, *J. Magn. Reson.*, 1990, **87**, 554.
30. B. Blümich, J. Jansen, H. Nilgens, P. Blümler, and G. L. Hoatson, *J. Magn. Reson. Med. Biol.*, 1993.
31. T. Prisner and K. P. Dinse, *J. Magn. Reson.*, 1989, **84**, 296.
32. J. Paff, B. Blümich, and R. Kaiser, in *Advances in Magnetic Resonance*, ed. J. S. Waugh, Academic Press, New York, 1992, Vol. 17, p. 1.
33. M. Schetzen, *The Volterra and Wiener Series of Nonlinear Systems*, Wiley, New York, 1980.
34. V. Volterra, *Theory of Functionals*, Dover, New York, 1951.
35. Y. W. Lee and M. Schetzen, *Int. J. Control*, 1965, **2**, 237.
36. J. Paff and B. Blümich, *Mol. Phys.*, 1989, **68**, 225.
37. B. Blümich and D. Ziessow, *Mol. Phys.*, 1983, **5**, 955.
38. B. Blümich, *Mol. Phys.*, 1983, **5**, 969.
39. J. Paff and B. Blümich, *Phys. Rev. A*, 1991, **43**, 225.
40. B. Blümich and R. Kaiser, *J. Magn. Reson.*, 1984, **58**, 149.
41. B. Blümich and R. Kaiser, *J. Magn. Reson.*, 1983, **54**, 486.
42. J. Jansen, *NMR-Bildgebung mit Rauschanregung*, Dissertation, Johannes-Gutenberg-Universität Mainz, 1992.
43. M. Greferath, B. Blümich, W. M. Griffith, and G. L. Hoatson, *J. Magn. Reson., Ser. A*, 1993, **102**, 73.
44. J. Jansen and B. Blümich, *J. Magn. Reson.*, 1992, **99**, 525.
45. M. Bernardo Jr., D. Chaudhuri, X.-R. Liu, and P. C. Lauterbur, *Proc. Soc. Magn. Reson. Med. 1985 Meet.*
46. H. Nilgens, P. Blümler, J. Paff, and B. Blümich, *J. Magn. Reson., Ser. A*, 1993, **105**.
47. R. R. Ernst, *Chimia*, 1972, **26**, 53.
48. A. A. Michelson, *Light Waves and Their Uses*, University of Chicago Press, Chicago, 1903.
49. B. Blümich, *Nichtlineare inkohärente Spektroskopie in der magnetischen Kernresonanz*, Habilitationsschrift, Johannes-Gutenberg-Universität Mainz, 1987.
50. B. Blümich, *Rev. Sci. Instrum.*, 1987, **58**, 911.
51. S. Asaka, H. Nakatsuoka, M. Fujiwara, and M. Matsuoka, *Phys. Rev. A*, 1984, **29**, 2286.
52. R. Beach and S. R. Hartmann, *Phys. Rev. Lett.*, 1984, **53**, 663.
53. M. Morita and T. Yajima, *Phys. Rev. A*, 1984, **30**, 2525.
54. K. P. Dinse, M. P. Winters, and J. L. Hall, *J. Opt. Soc. Am. B*, 1988, **5**, 1825.

Biographical Sketch

Bernhard Blümich. *b* 1952. Vordiplom, 1974, Technische Universität Berlin; M.S., 1976, Rensselaer Polytechnic Institute; Diplom, 1977, Technische Universität Berlin; Dr. rer. nat., 1981, Technische Universität Berlin; NATO postdoctoral fellow, University of New Brunswick at Fredericton, 1982–1983; Universität Bayreuth, 1983–1984; Max-Planck-Institut für Polymerforschung, 1984–1993; Habilitation, Johannes-Gutenberg-Universität Mainz, 1988; Visiting Professor, University of Massachusetts at Amherst, 1992–1993; Professor of Macromolecular Chemistry, Rheinisch-Westfälische Technische Hochschule Aachen, 1993–present. Introduced to NMR by Dieter Ziessow in 1974. Approximately 90 publications. Research interests; nonlinear incoherent spectroscopy, and methods and applications of solid state NMR spectroscopy and imaging in materials science.

Symmetry-Based Pulse Sequences in Magic-Angle Spinning Solid-State NMR

Malcolm H. Levitt

Chemistry Department, Southampton University, Southampton, UK

1 Introduction 1
2 Homonuclear Sequences 2
3 Heteronuclear Sequences 19
4 Applications 20
5 Conclusions 29
6 References 29

1 INTRODUCTION

Much modern solid-state NMR technology is based on two physical manipulations: (i) rotation of the sample in space, usually at a fixed frequency around a fixed axis, but sometimes using more complicated trajectories; and (ii) rotation of the nuclear spin polarizations using applied rf fields.

Magic-angle spinning was first demonstrated independently by Andrew and Lowe[1,2] in 1959. These researchers demonstrated a noticeable narrowing effect on the NMR spectra of abundant spins in solids when the sample was rotated at several kHz around an axis tilted by the angle $\arctan\sqrt{2} = 54.74^\circ$ with respect to the main magnetic field (see **Magic Angle Spinning,** Volume 5). However, the magic-angle spinning (MAS) method was not employed much at first because it was thought to be ineffective unless the spinning frequency greatly exceeded the size of the anisotropic nuclear spin interactions – a condition difficult to satisfy except for a limited number of samples. The situation changed at the end of the 1970s, when it was found that magic-angle spinning dramatically narrowed the proton-decoupled NMR peaks of isolated ^{13}C spins in organic solids.[3] The ^{13}C peaks split up into narrow 'spinning sidebands', even though the spinning frequency was much smaller than the chemical shift anisotropy (CSA). MAS, in combination with Hartmann–Hahn cross-polarization and heteronuclear decoupling, became a standard method for examining the NMR spectra of rare spin species such as ^{13}C and ^{15}N in solids.[4] Commercial NMR companies began to offer MAS equipment as options for their spectrometers, allowing an explosion of applications.

The use of nuclear spin rotations by applied rf fields developed in parallel. The basic technique of *hetero*nuclear decoupling was already introduced by Bloch,[5] and advanced rapidly in the context of solution NMR with the introduction of noise modulation[6] and composite pulse decoupling[7–9] (see **Decoupling Methods,** Volume 3). In solid-state NMR, on the other hand, heteronuclear decoupling methodology stagnated until the introduction of the two-pulse phase modulation (TPPM) by Griffin and co-workers.[10] The methodology of *homo*nuclear dipolar decoupling in solids received more attention from the start. This process started with the use of magic-angle off-resonance irradiation by Lee and Golburg[11] and continued with the pulse methods of Waugh, Huber and Haeberlen,[12,13] Mansfield,[14] Rhim and Vaughan,[15] Burum and co-workers[16] and many others (see **Average Hamiltonian Theory,** Volume 2). Advances in digital electronics made possible new approaches, such as the frequency-switched Lee–Goldburg (FSLG) method.[17] These methodological developments were accompanied by important theoretical advances such as the average Hamiltonian theory and its variants.[13,14,18]

For much of this period, the spatial and spin manipulations were treated separately. For example, the principles of homonuclear decoupling by applied rf fields were developed explicitly for static samples – the rotation of the sample during the rf pulse sequence, in the case of MAS, was regarded as a minor additional perturbation. Similarly, the principles of echo formation by sample rotation generally neglected the duration of applied rf pulses. This conceptual separation was made possible by an experimental separation of timescales. Routinely-available spinning frequencies were much smaller than routinely-available nutation frequencies under applied rf fields. This situation was not fundamentally changed even when the 'combined rotation and multiple pulse sequence' (CRAMPS) methods were introduced[19,20] (see **CRAMPS,** Volume 3). At the rather low spinning frequencies used initially, it was a reasonable approximation to ignore the MAS rotation during the rf pulse sequence. The enhanced narrowing effect of CRAMPS could be treated roughly by tacking the MAS rotation onto the end of a static average Hamiltonian calculation.

At the beginning of the 1980s, two developments highlighted the fact that rf pulse sequences and sample rotation could combine in unexpected and powerful ways. In the extraordinary sideband suppression and separation schemes of Dixon,[21,22] carefully-timed sequences of strong π pulses were applied to the rotating sample in order to manipulate the spinning sideband patterns generated by the subsequent free-induction decay. Around the same time, Waugh and co-workers applied a repetitive pulse train synchronous with the sample rotation, and showed that the averaging effect of the magic-angle rotation on the chemical shift anisotropy could be suppressed.[23] This would now be called a 'CSA recoupling' experiment.

The term 'recoupling' was first used in the *heteronuclear* context, when it was shown that the application of a continuous rf field to one spin species may restore the effect of the heteronuclear dipolar interaction to a second spin species, by counteracting the averaging effect of the magic-angle rotation.[24,25] This requires selection of the rf amplitude so that the magic-angle rotation frequency is a small integer multiple of the nutation frequency under the rf field, a condition termed 'rotary resonance'. It was also pointed out that the same effect could be produced by applying two strong 180° pulses every rotational cycle to one of the spin species.[25] This idea was developed independently by Schaefer et al., leading to the highly-successful rotational echo double resonance (REDOR) method[26,27] (see **REDOR & TEDOR,**

Volume 6). As discussed below, the REDOR scheme fits into the symmetry theory of rotor-synchronized pulse sequences (in the modern notation defined below, the symmetry of the usual version of REDOR is $R4_2^1$).

The next important advances were made by Tycko and co-workers.[28,29] It was shown that rotor-synchronized pulse sequences, in combination with sample rotation about a non-magic-angle axis, could be used to emulate a zero-field NMR experiment (see **Zero Field NMR,** Volume 8). In the context of the present article, it is important to note that Tycko used symmetry relationships to simplify the task of pulse sequence design. In the modern notation defined below, one would describe Tycko's 'zero-field in high-field' pulse schemes as having the symmetry $C5_1^1$.

The second development made by Tycko's group also had a wide impact. The dipolar recoupling at the magic angle (DRAMA) scheme[30–32] initiated the field of *homonuclear* dipolar recoupling in solids (see **Homonuclear Recoupling Schemes in MAS NMR,** Volume 4). DRAMA is a rather simple pulse sequence of strong 90° pulses separated by intervals and is not particularly robust. A partially successful attempt was made to improve it using symmetry-based arguments.[32] A popular alternative is the radio-frequency driven recoupling (RFDR) scheme of Griffin and co-workers, which is based on strong 180° pulses.[33,34] As discussed below, part of the success of RFDR may now be understood in terms of its symmetry properties (in modern notation, the symmetry of the usual version of RFDR is $R4_4^1$).

A different approach to dipolar recoupling was introduced with the double-quantum homonuclear rotary resonance (2Q-HORROR) method.[35] This was a development of the heteronuclear rotary resonance method, exploiting the additional resonance conditions associated with double-quantum transitions in homonuclear spin systems. The HORROR method showed for the first time that it is possible to achieve highly efficient 2Q excitation in a powder sample, in part by a tighter control of the orientation-dependence of the recoupled Hamiltonian. The appropriate property has come to be called "γ-encoding", and will be discussed below.

HORROR is only feasible for coupled spins with small chemical shift differences. It required a fresh theoretical approach to extend this method to more general systems while retaining the γ-encoded 2Q recoupling property. This effort lead to the C7 pulse scheme and its variants,[36–42] which are capable of efficient broadband double-quantum recoupling. In modern notation, these schemes have the symmetry $C7_2^1$. These methods were applied to a variety of problems, including the measurement of molecular torsional angles in a membrane protein.[43,44]

As well as being practically successful, the theory behind C7 was very powerful, and could be used for a variety of problems. A further extension of the symmetry theory led to a pallette of symmetries suitable for γ-encoded double-quantum recoupling, including methods which are applicable at high spinning frequencies.[39] The symmetry theorems were also used to treat the problem of heteronuclear decoupling in MAS solids, generating schemes competitive with the TPPM modulation method.[41,45]

In a related development, Spiess and co-workers showed that CRAMPS may be implemented at high MAS spinning frequencies by synchronizing the rf cycles with the sample rotation.[46,47] In modern notation, these schemes have the symmetry $C3_1^0$ and $C4_1^0$.

Schemes such as C7 are based on repeated radio-frequency cycles, shifted in phase and synchronized with the sample rotation. Each cycle is designed to return the nuclear spins to their initial states, if other spin interactions are ignored, i.e., each cycle provides a rotation through 0°, 360°, or 720°, etc. Although effective for double-quantum excitation, this construction scheme is too restrictive when applied to many other recoupling problems. A set of new symmetries were therefore developed, based on 180° rotation elements.[41] These symmetries, called R-symmetries, suggest many new classes of pulse sequence, and also help explain the operation of many existing schemes. As discussed below, many of the successful methods invented in the past, such as RFDR, REDOR, and TPPM conform to the R-symmetries. This is probably not a coincidence.

The invention of R-symmetries was anticipated by the through bond spectroscopy (TOBSY) method of Baldus and Meier.[48–52] These authors also used symmetry arguments to design their pulse sequences, which have the modern symmetry notation $R6_1^0$ and $R8_1^0$.

The discovery of the R-symmetries is still too recent to assess their full significance. Some of the promising recent applications are discussed below.

2 HOMONUCLEAR SEQUENCES

2.1 Spin Interactions

The symmetry-based approach to the design of rotor-synchronized pulse sequences exploits the rotational properties of the nuclear spin interactions. In general, each spin interaction may be expressed as a product of three terms, expressing the transformation properties of the interaction with respect to rotations of the molecular framework ('space'), rotations of the nuclear spin polarizations ('spin') and rotations of the external magnetic field. These rotational properties may be summarized in terms of the three *rotational ranks* which define each nuclear spin interaction. The set of rotational ranks forms the *rotational signature* of a nuclear spin interaction. The rotational signatures are summarized for the most important homonuclear interactions of spin-1/2 in Table 1.

As may be seen from Table 1, the significant nuclear spin interactions all have ranks 0, 1 or 2. For example, those interactions which are invariant to a particular type of rotation are assigned rank zero. Interactions which have the rotational symmetry of a p-orbital in atomic theory are assigned rank 1. Interactions which have the rotational symmetry of a d-orbital in atomic theory are assigned rank 2.

Consider, for example, the homonuclear dipolar interaction between nuclear spins. This has rank 2 with respect to both

Table 1 Rotational signatures of homonuclear spin interactions in diamagnetic systems of spin-1/2

Interaction	Space rank, l	Spin rank, λ	Field rank
Isotropic chemical shift	0	1	1
Chemical shift anisotropy	2	1	1
J-coupling	0	0	0
Dipole–dipole coupling	2	2	0

spatial and spin rotations, indicating, for example, that a rotation of the molecular framework by 180° does not change the interaction strength, while a rotation through 90° changes the sign of the interaction.

The chemical shift anisotropy interaction is more complicated, since it is a three-body interaction, involving the nuclear spins, the electronic environment and the external magnetic field. It has ranks 2, 1 and 1 with respect to molecular rotations, spin rotations, and external field rotations, respectively. This interaction changes sign if the nuclear spins are rotated by 180°, with the molecules and the field held fixed. The CSA interaction also changes sign if the external field is rotated through 180°, while the spin polarizations and the molecular environment are held fixed. The CSA interaction does not change sign, on the other hand, if the molecules are rotated through 180°, while the spins and the field are held fixed.

Many NMR textbooks conflate the 'spin' part and the 'field' part into one compound term, often called, confusingly, the 'spin part' of the interaction. This practice obscures the rotational properties and is best avoided.

There are also minor interactions such as the antisymmetric part of the chemical shift tensor (space, spin, field ranks of 1, 1 and 1), and the J-coupling anisotropy (space, spin, field ranks of 2, 2 and 0), which are omitted here for simplicity.

The spherical ranks listed in Table 1 are defined as follows: An irreducible spherical tensor of rank l has $2l + 1$ components, with a component index m running from $-l$ to $+l$ in integer steps. A rotation interconverts these $2l + 1$ components according to the transformation equation:

$$R(\Omega)T_{\lambda m}R(\Omega)^{\dagger} = \sum_{m'=-l}^{+l} T_{\lambda m'}D^{l}_{m'm}(\Omega) \qquad (1)$$

Here $R(\Omega)$ are rotation operators and $D^{l}_{m'm}(\Omega)$ is an element of the $(2l + 1)$-dimensional Wigner matrix. The symbol Ω indicates a triplet of Euler angles $\Omega = \{\alpha, \beta, \gamma\}$ defining a general three-dimensional rotation. Irreducible spherical tensors, Wigner matrices and Euler angles are discussed thoroughly in the literature.[4] A particularly useful compilation is given in Ref.[53] The article **Internal Spin Interactions & Rotations in Solids,** Volume 4, summarizes many key results.

The Wigner elements have the following form:

$$D^{l}_{m'm}(\Omega) = \exp\{-\mathrm{i}m'\alpha\}d^{l}_{m'm}(\beta)\exp\{-\mathrm{i}m\gamma\} \qquad (2)$$

where $d^{l}_{m'm}(\beta)$ is called a reduced Wigner matrix element.

Although the detailed form of the Wigner matrices and the spherical tensors depends on the rank, and the approach appears to be mathematically complicated at first sight, the transformation properties are always the same, which permits a universal approach to pulse sequence theory.

2.2 Reference Frames

The discussion of spin interactions in rotating solids is facilitated by defining a set of reference frames (Figure 1).

2.2.1 The Principal Axis Frame P^{Λ}

The *principal axis frame* P^{Λ} provides the simplest form of the spin interaction Λ. For example, consider the through-space dipole–dipole interaction (DD interaction) between two spins j and k. The z-axis of the principal axis frame P^{jk} is oriented along the vector joining the spins j and k. In this frame, the spherical tensor components with $m = \pm 1$ and $m = \pm 2$ vanish, leaving only the $m = 0$ component. For the CSA interaction of spin j, the $m = \pm 1$ components vanish in the principal axis frame P^{j}, while the $m = 0$ and $m = \pm 2$ components remain finite.

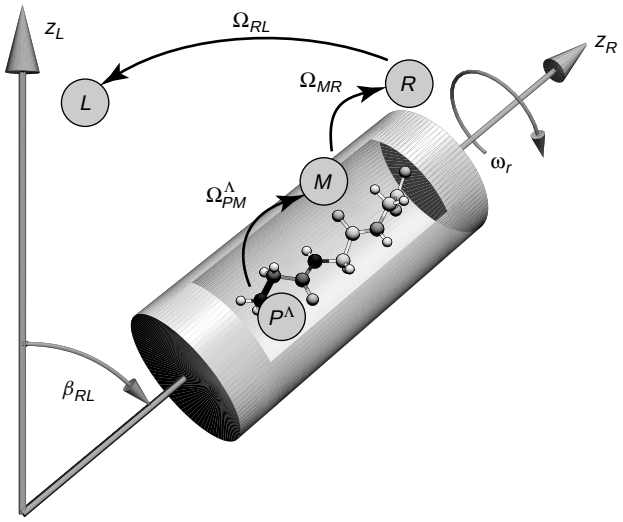

Figure 1 Definition of the reference frames in magic-angle spinning NMR experiments. (Adapted from Ref.[82])

In general, there are many different spin interactions, and each one has a different principal axis frame P^{Λ}.

2.2.2 The Molecular Frame M

The molecular reference frame M is fixed with respect to the molecular structure. It is usual to transform all of the different spin interactions into the common reference frame M before further manipulations are imposed.

A principal axis frame P^{Λ} is related to the molecular frame M by a set of three Euler angles, denoted $\Omega^{\Lambda}_{PM} = \{\alpha^{\Lambda}_{PM}, \beta^{\Lambda}_{PM}, \gamma^{\Lambda}_{PM}\}$. These Euler angles define the relative orientation of the frames P^{Λ} and M. In general, there are several spin interactions, each with a different set of Euler angles Ω^{Λ}_{PM}, specifying its orientation with respect to the common molecular frame M.

2.2.3 The Rotor Frame R

In a spinning solid, the orientation of the molecules with respect to the rotating sample holder ('rotor') is of great importance. The rotor-fixed frame R is defined such that its z-axis is along the rotational axis. The Euler angles $\Omega_{MR} = \{\alpha_{MR}, \beta_{MR}, \gamma_{MR}\}$ define the relative orientation of the molecular reference frame and the rotor frame.

If the sample were a single crystal, with only one molecule in the asymmetric unit of the crystal structure, then all molecules in the sample would have the same set of Euler angles Ω_{MR}. In practice, the sample usually has an orientational distribution of some kind, and in the extreme case of a disordered sample such as a powder, the Euler angles Ω_{MR} are distributed randomly. In such cases, the results of experiments must be analyzed by integrating spin dynamical calculations

over all possible values of the Euler angles Ω_{MR}. This is called powder averaging.

The Euler angle γ_{MR} has special significance in the theory of rotating solids. Molecules which have the same values of α_{MR} and β_{MR} but different values of γ_{MR} are related by a rotation around the rotor axis. This implies that the mechanical rotation of the sample causes such molecules to pass through the same cycle of laboratory frame orientations, but with a mutual time shift. This concept has been called a *carousel*,[54] since the riders on a playground carousel follow the same circular path, but are shifted with respect to each other in time.

In some samples, it is convenient to include one or more reference frames intermediate between M and R. For example, in crystalline solids, it is common to define a crystal-fixed reference frame C, and a set of Euler angles $\Omega_{MC} = \{\alpha_{MC}, \beta_{MC}, \gamma_{MC}\}$ defining the orientations of the molecules with respect to the crystal axes. If there is more than one more molecule in the crystal unit cell, then several sets of Euler angles Ω_{MC} are needed. The orientation of the crystal with respect to the rotor is defined through the Euler angles Ω_{CR}. In ordered samples such as fibres, on the other hand, it is useful to define a fibre director axis system D. The Euler angles Ω_{MD} relate the molecular axis system M to the fibre director system D, and a further set of Euler angles Ω_{DR} relate the fibre director to the rotor axis. By factorizing the problem in this way, it is possible to define independent orientation distributions for the molecules with respect to the fibre, and for the fibres with respect to the rotor. An example of this approach is found in Refs.[55,56] If the sample is a powder, these intermediate axis systems are unnecessary, and they will be omitted in the following discussion.

2.2.4 The Laboratory Frame L

The laboratory frame is chosen so that its z-axis is along the external magnetic field. The relative orientation of the sample holder and the field are defined by the Euler angles $\Omega_{RL} = \{\alpha_{RL}, \beta_{RL}, \gamma_{RL}\}$.

In magic-angle spinning NMR, the sample rotates at a fixed angular frequency ω_r about a fixed axis, subtending the magic angle $\theta_{\text{magic}} = \arctan\sqrt{2}$ with respect to the magnetic field. In these circumstances, the relevant Euler angles are given by

$$\begin{aligned} \alpha_{RL} &= \alpha^0_{RL} - \omega_r t \\ \beta_{RL} &= \theta_{\text{magic}} = \arctan\sqrt{2} \\ \gamma_{RL} &= \text{arbitrary} \end{aligned} \tag{3}$$

Here α^0_{RL} defines the orientation of the rotor at time point $t = 0$, which is rigorously defined as the start of signal acquisition (to be consistent with the normal definition of the Fourier transform, which involves an integral from $t = 0$ to $t = \infty$). If the rotation of the sample is not synchronized with the pulse sequence, the angle α^0_{RL} varies randomly from transient to transient. If necessary, the rotation of the sample may be synchronized optically with the pulse sequence, so as to obtain reproducible and controllable values of α^0_{RL}. This is usually unnecessary in powder samples.

The negative sign in the expression for α_{RL} is consistent with the usual definition of the Euler angles[53] and leads to a right-handed rotation of the sample in the case that ω_r is positive.

The second Euler angle β_{RL} is the angle between the rotor axis and the field. For exact magic-angle spinning it is exactly equal to θ_{magic}, but for other experiments, such as off-axis spinning, variable-axis spinning, or "zero-field in high-field" experiments, the angle β_{RL} may take other values. In the rest of this article, exact MAS is assumed.

In double rotation or dynamical angle spinning experiments,[57–59] the time-dependence of the Euler angles Ω_{RL} is more complicated (see **Double Rotation,** Volume 3). I ignore such possibilities here (double rotation may be handled neatly by introducing an 'outer rotor' frame as an intermediate between R and L).

2.3 Frame Transformations

The following 'chain rule' for the Wigner matrices greatly facilitates the transformations of spin interactions between the different frames:

$$D^l(\Omega_{AB})D^l(\Omega_{BC}) = D^l(\Omega_{AC}) \tag{4}$$

For example, a given spin interaction Λ may be transformed from its principal axis frame into the laboratory frame using equation (1) and the following chain:

$$D^l(\Omega^{\Lambda}_{PM})D^l(\Omega_{MR})D^l(\Omega_{RL}) = D^l(\Omega^{\Lambda}_{PL}) \tag{5}$$

Note the pattern of the subscripts. This notation greatly facilitates the task of concatenating multiple frame transformations.

2.4 Rf Euler Angles

The mathematics of spherical tensor rotations may also be applied to the rotations of the nuclear spin polarizations by resonant rf fields. In general, a sequence of resonant rf fields induces a time-dependent rotation of the resonant spins, which may be expressed as follows:

$$U_{\text{rf}}(t, t^0) = \exp\{-\text{i}\alpha_{\text{rf}}(t)I_z\}\exp\{-\text{i}\beta_{\text{rf}}(t)I_y\}\exp\{-\text{i}\gamma_{\text{rf}}(t)I_z\} \tag{6}$$

Here U_{rf} is the propagator under the applied rf fields, starting from the initial point of the pulse sequence, denoted t^0, up to an arbitrary time t, and $\{I_x, I_y, I_z\}$ are the total angular momentum operators of the resonant spin species. In general, the propagator may be determined by integrating the Schrödinger equation:

$$\frac{\text{d}}{\text{d}t}U_{\text{rf}}(t, t^0) = -\text{i}\mathcal{H}_{\text{rf}}(t)U_{\text{rf}}(t, t^0) \tag{7}$$

under the boundary condition $U_{\text{rf}}(t^0, t^0) = \mathbf{1}$. The operator $\mathcal{H}_{\text{rf}}$ is the spin Hamiltonian for the interaction with the rf field, and depends on the amplitude, phase and frequency of the applied rf field in the usual way.

In general, the rf Euler angles $\Omega_{\text{rf}} = \{\alpha_{\text{rf}}, \beta_{\text{rf}}, \gamma_{\text{rf}}\}$ do not have an *obvious* relationship with the applied rf pulse sequence. Nevertheless, these angles provide a convenient way of defining the symmetry properties of the spins under rf irradiation, and it is always possible to derive the Euler angle

trajectory from a given pulse sequence. Furthermore, it also possible to discover the pulse sequence that provides a desired trajectory of rf Euler angles.

2.5 Rotational Components

The mechanical rotation of the sample induces a time-dependent trajectory of the Euler angles $\Omega_{RL} = \{\alpha_{RL}, \beta_{RL}, \gamma_{RL}\}$, while the rf pulse sequence induces a time-dependent trajectory of the Euler angles $\Omega_{\mathrm{rf}} = \{\alpha_{\mathrm{rf}}, \beta_{\mathrm{rf}}, \gamma_{\mathrm{rf}}\}$. Suppose that a certain spin interaction has space rank l and spin rank λ. According to equation (1), the spatial rotation induces a mixing of the $(2l + 1)$ space components with $m = -l, -l + 1 \cdots + l$. Similarly, in the interaction frame of the rf field (see **Average Hamiltonian Theory,** Volume 2), the spin rotations induce a mixing of the $(2\lambda + 1)$ spin components with $\mu = -\lambda, -\lambda + 1 \cdots + \lambda$.

In the presence of sample rotation and resonant rf fields, each spin interactions may therefore be regarded as a superposition of $(2l + 1) \times (2\lambda + 1)$ components, characterized by quantum numbers m and μ:

$$\mathcal{H}^{\Lambda} = \sum_{m=-l}^{+l} \sum_{\mu=-\lambda}^{+\lambda} \mathcal{H}^{\Lambda}_{lm\lambda\mu} \tag{8}$$

In the case of exact magic-angle spinning, the components with $l = 2$ and $m = 0$ vanish, due to the following property of the magic angle:

$$d^2_{00}(\theta_{\mathrm{magic}}) = 0 \tag{9}$$

Explicit expressions for the components $\mathcal{H}^{\Lambda}_{lm\lambda\mu}$ may be found in Refs.[45,60]

A summary of the spin interaction components, in the case of exact magic-angle spinning, is given in Table 2.

2.6 Symmetry Classes

The space and spin trajectories may be synchronized so as to generate an average Hamiltonian containing desired combinations of quantum numbers $\{l, m, \lambda, \mu\}$ while other combinations are suppressed.

This is done by setting up periodic symmetry relationships between the mechanical and rf rotations. Consider two arbitrary time points, separated by an interval $n\tau_r/N$, where n and N are integers, and $\tau_r = |2\pi/\omega_r|$ is the rotational period of the sample. From equation (3), the continuous rotation of the sample imposes the following relationship on the spatial Euler angles:

$$\begin{aligned} \alpha_{RL}\left(t + \frac{n\tau_r}{N}\right) &= \alpha_{RL}(t) - \frac{2\pi n}{N} \\ \beta_{RL}\left(t + \frac{n\tau_r}{N}\right) &= \beta_{RL}(t) \end{aligned} \tag{10}$$

The rf pulse sequence imposes similar-looking rules on the rf Euler angles (equation (6)).

In the case of CN^{ν}_{n} sequences, the following Euler angle symmetry is imposed:

$$\begin{aligned} \beta_{\mathrm{rf}}\left(t + \frac{n\tau_r}{N}\right) &= \beta_{\mathrm{rf}}(t) \\ \gamma_{\mathrm{rf}}\left(t + \frac{n\tau_r}{N}\right) &= \gamma_{\mathrm{rf}}(t) - \frac{2\pi\nu}{N} \end{aligned} \tag{11}$$

where ν is an integer, possibly different from n.

In the case of RN^{ν}_{n} sequences, the Euler angle symmetry is slightly different:

$$\begin{aligned} \beta_{\mathrm{rf}}\left(t + \frac{n\tau_r}{N}\right) &= \beta_{\mathrm{rf}}(t) \pm \pi \\ \gamma_{\mathrm{rf}}\left(t + \frac{n\tau_r}{N}\right) &= \gamma_{\mathrm{rf}}(t) - \frac{2\pi\nu}{N} \end{aligned} \tag{12}$$

These symmetries apply to arbitrary time points within the pulse sequence.

The symbol CN^{ν}_{n} and RN^{ν}_{n} is called the *symmetry class* of the rotor-synchronized pulse sequence. The integers N, n and ν are called the *symmetry numbers* of the pulse sequence. As will be seen, the symmetry class defines a set of *selection rules* for the average Hamiltonian, which may be used to manipulate the recoupling and decoupling properties of the pulse sequence.

2.7 Rotor-Synchronized Pulse Sequences

The symmetries in equations (11) and (12) only refer to two Euler angles; the behavior of the third Euler angle α_{rf} is left completely free. This freedom implies that there are many inequivalent ways of implementing equations (11) and (12). Some simple possibilities are described below.

2.7.1 CN^{ν}_{n} Sequences

The CN^{ν}_{n} Euler angle symmetries [equations (10) and (11)] are generated by rotor-synchronized pulse schemes of the general form shown in Figure 2. The idea is that n rotational periods of the sample are subdivided into N equal intervals. Each interval contains a radio frequency pulse sequence which is a *cycle*, i.e., it induces a rotation of the nuclear spins through an integer multiple of 360° (including zero). The radio-frequency phases of subsequent cycles are shifted with respect to each other by the angle $2\pi\nu/N$, causing a repeated incrementation (or decrementation) of the radio-frequency phase as one proceeds through the sequence. The integers n and ν may therefore be interpreted as space and spin *winding numbers*.[39] The sample rotates bodily through n full rotations, in the same time that it takes the radio-frequency phases to

Table 2 Components of homonuclear spin interactions in the interaction frame of an applied rf field, in the case of exact magic-angle spinning

Interaction	Space rank, l	Space components, m	Spin rank, λ	Spin components, μ
Isotropic chemical shift	0	0	1	$\{-1, 0, 1\}$
Chemical shift anisotropy	2	$\{-2, -1, 1, 2\}$	1	$\{-1, 0, 1\}$
J-coupling	0	0	0	0
Dipole–dipole coupling	2	$\{-2, -1, 1, 2\}$	0	$\{-2, -1, 0, 1, 2\}$

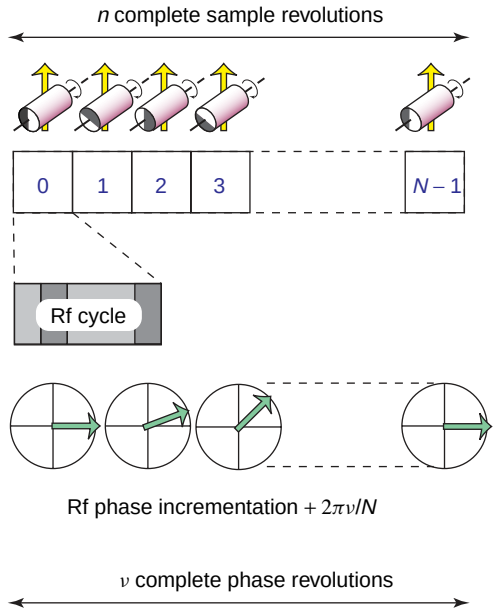

Figure 2 Construction of CN_n^{ν} sequences

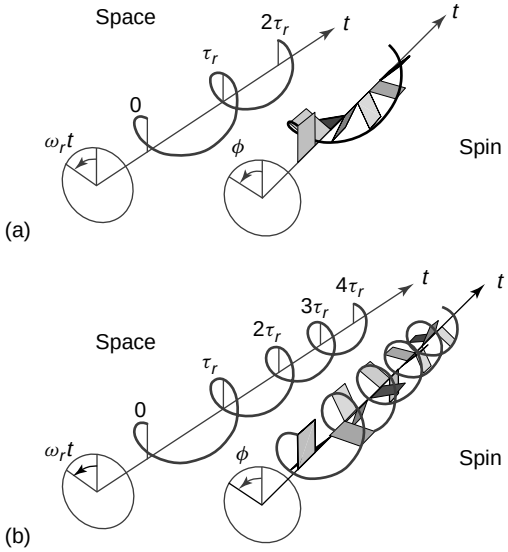

Figure 3 Visualization of the symmetry numbers for (a) $C7_2^1$ sequences, and (b) $C14_4^5$ sequences. The left-hand helices represent the spatial rotation of the sample as a function of time. The right-hand helices depict the modulation of the rf phase as a function of time. n spatial rotations are completed in the same time as ν spin rotations. The rf phase is modulated in N discrete steps, depicted by the planes in the right-hand diagrams. (Adapted from Ref.[39])

advance through ν full rotations, in N equal steps. This idea is conveyed for the cases of $C7_2^1$ and $C14_4^5$ in Figure 3.

These symmetry properties are independent of the internal structure of the rf cycles, providing that each cycle accomplishes a final rotation through an integer multiple of 360°.

For a proof that sequences with this structure generate the Euler angle symmetry given in equation (11), see Ref.[60]

For the sake of concreteness, consider a $C7_2^1$ sequence based upon the cyclic element $\mathcal{C} = 270_0 180_{180} 90_0$, where ξ_ϕ indicates a rectangular, resonant rf pulse with flip angle ξ and phase ϕ, and the angles are written in degrees. The full $C7_2^1$ sequence is as follows:

$$270_0 180_{180} 90_0 270_{51.43} 180_{231.43} 90_{51.43} 270_{102.86} 180_{282.86} 90_{102.86} -$$
$$270_{154.29} 180_{334.29} 90_{154.29} 270_{205.71} 180_{25.71} 90_{205.71} -$$
$$270_{257.14} 180_{77.14} 90_{257.14} 270_{308.57} 180_{128.57} 90_{308.57} \quad (13)$$

where the pulses are contiguous (no gaps in between). The rf field amplitude is chosen so that the entire sequence of 21 pulses fits exactly into two complete rotational periods of the sample. This requires that the spin nutation frequency in the rf field is exactly seven times the sample spinning frequency. The sequence in equation (13) is called POST-C7.[37]

2.7.2 RN_n^{ν} Sequences

A construction scheme for generating sequences with the Euler angle symmetries in equations (10) and (12) involves the following steps:

1. Select a sequence of rf pulses which rotates the nuclear spins through 180° about the x-axis. Call this element $\mathcal{R}$.
2. Change the *signs* of all rf phases within the element $\mathcal{R}$. Call this phase-inverted element $\mathcal{R}'$.
3. Select the rf amplitude so that N elements $\mathcal{R}$ occupy exactly the same time interval as n rotational periods of the sample. The number of elements N must be even in the case of RN_n^{ν} symmetry.
4. The RN_n^{ν} sequence consists of $N/2$ *pairs* of elements $\mathcal{R}_\phi \mathcal{R}_{-\phi}$, where ϕ is an overall phase shift, equal to $\phi = \pi\nu/N$ radians.

A simplified diagram of this procedure is shown in Figure 4 (step 2 above is omitted for simplicity). This looks similar to the set-up for a CN_n^{ν} sequence, but with the two differences that each element provides a 180° rotation, rather than a cycle, and that the rf phase is alternated between two values, rather than being incremented.

For a proof that sequences with this structure generate the Euler angle symmetry given in equation (12), see Ref.[60]

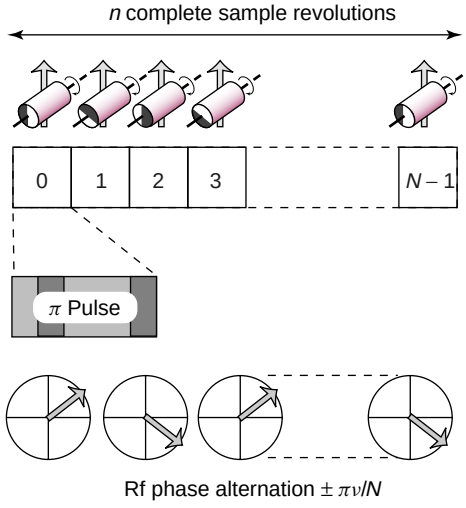

Figure 4 Construction of RN_n^{ν} sequences

As a concrete example, suppose that one would like to build a $R18_2^9$ sequence on the composite pulse $90_0 90_{90} 90_0$, which is known to have favorable homonuclear decoupling properties.[61] The first step is to establish whether this element induces a 180° rotation about the x-axis. This may be tested by rotating the three spin angular momentum operators, as follows:

$$\begin{aligned} I_x &\xrightarrow{90_0} I_x \xrightarrow{90_{90}} -I_z \xrightarrow{90_0} I_y \\ I_y &\xrightarrow{90_0} I_z \xrightarrow{90_{90}} I_x \xrightarrow{90_0} I_x \\ I_z &\xrightarrow{90_0} -I_y \xrightarrow{90_{90}} -I_y \xrightarrow{90_0} -I_z \end{aligned} \tag{14}$$

From this it may be seen that the $90_0 90_{90} 90_0$ sequence does transform I_z into $-I_z$, which is an appropriate property for a 180° rotation about the x-axis, but that it also exchanges the operators I_x and I_y, which is not appropriate. A little consideration leads to the conclusion that the $90_0 90_{90} 90_0$ sequence implements a rotation by 180° about an axis which is intermediate between the x-axis and the y-axis, i.e., phase shifted by 45°. This may also be proved by rotation operator algebra.[62]

This defect may be remedied by phase shifting the whole sequence by −45°. This leads to the element

$$\mathcal{R} = 90_{-45} 90_{45} 90_{-45} \tag{15}$$

which now implements the correct rotation. Changing the sign of all phases leads to

$$\mathcal{R}' = 90_{45} 90_{-45} 90_{45} \tag{16}$$

The desired $R18_2^9$ sequence requires additional phase shifts of $\phi = \pm\pi \times 9/18$ radians, or ±90°. The appropriate elements are therefore

$$\mathcal{R}_\phi = 90_{45} 90_{135} 90_{45} \tag{17}$$

and

$$\mathcal{R}'_{-\phi} = 90_{-45} 90_{-135} 90_{-45} \tag{18}$$

The full $R18_2^9$ sequence has the following structure:

$$R18_2^9(\text{version 1}) = \{90_{45} 90_{135} 90_{45} 90_{-45} 90_{-135} 90_{-45}\}^9 \tag{19}$$

where nine repetitions of the bracketed elements occupy exactly two rotational periods of the sample. If the phases are restricted to the interval 0–360°, we get

$$R18_2^9(\text{version 1}) = \{90_{45} 90_{135} 90_{45} 90_{315} 90_{225} 90_{315}\}^9 \tag{20}$$

If the element $\mathcal{R}$ contains no internal phase shifts, or when it only contains 180° phase shifts, then the conversion of $\mathcal{R}$ into $\mathcal{R}'$ may be ignored. For example, if a single 180_0 is used for the element $\mathcal{R}$, then the $R18_2^9$ sequence is as follows:

$$R18_2^9(\text{version 2}) = \{180_{90} 180_{270}\}^9 \tag{21}$$

where nine repetitions of the bracketed elements occupy exactly two rotational periods of the sample.

Although the construction principles of the RN_n^ν sequences appear to be quite complicated, the end result is sometimes very simple.

2.8 Effective Hamiltonian

In many circumstances, the behavior of the nuclear spins under a pulse sequence may be described using the theory described in **Average Hamiltonian Theory,** Volume 2. Suppose that the pulse sequence starts at time point t^0 and lasts until time point $t^0 + \tau$. Suppose also that the period of the pulse sequence is given by $T = n\tau_r$, where n is the space winding number. The propagator for the pulse sequence between the time points t^0 and $t^0 + \tau$ is written as

$$U(t^0 + \tau, t^0) \cong U_{\text{rf}}(t^0 + \tau, t^0) \exp\{-\text{i}\overline{\mathcal{H}}(t^0)\tau\} \tag{22}$$

where U_{rf} is the propagator for the rf field alone (equation (6)), $\overline{\mathcal{H}}(t^0)$ is the *effective Hamiltonian* of the internal spin interactions, for a pulse sequence starting at point t^0.

In a rotating sample, the effective Hamiltonian depends upon the starting time point t^0, since the orientation of the sample constantly changes.

The effective Hamiltonian may be approximated using the Magnus expansion:

$$\overline{\mathcal{H}}(t^0) \cong \overline{\mathcal{H}}^{(1)}(t^0) + \overline{\mathcal{H}}^{(2)}(t^0) + \cdots \tag{23}$$

where the first two terms are given by

$$\begin{aligned} \overline{\mathcal{H}}^{(1)}(t^0) &= T^{-1} \int_{t^0}^{t^0+T} \mathrm{d}t\, \mathcal{H}_{\text{int}}(t) \\ \overline{\mathcal{H}}^{(2)}(t^0) &= (2\text{i}T)^{-1} \int_{t^0}^{t^0+T} \mathrm{d}t_2 \int_{t^0}^{t_2} \mathrm{d}t_1 [\mathcal{H}_{\text{int}}(t_2), \mathcal{H}_{\text{int}}(t_1)] \end{aligned} \tag{24}$$

Here $\mathcal{H}_{\text{int}}$ is the internal spin Hamiltonian, expressed in the interaction frame of the rf field. This equation employs a consistent numbering system for the Magnus expansion terms, in which the kth Magnus term is proportional to a product of k Hamiltonians. Much literature uses a more awkward numbering, in which the indices start at zero.

The term $\overline{\mathcal{H}}^{(1)}$ is called the *average Hamiltonian*. The term $\overline{\mathcal{H}}^{(2)}$ is called the *second-order correction* to the average Hamiltonian, and so on.

If the internal spin Hamiltonian is small compared to the period T of the pulse sequence, then the average Hamiltonian expansion may be terminated after the first or second term.

Note that equation (22) represents the propagator over an arbitrary interval τ, while the average Hamiltonian terms in equation (24) involve integrals over the full period of the pulse sequence. This useful approximation allows results derived for entire periodic pulse sequences to be extended, with caution, to non-integral numbers of rf cycles. We have generally found this approximation to work well for the symmetry-based sequences.

2.9 First-Order Selection Rules

The interaction frame spin Hamiltonian is a sum of many rotational components, as in equation (8). The average Hamiltonian may therefore be written

$$\overline{\mathcal{H}}^{(1)}(t^0) = \sum_{lm\lambda\mu} \overline{\mathcal{H}}^{(1)}_{lm\lambda\mu}(t^0) \tag{25}$$

where

$$\overline{\mathcal{H}}^{(1)}_{lm\lambda\mu}(t^0) = T^{-1} \int_{t^0}^{t^0+T} \mathrm{d}t\, \mathcal{H}_{lm\lambda\mu}(t) \tag{26}$$

Each of these components is modulated by the spatial rotation of the sample, and the rotations of the spin polarizations induced by the rf field. If the pulse sequence is a member of the CN_n^ν or RN_n^ν symmetry classes, then the synchronized modulations possess the symmetry properties summarized in equations (10)–(12).

In Refs.[45,60] it is shown that these symmetry properties lead to *selection rules* on the average Hamiltonian terms:

2.9.1 Selection Rules for CN_n^ν Sequences

For CN_n^ν sequences, the following selection rule applies:

$$\overline{\mathcal{H}}^{(1)}_{lm\lambda\mu} = 0 \quad \text{if } mn - \mu\nu \neq NZ \tag{27}$$

where Z is any integer, including zero.

2.9.2 Selection Rules for RN_n^ν Sequences

For RN_n^ν sequences, the following selection rule applies:

$$\overline{\mathcal{H}}^{(1)}_{lm\lambda\mu} = 0 \quad \text{if } mn - \mu\nu \neq \frac{N}{2} Z_\lambda \tag{28}$$

Here Z_λ is any integer with the same *parity* as the spin rank λ. If λ is even, then Z_λ takes the values $0, \pm 2, \pm 4, \ldots$. If λ is odd, then Z_λ takes the values $\pm 1, \pm 3, \pm 5, \ldots$.

Equations (27) and (28) are the central results of symmetry-based pulse sequence theory. These two simple equations have wide consequences.

As a first example, consider a pulse sequence with symmetry $C7_2^1$. Let us examine the fate of double-quantum dipole–dipole terms with quantum numbers $\{l, m, \lambda, \mu\} = \{2, 1, 2, 2\}$. Equation (27) states that the average Hamiltonian of this term vanishes if the quantity $mn - \mu\nu$ is not equal to an integer multiple of N. Substituting in the values $m = 1$, $n = 2$, $\mu = 2$ and $\nu = 1$ we obtain $mn - \mu\nu = (1 \times 2) - (2 \times 1) = 0$. This is an integer multiple of $N = 7$, so the term $\{l, m, \lambda, \mu\} = \{2, 1, 2, 2\}$ is *symmetry allowed*. One cannot be sure whether this term actually exists without further calculation, but at least symmetry does not exclude it. Consider now the chemical shift anisotropy term with quantum numbers $\{l, m, \lambda, \mu\} = \{2, -2, 1, 1\}$. The expression $mn - \mu\nu$ evaluates to the value $mn - \mu\nu = ((-2) \times 2) - (1 \times 1) = -5$. This is not an integer multiple of 7, so this term is *symmetry forbidden* in the first-order average Hamiltonian.

Now consider the fate of the same two terms under the symmetry $R18_1^7$, using the rule in equation (28). The homonuclear dipole–dipole terms have a spin rank $\lambda = 2$, which is even. Equation (28) implies that a dipole–dipole term is symmetry-forbidden unless $mn - \mu\nu$ is equal to an even multiple of 9. For the term $\{l, m, \lambda, \mu\} = \{2, 1, 2, 2\}$, the expression $mn - \mu\nu$ evaluates to $(1 \times 1) - (2 \times 7) = -13$. This is not an even multiple of 9, so the term $\{2, 1, 2, 2\}$ is forbidden under the symmetry $R18_1^7$. For the chemical shift anisotropy term $\{l, m, \lambda, \mu\} = \{2, -2, 1, 1\}$, on the other hand, the expression $mn - \mu\nu$ evaluates to the value $mn - \mu\nu = ((-2) \times 1) - (1 \times 7) = -9$. This is an odd multiple of 9, and since the spin rank λ is also odd, this term is symmetry-allowed.

2.10 Space-Spin Selection Diagrams

The consequences of equations (27) and (28) are conveniently evaluated using *space-spin selection diagrams* (SSS diagrams). Two examples are given in Figure 5 and 6.

The branching lines in these diagrams show the possible values of $mn - \mu\nu$ for the particular class of spin interaction, split up into the 'space' part mn and the 'spin' part $\mu\nu$. The number of branches depends on the type of spin interaction, according to Table 2, while the spacing between the branches depends on the symmetry numbers n and ν. The right-hand side of each diagram shows a barrier containing holes spaced by the symmetry number N. Those pathways that are *blocked* by the barrier represent values of $mn - \mu\nu$ which *do* satisfy the inequalities in equations (27) and (28), and represent components that are symmetry-forbidden. Those pathways that *pass* through the holes in the barrier represent values of $mn - \mu\nu$ which *do not* satisfy the inequalities in equations (27) and (28), indicating components that are symmetry-allowed. The SSS diagrams allow the consequences of the inequalities in equations (27) and (28) to be visualized clearly.

The positions of the holes depend on the symmetry class. For the CN_n^ν class of symmetries, the holes in the barrier occur at levels $0, \pm N, \pm 2N, \ldots$. For the RN_n^ν class of symmetries, the positions of the holes depends on whether the spin rank λ is even or odd. For even ranks, the holes occur at levels $0, \pm N, \pm 2N, \ldots$, as in the case of CN_n^ν symmetries. For odd ranks, on the other hand, the holes occur at levels $\pm N/2, \pm 3N/2, \ldots$, where $N/2$ is an integer, since N is even.

2.10.1 SSS Diagrams for $C7_2^1$ Symmetry

The behavior of the chemical shift anisotropy (CSA) terms under $C7_2^1$ symmetry is shown in Figure 5(a). There are four branches in the space part, corresponding to the $m = \{-2, -1, 1, 2\}$ components indicated in Table 2. For clarity, only the branches with $m \leq 0$ are shown: the branches with negative m are mirror images. The $m = 0$ component vanishes in the case of exact magic-angle spinning. The 'space' branches are spaced vertically by two units, according to the winding number $n = 2$. Each of these branches splits into three spin components, with indices $\mu = \{-1, 0, 1\}$, and spaced vertically by one unit, according to the winding number $\nu = 1$. Since the value of N is 7, the barrier on the right contains holes at levels $0, \pm 7, \pm 14, \ldots$. There are no CSA pathways which pass through these holes, indicating that the average Hamiltonian contains no CSA terms. The SSS diagram shows immediately that the pulse sequence is compensated for the effects of CSA, to first order.

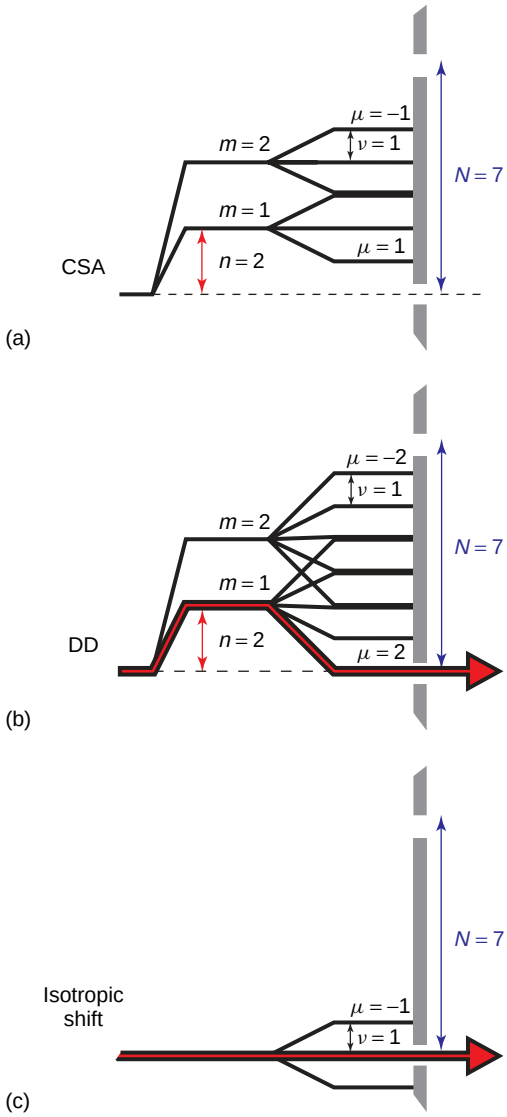

Figure 5 Space-spin selection diagram for $C7_2^1$ symmetry, omitting components with $m < 0$. (a) Behavior of the CSA terms. All terms are symmetry-forbidden. (b) Behavior of the homonuclear DD coupling terms. The component $\{l, m, \lambda, \mu\} = \{2, 1, 2, 2\}$ is symmetry-allowed. (c) Behavior of the isotropic chemical shift terms. The component $\{l, m, \lambda, \mu\} = \{0, 0, 1, 0\}$ is symmetry-allowed

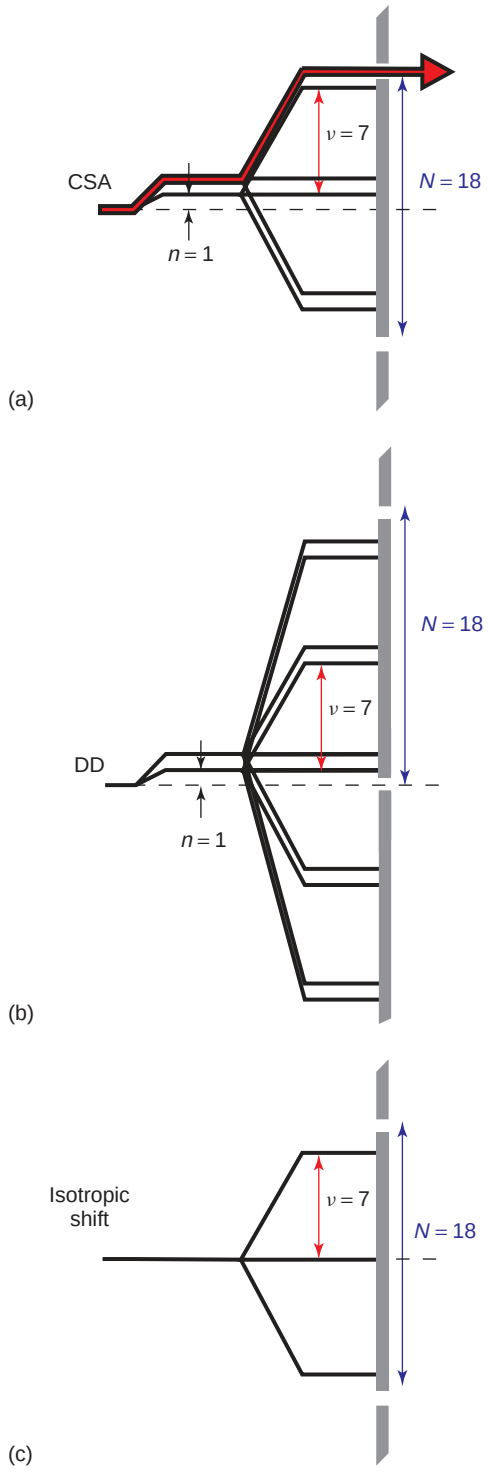

Figure 6 Space-spin selection diagram for $R18_1^7$ symmetry, omitting components with $m < 0$. (a) Behavior of the CSA terms. The component $\{l, m, \lambda, \mu\} = \{2, 2, 1, -1\}$ is symmetry-allowed. (b) Behavior of the homonuclear DD coupling terms. All components are symmetry-forbidden. (c) Behavior of the isotropic chemical shift terms. All components are symmetry-forbidden. Note that the positions of the holes change, depending on whether the spin rank λ is odd or even

The behavior of the dipole–dipole coupling (DD) terms under $C7_2^1$ symmetry is shown in Figure 5(b). Here too there are four branches in the space part, corresponding to the $m = \{-2, -1, 1, 2\}$ components in Table 2. Only the branches with non-negative m are shown, for the sake of clarity. Each of the space branches splits into five spin branches, with indices $\mu = \{-2, -1, 0, 1, 2\}$. As may be seen, the branch with $\{l, m, \lambda, \mu\} = \{2, 1, 2, 2\}$ passes through a hole in the barrier, indicating that this component is symmetry-allowed. The mirror-image branch with $\{l, m, \lambda, \mu\} = \{2, -1, 2, -2\}$ is also symmetry-allowed (not shown).

Since all the CSA terms are symmetry-forbidden, and the only symmetry-allowed DD terms have quantum numbers $\mu = \pm 2$, sequences with the symmetry $C7_2^1$ behave as *CSA-compensated double-quantum recoupling sequences*.

Now consider the SSS diagram for isotropic chemical shift terms, shown in Figure 5(c). Since the space and spin ranks are $l = 0$ and $\lambda = 1$, there is one space component, with $m = 0$,

and three spin components, with $\mu = \{-1, 0, 1\}$. The SSS diagram shows that the isotropic shift component $\{l, m, \lambda, \mu\} = \{0, 0, 1, 0\}$ is symmetry-allowed under $C7_2^1$ symmetry. This implies that $C7_2^1$ sequences are vulnerable to isotropic chemical shifts, unless additional precautions are taken. We return to this issue later.

2.10.2 SSS Diagrams for $R18_1^7$ Symmetry

The behavior of the CSA terms under $R18_1^7$ symmetry is shown in Figure 6(a). The left-hand side shows the two space branches with $m = 1$ and 2. The $m = 0$ component vanishes in the case of exact magic-angle spinning. The space branches are spaced vertically by 1 unit, according to the winding number $n = 1$. Each branch splits into three spin components, with indices $\mu = \{-1, 0, 1\}$, and spaced vertically by 7 units, according to the winding number $\nu = 7$. Since the spin rank λ of the CSA terms is equal to 1, which is an odd number, the barrier on the right contains holes at odd multiples of $N/2$, which is equal to 9 in this case. The holes in the barrier are therefore at levels $\pm 9, \pm 27, \ldots$. As may be seen, the CSA term $\{l, m, \lambda, \mu\} = \{2, 2, 1, -1\}$ passes through a hole, which indicates that $R18_1^7$ symmetry is a *CSA recoupling sequence*.

The behavior of the DD terms under $R18_1^7$ symmetry is shown in Figure 6(b). The space branches with $m = 1$ and 2 split into five spin components, with indices $\mu = \{-2, -1, 0, 1, 2\}$. In the case of DD couplings, the spin rank λ is equal to 2, which is an even number. As a result, the barrier on the right contains holes at even multiples of 9, i.e., $0, \pm 18, \pm 36, \ldots$. As may be seen, the barrier blocks all of the DD terms. This indicates that sequences with $R18_1^7$ symmetry are insensitive to homonuclear dipole–dipole couplings, to first order.

The behavior of the isotropic chemical shift terms under $R18_1^7$ symmetry is shown in Figure 6(c). None of the three components with $m = 0$ and $\mu = \{-1, 0, 1\}$ pass through the barrier. This indicates that sequences with $R18_1^7$ symmetry are insensitive to isotropic chemical shifts, to first order.

One may conclude that $R18_1^7$ sequences accomplish recoupling of the CSA interactions, compensated to first order for homonuclear DD couplings and isotropic chemical shifts.

2.11 Higher-Order Selection Rules

In many cases, the first-order Magnus term (the average Hamiltonian) is not a sufficiently good approximation to the effective Hamiltonian of a pulse sequence. Although the higher-order correction terms $\overline{\mathcal{H}}^{(2)}, \overline{\mathcal{H}}^{(3)}, \ldots$ are more complicated than the first-order terms, they are also subject to selection rules in the case of pulse sequence symmetry.

By analogy with equation (25), the second-order term $\overline{\mathcal{H}}^{(2)}$ may be written as a superposition of many rotational components:

$$\overline{\mathcal{H}}^{(2)}(t^0) = \sum_{l_2 m_2 \lambda_2 \mu_2} \sum_{l_1 m_1 \lambda_1 \mu_1} \overline{\mathcal{H}}^{(2)}_{l_2 m_2 \lambda_2 \mu_2, l_1 m_1 \lambda_1 \mu_1}(t^0) \tag{29}$$

where each component is given by

$$\overline{\mathcal{H}}^{(2)}_{l_2 m_2 \lambda_2 \mu_2, l_1 m_1 \lambda_1 \mu_1}(t^0) = (2\mathrm{i}T)^{-1} \int_{t^0}^{t^0+T} \mathrm{d}t_2 \int_{t^0}^{t_2} \mathrm{d}t_1 [\mathcal{H}_{l_2 m_2 \lambda_2 \mu_2}(t_2), \mathcal{H}_{l_1 m_1 \lambda_1 \mu_1}(t_1)] \tag{30}$$

The horrifying complexity is moderated by the following selection rules:

For CN_n^ν sequences, the following selection rule applies:

$$\overline{\mathcal{H}}^{(2)}_{l_2 m_2 \lambda_2 \mu_2, l_1 m_1 \lambda_1 \mu_1} = 0 \text{ if } \begin{cases} m_2 n - \mu_2 \nu \neq NZ \\ \text{AND} \\ m_1 n - \mu_1 \nu \neq NZ \\ \text{AND} \\ (m_2 + m_1) n - (\mu_2 + \mu_1) \nu \neq NZ \end{cases} \tag{31}$$

where Z is any integer, including zero.

For RN_n^ν sequences, the following selection rule applies:

$$\overline{\mathcal{H}}^{(2)}_{l_2 m_2 \lambda_2 \mu_2, l_1 m_1 \lambda_1 \mu_1} = 0 \text{ if } \begin{cases} m_2 n - \mu_2 \nu \neq \dfrac{N}{2} Z_{\lambda_2} \\ \text{AND} \\ m_1 n - \mu_1 \nu \neq \dfrac{N}{2} Z_{\lambda_1} \\ \text{AND} \\ (m_2 + m_1) n - (\mu_2 + \mu_1) \nu \neq \dfrac{N}{2} Z_{\lambda_2 + \lambda_1} \end{cases} \tag{32}$$

where Z_{λ_2} is an integer with the same parity as λ_2, Z_{λ_1} is an integer with the same parity as λ_1, and $Z_{\lambda_2+\lambda_1}$ is an integer with the same parity as $\lambda_2 + \lambda_1$.

These selection rules are proved in Refs.[45,60]

Although the second-order selection rules do not usually allow the elimination of all undesirable terms, they do greatly reduce the labor required to evaluate the terms. For example, in general, there are 208 components to the $\overline{\mathcal{H}}^{(2)}$ term involving commutators of dipole–dipole coupling and CSA interactions. In the presence of a $R14_2^6$ sequence, only 16 of these are symmetry-allowed.

The R-sequence selection rule equation (32) is more restrictive than that for C-sequences equation (31). As a result, R-sequences tend to have smaller numbers of higher-order terms than C-sequences, which often translates into improved performance.

The second-order selection rules allow a straightforward count of the number of symmetry-allowed terms of a particular type. Higher-order term counts may be used to get a feel for the qualitative performance of a particular symmetry, without performing detailed calculations.[41,45] However, this rather crude criterion should not be relied on completely.

It is possible to extend these second-order selection rules to arbitrarily high orders.[45]

2.12 Scaling Factors

The selection rules provide information on which terms are symmetry-forbidden. However, they provide no information on the magnitude of the symmetry-allowed terms.

In general, the form of a symmetry-allowed first-order term is as follows:

$$\overline{\mathcal{H}}^{\Lambda}_{lm\lambda\mu}(t^0) = \kappa_{lm\lambda\mu} [A^{\Lambda}_{lm}]^R \exp\{-\mathrm{i}m(\alpha^0_{RL} - \omega_r t^0)\} T^{\Lambda}_{\lambda\mu} \tag{33}$$

where $[A^{lm}_{\Lambda}]^R$ is a component of the spatial tensor of interaction Λ, expressed in the rotor-fixed frame R, and $T^{\Lambda}_{\lambda\mu}$ is a component of the spin tensor of interaction Λ, expressed in the laboratory frame. The factor $\kappa_{lm\lambda\mu}$ is called the *scaling factor* of the pulse sequence, and depends upon the symmetry class, as well as the detailed structure of the basic element upon which the pulse sequence is built.

The scaling factor may be a complex number. Its magnitude is always less than one, which indicates that the suppression of unwanted terms is always accompanied by a reduction in the magnitude of the symmetry-allowed terms.

2.12.1 Scaling Factor Formulae

General formulae for the scaling factors are given in Ref.[60] In the case of CN_n^ν sequences, the scaling factor for a symmetry-allowed term $\{l, m, \lambda, \mu\}$ is given by

$$\kappa_{lm\lambda\mu} = \tau^{-1} d^l_{m0}(\beta_{RL}) \int_0^\tau \mathrm{d}t\, d^\lambda_{\mu 0}(-\beta_{\mathrm{rf}}(t)) \exp\{\mathrm{i}(\mu\gamma_{\mathrm{rf}}(t) + m\omega_r t)\} \quad (34)$$

where $\tau = n\tau_r/N$ is the duration of a basic element $\mathcal{C}$, $\tau_r = |2\pi/\omega_r|$ is a rotor period, and $\beta_{\mathrm{rf}}(t)$ and $\gamma_{\mathrm{rf}}(t)$ are rf Euler angles [equation (6)]. The basic element C is assumed to extend from time $t = 0$ to $t = \tau$.

In the case of RN_n^ν sequences, the scaling factor is given by

$$\kappa_{lm\lambda\mu} = \tau^{-1} d^l_{m0}(\beta_{RL}) \times \int_0^\tau \mathrm{d}t\, d^\lambda_{\mu 0}(-\beta_{\mathrm{rf}}(t)) \exp\{\mathrm{i}(\mu\gamma_{\mathrm{rf}}(t) - \mu\frac{\pi\nu}{N} + m\omega_r t)\} \quad (35)$$

There is an extra complex factor in this case, since the first element of a RN_n^ν sequence is not the same as the basic element.

The scaling factor is calculated most readily if the basic elements of the pulse sequence do not contain any rf phase shifts, or if the phase shifts are integer multiples of 180°. This is the case of *amplitude-modulated* basic elements. For example, $\mathcal{C} = 270_0 180_{180} 90_0$ is an amplitude-modulated basic element, while $\mathcal{R} = 90_{-45} 90_{45} 90_{-45}$ is a *phase-modulated* basic element. In the case of amplitude-modulated basic elements, the rf Euler angles are given by

$$\beta_{\mathrm{rf}}(t) = \int_0^t \mathrm{d}t' \omega_{\mathrm{nut}}(t')$$
$$\gamma_{\mathrm{rf}}(t) = \pi/2 \quad (36)$$

where ω_{nut} is the amplitude of the rf field, expressed as a nutation frequency (180° phase shifts may be taken into account by reversing the sign of ω_{nut}).

The calculation of the scaling factor is more difficult if the basic element is phase modulated. General formulae are given in Ref.[60] Andreas Brinkmann has written a *Mathematica*[63] program which provides the scaling factors of general sequences of rectangular pulses. The program is available on the web (*http://www.soton.ac.uk/~mhl*).

2.12.2 Physical Interpretation

The formulae for the scaling factor, equations (34) and (35) contain three factors. The first term, $d^l_{m0}(\beta_{RL})$ is purely spatial, and concerns the transformation of spatial rank-l tensors by the physical rotation of the sample. This term depends on the tilt of the rotation axis with respect to the magnetic field. The second term $d^\lambda_{\mu 0}(-\beta_{\mathrm{rf}}(t))$ corresponds to the time-dependent transformation of rank-λ spin operators by the rf field. The third term (the complex exponential factor) takes into account the physical rotation of the sample within the duration of each pulse sequence element. The formula for the R-sequence scaling factor, equation (35), contains a further phase factor, which arises because the first element of a R-sequence is phase shifted with respect to the basic element $\mathcal{R}$.

In general, it is desirable that the magnitude of $\kappa_{lm\lambda\mu}$ is as large as possible. It helps if one develops a physical feel of how $\kappa_{lm\lambda\mu}$ is generated.

In most cases, the angle β_{RL} is equal to the magic angle, so that the first term $d^l_{m0}(\beta_{RL})$ is not open to manipulation (an exception is provided by the 'zero-field in high-field' pulse sequences, where the choice of the spinning angle is an important element of the pulse sequence design).

In many cases, the symmetry number N is much larger than n. In this case, the duration of each element is much less than a rotor period, and it is possible to ignore the rotation of the sample during the individual rf elements, as a first approximation. This corresponds to the neglect of the $m\omega_r t$ terms in equations (34) and (35). This is called the quasi-static approximation.

In the quasi-static limit, only the rf rotations affect the accumulating time average of $T_{\lambda\mu}$ spin operators. For example, consider the problem of double-quantum recoupling. The relevant Wigner element in this case is $d^2_{20}(\beta_{\mathrm{rf}})$, which is proportional to $\sin^2(\beta_{\mathrm{rf}})$. This term is always positive, and is maximized at $\beta_{\mathrm{rf}} = 90°$ and $\beta_{\mathrm{rf}} = 270°$. It follows that the main contributions to the scaling factor are obtained when the Euler angle β_{rf} is close to the values 90° or 270°. At the same time, the Euler angle γ_{rf} should be kept fixed. As shown in equation (36), this may be ensured by using an amplitude-modulated basic element.

The simplest cyclic element is $\mathcal{C} = 360_0$. The rotation under this pulse takes the Euler angle β_{rf} linearly from 0 to 360°. Double-quantum excitation is accomplished near the 'hot spots' at $\beta_{\mathrm{rf}} = 90°$ and $\beta_{\mathrm{rf}} = 270°$. No double-quantum excitation is achieved, on the other hand, at the 'cold spots' $\beta_{\mathrm{rf}} = 0$ and $\beta_{\mathrm{rf}} = 180°$. The element $\mathcal{C} = 360_0$ spends equal time near the 'hot' and 'cold' spots. Nevertheless, the appropriate Wigner element is always positive, so the scaling factor is satisfactory ($|\kappa_{2122}| = 0.157$ for the case of $C7_2^1$ symmetry).

The scaling factor may be improved by turning the rf field off near the 'hot spots' $\beta_{\mathrm{rf}} = 90°$ and $\beta_{\mathrm{rf}} = 270°$, allowing the double-quantum operators more time to accumulate. An example of this technique is given by the sequence

$$\mathcal{C} = 90_0 - \tau_\omega - 180_0 - \tau_\omega - 90_0 \quad (37)$$

where the 'window' duration τ_ω is selected so that the overall element occupies an interval $\tau = n\tau_r/N$. In the limit of infinitely strong and short pulses, the element in equation (37) provides a greatly improved scaling factor of $|\kappa_{2122}| = 0.308$ for the case of $C7_2^1$ symmetry. Although the scaling factor may be increased by introducing windows, this method has not been used very often, perhaps because the strong rf pulses make the problem of proton decoupling more acute (see below).

In practice, it is common to use elements which are locally compensated for rf inhomogeneity. This improves the robustness of the pulse sequence to rf amplitude deviations. The original version of the C7 pulse sequence used the locally-compensated element $\mathcal{C} = 360_0 360_{180}$ in a $C7_2^1$ symmetry

scheme.[36] In this case, each of the double-quantum 'hot spots' at $\beta_{\rm rf} = 90°$ and $\beta_{\rm rf} = 270°$ are traversed twice during each element. The scaling factor of $|\kappa_{2122}| = 0.155$ is almost the same as for the simple element $\mathcal{C} = 360_0$, which has $|\kappa_{2122}| = 0.157$. The values are slightly different because of the rotation of the sample during the rf element.

In the quasi-static limit, the efficiency of double-quantum recoupling is greatly reduced if the Euler angle $\gamma_{\rm rf}$ is allowed to vary. For example, the scaling factor for the phase-modulated element $\mathcal{C} = 360_0360_{120}360_{240}$ is given by $|\kappa_{2122}| = 0.047$ in the case of $C7_2^1$ symmetry.

If the values of N and n are comparable, the quasi-static approximation breaks down. In this case, it is necessary to think much more carefully about how the physical rotation of the sample and the spin rotations combine. Amplitude-modulated elements are no longer optimal as far as the scaling factor is concerned. For example, consider the symmetry $C7_5^1$, which provides similar selection rules to $C7_2^1$ (except that the $\{l, m, \lambda, \mu\} = \{2, \pm1, 2, \mp2\}$ terms are selected, rather than $\{2, \pm1, 2, \pm2\}$). In the case of $C7_5^1$ symmetry, the scaling factor for the allowed term $\{l, m, \lambda, \mu\} = \{2, 1, 2, -2\}$ is given by $|\kappa_{212-2}| = 0.064$ for the amplitude-modulated standard element $\mathcal{C} = 360_0360_{180}$. This low scaling factor is due to the considerable rotation of the sample during the $\mathcal{C}$ element, leading to a strong variation of the $\omega_r t$ term in equation (34).[39,40] The scaling factor may be greatly improved by using the phase-modulated element $\mathcal{C} = 360_0360_{120}360_{240}$. For the case of $C7_5^1$ symmetry, one obtains the value $|\kappa_{212-2}| = 0.144$.[39] The improvement in scaling factor arises because the modulations of the Euler angle $\gamma_{\rm rf}$ due to the rf phase shifts compensate the modulation of the $\omega_r t$ term, to a good approximation. Note that the phase shifts must be performed in the correct sense: The scaling factor for the element $\mathcal{C} = 360_0360_{240}360_{120}$, in the case of $C7_5^1$ symmetry, is only $|\kappa_{212-2}| = 0.044$.

In some cases, pulse sequences work even if the scaling factor is very small. For example, the most commonly-used version of the RFDR pulse sequence[33,34] employs XY phase cycling and conforms to $R4_4^1$ symmetry. This symmetry is appropriate for zero-quantum DD recoupling, since it allows the homonuclear DD terms $\{l, m, \lambda, \mu\} = \{2, \pm1, 2, 0\}$ and $\{2, \pm2, 2, 0\}$, while suppressing other DD terms and all chemical shift terms. However, the first reports of this pulse sequence used an $\mathcal{R}$ element consisting of a strong 180° pulse followed by a 'window' in which the rf field is turned off. This is a puzzling choice of basic element, since the scaling factors for all symmetry-allowed DD terms vanish if the rf pulses are infinitely short. In fact, this pulse sequence reasonably well because the rf pulses always have a finite duration, so that the scaling factor is small but finite. In addition, J-couplings and higher-order effects play a role. Recent implementations of RFDR take a more sophisticated approach.[64,65]

2.12.3 Vanishing Scaling Factors

In many cases, the scaling factors for some symmetry-allowed terms are deliberately set to zero. For example, the symmetry $C7_2^1$ allows the isotropic chemical shift term $\{l, m, \lambda, \mu\} = \{0, 0, 1, 0\}$. Pulse sequences with this symmetry are therefore vulnerable to isotropic shift variations. The basic elements $\mathcal{C} = 360_0$, 360_0360_{180} and $90_0360_{180}270_0$ set the scaling factor κ_{0010} to zero, compensating these pulse sequences for isotropic chemical shifts or resonance offset effects. R-symmetries such as $R14_2^6$ do not need this precaution, since all isotropic chemical shift terms are symmetry-forbidden in this case.

Another example is provided by the MELODRAMA sequence for homonuclear dipolar recoupling.[66] Some versions of this sequence are based on $C4_1^1$ symmetry. In these cases, the isotropic shift term $\{l, m, \lambda, \mu\} = \{0, 0, 1, 0\}$ is symmetry-allowed, but may be suppressed by using basic elements of the form $\mathcal{C} = (360k)_0$, where k is an integer. Other versions of the MELODRAMA sequence[66] have $R4_1^1$ symmetry, which suppresses all isotropic shift terms without extra precautions. None of these symmetries, however, remove all of the CSA terms.

The recently-described C-REDOR sequences[67] are remarkable examples of how the basic element may be designed so as to destroy undesirable symmetry-allowed terms. The main variants of C-REDOR sequences are based upon $C3_3^1$ and $C7_7^1$ symmetry. These symmetries allow CSA terms of the form $\{l, m, \lambda, \mu\} = \{2, \pm2, 1, 0\}$ and $\{2, \pm1, 1, 0\}$, the isotropic shift term $\{0, 0, 1, 0\}$, and also the homonuclear DD coupling terms $\{2, \pm2, 2, 0\}$ and $\{2, \pm1, 2, 0\}$. However, by choosing a basic element $\mathcal{C} = 90_0360_{180}270_0$, the scaling factors of all terms vanish, except for those belonging to the CSA terms $\{2, \pm1, 1, 0\}$. These sequences may therefore be used to selectively recouple CSA terms while suppressing the isotropic chemical shifts and homonuclear DD couplings. C-REDOR has been applied to the selective recoupling of heteronuclear DD interactions,[67] which behave in the same way as the CSA terms, if the rf field is resonant with only one spin species (see below).

The vanishing scaling factors of certain terms under specific pulse sequences is probably due to additional symmetries. This is a promising area for further theory.

2.13 Orientation Dependence

In most cases, the magnitudes of the recoupled spin interactions depend on the orientation of the molecular reference frame with respect to the rotor. The only exceptions are when isotropic spin interactions such as the J-coupling or the isotropic chemical shift are selected, or in the special case of 'zero-field in high-field' experiments.[28,29]

The orientation-dependence of the recoupled spin interactions creates both problems and opportunities. A powerful feature of the symmetry theory is that it allows the form of the orientation-dependence to be manipulated qualitatively by choosing certain combinations of symmetry numbers.

The recoupled spin Hamiltonian in equation (33) is proportional to the spatial tensor component in the rotor-fixed frame, defined through the transformation chain

$$[A_{lm}^{\Lambda}]^R = \sum_{m'',m'} [A_{lm''}^{\Lambda}]^P \, D^l_{m''m'}(\Omega_{PM}^{\Lambda}) D^l_{m'm}(\Omega_{MR}) \qquad (38)$$

Here $[A_{lm}^{\Lambda}]^P$ are components of the spatial tensor, expressed in its own principal axis frame. The expression in equation (38) depends on the three Euler angles $\Omega_{MR} = \{\alpha_{MR}, \beta_{MR}, \gamma_{MR}\}$ defining the orientation of the molecular reference frame with respect to the rotor frame. In general, the recoupled spin Hamiltonian is anisotropic, and depends upon all three orientational Euler angles.

2.13.1 γ-Encoding

Suppose that a particular set of quantum numbers $\{l, m, \lambda, \mu\}$ is symmetry-allowed in the average Hamiltonian. The spatial Wigner element has the following form:

$$D^{l}_{m'm}(\Omega_{MR}) = \exp\{-\mathrm{i}m'\alpha_{MR}\} d^{l}_{m'm}(\beta_{MR}) \exp\{-\mathrm{i}m\gamma_{MR}\} \quad (39)$$

This may be combined with equation (33) to show how a single recoupled term depends upon the Euler angle γ_{MR}, the time point t^0 at which the symmetry-based pulse sequence starts, and the rotor Euler angle α^0_{RL} at the time point $t = 0$:

$$\overline{\mathcal{H}}^{\Lambda}_{lm\lambda\mu}(\gamma_{MR}, t^0, \alpha^0_{RL}) = \overline{\mathcal{H}}^{\Lambda}_{lm\lambda\mu}(0, 0, 0) \times \exp\{-\mathrm{i}m(\gamma_{MR} + \alpha^0_{RL} - \omega_r t^0)\} \quad (40)$$

The three parameters γ_{MR}, t^0 and α^0_{RL} may be included in a single complex phase factor.

It follows that only the *phase*, and not the *magnitude*, of the single term $\overline{\mathcal{H}}^{\Lambda}_{lm\lambda\mu}$ depends on the orientational Euler angle γ_{MR}. This property is termed *γ-encoding* of the recoupled term $\overline{\mathcal{H}}^{\Lambda}_{lm\lambda\mu}$.

In general, there are several symmetry-allowed terms $\overline{\mathcal{H}}^{\Lambda}_{lm\lambda\mu}$ with the same value of l, λ and μ but different values of m. Each of these terms contains the same spin operator $T^{\Lambda}_{\lambda\mu}$, but with a different spatial coefficient. These multiple coefficients interfere in a complicated way. As a result, the *complete* recoupled spin Hamiltonian is usually not γ-encoded.

It is possible to maintain γ-encoding of the entire recoupled Hamiltonian, by imposing a *one-to-one correspondence* between the symmetry-allowed spatial quantum numbers $\{l, m\}$ and the symmetry-allowed spin quantum numbers $\{\lambda, \mu\}$. This prevents the interference of terms with the same value of μ but different values of m.

For example, consider the symmetry $C6^1_2$. This leads to double-quantum recoupling of the DD terms, with suppression of all CSA terms to first order. The symmetry-allowed DD terms have the quantum numbers $\{2, -2, 2, 2\}$, $\{2, -1, 2, -2\}$, $\{2, 1, 2, 2\}$ and $\{2, 2, 2, -2\}$. The average Hamiltonian is *not* γ-encoded, since each spin term $\mu = 2$ is associated with two spatial components, $m = -2$ and $m = 1$.

If the symmetry number N is increased from 6 to 7, the symmetry $C7^1_2$ is generated, which only allows the DD terms $\{2, -1, 2, -2\}$ and $\{2, 1, 2, 2\}$. Since each spin component is now associated with only a single spatial component, the recoupled spin Hamiltonian is γ-encoded. Some of the success of the C7 pulse sequence and its variants may be attributed to the γ-encoding of the average Hamiltonian. For example, the theoretical maximum efficiency of double-quantum filtering experiments is usually increased by around 20% by using a γ-encoded pulse sequence.[36] In addition, γ-encoded pulse sequences enjoy much greater freedom in the relative timing of the pulse sequence and the sample rotation (see below).

The orientation-dependence of γ-encoded and non-γ-encoded sequences are contrasted in Figure 7. For γ-encoded sequences, the magnitude of the recoupled Hamiltonian is cylindrically symmetrical around the sample rotation axis.

2.13.2 Non-γ-Encoded Sequences

Although γ-encoding is generally a positive feature, it does have some disadvantages. As explained above, γ-encoding is generally imposed by eliminating some components of the average Hamiltonian. This enhanced selectivity is generally accompanied by a reduction in the overall magnitude of the recoupled Hamiltonian. In some cases, for example in long-range distance measurements, this is a disadvantage, since the recoupled interactions compete with relaxation and other loss processes. As a result, non-γ-encoded pulse sequences are sometimes preferable if the largest possible recoupled Hamiltonian is required, and its orientation-dependence is of lesser importance.

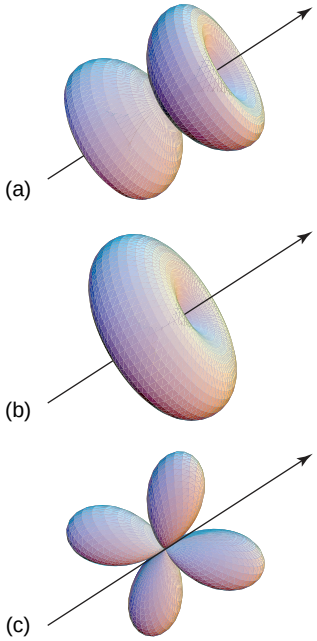

Figure 7 Polar plots showing the orientation-dependence of different dipolar recoupling sequences with respect to the magic-angle rotation axis (solid arrow). The direction of the external field is vertical. In each case, the magnitude of the recoupled Hamiltonian for a given orientation of the internuclear vector is proportional to the distance from the origin to the surface, in the direction of the vector. (a) γ-encoded recoupling of $m = \pm 1$ terms; (b) γ-encoded recoupling of $m = \pm 2$ terms; (c) non-γ-encoded recoupling

The complicated orientation-dependence of non-γ-encoded sequences may also be put to good use. Spiess and co-workers[68,69] have shown that the orientation-dependence generates characteristic signal modulations in certain two-dimensional experiments. These modulations may be matched with simulations in order to obtain structural information such as internuclear distances. In these applications, the recoupling pulse sequence must *not* be γ-encoded.

A further disadvantage of γ-encoding is that the construction of compensated supercycles is more difficult.

Some recoupled Hamiltonians *cannot* be γ-encoded within the framework of the symmetry theory described here. For example, consider the problem of zero-quantum recoupling in the presence of MAS. Since the selection rules are invariant to an overall sign change, it is not possible to allow terms of the form $\{l, m, \lambda, \mu\} = \{2, m, 2, 0\}$ without also allowing terms of the form $\{2, -m, 2, 0\}$. Since the $\mu = 0$ term is associated with two spatial terms $\pm m$, the resulting Hamiltonian is not γ-encoded. If desired, a γ-encoded zero-quantum DD Hamiltonian may be generated by rotational resonance,[70–72] which

is based on different principles (see **Rotational Resonance in Biology,** Volume 7).

2.13.3 β-Dependence

Consider the γ-encoded recoupling of dipole–dipole interactions between two spins j and k. Since the DD interaction is symmetrical, the tensor components $[A_{2m}^{jk}]^P$, written in the principal axis system of the DD interaction, vanish for the case $m \neq 0$. From equation (33), the recoupled DD interaction between spins j and k has the form

$$\overline{\mathcal{H}}_{2m2\mu}^{jk}(t^0) = \kappa_{2m2\mu}[A_{20}^{jk}]^P d_{0m}^2(\beta_{PR}^{jk}) \times \exp\{-\mathrm{i}m(\gamma_{PR}^{jk} + \alpha_{RL}^0 - \omega_r t^0)\}T_{2\mu}^{jk} \qquad (41)$$

Here β_{PR}^{jk} and γ_{PR}^{jk} are Euler angles relating the principal axis frame of the DD interaction to the rotor-fixed frame. For example, β_{PR}^{jk} is the angle subtended by the internuclear $j \rightarrow k$ vector and the rotation axis of the sample.

If the sequence implements γ-encoded recoupling, then equation (41) contains the entire orientation-dependence of the $T_{2\mu}^{jk}$ spin operator. As may be seen, the magnitude of the recoupled Hamiltonian depends on β_{PR}^{jk} according to the reduced Wigner function $d_{0m}^2(\beta_{PR}^{jk})$.

The relevant functions have the following form:

$$d_{00}^2(\beta) = \frac{1}{2}(3\cos^2\beta - 1)$$

$$d_{0\pm1}^2(\beta) = \pm\sqrt{\frac{3}{8}}\sin 2\beta$$

$$d_{0\pm2}^2(\beta) = \sqrt{\frac{3}{8}}\sin^2\beta \qquad (42)$$

The type of orientation-dependence may be selected by choosing the m-value of the symmetry-allowed component.

For example, consider the double-quantum recoupling sequences with symmetry $C7_2^1$. As discussed above, this symmetry implements γ-encoded recoupling with selection of the $\{l, m, \lambda, \mu\} = \{2, 1, 2, 2\}$ and $\{2, -1, 2, -2\}$ terms. Since the $m = \pm 1$ terms are symmetry-allowed, the magnitude of the recoupled Hamiltonian is proportional to $d_{01}^2(\beta_{PR}^{jk})$, and hence depends upon orientation according to the function $\sin(2\beta_{PR}^{jk})$. The recoupling effect is maximized at the angles $\beta_{PR}^{jk} = 45°$ and 135°, and vanishes at the orientations $\beta_{PR}^{jk} = 0$ or 180° (internuclear vector along the spinning axis) and also $\beta_{PR}^{jk} = 90°$ (internuclear vector perpendicular to the spinning axis). A sketch of the orientation dependence of the $C7_2^1$ recoupled Hamiltonian is shown in Figure 7(a).

The symmetry $C8_3^1$, on the other hand, implements γ-encoded double-quantum recoupling with selection of the terms $\{l, m, \lambda, \mu\} = \{2, -2, 2, 2\}$ and $\{2, 2, 2, -2\}$. In this case, the magnitude of the recoupled Hamiltonian is proportional to $d_{02}^2(\beta_{PR}^{jk})$, and hence depends upon orientation according to the function $\sin^2(\beta_{PR}^{jk})$. In this case, the recoupling effect is maximized at the angle $\beta_{PR}^{jk} = \pi/2$ (internuclear vector perpendicular to the spinning axis) and vanishes for the angles $\beta_{PR}^{jk} = 0$ and π (internuclear vector parallel to the spinning axis). A sketch of the orientation dependence of the $C8_3^1$ recoupled Hamiltonian is shown in Figure 7(b).

These orientation-dependences may be exploited in the magic-angle spinning of oriented materials.[55,56,73–75] Glaubitz has proposed a series of different recoupling experiments, in order to deduce the angles subtended by internuclear vectors and the spinning axis with a minimum of ambiguity.[75] This should enhance the molecular structural information which may be obtained from the magic-angle spinning NMR of oriented samples.

The symmetry-aided manipulation of orientation-dependence may also be useful in the NMR of disordered samples such as powders. It is possible to gain information on the relative orientation of pairs of interactions by correlating them with each other using multiple-dimensional NMR methods.[43,44,76–81] It should be possible to enhance the information content of such experiments, and resolve ambiguities, by using combinations of recoupling symmetries applied in different time intervals of a multidimensional experiment. At the moment, such experiments are still in the planning stage.

2.14 Phase-Time Relationships

The spin tensors transform in the following way when rotated about the z-axis:

$$\exp\{-\mathrm{i}\phi I_z\}T_{\lambda\mu}^{\Lambda}\exp\{-\mathrm{i}\phi I_z\} = T_{\lambda\mu}^{\Lambda}\exp\{-\mathrm{i}\mu\phi\} \qquad (43)$$

This equation may be combined with equation (40) to obtain the dependence of a recoupled Hamiltonian term on the orientational angles γ_{MR} and α_{RL}^0, the rf phase ϕ, and the initial time point t^0:

$$\overline{\mathcal{H}}_{lm\lambda\mu}^{\Lambda}(\gamma_{MR}, t^0, \alpha_{RL}^0, \phi) = \overline{\mathcal{H}}_{lm\lambda\mu}^{\Lambda}(0,0,0,0) \times \exp\{-\mathrm{i}[m(\gamma_{MR} + \alpha_{RL}^0 - \omega_r t^0) + \mu\phi]\} \qquad (44)$$

As discussed in Ref.[82], this relationship may be used to remove the dependence of the recoupled Hamiltonian on the initial time point t^0. The desired effect is achieved for the case $\mu \neq 0$ by shifting the overall rf phase according to the formula:

$$\phi = \frac{m}{\mu}\omega_r t^0 \qquad (45)$$

If this is done, then the average Hamiltonian term $\overline{\mathcal{H}}_{lm\lambda\mu}^{\Lambda}$ is independent of the initial time point t^0 at which the pulse sequence starts. Equation (45) is called a *phase-time relationship*.

In general, the recoupled Hamiltonian contains many symmetry-allowed terms, which may have different ratios of m and μ. If that is the case, then the formula in equation (45) cannot be implemented simultaneously for all of them, and it is impossible to compensate the full recoupled Hamiltonian for a change in the timing by a shift in the rf phase. This is clearly the case if the sequence is not γ-encoded.

If the sequence is γ-encoded, and if all the symmetry-allowed terms have the same ratio m/μ, then the pulse sequence may be applied at arbitrary time points in a pulse sequence, providing the overall rf phase is adjusted according to equation (45). This is an important practical principle of γ-encoded recoupling sequences, which has been applied in many different experimental contexts.[39,60,79,82–84]

A typical application is two-dimensional double-quantum spectroscopy. The pulse sequence consists of a preparation period, which may consist of a CN_n^ν recoupling sequence, followed by a variable evolution interval t_1, followed by a mixing interval, which might be a second CN_n^ν sequence, followed by signal detection.

In solution NMR, it is possible to vary the evolution interval t_1 in arbitrarily small steps, in order to obtain a sufficiently large spectral bandwidth in the double-quantum dimension. This is because the operation of the preparation and mixing sequences is independent of the times at which they are applied.

In magic-angle-spinning solid-state NMR, on the other hand, the situation is completely different, since the rotation of the sample modulates the spin Hamiltonian during the pulse sequence. In general, the average Hamiltonian generated by the second recoupling sequence depends on the time at which it is applied, and hence on the interval t_1. As a result, multi-dimensional experiments often display strong periodic modulations in the indirectly-detected dimension, which are due to the rotation of the sample during t_1 (see **Double-Quantum NMR Spectroscopy of Dipolar Coupled Spins Under Fast Magic-Angle Spinning**). It is easy to misinterpret these modulations as being due to the evolution of coherences in the interval t_1.

If the sequence is not γ-encoded, the only way to avoid these orientational modulations is to restrict t_1 to be integer multiples of a rotor period, so that the sample has the same orientation at the beginning and end of the evolution interval. However, this is a very strong restriction which in many cases greatly cramps the spectral width.

However, if the sequence is γ-encoded, and if all symmetry-allowed terms have the same ratio m/μ, then it is possible to vary the evolution interval completely freely by coupling the rf phase to the timing, according to the phase-time relationship equation (45). This allows multiple-quantum spectroscopy with an arbitrarily large bandwidth in the indirectly-detected dimension. Examples, including explicit formulae for the radio-frequency phases, are given in Refs.[39,60,79,82–84]

2.15 Incomplete Cycles

As mentioned before, the average Hamiltonian theory is strictly valid only for integer multiples of complete CN_n^ν or RN_n^ν cycles, i.e., complete multiples of n rotor periods. However, in most cases, the theory seems to work very well even when the full cycles are not completed. This allows a further degree of freedom in experimental design, since it becomes possible to adjust the recoupling intervals in relatively fine time steps.

This is an important advantage in experiments which aim to measure the magnitude of recoupled interactions. A fine time resolution of the recoupling interval is often a prerequisite for obtaining a result of the desired accuracy. Fine time resolution also makes it easier to maximize signal strength in multiple-quantum-filtering experiments.

There is an important complication associated with the use of incomplete recoupling cycles. In general, the pulse sequence propagator under a recoupling sequence is the product of two terms (equation (22)). The first term is the propagator for the rf field under the pulse sequence, while the second term concerns the average Hamiltonian of the internal spin interactions, which is subject to the selection rules discussed above. In the case of *complete* CN_n^ν or RN_n^ν sequences, the first term may be omitted, since the complete sequence behaves as a cycle, with an rf propagator proportional to the unity operator. However, this is not always the case for *incomplete* pulse sequences.

The CN_n^ν sequences present few problems in this respect, since the rf propagator for an incomplete CN_n^ν sequence is still proportional to the unity operator, providing that integer numbers of $\mathcal{C}$ elements are completed. As a result, only the average Hamiltonian must be taken into account for integer multiples of $\mathcal{C}$ elements.

Matters are more complicated for RN_n^ν sequences. If q elements $\mathcal{R}$ are completed, the rf propagator is given by

$$U_{\mathrm{rf}}(t^0 + q\tau_{\mathcal{R}}, t^0) = \exp\{-\mathrm{i}2q\phi I_z\}\exp\{-\mathrm{i}q\pi I_x\} \qquad (46)$$

where I_x and I_z is the longitudinal angular momentum operator of the irradiated spins, and the phase ϕ is given ideally by $\phi = \pi\nu/N$. The duration of each element is $\tau_{\mathcal{R}} = n\tau_r/N$, where τ_r is a rotor cycle.

In the case of even q, the rf propagator leads to an additional z-rotation of the spin operators, which must be taken into account by a compensatory rf phase shift of subsequent rf pulses. This phase shift must be added to the phase shifts imposed by the phase-time relationships, described above, as well as any phase shifts required in the phase cycling procedure, used to select NMR signals passing through certain orders of spin coherence.

In the case of odd q, there is a rotation of the spins by an odd multiple of π about the x-axis, as well as the phase rotation by $2q\phi$. The additional x-rotation may be taken into account by changing the *sign* of subsequent rf phases.

The overall implementation of these multiple phase shifts and phase inversions is quite complex. Refs.[39,60,79,82–84] give some practical examples with explicit formulae for the rf phases.

If these phase factors are taken into account correctly, it is possible to achieve fine time resolution of both the duration of the recoupling sequences and the intervals between them. In many cases, this is a decisive practical advantage.

2.16 Supercycles

In many cases, the performance of the recoupling sequences is enhanced by *supercycling*, which means repetition of the sequence with some variation of the rf phase shifts or the order of the pulse sequence elements.

The effect of supercycling is well understood on the level of the first-order average Hamiltonian. The higher order effects of supercycling, on the other hand, are currently not well researched, despite their importance. Some of the results sketched below should be regarded as preliminary. Refs.[39,60] contain some relevant theory.

Most of the supercycles used so far fall into the categories summarized below:

2.16.1 180° Phase Shift Supercycles

If a complete CN_n^ν or RN_n^ν sequence is repeated with a 180° phase shift, we get a two-step supercycle denoted $[\mathcal{S}]_0[\mathcal{S}]_{180}$.

Here $[\mathcal{S}]_\phi$ indicates an overall phase shift of all elements in the sequence $\mathcal{S}$ by the angle ϕ.

This supercycle cancels all components with odd values of μ in the first-order average Hamiltonian. The supercycle therefore implements an additional selection rule which is superimposed on the CN_n^ν or RN_n^ν selection rules.

For example, the symmetry $C5_2^1$ implements γ-encoded double-quantum homonuclear recoupling, with selection of the $\{l, m, \lambda, \mu\} = \{2, \pm1, 2, \pm2\}$ terms, similar to $C7_2^1$. However, $C5_2^1$ symmetry also allows CSA terms with quantum numbers $\{2, \pm2, 1, \mp1\}$ and single-quantum DD terms with quantum numbers $\{2, \pm2, 2, \mp1\}$. These undesirable terms all have odd values of μ and may be suppressed by building a supercycle of the form $[C5_2^1]_0[C5_2^1]_{180}$. The resulting sequence is called SPC5.[40] It has the same first-order average Hamiltonian properties as $C7_2^1$ but lower rf field requirements.[40] There are other ways of achieving the same result.[39]

Supercycles of the form $[\mathcal{S}]_0[\mathcal{S}]_{180}$ may be used whenever the desired components of the first-order average Hamiltonian have even values of μ. Even when this supercycle does not add to the selectivity of the first-order average Hamiltonian, it tends to reduce higher-order terms. For example, the CSA compensation of RN_n^ν sequences for homonuclear double-quantum recoupling is improved by using supercycles of the form $[RN_n^\nu]_0[RN_n^\nu]_{180}$.[85]

2.16.2 120° Phase Shift Supercycles

A higher degree of coherence order selectivity is implemented by using three-step phase cycles of the form $[\mathcal{S}]_0[\mathcal{S}]_{120}[\mathcal{S}]_{240}$. Supercycles of this type suppress all terms in the average Hamiltonian in which μ is not an integer multiple of 3. Since all spin interactions have μ values between 2 and -2, this supercycle $[\mathcal{S}]_0[\mathcal{S}]_{120}[\mathcal{S}]_{240}$ selects the $\mu = 0$ components in the average Hamiltonian, suppressing single-quantum and double-quantum terms.

This type of supercycle is useful for stabilizing zero-quantum recoupling sequences such as $R4_4^1$.[65]

2.16.3 Phase Inversion Supercycles

A different effect is achieved by supercycles of the form $\mathcal{SS}'$, where $\mathcal{S}'$ indicates the sign reversal of all rf phase shifts in the sequence $\mathcal{S}$. For example, if $\mathcal{S}$ consists of a $RN_n^{-\nu}$ sequence based on the elements $\mathcal{R} = 90_{-45}90_{45}90_{-45}$ and $\mathcal{R}' = 90_{45}90_{-45}90_{45}$, then $\mathcal{S}'$ consists of a RN_n^ν sequence based on the elements $\mathcal{R} = 90_{45}90_{-45}90_{45}$ and $\mathcal{R}' = 90_{-45}90_{45}90_{-45}$.

This type of supercycle replaces first-order average Hamiltonian terms of the form $aT_{\lambda\mu} + a^*T_{\lambda-\mu}$ by the expression $Re\{a\}(T_{\lambda\mu} + T_{\lambda-\mu})$. The effect is to convert the phase modulation of the average Hamiltonian into an amplitude modulation.

This type of supercycle cannot be used for γ-encoded sequences, but has been used with advantage for zero-quantum recoupling sequences, which cannot be γ-encoded.[65] It is used in many popular implementations of REDOR[26,27] and RFDR.[33,34]

2.16.4 Combined Phase Inversion and 180° Pulse Insertion Supercycles

It is possible to combine phase inversion with the insertion of strong 180° pulses, leading to supercycles of the form $\mathcal{S}\Pi_0\mathcal{S}'\Pi_{180}$, where Π_ϕ indicates the insertion of a strong, short, 180° pulse of phase ϕ.

If the inserted 180° pulses are ideal and infinitely short, this supercycle maintains the γ-encoding of the average Hamiltonian and also deletes average Hamiltonian terms with odd values of the spin rank λ. This type of supercycle is particularly useful for improving the chemical shift compensation of a pulse sequence.

Tycko used this type of supercycle to compensate 'zero-field in high-field' experiments for chemical shifts.[28,29]

In practice, 180° pulse insertion supercycles are awkward to implement, especially at high spinning frequencies, because the finite duration of real 180° pulses disturbs the timing of the other pulse sequence elements, breaking the pulse sequence symmetry.

2.16.5 Combined Phase Inversion and Cyclic Permutation Supercycles

A similar effect to the insertion of strong 180° pulses is achieved by *cyclically permuting* a 180° pulse sequence element. For example, the cyclic permutation of a 180° element $\mathcal{R}$ of the phase-inverted cycle $\mathcal{S}'$ may be denoted $\mathcal{R}^{-1}\mathcal{S}'\mathcal{R}$, where the notation $\mathcal{R}^{-1}\mathcal{S}'$ indicates the deletion of the element $\mathcal{R}$ from the beginning of the sequence $\mathcal{S}'$.

For example, consider a $C14_4^5$ sequence based on the simple element $\mathcal{C} = 360_0$, i.e.,

$$\mathcal{S} = 360_0360_{128.57}360_{257.14}360_{25.71}360_{154.29}360_{282.86}360_{51.43}- 360_{180}360_{308.57}360_{77.14}360_{205.71}360_{334.29}360_{102.86}360_{231.43} \quad (47)$$

spanning four rotational periods. The phase inverted cycle $\mathcal{S}'$ is as follows:

$$\mathcal{S}' = 360_0360_{231.43}360_{102.86}360_{334.29}360_{205.71}360_{77.14}360_{308.57}- 360_{180}360_{51.43}360_{282.86}360_{154.29}360_{25.71}360_{257.14}360_{128.57} \quad (48)$$

The sequence $\mathcal{R}^{-1}\mathcal{S}'\mathcal{R}$ derived by cyclically-permuting the element $\mathcal{R} = 180_0$ of $\mathcal{S}'$ is therefore

$$\mathcal{R}^{-1}\mathcal{S}'\mathcal{R} = 180_0360_{231.43}360_{102.86}360_{334.29}360_{205.71}360_{77.14}360_{308.57}- 360_{180}360_{51.43}360_{282.86}360_{154.29}360_{25.71}360_{257.14}- 360_{128.57}180_0 \quad (49)$$

This type of supercycle has almost the same effect as the combined phase inversion/180° pulse insertion supercycle discussed above. At the same time there is no need to apply very strong rf pulses. The timing complications associated with the inevitably finite duration of "strong" pulses are also avoided.

The cyclic permutation of an element creates a shift in the timing of the second sequence, disturbing the symmetry. In the case of γ-encoded pulse sequences, the timing shift may be compensated by modifying the rf phase of the second cycle, according to the phase-time relationship (equation (45)). This leads to the modified supercycle $[\mathcal{S}]_0[\mathcal{R}^{-1}\mathcal{S}'\mathcal{R}]_\delta$, where the overall phase shift δ is given by

$$\delta = -\frac{m}{\mu}\omega_r\tau_\mathcal{R} \quad (50)$$

Here $\tau_{\mathcal{R}}$ is the duration of the cyclically permuted element $\mathcal{R}$, and m/μ is the ratio of space and spin quantum numbers selected by the γ-encoded CN_n^ν sequence.

In the case of equation (49), the symmetry $C14_4^5$ selects the rotational components $\{l, m, \lambda, \mu\} = \{2, \pm 1, 2, \mp 2\}$, and the permuted element has a duration $\tau_{\mathcal{P}} = 2\tau_r/7$. The phase correction is therefore $\delta = \pi/7 = 25.71°$. The supercycle is

$$\begin{aligned}[\mathcal{S}]_0[\mathcal{R}^{-1}\mathcal{S}'\mathcal{R}]_\delta = {} & 360_0 360_{128.57} 360_{257.14} - \\ & 360_{25.71} 360_{154.29} 360_{282.86} 360_{51.43} 360_{180} - \\ & 360_{308.57} 360_{77.14} 360_{205.71} 360_{334.29} 360_{102.86} - \\ & 360_{231.43} 180_{25.71} 360_{257.14} 360_{128.57} 360_0 - \\ & 360_{231.43} 360_{102.86} 360_{334.29} 360_{205.71} - \\ & 360_{77.14} 360_{308.57} 360_{180} 360_{51.43} 360_{282.86} - \\ & 360_{154.29} 180_{25.71} \end{aligned} \tag{51}$$

This comprises one half of the SC14 sequence.[39]

This type of supercycle has beneficial effects on the CSA compensation of recoupling sequences, without destroying the γ-encoding.

2.16.6 Additional Supercycles

It is possible to construct supercycles by using consecutive CN_n^ν sequences based upon different basic elements $\mathcal{C}$. For example, Rienstra et al.[38] concatenated a $C7_2^1$ sequence based upon the basic cycle $\mathcal{C}_a = 360_0 360_{180}$ with a second $C7_2^1$ sequence based upon a different basic cycle $\mathcal{C}_b = 180_0 360_{180} 180_0$. Some higher-order error terms of the individual cycles cancel out in the mixed supercycle $C7_2^1(a)C7_2^1(b)$.

More complex supercycles may be created by superimposing the basic supercycle types, and by transposing, mixing, and permuting the elements. For example, the full SC14 supercycle[39] is

$$[[\mathcal{S}]_0[\mathcal{R}^{-1}\mathcal{S}'\mathcal{R}]_\delta]_0[[\mathcal{S}]_0[\mathcal{R}^{-1}\mathcal{S}'\mathcal{R}]_\delta]_{180} \tag{52}$$

where $\mathcal{S}$ is a $C14_4^5$ sequence using the basic element $\mathcal{C} = 360_0$, the element $\mathcal{R} = 180_0$ is cyclically permuted, and $\delta = 25.71°$. The CMR7 sequence[38] employs a particularly complicated supercycle structure.

At the moment, an empirical approach to supercycle construction prevails, since a complete higher-order theory has not yet been developed.

Supercycling should be implemented with care. In many cases, the supercycles are unnecessary, and readily harm the pulse sequence performance if they are used incorrectly.

2.17 Rf Imperfections

In practice, all rf pulse sequences are subject to various types of instrumental imperfection. Some typical imperfections of practical importance are:

1. Spatial inhomogeneity in the *amplitude* of the rf field over the sample volume;
2. Spatial inhomogeneity in the *direction* of the rf field over the sample volume, which translates into a phase modulation of the rf field as the sample rotates;[25,86,87]
3. Transients in the rf field upon changes in the driving field amplitude or phase, caused by the limited frequency bandwidth of the probe;[85,88]
4. Instability or droop in the rf field applied to the probe;
5. Errors in the values of rf phase shifts;
6. Phase instability of the rf field.

Many of these imperfections have been investigated rather thoroughly, and some fit well into the framework of the symmetry theory. In particular, rf amplitude inhomogeneity may be included by using a set of interaction frame Hamiltonian terms with the quantum numbers $l = 0$, $m = 0$, $\lambda^{\text{eff}} = Z_g$ and $\mu = \{-1, 0, +1\}$. Here λ^{eff} is the 'effective spin rank' of the rf inhomogeneity terms and Z_g is any *even* integer ('*g*' stands for *gerade*, which means 'even' in German).

It is surprising that the 'effective spin rank' λ^{eff} of the rf inhomogeneity terms is *even*, since the rf spin Hamiltonian actually contains rank 1 spin operators. This is because the rf inhomogeneity terms depend on the phase of the rf field, even before transformation into the interaction frame. As a result, these terms behave differently to the others.[89]

The rf inhomogeneity terms may be inserted into the selection rules and space-spin selection diagrams in the usual way. For example, it is easy to see that the rf inhomogeneity term $\{l, m, \lambda^{\text{eff}}, \mu\} = \{0, 0, Z_g, 0\}$ is symmetry-allowed under $C7_2^1$ and $R18_1^7$ sequences, while the terms $\{0, 0, Z_g, \pm 1\}$ are symmetry-forbidden. In order to achieve first-order rf compensation, one must therefore set the scaling factors for the symmetry allowed $\{0, 0, Z_g, 0\}$ terms to zero. This may be done by using amplitude-modulated basic elements $\mathcal{C}$ or $\mathcal{R}$. It follows that symmetries such as $C7_2^1$ and $R18_1^7$ have first-order compensation for rf inhomogeneity if they are based on amplitude-modulated elements.

In practice, higher-order terms are very important in determining the robustness of a pulse sequence with respect to rf amplitude deviations. These terms may be analyzed by using the selection rules equations (31) and (32). In many cases, it is simpler to use crude geometric arguments as a guideline.[39] For example, although the symmetry $C7_2^1$ is compensated for rf amplitude errors to first order (in the case of amplitude-modulated basic elements), geometrical arguments show that the second-order rf error terms are large.[39] As a result, $C7_2^1$ sequences must usually be based on elements which have a built-in rf error compensation, such as the original element $\mathcal{C} = 360_0 360_{180}$,[36] or the "POST" element $\mathcal{C} = 90_0 360_{180} 270_0$.[37] In Ref.[39] it is shown by geometrical arguments that the symmetry $C14_4^5$ has a higher degree of intrinsic rf error compensation, and that it is therefore feasible to use this symmetry together with the uncompensated basic element $\mathcal{C} = 360_0$. This provides a two-fold reduction in the rf field requirements for a given spinning frequency.

The effect of rf transients has also been analyzed.[85] A combination of electronic simulations and experimental measurements has led to the development of a simple analytical model for the transient behavior of the rf field at the sample. This model was used for accurate spin dynamical simulations during symmetry-based sequences, including the transient probe response. The effect of transients is minor, at least in the cases examined so far.

There is one common spectrometer imperfection which is a cause for real concern. In many contexts, the RN_n^ν class of

pulse sequences is extremely sensitive to the precise value of the rf phase shift. As described above, RN_n^ν sequences are composed of elements with the alternating phase values $\pm\pi\nu/N$. Even small deviations from this precise phase shift value may be disastrous.[85] A phase shift accuracy of $\pm 0.1^\circ$ or better is necessary for many applications of RN_n^ν sequences. In particularly demanding applications, such as long-range distance measurements, the phase shift accuracy should be an order of magnitude better still. Such extreme accuracy stretches current rf hardware. At the moment, only direct digital synthesis (DDS) of the rf wave produces sufficiently reliable and accurate phase shifts. Unfortunately, not all commercial spectrometers are equipped with such devices.

The extreme phase-shift sensitivity of RN_n^ν sequences may be understood using equation (46). This equation shows that a complete RN_n^ν sequence rotates resonant spins about the z-axis through the angle $2N\phi$. Since the value of the phase shift is ideally $\phi = \pi\nu/N$, the overall rotation angle generated by one RN_n^ν sequence is ideally $\Phi = 2\pi\nu$ radians. This is an integer multiple of 360°, and so has no effect on the spin system. If a set of K consecutive RN_n^ν sequences are applied, the overall rotation is through an angle $\Phi = 2\pi\nu K$, which also has no effect. However, if the value of ϕ is in error by a small angle Δ, then the overall rotation over K cycles is in excess by the angle $2NK\Delta$. For example, in the case of a $R14_2^6$ sequence, a phase deviation of only $\Delta = 0.1^\circ$ leads to an accumulating error of 2.8° per complete RN_n^ν sequence. Since a typical short-range pulse sequence employs around five complete sequences, the accumulated error rotation is about 14°. This is enough to degrade the double-quantum filtering efficiency significantly, especially since the double-quantum coherences are twice as sensitive as single-quantum coherences to phase shift errors. In a long-range application where around 50 complete sequences are used, the 0.1° phase shift error is disastrous.

CN_n^ν sequences are much less sensitive to phase shift errors, since there are no *accumulating* rotations in this case.

The extreme phase shift sensitivity of RN_n^ν sequences may be removed by using the supercycle $\mathcal{SS}'$. However, this method is only applicable to non-γ-encoded sequences. Work is under way towards a more general solution of this serious practical problem.

2.18 Selection of Sequences

Although the symmetry theory provides a sound framework for the search for suitable pulse sequences, this framework still allows enormous freedom. In order to develop a pulse sequence for a specific task, one must:

- Identify the space-spin components $\{l, m, \lambda, \mu\}$ which must be selected, and those that must be suppressed;
- Identify the set of suitable CN_n^ν or RN_n^ν symmetries;
- Identify the desired range of MAS frequencies;
- Identify a suitable basic element ($\mathcal{C}$ in the case of CN_n^ν symmetry, or $\mathcal{R}$ in the case of RN_n^ν symmetry);
- Identify a suitable supercycle, if required.

For each problem, there are usually a large number of feasible symmetries, and within each symmetry, there is an infinity of possible basic elements.

This great freedom is both a strength and a disadvantage: It is a strength because it allows one to design a sequence tailored to the specific requirements of the experiment; it is a disadvantage because there are too many possibilities for a complete search.

The first two steps are easy: The application itself defines the desired and undesired space-spin components, and it is a straightforward task to identify the set of appropriate symmetries. This may be done manually using space-spin selection diagrams, or by using a Mathematica program[63] developed for this purpose (available at *http://www.soton.ac.uk/∼mhl*).

The next stage is to choose the symmetry class and the basic element. Here one must pay attention to the following factors:

- The scaling factor for a given basic element $\mathcal{C}$ (or $\mathcal{R}$) under the symmetry class CN_n^ν (or RN_n^ν) should be reasonably high.
- The required rf field depends on the basic element and also the symmetry class (more specifically, the ratio of N to n). If the pulse sequence is intended to be broadband, it is usually desirable that the nutation frequency under the rf field should be as large as possible without being impractically large (see the subject of heteronuclear decoupling, discussed below).
- A rough guide to the relative performance of different symmetries is available by counting the number of symmetry-allowed higher-order terms, using the selection rules in equations (31) and (32).
- It is sometimes unnecessary for the pulse sequence symmetry to suppress all of the undesired rotational components. Undesired components may also be suppressed by using a basic element which provides a zero scaling factor for the undesired rotational components. Supercycling may also be used to suppress the undesired symmetry-allowed components. These strategies are used in the SPC5[40] and C-REDOR[67] schemes.

Previous experience in designing composite pulses[7–9,61,62] has been useful for guiding the choice of $\mathcal{C}$ and $\mathcal{R}$ elements (see **Composite Pulses,** Volume 2). For example, the composite pulse 360_0360_{180} is known to be a robust rf cycle with good rf amplitude compensation and reasonably broadband behavior with respect to isotropic chemical shifts. Its chemical shift performance may be enhanced considerably by cyclically-permuting a 90_0 pulse, leading to $\mathcal{C} = 90_0360_{180}270_0$. This 'permutationally offset-stabilized' (POST) element is a stalwart of liquid-state broadband decoupling experiments,[7–9] and was used in the design of the POST-C7 sequence.[37] Similarly, the element $\mathcal{R} = 90_0270_{180}$ is known as an offset-compensated 180° composite pulse,[7–9,61,62] and often proves to be a good choice in the context of RN_n^ν sequences.[41,60]

More recently, semi-automated computer searches have been used to identify suitable sequences. For example, Brinkmann[60] developed a combinatorial approach in which a large number of combinations of feasible symmetries, basic elements, and supercycle schemes are tested numerically by simulation under a variety of test situations.

The future may see a move towards more sophisticated basic elements, employing smoothly modulated pulse shapes rather than rectangular pulses. A full flowering of this field may require further improvements in the speed and flexibility of the electronic hardware.

3 HETERONUCLEAR SEQUENCES

In practice, most samples contain several nuclear spin species. The selection rules and design principles may be extended to the case of heteronuclear spin interactions.

3.1 Heteronuclear Spin Interactions

Suppose that the rotating sample contains two interacting spin species, denoted I and S, which are subjected to resonant rf fields at the corresponding nuclear Larmor frequencies. The nuclear spin interactions may be classified in terms of their spherical ranks under spatial (molecular) rotations, rotations of the I-spin polarizations by rf fields, rotations of the S-spin polarizations by rf fields, and rotations of the external magnetic field. The corresponding classification scheme is shown in Table 3. As may be seen, all interactions, with the exception of the homonuclear J-couplings, have different rotational properties. The symmetry theory of homonuclear rotor-synchronized pulse sequences is extended to the heteronuclear case by employing two different sets of spin quantum numbers.

In the presence of rf fields on both spin species I and S, the interaction frame Hamiltonian may be described as a superposition of many rotational components:

$$\mathcal{H}^{\Lambda} = \sum_{m=-l}^{+l} \sum_{\mu_I=-\lambda_I}^{+\lambda_I} \sum_{\mu_S=-\lambda_S}^{+\lambda_S} \mathcal{H}^{\Lambda}_{lm\lambda_I\mu_I\lambda_S\mu_S} \tag{53}$$

as listed in Table 4.

The fundamental design task in heteronuclear spin systems is to design pulse sequence symmetries which select a small number of combinations of these terms, while suppressing others.

Table 3 Rotational signatures of interactions in heteronuclear systems

Interaction	Space rank, l	I-Spin rank, λ_I	S-Spin rank, λ_S	Field rank
I-Spin isotropic shift	0	1	0	1
I-Spin CSA	2	1	0	1
I-Spin J-coupling	0	0	0	0
I-Spin DD-coupling	2	2	0	0
S-Spin isotropic shift	0	0	1	1
S-Spin CSA	2	0	1	1
S-Spin J-coupling	0	0	0	0
S-Spin DD-coupling	2	0	2	0
IS J-coupling	0	1	1	0
IS DD-coupling	2	1	1	0

3.2 Strong Heteronuclear Decoupling

A common method for heteronuclear decoupling at the same time as homonuclear recoupling involves the application of a CN_n^{ν} or RN_n^{ν} sequence on one channel while a strong resonant rf field is applied to the second channel. If the rf field is strong enough, this suppresses the heteronuclear spin interactions, so that the two spin species are *decoupled* from each other.

If the strong resonant irradiation is on the I-spin channel, the appropriate selection rules are:
Case of $CN_n^{\nu_S}$ sequences with I-spin decoupling:

$$\overline{\mathcal{H}}^{(1)}_{lm\lambda_I\mu_I\lambda_S\mu_S} = 0 \quad \text{if} \quad mn - \mu\nu_S \neq NZ \quad \text{or if } \lambda_I = 1 \tag{54}$$

Case of $RN_n^{\nu_S}$ sequences with I-spin decoupling:

$$\overline{\mathcal{H}}^{(1)}_{lm\lambda_I\mu_I\lambda_S\mu_S} = 0 \quad \text{if } mn - \mu\nu_S \neq \frac{N}{2}Z_{\lambda_S} \quad \text{or if } \lambda_I = 1 \tag{55}$$

Empirically, it is found that effective heteronuclear decoupling requires a relatively large ratio of the nutation frequencies of the spins under their corresponding rf fields, i.e., if the decoupling irradiation is applied to the I-spins, while a recoupling sequence is applied to the S-spins, the ratio of nutation frequencies should be at least $|\omega^I_{\text{nut}}/\omega^S_{\text{nut}}| > \sim 3$.[38]

In the absence of S-spin irradiation, two-pulse phase modulation (TPPM) of the decoupler field usually enhances the quality of the decoupling.[10] This does not usually appear to be the case when an rf field is also applied to the S-spins. Under some circumstances, however, the decoupling quality may be improved by placing the I-spin rf field well off-resonance, so as to approach or satisfy the Lee–Goldburg condition.[11] These effects are of great practical importance but are not fully understood.

Since many of the applications of the symmetry-based sequences are in isotopically-labelled organic solids, good heteronuclear decoupling is of great importance. The need for a very strong decoupler field is a strong constraint on the applications of these pulse sequences, since typical NMR probes cannot tolerate simultaneous resonant rf fields on two irradiation channels for very long. A typical practical limit corresponds to nutation frequencies of around 100 kHz

Table 4 Components of I and S-spin interactions in the interaction frame of two resonant rf fields, in the case of exact magic-angle spinning

Interaction	Space rank, l	Space components, m	I-Spin rank, λ_I	I-Spin components, μ_I	S-Spin rank, λ_S	S-Spin components, μ_S
I-Spin isotropic shift	0	0	1	$\{-1, 0, 1\}$	0	0
I-Spin CSA	2	$\{-2, -1, 1, 2\}$	1	$\{-1, 0, 1\}$	0	0
I-Spin J-coupling	0	0	0	0	0	0
I-Spin DD-coupling	2	$\{-2, -1, 1, 2\}$	2	$\{-2, -1, 0, 1, 2\}$	0	0
S-Spin isotropic shift	0	0	0	0	1	$\{-1, 0, 1\}$
S-Spin CSA	2	$\{-2, -1, 1, 2\}$	0	0	1	$\{-1, 0, 1\}$
S-Spin J-coupling	0	0	0	0	0	0
S-Spin DD-coupling	2	$\{-2, -1, 1, 2\}$	0	0	2	$\{-2, -1, 0, 1, 2\}$
IS J-coupling	0	0	1	$\{-1, 0, 1\}$	1	$\{-1, 0, 1\}$
IS DD-coupling	2	$\{-2, -1, 1, 2\}$	1	$\{-1, 0, 1\}$	1	$\{-1, 0, 1\}$

for the I-spin channel and around 50 kHz for the S-spin channel, applied for intervals of up to around 20 ms. Since the symmetry-based sequences require a fixed ratio of the nutation frequency to the spinning frequency, the limitation in the tolerable rf power restricts the operational spinning frequency. For example, the C7 pulse sequence is typically limited to spinning frequencies of 7 kHz or less.[36]

3.3 Single-Channel Sequences

If the rf field is only applied to one spin species, the opportunities for symmetry selection are restricted. For example, if rf fields are applied at the I-spin Larmor frequency, but not at the S-spin Larmor frequency, the S-spin quantum number is restricted to $\mu_S = 0$. In effect, only the first 5 columns in Table 4 are relevant. Under these circumstances, the rotational properties of the I-spin CSA and that of the IS DD coupling are indistinguishable: Both have $l = 2$ and $\lambda_I = 1$. Similarly, the I-spin isotropic shift and that of the IS J-coupling both have $l = 0$ and $\lambda_I = 1$.

The selection rules for symmetry-based pulse sequences with rf irradiation on the I-spin channel are:
Case of $CN_n^{\nu_I}$ sequences with no S-spin rf fields:

$$\overline{\mathcal{H}}^{(1)}_{lm\lambda_I\mu_I\lambda_S\mu_S} = 0 \quad \text{if } mn - \mu\nu_I \neq NZ \tag{56}$$

Case of $RN_n^{\nu_I}$ sequences with no S-spin rf fields:

$$\overline{\mathcal{H}}^{(1)}_{lm\lambda_I\mu_I\lambda_S\mu_S} = 0 \quad \text{if } mn - \mu\nu_I \neq \frac{N}{2}Z_{\lambda_I} \tag{57}$$

Here Z_{λ_I} is any integer with the same parity as the spin rank λ_I. These are the same as equations (27) and (28). The S-spin quantum numbers λ_S and μ_S are irrelevant.

It follows that if the rf irradiation is restricted to one channel, the same pulse sequences recouple the heteronuclear DD interactions and the CSA interactions of the resonant spins.

3.4 Dual Pulse Sequences

If rf fields are applied at the Larmor frequencies of both spin species, there are many more opportunities for symmetry selection. As described in Ref.[60] four different symmetry classes may be envisaged, denoted $CN_n^{\nu_I,\nu_S}$, $CRN_n^{\nu_I,\nu_S}$, $RCN_n^{\nu_I,\nu_S}$ and $RN_n^{\nu_I,\nu_S}$ Figure 8. The basic elements may be different on the two channels, although they must have the same duration $n\tau_r/N$. The phase shift scheme for the I-spin irradiation follows the usual construction rule for C-sequences (in the case of $CN_n^{\nu_I,\nu_S}$ or $CRN_n^{\nu_I,\nu_S}$), or for R-sequences (in the case of $RCN_n^{\nu_I,\nu_S}$ or $RN_n^{\nu_I,\nu_S}$), and depends on the symmetry numbers N, n and ν_I. Similarly, the phase shift scheme for the S-spin irradiation follows the construction rule for C-sequences (in the case of $CN_n^{\nu_I,\nu_S}$ or $RCN_n^{\nu_I,\nu_S}$), or for R-sequences (in the case of $CRN_n^{\nu_I,\nu_S}$ or $RN_n^{\nu_I,\nu_S}$), and depends on the symmetry numbers N, n and ν_S.

The selection rules for dual sequences may be derived by extension of the single-channel case, and are given by the following expressions:[60]

Case of $CN_n^{\nu_I,\nu_S}$ sequences:

$$\overline{\mathcal{H}}^{(1)}_{lm\lambda_I\mu_I\lambda_S\mu_S} = 0 \quad \text{if } mn - \mu_I\nu_I - \mu_S\nu_S \neq NZ \tag{58}$$

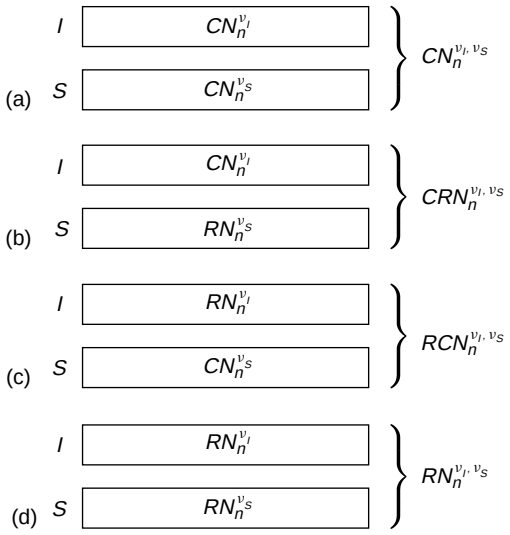

Figure 8 Naming convention for 2-channel heteronuclear pulse sequences

Case of $RCN_n^{\nu_I,\nu_S}$ sequences:

$$\overline{\mathcal{H}}^{(1)}_{lm\lambda_I\mu_I\lambda_S\mu_S} = 0 \quad \text{if } mn - \mu_I\nu_I - \mu_S\nu_S \neq \frac{N}{2}Z_{\lambda_I} \tag{59}$$

Case of $CRN_n^{\nu_I,\nu_S}$ sequences:

$$\overline{\mathcal{H}}^{(1)}_{lm\lambda_I\mu_I\lambda_S\mu_S} = 0 \quad \text{if } mn - \mu_I\nu_I - \mu_S\nu_S \neq \frac{N}{2}Z_{\lambda_S} \tag{60}$$

Case of $RN_n^{\nu_I,\nu_S}$ sequences:

$$\overline{\mathcal{H}}^{(1)}_{lm\lambda_I\mu_I\lambda_S\mu_S} = 0 \quad \text{if } mn - \mu_I\nu_I - \mu_S\nu_S \neq \frac{N}{2}Z_{\lambda_I+\lambda_S} \tag{61}$$

The consequences of these selection rules may be explored by extended space-spin selection diagrams, as described in Ref.[60] Expressions for the higher-order selection rules, and the dual-channel scaling factors, are also available.[60]

The dual-channel selection rules enable the design of pulse sequences which select interactions on the basis of their full rotational properties, as detailed in Table 4. For example, the symmetry $CR14_3^{2,2}$ suppresses all average Hamiltonian terms except those with the quantum numbers $\{l, m, \lambda_I, \mu_I, \lambda_S, \mu_S\} = \{0, 0, 0, 0, 0, 0\}$ and $\{2, \mp1, 1, \pm1, 1, \pm1\}$. This symmetry therefore enables γ-encoded double-quantum heteronuclear recoupling, with suppression of all homonuclear DD couplings, all chemical shift terms, and all heteronuclear J-couplings.[60]

In principle, the selection rules (equations (58)–(61)) permit the rational design of homonuclear recoupling sequences with simultaneous heteronuclear decoupling. In principle, this approach could avoid the severe power requirements of the strong heteronuclear decoupling method (see above). However, no dual sequences with significant advantages over conventional decoupling methods have been found yet.

4 APPLICATIONS

This section presents a brief summary of some of the published applications of the symmetry theory sketched above.

Sets of symmetry solutions appropriate for a number of different recoupling and decoupling problems are provided. The field is developing rapidly and these descriptions are by no means exhaustive.

4.1 Double-Quantum Homonuclear Recoupling

Double-quantum homonuclear recoupling has a number of important practical applications, including (see **Homonuclear Recoupling Schemes in MAS NMR,** Volume 4 and **Low-γ Nuclei in Solid Samples**):

- Passing signals through double-quantum coherences allows the suppression of signals from isolated spins-1/2. This is particularly useful, for example, in the spectroscopy of multiply-^{13}C-labelled macromolecules, since the 'background' signals from naturally-occurring isolated ^{13}C nuclei are suppressed, allowing the selective observation of the labelled spin clusters.[31,36,43,44]
- Double-quantum spectroscopy, and double-quantum filtered correlation spectroscopy, are useful for peak assignments.
- Double-quantum coherences are sensitive to the correlations between local magnetic fields. Double-quantum NMR allows the relative orientations of different spin interactions to be determined, and hence the estimation of interbond angles and torsional angles.[43,44,76–81,90,91]
- Double-quantum recoupling provides a route to the excitation of higher coherence orders.[81,92–94]

Double-quantum homonuclear decoupling sequences may be classified according to whether or not they provide a γ-encoded recoupled Hamiltonian.

4.1.1 γ-Encoded Double-Quantum Recoupling

Many CN_n^ν symmetries provide γ-encoded double-quantum recoupling. As described above, γ-encoding simplifies the orientation-dependence of the recoupling, improving the clarity of the dipolar oscillations and the efficiency of the double-quantum excitation, and improving the time resolution.

Some of the symmetries achieving γ-encoded double-quantum recoupling selectively recouple the $m = \pm 1$ terms (Table 5), while others recouple the $m = \pm 2$ terms (Table 6). In general, the former are more efficient. The isotropic chemical shift terms are symmetry-allowed so the scaling factors of these terms must be set to zero by a suitable choice of the basic element $\mathcal{C}$. Table 5 includes the symmetry $C7_2^1$, which was initially demonstrated with the basic element $\mathcal{C} = 360_0360_{180}$.[36] The 'POST' element $\mathcal{C} = 90_0360_{180}270_0$ is more robust with respect to chemical shift offsets and is now favored.[37] The symmetry $C14_4^5$ allows operation at high spinning frequencies, if it is stabilized by the use of supercycles.[39] A variant of $C7_2^1$ employing a complex supercycle structure has been described.[38] Sequences with the symmetry $C5_2^1$ have also been used, in conjunction with a two-step supercycle to remove the components $\mu = \pm 1$.[40]

The $C7_2^1$ sequences have already been applied to 'real' systems, such as membrane proteins. For example, $C7_2^1$ sequences were applied to a $^{13}C_2$-labelled sample of the photoreceptor protein bovine rhodopsin, allowing selective observation of the labelled sites with suppression of the background signals

Table 5 A set of CN_n^ν symmetries for γ-encoded homonuclear double-quantum recoupling, with selection of $\{l, m, \lambda, \mu\} = \{2, \pm 1, 2, \pm 2\}$ or $\{2, \pm 1, 2, \mp 2\}$ terms, and suppression of all CSA terms. The isotropic shift term $\{0, 0, 1, 0\}$ and the homonuclear J-coupling $\{0, 0, 0, 0\}$ are also symmetry-allowed. All inequivalent solutions in the range $N \leq 20, n \leq 10$ and $\nu \leq 10$ are shown

$C7_1^3$	$C9_1^4$	$C11_1^5$	$C13_1^6$	$C15_1^7$	$C17_1^8$
$C19_1^9$	$C7_2^1$	$C8_2^1$	$C8_2^3$	$C9_2^1$	$C10_2^1$
$C11_2^1$	$C12_2^1$	$C12_2^5$	$C13_2^1$	$C14_2^1$	$C15_2^1$
$C16_2^1$	$C16_2^7$	$C17_2^1$	$C18_2^1$	$C19_2^1$	$C20_2^1$
$C20_2^9$	$C7_3^2$	$C11_3^4$	$C13_3^5$	$C17_3^7$	$C19_3^8$
$C7_4^2$	$C9_4^2$	$C10_4^3$	$C11_4^2$	$C13_4^2$	$C14_4^5$
$C15_4^2$	$C17_4^2$	$C18_4^7$	$C19_4^2$	$C7_5^1$	$C9_5^2$
$C11_5^3$	$C13_5^4$	$C17_5^6$	$C19_5^7$	$C7_6^3$	$C8_6^1$
$C8_6^3$	$C10_6^3$	$C11_6^3$	$C13_6^3$	$C14_6^3$	$C16_6^3$
$C16_6^5$	$C17_6^3$	$C19_6^3$	$C20_6^3$	$C20_6^7$	$C9_7^1$
$C11_7^2$	$C13_7^3$	$C15_7^4$	$C17_7^5$	$C19_7^6$	$C7_8^3$
$C9_8^4$	$C10_8^1$	$C11_8^4$	$C13_8^4$	$C14_8^3$	$C15_8^4$
$C17_8^4$	$C18_8^5$	$C19_8^4$	$C7_9^1$	$C11_9^1$	$C13_9^2$
$C17_9^4$	$C19_9^5$	$C7_{10}^2$	$C8_{10}^1$	$C8_{10}^3$	$C9_{10}^4$
$C11_{10}^5$	$C12_{10}^1$	$C12_{10}^5$	$C13_{10}^5$	$C14_{10}^5$	$C16_{10}^3$
$C16_{10}^5$	$C17_{10}^5$	$C18_{10}^5$	$C19_{10}^5$		

Table 6 A set of CN_n^ν symmetries for γ-encoded homonuclear double-quantum recoupling, with selection of $\{l, m, \lambda, \mu\} = \{2, \pm 2, 2, \pm 2\}$ or $\{2, \pm 2, 2, \mp 2\}$ terms, and suppression of all CSA terms. The isotropic shift term $\{0, 0, 1, 0\}$ and the homonuclear J-coupling $\{0, 0, 0, 0\}$ are also symmetry-allowed. All inequivalent solutions in the range $N \leq 20, n \leq 10$ and $\nu \leq 10$ are shown

$C8_1^3$	$C10_1^4$	$C12_1^5$	$C14_1^6$	$C16_1^7$	$C18_1^8$
$C20_1^9$	$C10_2^3$	$C14_2^5$	$C18_2^7$	$C8_3^1$	$C10_3^2$
$C14_3^4$	$C16_3^5$	$C20_3^7$	$C10_4^1$	$C14_4^3$	$C18_4^5$
$C8_5^1$	$C12_5^1$	$C14_5^2$	$C16_5^3$	$C18_5^4$	$C10_6^1$
$C14_6^1$	$C8_7^3$	$C10_7^2$	$C12_7^1$	$C16_7^1$	$C18_7^2$
$C20_7^3$	$C10_8^3$	$C14_8^1$	$C18_8^1$	$C8_9^3$	$C10_9^4$
$C14_9^2$	$C16_9^1$	$C20_9^1$	$C14_{10}^3$	$C18_{10}^1$	

(see **Bacteriorhodopsin & Rhodopsin,** Volume 2). The evolution of the $^{13}C_2$ double-quantum coherences in the presence of local fields from the neighboring protons allowed determination of a H–C–C–H torsional angle in the retinylidene chromophore.[43] A conformational change could be detected in a trapped photointermediate.[44] The same experiment has also been demonstrated on carbohydrates.[77,78] The experiment may be extended to allow the determination of ^{15}N–^{13}C–^{13}C–^{15}N torsional angles in peptides and proteins.[79–81]

If double-quantum recoupling sequences are applied to single-quantum coherences in clusters of more than two spins, triple-quantum coherences are developed.[92] These triple-quantum coherences may also be used for torsional angle investigations.[81] The double-quantum recoupled spin dynamics in three-spin-1/2 clusters have been investigated by two-dimensional spectroscopy.[39] High orders of coherence have been excited by applying $C7_2^1$ sequences to abundant protons.[93] The relaxation of zero-quantum coherence has been studied by using a $C7_2^1$ sequence to excite double-quantum coherence,

followed by a coherence transfer into zero-quantum coherence using a selective pulse pair.[83]

$C7_2^1$ sequences have also been applied to glasses,[95–98] zeolites,[99] inorganic phosphates,[100–102] proteins[103] and drug molecules.[104]

Figure 9 shows a two-dimensional double-quantum ^{13}C spectrum of [U−^{13}C]-L-tyrosine, obtained using the SC14 pulse sequence at a spinning frequency of 20 kHz.[39] The utility of such spectra for peak assignment is obvious.

There are also a large number of RN_n^ν symmetries suitable for γ-encoded double-quantum recoupling. A set of symmetries which selectively recouple the $m = \pm 1$ terms are listed in Table 7. All of these symmetries suppress the isotropic chemical shift terms, and many of them are particularly robust with respect to chemical shift anisotropies. The symmetries $R14_2^6$ and $R22_4^9$ with $\mathcal{R} = 90_{180}270_0$ have been mainly used so far.[41,85] Measurement of the excitation dynamics of the double-quantum coherences allows the accurate estimation of ^{13}C–^{13}C bond lengths and medium-range distances in $^{13}C_2$-labelled systems, even in the presence of large CSA interactions.[85]

As discussed above, the orientation-dependence of the recoupling under the $m = \pm 1$ sequences (Tables 5 and 7) is different from that under the $m = \pm 2$ sequences (Table 6). This is expected to improve the information content of the NMR spectroscopy of rotating oriented samples.[75] Preliminary results have been obtained.[105]

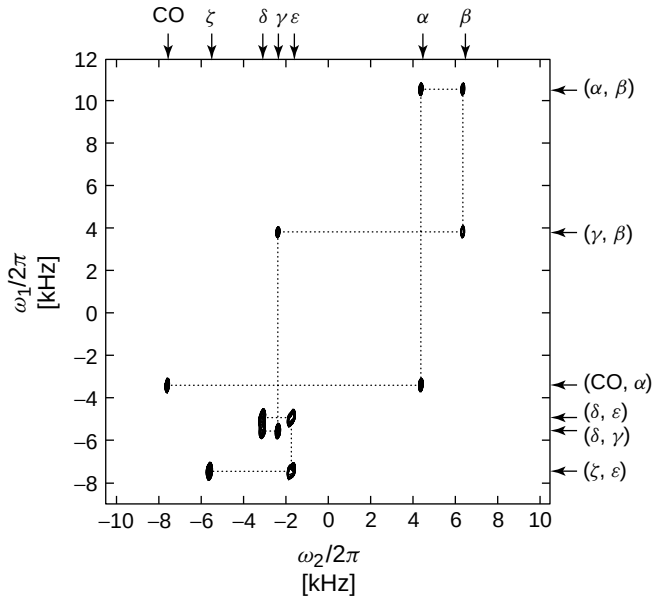

Figure 9 Two-dimensional double-quantum spectrum of [U−^{13}C]-L-tyrosine, obtained at a field of 9.4 T and a spinning frequency of 20 kHz, using the SC14 pulse sequence. The dashed lines are guides for the eye. (Adapted from Ref.[39])

Table 7 A set of RN_n^ν symmetries for γ-encoded homonuclear double-quantum recoupling, with selection of $\{l, m, \lambda, \mu\} = \{2, \pm 1, 2, \pm 2\}$ or $\{2, \pm 1, 2, \mp 2\}$ terms, and suppression of all isotropic shift and CSA terms. The homonuclear J-coupling $\{0, 0, 0, 0\}$ is also symmetry-allowed. All inequivalent solutions in the range $N \leq 20, n, \leq 10$ and $\nu \leq 10$ are shown

$R12_2^1$	$R12_2^5$	$R14_2^1$	$R14_2^6$
$R16_2^1$	$R16_2^7$	$R18_2^1$	$R18_2^8$
$R20_2^1$	$R20_2^9$	$R14_4^2$	$R14_4^5$
$R18_4^2$	$R18_4^7$		

4.1.2 *Non-γ-Encoded Double-Quantum Recoupling*

It is also possible to implement 2Q homonuclear recoupling without γ-encoding. An example is the back-to-back (BABA) recoupling sequence[102,106–108] which is given by

$$90_0 - \tau - 90_{180}90_{90} - \tau - 90_{270} \tag{62}$$

The rf pulses are assumed to be strong and short and the delay τ is adjusted so that the complete sequence lasts one rotor period. This sequence corresponds to the first two elements of a $C4_2^1$ sequence, using the basic element $\mathcal{C} = 90_0 - \tau - 90_{180}$. The $C4_2^1$ symmetry implements double-quantum recoupling, but also allows many unwanted terms, such as the isotropic chemical shift term $\{l, m, \lambda, \mu\} = \{0, 0, 1, 0\}$, CSA terms of the form $\{l, m, \lambda, \mu\} = \{2, \pm 2, 1, 0\}$, and zero-quantum DD terms of the form $\{l, m, \lambda, \mu\} = \{2, \pm 2, 2, 0\}$. However, the scaling factors for all of these terms vanish if the rf pulses are made infinitely short. In this limit, the only symmetry-allowed terms in the first-order average Hamiltonian are of the form $\{l, m, \lambda, \mu\} = \{2, \pm 1, 2, \pm 2\}$ and $\{2, \pm 1, 2, \mp 2\}$. In the limit of very strong rf fields, BABA therefore implements non-γ-encoded homonuclear DD recoupling with compensation for chemical shifts. Although the lack of γ-encoding has disadvantages, the same property allows the robustness of the sequence to be enhanced by constructing a $\mathcal{SS}'$ supercycle, i.e.,

$$\begin{aligned} &90_0 - \tau - 90_{180}90_{90} - \tau - 90_{270}90_0 - \tau - 90_{180} \\ &90_{270} - \tau - 90_{90} \end{aligned} \tag{63}$$

In addition, the absence of γ-encoding causes orientationally-induced modulations in 2D experiments, which may be analyzed in order to estimate internuclear distances.[68,69] The

Table 8 A set of CN_n^ν symmetries for non-γ-encoded homonuclear double-quantum recoupling. The symmetries $C6_2^1$ and $C6_8^1$ suppress all CSA terms and all homonuclear DD terms except $\{l, m, \lambda, \mu\} = \{2, \pm 2, 2, \mp 2\}$ and $\{2, \pm 1, 2, \pm 2\}$. The symmetries $C6_4^1$ and $C6_{10}^1$ suppress all CSA terms and all homonuclear DD terms except $\{l, m, \lambda, \mu\} = \{2, \pm 2, 2, \pm 2\}$ and $\{2, \pm 1, 2, \mp 2\}$. The isotropic shift term $\{0, 0, 1, 0\}$ and the homonuclear J-coupling $\{0, 0, 0, 0\}$ are symmetry-allowed. All inequivalent solutions in the range $N \leq 20, n \leq 10$ and $\nu \leq 10$ are shown

$C6_2^1$	$C6_4^1$	$C6_8^1$	$C6_{10}^1$

supercycled version of BABA has been applied to a variety of systems including phosphate networks[106,107] and glasses.[108]

There are several C-symmetries which provide non-γ-encoded 2Q recoupling with suppression of all CSA terms, even in the case of finite rf fields (see Table 8). The isotropic chemical shift terms are readily suppressed by an appropriate choice of the basic element. These C-sequences may provide an alternative to BABA in the case of limited rf field strength.

4.2 Zero-Quantum Homonuclear Recoupling

The radio-frequency-driven recoupling (RFDR) pulse sequence is widely used to transfer longitudinal magnetization between dipolar coupled spin sites in the solid state (see **Homonuclear Recoupling Schemes in MAS NMR,** Volume 4). The most common application is as the mixing interval in a two-dimensional experiment. If the J-couplings are neglected, the 2D spectrum displays cross peaks which indicate the spatial proximity of spin sites.

The most popular version of RFDR employs the so-called XY8 phase scheme.[33,34] This corresponds to a sequence of strong 180° pulses, spaced at intervals of one rotor period, with rf phases of $\{0, 90, 0, 90, 90, 0, 90, 0\}$. This corresponds to a $\mathcal{SS}'$ supercycle of a $R4_4^1$ sequence, with an overall 45° phase shift. This is indeed an appropriate symmetry for zero-quantum homonuclear recoupling, as may be seen from the list of solutions in Table 9. Symmetries such as $R4_4^1$ select terms of the form $\{l, m, \lambda, \mu\} = \{2, \pm1, 2, 0\}$ and $\{2, \pm2, 2, 0\}$. The recoupling is not γ-encoded, which harms its efficiency in a non-oriented sample, but the lack of γ-encoding permits the use of the stabilizing supercycle $\mathcal{SS}'$.

Table 9 A set of RN_n^ν symmetries for recoupling of the $\{l, m, \lambda, \mu\} = \{2, \pm2, 2, 0\}$ and $\{2, \pm1, 2, 0\}$ terms with suppression of all other homonuclear DD terms, CSA terms and isotropic shift terms. The homonuclear J-coupling $\{0, 0, 0, 0\}$ is symmetry-allowed. All inequivalent solutions in the range $N \leq 40, n \leq 10$ and $\nu \leq 20$ are shown

$R4_4^1$	$R6_6^1$	$R6_6^2$	$R4_8^1$
$R8_8^1$	$R8_8^3$	$R10_{10}^1$	$R10_{10}^2$
$R10_{10}^3$	$R10_{10}^4$		

The curious aspect of RFDR is that the scaling factor for the symmetry-allowed terms tends to zero in the limit of a strong rf field. Indeed, simulations show that the only reason RFDR works is because of the finite duration of practical rf pulses, interference from chemical shifts,[34] and the significant effect of J-couplings (which may even be dominant in some circumstances). Ishii[64] has given a symmetry-based analysis of RFDR with finite rf pulses, and proposed the use of symmetries such as $R4_4^1$ and $R6_6^1$. Brinkmann and Schmedt auf der Günne[65] have demonstrated additional symmetries and explored the use of more complex $\mathcal{R}$ elements in order to allow operation at high spinning frequencies. One recommended sequence involves the supercycle $[\mathcal{SS}']_0[\mathcal{SS}']_{120}[\mathcal{SS}']_{240}$ where $\mathcal{S}$ is a $R6_6^2$ sequence using the

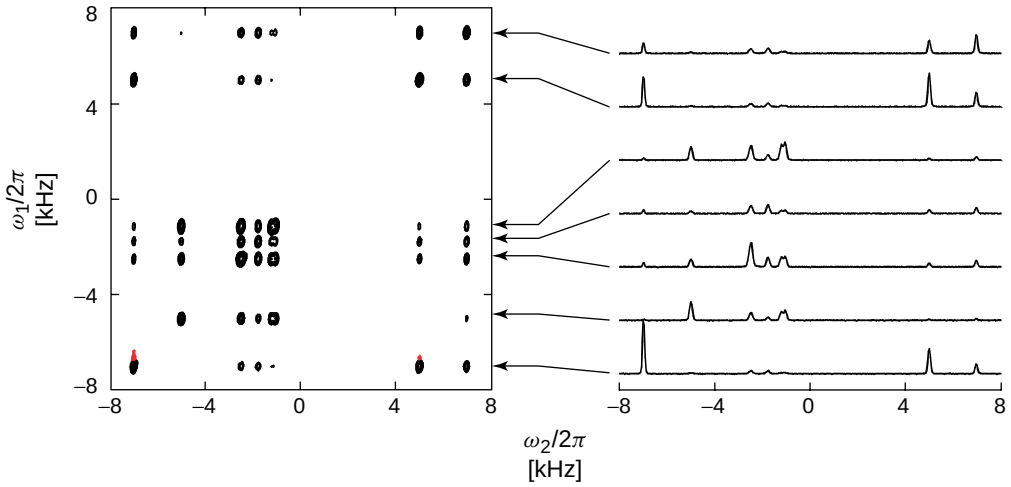

Figure 10 Two-dimensional correlation spectrum of [U−^{13}C]-L-tyrosine, obtained at a field of 9.4 T and a spinning frequency of 23 kHz, using a supercycled $R6_6^2$ pulse sequence, with a mixing interval of 9.9 ms. (Adapted from Ref.[65])

Table 10 A set of RN_n^ν symmetries for γ-encoded recoupling of the $\{l, m, \lambda, \mu\} = \{2, \pm2, 2, \pm1\}$ or $\{2, \pm2, 2, \mp1\}$ components of the homonuclear DD couplings with suppression of all other homonuclear DD terms, CSA terms and isotropic shift terms. The homonuclear J-coupling $\{0, 0, 0, 0\}$ is symmetry-allowed. All inequivalent solutions in the range $N \leq 20, n \leq 10$ and $\nu \leq 10$ are shown

$R10_1^2$	$R12_1^2$	$R14_1^2$	$R16_1^2$	$R18_1^2$	$R20_1^2$	$R14_2^4$	$R18_2^4$	$R10_3^4$	$R14_3^6$
$R16_3^6$	$R20_3^6$	$R14_4^8$	$R18_4^8$	$R12_5^{10}$	$R14_5^{10}$	$R16_5^{10}$	$R18_5^{10}$	$R14_6^{12}$	$R20_6^{12}$
$R10_7^4$	$R12_7^2$	$R16_7^{14}$	$R18_7^{14}$	$R20_7^{14}$	$R14_8^2$	$R18_8^{16}$	$R10_9^2$	$R14_9^4$	$R16_9^2$
$R20_9^{18}$	$R14_{10}^6$	$R18_{10}^2$							

Table 11 A set of CN_n^ν symmetries for selection of homonuclear J-couplings $\{l, m, \lambda, \mu\} = \{0, 0, 0, 0\}$ with suppression of all homonuclear DD couplings and CSA terms. Some isotropic shift terms are also symmetry-allowed. All inequivalent solutions in the range $N \leq 20, n \leq 10$ and $\nu \leq 10$ are shown

$C3_1^0$	$C4_1^0$	$C5_1^0$	$C6_1^0$	$C6_1^3$	$C7_1^0$	$C8_1^0$	$C8_1^4$	$C9_1^0$	$C9_1^3$
$C10_1^0$	$C10_1^3$	$C10_1^5$	$C11_1^0$	$C11_1^3$	$C11_1^4$	$C12_1^0$	$C12_1^3$	$C12_1^4$	$C12_1^6$
$C13_1^0$	$C13_1^3$	$C13_1^4$	$C13_1^5$	$C14_1^0$	$C14_1^3$	$C14_1^4$	$C14_1^5$	$C14_1^7$	$C15_1^0$
$C15_1^3$	$C15_1^4$	$C15_1^5$	$C15_1^6$	$C16_1^0$	$C16_1^3$	$C16_1^4$	$C16_1^5$	$C16_1^6$	$C16_1^8$
$C17_1^0$	$C17_1^3$	$C17_1^4$	$C17_1^5$	$C17_1^6$	$C17_1^7$	$C18_1^0$	$C18_1^3$	$C18_1^4$	$C18_1^5$
$C18_1^6$	$C18_1^7$	$C18_1^9$	$C19_1^0$	$C19_1^3$	$C19_1^4$	$C19_1^5$	$C19_1^6$	$C19_1^7$	$C19_1^8$
$C20_1^0$	$C20_1^3$	$C20_1^4$	$C20_1^5$	$C20_1^6$	$C20_1^7$	$C20_1^8$	$C20_1^{10}$	$C3_2^0$	$C5_2^0$
$C6_2^3$	$C7_2^0$	$C9_2^0$	$C9_2^3$	$C10_2^5$	$C11_2^0$	$C11_2^3$	$C11_2^5$	$C12_2^3$	$C13_2^0$
$C13_2^3$	$C13_2^5$	$C13_2^6$	$C14_2^3$	$C14_2^7$	$C15_2^0$	$C15_2^3$	$C15_2^5$	$C15_2^6$	$C15_2^7$
$C16_2^3$	$C16_2^5$	$C17_2^0$	$C17_2^3$	$C17_2^5$	$C17_2^6$	$C17_2^7$	$C17_2^8$	$C18_2^3$	$C18_2^5$
$C18_2^9$	$C19_2^0$	$C19_2^3$	$C19_2^5$	$C19_2^6$	$C19_2^7$	$C19_2^8$	$C19_2^9$	$C20_2^3$	$C20_2^5$
$C20_2^7$	$C4_3^0$	$C5_3^0$	$C7_3^0$	$C8_3^0$	$C8_3^4$	$C9_3^1$	$C9_3^2$	$C9_3^4$	$C10_3^0$
$C10_3^1$	$C10_3^5$	$C11_3^0$	$C11_3^1$	$C11_3^2$	$C12_3^1$	$C12_3^2$	$C12_3^4$	$C12_3^5$	$C13_3^0$
$C13_3^1$	$C13_3^2$	$C13_3^4$	$C14_3^0$	$C14_3^1$	$C14_3^2$	$C14_3^5$	$C14_3^7$	$C15_3^1$	$C15_3^2$
$C15_3^4$	$C15_3^5$	$C15_3^7$	$C16_3^0$	$C16_3^1$	$C16_3^2$	$C16_3^4$	$C16_3^7$	$C16_3^8$	$C17_3^0$
$C17_3^1$	$C17_3^2$	$C17_3^4$	$C17_3^5$	$C17_3^8$	$C18_3^1$	$C18_3^2$	$C18_3^4$	$C18_3^5$	$C18_3^7$
$C18_3^8$	$C19_3^0$	$C19_3^1$	$C19_3^2$	$C19_3^4$	$C19_3^5$	$C19_3^7$	$C19_3^9$	$C20_3^0$	$C20_3^1$
$C20_3^2$	$C20_3^4$	$C20_3^5$	$C20_3^8$	$C20_3^9$	$C20_3^{10}$	$C3_4^0$	$C5_4^0$	$C6_4^3$	$C7_4^0$
$C9_4^0$	$C9_4^3$	$C10_4^5$	$C11_4^0$	$C11_4^1$	$C11_4^5$	$C12_4^1$	$C12_4^3$	$C12_4^5$	$C13_4^0$
$C13_4^1$	$C13_4^3$	$C13_4^6$	$C14_4^1$	$C14_4^7$	$C15_4^0$	$C15_4^1$	$C15_4^3$	$C15_4^5$	$C15_4^6$
$C16_4^1$	$C16_4^3$	$C16_4^5$	$C16_4^7$	$C17_4^0$	$C17_4^1$	$C17_4^3$	$C17_4^5$	$C17_4^6$	$C17_4^7$
$C18_4^1$	$C18_4^3$	$C18_4^9$	$C19_4^0$	$C19_4^1$	$C19_4^3$	$C19_4^5$	$C19_4^6$	$C19_4^7$	$C19_4^9$
$C20_4^1$	$C20_4^3$	$C20_4^5$	$C20_4^7$	$C20_4^9$	$C3_5^0$	$C4_5^0$	$C6_5^0$	$C6_5^3$	$C7_5^0$
$C8_5^0$	$C8_5^4$	$C9_5^0$	$C9_5^3$	$C11_5^0$	$C11_5^2$	$C11_5^4$	$C12_5^0$	$C12_5^3$	$C12_5^4$
$C12_5^6$	$C13_5^0$	$C13_5^1$	$C13_5^2$	$C13_5^6$	$C14_5^0$	$C14_5^1$	$C14_5^3$	$C14_5^6$	$C14_5^7$
$C15_5^1$	$C15_5^2$	$C15_5^3$	$C15_5^4$	$C15_5^6$	$C15_5^7$	$C16_5^0$	$C16_5^1$	$C16_5^2$	$C16_5^4$
$C16_5^7$	$C16_5^8$	$C17_5^0$	$C17_5^1$	$C17_5^2$	$C17_5^3$	$C17_5^4$	$C17_5^8$	$C18_5^0$	$C18_5^1$
$C18_5^2$	$C18_5^3$	$C18_5^6$	$C18_5^7$	$C18_5^9$	$C19_5^0$	$C19_5^1$	$C19_5^2$	$C19_5^3$	$C19_5^4$
$C19_5^6$	$C19_5^8$	$C20_5^1$	$C20_5^2$	$C20_5^3$	$C20_5^4$	$C20_5^6$	$C20_5^7$	$C20_5^8$	$C20_5^9$
$C5_6^0$	$C7_6^0$	$C9_6^1$	$C9_6^2$	$C9_6^4$	$C10_6^5$	$C11_6^0$	$C11_6^2$	$C11_6^4$	$C13_6^0$
$C13_6^2$	$C13_6^4$	$C13_6^5$	$C14_6^5$	$C14_6^7$	$C15_6^1$	$C15_6^2$	$C15_6^4$	$C15_6^5$	$C15_6^7$
$C16_6^1$	$C16_6^7$	$C17_6^0$	$C17_6^1$	$C17_6^2$	$C17_6^4$	$C17_6^7$	$C17_6^8$	$C18_6^1$	$C18_6^5$
$C18_6^7$	$C19_6^0$	$C19_6^1$	$C19_6^2$	$C19_6^4$	$C19_6^5$	$C19_6^8$	$C19_6^9$	$C20_6^1$	$C20_6^5$
$C20_6^9$	$C3_7^0$	$C4_7^0$	$C5_7^0$	$C6_7^0$	$C6_7^3$	$C8_7^0$	$C8_7^4$	$C9_7^0$	$C9_7^3$
$C10_7^0$	$C10_7^1$	$C10_7^5$	$C11_7^0$	$C11_7^1$	$C11_7^5$	$C12_7^0$	$C12_7^3$	$C12_7^4$	$C12_7^6$
$C13_7^0$	$C13_7^2$	$C13_7^4$	$C13_7^5$	$C15_7^0$	$C15_7^2$	$C15_7^3$	$C15_7^5$	$C15_7^6$	$C16_7^0$
$C16_7^3$	$C16_7^4$	$C16_7^5$	$C16_7^6$	$C16_7^8$	$C17_7^0$	$C17_7^1$	$C17_7^2$	$C17_7^4$	$C17_7^6$
$C17_7^8$	$C18_7^0$	$C18_7^1$	$C18_7^3$	$C18_7^5$	$C18_7^6$	$C18_7^8$	$C18_7^9$	$C19_7^0$	$C19_7^1$
$C19_7^2$	$C19_7^3$	$C19_7^4$	$C19_7^8$	$C19_7^9$	$C20_7^0$	$C20_7^1$	$C20_7^2$	$C20_7^4$	$C20_7^5$
$C20_7^8$	$C20_7^9$	$C20_7^{10}$	$C3_8^0$	$C5_8^0$	$C6_8^3$	$C7_8^0$	$C9_8^0$	$C9_8^3$	$C10_8^5$
$C11_8^0$	$C11_8^1$	$C11_8^2$	$C12_8^1$	$C12_8^3$	$C12_8^5$	$C13_8^0$	$C13_8^1$	$C13_8^2$	$C13_8^6$
$C14_8^5$	$C14_8^7$	$C15_8^0$	$C15_8^2$	$C15_8^3$	$C15_8^5$	$C15_8^6$	$C17_8^0$	$C17_8^2$	$C17_8^3$
$C17_8^5$	$C17_8^6$	$C17_8^7$	$C18_8^3$	$C18_8^7$	$C18_8^9$	$C19_8^0$	$C19_8^1$	$C19_8^2$	$C19_8^5$
$C19_8^6$	$C19_8^7$	$C19_8^9$	$C20_8^1$	$C20_8^3$	$C20_8^5$	$C20_8^7$	$C20_8^9$	$C4_9^0$	$C5_9^0$
$C7_9^0$	$C8_9^0$	$C8_9^4$	$C10_9^0$	$C10_9^3$	$C10_9^5$	$C11_9^0$	$C11_9^3$	$C11_9^5$	$C12_9^1$
$C12_9^2$	$C12_9^4$	$C12_9^5$	$C13_9^0$	$C13_9^1$	$C13_9^3$	$C13_9^6$	$C14_9^0$	$C14_9^1$	$C14_9^3$
$C14_9^6$	$C14_9^7$	$C15_9^1$	$C15_9^2$	$C15_9^4$	$C15_9^5$	$C15_9^7$	$C16_9^0$	$C16_9^3$	$C16_9^4$

(*continued overleaf*)

Table 11 (*Continued*)

$C16_9^5$	$C16_9^6$	$C16_9^8$	$C17_9^0$	$C17_9^2$	$C17_9^3$	$C17_9^5$	$C17_9^6$	$C17_9^7$	$C19_9^0$
$C19_9^2$	$C19_9^3$	$C19_9^4$	$C19_9^6$	$C19_9^7$	$C19_9^8$	$C20_9^0$	$C20_9^3$	$C20_9^4$	$C20_9^5$
$C20_9^6$	$C20_9^7$	$C20_9^8$	$C20_9^{10}$	$C3_{10}^0$	$C6_{10}^8$	$C7_{10}^0$	$C9_{10}^0$	$C9_{10}^3$	$C11_{10}^0$
$C11_{10}^3$	$C11_{10}^4$	$C12_{10}^3$	$C13_{10}^0$	$C13_{10}^1$	$C13_{10}^2$	$C13_{10}^4$	$C14_{10}^1$	$C14_{10}^7$	$C15_{10}^1$
$C15_{10}^2$	$C15_{10}^3$	$C15_{10}^4$	$C15_{10}^6$	$C15_{10}^7$	$C16_{10}^1$	$C16_{10}^7$	$C17_{10}^0$	$C17_{10}^1$	$C17_{10}^2$
$C17_{10}^4$	$C17_{10}^6$	$C17_{10}^8$	$C18_{10}^3$	$C18_{10}^7$	$C18_{10}^9$	$C19_{10}^0$	$C19_{10}^2$	$C19_{10}^3$	$C19_{10}^4$
$C19_{10}^6$	$C19_{10}^7$	$C19_{10}^8$							

Table 12 A set of RN_n^ν symmetries for selection of homonuclear J-couplings $\{l, m, \lambda, \mu\} = \{0, 0, 0, 0\}$ with suppression of all homonuclear DD couplings, CSA terms and isotropic shift terms. All inequivalent solutions in the range $N \leq 20, n \leq 10$ and $\nu \leq 10$ are shown

$R6_1^0$	$R8_1^0$	$R10_1^0$	$R12_1^0$	$R12_1^3$	$R14_1^0$	$R14_1^3$	$R14_1^4$	$R16_1^0$	$R16_1^3$
$R16_1^4$	$R16_1^5$	$R18_1^0$	$R18_1^3$	$R18_1^4$	$R18_1^5$	$R18_1^6$	$R20_1^0$	$R20_1^3$	$R20_1^4$
$R20_1^5$	$R20_1^6$	$R20_1^7$	$R6_2^0$	$R10_2^0$	$R12_2^3$	$R14_2^0$	$R16_2^3$	$R16_2^5$	$R18_2^0$
$R18_2^3$	$R18_2^6$	$R20_2^3$	$R20_2^5$	$R20_2^7$	$R8_3^0$	$R10_3^0$	$R14_3^0$	$R14_3^2$	$R14_3^5$
$R16_3^0$	$R16_3^1$	$R16_3^4$	$R16_3^7$	$R18_3^1$	$R18_3^2$	$R18_3^4$	$R18_3^5$	$R18_3^7$	$R18_3^8$
$R20_3^0$	$R20_3^1$	$R20_3^2$	$R20_3^5$	$R20_3^8$	$R20_3^9$	$R6_4^0$	$R10_4^0$	$R12_4^1$	$R12_4^3$
$R12_4^5$	$R14_4^0$	$R18_4^0$	$R18_4^3$	$R18_4^6$	$R20_4^1$	$R20_4^3$	$R20_4^5$	$R20_4^7$	$R20_4^9$
$R6_5^0$	$R8_5^0$	$R12_5^0$	$R12_5^3$	$R14_5^0$	$R14_5^1$	$R14_5^6$	$R16_5^0$	$R16_5^1$	$R16_5^4$
$R16_5^7$	$R18_5^0$	$R18_5^2$	$R18_5^3$	$R18_5^6$	$R18_5^7$				

Table 13 A set of CN_n^ν symmetries for selection of isotropic chemical shift terms. All CSA terms and homonuclear DD coupling terms are suppressed. The homonuclear J-coupling $\{0, 0, 0, 0\}$ is symmetry-allowed. All inequivalent solutions in the range $N \leq 20, n \leq 10$ and $\nu \leq 10$ are shown

$C3_1^0$	$C4_1^0$	$C5_1^0$	$C6_1^0$	$C6_1^3$	$C7_1^0$	$C8_1^0$	$C8_1^4$	$C9_1^0$	$C9_1^3$
$C10_1^0$	$C10_1^3$	$C10_1^5$	$C11_1^3$	$C11_1^4$	$C12_1^3$	$C12_1^4$	$C12_1^6$	$C13_1^3$	$C13_1^4$
$C13_1^5$	$C14_1^3$	$C14_1^4$	$C14_1^5$	$C14_1^7$	$C15_1^3$	$C15_1^4$	$C15_1^5$	$C15_1^6$	$C16_1^3$
$C16_1^4$	$C16_1^5$	$C16_1^6$	$C16_1^8$	$C17_1^3$	$C17_1^4$	$C17_1^5$	$C17_1^6$	$C17_1^7$	$C18_1^3$
$C18_1^4$	$C18_1^5$	$C18_1^6$	$C18_1^7$	$C18_1^9$	$C19_1^3$	$C19_1^4$	$C19_1^5$	$C19_1^6$	$C19_1^7$
$C19_1^8$	$C20_1^3$	$C20_1^4$	$C20_1^5$	$C20_1^6$	$C20_1^7$	$C20_1^8$	$C20_1^{10}$	$C3_2^0$	$C5_2^0$
$C6_2^3$	$C7_2^0$	$C9_2^0$	$C9_2^3$	$C10_2^5$	$C11_2^3$	$C11_2^5$	$C12_2^3$	$C13_2^3$	$C13_2^5$
$C13_2^6$	$C14_2^3$	$C14_2^7$	$C15_2^3$	$C15_2^5$	$C15_2^6$	$C15_2^7$	$C16_2^3$	$C16_2^5$	$C17_2^3$
$C17_2^5$	$C17_2^6$	$C17_2^7$	$C17_2^8$	$C18_2^3$	$C18_2^5$	$C18_2^9$	$C19_2^3$	$C19_2^5$	$C19_2^6$
$C19_2^7$	$C19_2^8$	$C19_2^9$	$C20_2^3$	$C20_2^5$	$C20_2^7$	$C4_3^0$	$C5_3^0$	$C7_3^0$	$C8_3^0$
$C8_3^4$	$C9_3^1$	$C9_3^2$	$C9_3^4$	$C10_3^0$	$C10_3^1$	$C10_3^5$	$C11_3^1$	$C11_3^2$	$C12_3^1$
$C12_3^2$	$C12_3^4$	$C12_3^5$	$C13_3^1$	$C13_3^2$	$C13_3^4$	$C14_3^1$	$C14_3^2$	$C14_3^5$	$C14_3^7$
$C15_3^1$	$C15_3^2$	$C15_3^4$	$C15_3^5$	$C15_3^7$	$C16_3^1$	$C16_3^2$	$C16_3^4$	$C16_3^7$	$C16_3^8$
$C17_3^1$	$C17_3^2$	$C17_3^4$	$C17_3^5$	$C17_3^8$	$C18_3^1$	$C18_3^2$	$C18_3^4$	$C18_3^5$	$C18_3^7$
$C18_3^8$	$C19_3^1$	$C19_3^2$	$C19_3^4$	$C19_3^5$	$C19_3^7$	$C19_3^9$	$C20_3^1$	$C20_3^2$	$C20_3^4$
$C20_3^5$	$C20_3^8$	$C20_3^9$	$C20_3^{10}$	$C3_4^0$	$C5_4^0$	$C6_4^3$	$C7_4^0$	$C9_4^0$	$C9_4^3$
$C10_4^5$	$C11_4^1$	$C11_4^5$	$C12_4^1$	$C12_4^3$	$C12_4^5$	$C13_4^1$	$C13_4^3$	$C13_4^6$	$C14_4^1$
$C14_4^7$	$C15_4^1$	$C15_4^3$	$C15_4^5$	$C15_4^6$	$C16_4^1$	$C16_4^3$	$C16_4^5$	$C16_4^7$	$C17_4^1$
$C17_4^3$	$C17_4^5$	$C17_4^6$	$C17_4^7$	$C18_4^1$	$C18_4^3$	$C18_4^9$	$C19_4^1$	$C19_4^3$	$C19_4^5$
$C19_4^6$	$C19_4^7$	$C19_4^9$	$C20_4^1$	$C20_4^3$	$C20_4^5$	$C20_4^7$	$C20_4^9$	$C3_5^0$	$C4_5^0$
$C6_5^0$	$C6_5^3$	$C7_5^0$	$C8_5^0$	$C8_5^4$	$C9_5^0$	$C9_5^3$	$C11_5^2$	$C11_5^4$	$C12_5^3$
$C12_5^4$	$C12_5^6$	$C13_5^1$	$C13_5^2$	$C13_5^6$	$C14_5^1$	$C14_5^3$	$C14_5^6$	$C14_5^7$	$C15_5^1$
$C15_5^2$	$C15_5^3$	$C15_5^4$	$C15_5^6$	$C15_5^7$	$C16_5^1$	$C16_5^2$	$C16_5^4$	$C16_5^7$	$C16_5^8$
$C17_5^1$	$C17_5^2$	$C17_5^3$	$C17_5^4$	$C17_5^8$	$C18_5^1$	$C18_5^2$	$C18_5^3$	$C18_5^6$	$C18_5^7$
$C18_5^9$	$C19_5^1$	$C19_5^2$	$C19_5^3$	$C19_5^4$	$C19_5^6$	$C19_5^8$	$C20_5^1$	$C20_5^2$	$C20_5^3$

Table 13 (*Continued*)

$C20_5^4$	$C20_5^6$	$C20_5^7$	$C20_5^8$	$C20_5^9$	$C5_6^0$	$C7_6^0$	$C9_6^1$	$C9_6^2$	$C9_6^4$
$C10_6^5$	$C11_6^2$	$C11_6^4$	$C13_6^2$	$C13_6^4$	$C13_6^5$	$C14_6^5$	$C14_6^7$	$C15_6^1$	$C15_6^2$
$C15_6^4$	$C15_6^5$	$C15_6^7$	$C16_6^1$	$C16_6^7$	$C17_6^1$	$C17_6^2$	$C17_6^4$	$C17_6^7$	$C17_6^8$
$C18_6^1$	$C18_6^5$	$C18_6^7$	$C19_6^1$	$C19_6^2$	$C19_6^4$	$C19_6^5$	$C19_6^8$	$C19_6^9$	$C20_6^1$
$C20_6^5$	$C20_6^9$	$C3_7^0$	$C4_7^0$	$C5_7^0$	$C6_7^0$	$C6_7^3$	$C8_7^0$	$C8_7^4$	$C9_7^0$
$C9_7^3$	$C10_7^0$	$C10_7^1$	$C10_7^5$	$C11_7^1$	$C11_7^5$	$C12_7^3$	$C12_7^4$	$C12_7^6$	$C13_7^2$
$C13_7^4$	$C13_7^5$	$C15_7^2$	$C15_7^3$	$C15_7^5$	$C15_7^6$	$C16_7^3$	$C16_7^4$	$C16_7^5$	$C16_7^6$
$C16_7^8$	$C17_7^1$	$C17_7^2$	$C17_7^4$	$C17_7^6$	$C17_7^8$	$C18_7^1$	$C18_7^3$	$C18_7^5$	$C18_7^6$
$C18_7^8$	$C18_7^9$	$C19_7^1$	$C19_7^2$	$C19_7^3$	$C19_7^4$	$C19_7^8$	$C19_7^9$	$C20_7^1$	$C20_7^2$
$C20_7^4$	$C20_7^5$	$C20_7^8$	$C20_7^9$	$C20_7^{10}$	$C3_8^0$	$C5_8^0$	$C6_8^3$	$C7_8^0$	$C9_8^0$
$C9_8^3$	$C10_8^5$	$C11_8^1$	$C11_8^2$	$C12_8^1$	$C12_8^3$	$C12_8^5$	$C13_8^1$	$C13_8^2$	$C13_8^6$
$C14_8^5$	$C14_8^7$	$C15_8^2$	$C15_8^3$	$C15_8^5$	$C15_8^6$	$C17_8^2$	$C17_8^3$	$C17_8^5$	$C17_8^6$
$C17_8^7$	$C18_8^3$	$C18_8^7$	$C18_8^9$	$C19_8^1$	$C19_8^2$	$C19_8^5$	$C19_8^6$	$C19_8^7$	$C19_8^9$
$C20_8^1$	$C20_8^3$	$C20_8^5$	$C20_8^7$	$C20_8^9$	$C4_9^0$	$C5_9^0$	$C7_9^0$	$C8_9^0$	$C8_9^4$
$C10_9^0$	$C10_9^3$	$C10_9^5$	$C11_9^3$	$C11_9^5$	$C12_9^1$	$C12_9^2$	$C12_9^4$	$C12_9^5$	$C13_9^1$
$C13_9^3$	$C13_9^6$	$C14_9^1$	$C14_9^3$	$C14_9^6$	$C14_9^7$	$C15_9^1$	$C15_9^2$	$C15_9^4$	$C15_9^5$
$C15_9^7$	$C16_9^3$	$C16_9^4$	$C16_9^5$	$C16_9^6$	$C16_9^8$	$C17_9^2$	$C17_9^3$	$C17_9^5$	$C17_9^6$
$C17_9^7$	$C19_9^2$	$C19_9^3$	$C19_9^4$	$C19_9^6$	$C19_9^7$	$C19_9^8$	$C20_9^3$	$C20_9^4$	$C20_9^5$
$C20_9^6$	$C20_9^7$	$C20_9^8$	$C20_9^{10}$	$C3_{10}^0$	$C6_{10}^3$	$C7_{10}^0$	$C9_{10}^0$	$C9_{10}^3$	$C11_{10}^3$
$C11_{10}^4$	$C12_{10}^3$	$C13_{10}^1$	$C13_{10}^2$	$C13_{10}^4$	$C14_{10}^1$	$C14_{10}^7$	$C15_{10}^1$	$C15_{10}^2$	$C15_{10}^3$
$C15_{10}^4$	$C15_{10}^6$	$C15_{10}^7$	$C16_{10}^1$	$C16_{10}^7$	$C17_{10}^1$	$C17_{10}^2$	$C17_{10}^4$	$C17_{10}^6$	$C17_{10}^8$
$C18_{10}^3$	$C18_{10}^7$	$C18_{10}^9$	$C19_{10}^2$	$C19_{10}^3$	$C19_{10}^4$	$C19_{10}^6$	$C19_{10}^7$	$C19_{10}^8$	

Table 14 A set of RN_n^ν symmetries for selection of isotropic chemical shift terms. In all cases, the terms $\{l, m, \lambda, \mu\} = \{0, 0, 1, \pm 1\}$ are selected. All CSA terms and homonuclear DD coupling terms are suppressed. The homonuclear J-coupling $\{0, 0, 0, 0\}$ is symmetry-allowed. All inequivalent solutions in the range $N \leq 20, n \leq 10$ and $\nu \leq 10$ are shown

$R6_1^3$	$R8_1^4$	$R10_1^5$	$R12_1^6$	$R14_1^7$	$R16_1^8$	$R18_1^9$	$R20_1^{10}$
$R6_2^3$	$R10_2^5$	$R14_2^7$	$R18_2^9$	$R8_3^4$	$R10_3^5$	$R14_3^7$	$R16_3^8$
$R20_3^{10}$	$R6_4^3$	$R10_4^5$	$R14_4^7$	$R18_4^9$	$R6_5^3$	$R8_5^4$	$R12_5^6$
$R14_5^7$	$R16_5^8$	$R18_5^9$					

Table 15 A set of RN_n^ν symmetries for γ-encoded recoupling of CSA interactions, with selection of $\{l, m, \lambda, \mu\} = \{2, \pm 2, 1, \pm 1\}$ or $\{2, \pm 2, 1, \mp 1\}$ terms, and suppression of isotropic shift and homonuclear DD terms. The homonuclear J-coupling $\{0, 0, 0, 0\}$ is also symmetry-allowed. The same solutions implement γ-encoded heteronuclear recoupling if they are applied to only one spin species. All inequivalent solutions in the range $N \leq 20, n \leq 10$ and $\nu \leq 10$ are shown

$R10_1^3$	$R12_1^4$	$R14_1^5$	$R16_1^6$	$R18_1^7$	$R20_1^8$	$R14_2^3$	$R18_2^5$	$R10_3^1$	$R14_3^1$
$R16_3^2$	$R20_3^4$	$R14_4^1$	$R18_4^1$	$R12_5^4$	$R14_5^3$	$R16_5^2$	$R18_5^1$	$R14_6^5$	$R10_7^1$
$R12_7^4$	$R16_7^6$	$R18_7^5$	$R20_7^4$	$R14_8^5$	$R18_8^7$	$R10_9^3$	$R14_9^3$	$R16_9^6$	$R20_9^8$
$R14_{10}^1$	$R18_{10}^7$								

Table 16 A set of RN_n^ν symmetries for non-γ-encoded zero-quantum recoupling of CSA interactions, with selection of $\{l, m, \lambda, \mu\} = \{2, \pm 2, 1, 0\}$ terms, and suppression of all isotropic shift and homonuclear DD terms. The homonuclear J-coupling $\{0, 0, 0, 0\}$ is also symmetry-allowed. The same solutions implement zero-quantum heteronuclear recoupling if they are applied to only one spin species. All inequivalent solutions in the range $N \leq 20, n \leq 10$ and $\nu \leq 10$ are shown

$R12_3^1$	$R12_3^2$	$R12_3^4$	$R12_3^5$	$R16_4^1$	$R16_4^3$	$R16_4^5$	$R16_4^7$	$R20_5^1$	$R20_5^2$
$R20_5^3$	$R20_5^4$	$R20_5^6$	$R20_5^7$	$R20_5^8$	$R20_5^9$	$R12_9^1$	$R12_9^2$	$R12_9^4$	$R12_9^5$

element $\mathcal{R} = 90_{180}270_0$. An experimental correlation spectrum of [U–^{13}C]-L-tyrosine at a spinning frequency of 20 kHz is shown in Figure 10.

4.3 Homonuclear Single-Quantum Recoupling

Table 10 shows a set of symmetries for recoupling the $\mu = \pm 1$ components of the homonuclear DD interaction. These symmetries are expected to be useful in multiple-quantum spin counting experiments.[93,94,109,110]

4.4 Selection of J-Couplings

Compilations of symmetries appropriate for the selection of homonuclear J-couplings $\{l, m, \lambda, \mu\} = \{0, 0, 0, 0\}$ with suppression of homonuclear DD couplings and chemical shift anisotropies are given in Tables 11 and 12. The RN_n^ν symmetries in Table 12 also suppress isotropic chemical shift terms. For the CN_n^ν symmetries in Table 11, on the other hand, the scaling factors for the isotropic shift terms must be set to zero by an appropriate choice of $\mathcal{C}$.

These symmetries may be used in through-bond correlation spectroscopy (TOBSY) experiments.[48–52] The pulse sequence is used as the mixing interval in a two-dimensional experiment; The transfer of longitudinal magnetization generates cross peaks in the 2D spectrum, indicating spin sites with finite mutual J-couplings (see **Through-Bond Experiments in Solids**).

The original pulse sequences of this kind, suggested by Baldus and Meier[48–52] have symmetries $R6_1^0$ and $R8_1^0$. Two groups[50,51] have proposed a new range of pulse sequence, operational at higher spinning frequencies, which employ symmetries such as $C9_3^1$, $C9_6^1$ and others included in Table 11. Chan has demonstrated a $R30_6^{14}$ sequence which also has good performance at high spinning frequency.[52]

4.5 Selection of Isotropic Chemical Shifts

High-resolution isotropic shift spectra may be obtained in solids if all DD couplings and CSA terms are suppressed. In principle, this may be done by sufficiently rapid sample spinning. However, in practice, the required spinning frequencies are usually impractical. A well-designed rf pulse sequence may assist the spatial averaging, leading to acceptable resolution at practical spinning frequencies. The most common applications of such CRAMPS methods are in the high-resolution ^{1}H NMR of organic powdered solids (see **Line Narrowing Methods in Solids,** Volume 4).

Tables 13 and 14 show symmetry solutions for fast-spinning CRAMPS. All these symmetries suppress the homonuclear DD couplings and the CSA interactions, while allowing some isotropic shift terms. In this application it is particularly important that the scaling factors for the isotropic shift terms are as large as possible. This requires careful design of the element $\mathcal{C}$.

Spiess and co-workers employed $C3_1^0$ and $C4_1^0$ symmetries in fast-spinning CRAMPS experiments, using the known WHH4 cycles[12,13] as the basic element $\mathcal{C}$.[46,47] Recently, Madhu and Zhao demonstrated the use of $R18_2^9$ symmetry.[111] Figure 11 shows an experimental ^{1}H spectrum obtained at a spinning frequency of 20 kHz with a $R18_2^9$ sequence

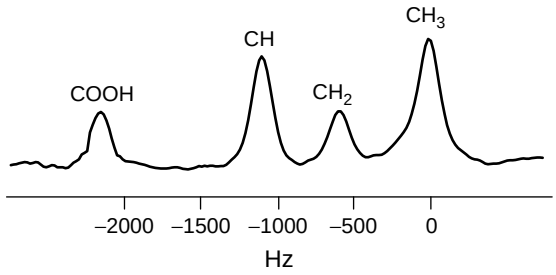

Figure 11 ^{1}H spectrum of monoethylfumarate, obtained at a field of 9.4 T and a spinning frequency of 20 kHz with a $R18_2^9$ sequence. After correcting for the pulse sequence scaling factor, the linewidths of all four peaks are given by approximately 0.9 ppm. (Adapted from Ref.[111])

constructed from basic elements $\mathcal{R} = 90_{-45}90_{45}90_{-45}$. Note the use of a phase-modulated basic element, in order to enhance the local averaging of the strong homonuclear interactions.

4.6 CSA Recoupling

Table 15 shows a set of symmetries leading to γ-encoded recoupling of CSA interactions, with suppression of isotropic chemical shifts and homonuclear DD couplings. The recoupled average Hamiltonian is transverse, i.e., it has the form $I_x \cos\phi + I_y \sin\phi$.

These sequences could be useful for measuring the CSA principal values of individual sites in coupled spin clusters.

Table 16 shows a set of symmetries leading to recoupling of the zero-quantum ($\mu = 0$) part of the CSA interaction, with suppression of isotropic chemical shifts and homonuclear DD couplings. In this case, the recoupling is not γ-encoded, and the recoupled average Hamiltonian is longitudinal, i.e., proportional to the operator I_z.

4.7 γ-Encoded Heteronuclear Recoupling

The solutions in Table 15 may also be used for the selective γ-encoded recoupling of heteronuclear DD interactions. If these sequences are applied repetitively at the Larmor frequency of one spin species, while the NMR signals from a coupled spin species are observed, the resulting spectrum displays a splitting, due to the recoupled heteronuclear interactions. Since the recoupling is γ-encoded, the splittings are prominent, even in orientationally-disordered systems such as powders.

Zhao has demonstrated the measurement of ^{13}C–^{1}H and ^{15}N–^{1}H DD couplings, using sequences with $R18_1^7$ and $R18_2^5$ symmetries.[112,113] An experimental example is shown in Figure 12. The figure shows the individual ^{15}N spectra of the two different NH groups in the imidazole ring of L-histidine hydrochloride monohydrate, obtained in a 2D experiment in which a $R18_2^5$ sequence is applied at the ^{1}H Larmor frequency.[113] There is a visible difference in the two splittings, which corresponds to a 4 pm difference in the two NH bond lengths. This difference is attributed to an intermolecular hydrogen bond formed by one of the NH groups. This result shows the potential of recoupling experiments for investigating the details of intermolecular interactions and other bonding

Table 17 A set of $CRN_n^{\nu_I,\nu_S}$ symmetries for γ-encoded double-quantum heteronuclear recoupling, with suppression of all CSA terms, isotropic chemical shift terms, homonuclear DD terms, and heteronuclear J-couplings. All symmetries recouple terms of the form $\{l, m, \lambda_I, \mu_I, \lambda_S, \mu_S\} = \{2, \mp 1, 1, \pm 1, 1, \pm 1\}$ The homonuclear J-couplings $\{0, 0, 0, 0, 0, 0\}$ are symmetry-allowed. All in-equivalent solutions in the range $N \leq 20, n \leq 9$ and $N/n \leq 7$ are shown

$CR14_3^{2,2}$	$CR14_3^{-5,-5}$	$CR16_3^{1,4}$	$CR16_3^{-4,-7}$	$CR18_3^{-1,7}$	$CR18_3^{1,5}$
$CR18_3^{-2,8}$	$CR18_3^{2,4}$	$CR18_3^{-4,-8}$	$CR18_3^{-5,-7}$	$CR20_3^{-1,8}$	$CR20_3^{-2,9}$
$CR20_3^{2,5}$	$CR20_3^{-5,-8}$	$CR20_4^{-1,7}$	$CR20_4^{1,5}$	$CR20_4^{-3,9}$	$CR20_4^{3,3}$
$CR20_4^{-5,-9}$	$CR20_4^{-7,-7}$	$CR14_5^{1,1}$	$CR14_5^{-6,-6}$	$CR16_5^{-1,4}$	$CR16_5^{-4,7}$
$CR18_5^{-2,6}$	$CR18_5^{2,2}$	$CR18_5^{-3,7}$	$CR18_5^{-7,-7}$	$CR16_6^{1,1}$	$CR16_6^{-7,-7}$
$CR20_6^{-1,5}$	$CR20_6^{-5,9}$	$CR16_7^{-3,4}$	$CR16_7^{-4,5}$	$CR18_7^{-1,3}$	$CR18_7^{1,1}$
$CR18_7^{-6,8}$	$CR18_7^{-8,-8}$	$CR20_7^{1,2}$	$CR20_7^{-2,5}$	$CR20_7^{-5,8}$	$CR20_7^{-8,-9}$
$CR20_8^{-1,3}$	$CR20_8^{1,1}$	$CR20_8^{-3,5}$	$CR20_8^{-5,7}$	$CR20_8^{-7,9}$	$CR20_8^{-9,-9}$
$CR14_9^{-1,-1}$	$CR14_9^{6,6}$	$CR16_9^{3,-4}$	$CR16_9^{4,-5}$	$CR20_9^{-3,4}$	$CR20_9^{-4,5}$
$CR20_9^{-5,6}$	$CR20_9^{-6,7}$				

Table 18 A set of $RN_n^{\nu_I,\nu_S}$ symmetries for γ-encoded double-quantum heteronuclear recoupling, with suppression of all CSA terms, isotropic chemical shift terms and homonuclear DD terms. All symmetries recouple terms of the form $\{l, m, \lambda_I, \mu_I, \lambda_S, \mu_S\} = \{2, \mp 1, 1, \pm 1, 1, \pm 1\}$ The homonuclear J-couplings $\{0, 0, 0, 0, 0, 0\}$ and heteronuclear J-coupling $\{0, 0, 1, 0, 1, 0\}$ are symmetry-allowed. All inequivalent solutions in the range $N \leq 20, n \leq 9$ and $N/n \leq 7$ are shown

$R14_3^{2,-5}$	$R16_3^{1,-4}$	$R16_3^{4,-7}$	$R18_3^{-1,-2}$	$R18_3^{1,-4}$	$R18_3^{2,-5}$
$R18_3^{4,-7}$	$R18_3^{5,-8}$	$R18_3^{7,8}$	$R20_3^{-1,-2}$	$R20_3^{2,-5}$	$R20_3^{5,-8}$
$R20_3^{8,9}$	$R20_4^{-1,-3}$	$R20_4^{1,-5}$	$R20_4^{3,-7}$	$R20_4^{5,-9}$	$R20_4^{7,9}$
$R14_5^{1,-6}$	$R16_5^{-1,-4}$	$R16_5^{4,7}$	$R18_5^{-2,-3}$	$R18_5^{2,-7}$	$R18_5^{6,7}$
$R16_6^{1,-7}$	$R20_6^{-1,-5}$	$R20_6^{5,9}$	$R16_7^{-3,-4}$	$R16_7^{4,5}$	$R18_7^{-1,-6}$
$R18_7^{1,-8}$	$R18_7^{3,8}$	$R20_7^{1,-8}$	$R20_7^{-2,-5}$	$R20_7^{2,-9}$	$R20_7^{5,8}$
$R20_8^{-1,-7}$	$R20_8^{1,-9}$	$R20_8^{-3,-5}$	$R20_8^{3,9}$	$R20_8^{5,7}$	$R14_9^{1,-6}$
$R16_9^{3,4}$	$R16_9^{-4,-5}$	$R20_9^{-3,-6}$	$R20_9^{-4,-5}$	$R20_9^{4,7}$	$R20_9^{5,6}$

perturbations, in systems that are unsuitable for crystallography or solution NMR.

The symmetry $C5_1^1$ has also been used for γ-encoded heteronuclear recoupling, although it does not fully suppress the homonuclear DD terms.[114–116] The performance of $C5_1^1$ is acceptable if it is used together with a basic element $\mathcal{C}$ with good local averaging properties for the homonuclear DD interactions. The frequency-switched Lee–Goldburg (FSLG)[17] and MREV[14,15] sequences have both been used.[114–116] Nevertheless, one expects some interference from the homonuclear DD couplings in the $C5_1^1$-based methods.

4.8 Non-γ-Encoded Heteronuclear Recoupling

The symmetries in Table 16 lead to zero-quantum recoupling of heteronuclear DD interactions, with suppression of chemical shift terms and homonuclear DD couplings. The recoupled heteronuclear interactions are proportional to the operator product $I_z S_z$.

If the RN_n^ν sequence is applied to the I-spin species, the S-spin NMR signals display a splitting which may be used to estimate the magnitude of the heteronuclear DD coupling. Since the recoupling is not γ-encoded, the splittings are relatively obscure in a powder sample.

Although the CSA interactions of resonant spins are recoupled at the same time as the heteronuclear DD interactions, the influence of the recoupled CSA terms is often minor, since the terms commute. In the single-quantum case of Table 15, on the other hand, the two recoupled interactions do not necessarily commute, and may interfere with each other in a complex way. The solutions in Table 15 are therefore only suitable for the heteronuclear recoupling of spins with small CSA interactions, while the solutions in Table 16 are more generally applicable.

The symmetries in Table 16 may be regarded as extensions of the REDOR pulse sequence.[26,27] Unlike REDOR, they implement homonuclear dipolar decoupling of the irradiated spin species, and should be applicable to systems with homonuclear dipolar interactions.

REDOR itself consists of two 180° pulses per rotor period, and therefore belongs to the symmetry class $RN_{N/2}^\nu$. The most common implementation of REDOR follows the XY8 phase scheme, which corresponds to the supercycle $\mathcal{SS}'$ of the symmetry $R4_2^1$. This symmetry implements selection of the $\{l, m, \lambda, \mu\} = \{2, \pm 1, 1, 0\}$ terms, just as the solutions in Table 16. However, the $R4_2^1$ symmetry also allows homonuclear DD terms of the form $\{2, \pm 2, 2, 0\}$, $\{2, \pm 1, 2, \pm 2\}$ and $\{2, \pm 1, 2, \mp 2\}$. These recoupled homonuclear DD interactions interfere with the operation of REDOR in non-dilute spin systems, a defect which should be reduced by the symmetries in Table 16.

Chan has discovered a different way of suppressing the homonuclear DD interactions in the REDOR method.[67] The

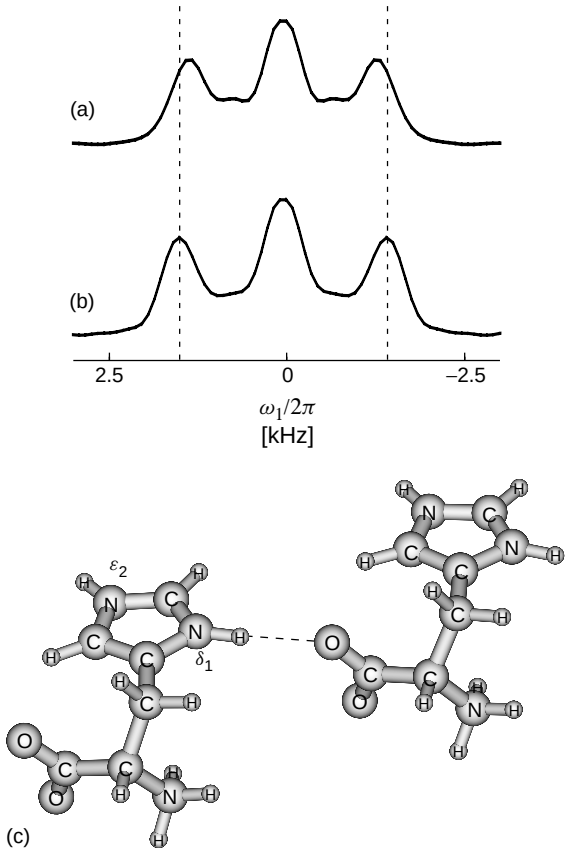

Figure 12 (a) Experimental ^{15}N spectrum of the δ_1 nitrogen site of [U$-^{13}$C,^{15}N]-L-histidinium hydrochloride monohydrate, obtained by a 2D experiment in the presence of $R18_2^5$ irradiation of the protons, at a magnetic field of 9.4 T and a spinning frequency of 20 kHz. The three-peak structure is due to the recoupled heteronuclear interaction between the ^{15}N and the directly-bonded ^{1}H. (b) Experimental ^{15}N spectrum of the ε_2 nitrogen site. Note that the splitting is slightly larger than in plot (a). These spectra show that the δ_1 NH bond is about 4 pm longer than the ε_2 NH bond. This elongation is attributed to the existence of an intermolecular hydrogen bond (see crystal structure in (c)). (Adapted from Ref.[113])

C-REDOR sequences are based upon the symmetries $C3_3^1$ and $C7_7^1$. These symmetries allow heteronuclear DD terms of the form $\{l, m, \lambda, \mu\} = \{2, \pm1, 1, 0\}$ and $\{2, \pm2, 1, 0\}$, and also the isotropic chemical shift term $\{0, 0, 1, 0\}$ and homonuclear DD terms of the form $\{2, \pm1, 2, 0\}$ and $\{2, \pm2, 2, 0\}$. This does not seem very promising since most of these terms are undesirable. However, by using the POST element $\mathcal{C} = 90_0360_{180}270_0$, the scaling factors for all of the symmetry-allowed terms with the exception of $\{2, \pm1, 1, 0\}$ and $\{0, 0, 0, 0\}$ may be made to vanish. The result is a REDOR-like average Hamiltonian with suppression of homonuclear DD couplings. This has been demonstrated experimentally.[67]

4.9 Double-Quantum Heteronuclear Recoupling by Dual Pulse Sequences

It is also possible to recouple heteronuclear interactions by applying synchronized rf irradiation to both spin species. This procedure allows γ-encoded recoupling of the heteronuclear interactions with the suppression of CSA interference.

The 'dual' selection rules in equations (58)–(61) may be used to generate the symmetry solutions. Sets of symmetries suitable for γ-encoded double-quantum heteronuclear recoupling are shown in Table 17 and 18. All of these symmetries recouple the terms of the form $\{l, m, \lambda_I, \mu_I, \lambda_S, \mu_S\} = \{2, \mp1, 1, \pm1, 1, \pm1\}$ with suppression of all isotropic chemical shift, homonuclear DD coupling and CSA terms. In the case of the $CRN_n^{\nu_I,\nu_S}$ symmetries in Table 17, the heteronuclear J-couplings are also suppressed.

Brinkmann[60] has shown that these symmetries may be used for the generation of heteronuclear multiple-quantum coherences, for the measurement of heteronuclear coupling constants, and for implementing magnetization transfer between spin species. For example, a sequence with the symmetry $R24_9^{5,10}$ has been used to obtain a heteronuclear multiple-quantum spectrum of a labelled amino acid.[60]

4.10 Heteronuclear Decoupling

The two-pulse phase modulation (TPPM) decoupling method[10] may also be understood qualitatively using the symmetry theory. The TPPM modulation scheme corresponds to a RN_n^ν sequence with a large ratio of N to n, although exact synchronization with the sample rotation does not appear to be important in this case. Edén has shown[41,45] that in many cases, a similar decoupling quality to TPPM may be achieved with exactly synchronized CN_n^ν and RN_n^ν sequences, and that the decoupling quality correlates reasonably well with higher-order term counts obtained by applying the rules in equations (31) and (32). In addition, there is evidence that the quality of heteronuclear decoupling is enhanced by implementing homonuclear *recoupling* at the same time, using symmetries such as $R24_2^1$.[41] This actually happens inadvertently in many implementations of TPPM. This observation is consistent with the well-known effect of 'self-decoupling', where strong homonuclear couplings within one spin species can narrow the peaks of a second, coupled, spin species.[4] (See **Heteronuclear Decoupling in Solids**.)

5 CONCLUSIONS

The symmetry theory sketched here is still in its infancy, although it is already clear that it provides much insight into the operation of many existing pulse sequences, as well as many new experimental possibilities. There remain many theoretical problems, such as the treatment of higher-order terms, and many practical problems, such as the phase-shift sensitivity of the RN_n^ν sequences. It is hoped that this summary will encourage many other research groups to explore the subject.

6 REFERENCES

1. E. R. Andrew, A. Bradbury, and R. G. Eades, *Nature*, 1959, **183**, 1802.
2. I. J. Lowe, *Phys. Rev. Lett.*, 1959, **2**, 285.
3. E. O. Stejskal, J. Schaefer, and J. S. Waugh, *J. Magn. Reson.*, 1977, **28**, 105.
4. M. Mehring, 'High Resolution NMR in Solids', 2nd edn., Springer: Berlin, 1982.

5. A. Abragam, 'The Principles of Nuclear Magnetism', Clarendon Press: Oxford, 1961.
6. R. R. Ernst, *J. Chem. Phys.*, 1966, **45**, 3845.
7. M. H. Levitt and R. Freeman, *J. Magn. Reson.*, 1981, **43**, 502.
8. J. S. Waugh, *J. Magn. Reson.*, 1982, **49**, 517.
9. M. H. Levitt, R. Freeman, and T. A. Frenkiel, *Adv. Magn. Reson.*, 1983, **11**, 47.
10. A. E. Bennett, C. M. Rienstra, M. Auger, K. V. Lakshmi, and R. G. Griffin, *J. Chem. Phys.*, 1995, **103**, 1.
11. M. Lee and W. I. Goldburg, *Phys. Rev. A*, 1965, **140**, 1261.
12. J. S. Waugh, M. L. Huber, and U. Haeberlen, *Phys. Rev. Lett.*, 1968, **20**, 180.
13. U. Haeberlen and J. S. Waugh, *Phys. Rev.*, 1968, **175**, 453.
14. P. Mansfield, *J. Phys. C*, 1971, **4**, 1444.
15. W. K. Rhim, D. D. Elleman, L. B. Schreiber, and R. W. Vaughan, *J. Chem. Phys.*, 1974, **60**, 4595.
16. D. P. Burum, M. Linder, and R. R. Ernst, *J. Magn. Reson.*, 1981, **44**, 173.
17. A. Bielecki, A. C. Kolbert, and M. H. Levitt, *Chem. Phys. Lett.*, 1989, **155**, 341.
18. M. Hohwy and N. C. Nielsen, *J. Chem. Phys.*, 1997, **106**, 1.
19. B. C. Gerstein, R. G. Pembleton, R. D. Wilson, and L. J. Ryan, *J. Chem. Phys.*, 1977, **66**, 361.
20. G. E. Maciel, C. E. Bronnimann, and B. Hawkins, *Adv. Magn. Reson.*, 1990, **14**, 125.
21. W. T. Dixon, *J. Chem. Phys.*, 1982, **77**, 1800.
22. O. N. Antzutkin, Z. Song, X. Feng, and M. H. Levitt, *J. Chem. Phys.*, 1994, **100**, 130.
23. Y. Yarim-Agaev, P. N. Tutunjian, and J. S. Waugh, *J. Magn. Reson.*, 1982, **47**, 51.
24. T. G. Oas, R. G. Griffin, and M. H. Levitt, *J. Chem. Phys.*, 1988, **89**, 692.
25. M. H. Levitt, T. G. Oas, and R. G. Griffin, *Isr. J. Chem.*, 1988, **28**, 271.
26. T. Gullion and J. Schaefer, *J. Magn. Reson.*, 1989, **81**, 196–200.
27. T. Gullion and J. Schaefer, *Adv. Magn. Reson.*, 1989, **13**, 57.
28. R. Tycko, *Phys. Rev. Lett.*, 1988, **60**, 2734.
29. R. Tycko, *J. Chem. Phys.*, 1990, **92**, 5776.
30. R. Tycko and G. Dabbagh, *Chem. Phys. Lett.*, 1990, **173**, 461.
31. R. Tycko and G. Dabbagh, *J. Am. Chem. Soc.*, 1991, **113**, 9444.
32. R. Tycko and S. O. Smith, *J. Chem. Phys.*, 1993, **98**, 932.
33. A. E. Bennett, J. H. Ok, R. G. Griffin, and S. Vega, *J. Chem. Phys.*, 1992, **96**, 8624.
34. D. K. Sodickson, M. H. Levitt, S. Vega, and R. G. Griffin, *J. Chem. Phys.*, 1993, **98**, 6742.
35. N. C. Nielsen, H. Bildsøe, H. J. Jakobsen, and M. H. Levitt, *J. Chem. Phys.*, 1994, **101**, 1805.
36. Y. K. Lee, N. D. Kurur, M. Helmle, O. G. Johannessen, N. C. Nielsen, and M. H. Levitt, *Chem. Phys. Lett.*, 1995, **242**, 304.
37. M. Hohwy, H. J. Jakobsen, M. Edén, M. H. Levitt, and N. C. Nielsen, *J. Chem. Phys.*, 1998, **108**, 2686.
38. C. M. Rienstra, M. E. Hatcher, L. J. Mueller, B. Sun, S. W. Fesik, and R. G. Griffin, *J. Am. Chem. Soc.*, 1998, **120**, 10 602–10 612.
39. A. Brinkmann, M. Edén, and M. H. Levitt, *J. Chem. Phys.*, 2000, **112**, 8539–8554.
40. M. Hohwy, C. M. Rienstra, C. P. Jaroniec, and R. G. Griffin, *J. Chem. Phys.*, 1999, **110**, 7983–7992.
41. M. Carravetta, M. Edén, X. Zhao, A. Brinkmann, and M. H. Levitt, *Chem. Phys. Lett.*, 2000, **321**, 205–215.
42. A. Brinkmann, M. Carravetta, X. Zhao, M. Edén, J. Schmedt auf der Günne, and M. H. Levitt, in 'Perspectives on Solid State NMR in Biology', eds S. Kühne and H. J. M. de Groot, Kluwer: Dordrecht, 2001.
43. X. Feng, P. J. E. Verdegem, Y. K. Lee, D. Sandström, M. Edén, P. Bovee-Geurts, W. J. de Grip, J. Lugtenburg, H. J. M. de Groot, and M. H. Levitt, *J. Am. Chem. Soc.*, 1997, **119**, 6853–6857.
44. X. Feng, P. J. E. Verdegem, M. Edén, D. Sandström, Y. K. Lee, P. Bovee-Geurts, W. J. de Grip, J. Lugtenburg, H. J. M. de Groot, and M. H. Levitt, *J. Biomol. NMR*, 2000, **16**, 1–8.
45. M. Edén and M. H. Levitt, *J. Chem. Phys.*, 1999, **111**, 1511–1519.
46. D. E. Demco, S. Hafner, and H. W. Spiess, *J. Magn. Reson. A*, 1995, **116**, 36.
47. S. Hafner and H. W. Spiess, *J. Magn. Reson. A*, 1996, **121**, 160.
48. M. Baldus and B. H. Meier, *J. Magn. Reson. A*, 1996, **121**, 65.
49. M. Baldus, R. J. Iulicci, and B. H. Meier, *J. Am. Chem. Soc.*, 1997, **119**, 1121–1124.
50. E. H. Hardy, R. Verel, and B. H. Meier, *J. Magn. Reson.*, 2001, **148**, 459–464.
51. A. S. D. Heindrichs, H. Geen, C. Giordani, and J. J. Titman, *Chem. Phys. Lett.*, 2001, **335**, 89–96.
52. J. C. C. Chan and G. Brunklaus, in press.
53. D. A. Varshalovich, A. N. Moskalev, and V. K. Kheronskii, 'Quantum Theory of Angular Momentum', World Scientific: Singapore, 1988.
54. M. H. Levitt, *J. Magn. Reson.*, 1989, **82**, 427.
55. Z. Song, O. N. Antzutkin, Y. K. Lee, S. C. Shekar, A. Ruppre-cht, and M. H. Levitt, *Biophys. J.*, 1997, **73**, 1539.
56. L. van Dam and M. H. Levitt, *J. Mol. Biol.*, 2000, **304**, 541–560.
57. A. Samoson, E. Lippmaa, and A. Pines, *Mol. Phys.*, 1988, **65**, 1013.
58. A. Llor and J. Virlet, *Chem. Phys. Lett.*, 1988, **152**, 248.
59. B. F. Chmelka and A. Pines, *Science*, 1989, **246**, 71.
60. A. Brinkmann and M. H. Levitt, *J. Chem. Phys.*, 2001, **115**, 357–384.
61. M. H. Levitt, *Prog. NMR Spectrosc.*, 1986, **18**, 61.
62. M. H. Levitt and R. Freeman, *J. Magn. Reson.*, 1981, **43**, 65.
63. S. Wolfram, 'Mathematica: A System for Doing Mathematics by Computer', Addison-Wesley: New York, 1991.
64. Y. Ishii, *J. Chem. Phys.*, 2001, **114**, 8473–8483.
65. A. Brinkmann, J. Schmedt auf der Günne, and M. H. Levitt, to be published.
66. B. -Q. Sun, P. R. Costa, D. Kocisko, P. T. Lansbury, and R. G. Griffin, *J. Chem. Phys.*, 1995, **102**, 702.
67. J. C. C. Chan, *Chem. Phys. Lett.*, 2001, **335**, 289–297.
68. H. Geen, J. J. Titman, J. Gottwald, and H. W. Spiess, *J. Magn. Reson. A*, 1995, **114**, 264.
69. R. Graf, D. E. Demco, S. Hafner, and H. W. Spiess, *Solid State Nucl. Magn. Reson.*, 1998, **12**, 139.
70. D. P. Raleigh, M. H. Levitt, and R. G. Griffin, *Chem. Phys. Lett.*, 1988, **146**, 71.
71. M. H. Levitt, D. P. Raleigh, F. Creuzet, and R. G. Griffin, *J. Chem. Phys.*, 1990, **92**, 6347.
72. M. Helmle, Y. K. Lee, P. J. E. Verdegem, X. Feng, T. Karlsson, J. Lugtenburg, H. J. M. de Groot, and M. H. Levitt, *J. Magn. Reson.*, 1999, **140**, 379–403.
73. G. S. Harbison and H. W. Spiess, *Chem. Phys. Lett.*, 1986, **124**, 128.
74. P. Tang, C. -L. Juang, and G. S. Harbison, *Science*, 1990, **249**, 70.
75. C. Glaubitz and A. Watts, *J. Magn. Reson.*, 1998, **130**, 305.
76. X. Feng, Y. K. Lee, D. Sandström, M. Edén, H. Maisel, A. Sebald, and M. H. Levitt, *Chem. Phys. Lett.*, 1996, **257**, 314.
77. S. Ravindranathan, X. Feng, T. Karlsson, G. Widmalm, and M. H. Levitt, *J. Am. Chem. Soc.*, 2000, **122**, 1102–1115.
78. S. Ravindranathan, T. Karlsson, K. Lycknert, G. Widmalm, and M. H. Levitt, *J. Magn. Reson.*, 2001, **151**, 136–141.
79. X. Feng, M. Edén, A. Brinkmann, H. Luthman, L. Eriksson, A. Gräslund, O. N. Antzutkin, and M. H. Levitt, *J. Am. Chem. Soc.*, 1997, **119**, 12 006–12 007.
80. P. R. Costa, J. D. Gross, M. Hong, and R. G. Griffin, *Chem. Phys. Lett.*, 1997, **280**, 95–103.
81. M. Edén, A. Brinkmann, H. Luthman, L. Eriksson, and M. H. Levitt, *J. Magn. Reson.*, 2000, **144**, 266–279.

82. A. Brinkmann, Ph.D. thesis, Stockholm University, 2001.
83. T. Karlsson, A. Brinkmann, P. J. E. Verdegem, J. Lugtenburg, and M. H. Levitt, *Solid State Nucl. Magn. Reson.*, 1999, **14**, 43–58.
84. M. Hong, *J. Magn. Reson.*, 1999, **136**, 86–91.
85. M. Carravetta, M. Edén, O. G. Johannessen, H. Luthman, P. J. E. Verdegem, J. Lugtenburg, A. Sebald, and M. H. Levitt, *J. Am. Chem. Soc.*, 2001, **123**, 10 628–10 638.
86. M. Goldman, V. Fleury, and M. Guron, *J. Magn. Reson. A*, 1996, **118**, 11.
87. P. Tekely and M. Goldman, *J. Magn. Reson.*, 2001, **148**, 135–141.
88. M. Mehring and J. S. Waugh, *Rev. Sci. Instrum.*, 1972, **43**, 649.
89. M. Carravetta, M. H. Levitt, and A. Brinkmann, to be published.
90. K. Schmidt-Rohr, *J. Am. Chem. Soc.*, 1996, **118**, 7601.
91. D. M. Gregory, M. A. Mehta, J. C. Shiels, and G. P. Drobny, *J. Chem. Phys.*, 1997, **107**, 28.
92. M. Edén and M. H. Levitt, *Chem. Phys. Lett.*, 1998, **293**, 173.
93. H. Geen, R. Graf, A. S. D. Heinrichs, B. S. Hickman, I. Schnell, H. W. Spiess, and J. J. Titman, *J. Magn. Reson.*, 1999, **138**, 167.
94. O. N. Antzutkin and R. Tycko, *J. Chem. Phys.*, 1999, **110**, 2749.
95. R. Witter, P. Hartmann, J. Vogel, and C. Jager, *Solid State Nucl. Magn. Reson.*, 1998, **13**, 189–200.
96. F. Fayon, C. Bessada, J. P. Coutures, and D. Massiot, *Inorg. Chem.*, 1999, **38**, 5212–5218.
97. A. Le Sauze, L. Montagne, G. Palavit, F. Fayon, and R. Marchand, *J. Non-Cryst. Solids*, 2000, **263**, 139–145.
98. D. Fayon, D. Massiot, K. Suzuya, and D. L. Price, *J. Non-Cryst. Solids*, 2001, **283**, 88–94.
99. D. F. Schantz, J. Schmedt auf der Günne, H. Koller, and R. F. Lobo, *J. Am. Chem. Soc.*, 2000, **122**, 6659–6663.
100. W. A. Dollase, M. Feike, H. Förster, T. Schaller, I. Schnell, A. Sebald, and S. Steuernagel, *J. Am. Chem. Soc.*, 1997, **119**, 3807.
101. X. Helluy, C. Marichal, and A. Sebald, *J. Phys. Chem. B*, 2000, **104**, 2836–2845.
102. W. Sommer, J. Gottwald, D. E. Demco, and H. W. Spiess, *J. Magn. Reson. A*, 1995, **113**, 131–134.
103. A. N. Appleyard, R. B. Herbert, P. J. F. Henderson, A. Watts, and P. J. R. Spooner, *Biochim. Biophys. Acta*, 2000, **1509**, 55–64.
104. D. A. Middleton, C. S. Le Du., X. Peng, D. G. Reid, and D. Saunders, *J. Am. Chem. Soc.*, 2000, **122**, 1161–1170.
105. C. Glaubitz, M. Carravetta, M. Edén, and M. H. Levitt, in 'Perspectives on Solid State NMR in Biology', eds S. Kühne and H. J. M. de Groot, Kluwer: Dordrecht, 2001.
106. M. Feike, D. E. Demco, R. Graf, J. Gottwald, S. Hafner, and H. W. Spiess, *J. Magn. Reson. A*, 1996, **122**, 214.
107. M. Feike, R. Graf, I. Schnell, C. Jäger, and H. W. Spiess, *J. Am. Chem. Soc.*, 1996, **118**, 9631.
108. R. Witter, P. Hartmann, J. Vogel, and C. Jäger, *Solid State Nucl. Magn. Reson.*, 1998, **13**, 189.
109. M. G. Munowitz and A. Pines, *Science*, 1986, **233**, 501.
110. D. Suter, S. B. Liu, J. Baum, and A. Pines, *Chem. Phys.*, 1987, **114**, 103–109.
111. P. K. Madhu, X. Zhao, and M. H. Levitt, *Chem. Phys. Lett.*, 2001, **346**, 142–148.
112. X. Zhao, M. Edén, and M. H. Levitt, *Chem. Phys. Lett.*, 2001, **342**, 353–361.
113. X. Zhao, J. L. Sudmeier, W. W. Bachovchin, and M. H. Levitt, *J. Am. Chem. Soc.*, in press.
114. J. D. Gross, P. R. Costa, and R. G. Griffin, *J. Chem. Phys.*, 1998, **108**, 7286–7293.
115. M. Hohwy, C. P. Jaroniec, B. Reif, C. M. Rienstra, and R. G. Griffin, *J. Am. Chem. Soc.*, 2000, **122**, 3218–3219.
116. B. Reif, M. Hohwy, C. P. Jaroniec, C. M. Rienstra, and R. G. Griffin, *J. Magn. Reson.*, 2000, **145**, 132–141.

Acknowledgements

I would like to thank my research group in Stockholm for helping develop and test these concepts, and for providing experimental results for this review, especially: Young Lee, Oleg Antzutkin, Mattias Edén, Andreas Brinkmann, Marina Carravetta, Xin Zhao, and P. K. Madhu. I would also like to thank Beat Meier, Jerry Chan, Hans Spiess and Yoshitaka Ishii for supplying results prior to publication.

Biographical Sketch

Malcolm Harris Levitt, *b* 1957. D. Phil. 1981, University of Oxford, England. Research associate, Weizmann Institute, Israel, 1981–1982, with S. Vega; ETH-Zürich, Switzerland, 1982–1986, with R. R. Ernst; Princeton University, USA, 1986, with W. S. Warren. Research Scientist at the Francis Bitter National Magnet Laboratory, Cambridge, MA, USA 1986–1990. Royal Society Research Fellow at the Interdisciplinary Research Centre for Superconductivity, Cambridge, England, 1990–1991. Lecturer at the Physical Chemistry Division, University of Stockholm, Sweden, 1992–1997. Professor in NMR Methodology, Physical Chemistry Division, University of Stockholm, Sweden, 1997–2001. Professor in Physical Chemistry, Southampton University, England, from 2001. Approx 120 publications. Current research interests: methodology and theory of NMR and its applications, especially to biological materials.

Brownian Motion and Correlation Times

Donald E. Woessner
The University of Texas Southwestern Medical Center at Dallas and Department of Radiology, The Mary Nell and Ralph B. Rogers Magnetic Resonance Center, Dallas, TX, USA

1	Introduction	1
2	Remarks on Models of Molecular Reorientation	2
3	Correlation Functions for a Rigid, Completely Asymmetric Ellipsoid	3
4	Correlation Functions for Axially Symmetric Ellipsoids with Internal Motion	5
5	Correlation Functions for InterGroup Magnetic Dipolar Relaxation with Internal Motion	7
6	'Model-Free' Correlation Functions for Flexible Macromolecules	9
7	Correlation Functions for Intermolecular Magnetic Dipolar Relaxation	10
8	Experimental and Theoretical Correlation Times of Rigid Molecules	10
9	Correlation Functions for a 'Nearly-Free' Rotor Attached to an Ellipsoid	16
10	Scrutiny of the Mathematical Form of Correlation Functions	16
11	Related Articles	17
12	References	17

1 INTRODUCTION

In nuclear magnetic resonance (NMR), the magnetic interaction between the nuclear magnetic dipole moment and the magnetic field $\boldsymbol{B}_0$ determines the nuclear spin energy levels. Nuclear spin interactions with the chemical structures in the local environment cause small shifts of the energy levels. Brownian molecular motions cause this local structure to fluctuate and as a result cause the energy levels to be time dependent. The frequency component of energy level fluctuation at the frequency difference between two energy levels induces nuclear spin transitions between the energy levels. The rate of such transitions depends on the intensity of the nuclear spin energy at the nuclear spin transition frequency. These transitions couple the spin system to the kinetic energy of the molecular system, enabling the spin system to reach thermal equilibrium (i.e. to relax). The relaxation times are inversely proportional to the transition rates. Therefore, we can use NMR relaxation time measurements to study molecular motions in liquids.

In the case of spin-$\frac{1}{2}$ nuclei, the spin interactions include magnetic interactions of the nuclear magnetic moment with the local magnetic field. The local magnetic field depends on the distance and position relative to neighboring nuclear spins and unpaired electrons, and on the effective local fields generated by the chemical shielding due to the surrounding electrons. Nuclei of spin $> \frac{1}{2}$ have an additional interaction, the electric interaction between the nuclear quadrupole moment and the surrounding electric changes. Both interactions depend on the length of the vector that joins the nucleus to the interacting entity and on the orientation of this interaction vector in the magnetic field $\boldsymbol{B}_0$. Such interactions are the mechanism by which the energy of the nuclear spins is coupled to the molecular system.

To illustrate the relationship between Brownian motion and NMR relaxation, we consider the cases of magnetic dipolar interaction between two identical spin-$\frac{1}{2}$ nuclei and of electric quadrupolar interaction of a spin 1 nucleus with an electric charge ze. In both instances, the relaxation times are given[1] by the expressions:

$$1/T_1 = H[J_1(\omega_0) + J_2(2\omega_0)] \tag{1}$$

$$1/T_2 = \tfrac{1}{4}H[J_0(0) + 10J_1(\omega_0) + J_2(2\omega_0)] \tag{2}$$

where T_1 is the spin–lattice relaxation time, T_2 is the transverse of spin–spin relaxation time, and ω_0 is the angular Larmor frequency. These equations apply in the motionally narrowed limit (see ***Relaxation Theory: Density Matrix Formulation***) which is appropriate for liquids.

In deriving these relationships, we express the time dependencies of the nuclear spin interactions $\mathcal{H}(t)$ in terms of the interaction constants H and the time correlation functions $\langle F_\mathrm{h}(t)F_\mathrm{h}^*(t+\tau)\rangle$ in which the $F_\mathrm{h}(t)$ terms are the spatial parts of the time-dependent nuclear spin interactions and the $\langle\ \rangle$ brackets denote ensemble average. The $J_\mathrm{h}(\omega)$ terms are Fourier intensities (or spectral densities) of the time correlation functions at the angular frequency ω as given by

$$J_h(\omega) = \int_{-\infty}^{+\infty} \langle F_\mathrm{h}(t)F_\mathrm{h}^*(t+\tau)\rangle \exp(\mathrm{i}\omega\tau)\,\mathrm{d}\tau \tag{3}$$

where $\mathrm{i} = (-1)^{\frac{1}{2}}$ and the asterisk denotes the complex conjugate. The interaction constants are $H = (9/8)\gamma^4\hbar^2$ for magnetic dipole–dipole interaction between two identical atomic nuclei and $H = (9/8)e^4Q^2z^2\hbar^2$ for the electric quadrupolar interaction. The physical quantities are: γ, the nuclear magnetogyric ratio; $\hbar$, Planck's constant divided by 2π; e, the unit electric charge; z, the number of unit charges in the electric charge; and Q, the nuclear quadrupole moment. For both interactions, the $F_\mathrm{h}(t)$ terms are related to the second-order spherical harmonics as given by:

$$F_0(t) = r(t)^{-3}[3\cos^2\theta(t) - 1] \tag{4a}$$

$$F_1(t) = r(t)^{-3}\{\sin\theta(t)\cos\theta(t)\exp[\mathrm{i}\phi(t)]\} \tag{4b}$$

$$F_2(t) = r(t)^{-3}\{\sin^2\theta(t)\exp[2\mathrm{i}\phi(t)]\} \tag{4c}$$

in which $r(t)$ is the length of the vector connecting the nucleus with the interacting unit, and $\theta(t)$ and $\phi(t)$ are the polar and azimuthal angles that describe the orientation of this vector in the laboratory rectangular coordinate system S (magnetic field $\boldsymbol{B}_0$ of the NMR spectrometer).

Different motions of molecules in liquids cause r, θ, and ϕ to be time dependent. We classify them as rotational and translational. The translational motions cause the molecules to move in three-dimensional space. The rotational motions cause

an axis in the molecule to change in orientation with respect to the axes of the fixed three-dimensional laboratory rectangular coordinate system. Many molecules contain chemical groups that can rotate with respect to the rest of the molecule. Methyl groups that reorient about the methyl threefold symmetry axis comprise a common example of molecular internal motion.

We commonly designate relaxation interactions as *intramolecular* or *intermolecular*, depending on whether the entity that interacts with the nucleus is part of the same molecule. This designation is related to the above classification of molecular motions. For a completely rigid molecule (Section 3), the intramolecular relaxation results only from the time dependences of θ and ϕ because r is constant. Then, we may remove r from equations (3) and (4) absorb it into a redefined H (i.e. H'), and redefine the $F_{\mathrm{h}}(t)$:

$$F_0(t) = 3\cos^2\theta(t) - 1 \tag{5a}$$

$$F_1(t) = \sin\theta(t)\cos\theta(t)\exp[\mathrm{i}\phi(t)] \tag{5b}$$

$$F_2(t) = \sin^2\theta(t)\exp[2\mathrm{i}\phi(t)] \tag{5c}$$

For magnetic dipolar relaxation of two identical nuclei with spin-$\frac{1}{2}$, $H' = (9/8)\gamma^4\hbar^2 r^{-6}$. For quadrupolar relaxation of a nucleus with spin 1, $H' = (9/8)e^4Q^2z^2\hbar^2r^{-6}$. Here, if all the electric charges result in a nuclear quadrupolar interaction with zero asymmetry parameter, $H' = (9/8)\pi^2\chi^2$. The same statement applies to intragroup relaxation of nuclei in a rigid group that rotates within an otherwise rigid ellipsoid (Section 4), such as a methyl group that rotates about its threefold symmetry axis that is fixed to the ellipsoid. However, intramolecular magnetic dipolar relaxation between a nucleus of such a rotating group and a nucleus on the remainder of the ellipsoid (Section 5) is more complex. Besides θ and ϕ, r also is time dependent. For intermolecular magnetic dipolar relaxation (Section 7), r, θ, and ϕ are all time dependent. A mathematical description of the correlation function is especially complex. It depends on the translational diffusion of the molecules and on the rotational motions of the molecule. We emphasize intramolecular NMR relaxation in this article and briefly treat intermolecular relaxation in Section 7.

As the NMR relaxation times are related to the molecular motions through the correlation function and the spectral densities, we need relationships between these quantities to analyze the relaxation times of liquids in terms of molecular motions. It is customary to invoke specific models of molecular motions and formulate correlation functions from these models. There are many different models that are based on different starting points and perturbations from them. Some are based on a quantum mechanical formulation and some are treated from the viewpoint of classical mechanics. No single, tractable model that describes all liquids has been found.

2 REMARKS ON MODELS OF MOLECULAR REORIENTATION

Molecules in the gaseous state undergo vibrational and rotational motions and exist in discrete vibrational–rotation energy levels with discrete frequencies. Molecular collisions cause transitions between the energy states and broaden the energy levels. In a condensed phase, such as a liquid or a solid, the 'collisions' between molecules occur much more frequently and the kinetic and potential energies of the different molecules are much more closely coupled. Consequently, we cannot calculate the correlation functions that are effective in NMR relaxation from the motions of isolated, noninteracting molecules. Rothschild[2] has presented a comprehensive, detailed account of the theoretical and experimental knowledge of the rotational and vibrational motions of small, nearly spherical molecules in liquids.

Many different models of molecular reorientation have been discussed. It is beyond the scope of this article to review these models in detail because the literature is extensive (see ***Spin–Rotation Relaxation Theory***). One approach is to start from an assembly of freely rotating molecules, as in a dilute gas. There are different ways of introducing the effects of the surrounding molecules. One way is to have collisions that introduce sudden or instantaneous changes in molecular angular momentum. Another way is to examine the potential energy of the molecule as a function of orientation. If the potential energy is independent of orientation, the molecule experiences no torques and rotates freely. The correlation function is that for an assembly of freely rotating molecules. If the potential energy does depend on orientation, the molecule experiences torques that depend on the molecular shape and on the shape, configuration, motions ('collisions'), and distances of the neighboring molecules. These torques quench or change the molecular rotation. The effective molecular shape could be that of a spherical top, a symmetric top, or a completely asymmetric rotor. The molecule might experience a constant torque or a torque that is significant only when the neighboring molecules attain specific configurations. In such approaches, the rotational inertia of the molecule is important in deciding the mathematical form of the correlation function.

Another approach is to assume that the environment of the molecule sets up an energy barrier that the molecule must surmount to rotate into an orientation in which its interaction energy with its neighbors is the next minimum. While in this potential well, the molecule undergoes low-amplitude rotational oscillations. A 'large' change in orientation occurs when a transition from one potential well to another takes place. The molecule is stationary except for occasional jumps to a different orientation. Some consider the jump to be instantaneous and others consider the jump velocity to be the rms average molecular rotational velocity obtained from kinetic energy considerations.

Clearly the rotational motion of molecules in liquids is a many-body problem and, to calculate the correlation functions, we must introduce approximate methods. We can view Brownian rotational motion as a random walk in coordinate space in which the molecular orientations are defined relative to a motionless laboratory coordinate system. Diffusion-type equations correctly describe the observed rms displacements after many random steps have taken place. The length of the step is an important parameter if solutions of diffusion-type equations are to be used to calculate the correlation functions. The average length of the step must be small compared with the correlation distance of the orientational function. Because the orientational functions undergo large changes with a one-radian change in orientation, the step must be much smaller than one radian.

The Debye theory[3] is a widely used model of molecular reorientation. The molecule is assumed to be a rigid sphere that

undergoes isotropic reorientations by infinitestimal rotations caused by thermal collisions with other molecules. Because the reorientation occurs by infinitesimal rotations, isotropic rotational diffusion motion is obtained. The rotational diffusion coefficient is related through Stokes's law to the viscosity of the fluid. This approach was used by Bloembergen, Purcell, and Pound[4] in their pioneering work on NMR relaxation.

Perrin[5] has developed an anisotropic model of molecular reorientation. The molecule reorients like a rigid ellipsoid that undergoes rotational diffusion by infinitesimal rotations about the different ellipsoid axes at different rates. Although the diffusion approximation may not be an exact model and molecules are not completely rigid, it does provide a reasonably reliable model for many liquids. Also, use of it yields equations that are well suited for straightforward data reduction. In the following sections, we assume that molecules are rigid bodies that follow the Perrin model and that internal motion is described by rigid groups that rotate about an axis that is fixed to the rigid body. This internal rotation is independent of the ellipsoid reorientation. Some consequences of vibrations and oscillations of the otherwise rigid bodies are noted in Section 8.1.

3 CORRELATION FUNCTIONS FOR A RIGID, COMPLETELY ASYMMETRIC ELLIPSOID

In formulating the spatial orientational correlation functions of nuclei in a completely asymmetric ellipsoid, it is convenient to express the $F_h(t)$ in terms of the direction cosines l, m, and n of the nuclear interaction vector with respect to the X, Y, and Z axes, respectively, of the laboratory coordinate system S. Rotational Brownian motions cause these direction cosines to fluctuate. The coordinate system S is fixed in space with its Z axis in the direction of $\boldsymbol{B}_0$. Using the definitions $l = \sin\theta\cos\phi$, $m = \sin\theta\sin\phi$, and $n = \cos\theta$, the $F_h(t)$ terms, as given by equation (5) in which r is constant, are:

$$F_0(t) = 1 - 3n^2 \tag{6a}$$

$$F_1(t) = (l + \mathrm{i}m)n \tag{6b}$$

$$F_2(t) = (l + \mathrm{i}m)^2 \tag{6c}$$

To include the fluctuations of these direction cosines, we use two additional rectangular coordinate systems. The first is S_0, a stationary reference frame, to describe the rotational motion of the ellipsoid. The other coordinate system is S' which is fixed to the ellipsoid and oriented such that the X', Y', and Z' axes of S' always coincide with the three major axes of the ellipsoid. We reference the direction cosines of the relaxation interaction vector in the ellipsoid directly to S'. At time t, these direction cosines are denoted by l', m', and n'. When there is no internal motion, the direction cosines always have these values. However, to allow for internal motion in later equations, we let l'', m'', and n'' be the respective direction cosines at the later time $t + \tau$.

We assume that all of the ellipsoids are equivalent. Since we are dealing with liquids, at any instant t there is a random orientation distribution of ellipsoids. Let us choose a particular ellipsoid. We orient S_0 of this ellipsoid so that, at time t, S_0 coincides with S' and the Euler angles (ϕ_0, θ_0, ψ_0) that describe the orientation of S' in S_0 are all zero. Since S_0 is stationary and S' is fixed to the ellipsoid, rotational Brownian motion of the ellipsoid causes ϕ_0, θ_0, and ψ_0 to become nonzero. The direction cosines of the relaxation interaction vector in S_0 at $t + \tau \geq 0$ are given by the following transformation that involves the change in the Euler angles of S' in S_0:

$$\begin{pmatrix} l_0 \\ m_0 \\ n_0 \end{pmatrix} = \begin{pmatrix} c_{11} & c_{12} & c_{13} \\ c_{21} & c_{22} & c_{23} \\ c_{31} & c_{32} & c_{33} \end{pmatrix} \begin{pmatrix} l'' \\ m'' \\ n'' \end{pmatrix} \tag{7}$$

where

$$\left.\begin{aligned} c_{11} &= \cos\psi\cos\phi - \cos\theta\sin\phi\sin\psi \\ c_{12} &= -\sin\psi\cos\phi - \cos\theta\sin\phi\cos\psi \\ c_{13} &= \sin\theta\sin\phi \\ c_{21} &= \cos\psi\sin\phi + \cos\theta\cos\phi\sin\psi \\ c_{22} &= -\sin\psi\sin\phi + \cos\theta\cos\phi\sin\psi \\ c_{23} &= -\sin\theta\cos\phi \\ c_{13} &= \sin\theta\sin\psi \\ c_{32} &= \sin\theta\cos\psi \\ c_{33} &= \cos\theta \end{aligned}\right\} \tag{8}$$

In this definition of the transformation matrix elements, the subscript of the Euler angles has been omitted for simplicity. Finally, the direction cosines of the interaction vector in S are given by the following transformation in Euler angles (ϕ, θ, ψ) that describe the orientation of S_0 in S:

$$\begin{pmatrix} l \\ m \\ n \end{pmatrix} = \begin{pmatrix} a_{11} & a_{12} & a_{13} \\ a_{21} & a_{22} & a_{23} \\ a_{31} & a_{32} & a_{33} \end{pmatrix} \begin{pmatrix} l_0 \\ m_0 \\ n_0 \end{pmatrix} \tag{9}$$

where the definitions of the a_{ij} are analogous to those of the c_{ij} in equation (8). We use the transformations shown in equations (7) and (9) to evaluate the functions $F_h(t + \tau)$ for $\tau \geq 0$. The initial conditions imply that $c_{ij}(t) = \delta_{ij}$ (the delta function). Consequently, the initial values at time t are:

$$F_0(t) = 1 - 3(a_{31}l' + a_{32}m' + a_{33}n')^2 \tag{10a}$$

$$F_1(t) = (A_1l' + A_2m' + A_3n')(a_{31}l' + a_{32}m' + a_{33}n') \tag{10b}$$

$$F_2(t) = (A_1l' + A_2m' + A_3n')^2 \tag{10c}$$

where

$$A_1 = a_{11} + \mathrm{i}a_{21} \tag{11a}$$

$$A_2 = a_{12} + \mathrm{i}a_{22} \tag{11b}$$

$$A_3 = a_{13} + \mathrm{i}a_{23} \tag{11c}$$

Because molecular orientations in a liquid are random, there is a random distribution of orientations of S_0 in S. The c_{ij} in all the S_0 are equivalent at all times $t + \tau \geq t$. The rotational Brownian motion of the ellipsoid causes the c_{ij} to be time dependent. Suppose $\Delta\alpha$, $\Delta\beta$, and $\Delta\gamma$ are the angular displacements of the ellipsoid about the X', Y', and Z', axes, respectively, of S' due to the Brownian motion. We assume that the elementary angular displacments are sufficiently small (see Section 8.2) so that the angular displacements during time τ are given by rotational diffusion relationships that involve rotational diffusion coefficients R_i as:

$$\langle(\Delta\alpha)^2\rangle = 2R_1\tau \tag{12a}$$

$$\langle(\Delta\beta)^2\rangle = 2R_2\tau \tag{12b}$$

$$\langle(\Delta\gamma)^2\rangle = 2R_3\tau \tag{12c}$$

and the motions are statistically independent, e.g., $\langle\Delta\alpha\Delta\beta\rangle = 0$. Internal motion within the ellipsoids, when it occurs, causes the direction cosines l'', m'', and n'' to be time dependent. Because we assume that the internal motion is statistically independent of the Brownian motion of the ellipsoid, we average separately over the two types of motion to obtain the final correlation functions. For each S_0, and for a given set of intramolecular parameters, the $F_{\rm h}(t)$ in the correlation function is a time independent multiplication factor and the autocorrelation function becomes:

$$\langle F_{\rm h}(t)F_{\rm h}^*(t+\tau)\rangle_{S_0} = F_{\rm h}(t)\langle F_{\rm h}^*(t+\tau)\rangle_{S_0} \tag{13}$$

In the calculation of the rotational Brownian motion parts of $\langle F_h^*(t+\tau)\rangle_{s_a}$, we find for each S_0 a sum of terms that are proportional to squares and products of the c_{ij} that appear in the transformation shown in equation (8). To calculate these terms, we use the time dependent probability density $P(\phi_0, \theta_0, \psi_0; \tau)$ for S' to be in orientation $(\phi_0, \theta_0, \psi_0)$ in S_0 at time $t + \tau$. This probability density is described[6] by the partial differential equation:

$$\partial P(\phi_0, \theta_0, \psi_0; \tau)/\partial\tau = \Lambda P(\phi_0, \theta_0, \psi_0; \tau) \tag{14}$$

where the operator Λ is given by:

$$\begin{aligned}\Lambda = {} & (R_1\cos^2\psi_0 + R_2\sin^2\psi_0)\left(\frac{\partial^2}{\partial\theta_0^2}\right) \\ & +(R_1\sin^2\psi_0 + R_2\cos^2\psi_0)\left(\cot\theta_0\frac{\partial}{\partial\theta_0} + \frac{1}{\sin^2\theta_0}\frac{\partial^2}{\partial\phi_0^2}\right. \\ & \left.+\cot^2\theta_0\frac{\partial^2}{\partial\psi_0^2} - \frac{2\cot\theta_0}{\sin\theta_0}\frac{\partial^2}{\partial\phi_0\partial\psi_0}\right) \\ & +2(R_1 - R_2)\frac{\cos\psi_0\sin\psi_0}{\sin\theta_0}\left(\frac{\partial^2}{\partial\theta_0\partial\phi_0} - \cos\phi_0\frac{\partial^2}{\partial\theta_0\partial\psi_0}\right. \\ & \left.+\frac{1+\cos^2\theta_0}{2\sin\theta_0}\frac{\partial}{\partial\psi_0} - \cot\theta_0\frac{\partial}{\partial\phi_0}\right) \\ & +R_3\frac{\partial^2}{\partial\psi_0^2}\end{aligned} \tag{15}$$

The properties of Λ are such that the time differential $\langle f\rangle$, the average value of any function f of the orientation of the ellipsoid, is given by the relationship

$$\mathrm{d}\langle f\rangle/\mathrm{d}\tau = \langle\Lambda f\rangle \tag{16}$$

The application of equation (15) yields:

$$\Lambda(c_{jj}c_{kk} + c_{jk}c_{kj}) = -(4R_i + R_j + R_k)(c_{jj}c_{kk} + c_{jk}c_{kj}) \tag{17}$$

$$\Lambda c_{ri}^2 = -2(R_j + R_k)c_{ri}^2 + 2R_j c_{rk}^2 + 2R_k c_{rj}^2 \tag{18}$$

where the indices i, j, and k are all different. With the condition $c_{ij} = \delta_{ij}$ (i.e. the delta function) when $\tau = 0$, the application of equations (16) yields the average values:

$$\langle c_{jj}c_{kk} + c_{jk}c_{kj}\rangle = \exp[-(4R_i + R_j + R_k)\tau] \tag{19}$$

The application of equations (16) and (18) in deriving the average values of the c_{ri}^2 yields three first-order linear differential equations that are related because $\sum_i C_{ri}^2 = 1$. The average values are:

$$\begin{aligned}\langle c_{ii}^2\rangle = {} & (\tfrac{1}{3}) + (\tfrac{1}{6})(2+\delta_i)\exp(-\tau/\tau_-) \\ & +(\tfrac{1}{6})(2-\delta_i)\exp(-\tau/\tau_+)\end{aligned} \tag{20}$$

$$\begin{aligned}\langle c_{jk}^2\rangle = {} & (\tfrac{1}{3}) - (\tfrac{1}{6})(1-\delta_i)\exp(-\tau/\tau_-) \\ & -(\tfrac{1}{6})(1+\delta_i)\exp(-\tau/\tau_+)\end{aligned} \tag{21}$$

where

$$\delta_i = (R_i - R)/(R^2 - L^2)^{1/2} \tag{22}$$

$$1/\tau_\pm = 6[R \pm (R^2 - L^2)^{1/2}] \tag{23}$$

in which

$$R = (\tfrac{1}{3})(R_1 + R_2 + R_3) \tag{24}$$

$$L^2 = (\tfrac{1}{3})(R_1R_2 + R_1R_3 + R_2R_3) \tag{25}$$

The final result, after averaging over all S_0, is[7]

$$\begin{aligned}\langle F_{\rm h}(t)F_{\rm h}^*(t+\tau)\rangle = {} & (\tfrac{1}{2})K_{\rm h}\langle C_+\exp(-|\tau|/\tau_+) + C_-\exp(-|\tau|/\tau_-) \\ & +C_1\exp(-|\tau|/\tau_1) + C_2\exp(-|\tau|/\tau_2) \\ & +C_3\exp(-|\tau|/\tau_3)\rangle_{\rm av}\end{aligned} \tag{26}$$

in which

$$K_0 = \tfrac{4}{5} \tag{27a}$$

$$K_1 = \tfrac{2}{1} \tag{27b}$$

$$K_2 = \tfrac{8}{15} \tag{27c}$$

$$1/\tau_1 = 4R_1 + R_2 + R_3 \tag{28a}$$

$$1/\tau_2 = 4R_2 + R_1 + R_3 \tag{28b}$$

$$1/\tau_3 = 4R_3 + R_1 + R_2 \tag{28c}$$

$$C_+ = d - e \tag{29a}$$

$$C_- = d + e \tag{29b}$$

$$C_1 = 6m'n'm''n'' \tag{29c}$$

$$C_2 = 6l'n'l''n'' \tag{29d}$$

$$C_3 = 6l'm'l''m'' \tag{29e}$$

in which

$$d = (\tfrac{1}{2})[3(l'^2 l''^2 + m'^2 m''^2 + n'^2 n''^2) - 1] \tag{30a}$$

$$\begin{aligned} e = (\tfrac{1}{2})[&\delta_1(l'^2 l''^2 + m'^2 n''^2 + n'^2 m''^2) \\ &+\delta_2(m'^2 m''^2 + l'^2 n''^2 + n'^2 l''^2) \\ &+\delta_3(n'^2 n''^2 + l'^2 m''^2 + m'^2 l''^2)] \end{aligned} \tag{30b}$$

Frequently, the shape of a molecule approximates an axially symmetric ellipsoid. In this case, given by $R_1 = R_2$, the correlation function in equation (26) is simplified to

$$\begin{aligned} \langle F_h(t) F_h^*(t+\tau)\rangle = (\tfrac{1}{2})K_h\langle &C_A \exp(-|\tau|/\tau_A) \\ &+C_B \exp(-|\tau|/\tau_B) + C_C \exp(-|\tau|/\tau_C)\rangle_{av} \end{aligned} \tag{31}$$

where

$$1/\tau_A = 6R_2 \tag{32a}$$

$$1/\tau_B = 5R_2 + R_3 \tag{32b}$$

$$1/\tau_C = 2R_2 + 4R_3 \tag{32c}$$

$$C_A = C_+ = (\tfrac{1}{2})(1 - 3n'^2)(1 - 3n''^2) \tag{33a}$$

$$C_B = C_1 + C_2 = 6n'n''(m'm'' + l'l'') \tag{33b}$$

$$C_C = C_- + C_3 = (\tfrac{3}{2})(l'^2 - m'^2)(l''^2 - m''^2) + 6l'l''m'm'' \tag{33c}$$

The operation $\langle\cdots\rangle_{av}$ on the right-hand side of equations (26) and (31) signifies the final average over molecular internal motions that introduce additional time dependencies into the correlation function. If there are no internal motions and the ellipsoid is rigid, this final averaging procedure is unnecessary. In this case, l'', m'', n'' are equal to l', m', n', respectively.

The correlation functions for a rigid, completely asymmetric ellipsoid are then

$$\begin{aligned} \langle F_h(t) F_h^*(t+\tau)\rangle = (\tfrac{1}{2})K_h[&C_+ \exp(-|\tau|/\tau_+) + C_- \exp(-|\tau|/\tau_-) \\ &+C_1 \exp(-|\tau|/\tau_1) + C_2 \exp(-|\tau|/\tau_2) \\ &+C_3 \exp(-|\tau|/\tau_3)] \end{aligned} \tag{34}$$

It is useful to note that $C_+ + C_- + C_1 + C_2 + C_3 = 2$. For a sphere, $R_1 = R_2 = R_3 = R_s$, where R_s is the rotational diffusion constant for the sphere and all of the correlation times are equal to the well-known result $\tau_c = 1/6R_s$.

Similarly, the correlation functions for a rigid, axially symmetric ellipsoid are

$$\begin{aligned} \langle F_h(t) F_h^*(t+\tau)\rangle = \ &(\tfrac{1}{2})K_h[C_A \exp(-|\tau|/\tau_A) \\ &+C_B \exp(-|\tau|/\tau_B) + C_C \exp(-|\tau|\tau_C)] \end{aligned} \tag{35}$$

In this case, the C_i simplify to:

$$C_A = (\tfrac{1}{2})(1 - 3n'^2)^2 \tag{36a}$$

$$C_B = 6n'^2(1 - n'^2) \tag{36b}$$

$$C_C = (\tfrac{3}{2})(1 - n'^2)^2 \tag{36c}$$

Note that the correlation functions are independent of l' and m'. The $J_h(\omega)$ depend only on the angle between the nuclear interaction vector and the motional symmetry axis.

The rotational correlation function is a sum of five (or three) simple exponential decay functions. This functional form is a consequence of the assumption of rotational diffusion that involves only infinitesimally small rotational steps.

4 CORRELATION FUNCTIONS FOR AXIALLY SYMMETRIC ELLIPSOIDS WITH INTERNAL MOTION

When the nuclear interaction vector reorients independently inside the ellipsoid, the direction cosines l', m', and n' of the interaction vector with respect to the rectangular coordinate system S' of the ellipsoid are time dependent and time dependent averaging on the right-hand side of equation (31)

must be performed to obtain the correlation functions. Because the internal rotational motion is independent of the rotational motions of the ellipsoid, we must evaluate the separate correlation functions (i.e. the C_i) in equation (33). To do this, it is convenient to express the internal motion in terms of spherical polar coordinates in S'. The relaxation vector rotates about the z' axis with a constant polar angle Δ and a time dependent azimuthal angle $\phi'(t)$. In the case of a methyl group, the z' axis is the threefold symmetry axis. The z' axis makes a constant angle α with the Z' symmetry axis of the ellipsoid. In the coordinate system of the ellipsoid,

$$C_{\mathrm{A}} = (\tfrac{1}{2})\langle[1 - 3\cos^2\theta(t)][1 - 3\cos^2\theta(t+\tau)]\rangle \tag{37a}$$

$$C_{\mathrm{B}} = (\tfrac{3}{2})\langle\sin 2\theta(t)\exp[\mathrm{i}\phi(t)]\sin 2\theta(t+\tau) \times \exp[-\mathrm{i}\phi(t+\tau)]\rangle \tag{37b}$$

$$C_{\mathrm{C}} = (\tfrac{3}{2})\langle\sin^2\theta(t)\exp[2\mathrm{i}\phi(t)]\sin^2\theta(t+\tau) \times \exp[-2\mathrm{i}\phi(t+\tau)]\rangle \tag{37c}$$

where $\theta(t)$ and $\phi(t)$ are the time dependent polar and azimuthal angles of the interaction vector in S'.

The quantities in brackets are products of spherical harmonics; the C_i can be expressed in terms of the constant angles α and Δ and of the time dependent angle $\phi'(t)$ by using the transformation formulas for spherical harmonics. The result of setting $\phi''(\tau) = \phi'(t + \tau) - \phi'(t)$ and averaging over the random distribution at time t is[8]

$$C_{\mathrm{A}} = C_{\mathrm{A1}} + C_{\mathrm{A2}}\langle\cos\phi''(\tau)\rangle + C_{\mathrm{A3}}\langle\cos 2\phi''(\tau)\rangle \tag{38a}$$

$$C_{\mathrm{A1}} = (\tfrac{1}{8})(1 - 3\cos^2\alpha)^2(1 - 3\cos^2\Delta)^2 \tag{38b}$$

$$C_{\mathrm{A2}} = (\tfrac{9}{16})\sin^2 2\alpha\sin^2 2\Delta \tag{38c}$$

$$C_{\mathrm{A3}} = (\tfrac{9}{16})\sin^4\Delta\sin^4\alpha \tag{38d}$$

$$C_{\mathrm{B}} = C_{\mathrm{B1}} + C_{\mathrm{B2}}\langle\cos\phi''(\tau)\rangle + C_{\mathrm{B3}}\langle\cos 2\phi''(\tau)\rangle \tag{39a}$$

$$C_{\mathrm{B1}} = (\tfrac{3}{8})\sin^2 2\alpha(3\cos^2\Delta - 1)^2 \tag{39b}$$

$$C_{\mathrm{B2}} = (\tfrac{3}{4})(\cos^2 2\alpha + \cos^2\alpha)\sin^2 2\Delta \tag{39c}$$

$$C_{\mathrm{B3}} = (\tfrac{3}{4})[\sin^2\alpha + (\tfrac{1}{4})\sin^2 2\alpha]\sin^4\Delta \tag{39d}$$

$$C_{\mathrm{C}} = C_{\mathrm{C1}} + C_{\mathrm{C2}}\langle\cos\phi''(\tau)\rangle + C_{\mathrm{C3}}\langle\cos 2\phi''(\tau)\rangle \tag{40a}$$

$$C_{\mathrm{C1}} = (\tfrac{3}{8})\sin^4\alpha(3\cos^2\Delta - 1)^2 \tag{40b}$$

$$C_{\mathrm{C2}} = (\tfrac{3}{4})[\sin^2\alpha + (\tfrac{1}{4})\sin^2 2\alpha]\sin^2 2\Delta \tag{40c}$$

$$C_{\mathrm{C3}} = (\tfrac{3}{16})[(1 + \cos^2\alpha)^2 + 4\cos^2\alpha]\sin^4\Delta \tag{40d}$$

Each of the three coefficients C_{A}, C_{B}, and C_{C} consists of a time-independent term (subscripted 1) and two terms that are time dependent because of the internal motion.

The internal motion determines the time dependence of $\phi''(\tau)$. One model for the time dependence is that of a terminal methyl group in an *n*-paraffin molecule in the *s-trans* configuration. Because there are three equivalent positions of the methyl group, the allowed values of $\phi''(\tau)$ are 0°, 120°, and 240°. Here, the internal motion occurs by random jumping of the methyl group from any of these equivalent positions to either of the two adjacent positions at an average rate of $(3\tau_{\mathrm{ci}})^{-1}$. With this type of motion,[9] we have

$$\langle\cos\phi''(\tau)\rangle = \langle\cos 2\phi''(\tau)\rangle = \exp(-|\tau|/\tau_{\mathrm{ci}}) \tag{41}$$

so that

$$C_{\mathrm{A}} = C_{\mathrm{A1}} + (C_{\mathrm{A2}} + C_{\mathrm{A3}})\exp(-|\tau|/\tau_{\mathrm{ci}}) \tag{42a}$$

$$C_{\mathrm{B}} = C_{\mathrm{B1}} + (C_{\mathrm{B2}} + C_{\mathrm{B3}})\exp(-|\tau|/\tau_{\mathrm{ci}}) \tag{42b}$$

$$C_{\mathrm{C}} = C_{\mathrm{C1}} + (C_{\mathrm{C2}} + C_{\mathrm{C3}})\exp(-|\tau|/\tau_{\mathrm{ci}}) \tag{42c}$$

As a result of this type of internal motion, the correlation function contains the three additional correlation times

$$1/\tau_{\mathrm{A23}} = 6R_2 + 1/\tau_{\mathrm{ci}} \tag{43a}$$

$$1/\tau_{\mathrm{B23}} = 5R_2 + R_3 + 1/\tau_{\mathrm{ci}} \tag{43b}$$

$$1/\tau_{\mathrm{C23}} = 2R_2 + 4R_3 + 1/\tau_{\mathrm{ci}} \tag{43c}$$

Another model of internal motion is a stochastic diffusion process among a very large number of equilibrium positions that are uniformly distributed from $\phi' = 0$ to 2π such that $\langle\phi''^2\rangle = 2R_{\mathrm{i}}\tau$, where R_{i} is the internal rotational diffusion coefficient. With this model[9] of internal motion,

$$\langle\cos\phi''(\tau)\rangle = \exp(-R_{\mathrm{i}}|\tau|) \tag{44a}$$

$$\langle\cos 2\phi''(\tau)\rangle = \exp(-4R_{\mathrm{i}}|\tau|) \tag{44b}$$

so that

$$C_{\mathrm{A}} = C_{\mathrm{A1}} + C_{\mathrm{A2}}\exp(-R_{\mathrm{i}}|\tau|) + C_{\mathrm{A3}}\exp(-4R_{\mathrm{i}}|\tau|) \tag{45a}$$

$$C_{\mathrm{B}} = C_{\mathrm{B1}} + C_{\mathrm{B2}}\exp(-R_{\mathrm{i}}|\tau|) + C_{\mathrm{B3}}\exp(-4R_{\mathrm{i}}|\tau|) \tag{45b}$$

$$C_{\mathrm{C}} = C_{\mathrm{C1}} + C_{\mathrm{C2}}\exp(-R_{\mathrm{i}}|\tau|) + C_{\mathrm{C3}}\exp(-4R_{\mathrm{i}}|\tau|) \tag{45c}$$

giving the six new correlation times

$$1/\tau_{\mathrm{A2}} = 6R_2 + R_{\mathrm{i}} \tag{46a}$$

$$1/\tau_{\mathrm{A3}} = 6R_2 + 4R_{\mathrm{i}} \tag{46b}$$

$$1/\tau_{B2} = 5R_2 + R_3 + R_i \tag{46c}$$

$$1/\tau_{B3} = 5R_2 + R_3 + 4R_i \tag{46d}$$

$$1/\tau_{C2} = 2R_2 + 4R_3 + R_i \tag{46e}$$

$$1/\tau_{C3} = 2R_2 + 4R_3 + 4R_i \tag{46f}$$

Frequently, the internal rotation axis lies along the symmetry axis of the ellipsoid so that $\alpha = 0$ in equations (38)–(40). Consequently, the value of many of these equations is zero and the correlation function is[7]

$$\langle F_h(t)F_h^*(t+\tau)\rangle = (\tfrac{1}{2})K_h[A\exp(-|\tau|/\tau'_A) + B\exp(-|\tau|/\tau'_B) + C\exp(-|\tau|/\tau'_C)] \tag{47}$$

in which

$$A = (\tfrac{1}{2})(1 - 3\cos^2\Delta)^2 \tag{48a}$$

$$B = (\tfrac{3}{2})\sin^2 2\Delta \tag{48b}$$

$$C = (\tfrac{3}{2})\sin^4\Delta \tag{48c}$$

For the internal jump model,

$$1/\tau'_A = 1/\tau_A = 6R_2 \tag{49a}$$

$$1/\tau'_B = 5R_2 + R_3 + \tau_{ci} \tag{49b}$$

$$1/\tau'_C = 2R_2 + 4R_3 + \tau_{ci} \tag{49c}$$

For the internal rotational diffusion model,

$$1/\tau'_A = 1/\tau_A = 6R_2 \tag{50a}$$

$$1/\tau'_B = 5R_2 + R_3 + R_i \tag{50b}$$

$$1/\tau'_C = 2R_2 + 4R_3 + 4R_i \tag{50c}$$

Generally, the correlation function of a nonspherical molecule that reorients at different rates about different molecular axes depends on many external and internal molecular motions. We can use NMR relaxation time measurements on nuclei that have different nuclear interaction vector orientations in the molecule to give information on the internal and external molecular motions.

5 CORRELATION FUNCTIONS FOR INTERGROUP MAGNETIC DIPOLAR RELAXATION WITH INTERNAL MOTION

In intramolecular magnetic dipolar relaxation between a nucleus of a rotating group and a nucleus on the remainder of the molecule, the length as well as the orientation of the nuclear interaction vector is time dependent. Consequently, we use the $F_h(t)$ as defined in equation (4). To restrict the calculation of the correlation function to simple but useful cases, we assume the following geometry.[10] The two nuclei rotate in parallel planes about the same perpendicular axis. The planes are separated by the distance b and the radii of rotation are a and c. This geometry describes the magnetic dipolar interaction between protons in different methyl groups in ethane, protons on neighboring carbon atoms in n-paraffins, methyl and ring protons in toluene, fluorine nuclei and protons in benzotrifluoride, etc.

Let us assume that the molecule is an axially symmetric ellipsoid and that the internal rotation axis is parallel to the ellipsoid symmetry axis. Because the internal motion causes simultaneous changes in the orientation and length of the internuclear vector, the correlation function is an extension of equations (31)–(33) to include a time dependent r.

$$\langle F_h(t)F_h^*(t+\tau)\rangle = (\tfrac{1}{2})K_h\langle C_{Ar}\exp(-|\tau|/\tau_A) + C_{Br}(-|\tau|/\tau_B) + C_{Cr}\exp(-|\tau|/\tau_C)\rangle_{av} \tag{51}$$

where

$$1/\tau_A = 6R_2 \tag{52a}$$

$$1/\tau_B = 5R_2 + R_3 \tag{52b}$$

$$1/\tau_C = 2R_2 + 4R_3 \tag{52c}$$

$$C_{Ar} = (\tfrac{1}{2})(1 - 3n'^2)(1 - 3n''^2)r'^{-3}r''^{-3} \tag{53a}$$

$$C_{Br} = 6n'n''(m'm'' + l'l'')r'^{-3}r''^{-3} \tag{53b}$$

$$C_{Cr} = [(\tfrac{3}{2})(l'^2 - m'^2)(l''^2 - m''^2) + 6l'l''m'm'']r'^{-3}r''^{-3} \tag{53c}$$

The operation $\langle\cdots\rangle_{av}$ on the right-hand side of equation (51) signifies the final average over the internal motions. These motions are statistically independent from the rotational motions of the ellipsoid. The values at time t are l', m', n', and r', and those at the later time $t + \tau$ are l'', m'', n'', and

r''. In terms of the geometry of the problem, the C quantities are:

$$C_{\mathrm{Ar}} = (\tfrac{1}{2})r'^{-5}r''^{-5}\{(a^2+c^2-2b^2)^2 - 2(a^3c+ac^3-2ab^2c) \times[\cos(\phi_1'-\phi_2') + \cos(\phi_1''-\phi_2'')] +4a^2c^2\cos(\phi_1'-\phi_2')\cos(\phi_1''-\phi_2'')]\} \tag{54a}$$

$$C_{\mathrm{Br}} = 6r'^{-5}r''^{-5}b^2\{c^2\cos(\phi_1'-\phi_1'') + a^2\cos(\phi_2'-\phi_2'') -ac[\cos(\phi_1'-\phi_2'') + \cos(\phi_2'-\phi_1'')]\} \tag{54b}$$

$$C_{\mathrm{Cr}} = (\tfrac{3}{2})r'^{-5}r''^{-5}\{c^4\cos(2\phi_1'-2\phi_1'') + a^4\cos(2\phi_2'-2\phi_2'') +4a^2c^2\cos(\phi_1'+\phi_2'-\phi_1''-\phi_2'') +a^2c^2[\cos(2\phi_1'-2\phi_2'') + \cos(2\phi_2'-2\phi_1'')] -2ac^3[\cos(2\phi_1'-\phi_1''-\phi_2'') + \cos(\phi_1'+\phi_2'-2\phi_1'')] -2a^3c[\cos(2\phi_2'-\phi_1''-\phi_2'') + \cos(\phi_1'+\phi_2'-2\phi_2'')]\} \tag{54c}$$

in which ϕ_1' and ϕ_2' are the azimuthal angles of the nuclei at time t and ϕ_1'' and ϕ_2'' are the angles at time $t+\tau$.

Calculating the time dependent average values $\langle C_{\mathrm{ir}}\rangle$ involves integrals of functions that approach the complete elliptic integrals at long τ values if $(\phi_1' - \phi_1'')$ and $(\phi_2' - \phi_2'')$ are allowed to have all values from 0 to 2π. The calculation is greatly simplified with the model in which one nucleus occupies three positions 120° apart and the other nucleus occupies three similar positions that are staggered with respect to those of the former nucleus. Here, there are only two different values of r, as given by the expressions:

$$r_{\mathrm{l}}^2 = a^2+b^2+c^2+2ac \tag{55a}$$

$$r_{\mathrm{s}}^2 = a^2+b^2+c^2-ac \tag{55b}$$

If each nucleus independently and randomly jumps among its three positions, the $\langle C_{\mathrm{ir}}\rangle$ are

$$\langle C_{\mathrm{Ar}}\rangle = C_{\mathrm{a1}} + C_{\mathrm{a2}}\exp[-|\tau|(1/\tau_1+1/\tau_2)] \tag{56a}$$

$$\langle C_{\mathrm{Br}}\rangle = C_{\mathrm{b1}}\exp[-|\tau|/\tau_1] + C_{\mathrm{b2}}\exp[-|\tau|/\tau_2] +C_{\mathrm{b3}}\exp[-|\tau|(1/\tau_1+1/\tau_2)] \tag{56b}$$

$$\langle C_{\mathrm{Cr}}\rangle = C_{\mathrm{c1}}\exp[-|\tau|/\tau_1] + C_{\mathrm{c2}}\exp[-|\tau|/\tau_2] +C_{\mathrm{c3}}\exp[-|\tau|(1/\tau_1+1/\tau_2)] \tag{56c}$$

where

$$C_{\mathrm{a1}} = (\tfrac{1}{18})[(a^2+c^2-2b^2)^2Q_1 + 4a^2c^2Q_2 -4(a^3c+ac^3-2ab^2c)Q_3] \tag{57a}$$

$$C_{\mathrm{a2}} = (\tfrac{1}{9})[(a^2+c^2-2b^2)^2Q_2 + a^2c^2Q_5 -2(a^3c+ac^3-2ab^2c)Q_4] \tag{57b}$$

$$C_{\mathrm{b1}} = (\tfrac{2}{3})b^2(c^2Q_1 + a^2Q_2 - 2acQ_3) \tag{57c}$$

$$C_{\mathrm{b2}} = (\tfrac{2}{3})b^2(c^2Q_2 + a^2Q_1 - 2acQ_3) \tag{57d}$$

$$C_{\mathrm{b3}} = (\tfrac{2}{3})b^2(a+c)^2Q_2 \tag{57e}$$

$$C_{\mathrm{c1}} = (\tfrac{1}{6})(c^4Q_1 + a^4Q_2 + 6a^2c^2Q_6 - 4ac^3Q_3 + 4a^3cQ_2) \tag{57f}$$

$$C_{\mathrm{c2}} = (\tfrac{1}{6})(c^4Q_2 + a^4Q_1 + 6a^2c^2Q_6 + 4ac^3Q_2 - 4a^3cQ_3) \tag{57g}$$

$$C_{\mathrm{c3}} = (\tfrac{1}{6})(c^4Q_2 + a^4Q_2 + 6a^2c^2Q_7 - 4ac^3Q_3 - 4a^3cQ_3) \tag{57h}$$

in which

$$Q_1 = 4r_{\mathrm{s}}^{-10} + r_{\mathrm{l}}^{-10} + 4r_{\mathrm{s}}^{-5}r_{\mathrm{l}}^{-5} \tag{58a}$$

$$Q_2 = r_{\mathrm{s}}^{-10} + r_{\mathrm{l}}^{-10} - 2r_{\mathrm{s}}^{-5}r_{\mathrm{l}}^{-5} \tag{58b}$$

$$Q_3 = 2r_{\mathrm{s}}^{-10} - r_{\mathrm{l}}^{-10} - r_{\mathrm{s}}^{-5}r_{\mathrm{l}}^{-5} \tag{58c}$$

$$Q_4 = r_{\mathrm{s}}^{-10} - 2r_{\mathrm{l}}^{-10} + r_{\mathrm{s}}^{-5}r_{\mathrm{l}}^{-5} \tag{58d}$$

$$Q_5 = r_{\mathrm{s}}^{-10} + 4r_{\mathrm{l}}^{-10} + 4r_{\mathrm{s}}^{-5}r_{\mathrm{l}}^{-5} \tag{58e}$$

$$Q_6 = r_{\mathrm{l}}^{-10} - r_{\mathrm{s}}^{-5}r_{\mathrm{l}}^{-5} \tag{58f}$$

$$Q_7 = 3r_{\mathrm{s}}^{-10} + r_{\mathrm{l}}^{-10} + 2r_{\mathrm{s}}^{-5}r_{\mathrm{l}}^{-5} \tag{58g}$$

The correlation time of internal motion of the nucleus associated with ϕ_1 and c is τ_1 and that of the nucleus associated with ϕ_2 and a is τ_2.

The final correlation times are given by:

$$1/\tau_{\mathrm{a1}} = 1/\tau_{\mathrm{A}} = 6R_2 \tag{59a}$$

$$1/\tau_{\mathrm{a2}} = 6R_2 + 1/\tau_1 + 1/\tau_2 \tag{59b}$$

$$1/\tau_{\mathrm{b1}} = 5R_2 + R_3 + 1/\tau_1 \tag{59c}$$

$$1/\tau_{b2} = 5R_2 + R_3 + 1/\tau_2 \tag{59d}$$

$$1/\tau_{b3} = 5R_2 + R_3 + 1/\tau_1 + 1/\tau_2 \tag{59e}$$

$$1/\tau_{c1} = 2R_2 + 4R_3 + 1/\tau_1 \tag{59f}$$

$$1/\tau_{c2} = 2R_2 + 4R_3 + 1/\tau_2 \tag{59g}$$

$$1/\tau_{c3} = 2R_2 + 4R_3 + 1/\tau_1 + 1/\tau_2 \tag{59h}$$

Use of this simple model of internal motion with magnetic dipolar relaxation interaction increases the number of correlation times for the axially symmetric ellipsoid from three to eight. If the internal rotational axis were not parallel to the ellipsoid symmetry axis, then more than eight correlation times would result. Even in this simple case, many simplifications occur if the molecule rotates with spherical symmetry, if $\tau_1 = \tau_2$, or if either of the two nuclei does not rotate internally.

Examination of the sum of the eight coefficients given by equation (57) reveals insight into the effects of internal motion. This sum is $(4/3)r_s^{-6} + (2/3)r_1^{-6}$, which is twice the weighted average of r^{-6}. The corresponding sum for a rigid molecule, obtained from the sum of equation (53) when the single-primed and double primed quantities are equal, is $2r^{-6}$. The effect of the internal motion, then, is to split r^{-6} into several terms. Most of these terms have shorter correlation times than for a rigid molecule. One of the terms is independent of the internal motion and it gives rise to the 'order parameter' that represents a kind of order in a large, flexible molecule.

6 'MODEL-FREE' CORRELATION FUNCTIONS FOR FLEXIBLE MACROMOLECULES

Modern applications of NMR include the use of relaxation time measurements to investigate the dynamics of flexible macromolecules, such as polymers, lipids, and proteins (see ***Protein Dynamics from NMR Relaxation***), in solution. Clearly, the correlation function for such systems is extremely complex because many different correlation times and associated preexponential factors are involved in its formulation. In addition, we must assume structural and dynamical models to make the formulation. Even with such a formulation, the typical NMR relaxation time measurement does not allow for the experimental evaluation of all the parameters that are in the assumed models.

We can use the expressions presented in this article with various assumed dynamics and structures to formulate the correlation functions for a complex flexible molecule and compute values of relaxation times. We can use these values to validate simplified expressions for the spectral density to figure out (a) what is the unique information in a set of relaxation time data and (b) how can we extract this information from the data?

Such simplified expressions are called[11–13] 'model-free' because the analysis of relaxation time data using these expressions does not require the adoption of a physical model. However, the derivation and productive use of these expressions do require the assumption of certain limiting cases. The description of the motion of the flexible macromolecule is that of overall reorientation of the molecular framework and internal motions within this framework that are independent of the reorientation of the framework. To illustrate this approach, we factor equation (47) as

$$\langle F_h(t)F_h^*(t+\tau)\rangle = (\tfrac{1}{2})K_h[\exp(-|\tau|/\tau_{ov})] \times[A + B\exp(-|\tau|/\tau_{i1}) + C\exp(-|\tau|/\tau_{i2})] \tag{60}$$

in which $A + B + C = 2$. When the internal motion is rotational diffusion, for example, the correlation times are:

$$1/\tau_{ov} = 1/\tau_A = 6R_2 \tag{61a}$$

$$1/\tau_{i1} = -R_2 + R_3 + R_i \tag{61b}$$

$$1/\tau_{i2} = -4R_2 + 4R_3 + 4R_i \tag{61c}$$

We can view equation (60) as the product of a correlation function $C_{ov}(\tau)$ that depends only on overall motion, and a correlation function $C_{in}(\tau)$ that contains a constant term and terms that involve the internal motion, so that

$$\langle F_h(t)F_h^*(t+\tau)\rangle = K_h C_{ov}(\tau)C_{in}(\tau) \tag{62}$$

where

$$C_{ov}(\tau) = \exp(-|\tau|/\tau_{ov}) \tag{63a}$$

$$C_{in}(\tau) = (\tfrac{1}{2})[A + B\exp(-|\tau|/\tau_{i1}) + C\exp(-|\tau|/\tau_{i2})] \tag{63b}$$

The model-free approach is to approximate $C_{in}(\tau)$ as

$$C_{in}(\tau) = \zeta^2 + (1-\zeta^2)\exp(-|\tau|/\tau_{eff}) \tag{64}$$

where ζ is called an order parameter, equal to $(A/2)^{\frac{1}{2}}$ in the present example, and τ_{eff} is an effective correlation time as given by the definition:

$$\tau_{eff} = (1-\zeta^2)^{-1}\int_0^\infty [C_{in}(\tau) - \zeta^2]\,d\tau \tag{65}$$

When the internal motions are rapid so that $2\omega_0/R_i \ll 1$, use of this definition in the spectral density function provides an excellent approximation.

In considering the consequences of the fluctuations of internuclear separation on magnetic dipolar relaxation that are

caused by the internal motion, we can use equations (56)–(59) to factor equation (51) as

$$\begin{aligned}\langle F_{\rm h}(t)F_{\rm h}^*(t+\tau)\rangle &= (\tfrac{1}{2})K_{\rm h}[\exp(-|\tau|/\tau_{\rm ov})]\\ &\times[C_{\rm a1}+C_{\rm a2}\exp(-|\tau|/\tau_{\rm i1})\\ &+C_{\rm b1}\exp(-|\tau|/\tau_{\rm i2})+C_{\rm b2}\exp(-|\tau|/\tau_{\rm i3})\\ &+C_{\rm b3}\exp(-|\tau|/\tau_{\rm i4})+C_{\rm c1}\exp(-|\tau|/\tau_{\rm i5})\\ &+C_{\rm c2}\exp(-|\tau|/\tau_{\rm i6})+C_{\rm c3}\exp(-|\tau|/\tau_{\rm i7})]\end{aligned} \tag{66}$$

in which

$$1/\tau_{\rm ov} = 6R_2 \tag{67a}$$

$$1/\tau_{\rm i1} = 1/\tau_1 + 1/\tau_2 \tag{67b}$$

$$1/\tau_{\rm i2} = -R_2 + R_3 + 1/\tau_1 \tag{67c}$$

$$1/\tau_{\rm i3} = -R_2 + R_3 + 1/\tau_2 \tag{67d}$$

$$1/\tau_{\rm i4} = -R_2 + R_3 + 1/\tau_1 + 1/\tau_2 \tag{67e}$$

$$1/\tau_{\rm i5} = -4R_2 + 4R_3 + 1/\tau_1 \tag{67f}$$

$$1/\tau_{\rm i6} = -4R_2 + 4R_3 + 1/\tau_2 \tag{67g}$$

$$1/\tau_{\rm i7} = -4R_2 + 4R_3 + 1/\tau_1 + 1/\tau_2 \tag{67h}$$

The analogous order parameter $\zeta_{\rm r}$ for internal motion with equation (62) is similarly defined by:

$$C_{\rm in}(\tau) = \zeta_{\rm r}^2 + (1-\zeta_{\rm r}^2)\exp(-|\tau|/\tau_{\rm er}) \tag{68}$$

in which $\zeta_{\rm r}$ is equal to $(C_{\rm a1}/2)^{\frac{1}{2}}$ and $\tau_{\rm er}$ is the effective correlation time that is defined in the same fashion as $\tau_{\rm eff}$.

When the internal motions are rapid compared with the overall molecular reorientation rate and obey the condition $2\omega_0/R_{\rm i} \ll 1$, the correlation function is the sum of two terms. One of these terms involves the overall correlation time and the other term involves the effective correlation time that depends on the internal motions. The term that is dependent on the overall molecular motion is weighted by the order parameter.

7 CORRELATION FUNCTIONS FOR INTERMOLECULAR MAGNETIC DIPOLAR RELAXATION

Magnetic dipolar NMR relaxation between nuclei of different molecules is an important relaxation mechanism that depends on Brownian motion. The values of r, θ, and ϕ are time dependent because of translational diffusion of the molecular centers and rotation of the molecules about their centers. If the interacting nuclei are at the centers of spherical molecules, the correlation functions can be calculated[1] from classical diffusion theory. The correlation function is[1]

$$\langle F_{\rm h}(t)F_{\rm h}^*(t+\tau)\rangle = \frac{\alpha_{\rm h}N}{d^3} \times \int_0^\infty [J_{3/2}(u)]^2 \exp\left[-\left(\frac{2D}{d^2}u^2\tau\right)\right]\frac{{\rm d}u}{u} \tag{69}$$

where N is the number of nuclear spins per cm^3, D is the translational diffusion coefficient, d is the minimum distance of approach between nuclei on different molecules, $J_{3/2}$ is a Bessel function, $\alpha_{\rm h}$ is a numerical factor that depends on h, and u is a dummy integration parameter. The spectral energy densities are then

$$J_{\rm h}(\omega) = \frac{\alpha_{\rm h}N}{dD}\int_0^\infty [J_{3/2}(u)]^2 \frac{u\,{\rm d}u}{u^4+\omega^2\tau^2} \tag{70}$$

where $\tau = d^2/2D$. The effects on $J_{\rm h}(\omega)$ in the case of off-center nuclei[14] depend on the ratio $\tau/\tau_{\rm c}$ and they are not insignificant.

8 EXPERIMENTAL AND THEORETICAL CORRELATION TIMES OF RIGID MOLECULES

8.1 Evaluation of Correlation Times from NMR Relaxation Data

We can express the correlation functions in the preceding sections of this article (except for Section 7) as the following sum of exponential functions:

$$\langle F_{\rm h}(t)F_{\rm h}^*(t+\tau)\rangle = (\tfrac{1}{2})\langle F_{\rm h}(t)F_{\rm h}^*(t)\rangle \sum_j C_j \exp(-|\tau|/\tau_{cj}) \tag{71}$$

in which $\Sigma_j C_j = 2$. The values of the correlation times τ_{cj} depend on the rates of molecular motions, and the number and values of the C_j depend on the details of molecular structure and motion. Because equation (71) is a sum of exponential functions, the spectral densities $J_{\rm h}(\omega)$ in equation (3) are given by the sum of Lorentzian functions

$$J_{\rm h}(\omega) = \langle F_{\rm h}(t)F_{\rm h}^*(t)\rangle \sum_j C_j[\tau_{cj}/(1+\omega^2\tau_{cj}^2)] \tag{72}$$

Note that the spectral densities for intermolecular magnetic dipolar relaxation in Section 7 are not sums of Lorentzian functions because equation (69) is not a sum of exponential functions.

The models presented in the preceding sections do not explicity include various motions, such as high frequency, small amplitude bond stretching vibrations, as well as torsional oscillations about temporary equilibrium positions that change because of Brownian motion. The inclusion of such motions would increase the number of terms in equations (71) and (72) and could decrease the spectral density. If the decrease in spectral density is significant, the application of the preceding models to relaxation time data could lead to inconsistencies of interpretation. In the case of magnetic dipolar relaxation of CH_3 groups, the predicted decrease due to torsional ocillations agrees[15] with experiment.

The study of Brownian motions by means of NMR relaxation time measurements involves the evaluation of the τ_{cj} from $J_h(\omega)$ values that are obtained from the measured relaxation times. These relaxation times should be from different nuclei that have different orientations of relaxation interaction vector with respect to the various axes of the ellipsoidal molecule.

There can be an ambiguity in evaluating correlation times from relaxation data, especially for large molecules with relatively small R_i values. Because the function $\tau_{cj}/(1 + \omega^2\tau_{cj}^2)$ is at its maximum value $1/\omega$ at $\omega\tau_{cj} = 1$, there is an ambiguity of τ_{cj} values when the 'experimental' value of $\tau_{cj}/(1 + \omega^2\tau_{cj}^2)$ is less than $1/\omega$. This ambiguity does not occur if, for example, all of the τ_{cj} values are small compared to $1/\omega$. In ordinary NMR spectrometers, this condition is met for nonviscous liquids. For example, $2\omega_0\tau_c \approx 0.05$ for protons in liquid water at 0 °C in a 750 MHz NMR spectrometer. Clearly, the simplest circumstance is a rigid, spherical molecule of a nonviscous liquid so that there is only one correlation time. We can compare the correlation time obtained from the analysis of the NMR relaxation time to the value that is predicted from liquid properties and molecular parameters.

8.2 Relationship of Rotational Correlation Times to Brownian Motion

In the preceding sections of this article, the correlation functions for a rigid ellipsoid are expressed in terms of the rotational diffusion coefficients R_i. The R_i values can be determined from the analysis of the proper relaxation time measurements. The next step is to relate the R_i to Brownian motion in the liquid. Molecules in the liquid undergo random collisions with other molecules. Perrin's exquisitely detailed description of the translational and rotational motion of an ellipsoid that is immersed in a liquid and experiencing collisions with the liquid molecules[5] is useful in establishing this relationship.

It is assumed that the average action of molecular collisions on the ellipsoid gives rise to the friction of viscosity. Fluctuations of these collisions produce impulses of torque that affect the rotation of the ellipsoid. These impulses couple the rotational kinetic energy of the ellipsoid to the kinetic energy of its surroundings so that thermodynamic equilibrium obtains and the average kinetic energy for each degree of freedom is equal to $kT/2$, where T is the absolute temperature of the fluid and k is Boltzmann's constant.

Let ω_1, ω_2, and ω_3 be the angular velocities of the ellipsoid about the X, Y, and Z axes and I_1, I_2 and I_3 be the moments of inertia about these axes, respectively. Similarly, let α_1, α_2, and α_3 be small rotation angles about these axes. In the following discussion, designate the subscripts 1, 2, and 3 as the subscript i. If K is the kinetic energy of the particle, the angular momenta λ_i are the partial derivatives of K with respect to the angular velocities ω_i:

$$\lambda_i = \partial K/\partial\omega_i \tag{73}$$

At each instant, the collisions with the surrounding molecules produce a torque L_i about the respective ellipsoid axes. Each L_i is the sum of the frictional torque $-\mathcal{C}_i\omega_i$ that results from viscosity and a variable torque Γ_i that is caused by fluctuations of the collisions. This torque causes changes in angular momenta as given by

$$d\lambda_i/dt = -\mathcal{C}_i\omega_i + \Gamma_i \tag{74}$$

We take time intervals Δt that are sufficiently great so that there is almost complete statistical independence of the angular displacements that are produced by torque Γ_i during two consecutive time intervals, and nevertheless, sufficiently small so that the rotation during each interval is very small. If α_i are the very small angles that are needed to describe the changes in orientation from its initial position to its orientation at the end of time interval Δt, to a first approximation the angular velocities are

$$\omega_i = d\alpha_i/dt \tag{75}$$

Under these conditions, the angular displacements that result from successive impulses due to the thermal motions of the liquid are independent and simply additive. If we divide the time interval Δt into very small successive intervals δt, the variable couple Γ_i communicates to the ellipsoid an impulse $\mathcal{L}_i$ that is the integral of Γ_i over the interval δt,

$$\mathcal{L}_i = \int_0^{\delta t} \Gamma_i\, dt \tag{76}$$

Also, to calculate the net angular displacement that results from these impulses, it suffices to calculate the displacement that results from each impulse, assuming action on the initially immobile particle, and take the sum of these small displacements as if they are not superposed in time.

Because $\omega_i = d\alpha_i/dt$ and $d\lambda_i/dt = -\mathcal{C}_i\omega_i + \Gamma_i$

$$d\lambda_i/dt = -\mathcal{C}_i(d\alpha_i/dt) + \Gamma_i \tag{77}$$

Integration between the initial time t_0 and the final time t gives:

$$\lambda_i - \lambda_{i0} = -\mathcal{C}_i(\alpha_i - \alpha_{i0}) + \int_{t_0}^{t} \Gamma_i\, dt \tag{78}$$

The ellipsoid is assumed to be immobile at time t_0 so that $\lambda_0 = 0$. If the torque Γ_i acts on the particle only during the time interval δt,

$$\lambda_i = -\mathcal{C}_i(\alpha_i - \alpha_{i0}) + \mathcal{L}_i \tag{79}$$

If t is large enough so that the particle is now practically stopped due to the friction, the rotational displacement of the particle that results from the total of the angular impulses $\mathcal{L}$ is

$$\delta\alpha_i = \mathcal{L}_i/\mathcal{C}_i \tag{80}$$

The displacement does not depend on the moments of inertia, I_i; it depends only on the coefficients of friction $\mathcal{C}_i$. However, this result is true only if the preceding approximations are justified by the smallness of the angular displacements.

If the time interval Δt is sufficiently great, the displacement is that which results from the n successive intervals δt that compose it. If the intervals δt are not too small, the successive corresponding impulses are nearly statistically independent, and the net angular displacement $\Delta\alpha_i$ over time Δt is given by:

$$\langle\Delta\alpha_i^2\rangle = (1/\mathcal{C}_i^2)\sum_k\langle\mathcal{L}_{ik}^2\rangle = n\langle\mathcal{L}_i^2\rangle/\mathcal{C}_i^2 \tag{81}$$

because the average values for time intervals of the same duration δt are equal. Also, the average values of cross terms $\Delta\alpha_i\Delta\alpha_j$ are zero.

The average values of the $\Delta\alpha_i{}^2$ quantities can be found by noting that the impulses received by the particle maintain statistically a state of agitation that corresponds to the average kinetic energy that, from the equipartition theorem of statistical mechanics, is given by:

$$\langle\lambda_i\omega_i\rangle = kT \tag{82}$$

If the time interval δt is sufficiently small so that the rotational velocity ω_i is nearly constant, integration of equation (74) over δt gives:

$$\lambda_i' = \lambda_i - \mathcal{C}_i\omega_i\delta t + \mathcal{L}_i \tag{83}$$

where λ_i and λ_i' are angular momenta at the beginning and end of the interval δt. After squaring and taking the average,

$$\begin{aligned}\langle\lambda_i'^2\rangle = {} & \langle\lambda_i^2\rangle + \mathcal{C}_i^2\langle\omega_i^2\rangle\delta t^2 + \langle\mathcal{L}_i^2\rangle \\ & -2\mathcal{C}_i\langle\lambda_i\omega_i\rangle\delta t + 2\langle\lambda_i\mathcal{L}_i\rangle - 2\mathcal{C}_i\langle\omega_i\mathcal{L}_i\rangle\delta t\end{aligned} \tag{84}$$

Several characteristics allow us to simplify this expression. Since the system is in steady-state conditions, $\langle\lambda_i'^2\rangle = \langle\lambda_i^2\rangle$. The impulses $\mathcal{L}_i$ do not depend directly on the angular velocities, and the intervals δt are assumed to be sufficiently long in order than the impulses may be independent of the previous impulses that have influenced the angular velocities. Therefore, the average values of products of impulses and angular velocities and of products of impulses and angular momenta are null. Finally, the terms in δt^2 are negligible. Equation (84) then reduces to:

$$\langle\mathcal{L}_i^2\rangle = 2\mathcal{C}_i\langle\lambda_i\omega_i\rangle\delta t \tag{85}$$

and use of equation (82) gives the relation:

$$\langle\mathcal{L}_i^2\rangle = 2\mathcal{C}_i kT\delta t \tag{86}$$

Then, because $n\delta t = \Delta t$ equation (81) gives:

$$\langle\Delta\alpha_i^2\rangle = 2(kT/\mathcal{C}_i)\Delta t \tag{87}$$

and $\Delta\alpha_i$ changes with time as described by the rotational diffusion coefficient

$$R_i = kT/\mathcal{C}_i \tag{88}$$

In an analogous fashion, Einstein[16] considered the translational Brownian motion of colloidal particles and showed that the translational diffusion coefficient D in an infinitely dilute solution is given by the equation:

$$D = kT/f \tag{89}$$

where f is the frictional coefficient of the particle.

8.3 Relationships between Friction Coefficients and Properties of Molecules and Liquids

8.3.1 Hydrodynamic Models

The strategy to evaluate the $\mathcal{C}_i$ and f friction coefficients for *molecules* in ordinary liquids is not completely straightforward. Usually, the results of classical hydrodynamics are used. Stokes[17] considered the special case of the motion of a macroscopic spherical particle of radius a moving with uniform velocity in a continuous fluid (i.e. infinitesimally small particles) of viscosity η. He assumed that the moving sphere carries along with it, *with no slippage*, the layer of fluid in contact with it (i.e. the surface of the sphere is 'wetted' by the fluid medium). Parenthetically, using this assumption avoids the problems of evaluating the friction coefficient between two different materials, the surface of the smooth sphere and the adjacent surface of the fluid medium. Using classical hydrodynamical principles, such as perfect streamline flow, etc., he showed that the translational movement of the sphere is impeded by the sum of two forces: (1) the force ($=4\pi\eta a$) due to pressure built up in front of it, and (2) a frictional force ($=2\pi\eta a$) parallel to its surface. Then, the friction coefficient f_0 is given by

$$f_0 = 6\pi\eta a \tag{90}$$

Einstein[16] noted that *if* one can assume that this equation applies to spherical *molecules* of radius a, the resulting value of the molecular diffusion coefficient is given by the equation

$$D = kT/6\pi\eta a \tag{91}$$

which is known as the Stokes–Einstein equation. This relationship has been experimentally verified many times for particles whose size can be measured directly, including latex particles of only 1300 Å radius in water. The increase in size

due to the monolayer of water molecules is negligible for spheres of such size.

For the case of a sphere rotating uniformly in the continuous medium, the Stokes approach gives the rotational friction coefficient

$$\mathcal{C}_i = 8\pi\eta a^3 \tag{92}$$

Following Einstein's lead in assuming that the translational friction coefficient of a molecule obeys the classical hydrodynamic formulation, Debye[3] made the analogous assumption that the rotational motion of a spherical molecule is described by rotational diffusion with the classical rotational friction coefficient given above.

Edwardes extended Stokes's calculation of the single rotational friction coefficient of a rotating sphere to evaluate the three friction coefficients for an asymmetric ellipsoid rotating in a continuous fluid. The results, as corrected by Perrin,[5] are:

$$\mathcal{C}_1 = 16\pi\eta(b^2 + c^2)/[3(b^2Q + c^2R)] \tag{93a}$$

$$\mathcal{C}_2 = 16\pi\eta(c^2 + a^2)/[3(c^2R + a^2P)] \tag{93b}$$

$$\mathcal{C}_3 = 16\pi\eta(a^2 + b^2)/[3(a^2P + b^2Q)] \tag{93c}$$

where a, b, and c are the X', Y', and Z' semiaxes of the ellipsoid, and P, Q and R are the elliptic integrals

$$P = \int_0^\infty (a^2 + s)^{-3/2}(b^2 + s)^{-1/2}(c^2 + s)^{-1/2}\,\mathrm{d}s \tag{94a}$$

$$Q = \int_0^\infty (b^2 + s)^{-3/2}(a^2 + s)^{-1/2}(c^2 + s)^{-1/2}\,\mathrm{d}s \tag{94b}$$

$$R = \int_0^\infty (c^2 + s)^{-3/2}(a^2 + s)^{-1/2}(b^2 + s)^{-1/2}\,\mathrm{d}s \tag{94c}$$

These quantities are related by the equations:

$$P + Q + R = 2/(abc) \tag{95}$$

$$a^2P + b^2Q + c^2R = S \tag{96}$$

where

$$S = \int_0^\infty [(a^2 + s)(b^2 + s)(c^2 + s)]^{-1/2}\,\mathrm{d}s \tag{97}$$

For the axially symmetric ellipsoid, with $a = b$ so that $R_1 = R_2$, the $\mathcal{C}_i$ simplify to

$$\mathcal{C}_1 = \mathcal{C}_2 = 32\pi\eta(c^4 - b^4)/\{3[(2c^2 - b^2)S - 2c]\} \tag{98a}$$

$$\mathcal{C}_3 = 32\pi\eta b^2(c^2 - b^2)/[3(2c - b^2S)] \tag{98b}$$

Also, for $b > c$,

$$S = 2(b^2 - c^2)^{-1/2}\tan^{-1}[(b^2 - c^2)^{1/2}/c] \tag{99a}$$

and for $b < c$,

$$S = 2(c^2 - b^2)^{-1/2}\ln\{[c + (c^2 - b^2)^{1/2}]/b\} \tag{99b}$$

For a sphere, where $a = b = c$, all the the $\mathcal{C}_i$ are equal to $8\pi\eta a^3$.

The relationships given above can be used to calculate the NMR correlation times for rigid molecules of a variety of shapes. Generally, for pure liquids and for solutes in solutions in which the solute molecules are not large compared to the solvent molecules, the calculated correlation times are approximately an order of magnitude greater than the values obtained from analysis of NMR relaxation time data. The discrepancy is especially great for small, nearly spherical molecules. Also, the calculated translational diffusion coefficients for such systems are significantly smaller than measured D values.[18]

8.3.2 Gierer–Wirtz Microviscosity Factor

Two difficulties will arise from use of these hydrodynamic friction coefficients. One difficulty is uncertainty of the size of small molecules. Because of the free space between molecules in a liquid, it is not sufficient to equate the molecular volume to the molar volume divided by Avogadro's number. For example, a crystal made up of closely packed spheres is 26% empty volume. Accordingly, 74% of the above molecular volume is commonly used in calculating the molecular radius for rotational correlation time estimates. Several other methods are described[18] for use in the Stokes–Einstein equation. However, using any realistic method of calculating molecular size does not solve the problem. The inclusion of a 'wetting' or 'sticking' layer of molecules would make the situation worse, because even smaller molecular volumes are generally needed to fit the experimental results to equations (91) and (92).

Another problem is that the molecule of interest is surrounded by particles of comparable size instead of a continuous fluid of infinitesimally small particles. Gierer and Wirtz[19] estimated the rotational and translational friction coefficients of a 'solute' sphere surrounded by 'solvent' spheres by formulating the liquid viscosity in terms of the kinetics of the spheres. They regard the given molecule of interest to be a sphere of radius r and the surrounding molecules to be spheres of radius r_1. The surrounding molecules form spherical layers, each of thickness $2r_1$, around the given molecule. If this central molecule is set rotating about the z axis with angular velocity ω, each layer will eventually acquire an angular velocity because of the friction between layers. In the steady state, the mth layer will have angular velocity ω_m. At equilibrium the total torque acting on the mth layer will be equal to the resistive torque on the central molecule, which is zero. The rotational friction coefficient for the central molecule is given by

$$\mathcal{C}_\mathrm{s} = 8\pi\eta r^3 f_\mathrm{r} \tag{100}$$

where

$$f_r = \frac{\rho}{6}\left[\sum_m (1+2m\rho)^{-4}\right]^{-1} \approx \left[6\rho + \frac{1}{(1+\rho)^3}\right]^{-1} \quad (101)$$

in which f_r is the rotational 'microviscosity factor', the summation is from $m = 0$ to $m = \infty$, and $\rho = r_1/r$. For translational motion, the Stokes–Einstein friction coefficient is multiplied by the microviscosity factor

$$f_t = [(3/2)\rho + 1/(1+\rho)]^{-1} \quad (102)$$

The value for pure liquids is $f_r = 0.164$. Use of these microviscosity correction factors gives correlation times and diffusion coefficients that are generally close to experimental values when the assumed molecular volume is 0.74 times the molar volume divided by Avogadro's number. However, when ρ differs from unity, the experimental f_r depends more strongly on ρ than equation (101) predicts. Generally, $\rho \neq 1$ for molecules in solutions.

8.3.3 Mutual Viscosity Formulation

The preceding calculations of the friction coefficient $\mathcal{C}_i$ use the viscosity of the fluid. This usage represents a deficiency of approach. As discussed by Hill,[20] every molecule in a pure liquid is surrounded by molecules of the same kind and the interactions between these like molecules determine both the liquid viscosity η and the friction coefficient $\mathcal{C}_i$. Despite the particular argument by which η and $\mathcal{C}_i$ are related, it is expected that they will vary in a similar manner from one substance to another. But in a dilute solution, η is determined almost entirely by the interactions between the solvent molecules while $\mathcal{C}_i$ is determined almost entirely by interactions between the solute and solvent molecules. Therefore, there is no reason to expect a general, simple relationship between η and $\mathcal{C}_i$ for solutions of different substances. To obtain an improved relationship, it is necessary to consider more closely the interactions that determine these quantities.

In the Andrade theory of liquid viscosity, the molecules in a liquid are regarded as vibrating with a frequency ν about equilibrium positions that change slowly with time. The transfer of momentum that occurs in a viscous liquid between layers moving with different velocities is due to temporary unions or collisions of adjacent molecules. These unions occur at the extremes of each vibrational swing so that, for an infinitesimal time, the two molecules move as one. Hill[20] applied this approach to a mixture of two liquids and found that the viscosity η_m of the mixture is:

$$\eta_m = f_A^2 \eta_A \sigma_A/\sigma_m + f_B^2 \eta_B \sigma_B/\sigma_m + 2 f_A f_B \eta_{AB} \sigma_{AB}/\sigma_m \quad (103)$$

where η_A and η_B are the viscosities of the pure liquids A and B, η_{AB} is the 'mutual viscosity', σ_A and σ_B are the average distances between molecules in the liquids A and B, σ_m is the average distance between molecules in the mixture, and σ_{AB} is the mean distance between a molecule of type A and an adjacent molecule of type B in the mixture. The resultant value of $\mathcal{C}_s$ for a molecule of type B is:

$$\begin{aligned}\mathcal{C}_s = {} & 6 f_A \{[(I_{AB} I_B)/(I_{AB} + I_B)] \\ & \times [(m_A + m_B)/(m_A m_B)]\} \eta_{AB} \sigma_{AB} \\ & + 3(3 - \sqrt{2})\, f_B \{[(I_{BB} I_B)/(I_{BB} + I_B)] \\ & \times [(m_B + m_B)/(m_B m_B)]\} \eta_B \sigma_B\end{aligned} \quad (104)$$

where I_B is the moment of inertia of a type B molecule, m is the mass of a molecule, and I_{AB} is the moment of inertia of molecule A about the center of mass of molecule B at the instant of collision. For a pure liquid ($f_B = 1$), the results are nearly the same as the Gierer and Wirtz approach, but for an infinitely dilute solution ($f_A = 1$), the viscosity is the mutual viscosity η_{AB} instead of the solvent viscosity. This approach explains[20] the different correlation times, found from dielectric relaxation measurements, for one solute in a variety of solvents having the same viscosity and for the relatively short correlation times found for solutes in high viscosity solvents.

In studies of the dielectric relaxation times of molecules of a wide range of size in solution, the use of equation (92) gives friction coefficients that agree[21] with experiment when the molecular volume is at least three times that of the solvent molecule. Furthermore, the Hill theory is inferior for large solute molecules but it is superior for small solute molecules. Therefore, use of the rotational friction coefficients that are given in equations (92)–(99) to evaluate the correlation times for rotational diffusion of ellipsoids should provide a good approximation for large molecules in a solvent of small molecules.

8.4 Deficiencies of Viscosity/Rotational Diffusion Models

Since the earliest studies on molecular reorientational phenomena by nuclear magnetic relaxation, many have attempted to find a fundamental connection between orientational correlation times and macroscopic viscosity. Macroscopic viscosity, or shear viscosity, is defined as the resistance to shear if a thin liquid layer is moved ('sheared') between parallel plates. The physical dimension of viscosity is force times time divided by area. This tells us that we deal with momentum transfer. The momentum transfer tries to equalize the velocities of the moving layers. As indicated in Section 8.3.1, the hydrodynamic boundary conditions for the viscosity dependence of the orientational function of a spherical molecule have been defined in terms of a 'rough sphere'; the surface of the reorienting molecule entrains its neighbors. A perfectly slipping sphere would have zero viscosity. On the other hand, we know that, on the molecular level, interactions take place through impulsive collisions between only a few neighbors. It is therefore not surprising that such a macroscopic rough sphere model overestimates $\mathcal{C}_s$. The microviscosity and mutual viscosity approaches are different attempts to formulate relationships that retain the idea of smooth spheres that, nevertheless, have surface friction. The situation is simpler for systems of small molecules of ellipsoidal shape since their reorientational motion displaces their neighbors; the rotational motion of a perfectly slipping ellipsoid would show a viscosity dependence.

The NMR relaxation behavior of several pure liquids of small molecules provides instructive cases. When the

molecules are rigid, all of the rotational diffusion models described above predict that the correlation times are directly proportional to the quantity η/T. However, this relationship is not always obeyed. Perdeuterobenzene provides a good example of this behavior. The temperature dependence of the deuteron T_1 value obeys[22] an Arrhenius equation with an apparent activation energy E_a = 7.78 kJ mol^{-1}. On the other hand, the temperature dependence of η/T is much greater; an Arrhenius equation is obeyed, but with E_a = 13.05 kJ mol^{-1}. Besides varying temperature, the viscosity can be adjusted by changing the pressure on the liquid. The pressure dependence of the benzene viscosity[23] is described by an activation volume of 20.5 cm^3 mol^{-1}. The pressure dependence of the deuteron T_1 of perdeuterobenzene is much less,[24] described by an activation volume of only 0.44 cm^3 mol^{-1}. On the other hand, the pressure dependence of the translational diffusion coefficient of benzene[25] obeys an activation volume of 20.0 cm^3 mol^{-1}, nearly identical to that of the viscosity. This means that the translational frictional coefficient is directly coupled to the viscosity, but the effective rotational friction coefficient is largely decoupled from the viscosity.

Acetonitrile, CH_3CN,[26] is another instructive case. In the temperature range from 20 °C to 50 °C, the temperature dependence of η/T obeys an Arrhenius equation with E_a = 8.66 kJ mol^{-1}. This molecule has an electric dipole moment that is parallel to the C–N axis of the molecule and the ^{14}N nucleus experiences an electric quadrupole interaction in the same direction. The temperature dependence of the dielectric relaxation time (E_a = 8.28 kJ mol^{-1}) and of the ^{14}N T_1 (7.9 kJ mol^{-1}) are nearly equal to the above value for η/T. This shows that the rotational friction coefficient for reorientation of the C–N molecular axis at a given temperature is directly proportional to the viscosity. Also, the microviscosity model of Gierer and Wirtz,

$$\tau_c \equiv V\eta/6kT \tag{105}$$

where V is the molecular volume, yields at room temperature τ_c = 0.89 × 10^{-2} s. This value is close (81%) to the value found from the ^{14}N measurements of T_1. The deuteron T_1 values of CD_3CN, however, have a smaller temperature dependence with E_a = 5.73 kJ mol^{-1}. This temperature dependence behavior shows that the rotational friction coefficient of the C–N axis of the molecule is directly proportional to the viscosity but that of the other molecular axes is relatively uncoupled from the viscosity. Also, at 25 °C, the effective deuteron correlation time is 0.340 × 10^{-12} s, which is much smaller than the value 1.104 × 10^{-12} s for ^{14}N. Evidently, the molecular reorientation rate about the C–N axis is much greater than that about an axis that is perpendicular to the C–N direction. If the molecule reorients like a rigid axially symmetric ellipsoid, use of equations (32) and (34)–(36) gives R_3 = 10.35 × R_2. Also, the temperature dependence of R_3 is small, described by an Arrhenius equation with E_a = 3.05 kJ mol^{-1}.

Toluene provides another informative case[27] of motions of small molecules. The temperature dependence of η/T is well described by an Arrhenius equation with E_a = 11.51 kJ mol^{-1}. This value is larger than that of the T_1 of the ring deuterons of perdeuterotoluene (8.20 kJ mol^{-1}) and that of the methyl group deuterons of perdeuterotoluene (5.77 kJ mol^{-1}). Toluene has a small electric dipole moment (0.3–0.4 D) that is parallel to the methyl group symmetry axis. The dielectric relaxation time is approximately three times the NMR correlation time of the ring deuterons and its temperature dependence is essentially the same as that of this correlation time. Also, the T_1 values of the *ortho* and *para* ring deuterons are apparently equal. These dielectric and NMR relaxation results indicate that the ring of the toluene molecule reorients approximately like a sphere with $R_1 = R_2 = R_3$. However, the observation that the activation energy for the dielectric and NMR relaxation times is significantly smaller than that of η/T suggests that the molecular rotational friction coefficients of the ring are not directly related to the liquid viscosity.

Another significant observation is that the methyl deuterons have a much longer T_1 than the ring deuterons (4.88 s compared with 0.943 s). This longer T_1 and the smaller activation energy mean that the methyl group of the toluene molecule is internally reorienting rapidly about its symmetry axis. The intramolecular energy barrier to internal rotation of the methyl group in molecules such as toluene is very small, only 0.059 kJ mol^{-1},[28] especially in comparison with the hinderance from interactions with neighboring molecules. Here, reorientation of the methyl group about its symmetry axis is completely independent from the reorientation of the remainder of the molecule, and the terms involving R_3 in equations (49) and (50) are omitted. Analysis[27] of the data using the 'internal' rotational diffusion model gives an apparent activation energy of 3.47 kJ mol^{-1}. Use of the 'internal' 120° jump model gives a similar value, 3.89 kJ mol^{-1}. Many other molecules have rapid internal reorientation of the methyl group, including methanol, acetone, acetic anhydride, ethanol, acetic acid, *t*-butanol, *p*-xylene, and acetophenone.

The rapid reorientation of the methyl group about its symmetry axis, the low values of apparent activation energy of this motion, and the decoupling of the rotational friction coefficient of benzene from the liquid viscosity may show that the model of rotational diffusion of a rigid ellipsoid may provide an incomplete description of molecular rotation of small molecules.

Relationships among viscosity, molecular reorientational motions, and molecular translational diffusion depend on the physical model that is assumed in the derivation. The Stokes–Einstein–Debye–Perrin model is based on the idea of particles surrounded by a continuous medium that is characterized by viscosity. The Gierer–Wirtz and Hill methods assume that the molecule of interest is surrounded by other particles and use specific physical models of interactions of spheres to interrelate the quantities. In all models, the system is at thermal equilibrium and subject to the general laws of thermodynamics and statistical mechanics. Different models may be appropriate for different molecular liquids. Steric considerations and the NMR observation[29] that benzene molecules rotate in the solid state suggest that liquid benzene molecules could rotate much faster about the C_6 molecular symmetry axis than about a C_2 axis. Such C_6 rotation requires less accommodation of the surrounding molecules than is required by a C_2 rotation. Similarly, for such molecules as toluene and acetonitrile, the rotation of a methyl group about its C_3 symmetry axis requires less accommodation by the surroundings than the rotation of the symmetry axis itself. Because the viscosity is likely to reflect the motions

that experience the greatest hindrances, the above C_6 and C_3 rotations could be largely uncoupled from the liquid viscosity. However, these rotations need not be completely free or frictionless. For example, the electric dipole moments of the individual C–H or C–D bonds could interact with the fluctuating local electric dipole fields due to the nearby molecules and hinder this motion.

9 CORRELATION FUNCTIONS FOR A 'NEARLY-FREE' ROTOR ATTACHED TO AN ELLIPSOID

The rotational diffusion model is a limiting case of the Langevin model. The internally reorienting part of the molecule may be treated as a classical rigid rotor that rotates about one axis. This rotational problem is analogous[30] to the case of translational motion.[31] The distribution of rotational angular velocities follows the Boltzmann energy distribution law. The angular frequency ω of a rotor changes in time as described by

$$\mathrm{d}\omega/\mathrm{d}t = -[\xi\omega + F(t)]/I \tag{106}$$

where ξ is a rotational friction coefficient, I is the moment of inertia, and $F(t)$ is a randomly fluctuating torque. The fluctuating part is an instantaneous angular velocity independent, statistically defined force (its autocorrelation function decays much faster than that of the angular frequency) that causes random changes in the angular frequency. The value of the rotational angle $\phi''(\tau)$ of a rotor with initial angular velocity ω_i obeys a normal Gaussian distribution with a mean value

$$\langle\phi''(\tau)\rangle = \omega_\mathrm{i}(I/\xi)\{1 - \exp[-(\xi/I)\tau]\} \tag{107}$$

When ξ is small, the value of $\langle\phi''(\tau)\rangle$ is $\omega_\mathrm{i}\tau$. The averages $\langle\cos\phi''(\tau)\rangle$ and $\langle\cos 2\phi''(\tau)\rangle$ that appear in equations (38)–(40), obtained by a final averaging over the distribution of ω_i values, are:

$$\langle\cos\phi''(\tau)\rangle = \exp\{-(IkT/\xi^2)[\xi\tau/I + \exp(-\xi\tau/I) - 1]\} \tag{108a}$$

$$\langle\cos 2\phi''(\tau)\rangle = \exp\{-4(IkT/\xi^2)[\xi\tau/I + \exp(-\xi\tau/I) - 1]\} \tag{108b}$$

When the rotational friction coefficient is sufficiently great, we obtain an exponentially decaying function in τ as given in equation (44) with $R_\mathrm{i} = kT/\xi$. This is the rotational diffusion limit. However, when the friction coefficient is sufficiently small, at short τ values we obtain exponentially decaying functions in τ^2 as given by

$$\langle\cos\phi''(\tau)\rangle = \exp[-(kT/2I)\tau^2] \tag{109a}$$

$$\langle\cos 2\phi''(\tau)\rangle = \exp[-(2kT/I)\tau^2] \tag{109b}$$

In this limit, the average values are independent of the friction coefficient and inertial effects dominate. The rotational motions are decoupled from the viscosity of the liquid. The temperature dependencies predicted for these limiting cases are greatly different. Because the friction coefficient is likely to decrease with an increase in temperature, the temperature dependence in the rotational diffusion limit is expected to be much greater than in the inertial limit.

Although the temperature dependence may be used as a criterion between the applicability of these models, the value of R_i obtained from data analysis with the average angular velocity $(kT/I)^{\frac{1}{2}}$ provides another criterion. The rotational diffusion case may apply when the time required for the internal orientation to change by one radian calculated from the value of R_i obtained from data analysis, $(1/2R_\mathrm{i})$, is large compared to the time required by free rotation, $(I/kT)^{\frac{1}{2}}$. The motion of of the methyl groups (CD_3) at room temperature falls between these two limits.[27] Further information about methyl group reorientation is available as follows. Equation (108) shows that I/ξ is the time constant for frictional changes in the rotational velocity of the CD_3 rotor. The quantity $(kT/I)^{\frac{1}{2}}$ is the average rotational angular velocity. The product of these two quantities, $(IkT/\xi^2)^{\frac{1}{2}}$, is the number of radians through which the CD_3 group rotates before its angular velocity changes appreciably. For the CD_3 groups of perdeuterotoluene at 298 K, this angle is 16°. This value is too large for rigorous application of the rotational diffusion model. Nevertheless, it is sufficiently small so that this model provides a convenient mathematical form for data analysis.

The experimental correlation times for many small rigid molecules in pure liquids and solutions obey a linear relationship with the liquid viscosity but have a nonzero intercept at zero viscosity. The intercept yields a correlation time[2] that appears to equal the time interval $(2\pi/9)(I/kT)^{\frac{1}{2}}$. This is the time required for a freely rotating molecule to turn through an angle of 41°, the angle for the correlation function of a second-order Legendre polynomial to drop to 1/e of its original (at $\tau = 0$) value. This result, which also shows that the correlation time is not directly proportional to viscosity at constant temperature, provides another indication that rotational diffusion may not accurately describe the motions of small molecules and the inertial effects are important in the rotational motions of small liquid molecules.

10 SCRUTINY OF THE MATHEMATICAL FORM OF CORRELATION FUNCTIONS

Realistically, at short enough times molecular collisions have not yet occurred and, consequently, molecular motion is purely kinetic. Because of this, the real correlation function has no first-order term in τ(it has zero slope at $\tau = 0$). Consequently, the rotational diffusion model fails with the first-order term and the spectral density derived from it is in error. We cannot use it to give a credible description of the details of molecular motion, especially for small molecules, since it is invalid for initial time intervals where the correlation function is least 'scrambled' by complicated orientation–collision events. This is dramatically shown by the nonexponential infrared and Raman spectral correlation functions[2] obtained in measurements on small molecules. NMR relaxation measurements made over a range

of frequencies do not reveal this dramatic behavior because the spectral density at ordinary Larmor frequencies is merely the integral of the correlation function. However, at sufficiently 'high' Larmor frequencies, the Lorentzian spectral density equation would not be obeyed. When this happens, and if the Larmor frequency is varied on both sides of the 'T_1 minimum', serious errors could occur if we interpret the relaxation data by use of the Lorentzian spectral density equation.

When the angle of free rotation is very large, the correlation functions derived for rotational diffusion of an asymmetric ellipsoid are no longer a reasonable approximation. In the spirit of Brownian rotational motion that is based on the Langevin equation in Section 9, the correlation functions for a rotating sphere with three degrees of rotational freedom are given by:

$$\langle F_{\mathrm{h}}(t)F_{\mathrm{h}}^{*}(t+\tau)\rangle = \langle F_{\mathrm{h}}(t)F_{\mathrm{h}}^{*}(t)\rangle \exp\{-6(IkT/\mathcal{C}_{\mathrm{s}}^{2}) \times[\mathcal{C}_{\mathrm{s}}\tau/I + \exp(-\mathcal{C}_{\mathrm{s}}\tau/I) - 1]\} \quad (110)$$

At long times, this function decays exponentially with time. At very short times, the results for a freely rotating sphere are obtained. At 'low' frequencies a plot of spectral density vs. friction coefficient $\mathcal{C}_{\mathrm{s}}$ has a nonzero intercept equal to $(\pi/12)^{\frac{1}{2}}(I/kT)^{\frac{1}{2}}$. The spectral density function at high frequencies would deviate significantly from a Lorentzian function. When the friction is very large so that $\mathcal{C}_{\mathrm{s}}\tau/I \gg 1$, we obtain from equation (110) the results for rotational diffusion of a sphere.

There is a wide variety of correlations between NMR spectral densities of liquid molecules and macroscopic liquid properties such as viscosity. These correlations are sensitive to molecular size and intermolecular interactions. The spectral densities of large molecules appear to obey rotational diffusion equations with friction coefficients calculated with hydrodynamic models. Those for small molecules may be approximated by microviscosity and mutual viscosity formulations. Experiments that include NMR relaxation measurements at very high B_0 values and wide temperature ranges may yield more information on the rotational motions of molecules in liquids.

11 RELATED ARTICLES

Coupled Spin Relaxation in Polymers; Molecular Motions: T_1 Frequency Dispersion in Biological Systems; Polymers: Relaxation and Dynamics of Synthetic Polymers in Solution; Protein Dynamics from NMR Relaxation; Protein Structures: Relaxation Matrix Refinement; Relaxation: An Introduction; Relaxation of Coupled Spins from Rotational Diffusion; Relaxation Processes: Cross Correlation and Interference Terms; Relaxation Theory: Density Matrix Formulation; Relaxation Theory for Quadrupolar Nuclei; Relaxation of Transverse Magnetization for Coupled Spins; Relaxometry of Tissue; Spin–Rotation Relaxation Theory

12 REFERENCES

1. A. Abragam, *The Principles of Nuclear Magnetism*, Clarendon Press, Oxford, 1961.
2. W. G. Rothschild, *Dynamics of Molecular Liquids*, John Wiley & Sons, New York, 1984.
3. P. Debye, *Polar Molecules*, Dover Publications, New York, 1945.
4. N. Bloembergen, E. M. Purcell, and R. V. Pound, *Phys. Rev.*, 1948, **73**, 679.
5. F. Perrin, *J. Phys. Radium*, 1934, **5**, 497.
6. F. Perrin, *J. Phys. Radium*, 1936, **7**, 1.
7. D. E. Woessner, *J. Chem. Phys.*, 1962, **37**, 647.
8. D. E. Woessner, B. S. Snowden, Jr., and G. H. Meyer, *J. Chem. Phys.*, 1969, **50**, 719.
9. D. E. Woessner, *J. Chem. Phys.*, 1962, **36**, 1.
10. D. E. Woessner, *J. Chem. Phys.*, 1965, **42**, 1855.
11. G. Lipari and A. Szabo, *J. Am. Chem. Soc.*, 1982, **104**, 4546.
12. G. Lipari and A. Szabo, *J. Am. Chem. Soc.*, 1982, **104**, 4559.
13. M. Dellwo and A. J. Wand, *J. Am. Chem. Soc.*, 1993, **115**, 1886.
14. J. F. Harmon, *J. Magn. Reson.*, 1978, **31**, 411.
15. C. S. Johnson, Jr., *J. Magn. Reson.*, 1976, **24**, 63.
16. A. Einstein, *Ann. Phys.*, 1905, **17**, 549.
17. G. Stokes, *Trans. Cambridge Philos. Soc.*, 1856, **9**, 5.
18. J. T. Edward, *J. Chem. Educ.*, 1970, **47**, 261.
19. A. Gierer and K. Wirtz, *Z. Naturforsch.*, 1953, **8a**, 532.
20. N. E. Hill, *Proc. Phys. Soc. London*, 1954, **B67**, 149.
21. R. J. Meakins, *Trans Faraday Soc.*, 1958, **54**, 1160.
22. D. E. Woessner, *J. Chem. Phys.*, 1964, **40**, 2341.
23. P. W. Bridgman, *Proc. Am. Acad. Arts Sci.*, 1926, **61**, 57.
24. D. E. Woessner and B. S. Snowden, Jr., *J. Chem. Phys.*, 1970, **52**, 1621.
25. D. W. McCall, D. C. Douglass, and E. W. Anderson, *J. Chem. Phys.*, 1959, **31**, 1555.
26. D. E. Woessner, B. S. Snowden, Jr., and E. Thomas Strom, *Mol. Phys.*, 1958, **14**, 265.
27. D. E. Woessner and B. S. Snowden, Jr., *Adv. Mol. Relaxation Processes*, 1972, **3**, 181.
28. H. D. Rudolph, H. Breizler, A. Jaeschke, and P. Wendling, *Z. Naturforsch.*, 1967, **22a**, 940.
29. E. R. Andrew and R. G. Eades, *Proc. R. Soc. London*, 1953, **A218**, 537.
30. W. A. Steele, *J. Chem. Phys.*, 1963, **38**, 2404.
31. G. Uhlenbeck and L. S. Ornstein, *Phys. Rev.*, 1930, **36**, 823.

Biographical Sketches

Donald E. Woessner. *b* 1930. A.B., 1952, Ph.D. (supervisor Herbert Gutowsky), 1957, Chemistry, University of Illinois, USA. Postdoctoral work at University of Illinois (with Herbert Gutowsky). Successively senior research chemist, research associate, senior research associate, Mobil Research and Development Corporation, Dallas, Texas, USA. Currently Adjunct Assistant Professor of Radiology, The University of Texas Southwestern Medical Center at Dallas, 1992–present. Approx. 72 publications. Research specialties: NMR relaxation and molecular motions in liquids, relationships of NMR relaxation of hydrogen and ionic nuclei to motions, structure, and order in aqueous heterogeneous systems and biological tissue.

Carbon-13 Relaxation Measurements: Organic Chemistry Applications

George C. Levy and Deborah J. Kerwood

Informatrix Inc., Ann Arbor, MI, USA

1	Introduction	1
2	Measurements of ^{13}C Relaxation Parameters	5
3	Overview of Applications for ^{13}C Spin Relaxation Measurements	6
4	Summary	9
5	References	9

1 INTRODUCTION

Paralleling other developments in ^{13}C NMR,[1,2] interest in ^{13}C spin relaxation data increased greatly with the availability in the early 1970s of Fourier transform methods.[1–3] This interest initially arose for two reasons. First, it was necessary to have information about spin relaxation behavior in order to achieve sensitivity advantages approaching those theoretically possible in Fourier transform NMR experiments. Second, spin relaxation data can give chemical and dynamic molecular structural data that are either difficult or impossible to obtain from other kinds of measurements.

The ^{13}C nucleus is particularly well suited for spin relaxation studies for several reasons:

1. Since carbon atoms are usually found at the backbone of molecules, interpretation of ^{13}C relaxation behavior is generally not complicated by intermolecular relaxation processes, unlike the situation for ^{1}H and ^{19}F nuclei.
2. ^{13}C spectra are primarily observed under proton-decoupled conditions, where each carbon in the molecule is represented by a single spectral line whose spin–lattice (T_1) and spin–spin (T_2) relaxation times can be governed by single exponential time constants.[4]
3. The rather large chemical shift range of the ^{13}C nucleus makes it possible to resolve virtually all individual carbons, even in complex molecules. Thus, multiple sites are often available at which to probe a molecule's overall and internal motions.
4. Since ^{13}C is a rare spin (low natural abundance), consideration of ^{13}C–^{13}C dipolar interactions or of the phenomenon of spin diffusion[5] is usually not necessary. This greatly simplifies the interpretation of ^{13}C relaxation rates.

Carbon-13 relaxation times provide significant information in many areas of chemistry. Interpretation of ^{13}C relaxation data in terms of molecular dynamics (e.g. internal and overall molecular motions) provides the chemist with a unique and powerful probe into the detailed structure of organic molecular systems, and provides the theoretician with much needed motional data with which to test models for the microdynamic behavior of molecular systems. This potential for chemical insight, coupled with the ease of obtaining ^{13}C relaxation data on commercially available FT NMR spectrometers, argues for a basic understanding of NMR spin relaxation parameters by most chemists. This article considers the topic of ^{13}C spin relaxation in three overall parts: (1) a description of ^{13}C spin relaxation processes, (2) a short section outlining experimental methods, and (3) discussions of several types of applications in organic chemistry.

The magnetic resonance parameters that are relevant to molecular dynamics are the nuclear spin relaxation times T_1 and T_2 and (usually) for the ^{13}C nucleus, the ^{13}C–^{1}H nuclear Overhauser effect (NOE).

For a nucleus with a spin quantum number equal to $\frac{1}{2}$ (e.g., ^{1}H, ^{13}C, ^{19}F, ^{31}P, etc), there are two allowed orientations for each magnetic moment vector relative to an applied field, $\boldsymbol{B}_0$. If it is assumed that the spin system is in thermal contact with its environment and the nuclei do not strongly interact with one another, then in the absence of additional irradiation, a Boltzmann distribution of nuclei will be established among the two resultant energy states. The redistribution of populations arises from interactions of the nuclei with their surroundings. This interaction is the so-called spin–lattice relaxation process and is characterized by a relaxation time T_1, which represents the timescale for energy transfer between the spin system and the lattice or environment. (For a liquid, the term 'lattice' is taken essentially as the translational, rotational, and other degrees of freedom of the molecular system.)

The resonant condition in NMR is accomplished by imposing a radiofrequency field $\boldsymbol{B}_1$ at right angles to $\boldsymbol{B}_0$. When B_1 is equal to the nuclear Larmor frequency, two effects occur in the spin system. First, some nuclei in the lower energy state absorb energy from $\boldsymbol{B}_1$, which results in a transition to the upper energy state and a decrease in the net population difference between the states. This process decreases the value of M_z, the magnetization along the z axis coincident with $\boldsymbol{B}_0$. The second effect of B_1 is to generate a phase-coherent magnetization in the transverse plane, M_{xy}. After excitation, the nuclei tend to get out of phase again, thereby decreasing M_{xy}. The time constant for this process is the spin–spin relaxation time, T_2. Loss of phase coherence arises because fluctuating local magnetic fields augment or decrease $\boldsymbol{B}_0$, thus causing a spread of precessional frequencies among the individual nuclei and a corresponding loss of phase coherence. A second process tending to destroy the phase coherence arises from a mutual spin flip of two nuclei, if they are initially antiparallel and have precessing magnetic fields at the proper frequency. Although this interaction conserves the energy of the spin system, it does produce an uncertainty in the energy since it limits the lifetime of a state. The magnetization M_{xy} will decay to zero as the spins resume a random precession. When $M_{xy} = 0$, the net magnetization vector lies along the z direction; thus $\boldsymbol{M} = M_z$. However M_z may or may not at that moment equal $\boldsymbol{M}_0$. Simultaneous with the decay of M_{xy} is the restoration of M_z magnetization. The timescale for M_z to reassume the value $\boldsymbol{M}_0$ is determined by the spin–lattice relaxation time. From the above arguments, $T_1 \geq T_2$.

Bloch viewed both of the magnetic relaxation processes as first-order decays. The usual equations for describing these decays are

$$\frac{\mathrm{d}M_z}{\mathrm{d}t} = \frac{-(M_z - M_0)}{T_1} \qquad (1)$$

and

$$\frac{dM_{xy}}{dt} = \frac{-M_{xy}}{T_2} \tag{2}$$

These simple equations have been found to provide, in most cases, a good description of relaxation phenomena pertinent to much liquid-phase ^{13}C NMR.[6,7] The primary concern of this article will be the spin–lattice relaxation time, T_1, and the associated $^{13}C-^{1}H$ NOE; in general, it is more difficult to measure ^{13}C T_2 values accurately.

Unlike most molecular relaxation processes in liquids, the timescale for the spin–lattice relaxation process is relatively long because the nuclear spin system is only weakly coupled to the other motions of the system. Experimental values of ^{13}C T_1 values are correspondingly of the order of 10^{-2}–10^{2} s and are usually in the range of 0.1 s to several seconds for typical organic compounds as neat liquids or in solution[6,7] (provided the system is free of paramagnetic impurities). While this order of time constant indicates that the interactions governing the spin–lattice relaxation process are relatively inefficient, it is nevertheless only because of these weak interactions that nuclear spin relaxation occurs.

The coupling of the nuclear spin system to the lattice originates from the interaction of individual nuclear moments with fluctuating local magnetic fields, $\boldsymbol{B}_{loc}$, produced by the lattice at the nuclear site. If the various $\boldsymbol{B}_{loc}$ quantities have frequency components at values appropriate to the nuclear spin transition frequency, then energy can be transferred to the lattice and spin relaxation induced. The time dependence of the local fields arises from the overall and internal motions of the molecule, and other dynamic processes. To develop this link conceptually between $\boldsymbol{B}_{loc}$ and T_1, it is necessary to consider the origin and some of the properties of the lattice fields.

In fluids, typical sources of $\boldsymbol{B}_{loc}$ are nuclear and electromagnetic dipoles, electric quadrupoles (for nuclei with spin $I > \frac{1}{2}$), anisotropy of the chemical shielding tensor, modulation of scalar coupling, and rotation of the molecule or group itself (spin rotation). The efficiency of any one of these sources in causing relaxation depends on both the amplitude of the fluctuations in $\boldsymbol{B}_{loc}$ and the timescale of those fluctuations. The mathematical description of the interaction of the spin with $\boldsymbol{B}_{loc}$ is similar for each relaxation mechanism.

Since the interaction of a ^{13}C nucleus with the magnetic field arising from an attached proton ($^{13}C-^{1}H$ nuclear dipole–nuclear dipole interaction) is most often the pathway useful in broad applications of ^{13}C spin–lattice relaxation,[1,6,7] a brief account of the origin of the equation relating T_1 to this interaction is given immediately below.

1.1 The Dipole–Dipole Relaxation Mechanism

The prime source of ^{13}C spin relaxation in most diamagnetic liquids arises from the local magnetic fields produced by bonded or nearby protons. The instantaneous dipolar magnetic field (which may be as large as several gauss) that induces T_1 relaxation is proportional to the square of the magnetogyric ratios of both spins.

For a rigid system of intramolecular dipoles, molecular tumbling imparts the time-dependence to $\boldsymbol{B}_{loc}$ through the angle Θ between the through-space vector between the two dipoles, and $\boldsymbol{B}_0$ (for carbons with directly bonded protons, this vector is of course coincident with the C–H bond itself). For the intermolecular case, and for intramolecular relaxation in flexible molecules, both the angle Θ and the distance between the dipoles are time-dependent, owing to relative translation as well as rotational motion. Intermolecular interactions tend to be attenuated rapidly owing to the r^{-3} dependence of $\boldsymbol{B}_{loc}$ for the two spins and the consequent r^{-6} dependence for T_1 relaxation of the ^{13}C nucleus. This result has important consequences for ^{13}C relaxation.

Another case of dipolar interaction is where the relaxing field has its origin with an unpaired electronic spin rather than a nuclear spin: for example, from any paramagnetic species present in the sample. Since the magnetic moment of the electron is roughly three orders of magnitude greater than nuclear moments, the fields are correspondingly more intense. When modulated by molecular tumbling, such fields can then induce very efficient nuclear spin relaxation, even at low concentration in a sample.

1.1.1 Properties and Formal Description of $\boldsymbol{B}_{loc}$

By assuming that the molecules constituting the liquid can be described as particles undergoing Brownian motion, the local dipolar field then has the following properties:[8]

1. $\langle \boldsymbol{B}_{loc}(t_0) \rangle = 0$, where $\langle\ \rangle$ is an average over time.
2. $\langle \boldsymbol{B}_{loc}{}^{2}(t) \rangle \neq 0$; i.e., the mean of the square is nonzero.
3. $\langle \boldsymbol{B}_{loc}(t_0) \cdot \boldsymbol{B}_{loc}(t + \tau) \rangle = 0$, provided that τ is sufficiently long.

At long τ, the value of $\boldsymbol{B}_{loc}$ at time $t + \tau$ does not in any manner depend on the value at time t. If τ is sufficiently short, then the quantity is expected to have a nonzero value.

Mathematically, these characteristics are embodied in the so-called time-dependent correlation function $G(t)$ of $\boldsymbol{B}_{loc}$.[9] In a qualitative sense, such a function describes the persistence of a dynamical property of the system before being averaged out by molecular motions in the liquid, and is of particular value when two physical systems are weakly coupled, as is the case for the nuclear spin system and its lattice. The autocorrelation function of $\boldsymbol{B}_{loc}$ is given by the ensemble average

$$G(t) = \langle \boldsymbol{B}_{loc}(t_0) \cdot \boldsymbol{B}_{loc}(t_0 + \tau) \rangle_t \tag{3}$$

where the time-dependence is that produced by the molecular motion. The average is over an ensemble at the reference time t. Since $\langle \boldsymbol{B}_{loc}(t) \cdot \boldsymbol{B}_{loc}(t + \tau) \rangle$ is independent of the reference time, $G(t)$ is designated a correlation function of a stationary random process; $G(t)$ is independent of t_0 and is both a real and even function of τ.[9] If the time origin is taken as $t = 0$, then

$$G(\tau) = \langle \boldsymbol{B}_{loc}(0) \bullet \boldsymbol{B}_{loc}(\tau) \rangle_0 \tag{4}$$

and $G(\tau)$ then describes the timescale for the decay of inherent motional order in the system. Information on the molecular system is dependent on the existence of $G(\tau)$, and as $G(\tau)$ decays toward zero so does knowledge of the dynamical processes at the prior time.

The Fourier transform of $G(\tau)$, the spectral density function, $J(\omega)$ provides the means of characterizing the frequency distribution and magnitude of the fluctuations in $\boldsymbol{B}_{loc}$; $J(\omega)$

represents a transformation from the time to the frequency domain. It is given by

$$J(\omega) = \int_{-\infty}^{+\infty} G(\tau) e^{i\omega\tau} \, d\tau \tag{5}$$

and represents the power available at angular frequency ω to relax the spin system. Equation (5) indicates that, if $G(\tau)$ decays slowly, information [through $J(\omega)$] will persist for a long time and the spectral lines will be narrow. If $G(\tau)$ decays rapidly, information is lost quickly and the spectral peaks will be broad.

Evaluation of equation (5) requires a description of the decay of $G(\tau)$. For a liquid, assuming exponential decay for $G(\tau)$

$$G(\tau) = \langle B_{loc}^2(0) \rangle_0 e^{-\tau/\tau_e} \tag{6}$$

where τ_e is the characteristic exponential time constant (correlation time) in which it is assumed motional order decays out of the system. It can be further assumed that the different spatial components of $\boldsymbol{B}_{loc}$ are uncorrelated, i.e., $\langle \boldsymbol{B}_{loc}(x) \boldsymbol{B}_{loc}(y) \rangle = 0$ but for isotropic motion they share the same correlation time, τ_c. Substitution of equation (6) into equation (5) and integration results in

$$J(\omega) = \langle B_{loc}^2(0) \rangle \frac{2\tau_c}{1 + \omega^2 \tau_c^2} \tag{7}$$

From equation (7) it is evident that $J(\omega)$ is a maximum at $\omega = 0$ and is approximately constant over the range $\tau_c < \omega$; it decreases with increasing frequency as ω approaches $1/\tau_c$. The total spectral density, as a sort of probability distribution, is constant and independent of τ_c. Thus, variation in τ_c merely changes the distribution of 'spectral density' over the entire frequency spectrum.

This result indicates that T_1 goes through a minimum as a function of τ_c. Plots of T_1 versus τ_c as a function of spectrometer operating frequency are given in Figure 1. The left side of Figure 1, where T_1 is independent of spectrometer frequency, is called the region of motional narrowing. In this regime $J(\omega)$ is given by

$$J(\omega) = 2\langle B_{loc}^2(0) \rangle \tau_c \tag{8}$$

Liquids or solutions for which τ_c is within the motional narrowing limit include many organic molecules at or above room temperature. Use of increasing NMR magnetic field strengths, however, places more molecules outside the motional narrowing limit (see Figure 1). When the motional narrowing limit is valid, and when motion is isotropic, $^{13}C-^{1}H$ dipole–dipole relaxation is described by

$$\frac{1}{T_1} = \sum_{i=1}^{n} \frac{\gamma_C^2 \gamma_H^2 \hbar^2}{r_{CH}^6} \tau_c \tag{9}$$

where the summation is over all nearby protons, and the $r^6{}_{CH}$ values reflect the various ^{13}C,H internuclear distances.

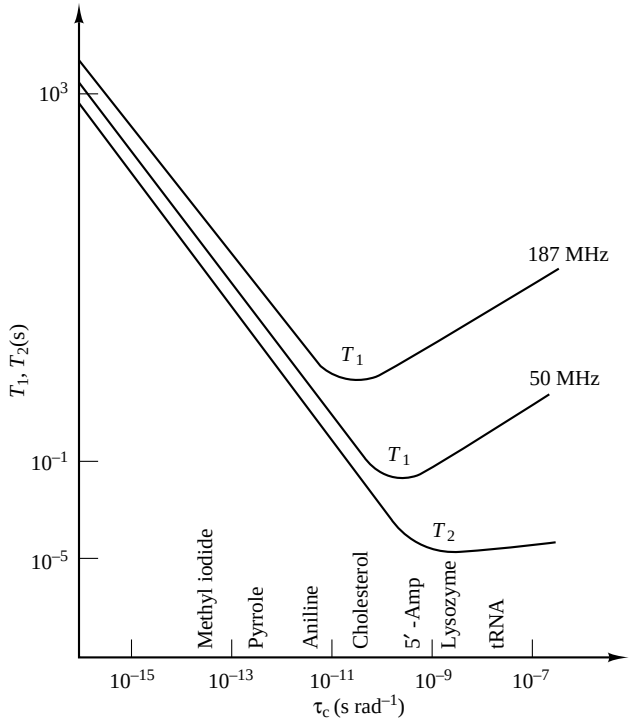

Figure 1 Spectral density $J(\omega)$ as a function of frequency for various values of the correlation time, τ_c (ω_0 corresponds to the nuclear Larmor frequency)

In the case of a ^{13}C nucleus that has one or more directly attached protons, longer range proton interactions can generally be ignored and equation (9) simplifies to:

$$\frac{1}{T_1} = \frac{N_H \hbar^2 \gamma_C^2 \gamma_H^2 \tau_c}{r_{CH}^6} \tag{10}$$

where N_H is the number of directly attached protons and $r_{CH}{}^{-6}$ is the C–H bond length. In those cases where the molecular tumbling is anisotropic or where internal motions are present, ^{13}C dipolar relaxation (T_1 and T_2) is described by more complex equations, described elsewhere.[8] Many applications can utilize equation (10), or approximate treatments that model motional anisotropy in terms of three orthogonal rotational diffusion constants (D_x, D_y, D_z).

1.2 Other ^{13}C Spin Relaxation Mechanisms

As described above, many carbons, particularly CH_x carbons, are relaxed completely by $^{13}C-^{1}H$ dipole–dipole interactions. However, at increasingly high magnetic fields, and for other selected cases, a given carbon's relaxation may be dominated by other mechanisms.[10] In applications of spin relaxation, it is of *paramount importance for the correct interpretation of results, that the investigator recognize all significant contributions to relaxation for the specific ^{13}C nuclei being examined.*

Briefly, the other ^{13}C spin relaxation mechanisms commonly encountered are: (a) dipolar interactions (DD) with other nuclides (e.g., ^{19}F, ^{31}P, sometimes ^{13}C, metal nuclei, etc.);

(b) dipolar interactions with unpaired electron spins (added paramagnetic agents, dissolved oxygen, etc.); (c) chemical shift anisotropy (CSA) relaxation of ^{13}C nuclei which occurs through the anisotropy of the ^{13}C shielding tensor; because CSA relaxation depends on $B_0{}^2$ as well as the square of the shielding anisotropy, it is significant, especially at higher $\boldsymbol{B}_0$, for sp^2 and sp carbons, and is often dominant at high $\boldsymbol{B}_0$ for those carbons not having directly attached protons; (d) ^{13}C relaxation through scalar interactions is common for spin–spin relaxation (linewidths), but the formalism restricts scalar T_1 relaxation to carbons scalar-coupled (SC) with nuclei having a closely similar resonance frequency and/or a very large scalar coupling constant; carbons bonded to bromine atoms, for example, can have highly efficient scalar relaxation to ^{79}Br, whose resonance frequency is only 0.3% different from ^{13}C (for ^{81}Br the Δ frequency is 7.4%); and (e) spin rotation (SR) relaxation, which in very small molecules or for freely rotating groups such as the methyl group of toluene, can dominate ^{13}C relaxation. This mechanism is more common for heavy nuclides.

1.3 Relationship of T_1 to Individual Relaxation Mechanisms

In a particular compound, all or any combination of the ^{13}C relaxation mechanisms discussed above may be of potential importance. However, only a single relaxation time is measured for each carbon. This is assumed to be related to the individual mechanisms via the reciprocal relationship:

$$\frac{1}{T_1^{\text{obs}}} = \frac{1}{T_1^{\text{DD}}} + \frac{1}{T_1^{\text{SR}}} + \frac{1}{T_1^{\text{CSA}}} + \frac{1}{T_1^{\text{SC}}} + \frac{1}{T_1^{\text{other}}} \qquad (11)$$

This equation ignores cross correlation between relaxation processes. Cross correlation relaxation can be important and useful.[4b,c] It can be significant particularly between CSA and dipolar processes, but there are experimental methods for separating these effects.[11] Extraction of the relevant molecular information from measured T_1 values requires evaluation of the contributions from individual relaxation mechanisms.

In 1973, Levy, Cargioli, and Anet published a paper[10] describing ^{13}C spin relaxation in benzene and a variety of substituted benzenoid compounds. In that early paper, evidence was found for different individual carbons having their spin relaxation controlled by each of the available spin relaxation mechanisms: dipole–dipole interactions, chemical shift anisotropy, spin rotation, and scalar interactions. It was seen that most carbons had their spin relaxation controlled by dipole–dipole interactions to attached or nearby hydrogens, except that for nonprotonated sp^2 carbons at (then) high fields (in 1973, 63 MHz operation for ^{13}C was considered high field) there were significant contributions from chemical shift anisotropy relaxation.

Another interesting exceptional case was found for the *ipso* ring carbon in bromobenzene, where the attached bromine was highly effective in producing scalar spin relaxation, at least for the ^{79}Br isotope. Because both ^{79}Br and ^{81}Br are present in roughly comparable amounts, the T_1 magnetization recovery was seen to be nonexponential (a combination of two dissimilar spin relaxation rates).[12]

In the 1973 paper on substituted benzenes,[10] there was an expansion on work from Grant and others on free methyl rotation. The methyl carbon in toluene was observed to have effective spin rotation relaxation, as confirmed by variable temperature measurements. The effect of dissolved oxygen from the air was noted for these benzenoid compounds. In the case of the smaller nonpolar compounds, and for nonprotonated carbons in some of the larger substituted benzenes, oxygen from the air contributed significantly to ^{13}C overall spin relaxation. In benzene itself, dissolved oxygen resulted in a contribution of approximately 25% to the ^{13}C relaxation rate at 38 °C, while spin rotation relaxation had a comparable contribution. Observation of several phenylacetylene compounds showed that chemical shift anisotropy relaxation was a major contributor for nonprotonated sp carbons, even at modest magnetic fields.

1.3.1 ^{13}C–^{1}H Dipole–Dipole Relaxation Outside of the Motional Narrowing Limit

For synthetic and biopolymers, where motion is slow and the $^{13}C-^{1}H$ dipolar T_1 (and NOE) becomes field-dependent, it is more difficult to quantify $^{13}C-^{1}H$ dipolar relaxation versus other contributors. However, especially for proton-bearing sp^3 carbons, it can usually be assumed that $^{13}C-^{1}H$ dipolar relaxation is the only significant operating mechanism.

In these cases, when dipolar T_1 and observed NOE show complex behavior as a function of the NMR observed frequency (magnetic field), it is possible to model molecular dynamics in terms of the complex overall and internal motions occurring at various frequencies and, in the case of internal motions, of varying angular amplitudes. A number of models have been proposed,[13] but many groups prefer to use a model-free description of complex dynamics initially proposed by Lipari and Szabo.[14] While the model-free approach does not explain specific conformational motions, it is quite useful for the assessment of local conformational mobility in synthetic and biopolymers.[15,16]

1.3.2 Complex Dynamics of Small Molecules; Nonexponential Decay of $G(\tau)$

In the mid-1970s it was recognized that, under a range of circumstances, the ^{13}C dipole–dipole T_1 values apparently indicative of motional narrowing in fact showed marked field-dependence.[17] This occurs when there are cooperative motions, as in some samples of aggregated molecules having relatively freely moving side chains. In the first ^{13}C study of this type, the ^{13}C dipolar T_1 values for all 10 carbons in 1,2-decanediol were found to have a strong field-dependence despite being fully due to $^{13}C-H$ dipolar interactions, and where lines were sharp and ^{13}C T_1 values were as long as 5 s (corresponding to a τ_c well within motional narrowing). The ^{13}C T_1 results of the 1,2-decanediol study[17] are summarized in Table 1, along with T_1 values for 1-decanol, which can be used for comparison purposes.

The important and unexpected thing to note in Table 1 is the large difference between the 22.6 MHz and 67.9 MHz ^{13}C T_1 values of decanediol. By contrast, the ^{13}C T_1 values of 1-decanol show no field dependence, in accordance with standard theories for molecules undergoing rapid reorientation

Table 1 ^{13}C Spin–Lattice Relaxation Data for 1,2-Decanediol and 1-Decanol

Compound[a]	Temp (° C)[b]	Frequency (MHz)	^{13}C T_1 values (s)[c]									
			C-1	C-2	C-3	C-4	C-5	C-6	C-7	C-8	C-9	C-10
1,2-Decanediol	54	22.6	0.27	0.41	0.3	0.37	0.3	0.4	0.5	0.95	1.5	3.4
	54	67.9	0.5	0.7	0.5	0.6	0.6	0.7	1.0	1.8	2.7	5.3
1-Decanol	36	22.6	0.7	0.7	0.7		~1.0[d]			1.5	2.4	3.9
	36	67.9	0.6	0.6	0.7		~1.0[d]			1.4	2.3	3.8

[a]Samples neat unless noted.
[b]Temperatures ±1 °C, measured directly before and after data collection.
[c]Maximum probable error ±5%–10%. Decanediol and decanol data, average of two to four runs.
[d]Peaks insufficiently resolved for individual T_1 assignment.

in solution. These results can be interpreted in terms of a distribution of τ values for overall motion [or, equivalently, a nonexponential autocorrelation function $G(\tau)$] at the H-bond restricted end of the diol, with effective transmission of this nonideality to all the other carbons along the alkyl chain, either by the inherent intramolecular characteristics[13b] of the chain segmented motion, or through intermolecular transmission from chain–chain entanglements.

1-Decanol is extensively hydrogen bonded in neat solution. The ^{13}C T_1 values of 1-decanol given in Table 1 do not show a significant field dependence. The two field T_1 data for decanol at 36 °C thus do not require invocation of a complex cooperative motional description as in 1,2-decanediol.

The type of effect observed for the end carbons (C_7–H_{10}) of 1,2-decanediol may be observed in organized molecules, e.g., micelles, etc, and it is characteristic of complex dynamics in large biological or synthetic polymers, where relatively freely moving side groups can continue to show marked field dependence. For these cases, multiple field (frequency) ^{13}C T_1, NOE and, where practical, T_2 measurements can provide an extremely sensitive probe of molecular dynamics, in favorable cases uniquely differentiating similar models for overall and internal dynamics.

2 MEASUREMENTS OF ^{13}C RELAXATION PARAMETERS

Pulsed Fourier transform NMR methods are available for accurately determining spin–lattice relaxation times and NOEs. In one-dimensional ^{13}C NMR, these methods have been used for over 25 years in order to determine simultaneously T_1 values for all carbons in the spectrum. Even though the measurements can be considered as routine on modern day spectrometers, there are many factors that can make the experimental values that are determined inaccurate.[18] These factors include: (i) the choice of measurement pulse sequence; (ii) stability and accuracy of pulses and the spectrometer stability as a whole; (iii) data processing method used for calculation of the time constants from the experimental data; (iv) the presence of sample impurities; (v) temperature or solvent variation between experiments to be compared; (vi) sample geometry; and (vii) unusual spin relaxation characteristics, e.g., nonexponential relaxation.

Measurement of nuclear Overhauser effects similarly depends on the control of variables such as sample state and temperature, the application of radiofrequency pulses and timing, and care in data processing. Further, both ^{13}C spin–lattice relaxation measurements and NOE experiments may become difficult for carbons having very long spin relaxation times, where the sample is limited in quantity, or where solubility is very low.

Various pulse sequences have been used to establish a nonequilibrium condition and monitor the magnetization as a function of the time variable τ, thereby measuring T_1. Several pulse sequences directly measure NOE values, and one version of this experiment can simultaneously measure T_1s and NOEs for all carbons (although the efficiency of this last experiment is not high). There are existing discussions of necessary precautions that should be taken in these measurements. Table 2 summarizes some of the experiments used for ^{13}C spin relaxation measurements.

Most of the experiments listed in Table 2 are straightforward; the experiments listed for the measurement of T_1 all produce a nonequilibrium magnetization with subsequent time recovery towards equilibrium being monitored by a 90° pulse. The IRFT[19] and the pulse sequences most commonly used are relatively forgiving, experimentally. However, IRFT experiments can be quite lengthy when one or more carbons that are being measured have one long T_1 value. In these cases the shorter FIRFT experiment is preferred. The progressive saturation method was used in the early days of ^{13}C NMR but it is not generally used today because the technique is not as accurate in the case of mis-set pulse angles. Both progressive saturation and saturation recovery techniques utilize in most cases homospoil pulses (z homospoil) (indicated as HS in Table 2). The saturation recovery technique avoids some of the experimental problems of progressive saturation but the magnetization change measured is only half that of full inversion–recovery technique, leading to the choice of the latter in most cases. One advantage of the FIRFT pulse sequence is that for different ^{13}C nuclei in the same sample, the magnetization change being monitored can range from full inversion–recovery to essentially half of that value for very long T_1 values.

NOE measurements for ^{13}C are easily performed in most cases. Care must be taken in high dielectric samples not to heat the sample differently during relaxation pulse intervals, and in some cases authors have utilized decoupling power at a constant level but have offset the frequency sufficiently such that the protons in the sample are not affected.

Pulse sequences have been proposed to improve IRFT-type measurements[24] and to remove the effects of cross correlation between dipolar and chemical shift anisotropy relaxation.[25] Use of indirect observation (through the ^1H channel) to

Table 2 Some Methods for Determining ^{13}C Spin Relaxation Data

Method	Pulse sequence[a]	Comments	References
(a) T_1 Measurements			
Inversion recovery (IRFT)	$(180^\circ, \tau, 90^\circ, \text{AT}, \text{PD})_n$	PD > 4 × longest T_1 to be measured	19
Fast inversion recovery (FIRFT)	$(180^\circ, \tau, 90^\circ, \text{AT}, \text{PD})_n$	PD > T_2* but short relative to T_1; first FID is discarded	20
Progressive saturation (PSFT)	$(90^\circ, \tau, 90^\circ, \text{HS})_n$		21
Saturation recovery	$(90^\circ, \text{HS}, \tau, 90^\circ, \text{AT}, \text{HS})_n$		22
(b) NOE Measurements			
Gated decoupling	$(90^\circ, \text{AT}, \text{PD})$	PD with and without decoupling	23
NOE build-up	$(\tau, 90^\circ, \text{AT}, \text{PD})$	Decoupling only during τ and AT. PD varies from 0 to >12-times T_1s of interest. Simultaneously measures T_1s for carbons having appreciable NOEs.	23

[a]AT = acquisition time; PD = pulse delay; HS = z homospoil pulse.

measure ^{13}C T_1 and T_2 values has been demonstrated.[26] New variations on direct T_2 pulse schemes have been proposed that improve their accuracy.[27]

3 OVERVIEW OF APPLICATIONS FOR ^{13}C SPIN RELAXATION MEASUREMENTS

Utilization of carbon-13 spin relaxation data for both structural and dynamic information has been widespread in the literature over the past 20 years. Molecular systems that have been examined range from one-carbon molecules to highly complex synthetic and biological macromolecules, as well as simple and complex organometallics. The theoretical underpinnings for these measurements have advanced over this time period, but the simplest theories of spin relaxation are still sufficient in many applications. This has not caused special difficulty, since cross correlation has shown the greatest effect in the simplest molecules, usually under conditions that are not pertinent to most experiments (for example, in experiments not utilizing proton decoupling). By contrast, learning the intimate details of complex molecular dynamics can require highly sophisticated treatment of relaxation data.

Use of ^{13}C spin relaxation data to obtain qualitative dynamic information is quite facile; quantitative interpretation requires more care in terms of both experiment and elucidation of the dynamics through model assumptions, even in the case of model-free approaches. For molecules that are highly associated, or that are large enough inherently to be outside the extreme spectral narrowing limit, proper interpretation of the data is best done utilizing spin relaxation data obtained across dispersed frequencies (utilizing spectrometers operating at several magnetic fields).

3.1 Structure Determination

Carbon-13 spin relaxation data can be used as primary or confirmatory evidence for the assignment of chemical structures. The inverse sixth power relationship between $^{13}C-^{1}H$ distances and the usual observed ^{13}C dipolar T_1 values can be converted into spectral assignment information, particularly for carbons not having directly attached hydrogens and yet dipolar-relaxed from protons on adjacent or nearby carbons, or from protons in the solvent. For carbons that have one or more directly attached hydrogens, the spin relaxation data may still be useful for spectral assignments, in many cases adding an independent check on assignments made by other methods. For molecules that are globular in shape and close to isotropic in tumbling behavior, the protonated carbon T_1 values often fall into three groups: CH_2 carbons with the shortest T_1s, CH carbons having T_1s approximately twice that of the CH_2 carbons (the relaxation rate is half because only one hydrogen contributes to the carbon's spin relaxation), and CH_3 T_1s ranging from 1.5-times shorter than those found for CH_2 (occasionally, for a methyl that is not rotating) to T_1 values that are longer than T_1 values observed for the CH carbons in that molecule (rapidly rotating CH_3 groups).

An early example of the use of ^{13}C T_1 values to differentiate carbons not having directly attached hydrogens, is the molecule mescaline (**1**). The three types of nonprotonated carbons on the benzene ring of mescaline have differing numbers of hydrogens in the *ortho* ring position, as shown in structure (**1**). The ^{13}C T_1s reflect this, the longest value belonging to the carbon having no adjacent ring *ortho* hydrogens. An example showing the ^{13}C T_1s of protonated carbons varying with the numbers of directly attached hydrogens is the molecule cholesterol (**2**). Cholesterol shows T_1 values around 0.3 s for CH_2 carbons of the steroid ring skeleton while CH ring carbons show ^{13}C T_1 values closer to 0.55 s and methyl carbons (in this case, with considerable internal mobility) have T_1 values of approximately 1 s.[28] In

cholesterol, group segmental motion is also demonstrated; the carbon T_1 values of the cholesterol side chain increase with removal from the fused four-ring structure. Note that the side-chain carbons close to the steroidal skeleton maintain the expected ^{13}C T_1 values but near the end of the chain the CH_2 and CH carbons have significantly longer T_1s, indicative of considerable group segmental motion. (The 1.6 s T_1 observed for the pendant methyl carbons results from combined segmental and methyl group internal rotation.)

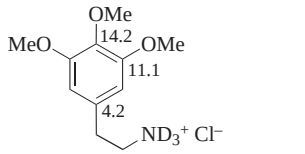

(1)

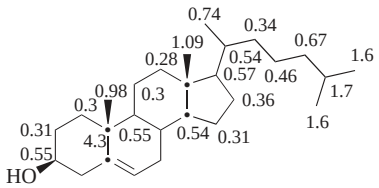

(2)

Another early example of the utilization of ^{13}C spin relaxation times to assist spectral assignments was the study of the tetrasaccharide stachyose (**3**).[29] Stachyose contains two galactose residues and the carbon lines were differentiated as a result of segmental motion increasing the T_1 values of the terminal galactose relative to the internal galactose residue.

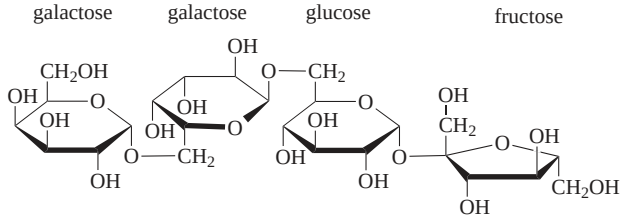

(3)

3.2 Dynamics of Small Molecules

Following pioneering work by the groups of David Grant[4] and Endel Lippmaa,[30] both examining ^{13}C spin relaxation in very small organic molecules, studies began on organic systems of moderate complexity, including examination of group internal mobility and steric effects, solvent effects and hydrogen bonding, ionization, and microphase changes, such as occur in micelles or other ordered phases.

One of the interesting results reported in the 1973 substituted-benzenes paper[10] related that preferred rotational motion around the axis coincident with the phenyl substituent was reflected in significantly shorter ^{13}C T_1 values for the protonated ring carbon *para* to the substituent, versus longer values for the carbons *ortho* and *meta* to the substituent. This effect was marked when the substituent was large or highly solvated, restricting motion through solvent–solute interactions or, in some cases, ion-pair formation. The 60° angular relationship for the *ortho* and *meta* CH vectors with respect to preferred overall rotation around the symmetry axis coincident with the substituent (or, equivalently from the point of view of the ^{13}C T_1s, for internal benzene ring spinning around the same axis), provides a sensitive probe of structure and solvation effects.[10] It was reported for the long molecule 1,4-diphenyldiacetylene that the ^{13}C T_1s for the *ortho* and *meta* carbons, approximately 5.3 s, were almost five-times longer than the ^{13}C T_1 values for the *para* carbon at 1.1 s. These results have some analogies to earlier work on methyl rotational rates, but the substituted-benzene structural unit allows for studies of a broader range of physical and chemical phenomena.

The 1973 paper also gave results for the phenol molecule, which when concentrated in solution is highly associated, giving shortened T_1s, reflecting slow overall motion of the molecule. Further, the anisotropy of tumbling was shown to be higher in these concentrated solutions, where aggregation was important. The aniline molecule was also studied, as a neat sample, in several solvents, and as the anilinium cation. In the latter case, motion was restricted by roughly an order of magnitude and the anisotropy of overall and internal phenyl ring motion approached that in diphenyldiacetylene.[10]

Another early paper giving information about group internal rotations for ring compounds was published in 1972.[31] In that study, two monosubstituted ferrocenes were examined. In both cases, ^{13}C T_1s of the substituted ring carbons were approximately half that of T_1 for the carbons of the unsubstituted ring. Most of this differential was considered to be due to free internal rotation of the unsubstituted planar five-membered aromatic ring, around the ring–Fe bond. One of the molecules, *n*-butylferrocene, also displayed chain segmental motion, where the γ-methylene and δ-methyl carbon T_1 values indicated increased mobility.

In other early work, alkyl chain mobility and steric effects were examined for amides and oximes[32] and in *n*-butylamine and the *n*-butylammonium ion.[33] In the study of several alkyl amides, differential effects were noted for group segmental motions *syn* and *anti* to the oxime function, and marked chain segmental motion was noted for *N,N*-di-*n*-butylacetamide, with ^{13}C T_1s for the four carbons being observed to be comparable to the last four carbons in the hydrogen-bonded molecule decanol. In the case of the acetamide, restriction of chain motion results from the molecular mass centered at the nitrogen and not from hydrogen-bonding interactions. In the *n*-butylammonium ion, ^{13}C T_1 values were observed to decrease by over an order of magnitude in changing from the relatively nonpolar amine to the protonated species, with associated counterion and strong solvation. In *n*-butylamine itself, methylene group segmental motion along the four carbon chain was masked by rapid overall molecular tumbling, but the data for the *n*-butylammonium ion showed ^{13}C T_1s comparable to those observed for the four carbon chain of *N,N*-di-*n*-butylacetamide, and also carbons 7 through 10 of 1-decanol.

3.3 Dynamics of Large Molecules

In the study of biological functions of macromolecules, it is essential to determine the nature and rate of internal motions of the molecule, as well as the overall average structure. Carbon-13 spin–lattice relaxation measurements, in conjunction with

NOE and when possible spin–spin relaxation measurements, have proven to be an important atomic probe of these internal motions. The relaxation of protonated ^{13}C nuclei is primarily dominated by the dipole–dipole interaction with the attached proton according to the following equation (valid inside or outside of the extreme narrowing limit):

$$\frac{1}{T_1} = R_1 = \frac{N_H}{20}\left(\frac{\mu_0\gamma_C\gamma_H\hbar}{4\pi r^3}\right)^2 \times [J(\omega_C - \omega_H) + 3J(\omega_C) + 6J(\omega_C + \omega_H)] \quad (12)$$

where N_H is the number of directly bonded hydrogens, r is the average C–H bond distance, and $J(\omega)$ is the spectral density function at the three indicated frequencies.

Relaxation parameters are related to the overall and internal motions of a molecule through their dependence on the spectral density functions. For large or aggregated molecules that reorient slowly compared with the extreme narrowing limit, the description of the function for a large molecule undergoing overall isotropic motion with fast internal motion is the model-free approach by Lipari and Szabo[14] in which the spectral density function is given by

$$J(\omega) = S^2\left(\frac{\tau_c}{1 + (\omega\tau_c)^2}\right) + (1 - S^2)\left(\frac{2\tau}{1 + (\omega\tau)^2}\right) \quad (13)$$

where S^2 is a generalized order parameter describing the amplitude of the internal motion and τ_c is the overall correlation time. The quantity τ is related to the overall and effective correlation time for the internal motion by $\tau^{-1} = \tau_c{}^{-1} + \tau_e{}^{-1}$. This two-parameter fit of the relaxation data has yielded good success in describing the internal motion of certain residues in macromolecules. Clore et al.[34] found it necessary to expand the above equation to include the internal motions of two uncoupled processes:

$$J(\omega) = S^2\left(\frac{\tau_c}{1 + (\omega\tau_c)^2}\right) + (1 - S_f^2)\left(\frac{2\tau_f}{1 + (\omega\tau_f)^2}\right) + (S^2 - S_f^2)\left(\frac{2\tau_s}{1 + (\omega\tau_s)^2}\right) \quad (14)$$

where 'f' refers to the fast motion and 's' to slower motion that may not be outside the extreme narrowing limit.

The motion of large molecules can also be complicated by overall molecular shape. For globular proteins or polynucleotides of the order of 5–7 base pairs (where the length of the chain is roughly equal to the diameter), the overall motion can be described as isotropic, but with molecules in which the shape is not close to spherical the molecule itself undergoes anisotropic motion. Equation (14) can also be used to describe anisotropic motion with internal motion. In addition to this model-free formalism, a number of different equations of spectral densities have been proposed for anisotropic motion,[35] multiple internal rotations and restricted diffusion,[36] and librational motions.[37]

Early work on the spin–lattice relaxation of carbon-13 of biological molecules provided a fragmentary analysis of internal motion. Instead of analyzing the relaxation data of a single ^{13}C resonance, usually composite ^{13}C resonances had to be studied. James[38] determined the internal motion of 23 Thr residues of chymotrypsinogen to 20 ns based on the combination of spin–lattice relaxation, NOE, and off-resonance rotating frame spin–lattice relaxation techniques. These findings suggested that, on the average, the rate of motion of the Thr residues is limited, possibly by steric hindrance or by interaction of the polar hydroxy with other polar groups. Levy et al.[39] looked at the relaxation data for the interaction of ethidium bromide with nucleosome core length DNA, of ca. 145 bp, and determined that the overall conformational dynamics were not altered by low to moderate levels of ethidium. In addition, the flexibility of the sugar rings was reduced when ethidium intercalated in DNA. Levy et al.[40] also found that the ^{13}C relaxation parameters of double-stranded DNA molecules of 100–300 bp were well fitted by a model which assumed that DNA undergoes rapid local motions such that the C–H vectors wobble inside a conic boundary with a half angle of 20–25°. In addition to these rapid local motions, slower overall axially symmetric rotation occurs. These are a few examples of early studies of ^{13}C relaxation in which qualitative or semiquantitative dynamic information could be ascertained from a combination of different relaxation techniques.

A comprehensive interpretation of ^{13}C relaxation data had been hampered by the inherent low sensitivity of the carbon-13 nucleus, the low natural abundance of carbon-13, and the low resolution of one-dimensional spectra. These problems have been alleviated to a certain extent by the development of proton-detected two-dimensional heteronuclear relaxation experiments,[41] which increase the sensitivity by approximately $(\gamma_H/\gamma_C)^{5/2}$ [42] and afford increased resolution by the addition of the second dimension. The pulse sequence consists of an initial DEPT sequence[43] to transfer the magnetization from protons to the carbon, a relaxation period T that is varied between the two-dimensional data sets, and the evolution time, followed by a second DEPT sequence in which the magnetization is transferred back from the carbon to the protons for detection. The intensities of the peaks, $I(T)$, are described by the usual T_1 equation of the inversion–recovery experiment.

Palmer et al.[44] have used this method, along with spin–spin relaxation and NOE studies, to characterize the intramolecular dynamics of Xfin-31, which is a 25-residue synthetic zinc finger peptide that is capable of binding nucleic acids and is recurrent in regulatory proteins. The studies suggest that the motion of the backbone carbons, excluding the terminal residues, are highly restricted, but with the residues forming a loop between the β-sheet and the helix showing slightly higher mobility. The motion of the side chains of the hydrophobic residues, Val and Leu, are also restricted, although they are more mobile than the backbone. These results suggest that the peptide is quite compact.

An additional development that has allowed comprehensive analysis of T_1 relaxation is site-specific ^{13}C enrichment. This has permitted certain sites in a macromolecule to be extensively studied. Nicholson et al.[45] have ^{13}C-enriched 11 leucine residues of the protein staphyloccal nuclease, which is a small enzyme of M_r = 16800. The leucines, which are nearly all buried within the closely packed interior, were studied with, and without, ligand binding by two-dimensional relaxation methods as described above. The parameters were fitted using the formalism of Lipari and Szabo[14] [equation (14)]. The results showed a rapid rotation of the methyl group

about the $C^{\gamma}-C^{\delta}$ bond, plus a slower motion associated with the reorientation of the $C^{\gamma}-C^{\delta}$ bond axis itself. A significant increase in the order parameter, S^2, was seen upon binding of the ligand to leucine in the vicinity of either Ca^{2+} or the pdTp heavy atoms, which indicates a localized restriction of motion in the vicinity of the ligand-binding sites.

Many groups have used relaxation data in order to characterize the motion of synthetic polymers.[46,47] Early on, Jacob Schaefer,[13a] using the results of carbon-13 spin–lattice relaxation times, linewidths, and NOE factors for isotactic polystyrene, *cis*-polyisoprene, and *cis*-polybutadiene, proposed a log χ^2 density function to describe the distribution of motion. The width of the distribution is a relative measure of the extent of cooperative segmental motion of the chain. In this 1973 study, it was shown that polybutadiene exhibits more long-range cooperative motions than the other two polymers studied.

3.4 Solvent Effects and Intermolecular Interactions

Unlike ^{15}N, in which intermolecular dipolar relaxation can contribute significantly to the nitrogen T_1 values carbon-13 intermolecular effects are usually negligible. Therefore, the use of ^{13}C spin–lattice relaxation to study intermolecular interactions, such as solvent effects hydrogen bonding, and ion–dipole pairing depends on the fact that the localized motions around the site of the interaction are restricted and the overall tumbling decreases due to the increased size of the complex. Both of these effects will result in a decrease in the ^{13}C spin–lattice relaxation times. These effects have been seen upon molecular association[48] and solute-solvent interactions[49] via hydrogen-bond formation.

In a study of molecular association, it was shown in 1971 by Alger, Grant, and Lyerla[48] that the carbon nuclei of formic and acetic acids have shorter T_1s, therefore relax faster, than the corresponding methyl esters. The carboxylic acid, which is dimerized by hydrogen bonding, rotates more slowly than the methyl esters. This behavior is seen in long- and branch-chain alcohol and acids, such as decanoic acid, decanol, and 3,7-dimethyloctanol, in which the hydrophobic end shows increased mobility, i.e. longer T_1s than the polar end which is hydrogen bonded and therefore less mobile. Other solvent effect studies had been discussed earlier.[10,17]

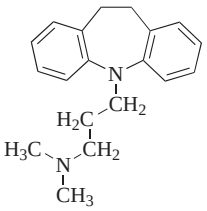

(4)

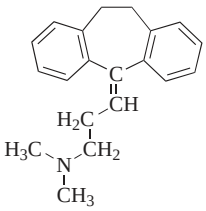

(5)

The intermolecular interaction of biological molecules in solution is of biological significance. Casarotto and Craik[50] looked at the interaction of tricyclic antidepressant drugs imipramine (**4**) and amitriptyline (**5**) with sodium dodecyl sulfate (SDS) (**6**) micelles. The ^{13}C relaxation parameters, including T_1 and NOE measurements at two different field strengths, were fitted to the model-free formalism of Lipari and Szabo.[14] The smallest T_1 value occurs in the middle of the aliphatic chain of neat SDS with a slight increase near the headgroup and a significant increase near the terminal methyl region. This corresponds to a low value for the order parameter for the terminal methyl, which reflects increased amplitude of mobility at the end. Upon addition of the drugs, there was a significant decrease in the T_1 values with an overall increase in the S^2 values. The aromatic carbons of the drugs showed the greatest change in T_1 upon association with the micelles. This indicated a marked decrease in overall tumbling rate. The rapid internal bridge flipping of the seven-membered ring is not significantly affected in the micelles. It was concluded from the relaxation studies that there is a notable increase in the micellar volume with a reduction of motion in the SDS alkyl chains. The drugs become extended in the micelles with the tricyclic moiety occupying the hydrophobic region of the micelle and the terminal dimethylammonium ion interacting at the micelle–water interface.

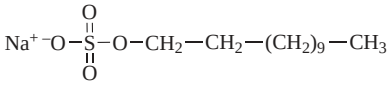

(6)

4 SUMMARY

Carbon-13 relaxation data provide unique insight into the structure and, especially, the structural dynamics of organic molecular systems, including complex biomolecules. The ability of these studies to probe molecules at each atomic site, and quantitatively to reflect dynamical information, is made especially useful by the central role of carbon atoms in these molecules and by the relatively simple mechanistic relaxation pathway for most ^{13}C nuclei. Carbon-13 relaxation complements other techniques in yielding to scientists the most basic structural secrets of complex molecules.

5 REFERENCES

1. G. C. Levy and G. L. Nelson, *Carbon-13 Nuclear Magnetic Resonance for Organic Chemists*, Wiley-Interscience, New York, 1972.
2. F. A. L. Anet and G. C. Levy, *Science*, 1973, **180**, 141.
3. R. R. Ernst and W. A. Anderson, *Rev. Sci. Instrum.*, 1966, **37**, 93.
4. (a) Early references: K. F. Kuhlmann, D. M. Grant, and R. K. Harris, *J. Chem. Phys.*, 1970, **52**, 3439; but see also (b) L. G. Werbelow and D. M. Grant, *Adv. Magn. Reson.*, 1977, **9**, 89; (c) D. M. Grant, C. L. Mayne, F. Liu, and T.-X. Xiang, *Chem. Rev.*, 1991, **91**, 1591.
5. R. Freeman, *A Handbook of Nuclear Magnetic Resonance*, Longman, Hanlow, UK, 1987, p. 147.
6. G. C. Levy, R. L. Lichter, and G. L. Nelson, *Carbon-13 Nuclear Magnetic Resonance Spectroscopy*, 2nd edn., Wiley-Interscience, New York, 1980.
7. H.-O. Kalinowski, S. Berger, and S. Braun, *Carbon-13 NMR Spectroscopy*, Wiley, Chichester, UK, 1988, Chap. 5

8. D. A. Wright, D. E. Axelson, and G. C. Levy, *Topics in Carbon-13 NMR Spectroscopy*, ed. G. C. Levy, Wiley, New York, 1979, Vol. 3, Chap. 2
9. A. Abragam, *The Principles of Nuclear Magnetism*, Oxford University Press, Oxford, UK, 1961.
10. G. C. Levy, J. D. Cargioli, and F. A. L. Anet, *J. Am. Chem. Soc.*, 1973, **95**, 1527.
11. L. E. Kay, L. K. Nicholson, F. Delaglio, A. Bax, and D. A. Torchia, *J. Magn. Reson.*, 1992, **97**, 359.
12. G. C. Levy, *J. Chem. Soc., Chem. Commun.*, **1972**, 352.
13. (a) J. Schaefer, *Macromolecules*, 1973, **6**, 882; (b) A. Kumar and G. C. Levy, *J. Chem. Phys.*, 1986, **85**, 485.
14. G. Lipari and A. Szabo, *J. Am. Chem. Soc.*, 1982, **104**, 4546, 4559.
15. L. M. Bull, D. G. Gillies, S. J. Matthews, L. H. Sutcliffe, and A. J. Williams, *Magn. Reson. Chem.*, 1991, **29**, 273.
16. P. N. Borer, S. R. LaPlante, A. Kumar, N. Zanatta, A. Martin, A. Hakkinen, and G. C. Levy, *Biochemistry*, 1994, **33**, 2441.
17. G. C. Levy, M. P. Cordes, J. S. Lewis, and D. E. Axelson, *J. Am. Chem. Soc.*, 1977, **99**, 5492.
18. G. C. Levy and I. R. Peat, *J. Magn. Reson.*, 1975, **18**, 500.
19. R. L. Vold, J. S. Waugh, M. P. Klein, and D. E. Phelps, *J. Chem. Phys.*, 1968, **48**, 3831.
20. D. Canet, G. C. Levy, and I. R. Peat, *J. Magn. Reson.*, 1975, **18**, 199.
21. R. Freeman and H. D. W. Hill, *J. Chem. Phys.*, 1971, **54**, 3367.
22. J. L. Markley, W. J. Horsley, and M. P. Klein, *J. Chem. Phys.*, 1971, **55**, 3604.
23. R. Freedman, H. D. Hill, and R. Kaptein, *J. Magn. Reson.*, 1972, **7**, 327.
24. A. Ejchart, P. Oleski, and K. Wroblewski, *J. Magn. Reson.*, 1986, **68**, 207.
25. L. E. Kay, L. K. Nicholson, F. Delaglio, A. Bax, and D. A. Torchia, *J. Magn. Reson.*, 1992, **97**, 359.
26. L. E. Kay, T. E. Bull, L. K. Nicholson, C. Griesinger, H. Schwable, A. Bax, and D. A. Torchia, *J. Magn. Reson.*, 1992, **100**, 538.
27. J. W. Peng, V. Thanabal, and G. Wagner, *J. Magn. Reson.*, 1991, **95**, 421.
28. H.-O. Kalinowski, S. Berger, and S. Braun, *Carbon-13 NMR Spectroscopy*, Wiley, Chichester, UK, 1988.
29. A. Allerhand and D. Doddrell, *J. Am. Chem. Soc.*, 1971, **93**, 2777.
30. (a) E. Lippmaa and M. Alla, *Eesti NSV Tead. Akad. Toim., Fuus., Mat., Tehnikatead. Seer.*, 1966, **3**, 473; (b) E. Lippmaa and M. Alla, *Eesti NSV Tead. Akad. Toim., Fuus., Mat.*, 1968, **17**, 117; (c) E. Lippmaa, M. Alla and A. Sugis, *Eesti NSV Tead. Akad. Toim., Fuus., Mat.*, 1967, **16**, 385.
31. G. C. Levy, *Tetrahedron Lett.*, 1972, 3709.
32. G. C. Levy and G. L. Nelson, *J. Am. Chem. Soc.*, 1972, **94**, 4897.
33. G. C. Levy, *J. Chem. Soc., Chem. Commun.*, 1972, 768.
34. G. M. Clore, A. Szabo, A. Bax, L. E. Kay, P. C. Driscoll, and A. M. Gronenborn, *J. Am. Chem. Soc.*, 1990, **112**, 4989.
35. D. E. Woessner, *J. Chem. Phys.*, 1962, **36**, 1.
36. (a) R. J. Wittebort and A. Szabo, *J. Chem. Phys.*, 1978, **69**, 1722; (b) R. E. London and J. Avitabile, *J. Am. Chem. Soc.*, 1978, **100**, 7159.
37. O. W. Howarth, *J. Chem. Soc., Faraday Trans. 2*, 1978, **74**, 1031.
38. T. L. James, *J. Magn. Reson.*, 1980, **39**, 141.
39. G. C. Levy, A. Ejchart, P. S. Marchetti, and R. L. Rill, *J. Magn. Reson.*, 1984, **57**, 130.
40. (a) G. C. Levy, P. R. Hillard, L. F. Levy, R. L. Rill, and R. Inners, *J. Biol. Chem.*, 1981, **256**, 9986; (b) P. R. Hillard, R. L. Rill, G. C. Levy, and L. F. Levy, in *ACS Symp. Ser. No. 191*, ed. G. C. Levy, Am. Chem. Soc., Washington, DC, 1982.
41. (a) V. Sklenar, D. Torchia, and A. Bax, *J. Magn. Reson.*, 1987, **73**, 375; (b) L. E. Kay, T. L. Jue, B. Bangerter, and P. C. Demon, *J. Magn. Reson.*, 1987, **73**, 558.
42. S. C. Kim and M. Garwood, *J. Magn. Reson.*, 1992, **99**, 660.
43. D. M. Doddrell, D. T. Pegg, and M. R. Bendall, *J. Magn. Reson.*, 1982, **48**, 323.
44. A. G. Palmer III, M. Rance, and P. E. Wright, *J. Am. Chem. Soc.*, 1991, **113**, 4372.
45. L. K. Nicholson, L. E. Kay, D. M. Baldisseri, J. Arango, P. E. Young, A. Bax, and D. A. Torchia, *Biochemistry*, 1992, **31**, 5253.
46. (a) G. C. Levy, *J. Am. Chem. Soc.*, 1973, **95**, 6117; (b) G. C. Levy, P. L. Rinaldi, J. J. Dechter, D. E. Axelson, and L. Mandelkern, *ACS Symp. Ser. No. 142* Am. Chem. Soc., Washington DC, 1980, p. 119; (c) G. C. Levy and D. Wang, *Macromolecules*, 1986, **19**, 1013.
47. (a) F. A. Bovey and L. W. Jelinski, *J. Phys. Chem.*, 1985, **89**, 571; (b) F. Heatley, *Prog. Nucl. Magn. Reson. Spectrosc.*, 1979, **13**, 47.
48. T. D. Alger, D. M. Grant, and J. R. Lyerla, *J. Phys. Chem.*, 1971, **75**, 2539.
49. R. E. Waysleshan and B. A. Pettitt, *Can. J. Chem.*, 1977, **55**, 2564.
50. M. G. Casarotto and D. J. Craik, *J. Phys. Chem.*, 1991, **95**, 7093.

Biographical Sketches

George C. Levy. *b* 1944. A.B., 1965, Ph.D., 1968, Chemistry, U.C.L.A., USA. General Electric Corporate R & D staff, 1968–73, Faculty member Florida State University, 1973–81. Faculty member and Science and Technology Professor, Syracuse University, 1981–94. In 1983, founded New Methods Research, Inc., the first company to develop and market NMR data processing and NMR laboratory networking software based on general purpose computers and workstations. Approximately 240 publications. Co-authored with Gordon Nelson the first published ^{13}C NMR book. Research specialties: ^{13}C NMR, data processing methods for one- and multidimensional NMR, utilization and commercialization of technology.

Deborah J. Kerwood, *b* 1959. B.S., 1981, Ph.D., 1986, Chemistry, Wesleyan University, USA. Postdoctoral research scientist, University of California at San Francisco, Research Scientist, Veterans Administration Hospital, San Francisco, NMR Laboratory Operational Manager, Syracuse University, 1992–present. Approx. 15 publications. Research specialties: structure determination via NMR techniques, ^{13}C-relaxation NMR.

Coupled Spin Relaxation in Polymers

Michael M. Fuson
Denison University, Granville, OH, USA

1	Introduction	1
2	Spin–Lattice Relaxation of $^{13}CH_2$	1
3	Obtaining Motional Information from Coupled Spin Relaxation Data	2
4	Experimental Methods for Polymer Studies	3
5	Results from Polymer Studies	4
6	Related Articles	6
7	References	6

1 INTRODUCTION

Coupled spin relaxation is the generally accepted term for the spin–lattice relaxation of a scalar-coupled spin system such as a ^{13}C-containing methylene group, $^{13}CH_2$. It is a powerful method to probe motional dynamics in solution, particularly in molecules with internal motions such as polymers.

Nuclear spin relaxation was recognized as a powerful probe of motional dynamics since the observation of unexpectedly sharp resonance lines in liquids in the early days of magnetic resonance spectroscopy in the 1940s. These phenomena were explained almost immediately in terms of the effect of thermal motion by Bloembergen, Purcell, and Pound.[1] This sensitivity to motion has its basis in the fact that the energy of a spin state in a static magnetic field usually depends on an orientation, whether it is the orientation of a chemical shift tensor or a dipole–dipole interaction between two spins or a quadrupole coupling tensor. Orientational fluctuations, that is 'motional dynamics', cause fluctuations in the spin energy levels that can couple to each other or the surrounding lattice to produce the various phenomena of spin relaxation. Measurement of spin relaxation times in order to obtain information about dynamics has been widely exploited (see ***Carbon-13 Relaxation Measurements: Organic Chemistry Applications***, etc.).

In the 1960s Woessner, amongst others, recognized the potential of using a series of relaxation interactions that are rigidly oriented relative to each other to obtain information about the anisotropy, or relative rates in different directions, of motion (see ***Brownian Motion and Correlation Times***). The requirement of a series of independent spin systems all oriented rigidly relative to each other in a molecule is a stringent one however, and the method did not receive wide application.

In the 1970s several groups showed that a more productive approach was to use the multiplicity of interactions amongst a *single* spin system of three or more scalar-coupled spins to generate sufficient information to determine the full diffusion tensor of a small molecule[2,3] (see ***Relaxation Processes in Coupled-Spin Systems***). In addition, coupled spin relaxation has the advantage that a three spin system such as $^{13}CH_2$ can be incorporated in a flexible chain and thus provides a powerful probe of internal motion. Application of these techniques to internal dynamics in small molecules has recently been reviewed.[4]

The basis for the method can be summarized briefly. The relaxation of dipolar coupled spins is generally described in terms of autocorrelation spectral densities which are the Fourier transforms of correlation functions relating the orientation of an internuclear dipole to itself at a later time. For multiple coupled spins, for example $^{13}CH_2$, a complete description of the relaxation also includes cross-correlation terms between *pairs* of dipolar vectors. The traditional approach has been to regard these as unimportant and, using our example, to decouple the ^{1}H spins to enhance the ^{13}C sensitivity. Invariably, the proton-decoupled methylene ^{13}C spin will relax with an 'effective' single exponential recovery law as the multiple exponential relaxation behavior of the coupled spins is obscured with the collapse of the proton-induced multiplet under decoupling.

Study of the fully coupled multiplets provides significant additional information. For a methylene group, four independent spectral densities are required to describe the relaxation, even in the extreme narrowing limit. These can be used to calculate four correlation times describing reorientation of the x, y, and z axes of a molecule fixed reference frame.

This article describes the application of coupled spin relaxation to the reorientational dynamics of polymer chains in solution. These dynamics have been of considerable interest in recent years. Technologically important properties such as elasticity, phase transition temperatures, and solution and melt viscosities are thought to be correlated with molecular motion.[5] Thus, understanding the relationship between chain structure and chain motion is an important factor in predicting polymer properties.

Spin–lattice relaxation has been widely used to investigate such systems and, typically, in these studies the ^{1}H or ^{13}C T_1 values of the polymer are studied as a function of temperature and/or field strength. The results are then fitted to expressions derived from the theoretical models. Discrimination between models has been difficult, however. While experiments such as those described are very sensitive to the motional *timescales*, they lack descriptive details of the *geometry* of motion. This latter information is often needed to discriminate one model from another and can be provided by coupled spin relaxation methods.

In addition, computer simulations of the dynamics of simple polymers are now practical. Recent simulations of chain dynamics have included studies of polyethylene (PE), polyisoprene, and poly(ethylene oxide) (PEO).[6] The Cartesian correlation times (described below) calculated from coupled spin relaxation measurements can be obtained directly from such simulated dynamics trajectories.

Coupled spin relaxation methods have now been applied to a series of linear polymers, most notably polyoxides. In the following, the theory and methods used in these studies are described and recent results are then summarized. The results show quite strikingly the dependence of dynamic properties on chain structure.

2 SPIN–LATTICE RELAXATION OF $^{13}CH_2$

As noted above, the $^{13}CH_2$ spin system makes an excellent probe of chain dynamics. The relative positions of the nuclei

in the methylene group are independent of the orientation or rotational state of the chain. Spin relaxation of the group then depends on its overall reorientation, not the motion of the three nuclei relative to each other. Dipole–dipole interactions among the ^{13}C and ^{1}H spins are sufficiently strong that they are the dominant relaxation mechanisms under most circumstances. These characteristics make the spin relaxation behavior itself relatively simple to interpret. In addition, there are experimental advantages to this spin system. The coupled spin relaxation can be characterized entirely from observing the ^{1}H coupled ^{13}C multiplet and individual ^{13}C signals are often easily resolved, even in complex samples. The ability to excite ^{13}C and ^{1}H spins separately makes it possible to dispense with most selective excitation experiments.

Relaxation in scalar-coupled spin systems has been described using Bloch–Redfield theory and then recasting the density matrix in terms of 'magnetization modes'. A full description is given elsewhere and will not be repeated here except to summarize pertinent details (see ***Relaxation Processes in Coupled-Spin Systems*** and ***Relaxation Mechanisms: Magnetization Modes***).

An energy level diagram for the AX_2 spin system (of which $^{13}CH_2$ is an example) is given in Figure 1. Application of Bloch–Redfield theory to the AX_2 spin system in the eigenstate representation yields an expression for the time evolution of the populations of the various states, N_κ,

$$\frac{\mathrm{d}\boldsymbol{N}}{\mathrm{d}t} = \mathbf{W}[\boldsymbol{N} - \boldsymbol{N}(\infty)] \tag{1}$$

where the elements of $\boldsymbol{N}$ are the diagonal members of the spin density matrix: $N_\kappa = \sigma_{\kappa\kappa} = \langle\kappa|\hat{\sigma}|\kappa\rangle$. The elements of the matrix $\mathbf{W}$ are a subset of the full Redfield matrix, $W_{\kappa\lambda} = R_{\kappa\kappa\lambda\lambda}$, and may be considered as simple transition probabilities.

For convenience magnetization modes, ν, corresponding to a maximum number of observables are constructed by taking linear combinations of the diagonal density matrix elements. Thus

$$\nu_\kappa = \sum_\lambda T_{\kappa\lambda} N_\lambda \quad \text{or} \quad \boldsymbol{\nu} = \mathbf{T}\boldsymbol{N} \tag{2}$$

where $T_{\kappa\lambda}$ are the elements of the transformation matrix. If $\mathbf{\Gamma} = \mathbf{TWT}^{-1}$, then

$$\frac{\mathrm{d}\boldsymbol{\nu}}{\mathrm{d}t} = \mathbf{\Gamma}[\boldsymbol{\nu} - \boldsymbol{\nu}(\infty)] \tag{3}$$

As line intensities depend on the difference between diagonal density matrix elements, the magnetization modes can also be expressed as combinations of line intensities. The members of a convenient set of modes for the AX_2 spin system which are observable in isotropic solution are:

$$\left.\begin{aligned}
{}^{\mathrm{a}}\nu_{\mathrm{A}} &= \tfrac{1}{k_{\mathrm{A}}}(L_1 + L_2 + L_3) \\
{}^{\mathrm{a}}\nu_{\mathrm{X}} &= \tfrac{1}{k_{\mathrm{X}}}(L_4 + L_5) \\
{}^{\mathrm{a}}\nu_{+-+} &= \tfrac{1}{k_{\mathrm{A}}}(L_1 - L_2 + L_3) \\
{}^{\mathrm{a}}\nu_{\pm\mp} &= \tfrac{1}{k_{\mathrm{X}}}(L'_4 - L''_4 - L'_5 + L''_5) \\
&= \tfrac{1}{k_{\mathrm{A}}}(L_1 - 2L'_2 + L_3) \\
{}^{\mathrm{s}}\nu_{+0-} &= \tfrac{1}{k_{\mathrm{A}}}(L_1 - L_3) = \tfrac{1}{k_{\mathrm{X}}}(L_4 - L_5)
\end{aligned}\right\} \tag{4}$$

where line labels are given in Figure 1 and k_{A} and k_{X} are scaling factors. The quantities ${}^{\mathrm{a}}\nu_{\mathrm{A}}$, ${}^{\mathrm{a}}\nu_{+-+}$, and ${}^{\mathrm{s}}\nu_{+0-}$ are all directly observable from the A spectrum (^{13}C in a $^{13}CH_2$ study). The quantity ${}^{\mathrm{a}}\nu_{\mathrm{A}}$ is proportional to the the sum of the intensities of all the lines in the A multiplet. The quantity ${}^{\mathrm{a}}\nu_{+-+}$ is proportional to the difference between the intensities of the outer and inner lines of the multiplet, while ${}^{\mathrm{s}}\nu_{+0-}$ is related to the difference between the two outer lines of the multiplet. The quantity ${}^{\mathrm{a}}\nu_{\mathrm{X}}$ is simply the total X (^{1}H) magnetization. Application of a 90° X pulse simultaneous with an observe pulse on the A spins exchanges triplet intensities in the A manifold and allows, by difference, evaluation of ${}^{\mathrm{a}}\nu_{\pm\pm}$.

The elements of the relaxation matrix, $\mathbf{\Gamma}$, are made up of linear combinations of spectral densities arising from the interactions important in the system under study. These might include dipole–dipole, chemical shift anisotropy, spin rotation, and random field interactions among others. The relaxation matrix for the AX_2 spin system including only contributions from dipole–dipole and random field interactions and corresponding to the set of magnetization modes used here is given in full elsewhere.[4]

In the limit of extreme narrowing, the dipolar relaxation of an AX_2 or $^{13}CH_2$ spin system is completely described by four frequency-independent spectral densities. Two of these are autocorrelation terms related to the CH or HH′ internuclear vectors (J_{CH} and J_{HH}). The others are cross-correlation terms relating one CH vector to the other (J_{HCH}) or to the HH′ vector (J_{CHH}). A complete set of random field spectral densities would include an autocorrelation term at the carbon (j_{C}), an autocorrelation term at each hydrogen (j_{H}), and a cross-correlation term between the two hydrogens (j_{HH}).

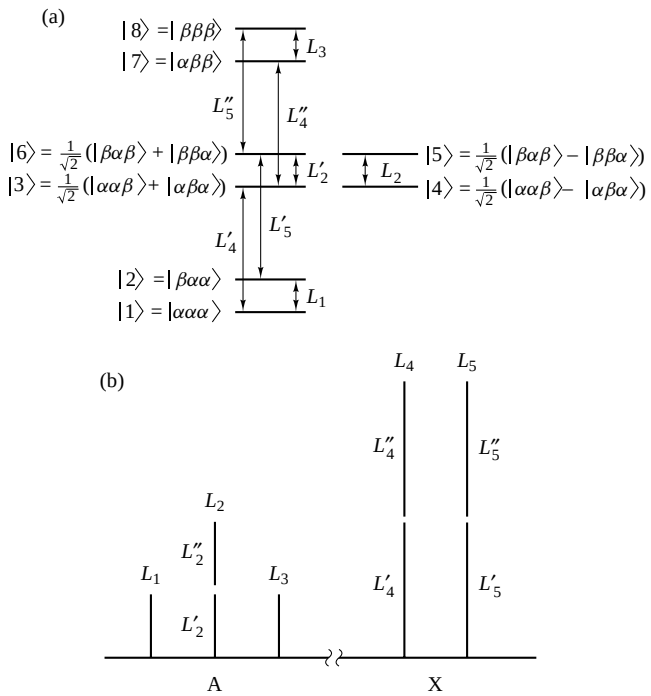

Figure 1 (a) The energy level diagram and eigenstates of the static Hamiltonian, $\hat{\mathcal{H}}_0$, for an AX_2 spin system. The first label gives the state of the A spin and subsequent labels the states of the two X spins. Allowed single quantum transitions are labeled. (b) A schematic diagram of the AX_2 spectrum in isotropic solution

3 OBTAINING MOTIONAL INFORMATION FROM COUPLED SPIN RELAXATION DATA

As noted above, the spectral densities are the Fourier transforms of correlation functions relating the orientation of an internuclear dipole to a second dipole at a later time. In the simplest case, these correlation functions decay as simple exponentials which can be characterized by a correlation time, τ_c. The value of the spectral density then depends on the magnitude of τ_c and the frequency at which it is sampled. When the dynamics are more complex, the correlation function can be a complex sum of exponentials with various time constants. The resulting spectral densities do not reflect the values of these time constants in any simple way.

Two general approaches to this problem have been established. One is to sample a spectral density function at a range of frequencies, perhaps by performing conventional T_1 experiments at several field strengths. This is often effective in enabling the investigator to estimate the timescales involved in a dynamic process, but is less effective in establishing the associated geometrical factors. The other approach, embodied in the coupled spin relaxation experiment, is to sample a wider variety of spectral density functions. The ratios of the different spectral densities at a given frequency are often a sensitive function of the geometry of the motion.

It remains to establish the relationship between the measured spectral densities and appropriate motional parameters. Again, two approaches have been used. The first, dating to the very first use of spin relaxation to elucidate dynamic parameters, is to assume a particular motional model and then calculate the associated correlation function and, by taking the Fourier transform, spectral density function. The assumption of diffusive isotropic motion, which leads to an exponential correlation function and a Lorentzian spectral density function, is the classic example of this approach, but it has also been applied to much more complex models.

A second approach that has been used recently is to take the four spectral densities measured in the coupled spin relaxation experiment (J_{CH}, J_{HH}, J_{HCH}, and J_{CHH}) and to reexpress them in terms of four autocorrelated Cartesian spectral densities, which are in turn simply related to four correlation times (τ_{xx}, τ_{yy}, τ_{zz}, and τ_{xy}).[7] These transformations are model-independent and are extremely useful in several ways. First, the difficulty of interpreting cross-correlation functions is removed. Second, the results are presented in a molecule fixed Cartesian axis system commonly used in dynamics simulations (see Figure 2) and are readily interpretable. The correlation times describe the reorientation of geometrical constructs having the shape of d orbitals. Thus τ_{xx} represents the motion of a d_0 construct fixed on the x axis or the bisector of the HCH angle. Lastly, it should be emphasized that in the transformation to this basis no biases or assumptions about the dynamical behavior of the molecule are introduced, as are encountered in using diffusional models.

As will be discussed below, in spin relaxation studies of unlabeled polymers it is difficult to determine J_{HH} reliably. Under these circumstances some assumption must be made in order accomplish the transformation. A reasonable assumption is to set τ_{xx} and τ_{yy} equal to each other and defining a $\tau_\perp$ term. The quantities τ_{xx} and τ_{yy} have been shown to be very similar in value in simulations of flexible chains.

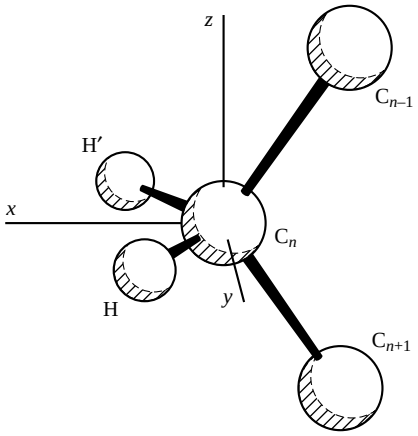

Figure 2 Orientation of the Cartesian axis system in the frame of reference of the methylene group

Reduced spectral densities are defined as

$$\hat{J}_{ijkl} = \frac{20}{9K_{ijkl}} J_{ijkl}(\omega = 0) \tag{5}$$

where $K_{ijkl} = \gamma_i\gamma_j\gamma_k\gamma_l h^2/r_{ij}^3 r_{kl}^3$ and i, j, k, and l represent the spins involved. If the reduced autocorrelation spectral densities $\hat{J}_{xx}$ and $\hat{J}_{yy}$ are set equal to each other than it can be shown:

$$\left.\begin{aligned} \tau_\perp = \tau_{xx} = \tau_{yy} &= \tfrac{3}{4(\alpha^4-\beta^4)}(\hat{J}_{AX} + \hat{J}_{XAX} - 4\beta^2\hat{J}_{AXX}) \\ \tau_\parallel = \tau_{zz} &= \tfrac{3}{2\alpha^2}(\hat{J}_{AX} + \hat{J}_{XAX} - (2-4\beta^2)\hat{J}_{AXX}) \\ \tau_{xy} &= \tfrac{1}{4\alpha^2\beta^2}(\hat{J}_{AX} - \hat{J}_{XAX}) \end{aligned}\right\} \tag{6}$$

where $\alpha = \cos(\theta/2)$, $\beta = \sin(\theta/2)$, and θ = HCH angle.

4 EXPERIMENTAL METHODS FOR POLYMER STUDIES

Spectroscopic samples are typically 1% w/v polymer in good solvents. Samples are degassed either by flushing the solvent with dry nitrogen and then assembling and sealing the sample under nitrogen, or by subjecting the sample to five freeze–pump–thaw cycles and then sealing under vacuum.

Spin relaxation measurements use variations on the inversion recovery pulse sequence. Four different initial perturbations of the coupled $^{13}CH_2$ spin system are used: (1) a ^{13}C 180° pulse inverting the ^{13}C triplet; (2) a ^1H 180° pulse inverting the proton doublet; (3) a low power ^1H pulse inverting only the low-frequency line of the ^1H doublet; and (4) a J pulse preparation on the ^1H magnetization (resembling a spin echo) resulting in the inversion of the outer lines of the ^{13}C triplet. In each case the initial perturbation of the spin system is followed by a variable delay period and a ^{13}C sampling pulse as in a normal inversion recovery experiment. For each experiment 17 or 18 different delay times are used. The delay times are ordered randomly to reduce systematic errors. Recycle delays are adjusted to be at least 10-times the nominal T_1 value of the sample.

FIDs are subjected to appropriate exponential multiplication before Fourier transformation. Line amplitudes are then obtained, typically after applying a linear baseline correction over a 500 Hz region centered on the appropriate ^{13}C multiplet. Relaxation parameters are obtained from a multiparameter least squares curve fitting routine using an implementation of the Levenberg–Marquardt algorithm. Theoretical values of the intensities of the modes are calculated first using the normalized, symmetric set of modes described by Werbelow and Grant[8] and then taking appropriate linear combinations to generate the modes described here. Parameters for the fit include not only dipolar and random field spectral densities, but also several experimental parameters.[9] To account for any systematic instrumental imperfections or differences in widths of inner and outer lines of the multiplet, the line amplitudes for each data set are scaled by two parameters β and δ such that the ^{13}C multiplet has the expected 1:2:1 intensity ratio when fully relaxed. The term L_3 (see Figure 1) is multiplied by δ to equalize the outer line intensities and then both outer lines are multiplied by β to equalize the intensities of the sum of the outer lines and the inner line of the multiplet. A third parameter associated with each data set is a normalization constant such that $^{a}\nu_c(\infty)$ is scaled to unity. Additional parameters are pulse efficiencies and differential pulse efficiencies.

Spectral densities included in the fit include four frequency independent spectral densities describing the dipolar relaxation of a methylene group ($^{13}CH_2$) in the limit of extreme narrowing (J_{CH}, J_{HH}, J_{HCH}, and J_{CHH}). Random field spectral densities are also included to account for other relaxation mechanisms operating in the sample, primarily remote dipolar interactions. For the methylene spin system, a complete set of random field spectral densities would include an autocorrelation term at the carbon (j_C), an autocorrelation term at each hydrogen (j_H), and a cross correlation term between the two hydrogens ($j_{HH'}$). At high fields or in a more anisotropic electronic environment caused by insertion of an oxygen into the polymer chain, cross correlation between chemical shift anisotropy (CSA) and dipolar relaxation mechanisms is possible. Where appropriate, this requires inclusion of four more spectral densities in the fit: $J_{CH,C}$, the cross term between the CH dipolar interaction and the carbon CSA; $J_{CH,H}$, the cross term between the CH dipolar interaction and the proton CSA; $K_{CH,H'}$, the cross term between the CH dipolar interaction and the CSA on the other proton (H′); and finally $J_{HH,H}$, the cross term between the HH dipolar interaction and the proton CSA.[10]

Rigorous characterization of dipolar interactions as random fields requires that both the rotational and translational motion of the interacting spins be independent. This independence of motion is not satisfied for protons bonded to carbons adjacent to the methylene group of interest. A study of isotopomers of 5-^{13}C nonane has shown that inclusion of random field terms in the relaxation matrix is not enough to allow accurate measurement of all four dipolar spectral densities in the presence of protons on neighboring carbons.[9] However, that study showed that as long as the random field term j_C is held equal to zero in the fitting procedure, then J_{CH}, J_{HCH}, and J_{CHH} may be reliably evaluated; J_{HH} remains strongly correlated to j_H. The results reported here follow this practice.

5 RESULTS FROM POLYMER STUDIES

These methods have been applied to a series of homologous polyethers with increasing numbers of methylenes between the oxygens: poly(oxymethylene) (POM),[11] poly(ethylene oxide) (PEO),[12] and poly(tetramethylene oxide) (PTMO),[12] and to poly(*cis*-1,4-butadiene) (CBD).[13] In the absence of data on polyethylene, CBD serves as a model for the dynamics of the infinite polymethylene chain. Recent simulations of polyethylene and polyisoprene suggest the dynamics are quite similar despite the structural differences and justify this analogy.[6] Data from the smaller hydrocarbon [11-^{13}C]heneicosane are also included for comparison.[14] These polymers exhibit a wide range of equilibrium conformations with POM most stable in a helical conformation and CBD in an extended, all-*trans* conformation. PEO and PTMO are more flexible and intermediate in conformational preferences. As such they provide an interesting opportunity to probe the impact of chain conformation on dynamics with only minimal variations in structure.

Each of the polymers studied has a single type of methylene group, except for PTMO which has two distinct types of methylene groups with the carbons adjacent to the oxygen (C-α) absorbing at 67.4 ppm and the central carbons (C-β) absorbing at 25.3 ppm. Only POM and heneicosane were isotopically labeled to provide truly isolated $^{13}CH_2$ spin systems.

Three 'magnetization nodes' of each $^{13}CH_2$ spin system can be obtained while observing only the ^{1}H coupled ^{13}C spectrum of a given polymer: $^{a}\nu_C$, the total ^{13}C magnetization; $^{a}\nu_{+-+}$, the difference between the inner and outer line intensities of the ^{13}C triplet; and $^{s}\nu_{+0-}$, the difference between the intensities of the outer two lines of the ^{13}C triplet. Figure 3 shows typical relaxation curves for C-α of PTMO.

The three dipolar spectral densities which have been reliably evaluated in all cases can be reexpressed in terms of three second rank autocorrelation times ($\tau_\perp = \tau_{xx} = \tau_{yy}$, τ_{zz}, and τ_{xy}). The transformation to Cartesian correlation times requires that the geometry of the spin system be known. In most cases these geometries must be inferred from small molecule analogs. As hydrogens are not located accurately in most X-ray diffraction studies, it is generally necessary to rely on other structural techniques such as electron or neutron diffraction. For methylenes in hydrocarbon chains, electron diffraction studies of small alkanes provide the HCH angle of 108.5° and a CH distance of 1.12 Å. For protons bonded to carbons adjacent to oxygen, the value of 1.11 Å for the CH distance given by the electron diffraction study of the small molecule analog 1,2-dimethoxyethane has been adopted. The HCH angle was not determined in that study. The Cartesian correlation times calculated using these parameters are given in Table 1. Uncertainties reported are standard errors in the last significant figure of the associated value.

The timescales of tens of picoseconds reported in Table 1 are consistent with those generally found for local segmental motion of polymers in dilute solution. Because of differences in temperature and viscosity among the samples, comparing the absolute values of the correlation times is not as interesting as comparing ratios of correlation times which gives insight into the anisotropy of motion. Table 2 gives these ratios.

If we examine the anisotropies of motion of the most conformationally distinct polymers, POM and CBD, we see

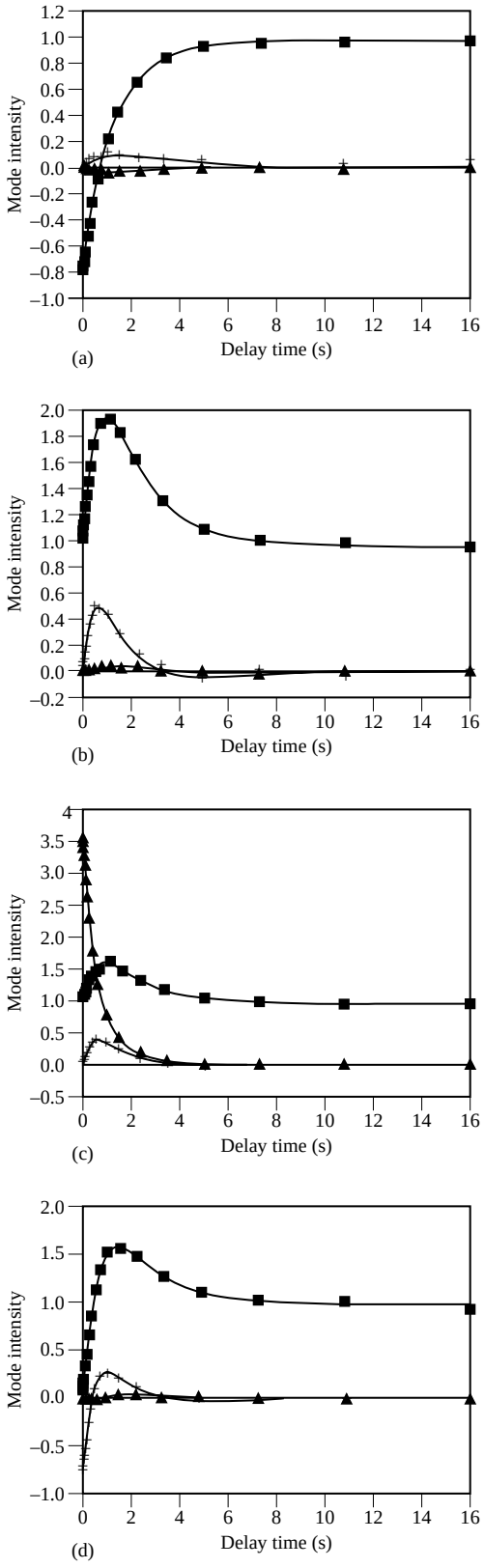

Figure 3 Magnetization mode intensities for C-α of PTMO. Intensity units are defined by setting $^{a}\nu_{C}$ (∞) to unity. Experimental values for $^{a}\nu_{C}$, ■; experimental values for $^{a}\nu_{+-+}$, +; experimental values for $^{s}\nu_{+0-}$, ▲. Solid lines are calculated from fitted parameters. (a) After ^{13}C inversion. (b) After ^{1}H inversion. (c) After selective inversion of one line of the ^{1}H doublet. (d) After J pulse preparation of the ^{1}H spins, resulting in ^{1}H inversion and inversion of the outer lines of the ^{13}C multiplet

Table 1 Cartesian Correlation Times of Polymers in Solution

	$\tau_{\perp}$ (ps)	τ_{zz} (ps)	τ_{xy} (ps)
POM (phenol-d_6, 86 °C)	21(1)	36(6)	12.1(8)
PEO (D_2O, 25 °C)	42(9)	115(11)	44(3)
PTMO(C-α) (toluene-d_8, 28 °C)	21(2)	64(3)	10.4(6)
PTMO(C-β) (toluene-d_8, 28 °C)	15(2)	45(2)	15.2(6)
CBD (CD_2Cl_2, 20 °C)	23(2)	55(6)	11(1)
C11-heneicosane (diglyme-d_{14}, 40 °C)	21(1)	48(3)	9(1)

Table 2 Motional Anisotropies of Polymers in Solution

	$\tau_{zz}/\tau_{\perp}$	τ_{zz}/τ_{xy}	$\tau_{\perp}/\tau_{xy}$
POM	1.6	2.6	1.6
PEO	2.7	2.6	1.0
PTMO(C-α)	3.0	6.2	2.0
PTMO(C-β)	3.0	3.0	1.0
poly(*cis*-1,4-butadiene)	2.4	5.0	2.1
C11-heneicosane	2.3	5.1	2.2

that they are quite different. POM has reduced anisotropies of motion compared with CBD methylenes, which in turn have anisotropies of motion which are very similar to those of the central methylene of the smaller hydrocarbon heneicosane. These differences have been interpreted in terms of the relative importance of transitions between rotational isomeric states and librational motion within a given potential energy well in the spin relaxation of these polymers. The lowest energy conformation of POM in solution is predicted to be helical, with no readily available rotational transitions that do not involve major chain translocation. In such a situation it is reasonable to expect librational motion to be an important relaxation mechanism. In CBD the extended chain structure make possible 'crankshaft'-type correlated motions of a few bonds. Supporting the interpretation that these might be important are simulations of hydrocarbon chains which show contributions from both correlated and uncorrelated chain motions. The correlated motions in these simulations have a similar ratio of $\tau_{zz}/\tau_{\perp}$ to that observed for CBD and heneicosane.[15]

New patterns emerge when examining the anisotropies of motion for PEO and PTMO. Overall the pattern for C-α of PTMO is much like those seen previously in hydrocarbons, although with slightly greater anisotropies. PEO and the C-β position of PTMO have very similar anisotropies of a reduced magnitude and a much different pattern from any observed previously. The ratios $\tau_{zz}/\tau_{\perp}$ and τ_{zz}/τ_{xy} are nearly identical and the ratio $\tau_{\perp}/\tau_{xy}$ is essentially unity. The relative anisotropies of C-α and C-β of PTMO are the opposite of what might be naively expected. Based on the similarity of the energetics of conformations involving C-α and its adjacent atoms to those in PEO, and of conformations involving C-β to those in PE, one might expect the opposite result.

Do the differences in dynamics in PEO and PTMO originate at the librational level or in transitions between rotational isomeric states? It is difficult to imagine that the differences in

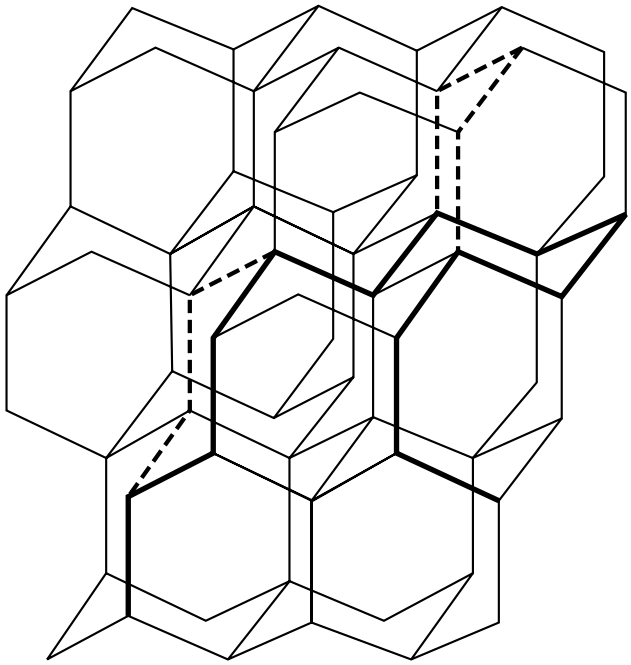

Figure 4 Examples of chain motion on a tetrahedral lattice. An example of three bond motion is at the bottom and of four bond motion is at the top

librational motion between C-α and C-β, adjacent carbons in the PTMO chain, are large enough to give rise to the measured difference in anisotropies. A plausible model does exist for differences in rotational transitions.

Geny and Monnerie have simulated the motion of the various linear polyoxides as motions involving three or four bonds on a tetrahedral lattice.[16] Examples of such motions are shown in Figure 4. The three bond motions are essentially the 'crankshaft'-type motions referred to above. Four bond motions involve the pivoting of a segment back and forth, without the option of continuing around the chain axis. Three bond motions occur in all their simulations of the polyoxides although with markedly less 'efficiency' in POM due to the stability of its helical form. Four bond motions such as shown are forbidden in PE due to the 'pentane effect' (which rules out g^+g^- sequences because of steric interactions of the hydrogens on carbon i and i + 4 along the chain). In the polyoxides these motions are allowed as long as at least one oxygen atom is at the 'foot' of the pivoting segment. Geny and Monnerie found these motions even more common than three bond motions in PEO, significant in PTMO, and again rarely observed in POM.

Of course, full recognition must be given to the limitations of the model of the polymer chain as moving on a tetrahedral lattice. In this model all motions must be cooperative, in the sense that any configurational transition is accompanied by compensatory transitions elsewhere in order not to force large motions of the chain. In contrast, Brownian dynamics simulations of the PE chain showed that at least two-thirds of the configurational transitions in PE were 'isolated' rotations about bonds along the chain accompanied by orientational relaxation of neighboring segments. Simulations of polyisoprene suggest that three bond motions are largely absent in polyisoprene. Furthermore, analysis of the motion in isolated configurational transitions and in 'three bond motions' in PE finds them to be nearly identical, leading into question the importance of cooperative motions in analyzing polymer dynamics.

Even so, the reduced anisotropy of PEO relative to the hydrocarbons may be due to the combination of three- and four-bond motions available to the former. In particular, the ratio $\tau_\perp/\tau_{xy}$ becomes unity only when there is efficient averaging with respect to the z axis of the coordinate system we have defined. Remembering that the z axis is perpendicular to the HCH plane or parallel to the vector between adjacent atoms on either side of the methylene along the polymer chain, efficient averaging around this axis occurs whenever the methylene is located at the 'point' of the four bond section which is pivoting.

The results for PTMO may then be explained by noting that only C-β can be at the 'point' of the pivoting section when there is an oxygen at the 'foot', making the four bond motion possible. The motion of a methylene at the 'side' of the four bond segment is similar to that caused by a three bond motion and thus although PTMO as a whole appears to undergo three and four bond motions, C-α can only experience 'three bond like' motion and thus is very similar in anisotropy to hydrocarbons studied previously. Thus while four bond motions may be minor components of the overall dynamics, by introducing a distinctly different reorientational motion they may have an apparently disproportionate impact on the measured anisotropy. A more complete analysis of the importance of these motions must await more realistic simulations of the polyoxide chains. A molecular dynamics simulation of PEO in water has been published recently, but it was on a fairly short chain (13 units) and the question of cooperative transitions was not addressed.

6 RELATED ARTICLES

Brownian Motion and Correlation Times; Carbon-13 Relaxation Measurements: Organic Chemistry Applications; Protein Dynamics from NMR Relaxation; Relaxation Mechanisms: Magnetization Modes; Relaxation Processes in Coupled-Spin Systems; Relaxation Processes: Cross Correlation and Interference Terms; Relaxation Theory: Density Matrix Formulation

7 REFERENCES

1. N. Bloembergen, E. M. Purcell, and R. V. Pound, *Phys. Rev.*, 1948, **73**, 679.
2. L. G. Werbelow and D. M. Grant, *Adv. Magn. Reson.*, 1977, **9**, 189.
3. R. L. Vold and R. R. Vold, *Prog. Nucl. Magn. Reson. Spectrosc.*, 1978, **12**, 79.
4. D. M. Grant, C. L. Mayne, F. Liu, and T.-X. Xiang, *Chem. Rev.*, 1991, **91**, 1591.
5. L. Monnerie, *Makromol. Chem., Macromol. Symp.*, 1991, **48–49**, 125.
6. M. D. Ediger and D. B. Adolf, *Adv. Polym. Sci.*, 1994, **116**, 73.
7. M. M. Fuson, M. S. Brown, D. M. Grant, and G. T. Evans, *J. Am. Chem. Soc.*, 1985, **107**, 6695.
8. L. G. Werbelow and D. M. Grant, *J. Chem. Phys.*, 1976, **63**, 544.
9. M. M. Fuson and A. M. Belu, *J. Magn. Reson., Ser. A*, 1994, **107**, 1.

10. Z. Zheng, C. L. Mayne, and D. M. Grant, *J. Magn. Reson., Ser. A,* 1993, **103**, 268.
11. M. M. Fuson and D. M. Grant, *Macromolecules*, 1991, **24**, 2594.
12. M. M. Fuson and J. B. Miller, *Macromolecules*, 1993, **26**, 3218.
13. M. M. Fuson and D. M. Grant, *Macromolecules*, 1988, **21**, 944.
14. M. S. Brown, D. M. Grant, W. J. Horton, C. L. Mayne, and G. T. Evans, *J. Am. Chem. Soc.*, 1985, **107**, 6698.
15. T. A. Weber and E. Helfand, *J. Chem. Phys.*, 1983, **78**, 2881.
16. F. Geny and L. Monnerie, *J. Polym. Sci., Polym. Phys. Ed.*, 1979, **17**, 131, 147, 173.

Biographical Sketch

Michael M. Fuson. *b* 1954. B.A., 1976, Haverford, Ph.D., 1982, Yale (supervisor J. H. Prestegard). Postdoctoral studies at the University of Utah (with D. M. Grant). Faculty in Chemistry at Wabash College (1984–89) and Denison University (1989–present). Approx. 10 publications. Research interests: coupled spin relaxation and molecular motion in macromolecules.

Field Cycling Experiments

Friedrich Noack

Universität Stuttgart, Physikalisches Institut, Stuttgart, Germany

1	Introduction	1
2	Basic FC Principles	1
3	Technical Problems and Instruments	3
4	Refinement and Extensions	6
5	Selected Examples	8
6	Related Articles	9
7	References	9

1 INTRODUCTION

In conventional NMR experiments the spin resonance is observed by irradiating selected nuclear magnetic spins of a sample material, which is exposed to a fixed high magnetic flux density $\boldsymbol{B}_0$ (Zeeman field, magnetic induction), with appropriate time-dependent rf fields $\boldsymbol{B}_1(t)$ tuned in resonance with the Larmor frequency $\nu \sum \omega/2\pi$ of the nuclei considered. This resonance frequency ν usually varies linearly with the magnitude of the Zeeman field $\boldsymbol{B}_0$ according to the Larmor condition $\nu = \gamma B_0/2\pi$, where γ is the characteristic magnetogyric ratio of the nuclear spin species; therefore, with decreasing field strength the standard procedures become more and more impracticable or even impossible for several reasons. The difficulties are primarily due to the related well known weakening of the NMR induction signal, which for a constant number of nuclei falls approximately as $B_0^{3/2}$, but serious problems also occur due to the tendency of the resonance to become broader at lower frequencies for a given linewidth. Hence it is not surprising that, generally, instruments operating at $\boldsymbol{B}_0$ fields or Larmor frequencies ν as high as possible are favored, and most endeavours in the past were concerned with ways to strengthen $\boldsymbol{B}_0$ to improve the signal quality. Presently, most spectrometers work under high-field conditions in the range between about 4 MHz up to 800 MHz for protons and up to 100 MHz for several spins with smaller γ, corresponding to a maximum Zeeman field of nearly 20 T. However, many good reasons can be given to support the less spectacular developments which oppose this familiar trend, that is, how to overcome the physical and technical barriers connected with NMR frequencies below the common megahertz range. The Earth's magnetic field $B_{\text{Earth}} \approx 5 \times 10^{-5}$ T can be easily compensated for to less than 1% of its value, allowing NMR spectroscopy with Larmor frequencies as low as, for example, 20 Hz for protons to be performed.

Numerous techniques have been successfully realized to solve the problems of NMR under low-field conditions below $\nu \approx 1$ MHz, ranging from simple enlargement of samples to sophisticated polarization transfer. One of these techniques, which is still relatively rarely used despite the great instrumental progress in recent years, is field cycling (FC) magnetic resonance or, more correctly, fast field cycling, where $\boldsymbol{B}_0$ is not fixed but periodically cycled. Several reviews on the subject have been published.[1–3] FC primarily makes it possible to extend the scope of frequency-dependent relaxation measurements from the megahertz regime to almost zero Larmor frequency. FC devices also, however, supplement or even replace presently used standard procedures, because once in operation the new approach is often less time-consuming than common practice: changes of the Larmor frequency do not require inconvenient retuning of electric circuits. Furthermore, the FC principle is very versatile, since cycling of both the strength and orientation of the Zeeman field $\boldsymbol{B}_0$, combined with special $\boldsymbol{B}_1(t)$ sequences, allows for possibilities which go far beyond the original intentions.[1,2] Typical subjects of FC studies are concerned with, for example, frequency-dependent relaxation times (relaxation dispersion), zero field spectra (resolution improvement), heteronuclear cross-relaxation effects (quadrupole dips), diffusion constants (magic angle averaging), and the angular dependence of these and related NMR parameters where lower Larmor frequencies introduce more favorable spectoscopic timescales than conventional magnetic resonance methods.

The origins of the FC technique go back to the early 1950s, when several groups started low-field work and searched for ways to improve the results. A simple yet slow mechanical field switch was first described in 1951 by Pound.[4] However, it took more than 10 years to develop instruments which allowed the FC principle to be applied to other than the most convenient cases. Essentially based on the pioneering concepts of Redfield et al.,[5] several laboratories succeeded in developing fast, versatile FC devices for measurements of fast relaxing signals of liquids and solids, and various prototypes of flexible, powerful machines have been described in the literature.[1–3,6–13] However, a commercial apparatus is not yet available. Due to the peculiar spin dynamics of some particularly ordered systems such as organic conductors[7] (spin waves) or anisotropic liquids[11] (order fluctuations), where as a rule a dramatic shortening of the longitutinal spin relaxation time occurs at low fields, studies of such materials require very fast cycling devices, which are difficult to construct. However, the presently available equipment will allow the application of FC NMR in most cases,

2 BASIC FC PRINCIPLES

2.1 Field Periods

FC requires the sample material to be in different Zeeman fields (two or more) at different times t. This implies that the normally constant external flux density $\boldsymbol{B}_0 \sum \mu \boldsymbol{H}_0$ or magnetic field $\boldsymbol{H}_0$ (μ is the permeability of the sample) has to be modulated periodically (cycled) in strength or direction (ideally both) in an adequately fast manner in a definite way (Figure 1). In the simplest case the nuclear spins are polarized and detected as usual by means of a field sufficiently high to yield a satisfactory signal quality. Unlike standard high-field NMR, however, between the period of polarization and the period of detection one inserts a period of evolution, during which the external field is decreased from the selected high value to an adjustable lower level. In this way any related Larmor frequency can be tuned easily over a broad range $\nu_{\min} < \nu < \nu_{\max}$, where the limits are mainly determined

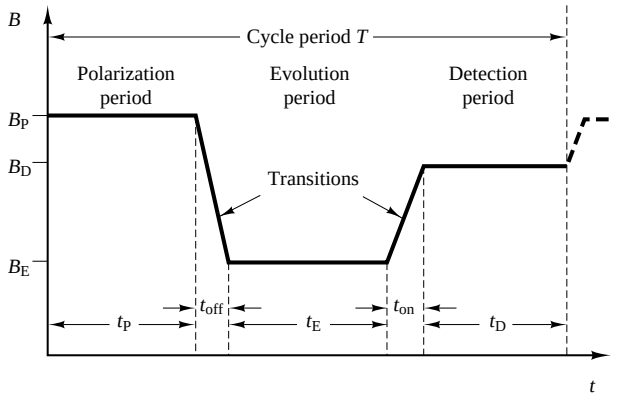

Figure 1 Typical $\boldsymbol{B}_0$ field cycle with polarization, evolution, and detection periods, and transition intervals from high to low and low to high

by the properties of the available magnet system and the exactness of the Earth's field compensation. As a consequence, features characteristic of the spins for frequencies between almost zero and an upper limit ν_{max}, at present typically 10–50 MHz, can be conveniently studied by well established high-field detection methods at a single fixed field. Obviously, the primary sensitivity problem is now transformed into the exacting task of switching an adequately high magnetic induction rapidly and reproducibly with sufficient accuracy. Sometimes it proves advantageous to use the highest accessible $\boldsymbol{B}_0$ not for the polarization and detection period, but only for the shorter evolution state, so that FC is a technique for both lowering and increasing the Larmor frequency compared with the fixed detection field.[3,11] During the different phases of the cycle the sample has to be irradiated by standard magnetic rf sequences $\boldsymbol{B}_1(t)$ to prepare and observe the nuclear magnetization or spin order, to determine the underlying frequency dependent spin parameters such as relaxation times, coupling constants, spectral shifts, jumping rates, etc.[1,2]

2.2 $\boldsymbol{B}_0$ Field Switches

To keep such experiments as flexible and transparent as possible, the cycle must fulfill several conditions on the level and speed of the field changes. It is obvious that both $\boldsymbol{B}_0$ and its time derivative $\mathrm{d}\boldsymbol{B}_0/\mathrm{d}t$ at the transitions should be made as large as is technically feasible to obtain good signals in the presence of fast magnetization decays. However, there are exceptions where it is necessary to slow down the switching to avoid effects on the spin order (see Section 2.4). Originally, the cycles were produced mechanically by moving or shooting the sample between a strong and a weak magnet[4] [Figure 2(a)]. This technique is relatively simple to realize, and is therefore still used,[14–16] taking advantage of strong cryomagnets for the high-field states, but it has some significant drawbacks. Above all, the switching times t_s (typically $t_{off} \approx t_{on} \geq 0.1\,s$) are generally too long for work on fast relaxing spins. The more powerful alternative[5] is to generate the transitions by quickly turning the current on or off through a magnet coil by means of an electronic switch [Figure 2(b)]. To understand the main problem of such a device one has to recall some elementary physics. If a voltage U is applied to a coil with inductance L and series resistance R_s, the current I through the coil, and

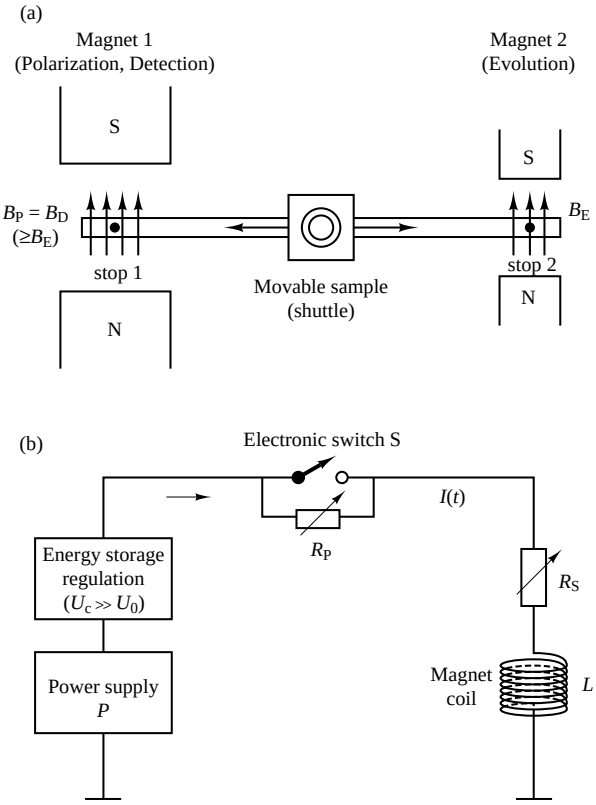

Figure 2 $\boldsymbol{B}_0$ field switch devices using either (a) a shuttle between two magnets (mechanical switch) or (b) a fast power supply control of the electric current I through a magnet coil (electronic switch)

hence the related field $\boldsymbol{B}_0$, increase exponentially with the time constant L/R_s. Owing to this increase, an equilibrium state is obtained more rapidly with a higher damping resistance, but this does not mean that the switching becomes faster by increasing R_s. Consideration of Faraday's induction law shows us that the fastest current change in the magnet is independent of R_s and determined by $(\mathrm{d}I/\mathrm{d}t)_{max} = U/L$; this maximum slope is maintained longer for a smaller R_s, and hence in principle a cryomagnet with $R_s = 0$ should give the best results. However, other features of cryomagnets, e.g. the maximum allowed current density, are less favorable. So to obtain fast field transitions one has to be concerned with high driving voltages U, and magnets with both low inductance L and low resistance R_s, i.e. with high-current air-cored coils instead of iron magnets. Since the highest electric power $P = UI$ is needed only for the (short) transition intervals, it is most effectively provided by an energy storage control which supplies a higher voltage (U_c) for the transition than for the steady states (U_0). All this was already known to Redfield,[5] but in 1968 adequate electronic components to build a powerful FC network were not available.

2.3 T_1 Cycle

A typical frequency-dependent FC measurement of the longitudinal relaxation time T_1 can be performed by combining a $\boldsymbol{B}_0$ cycle with standard $\boldsymbol{B}_1$ rf pulses as shown in Figure 3. When the Zeeman field is switched from its maximum value B_P to a selectable lower level B_R (in this case called the

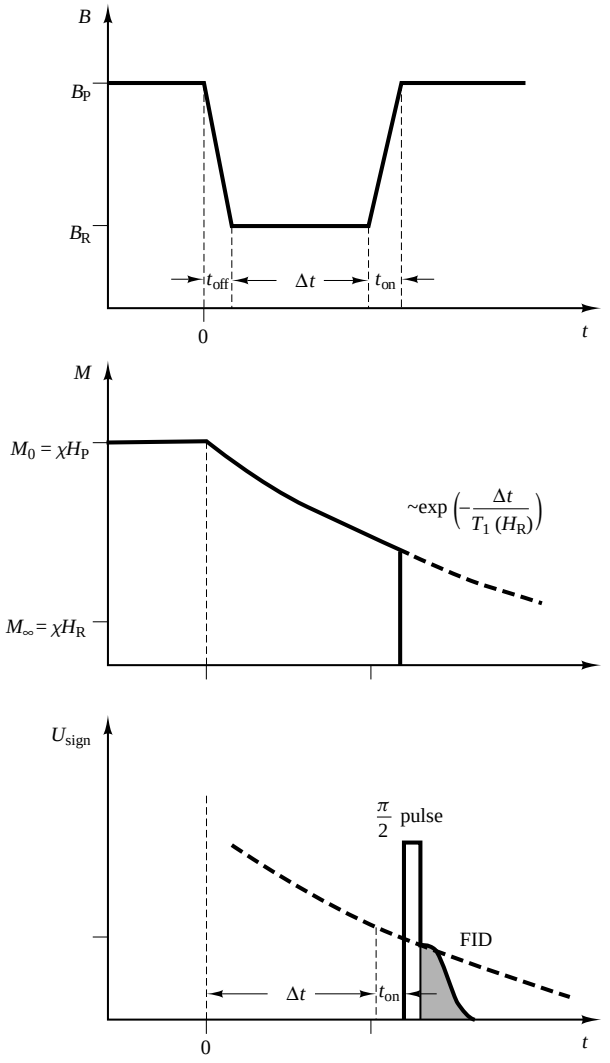

Figure 3 The FC principle for frequency- (or field-) dependent measurements of the longitudinal relaxation time $T_1(\nu)$ or $T_1(B)$. The diagram illustrates the $\boldsymbol{B}_0(t)$ cycle, the related magnetization decay $M(t)$ from M_0 to M_∞, and the FID signal $U_{sign}(t)$ after a $\pi/2$ $\boldsymbol{B}_1$ rf pulse

relaxation period), the initial longitudinal magnetization $\boldsymbol{M}_0 = \chi \boldsymbol{H}_0 = (\chi/\mu)\boldsymbol{B}_0$ along the external magnetic field $\boldsymbol{H}_0$ of, say, proton spins (χ is the nuclear spin susceptibility) decays exponentially with a time constant $T_1(H_R)$, characteristic of the Larmor frequency ν_R in the adjustable field H_R, to the new equilibrium $M_\infty = \chi H_R$. This decay is sampled as a function of the relaxation interval Δt by the FID amplitude after a $\pi/2$ rf pulse, applied in resonance with the Larmor frequency ν of the high detection field $B_D = B_P$, immediately after the transition to this detection state. Then the procedure is repeated over the available range of ν_Rs to give the full dispersion profile $T_1(\nu_R)$. If ν_R is near to ν_{max} and hence $M_0 - M_\infty$ becomes small, it is advantageous to precede the off switch by a π or $\pi/2$ rf pulse, which enhances the $M(t)$ change. The field switching times t_{off} and t_{on} must be shorter or at least comparable to the considered relaxation interval Δt and the observed T_1 value to get exact results. All these steps and the necessary data acquisition and processing, including the frequency changes, do not require hardware readjustments and can be conveniently made computer controlled. Frequency-dependent studies of other relaxation processes, e.g. transverse to $\boldsymbol{B}_0$ (T_2) or along the dipolar field $\boldsymbol{B}_d$ (T_{1d}), are less common in the literature and require more sophisticated cycles and different rf pulse sequences,[1–3] which are briefly commented on later in this article.

2.4 Adiabatic Condition

The main purpose of making the $\boldsymbol{B}_0$ field switches of a cycle fast is to avoid uncontrolled magnetization decay and hence signal losses by relaxation. For a T_1 cycle this essentially requires t_{off}, $t_{on} \leq T_1$. However, it is often overlooked that too fast transitions may also modify the magnetization or spin order undesirably in spite of negligible relaxation effects, namely by changing the angle of the magnetization $\boldsymbol{M}$ relative to the Zeeman field, and thus by inducing transitions between different Zeeman levels. Field changes preserving the initial angle during the transitions, which for normal FC T_1 measurements should be zero, for example, are called adiabatic, whereas nonadiabatic transitions perturb the angle.[1,2] Both types of switches are applied in FC experiments: standard relaxation studies demand adiabatic cycles;[1–3] nonadiabatic cycles[2,14,15] are mainly practised in zero field and Earth's field FC NMR, where rotations of $\boldsymbol{M}$ are necessary. The condition for adiabaticity requires that field variations perpendicular to the initial Zeeman field $\boldsymbol{B}_0$ must be slow compared with the effective Larmor frequency $\nu = \gamma B$ according to[1,2]

$$\frac{|\boldsymbol{B} \times \mathrm{d}\boldsymbol{B}/\mathrm{d}t|}{B^2} \ll \gamma B = 2\pi\nu \qquad (1)$$

which restricts the time derivative $\mathrm{d}\boldsymbol{B}/\mathrm{d}t$ if the direction is perpendicular to $\boldsymbol{B}$ because of the finite value of ν, particularly at low frequencies. Obviously, equation (1) is always valid, independent of the magnitude of $\mathrm{d}\boldsymbol{B}/\mathrm{d}t$, so long as the orientation of $\boldsymbol{B}$ is not changed. The condition becomes critical in the case of angular-dependent measurements, and in any case at low Larmor frequencies near $\nu \approx 10$ kHz, where for solids internal local field contributions $\boldsymbol{B}_{loc}$ are comparable in magnitude to the external field $\boldsymbol{B}$, and thus locally fast field rotations come into play. Similar effects may occur if the Earth's field is not properly compensated for or not correctly adjusted parallel to the Zeeman field of the spectrometer. Such problems have frequently been neglected and need more careful study. Adiabaticity sometimes requires that the cycle transition must be slowed down in the low-field range by appropriate current regulation, though such a step entails a dilemma between signal losses at transitions by either nonadiabaticity or by relaxation.

3 TECHNICAL PROBLEMS AND INSTRUMENTS

3.1 Magnet Switch Optimization

Magnets for fast FC NMR should provide the following from a given electric power P: (i) a magnetic flux density (induction) B or the related magnetic field $H = B/\mu$ as high as possible; (ii) the large flux variation rate $\mathrm{d}B/\mathrm{d}t$ needed for the cycle; and, in addition, (iii) a satisfactory field homogeneity

$B/\Delta B$ over the sample volume. These three requirements are strongly interrelated, and the problems of finding the most favorable switching network and coil geometry have still not been solved completely. This explains why many constructions described in the literature[5–13] are more or less based on semiempirical rules concerning the magnet system, though there are some sophisticated approaches. The basic aspect of the optimization problem is well demonstrated by considering estimations of B and dB/dt for a simple, long cylindrical coil with inductance L, resistance R_S, and field volume V in the solenoid approximation (length $\gg$ diameter), where the field is assumed to be constant over the whole coil volume, i.e. its inhomogeneity $\Delta B/B$ is neglected. If such a solenoid is driven by a power supply with maximum current I_{max} and maximum voltage U_{max} during the transitions, the greatest possible flux density and flux variation rate following from Maxwell's equations are determined by[1,2]

$$(B)_{max} = (\mu L/V)^{1/2} I_{max} = (\mu L/V)^{1/2}(U_0/R_S) \qquad (2)$$

$$(dB/dt)_{max} = (\mu/LV)^{1/2} U_{max} = (\mu/V)(P_{max}/B_{max}) \qquad (3)$$

with $P_{max} \sum I_{max}U_{max}$, $I_{max} \sum U_0/R_S$, and U_0 the steady state supply voltage. These relationships illustrate the intricate role of the magnet inductance L when trying to optimize the switch characteristics, i.e. to maximize both B and dB/dt, since the field strength increases with $L^{\frac{1}{2}}$, whereas dB/dt decreases with $1/L^{\frac{1}{2}}$. Essentially, equations (2) and (3) show the merits of high-current magnets in comparison with low-current coils, and also establish that the available electric power, the maximum field, and the field volume limit the switching or transition times t_{off}, t_{on} of the cycle. The time $t_S = (dt/dB)\ B$ for a transition from zero to B_{max}, or the inverse, becomes larger in the considered approximation ($\propto B_{max}^2$ and V), but smaller with higher power ($\propto 1/P_{max}$). Therefore the technical progress achieved in recent years is due to a great extent to the improved knowledge of handling smaller, yet still homogeneous magnet coils in combination with more powerful electric current supplies; advanced supplies typically should provide [11–13] an average power of 10–50 kW and a peak power of 100–500 kW to obtain fields of the order of 1–2 T, with switching times better than 1–10 ms and a homogeneity up to some 10^4 over 1 cm^3. One should note that equations (2) and (3) involve an interesting dependence on the permeability μ, which, however, has not been exploited in practice due to the technical problems of filling the coil volume around the sample with a magnetic material.

3.2 Energy Storage

Since the switching power $P_S = P_{max} = I_{max}U_{max}$ is only needed over the rather short field transition times, and both the power $P_0 = I_{max}U_0$ and voltage U_0 to maintain the stationary high-field states of the cycle are much lower than P_{max} and U_{max}, respectively (in the case of a superconducting magnet P_0 is zero!), it is advantageous to separate the driving networks for the transitions and for the steady states. This concept was first introduced by Redfield et al.,[5] but in a rather elementary way. Its main advantage comes from the fact that though P_S must be made extremely high (up to many hundreds of kilowatts) the related average energy $\langle E_S \rangle = P_S t_S$ is still relatively small because of the short switching time, typically of the order of milliseconds. Therefore, it is possible to take this switching energy and voltage from a precharged, sufficiently large high-voltage capacitor, C, which allows the collection and storage of the required energy over the whole cycle period from a comparably small auxiliary electric supply. Such a storage capacitor and suitable switching networks[6–13] can very effectively provide much higher driving voltages for the field transitions than the main lower-voltage current system, and thus achieve the fast current changes where desired. This is the well known energy storage principle of Redfield.[5] Since its original application the concept has been extended and refined in such a way that the magnetic energy of the coil is used to charge and recharge the storage capacitor during the field switch-off intervals instead of dissipating it in a damping resistor as in Redfield's work.[8,10,11] After the initial charging of the capacitor by the auxiliary supply, the switching device transforms magnetic coil energy to electric field energy and vice versa, so that the average additional power needed to generate the fast cycle transitions remains relatively low, typically less than a few percent of the main system. Essentially, only the ohmic losses of the circuits have to be compensated.

3.3 MOSFET–GTO Switching Networks

Figure 4 illustrates the basic components of an advanced fast FC network,[8–13] using high-voltage field effect transistors (MOSFETs) to regulate the magnet current for the stationary field states, and high-voltage gate turn-off thyristors (GTOs) to control the current paths of the energy storage during the transition periods. These and similar devices reported in the literature operate in general as follows. The current through the magnet coil, from a high-power low-voltage dc supply, is regulated by a MOSFET bank network, which tolerates the high-voltage peaks induced by the current switching of up to more than 1 kV without being damaged. To reduce the magnet current at the end of the polarization period, the gates of the MOSFETs are regulated to a selected level, and thus the decreasing current is partially driven by the storage capacitor, which is precharged by an additional high-voltage, low-current source up to the limits of the components, characteristically 1 kV. This auxiliary supply provides an adjustable voltage for the field transitions, so that the ratio U_C/L responsible for the slope of the current changes can be made considerably larger than the ratio U_0/L determined by the main current source, and consequently the transit from high to low becomes faster by a factor U_C/U_0. Similarly, to increase the current through the coil from a given lower level, the MOSFET gates are opened again, and simultaneously the high voltage of the storage capacitor is connected with the correct polarity to the coil by firing the GTO thyristor. In this way the current turn-off and turn-on can be driven by the same voltage $U_C \gg U_0$. Finally, as soon as the detection field level is reached, the GTO is switched off and the MOSFETs begin to stabilize the new detection state of the cycle. Figure 4 includes the different current paths for the four individual regulations of the switching network. In the high to low step the device transforms the magnetic coil energy to the electric field energy of the storage capacitor, and in the low to high step the process

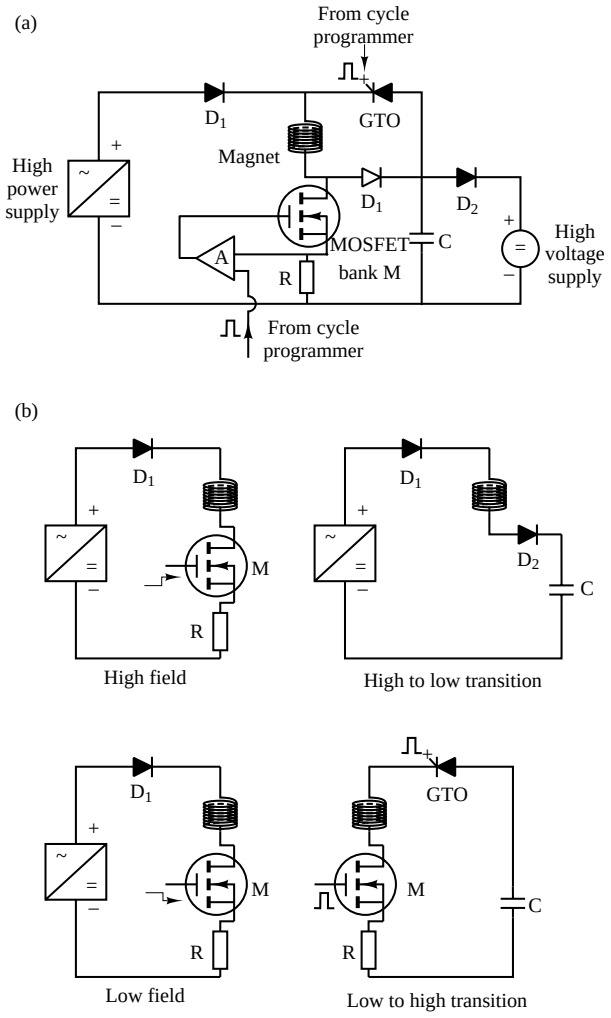

Figure 4 Basic components of a fast FC network with energy storage, making use of a MOSFET bank to regulate the current of the main power supply through the magnet coil, and a GTO to control the auxiliary high-voltage supply and the energy storage by the capacitor C. The figure illustrates (a) the basic network and (b) the four individual current paths for the transitions and steady states of the field cycle, timed by a cycle programmer

is inverted. By this means it has become possible to obtain maximum fields of more than 1 T with switching times of approximately 1 ms,[7–13] i.e. much more powerful and faster cycling instruments are possible than without energy storage. Unfortunately, commercial help for building such FC devices is still rather poor. Improvements to noncommercial switching networks, however, have become more and more facile by the availability of novel and less expensive semiconductor components such as POWER-MOSFET and POWER-IGBT (insulated gate bipolar transistor) packages,[17,18] which have properties similar to individual field effect transistors, but can handle higher currents without the need to connect an inconveniently large number of them in parallel.

3.4 Magnet Coil Geometries

Many different forms of air-cored coils have been considered and tried for FC spectrometers.[1,2] Originally, the Helmholtz ring pair arrangement was highly favored because of the well understood mathematics and the convenient radial access to the center of the magnet. However, the field at this center is markedly weakened relative to the strength near the inner surface of the conductor rings because of the wide air gap. Furthermore, even in the ideal case of negligible conductor cross section relative to the gap area, good homogeneity is confined to a rather small space around the midpoint region, and deviations from the ideal Helmholtz geometry are hard to correct. This circumstance, together with the poorer theoretical B/I ratio compared with cylindrical geometries, has made it evident that Helmholtz-type coils are not a good solution for FC magnets. Cylindrical coils can be designed that are superior to ring pairs with regard to many critical specifications such as maximum flux density, homogeneity, and total field volume, as was pointed out in the historic paper of Hak;[19] this result has long been overlooked. To take advantage of the cylinder geometry, however, one has to accept the inconvenience of having only axial access to the field center, which is why only later developments concentrated on such magnets. The ideal cylinder (solenoid, length $\gg$ diameter) theoretically gives a zero field gradient at its center, yet demands an unreasonable length and field volume, and hence it is necessary to look for short systems with suitable refinements of the field homogeneity. Various practicable ways exist to increase the current density at the ends of short cylindrical coils in order to diminish the field gradient over the central region by modifications to the conductor construction.[1,2,19–22] The most important of these modifications are shown in Figure 5, and are namely a linearly increasing number of conductor loops (linearly varied winding), a reduced number of loops (or even a gap) in the central part (outer notch), decreasing loop separations toward the coil ends (graduated current density), and conductor loops with a continuously variable cross section (optimized current

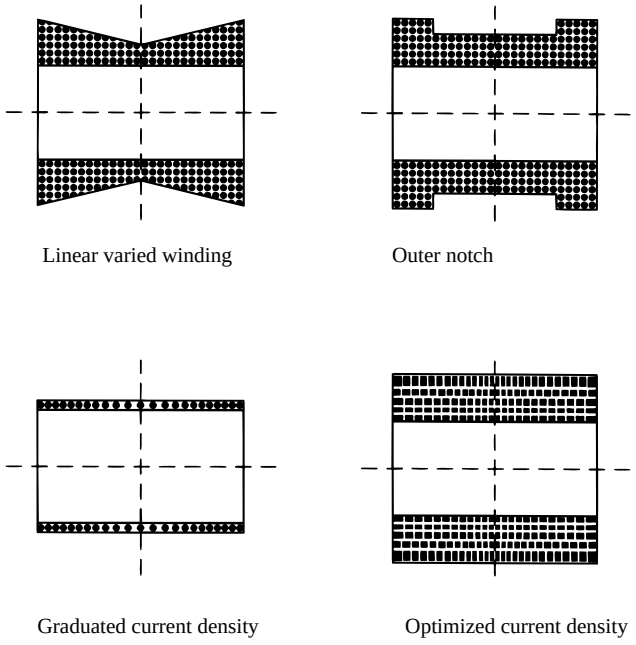

Figure 5 Cylindrical air core coil geometries to increase the field homogeneity of short FC magnets with small field volume

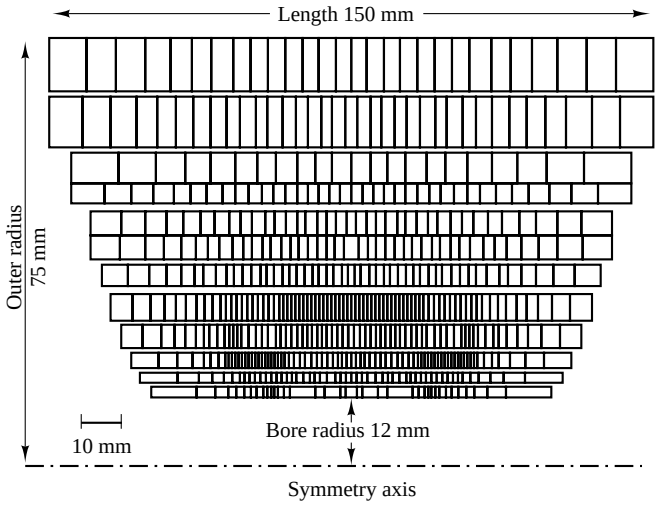

Figure 6 Conductor cross-section distribution (upper half) of a 2.4 T/50 kW FC magnet with optimized current density

density). By far the best results have been obtained using the last approach, which makes use of a novel Lagrange formalism[21] to calculate the most efficient coil and loop geometry under selectable constraints; i.e. it evaluates the conductor distribution that maximizes the field B for a given electric power P by simultaneously observing selectable target points (constraints) on the field homogeneity $B/\Delta B$ and the field volume V, i.e. indirectly on the inductance L. This Lagrange minimization procedure allows an inversion of the Biot–Savart law [$B(I)$ relationship] to a current–field law [$I(B)$ relationship] for conductor segments with an arbitrarily high number of adjustable coil parameters, and so gives an explicit (numeric) solution for the optimized current distribution. Several prototypes of such powerful FC magnets have been fabricated by cutting the calculated conductor rings from suitable copper and aluminum tubes. The cutting was performed either mechanically with isolating gaps as fine as 0.1 mm by means of a computer-controlled turning lathe,[11,21,22] or with less narrow gaps by computer-controlled spark erosion techniques.[12] Figure 6 represents the conductor cross sections of a 2.4 T/50 kW magnet manufactured in the author's laboratory.[22] The coil has 12 layers with about 20 000 parameters and an air bore of 24 mm diameter. The inner windings were cut from copper tubes, and the outer ones from aluminum tubes to lessen cutting problems.

4 REFINEMENT AND EXTENSIONS

FC is a particularly useful technique if the NMR properties to be investigated and the models involved depend on the Larmor frequency ν or the related magnetic energy splittings, and thus allow scaling of other frequencies, reorientation rates, coupling constants, and interaction energies of the spin system. Originally, FC was primarily used to study the frequency or field dependence of relaxation times in liquids, in order to analyze molecular motions by relaxation models; after numerous instrumental improvements, however, the technique can also be applied to quite different aims and problems. Though only relatively few laboratories have contributed systematically to instrumental developments, there has been a remarkable increase in the number of research groups working with FC, and numerous papers have now been published in this subject area.[1–16] Results are available for many types of materials, such as pure liquids, diamagnetic and paramagnetic solutions, liquid crystals, biological systems, molecular and ionic crystals, polymers, metals, alloys, and both classical and high-temperature superconductors. A large number of the earlier contributions have been summarized in several reviews[1–3] about both the technical concepts and physical findings of FC studies. Broadly, one can distinguish four types of applications, which require somewhat different spectrometers for suitable $\boldsymbol{B}_0$ cycles (Figure 7), rf pulse sequences $B_1(t)$, and data-processing methods. Some of these special FC subjects are described in related articles in this Encyclopedia.

4.1 Relaxation Dispersion

The main intention here is to study atomic or molecular motions by the frequency dependence of spin relaxation times[1–3] (relaxation spectroscopy, or relaxometry), commonly by $T_1(\nu)$ (longitudinal to $\boldsymbol{B}_0$, see Figure 3) and more rarely also by $T_2(\nu)$ (transverse to $\boldsymbol{B}_0$, see Figure 7). The interesting combination of FC with other spin relaxation processes such as $T_{1\rho}$ (rotating frame), $T_{1\mathrm{d}}$ (dipolar), or $T_{1\mathrm{q}}$ (quadrupolar), i.e. with more sophisticated spin preparation rf pulses, is still in its early stages.[23] In recent years, relaxation spectroscopy of solid-type signals has been extended from protons to other less sensitive but weaker coupled nuclei, e.g. deuterons, essentially to allow selective frequency-dependent measurements for different sites on a molecule by means of fast Fourier transform data processing.[11,24,25] The inclusion of this standard high-field NMR practice in fast electronic FC methods was an old but hard to realize challenge, and the experimental problems for this aim, which requires better magnet stability and homogeneity than previous nonselective work, have not yet been solved satisfactorily. Another fascinating recent development originated from the combination of relaxation spectroscopy with imaging procedures,[16] whereby using very inhomogeneous relaxation fields the T_1 dispersion over a broad range is spatially encoded in the sample; thus with adequate imaging rf pulses it is feasible to determine $T_1(\nu)$ in principle by one single B_R adjustment, i.e. by one single cycle. Obviously, these two refinements need almost opposite magnet specifications.

4.2 Zero Field NMR

In this case the original purpose was to enhance the spectral resolution[14,15,26] for polycrystalline or powdered samples through the phenomenon that in a zero magnetic field the Zeeman energy, and consequently also the line broadenings caused by the orientational distribution of dipolar or quadrupolar coupling tensors relative to the external Zeeman field $\boldsymbol{B}_0$, become irrelevant. In a zero field these interactions are made the dominant energy terms of the spin Hamiltonian, which can entail more favorable transition rules and thus simplify the NMR spectrum.[26] Almost all reported measurements were performed by mechanical FC

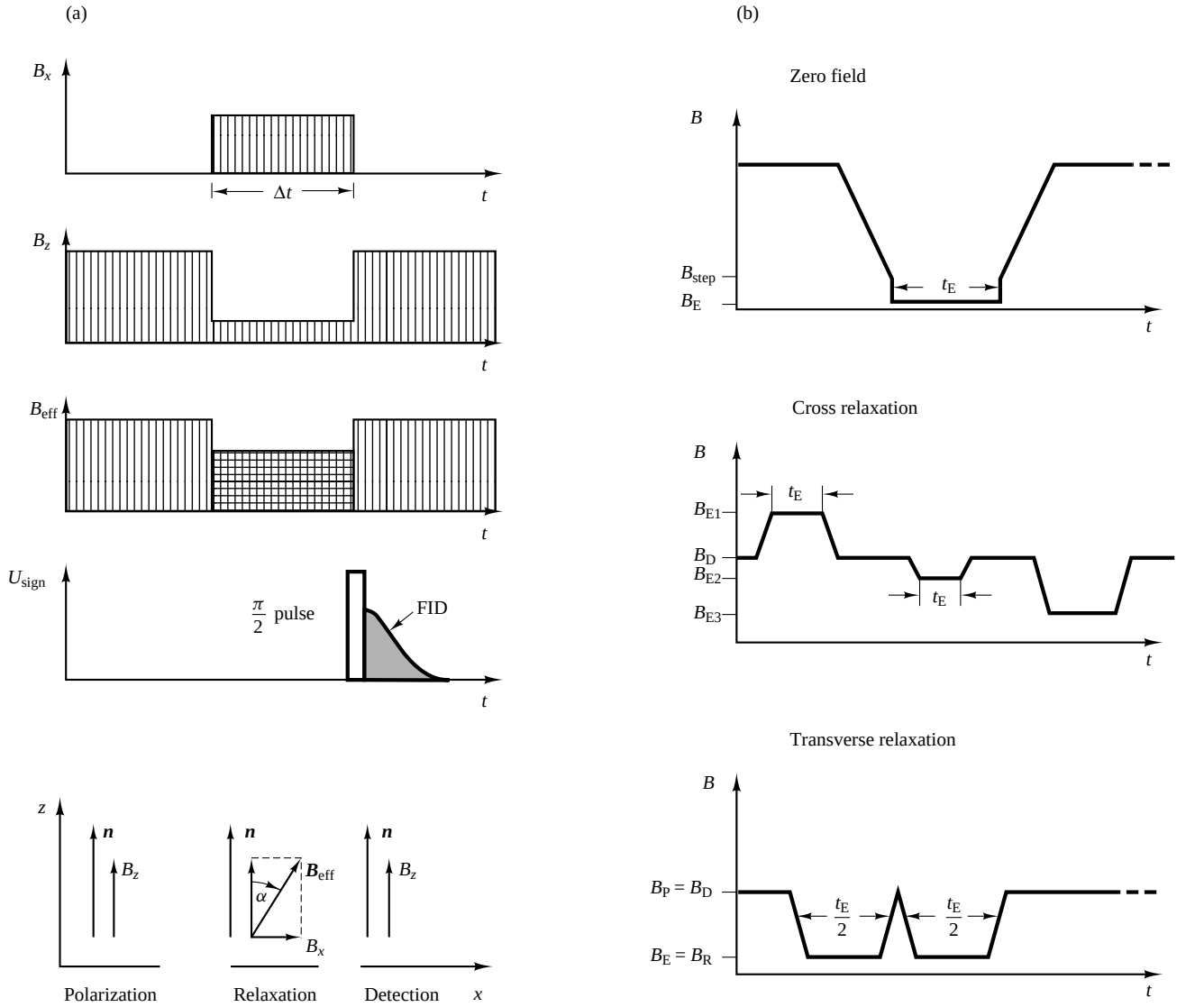

Figure 7 Advanced forms of $\boldsymbol{B}_0$ field cycles for (a) angular-dependent NMR measurements, making use of two perpendicular fields B_x, B_z, and (b) zero field, cross relaxation and transverse relaxation studies

instruments[14,15] and so are restricted to samples with long relaxation times T_1 ($\geq$0.1 s), which excludes, for example, biological membranes and liquid crystals. Unfortunately, the few experiments known so far for such samples with short T_1 s (millisecond range) in a zero field have proved rather disappointing,[27,28] because the expected resolution improvement could not be achieved; it seems to be hidden by the relaxation broadening and by experimental errors.

4.3 Cross-Relaxation Spectroscopy

Relaxation rates often involve a resonant increase in particular Zeeman fields where, as a function of $\boldsymbol{B}_0$, different energy levels of the spin system have a crossing point. The advantage of the FC method is to make use of such resonant exchange effects between dipolar, quadrupolar, Zeeman, and other (e.g. vibrational) splittings by properly adjusting the field to the resonance conditions[29–33] of multiple, different level crossing mechanisms. Using this method it has become possible to detect directly very small cross couplings between unlike spins or between like spins in different surroundings. These include interactions between protons and quadrupolar deuterons, nitrogens or chlorines,[2,29,30] between protons and vibrational modes in tunnel systems such as methyl groups,[9,31] or between quadrupolar spins in a highly symmetric crystal lattice and a less symmetric defect structure.[13,32,33] In the last case the technique is generally combined with selective irradiation of quadrupole transition frequencies at low fields to enhance the cross-coupling effects (nuclear quadrupole double resonance, NQDR). In addition to relaxation dispersion, several variants of NQRD belong to the most widely used FC applications.[13]

4.4 Angular Dependent FC

Originally, rotations of the field direction were introduced as a means of measuring relaxation times, which are angular dependent relative to special crystal axes,[2,34] for clearer

model discrimination, as illustrated in Figure 7. Later, the method initiated quite different types of work,[35–38] where fast electronic field switching is capable of extending considerably the previously used slower alternatives. For example, by changing the magnetic field direction relative to the symmetry axis (director) of liquid crystals, it becomes possible to study the short-time behavior of anisotropic flow processes, particularly the alignment of the director field parallel to $\boldsymbol{B}_0$, and thus the many anisotropic viscosities and elastic constants.[36] Similarly, one can reduce the dipolar coupling of spins by a fast magic angle orientation of $\boldsymbol{B}_0$ relative to the director and thus lengthen the effective transverse relaxation time T_2. In this way, the NMR pulsed field gradient (PFG) diffusion method has been successfully combined with FC for direct measurements of diffusion constants, even those that are angular-dependent, where normal solid-like FIDs are much too short to detect the contribution of the Fick's law signal decay more conventionally.[37,38]

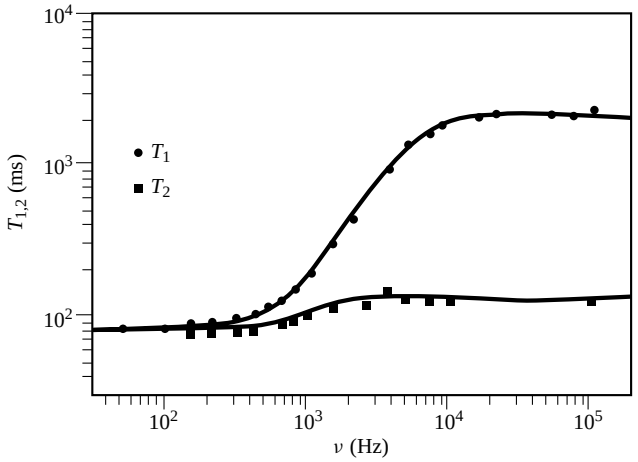

Figure 8 Proton spin relaxation dispersion of pure H_2O enriched with 4% ^{17}O (pH 7 and 26 °C) at low Larmor frequencies in the sub-Earth's field range. Lines are model fits[6,41]

5 SELECTED EXAMPLES

By far the most extensive applications of FC described in the literature are concerned with biological systems, polymers, and liquid crystals.[1–3] In these cases the usual NMR approach of determining molecular motions at a constant Larmor frequency by variation of the sample temperature suffers from limitations of the temperature ranges available without changing or degrading the phase of the materials. The following two examples were chosen from the numerous reported results because they required more sophisticated FC techniques than are commonly available.

5.1 Proton Relaxation Dispersion of Water

The mobilities of H_3O^+ and OH^- ions in pure H_2O are known to be considerably greater than those of any other univalent ions. This anomaly is understood to be a consequence of hydrogen bonds between water molecules and the ionic species under the premise that such links facilitate the rapid transfer of protons; for instance, one of the protons of an H_3O^+ ion can jump along the hydrogen bond to combine with an adjacent H_2O molecule faster than without the link. It was recognized by Meiboom as early as 1961[39] that the various time constants characteristic for the proton transfer reactions, in particular the mean proton exchange time τ_{ex} of a water molecule, can have a significant effect on the longitudinal and transverse spin relaxation times (T_1, T_2) of both the hydrogen (^1H) and oxygen (^{17}O) atoms (the more abundant isotopes ^{16}O and ^{18}O have no magnetic dipole moment). This additional relaxation rate is essentially due to a scalar magnetic coupling between neighboring ^1H and ^{17}O spins, which unlike the normal dipolar ^1H–^1H interaction is not averaged by the fast rotational and translational tumbling of H_2O molecules in the liquid state. According to standard relaxation models[40] the proton exchange statistically modulates the scalar coupling energy and leads to frequency-dependent proton relaxation times T_1 and T_2 at Larmor frequencies ν where $2\pi\nu\tau_{scal} \approx 1$. However, since the natural abundance of ^{17}O is only 0.037%, the dispersion step is extremely small in normal water (only ≈ 25%), but it could be observed[6,41] at low frequencies between 100 Hz and 2 kHz, i.e. for Zeeman fields below the Earth's magnetic field. By performing the measurements on ^{17}O-enriched samples, the scalar relaxation contribution is significantly increased, and more powerful FC instruments are needed to observe the full dispersion profiles at low fields. Figure 8 illustrates results for H_2O, enriched with 4% ^{17}O, at room temperature (26 °C) and pH 7. Note that near 100 Hz both T_1 and T_2 become shorter than 10 ms. The solid lines are fits of a two-spin relaxation model[40] with both dipolar ^1H–^1H and scalar ^1H–^{17}O couplings, and yield a correlation time τ_{scal} = 2.20 ms.[8,41] This is slightly shorter than literature data[39] for τ_{ex}, and indicates that the scalar interaction is also affected by mechanisms other than proton exchange, such as the ^{17}O spin relaxation. More details are given in the original papers.[6,8,41]

5.2 Proton and Deuteron Relaxation Dispersion of Liquid Crystals

Liquid crystalline mesophases have challenged NMR groups with FC equipment since the early 1970s, shortly after theoretical predictions became known that order director fluctuations (ODF, OF), i.e. collective thermal molecular excitations of the long-range orientational order (director field), may play an important role in nuclear spin relaxation. Unique to these materials, which contain rod-like or disk-like, i.e. anisotropic, molecules, it was predicted that such thermal fluctuations of the director should entail rather peculiar T_1 dispersion profiles. In the case of nematic order, they should produce a square root law frequency dependence of the longitudinal spin relaxation time, i.e. $T_1 \sim \nu^{1/2}$, which is a very unusual dispersion behavior[42,43] for low-viscosity liquids. Since the collective motions are superimposed on noncollective rotational and translational reorientation processes of individual molecules, it took a long time to separate the more common from the characteristic liquid crystalline phenomena. Controversies arose because the range of Larmor frequencies available to conventional spectrometers made the clear distinction of the different superimposed relaxation rates virtually impossible. With the development of fast T_1 FC devices capable of extending measurements of short T_1s to a regime where the

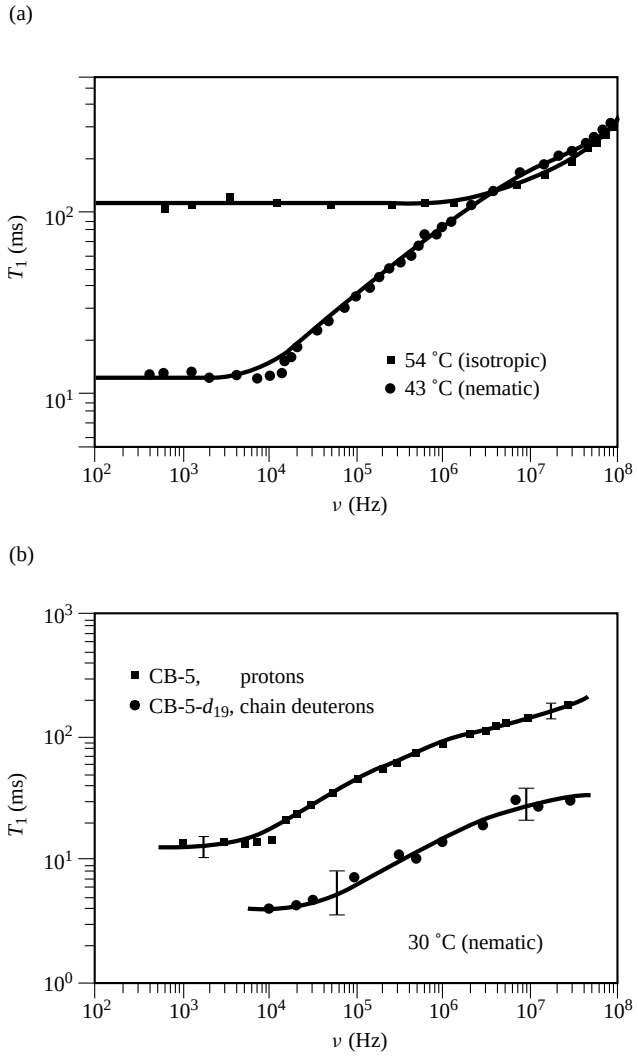

Figure 9 Proton and deuteron spin relaxation dispersion of nematogen liquid crystals. (a) Comparison of the proton T_1 for PCH-5 in the nematic and isotropic phase. (b) Comparison of the proton and chain deuteron T_1 values for normal and perdeuterated CB-5. Solid lines are model fits[11,24,25]

square root law dominates other competing terms (note that $T_1 \sim \nu^{1/2}$ gives $1/T_1 \to \infty$ for $\nu \to 0$), and which furthermore opened the way for angular-dependent studies under such conditions, a more reliable separation of the significant relaxation processes emerged. The results leave no doubt that the theoretical concept about relaxation by collective molecular fluctuations in liquid crystals at low ν values is basically correct. Figure 9 shows typical T_1 dispersion profiles[2,11,24,25] for two nematogen liquids: PCH-5 (pentyl**p**henyl**c**yclo**h**exane) and CB-5 (pentyl**c**yano**b**iphenyl). In both systems $T_1(\nu)$ exhibits at least three different frequency ranges where distinct mechanisms determine the total relaxation rate, in particular the broad square root law profile below the conventional Larmor frequency range. As expected, the $\nu^{1/2}$ contribution vanishes for the isotropic phase of the materials, and in deuterated molecules it is seen for both proton and deuteron spins. This idea allows acceptable theoretical fits[25,28] (solid lines in Figure 9) to the measured data. However, the detailed analysis of deuteron low-frequency results is only beginning, because of technical problems involved in selective deuteron FC experiments. The theoretical background of relaxation in liquid crystals and further experiments are discussed in other articles (***Amphiphilic Liquid Crystalline Samples: Nuclear Spin Relaxation***, ***Deuteron Relaxation Rates in Liquid Crystalline Samples: Experimental Methods***, and ***Liquid Crystalline Samples: Relaxation Mechanisms***).

6 RELATED ARTICLES

Amphiphilic Liquid Crystalline Samples: Nuclear Spin Relaxation; Brownian Motion and Correlation Times; Coupled Spin Relaxation in Polymers; Deuteron Relaxation Rates in Liquid Crystalline Samples: Experimental Methods; Diffusion Measurements by Magnetic Field Gradient Methods; Double Resonance; Dynamics of Water in Biological Systems: Inferences from Relaxometry; Fast Ion Conductors; Flow NMR; Liquid Crystalline Samples: Deuterium NMR; Liquid Crystalline Samples: Diffusion; Liquid Crystalline Samples: Relaxation Mechanisms; Paramagnetic Relaxation in Solution; Molecular Motions: T_1 Frequency Dispersion in Biological Systems; Polymer Dynamics and Order from Multidimensional Solid State NMR; Quantum Tunneling Spectroscopy; Relaxation Processes: Cross Correlation and Interference Terms; Relaxation Theory: Density Matrix Formulation; Relaxometry of Tissue; Slow and Ultraslow Motions in Biology; Zero Field NMR.

7 REFERENCES

1. R. Kimmich, *Bull. Magn. Reson.*, 1980, **1**, 195.
2. F. Noack, *Progr. Nucl. Magn. Reson. Spectrosc.*, 1986, **18**, 171.
3. S. H. Koenig and R. D. Brown, *Progr. Nucl. Magn. Reson. Spectrosc.*, 1990, **22**, 487.
4. R. Pound, *Phys. Rev.*, 1951, **81**, 156.
5. A. G. Redfield, W. Fite, and H. E. Bleich, *Rev. Sci. Instrum.*, 1968, **39**, 710.
6. S. P. Conti, Thesis, University of Geneva, 1984.
7. K. J. Glover, Thesis, University of California, Los Angeles, 1986.
8. E. Rommel, K. Mischker, G. Osswald, K.-H. Schweikert, and F. Noack, *J. Magn. Res.*, 1986, **70**, 219.
9. G. Vandemaele, P. Coppens, and L. van Gerven, *Proceedings of the 22nd Congress AMPERE, Zürich, 1984*, p. 398.
10. M. Blanz, G. Q. Chen, H. Birli, and R. Messer, *Proceedings of the 22nd Congress AMPERE, Zürich, 1984*, p. 596.
11. K. H. Schweikert, Thesis, Universität Stuttgart, 1991.
12. M. Blanz, T. J. Rayner, and J. A. S. Smith, *Meas. Sci. Technol.*, 1993, **4**, 48.
13. M. Notter, K. Konzelmann, G. Majer, and A. Seeger, *Z. Naturforsch., Teil A*, 1994, **49**.
14. D. B. Zax, A. Bielecki, K. W. Zilm, A. Pines, and D. P. Weitekamp, *J. Chem. Phys.*, 1985, **83**, 4877.
15. R. Kreis, A. Thomas, W. Studer, and R. R. Ernst, *J. Chem. Phys.*, 1988, **89**, 6623.
16. S. D. Swanson and S. D. Kennedy, *J. Magn. Res. A*, 1993, **102**, 375.
17. Harris Semiconductor, Product Selection Guide, 1992, Melbourne, USA.

18. Advanced Power Technology, Product Catalogue, 1992, Bend, USA.
19. J. Hak, *Arch. Elektrotech.*, 1936, **30**, 736.
20. G. Grössl, F. Winter, and R. Kimmich, *J. Phys. E.*, 1967, **18**, 358.
21. K. H. Schweikert, R. Krieg, and F. Noack, *J. Magn. Reson.*, 1988, **78**, 77.
22. St. Becker, K. H. Schweikert, and F. Noack, *Proceedings of the 25th Congress AMPERE, Stuttgart, 1990*, p. 458.
23. M. Reinöhl, Diploma Thesis, Universität Stuttgart, 1994.
24. K. H. Schweikert and F. Noack, *Mol. Cryst. Liq. Cryst.*, 1992, **212**, 33.
25. R. Köllner, K. H. Schweikert, F. Noack, and H. Zimmermann, *Liq. Cryst.*, 1993, **13**, 483.
26. J. W. Hennel, A. Birczyński, S. F. Sagnowski, M. Stachurowa, *Z. Phys. B*, 1985, **60**, 49.
27. E. Rommel, Thesis, Universität Sttutgart, 1988.
28. F. Noack, M. Notter, and W. Weiss, *Liq. Cryst.*, 1988, **3**, 907.
29. F. Winter and R. Kimmich, *Mol. Phys.*, 1982, **45**, 33.
30. D. J. Pusiol, R. Humpfer, and F. Noack, *Z. Naturforsch., Teil A*, 1992, **47**, 1105.
31. P. Coppens, L. van Gerven, S. Clough, and A. J. Horsewill, *J. Phys. C*, 1983, **16**, 567.
32. D. T Edmonds, *Phys. Rep.*, 1977, **29**, 233.
33. J. Seliger, *Proc. AMPERE Summer Institute on Advanced Techniques in Experimental Magnetic Resonance, Portorož, 1993*, p. 46.
34. J. Struppe and F. Noack, *22te Freiburger Arbeitstagung Flüssigkristalle, 1993*, p. 15.
35. A. F. Martins, P. Esnault, and F. Volino, *Phys. Rev. Lett.*, 1986, **57**, 1745.
36. H. Gotzig and F. Noack, *Abstracts of the 11th EENC, Lisbon 1992*, p. 88.
37. F. Noack, *Mol. Cryst. Liq. Cryst.*, 1984, **113**, 247.
38. J. Mager, Thesis, Universität Stuttgart, 1994.
39. S. Meiboom, *J. Chem. Phys.*, 1961, **34**, 375.
40. A. Abragam, *The Principles Of Nuclear Magnetism*, Oxford University Press, Oxford, 1961.
41. V. Graf, F. Noack, and G. J. Béné, *J. Chem. Phys.*, 1980, **72**, 861.
42. P. Pincus, *Solid State Commun.*, 1969, **7**, 415.
43. R. Blinc, D. L. Hogenboom, D. E. O'Reily, and E. M. Peterson, *Phys. Rev. Lett.*, 1969, **23**, 969.

Biographical Sketch

Friedrich Noack. *b* 1932. Ph.D., 1966, Physics, University of Stuttgart. Professor, 1978–present. Approx. 200 publications. Special interests are teaching of basic physics, developments of novel experimental NMR techniques such as field cycling, applications of NMR methods to investigate the molecular dynamics of liquid crystals and biological systems, and the critical analysis of scientific software.

Gas Phase Studies of Intermolecular Interactions and Relaxation

Cynthia J. Jameson

University of Illinois, Chicago, IL, USA

1	Introduction	1
2	Intermolecular Effects on Chemical Shifts	1
3	Temperature Dependence of Nuclear Shielding in the Isolated Molecule	4
4	Spin Relaxation in the Gas Phase	5
5	Related Articles	10
6	References	10

1 INTRODUCTION

The nuclear magnetic moment is a very sensitive site-specific probe of electronic environment and of dynamics in the gas, liquid, or solid phase. In this article, we specifically consider the nature of the information that can be obtained in the gas phase. Why should one do NMR spectroscopy in the gas phase? In the binary collision limit and in the zero-pressure limit, experimental measurements can be directly connected to quantities that can be calculated from first principles. Gas phase measurements therefore provide direct stringent tests of calculations of molecular electronic properties of the isolated molecule such as the rovibrationally averaged chemical shift, tests of intermolecular shielding surfaces and intermolecular potential surfaces from density and temperature dependence of chemical shifts in the binary collision limit, tests of relaxation theory near the T_1 minimum, and experimental values of cross sections for relaxation, which have a direct connection with the anisotropy of intermolecular potentials. Gas phase NMR measurements also provide cross sections for chemical reactions and intermolecular vibrational energy transfer, which are discussed in ***Gas Phase Studies of Chemical Exchange Processes***. The gas phase allows us to do experiments in theoretically tractable systems, then carry over the understanding to the less tractable condensed phase systems where possible.

Variable temperature studies can be carried out in the gas phase, where density is a variable that is independent of temperature. Equivalent experiments in the liquid phase would require high-pressure studies. The ability to work in a regime where only two-body effects are important permits the quantitative characterization of the observations with well-defined quantities such as the second virial coefficient of the chemical shift, which is a direct test of intermolecular shielding surfaces. The linear density region provides collision cross sections for molecular reorientation, or rotational angular momentum transfer, or intermolecular vibrational energy transfer leading to unimolecular reaction. These provide stringent tests of anisotropic intermolecular potentials, distinguishing between superficially similar potentials, and, in favorable cases, permitting refinement of the best available ones entirely on the basis of gas phase relaxation data. Furthermore, one can extrapolate the measured quantities to the zero-pressure limit to obtain the properties that are characteristic of the nearly isolated molecule, such as chemical shifts and coupling constants, which in turn can be related to intramolecular shielding and J coupling surfaces. At this limit, the intrinsic rate with which an energized molecule in the absence of collisions undergoes a unimolecular reaction such as ring inversion can also be obtained (see ***Gas Phase Studies of Chemical Exchange Processes***). A recent review of gas phase NMR studies spanning the density range 10^{16}–10^{21} molecules cm^{-3} and pressures from under 1 torr to 50 atm provides an overview, including experimental details.[1] In this article, we shall discuss only the intermolecular effects on chemical shifts, the temperature dependence of chemical shifts in nearly isolated molecules, and spin relaxation in the gas phase.

2 INTERMOLECULAR EFFECTS ON CHEMICAL SHIFTS

The nuclear magnetic shielding σ is determined by the electronic distribution around the nucleus of interest. Since interactions between molecules necessarily affect this distribution to some extent, there are observable effects of intermolecular interactions on σ. These intermolecular shifts can be rather large, and are usually observed as gas-to-liquid shifts or solvent shifts, which are difficult to describe quantitatively and interpret theoretically because they are dependent on the structure of the liquid. A table of gas-to-liquid shifts is given in ***Chemical Shift Scales on an Absolute Basis***. On the other hand, in a gas of modest density, the nuclear magnetic shielding σ, like other molecular electronic properties, can be expressed in terms of a virial expansion in density ρ:[2]

$$\sigma(T, \rho) = \sigma_0(T) + \sigma_1(T)\rho + \sigma_2(T)\rho^2 + \cdots \qquad (1)$$

Here, the terms dependent on the gas density ρ characterize the intermolecular effects, while the independent molecule value of the shielding, $\sigma_0(T)$, is a function of temperature owing to averaging over intramolecular motions (vibrations and rotations).[3] By analogy with the second virial coefficient in the usual expansion for PV/RT, $\sigma_1(T)$ may be called a second virial coefficient of the nuclear shielding. Both $\sigma_0(T)$ and $\sigma_1(T)$ can be obtained from experiments in the gas phase.[4] In a mixture of gases, $\sigma_1(T)$ due to A–A collisions and $\sigma_1(T)$ due to A–B collisions can be determined separately in a series of experiments. The sign of the intermolecular shielding effects has been found to be uniformly negative,[3,5]

$$[\sigma(T, \rho) - \sigma_0(T)] < 0 \qquad (2)$$

that is, intermolecular effects are deshielding, with only a few exceptions such as the nitrogen shielding in nitriles, pyridine and other similar nuclear sites involving n $\rightarrow \pi^*$ excited states.[6]

2.1 Second Virial Coefficient of Nuclear Shielding

Operationally, $\sigma_1(T)$ is obtained as

$$\sigma_1(T) = -\frac{1}{\nu_0} \lim_{\rho \to 0} \left(\frac{\partial \nu}{\partial \rho} \right)_T \tag{3}$$

Since the gas phase measurements are not carried out on spherical samples, the measured $\sigma_1(T)$ have to be corrected for the bulk susceptibility, given to a good approximation by $\sigma_{1\text{bulk}} = \frac{2}{3}\pi\chi_{\text{mol}}$ or $-\frac{4}{3}\pi\chi_{\text{mol}}$ for the perpendicular or parallel arrangement of a cylindrical sample in the magnet, where χ_{mol} is the molar magnetic susceptibility of the sample. This is the same for all nuclei in the sample, and is a sizable fraction of the observed apparent $\sigma_1(T)$ for nuclei such as ^{1}H and ^{13}C, whereas it is a very small fraction for ^{129}Xe. Observed values of σ_1 range from -1×10^{-3} to about -1 ppm amagat^{-1} (1 amagat = 2.687 $\times$ 10^{25} molecules m^{-3}, the density of an ideal gas at 1 atm and 273.16 K). The range of values of σ_1 for a given nucleus not unexpectedly reflects the chemical shift range of the nucleus.[3] Xenon-129 in the Xe atom is found to be an ideal probe of intermolecular interactions. Xe intermolecular chemical shifts are very large in comparison with other nuclei.[7] After correction for bulk susceptibility, typical values of σ_1 at room temperature are[3,8,9] as shown in Table 1.

A summary of second virial coefficients of shielding for ^{19}F in various molecules has been given by Jameson.[1]

2.2 The Intermolecular Shielding Surface

For ^{129}Xe in dilute xenon gas, we can explicitly write $\sigma_1(T)$ in terms of the intermolecular potential function for Xe–Xe interactions and the nuclear shielding function for a Xe atom in a pair of interacting Xe atoms:

$$\sigma_1(T) = \int_0^\infty 4\pi r^2 \, \mathrm{d}r[\sigma(r) - \sigma(\infty)] \exp\left[-\frac{V(r)}{k_B T}\right] \tag{4}$$

where $\sigma(\infty)$ is the nuclear shielding of the isolated Xe atom and $\sigma(r)$ is the shielding of the Xe atom under the influence of a neighboring Xe atom at distance r from it. The expression applies to any pair of rare gas atoms, like or unlike.

A mean field long-range model for $[\sigma(r) - \sigma(\infty)]$ had been advanced by Raynes, Buckingham and Bernstein[10] (RBB) for a molecule in the presence of a neighbor at distance r and orientations given by θ_1, θ_2, ϕ_1, ϕ_2:

$$[\sigma(r, \theta_1, \theta_2, \phi_1, \phi_2) - \sigma(\infty)] = \sigma_a + \sigma_E + \sigma_W \tag{5}$$

They include a magnetic anisotropy term σ_a, electrical terms due to permanent electric moments on the neighbor σ_E, and a 'van der Waals term' σ_W, the intermolecular contributions to shielding due to dispersion, which was modeled by fluctuating electric fields produced at the molecule by mutual interactions with the neighbor in accordance with the London model of dispersion forces. The latter was taken to be of the form $-B\alpha_2 I_2 r^{-6}$, involving the polarizability and the ionization potential of the neighbor molecule and an empirical parameter B, which was taken to be the same as the average B in the quadratic response of the shielding in a molecule to a uniform static electric field. Later refinements involve the polarizability and ionization potential of the observed molecule as well, for example, $-3B\alpha_2 I_1 I_2 r^{-6}/2(I_1 + I_2)$. This is the only term in the model that applies to a pair of rare gas atoms. However, the magnitude of the average B that has been obtained by ab initio calculations[11] for ^{129}Xe in a Xe atom in a static uniform field when used in this model gives a value much too small to account for the observed $\sigma_1(T)$. Therefore, if the model is to be used in this form, the B parameter in it can no longer be identified with the average B in the shielding response to a uniform static electric field. Indeed, when the model is used, the empirical B parameter found in fitting the RBB equation, equation (5), to experiment is at least an order of magnitude larger, because this term in the model makes up for the shielding change due to overlap and exchange—terms that are missing in the long-range model, and which can only be obtained by ab initio calculations on the 'supermolecule' (the interacting pair of molecules).

Ab initio calculations of the intermolecular shielding function for ^{39}Ar in the argon atom interacting with another argon have revealed that dispersion contributions are not as important as was originally thought, and constitute only a minor correction when second-order correlation effects on shielding are included in the supermolecule calculation,[12] despite the nearly r^{-6} dependence of the shielding function in the region of interest (i.e., those values of r favored by the exp $[-V(r)/k_B T]$ weighting). Therefore, to the extent that ab initio shielding calculations at the level that includes second-order correlation effects are the basis for the inclusion of dispersion contributions, one may conclude that there are only very small contributions from dispersion in the intermolecular shifts of rare gases. The shape of the intermolecular shielding function for Ar–Ar is shown in Figure 1. This is the same shape as has been found for the shielding of ^{39}Ar in the Ar atom under the influence of Ne, and for ^{21}Ne shielding in the Ne atom in the presence of another Ne atom or a He atom.[13] It has been found that when this shielding function is scaled up to ^{129}Xe in various Xe–rare gas pairs, it is possible to reproduce quantitatively the $\sigma_1(T)$ observed for ^{129}Xe in pure xenon, and also for Xe with Kr and for Xe with Ar, in their signs, magnitudes, and temperature dependences.[12] The relative magnitudes of the temperature dependences in these three systems are also reproduced.

Table 1 Second Virial Coefficients of Nuclear Shielding

	$-\sigma_1$(ppm amagat^{-1})
^{1}H	0.0003–0.008
^{11}B	0.0085 (in BF_3)
^{13}C	0.0022–0.0105
^{15}N	0.0026–0.04
^{19}F	0.006–0.05
^{31}P	0.0023–0.266
^{77}Se	0.007 (in SeF_6)
^{83}Kr	0.131
^{125}Te	0.01 (in TeF_6)
^{129}Xe	0.166–0.75

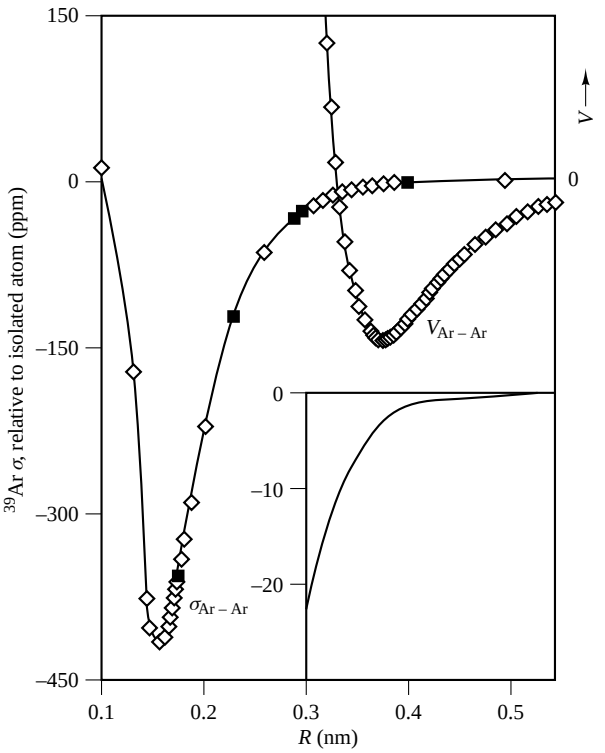

Figure 1 Intermolecular shielding function for ^{39}Ar in Ar–Ar obtained from ab initio calculations. Adapted from Jameson and de Dios[12] by permission. The values denoted by ■ include second-order correlation contributions, all other values are from a coupled Hartree–Fock calculation, using the local origins method described in the article ***Chemical Shift Calculations by the LORG & SOLO Approaches***

2.3 The Nuclear Site Effect

Intermolecular shieldings are different for different nuclear sites in a molecule under the influence of a solvent molecule. In averaging over all the orientations of the molecule bearing the observed nuclei, the peripheral nuclei suffer larger intermolecular effects than nuclei located in the interior. That is why relatively protected nuclei such as ^{77}Se in SeF_6 or ^{125}Te in TeF_6 have fairly small intermolecular shifts compared with ^{77}Se in H_2Se or ^{125}Te in H_2Te. A direct comparison is possible when the nuclei are the same type and in the same molecule, such as the two N nuclei in the NNO molecule or the three different ^{19}F nuclei in $F_2C{=}CFH$. A simple model by Rummens et al.[14] depends on the averaging of r_{NS}^{-6} distances between nucleus N and solvent S, while the isotropic intermolecular potential is expressed in terms of the separation R_{CS} between the center of mass of the molecule and the solvent. The average intermolecular shift can then be expressed in terms of the distance d between the nuclear site and the center of mass of the molecule. The distance d changes systematically for each of the three types of F nuclear sites in $F_2C{=}CFX$, where X varies as H, F, Cl, Br, and I. It has been demonstrated that in this series of molecules, this model provides semiquantitative agreement with experiment in the pure gases; the $\sigma_1(T)$ for the three different ^{19}F nuclei vary with the respective values of d for the nuclear site as expected.[15] Similarly, in the NNO molecule, the end nitrogen nucleus has a larger intermolecular shift in pure NNO, and in NNO–rare gas, and NNO–SF_6 mixtures.

2.4 Intermolecular Contact Shifts

The ^{129}Xe chemical shifts for Xe in the paramagnetic gases O_2 and NO exhibit a linear dependence on the density of O_2 (or NO) with unusually large slopes.[16,17] There is, of course, the bulk susceptibility contribution to the apparent $\sigma_1(T)$, but this can easily be corrected for, using

$$\chi_{mol} = N_{Avo}\langle\mu_{eff}^2\rangle/3k_BT \tag{6}$$

where $\langle\mu_{eff}^2\rangle$ is a very nearly temperature-independent 8 Bohr magnetons for O_2 and a strongly temperature dependent average value for NO. In addition to this bulk susceptibility contribution, there is a strongly temperature-dependent true $\sigma_1(T)$, which has a very different behavior from that in the ^{129}Xe $\sigma_1(T)$ for Xe in Ar, for example. This $\sigma_1(T)$ includes, in addition to the usual intermolecular shielding contribution, a contact shift that arises from the finite electron spin density ρ_{spin} at the ^{129}Xe nucleus from the interaction of the Xe with O_2 or NO, which Buckingham and Kollman[18] attributed to the overlap of the $O_2(\pi_g{*})$ or NO($\pi{*}$) orbitals with the Xe(5s). That is,

$$\sigma_1(\text{contact}) = -\frac{4}{3}\pi\frac{\langle\mu_{eff}^2\rangle}{3k_BT}\int_0^\infty 4\pi r^2\,dr\rho_{spin}\exp\left[-\frac{V(r)}{k_BT}\right] \tag{7}$$

It was found that if the normal ^{129}Xe $\sigma_1(T)$ for Xe in hypothetically diamagnetic O_2 or NO were taken to be the same as the observed ^{129}Xe $\sigma_1(T)$ for Xe in Ar and the distance dependence of the shielding change due to contact shift were similar to that of the $\sigma(r)$ for ^{129}Xe in Ar, then the limiting temperature dependence of the contact shift could be extracted. The latter is found to be $1/T$ at the lower temperatures, just as the Curie law behavior predicts, and the magnitude of the intermolecular contact shielding is roughly three times that of the ^{129}Xe $\sigma(r)$ for Xe in Ar. The integrals shown above can be extracted empirically from the observed density and temperature dependence of the shifts, and are found to have a ratio 1.25 for NO/O_2, which agrees with the ratio calculated by Buckingham and Kollman.

2.5 Many Body Terms

The dependence on density becomes nonlinear as the densities approach liquid densities.[19] The intermolecular shielding contributions from the many body terms are found to be opposite in sign to the two-body second virial coefficient of shielding that is found in the dilute gas.[1] That is, the effective density coefficient of shielding for liquids is smaller in magnitude than the σ_1 obtained in the dilute gas. Both are deshielding (excepting the cases of nitrile or pyridine nitrogen nuclei already mentioned), but liquids are less deshielded than one might expect from direct extrapolation to liquid densities. The gas-to-liquid shift thus gives an estimate of σ_1 that is somewhat too small in magnitude, but nevertheless provides a reasonable estimate of σ_1 when density dependence measurements cannot be carried out. The general shape of ab initio intermolecular shielding surfaces and assumption of

largely pairwise-additive shielding contributions are found to be consistent with the signs and general magnitudes of gas-to-liquid and gas-to-solution shifts and adsorption shifts.[20] A favorable example is the set of chemical shifts and their temperature dependence in Xe, Xe_2, Xe_3, ... , Xe_8 clusters trapped in zeolite NaA, which have been reproduced by using grand canonical Monte Carlo averaging of ^{129}Xe shieldings assuming pairwise additive isotropic shieldings based on ab initio shielding functions in rare gas pairs.[21]

3 TEMPERATURE DEPENDENCE OF NUCLEAR SHIELDING IN THE ISOLATED MOLECULE

After extrapolation to zero density, there should be no remaining temperature dependence in the case of xenon. However, it was discovered during measurements of σ_1 that the zero-density intercept of the chemical shift changed with temperature when the molecule bearing the nucleus had internal degrees of freedom, and dramatically so for ^{19}F nuclei.[4] In practice, the temperature dependence in the limit of zero density is not obtained from the intercepts; rather, the $\sigma_1(T)$ function is fully characterized experimentally from the density dependence of the chemical shift in several samples and then $\sigma_1(T)\rho$ is subtracted from every data point to correct each to the zero-density limit, thereby obtaining $[\sigma_0(T) - \sigma_0(300\,\mathrm{K})]$. The general shape of these functions is that the nucleus becomes more deshielded with increasing temperature, usually with a nonlinear temperature dependence, although in the cases of ^{13}C in CO and ^{15}N in N_2 the function is a linear one.[22] The magnitude of the temperature coefficient depends on the nucleus—larger for ^{31}P and ^{19}F than for ^{13}C. Some examples are shown in Table 2. There is some evidence that the temperature coefficient is very large for transition metal nuclei, although these have been studied in solution rather than in the limit of zero-density gas. For a given nucleus, the temperature coefficient correlates with the shielding, and is larger for less shielded environments.

The temperature dependence of the shielding results from the same rotational and vibrational averaging that is responsible for isotope shifts. In the context of the Born–Oppenheimer approximation, the separation of the electronic from the nuclear motion allows an intramolecular potential surface to be defined, which is then used in finding the vibrational states and functions. In the same context, the nuclear shielding surface is defined: this is a mathematical surface containing the values of the shielding as a function of the positions of the nuclei in the molecule. Some examples of shielding surfaces are given in ***Isotope Effects on Chemical Shifts and Coupling Constants***. The entire shielding tensor changes with the molecular internal geometry, but only the isotropic average about all orientations of the molecule with respect to the external magnetic field concerns us in the gas phase. Thus, the isotropic shielding surface can be described in terms of an expansion of the shielding in powers of the nuclear displacement coordinates such as bond stretches and bond angle deformations and the derivatives of the shielding with respect to these stretches and deformations:

$$\begin{aligned}\sigma(\mathrm{F}_1) = \sigma_\mathrm{e} &+ \left(\frac{\partial\sigma}{\partial r_1}\right)_\mathrm{e}\Delta r_1 + \left(\frac{\partial\sigma}{\partial r_2}\right)_\mathrm{e}\Delta r_2 \\ &+ \sum_{i=3}^{6}\left(\frac{\partial\sigma}{\partial r_i}\right)_\mathrm{e}\Delta r_i + \left(\frac{\partial^2\sigma}{\partial r_1^2}\right)_\mathrm{e}(\Delta r_1)^2 + \left(\frac{\partial^2\sigma}{\partial r_2^2}\right)_\mathrm{e}(\Delta r_2)^2 \\ &+ \sum_{i=3}^{6}\left(\frac{\partial^2\sigma}{\partial r_i^2}\right)_\mathrm{e}(\Delta r_i)^2 + \left(\frac{\partial^2\sigma}{\partial\alpha_{12}\partial r_1}\right)_\mathrm{e}\Delta r_1\Delta\alpha_{12} + \cdots \end{aligned} \quad (8)$$

for ^{19}F in an MF_6 molecule, for example. The thermal average of σ then gives $\sigma_0(T)$. The thermal averages of the nuclear displacement coordinates can be obtained if the intramolecular force field is available, as they are for SF_6, for example. In ***Isotope Effects on Chemical Shifts and Coupling Constants***, it is shown how these averages are

Table 2 Temperature Coefficients of the Shielding for Molecules in the Zero-Pressure Limit at 300 K

	Molecule	$d\sigma_0(T)/dT$ (ppb K^{-1})		Molecule	$d\sigma_0(T)/dT$ (ppb K^{-1})
^{13}C	CH_4	−0	^{15}N	N_2	−0.85
	CO	−0.29		NNO	−3.5, −8.8
	CO_2	−0.54	^{19}F	BF_3	−1.33
^{19}F	SiF_4	−3.81		$CFCl_3$	−11.6
	CF_4	−5.01		CF_2HCl	−4.86
	POF_3	−5.65		$CFHCl_2$	−5.92
	PF_3	−6.73		CF_3CH_3	−10.3
	PF_5	−9.79		CF_2HCH_3	−10.8
	ClF	−10.4		CF_3CF_3	−11.4
	SF_6	−12.1		CF_3CF_2Cl	−11.3
	TeF_6	−16.1		CF_2ClCF_3	−13.1
	SeF_6	−22.9		OCF_2	−4.33
	WF_6	−23.3		$CF_2{=}CH_2$	−4.07
	NF_3	−20.0		$CF_2{=}CF_2$	−8.13
	F_2	−34.0		$CF_2{=}CFH$	−5.06, −5.11, −6.76
	CH_3F	−1.76		$CF_2{=}CFCl$	−7.87, −8.73, −10.6
	CH_2F_2	−2.89		$CF_2{=}CFBr$	−8.04, −9.07, −11.5
	CF_3H	−5.60		$CF_2{=}CFI$	−6.98, −8.77, −12.8
	CF_3CN	−7.57	^{31}P	PH_3	−0.5
	CF_3I	−9.25		PF_3	−1.7
	CF_3Br	−10.2		POF_3	−1.4
	CF_3Cl	−6.78	^{77}Se	SeF_6	−14
	CF_2Cl_2	−9.06	^{125}Te	TeF_6	−10

obtained in general. Given the ab initio surface, or the shielding derivatives, and the intramolecular force field, the $\sigma_0(T)$ can be calculated and compared with experiment. It is generally not possible to obtain accurate derivatives of shielding directly from the experimentally observed $\sigma_0(T) - \sigma_0(300\,\mathrm{K})$ functions even using very accurate force fields, since the nature of the experimental data allows typically only one, at most two, parameters to be determined empirically. The empirical shielding derivatives that have been estimated from the temperature dependence of the shielding of ^{19}F have made use of the assumption that the bond extension terms completely dominate the shielding. In this way, estimates of the shielding derivatives in the fluoromethanes, fluoroethenes, and MF_6 type molecules have been made. The observed temperature coefficients $d\sigma_0(T)/dT$ for a series of related compounds such as for ^{19}F in substituted fluoromethanes, and generally for ^{19}F in binary fluorides, correlate with the ^{19}F chemical shifts in these compounds, and the least shielded environments show the largest temperature coefficients. The correlation is even better with the paramagnetic part of the shielding.[9] Although the derivatives in these particular molecules have not been provided by ab initio calculations, it has been found that, for a large number of molecules, the ab initio shielding derivatives for ^{19}F generally correlate with the shielding itself.[20,23] In the case of F_2, the shielding derivative estimated from the temperature dependence appears to be too large compared with the ab initio calculations. In N_2 and CO, the shielding first derivatives estimated from the temperature dependences of the ^{15}N and ^{13}C nuclei, respectively, are roughly the same as those calculated from the ab initio surfaces for these molecules.

4 SPIN RELAXATION IN THE GAS PHASE

Spin relaxation in the gas phase provides qualitatively different information from that in the liquid phase. Since the intermolecular dynamics in the gas phase can be modeled more accurately, the gas phase provides critical tests of relaxation theories, allows quantitative separation of two or more contributing mechanisms, and provides a direct connection with the anisotropy of intermolecular potentials.

4.1 Theoretical Treatments of Relaxation and the Connection with Intermolecular Potentials

NMR studies of spin relaxation in molecular gases provide a very sensitive probe of the anisotropic part of the intermolecular potential surfaces. As a function of gas density ρ, the spin–lattice relaxation time T_1 is long at low densities, for which the collision frequency is very low, passes through a characteristic minimum corresponding to a matching between the collision and spin precession frequencies, and then passes into a regime in which it increases linearly with gas density, the so-called 'extreme narrowing' regime. As the density increases, there is a less efficient communication through the weak intermolecular coupling between the rotational degrees of freedom (the 'lattice') and the nuclear spin system of the effects of reorienting molecular collisions to the nuclear spins. The region of the T_1 minimum permits a measurement of the strength of the interaction that couples the nuclear spin system to the lattice degrees of freedom. Bloch's phenomenological equations (***Relaxation: An Introduction***) provide a description of nuclear magnetic relaxation in gas phase systems. In order to make the connection with intermolecular potential energy surfaces, it is necessary to express the relaxation times T_1 and T_2 in Bloch's equations in terms of quantities that may be directly calculated once an intermolecular potential energy surface has been specified. There are several approaches: the traditional one is to apply correlation function theory to a master equation. This is the approach used by Abragam[24] and by Bloom and Oppenheim.[25,26] Another approach is to employ the kinetic theory of gases in the context of a generalized Boltzmann equation.[27] It has been demonstrated by McCourt et al.[28,29] that the most useful features of each method can be retained in a unified theory by utilizing a projection operator formalism to obtain a memory equation for that part of the distribution function density matrix characterizing the gaseous system and proportional to the nuclear spin operator $\hat{\boldsymbol{I}}$. The memory equation thus obtained is utilized to obtain an integral equation governing the time dependence of the nonequilibrium part of the nuclear magnetization in terms of a kernel having the form of an autocorrelation function.

In the single relaxation time approximation (SRTA), a common correlation time is assumed for all the rotational levels. A multiple relaxation time approximation (MRTA) uses a distribution of correlation times, and has been shown to be necessary in the accurate analysis of the proton relaxation in HCl and in NH_3 molecules in the range of densities including the T_1 minimum, which then provides spin rotation tensor elements that are in excellent agreement with molecular beam values.[30] General multilevel expressions for the contributions to the nuclear magnetic relaxation from spin rotation, dipolar, intramolecular, and quadrupolar mechanisms have been given independently by Gordon[31,32] and by McCourt[29] which we shall illustrate here using the example of the D_2 molecule, since it includes three major relaxation mechanisms: spin–rotation, intramolecular dipolar, and quadrupolar mechanisms.

The relaxation of nuclei of rare gas atoms is strictly intermolecular.[33] Although both intermolecular and intramolecular relaxation mechanisms contribute in general to the relaxation of nuclei in molecular gases, intramolecular relaxation dominates by five or so orders of magnitude (excepting the intermolecular relaxation due to a paramagnetic collision partner, which we shall consider later). It is also typical of the molecular gases that have been studied that shielding anisotropy and scalar coupling mechanisms are not important. We shall also only show here the theoretical expressions (following McCourt[29,34,35]) appropriate to the *linear density regime* (extreme narrowing conditions), which provide the connection with the anisotropy of intermolecular potential surfaces. This regime is characterized by T_1/ρ. In H_2, only the spin rotation and dipolar mechanisms, and in D_2, spin–rotation, dipolar and quadrupolar mechanisms have to be considered. For H_2, only the *ortho* modification has a nonzero total nuclear spin, whereas in D_2, *para* and *ortho* modifications have to be considered separately:

$$\left(\frac{\rho}{T_1}\right)_{\mathrm{lin}} = \left(\frac{\rho}{T_1}\right)_{\mathrm{lin,sr}} + \left(\frac{\rho}{T_1}\right)_{\mathrm{lin,dq}} \tag{9}$$

The expressions for H_2(*ortho*) are

$$\left(\frac{\rho}{T_1}\right)_{\mathrm{lin,sr}} = \frac{2}{3}\frac{(\omega_{\mathrm{sr}}^{\mathrm{H}})^2}{L_0\langle \mathrm{v}\rangle}\,\boldsymbol{d}^{(1)\mathrm{T}} \cdot \langle \boldsymbol{\sigma}_{\mathrm{v}}\rangle^{-1} \cdot \boldsymbol{P} \cdot \boldsymbol{d}^{(1)} \tag{10}$$

$$\left(\frac{\rho}{T_1}\right)_{\text{lin,d}} = \frac{(\omega_{\text{d}}^{\text{H}})^2}{L_0\langle \text{v}\rangle}\, \boldsymbol{d}^{(2)\text{T}} \cdot \langle \boldsymbol{\sigma}_{\text{T}}\rangle^{-1} \cdot \boldsymbol{P} \cdot \boldsymbol{d}^{(2)} \tag{11}$$

whereas for the D_2 molecule,

$$\left(\frac{\rho}{T_1}\right)_{\text{lin,sr}} = \frac{2}{3}\frac{(\omega_{\text{sr}}^{\text{D}})^2}{L_0\langle \text{v}\rangle}\, \boldsymbol{d}^{(1)\text{T}} \cdot \langle \boldsymbol{\sigma}_{\text{v}}\rangle^{-1} \cdot \boldsymbol{P} \cdot \boldsymbol{d}^{(1)} \tag{12}$$

$$\left(\frac{\rho}{T_1}\right)_{\text{lin,dq}} = \frac{(\omega_{\text{dq}}^{\text{D}})^2}{L_0\langle \text{v}\rangle}\, \boldsymbol{d}^{(2)\text{T}} \cdot \langle \boldsymbol{\sigma}_{\text{T}}\rangle^{-1} \cdot \boldsymbol{P} \cdot \boldsymbol{d}^{(2)} \tag{13}$$

The gas density ρ is measured in amagats, $L_0 = 2.687 \times 10^{25}$ molecules m^{-3}, the number density corresponding to 1 amagat, $\langle \text{v}\rangle$ is the mean relative velocity $(8k_{\text{B}}T/\pi\mu)^{1/2}$, with μ the reduced mass of the colliding pair. The other quantities are described below. The intramolecular spin–rotation and dipolar frequencies come from the intramolecular interaction Hamiltonian in terms of first- and second-rank irreducible tensors:

$$\hat{\mathcal{H}} = -\hbar\omega_{\text{sr}}^{\text{D}}\hat{\boldsymbol{I}}\cdot\hat{\boldsymbol{J}} - \hbar\omega_{\text{d}}^{\text{D}}\overline{\boldsymbol{I}_1\boldsymbol{I}_2}:\overline{\boldsymbol{JJ}} - \hbar\omega_{\text{q}}^{\text{D}}(\overline{\boldsymbol{I}_1\boldsymbol{I}_1} + \overline{\boldsymbol{I}_2\boldsymbol{I}_2}):\overline{\boldsymbol{JJ}} \tag{14}$$

The off-diagonal matrix elements of $\overline{\boldsymbol{JJ}}$ lead to high-frequency effects in NMR,[26,29,36] which will only affect the NMR relaxation process at densities in which the collision frequencies are comparable to any of the rotational frequencies, at which densities the *O* and *S* branches of the Raman spectrum are sufficiently collisionally broadened to overlap with the *Q* branch. This is usually the case in liquids. For H_2, such an overlap does not occur even up to densities of 1000 amagat. For dilute gases, the high-frequency terms arising from the off-diagonal matrix elements of $\overline{\boldsymbol{JJ}}$ do not play a significant role in the relaxation; thus, only the diagonal part of $\overline{\boldsymbol{JJ}}$ is taken into account:

$$\hat{\mathcal{H}} = -\hbar\omega_{\text{sr}}^{\text{D}}\hat{\boldsymbol{I}}\cdot\hat{\boldsymbol{J}} + \frac{\hbar\omega_{\text{d}}^{\text{D}}\overline{\boldsymbol{I}_1\boldsymbol{I}_2}:\overline{\boldsymbol{JJ}}}{(4\boldsymbol{J}^2-3)} - \frac{\hbar\omega_{\text{q}}^{\text{D}}(\overline{\boldsymbol{I}_1\boldsymbol{I}_1}+\overline{\boldsymbol{I}_2\boldsymbol{I}_2}):\overline{\boldsymbol{JJ}}}{4\boldsymbol{J}^2-3} \tag{15}$$

It has been shown that the last two terms give the combined dipolar/quadrupolar coupling Hamiltonian in terms of the total spin $\hat{\boldsymbol{I}}$, $-\hbar\omega_{\text{dq}}\overline{\boldsymbol{II}}:\overline{\boldsymbol{JJ}}/(4\boldsymbol{J}^2-3)$ in which

$$\omega_{\text{dq}}^{\text{D}}(para) = 2\omega_{\text{d}}^{\text{D}} - \tfrac{3}{2}\omega_{\text{q}}^{\text{D}} \tag{16}$$

$$\omega_{\text{dq}}^{\text{D}}(ortho) = \tfrac{12}{5}(\omega_{\text{d}}^{\text{D}})^2 - \tfrac{6}{5}\omega_{\text{d}}^{\text{D}}\omega_{\text{q}}^{\text{D}} + \tfrac{9}{4}(\omega_{\text{q}}^{\text{D}})^2 \tag{17}$$

The matrices $\langle \boldsymbol{\sigma}_{\text{v}}\rangle$ and $\langle \boldsymbol{\sigma}_{\text{T}}\rangle$ contain the state-to-state reorientation effective collision cross sections, averaged over a Boltzmann distribution of translational energies, associated with the irreducible first-rank tensor operator $\hat{\boldsymbol{J}}$ and the second-rank irreducible tensor operator $\overline{\boldsymbol{JJ}}/(4\boldsymbol{J}^2-3)$ respectively. The population matrix $\boldsymbol{P}$ is diagonal, with the jth element being the fractional population per state associated with the jth rotational manifold, $e^{-E_j/k_BT}/\sum_j(2j+1)e^{-E_j/k_BT}$, while $\boldsymbol{d}^{(1)}$ and $\boldsymbol{d}^{(2)}$ are vectors whose jth elements are the reduced matrix elements of $\hat{\boldsymbol{J}}$ and $\overline{\boldsymbol{JJ}}/(4\boldsymbol{J}^2-3)$ respectively, in the Edmonds convention:

$$d_j^{[1]} = \langle j\|\hat{\boldsymbol{J}}\|j\rangle = [j(j+1)(2j+1)]^{1/2} \tag{18}$$

$$d_j^{[2]} = \langle j\|\overline{\boldsymbol{JJ}}/(4\boldsymbol{J}^2-3)\|j\rangle = \frac{[j(j+1)(2j+1)]^{1/2}}{[6(2j-1)(2j+3)]^{1/2}} \tag{19}$$

These are equivalent to the equations derived by Gordon.[32,36] The correspondence with Gordon's notation is shown by Lemaire et al.[35] The cross-relaxation terms only become important at pressures below the T_1 minimum. Furthermore, with the *ortho* relaxing at least three times more slowly than the *para* D_2 and being favored in the 5:1 equilibrium ratio of these two modifications, only the relaxation of the *ortho* D_2 is observed experimentally. The equations for the relaxation behavior of D_2 are also applicable to $^{14}N_2$; however, for ^{14}N, the quadrupolar interaction dominates to the extent that the other nuclear spin interactions can be totally ignored, so that the relaxation rates for *ortho* and *para* modifications of N_2 are equal.

It has been demonstrated that the $(T_1/\rho)_{\text{lin}}$ data of H_2 and its isotopomers at infinite dilution in a rare gas are capable of distinguishing between the various proposed potential surfaces of H_2–rare gas (He, Ne, Ar).[34,35,37–39] Potential energy surfaces did not differ significantly in their ability to reproduce various experimental quantities such as virial coefficients, molecular beam scattering, transport properties and their field effects, and yet provide different results for T_1/ρ versus temperature data. The sensitivity of the computed spin relaxation times to different parts of the H_2–He potential has been examined in detail.[40] Both types of cross sections obtained from relaxation data in dilute gas are very sensitive to both the isotropic part of the potential and the $P_2(\cos\theta)$ terms, and sensitive to the $P_4(\cos\theta)$ terms, but less sensitive to higher orders. In a further example, the ^{15}N and ^{14}N spin relaxation data for N_2 in Ar have been used to distinguish between potential surfaces and to refine the best available one.[41] While quantum scattering calculations are essential for the hydrogen case, it has been shown that classical trajectory calculations are quite reliable for the case of the nitrogen molecule.

In the single relaxation time approximation (SRTA), in the extreme narrowing limit, $\boldsymbol{d}^{(1)\text{T}} \cdot \langle \boldsymbol{\sigma}_{\text{v}}\rangle^{-1} \cdot \boldsymbol{P} \cdot \boldsymbol{d}^{(1)}$ becomes $\langle j(j+1)\rangle/\sigma_{\text{J}}$, where σ_{J} [or $\mathfrak{S}'(01)$ in the literature on kinetic theory of polyatomic gases[29]] is a density-independent cross section for spin–rotation relaxation. In the same limit, $\boldsymbol{d}^{(2)\text{T}} \cdot \langle \boldsymbol{\sigma}_{\text{T}}\rangle^{-1} \cdot \boldsymbol{P} \cdot \boldsymbol{d}^{(2)}$ becomes $\frac{1}{6}\langle j(j+1)/(2j-1)(2j+3)\rangle/\sigma_{\theta,2}$, where $\sigma_{\theta,2}$ [or $\mathfrak{S}'(02)$ in the kinetic theory literature] is a density-independent cross section for molecular reorientation, the cross section associated with both dipolar and quadrupolar relaxation. This cross section differs from that for depolarized Rayleigh light scattering, σ_{DPR} (or $\mathfrak{S}_{\text{DPR}}$), only in that the latter includes contributions from a rotating collision partner, which means that $\sigma_{\theta,2}$ and σ_{DPR} are identical when the collision partner is a rare gas atom. Therefore, for a linear molecule,

$$\left(\frac{\rho}{T_1}\right)_{\text{lin,sr}} = \frac{2}{3}\frac{(\omega_{\text{sr}})^2}{L_0\langle \text{v}\rangle\sigma_{\text{J}}}\langle j(j+1)\rangle \tag{20}$$

In the 'high-temperature' or classical limit, $\langle j(j+1)\rangle = 2I_0k_{\text{B}}T$ for linear molecules, where I_0 is the molecular moment of inertia. For homonuclear dipolar relaxation,

$$\left(\frac{\rho}{T_1}\right)_{\text{lin,d}} = \frac{4}{3}I_2(I_2+1)\frac{(\omega_{\text{d}})^2}{L_0\langle \text{v}\rangle\sigma_{\theta,2}}\frac{1}{6}\left\langle\frac{j(j+1)}{(2j-1)(2j+3)}\right\rangle \tag{21}$$

For a quadrupolar nucleus, when the dipolar and the cross relaxation between dipolar and quadrupolar are negligible compared with the quadrupolar relaxation rate,

$$\left(\frac{\rho}{T_1}\right)_{\text{lin,q}} = \frac{(\omega_q)^2}{L_0\langle v\rangle\sigma_{\theta,2}}\frac{1}{6}\left\langle\frac{j(j+1)}{(2j-1)(2j+3)}\right\rangle \tag{22}$$

The average $\langle j(j+1)/(2j-1)(2j+3)\rangle$ goes to $\frac{1}{4}$ at the high-temperature limit, so that the above relationships, using the definitions of ω_d and ω_q, become the familiar

$$\left(\frac{\rho}{T_1}\right)_{\text{lin,d}} = \frac{1}{2}I_2(I_2+1)\frac{\gamma^4\hbar^2\langle r^{-3}\rangle^2}{L_0\langle v\rangle\sigma_{\theta,2}} \tag{23}$$

$$\left(\frac{\rho}{T_1}\right)_{\text{lin,q}} = \frac{3}{160}\frac{2I_1+3}{I_1^2(2I_1-1)}\frac{(eqQ/\hbar)^2}{L_0\langle v\rangle\sigma_{\theta,2}} \tag{24}$$

which were first derived by Gordon.[42]

In a dilute gas, the concept of a correlation time τ is physically obvious. Since a collision is itself a very short time event, the correlation time, the time it takes for a molecule to lose memory of the orientation of its angular momentum vector, is just the average time between those collisions that change the orientation of the rotational angular momentum vector:

$$\tau_J = [\rho\langle v\rangle\sigma_J]^{-1} \quad \text{or} \quad \tau_2 = [\rho\langle v\rangle\sigma_{\theta,2}]^{-1} \tag{25}$$

where σ_J and $\sigma_{\theta,2}$ are the effective cross sections for collisions that change the rotational angular momentum vector or its orientation, defined explicitly above, and can be calculated by quantum scattering or classical trajectories. The conventional definition of correlation time $\tau_{\theta,2}$ (as most often used in the liquid phase) is thus $\frac{1}{4}\tau_2$ for dipolar and quadrupolar relaxation in linear molecules in a dilute gas.[29,43,44]

Between collisions, the molecule is rotating freely. The spin–rotation interaction is not affected by the precession of the molecular symmetry axis about $\boldsymbol{J}$ between collisions. On the other hand, in dipolar relaxation, since the spin precession in the magnetic field is slow compared with molecular rotation frequencies, only the conserved or rotationally averaged component of the intramolecular dipolar magnetic field, modulated by collisions, contributes to the spin relaxation.[43] For nuclei with electric quadrupole moments, the relaxation depends on the coupling to the conserved part of the electric field gradient tensor, modulated by collisions. The averaging of second-rank tensor types of interactions leads to a factor of $\frac{1}{4}$ for linear molecules and $\frac{1}{5}$ for tetrahedral spherical tops. Similarly the symmetry axis of a symmetric top molecule precesses many times about $\boldsymbol{J}$ between collisions, thus resulting in an averaging of the spin–lattice interaction for a tensor of rank 2 by an amount $P_2(\cos\theta_0)$, where θ_0 is the angle that the dipolar axis or the electric field gradient symmetry axis makes with the molecular symmetry axis. These important and dramatic geometrical effects on the T_1/ρ values for the D spins in CD_3H, CD_2H_2, CDH_3, and CD_4 have been observed.[26] Such geometrical effects arising from averaging of the interaction during the free rotation between collisions in the gas phase do not apply to the spin–rotation mechanism, as mentioned above, so the proton relaxations in these systems have only the very small differences associated with the variation of $\langle j(j+1)\rangle$ with rotational constants.

In the language of correlation functions, Bloom et al.[26] emphasized the physical origin of this factor of $\frac{1}{4}$ by writing the correlation time as $f_2\tau_2$, where f_2 has a different numerical value for molecules of different geometry or for different nuclear sites in the same molecule. In the language of correlation functions,

$$\tau_{\theta,2} = \int_0^\infty g(t)\,dt, \quad \text{where} \quad g(t) = [g(t)]_{\text{free rot}}[g(t)]_{\text{coll}} \tag{26}$$

$$\tau_2 = \int_0^\infty [g(t)]_{\text{coll}}\,dt, \quad f_2 = \int_0^\infty [g(t)]_{\text{free rot}}\,dt \tag{27}$$

where the oscillatory nature of the correlation function for the free rotation between collisions gives rise to the factor $f_2 = \frac{1}{4}$ for linear molecules and $\frac{1}{5}$ for tetrahedral spherical tops. For a given collision pair, for example, CH_3D–Ar, the geometrical effects on ^1H or D relaxation are different; nevertheless, the cross section $\sigma_{\theta,2}$, which is a property of the CH_3D molecule with Ar, should be the same whether derived from ^1H or D spin relaxation.

4.2 Analysis of T_1 Measurements

A review of T_1 studies in the gas phase by Armstrong[45] provides some interesting examples in the region of the T_1 minimum. The effects of centrifugal distortion can be incorporated into the T_1 expression, as was found to be necessary in the interpretation of the low-density data for proton relaxation in CH_4 and SiH_4. In the region of the T_1 minimum, the assumption of a single relaxation time for all rotational levels (SRTA) gives a poorer fit to experimental data than multiple relaxation times (MRTA). In some cases, it is found that a distribution of correlation times τ_J leads to a better fit to the data and to a more accurate spin–rotation tensor from the T_1 minimum. Beyond the T_1 minimum, T_1/ρ should be a constant independent of ρ for a given temperature. However, in some cases, dimers formed by van der Waals interactions can result in contributions to the relaxation by the rotational states of the observed molecule, as was found in H_2–Ar.[39] This leads to a maximum in the T_1/ρ versus ρ curve, which can be fitted theoretically by considering the dynamics of formation and annihilation of the dimers.

Separate relaxation of nuclei in magnetically inequivalent sites has been measured in SF_4 and in NNO. The former was carried out in the region of the T_1 minimum. The different relaxation rates are characteristic of the different paramagnetic shieldings at the two sites, which have known relationships to the respective spin–rotation tensors.[46] When measurements are made beyond the T_1 minimum in two or more nuclear sites in the molecule, the same σ_J and $\sigma_{\theta,2}$ cross sections (which are characteristic of the molecule and independent of which nucleus is observed) should result from the analysis. This was the case for NNO. Similarly, both ^1H and ^{13}C provide the same σ_J cross section for CH_4. Relaxation information for more than one nuclear site in the same molecule provides redundancy of information. Cross sections obtained from different isotopomers have different kinematic factors and should be slightly different; scattering calculations have to be carried out for each isotopomer.

In a mixture of two gases, the analysis provides cross sections for the unlike pair of molecules if the pure gas experiment has been done, since the relaxation times in the extreme narrowing limit due to two types of collision partners are additive:[42]

$$T_1(\mathrm{A}) = (T_1/\rho)_{\mathrm{A\text{-}A}}\rho_{\mathrm{A}} + (T_1/\rho)_{\mathrm{A\text{-}B}}\rho_{\mathrm{B}} \tag{28}$$

The characteristic $(T_1/\rho)_{\mathrm{A-B}}$ provides $\sigma_J(\mathrm{A-B})$ or $\sigma_{\theta,2}(\mathrm{A-B})$.

4.3 Spin–Rotation Relaxation

In most molecules, the nuclear spin angular momentum of the ^{19}F nucleus is coupled to the molecular rotational angular momentum by a rather large spin–rotation constant, so that the ^{19}F nuclear spin is relaxed predominantly by the rotational magnetic fields. In the extreme narrowing regime, in the gas phase,

$$\left(\frac{\rho}{T_1}\right)_{\mathrm{lin.sr}} = \frac{2}{3}\frac{(\omega_{\mathrm{sr}})^2}{L_0\langle \mathrm{v}\rangle\sigma_J}\langle\, j(j+1)\rangle \tag{29}$$

where

$$(\omega_{\mathrm{sr}})^2 = C_{\mathrm{eff}}^2 = [\tfrac{1}{3}(C_\parallel + 2C_\perp)]^2 + \tfrac{4}{45}(C_\parallel - C_\perp)^2 \tag{30}$$

involving the spin–rotation tensor components, and $\langle j(j+1)\rangle = 3I_0/k_{\mathrm{B}}T$ for spherical tops such as CF_4, SiF_4, SF_6, SeF_6, and TeF_6, whereas for a linear molecule, $C_{\mathrm{eff}}^2 = C_\perp^2$ and $\langle j(j+1)\rangle = 2I_0/k_{\mathrm{B}}T$. The assumptions that allow the above T_1 equation to be used are that

1. the Larmor frequency is small compared with the collision frequency;
2. the duration of a collision is short compared with the average time between collisions;
3. the interactions among the collision partners do not significantly influence their collisions with the observed molecule;
4. bound states between the observed molecule and the collision partner have no significant effect on the spin relaxation.

Independent knowledge of the spin–rotation tensors from molecular beam electric or magnetic resonance or high-resolution microwave spectroscopy leads to $\sigma_J(T)$ directly from measurements of T_1. The temperature dependence of these cross sections appears to be described well enough by a power law:

$$\sigma_J(T) = \sigma_J(300\ \mathrm{K})(T/300\ \mathrm{K})^{-m} \tag{31}$$

These cross sections have been measured in NNO, CO_2, CO, N_2, CF_4, CH_4, SF_6, SeF_6, and TeF_6 molecules in collisions with self, Ar, Kr, Xe, N_2, CO, CO_2, HCl, CH_4, CF_4, and SF_6 molecules. Cross sections ranged from 0.09 nm^2 for SF_6 in CH_4 to 1.29 nm^2 for TeF_6 in pure TeF_6 at 300 K. The temperature exponent ranged from $m = 0.44$ for ^{13}CO in SF_6 to 1.62 for TeF_6 in SF_6, not uniformly $m = 1$ as was originally expected. Two $\sigma_J(T)$ sets for one interacting pair help to test the anisotropy of one interaction potential, offering the possibility of probing different parts of the potential surface; for example, $\sigma_J(T)$ of ^{13}CO in N_2–CO provides the anisotropy around CO, primarily $\mathrm{d}V/\mathrm{d}\theta_1$, where θ_1 is the angle that the CO molecule makes with the line connecting the centers of mass of the two molecules, and $\sigma_J(T)$ of $^{15}N_2$ in N_2–CO provides the anisotropy around N_2, primarily $\mathrm{d}V/\mathrm{d}\theta_2$, where θ_2 is the angle that the N_2 molecule makes with the intermolecular axis. A summary of σ_J cross sections and exponents m has been published.[1]

Each cross section is determined uniquely by the nature of interaction of the collision pair. As we have seen, the theoretical formalism provides the means, given the potential energy surface (PES), to calculate directly, via quantum scattering or classical trajectory methods, the observed cross sections. Nevertheless, there are interesting general observations that an examination of these cross sections reveals.[47]

1. Collision efficiencies can be defined in terms of the collision cross section divided by a geometric cross section, to take into account the relative sizes of the molecules. We have been using $(\sigma_J/\pi d_{12}{}^2)$, where d_{12} is taken from the distance scaling parameter in the conformal isotropic potential functions, the value of r at which $V = 0$. In comparing across the various observed molecules, it appears that the most important factor determining the absolute magnitude of the observed efficiencies of angular momentum change in the target molecule 1 by collision partner 2 is the anisotropy of the electronic distribution of the target molecule. For any given collision partner, the largest efficiencies are observed for the NNO molecule, followed by CO_2 and CO. To an approaching projectile, the anisotropy of the NNO molecule appears the greatest, followed by CO_2 and CO, in that order. The shape of the projectile molecule appears to be of secondary importance. Having corrected for the geometric sizes, projectiles Ar and HCl are observed to have about the same effect as do CF_4 and Xe on a nearly isotropic target such as SF_6.
2. The collision cross section for any given observed molecule increases with increasing mass (and number of electrons) of the collision partner—not unexpectedly, because of the geometric sizes. Having been corrected for the geometric sizes, the collision efficiencies also increase with increasing mass and number of electrons of the collision partner. Part of this has to do with the kinematic factors, which can be modeled by classical collisions between hard bodies, as in Chandler's perfectly rough hard spheres model.[48] The collision efficiency involves a kinematic factor containing only reduced masses and moments of inertia of the form

$$\left\{\frac{I_0(1)}{\mu_{12}d_{11}^2} + \frac{1}{2}\left[1 + \frac{I_0(1)d_{22}^2}{I_0(2)d_{11}^2}\right]\right\}^{-1} \tag{32}$$

   which applies to linear or spherical top target molecules and molecular collision partners (not rare gas atoms). The other part can be attributed to attractive forces increasing roughly with increasing number of electrons of the partner.
3. The observed collision efficiencies of the CH_4 molecule are nearly the same for nearly all partners, with the small mass of CH_4 having a leveling effect, making the reduced mass of the collision pair nearly the same for all partners.
4. Electrical moments of the collision partner enhance collision efficiencies by introducing sizable angle-dependent terms in the intermolecular potential. Thus, collision efficiencies involving HCl as a partner are higher than might be expected for its number of electrons; so do those involving CO_2 and NNO, which have large electric quadrupole moments.
5. Despite the similarities of kinematic factors for NNO with CO_2 or CO with N_2, there are clear differences in their

Table 3 Thermal Average Cross Sections for Molecular Reorientation, $\sigma_{\theta,2}$ (300 K)[51]

	$\sigma_{\theta,2}$ (nm^2)			$\sigma_{\theta,2}/\sigma_j$		
Collision partner	$^{14}N_2$	^{14}NNO	CD_4	N_2	NNO	CD_4
CH_4 or CD_4	0.31	0.452	0.391	2.2	1.67	2.1
N_2	0.293	0.430	0.390	2.0	1.46	2.4
CO	0.32	0.470	0.381	2.1	1.42	2.4
Ar	0.32	0.474	0.354	2.1	1.26	2.5
Kr	0.41	0.656	0.459	2.3	1.18	2.5
HCl	0.36	0.634	0.536	2.0	1.22	2.3
Xe	0.44	0.762	0.520	2.2	1.18	2.3
CO_2	0.59	0.754	0.599	2.0	1.26	2.5
NNO		0.755			1.27	
CF_4	0.59	0.798	0.614	2.0	1.11	2.5
SF_6	0.73	0.994	0.779	1.9	0.96	2.3

cross sections that cannot be accounted for by the very small electric dipole moments in NNO and CO. This is an indication of the sensitivity of the σ_J cross sections to the details of the anisotropy of the intermolecular potential.

6. There is a rough correlation between the magnitude of the temperature exponent of $\sigma_J(T)$ and the well depth ε_{12} for the collision pair. This is consistent with Chandler's model,[49] in which the collision efficiencies are multiplied by an exponential factor exp (ε_{12}/k_BT) to include the effects of attractive forces.

4.4 Quadrupolar Relaxation

The ^{14}N nucleus in $^{14}N_2$ and the end ^{14}N nucleus in $^{14}N^{14}NO$ relax entirely by the quadrupolar mechanism, which allows us to characterize quadrupolar relaxation cross sections in the gas phase.[50,51] On the other hand, the much smaller electric field gradient for the middle nitrogen in NNO leads to a competing spin–rotation and quadrupolar mechanism for this nucleus. Nevertheless, $\sigma_{\theta,2}(T)$ for the $^{14}N^{14}NO$ molecule [and also $\sigma_J(T)$] should be independent of whether the end or the middle nitrogen is used to determine the cross section. Similarly, the D relaxation in CD_4 is a combination of spin–rotation and quadrupolar. Whenever more than one mechanism makes a significant contribution to the relaxation, the separation of the two leads to greater errors in the cross sections.

It has been demonstrated by McCourt and co-workers that $\sigma_J(T)$ and $\sigma_{\theta,2}(T)$ are sensitive to different parts of the anisotropic potential, thus providing independent tests. Classical trajectory calculations for $\sigma_J(T)$ and $\sigma_{\theta,2}(T)$ in the N_2–Ar system have provided agreement with the experimental values, upon refining the PES.[41] $\sigma_{\theta,2}(T)$ is found to be most sensitive to variations in the anisotropy of r_{min} of the PES, and $\sigma_J(T)$ is found to be fairly sensitive to variations both in the anisotropy of r_{min} and the angular dependence of the repulsive wall of the PES.

A summary of the results of quadrupolar relaxation in gases is given in Tables 3 and 4. A very interesting result is that for $^{14}N_2$ and $^{15}N_2$, the ratio $\sigma_{\theta,2}/\sigma_J$ is very close to 2.0, with 10 different collision partners (ranging from 1.9 to 2.3, with an average of 2.1) and m_J ranges from 0.6 to 1.0, with an average of 0.74 while $m_{\theta,2}$ ranges from 0.62 to 0.91, with an average of 0.71. On the other hand, the ratio $\sigma_{\theta,2}/\sigma_J$ for NNO is somewhat more variable, ranging from 0.96 to 1.67, with an average of 1.27, m_J ranges from 0.47 to 1.29, with an average of 0.88, and $m_{\theta,2}$ ranges from 0.66 to 0.95 with an average of 0.80. The relaxation of D in CD_4 and H in CH_4 can also be compared for 10 different collision partners, resulting in $\sigma_{\theta,2}/\sigma_J$ ranging from 2.1 to 2.5 (average 2.4), m_J ranging from 0.79 to 1.06 (average 0.88), and $m_{\theta,2}$ ranging from 0.56 to 0.75 (average 0.64).[51] Of course, the kinematic factors are slightly different for the different isotopomers, and we have already seen that kinematic factors such as moments of inertia and reduced masses play a role. In these examples, classical trajectory calculations will have to be carried out for both isotopomers in order to obtain an accurate $\sigma_{\theta,2}/\sigma_J$ ratio for each isotopomer. Other examples are $\sigma_{\theta,2}/\sigma_J$ = 1.38 in pure ClF gas at 295 K[52] and $\sigma_{\theta,2}/\sigma_J$ = 1.6 in pure D_2 at 293 K, increasing to very nearly 2.0 at 171 K,[53] and for CF_4 in the pure gas, the ratio is very close to 4.0, with $\sigma_{\theta,2}$ obtained from depolarized light scattering. In general, $\sigma_{\theta,2}/\sigma_J > 1.0$ has been found experimentally. Results of classical trajectory calculations with a variety of PES are generally consistent with $\sigma_{\theta,2}/\sigma_J > 1.0$. In general, $m_J > m_{\theta,2}$ has been found experimentally. The greater temperature dependence of σ_J compared with $\sigma_{\theta,2}$ is consistent with the finding by McCourt et al. that σ_J is fairly sensitive to variations in the angular dependence of the repulsive wall, whereas $\sigma_{\theta,2}$ is not, and the general observations by Gordon that σ_J contains information mainly about the higher j states, and is determined both by changes in the magnitude of the rotational angular momentum

Table 4 Temperature Dependence of Collision Cross Sections for Molecular Reorientation $\sigma_{\theta,2}(T) = \sigma_{\theta,2}(300\,K)\,(T/300\,K)^{-m}$

	m		
Collision partner	$^{14}N_2$	^{14}NNO	CD_4
CH_4 or CD_4	0.76	0.79	0.65
N_2	0.62	0.77	0.60
CO	0.69	0.82	0.58
Ar	0.71	0.73	0.65
Kr	0.70	0.80	0.67
HCl	0.78	0.95	0.59
Xe	0.63	0.77	0.75
CO_2	0.91	0.93	0.71
NNO		0.85	
CF_4	0.66	0.69	0.66
SF_6	0.63	0.66	0.56

and by changes in its direction, whereas $\sigma_{\theta,2}$ are affected strongly by reorientation and only to a minor extent by changes in j.[32,41]

4.5 Intermolecular Dipole–Dipole Relaxation

In intramolecular relaxation mechanisms such as those discussed above, the interactions involved in the spin relaxation are always present within the molecule of interest; collisions interrupt molecular rotation, and thereby introduce the fluctuations of local magnetic fields or electric field gradient tensors that lead to nuclear spin relaxation. In an intermolecular mechanism, the interaction is 'on' only during a collision. By their nature, the dependence of intermolecular mechanisms on density, temperature, and magnetic field are very different from those of intramolecular mechanisms in the gas phase. It has been shown that it is possible to take advantage of such differences to separate the intermolecular mechanisms precisely from the ever-present intramolecular ones.[54–56]

In the gas phase, nuclear spin relaxation by intermolecular magnetic dipolar coupling is usually not an important mechanism. The exception is when the magnetic dipole on the collision partner is from an electron spin. The presence of the electron spin on the collision partner also generates a scalar intermolecular nuclear spin–electron spin interaction, which is responsible for the observed contact shifts discussed in Section 2.4. However, it has been shown that in the case of ^{129}Xe, this scalar mechanism[24] accounts for no more than 0.3% of the observed value of $1/T_1$ for ^{129}Xe in O_2 gas.[57] Under ideal conditions, the separation of the intermolecular dipolar from the other dominant mechanism (e.g., spin–rotation) has been quantitative, permitting the characterization of the intermolecular dipolar mechanism. This was possible for ^{1}H in CH_4, ^{19}F in CF_4, SiF_4, SF_6, SeF_6, and TeF_6 in oxygen gas.[54–56] After the spin–rotation contributions (which are proportional to $1/\rho$) were taken out, the remainder of the relaxation rate was found to be proportional to the density of oxygen for all temperatures and all fields. For example, for ^{19}F in mixtures of CF_4 in O_2, the relaxation rates ranged from 10% DD/90% SR up to 80% DD/20% SR.

There is a magnetic field dependence of the intermolecular dipolar relaxation. The duration of a collision, during which time the CF_4 and O_2 molecules are close enough for the electron spin–nuclear spin dipole interaction to cause nuclear spin transition, lasts for only a tiny fraction (1 part in 10^4) of the Larmor period of the ^{19}F nucleus, but a sizable fraction (0.04–0.2) of the Larmor period of the electron spin at typical fields 1.9–9.4 T. It has been found that a field dependence of the form

$$(1/T_1^{\mathrm{DD}}) = (1/T_1^{\mathrm{DD}})_0[1 - f(T)\omega_{\mathrm{I}}^{1/2}] \tag{33}$$

is consistent with the experimental data for ^{129}Xe, ^{1}H in CH_4, ^{19}F in CF_4, SiF_4, SF_6, SeF_6, and TeF_6 in oxygen gas,[54–57] where $(1/T_1{}^{\mathrm{DD}})_0$ corresponds to the zero-field limit. All these results were in the low-frequency limit; that is, the nuclear spin-bearing molecule suffers several collisions during one Larmor precession, and the duration of a collision is a fraction less than one of a Larmor cycle of the electron spin.

In the extreme narrowing limit, the correlation function approach[26] and the quantum mechanical formulation of molecular kinetic theory[27,33] both lead to

$$(1/T_1^{\mathrm{DD}})_0 = \tfrac{16}{3}S(S+1)\gamma_I^2\gamma_S^2\frac{\hbar^2}{d^2}\left(\frac{\pi\mu}{8k_{\mathrm{B}}T}\right)^{1/2} N_S \cdot F\,(V/k_{\mathrm{B}}T) \tag{34}$$

where N_S is the number density of S-bearing molecules, d is the characteristic length of the intermolecular interaction, loosely referred to as the molecular diameter, and $(\pi\mu/8k_{\mathrm{B}}T)^{\frac{1}{2}}$ is the reciprocal mean relative velocity $\langle \mathrm{v}\rangle^{-1}$. The dependence of the intermolecular dipolar relaxation on the intermolecular PES is contained in $F(V/k_{\mathrm{B}}T)$, which can be viewed as a measure of collision efficiency; i.e., the intermolecular dipolar relaxation rate is proportional to an *effective* collision frequency, which is a factor $F(V/k_{\mathrm{B}}T)$ times that for hard spheres of diameter d at the high translational energy limit. At 300 K, $F(V/k_{\mathrm{B}}T)$ is 2.04, 2.83, 3.16, 2.95, 3.66, and 3.75, respectively, for CH_4, CF_4, SiF_4, SF_6, SeF_6, and TeF_6 with O_2, and the temperature dependence is as $T^{-0.4}$. These $F(V/k_{\mathrm{B}}T)$ functions are expected to serve as good tests of potential energy surfaces involving interaction with the O_2 molecule, as clearly indicated by the failure of a square well approximation to provide values of the correct order of magnitude.

The experimental results of the field dependence, obtained empirically without making any assumptions as to the form— only with the assumption that $(1/T_1{}^{\mathrm{DD}})_0$ is field-independent— show that $f(T)$ is closely approximated by the form

$$f(T) \approx \frac{1}{24}\left(\frac{d_{\mathrm{eff}}}{\langle \mathrm{v}\rangle}\right)^{1/2}\left[3 + 7\left(\frac{\gamma_S}{\gamma_I}\right)^{1/2}\right] \tag{35}$$

This was arrived at by replacing the translational correlation time ($\tau_{\mathrm{trans}} = d^2/D$ in liquid models) by the analogous characteristic time in the gas phase ($d_{\mathrm{eff}}/\langle \mathrm{v}\rangle$). It appears that $\pi d_{\mathrm{eff}}{}^2 \approx \pi d^2 \cdot F(V/k_{\mathrm{B}}T)$ gives a reasonable fit to the experimental field dependence. At 300 K, the values of $f(T)$ ranged from 0.0157 to 0.0243 $\mathrm{MHz}^{-\frac{1}{2}}$ whereas the above expression leads to values of 0.0155–0.0240 $\mathrm{MHz}^{-\frac{1}{2}}$ for CH_4, CF_4, SiF_4, and SF_6.

5 RELATED ARTICLES

Chemical Shift Scales on an Absolute Basis; Gas Phase Studies of Chemical Exchange Processes; Isotope Effects on Chemical Shifts and Coupling Constants; Relaxation: An Introduction; Relaxation Theory for Quadrupolar Nuclei; Spin–Rotation Relaxation Theory.

6 REFERENCES

1. C. J. Jameson, *Chem. Rev.*, 1991, **91**, 1375.
2. A. D. Buckingham and J. A. Pople, *Discuss. Faraday Soc.*, 1956, **22**, 17.
3. C. J. Jameson, *Bull. Magn. Reson.*, 1980, **3**, 3.
4. C. J. Jameson, A. K. Jameson, and S. M. Cohen, *J. Chem. Phys.*, 1977, **67**, 2771.

5. F. H. A. Rummens, in *NMR Basic Principles and Progress*, eds. P. Diehl, E. Fluchs, and R. Kosfeld, Springer-Verlag, Berlin, 1975, Vol. 10, p. 1.
6. C. J. Jameson, A. K. Jameson, D. Oppusunggu, and S. Wille, *J. Chem. Phys.*, 1982, **76**, 152.
7. A. K. Jameson, C. J. Jameson, and H. S. Gutowsky, *J. Chem. Phys.*, 1970, **53**, 2310.
8. B. Bennett and W. T. Raynes, *Magn. Reson. Chem.*, 1991, **29**, 946.
9. C. J. Jameson, A. K. Jameson, and D. Oppusunggu, *J. Chem. Phys.*, 1986, **85**, 5480.
10. W. T. Raynes, A. D. Buckingham, and H. J. Bernstein, *J. Chem. Phys.*, 1962, **36**, 3481.
11. D. M. Bishop and S. M. Cybulski, *J. Magn. Reson., A*, 1994, **107**, 99.
12. C. J. Jameson and A. C. de Dios, *J. Chem. Phys.*, 1992, **97**, 417.
13. C. J. Jameson and A. C. de Dios, *J. Chem. Phys.*, 1993, **98**, 2208.
14. F. H. A. Rummens, W. T. Raynes, and H. J. Bernstein, *J. Phys. Chem.*, 1968, **72**, 2111.
15. C. J. Jameson, A. K. Jameson, and D. Oppusunggu, *J. Chem. Phys.*, 1984, **81**, 2313.
16. C. J. Jameson, A. K. Jameson, and S. M. Cohen, *J. Chem. Phys.*, 1976, **65**, 3397.
17. C. J. Jameson, A. K. Jameson, and S. M. Cohen, *Mol. Phys.*, 1975, **29**, 1919.
18. A. D. Buckingham and P. A. Kollman, *Mol. Phys.*, 1972, **23**, 65.
19. C. J. Jameson, A. K. Jameson, and S. M. Cohen, *J. Chem. Phys.*, 1973, **59**, 4540.
20. A. C. de Dios and C. J. Jameson, *Annual Reports on NMR Spectroscopy*, ed. G. A. Webb, Academic Press, London, 1994, Vol. 29, p. 1.
21. C. J. Jameson, A. K. Jameson, B. I. Baello, and H. M. Lim, *J. Chem. Phys.*, 1994, **100**, 5965.
22. C. J. Jameson, A. K. Jameson, S. Wille, and P. M. Burrell, *J. Chem. Phys.*, 1981, **74**, 853.
23. D. B. Chesnut and D. W. Wright, *J. Comput. Chem.*, 1991, **12**, 546.
24. A. Abragam, *Principles of Nuclear Magnetism*, Clarendon Press, Oxford, 1961.
25. M. Bloom and I. Oppenheim, *Adv. Chem. Phys.*, 1967, **12**, 549.
26. M. Bloom, in *MTP International Review of Science: Magnetic Resonance*, Butterworths, London, 1972, p. 505.
27. F. M. Chen and R. F. Snider, *J. Chem. Phys.*, 1967, **46**, 3937.
28. F. R. W. McCourt, T. E. Raidy, T. Rudensky, and A. C. Levi, *Can. J. Phys.*, 1975, **53**, 2463.
29. F. R. W. McCourt, J. J. M. Beenakker, W. E. Kohler, and I. Kuscer, *Nonequilibrium Phenomena in Polyatomic Gases*, Oxford University Press, Oxford, 1990, pp. 505–552.
30. C. Lemaire and R. L. Armstrong, *J. Chem. Phys.*, 1984, **81**, 1626.
31. R. G. Gordon, *Adv. Magn. Reson.*, 1968, **3**, 1.
32. W. B. Neilsen and R. G. Gordon, *J. Chem. Phys.*, 1973, **58**, **4131**, 4149.
33. B. Shizgal, *Can. J. Phys.*, 1976, **54**, 164.
34. R. L. Armstrong, M. Bogdan, K. R. Jeffrey, C. Bissonnette, and F. R. W. McCourt, *J. Chem. Phys.*, 1993, **99**, 5754.
35. C. Lemaire, R. L. Armstrong, and F. R. W. McCourt, *J. Chem. Phys.*, 1984, **81**, 5275.
36. R. G. Gordon, *J. Chem. Phys.*, 1966, **45**, 1649.
37. R. S. Wagner, R. L. Armstrong, E. C. Bissonnette, and F. R. W. McCourt, *J. Chem. Phys.*, 1990, **92**, 5907.
38. R. S. Wagner, R. L. Armstrong, C. LeMaire, and F. R. W. McCourt, *J. Chem. Phys.*, 1986, **84**, 1137.
39. C. Lemaire, R. L. Armstrong, and F. R. W. McCourt, *J. Chem. Phys.*, 1987, **87**, 6499.
40. M. J. Smith, S. Shi, H. Rabitz, and F. R. W. McCourt, *J. Chem. Phys.*, 1991, **94**, 7125.
41. L. Beneventi, P. Casavecchia, G. G. Volpi, C. C. K. Wong, and F. R. W. McCourt, *J. Chem. Phys.*, 1993, **98**, 7926.
42. R. G. Gordon, *J. Chem. Phys.*, 1966, **44**, 228.
43. R. G. Gordon, *J. Chem. Phys.*, 1966, **45**, 1635.
44. M. Bloom, F. B. Bridges, and W. N. Hardy, *Can. J. Phys.*, 1967, **45**, 3533.
45. R. L. Armstrong, *Magn. Reson. Rev.*, 1987, **12**, 91.
46. C. J. Jameson, A. K. Jameson, J. K. Hwang, and N. C. Smith, *J. Chem. Phys.*, 1988, **89**, 5642.
47. C. J. Jameson and A. K. Jameson, *J. Chem. Phys.*, 1990, **93**, 3237.
48. D. Chandler, *J. Chem. Phys.*, 1974, **60**, **3500**, 3508.
49. H. C. Andersen, D. Chandler, and J. D. Weeks, *Adv. Chem. Phys.*, 1976, **34**, 105.
50. C. J. Jameson, A. K. Jameson, and M. A. ter Horst, *J. Chem. Phys.*, 1991, **95**, 5799.
51. M. A. ter Horst, *Ph.D. Thesis, University of Illinois*, 1993.
52. K. T. Gillen, D. C. Douglass, and J. E. Griffiths, *J. Chem. Phys.*, 1978, **69**, 461.
53. M. Bogdan, K. R. Jeffrey, and R. L. Armstrong, *J. Chem. Phys.*, 1993, **98**, 6154.
54. C. J. Jameson, A. K. Jameson, J. K. Hwang, and D. Dabkowski, *J. Phys. Chem.*, 1988, **92**, 5937.
55. C. J. Jameson, A. K. Jameson, and J. K. Hwang, *J. Phys. Chem.*, 1989, **93**, 634.
56. C. J. Jameson, A. K. Jameson, and J. K. Hwang, *J. Chem. Phys.*, 1991, **94**, 172.
57. C. J. Jameson, A. K. Jameson, and J. K. Hwang, *J. Chem. Phys.*, 1988, **89**, 4074.

Biographical Sketch

Cynthia J. Jameson. *b* 1937. B.S., University of the Philippines; Ph.D., 1963, University of Illinois at Urbana-Champaign. Introduced to NMR by Herb Gutowsky. Faculty in Chemistry, University of Illinois at Chicago, 1968–present. Approx. 130 publications. Research interests include theoretical and experimental studies of the chemical shift in simple systems in the gas phase and in molecules absorbed in microporous solids, with particular emphasis on intramolecular and intermolecular shielding surfaces and averages therein; also, spin relaxation in gases and their connection with the anisotropy of intermolecular potentials and molecular dynamics.

Micellar Solutions and Microemulsions

Olle Söderman and Ulf Olsson
University of Lund, Lund, Sweden

1	Introduction	1
2	Self-Diffusion Studies	1
3	Relaxation Studies	5
4	Related Articles	11
5	References	11

1 INTRODUCTION

Surfactants are molecules with two distinctively different parts, one of which is hydrophilic and one which is hydrophobic. This feature of surfactants determines their properties in aqueous or oleic solutions. At low enough concentrations they form molecularly dispersed solutions. As the concentration is increased, they self-assemble into aggregates at a rather well-defined concentration, which is termed the *critical micellar concentration* (cmc) on account of the fact that the aggregates formed are termed *micelles*. As the concentration of surfactant is further increased, the aggregates crystallize into liquid crystalline phases with long-range order, the structures of which may vary rather substantially. The addition of a third component, giving rise to a water–oil–surfactant (where 'oil' is taken to be a generic term for an oleic component) system, results in an amazingly rich phase behavior, involving both liquid crystalline phases and liquid solution phases.

The present contribution will be concerned with the characterization by means of NMR techniques of two particular types of liquid solution of surfactant, the first being micellar solutions and the second being microemulsions. Having said this, we run into a problem of definition. How do we decide whether a particular solution belongs to one of these classes or perhaps to yet another class of solutions? Commonly, microemulsions are defined as thermodynamically stable solutions containing a surfactant (where 'surfactant' is a generic term for a single surfactant or mixtures of different amphiphilic molecules), water and oil. We shall adhere to this definition. Consequently, a micellar solution is one containing a surfactant and water (possibly with added salt) or oil, while the addition of oil or water to a micellar solution turns it into a microemulsion. Possible ambiguities of these definitions will be pointed out as we go along. [The name 'microemulsion' is somewhat unfortunate as it implies that the structure in the solution is one of discrete droplets of either water in oil (W/O) or oil in water (O/W). This is only partly true, as a rich variety of structures can indeed be found in addition to these two droplet structures. The literature is abundant with contributions which ignore this fact and only treat the two droplet structures.]

Studies of surfactant solution systems have had a central place in physical chemistry ever since the pioneering work of McBain at the beginning of this century,[1–4] not least due to the fact that these systems have important roles in a variety of applied processes. Questions asked pertain to the structure of the aggregates formed as well as the properties on a molecular level of the molecules comprising the systems.

It is fair to state that NMR has played a central role as a tool in tackling these questions, and much of our current understanding of surfactant solutions derives from NMR studies where two NMR methods have been especially important. The first of these is NMR relaxation studies, which have evolved to become an indispensable tool in studies of liquid surfactant solutions. The second one is measurements of self-diffusion coefficients by means of pulsed field gradients (PFG), an experiment which yields direct and easily interpretable information regarding many different aspects of surfactant solutions. In fact, our present understanding of the structure in microemulsions is to a large extent derived from PFG work in combination with various scattering approaches.

In the present article we discuss the two NMR approaches and describe applications which we consider to be those where NMR has contributed significantly to our present understanding of liquid solution phases of surfactants.

2 SELF-DIFFUSION STUDIES

Measurements of self-diffusion coefficients by means of PFG techniques have evolved to become one of the most important tools in the characterization of liquid surfactant systems. There are essentially two reasons for this, one of which has to do with the measuring technique itself. Thus the PFG approach offers a convenient method of determining self-diffusion coefficients. The technique is outlined in another article in this Encyclopedia (see ***Diffusion Measurements by Magnetic Field Gradient Methods***) and has also been described in a number of review articles.[5,6] Thus we shall not dwell on the technical aspects here. Suffice is to say that the technique requires no isotopic labeling (thus avoiding possible disturbances due to addition of probes); furthermore, it gives component resolved diffusion coefficients with great precision in a minimum of measuring time.

The second reason for its success rests on the fact that the method monitors transport over macroscopic distances (typically of the order of micrometers), and therefore the determined diffusion coefficients reflect aggregate sizes and obstruction effects, yielding information which is easily interpretable in terms of the microstructure of surfactant solutions. The fact that the information is obtained without the need to invoke complicated models, as is the case in the NMR relaxation approach, is particularly important. In this context it should be stressed that the PFG approach measures the self-diffusion rather than the collective diffusion coefficient.

The foundation for the use of NMR to monitor diffusion was laid in 1950 in the seminal paper by Hahn.[7] Another milestone occurred in the mid-1960s when Stejskal and Tanner demonstrated,[8] following a suggestion by Douglass and coworkers,[9] the use of pulsed gradients. Finally, towards the end of the 1960s the method became component resolved when the FT approach was introduced.[10]

In its simplest version, the method consists of two equal and rectangular gradient pulses of magnitude g and length δ, sandwiched on either side of the 180° rf pulse in a simple Hahn

echo experiment. For molecules undergoing free (Gaussian) diffusion characterized by a diffusion coefficient of magnitude D, the echo attenuation due to diffusion is given by[8,11]

$$I(\Delta, \delta, g) = I_0 \exp\left[-\gamma^2 g^2 \delta^2 \left(\Delta - \frac{\delta}{3}\right) D\right] \qquad (1)$$

where Δ represents the distance between the two gradient pulses, γ is the magnetogyric ratio of the monitored spin, and I_0 denotes the echo intensity in the absence of any field gradient. By varying either g, δ, or Δ (while at the same time keeping the distance between the two rf pulses constant), D can be determined by fitting equation (1) to the observed intensities.

In the following we use some illustrative examples to show how the PFG approach can be used to obtain information on surfactant solutions.

2.1 Micellar Solutions

2.1.1 The Micellization Process

The PFG method provides a unique way of investigating the process of micellization. The approach is based on the fact that the observed surfactant self-diffusion rates constitute a population weighted average between micellized and monomeric surfactant. This follows since the surfactant lifetime in the micelle is short on the relevant NMR timescale (which is essentially Δ in equation (1), and thus typically around 100 ms). Thus the observed surfactant diffusion coefficient is given by

$$D_{\text{obs}} = p_{\text{mic}} D_{\text{mic}} + (1 - p_{\text{mic}}) D_{\text{free}} \qquad (2)$$

where D_{mic} and D_{free} represent the diffusion coefficients of micellized and free surfactant, respectively, and p_{mic} is the fraction of micellized surfactant. Equation (2) can be rearranged to

$$p_{\text{mic}} = \frac{D_{\text{free}} - D_{\text{obs}}}{D_{\text{free}} - D_{\text{mic}}} \qquad (3)$$

Clearly, one can obtain the degree of micellization as a function of total surfactant concentration from the concentration dependence of D_{obs}, provided that D_{free} and D_{mic} are known. D_{free} can be obtained from measurements below cmc, while D_{mic} can be obtained from the diffusion coefficient of a hydrophobic probe which is solubilized into the micelles and for which p_{mic} is unity. A suitable probe is hexamethyldisilane (HMDS) which, if it is added in small amounts (on average one probe per micelle is a recommended concentration), seems only negligibly to disturb the micelles (although for some systems it should be used with some care[12]). Once D_{free} and D_{mic} are known, p_{mic} is obtained without the need to invoke any model for the micellization process. For ionic surfactants the same approach can also be used to obtain the degree of counterion association with the micelles, provided that the counterions contain nuclei suitable for PFG work, which is the case for surfactants with organic counterions.

The result of the approach outlined above is shown in Figure 1, in which a textbook example of the micellization process is presented. Data are obtained for a system with an organic counterion.[13] It is difficult to conceive of any other method that would give the same richness of detail concerning the micellization process. Data such as those presented in Figure 1 have been instrumental in testing various models for describing the micellization process. For instance, approaches based on the Poisson–Boltzmann equation have been very successful in rationalizing the process of micellization for ionic surfactants.[14,15]

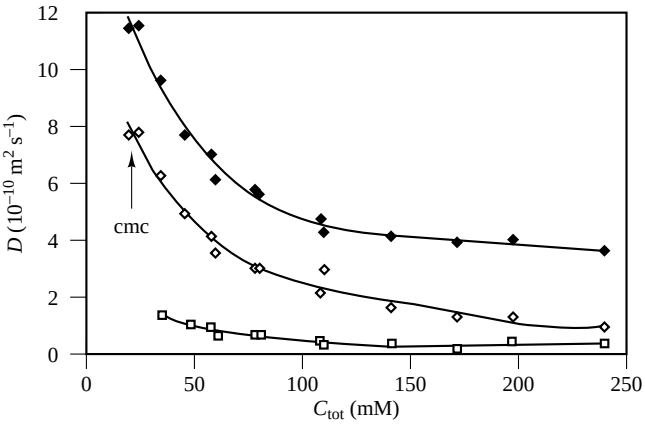

Figure 1 Self-diffusion data for the surfactant ion ($C_{10}H_{21}ND_3^+$) (◊) and counterion ($CHCl_2COO^-$) (♦) of a cationic surfactant with an organic counterion. Also given are the diffusion coefficients of the micelles (□), as measured by solubilizing a small amount of HMDS into the micelles. By applying the two-site model given by equation (3) one can estimate both the fraction of micellized surfactant and the degree of counterion binding to the micelles from the diffusion coefficients. For instance, at 140 mM total concentration of surfactant p_{mic} = 0.8, while the degree of counterion binding (defined as the ratio of the concentration of micelle associated counterions to the concentration of micellized surfactant cations) is 0.8. (Data from Jansson and Stilbs.[13])

2.1.2 Micellar Size and Structure

Questions pertaining to micellar size and structure may be tackled in two ways by means of PFG studies. The first concerns the measurement of self-diffusion of water (or other small molecules) in the system. Any aggregate present obstructs the diffusion of the water and, as the degree of obstruction depends on the volume fraction of the particles present as well as their geometry, information concerning the latter may be obtained. The mathematical description of such obstruction effects was worked out by Jönsson et al.,[16] who presented results for spheres, prolates, and oblates of different sizes and solution volume fractions.

The other approach to investigating micellar structure is based on Einstein's law, in which the (micellar) diffusion coefficient is related to the frictional factor f through

$$D = \frac{k_{\text{B}} T}{f} \qquad (4)$$

where k_{B} is the Boltzmann constant, and T is the absolute temperature.

The friction coefficient depends on the geometry and size of the diffusing particle as well as on the solvent viscosity η. Expressions relating f to the dimensions exist for several

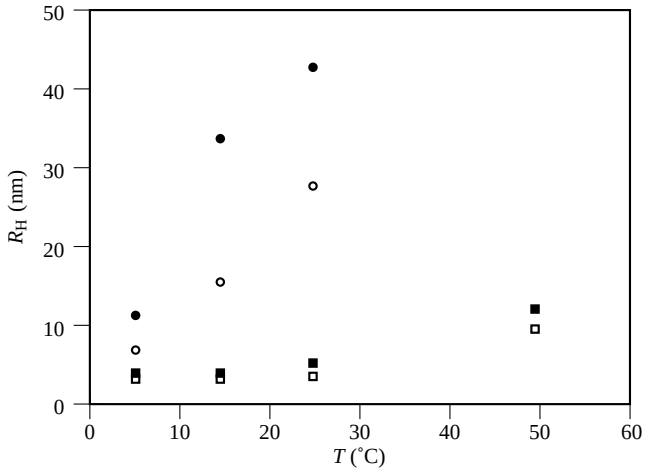

Figure 2 Micelle hydrodynamic radii for two concentrations of $C_{12}H_{25}(OCH_2CH_2)_5OH$ [(●) 2.73 wt%, (○) 0.92 wt% surfactant] and $C_{12}H_{25}(OCH_2CH_2)_8OH$ [(■) 3.06 wt%, (□) 1.02 wt%]. (Data from Nilsson et al.[18,19])

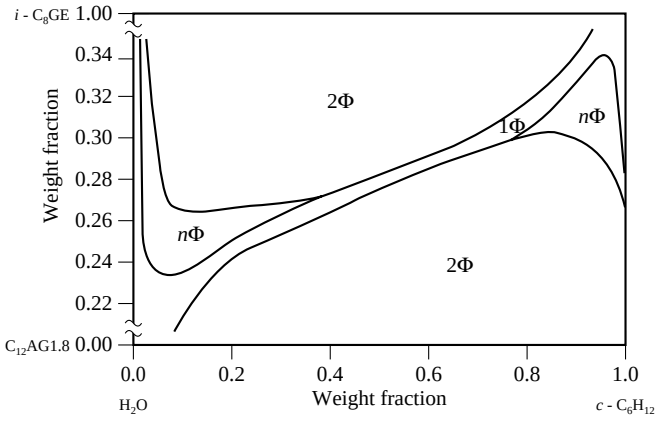

Figure 3 Phase diagram of an alkylpolyglucoside/cosurfactant/water/cyclohexane system at 25 °C with a total surfactant + cosurfactant concentration of 4 wt%. The number of phases present in the various regions of the phase diagram is indicated (for example, the one-phase microemulsion is denoted by 1Φ). (Reproduced with permission from Fukuda et al.[24])

different geometries, the simplest being that for a sphere of hydrodynamic radius R_H, which is:

$$f = 6\pi\eta R_H \tag{5}$$

For cases where the geometry is not known, one often uses equation (5) and computes a hydrodynamic radius, on the assumption that the diffusing species is a sphere. An example of this approach is shown in Figure 2, which gives the hydrodynamic radii for micelles formed by nonionic surfactants of the oligo(ethylene oxide) type as a function of temperature. Questions pertaining to the aggregate growth as a function of temperature and concentration in these systems have been the subject of rather lively discussion over the years.[17] Clearly, data such as those presented in Figure 2 are important in this context.[18–20]

Although the method outlined above is certainly useful, one should be aware of the limitations inherent in the approach. First, equations (4) and (5) assume infinite dilution. As micelles are self-assembled units, one must be aware of the fact that dilution may change their properties. At higher concentrations particle–particle obstruction effects become important, and these must be taken into account.[21,22]

2.2 Microemulsions

Microemulsions are defined as thermodynamically stable systems containing an oleic solvent (in most basic research a simple hydrocarbon is used), a hydrophilic solvent (most often water or brine), and a surfactant (which can be a combination of several amphiphilic molecules). For weakly amphiphilic molecules the system is molecularly dispersed; this will not be discussed here.

Of particular interest are systems in which small amounts of surfactant may bring equal volumes of oil and water into solution. This can be achieved with less than 1% surfactant, and such systems are usually termed 'balanced'.[23] In many of these systems one may vary the oil to water volume ratio extensively without ever leaving the one-phase microemulsion region. This is achieved by varying some parameter. Such a parameter is constituted by the temperature in the case of nonionic surfactants of the C_xE_y type, the salinity of the water for ionic surfactants, and the cosurfactant/surfactant ratio in a mixed surfactant system. An example of such behavior is shown in Figure 3, where a recently compiled phase diagram for an alkylpolyglucoside surfactant is displayed. In this case it is the proportion of the cosurfactant (which is a branched alkyl glycerol monoether) in the surfactant mixture which was varied.[24]

It is a considerable challenge to model such a system, and a prerequisite for such an endeavor is the availability of structural information. It is perhaps in this context that the PFG approach has achieved its most spectacular successes, not least due to the fact that very few other methods can yield such information for microemulsions. How then do we infer structural information from self-diffusion coefficients which are dynamic quantities? The basis of the approach is the fact that the mean distance traveled by the molecules is of the order of $\sqrt{\Delta D}$, which quantity is of the order of micrometers for low molecular weight liquids. Thus any obstruction effects or confinement to droplets of colloidal dimensions affects the diffusion coefficient.

Broadly speaking, one can differentiate between a microstructure of closed particles, whether they are normal (enclosing the oil component) or reversed (enclosing the water), and a microstructure which is bicontinuous. The latter term is often used without being properly defined. We shall take it to imply that a large fraction of both the oil and water molecules exists in domains which span macroscopic distances in three dimensions.

For the case of discrete particles, the continuous phase displays a diffusion behavior similar to that of the neat liquid. There will be solvation effects, i.e. some of the continuous solvent may be associated with the surfactant and, as a consequence, will have an altered diffusional behavior. However, for low surfactant concentration this effect is negligible. Thus any reduction in the reduced diffusion coefficient for the continuous solvent (in PFG studies of microemulsions one preferably reports the reduced diffusion

coefficient, defined as D/D_0, where D_0 is the bulk diffusion coefficient of the neat liquid at the same temperature) can be attributed to particle obstruction effects (see above). If both the dispersed phase and the surfactant have negligible solubility in the continuous phase, their diffusion is given by the particle diffusion, and so both have the same diffusion coefficient, the value of which can be used to estimate the size of the diffusion particle from equation (4), while the concentration dependence of the diffusion coefficient can be used to infer information about the interaggregate interactions.[22]

Turning to the bicontinuous case we note first that both the water and the oil component diffuse rapidly. Careful PFG work using mixtures of oil has revealed that the diffusion process of the oil component is very similar to the diffusion in neat oil.[25,26] The same holds for the water component.[27] This is an important observation, which implies that any reduction in the reduced diffusion coefficient can be attributed to the obstruction effects due to the presence of the surfactant film. Effects such as exchange between droplets and fusion–fission processes cannot explain the rapid oil and water diffusion. Any structural model of microemulsions must not be at variance with this statement. It should be emphasized that, at present, the PFG method is the only way in which bicontinuity may be proved or disproved. Two-dimensional images cannot prove bicontinuity, since it cannot exist in two dimensions.[28]

Let us now investigate whether the diffusion data for the system in Figure 3 is in line with this reasoning. Figure 4 shows the reduced diffusion coefficients for the water and oil components in the system shown in Figure 3 as a function of the volume fraction of hydrocarbon in the solvent mixture (Φ_{oil}). The data in Figure 4 are typical for microemulsions where the oil content can be varied continuously from no oil to pure oil. Thus the water and oil component diffusion changes continuously from rapid to slow as the fraction of each component is decreased, and the plots of the reduced diffusion coefficients versus the volume fraction of oil in the solvent mixture show a rather characteristic 'sigmoidal' curve for both components. At equal volume fractions of oil and water the curves intersect, and the value of both reduced diffusion coefficients is around 0.6 at the point of intersection. In line with the discussion above, this points to discrete particles at low and high values of Φ_{oil} and a bicontinuous structure in between. Based on the information inherent in PFG data such as those presented in Figure 4, how should we picture the bicontinuous microemulsions?

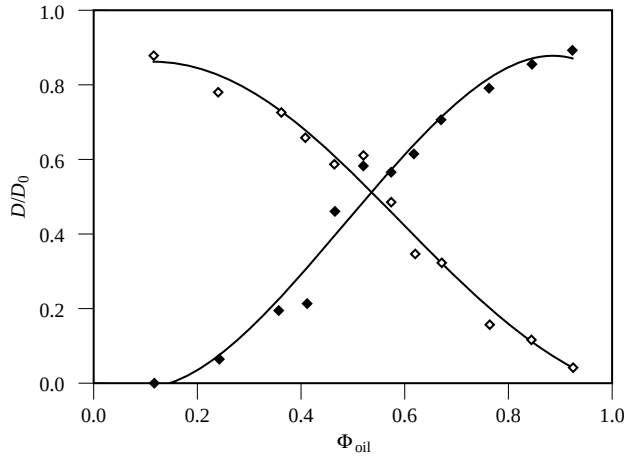

Figure 4 The relative self-diffusion coefficients of water (◊) and hydrocarbon (♦) as a function of the volume fraction, Φ_{oil} of hydrocarbon in the solvent mixture, for microemulsions formed in the alkylpolyglucoside/cosurfactant/water/cyclohexane system, the phase diagram of which is shown in Figure 3. (Data from Fukuda et al.[24])

A most fruitful way of looking at these phases is due to Scriven[29] who proposed the idea that the structure could be described as a melted liquid crystalline cubic phase, for which the structure is known on account of the scattering studies that can be performed on these systems [cubic phases come in two varieties (discrete and bicontinuous); Scriven had the latter class in mind]. These are formed by two interwoven subvolumes of the same material (polar or nonpolar), which are separated by a film of the opposite material. This dividing film is described as a 'minimal surface', having zero mean curvature.

Now, allow this structure to melt, so that the long range order is lost, but locally the structure is retained. When the material on both sides is equal, L_3 phases or bicontinuous micellar solutions (see below) are formed, and the dividing film is a bilayer, while for the case where the two subvolumes are not equal, microemulsions are formed. For this case the dividing film is a monolayer, with a curvature towards the oil or water depending on the volume fraction of the two components.

In an important contribution, Anderson and Wennerström[30] have computed the obstruction effect for components in the subvolumes and for components diffusing along the dividing surface. Indeed, these workers found that the reduced diffusion coefficient for a bicontinuous microemulsion with roughly equal oil and water volume fractions is around 0.6, giving further credence to Scriven's suggestion.

Finally, we note that, when measurements are possible, the value of the surfactant self-diffusion coefficient often displays a maximum with respect to changes in the solvent composition at equal oil and water volume fractions. This observation is more difficult to interpret in terms of a particular microstructure, owing to the difficulties of finding a suitable reference value for the lateral diffusion coefficient for the surfactant along the surfactant film, but it does indicate that the surfactant is diffusing over surfaces that extend over several micrometers with only minor disturbances for diffusions. Consider, for example, the case of a sodium dodecyl sulfate (SDS) microemulsion,[31] where D for the surfactant was found to be $1.5 \times 10^{-10}\,m^2\ s^{-1}$ at 27 °C, a value which is in good agreement with the values found for lateral diffusion of SDS over a micellar surface of spherical[32] ($D = 1.0 \times 10^{-10}\,m^2\ s^{-1}$ at 30 °C) and cylindrical[33] ($D = 1.69 \times 10^{-10}\,m^2\ s^{-1}$ at 30 °C) geometry, where the diffusion is indeed unhindered.

2.3 L_3-Phases and Bicontinuous Micellar Solutions

The properties of L_3 phases and bicontinuous micellar solutions have been discussed extensively, and they constitute an illustrative example of the power of the PFG method in unravelling solution structure. Both types of solution have a connected structure, and again a fruitful starting point is the (known) structure of the cubic phases. If a cubic phase is diluted with the material of the subvolumes, an L_3 phase

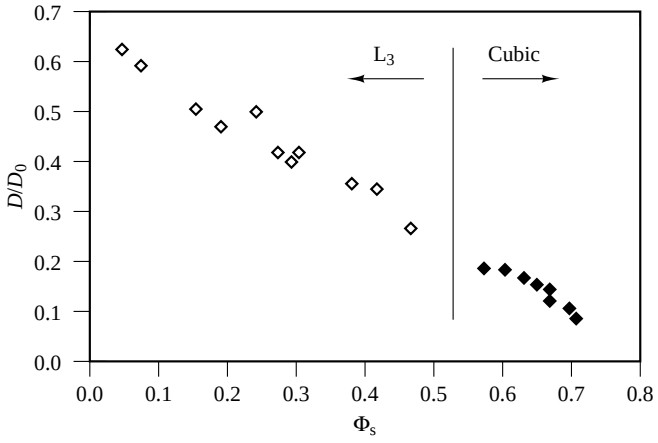

Figure 5 Variation in the reduced water diffusion coefficient with the volume fraction of surfactant in the L_3 (◊) and cubic (♦) phases formed in the AOT/water/NaCl system. (Data from Balinov et al.[34])

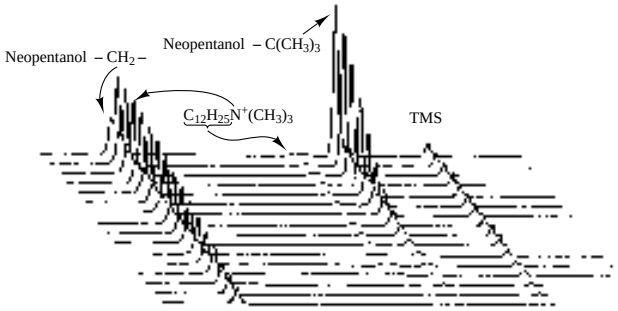

Figure 6 A ^{1}H NMR FT PFG experiment at 100 MHz on the solubilization of neopentanol into dodecyltrimethylammonium chloride micelles (solvent D_2O). The degree of solubilization is obtained directly from the evaluated D values for neopentanol in the micellar solution and in an aqueous solution [see equation (3)]. The value for the micellar diffusion coefficient, which is obtained from a small amount of solubilized tetramethylsilane (TMS), is also needed. The gradient current was varied linearly between successive spectra, which were obtained at fixed intergradient (Δ) and rf pulse (τ) intervals

(sometimes known as L* or 'sponge' phase) is formed, while dilution with the material of the dividing film gives rise to a bicontinuous micellar solution. Let us consider the L_3 phase formed in the sodium bis(2-ethylhexyl)sulfosuccinate (AOT)/brine system. In this system, the L_3 phase is in equilibrium with a bicontinuous cubic phase via a two-phase region.[34] Figure 5 gives the reduced diffusion coefficients for the water as a function of the surfactant volume fraction Φ_s in both the L_3 and the cubic phase.

There are two noteworthy features of the data shown in Figure 5. First, there is a continuous change in D/D_0 with Φ_s over the two-phase area between the L_3 and cubic phases. Secondly, at high dilution, a limiting value of D/D_0 of around 0.65 is obtained. The first observation indicates that the microstructures in the two phases are similar, since the translational diffusion of water reflects the microstructure of the solution. The second point can be used to infer information about the microstructure in a slightly more rigorous way. Consider a structure of discrete particles. According to the obstruction factors derived by Jönsson et al.,[16] the only geometry that would give rise to a reduction in D/D_0 from 1 to 0.65 would be large disks with an axial ratio in excess of 100:1. This is not in agreement with the surfactant diffusion, which, for the case of disks, implies an axial ratio of 12:1. Thus we are forced to think of alternative microstructures. Following the suggestion inherent in the first feature of the data in Figure 5, i.e. that the microstructures are similar in the L_3 and cubic phases, let us consider the case of a bilayer continuous structure. As noted above, this case has been treated by Anderson and Wennerström,[30] who obtained a value of 0.65 for the reduced diffusion coefficient for the solvent diffusion at low volume fraction of bilayer (in fact, for an infinitely thin multiply connected bilayer, the limiting value is $\frac{2}{3}$, on account of the dimensionality of the bilayer). Moreover, by analyzing the dependence of D/D_0 on Φ_s, information can be obtained regarding the coordination number of the obstructing surface.[35]

The analysis of the bicontinuous micellar solution structure as based on PFG data follows the same approach as the one described above. Readers interested in this particular micellar solution are referred to the paper by Monduzzi et al.[36]

2.4 Solubilization

As a final illustration of the power of the PFG approach, we consider the topic of solubilization. By 'solubilization' we mean the incorporation of molecules which are not water soluble into the micellar subvolume of a micellar solution. An important question pertaining to the phenomenon of solubilization concerns the degree of partitioning between the micelles and the water. This question is related to that pertaining to the micellization process (see above), and the same approach used to study that process can be used to investigate solubilization. Thus the degree of solubilization p can be determined by measuring the diffusion coefficient of the solubilizate in the absence and presence of micelles, and determining the diffusion coefficient for the micelle (using the approach outlined above) by using equation (3). From the volume or weight fraction of the micellar subvolume and the value of p, one can then determine the desired partition coefficient. A typical PFG solubilization experiment is shown in Figure 6.[37]

There are several advantages of the PFG approach as compared with other techniques for studying solubilization. The experiment is simple as well as selective. The latter point is particularly important, as one can determine the solubilization of several different solubilizates simultaneously, and each individual value of p can be determined. The presence of impurities is normally not a problem. The quantity p is well defined and easily interpreted. Finally, by measuring the surfactant diffusion one can independently check whether the micelles as such are altered by the presence of solubilizates. Clearly, the whole topic of solubilization becomes somewhat less meaningful if one does not have control over the state of the micelles.

3 RELAXATION STUDIES

NMR relaxation has proven to be a useful experimental technique for studying surfactant aggregation in liquid solutions

and liquid crystals.[20,38–40] The experiment yields information on the local dynamics and conformational state of the surfactant hydrocarbon chain and has demonstrated the liquid-like interior of surfactant micelles. However, the main purpose of NMR relaxation studies of isotropic micellar solutions and microemulsions has been to study properties such as the aggregate size.

The reorientation dynamics of aggregated surfactant molecules, which are discussed in more detail below, are characterized by the fact that they locally have a preferred orientation, forming essentially a monomolecular film of oriented molecules. Locally, surfactant molecules undergo rapid internal motions, such as *trans–gauche* isomerizations in the hydrocarbon chain. These motions are, due to the preferred orientation, slightly anisotropic. The situation can be pictured as the polar headgroups being anchored at the polar–apolar interface, leaving room for dangling motions of the hydrocarbon chains, with certain restrictions on the number of conformations due to packing constraints in the film. In isotropic solutions the residual interaction or anisotropy is further averaged by the thermal tumbling of the aggregates in combination with the diffusion of surfactant molecules within the curved surfactant film.

NMR spectra from surfactants in micellar solutions and microemulsions are generally in the motional narrowing regime, and the spin dynamics are characterized by well-defined relaxation times. Exceptions can be found in solutions of very long ($>10^2$ nm) wormlike cylindrical micelles where the large size in connection with steric overlap gives rise to a very slow (about 10^{-4} s) aggregate reorientation.[41,42] On the other hand, the dynamics are typically outside the extreme narrowing regime, and one often observes $R_2 \gg R_1$, where R_1 and R_2 are the longitudinal and transverse relaxation rates, respectively. Micellar aggregates reorient on a timescale of 10^{-9} s or slower. Thus, at conventional magnetic field strengths, the essential information on the surfactant aggregates is stored in the transverse relaxation rate R_2.

A hydrocarbon, typically an alkyl chain of 12–16 carbon atoms, constitutes the major part of surfactant molecules, offering ^{1}H and ^{13}C nuclei for NMR studies. Being spin-$\frac{1}{2}$ nuclei, the relaxation is mainly due to dipole–dipole interactions (although chemical shift anisotropy and scalar interaction can sometimes be important in the case of ^{13}C). The easy access and the relatively high sensitivity (which was particularly important in early CW NMR studies) has made ^{1}H NMR (in particular bandwidth measurements) studies particularly popular. Micellar growth can easily be studied qualitatively by monitoring the bandwidth of aliphatic ($-CH_2-$) protons in the spectrum. Quantitative analysis is, however, complicated by the coupling of the various protons having locally different motional characteristics along the alkyl chain. In an alkyl chain of, say, 16 carbon atoms, the protons constitute a coupled spin system of approximately 2^{16} spin states, which can have a broad spectrum of transition rates, resulting in significant deviations from a Lorentzian bandshape of the CH_2 resonance.[41,43] This complexity can, however, be turned into an advantage in that it allows for a continuum description of the transition rate spectrum. The ^{1}H bandshape problem was analyzed by Wennerström et al.[41,43] within the two-step formalism (see below), and quantitative ^{1}H bandshape analyses have been performed in systems of large, slowly reorienting micelles.[41,42] In contrast to the non-Lorentzian band shape, one often observes an exponential longitudinal relaxation due to rapid internal equilibration of the spin system (spin diffusion), and the frequency dependence of R_1 has been measured by using field cycling techniques.[44,45]

In an alkyl chain, the ^{13}C nuclei are relaxed by the fluctuating dipole–dipole coupling to the directly bound protons. The various carbon atoms along the chain are normally resolved. Usually, one applies broadband proton decoupling, resulting in exponential longitudinal relaxation of the individual ^{13}C magnetizations, and it is possible to determine R_1 and the nuclear Overhauser enhancement of the different methylene segments. On the other hand, it is difficult to measure R_2 on ^{13}C. Therefore, ^{13}C is mainly useful for studying local chain dynamics and segmental order, since the aggregate dynamics occur on timescales which are normally long relative to the inverse ^{13}C resonance frequency.

Certain surfactants carry phosphate or ammonium polar headgroups, offering ^{31}P and ^{14}N nuclei, respectively, for relaxation studies. The phosphate ^{31}P ($I = \frac{1}{2}$) has a relatively large chemical shift anisotropy which is strongly dependent on the pH (degree of protonation), complicating the analysis of relaxation data. ^{14}N is a $I = 1$ nucleus and its relaxation is dominated by the strong quadrupolar interaction. Except for the case of quaternary ammonium groups, the magnitude and asymmetry of the quadrupolar coupling is also pH dependent, and special care has to be taken.

The most suitable nucleus for relaxation studies of surfactant systems is ^{2}H, which can be incorporated synthetically into the hydrocarbon chain of the surfactant molecule. Normally, one selectively labels a single methylene segment, typically one adjacent to the polar headgroup, in order to avoid resonance overlap in the spectrum. ^{2}H is a $I = 1$ nucleus, and the dominating interaction governing the relaxation is the strong quadrupolar interaction. For aliphatic ($C-^2H$) deuterons, the analysis is further simplified by the fact that the electric field gradient tensor has essentially cylindrical symmetry around the $C-^2H$ bond direction, resulting in a vanishing asymmetry parameter. The ease with which both R_1 and R_2 can be accurately measured, the relatively simple interaction Hamiltonian, and the sufficiently high sensitivity allowing measurements to be made at low resonance frequencies (down to 2 MHz using variable field electromagnets), give ^{2}H NMR relaxation a particularly important role among the different experimental tools available for studying surfactant systems.

The utility of the NMR technique as an experimental tool in surfactant science can be made apparent by comparing the strengths and weaknesses of the NMR relaxation technique with those of other experimental techniques. In comparison with other experimental methods used in studying, for example, micellar size, the NMR relaxation technique has two major advantages, both of which are associated with the fact that it is reorientational motions which are measured. One is that the relaxation, i.e. R_2, is sensitive to small variations in micellar size. Consider, for example, a sphere for which the rotational correlation time is proportional to the cube of the radius. This can be compared with the translational self-diffusion coefficient which varies linearly with the radius. The second, and perhaps most important advantage is the fact that the rotational diffusion of particles in solution is essentially independent of interparticle interactions (electrostatic and hydrodynamic). This is in contrast to most

other techniques (such as viscosity, collective and self-diffusion, scattered light intensity, etc.) available for studying surfactant systems or colloidal systems in general. In this latter respect, NMR relaxation experiments are comparable with form factor determinations with small angle X-ray or neutron scattering experiments. A weakness of the NMR relaxation approach to aggregate size determinations, compared with form factor determinations, would be the difficulties of absolute calibration, since the transformation from information on dynamics to information on structure must be performed by means of a motional model.

3.1 Timescale Separation: The Two-Step Model

In this section we discuss a motional model[46–48] of aggregated surfactant molecules, which involves a timescale separation of fast local and slow global motions. This model has been applied extensively to, and shown to rationalize, NMR relaxation data from aggregated surfactant systems. We discuss the model in connection with ^{2}H relaxation experiments, since the most extensive experimental studies have been performed on ^{2}H-labeled surfactants. We begin by recalling that the longitudinal (R_1) and transverse (R_2) relaxation rates of an $I = 1$ nucleus, due to the quadrupolar interaction in an isotropic solution, are given by[49]

$$R_1 = \frac{3\pi^2}{40}\chi^2[2j(\omega_0) + 8j(2\omega_0)] \tag{6a}$$

$$R_2 = \frac{3\pi^2}{40}\chi^2[3j(0) + 5j(\omega_0) + 2j(2\omega_0)] \tag{6b}$$

where χ is the quadrupolar coupling constant, and $j(\omega_0)$ is the reduced spectral density function evaluated at the Larmor frequency ω_0.

Based on existing knowledge of surfactant aggregate structures, Wennerström and co-workers[46–48] suggested that the reorientational motion of surfactant molecules can be divided into: (i) fast local motions (equilibration of internal modes), which are slightly anisotropic due to the preferred orientation of the surfactant molecules; and (ii) slow isotropic motions, associated with the aggregate tumbling and the lateral diffusion of surfactant molecules within the aggregates. If these two motions occur on significantly different timescales, the fast motions generate a well-defined residual anisotropy to be averaged by the slow motions, and the spectral density can be written as a weighted sum of the fast and the slow components

$$j(\omega_0) = (1 - S^2)j_f(\omega_0) + S^2 j_s(\omega_0) \tag{7}$$

where $j_f(\omega_0)$ and $j_s(\omega_0)$ are the reduced spectral density functions describing the fast and slow motions, respectively. The parameter S is often referred to as an 'order parameter' and is given by the average

$$S = \tfrac{1}{2}\langle 3\cos\theta_{MD} - 1\rangle_f \tag{8}$$

where θ_{MD} is the angle between the axis of the maximum component of the electric field gradient tensor and the director axis.

The situation for the case of a ^{2}H-labeled methylene segment of a surfactant molecule residing in a micelle is illustrated in Figure 7. The director axis Z_D corresponds to the micellar surface normal. The field gradient tensor is cylindrically symmetric around the C–D bond axis, with the maximum component in the bond axis direction Z_M.

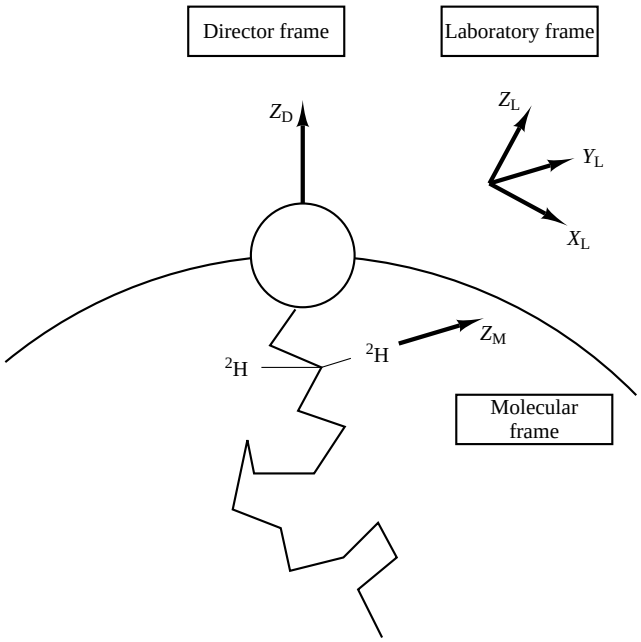

Figure 7 Schematic illustration of the various coordinate frames considered within the two-step model, for the case of a specifically ^{2}H-labeled methylene segment in the surfactant hydrocarbon chain. The laboratory frame (L) is set by the direction of the external magnetic field, where Z_L is the field direction. In this frame the nuclear quadrupolar moment tensor is diagonal. The director frame (D) is associated with the micellar aggregate, where Z_D specifies the micellar surface normal. It is assumed that the fast local dynamics occur with an essentially cylindrical symmetry around Z_D. The molecular frame (M) corresponds to the principal axis of the electric field gradient tensor. For the case of a methylene segment, Z_M specifies the maximum component of the field gradient tensor, which is also cylindrically symmetric around Z_M

In equation (7) it is also assumed that the fast motions have an effective three-fold or higher symmetry around the director. For most situations, however, one may expect an effectively cylindrical symmetry. For lower than three-fold symmetry, equation (7) must be extended to include a second-order parameter, describing the residual order in the plane perpendicular to the director. A similar extension is also necessary when the electric field gradient has a nonvanishing asymmetry parameter (for an extensive discussion, see Halle and Wennerström[48]).

3.2 Frequency Dependent Relaxation Studies of Small Spherical Micelles

The fast motions, described by the spectral density function $j_f(\omega_0)$, are expected to occur on a similar timescale ($\tau_f \approx 10^{-11}$ s) as in the corresponding liquid alkane. Thus this motion is in extreme narrowing ($\tau_f \ll 1/\omega_0$) in the accessible frequency range, and we may assume that $j_f(2\omega_0) \approx j_f(\omega_0) \approx j_f(0) = 2\tau_f$, where τ_f should be considered as an effective correlation time, representing the integral over a nonexponential correlation function.

The slow motion is a combination of micelle tumbling and the lateral diffusion of surfactant molecules within the surfactant film. For spherical aggregates, this motion is described by a Lorentzian spectral density function:

$$j_s(\omega_0) = \frac{2\tau_s}{1 + (\omega_0\tau_s)^2} \tag{9}$$

where τ_s is the correlation time. The tumbling and the lateral diffusion are expected to be statistically independent, in which case the correlation function can be factorized:

$$G_s = G_t G_d = e^{-t/\tau_t}\, e^{-t/\tau_d} = e^{-t/\tau_s} \tag{10}$$

where subscripts t and d refer to tumbling and lateral diffusion, respectively, and the slow correlation time can be written as

$$\frac{1}{\tau_s} = \frac{1}{\tau_t} + \frac{1}{\tau_d} \tag{11}$$

The correlation time associated with the tumbling of a sphere of radius R is given by

$$\tau_t = \frac{4\pi\eta R^3}{3k_B T} \tag{12}$$

where η represents the solvent viscosity, and $k_B T$ is the thermal energy. The effect of lateral diffusion can be described in terms of diffusion on the surface of a sphere of radius R. In this case, the correlation time can be written as

$$\tau_d = \frac{R^2}{6D_{lat}} \tag{13}$$

where D_{lat} is the lateral diffusion coefficient.

With the assumptions of (i) extreme narrowing conditions for the fast motions and (ii) a Lorentzian spectral density function of the slow motion, the expressions for the relaxation rates become, with equation (7)

$$R_1 = \frac{3\pi^2}{40}\chi^2 \left\{ (1 - S^2)20\tau_f + S^2 \times \left[\frac{4\tau_s}{1 + (\omega_0\tau_s)^2} + \frac{16\tau_s}{1 + (2\omega_0\tau_s)^2} \right] \right\} \tag{14a}$$

$$R_2 = \frac{3\pi^2}{40}\chi^2 \left\{ (1 - S^2)20\tau_f + S^2 \times \left[6\tau_s + \frac{10\tau_s}{1 + (\omega_0\tau_s)^2} + \frac{4\tau_s}{1 + (2\omega_0\tau_s)^2} \right] \right\} \tag{14b}$$

Equations (14a) and (14b) have been applied in a large number of ^{2}H NMR relaxation studies of micellar systems. It turns out that frequency dependent relaxation studies are particularly useful for studying small spherical micelles, which typically have a radius of about 2 nm. Using the water viscosity and equation (12) we obtain $\tau_t \approx 7$ ns at room temperature (25 °C). Including the effect of lateral diffusion, a typical value of the slow correlation time is $\tau_s \approx 5$ ns. Thus, the relaxation dispersion from the slow motion occurs around $\nu_0 \approx (2\pi\tau_s)^{-1} \approx 30$ MHz, which is well within the accessible Larmor frequency range for ^{2}H.

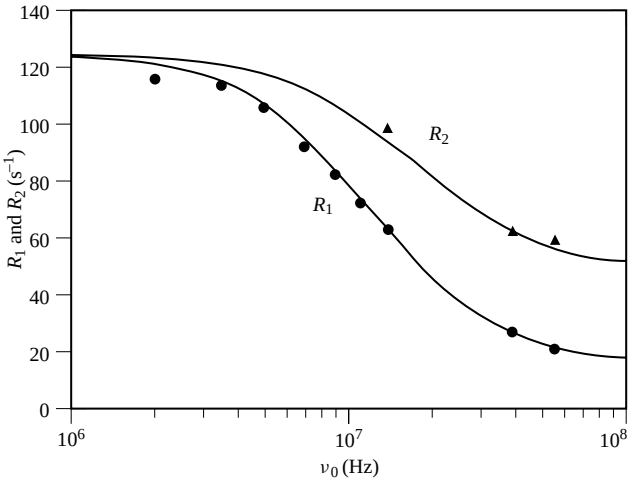

Figure 8 The variation in R_1 and R_2 with the Larmor frequency for ^{2}H nuclei bound to the α-methylene segment of the surfactant hexadecyltrimethylammonium chloride. The sample was an aqueous micellar solution containing 13 wt% of the surfactant. Experiments were performed at 27 °C. (Data from Söderman et al.[51])

To investigate the applicability of the motional model, Söderman and co-workers[50,51] studied aqueous micellar systems of alkyltrimethylammonium chloride surfactants of two different alkyl chain lengths: dodecyl and hexadecyl chains. The alkyl chains were ^{2}H labeled in the α-methylene segment, adjacent to the ammonium polar headgroup, and the relaxation rates R_1 and R_2 were measured in the Larmor frequency range 2–55 MHz, in order to cover the dispersion of the slow motion. The lower frequencies were obtained by using a variable field electromagnet. The results[51] obtained for the hexadecyltrimethylammonium chloride micelles (concentration 13 wt%) are shown in Figure 8. The solid lines are best fits of equations (14a) and (14b) to the whole data set, using τ_f, τ_s, and S as adjustable parameters. As can be seen from Figure 8, the data are well described by a Lorentzian spectral density function superimposed on a constant offset in the investigated frequency range, thus supporting the assumption of timescale separation. The fit yielded $\tau_f = 42 \pm 1$ ps, $\tau_s = 7.6 \pm 0.4$ ns, and $S = 0.186 \pm 0.003$, where the uncertainties correspond to an approximately 80% confidence interval taking only random errors into account, and a value of $\chi = 167$ kHz was used for the quadrupolar coupling constant.

The slow correlation time was interpreted in terms of equations (11)–(13), which contain two unknown parameters, R and D_{lat}. However, D_{lat} can be measured in phases of extended surfactant films, such as bicontinuous cubic phases, and R is expected to be close to the overall length of the surfactant molecule. Using $D_{lat} \approx 1 \times 10^{-11}$ m^2 s^{-1}, as measured in a bicontinuous cubic phase of the similar surfactant hexadecylammonium fluoride, and the radius $R = 2.37$ nm, a slow correlation time of approximately 10 ns was calculated from equations (11)–(13), which is in reasonable agreement with the experimentally determined value.

The applicability of the two-step model receives further support when comparing the S value obtained from the fit to the relaxation dispersion with that measured from quadrupolar

splittings in liquid crystalline phases formed at higher surfactant concentrations. In the liquid crystalline phases, extended surfactant aggregates are 'locked' in a crystalline array. Two very common structures are the lamellar phase, where surfactant bilayers are stacked with one-dimensional order, and the hexagonal phase, where cylindrical aggregates are packed on a two-dimensional hexagonal lattice. In these phases one has effectively frozen the slow motion, and the nuclei experience a static quadrupolar Hamiltonian $\langle\hat{\mathcal{H}}_Q\rangle_f$ in addition to the Zeeman term, where the average is taken over the fast local motions. This results in a quadrupolar splitting of magnitude[46]

$$\Delta_{lam} = \tfrac{3}{4}\chi|S| \tag{15}$$

in the lamellar phase with planar films. In the hexagonal phase, the rapid surfactant diffusion around the cylinder axis results in an additional averaging of the interaction by a factor of 2 and the splitting is given by

$$\Delta_{hex} = \tfrac{3}{8}\chi|S| \tag{16}$$

One may expect that the local motions, and hence the S value, should be similar in the liquid crystalline surfactant aggregates and the micelles in the dilute solution phase. This is in fact found to be the case. As mentioned above, the S value obtained from the fit to the relaxation dispersion (Figure 8) was found to be $S = 0.186$. A very similar value (0.192) was measured in the hexagonal phase at higher concentrations.[51]

3.3 Larger Aggregates: Use of the Zero Frequency Spectral Density

The small spherical micelles ($R \approx 2$ nm) can be seen as a limiting case, and in general surfactant aggregates have much larger extensions. When the size of the aggregates increases, τ_s increases as well, and the relevant relaxation dispersion moves out of the accessible frequency window. In some extreme cases, for example with long, entangled wormlike micelles, the dynamics may even move out of motional narrowing, showing slow motion effects in the NMR spectrum.[42] However, for most micellar and microemulsion systems, the motional narrowing condition applies. In these cases, valuable information may be obtained by measuring R_1 and R_2 for ^{2}H-labeled surfactants at a single Larmor frequency. For larger aggregates, the relevant information on the aggregate size is contained in the zero frequency spectral density only. Assuming that the fast motions are in extreme narrowing, in which case they contribute to a constant offset of both R_1 and R_2, it is useful to consider the difference $\Delta R = R_2 - R_1$ which then depends only on the slow motions. For the case of very slow motions, we also have $j_s(0) \gg j_s(\omega_0) \approx j_s(2\omega_0)$, and ΔR can be approximated by

$$\Delta R = \frac{9\pi^2}{40}(\chi S)^2 j_s(0) \tag{17}$$

This expression has been used to study variations in the shape of surfactant aggregates in different microemulsion systems.[52,53] Here, the micellar aggregates are swollen by the addition of a third component (normal micelles in aqueous solution are swollen by oil; reverse micelles in oil are swollen by water), where spherical aggregates can have radii of the order of 10 nm. Quantitative applications of equation (17) require reliable determinations of S from adjacent liquid crystalline phases. Furthermore, they require assumptions concerning the aggregate shape, and a knowledge of D_{lat}, to determine, for example, an aggregate radius of spherical aggregates. So, obviously, there are some uncertainties involved concerning the 'absolute calibration' of the method.

The situation can, however, be optimized by noting that the aggregates are formed under the constraint of a constant average interfacial area/enclosed volume ratio, set by the surfactant/internal component concentration ratio. With this constraint, the minimum aggregate size corresponds to a spherical shape. Due to the entropy of mixing, spherical aggregates, representing the minimum aggregate size, will always be stable at high dilutions, where the experiment can be calibrated. In many cases, D_{lat} is also known quite accurately from the various bicontinuous phases of the different systems.

Deviations from spherical shape can be modeled as a growth into prolate or oblate shapes. The interfacial area/enclosed volume constraint implies a constraint on the possible values of the two semiaxes describing the particle size. Halle[54] has calculated the correlation functions for the combined particle tumbling and surface diffusion of prolate and oblate particles. His results have been applied to, for example, microemulsion systems,[52,53] focusing on the ratio $j_{s,pr}(0)/j_{s,sph}(0)$, where the subscripts pr and sph refer to prolate and spherical particles, respectively. For a given interfacial area/enclosed volume ratio, which specifies the radius R of the sphere, $j_{s,pr}(0)/j_{s,sph}(0)$ is a function of the prolate axial ratio D_{lat}, and R. Knowing D_{lat} and R from other experiments it is possible to determine the aggregate axial ratio from the relaxation experiment.

As mentioned above, the strength of the NMR relaxation technique in comparison to other (e.g. scattering) techniques for studying micelles and microemulsions is related to the fact that rotational dynamics are monitored. This has the advantages that (i) the dynamics are sensitive to small size variations, and (ii) the dynamics are essentially independent of interactions. In an extensive study of a three-component microemulsion system composed of the nonionic surfactant pentaethyleneoxide dodecyl ether, water, and decane, oil swollen micelles dispersed in water were investigated over a large concentration range.[52]

With a nonionic surfactant, spherical aggregates are formed at lower temperatures, while the aggregates grow in size with increasing temperature.[17] Figure 9 shows the variation of ΔR with temperature for two compositions, $\Phi = 0.12$ and 0.23, in the microemulsion phase.[52] Here, $\Phi = \Phi_s + \Phi_O$ is the total volume fraction of surfactant (Φ_s) and oil (Φ_O), and the ratio $\Phi_s/\Phi_O = 0.815$ was kept constant.

The value of ΔR decreases when the temperature is decreased in the microemulsion phase and levels off at lower temperatures at a minimum value ΔR_{min}, when the aggregates have reached the limiting spherical shape, corresponding to the minimum size. Note that the minimum ΔR value is the same for the two concentrations, as is expected because the radius, dictated by Φ_s/Φ_O, should be the same. By considering

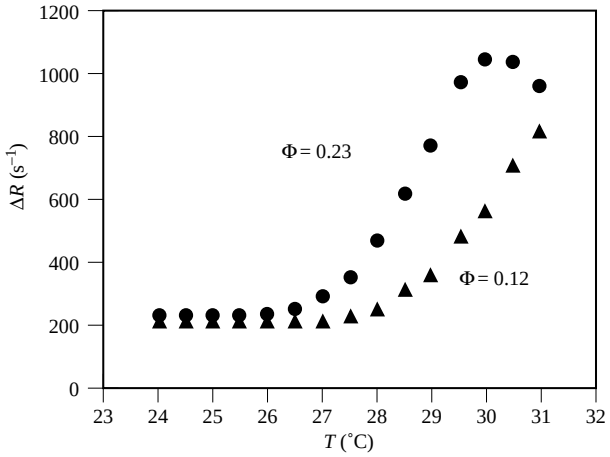

Figure 9 Variation in ^{2}H $\Delta R = R_2 - R_1$ with temperature of the ^{2}H-labeled nonionic surfactant pentaethyleneoxide dodecyl ether $[CH_3(CH_2)_{10}C^2H_2(OCH_2CH_2)_5OH]$ in a ternary system with water and decane. The ratio Φ_s/Φ_O is 0.815, where Φ_s and Φ_O are the surfactant and oil volume fractions, respectively. The concentrations are $\Phi=\Phi_s + \Phi_O$ = 0.12 and 0.23, respectively. (Data from Leaver et al.[52])

the reduced ΔR value, $\Delta R/\Delta R_{min} = j_{s,pr}(0)/j_{s,sph}(0)$, it was possible to calculate the increase in the axial ratio of the aggregates with increasing temperature, assuming a growth into prolate aggregates. The variation in the axial ratio obtained is shown in Figure 10.

Very large micelles may also form in binary surfactant systems. These are long wormlike micelles which become entangled at higher concentrations, giving rise to rheological properties similar to those in polymer solutions. Such systems have been examined by means of ^{1}H bandshape analysis.[41,42] The protons of the surfactant hydrocarbon chain form a very large dipolar coupled spin system, with essentially a continuum distribution of transverse relaxation rates. The distribution of relaxation rates is related to the distribution of order parameters,[43] which can be obtained from analyzing the bandshape in the liquid crystalline (lamellar or hexagonal) phases, where the bandshape is associated with a continuum distribution of residual dipolar splittings.[55]

Slow motions have also been studied by measuring the differential line broadening (DLB) of proton J coupled ^{13}C nuclei.[56] Here the difference in bandwidth of the different resonances in a ^{13}C multiplet can be attributed to the interplay between the dipole–dipole and chemical shift anisotropy relaxation mechanisms, and by analyzing the difference, information on the slow motion may be obtained.

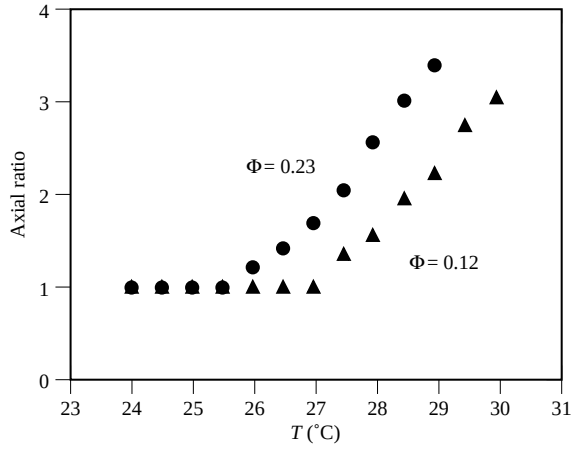

Figure 10 Variation in the micellar axial ratio with temperature, assuming a monodisperse prolate growth, as deduced from the relaxation data in Figure 9 by using the correlation function due to Halle,[54] for the combined motion of aggregate tumbling and surface diffusion

3.4 Relaxation Measurements on Water and Counterion Nuclei

Relaxation measurements on water and counterion nuclei may also give information about the surfactant aggregate size and shape. Such measurements may be particularly useful in reverse micellar systems, where water and surfactant counterions are contained in small water pools covered by a surfactant monolayer. In a ^{23}Na ($I = \frac{3}{2}$) spin relaxation study of a reverse micellar system, the presence of slow motions was found to result in a biexponential free induction decay (FID).[57] Using the two transverse relaxation rates and an effective longitudinal relaxation rate, it was possible to determine all three spectral density values: $j(0)$, $j(\omega_0)$, and $j(2\omega_0)$. From the fit of the imaginary part of the FID it was also possible to determine the second-order quadrupolar dynamic shift, allowing for an additional test of the motional model invoked in the interpretation of the data.

An interesting application of water nuclei relaxation in microemulsions concerns the so-called 'nuclear spin quenching' studied by Carlström and Halle.[58] Here, the effect of chemical exchange of water protons, mediated by the presence of prototropic ions, H_3O^+ and OH^-, on the ^{17}O bandshape in a reverse micellar system was investigated. By careful analysis of the ^{17}O bandshape, information on the water exchange kinetics between droplets as well as the droplet size was obtained.

3.5 Surfactant Hydrocarbon Chain Conformations in Micelles

The early findings of narrow ^{1}H bands from the surfactant hydrocarbon chains in small spherical micelles revealed that the micellar interior is in a liquid-like state. Magnetic field dependent ^{13}C R_1 relaxation experiments confirmed those ideas, and a segmental order parameter profile, similar to that obtained from ^{2}H quadrupolar splittings in lipid bilayer systems, was obtained within the two-step formalism.[59] By studying the dynamics of a symmetric probe molecule solubilized in micelles, it was concluded that the micellar interior was characterized by an effective viscosity similar to that of the neat hydrocarbon.[60]

Chachaty and co-workers[40,61] have studied the enhanced relaxation rate due to the presence of paramagnetic counterions. The multivalent paramagnetic counterion is expected to be selectively adsorbed onto the charged micellar surface. Thus, by analyzing the effect on the ^{13}C relaxation along the chain, the distribution in the distance from the micellar surface could be estimated for the various methylene segments.

A conceptually similar study was reported recently by Palmas et al.[62] Here, cross relaxation effects between ^{13}C and nondirectly bonded protons were examined by two-dimensional heteronuclear Overhauser effect spectroscopy (HOESY). This study revealed the significance of intermolecular $^{1}H-^{13}C$ dipolar interactions. Correlations between carbon atoms and protons belonging to different segments were observed in the lower part of the hydrocarbon chains, while they were found to be absent in the vicinity of the polar headgroup, where the chain configuration is more rigid.

4 RELATED ARTICLES

Amphiphilic Liquid Crystalline Samples: Nuclear Spin Relaxation; Bilayer Membranes: Deuterium and Carbon-13 NMR; Brownian Motion and Correlation Times; Colloidal Systems; Diffusion Measurements by Magnetic Field Gradient Methods; Liquid Crystalline Samples: Diffusion; Liquid Crystalline Samples: Structure of Nonrigid Molecules.

5 REFERENCES

1. J. W. McBain and M. Taylor, *Ber.*, 1910, **43**, 321.
2. J. W. McBain, E. C. V. Cornish, and R. C. Bowden, *J. Chem. Soc.*, 1912, **101**, 2042.
3. J. W. McBain, *Trans. Faraday Soc.*, 1913, **9**, 99.
4. J. W. McBain and C. S. Salmon, *J. Am. Chem. Soc.*, 1920, **42**, 426.
5. P. T. Callaghan, C. M. Trotter, and K. W. Jolley, *J. Magn. Reson.*, 1980, **37**, 247.
6. P. Stilbs, *Prog. Nucl. Magn. Reson. Spectrosc.*, 1987, **19**, 1.
7. E. L. Hahn, *Phys. Rev.*, 1950, **80**, 580.
8. E. O. Stejskal and J. E. Tanner, *J. Chem. Phys.*, 1965, **42**, 288.
9. D. W. McCall, D. C. Douglass, and E. W. Anderson, *Ber. Bunsenges. Phys. Chem.*, 1963, **67**, 336.
10. R. L. Vold, J. S. Waugh, M. P. Klein, and D. E. Phelps *J. Chem. Phys.*, 1968, **48**, 3831.
11. J. E. Tanner, Thesis, University of Wisconsin, Madison, WI, USA, 1966.
12. G. Oraedd, G. Lindblom, L. B. A. Johansson, and G. Wikander, *J. Phys. Chem.*, 1992, **96**, 5170.
13. M. Jansson and P. Stilbs *J. Phys. Chem.*, 1985, **89**, 4868.
14. G. Gunnarsson, B. Jönsson, and H. Wennerström, *J. Phys. Chem.*, 1980, **84**, 3114.
15. H. Hagslätt, O. Söderman, B. Jönsson, and L. Johansson, *J. Phys. Chem.*, 1991, **95**, 1703.
16. B. Jönsson, H. Wennerström, P. Nilsson, and P. Linse, *Colloid Polymer Sci.*, 1986, **264**, 77.
17. B. Lindman and H. Wennerström, *J. Phys. Chem.*, 1991, **95**, 6053.
18. P. G. Nilsson, H. Wennerström, and B. Lindman, *J. Phys. Chem.*, 1983, **87**, 1377.
19. P. G. Nilsson, H. Wennerström, and B. Lindman, *Chem. Script.*, 1985, **25**, 67.
20. B. Lindman, O. Söderman, and P. Stilbs, in *Surfactants in Solutions*, ed. K. L. Mittal, Plenum, New York, 1989, Vol. 7.
21. O. Söderman, E. Hansson, and M. Monduzzi, *J. Colloid Interface Sci.*, 1991, **141**, 512.
22. U. Olsson and P. Schurtenberger, *Langmuir*, 1993, **9**, 3389.
23. K. Shinoda and B. Lindman, *Langmuir*, 1987, **3**, 135.
24. K. Fukuda, O. Söderman, B. Lindman, and K. Shinoda, *Langmuir*, 1993, **9**, 2921.
25. U. Olsson, K. Nagai, and H. Wennerström, *J. Phys. Chem.*, 1988, **92**, 6675.
26. U. Olsson, M. Jonströmer, K. Nagai, O. Söderman, H. Wennerström, and G. Klose, *Prog. Colloid Polym. Sci.*, 1988, **76**, 75.
27. M. Jonströmer, W. O. Parker, and U. Olsson, *Langmuir*, 1995, **11**, 61.
28. B. Lindman, K. Shinoda, U. Olsson, D. Anderson, G. Karlström, and H. Wennerström, *Colloid Surfaces*, 1989, **38**, 205.
29. L. E. Scriven, *Nature*, 1976, **263**, 123.
30. D. M. Anderson and H. Wennerström, *J. Phys. Chem.*, 1990, **94**, 8683.
31. M. T. Clarkson, D. Beaglehole, and P. T. Callaghan, *Phys. Rev. Lett.*, 1985, **54**, 1722.
32. O. Söderman, G. Carlström, U. Olsson, and T. C. Wong, *J. Chem. Soc., Faraday Trans. 1*, 1988, **84**, 4475.
33. P.-O. Quist, B. Halle, and I. Furo, *J. Chem. Phys.*, 1991, **95**, 6945.
34. B. Balinov, U. Olsson, and O. Söderman, *J. Phys. Chem.*, 1991, **95**, 5931.
35. U. Olsson, B. Balinov, and O. Söderman, in *The Structure and Conformation of Amphiphilic Membranes* (*Springer Proceedings in Physics, Vol. 66*), ed. R. Lipowsky and K. Kremer, Springer, Berlin, 1992.
36. M. Monduzzi, U. Olsson, and O. Söderman, *Langmuir*, 1993, **9**, 2914.
37. P. Stilbs, in *Solubilization* (*Surfactant Science Series*), ed. D. Christian and J. F. Scamehorn, M. Dekker, New York, 1994.
38. B. Lindman, O. Söderman, and H. Wennerström, in *Surfactant Solutions. New Methods of Investigation*, ed. R. Zana, M. Dekker, New York, 1987, p. 295.
39. B. Lindman, O. Söderman, and H. Wennerström, *Ann. Chim. (Rome)*, 1987, **77**, 1.
40. C. Chachaty, *Prog. Nucl. Magn. Reson. Spectrosc.*, 1987, **19**, 183.
41. J. Ulmius and H. Wennerström, *J. Magn. Reson.*, 1977, **28**, 309.
42. U. Olsson, O. Söderman, and P. Guéring, *J. Phys. Chem.*, 1986, **90**, 5223.
43. H. Wennerström and J. Ulmius, *J. Magn. Reson.*, 1976, **23**, 431.
44. F. Noack, *Prog. Nucl. Magn. Reson. Spectrosc.*, 1986, **18**, 171.
45. W. Kühner, E. Rommel, F. Noack, and P. Meier, *Z. Naturforsch., Teil A*, 1987, **42**, 127.
46. H. Wennerström, G. Lindblom, and B. Lindman, *Chem. Script.*, 1974, **6**, 97.
47. H. Wennerström, B. Lindman, O. Söderman, T. Drakenberg, and J. B. Rosenholm, *J. Am. Chem. Soc.*, 1979, **101**, 6860.
48. B. Halle and H. Wennerström, *J. Chem. Phys.*, 1981, **75**, 1928.
49. A. Abragam, *The Principles of Nuclear Magnetism*, Clarendon, Oxford, 1961.
50. O. Söderman, H. Walderhaug, U. Henriksson, and P. Stilbs, *J. Phys. Chem.*, 1985, **89**, 3693.
51. O. Söderman, U. Henriksson, and U. Olsson, *J. Phys. Chem.*, 1987, **91**, 116.
52. M. S. Leaver, U. Olsson, H. Wennerström, and R. Strey, *J. Phys. II*, 1994, **4**, 515.
53. R. Skurtveit and U. Olsson, *J. Phys. Chem.*, 1992, **96**, 8640.
54. B. Halle, *J. Chem. Phys.*, 1991, **94**, 3150.
55. H. Wennerström, *Chem. Phys. Lett.*, 1973, **18**, 41.
56. L. Hwang, P. Wang, and T. C. Wong, *J. Phys. Chem.*, 1988, **92**, 4753.

57. P. H. Kenez, G. Carlström, I. Furo, and B. Halle, *J. Phys. Chem.*, 1992, **96**, 9524.
58. G. Carlström and B. Halle, *Mol. Phys.*, 1988, **64**, 659.
59. H. Walderhaug, O. Söderman, and P. Stilbs, *J. Phys. Chem.*, 1984, **88**, 1655.
60. P. Stilbs, H. Walderhaug, and B. Lindman, *J. Phys. Chem.*, 1983, **87**, 4762.
61. Y. Chevalier and C. Chachaty, *J. Phys. Chem.*, 1985, **89**, 875.
62. P. Palmas, P. Tekely, P. Mutzenhardt, and D. Canet, *J. Chem. Phys.*, 1993, **99**, 4775.

Biographical Sketches

Olle Söderman. *b* 1951. B.Sc., 1976, Ph.D. (supervisor Göran Lindblom), 1981, Lund Institute of Technology. Introduced to NMR by S. Forsén and G. Lindblom. Visiting graduate student at University of British Columbia (with Myer Bloom). Joined Faculty of Physical Chemistry, University of Lund, 1981. Currently, lecturer, University of Lund. Approx. 80 publications. Current research interests: pulsed field gradient NMR applied to colloidal systems.

Ulf Olsson. *b* 1957. B.Sc., 1981, Ph.D. (supervisor Olle Söderman), 1988, Lund University. Postdoctoral research, Centre de Recherche Paul Pascal, Pessac France, 1989. Faculty of Physical Chemistry, Lund University, 1989. Approx. 40 publications. Current research interests: structure and phase equilibria of surfactant/water/oil systems.

Molecular Motions: T_1 Frequency Dispersion in Biological Systems

Rainer Kimmich
Universität Ulm, Germany

1	Introduction	1
2	Fluctuations in Proteins	1
3	Fluctuations in Lipid Bilayers	2
4	Deuteron T_1 Frequency Dispersion of Protein Solutions in D_2O	2
5	Critical Water Contents	4
6	Proton T_1 Frequency Dispersion of Tissue	5
7	$T_{1\rho}$ Frequency Dispersion Imaging	5
8	Related Articles	6
9	References	6

1 INTRODUCTION

The information provided by the frequency dependence ('dispersion') of spin–lattice relaxation times (or rates) in the laboratory frame T_1 (T_1^{-1}), or in the rotating frame $T_{1\rho}$ ($T_{1\rho}^{-1}$), is the type and the timescale of molecular motion. Studies of this sort are mainly based on the field cycling [or NMR dispersion (NMRD)] technique[1,2] often supplemented by rf pulse experiments in stationary magnetic fields. Molecular dynamics can be specified on this basis in great detail, although chemical shift distributions normally cannot be resolved.

The essence of the field cycling principle is to generate nonequilibrium spin populations by switching the magnetic field to a variable relaxation field, the flux density of which is normally lower than that of the polarization field. The relaxation curve of the magnetization is then probed point by point by switching to a fixed detection field, where the magnetization is read out in the form of a FID or a spin echo. A prerequisite of the technique is that relaxation during the switching intervals is minor. The maximum frequency is determined by technical restrictions, whereas the lower frequency limit is given by the local fields within the sample or by incompletely compensated external fields such as the Earth field. Operational order-of-magnitude ranges of the frequency are $10^3 < \nu < 10^8$ Hz for protons and $10^2 < \nu < 10^7$ Hz for deuterons.

Molecular motions cause fluctuations of the spin interactions; these are normally the dipolar interaction among the spin-bearing particles or the coupling of quadrupole nuclei to electric field gradients. The fluctuating interactions induce spin transitions, making the ensemble relax towards equilibrium. The spin–lattice relaxation rate $1/T_1$ in *homogeneous systems* is given by intensity functions (or spectral densities) $I(\omega)$ at the transition frequencies ω of the spin system.[3] These functions are proportional to the FTs of the time autocorrelation functions of spherical harmonics of order 2, $G(t)$. The fluctuations of quadrupolar interactions and the low-frequency part of fluctuations of dipolar interactions are normally dominated by intramolecular contributions. The T_1 frequency dispersion thus probes the correlation function (or the corresponding intensity function) of molecular reorientations and, in certain circumstances, translations.

Systems of biological origin tend to be *heterogeneous* in the sense that the investigated nuclei occur in different environments with different molecular dynamics and spin interactions. It is then a matter of exchange rates whether spin–lattice relaxation is determined by average intensity functions ('fast exchange' relative to relaxation times) so that monoexponential relaxation decays arise, or whether multiexponential distributions occur.[4] In the context of water relaxation in biological systems, the two-site fast exchange model turned out to be very successful. Note, however, that the term 'exchange' refers to material transport as well as to (immaterial) spin diffusion or magnetization transfer.[12,13]

The element usually detected in T_1 frequency dispersion experiments is hydrogen, via proton or deuteron resonance. (In exceptional cases, ^{31}P relaxation studies might also be feasible.[5]) Other nuclear species can be probed indirectly via cross relaxation if their relaxation rates are fast enough to act in combination with proton spin diffusion as relaxation sinks. This can be expected in particular with quadrupole nuclei. The cross relaxation then manifests itself as 'quadrupole dips' at the resonance crossing frequencies,[6] as demonstrated in Figure 1 for polyalanine protons cross relaxed by the amide ^{14}N relaxation sinks.

The T_1 frequency dispersion may be influenced further by electron paramagnetic constituents such as, for example, molecular oxygen,[8] paramagnetic ions,[9,10] or heme groups.[7,11] Relaxation mechanisms of this sort, however, are not considered in this article.

T_1 frequency dispersion studies have been performed with many different (diamagnetic) systems of biological origin, including: dissolved,[12,14] wet,[15] or dry[16] proteins; DNA;[6] lipid bilayers;[17,18] tissue;[15] eye lenses;[19] and small animals in vivo.[20]

The dominant constituents of biological systems are biopolymers (or oligomers) and water. The water component (including all exchangeable hydrogen atoms of the biopolymers) can be conveniently prepared in deuterated form so that separate studies of the dynamics in the two components can be performed. Figure 2 shows the T_1 frequency dispersions of water deuterons and of nonexchangeable biopolymer protons measured in a solution of bovine serum albumin (BSA) in D_2O as a typical system.[21] The entirely different nature of the fluctuations within the two constituents is obvious.

2 FLUCTUATIONS IN PROTEINS

Molecular motions of proteins can comprise main chain ('backbone') fluctuations, side-group motions and tumbling of the whole macromolecule. The latter can easily be identified by considering the concentration dependence of the reorientation rates (see below). Side-group motions, such as restricted rotational diffusion and ring flips, are a matter of the local structure and chemical composition. Proteins, for instance, therefore tend to be characterized by a broad distribution of the side-group correlation times.

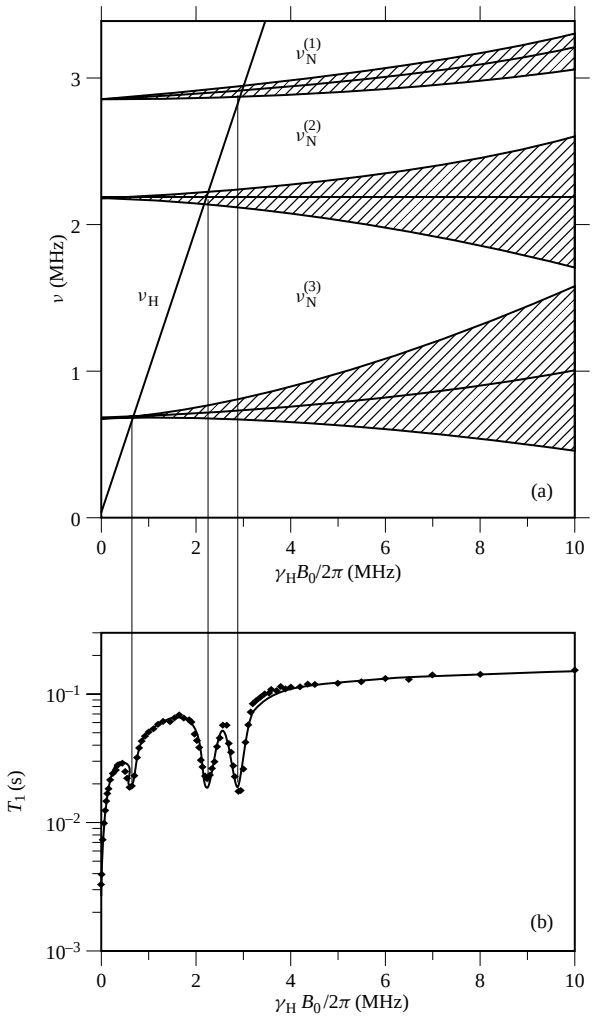

Figure 1 (a) Field dependence of the ^{1}H and ^{14}N resonance frequencies of amide groups. The hatched areas indicate the range covered in a powdery sample. The solid lines within these areas represent the powder averages. The magnetic flux density $\boldsymbol{B}_0$ is expressed in units of the proton Larmor frequency. (b) T_1 frequency dispersion of poly-L-alanine at $-1\,^\circ$C. The three ^{14}N–^{1}H quadrupole dips at the resonance crossings are obvious. (Reproduced by permission of Academic Press from R. Kimmich, F. Winter, W. Nusser, and K.-H. Spohn, *J. Magn. Reson.*, 1986, **68**, 263)

Backbone fluctuations in proteins and polypeptides, on the other hand, appear to be governed by homogeneous modes leading to an apparently universal T_1 dispersion behavior at low frequencies where side-group motions are of minor importance. The frequency dependence in the absence of molecular tumbling can be described over a wide range by the power law[6] $T_1 \propto \nu^{0.74\pm0.06}$, which can be explained by one-dimensional multiple trapping diffusion of defects locally dilating the structure.[16] The corresponding correlation function is given by the error function ('erf') expression:

$$G_{\mathrm{mtd}}(t) = a_1 \left\{ \mathrm{erf}\left(\frac{b^2}{2\langle\xi^2\rangle}\right)^{1/2} - \left(\frac{2\langle\xi^2\rangle}{\pi b^2}\right)^{1/2} \times \left[1 - \exp\left(-\frac{b^2}{2\langle\xi^2\rangle}\right)\right]\right\} + a_2 \qquad (1)$$

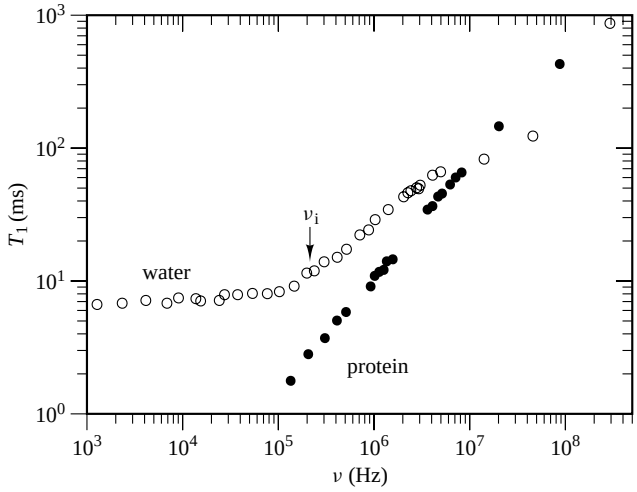

Figure 2 Frequency dependence of the proton (•) and deuteron (○) spin–lattice relaxation times of a D_2O solution of bovine serum albumin (35 wt.%) at 291 K. The data in the vicinity of the ^{14}N–^{1}H quadrupole dips are omitted. The different T_1 frequency dispersions indicate different fluctuation processes dominant for water (including exchangeable hydrogen atoms) and for the protein molecules. (Reproduced by permission of the American Chemical Society from W. Nusser and R. Kimmich, *J. Phys. Chem.*, 1990, **94**, 5637)

where $a_2 = 1 - a_1$ represents the residual correlation at long times, b represents the extension of the defect, and $\langle\xi^2\rangle \propto t^{\frac{1}{2}}$ represents the (anomalous) mean-square displacement of the defects in a time interval t.

3 FLUCTUATIONS IN LIPID BILAYERS

Lipid bilayers form another system whose dynamics are governed by dynamic modes. In experiments with partially deuterated samples, one can distinguish between the alkyl chain and the headgroup part of the bilayers. In the gel phase, one-dimensional restricted diffusion of defects (chain orientation conserving rotational isomers) permits the perfect description of the T_1 frequency dispersion of the alkyl chains.[17] The corresponding intensity function for defect diffusion is characterized by the limits

$$I_{\mathrm{dd}}(\omega) = \begin{cases} \frac{2}{3}(\tau_b^{1/2}\tau_d^{1/2} - \tau_b) & \text{for } \omega\tau_d \ll 1 \\ \frac{\tau_d\tau_b^{1/2} - 2\tau_b\tau_d^{1/2}}{(\tau_d^{1/2} - \tau_b^{1/2})^2}\omega^{-1/2} & \text{for } \omega\tau_b \ll 1 \ll \omega\tau_d \\ \frac{\tau_d^{1/2}}{\tau_d^{1/2}\tau_b^{1/2} - \tau_b}\omega^{-3/2} & \text{for } \omega\tau_b \gg 1 \end{cases} \qquad (2)$$

where τ_d is the mean diffusion time across the bilayer (from headgroup to headgroup) and τ_b is the mean diffusion time over a length equal to the width of the defect.

In the liquid crystalline phase, collective modes ('director fluctuations') tend to dominate at low frequencies.[18] The behavior is, however, much more complex because other mechanisms such as rotational isomerism, chain rotations, and diffusion along the curved shape of the bilayer are superimposed.

4 DEUTERON T_1 FREQUENCY DISPERSION OF PROTEIN SOLUTIONS IN D_2O

The proton signals observed in tissue, diluted aqueous biopolymer solutions, and diluted aqueous lipid bilayer dispersions tend to be dominated by water. In such systems, the polar surfaces of the macromolecular constituents are covered by hydration shells; however, these shells form only a minor fraction of the total water. Nevertheless, a strong enhancement of the spin–lattice relaxation of water occurs as first observed in protein solutions.[22]

Also at a rather early stage, it was found by means of NMR spectroscopy that water molecules in the hydration shell are oriented relative to the biopolymer surface[23,24] and congeal far below the freezing point of bulk water.[25] Nonfreezing water actually may be an operational definition of hydration water, the fraction of which can be quantitatively determined in this way.

Another striking finding is that translational diffusion within the hydration shells is relatively fast. Even in frozen protein solutions not far below 0 °C, where diffusion is restricted to thin (about a monolayer thick) films of liquid water on the surface of the macromolecules, the diffusion coefficient is merely reduced by one order of magnitude relative to liquid bulk water.[26] On the other hand, orientation correlation times up to six orders of magnitude longer than those in bulk water must be concluded from T_1 frequency dispersion experiments.[15]

The T_1 frequency dispersion of the water phases in protein/D_2O solutions was measured selectively using deuteron resonance.[15] In the frame of the two-site fast exchange model, the effective water spin–lattice relaxation rate is given by:

$$\frac{1}{T_1} \approx \frac{1 - p_h}{T_1^f} + \frac{p_h}{T_1^h} \tag{3}$$

where T_1^f and T_1^h are the spin–lattice relaxation times in the 'free' (i.e. bulk) and 'hydration' water phases, respectively, and p_h is the fraction of hydration water.

The description of the T_1 frequency dispersion of hydration water is principally based on four competitive mechanisms:

1. Tumbling of the macromolecule including its hydration shell (correlation time τ_t).
2. Restricted rotational diffusion of water molecules about axes perpendicular to the local surface (correlation time τ_r).
3. Exchange between free and hydration water (correlation time = residence time in the hydration shell $\tau_\perp$).
4. Reorientations mediated by translational displacements (RMTDs) along the more or less rugged and curved surface of the macromolecule: water molecules diffuse along the surface and, as a consequence, alter their orientations which are defined by the local surface structure. The longest correlation of this mechanism is designated by $\tau_\parallel$.

Using the orientational structure factor formalism,[27] the RMTD correlation function was derived as:

$$G_{RMTD}(t) = \frac{1}{2(k_u - k_l)}\sqrt{\frac{\pi}{Dt}}[\mathrm{erf}(\sqrt{Dt}k_u) - \mathrm{erf}(\sqrt{Dt}k_l)] \tag{4}$$

where k_u and k_l are the upper and lower cut-off wavenumbers of the equipartition distribution assumed for the surface structure. D is the average translational water diffusion coefficient in the hydration shell. The lower cut-off wavenumber is connected with a cut-off correlation time:

$$\tau_\parallel = (Dk_l^2)^{-1} \tag{5}$$

revealing itself as the 'inflection point' $2\pi\nu_i\tau_\parallel \approx 1$ in the absence of molecular tumbling (see Figure 3). Equation (4) produces the square root frequency dependence typical for water relaxation in aqueous protein solutions at intermediate frequencies.

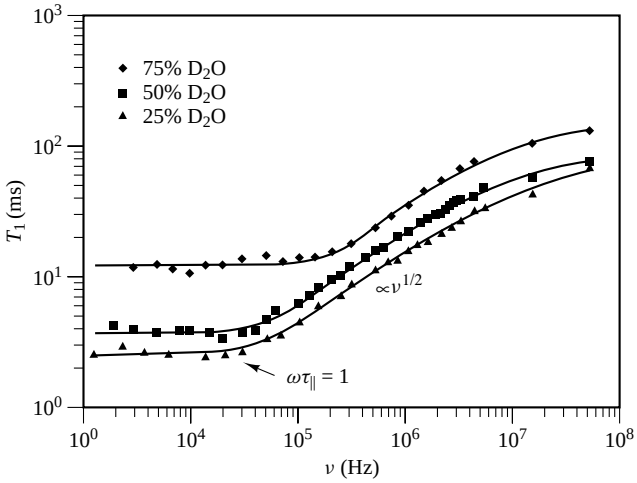

Figure 3 Deuteron T_1 frequency dispersion of D_2O solutions of bovine serum albumin at 291 K. The solid lines were calculated using the RMTD formalism taking into account protein tumbling [equation (8)] and restricted rotational diffusion of the water molecules (high-frequency regime). Note that the T_1 frequency dispersions at a water content of 25 wt.% (no free water) and 50 wt.% (with free water) are qualitatively the same, apart from differences in the absolute values of the relaxation times. In these cases, the low-frequency dispersion is dominated by RMTD. At 75 wt.%, the inflection point is shifted to higher frequencies due to the competitive action of protein tumbling. (Reproduced by permission of Elsevier from R. Kimmich, W. Nusser, and T. Gneiting, *Colloids Surf.*, 1990, **45**, 283)

Restricted rotational diffusion, exchange with free water and macromolecular tumbling can be represented by exponential correlation function. Restricted rotational diffusion is only important for the high-frequency dispersion, whereas the exchange mechanism is normally too slow (relative to the other contributions) to affect the reorientation behavior. What remains as a mechanism effective in the low-frequency regime is macromolecular tumbling and RMTD.

On the basis of this scheme, the deuteron T_1 frequency dispersion of D_2O in aqueous protein solutions can be described perfectly.[15] Inserting the water diffusion coefficient experimentally determined with the NMR field gradient technique, a length scale can be estimated from the RMTD correlation time $\tau_\parallel$ [equation (5)] revealing itself via the inflection point in the absence of macromolecular tumbling. The result is half the protein circumference, as required by RMTD.[27] In other words, the mean diffusion time around half the circumference of the protein molecule is calculated, on the basis of the experimental diffusion coefficient and the known short and long axes of the protein, to be of the order of 10^{-6} s, which is in perfect agreement with the inflection point measured in the absence of macromolecular tumbling.

The RMTD mechanism accounts very well for the weak temperature dependence of spin–lattice relaxation. Transient irrotational binding of a small percentage of the hydration water at certain sites, as suggested in several studies,[22,28] would require binding energies twice as high as the apparent activation energies estimated from the experimental T_1 data. With RMTD, long correlation times are due to the geometry of the system rather than to high binding energies at certain sites. Furthermore, transient irrotational binding would result in slopes of the T_1 frequency dispersion at intermediate frequencies which are four times as high as found experimentally.

Another question is the origin of the long residence times of water molecules in the hydration shells. This, of course, is no problem, in principle, if free water is absent or frozen. Adding more and more water to a protein sample which initially has saturated hydration shells but no free water, does not change the qualitative behavior of relaxation or diffusion.[15,26] With the exception of the onset of macromolecular tumbling (described below), there is no evidence for new relaxation mechanisms of hydration water due to the presence of free water.

The relaxation scheme outlined above can also be applied to a certain degree to systems modeling hydrated globular proteins. Water adsorbed on agglomerates of fine particles of silica of a similar diameter again shows a T_1 frequency dispersion reflecting the surface structure.[30]

While the surfaces of fine particles of silica are expected to be smooth and chemically homogeneous, those of proteins are extremely heterogeneous with respect to polarity and hydrogen binding ability. On such surfaces water diffusion is more likely to resemble a hopping process among the preferential binding sites or areas. Translational displacements may then be governed by waiting time and step-length distributions.[31] Nevertheless, in timescales that are long compared with typical waiting times, i.e. in the fast-jump limit, an effective diffusion coefficient can be defined. This also includes exchange processes in the sense that molecules (or hydrogen atoms) leave and reenter the hydration shell to and from other environments such as free water or sites within the protein. In this case, the surface is probed only selectively by a set of discrete binding sites. Correspondingly, the spin–lattice relaxation then originates from reorientation jumps.

From the experimental point of view, the fast jump/exchange limit reveals itself by giving monoexponential attenuation curves in diffusion as well as in spin–lattice relaxation experiments. This is what one normally observes, to a reasonably good approximation.[26] In this case, effective diffusion coefficients D_{eff} and effective spin–lattice relaxation times $T_{1,\text{eff}}$ can be evaluated.

The microphases (or molecular environments) can be characterized by weights p_i, diffusion coefficients D_i, and spin–lattice relaxation times $T_{1,i}$. The following exchange formulas are then valid:

$$D_{\text{eff}} = \sum_i p_i D_i \tag{6}$$

$$\frac{1}{T_{1,\text{eff}}} = \sum_i \frac{p_i}{T_{1,i}} \tag{7}$$

where $\Sigma_i\, p_i = 1$.

D_{eff} tends to be governed by environments with high molecular mobility, whereas $1/T_{1,\text{eff}}$ is dominated by the slowly reorienting molecules, that sit for relatively long periods on sites with certain orientations. Thus, high effective diffusion coefficients, long orientation correlation times, and low thermal activation energies do not contradict each other a priori.

If distributions of microphases exist, the continuous-diffusion treatment must be regarded as an approximate description of phenomena that tend to be discrete in reality. RMTD in this case probes only those sites of the surface at which spin–lattice relaxation effectively takes place (irrespective of the exchange pathways that the molecules or atoms follow in between). In principle, the applicability of the concept comprises continuous and step-by-step, surface-bound and multiphase diffusion, as long as the experiments provide *effective* diffusion coefficients and spin–lattice relaxation times.

5 CRITICAL WATER CONTENTS

In the limit of low frequencies, the T_1 frequency dispersion of water in protein solutions terminates at a certain 'inflection frequency' ν_i in a plateau (see Figure 2 and Figure 3). As an indication of the competitive nature of RMTD and macromolecular tumbling, this quantity depends strongly on the water content c_w (Figure 4).[29]

Tumbling can only take place if the water content exceeds the saturation concentration c_s defined by the saturation of

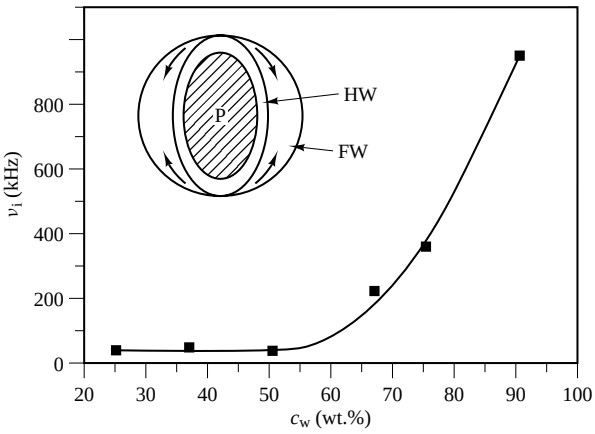

Figure 4 Inflection frequency of the deuteron T_1 dispersion of BSA/D_2O solutions at 291 K versus water content. This dependence can be described by the 'free-water volume' model of macromolecular tumbling illustrated in the upper left-hand corner of the diagram. A protein molecule (P) including hydration water (HW) can only tumble if sufficient free water (FW) is available. The minimum free-water volume corresponds to the circumscribing sphere. Below a critical water content $c_0 \approx 65$ wt.%, macromolecular tumbling is slower than the RMTD process of water on the surface, so that the inflection frequency is governed by RMTD. Above c_0, tumbling becomes faster than this limit. The inflection frequency is then determined by the tumbling rate of the macromolecules. The experimental data were evaluated directly from the T_1 dispersion curves, the solid line was calculated on the basis of the formalism described in the text. (Reproduced by permission of Hüthig & Wepf from R. Kimmich, *Makromol. Chem., Macromol. Symp.*, 1990, **34**, 237)

the hydration shells. In this case 'free water' is present so that, with a certain probability, a macromolecule is surrounded by enough free water for rotational jumps. The 'free-water volume' formalism[15] leads to a macromolecular tumbling correlation time:

$$\tau_t = \tau_t^0 \exp\left[\gamma^*(r-1)\frac{1-c_w+c_s}{c_w-c_s}\right] \quad (c_w \rangle c_s) \qquad (8)$$

where $\tau_t^0 = \eta(v_p + v_s)/(k_B T)$ is the Stokes–Einstein expression for tumbling of a particle with volume $v_p + v_s$ (bare protein plus the saturated hydration shell) in a solvent with viscosity η; $0.5 < \gamma^* < 1$ is a numerical constant; and r is the ratio of the volumes of the circumscribing sphere and the hydrated protein molecule itself approximated by an ellipsoid (see Figure 4). The critical water content c_0 at which macromolecular tumbling becomes competitive to the correlation time $\tau_\parallel$ corresponding to the lower cut-off wavenumber k_1 of the RMTD process, is then defined by the condition $\tau_\parallel = \tau_t$. From this, one finds that

$$c_0 = c_s + \frac{\tilde{\gamma}}{1+\tilde{\gamma}} \qquad (9)$$

where $\tilde{\gamma} = (r-1)\gamma * / \ln(\tau_\parallel/\tau_t^0)$. For aqueous bovine serum albumin (BSA) solutions, $c_s \approx 30$ wt.% and $c_0 \approx 65$ wt.%, that is $\tilde{\gamma} \approx 0.5$.

6 PROTON T_1 FREQUENCY DISPERSION OF TISSUE

Although water is normally the most abundant compound in tissue, and therefore provides the dominant contribution to hydrogen signals recorded in relaxation experiments, the behavior observed in tissue is determined by the interaction and the cross relaxation with the macromolecular constituents. The description must therefore refer to fluctuations in the water phases as well as in the macromolecules. Assuming fast exchange between all components, it is possible to reproduce the experimental T_1 frequency dispersion of tissue by considering the combined action of RMTD in the hydration shells, tumbling and backbone fluctuations of the proteins, restricted rotational diffusion of hydration water molecules, and (with regard to the quadrupole dip frequency region) $^{14}N^1H$ cross relaxation. Figure 5 shows two representative data sets.[15]

Treatments of this sort are crucial for our understanding of the basic mechanisms contributing to relaxation in tissue. For the practical characterization of tissue, it may be more useful to describe the T_1 frequency dispersion by empirical intensity functions or just qualitatively. The T_1 frequency dispersion of a number of different tissues have been characterized in this way, showing significant differences.[32–34]

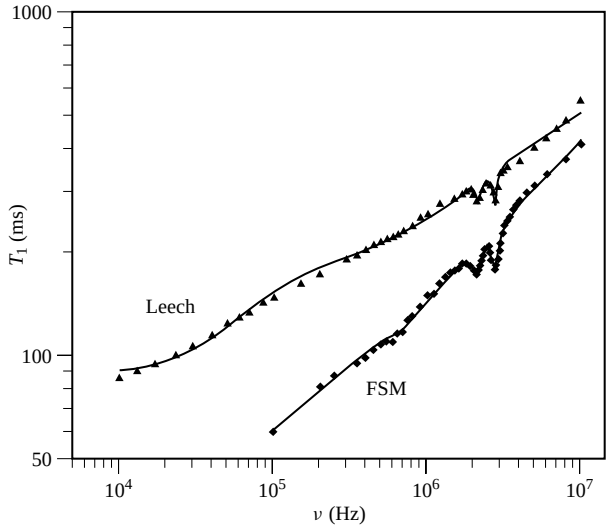

Figure 5 Proton T_1 frequency dispersion of a leech (in vivo) and freshly excised frog sartorius muscle (FSM) in the relaxed state in vitro. The solid lines were calculated on the basis of macromolecular tumbling, RMTD, restricted rotational diffusion of hydration water, protein backbone fluctuations and terms representing the $^{14}N-^1H$ cross relaxation quadrupole dips. (Reproduced by permission of Elsevier from R. Kimmich, W. Nusser, and T. Gneiting, *Colloid. Surf.*, 1990, **45**, 283)

7 $T_{1\rho}$ FREQUENCY DISPERSION IMAGING

The molecular motions revealing themselves in the T_1 frequency dispersion are substantial for image contrasts in

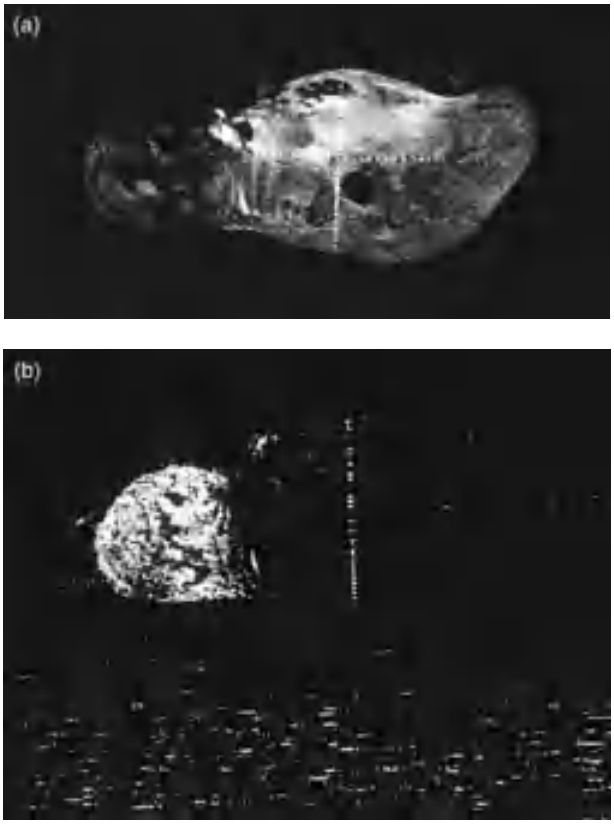

Figure 6 Cross-sectional NMR images of a mouse with an implanted tumor (left). (a) Conventional two-dimensional spin echo FT image. (b) Rotating frame dispersion image (RODI) rendering the $T_{1\rho}$ frequency dispersion as gray scale contrasts. The tumorous tissue (left) can be clearly distinguished from muscle tissue (right). (Reproduced by permission of Academic Press from E. Rommel and R. Kimmich, *Magn. Reson. Med.*, 1989, **12**, 390)

NMR tomography. At conventional magnetic flux densities, the relaxation contrasts originate from relative fast motions and represent the relaxation rates rather than the T_1 frequency dispersion. Using on- and off-resonance variants of spin–lattice relaxation in the rotating frame, an imaging sequence was proposed that gives directly the spatial distribution of the $T_{1\rho}$ frequency dispersion,[35,36] which is indicative for slow motions, macromolecular tumbling, and RMTD.

Figure 6 shows images of a tumorous mouse recorded with this rotating frame dispersion imaging (RODI) technique and conventional tomography for comparison. Striking differences are obvious. RODI provides strong contrast of the tumorous tissue, whereas muscle tissue is suppressed. In the conventional spin echo FT image, on the other hand, both sorts of tissue are rendered with equivalent intensity. Thus biomedical applications of the low-frequency dispersion of spin–lattice relaxation suggest themselves.

8 RELATED ARTICLES

Dynamics of Water in Biological Systems: Inferences from Relaxometry; Field Cycling Experiments; Protein Hydration; Relaxation Theory: Density Matrix Formulation; Relaxometry of Tissue; Rotating Frame Spin–Lattice Relaxation Off-Resonance; Slow and Ultraslow Motions in Biology; Whole Body Studies Involving Spin-Lattice Relaxation in the Rotating Frame.

9 REFERENCES

1. R. Kimmich, *Bull. Magn. Reson.*, 1980, **1**, 195.
2. F. Noack, *Prog. NMR Spectrosc.*, 1986, **18**, 171.
3. A. Abragam, *The Principles of Nuclear Magnetism*, Clarendon, Oxford, 1961.
4. J. R. Zimmerman and W. E. Brittin, *J. Phys. Chem.*, 1957, **61**, 1328.
5. G. Schauer, W. Nusser, M. Blanz, and R. Kimmich, *J. Phys. E: Sci. Instrum.*, 1987, **20**, 43.
6. R. Kimmich, F. Winter, W. Nusser, and K.-H. Spohn, *J. Magn. Reson.*, 1986, **68**, 263.
7. R. Kimmich, *Z. Naturforsch., Teil b*, 1971, **26**, 1168.
8. R. Kimmich and A. Peters, *Chem. Phys. Lipids*, 1975, **14**, 350.
9. S. H. Koenig and W. E. Schillinger, *J. Biol. Chem.*, 1969, **244**, 6520.
10. S. D. Kennedy and R. G. Bryant, *Biophys. J.*, 1986, **50**, 669.
11. S. H. Koenig, R. D. Brown III, and T. R. Lindstrom, *Biophys. J.*, 1981, **34**, 397.
12. R. Kimmich and F. Noack, *Z. Naturforsch., Teil a*, 1970, **25**, 1680.
13. H. T. Edzes and E. T. Samulski, *J. Magn. Reson.*, 1978, **31**, 207.
14. S. H. Koenig and W. E. Schillinger, *J. Biol. Chem.*, 1969, **244**, 3283.
15. R. Kimmich, W. Nusser, and T. Gneiting, *Colloid. Surf.*, 1990, **45**, 283.
16. W. Nusser, R. Kimmich, and F. Winter, *J. Phys. Chem.*, 1988, **92**, 6808.
17. R. Kimmich, G. Schnur, and A. Scheuermann, *Chem. Phys. Lipids*, 1983, **32**, 271.
18. E. Rommel, F. Noack, P. Meier, and G. Kothe, *J. Phys. Chem.*, 1988, **92**, 2981.
19. S. H. Koenig, R. D. Brown III, A. K. Kenworthy, A. D. Magid, and R. Ugolini, *Biophys. J.*, 1993, **64**, 1178.
20. R. Kimmich, W. Nusser, and F. Winter, *Phys. Med. Biol.*, 1984, **29**, 593.
21. W. Nusser and R. Kimmich, *J. Phys. Chem.*, 1990, **94**, 5637.
22. O. K. Daszkiewicz, J. W. Hennel, and B. Lubas, *Nature*, 1963, **200**, 1006.
23. H. J. C. Berendsen, *J. Chem. Phys.*, 1962, **36**, 3297.
24. C. Migchelson and H. J. C. Berendsen, *J. Chem. Phys.*, 1973, **59**, 296.
25. I. D. Kuntz and W. Kauzmann, *Adv. Protein Chem.*, 1974, **28**, 239.
26. R. Kimmich, F. Klammler, V. D. Skirda, I. A. Serebrennikova, A. I. Maklakov, and N. Fatkullin, *Appl. Magn. Reson.*, 1993, **4**, 425.
27. R. Kimmich and H. W. Weber, *Phys. Rev. B*, 1993, **47**, 11 788.
28. S. H. Koenig, R. D. Brown III, and R. Ugolini, *Magn. Reson. Med.*, 1993, **29**, 77.
29. R. Kimmich, *Makromol. Chem., Macromol. Symp.*, 1990, **34**, 237.
30. S. Stapf, R. Kimmich, and J. Niess, *J. Appl. Phys.*, 1994, **75**, 529.
31. J. Noolandi, *Phys. Rev. B*, 1977, **16**, 4474.
32. G. Held, F. Noack, V. Pollak, and B. Melton, *Z. Naturforsch., Teil c*, 1973, **28**, 59.
33. S. H. Koenig, R. D. Brown III, D. Adams, D. Emerson, and D. G. Harrison, *Inv. Radiol.*, 1984, **19**, 76.
34. H. W. Fischer, Y. van Haverbeke, P. A. Rinck, I. Schmitz-Feuerhake, and R. N. Muller, *Magn. Reson. Med.*, 1989, **9**, 315.
35. E. Rommel and R. Kimmich, *Magn. Reson. Med.*, 1989, **12**, 390.
36. E. Rommel, R. Kimmich, H. Körperich, C. Kunze, and K. Gersonde, *Magn. Reson. Med.*, 1992, **24**, 149.

Biographical Sketch

Rainer Kimmich. *b* 1941. Dipl.-Phys., (Technical) Universities of Munich and Stuttgart, 1967; Dr. rer. nat., University of Stuttgart, 1971. Introduced to NMR by F. Noack; Priv.-Doz., Ulm, 1975. Professor of Physics at the University of Ulm 1976–present. Approx. 170 publications. Research specialties: NMR field cycling relaxation spectroscopy, NMR field gradient diffusion studies, NMR microscopy and localized spectroscopy in liquid and solid systems, porous media, polymers, and biological systems.

Nuclear Overhauser Effect

David Neuhaus

MRC Laboratory of Molecular Biology, Cambridge, UK

1	Introduction	1
2	Cross Relaxation and the Origin of the NOE	1
3	Multispin Systems	4
4	Steady-State NOE Experiments with Small Molecules	4
5	Kinetic NOE Experiments with Large Molecules	6
6	The Rotating Frame NOE	9
7	The Heteronuclear NOE	9
8	Exchanging Systems and the Transferred NOE	10
9	Related Articles	11
10	References	11

1 INTRODUCTION

The nuclear Overhauser effect is defined as the change in the overall intensity of one resonance that occurs when another resonance is saturated. Generally it is expressed as the fractional enhancement:

$$f_I\{S\} = \frac{I - I^0}{I^0} \tag{1}$$

where I is the intensity of the observed resonance when the spin S is saturated and I^0 is the equilibrium intensity of the I resonance. Conventionally, the observed spin is called I and the saturated spin is called S. However, particularly for heteronuclear cases, the NOE is often also expressed as the enhancement ratio:

$$\eta = \frac{I}{I^0} = f_I\{S\} + 1 \tag{2}$$

Detection of an appreciable NOE between two spins indicates that there is a relatively short internuclear distance between them, generally less than about 4 or 5 Å. It is this through-space dependence, which is completely independent of the nature of the covalent bonding network between the two interacting spins, that makes the NOE extremely powerful for characterizing molecular stereochemistry and conformation. However, the dependence on the internuclear separation between I and S is complicated by a dependence on several other factors, particularly the rates of molecular motions. For this reason, a truly quantitative interpretation of NOE enhancements is difficult, and the effect is usually interpreted at a semiquantitative level when deriving structural information, as will be discussed below.

The original prediction by Overhauser concerning the enhancement of nuclear spin polarization in metals upon saturation of the electron spins was published in 1953,[1] and the nuclear analog was described by Solomon in 1955.[2] The first applications to structure determination were by Anet and Bourne in 1965,[3] and for 10 years or so the method found applications mainly in organic chemistry.[4] Detection of NOE enhancements using repeated integration of CW-detected one-dimensional spectra imposed a detection limit in the region of 5%, but the introduction of new measurement techniques together with high-field, computer-assisted Fourier transform NMR spectrometers in the mid-1970s revolutionized the whole area. Now two experiments in particular, NOE difference spectroscopy and NOESY, have greatly improved sensitivity and allow very much more extensive use to be made of the NOE in structure determination than was possible previously. The technique is very widely used to determine stereo- and regiochemical isomerism in small and medium-sized natural and synthetic molecules, and more recently it has become the basis for a whole area of NMR, namely the structure determination of biological macromolecules, particularly proteins, in solution.[5]

2 CROSS RELAXATION AND THE ORIGIN OF THE NOE

The origin of the NOE lies in population changes caused by a particular form of longitudinal relaxation, namely dipole–dipole cross relaxation (see also ***Relaxation Processes in Coupled-Spin Systems***). Longitudinal relaxation involves energy exchange events between the nuclear spin states and the 'lattice', which term is used to depict the continuum of translational and rotational energy levels of the system as a whole. If the population of the high-energy state of a particular nuclear spin transition is larger than its equilibrium value, it will relax back towards equilibrium through events in which individual nuclei flip from high-energy to low-energy spin state while the lattice accepts the energy released, for instance by accelerating either the overall rotation or some internal motion of the molecule in which the nuclear spin transition occurred. Similarly, if the population of the high-energy state were smaller than its equilibrium value, then corresponding decelerations of molecular motions would provide energy to promote spins to the high-energy state.

However, such relaxation events can only occur if there exists a mechanism to couple the motions of the molecule to the nuclear spin states. In practice this means that the motion must itself cause a varying transverse magnetic field at the site of the nucleus it is to relax, and that this magnetic field variation must have an appreciable frequency component corresponding to the frequency of the nuclear spin transition. In the case of dipole–dipole relaxation, this 'local field' originates from the magnetic dipoles of other neighboring spins. Because in this case the local field itself originates from a spin, this opens the possibility for cooperative relaxation events in which *both* spins simultaneously flip, while the lattice accepts or provides energy corresponding to the net change. This is dipole–dipole cross relaxation. The various possible transitions for the simplest case of a two-spin system are summarized in Figure 1.

Two types of cross relaxation event are possible. In one, characterized by the transition probability W_2, both spins flip in the same sense, and the energy change accommodated by the lattice corresponds to the *sum* of the energies of the individual spin transitions. For these 'W_2 transitions' to occur, the local field resulting from lattice motions must contain fluctuations

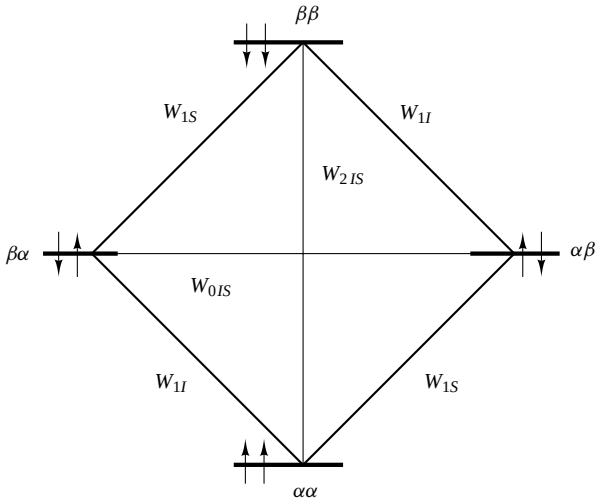

Figure 1 Energy level for a two-spin system, showing the definitions of transition probabilities (W_0, W_1, and W_2) and spin states ($\alpha\alpha$, $\alpha\beta$, $\beta\alpha$, and $\beta\beta$). Spin states are written with the state of I first and that of S second, i.e. $\alpha\beta$ means spin I is in the α state, and spin S in the β

at the sum frequency ($\omega_I + \omega_S$). In the other type of transition, characterized by the transition probability W_0, the spins flip in opposite senses. In the homonuclear case, this implies that a very much smaller energy change is accommodated by the lattice, corresponding to the *difference* between the energies of the individual transitions. For 'W_0 transitions', the local field must contain fluctuations at the difference frequency ($\omega_I - \omega_S$).

These two types of cross relaxation event are crucially different in their influence on the NOE. Suppose that spin S is saturated, thereby equalizing the populations of states $\alpha\alpha$ and $\alpha\beta$, and (separately) equalizing the populations of the states $\beta\alpha$ and $\beta\beta$. For all of the relaxation transitions involving S there will now be an excess of downward transitions (i.e. high $\rightarrow$ low energy), since there are more spins in the high-energy state than would be the case at equilibrium. The excess of downward single spin flips of S (W_1 transitions) has no effect on the intensity of I. However, if spin S flips downwards during a W_2 transition, spin I also flips downwards, thereby *increasing* the population difference across the I spin transition. Thus when W_2 transitions predominate over W_0 transitions, saturation of S causes the intensity of I to increase, which corresponds to a positive NOE enhancement. Conversely, for a W_0 transition, if spin S flips downwards then spin I must flip upwards, thereby *decreasing* the population difference across the I spin transitions. Therefore if W_0 transitions predominate over W_2 transitions, saturation of S causes the intensity of I to decrease, implying a negative NOE enhancement. If there are equal numbers of W_2 and W_0 transitions, the opposing effects cancel and there is no NOE at all.

2.1 The NOE for an Isolated Two-Spin System

These points may be expressed more formally using the Solomon equations, which form the basis for the theory of the NOE. For a system of two isolated spins $\frac{1}{2}$, the equation of motion for the longitudinal component of I spin magnetization is given by[2,6]

$$\frac{dI_z}{dt} = -(I_z - I_z^0)(W_{0IS} + 2W_{1I} + W_{2IS}) - (S_z - S_z^0)(W_{2IS} - W_{0IS}) \quad (3)$$

If S is saturated until steady state is reached, then dI_z/dt and S_z may both be set to zero, whereupon rearrangement and substituting $I_z^0 = (\gamma_I/\gamma_S)S_z^0$ gives

$$f_I\{S\} = \frac{I_z - I_z^0}{I_z} = \frac{\gamma_S}{\gamma_I}\frac{W_{2IS} - W_{0IS}}{W_{0IS} + 2W_{1I} + W_{2IS}} \quad \text{(two-spin)} \quad (4)$$

where $f_I\{S\}$ is the fractional steady state NOE enhancement measured at I upon completely saturating S. For the case of two spins $\frac{1}{2}$ relaxing exclusively via their mutual dipole–dipole interaction, the values of the various transition probabilities can be shown to be[7]

$$\left.\begin{aligned} W_{0IS} &= \tfrac{1}{20}K^2J(\omega_I - \omega_S) \\ W_{1I} &= \tfrac{3}{40}K^2J(\omega_I) \\ W_{2IS} &= \tfrac{3}{10}K^2J(\omega_I + \omega_S) \end{aligned}\right\} \quad \left(\begin{array}{c}\text{dipole}\\ \text{only,}\\ \text{extreme}\\ \text{narrowing}\end{array}\right) \quad (5)$$

where $K = (\mu_0/4\pi)\hbar\gamma_I\gamma_S r_{IS}^{-3}$. Given that K always appears as its square, this shows that all of these intramolecular dipole–dipole transition probabilities depend linearly on the minus sixth power of the internuclear distance r_{IS}. The various spectral density functions $J(\omega_x)$ each describe the power available at the corresponding frequency ω_x from molecular motions to stimulate relaxation. These spectral density functions provide the vital link between transition probabilities and molecular tumbling properties. If it is assumed that molecular tumbling is isotropic, and that it can be described by a correlation function that is a simple exponential decay with a rate constant τ_c, then the spectral density functions are given by

$$J(\omega_X) = \frac{2\tau_c}{(1 + \omega_X^2\tau_c^2)} \quad (6)$$

For small molecules molecular tumbling is very rapid, τ_c is very short and $\omega_X\tau_c < 1$. This is called the 'extreme narrowing' condition, and in this limit the denominators of the various spectral density expressions can all be set to unity, leading to much simpler expressions for the transition probabilities in equation (5). When these are substituted into equation (4), we have

$$f_I\{S\} = \frac{\gamma_S}{\gamma_I}\frac{\frac{3}{5}K^2\tau_c - \frac{1}{10}K^2\tau_c}{\frac{1}{10}K^2\tau_c + \frac{3}{10}K^2\tau_c + \frac{3}{5}K^2\tau_c} = \frac{\gamma_S}{2\gamma_I} \quad \left(\begin{array}{c}\text{two-spin}\\ \text{dipole only,}\\ \text{extreme}\\ \text{narrowing}\end{array}\right) \quad (7)$$

which, in the homonuclear case, is just +50%.

As molecular weight increases and tumbling becomes slower, the spectrum of rates of molecular motions becomes

more and more concentrated at low frequencies. The spectral densities $J(\omega_I + \omega_S)$ and $J(\omega_I)$ thus become progressively smaller until they cease to make any significant contribution to relaxation; in other words, the local field produced by motions of neighboring dipoles in large molecules has no frequency component high enough to stimulate W_2 or W_1 transitions. In heteronuclear systems, the same fate eventually overtakes $J(\omega_I - \omega_S)$ also [indeed, if γ_S and γ_I have opposite signs, $J(\omega_I + \omega_S)$ will diminish before $J(\omega_I - \omega_S)$, and for $S = {}^1\mathrm{H}$, ω_I is generally smaller than $(\omega_I - \omega_S)$ or $(\omega_I + \omega_S)$], but in homonuclear cases the difference frequency $(\omega_I - \omega_S)$ is so low (being just a difference of chemical shifts in this case) that $J(\omega_I - \omega_S)$ always remains large.

Thus, although in the extreme narrowing limit there are six times as many W_2 transitions as W_0 transitions, where $\omega\tau_c \approx 1$ (for a homonuclear system) the numbers of W_2 and W_0 transitions are nearly equal, resulting in small or zero NOE enhancements irrespective of the internuclear distances involved. For homonuclear systems in still larger molecules where $\omega\tau_c \gg 1$, all the spectral densities other than $J(\omega_I - \omega_S)$ become insignificant, dipolar relaxation is completely dominated by W_0 transitions and NOE enhancements are all negative. This limit is known as the 'spin diffusion' limit, for reasons that will become apparent shortly.

The overall dependence of the NOE on $\omega_I\tau_c$ for an ideal two-spin system relaxing exclusively through mutual dipole–dipole interactions can be calculated from equations (4)–(6). This function, often called η_{max}, is actually *independent* of the internuclear distance r, since all of the terms in equation (4) have an identical dependence on r^{-6} that cancels out. Conceptually, η_{max} represents the theoretical maximum NOE enhancement observable between two spins in the absence of other spins and external relaxation. Figure 2 shows η_{max} for a homonuclear system.

To simplify later equations, it is convenient to introduce here the cross-relaxation rate σ_{IS} and the direct relaxation rate ρ_{IS}, defined by

$$\sigma_{IS} = W_{2IS} - W_{0IS}; \quad \rho_{IS} = W_{0IS} + 2W_{1I} + W_{2IS} \qquad (8)$$

In this way, η_{max} can be reexpressed as

$$\eta_{max} = \frac{\gamma_S}{\gamma_I}\frac{\sigma_{IS}}{\rho_{IS}} \qquad (9)$$

2.2 Competition from Other Relaxation Mechanisms

Of course, in real situations, there will be relaxation mechanisms other than intramolecular dipole–dipole operating, and there will generally be more than two spins in the system. Almost without exception, other relaxation mechanisms do not contribute to cross relaxation at all, so their only influence is to dilute the contribution of dipolar relaxation to the whole. Such additional relaxation is often referred to as 'leakage', and in the equations the 'leakage rate' ρ^*_I is introduced as a *purely empirical* correction factor to allow for it; the subscript I is required since, in principle, every spin could have a different leakage rate.

$$f_I\{S\} = \frac{\gamma_S}{\gamma_I}\frac{\sigma_{IS}}{\rho_{IS} + \rho^*_I} \quad \text{(two-spin)} \qquad (10)$$

Significantly, for most systems leakage is much more important for small molecules than for large. This is because dipolar relaxation becomes steadily more efficient as tumbling rates diminish, whereas the leakage rate is often not greatly affected by solute tumbling rate. For instance, in many cases the dominant source of leakage is intermolecular dipole–dipole interactions between spins on the solute and unpaired electrons of dissolved oxygen molecules (see also ***Paramagnetic Relaxation in Solution***). This interaction is likely to be largely independent of solute tumbling rate, since the relative positions of the electron and nuclear spins will always vary rapidly as the oxygen molecule tumbles. Figure 3 shows how the ideal homonuclear two-spin NOE η_{max} is reduced more severely for small molecules than for large, assuming various constant leakage rates.

For spin systems involving nuclei with $I > \frac{1}{2}$, efficient quadrupolar relaxation usually leads to very high leakage rates,

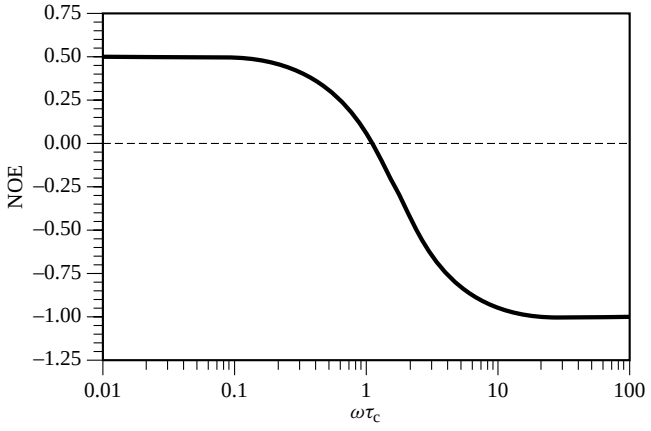

Figure 2 Maximum theoretical homonuclear NOE enhancement (η_{max}) for a two-spin system relaxing exclusively via dipolar interaction, as a function of $\omega\tau_c$. For small rapidly tumbling molecules where $\omega\tau_c \ll 1$, the maximum NOE enhancement is +50%, while for large, slowly tumbling molecules where $\omega\tau_c \gg 1$, the maximum enhancement is −100%

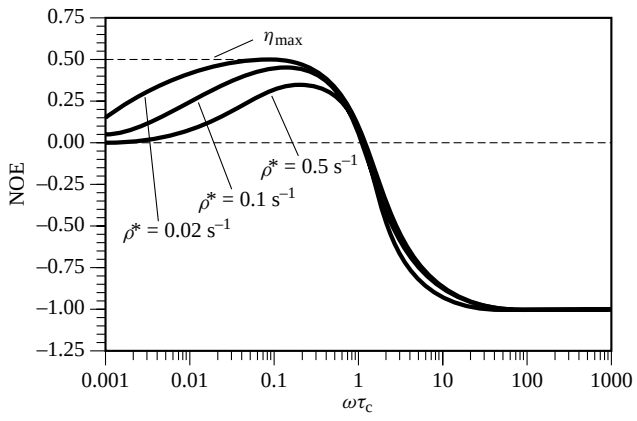

Figure 3 Reduction in η_{max} resulting from leakage, e.g. due to intermolecular relaxation by dissolved oxygen. The different curves are calculated according to equation (10) using the indicated values for ρ^*_I, assumed to remain constant as a function of solute tumbling rate, and taking an internuclear distance r_{IS} of 2 Å and a spectrometer frequency of 300 MHz

so that little or no NOE is detectable (see also ***Relaxation of Quadrupolar Nuclei Measured via Multiple Quantum Filtration***).

3 MULTISPIN SYSTEMS

In multispin systems, two further points need to be considered. Firstly, spin I will be relaxed not only by spin S but also potentially by all the other spins in the system (here collectively denoted X), depending on their distances from I. This adds further terms to the direct relaxation rate of I, diluting the NOE in much the same way as does ρ_I*. Thus, the total relaxation rate of I becomes

$$R_I = \rho_{IS} + \sum_X \rho_{IX} + \rho_I^* \tag{11}$$

Note that there is an implicit assumption made in equation (11) and in all the theory for multispin NOE enhancements that follows, namely that the total relaxation behavior of the system can be obtained by a simple summation over all possible pairwise interactions. This amounts to neglecting the cross correlation that must exist between the random motions of one spin pair and another within the same molecule. This assumption is almost universally made throughout applications of the NOE, and various authors have shown that it actually introduces little error into conventional interpretations (see also ***Relaxation Processes: Cross Correlation and Interference Terms***).[8]

Note also that the inclusion of ρ^*_I in this definition implies that R_I corresponds to the reciprocal of the *experimentally measured* selective T_1. In all the equations involving R_I that follow, one may in principle either include or exclude ρ^*_I. If it is included, the equations relate directly to measured results, but they require that measured values or at least estimates of leakage rates are available. If ρ^*_I is excluded, the equations relate to a hypothetical spin system with no leakage, allowing idealized NOE properties to be calculated provided only that the relevant internuclear distances are known.

The second important point for the NOE in multispin systems is the possibility of indirect enhancements. Once spins close to S have themselves received NOE enhancements, their own populations are no longer at equilibrium. This in turn disturbs the balance of their cross relaxation with their own neighboring spins, thereby creating additional NOE enhancements often called *indirect* enhancements. Such indirect enhancements can themselves cause further enhancements, and so on, until at steady state the original population disturbance at S may cause intensity changes to a greater or lesser extent throughout the spin system. For a multispin system, the relevant Solomon equation is

$$\begin{aligned}\frac{\mathrm{d}I_z}{\mathrm{d}t} = &-(I_z - I_z^0)(W_{0IS} + 2W_{1I} + W_{2IS}) - (S_z - S_z^0) \\ &\times (W_{2IS} - W_{0IS}) - \sum_X (X_z - X_z^0) \\ &\times (W_{2IX} - W_{0IX})\end{aligned} \tag{12}$$

Setting $\mathrm{d}I_z/\mathrm{d}t$ and S_z to zero as before, then rearranging and substituting $I_z^0 = (\gamma_I/\gamma_S)S_z^0 = (\gamma_I/\gamma_X)X_z^0$ gives the steady state enhancement as

$$f_I\{S\} = \frac{\gamma_S}{\gamma_I}\frac{1}{R_I}\left[\sigma_{IS} - \sum_X \frac{\gamma_X}{\gamma_S} f_X\{S\}\sigma_{IX}\right] \tag{13}$$

where all the indirect contributions to $f_I\{S\}$ are represented by the summation over the other spins X. Thus, in general, the theoretical steady state enhancements (i.e. assuming no leakage) upon saturating S in an N-spin system where the distances are all known can be calculated from a set of $(N - 1)$ linear simultaneous equations of the form of equation (12).[9] Note particularly that steady state enhancements are not controlled only by the internuclear distance between I and S, but are a function of many (potentially all) of the internuclear distances in the system. This crucially important point is all too often ignored in naïve interpretations of NOE experiments, particularly those involving small molecules.

The significance of indirect enhancements depends very much on the tumbling rate of the molecule under study, as will be illustrated in the following sections.

4 STEADY-STATE NOE EXPERIMENTS WITH SMALL MOLECULES

For homonuclear systems in small molecules, direct enhancements are positive, so that a directly enhanced signal can itself be thought of as being 'negatively saturated'. Spins that are significantly closer to such a directly enhanced spin than they are to the saturated spin therefore receive a *negative* enhancement from the directly enhanced spin, often called a 'three-spin effect'. However, at extreme narrowing, σ is significantly smaller than R_I, so that the transmission of enhancements down a chain of spins is a relatively inefficient process, even in the absence of leakage. In practice, efficient leakage reduces the transmission of indirect effects still further, and effects transmitted over more than one intermediate spin are almost never observed in small molecules. Given the sign distinction between direct and three-spin effects, this makes distinguishing indirect effects a relatively trivial matter.

Clearly, the geometry of a spin system is crucial in determining what effects will actually be seen. Substantial three-spin effects are generally associated with spins in a nearly linear arrangement, and it also follows that for some arrangements of spins, appreciable direct and indirect effects cancel leaving a small or zero net enhancement despite a short *IS* internuclear distance. These points are illustrated by the theoretical enhancements shown for some particular geometries in Figure 4.

4.1 NOE Difference Spectroscopy

The experiment that is now most widely used to measure steady state enhancements in small molecules is the NOE difference experiment, the pulse sequence for which is summarized in Figure 5. Two datasets are acquired, in one of which selective, low-power preirradiation is applied to the target resonance S. In the other experiment (the control), all details are identical to the first except that the preirradiation is applied in a blank area of the spectrum. Subtraction of

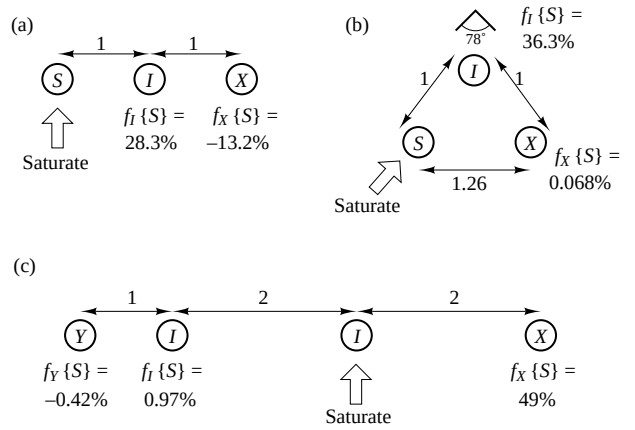

Figure 4 Theoretical NOE intensities ($\rho^*_I = 0$) for various simple multispin systems at the extreme narrowing limit ($\omega\tau_c \ll 1$). (a) Illustration of the transmission of a three-spin effect (here $f_X\{S\}$) in a linear spin system. (b) Illustration of how substantial direct and indirect contributions can cancel, leaving a very small net enhancement ($f_X\{S\}$) despite short distances. (c) Illustration as to how two direct effects corresponding to the same distance can differ drastically when one enhanced spin is rapidly relaxed by another near neighbor, and the other enhanced spin is not

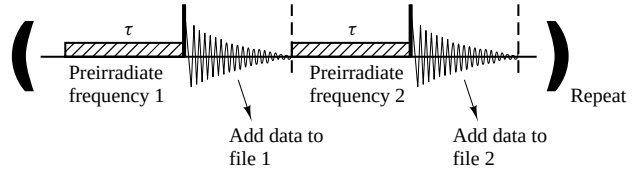

Figure 5 Pulse sequence for the one-dimensional NOE difference experiment

the control spectrum from that in which S is preirradiated yields a difference spectrum containing only those signals that changed intensity upon preirradiation of S. Note that, since the saturating field is switched off during acquisition of the FID, no coherent decoupling effects are present to complicate the data, and (ideally) only population effects can contribute to the difference spectrum.

In order to minimize unwanted differences between the datasets arising from instrumental instabilities, acquisition of the two datasets is usually carried out in an interleaved manner. If, as is usual, a series of experiments is to be carried out, a list is constructed of frequencies corresponding to the various preirradiation targets. Since, in principle, the control data are identical for all the different preirradiation targets, generally only one or two control entries are included in this list. The spectrometer then cycles repeatedly through the whole list, typically acquiring two or four dummy scans followed by eight or 16 transients at each frequency on each pass, until the available experimental time has been filled. A separate dataset is maintained for each preirradiation frequency, and incoming data are always added to data acquired at the same frequency on previous cycles. Careful attention to temperature equilibration and stability are also crucial to obtaining high-quality data. Long preirradiation periods (5–10 s or more) are often useful in NOE difference experiments, since then informative three-spin effects are allowed to become significant. However, when sensitivity for measuring relatively strong direct effects is the only issue, somewhat shorter preirradiation periods of $(1-3)T_1$ are often used in conjunction with an increased number of scans. Note also that there is no need whatsoever for a relaxation delay between acquisition and the start of the next preirradiation.

Preirradiation power is generally set extremely low, in order to avoid unwanted saturation of neighboring resonances. This can result in the target resonance being only partially saturated, which leads to NOE enhancements being only partially excited in direct proportion. However, this is of little real consequence since the absolute size of the enhancement rarely needs to be interpreted quantitatively in steady state experiments, the only real loss being one of sensitivity. Various techniques are available for saturating multiplets evenly without using high powers, for instance by cycling the preirradiation frequency around the multiplet components during each preirradiation period. These methods help to minimize the unwanted effects of selective population transfer (SPT) that arise at scalar coupling partners of the irradiated signal if the multiplet components of S are unevenly saturated (e.g. see Figure 6); these appear as intense antiphase signals at the coupled signals, and are completely unrelated to the NOE. Further suppression of SPT effects can be achieved by using a composite 90° pulse to excite the spectrum.

With care and long acquisition periods, enhancements well below the 1% level may now be quite routinely detected using

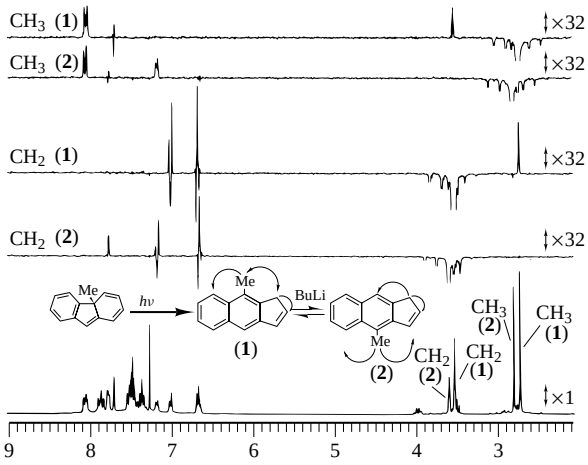

Figure 6 NOE difference and control spectra of a mixture of 4- and 9-methylcyclopenta[*b*]naphthalenes [compounds (**1**) and (**2**), obtained by photolysis of 4a-methyl-4a*H*-fluorene followed by treatment with butyllithium] in $CDCl_3$ solution, recorded at ambient temperature and 250 MHz (preirradiation period 5 s).[11] For each NOE difference trace, the preirradiation target is indicated on the left, and the relative vertical scaling on the right. The enhancements between the CH_2 and CH_3 signals in compound (**1**), and the enhancements $H_9\{CH_2\}$ and $H_3\{CH_3\}$ in compound (**2**), established the relative assignment of signals from the two isomers, thereby allowing compound (**1**) to be identified as the one that was initially formed in the photolysis step (the small peaks near 2.9 ppm and 3.9 ppm are due to impurities). This example also demonstrates the use of NOE difference experiments in analyzing mixtures in cases where spectral overlap is not too severe, and the appearance of SPT artifacts at coupling partners of the preirradiated signals (these spectra were recorded before the methods of SPT suppression referred to in the text had been introduced). Adapted with permission from Neuhaus[11]

the NOE difference technique (but such experiments are a particularly demanding test of instrumental stability).[10]

4.2 Applications to Small Molecules

One-dimensional NOE difference spectroscopy has now become an essential and routine tool for the determination of regio- and stereochemical isomerism in small and medium-sized molecules. However, a major and unavoidable limitation to the approach is imposed by molecular flexibility. The NOE can only distinguish between two or more possible structures or conformations if there is some significant and *consistently maintained* difference between internuclear distances corresponding to measurable NOE enhancements in the various cases. In this context, it is largely irrelevant whether the formal difference between the possibilities is one of covalently bonded structure or one of noncovalently stabilized conformation, provided that the relative spatial arrangement of protons is preserved.

Some of the simplest applications of the NOE involve the determination of aromatic ring and olefinic double-bond substitution patterns. Interpretation of the NOE enhancements in these essentially flat molecules is particularly simple, since the differences between internuclear distances in various possible structures are usually extremely clear cut. Aromatic ring fusion patterns are also usually quite straightforward to establish, provided, as in the case of substitution patterns, that there are strategically located protons at or near the sites that differ between the structures needing be distinguished (e.g. on each side of ring junctions). A simple example is shown in Figure 6.

Saturated systems often require a somewhat more sophisticated analysis, since differences between internuclear distances in various structures may be more subtle, and the importance of relaxation from other nearby protons in determining the relative sizes of enhancements may be less obvious. Substitution positions and ring fusion patterns are more likely to be available from coupling connectivities in such cases, so it is more often *stereochemical* information that is required from the interpretation of the NOE results. Applications to five-membered rings are perhaps more common than to six-membered rings, presumably due to the relative difficulty of using coupling constant magnitudes to distinguish whether protons are *cis* or *trans* in a five-membered ring. Rigidity is again crucial to the successful application of the technique, so applications to medium-sized or larger ring systems are more difficult, unless flexibility is limited, e.g. by fusion to another ring.

In larger systems, rigidity may be maintained in more complicated ways, e.g. by a specific, intramolecular network of hydrogen bonds that may, in effect, convert an acyclic portion of a molecule into a cyclic one. In combination with other NMR techniques, the NOE has been used to define largely or completely the stereochemistry and conformation of many complicated natural products, including steroids and other terpenoids, alkaloids, saccharides, small cyclic peptides, and various other types of natural macrocycles (see also ***Carbohydrates and Glycoconjugates***).[15]

Applications to characterizing conformational equilibria have been much less common. Accurate quantitation and very careful analysis are essential, and several unavoidable assumptions render analysis of even the simplest systems extremely approximate. In particular, if averaged NOE data from a rapidly exchanging system are to be fitted to try to find the relative proportions of two or more conformers, then the r^{-6} dependence of enhancements implies that the fit will be critically dependent on having very accurate internuclear distances available from models of the contributing conformers. The outlook for improvement in this situation remains bleak.

A few representative examples of applications of the NOE to problems of structure determination in small and medium-sized molecules are summarized in Figure 7.

5 KINETIC NOE EXPERIMENTS WITH LARGE MOLECULES

In complete contrast to the situation for small molecules, for homonuclear experiments with large molecules direct and

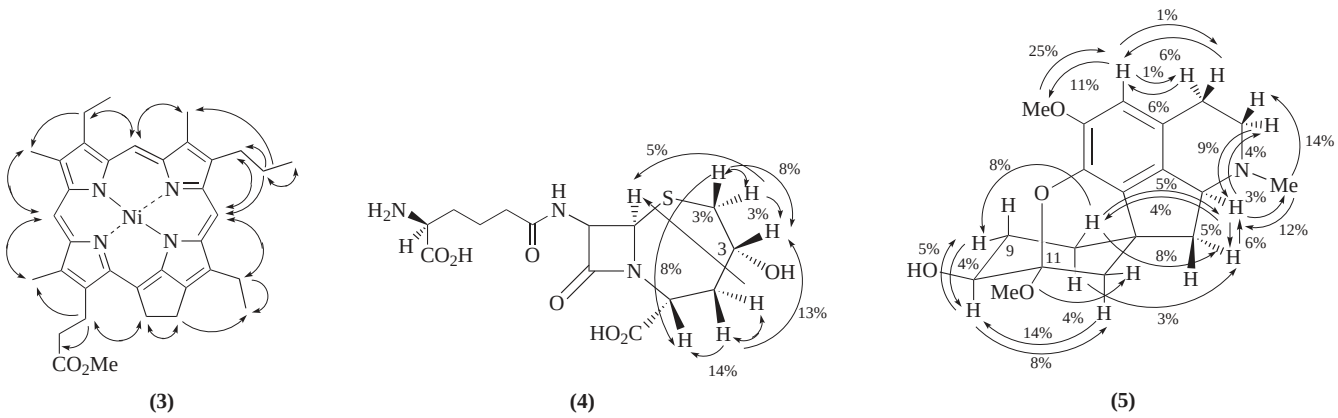

(3) (4) (5)

Figure 7 A few representative examples of structural applications of the NOE in small molecules. Compound (**3**) is a petroporphyrin whose substitution pattern was determined by the NOE enhancements shown.[12] Compound (**4**) is a hydroxyhomocepham isolated during work on penicillin biosynthesis, in which the stereochemistry at C-3 was established by the enhancements shown.[13] Compound (**5**) is a benzylisoquinoline alkaloid called misramine, the structure of which was established by a combination of spectroscopic techniques, and including the NOE enhancements shown.[14] In this case the enhancement data helped to link together partial ^{1}H spin systems determined by decoupling experiments, to determine the stereochemistry, and to determine that the site of the acetal function was C-11 rather than C-9

indirect enhancements are all negative, and the predominance of W_0 transitions over all others means that indirect enhancements can be transmitted efficiently down a chain of spins. In the limit of slow tumbling, saturation of any spin in a homonuclear multispin system will, at steady state, cause a -100% enhancement of every other spin; in other words, the entire spectrum will become saturated and disappear. This is the ultimate demonstration of the process known as 'spin diffusion', whereby enhancements in large molecules lose their specificity by dissipating onto other nearby spins.

Spin diffusion renders steady state homonuclear experiments on large molecules completely useless in terms of determining structures. Even limited spin diffusion poses a severe problem for interpretation, since direct and indirect enhancements cannot be distinguished a priori, being all negative, making it impossible to equate a given strength of enhancement with a given distance even approximately. In order to overcome this problem, NOE enhancements for such molecules are measured not at steady state but rather during the early stages of their build up.

Two types of simple kinetic experiment are possible. In the first, generally called the truncated driven Overhauser experiment or TOE, the NOE is driven by continuous saturation of the S signal throughout a short, variable period of NOE evolution. This experiment is essentially identical to the NOE difference experiment, except that the period of preirradiation during which the NOE evolves is kept much shorter. In the second type of kinetic experiment, perturbation of the S spin populations is achieved effectively instantaneously using pulses, and the NOE is then allowed to evolve for a short variable period in the absence of saturation. Experiments in this latter category include the two-dimensional NOESY experiment (see ***NOESY***) and all its variants (see also ***Homonuclear Three-Dimensional NMR of Biomolecules***), and also various transient one-dimensional experiments based on allowing the NOE to evolve after a selective inversion pulse to the signal corresponding to S (note, however, that there can be no true two-dimensional analog of the steady state or TOE experiments).

The period of NOE evolution in any kinetic experiment is generally called the mixing time, or τ_{m}. Provided that τ_{m} is sufficiently short, direct enhancements never become large enough to cause substantial indirect enhancements, and the process of spin diffusion has no chance to begin. This limit is known as the 'initial rate approximation'. The limiting form of equation (12) at short times may be found by substituting $S_z = 0$, $I_z = I_z^0$, and $X_z = X_z^0$, leaving

$$\left.\frac{\mathrm{d}I_z}{\mathrm{d}t}\right|_{t=0} = \sigma_{IS} S_z^0 \tag{14}$$

(for experiments where S is selectively inverted rather than saturated, the appropriate initial condition is $S_z = -S_z^0$, leading to an initial rate of $2\sigma_{IS}S_z^0$).

Thus the initial rate of NOE buildup is directly proportional to σ_{IS}, and therefore also to r^{-6}. It is this simple proportionality that forms the basis for most uses of the NOE in the structure determination of large molecules. At later times, once an appreciable enhancement has built up at I, then relaxation of the I spins at a rate determined by R_I starts significantly to oppose the buildup of the enhancement, and the steady state represents the balance that is eventually reached between these processes and also the influence of indirect enhancements. This also shows that the period of validity of the initial rate approximation depends on R_I, and may thus be different for different spins. However, broadly speaking, it is the molecular tumbling rate that is the main factor that determines how short mixing times must be if the direct proportionality between NOE intensity and r^{-6} is to be at least approximately preserved; the more slowly the solute tumbles, the faster longitudinal relaxation will occur and the shorter the validity of the initial rate approximation will last.

Although most interpretation of NOESY data and other kinetic NOE experiments is based on the assumption (or hope) that the initial rate approximation is still valid at the particular values of τ_{m} used, it is also possible to calculate the whole time-course for the evolution of NOE enhancements in multispin systems of known geometry. The relaxation behavior of a multispin system can be fully described in terms of the relaxation matrix $\mathbf{R}$, defined by

$$\mathbf{R} = \begin{bmatrix} R_1 & \sigma_{12} & \sigma_{13} & \cdots & \sigma_{1N} \\ \sigma_{21} & R_2 & \sigma_{23} & \cdots & \sigma_{2N} \\ \sigma_{31} & \sigma_{32} & R_3 & \cdots & \sigma_{3N} \\ \vdots & \vdots & \vdots & \ddots & \\ \sigma_{N1} & \sigma_{N2} & \sigma_{N3} & & R_N \end{bmatrix} \tag{15}$$

The intensities of the NOESY cross peaks at time τ_{m} are then given by:

$$\mathbf{a}(\tau_{\mathrm{m}}) = \exp(-\mathbf{R}\tau_{\mathrm{m}})\,\mathbf{a}(0) = \mathbf{T}\exp(-\mathbf{D}\tau_{\mathrm{m}})\,\mathbf{T}^{-1}\,\mathbf{a}(0) \tag{16}$$

where $\mathbf{a}(\tau_{\mathrm{m}})$ is the matrix of cross peak intensities at mixing time τ_{m}, $\mathbf{a}(0)$ is the corresponding matrix at zero mixing time, $\mathbf{D}$ is the diagonal matrix comprised of the eigenvalues of $\mathbf{R}$, and $\mathbf{T}$ is the matrix comprised of the eigenvectors of $\mathbf{R}$. The matrix $\mathbf{a}(0)$ is of course diagonal, and is needed only for normalization. Figure 8 shows how the intensities of the cross peaks and diagonal peaks in the NOESY spectrum vary as a function of τ_{m}, for a two-spin system in the extreme narrowing limit, and for one near the spin diffusion limit.

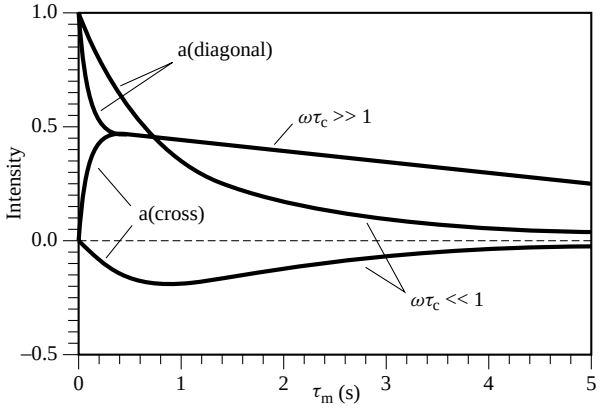

Figure 8 Simulated time course for cross-peak and diagonal peak intensity in a NOESY experiment for an isolated two-spin homonuclear system, as a function of mixing time (τ_{m}) for two different motional regimes. In a rapidly tumbling molecule ($\omega\tau_{\mathrm{c}} \ll 1$) the cross peak is negative relative to the diagonal, and builds up and decays slowly, whereas for a slowly tumbling molecule ($\omega\tau_{\mathrm{c}} \gg 1$) the cross peak is positive and builds up rapidly before decaying slowly

A slightly more complicated matrix equation also exists for describing the time-course of TOE experiments:

$$\mathbf{f} = [\mathbf{R}'^{-1}\,\boldsymbol{\sigma}] - [\mathbf{T}'\exp(-\mathbf{D}'\tau_{\mathrm{m}})\,\mathbf{T}'^{-1}\,\mathbf{R}'^{-1}\,\boldsymbol{\sigma}] \qquad (17)$$

where $\mathbf{f}$ is the column matrix of enhancements $f_I\{S\}$, σ is the column matrix of cross-relaxation rates involving S, and $\mathbf{R}'$, $\mathbf{T}'$, and $\mathbf{D}'$ are matrices analogous to $\mathbf{R}$, $\mathbf{T}$, and $\mathbf{D}$ in equation (16), but reduced by the elimination of all entries involving spin S. In addition to these matrix formulations, there are iterative numerical approaches to calculating the time course of NOESY and TOE experiments.[16,17]

At a practical level, if quantitative intensities are required for estimating internuclear distances, it is important that the spin populations be at equilibrium at the start of each pass through the pulse sequence. This is one reason why such kinetic experiments are used mainly for large molecules; for small molecules, this condition implies that long relaxation delays (tens of seconds) are required, making overall experiment times very long.

5.1 Applications to Biological Macromolecules

Generally, structure determinations of biological macromolecules rely on the assignment and classification of a large number of NOESY cross peaks linking individual spin pairs, followed by the calculation of a family of structures consistent with these data. Methods for assigning such spectra are discussed elsewhere.[18] The simple interpretation of data derived from NOESY spectra is usually based on an assumed validity of the initial rate approximation, so that the intensities of individual cross peaks are identified exclusively with the corresponding internuclear distance. In this context, this approximation is often known as the 'isolated spin-pair approximation', or ISPA. Cross peaks are classified semiquantitatively into groups such as 'strong', 'medium', and 'weak', and each category is interpreted as corresponding to a particular range of internuclear distances, following calibration by comparison with cross peaks corresponding to known distances. Usually, only the upper bound of each distance range is defined by the NOE intensity, in order to allow for the possibility that enhancements due to spins that are actually close together are made weaker by internal motions.

Various types of computer program are then used to generate a structure from the NMR data in conjunction with the known covalent connectivity and ideal covalent geometry. Although the bulk of the NMR data comprise NOE-derived distance constraints, it is common also to use torsion angle constraints derived from scalar coupling constant measurements and hydrogen bonding constraints derived from identification of slowly exchanging NH protons. Methods used for calculating biological macromolecular structures include distance-geometry, simulated annealing, and restrained molecular dynamics calculations, and also probabilistic model-building approaches; details may be found elsewhere (see also ***Distance Geometry***).[19] Normally an ensemble of calculations is run with each member starting from a randomly different set of initial conditions. Comparing the structures by superposition identifies which regions are well defined by the data, since only such regions are conserved across the ensemble.

Full matrix calculations of the NOE intensities can also be used to refine structures based on ISPA calculations, since they allow at least limited spin-diffusion to be accounted for explicitly (see ***Protein Structures: Relaxation Matrix Refinement***). Although equation (16) allows the prediction of NOE intensities at any point during their evolution for a known structure, the reverse process, calculation of all the internuclear distances directly from the NOE intensities, would require that the *complete* NOESY intensity matrix be known, including all of the diagonal elements. Given that, in practice, such complete information is never available for complicated spectra of macromolecules, various iterative approaches have been developed that improve the fit of a starting structure to the available NOE data, either by progressively modifying the structure (e.g. the program IRMA[20]), or by iterating on the internuclear distances themselves (e.g. the program MARDIGRAS[21]).

The whole field of application of the NOE to macromolecules has seen a huge growth since the first three-dimensional protein structure derived from NMR (that of BUSI-IIA) was published by Williamson et al. in 1986.[22] The size of proteins that can be tackled is limited principally by the assignment problem, both in terms of assigning all the ^{1}H chemical shifts within the protein, and in terms of assigning each individual NOE cross peak; the latter becomes a severe problem in its own right for proteins that exhibit extensive chemical shift degeneracy. The homonuclear experiments used for making assignments in unlabeled proteins begin to fail when ^{1}H linewidths become significantly greater than the values of typical (^{1}H,^{1}H) coupling constants, implying that for nonaggregated globular proteins this methodology is usually applicable up to polypeptide chain lengths of a little over 100 residues (see also ***Structures of Larger Proteins, Protein-Ligand, and Protein-DNA Complexes by Multi-Dimensional Heteronuclear NMR***).[18]

More recently, it has become practical to obtain protein samples in which all (<98%) carbon atoms are isotopically substituted with ^{13}C, and all nitrogens with ^{15}N; this is achieved by overexpression of the protein in a bacterial system growing in an appropriately isotopically enriched medium. This has opened the door to a whole barrage of new NMR techniques for the assignment of signals and NOE cross peaks, the details of which may be found elsewhere (see also ***Half-Filter Experiments: Proton–Carbon-13***; ***Three- and Four-Dimensional Heteronuclear Magnetic Resonance***; ***Three-Dimensional HMQC-NOESY, NOESY-HMQC, and NOESY-HSQC***).[23] These make use of the much larger one-bond heteronuclear and (^{13}C,^{13}C) couplings to detect through-bond connectivities and disperse crowded spectra in three or four frequency dimensions. It is not really clear yet what the upper size limit is for studying such isotopically enriched proteins, but systems approaching 200 residues have already been solved and it seems likely that larger ones will follow.

Although perhaps the most spectacular results have been obtained with proteins, related studies for DNA oligonucleotides have yielded much structural information,[24] although reliable identification of sequence-dependent conformation of double-helical DNA has proved somewhat elusive due to the essentially linear nature of the DNA molecule (see ***DNA Triplexes, Quadruplexes, and Aptamers***; ***DNA: A-, B-, and Z-***; ***Nucleic Acid Structures in Solution: Sequence Dependence***; ***Nucleic Acids: Spectra, Structures, and Dynamics***). Very

recently, NOE-based structure determinations of small RNA molecules have been reported, some making use of global isotopic labeling in a similar fashion to that used for proteins,[25] and the first solution structures of protein–nucleic acid complexes are now beginning to appear.[26]

6 THE ROTATING FRAME NOE

As Figure 2 makes clear, for homonuclear spin systems where $\omega\tau_c \approx 1$, all conventional NOE enhancements are small or zero, irrespective of the internuclear distances involved, representing a severe problem for studies of intermediate-sized molecules. However, this problem can be avoided by carrying out a different type of NOE experiment, in which NOE enhancements evolve not between elements of longitudinal magnetization as in the conventional experiment, but rather between elements of transverse magnetization during a period of spin locking.

Spin locking suppresses the *relative* precession of chemically shifted resonances within the spectrum; in other words, while the spin locking field is switched on, all the transverse magnetization components from the different signals in the spectrum precess *together*, with a constant relative phase. The simplest spin locking sequence comprises a hard 90° pulse followed by application of a spin locking field 90° out of phase with the pulse. If, prior to the 90° pulse, the system is prepared by inverting a particular signal S, then transverse cross relaxation during the spin locking period will lead to a transient rotating frame Overhauser effect, accumulating at signals corresponding to the cross-relaxation partners of S. This is exactly analogous to a conventional one-dimensional transient NOE experiment, in which the S signal is inverted prior to a period for evolution of longitudinal NOE enhancements. The role of the spin locking field is perhaps best viewed as maintaining a constant phase relationship between the inverted signal and the others; had the spin locking field been absent, relative precession due to chemical shifts would have prevented any *net* accumulation of enhancement. Most commonly, ROE enhancements are measured using the two-dimensional ROESY experiment, which is the ROE analog of NOESY (see ***ROESY***). Note that since there is no frequency difference between any of the spins while the ROE enhancements are evolving during the spin locking period, it is not possible to saturate selectively any of them separately during this time. There can therefore be no ROE analog of the conventional steady-state experiment.

The reason why ROE experiments differ fundamentally from longitudinal ones is that the transition probabilities for spin locked dipolar relaxation are based on different spectral densities. The transverse cross-relaxation rate σ_2 and transverse direct relaxation rate ρ_2 are given by[27]

$$\sigma_2 = \tfrac{1}{40}K^2[\tfrac{9}{2}J(2\omega_1) - \tfrac{1}{2}J(0) + 6J(\omega_0)] \quad (18)$$

$$\rho_2 = \tfrac{1}{40}K^2[\tfrac{9}{2}J(2\omega_1) + \tfrac{1}{2}J(0) + 9J(\omega_0) + 6J(2\omega_0)] \quad (19)$$

where ω_0 is the Larmor frequency and ω_1 is the frequency of precession about the $\boldsymbol{B}_1$ field. For comparison, the equivalent expressions for their longitudinal counterparts, obtained by substituting into equation (8), are

$$\sigma_1 = \tfrac{1}{20}K^2[-J(\omega_I - \omega_S) + 6J(2\omega_0)] \quad (20)$$

$$\rho_1 = \tfrac{1}{20}K^2[J(\omega_I - \omega_S) + 3J(\omega_0) + 6J(2\omega_0)] \quad (21)$$

Note that for slowly tumbling molecules where terms in $J(\omega_0)$ and $J(2\omega_0)$ are insignificant, σ_2 is twice σ_1. If NOESY and ROESY data are to be compared directly in such cases, τ_m should therefore be set twice as long in the NOESY experiment as in the ROESY.

The key difference between these expressions is that, unlike σ_1, σ_2 cannot become negative unless the extreme narrowing approximation breaks down *with respect to* ω_1. Typical spin locking field strengths in ROE experiments are between about $\omega_1 = 2$ kHz and $\omega_1 = 10$ kHz, implying that molecular motions in liquid samples will never be significantly slower than this so that direct ROE enhancements are always positive. Another key difference to the conventional experiment concerns spin diffusion. In effect, any size of molecule behaves in an ROE experiment as though it were a small molecule in a conventional NOE experiment (hence the original acronym CAMELSPIN for the experiment;[28] this stands for cross relaxation appropriate for mini-molecules emulated by spin locking). Thus, there is an alternation of sign for each intermediate spin over which an indirect enhancement is transmitted, and the transmission of indirect effects is relatively inefficient due to the loss that occurs at each step. For a large molecule, the influence of spin diffusion is markedly reduced in an ROE experiment relative to the corresponding NOE experiment, and what spin diffusion there is can usually readily be identified from the relative sign of the corresponding cross peaks.

Against these advantages, there are some difficulties that arise from the application of the spin locking field. Significant resonance offset effects are inevitable at the relatively low spin locking field strengths that can be applied in practice, implying that the cross relaxation controlling cross-peak intensities will, in general, be a composite of longitudinal and transverse contributions. Also, for coupled spins that are symmetrically disposed about the spin lock frequency, or are both close to it, a net transfer of magnetization may occur through the scalar coupling via the homonuclear Hartmann–Hahn (HOHAHA) interaction. Multistep mechanisms involving both HOHAHA transfer and ROE transfer may also occur, making the interpretation of ROESY data potentially quite complicated (see also ***TOCSY in ROESY and ROESY in TOCSY***).[29]

Nonetheless, there have been many applications of the ROE in the decade or so since its discovery. Mainly, these have been to intermediate-sized molecules, such as small peptides, that often give very poor NOESY spectra. However, it may also be worthwhile running a series of conventional steady state NOE difference spectra, since these are often significantly more sensitive than NOESY for such systems. For macromolecules, although clearly ROESY does not supplant NOESY for obtaining internuclear distance constraints, it can be very useful to compare NOESY and ROESY data in order to help identify spin diffusion pathways in the former.

7 THE HETERONUCLEAR NOE

Figure 9 shows the maximum theoretical steady-state heteronuclear two-spin NOE enhancement (η_{max}) for the

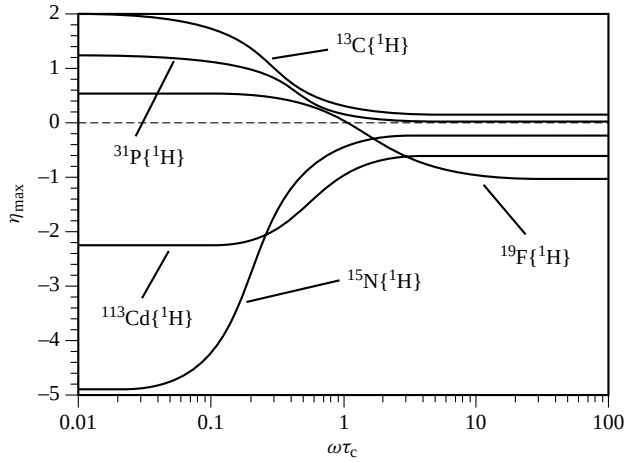

Figure 9 Maximum theoretical two-spin NOE enhancements (η_{max}) for various heteronuclear systems relaxing exclusively via dipolar interaction, as a function of $\omega\tau_c$. Note that for ^{15}N, the NOE can be negative, and that for ^{13}C and ^{31}P the NOE becomes very small for large molecules

more important heteronuclei and hydrogen, calculated using equations (4)–(6). The commonest application of these heteronuclear NOE enhancements is for sensitivity improvement during direct observation of heteronuclear signals, e.g. the application of ^1H decoupling when acquiring ^{13}C spectra of small molecules (at the extreme narrowing limit, η_{max} for the $^{13}C\{^1H\}$ NOE is 199%, corresponding to a threefold gain in signal). Note that η_{max} also corresponds to the theoretical NOE ($\rho^* = 0$) seen in a multispin system when all spins but one are saturated (provided all the saturated spins have the same γ).[5] However, any value of η_{max} between 0% and −200% means that saturation of the protons causes a *reduced* intensity for the X resonances, and a value of −100% means they are destroyed altogether. Inspection of the curves in Figure 9 shows that such circumstances do occur in some cases where γ_X is negative, e.g. for $^{15}N\{^1H\}$ with $\omega_N\tau_c \approx 0.5$. In such cases, if proton decoupling is to be used to collapse the X resonance multiplet structures, it should be applied in a gated fashion during the acquisition time only, and be switched off during the relaxation delay. In several other cases, the heteronuclear NOE becomes very small for slowly tumbling molecules, e.g. at the spin diffusion limit η_{max} for the $^{13}C\{^1H\}$ NOE is 15.4%, and for the $^{31}P\{^1H\}$ NOE it is only 2.2%. For these cases, there is of course virtually no sensitivity gain to be had from the heteronuclear NOE.

Measurements of specific heteronuclear enhancements to aid in structure determination are much less common than homonuclear applications because the sensitivity of the experiments is much lower, but several applications to small molecules have appeared.[30] Although the NOE observed on protons is a lot smaller than that observed on the X resonance, it is still often preferable to use proton observation as the sensitivity gain from detecting the higher frequency nucleus more than compensates; however, such ^1H-detected (inverse) NOE experiments may be compromised by inferior subtraction quality if the X nucleus is a dilute spin. Another factor that makes heteronuclear NOE experiments difficult is that the buildup rate σ_{XH} is slower than the corresponding interproton rate by a factor of $(\gamma_H/\gamma_X)^2$, for the same internuclear separation. Thus specific steady-state heteronuclear NOE difference experiments with small molecules can be extremely time-consuming, while experiments with macromolecules are usually precluded by the small values of η_{max}. Even in cases where η_{max} appears to behave quite similarly to that for the interproton NOE (e.g. for $^{19}F\{^1H\}$), one must remember that in the spin diffusion limit W_0 transitions will always be more efficient for the homonuclear case, since for sufficiently large molecules the tumbling rate will always be slower than the heteronuclear frequency difference ($\omega_I - \omega_S$). Thus, for example, in a $^1H\{^{19}F\}$ NOE experiment where a single fluorine resonance is saturated in a macromolecule, the buildup of heteronuclear enhancements at the nearest protons will be much slower than the dissipation of those enhancements onto other protons via homonuclear spin diffusion.

Recently, one of the more significant uses for heteronuclear NOE measurements (in conjunction with X nucleus T_1 and T_2 values) has been in the determination of local flexibility in macromolecules (see ***Protein Dynamics from NMR Relaxation***). Typically, for each ^{15}N resonance in a ^{15}N-labeled protein, the corresponding T_1, T_2, and $^{15}N\{^1H\}$ steady-state NOE would be measured, and these data analyzed using a suitable formalism, most commonly the 'model-free' formalism of Lipari and Szabo.[31] For internal motions of the ^{15}N–^1H vector that are faster than the overall molecular tumbling, this approach yields an 'order parameter' S^2 that describes the geometric extent of the internal motion relative to the molecular frame; $S^2 = 1$ implies complete rigidity, while $S^2 = 0$ implies the internal motion is isotropic relative to the molecular frame.

8 EXCHANGING SYSTEMS AND THE TRANSFERRED NOE

There are many types of exchange that can affect NMR spectra, including chemical exchange of labile protons (OH, NH, etc.) in protic solvents, conformational equilibria, and exchange of a solute between free and bound states. The effects that these processes have on NOE experiments depends mainly on their rate, relative both to the T_1 timescale and to the chemical shift timescale (see also ***Relaxation Effects of Chemical Exchange***). If exchange is slow relative to T_1, then NOE enhancements will evolve largely unaffected by the exchange process. However, if exchange is fast relative to T_1, then many exchange events will occur during NOE evolution, causing the various relaxation rates themselves to be averaged, and it will be as though the NOE had evolved in an 'averaged molecule'. Thus, if two resonances are linked by exchange that is faster than T_1, irradiation of one will result in saturation of both (saturation transfer), and if one resonance receives an NOE enhancement, exchange will transfer the enhancement onto the second resonance also. Under these circumstances, NOE enhancements will reflect so-called '$\langle r^{-6}\rangle$ average' distances, defined as

$$\langle r_{IS}^{-6}\rangle = \left[\frac{1}{N}[(r_{IS}^{A})^{-6} + (r_{IS}^{B})^{-6} + \cdots (r_{IS}^{N})^{-6}]\right]^{-1/6} \quad (22)$$

where r_{IS}^{A}, r_{IS}^{B}, etc. represent the IS internuclear distance in each of the N exchanging forms of the system. For internal

motions faster than overall molecular tumbling, it transpires that $\langle r^{-3} \rangle$ averaging of distances is appropriate, and that in addition there is a geometry-dependent reduction of NOE enhancements caused by the anisotropy of the internal motion with respect to the molecular frame; this situation usually applies for methyl group rotations.[32]

Note that the rate of exchange relative to $\Delta\delta$ (the chemical shift difference for the same spin in its two environments, for the case of two-site exchange) does not directly affect the NOE intensities at all; however, it does affect the number of separate resonances in the spectrum, and thereby dictates what NOE interactions can be measured separately. In cases of exchange which is slow relative to $\Delta\delta$, where separate signals are seen for each exchanging species, exchange can provide an additional mechanism for magnetization transfer in NOE experiments. For large molecules in conventional NOE experiments, exchange that is fast on the T_1 timescale causes saturation transfer signals that have the same sign as the NOE-enhanced signals; a distinction between the two types of signal can generally only be made on grounds of intensity or buildup rate. Conversely, for conventional NOE experiments with small molecules, and for ROE experiments with any size of solute, exchange will lead to signals of opposite sign to direct enhancements. Although this implies that they have the same sign as indirect enhancements transmitted over one intermediate spin, in the context of a general interpretation of all the cross peaks, the distinction between these two types of signal is usually quite straightforward.

More insidious than the signals due to exchange itself, however, is the possibility that conformational averaging affects the NOE intensities, giving results that reflect an 'averaged structure'. This can lead to data that are inconsistent with any single structure. In the case of slow exchange on the chemical shift timescale there is likely to be warning of the danger since multiple resonances are observed, but in the case of fast exchange on the chemical shift timescale there may be no indication of conformational exchange other than mutual inconsistencies amongst the NOE intensities. If models of the separate exchanging conformers are available from some other source, then in principle it is possible to fit the NOE data, using the relative proportions of the conformers as one of the fitting variables; however, this process is difficult and, given the r^{-6} dependence of the NOE, very heavily dependent upon the accuracy of the initial models. In large molecules, the main issue concerning conformational exchange is usually how to allow for relatively small-scale local motions when interpreting NOE data. These have two principal effects: they reduce the size of the enhancements, by making the effective τ_c shorter, and they change relative intensities by altering the values of $\langle r^{-6} \rangle$. For small-scale motions, these effects are both taken into account, at least approximately, by specifying NOE-derived distance constraints as ranges rather than specific distances, as mentioned earlier.

A particularly significant case of the influence of exchange is in the transferred NOE, or TRNOE experiment. Suppose a small ligand binds to a large molecule, and that exchange between the free and bound states is fast both on the T_1 and chemical shift timescales. The ligand resonances and also its intramolecular NOE enhancements will be averaged over the free and bound states by such an exchange. If the ligand is present in moderate excess, then the averaged ligand resonances will largely retain the narrow linewidths associated with the free ligand. However, because the tumbling rate of the ligand when bound to the large molecule is very much slower than in the free state, dipolar relaxation rates will be very much faster for the bound ligand than for the free [equations (4)–(6)]. Therefore, the observed NOE interactions will be dominated by the bound state, and thus reflect the bound conformation of the ligand, even though the free ligand concentration is higher than the bound. Although the first applications involved one-dimensional experiments, TRNOE experiments are now usually carried out using either NOESY or ROESY. Typical applications include studies of inhibitors bound to enzymes and small peptides bound to immunoglobulins; however, the generality of the technique is somewhat limited by the requirements for suitable exchange rates for the ligand–macromolecule interaction.[33] More recently, related experiments have been used to investigate protein hydration using intermolecular NOE enhancements between the protein surface and water protons (see ***Protein Hydration***).

9 RELATED ARTICLES

Biological Macromolecules: Structure Determination in Solution; Biological Macromolecules; Carbohydrates and Glycoconjugates; NOESY; Nucleic Acid Structures in Solution: Sequence Dependence; Relaxation Processes in Coupled-Spin Systems; ROESY; Selective NOESY; Structures of Larger Proteins, Protein-Ligand, and Protein-DNA Complexes by Multi-Dimensional Heteronuclear NMR.

10 REFERENCES

1. A. W. Overhauser, *Phys. Rev.*, 1953, **89**, 689.
2. I. Solomon, *Phys. Rev.*, 1955, **99**, 559.
3. F. A. L. Anet and A. J. R. Bourne, *J. Am. Chem. Soc.*, 1965, **87**, 5250.
4. J. H. Noggle and R. E. Schirmer, *The Nuclear Overhauser Effect; Chemical Applications*, Academic Press, New York, 1971.
5. D. Neuhaus and M. P. Williamson, *The Nuclear Overhauser Effect in Structural and Conformational Analysis*, VCH, New York, 1989.
6. Ref. 5, pp. 27–29.
7. Ref. 5, Appendix II.
8. T. E. Bull, *J. Magn. Reson.*, 1987, **72**, 379, and references therein.
9. Ref. 5, p. 76.
10. Further practical details concerning NOE difference spectroscopy may be found in Ref. 5, Chap. 7
11. D. Neuhaus, Ph. D. Thesis, University of London, 1982; see also D. Neuhaus and C. W. Rees, *J. Chem. Soc., Chem. Commun.*, 1983, 318.
12. R. Ocampo, H. J. Callot, and P. Albrecht, *J. Chem. Soc., Chem. Commun.*, 1985, 200.
13. A. E. Derome, *Modern NMR Techniques for Chemistry Research*, Pergamon Press, Oxford, 1987, pp. 124–127.
14. S. El-Masry, Z. Mahmoud, M. Amer, A. J. Freyer, E. Valencia, A. Patra, and M. Shamma, *J. Org. Chem.*, 1985, **50**, 729.
15. Ref. 5, Chap. 10
16. M. P. Williamson, *Magn. Reson. Chem.*, 1987, **25**, 356.

17. M. J. Forster, *J. Comput. Chem.*, 1991, **12**, 292.
18. K. Wüthrich, *NMR of Proteins and Nucleic Acids*, Wiley, New York, 1986.
19. M. J. Sutcliffe, in *NMR of Macromolecules; A Practical Approach*, ed. G. C. K. Roberts, IRL Press at Oxford University Press, Oxford, 1993, Chap. 11
20. R. Boelens, T. M. G. Konig, and R. Kaptein, *J. Mol. Struct.*, 1988, **173**, 299.
21. B. A. Borgias and T. L. James, *J. Magn. Reson.*, 1990, **87**, 475.
22. M. P. Williamson, T. F. Havel, and K. Wüthrich, *J. Mol. Biol.*, 1985, **182**, 295.
23. G. M. Clore and A. M. Gronenborn, *Prog. NMR Spectrosc.*, 1991, **23**, 43.
24. F. J. N. Van De Wen. and C W. Hilbers, *Eur. J. Biochem.*, 1988, **178**, 1.
25. G. Varani and I. Tinoco, Jr., *Q. Rev. Biophys.*, 1991, **24**, 479.
26. J. G. Omichinski, G. M. Clore, O. Schaad, G. Felsenfeld, C. Trainor, E. Appella, S. J. Stahl, and A. M. Gronenborn, *Science*, 1993, **261**, 438.
27. Ref. 5, p. 316.
28. A. A. Bothner-By, R. L. Stephens, J.-M. Lee, C. D. Warren, and R. W. Jeanloz, *J. Am. Chem. Soc.*, 1984, **106**, 811.
29. Ref. 5, pp. 312–327.
30. M. F. Aldersley, F. M. Dean, and B. E. Mann, *J. Chem. Soc., Chem. Commun.*, 1983, 107.
31. G. Lipari and A. Szabo, *J. Am. Chem. Soc.*, 1982, **104**, 4546, and following paper.
32. J. Tropp, *J. Chem. Phys.*, 1980, **72**, 6035.
33. For a recent review, see B. D. Sykes and A. P. Campbell, *Biophys. Biomol. Struct.*, 1993, **22**, 99.

Biographical Sketch

David Neuhaus. *b* 1956. B.A., 1978, Oxford University, Ph.D., 1982, Imperial College of Science and Technology, London (supervisor Prof. Charles Rees). Postdoctoral visits to Professor Kurt Wüthrich, ETH Hönggerberg, Zürich, Switzerland (1983) and Dr. Ray Freeman, Physical Chemistry Laboratory, Oxford University (1984). NMR spectroscopist for Parke Davis Research Centre, Cambridge, 1985–88; staff scientist and NMR facility manager for MRC Laboratory of Molecular Biology, Cambridge, 1988–present. Approx. 40 publications. Research interests: structure determination of proteins and protein–nucleic acid complexes using NMR.

Paramagnetic Relaxation in Solution

Jozef Kowalewski
Stockholm University, Sweden

1	Introduction	1
2	Theory	1
3	Experimental Methods	4
4	Related Articles	6
5	References	6

1 INTRODUCTION

Paramagnetic systems are materials with positive magnetic susceptibility, normally associated with unpaired electrons. Chemically, paramagnetic systems of relevance for this article are dilute aqueous or organic solutions of free radicals and transition metal ions or their complexes, including metalloproteins. The presence of unpaired electron spins has a profound influence on the NMR spectra of such solutions. The origin of the effects is to be found in the large value of the electronic magnetic moment, about 650 times that of the proton.

The influence of the paramagnetic species on NMR spectra of liquids may be two-fold. First, the nuclear spin relaxation rates are enhanced. The paramagnetic relaxation enhancement (PRE) is caused by random variation of the electron spin–nuclear spin interactions, which opens new pathways for longitudinal as well as transverse relaxation. The PRE is most often studied for $I = \frac{1}{2}$ nuclei, but oxygen-17 applications are not uncommon. Second, the NMR signals may be shifted, provided the relevant electron spin–nuclear spin interaction has a nonzero average. Paramagnetic complexes in solution often contain exchangeable ligands, and the exchange phenomena (see***Chemical Exchange Effects in Biological Macromolecules***), together with the intrinsic relaxation rates and shifts, contribute to the observed lineshapes and line positions. The paramagnetic effects have been used for several decades by chemists and biochemists as a source of structural, thermodynamic, and dynamic information. Applications of this type have been described in numerous books, recently by Bertini and Luchinat[1] and by Banci et al.[2] A more recent application of PRE is the use of paramagnetic compounds as contrast agents in MRI (see ***Contrast Agents in Whole Body Magnetic Resonance: An Overview*** and ***Contrast Agents in Magnetic Resonance: Operating Mechanisms***).

2 THEORY

The theory of nuclear relaxation in paramagnetic systems contains many intricate points, described some years ago in a review article.[3] Here, we concentrate on the most important issues and begin by formulating the relationships between the measured macroscopic PRE and the microscopic quantities. We then proceed with the theory for relaxation times for nuclei residing in the ligands in paramagnetic complexes and conclude the theory section by a brief discussion of intermolecular relaxation.

2.1 The Macroscopic and Microscopic Quantities

The PRE experiments are often performed with a considerable excess of a ligand (e.g. solvent) over the paramagnetic centers (e.g. transition metal ions). The type of information obtainable from PRE measurements in solution depends on the relative magnitudes of the exchange rates, the intrinsic relaxation rates, and shifts. The set of equations relating the relaxation, shift, and lifetime properties of the nuclei in paramagnetic complexes to the observables of the NMR experiments has been derived by Swift and Connick[4] and by Luz and Meiboom:[5]

$$T_{1\mathrm{P}}^{-1} = \frac{P_\mathrm{M}}{\tau_\mathrm{M} + T_{1\mathrm{M}}} \tag{1}$$

$$T_{2\mathrm{P}}^{-1} = \frac{P_\mathrm{M}}{\tau_\mathrm{M}} \left[\frac{T_{2\mathrm{M}}^{-2} + (T_{2\mathrm{M}}\tau_\mathrm{M})^{-1} + \Delta\omega_\mathrm{M}^2}{(T_{2\mathrm{M}}^{-1} + \tau_\mathrm{M}^{-1})^2 + \Delta\omega_\mathrm{M}^2} \right] \tag{2}$$

$$\Delta\omega_\mathrm{P} = \frac{P_\mathrm{M}\Delta\omega_\mathrm{M}}{(\tau_\mathrm{M}/T_{2\mathrm{M}} + 1)^2 + \tau_\mathrm{M}^2\Delta\omega_\mathrm{M}^2} \tag{3}$$

$T_{1\mathrm{P}}{}^{-1}$, $T_{2\mathrm{P}}{}^{-1}$, and $\Delta\omega_\mathrm{P}$ are the excess (see Section 3) spin–lattice relaxation rate, spin–spin relaxation rate and shift measured for the ligand in solution, while the properties with index M refer to the ligand in the paramagnetic complex. τ_M is the lifetime of the ligand in the complex and P_M is the mole fraction of ligand nuclei in bound positions.

2.2 The Modified Solomon–Bloembergen Equations

The nuclear spin relaxation in a paramagnetic complex arises through the electron–nucleus hyperfine interaction (see ***Electron-Nuclear Interactions***) between the nuclear spin I and the electron spin S. The hyperfine interaction consists of two parts. The first term is the dipole–dipole interaction between the nuclear magnetic moment and the electron spin of the electron outside of the nucleus; the second term is the scalar interaction or Fermi contact coupling between the nuclear magnetic moment and the spin of s electrons at the site of the nucleus. Each of these terms can be modulated by random processes and can contribute to the nuclear relaxation rates. The dipole–dipole part of the hyperfine interaction is modulated by reorientation of the spin–spin axis, by changes in the orientation of the electron spin (electron spin relaxation) and by ligand exchange. The scalar interaction part remains unaffected by reorientation of the molecule and is only modulated by electron relaxation and ligand exchange.

These qualitative ideas are reflected in the set of equations for nuclear relaxation rates in paramagnetic complexes, known as the ‘modified Solomon–Bloembergen equations’:

$$T_{1M}^{-1} = (T_{1M}^{SC})^{-1} + (T_{1M}^{DD})^{-1}$$
$$= \frac{2}{3}\left(\frac{A}{\hbar}\right)^2 S(S+1)\frac{\tau_{e2}}{1+(\omega_S-\omega_I)^2\tau_{e2}^2}$$
$$+\frac{2}{15}\left(\frac{\mu_0}{4\pi}\right)^2 S(S+1)\hbar^2\gamma_I^2\gamma_S^2 R^{-6}$$
$$\times\left[\frac{\tau_{c2}}{1+(\omega_S-\omega_I)^2\tau_{c2}^2}+\frac{3\tau_{c1}}{1+\omega_I^2\tau_{c1}^2}\right.$$
$$\left.+\frac{6\tau_{c2}}{1+(\omega_S+\omega_I)^2\tau_{c2}^2}\right] \quad (4)$$

and

$$T_{2M}^{-1} = (T_{2M}^{SC})^{-1} + (T_{2M}^{DD})^{-1} = \frac{1}{3}\left(\frac{A}{\hbar}\right)^2 S(S+1)$$
$$\times\left(\tau_{e1}+\frac{\tau_{e2}}{1+(\omega_S-\omega_I)^2\tau_{e2}^2}\right)$$
$$+\frac{1}{15}\left(\frac{\mu_0}{4\pi}\right)^2 S(S+1)\hbar^2\gamma_I^2\gamma_S^2 R^{-6}$$
$$\times\left[4\tau_{c1}+\frac{3\tau_{c1}}{1+\omega_I^2\tau_{c1}^2}+\frac{\tau_{c2}}{1+(\omega_S-\omega_I)^2\tau_{c2}^2}\right.$$
$$\left.+\frac{6\tau_{c2}}{1+\omega_S^2\tau_{c2}^2}+\frac{6\tau_{c2}}{1+(\omega_S+\omega_I)^2\tau_{c2}^2}\right] \quad (5)$$

where

$$\tau_{ci}^{-1} = \tau_R^{-1} + \tau_M^{-1} + T_{ie}^{-1} \quad (i = 1, 2) \quad (6)$$

$$\tau_{ei}^{-1} = \tau_M^{-1} + T_{ie}^{-1} \quad (7)$$

τ_R is an isotropic rotational correlation time of the complex, T_{ie} (i = 1 or 2) is the electron spin relaxation time, and S is the electron spin quantum number, $A/\hbar$ is the isotropic scalar coupling constant, μ_0 is the permeability of vacuum, R is the distance between the nuclear spin and the electron spin (considered as a point dipole), and γ_S equals $g_{eff}\beta/\hbar$, where g_{eff} is the effective g factor of the electron in the complex under consideration and β is the Bohr magneton. ω_S and ω_I are the electronic and nuclear Larmor frequencies. The electronic Larmor frequency is so much larger than the nuclear Larmor frequency that the latter can be neglected in the terms involving the sum and difference frequencies, and some of the terms in the dipole–dipole parts of equations (4) and (5) can be brought together. Note the peculiar dual role that the exchange can play in the PRE: in equations (4)–(7) the τ_M acts as a correlation time, while its role in equations (1)–(3) is that of a relaxation time.

The modified Solomon–Bloembergen equations were first presented in the papers by Connick and Fiat[6] and by Reuben et al.[7] The formal derivation of the equations is fairly complicated and was in fact published much later.[8] It is based on the Redfield relaxation theory for the nuclear spin and involves two critical assumptions. The first one is that the electron relaxation (which is a motion in the electron spin space) is uncorrelated with molecular reorientation (which is a spatial motion influencing the dipole coupling). The second assumption is concerned with the description of the dynamics in the electron spin space. It is assumed that the electron spin system is dominated by the electronic Zeeman interaction. Other interactions lead to relaxation, which can be described in terms of the longitudinal and transverse relaxation times T_{1e} and T_{2e}. This point is elaborated on in Section 2.3. In this sense, one can call the modified Solomon–Bloembergen equations a 'Zeeman-limit theory'. If the second assumption is fulfilled, then the scalar interaction parts in equations (4) and (5) become analogous to the equations describing scalar relaxation originating from the modulation of the nuclear spin–spin coupling, with the hyperfine coupling constant $A/\hbar$ replacing the J coupling constant. The first assumption does not directly influence the scalar interaction term, but the failure to fulfil it will lead to an additional interference (cross correlation) term between the dipole–dipole and the scalar interactions. The validity of both the above assumptions is questionable in many cases of practical importance.

Apart from these two main assumptions, equations (4) and (5) contain several additional approximations, the most important of which are the following:

1. The electron spin is assumed to be a point dipole centered at the metal ion. The validity of this assumption can be tested by ab initio quantum-chemical calculations, which indicate that it is reasonable for protons but may cause errors for heavier nuclei, in particular if the atoms where they reside are involved in bonding with the paramagnetic metal center.[9]
2. The electron g tensor is assumed to be isotropic. The effects of deviations from this assumption were first investigated by Sternlicht.[10]
3. It is assumed that the reorientation of the nuclear–electron spin vector can be described by a single correlation time, τ_R. This amounts to neglecting the effects of internal motion and anisotropic reorientation.
4. It is assumed that chemical exchange is uncorrelated with the remaining motions in the lattice. This assumption seems to be easy to fulfil. We return to the exchange effects in Section 3.1.

2.3 The Bloembergen–Morgan Theory for Electron Spin Relaxation

As one can see in equations (4) and (5), the magnitude of the PRE for the ligand nuclei depends on the energy level splittings and the relaxation behavior of the electron spin system of the transition metal ion in the magnetic field. For discussing the splittings, the spin Hamiltonian formalism, developed originally for the interpretation of ESR spectra,[11] normally constitutes an appropriate framework. The spin Hamiltonian is an operator involving only nuclear and electron spin operators and parameters characterizing the spin system under consideration. Neglecting the terms containing only nuclear spins and the hyperfine coupling to the ligand nuclei, the spin Hamiltonian can be written:

$$\hat{\mathcal{H}}_S = \hat{\boldsymbol{S}}\cdot\boldsymbol{g}\cdot\hat{\boldsymbol{B}}_0\cdot + \hat{\boldsymbol{S}}\cdot\boldsymbol{D}\cdot\hat{\boldsymbol{S}} + \hat{\boldsymbol{S}}\cdot\boldsymbol{A}\cdot\hat{\boldsymbol{I}}_M \quad (8)$$

$\hat{\boldsymbol{S}}$ is the electron spin operator. The first term describes the electron Zeeman interaction and the second the zero-field splitting (ZFS) interaction, which only has to be considered for systems with electron spin quantum number $S \geq 1$. The last term corresponds to the hyperfine interaction with the metal nucleus, if it has nonzero spin ($\hat{\boldsymbol{I}}_{\mathrm{M}}$ is the nuclear spin operator for the metal). The molecular parameters are the three second-rank tensors: the g tensor $\boldsymbol{g}$, the ZFS tensor $\boldsymbol{D}$ and the hyperfine coupling tensor $\boldsymbol{A}$. The combined effect of the electrostatic interactions and spin–orbit coupling renders the Zeeman interaction anisotropic and makes the average effective g value (equal to one-third of the trace of the g tensor) different from the free electron value of 2.0023. The effect of the g tensor on ESR spectra is similar to the effect of the shielding tensor in NMR.

The zero-field splitting tensor also has its origin in the intermingling of the electrostatic and spin–orbit interactions. In addition, the dipolar coupling between the electron spins can contribute to the ZFS, but this contribution is believed to be minor for transition metal complexes.[12] The ZFS tensor is traceless and can be characterized, in its principal axis system, by two constants:

$$D = D_{zz} - \tfrac{1}{2}(D_{xx} + D_{yy}) \tag{9a}$$

$$E = \tfrac{1}{2}(D_{xx} - D_{yy}) \tag{9b}$$

The ZFS interaction has a form similar to the quadrupolar interaction in NMR.

The modulation of various terms in equation (8) by random processes in liquids leads to electron spin relaxation. The rotational modulation of the anisotropies of the g and hyperfine tensors are important sources of electron relaxation for $S = \frac{1}{2}$ systems. Still another relaxation mechanism for $S = \frac{1}{2}$ systems, in analogy with the case of nuclear relaxation, is the spin–rotation coupling. The electron relaxation in $S = \frac{1}{2}$ systems is discussed at length in the book by Muus and Atkins[13] and is summarized in the book by Banci et al.[2]

For systems with $S \geq 1$, the electron spin relaxation is usually so fast (often on the picosecond timescale) that it competes effectively with complex reorientation as the main modulation mechanism for the dipole–dipole part of the modified Solomon–Bloembergen equations, even in small complexes. Bloembergen and Morgan[14] presented, as early as the early 1960s, a Redfield-type theory (see ***Relaxation Theory: Density Matrix Formulation***) where they related this efficient electronic relaxation in hexaaquo complexes of transition metal ions to the modulation of the ZFS by the distortion of the hydration shell. The Bloembergen–Morgan equations for $T_{1\mathrm{e}}$ and $T_{2\mathrm{e}}$ are often written as

$$T_{1\mathrm{e}}^{-1} = \frac{\Delta^2}{25}[4S(S+1) - 3]\left(\frac{\tau_v}{1 + \tau_v^2\omega_S^2} + \frac{4\tau_v}{1 + 4\tau_v^2\omega_S^2}\right) \tag{10}$$

$$T_{2\mathrm{e}}^{-1} = \frac{\Delta^2}{50}[4S(S+1) - 3] \times \left(3\tau_v + \frac{5\tau_v}{1 + \tau_v^2\omega_S^2} + \frac{2\tau_v}{1 + 4\tau_v^2\omega_S^2}\right) \tag{11}$$

where τ_v is the correlation time for the collision-related modulation of the ZFS, and Δ^2 is the trace of the square of the transient ZFS tensor:

$$\Delta^2 = D_{xx}^2 + D_{yy}^2 + D_{zz}^2 = \tfrac{2}{3}D^2 + 2E^2 \tag{12}$$

The combination of the modified Solomon–Bloembergen equations with the Bloembergen and Morgan theory for electron spin relaxation rates provides a complete theory for the magnetic field dependence of the PRE, known in the literature as the Solomon–Bloembergen–Morgan (SBM) theory.

The Bloembergen–Morgan theory has rather severe validity conditions, very clearly stated in the original paper. The most important limitation is the validity requirement for the Redfield-type or perturbative approach, which can generally be formulated as $\tau_v{}^2\Delta^2 \ll 1$. It is unfortunately rather common in the literature to use equations (10) and (11) uncritically, also beyond the limits of their validity. Analogous equations have also been derived for the case of rotational modulation of a static ZFS.[15] This case should be handled with care in the context of PRE, because it violates the requirement of no correlation between rotation and electron relaxation. An improvement of the SBM theory, within the same general framework and with the same validity limits, has been proposed by Rubinstein et al.[16] They noted that for systems with $S \geq \frac{3}{2}$ one may have more than one electronic T_1 or T_2, and they elegantly described the collision modulation of the ZFS as a pseudorotation process.

The issue of the electron spin relaxation for $S \geq 1$ in solution is not really settled, on the fundamental level of the applicability of the spin Hamiltonian formalism. An interesting line of thought, which still awaits a quantitative formulation, is that the electronic relaxation in liquids might in fact be similar to that in solids, where one talks about mechanisms involving interactions between the electron spin and phonons, mediated by the spin–orbit coupling.[2]

2.4 Beyond the Solomon–Bloembergen–Morgan Theory

During the last decade, significant effort has been invested into moving the paramagnetic relaxation theory beyond the limitations of the SBM theory. Two main approaches can be discerned. One of them can be referred to as 'low-field theories'. These are designed to handle cases when the electron Zeeman interaction does not dominate the energy level structure, either because the slow reorientation does not average out the anisotropic term in equation (8) or because another interaction (in the first place the ZFS interaction) simply is stronger and determines the quantization direction of the electron spin. This approach was originally proposed by Lindner[17] and was subsequently developed by Bertini and co-workers[1,2] and by Sharp.[18] The form of the resulting equation for $T_{1\mathrm{M}}{}^{-1}$ is similar to equation (4), in the sense that it consists of a sum of terms containing spectral density functions at the transition frequencies in the combined nuclear spin–electron spin system. The coefficients of the various spectral densities depend on the angle between the two molecule–fixed axis systems: the dipole–dipole axis and the principal axis of the anisotropic interaction. The electron spin relaxation enters the theories of this type in the simple form of 'electron relaxation

time', $\tau_S = T_{1e} = T_{2e}$, i.e. the electron spin is assumed to be in the Redfield limit. In addition, a frequency dependence of τ_S, similar to that given by the Bloembergen–Morgan theory, is sometimes used.

The other approach tries to solve the problem using more general, and more cumbersome, methods[3,8,19,20] based on the stochastic Liouville equation (see ***Liouville Equation of Motion***).[13] This formulation is often referred to as the 'slow-motion approach'. The nuclear spin is considered to be weakly coupled (in the sense that the Redfield formalism is valid) to a composite lattice, containing the electron spin degree of freedom as well as rotations and possibly other classical degrees of freedom. The electron spin and the classical degrees of freedom are coupled through the ZFS interaction of arbitary strength. The dynamics in the composite lattice can be described in terms of a spectral density function, and the nuclear T_1 is determined by the value of the spectral density at the nuclear Larmor frequency, while the nuclear T_2 depends on the spectral density at the nuclear Larmor frequency and at zero frequency. There is no need to invoke the concept of electronic relaxation time, even though the result of numerical calculations becomes identical to the SBM theory under appropriate limiting conditions. The disadvantage of the approach is its complexity: the composite lattice spectral density is obtained by the inversion of a complex matrix, in principle of infinite dimensions.

The magnetic field dependences of the nuclear spin–lattice relaxation rate, calculated using the methods of Bertini et al.[2] and of Benetis et al.,[8] have been compared with each other, imposing on the latter model the additional assumption of exponential electron spin relaxation.[2] For the case of large ZFS, the results of the two methods are identical and very different from the predictions of the SBM theory (Figure 1).

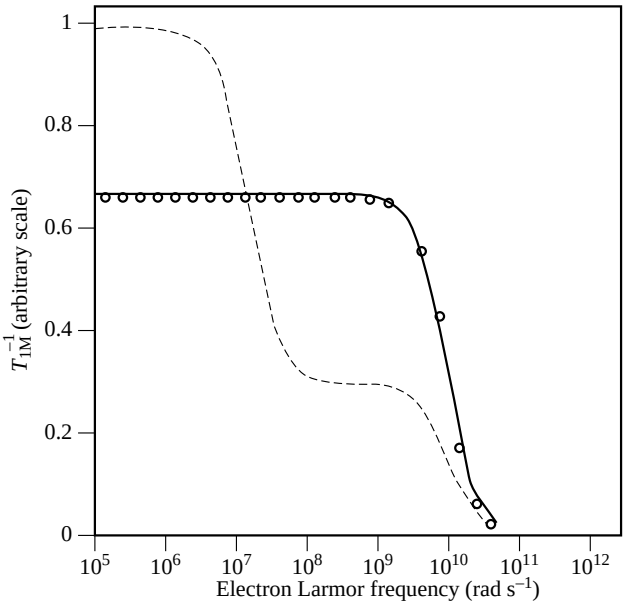

Figure 1 Calculated magnetic field dependence of proton $T_{1M}{}^{-1}$ in an $S = 1$ system according to the modified Solomon–Bloembergen equations (----), a low-field theory (—), and the slow-motion approach (○). (Reproduced by permission of VCH from L. Banci, I. Bertini, and C. Luchinat, 'Nuclear and Electron Relaxation', Weinheim, 1991)

2.5 The Curie Spin Relaxation

Gueron, Fiat, and Vega[21] have proposed an additional mechanism for the PRE, due to dipolar coupling of the nuclear spin with the thermally averaged electron magnetic moment. This average 'Curie spin' is aligned along the external magnetic field and is proportional to its magnitude. The interaction between the nuclear spin and the Curie spin is modulated by reorientation and exchange, but not by the electron spin relaxation. If the electron relaxation is much faster than the reorientation and exchange, and if the magnetic field is high, the Curie spin relaxation can become important (in particular for T_{2M}) in spite of the fact that the average electronic magnetic moment is of course much smaller than the real, rapidly oscillating one.

2.6 Intermolecular Relaxation

The above-mentioned theories of intramolecular nuclear spin relaxation due to dipole–dipole interaction assume that the distance R between the I and S spins is constant. The chemical exchange can be thought of as an extremely crude way of incorporating possible intermolecular effects or modulation of the dipole–dipole interaction by the variation of the interspin distance; it is allowed to be given a value of either R or infinity. For many transition metal complexes, this essentially intramolecular approach is sufficient. For other systems, where the paramagnetic centers in solution are either transition metal complexes with a nonlabile coordination sphere, or stable organic radicals, the relaxation of the solvent nuclei is predominantly intermolecular in nature (the concept of outer sphere relaxation is also used), and a more refined approach to the modulation of the spin–spin distance by translational diffusion is required. The problem can be solved at different levels of sophistication. The earlier development has been reviewed by Kowalewski et al.[3] Among more recent contributions, one should mention the work of Bayburt and Sharp[22] dealing with the limiting case of ZFS dominating over the electron Zeeman interaction.

3 EXPERIMENTAL METHODS

Most experimental work on PRE is technically very simple. Basically, one measures the nuclear spin–lattice or spin–spin relaxation rate (the latter is commonly estimated from the linewidth) for ligand nuclei in the presence and in the absence of the paramagnetic reagent, and one obtains the PRE by subtraction. The experiments are often performed to yield the result as a function of concentration of the paramagnetic species, temperature, pressure, or magnetic field. Variable concentration work can provide information on complexation equilibria. Variable temperature measurements can be used to clarify the relationships between the relaxation and exchange processes. Variable pressure experiments provide mechanistic information on the exchange processes (see ***Kinetics at High Pressure***). Variable field measurements are PRE experiments *par excellence*, if one is interested in verifying theoretical models. The variable temperature and variable field measurements are discussed in the following two sections, and the experimental section is concluded by a brief presentation of

the paramagnetic relaxation effects in certain two-dimensional experiments.

3.1 Variable Temperature: Fast and Slow Exchange

As can be seen from equations (1)–(3), the relationship between relaxation and exchange is simplest for the spin–lattice relaxation, where one can easily define two limiting conditions: fast exchange, $\tau_M \ll T_{1M}$; and slow exchange, $\tau_M \gg T_{1M}$. Assume a simple case of a small complex in low viscosity solution, with T_{1M} dominated by the dipole–dipole interaction and with the reorientation of the complex determining τ_{c1} and τ_{c2}. For such a case, we are likely to have $(\tau_{c1}\ \omega_I)^2 \ll 1$ and $[\tau_{c2}\ (\omega_S \pm \omega_I)]^2 \ll 1$ and, as the rate of reorientation increases with increasing temperature, the nuclear relaxation rate decreases. The opposite is true for the ligand exchange—the rate is going to increase with increasing temperature. The measurements of the PRE in the slow exchange regime give directly the exchange lifetime and its temperature dependence/activation parameters. Measurements in the fast exchange limit provide the relaxation rate in the paramagnetic complex which, given a suitable theoretical model, can yield information on structural as well as dynamic parameters. The slow and fast exchange conditions can also be formulated for paramagnetic line broadening, a quantity commonly measured in variable temperature studies. An example of variable temperature ^{17}O line-broadening data, taken from the work of Hugi et al.,[23] is shown in Figure 2.

3.2 Variable Field: Physics of Relaxation

When one wishes to reach a deeper understanding of the details of the relaxation mechanism, a variable field [nuclear magnetic relaxation dispersion (NMRD)] study is a very powerful tool. Changing the magnetic field provides a direct way of measuring the frequency dependence of the relevant spectral densities.

Figure 2 gives an example of a variable field T_2 study. More commonly, the variable field studies are concentrated on T_1 measurements. Besides performing the regular inversion–recovery experiments at as many high-field spectrometers as possible, it is useful to apply field cycling experiments (see ***Field Cycling Experiments***) to obtain the PRE also at very low magnetic fields. An illustrative example of the use of NMRD over a very wide range of magnetic fields is provided by the water proton relaxation in an aqueous solution of Mn(II) ions. The first field cycling experiments for this system were reported as early as the 1960s.[24] More recent data, as a function of solution viscosity varied by means of adding glycerol, are shown in Figure 3, taken from Bertini et al.[25] The Mn(II) ion is characterized by very small ZFS and slow electron spin relaxation; the data in Figure 3 can be interpreted successfully using the SBM theory. The scalar relaxation is observed at low field, because the electron relaxation is slow. In pure water, the scalar contribution disperses at ω_I of about 0.1 MHz, where $(T_{2e}\omega_S)^2$ becomes larger than unity. At higher fields, the dipolar relaxation dominates, and the second dispersion at ω_I of about 10 MHz corresponds to the condition $\omega_S\tau_R = 1$. Upon increasing the glycerol content, the viscosity increases, and both τ_R and τ_v increase with it, which changes the NMRD profiles.

A different case is presented by the PRE of water protons in an aqueous solution of another divalent first-row transition metal ion, Ni(II). An NMRD curve for this system, taken from work by Kowalewski et al.,[26] is shown in Figure 4. Here, the field dependence of the PRE is much weaker. The origin of this different behavior is to be sought in the electron relaxation in Ni(II), much faster than in the case of Mn(II). In fact, the nuclear and electron relaxation in aqueous Ni(II) is beyond the validity region of the SBM theory, and the details of the analysis of the data in Figure 4 are still not

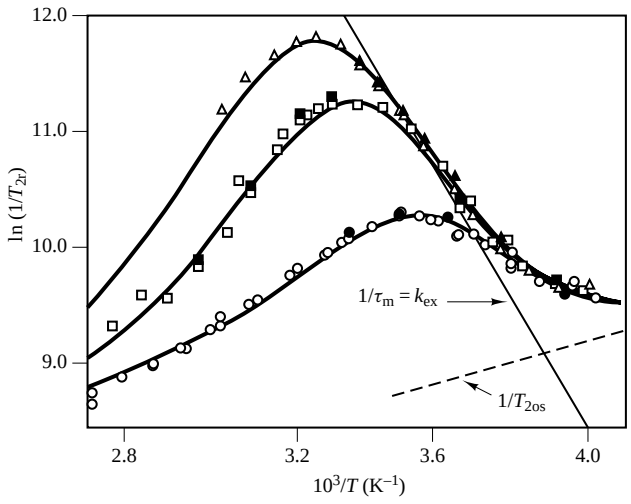

Figure 2 Oxygen-17 T_{2r}^{-1} in aqueous solution of a Ti(III) salt as a function of reciprocal temperature. Measurements were made at: (△, ▲) 8.4 T, (□, ■) 4.7 T, and (○, ●) 1.4 T. Open and filled symbols refer to different pH values. (Reproduced by permission of the American Chemical Society from A. D. Hugi, L. Helm, and A. E. Merbach, *Inorg. Chem.*, 1987, **26**, 1763)

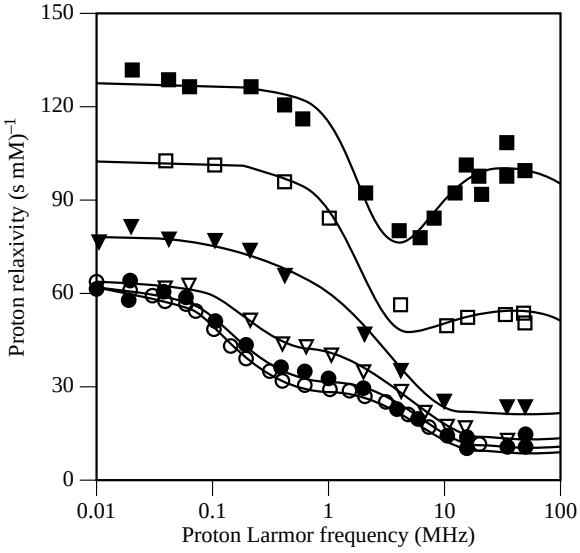

Figure 3 Water ^1H NMRD profiles of Mn(II) solutions in pure water (○) and with increasing amounts of deuterated glycerol [(●) 10%, (▼) 20%, (▼) 35%, (□) 55%, (■) 65%]. (Reproduced by permission of Academic Press from I. Bertini, F. Briganti, Z. C. Xia, and C. Luchinat, *J. Magn. Reson., Ser. A*, 1993, **101**, 198)

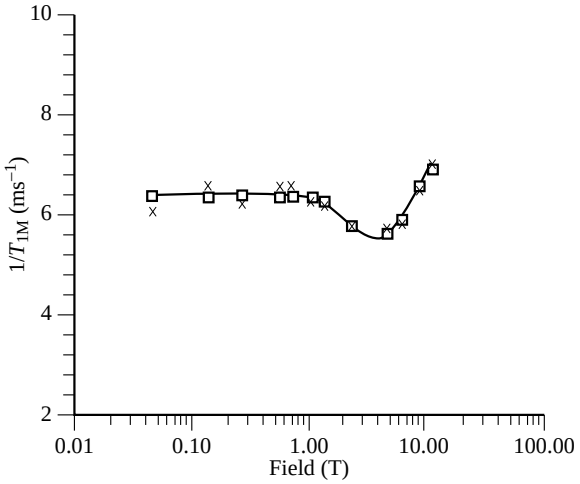

Figure 4 Water ^{1}H NMRD profile in aqueous Ni(II) solution [(×) experimental points, (□) slow-motion calculations, (—) SBM theory]. (Reproduced by permission of Academic Press from J. Kowalewski, T. Larsson, and P.-O. Westlund, *J. Magn. Reson.*, 1987, **74**, 56)

completely settled.[18,20,26] The flatness of the NMRD curve is caused by the rapid electron relaxation, which makes the scalar contribution negligible and reduces the efficiency of the dipole–dipole contribution. The weak increase of PRE at high field can be related to the onset of the dispersion of the electron relaxation.

The NMRD measurements are by no means limited to low-molecular-weight paramagnetic systems. A large number of data for metalloproteins in solutions can be found in the book by Banci et al.[2] and in a review by Koenig and Brown.[27]

3.3 Novel Experiments

The last few decades have seen a tremendous growth in the number of available NMR experiments. In many of these experiments the paramagnetic relaxation effects are a nuisance, and are carefully avoided by removing oxygen and paramagnetic impurities from the samples. In some cases, however, paramagnetic systems can be studied, and special features introduced into common two-dimensional techniques (NOESY and COSY) by the paramagnetic relaxation are worth mentioning.

The NOESY experiment suffers from the PRE in the sense that the cross-relaxation rates involving nuclei close to paramagnetic centers become much smaller than the leakage rates, which reduces the intensity of the cross peaks. As demonstrated, by Emerson and La Mar[28] among others, it is nevertheless possible to perform NOESY studies of the active site regions of fairly large paramagnetic proteins. The COSY experiments suffer from the PRE because of rapid relaxation and excessive signal cancellation when the linewidth is much larger than the J coupling. COSY cross peaks have nevertheless been reported in paramagnetic proteins. The results may, however, require a reevaluation in the light of the recent work by Bertini et al.,[29] who have demonstrated that the cross peaks may actually arise through relaxation-allowed coherence transfer, originating from cross correlation of the dipole–dipole and Curie relaxation mechanisms, rather than through J couplings.

4 RELATED ARTICLES

Chemical Exchange Effects on Spectra; Cobalt(II)- and Nickel(II)-Substituted Proteins; Contrast Agents in Whole Body Magnetic Resonance: An Overview; Contrast Agents in Magnetic Resonance: Operating Mechanisms; Copper Proteins; Electron–Nuclear Hyperfine Interactions; Electron–Nuclear Multiple Resonance Spectroscopy; Field Cycling Experiments; Iron—Sulfur Proteins; Kinetics at High Pressure; Liouville Equation of Motion; Myoglobin; Nonheme Iron Proteins; Relaxation Theory: Density Matrix Formulation; Transferrins.

5 REFERENCES

1. I. Bertini and C. Luchinat, *NMR of Paramagnetic Molecules in Biological Systems*, Benjamin/Cummings, Menlo Park, 1986.
2. L. Banci, I. Bertini, and C. Luchinat, *Nuclear and Electron Relaxation*, VCH, Weinheim, 1991.
3. J. Kowalewski, L. Nordenskiöld, N. Benetis, and P.-O. Westlund, *Progr. NMR Spectrosc.*, 1985, **17**, 141.
4. T. J. Swift and R. E. Connick, *J. Chem. Phys.*, 1962, **37**, 307.
5. Z. Luz and S. Meiboom, *J. Chem. Phys.*, 1964, **40**, 2686.
6. R. E. Connick and D. Fiat, *J. Chem. Phys.*, 1966, **44**, 4103.
7. J. Reuben, G. H. Reed, and M. Cohn, *J. Chem. Phys.*, 1970, **52**, 1617.
8. N. Benetis, J. Kowalewski, L. Nordenskiöld, H. Wennerström, and P.-O. Westlund, *Mol. Phys.*, 1983, **48**, 329.
9. D. Waysbort and G. Navon, *J. Chem. Phys.*, 1975, **62**, 1021; L. Nordenskiöld, A. Laaksonen, and J. Kowalewski, *J. Am. Chem. Soc.*, 1982, **104**, 379; N. Sahoo and T. P. Das, *J. Chem. Phys.*, 1989, **91**, 7740.
10. H. Sternlicht, *J. Chem. Phys.*, 1965, **42**, 2250.
11. A. Abragam and B. Bleaney, *Electron Paramagnetic Resonance of Transition Ions*, Clarendon, Oxford, 1970.
12. J. S. Griffith, *The Theory of Transition-Metal Ions*, Cambridge University, Cambridge, 1961.
13. L. T. Muus and P. W. Atkins (eds), *Electron Spin Relaxation in Liquids*, Plenum, New York, 1972.
14. N. Bloembergen and L. O. Morgan, *J. Chem. Phys.*, 1961, **34**, 842.
15. A. Carrington and G. R. Luckhurst, *Mol. Phys.*, 1964, **8**, 125; A. D. McLachlan, *Proc. R. Soc. London, Ser. A*, 1964, **280**, 271.
16. M. Rubinstein, A. Baram, and Z. Luz, *Mol. Phys.*, 1971, **20**, 67.
17. U. Lindner, *Ann. Phys. (Leipzig)*, 1965, **16**, 319 (Chem. Abstr., **64**: 14973c).
18. R. R. Sharp, *J. Chem. Phys.*, 1993, **98**, 912.
19. L.-P. Hwang and C.-Y. Ju, *J. Chem. Phys.*, 1985, **83**, 3775.
20. P.-O. Westlund, T. P. Larsson, and O. Teleman, *Mol. Phys.*, 1993, **78**, 1365.
21. M. Gueron, *J. Magn. Reson.*, 1975, **19**, 58; A. J. Vega and D. Fiat, *Mol. Phys.*, 1976, **31**, 347.
22. T. Bayburt and R. R. Sharp, *J. Chem. Phys.*, 1990, **92**, 5892.
23. A. D. Hugi, L. Helm, and A. E. Merbach, *Inorg. Chem.*, 1987, **26**, 1763.
24. R. Hausser and F. Noack, *Z. Phys.*, 1964, **182**, 93.
25. I. Bertini, F. Briganti, Z. C. Xia, and C. Luchinat, *J. Magn. Reson., Ser. A.*, 1993, **101**, 198.
26. J. Kowalewski, T. Larsson, and P.-O. Westlund, *J. Magn. Reson.*, 1987, **74**, 56.

27. S. H. Koenig and R. D. Brown, *Progr. NMR Spectrosc.*, 1990, **22**, 487.
28. S. D. Emerson and G. N. La Mar, *Biochemistry*, 1990, **29**, 1545.
29. I. Bertini, C. Luchinat, and D. Tarchi, *Chem. Phys. Lett.*, 1993, **203**, 445.

Biographical Sketch

Jozef Kowalewski. *b* 1947. B.Sc., 1969, Ph.D. (supervisors Ragnar Vestin and Björn Roos), 1975, Stockholm University. Postdoctoral work, Florida State University (with George Levy). Faculty, Stockholm University, 1977–present; Professor of Physical Chemistry, 1986–present. Approx. 100 publications. Research specialties: spin relaxation and molecular dynamics, cross-correlation effects, and paramagnetic systems.

Protein Dynamics from NMR Relaxation

Dennis A. Torchia

National Institutes of Health, Bethesda, MD, USA

1	Introduction	1
2	Theoretical Considerations	1
3	Pulse Sequences and Data Analysis	2
4	Two-Dimensional Heteronuclear Relaxation Studies of Proteins	4
5	Summary of ^{15}N Work and Prospects for ^{13}C Measurements	5
6	Related Articles	5
7	References	5

1 INTRODUCTION

Triple resonance (^{1}H, ^{13}C, ^{15}N) NMR techniques[1] have greatly reduced the effort required to obtain protein signal assignments as well as interproton distance and dihedral angle restraints.[2] This development has enhanced the prospects of obtaining information about protein structure. Such information is of widespread interest because it is fundamental for understanding protein function. However, proteins are not rigid bodies, but rather execute internal motions on a wide range of timescales.[3] In order to understand important aspects of protein function such as folding, molecular recognition, and enzyme action, detailed knowledge about protein dynamics is essential. At a more fundamental physical level, experimental information about the amplitudes and rates of internal motions in proteins can be used to check the predictions of molecular dynamics trajectories. Such tests of theoretical calculations should result in improved formulas for the potential functions used in the computations.

Protein structures in solution are derived using restraints obtained almost exclusively from proton J couplings and NOEs,[4,5] whereas information about the internal motions of proteins is derived most directly from measurements of spin relaxation rates of nuclei such as ^{15}N and ^{13}C (designated A spins herein).[6–8] Although ^{13}C relaxation studies of proteins were initiated over a decade ago,[8] these early studies were limited by the lack of sequential assignments as well as by the low resolution and sensitivity afforded by one-dimensional NMR spectra recorded with A spin detection. Fortunately, triple resonance experiments[1] provide sequential assignments of ^{15}N and ^{13}C nuclei along with those of protons. Hence, proton-detected two-dimensional heteronuclear relaxation experiments[9–16] are a means of measuring A spin relaxation rates with high sensitivity and resolution.

2 THEORETICAL CONSIDERATIONS

2.1 Relaxation Equations

Elegant general formalisms relating nuclear spin relaxation to molecular motion have been provided by Abragam[17] and Redfield.[18] In the case of a spin $I = \frac{1}{2}$ A nucleus such as ^{13}C or ^{15}N directly bonded to N protons (designated X), the AX_N dipolar interactions and A-spin chemical shift anisotropy, CSA, are the significant relaxation mechanisms. Provided that cross correlations can be neglected, the A-spin longitudinal relaxation time, T_1, transverse relaxation time, T_2, and A-{X} NOE, are given by[9,17]

$$1/NT_1 = d^2[J(\omega_A - \omega_X) + 3J(\omega_A) + 6J(\omega_A + \omega_X)] + c^2 J(\omega_A) \quad (1)$$

$$1/NT_2 = 0.5d^2[4J(0) + J(\omega_A - \omega_X) + 3J(\omega_A) + 6J(\omega_X) + 6J(\omega_A + \omega_X)] + \tfrac{1}{6}c^2[4J(0) + 3J(\omega_A)] \quad (2)$$

$$\mathrm{NOE} = 1 + (\gamma_A/\gamma_X)d^2[6J(\omega_A + \omega_X) + J(\omega_A - \omega_X)]NT_1 \quad (3)$$

where ω_i is the Larmor frequency of spin i, $J(\omega)$ is the spectral density function, γ_i is the gyromagnetic ratio of spin i, $d^2 = 0.1[(\mu_0/4\pi)\gamma_A\gamma_X h/(2\pi\langle 1/r_{AX}^3\rangle)]^2$, $c^2 = \frac{2}{15}[\omega_A(\sigma_{vert} - \sigma_\perp)]^2$, h is Planck's constant, r_{AX} is the AX bond length (0.102 nm for NH and 0.109 nm for CH), and $\sigma_\parallel$ and $\sigma_\perp$ are principal components of the axially symmetric CSA tensor. For the amide ^{15}N, the CSA is about 160 ppm,[19] and at 11.7 T contributes nearly 20% to the ^{15}N relaxation rate. In contrast, the CSA contribution is much smaller in the case of aliphatic carbons. For example, the CSAs of rotating methyl and backbone α-carbons are about 25 and 35 ppm respectively, and, at 11.7 T, contribute less than 2.5% to ^{13}C spin relaxation.

As noted above, equations (1)–(3) are valid only when the effects of cross correlations are negligible. Although rf pulses can eliminate cross correlation of AX dipolar A-spin CSA interactions,[11] such pulses cannot completely eliminate the effects of dipolar cross correlations in AX_2 and AX_3 spin systems.[20] In general, A-spin magnetization relaxes in multiexponential fashion in AX_2 and AX_3 spin systems, and equations (1) and (2) yield the initial decay rates of longitudinal and transverse magnetization, respectively.[20]

2.2 The Model-Free Formulation of the Spectral Density Function

In equations (1)–(3), the spectral density function contains the information about molecular motion. However, if experiments are recorded at a single external field, only three experimental parameters are measured, and hence the data are insufficient to determine the spectral density function at five frequencies. In principle, spectral densities at 11 frequencies can be determined from the set of 12 A-spin T_1, T_2, and NOEs measured at four magnetic fields: $\gamma_A\omega$, $\gamma_H\omega$, $(\gamma_H \pm \gamma_A)\omega$, where ω is the A-spin Larmor frequency at the lowest

field employed. However, the large value of γ_H/γ_A, requires that one data set be obtained at low field (<3.5 T) where sensitivity and resolution are poor. Spectral densities have been determined for eglin c from spectra recorded at a single high field by measuring an expanded set of relaxation parameters that include the relaxation of certain two-spin coherences and the selective proton longitudinal relaxation.[16] A potential limitation of this approach is that the relaxation of the two-spin coherences contain a large contribution from the selective proton relaxation. This contribution must be subtracted from the two-spin relaxation in order to obtain reliable values of $J(\omega_i)$.

An alternative to direct determination of the spectral density functions is afforded by the model-free approach.[6,7] According to this formalism, the spectral density function is expressed in terms of three motional parameters according to

$$J(\omega) = S^2\tau_m/(1+\omega^2\tau_m^2) + (1-S^2)\tau/(1+\omega^2\tau^2) \quad (4)$$

where S is the generalized order parameter, τ_m is the overall correlation time, and $1/\tau = 1/\tau_m + 1/\tau_e$, where τ_e is an effective correlation time characterizing the internal motions of the protein. Equation (4) is an exact expression provided that (a) the overall motion of the protein is isotropic and is not correlated with the internal motions, and (b) all correlation times associated with the internal motions are in the extreme narrowing limit. When internal motions take place on two significantly different timescales, a useful, approximate, generalization of equation (4) is

$$J(\omega) = S^2\tau_m/(1+\omega^2\tau_m^2) + (1-S_f^2)\tau_1/(1+\omega^2\tau_1^2) + S_f^2(1-S_s^2)\tau_2/(1+\omega^2\tau_2^2) \quad (5)$$

where S_f, τ_1 and S_s, τ_2 are order parameters and effective correlation times associated with the 'fast' and 'slow' (outside the extreme narrowing limit) internal motions, and $S = S_fS_s$.[21]

The analysis of relaxation data using the model-free approach yields the overall correlation time of the protein as well as values of S^2 and τ_e for individual amino acid residues in the protein. Because τ_e is, in general, a complex combination of geometric factors and internal correlation times it cannot be interpreted in a quantitative manner. However, its determination does provide an estimate of the timescale of the internal motion at a particular site in the protein. In contrast, the order parameter is precisely related to the amplitude of the internal motion.[6,7] When the interaction responsible for relaxation is axially symmetric, with the symmetry axis along the AX bond, (rigorously true for the AX dipolar interaction and approximately so for the ^{15}N amide CSA interaction) S^2 is given by

$$S^2 = \int d\Omega_1\, p_{eq}(\Omega_1) \int d\Omega_2\, p_{eq}(\Omega_2) P_2(\cos\theta_{12}) \quad (6)$$

where $p_{eq}(\Omega)\, d\Omega$ is the equilibrium probability that the unit vector along the AX bond axis has orientation $d\Omega$, $\Omega = (\theta, \phi)$, in a coordinate system fixed in the protein, θ_{12} is the angle between two such vectors, and $P_2(x) = (3x^2 - 1)/2$. The advantage of the model-free approach derives from the fact that values of S^2 are obtained for numerous sites in the protein without the need to assume an explicit model of the internal motion. Using equation (6) values of S^2 can be calculated for any model of interest. Then, it can be determined if the model does indeed yield order parameters in agreement with experiment, and if the order parameters correspond to physically reasonable values of angular amplitudes of internal motion.

A useful and popular model of internal motion is diffusion in a cone, in which the AX bond axis is thought to diffuse freely in the angular region $0 \le \theta \le \theta_0$, $0 \le \phi \le 360^\circ$, where θ and ϕ are spherical, polar angles. For this model,

$$S^2 = [0.5\cos\theta_0\,(1+\cos\theta_0)]^2 \quad (7)$$

so that the cone semiangle can be derived from the order parameter. Equation (7) reveals several general features about the relationship between the amplitude of angular reorientation and S^2. S^2 equals unity when θ_0 is zero, diminishes as θ_0 increases, and vanishes when $\theta_0 = 180^\circ$, i.e., isotropic motion. Note however that S^2 is not a monotonic function of θ_0, and vanishes when motion is not isotropic, $\theta_0 = 90^\circ$. In general, S^2 is large for a small amplitude motion, but the converse need not be true; for example, S^2 equals unity if the AX bond reorients by a two-site jump of 180°. Analytical expressions for S^2 are available for other plausible models of internal motion.[6,7]

3 PULSE SEQUENCES AND DATA ANALYSIS

Two-dimensional heteronuclear pulse sequences designed to measure A-spin T_1, T_2, and NOE values in AX spin systems (A = ^{13}C or ^{15}N, X = ^{1}H) are depicted in Figure 1.[9,14] In order to maximize sensitivity, A-spin magnetization is derived from proton magnetization using an INEPT scheme in the T_1 and T_2 pulse sequences, and proton detection is employed in all three experiments. The application of 180° proton pulses during the relaxation delay period, T, suppresses cross correlation of AX dipolar and A-spin CSA interactions. The NOE experiment is the least sensitive of the three measurements because one must record spectra starting with equilibrium A-spin magnetization (in the absence and presence of proton saturation), and it is necessary to wait a long period between scans ($\ge 3T_L$, where T_L is the larger of either the proton or the A-spin T_1 value) to ensure that the A-spin magnetization attains equilibrium. Also, when the spectrum is recorded in H_2O without a NOE, water saturation must be achieved quickly in order to minimize transfer of saturation from water to protein protons. Recently it has been shown that one can avoid water saturation in the NOE experiment using pulsed field gradients and water flip-back pulses.[22]

Pulse sequences for measuring methyl ^{13}C relaxation parameters, while similar to those depicted in Figure 1, differ from them in several significant respects.[12,13,23] First, one must use magic angle delays in INEPT- or DEPT-type transfer steps in order to avoid complications that arise from dipolar cross correlations[12] and to ensure that carbon magnetization in $\frac{3}{2}$ and $\frac{1}{2}$ proton manifolds is faithfully transferred back to protons[13] in the reverse INEPT or DEPT portions of the sequences. Second, a sequence of 125° proton pulses should be applied during the CPMG period in order to eliminate dipolar cross correlations from ^{13}C transverse relaxation within the $\frac{3}{2}$ manifold. Third, the final delays, Δ, in the reverse INEPT portion of the sequence should be set to a short value, about

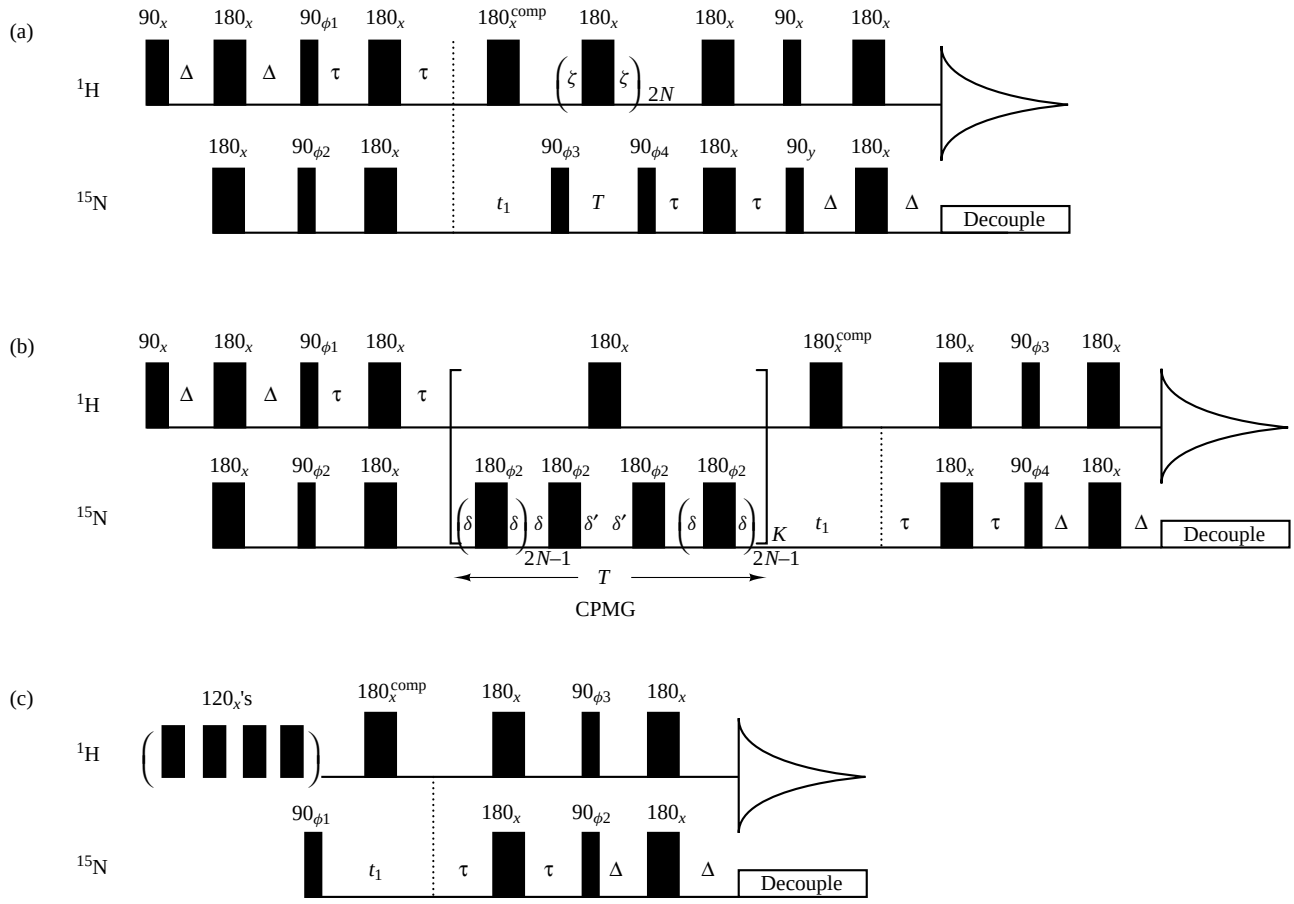

Figure 1 Pulse sequences used to measure A-spin (a) T_1, (b) T_2, and (c) A{-X} NOE in AX spin systems. The sequences are discussed in Kay et al.[14]

$1/[8J(\mathrm{C, H})]$, to minimize the effect of rapid proton relaxation upon the measurement of the ^{13}C relaxation rates. Finally, because the methyl ^{13}C NOE is large, there is no sensitivity loss in saturating the protons and initiating the T_1 and T_2 experiments with ^{13}C magnetization. Sequences for measuring methyl carbon relaxation have been discussed in detail,[12,13,23] and Kay et al.[13] have discussed the errors in T_2 measurements that are caused by (a) missetting the magic angle, and (b) rapid relaxation of proton magnetization in the $\frac{3}{2}$ manifold, when INEPT- and DEPT-type sequences are recorded without applying 125° pulses during the CPMG period. Application of 125° pulses, during the CPMG period, decreases (increases) the error in the T_2 measurement in the INEPT (DEPT)-type experiment caused by magic angle misset, and increases (decreases) error in the INEPT (DEPT) experiment caused by rapid proton relaxation.

Although the pulse schemes used to measure methyl relaxation minimize the effects of dipolar cross correlation, rf pulses cannot mix the $\frac{3}{2}$ and $\frac{1}{2}$ proton manifolds and therefore cannot completely eliminate such effects. Fortunately, dipolar cross correlations make very small contributions to T_1 and NOE of rapidly rotating methyl carbons in proteins in the 5–40 kDa molecular weight range.[24] Hence, equations (1) and (3) can be applied in the analysis of methyl carbon relaxation in proteins. However, the effects of dipolar cross correlations are significant in the case of transverse relaxation, and equation (2) provides the rate of the initial decay of the methyl carbon transverse magnetization. Finally, we note that chemical exchange often contributes to T_2 relaxation in proteins. Because accurate T_2 values are obtained by the CPMG method only when $\delta \ll 1/[2J(\mathrm{A, X})]$,[9,14,16] small δ values are employed in the CPMG sequence. For this reason, and because the maximum spin lock field that can be safely applied to protein solutions is about 10 kHz, chemical exchange often affects T_2 and $T_{1\rho}$ in a similar way. Therefore, even in the presence of chemical exchange, T_2 may be equal to $T_{1\rho}$. A significant increase in $1/T_2$, as the external field increases, is strong evidence that fast chemical exchange contributes to transverse relaxation.

In view of the large amount of data that is required to determine residue-specific relaxation parameters in proteins, surface fitting routines are an extremely useful means of determining signal positions and intensities in individual two-dimensional spectra. The derived signal intensities are fit to an equation of the form $y = A\exp(-t/T_i)$, $i = 1$, 2, using conjugate gradient minimization techniques,[25] and standard errors in A and T_i are obtained using a Monte Carlo approach.[26] The NOE values are determined by measuring the ratio of signal intensities in the presence and absence of proton saturation. The standard error in the NOE measurement is derived from the rms noise measured in a signal-free region of the spectrum.

Although the model-free approach can be applied when the overall motion of the protein is anisotropic,[6,7,27] most globular

proteins have approximately spherical shapes, and it is usually assumed that the overall motion of the protein is characterized by a single overall correlation time, τ_m. In the framework of the model-free formalism, each NMR parameter is then related to three parameters: the global parameter τ_m, and two residue-specific internal motion parameters, S^2 and τ_e. A general approach to determine the three model-free parameters consists of minimizing the function[25,28,29]

$$\chi^2 = \sum_i \{[(T_{1i}^{obs} - T_{1i}^{cal})/\sigma_{1i}]^2 + [(T_{2i}^{obs} - T_{2i}^{cal})/\sigma_{2i}]^2 + [(NOE_i^{obs} - NOE_i^{cal})/\sigma_{NOEi}]^2\} \quad (8)$$

where the summation is over the residues in the protein, the superscripts indicate observed and calculated parameters, and σ is the standard error in the measured parameter. A single value of τ_m is assigned to all residues in the protein and then the set of $\{S_i^2, \tau_{ei}\}$ values that minimize χ^2 is found using conjugate gradient minimization.[25] This process is repeated, incrementing τ_m until the minimum value of χ^2 is attained. Then, several hundred synthetic data sets are used in a Monte Carlo approach[23,26,29] to determine the uncertainties in the model-free parameters.

In analyzing relaxation data, residues that have unusually small T_2 values should be noted, because a small T_2 suggests that chemical exchange contributes to transverse relaxation. In contrast, unusually large T_2 values indicate the presence of large-amplitude, rapid internal motions that may not be well fit by a single internal correlation time. It is probably best to exclude residues with unusual T_2 values from the initial determination of τ_m using equation (8). Once the value of τ_m is determined, residues having anomalous T_2 values can be analyzed to see if an exchange term is required to account for a small T_2 or if an analysis involving more than one internal correlation time is required to account for relaxation data of residues having large T_2 values. An approach has been presented,[29] based upon statistical criteria, for systematically adding parameters to analyze relaxation data within the framework of the model-free formalism.

4 TWO-DIMENSIONAL HETERONUCLEAR RELAXATION STUDIES OF PROTEINS

4.1 Staphylococcal Nuclease (SNase)

Staphylococcal nuclease is a 17 kDa phosphodiesterase that efficiently hydrolyzes strands of both DNA and RNA. Relaxation studies of a uniformly ^{15}N-labeled protein yielded an overall correlation time of 8.3–8.5 ns,[30] while ^{13}C relaxation measurements[31] of samples labeled at alanine (Ala) C-α sites yielded a somewhat larger value of τ_m in the range 9.2–9.5 ns. The larger value of τ_m, obtained from the carbon relaxation data has been ascribed to the fact that the viscosity of the solvent (D_2O) is about 20% greater than the solvent (H_2O) used in the ^{15}N study. The residue-specific order parameters of the Ala ^{15}N amide and C-α sites were in good agreement. Moreover, values of S^2 were in the range 0.8–0.95 for nearly all amino acids in the protein. This result showed that internal motion of the SNase backbone is limited to rapid small-amplitude motions. Exceptions to this statement are (a) highly flexible residues in the N- and C-termini which have large T_2 values, and (b) several residues in the functionally important Ω loop which have unusually small T_2 values. In the X-ray structure of SNase[32] residues in the Ω loop have weak electron density and large B factors. In solution, the loop is highly flexible, as evidenced by the broad lines and missing amide signals of residues in, or adjacent to, the loop. Although the Ω loop is flexible, it has a significant role in catalysis, as constructs of SNase lacking the loop have virtually the same structure as the parent molecule, but significantly lower levels of activity.

Although the side chains of all 11 leucine (Leu) residues in SNase are in well-structured regions of the protein, the values of S^2 of the Leu methyl sites fall into two distinct classes.[23,30] In the presence of stabilizing ligands, thymidine 3′,5′-bisphosphate and Ca^{2+}, four residues have values of S^2, approx. 0.4–0.5, that are substantially less than the values of S^2, approx. 0.8–0.9, of six of the remaining residues. This result indicates that there is a significant range in the flexibility of the large, hydrophobic side chains in SNase. Furthermore, it was found that the flexibility of the Leu methyl groups was sensitive to ligand binding, with side chains in the neighborhood of the ligand binding sites increasing in flexibility in the absence of the ligands.

4.2 Calmodulin and Calbindin D_{9k}

Calmodulin is a 148-residue protein that couples fluctuations in Ca^{2+} concentration to cellular activity. In the crystalline state the protein has the shape of a dumbbell in which two globular domains are connected by a continuous 26-residue α-helix. However, a ^{15}N relaxation study has shown that residues in the center of this helix have small order parameters, in the 0.5–0.6 range.[33] In addition, the relaxation data showed that the N- and C-terminal globular domains tumble nearly isotropically with slightly different correlation times. These results are strong evidence that the central helix is flexible in solution, a result that structural studies of the calmodulin/M19 complex have confirmed.[34]

Calbindin D_{9k} is a 75-residue member of the calmodulin superfamily of calcium-binding proteins, containing two calcium binding sites. A careful comparison of ^{15}N relaxation measurements[35] made on the apo protein, the protein with Ca^{2+} in binding site II, and the protein with ions in both sites I and II, has shown that ion binding has very small effects on amide order parameters, with the notable exception of residues in binding site II. The order parameters of these residues increase from 0.6 to 0.85 when an ion is bound in site II. In contrast, residues in site I have large order parameters, S^2 approx. 0.8–0.85, in the absence and presence of bound ions. The asymmetry in the dynamic behavior of the two Ca^{2+} binding sites may be related to the fact that site I is not a typical EF hand (Ca^{2+}-binding loop), and is being characterized by further work on protein samples, half saturated with Ca^{2+}.

4.3 Interleukins, IL-1β, IL-4, and IL-8

High-resolution crystal and solution structures, as well as backbone amide order parameters are available[36] for IL-1β, IL-4, and IL-8. Analysis of these extensive data has

shown that amide nitrogen order parameters correlate with the inverse of (a) rms deviation (rmsd) values of the amide nitrogen coordinates, derived from the NMR structures, and (b) the amide nitrogen crystallographic *B* factors. While the correlations show significant scatter, this is to be expected because internal motions on a timescale slower than τ_m will not usually affect S^2 but will affect the other two parameters. Furthermore, crystal contacts may hinder motions that occur in solution. In general, it was found that amide nitrogen sites, having small *B* factors and small rmsd values in NMR structures, are strongly correlated with amide nitrogen sites that have large values of S^2.

4.4 Bovine Pancreatic Trypsin Inhibitor, BPTI

Bovine pancreatic trypsin inhibitor (BPTI) was one of the first proteins whose internal dynamics were characterized by NMR lineshape and relaxation studies. More recently, measurement of transverse relaxation rates using natural abundance two-dimensional $^1H-^{13}C$ heteronuclear techniques has provided evidence for slow internal motions involving cysteine (Cys) 14 and Cys-38.[10] A thorough investigation of this process in wild-type BPTI and in a mutant protein, BPTI(G36S), showed that the protein is an equilibrium mixture of interconverting isomers of the Cys-14–Cys-38 disulfide bond.[37] The rate of interconversion of the two isomers, as determined by measurements of the ^{15}N $T_{1\rho}$ of Cys-38 and of Arg-39, as a function of the spin lock field,[38] was in reasonable agreement with the rate of conformational exchange determined independently using two-spin-order exchange experiments and from measurements of chemical exchange line broadening. This work also demonstrates that, because of the inherent limited sensitivity of protein NMR spectra, slow dynamic processes in proteins are difficult to observe and may be more common than has been supposed.

5 SUMMARY OF ^{15}N WORK AND PROSPECTS FOR ^{13}C MEASUREMENTS

Unfortunately, space does not permit even brief individual reviews of the substantial number of other interesting proteins that have been studied using ^{15}N relaxation measurements. However, a few general comments about backbone mobility, based upon the ^{15}N relaxation work, can be made. Internal motions of the amide backbone are small in amplitude, with order parameters typically greater than 0.8 for amino acids in regions of regular secondary structure. In contrast, residues in either the terminal regions of the protein sequence or in small external loops often exhibit large amplitude, $S^2 < 0.6$, rapid internal motions, with $\tau_e \ll \tau_m$. Much slower motions, on the chemical shift timescale, are most commonly seen for large loops or segments near the protein surface, that often contain amino acid residues implicated in the function of the molecule.

While the ^{15}N studies have provided the first comprehensive view of internal dynamics of the protein backbone in solution, internal motions of protein side chains are likely to be considerably more varied and interesting. While the use of specifically ^{13}C-labeled samples is a means of studying such motions, it would be much more efficient to use uniformly ^{13}C-labeled samples, provided that the pulse sequences can be developed that suppress effects of carbon–carbon coupling. Labeling a protein with ^{13}C at alternate carbon sites has also been proposed[39] to achieve this goal. Elimination of the effects of dipolar cross correlation ^{13}C relaxation measurements is also highly desirable. This has been done for glycine (Gly) C-α H_2 sites in *Escherichia coli* thioredoxin by preparing a sample labeled with 50% [U-^2H, 2-^{13}C]Gly,[39] and recording spectra using pulse sequences that (a) select for Gly α-carbons bonded to a single proton, and (b) decouple deuterons. Deuteration also has the advantage that both carbon and proton T_2 values are significantly larger than in the protonated protein. Although it will require considerably more effort to measure relaxation parameters of protein uniformly labeled with ^{13}C than with ^{15}N, the wealth of information about protein side-chain motions that will be provided by the ^{13}C experiments should fully reward the effort required.

6 RELATED ARTICLES

Motional Effects on Protein Structure: Acyl Carriers; Protein Dynamics from Solid State NMR; Selective Relaxation Techniques in Biological NMR.

7 REFERENCES

1. A. Bax and S. Grzesiek, *Acc. Chem. Res.*, 1993, **26**, 131.
2. S. J. Archer, V. K. Vinson, T. D. Pollard, and D. A. Torchia, *Biochemistry*, 1993, **32**, 6680.
3. M. Karplus and J. A. McCammon, *Sci. Am.*, 1986, **254**, 42.
4. K. Wüthrich, *NMR of Proteins and Nucleic Acids*, Wiley, New York, 1986.
5. G. M. Clore and A. M. Gronenborn, *Crit. Rev. Biochem. Mol. Biol.*, 1989, **24**, 479.
6. G. Lipari and A. Szabo, *J. Am. Chem. Soc.*, 1982, **104**, 4546.
7. G. Lipari and A. Szabo, *J. Am. Chem. Soc.*, 1982, **104**, 4559.
8. R. E. London, *Methods Enzymol.*, 1989, **176**, 358.
9. L. E. Kay, D. A. Torchia, and A. Bax, *Biochemistry*, 1989, **28**, 8972.
10. N. R. Nirmala and G. Wagner, *J. Magn. Reson.*, 1989, **82**, 659.
11. J. Boyd, U. Hommel, and I. D. Campbell, *J. Chem. Phys.*, 1990, **175**, 477.
12. A. G. Palmer, III, P. E. Wright, and M. Rance, *Chem. Phys. Lett.*, 1991, **185**, 41.
13. L. E. Kay, T. E. Bull, L. K. Nicholson, C. Griesinger, H. Schwalbe, A. Bax, and D. A. Torchia, *J. Magn. Reson.*, 1992, **100**, 538.
14. L. E. Kay, L. K. Nicholson, F. Delaglio, A. Bax, and D. A. Torchia, *J. Magn. Reson.*, 1992, **97**, 359.
15. A. G. Palmer, N. J. Skelton, W. J. Chazin, P. E. Wright, and M. Rance, *Mol. Phys.*, 1992, **75**, 699.
16. J. W. Peng and G. Wagner, *J. Magn. Reson.*, 1992, **98**, 308.
17. A. Abragam, *The Principles of Nuclear Magnetism*, Oxford University Press, Oxford, 1961.
18. A. G. Redfield, *Adv. Magn. Reson.*, 1965, **1**, 1.
19. Y. Hiyama, C. H. Niu, J. V. Silverton, A. Bavoso, and D. A. Torchia, *J. Am. Chem. Soc.*, 1988, **110**, 2378.
20. L. G. Werbelow and D. M. Grant, *Adv. Magn. Reson.*, 1977, **9**, 189.

21. G. M. Clore, A. Szabo, A. Bax, L. E. Kay, P. C. Driscoll, and A. M. Gronenborn, *J. Am. Chem. Soc.*, 1990, **112**, 4989.
22. S. Grzesiek and A. Bax, *J. Am. Chem. Soc.*, 1993, **115**, 12 593.
23. L. K. Nicholson, L. E. Kay, D. M. Baldisseri, J. Arango, P. E. Young, A. Bax, and D. A. Torchia, *Biochemistry*, 1992, **31**, 5253.
24. L. E. Kay and D. A. Torchia, *J. Magn. Reson.*, 1991, **95**, 536.
25. W. H. Press, B. P. Flannery, S. A. Teukolsky, and W. T. Vetterling, *Numerical Recipes in C*, Cambridge University Press, Cambridge, 1988.
26. U. Kamath and J. W. Shriver, *J. Biol. Chem.*, 1989, **264**, 5586.
27. D. M. Schneider, M. J. Dellwo, and A. J. Wand, *Biochemistry*, 1992, **31**, 3645.
28. M. J. Dellwo and A. J. Wand, *J. Am. Chem. Soc.*, 1989, **111**, 4571. 4578.
29. M. J. Stone, W. J. Fairbrother, A. G. Palmer, III, J. Reizer, M. H. Saier, Jr., and P. E. Wright, *Biochemistry*, 1992, **31**, 4394.
30. D. A. Torchia, L. K. Nicholson, H. B. R. Cole, and L. E. Kay, in *NMR of Proteins*, eds. G. M. Clore and A. M. Gronenborn, Macmillan, London, 1993, pp. 190–219.
31. L. K. Nicholson, L. E. Kay, and D. A. Torchia, in *NMR Spectroscopy and its Application to Biomedical Research*, ed. S. K. Sarkar, Elsevier, Amsterdam, 1995.
32. P. J. Loll and E. E. Lattman, *Proteins Struct. Funct. Genet.*, 1989, **5**, 183.
33. G. Barbato, M. Ikura, L. E. Kay, R. W. Pastor, and A. Bax, *Biochemistry*, 1992, **31**, 5269.
34. M. Ikura, G. M. Clore, A. M. Gronenborn, G. Zhu, C. B. Klee, and A. Bax, *Science*, 1992, **256**, 632.
35. J. Kördel, N. J. Skelton, M. Akke, A. G. Palmer, III, and W. J. Chazin, *Biochemistry*, 1992, **31**, 4856.
36. R. Powers, G. M. Clore, D. S. Garrett, and A. M. Gronenborn, *J. Magn. Reson., Ser. B*, 1993, **101**, 325.
37. G. Otting, E. Liepinsh, and K. Wüthrich, *Biochemistry*, 1993, **32**, 3571.
38. T. Szyperski, P. Luginbühl, G. Otting, P. Guntert, and K. Wüthrich, *J. Biomol. NMR*, 1993, **3**, 151.
39. D. M. Kushlan and D. M. LeMaster, *J. Am. Chem. Soc.*, 1993, **115**, 11026.

Biographical Sketch

Dennis A. Torchia. *b* 1939. B.A., 1961, physics, University of California, Ph.D., 1967, Physics, Yale University. Postdoctoral fellow, Harvard Medical School, 1967–1969 with Elkan Blout; Bell Laboratories, 1969–1971, with Frank Bovey. Staff member, National Bureau of Standards, 1971–1974. Dental Institute, NIH, 1974–present. Currently, Chief, Protein Biophysics Section, Bone Research Branch. Approx. 125 publications. Current research specialty: application of solution state heteronuclear NMR techniques to study protein structure and dynamics.

Protein Structures: Relaxation Matrix Refinement

Alexandre M. J. J. Bonvin, Rolf Boelens and Robert Kaptein

Utrecht University, Utrecht, The Netherlands

1	Introduction	1
2	The Nuclear Overhauser Effect	1
3	Structure Calculations	5
4	Quality of the Structures	7
5	Application: The ARC Repressor	7
6	Conclusion	9
7	Related Articles	9
8	References	9

1 INTRODUCTION

In the last decade, NMR spectroscopy has become an important alternative to X-ray crystallography for the structural studies of molecules of biological interest. The principal advantage of NMR is that it allows the study of biomolecules in solution, thus closer to their real physiological environment. The method is limited, however, to biomolecules of relatively small size due to limitations in spectral resolution and line-broadening effects. The upper limit is presently situated around molecular weights of 30 kDa. Knowledge of three-dimensional (3D) structures might lead, for example, to a better understanding of structure–function relationships or recognition processes. For this purpose, accurate structures are required and, as we shall see, the use of so-called relaxation matrix approaches provides a means of improving the accuracy of the method.

The process of structure determination based on NMR data can be divided into four stages:

1. assignments of the proton resonances,
2. determination of structural constraints from NOE and J coupling data,
3. generation of structures,
4. refinement of these structures.

The first and laborious task of assigning proton resonances is still the main bottleneck of the structure determination, but progress is being made in this area by the development of new multidimensional NMR techniques [3D and four-dimensional (4D)][1–6] and the use of labeled samples (^{15}N, ^{13}C). Computational approaches are also being developed toward an automatic assignment of the NMR spectra (see ***Analysis of Spectra: Automatic Methods***). We will not treat this aspect of the problem here, but concentrate on the last three stages involving the determination of structural constraints (distances, dihedral angles) and the generation and refinement of the structures.

Structure determination by NMR is based primarily on the nuclear Overhauser effect (NOE)[7] (see ***Nuclear Overhauser Effect***). Its origin is dipolar cross relaxation between protons, which is a function of distances and molecular motions. Because of the approximate r^{-6} dependence of the NOEs on the interproton distances, these can only be measured between protons relatively close in space ($<$ about 0.5 nm). NOEs are generally transformed into distance constraints which are then used, together with dihedral angle constraints obtained from J coupling data, for the generation of structures using Distance Geometry (DG)[8] (see ***Distance Geometry***) or Simulated Annealing (SA) techniques.[9,10] These structures are then usually refined with a combination of restrained Energy Minimization and Molecular Dynamics (MD) simulations.[11] Genetic algorithms[12] and heuristic methods based on Kalman filter techniques[13] can also be used for this purpose. Several approaches have been proposed for the interpretation of NOEs in terms of distances. The simplest one classifies the NOEs into strong, medium, and weak peaks and attributes corresponding distance ranges to these three categories. However, more accurate distances can be obtained from relaxation matrix calculations, which take into account all indirect magnetization transfers ('spin diffusion').[14–23] A more direct method for refinement was proposed by Yip and Case,[24] in which NOE intensities are directly used as structural constraints, thus avoiding the transformation into distances. In this method, the structures are directly refined against experimental NMR data by comparison of theoretical and experimental NOE intensities.

In addition to NOEs and J couplings, chemical shifts can also provide structural information on biomolecules. Recent developments that permit the prediction of ^{1}H, ^{13}C, ^{15}N, and ^{19}F chemical shifts should open new avenues to the structure refinement of proteins[25–29] (see ***Amino Acids, Peptides and Proteins: Chemical Shifts***; ***Chemical Shifts in Biochemical Systems***).

In this review, we will first discuss the underlying theory of the NOE, including a description of intramolecular motions. The use of NOEs as structural constraints, indirectly by conversion into distances or directly by comparison of experimental and theoretical intensities, will be presented together with the most common methods used to generate and refine structures. This will be illustrated with results from our laboratory for the structure determination and refinement of the Arc repressor of phage P22, a dimeric DNA-binding protein (2×53 residues).

2 THE NUCLEAR OVERHAUSER EFFECT

2.1 Relaxation Matrix Theory

Multispin relaxation in a biomolecule in solution can be approximately described by the generalized Bloch equations. The evolution of the longitudinal magnetization components in a system of N spins is governed by a set of coupled differential equations of the form[30]

$$\frac{\mathrm{d}}{\mathrm{d}t}\Delta \boldsymbol{M}(t) = -\mathbf{R}\Delta \boldsymbol{M}(t) \qquad (1)$$

where the vector $\Delta \boldsymbol{M}(t)$ comprises the deviations from thermal equilibrium for all spins i

$$\Delta M(t)_i = [M_z(t) - M_0]_i \qquad (2)$$

and **R** is the relaxation matrix. It comprises contributions from cross relaxation and from external relaxation. For a system of dipolar-coupled spins, neglecting cross correlation, **R** has the dimension of the number of spins N in the systems. Since the dipolar interaction is a function of time, the relaxation rates are intimately connected with the molecular motion. The elements of **R** can be expressed as[7,30]

$$R_{ii} = \rho_{ii} = K \sum_{j \neq i} [J_{ij}^0(0) + 3J_{ij}^1(\omega_0) + 6J_{ij}^2(2\omega_0)] + R_{\text{leak}}$$

$$R_{ij} = \sigma_{ij} = K[-J_{ij}^0(0) + 6J_{ij}^2(2\omega_0)] \tag{3}$$

where ω_0 is the Larmor frequency and $K = (2\pi/5)\gamma^4\hbar^2$; ρ_{ii} is the auto relaxation rate, with R_{leak} as an additional term to account for all nondipolar relaxation mechanisms, and σ_{ij} is the cross-relaxation rate between spins i and j. ${J_{ij}}^m(\omega)$ denotes the spectral densities at multiple values of the spin Larmor frequency [$(m \times \omega_0)$ with $m = 0, 1, 2$]. Cross relaxation is normally measured by observing intensity changes upon saturation or inversion of spins. Two-dimensional (2D) NMR techniques have been developed to investigate the resulting NOEs[31] (see ***Nuclear Overhauser Effect***; ***NOESY***). The integrated intensities I_{ij} in a 2D NOE spectrum recorded with mixing time τ_m, are given by the matrix equation[31]

$$\mathbf{I}(\tau_m) = \exp(-\mathbf{R}\tau_m)\boldsymbol{M}(0) = \mathbf{A}\boldsymbol{M}(0) \tag{4}$$

which is the formal solution of the differential equation (1) where $\boldsymbol{M}(0)$ specifies the starting conditions. This defines the exponential matrix of normalized NOE intensities **A**,

$$\mathbf{A} = \exp(-\mathbf{R}\tau_m) \tag{5}$$

that will be referred to as 'the NOE matrix'.

The spectral densities ${J_{ij}}^m(\omega)$ in the definitions of the relaxation rates ρ_{ii} and σ_{ij} are cosine Fourier transforms

$$J_{ij}^m(\omega) = \int_0^\infty C_{ij}^m(t)\cos(\omega t)\,\mathrm{d}t \tag{6}$$

where the $C(t)$ are correlation functions describing the time evolution of the dipolar interaction. Assuming that the molecule is a rigid body moving isotropically in solution, the correlation functions in equation (6) can be described by a simple exponential of the form $\exp(-t/\tau_c)$, τ_c being the correlation time for the overall rotation of the molecule. With this simple definition, the spectral density ${J_{ij}}^m(\omega)$ becomes

$$J_{ij}^m(\omega) = \frac{1}{4\pi r_{ij}^6}\left[\frac{\tau_c}{1+(\omega\tau_c)^2}\right] \tag{7}$$

If the assumption of a rigid body is not valid, which is usually the case for biomolecules, the description of $C(t)$ by a simple exponential is no longer correct. The correlation function should then be defined in a more general form as

$$C_{ij}^m(t) = \left\langle \frac{Y_{2m}[\Phi_{ij}^{\text{lab}}(t_0+t)]Y_{2m}^*[\Phi_{ij}^{\text{lab}}(t_0)]}{r_{ij}^3(t_0+t)r_{ij}^3(t_0)} \right\rangle \tag{8}$$

Here the angular brackets indicate a time average over t_0 (which is equivalent to an ensemble average); Y_{2m} are the second-order spherical harmonics and r and Φ^{lab} denote the length and polar angles of the interproton vector in the laboratory frame of coordinates. The form of the spectral density functions ${J_{ij}}^m(\omega)$ could be obtained experimentally from relaxation measurements. The feasibility of this approach has been recently demonstrated by Peng and Wagner[32,33] who mapped the spectral densities of N–H vectors using heteronuclear relaxation experiments. In theory, this function can also be computed from a long MD trajectory. With present-day computational facilities $C(t)$ can only be computed with sufficient statistical accuracy for t values of the order of 0.1–1.0 ns. Fortunately, for many interproton vectors $C(t)$ is observed to reach a plateau value after a few ps, indicating that fast picosecond motions are well separated from slower processes.[34,35]

Following the approach developed by Lipari and Szabo,[36,37] a 'model-free' description of $C(t)$ can be set up in terms of two characteristic times, τ_p, the time in which $C(t)$ decays to the initial plateau value due to the fast internal motions, and τ_c, the correlation time for the overall rotation of the molecule. Assuming isotropic tumbling, and transforming to molecule fixed coordinates Φ^{mol} one has[34]

$$C_{ij}^m(t) = \frac{\exp(-t/\tau_c)}{4\pi} C_{ij}^{\text{int}}(t) \tag{9}$$

where the internal motion correlation functions $C^{\text{int}}(t)$ are defined as

$$C_{ij}^{\text{int}}(t) = \frac{4\pi}{5}\sum_{n=-2}^{2}\left\langle \frac{Y_{2n}[\Phi_{ij}^{\text{mol}}(t_0+t)]Y_{2n}^*[\Phi_{ij}^{\text{mol}}(t_0)]}{r_{ij}^3(t_0+t)r_{ij}^3(t_0)} \right\rangle \tag{10}$$

According to the addition theorem ${C_{ij}}^{\text{int}}(0) = \langle {r_{ij}}^{-6}\rangle$. The plateau value of the correlation function, ${C_{ij}}^{\text{int}}(t)$, can thus be defined quite generally as ${S_{ij}}^2\langle {r_{ij}}^{-6}\rangle$, where ${S_{ij}}^2$ is a generalized order parameter. It has a value between 0 and 1, and can be calculated from an MD trajectory by using equation (10) and estimating the plateau value for each interproton vector. Within this simplified model the functions ${C_{ij}}^{\text{int}}(t)$ can be written as

$$C_{ij}^{\text{int}}(t) = \left\langle \frac{1}{r_{ij}^6} \right\rangle [S_{ij}^2 + (1 - S_{ij}^2)\exp(-t/\tau_p)] \tag{11}$$

where the initial decay has been written as an exponential. Combining equations (6) and (8)–(11), one arrives at[34,35]

$$J_{ij}^m(\omega) = \frac{1}{4\pi}\left\langle \frac{1}{r_{ij}^6} \right\rangle \left[\frac{S_{ij}^2\tau_c}{1+(\omega\tau_c)^2} + \frac{(1-S_{ij}^2)\tau_{cp}}{1+(\omega\tau_{cp})^2} \right] \tag{12}$$

with ${\tau_{cp}}^{-1} = {\tau_c}^{-1} + {\tau_p}^{-1}$. Assuming that $\tau_p \ll \tau_c$, the second term in equation (12), related to the initial decay, vanishes and ${J_{ij}}^m(\omega)$ becomes

$$J_{ij}^m(\omega) = \frac{1}{4\pi}\left\langle \frac{1}{r_{ij}^6} \right\rangle \frac{S_{ij}^2\tau_c}{1+(\omega\tau_c)^2} \tag{13}$$

Besides the effects of fast local motions, other dynamic processes like, for example, methyl group rotation and aromatic ring flips can affect the relaxation behavior of

biomolecules. Their inclusion in the calculation of the theoretical NOE intensities has been described in detail by Koning et al.[38]

2.2 Computational Aspects

Basically two methods are available for the computation of theoretical NOE intensities. These have been reviewed by Forster.[39] The first involves finding the eigenvectors and eigenvalues of the real symmetrical matrix **R** by standard matrix techniques:[14]

$$\Lambda = \mathbf{X}^{-1}\mathbf{R}\mathbf{X} \tag{14}$$

Combining this expression with equation (5) leads to

$$\mathbf{A} = \exp(-\mathbf{R}\tau_m) = \mathbf{X}\exp(-\Lambda\tau_m)\mathbf{X}^{-1} \tag{15}$$

The matrix diagonalization scales as N^3, where N is the dimension of the matrix **R**, and can become extremely time-consuming when N increases. The calculations can be speeded up by making use of the sparseness of the relaxation matrix; due to the r^{-6} dependence on the distances of the cross-relaxation rates, only a few elements of **R** are significantly larger than zero. Thus, it is possible to apply a spherical cutoff around each proton pair defining a subset of NOEs with only the neighbors. In this way, for each peak, a small eigenvalue problem can then be solved. The second approach[40] for the calculation of theoretical intensities is based on a numerical integration of the differential equations [equation (1)] describing the time dependence of the NOE intensities. Several integration schemes exist (Taylor series integration, Euler algorithm, various Runge–Kutta methods) and their accuracy and performance have been addressed by Forster.[39] A choice between the various methods has to be made depending on the dimension of the system and on the purpose of the NOE calculation; for example, numerical integration is no longer suitable if eigenvalues and/or eigenvectors are required (e.g. for the analytical NOE gradient; see Section 2.4).

2.3 From NOEs to Distances

2.3.1 Two-Spin Approximation

Proton–proton distance constraints are most conveniently derived from cross-peak intensities in 2D NOE spectra taken at various short mixing times. The initial buildup rate of these peaks is proportional to the cross-relaxation rates σ_{ij} between protons i and j.[41] Therefore, these cross-relaxation rates can be measured either from a single 2D NOE spectrum taken with a sufficiently short mixing time or, more accurately, from a buildup series recorded with various mixing times.[41–43] For a large molecule, assuming isotropical tumbling and no internal motions, the $J_{ij}^0(0)$ term in equation (3) dominates the cross-relaxation rate σ_{ij} which becomes simply related to the distance r_{ij} and the correlation time τ_c:

$$\sigma_{ij} \propto -\tau_c r_{ij}^{-6} \tag{16}$$

Therefore, with a known calibration distance r_{cal}, the proton–proton distances follow from the relationship

$$r_{ij} = r_{cal}(\sigma_{cal}/\sigma_{ij})^{1/6} \tag{17}$$

In practice equations (16) and (17) are only approximately valid. There are two main problems associated with accurate determination of proton–proton distances. The first is that proteins are not rigid bodies, and intramolecular mobility leads to nonlinear averaging of distances and to different effective correlation times for the different interproton vectors in the molecule. The second is that of indirect magnetization transfer or 'spin diffusion'.[44] In reality the NOE cross peaks are the result of multispin relaxation and only in the limit of extremely short mixing times (where the signal-to-noise ratio is poor) is the two-spin approximation of equation (16) valid. For these reasons, a common approach is that of translating the NOE intensities into distance ranges (e.g. 0.2–0.3, 0.2–0.4, 0.2–0.5 nm for strong, medium, and weak NOEs, respectively) rather than attempting to obtain precise distances.[45]

It has become possible to circumvent the spin diffusion problem by the use of relaxation matrix calculations, which take into account all indirect magnetization transfers. These methods will be developed in the next section.

2.3.2 Relaxation Matrix Approaches

When a model for the structure and dynamics of a molecule is available, the NOEs can be calculated from the spectral densities as shown above [see equations (3), (5), (14), and (15)]. The opposite route from experimental NOEs to relaxation parameters is also possible. The relaxation matrix **R** can be obtained after diagonalization of the NOE matrix **A**.[15]

$$\mathbf{X}^{-1}\mathbf{A}\mathbf{X} = \mathbf{D} = \exp(-\Lambda\tau_m) \tag{18}$$

$$\mathbf{R} = -\mathbf{X}\left(\frac{\ln \mathbf{D}}{\tau_m}\right)\mathbf{X}^{-1} \tag{19}$$

Thus, theoretically the matrix **R** can be obtained directly from 2D NOE experiments taken at suitably chosen mixing times. In practice, this is not possible for large molecules, since the experimental NOE matrix is incompletely known due to overlap and missing assignments. Hybrid matrix methods have been proposed to circumvent this problem, in which the experimental data are supplemented by theoretical NOEs calculated from a model structure as implemented in IRMA,[16,17] MARDIGRAS,[18] MORASS,[46] FIRM,[22] and CROSREL.[23] An overview of the Iterative Relaxation Matrix Approach (IRMA) is given in Figure 1.

The starting point for the calculations can be a single structure or an ensemble of structures, the relaxation matrix being built from the distances of the corresponding contributions averaged as $\langle r^{-6}\rangle$ in the latter case. A theoretical NOE matrix is then computed using standard matrix techniques [cf. equation (14) and equation (15)] and combined with the experimental data. The resulting matrix can then be transformed back to a corrected relaxation matrix from which new distances are calculated. These distances are used to generate an improved model. The whole process is repeated until convergence is obtained. In other implementations (MARDIGRAS, MORASS, FIRM), the theoretical information is progressively introduced in the hybrid matrix and the back-calculated corrected relaxation matrix is directly used to calculate new NOE

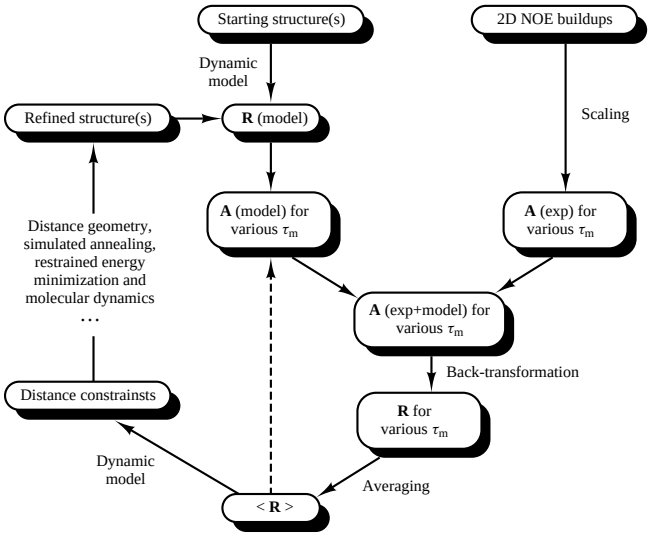

Figure 1 Overview of the IRMA scheme. [The broken line indicates the possible direct use of the back-calculated relaxation matrix for the computation of new theoretical NOEs for a progressive mixing of theoretical and experimental NOE data as found in other implementations (see text)]

matrices (broken line path in Figure 1). Only after a few cycles are distances calculated and used to generate new structures. To increase the accuracy, the calculations can be performed for a series of mixing times; upper and lower bound margins can then be related to the precision with which the elements of $\langle \mathbf{R} \rangle$ can be calculated, i.e. their variation with the mixing time. It has been shown that distances obtained from these relaxation matrix procedures result in an increased accuracy of the structures.[47,48]

Similar procedures have been developed that do not rely on a starting model.[19–21] We have shown, however, that the choice of the model structure in IRMA has little effect on the calculated distances:[48] for crambin, a 46 amino acid protein, distances obtained from a linear chain of crambin and from the well-refined crystal structure only differ on average by 0.015 nm, with a maximum deviation of 0.065 nm for long-range contact in a β-sheet. In general, however, relaxation matrix calculations will usually start from low-resolution model structures that have been obtained at previous structure determination stages from qualitative distance restraints.

2.4 Direct Use of NOEs as Structural Constraints

2.4.1 2D NOE Intensities

Yip and Case[24] proposed a method for structure refinement based on a direct comparison of experimental and theoretical NOE intensities, avoiding the conversion to distance constraints. The experimental NOE intensities are directly introduced as constraints in a refinement procedure using a penalty function of the form:

$$V_{\mathrm{NOE}} = \sum w_{ij}[(f A_{ij}^{\mathrm{theo}})^x - (A_{ij}^{\mathrm{exp}})^x]^y \qquad (20)$$

where $A_{ij}{}^{\mathrm{exp}}$ and $A_{ij}{}^{\mathrm{theo}}$ represent the experimental and theoretical NOE intensities between protons i and j, respectively, f is a scaling factor, and w_{ij} a weighting function. Often a quadratic potential is used ($y = 2$), directly with the NOE intensities ($x = 1$)[24,49–51] or with their sixth-root ($x = \frac{1}{6}$)[52] or inverse sixth-root ($x = -\frac{1}{6}$),[53] the last two definitions being closer to a standard distance-based potential. To account for the fact that NMR experimental data are collected as time- and ensemble-averaged quantities, the theoretical intensities in equation (20) can be replaced by their time- or ensemble-averages denoted as $\overline{A_{ij}^{\mathrm{theo}}}$ in a similar way as for distances[54,55] and J coupling restraints.[56] The averaged intensities, and no longer those calculated from a single static structure, are now required to satisfy the experimental constraints.[57]

2.4.1.1 Calculation of the NOE Forces. Calculation of the NOE forces requires the calculation of the gradient of the NOE potential function of equation (20) and therefore the calculation of the gradient of the NOE intensities ∇A^{theo}. An analytical solution of this gradient has been proposed by Yip and Case,[24] which has since been implemented also by others:[51,52,58]

$$\begin{aligned} \nabla_\mu A_{ij}^{\mathrm{theo}} &= \sum_{rstu} X_{ir} X_{rs}^{-1} (\nabla_\mu R)_{st} X_{tu} X_{uj}^{-1} f_{ru} \\ f_{ru} &= \frac{\exp(-\Lambda_r \tau_{\mathrm{m}}) - \exp(-\Lambda_u \tau_{\mathrm{m}})}{(\Lambda_r - \Lambda_u)} \quad (r \neq u) \\ f_{rr} &= -\tau_{\mathrm{m}} \exp(-\Lambda_r \tau_{\mathrm{m}}) \end{aligned} \qquad (21)$$

Another approach is based on a numerical evaluation of ∇A^{theo}.[49,59] Both methods are time consuming. An approximation for the calculation of ∇A^{theo} can be based on the first two terms of the power series of the exponential of equation (5)[50]

$$\mathbf{A} = \exp(-\tau_{\mathrm{m}}\mathbf{R}) = 1 - \tau_{\mathrm{m}}\mathbf{R} + \frac{1}{2}\tau_{\mathrm{m}}^2\mathbf{R}^2 \cdots \qquad (22)$$

and the gradient becomes

$$\nabla A_{ij} = \nabla(1 - \tau_{\mathrm{m}}\mathbf{R})_{ij} = -\tau_{\mathrm{m}} \nabla R_{ij} \qquad (23)$$

With this simple approximation, the NOE forces F_{NOE} can be computed rapidly, each NOE peak only giving rise to forces on the corresponding protons. The computational costs are considerably reduced in comparison with those for an analytical evaluation of the gradient, the time consuming part becoming the computation of the theoretical NOE intensities. The entire procedure scales as an N^3 problem if a diagonalization method is used for calculating the NOEs. This can be reduced by the use of a spherical cutoff around each proton pair ij defining an experimental NOE peak. With this approximation the spin diffusion contributions of all neighbors within two spheres around the two protons defining an NOE peak are taken into account. For each NOE a small relaxation matrix is calculated.

Recently, new methods have been proposed for an efficient and exact calculation of the NOE gradient[60,61] that should allow a further speed-up of the computations. Particularly promising is the method proposed by Yip[61] based on an integral expression of the NOE gradient using standard perturbation expansion techniques as in quantum mechanics.

The derivative of A_{ij} with respect to the relaxation matrix element R_{kl} is defined as:

$$\frac{\partial A_{ij}}{\partial R_{kl}} = \lim_{h \to 0} \frac{A(\mathbf{R} + \mathbf{D})_{ij} - A(\mathbf{R})_{ij}}{h} \tag{24}$$

where $A(\mathbf{R} + \mathbf{D}) = \exp[-(\mathbf{R} + \mathbf{D})\tau_m]$ and $\mathbf{D}$ is a perturbation of $\mathbf{R}$ whose only nonvanishing component is h. By using standard quantum-mechanics perturbation expansion techniques one can identify the NOE matrix $\mathbf{A}$ as the evolution operator, the relaxation rate matrix $\mathbf{R}$ as the Hamiltonian, and τ_m as the imaginary time i. $A(\mathbf{R} + \mathbf{D})_{ij}$ can then be approximated to first-order in h as

$$A(\mathbf{R} + \mathbf{D})_{ij} = A(\mathbf{R})_{ij} - h \int_0^{\tau_m} \exp[-\mathbf{R}(\tau_m - s)]_{ik} \exp(-\mathbf{R}s)_{lj}\, ds \tag{25}$$

Substituting this expression in equation (23) gives the derivative of the NOE with respect to R_{kl}:

$$\frac{\partial A_{ij}}{\partial R_{kl}} = -\int_0^{\tau_m} \exp[-\mathbf{R}(\tau_m - s)]_{ik} \exp(-\mathbf{R}s)_{lj}\, ds \tag{26}$$

The integral in equation (26) can be computed efficiently with numerical integration techniques. In addition, since no eigenvectors of $\mathbf{R}$ are required as for the expression in equation (21) any technique that allows a fast and accurate evaluation of the NOE intensities can be used in place of the diagonalization method. The derivative in equation (26) has been shown to be equivalent to the analytical expression proposed by Yip and Case[24] [equation (21)] and, from preliminary results, appears to be significantly faster than the expression in equation (21).[61]

2.4.2 3D NOE–NOE Intensities

For larger molecules considerable overlap can exist in 2D spectra. This overlap can be overcome by spreading the peaks in a third dimension and new multidimensional NMR techniques were therefore developed.[1–6] A similar procedure as with the refinement of NOE data from one-dimensional and 2D spectra can be followed for the treatment of NOE intensities from 3D spectra.

The intensities of cross peaks in a 3D spectrum are proportional to the transfer efficiencies of the two mixing periods of the experiment. The net transfer can be described in general as:

$$T_{ijk}^{3D} = T_{ij}(1) T_{jk}(2) \tag{27}$$

where $T_{ij}(1)$ and $T_{jk}(2)$ describe the magnetization transfer efficiencies for each separate mixing period and correspond to NOE transfer, exchange, or J transfer. The use of cross-peak intensities in a structure refinement procedure requires calculation of the gradients of these 3D intensities with respect to the coordinates of the protons in a molecule. The gradient of a 3D peak can be written as the sum of two terms containing the separate gradients of $T_{ij}(1)$ and $T_{jk}(2)$:

$$\nabla T_{ijk}^{3D} = T_{jk}(2) \nabla T_{ij}(1) + T_{ij}(1) \nabla T_{jk}(2) \tag{28}$$

These equations can be generalized for even higher dimensional experiments. Thus, given a valid model for the calculation of the magnetization transfer efficiencies and their derivatives, 3D peaks can be used as constraints in a direct refinement procedure.

In particular, 3D NOE–NOE spectra appear to be suitable for this purpose. This latter technique was developed for the direct observation of indirect NOE magnetization transfer ('spin diffusion') as occurs in larger biomolecules.[62] Kessler et al.[63] and Habazettl et al.[64] described the quantitative use of 3D NOE–NOE cross peaks for obtaining distance constraints, which are used by DG or restrained MD computations. It is also possible to use the intensities of such 3D spectra as direct constraints for structure refinement.[65] In a 3D NOE–NOE spectrum the 3D cross-peak intensities $A_{ijk}{}^{3D}$ can be calculated from their separate 2D NOE transfer efficiencies. The computation of the 3D NOE–NOE intensity $A_{ijk}{}^{3D}$ then amounts to the multiplication of the calculated 2D contributions A_{ij} and A_{jk}. A similar NOE restraining potential function can be defined as for the direct refinement with 2D NOE data.[65] The same approximations as for 2D data can be used for the computation of the 3D NOE–NOE forces.

The feasibility of direct NOE refinement with 3D NOE–NOE data was demonstrated by Bonvin et al.[65] for a small peptide with synthetic 3D data using a simple approximation for the derivative of the NOE intensity based on the first two terms of the expansion of the exponential function [equation (23)].[65] A similar approach has been developed since by Habazettl et al.[66] and applied to the structure refinement of a few proteins [*Cucurbita maxima* trypsin inhibitor I (CMTI-I), hisactophilin, mucous protease inhibitor (MPI)].[66,67] The main problem with the application of the method lies in the assignment of cross peaks of a 3D NOE–NOE spectrum. The huge amount of data contained in a 3D experiment requires an efficient program for automatic assignment and peak-picking before a refinement based on 3D NOE–NOE intensities can be undertaken.

3 STRUCTURE CALCULATIONS

3.1 Distance Geometry (DG)

The metric matrix DG algorithm[68,69] was known well before structure determination by NMR became possible.[70,71] This method does not rely on a starting conformation, is free from operator bias in this respect, and is therefore very attractive for structure determination. The DG procedure amounts to the following. First, upper and lower bound matrices $\mathbf{U}$ and $\mathbf{L}$ are set up for all atom–atom distances of the molecule. Some of the elements u_{ij} and l_{ij} follow from standard bond lengths and bond angles of the covalent structure and from experimentally found distance ranges from NOEs and J coupling constants. A bound smoothing procedure using triangle inequalities extends the constraints to all elements of $\mathbf{U}$ and $\mathbf{L}$. This procedure can even be extended to satisfy tetrangle inequalities as for example implemented in the DG-II package[8] (see ***Distance Geometry***). Then, a distance matrix $\mathbf{D}$ is set up with distances chosen randomly between upper and lower bounds, $l_{ij} \leq d_{ij} \leq u_{ij}$. The elements of $\mathbf{D}$ can be chosen in such a way that they not only lie between their respective upper and lower

bounds, but also themselves obey the triangle inequalities; this latter technique is known as *random metrization*. The so-called 'embedding' algorithm then finds the best 3D structure consistent with the distances d_{ij}. This structure must be optimized with an error function consisting of chirality and distance constraints. This forces the amino acid side chains to adopt the correct chirality and the distances to satisfy the upper and lower bound criteria, although usually the DG structures still contain a number of violations of the distance bounds. By repetition of the DG calculations with randomly chosen distance matrices **D**, families of structures can be obtained that allow one to judge how uniquely the structure is determined by the constraints.

Another method, also termed distance geometry, but using a quite different mathematical procedure, was suggested by Braun and Gō.[72] Here, the biomolecular conformation is calculated by minimizing a distance constraint error function. Special features of the method are that dihedral angles are used as independent variables rather than Cartesian coordinates and that it uses a variable target function, first satisfying local constraints (between amino acids nearby in the polypeptide chain) and later including long-range constraints. This approach avoids becoming trapped in a local minimum of the target function. Usually one starts with various initial conformations obtained by taking random values for the dihedral angles. This method, which has been implemented since in various programs, e.g. DISMAN[72] and more recently DIANA,[73] has rather similar efficiency and convergence properties as the metric matrix distance-geometry algorithm.

3.2 Simulated Annealing (SA)

Although the DG methods do not need starting structures and are therefore not subject to operator bias, this does not mean that they sample the allowed conformational space (consistent with the bounds) in a truly random fashion. Simplified MD calculations with only geometric constraints were developed to increase the sampling of the DG methods. These are termed, in general, simulated annealing (SA) procedures. Although these can be directly used to generate structures starting from random coordinates, they are most commonly combined with DG calculations, the starting structures for the SA stage being obtained by DG embedding. Simulated annealing involves raising the temperature of the system followed by slow cooling in order to overcome local minima and locate the region of the global minimum of the target function V_{tot} (cf. Nilges et al.)[9]. This is achieved by solving Newton's equations of motion

$$m_i \ddot{\boldsymbol{r}}_i = \boldsymbol{F}_i \tag{29}$$

with the forces given by

$$\boldsymbol{F}_i = -\partial V_{\text{tot}}/\partial \boldsymbol{r}_i \tag{30}$$

The potential V_{tot} usually contains the following terms:

$$V_{\text{tot}} = V_{\text{covalent}} + V_{\text{repel}} + V_{\text{disre}} + V_{\text{dihre}} + V_{\text{NOE}} \tag{31}$$

V_{covalent} is a potential to maintain correct bond lengths, angles, planes and chirality, V_{repel} is a simple repulsion term to prevent unduly close nonbonded contact, V_{disre} and V_{dihre} represent the experimental NOE distance and dihedral angle constraints, respectively, and V_{NOE} is an extra term for direct comparison of theoretical and experimental NOE intensities as defined in equation (20). Usually the NOE distance constraints are represented by a flat well potential of the form

$$V_{\text{disre}} = \begin{cases} \frac{1}{2}K_{\text{disre}}(d_{ij} - l_{ij})^2 & 0 \le d_{ij} \le l_{ij} \\ 0 & l_{ij} \le d_{ij} \le u_{ij} \\ \frac{1}{2}K_{\text{disre}}(d_{ij} - u_{ij})^2 & u_{ij} \le d_{ij} \end{cases} \tag{32}$$

where l_{ij} and u_{ij} are the value of lower and upper limits of the target distances, respectively. Other forms that contains a linear part at long distances are also used[74] to avoid too large energies, which may give computational problems. A similar definition as in equation (32) can be used for dihedral angle constraints, but other forms have also been proposed such as:[75]

$$V_{\text{dihre}} = K_{\text{dihre}}[1 - \cos(\phi - \phi_0)] \tag{33}$$

where ϕ_0 represents the dihedral angle value obtained from J coupling data. The various terms in equation (31) have variable force constants, which can be progressively increased during the annealing.

The combination of DG, for generating starting structures with an approximate folding by embedding a subset of atoms, and SA calculations, provides a powerful and efficient tool for the structure determination of biomolecules.[9,76] This hybrid method should be particularly useful for solving the structure of large proteins for which computational costs may become a limiting factor.

3.3 Restrained Molecular Dynamics and Energy Minimization (RMD, REM)

The quality of biomolecular structures based on geometric constraints can be improved by taking energy considerations into account. For instance, in DG structures amino acid side chains often adopt eclipsed conformations. Also, hydrogen bonds and salt bridges may not be formed unless they are specifically introduced as constraints. In RMD refinement structures are optimized simultaneously with respect to a potential energy function and a set of experimental restraints. Of course the success of this method now depends to a large extent on the quality of the force field used. It is therefore important to realize the limitations and approximate nature of this force field, especially when the calculations do not include solvent molecules.

In RMD calculations, equation (29) and equation (30) are integrated with the potential function given by

$$\begin{aligned} V_{\text{tot}} = {} & V_{\text{bond}} + V_{\text{angle}} + V_{\text{torsion}} + V_{\text{vdW}} \\ & + V_{\text{Coulomb}} + V_{\text{disre}} + V_{\text{dihre}} + V_{\text{NOE}} \end{aligned} \tag{34}$$

The first two terms tend to keep bond lengths and angles at their equilibrium values. V_{torsion} is a sinusoidal potential describing rotations about bonds; for V_{vdW} (the van der Waals interaction) usually a Lennard–Jones potential is taken, and V_{Coulomb} describes the electrostatic interactions. The three last

terms, similar to those in equation (31), distinguish RMD from more conventional MD simulations.

An RMD simulation is usually preceded and followed by REM using steepest descent or conjugated gradient methods to bring the energy down to an acceptable level. Using the same potential energy function as RMD [equation (34)] REM usually induces only small changes in the structures by driving them to the closest minimum and is not able to take them out of this. By contrast, RMD is able to overcome barriers of the order of kT because of the kinetic energy in the system and therefore has a much larger radius of convergence. The RMD method works as an efficient minimizer, since excess potential energy, converted to kinetic energy, is drained off by coupling the system to a thermal bath of constant temperature. Sampling of the conformational space consistent with the experimental constraints can be increased by using high-temperature simulations[77] or potential energy annealing conformational search methods (PEACS)[78] in which the potential energy is coupled to a reference energy bath whose energy level is progressively decreased over the run, or by introducing a fourth dimension[79] as recently implemented in GROMOS (4D MD),[80] which, by increasing the number of degrees of freedom in the system, allows one to circumvent energy barriers present in the 3D potential energy hypersurface.

Further extensions of the method, especially useful for highly mobile structures, include time-averaging[54] or ensemble-averaging[55] of the experimental restraints. In these methods, V_{disre} is calculated from time- or ensemble-averaged distances instead of instantaneous ones. Forces are thus applied on the corresponding protons only if the *averaged* distance violates the restraint. These methods allow a larger conformational freedom consistent with the NOE restraints. The use of time-averaged restraints has recently been described for direct structure refinement with J coupling[56] and NOE[57] data.

4 QUALITY OF THE STRUCTURES

Important factors for assessing the quality of the NMR structures usually obtained with a combination of the above described methods are the number and distribution of the NOE and dihedral angle constraints and the number of stereospecific assignments. Several other criteria have also to be considered, but these will all depend, to some extent, on the factors mentioned above. The precision of the structure is generally given by the average root mean squared deviations (rmsd) (pairwise or from the average coordinates). These are usually calculated for the backbone and all atoms, respectively, and sometimes on a substructure. The rmsd as a function of the residue sequence can also be useful for identifying less well-defined regions in a structure. Another useful parameter to assess the precision of solution structures is the angular order parameter proposed by Hyberts et al.[81]

$$S_{\phi}^{\text{angle}} = \frac{1}{N_{\text{struc}}}\left[\left(\sum \cos\phi\right)^2 + \left(\sum \sin\phi\right)^2\right]^{1/2} \quad (35)$$

It has the advantage that, contrary to rmsd, it does not require the superimposition of the structures. Angular order parameters (S^{angle}) are generally given as a function of the residue sequence for backbone ϕ, ψ and side-chain χ_1 dihedral angles. S^{angle} values of 0.9 and 0.8, for example, indicate very well-defined dihedral angles with fluctuations of $\pm 24^\circ$ and $\pm 40^\circ$, respectively. We have to keep in mind, however, that the rmsd etc and angular order parameters give an indication of the precision of the structure, but are not a direct indication of its accuracy. Structures with very low rmsd can still be wrong! To judge the quality, we have to take several other criteria into account: the stereochemical quality (e.g. via ϕ, ψ Ramachandran plots), the deviations from the idealized covalent geometry, the conformational energy, residual restraints violations, the presence of hydrogen bonds, and a good packing of the structures; these are criteria commonly used for this purpose. Studies of the stereochemical quality of crystal and NMR protein structures have resulted in useful criteria to assess the quality of these structures.[82,83] These criteria, among which are the percentage of residues in the favorable area of the Ramachandran plot and the χ_1 dihedral angles- and hydrogen-bond energy standard deviations, can be easily checked with the program PROCHECK,[82] which allows a fast and simple evaluation of the stereochemical quality of a protein structure. Another criterion to assess the quality of the structures obtained from NMR data is directly to compare calculated and experimental NOEs. The fit can be described by a residual index or R factor in a similar manner as in X-ray crystallography. Several R factor definitions have been proposed[47,84,85] and can all be represented by a general equation of the form:

$$R = \frac{\sum_i w_i |N_i^{\text{theo}} - N_i^{\text{exp}}|}{\sum_i w_i |N_i^{\text{ref}}|} \quad (36)$$

where $N_i = A_i$ or $N_i = (A_i)^{\frac{1}{6}}$ with, in the denominator, N_i^{ref} defined as $N_i^{\text{ref}} = N_i^{\text{exp}}$ or $N_i^{\text{ref}} = \frac{1}{2}(N_i^{\text{exp}} + N_i^{\text{theo}})$, w_i are weighting factors that can be chosen equal to the mixing times, since NOEs measured at longer mixing times are expected to have a better signal-to-noise ratio. The simplest one, with $N_i = A_i$ and $N_i^{\text{ref}} = N_i^{\text{exp}}$, is similar to the X-ray definition.[84] For NMR, however, other functions may be more appropriate since we are dealing principally with two problems. First, the range of NOE intensities is quite extended (by more than a factor of 1000) and R might be dominated by strong peaks, corresponding to short distances in the structures which are expected to be less important for determining the 3D structure. A sixth-root residual index, $R^{\frac{1}{6}}$, where $N_i = (A_i)^{\frac{1}{6}}$, allows for a more even contribution of weak and strong NOEs in the R factor.[47,84] The second problem inherent to the R factor comes from the approximate r^{-6} dependence of the NOEs. Because of this extreme distance dependence, the R factor function is asymmetric, the error increasing strongly when the distances are shorter than the target distances. Normalizing the errors by the sum of both experimental and theoretical NOE intensities, $N_i^{\text{ref}} = \frac{1}{2}(N_i^{\text{exp}} + N_i^{\text{theo}})$, should avoid this problem.[85] To give a better picture of the quality of the structures, a distinction can be made between intra- and interresidue peaks and the R factors can be calculated as a function of the residue sequence, which allows one to recognize problem regions in the structures.

5 APPLICATION: THE ARC REPRESSOR

The structure refinement process using relaxation matrix calculations can be best illustrated using a specific example: the Arc repressor. The solution structure of the Arc repressor of *Salmonella* bacteriophage P22, a dimeric sequence-specific DNA-binding protein,[86] has been determined from 2D NMR data using an 'ensemble' IRMA followed by direct NOE refinement with DINOSAUR.[87]

An 824 NOE buildup series in H_2O and D_2O and 130 additional qualitative distance constraints were collected for Arc. This resulted in a set of 954 constraints consisting of 350 intraresidue, 215 sequential, 181 medium range, and 208 long-range constraints; 144 of the total set correspond to intermonomer constraints. Twenty-four hydrogen bonds were also explicitly defined. The constraints were duplicated to account for the dimeric nature of Arc giving a total set of 2004 constraints (NOEs + hydrogen bonds). Of the set of 954 constraints per monomer, 824 NOEs with good quality buildup curves were used in the IRMA and DINOSAUR calculations, the others being introduced as qualitative constraints. From the stereospecific assignment procedure, which resulted in the assignment of 16 β-methylene diastereotopic proton pairs (40%) and of the methyl groups of four valine residues, constraints could be imposed on 21 χ_1 dihedral angles.

In the initial stage, a set of 51 structures was generated with DG and further refined with a combination of REM and RMD using the GROMOS force field[88] in a parallel refinement protocol. Distance constraints were obtained from the set of 854 NOE buildups via relaxation matrix calculations from the ensemble of structures, except for the initial cycle in which a structure obtained by Breg et al.[89] was chosen as the model. Methyl group rotation, aromatic ring flips, and internal mobility effects (via order parameters obtained from a free MD run in water) were included in these calculations. Convergence was obtained after three IRMA cycles. The best 16 structures were finally refined with direct NOE constraints following a slow-cooling SA protocol from 600 to 1 K in 1.5 ps followed by REM.[88] In this final refinement stage, theoretical NOE intensities were directly compared with the experimental data using a simple quadratic restraining potential [$x = 1$, $y = 2$ in equation (20)] with, as weighting factor, an experimental error defined as $w_{ij} = (N + \varepsilon A_{ij}^{\exp})^{-2}$.[50] N corresponds to a noise level and ϵ to a relative error on the experimental intensities. The forces were derived using the simple two-spin approximation for the gradient of the NOE function [equation (23)]. Dynamic assignment was applied to the peaks involving unassigned diastereotopic groups.

A view of the backbone of the 16 best Arc structures at various stages during the refinement (DG/SA, IRMA 1st, 2nd, and 3rd cycles, and DINOSAUR) is presented in Figure 2, which clearly shows the improvement of the structures. The precision of the well-defined region of Arc (residues 8–48) including the β-sheet and the two α-helices increases during the IRMA refinement as confirmed by the rmsd (from the average) shown in Figure 3(a). The rmsd for the backbone atoms decreases from 1.0 Å for the DG/SA structures to 0.50 Å for the structures obtained after the third IRMA cycle. This value increases slightly to 0.55 Å after the direct NOE refinement indicating that the use of direct NOE constraints might introduce more variability in the structures (due to spin diffusion effects there are more ways to fulfill a NOE constraint than a distance constraint). The R factors ($Q^{\frac{1}{6}}$ definition),[87] however, show a substantial decrease during the DINOSAUR refinement step as can be seen from Figure 3(b). The final structures satisfy the NMR constraints with no significant deviations from dihedral angle restraints obtained from J coupling data and very low R factors, indicating a very good agreement with the experimental NOE data.

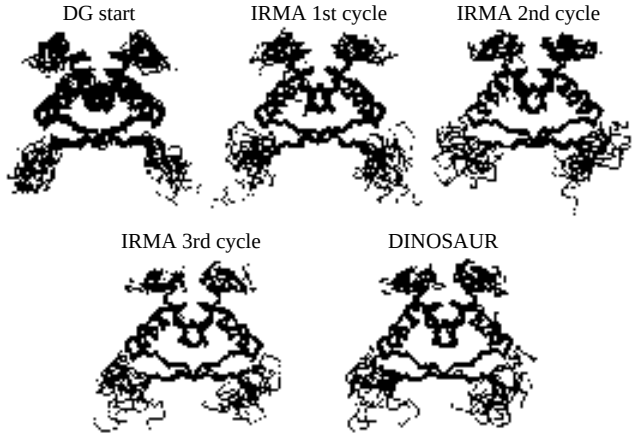

Figure 2 View of the Arc repressor structures during the refinement with NMR constraints. The structures corresponding to the 16 best final conformations are shown directly after the DG/SA calculations in the first IRMA cycle, after each IRMA cycle, and after direct NOE refinement with DINOSAUR. The structures were superimposed on C-α,C,N atoms of the well-defined region of Arc (residues 8–48 of each monomer)

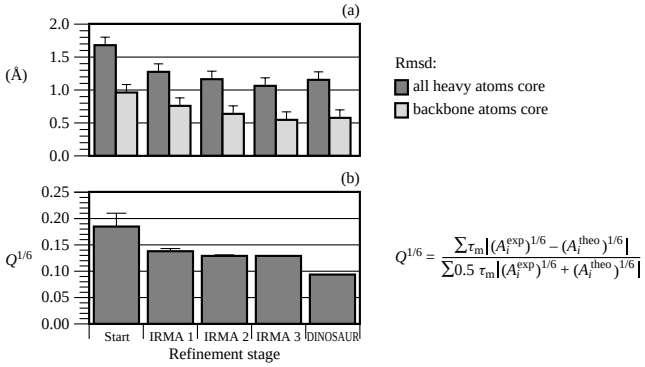

Figure 3 (a) All heavy atom and backbone atom rmsd from the average for the well-defined region of the Arc repressor (residues 8–48 of each monomer) calculated for an ensemble of 16 structures as a function of the refinement. The structures were superimposed on backbone atoms of the well-defined core. (b) R factors ($Q^{\frac{1}{6}}$ definition) of the Arc structures as a function of the refinement

The distribution of the experimental constraints as a function of the residue sequence is plotted in Figure 4, together with the precision (rmsd on C-α and all heavy atoms), the backbone angular order parameters [equation (35)] and the $Q^{\frac{1}{6}}$ factors. A correlation can be noticed between the number of constraints and the precision per residue, but no such relationship can be found for the $Q^{\frac{1}{6}}$ factors which all represent low values (~0.05) (for comparison, the $Q^{\frac{1}{6}}$ factors for a linear chain of Arc have values of around 0.55). Regions of high variability are found in the N- and C-terminal parts for which few

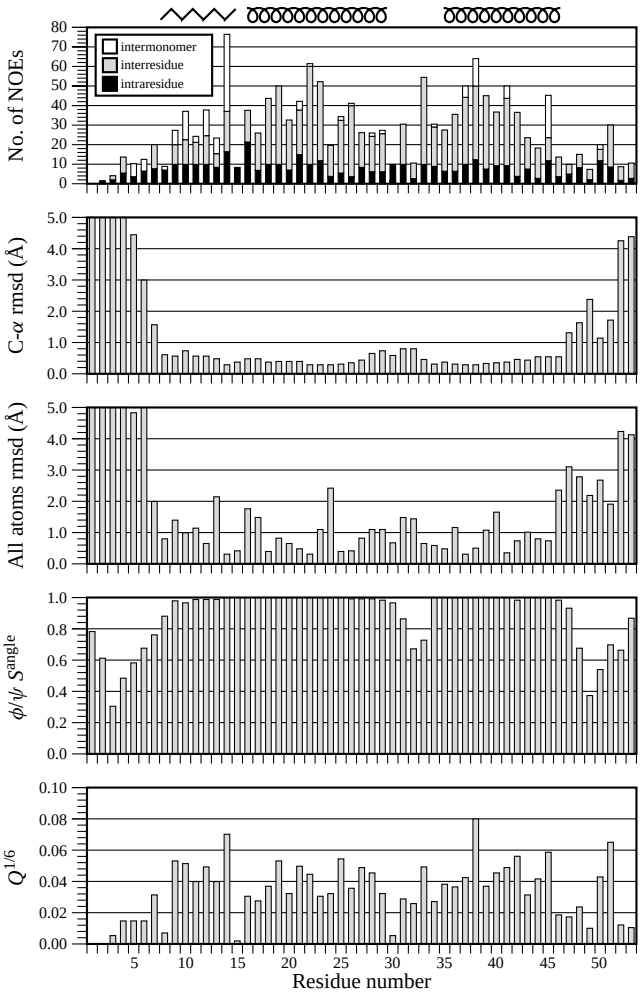

Figure 4 Number of constraints, rmsd (from the average) on C-α atoms and on all heavy atoms [the structures were superimposed on C-α,C,N atoms of the well-defined region of Arc (residues 8–48 of each monomer)], backbone angular order parameters (averages from ϕ and ψ angular order parameters) [equation (35)], and $Q^{\frac{1}{6}}$ factors as a function of the residue sequence for the final Arc structures. Secondary structure elements in Arc are indicated. (The rmsd of the first four residues are off-scale and have values of up to 10 Å)

constraints are available. The structures, which have been deposited in the Brookhaven Protein Data Bank (entry 1ARR), have good stereochemical qualities and present an extensive pattern of hydrogen bonds and a good packing with a very well defined core.

6 CONCLUSION

The use of relaxation matrix calculations for the refinement of protein structures from NMR, as illustrated here for the Arc repressor, should result in a more accurate representation of the solution structure of a biomolecule. In addition, such methods also offer a tool to identify errors or overinterpretation in distance constraints and assess the quality of the NMR structures by a direct comparison of theoretical and experimental data. They should however not be used as single criteria for accuracy, but should be used together with others, such as the stereochemical quality of the structure. An adequate description of motional effects like internal mobility (e.g. via order parameters, fast methyl group rotation, and aromatic ring flips) or conformational heterogeneity, allows a dynamic description of the structure in solution. A treatment of the experimental NMR data as time- and/or ensemble-averaged restraints should even lead us further toward a more realistic description of solution structures. Additional work is however required in this direction since the motional model is the most controversial point in the use of relaxation matrix calculations. The new developments both in software and hardware should extend the range of such computations to proteins of increasing size and allow the use of more detailed motional models for a better description of solution structure.

7 RELATED ARTICLES

Amino Acids, Peptides and Proteins: Chemical Shifts; Analysis of Spectra: Automatic Methods; Chemical Shifts in Biochemical Systems; Distance Geometry; NOESY; Nuclear Overhauser Effect.

8 REFERENCES

1. C. Griesinger, O. W. Sørensen, and R. R. Ernst, *J. Magn. Reson.*, 1989, **84**, 14.
2. L. E. Kay, D. Marion, and A. Bax, *J. Magn. Reson.*, 1989, **84**, 72.
3. S. W. Fesik and E. R. P. Zuiderweg, *Q. Rev. Biophys.*, 1990, **23**, 97.
4. R. Boelens, C. Griesinger, L. E. Kay, D. Marion, and E. R. P. Zuiderweg, in *Computational Aspects of the Study of Biological Macromolecules by Nuclear Magnetic Resonance Spectroscopy*, ed. J. C. Hoch et al., Plenum, New York, 1991, pp. 127–150.
5. G. M. Clore and A. M. Gronenborn, *Prog. NMR Spectrosc.*, 1991, **23**, 43.
6. A. Bax and C. Grzesiek, *Acc. Chem. Res.*, 1993, **26**, 131.
7. D. Neuhaus and M. Williamson, *The Nuclear Overhauser Effect in Structural and Conformational Analysis*, VCH, New York, 1989.
8. T. F. Havel, *Prog. Biophys. Mol. Biol.*, 1991, **56**, 43.
9. M. Nilges, G. M. Clore, and A. M. Gronenborn, *FEBS Lett.*, 1988, **229**, 317.
10. R. M. Scheek, W. F. van Gunsteren, and R. Kaptein, *Methods Enzymol.*, 1989, **177**, 204.
11. A. Brünger and M. Karplus, *Acc. Chem. Res.*, 1991, **24**, 54.
12. M. J. J. Blommers, C. B. Lucasius, G. Kateman, and R. Kaptein, *Biopolymers*, 1992, **32**, 45.
13. R. Pachter, R. B. Altman, and O. Jardetzky, *J. Magn. Reson.*, 1990, **89**, 578.
14. J. W. Keepers and T. L. James, *J. Magn. Reson.*, 1984, **57**, 404.
15. E. T. Olejniczak, R. T. Gampe, Jr., and S. W. Fesik, *J. Magn. Reson.*, 1986, **67**, 28.
16. R. Boelens, T. M. G. Koning, and R. Kaptein, *J. Mol. Struct.*, 1988, **173**, 299.
17. R. Boelens, T. M. G. Koning, G. A. van der Marel, J. H. van Boom, and R. Kaptein, *J. Magn. Reson.*, 1989, **82**, 290.
18. B. A. Borgias, M. Cochin, D. J. Kerwood, and T. L. James, *Prog. NMR Spectrosc.*, 1990, **22**, 83.

19. P. Koehl and J.-F. Lefèvre, *J. Magn. Reson.*, 1990, **86**, 565.
20. M. Madrid, E. Llinás, and M. Llinás, *J. Magn. Reson.*, 1991, **93**, 329.
21. F. J. M. Van de Ven, M. J. J. Blommers, R. E. Schouten, and C. W. Hilbers, *J. Magn. Reson.*, 1991, **94**, 140.
22. S. P. Edmonson, *J. Magn. Reson.*, 1992, **98**, 283.
23. B. R. Leeflang and L. M. J. Kroon-Batenburg, *J. Biomol. NMR*, 1992, **2**, 495.
24. P. Yip and D. A. Case, *J. Magn. Reson.*, 1989, **83**, 643.
25. K. Ösapay and D. Case, *J. Am. Chem. Soc.*, 1991, **113**, 9436.
26. D. S. Wishart, B. D. Sykes, and F. M. Richards, *J. Mol. Biol.*, 1991, **222**, 311.
27. M. P. Williamson, T. Asakura, E. Nakamura, and M. Demura, *J. Biomol. NMR*, 1992, **2**, 83.
28. A. C. de Dios, J. G. Pearson, and E. Oldfield, *Science*, 1993, **260**, 1491.
29. T. S. Harvey and W. F. van Gunsheren, *Techniques in Protein Chemistry*, Academic Press, New York, 1993, p. 615.
30. I. Solomon, *Phys. Rev.*, 1955, **99**, 559.
31. S. Macura and R. R. Ernst, *Mol. Phys.*, 1980, **41**, 95.
32. J. W. Peng and G. Wagner, *J. Magn. Reson.*, 1992, **98**, 308.
33. J. Peng and G. Wagner, *Biochemistry*, 1992, **31**, 8571.
34. E. T. Olejniczak, C. M. Dobson, M. Karplus, and R. M. Levy, *J. Am. Chem. Soc.*, 1984, **106**, 1923.
35. T. M. G. Koning, R. Boelens, G. A. van der Marel, J. H. van Boom, and R. Kaptein, *Biochemistry*, 1991, **30**, 3787.
36. G. Lipari and A. Szabo, *J. Am. Chem. Soc.*, 1982, **104**, 4546.
37. G. Lipari and A. Szabo, *J. Am. Chem. Soc.*, 1982, **104**, 4559.
38. T. M. G. Koning, R. Boelens, and R. Kaptein, *J. Magn. Reson.*, 1990, **90**, 111.
39. M. J. Forster, *J. Comput. Chem.*, 1990, **12**, 292.
40. D. Marion, M. Genest, and M. Ptak, *Biophys. Chem.*, 1987, **28**, 235.
41. A. Kumar, G. Wagner, R. R. Ernst, and K. Wüthrich, *J. Am. Chem. Soc.*, 1981, **103**, 3654.
42. G. Wagner and K. Wüthrich, *J. Magn. Reson.*, 1979, **33**, 675.
43. C. M. Dobson, E. T. Olejniczak, F. M. Poulsen, and R. G. Ratcliffe, *J. Magn. Reson.*, 1982, **48**, 97.
44. A. Kalk and H. J. C. Berendsen, *J. Magn. Reson.*, 1976, **24**, 343.
45. K. Wüthrich, *NMR of Proteins and Nucleic Acids*, Wiley, New York, 1986.
46. C. B. Post, R. P. Meadows, and D. G. Gorenstein, *J. Am. Chem. Soc.*, 1990, **112**, 6796.
47. P. D. Thomas, V. J. Basus, and T. L. James, *Proc. Natl. Acad. Sci. USA*, 1991, **88**, 1237.
48. A. M. J. J. Bonvin, J. A. C. Rullmann, R. Boelens, and R. Kaptein, *Proteins Struct. Funct. Genet.*, 1993, **15**, 385.
49. J. D. Baleja, J. Moult, and B. D. J. Sykes, *J. Magn. Reson.*, 1990, **87**, 375.
50. A. M. J. J. Bonvin, R. Boelens, and R. Kaptein, *J. Biomol. NMR*, 1991, **1**, 305.
51. J. E. Mertz, P. Güntert, K. Wüthrich, and W. Braun, *J. Biomol. NMR*, 1991, **1**, 257.
52. M. Nilges, J. Habazettl, A. T. Brünger, and T. A. Holak, *J. Mol. Biol.*, 1991, **219**, 499.
53. B. Stawarz, M. Genest, and D. Genest, *Biopolymers*, 1992, **32**, 633.
54. A. E. Torda, R. M. Scheek, and W. F. van Gunsteren, *Chem. Phys. Lett.*, 1989, **157**, 289.
55. R. M. Scheek, A. E. Torda, J. Kemmink, and W. F. van Gunsteren, in *Computational Aspects of the Study of Biological Macromolecules by NMR*, ed. J. C. Hoch, F. M. Poulsen, and C. Redfield, Plenum, New York, 1991, pp. 209–217.
56. A. E. Torda, R. M. Brunne, T. Huber, H. Kessler, and W. F. van Gunsteren, *J. Biomol. NMR*, 1993, **3**, 55.
57. A. M. J. J. Bonvin, R. Boelens, and R. Kaptein, *J. Biomol. NMR*, 1994, **4**, 143.
58. J. Pothier, J. Gabarro-Arpa, and M. Le Bret, *J. Comput. Chem.*, 1993, **14**, 226.
59. J. D. Baleja, *J. Magn. Reson.*, 1992, **96**, 619.
60. E. N. Nesterova and V. P. Chuprina, *J. Magn. Reson.*, 1993, **B101**, 94.
61. P. F. Yip, *J. Biomol. NMR*, 1993, **3**, 361.
62. R. Boelens, G. W. Vuister, T. M. G. Koning, and R. Kaptein, *J. Am. Chem. Soc.*, 1989, **111**, 8525.
63. H. Kessler, S. Seip, and J. Saulitis, *J. Biomol. NMR*, 1991, **1**, 83.
64. J. Habazettl, A. Ross, H. Oschkinat, and T. A. Holak, *J. Magn. Reson.*, 1992, **97**, 511.
65. A. M. J. J. Bonvin, R. Boelens, and R. Kaptein, *J. Magn. Reson.*, 1991, **95**, 626.
66. J. Habazettl, M. Schleicher, J. Otlewski, and T. A. Holak, *J. Mol. Biol.*, 1992, **228**, 156.
67. R. Bernstein, A. Ross, C. Cieslar, and T. A. Holak, *J. Magn. Reson.*, 1993, **B101**, 185.
68. L. M. Blumenthal, *Theory and Application of Distance Geometry*, Chelsea, New York, 1970.
69. G. M. Crippen and T. F. Havel, *Acta Crystallogr., Sect. A*, 1978, **34**, 282.
70. T. F. Havel, I. D. Kuntz, and G. M. Crippen, *Bull. Math. Biol.*, 1983, **45**, 665.
71. T. F. Havel and K. Wüthrich, *Bull. Math. Biol.*, 1984, **46**, 673.
72. W. Braun and N. Gō, *J. Mol. Biol.*, 1985, **186**, 611.
73. P. Güntert, W. Braun, and K. Wüthrich, *J. Mol. Biol.*, 1991, **217**, 517.
74. R. Kaptein, E. R. P. Zuiderweg, R. M. Scheek, R. Boelens, and W. F. van Gunsteren, *J. Mol. Biol.*, 1985, **182**, 179.
75. J. De Vlieg, R. Boelens, R. M. Scheek, R. Kaptein, and W. F. van Gunsteren, *Isr. J. Chem.*, 1986, **27**, 181.
76. T. A. Holak, D. Gondol, J. Otlewski, and T. Wilusz, *J. Mol. Biol.*, 1989, **210**, 635.
77. R. E. Bruccoleri and M. Karplus, *Biopolymers*, 1990, **29**, 1847.
78. R. C. Van Schaik, W. F. van Gunsteren, and H. J. C. Berendsen, *J. Comput.-Aided Mol. Des.*, 1992, **6**, 97.
79. G. M. Crippen, *J. Comput. Chem.*, 1982, **3**, 471.
80. R. C. Van Schaik, H. J. C. Berendsen, A. E. Torda, and W. F. van Gunsteren, *J. Mol. Biol.*, 1993, **234**, 751.
81. S. G. Hyberts, M. S. Goldberg, T. F. Havel, and G. Wagner, *Protein Sci.*, 1992, **1**, 736.
82. A. L. Morris, M. W. MacArthur, E. G. Hutchinson, and J. M. Thornton, *Proteins Struct. Funct. Genet.*, 1992, **12**, 345.
83. M. W. MacArthur and J. M. Thornton, *Proteins Struct. Funct. Genet.*, 1993, **17**, 232.
84. C. Gonzalez, J. A. C. Rullmann, A. M. J. J. Bonvin, R. Boelens, and R. Kaptein, *J. Magn. Reson.*, 1991, **91**, 659.
85. J. M. Withka, J. Srinivasan, and P. H. Bolton, *J. Magn. Reson.*, 1992, **98**, 611.
86. J. U. Bowie and R. T. Sauer, *Proc. Natl. Acad. Sci. USA*, 1989, **86**, 2152.
87. W. F. Van Gunsteren and H. J. C. Berendsen, *Groningen Molecular Simulation (GROMOS) Library Manual*, Biomos BV, Nijenborgh 16, 9747 AG Groningen, The Netherlands, 1987.

88. A. M. J. J. Bonvin, R. Boelens, and R. Kaptein, *Biopolymers*, 1994, **34**, 39.
89. J. N. Breg, J. H. J. van Opheusden, M. J. M. Burgering, R. Boelens, and R. Kaptein, *Nature (London)*, 1990, **346**, 586.

Biographical Sketches

Alexandre M. J. J. Bonvin. *b* 1964. B.S., 1989, Lausanne, Switzerland; Ph.D., 1993, Utrecht. Introduced to NMR by G. Bodenhausen. Postdoctoral associate of Professor Dr. A. T. Brünger, Yale University. Approx. 16 publications. Research interests include molecular modeling, development and application of new methods for biomolecular structure determination by NMR, and dynamic studies of proteins by molecular dynamics simulations.

R. Boelens. *b* 1951. B.S., 1977, University of Groningen, Ph.D., University of Amsterdam, Ph.D., 1984, biochemistry. Postdoctoral associate with R. Kaptein, Groningen. Associate professor at Utrecht University, 1987–present. Approx. 130 publications. Research specialties: NMR method development, structure determination of biomolecules by NMR and studies on protein–DNA interaction.

Robert Kaptein. *b* 1941. M.S., 1965, Ph.D., Leiden, 1971; postdoctoral fellow with Ray Freeman, Varian 1971–72; Shell Research Laboratory, Amsterdam, 1972–75; Groningen University, 1975–87; Utrecht University, Professor of Chemistry 1987–present. Research interests: biomolecular structure determination, NMR methodology, protein–DNA interactions.

Selective Relaxation Techniques in Biological NMR

Claudio Rossi
University of Siena, Siena, Italy

1	Introduction	1
2	Selective Pulse Excitation	1
3	The Dipolar Relaxation Mechanism	1
4	General Remarks on Selective Relaxation Experiments	3
5	Application of Selective Relaxation Techniques in Biological Systems	4
6	Related Articles	8
7	References	9

1 INTRODUCTION

Interest in selective relaxation experiments was aroused when it emerged that it was possible to interpret experimental selective relaxation parameters in terms of different relaxation contributions. Considering the dipole–dipole interaction between $I = \frac{1}{2}$ nuclei as the dominant relaxation contribution of biomolecules in solution, selective relaxation experiments can be used to calculate both selective 'cross-relaxation' rates σ_{ij} and individual, direct self-relaxation rates ρ_i. The observation of specific dipolar connectivities can provide useful information on several aspects of the chemical behavior of biomolecules, especially molecular structures and organization, solution dynamics, and biomolecular interactions.

2 SELECTIVE PULSE EXCITATION

Any selective relaxation experiment is performed with a specific pulse sequence which contains at least one selective excitation period. An ideal selective pulse should have the following features:[1,2]

1. good frequency selectivity (i.e. uniform excitation of a limited spectral region);
2. short duration (to avoid effects such as relaxation, chemical shift, and coupling evolution during the pulse);
3. uniform phase behavior of the magnetization.

Several approaches, recently reviewed,[1–3] have been developed, to generate excitation profiles to yield selective perturbation, starting from the pioneering work of Alexander.[4] The pulse sequences proposed for selective excitation can be regarded as belonging to the following categories:

1. rectangular sequence;
2. DANTE sequence;
3. shaped sequence.

2.1 Rectangular Sequences

Rectangular sequences are single, soft pulses obtained like an ordinary hard pulse but with low-amplitude power of the radiofrequency field and a long pulse duration. Two main disadvantages are the low-frequency selectivity and the long excitation time.[5]

2.2 DANTE Sequence[6,7]

The DANTE sequence is an ingenious system for selective excitation using high-power pulses. It consists of a sequence of 10–100 short, high-power pulses with a pulse angle $\phi < \pi/2$ and a repetition frequency $1/\tau$. The effect generated on a magnetic moment vector is similar to that of a soft rectangular pulse with a larger selectivity that improves as the number of pulses in the pulse train is increased. With respect to the soft rectangular pulse, the DANTE sequence generates a set of excitation bands at a frequency n/τ (where n is an integer 1, 2, 3, etc.) symmetrical with the transmitter frequency ω_o.

Important improvements to the original DANTE sequence have increased the frequency selectivity (reducing the effect of side lobes of the excitation function) by pulse-shaping with DANTE[8] and have enabled selective simultaneous excitation of two frequencies by double-DANTE sequences.[9]

2.3 Shaped Pulses

Selective relaxation experiments require the generation of sharp selective pulses that cannot be obtained from soft rectangular pulses. An almost ideal excitation profile requires smoothing of the side lobes in the frequency domain. This is now achieved by appropriate pulse-shaping procedures, which usually require a pulse-shaping spectrometer device.

Gaussian pulse shaping was one of the first shaping functions to be used.[5,10,11] Now a number of different shaping functions are available to generate selective soft pulses for any multidimensional relaxation experiment. Tables 1 and 2 (from Kessler et al.)[1] show the main characteristics of the different soft excitation pulses and their 'recommended' applications.

3 THE DIPOLAR RELAXATION MECHANISM

In solution the exchange of magnetic energy between excited nuclei and the lattice occurs mainly through dipole–dipole interactions between $I = \frac{1}{2}$ nuclei. The efficiency of energy diffusion from 'hot' nuclei (excited) to the 'cold' lattice is a function of internuclear distances between spin-$\frac{1}{2}$ nuclei and the modulation of these internuclear vectors by dynamic processes, typical of molecules in solution. The time evolution of the z component magnetization of two spins I and S in a dipolar interaction has the form[12,13]

$$\frac{d\langle I_z\rangle}{dt} = -\rho_I(\langle I_z\rangle - I_o) - \sigma_{IS}(\langle S_z\rangle - S_0) \quad (1)$$

$$\frac{d\langle S_z\rangle}{dt} = -\rho_S(\langle S_z\rangle - S_o) - \sigma_{SI}(\langle I_z\rangle - I_0) \quad (2)$$

where $\langle I_z\rangle$ and $\langle S_z\rangle$, and S_0 and I_0 are the z components and the equilibrium values of magnetization of spins I and S, ρ_I

Table 1 Characteristics of the Soft Excitation Forms

Form of soft excitation	Special hardware requirements[a]	Excitation function (frequency domain)		Offset-dependent phase gradient	Selectivity[b]	Side lobes	Comments
		Absorptive component	Dispersive component				
Hermite	Pulse-shaping device	Gaussian	Yes	Large, linear	Similar	No	
Rectangular	None	flattened top sinc	Yes	Large, linear	Worse	Yes	
DANTE[c]	None	sinc	Yes	Large, linear	Worse	Yes	Main band and sidebands
90° Gaussian	Pulse-shaping device	Gaussian	Yes	Large, linear		No[d]	
Half Gaussian	Pulse-shaping device	Almost Gaussian	Yes	Large, nonlinear	Worse	No	Dispersive component shows low selectivity
Purged half Gaussian	Pulse-shaping device	Almost Gaussian	No	None	Better	No	
$90° - \alpha_{sel}$	None[e]	$sinc^2$ (near resonance)	No	None	Worse Worse	Yes[e] Yes[e]	Low sensitivity to $\boldsymbol{B}_1$ inhomogeneity
270° Gaussian	Pulse-shaping device	Almost Gaussian	Yes	Small, linear[f]	Worse	Yes	Slightly higher[b] sensitivity to $\boldsymbol{B}_1$ inhomogeneity[b]
Pulse shaping by DANTE	None	Any desired function	[g]	[g]	[g]	[g]	Main band and sidebands
Tailored excitation	None None	Any desired function	[g]	[g]	[g]	[g]	[g]

[a]In general pulse shaping by DANTE possible for all of the shaped pulses.
[b]In comparison with the Gaussian.
[c]'Rectangular' without modulation.
[d]After application of phase correction.
[e]Depends on the soft pulse used.
[f]Only in a small area in the center of the excitation band.
[g]Depends on the excitation sequence.

Table 2 Recommended Applications of the Different Soft Excitation Forms

Form of soft excitation	Recommended application	Evolution of J and Ω during the pulse
Hermite	In cases where uniform excitation is needed	Yes
Rectangular	Only for experiments with low demand on selectivity	Yes
DANTE	For simultaneous excitation of two resonances; excitation of an off-resonance signal	Yes
DANTE	by a side band	Yes
90° Gaussian	Pulse sequence that requires antiphase magnetization for mixing	Yes
Half Gaussian	Pulse sequence that requires antiphase magnetization for mixing; purging of dispersive	Negligible at the end
Half Gaussian	component accomplished by mixing sequence[a]	Negligible at the end
Purged half Gaussian	As above, but experiments with need for explicit purging[b]	Negligible at the end
$90° - \alpha_{sel}$	Pulse sequence starting with antiphase magnetization for mixing	Yes
270° Gaussian	As for the purged half Gaussian in cases with no high selectivity requirements	Partially refocused
Pulse shaping by DANTE	[c]	[c]
Tailored	Solvent peak suppression; excitation of arbitrary spectral regions; hole burning	[c]

[a]E.g. TOCSY or by the phase cycling of 90° pulse before the NOESY mixing.
[b]E.g. ROESY.
[c]Depends on the excitation sequence.

and ρ_S the direct self-relaxation rates, and $\sigma_{IS} = \sigma_{SI}$ the 'cross-relaxation' rates. In this case the relaxation process assumes an exponential decay with a rate constant R_1, the spin–lattice relaxation rate:

$$R_1^i = \rho_i + \sigma_{ij} \quad (i = I, S), (j = S, I) \tag{3}$$

For multispin interaction, as occurs in complex systems of biomolecules, the 'nonselective' spin–lattice relaxation rate ${R_1}^{NS}$ of an i nucleus interacting with neighboring j nuclei can be described by a modified version of Equation (3):

$$R_1^{NS} = \sum_{i \neq j} \rho_{ij} + \sum_i \sigma_{ij} + R^* \tag{4}$$

with the approximation of independent pairwise interactions and considering the contribution of nondipolar relaxation processes R^*.

The explicit form of ρ_{ij} and σ_{ij} in the case of intramolecular dipolar interactions are:

$$\rho_{ij} = \frac{1}{10}\frac{\gamma_H^4\hbar^2}{r_{ij}^6}\left(\frac{3\tau_c}{1+\omega_H^2\tau_c^2} + \frac{6\tau_c}{1+4\omega_H^2\tau_c^2} + \tau_c\right) \quad (5)$$

$$\sigma_{ij} = \frac{1}{10}\frac{\gamma_H^4\hbar^2}{r_{ij}^6}\left(\frac{6\tau_c}{1+4\omega_H^2\tau_c^2} - \tau_c\right) \quad (6)$$

where $\hbar$ is the reduced Planck's constant, γ_H and ω_H are the proton magnetogyric ratio and Larmor frequency respectively, r_{ij} the internuclear distance, and τ_c the effective correlation time which modulates the $i-j$ magnetic interaction.

When the excited i nucleus relaxes with j nuclei at their thermal equilibrium, the 'cross-relaxation' term vanishes[14–16] [as the difference between the second terms of equations (1) and (2) becomes zero] and equation (4) becomes:

$$R_{1i}^{SE} = \sum_{i\neq j}\rho_{ij} \quad (7)$$

where R_{1i}^{SE} is the selective spin–lattice relaxation rate.

Selective excitation of two (or more) resonances adds a selective cross-relaxation term to equation (7) and the relaxation process is driven by the biselective spin–lattice relaxation rate[17] R_{1i}^{BS}:

$$R_{1i}^{BS} = \sum_{i\neq j}\rho_{ij} + \sigma_{ij} \quad (8)$$

Proton and ^{13}C nuclei can be regarded as limiting examples of complexity for dipolar relaxation analysis and, in both cases, the possibility of using spin–lattice relaxation rates for conformational investigations is based on the ability to dissect the complex relaxation process of a multispin system.

In principle, internuclear distances can be measured for biomolecules in solution provided that (1) they have a single predominant structure or a limited number of conformers and (2) a single ρ_{ij} or σ_{ij} can be experimentally measured. This can be achieved by selective spin–lattice relaxation techniques and by combining selective relaxation rates and nuclear Overhauser effects (NOEs) as described below.

As shown by equation (4) in nonselective spin–lattice relaxation experiments on proton nuclei, the measured relaxation rate is the sum of many terms related to all the direct and σ_{ij} cross-relaxation contributions. Thus, only limited information on molecular conformation and dynamics can be obtained from nonselective proton relaxation data since several different internuclear distances and correlation times determine the experiment rate. No structural information can be obtained from the conventional ^{13}C selective relaxation of protonated carbon atoms since the one-bond C–H interaction dominates the relaxation process, and conformational analysis by studying the relaxation of quaternary carbons is complicated by the multiplicity of long-range C–H interactions.[18,19]

The selective excitation of single (or double) protons simplifies the nuclear relaxation pathway and can be performed by a variety of techniques.[1,2,4,20] If the experimental conditions are such that the selective relaxation process of a nucleus involved in dipole–dipole interactions is described by the above equations, simple and reliable methods of calculation of relaxation parameters from selective relaxation measurements can be used, and structural and/or dynamic information can be obtained.

Although selective relaxation parameters can be efficiently used as tools to investigate conformational properties and biomolecular interactions in small and medium-size molecules, cross-relaxation processes may be profoundly altered under the slow motion conditions ($\omega_0\tau_c \gg 1$) typical of large biomacromolecules such as proteins, nucleic acids, and polysaccharides. When these dynamic conditions apply, the rate of transfer of spin energy between nuclei becomes much larger than the rate of transfer of energy to the lattice. The process of propagation of the magnetization in the network of dipolar-coupled spins, known as 'spin diffusion',[21] has the effect of destroying differences in spin–lattice relaxation rates in the molecules so that all tend to the same value.[22–24]

Analyzing the relaxation process on a short timescale, i.e. using the 'initial rate approximation', it has been possible to simplify the interpretation of the results on the basis of a hypothetical two-spin system, but large problems still remain due to the extensive overlapping resonances typical of biomacromolecular spectra.

Some novel one-dimensional (1D)[25–27] and two-dimensional (2D)[28–30] methods have recently eliminated the 'spin diffusion' process by exclusion of selected nuclei from the dipolar-coupled bulk proton network[29,30] or by removing the interference of all protons other than the selected pair.[25–27] In the era of 1D, 2D, three-dimensional, and multidimensional NMR these methods can open up a new age for the application of selective relaxation measurement to study large biomacromolecules.

4 GENERAL REMARKS ON SELECTIVE RELAXATION EXPERIMENTS

In order to perform selective relaxation experiments, the use of pulse sequences able to perturb the nuclear spin population is required. Initial relaxation rates can be obtained provided that the experiment is correctly carried out and that theoretical problems do not quench the dipolar relaxation strategy. As the recovery of the longitudinal component of nuclear magnetization very rarely follows a true exponential decay, it is important to analyze under what circumstances these undesired effects can be avoided. Unfortunately the main effects that alter the exponential behavior of the magnetization are intrinsic, as they arise in coupled spin systems and are due to dipole–dipole 'cross-relaxation' effects and scalar coupling.[31,32]

4.1 Cross-Relaxation Effects

As shown by equations (1) and (2), the recovery of the longitudinal component of the magnetization is usually described by two constant rates ρ and σ, and only under special conditions is this behavior a pure exponential. This is the case

for ^{13}C magnetization measured under conditions of continuous broadband proton decoupling, where proton irradiation sets up and maintains a constant spin population of allowed energy levels such that cross relaxation no longer affects the recovery curve. Similar behavior is expected for selective proton relaxation in cases of weak dipolar coupling or when the effect of cross-relaxation diffusion is truncated using the initial slope approximation. In the latter case the experimental relaxation parameter is calculated by measuring the initial rates in the semi-logarithmic plot of reduced intensity $(I_0 - I_z)/2I_0$ vs. delay times. In more general cases, especially in biological systems, the presence of a network of dipolar-coupled spins induces cross-relaxation contributions that change the pure exponential decay. Nevertheless, at least for small and medium-size biomolecules and for dipolar interactions within a 3.5 distance, the initial rate approximation can be used to interpret the data in terms of two-spin systems and to calculate by numerical simulation the direct self-relaxation rate and the 'cross-relaxation' contributions. A more complex situation occurs when the fast motion conditions $\omega_0{}^2\tau_c{}^2 \ll 1$ do not hold, as in large biomolecules. Under these conditions, due to spin diffusion, the initial slope approximation is no longer valid, especially for long-range interactions, and only recently has it been possible to determine by virtue of synchronous nutation experiments[25–27] the structural properties of proteins from cross-relaxation data obtained by selective relaxation measurements.

4.2 Scalar Coupling

In strongly coupled spin systems, the transition probabilities for the components of a spin multiplet are no longer equal. An important element of symmetry is thus lost, even though the excitation pulse acts equally on all multiplet components. Even for a single two-spin system AB, the zero quantum, single quantum and the double quantum transition probabilities do not assume the classical form,[31–33] but a mixing term W_{AB} appears. It is this last term W_{AB} that causes different recovery curves for the components of a spin multiplet with a specific deviation from pure exponential magnetization decay.

However the perturbative effect of scalar coupling on the behavior of the magnetization recovery curve can be considered a priori. Moreover the 'classical' relaxation equations are still valid when $\Delta\omega/J > 10$, where $\Delta\omega$ is the difference in chemical shift between two spins and J is their scalar coupling constant. This is a general condition met in studying biological systems. Again the synchronous nutation experiment[27] has simplified the problem of correctly calculating the relaxation parameter in the presence of strong scalar coupling, by removing all scalar interactions between spins that are irradiated (active) and at Boltzmann equilibrium (passive). Although the effect of strong scalar coupling between irradiated (active) spins can still affect the recovery curve, its contribution can be taken into account by simple numerical analysis.

5 APPLICATION OF SELECTIVE RELAXATION TECHNIQUES IN BIOLOGICAL SYSTEMS

Many papers have fairly recently been published[25,34–38] proposing the use of selective relaxation experiments to investigate biological systems. For simplicity, proton homonuclear and heteronuclear interactions and their field of application will be treated separately.

5.1 Homonuclear Selective Relaxation Experiments

In ^1H homonuclear spin systems, the nonselective inversion recovery, 180°-τ-90° pulse sequence gives partially relaxed spectra in which it is possible to follow the recovery of the Boltzmann equilibrium for each resonance by individual constant rates (R_1^{NS}) which are the sum of two contributions: the direct and the cross-relaxation terms [as described by equation (4)]. It has been shown by Freeman et al.[14] that cross relaxation may be negligible provided that the 180° pulse selectively excites single-proton resonances. In particular, if the initial relaxation is monitored after selective population inversion of proton i, i.e., short delays are used between the selective and the nonselective observing 90° pulse, the initial recovery rate of the magnetization (R_{1i}^{SE}) is described by equation (7). At longer delay times, cross relaxation becomes significant, as can be observed from the intensity changes of the resonances of protons dipolarly coupled to the excited proton. It follows that selective excitation techniques can be used to achieve a simplification of the proton relaxation process and to calculate the selective dipolar relaxation contribution to the observed spin–lattice relaxation rate.

The initial selective relaxation rate R_{1i}^{SE} is an important parameter which can be used to obtain information on: (1) relaxation mechanisms, (2) molecular dynamics, and (3) molecular conformations.

1. In molecular systems which satisfy the extreme narrowing condition $(\omega_0\tau_c)^2 \ll 1$, for proton i, the ratio between the nonselective relaxation, R_1^{NS}, and R_{1i}^{SE} is diagnostic of the efficiency of the dipole–dipole relaxation mechanism, since this ratio, F_i, is equal to 1.5 for a relaxation pathway completely dominated by the i–j proton dipolar interactions.[39]
2. As shown in Figure 1, F_i also depends on $\omega_0\tau_c$ and, hence, for rigid isotropically reorienting molecules, motions can be quantified from the latter parameter.[39]
3. The combined use of R_{1i}^{SE} and homonuclear Overhauser effects, NOEs, yields an absolute evaluation of σ_{ij} rates since, neglecting cross-polarization effects, the following relationship holds[40]

$$\mathrm{NOE} = \sigma_{ij}/R_i(\mathrm{SE}) \tag{9}$$

where NOE is the Overhauser effect on proton i upon selective excitation of proton j.

The calculation of the cross-relaxation rate relative to a single i–j dipolar interaction is also possible by the simultaneous double excitation of protons i and j. If selectivity in the double excitation can technically be achieved, the relaxation process is driven by the biselective relaxation rate, $R_{1i}{}^{BS}$, as shown by equation (8).

It should be noted that the initial conditions for the evaluation of $R_{1i}{}^{BS}$ are critically important because the peak intensities observed in the partially relaxed spectra are determined by the relaxation process and the time-dependent i–j NOE.[31,41]

Homonuclear selective relaxation experiments are widely used to investigate different properties of biological systems. The most interesting approaches are related to the analysis of:

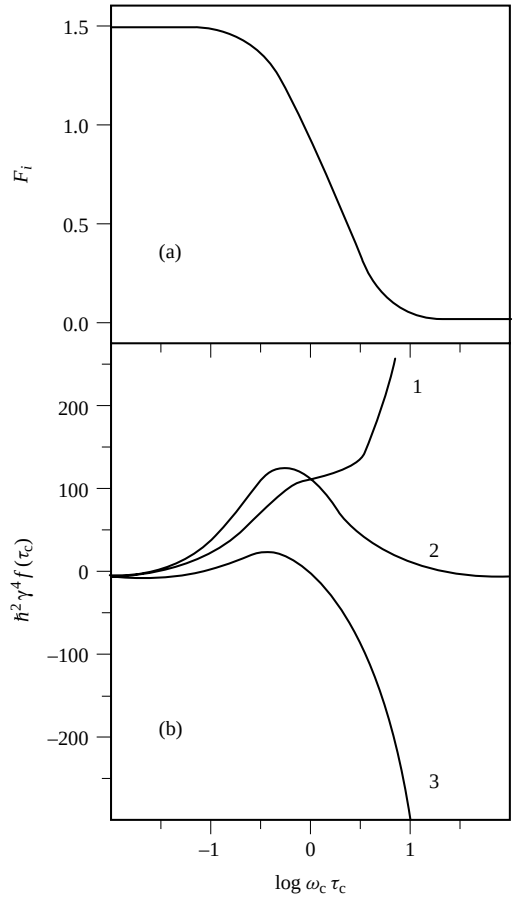

Figure 1 (a) Dependence of $F = R_i(\mathrm{NS})/R_i(i)$ versus log $\omega_0\tau_c$. (b) Behavior of *R*SE/1 (1), *R*NS/1 (2), and σ_{ij} (3) for a two-spin system under different dynamic conditions; (1), (2), and (3) are readily generalized for proton i, involved in multiple interactions with several protons, $i \neq j$. (Reproduced by permission of Academic Press from N. Niccolai et al.[39])

1. conformational and dynamic properties of biomolecules in solution;
2. the interaction process between ligand and biological receptors;
3. the behavior of water in the presence of large, organized biological systems.

5.1.1 Conformational and Dynamic Properties of Biomolecules in Solution

The network of intramolecular dipolar connectivities in small to medium-size biomolecules can be easily evaluated by selective relaxation experiments. The most suitable approach consists first of calculating the cross-relaxation rates between selective proton pairs as the difference between selective and biselective relaxation experiments:

$$\sigma_{ij} = R_{1i}^{\mathrm{BS}} - R_{1i}^{\mathrm{SE}} \tag{10}$$

$$\sigma_{ji} = R_{1j}^{\mathrm{BS}} - R_{1j}^{\mathrm{SE}} \tag{11}$$

in which $\sigma_{ij} = \sigma_{ji}$ are the cross-relaxation values obtained from analysis of the relaxation properties of the i and j nuclei, respectively. Selective homonuclear NOE experiments can also be used to evaluate σ_{ij}. Figure 2 shows an example of proton-selective and biselective experiments used for calculating σ_{ij}. The effect of the additional cross-relaxation contribution to the magnetization recovery process in the biselective experiment, is evident.

As shown by equation (6) and Figure 3, σ_{ij} contains both structural (r_{ij}) and dynamic (τ_c) information.[42] Constant calibration distances are required for the calculation of the effective correlation time τ_c. This is easily achieved by considering independent conformational distances as geminal interactions of CH_2 groups, *ortho* protons of aromatic residues, etc.

As shown in Figure 1, $F_1 = R_{1i}^{\mathrm{NS}}/R_{1i}^{\mathrm{SE}}$ can be used as a probe for molecular motion assuming as dominant the intramolecular dipolar mechanism. Carbon-13 relaxation measurements (see next section) obtained under broad-band proton decoupling can also be used to map the distribution of motions along a biomolecule or to verify isotropic tumbling in systems with restricted internal flexibility. A detailed description of the modulation of the dipole–dipole interaction allows selected interproton distances, from which the solution conformation can be derived, to be calculated with confidence. From the first papers[39,43,44] in which this approach was proposed, nearly every class of biological molecule was investigated: amino acids,[43,45] peptides,[42] carbohydrates,[46] oligosaccharides,[47,48] drugs,[49,50] natural products,[37,51,52] etc.

Recently when the 2D approach for studying dipolar networks seemed to diminish the importance of these selective relaxation studies, a new selective experiment was proposed which enabled large macromolecules such as proteins to be investigated[25] (Figure 4). According to this new approach, one or two proton resonances are simultaneously excited by an amplitude modulated radiofrequency field which forces the magnetization vectors to undergo simultaneous motion defined as 'synchronous nutation'.[25–27] Time-dependent analysis under different initial conditions allows calculation of the direct self-relaxation rate or the 'cross-relaxation' term. In the 'synchronous nutation' experiment, the neighboring spins do not affect the magnetization behavior of the selectively isolated spin system even in the presence of the spin diffusion typical of slow molecular tumbling $\omega_0\tau_c \gg 1$ conditions. Conformational studies (through selected-pair distance determination) by selective relaxation measurements in large biomacromolecules appear to be a valid alternative to the classical approach based on 2D analysis of dipolar-coupled spin systems.

5.1.2 Intermolecular Interaction: Ligand–Macromolecular Receptor

Ligand–macromolecule interactions can be detected by selective relaxation measurements. The formation of intermolecular adducts affects nonselective and selective spin–lattice relaxation rates to different extents, assuming that fast chemical exchange occurs between the bound and free environments with respect to both the chemical shift difference and the proton relaxation rate.[53]

If only two environments are considered, the relaxation parameters are expressed by:

$$R_{1\mathrm{obs}}^{\mathrm{A}} = \chi_{\mathrm{f}} R_{1\mathrm{f}}^{\mathrm{A}} + \chi_{\mathrm{b}} R_{1\mathrm{b}}^{\mathrm{A}} \tag{12}$$

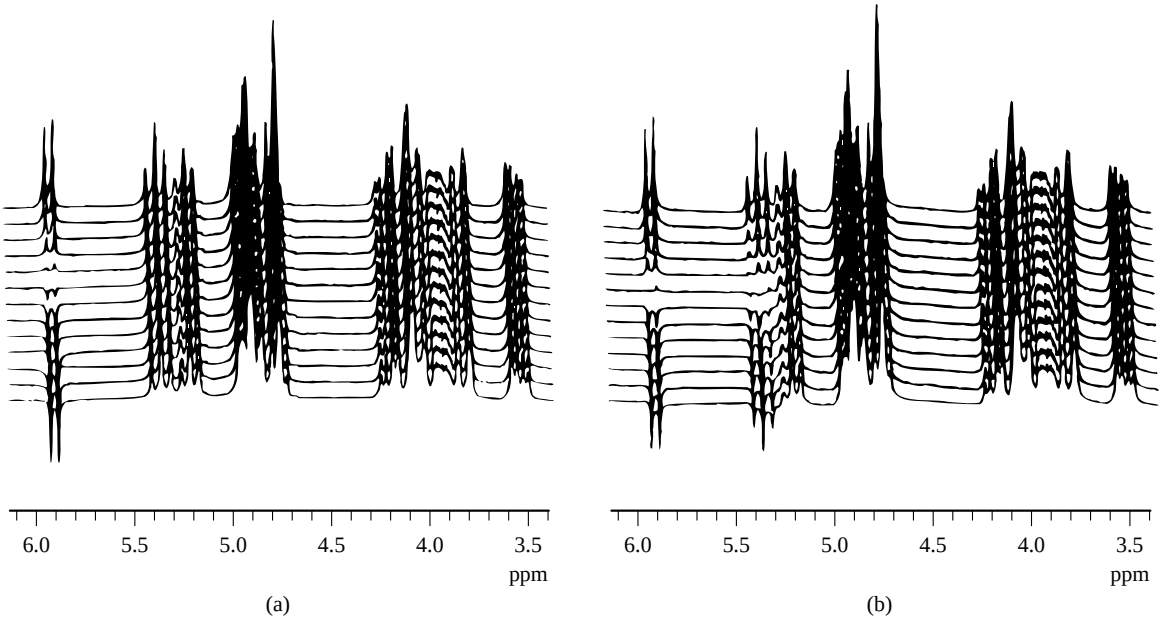

Figure 2 Proton-selective and biselective partially relaxed spectra obtained by selective inversion of the magnetization of H-1′ (a) and of both H-1′–H-3 (b) protons of a 0.15 mol dm^{-3} gentiobiose octaacetate solution in dimethyl sulfoxide-d_6. T = 300 K. The delay values between the selective and nonselective pulses were: 5, 10, 20, 40, 80, 100, 200, 400, 600, 800, 1000, 2000, and 10 000 ms

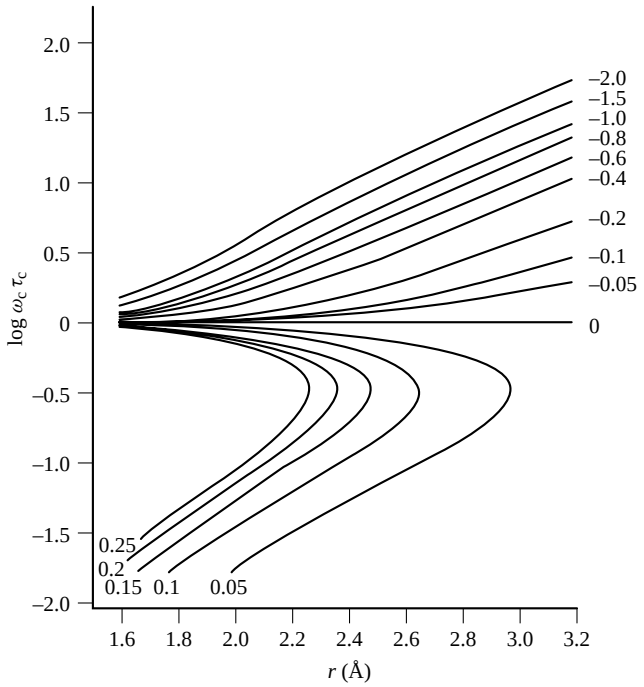

Figure 3 Isosigma contours for log $\omega_0\tau_c$ vs. interproton distances calculated from equation [6]; the selected σ values are expressed in s^{-1}. (Reproduced by permission of Elsevier from N. Niccolai, L. Pogliani, C. Rossi, P. Corti, and W. A. Gibbons, *Biophys. Chem.*, 1984, **20**, 217)

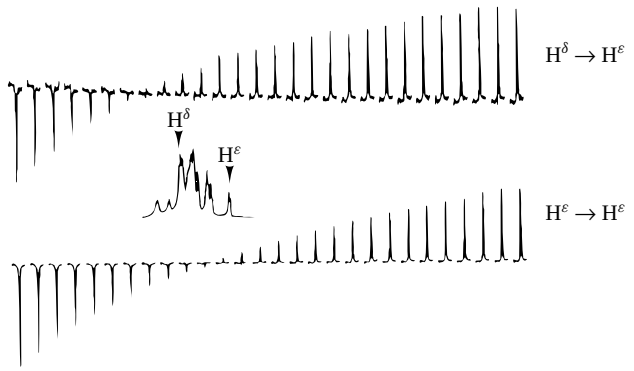

Figure 4 Selective inversion–recovery measurements of the aromatic protons H^δ and H^ε of the tyrosine (Tyr) residue in bovine pancreatic trypsin inhibitor dissolved in ^2H_2O at 327 K. The inset shows the aromatic region (between 8.2 and 5.8 ppm) of the 1D spectrum (eight scans); the arrows indicate the shifts of H^ε at 6.30 ppm and of H^δ at 7.20 ppm. Lower part: normal inversion–recovery measurement of H^ε in Tyr[23] using selective pulses and direct observation of H^ε. Upper part: inversion–recovery of H^δ using selective pulses and Hartmann–Hahn transfer from H^δ to H^ε. (Reproduced by permission of the American Chemical Society from B. Boulat, R. Konrat, I. Burghardt, and G. Bodenhausen, *J. Am. Chem. Soc.*, 1992, **114**, 5412)

where χ_f and χ_b are the ligand fractions in the free and bound environments. Since $\chi_f + \chi_b = 1$ and taking $\chi_b \ll 1$, equation (12) becomes:

$$R_{1\text{obs}}^{\text{A}} = R_{1\text{f}}^{\text{A}} + \chi_{\text{b}} R_{1\text{b}}^{\text{A}} \qquad (13)$$

where A = SE or NS. From equation (13) it emerges that only experimental parameters broadly affected by the ligand–macromolecular interaction make the second term of equation (13) significant. Binding of a ligand to a macromolecular receptor slows down its reorientation motion from $\omega_0\tau_c \ll 1$ to $\omega_0\tau_c \gg 1$. In diamagnetic systems where the dipole–dipole interaction is the dominant relaxation mechanism, entering into the slow-motion region does not significantly alter the nonselective spin–lattice relaxation rates [equation (4)]. On the contrary, the selective relaxation of the bound ligand can be expected to be quite different from that

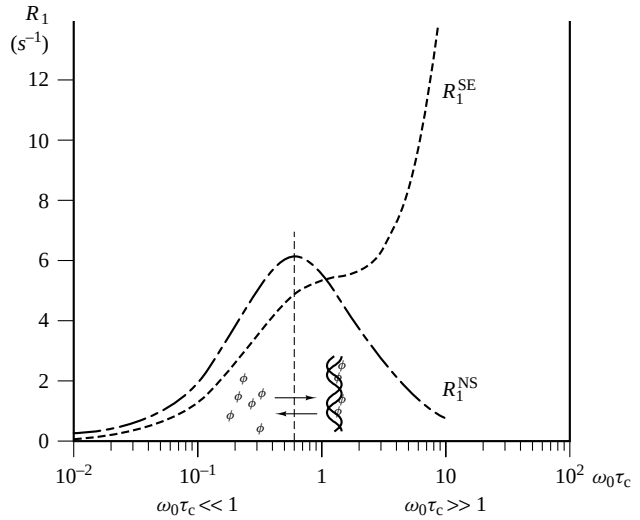

Figure 5 *R*NS/1 and *R*SE/1 of a proton pair versus $\omega_0\tau_c$ assuming a constant r_{i-j} distance (1.77 Å) for the $i-j$ dipolar interaction. The equilibrium between the ligand molecules in the bulk ($\omega_0\tau_c \ll 1$) and DNA-bonded ($\omega_0\tau_c \gg 1$) is also shown. (Reproduced by permission of Elsevier from C. Rossi, A. Donati, and M. R. Sansoni, *Chem. Phys. Lett.*, 1992, **189**, 278)

of the free ligand in solution as shown in Figure 5 for a ligand–DNA interaction.[36]

Since the study of biomolecular interactions by selective relaxation measurement is based on a slowing of ligand molecular motion, the effect of the macromolecular receptor on the viscosity of the system must be considered. Temperature-dependent analysis of R_1^{NS} can address this point. In fact as seen in Figure 5, fast-motion ($\omega_0\tau_c \ll 1$) and slow-motion ($\omega_0\tau_c \gg 1$) conditions show opposite slopes, so hypothetical, drastic changes in viscosity due to the receptor site can be monitored simply by following R_1^{NS} dependence on temperature.[36,54] This method is very powerful since is has a wide range of applications in biological systems. As the information is gained from selective relaxation rates of the ligand, ill-defined receptors in biological samples[55] such as blood whole cells etc. can be investigated and receptor purification followed.

A wide range of ligand–biomacromolecule interactions have been investigated by selective spin–lattice relaxation rate analysis;[56] these include enzyme–substrate,[53] drug–membrane interactions,[57] and recently ligand–DNA,[36] for the purpose of identifying potential mutagens and toxic compounds. This approach can also be used to calculate the association constant for the interaction processes.[58]

5.1.3 Water Selective Relaxation in Large Organized Biological Systems

Water proton relaxation rates have been found to correlate with the physiological and pathological state of the cell as well as to the conformational state of cell constituents.[59–61] Experimental evidence that water selective relaxation is faster than nonselective water relaxation rates in protein solutions and cell suspensions has focused attention on the relaxation mechanism of water protons in large organized systems.[38,62–65] The water spin–lattice relaxation (R_{1W}) may be described as the sum of two contributions:[66]

$$R_{1W} = R_{1A} + R_{1B} \tag{14}$$

where R_{1A} and R_{1B} are the intra- and inter-molecular relaxation rates. The intramolecular term is due to:

$$R_{1B} = R_{1WW} + R_{1WM} \tag{15}$$

R_{1WW} is the dipolar contribution due to intramolecular water–water interactions and R_{1WM} that arising from water–macromolecule (or cell constituent) interactions.[31] The latter interaction can yield direct ρ_{WM} and cross-relaxation σ_{WM} contributions from simultaneous water and macromolecule proton excitation:

$$R_{1WM} = \sum \rho_{WM} + \sum \sigma_{WM} \tag{16}$$

If the water relaxation rate is measured in the selective mode, only a small fraction of the macromolecule protons are excited and the σ_{WM} term disappears. It follows that in the presence of large biological surfaces:[65]

$$R_{1W}^{NS} - R_{1W}^{SE} = \sum \sigma_{WM} \tag{17}$$

where R_{1A} and R_{1WW} are constants in nonselective and selective experiments respectively. Experimental evidence obtained for protein solutions and cell culture suspensions shows that the difference between nonselective and selective relaxation rates [equation (17)] are not only due to the dynamic change in the solvent molecules but also to dipolar intermolecular connectivities between the solvent and the surface of hydrophilic regions of macromolecules. This suggests that it would be useful to use the complete set of relaxation parameters, such as $R_{1W}^{NS}R_{1W}^{SE}$, and σ_{WM} to investigate the physiological and pathological state of cells or to study drug–cell and virus–cell interactions:[67] R_{1W}^{NS} to probe essentially dynamic features of the heterogeneous systems, and R_{1W}^{SE} and σ_{WM} to study the water–macromolecule magnetic energy transfer process, which is intimately linked to the solvent exposed interface structure assumed by the biological material.

5.2 Heteronuclear Selective Relaxation Experiments

Our discussion will be limited to the ^{13}C nucleus, due to its importance for verifying dynamic and structural information on biological systems.

In spite of the low sensitivity of heteronuclei with respect to protons, several advantages exist. Carbon-13 signals are spread over a large chemical shift range (over 300 ppm). The carbon resonances can be treated as single resonances removing proton scalar coupling by a broadband decoupling pulse. Under these conditions the carbon relaxations can be regarded as pure exponential, determined by a single contribution: the direct self-relaxation term. Furthermore, relaxation contributions due to intermolecular interactions are seldom significant (as the carbons are shielded by the proton surface) and, in natural abundance experiments, homonuclear $^{13}C-^{13}C$ dipolar interactions are rare due to ^{13}C isotopic dilution. These properties make carbon relaxation a suitable parameter for investigating solution properties of biomolecules.

5.2.1 ^{13}C Selective Relaxation

In conventional ^{13}C relaxation experiments (obtained by broadband proton decoupling), cross relaxation between carbon nuclei is ignored and the measurement gives the selective, direct carbon spin–lattice relaxation rate:

$$R_{1C}^{SE} = \sum \frac{1}{10} \frac{\hbar^2 \gamma_H^2 \gamma_C^2}{r_i^6} \left[\frac{3\tau_c}{1+\omega_C^2\tau_c^2} + \frac{6\tau_c}{1+(\omega_H+\omega_C)^2\tau_c^2} + \frac{\tau_c}{1+(\omega_H-\omega_C)^2\tau_c^2} \right] \quad (18)$$

R_{1C}^{SE} of protonated carbons are dominated by the dipolar interaction between bonded proton–carbon nuclei.[17,18] In this case the internuclear proton–carbon distance can be assumed to be constant and the effective correlation time calculated. In flexible molecules, a mapping of dynamic properties may be obtained from the R_{1C}^{SE} of different carbons. If continuous broadband proton decoupling is replaced by a selective 180° proton pulse, applied to the i nucleus, with the first 180° carbon pulse the initial rate of the longitudinal magnetization of carbon is:[68–70]

$$R_{1C}^{BS} = R_{1C}^{SE} + \xi\sigma_{CH_i} \quad (19)$$

where R_{1C}^{BS} is the biselective carbon relaxation rate $\xi = \gamma_H/\gamma_C$ and σ_{CH} the single proton–carbon 'cross-relaxation' term. When the selective 180° proton pulse is replaced by a proton perturbation which can invert the spin equilibrium of the entire proton population, the carbon relaxation is described by:[69–71]

$$R_{1C}^{NS} = R_{1C}^{SE} + \xi \sum \sigma_{CH_i} \quad (20)$$

The following dynamic and structural information is obtained by comparing R_{1C}^{SE}, R_{1C}^{BS}, and R_{1C}^{NS} measurements.

5.2.1.1 Dynamic analysis. The R_{1C}^{NS}/R_{1C_i} ratio takes a value in the range 2.99–1, depending on the molecular motion. In this way the value of the R_{1C}^{NS}/R_{1C_i} ratio allows the correlation times for each molecular moiety to be determined (or at least the limit value of τ_c). The R_{1C}^{NS}/R_{1C_i} ratio in particular is a very useful parameter for evaluating the effective correlation time of nonprotonated carbon atoms.

5.2.1.2 Structural analysis. The difference between R_{1C}^{BS} and R_{1C}^{SE} gives the cross relaxation term $\sigma_{C_iH_A}$ for each $^1H-^{13}C$ magnetic interaction which contains distance information. This method has been demonstrated with different natural products, giving reliable results.[69–71]

5.2.2 Selective Proton–Carbon NOEs

Several authors have shown that selective proton–carbon NOEs, $(^1H)^{13}C$-NOE, can be generated.[72–74] When a selective pulse is used to saturate a single proton then 'cross relaxation' between the irradiated proton and the carbon microenvironment occurs. The $(^1H)^{13}C$-NOE is described by:[75,76]

$$(^1H_A)^{13}C_i - \text{NOE} = \frac{\sigma_{C_iH_A}}{R_{1C}^{SE} + R_{1C}^{*}} \quad (21)$$

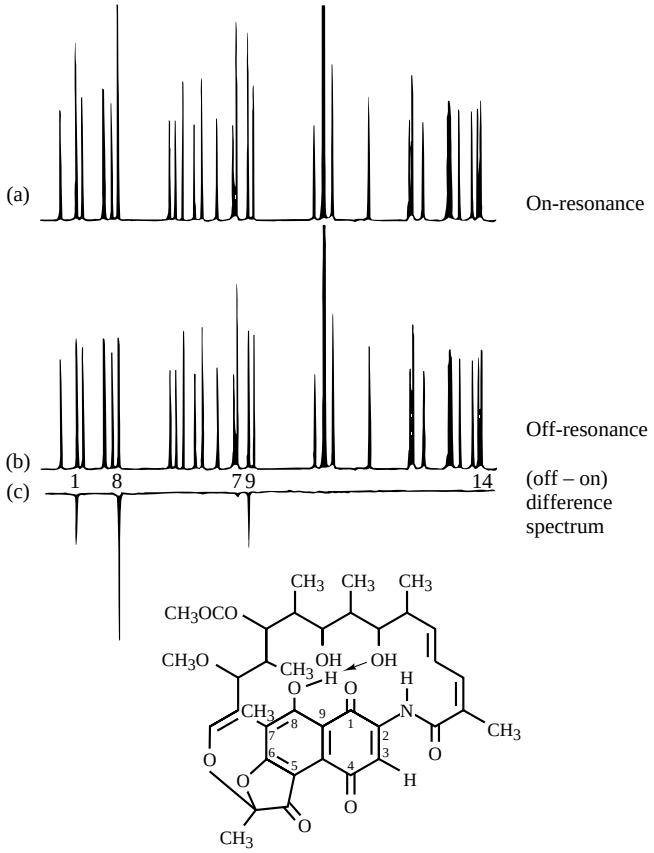

Figure 6 Carbon-13 spectra of 0.5 mol dm^{-3} rifamycin in $CDCl_3$ recorded on a Varian XL-200 spectrometer at 296 K: (a) ^{13}C spectrum after irradiation of the phenolic hydroxyl proton; (b) as (a) but with the decoupler set 'off-resonance'. (c) Difference spectrum (b)–(a). The presaturation selective pulse on the phenolic hydroxyl proton had a 10 s duration and 0.5 W power. During the acquisition of the FIDs the decoupler was on with a power of 4 W in the broadband mode. The structure of rifamycin S is shown. (Reproduced by permission of the American Chemical Society from N. Niccolai et al.[75])

where $\sigma_{C_iH_A}$ is the selective 'cross relaxation', R_{1C}^{SE} the selective carbon relaxation rate, and R_1* the relaxation contribution due to nondipolar interactions [in paramagnetic systems this term often quenches the $(^1H)^{13}C$-NOE]. Thus by combining selective NOEs with carbon relaxation rates, specific distance calculations can be obtained.

Although care must be taken in dealing with large macromolecules when magnetization diffusion occurs between spins, this method has been usefully applied to investigate the conformation of biological molecules such as antibiotics, peptides, natural components,[77–79] etc. Figure 6 illustrates the capacity of $(^1H)^{13}C$ - NOE to discriminate the carbon microenvironment by selective proton perturbation.[75]

6 RELATED ARTICLES

Biological Macromolecules: Structure Determination in Solution; Molecular Motions: T_1 Frequency Dispersion in Biological Systems; Nuclear Overhauser Effect; Relaxation: An Introduction; Relaxation Mechanisms: Magnetization Modes; Selective Pulses.

7 REFERENCES

1. H. Kessler, S. Mronga, and G. Gemmecker, *Magn. Reson. Chem.*, 1991, **29**, 527.
2. R. Freeman, *Chem. Rev.*, 1991, **91**, 1397.
3. E. Gaggelli and G. Valensin, *Concepts Magn. Reson.*, 1992, **4**, 339.
4. S. Alexander, *Rev. Sci. Instrum.*, 1961, **32**, 1066.
5. C. Bauer, R. Freeman, T. Frenkiel, J. Keeler, and A. J. Shaka, *J. Magn. Reson.*, 1984, **58**, 442.
6. G. A. Morris and R. Freeman, *J. Magn. Reson.*, 1978, **29**, 433.
7. G. Bodenhausen, R. Freeman, and G. A. Morris, *J. Magn. Reson.*, 1976, **23**, 171.
8. J. Friedrich, S. Davies, and R. Freeman, *J. Magn. Reson.*, 1987, **75**, 390.
9. H. Geen, X.-L. Wu, P. Xu, J. Friedrich, and R. Freeman, *J. Magn. Reson.*, 1989, **81**, 646.
10. R. J. Sutherland and J. M. S. Hutchinson, *J. Phys. E*, 1978, **11**, 79.
11. J. M. Hutchinson, R. J. Sutherland, and J. R. Mallard, *J. Phys. E*, 1978, **11**, 217.
12. F. Bloch, *Phys. Rev.*, 1957, **105**, 1206.
13. I. Solomon, *Phys. Rev.*, 1955, **99**, 559.
14. R. Freeman, H. D. W. Hill, B. L. Tomlinson, and L. D. Hall, *J. Chem. Phys.*, 1974, **61**, 4466.
15. J. H. Noggle and R. E. Shirmer, *The Nuclear Overhauser Effect; Chemical Applications*, Academic Press, New York, 1971.
16. D. Neuhans and M. P. Williamson, *The Nuclear Overhauser Effect in Structural and Conformational Analysis*, VCH, Berlin, 1989.
17. A. Abragam, *The Principles of Nuclear Magnetism*, Oxford University Press, London, 1961.
18. A. Allerhand, D. Doddrell, and R. Komoroski, *J. Chem. Phys.*, 1971, **55**, 189.
19. L. G. Werbelow and D. M. Grant, *J. Chem. Phys.*, 1975, **63**, 544.
20. C. J. Turner, *Prog. NMR Spectrosc.*, 1984, **16**, 311.
21. A. Kalk and H. J. C. Berendsen, *J. Magn. Reson.*, 1975, **24**, 343.
22. W. Massefski Jr. and A. G. Redfield, *J. Magn. Reson.*, 1988, **78**, 150.
23. V. V. Krishnan, N. Murali, and A. Kumar, *J. Magn. Reson.*, 1989, **84**, 255.
24. V. V. Krishnan, U. Hedge, and A. Kumar, *J. Magn. Reson.*, 1991, **94**, 605.
25. B. Boulat, R. Konrat, I. Burghardt, and G. Bodenhausen, *J. Am. Chem. Soc.*, 1992, **114**, 5412.
26. B. Boulat, I. Burghardt, and G. Bodenhausen, *J. Am. Chem. Soc.*, 1992, **114**, 10 679.
27. I. Burghardt, R. Konrat, B. Boulat, S. J. F. Vincent, and G. Bodenhausen, *J. Chem. Phys.*, 1993, **98**, 1721.
28. J. Fejzo, W. M. Westler, S. Macura, and J. L. Markley, *J. Magn. Reson.*, 1991, **92**, 195.
29. J. Fejzo, W. M. Westler, S. Macura, and J. L. Markley, *J. Magn. Reson.*, 1991, **92**, 20.
30. J. Fejzo, W. M. Westler, S. Macura, and J. L. Markley, *J. Am. Chem. Soc.*, 1992, **114**, 1523.
31. I. D. Campbell and R. Freeman, *J. Magn. Reson.*, 1973, **11**, 143.
32. I. D. Campbell, C. M. Dobson, R. G. Ratcliffe, and R. J. P. Williams, *J. Magn. Reson.*, 1978, **29**, 397.
33. R. L. Vold and R. R. Vold, *Prog. NMR Spectrosc.*, 1978, **12**, 79.
34. N. Niccolai and C. Rossi, *Methods in Enzymol.*, 1989, **176**, 184.
35. N. Marchettini and G. Valensin, *J. Phys. Chem.*, 1990, **94**, 4507.
36. C. Rossi, A. Donati, and M. R. Sansoni, *Chem. Phys. Lett.*, 1992, **189**, 278.
37. M. Sugiura, T. Sai, M. Ichimaru, A. Kato, and N. Takao, *Magn. Reson. Chem.*, 1991, **29**, 755.
38. B. P. Hills, *Mol. Phys.*, 1992, **76**, 489.
39. N. Niccolai, M. P. Miles, and W. A. Gibbons, *Biochem. Biophys. Res. Commun.*, 1979, **91**, 157.
40. C. R. Jones, C. T. Sikakana, S. Hehir, M.-C. Kuo, and W. A. Gibbons, *Biophys. J.*, 1978, **24**, 815.
41. C. Rossi and N. Niccolai, *Chem. Phys. Lett.*, 1989, **156**, 438.
42. N. Niccolai, L. Pogliani, C. Rossi, P. Corti, and W. A. Gibbons, *Biophys. Chem.*, 1984, **20**, 217.
43. N. Niccolai, M. P. de Leon de Miles, S. P. Hehir, and W. A. Gibbons, *J. Am. Chem. Soc.*, 1978, **100**, 6528.
44. N. Niccolai, A. K. Schnoes, and W. A. Gibbons, *J. Am. Chem. Soc.*, 1980, **102**, 1513.
45. C. Rossi, L. Pogliani, F. Laschi, and N. Niccolai, *J. Chem. Soc., Faraday Trans. 1*, 1983, **79**, 2955.
46. T. R. Brown and S. Ogawa, *Proc. Natl. Acad. Sci. U.S.A.*, 1977, **74**, 3627.
47. C. Rossi, L. Pogliani, S. Masi, C. Ceccarini, and N. Niccolai, *J. Biomol. Struct. Dyn.*, 1984, **2**, 481.
48. C. Rossi, S. Ulgiati, and N. Marchettini, *J. Chem. Soc., Faraday Trans. 1*, 1989, **85**, 2149.
49. T. Sai, N. Takao, and M. Sugiura, *Magn. Reson. Chem.*, 1992, **30**, 1041.
50. E. Gaggelli, N. Gaggelli, G. Valensin, and A. Vivi, *Can. J. Chem.*, 1993, **71**, 738.
51. W. Chen, X.-H. Zhu, M. J. Avison, and R. G. Shulman, *Biochemistry*, 1993, **32**, 9417.
52. C. Anselmi, M. Centini, M. Scotton, and A. Sega, *Magn. Reson. Chem.*, 1992, **30**, 994.
53. G. Valensin, T. Kushnir, and G. Navon, *J. Magn. Reson.*, 1982, **46**, 23.
54. C. Rossi, M. R. Sansoni, and A. Donati, *Trends Ecol. Phys. Chem.*, 1993, **57**.
55. I. Barni-Comparini, E. Gaggelli, N. Marchettini, and G. Valensin, *Biophys. J.*, 1985, **48**, 247.
56. G. Uccello-Barretta, C. Bertucci, E. Domenici, and P. Salvadori, *J. Am. Chem. Soc.*, 1991, **113**, 7017.
57. G. Valensin, A. Casini, A. Lepri, and E. Gaggelli, *Biophys. Chem.*, 1983, **17**, 297.
58. E. Gaggelli, G. Valensin, T. Kushnir, and G. Navon, *Magn. Reson. Chem.*, 1992, **30**, 461.
59. D. E. Woessner, *Mol. Phys.*, 1977, **34**, 899.
60. R. Damadian, *Science*, 1971, **171**, 1151.
61. P. T. Beall, C. F. Hazlewood, and P. N. Rao, *Science*, 1976, **192**, 904.
62. D. C. Chang and D. E. Waessner, *Science*, 1978, **198**, 1180.
63. G. Valensin and N. Niccolai, *Chem. Phys. Lett.*, 1981, **79**, 47.
64. N. Niccolai, C. Rossi, and E. Tiezzi, *Chem. Phys. Lett.*, 1983, **96**, 154.
65. N. Niccolai, L. Pogliani, and C. Rossi, *Chem. Phys. Lett.*, 1984, **110**, 294.
66. J. A. Glasel, *Water. A Comprehensive Treatise*, ed. F. Franks, Plenum Press, New York, 1975, Vol. 1, p. 215.
67. G. Valensin, E. Gaggelli, E. Tiezzi, P. F. Valensin, and M. L. Bianchi-Bandinelli, *Biophys. Chem.*, 1979, **10**, 143.
68. I. D. Campbell and R. Freeman, *J. Chem. Phys.*, 1973, **58**, 2666.
69. C. Rossi, *J. Chem. Phys.*, 1986, **84**, 6581.
70. K. E. Kövér and G. Batta, *Prog. NMR Spectrosc.*, 1987, **19**, 223.
71. C. Rossi, N. Marchettini, L. Pogliani, F. Laschi, and N. Niccolai, *Chem. Phys. Lett.*, 1987, **136**, 506.

72. K. F. Kuhlmann, D. M. Grant, and R. K. Harris, *J. Chem. Phys.*, 1970, **52**, 3439.
73. S. Takeuchi, J. Uzawa, H. Seto, and H. Yonehara, *Tetrahedron Lett.*, 1977, 2943.
74. J. J. Ford, W. A. Gibbons, and N. Niccolai, *J. Magn. Reson.*, 1982, **47**, 522.
75. N. Niccolai, C. Rossi, V. Brizzi, and W. A. Gibbons, *J. Am. Chem. Soc.*, 1984, **106**, 5732.
76. N. Niccolai, C. Rossi, P. Mascagni, W. A. Gibbons, and V. Brizzi, *J. Chem. Soc., Perkin Trans. 1*, 1985, 239.
77. M. F. Aldersley, F. M. Dean, and B. E. Mann, *J. Chem. Soc., Chem. Commun.*, 1983, 107.
78. N. Niccolai, C. Rossi, P. Mascagni, P. Neri, and W. A. Gibbons, *Biochem. Biophys. Res. Commun.*, 1984, **124**, 739.
79. C. Rossi, N. Niccolai, and F. Laschi, *J. Phys. Chem.*, 1987, **91**, 3903.

Biographical Sketch

Claudio Rossi. *b* 1952. Ph.D., University of Siena, Italy (Supervisor Professor Enzo Tiezzi, 1977). Postdoctoral work at the Biochemistry Department, University of Wisconsin, Madison (Prof. William A. Gibbons), 1981, and at the Pharmaceutical Chemistry Department, University of California at San Francisco (Prof. Thomas L. James), 1985–86. Successively research associate and associate professor at the University of Siena, 1987–93. Currently full Professor of Physical Chemistry, Department of Chemistry, University of Siena, 1994–present. Approx. 100 publications. Research specialities: ^{1}H and ^{13}C selective relaxation experiments and their applications to biological systems.

Supercritical Fluids

Craig M. V. Taylor and Gunilla B. Jacobson

Los Alamos National Laboratory, Los Alamos, NM, USA

1 Introduction to Supercritical Fluids 1
2 Supercritical Fluids 1
3 Instrument Requirements for High-Pressure NMR 7
4 Supercritical Fluid Applications 8
5 References 9

1 INTRODUCTION TO SUPERCRITICAL FLUIDS

While the existence of the supercritical 'phase' has been known for over 150 years it has been only in the last 20 years that the value of supercritical fluids (SCFs) as a medium for extraction, cleaning and synthesis has been recognized. It is now clear that SCF processes are often constrained to very narrow regions of economic feasibility due to the phase behavior of the solute-solvent system. As a result, there needs to be very tight controls over any industrial process employing SCFs. If the process parameters must be more exact, then so does the information required to generate the design parameters, which includes experimental measurements, theories, and the correlations that result in predictability in a given system. In an effort to expand the current understanding of SCFs and their applications, intensive studies are ongoing using nuclear magnetic resonance (NMR). In an effort to further explain the physical chemistry inherent to possible applications of SCFs, a brief introduction is given to this odd and often ignored 'phase' of substances. Following that is an introduction to NMR as it pertains to the study of SCF applications.

2 SUPERCRITICAL FLUIDS

2.1 General Properties

The supercritical state is defined by the critical pressure (P_c) and critical temperature (T_c). One of the most common phenomenological definitions describes critical pressure as the pressure above which, regardless of the applied temperature, a liquid cannot be made to boil. In a similar way, the critical temperature can be thought of as the temperature above which, regardless of the applied pressure, a gas cannot be converted into a liquid. Hence, above the critical point there is no longer a phase boundary between the liquid and the vapor. A liquid/vapor phase boundary represents a coexistence line so that material crossing it requires the expenditure of the latent heat of vaporization.

The concept of the supercritical state can be illustrated by a physical example. Consider a closed container of constant volume. Inside the container we start with some amount of pure liquid. The space above this pure liquid will be filled with pure vapor at the liquid's equilibrium vapor pressure. Now assume that we begin to heat up this container slowly and uniformly. The density of the liquid will begin to decrease through normal thermal expansion. Meanwhile, the density of the vapor phase begins to increase since more molecules are leaving the liquid to enter the vapor phase. Continued heating results in a further decrease of the liquid density and an increase in the vapor density. Eventually, at some temperature, T_c (and resulting, uniform pressure, P_c), the density of the liquid and vapor phases reach the same value, and the vapor and liquid 'phases' have identical compositions and identical densities.

Is this supercritical fluid phase to be considered a liquid or a gas? The answer is that a supercritical fluid reflects properties of both. Table 1 shows relative values of the density, diffusion coefficient, and viscosity for a typical liquid, gas, and supercritical fluid. These values indicate the mass transport properties (i.e., diffusivity) are similar to a gas, while the mechanical properties (viscosity and density) are similar to those of a liquid. This unique combination of properties makes supercritical fluids attractive for use as solvents. The high diffusivity and low viscosity allows the fluid to penetrate easily into matrices which are in the form of loose powders, compacted powders, or even fully cemented pre-forms. Further, the ability of a solvent to dissolve other liquids is, to a first approximation, related to the density of the solvent. The relatively high density of supercritical fluids, relative to gases, increases the useful levels of solubility that may be attained.

2.2 Supercritical CO_2

As a result of the law of corresponding states the physical properties of supercritical CO_2 apply to all fluids in the supercritical state. The critical values of temperature and pressure are unique for each gas/liquid and are determined by the type of intermolecular interactions occurring between

Table 1 Comparison of physico-chemical properties of a typical organic fluid in the liquid, gas, and supercritical fluid state

	Liquid	Supercritical fluid	Gas
Density ($g\,cm^{-3}$)	1	0.1–1	10^{-3}
Viscosity (Pa·s)	10^{-3}	10^{-4}–10^{-5}	10^{-5}
Diffusivity ($cm^2\,s^{-1}$)	10^{-5}	10^{-3}	10^{-1}

Table 2 Critical temperature, T_c, and Pressure, P_c, for some common fluids

Fluid	T_c (°C)	P_c (psi)
Neon, Ne	−229	400
Nitrogen, N_2	−147	492
Argon, Ar	−122	706
Xenon, Xe	17	858
Carbon dioxide, CO_2	31	1072
Sulfur hexafluoride, SF_6	46	545
Propane, C_3H_8	97	617
Ammonia, NH_3	133	1654
Water, H_2O	374	3209

the individual molecules. Table 2 gives the critical temperature and pressure of some common fluids. For example, the critical temperature and pressure required to transform water (H_2O) into a supercritical fluid are 374 °C and 218 atmospheres. These values are much higher than those for CO_2 because the water molecules exert an attractive force on each other, making the solid and liquid phases particularly stable. CO_2 molecules, on the other hand, have much weaker intermolecular attractive forces. It is important to note that, in the SCF region, attractive forces between molecules are minimized.

In the solid form CO_2 has a high density and a very high viscosity. Similarly, the liquid has a high density and a reasonably high viscosity, and the gas has a low density and low viscosity. Conversely, the supercritical fluid phase has a high density but a relatively low viscosity. The density of supercritical CO_2 can vary over a wide range from gas values, around 0.1 g cm^{-3}, to liquid values of about 2.0 g cm^{-3}. In other words, the density of supercritical CO_2 can be changed by over 2000% simply by varying the temperature and pressure within the supercritical region. A supercritical fluid is by definition both liquid and gas-like, and hence it is compressible. Thus, relatively small changes in temperature and/or pressure can significantly affect the density, as seen in Figure 1.

As the density of the CO_2 becomes more liquid-like, so do the solvent properties of the fluid. To a first approximation, the ability of a supercritical fluid to dissolve other fluids can be related to its density in the supercritical region. When operating in the supercritical region, therefore, both temperature and pressure can be used to vary the density, and therefore, the dissolving power of the fluid. It is this ability to alter the solvent power that makes supercritical CO_2 such an attractive solvent. To make the potential for SCFs even more promising, small additions of other components, called co-solvents or entrainers, often modify the observed phase equilibria dramatically. Again this special property affords the chemist the opportunity to *tailor* solvents to achieve a variety of goals, either in separations or reactions.

The viscosity of carbon dioxide is observed to change rapidly in the critical region, as is the case also for diffusivity. Even at high pressures of 300–400 atm it is still only about 0.09 centipoise, an order of magnitude below typical organic solvents. Because of these density and viscosity properties, supercritical CO_2 possesses certain other characteristics, which enhance its attractiveness as a solvent. In addition to possessing liquid-like densities over much of the temperature and pressure range of interest to industry, it exhibits the gas-like property of diffusivity with a zero value for the surface tension. These features alter the transport to allow for easy penetration of SCFs into nano-dimensional spaces.

The self-diffusion coefficient for carbon dioxide (which is approximately the same for similar sized molecules diffusing through carbon dioxide) is about one to two orders of magnitude higher than the diffusivities of comparable solutes in typical organic liquids.

2.3 NMR of Supercritical Fluids

The interactions of a nuclear moment with other nuclei and the electrons surrounding it provide a very sensitive site specific probe into the structure and dynamics in the solid, liquid, and gas phase. This work will concern itself with NMR in the supercritical fluid state of carbon dioxide. As mentioned above, these states exhibit properties of both the liquid and the gas phases. Thus, techniques and theory from work in both phases combine in these unique applications. Thorough reviews have been published on the unique information which can be obtained in the gas phase.[1,2] Other reviews have been published on experimental techniques and applications of high pressure NMR.[3,4] These reviews were published on or before

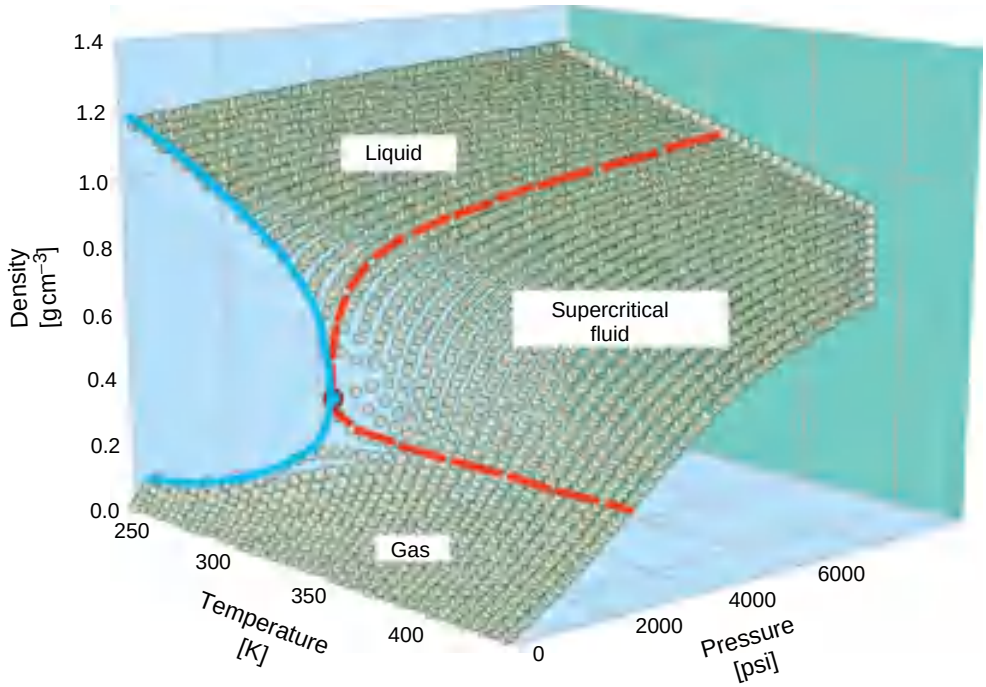

Figure 1 Pressure–temperature–density surface of pure CO_2

1991. We will discuss primarily studies published later, with information as it relates specifically to NMR determination of the dynamics and structure in the SCF state.

Although the application of high pressure NMR to simple fluids leads to some interesting additional complications, the information gained from the technique more than justifies its use. The pressure axis provides an additional dimension to the experimental matrix. For a liquid it is commonly known that temperature changes at constant pressure will effect the molecular motion via kinetic energy and molecular average volume collisional arguments. One can separate the effects of density and temperature on the molecular motion only if both the temperature and pressure are controlled variables in the NMR experiment. Increased pressure also allows for the experimental range to expand well above the normal boiling point and into the compressible supercritical fluid regime. Some examples of the usefulness of high pressure NMR will be given.

2.4 Introduction to the Basics of High-pressure NMR

The motions of molecules in liquids is accessible only through a large number of various models that depend upon phenomenological parameters such as the coefficient of rotational diffusion, the frequency of collisions, the time between jumps, etc. Three such theories: the random walk theory of Torrey,[5] the rotational diffusion theory of Abragam,[6] and the rotational Brownian motion of McConnell[7] form the basis upon which most NMR relaxation models in liquids are based. Other methods of studying molecular motion (optical, dielectric, neutron scattering, etc.) can in principal give additional detailed information. However, as a consequence of the many-particle effects present in these methods, the interpretation of the experimental results for liquids is often ambiguous. In NMR, the weak coupling of the spin system with the lattice allows one to focus better on isolated molecular motions to describe relaxation in liquids.[8] Information on the rotational motion of molecules in liquids of low viscosity, given by NMR, is obtained in the form of the integrals of the time correlation functions, i.e., the correlation times. This section will discuss the effects of dense gas and supercritical fluid states on the correlation times, and what this means to the NMR spectroscopist.

2.5 The Origin of Nuclear Spin Relaxation

Direct time dependant interactions have been shown to cause spin relaxation. However any static interaction can simply be treated as part of the normal spin Hamiltonian, altering the positions and intensities of the spectral lines. For example, a nuclear spin may experience a local magnetic field from the spins of other nuclei moving in its vicinity, from an unpaired electron, or from a variety of other mechanisms, such as the spin–rotation interaction in which the rotation of the molecular electrons generates a magnetic field at the nucleus. In general, rotational and diffusional motions are important sources of relaxation in fluids. Some mechanisms that make contributions to spin–lattice relaxation will be discussed.

2.5.1 Nuclear Spin Relaxation Mechanisms

There are a number of processes that provide the basis for nuclear spin relaxation. These include the nuclear magnetic dipole–dipole interactions (DD), the spin–rotation interactions (SR), the quadrupolar interactions (Q), and the chemical shift interactions, (CSA). The overall relaxation rate can be expressed as a sum of contributions from each mechanism.

2.5.2 Dipole–Dipole Interaction

The magnetic nuclei in molecules provide magnetic dipole fields that are proportional to the magnetic moments of the nuclei. These fields fluctuate in magnitude and direction as the molecule tumbles through space. When these random oscillating fields have magnetic field components at the Larmour frequency, the nuclear spin relaxes. This interaction depends upon the correlation time of the tumbling molecule as well as the distance between the interacting nuclei. The dipole interactions can be divided into intramolecular and intermolecular interactions. For both of these types of interactions there is a homo, and hetero-nuclear sub-interaction. These are reflected in the following equations

$$\text{For intra-homo:} \quad \frac{1}{T_1^{\mathrm{DD}}} = \frac{3\gamma_A^4\hbar^2\tau_c}{2r^6}$$

$$\text{For intra-hetero:} \quad \frac{1}{T_1^{\mathrm{DD}}} = \frac{\gamma_A^2\gamma_X^2\hbar^2\tau_c}{r^6} \tag{1}$$

$$\text{For inter-hetero:} \quad \frac{1}{T_1^{\mathrm{DD}}} = \frac{2N_x\gamma_A^2\gamma_X^2\hbar^2}{Da}$$

where r is the distance between the interacting nuclei, D is a mutual translational self-diffusion coefficient for the molecules containing A and X, and a is the distance of closest approach between A and X. τ_c is a rotational diffusion correlation time for molecular tumbling. This corresponds to the average time it takes for a molecule to rotate through one radian.

2.5.3 The Spin–Rotation (SR) Interaction

Spin–rotation relaxation of the nuclear magnetization in molecules is due to the intramolecular coupling of the individual nuclear spins to the molecular angular momentum. A fluctuating local magnetic field, which relaxes the nuclear spins, is the result of the collisional reorientation of the molecular rotational angular momentum. For linear molecules such as CO_2, the spin–rotation contribution to the total spin–lattice relaxation can be expressed as

$$\frac{1}{T_1^{\mathrm{SR}}} = \frac{4C_\perp^2 IkT\tau_j}{3\hbar^2} \tag{2}$$

$C_\perp$ is the spin–rotation constant and I is the moment of inertia. For a spherical top molecule, the relaxation rate has the form

$$\frac{1}{T_1^{\mathrm{SR}}} = \frac{2C_{\mathrm{eff}}^2 IkT\tau_j}{\hbar^2} \tag{3}$$

C_{eff} is the effective spin–rotation tensor. The τ_j is the correlation time for angular momentum transfer and therefore is closely related to the average time between collisions. The higher the temperature the faster the molecule reorients in accordance with the kT term. The result is that the spin–rotation contribution to the total spin–lattice relaxation

increases with temperature. This is quite the opposite in all other mechanisms examined in this work.

2.5.4 Quadrupolar Relaxation

Quadrupolar occurs when the nuclear electric quadrupole moment, interacts with electric field gradients to provide a very efficient nuclear relaxation process. The equation for these interactions is similar in form to that of the dipole interaction. The electric quadrupolar interaction between spin I and an electric field gradient can be written in the form given in equation (4).

$$\frac{1}{T_1^{\mathrm{Q}}} = \frac{3\pi^2(2I+3)\chi^2\tau_{\mathrm{c}}}{10[I^2(2I-1)]} \tag{4}$$

where χ is known as the nuclear quadrupolar coupling constant and is in units of frequency. The τ_{c} here is the rotational diffusion correlation time as it appeared in the dipolar equation. Because of its relative efficiency the quadrupolar interaction nearly dominates when quadrupolar nuclei are present.

2.5.5 Chemical Shift Anisotropy

Anisotropic shielding at the nucleus changes with the orientation of the molecule in a static field. Therefore the molecular tumbling modulates the local magnetic field resulting in relaxation. The spin–lattice relaxation rate due to this interaction is proportional to the square of the magnetic field:

$$\frac{1}{T_1^{\mathrm{CSA}}} = \frac{2}{15}\gamma_A^2 B^2 \Delta\sigma^2 \tau_{\mathrm{c}} \tag{5}$$

where Δ is the chemical shielding anisotropy of the nucleus and τ_{c} has the same meaning as before.

The spin–lattice relaxation can be measured and contributions from each of the mechanisms decoupled to yield dynamic and structural information pertaining to the species of interest. Each of the following sections will contain specific observation techniques and theoretical treatments used to provide insight into the often strange and unpredictable world of supercritical fluids.

Extensive studies have been performed on nuclear magnetic spin lattice relaxation and its dependence on molecular structure and dynamics. This is the subject of several review articles.[9–12] Decoupling techniques are often used to enhance the signal and to simplify the resulting spectrum. Such decoupling studies also yield the nuclear Overhauser enhancement (NOE), which allows the unique separation of the dipolar interaction from other relaxation interactions. However, decoupling also eliminates multiplet splittings from scalar couplings, thereby preventing direct measurement of some of the spectral features that are required to completely describe the relaxation of coupled nuclear spin systems.

Spin-coherent double-resonance experiments, which avoid this loss of information, and a general numerical method for analyzing the data obtained in relaxation studies of this type may be used.[13,14] Relaxation processes, described by a system of coupled linear differential equations, determine a variety of time-independent relaxation parameters that contain information on the molecular structure, and dynamic features of the motion. The relaxation parameters in the equations of motion can then be extracted from the experimental data using standard least squares methods.[13,14]

For polyatomic gases, nuclear spin relaxation proceeds primarily from the collisional modulation of the molecular rotational angular momentum coupled to the angular momentum of the nuclear spins. Reorientations of molecular angular momentum by collision then give rise to fluctuating internal magnetic fields, that effect the nuclear spins through intramolecular spin–rotation couplings. In addition to the spin–rotation mechanism molecular motional modulation of the chemical shift anisotropy, dipole-dipole and quadrupolar couplings also affect the relaxation rates.

In low-viscosity liquids and gases, spin–lattice relaxation may be treated as a temporal modulation associated with the thermal reorientation of the molecule. The study of spin lattice relaxation contributes to an understanding of molecular dynamics.[15] In dilute gaseous samples of small molecules where the interactions mediating spin relaxation are primarily intermolecular,[16,17] and the various interaction parameters are known accurately,[18–21] the study of relaxation reveals features of collisional processes responsible for reorientation of the molecules.[22–24]

2.6 Line Narrowing

All polyatomic gases possess more than one intramolecular relaxation mechanism. Even the molecule H_2, for instance, has two competing mechanisms: the spin–rotation and the direct dipole–dipole interaction. In condensed phase molecular hydrogen the contribution of the dipole–dipole mechanism is comparable to that of spin rotation because the distance between the protons is short enough for the dipole–dipole relaxation to be appreciable. In a gaseous system, however, spin rotation is normally the dominant relaxation mechanism. In such experiments high density carbon dioxide can be added to hydrogen isotopomers such as hydrogen deuteride, as suggested by Johnson and Waugh,[23] to shorten the rotational correlation times and thereby lengthen the spin–rotation relaxation time and narrow the resonances in the high-resolution spectra. The H_2 system is difficult to study because of the indistinguishability of the two particles. Thus research on the lower HD symmetry[18,19,21–23,25–28] provides more information from both the proton and deuteron resonances arising from indirect spin-spin couplings.

Supercritical fluids generally have viscosities 10–100 times lower than that of the normal liquid phase and self diffusion coefficients 10–100 times greater. To the NMR spectroscopist, these properties are of significant benefit in studying quadrupolar nuclei, since the quadrupolar linewidth is proportional to the rotational correlation time. The utility of NMR to study many quadrupolar nuclei has been somewhat limited. Quadrupolar relaxation can be very efficient, leading to broad lines and low sensitivities. In the extreme narrowing limit, the linewidth of these nuclei,$(1/\pi T_2)$ can be written as

$$\frac{1}{\pi T_2} = \frac{3}{8}\left(\frac{e^2qQ}{h}\right)^2\left(1+\frac{\eta^2}{3}\right)\tau \tag{6}$$

where e^2qQ/h is the quadrupolar coupling constant, τ is the rotational correlation time for the molecular motion, and η is the asymmetry parameter of the electric field gradient

tensor. Various studies have demonstrated the validity of the Stokes–Einstein–Debye equation.[29]

$$\tau = \frac{A\eta}{T + \tau_0} \tag{7}$$

in which τ is the rotational correlation time, η is the solvent viscosity, T is the temperature and τ_0 is the high temperature intercept. This equation predicts a linear relation between τ and η/T to a limiting value τ_0 attained in the limit as $\eta/T \rightarrow 0$. Comparisons with above equation show that NMR line widths should decrease with decreasing viscosity to a limiting value expected to be related to the free rotor correlation time given by

$$\tau_{\mathrm{FR}} = \left(\frac{2\pi I}{9kT}\right)^{1/2} \tag{8}$$

where I is the moment of inertia about the rotational axis.

2.7 NMR Determination of Structural Dynamics in High-Pressure Fluids

There have been direct spectroscopic probes of the local solvent structure around solutes in supercritical fluids. These include using the solvatochromic scales as in the ultraviolet-visible (UV) absorption of phenol blue in ethylene[30] and the fluorescence spectroscopy of pyrene in carbon dioxide.[31] The use of spectroscopic methods to study the local environment surrounding solute molecules in dilute supercritical fluid mixtures has been reviewed.[32] However the use of NMR to determine the local structure within supercritical fluids has thus far been sparse in the literature.

2.7.1 High Pressure NMR Studies of Hydrogen Bonded Liquids

An understanding of molecular interactions between solute and solvent molecules in supercritical fluids (SCF) is essential to an explanation of clustering phenomena, considered responsible for the unique SCF solvating characteristics compared to gases.[33–35] Although both theoretical[36–38] and experimental efforts[39–46] have been made to increase the understanding of these phenomena, a complete picture of clustering in SCFs is still evolving. The accumulation of experimental NMR relaxation data is expected to improve our physical picture of solvent clustering in SCF. Because the nuclear spin–lattice relaxation rates depend on the fluctuating molecular reorientation and molecular collision frequency, their measurement proves to be an effective method for studying such molecular interactions and dynamics in fluids.[47] One of the advantages of utilizing NMR relaxation data is that they provide not only information, similar to optical methods, on overall molecular motions but also site-specific information on intramolecular motions. The ^{13}C spin–lattice relaxation processes in CO_2 are dominated by spin–rotation interactions.[48–50] Nuclear spin–lattice relaxation rates have been measured under SCF conditions by Lamb et al.[51] and Etesse et al.[52–54] for various SCF mixtures. NMR chemical shift measurements[55] were also used to relate ^{129}Xe chemical shift data to the local solvent structures of SCF Xe. SCF fluid structures in pure methanol,[56] CO_2–methane,[39] CO_2–methanol,[40] and CO_2–decanol[40] mixtures have recently been made. The function of the hydroxyl group in solute-induced solvent clustering in SCF CO_2 appears to be especially important. Earlier developments in high pressure NMR studies of hydrogen bonded liquids may be found in a review article by Lang and Ludemann.[57]

Information on the nature and average rate of molecular motions may be obtained by determining the nuclear spin–lattice relaxation rates of nuclei in the molecules under investigation. The nuclear spin relaxation rate, $1/T_1$, depends on fluctuations in molecular reorientations as a consequence of molecular collisions, where T_1 is the time constant defining the exponential return of a perturbed nuclear spin to its equilibrium state. Many nuclear spin interaction mechanisms affect T_1 values. Among them, spin–rotation, quadrupolar and dipolar interactions are the most important ones at sub- and supercritical densities. Detailed descriptions of spin–rotation, quadrupolar and dipolar interactions may be found in the review articles by Grant et al.[58] and Jameson.[59] Briefly, determination of NMR nuclear relaxation rates provides the angular momentum[59] and rotational reorientation correlation times[58] from the spin–rotation and quadrupolar/dipolar interactions, respectively. Spin–rotation interactions are directly related to molecular collision frequencies and depend on macroscopic properties such as fluid density and temperature. Dipolar and quadrupolar interactions, however, are often related to fluid viscosity and temperature. Since the fluid viscosity may be treated as a function of local density in the compressible regions of CO_2, both correlation times may be considered as functions of local densities. Therefore, clustering phenomena in SCF resulting in fluctuations of local density may in principle be observed by NMR relaxation measurements.

The magnitude of the NOE effect is given by[60]

$$\mathrm{NOE}(A\{X\}) = \frac{I_A^*}{I_A^0} \tag{9}$$

where I_A^* is the integrated intensity of a decoupled spectrum with saturation of the nucleus X, and I_A^0 is the equilibrium intensity of A in the coupled spectrum. The maximum possible NOE of ^{13}C{^{1}H} occurs when ^{13}C and ^{1}H relax only by the dipolar mechanism given by[60] and is given by

$$\mathrm{NOE(max)} = 1 + \left(\frac{\gamma_{\mathrm{H}}}{2\gamma_{\mathrm{C}}}\right) = 2.988 \tag{10}$$

where γ_{H} and γ_{C} are the magnetogyric ratios for ^{1}H and ^{13}C, respectively. The NOE effect may be determined as a ratio of spectral intensities with proton decoupling to that of gated proton decoupling. Since the ^{13}C in CO_2 does not exhibit an NOE, its signal intensity may be used as a fiducial reference.

2.8 Significant Mechanism in Spin–Lattice Relaxation: Overall Rotational Motion

In general, the overall rotational motions of solute molecules depend on the intermolecular frictional forces between the solute and solvent molecules and, therefore, are dependent upon the solvent viscosity. The solvent viscoelastic response, in turn, is also dependent on various relaxation mechanisms of solvent molecules. Internal rotational motions including various local isomerization movements are driven by torsional forces.[61]

The rotational reorientation correlation time, τ_c, may be extracted from NMR spin–lattice relaxation time measurements, within the *extreme narrowing* limit, using the following expression[60]

$$T_{1,\mathrm{DD}}^{-1}(^{13}\mathrm{C}) = \frac{\upsilon\gamma_C^2\gamma_H^2\hbar^2\tau_c}{r^6} \tag{11}$$

where r is the bond distance between ^{1}H and ^{13}C (measured as 1.085 Å), and υ is the number of protons directly attached to the ^{13}C nucleus. The dipole–dipole relaxation rate, may be obtained from the standard relationship between the overall T_1 and NOE measurements:[60]

$$\mathrm{NOE} = 1 + \frac{\gamma_H}{2\gamma_C}\frac{T_{1,\mathrm{DD}}^{-1}(^{13}\mathrm{C})}{T_{1,\mathrm{Tot}}^{-1}(^{13}\mathrm{C})} \tag{12}$$

The reorientation correlation time obtained in this manner is an average assuming isotropic reorientation. This correlation time may be related to a rotational diffusion coefficient by assuming that each nuclear environment is roughly spherical and rotates randomly.[62]

$$\tau_c = \frac{1}{6D} \tag{13}$$

From the temperature dependence of rotational diffusion coefficients at fixed viscosity, one can determine effective rotational activation energies.

2.9 CO_2 Clustering

The rotational reorientation correlation time, τ_c, can be expressed by a modified Stokes–Einstein–Debye (SED) equation[63]

$$\tau_c = \frac{\eta V_p}{kT} f_{\mathrm{stick}} C + \tau_0 \tag{14}$$

where η is the fluid viscosity, V_p is the volume of solute molecule, f_{stick} is a well-defined shape parameter dependent only on the structure of solute molecules,[64] C is a boundary parameter dependent on the nature of the solute and solvent and upon their concentration, and finally τ_0 is the free-rotor correlation time. The success of this model strongly depends on the selection of parameters C and f_{stick}. Recently, Roy et al.[64] noted that the Dote, Kivelson, and Schwartz (DKS) model[63] is the best model for predicting reorientational correlation times for solutes with radii up to about 4.5 Å. Anderson and Kauffman[65] further modified the calculation of the smallest volume of free space per solvent molecule, ΔV, in the DKS model, and more recently, these two workers[66] related fluid viscosity and the parameter C in the SED model to the local density by introducing a radial distribution function into the hydrodynamic model. These modifications[65,66] by Anderson and Kauffman are referred to as the AK model.

In the AK model, the viscosity for a fluid is expressed as a function of local density ρ_{12}^1 by equation 4.7 described by Jossi et al.[67]

$$[(\eta - \eta_0)\xi_T^y + 1]^{1/4} = 1.023 + 0.23364\rho_r + 0.58533\rho_r^2 - 0.40758\rho_r^3 + 0.09324\rho_r^4 \tag{15}$$

where $\rho_r = \rho_{12}^1/\rho_c$ and $\xi_T = (T_c/M^3P_c^4)^{1/6}$. ρ_c, T_c, and P_c represent the critical density, temperature, and pressure, respectively. M is the molecular weight in the unit of g mol^{-1}. The local density of is related to the bulk density ρ by a radial distribution formalism

$$\rho_{12}^1 = \rho\{1 + F[g_{12}(r)]\} \tag{16}$$

where $F[g_{12}(r)]$ is an integral equation in the pair distribution function, $g_{12}(r)$, over the spatial coordinates and r is the distance between solvent and solute molecules. $F[g_{12}(r)]$ is a measure of the excess solvent density near the solute molecule and is treated as an adjustable parameter in the AK model. When $F[g_{12}(r)] = 0$, the local density equals the bulk density, and when $F[g_{12}(r)] = 1.0$, the local density is twice the bulk density.

In the AK model, the parameter $C(\rho_{12}^1)$ equivalent to C in the SED model, is also treated as a function of local density. According to the DKS model

$$C(\rho_{12}^1) = \frac{f_{\mathrm{slip}}V_p}{f_{\mathrm{slip}}V_p + \gamma V_p} \tag{17}$$

where f_{slip} is a factor for the slip boundary condition whose value estimated from f_{stick} by the method reported by Hu and Zwanzig[68] and γ is defined as

$$\gamma = \left(\frac{\Delta V}{V_p}\right)\left[4\left(\frac{V_p}{V_s}\right)^{\frac{2}{3}} + 1\right] \tag{18}$$

In equation (18), V_s is the solute molecular volume and ΔV is the free space volume for a solvent molecule. For supercritical fluids in their compressible regions, a large variation in the free space is expected, and ΔV is given by equation (19) relating molecular weight (MW) and local density:

$$\Delta V = \frac{\mathrm{MW}}{\rho_{12}^1} - V_s \tag{19}$$

Therefore, the parameter $C(\rho_{12}^1)$ is expressed as a function of local density ρ_{12}^1 though the free space volume ΔV.

Combining equations (18) and (19), the AK version of the SED equation may be expressed as[66]

$$\tau_c \equiv \frac{\eta(\rho_{12}^1)V_p}{kT} f_{\mathrm{stick}} C(\rho_{12}^1) + \tau_0 \tag{20}$$

Equation (20) relates the reorientation correlation time, τ_c, to the solvent local density at a given temperature. By performing a comparison experiment on *trans*,*trans*-1,4-diphenylbutadiene (DPB) solute in CO_2, Anderson and Kauffman[66] also observed that CO_2 solvent clustering only occurs in the vicinity of *trans*-4-(hydroxymethyl)stilbene (HMS) molecules. Because the extended π-electron systems existing in DPB and HMS are similar, Anderson and Kauffman concluded that the OH group in HMS is responsible for the association between the solute and solvent molecules. The one-to-one association between solute and solvent molecules may initiate further CO_2 clustering whenever strong many-body interactions affect the solvent structure in supercritical

fluids in the compressible density region. The CO_2 clustering gradients observed along the aliphatic chain of l-decanol molecules in the Bai et al.[39] study appear to support the observations by Anderson and Kauffman.

To verify further the importance of alcohol enhanced clustering, the same procedure was applied to a CO_2–methanol mixture,[69] where a specific association between CO_2 and CH_3OH has been observed also by the IR studies.[42] Such solvent-solute interactions may initiate CO_2 solvent clustering.[66] The low-pressure limit free-rotor correlation time can be calculated using the following expression[70]

$$\tau_0 = \frac{2\pi}{9}\left(\frac{I_\perp}{kT}\right)^{1/2} \tag{21}$$

where is the perpendicular component of the moment of inertia for methanol molecules. The calculated τ_0 from equation (21) is 0.20 ps, which agrees well with the 0.17 ps from fitting the low-density data.

2.10 More Evidence for the Formation of CO_2 Clusters in the Vicinity of Methanol

As stated above, NOE measurements allow the separation of the dipole–dipole contributions to spin–lattice relaxation rates from other mechanistic contributions. For methanol, the remaining relaxation contributions result essentially from the spin–rotation mechanisms described previously.[69] These spin–rotation relaxation rates allow one to calculate an angular momentum exchange correlation time, τ_J, which is strongly dependent on the fluid density. Methanol is a quasi-symmetric top molecule, but the relation between ρ, and spin–rotation relaxation rates for symmetric top molecules may be used as a good approximation for T_1^{SR}. The expression[71] is

$$\frac{1}{T_1^{SR}} = \frac{2\pi^2}{\alpha} C_{\text{eff}}{}^2 \tau_J \tag{22}$$

where pull down $\alpha = \hbar^2/(2kTI_\perp)$ and $I_\perp$ is the perpendicular part of the moment of inertia for methanol. The effective spin–rotation, C_{eff}, may be expressed as

$$C_{\text{eff}}{}^2 = k_1 C_a^2 + k_2 C_a C_d + k_3 C_d^2 \tag{23}$$

In equation (23), the structure parameters, k_i, only depend on molecular structure. C_a and C_d are the isotropic and anisotropic components of the spin–rotation tensor. Therefore, in principle, an experimental angular momentum correlation time, τ_J, may be estimated using equation (22). Since τ_J is linearly related to the time between molecular collisions, τ_{BC}, one may calculate τ_J using a gas kinetic theory. The slope of this linear relationship, called an effective collision number and referred to as Z,[72] provides the average number of collisions needed for an effective molecular angular momentum exchange. This number is found to be between 1.4 and 3.4 for many collision pairs (cf. Table 3 in Ref.[72]). In the use of a hard-sphere model (HSM) for calculating cross sections, choosing the effective collision number of two appeared to be a good approximation in the work of Maryott, Malmberg, and Gillen,[72] and therefore, this value is used in the following discussion. The expression for computing τ_J is given by[73]

$$\tau_J = \frac{Z}{\rho \overline{v} \sigma_K} \tag{24}$$

where ρ is fluid density, $\overline{v}$ is the average velocity of molecules, and ρ_K is the kinetic collisional cross section between solute and solvent molecules. Both $\overline{v}$ and σ_K may be estimated from molecular properties of the solute and solvent. If the density term, ρ, in equation (24) is replaced by a local density [cf. equation (16)], the estimated τ_J becomes a function of the excess solvent density parameter, $F[g_{12}(r)]$. In this case, equation (24) becomes

$$\tau_J = \frac{Z}{\rho\{1 + F[g_{12}(r)]\}\overline{v}\sigma_K} \tag{25}$$

There is good agreement between theoretical and experimental data when an increase in local density is employed in the predictions of τ_J. This provides additional evidence for the formation of SCF solvent clustering in the vicinity of hydrogen bonding solute molecules. Supposedly, these interactions are induced by the hydroxyl functional group present in alcohol molecules.

2.11 NMR Determination of Self-diffusion Coefficients in High-pressure Fluids

Many methods exist for measuring the diffusion coefficients of fluids. However, the experimental accuracy of many of these is quite limited.[74,75] Furthermore, methods that give reliable results in the low pressure regime are not always suitable at high pressures because the inverse dependence of the diffusion coefficient on pressure makes for experiments that take an inordinately long time. The most widely reported method for the measurement of diffusion coefficients in the SCF state is a gas chromatographic method based on Taylor dispersion, which has proven unreliable at lower pressures.[76–78]

The only other methods that can be utilized for this measurement in SCFs are photon correlation spectroscopy[79,80] and NMR.[81,82] They are not widely used at this time because the equipment is very expensive and their application to industrially important SCF's is still in its infancy. The use of the NMR technique has been confined to the measurement of self diffusion coefficients.[81,82]

3 INSTRUMENT REQUIREMENTS FOR HIGH-PRESSURE NMR

In order to perform NMR experiments under high pressure, it is necessary to devise a convenient means to control the pressure, temperature and sample concentration while it is inside the magnet. Two basic approaches to the design of high pressure NMR experiments have been reported: (1) construction of a probe which is capable of achieving the necessary pressures, referred to as the *high pressure probe technique*,[83] or (2) fabrication of a high pressure cell which can be used in a standard commercial NMR probe, referred to as the *high pressure cell technique*.

The very first high pressure NMR experiment was performed in 1954 by Benedek and Purcell.[84] They used a

hydrostatic high pressure probe capable of holding pressures up to 10 000 atm. For deformable samples the high pressure probe technique requires a sealed sample cell which incorporates a volume change mechanism such as bellows or a mercury column.[85] The cell is surrounded by a RF coil and is located inside a pressure vessel small enough to fit inside the NMR magnet. The high pressure probe technique usually offers higher sensitivity because of a better filling factor for the receiver coil. It also allows for higher pressures and is usually safer to work with. The disadvantages are that they require a more elaborate and expensive design and are therefore not suitable for a routine NMR laboratory. The approach to a high pressure probe has continually been developed by Jonas et al.[86] with improvements to pressure vessel design and electrical feed-throughs. The most recent advances to the probe design for studying supercritical fluids include the toroidal coil[87] and cavity[88] design by Rathke et al.

The high pressure cell technique allows the experiments to be performed in a commercial NMR probehead, thereby eliminating the need to alter the basic probe design. The earlier versions of high pressure cells experienced lower sensitivity and reduced working pressures. Yonker et al. designed a simple and safe method by coiling a fused silica capillary tube inside a commercial 5-mm NMR tube.[89] Newer cell designs have improved these limitations providing a more convenient and cost-effective means of carrying out high pressure NMR experiments. Roe et al.[90] designed the first cell made of single crystal sapphire and Horvath et al. later improved this design.[91,92] Pressure control while the cell is in the magnet is a major issue in the cell design. The previously reported designs of the sapphire NMR cells were unable to independently control both the sample temperature and pressure. In the Bai et al. design[93] a movable piston is used to control the sample pressure (see Figure 2). With this design it is possible to control temperature and pressure independently over a wide range of conditions while keeping the relative molar concentration ratios of the sample mixture intact. The sample volume must be restricted to the active coil in order to eliminate errors introduced through molecular diffusion between polarized and nonpolarized volume elements within the cell. Recently a high pressure cell constructed of high-performance polymers, such as poly(etherether ketone) (PEEK), was developed by Wallen et al.[94] with the purpose of simplifying the cell design to allow for more routine experiments on supercritical fluids.

The very first high pressure probe was made of a beryllium copper alloy (Berylco 25). This alloy was used due its strength and nonmagnetic properties, but does require special heat treatment and can have significant variations in the level of paramagnetic impurities. Berylco 25 is stable up to 10 000 atm and permits a temperature range of $-10\,^{\circ}\mathrm{C}$–$80\,^{\circ}\mathrm{C}$. Titanium alloys (IMI-680) are now more commonly used as they require no special heat treatment during machining and retain their strength up to 400 °C and 5000 atm. For even higher pressures, up to 100 kbar, the diamond anvil method can be used.[95] This method can only be used with very small samples so most studies concern sensitive nuclei, although a study on ^{13}C has been reported.

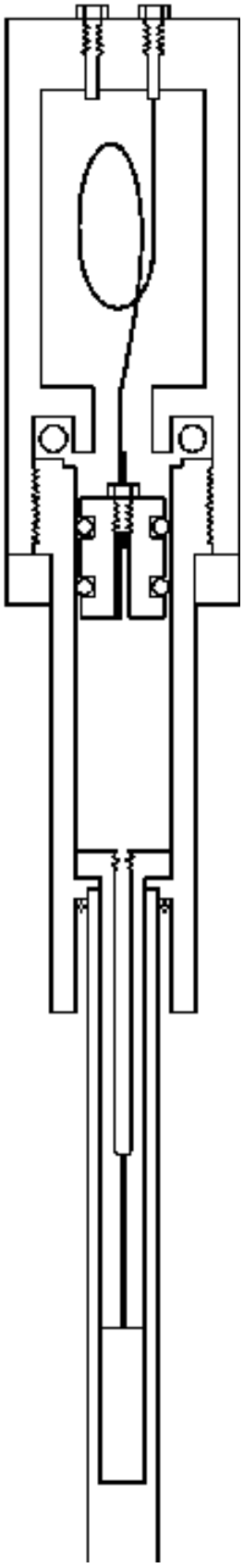

Figure 2 Schematic diagram of the high pressure piston NMR cell capable of independently controlling temperature, pressure and sample concentration

4 SUPERCRITICAL FLUID APPLICATIONS

Most of the high pressure NMR studies of supercritical fluids have involved measuring chemical shifts, such as ^{1}H,[96]

of both polar and nonpolar solute molecules in the dense phase fluid. Increased reaction rates of certain reactions in supercritical fluids has been attributed to specific solvent-solute and solute–solute interactions. By studying these specific interactions by NMR further insight into the variation of the surroundings of the solute molecules with the density of the supercritical fluid is obtained and can be compared to other experimental techniques, such as UV and vibrational spectroscopy.

Using a fused silica capillary cell an in situ photolysis study of organometallics in supercritical fluids was performed where the ligand exchange with the metal center was directly observed.[97] High pressure NMR was also used to determine the fundamental dynamic and electronic properties of the organometallic complexes in the SCF through the investigation of the spin–lattice relaxation times, T_1, and NMR magnetic shielding constants, σ.

Another interesting application of supercritical fluids is to use them as solvents for comprehensive NMR studies of large proteins. In conventional solvents large proteins (over 30 kDa) tumble too slowly and correspondingly the spin–spin relaxation times (T_2) become shorter, making some standard experiments unreliable. By encapsulating the protein in a reverse micelle dispersed in a low viscosity fluid, such as a supercritical fluid, the tumbling correlation time (τ_m) of the protein is reduced thereby increasing T_2.[98] This results in narrower lines in the spectrum.

High pressure NMR has also been used to investigate phase behavior of binary solvent systems in order to obtain vapor–liquid equilibrium (VLE) values. Usually VLE values of supercritical fluid solutions are obtained using variable volume view cells and off-line analysis techniques. By using NMR, this process can be simplified and made more efficient for numerous solvent systems. This technique is especially suitable for hydrocarbon containing solvent molecules as detection of solvent protons in both the liquid and vapor phase can be detected simultaneously.[99]

An advantage of using supercritical fluids as reaction media for chemical reactions is that gaseous reagents are completely miscible with the solvent. In catalytic reactions such as hydrogenations and hydroformylations where H_2 and CO are reactants this can have a significant impact on both the yield and selectivity of the desired products. Since only one phase is present in the supercritical system, stirring to achieve gas–liquid mixing is unnecessary. By studying these reactions in situ by NMR valuable information regarding the mechanism can be obtained.[100] In situ NMR was used to optimize the iridium catalyzed enantioselective hydrogenation of imines in supercritical CO_2. By studying the specific interactions between substrates and products with CO_2 conclusions about the different reactivities of structurally similar substrates were obtained.[101]

5 REFERENCES

1. C. J. Jameson, *Chem. Rev.*, 1991, **91**, 1375–1395.
2. R. L. Armstrong, *Magn. Reson. Rev.*, 1987, **12**, 91.
3. J. Jonas, ed, 'NMR Basic Principles and Progress', Springer Verlag: Berlin, 1991, Vol. 24 of High Pressure NMR.
4. I. T. Horvath and J. M. Millar, *Chem. Rev.*, 1991, **91**, 1339–1351.
5. H. C. Torrey, *Phys. Rev.*, 1953, **92**, 962.
6. A. Abragam, 'The Principals of Nuclear Magnetism', The Clarendon Press: Oxford, 1961.
7. J. McConnell, 'Rotational Brownian Motion and Dielectric Theory', Academic Press: London, 1980.
8. J. McConnell, 'The Theory of Nuclear Magnetic Resonance Relaxation in Liquids', Cambridge University Press: Cambridge, 1987.
9. S. W. Collins, T. D. Alger, D. M. Grant, K. F. Kuhlman, and J. C. Smith, *J. Phys. Chem.*, 1975, **79**, 2031.
10. C. L. Mayne, D. W. Alderman, and D. M. Grant, *J. Chem. Phys.*, 1975, **63**, 2514.
11. G. A. Gray and S. E. Cremer, *J. Magn. Reson.*, 1973, **12**, 5.
12. D. M. Grant, R. J. Pugmire, E. P. Black, and K. A. Christensen, *J. Phys. Chem.*, 1973, **95**, 8465.
13. D. M. Grant, C. L. Mayne, F. Liu, and T.-X. Xiang, *Chem. Rev.*, 1991, **91**, 1591–1624.
14. D. Canet, *Prog. NMR Spectrosc.*, 1989, **21**, 237.
15. D. M. Grant, C. L. Mayne, F. Liu, and T.-X. Xiang, *Chem. Rev.*, 1991, **91**, l591–1624.
16. N. Bloembergen, E. M. Purcell, and R. V. Pound, *Phys. Rev.*, 1948, **73**, 679.
17. A. Abragam, 'Principles of Nuclear Magnetism', Clarendon Press: Oxford, 1961, p. 1581.
18. N. F. Ramsey and H. R. Lewis, *Phys. Rev.*, 1957, **108**, 1246.
19. N. J. Harrick, R. G. Barnes, P. J. Bray, and N. F. Ramsey, *Phys. Rev.*, 1953, **90**, 260.
20. N. F. Ramsey, 'Molecular Beams', Clarendon Press: Oxford, 1956, p. 1454.
21. W. E. Quinn, J. M. Baker, J. T. LaTourrette, and N. F. Ramsey, *Phys. Rev.*, 1958, **112**, 1929.
22. J. R. Gains, P. C. Souers, E. M. Fearon, J. D. Sater, and E. R. Mapoles, *Phys. Rev. B*, 1989, **39**, 3943.
23. C. S. Johnson, Jr. and J. S. Waugh, *J. Chem. Phys.*, 1962, **36**, 2266.
24. P. R. McCourt, in 'NMR Basic Principles and Progress', eds P. Diehl, B. Fluck, and R. Kosfeld, Springer Verlag: Berlin, 1976, p. 56.
25. B. D. Nageswara Rao and L. R. Anders, *Phys. Rev.*, 1967, **140**, A112.
26. P. C. Souers, E. M. Fearon, J. D. Sater, E. R. Mapoles, J. R. Gaines, and P. A. Fedders, *J. Voc. Sci. Tec. A.*, 1991, **9**, 232.
27. R. S. Wagner, R. L. Armstrong, E. C. Bissonette, and F. R. W. McCourt, *J. Chem. Phys.*, 1990, **92**, 5907.
28. J. M. Deutch and I. Oppenheim, in 'Advances in Magnetic Resonance', ed J. S. Waugh, Academic Press: New York, 1966, p. 225.
29. R. B. Bird, W. E. Stewart, and L. N. Lightfoot, 'Transport Phenomena', Wiley: New York, 1960, Chapter 16.
30. S. Kim and K. P. Johnston, *Ind. Eng. Chem. Res.*, 1987, **26**, 1206.
31. J. F. Brennecke and C. A. Eckert, in *Proceedings of the International Symposium on Supercritical Fluids*, Nice, October, 1988.
32. K. P. Johnston, S. Kim, and J. Coombes, in 'Supercritical Fluid Science and Technology', eds K. P. Johnston and J. Penninger, ACS Symposium Series No. 406, American Chemical Society: Washington, DC, 1989.
33. P. G. Jessop, T. Ikariya, and R. Noyori, *Science*, 1995, **269**, 1065–1069.
34. T. J. Bruno and J. F. Ely, eds, 'Supercritical Fluid Technology – Reviews in Modern Theory and Applications', CRC Press: Boca Raton, FL, 1991.
35. E. Klesper, *Angew. Chem. Int. Ed. Engl.*, 1978, **17**, 738–746.
36. (a) J. W. Tom and P. G. Debenedetti, *Ind. Eng. Chem. Res.*, 1993, **32**, 2118–2128; (b) P. G. Debenedetti, *Chem. Eng. Sci.*, 1987, **42**, 2203–2212.
37. S. Kim and K. P. Johnston, *Ind. Eng. Chem. Res.*, 1987, **26**, 1206–1213.

38. (a) H. D. Cochran and L. L. Lee, in 'Supercritical Fluid Science and Technology – Reviews in Modern Theory and Applications', eds T. J. Bruno and J. F. Ely, CRC Press: Boca Raton, FL, 1991; (b) K. P. Johnston and J. Penninger, eds, 'Supercritical Fluid Science and Technology', ACS Symposium Series No. 406, American Chemical Society: Washington, DC, 1989, Chapter 3.
39. S. Bai, C. M. V. Taylor, F. Liu, C. L. Mayne, R. J. Pugmire, and D. M. Grant, *J. Phys. Chem. B*, 1997, **101**, 2923–2928.
40. C. M. V. Taylor, S. Bai, C. L. Mayne, and D. M. Grant, *J. Phys. Chem. B*, 1997, **101**, 5652–5658.
41. J. P. Blitz, C. R. Yonker, and R. D. Smith, *J. Phys. Chem.*, 1989, **93**, 6661–6665.
42. J. L. Fulton, G. G. Yee, and R. D. Smith, *J. Am. Chem. Soc.*, 1991, **113**, 8327–8334.
43. C. R. Yonker, S. L. Frye, D. R. Kalkwarf, and R. D. Smith, *J. Phys. Chem.*, 1986, **90**, 3022–3026.
44. C. R. Yonker and R. D. Smith, *J. Phys. Chem.*, 1988, **92**, 2374–2378.
45. J. Zagrobelny and F. V. Bright, *J. Am. Chem. Soc.*, 1993, **115**, 701–707.
46. T. A. Betts, J. Zagrobelny, and F. V. Bright, *J. Am. Chem. Soc.*, 1992, **114**, 8163–8171.
47. D. M. Grant, C. L. Mayne, F. Liu, and T. X. Xiang, *Chem. Rev.*, 1991, **91**, 1591–1624.
48. P. Etesse, J. A. Zega, and R. Kobayashi, *J. Chem. Phys.*, 1992, **97**, 2022–2029.
49. S. Bai, C. L. Mayne, R. J. Pugmire, and D. M. Grant, *J. Chem. Phys.*, 1997, **101**, 2923–2928.
50. C. J. Jameson, A. K. Jameson, N. C. Smith, and K. Jackowski, *J. Chem. Phys.*, 1987, **86**, 2717–2722.
51. D. M. Lamb, S. T. Adamy, K. W. Woo, and J. Jonas, *J. Phys. Chem.*, 1989, **93**, 5002–5005.
52. P. Etesse, J. A. Zega, and R. Kobayashi, *J. Chem. Phys.*, 1992, **97**, 2022–2029.
53. P. Etesse, A. M. Ward, and R. Kobayashi, *Physica B*, 1993, **183**, 45–52.
54. P. Etesse, W. G. Chapman, and R. Kobayashi, *Mol. Phys.*, 1993, **80**, 1145–1164.
55. D. M. Pfund, T. S. Zemanian, J. C. Linehan, J. L. Fulton, and C. R. Yonker, *J. Phys. Chem.*, 1994, **98**, 11 846–11 857.
56. S. Bai and C. R. Yonker, *J. Phys. Chem. A*, 1998, **102**, 8641–8647.
57. E. W. Lang and H. D. Ludemann, *Prog. NMR Spectrosc.*, 1993, **25**, 507.
58. D. M. Grant, C. L. Mayne, F. Liu, and T. X. Xiang, *Chem. Rev.*, 1991, **91**, 1591–1624.
59. C. J. Jameson, *Chem. Rev.*, 1991, **91**, 1375–1395.
60. R. K. Harris, 'Nuclear Magnetic Resonance Spectroscopy', The Bath Press: Avon, UK, 1986, Chapter 4.
61. F. Liu, W. J. Horton, C. L. Mayne, T. X. Xiang, and D. M. Grant, *J. Am. Chem. Soc.*, 1992, **114**, 5281–5294.
62. Y. J. Kim and J. Jonas, *J. Phys. Chem.*, 1995, **99**, 6777–6788.
63. J. L. Dote, D. Kivelson, and R. N. Schwartz, *J. Phys. Chem.*, 1981, **85**, 2169–2180.
64. M. Roy and S. Doraiswamy, *J. Chem. Phys.*, 1993, **98**, 3213–3223.
65. R. M. Anderson and J. F. Kauffman, *J. Phys. Chem.*, 1994, **98**, 12 117–12 124.
66. R. M. Anderson and J. F. Kauffman, *J. Phys. Chem.*, 1995, **99**, 13 759–13 762.
67. J. A. Jossi, L. I. Stiel, and G. Thodos, *AIChE J.*, 1961, **7**, 625.
68. C.-M. Hu and R. Zwanzig, *J. Chem. Phys.*, 1974, **60**, 4354–4357.
69. S. Bai, C. M. V. Taylor, F. Liu, C. L. Mayne, R. J. Pugmire, and D. M. Grant, *J. Phys. Chem. B.*, 1997, **101**, 2923–2928; C. M. V. Taylor, S. Bai, C. L. Mayne, and D. M. Grant, *J. Phys. Chem. B*, 1997, **101**, 5652–5658.
70. D. Ben-Amotz and T. W. Scott, *J. Chem. Phys.*, 1987, **87**, 3739.
71. B. L. Armstrong and J. Courtney, *Can. J. Phys.*, 1972, **50**, 1262–1272.
72. A. A. Maryott, M. S. Malmberg, and K. T. Gillen, *Chem. Phys. Lett.*, 1974, **25**, 169–174.
73. P. Etesse, J. A. Zega, and R. Kobayashi, *J. Chem. Phys.*, 1992, **97**, 2022–2029.
74. J. Kestin and W. A. Wakeham, in 'Transport Properties of Fluids: Thermal Conductivity, Viscosity and Diffusion Coefficients', CINDAS Data Series Material Properties, ed C. Y. Ho, Hemisphere Publishing: New York, 1988, Vol. 1.
75. T. R. Marrero and E. A. Mason, *J. Phys. Chem. Ref. Data*, 1972, **1**, 1.
76. I. Swaid and G. M. Schneider, *Ber. Bunsenges. Phys. Chem.*, 1979, **83**, 969.
77. R. Feist and G. M. Schneider, *Sep. Sci. Technol.*, 1980, **17**, 261.
78. Z. Balenovic, M. Myers, and J. C. Giddings, *J. Chem. Phys.*, 1970, **52**, 915.
79. H. Saad and E. Gulari, *Ber. Bunsenges. Phys. Chem.*, 1984, **88**, 834.
80. H. Saad and E. Gulari, *J. Phys. Chem.*, 1984, **88**, 136.
81. J. Jonas and D. M. Lamb, in 'ACS Symposium Series No. 329', eds T. G. Squires and M. E. Paulaitis, American Chemical Society: Washington, DC, 1987.
82. W. J. Lamb, G. A. Hoffmann, and J. Jonas, *J. Chem. Phys.*, 1981, **74**, 6875.
83. I. T. Horváth and J. M. Millar, *Chem. Rev.*, 1991, **91**, 1339–1351.
84. G. B. Benedek and E. M. Purcell, *J. Chem. Phys.*, 1954, **22**, 2003.
85. M. E. Smith and J. H. Strange, *Meas. Sci. Technol.*, 1997, **7**, 449–475.
86. B. Lance and J. Jonas, *Annu. Rep. NMR Spectrosc.*, 1997, **33**, 115–150.
87. J. W. Rathke, *J. Magn. Reson.*, 1989, **85**, 150–155.
88. K. Woelk, R. W. Rathke, and R. J. Klinger, *J. Magn. Reson. A*, 1994, **109**, 137–146.
89. C. R. Yonker, T. S. Zemanian, S. L. Wallen, J. C. Linehan, and J. A. Franz, *J. Magn. Reson. A*, 1995, **113**, 102.
90. D. C. Roe, *J. Magn. Reson.*, 1985, **63**, 388.
91. I. T. Horvath and E. C. Ponce, *Rev. Sci. Instrum.*, 1991, **62**, 1104.
92. I. T. Horvath and J. M. Millar, *Chem. Rev.*, 1991, **91**, 1339.
93. S. Bai, C. M. Taylor, C. L. Mayne, R. J. Pugmire, and D. M. Grant, *Rev. Sci. Instrum.*, 1996, **76**, 240–243.
94. S. L. Wallen, L. K. Schoenbachler, E. D. Dawson, and M. A. Blatchford, *Anal. Chem.*, 2000, **72**, 4230–4234.
95. R. Bertani, M. Mali, J. Roos, and D. Brinkmann, *Rev. Sci. Instrum.*, 1992, **63**, 3303.
96. M. Kanakubo, T. Aizawa, T. Kawakami, O. Sato, Y. Ikushima, K. Hatakeda, and N. Saito, *J. Phys. Chem. B*, 2000, **104**, 2749–2758.
97. J. C. Linehan, S. L. Wallen, C. R. Yonker, T. E. Bitterwolf, and J. T. Bays, *J. Am. Chem. Soc.*, 1997, **119**, 10 170–10 177.
98. M. R. Ehrhardt, P. F. Flynn, and A. J. Wand, *J. Biomol. NMR*, 1999, **14**, 75–78.
99. C. R. Yonker, J. C. Linehan, and J. L. Fulton, *J. Supercrit. Fluids*, 1998, **14**, 9–16.
100. J. W. Rathke, R. J. Klinger, R. E. Gerald II, K. W. Kramarz, and K. Woelk, *Prog. NMR Spectrosc.*, 1997, **30**, 209.
101. S. Kainz, A. Brinkmann, W. Leitner, and A. Pfalz, *J. Am. Chem. Soc.*, 1999, **121**, 6421–6429.

Biographical Sketches

Gunilla B. Jacobson, *b* 1969. Ph.D. 1996, Organic Chemistry, University of Uppsala, Sweden. Postdoctoral Research Associate with Keith P. Johnston, Univ. of Texas, Austin, 1997–1998. Research

Associate with William Tumas, Los Alamos National Laboratory, 1998–1999. Technical Staff Member, Los Alamos National Laboratory, 2000–present. Approx 30 publications. Current research interests: reactions, separations, and materials modifications using supercritical fluid technology.

Craig M. V. Taylor, *b* 1962. M.S., 1987 Organometallic Chemistry, New Mexico Institute of Mining and Technology, Ph.D. 1999, Physical Chemistry, University of Utah (supervisor David M. Grant) 1985–87 Research Associate on Supercritical Fluid Tertiary Oil Recovery, Petroleum Recovery Research Center Socorro New Mexico. 1987–94 Scientist Los Alamos National Laboratory (LANL). 1994–98 Principal Investigator Supercritical Fluids Facility, LANL. Leader of Applied Chemical Technologies Group, Chemistry Division, LANL 1998–present. Approx 25 publications. Current research interests: Supercritical Fluids Applications.

Transferrins

Claudio Luchinat and Marco Sola
University of Bologna, Bologna, Italy

1	Introduction	1
2	The Role of NMR in the Chemistry of Transferrins: Achievements	2
3	The Role of NMR in the Chemistry of Transferrins: Future Prospects	7
4	Related Articles	8
5	References	8

1 INTRODUCTION

Transferrins are a family of metal binding glycoproteins which play a fundamental role in iron metabolism in vertebrates and invertebrates.[1] Transferrin from serum (Tf hereafter) acts as the principal iron carrier in plasma, binding the Fe^{3+} ion strongly and reversibly and shuttling it from the sites of metal uptake to those of iron–proteins biosynthesis and iron storage. Ovotransferrin from avian egg white (Otf), and lactoferrin (Ltf) found in many secretory fluids and in leukocytes, are mainly iron-sequestering proteins which exert a bacteriostatic and detoxifying function. Transferrins are monomeric proteins of about 700 residues with molecular weight close to 80 kDa. They are related by a sequence homology of about 50%. The X-ray structural information[2,3] indicates that the polypeptide chain is organized into two nearly equal-sized and about 40% homologous globular lobes connected by a short peptide segment, each containing one chain terminus (hence termed N-lobe and C-lobe), and one metal site (Figure 1). Each lobe is in turn structured into two domains. The metal lies at the bottom of the cleft between the two domains, about 10 Å from the protein surface. Both metals are bound by two tyrosines, one histidine, and one aspartate in a pseudooctahedral coordination which is completed by a bidentate carbonate ion hydrogen bonded to some protein groups (Figure 1).[2,3] X-ray data also indicate the absence of metal-coordinated water in the crystal.

The requirement of a concomitant (synergistic) binding of an anion (besides carbonate, carboxylate anions with a second donor group are also active) for specifically loading the metal in the two sites is a unique feature of the biochemistry of transferrins. In recent years X-ray crystallography and NMR have allowed the elucidation of several molecular details of the metal sites. It is apparent that the formation of the ternary complex at both sites proceeds through initial anion binding to the protein: the anion is most probably required to reduce the net positive charge in the binding cavity, due to the presence of a number of cationic residues, and for increasing the overall stability of the adduct by further anchoring the metal to the protein. Overall, it functions as a bridge between the metal and the protein. The synergistic anion appears to play a central role in the reactivity of the metal centers, acting as the key for the processes of metal uptake and release. The associated protein conformational changes are also being extensively studied, in particular the open–close equilibrium of the interdomain cleft at each lobe, with metal binding and removal occurring only in the open form.

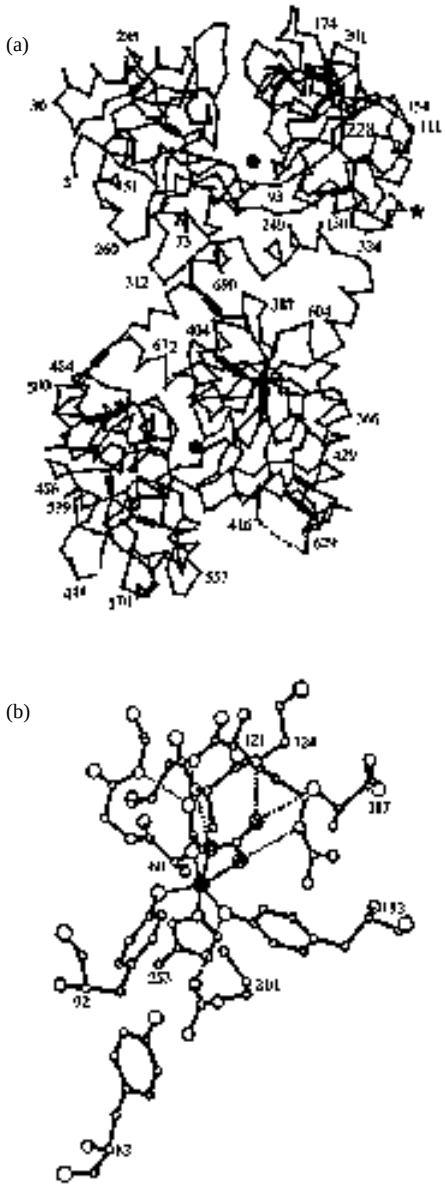

Figure 1 (a) C^{α} plot of the lactoferrin molecule showing its subdivision into two lobes, the N-lobe (top) and C-lobe (bottom). The iron atoms are shown as filled circles bound in the cleft between the two domains in each lobe. (b) The metal- and anion-binding site in lactoferrin (N-lobe). The carbonate anion is shown by hatched circles. Hydrogen bonds are indicated by dotted lines. (Reproduced by permission of Academic Press from B. F. Anderson, H. M. Baker, G. E. Norris, D. W. Rice, and E. N. Baker, *J. Mol. Biol.*, 1989, **209**, 711)

The two metal sites of transferrins are, in general, spectroscopically slightly inequivalent and differ, although most often not dramatically, in metal binding affinity. The relative binding strength of the two sites is sensitive to pH, synergistic anion, and ionic composition of the medium, and may vary toward different metals. However, the C-site almost invariably shows a greater metal affinity than the N-site at acidic pH. The structural bases of these differences are still not unequivocally

established (although the disulfide bridge content of the two lobes appears to be relevant in this respect). Their physiological relevance is also under investigation. The biological requirement for the structural 'doubleness' of transferrins is nowadays a central issue.

Transferrins can firmly bind a large number of transition, nontransition, and lanthanide ions. Several metals have served as spectroscopic probes for investigating the structural features of the metal sites, but some of the adducts also have a biological relevance since serum transferrin, being only about 30% saturated with iron in vivo, may function as an efficient carrier for metals other than iron.

2 THE ROLE OF NMR IN THE CHEMISTRY OF TRANSFERRINS: ACHIEVEMENTS

It should be recalled that for a protein of the size of transferrin full structural studies in solution (see ***Biological Macromolecules: Structure Determination in Solution***; ***Biological Macromolecules***; ***Biological Macromolecules: NMR Parameters***; ***Multidimensional Spectroscopy: Concepts***; ***Structures of Larger Proteins, Protein-Ligand, and Protein-DNA Complexes by Multi-Dimensional Heteronuclear NMR***) are not yet feasible. The NMR of transferrins was until recently mainly devoted to the elucidation of the molecular details of the ternary adducts at the metal sites with the following methodological approaches: (a) ^{13}C NMR of protein derivatives of diamagnetic metals with ^{13}C-enriched anions; (b) observation of protein-bound NMR active metal nuclei; (c) observation of ^{1}H NMR hyperfine-shifted resonances arising from the protons surrounding a bound paramagnetic metal (see ***Electron–Nuclear Hyperfine Interactions***; ***Cobalt(II)- and Nickel(II)-Substituted Proteins***; ***Electron– Nuclear Multiple Resonance Spectroscopy***); (d) NMRD profiles. Only in recent years, has one- and two-dimensional ^{1}H NMR at high field (see ***Multidimensional Spectroscopy: Concepts***) succeeded in handling, at least partially, the largely unresolved proton spectrum and proved to be of use in monitoring metal binding to the protein and the related conformational changes. In what follows we have outlined the contribution of NMR to the understanding of the main issues of the metallobiochemistry of transferrins.

2.1 Identification of the Metal-Binding Residues

The involvement of tyrosine residues in metal binding at both sites of transferrins, indicated by a number of spectroscopic and chemical modification studies, has been conclusively supported by ^{1}H NMR since the early 1970s from the shift induced in the corresponding resonances by Ga^{3+} binding, and their paramagnetic broadening upon Fe^{3+} binding (see ***Paramagnetic Relaxation in Solution***).[4] In addition, two histidines were also proposed as metal ligands from the detection of the C(2)H resonances which did not titrate with pH in the Ga^{3+} ternary complexes[5] of either intact or half molecules of Otf and human Tf[6,7] (Ga^{3+} has proved to be a good diamagnetic substitute for the Fe^{3+} ion, owing to the similarity of the ionic radius and to a similar binding affinity for transferrins). Metal binding of two histidines and two tyrosines was also consistent with the hyperfine shifted ^{1}H resonances in the mono- and bis-Co^{2+} derivatives of Otf.[8,9] The spread of the hyperfine shifted signals and their relatively long relaxation times[10] (see ***Paramagnetic Relaxation in Solution*** and ***Cobalt(II)- and Nickel(II)-Substituted Proteins***) suggested octahedral coordination around the metal ions.[8,9]

The X-ray structure later confirmed octahedral coordination and the presence of two tyrosine ligands, but showed that only one of histidine is involved in the metal binding site.[2,3] The identity of the additional nontitrating histidine in the Ga^{3+} derivative remains unknown, while the additional hyperfine shifted exchangeable proton in the spectrum of the Co^{2+} derivative could well arise, in retrospect, from one of the NH protons H bonded to the metal-coordinated carbonate ion.

Cadmium-113 NMR[11] (see ***Cadmium-113 NMR: A Surrogate Probe for Zinc and Calcium in Proteins***) and ^{205}Tl NMR data[12] (see ***Thallium NMR***) are in full agreement with the presence of only one histidine in the binding set. Aspartate coordination invariably went undetected, most probably due to the rather elusive ^{1}H NMR spectral changes in the crowded aliphatic region upon metal binding and the impossibility of metal NMR to discriminate it from other potential oxygen donors.

2.2 Exchangeable Protons in the Metal Sites

The issue of possible water coordination was tackled through water proton relaxation measurements. Early studies of water T_1 measurements in solutions of the Fe^{3+} adducts of Htf and Otf simply showed the accessibility of both sites to water molecules.[13,14] This was substantiated later by measurements of the field dependence of the longitudinal nuclear magnetic relaxation rates of water protons (NMRD profiles) on the iron adduct of Htf, also carried out for comparative purposes on the apoprotein and the diamagnetic analog containing Co^{3+}, which were interpreted as indicative of a water molecule only loosely bound to the metal in each site.[15,16] Analogously, one water molecule axially bound to the metal was also proposed for the Cu^{2+} derivative of Htf.[17] It was later shown that for slowly rotating protein complexes the anisotropic structure of the ligand fields of the complexed metals is not averaged out as it is for fast rotating aqua ions or small complexes.[18,19] The NMRD profiles for Cu^{2+} and VO^{2+} complexes of Htf were then evaluated with computations that included the anisotropic hyperfine interaction of metal ions with their own nuclei (see ***Electron–Nuclear Hyperfine Interactions***).[20] It was found that relaxation occurs through exchange of bulk water with a second coordination sphere water molecule. This was also confirmed for the Gd^{3+}–Htf complex[21] (see ***Gadolinium Chelates: Chemistry, Safety and Behavior***) and demonstrated later by the X-ray structure of human Ltf.[3] Recent[22] more quantitative interpretation of the NMRD data for Fe^{3+}–Htf,[23] taking into account zero field splitting of the iron ion,[18,19,24] suggests the presence of slowly exchanging protons (possibly from the protein) and of fast exchanging water at about 4–5 Å from the metal ion. NMRD data on Cu^{2+}–transferrin were also instrumental in demonstrating rotation-independent electronic relaxation mechanisms for Cu^{2+} in solution.[25]

2.3 Synergistic Anions in the Metal Sites

Elucidation of the anion binding arrangement in the metal sites was obtained from a number of ^{13}C NMR data using

Table 1 ^{13}C NMR Chemical Shifts for ^{13}C-Enriched Synergistic Anions in Various Metal–Transferrin Derivatives[a]

Derivative	Chemical shift[b]	
Carbonate derivatives		
Co^{3+}–Htf[27]	169.5	169.3
Al^{3+}–Otf[30]	165.7 (N)	165.5(C)
Al^{3+}–Htf[29]	165.4	
Ga^{3+}–Otf[29]	166.3	
Ga^{3+}–Htf[29]	166.5	
Tl^{3+}–Htf[12]	165.98 (N)	166.22 (C)
Tl^{3+}–Otf[12]	165.92	
Sc^{3+}–Otf[38]	166.74 (N)	166.61 (C)
Sc^{3+}–Htf[38]	167.19	166.76
Zn^{2+}–Otf[29]	168.2	
Zn^{2+}–Htf[29]	168.5	
Cd^{2+}–Otf[11]	168.2	
Cd^{2+}–Htf[11]	168.2	
Oxalate derivatives		
	C-1	C-2
Al^{3+}–Otf[30]	168.42 (C)	165.33 (C)
	168.47 (N)	165.89 (N)
Al^{3+}–Htf[36]	168.58	166.07
	168.40	165.33
Al^{3+}–Ltf[36]	168.55	166.0
	168.24	166.0
Ga^{3+}–Otf[29]	168.4 (C)	165.7 (C)
	168.4 (N)	166.2 (N)
Tl^{3+}–Otf[12]	167.80 (C)	165.35 (C)
	167.91 (N)	165.99 (N)
Tl^{3+}–Htf[12]	167.88 (N)	165.62 (N)
Sc^{3+}–Otf[38]	170.52 (C)	167.00 (C)
	170.60 (N)	167.68 (N)
Zn^{2+}–Otf[29]	169.6	
Cd^{2+}–Htf[32]	168.5 (C)	169.9 (N)

[a]Htf: human serum transferrin; Otf: ovotransferrin; Ltf: human lactoferrin. Assignments to the N- and C-site are reported in parentheses, when available.
[b]In ppm from Me_4Si.

^{13}C-enriched anions (mainly carbonate and oxalate) and/or NMR-active nuclei loaded in the protein sites. The spectral parameters and resonance assignments to individual sites, where available, have been collected in Table 1 and 2. The broadening beyond detection of the ^{13}C NMR resonance of isotopically-enriched bicarbonate bound to Fe^{3+}–Tf[26] allowed an estimate to be made of an upper limit of 9 Å for the Fe–^{13}C distance, which was later reduced to 4.5 Å[27] thanks to instrumental developments, consistent with the presence of the anion in the first coordination sphere of the metal. The latter study also indicated that the anion, most probably carbonate rather than bicarbonate as judged by the ^{13}C chemical shift value, was specifically bound in both metal binding sites of the diamagnetic Co^{3+} derivative and of the apoenzyme, giving rise in both cases to resonances in slow exchange with that of free bicarbonate (see ***Chemical Exchange Effects on Spectra***).[27] Specific anion binding to the apoprotein was taken as indicative that anion binding to the sites may precede metal binding, which is now indeed a widely accepted step in the mechanism of metal uptake of transferrins. A positively charged arginine residue was suggested as one of the anion binding groups for carbonate,[27] as later confirmed by X-ray data. The pH dependence of the ^1H NMR resonances of the histidine C(2)H protons in diamagnetic Ga(III) derivatives of Otf, Htf, and their half-molecules in the presence of dicarboxylic acids as synergistic anions indicated a histidine as the likely anion binding group in each site.[5–7,28] Interestingly, the X-ray structure of human Ltf allows for binding of anions larger than carbonate not to the arginine involved in the carbonate derivative, but to polar residues of a cavity beyond such a residue, which actually also includes a histidine residue.[3]

Further ^{13}C NMR studies of diamagnetic Al^{3+}–, Ga^{3+}– and Zn^{2+}–transferrin derivatives with carbonate and oxalate as the synergistic anion[29,30] were interpreted in terms of the anion bridging the metal and a positively charged group of the protein, in line with the 'interlocking-sites' model (Figure 2).[31] Oxalate bound in the Ga^{3+}– and Al^{3+}–Otf derivatives gave rise to two partially overlapped AB signal patterns.[29] The inequivalence of the two carbon atoms was assumed to arise from oxalate binding to the metal via only one carboxylate group, the other interacting with a positive residue of the site. Reference to ^{13}C chemical shift data of simple inorganic oxalate complexes allowed the assignment of the resonances of the protein-bound and metal-bound carbons of each oxalate molecule.[29,30] In the case of Zn^{2+}–[29] and Cd^{2+}–Otf–oxalate derivatives,[32] the effect of the metal on the shielding of the carbon atom is more similar to that of the protein residue, leading to the equivalence of the two carbon atoms (see ***Magnetic Equivalence***), hence to the observation of a single signal for each protein-bound anion.

Overall, although subject to a successive reevaluation (see below), these ^{13}C NMR data strongly supported the bridging arrangement of the synergistic anion prior to publication of the X-ray data.[2,3] Moreover, more recent ^{113}Cd NMR spectra of the ^{113}Cd–Otf derivative with glycine as the synergistic anion unequivocally indicated the binding of the amino group of the amino acid to the metal, fully in line with the interlocking sites model.[33]

Observation of the magnetic coupling between an $I = \frac{1}{2}$ metal and the carbon atom of the anion in both metal sites yielded conclusive spectroscopic evidence of a direct metal–ion linkage. In particular, this was achieved by using ^{205}Tl and ^{113}Cd ions loaded in one or both metal sites (Figure 3).[11,12,34] The ^2J coupling constants are collected in Table 2.

Thallium–transferrin derivatives allowed a reevaluation of the binding mode of oxalate, and led to further insight into the chemistry of the ternary adduct in the protein sites. The ^{13}C NMR signals of bound oxalate in each site of the $^{205}Tl^{3+}$ derivatives of human Tf and Otf are split into a doublet of doublets due to carbon–carbon and thallium–carbon coupling.[12] The comparable values of the ^{13}C–metal coupling constants for the two oxalate carbons (Table 2) indicate that the anion binds to the metal in a 1,2-bidentate mode at both sites. This is likely to be the case for all the oxalate adducts of transferrins with tripositive metals, as recently suggested from the similarity of the ^{13}C NMR spectral patterns for these adducts.[12] This view receives conclusive support from the X-ray structure of the Cu^{2+}–oxalate ternary adduct with the C-terminal half-molecule of Ltf,[35] which confirms the 1,2-bidentate bridging arrangement of the oxalate anion and indicates that the spectral inequivalence of the two carbon

Table 2 Spectral Parameters for Metal NMR Resonances and M–^{13}C Coupling Constants for Various Metal–Transferrin Derivatives[a]

Derivative	Chemical shift (ppm)[b]	$\Delta\nu_{\frac{1}{2}}$(Hz)	^2J(M,^{13}C) (Hz)
$^{27}Al^{3+}$–Otf–CO_3^{2-}[c] **30, 36, 37**	−2.3 (N)	140	
	−3.8 (C)	170	
$^{27}Al^{3+}$–Tf–CO_3^{2-}[c] **36**	−2.8	180	
$^{27}Al^{3+}$–Ltf–CO_3^{2-}[c] **36**	−4.3	200	
$^{27}Al^{3+}$–Otf–$C_2O_4^{2-}$[c] **30**	−4.4 (N)	170	
	−5.7 (C)	200	
$^{205}Tl^{3+}$–Htf–CO_3^{2-}[d] **34, 43**	2055 (C)	100	265
	2075 (N)	100	290
$^{205}Tl^{3+}$–Htf–CO_3^{2-}[e] **12**	2055 (C)		285
	2072 (N)		278
$^{205}Tl^{3+}$–Otf–CO_3^{2-}[e] **12**	2054 (C)		281
	2075 (N)		281
$^{205}Tl^{3+}$–Otf–$C_2O_4^{2-}$[e] **12**	2100 (C)		32, 21[f]
	2103 (N)		28, 14[f]
$^{205}Tl^{3+}$–Htf–$C_2O_4^{2-}$[e] **12**	–		27, 15[f,g]
$^{51}V^{5+}$–Htf–CO_3^{2-}[c] **39, 40**	−529.5 (C)	200	
	−531.5 (N)	310	
$^{45}Sc^{3+}$–Otf–CO_3^{2-}[c] **38**	77 (C)	940	
	85 (N)	740	
$^{45}Sc^{3+}$–Htf–CO_3^{2-}[c] **38**	76	1020	
$^{45}Sc^{3+}$–Otf–$C_2O_4^{2-}$[c] **38**	65 (C)	1030	
	70 (N)	1160	
$^{113}Cd^{2+}$–Otf–CO_3^{2-}[e] **11**	21.6	100	22
$^{113}Cd^{2+}$–Htf–CO_3^{2-}[e] **11**	11.7	100	20
$^{113}Cd^{2+}$–Htf–CO_3^{2-}[c] **54**	38.1 (N)	313	
	43.6 (C)	377	
$^{113}Cd^{2+}$–Otf–$C_2O_4^{2-}$[e] **32**	54 (C)	150	
	– (N)[h]		
$^{113}Cd^{2+}$–Otf–Gly[e] **33**	139	320	

[a]Htf: human serum transferrin; Otf: ovotransferrin; Ltf: human lactoferrin. Assignments to the N- and C-site are reported in parentheses.
[b]The following references were used: ^{27}Al: 1 M $Al(NO_3)_3$ in D_2O; ^{205}Tl: Tl^+ ion at infinite dilution; ^{51}V: $VOCl_3$; ^{45}Sc: 0.1 M $Sc(H_2O)_6^{3+}$; ^{113}Cd: 0.1 M $Cd(ClO_4)_2$ in D_2O. Assignment to the N- and C-site are reported in parentheses, when available.
[c]11.7 T.
[d]1.4 T.
[e]4.7 T.
[f]Inequivalent carbons.
[g]N-terminal half-molecule.
[h]Broadened beyond detection.

atoms in the ternary adducts with tripositive metals arises from differences in the protein residues H bonded to the two carboxylate groups. In the light of these results, the ^{13}C spectra of the $^{113}Cd^{2+}$–oxalate adduct of Otf, for which, unlike the carbonate derivative,[11] no ^{113}Cd–^{13}C coupling could be detected,[32] consistent with a longer metal–carbon distance, can also be interpreted in terms of the above anion arrangement.

Recent work on NMR of quadrupolar metal nuclei (^{51}V, ^{27}Al, and ^{45}Sc) (see ***Aluminum-27 NMR of Solutions***; ***Quadrupolar Transition Metal and Lanthanide Nuclei***) loaded in the sites of transferrins deserve a special mention.[12,30,36–40] For an $I = \frac{n}{2}$ nucleus (n = 3, 5, 7) firmly bound to a slowly rotating macromolecule, far from the extreme narrowing limit, it is shown that only the central $\frac{1}{2} \rightarrow -\frac{1}{2}$ nuclear spin transition can be observed (see ***Quadrupolar Interactions***) (Figure 4). Under these conditions the field dependence of the linewidth and chemical shift (see ***Dynamic Frequency Shift***) provides the values of the quadrupole coupling constant, χ, and of the rotational correlation time, τ_c, for the protein-bound metals, and hence yields information on the symmetry of the metal coordination environment. For example, independent of the synergistic anion, the Al^{3+} ion appears to be octahedrally coordinated in both sites, with a higher degree of symmetry in the N-site as compared to the C-site.[30] Moreover, the metal sites of the Sc^{3+}–Otf derivative show a higher symmetry than those in the homologous Al^{3+} derivative.[38]

Since detection of the resonances of these quadrupolar nuclei is facilitated by increasing the magnetic field and the molecular size of the protein, the technique is of general interest for probing the properties of the metal binding sites of large metalloproteins.

2.4 The (In)Equivalence of the Two Binding Sites

Early water proton relaxation measurements of Fe^{3+} binding to Otf, coupled with electrophoretic profiles, failed to detect the difference in iron binding ability of the two sites,[41] indicating a random distribution of iron in the two lobes.[14] Inequivalences can be detected with the aid of paramagnetic

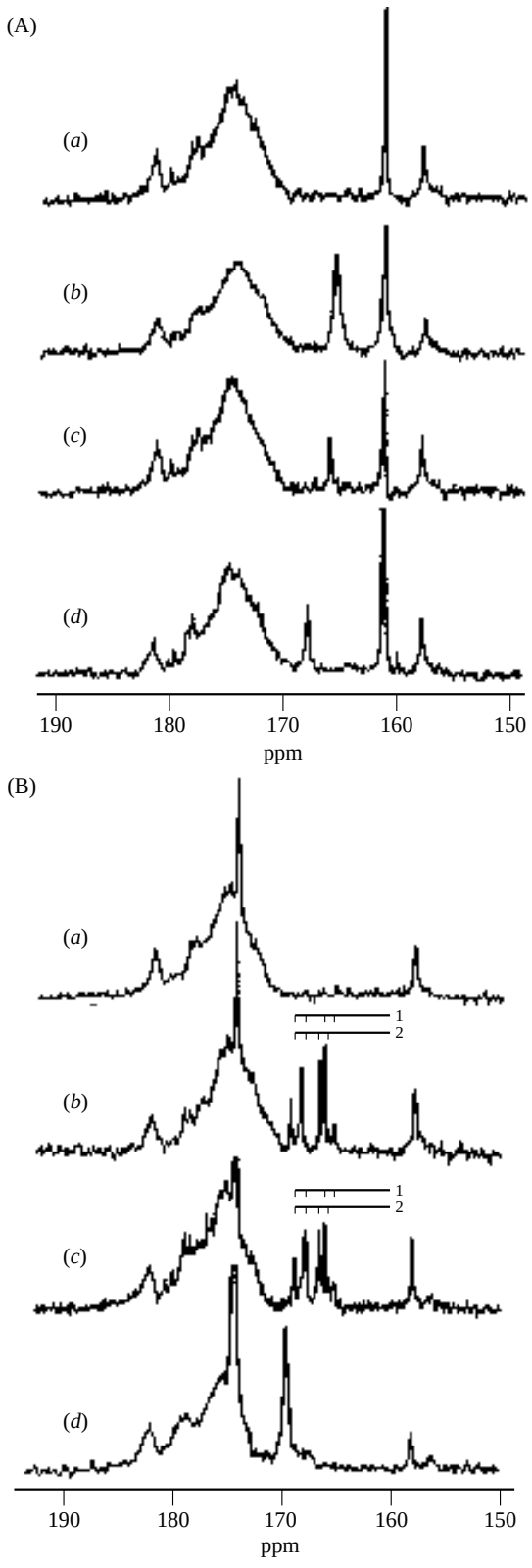

Figure 2 75.4 MHz ^{13}C NMR spectra of the carbonyl region of (A) Otf–carbonate–metal complexes and (B) Otf–oxalate–metal complexes in the presence of excess anion, pH 8 (protein concentration 1.5 mM): (*a*) apoprotein; (*b*) Al^{3+} derivatives; (*c*) Ga^{3+} derivatives; and (*d*) Zn^{2+} derivatives. (Reproduced by permission of the American Chemical Society from I. Bertini, C. Luchinat, L. Messori, A. Scozzafava, G. C. Pellacani, and M. Sola, *Inorg. Chem.*, 1986, **25**, 1782)

metals like Co^{2+} [8,9] and lanthanides,[42] taking advantage of the sensitivity of hyperfine shifts to even slight changes in the coordination sphere.[10] The advent of high-field Fourier transform spectrometers allowed the safe determination of site (in)equivalence simply from the presence of either one or two NMR signals (or signal patterns) due to the ^{13}C-labeled synergistic anion and/or NMR-active diamagnetic metals bound to the protein. A metal titration then generally indicated if sequential metal binding had occurred, and in some instances assignment of the NMR resonances to the individual sites allowed the site with higher metal affinity to be determined. This approach has been followed for the derivatives of Otf and Htf with Co^{3+}, Ga^{3+}, Al^{3+}, Tl^{3+}, Sc^{3+}, V^{5+}, Cd^{2+}, Zn^{2+} in combination with different synergistic anions, most often carbonate and oxalate. The NMR-active metals and the ^{13}C-labeled synergistic anion loaded in the two sites led to either overlapping peaks or distinct, but invariably closely spaced, resonances indicative of equivalent (within the resolution available) or slightly different chemical environments, respectively (Table 1 and 2). The higher metal affinity of the C-site over the N-site at acidic pH was, in general, exploited to obtain resonance assignment to individual sites, although recently the use of proteolytically-obtained half-molecules has proved to be a safer means for such an assignment. This was evidenced for the derivatives of human Tf and Otf with Al^{3+}, Tl^{3+}, and Sc^{3+}, for which the metal resonances and the ^{13}C signals of the synergistic anion in the bimetallic derivative were invariably found to exactly superimpose the signals of the two one-sited half-molecules.[12,30,36–38]

These extensive NMR data concurred to indicate that the relative properties of the two sites for a given transferrin vary with the nature of the metal, the synergistic anion, pH, and medium composition, and may differ from those of other transferrins. The following selected examples are worth mentioning. Aluminum–27 and ^{13}C NMR showed that in the presence of carbonate the two aluminum metal sites of Otf are slightly inequivalent and that Al^{3+} binds preferentially to the N-site at pH 8, while the site preference is reversed with oxalate.[30] In contrast, spectroscopically equivalent sites are detected in the homologous derivatives of human Tf and Ltf.[36] At pH values slightly above neutrality in the presence of carbonate, the Tl^{3+} ion was shown at an early stage,[43] unlike Al^{3+}, to bind more strongly to the C-site of human Tf, and more recently to bind with the same affinity to both sites of Otf.[12] Moreover, Sc^{3+} showed no site preference toward Otf with either carbonate or oxalate as synergistic anions,[38] and site inequivalence in the Cd^{2+} derivative of Tf with oxalate appeared more pronounced than in the homologous Zn^{2+} derivative.[11,32]

Although this overview demonstrates NMR to be a powerful tool for probing the differences in structural properties and binding affinity of the two metal sites, at present, as noted elsewhere,[44] it does not address unequivocally the question of the presence of a functional association between the lobes. The above-mentioned near-identity of the spectral properties of a given site in the half and intact transferrin molecules does not necessarily imply that the metal affinity of the sites remains unchanged upon proteolytic cleavage.

The application of resolution enhancement techniques, although allowing resolution of only a small fraction of the total proton resonances, particularly those belonging

to relatively mobile portions of the protein, has recently enabled one- and two-dimensional ^{1}H NMR (see ***COSY Two-Dimensional Experiments***; ***Multidimensional Spectroscopy: Concepts***; ***NOESY***) to monitor the binding of diamagnetic metals to whole and half-transferrin molecules.[45–47] Low-frequency methyl peaks probably experiencing aromatic ring current shifts, glycan *N*-acetyl and sugar ring protons, Lys/Arg ϵ/δ-CH_2 protons, and His C-2,H resonances could be resolved in the apo form of human Tf.[47] The disappearance of some of these peaks and the rise of new resonances in a slow exchange regime upon metal titration of the apo form of whole human Tf and its N-lobe (HTf/2N hereafter) allowed the detection of the sequential binding of Al^{3+} and Ga^{3+} to Tf, with preferential binding of the former metal to the N-site (in the presence of carbonate, pH 8.8),[46] and of the latter to the C-site (with oxalate as a synergistic anion, pH 7.2).[45] Examples of one- and two-dimensional proton spectra are illustrated in Figure 5.[45]

Since X-ray data indicate that the structural features of the N-lobe are likely to be closely similar in the intact protein and in the isolated lobe,[2] the lack of a perfect match between the spectral features of the apo form and the Al^{3+} adducts of Tf and Tf/2N was interpreted as indicative of an interaction between the lobes in the intact protein.[46] This approach also allowed a determination of the apparent binding constant of oxalate to apo-HTf/2N ($\log K = 4.04 \pm 0.09$) from the shift of some resonances induced by the weak binding of the anion, as a consequence of the fast exchange between the free and anion bound species on the NMR timescale.[45] Moreover, the time course of the paramagnetic broadening of the proton resonances in the Ga^{3+}–oxalate–HTf/2N adduct upon Fe^{3+} addition allowed the kinetics of Ga^{3+} displacement (k_{obs} = 0.162 h^{-1} at 310 K) to be determined.[45]

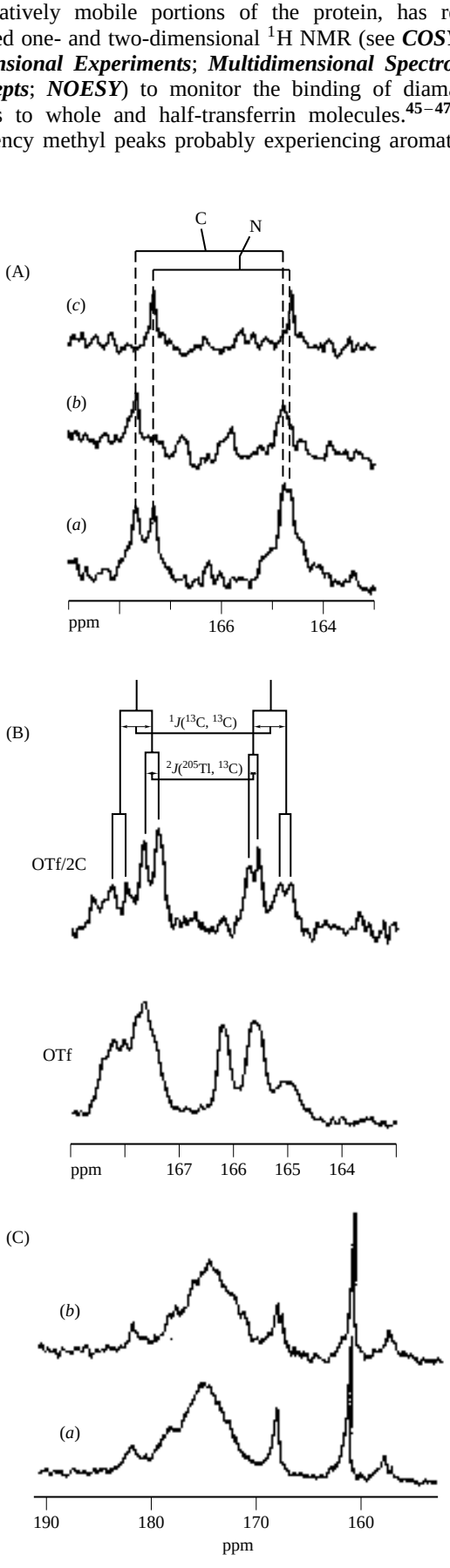

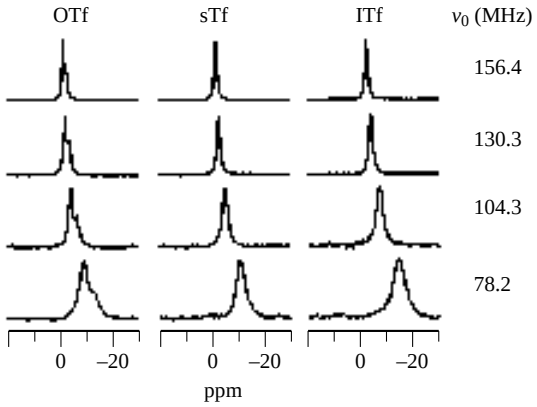

Figure 4 ^{27}Al NMR spectra of the Al_2 derivatives of Otf, human Tf, and human Ltf at different magnetic fields. (Reproduced by permission of the American Chemical Society from J. M. Aramini, M. W. Germann, and H. J. Vogel, *J. Am. Chem. Soc.*, 1993, **115**, 9750)

Figure 4 (A) Expanded carbonyl region of the 100.6 MHz ^{13}C NMR spectra of (*a*) Tl_2–Tf–CO_3^{2-} derivative; (*b*) Tl–Tf–carbonate derivative with Tl^{3+} loaded in the C-site; (*c*) Tl–Tf/2N–carbonate derivative. (Reproduced by permission of the American Chemical Society from J. M. Aramini, P. H. Krygsman, and H. J. Vogel, *Biochemistry*, 1994, **33**, 3304). (B) Expanded carbonyl regions of the 125.7 MHz ^{13}C NMR spectra of the Tl_2–Otf–oxalate derivative and of the Tl–Otf/2C–oxalate derivative. (Reproduced by permission of the American Chemical Society from J. M. Aramini, P. H. Krygsman, and H. J. Vogel, *Biochemistry*, 1994, **33,** 3304). (C) Carbonyl regions of the 50.3 MHz ^{13}C NMR spectrum of the Cd_2–Otf–carbonate derivatives containing (*a*) natural-abundance Cd^{2+} ion and (*b*) isotopically-enriched $^{113}Cd^{2+}$ ion. (Reproduced by permission of the American Chemical Society from M. Sola, *Inorg. Chem.*, 1990, **29**, 1113)

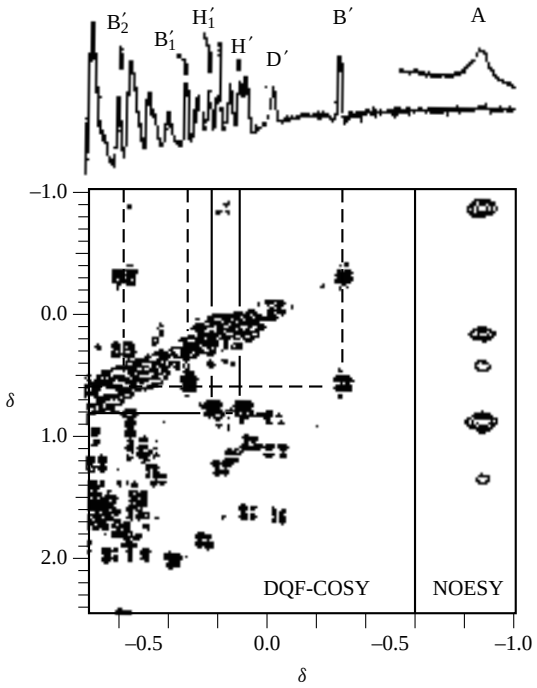

Figure 5 600-MHz phase-sensitive DQF-COSY ^{1}H NMR spectrum (subject to resolution enhancement) of the Ga^{3+}–Tf–oxalate adduct, together with a NOESY spectrum for the lowest frequency peak. (Reproduced by permission of the American Chemical Society from G. Kubal, A. B. Mason, S. U. Patel, P. J. Sadler, and R. C. Woodworth, *Biochemistry*, 1993, **32**, 3387)

2.5 Other Structural Features in Solution

Tentative assignments of the low-frequency methyl proton resonances to individual Leu, Val, and Ile residues were proposed for human Tf and its N-lobe through 2D COSY techniques (see ***COSY Two-Dimensional Experiments***) and calculation of the shifts induced by the ring currents of nearby aromatic groups (see ***Shielding: Overview of Theoretical Methods***).[45,46] The shifts of these resonances upon metal binding appear to be related to changes in their orientation toward the aromatic groups which reside in relatively mobile, yet structured hydrophobic domains possibly involved in conformational changes related to the closure of the interdomain cleft.[45] Unambiguous signal assignments and determinations of the precise movements of single residues are still unavailable, but much effort is being devoted toward this end.

Nonsynergistic anions like chloride, perchlorate, thiocyanate, and pyrophosphate are known to decrease the stability of various metal–transferrin derivatives, and, the chloride ion in particular, to affect the relative metal binding affinity of the sites.[48] They most probably bind to positively charged residues in the proximity of the metal site, altering the network of salt bridges and hydrogen bonds that stabilize the complex. The effect of perchlorate in decreasing the stability of the metal complexes was clearly monitored by the decrease of the ^{13}C and ^{113}Cd NMR resonances of the $^{113}Cd_2$–Otf–CO_3^{2-} adduct upon anion addition, due to dissociation of the complex.[11] Chlorine-35 and ^{14}N NMR linewidth measurements of chloride, perchlorate, and nitrate anion binding to human Tf in a fast exchange regime allowed the determination of a 2:1 stoichiometry for V^{5+} binding to the protein, since the formation of the ternary metal–carbonate complex at the sites determines the specific anion binding to the protein and hence leads to a decrease in quadrupolar relaxation (see ***Relaxation Theory for Quadrupolar Nuclei***).[49]

Proton NMR has also played an important role in the determination of the primary structure on the glycan moieties of a variety of transferrins and in the determination of solution conformation through 2D techniques.[50–53] Studies were carried out on glycopeptides obtained by proteolytic digestion or on the intact oligosaccharide chain detached from the protein by hydrazinolysis. Readers are referred to the original literature as far as the assignment procedures are concerned. However, it is worth mentioning that recent ^{1}H NMR studies on Ga^{3+} binding to human Tf indicate that metal binding alters the shift of the resonances of the *N*-acetylated sugar residues of both glycan chains, suggesting that the transmission of the perturbation to the carbohydrate chains may have significance for cell receptor recognition of the metal-loaded protein.[45]

3 THE ROLE OF NMR IN THE CHEMISTRY OF TRANSFERRINS: FUTURE PROSPECTS

The applicability of NMR techniques becomes less and less trivial with increase in molecular size. From this point of view, molecules of the size of transferrins represent a challenge. Multidimensional NMR, coupled with resolution enhancement techniques, of either intact and half-transferrin molecules, appear as a promising approach for detecting structural changes in the individual lobes upon metal uptake or release and ionization equilibria, and should be of use for monitoring the protein behavior toward the binding of a variety of metals and synergistic anions, under different conditions of pH and medium composition. The bottom line is to understand whether the two lobes undertake different roles in metal uptake and release processes, and whether they are functionally associated, and hence to address one of the most intriguing points of the biochemistry of transferrins related to their structural 'doubleness'. The advent of very high field spectrometers (750 MHz or higher) would greatly enhance the diagnostic power of this approach, together with the feasibility of NMR of quadrupolar metal nuclei which has proved highly sensitive to the structural features of the metal sites. The use of genetically-engineered proteins containing either amino acid substitutions, deletions, or labeled residues could also add essential information. Nitrogen-15 and/or ^{13}C selective and nonselective labeling is indeed providing a breakthrough to structural studies on medium sized proteins (see ***Heteronuclear Assignment Techniques***; ***Heteronuclear Shift Correlation Spectroscopy***).

Besides metal binding, NMR should also be a valuable means of monitoring the potential ability of transferrins to accommodate small molecules in the binding cleft.[3] Overall, the application of ^{1}H NMR to determine protein structure in solution, coupled with molecular dynamics calculations (although the size of transferrin would set this as a long-term project) appears to be the main research direction toward the elucidation of the structure–function relationships in this class of proteins.

4 RELATED ARTICLES

Calcium-Binding Proteins; Carbonic Anhydrase; Cobalt(II)- and Nickel(II)-Substituted Proteins; Copper Proteins; Field Cycling Experiments; Heme Peroxidases; Hemoglobin; Iron—Sulfur Proteins; Mitochondrial Cytochrome c; Myoglobin; Nonheme Iron Proteins; Proteases.

5 REFERENCES

1. D. C. Harris and P. Aisen, in *Physical Bioinorganic Chemistry*, ed. T. M. Loehr, VCH Publishers, New York, 1989, Vol. 2, p. 239
2. R. Sarra, R. Garratt, B. Gorinski, H. Jhoti, and P. Lindley, *Acta Crystallogr.*, 1990, **B46**, 763.
3. B. F. Anderson, H. M. Baker, G. E. Norris, D. W. Rice, and E. N. Baker, *J. Mol. Biol.*, 1989, **209**, 711.
4. R. C. Woodworth, K. G. Morallee, and R. J. P. Williams, *Biochemistry*, 1970, **9**, 839.
5. B. M. Alsaadi, R. J. P. Williams, and R. C. Woodworth, *J. Inorg. Biochem.*, 1981, **15**, 1.
6. A. A. Valcour and R. C. Woodworth, *Biochemistry*, 1987, **26**, 3120.
7. R. C. Woodworth, N. D. Butcher, S. A. Brown, and A. Brown Mason, *Biochemistry*, 1987, **26**, 3115.
8. I. Bertini, C. Luchinat, L. Messori, R. Monnanni, and A. Scozzafava, *J. Biol. Chem.*, 1986, **261**, 1139.
9. L. Messori and M. Piccioli, *Inorg. Chim. Acta*, 1990, **174**, 137.
10. I. Bertini and C. Luchinat, *NMR of Paramagnetic Molecules in Biological Systems*, Benjamin/Cummings, Menlo Park, CA, 1986.
11. M. Sola, *Inorg. Chem.*, 1990, **29**, 1113.
12. J. M. Aramini, P. H. Krygsman, and H. J. Vogel, *Biochemistry*, 1994, **33**, 3304.
13. A. Wishnia, *J. Chem. Phys.*, 1960, **32**, 871.
14. P. Aisen, A. Leibman, and H. A. Reich, *J. Biol. Chem.*, 1966, **241**, 1666.
15. S. H. Koenig and W. E. Schillinger, *J. Biol. Chem.*, 1969, **244**, 3283.
16. S. H. Koenig and W. E. Schillinger, *J. Biol. Chem.*, 1969, **244**, 6520.
17. B. P. Gaber, W. E. Schillinger, S. H. Koenig, and P. Aisen, *J. Biol. Chem.*, 1970, **245**, 4251.
18. I. Bertini, C. Luchinat, M. Mancini, and G. Spina, in *Magneto-Structural Correlations in Exchange-Coupled Systems*, ed. D. Gatteschi, O. Kahn, and R. D. Willet, Reidel, Dordrecht, 1985, p. 421.
19. L. Banci, I. Bertini, and C. Luchinat, *Nuclear and Electron Relaxation. The Magnetic Nucleus–Unpaired Electron Coupling in Solution*, VCH, Weinheim, 1991.
20. I. Bertini, F. Briganti, S. H. Koenig, and C. Luchinat, *Biochemistry*, 1985, **24**, 6287.
21. P. B. O'Hara and S. H. Koenig, *Biochemistry*, 1986, **25**, 1445.
22. I. Bertini, O. Galas, C. Luchinat, L. Messori, and G. Parigi, *J. Phys. Chem.*, in press.
23. S. H. Koenig and R. D. Brown, III, in *The Coordination Chemistry of Metalloenzymes*, ed. I. Bertini, R. S. Drago and C. Luchinat, Reidel, Dordrecht, 1983, p. 19.
24. I. Bertini, C. Luchinat, M. Mancini, and G. Spina, *J. Magn. Reson.*, 1984, **59**, 213.
25. I. Bertini, C. Luchinat, R. D. Brown, III, and S. H. Koenig, *J. Am. Chem. Soc.*, 1989, **111**, 3532.
26. D. C. Harris, G. A. Gray, and P. Aisen, *J. Biol. Chem.*, 1974, **249**, 5261.
27. J. A. Zweier, J. B. Wooten, and J. S. Cohen, *Biochemistry*, 1981, **20**, 3505.
28. R. C. Woodworth, *J. Inorg. Biochem.*, 1986, **28**, 245.
29. I. Bertini, C. Luchinat, L. Messori, A. Scozzafava, G. C. Pellacani, and M. Sola, *Inorg. Chem.*, 1986, **25**, 1782.
30. J. M. Aramini and H. J. Vogel, *J. Am. Chem. Soc.*, 1993, **115**, 245.
31. G. W. Bates and M. R. Schlabach, *J. Biol. Chem.*, 1975, **250**, 2177.
32. M. Sola, *Eur. J. Biochem.*, 1990, **194**, 349.
33. G. Battistuzzi and M. Sola, *Biochim. Biophys. Acta*, 1992, **1118**, 313.
34. I. Bertini, L. Messori, G. C. Pellacani, and M. Sola, *Inorg. Chem.*, 1988, **27**, 761.
35. M. S. Shongwe, C. A. Smith, E. W. Ainscough, H. M. Baker, A. M. Brodie, and E. N. Baker, *Biochemistry*, 1992, **31**, 4451.
36. J. M. Aramini, M. W. Germann, and H. J. Vogel, *J. Am. Chem. Soc.*, 1993, **115**, 9750.
37. J. M. Aramini and H. J. Vogel, *Bull. Magn. Reson.*, 1993, **15**, 84.
38. J. M. Aramini and H. J. Vogel, *J. Am. Chem. Soc.*, 1994, **116**, 1988.
39. A. Butler and H. Eckert, *J. Am. Chem. Soc.*, 1989, **111**, 2802.
40. A. Butler and M. J. Danzitz, *J. Am. Chem. Soc.*, 1987, **109**, 1864.
41. P. Aisen, A. Leibman, and J. Zweier, *J. Biol. Chem.*, 1978, **253**, 1930.
42. L. Messori and M. Piccioli, *J. Inorg. Biochem.*, 1991, **42**, 185
43. I. Bertini, C. Luchinat, and L. Messori, *J. Am. Chem. Soc.*, 1983, **105**, 1347.
44. M. Sola, *Chemtracts—Inorg. Chem.*, 1993, **5**, 201.
45. G. Kubal, A. B. Mason, S. U. Patel, P. J. Sadler, and R. C. Woodworth, *Biochemistry*, 1993, **32**, 3387.
46. G. Kubal, A. B. Mason, P. J. Sadler, A. Tucker, and R. C. Woodworth, *Biochem. J.*, 1992, **285**, 711.
47. G. Kubal and P. J. Sadler, *J. Am. Chem. Soc.*, 1992, **114**, 1117.
48. N. D. Chasteen, *Adv. Inorg. Biochem.*, 1983, **5**, 201.
49. N. D. Chasteen, J. K. Grady, and C. E. Holloway, *Inorg. Chem.*, 1986, **25**, 2754.
50. S. W. Homans, R. A. Dwek, D. L. Fernandes, and T. W. Rademacher, *Biochim. Biophys. Acta*, 1983, **760**, 256.
51. H. Van Halbeek, L. Dorland, J. F. G. Vliegenthart, G. Spik, A. Cheron, and J. Montreuil, *Biochim. Biophys. Acta*, 1981, **675**, 293.
52. L. Dorland, J. Haverkamp, J. F. G. Vliegenthart, G. Spik, B. Fournet, and J. Montreuil, *Eur. J. Biochem.*, 1979, **100**, 569.
53. L. Dorland, J. Haverkamp, B. L. Schut, J. F. G. Vliegenthart, G. Spik, G. Strecker, B. Fournet, and J. Montreuil, *FEBS Lett.*, 1977, **77**, 15.
54. W. Kiang, P. J. Sadler, and D. G. Reid, *Magn. Reson. Chem.*, 1993, **31**, 5110.

Biographical Sketches

Claudio Luchinat. *b* 1952. Doctor in Chemistry, 1976, University of Florence. Introduced to NMR by I. Bertini. Faculty positions at University of Florence, 1981–86. Professor of Chemistry, University of Bologna, 1986–present. More than 200 publications and two books. Research interests: NMR of paramagnetic species, theory of electron

and nuclear relaxation, biological applications of NMR, bioinorganic, biophysical and environmental chemistry.

Marco Sola. *b* 1957. B.S., 1984, University of Modena, Ph.D., 1987, University of Parma. Introduced to NMR by I. Bertini and C. Luchinat. Faculty in Chemistry, University of Modena, 1990–92. Associate Professor of Chemistry, University of Basilicata, 1992–1994. University of Bologna, 1994–present. More than 60 publications. Research interests: NMR of hydrolytic enzymes and metalloproteins involved in metal transport and electron transport, and NMR of model complexes.

Ultraslow Motions in Solids

David C. Ailion

University of Utah, Salt Lake City, UT, USA

1	Introduction	1
2	Spin–Lattice Relaxation in the Rotating Frame ($T_{1\rho}$)	1
3	Dipolar Relaxation in the Laboratory Frame (T_{1D})	3
4	Dipolar Relaxation in the Rotating Frame ($T_{1D\rho}$)	5
5	Experimental Results using Ultraslow Motion Techniques	5
6	Conclusions	7
7	Related Articles	7
8	References	8

1 INTRODUCTION

The use of conventional NMR relaxation measurement techniques for studying moderately rapid atomic motions may result in observation of the following phenomena:

1. a decrease (or a minimum)[1] of the spin–lattice relation time T_1 in a plot of T_1 versus temperature;
2. motional narrowing of the resonance linewidth[2] (or motional lengthening of the free induction decay or the spin–spin relaxation time T_2);
3. a decrease[2] in the Hahn echo decay time compared to the Carr–Purcell–Meiboom–Gill (CPMG)[3] time constant (see ***Diffusion Measurements by Magnetic Field Gradient Methods***).

The term ultraslow motions[4] refers to motions that are observable by NMR but are sufficiently infrequent that they produce no motional narrowing of the resonance line and make no measurable contribution to the spin–lattice relaxation rate. Typical T_1 minima correspond to motions for which the mean atomic jump rate $1/\tau_c$ is of the order of the nuclear precession frequency Ω_0 ($\approx 10^8$ s^{-1}, typically).[1] Motions having jump frequencies one or two orders of magnitude higher or lower than that for the minimum usually still give measurable contributions to the relaxation rate. Since the condition for motional narrowing is that the atomic jump time τ_c be less than T_2, ultraslow motions are typically those for which $T_2 < \tau_c < T_1$.[4] A very wide range of atomic motions falls under this classification, since $T_2 \approx 10^{-4}$–10^{-5} s in solids, while T_1 can be as long as several seconds to hours in length.

It is clearly desirable to extend to lower frequencies the frequency range (and thus the temperature range) of motions that can be studied. One advantage of studying a wider range of atomic motions is that motions having slightly different activation energies may be distinguished if they are observed over a sufficiently wide temperature range. Also, motions associated with a particular phenomenon, like a phase transition, may occur only in a particular temperature region.

The basic idea of the ultraslow motion techniques can be understood by considering what happens to a T_1 minimum if the field B_0, and thus the resonant frequency, is greatly reduced. According to the Bloembergen, Purcell, and Pound (BPP) theory,[1] atomic diffusion or molecular reorientations will cause fluctuations in the dipolar interactions that can be treated as perturbations on the Zeeman levels, and, furthermore, these fluctuations can be described by an exponential correlation function. BPP derived for T_1 an expression of the form

$$\frac{1}{T_1} \approx \frac{\Omega_d^2 \tau_c}{1 + \Omega_0^2 \tau_c^2} \tag{1}$$

where Ω_0 is the Larmor angular frequency and Ω_d is the angular frequency corresponding to a typical dipolar splitting. (Actually, there are additional terms of similar form. For interactions involving identical spins, there is an extra term proportional to $1/(1 + 4\Omega_0^2\tau_0^2)$; for heteronuclear systems, there are also terms having $[1 + (\Omega_I - \Omega_S)^2\tau_c^2]$ and $[1 + (\Omega_I + \Omega_S)^2\tau_c^2]$ in the denominator.) Equation (1) predicts that, in a temperature plot of T_1, there will be a minimum value for T_1 at the temperature for which $\tau_c \approx \Omega_0^{-1}$, in agreement with the idea that the transition probability $1/T_1$ arises largely from frequency components in the perturbation that equal the energy level spacing divided by $\hbar$. If Ω_0 is reduced, the minimum will correspond to a longer value of τ_c, and thus to lower frequency motions. For a typical diffusion mechanism, atomic jumps become less frequent as the temperature is lowered. Thus the T_1 minimum in a low field will occur at a lower temperature than would the T_1 minimum at a higher field.

There are experimental problems associated with attempting to study relaxation in very weak fields where the NMR signal might be very small (see ***Zero Field NMR***). There are also theoretical difficulties, since the theory underlying equation (1) is a perturbation theory that treats the fluctuating dipolar Hamiltonian due to diffusion as a perturbation on the Zeeman Hamiltonian; such an assumption may not be valid in very weak applied fields. Solutions to both these problems will now be discussed. Ultraslow motion techniques have been reviewed by Ailion.[5–7]

2 SPIN–LATTICE RELAXATION IN THE ROTATING FRAME ($T_{1\rho}$)

One approach to studying relaxation in weak applied fields and yet having the strong signal strength for a large field is to use the field cycling method[8,9] (see ***Field Cycling Experiments***), in which the external magnetic field is reduced adiabatically to a small value and subsequently increased adiabatically back to the original value, where the signal is measured. If there are no irreversible processes, the entropy will be constant, and the full signal will be measured after the remagnetization. However, atomic diffusion constitutes an irreversible process, which will cause a loss of dipolar order. Thus, by plotting the signal strength versus time in the demagnetized state, the weak field relaxation can in principle be measured. One difficulty with this approach is that it may be difficult to satisfy the requirement that the demagnetization and remagnetization processes be sufficiently slow that the adiabatic condition is satisfied and yet be rapid compared with T_1.

An alternate approach is to measure $T_{1\rho}$, the spin–lattice relaxation time in the rotating frame of the rf field $\boldsymbol{B}_1$ (see ***Magnetization Transfer between Water and Macromolecules in Proton MRI***). According to Redfield,[10] a spin system

in an rf field strong enough to saturate the resonance line (i.e., $\gamma^2 B_1^2 T_1 T_2 \gg 1$) will form a canonical distribution among energy levels separated by γB_{eff} rather than γB_0, where the effective field $\boldsymbol{B}_{\text{eff}}$ in a frame rotating at angular frequency ω is given by

$$\boldsymbol{B}_{\text{eff}} = B_1 \boldsymbol{i} + (B_0 - \omega/\gamma)\boldsymbol{k} \tag{2}$$

In this case, the spins will, after equilibrium has been achieved, be characterized by a 'spin temperature in the rotating frame', which means that Curie's law will hold, but with $\boldsymbol{M}_{\text{eq}} = C\boldsymbol{H}_{\text{eff}}/T$. The significance is that, at exact resonance ($B_0 = \omega/\gamma$), the equilibrium magnetization $\boldsymbol{M}_{\text{eq}}$ will be parallel to $\boldsymbol{B}_1$ rather than to $\boldsymbol{B}_0$. The $T_{1\rho}$ minimum will then occur when $\gamma B_1 \tau_c \approx 1$, for B_0 at exact resonance. Since B_1 is typically of order 1–50 G, this minimum arises from much lower frequency motions than does the normal T_1 minimum. If B_1 is much larger than the magnetic dipolar or electric quadrupolar local fields, the dipolar and quadrupolar fluctuations can still be treated by perturbation theory (this approach is called the 'weak collision' theory).[11] If, on the other hand, B_1 is comparable to or less than the dipolar or quadrupolar local fields, perturbation theory fails, and a different theory, called the 'strong collision' theory,[12] must be used. In this article, we shall consider the case for a spin-$\frac{1}{2}$ nucleus or one in which quadrupolar interactions can be neglected; the inclusion of quadrupolar interactions in the strong collision theory has been described by Ailion.[5]

2.1 Weak Collision Theory

All of the weak collision calculations are applications of the BPP theory in which the fluctuating dipolar Hamiltonian is treated as a perturbation on the Zeeman system. The only important difference is that the basic laboratory frame Hamiltonian is replaced by a rotating frame Hamiltonian in which $\boldsymbol{B}_0$ is replaced by $\boldsymbol{B}_{\text{eff}}$, as given by equation (2). At exact resonance, this theory predicts that $T_{1\rho}$ should exhibit a low-frequency minimum of the form

$$\frac{1}{T_{1\rho}} = K \frac{\tau_c}{1 + 4\Omega_1^2 \tau_c^2} \tag{3}$$

where Ω_1 (= γB_1) is proportional to the energy level splitting in the rotating frame. Thus the $T_{1\rho}$ minimum occurs when $\tau_c \approx (2\Omega_1)^{-1}$, which may be several orders of magnitude longer than the value of τ_c at a typical T_1 minimum. Accordingly, a $T_{1\rho}$ minimum is deeper than a T_1 minimum, and corresponds to slower atomic motions occurring at lower temperatures, as shown in Figure 1.

2.2 Strong Collision Theory

In order to get even more effective relaxation so as to observe even lower frequency motions, B_1, and thus Ω_1 in equation (3), can be reduced to a value comparable to the local dipolar field, or even to zero (e.g., by adiabatic demagnetization in the rotating frame (ADRF),[13] which is discussed in Section 3.3). In this case, equation (3) would predict that the minimum would not occur unless τ_c were infinite. However, perturbation theories like BPP and the weak collision theory will not be valid, since the perturbation

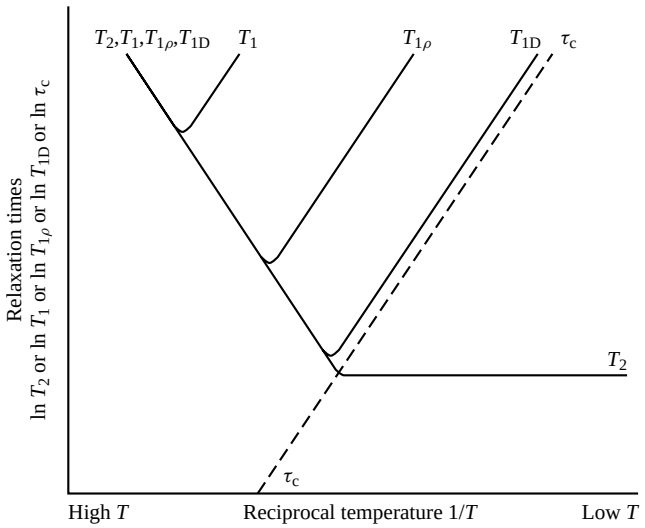

Figure 1 Temperature plot of relaxation times (T_2, T_1, $T_{1\rho}$, and T_{1D}) and atomic jump time τ_c. (Reproduced by permission of Academic Press from D. C. Ailion, in 'Methods of Experimental Physics', ed. J. N. Mundy, S. J. Rothman, M. J. Fluss, and L. C. Smedskjaer, Academic Press, Orlando, 1983, Vol. 21, Chap. 6)

(the dipolar Hamiltonian) in this case is comparable to or larger than the unperturbed Hamiltonian (the Zeeman Hamiltonian). Nevertheless, the condition for the relaxation time minimum in zero magnetic field can still be easily understood. The underlying physical basis for all relaxation time minima is that the most effective relaxation (and thus the minimum) occurs when the principal frequency components of the fluctuating Hamiltonian are comparable to the energy level splitting (in units of $\hbar$). We have seen, for Zeeman relaxation in the laboratory or rotating frames, that this requirement is equivalent to requiring that $1/\tau_c \approx \Omega_0$ or $1/\tau_c \approx \Omega_1$, respectively. For relaxation due to a fluctuating dipolar Hamiltonian in zero field, the energy level splittings $\hbar\Omega_d$ are determined by dipolar interactions. Thus the minimum in zero field occurs when $1/\tau_c \approx \Omega_d$ or $\tau_c \approx T_2$, which is at the onset of motional narrowing. The zero field relaxation time for the case in which quadrupolar interactions can be neglected is commonly called the dipolar relaxation time T_{1D},[14] and is also shown in Figure 1.

In order to study the dynamics of the atomic motions, it is desirable to obtain theoretical expressions that relate the measured relaxation time $T_{1\rho}$ or T_{1D} to the atomic jump time τ_c throughout the temperature range of observations. Experimental procedures for measuring these relaxation times are described in Sections 2.3 and 3.3, respectively. The strong collision theory, originally developed by Slichter and Ailion[12] for low-field relaxation, is not a perturbation theory, but is based on the assumption that sufficient time elapses between diffusion jumps to allow the dipolar and rotating frame Zeeman interactions to cross relax to a common spin temperature between each jump. This temperature is then disturbed by the sudden change in dipolar energy resulting from a jump, but reequilibrates in a time of order T_2 to a new value prior to the next jump. This spin temperature assumption is thus equivalent to requiring that $\tau_c \gg T_2$; hence the strong collision theory will be valid in the 'rigid lattice' below both the $T_{1\rho}$ minimum and the temperature for motional narrowing. If the

ADRF process is complete so that $\boldsymbol{B}_1$ is reduced to zero in the demagnetized state, the ADRF process will have transferred long-range Zeeman order due to spins aligned preferentially along $\boldsymbol{B}_{\text{eff}}$ to short-range dipolar order from spins aligned along their individual local fields. A single diffusion jump per spin will then have a major effect on the relaxation so that, in zero B_1, we should expect $T_{1\rho}$ (= $T_{1\text{D}}$ for zero field) to be of order τ_{c}. In the weak collision regime, much less of the order is dipolar and much more is Zeeman; accordingly, it will take many jumps to relax the magnetization, and $T_{1\rho}$ will be much larger than τ_{c}. Both these effects are shown in Figure 1.

The actual strong collision result[12] for $T_{1\rho}$ at exact resonance due to dipolar fluctuations of a homonuclear (i.e., having only one nuclear species) system in a field B_1 is

$$\frac{1}{T_{1\rho}} = \frac{1}{T_{1\text{D}}} \frac{B_{\text{D}}^2}{B_1^2 + B_{\text{D}}^2} \tag{4}$$

where B_{D} is the dipolar local field. We see that $T_{1\rho}$ reduces to $T_{1\text{D}}$ in the limit as B_1 approaches zero. Note that the local field B_{D} can be determined experimentally by measuring $T_{1\rho}$ versus B_1^2 for fixed $T_{1\text{D}}$ (i.e., at a fixed temperature).

2.3 Experimental Techniques for Measuring $T_{1\rho}$

Essentially all methods for measuring $T_{1\rho}$ start by tipping the magnetization from its original direction (the z direction) to a direction parallel to $\boldsymbol{B}_{\text{eff}}$ in the rotating frame, a procedure called spin locking. For exact resonance, the magnetization would then be aligned parallel to $\boldsymbol{B}_1$ (in contrast to the situation immediately after a $\frac{1}{2}\pi$ pulse, when the magnetization would be perpendicular to $\boldsymbol{B}_1$). $T_{1\rho}$ can then be determined by measuring the magnetization as a function of time τ in the aligned state, since $T_{1\rho}$ is given by

$$M_x = M_0 \exp(-\tau / T_{1\rho}) \tag{5}$$

where M_x is the height of the FID following the turn-off of the variable length B_1 pulse. Figure 2 shows several different pulse sequences for measuring $T_{1\rho}$.

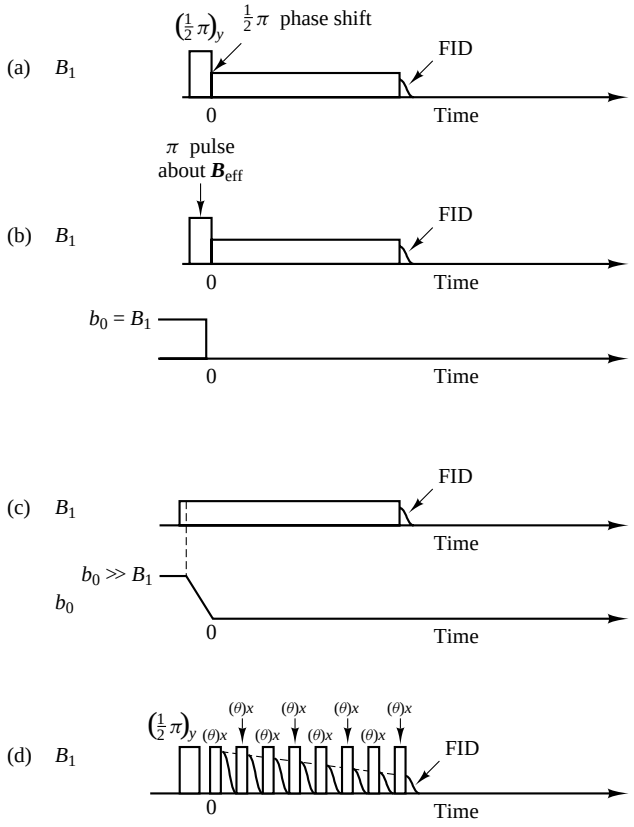

Figure 2 Pulse sequences for measuring $T_{1\rho}$. (a), (b), and (c) all have a spin locking sequence followed by a long rf pulse. The spin locking in (a) consists of a $\frac{1}{2}\pi$ pulse followed by a $\frac{1}{2}\pi$ phase shift. In (b), spin locking is achieved by a π pulse about $\boldsymbol{B}_{\text{eff}}$ (at an angle of 45° with respect to the z direction). In (c), $\boldsymbol{B}_1$ is turned on when the z field (or frequency) is far off resonance, and spin locking is achieved as a result of an adiabatic return to resonance. In (d), spin locking is achieved, as in (a), by a $\frac{1}{2}\pi$ pulse followed by a $\frac{1}{2}\pi$ phase shift; $T_{1\rho}$ is measured by monitoring the FID following short pulses of duration θ. (Reproduced with modifications by permission of Academic Press from D. C. Ailion, in 'Methods of Experimental Physics', ed. J. N. Mundy, S. J. Rothman, M. J. Fluss, and L. C. Smedskjaer, Academic Press, Orlando, 1983, Vol. 21, Chap. 6)

3 DIPOLAR RELAXATION IN THE LABORATORY FRAME ($T_{1\text{D}}$)

3.1 Homonuclear Systems

For homonuclear systems, $T_{1\text{D}}$ can be calculated by considering the fractional change in dipolar energy per jump for N jumping atoms with a time τ_{c} between jumps

$$\frac{1}{T_{1\text{D}}} = \frac{N}{\tau_{\text{c}}} \frac{E_{\text{Df}} - E_{\text{Di}}}{E_{\text{Di}}} = \frac{N}{\tau_{\text{c}}} \frac{\langle \hat{\mathcal{H}}_{\text{Df}}^{(0)} \rangle - \langle \hat{\mathcal{H}}_{\text{Di}}^{(0)} \rangle}{\langle \hat{\mathcal{H}}_{\text{Di}}^{(0)} \rangle} \tag{6}$$

where E_{Di} and E_{Df} are, respectively, the dipolar energies before and after a jump. $\hat{\mathcal{H}}_{\text{Di}}^{(0)}$ and $\hat{\mathcal{H}}_{\text{Df}}^{(0)}$ are, similarly, the secular parts of the dipolar Hamiltonian (i.e., those parts that commute with the Zeeman Hamiltonian), and the angle brackets indicate expectation values. If the system can be characterized by a spin temperature before each jump, the expectation values can be expressed as traces of the quantum mechanical operators, and the following expression is obtained in the high-temperature approximation:[2]

$$\frac{1}{T_{1\text{D}}} = \frac{N}{\tau_{\text{c}}} \frac{\text{Tr}(\hat{\mathcal{H}}_{\text{Di}}^{(0)})^2 - \text{Tr}(\hat{\mathcal{H}}_{\text{Di}}^{(0)} \hat{\mathcal{H}}_{\text{Df}}^{(0)})}{\text{Tr}(\hat{\mathcal{H}}_{\text{Di}}^{(0)})^2} \tag{7}$$

This equation can be rewritten as

$$\frac{1}{T_{1\text{D}}} = \frac{2(1-p)}{\tau_{\text{c}}} \tag{8}$$

where $1 - p$ is a calculable geometrical factor of order unity that characterizes the fractional change in energy resulting from a diffusion jump. Because of this factor, $T_{1\text{D}}$ shows a 10–20% dependence on the orientation of the field $\boldsymbol{B}_0$ relative to the crystal axes, and, furthermore, this anisotropy depends on diffusion mechanism.[15] We also note that $T_{1\text{D}}$ is of order τ_{c}, as we have seen intuitively. Diffusion can be studied by measuring either $T_{1\text{D}}$ or $T_{1\rho}$, provided the relaxation rate due to diffusion is greater than the relaxation rate due to other T_1

processes. The condition for observability of diffusion effects is then that $\tau_c < T_1$. Since T_1 values are typically 10^{-3}–10^3 s, this condition is much less stringent than the condition for motional narrowing ($\tau_c < T_2$).

We should note that the strong collision formula, equation (8), can be used to obtain τ_c from the measured relaxation time, assuming $\tau_c \gg T_2$. BPP-type theories can be used to determine τ_c in the motionally narrowed region where $\tau_c \ll T_2$. In the vicinity of the T_{1D} minimum, neither theory is valid.

3.2 Heteronuclear Systems

A problem arises in the interpretation of T_{1D} measurements for heteronuclear systems in which one nuclear species is diffusing and the others are stationary. For simplicity, consider a system containing two species of comparable abundance and gyromagnetic ratio, whose spin quantum numbers are labeled I and S. Assume further that the I and S spins are in strong contact. (A good example would be the alkali halide LiF, in which every lithium atom is surrounded by fluorines, and vice versa.) The problem is that if the I spins are irradiated and T_{1D} is measured, the result will be the same as when the S spins are irradiated and their T_{1D} measured, independent of which spin is actually diffusing.[16] Hence, from a T_{1D} measurement alone, it would not be possible in this case to determine which species is diffusing. This feature arises because there is normally strong coupling between parts of the dipolar interaction involving different species (i.e., the I–I and S–S dipolar terms are strongly coupled through the I–S interaction). So, if an S spin undergoes a jump, there will be rapid cross relaxation between I–I and S–S terms, which will result in the local heating being transferred rapidly to the entire spin system. Thus, in the strong collision limit, the entire dipolar reservoir is describable by a single temperature prior to a diffusion jump, but either spin species alone is not.

Fortunately, there is a way to determine in a T_{1D} experiment which spin species is diffusing for the case where the S spins are weakly magnetic (small γ_S) compared with the more strongly magnetic I spins (large γ_I). If the relaxation is due to the motion of S spins, T_{1D} will have an enormous anisotropy, whereas for diffusion of I spins the anisotropy will be very small [arising only from the $1 - p$ factor in equation (8)]. A more general strong collision theory,[17] appropriate for heteronuclear systems, shows that, for the case in which the strongly magnetic I spins are diffusing, only the I–I interaction terms need be kept. The resulting expression for $1/T_{1D}$ is similar to equation (8), only with p replaced by p_{II} and τ_c by τ_I:

$$\frac{1}{T_{1D}} = \frac{2(1 - p_{II})}{\tau_I} \tag{9}$$

However, if T_{1D} is due to the diffusion of weakly magnetic S spins then the diffusion produces significant changes in the I–S interaction, with the result that

$$\frac{1}{T_{1D}} = \frac{1 - p_{SI}}{\tau_S} \frac{B_{DIS}^2}{B_{DII}^2} \tag{10}$$

where B_{DIS} and B_{DII} are the I–S and I–I contributions to the dipolar local fields and τ_S is the time between jumps of the S spins. The precise definitions of these local fields and the parameters p_{II} and p_{SI} are given by Stokes and Ailion.[17] equation (10) predicts a strong anisotropy, arising from the factor B_{DIS}^2/B_{DII}^2, which is absent for motion by I atoms. The observation of this anisotropy would confirm that the diffusion arises from the motion of weakly magnetic spins. The experimental verification of this idea is shown in Figure 7 in Section 5 below.

3.3 Experimental Techniques for Measuring T_{1D}

There are basically two commonly used methods for measuring T_{1D}, and each involves transferring order to the dipolar system and then monitoring the decrease in dipolar order arising from dipolar relaxation. The first technique consists in following a spin locking sequence by an adiabatic demagnetization–remagnetization cycle of the rf field.[5] The second consists in creating a state of dipolar order by a pair of phase-shifted pulses and then using a third pulse to monitor the decrease in dipolar order due to the relaxation.[14] Both are shown in Figure 3.

3.3.1 Adiabatic Demagnetization in the Rotating Frame (ADRF)

This method, illustrated in Figure 3(a), is similar to the methods for measuring $T_{1\rho}$, shown in Figure 2(a)–(c), except that spin locking is now followed by an adiabatic demagnetization of B_1 to zero followed a variable time later by an adiabatic remagnetization, so that the NMR signal can be measured. The adiabatic demagnetization transfers order from Zeeman order in the rotating frame to dipolar order (in alignment of the spins along the local fields). The subsequent remagnetization converts the remaining dipolar order (not destroyed by the dipolar relaxation) back to Zeeman order, where it is observed in the form of an FID following the turn-off of the rf pulse. Dipolar relaxation results in a reduction in this FID.

One limitation of this technique arises from the conflicting requirements that the B_1 sweep be adiabatic yet that it also be

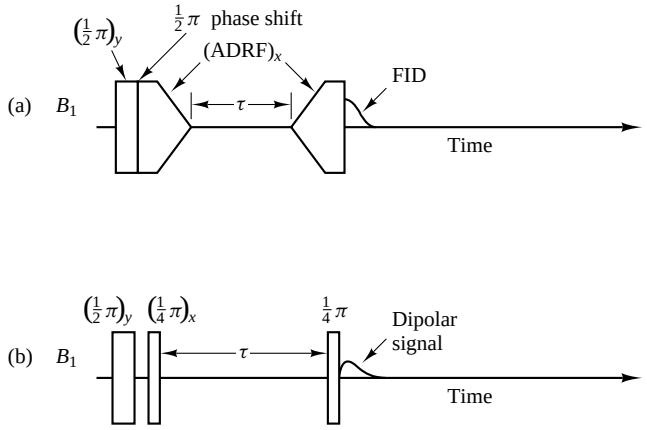

Figure 3 Pulse sequences for measuring T_{1D}. (a) The ADRF sequence showing demagnetization of B_1 following spin locking. (b) The phase-shifted pulse pair sequence. The first two pulses are separated by a time that is approximately T_2 for maximum signal. (Reproduced with modifications by permission of Academic Press from D. C. Ailion, in 'Methods of Experimental Physics', ed. J. N. Mundy, S. J. Rothman, M. J. Fluss, and L. C. Smedskjaer, Academic Press, Orlando, 1983, Vol. 21, Chap. 6)

completed in a time short compared with T_{1D}. This limitation makes it difficult to measure a T_{1D} less than about 0.1–1 ms.

3.3.2 *Phase-Shifted Pulse Pair*

This method, shown in Figure 3(b), avoids the difficulty in measuring a short T_{1D} inherent in ADRF. In this technique, a state of dipolar order is created by applying two closely spaced pulses that are 90° out of phase. The dipolar order is observed by applying a third pulse of arbitrary phase in the (x,y) plane. The dipolar signal that appears after the third pulse is proportional to the time derivative of the FID.

A major disadvantage of this technique is that the maximum efficiency for transfer of order is only about 56%, in contrast to the 100% efficiency theoretically obtainable with ADRF.

In summary, the ADRF technique is superior when measuring longer relaxation times or when $T_{1\rho}$ measurements are also desired, while the phase-shifted pulse pair method is better for very short T_{1D} measurement.

4 DIPOLAR RELAXATION IN THE ROTATING FRAME ($T_{1D\rho}$)

The last paragraph of Section 3.2 described the possibility of using a measurement of the anisotropy of T_{1D} in a single crystal to verify that a weakly magnetic spin species is diffusing. There are two disadvantages of this approach:

1. single crystals are not always available;
2. even though S spins are diffusing, they may not be dominating T_{1D} if they are sufficiently weakly magnetic or low in abundance.

This second feature can be seen in equation (10), since, for $B_{DIS} \ll B_{DII}$, we have $T_{1D} \gg \tau_S$ for weak (S) spin motion. In contrast, for strong (I) spin motion, $T_{1D} \approx \tau_I$. These results arise from the fact that the heat capacities of the terms involving S spins are much smaller than the I–I heat capacities. Accordingly, it may be very difficult, or even impossible, in many cases to study the diffusion of sufficiently weak S spins in a T_{1D} experiment.

In order to determine the diffusing species in a slow motion experiment, it is necessary to identify a parameter that is sensitive to which species is diffusing. If this parameter can be varied by the experimenter then the diffusing species can be identified and studied. Furthermore, for the case of diffusion by spins that are so weakly magnetic as to preclude their study through direct T_{1D} measurement, it is desirable to vary the parameter so as to enhance the temperature change of the entire system resulting from the weak spins' motions. A way to perform such experiments is to observe the dipolar relaxation in the rotating frame of one of the species, say, the I spins. In this frame, only part of the original dipolar Hamiltonian will be secular. The symbol $T_{1D\rho}$ is used for the relaxation time of this secular part of the rotating-frame Hamiltonian, in analogy to T_{1D}, which is the relaxation time for the secular part of the laboratory-frame dipolar Hamiltonian. $T_{1D\rho}$ may be considered to be the dipolar relaxation time in the rotating frame, whereas T_{1D} is the dipolar relaxation time in the laboratory frame. In contrast to T_{1D}, $T_{1D\rho}$ may depend on the angle θ_I between $\boldsymbol{B}_{\text{eff}}$ and $\boldsymbol{B}_0$ in the rotating reference frame. For diffusion by the strong I spins, $T_{1D\rho} = T_{1D}$ and is described by equation (9) for all θ_I except near the magic angle θ_m (defined by $\cos^2\theta_m = \frac{1}{3}$), where there is a small change.[17] However, for diffusion by weak S spins, the following expression is obtained for $T_{1D\rho}$:[17]

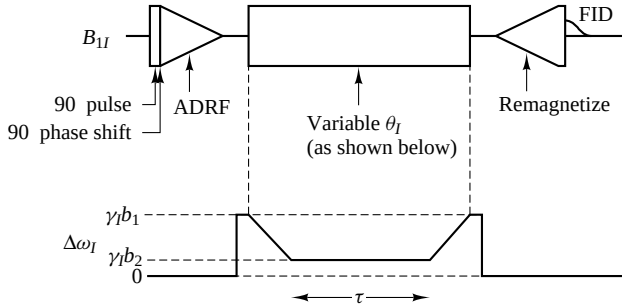

Figure 4 Pulse sequence for measuring $T_{1D\rho}$. The lower part of the figure shows the variation of $\Delta\omega_I = \gamma_I B_0 - \omega_I$, the off-resonance frequency of B_{1I}. (Reproduced with modifications by permission of the American Physical Society from H. T. Stokes and D. C. Ailion, *Phys. Rev. B*, 1978, **18**, 141)

$$\frac{1}{T_{1D\rho}(\theta_I)} = \frac{1}{\tau_S}\,\frac{\cos^2\theta_I B_{DIS}^2(1-p_{SI}) + 2B_{DSS}^2(1-p_{SS})}{[\frac{1}{2}(3\cos^2\theta_I - 1)^2]^2 B_{DII}^2 + \cos^2\theta_I B_{DIS}^2 + B_{DSS}^2} \quad (11)$$

where $1 - p_{SI}$ and $1 - p_{SS}$ are geometrical factors of order unity (analogous to p of the conventional strong collision theory). In contrast to the result obtained in the case of diffusion by the strong I spins, this expression predicts a very strong dependence of $T_{1D\rho}$ on θ_I, which can be observed experimentally, using the pulse sequence described in the next section.

4.1 Experimental Technique for Measuring $T_{1D\rho}$

Figure 4 shows a pulse sequence that can be used to measure $T_{1D\rho}$.[17] A spin locking sequence followed by an ADRF is applied on resonance to the I spins. This step transfers Zeeman order, which was originally along $\boldsymbol{B}_0$, to dipolar order. A large off-resonance pulse is then applied, which does not change the dipolar order but rather changes its reference frame from the laboratory frame to the rotating frame. After establishing a spin temperature in the rotating frame, the frequency of the rf pulse is then reduced adiabatically toward resonance, thereby reducing B_{eff} and changing θ_I. By reversing this sequence, the remaining order is transferred back to laboratory-frame Zeeman order, where it appears as an FID following the turn-off of the rf pulse. If one increases the time τ in the state at θ_I, the magnitude of the resulting FID will be reduced, owing to $T_{1D\rho}$ relaxation. A plot of magnetization versus τ on a semilogarithmic plot will yield a straight line of slope $-1/T_{1D\rho}(\theta_I)$. To vary θ_I, one merely needs to vary the frequency of the pulse (and thus b_2) in the variable time interval τ.

5 EXPERIMENTAL RESULTS USING ULTRASLOW MOTION TECHNIQUES

Ultraslow motions have been widely studied in the last 30 years, generally via $T_{1\rho}$ and T_{1D} measurements. It would be impossible in this article to summarize all the applications. Instead, just a few examples will be given to confirm various

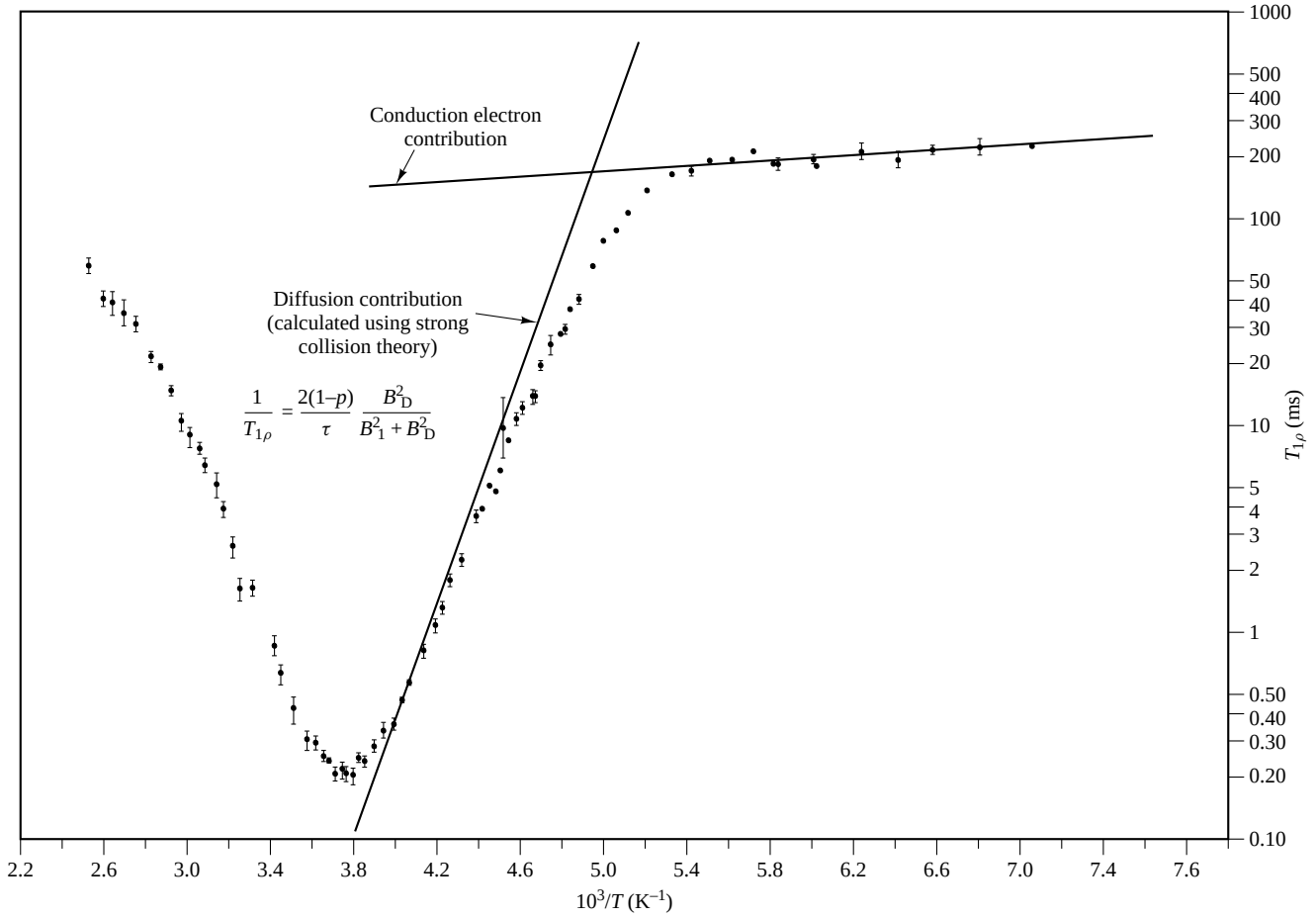

Figure 5 $T_{1\rho}$ versus reciprocal temperature in metallic lithium, with $B_1 = 1.3 \times 10^{-4}$ T. (Reproduced with modifications by permission of the American Physical Society from D. C. Ailion and, C. P. Slichter, *Phys. Rev.*, 1965, **137**, A235)

features of the previous discussion and illustrate the kinds of additional information that may be obtained from such measurements.

Figure 5 shows the original $T_{1\rho}$ data of Ailion and Slichter[18] in metallic lithium. The principal feature is that the $T_{1\rho}$ minimum is symmetric and occurs at the onset of motional narrowing. Furthermore, the minimum value of $T_{1\rho}$ is within an order of magnitude of T_2, as expected from the strong collision theory. Figure 6 shows a plot of the atomic jump time obtained from the experimental $T_{1\rho}$ values, using the strong collision theory. As can be seen, the data exhibit Arrhenius behavior over eight orders of magnitude, and correspond to extremely slow diffusion (of the order of one atomic jump per second) at the lowest temperatures.

Figure 7 shows the verification of the prediction of a very strong anisotropy in T_{1D} described in Section 3.2 for a system having diffusion dominated by weakly magnetic spins. These measurements were performed on a single crystal of KF doped with 0.1% CaF_2. In this case, mobile potassium vacancies are created to compensate for the extra charge of the Ca^{2+}. We thus have a case in which the diffusion of weak spins (potassium) dominates T_{1D} (of fluorine). The solid curve is the calculated anisotropy of the local field factor of equation (10).

Figure 8 shows experimental verification of the strong collision theory for $T_{1D\rho}$. The sample used in this experiment is the same KF:0.1% CaF_2 single crystal used for the data of Figure 7. The curve is calculated from equation (11). All the strong dependence of $T_{1D\rho}$ on θ_I (described earlier) appears, thereby indicating that the weak S spins (in this case, ^{39}K) are diffusing rather than the strong I spins (^{19}F here).

A possibly important potential application of this $T_{1D\rho}$ technique is the study of impurity diffusion. In this case, the S spins are weak because their concentration N_S is small (but γ_S may be large). As in the case of small γ_S, diffusion by the weak S spins should again be characterized by a sharp dip in $T_{1D\rho}$ at the magic angle. For this application to be fruitful, an abundant, easily observable I spin species must exist and be in good thermal contact with the S spins. However, it has been shown[19] that nonadiabatic effects will also give rise to a dip in $T_{1D\rho}$ at the magic angle, which could mask the effect of the S spins' diffusion. Nevertheless, by appropriately modifying the 'adiabatic' sweeps of Figure 4, these effects can be minimized.[19]

An interesting new application of ultraslow motion NMR has been developed[20] to study the ultraslow hopping of selenium atoms between two sites in crystalline Se having well-resolved separate NMR lines. By selective excitation, one of the lines is saturated. Then, as the ^{77}Se atoms jump between the two sites, the magnetization of the previously saturated site builds up and the magnetization of the previously unsaturated site decreases. By measuring the time constant for these decays, the jump time τ_c and the diffusion constant D can

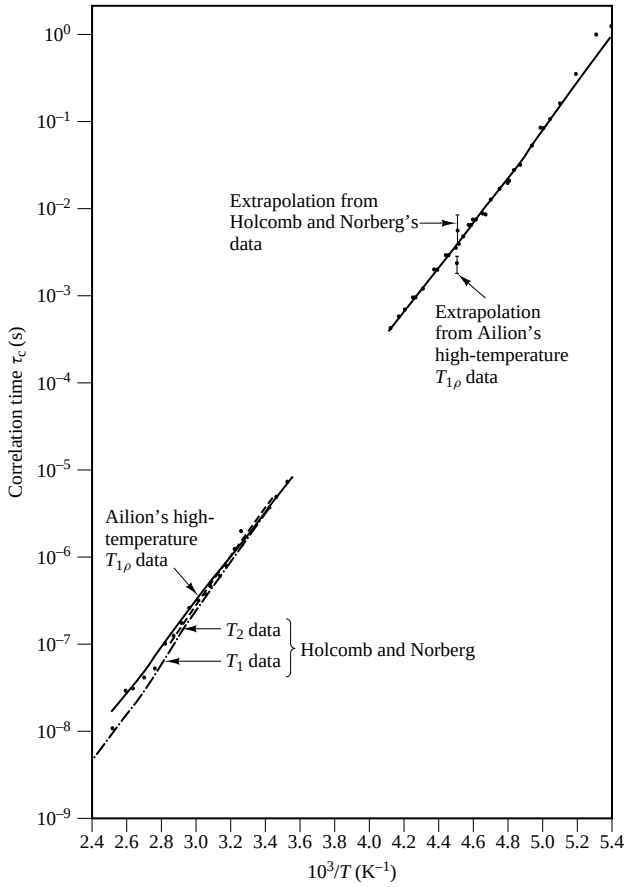

Figure 6 τ_c versus reciprocal temperature in metallic lithium. The experimental points were obtained from the data of Figure 5 using the strong collision theory in the low-temperature region and the weak collision theory in the high-temperature region. The 'gap' in the middle corresponds to the region around the $T_{1\rho}$ minimum where neither theory is valid. In the high temperature region, values of τ_c obtained from Holcomb and Norberg[21] were also plotted. (Reproduced with modifications by permission of the American Physical Society from D. C. Ailion and C. P. Slichter, *Phys. Rev.*, 1965, **137**, A235)

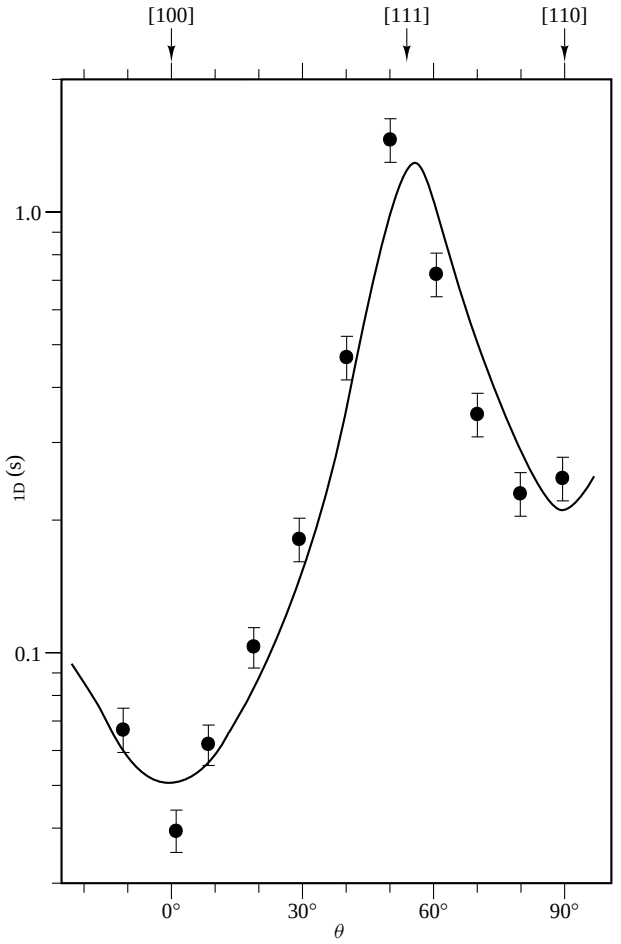

Figure 7 T_{1D} anisotropy in KF:0.1% CaF_2 at 227 °C. The crystal was rotated about its [110] axis. The curve is the calculated anisotropy of $B2/DII/B2/DIS$. (Reproduced by permission of the American Physical Society from H. T. Stokes and D. C. Ailion, *Phys. Rev. B*, 1978, **18**, 141)

both be directly determined. Excellent agreement was found between D measured by this NMR approach and D measured by radioactive tracers. As with the T_{1D} measurements, this technique will be able to observe jump times limited by T_1 for these specialized systems.

6 CONCLUSIONS

The most obvious advantage of the slow motion methods is to extend downward in temperature the range over which atomic diffusion can be studied. As a result, diffusion mechanisms occurring only at lower temperatures can be observed. Moreover, since the effect of diffusion on the dipolar relaxation time will be much greater than its effect on the spin–lattice relaxation time, going to zero field magnifies the relaxation effects, thereby making possible the observation of diffusion whose relaxation effects might otherwise be too weak to be observable. A measurement of the frequency dependence of the relaxation time can determine the relaxation mechanism and can check the validity of the theory used, such as the assumption of an exponential correlation function, underlying equation (1). $T_{1\rho}$ and T_{1D} measurements greatly increase the frequency range available, since they are effectively very low frequency measurements (of order 10^3 Hz), in contrast to typical T_1 measurements (of order 10^7 Hz). Finally, by having a wider temperature range available, it is possible to observe the onset of other diffusion mechanisms having different activation energies. $T_{1D\rho}$ measurements can be used to enhance the NMR effects arising from the ultraslow motions of weakly magnetic nuclei and, possibly, impurities.

7 RELATED ARTICLES

Brownian Motion and Correlation Times; Diffusion Measurements by Magnetic Field Gradient Methods; Diffusion in Rare Gas Solids; Diffusion in Solids; Double Resonance; Field Cycling Experiments; Low Spin Temperature NMR; Magnetization Transfer between Water and Macromolecules in Proton MRI; Relaxation Theory: Density Matrix Formulation; Rotating Frame Spin–Lattice Relaxation Off-Resonance; Slow and Ultraslow Motions in Biology; Zero Field NMR.

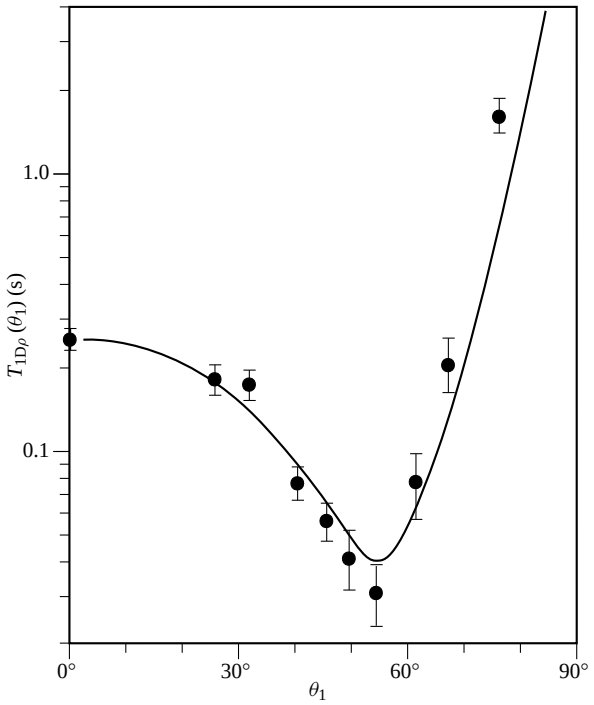

Figure 8 $T_{1D\rho}$ as a function of θ_I in KF:0.1% CaF_2 at 200 °C. The curve was calculated from equation (11). Note that the data point at $\theta_I = 0$ is T_{1D}. (Reproduced by permission of the American Physical Society from H. T. Stokes and D. C. Ailion, *Phys. Rev. B*, 1978, **18**, 141)

8 REFERENCES

1. N. Bloembergen. E. M. Purcell, and R. V. Pound, *Phys. Rev.*, 1948, **73**, 679.
2. C. P. Slichter, *Principles of Magnetic Resonance*, 3rd edn., Springer-Verlag, Berlin, 1990.
3. H. Y. Carr and E. M. Purcell, *Phys. Rev.*, 1954, **94**, 630; S. Meiboom and D. Gill, *Rev. Sci. Instrum.*, 1958, **29**, 6881.
4. D. C. Ailion and C. P. Slichter, *Phys. Rev. Lett.*, 1964, **12**, 168.
5. D. C. Ailion, in *Advances in Magnetic Resonance*, ed. J. S. Waugh, Academic Press, New York, 1971, Vol. 5, Chap. 4
6. D. C. Ailion, in *Methods of Experimental Physics*, ed. J. N. Mundy, S. J. Rothman, M. J. Fluss, and L. C. Smedskjaer, Academic Press, Orlando, 1983, Vol. 21, Chap. 6
7. D. C. Ailion, in *Proceedings of 10th Ampère Summer School and Symposium*, ed. R. Blinc, M. Vilfan, and J. Slak, J. Stefan Institute, Ljubljana, 1988, p. 47.
8. L. C. Hebel and C. P. Slichter, *Phys. Rev.*, 1959, **113**, 1504; A. G. Anderson and A. G. Redfield, *Phys. Rev.*, 1959, **116**, 583.
9. F. Noack, in *Progress in Nuclear Magnetic Resonance Spectroscopy*, ed. J. W. Emsley, J. Feeney, and L. H. Sutcliffe, Pergamon Press, Oxford, 1986, Vol. 18, p. 171.
10. A. G. Redfield, *Phys. Rev.*, 1955, **98**, 1787.
11. D. C. Look and I. J. Lowe, *J. Chem. Phys.*, 1966, **46**, 2995.
12. C. P. Slichter and D. C. Ailion, *Phys. Rev.*, 1964, **135**, A1099.
13. C. P. Slichter and W. C. Holton, *Phys. Rev.*, 1961, **122**, 1701.
14. J. Jeener and P. Broekaert, *Phys. Rev.*, 1967, **157**, 232.
15. D. C. Ailion and P. Ho, *Phys. Rev.*, 1968, **168**, 662.
16. H. T. Stokes and D. C. Ailion, *Phys. Rev. B*, 1977, **16**, 4746.
17. H. T. Stokes and D. C. Ailion, *Phys. Rev. B*, 1978, **18**, 141.
18. D. C. Ailion and C. P. Slichter, *Phys. Rev.*, 1965, **137**, A235.
19. B. Günther and D. C. Ailion, *J. Magn. Reson.*, 1985, **61**, 482.
20. B. Günther and O. Kanert, *Phys. Rev. B*, 1985, **31**, 20.
21. D. F. Holcomb and R. F. Norburg, *Phys. Rev.*, 1955, **98**, 1074.

Biographical Sketch

David C. Ailion. *b* 1937. A.B., 1956, M.S., 1958, Ph.D., 1964, Physics, University of Illinois, under supervision of C. P. Slichter. Faculty member (currently Professor of Physics) University of Utah, 1964–present. Fellow of American Physical Society, Humboldt Senior Research Award (1994–6), University of Utah Distinguished Research Award (1995), NIH Special Fellow (1971–2), Guest Member of AMPERE Committee. Approx. 130 publications. Current research specialties: magnetic resonance imaging of lungs, NMR of partially disordered systems (incommensurate insulators and glasses).

Diffusion and Flow in Fluids

Ken J. Packer

Department of Chemistry, University of Nottingham, UK

1	Introduction	1
2	Spin Echoes in the Presence of Magnetic Field Gradients	1
3	Hindered, Anisotropic, and Restricted Diffusion	6
4	PGSE Characterization of Flowing Fluids	9
5	Related Articles	11
6	References	11

1 INTRODUCTION

The translational displacement of molecules in fluids and fluid-containing systems is of significance for many biological, chemical, and physical processes, encompassing phenomena such as the circulation and performance of body fluids, the functioning of living cells, the behavior of macromolecular systems, the properties of organized and ordered fluids such as thermotropic and lyotropic liquid crystals, and the permeation of fluids through porous adsorbents such as catalysts, oil reservoir rocks, etc., to mention just a few. From its earliest days NMR has developed approaches to enable these translational movements to be characterized, with a considerable degree of detail and subtlety, over spatial and temporal scales not accessed in general by other techniques. In this article we examine the ways in which NMR can be used to probe these processes, usually described as either 'diffusion' or 'flow'. The use of these two terms reflects the two main driving forces for the processes: the internal thermal energy, which produces the chaotic and randomly directed diffusional displacements of molecules; and any macroscopic, usually external, constraint, such as a pressure, temperature, or density gradient, which leads to movement of fluids in a more directed and, to a greater or lesser extent, coherent manner.

Diffusion can be an important factor in determining the spin relaxation behavior in nuclear spin systems and, as such, measurements of relaxation characteristics can give information about the diffusion, albeit via indirect physical models for the relaxation process. This article, however, is concerned with NMR methods which access directly information on the translational displacements of spin-bearing molecules and ions without the requirement for such models. The principle underlying the majority of these applications of NMR to the characterization of diffusion and flow processes is very simple. It is that the spatial coordinates of spins can be distinguished and labeled by the application of magnetic field gradients. This makes the NMR frequency of the spins a function of their coordinates. Movement of the spins through this frequency-labeled space is characterized by their acquisition of phase shifts in their precession, these reflecting their frequency, and hence, their spatial coordinates' history. The statistics of these phase shifts reflect directly the nature of the translational displacements the spins experience. Space-labeling with field gradients is, of course, the basis of MRI and the topics covered in this article have relevance to aspects of both the power and certain limitations of MRI. The reader is referred to the many articles on this topic contained in this Encyclopedia.

In order for the statistics of the phase shifts, and hence translational displacements, mentioned above to be measured, the spins have to have a collective phase coherence imposed on them to start with, rather like runners being called to the starting line on a race track. It was in this context that in 1950 Hahn[1] described for the first time the formation of spin echoes, through the application of two or more rf pulses to a spin system in an inhomogeneous magnetic field, and discussed, inter alia, the effects of diffusion through this inhomogeneous field on the echo formation. Subsequently, Carr and Purcell[2] derived in more detail the expression for the effect of self-diffusion on spin echo formation in the presence of an applied linear field gradient, demonstrated the measurement of self-diffusion coefficients using this phenomenon, and established the effects of convection, which is a flow process in our terms, on both single and multiple echo formation. These two papers form the foundations on which all that follows rests.

A second type of space labeling involves saturation of longitudinal magnetization which, coupled with time-of-flight/MRI methods of observation, can also be used for the characterization of diffusion and flow processes. These are not covered in this article, but can be accessed through the reviews cited.

2 SPIN ECHOES IN THE PRESENCE OF MAGNETIC FIELD GRADIENTS

The early work referred to above considered the effects of diffusion and flow in the presence of a time-independent magnetic field gradient. In practice, it turns out to be advantageous from a number of standpoints to apply the gradient in the form of pulses, usually rectangular. Figure 1 illustrates the simplest form of the experiment used to study diffusion and flow.

This pulsed gradient spin echo (PGSE) experiment comprises a $90^\circ_x - \tau - 180^\circ_y - \tau$ echo sequence with two identical field gradient pulses (FGP) applied. These have duration δ, amplitude $|\boldsymbol{g}|$, and are separated by a time Δ. Also shown is a steady gradient $\boldsymbol{g}_0$. In many situations such a steady gradient is unavoidable arising, for example, from inhomogeneities in the $\boldsymbol{B}_0$ field or from internal inhomogeneities in the sample. The applied gradient $\boldsymbol{g}$ and the steady gradient $\boldsymbol{g}_0$ are not necessarily colinear. Indeed, there may be a distribution of angles between them if $\boldsymbol{g}_0$ has a distribution of directions. In general, applied gradients are taken as linear, i.e. for $\boldsymbol{g}_x = \{\delta B/\delta x\}$:

$$\omega(x) = \gamma B(x) = \gamma B_0 + \gamma g_x x \tag{1}$$

where γ is the magnetogyric ratio of the spins. Note that the term 'gradient' means the spatial derivatives of the static field $\boldsymbol{B}_0$.

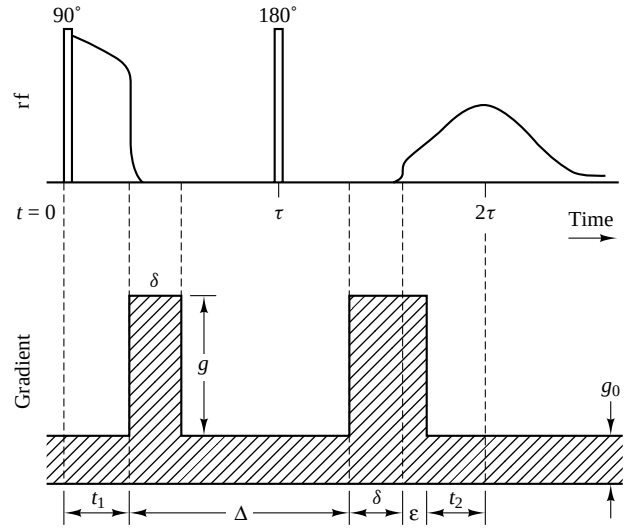

Figure 1 The basic pulsed magnetic field gradient spin echo experiment, comprising a $90°-\tau-180°$ spin echo sequence with two FGPs superimposed. The first FGP labels the position of spins in the gradient direction through phase shifts which cause the loss of signal at around t_1. The second FGP, together with the 180° rf pulse, refocuses these phase shifts and regenerates a signal which reflects the degree to which spins have moved to different positions in the gradient direction during the time Δ. The imbalance in FGP width shown as ϵ is important in considering the experimental behavior (see Section 2.3)

2.1 Phase Shifts and Translational Displacements

The PGSE experiment was first analyzed and demonstrated experimentally by Stejskal and Tanner.[3,4] Whilst there have been a number of approaches to analyzing the response of spin echo experiments to translational motions of the spins, here a simple approach will be followed initially, concentrating on the effects of the FGPs only. This gives a particularly clear physical picture.

The assumption is made that the FGPs are of negligible duration with regard to the movements of the spins along the gradient direction. In practice this means it is assumed that spins remain fixed in their positions during the FGPs. The $90°_x$ rf pulse (see Figure 1) creates the required initial phase coherence in the spin system. The natural decay timescale of this coherence, the transverse relaxation time T_2, sets the limit for the time available in this particular experiment for the observation of the translational movements. In addition, the formation of an echo, as illustrated, arises from the refocusing by the $180°_y$ rf pulse of the dephasing of the FID due, inter alia, to the effects of $\boldsymbol{g}_0$.

Neglecting these relaxation processes for the moment, the first FGP gives to the spins phase shifts proportional to their position in the gradient direction at that time (taken as the origin of time, i.e. $\Delta = 0$, for the characterization of the translational motions), e.g. for the ith spin with position $x_i(0)$ at the time of application of the first FGP,

$$\phi_i(0) = \gamma \delta g_x x_i(0) \tag{2}$$

The spins are now labeled in terms of their x coordinate at $\Delta = 0$ through this phase shift. The effect of the $180°_y$ rf pulse is to make the second FGP, applied a time Δ after the first, act as if it were of reverse polarity, i.e. $-g_x$. (NB: The experiment could be carried out using only two, opposite polarity, FGPs without the $180°_y$ rf pulse.) Following this, the ith spin has the resultant phase shift

$$\phi_i(\Delta) = \gamma \delta g_x [x_i(\Delta) - x_i(0)] = \gamma \delta g_x X_i(\Delta) \tag{3}$$

What is clear from equation (3) is that if all spins have not changed their x coordinates in the time Δ [i.e. $X_i(\Delta) = 0$ for all i], they all have no net phase shift and the coherence, apparently destroyed by the first FGP [i.e. the NMR signal will have disappeared at this point (see Figure 1)], is recovered. If the spins have experienced finite displacements in the time Δ, then each contributes to the NMR signal following the second FGP by the amount

$$s_i(g_x, \delta, \Delta) = \exp[\mathrm{i}\phi_i(\Delta)] = [\cos\phi_i(\Delta) + \mathrm{i}\sin\phi_i(\Delta)] \tag{4}$$

where the real and imaginary components correspond to the y and x components of the magnetization in the rotating frame defined by the x/y rf pulses. The total NMR signal following the second FGP is then the sum over all the spins:

$$S(g_x, \delta, \Delta) = \sum_i s_i(g_x, \delta, \Delta) = \langle \exp[\mathrm{i}\phi(\Delta)] \rangle \tag{5}$$

where $\langle \ldots \rangle$ represents an ensemble average.

Clearly, the result of equation (5) depends on the statistics of the displacements $X_i(\Delta)$. For example, in the simplest possible case in which all spins experience the same displacement (this would represent 'plug flow') the NMR signal would be recovered unchanged in amplitude, as all the spins would be in phase immediately after the second FGP, but would be phase shifted by an amount

$$\phi^{\mathrm{PF}}(\Delta) = \gamma \delta g_x X^{\mathrm{PF}}(\Delta) = \gamma \delta g_x \Delta v \tag{6}$$

where the superscript PF designates plug flow, and v is the velocity in the gradient direction.

For this case the full NMR signal behaves according to equation (4) with ϕ^{PF} given by equation (6). In general, however, the molecules carrying the spins experience a distribution of displacements $P[X_i(\Delta)]$ during the observation time Δ. This, in turn, results in a distribution of phase shifts $P[\phi(\Delta)]$ and an NMR signal which has the form

$$S(g_x, \delta, \Delta) = \int P[\phi(\Delta)] \exp[\mathrm{i}\phi(\Delta)]\, \mathrm{d}\phi \tag{7}$$

which may be expressed as

$$S(g_x, \delta, \Delta) = \int \mathrm{d}x_0 \int \mathrm{d}x\, P(x_0) P(x, \Delta; x_0) \times \exp\{\mathrm{i}\gamma \delta g_x [x(\Delta) - x_0]\} \tag{8}$$

or, more generally,

$$S(\boldsymbol{q}, \Delta) = \int \mathrm{d}\boldsymbol{r}_0 \int \mathrm{d}\boldsymbol{r}\, P(\boldsymbol{r}_0) P(\boldsymbol{r}, \Delta; \boldsymbol{r}_0) \times \exp[\mathrm{i}2\pi \boldsymbol{q} \cdot (\boldsymbol{r} - \boldsymbol{r}_0)] \tag{9}$$

where $\boldsymbol{q} = (2\pi)^{-1}\,\gamma\delta\boldsymbol{g}$ and $P(x, \Delta; x_0)$ and $P(\boldsymbol{r}, \Delta; \boldsymbol{r}_0)$ are the conditional probabilities for displacements $(x - x_0)$ and $(\boldsymbol{r} - \boldsymbol{r}_0)$, respectively, in time Δ; i.e. the probability that, given a starting position x_0 or $\boldsymbol{r}_0$, spins will reach position x or $\boldsymbol{r}$ in time Δ. As, in general, these conditional probabilities can depend on the starting position, they must be treated as functions of these, hence the integration over the probability density for starting positions, $P(x_0)$ or $P(\boldsymbol{r}_0)$. These latter terms are merely the spatial spin density distributions.

Equation (9) may also be written in terms of what Kärger and Heink[5] called the 'average propagator', $\langle P[X(\Delta)]\rangle$, i.e.

$$S(q, \Delta) = \int \langle P[X(\Delta)]\rangle \exp[\mathrm{i}2\pi q X(\Delta)]\,\mathrm{d}X \qquad (10)$$

where the average propagator is given by

$$\langle P[X(\Delta)]\rangle = \int P(x, \Delta; x_0) P(x_0)\,\mathrm{d}x_0 \qquad (11)$$

and $q = |\boldsymbol{q}|$.

Equation (10) shows that $S(q, \Delta)$ and $\langle P[X(\Delta)]\rangle$ are a Fourier pair and that determination of $S_\Delta(q)$ (i.e. the q dependence of the NMR signal at fixed observation time Δ) allows the direct measurement of $\langle P[X(\Delta)]\rangle$ by Fourier transformation of $S_\Delta(q)$ with respect to q.

The definition of $\boldsymbol{q}$ (note that it has dimensions of inverse distance) and its role in equations (9) and (10) is analogous to that of a wavevector in diffraction and scattering phenomena. This viewpoint is described by Callaghan[6] in his review of this field and has recently found more favor through the application of these NMR methods to the diffusion of fluids in porous solids.[7–9]

2.2 Unrestricted Self-Diffusion and the PGSE Experiment

Self-diffusion is the translational displacement of molecules driven by internal kinetic energy. It is chaotic and random in character and can be thought of in terms of a random walk process. The statistics of displacements for such a random walk are Gaussian, i.e. in one dimension,

$$P[X(\Delta)] = (4\pi D\Delta)^{-1/2} \exp[-X(\Delta)^2/4D\Delta] \qquad (12)$$

where D is the self-diffusion coefficient. Equation (12) provides a phenomenological definition of D through the mean squared displacement:

$$\langle X^2(\Delta)\rangle = nD\Delta \qquad (13)$$

(n = 2, 4, or 6 for one, two, or three dimensions) and is a solution of Fick's diffusion equation:

$$\mathrm{d}P/\mathrm{d}t = D(\mathrm{d}^2P/\mathrm{d}x^2) \qquad (14)$$

A statistical mechanical definition of D is through the velocity correlation function

$$D = \int_0^\infty \langle v(t)\cdot v(0)\rangle\,\mathrm{d}t \qquad (15)$$

A detailed discussion of the relationship between self-diffusion and the mutual diffusion coefficient in a binary system is given by Mills et al.[10]

Equation (12) is valid under the condition that $\Delta \ll L^2/D$, where L is the size scale separating any barriers to the free diffusion process.[9] Under these conditions the diffusion is described as 'unrestricted'.

For the PGSE experiment, the substitution of equation (12) into equation (8) gives

$$S(q, \Delta) = S_0 \exp(-4\pi^2 q^2 \Delta D) \qquad (16)$$

where S_0 is the NMR signal measured in the absence of the FGPs. In general, because the background gradients cause echo formation around 2τ, it is normal to measure the echo amplitude at this time, with and without the gradient pulses applied, in which case $S_0 = S(2\tau)$. The role of the background gradients is important and is discussed below. If the PGSE experiment is carried out under high-resolution conditions (i.e. the effects of background gradients are eliminated) then the signal $S(q, \Delta, t)$, where t runs from 2τ onwards, may be measured and Fourier transformed with respect to t to give a high-resolution spectrum in which each resolved peak suffers attenuation according to equation (16), with a value of D appropriate to the molecular species. This area has been reviewed by Stilbs.[11]

Equation (16) is based on equation (8), which assumes no movement of the spins during the FGPs. This is equivalent to $\Delta \gg \delta$. If this is not the case, a more general treatment shows that the exact result is

$$S(q, \Delta) = S_0 \exp[-4\pi^2 q^2(\Delta - \delta/3)] \qquad (17)$$

In the limit when $\Delta = \delta = \tau$, i.e. the case when there is a constant gradient present throughout the spin echo experiment, equation (17) becomes

$$S(g, \tau) = S_0 \exp(-2\gamma^2 g^2 \tau^3/3) \qquad (18)$$

This is the original equation derived by Hahn[1] and Carr and Purcell.[2]

Equations (16)–(18) form the basis for the measurement of the self-diffusion coefficients of spin-bearing molecules. The spin echo amplitude is determined as a function of the FGP parameters q and Δ, and a fit to the appropriate equation (given that g is known) gives D. An example of a typical set of data for simple fluids is shown in Figure 2. The range of D accessible to measurement depends on the nucleus used, the spin relaxation properties of the system, and the FGP amplitude/width capability of the spectrometer. In general, it is relatively straightforward to measure D for fairly mobile liquids ($D \geq 10^{-10}\,\mathrm{m^2\ s^{-1}}$). However, for systems with higher viscosities the difficulties in determining D multiply. This is because, as D becomes smaller, T_2 tends to get smaller, which means that to generate a given attenuation of the echo signal more gradient area is required but with less time in which to apply it. Gradient amplitudes of the order of $10\,\mathrm{T\ m^{-1}}$ or more can be generated but require specialized design of coils, current sources, etc. Aspects of these experimental issues are mentioned later. Values of D of the order of 10^{-11} to $10^{-12}\,\mathrm{m^2\ s^{-1}}$ can be measured without too much difficulty. Smaller values offer increased

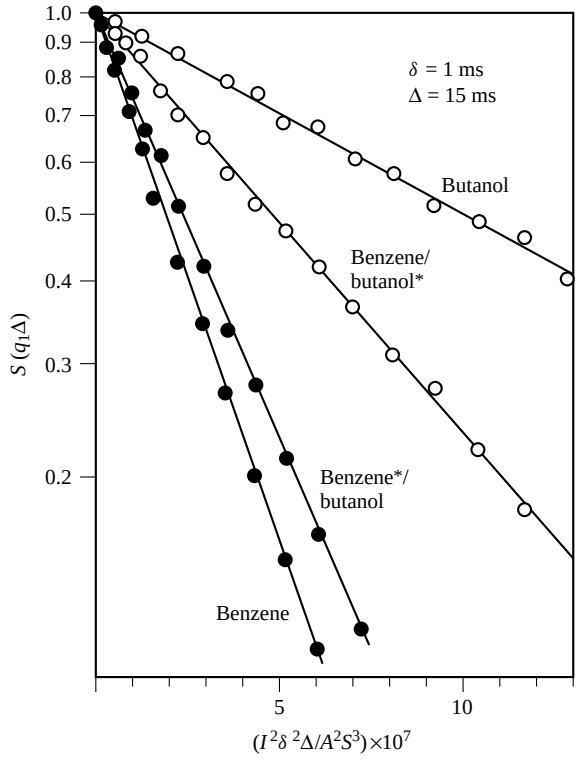

Figure 2 Typical PGSE echo signal decays used to determine the self-diffusion coefficients of the constituents benzene and butanol. The data are plotted as a function of $I^2\delta^2\Delta$ with the current I proportional to g. The diffusion coefficients are obtained from the slope of the lines according to equation (16). (Reproduced by permission of CSIRO from P. T. Callaghan, *Aust. J. Phys.*, 1984, **37**, 359)

experimental challenges, with values as low as $10^{-14}\,\mathrm{m^2\ s^{-1}}$ probably representing the limit. Use of nuclei other than protons is possible, although the dependence of the echo attenuation on γ^2 implies a considerable penalty. For ^{13}C, for example, this requires an increase of a factor of 4 in the FGP area to maintain the same echo attenuation compared with a measurement using ^{1}H with the same diffusion coefficient. Use of multiple quantum coherences can be partly successful in regaining the sensitivity,[12] as a coherence of order n has an effective precession frequency of $n\omega_0$.

The accuracy of the determination of D again depends on a number of factors.[13] Perhaps most critical is whether g is determined directly, in which case this is usually the limiting factor, or whether g is calibrated through use of a sample of known D, determined by another method. Linearity and stability of the gradient generation system and the rf amplifiers and detectors can also play an important role in limiting accuracy and precision (see Section 2.3).

2.3 Finite Width FGPs and Effects of Background Gradients

Equations (8) and (9) are valid in the limit $\delta \to 0$ with $g\delta$ remaining finite, or, in a practical sense, when evolution of $P(x, \Delta; x_0)$ during δ is negligible. To calculate the response of the PGSE and other pulse sequences when these conditions are not satisfied requires that the phase shifts of the spins are calculated by integration over their gradient/coordinate histories:

$$\phi_i(t) = \int \Omega_i(t')\,\mathrm{d}t' \tag{19}$$

where $\Omega_i(t') = [\omega_i(t') - \omega_0]$.

One approach to the solution of this problem was that used by Douglass and McCall[14] for the case of a constant gradient. This was also used by Neuman[15] and Murday and Cotts[16] for restricted diffusion (see Section 3.1). The essence of this approach is the assumption that the phase probability distribution $P[\phi(\Delta)]$ [see equation (7)] is Gaussian for all Δ. This gives the spin echo amplitude as

$$S(2\tau) = S_0\ \exp[-\langle\phi^2(2\tau)\rangle/2] \tag{20}$$

where

$$\langle\phi^2(2\tau)\rangle = \gamma^2 g_0^2\Big[\int_0^\tau \mathrm{d}t \int_0^\tau \mathrm{d}t' - 2\int_0^\tau \mathrm{d}t \int_\tau^{2\tau} \mathrm{d}t' + \int_\tau^{2\tau} \mathrm{d}t \int_\tau^{2\tau} \mathrm{d}t'\Big]\langle x(t)x(t')\rangle \tag{21}$$

and where the position correlation function has the general form[15]

$$\langle x(t)x(t')\rangle = \int \mathrm{d}\boldsymbol{r}_0 \int \mathrm{d}\boldsymbol{r} \int \mathrm{d}\boldsymbol{r}'(\boldsymbol{r} - \boldsymbol{r}_0)_x(\boldsymbol{r}' - \boldsymbol{r}_0)_x P(\boldsymbol{r}_0) \times P(\boldsymbol{r}, t; \boldsymbol{r}_0)P(\boldsymbol{r}', t' - t; \boldsymbol{r}) \tag{22}$$

in which the $P(\boldsymbol{r}, t; \boldsymbol{r}')$, etc., are the usual conditional probabilities. For unbounded self-diffusion this leads directly to equation (18). Recently, the question concerning the generality of the assumption of Gaussian character for $P[\phi(t)]$ for restricted diffusion[15] has been investigated for the case of plane parallel and spherical barriers (see Section 3.1).

An alternative approach, used by Stejskal and Tanner,[3,4] starts with addition of a diffusion term to the Bloch equation describing the time dependence of the transverse magnetization:

$$\mathrm{d}M/\mathrm{d}t = [\mathrm{i}\omega_0 - (1/T_2) - \mathrm{i}\gamma(\boldsymbol{r}\cdot\boldsymbol{g}) - D\nabla^2]M \tag{23}$$

The contribution of diffusion is emphasized by defining ψ as

$$\psi = M\ \exp[-\mathrm{i}\omega_0 t + (1/T_2)] = A(t)\ \exp(-\mathrm{i}\gamma\boldsymbol{r}\cdot\boldsymbol{F}) \tag{24}$$

where

$$\boldsymbol{F}(t) = \int \boldsymbol{g}(t')\,\mathrm{d}t' \tag{25}$$

and the effects of diffusion are contained in $A(t)$ through

$$\mathrm{d}A(t)/\mathrm{d}t = -\gamma^2 D[\boldsymbol{F} + (\xi - 1)\boldsymbol{f}]^2 A \tag{26}$$

in which $\xi = -1$ for $t > \tau$ and +1 for $t < \tau$. For the sequence in Figure 1, $\boldsymbol{f} = \boldsymbol{F}(\tau)$. The echo amplitude at 2τ for this sequence is given by

$$\ln[A(2\tau)/A(0)] = -\gamma^2 D\{2\tau^3 g_0^2/3 + \delta^2(\Delta - \delta/3)g^2 - \delta[(t_1^2 + t_2^2) + \delta(t_1 + t_2) + 2\delta^2/3 + 2\tau^2]\boldsymbol{g} \cdot \boldsymbol{g}_0\} \quad (27)$$

As indicated above, the presence of a steady field gradient $\boldsymbol{g}_0$ is almost inevitable, except for homogeneous liquid samples studied using a high-resolution spectrometer.[11] Such 'background' gradients can arise from intrinsic inhomogeneity in the applied static field, may be generated deliberately by passing a steady current through the coils used to apply the pulsed gradients or coils used to shim the main field, or may be induced within the sample if this has significant spatial variations in its magnetic susceptibility. In probing the translational displacements of spins using the PGSE experiments, account must generally be taken of the interplay between $\boldsymbol{g}$ and $\boldsymbol{g}_0$, whether the aim is to extract accurate transport coefficients [e.g. using equation (27)], to minimize the impact of $\boldsymbol{g}_0$, or to exploit it. A detailed analysis of the role of $\boldsymbol{g}_0$ on PFG experiments has been presented by Hrovat and Wade,[17] whilst Williams et al.[18] and Karlicek and Lowe[19] have devised pulse sequences which aim to remove the effects of diffusion through $\boldsymbol{g}_0$ whilst discriminating in favor of the effects of the applied FGPs (see below). These have been further developed by Latour et al.[20]

A feature of the PGSE experiment is that the amplitudes and time of occurrence of the spin echo maxima can show variability, although careful attention to equipment design can reduce these considerably.[21] This sensitivity can be understood in qualitative terms by recognizing that, even for a modest FGP amplitude and a sample with dimensions of the order of 1 cm, the difference in phase produced at either side of the sample by a typical FGP can be several thousand radians. The second FGP must be capable of refocusing shifts of this order such that the full signal is recovered to certainly better than 1% or so. This requires very careful balancing of the two (or more) FGPs and, as already indicated, careful attention to apparatus design and construction.

Understanding the effects of imbalance in the gradient pulses is important and, using similar terminology to that in equation (24)–(27), Hrovat and Wade[17] have described the effects of this imbalance in the length of the FGPs. This imbalance, shown in Figure 1 as an extra width ϵ in the second FGP, leads to a reduction in the amplitude of the echo and a shift in the time of the echo maximum t_e from 2τ. Typically, for a cylindrical sample of radius R, with the gradient applied perpendicular to the cylinder axis, the echo amplitude at the maximum ($t = t_e$) is given by

$$S(t_e) = 2J_1(\gamma Rg\epsilon \sin\alpha)/\gamma Rg\epsilon \sin\alpha \quad (28)$$

where J_1 is the first-order Bessel function, and α is the angle between $\boldsymbol{g}_0$ and $\boldsymbol{g}$. This shows that even small imbalances in the two FGPs can give significant amplitude reductions, quite unrelated to diffusion. Similarly, the shift of t_e from 2τ is found to be $g\epsilon \cos\alpha/g_0$. In general, the FGPs are balanced empirically and the criterion which should be used is found to be maximizing the echo intensity rather than forcing t_e as close as possible to 2τ. It is also found, consistent with experimental observation, that the presence of a significant $\boldsymbol{g}_0$ parallel to $\boldsymbol{g}$ produces a stabilization of the position of the echo when its width is dominated by $\boldsymbol{g}_0$.

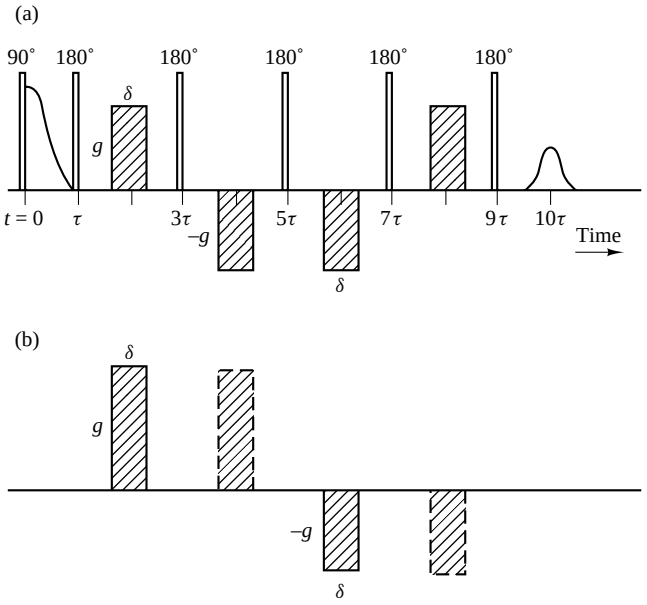

Figure 3 (a) The simplest of the alternating gradient multiple pulse sequences devised by Karlicek and Lowe[19] to allow the measurement of diffusion processes in systems with significant internal magnetic field gradients. (b) The effective polarity of the four FGPs applied during this sequence. The effect of the background gradients is reduced through the effects of the multiple echo formation

Figure 3(a) shows the simplest of the alternating PFG spin echo experiments devised by Karlicek and Lowe[19] to allow the measurement of diffusion coefficients in materials which have strong internal steady field gradients.

It is a CPMG-type multiple echo sequence involving five 180° pulses. As mentioned above, the effect of a 180° pulse is effectively to reverse the polarity of a following FGP relative to that before it. The applied FGPs in this sequence alternate in sign with a mirror reflection at the central 180° pulse. As the switching in polarity occurs at each 180° pulse the nett effect is to produce the equivalent of a bipolar applied FGP [Figure 3(b)] which then produces a full effect in terms of diffusional attenuation of the final echo. The effect of the multiple echo sequence on the internal (or background) gradient, however, is to reduce its effectiveness (see Section 2.4) and also to remove the $\boldsymbol{g} \cdot \boldsymbol{g}_0$ contribution of equation (27).

2.4 The Stimulated Echo and Other Alternative Pulse Sequences

The Karlicek and Lowe sequence, mentioned above, makes use of the fact that, inter alia, diffusion through existing gradients in the sample can be discriminated against by use of a multiple echo sequence. In fact Carr and Purcell[2] showed that the echo at time $t = 2n\tau$ in their $90°-\tau-(180°-2\tau-)_n$

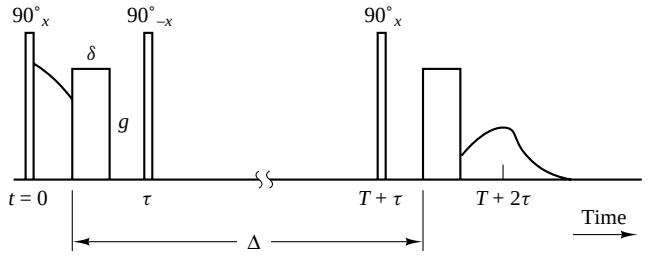

Figure 4 The pulsed gradient stimulated echo (PGSTE) sequence used to study diffusion and flow. It is particularly useful in systems where $T_1 \gg T_2$. During the time T the signal which gives rise to the stimulated echo relaxes at a rate determined by T_1, which allows Δ to be made larger than for the corresponding PGSE experiment for the condition $T_1 \gg T_2$

sequence in the presence of a static field gradient $\boldsymbol{g}_0$ was

$$S(t = 2n\tau) = S(0)\ \exp[-(1/T_2 + \gamma^2 g_0^2 D\tau^2 t/3)] \qquad (29)$$

which indicates that if the pulse separation is made small enough the effects of diffusion through the gradient may be eliminated. If combined with applied FGPs, this rf pulse sequence can be thought of as modifying the intrinsic relaxation properties of the sample (in this case produced by internally generated gradients) in order to allow the controlled use of the PFG approach with maximum time for observation of the diffusional displacements, i.e. T_2 as compared with T_2* (or something close to this). In fact many possibilities exist for using the variety of rf pulse sequences which allow different relaxation behaviors to determine the timescales over which the translational displacements may be observed. Probably the most used of such alternative sequences is the stimulated echo (STE) sequence which is shown in its PFG version in Figure 4.

The use of this for diffusion measurements was first suggested and demonstrated by Tanner.[22] The essence of the STE sequence, originally discussed by Hahn,[1] is that in a general three-rf-pulse sequence five echoes are produced. Of these, that occurring at a time τ following the third pulse, i.e. $t = (T + 2\tau)$ in Figure 4 is the important echo for the purposes of diffusion and flow studies. It is known as the stimulated echo and arises from magnetization which is stored in the longitudinal ($\boldsymbol{B}_0$) direction in the period between the second and third rf pulses. In terms of relaxation its amplitude is given by

$$S(T + 2\tau) = [S(0)/2]\ \exp[-(2\tau/T_2 + T/T_1)] \qquad (30)$$

which means that, for systems in which $T_1 \gg T_2$, it can be advantageous to use this sequence despite the fact that the STE has a maximum intensity only half that of the normal spin echo in Figure 1. The attenuation of the pulsed gradient stimulated echo (PGSTE) arising from diffusion has the form

$$S(T + 2\tau) = 0.5S(0)\ \exp[-\gamma^2 g^2 \delta^2 D(\Delta - \delta/3)] \qquad (31)$$

but with the accessible range of Δ now being determined in the main by T_1, particularly when $T_1 \gg T_2$. The choice of when to use the PGSTE or other pulse sequences rather than the simple PGSE method is dictated by the nature of the spin relaxation characteristics of the sample under study. A fuller discussion of the use of the STE and other pulse sequences for the study of diffusion may be found in Section V of the review by Kärger et al.[23]

3 HINDERED, ANISOTROPIC, AND RESTRICTED DIFFUSION

In Section 2, discussion of diffusion was limited to a Gaussian propagator, i.e. equation (12) for which the mean squared displacement increases linearly with time Δ [equation (13)]. The power of the PGSE method is that, through the dependence of the NMR signal on $\boldsymbol{q}$ and Δ, it provides a means of probing the translational propagator over a range of spatial and temporal scales. The accessible ranges of these scales in any material are determined by, on the one hand, the intrinsic diffusion coefficients and the spin relaxation characteristics (the latter constraining the range of Δ) and, on the other, the values of $\boldsymbol{q}$ achievable—usually dictated by instrumental design characteristics.

In homogeneous solutions of small molecules of generally similar size, any deviations from Gaussian behavior of the propagator are dissipated on a distance scale for displacements which are of the order of a molecular diameter d, and hence on timescales of the order of (d^2/D), which will be nanoseconds or less. As discussed by Callaghan and Coy[24] this is the province of neutron scattering. On the other hand, for small molecules diffusing through systems which have structural features or obstacles to diffusion of the order of micrometers, timescales are of the order of milliseconds and this brings such effects within the normal range of the PGSE and related experiments. Typically, Δ can cover the range 0.1–1000 ms, corresponding to mean squared displacements in mobile fluids in the range 0.5–50 μm.

The use of the terms 'hindered' and 'restricted' in the heading of this section is intended to draw a qualitative distinction between two limiting situations. Restricted diffusion is usually taken to be that in which the molecular translational displacements are constrained by impermeable barriers to remain trapped within finite regions of space, these regions being of a size such that the diffusing molecules may encounter and be reflected by the barriers within the timescale Δ. 'Hindered' is not a widely employed term, but is one which might be used to describe those situations in which the mean squared displacement of the diffusing molecules is not bounded but, nonetheless, suffers a change in its effective rate of change over the timescale Δ. In reality, there is a continuity of behavior from restricted through to completely free diffusion. The term 'anisotropic' is self-explanatory—the diffusion occurs at different rates in different directions in space. These spatial directions are usually defined within the material under study by its structure and organization. There may be a distribution of orientations of these internal features with respect to the applied field gradient direction.

Before introducing certain quantitative descriptions of these restricted non-Gaussian diffusion effects, it is helpful to consider, qualitatively, a simple model with the aims of discriminating the roles of $\boldsymbol{q}$ and Δ and of illustrating the general behavior of the PGSE NMR signal in the presence of such effects. Figure 5 shows molecules diffusing between

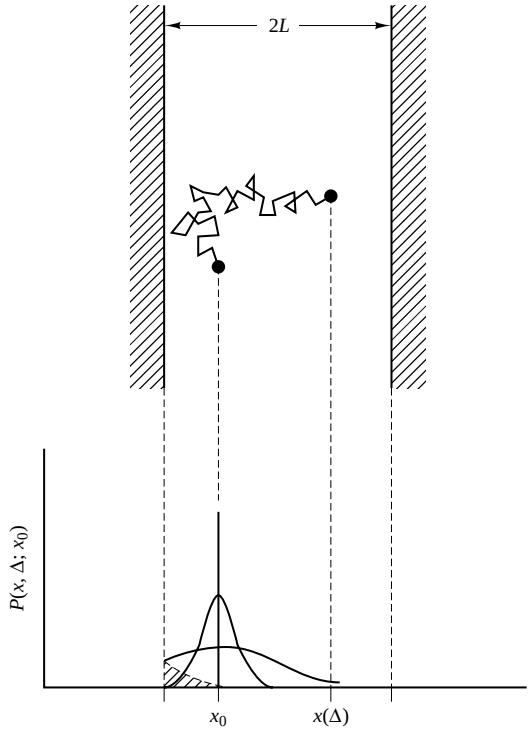

Figure 5 A typical trajectory of a spin undergoing diffusion between plane parallel impenetrable barriers showing reflection at the barrier. Also shown is the general behavior of the propagator for displacements for a spin starting at x_0. It is clear that the propagator will be a function of starting position with spins starting near the walls experiencing their effect sooner and to a greater extent in that earlier period than those starting further away

two parallel planar and impermeable barriers, separated by a distance $2L$. The PFG $\boldsymbol{g}$, and hence $\boldsymbol{q}$, is taken as being perpendicular to the planes. Molecules starting at x_0 explore the surrounding space. The propagator $P(x, \Delta; x_0)$, representing an average over all possible trajectories, evolves in a Gaussian fashion until it encounters the barrier which reflects it back into the space between the barriers. It is clear immediately that the behavior of the propagator is a function of starting position x_0. At times Δ such that $(2D\Delta)^{1/2} \ll (L - x_0)$ spins starting at x_0 diffuse without being influenced significantly by the barriers, and the echo signal obeys equation (16) to a good approximation. The smaller $(L - x_0)$, the sooner (on average) the spins experience the effects of the constraining barriers. Indeed, in the limit of low $\boldsymbol{q}$ (defined by $qL \ll 1$), the short-time behavior of such a system has been shown[25,26] to be consistent with the result

$$[D_{\text{eff}}(\Delta)/D(0)] = 1 - (4/9\sqrt{\pi})(S/V)D^{1/2}\Delta^{1/2} + \text{higher terms} \tag{32}$$

where $D_{\text{eff}}(\Delta)$ is obtained from the variation with q of the signal at fixed Δ according to

$$S_\Delta(q) = S_\Delta(0)\ \exp[-4\pi^2 q^2 \Delta D_{\text{eff}}(\Delta)] \tag{33}$$

and where S/V is the surface-to-volume ratio of the obstacles to diffusion.

In the limit of long observation times ($\Delta \geq L^2/D$) all spins, regardless of their x_0 value, encounter the barriers and, for each x_0, the propagator tends to the spin density function $P(x_0)$:

$$P(x, \infty; x_0) \rightarrow P(x_0) \tag{34}$$

This makes the average propagator the autocorrelation function of the spin density:

$$\langle P[X(\infty)]\rangle = \int P(x_0 + X)P(x_0)\,\mathrm{d}x_0 \tag{35}$$

The Wiener–Khintchine theorem[27] shows that the Fourier transform of an autocorrelation function of a property is the power spectrum of that property and, since $S(q, \Delta)$ is the q-space Fourier transform of the average propagator, this means that for this planar barrier model

$$S(q, \infty) = |\text{sinc}\,(\pi q L/2)|^2 = |I(q)|^2 \tag{36}$$

where

$$I(q) = \int P(x_0)\ \exp(\text{i}2\pi q x_0)\,\mathrm{d}x_0 \tag{37}$$

which is the same quantity measured in conventional NMR imaging. As was first pointed out by Cory and Garroway,[28] this behavior is analogous to the optical intensity diffraction pattern arising from a single slit of width $2L$.

This discussion leads to a general understanding of the roles of Δ and $\boldsymbol{q}$ in the PGSE experiment for situations in which diffusion occurs through systems which impose some spatially distributed obstacles or barriers. To access information dominated by diffusive motion, the condition $qL \ll 1$ must be approached in general. For short observation times Δ it can be shown[24] that the PGSE response has the form

$$S(\Delta, q \ll L^{-1}) \approx 1 - (1/2!)(2\pi q)^2\langle X^2(\Delta)\rangle + \ldots \tag{38}$$

where $\langle X^2(\Delta)\rangle$ is the mean squared displacement at time Δ.

For a system which has obstacles to diffusion on a spatial scale L, measurements when $\Delta < L^2/D$ with $qL \ll 1$, will give a diffusivity which tends to that of the bulk fluid together with information on the surface-to-volume ratio of the obstacles [equation (32)]. For $\Delta \geq L^2/D$, on the other hand (with $qL \ll 1$ still), the diffusivity measured increasingly incorporates the influence of the obstacles.

Varying q such that $qL \geq 1$ probes the structural arrangement and features of the obstacles, as seen by the displacements $X(\Delta)$. So, for $\Delta \ll L^2/D$, the q dependence will be weak, since few spins have encountered the effects of the obstacles, whereas once $\Delta \geq L^2/D$ varying q such that $qL \geq 1$ imposes strong structure-related behavior on the PGSE signal. For structures with some periodicity or local order this can have the form of diffraction-like effects with coherences appearing when $qL \approx$ integer (see Section 3.2). Figure 6 gives an example of such behavior. It is interesting to realize that, despite the long history of this experiment and the obvious similarity of its mathematical formulation to diffraction and

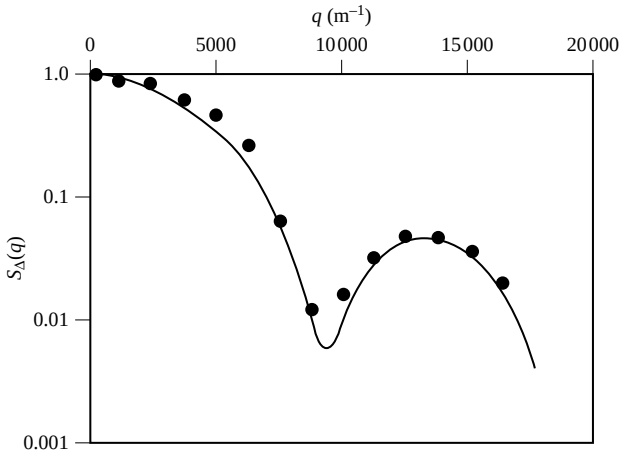

Figure 6 The spin echo amplitude $S_\Delta(q)$ as a function of q for protons in liquid pentane diffusing in a structure made up of rectangular microcapillaries with a separation of approximately 100 μm. Δ = 950 ms. The diffraction-like effects are clearly visible. The solid line is a fit to equation (39) which gives $2L$ = 107 μm and $D = 5 \times 10^{-9}$ m^2 s^{-1} (see Figure 5). (Reproduced by permission of Kluwer from Callaghan and Coy in NMR Probes of Molecular Dynamics, ed. R. Tycko, Dordrecht, 1994)

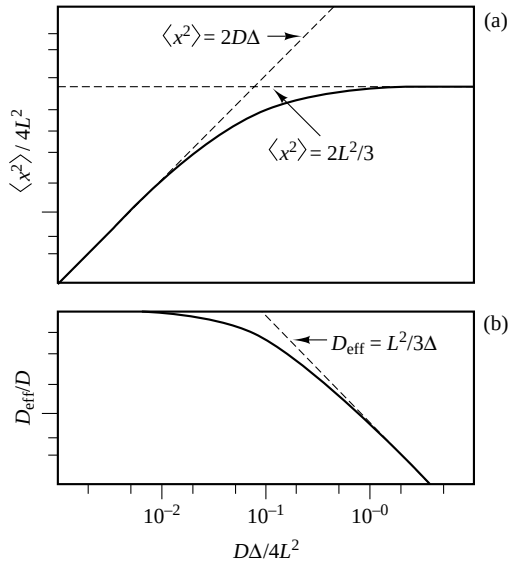

Figure 7 Mean squared displacement and effective diffusion coefficient for spins diffusing between planar parallel impenetrable barriers of separation $2L$. (Adapted and reproduced by permission of Academic Press Ltd. from J. Kärger, H. Pfeifer and W. Heink, *Adv. Magn. Reson.*, 1988, **12**, 1)

scattering phenomena in general, it was only recently recognized and demonstrated[7,8,28] that an essentially dissipative process, i.e. self-diffusion, could result in the growth of an NMR coherence as well as the usually expected decay.

3.1 Restricted Diffusion

The general problem of calculating the echo response for restricted diffusion has been approached in a number of ways. In general, solutions have to be found for the diffusion equation with the appropriate boundary conditions and these solutions used to calculate the phase shift distributions of spins in the applied gradient. The results for the plane parallel barrier case will be used as an example. Full details of other geometries and models can be found in the many excellent reviews.[4,6,11,23,24,29]

The echo attenuation arising from diffusion in the plane parallel barrier case of Figure 5 was first analyzed by Stejskal and Tanner.[30] The general result has the form:

$$S(q,\Delta) = (\mathrm{sinc}\, 2\pi qL)^2 + (8\pi qL)^2 \sum_{n=1}^{\infty} \exp(-n^2\pi^2 D\Delta/4L^2) \times \{[1-(-1)^n \cos(4\pi qL)]/[(4\pi qL)^2 - (n\pi)^2]^2\} \quad (39)$$

In the short- and long-time limits ($\Delta \ll 4L^2/D$ and $\Delta \gg 4L^2/D$) equation (39) reduces, as expected, to equation (16) and equation (36), respectively. Figure 7 illustrates the general behavior of equation (39) in terms of the mean squared displacement $\langle X^2(\Delta)\rangle$ and the variation of $D_{\mathrm{eff}}(\Delta)$ with Δ for the plane parallel barrier case shown in Figure 5.

Figure 7(a) shows that for $\Delta D < 4L^2$, $\langle X^2(\Delta)\rangle$ increases linearly with Δ but when $\Delta D > 4L^2$ it tends to a limit of $2L^2/3$. The value of D_{eff} undergoes a transition from D to $L^2/3\Delta$, as illustrated in Figure 7(b). A typical set of experimental

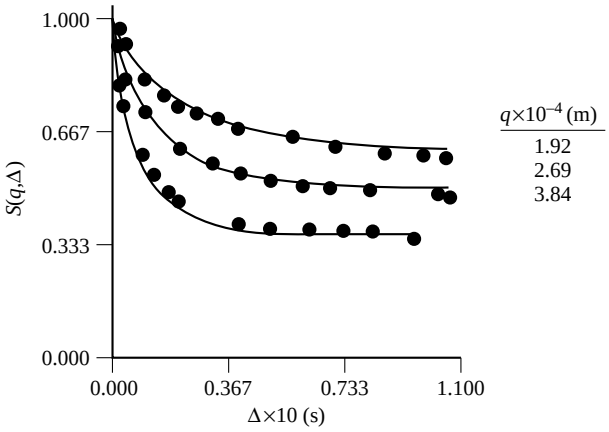

Figure 8 A typical set of echo attenuation data for restricted diffusion in an emulsion. The data are plotted as a function of observation time Δ for different gradient intensities q. This shows the change of effective diffusion coefficient with both these variables. The lines are fits to theoretical expressions for diffusion in spherical containers with a log–normal distribution of diameters. (Adapted and reproduced by permission of Academic Press Inc., from K. J. Packer and C. Rees, *Colloid Interface Sci.*, 1972, **40**, 206)

data for restricted diffusion is shown in Figure 8. The echo attenuation is displayed as a function of the diffusion time Δ, for different gradient strengths. It can be seen that the characteristic of restricted diffusion is that the echo attenuation reaches a limiting value (when $\Delta \gg L^2/D$), and that this limit and the echo attenuation in general are functions of q and Δ as independent variables.

As pointed out above (Section 2.3), in cases other than that of plane parallel barriers, calculation of the echo response for restricted diffusion has required the assumption of a Gaussian distribution of phases at all times.[14,15] As mentioned in

Section 2.3, this assumption, and the accuracy of the short gradient pulse limit has been studied by Balinov et al.[31] using computer simulations.

PGSE experiments in situations where diffusion is restricted may be used to characterize the distributions of sizes of such barriers to diffusion, usually with some assumed form of the distribution.[32,33] A complication which has only recently begun to be addressed is that, in many systems containing barriers to diffusion on the micrometer scale, the spin relaxation behavior may also be dominated by diffusion to the surface of the barriers.[34,35] In order to determine accurately information concerning the compartment sizes bounding the diffusion, the PGSE experiment must be analyzed taking these surface relaxation effects into account.

3.2 Hindered and Anisotropic Diffusion

As indicated above, hindered diffusion is taken as describing any situation in which the propagator $P(\boldsymbol{r}, \Delta; \boldsymbol{r}_0)$ evolves in a non-Gaussian fashion and the mean-squared displacements are not bounded. Examples of this could be permeable barriers such as membranes or polymers,[23,36] intra- and inter-crystallite diffusion in zeolites and related materials,[23] polymer solutions and melts,[36,37] fluids contained in porous solids,[7–9,24] and colloidal and multiphase systems.[11] A number of approaches have been developed to allow the interpretation of PGSE data arising from such situations.[6–9,24–26,28,35,37] It is not the purpose of this article to provide a detailed account of all these aspects, and many of the ideas and principles involved have been introduced earlier. However, as an illustration, the case of diffusion through a porous solid will be described. Typically, this might concern the diffusion of molecules through an array of pores, these having a characteristic dimension a, which are connected in some manner in three dimensions with a separation b. Under the so-called 'pore equilibration assumption',[8] which requires that once a molecule transfers to a neighboring pore its spatial distribution is immediately taken to be the pore volume, the PGSE response has the form

$$S(q, \Delta) = |I(q)|^2 \, F(q, \Delta) \tag{40}$$

where $I(q)$, the structure factor of a single pore, is given by equation (37) and $F(q, \Delta)$ describes the details of the motions between pores. For an array of pores which have the nature of a single crystal and using a pore hopping formalism to describe the diffusion between pores, it was found that

$$F(q, \Delta) = \exp[-(4D_{\text{eff}}\Delta/b^2) \, \sin^2(\pi q b)] \tag{41}$$

whereas for a pore glass configuration in which the pore hops produce a distribution of displacements in the gradient direction,

$$F_G(q, \Delta) = \exp\{-(6D_{\text{eff}}\Delta/b^2)[1 - \sin(2\pi q b)/2\pi q b]\} \tag{42}$$

Equation (41) shows that when qb = Integer, $F(q, \Delta) = 1$ and all dependence of $S(q, \Delta)$ on Δ disappears, whereas for the pore glass there is no such unique condition. Comparison of these analytic results with random walk computer simulations showed that agreement was exact for qb = integer, with deviations at intermediate qb values which were more significant for more open structures, i.e. when the connections between pores become of increasing importance in terms of fluid content and close in dimensions to the pores themselves. Mitra et al.[9] derived an alternative description of the behavior for such systems which was exact for the short Δ regime [cf. equation (32)] and, via an anzatz, derived a model for propagator behavior on all Δ and q scales which they suggest is better able to describe diffusion in more open structures. In another approach, describing the combined effects of both diffusion and relaxation in structured systems, typical of cellular biological materials, Hills and Snaar[35] showed the necessity of characterizing $S(q, \Delta, \tau)$ (τ being a timescale over which relaxation is occurring in the experiment) over as wide a range of the three variables as possible in order to interpret the data in terms of the structure and dynamics of the systems.

The case of anisotropic diffusion is summarized in the review by Callaghan[6] as are other forms of nonisotropic diffusion such as curvilinear behavior which might be found in the diffusion of polymer molecules over timescales spanning the tube renewal time.[37] The key to distinguishing these situations from restricted/hindered diffusion, is that although $S(q, \Delta)$ is not a simple exponential decay [such as equation (16)] and, typically, may show curved semilogarithmic behavior, it is a function of only the single combined variable $q^2\Delta$.

4 PGSE CHARACTERIZATION OF FLOWING FLUIDS

As pointed out by Callaghan in 1984,[6] at that time studies of flow using the PGSE approach had not attracted the same level of attention as diffusion. The rapid development of MRI has since changed that situation because of the clinical importance of the flow of fluids throughout the body. As MRI investigations of flow are covered elsewhere in this Encyclopedia, the aim of this section is to provide a basis for understanding the way in which flow processes affect PGSE-type experiments.

The possibility of NMR characterization of flow using spin echoes in the presence of gradients was first proposed by Hahn.[38] The area has been reviewed regularly and the reader is referred to the recent account by Caprihan and Fukushima[39] for a survey of such reviews and a comprehensive discussion of all aspects of flow measurement using NMR methods. In particular, time-of-flight and MRI approaches may be accessed through this review.

Characterization of the flow of fluids by NMR can probe a wide range of behaviors, including the magnitudes and distributions of flow velocities (which can range from micrometers to meters per second), the detailed nature of the displacements of fluid produced by the flow, whether this be laminar, time varying streamline or turbulent, and the time and spatial scale dependence of these qualities. The general principles governing the PGSE response to flow are those described in Section 2. As pointed out there, the differences between diffusion and flow are to be found in the nature of the propagator $P(x, \Delta; x_0)$, with flow, being to a degree a directed and coherent process, producing assymetric development of the propagator with respect to $(x - x_0)$.

4.1 Measurement of Time-Independent Velocities

As discussed in Section 2 [equation (4) and (6)] for a system in which all spins move with the same and time-independent velocity in the gradient direction during the time Δ, referred to as 'plug flow', the PGSE response has the form:

$$S(q, \Delta) = S(0)\ \exp(\mathrm{i}q\Delta v) \tag{43}$$

Thus, the echo amplitude, detected with a phase sensitive detector, will exhibit a sinusoidal variation with $q\Delta$. Note that the magnitude of the signal is unaffected by plug flow and, under these conditions, would be damped only by spin relaxation processes.

In the case of laminar flow of a fluid there always exists a distribution of velocities $P(v)$, the form of which is characteristic of the geometry of the flow channel. The echo response of the PGSE experiment under these circumstances is:

$$S(q, \Delta) = S(0) \int P(v)\ \exp(\mathrm{i}q\Delta v)\, \mathrm{d}v \tag{44}$$

i.e. the Fourier transform of $P(v)$. Thus, for example, for laminar flow in a circular pipe with the gradient oriented along the pipe axis

$$S(q, \Delta) = S(0)\, \mathrm{sinc}\, (4\pi q \Delta \langle v \rangle) \tag{45}$$

This can be deduced quite simply from equation (44) by noting that, for this flow situation, $P(v)$ is rectangular, having uniform intensity ($\frac{1}{2}\langle v \rangle$) up to $v = v_{\max} = 2\langle v \rangle$, where $\langle v \rangle$ is the average velocity.[40] The Fourier transform of such a rectangular function is the sinc function.[27] equation (45) shows that, in general, the presence of a velocity distribution, produces a damping of the PGSE signal, proportional to the inverse of the width of $P(v)$, and a net phase shift.

4.2 Effects of Time-Dependent Velocities

In many systems of interest, medical, biological or physicochemical, fluid flow occurs such that the velocity of any fluid element projected onto the gradient direction will exhibit some time dependence. For example, fluid moving through a channel which varies in dimensions will have a time varying velocity. Similarly, if the flow channel direction changes, the projection of the fluid velocity onto the gradient will be time dependent. For slow flows, diffusion can cause spins to sample a range of velocities within $P(v)$, whilst turbulence also introduces time dependence. In a qualitative sense, such time dependence of velocity could be thought of in terms of a diffusion-like process and indeed the term 'pseudodiffusion' has been used in this context.[41–43] As such, it might be expected that this would introduce a further damping of the echo signal. However, relative to the effects of a given time-independent $P(v)$, time-dependent sampling by spins of this $P(v)$ during Δ will have an effect similar to motional narrowing of spectral lines and will cause a reduction in the loss of phase memory which, in the limit, will average to a narrowed effective $P(v)$ corresponding to a single average velocity.

In the MRI literature an approach to time varying velocities has been developed[43] which starts from the requirement to calculate the phase shift from the expression

$$\phi = \int x(t) g(t)\, \mathrm{d}t \tag{46}$$

which allows for finite gradient durations. The position $x(t)$ is expanded as a power series

$$x(t) = x_0 + vt + \tfrac{1}{2}at^2 + \tfrac{1}{6}jt^3 + \cdots \tag{47}$$

where v, a, and j are the first, second and third time derivatives of $x(t)$ corresponding to velocity, acceleration, and 'jerk', respectively. This analysis leads to the design of gradient pulse profiles which can be used either to null specific orders in this series or to sensitize experiments to these orders.[43]

For the case in which fluid moves through small vessels with a mean velocity $\langle v \rangle$, and where these paths change direction at random with a characteristic length I, the pseudodiffusion coefficient is given by:[41–43]

$$D_{\mathrm{p}} = \langle v \rangle I/6 \tag{48}$$

Further discussion of these and related situations, including turbulent flow, are given by Caprihan and Fukushima.[39]

4.3 Multiple Pulse and Other Sequences for Characterizing Flow

The simple PGSE and related PGSTE sequences have the disadvantage, for both diffusion and flow, that they must be repeated for appropriate ranges of the variables q and Δ. As such, they are time consuming and, for the case of flowing systems, this can lead to problems with non-steady-state phenomena. Use of sequences which capture the effects of flow in as short a time as possible are therefore desirable. Carr and Purcell[2] showed that in the $90^\circ - \tau - (-180^\circ - 2\tau -)_n -$multiple echo sequence, only odd numbered echoes were affected by flow (convection), the even echoes decaying solely through T_2 effects and diffusion. This realization led to the development of new multiple pulse sequences which, in the presence of applied gradients, allowed a cumulative effect of flow on echo amplitudes to be achieved.[44,45] More recently, use of the Carr–Purcell type sequence together with the Karlicek and Lowe alternating gradient concept has been used to allow the effects of flow to be maximized, whilst discriminating against the effects of diffusion through internal gradients.[46]

Other approaches to enhancing the capability to measure flow, particularly for low velocities, include the direct measurement of time shifts of the echoes measured with a frequency offset, which has been used to measure directly the drift motion of ions in solution driven by an electric field,[47,48] and the development of two-dimensional methods.[48,49]

These latter developments are of considerable interest and, whilst details are available elsewhere in this Encyclopedia and in the references cited in this article, some general points are worth highlighting in this introductory account. In the development of what is termed 'electrophoretic NMR', Johnson and He[48] have pointed to the close analogy in formalism between the optical method of holographic

relaxation spectroscopy (HRS) and the PGSTE experiment in which the echo signal is measured in the presence of a gradient.[50] This can be appreciated by considering the nature of $M_z(x)$, the magnetization existing during the time T in the PGSTE sequence (Figure 4) and from which the STE derives. $M_z(x)$ has the form

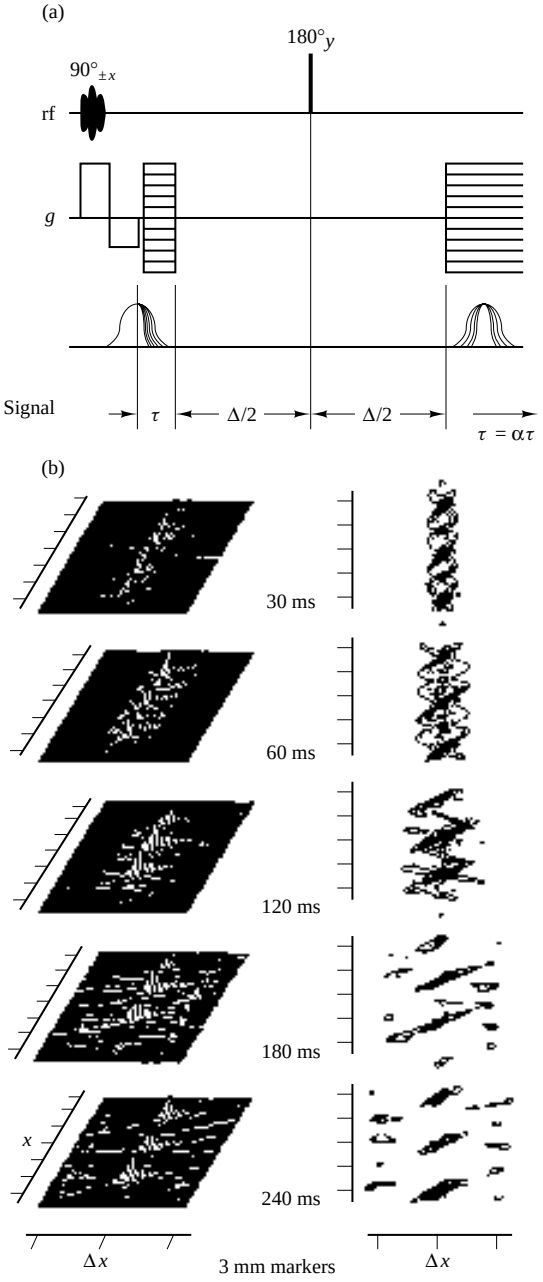

Figure 9 (a) The pulse sequence used to determine the correlation between the starting position x_0 and diffusional displacement $X(\Delta)$ $[=x(\Delta) - x_0]$. A slice selection is used to define a plane of spins and this is followed by a PGSE experiment in which the echo is recorded in the presence of the second gradient pulse. (b) Two-dimensional plots showing the correlations for Taylor–Couette flow. (Reproduced by permission of Academic Press Inc. from L. Frydman, J. S. Harwood, D. N. Garnier, and G. C. Chingas, *J. Magn. Reson. Ser. A*, 1993, **101**, 240)

$$M_z(x) = 0.5M_0 \cos(2\pi qx) \tag{49}$$

which is analogous to the transient grating produced optically in HRS. In both cases, diffusion or flow either damp or shift the gratings, and these effects may be imaged through application of a 'read' gradient in the place of the second gradient pulse or, for HRS, by laser diffraction. The concept of imaging the spatial magnetization distribution in PFG-type experiments (as distinct from MRI) is of interest both for the insight it generates, through analogies with optical phenomena, and for the additional information it makes available. This is shown clearly by the use of this approach by Frydman et al.[49] for the characterization of flow.

The sequence used by Frydman et al. is essentially that shown in Figure 1, except that the echo is captured in the presence of a gradient. Their actual experiment is shown in Figure 9(a), whilst Figure 9(b) illustrates the characteristic two-dimensional plots obtained which correlate the separately-determined x_0 and $X(\Delta)$ for the case of Taylor vortices in Taylor–Couette flow. As pointed out,[49] this approach has the merits of providing a global view of the particle displacements, yielding a Lagrangian, as compared to an Eulerian, view of the flow behavior.

5 RELATED ARTICLES

Anisotropically Restricted Diffusion in MRI; Brownian Motion and Correlation Times; Colloidal Systems; Diffusion: Clinical Utility of MRI Studies; Diffusion Measurements by Magnetic Field Gradient Methods; Diffusion and Perfusion in MRI; Diffusion in Porous Media; Electrolytes; Electrophoretic NMR; Field Gradients and Their Application; Flow NMR; Whole Body Magnetic Resonance Angiography; Gradient Coil Systems; Liquid Crystalline Samples: Diffusion; Micellar Solutions and Microemulsions; Pulsatility Artifacts Due to Blood Flow and Tissue Motion and Their Control.

6 REFERENCES

1. E. L. Hahn, *Phys. Rev.*, 1950, **80**, 580.
2. H. Y. Carr and E. M. Purcell, *Phys. Rev.*, 1954, **94**, 630.
3. E. O. Stejskal and J. E. Tanner, *J. Chem. Phys.*, 1965, **42**, 288.
4. E. O. Stejskal, *Adv. Mol. Relaxation Proc.*, 1972, **3**, 27.
5. J. Kärger and W. Heink, *J. Magn. Reson.*, 1983, **51**, 1.
6. P. T. Callaghan, *Aust. J. Phys.*, 1984, **37**, 359.
7. P. T. Callaghan, A. Coy, D. MacGowan, K. J. Packer, and F. O. Zelaya, *Nature* 1991, **351**, 467.
8. P. T. Callaghan, A. Coy, T. P. J. Halpin, D. MacGowan, K. J. Packer, and F. O. Zelaya, *J. Chem. Phys.*, 1992, **97**, 651.
9. P. P. Mitra, P. N. Sen, L. M. Schwartz, and P. Le Doussal, *Phys. Rev. Lett.*, 1992, **68**, 3555.
10. R. Mills and H. G. Hertz, *J. Phys. Chem.*, 1980, **84**, 220.
11. P. Stilbs, *Prog. NMR Spectrosc.*, 1987, **19**, 1.
12. B. E. Chapman and P. W. Kuchel, *J. Magn. Reson. A.*, 1993, **102**, 105.

13. K. R. Harris, R. Mills, P. J. Back, and D. S. Webster, *J. Magn. Reson.*, 1978, **29**, 473.
14. D. C. Douglass and D. W. McCall, *J. Phys. Chem.*, 1958, **62**, 1102.
15. C. H. Neuman, *J. Chem. Phys.*, 1974, **60**, 4508.
16. J. S. Murday and R. M. Cotts, *J. Chem. Phys.*, 1968, **48**, 4938.
17. M. I. Hrovat and C. G. Wade, *J. Magn. Reson.*, 1981, **44**, 62; 1981, **45**, 67.
18. W. D. Williams, E. F. W. Seymour, and R. M. Cotts, *J. Magn. Reson.*, 1978, **31**, 271.
19. R. F. Karlicek and I. J. Lowe, *J. Magn. Reson.*, 1980, **37**, 75.
20. L. L. Latour, L. Li, and C. H. Sotak, *J. Magn. Reson. B*, 1993, **101**, 72.
21. P. T. Callaghan, K. W. Jolley, and C. M. Trotter, *J. Magn. Reson.*, 1980, **39**, 525; 1980, **37**, 247.
22. J. E. Tanner, *J. Chem. Phys.*, 1970, **52**, 2523.
23. J. Kärger, H. Pfeifer, and W. Heink, *Adv. Magn. Reson.*, 1988, **12**, 1.
24. P. T. Callaghan and A. Coy, in *NMR Probes of Molecular Dynamics*, ed. R. Tycko, Kluwer, Dordrecht, 1994, p. 489.
25. P. P. Mitra, P. N. Sen, and L. M. Schwartz, *Phys. Rev. B.*, 1993, **47**, 8565.
26. L. L. Latour, P. P. Mitra, R. L. Kleinberg, and C. H. Sotak, *J. Magn. Reson. A*, 1993, **101**, 342.
27. D. C. Champeney, *Fourier Transforms and their Applications*, Academic, New York, 1973.
28. D. G. Cory and A. N. Garroway, *Magn. Reson. Med.*, 1990, **14**, 435.
29. L. W. Reeves, *Dynamic Magnetic Resonance*, L. M. Jackman and F. A. Cotton, Academic, London, 1975, p. 83.
30. E. O. Stejskal and J. E. Tanner, *J. Chem. Phys.*, 1968, **49**, 1768.
31. B. Balinov, B. Jönsson, P. Linse, and O. Soderman, *J. Magn. Reson. A.*, 1993, **104**, 17.
32. J. E. Tanner, Ph. D. Thesis, University of Wisconsin, University Microfilms, Ann Arbor, MI, 1966.
33. K. J. Packer and C. Rees, *Colloid Interface Sci.*, 1972, **40**, 206.
34. J. E. M. Snaar and H. van As, *J. Magn. Reson. A*, 1993, **102**, 318.
35. B. P. Hills and J. E. M. Snaar, *Mol. Phys.*, 1992, **76**, 979.
36. E. D. von Meerwall, *Adv. Polym. Sci.*, 1983, **54**, 1.
37. P. T. Callaghan and A. Coy, *Phys. Rev. Lett.*, 1992, **68**, 3176.
38. E. L. Hahn, *J. Geophys. Res.*, 1960, **65**, 776.
39. A. Caprihan and E. Fukushima, *Phys. Rep.*, 1990, **198**, 195.
40. R. J. Hayward, K. J. Packer, and D. J. Tomlinson, *Mol. Phys.*, 1972, **23**, 1083.
41. D. Le Bihan, E. Breton, D. Lallemand, P. Grenier, E. A. Cabanis, and M. Laval-Jeantet, *Radiology*, 1986, **161**, 401.
42. R. Turner, in *Cerebral Blood Flow* eds A. Rescigno and A. Boicelli, Plenum, New York, 1988, p. 245.
43. R. Turner and P. Keller, *Prog. NMR Spectrosc.*, 1991, **23**, 94.
44. K. J. Packer, *Mol. Phys.*, 1969, **17**, 355.
45. A. N. Garroway, *J. Phys. D, Appl. Phys.*, 1974, **7**, L159.
46. D. N. Guilfoyle, P. Mansfield, and K. J. Packer, *J. Magn. Reson.*, 1992, **97**, 342.
47. M. Holz, C. Müller, and A. M. Wachter, *J. Magn. Reson.*, 1986, **69**, 108.
48. C. S. Johnson, Jr, and Qiuhong He, *Adv. Magn. Reson.*, 1989, **13**, 131.
49. L. Frydman, J. S. Harwood, D. N. Garnier, and G. C. Chingas, *J. Magn. Reson, Ser. A*, 1993, **101**, 240.
50. T. R. Saarinen and C. S. Johnson, Jr, *J. Magn. Reson.*, 1988, **78**, 257.

Biographical Sketch

Ken J. Packer. *b* 1938. B.Sc., 1959, Chemistry, Imperial College, London, Ph.D., 1962, Cambridge University. Introduced to NMR by making a new compound and collaborating with fellow graduate student (Robin Harris) in the analysis of its spectrum. Reinforced by a postdoctoral year with Earl Muetterties at the duPont Experimental Station, Wilmington. 1963–84, School of Chemical Sciences, University of East Anglia; 1984–93, BP Research, Chief Research Associate in Spectroscopy and latterly Chief Scientist. Currently, Research Professor in Chemistry, Department of Chemistry, University of Nottingham. Approx 120 publications including book 'NMR of Solid Polymers' with V. J. McBrierty. Current research interests: NMR/MRI applied to heterogeneous catalysts, solid polymers, and fluid transport processes in porous solids.

Diffusion in Porous Media

Jörg Kärger

Leipzig University, Germany

1 Introduction 1
2 Pieces of Information 1
3 Principles of PFG-NMR 2
4 Diffusion in Microporous Crystallites (Zeolites) 5
5 Related Articles 7
6 References 7

1 INTRODUCTION

Porous media are of considerable interest in a very diverse range of activities. Porous media comprise a wide variety of substances—plastics, ceramics, cements, clays, rocks, porous glasses, carbons, silica gels, and zeolites. Even biological tissues may share many features of porous media. Depending on the given nature, the pore diameters in these substances may range from the subnanometer region up to macroscopic dimensions. The efficiency of their technical use is intimately connected with their transport properties. Diffusion measurements in porous systems are therefore of direct practical relevance. Moreover, systematic diffusion studies in such systems may contribute to a better understanding of such fundamental questions as the interaction between molecules and solid surfaces,[1–3] and the behavior of molecular systems of reduced dimensionality.[4]

Among the methods of studying molecular diffusion in porous media, NMR spectroscopy is of particular relevance. As a noninvasive method, it allows the observation of molecular transportation without interfering with the internal processes. The technique may be applied under both equilibrium and nonequilibrium conditions. Using different NMR techniques, various aspects of molecular transport may be investigated, including the elementary processes of diffusion and the rate of molecular propagation over microscopic and macroscopic distances. A review of the principles of these techniques and examples of their application is given in Section 2. Probably the most powerful NMR method for studying molecular propagation is the pulsed field gradient method (PFG-NMR), and this is described in more detail in Section 3. The capability of PFG-NMR to trace indications of anomalous diffusion in porous media is discussed in Section 4. Finally, as an illustration of the versatility of PFG-NMR, Section 5 summarizes the information provided by this method about molecular diffusion in beds of microporous crystallites (zeolites).

2 PIECES OF INFORMATION

The most straightforward way of applying NMR to study diffusion in porous media is based on the fact that the intensity of an NMR signal is directly related to the number of the observed nuclei. Using this correlation it was possible to measure the rate of molecular exchange between zeolite crystallites of type ZSM-5[5] and NaX,[6] loaded with ordinary (i.e. hydrogen containing) benzene and the surrounding atmosphere of deuterated benzene. The intracrystalline diffusivities estimated on the basis of the measured exchange rates were in excellent agreement with the data determined directly by PFG-NMR in the identical sample and verified the equivalency of macroscopically and microscopically measured diffusivities.

The information provided by the NMR signal intensity is significantly enhanced when the measurements are performed under the influence of well defined inhomogeneities of the magnetic field. Under such conditions, the resonance frequency becomes space dependent, so that the NMR spectrum may be directly correlated with the distribution of the nuclei under consideration within the sample. This method has become popular under the names ‘NMR tomography’ or ‘NMR spin mapping’, due to its spectacular progress in application to anatomical imaging in medicine[7] (cf. articles on biomedical applications in this Encyclopedia). However, its application is certainly not confined to biomedicine; in particular, a wide variety of NMR imaging studies have been concerned with molecular propagation in porous media.[8,9] A summary of the most recent results may be found in the proceedings of the ‘International Meeting on Recent Advances in NMR Applications to Porous Media’, Bologna, 1990,[10] and Canterbury, 1993.[11]

An interesting possibility of tracing mass transfer in porous systems is provided by ^{129}Xe NMR.[12] For this purpose, the system under study is brought into contact with a xenon atmosphere. Since, besides the pore architecture and the chemical composition of the pore surface, the chemical shift of ^{129}Xe NMR also depends on the nature and the concentration of the molecules in the interior of the porous system, the ^{129}Xe NMR spectrum reflects the distribution function of molecular concentrations within the sample. If there are, for example, two regions of different concentration of the molecular species under study, the ^{129}Xe NMR spectrum should consist of two different lines. Obviously, the merging rate of the two lines is directly correlated with the rate of equilibration of the internal concentration, and provides direct information about the intrinsic diffusivities. This measuring principle has been used to study molecular transportation in both the micropores[13] and the macropores[14,15] in zeolitic adsorbate–adsorbent systems.

In the methods so far mentioned, we have exclusively considered samples that are not at equilibrium, either in the strict macroscopic sense, or at least with respect to the different isotopes involved. As soon as equilibrium is attained, these methods cannot provide any information about molecular diffusion. It is one of the great advantages of NMR spectroscopy to be able to follow even the molecules themselves on their individual diffusion paths. The information thus obtained may concern the elementary steps of diffusion as well as the rate of molecular propagation over much larger distances. Information about the elementary steps of diffusion of molecules under the influence of the internal system of porous media may be deduced from an analysis of the nuclear magnetic relaxation times and the NMR spectra.

Proton magnetic relaxation studies offer the advantage that most molecules of interest in diffusion studies of porous media

contain hydrogen atoms, and that, except for the non-naturally-occurring tritium, the magnetogyric ratio, and hence the signal-to-noise ratio, is largest for the hydrogen nucleus.[16] Proton magnetic relaxation of molecules in contact with solid surfaces is mainly determined by magnetic dipole interaction with protons of the same molecule (intramolecular proton–proton interaction), with protons of other molecules (intermolecular proton–proton interaction), and with paramagnetic ions. The different contributions may be separated by a 'relaxation analysis'.[17] Except for extremely pure substances, longitudinal relaxation is controlled by the magnetic dipole interaction with paramagnetic ions. If the longitudinal electron spin relaxation time of these paramagnetic ions is much greater than the mean residence time between subsequent diffusion jumps, then proton magnetic relaxation is affected by the translational motion of the molecules with respect to the ions, and the temperature dependence of the longitudinal relaxation time is found to pass a distinct minimum, which is characterized by the condition that at this temperature the mean residence time is of the order of the reciprocal of the resonance frequency.[17]

The problem of separating the various contributions to nuclear magnetic relaxation can be overcome to a certain degree by studying the deuteron magnetic resonance. This is due to the almost completely dominant interaction energy of the electric quadrupolar moment of the deuteron with the intramolecular electric field gradient at the nuclear site in comparison with the various magnetic coupling energies. Since the deuteron magnetic resonance frequency depends on the orientation of this electric field gradient with respect to the external magnetic field, molecular reorientations with time constants of the order of the reciprocal of the linewidths will lead to characteristic changes in the NMR spectra, including a narrowing of the total spectrum.[18,19] The thus-estimated reorientation times for several hydrocarbons in X-type zeolites were found to be in excellent agreement with the directly measured diffusivity, if one assumes that the molecular mean jump lengths are of the order of the distance between neighboring supercages.[20]

In an identical manner, molecular reorientation also leads to a narrowing of NMR lines in the case of chemical shift anisotropy. Measurements of this type have been carried out with various nuclei (^{13}C and ^{31}P), and numerical simulations have been developed to allow the measured spectra to be attributed to the corresponding reorientation times in the relevant geometry.[21,22]

Since the confinement of the molecules to the internal surface of porous media often leads to a preferential orientation of the molecules, the orientation correlation function will generally not decay to zero by mere local reorientation. Rather, the complete decay to zero necessitates molecular migration to positions with changed orientational preference. This process of 'reorientation mediated by translational displacements' (RMTD)[23] may be traced by measuring the longitudinal nuclear magnetic relaxation times in the range of low resonance frequencies (in particular by the field cycling technique[24]), corresponding to the large correlation times of this process. Tracing RMTD has been shown to be an informative tool for studying both molecular dynamics and structural properties in micrometer and submicrometer length scales of porous systems.[23,25]

In more open porous structures, overall nuclear magnetic relaxation is significantly influenced by the rate of exchange between the region of intense relaxation (the magnetization 'sinks') and the bulk phase. The theoretical analysis of this situation[26,27] shows that the relaxation pattern is controlled by the relationship between the mean diffusion time over a characteristic length scale of the individual pores (e.g. their radius) and the overall relaxation time to be expected under the condition of fast exchange. For diffusion times exceeding the (hypothetical) overall relaxation time, the observed relaxation behavior depends notably on the exchange conditions, yielding information about both the pore sizes and the intrinsic diffusivities.[26–28]

At the beginning of this section ^{129}Xe NMR was introduced as a tool for following the evolution of molecular concentration profiles within porous media. This technique clearly includes the observation of the distribution of the xenon atoms themselves. In microporous materials where the individual cavities are separated by narrow 'windows', the population distribution of the xenon atoms within the individual cavities may be determined.[29] In addition to this local structural information, by using a second time dimension in the NMR experiments (two-dimensional exchange NMR), one may even determine the rate of molecular exchange between cavities of different occupation numbers. This method has been successfully applied to the study of intracrystalline diffusion of xenon in NaA-type zeolites.[30]

Common to all the methods so far considered is the fact that the information about molecular self-diffusion is based on the applicability of certain models. There is, however, the possibility of monitoring directly the probability distribution of molecular propagation. This possibility is provided by transient NMR measurements in a magnetic field with well-defined inhomogeneities of large intensity. The most important representative of these techniques, PFG-NMR, is described in more detail in the rest of this article.

3 PRINCIPLES OF PFG-NMR

The principles of diffusion measurement by NMR may be easily visualized by using the classical concept of nuclear magnetism. According to this concept, any individual spin will carry out a precessional motion about the direction of the constant magnetic field with a precessional frequency given by the Larmor relationship:

$$\omega = -\gamma B \tag{1}$$

where γ is the magnetogyric ratio. In PFG-NMR, the constant magnetic field is superimposed over two short time intervals δ by an inhomogeneous field

$$B_{\mathrm{add}}(\boldsymbol{r}) = \boldsymbol{g} \cdot \boldsymbol{r} \tag{2}$$

the so-called 'field gradient pulses'. According to equation (1) these pulses have the effect that the positions of the individual spins at the instants of the field gradient pulses are recorded by the precessional phases

$$\phi(\boldsymbol{r}) = \int \omega \, \mathrm{d}t = -\gamma(B + \boldsymbol{g} \cdot \boldsymbol{r})\delta \tag{3}$$

accumulated during these time intervals. The two field gradient pulses are generally incorporated into the classical $\pi/2-\tau-\pi$ rf pulse sequence which gives rise to a transient NMR signal (the 'spin echo') at time 2τ after the initial $\pi/2$ pulse. Being proportional to the total magnetization, the intensity of the spin echo depends on the dephasing of the precessional phases of the individual spins at time 2τ. Since the dephasing effected by the first field gradient pulse according to equation (3) is inverted by the π pulse, for immobile spins it is exactly compensated by the second field gradient pulse which is applied after the π pulse. However, if the individual molecules (and with them the spins) have moved during the time interval between the field gradient pulses, the refocusing will be incomplete and the intensity of the transverse magnetization will not be fully restored to its original value. NMR signal attenuation must therefore be expected to increase with increasing displacements during the 'observation time' (i.e. the time interval between the two field gradient pulses), and with increasing width δ and amplitude g of the field gradient pulses.

For a quantitative analysis we consider a particular spin which has been at positions $\boldsymbol{r}_1$ and $\boldsymbol{r}_2$ during the first and second field gradient pulses, respectively. According to equation (3), the phase shift of such a spin in comparison with a spin fixed in space is equal to $\gamma\delta\boldsymbol{g}\cdot(\boldsymbol{r}_2-\boldsymbol{r}_1)$. The total magnetization is the vector sum of the dipolar moments of the individual spins. Thus, in complex notation, the vector sum of the transverse nuclear magnetic moments of all spins involved yields

$$\Psi = \int\int \exp[\mathrm{i}\gamma\delta\boldsymbol{g}\cdot(\boldsymbol{r}_2-\boldsymbol{r}_1)]\, p(\boldsymbol{r}_1) P(\boldsymbol{r}_2, \boldsymbol{r}_1, \Delta)\, \mathrm{d}\boldsymbol{r}_1\, \mathrm{d}\boldsymbol{r}_2 \tag{4}$$

where Ψ denotes the ratio between the NMR signal intensity observed with and without magnetic field gradient pulses, $p(\boldsymbol{r}_1)$ denotes the probability (density) of finding a spin at position $\boldsymbol{r}_1$ (i.e. during the first magnetic field gradient pulse), and $P_2(\boldsymbol{r}_2, \boldsymbol{r}_1, \Delta)$ denotes the probability (density) that a spin which has been at position $\boldsymbol{r}_1$ during the first field gradient pulse will have come to $\boldsymbol{r}_2$ after a time interval Δ(i.e. during the second field gradient pulse). As it contains the complete information about the process of molecular propagation, the function $P(\boldsymbol{r}_2,\boldsymbol{r}_1,\Delta)$ has been termed the 'propagator'. (This expression must clearly not be confused with the operator $\hat{U}(t)$ which is generally termed in the same way and describes the evolution of the ensemble of the magnetically resonant nuclei under study.) Integrating over all possible starting positions $\boldsymbol{r}_1$, one may introduce a mean propagator[31]

$$P(\boldsymbol{r}, \Delta) = \int p(\boldsymbol{r}_1) P(\boldsymbol{r}_1 + \boldsymbol{r}, \boldsymbol{r}_1, \Delta)\, \mathrm{d}\boldsymbol{r}_1 \tag{5}$$

which denotes the probability that during time Δ an arbitrarily selected molecule within the sample will be displaced over $\boldsymbol{r}$. With this notation, equation (4) becomes

$$\Psi = \int \exp\{\mathrm{i}\gamma\delta\boldsymbol{g}\cdot\boldsymbol{r}\} P(\boldsymbol{r}, \Delta)\, \mathrm{d}\boldsymbol{r} \tag{6}$$

Since equations (4) and (6) formally coincide with the expressions for the intermediate incoherent scattering function in neutron scattering, PFG-NMR has been repeatedly interpreted as a scattering experiment[32–35] with a generalized scattering vector

$$\boldsymbol{k} = \gamma\delta\boldsymbol{g} \tag{7}$$

The maximum value of this quantity is of the order of $10^7\ \mathrm{m}^{-1}$, yielding a lower limit of about 100 nm for the space scale covered in PFG-NMR experiments. The much larger scattering vectors in neutron scattering experiments confine diffusion measurements by this technique to maximum displacements of the order of only a few nanometers. Hence, for the observation of molecular transportation phenomena on the micrometer scale, PFG-NMR represents a unique method.

PFG-NMR has been successfully applied to the study of molecular diffusion in a wide spectrum of substances, including pure liquids and gases, polymers, liquid crystals, membranes, biological tissues, as well as the vast group of porous media. Detailed introductions to the experimental procedure with special emphasis on the various techniques which may be applied to enhance the sensitivity of this method and to circumvent the omnipresent pitfalls in experimental work may be found in the literature.[33–39] In most cases, molecular diffusion, as observed by PFG-NMR, is considered to follow the laws of ordinary diffusion. The validity of this assumption is considered in the next section.

4 ORDINARY VS ANOMALOUS DIFFUSION

The total molecular displacement of any molecule during the observation time Δ of a PFG-NMR experiment may be understood as the result of the displacements of this molecule during the different time intervals into which the observation time Δ may be subdivided. Under the assumption that subsequent displacements are independent of each other and are controlled by the same probability distribution then, according to the central limit theorem of statistics for a sufficiently large number of time intervals, the distribution of the sum of these displacements will be given by a Gaussian function with a mean square distribution being proportional to the number of time intervals considered and, hence, to the observation time. Since this probability distribution is in fact the propagator, in the case of three-dimensional diffusion, for example, we may thus write

$$P(\boldsymbol{r}, \Delta) = (4\pi D\Delta)^{-3/2} \exp(-r^2/4D\Delta) \tag{8}$$

where the self-diffusion coefficient D has been introduced via the required proportionality between the mean square displacement and the observation time:

$$\langle r^2(\Delta)\rangle = 6D\Delta \tag{9}$$

Molecular random walk following equation (8) [and hence equation (9)] is called 'ordinary diffusion'. It is completely described by the self-diffusion coefficient D. The definition of the self-diffusion coefficient by the Einstein relationship [equation (9)] is equivalent to that by Fick's first law:[40]

$$\boldsymbol{j}^* = -D\ \nabla\ c^* \tag{10}$$

where the self-diffusion coefficient is introduced as the factor of proportionality between the negative concentration gradient and the flux density of labeled molecules at macroscopic equilibrium. Inserting equation (8) into equation (6), one obtains for the signal attenuation in PFG-NMR for ordinary diffusion:

$$\Psi = \exp(-\gamma^2\delta^2 g^2 D\Delta) \tag{11}$$

With equation (9), signal attenuation may also be expressed as a function of the mean square displacement:

$$\Psi = \exp(-\gamma^2\delta^2 g^2 \langle r^2\rangle/6) \tag{12}$$

In deriving equation (4) [and hence equations (11) and (12)] it has implicitly been assumed that the molecular displacements during the field gradient pulses are much smaller than those in the interval between the two gradient pulses (narrow-pulse limit).[33] Only under this assumption can the NMR signal attenuation be related to the propagator in such a straightforward way. In the case of ordinary diffusion, the finite field gradient pulse width may be exactly taken into account by replacing Δ by an 'effective' observation time $\Delta - \delta/3$.

Any violation of the conditions for the applicability of the central limit theorem must be expected to lead to deviations from ordinary diffusion. Very often, in particular considering molecular diffusion in fractal networks, in the case of 'anomalous' diffusion the mean square displacement should obey a simple scaling law

$$\langle r^2(t)\rangle \propto t^{\kappa} \tag{13}$$

where now, in contrast to ordinary diffusion, the time exponent κ is smaller than 1. It may be shown[40] that the fractal dimension of the trajectory of a random walker obeying equation (13) is equal to $2/\kappa$. As a simple inversion of the central limit theorem, one may conclude that in the case of anomalous diffusion subsequent displacements must be correlated. Analytical expressions for this correlation may be deduced from equation (13).[41] By using these expressions it can be shown that in the narrow-pulse approximation for anomalous diffusion the PFG-NMR spin echo attenuation is also given by equation (12). For finite pulse widths δ, the expression for the spin echo attenuation is more complicated[41] and cannot be deduced from the narrow-pulse approximation by simply introducing an effective observation time.

The search for indications of anomalous diffusion is a current topic of PFG-NMR. Recent progress in the sensitivity towards smaller molecular displacements, in particular including the possibilities of the stray-field modification of the steady-gradient spin echo NMR method,[42] did in fact allow the observation of anomalous diffusion in polymer melts and solutions.[34,43,44] Scaling laws with time exponents κ differing in the range 0.25–0.5 could be confirmed, partially by varying the observation time over orders of magnitude. No similar breakthrough in detecting indications of anomalous diffusion in porous media has yet been achieved. As an example, Figure 1 shows the mean square displacement of *n*-hexadecane adsorbed on active carbon as a function of the observation time.[45] Over two orders of magnitude the observed time dependence is in complete agreement with that of ordinary diffusion,

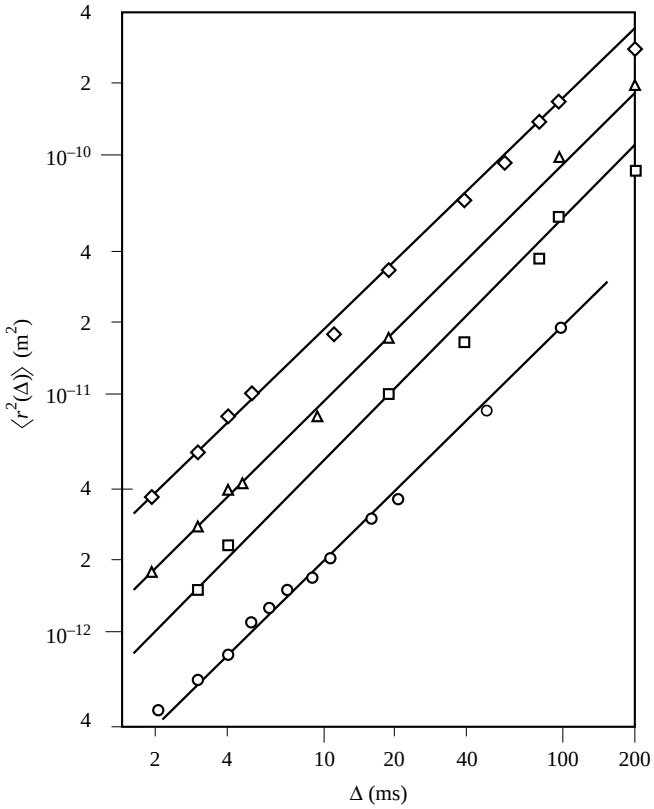

Figure 1 Mean square displacement of *n*-hexadecane adsorbed on active carbon at a pore filling factor of 0.43 versus observation time Δ at: (○) 291 K, (□) 323 K, (△) 363 K, and (◇) 413 K. The straight line indicates the dependence[45] $\langle r^2(\Delta)\rangle \propto \Delta$

although the internal pore system can be described by introducing fractal dimensions. One should note, however, that in the measurements there was only a very small overlap between the pore distribution function and the minimum displacements observable by PFG-NMR.

Molecular transportation in porous crystallites over distances sufficiently exceeding the dimensions of the elementary units clearly fulfils the conditions for the application of the central limit theorem. It is not surprising, therefore, that PFG-NMR measurement of intracrystalline diffusion in zeolites has not thus shown any deviation from ordinary diffusion. There is, however, an intriguing exceptional case, where even in zeolites molecular transportation must be expected to deviate from ordinary diffusion. Such a situation may occur when the zeolite pore system consists of parallel channels, as for example in zeolites ZSM-12 or $AlPO_4$-5. As soon as the channel diameters are so small that the molecules cannot pass each other, by theoretical considerations[46] the molecular mean square displacement may be shown to be proportional to the square root of the observation time rather than to the observation time itself. The experimental verification of this phenomenon of 'single-file' diffusion[47] is a task for PFG-NMR.

In the following final section, by reviewing selected PFG-NMR studies on zeolites, typical examples are given of the application of this NMR technique to diffusion measurements in porous systems. The variety of attainable information will demonstrate that the confinement to ordinary diffusion in these

substances in no way diminishes the attractiveness of such investigations.

5 DIFFUSION IN MICROPOROUS CRYSTALLITES (ZEOLITES)

According to the original definition, zeolites are microporous crystalline aluminosilicates. In the last few years, dramatic progress in zeolite synthesis has made possible the production of a large number of zeolite structure types with the aluminum and/or silicon atoms replaced by other components such as phosphorus, gallium, germanium, boron, and beryllium. Moreover, with these new structural components, a number of new structure types have been realized which have no equivalent among the aluminosilicates.[48] It has become common use, therefore, to apply the term 'zeolites' quite generally to microporous crystalline solids. The diameters of the zeolite crystallites are typically in the micrometer range. Therefore, molecular propagation within beds of zeolite crystallites proceeds both within the individual crystallites (in the 'micropores') and in the intercrystalline space (the macropores or transport pores). In the case of gas phase adsorption, which we shall consider exclusively in the following discussion, molecular concentration in the intercrystalline space is negligibly small in comparison with intracrystalline concentration.

A survey of the different features of molecular transportation as accessible by PFG-NMR under such conditions is provided by the propagator representation. As an example, Figure 2 shows the mean propagator of ethane in zeolite NaCaA[31] for two different crystallite sizes at three different temperatures, determined from the measured spin echo attenuations by using the inversion of equation (6). Depending on the crystallite size, the observation time and the temperature, the observed mean propagator may be exclusively determined by intracrystalline diffusion [e.g. in Figure 2(a) at 153 K] or by migration through the bed of crystallites ['long-range' diffusion, in Figure 2(b) at 293 K]. In the intermediate range between these two limiting cases, the propagator additionally depends on the rate of molecular exchange between the intra- and intercrystalline spaces. Under appropriate conditions, PFG-NMR is therefore able to provide three different dynamic quantities: the coefficients of intracrystalline and of long-range self-diffusion, and the intracrystalline mean lifetime.

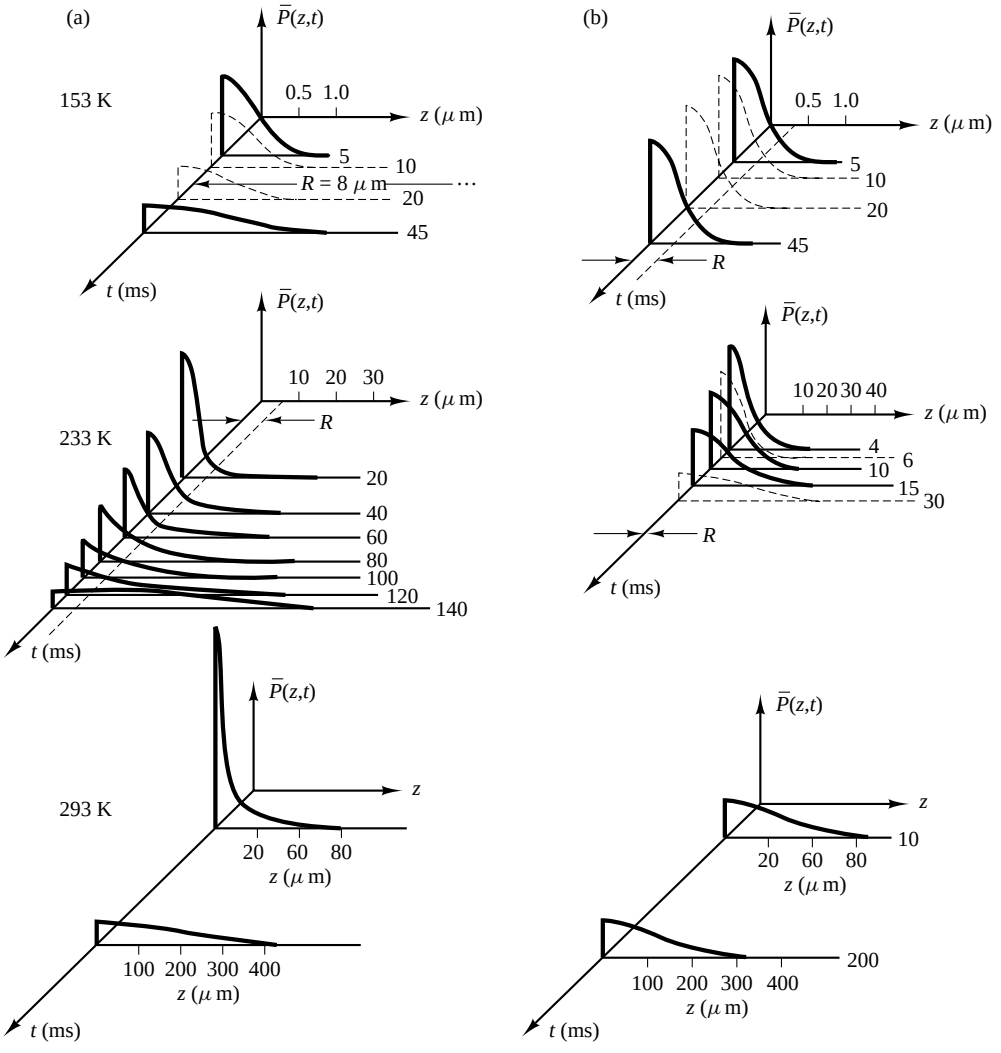

Figure 2 Propagator representation for the self-diffusion of ethane in NaCaA zeolites: (a) 40 mg g^{-1}, $R \approx 8$ μm; (b) 58 mg g^{-1}, $R \approx 0.4$ μm[31]

A detailed description of the procedure and examples of application may be found in the literature.[40,49]

At sufficiently low temperatures, the thermal energy of the adsorbate molecules is not high enough to allow them to overcome the step in the potential energy from the intracrystalline to the intercrystalline space. The molecules are confined, therefore, to the interior of the individual crystallites, and the situation is comparable to that within a pore with impenetrable walls,[50] where now the pore size corresponds to the size of the crystallites. Following the scattering analogy, the PFG-NMR spin echo attenuation due to diffusion between connected pores has been used to analyze the pore distribution and connectivity.[51,52] It is a challenge for PFG-NMR to adopt this concept to study molecular exchange between the different crystallites in the transition range between 'restricted' and long-range diffusion.

One of the most remarkable features of intracrystalline diffusion is the large variety of patterns of concentration dependence. So far, at least five different types of concentration dependence have been observed. Examples of adsorbate–adsorbent systems that follow these different patterns are presented in Figure 3.[40] It is an attractive task for molecular dynamics simulations to correlate the different patterns with possible microdynamic models.[53–55]

A large number of zeolite structure types are of noncubic symmetry, so that intracrystalline molecular migration must be described by a diffusion tensor rather than by a diffusion coefficient, i.e. a scalar quantity. As a consequence of the microscopic size of the crystallites, only recently have PFG-NMR measurements of diffusion anisotropy in zeolites become possible. The measurements have been carried out in two different ways: (i) by introducing the zeolite crystallites into an array of parallel capillaries with their longitudinal extension preferentially parallel to the capillary axes; and (ii) by analyzing the shape of the signal decay function.[56,57] In both cases, the measured diffusivities (methane and ethane in zeolite ZSM-5) were found to be in satisfactory agreement with the results of molecular dynamics simulations.[53,54]

As a noninvasive method, PFG-NMR represents an excellent tool for the in situ observation of molecular transportation under reaction conditions. As an example, Figure 4 represents the results of Fourier transform PFG-NMR measurements[56,58] of the time dependence of the diffusivities of the reactant and the product molecules during the conversion of cyclopropane to propene on zeolite NaX.[59] In addition, Figure 4 also shows the relative amount of both species as determined by analyzing the free induction decay. Comparing the intrinsic reactivities with the rather high intracrystalline mobilities, any essential influence of molecular transport on the rates of molecular conversion in flow reactors may be excluded. Using zeolite crystallites of different size, this prediction could in fact be confirmed by direct measurement in flow reactors.[59]

Since the first applications of PFG-NMR to study intracrystalline diffusion in zeolites, repeatedly dramatic differences between these data and the results of conventional sorption measurements have been stated.[17,40] This discrepancy led to a critical reexamination of the earlier sorption data, which revealed that in many cases the effects of external heat- and mass-transfer resistances in limiting the adsorption–desorption rates were far greater than originally assumed, and the discrepancy with the NMR data could be explained on this

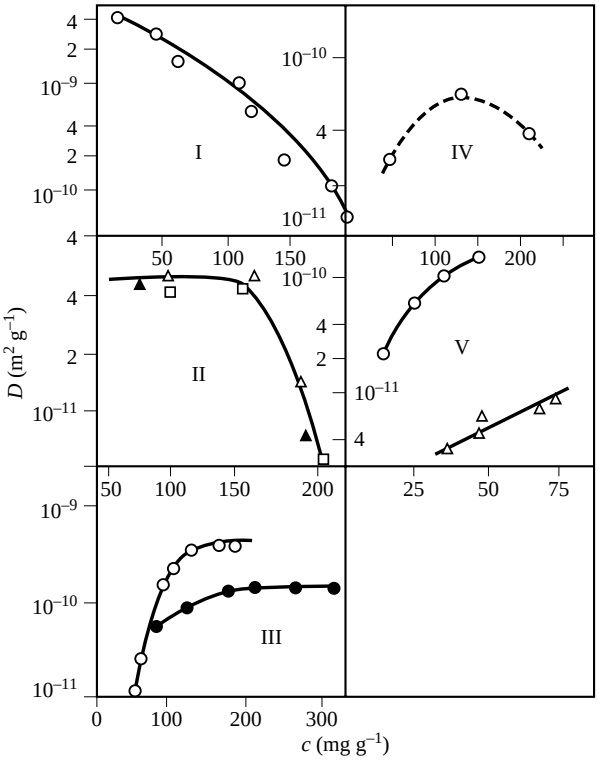

Figure 3 Patterns of the concentration dependence of intracrystalline diffusivities. I, *n*-Hexane in NaX at 358 K. II, (△) *ortho*-, (□) *meta*-, and (▲) *para*-xylenes in NaX at 393 K. III, Ammonia (○) and water (●) in NaX at 298 K. IV, Acetonitrile in NaX at 393 K. V, (○) Ethane at 173 K and (△) propane at 413 K in NaCaA[40]

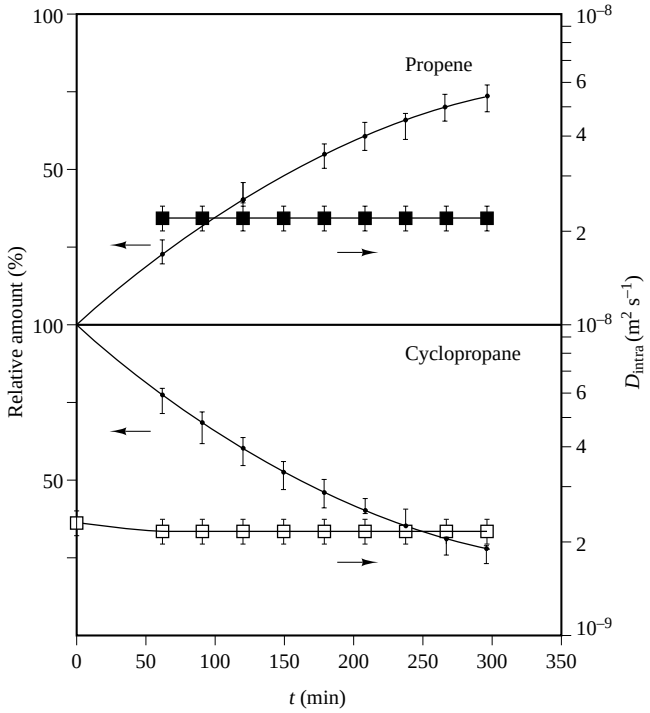

Figure 4 Time dependence of the relative amounts of cyclopropane and propene during the conversion of cyclopropane to propene in NaX and their self-diffusion coefficients at 473 K[59]

basis. Moreover, as the PFG-NMR data are in satisfactory agreement with the results of quasielastic neutron scattering experiments[60] and with molecular dynamics simulations,[53,54] there should be no doubt that PFG-NMR yields the correct values for the intracrystalline mobility under equilibrium conditions.

A comparison with the results of adsorption–desorption measurements is complicated by the fact that the latter experiments are carried out under nonequilibrium conditions, yielding transport- rather than self-diffusivities.[40] However, being based on the same elementary processes, i.e. the stochastic movement of the individual molecules, at least for small concentrations, agreement between the transport- and self-diffusivities should be expected. For A-type zeolites this agreement has in fact repeatedly been confirmed.[40,61,62] Remaining differences, mainly observed for zeolites NaX and ZSM-5, are difficult to explain. Following the adsorption process of *n*-hexane in beds of zeolites NaX by space- and time-resolved PFG-NMR, the molecular mobility of the *n*-hexane molecules immediately after adsorption was found to coincide with that at equilibrium.[63] Therefore, as a possible explanation of this discrepancy, it must also be excluded that the diffusivities as obtained by PFG-NMR with sealed samples are only attained after some period of relaxation within the adsorbate–adsorbent system. It is one of the current tasks of zeolite research to decide whether the remaining differences are real indications of different transport properties under equilibrium and nonequilibrium conditions, or whether they are mere consequences of not yet revealed shortcomings in the experimental procedure.

6 RELATED ARTICLES

Anisotropically Restricted Diffusion in MRI; Brownian Motion and Correlation Times; Complex Radiofrequency Pulses; Diffusion: Clinical Utility of MRI Studies; Diffusion and Flow in Fluids; Diffusion Measurements by Magnetic Field Gradient Methods; Diffusion and Perfusion in MRI; Diffusion in Rare Gas Solids; Imaging Techniques for Solids and Quasi-Solids; Intercalation Compounds; Microporous Materials and Xenon-129 NMR; Molecular Motions: T_1 Frequency Dispersion in Biological Systems; Molecular Sieves: Crystalline Systems; Oil Reservoir Rocks Examined by MRI; Reactions in Zeolites.

7 REFERENCES

1. H. Pfeifer, *NMR Basic Principles Prog.*, 1994, **31**, 31.
2. G. Ertl, *Langmuir*, 1987, **3**, 4.
3. H. Pfeifer and H. Ernst, *Ann. Rep. NMR Spectrosc.*, in press.
4. D. Avnir (ed.), *The Fractal Approach to Heterogeneous Chemistry*, Wiley, New York, 1989.
5. C. Förste, J. Kärger, H. Pfeifer, L. Riekert, M. Bülow, and A. Zikánová, *J. Chem. Soc., Faraday Trans.*, 1990, **86**, 881.
6. C. Förste, J. Kärger, and H. Pfeifer, *J. Am. Chem. Soc.*, 1990, **112**, 7.
7. P. Mansfield and P. G. Morris, *NMR Imaging in Biomedicine*, Academic, New York, 1982.
8. W. Heink, J. Kärger, and H. Pfeifer, *Chem. Eng. Sci.*, 1978, **33**, 1019.
9. G. Guillot, G. Kassab, J. P. Hulin, and P. Rigord, *J. Phys. D: Appl. Phys.*, 1991, **24**, 763.
10. G. C. Borcia, R. J. S. Brown, P. Fantazzini, J. Gore, P. Mansfield, B. Maraviglia, E. Mesini, and L. Sgubini (eds.), *Magn. Reson. Imaging*, 1991, 9(5).
11. G. C. Borgia, P. Fantazzini, J. C. Gore, M. E. Smith, and J. H. Strange (eds), *Magn. Reson. Imaging*, 1994, 12(2).
12. J. Fraissard and T. Ito, *Zeolites*, 1988, **8**, 350.
13. J. Kärger, H. Pfeifer, T. Wutscherk, S. Ernst, and J. Weitkamp, *J. Phys. Chem.*, 1992, **96**, 5059.
14. B. F. Chmelka, J. V. Gillis, E. E. Petersen, and C. J. Radke, *AIChE J.*, 1990, **36**, 1562.
15. N. Bansal and C. Dybowski, *J. Magn. Reson.*, 1990, **89**, 21.
16. H. Pfeifer, in *NATO ASI Ser. B*, 1991, **265**, 151.
17. H. Pfeifer, *Phys. Rep.*, 1976, **26**, 293.
18. H. W. Spiess, *NMR Basic Principles Prog.*, 1978, **15**, 55.
19. B. Zibrowius, J. Caro, and H. Pfeifer, *J. Chem. Soc., Faraday Trans. 1*, 1988, **84**, 2347.
20. B. Boddenberg and R. Burmeister, *Zeolites*, 1988, **8**, **480**, 488.
21. H. W. Spiess, *Chem. Phys.*, 1974, **6**, 217.
22. B. Zibrowius, M. Bülow, and H. Pfeifer, *Chem. Phys. Lett.*, 1985, **120**, 420.
23. R. Kimmich, W. Nusser, and T. Gneiting, *Colloid. Surf.*, 1990, **45**, 283.
24. F. Noack, *Prog. NMR Spectrosc.*, 1986, **18**, 17.
25. R. Kimmich, T. Gneiting, K. Kotitschke, and G. Schnur, *Biophys. J.*, 1990, **58**, 1183.
26. D. Michel and H. Pfeifer, *Z. Naturforsch., Teil a*, 1965, **20**, 220.
27. K. R. Brownstein and C. E. Tarr, *Phys. Rev. A*, 1979, **19**, 2446.
28. G. C. Borgia, R. J. S. Brown, P. Fantazzini, and E. Mesini, *Nuov. Cim. D*, 1993, **15**, 1025.
29. B. F. Chmelka, D. Raftery, A. V. McCormick, L. C. de Menorval, R. D. Levine, and A. Pines, *Phys. Rev. Lett.*, 1991, **66**, 580.
30. R. G. Larsen, J. Shore, K. Schmidt-Rohr, L. Emsley, H. Long, A. Pines, M. Janicke, and B. F. Chmelka, *Chem. Phys. Lett.*, 1993, **214**, 220.
31. J. Kärger and W. Heink, *J. Magn. Reson.*, 1983, **51**, 1.
32. D. G. Cory and A. N. Garroway, *Magn. Reson. Med.*, 1990, **14**, 435.
33. P. T. Callaghan, *Principles of Nuclear Magnetic Resonance Microscopy*, Clarendon, Oxford, 1991.
34. G. Fleischer and F. Fujara, *NMR Basic Principles Prog.*, 1994, **30**, 159.
35. R. M. Cotts, *Nature*, 1991, **351**, 443.
36. P. Stilbs, *Prog. NMR Spectrosc.*, 1986, **19**, 1.
37. J. Kärger, H. Pfeifer, and W. Heink, *Adv. Magn. Reson.*, 1988, **12**, 1.
38. J. Kärger, *Adv. Colloid Interface Sci.*, 1985, **23**, 129.
39. M. Silva-Crawford, B. C. Gerstein, A.-L. Kuo, and C. G. Wade, *J. Am. Chem. Soc.*, 1980, **102**, 3728.
40. J. Kärger and D. M. Ruthven, *Diffusion in Zeolites and Other Microporous Solids*, Wiley, New York, 1992.
41. J. Kärger, H. Pfeifer, and G. Vojta, *Phys. Rev. A*, 1988, **37**, 4514.
42. R. Kimmich, W. Unrath, G. Schnur, and E. Rommel, *J. Magn. Reson.*, 1991, **91**, 136.
43. P. T. Callaghan and A. Coy, *Phys. Rev. Lett.*, 1992, **68**, 3176.
44. M. Appel, G. Fleischer, J. Kärger, and F. Fujara, *Macromolecules*, 1994, **27**, 4274.
45. J. Kärger and H. Spindler, *J. Am. Chem. Soc.*, 1991, **113**, 7571.

46. J. Kärger, *Phys. Rev. A*, 1992, **45**, 4173; *Phys. Rev. E*, 1993, **47**, 1427.
47. J. Kärger, M. Petzold, H. Pfeifer, S. Ernst, and J. Weitkamp, *J. Catal.*, 1992, **136**, 283.
48. R. von Ballmoos, J. B. Higgins, and M. H. J. Treacy (eds.), *Proceedings of the 9th International Zeolite Conference, Montreal 1992*, Butterworth-Heinemann, Boston, MA, 1993.
49. J. Kärger and H. Pfeifer, in *NMR and Catalysis*, eds. A. Pines and A. Bell, Marcel Dekker, New York, 1994, p. 69.
50. S. Frey, J. Kärger, H. Pfeifer, and P. Walther, *J. Magn. Reson.*, 1988, **79**, 336.
51. P. T. Callaghan, A. Coy, D. MacGowan, K. J. Packer, and F. O. Zelaya, *Nature*, 1991, **351**, 467.
52. P. T. Callaghan, A. Coy, T. P. J. Halpin, D. MacGowan, K. J. Packer, and F. O. Zelaya, *J. Chem. Phys.*, 1992, **97**, 651.
53. P. L. June, A. T. Bell, and D. N. Theodorou, *J. Phys. Chem.*, 1990, **94**, **1508**, 8232.
54. S. D. Picket, A. K. Nowak, J. M. Thomas, B. K. Peterson, J. F. P. Swift, A. K. Cheetham, C. J. J. den Ouden, B. Smit, and M. F. M. Post, *J. Phys. Chem.*, 1990, **94**, 1233; 1992, **95**, 848.
55. S. Fritzsche, R. Haberlandt, J. Kärger, H. Pfeifer, and K. Heinzinger, *Chem. Phys.*, 1993, **174**, 229.
56. U. Hong, J. Kärger, R. Kramer, H. Pfeifer, G. Seiffert, U. Müller, K. K. Unger, H.-B. Lück, and T. Ito, *Zeolites*, 1991, **11**, 816.
57. D. Fenzke and J. Kärger, *Z. Phys. D. Atom. Mol. Cluster.*, 1993, **25**, 345.
58. U. Hong, J. Kärger, and H. Pfeifer, *J. Am. Chem. Soc.*, 1991, **113**, 4812.
59. U. Hong, J. Kärger, B. Hunger, N. N. Feoktistova, and S. P. Zhdanov, *J. Catal.*, 1992, **137**, 243.
60. H. Jobic, M. Bée, J. Kärger, H. Pfeifer, and J. Caro, *J. Chem. Soc., Chem. Commun.*, **1990**, 341.
61. D. M. Ruthven, *Zeolites*, 1993, **13**, 594.
62. F. Stallmach, J. Kärger, and H. Pfeifer, *J. Magn. Reson. A*, 1993, **102**, 270.
63. J. Kärger, G. Seiffert, and F. Stallmach, *J. Magn. Reson. A*, 1993, **102**, 327.

Acknowledgments

The development of PFG-NMR for the study of molecular diffusion in porous media, particularly in zeolites, has profited significantly from the continuous engagement of Harry Pfeifer, one of the pioneers of NMR in Central Europe (see ***Pfeifer, Harry: Leipzig, Summer 1951***). I have had the privilege of personal contact and many stimulating discussions with him over many years, and I would like to thank him for his continuous help and encouragement and for countless discussions

Biographical Sketch

Jörg Kärger. *b* 1943. Ph.D. (supervisor Harry Pfeifer), 1970; Habilitation, Leipzig University, 1978. Lecturer, 1982–89 Professor of Experimental Physics, 1989–present, Leipzig University. Approx. 200 publications, including *Diffusion in Zeolites and Other Microporous Solids* (with Douglas M. Ruthven). Research interests include various topics within the field of molecular dynamics at interfaces, in particular in adsorbate–adsorbent systems.

Diffusion in Rare Gas Solids

Richard E. Norberg
Washington University, St. Louis, MO, USA

1	Introduction	1
2	Neon	1
3	Krypton	2
4	Xenon	3
5	Self-Diffusion in Rare Gas Solids	4
6	Hydrogen in Rare Gas Solids	5
7	Related Articles	6
8	References	6

1 INTRODUCTION

NMR measurements of diffusion in rare gas solids offer the opportunity for comparisons[1,2] with the predictions of theory, with tracer results, and with beautiful non-NMR data on energies of vacancy formation. The employment of NMR studies of ultraslow motion[3–4] has produced diffusion data over ranges of nine orders of magnitude.

Pure neon, argon, krypton, and xenon form face-centered cubic (f.c.c.) solids. Self-diffusion proceeds via thermally-activated monovacancy diffusion, with a divacancy population negligible even at the melting point. The temperature variation of the diffusion coefficient follows an Arrhenius relationship with an activation energy which reflects the monovacancy formation and mobility energies:

$$E_{\mathrm{D}} = E_{\mathrm{F}} + E_{\mathrm{M}} \tag{1}$$

NMR measurements on diffusion in solid neon, krypton, and xenon have been reported on the nuclides ^{21}Ne, ^{83}Kr, ^{129}Xe, and ^{131}Xe. ^{129}Xe has spin $\frac{1}{2}$; ^{21}Ne and ^{131}Xe have spin $\frac{3}{2}$; and ^{83}Kr has spin $\frac{9}{2}$. NMR diffusion results have been inferred from the temperature variations of relaxation times T_1, T_2, and $T_{1\rho}$. The present article also touches upon the impurity diffusion of N_2, H_2, and HD in various rare gas solids. Solid helium is not included in the discussion.

Reported measurements[5–7] of lengths and lattice parameters have yielded vacancy formation energies E_{F}. In the case of ^{83}Kr, NMR experiments yield $E_{\mathrm{F}} - E_{\mathrm{M}}$ as well as E_{D}. For spin-$\frac{1}{2}$ ^{129}Xe diffusion parameters are inferred from motional narrowing of the dipolar broadened resonance line. For the quadrupolar nuclides ^{21}Ne, ^{83}Kr, and ^{131}Xe the linewidths include both dipolar and quadrupolar contributions. Intraspin cross relaxation effects[8] are crucial for understanding the diffusional effects in ^{83}Kr NMR.

2 NEON

Relaxation times T_1 and T_2 have been measured[9] for ^{21}Ne in warm polycrystalline solid neon, isotopically enriched to 51 atom.% ^{21}Ne. The open circles in Figure 1 show T_2 from spin echo envelopes and, below 18 K, from free induction decays. Above 19 K compound envelopes were observed for the spin echoes. The slower component, shown in Figure 1, was interpreted in terms of adiabatic narrowing of the motionally-resolved central ($-\frac{1}{2} \leftrightarrow \frac{1}{2}$) transition.

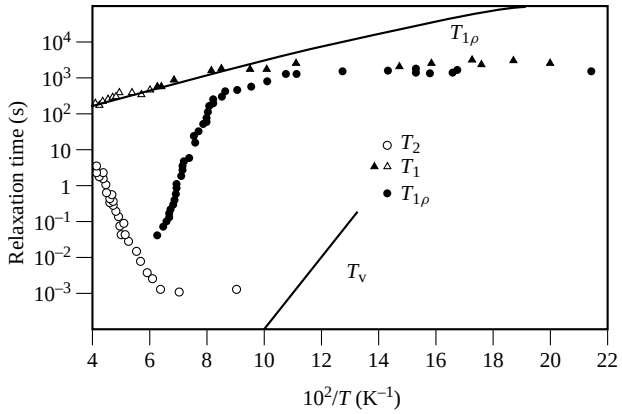

Figure 1 ^{21}Ne spin relaxation times in solid neon. The solid line indicates the temperature dependence anticipated for quadrupolar T_1. (Reproduced with permission from B. E. Sirovich and R. E. Norberg, *Phys. Rev. B.*, 1977, **15**, 5107)

In the adiabatic limit ($\omega_0\tau_{\mathrm{c}} \gg 1$) it is useful to employ the expression[10]

$$\left(\frac{1}{T_2}\right)^2 = \frac{4\ \ln\ 2}{\pi}\sigma^2 \tan^{-1}\left[\frac{\pi\tau_{\mathrm{c}}}{(4\ \ln\ 2)T_2}\right] \tag{2}$$

in which T_2 is the reciprocal of the halfwidth at half-maximum of the motionally-narrowed Lorentzian resonance line. For the well-narrowed line ($\tau_{\mathrm{c}}\sigma \ll 1$), equation (2) reduces to[11]

$$\frac{1}{T_2} = \sigma^2\tau_{\mathrm{c}} \tag{3}$$

The data were analyzed in terms of spin–spin relaxation in the case of monovacancy diffusion on an f.c.c. lattice.[12] In the weak-collision limit the result may be written

$$\frac{1}{T_2} = 0.9628\ f\alpha\tau \times 2^6/a_0^6 \tag{4}$$

Here f = 0.51 is the ^{21}Ne abundance, $\alpha = \frac{3}{2}\gamma\ ^4\hbar^2 I(I+1)$, and a_0 is the f.c.c. cube edge lattice parameter. Equation (4) corresponds to the expression

$$\frac{1}{T_2} = \tfrac{4}{3}\sigma_{\mathrm{d}}^2\tau \tag{5}$$

Here $\sigma_{\mathrm{d}}{}^2$ is the Van Vleck dipolar second moment. Equation (5) states that $1/T_2$ is just $\frac{4}{3}$ times the Anderson–Weiss[11] expression for adiabatic narrowing. The τ analysis used the expression

$$\frac{1}{T_2} = 0.85 \times \tfrac{4}{3}\sigma_{\mathrm{d}}^2\tau \tag{6}$$

where the factor 0.85 is a compromise between the 'like' coefficient 0.90 and the 'semi-like' coefficient 0.80 for quadrupolar modification of the central line.[13]

The coefficient of atomic self-diffusion based on T_2 for warm solid neon can be computed from τ by using the relationship $D = {a_0}^2/12\tau$ for diffusion in a f.c.c. lattice of cube edge a_0. The result i s $D = D_0 \exp(-E_D/T)$ with

$$D_0 = 0.15^{+0.20}_{-0.07}\ \mathrm{cm}^2\ \mathrm{s}^{-1}, \quad E_D = 475 \pm 19\ \mathrm{K} \qquad (7)$$

where the error estimates include both statistical errors and estimated errors on individual data points.

The study of neon diffusion was extended[14] to include ultraslow motions in the cold solid below 15.5 K. The solid circles in Figure 1 indicate $T_{1\rho}$ times measured upon adiabatic demagnetization in the rotating frame (ADRF) to zero $\boldsymbol{B}_1$.

In the strong-collision approximation the spin–lattice relaxation rate in the rotating frame may be written[15]

$$\frac{1}{T_{1\rho}} = \frac{1}{B_d^2 + B_q^2 + B_{eff}^2}\left(B_d^2 \frac{1-p_d}{\tau^d} + B_q^2 \frac{1-p_q}{\tau^q}\right) \qquad (8)$$

where τ^d and τ^q are, respectively, the characteristic times for significant fluctuations in the dipolar pair energy and the quadrupolar interaction. For uncorrelated self-diffusion $\tau^d = \frac{1}{2}\tau$, where τ is the characteristic time for the atomic diffusion. The dipolar order parameter p_d can be defined as the average dipolar energy per spin after an atomic jump divided by the average dipolar energy before a jump. Similarly, p_q is the ratio of average quadrupolar energies after and before a jump. If the field gradient sources of interest are stationary and the spins move randomly then equation (7) becomes[16]

$$\frac{1}{T_{1\rho}} = \frac{1}{B_d^2 + B_q^2 + B_{eff}^2}\frac{1}{\tau}[2(1-p_d)B_d^2 + (1-p_q)B_q^2] \qquad (9)$$

The inclusion of correlations among the motions of spins in the local environment of a particular spin corrects the factor $2(1 - p_d)$ to the powder average value 0.882 for vacancy diffusion on a f.c.c. lattice[17] in the case $\tau_v \ll {T_2}^{RL} \ll \tau \ll T_1$. Here τ_v is the characteristic time for vacancy motion, and equation (9) becomes

$$T_{1\rho} = \tau \frac{B_d^2 + B_q^2 + B_{eff}^2}{0.882 B_d^2 + (1-p_q)B_q^2} \qquad (10)$$

The ^{21}Ne $T_{1\rho}$ data indicated that the static electric field gradients arise from randomly distributed remote defects and that the correlation factor p_q is unity. Equation (10) and the $T_{1\rho}$ data in Figure 1 then produce the self-diffusion results shown in Figure 2 along with those inferred from the T_2 data and equation (6). These data extend over nine orders of magnitude and yield a single Arrhenius result for neon:[14]

$$D_0 = 0.15^{+0.03}_{-0.02}\,\mathrm{cm}^2\,\mathrm{s}^{-1}; \qquad E_D = 475 \pm 3\,\mathrm{K} \qquad (11)$$

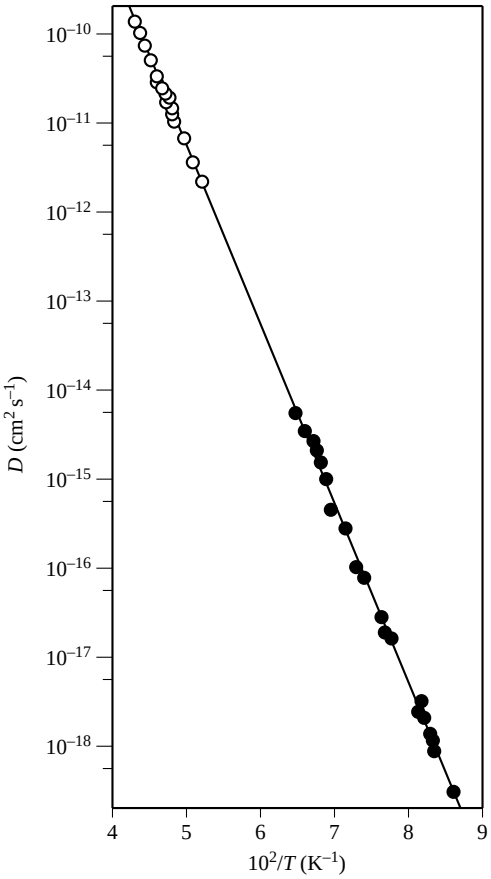

Figure 2 Coefficient of atomic self-diffusion in solid neon: (•) from $T_{1\rho}$; (○) from T_2. (Reproduced with permission from B. E. Sirovich and R. E. Norberg, *Phys. Rev. B.*, 1977, **15**, 5107)

3 KRYPTON

NMR measurements have been made[18,19] on ^{83}Kr in both krypton of normal 11.55% abundance and isotopically enriched to 73.1% ^{83}Kr. Low-frequency (1.55 MHz) measurements[19] were in a more homogeneous static field, which permitted ADRF measurements, even at normal abundance. Motional narrowing of the central $\frac{1}{2} \rightleftarrows -\frac{1}{2}$ line terminated at $T_2 = T_1/6.25$. The effects of intraspin cross relaxation[8] in the presence of a large first-order quadrupole interaction predict a $T_1/6.25$ factor as a limit for spin $\frac{9}{2}$ in the presence of an independent quadrupolar T_1 process such as the thermal phonon-quadrupole mechanism present in krypton. Inclusion of the intraspin cross-relaxation effect increases the useful range of motionally-narrowed central T_{2c} data by two orders of magnitude. The krypton diffusion experiments were extended[19] to much lower temperatures and to ultraslow motions by means of spin lock and ADRF $T_{1\rho}$ measurements on both the central and noncentral components of the ^{83}Kr line in solid krypton. Figure 3 summarizes some of the relaxation rates for a reasonably clean (35 ppm N_2) krypton sample.

Figure 3 shows the spin–lattice relaxation rates R_1 for the whole line, central and noncentral widths R_{2c} and R_{2q}, and central and noncentral rotating frame rates $R_{1\rho c}$(ADRF) and $R_{1\rho q}$ (ADRF). On the left of the figure, the motionally-narrowed R_{2c} rates limit in the warm solid at $6.25R_1$, where the $R_{1\rho q}$ (ADRF) rates limit at $4.0R_1$. Near $10^3/T$ = 11.8

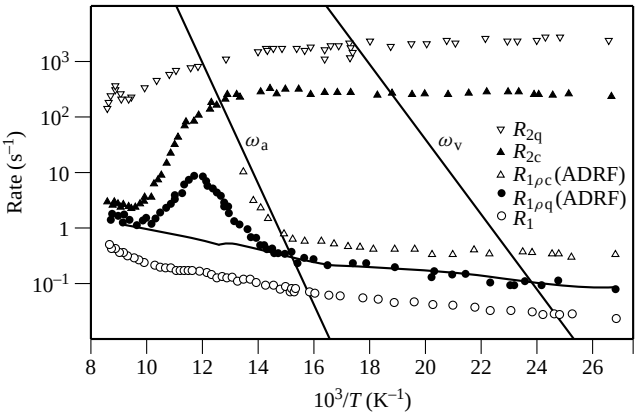

Figure 3 Summary of some of the ^{83}Kr nuclear spin relaxation rates observed in a solid krypton sample N (35 ppm N_2). Sloping lines indicate the deduced characteristic frequencies for atomic (ω_a) and vacancy (ω_v) motion. The curved solid line is $4R_1$. (Reproduced with permission from E. I. Madras and R. E. Norberg, *Phys. Rev. B.*, 1986, **33**, 5999)

the narrowing of R_{2c} shows a significant offset, which is examined in more detail in Figure 4. The offset is a ($I = \frac{9}{2}$) multiplicative factor of 5.96, predicted[8] for R_{2c} at the onset of the effect of quadrupolar intraspin cross relaxation on the motionally narrowed dipolar interaction as the atomic hopping frequency (ω_a in Figure 3) becomes larger than the residual static quadrupole frequency $\omega_q = R_{2q}$. The correction is essential in order to infer the correct $l = 1$, $m = 1$ decay rate $R_{1,1} = (T_2)^{-1}$. The inverted triangles in Figure 4 represent $6.25R_1$, demonstrating excellent agreement with the R_{2c} data near the melting point. Correct diffusional analysis of the R_{2c} results[19] involves: use of equation (2) in order to include data near $10^3/T = 13$; use of equation (5) for the case of the weak collision limit[12] of correlated motion on a f.c.c. lattice; and the intraspin cross relaxation 5.96 offset and $6.25R_1$ correction.[8] Combination of the analyzed temperature variations of R_{2c}, $R_{1\rho}$ (spin lock), and $R_{1\rho}$ (ADRF) yields the coefficient of atomic self-diffusion in clean solid krypton (Figure 5). Here, as in neon, the quadrupolar correlation factor p_q was found to be unity. The line in Figure 5 shows the least-squares fit which corresponds to

$$D_0 = 8.7^{+3.0}_{-2.2}\ \text{cm}^2\ \text{s}^{-1}, \quad E_d = 2612 \pm 25\ \text{K} \qquad (12)$$

A resolvable contribution to the temperature variation of R_{2q} between 80 and 108 K (Figure 3) provides a direct NMR measure[19] of the energy difference $E_M - E_F = 654 \pm 50$ K. This result, combined with equation (12), $E_D = E_M + E_F = 2612 \pm 25$ K, yields an NMR measure of the monovacancy mobility and formation energies in solid krypton:

$$E_M = 1633 \pm 38\ \text{K} \qquad (13)$$

$$E_F = 978 \pm 38\ \text{K} \qquad (14)$$

The E_F result is in reasonable agreement with the formation energies reported[1] by Losee and Simmons[5] (896 ± 100 K)

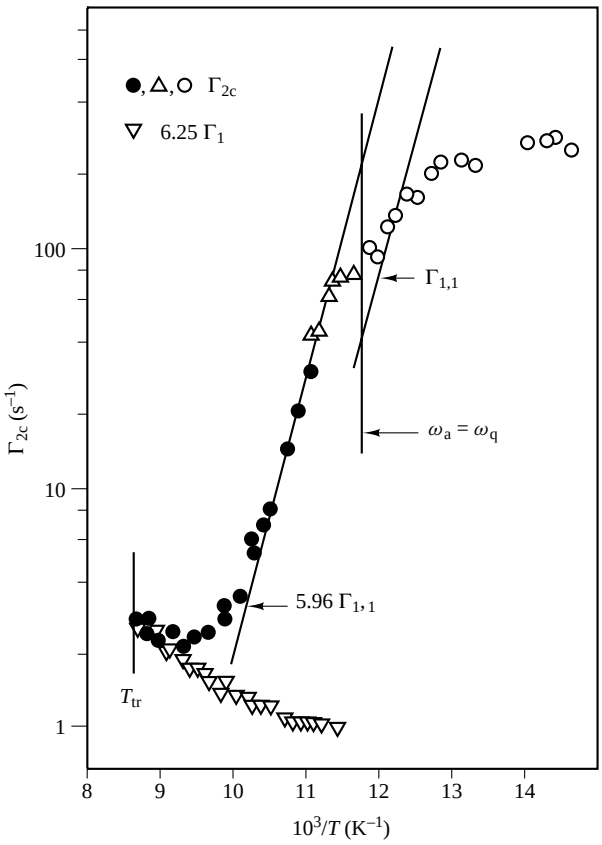

Figure 4 Krypton sample N central component rates R_{2c}. (●) Exponential spin echo rates. (△, ○) Exponential and Gaussian free induction decay rates. A multiplicative 5.96 offset occurs near $10^3/T = 11.8$ where ω_a passes through ω_q. (▽) Warm sample R_1 data of Figure 3, each multiplied by 6.25. (Reproduced with permission from E. I. Madras and R. E. Norberg, *Phys. Rev. B.*, 1986, **33**, 5999)

and by Korpium and Coufal[6] (956 ± 100 K). The NMR detection of vacancy motion occurs because, in the regime where the concentration of thermal vacancies ranges from 10^{-4} to 10^{-3}, an asymmetric R_{2q} relaxation peak occurs[20–22] as the characteristic vacancy hopping rate becomes equal to twice the strength of the ^{83}Kr–vacancy quadrupole interaction. In the Arrhenius approximation, the high temperature side of the R_{2q} peak has a slope $E_M - E_F$.

The addition of 190–4000 ppm N_2 impurity produced[19] increased rates R_1 and R_{2c}, to above 90 K. This additional relaxation arises from ^{83}Kr quadrupolar interaction with the electric field gradients of codiffusing impurities. The additional relaxation shows an Arrhenius behavior with an activation energy of 2214 K. The added impurities also increase the magnitude of quadrupolar $R_{1\rho}$ peaks near 90 K (Figure 3) and this additional relaxation is again consistent with 2214 K for the N_2 codiffusion.

4 XENON

Both ^{129}Xe and ^{131}Xe have been examined[23,24] in solid xenon of natural abundance (26.24 at.% ^{129}Xe and 21.24 at.% ^{131}Xe). The spin-$\frac{1}{2}$ ^{129}Xe dipolar-broadened line narrows exponentially over more than three orders of magnitude

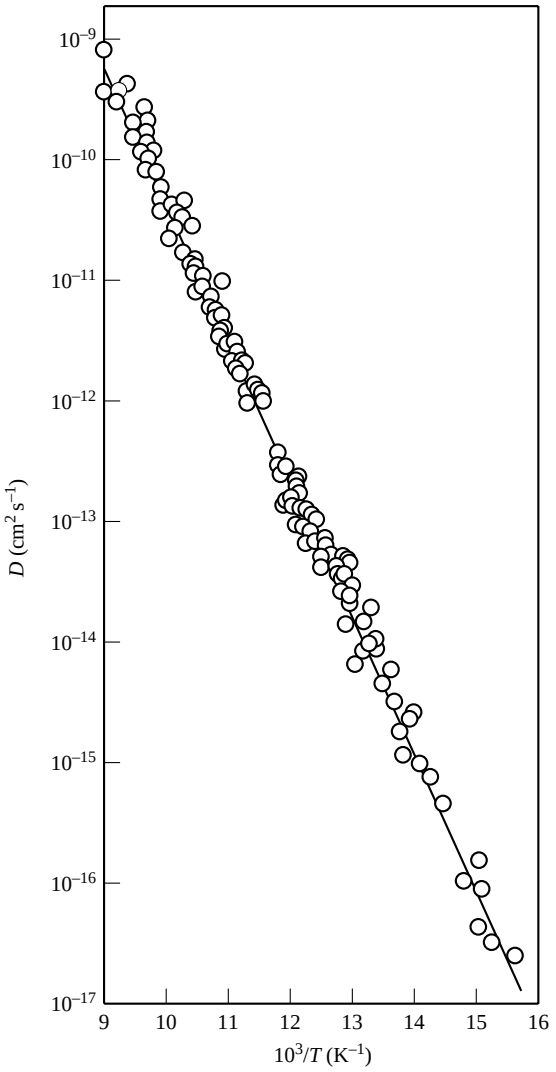

Figure 5 Coefficient of atomic self-diffusion in solid krypton. (Reproduced with permission from E. I. Madras and R. E. Norberg, *Phys. Rev. B.*, 1986, **33**, 5999)

between 117 K and the 161 K triple point. Figure 6 shows Carr–Purcell echo envelope T_2 values, which reflect exponential envelope decays above 125 K. Analysis of the adiabatic narrowing, including correlation effects and diffusion on a f.c.c. space lattice employs equations (4) and (5). The dipolar second moment arises 86.4% from like-spin 129–129 interaction and 13.5% from 129–131 unlike-spin interaction. The T_2 data in Figure 6 yield[18,23] the following xenon diffusion coefficients:

$$D_0 = 9.7^{+0.5}_{-0.3} \text{ cm}^2 \text{ s}^{-1},\ E_0 = 3724 \pm 25 \text{ K} \qquad (15)$$

It is notable in Figure 6 that there is no evident deviation from an Arrhenius-described monovacancy diffusion mechanism, even in the vicinity of the triple point.

Measurements on ^{131}Xe in xenon of natural abundance showed[24] a central transition line that was appreciably second-order quadrupole broadened by interaction with remote defects in the rigid lattice. The onset and progression of motional narrowing agreed with the ^{129}Xe diffusion coefficient results of equation (15).

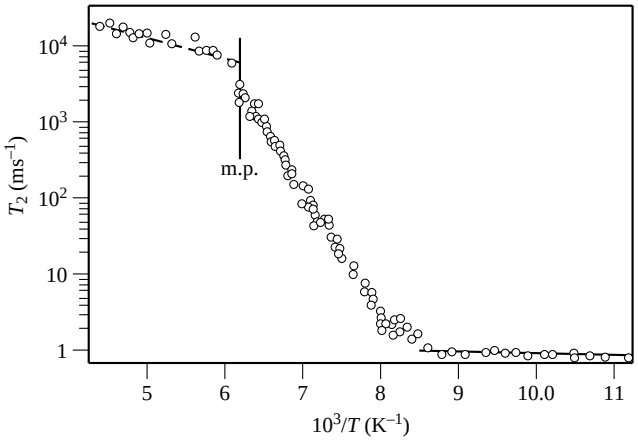

Figure 6 Spin–spin relaxation times for ^{129}Xe in liquid and solid xenon. (Reproduced with permission from W. M. Yen and R. E. Norberg, *Phys. Rev.*, 1963, **131**, 269)

5 SELF-DIFFUSION IN RARE GAS SOLIDS

Table 1 lists the best value NMR-determined self-diffusion coefficients for neon, krypton, and xenon. Radioactive tracer results also are listed for argon and krypton. The activation energies for self-diffusion are nearly twice the lattice sublimation energies. Thus, E_D in rare gas solids is nearly the same as the work required to remove a single atom from the lattice to infinity.

Application of the law of corresponding states to an examination of the properties of neon presents the interesting question of the effects of an appreciable deviation from classical behavior. Table 2 summarizes a set of molecular parameters ϵ and σ appropriate for a Lennard–Jones (6–12) interatomic two-body potential and the deBoer quantum parameter [$\Lambda^* = h/\sigma\ (me)^{1/2}$] for the rare gases.[25]

According to the classical law of corresponding states, the lattice cohesive energies and the activation energies for self-diffusion have the reduced forms $L_0^* = L_0/\epsilon$ and $E_D^* = E_D/\epsilon$, respectively. As Table 2 indicates, E_D^* and $2L_0^*$ vary by less than 5% among Ar, Kr, and Xe, but are some 20% smaller in Ne.

Bernardes[26] applied a quantum mechanical law of corresponding states to the description of the effects of zero point motion on the properties of rare gas solids. His results include a variation with the deBoer quantum parameter of the reduced

Table 1 Coefficients of Atomic Self-Diffusion for Rare Gas Solids

	D_0/cm^{2}s	E_D/K	$2L_0$/K
Ne	$0.15^{+0.03}_{-0.05}$	475 ± 3 (NMR)	451[a]
Ar	$0.20^{+0.035}_{-0.14}$[b]	1812 ± 75[b] (tracer)	1870[a]
Kr	3^{+4}_{-2}[b]	2415 ± 100[b] (tracer)	2683[a]
	$8.7^{+3.0}_{-2.2}$	2612 ± 25 (NMR)	
Xe	$9.7^{+0.5}_{-0.3}$	3724 ± 25 (NMR)	3853[a]

[a]Henry and Norberg[9] and Pollack.[25]
[b]Chadwick and Glyde.[1]

Table 2 Comparison of Reduced Corresponding States Parameters

	ϵ/K	σ/nm	Λ	E_D*	$E_D/2L_{00}$*	$2L_0$*	L_0*/L_{00}*
Ne	36.7[a]	0.2789[a]	0.577[c]	12.95 ± 0.5	0.752	12.29	0.713
Ar	120	0.3403	0.186	15.13 ± 0.6[b]	0.879	15.61	0.906
Kr	164	0.3638	0.102	14.72 ± 0.7[b]	0.855	16.36	0.950
				15.92 ± 0.15	0.925		
Xe	231	0.3961	0.0635	16.12 ± 0.1	0.936	16.68	0.969

[a]Data in the first three columns are from Henry and Norberg[9] and Pollack.[25] The last four columns are calculated from the data in Table 1.
[b]Chadwick and Glyde.[1]

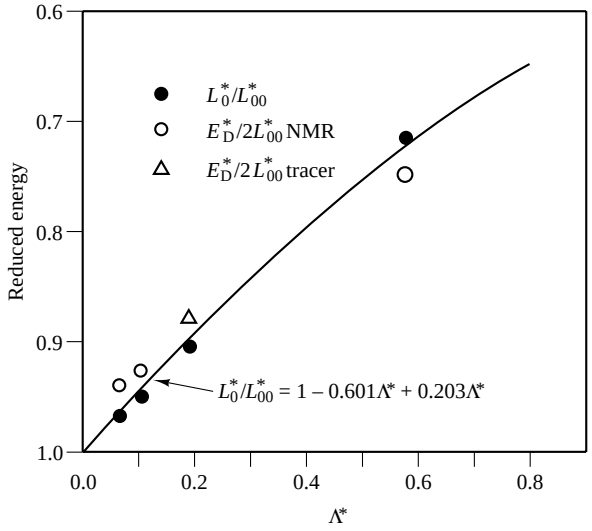

Figure 7 Variation of reduced activation energies as a function of the deBoer quantum parameter Λ^*. (•) Reduced latent heats of sublimation ($L^*/0/L^*/00$); (○, △) reduced diffusion energies ($E^*/D/2L^*/00$). (Modified from Henry and Norberg[9])

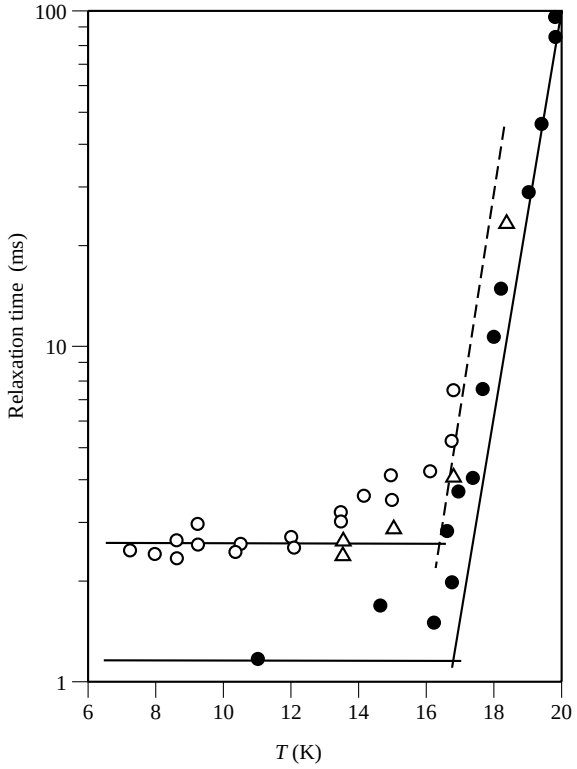

Figure 8 Temperature variation of the proton intermolecular T_2 for 52 ppm o-H_2 in solid neon. (○) FID; (△) spin echo; (•) T_2 results for ^{21}Ne from Figure 1 for comparison. (Reproduced with permission from M. S. Conradi, K. Luszczynski, and R. E. Norberg, *Phys. Rev.*, 1979, **20**, 2594)

lattice cohesive energies, according to the approximate expression

$$L_0^* = L_{00}^*(1 - 0.601\Lambda^* + 0.203\Lambda^{*^2}) \qquad (16)$$

where L_{00}* = 8.61 is the classical reduced cohesive energy for a close-packed solid having no zero-point energy. Table 2 includes the quantities E_D*/$2L_{00}$* and L_0*/L_{00}*, which are also plotted as a function of Λ* in Figure 7 (which corresponds to Figure 2 in Bernardes' paper[26]). The line indicated in Figure 7 corresponds to equation (16) and one sees that the quantum mechanical modification of the law of corresponding states accounts very well for the variation in the observed diffusion activation energies among the rare gas solids.

6 HYDROGEN IN RARE GAS SOLIDS

Conradi et al.[27] performed novel relaxation studies of dilute o-H_2 distributed in rare gas solids. The object of the experiments was to examine spin–lattice relaxation for the matrix-isolated o-H_2 molecules. In the course of the work it was found that the proton transverse rate T_2^{-1} contained both intermolecular and molecular–host contributions which were narrowed out as diffusion set into the warm rare gas solids. Figures 8 and 9 compare the motional narrowing of the o-H_2 proton line with narrowing of the ^{21}Ne and ^{83}Kr lines by self-diffusion in solid neon and krypton (Figures 1 and 3). Similar results were observed for o-H_2 in solid argon. In each case the proton narrowing corresponds to a codiffusion coefficient approximately equal to the host self-diffusion coefficient. Evidently translational motion of the molecular hydrogen requires the adjacent presence of a thermal monovacancy in the rare gas host.

A similar lattice control of molecular hydrogen diffusion has been observed for dilute molecular HD in solid argon and krypton. Deuteron and proton T_1 times have been measured[28–30] for these systems. Figure 10 shows HD deuteron T_1 data, which decrease with increasing temperature from very long times at low temperature (more than 10^3 s

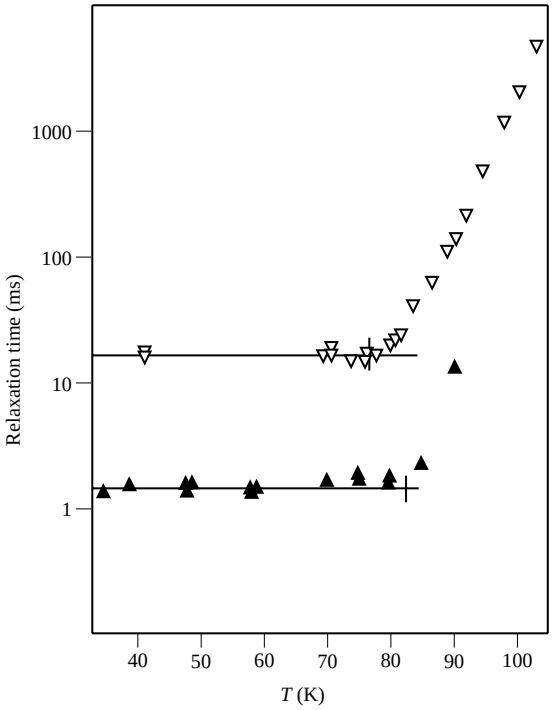

Figure 9 Motional narrowing of the proton line for ca. 300 ppm o-H_2 in warm solid krypton. (▲) Residual T_2 arising from H–^{83}Kr interactions; (▽) ^{83}Kr dipolar T_2 results (Figure 3). (Reproduced with permission from M. S. Conradi, K. Luszczynski, and R. E. Norberg, *Phys. Rev. B*, 1979, **20**, 2594)

below 10 K). The decrease is dominated by the Boltzmann factor for the increasing population of the HD $J = 1$ rotational state (128 K above the $J = 0$ ground state).[30] Above 40 K in argon (and 65 K in krypton) a more rapid T_1 decrease occurs as the onset of appreciable rare gas host self-diffusion permits diffusion of the HD molecules which then lose their matrix isolation and begin to experience additional spin–lattice relaxation via intermolecular interactions. As in the case of o-H_2, the warm-sample temperature relaxation time variations in Figure 10 are well fitted by the host self-diffusion coefficients.

7 RELATED ARTICLES

Hydrogen Molecules; Ortho–Para Hydrogen at Low Temperature.

8 REFERENCES

1. A. V. Chadwick and H. R. Glyde, in *Rare Gas Solids*, ed. M. L. Klein and J. A. Venables, Academic, London, 1977, Chap. 19
2. R. E. Norberg, in *Rare Gas Solids* (*Springer Tracts in Modern Physics Vol. 103*), ed. G. Höhler, Springer, Berlin, 1984.
3. C. P. Slichter and D. Ailion, *Phys. Rev.*, 1964, **135**, 1049.
4. D. C. Look and J. J. Lowe, *J. Chem. Phys.*, 1966, **44**, 2995.
5. D. L. Losee and R. O. Simmons, *Phys. Rev.*, 1968, **172**, 934.
6. P. Korpium and H. J. Coufal, *Phys. Stat. Solidi*, 1971, **62**, 187.
7. W. E. Schoknecht, Ph.D. Thesis, University of Illinois, 1971 (unpublished).
8. P. A. Fedders, *Phys. Rev. B*, 1972, **13**, 2768.

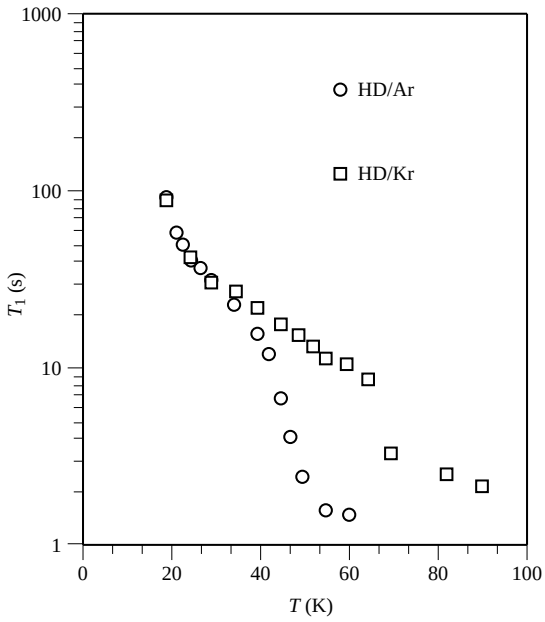

Figure 10 Deuteron T_1 for ca. 500 ppm HD in solid argon and krypton. The step decreases reflect intermolecular interactions which accompany the onset of host self-diffusion. (From Lyou[28])

9. R. Henry and R. E. Norberg, *Phys. Rev. B*, 1972, **6**, 1645.
10. R. Kubo and K. Tomita, *J. Phys. Soc. Jpn.*, 1954, **9**, 888.
11. R. W. Anderson and P. R. Weiss, *Rev. Mod. Phys.*, 1953, **25**, 269.
12. D. Wolf, *Phys. Rev. B*, 1974, **10**, 2710.
13. A. Abragam, *The Principles of Nuclear Magnetism*, Clarendon, Oxford, 1961, Chap. IV.
14. B. E. Sirovich and R. E. Norberg, *Phys. Rev. B*, 1977, **15**, 5107.
15. D. Wolf, *Phys. Rev. B*, 1976, **14**, 932.
16. T. J. Rowland and F. Y. Fradin, *Phys. Rev.*, 1969, **182**, 760.
17. D. Wolf, *Phys. Rev. B*, 1974, **10**, 2724.
18. D. F. Cowgill and R. E. Norberg, *Phys. Rev. B*, 1976, **13**, 2773.
19. E. I. Madaras and R. E. Norberg, *Phys. Rev. B*, 1986, **33**, 5999.
20. D. Wolf, *Spin Temperature and Nuclear Spin Relaxation in Matter*, Clarendon, Oxford, 1979.
21. M. Eisenstadt, *Phys. Rev.*, 1964, **133**, 191.
22. F. Reif, *Phys. Rev.*, 1955, **100**, 1597.
23. W. M. Yen and R. E. Norberg, *Phys. Rev.*, 1963, **131**, 269.
24. W. W. Warren and R. E. Norberg, *Phys. Rev.*, 1967, **154**, 277.
25. G. L. Pollack, *Rev. Mod. Phys.*, 1964, **36**, 748.
26. N. Bernardes, *Phys. Rev.*, 1960, **120**, 807.
27. M. S. Conradi, K. Luszczynski, and R. E. Norberg, *Phys. Rev. B*, 1979, **20**, 2594.
28. J. H. Lyou, Ph.D. Thesis, Washington University, St. Louis, 1991, (unpublished).
29. Z. Yan, Ph.D. Thesis, Washington University, St. Louis, 1994 (unpublished).
30. J. Ganem, P. A. Fedders, and R. E. Norberg, *Phys. Rev. B*, 1993, **47**, 2581.

Acknowledgments

It is a pleasure to acknowledge conversations with M. S. Conradi and P. A. Fedders. Continuing partial support has been provided by the National Science Foundation under DMR 93-05344.

Biographical Sketch

Richard E. Norberg. *b* 1922. B.A., 1943, Ph.D., 1951, Physics, University of Illinois, USA, where he was introduced to NMR by Charles Slichter and Erwin Hahn. Postdoctoral work, University of Illinois, 1951–54. Faculty in Physics, Washington University, 1954–present. Approx. 100 publications. Research specialties: NMR at high pressure, for physisorbed species, in amorphous semiconductors, in condensed rare gases, in metal–hydrogen systems, for matrix isolated H_2, HD, and D_2.

Diffusion in Solids

Robert M. Cotts
Cornell University, Ithaca, NY, USA

1	Introduction	1
2	Spin Relaxation and Diffusion	2
3	Direct Measurement of Diffusion Coefficients Using Magnetic Field Gradients	9
4	Applications of NMR to Diffusion in Solids	11
5	Further Reading	14
6	Related Articles	14
7	References	14

1 INTRODUCTION

Soon after the first observations[1,2] of nuclear magnetic resonance (NMR) in condensed matter it became clear that this new experiment had promising potential for the measurement and study of atomic transport. Two of the early questions asked about nuclear spin systems were: 'How does a spin system reach the temperature of the surrounding "lattice" ', and 'How long does it take to reach this thermal equilibrium?'. Here, the term 'lattice' is used to represent all the other degrees of freedom of the material, be it a solid or liquid, containing the spin system. In his phenomenological equations describing the interaction between the nuclear spins and applied static and time-dependent magnetic fields, Bloch[3] identified the spin–lattice, or longitudinal, relaxation time T_1, and the spin–spin, or transverse, relaxation time T_2. In the presence of a large constant magnetic field, the difference between the instantaneous nuclear spin system's magnetization and its equilibrium magnetization decays exponentially with the time contant T_1, while T_2 is the time constant for exponential decay of the magnitude of the coherent component of the magnetization transverse to the large field.

Only 2 years after the publications of discovery of NMR, the first comprehensive description of the relationship between the nuclear spin relaxation rates and atomic motion came in the definitive paper of Bloembergen, Purcell, and Pound,[4] which identified the relationship between the relaxation rates ${T_1}^{-1}$ and ${T_2}^{-1}$ and the modulation of the nuclear dipolar interactions caused by diffusive motion. They showed that each rate could be expressed by a linear combination of spectral density functions evaluated, for like nuclei, at the Larmor frequency and at twice that frequency. Each such function was expressed as the Fourier transform of pair correlation functions for interacting nuclear dipole moments. There are two distinct classifications of NMR experiments used to measure fundamental parameters of translational diffusion of atoms or molecules in solids; both are associated with spin system relaxation times.

The first technique is the measurement of the dependence of relaxation times upon temperature and the Larmor precession frequency. These measurements may be analyzed to yield the temperature dependence of the mean residence time τ_d of the diffusing entity on a lattice site. The second is the measurement at one temperature of the attenuation of the spin echo in the presence of applied magnetic field gradients, from which the tracer diffusion coefficient D is deduced. The first method relies on having good theoretical understanding of the relationship between the mean residence time, the Larmor frequency and the measured relaxation time. The second technique is simpler theoretically, since it relies only on the assumption that the solution to the diffusion equation holds for the spin system, and it yields the diffusion coefficient directly. A disadvantage of the second technique is that it is more difficult and limited experimentally. It also requires higher diffusivity than does the measurement of some relaxation times.

This use of NMR to measure D directly was suggested by Hahn.[5] Some kind of atomic or molecular label is needed to measure the diffusion coefficient. In Hahn's proposal, the atom's position along a particular direction was effectively labeled by making its Larmor frequency linearly dependent upon position through application of a uniform gradient of the magnitude of the applied magnetic field. With a very small gradient, the precession frequency of each spin is essentially constant. This constancy makes the spin echo[5,6] experiments possible with echo attenuation limited only by the decay due to T_2. When diffusion occurs in a sufficiently strong gradient, diffusive motion of each spin makes its precession frequency unpredictably time dependent, so that at the time of echo formation the accumulated disorder in the phases of spins in the transverse plane causes a spin echo attenuation given by[6]

$$S(t)/S(0) = \exp(-t/T_2 - \tfrac{1}{12}\gamma^2 G^2 t^3 D) \qquad (1)$$

where γ is the nuclear magnetogyric ratio, G is the magnitude of the applied magnetic field gradient, τ is the time between the first and second rf pulses, and $t = 2\tau$. Echo attenuation may be measured as a function of G, and the resulting data are analyzed to determine D. The measured D is the tracer diffusion coefficient because the effect of the applied magnetic field gradient is to produce a nearly zero gradient in the chemical potential of the atoms in the system. As noted by Carr and Purcell,[6] 'A more innocuous label would be difficult to imagine'.

In terms of the tracer correlation factor f_t ($0 < f_t \leq 1$) and the step length l, D for a crystalline solid is given by

$$D = f_t l^2/6\tau_d \qquad (2)$$

From independent determinations of τ_d (from relaxation times) and D, the product, $f_t l^2$, can be determined and used to test models for diffusion paths in the solid. For such detailed study, accurate theory for the relationships between relaxation rates and mean residence times are needed and have been calculated for common crystal structures. With these tools at hand, step lengths have been determined, and mixed monovacancy and divacancy diffusion mechanisms and effects of interactions between diffusing atoms have been identified; these topics are discussed below. Sophisticated pulsed gradient techniques have greatly extended the possibilities for measuring D in solids, and some of their applications are presented.

This review is presented in three parts, with the use of relaxation rates in Section 2, measurements of D in Section 3, and applications of these two in Section 4.

2 SPIN RELAXATION AND DIFFUSION

2.1 Introduction

Bloembergen, Purcell, and Pound[4] (BPP) identified the nuclear dipolar coupling as a strong interaction for inducing spin relaxation. The interaction between two nuclear moments having spins I and S,

$$\hat{\mathcal{H}}_{\mathrm{D}} = \frac{\hbar^2 \gamma_I \gamma_S}{r_{IS}^3}\left[\hat{\boldsymbol{I}}\cdot\hat{\boldsymbol{S}} - \frac{3(\hat{\boldsymbol{I}}\cdot\boldsymbol{r}_{IS})(\hat{\boldsymbol{S}}\cdot\boldsymbol{r}_{IS})}{r_{IS}^2}\right] \tag{3}$$

varies in time as the internuclear vector $\boldsymbol{r}_{\mathrm{IS}}$ changes because of the diffusive motion of one or both atoms. BPP described how that motion produced Fourier components of fluctuating dipolar fields at the precession frequencies and their sum and difference frequencies needed to induce spin transitions of one or both spins. Transitions in which both spins flip or one spin flips are driven by the raising and lowering operators $\hat{I}^+$, $\hat{I}^-$, S^+, or S^-, implicitly contained in equation (3). Therefore, Fourier components which drive spin lattice relaxation of the I spin system are ω_{0I}, $2\omega_{0I}$, $(\omega_{0I} + \omega_{0S})$, and $(\omega_{0I} - \omega_{0S})$, where ω_{0I} and ω_{0S} are the resonant frequencies of the I and S spin systems, respectively. General theory of spin system relaxation is available.[7,8]

For nuclei with $I > \frac{1}{2}$, the nuclear electric quadrupole interaction may, for the same reasons, be an effective relaxation mechanism. Here, atomic motion modulates the electric field gradient,[9] and in some circumstances, the quadrupolar mechanism is stronger than magnetic dipolar relaxation. However, for measuring parameters of diffusion, utilization of the dipolar mechanism is, when possible, usually preferred because of high uncertainties in the knowledge of electric field gradients in the solid of interest.

As noted above, for accurate analysis of relaxation data, what is needed are accurate calculations, specific to each crystal structure, that relate relaxation rates to a characteristic diffusion parameter, i.e. the mean residence time of the diffusing atom on a crystal site. Relaxation rate theories are calculated in the weak or the strong collision regime. In the strong collision regime, the dipolar correlation time τ_{d} is greater than the thermal mixing time τ_{m} for the spin system. τ_{m} is the characteristic time needed for the Zeeman spin reservoir to come to a common spin temperature with the dipole spin reservoir.[10] This process requires that the Zeeman field be smaller than characteristic dipolar fields, which is a relevant issue in the rotating coordinate system. The book by Goldman[11] treats the spin temperature concept in detail. Comments on strong collision experiments are reserved here until after the presentation of weak collision theory.

Weak collision theory applies when the Zeeman field is much larger than the characteristic dipolar field. In this regime $\tau_{\mathrm{d}} \ll \tau_{\mathrm{m}}$. This theory applies to many spin systems and temperatures where (depending upon the magnitude of γ) $\tau_{\mathrm{d}} < 10^{-5}$ s, but strong collision theory extends to slower motion where 10^{-5} s $< \tau_{\mathrm{d}} < 10^{-1}$ s.

2.2 Weak Collision Theory

The spectral density functions are defined by[7,8]

$$J^{(q)}(\omega) = 2\int_0^\infty G^{(q)}(t)\cos(\omega t)\,\mathrm{d}t \tag{4}$$

where $\boldsymbol{G}^{(\mathrm{q})}(t)$ is an ensemble average correlation function for the spatial coordinates of the dipolar interaction, and

$$G^{(q)}(t) = \sum_j \overline{F_{ij}^{(q)}(0)F_{ij}^{(q)*}(t)} \tag{5}$$

where the bar indicates the ensemble average. The functions $F_{ij}^{(q)}(t) = d_q Y_{2q}(\Omega_{ij})/r_{ij}^3$ are the dipolar interactions between spins i and j separated by $(r,\Omega)_{ij}$ at time t, and where $Y_{2q}(\Omega)$ are the normalized spherical harmonics having the z axis along the applied magnetic field, $\boldsymbol{B}_0$. The d factors are: ${d_0}^2 = (16\pi/5)$, $d_1^2 = (8\pi/15)$, and $d_2^2 = (32\pi/15)$. The spin operators have been incorporated in the expressions for the relaxation rates,[7,12,13] given here for identical (like) spins:

$$\frac{1}{T_1} = R_1 = \tfrac{3}{2}\gamma^4\hbar^2 I(I+1)[J^{(1)}(\omega_0) + J^{(2)}(2\omega_0)] \tag{6}$$

$$\frac{1}{T_{1\rho}} = R_{1\rho} = \tfrac{3}{8}\gamma^4\hbar^2 I(I+1) \times[J^{(0)}(2\omega_1) + 10J^{(1)}(\omega_0) + J^{(2)}(2\omega_0)] \tag{7}$$

$$\frac{1}{T_2} = R_2 = \tfrac{3}{8}\gamma^4\hbar^2 I(I+1) \times[J^{(0)}(0) + 10J^{(1)}(\omega_0) + J^{(2)}(2\omega_0)] \tag{8}$$

where $T_{1\rho}$ is the spin–lattice relaxation time in the rotating frame[12] and ω_1 is the precession frequency in the rotating field $\boldsymbol{B}_1$. The correlation functions are given by:[14]

$$G^{(q)}(t) = d_q^2 \sum_{\alpha,\beta} \frac{Y_{2q}^*(\Omega_\alpha)^*}{r_\alpha^3}\frac{Y_{2q}(\Omega_\beta)}{r_\beta^3}P(\boldsymbol{r}_\alpha, \boldsymbol{r}_\beta, t) \tag{9}$$

where $P(\boldsymbol{r}_\alpha, \boldsymbol{r}_\beta, t)$ is the probability of a pair of spins being separated by $\boldsymbol{r}_\beta$ at a time t given that they were separated by $\boldsymbol{r}_\alpha$ at time zero, and $P(\boldsymbol{r}_\alpha, \boldsymbol{r}_\beta, t)$ is determined by the diffusive motion in the solid. The correlation function decays with a characteristic time τ_{c}, which for translational diffusion should be approximately the mean residence time. The above expressions apply directly to a single crystal, but can also be averaged over all orientation angles for polycrystalline samples.

It is convenient to express the spherically averaged rates in terms of a single dimensionless spectral function $F(\omega\tau_{\mathrm{c}})$, which applies to any spin transition (parameter q). Equations (6)–(8) then become (for like spins only):

$$\frac{1}{T_1} = R_1 = \tfrac{2}{3}M_{II}^2\tau_{\mathrm{c}}[F(\omega_0\tau_{\mathrm{c}}) + 4F(2\omega_0\tau_{\mathrm{c}})] \tag{10}$$

$$\frac{1}{T_{1\rho}} = R_{1\rho} = \tfrac{1}{3}M_{II}^2\tau_c[3F(\omega_1\tau_c) + 5F(\omega_0\tau_c) + 2F(2\omega_0\tau_c)] \quad (11)$$

$$\frac{1}{T_2} = R_2 = \tfrac{1}{3}M_{II}^2\tau_c[3F(0) + 5F(\omega_0\tau_c) + 2F(2\omega_0\tau_c)] \quad (12)$$

where

$$M_{II}^2 = (\mu_0/4\pi)^2\tfrac{3}{5}\gamma^4\hbar^2 I(I+1)\sum_i r_i^{-6} \quad (13)$$

is, here, the dipole second moment for like spin interactions only.

2.2.1 The BPP Model

A simple assumption of an exponential decay was made by BPP for $\boldsymbol{G}^{(q)}(t)$:

$$G^{(q)}(t) = G^{(q)}(0)\exp\left(-\frac{t}{\tau_c}\right) \quad (14)$$

It follows that the spectral density has the form

$$J^{(q)}(\omega) = \frac{G^{(q)}(0)2\tau_c}{[1+(\omega\tau_c)^2]} \quad (15)$$

Torrey[15] pointed out that, for like spins, the *relative* motion of spins contributes to the decay of $G^{(q)}(t)$, and therefore $\tau_c = \tau_d/2$. The relatively simple BPP form of $J^{(q)}(\omega)$ has made it a very useful, though approximate, model for analysis of data. In the low frequency, or short correlation time, regime ($\omega\tau_d \ll 1$), $J^{(q)}(\omega)$ is essentially independent of frequency, and for like spins $J^{(q)}(\omega) \approx G^{(q)}(0)\tau_d[1-(\omega\tau_d/2)^2]$. At high frequencies, or long correlation times $\omega\tau_d \gg 1$, and again for like spins, $J^{(q)} \approx 4G^{(q)}(0)/(\omega^2\tau_d)$.

The low-frequency behavior of the BPP model is inconsistent with the solution to the diffusion equation when applied to calculation of $J^{(q)}(\omega)$, which for solids[16] or liquids[17] is

$$J^{(q)}(\omega) \approx J^{(q)}(0)[1 - c_1\omega^{1/2}] \quad (16)$$

where $J^{(q)}(0) \propto \tau_d$ and c_1 is a constant, different for solids than for liquids. In fact, c_1 specifically depends on D, so that in principle D could be determined from the frequency dependence of $J^{(q)}(\omega)$ in the short correlation time regime.[16] [For two-dimensional diffusion[16] there is a much stronger frequency dependence at $\omega\tau_d \ll 1$. Here, $J^{(q)}(\omega) \approx c_2\tau_d \ln(\omega)^{-1}$, where c_2 is dependent upon D and the structure of the solid.] In the very low and high frequency limits, accurate calculations show that $J^{(q)}(\omega)$ is proportional to τ_d and to $(\omega^2\tau_d)^{-1}$, respectively, as in the BPP model, but the constants of proportionality in the BPP model can be in error[16,18] by up to a factor of 3. For thermally activated diffusion $\tau_d = \tau_0 \exp(E_a/RT)$, where E_a is the activation energy (per mole) for diffusion. It is usually convenient experimentally to hold the NMR frequency constant and vary the temperature. In such an experiment a graph of the relaxation rate, R_1 versus $(1/T)$, would have slope $+(E_a/R)$ at very high temperatures and $-(E_a/R)$ at low temperatures. On such a graph the maximum of R_1 in the BPP model occurs for a system of like spins, at $(\omega\tau_d) = 1.23$. Although the BPP model is an approximation and not specific to any crystal lattice, it is highly regarded for its ease in applicability and its utility. It is seen in the next section that the errors noted above may be significantly reduced if it is assumed that for like spins $\tau_c = \tau_d$. The dependences of R_1, $R_{1\rho}$, and R_2, upon $\omega\tau_d$ in the BPP model are shown in Figure 1. On the low-temperature side of the peak in R_1, the transverse rate, $R_2 \propto \tau_d$. Using this relationship, Hultsch and Barnes[19] measured the pressure dependence of T_2 of ^{7}Li and ^{23}Na in solid lithium and sodium, respectively, and determined the activation volumes for self-diffusion in these solids.

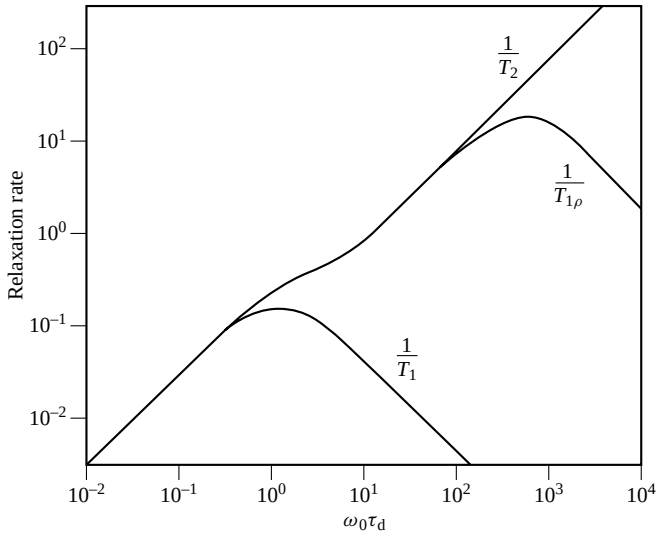

Figure 1 Relaxation rate (in arbitrary units) as a function of $\omega_0\tau_d$ for R_1, $R_{1\rho}$ and R_2 in the BPP model with $\omega_0 = 500\ \omega_1$

2.2.2 Lattice-Specific Models

In many solids, translational diffusion is enabled by vacancies, (empty lattice sites) in the solid. Only atoms next to a site vacancy can move. For most solids, vacancies must be thermally activated. Typically, vacancy concentrations are very small, increase strongly with temperature, but reach fractional concentrations of only about 10^{-4} to 10^{-3} near the melting point. When a vacancy encounters an atom the atom can move, but its motion during the encounter is not random in that it has a significant probability of jumping back to take the place of a vacancy immediately after it has exchanged sites with it. The effect of this correlated motion[20] on the NMR spectral density is distinguishable from an uncorrelated random walk process that would occur with low atom concentration on an otherwise empty lattice. The interstitialcy mechanism has also been considered in lattice-specific calculations.

High vacancy concentrations are characteristic of a number of systems, such as hydrogen in metals and fast ionic conductors. For example, in the α' phase of the VH_x, NbH_x, and TaH_x systems, hydrogen atoms occupy the tetrahedral interstitial sites and the solubility of hydrogen atoms in this phase ranges from $x = 0$ to about 0.7, depending on the host metal. Therefore, there is interest in knowing $J^{(q)}(\omega, \tau_d)$ for the full range of atomic concentration, c. Figure 2 shows a plot

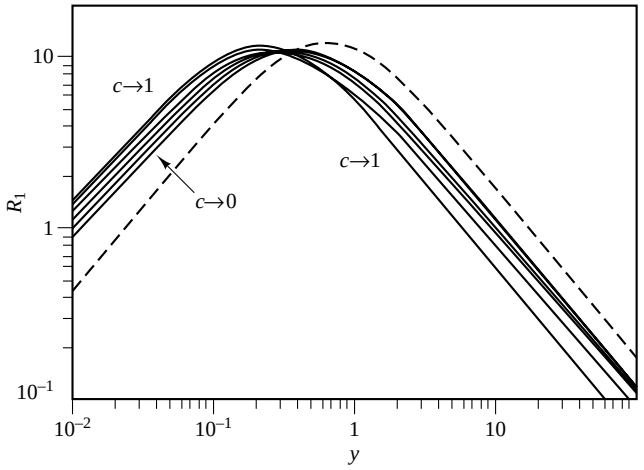

Figure 2 Angular average of the spin–lattice relaxation rate (in arbitrary units), divided by c, as a function of $y = \omega_0\tau_d/2$ for like spins on the simple cubic lattice. (- - - -) The BPP model. (——) Lattice-specific models for atom concentrations, from left to right: $c \rightarrow 1$, 0.99, 0.90, 0.70, 0.50, and $c \rightarrow 0$, respectively. (Reproduced by permission of IOP Publishing Ltd from C. A. Scholl, *J. Phys. C: Solid State Phys.*, 1988, **21**, 319)

of R_1 versus $(\omega\tau_d/2)$ calculated from lattice-specific models[14] for the simple cubic lattice. It can be seen in Figure 2 that letting $\tau_c = \tau_d$ in the BPP model moves the BPP curve a factor of 2 to the left and into better agreement with the others. Many calculations of $J^{(q)}(\omega, \tau_d)$ must be done numerically.

The relationships between relaxation rates and the mean residence time, τ_d have been calculated specifically for the more common crystal structures, for example: simple cubic (s.c.); body-centered cubic (b.c.c.); and face-centered cubic (f.c.c.). These relationships do indeed differ perceptibly from one lattice to another. It is known that the dependence of R_1 upon τ_d for a given lattice changes with the microscopic diffusion mechanism, but that these differences are small. Measurements of high precision on spin systems with very well understood relaxation mechanisms are needed before one can hope to use experimental data to rule out a contending microscopic mechanism.

The first lattice-specific relaxation rate theoretical calculations for R_1 and R_2 were made by Torrey[15] and Resing and Torrey.[21] In these calculations, nuclear dipoles were assumed to move by an uncorrelated random walk by nearest neighbor jumps through the lattice. The average of relaxation rates over all crystalline directions were approximated by the use of an isotropic diffusion model. Relaxation rates were calculated numerically for like spins only; their most accurate results are presented in Resing and Torrey[21] in tabular form for the b.c.c. and f.c.c. lattices. At fixed frequency, R_1 reaches a maximum at $\omega\tau_d = 1.06$ and 1.04 for the f.c.c. and b.c.c. lattices, respectively. Because of the assumption of uncorrelated motion, these results would be expected to be applicable at low concentrations of atoms on a crystal lattice, or sublattice.

Before it appeared in print, the Torrey model was applied to analyze data in the first comprehensive set of pulsed NMR experiments[22] measuring effects of diffusion on NMR relaxation rates in alkali metals. Holcomb and Norberg[22] convincingly demonstrated the applicability of NMR to the study of diffusion in solids. Their most extensive data were

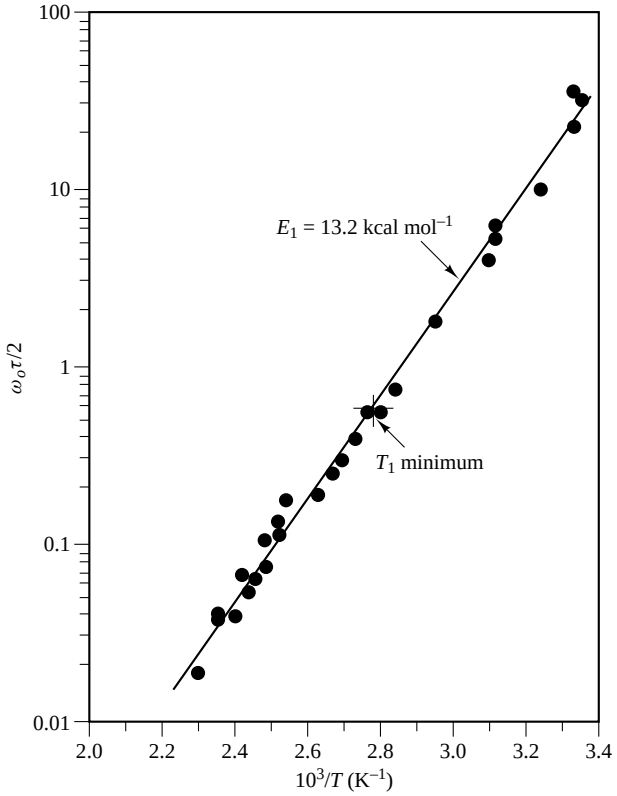

Figure 3 Plot of $\omega_0\tau/2$, where $\tau = \tau_d$, against $10^3/T$ for ^{7}Li in solid lithium. Values of τ were obtained from analysis of R_1 data at 3 MHz using the Torrey theory. The slope is 13.2 kcal mol^{-1} = 55.2 kJ mol^{-1}. (Reproduced by permission of The American Physical Society from D. F. Holcomb and R. E. Norberg, *Phys. Rev.*, 1955, **98**, 1074)

from ^{7}Li with temperature dependence of T_1 measured at 3, 6, 9, and 15 MHz. ^{7}Li data at 3 MHz were analyzed by trying both the BPP and the Torrey theory. The better fit to the data, shown in Figure 3 came from Torrey theory for the b.c.c. lattice, and from it they found that $E_a = 55.2 \pm 2$ kJ mol^{-1}.

Sholl[23,24] and Wolf[25] addressed the random walk problem without the approximation of isotropic diffusion. Both took the discrete nature of the lattice into account for both single and polycrystalline materials. The papers of Barton and Sholl,[26] provide good perspective on the random walk model and include tables that conveniently allow calculation of R_1, $R_{1\rho}$, or R_2, for any product of $\omega\tau_d$ in s.c., b.c.c., or f.c.c. lattices. These improved calculations have, for like spins in a polycrystalline sample, the maximum in R_1 occurring at $\omega\tau_d = 1.04$, 0.99, and 0.92 for f.c.c., b.c.c., and s.c. lattices, respectively.

While few real systems were expected to have atoms diffusing by random walk, these lattice-specific calculations were still important in the development of the theory. The shape of the R_1 versus τ_d curve for random walk fit the data better than the shape of the BPP curve did. A second improvement to the random walk came with the mean field model[27] which accounted for the effects of site blocking. That is, it excluded the possibility of having two atoms on the same site. The mean field theory is exact where a single jump for a pair of spins is relevant, in the low-temperature (high-frequency) limit, except where the fractional atom concentration is $c \rightarrow 1$. It is also exact in the dilute

limit as $c \rightarrow 0$, and the model was expected to be a good approximation for most concentrations except[26] as $c \rightarrow 1$. In the mean field model, for like spins in a polycrystalline sample, the maximum in R_1 occurs at $\omega\tau_d = 0.95$, 0.89, and 0.77 for f.c.c., b.c.c., and s.c. lattices, respectively.

2.2.3 Monovacancy Diffusion

Diffusion enabled by vacancies at extremely low concentration is known as 'monovacancy diffusion'. Wolf[28] provided the first relaxation rate theory applicable to this mechanism. At their characteristically low concentration, vacancies move with random walk and atoms are displaced only through encounters with vacancies. Eisenstadt and Redfield[29] identified the encounter model and its role in NMR relaxation in their study of diffusion in ionic crystals.

Wolf[30] calculated relaxation rates in the encounter model for both the weak and strong collision regimes, and he identified characteristic features of temperature-dependent experimental data that could, in principle, be applied to identify microscopic diffusion mechanisms. He emphasized the valuable information contained in the anisotropy of relaxation rates,[28,30,32] especially $R_{1\rho}$, for single crystal samples. For polycrystalline or single crystal samples, Wolf et al.[32] defined measures of the width and asymmetry of the relaxation peak that were dependent upon the mechanism of diffusion.

A comprehensive series of experiments were performed by Figueroa and Strange and reported with Wolf[32,33] on the NMR of ^{19}F in pure BaF_2 and crystals doped with K^+ to control F^- vacancy concentrations, or with La^+ to control number of interstitial F^-. This element of control made it possible to determine the activation energies for migration of F^- by vacancies (E_{mv} = 59 kJ mol^{-1}) and by interstitials (E_{mi} = 74 kJ mol^{-1}). From the pure BaF_2 data (Figure 4), the energy of formation of Frenkel anion pairs (E_f = 174 kJ mol^{-1}) was determined. Comparison with conductivity data[34] showed satisfactory agreement with diffusion parameters obtained by the two techniques. In their analysis of the NMR data, there was clear agreement with the encounter model but not the random walk model. Even though the data appear to have little scatter, especially considering the very high temperatures at which much of it was recorded, the difference between the interstitialcy and monovacancy mechanisms could not be distinguished.

Building upon previous calculations on relaxation rate theory,[16,35] MacGillivray and Sholl[36] improved the accuracy of the encounter model in the monovacancy limit to better than 4% and 1% in the low- and high-frequency regimes, respectively. Their paper contains numerical tables from which spectral densities $J^{(q)}(\omega, \tau_d)$ can conveniently be calculated for s.c., b.c.c., and f.c.c. lattices. From these, more accurate predictions of the width and asymmetry of relaxation rate peaks can be made. In the monovacancy limit, the peaks in the spin–lattice relaxation rate R_1 for like spins occur at[35] $\omega\tau_d = 0.57$, 0.51, and 0.42 for the f.c.c., b.c.c., and s.c. lattices, respectively. All these peaks in R_1 occur at significantly lower values of $\omega\tau_d$ than in the random walk or the mean field models. This means that if NMR data for R_1 or $R_{1\rho}$ from a solid having monovacancy diffusion were analyzed with the random walk, mean field, or the BPP models, the deduced τ_d at temperatures near maximum relaxation rates would be too large by at least 67% for the first two, and by more than 100% for the BPP model. But the error in the activation energy would probably be very small for the first two models because they give essentially the same shape for the relaxation peaks. However, since the peak is narrower in the BPP model, the activation energy derived from its use could be systematically too small by an amount that depends upon the range of temperature over which data were available (see Section 2.2.5).

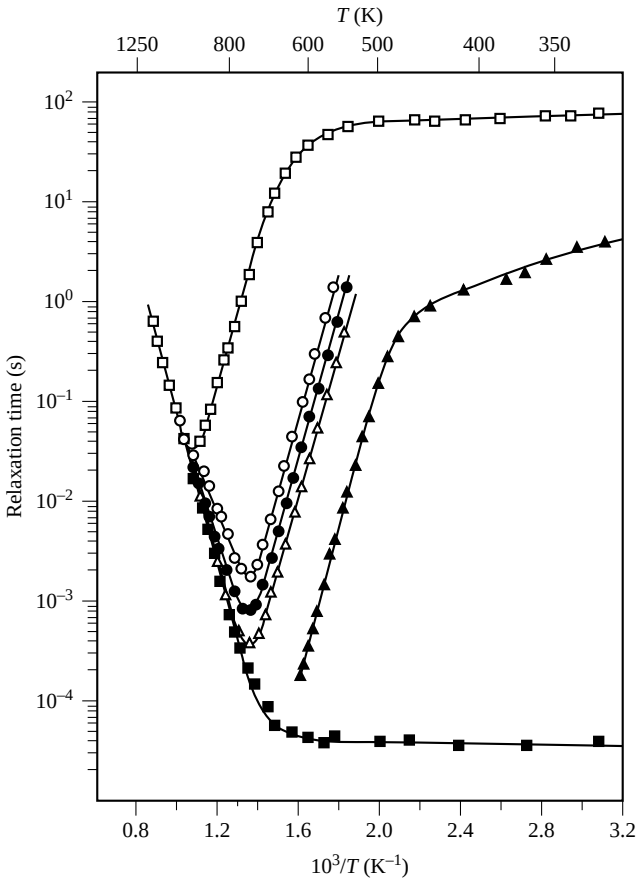

Figure 4 Relaxation times plotted against $10^3/T$ for ^{19}F in a pure BaF_2 single crystal. (□) T_1 taken at 10 MHz; (○, ●, △) $T_1\rho$, B_1 = 1.2×10^{-3} T, for three different crystal orientations; (▲) $T_{1\,Dipolar}$; (■) T_2. Details on crystal orientations may be found in Figreroa et al.[33] (Reproduced by permission of The American Physical Society from D. R. Figueroa, J. H. Strange, and D. Wolf, *Phys. Rev. B*, 1979, **19**, 148)

2.2.4 Models for Arbitrary Concentrations

In 1978, Fedders and Sankey[18] published their multiple scattering theory for the s.c. lattice using a reciprocal space formalism that can be applied to any concentration from c = 0 to nearly the monovacancy limit. They published their numerical results for the spectral densities in the low- and high-frequency limits for $c = 0$ to $c \rightarrow 1$ in steps of $\Delta c = 0.2$. While they gave no numerical tables for the spectral densities at arbitrary $\omega\tau_d$, they offered to supply tables of T_1 versus $\omega\tau_d$ upon request. It is pointed out that the lattice-specific relaxation function (Figure 5) approaches its high- and low-temperature limits more gradually than the BPP model does. Results for the f.c.c. lattice were reported in a later paper.[37] An interesting product of their formalism is a simple analytic

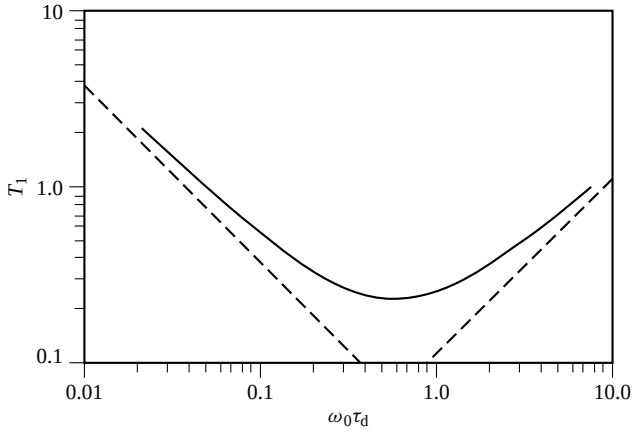

Figure 5 Angular average of spin–lattice relaxation time (in arbitrary units) for like spins on the s.c. lattice as a function of $\omega_0\tau_d$ calculated for the multiple scattering theory with atomic concentration c = 0.85. (- - - -) Asymptotic limits for $\omega_0\tau_d$ sufficiently large and small; they show how gradually the curve approaches each line. (Reproduced by permission of The American Physical Society from P. A. Fedders and O. F. Sankey, *Phys. Rev. B*, 1978, **18**, 5938)

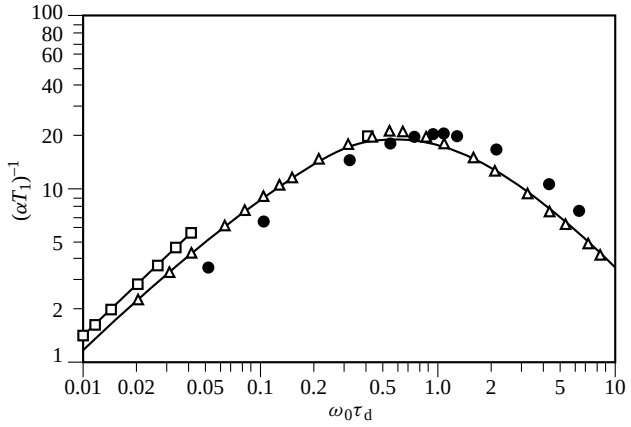

Figure 6 Angular average of spin–lattice relaxation rates as a function of $\omega_0\tau_d$, as calculated for like spins from simple cubic lattice theories. (□) Monovacancy encounter model;[10] (•) random walk model;[26] (△) vacancy concentration, c_v = 0.15.[18] (——) Monte Carlo for c_v = 0.15. (Reproduced by permission of The American Physical Society from L. D. Bustard, *Phys. Rev. B*, 1980, **22**, 1))

expression (accurate to about 1%) for the tracer correlation factor for atoms at concentration c in a simple cubic lattice:

$$f_t = 0.7882[1 + 0.1059(6c - 4)/(2 - c)] \qquad (17)$$

Fedders[38] also considered the effect that interactions between mobile atoms would have on the dipolar relaxation mechanism. These interactions are more likely to be important in systems having intermediate concentrations of diffusing atoms (with number of vacancies exceeding 10% of the number of lattice sites), as in metal hydrides. At short distances, the H–H interaction is repulsive, and in some metals, (for example, the group V transition metals) it is sufficiently strong to prevent simultaneous occupation of nearest neighbor interstitial sites. In the BPP model, one would be tempted to compensate for this interaction by simply removing nearest neighbor terms from the lattice sums contained in calculating the second moment of the hydrogen spin system. Doing this underestimates the dipolar interaction strength in the low-frequency (high-temperature) regime because here the motions of atoms further from each other than the nearest neighbor positions are the most effective in inducing spin transitions. For this motion short-range repulsive reactions are irrelevant.[38] On the high-frequency (low-temperature) side of the relaxation rate peak, single steps of atoms account for the decay of the pair correlation function and the reduction of the second moment is a good approximation[38] to the effects of the above repulsive interaction.

2.2.5 Monte Carlo Simulations

For any crystal structure, the pair correlation functions $G^{(q)}(t, \tau_d)$ can be computed numerically by simulating motion with the Monte Carlo technique. Bustard[39] established an s.c. lattice having 8000 sites (20 lattice constants on each side) and assumed periodic boundary conditions. Using the Monte Carlo technique he calculated numerically T_1^{-1} versus $\omega\tau_d$ for like spins on this s.c. lattice with vacancy concentrations, c_v = 3.75 × 10^{-4}, 0.15, 0.225, and 0.90, and published the appropriate tables for these concentrations. The Monte Carlo results are in substantial agreement with multiple scattering theory[18] for c_v = 0.15 (Figure 6) and with mean field theory[26] for c_v = 0.90. A difficulty in the Monte Carlo calculations is their inaccuracy in the low-frequency regime. Bustard[39] dealt with this by making a least-squares fit to $G^{(q)}(t, \tau_d)$ with a sum of decaying exponentials. This substitution facilitated making the Fourier transform to $J^{(q)}(\omega, \tau_d)$ but, since the long time tails of the exponential decay curves decay faster than the actual[16] $t^{-3/2}$ form of the tail of $\boldsymbol{G}^{(q)}(t, \tau_d)$, Bustard's Monte Carlo magnitudes of R_1 and $R_{1\rho}$ were too small where $\omega\tau_d \ll 1$. Nevertheless, the calculations were accurate enough for R_1 data to be analyzed at two NMR frequencies in order to obtain the temperature dependences of τ_d for ^{1}H in $TiH_{1.55}$ and $TiH_{1.70}$, where c_v = 0.225 and 0.15 on the interstitial s.c. lattice, respectively. These results for τ_d were combined with direct NMR measurements[40] of the diffusion coefficient D using the pulsed field gradient technique in the stimulated echo experiment, so that the mean squared jump length l^2 could be determined from $D = f_t l^2/(6\tau_d)$. It was found that hydrogen atoms jump to their nearest neighbor sites and not to their third nearest neighbor sites as had been found theoretically to be feasible.[41] Similar sets of experiments have recently been done for the isomorphic system ZrH_x,[42] analyzing R_1 data with more recent Monte Carlo calculations[43] for τ_d, and reaching the same conclusion.

Faux et al.[43] made Monte Carlo calculations for like spins moving according to the simple hopping model on f.c.c., b.c.c. and s.c. lattices. They fitted their numerical calculations of $J^{(q)}(\omega, \tau_d)$ in the low- and high-frequency limiting cases to the corresponding expected frequency dependences calculated earlier by Sholl.[16] This fitting also checked the accuracy of their Monte Carlo numerical procedures.[43] Numerical tables provide spectral densities and R_1 at many selected values of $\omega\tau_d$ for concentrations c approaching 0, 0.5, 0.7, 0.9, and 0.99. For $c \leq 0.4$, application of mean field theory might be an

acceptable and convenient approximation, since its difference from the Monte Carlo results is quite small.[43]

Because use of numerical tables is not as convenient as an analytic expression (such as that for the BPP model) in fitting experimental data, analytic approximations to the numerical tables given by Faux et al.[43] for intermediate concentrations, by Barton and Sholl[26] for mean field theory, and by MacGillivray and Sholl[36] for monovacancy diffusion have been developed by Sholl.[14] Faux et al.[43] and Sholl[14] provide an overview of the dependences of the relaxation rates upon atom concentration on the f.c.c., b.c.c., and s.c. lattices from $c \rightarrow 0$ to $c \rightarrow 1$. Figure 2 shows R_1 versus $\omega\tau_d/2$ for the full range of concentration on a simple cubic lattice plotted from the analytic expressions given by Sholl[14] and, for comparison, the BPP model. It is seen here, and is apparent for all cubic lattices, that the relaxation peak is narrower in the BPP model than for any concentration of the lattice-specific models. There is little concentration or model dependence in the maximum relaxation rates shown in Figure 2. For all the lattice-specific relaxation rate curves, their peaks are located at significantly lower values of $\omega\tau_d$ than for the BPP model (using $\tau_c = \tau_d/2$). It can be seen in Figure 7 that

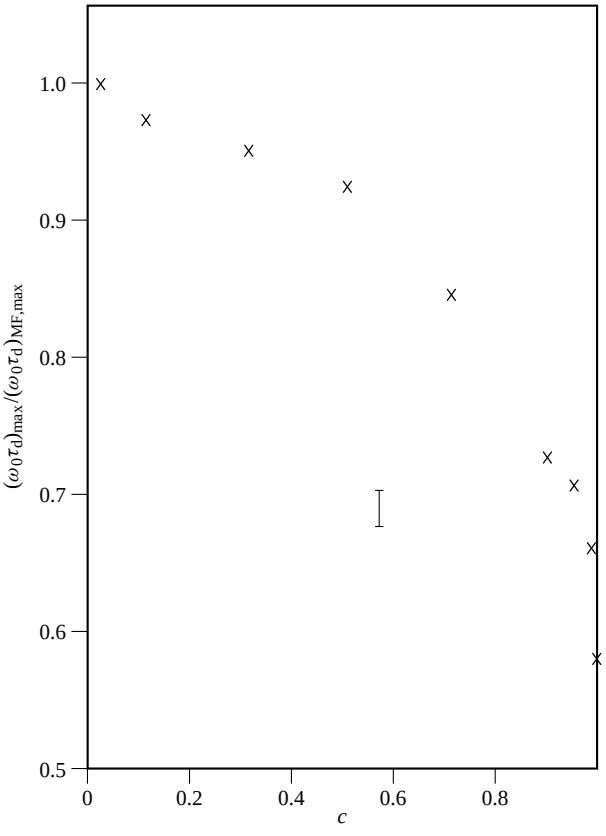

Figure 7 The value of $(\omega_0\tau_d)_{max}$ at the maximum of the R_1 versus $\omega_0\tau_d$ curve, plotted against atom concentration c for a polycrystalline b.c.c. lattice. The $(\omega_0\tau_d)_{max}$ values are normalized to the mean field theory value of 0.89. The point at $c = 1$ is for the monovacancy limit. The bar is the estimated error of the Monte Carlo results. The points for the f.c.c. and s.c. lattices lie above and below these points, respectively. On this graph, the points for the BPP model would be at 1.38, independent of c. (Reproduced by permission of IOP Publishing Ltd from D. A. Faux, D. K. Ross, and C. A. Sholl, *J. Phys. C: Solid State Phys.*, 1986, **19**, 4115)

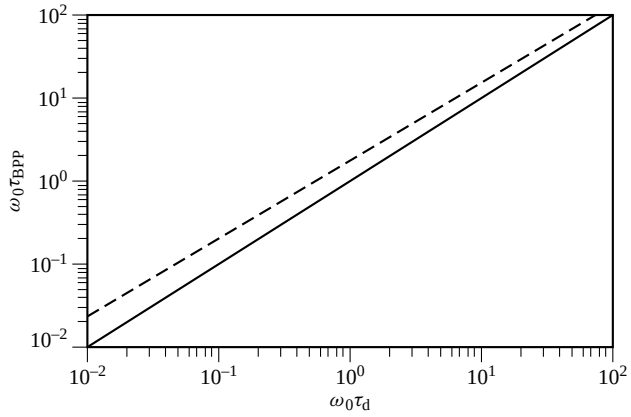

Figure 8 (- - - -) $\tau_d = \tau_{BPP}$, obtained by analyzing the R_1 relaxation results of the mean field theory using the BPP model. The horizontal axis shows τ_d in the mean field theory, and $(\omega_0\tau_d)_{max}$ is approximately centered. The solid line has the 'correct' slope. In the limits of large and small τ_d, the two lines are parallel, but over the region shown, the average slope of the dashed line is seen to be the smaller one. (Reproduced by permission of Sci-Tech Publications from C. A. Scholl, *Diffus. Defect Data, Solid State Data A, Defect Diffus. Forum*, 1993, **95–98**, 91)

the value of $\omega\tau_d$ at the peak decreases monotonically from the $c = 0$ limit to the $c = 1$ limit, with most of the change coming between $c = 0.5$ and $c = 1.0$. Because the value of $\omega\tau_d$ at the peak may be used to set the absolute values of the determinations of τ_d from experimental R_1 data, Figure 2 is useful for estimating the relative error resulting from application of an inappropriate model. The activation energies determined by application of the BPP model should be accurate if there are experimental data extending far into the wings of the relaxation peak. However, often the data are most accurate or only available near the peak where there is relatively less competition from other relaxation mechanisms. In this regime, the narrowness of the peak in the BPP model means that if it were used to analyze data obtained with a lattice-specific model, the resulting values of τ_d (shown as τ_{BPP} in Figure 8) might be interpreted in terms of an activation energy that would be too small. The resulting systematic error in E_a could exceed 10%.[44]

2.2.6 Quadrupolar Relaxation Mechanisms

As noted earlier, nuclear electric quadrupolar interactions may be an effective mechanism for spin relaxation where the interaction is modulated by atomic motion. Its utilization for the study of diffusion is more complicated than the dipolar mechanism because: (1) the electric field gradient (EFG) might be unknown; and (2) the spin system's recovery might be multiexponential. Lack of knowledge of the magnitude of the EFG might be acceptable, since it mainly affects the magnitude of spin–lattice relaxation rates, but it might have a temperature dependence strong enough to complicate data interpretation. The recovery through spin–lattice relaxation will be a single exponential[7] if the spin $I = 1$, if the motion is so fast that $\omega_0\tau_d \ll 1$, or if the dipolar interaction can maintain a spin temperature in the spin system.[10] Otherwise, the recovery is the sum of exponentials the number of which depends upon I.[45] If the spin system has a static quadrupole interaction,

establishment of a spin temperature is unlikely outside of thermal equilibrium with the lattice.

Without a static quadrupole interaction, it is likely that the dipolar interactions within the spin system can maintain a spin temperature during recovery. If so, the recovery occurs with the relaxation rate[7,10]

$$\frac{1}{T_{1Q}} = R_{1Q} = C_Q[J_Q^{(1)}(\omega_0) + J_Q^{(2)}(2\omega_0)] \tag{18}$$

where

$$C_Q = (9/160)(eQ/\hbar I)^2(2I+3)/(2I-1) \tag{19}$$

and the dynamic EFG is contained in the spectral densities, $J_Q{}^{(i)}(\omega_0)$. If the dynamic EFG is due to point charges, as in ionic compounds, the spectral densities will depend upon normalized spherical harmonics as do those for dipolar interactions. But the quadrupolar spectral densities may differ from the dipolar because of the potential importance of three particle correlation functions in many solids.[46] A difference in principle is that the $J_Q^{(2)}(2\omega_0)$ term in quadrupolar relaxation corresponds to $\Delta m = \pm 2$ of one spin, but in dipolar relaxation it means Δm = nbsp;±1 for a *pair* of spins If a spin temperature is not maintained during recovery, the recovery is a combination of I exponentials for integral spins and $(I + \frac{1}{2})$ exponentials for half-integral spins.[45] For a system with a static quadrupole interaction, the mix of exponentials is expected to be similar to that with no static interaction except that the spectral density functions would have arguments different from ω_0 and $2\omega_0$. The mix would depend upon the initial conditions of the spin system at the start of the recovery as established by the rf pulse sequence used and the energy levels to which it was applied. Gordon and Hoch[45] present results for excitation of the central transition only.

Because of the uncertainties of the magnitude of the dynamic quadrupole interactions, and because static interactions often occur in the less common crystal structures and in disordered solids, very few lattice-specific calculations are available for data analysis. The BPP model is often applied to obtain numerical values of diffusion parameters from these experiments.

2.2.7 Disordered Solids

In disordered solids, such as alloys or glasses, it would be expected that each atom of a given type would have different probabilities for jumping in each of its likely jump directions because of different barrier heights and vibration frequencies. Also, there would be a distribution of site binding energies, and, ignoring other possible effects of the disorder, it is still not obvious how these variations would affect the temperature and frequency dependences of NMR relaxation rates.

It is commonly found experimentally that at fixed frequency, when the relaxation rate due to translational diffusion has been plotted against T^{-1}, the characteristic peak in the rate has a lower magnitude slope on the low-temperature side than on the high-temperature side. In systems where, for example, the mean squared dipolar interaction is known through independent measurement of the second moment of the NMR line, the maximum relaxation rate may be reduced from the rate estimated from the known second moment. These characteristics may be emulated in the calculation of a mean relaxation rate for a distribution of activation energies where the dependence of R_1 upon E_a follows from its dependence upon τ_d and the Arrhenius relationship:

$$\tau_d = \tau_0 \exp(E_a/RT) \tag{20}$$

Assuming a distribution of activation energies, $g(E_a)$, the mean relaxation rate is

$$\left\langle \frac{1}{T_1} \right\rangle = \int g(E_a) R_1(E_a)\, d(E_a) \tag{21}$$

There are other models for NMR relaxation in disordered systems. Beckmann[47] has reviewed many and presented them in a format readily applied to NMR. The question for each is: what is the physical significance of the parameters that would be derived from a fit to NMR relaxation data? McDowell[48] has applied Monte Carlo techniques to solids disordered with distributions of site energies and, separately, with distributions of barrier height energies. He has found that in the Monte Carlo simulations the observed asymmetry of the relaxation peak occurs with the barrier height distribution but not with the site energy distribution.

The Kohlrausch–Williams–Watts (KWW) model[47] has seen considerable application. It produces the characteristic asymmetric shape of the relaxation peak and is known as the 'stretched exponential' for the form of its correlation function, which is proportional to $\exp[-(t/\tau^*)^{1-n}]$, where $n < 1$. Ngai and Martin[49] argue that at long times, decay of the correlation function is slowed down due to dynamic correlations among the atoms that arise from their mutual interactions.

Elliot's diffusion controlled relaxation (DCR) model[50] has recently been applied to NMR in ionic conducting glasses.[51] The transport mechanism involves the motion of interstitialcies followed by ionic relaxation in the vicinity of a recently arrived interstitial atom. The form of the correlation function can be viewed as a stretched exponential, but the power β to which the time t is raised would be itself time dependent.

No one model is expected to be applicable to all disordered systems, and more than one model might fit the data of one system. What remains to be seen is which models can be convincingly identified with the structure and dynamic processes in glasses. A good test of the applicability of a spin relaxation model is to compare its predictions of the diffusion coefficient of the mobile atom, based on relaxation rate measurements, to an independent set of measurements of D obtained from, for example, NMR pulsed field gradient measurements, or from electric conductivities, preferably in the same temperature range, although this cannot always be realized because of the limitations in measuring low values of D.

2.3 Strong Collision Theory and Experiments

The strong collision regime, defined by Slichter and Ailion,[52] is characterized by fast thermal mixing between the dipolar and Zeeman energy reservoirs that meets the condition $\tau_m \ll \tau_c$, where τ_m is the mixing time, and $\tau_c = (\tau_d/2)$ for a system of like spins in the solid. This energy exchange cannot occur if $B_1 > B_{D\rho}$, where $B_{D\rho}$ is the measure of the

nuclear dipolar field in the rotating frame. At sufficiently low temperatures, $\tau_m^{-1} \approx \gamma B_{D\rho}$, so that the inequality, $\tau_m \ll \tau_c$ requires that the lattice temperature be below the motional narrowing temperature of the solid.[8] Under these conditions, Slichter and Ailion find

$$R_{1\rho} = \frac{2(1-p)}{\tau_d} \frac{B_{D\rho}^2}{B_1^2 + B_{D\rho}^2} \tag{22}$$

where p is a parameter which represents the fact that the local field is not completely random after a single atom jump. The important concept in the strong collision regime is that the correlation time is essentially determined by single jumps. In the rotating frame experiment, the relatively high degree of order in the spin polarization, originally along the large applied field in the laboratory frame, becomes transferred to dipolar and Zeeman order in the rotating frame. This order is locally disrupted when an atom jumps to a neighboring site and may be gradually eroded by some other spin–lattice relaxation mechanism. The latter limits $T_{1\rho}$, which puts an upper limit on τ_d that is measurable. In the Slichter and Ailion experiment[53] on ^{7}Li in lithium metal, relaxation by conduction electrons limited observation to temperatures above about 190 K where $\tau_d \leq 1$ s, a very long time in translational diffusion. The values of τ_d obtained in this regime were found to be consistent with those found from T_1 measurements by Holcomb and Norberg.[22]

The strong collision theory is lattice specific in that the parameter p must be carefully calculated for each lattice. In their experimental paper,[53] Slichter and Ailion derived p for the b.c.c. lattice and found $p = 0.2663$. Of course, $B_{D\rho}$ is also lattice dependent (see ***Ultraslow Motions in Solids***).

3 DIRECT MEASUREMENT OF DIFFUSION COEFFICIENTS USING MAGNETIC FIELD GRADIENTS

3.1 Introduction

Analysis of measurements of the temperature and frequency dependence of nuclear spin relaxation rates yields the temperature dependence of the mean residence time of atoms in the solid. For a known structure of the solid, and from an assumed or known mechanism of diffusion and its tracer correlation factor, D can be calculated using equation (2). But it is not necessary to rely upon theory to obtain D, because it is directly measurable with NMR from echo attenuation caused by application of uniform magnetic field gradients in a selected spin echo experiment. As noted in Section 1, the field gradient provides the label needed in the measurement of the tracer D. At a coordinate, $\boldsymbol{r}$, the precession frequency is given by $\omega(\boldsymbol{r}) = \gamma B_0 + \gamma \boldsymbol{G}\cdot\boldsymbol{r}$, where $\boldsymbol{B}_0$ is the applied magnetic field, $\boldsymbol{G}$ is the applied gradient, and $\boldsymbol{G} = \nabla B_z$. Usually only the z component of ∇B_z is applied in measuring D, although the others might be used to measure diffusivity in directions normal to $\boldsymbol{B}_0$. (Unless otherwise stated, D is assumed to be isotropic.) In addition to the applied gradient, there is usually a background gradient $\boldsymbol{G}_0$, which includes the inhomogeneity of $\boldsymbol{B}_0$ and constant gradients in the sample due to the sample material susceptibility and its shape.

3.2 Application of a Constant Field Gradient

Although it is possible through extraordinary measures to remove the dipolar interaction in solids with multiple pulse techniques, most diffusion measurements are made at temperatures where the dipolar interactions are motionally narrowed. For the Hahn spin echo, the echo attenuation for gradients constant in time, is given by[6]

$$S(t) = 2\tau/S(0) = \exp[-(2\tau/T_2) - \tfrac{2}{3}\gamma^2 D\tau^3(\boldsymbol{G} + \boldsymbol{G}_0)^2] \tag{23}$$

where τ is the time between the $\pi/2$ and the π rf pulses. At a fixed echo time, the numerical value of D may be obtained from dependence of the echo attenuation upon the magnitude of $\boldsymbol{G}$. This method is relatively easy to implement especially in application to fluid samples where D is large. For example, for ^{1}H in water where $D \approx 2 \times 10^{-9}$ m^2 s^{-1}, and $\tau = 30$ ms, $G \geq 2 \times 10^{-2}$ T m^{-1} to attenuate the echo by a factor 1/e, and it has been assumed that $G \gg G_0$. In solids, where D may be much smaller, considerably larger field gradients would be needed for acceptable echo attenuations.

The need for larger constant gradients presents two experimental problems, beyond the nontrivial ones of gradient coil design and coil cooling, which are: (1) the need for high rf power to provide the larger tipping field in the rotating coordinate system; and (2) the need for broader bandwidth, $\Delta\omega_{rec}$ for the rf receiver in the NMR spectrometer to accompany the broader spectrum of the spin system being observed. The NMR linewidth will be broadened by the gradient field by approximately $\Delta B \approx GR$, where R is the radius of the sample. Therefore, the tipping field B_1 must be increased as G is increased, and the rf power must increase as G^2 is increased. To avoid having the observed echo shape distorted, $\Delta\omega_{rec}$ must exceed the spectral width of the spin system observed. An increased $\Delta\omega_{rec}$ increases the noise observed with the echo and, therefore, reduces the signal-to-noise ratio and increases the accumulation time needed for an acceptable signal-to-noise ratio. These experimental problems are so severe that the constant gradient has not seen much use for solids.

3.3 Application of Pulsed Field Gradients

3.3.1 The Spin Echo Pulsed Field Gradient Experiment

The solution to these problems, turning off the field gradient during rf pulses and during signal accumulation, was proposed by Stejskal and Tanner in their definitive paper[54] describing the use of pulsed field gradients (PFGs) for the measurement of D. The timing of the gradient pulses in the spin echo experiment is shown in Figure 9 where a gradient pulse of amplitude $\boldsymbol{G}$ is applied at a time t_1 after the $\pi/2$ pulse and again after the π pulse at a time Δ after the start of the first gradient pulse. The width of each gradient pulse is δ. Using the calculation method of Torrey[55] and Abragam,[7] Stejskal and Tanner derived the expression for echo attenuation for their two-pulse PFG:

$$\begin{aligned} F(t = 2\tau) = \exp\{-(t/T_2) - \gamma^2 D[&\delta^2(\Delta - \tfrac{1}{3}\delta)G^2 + \tfrac{2}{3}\tau^3 G_0^2 \\ &-\delta\left(t_1^2 + t_2^2 + \delta(t_1 + t_2)\right. \\ &\left.+\tfrac{2}{3}\delta^2 - 2\tau^2\right)\boldsymbol{G}\cdot\boldsymbol{G}_0]\} \end{aligned} \tag{24}$$

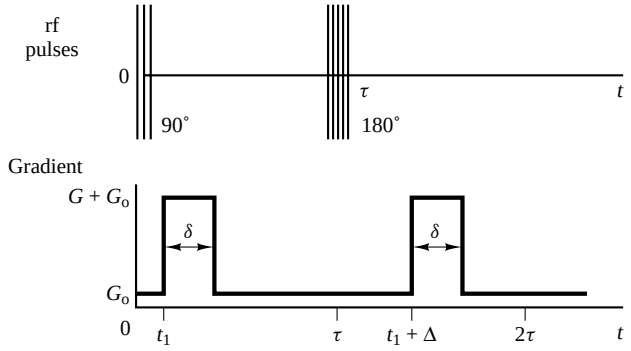

Figure 9 Timing of rf and magnetic field gradient pulses in the PFG spin echo experiment. G is the applied gradient, G_0 is the background gradient, and the spin echo (not shown) occurs at $t = 2\tau$

where $t_2 = 2\tau - (t_1 + \delta + \Delta)$. Other parameters are defined in Figure 9. The G_0^2 term is the usual one for a constant gradient. The $\boldsymbol{G}\cdot\boldsymbol{G}_0$ (cross) term arises in the Stejskal and Tanner derivation of $F(t = 2\tau)$. To ignore the $\boldsymbol{G}_0$ terms, it is necessary that $\delta G \gg \tau G_0$. Under these conditions the cross term is larger than the ${G_0}^2$ term, and if G_0 were essentially uniform across the sample, the cross term would make a plot of $\ln F(t = 2\tau)$ versus G^2 nonlinear.

There are stringent requirements for generating the pulsed currents that create the field gradients. The coils and sample must be firmly supported in order to minimize mechanical vibration caused by the large magnetic forces that act on the gradient coils. Since the first pulse defocuses the spins and the second refocuses them, their areas, $G\delta$ must match each other to high precision. For example, at a maximum gradient strength of 0.1 T m^{-1} with a 0.2 cm diameter sample and pulse widths of the order of 10 ms, one pulse gives ^{1}H spins an angular displacement of more than 10^4 rad. Therefore the matching precision must be better than 10 ppm for reproducible echo amplitudes. Callaghan[56] recently proposed a sequence to improve this pulse matching.

3.3.2 Background Gradients

The G_0 associated with a very homogeneous applied field B_0 is usually negligible. But in samples that are heterogenous on a small length scale, background gradients can be large. The apparently anomalous rapid transverse decay of the ^{7}Li spin envelope of liquid lithium was attributed by Zamir et al.[57] to diffusion in the distribution of background gradients in closely, but randomly, packed spherical lithium particles in oil. Similar effects were observed[58] in the NMR of ^{1}H in small granules of $NbH_{0.7}$. The importance of particle size is evident in their estimate of the typical $G_0 \approx 3\chi_0 B_0/R$, where χ_0 is the magnetic susceptibility of lithium and R is a typical particle radius. In lithium, for $B_0 = 1.0$ T, G_0 exceeds 0.1 T m^{-1} (10 G cm^{-1}) for particle radii of about 10^{-5} m. If the distribution of values of G_0 is symmetric about zero, the effect of the cross term would vanish for $\delta G \gg \tau G_0$. The effect of the cross term in second order is to reduce the *apparent* value of D deduced from the data.[59] G_0 can be reduced by reducing B_0 or by using larger particles. For metals, small particles are needed for penetration of the rf field and a good coil filling factor. This and a loss of signal-to-noise ratio at lower fields work against reduction of G_0. Pulse techniques for reducing or eliminating the cross term are listed in Section 3.3.4

3.3.3 Restricted Diffusion

In the derivations of the echo attenuation, it is assumed that the sample has infinite extent. For the PFG experiment, this means that $(2D\Delta)^{1/2} \ll d$, where d is the spacing between sample boundaries in the direction of the gradient. If this condition is not well met, the apparent value of D will be less than the true value. For some high diffusivity solids such as metal hydrides and fast ion conductors, diffusion might be restricted in the time of PFG measurements. A practical expression for echo attenuation in the PFG experiment on samples with spherical boundaries has been calculated by Murday and Cotts[59] who adapted the 'constant gradient' model of Newman.[60] Tanner and Stejskal[61] have calculated expressions for PFG echo attenuation for planar, cylindrical and spherical boundaries in the approximation that $\delta \ll \Delta$. Kärger, Pfeifer, and Heink[62] have reviewed the principles and applications of diffusion measurements by NMR.

3.3.4 Other Pulse Sequences

In the PFG spin echo experiment, the minimum measurable diffusion coefficient is inversely proportional to the diffusion time Δ, and Δ is limited by T_2 of the spin system. In systems where $T_1 \gg T_2$, the stimulated spin echo experiment can provide a greater diffusion time, since the time between the defocusing and refocusing intervals is limited by T_1. Tanner[63] proposed the stimulated echo sequence shown in Figure 10. In this sequence δ is still limited by T_2, but the diffusion time is limited by T_1. The cost of gaining an increase in Δ is an intrinsic reduction in the echo amplitude by a factor of $\frac{1}{2}$ created by the 'storage' of the spin magnetization along the z axis between second and third rf pulses. Tanner calculated the echo attenuation for the stimulated spin echo PFG experiment to be

$$F[t = (\tau_1 + \tau_2)] = -\gamma^2 D\{\delta^2(\Delta - \tfrac{1}{3}\delta)G^2 + \tau_1^2(\tau_2 - \tfrac{1}{3}\tau_1)G_0^2 - \delta[t_1^2 + t_2^2 + \delta(t_1 + t_2) + \tfrac{2}{3}\delta^2 - 2\tau_1\tau_2]\boldsymbol{G}\cdot\boldsymbol{G}_0\} \quad (25)$$

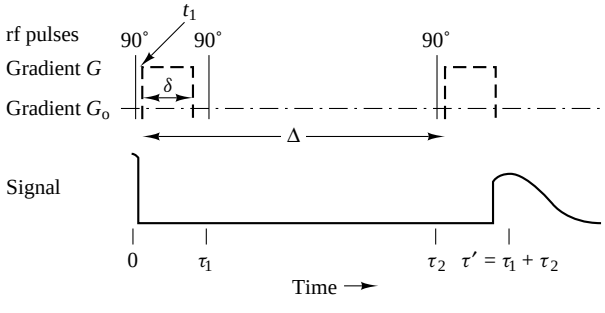

Figure 10 Timing of rf and magnetic field gradient pulses for the PFG stimulated echo experiment. The applied gradient is G, and G_0 is the background gradient. The stimulated echo is shown peaking at $t = (\tau_1 + \tau_2)$. (Reproduced by permission of The American Institute of Physics from J. E. Tanner, *J. Chem. Phys.*, 1970, **52**, 2523)

where $t_2 = \tau' - (t_1 + \delta + \Delta)$. The times in equation (21) are defined in Figure 10. The diffusion time Δ is approximately $(\tau_2 - \tau_1)$.

A number of techniques have been developed to reduce or eliminate effects of the cross term in equations (20 and 21). Karlicek and Lowe[64] invented a very effective pulse sequence that *eliminates* the cross term and substantially reduces the effect of the G_0^2 term relative to the G^2 term. It requires bipolar (or alternating) gradient pulses, and utilizes the Carr–Purcell[6] spin echo train with one gradient pulse inserted between each pair of π pulses; that is, δ is limited by 2τ instead of τ. In this scheme, the minimum usable Carr–Purcell sequence has five π pulses, and it can be extended by units of four such pulses at a time. The technical requirement of bipolar current pulses is not insignificant.

The Karlicek–Lowe concept has been extended to the stimulated echo experiment,[65] with three different sequences that eliminate the cross term in the expression for echo attenuation. All these sequences use bipolar gradient pulses. One simple unipolar sequence reduces the ratio of the cross term to the G^2 term by a factor of about τ/Δ, which is less than the factor of about unity in the Tanner stimulated echo PFG experiment. In summary, the systematic errors due to background gradients can be nearly eliminated in diffusion coefficient measurements (see ***Diffusion Measurements by Magnetic Field Gradient Methods***).

4 APPLICATIONS OF NMR TO DIFFUSION IN SOLIDS

4.1 Solids with Low Vacancy Concentrations

4.1.1 Lithium

Solid lithium is a good example of a simple elemental low-vacancy solid which has been investigated by relaxation rate and PFG diffusion coefficient measurements. Lithium has the b.c.c. structure from about 77 K to its melting point at 454 K. The ^{7}Li relaxation times have been measured over this full temperature range, covering both the strong and weak collision regimes, and they have been analyzed over eight decades of lithium jump rates from about $3\,s^{-1}$ to $3 \times 10^8\ s^{-1}$ between 200 K and the melting point.[66] (Messer and Noack[66] give references to earlier works.) Direct PFG measurements of D in the solid have been made by Mali et al.[67] at temperatures above about 350 K where $D > 10^{-13}\,m^2\ s^{-1}$ for both ^{6}Li and ^{7}Li in nearly isotopically pure and mixed samples. There is consistency between these D measurements and lithium atomic jump rates analyzed from relaxation data using lattice specific encounter models. These results demonstrate the importance of assembling relaxation data over a wide range of NMR frequencies as well as temperature. An exemplary data set[68] for R_1 and $R_{1\rho}$ is shown in Figure 11.

Messer and Noack[66] combined the R_1 data of Figure 11 with $R_{1\rho}$ data[69] at one ω_1 and strong collision data.[53] These data were analyzed with the monovacancy encounter theory of Wolf[28] and the encounter model with divacancies,[70] for the self-diffusion coefficient with the following expected temperature dependence:

$$D_{SD} = D_{10} \exp(-E_1/RT)[1 + D_{12} \exp(-E_{12}/RT)] \quad (26)$$

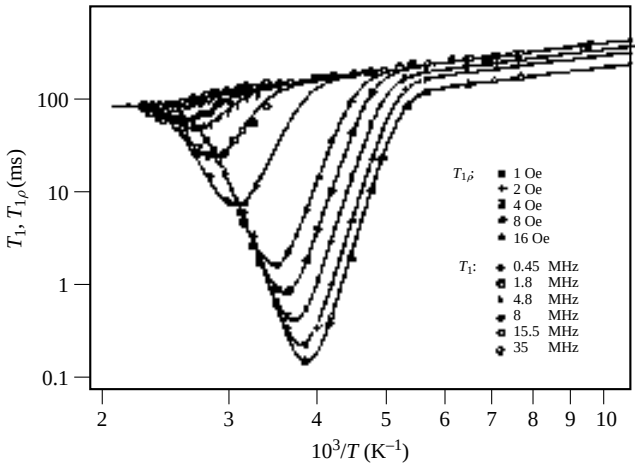

Figure 11 Temperature dependences of T_1 and $T_{1\rho}$ of ^{7}Li in solid lithium. The T_1 curves are labeled with the NMR frequency, and the $T_{1\rho}$ curves list the rotating frame magnetic field in oersteds (1 Oe $\equiv 1 \times 10^{-4}$ T). The upper limits on values of relaxation times is set by the conduction electron relaxation mechanism. (From Messer[68])

D_{SD} simply expresses the mean jump rate τ_d^{-1} of lithium atoms in that, by definition,[66] $D_{SD} = l^2/(6\tau_d)$, where l is the nearest neighbor distance in the b.c.c. lattice. Results of the analysis are plotted in Figure 12. The evident deviation from the Arrhenius relationship in equation (22) at high temperatures is attributed to divacancies and is offered as the explanation of the form of the curve in Figure 12. They obtained $E_1 = 50.2\,kJ\ mol^{-1}$, $E_{12} = 16.7\,kJ\ mol^{-1}$, $D_1 = 3.8 \times 10^{-6}\,m^2\ s^{-1}$, and $D_{12} = 2.5 \times 10^{-2}\,m^2\ s^{-1}$. Using the set of data in Figure 11 with a modified formula for the strong collision regime, Messer[68] obtained values of D_{SD} a factor of about 1.5 greater than those he reported previously.[66] A similar analysis has been done in solid sodium,[71] but without the availability of R_1 data which were masked because of the stronger conduction relaxation rate in sodium.

PFG measurements[67] of D are given in Figure 13 for three lithium samples having different isotopic composition. These data occur in the high temperature range where the divacancy term in equation (22) appears to be in evidence. The PFG measurements[67] of D have been compared with the two sets of D_{SD} from Messer and Noack[66] and Messer.[68] Theoretically, for the b.c.c. lattice with monovacancies only, $(D/D_{SD}) = f_t = 0.727$. Mali et al.[67] found values of this ratio to be between about 0.33 and 0.60, depending on temperature for the data analysis used by Messer and Noack.[66]

4.1.2 Fluorides

As noted in Section 2.2.3, the work[32–34] on pure and doped BaF_2 represents a very successful application of NMR to a low-vacancy system. The comparison made by Figueroa et al.[34] between values of D calculated by analysis of relaxation rate data and values of D deduced from electrical conductivity is shown in Figure 14 (from the review by Chadwick).[72] Experimentalists who have ever taken NMR data from samples at temperatures within a few hundred degrees of these high temperatures (up to about 1200 K) will especially appreciate Figure 14. The same research group settled many questions regarding the interpretation of relaxation rates in PbF_2 at high

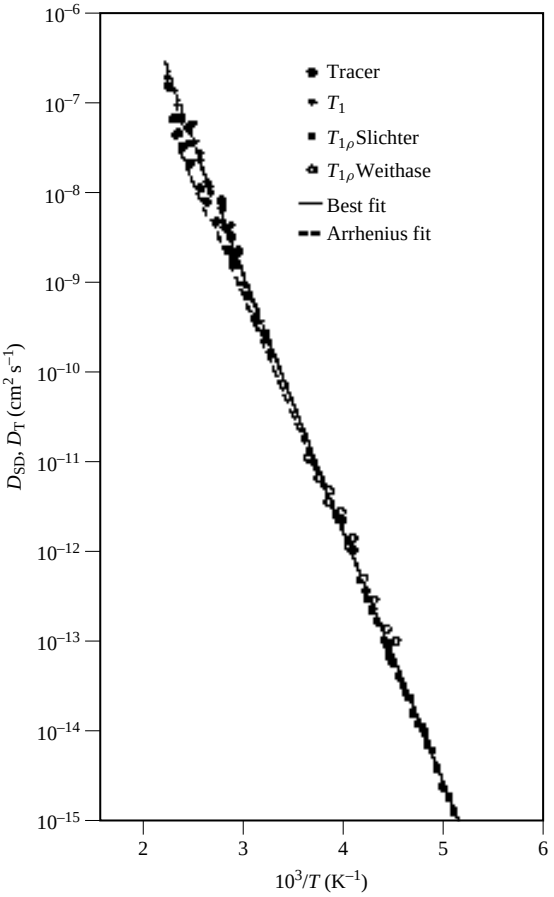

Figure 12 Temperature dependence of the self-diffusion coefficient D_{SD} based on ^{7}Li relaxation times measured in solid lithium. (+) T_1 from Messer and Noack;[66] (■) $T_{1\rho}$ from Ailion and Slichter;[53] (○) $T_{1\rho}$ from Weithase and Noack;[69] (●) mass spectroscopy tracer diffusion coefficients; (—) D_{SD} fit to equation [22]; (- - -) Arrhenius fit. (Reproduced by permission of Springer-Verlag from R. Messer and F. Noack, *Appl. Phys.*, 1975, **6**, 79)

temperatures by making direct PFG diffusion measurements of fluoride ions and showing their agreement with D deduced from conductivity measurements.[73]

4.1.3 Plastic Crystals

Some molecular crystals with approximately spherical molecules, e.g. adamantane, have a plastic phase just below the melting point in which the molecules are in a state of rapid reorientation combined with translational diffusion. Many of these solids have low melting points, and so the transition to the plastic phase limits the temperature range for their study. The rapid reorientation effectively averages out the intramolecular dipole interaction and provides the fluctuating fields needed for spin relaxation. The understanding of the rotational motion has relied on analysis of NMR relaxation rate measurements. Analyses of the several spin relaxation rates have identified translational jumping rates of the rotators in the plastic phase, but the jump rates are usually so low near the melting point that PFG measurements of D have not been practical. Typically, the plastic crystal has f.c.c. or b.c.c. structure, considering the equilibrium sites of the rotators, and

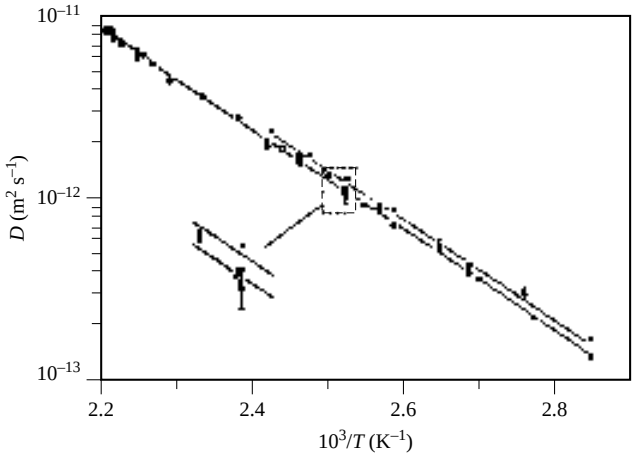

Figure 13 Temperature dependence of ^{7}Li diffusion coefficients in solid lithium measured with the PFG spin echo technique. (○, ●) Natural lithium (92.6%^{7}Li, 7.4%^{6}Li); (▲) sample with 99.97%^{7}Li; (×) sample with 95.5%^{6}Li, 4.5%^{7}Li. (○) Magnetic field $\boldsymbol{B}_0$ = 2.11 T; for all other symbols, $\boldsymbol{B}_0$ = 5.17 T. The data near 400 K are shown enlarged in order better to display the error bars. (Reproduced by permission of IOP Publishing Ltd from M. Mali, J. Roos, M. Sonderegger, D. Brinkmann, and P. Heithjans, *J. Phys. F: Met. Phys.*, 1988, **18**, 403)

monovacancy diffusion obtains in these systems. Observations of R_2 and the peak(s) in $R_{1\rho}$ at one or more values of ω_1 have been most useful in exposing diffusion because τ_d is usually too long to allow observation of the peak in R_1 at the selected NMR operating frequencies. Figure 15 shows relaxation time data for the ordered and the b.c.c. plastic phase

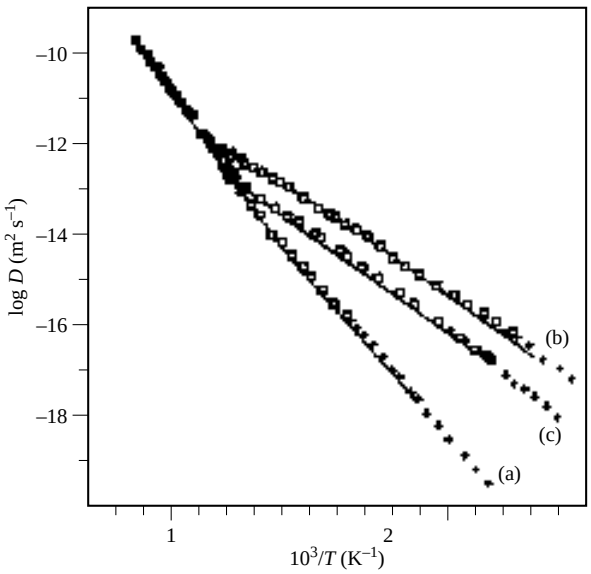

Figure 14 Temperature dependence of ^{19}F diffusion coefficients in BaF_2 single crystals: (a) pure; (b) doped with 0.04 mol% KF; (c) doped with 0.05 mol% LaF_3. Diffusion coefficients were calculated from relaxation time measurements using the monovacancy encounter model. (■) From T_1; (□) from $T_{1\rho}$; (+) from $T_{1\text{Dipolar}}$; (—) calculated from the ionic conductivity. The changes in slope occur between the extrinsic and intrinsic regions.34, 72 (Reproduced by permission of the Royal Society of Chemistry from A. V. Chadwick, *J. Chem. Soc. Faraday Trans.*, 1990, **86**, 1157)

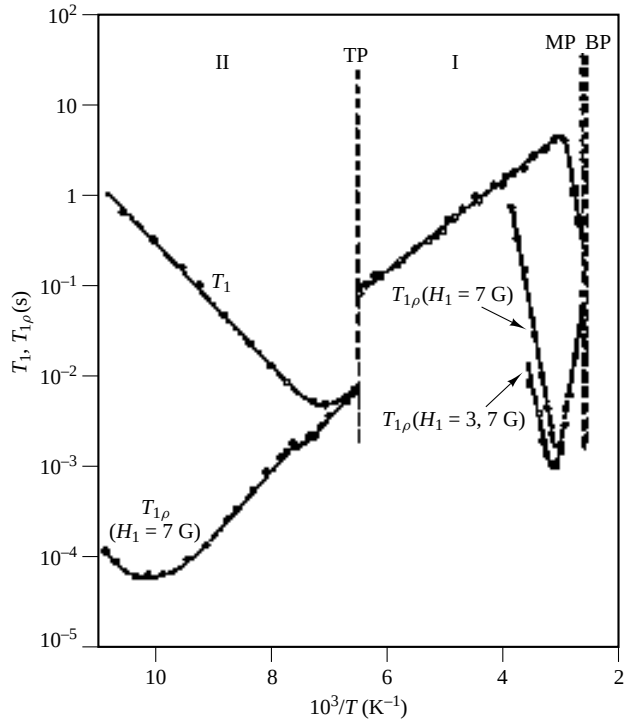

Figure 15 Temperature dependences of T_1 and $T_{1\rho}$ for ^{1}H in hexamethylethane. Region I is the plastic crystal phase, and region II is the ordered phase. The NMR frequency is 14.3 MHz. The temperature increases from left to right. (Reproduced by permission of Taylor & Francis Ltd. from J. M. Chezeau, J. Dufourcq, and J. H. Strange, *Mol. Phys.*, 1971, **20**, 305)

of hexamethylethane (HME).[74] The reorientational motion in the low-temperature phase produces the minimum in T_1 and in $T_{1\rho}$, and the effects of the translational motion in the plastic phase is similarly evident. In the plastic phase, second moment measurements indicated isotropic molecular reorientation.

From the encounter model for monovacancies,[25,28] estimates of D deduced from NMR relaxation times for three compounds have been compared with D obtained from radiotracer results, with acceptable agreement.[75] In HME, $D \approx 1 \times 10^{-12}$ m^2 s^{-1} at the melting point (374 K). Boden has prepared a review of NMR in plastic crystals.[76]

4.2 High-Vacancy Solids

4.2.1 Metal Hydrides

Nearly half of the transition metals, the rare earth metals, and many intermetallic compounds and alloys can absorb large amounts of hydrogen, which for some systems can exceed three hydrogen atoms for each metal (M) atom. Usually the hydrogen resides as atoms in one set of interstitial sites of the metal host lattice, though not necessarily the lattice of the pure, unhydrided metal. Norberg[77] explored the application of NMR early to metal hydrides by conducting pulsed and continuous wave experiments on PdH_x and identifying motional narrowing, susceptibility shifts, and testing for the conduction electron relaxation mechanism.

High diffusivities of the hydrogen atoms (i.e. those exceeding 10^{-9} m^2 s^{-1}) can occur in these metal–hydrogen (M–H) systems. Wide ranges of hydrogen solubility exist wherein hydrogen atoms reside nearly randomly (subject to site-blocking effects) on one set of sites. Vacancy concentrations can be large. Fractional concentrations exceeding 0.2 are not unusual, but 'monovacancy' levels are rare. This means that there are opportunities in M–H systems to use mean field,[26] multiple scattering,[18] or Monte Carlo[39]emrstm0123-bib-0043 models in relaxation rate analyses. Because of its low atomic number, hydrogen has a weak conduction electron relaxation mechanism[78] to compete with relaxation due to diffusion. T_1 and T_2 are sufficiently long to allow use of the PFG methods for measuring D.

Most M–H systems are good metals. As noted earlier, systematic errors in PFG measurements are reduced if metal particles are made as large as possible. This consideration favors lower laboratory frame NMR frequencies, so that 7 MHz was selected[40] for the determination of the step length of hydrogen in the subdihydrides of TiH_x. In the first PFG measurement[79] of D for hydrogen in the metal hydride, $NbH_{0.6}$, a cylindrical single crystal was used partly to avoid the concerns over small particles. This experiment[79] also combined R_1 and D measurements to determine the step length. In a series of measurements on b.c.c. hydrides, summarized by Sevilla and Cotts,[80] two special PFG sequences[64,81] were used to eliminate the $\boldsymbol{G}\cdot\boldsymbol{G}_0$ cross term. Hydrogen is found to be more mobile in the b.c.c. host metals than in those with more closely packed metal atoms.[80]

The combining of measurements of D and R_1 to learn about step lengths has been done impressively by a collaboration between the Stuttgart Max Planck Institute and Iowa State University groups. Majer et al.[42,82] have measured D for ^{1}H using the PFG stimulated echo[63] for five concentrations of hydrogen in the subdihydride ZrH_x at temperatures from 600 to 950 K using applied gradients up to 25 T m^{-1}. Their results are shown in Figure 16. Using lattice specific R_1 theories,[14,18,43] combined with R_1 measurements by Han et al.[83] on the same samples, it was demonstrated that hydrogen atoms jump between nearest neighbor tetrahedral interstitial sites.

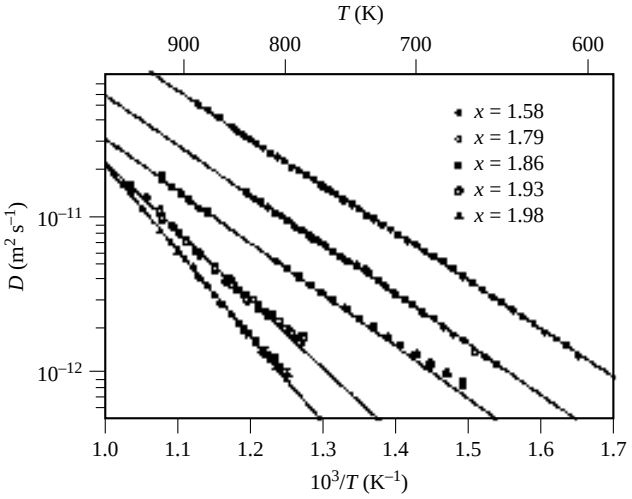

Figure 16 Temperature dependences of diffusion coefficient of hydrogen in five samples of ZrH_x measured by the ^{1}H PFG stimulated echo. (——) Fits to the data with the Arrhenius equation. (Reproduced by permission of IOP Publishing, Ltd from G. Majer, W. Renz, and R. G. Barnes, *J. Phys. Condens. Matter*, 1994, **6**, 2935)

Non-Arrhenius plots at high temperatures for high concentration samples have been attributed to having a small fraction of hydrogen atoms located on a second, but as yet unidentified, site. References cited by Han et al.[83] offer a good introduction to the literature on applications of NMR in metal hydrides (see ***Hydrogen–Metal Systems***).

4.2.2 Fast Ion Conductors

In the more than 20 years that there has been a high level of interest in understanding ionic conductivity in solids, NMR has been an important tool for the study of structure and ionic motion in what are regularly known as 'solid electrolytes' or 'superionic conductors'. The work on the fluorides which has already been mentioned[32–34,74,75] is representative of the application of NMR in this field. The search for high ionic conductivity has identified a wide variety of solids that meet the necessary criterion. These include crystals, glasses and polymer electrolytes. The recent report by Brinkmann[84] provides an informative and comprehensive review of NMR in this field.

Interesting examples of combining R_1 measurements with the PFG technique for D are found in the work by the University of Zürich group on ^{109}Ag ($I = \frac{1}{2}$) in fast ion conductors. Because nuclear moments of both silver isotopes are less than one-twentieth of that of ^{1}H, it is necessary to have access to high magnetic fields to get the NMR frequency into a workable range (above 10 MHz). However, even in this frequency range signals will be low because of the low magnetogyric ratio of ^{109}Ag. Compared to working with large γ spins such as those of ^{1}H, ^{7}Li, ^{19}F, or ^{23}Na, doing the PFG experiment on silver at first appears daunting because of the γ dependence of the important exponent in the echo attenuation expression in equation (20): $[\gamma^2 D\delta^2(\Delta - \frac{1}{3}\delta)G^2]$. This term should equal or exceed unity in order effectively to attenuate the echo. However, because γ of ^{109}Ag is small, its relaxation rates are also reduced, so the difference can be made up by increasing the times δ and Δ in the sequence. Nevertheless, the long relaxation times and the lower NMR signal amplitudes mean longer signal accumulation times for an acceptable signal-to-noise ratio and good data.

Looser et al.[85] used the PFG spin echo technique to measure D in the two isostructural crystals $RbAg_4I_5$ and KAg_4I_5 from 150 to 300 K covering the α and β phases of these crystals. They found little difference in D between these crystals except in the $\alpha-\beta$ phase transition temperatures, which are visible in Figure 17. From comparison between D measured by the PFG and D_σ deduced from conductivity data, they concluded that there was increased correlation of the silver motion in the β phase.

In their work on β-Ag_3SBr, Huber et al.[86] brought together experimental data on the temperature, pressure, and NMR frequency dependence of the silver R_1 and PFG D measurements. Having the diffusion data allowed them to identify a model for silver motion that includes local hopping between the four silver sites within one face of the cubic unit cell and diffusional jumps between neighboring faces.

5 FURTHER READING

Review papers provide special perspectives on their selected applications of NMR and references to other works of interest.

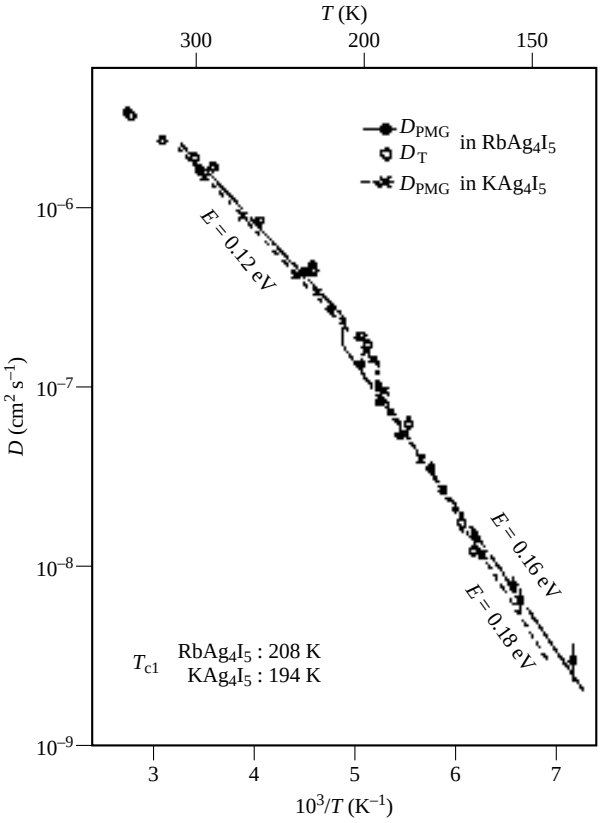

Figure 17 Temperature dependences of diffusion coefficients of silver in fast ion conductors, $RbAg_4I_5$ and KAg_4I_5. ^{109}Ag PFG spin echo measurements: (•) $RbAg_4I_5$; (×) KAg_4I_5; (○) radioactive tracer data. The positions of the $\alpha-\beta$ phase transitions are visible. (Reproduced by permission of Elsevier Science Publishers B.V. From Looser et al.[85])

Polymer systems have been reviewed by von Meerwall.[87] Boden et al.[88] have discussed model polymer electrolytes. Both polymer electrolytes and glasses have been discussed by Brinkmann.[84] Seymour[89] and Barnes[90] have reviewed metal hydrides, and Strange[91] has summarized work on ionic transport. Chadwick's paper[72] is broader in its coverage of mass transport in a number of solids.

6 RELATED ARTICLES

Diffusion Measurements by Magnetic Field Gradient Methods; Diffusion in Rare Gas Solids; Fast Ion Conductors; Field Gradients and Their Application; Hydrogen–Metal Systems; Liquid Crystalline Samples: Diffusion; Polymer Dynamics and Order from Multidimensional Solid State NMR; Radiofrequency Gradient Pulses; Relaxation Theory: Density Matrix Formulation; Spin Diffusion in Solids; Ultraslow Motions in Solids.

7 REFERENCES

1. E. M. Purcell, H. C. Torrey, and R. V. Pound, *Phys. Rev.*, 1946, **69**, 37.
2. F. Bloch, W. W. Hansen, and M. Packard, *Phys. Rev.*, 1946, **69**, 127.

3. F. Bloch, *Phys. Rev.*, 1946, **70**, 460.
4. N. Bloembergen, E. M. Purcell, and R. V. Pound, *Phys. Rev.*, 1948, **73**, 679.
5. E. L. Hahn, *Phys. Rev.*, 1950, **80**, 580.
6. H. Y. Carr and E. M. Purcell, *Phys. Rev.*, 1954, **94**, 630.
7. A. Abragam, *The Principles of Nuclear Magnetism*, Clarendon, Oxford, 1961.
8. C. P. Slichter, *Principles of Magnetic Resonance*, 3rd edn, Springer, Berlin, 1990.
9. S. W. Kelly and C. A. Sholl, *J. Phys.: Condens. Matter*, 1992, **4**, 3317, and references therein.
10. D. Wolf, *Spin-temperature and Nuclear-spin Relaxation in Matter*, Clarendon, Oxford, 1979.
11. M. Goldman, *Spin Temperature and Nuclear Magnetic Resonance*, Oxford, London, 1970.
12. D. C. Look and I. J. Lowe, *J. Chem. Phys.*, 1966, **44**, 2995.
13. R. Kubo and K. Tomita, *J. Phys. Soc. Jpn*, 1954, **9**, 888.
14. C. A. Sholl, *J. Phys. C: Solid State Phys.*, 1988, **21**, 319.
15. H. C. Torrey, *Phys. Rev.*, 1953, **92**, 962.
16. C. A. Sholl, *J. Phys. C: Solid State Phys.*, 1981, **14**, 447.
17. J. F. Harrmon and B. H. Muller, *Phys. Rev*, 1969, **182**, 400.
18. P. A. Fedders and O. F. Sankey, *Phys. Rev. B*, 1978, **18**, 5938.
19. R. A. Hultsch and R. G. Barnes, *Phys. Rev.*, 1962, **125**, 1832.
20. K. Compaan and Y. Haven, *Trans. Faraday Soc.*, 1956, **52**, 786.
21. H. A. Resing and H. C. Torrey, *Phys. Rev.*, 1963, **131**, 1102.
22. D. F. Holcomb and R. E. Norberg, *Phys. Rev.*, 1955, **98**, 1074.
23. C. A. Sholl, *J. Phys. C: Solid State Phys.*, 1974, **7**, 3378.
24. C. A. Sholl, *J. Phys. C: Solid State Phys.*, 1975, **8**, 1737.
25. D. Wolf, *J. Magn. Reson.*, 1975, **17**, 1.
26. W. A. Barton and C. A. Sholl, *J. Phys. C: Solid State Phys.*, 1976, **9**, 4315; 1978, **11**, 4405.
27. W. A. Barton and C. A. Sholl, *J. Phys. C: Solid State Phys.*, 1980, **13**, 2579.
28. D. Wolf, *Z. Naturforsch., Teil a*, 1971, **26**, 1816; *Phys. Rev. B*, 1974, **10**, 2710.
29. M. Eisenstadt and A. G. Redfield, *Phys. Rev.*, 1963, **132**, 635.
30. D. Wolf, *Phys. Rev. B.*, 1974, **10**, 2724.
31. D. C. Ailion and P. P. Ho, *Phys. Rev.*, 1968, **168**, 662.
32. D. Wolf, D. R. Figueroa, and J. H. Strange, *Phys. Rev. B*, 1977, **15**, 2545.
33. D. R. Figueroa, J. H. Strange, and D. Wolf, *Phys. Rev. B*, 1979, **19**, 148.
34. D. R. Figueroa, A. V. Chadwick, and J. H. Strange, *J. Phys. C: Solid State Phys.*, 1978, **11**, 55.
35. C. A. Sholl, *J. Phys. C: Solid State Phys.*, 1982, **15**, 1177.
36. I. R. MacGillivray and C. A. Sholl, *J. Phys. C: Solid State Phys.*, 1986, **19**, 4771.
37. O. F. Sankey and P. A. Fedders, *Phys. Rev. B.*, 1979, **20**, 39.
38. P. A. Fedders, *Phys. Rev. B*, 1982, **25**, 78.
39. L. D. Bustard, *Phys. Rev. B.*, 1980, **22**, 1.
40. L. D. Bustard, R. M. Cotts, and E. F. W. Seymour, *Phys. Rev. B.*, 1980, **22**, 12.
41. C. L. Bisson and W. D. Wilson, in *Effect of Hydrogen on the Behavior of Matter.*, ed. A. W. Thompson and I. M. Bernstein, AIME, New York, 1976, p. 416.
42. G. Majer, W. Renz, A. Seeger, and R. G. Barnes, *Z. Phys. Chem.*, 1993, **181**, 187.
43. D. A. Faux, D. K. Ross, and C. A Sholl, *J. Phys. C: Solid State Phys.*, 1986, **19**, 4115.
44. C. A. Sholl, *Diffus. Defect Data, Solid State Data A, Defect Diffus. Forum*, 1993, **95–98**, 91.
45. E. R. Andrew and D. P. Tunstall, *Proc. R. Soc.*, 1961, **78**, 1; M. I. Gordon and M. J. R. Hoch, *J. Phys. C: Solid State Phys.*, 1978, **11**, 783; P. S. Hubbard, *J. Chem. Phys.*, 1970, **33**, 985; and S. W. Kelly and C. A. Sholl, *J. Phys. Condens. Matter*, 1992, **4**, 3317.
46. W. A. Barton, *J. Phys. C: Solid State Phys.*, 1982, **15**, 5123.
47. P. A. Beckmann, *Phys. Rep.*, 1988, **171**, 85.
48. A. F. McDowell, Ph.D. Thesis, Cornell University, 1993 (unpublished).
49. K. L. Ngai and S. W. Martin, *Phys. Rev. B*, 1989, **40**, 10 550.
50. S. R. Elliot, *Solid State Ionics*, 1988, **27**, 131.
51. S. R. Elliot and A. P. Owens, *Phys. Rev. B*, 1991, **44**, 47.
52. C. P. Slichter and D. Ailion, *Phys. Rev. A*, 1964, **135**, 1099.
53. D. Ailion and C. P. Slichter, *Phys. Rev. A*, 1965, **137**, 235.
54. E. O. Stejskal and J. E. Tanner, *J. Chem. Phys.*, 1965, **42**, 288.
55. H. C. Torrey, *Phys. Rev.*, 1956, **104**, 563.
56. P. T. Callaghan, *J. Magn. Reson.*, 1990, **88**, 493.
57. D. Zamir, R. C. Wayne, and R. M. Cotts, *Phys. Rev. Lett.*, 1964, **12**, 327.
58. D. Zamir and R. M. Cotts, *Phys. Rev.*, 1964, **134**, A666.
59. J. S. Murday and R. M. Cotts, *Z. Naturforsch., Teil a*, 1971, **26**, 85; *J. Chem, Phys.*, 1968, **48**, 4938.
60. C. H. Newman, *J. Chem. Phys.*, 1974, **60**, 4508.
61. J. E. Tanner and E. O. Stejskal, *J. Chem. Phys.*, 1968, **49**, 1768; J. E. Tanner, Ph.D. Thesis, University of Wisconsin, 1966.
62. J. Kärger, H. Pfeifer, and W. Heink, *Adv. Magn Reson.*, 1988, **12**, 1.
63. J. E. Tanner, *J. Chem. Phys.*, 1970, **52**, 2523.
64. R. F. Karlicek, Jr and I. J. Lowe, *J. Magn. Reson.*, 1980, **37**, 75.
65. R. M. Cotts, M. J. R. Hoch, T. Sun, and J. T. Markert, *J. Magn. Reson.*, 1989, **83**, 252.
66. R. Messer and F. Noack, *Appl. Phys.*, 1975, **6**, 79.
67. M. Mali, J. Roos, M. Sonderegger, D. Brinkmann, and P. Heithjans, *J. Phys. F: Met. Phys.*, 1988, **18**, 403.
68. R. Messer, *1976 Magnetic Resonance and Related Phenomena, Proceedings of the 19th Congress Ampère, Heidelberg*, ed. H. Brunner et al. Groupment Ampère, Heidelberg, p. 269.
69. M. Weithase and F. Noack, *Phys. Stat. Sol. (b)*, 1973, **57**, K111.
70. E. Cavelius, *Phys. Stat. Sol. (b)*, 1974, **65**, 181.
71. G. Brünger, O. Kanert, and D. Wolf, *Phys. Rev. B*, 1980, **22**, 4247.
72. A. V. Chadwick, *J. Chem. Soc. Faraday Trans.*, 1990, **86**, 1157.
73. R. E. Gordon and J. H. Strange, *Faraday Symp. Chem. Soc.*, 1978, **13**, 154; *J. Phys. C: Solid State Phys.*, 1978, **11**, 3213.
74. J. M. Chezeau, J. Dufourcq, and J. H. Strange, *Mol. Phys.*, 1971, **20**, 305.
75. A. R. Britcher and J. H. Strange, *Mol. Phys.*, 1979, **37**, 181.
76. N. Boden, *The Plastically Crystalline State*, ed. J. N. Sherwood, Wiley, New York 1979, p. 147.
77. R. E. Norberg, *Phys. Rev.*, 1952, **86**, 745.
78. C. Korn and D. Zamir, *J. Phys. Chem. Sol.*, 1970, **31**, 489.
79. O. J. Zogal and R. M. Cotts, *Phys. Rev. B*, 1975, **11**, 2443.
80. E. H. Sevilla and R. M. Cotts, *J. Less-Common Metals*, 1987, **129**, 223.
81. W. D. Williams, E. F. W. Seymour, and R. M. Cotts, *J. Magn. Reson.*, 1978, **31**, 271.
82. G. Majer, W. Renz, and R. G. Barnes, *J. Phys. Condens. Matter*, 1994, **6**, 2935.

83. J.-W. Han, D. R. Torgeson, R. G. Barnes, and D. T. Peterson, *Phys. Rev. B*, 1991, **44**, 12 353.
84. D. Brinkmann, *Prog. NMR Spectrosc.*, 1992, **24**, 527.
85. H. Looser, M. Mali, J. Roos, and D. Brinkmann, *Solid State Ionics*, 1983, **9/10**, 1237.
86. H. Huber, M. Mali, J. Roos, and D. Brinkmann, *Phys. Rev. B*, 1988, **37**, 1441; *Solid State Ionics*, 1986, **18/19**, 1188.
87. E. D. von Meerwall, *J. Non-Cryst. Solids*, 1991, **131–133**, 735.
88. N. Boden, S. A. Leng, and I. M. Ward, *Solid State Ionics*, 1991, **45**, 261.
89. E. F. W. Seymour, *J. Less-Common Met.*, 1982, **88**, 323.
90. R. G. Barnes, in *Hydrogen in Metals*, ed. H. Wipf, Springer, Berlin, Vol. 3, in press.
91. J. H. Strange, *Crystal Lattice Defects Amorph. Mater.*, 1987, **14**, 183.

Biographical Sketch

Robert M. Cotts. *b* 1927. B.S., Wisconsin, Madison, 1950; Ph.D., California, Berkeley, 1954. Introduced to NMR by Walter D. Knight. Instructor–research associate (with Felix Bloch), Stanford University, 1954–57; Faculty, Cornell University, 1957–present. Approx. 55 publications. Research interests: the physics of condensed matter, including applications of NMR and NQR; translational diffusion in solids and liquids; and motion and siting of hydrogen in transition and rare earth metals.

Diffusion Measurements by Magnetic Field Gradient Methods

Charles S. Johnson Jr

University of North Carolina, Chapel Hill, NC, USA

1	Introduction	1
2	Effects of Translational Motion in NMR	2
3	Pulsed Field Gradient NMR	4
4	The FT-PFG-NMR Method and Diffusion Ordered Two-Dimensional NMR Spectroscopy	9
5	The Average Propagator and the Scattering Analogy	11
6	Restricted Diffusion and Diffusive Diffraction	13
7	Anisotropic Diffusion	14
8	Chemical Exchange Involving Diffusing Molecules	14
9	Large Gradients and the Measurement of Small Displacements	15
10	Data Analysis and Polydispersity	16
11	Mass and Size Distributions from NMR Diffusion Data	17
12	Literature Sources for NMR Diffusion Measurements	17
13	Related Articles	18
14	References	18

1 INTRODUCTION

Diffusion measurements by field gradient methods in this article refer to the measurement of translational diffusion. Rotational diffusion and spin diffusion by means of mutual spin flips are treated elsewhere. Measurements of translational diffusion are important in the determination of sizes and shapes of molecules and molecular aggregates, and NMR in the presence of magnetic field gradients is a uniquely powerful method for making such measurements. The NMR method also provides a means for correlating diffusion coefficients with chemical shifts, characterizing the microgeometry of porous materials, investigating anisotropy of organized phases, and determining degrees of solubilization, to list only a few applications. In this article we present the principles of NMR diffusion measurements and discuss some useful techniques. This represents only a sampling of an extensive field, and we rely on recent review articles to fill in some of the gaps. Also, recent advances that offer new insights and expand the range of applications are emphasized at the expense of some important older contributions. Although some applications appear as examples, a review of applications is not intended. Appropriate textbooks and reviews are cited in the various sections, and Section 12 is devoted to sources for background material and additional reading.

1.1 Fick's Laws

According to Fick's first law of diffusion, the particle flux $\boldsymbol{J}$ at position $\boldsymbol{r}$ is proportional to the gradient of the concentration. Thus,

$$\boldsymbol{J}(\boldsymbol{r}, t) = -D\nabla c(\boldsymbol{r}, t) \tag{1}$$

where D is the diffusion coefficient and $c(\boldsymbol{r}, t)$ is the concentration in number of particles per unit volume. The conservation of mass is assured by the equation of continuity,

$$\frac{\partial c(\boldsymbol{r}, t)}{\partial t} = -\nabla \cdot \boldsymbol{J}(\boldsymbol{r}, t) \tag{2}$$

and this equation can be combined with equation (1) to obtain Fick's second law of diffusion:[1]

$$\frac{\partial c(\boldsymbol{r}, t)}{\partial t} = D\nabla^2 c(\boldsymbol{r}, t) \tag{3}$$

It is assumed that D has at most a weak dependence on the concentration and that the concentration is low. However, equation (3) is useful over a wide range of concentrations.

In the following it is convenient to introduce the conditional probability $P(\boldsymbol{r}_0 \mid \boldsymbol{r}, t)$ that a particle initially at $\boldsymbol{r}_0$ will be at $\boldsymbol{r}$ at time t, and it is reasonable to assume that $P(\boldsymbol{r}_0 \mid \boldsymbol{r}, t)$ also obeys the diffusion equation so that:

$$\frac{\partial P(\boldsymbol{r}_0 \mid \boldsymbol{r}, t)}{\partial t} = D\nabla^2 P(\boldsymbol{r}_0 \mid \boldsymbol{r}, t) \tag{4}$$

The solution of equation (4) by standard means for unrestricted diffusion with the initial condition $P(\boldsymbol{r}_0 \mid \boldsymbol{r}, 0) = \delta(\boldsymbol{r}_0 - \boldsymbol{r})$ yields the expected Gaussian dependence on the displacement:

$$P(\boldsymbol{r}_0 \mid \boldsymbol{r}, t) = (4\pi Dt)^{-3/2} \exp[-(\boldsymbol{r} - \boldsymbol{r}_0)^2/4Dt] \tag{5}$$

The calculation of the average square displacement by means of equation (5) gives the Einstein–Smoluchowski equation:

$$\langle(\boldsymbol{r} - \boldsymbol{r}_0)^2\rangle = 6Dt \tag{6}$$

Thus, molecular displacement resulting from diffusion is simply related to the diffusion coefficient.

1.2 The Stokes–Einstein Equation and Tracer Diffusion

Much of the interest in diffusion arises because of the connection between D and molecular size. For macromolecules, at least, this connection is usually made through the Stokes–Einstein equation:[2]

$$D = k_{\mathrm{B}}T/f \tag{7}$$

where f is the friction factor. For a spherical particle with hydrodynamic radius R_{h} immersed in a fluid of viscosity η, Stokes's law gives $f = 6\pi\eta R_{\mathrm{h}}$. Analytical expressions are also available for the friction factors of oblate and prolate ellipsoids and approximate results have been reported for complex structures made of identical subunits.[3]

The diffusion coefficient of interest here is the tracer diffusion coefficient, sometimes called the self-diffusion or intra-diffusion coefficient.[2] Nuclear spin states provide perfect labels that have almost no effect on the hydrodynamic properties of molecules. The samples under study are homogeneous and the translational motion of nuclear spins can be detected directly as described below. In a mixture with $N + 1$ components (including the solvent) there are $N + 1$ distinct tracer diffusion coefficients. This must be contrasted with the situation in which there are concentration gradients, and molecular species diffuse into each other in a process called 'interdiffusion'. The diffusion coefficients measured in such systems are known as the 'mutual diffusion' or 'interdiffusion' coefficients. In the limit of infinite dilution, tracer and mutual diffusion coefficients are equal, but at higher concentrations they may be quite different. Also, mutual diffusion in mixtures invariably involves coupled flows, and in a volume fixed frame a system with $N + 1$ components has $N(N + 1)/2$ independent Onsager diffusion coefficients.

Dynamic light scattering (DLS), a method that depends on concentration fluctuations, is often used to measure mutual diffusion coefficients.[4,5] DLS is a standard method, even though the diffusion coefficients obtained are not necessarily equal to the mutual diffusion coefficients that are measured with macroscopic concentration gradients.[6] At low concentrations NMR and DLS give similar diffusion coefficients for macromolecules in solution, but the dependence on concentration is usually much stronger for tracer diffusion coefficients than for mutual diffusion coefficients. In contrast to equation (7), the mutual diffusion coefficient D_{m} for a macromolecule can be expressed as

$$D_{\mathrm{m}} = \frac{k_{\mathrm{B}}T}{f}\left(1 + \frac{\partial \ \ln \ \gamma'}{\partial \ \ln \ c}\right)(1 - \phi') \tag{8}$$

where γ' is the activity coefficient and ϕ' is the volume fraction of solute.[7,8] Primes have been used here since the same symbols are used elsewhere for different quantities. The last two factors on the right-hand side of equation (8) largely account for the difference between mutual and tracer diffusion coefficients, but in principle the friction factors for mutual and tracer diffusion are not equal.[9]

2 EFFECTS OF TRANSLATIONAL MOTION IN NMR

The ability of NMR to detect translational motion and to image spin density depends on two essential facts: (1) a nucleus at position $\boldsymbol{r}$ precesses with the frequency

$$\omega(\boldsymbol{r}) = -\gamma B(\boldsymbol{r}) \tag{9}$$

where γ is the magnetogyric ratio and $B(\boldsymbol{r})$ is the magnitude of the local magnetic field (flux density), and (2) the local fields can be manipulated through the use of magnetic field gradients so that the spatial positions of nuclei can be encoded. The spin echo experiment is the basis of NMR diffusion measurements, since this experiment involves the refocusing of magnetization in inhomogeneous magnetic fields, a process that is extremely sensitive to the translational motion of spins.

2.1 Spin Echoes and Magnetization Helices

Consider the experiment illustrated in Figure 1(a) for a sample with a single resonance line. The applied magnetic field is in the z direction and a hard 90°_x rf pulse at $t = 0$ rotates magnetization from all parts of the NMR active volume into the y direction. Here x and y refer to a reference frame rotating about the field direction at the average precession frequency ω_0 for spins in the applied field $\boldsymbol{B}_0$. The resultant magnetization in each differential volume element is described by a vector (known as an 'isochromat') that precesses in the xy plane at a frequency that depends on the local field as indicated by equation (9). The interpretation is simpler if the inhomogeneity results from a constant field gradient $\boldsymbol{g}$ applied and controlled externally. Such a gradient is described by:

$$\boldsymbol{g} = \frac{\partial B_z}{\partial x}\boldsymbol{i} + \frac{\partial B_z}{\partial y}\boldsymbol{j} + \frac{\partial B_z}{\partial z}\boldsymbol{k} \tag{10}$$

where $\boldsymbol{i}$, $\boldsymbol{j}$, and $\boldsymbol{k}$ are unit vectors in the x, y, and z directions, respectively. Thus the magnitude of the total external magnetic field at $\boldsymbol{r}$ is given by:

$$B = B_0 + \boldsymbol{g} \cdot \boldsymbol{r} \tag{11}$$

In the following we assume that only a z gradient of magnitude $g = \boldsymbol{g}\cdot\boldsymbol{k}$ is present. In the presence of this gradient, isochromats with different frequencies are associated with different values of z, and it is instructive to represent the magnetization immediately after the 90°_x pulse as a ribbon formed by the isochromats with their tails on the centerline of the sample. Initially, the resultant magnetization in the y direction is equal to M_0, the magnitude of the equilibrium magnetization prior to the rf pulse. The effect of the gradient is to give the isochromat at coordinate z a phase angle $\phi(z) = \gamma gzt$ with respect to the yz plane at time t. This is represented in Figure 1(b) by the magnetization helices with pitches given by $\Lambda = 2\pi/(\gamma gt)$.[10] The detected signal, that is proportional to the resultant magnetization in the y direction, decays to zero with increasing time as illustrated by the FID in Figure 1(a). In the absence of diffusion the interpretation of the experiment is straightforward. The 180°_y pulse at τ rotates each isochromat about the y axis and thus changes the phase angle of the isochromat at z by the amount $-2\gamma gz\tau$. Precession then continues as before since the local magnetic field is unaffected by the rf pulse. In the period between τ and 2τ the helix unwinds so that the resultant is again directed along the y axis (in the absence of directed flow) and a spin echo signal is created. Thus, the isochromats have been refocused and the only attenuation of the echo results from the intrinsic T_2 of the sample, i.e. the echo amplitude is proportional to $M_0 \exp(-t/T_2)$.

2.2 Bloch Equations including Diffusion

As emphasized in Figure 1(b), the effect of the 90°_x pulse followed by the z gradient is to create a magnetization pattern in the sample. Diffusion smears out this pattern and leads to attenuation of the spin echo. The tightly wound helices are more easily disturbed by diffusion, and analytical equations

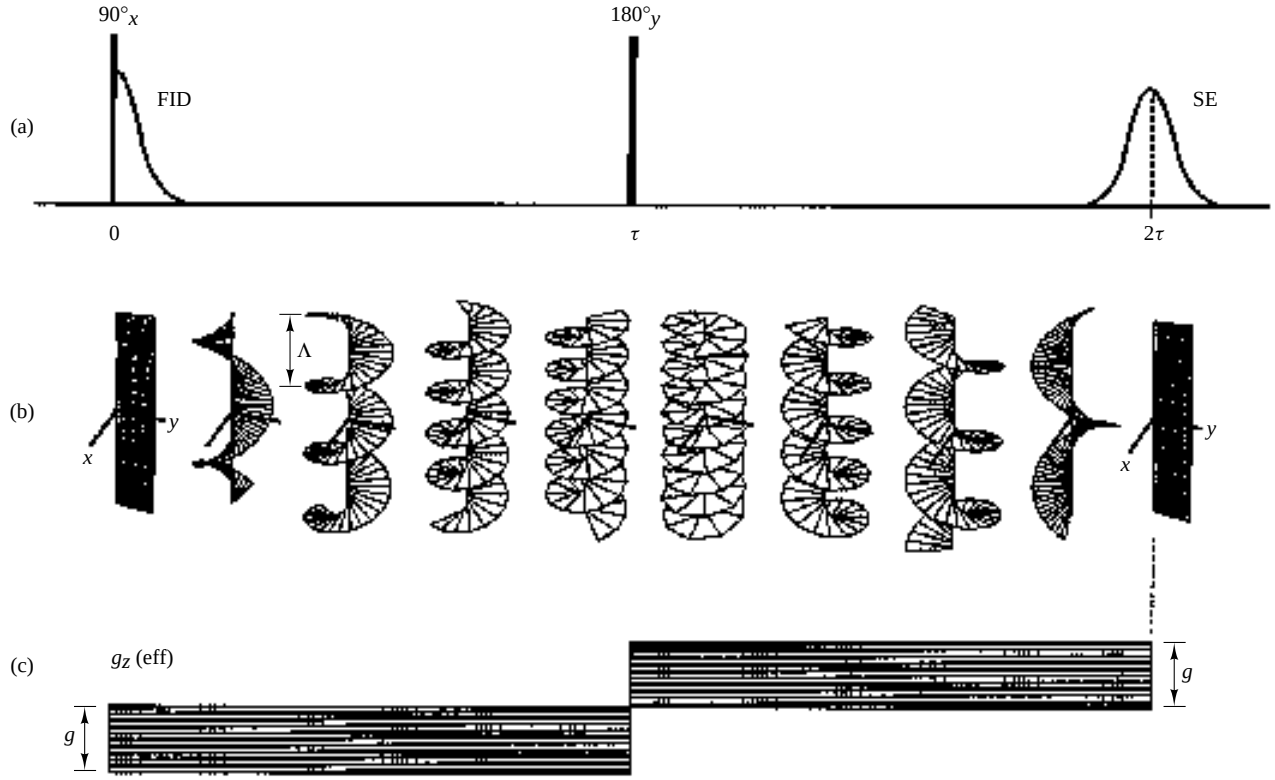

Figure 1 Spin echoes with a constant gradient: (a) the Hahn spin echo pulse sequence; (b) magnetization helices formed by isochromats; and (c) the effective gradients in the presence of a 180° rf pulse

can be derived to describe this effect. In the standard mathematical description of this experiment a term describing the rate of translational diffusion of magnetization is added to the Bloch equations to obtain a macroscopic theory of diffusion effects in NMR. Following the notation of Abragam[11] this gives,

$$\frac{\partial \boldsymbol{M}(\boldsymbol{r},t)}{\partial t} = \gamma \boldsymbol{M} \times \boldsymbol{B}(\boldsymbol{r},t) - \frac{M_x \boldsymbol{i}' + M_y \boldsymbol{j}'}{T_2} - \frac{(M_z - M_0)\boldsymbol{k}'}{T_1} + D\nabla^2 \boldsymbol{M} \qquad (12)$$

A more convenient equation for the investigation of transverse magnetization is obtained from equation (12) by defining the complex magnetization $M_+ = M_x + \mathrm{i}M_y$, setting $B_x = B_y = 0$, and denoting the magnitude of the average precession frequency in the sample by $\omega_0 = \gamma B_0$. The resulting equation is

$$\frac{\partial M_+}{\partial t} = \mathrm{i}\omega_0 M_+ - \frac{M_+}{T_2} - \mathrm{i}\gamma(\boldsymbol{g}\cdot\boldsymbol{r})M_+ + D\nabla^2 M_+ \qquad (13)$$

The uninteresting parts of the time dependence are then transformed away by means of the substitution

$$M_+ = \psi \exp(\mathrm{i}\omega_0 t - t/T_2) \qquad (14)$$

to yield the equation[12]

$$\frac{\partial \psi}{\partial t} = -\mathrm{i}\gamma g z \psi + D\nabla^2 \psi \qquad (15)$$

In the absence of diffusion equation (15) is easily solved for the magnetization in the rotating frame as a function of z and t. If the initial condition is a coherent state created by a 90° rf pulse, the magnetization pattern evolving under the influence of g is just the helix previously described. A gradient pulse with amplitude g and duration δ is said to have an area of $q = \gamma g \delta$, and the helix at the end of the pulse is described by $S(z) = m \exp(-\mathrm{i}qz)$, where m is the magnetization density per unit length in the z direction. The integral of the effective gradient areas at the time of the echo must be zero so that the pitch of the helix becomes much larger than the active volume. This can be achieved either by reversing the direction of the gradient to obtain a 'gradient echo' or by applying a $180°_y$ pulse to set back the phase to achieve a spin echo. In fact, it is convenient in mathematical derivations to replace $180°_y$ rf pulses by the inversion of previous gradient pulses.[13] The complete sequence of rf and gradient pulses can then be described by an effective $g(t)$. With this approach it has been shown that the solution of equation (15) in the presence of diffusion and a time dependent gradient can be written as

$$\ln \psi = -D\left[\int_0^t q^2(t')\,\mathrm{d}t'\right] \qquad (16)$$

where

$$q(t') = \int_0^{t'} \gamma g(t'')\,\mathrm{d}t'' \qquad (17)$$

It is important to note that gradient echoes and spin echoes have quite different properties in many experiments. The 180°

rf pulse refocuses phase dispersion resulting from background gradients, chemical shifts, susceptibility effects in heterogeneous samples, etc., while the reversed gradient pulse only refocuses phase dispersion resulting from a previously applied gradient pulse.

2.3 Diffusion Effects on Magnetization Patterns

According to Figure 1, the projection of the helix onto either the *xz* or the *yz* plane yields a simple sinusoidal grating function, e.g. Re $[S(z)] = m \cos(qz)$ for the *yz* plane. The effect of diffusion (in the direction of the gradient) on such a grating can be obtained immediately through the use of equation (5). First we integrate over the x and y coordinates to obtain

$$P(z_0 \mid z, t) = (4\pi Dt)^{-1/2} \exp[-(z - z_0)^2/4Dt] \tag{18}$$

Then $P(0 \mid z,t)$ is convoluted with $S(z)$ to obtain an expression for the time dependent gratings. The effect of diffusion is to 'smear out' the spatial gratings, and the time dependent helix is described by $S(z, t) = S(z) * P(0 \mid z, t)$, where '*' means convolution, and we can write

$$S(z, t) = \frac{m}{(4\pi D\Delta)^{1/2}} \int_{-\infty}^{\infty} \exp(-\mathrm{i}qz') \exp[(z - z')^2/4Dt]\, \mathrm{d}z' \tag{19}$$

Equation (19) can be evaluated directly or by means of the convolution theorem to obtain

$$S(z, t) = m \exp(-\mathrm{i}qz) \exp(-Dq^2 t) \tag{20}$$

This expression includes the amplitude attenuation resulting from diffusion for a helix with a constant q value, i.e. a constant pitch. The attenuation factor can also be recognized as $F(q, t)$, the spatial Fourier transform of $P(0 \mid \boldsymbol{r}, t)$:

$$F(q, t) = \int_0^{\infty} P(0 \mid \boldsymbol{r}, t) \exp(-\mathrm{i}q \cdot \boldsymbol{r})\, \mathrm{d}\boldsymbol{r} \tag{21}$$

The time evolution of $F(q, t)$ is described by the spatial Fourier transform of equation (4). This gives

$$\frac{\partial F(q, t)}{\partial t} = -Dq^2 F(q, t) \tag{22}$$

and we again find that $F(q,t) = F(q,0) \exp(-Dq^2 t)$. Note that the right-hand side of equation (21) can be interpreted as an average of the phase factor over the distribution of displacements. This viewpoint is explored in Section 5.

2.4 Echo Attenuation in a Constant Gradient

When gradients are present and q is time dependent, $S(z, t)$ in equation (20) describes the evolution of the attenuation factor at a specific time, and the cumulative attenuation is obtained by multiplying together the attenuation factors for the differential time increments. As expected, this procedure yields the diffusion factor displayed in equation (16).

As an illustration of the use of equation (16), consider the echo attenuation for the simple $90^\circ_x - \tau - 180^\circ_y - \tau$ echo experiment shown in Figure 1. In the regions 0 to τ and τ to 2τ the effective gradient amplitudes are $-g$ and g, respectively, as shown in Figure 1(c), and equation (17) gives

$$q(t) = -\int_0^t \gamma g\, \mathrm{d}t', \quad 0 < t < \tau$$
$$q(t) = -\gamma g\tau + \int_\tau^t \gamma g\, \mathrm{d}t', \quad \tau < t < 2\tau \tag{23}$$

q(t) from equation (23) is then substituted into equation (16) to obtain

$$\ln\ \psi(2\tau) = -D(\gamma g)^2 \left[\int_0^{\tau} (t')^2\, \mathrm{d}t' + \int_\tau^{2\tau} (t' - 2\tau)^2\, \mathrm{d}t' \right] \tag{24}$$

Therefore, the attenuation resulting from diffusion at the echo time 2τ is found to be

$$\ln\ \psi(2\tau) = \tfrac{1}{12} D\gamma^2 g^2 (2\tau)^3 \tag{25}$$

and the total echo amplitude $S(2\tau)$ is given by

$$S(2\tau) = M_0 \exp(-2\tau/T_2) \exp[-D\gamma^2 g^2 (2\tau)^3/12] \tag{26}$$

The well-known τ^3 dependence of the exponent in the diffusion factor is the reason why the simple spin echo experiments are usually not satisfactory for the measurement of T_2.[14,15]

3 PULSED FIELD GRADIENT NMR

The introduction of pulsed field gradients (PFGs) in place of steady gradients for diffusion measurements greatly improves the spin echo diffusion experiment and opens a wide range of applications.[12] The basic Stejskal–Tanner experiment, illustrated in Figure 2, has two major advantages over constant gradient methods. First, by confining the gradients to relatively narrow time intervals, this experiment permits gradient areas to be varied without changing the echo time, so that the attenuation resulting from relaxation can be held constant. Second, the echo can be recorded in a homogeneous magnetic field. Spectral information is, therefore, retained and frequency resolved diffusion measurements are possible. These advantages are widely acknowledged, and almost all modern NMR diffusion measurements are made with some form of pulsed gradient experiment. However, a disadvantage of pulsed experiments should be noted. The switched gradient experiments require current pulses that inevitably produce heat, mechanical forces, and eddy currents.

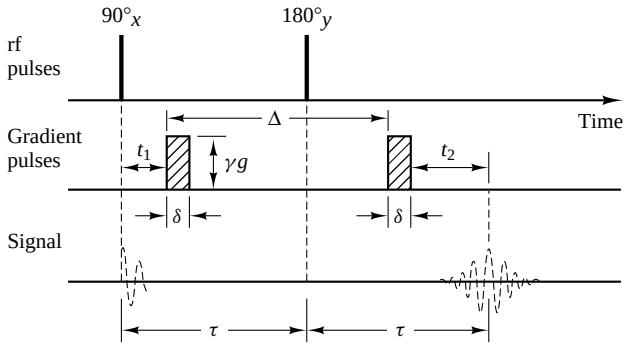

Figure 2 The Stejskal–Tanner pulsed field gradient spin echo diffusion experiment

3.1 The Spin Echo SE Diffusion Experiment

The echo attenuation resulting from diffusion with the sequence shown in Figure 2 can be obtained by direct application of equation (16). The total echo amplitude is given by[12]

$$S(2\tau) = M_0 \exp(-2\tau/T_2) \exp[-Dq^2(\Delta - \delta/3)] \qquad (27)$$

where $q = \gamma g \delta$ and the effect of transverse relaxation has been included. The attenuation factor $\psi(2\tau)$ for diffusion alone is easily isolated by taking the ratio of the echo amplitude with applied gradient switched on, $S(2\tau)$, to the amplitude with gradient switched off, $S_0(2\tau)$. Thus $\psi(2\tau) = S(2\tau)/S_0(2\tau)$. However, transverse relaxation diminishes the signal-to-noise ratio and may present a serious problem for slowly tumbling macromolecules and molecular aggregates where T_2 values tend to be short. Transverse relaxation and J modulation effects present special problems for coupled spin systems.[16,17] T_2 is often much shorter for coupled spins than expected from the rotational correlation times alone, and spin coupling in homonuclear spin systems can prevent complete refocusing of the spin echo. The latter effect arises because hard rf pulses exchange the spin states of nuclei that are coupled to the nuclei under observation. Precession frequencies change, and refocusing depends on the magnitude of the spin coupling constant J. For a coupled pair of spin-$\frac{1}{2}$ nuclei this leads to echo maxima when $\tau = n/J$ and negative echoes when $\tau = n/(2J)$, where n is an integer and J is in hertz.

Equation (27) is appropriate for the analysis of experimental data when the magnetic field $\boldsymbol{B}_0$ is homogeneous and the gradient pulses are well matched. It may be possible to approximate the effect of an inhomogeneous magnetic field by a constant background gradient $\boldsymbol{g}_0$. The effective gradient is then $\boldsymbol{g} + \boldsymbol{g}_0$ and a complete analysis gives the diffusion factor:[12]

$$\begin{aligned}\psi(t) = \exp\{-D\gamma^2[&g^2\delta^2(\Delta - \delta/3) + 2g_0^2\tau^3/3 \\ &-\boldsymbol{g}\cdot\boldsymbol{g}_0\delta(t_1^2 + t_2^2 + \delta(t_1 + t_2) \\ &+2\delta^2/3 - 2\tau^2)]\}\end{aligned} \qquad (28)$$

Gradient pulse mismatch changes the position and intensity of the echo. Some investigators have resorted to adjusting the width of the second gradient pulse to reposition the echo, but this is not a practical solution in experiments where the gradient areas are automatically ramped through a series of values and the signal is recorded starting from the center of the echo. A detailed analysis shows that sensitivity to the gradient pulse mismatch is decreased by the application of a constant gradient parallel to the gradient pulses.[18]

3.2 The Stimulated Echo Diffusion Experiment

A sequence containing three 90° rf pulses was among the first echo forming sequences studied by Erwin Hahn in his pioneering work on time dependent NMR.[14] He found that five echoes are formed in a steady gradient experiment. As shown in Figure 3(a) they are the primary echo (PE) at $2\tau_1$, the stimulated echo (STE) at $\tau_1 + \tau_2$, and three secondary echoes that are usually not of interest. The effect of diffusion on the STE has been investigated for a steady gradient[19] and for gradient pulses.[20] Both versions of the experiment are of current interest (Section 9), but this section focuses on pulsed gradients.

An intuitive understanding of the formation of the stimulated echo can be gained from the graphical representation of the isochromats shown in Figure 3(b). Here the superscripts (−) and (+) indicate 'immediately before' and 'immediately after' the rf pulse at the indicated time. The magnetization ribbon at 0^+, characterized by $q = 0$, is wound up by the action of the first gradient pulse so that at τ_1^- the pitch of the resulting helix is $\Lambda = 2\pi/q$. In the presence of the gradient pulse and a very weak background gradient, $q \approx \gamma g \delta$. The new feature here is the rf pulse at time τ_1 that rotates each isochromat through 90° about the $-x$ axis so that its y component is stored in the z direction. The resulting pattern of z magnetization is responsible for the STE. At τ_2 the third 90° rf pulse rotates the z magnetization back into the yx plane. If this pulse is directed along the x axis, the isochromats all become collinear with the y axis so that the magnetization lies in the yz plane as represented by the cos (qz) function shown in Figure 3(b). The refocusing effect necessary to form the STE results from twisting action of the second gradient on this pattern. At the time of the STE the y components of the isochromats are all positive and their resultant reaches a maximum along the y direction, even though they do not all lie in the yz plane. In fact, the projection of the tips of the isochromats onto the xy plane gives a circle tangent to the xz plane. Note that the STE results from a pattern of magnetization density in the z direction, regardless of the source of the pattern. A specially prepared sample with alternating layers having different spin densities can give an STE in an experiment with a single rf pulse.

The magnetization components remaining in the x and y directions after the second rf pulse are responsible for the primary echo and secondary echoes. These components result from the x and z components of the magnetization at τ_1^-. In the pulsed gradient experiment the PE and the secondary echoes do not refocus.

The primary advantage of the STE sequence is that the transverse evolution time for magnetization can be reduced. This is especially important when T_2 is small but, as mentioned above, can also be used to minimize the effects of J modulation. In the absence of a significant background

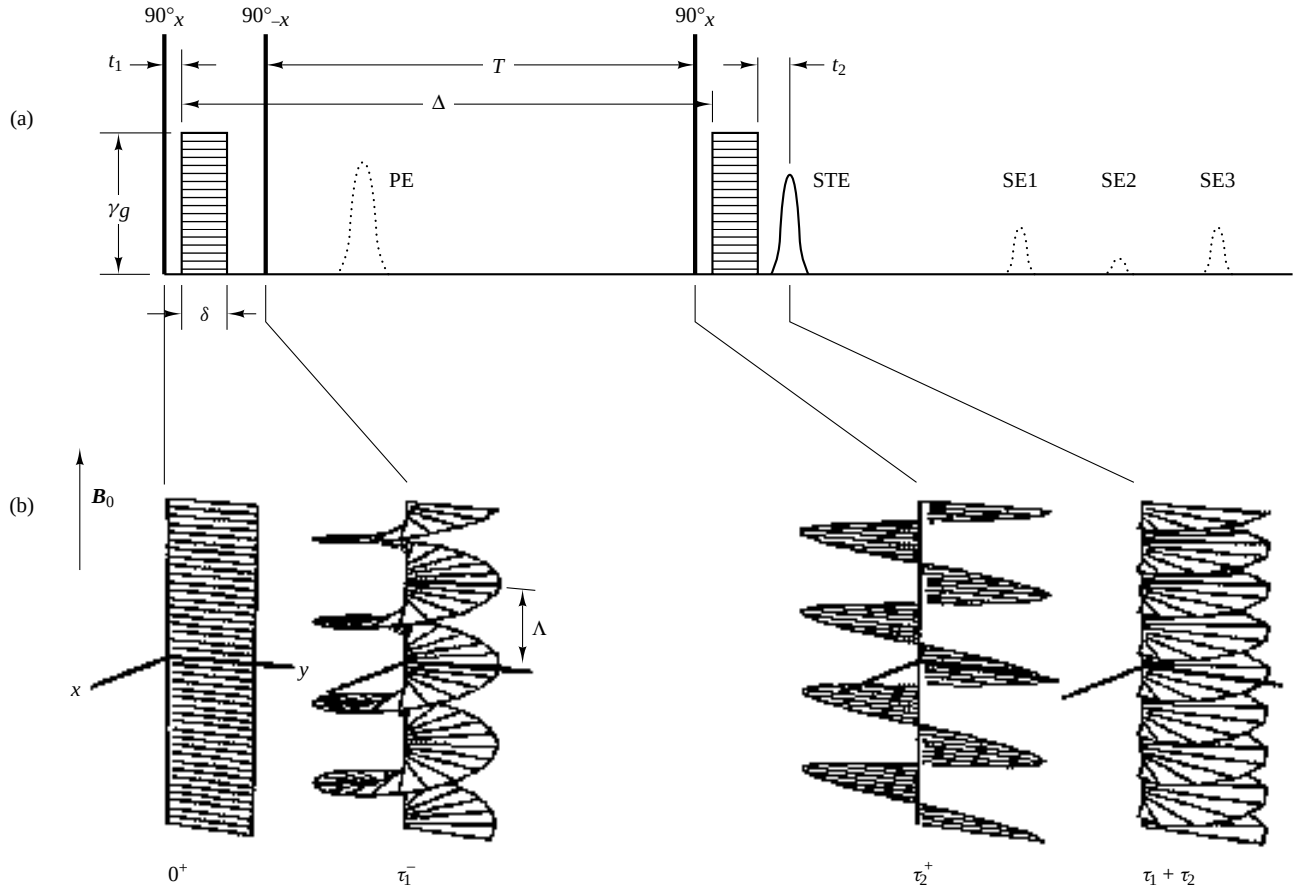

Figure 3 The pulsed field gradient stimulated echo (STE) diffusion experiment: (a) the pulse sequence and echoes; (b) evolution of the isochromats

gradient, i.e. when $g_0 \approx 0$, the total amplitude of the STE is given by

$$S(T + 2\tau_1) = (M_0/2)\exp(-2\tau_1/T_2 - T/T_1) \times \exp[-Dq^2(\Delta - \delta/3)] \quad (29)$$

Equation (29) also shows the major disadvantage of STE experiments, namely the amplitude of the echo is reduced by a factor of 2 relative to a spin echo (SE) if T_1 and T_2 are equal. The reason for this loss is obvious from Figure 3(b). The second rf pulse only stores the y components, and the second gradient only partially refocuses the magnetization for the STE. This loss may be recovered many times over depending on the ratio of T_2 to T_1 and the amount of attenuation. For example, when T_2/T_1 = 0.5 and T/T_1 = 0.1 the STE signal is 23% larger than an SE with the same echo time (TE), and when T/T_1 = 0.5 the STE is 45 times as large as the SE. It is also advantageous to keep $\tau \ll 1/J$ for spin coupled systems, in order to minimize the modulation of intensities and to make sure that all signals are positive. In general, the advantages of the STE experiment outweigh the loss of signal resulting from the factor of 0.5, and STE is becoming the standard method for diffusion measurements.

3.3 Special Sequences for Heterogeneous Samples

In some cases background gradients cannot be ignored. When the background gradients are uniform, corrections can be applied to the attenuation factor as shown in equation (28) for the spin echo experiment. However, in heterogeneous samples where the backgrounds gradients $\boldsymbol{g}_0$ have random magnitudes and directions and may be comparable in magnitude to the applied gradients, simple corrections are not possible. Fortunately, pulse sequences can be designed to minimize the corrupting effects of the background gradients. A useful principle is that a 180° rf pulse refocuses isochromats dispersed by a time independent gradient, but that refocusing of the effects of an applied gradient $\boldsymbol{g}_A$ can be avoided either by changing the polarity of the gradient or by applying the gradient pulse on one side of the 180° rf pulse. A number of sequences have been proposed to minimize the effect of the cross term $\boldsymbol{g}_0 \cdot \boldsymbol{g}_A$. Here two schemes are used as illustrations, one for SE and one for STE experiments.

The Karlicek–Lowe (KL) alternating PFG sequence is shown in Figure 4.[21] Background gradients are effectively reversed by the second 180° rf pulse, but the effective applied gradient $\boldsymbol{g}_A$ is unchanged. The third 180° pulse begins the refocusing period, since the applied gradient is not reversed this time. Note that the intervals δ_1 and δ_2 have been introduced in the pulse sequence so that the rf pulses and the gradient pulses will not overlap. The general version of this sequence has n 180° pulses and the echo occurs at $2n\tau$. The cross term $\boldsymbol{g}_0 \cdot \boldsymbol{g}_A$ is avoided by requiring that the number of positive $\boldsymbol{g}_A$ intervals equal the number of negative $\boldsymbol{g}_A$ intervals, thus restricting n to the values (5, 9, ... , $4m$ +

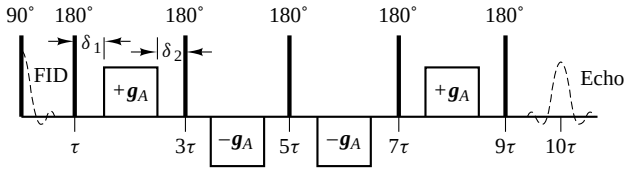

Figure 4 The Karlicek–Lowe alternating pulsed field gradient experiment for minimizing the effects of background gradients[21]

1; m = 1, 2, 3, ...). The effect of the complete sequence on the echo amplitude can be calculated by means of equation (16), with the simplifying assumption that 180° pulses can be replaced with gradient reversals. The solution for the general sequence is:

$$\ln[\psi(2n\tau)] = \frac{-2\gamma^2 D}{3}\left\{ng_0^2\tau^3 + (n-1)^3 g_A^2 \left[\tau - \frac{(\delta_1+\delta_2)}{2}\right]^2\left[\tau + \frac{(\delta_1+\delta_2)}{(n-1)^2}\right]\right\} \quad (30)$$

This sequence has been demonstrated with heterogeneous samples having g_0 values of nearly 3 kG cm^{-1}. It has also been used in imaging applications to determine the spatial distribution of diffusion coefficients.[21]

The KL sequence is effective, but is at a disadvantage for samples having T_2 much smaller than T_1. In order to deal with short transverse relaxation times Cotts et al.[22] have proposed a number of sequences based on the STE diffusion experiment. The standard STE pulsed gradient diffusion sequence in the presence of a background gradient $\boldsymbol{g}_0$ is shown in Figure 5(a) and the attenuation factor obtained by Tanner is given by[20,22]

$$\ln\ \psi[(\Delta+2\tau)] = -\gamma^2 D\left\{\delta^2\left(\Delta+\tau-\frac{\delta}{3}\right)g_A^2 + \delta\left[2\tau\Delta + 2\tau^2 - \frac{2\delta^2}{3} - \delta(\delta_1+\delta_2) - (\delta_1^2+\delta_2^2)\right]\times \boldsymbol{g}_A\cdot\boldsymbol{g}_0 + \tau^2\left(\Delta+\frac{2\tau}{3}\right)g_0^2\right\} \quad (31)$$

A sequence that eliminates the cross term $\boldsymbol{g}_0\cdot\boldsymbol{g}_A$ when $\delta_1 = \delta_2$ and reduces the effect of g_0^2 is shown in Figure 5(b). The attenuation factor calculated for this 13 interval sequence is

$$\ln[\psi(\Delta+4\tau)] = -\gamma^2 D\left[\delta^2\left(4\Delta+6\tau-\frac{2\delta}{3}\right)g_A^2 + 2\tau\delta(\delta_1-\delta_2)\boldsymbol{g}_A\cdot\boldsymbol{g}_0 + \frac{4\tau^3 g_0^2}{3}\right] \quad (32)$$

A number of more effective but also more complicated sequences have been designed. For example, a 17 interval sequence that is the STE version of the KL sequence with storage at 6τ and recovery of transverse magnetization at Δ + 6τ has the advantages of the 13 interval sequence but gives a larger coefficient for g_A^2. An extension to n pairs of gradient pulses ($n \leq 12$) has been found to be even more effective in eliminating the effects of g_0.[23]

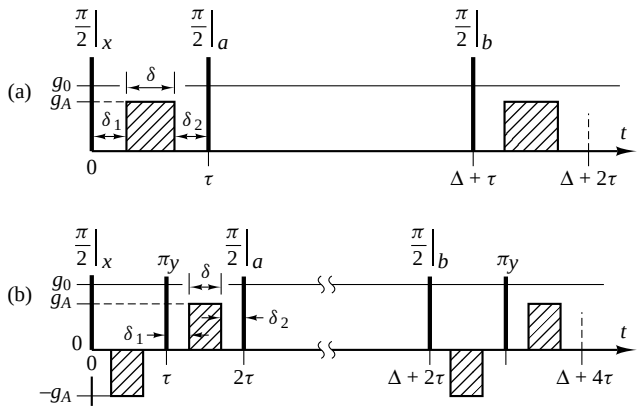

Figure 5 (a) The standard stimulated echo (STE) sequences with a background gradient. (b) A 13 interval STE sequence for minimizing the effects of background gradients[22]

3.4 Modulated Gradients

Modulated gradients, in particular gradients with sinusoidal time dependence, have been suggested as alternatives to pulsed gradients.[12,24] Modulated gradients may be easier to implement than pulsed gradients and may cause less trouble with eddy currents in metal magnet structures. These advantages have not yet attracted many users. However, modulated gradients should be of interest for another reason: they introduce flexibility into NMR studies of motion and may permit frequency-dependent diffusion coefficients to be studied that are inaccessible with conventional PFG-NMR experiments.[25,26]

In transport theory the frequency dependent self-diffusion tensor is defined as the spectrum of the velocity correlation function:

$$D_{\alpha,\beta}(\omega) = \frac{1}{2}\int_{-\infty}^{\infty} \overline{v_\alpha(0)v_\beta(t)}\exp(\mathrm{i}\omega t)\,\mathrm{d}t \quad (33)$$

where α and β represent the Cartesian coordinates x, y, z. In order to investigate the frequency dependence of $D_{\alpha\beta}(\omega)$, Stepisnik[26] has developed a general theory for the echo attenuation exponent $\alpha(t)$, defined by $\psi \propto \exp[-\alpha(t)]$, in the presence of a modulated gradient. Under certain conditions $\alpha(t)$ can be expressed as

$$\alpha(t) = \frac{1}{2\pi}\gamma^2\int_{-\infty}^{\infty} D_{zz}(\omega)S(\omega,t)\,\mathrm{d}\omega \quad (34)$$

where

$$S(\omega,t) = \frac{|\boldsymbol{g}(\omega,t)|^2}{\omega^2}, \quad \boldsymbol{g}(\omega,t) = \int_0^t \boldsymbol{g}_{\mathrm{eff}}(t')\exp(-\mathrm{i}\omega t')\,\mathrm{d}t' \quad (35)$$

Here $\boldsymbol{g}_{\mathrm{eff}}(t)$ includes inversions to account for 180° pulses, as discussed in Section 2.2. Equation (34) shows that echo

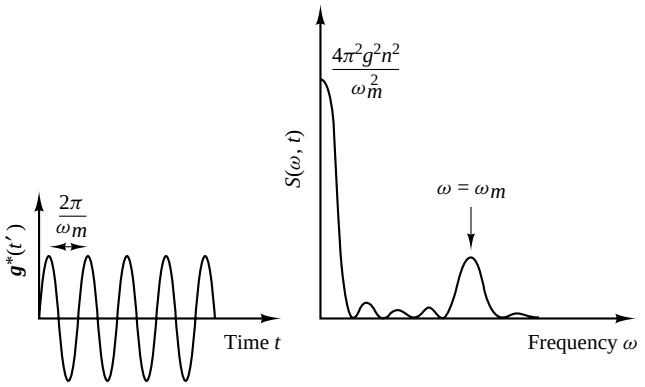

Figure 6 Sinusoidal modulation: the gradient $\boldsymbol{g}_{\text{eff}}(t)$ and its spectrum $S(\omega, t)$[25]

attenuation depends on the spectral density of molecular motion and the spectrum of the gradient.

This 'gradient spectrum' formulation is consistent with the Stejskal–Tanner result for the conventional gradient echo experiment that depends on $\boldsymbol{D}(0)$. The power of Stepisnik's method is revealed with modulated gradients that offer the possibility of probing the frequency dependence of $\boldsymbol{D}(\omega)$. For example, Figure 6 shows a sinusoidal gradient with amplitude $\boldsymbol{g}$ and its spectrum, and the application of equation (34) gives:

$$\alpha(t) = \frac{\gamma^2 \boldsymbol{g}^2}{\omega_{\text{m}}^2} t[D_{zz}(0) + \tfrac{1}{2} D_{zz}(\omega_{\text{m}})] \qquad (36)$$

Therefore, $\boldsymbol{D}(\omega)$ can be investigated by measuring $\alpha(t)$ for different modulation frequencies. It has been pointed out that this technique permits rapid motions to be investigated without reducing the evolution period.

3.5 Radiofrequency Field Gradients

The difficulties encountered in producing large pulsed gradient fields and in controlling the induced eddy currents are well known. A method that avoids these problems, albeit at some cost, is the use of rf field gradients in place of B_z gradients. This is essentially an extension of the rotary echo method to diffusion measurements.[27] A single turn rf coil around the x axis in the laboratory frame provides a $\boldsymbol{B}_1$ field gradient, $\boldsymbol{g}_1$ perpendicular to the $\boldsymbol{B}_0$ field. The result is phase encoding of x positions, so that a helix of magnetization lies along the x axis. One implementation of this method (Figure 7) uses two rf coils to produce homogeneous and inhomogeneous rf fields.[28] An inhomogeneous pulse of length δ imparts the phase angle $\gamma g_1 x \delta$ in the yz plane at x. A homogeneous (hard) 180°_y pulse reverses the sign of the phase, and the second inhomogeneous pulse unwinds the helix to refocus magnetization along the z axis. Finally, a hard 90°_x pulse rotates the magnetization into the y direction in the rotating frame so that the signal can be detected.

The effect of diffusion is to smear out the helix as in the conventional PFG-SE experiment, and the same arguments lead to the exponential attenuation factor in equation (27). However, the effect of spin relaxation is different with rf gradients. If $T_2 \gg \Delta$, the magnetization is completely recovered by the second gradient pulse in the absence of

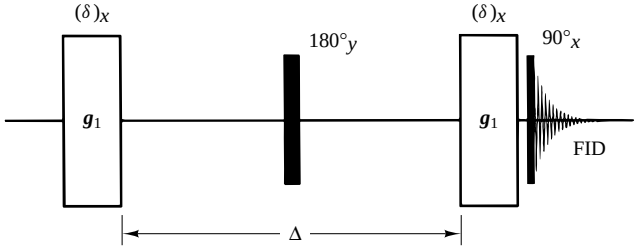

Figure 7 Sequence for rf gradient diffusion measurements with two coils: rf gradients $\boldsymbol{g}_1$ and hard 90° and 180° pulses are shown[28]

diffusion. However, with $T_2 \ll \Delta$ the isochromats are parallel to the z axis at the beginning of the second inhomogeneous pulse and refocusing only recovers half of the initial magnetization as recovered in STE experiments. Net transverse magnetization can also be removed by means of an inhomogeneous $\boldsymbol{B}_0$ field during Δ to ensure the rotary equivalent of the STE experiment. The signal at $\Delta + \delta$ is known as a 'stimulated rotary echo' (SRE).[29] There is also an echo at 2Δ that is T_2-weighted but may be useful for diffusion measurements. It turns out that the SRE experiment can be implemented with a single rf coil and without the hard 180_x and 90°_x rf pulses. As in the STE experiment the 180_x pulse is not needed, and in place of the 90°_x rf pulse the second inhomogeneous pulse can be lengthened by the amount τ that corresponds to a 90° rotation for isochromats at the center of the sample.

The rf gradient experiments are successful and provide convenient gradient switching without harmful eddy currents. Unfortunately, the gradient amplitudes are limited. The largest g_1 reported to date is 15.2 G cm^{-1}, and the measurement of small diffusion coefficients requires rf pulse lengths greater than 10 ms. Still a diffusion coefficient of 3.3×10^{-8} cm^2 s^{-1} has been measured to within 5%, and the method is promising.[29]

3.6 Multiple Quantum Diffusion Measurements

Multiquantum (MQ) NMR experiments have the following advantages for the study of molecular diffusion: (a) precession frequencies increase linearly with the order $n = \Delta m$ of the coherence; (b) MQ spectra are simplified with respect to the single quantum spectrum; and (c) for N coupled protons the N-quantum transition is free of dipolar couplings. The possible limitations are that the spectrum must show splittings from scalar, dipolar, or quadrupolar coupling; and that, except for double quantum excitations, there is a loss of sensitivity because of the inefficient transfer of magnetization.

The first two demonstrations of MQ diffusion measurements involved solutes in liquid crystal solvents where dipolar splittings are evident.[30,31] For example, benzene in a nematic phase diffusion permits measurements to be made with n = 1 to 6 by means of the pulse sequence shown in Figure 8.[31] In this sequence MQ orders are present during the diffusion period Δ and at the MQ echo. A short gradient pulse after the echo, but during the MQ evolution, and a set of n gradient pulses after recall of single quantum coherence provide the n-quantum filter. The effective gradient is increased by a factor

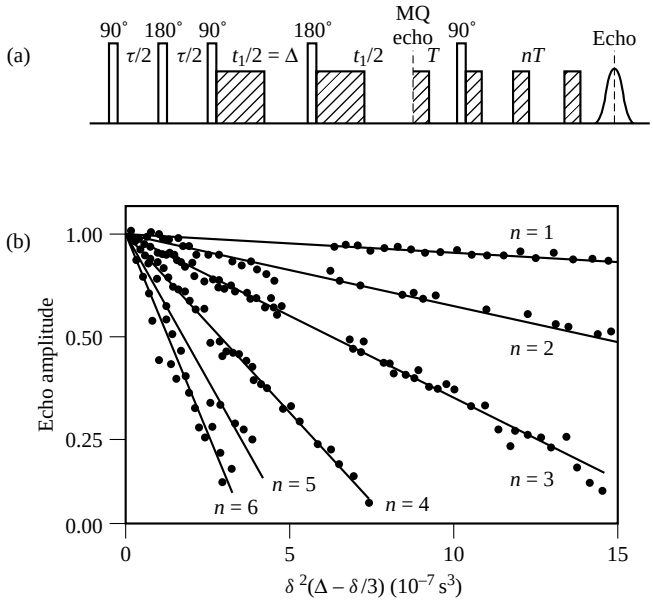

Figure 8 The multiquantum (MQ) diffusion experiment: (a) sequence for multiquantum excitation and n-quantum filtering; (b) echo intensities for coherences with n = 1 to 6 for benzene in a nematic solvent[31]

of n for the n-quantum coherence and the echo attenuation factor becomes:

$$\psi(t_1) = \exp[-n^2\gamma^2 g^2 \delta^2 D(\Delta - \delta/3)] \qquad (37)$$

This effect is elegantly illustrated by the plot of echo amplitudes for benzene shown in Figure 8(b). While this experiment may be most valuable for slow moving molecules in anisotropic environments, it can also provide enhanced gradients and MQ filtering in isotropic phases when scalar coupling is present.[32,33]

The use of zero quantum coherences in diffusion studies has been discussed in connection with the use of static gradients and the avoidance of eddy current effects.[34] However, high resolution is still obtained by switching off the gradient before data acquisition.

4 THE FT-PFG-NMR METHOD AND DIFFUSION ORDERED TWO-DIMENSIONAL NMR SPECTROSCOPY

The measurement of spin relaxation in complex systems by FT methods was suggested and demonstrated by Vold et al.[35] Their example was an inversion recovery experiment for the measurement of T_1, but frequency resolved measurements of transverse relaxation and diffusion rates were also discussed. The simultaneous measurement of diffusion coefficients for all components in a mixture was demonstrated by James and McDonald[36] with a spin echo experiment similar to that illustrated in Figure 2 except that the gradient was on almost the full time between the rf pulses. The second half of the spin echo at 2τ was Fourier transformed to obtain the complete spectrum of a mixture of dimethyl sulfoxide (DMSO) and water, and the experiment was repeated for 10 values of τ. The ratios of the peak intensities with and without the gradient pulses then gave the diffusion factor $\psi(2\tau)$ for each line. This type of experiment has been implemented on FT NMR spectrometers and applied to a variety of chemical systems.[37–39] The work of Stilbs and coworkers in particular stimulated much interest in diffusion measurements. An early example of the FT-PFG-NMR experiment for a mixture containing chloroform, benzene, dichloroethane, 1,4-dioxane, acetone, cyclopentane, cyclohexane, and tetramethylsilane is shown in Figure 9.[40] The gradient pulse amplitude was approximately 1.2 G cm^{-1} and the different values of q were obtained by varying the duration δ as shown on the right-hand side of the figure.

FT-PFG-NMR experiments demonstrate that information about diffusion and flow can be encoded into high-resolution data sets. This is very important because it addresses the shortcoming of NMR as an analytical tool. High-resolution NMR is highly selective because it reports on details of the local environments of nuclei, i.e. short range interactions. However, NMR is not sensitive to long range interactions of nuclei (>1 nm) and is only indirectly affected by the overall sizes and charges of macromolecules and molecular aggregates. Therefore, NMR is not particularly good for the analysis of complex mixtures. However, hydrodynamic properties do depend on size and charge, and FT-PFG-NMR opens the door to the utilization of this information in NMR analysis.

Diffusion ordered two-dimensional NMR (DOSY) is primarily concerned with the analysis and display of data obtained in FT-PFG-NMR experiments.[41] Plots of signal intensities versus gradient pulse lengths, or areas, are somewhat analogous to FIDs. The data sets can be analyzed to determine one or possibly more diffusion coefficients, but the results are not obvious by inspection of the decay curves. Just as FIDs are Fourier transformed to obtain 'user-friendly' frequency spectra, diffusion dependent decays can be transformed to obtain 'diffusion spectra'. DOSY experiments are designed to acquire automatically high-resolution NMR data sets for an exponentially spaced set of q values. The frequency spectra are obtained by Fourier transformations and the data sets at each chemical shift are inverted by approximate inverse Laplace transforms (ILTs) with respect to q^2 to generate two-dimensional diffusion spectra.

Signal stability is crucial in DOSY, and the following features have been incorporated: (i) the gradient pulses are matched within 10 ppm so that the echo positions do not vary as q is changed;[42] (ii) currents induced by the gradient pulses are minimized through the use of actively shielded gradient coils;[43,44] and (iii) signal distortions resulting from residual eddy currents are avoided through storage of the echo signal while the eddy currents decay. The pulse sequence chosen for this experiment is the 'longitudinal eddy delay' (LED) sequence shown in Figure 10.[45] This is a modified STE sequence with a fourth rf pulse to store the STE and a fifth rf pulse to recall the magnetization after the eddy current settling period. The gradient prepulses establish a steady state response so that the fourth and fifth gradient pulses will have equivalent effects.[46] Note that $\Delta = T + \tau$ and, in general, $\tau \ll T$, so that the evolution period for transverse magnetization between the first rf pulse and the STE is negligible. Also, phase cycling of the five rf pulses and a homospoil gradient pulse during T_e are used to eliminate the secondary echoes. With this

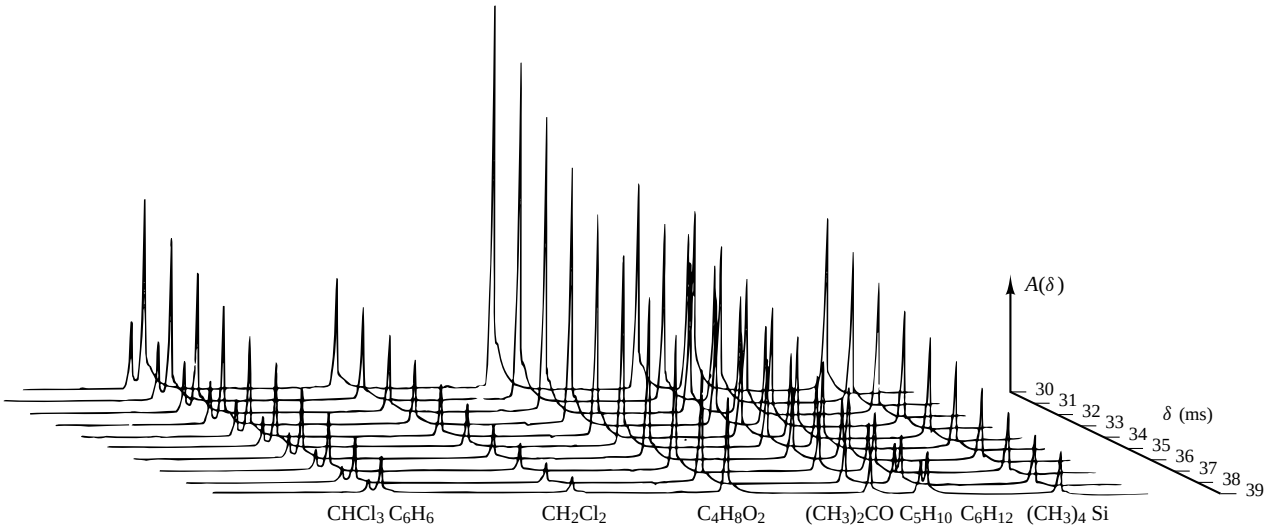

Figure 9 FT-PFG-NMR stack plot for a multicomponent mixture. The gradient pulse amplitude is constant, and the pulse duration δ increases from back to front[40]

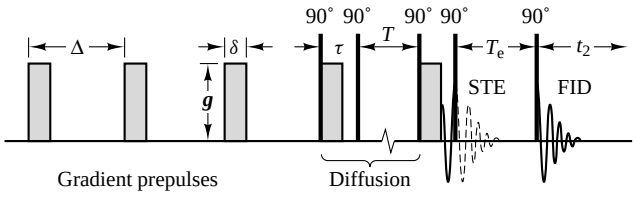

Figure 10 The LED pulse sequence. The phase cycling and homospoil pulse during T_e are not shown

system diffusion coefficients down to 10^{-10} cm^2 s^{-1} have been measured for gel stabilized samples. The lower limit for low viscosity samples is usually determined by convection currents resulting from temperature gradients.[47]

In DOSY, FIDs are acquired for 20–50 exponentially spaced q values and are Fourier transformed to obtain frequency spectra. The result is a two-dimensional data set of the form

$$f(q, \nu) = \sum_{j=1}^{N_\lambda} A_j(\nu) \exp[-D_j(\Delta - \delta/3)q^2] \qquad (38)$$

where $A_j(\nu)$ is the one-dimensional NMR spectrum of the jth diffusing species when $q = 0$ (taking into account transverse and longitudinal relaxation), D_j is the associated tracer diffusion coefficient, and N_λ is the number of components required for the fit. The aim is to analyze the data set for each frequency ν so that a set of amplitudes A_j and diffusion coefficients D_j is obtained. This set is then used to generate a diffusion spectrum with peak positions and amplitudes that correspond to the D_j and A_j values, respectively.

Unfortunately, the fitting of data (with noise) with an equation of the form of equation (38) is an ill-conditioned problem, and infinitely many sets of solutions may fit the data very well (see Section 10). Since it is not sufficient to fit the data, additional information must be introduced to aid in selecting the most likely solution for a real mixture. The first decision is whether the sample contains components with well defined (discrete) diffusion coefficients or if continuous distributions, i.e. polydispersity, must be considered. In the discrete case, data inversion programs such as DISCRETE[48,49] and SPLMOD[50,51] are appropriate for automated analysis since they do not require initial estimates of the parameters, but they must be supplemented with prior knowledge about the nature of the acceptable solutions. For example, signal amplitudes in LED experiments (with $\tau \ll \Delta$) and decay constants (diffusion coefficients) must be nonnegative. Also, the range of physically acceptable diffusion coefficients, the diffusion coefficients accessible to the PFG-NMR experiment, and the resolving power of the SPLMOD analysis are known. This knowledge combined with data analysis experience led to the following conservative set of acceptability criteria:

1. Diffusion coefficients must be feasible and experimentally accessible.
2. Standard errors in diffusion coefficients reported by SPLMOD must be less than 30%.
3. Diffusion coefficients of components at the same chemical shift must differ by a factor of more than 2.

These rules are included in a computer algorithm so that frequently occurring artifacts can be rejected.

When a solution has been found that meets the criteria at each frequency in the NMR spectrum, the DOSY display is generated with normalized Gaussians having center positions and intensities equal to the derived diffusion coefficients and amplitudes, respectively. Thus, the DOSY display has the form

$$F(D, \nu) = \sum_{j=1}^{N_\lambda} A_j(\nu) G_j(D) \qquad (39)$$

where

$$G_j = \frac{1}{\sqrt{2\pi\sigma_j^2}} \exp\left[-\frac{(D - D_j)^2}{2\sigma_j^2}\right] \qquad (40)$$

Here σ_j is derived from the error reported by the analysis program with an allowance for systematic errors. An example

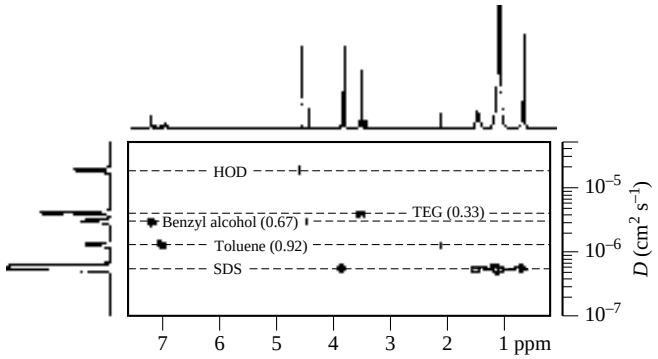

Figure 11 DOSY display processed with SPLMOD for a mixture containing toluene, benzyl alcohol, tetraethylene glycol (TEG), and SDS micelles in D_2O.[52] The degrees of solubilization p_j are given in parentheses

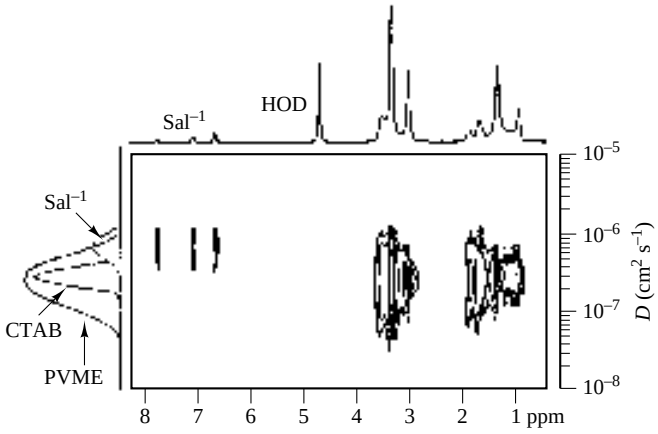

Figure 12 DOSY display precessed with CONTIN for a mixture containing CTAB, PVME, and NaSal (see text)[57]

of the application of DOSY to a discrete mixture is shown in Figure 11.[52] The various solutes are solubilized by the surfactant sodium dodecyl sulfate (SDS). The solutes exchange between SDS micelles and the bulk solution so rapidly that the PFG-NMR experiment reports only the time averaged diffusion coefficient for each species. Therefore, for the jth solute the observed diffusion coefficient D_j is given by[53,54]

$$D_j = p_j D_j^{\text{mic}} + (1 - p_j) D_j^{\text{free}} \tag{41}$$

where p_j is the degree of solubilization, and D_j^{mic} and D_j^{free} are the tracer diffusion coefficients for solubilized and free molecules, respectively. The diffusion coefficients in this example are so similar that resolution in the NMR dimension is essential for a complete analysis. High-resolution spectra were obtained in this experiment by means of a stop-and-go spinner system that permitted the sample to be stationary during the diffusion time Δ but to spin during data acquisition.[55]

Continuous distributions are encountered with many systems of interest. Examples include micelles, microemulsion droplets, vesicles, and polymers. Equation (38) can be rewritten to emphasize the continuous distribution $g(\lambda)$ of diffusion coefficients contributing to the data set at a particular frequency ν. Thus

$$G(s) = \int_0^\infty g(\lambda) \exp(-\lambda s)\, \mathrm{d}\lambda \tag{42}$$

where $\lambda = D$ and $s = q^2(\Delta - \delta/3)$. The factoring of the exponent in equation (38) is a matter of convenience, and in cases where $(\Delta - \delta/3)$ is constant one might choose $s = q^2$. The inversion of a data set $G(s)$ containing noise to obtain the diffusion spectrum $g(\lambda)$ is a long-standing problem in data analysis, and its ill-posed nature has been emphasized repeatedly. A large body of literature has been devoted to this problem (see Section 10). The ill-conditioned inverse Laplace transform ILT has been approached by a variety of methods including regularized least-squares (CONTIN) and maximum entropy (MEM). Thus far only CONTIN has been applied to DOSY analyses.[41,56] In this program the linear least-squares method is augmented with prior knowledge about the nature of the solutions and the principle of parsimony. We know that the decay constants (diffusion coefficients) are nonnegative and that the decay kernels are exponential. Also, as noted above, the LED experiment ensures that the signal amplitudes are positive. Parsimony implies that the simplest (smoothest) solution consistent with a priori information and the data is selected. This amounts to discriminating against solutions with high-frequency components (wiggles) by introducing a term to penalize such solutions. The weight given to the penalty is the regularization parameter α that is determined on the basis of the Fisher F-test or by input from the user. Therefore, CONTIN provides an automatic analysis that has some capability to handle multimodal distributions. The primary shortcoming is that enforced smoothness reduces the ability to resolve peaks in the diffusion spectrum and leads to overestimation of the widths of narrow peaks.

The generation of DOSY displays with CONTIN is straightforward. The $G(s)$ versus s data sets are analyzed at every frequency point where the signal-to-noise ratio exceeds a predetermined threshold value to obtain new data sets of intensities versus values of D. Stack plots or contour plots are then constructed without any additional data manipulation. An example of a CONTIN analysis is provided by the DOSY display in Figure 12 for a sample containing 25.0 mM hexadecyltrimethylammonium bromide (CTAB), 15.0 mM sodium salicylate (NaSal), and 7.40 g L^{-1} poly(vinyl methyl ether) (PVME) at 30 °C.[57] The projections on the left-hand side show diffusion distributions for PVME, CTAB, and NaSal. The addition of PVME to the viscoelastic CTAB/NaSal sample resulted in a marked reduction in the viscosity. It is thought that the polymer reduces the length of threadlike CTAB micelles by wrapping around the micelles. Note that the polydispersity of the polymer is consistent with the width of the distribution, but that the associated CTAB shows a much narrower distribution. The width for CTAB results primarily from regularization in the analysis, since CTAB molecules exchange rapidly between aggregates associated with different PVME molecules and exchange narrowing is expected. Figure 12 also shows the smoothing effect of CONTIN on the distribution for NaSal which is monodisperse and should have a vanishingly small width. When preliminary analysis indicates that a relatively narrow unimodal distribution of diffusion coefficients is present at a particular chemical shift, the direct cumulants analysis method may be preferable to CONTIN (see Section 10).

5 THE AVERAGE PROPAGATOR AND THE SCATTERING ANALOGY

In the short gradient pulse limit ($\delta \ll \Delta$) the equations given in Section 2 for the echo amplitude can be recast in a useful and instructive form. Consider the SE experiment illustrated in Figure 2 with gradient pulses of amplitude g in the z direction. The first gradient pulse instantaneously encodes the phase shift $-\gamma\delta g z_0$ for spins at position z_0. During the interval Δ the spins diffuse a distance Z parallel to the gradient to the position $z_0 + Z$, and finally the second gradient pulse, inverted relative to the first one or effectively inverted by a 180° rf pulse, gives the additional phase shift $\gamma\delta g(z_0 + Z)$. Thus, the net phase shift is $\gamma\delta g Z$ for spins starting at time zero. Of course, the echo arises from all of the excited spins and depends on both the initial spatial distribution of spins $\rho(z_0)$ and the conditional probability $P(z_0 \mid z_0 + Z, \Delta)$ that a spin at z_0 at time zero will be at $z_0 + Z$ at time Δ. The sum over all NMR active spins leads to the expression[58]

$$\psi = \int\int \rho(z_0) P(z_0 \mid z_0 + Z, \Delta) \exp(\mathrm{i}qZ)\, \mathrm{d}(z_0 + Z)\, \mathrm{d}z_0 \tag{43}$$

where again $q = \gamma\delta g$ and spin relaxation has been neglected.

We now define the 'average propagator'

$$\overline{P}(Z, \Delta) = \int \rho(z_0) P(z_0 \mid z_0 + Z, \Delta)\, \mathrm{d}z_0 \tag{44}$$

so that the echo amplitude can be written as

$$\psi(q) = \int \overline{P}(Z, \Delta) \exp(\mathrm{i}qZ)\, \mathrm{d}Z \tag{45}$$

This reveals the Fourier transform relationship between $\psi(q)$ and $\overline{P}(Z, \Delta)$ and indicates that $\overline{P}(Z, \Delta)$ can be obtained as the Fourier transform of the echo amplitude.[59,60] Note that for free diffusion in a homogeneous sample, the average propagator is simply the Gaussian function shown in equation (18) with Δ in place of t. Substitution of equation (18) into equation (45) gives

$$\psi(q) = 2(4\pi D\Delta)^{-1/2} \int_0^\infty \exp(-Z^2/4D\Delta) \cos(qZ)\, \mathrm{d}Z \tag{46}$$

and evaluation of equation (46) shows that the echo amplitude is just $\psi(q) = \exp(-Dq^2\Delta)$, as previously derived. In general, the shape of the propagator $\overline{P}(Z, \Delta)$ is determined by average molecular displacements in the sample under study. An example is provided by the diffusion of ethane in NaCaA zeolites;[59] for further information see ***Diffusion in Porous Media***.

It has been pointed out that the Fourier transformation of $\psi(q)$ provides an image of the propagator analogous to the image of spatial positions provided by magnetic resonance imaging (MRI). The q space introduced here is conjugate to the dynamic displacement space $\boldsymbol{R}$ or Z.

Equation (46) suggests an analogy with scattering experiments, in particular dynamic light scattering (DLS), neutron scattering, and holographic relaxation spectroscopy (HRS). In the idealized scattering experiment an incident plane wave having the wave vector $\boldsymbol{k}_\mathrm{i}$ of magnitude $2\pi/\lambda$ is scattered through an angle θ_s by suspended particles. The scattered wave is described by the wave vector $\boldsymbol{k}_\mathrm{s}$ that has a different direction but the same magnitude as the wave vector of the incident wave. In DLS we are concerned with the relative phase ϕ_j of the electric field E_s of the light scattered by the jth scatterer at the detector. This phase angle depends on the path lengths and, as illustrated in Figure 13,

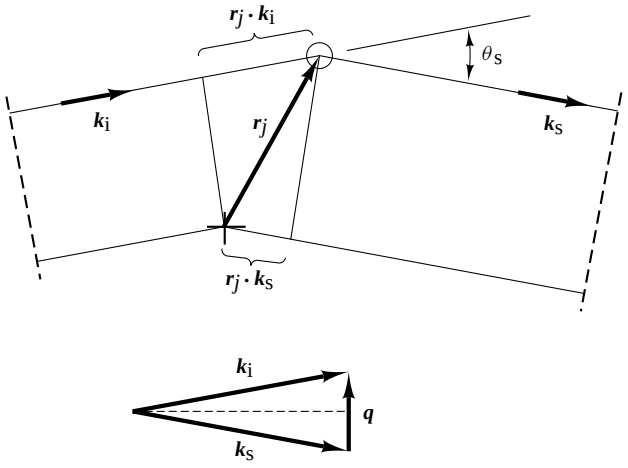

Figure 13 Scattering of a plane wave from a particle at $\boldsymbol{r}_j$ and the reference point (+)

$$\phi_j = \boldsymbol{k}_\mathrm{i} \cdot \boldsymbol{r}_j - \boldsymbol{k}_\mathrm{s} \cdot \boldsymbol{r}_j = \boldsymbol{q} \cdot \boldsymbol{r}_j \tag{47}$$

where elementary trigonometry shows that $|\, q \,| = (4\pi/\lambda) \sin(\theta_\mathrm{s}/2)$. The quantity derived from DLS data is the reduced first-order correlation function $g^{(1)}(\tau)$ defined by

$$g^{(1)}(\tau) = \frac{\langle E_\mathrm{s}^*(0) E_\mathrm{s}(\tau)\rangle}{\langle |E_\mathrm{s}(0)|^2\rangle} \tag{48}$$

If the motions of the scatterers are independent and certain other conditions are satisfied, only 'self-correlation' terms are important and equations (47) and (48) can be combined to obtain:[5,61]

$$|g^{(1)}(\tau)| = \langle \exp\{\mathrm{i}\boldsymbol{q} \cdot [\boldsymbol{r}_j(\tau) - \boldsymbol{r}_j(0)]\}\rangle \tag{49}$$

where $\langle\ \rangle$ represents an average over all scattering particles. This, of course, is equivalent to equation (43) for a uniform distribution of scatterers with τ in place of Δ. The discussion of DLS also applies to neutron inelastic scattering, except that the self-correlation function is available directly without assumptions about independent motions of scatterers from the neutron scattering function for the incoherent fraction.

In DLS the scattering angle determines the magnitude of $\boldsymbol{q}$ and $\sin(\theta_\mathrm{s}/2)$ plays a role similar to that of the gradient area in NMR. Similarly, the diffraction spot in DLS is analogous to the spin echo in NMR. This analogy can be pursued to show why DLS and PFG-NMR measure different types of diffusion coefficient. The key to the difference is the condition necessary for there to be a signal. In the case of light scattering a perfectly uniform distribution of scatterers, as for example in a perfect crystal, cannot produce a diffraction spot since light

scattered by the different scattering centers will interfere and cancel at the detector. The way to get around this problem is to arrange the scatterers so that they behave as a diffraction grating and produce intensity at the desired scattering angle. That is what actually happens in a solution or suspension of particles. Instantaneous concentration fluctuations have Fourier components that scatter light in various directions. This is why a grainy pattern of twinkling speckles is observed when light from a laser beam is scattered by a solution onto a flat surface. The important point is that the concentration of scatterers must vary with position, and time-dependent concentration changes result from mutual diffusion in the presence of concentration gradients.

In NMR it is well known that a single 90° rf pulse cannot produce a spin echo for a uniform sample. After the FID there is complete interference and the isochromats do not refocus. A close analogy with the optical case is found in the STE experiment. Here the magnetization pattern, created prior to the third 90° pulse, plays the role of a 'diffraction grating'. The 90° rf pulse rotates the isochromats into the *xy* plane where they evolve under the influence of a gradient until an echo is formed. The vector addition problem is identical to that found for the electric field in small angle light scattering. However, STE formation does not require spatial variations in the concentrations of particles but rather in the spin polarization (or phases) of the nuclei. Therefore, PFG-NMR detects tracer diffusion. It is, of course, possible to measure mutual diffusion with NMR by creating a periodic concentration pattern, as discussed in Section 3.2.

HRS provides an even more obvious analogy with the STE experiment.[10,62,63] In HRS two monochromatic laser beams are crossed at a small angle in a sample to form an interference pattern that in turn produces a volume hologram of photoproducts. In the low intensity limit the concentration of the jth photoproduct can be expressed as:

$$c_j(z,t) = \langle c_j \rangle + c_{1j} \cos(qz) \tag{50}$$

where $\langle\ \rangle$ represents an average over space and c_{1j} is the amplitude of the grating. The time evolution of the grating is monitored by a laser probe beam incident on the sample at the Bragg angle. In a heterodyne experiment where the diffracted light is mixed with a reference beam, the electric field of the diffracted light is determined and the amplitude of the grating can be mapped as a function of time. If photoexcitation changes optical properties and not hydrodynamic properties, this experiment permits tracer diffusion rates to be measured.

Analogies also appear in the spatial imaging of gratings. In the optical grating experiment a Fourier transformation of the electric field of the diffracted light with respect to the scattering angle yields an image of the diffracting grating. In the simplest case the diffraction spot is represented by a delta function at the angle θ_s and the grating is a cosine function. In the STE experiment an image of the magnetization grating can be obtained by reading out the stimulated echo in the presence of a constant gradient and Fourier transforming the signal with respect to time measured from the third 90° rf pulse. Images of transient magnetization gratings (TMGs) are useful for monitoring the spatial dependence of diffusion and flow.[10] In the medical literature this method is known as 'spatial manipulation of magnetization' (SPAMM).[64]

6 RESTRICTED DIFFUSION AND DIFFUSIVE DIFFRACTION

A significant fraction of NMR diffusion studies have been devoted to the restricted diffusion of fluids since Woessner's studies of porous materials with CW gradients.[65] PFG-NMR studies of restricted diffusion date from the pioneering work of Tanner and Stejskal.[66] Their procedure was to solve the diffusion equation with appropriate boundary conditions for $P(r \mid r', t)$ and to determine the echo amplitude by means of equation (43). Echo amplitudes have been derived for systems where diffusion is restricted by reflecting surfaces in the form of parallel planes, cubic cavities, cylinders, and spheres for steady gradients[67] and pulsed gradients.[66,68] There is much current interest in the study of porous materials by means of PFG-NMR.

The spherical cavity provides an important model for restricted motion in pores and in biological cells and vesicles. This case was treated by Neuman[67] for a steady gradient assuming a Gaussian distribution of phases at the time of the echo, and the calculation was later extended by Murday and Cotts[68] to the pulsed gradient SE experiment. The pulsed gradient solution is shown in equation (51) for a sphere of radius R:

$$\ln[\psi(q)] = -2\gamma^2 g^2 \sum_{m=1}^{\infty} \frac{1}{\alpha_m^4 D(\alpha_m^2 R^2 - 2)} \times \left(2\delta - \frac{2 + x_m^{\tau-\delta} - 2x_m^{\delta} - 2x_m^{\tau} + x_m^{\tau+\delta}}{\alpha_m^2 D}\right) \tag{51}$$

Here $x_m = \exp[-(\alpha_m{}^2 D)]$ and α_m is the mth root of the equation

$$(\alpha_m^2 R^2 - 2)\sin(\alpha_m R) + 2\alpha_m R \cos(\alpha_m R) = 0 \tag{52}$$

The parameters τ, δ, and g are defined in Figure 2, except that here $\tau = \Delta$. In the short time limit ($\Delta \ll R^2/2D$), equation (51) gives $\psi(q) = \exp(-Dq^2\Delta)$ as expected for unbounded diffusion; in the long time limit ($\Delta \gg R^2/2D$), $\psi(q) = \exp(-q^2R^2/5)$. Comparison of these results suggests that the effective diffusion coefficient in the long time limit is $D_{\text{eff}} = R^2/5\Delta$. This turns out to be precisely the mean square displacement $\langle Z^2 \rangle$ divided by 2Δ. The exact solution for $\psi(q)$ in the long time limit obtained by adapting results from the literature of heat diffusion is

$$\psi(q) = 9[qR\cos(qR) - \sin(qR)]^2/(qR)^6 \tag{53}$$

The long time limit of equation (51) agrees with exact result for small values of qR and the deviation is only 0.29% at $qR = 1$.

It is instructive to investigate the long time limit in more detail. If the fluid has the initial density distribution $\rho(z_0)$, in the limit $\Delta \to \infty$ we expect that $P(z_0 \mid z_0 + Z)$ will equal $\rho(z_0 + Z)$. Therefore, the average propagator can be written as

$$\overline{P}(Z,\infty) = \int \rho(z_0)\rho(z_0 + Z)\,\mathrm{d}z_0 \tag{54}$$

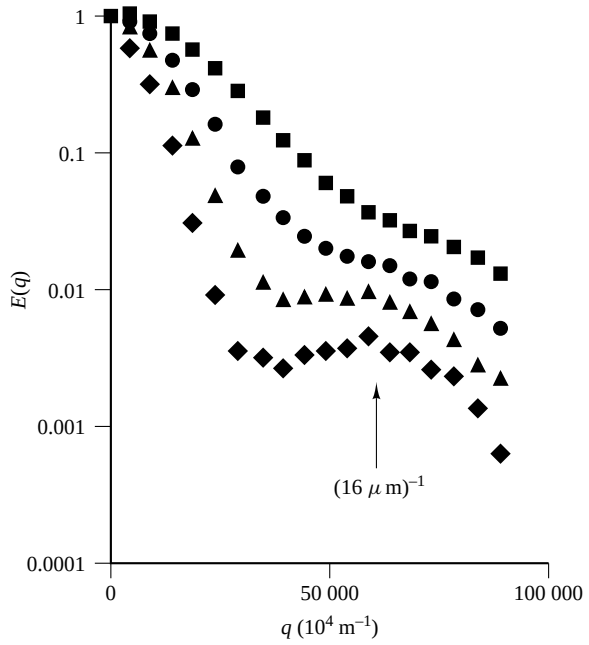

Figure 14 Echo amplitudes versus q^2 for pore glass. The data sets were obtained with Δ = 20 (■), 40 (●), 70 (▲), and 110 (♦) ms. (q in this figure is defined as $1/\Lambda$)[70]

and $\bar{P}(Z,\infty)$ is just the autocorrelation function of the molecular density or the convolution of the density with itself. It is also easy to show that equation (45) takes the form

$$\psi_\infty(q) = \left| \int \rho(z_0) \exp(-\mathrm{i}qz_0)\, \mathrm{d}z_0 \right|^2 \qquad (55)$$

Equations (45) and (54) show that the inverse Fourier transform of the echo intensity provides an image of the autocorrelation function of the density in real space.[69,70] This is the origin of diffraction-like effects in NMR diffusion studies, an idea that has led to a powerful method for the investigation of the structure of porous materials. For example, a 'pore glass' consisting of water in the presence of monodisperse spheres gives the echo intensities versus q shown in Figure 14.[70] At short times there is little indication that a water molecule samples more than one pore, while at longer times the diffraction effect resulting from neighboring pores is clearly visible. A Fourier transformation of an echo curve gives an image of the autocorrelation function. Note that this type of imaging gives resolution several orders of magnitude higher than MRI, since intensity is provided by the entire sample rather than a small voxel; but the information is limited to average features of local structure rather than positions of individual molecules in space.

Other important restricted diffusion problems include motion near an attracting center, diffusion in the presence of permeable walls and surface relaxers, inhomogeneous initial magnetization, and the effect of surface to volume ratios on the time dependence of the average propagator. These topics have been reviewed elsewhere,[25] except for the last one involving microgeometry and surface relaxation, a topic of considerable current interest in connection with the determination of pore size distributions.[71–73]

7 ANISOTROPIC DIFFUSION

Anisotropic environments are found in organized phases such as liquid crystals and zeolite crystallites. The description of diffusion in such systems requires the diffusion tensor $\boldsymbol{D}_{\alpha,\beta}$ in place of the scalar coefficient D. As a consequence, the flux defined in equation (1) depends on orientation and the right-hand side of equation (4) becomes $-\nabla \cdot \boldsymbol{D} \cdot \nabla P(\boldsymbol{r}_0|\boldsymbol{r}, t)$. The attenuation factors have the same forms as previously found except that g^2D is replaced by $\boldsymbol{g} \cdot \boldsymbol{D} \cdot \boldsymbol{g}$. Therefore, if D_x, D_y, and D_z are defined as the principal values of the diffusion tensor the attenuation factor has the form

$$\psi(\theta, \phi) = \exp[-q^2(D_x \cos^2\phi \sin^2\theta + D_y \sin^2\phi \sin^2\theta + D_z \cos^2\theta)\Delta] \qquad (56)$$

where θ and ϕ indicate the orientation of the gradient with respect to the principal axes of the diffusion tensor. For an axially symmetric diffusion tensor with $D_x = D_\perp$ and $D_z = D_\parallel$, we find that the mean square displacement in the direction of the gradient is proportional to $D_\parallel \cos^2\theta + D_\perp \sin^2\theta$. This type of treatment is appropriate for D_2O partially oriented in the lamellar phase of potassium palmitate/D_2O.[74] In this system water diffusion is relatively unrestricted parallel to the bilayers but is limited in the direction of the director.

Unfortunately, the organized systems of interest for PFG-NMR studies are likely to present problems because of severe dipolar and quadrupolar broadening. Both quadrupolar[75] and solid echoes[76] may be useful replacements for the Hahn echo in such cases. Also, a Waugh-type line-narrowing sequence, modified to permit refocusing in the presence of gradient pulses, has been used to measure the anisotropy of a diffusion tensor of liquid crystal molecules in smetic-A and smetic-C phases.[77] These and other examples of measurement of anisotropic diffusion have recently been reviewed by Callaghan.[25]

8 CHEMICAL EXCHANGE INVOLVING DIFFUSING MOLECULES

Chemical rate processes are detected by NMR when nuclei exchange between sites characterized by different spin Hamiltonians.[78] It is also possible that the sites will have similar spin Hamiltonians but will differ in hydrodynamic properties. In such cases the one-dimensional NMR spectrum is unaffected by exchange, but diffusion measurements may reveal the exchange process and permit it to be studied. Examples include: (i) association equilibria in which molecules diffuse freely or in association with larger, more slowly diffusing particles; and (ii) samples composed of subregions that are characterized by different numbers of spins and different diffusion coefficients.

Consider an FT-PFG-NMR experiment of the SE or STE type on a sample in which nuclei in various 'exchanging' sites all contribute to the same NMR line. In the slow exchange limit where exchange between sites is unlikely during the diffusion time Δ the signal amplitude can be described by a sum of exponentials as shown in equation (38). At the other extreme where many exchanges occur during Δ, a single exponential decay is found with a weighted average diffusion

coefficient. For intermediate exchange rates in the absence of strong spin coupling a simple theory of exchange, based on Bloch equations with diffusion and exchange terms, can be used to describe the evolution of longitudinal magnetization during the diffusion sensitive time interval $T = \Delta$ with $\tau, \delta \ll \Delta$. In this formulation the 'on resonance' magnetization $M_n(r, \Delta)$ for the nth species with spatial coordinates r is described by

$$\frac{\mathrm{d}M_n(r,T)}{\mathrm{d}T} = -\frac{1}{T_{1n}}M_n(r,T) - \nabla \cdot \boldsymbol{J}_n(r,T) + \sum_m K_{nm}M_m(r,T) \quad (57)$$

where the rate constants are given by $k_n = -K_{nn}$ and $k_{nm} = K_{nm}$. The flux $\boldsymbol{J}_n(r,T)$ is defined by

$$\boldsymbol{J}_n(r,T) = -D_n\nabla M_n(r,T) + M_n(r,T)v_n(r,T) \quad (58)$$

where D_n and $\boldsymbol{v}_n(r,T)$ are the diffusion coefficient and velocity for the nth species, respectively. The calculation of the signal is simplified by taking the spatial Fourier transform of equation (57) to obtain

$$\frac{\mathrm{d}M_n(q,T)}{\mathrm{d}T} = (\mathrm{i}\Omega_n - R_n)M_n(q,T) + \sum_m K_{nm}M_m(q,T) \quad (59)$$

where

$$M_n(q,T) = \int \exp(-\mathrm{i}\boldsymbol{q}\cdot\boldsymbol{r})\,M_n(r,T)\,\mathrm{d}r \quad (60)$$

Here $R_n = 1/T_{1n} + D_nq^2$ is a relaxation term, and $\Omega_n = \boldsymbol{q}\cdot\boldsymbol{v}_n$ describes the change in phase angle that results from flow, but for this discussion $1/T_{1n}$ and Ω_n are neglected. These equations and their solutions in special cases have been discussed by Kärger et al.,[60] and similar equations have been derived and studied for nuclear magnetic relaxation in multiple phase systems.[79]

Most attention has been focused on the two-site exchange case that can be solved exactly. The fast and slow exchange limits can be recovered from the solutions and useful simple equations can be derived for special cases, but in general one must resort to numerical solutions. Special problems may arise in the application of the exchange model to porous systems since the transport processes may not be adequately described by equation (59), samples may not be sufficiently uniform in properties including spin relaxation rates, and susceptibility differences may distort local magnetic fields. However, exchange in liquids is free of such complications and should be well described by equation (59).

Chemical exchange in liquid mixtures is of interest in connection with DOSY.[54] In order to simulate diffusion spectra with exchange, the ILT of $M_n(q,T)$ must be obtained. In the two-site case the inversion can be performed analytically, and whenever equations are available for $M_n(q,T)$ the Fourier transform method (q^2 replaced with $\mathrm{i}\omega$) can be used to obtain the ILT. The important quantity is the mean number of exchanges N that occur during the diffusion time T. In the slow exchange limit ($N \ll 1$) the diffusion spectrum consists of delta functions at the various diffusion coefficients, and as the exchange rate increases the spectrum evolves into a single Gaussian peak centered on the average diffusion coefficient. For example, if spins exchange between two sites (A and B) with populations p_A and p_B and diffusion coefficients D_A and D_B, respectively, the peak is centered at $\langle D\rangle = p_AD_A + p_BD_B$. The distribution of diffusion rates results from the sequences of N exchanges that occur during T and the fraction of the time that a spin occupies each site. A simple calculation for $N \gg 1$ of the number of independent sequences associated with each diffusion coefficient gives a Gaussian distribution with the square deviation $\sigma^2 = \Delta D^2 p_A(1 - p_A)/N$ where $\Delta D = D_A - D_B$. Therefore, the width of the distribution depends on the exchange rate and offers the possibility of measuring this rate.

The fast and slow exchange limits are frequently encountered and recognized, but the intermediate exchange region is difficult to identify. The amplitude of the diffusion spectrum is low in the intermediate region, and as T/N increases the linewidth decreases and becomes difficult to measure. It is also difficult to distinguish between polydispersity and exchange broadening. However, the diffusion time T can be varied, and it may be possible in some cases to determine exchange rates by means of PFG-NMR. In fact, plots of the attenuation factor Ψ versus q^2 have been used in special cases to estimate the mean lifetime in a site.[60] But it should be clear that measurements of diffusion coefficients in the slow and fast limits give no information about exchange rates.

9 LARGE GRADIENTS AND THE MEASUREMENT OF SMALL DISPLACEMENTS

The measurement of small diffusion coefficients ($D \leq 10^{-11}$ cm^2 s^{-1}) requires large values of the 'scattering vector' $\boldsymbol{q}$. Typically this is accomplished by increasing the amplitude of the gradient pulses. Modern gradient drivers for use with high-resolution spectrometers deliver 20–50 A for durations of a few milliseconds with pulse area matching to 10 ppm.[42] The gradient coils, either Maxwell pairs or quadrupolar coils, then produce gradients of a few hundred gauss per centimeter.[80,81] Much higher gradients have been reported, but usually at the cost of imperfect matching. However, even at the lower levels the pulsed gradient systems suffer from joule heating, vibrations, and pulse induced eddy currents in the metal components of the probe and neighboring magnet structures. Each of these problems can be minimized by special probe designs, but still the useful limit for stable gradient pulses appears to be approximately 10^3 G cm^{-1} in a narrow bore (5 cm) solenoid.

One way around the problem of gradient mismatch and sample motion is to accept phase variation from experiment to experiment and to correct the acquired data. A scheme to do this is called modulus addition using spatially separated echo spectroscopy (MASSEY), and the idea is as follows.[82] A phase error resulting from gradient mismatch means that the magnetization helix is not exactly unwound at the echo time. Therefore, if the echo is read out in the presence of a small read gradient g_r, a coherent superposition will occur in the vicinity of the expected echo center. One should then Fourier transform the echo with respect to $\gamma g_r t$, where t is

measured from the beginning of the read gradient, and use the modulus spectrum to measure the echo amplitude. The procedure of Fourier transformation prior to signal averaging permits displacements in the range of 1–10 nm to be measured, but does lead to a loss in the signal-to-noise ratio.

In a very different approach Kimmich et al.[83] have reported diffusion experiments in the fringe field of a superconducting magnet. Gradients of up to 42 T m^{-1} were obtained in a 4.7 T, 40 cm bore solenoid, and consistent results have been obtained in narrow bore solenoids. Thus, gradients of extremely high stability are obtained without heating, vibrations, and eddy currents. The supercon fringe field (SFF) experiment is remarkably easy to perform in any spectrometer system since one only needs the amplifier, receiver, and probe for the appropriate frequency in the fringe field. However, in its original form the SFF experiment has two major disadvantages. First, all frequency resolution is lost since the signal is acquired in the presence of the gradient. This is a serious loss, but useful information can still be obtained for specially selected systems. We note that successful experiments have been performed on polymer solutions and melts.[84] Second, the frequency gradient is approximately 2 MHz mm^{-1}, and a 1 μs rf pulse only excites a layer 0.5 mm thick. This results in very poor filling factors and small signal-to-noise ratios.

Both SE or STE diffusion experiments are easy in the fringe field, but the STE experiment is more flexible. As illustrated in Figure 3, the gradient in the STE experiment is only effective for phase encoding and decoding during the time intervals τ_1 after the first and third rf pulses, and the result is identical to a pulsed gradient experiment with pulses of duration $\delta = \tau_1$. An estimate of the lowest accessible diffusion coefficient $D_{\min}$ can be made by demanding that the attenuation caused by diffusion be equal to that resulting from relaxation. The result of this calculation is

$$D_{\min} \simeq \frac{1}{\gamma^2 g^2} \frac{1}{\delta^3(2/3 + T/\delta)} \left(\frac{T}{T_1} + \frac{2\delta}{T_2}\right) \qquad (61)$$

If τ_1 and T are of the order of T_2 and T_1, respectively, and g = 42 T m^{-1}, equation (61) gives $D_{\min} \approx 2 \times 10^{-20}/(T_1 T_2{}^2)$ in m^2 s^2. An improved STE experiment that permits the effective gradient duration to be varied without affecting relaxation is shown in Figure 15.[85] The introduction of 180° pulses in the encode and decode intervals partially refocuses the magnetization and cancels part of the effective gradient.

While the gradient amplitudes achieved in SFF are accessible with pulsed field gradients, the freedom from complications and the absence of rise and decay times for gradient pulses makes SFF a very powerful technique. The shortcomings mentioned above are already being addressed. For example, small excitation volumes can be used to advantage by exciting nonoverlapping slices without having to wait for T_1 recovery. Also, shaped rf pulses can be used to permit different pulse lengths while maintaining the same bandwidth. The loss of resolution appears to be intractable unless the sample can be moved into a homogeneous field for data acquisition. A shuttle system of the type developed for zero field spectroscopy can satisfy this requirement for samples with $T_1 > 100$ ms.

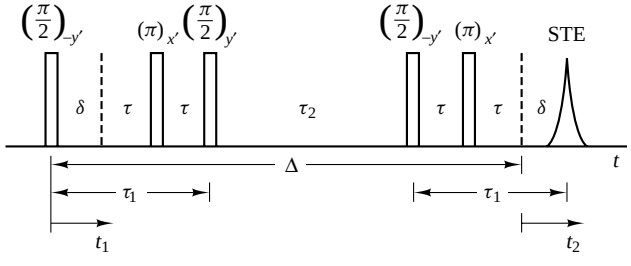

Figure 15 The five pulse STE sequence for SFF experiments. The effective gradient for encoding and decoding spatial positions has the duration δ[85]

10 DATA ANALYSIS AND POLYDISPERSITY

Data sets from PFG-NMR (SE and STE) experiments are usually in the form of a signal versus q^2 or $q^2\Delta$. For a monodisperse sample a single exponential decay as shown in equations (27) and (29) is expected. The logarithm of the signal can be fit as a linear function, but this emphasizes noise as the signal approaches zero and complicates the problem of proper weighting factors for the data points. It is better to use a nonlinear regression method to fit the exponential function directly. The Levenberg–Marquardt method is popular for this purpose.[86]

The problem may be much more difficult when more than one diffusing species contributes to the observed decay. The discrete and continuous distributions of diffusion coefficients as described by equations (38) and (42), respectively, were discussed in connection with automated analysis to obtain diffusion ordered spectra. The same analysis problem has played a major role in the development of dynamic light scattering and the extensive reviews can be found in the literature of DLS. Highly recommended sources are the analysis chapters in the monographs by Schmitz[87] and Chu[4] and the recent review by Štěpánek.[88] In general, the analysis problem is intractable. Exact answers cannot be extracted from the data and sometimes a wide variety of parameter sets fits the data within experimental error. There are, of course, some special cases where accurate answers can be determined easily or where the limited information required to characterize a distribution can be measured quite directly.

The discrete two-component decay, i.e. equation (38) with N_λ = 2, requires two decay constants, two amplitudes, and perhaps a baseline. Analysis is easy only when the decay constants differ by a large factor, the amplitudes are comparable, and the signal-to-noise ratio is high. When the answers are not obvious from a log plot, nonlinear regression procedures are sometimes used, but the latter do not provide a reliable procedure for multicomponent exponential decays, even when the number of components is known. The problem is that initial guesses of the parameters are required, and these may determine the outcome. For objective conclusions about the answers or even about the intractability of the problem, it is essential that the analysis not be biased by the user. A reasonable alternative is to use the program DISCRETE, which determines initial parameters by a Fourier method and then applies the least-squares method.[48,49] The program SPLMOD is similar but faster, and it permits the simultaneous analysis of multiple data sets.[50,51]

The continuous case requires, in principle, an ILT to determine the distribution of diffusion coefficients. There

appears to be only one simple case. If the distribution is unimodal and the distribution is narrow, a direct cumulant analysis may suffice. This method, introduced by Koppel,[89] is based on the expansion of the exponential function in equation (42) about the average decay constant $\langle\lambda\rangle$. The result is

$$G(s) = \exp\left[-\langle\lambda\rangle s + \frac{\mu_2}{2!}s^2 - \frac{\mu_3}{3!}s^3 + \frac{(\mu_4 - 3\mu_2^2)}{4!}s^4 + \ldots\right] \quad (62)$$

where

$$\langle\lambda\rangle = \int_0^\infty \lambda g(\lambda)\,\mathrm{d}\lambda, \quad \mu_n = \int_0^\infty (\lambda - \langle\lambda\rangle)^n g(\lambda)\,\mathrm{d}\lambda \quad (63)$$

A fit of equation (62) to the experimental data set, $G(s)$ versus s, by means of nonlinear regression typically yields $\langle D\rangle$ and $\mu_2 = (\langle D^2\rangle - \langle D\rangle^2)/\langle D\rangle^2$ with reasonable accuracy. The higher moments are less reliable. The ratio $\mu_2/\langle D\rangle^2$ is commonly used as an index of polydispersity; but, when this ratio exceeds 0.3, equation (62) is not justified.

When broad or multimodal distributions are expected, general ILT analyses are required. Seven schemes have recently been compared by Štěpánek.[88] The most widely used methods are constrained regularization (CONTIN), nonlinear regularization (REPES), maximum entropy (MEM), and exponential sampling. Prospective users should study the reviews to become familiar with the types of artifacts characteristic of these methods. Also, it is strongly advised that simulated data similar to the data of interest be analyzed to obtain experience with limitations of the analyses. When noise is present, the information content of the PFG-NMR data sets is simply not sufficient to provide an exact image of the distribution. One must be satisfied with a reasonable estimate rather than no solution at all.

11 MASS AND SIZE DISTRIBUTIONS FROM NMR DIFFUSION DATA

The PFG-NMR data set $G(s)$ collected at a specific chemical shift for a polydisperse sample has the form (see Section 4.1):

$$G(s) = \int_0^\infty g_\kappa(\kappa)\exp[-D(\kappa)s]\,\mathrm{d}\kappa \quad (64)$$

If $\kappa = D$ then $D(\kappa) = D$ and equations (64) and (42) are identical, but equation (64) is more general since κ may represent another molecular parameter of interest, e.g. molecular radius R or molar mass M. For example, the ILT of $G(q^2)$ gives $g_D(D)$, but $g_M(M)$ the distribution function for molar mass may be of interest. Equation (64) indicates that the normalized distribution for molar mass is given by $g_M(M) = g_D(D)\,|\mathrm{d}D/\mathrm{d}M|$.[4] For linear polymers this transformation can be carried out with the assumption that $D(M) = KM^{-\alpha}$, where K is a constant. Here α ranges from 0.6 for dilute solutions to 2.0 for melts when the 'reptation' model holds.[90] However, this treatment ignores possible spin relaxation effects that may depend on the mass. In general, the distribution functions should include a relaxation factor, e.g. $g_M(M)$ becomes $A_0(M)g_M(M)$, where $A_0(M)$ depends on T_1 and T_2. The small molecules tend to have longer relaxation times and, therefore, contribute disproportionately to the measured diffusion coefficient. Therefore, the neglect of $A_0(M)$ leads to higher apparent diffusion coefficients.

Unfortunately, equation (64) is not always appropriate. A number of experimental studies of polymer mixtures have found essentially exponential attenuation curves and, therefore, much less indication of polydispersity than predicted.[91,92] The important point is that equation (64) only holds when the diffusion rate of a polymer molecule is independent of the lengths of the neighboring polymer chains.[93] This condition is satisfied in very dilute solutions[94] and in the melts when diffusion can be described by the 'reptation' model.[90] Otherwise, little information can be obtained from $G(s)$ about $g_M(M)$. The averaging effect resulting from interactions with neighbors has been called 'microscopic' averaging.[92]

Another aim of diffusion studies is to size particles, i.e. to determine $g_R(R)$. As shown above $g_R(R)$ can be obtained from $g_D(D)$ if the relation between D and R is known. For spherical particles equation (7) with appropriate corrections for volume fraction can be assumed and $g_R(R)$ can be derived. However, this distribution is weighted by the number of nuclei contributing to the signal, i.e. the number of nuclei with diffusion coefficients in the range D to $D + \mathrm{d}D$. The number of particles in the range D to $D + \mathrm{d}D$ may be the quantity of interest, and these distributions can be related if the number of nuclei can be determined as a function of R. For example, for vesicles the number of molecules in the bilayer increases roughly with R^2 while the number of molecules entrapped in the aqueous cavity increases with R^3.[56] Therefore, the unnormalized distribution function for the number of nuclei associated with radii in the range R to $R + \mathrm{d}R$ is proportional to $R^n g_R(R)$, with $n = 2$ or 3 depending on the source of the signal. Also, the relaxation factor $A_0(R)$ is important here since T_2 is short for bilayer protons and depends on R through the rotational correlation time. The result is that the uncorrected diffusion coefficients determined from bilayer signals are much higher than those obtained with signals from molecules entrapped in the aqueous cavity. In addition, the microscopic averaging effect mentioned above may reduce the effect of polydispersity on the observed signals. All of these problems are compounded because data inversion methods often yield inaccurate estimates of $g_R(R)$.

Similarities between NMR and DLS analyses have been noted, but it should be kept in mind that different kinds of averaging processes are involved. When relaxation can be ignored NMR intensities depend on the number of nuclei involved in the resonance and this number may be proportional to the molecular weight of a molecule, the volume of an entrapped fluid, etc. In DLS the intensity is proportional to the number of scatterers, but each scatterer is weighted by the square of the number of electrons. In some cases the number of electrons is proportional to the mass and to the volume of a molecule. This is the origin of the well-known rule that scattering from a particle is proportional to the square of its volume. Therefore, in the limit of infinite dilution where tracer and mutual diffusion coefficients are equal, NMR and DLS may still give different average diffusion coefficients for polydisperse samples. Also, as a practical matter, PFG-NMR data sets usually have fewer points and lower signal-to-noise ratios than data sets obtained in DLS.

12 LITERATURE SOURCES FOR NMR DIFFUSION MEASUREMENTS

The most complete, up-to-date treatment of translational dynamics and its study by NMR is found in the book by Callaghan.[25] The experimental and theoretical aspects of diffusion in liquids are treated in the monograph by Tyrrell and Harris,[2] and Crank's book[1] is still the standard reference for the mathematics of diffusion. The principles and applications of PFG-NMR have been reviewed by Kärger et al.,[60] and Stilbs[39] has provided a detailed review of FT diffusion studies. NMR studies of diffusion in polymer systems have been reviewed by von Meerwall.[95,96] Wade[97] has reviewed lateral diffusion in lipids including NMR measurements, and Chachaty[98] has reviewed NMR relaxation and diffusion studies of micellar solutions. Molecular diffusion in NMR imaging has been reviewed by Le Bihan[99] (note that the references in this review incorrectly replace *Phys*. with *Physiol*. in several places). Multiple-quantum methods including sensitivity to gradients and use in diffusion studies have been reviewed by Norwood.[100]

13 RELATED ARTICLES

Chemical Exchange Effects on Spectra; Diffusion: Clinical Utility of MRI Studies; Diffusion and Flow in Fluids; Diffusion and Perfusion in MRI; Diffusion in Porous Media; Diffusion in Rare Gas Solids; Diffusion in Solids; Electrophoretic NMR; Field Gradients and Their Application; Flow NMR; Gradient Coil Systems; Liquid Crystalline Samples: Diffusion; NMR Microscopy: Resolution; Radiofrequency Gradient Pulses; Spin Echo Spectroscopy of Liquid Samples

14 REFERENCES

1. J. Crank, *The Mathematics of Diffusion*, 2nd edn, Oxford University Press, Oxford, 1975.
2. H. J. V. Tyrrell and K. R. Harris, *Diffusion in Liquids: A Theoretical and Experimental Study*, Butterworths, London, 1984.
3. C. R. Cantor and P. R. Schimmel, *Biophysical Chemistry, Part II: Techniques for the Study of Biological Structure and Function*, W. H. Freeman and Co., San Francisco, 1980.
4. B. Chu, *Laser Light Scattering: Basic Principles and Practice*, Academic, Boston, 1991.
5. C. S. Johnson, Jr, and D. A. Gabriel, *Laser Light Scattering*, Dover, New York, 1994.
6. D. G. Leaist and L. Hao, *J. Phys. Chem.*, 1993, **97**, 7763.
7. L. Onsager and R. M. Fuoss, *J. Phys. Chem.*, 1932, **36**, 2689.
8. J. G. Kirkwood, R. L. Baldwin, P. J. Dunlop, L. J. Gosting, and G. Kegeles, *J. Chem. Phys.*, 1960, **33**, 1505.
9. J. A. Marqusee and J. M. Deutch, *J. Chem. Phys.*, 1980, **73**, 5396.
10. T. R. Saarinen and C. S. Johnson, Jr, *J. Magn. Reson.*, 1988, **78**, 257.
11. A. Abragam, *The Principles of Nuclear Magnetism*, Oxford University Press, London, 1961.
12. E. O. Stejskal and J. E. Tanner, *J. Chem. Phys.*, 1965, **42**, 288.
13. R. F. Karlicek and I. J. Lowe, *J. Magn. Reson.*, 1980, **37**, 75.
14. E. L. Hahn, *Phys. Rev.*, 1950, **80**, 580.
15. H. Y. Carr and E. M. Purcell, *Phys. Rev.*, 1954, **94**, 630.
16. R. L. Vold and R. R. Vold, *J. Am. Chem. Soc.*, 1974, **96**, 4043.
17. R. L. Vold and R. R. Vold, *Prog. Nucl. Magn. Reson. Spectrosc.*, 1978, **12**, 79.
18. M. I. Hrovat and C. G. Wade, *J. Magn. Reson.*, 1981, **44**, 62.
19. D. E. Woessner, *J. Chem. Phys.*, 1961, **34**, 2057.
20. J. E. Tanner, *J. Chem. Phys.*, 1970, **52**, 2523.
21. J. Lian, D. S. Williams, and I. J. Lowe, *J. Magn. Reson., Ser. A*, 1994, **106**, 65.
22. R. M. Cotts, M. J. R. Hoch, T. Sun, and J. T. Marker, *J. Magn. Reson.*, 1989, **83**, 252.
23. L. L. Latour, L. Li, and C. H. Sotak, *J. Magn. Reson., Ser. B*, 1993, **101**, 72.
24. B. Gross and R. Kosfeld, *Messtechnik*, 1969, **7/8**, 171.
25. P. T. Callaghan, *Principles of Nuclear Magnetic Resonance Microscopy*, Oxford University Press, Oxford, 1991.
26. J. Stepisnik, *Prog. NMR Spectrosc.*, 1985, **17**, 187.
27. I. Solomon, *Phys. Rev. Lett.*, 1959, **2**, 301.
28. D. Canet, B. Diter, A. Belmajdoub, J. Brondeau, J. C. Boubel, and K. Elbayed, *J. Magn. Reson.*, 1989, **81**, 1.
29. R. Dupeyre, P. Devoulon, D. Bourgeois, and M. Decorps, *J. Magn. Reson.*, 1991, **95**, 589.
30. J. F. Martin, L. S. Selwyn, R. R. Vold, and R. L. Vold, *J. Chem. Phys.*, 1982, **76**, 2632.
31. D. Zax and A. Pines, *J. Chem. Phys.*, 1983, **78**, 6333.
32. L. E. Kay and J. H. Prestegard, *J. Magn. Reson.*, 1986, **67**, 103.
33. C. H. Sotak, *J. Magn. Reson.*, 1990, **90**, 198.
34. T. J. Norwood, *J. Magn. Reson.*, 1992, **99**, 208.
35. R. L. Vold, J. S. Waugh, M. P. Klein, and D. E. Phelps, *J. Chem. Phys.*, 1968, **48**, 3831.
36. T. L. James and G. G. McDonald, *J. Magn. Reson.*, 1973, **11**, 58.
37. J. Kida and H. Uedaira, *J. Magn. Reson.*, 1977, **27**, 253.
38. P. Stilbs and M. E. Moseley, *Chem. Script.*, 1979, **13**, 26.
39. P. Stilbs, *Prog. Nucl. Magn. Reson. Spectrosc.*, 1987, **19**, 1.
40. P. Stilbs and M. E. Moseley, *Chem. Script.*, 1980, **15**, 176.
41. K. F. Morris and C. S. Johnson, Jr, *J. Am. Chem. Soc.*, 1993, **115**, 4291.
42. R. M. Boerner and W. S. Woodward, *J. Magn. Reson., Ser. A*, 1994, **106**, 195.
43. P. Mansfield and B. Chapman, *J. Magn. Reson.*, 1986, **66**, 573.
44. S. J. Gibbs, K. F. Morris, and C. S. Johnson, Jr, *J. Magn. Reson.*, 1991, **94**, 165.
45. S. J. Gibbs and C. S. Johnson, Jr, *J. Magn. Reson.*, 1991, **93**, 395.
46. E. von Meerwall and M. Kamat, *J. Magn. Reson.*, 1983, **83**, 309.
47. W. J. Goux, L. A. Verkruyse, and S. J. Salter, *J. Magn. Reson.*, 1990, **88**, 609.
48. S. W. Provencher, *J. Chem. Phys.*, 1976, **64**, 2772.
49. S. W. Provencher, *Biophys. J.*, 1976, **16**, 27.
50. S. W. Provencher and R. H. Vogel, in *Numerical Treatment of Inverse Problems in Differential and Integral Equations*, eds. P. Deuflhard and E. Hairer, Birkhauser, Boston, 1983, p. 304.
51. R. H. Vogel, SPLMOD Users Manual (Technical Report DA06), European Molecular Biology Laboratory, Heidelberg, 1983.
52. K. F. Morris, P. Stilbs, and C. S. Johnson, Jr, *Anal. Chem.*, 1994, **66**, 211.

53. P. Stilbs, *J. Colloid Interface Sci.*, 1982, **87**, 385.
54. C. S. Johnson, Jr. *J. Magn. Reson., Ser. A*, 1993, **102**, 214.
55. D. Wu, W. S. Woodward, and C. S. Johnson, Jr, *J. Magn. Reson., Ser. A*, 1993, **104**, 231.
56. D. P. Hinton and C. S. Johnson, Jr, *J. Phys. Chem.*, 1993, **97**, 9064.
57. K. F. Morris, C. S. Johnson, Jr, and T. C. Wong, *J. Phys. Chem.*, 1994, **98**, 603.
58. E. O. Stejskal, *J. Chem. Phys.*, 1965, **43**, 3597.
59. J. Kärger and W. Heink, *J. Magn. Reson.*, 1983, **51**, 1.
60. J. Kärger, H. Pfeifer, and W. Heink, in *Advances in Magnetic Resonance*, ed. W. W. Warren, Academic, New York, 1988, Vol. 12, p. 1.
61. B. J. Berne and R. Pecora, *Dynamic Light Scattering*, Wiley, New York, 1976.
62. H. J. Eichler, P. Gunter, and D. W. Pohl, *Laser-induced Dynamic Gratings*, Springer, Berlin, 1986.
63. H. Hervet, W. Urbach, and F. Rondelez, *J. Chem. Phys.*, 1978, **68**, 2725.
64. L. Axel, *Radiology*, 1989, **171**, 841.
65. D. E. Woessner, *J. Phys. Chem.*, 1963, **67**, 1365.
66. J. E. Tanner and E. O. Stejskal, *J. Chem. Phys.*, 1968, **49**, 1768.
67. C. H. Neuman, *J. Chem. Phys.*, 1974, **60**, 4508.
68. J. S. Murday, and R. M. Cotts, *J. Chem. Phys.*, 1968, **48**, 4938.
69. D. G. Cory and A. N. Garroway, *Magn. Reson. Med.*, 1990, **14**, 435.
70. P. T. Callaghan, A. Coy, D. MacGowan, K. J. Packer, and F. O. Zelaya, *Nature*, 1991, **351**, 467.
71. P. P. Mitra and P. N. Sen, *Phys. Rev. B*, 1992, **45**, 143.
72. P. P. Mitra, P. N. Sen, L. M. Schwartz, and P. L. Doussal, *Phys. Rev. Lett.*, 1992, **68**, 3555.
73. J. E. M. Snaar and H. Van As, *J. Magn. Reson., Ser. A*, 1993, **102**, 318.
74. P. T. Callaghan, M. A. Le Gros, and D. N. Pinder, *J. Chem. Phys.*, 1983, **79**, 6372.
75. J. H. Davis, K. R. Jeffrey, M. Bloom, M. I. Valic, and T. P. Higgs, *Chem. Phys. Lett.*, 1976, **42**, 390.
76. G. J. Kruger, H. Spiesecke, R. von Steenwinkle, and F. Noack, *Mol. Cryst. Liq.*, 1977, **40**, 103.
77. R. Blinc, M. Burgar, M. Luzar, J. Pirs, I. Zupanzic, and S. Zumer, *Phys. Rev. Lett*. 1974, **33**, 1192.
78. C. S. Johnson, Jr, in *Advances in Magnetic Resonance*, ed. J. S. Waugh, Academic, New York, 1965, Vol. 1, p. 33.
79. J. R. Zimmerman and W. E. Brittin, *J. Phys. Chem.*, 1957, **61**, 1228.
80. J. E. Tanner, *Rev. Sci. Instrum.*, 1965, **36**, 1086.
81. D. S. Webster and K. H. Marsden, *Rev. Sci. Instrum.*, 1974, **45**, 1232.
82. P. T. Callaghan, *J. Magn. Reson.*, 1990, **88**, 493.
83. R. Kimmich, W. Unrath, G. Schnur, and E. Rommel, *J. Magn. Reson.*, 1991, **91**, 136.
84. G. Fleischer, F. Fujara, and B. Stuehn, *Macromolecules*, 1993, **26**, 2340.
85. R. Kimmich and E. Fischer, *J. Magn. Reson., Ser. A*, 1994, **106**, 229.
86. W. H. Press, S. A. Teukolsky, W. T. Vettering, and B. P. Flannery, *Numerical Recipes in FORTRAN*, Cambridge University Press, New York, 1992.
87. K. S. Schmitz, *An Introduction to Dynamic Light Scattering by Macromolecules*, Academic, Boston, 1990.
88. P. Štěpánek, in *Dynamic Light Scattering: The Method and Some Applications*, ed. W. Brown, Clarendon, Oxford, 1993, p. 177.
89. D. E. Koppel, *J. Chem. Phys.*, 1973, **57**, 4814.
90. R. Bachus and R. Kimmich, *Polymer*, 1983, **24**, 964.
91. R. Raghavan, T. L. Maver, and F. D. Blum, *Macromolecules*, 1987, **20**, 814.
92. P. T. Callaghan and D. N. Pinder, *Macromolecules*, 1985, **18**, 373.
93. G. Fleischer, *Polymer* 1985, **26**, 1677.
94. E. D. von Meerwall, *J. Magn. Reson.*, 1982, **50**, 409.
95. E. D. von Meerwall, *Adv. Polym. Sci.*, 1983, **54**, 1.
96. E. D. von Meerwall, *Rubber Chem. Technol. (Rubber Rev.)*, 1985, **58**, 527.
97. C. G. Wade, in *Structure and Properties of Cell Membranes*, ed. G. Benga, CRC Boca Raton, FL, 1985, Vol. 1, p. 51.
98. C. Chachaty, *Prog. NMR Spectrosc.*, 1987, **19**, 183.
99. D. Le Bihan, *Magn. Reson. Quart.*, 1991, **7**, 1.
100. T. J. Norwood, *Prog. NMR Spectrosc.*, 1993, **24**, 295.

Biographical Sketch

Charles S. Johnson, Jr. *b* 1936. B.S., 1958, Georgia Institute of Technology, Ph.D., 1961, Massachusetts Institute of Technology, (supervisor John Waugh). NAS-NRS Postdoctoral fellow and instructor at Illinois (with Herb Gutowsky). Faculty member Yale University 1962–67, University of North Carolina, Chapel Hill, 1967–present. Research interests include dynamic light scattering (DLS), electrophoretic NMR, diffusion-ordered 2D NMR, and applications of DLS and NMR to complex liquid mixtures.

Diffusion-Ordered Spectroscopy (DOSY)

Gareth A. Morris

University of Manchester, Manchester, UK

1 Introduction 1
2 Historical Background 2
3 Data Analysis 3
4 Experimental Methods 4
5 Examples 8
6 Related Articles in this Volume 9
7 Related Articles in Volumes 1–8 9
8 References 9

1 INTRODUCTION

High resolution NMR spectroscopy is one of the most powerful tools available for chemical structure elucidation. The great majority of high resolution NMR experiments are carried out on more or less pure materials, in which the signals of a single species dominate. NMR has until recently been much less widely used in the study of mixtures, but two techniques are changing this. The first is HPLC-NMR, in which NMR experiments are performed directly on the eluent stream from a chromatography column, in either continuous- or stopped-flow mode. HPLC-NMR is capable of handling complex mixtures, and offers great flexibility through the use of different stationary and mobile phases, but requires special hardware and is expensive both in instrument time and in solvent consumption. In the second, diffusion-ordered spectroscopy (DOSY), the results of pulsed field gradient spin echo experiments are analyzed to determine diffusion coefficients for the individual signals in a spectrum, and hence to distinguish between the signals of different components in a mixture. In most applications, two- or three-dimensional spectra are synthesized in which signals are dispersed in one dimension according to their diffusion coefficients. DOSY uses standard spectrometer hardware and sample handling, requiring only the additional software for data analysis and spectrum synthesis; the field has been authoritatively reviewed by Johnson.[1]

DOSY and HPLC-NMR may be viewed as analogues, DOSY effecting a virtual separation as opposed to the true physical separation used by HPLC. The versatility that changes in stationary and mobile phase afford when separating substances by HPLC is to some extent paralleled by the possibility of manipulating the relative diffusion coefficients of different species by changing solvent, or by adding agents to bind species preferentially. The two techniques are largely complementary, HPLC-NMR generally being the more powerful but slower and more expensive technique. In principle it would be possible to achieve higher resolution by combining stopped-flow HPLC-NMR with DOSY than either technique can provide in isolation.

Figures 1 and 2 illustrate some of the basic principles of DOSY. A series of measurements is made of pulsed field gradient stimulated echo spectra (Figure 1), in which diffusion causes signals to be attenuated. Fitting the signal peak heights as a function of gradient pulse area to the theoretical Gaussian form allows a diffusion coefficient and a standard error to be calculated for each peak in the spectrum. A two-dimensional diffusion-ordered spectrum can then be synthesized (Figure 2) in which the normal spectrum (top) is used to determine the horizontal (chemical shift) domain lineshape for each peak, and the diffusion coefficient and standard error are used to define the position and width of a Gaussian lineshape in the vertical (diffusion) domain. All signals for a given molecule should then appear in a horizontal line, at the same diffusion coefficient D; cross-sections through the 2D spectrum at different values of D then separated subspectra for the different species in a mixture. This simple and effective approach is however restricted to the high resolution case where peaks are well-resolved in the chemical shift domain: where signals overlap in the normal spectrum, analysis can be much more problematic.

The name DOSY deliberately invites comparison with 2D NMR methods such as COSY (correlation spectroscopy) and NOESY (nuclear Overhauser effect spectroscopy). There is however an important distinction to be drawn between the true 2D techniques, in which the positions of signals in the indirectly detected frequency domain (F_1) are encoded as frequencies of amplitude or phase oscillation as a function of the evolution time t_1, and DOSY, in which the positions of signals in the diffusion domain must be determined from the rate with which signal amplitude decreases as the strength of the applied magnetic field gradients is increased. F_1 frequencies in COSY etc. may be straightforwardly and unambiguously obtained by Fourier transformation of the signal oscillations as a function of t_1 (as well as by more sophisticated techniques such as linear prediction, maximum entropy or the filter diagonalization method), but there is no such general way to invert the corresponding experimental data in DOSY experiments. The Fourier transform is highly effective at unraveling superimposed oscillations, which may be treated as complex exponentials, but unfortunately the corresponding method for superimposed real exponential decays, the inverse Laplace transform, is numerically intractable.

DOSY therefore is forced to rely on simplifying approximations when attempting to interpret signal decay in terms of diffusion. By far the most common approximation is to assume, as in Figure 2 above, that each signal originates from a single species; this can allow very accurate estimation of diffusion coefficient, but risks misleading the experimenter if a given signal actually contains contributions from more than one species. Where two signals with different diffusion coefficients overlap, fitting the data to the form expected for a single decay will yield a compromise diffusion coefficient intermediate between the two true values. It seems unlikely that a practical, general solution will be found to the problem of unambiguously inverting an experimental decay of signal amplitude with gradient pulse area into an accurate distribution of signal strength as a function of diffusion coefficient, but a number of useful approximations are available.

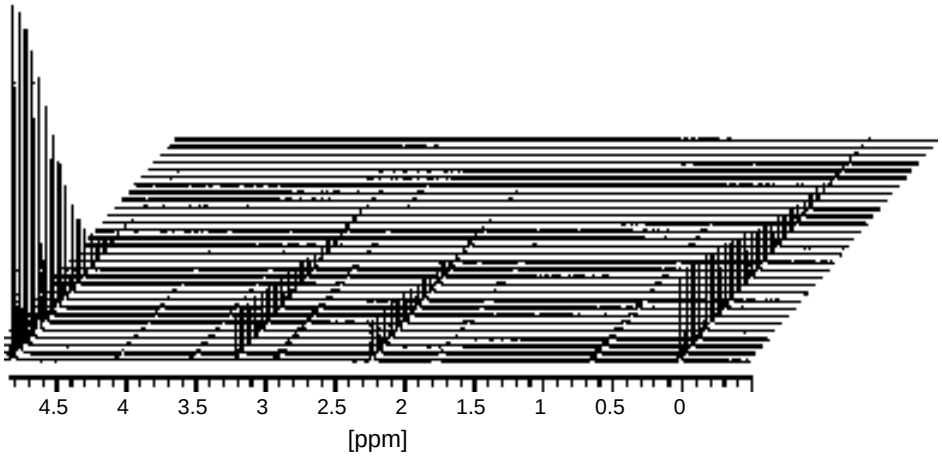

Figure 1 500 MHz ^{1}H pulsed field gradient spin echo spectra for a mixture of acetone (A), choline (C) and DSS (2,2-dimethyl-2-silapentane-5-sulfonate sodium salt, D) in D_2O; a signal is also seen for residual HDO (W). 30 spectra were acquired using the PFGLED sequence of Figure 3(b) using gradient strengths incremented linearly from 0.5 to 15 G cm^{-1}

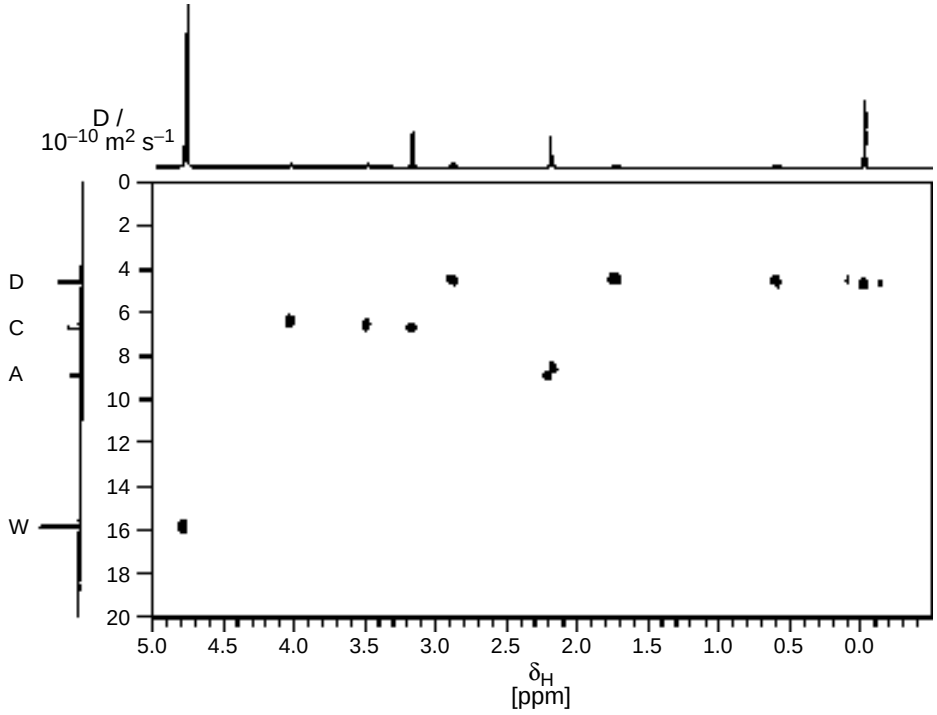

Figure 2 DOSY spectrum calculated from the data of Figure 1

DOSY is, in essence, nothing more than a new form of data presentation applied to a much older family of techniques, that of pulsed field gradient measurements of diffusion coefficient. However, by highlighting the use of such methods for the analysis of mixtures and focusing attention on some of their limitations, DOSY has led both to significant improvements in techniques for diffusion measurement and to a much wider range of applications.

2 HISTORICAL BACKGROUND

It was recognized very early in the development of NMR that diffusion contributes to the attenuation of spin echo signals when experiments are performed in an inhomogeneous magnetic field. Spins that move through a spatially-varying magnetic field during a spin echo experiment will suffer changes in Larmor frequency, leading to changes in signal phase that depend on the motion undergone. Diffusive motion will lead to a distribution of different signal phases, and hence to a diminution in net signal. This principle has been extensively exploited, and NMR remains one of the most widely-used of techniques for measuring diffusion.[2,3]

Experiments carried out using a static field which remains inhomogeneous throughout are limited in application, as the line broadening caused by the field inhomogeneity leads to signal overlap and reduces signal-to-noise ratio. The introduction

of pulsed magnetic field gradients allowed spin echo signals to be measured under high resolution conditions, retaining high sensitivity and allowing signals with different Larmor frequencies to be distinguished. Pulsed field gradient spin echo experiments come in a variety of forms, but all share the same basic features. After initial excitation, the evolution of the spins falls into three distinct phases: a defocusing period, in which field gradient pulses are used to give each spin a position-dependent phase; a delay, during which diffusion takes place; and a refocusing period, in which gradient pulses are applied to reverse the original phase encoding. For a single rectangular field gradient pulse of width δ and amplitude G, the extent of defocusing or refocusing produced is described by the gradient pulse area $q = \gamma\delta G$; an effective gradient pulse area may be defined for more complex sequences of gradient pulses. Spins that experience no net movement during the diffusion period refocus exactly, but where diffusion takes place, a distribution of signal phases results and the net magnetization is therefore attenuated. The net signal attenuation as a result of unrestricted diffusion shows a Gaussian dependence on q (an exponential dependence on q^2):

$$\mathrm{S}(q) = \mathrm{S}(0)\exp[-D\Delta' q^2] \tag{1}$$

where D is the diffusion coefficient, and the effective diffusion time Δ' is the time Δ between the midpoints of the defocusing and refocusing periods less a small correction for diffusion during the gradient pulses. It is important to choose values for q^2 that give an accurate record of diffusional attenuation for all species of interest, without wasting time acquiring spectra which are uninformative.[1]

The idea that pulsed field gradient echo spectra could be used for the analysis of mixtures dates back at least to the 1981 work of Stilbs,[4] but the concept of a diffusion-ordered spectrum was only introduced by Johnson in 1992.[5] Two distinct strands may be distinguished in the development of DOSY: high resolution DOSY, in which relatively complex mixtures can be analyzed with good diffusion accuracy using well-resolved spectra where the majority of peaks arise from a single species, and low resolution DOSY, in which the overlap or complete superimposition of signals limits the reconstruction of the diffusion dimension of the DOSY spectrum to a relatively low resolution. Between these two poles a variety of approaches may be used to constrain the analysis in order to maximize the amount of chemically useful information to be obtained from the experimental data.

3 DATA ANALYSIS

3.1 High Resolution DOSY

The simplest approach to analyzing the results of DOSY experiments is to assume that each individual peak in the NMR spectrum arises from a single species, and hence has an amplitude which varies with gradient pulse area according to equation (1). In simple mixtures with well-resolved signals this is straightforward, and gives the maximum interpretable information for a minimum of effort. The basic data processing follows the pattern described briefly in the Introduction. After measurement, experimental free induction decays are weighted and Fourier transformed as normal; where most signals have the same common linewidth, mild resolution enhancement may be useful. Careful baseline correction is then carried out, to minimize distortions of the diffusion spectrum caused by instrumental shortcomings and crosstalk between signals. Peak heights are tabulated as a function of gradient pulse area for each peak identified in the spectrum, and two-parameter exponential least squares fitting as a function of q^2 is carried out. This yields an apparent diffusion coefficient and a standard error for each peak, which may then be used in synthesizing a DOSY spectrum. For each peak j in the normal spectrum (for convenience, the spectrum with lowest q is generally used) a two-dimensional peak is constructed which has the same shape in the NMR dimension as that $\mathrm{S}_j(F)$ in the normal spectrum, a volume proportional to the peak height in the normal spectrum, and a Gaussian shape in the diffusion dimension which is centered on the fitted diffusion coefficient D_j and has a width determined by the standard error σ_j. The final 2D DOSY spectrum is then the sum of N such 2D peaks:

$$\mathrm{S}(D, F) = \sum_{j=1}^{N} \frac{\mathrm{S}_j(F)}{\sqrt{2\pi\sigma_j^2}} \exp\left[\frac{-(D - D_j)^2}{2\sigma_j^2}\right] \tag{2}$$

Several refinements of this basic approach are possible. Even the best available spectrometer hardware is unable to switch as rapidly as required between a field gradient pulse and high resolution conditions, with the result that spectra show small distortions because of the slow recovery of the main magnetic field B_0 to maximum homogeneity. These distortions may be corrected by reference deconvolution[6] (qv) if there is a suitable reference signal available in the spectrum. To the normal requirement that the reference signal should be a strong, well-resolved singlet, must be added the stipulation that the reference material should preferably diffuse no more rapidly than the slowest of the species under study, so that the reference signal remains strong in all the experimental spectra. One candidate for such a material in non-polar solvents is polydimethylsiloxane. In practice, 2–3 fold improvements in diffusion resolution may readily be obtained using reference deconvolution.

Another common instrumental shortcoming that reduces resolution in the diffusion domain of a DOSY spectrum is non-uniformity of the pulsed linear field gradient, i.e., the presence of gradients of higher orders than one. Variations of 10% across the active volume of the probe are common, with larger discrepancies outside the observe coil. The effect of such variation is make the signal attenuation dependence on q deviate from a Gaussian: effectively the decay becomes the sum of different Gaussians from different regions of the sample. For signals that are only mildly attenuated this is of little consequence: relatively clean Gaussian behavior is seen, corresponding to a gradient strength averaged over the sample. Where, however, signals undergo severe attenuation, the weaker gradient in some parts of the sample leads to significantly stronger signals than expected at high nominal gradient strengths. These deviations from Gaussian behavior lead to an increased error in the fitting process, and are one of the causes of the common observation that DOSY signals are broader in the diffusion domain at high diffusion coefficient. The loss of resolution can be reduced by empirically adjusting the apparent values of q^2 to force the experimental signal decay to adopt the expected Gaussian shape: this improves

the accuracy of fit, and hence the accuracy with which relative diffusion coefficients are determined, at the expense of a small loss in absolute accuracy. A much more effective solution, however, is to determine the form of the distribution of signal strength as a function of gradient strength, and then use this information to calculate the predicted form of the signal attenuation curve as a function of q^2. This may conveniently be done by mapping the experimental distributions of signal strength and gradient strength as functions of position within the sample, and then integrating over the sample to find the overall signal attenuation curve. Fitting to this function, which may conveniently be represented as the exponential of a power series, rather than to a Gaussian, then gives much better statistics for signals that experience strong attenuation. The benefits are particularly apparent when studying mixtures with a wide range of diffusion coefficients, since at high q the signal intensities of rapidly diffusing species will be dominated by contributions from the regions of the samples experiencing the lowest gradients.

Data processing strategies in DOSY depend on the nature of the sample, the characteristics of the spectrum, and the signal-to-noise ratio of the NMR data. Where resolution is good but signal-to-noise ratio poor, as for example with ^{13}C or ^{29}Si, there is little need for baseline correction and little advantage in using reference deconvolution. Conversely, for ^{1}H systems with very high signal-to-noise ratios, baseline correction is important and the improvement in diffusion resolution obtainable by combining reference deconvolution and gradient mapping can approach an order of magnitude.

3.2 Low Resolution DOSY

The problem of identifying an arbitrary distribution of signal intensity as a function of diffusion coefficient (a "diffusion spectrum") from measurements of signal attenuation as a function of gradient pulse area is one that has already been intensively studied in a different context, that of dynamic light scattering. Given the absence of a method for computing accurate inverse Laplace transforms from experimental data, the challenge is to use suitable approximations, constraints and prior knowledge to enable realistic diffusion spectra to be constructed. For polydisperse systems, where there is a continuous distribution of diffusion coefficients, only very general constraints can be applied, typically that the diffusion spectrum remain positive and that it be as simple and featureless as is compatible with the experimental data. This conservative approach minimizes the risk of misinterpretation, but yields large uncertainties in the diffusion coefficients of any monodisperse components in a mixture. The two approaches that have proved most successful in DOSY analysis of polydisperse systems are CONTIN[7] and maximum entropy.[8]

3.3 Intermediate Approximations

Many mixture analysis problems lie between the two extremes of a fully-resolved and an unresolved NMR spectrum. Some spectral lines are well-resolved, others are the sum of two or more components, which may be partially resolved. Under such circumstances low resolution DOSY has little to offer unless the system exhibits only a few diffusion coefficients which are of very different magnitudes. The straightforward monoexponential analysis as a function of q^2 described above is more successful in providing useful chemical information, since where two signals with different diffusion coefficients contribute to a given peak the apparent diffusion coefficient will be intermediate between the two values. Since the effects of overlap are simple where only two signals are involved, DOSY spectra with a minority of signals overlapping are relatively straightforward to interpret, but the ability to extract a complete subspectrum for a given diffusion coefficient is lost.

Between the Procrustes bed of a single exponential fit and the open-ended analyses of CONTIN and maximum entropy lie a range of methods designed to fit the experimental data to more or less constrained models, using prior knowledge of the likely form of the diffusion spectrum to allow the maximum of useful information to be extracted from the experimental data. In moderately crowded spectra the majority of cases of overlap will only involve two signals, so a logical first step is to replace monoexponential fitting with biexponential. Simple four parameter biexponential fitting can be quite satisfactory provided that the two diffusion coefficients differ by a factor of two or more, but the generation of initial guesses for the iterative fitting risks introducing bias. A safer solution is the general package for multiexponential fitting SPLMOD (SPLine Model), which has been used successfully[9] for DOSY by incorporating pragmatic rules for the rejection of spurious fits. A variety of more sophisticated approaches to analyzing multiple overlapping exponentially decaying spectra have been proposed, including the DECRA (direct exponential curve resolution algorithm),[10] MCR (multivariate curve resolution)[11] and CORE (component resolved NMR)[12] methods, but have yet to be widely applied.

4 EXPERIMENTAL METHODS

4.1 Homonuclear 2D DOSY

The earliest experiments used the basic Carr-Purcell pulse sequence in the presence of a continuous field gradient. The introduction of pulsed field gradients has already been mentioned; the next improvement was the shift to using a stimulated $(90 - \tau - 90 - \Delta - 90 - \tau)$ rather than a Carr-Purcell $(90 - \tau - 180 - \tau)$ echo sequence. This carries a factor of two penalty in sensitivity, since on average only half of the initial transverse magnetization is refocused in a stimulated echo, but minimizes the time for which the magnetization remains transverse. This is of value for systems where T_2 is significantly shorter than T_1, but is particularly useful for systems with homonuclear scalar coupling. Restricting the time that magnetization spends in the transverse plane minimizes the impact of J modulation, and hence avoids the introduction of multiplet phase errors. Since high resolution DOSY generally relies on peak heights as a guide to signal intensity, any dispersion mode character to the experimental lineshape greatly increases the risk of signal overlap, and hence of crosstalk between adjacent peak heights and distortion of the diffusion spectrum.

The parent pulse sequence for most DOSY experiments is the pulsed field gradient stimulated echo (PFGSTE) sequence of Figure 3(a), in which the delays τ are just long enough to encompass the transmitter pulse fall time, the width δ of the gradient pulse, and the recovery time for the gradient pulse.

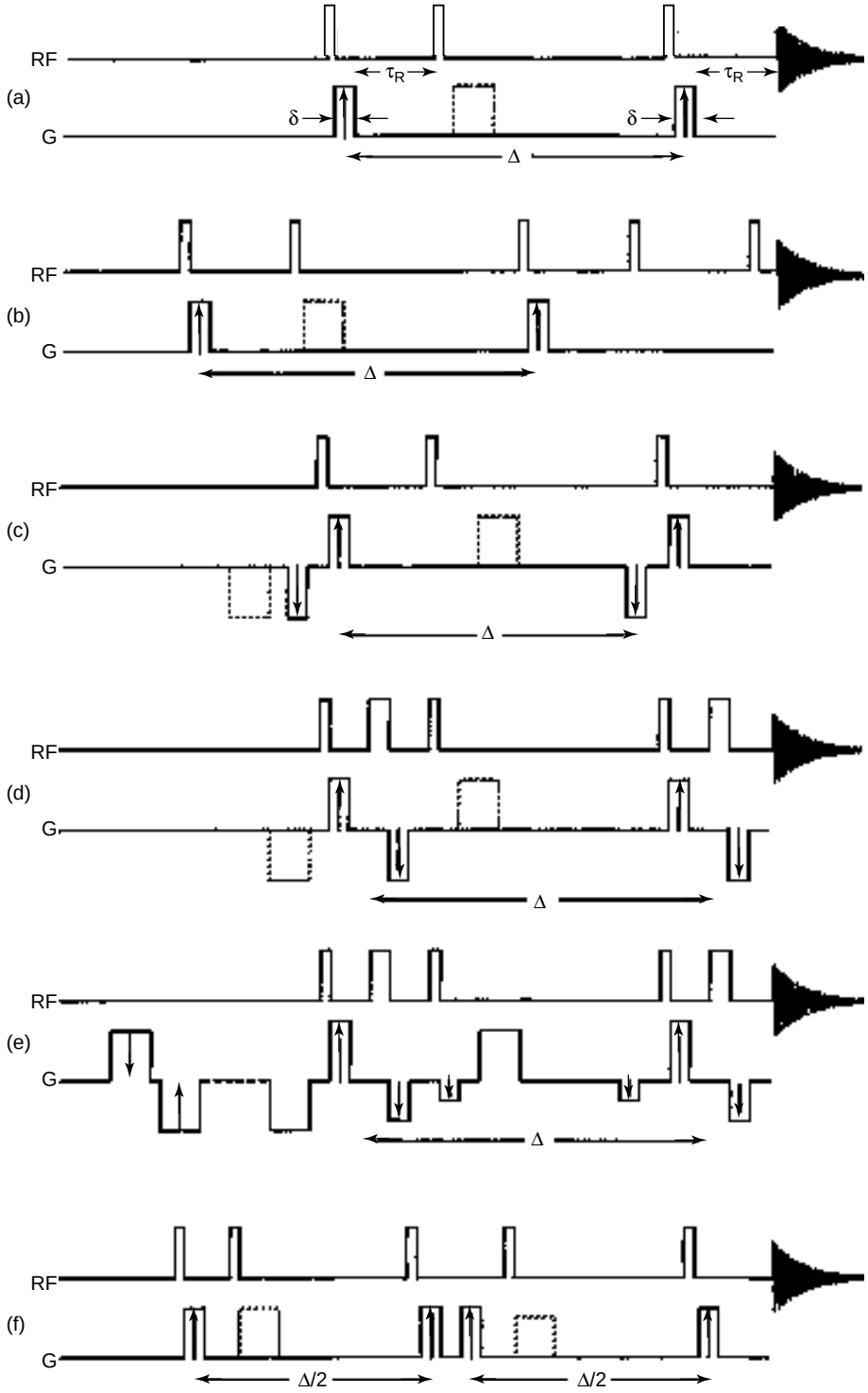

Figure 3 Radiofrequency (RF) and gradient (G) pulse sequences for DOSY: (a) pulsed field gradient stimulated echo (PFGSTE); (b) pulsed field gradient longitudinal echo delay (PFGLED); (c) gradient compensated stimulated echo sequence (GCSTE); (d) bipolar pulse pair stimulated echo (BPPSTE); (e) one-shot BPPSTE; (f) convection compensated double stimulated echo. 90° pulses are indicated by narrow rectangles in the RF traces and 180° by broad. Purge/homospoil pulses as an alternative or adjunct to phase cycling are indicated with dotted lines; up/down arrows indicate gradient pulse amplitudes that are increased/decreased to obtain increased diffusional weighting of signals. In the defocusing and refocusing periods, the spacing between RF pulses is given by the sum of the gradient pulse width δ and the gradient recovery delay τ_R, as shown for sequence (a)

If the diffusion delay Δ is defined as the time between the midpoints of the two gradient pulses, the correction to the diffusion time for diffusion during the gradient pulses is $-\delta/3$, giving $\Delta' = \Delta - \delta/3$ and the familiar attenuation expression

$$S(q) = S(0)\exp[-Dq^2(\Delta - \delta/3)] \quad (3)$$

This basic sequence is perfectly serviceable for many purposes, but is capable of considerable improvement. Two problems which are of particular importance under high resolution NMR conditions are those of slow main field recovery from the gradient pulses, causing distortion of the early part of the free induction decay, and interference with the deuterium field frequency lock. In general the former effect is brief, giving a broad distorted base to lines, and the latter relatively long-lived, giving sharp but "unphaseable" lineshapes.

The problem of main field disturbance, usually due to eddy currents induced in the probe and magnet metalwork, is much less severe in modern instruments, which have self-shielded ("actively shielded") gradient coils. These minimize magnetic flux leakage outside the gradient coil, and hence give rise to much weaker eddy currents. For probes with unshielded gradient coils, a very effective way to circumvent problems from eddy currents is to add a z-filter to the stimulated echo sequence, storing the refocused magnetization for some tens of ms until the field is stable. Such a LED (longitudinal echo delay)[13] step may be included in a variety of DOSY pulse sequences; the simplest is the PFGLED sequence of Figure 3(b).

A more general solution to the problem of eddy currents in modern high resolution spectrometers, which also deals with the problem of gradient pulses suppressing the deuterium lock signal and hence introducing slow B_0 shifts, is to use bipolar pairs of field gradient pulses. Using closely-spaced matched pairs of gradient pulses of opposite polarity cancels eddy current effects to first order, and refocuses the deuterium lock signal in a gradient echo. Such opposed pulse pairs may have one partner outside the defocusing/refocusing periods, or have both pulses within the defocusing/refocusing period but bracketing a 180° radiofrequency pulse. Sequences using the latter construct are generally referred to as bipolar sequences, since the diffusion encoding is carried out by the bipolar pulse pair; such sequences have a number of advantages. In second-order scalar coupled systems, relaxation effects can lead to zero quantum coherence causing phase errors in simple stimulated echo pulse sequences; by refocusing chemical shifts, bipolar sequences avoid exciting such coherences and hence do not suffer from phase errors in strongly coupled multiplets. Bipolar sequences also reduce contributions to diffusion-encoding from static background field gradients; these are not a problem under high resolution conditions, but in heterogeneous systems with strong internal field gradients caused by magnetic susceptibility differences they can complicate matters significantly. Adding balancing gradient pulses to the PFGSTE sequence gives the gradient compensated stimulated echo (GCSTE) sequence of Figure 3(c), which is a good general purpose sequence for systems lacking strong coupling; in the latter case the bipolar pulse pair stimulated echo (BPPSTE) sequence of Figure 3(d) is preferable.

With all pulse sequences for high resolution DOSY it is important to ensure that the desired coherence transfer pathway is followed. At first sight this might seem unimportant for a sequence such as PFGSTE, since the gradient pulses might be expected to suppress the coherence transfer antiecho. However, even with strong gradient pulses the attenuation envelope for rejected signals only decays as the inverse of the pulse area. Small amounts of unwanted signal can therefore survive the pulse sequence, causing small intensity and phase anomalies and distorting the resultant diffusion spectrum. For the best results with PFGSTE-based sequences it is therefore important to use phase cycling. With BPPSTE, the issue is more critical, since without phase cycling any magnetization that does not experience perfect 180° pulses during the defocusing and refocusing periods will form a gradient echo over the relevant period and will not experience significant diffusional attenuation.

Where speed of measurement is important – and useful DOSY data can be obtained in as little as 30 s – a purge/homospoil pulse may be used in the diffusion delay to enforce zero coherence order in this period, and in bipolar sequences the positive and negative gradient pulses may be unbalanced in order to dephase magnetization not refocused by the 180° pulses. A final refinement is to add dummy pulses, where gradient amplifier duty cycle permits, before the start of a pulse sequence. These may be ramped down in amplitude as the diffusion-encoding pulses are ramped up, in order to keep the net energy dissipated the same for each transient; the pulses precondition the gradient amplifier and coil, and reduce gradient pulse area mismatch problems. A bipolar sequence which incorporates all three of these modifications and is suitable for "one-shot" (single transient per gradient value) use is shown in Figure 3(e).

The limitations imposed by non-uniformity of the pulsed field gradient are most effectively dealt with as described in Data Analysis, since this retains full sensitivity and resolution in the NMR data. A much simpler method of reducing the impact of gradient non-uniformity is to restrict the active volume of the sample to the most homogeneous region of the gradient (i.e., the region where the applied gradient is closest to linear). This may be achieved either by using selective excitation in the presence of a field gradient to select just a slice of the sample, or by physically restricting the length of the sample. In the former case care must be taken to avoid spurious echo phenomena, while in the latter case even the best susceptibility matching still results in a substantial degradation of the NMR lineshape.

A more serious limitation on DOSY measurements is the requirement that the motion of the spins in the sample be dominated by diffusion. Typical high resolution DOSY experiments use diffusion times Δ of a few tenths of a second, so for small molecules the mean square displacement over the timescale of the experiment is about 20 μm. Coherent motion of the spins with a velocity of the order of 1 $\mu m\,s^{-1}$ is thus sufficient to interfere with diffusion measurements even for small molecules; studies on macromolecules, and on nuclei with low magnetogyric ratio, can be vitiated by much slower motion (of the same order as continental drift). There is thus a severe potential problem of convection when attempting to use DOSY at temperatures above or below room temperature.

Where mobile solvents such as methanol or acetone are used, the onset of convection in a normal NMR tube with commercial probes is typically only a few degrees away from the quiescent sample temperature. The first sign of convection is usually the appearance of small phase errors

at higher gradient strengths; for low velocities, the phase error is proportional to the product of the gradient pulse width, diffusion time and gradient amplitude. Unfortunately, apparent phase errors are a common symptom of other instrumental problems, including lock disturbance, slow B_0 recovery, and gradient pulse area mismatch. The onset of convection can be delayed by using a capillary tube, particularly if the capillary is surrounded by a mobile (but NMR-silent) solvent, since the convection of the outer liquid helps reduce the temperature gradient along the capillary sample. A more general solution to the problem of coherent motion of the spins during DOSY experiments is to build velocity compensation into the pulse sequence. The sequence of Figure 3(f) uses a double stimulated echo[14] to refocus the phase gradient caused by coherent motion. Such sequences, which can be extended by analogy with sequence 3(e) to avoid lock disturbance and hence give improved lineshapes, allow DOSY measurements to be performed over a much wider temperature range.

4.2 Heteronuclear 2D DOSY

The principal factor limiting the application of DOSY to the analysis of complex mixtures is the requirement that spectra be well-resolved if good diffusion resolution, and hence good discrimination between mixture components, is to be obtained. One way to improve resolution is to select for observation a nucleus such as carbon-13 that has a relatively high ratio of chemical shift dispersion to linewidth. Unfortunately there is a double price to pay on moving from protons to carbon-13, in the form of greatly reduced signal-to-noise ratio and a four-fold decrease in sensitivity to field gradients. The latter problem can be eliminated, and the former somewhat reduced, if the carbon-13 signals measured are the result of polarization transfer from protons. Combining a proton pulsed field gradient stimulated echo sequence with INEPT (insensitive nuclei enhanced by polarization transfer) or DEPT (distortionless enhancement by polarization transfer) transfer to carbon-13 allows carbon signals to be measured which enjoy the usual signal enhancement and recycle time advantages of polarization transfer techniques, and show the same sensitivity to diffusion as proton signals. DOSY-DEPT and DOSY-INEPT[15] can, where sensitivity permits, be very effective mixture analysis tools. One complication is the need to keep power deposition in the sample from decoupling to a minimum, since quite modest decoupling powers are sufficient to generate convection in mobile solvents.

4.3 3D DOSY

A more general approach to improving spectral resolution in DOSY is to extend experiments into a further spectral dimension. 3D DOSY experiments involve the measurement of a series of conventional two-dimensional spectra with increasing diffusion weighting, typically by prepending a pulsed field gradient stimulated echo sequence to the preparation period of a normal 2D experiment. Cross- and diagonal-peak volumes are then fitted to extract diffusion coefficients and standard errors and a 3D DOSY spectrum synthesized in a manner exactly analogous to 2D DOSY. DOSY-COSY,[16] DOSY-NOESY[17] and DOSY-TOCSY (total correlation spectroscopy)[18] experiments have all been described, although most applications have been restricted to labeling 2D peaks with diffusion coefficients rather than carrying out the synthesis of a full 3D spectrum. The highest

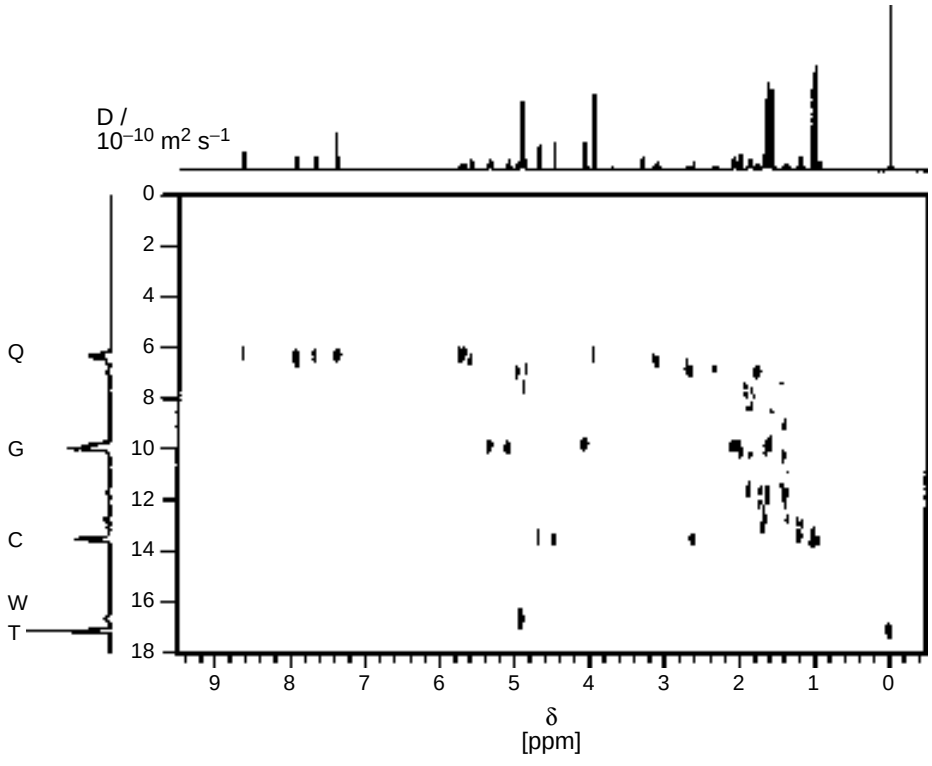

Figure 4 400 MHz proton DOSY spectrum of a mixture of quinine (Q), geraniol (G) and camphene (C) in deuteriomethanol; signals are also seen for HDO (W) and TMS (T)

net resolution technique reported to date is DOSY-HMQC (heteronuclear multiple quantum coherence),[19] which disperse signals according to proton shift, carbon-13 shift and diffusion coefficient.

5 EXAMPLES

Figure 4 shows a typical high resolution proton 2D DOSY spectrum for a simple mixture, illustrating some of the strengths and weaknesses of DOSY as a tool for the analysis of simple mixtures. The sample, a mixture of quinine, geraniol and camphene in deuteriomethanol, also contained TMS (tetramethylsilane) as reference, and residual water and monoprotiomethanol. Spectral data were acquired at 400 MHz using the GCSTE sequence of Figure 3(c); 10 spectra of 16 transients covering the range 0.6–10 G cm^{-1} in equal steps of gradient squared were measured with a diffusion time Δ of 0.5 s and gradient pulse widths δ of 2 ms, in a total time of 45 min. These parameters were chosen to give only modest (ca. 50%) attenuation for the signals of the slowly-diffusing quinine, in order to ensure that there was sufficient TMS signal for reference deconvolution at the higher gradient strengths. Spectra were processed with reference deconvolution based on the TMS line to give a Lorentzian lineshape of 1 Hz at half height, baseline corrected using cubic spline interpolation, and fitted with a modified exponential derived from gradient mapping experiments as described in Section 3.1.

Overall, the distribution of signals in the diffusion domain of spectrum of Figure 4 is dominated as expected by the

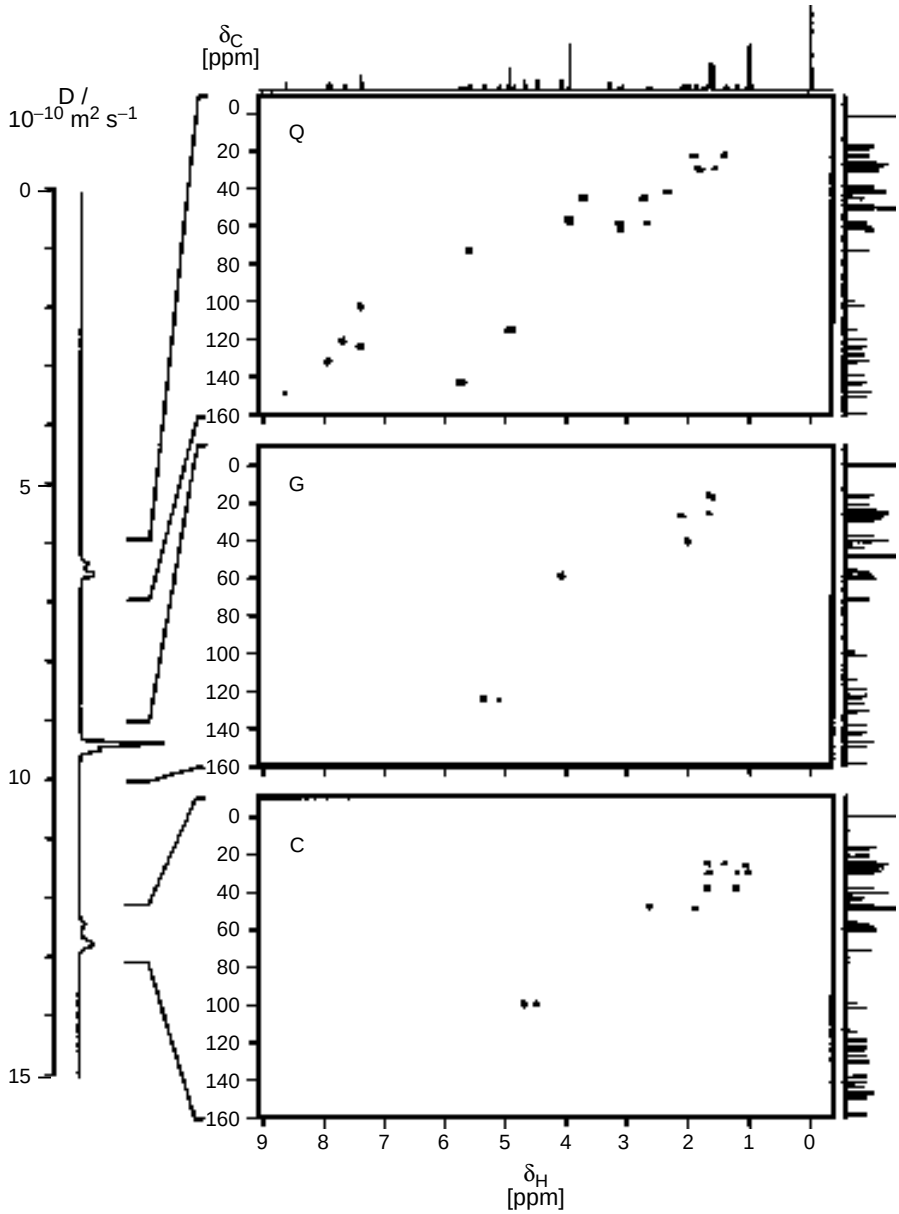

Figure 5 400 MHz ^{1}H-^{13}C DOSY-HMQC data for the same mixture as Figure 4, with (left) the integral projection of the 3D spectrum onto the diffusion axis, and (right, from top) integral projections onto the ^{1}H-^{13}C plane for the diffusion regions 5.9–6.9 × 10^{-10} (quinine, Q), 9.0–10.0 × 10^{-10} (geraniol, G), and 12.1–13.1 × 10^{-10} m^2 s^{-1} (camphene, C)

diffusion coefficients of the four main species present, quinine, geraniol, camphene and TMS. These appear as four strong distinct peaks in the integral projection of the spectrum onto the diffusion axis, shown at the left. Above 2 ppm, all of the signals appear at the expected positions in the diffusion domain, with one exception. At 4.9 ppm the quinine multiplet lies on top of the broader residual water signal, with the result that the apparent diffusion coefficients of the quinine signals are increased and that of the water slightly decreased. This effect can be reduced but not eliminated by the use of resolution enhancement to reduce the overlap between the signals; however, the shifts in the signals are simple, predictable and easily accounted for, and do little to damage the interpretability of the spectrum. Below 2 ppm the large number of aliphatic proton signals from the three main species gives rise to more severe overlap, with the result that a significant number of signals are displaced to lie at averaged apparent diffusion coefficients. As the diffusion projection shows, 95% of the overall signal intensity remains at the correct diffusion coefficient; in this sample only low intensity signals show significant deviations from their expected positions, although the difficulty of reproducing contour plots for spectra with such high chemical shift resolution exaggerates their apparent importance.

Where sensitivity considerations permit, 3D DOSY methods offer a large improvement in resolution. Figure 5 shows data from a 3D DOSY-HMQC (heteronuclear multiple quantum coherence) experiment[19] on a similar sample of quinine, geraniol and camphene. Five diffusion-weighted HMQC datasets of 512×1024 complex data points were acquired in a total time of 17 h, with a diffusion time of 45 ms and pulse gradient strengths from 1 to 30 G cm^{-1}. Peak volumes were determined for all cross peaks and fitted to a simple exponential as a function of q^2. The extra resolution afforded by separating signals according to both ^{1}H and ^{13}C chemical shifts now ensures that all signals, including those for the aliphatic protons, are well-resolved. Thus while the relative accuracy with which diffusion coefficients are determined is reduced compared to Figure 4 because of the small number of different gradient strengths used, the 3D experiment nevertheless successfully resolves all the signals in the mixture.

6 RELATED ARTICLES IN THIS VOLUME

Diffusion-Based Studies of Aggregation, Binding and Conformation of Biomolecules: Theory and Practice; Reference Deconvolution.

7 RELATED ARTICLES IN VOLUMES 1–8

Diffusion & Flow in Fluids, Volume 3; Diffusion Measurements by Magnetic Field Gradient Methods, Volume 3; Electrophoretic NMR, Volume 3; Field Gradients & Their Application, Volume 3.

8 REFERENCES

1. C. S. Johnson Jr., *Prog. NMR Spectrosc.*, 1999, **34**, 203.
2. W. S. Price, *Concepts Magn. Reson.*, 1997, **9**, 299.
3. W. S. Price, *Concepts Magn. Reson.*, 1998, **10**, 197.
4. P. Stilbs, *Anal. Chem.*, 1981, **53**, 2135.
5. K. F. Morris and C. S. Johnson Jr., *J. Am. Chem. Soc.*, 1992, **114**, 3139.
6. G. A. Morris, H. Barjat, and T. J. Horne, *Prog. Nucl. Magn. Reson. Spectrosc.*, 1997, **31**, 197.
7. K. F. Morris and C. S. Johnson Jr., *J. Am. Chem. Soc.*, 1993, **115**, 4291.
8. M. A. Delsuc and T. E. Malliavin, *Anal. Chem.*, 1998, **70**, 2146.
9. K. F. Morris and C. S. Johnson Jr., *J. Am. Chem. Soc.*, 1993, **115**, 4291.
10. B. Antalek and W. Windig, *J. Am. Chem. Soc.*, 1996, **118**, 10 331.
11. L. C. VanGorkom and T. M. Hancewiecz, *J. Magn. Reson.*, 1998, **130**, 125.
12. P. Stilbs, K. Paulsen, and P. C. Griffiths, *J. Phys. Chem.*, 1996, **100**, 8180.
13. S. J. Gibbs and C. S. Johnson Jr., *J. Magn. Reson.*, 1991, **93**, 395.
14. A. Jerschow and N. Müller, *J. Magn. Reson.*, 1997, **125**, 372.
15. D. Wu, A. Chen, and C. S. Johnson Jr., *J. Magn. Reson., A* 1996, **123**, 215.
16. D. Wu, A. Chen, and C. S. Johnson Jr., *J. Magn. Reson., A* 1996, **121**, 88.
17. E. K. Gozansky and D. G. Gorenstein, *J. Magn. Reson., B* 1996, **111**, 94.
18. A. Jerschow and N. Müller, *J. Magn. Reson., A* 1996, **123**, 222.
19. H. Barjat, G. A. Morris, and A. G. Swanson, *J. Magn. Reson.*, 1998, **131**, 131.

Biographical Sketch

Gareth A. Morris, *b* 1954. M.A. (Nat. Sci.), Ph.D. (supervisor Ray Freeman) 1978, Oxford University, UK. Fellow by Examination, Magdalen College, Oxford, 1978–1981; Izaak Walton Killam Postdoctoral Fellow, University of British Columbia (with Laurie Hall) 1978–79. Lecturer (1982–1989) and Reader (1989–1997) in Chemistry, Professor of Physical Chemistry (1998 to date), University of Manchester, UK. Approx. 130 publications. Current research interests: development of novel NMR techniques and their application to problems in chemistry, biochemistry and medicine.

Field Gradients and Their Application

Ralph E. Hurd
GE Medical Systems, Fremont, CA, USA

1	Introduction	1
2	Early Applications	1
3	Gradient Hardware Considerations	1
4	The Effect of Magnetic Field Gradients	2
5	Coherence Pathway Selection	2
6	Homonuclear Applications	4
7	Proton Detected Heteronuclear Applications	6
8	Water Elimination	8
9	Phase Sensitive Methods	9
10	Spatial Tools	13
11	Summary	14
12	Related Articles	15
13	References	15

1 INTRODUCTION

Pulsed magnetic field gradients can be used in NMR to suppress unwanted magnetization, or to encode space, motion, and coherence order. These applications, which are central elements of in vivo magnetic resonance, can also be used to enhance high-resolution NMR spectroscopy. There are several ways in which a conventional NMR experiment can benefit from pulsed field gradients. Coherence pathway selection using field gradient pulses instead of phase cycling can minimize data collection time, reduce artifacts, and avoid signal loss associated with traditional water elimination methods. Differences in the rates of molecular motion between solvent and macromolecules can be exploited to achieve linewidth and lineshape independent water suppression. The consequences of poor homogeneity can be reduced using spatially selective excitation, and spoiler gradients can be used to selectively eliminate unwanted magnetization. The present article describes the development and application of $\boldsymbol{B}_0$ pulse field gradients in high resolution NMR spectroscopy. For a description of $\boldsymbol{B}_1$ gradient applications see ***Radiofrequency Gradient Pulses*** .

2 EARLY APPLICATIONS

The first report of using pulsed field gradients was published in 1955 and described the potential of magnetic resonance for information storage.[1] This work detailed the use of gradient pulses in multipulse, multiecho NMR to eliminate selectively unwanted signal. In this paper, bracketing a 180° refocusing pulse with a symmetric gradient pair was introduced as an efficient way to avoid spurious echoes. Further, the application of a gradient pulse during a z axis storage interval was introduced as a way to select for stimulated echoes. These early pulsed gradient applications are still used in contemporary NMR, especially in imaging and localized spectroscopy, where they have taken on names such as primer−crusher pairs, crushers, and spoiler gradients. These concepts are also important for the application of pulsed gradients in high-resolution NMR spectroscopy.

The use of pulsed field gradients to measure molecular diffusion was introduced in 1965 by Stejskal and Tanner.[2] This approach overcame severe bandwidth limitations associated with earlier static gradient measurements. In this method, transverse magnetization is encoded with spatially dependent phase by application of an initial gradient pulse, allowed to stay encoded for a fixed period of time, and then rephased by a second gradient pulse. The loss of recoverable signal due to the movement of spins is related to the diffusion coefficient by the Stejskal−Tanner equation:

$$\ln(S/S_0) = -\gamma^2 g^2 \tau^2 (\Delta - 1/3\tau) D \qquad (1)$$

where γ is the magnetogyric ratio, g is the strength and τ the duration of the gradient pulse pair, Δ is the time between gradient pulses, and D is the diffusion coefficient (see also ***Diffusion Measurements by Magnetic Field Gradient Methods***). The large difference in D for macromolecules relative to solvent water provides the basis for the use of diffusion gradients in spectroscopy.

In 1968, Vold and co-workers[3] used a spoiler gradient to overcome imperfect 180° inversion in a T_1 recovery sequence. Shortly thereafter, the benefits of using spoiler gradients, or homospoil pulses, as they sometimes became to be known, were reported by a number of groups. One of the best known applications has been as a mix time spoiler in the NOESY experiment (see also ***NOESY***).

Even spatial resolution has shown potential value in high-resolution spectroscopy. As will be discussed later in this article, slice selection can be used to reduce end effects from sample and coil, and field maps may provide a way to optimize homogeneity. For a description of the development of spatial applications of pulsed field gradients see ***Magnetic Resonance Imaging: A Historical Overview*** .

In 1977, Wokaun and Ernst[4] described the relationship between coherence order and the effect of a gradient pulse. The idea of using gradients for coherence pathway selection was further developed by the studies of several groups.[5–8]

3 GRADIENT HARDWARE CONSIDERATIONS

3.1 Eddy Current Compensation

In early studies, potential benefits of using pulsed gradients were often overshadowed by drawbacks such as long gradient recovery times, increased phase instability, peak shape distortion, and, for high-resolution applications, disturbance of the field/frequency lock system. The problem is with the induced eddy currents generated in conductive materials by the switched gradient field. This may include such items as the magnet cryoshields, the bore tube, and the coil itself. The transient fields generated by eddy currents have a variety of decay times which may be of the order of milliseconds, or can persist for seconds. To reduce this problem, the gradient

amplifier can be overdriven to compensate for these undesirable fields. This approach, referred to as preemphasis, is in common use on almost all modern gradient systems, but does not completely overcome the problem (***Eddy Currents and Their Control***).

3.2 Gradient Amplifier Noise

With the incorporation of strong ($>200\,\mathrm{mT\ m^{-1}}$) pulsed gradient systems into the NMR experiment, it is important to consider the dynamic range of the gradient amplifier. For example, a $1\,\mathrm{T\ m^{-1}}$ gradient is capable of producing 425 800 2π radians $\mathrm{s^{-1}}$ gradient across a 1 cm sample. The tolerance of most experiments requires that any variation of the amplifier quiescent state (the noise floor) be significantly less than 10^{-7} of this peak value. For many experiments, especially those in which a nonrectangular gradient wave form is used, 16-bit control of the gradient amplitude is also desirable.

3.3 Actively Shielded Gradients

One of the most important improvements in gradient technology for NMR has been the introduction of actively shielded gradients (see ***Gradient Coil Systems***). The basic idea is to provide a second coil of opposite polarity outside the primary gradient coil, which is then driven to buck the stray field generated outside the primary coil. In practice the combination of active shielding and preemphasis gives the best performance.

Phase error can also come from movement of the coil during sharp gradient transitions. This is the source of the characteristic sound made by gradient pulses, sometimes referred to as the speaker-coil effect. It is often desirable to attenuate the amplitude and ring down time of this vibration. Reduced mechanical noise from the gradients is usually accomplished by potting the coils in a nonconductive material such as concrete or epoxy. These coils must also be designed to dissipate the significant heat that can be generated by gradient experiments.

3.4 Single-Axis versus Three-Axis Gradients

In any experiment which consists of multiple rf and multiple gradient pulses, care must be taken to avoid recovering unwanted signal dephased earlier in the pulse sequence. This is relatively straightforward, and can be achieved by prudent choice of sign, amplitudes, or durations of the gradient pulses. If multiple axes are available, gradient cycling has been shown to be effective.[9] In practice, single z axis gradient coils have been more widely available for high-resolution applications, and have proven sufficient to provide improvements over conventional phase cycled methods. Unfortunately, in some cases the static gradients generated by the homogeneity shims can create a problem. Although weak in comparison to the applied gradient pulses, these static gradients may have over 1 s (e.g. acquisition time) to rephase the effect of a 1 ms or shorter gradient interval.

In 1971, Redfield and Gupta[10] commented on the formation of unwanted gradient echoes when using spoiler gradients. The misadjustment of shims, in the same direction as the applied gradient, is suggested as a way to prevent this accidental rephasing by the static shim gradients during acquisition. Misadjustment of shims, however, is rarely desirable. Further, in the case of high order z shims, the rephased signal may be from a small part of the NMR sample. An effective approach to reducing this problem is to avoid application of a pure z pulsed gradient, using additional x and/or y gradients to provide an off z axis distribution of phase.[11]

3.5 Sample Spinning and Field Frequency Locking

Although the effect of a gradient pulse on a deuterium field/frequency lock system is reduced relative to protons by γ_D/γ_H, lock blanking during the gradient pulse can be valuable. Recovery of the steady-state lock signal is determined primarily by the sensitivity of the lock as reflected in the M_{xy}/M_z of the deuterium spins, and by the T_2 relaxation rates of the deuterium solvent. Lock recovery rates can be very favorable for strong lock solvents such as the 5–10% D_2O commonly used for biochemical studies.

Sample spinning is only compatible with z axis gradient application, and even there care must be taken to avoid vortexing of the sample. Any increased mixing leads to signal loss in both diffusion weighted and in gradient coherence selection methods. Also, in practice, sample spinning has been observed to reintroduce t_1 noise, partially negating one of the benefits of using gradients in the first place. Fortunately, full performance can be achieved nonspin for most biochemical samples.

4 THE EFFECT OF MAGNETIC FIELD GRADIENTS

4.1 Dephasing

The application of a pulsed field gradient generates a reversible distribution of phase

$$\phi_r = \gamma(g\tau)rp \tag{2}$$

where γ is the magnetogyric ratio, g is the gradient strength, τ is the gradient duration, r is the distance from gradient isocenter, and p is the coherence order. This effect can be visualized by mapping the effect of gradient pulse on a phase sensitive proton image as shown in Figure 1. As expected the application of a rectangular, $10\,\mathrm{mT\ m^{-1}}$ gradient of 1 ms in duration generates approximately three 2π cycles of phase along the z axis of a 1.5 cm long water sample. If not resolved in space, the signal from the volume of spins self-cancels. The effectiveness of cancellation increases with gradient integral $g\tau$.

The amount of gradient needed for complete signal dephasing is variable and depends strongly on factors such as $\boldsymbol{B}_1$ homogeneity and bulk magnetic susceptibility shifts. Although these would appear to be well controlled in a typical high-resolution NMR experiment, small deviations can make a significant difference when the amount of unwanted signal is large, as it is for most dilute biochemical samples in 90–95% H_2O. The largest variations in $\boldsymbol{B}_1$ are in the transition bands, at the ends of the rf coil, where $\boldsymbol{B}_1$ goes from maximum to zero. Short samples and bubbles can lead to localized frequency shifts, which also lead to inefficiency in self-cancellation.

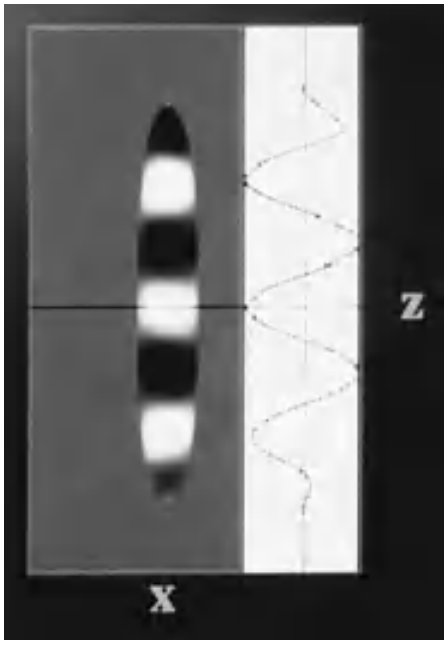

Figure 1 Phase sensitive image of a water sample in a standard 5 mm NMR tube. The effect of a 1 ms 10 mT m^{-1} rectangular z gradient pulse is recorded. The height of the detected volume is about 1.5 cm. As illustrated by the image and accompanying profile, the expected phase distribution is encoded by the applied gradient pulse. The curvature at the ends of the sample is the fall-off of x gradient strength as a function of z

5 COHERENCE PATHWAY SELECTION

Coherence selection using gradients takes advantage of the field dependence of coherence order. This dependence is described in terms of the phase generated by an applied gradient as shown in equation (2). In its simplest form, a sequence of rf pulses and delays generate multiple coherence pathways. A particular pathway can be selected, for example, by application of a gradient pulse to coherence order label the spins during an evolution or mixing delay interval, followed by the application of a read gradient just prior to data acquisition to rephase the desired pathway. This assumes that the chosen pathway will have zero net phase gradient and that the unwanted pathways will have a net distribution of phase, and therefore self-cancel. In general, signal will only be observed from pathways in which

$$\sum_i G_i p_i = 0 \tag{3}$$

where G_i represents the integral ($g\tau$, for a rectangular gradient pulse) of each gradient interval, i, and p_i is the coherence order during each interval, i.

5.1 Density Operator Description

The effect of a pulsed magnetic field gradient on the nuclear spin can be understood by describing the state of the spin system in terms of density operators. Many different formalisms express the density operator in matrix elements of appropriate sets of operators in a Cartesian or spherical basis. A detailed description of the effect of magnetic field gradients on the magnetization or coherence component is given by Counsell et al.[8]

For the purpose of describing the effects of magnetic field gradients, it is convenient to classify the density operator $\rho(t)$ of the spin system at any time t according to its various coherence orders or components:

$$\rho(t) = \sum_p \rho^p(t) \tag{4}$$

where p and ρ^p represent a particular coherence order and the density operator component corresponding to that coherence order. The spin coherences undergo precession during a gradient pulse, and the extent of precession depends on the spatial coordinate r of the spin, and the coherence order p of that particular component. Hence the Hamiltonian of the spin system during the gradient pulse is predominantly from Zeeman contributions. The Zeeman fields experienced by the various spins in the sample vary according to their spatial coordinates. The precession or rotation can be represented by $\exp\{-i\omega_z(r)F_z\tau\}$, where $\omega_z(r)$ is the precession frequency at a spatial position r, and τ is the duration of the field gradient pulse, and F_z is the z component of the total angular momentum. Classification of the density operator into the various coherence order components is convenient, since the effect of the field gradient pulse can be written as

$$\rho^p(t-) \xrightarrow{\exp\{i\omega_z(r)F_z\tau\}} \exp\{-ip\omega_z(r)\tau\}\rho^p(t+) \tag{5}$$

which describes the transformation of the pth component of the density operator ρ. $\rho(t-)$ and $\rho(t+)$ are used to label the density operator before and after the gradient pulse. As the right hand side shows, the effect of the gradient pulse is to modulate the density operator component by a complex phase factor. This phase factor depends on the coherence order of the component and on the integral of the gradient pulse. In other words, the phase of each magnetization component is modified by a factor which depends on the coherence order of the component, spatial position of that particular spin and also on the duration and amplitude of the applied field gradient. If we consider heteronuclear spins, the phase factor would also take into account the magnetogyric ratio of the nuclear spin. Essentially, the effect of the gradient pulse is to defocus the coherence by a controlled amount. Each of the coherence pathways can be thought to be coherence order labeled by the gradient pulse. Selection of a particular pathway or decoding is then accomplished by applying a rephasing gradient pulse with amplitude and duration $\omega_z^{\mathrm{R}}(r)\tau^{\mathrm{R}}$, which transforms the density operator described by

$$\sum_k C_k \rho^{(-1)} \exp\{-i\phi_k\} \tag{6}$$

where k is the index for a particular coherence pathway in the experiment, ϕ_k is the cumulative phase dispersal for that particular pathway, C_k denotes all of the time dependence and $\rho^{(-1)}$ denotes the observable component of the density operator, corresponding to coherence order $p = -1$. This can

be written as

$$\sum_k C_k \rho^{(-1)} \xrightarrow{\exp\{-\mathrm{i}\omega_z^{\mathrm{R}}(r)F_z\tau^{\mathrm{R}}\}} C_1\rho^{(-1)} + \sum_{k\neq 1} C_k\rho^{(-1)}\exp\{-\mathrm{i}(\phi_k + \omega_z^{\mathrm{R}}(r)\tau^{\mathrm{R}})\} \tag{7}$$

where 1 denotes the desired coherence pathway in the experiment. The first term on the right hand side $k = 1$, corresponds to the pathway which has been exactly decoded, and hence observed since

$$\phi_k = -\omega_z^{\mathrm{R}}(r)\tau^{\mathrm{R}} \tag{8}$$

The second term denotes all the other pathways which are still defocused and are not observable. Equation (5) describes the most important feature of all coherence transfer selection schemes, including rf phase cycling, $\boldsymbol{B}_0$ and $\boldsymbol{B}_1$ gradient methods. In conventional rf phase cycling methods, each coherence component accumulates phase factors during the various cycles of the phase cycle. The receiver phase cycle is then determined such that only the desired pathways yield a signal (see also ***Phase Cycling***). In the case of pulsed field gradients, each of the gradient pulses contributes to the cumulative phase factors of the various coherence components. The desired pathway is then selected by choosing the appropriate rephasing gradient integral (the product of amplitude and duration for rectangular gradient pulses) prior to data acquisition. A major feature of gradient selection of coherence pathways is that the selection is accomplished in a single acquisition, unlike rf phase cycling, where multiple acquisitions are required. It can be thought of as phase cycling in space rather than time. Also, the major limitation of gradient pathway selection has been the loss of all but a single pathway, resulting in lower sensitivity.

5.2 Coherence Pathway Diagrams

Coherence pathway diagrams[12,13] are a convenient way to visualize the use of gradients. This is illustrated with the homonuclear correlation experiment, COSY, in Figure 2. The spin system starts at thermal equilibrium with $p = 0$ and is detected in quadrature with $p = -1$. For this rf sequence there are two coherence pathways, $p = (0, -1, -1)$ and $p = (0, +1, -1)$. According to equation (3), a pathway will be selected only if $p_1G_1 + p_2G_2 = 0$. For the first pathway, where p_1 and p_2 are of the same sign, the gradient integral G_2 must be the negative of G_1. For the second pathway, where $p_2 = -p_1$, G_1 and G_2 must be identical. In a similar way, a pair of identical gradient pulses eliminates spurious signals in a spin echo experiment by selecting for a sign change in coherence order (e.g. $p = +1$ to -1 and $p = -1$ to $+1$). Unwanted signal excited by an imperfect 180° pulse will be dephased, $p_2G_2 \neq 0$.

For the multiple quantum experiments a third rf pulse adds another coherence transfer interval, and adds the possibility of using DQ coherence levels $p = \pm 2$. For the double quantum filtered correlations (DQF) COSY sequence illustrated in Figure 3, a gradient ratio, G_1:G_2:G_3 of 1:1:3, selects for one of the four DQ coherence pathways (0, +1, +2, −1).

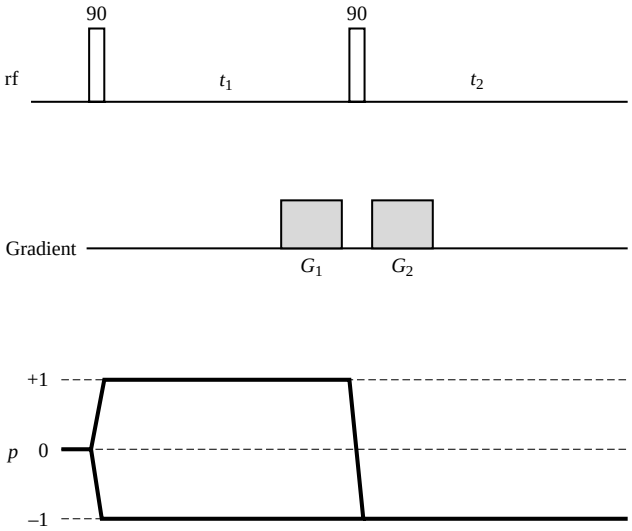

Figure 2 Pulse sequence and coherence pathway diagrams for the incorporation of pulse field gradients in COSY. P type (0, −1, −1) COSY is selected when $G_2 = G_1$ and N type (0, +1, −1) is selected when $G_2 = -G_1$

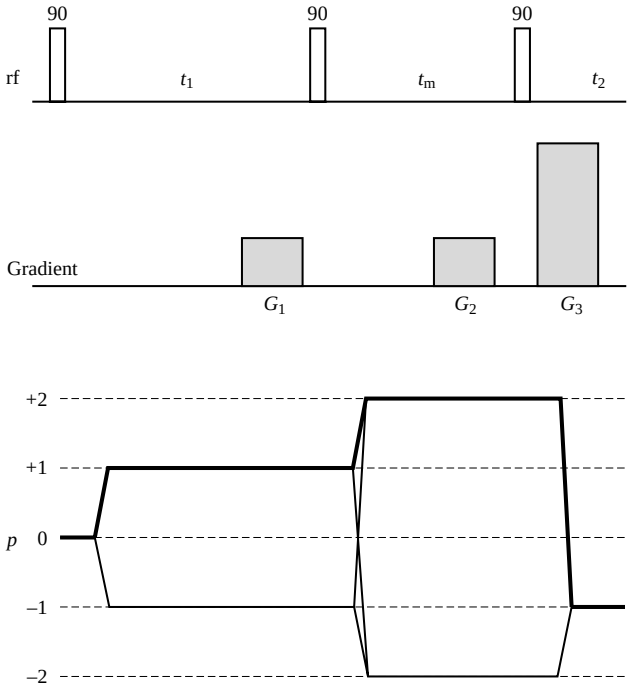

Figure 3 Pulse sequence and coherence pathway diagram for gradient enhanced DQF COSY. One of the four possible DQ pathways is selected

6 HOMONUCLEAR APPLICATIONS

For small organic molecule NMR, the major use of pulse field gradients is speed and reduction of artifacts in simple 2D NMR. For aqueous based proton NMR, gradient selection of multiple quantum pathways to discriminate against water, is an important application.

The uncoupled spins of water cannot generate $p = \pm 2$ coherence order, and can easily be left dephased during the detection period. This has been an advantage for in

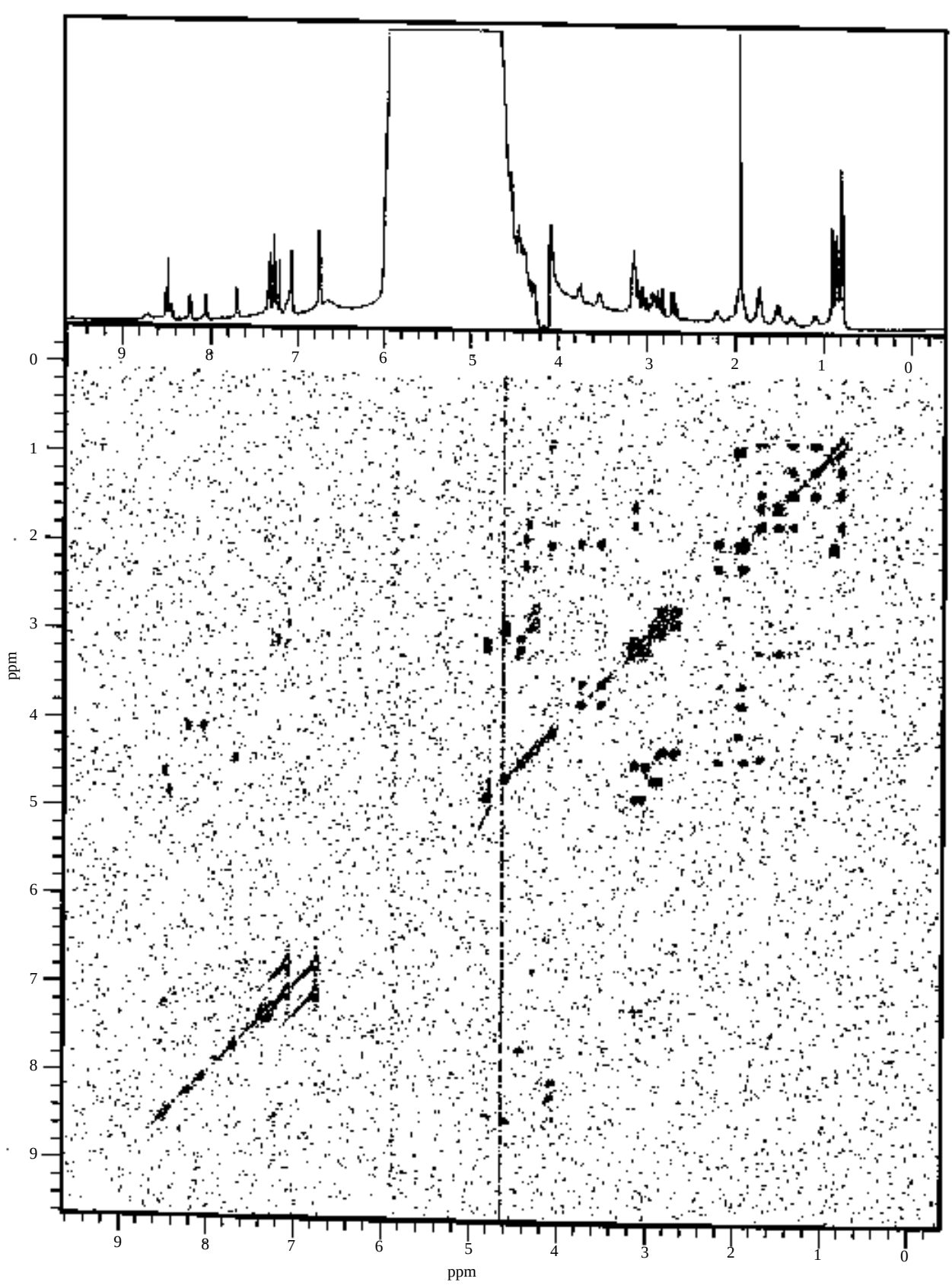

Figure 4 Noise floor contour plot of 400 MHz GE DQF COSY spectrum of 8 mM angiotensin II in H_2O. An 800-fold vertical expansion of the reference one-pulse spectrum is shown above the contour plot. 2D data were collected at 4 Hz resolution in ω_1 and ω_2 without phase cycling. A transmitter zero-frequency artifact, not residual water, is responsible for the intensity at 4.6 ppm. (Adapted by permission of Academic Press from Hurd[15])

vivo detection of lactate.[14] The single-shot selection process avoids the motion related subtraction errors that can be a problem in vivo. The further addition of rf selective coherence transfer provides extraordinary discrimination between the lactate methyl signal and the overlapping lipid CH_2 in a 2D DQ sequence.[11] Success of the in vivo results obtained using actively shielded gradients led to experiments with this technology on high-resolution NMR systems. Not surprisingly, one of the first experiments was gradient enhanced GE DQF COSY.[15] As illustrated by the noise floor contour plot shown in Figure 4, this approach to solvent suppression does not perturb signals close to or at the water chemical shift. It is also apparent that the nonsubtractive nature of gradient coherence pathway selection reduces the problem of t_1 noise.

7 PROTON DETECTED HETERONUCLEAR APPLICATIONS

7.1 GE HMQC

Proton detection of low γ nuclei is a good example of a method in which the desired signal is but a small part of the overall proton magnetization. As such, this type of experiment lends itself well to the application of gradients. The pulse sequence and modified coherence pathway diagram for a gradient enhanced version of a heteronuclear correlation experiment GE HMQC[16] are shown in Figure 5. In this diagram, shared coherence levels are drawn using a γ_H normalized coherence order

$$p' = p(^1\mathrm{H}) + p(\mathrm{X})\gamma_X/\gamma_H \tag{9}$$

Since phase distribution is proportional to the product of p' and gradient integral G, signal will only be observed for transverse magnetization from pathways for which the sum of the effects from all of the individual gradient pulses goes to zero:

$$\sum p'[i]G[i] = 0 \tag{10}$$

For $^1H/^{13}C$ experiments, $\gamma_X/\gamma_H = 0.25$. This means, for example, that $^1H[+1]^{13}C[-1]$ zero-quantum coherence will have a normalized order $p' = 0.75$. A gradient, G_1, applied during such an interval will cause a coherence pathway through this zero quantum level to be encoded with a distribution of phase, $\phi = 0.75G_1$. To select for this pathway, a read ($p' = -1$) gradient, G_3 must be set to $0.75G_1$. This pathway, H[0]C[0] $\rightarrow$ H[+1]C[0] $\rightarrow$ H[+1]C[-1] $\rightarrow$ H[-1]C[-1] $\rightarrow$ H[-1], can also be selected using alternate ratios of gradients G_1:G_2:G_3. These sequences can be optimized for best use of available gradient strength for dephasing (2:2:1) or can be optimized to avoid certain artifacts.[17]

In natural-abundance carbon experiments, more than 99% of the signal must be subtracted out to reveal the protons attached to the 1% abundant ^{13}C nuclei. With gradient selection, protons attached to ^{12}C and from solvents such as water are not detected, thus avoiding subtraction and dynamic range limitations. The effectiveness of this suppression is illustrated in Figure 6 by a noise floor contour plot of a single acquisition

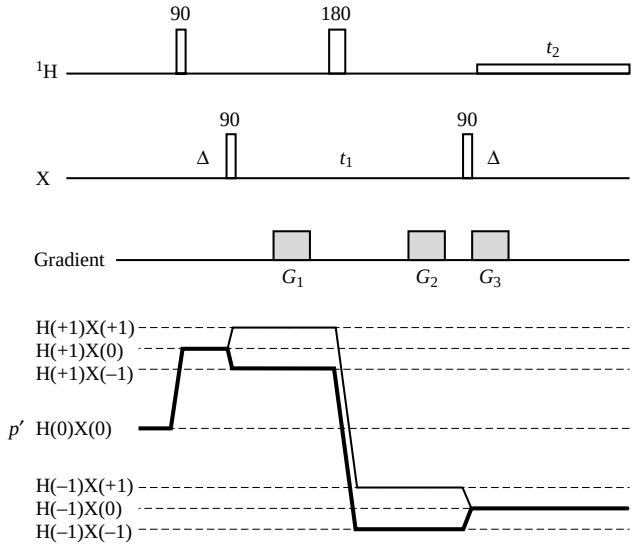

Figure 5 Pulse sequence and coherence pathway diagram for GE HMQC

per block ^1H[natural abundance ^{13}C] GE HMQC spectrum of sucrose in water. In this example, without broadband ^{13}C decoupling, the correlations are observed as ^{13}CH doublets. The absence of signal at the ^{12}C proton chemical shifts and at the water chemical shift in this spectrum demonstrate the complete cancellation of signal from protons not attached to ^{13}C. Another good application is in the long range heteronuclear multiple bond correlation (HMBC) experiment where t_1 noise from the uncoupled protons may obscure weak long range $^{13}C-^1H$ correlations in a conventional experiment.

7.2 3D and 4D Applications

It was recognized from early on that the reduction in the phase cycle requirement and the concomitant reduction in total data collection time would be a significant reason to use pulse field gradients in 3D and 4D applications. These experiments usually require large numbers of acquisitions just to achieve adequate resolution in the evolution domains. In fact, in some cases, it is the phase cycle and not the signal-to-noise ratio (S/N) which dictates the length of data collection time. A number of multidimensional methods have been developed to take advantage of the reduced data collection time, water suppression characteristics, and fewer artifacts.[18–23] Others have taken advantage of reduced phase cycle to increase resolution in the evolution dimensions.[24]

One of the first 3D gradient sequences was a modification of HMQC–COSY. The GE HMQC–COSY sequence[18] is a combination of a gradient-enhanced HMQC experiment, in which heteronuclear zero quantum magnetization is coherence order labeled and then selectively rephased via a 4:$-$3 gradient pair surrounding the final carbon 90° pulse, and a gradient-enhanced COSY experiment in which quadrature in the COSY dimension is selected with a 1:1 gradient pair around the final 90° pulse. The resulting gradient integrals are 4:$-$2:1. The asymmetry of this gradient pulse scheme leaves protons which are not at least indirectly connected to ^{13}C dephased and unobserved. This method provides editing, simple pattern

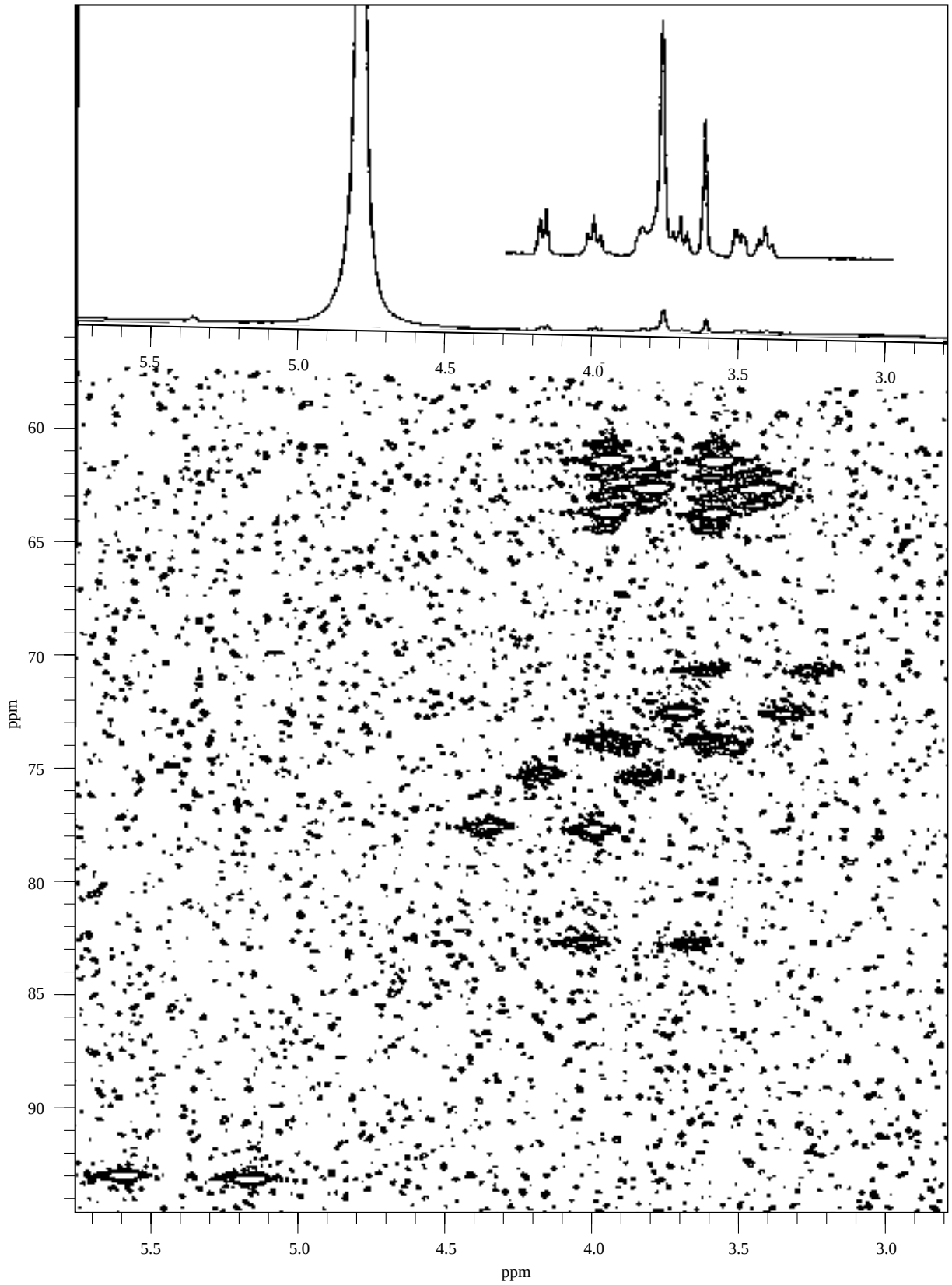

Figure 6 Noise floor contour plot of a 2 min total acquisition time $^{1}H[^{13}C$ natural abundance] GE HMQC spectrum of sucrose in water shows complete elimination of ^{12}C protons and solvent water

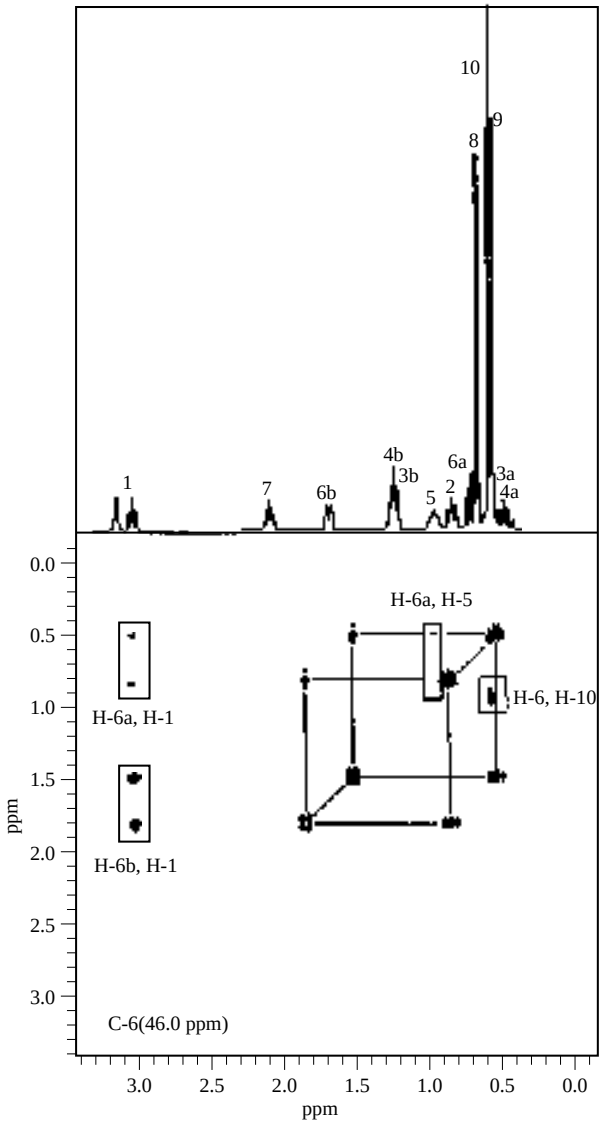

Figure 7 C-6 plane from a 512 × 128 × 128 GE HMQC–COSY spectrum of menthol collected in less than 7 h. Simple correlation patterns are observed for direct and remotely coupled protons. (Reproduced by permission of Academic Press from Hurd and John[18])

recognition features, and in some cases additional resolution. Without the need for phase cycling, a moderate resolution 512 × 128 × 128 spectrum can be obtained in just a few hours. As illustrated by the C-6 plane of menthol, shown in Figure 7, protons directly attached to carbon are observed as J(C,H) doublets along the $\omega_3 = \omega_2$ diagonal. A proton attached to a directly adjacent carbon (^{12}C) is observed at its ^{12}C proton chemical shift in ω_3, and at the frequencies of the directly (^{13}C) attached proton in ω_2 (see, for example, the H-6b,H-1 correlation). Proton connectivities from two carbon bonds away are observed as single correlations at the ^{12}C proton chemical shift in ω_3 and at the ^{12}C proton chemical shift of the intermediary proton in ω_2 (see, for example, H-6,H-10). The inequivalent CH_2 protons of C-6 (H-a,H-b and H-b,H-a correlations) remain coupled in both ω_2 and ω_3 to give a parallel squares pattern. This occurs because both protons are attached to the same ^{13}C nuclei.

Proton detected 3D SQ–DQ COSY of ^{13}C enriched sugars has been reported to be more useful with the incorporation of pulse field gradients, yielding 'unsurpassed' resolution plus better overall artifact suppression.[24]

7.3 Protein NMR Applications

The analysis of protein structure by NMR has been a driving force in the development of proton-detected multidimensional methods. The success of these applications often depends on the ability to identify, assign, and obtain distance information from C-α,H resonances. The proximity of these signals to the water chemical shift can be a problem in some cases. Traditional methods of water suppression often exhibit an inherent disadvantage. Selective excitation often results in the loss or attenuation of desired signals near the water resonance and, when presaturation is used, magnetization transfer and proton exchange can lead to a loss of signal intensity throughout the spectrum. Although these issues can be managed, in part, by compromises in solvent conditions and temperature, gradient based coherence selection offers an alternative. GE HMQC–TOCSY and GE HMQC–NOESY give full unobscured C-α,H correlations at water chemical shift.[19] These experiments were also among the first gradient coherence selection experiments run using a field/frequency lock and variable temperature; these are key requirements for routine use of gradients.

8 WATER ELIMINATION

Removal of the large unwanted water signal without perturbing the desired signal has been one of the great technical challenges of biomolecular proton NMR. Potential difficulties include exchangeable protons, a crowded water chemical shift region, and correlation times which allow signal loss via magnetization transfer. Gradients have had an increasingly important role in this area. The advantage relative to presaturation has been quantitatively measured using gradient versions of the heteronuclear single quantum correlation (HSQC) experiment.[25,26] As illustrated in Figure 8, the retention of signal is most significant for proteins in the physiologically important pH range of 6.5–7.5.[26] Elimination of the presaturation effect reveals the smaller loss of signal due to a 'short' recycle delay. This second effect is presumably due to an increased rate of exchange with long T_1 water protons at higher pH. In addition to multiple quantum coherence pathway selection, there are several other gradient based methods which can be used for water suppression. Spoiler gradients can be used in combination with selective rf excitation as an effective replacement of conventional presaturation, gradient pairs can be used to improve selective spin echo methods, and diffusion weighted methods can provide lineshape independent water reduction (***Water Signal Suppression in NMR of Biomolecules***).

8.1 CHESS

In a method sometimes referred to as a *che*mical *s*hift *s*elective (CHESS)[27] pulse, water is selectively excited and

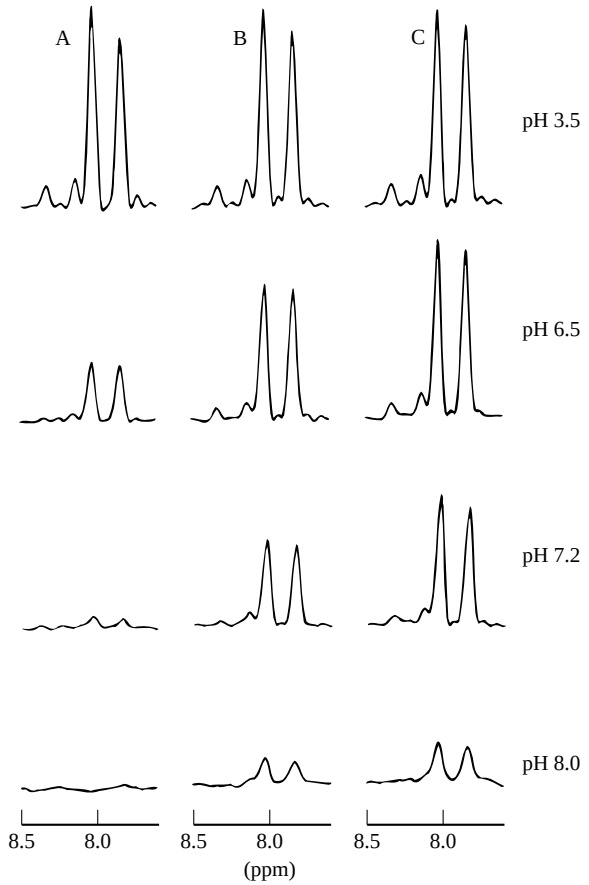

Figure 8 1D $^{15}N-^{1}H$ PFG HSQC spectra showing saturation transfer between solvent H_2O and the ^{15}N-labeled amide protons of 0.8 mM Ac–L-Asn–L-Pro–L-[^{15}N]Tyr–NHMe at various pH values and a temperature of 30 °C. (A) PGF HSQC spectra recorded with 1.3 s of water presaturation and total recycle time of 3.3 s. (B) PFG HSQC spectra recorded without presaturation and with a total recycle time of 3.3 s. (C) PFG HSQC spectra recorded without presaturation and with a total recycle time of 15.3 s. (Reproduced by permission of Academic Press from Li and Montelione[26])

then spoiled by application of a pulsed field gradient. For optimum elimination the tip angle of the excitation pulse must be adjusted for water T_1 relaxation which occurs during the excitation–dephase intervals. For high-resolution applications, this delay period can be increased to allow for recovery of shorter T_1 signals of interest at the water chemical shift.[28] When used for in vivo applications, where the volume of interest usually has multiple water T_1 values, a series of intervals (usually three) is used to provide the optimum water elimination. In practice, multiple CHESS pulses also improve water elimination in high-resolution NMR applications. This is likely due to $\boldsymbol{B}_1$ rather than T_1 heterogeneity. In the case of multiple CHESS pulses, care must be taken to avoid the rephasing of water. This can be accomplished by using spoiler gradients with different intensities, durations, or axes. This method is not only dependent on gradient performance, but also on selective rf pulse design. Desirable features of these rf pulses are minimum out-of-band excitation and sharp transition bands. Since the water signal is to be dephased anyway, the phase in the excitation band is unimportant and can be sacrificed in pulse design.[28]

8.2 Spin Echoes and Gradient Pairs

Elimination of the unwanted signals generated by the non-π character of selective time reversal pulses is an important application of pulse field gradients. A pair of gradients placed on either side of a 180° pulse to avoid spurious signal, one of the first applications of pulse field gradients, can provide significant improvement in modern high-resolution NMR. Placed on either side of a nonselective 180° refocusing pulse, a gradient pair eliminates unwanted signal from imperfections in $\boldsymbol{B}_1$ that would ordinarily have to be eliminated by phase cycling. This effect can be even more dramatic with frequency selective π pulse methods. Figure 9 illustrates the benefit of a gradient pair in the performance of *g*radient *e*nhanced *s*pin *e*cho *w*ater *s*uppression (GE SEWS), a selective 1–1 spin echo experiment.

8.2.1 WATERGATE

In a related experiment dubbed WATERGATE,[29] *water* suppression by *gra*dient-*t*ailored *e*xcitation is also accomplished using a gradient pair to improve a frequency selective spin echo. In this case, the frequency selectivity is achieved using a nonselective 180° pulse/water selective 180°($-x$) pulse combination. This has the advantage that peaks away from the water signal see only a nonselective spin echo. The disadvantage of these frequency selective methods is that they give up the chemical shift region near water.

8.3 Diffusion Weighted Water Suppression

The difference between the translational diffusion of a large solute molecule such as a protein and that of solvent water is the basis of the DRYCLEAN water suppression method.[30] DRYCLEAN comes from *d*iffusion-*r*educed water signals in spectroscopy of molec*u*les moving s*l*ow*e*r th*an* water. The idea is that water will move far enough in the time between the encode and the decode gradient pulses to remain dephased, while the large solute molecule will not move very far and will be largely rephased. According to equation (1), for a modest 20-fold difference in diffusion constant, D, a gradient pair could be selected to preserve over 70% of solute signal, while suppressing water by 1000-fold.

9 PHASE SENSITIVE METHODS

Modern multidimensional spectra are almost always recorded in pure absorption mode. The primary reasons are improved resolution and lineshape, and an increase of root-2 (about 40%) in S/N compared with magnitude mode. Absorption mode spectra are also phase sensitive.

Typically, pure absorption phase is obtained by amplitude modulation of the signal as a function of the evolution period t_1, in contrast to phase modulation in the magnitude methods. Amplitude modulation yields separable phases (separable to absorption and dispersion), but loses the ability to discriminate between positive and negative frequencies. Frequency discrimination can be obtained by independent collection of the real and imaginary parts in t_1 (quadrature

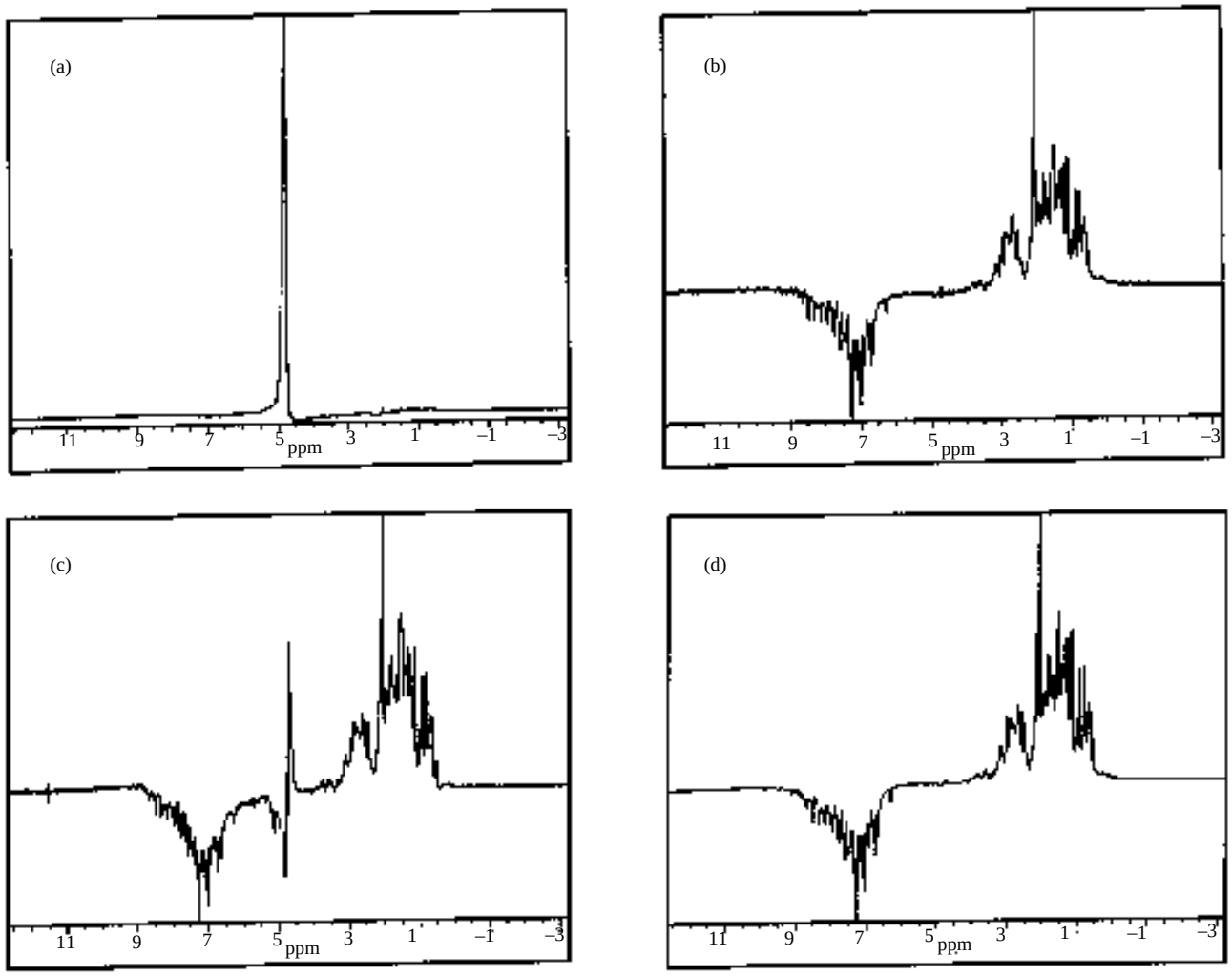

Figure 9 GE SEWS: comparison of spin echo water suppression (a, c) without and (b, d) with a gradient pair bracketing the semiselective 1–1 refocusing pulse. Suppression is shown for the 90% H_2O in a 2.6 mM sample of ^{15}N-enriched bovine pancreas trypsin inhibitor (BPTI). A single acquisition without gradient pair shown in (a) reduces water only by a factor of 50 and thereby limits optimization of receiver gain and ultimate SNR. In (b) complete suppression is obtained in a single acquisition using the gradient method allowing optimum setting of receiver gain. Although phase cycling improves the water suppression in the method without gradients (c), neither suppression or S/N matches the level achieved using the gradient pair (d). (Reproduced by permission of GE NMR Instruments)

data in t_1). Complex Fourier transformation of these data in t_1 produces spectra with quadrature detection in ω_1. By acquiring mirror image pathways (+1) and (−1) in t_1, this approach provides pure absorption shapes for the correlation peaks, and quadrature detection in the evolution dimension(s).

In the case of phase sensitive detection in gradient spectroscopy, there can exist a fundamental limitation. The single-shot selection of a unique coherence pathway precludes the acquisition of the mirror image pathways of (+1) and (−1). If both pathways are not acquired, mixed phase (absorption and dispersion components mixed in an inseparable manner) results for the correlation peaks. Hence the earlier gradient spectroscopy experiments were carried out in the magnitude mode. The requirement for selection of mirror image pathways for pure absorption mode can be at odds with that for improved dynamic range performance which requires selection of a unique pathway in a single acquisition.

The methods developed for pure absorption spectra in gradient spectroscopy adopted a compromise approach. The techniques can be broadly classed as: (a) those which acquire both the mirror image coherence pathways simultaneously by not applying a field gradient during the evolution dimension, albeit, using gradients elsewhere in the pulse sequence; (b) those which acquire both mirror image coherence pathways (+1) and (−1) in the evolution dimension, independently, and then combine both of these signal components in the time domain or in the frequency domain, to yield pure absorption spectra; (c) methods which use gradients as spoilers only and not for coherence pathway selection; and (d) methods which switch between the signals from the two mirror image pathways during the acquisition time.

9.1 Phase Sensitive GE DQF COSY

The DQF COSY experiment proposed by Davis et al.[31] falls into category (a). In this experiment, gradients are used to select DQ coherence transfer. However, gradients are not

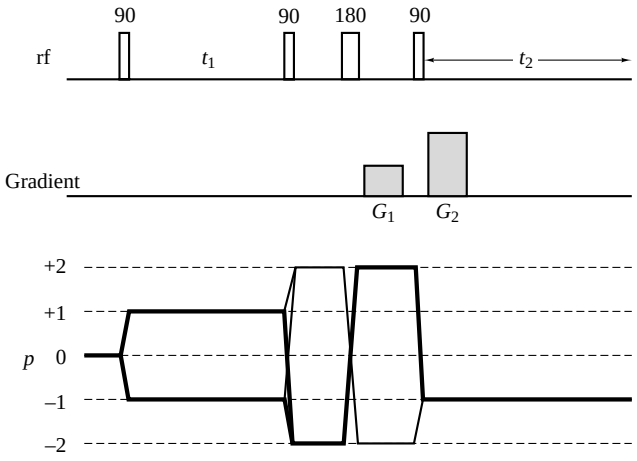

Figure 10 Pulse sequence and coherence pathway diagram for phase sensitive GE DQF COSY as described by Davis and co-workers[31]

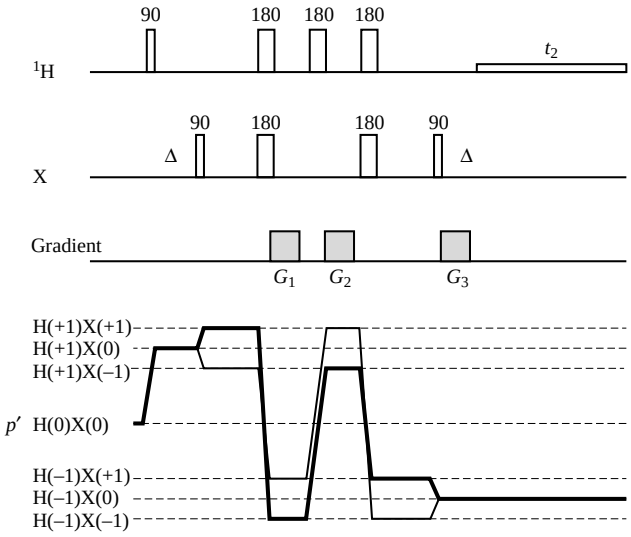

Figure 11 Pulse sequence and modified coherence pathway diagram for phase sensitive pulse field gradient HMQC described by Tolman et al.[33]

applied during the evolution period. With this modification, both mirror image coherence pathways are allowed during t_1 and pure absorption lineshapes can be obtained in the 2D spectrum. This work also addresses the problem of time dependent phase errors associated with chemical shift precession during the gradient pulse. In this pulse sequence as shown in Figure 10, these phase errors are refocused by the addition of a 180° rf pulse. The DQ selection is made using a pair of gradients G_1 and G_2 about the read pulse with a ratio of 1:2. The gradient sequence selects two of the four possible DQ pathways and hence the S/N of the experiments is root-2 (40%) lower than that of conventional phase cycled DQF COSY. Some of the loss can be avoided by use of an optimized tip angle for the read pulse. Frequency discrimination in t_1 is obtained in the normal manner.

The addition of a CHESS pulse (water selective excitation–gradient dephase interval), as described in the previous section, allows reduced gradient coherence selection intervals, and makes this an attractive approach for the study of biomolecules in water.

9.2 Phase Sensitive GE HMQC and GE HSQC

There are a variety of methods which belong in category (b), where the mirror image components corresponding to (+1) and (−1) coherence orders are acquired separately and then recombined in the time or frequency domain. Most of the proposed methods for gradient enhanced proton detected heteronuclear correlation[32–36] fall into this category. One example is the phase sensitive ^{1}H–^{13}C HMQC experiment described by Tolman et al.[33] The sequence consists of a HMQC sequence with three gradients G_1, G_2, and G_3, as shown in Figure 11. G_1 and G_2 are applied during the multiple quantum period on either side of the central proton 180. Additional 180° pulses on both ^{1}H and ^{13}C are applied to refocus chemical shift precession that has occurred during the gradient intervals. The final gradient G_3 is applied after the last ^{13}C 90. The sign of the final gradient is changed to retrieve the mirror image pathway. These two pathways correspond to mirror images in t_1, and are collected separately and subtracted to produce the real part of t_1 and are added to produce the imaginary part of

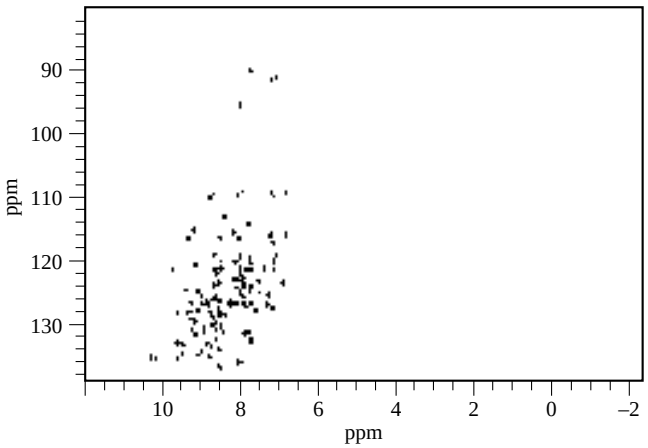

Figure 12 Phase sensitive ^{15}N–^{1}H GE HMQC spectrum of 100 μM ketosteroid isomerase (KSI) (27 kDa dimer) in 90% H_2O at 37 °C obtained at 500 MHz. (Sample provided by courtesy of M. Summers, University of Maryland)

t_1. Ross et al.[36] avoid the use of additional refocusing pulses by back-prediction of the t_1 domain. The method described by Tolman et al.[33] was used to collect the phase sensitive GE HMQC spectrum of the dilute (100 μM in 90% H_2O) protein sample shown in Figure 12. Here again, the addition of a CHESS pulse interval allows the use of shorter coherence selection intervals and allows for the study of larger, more dilute molecules. The unmatched level of water suppression is characteristic of the coherence selective $\boldsymbol{B}_0$ gradient methods.

9.3 Heteronuclear *zz* Filters

The most compelling benefit arising from the use of gradient coherence pathway selection in proton detected heteronuclear correlation experiments is the nearly complete elimination of signal from protons not attached to the

heteronuclear spins. This advantage is especially important for the suppression of water protons since conventional methods such as presaturation and most of the selective excitation methods can lead to loss of desired signal. Unfortunately, some of the benefits of these experiments are offset by the loss of a factor of root-2 in the S/N that results from the selection of a single or limited number of coherence pathways. On the other hand, the suppression of protons not attached to the X nucleus, and of the solvent proton resonance, can be a challenging task in the conventional, phase cycled methods. One approach to reduce this problem, which belongs in category (c) above, was described by Brühwiler and Wagner.[37] This approach takes advantage of the heteronuclear longitudinal spin order (described by the density operator I_zS_z, and also termed heteronuclear *zz* magnetization) which is formed by the sequence fragment $90_x(^1\text{H})-\tau-180_x(^1\text{H, X})-\tau-90_y(^1\text{H})$ where τ is $1/4J(\text{X,H})$. In this method, referred to here as the heteronuclear *zz* filter, protons not attached to the X spins remain in the transverse plane following this interval and are eliminated by application of a spoiler gradient. Although this method maintains full sensitivity, it is not overly effective at eliminating magnetization from protons that are not attached to the X nucleus, and especially those for H_2O solvent.

This approach has been successfully applied in combination with other suppression schemes.[38–43] The symmetry of the HSQC sequence allows for incorporation of two *zz* filters.[40] This approach maintains full sensitivity and pure absorption peak shapes, since all the necessary coherence pathways are selected. A HSQC sequence with gradient *zz* filters is shown in Figure 13. The gradient G_3 dephases the transverse magnetization while the desired components are stored along the *z* axis. As in the conventional HSQC experiment, X chemical shift labeling occurs in the evolution time, t_1, between the two 90°(X) pulses, and the application of the 180°(^{1}H) pulse in the center of the evolution time removes the J(X,H) coupling from the evolution dimension. The frequency labeled magnetization is transferred back into heteronuclear longitudinal *zz* order by the second 90°(X) pulse, and the spoiler gradient G_4 is applied further to eliminate unwanted signals. To improve the suppression of the water signal, a pair of CHESS pulses can be applied at the beginning of the sequence. As described previously, the water resonance can be partially inverted allowing for recovery of desired signal at the water chemical shift. In the implementation shown here, spoiler gradients, G_1 and G_2, are applied along the *x* and *y* axes, respectively, while the G_3 and G_4 gradients are applied along the *x*, *y*, and *z* axes simultaneously to minimize any residual water signal that may arise from accidental gradient rephasing.

This approach provides an optimum S/N and peak shapes but is inferior in performance to gradient coherence selection techniques for water elimination.

9.4 Gradient-Enhanced *z* Filter

To improve on the HSQC with *zz* filters, a gradient form of the *z* filter was developed and added to the sequence as shown in Figure 13.[40] This filter consists of two 90°(^{1}H) pulses with a gradient in between. The first pulse of the filter, $90°_y(^1\text{H})$, rotates the in-phase magnetization (i.e. protons coupled to X) to the *z* axis. The unwanted magnetization is left in the transverse plane, which is then dephased by the spoiler gradient G_5. The desirable component of the magnetization, which is aligned along the *z* axes is then read by the final 90°(^{1}H) pulse. This filter resembles a conventional *z* filter,[45] but has the advantage of full sensitivity, since the desired magnetization that enters the filter is completely aligned along a single axis. Unlike conventional *z* filters which use multiple delays and hence require multiple acquisitions, the gradient *z* filter accomplishes the filtering in a single acquisition. As illustrated in Figure 14, this method yields full sensitivity, pure absorption peak shapes, and good elimination of water. Furthermore, loss of signal associated with conventional water suppression and the requirement for additional phase cycling to improve suppression is avoided. This method, applied without the CHESS pulse and with *z* axis only gradients, was found to outperform nongradient methods in terms of solvent and artifact suppression, based on a comparable recording time.[42]

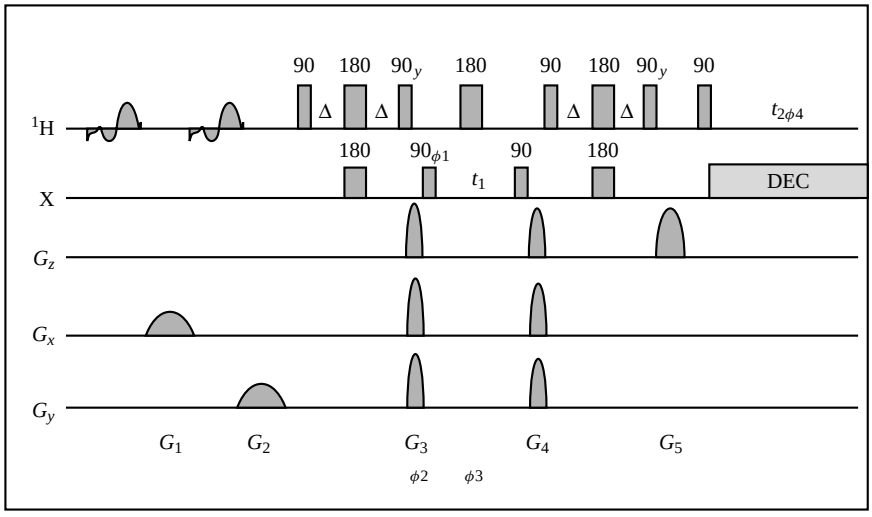

Figure 13 Pulse sequence for gradient-enhanced *z*-filtered (GEZ) HSQC. This sequence contains two gradient zz filters G_3 and G_4 and one gradient-enhanced *z* filter G_5. Additional water elimination can be achieved via the two CHESS pulses (G_1 and G_2) which precede the sequence. (Reproduced by permission of Academic Press from John et al.[40])

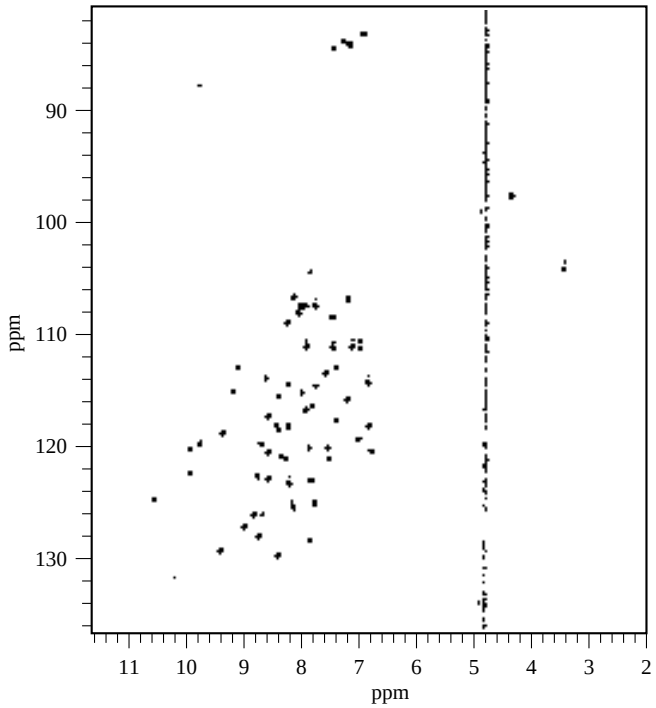

Figure 14 $^{15}N-^{1}H$ GEZ HSQC spectrum of 2.6 mM BPTI in 90% H_2O. (Reproduced by permission of Academic Press from John et al.[40])

Gradient *z* and *zz* units have also been used to improve ^{13}C resolution in an HSQC–NOESY experiment.[44]

9.5 SWAT Gradients

In the *sw*itched *a*cquisition *t*ime (SWAT) gradient method,[45] the N type (0, +1, . . . , −1) and P type (0, −1, . . . , −1) coherence pathway signals are alternately and individually acquired on alternate sampling points of the digitizer. Since the signals from the N type and P type pathways are in an easily separable format, pure phase 2D spectra with quadrature detection in both dimensions can be reconstructed from a single acquisition. The basic idea of the SWAT gradient method is to sample at twice the Nyquist frequency, inserting appropriate gradient pulses between digitizer sampling points, to rephase alternatively the desired coherence. Ordinarily, in a gradient COSY spectrum, either the N type or the P type coherence pathway would remain dephased and unobserved during the acquisition period. The data can be processed to yield pure absorption lineshapes in a number of ways. Although, the SWAT method is quite demanding on gradient switching time, it is the only method which achieves pure phase fully quadrature multidimensional data in a single acquisition per t_1 frame.

10 SPATIAL TOOLS

The rf coils used in high resolution NMR are designed to produce a homogeneous $\boldsymbol{B}_1$ magnetic field. In practice, homogeneous $\boldsymbol{B}_1$ fields are achievable in the transverse plane of sample volume and over most the detectable volume along the *z* axis. Normally, the transition band, the region of sample volume in which the $\boldsymbol{B}_1$ field strength goes from its maximum value to zero, is responsible for the $\boldsymbol{B}_1$ inhomogeneity that can lead to artifacts in multiple pulse NMR experiments. A separate problem that can occur at the coil extremes is that the lineshape of the NMR signal can be distorted by bulk magnetic susceptibility effects from the ends of the sample volume and the end of the NMR sample tube. Like $\boldsymbol{B}_1$ inhomogeneity, this lineshape distortion can be a problem, especially for observation of protons in aqueous solutions where the water signal must be eliminated or reduced. The principle of slice selection can be applied to eliminate this $\boldsymbol{B}_1$ inhomogeneous signal in high-resolution NMR.

10.1 $\boldsymbol{B}_1$ Inhomogeneity and Transition Band Suppression

Gross rf coil inhomogeneity can be visualized via spatial projections along the *z* axis (so-called *z* profiles). A *z* profile of a 180° pulse generated by a typical rf coil is shown in Figure 15(a). Comparison with the 90° pulse *z* profile from the same coil [Figure 15(b)] illustrates the gradient of $\boldsymbol{B}_1$ field (transition bands) that occurs at the top and bottom of the coil. In the 180° pulse profile, signal is not detected where a 180° rotation of

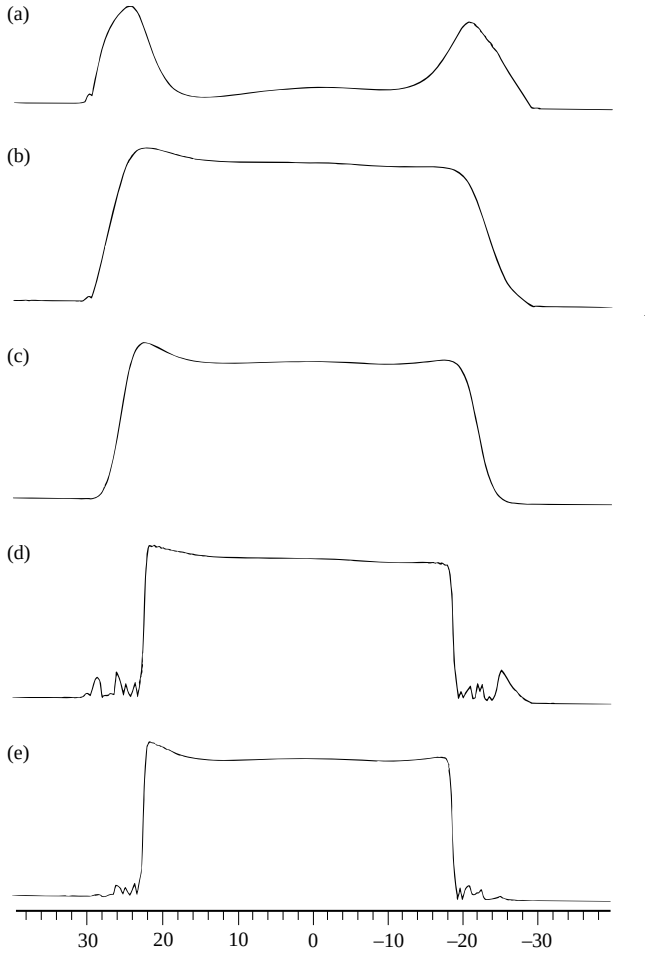

Figure 15 *z* profiles of an (a) 180° rf pulse, (b) 90° rf pulse, (c) composite 90° rf pulse, (d) 90° rf pulse following transition band suppression (TBS), and (e) composite 90° rf pulse following TBS

spins has occurred, but is detected in the sample volume which does not experience a 180° flip. These transition band regions can be reduced slightly by employing a composite 90° pulse as illustrated by the z profile in Figure 15(c). In the transition band suppression (TBS) method,[46] signals from these regions of coil volume are selectively excited and then eliminated by gradient dephasing. Slice selection is achieved by application of one or more frequency selective pulses during a constant z gradient. In practice, multiple pulses work better because of the differences in $\boldsymbol{B}_1$ of the region to be suppressed. While this effectively eliminates signal from these unwanted regions of the coil volume, care must be exercised in choice of pulse design to avoid excitation of the spins within the region of homogeneous $\boldsymbol{B}_1$. Figure 15(d) shows a 90° pulse profile of the sample following application of TBS, and Figure 15(e) shows the combined effect of TBS and a composite 90° pulse.

10.2 Improvements in WEFT and Reduction of Susceptibility Artifacts

One application of TBS is the reduction in the susceptibility water hump which is often observed in a very short samples. In essence, this is the slice selective version of a matched susceptibility plug.

Spatial differences in both $\boldsymbol{B}_0$ and $\boldsymbol{B}_1$ homogeneity also limit the effectiveness of water suppression by T_1 inversion recovery methods such as WEFT. A water elimination technique was described earlier using gradient dephasing in which the duration of the relaxation delay is used to recover the biopolymer spins at the water chemical shift. The TBS approach can be used to limit the effects of $\boldsymbol{B}_1$ inhomogeneity and significantly reduce the amount of signal left at the water 'null'.

The first practical test of TBS was its incorporation into the phase sensitive version of gradient enhanced DQF COSY. The pulse sequence is shown in Figure 16. Water is first selectively excited using a crafted rf pulse and dephased by application of an x gradient. The residual water spins are then partially inverted and transverse magnetization dephased by application of a y gradient pulse. This is followed by a recovery period during which the inverted water spins relax to a 'null'. During this recovery period, typically 200 ms, the transition band slices are excited and dephased using a z slice gradient. The water elimination is followed by a phase sensitive gradient enhanced DQF COSY sequence. Coherence is selected using a $1{:}-2$ ratio of gradients applied simultaneously along the x, y, and z axes. The careful choice of gradient axes during the water elimination period and for coherence selection is important to avoid unwanted rephasing of water signal. This approach was tested on a 1 mM sample of ubiquitin in 90% H_2O. As demonstrated by the contour plots of these data shown in Figure 17, water is nearly eliminated and correlations are observed unperturbed, even at or near the water chemical shift.

10.3 Field Maps and Shimming

One advantage of gradients is that you can make images with them. 3D phase or frequency maps are in effect images of the inhomogeneity experienced by the sample. Shim coil fields can also be directly characterized by measurement of a set of field maps with known shim current offsets. The foregoing information should be sufficient to determine in a noniterative way, the optimum corrected field. This approach to shimming, common to in vivo NMR, may become a significant advantage for three-axis gradient systems in high resolution NMR (***Shimming of Superconducting Magnets***).

11 SUMMARY

By effectively replacing the functions of phase cycling with a single-step, pulse field gradients are used to suppress artifacts, extend resolution in the evolution domains of multidimensional NMR and, where S/N allows, reduce total data collection time. Further, $\boldsymbol{B}_0$ field gradients provide unmatched levels of water elimination, with reduced dependence on the effects of lineshape, magnetization transfer, and dynamic range. With continued improvements in performance and availability, gradients are likely to become a routine part of high-resolution NMR.

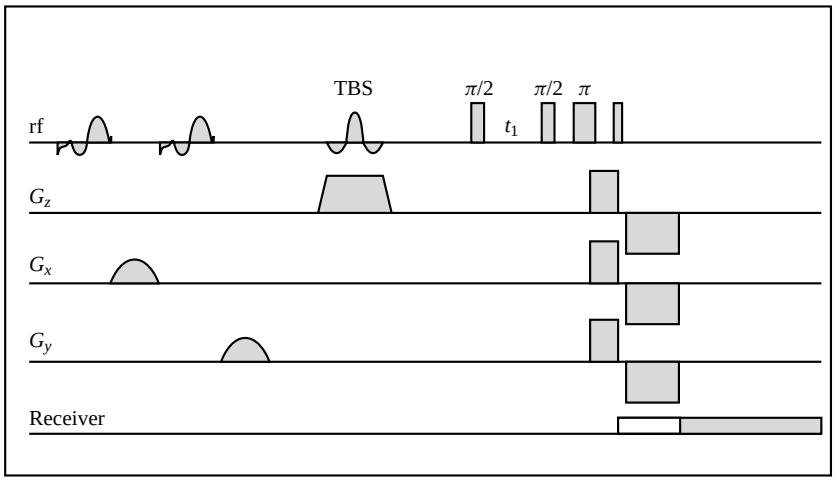

Figure 16 Pulse sequence for phase sensitive GE DQF COSY incorporating crafted rf CHESS pulses and TBS. (Reproduced by permission of Academic Press from Hurd et al.[47])

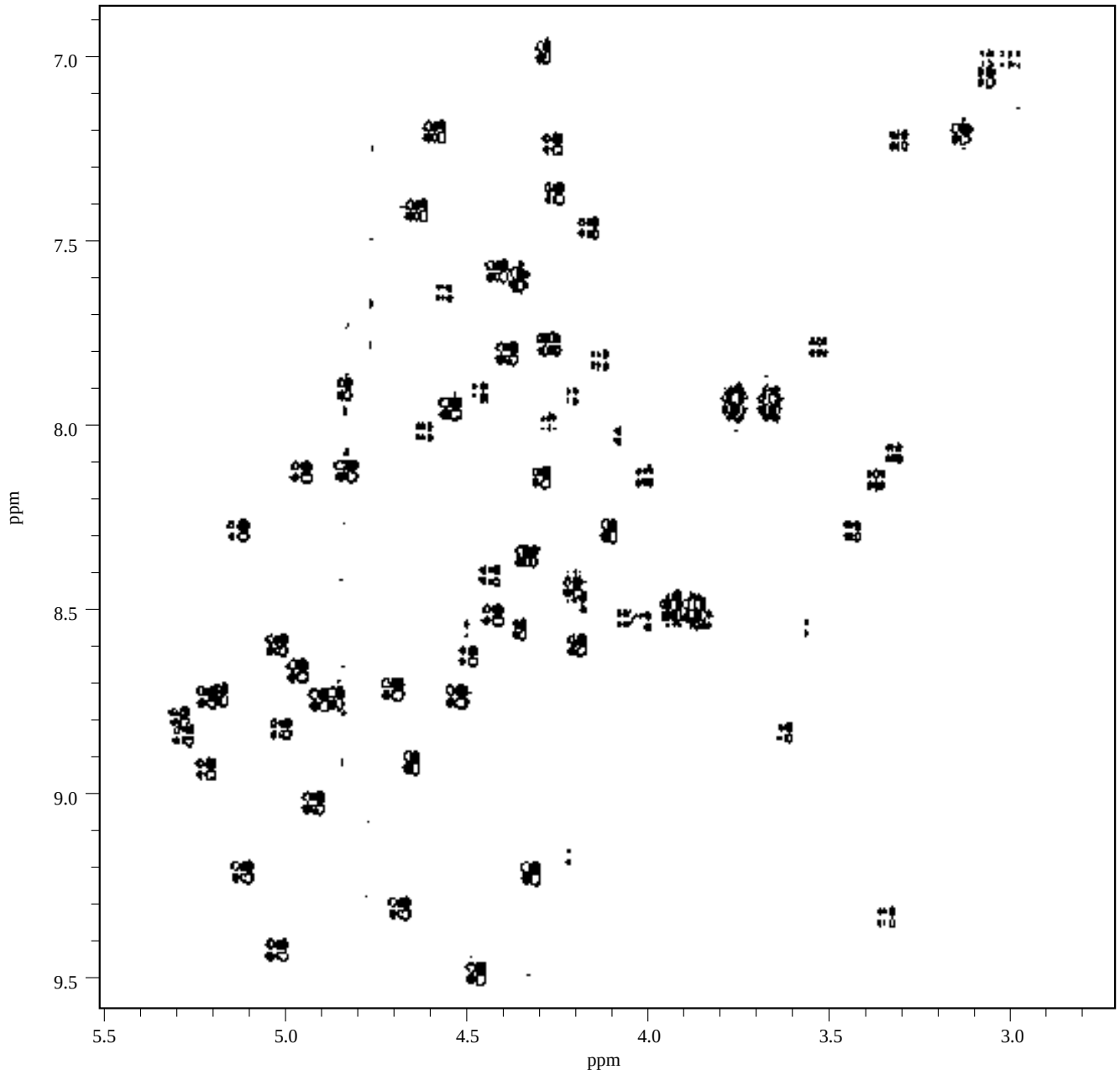

Figure 17 Phase sensitive GE DQF COSY contour plot of a 1 mM ubiquitin sample in 90% H_2O. Expansion of the fingerprint region shows nearly complete suppression of water at 4.7 ppm in ω_2 and unreduced correlations at that chemical shift. (Reproduced by permission of Academic Press from Hurd et al.[47])

12 RELATED ARTICLES

Diffusion Measurements by Magnetic Field Gradient Methods; Double Quantum Coherence; Eddy Currents and Their Control; Gradient Coil Systems; Heteronuclear Shift Correlation Spectroscopy; Magnetic Resonance Imaging: A Historical Overview; Multiple Quantum Coherence Imaging; Multiple Quantum Spectroscopy of Liquid Samples; NOESY; Phase Cycling; Radiofrequency Gradient Pulses; Shimming of Superconducting Magnets; Three- and Four-Dimensional Heteronuclear Magnetic Resonance; Water Signal Suppression in NMR of Biomolecules; Water Suppression in Proton MRS of Humans and Animals.

13 REFERENCES

1. A. G. Anderson, R. L. Garwin, E. L. Hahn, J. W. Horton, G. L. Tucker and R. M. Walker, *J. Appl. Phys.*, 1955, **26**, 1324.
2. E. O. Stejskal and J. E. Tanner, *J. Chem. Phys.* 1965, **42**, 288.
3. R. L. Vold, J. S. Waugh, M. P. Klein, and D. E. Phelps, *J. Chem. Phys.*, 1968, **48**, 3831.
4. A. Wokaun and R. R. Ernst, *Chem. Phys. Lett.*, 1977, **52**, 407.
5. A. A. Maudsley, A. Wokaun, and R. R. Ernst, *Chem. Phys. Lett.*, 1978, **55**, 9.
6. A. Bax, P. G. deJong, A. F. Mehlkopf, and J. Smidt, *Chem. Phys. Lett.*, 1980, **69**, 567.
7. P. Barker and R. Freeman, *J. Magn. Reson.*, 1985, **64**, 334.

8. C. J. R. Counsell, M. H. Levitt, and R. R. Ernst, *J. Magn. Reson.*, 1985, **64**, 470.
9. D. M. Doddrell, G. J. Galloway, W. M. Brooks, J. Field, J. M. Bulsing, M. G. Irving and H. Baddeley, *J. Magn Reson.*, 1986, **70**, 176.
10. A. G. Redfield and R. K. Gupta, *Adv. Magn. Reson.*, 1971, **5**, 81.
11. R. E. Hurd and D. M. Freeman, *Proc. Natl. Acad. Sci. U.S.A.*, 1989, **86**, 4402.
12. A. D. Bain, *J. Magn. Reson.*, 1984, **56**, 418.
13. G. Bodenhausen, H. Kogler, and R. R. Ernst, *J. Magn. Reson.*, 1984, **58**, 370.
14. D. M. Freeman and R. E. Hurd, *NMR: Basic Princ. Prog.*, 1992, **27**, 200.
15. R. E. Hurd, *J. Magn. Reson.*, 1990, **87**, 422.
16. R. E. Hurd and B. K. John, *J. Magn. Reson.*, 1991, **91**, 648.
17. J. Ruiz-Cabello, G. W. Vuister, C. T. W. Moonen, P. van Gelderen, J. S. Cohen and P. C. M. van Zijl, *J. Magn. Reson.*, 1992, **100**, 282.
18. R. E. Hurd and B. K. John, *J. Magn. Reson.*, 1991, **92**, 658.
19. B. K. John, D. Plant, S. Heald, and R. E. Hurd, *J. Magn. Reson.*, 1991, **94**, 664.
20. G. W. Vuister, R. Boelens, R. Kaptein, R. E. Hurd, B. John, and P. C. M. van Zijl, *J. Am. Chem. Soc.*, 1991, **113**, 9688.
21. A. L. Davis, R. Boelens, and R. Kaptein, *J. Biomol. NMR*, 1992, **2**, 395.
22. L. E. Kay, *J. Am. Chem. Soc.*, 1993, **115**, 2055.
23. G. W. Vuister, G. M. Clore, A. M. Gronenborn, R. Powers, D. S. Garrett, R. Tschudin, and A. Bax, *J. Magn. Reson., Ser. B*, 1993, **101**, 210.
24. J. Chung, J. R. Tolman, K. P. Howard, and J. H. Prestegard, *J. Magn. Reson., Ser. B*, 1993, **102**, 137.
25. L. E. Kay, P. Keifer, and Tim Saarinen, *J. Am. Chem. Soc.*, 1992, **114**, 10 663.
26. Y.-C. Li and G. T. Montelione, *J. Magn. Reson., Ser. B*, 1993, **101**, 315.
27. A. Haase, J. Frahm, W. Hanicke, and D. Matthaie, *Phys. Med. Biol.*, 1985, **30**, 341.
28. B. K. John, D. Plant, P. Webb, and R. E. Hurd, *J. Magn. Reson.*, 1992, **98**, 200.
29. M. Piotto, V. Saudek, and V. Sklenár, *J. Biomol. NMR*, 1992, **2**, 661.
30. P. C. M. van Zijl and C. T. W. Moonen, *J. Magn. Reson.*, 1990, **87**, 18.
31. A. L. Davis, E. D. Laue, J. Keeler, D. Moskau, and J. Lohman, *J. Magn. Reson.*, 1991, **94**, 637.
32. A. L. Davis, J. Keeler, E. D. Laue, and D. Moskau, *J. Magn. Reson.*, 1992, **98**, 207.
33. J. R. Tolman, J. Chung, and J. H. Prestegard, *J. Magn. Reson.*, 1992, **98**, 462.
34. J. Boyd, N. Soffe, B. K. John, D. Plant, and R. E. Hurd, *J. Magn. Reson.*, 1992, **98**, 660.
35. G. W. Vuister, J. Ruiz-Cabello, and P. C. M. van Zijl, *J. Magn. Reson.*, 1992, **100**, 215.
36. A. Ross, M. Czisch, C. Ciesslar, and T. A. Holak, *J. Biomol. NMR*, 1993, **3**, 215.
37. D. Brühwiler and G. Wagner, *J. Magn. Reson.*, 1986, **69**, 546.
38. E. R. P. Zuiderweg, *J. Magn. Reson.*, 1987, **71**, 283.
39. A. Bax and S. S. Pochapsky, *J. Magn. Reson.*, 1992, **99**, 638.
40. B. K. John, D. Plant, and R. E. Hurd, *J. Magn. Reson., Ser. A*, 1993, **101**, 113.
41. L. E. Kay, G.-Y. Xu, A. U. Singer, D. R. Muhandiram, and J. D. Forman-Kay, *J. Magn. Reson., Ser. B*, 1993, **101**, 333.
42. G. Wider and K. Wütrich, *J. Magn. Reson. B*, 1993, **102**, 239.
43. V. Sklenár, M. Piotto, R. Leppik, and V. Saudek, *J. Magn. Reson., Ser. A*, 1993, **102**, 241.
44. A. Majumdar and E. R. P. Zuiderweg, *J. Magn. Reson., Ser. B*, 1993, **102**, 242.
45. O. W. Sorensen, M. Rance, and R. R. Ernst, *J. Magn. Reson.*, 1984, **56**, 527.
46. R. E. Hurd, B. K. John, and D. Plant, *J. Magn. Reson.*, 1991, **93**, 666.
47. R. E. Hurd, B. K. John, P. Webb, and D. Plant, *J. Magn. Reson.*, 1991, **99**, 632.

Biographical Sketch

Ralph E. Hurd. *b* 1950. B.A., 1973, Chemistry, CSUSB, Ph.D., 1977, Biochemistry, University of California, Riverside (advisor Brian R. Reid). Joined Nicolet Magnetics in 1980 (working with LeRoy Johnson on HR applications of NMR); 1983, manager CSI Applications, GE Medical Systems (formerly Nicolet Magnetics); 1989, manager Combined CSI and HR Applications; since 1990, manager Spectroscopy Research and Development. Approx. 60 publications, 4 patents. Current research: clinical MR spectroscopy.

Flow NMR

Harry C. Dorn
Virginia Polytechnic Institute and State University, Blacksburg, VA, USA

1	Introduction	1
2	Monitoring Chemical Reactions and Intermediates in Flowing Liquids	2
3	Direct Coupling of Liquid Chromatography and NMR (LC–NMR)	5
4	Signal Enhancement	6
5	Related Articles	10
6	References	10

1 INTRODUCTION

1.1 Historical Aspects

NMR of flowing systems has been of interest since the early 1950s. For example, Suryan's study[1] in 1951 demonstrated a fivefold increase in the intensity of flowing water in comparison with a static water sample. This increase in signal strength is observed only when there is sufficient time for equilibration of the magnetization in the magnetic field before the signal is monitored (vide infra). An early general review of the subject of flow NMR is contained in a book by Zhernovoi and Latyshev[2] as well as a later review by Jones and Child.[3] During the 1950–1970s, pulsed NMR techniques were developed to measure flow rates, study dynamic flow patterns (laminar, plug, etc.), and measure (or alter) nuclear spin–lattice relaxation rates in flowing fluids. For example, the Carr–Purcell pulse sequence (90°_x, τ, 180°_x, 2τ, 180°_x, 2τ, ...), and related spin echo sequences in the presence of PFGs, evolved as common tools to study both flow and self-diffusion. The amplitude and phase of the echo after the 180° pulse are dependent on the dynamic process involved. A well known distinction between the spin echo generated by flow (coherent) and self-diffusion (dissipative) is the attenuation of the spin echo and phase shift, respectively, for these two dynamic processes. Seminal studies by Singer,[4] Packer,[5] Stejskal,[6] Garroway,[7] and Hemminga and deJager [8] led to the development of techniques for measuring self-diffusion, flow rates, and flow patterns (e.g. plug versus laminar flow) during the 1960s and 1970s for both static and flowing samples. For more depth on these topics, the reader should consult ***Diffusion and Flow in Fluids***; ***Diffusion Measurements by Magnetic Field Gradient Methods***; ***Diffusion in Porous Media***, and ***Diffusion in Rare Gas Solids*** (as well as recent reviews by Stepišnik,[9] Caprihan,[10], Chingas,[11] and Altobelli.[12]

During the 1970s, Sykes[13] and Fyfe[14] pioneered the development of flow NMR approaches to follow the intermediates in chemical reactions. One of the most significant developments during this time period was the advent of the pulsed FT technique by Ernst and Anderson.[15] The FT NMR technique helped facilitate flow chemical reaction monitoring and on-line NMR detection of liquid chromatography (LC–NMR) fractions. This major development coupled with the advent of mass data storage devices accelerated the implementation of these flow NMR techniques. During the next two decades, flow NMR instruments and probes were developed for a wide range of experimental conditions, including: (1) NMR measurements at high pressure and temperatures, (2) surface coils for in situ flow monitoring, and (3) homogeneous higher field superconducting magnets with large volumes.

During the 1980–1990s, MRI techniques were reported for the measurement of blood flow profiles in animal and human subjects. A number of methods for magnetic and chemical 'tagging' of a flowing bolus have been introduced. For biological flow studies, infusion of water (^{2}H, ^{17}O labeled), trifluoromethane (^{19}F), sodium (^{23}Na), and phosphorus (^{31}P) compounds have been reviewed by Neil.[16] The use of MRI and improved PFG techniques have further extended the types of flow velocity patterns (turbulent flow, granular flow, etc.) that can be studied. These latter topics are discussed in detail elsewhere in the Encyclopedia (see ***Diffusion: Clinical Utility of MRI Studies***; ***Diffusion and Perfusion in MRI*** and ***Whole Body Magnetic Resonance Angiography***).

1.2 Basic Concepts of Flow NMR

In order to appreciate some of the basic differences between static and flow NMR experiments, consider a flowing bolus (rounded mass) in the detector region (Figure 1). If we define a simple plug flow pattern ($F = V/t$), a given bolus has residence times t_a, t_b, and t_c in regions A, B, and C, respectively. If a given bolus resides for a relatively short time, $t_a \ll T_{1a}^x$ in region A, and the low magnetic field B_0^L is small ($B_0^L \sim$ Earth's magnetic field), the magnetization monitored will be determined by the high magnetic field magnetization.

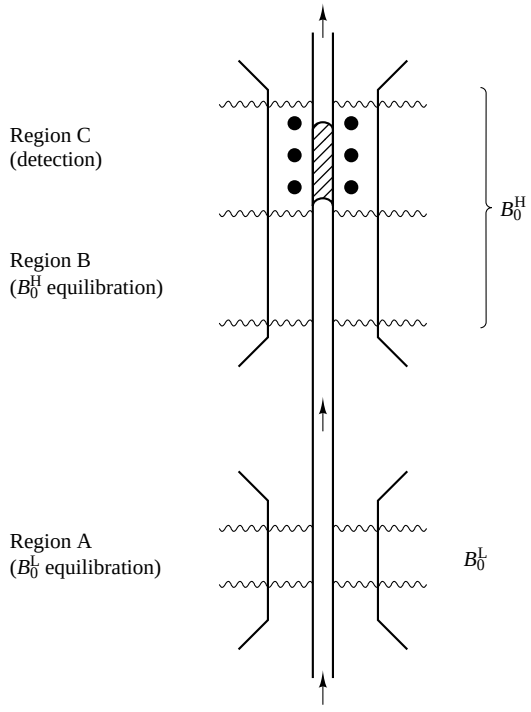

Figure 1 A flowing bolus in the detector region of an NMR instrument

In order to achieve a monitored signal that approaches the full equilibrium Boltzmann magnetization (M_0^{H}), it is clearly necessary to have a long residence time in the high magnetic field relative to the high field spin–lattice relaxation time, $t_{\mathrm{t}} \gg T_{1\mathrm{bc}^x}$. This is also sometimes expressed by treating flow as a relaxation process.[2,3] For example, the observed flow spin–lattice relaxation rate ($1/T_1$) flow in the presence of flow can be defined as

$$\left(\frac{1}{T_1^x}\right)_{\mathrm{obsd}} = \left(\frac{1}{T_1^x}\right)_{\mathrm{static}} + \frac{1}{t_{\mathrm{t}}} \qquad (1)$$

For nuclei with long spin–lattice relaxation times (e.g. ^{13}C, $T_1^x = 10$–100 s), the observed relaxation rate is dictated by the total residence time in the high magnetic field, before detection ($t_{\mathrm{t}} = t_{\mathrm{b}} + t_{\mathrm{c}}$). Thus, measuring the monitored magnetization as a function of flow rate is one method of measuring spin–lattice relaxation times [equation (1)]. On the other hand, it is sometimes desirable to circumvent this T_1 'bottleneck' by installing a large equilibration volume before the detector cell (region B). A second approach is to have the bolus flow over a stable free radical system (e.g. a silica immobilized nitroxide) in region B. In this manner, it is possible to enhance significantly the spin–lattice relaxation rate by strong nuclear–electron interactions. In either of these approaches, the intent is to recover the full equilibrium Boltzmann magnetization independent of the flow rate.

It is also useful to consider a second experiment when B_0^{L} is not zero. In this case, it is assumed that the sample has equilibrated in the lower magnetic field for a time that is long relative to the low magnetic field spin–lattice relaxation time, $t_{\mathrm{a}} \gg T_{1\mathrm{a}}^x$. The monitored magnetization in the high magnetic field (B_0^{H}) will now consist of low and high magnetic field magnetization components (M_{xy}^{L} and M_{xy}^{H}). In fact, the monitored magnetization (region C) can be dominated by the low magnetic field magnetization M_{xy}^{L}, if the volumes in regions B and C are small and flow transfer is rapid, $t_{\mathrm{t}} \ll T_{1\mathrm{bc}}^x$ (see Section 4.2). Under these conditions, the monitored magnetization is linearly dependent on B_0^{L}. This suggests one of the simplest methods for 'magnetic tagging' and provides a convenient method of monitoring the low field magnetization, but with high magnetic field spectral resolution. An alternative experiment can also be employed in which the flow is reversed and the flowing bolus is allowed to develop the high magnetic field magnetization (M_0^{H}), but is monitored in a low magnetic field (e.g. the Earth's magnetic field).

One can also envision several other possible methods for flow rate measurements by magnetic tagging of a given bolus (Figure 2). In one simple experiment, a uniformly homogeneous magnetic field (B_0) for both the upstream and downstream coils is employed in a two-coil system. In this approach, the upstream coil (region A) tags a flow segment by inverting the magnetization. If significant spin–lattice relaxation does not occur before the flow segment reaches the monitoring detector (region B), the inverted segment can be detected and the flow rate determined. There are many variations on this basic approach which have been reported for 'tagging' a flowing bolus.

A second consequence of flow is the effective residence time of the bolus in the detector cell, t_{c}. The average residence time

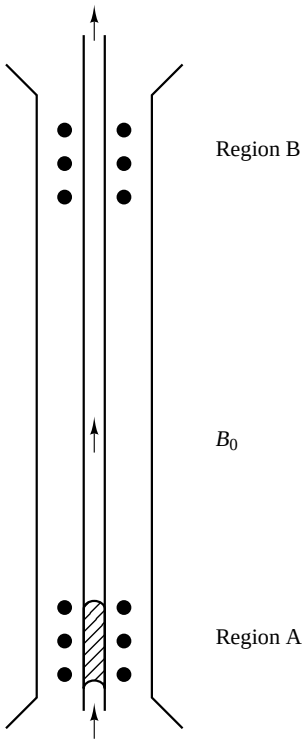

Figure 2 Flow rate measurement by magnetic tagging of a bolus using a two-coil system

of the bolus in the detector cell, V_{cell}, can be expressed as

$$t_{\mathrm{c}} = \frac{V_{\mathrm{cell}}}{\bar{v}} \qquad (2)$$

where the mean velocity ($\bar{v}$) must be used. The mean velocity is defined because for other flow patterns (e.g. laminar) the velocity is a function of the distance from the detector cell walls. Once again, treating flow as a relaxation process, the 'lifetime broadening' can be expressed as

$$\left(\frac{1}{T_2^x}\right)_{\mathrm{obs}} = \left(\frac{1}{T_2^x} + \frac{1}{T_2'}\right)_{\mathrm{static}} + \frac{1}{t_{\mathrm{c}}} \qquad (3)$$

It is apparent from equation (3) that the observed NMR linewidth ($\Delta\nu_{\frac{1}{2}}$) can be significantly broadened at high flow rates since the static component contains contributions from the spin–spin relaxation rate and the magnetic field inhomogeneity. For example, Fyfe[17] has reported ^{1}H NMR linewidth data for flowing ethylbenzene using a 5 mm o.d. flow tube. A linear plot [equation (3)] was obtained as a function of flow rate with linewidths ranging from 2.2 Hz (static) to 8 Hz (flow, 120 mL min^{-1}).

The simple models illustrated (Figures 1 and 2) provide only a cursory understanding of some of the basic concepts in the flow NMR experiment, and are rarely an adequate description of flow NMR under most experimental conditions. The experimental picture is generally more complicated because of the presence of laminar, turbulent, or other more complex flow patterns. In addition, self-diffusion effects of the flowing bolus cannot be ignored. The reader should consult other articles in the Encyclopedia for other treatments of this subject (see ***Diffusion and Flow in Fluids***).

2 MONITORING CHEMICAL REACTIONS AND INTERMEDIATES IN FLOWING LIQUIDS

2.1 Chemical Reaction Kinetics and Labile Intermediates

The spectroscopic investigation of chemical reaction intermediates has provided a wealth of information regarding the kinetics and mechanisms of chemical reactions. In situ spectroscopic approaches have the advantage of monitoring labile intermediates without the necessity of direct isolation from reaction mixtures. Although many spectroscopic approaches have better sensitivity than NMR, the diagnostic character of NMR provides unique spectroscopic characterization of intermediates in organic, inorganic, and biological systems. The flow and stopped flow NMR experiments enable chemical reaction intermediates to be monitored and kinetic measurements performed for reaction times down to the millisecond timescale. In 1972, an apparatus for flow NMR studies of reaction intermediates was described by Bargon.[18] In the same year, Asahi and Mizuta[19] reported flow ^{1}H NMR results for the reaction of thiamine with the hydroxide ion.

Although the advent of FT NMR instrumentation has enabled fast acquisition of rate data, nuclei with long relaxation times still require equilibration in the magnetic field for long periods of time relative to the spin–lattice relaxation time (see Section 1.2). Kühne et al.[20] have presented a theoretical formalism for the lineshape analysis of transient intermediates in nonequilibrium chemical reactions (A $\rightarrow$ B) and reported a stopped flow ^{1}H NMR study demonstrating this approach. It is noteworthy that their treatment not only includes lineshape changes due to the finite lifetime of the molecule, but also the phase and dispersive lineshape changes for the corresponding product molecule. The basic hydrolysis (NaOH) reaction of methyl formate in D_2O was used as an experimental test of their approach (Scheme 1).

Excellent agreement was observed between the experimental and theoretical lineshapes for the methyl hydrogen resonance [Figures 3(a) and (b)] and the formate hydrogen resonance [Figures 3(c) and (d)]. From their data, a second order rate constant of $k_{av}^{(2)} = 80 \pm 10$ L mol^{-1} s^{-1} (D_2O, 28.8 °C) was obtained. A minimum dead time for their apparatus was ~2 ms.

In 1978, Fyfe et al. reviewed flow and stopped flow NMR studies of reaction intermediates in chemical reactions.[14] In one of their studies, they examined the reaction of 3,5-dinitrocyanobenzene (**1**) with one equivalent of solution methoxide.[21] As illustrated in Figure 4, the static spectrum [compound (**1**)] exhibits two resolved ^{1}H NMR signals, whereas, at a flow rate of 30 mL min^{-1} five ^{1}H NMR signals were observed. The three signals of nearly equal intensity in this spectrum were assigned to the aromatic hydrogen in complex (**2**). The other two aromatic signals (2:1 ratio) were assigned to the thermodynamically less stable isomer (**3**). At higher flow rates (50 mL min^{-1}) the relative intensities of the isomer (**3**) increase; however, when the flow was stopped

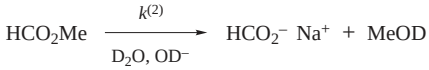

Scheme 1

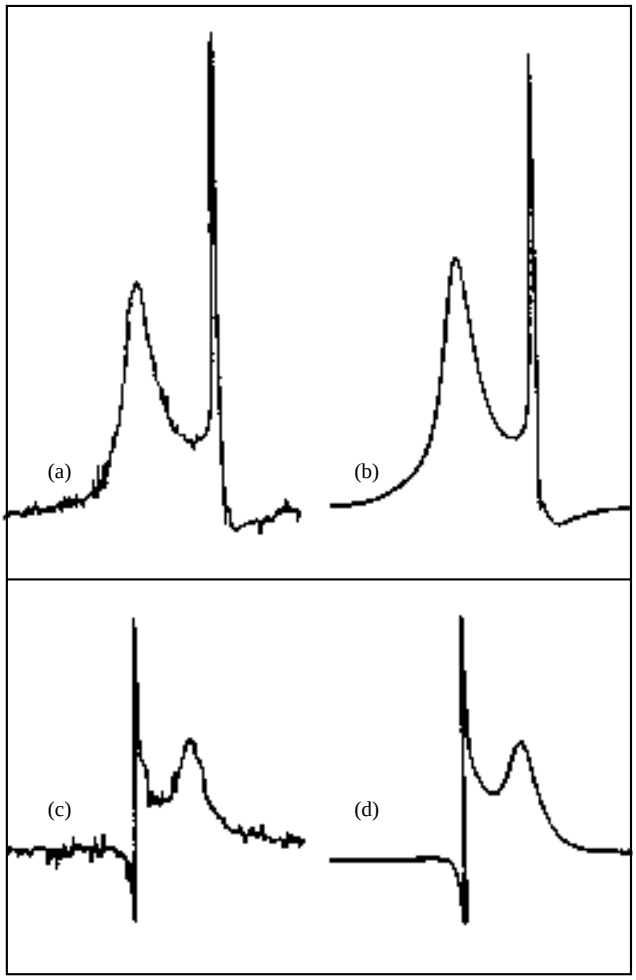

Figure 3 Experimental and fitted theoretical lineshapes for the hydrolysis of 0.15 M methyl formate with 0.63 M deuterated sodium hydroxide in D_2O. The fitted parameters were $k_1 = 45$ s^{-1} and $t_d = 3$ ms. (a) Experimental and (b) theoretical methyl proton resonance, and (c) experimental and (d) theoretical formate proton resonance lineshapes. (Reprinted by permission from Kühne et al.[20])

(Figure 4, bottom spectrum), only the signals due to the more stable complex (**2**) were observed. By varying the flow rate, and monitoring signal intensities a description of the kinetics of the system was obtained. In this manner, the halflife for the complex (**3**) was found to be 0.94 s at 30 °C. A minimum mixing time of ~20 ms was estimated for their apparatus (Scheme 2).

In a more recent study by Trahanovsky and Fischer,[22] the unstable molecule benzocyclobutadiene (**5**) was monitored for the first time by flow ^{1}H NMR (Figure 5). At high flow rates (45 mL min^{-1}) only (**5**) is observed; however, at low flow rates (**5**) has been shown to dimerize to (**6**) (Scheme 3).

Although (**5**) has been isolated in an argon matrix at 20 K, the high reactivity of this labile molecule has made it difficult to study at ambient temperatures. Several other intermediates in organic and inorganic reactions have been monitored by the flow and stopped flow NMR technique. For example, Trahanovsky and co-workers[23] have also utilized flow ^{1}H NMR to observe the labile molecule *o*-xylylene generated from *o*-quinodimethane. Tan and Cocivera[24,25] have studied the reaction of 4-formylpyridine with amino acids, imidazole, and

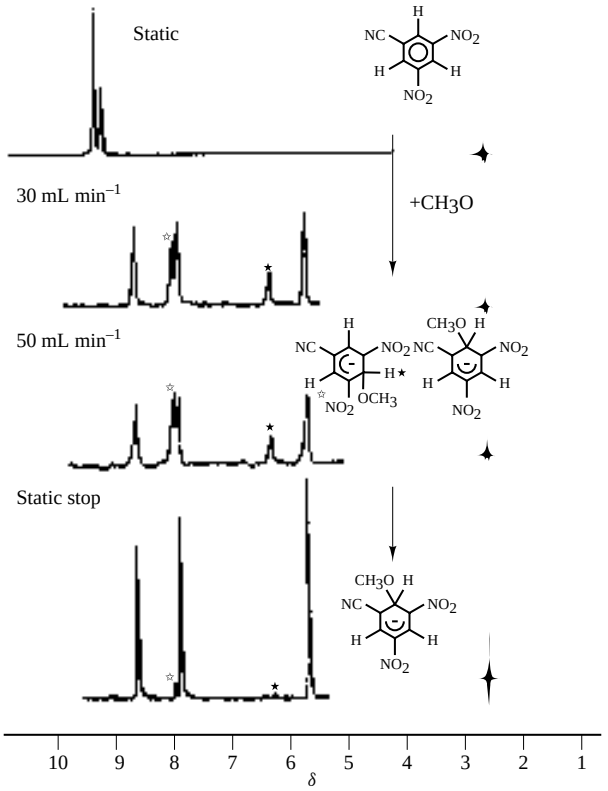

Figure 4 Representative ^{1}H NMR spectra recorded at 100 MHz, 0.5 M in DMSO, showing the ring proton absorptions of 3,5-dinitrocyanobenzene alone (top spectrum) and during its reaction with one equivalent of the methoxide ion (in 87.5% DMSO/12.5% MeOH) under the conditions of flow rate indicated. (Reprinted by permission from Fyfe et al.[14])

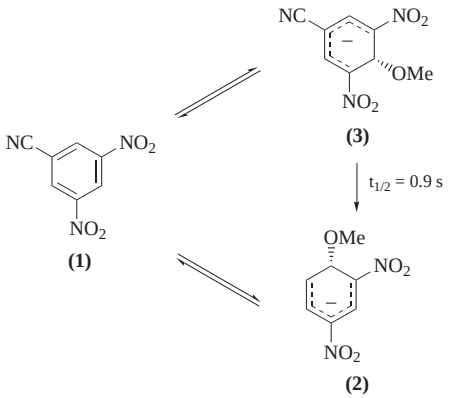

Scheme 2

DL-alanylglycine using the stopped flow ^{1}H NMR approach. In another study, Cocivera examined the dehydrohalogenation reaction of 2-chloropropanoyl chloride.[26]

Recently, Funahashi and co-workers[27] have designed a high-pressure ^{1}H NMR probe for stopped flow measurements at pressures <200 MPa. In this study, the substitution reactions of $(CH_3)_4Sn$ with I_2 in $HCCl_3$ and the solvent exchange reaction of the Al^{3+} ion with dimethylformide were examined. The volumes of activation measured by this approach were -2.2 ± 0.8 and $-24.9 \pm 3.8\,cm^3\,mol^{-1}$, respectively. Albert[28]

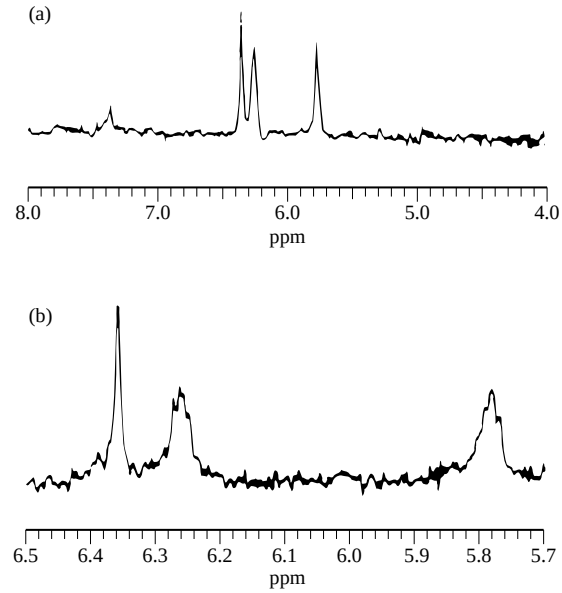

Figure 5 Proton NMR spectra (300 MHz) (a) formed by mixing 10^{-3} M (**4**) in CD_3CN with 5×10^{-2} M TBAF in CD_3CN (flow rate, 45 mL min^{-1}; number of scans, 512; pulse interval, 0.127 s) and (b) by mixing 10^{-3} M (**4**) in CD_3CN with 5×10^{-2} M TBAF in CD_3CN (flow rate, 3 mL/min; number of scans, 1105; pulse interval, 1.016 s). (Reprinted by permission from Trahanovsky et al.[22])

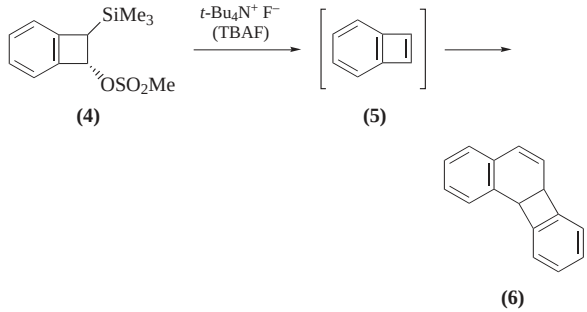

Scheme 3

has reported monitoring the electrochemical reaction of 2,4,6-tri-*t*-butylphenol by continuous flow ^{13}C NMR. Davis and co-workers[29] have reported in situ continuous monitoring of the vapor phase reaction of ^{13}C labeled 2-propanol vapor on a zeolite HZSM-5 catalyst at 100–180 °C. In 1986, flow and stopped flow NMR studies were reviewed by Selivanov and Ershov.[30]

2.2 Biochemical Reaction Monitoring

Although NMR is an excellent tool for monitoring chemical reactions, the technique is usually limited to nuclei with high sensitivity (e.g. ^{1}H, ^{31}P) or samples which can be isotopically enriched (e.g. ^{13}C). The noninvasive nature of the NMR approach is an attractive feature of this approach and is especially applicable to monitoring biological reactions. In addition, the NMR experiment can provide unique information regarding conformational changes, ligand binding, and exchange rates, as well as monitoring complex reactions.

In this area, Grimaldi and Sykes[13] reported a pioneering study of conformational changes of concanavalin A in the presence of Mn^{2+}, Ca^{2+}, and α-methyl-D-mannoside using stopped flow NMR.

Biochemical processes have been extensively monitored utilizing stopped flow and flow ^{31}P NMR. The high NMR sensitivity and large chemical shift range are inherent advantages of the ^{31}P nuclide. Jardetzky and co-workers[31] have reported continuous flow ^{31}P NMR experiments designed to monitor changes in mammalian cells (Chinese hamster ovary cells) in response to stresses, such as starvation, low temperature, and pH. In another study, extracorporeal observation of blood flow under in vivo conditions was described using a bypass from the animal (e.g. a dog). In this manner, phosphorus metabolites [e.g. adenosine triphosphate (ATP)] were continuously monitored.[32] More recently, Graaf et al.[33] have described a continuous flow NMR bioreactor for in vivo studies of microbial cell suspensions. Chen and Bailey[34] have reported a similar on-line NMR system for monitoring bacterial suspensions under aerobic and anaerobic conditions. To illustrate this approach, the ^{31}P NMR spectra obtained for an *Escherichia coli* culture (MG1655) at cell densities of 45 g dry weight L^{-1} under aerobic and anaerobic conditions are provided (Figure 6). Significant changes in these ^{31}P spectra are evident following the switch from aerobic to anaerobic conditions. For example, the intracellular NTP levels decrease in the shift from aerobic to anaerobic conditions. It was concluded that anaerobic glycolyzing cells contained a much smaller amount of NTP (20–50% lower) than cells in aerobic conditions. An in vivo flow ^{31}P NMR study of a functional phosphagen in the metabolism of a microscopic nematode, *Steinernema carpocapase*, has also been reported.[35]

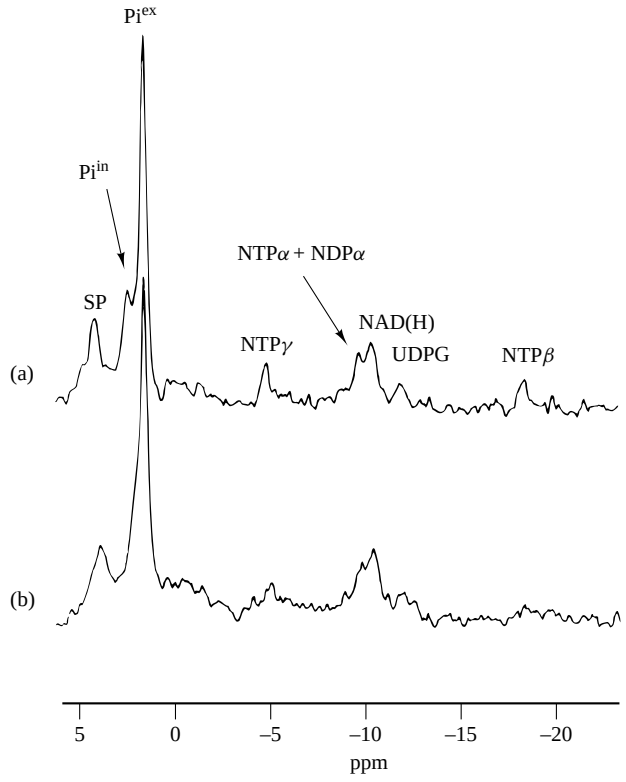

Figure 6 Phosphorus-31 spectra during aerobic and anaerobic glucose glycolysis of *E. coli* in early stationary phase: (a) aerobic spectrum and (b) anaerobic spectrum, both acquired at a cell density of about 45 g dry weight L^{-1} SP, sugar phosphate; Pi^{in}, intracellular inorganic phosphate; Pi^{ex}, extracellular inorganic phosphate; NTP, nucleoside triphosphate; NDP, nucleoside diphosphate; NAD(H), nicotinamide adenine dinucleotide; UDPG, uridine diphosphoglucose. (Reprinted by permission from Chen and Bailey[34])

The development of surface coils in the early 1980s by Ackerman et al.[36] provided new technology for in situ measurements of blood flood, oxygen uptake, and phosphorus metabolism in small animals.[36–38] For example, Eleff et al.[37] employed surface coils to measure in situ cerebral blood flow in cat brains. The high energy phosphate metabolites, phosphocreatine, inorganic phosphate, and ATP, were monitored by ^{31}P NMR. In addition, ^{19}F (blood flow via HCF_3), ^{23}Na, and ^{1}H (lactate) NMR techniques were employed in this multinuclear flow magnetic resonance study. In another study by Ackerman et al.,[38] ^{2}H NMR and ^{31}P NMR were used to investigate blood flow and metabolism of rat hind limb muscle during sepsis.

Although limited by sensitivity, studies of biological monitoring with less sensitive NMR nuclides (^{13}C) have been reported.[39–41] Albert and Bayer[39] have reported in vivo metabolism studies of ^{13}C-labeled phenacetin in an isolated perfused rat liver by continuous flow ^{13}C NMR. Also, a study of Ca^{2+} ion binding to β-trypsin and α-chromatotrypsin using ^{43}Ca and ^{113}Cd flow NMR was reported.[41] Other examples of monitoring biological processes under flow (and nonflow) conditions are discussed in MRI articles of the Encyclopedia.

3 DIRECT COUPLING OF LIQUID CHROMATOGRAPHY AND NMR (LC–NMR)

In 1978, Watanabe and Niki[42] reported the results for direct coupling of high-performance liquid chromatography (HPLC) to ^{1}H NMR with stopped flow detection. During the next 2 years, Bayer et al.,[43] Buddrus and Herzog,[44] and Haw and Dorn[45] extended the approach, but with continuous flow ^{1}H NMR detection (LC–^{1}H NMR). During the last 15 years, numerous LC–NMR studies have been reported, with reviews written in 1984, 1986, and 1988.[46–48] One of the major advantages of NMR in comparison with other commonly employed chromatographic detectors is the high information content present in the NMR chemical shift dimension. The inherent advantage of monitoring the local electronic environment at each nonequivalent nuclear site in a molecule has distinct advantages in comparison with other chromatographic detectors (ultraviolet, refractive index etc.). This is a particularly relevant point for those applications involving isomer identification and/or analysis of complex nonvolatile mixtures. The noninvasive nature of the NMR detector also has distinct advantages for characterization of air sensitive and/or light sensitive labile compounds.

The major limitation of NMR as a chromatographic detector is the detection limits (Table 1). Even with the advent of higher magnetic field NMR spectrometers (500–600 MHz, 11.8–14.1 T), typical detection limits for continuous flow ^{1}H NMR are in the 10^{-5}–10^{-6} g range for chromatographic time windows of 15–30 s. As noted in Table 1, fluorescence and mass spectrometry detectors have a significant sensitivity advantage, but the structural information available from

Table 1 Approximate Detection Limits for Various Spectroscopic Approaches

Technique	Detection Limit (g)
Mass spectrometry	10^{-10}–10^{-12}
Fluorescence spectrometry	$\sim 10^{-12}$
Infrared spectrometry	10^{-6}–10^{-9}
Inductively coupled plasma–atomic emission spectrometry	10^{-6}–10^{-9}
Refractive index	$\sim 10^{-6}$
NMR	10^{-4}–10^{-6}

these detectors is limited. In fact, most of these common spectroscopic detectors have a 10^2–10^6 advantage in comparison with even the favorable ^{1}H nuclide. Because of this sensitivity limitation, the coupling of liquid chromatography and NMR spectroscopy usually requires larger sample injection volumes (100–500 μL) in comparison with most HPLC experiments. These higher injection volumes can also lead to degradation of resolution in the chromatographic dimension and corresponding peak band broadening. For flow cell volumes of 20–200 μL, typical flow rates of 1–4 mL min^{-1} generally do not cause significant lifetime line broadening in the ^{1}H NMR chemical shift dimension.[46–48] As previously discussed, an important requirement is equilibration of the flowing bolus in the magnetic field before NMR detection. These and other conditions necessary for quantitative flow LC–NMR measurements have been reported.[49]

A second problem originally anticipated for the LC–^{1}H NMR technique was the limited choice of solvents compatible for chromatography analysis. Specifically, chromatographic solvents which do not contain extensive ^{1}H NMR background signals are certainly more desirable. This problem has been largely alleviated by the use of deuterated, chlorinated, and/or fluorinated solvents. In another approach supercritical fluid chromatography (SFC) coupled with ^{1}H NMR has the advantage that certain common supercritical solvents (e.g. CO_2) do not contain hydrogen.[50] However, for certain chromatographic separations (e.g. reversed phase), large residual ^{1}H NMR background signals are usually present in solvents, such as (D_2O, H_2O) or (CD_3OD, CD_3OH). In these cases, solvent suppression sequences have been successfully employed to eliminate one or more remaining spectral lines. Laude and Wilkins have utilized a 1–1 hard pulse sequence for solvent suppression (97:3, D_2O/acetonitrile) in a reverse phase LC–^{1}H NMR separation of the nucleosides uridine, cytidine, and adenosine.[51,52] More recently, Albert and Bayer have employed a binomial 1331 sequence for solvent suppression of a 50/50 water/acetonitrile solvent system in a reversed phase separation of several aromatic compounds (70 μg each).[53] The LC–^{1}H NMR (500 MHz) contour plot for this separation is illustrated in Figure 7. In other work by this group, LC–^{1}H NMR stopped flow 2D COSY data were obtained for a metabolite of 2-[(dicyclopropylmethyl)amino]-Δ^2-oxazoline dihydrogenophosphate.[54] Also, a French group[55] has reported an LC–^{1}H NMR study of an epoxy–amine system.

One of the more exciting recent developments in the area of LC–NMR is the work reported by Hatada and co-workers. In several studies, this group utilized gel permeation chromatography directly coupled to ^{1}H NMR (GPC–^{1}H NMR) to analyze several different soluble homopolymers, copolymers, and oligomers.[56–59] In one study, chloral oligomers

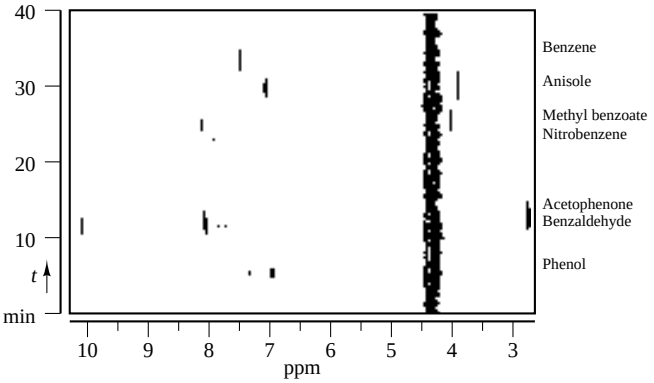

Figure 7 Proton NMR chromatogram (contour plot, 500 MHz) of a separation of phenol (t_R = 6 min), benzaldehyde (t_R = 12 min), acetophenone (t_R = 13 min), nitrobenzene (t_R = 23 min), methyl benzoate (t_R = 25 min), anisole (t_R = 30 min), and benzene (t_R = 34 min) (70 μg each; column, 250 × 4.0 mm; flow-rate 1 mL min^{-1}). (Reprinted by permission from Albert and Bayer[48])

were separated in both the chromatographic and ^{1}H chemical shift domains into dimer, trimer, tetramer, pentamer, hexamer, and heptamer fractions in the GPC–^{1}H NMR profile.[56] In a GPC–^{1}H NMR study of isotactic PMMAs containing a single *t*-butyl end group, the molecular weights were directly determined from integration of the *t*-butyl and methoxy ^{1}H NMR signals.[59] The on-line GPC–^{1}H NMR profile for isotactic PMMA is shown in Figure 8, and the corresponding ^{1}H NMR detected GPC curves are shown in Figure 9. In the latter figure, the refractive index curves are similar to the NMR data, but displaced in time because of differences in the void volumes of the two detectors. A linear plot of log($\bar{M}_n$) versus elution time was obtained from the ^{1}H NMR data profile.

To date, the LC–NMR technique has been employed for all common liquid chromatographic modes, including normal phase, gel permeation, reversed phase, and supercritical fluid chromatography. The technique has also been extended to other nuclei with good sensitivity (LC–^{19}F NMR).[60] Sensitivity constraints will undoubtedly continue to limit extension of the LC–NMR technique to other nuclei with lower sensitivity (e.g. ^{13}C). Nevertheless, anticipated further instrumentation advancements could help alleviate this situation (vide infra).

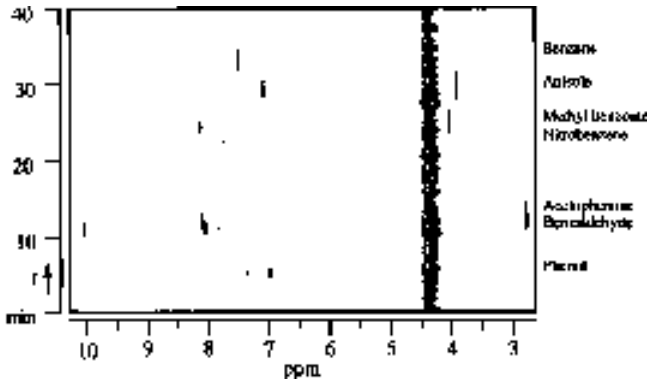

Figure 8 On-line GPC–NMR data of isotactic PMMA ($\bar{M}_n$ = 12 600). Cross section at 3.60 ppm (*) where the methoxy proton resonates give the ^{1}H NMR detected GPC curve (see Figure 9). (Reprinted by permission from Hatada et al.[59])

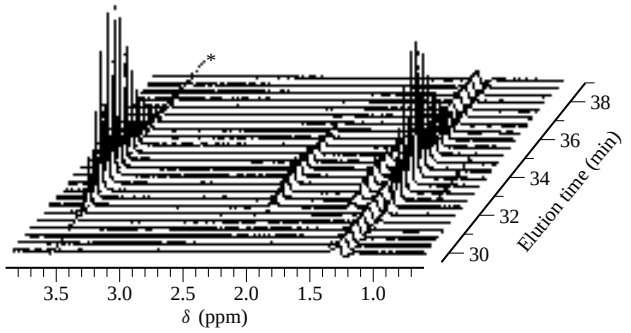

Figure 9 The ^{1}H NMR detected GPC curves of the isotactic PMMAs with $\bar{M}_n$ values of 12 600, 5260, and 3160. These curves were obtained by plotting the intensity of the methoxy proton signal (3.60 ppm) against elution time. The refractive index (RI) detected GPC curves are also shown. (Reprinted by permission from Hatada et al.[59])

4 SIGNAL ENHANCEMENT

4.1 Recycled Flow

As previously indicated, Suryan's observation of a fivefold increase in the intensity of a flowing water sample represents one of the first applications of flow NMR.[1] A similar enhancement (threefold) for a flow ^{13}C NMR study of benzene was observed by Forsén and Rupprecht.[61] Mitchell and Phillips[62] also utilized a flow system to detect low levels of H_2O (in D_2O) with higher rf power levels. In another early flow ^{1}H and ^{19}F NMR study by McIvor, signal enhancements for fluorinated hydrocarbons were reported.[63] It is noteworthy that these increases in the signal-to-noise ratio are per unit time and are only possible when there is sufficient sample quantity for magnetic field equilibration prior to monitoring in the active region (see Section 1.2). Thus, this flow method of enhancement is only possible by the continual influx of 'freshly equilibrated' spins. More recently, the same experiment has been described in terms of a recycled flow NMR experiment. Wilkins and Laude have reported reduced measurement times for long-relaxing nuclei, such as, carbonyl and quaternary carbon atoms in recycled flow ^{13}C NMR.[64–67] Laude and Wilkins have also utilized a recycled flow ^{29}Si NMR experiment for end-group analysis of siloxane polymers ($\bar{M}_n$ values, 495–3773).67 The flow NMR method was found to be more effective than using paramagnetic relaxation reagents for leveling spin–lattice relaxation times and minimizing nuclear Overhauser effects. A factor of 3–5 improvement in analysis time was reported by this group in comparison with static NMR measurements.

Fyfe and co-workers[68] introduced a different method of leveling spin–lattice relaxation times in flowing NMR studies which avoids the use of large equilibration volumes in the magnetic field. Specifically, their approach employed the use of stable free radicals (nitroxides) immobilized on a substrate (silica) placed in the flowing stream before detection. The flowing liquid exhibited significant increases in the effective nuclear relaxation rates because of efficient electron–nuclear relaxation processes at the liquid–substrate interface. The approach was not only important for decreasing spin–lattice relaxation times for the flowing fluid, but quantitative peak intensities were also obtained.

4.2 Flow DNP

Dorn and co-workers have reported[69–73] a transfer DNP experiment for signal enhancement which was originally suggested by Motchane[74] and later by Richards.[75] The experiment involves polarizing a flowing bolus in a low magnetic field, but monitored in a high magnetic field. (In some respects this experiment is similar to field cycling experiments—see ***Field Cycling Experiments***.) Sagdeev and co-workers have also reported a similar low to high magnetic field flow transfer apparatus for CIDNP and DNP experiments.[76] This approach provides dramatic improvements in signal enhancement when compared with the classic static DNP experiment.

As background to this approach, numerous static DNP studies have been reported and reviews written for both liquid[75–79] and solid[80] samples. Although the DNP technique holds great promise as a means of enhancing the signal for many NMR nuclides (e.g. ^{13}C, ^{31}P, ^{15}N, etc.), a number of difficulties have hampered the widespread use of the DNP technique. The DNP polarization A can be expressed in the following simplified form[75,77–79] for the time dependent Overhauser effect:

$$A = \left[\frac{\bar{M}_z - M_0}{M_0}\right] = \rho f s \left(\frac{\gamma_e}{\gamma_I}\right) \tag{4}$$

where γ_I and γ_e are the magnetogyric ratios for the nuclear and electron spins, respectively, and the coupling (ρ) and leakage (f) factors are defined in terms of the appropriate transition probabilities W_2^D, W_0^D, W_1^D, etc., for the nuclear–electron interaction,

$$\rho = \frac{(W_2^D - W_0^D - W_0^{Sc})}{(W_2^D + W_0^D + W_0^{Sc} + 2W_1^D)} \tag{5}$$

The coupling factor for the Overhauser effect can have any value between −1.0 for a purely scalar interaction, to a dominant dipolar interaction $W_0^{Sc} \simeq 0$, which has a limiting value of + 0.5 in the extreme narrowing limit, $\omega_e \tau_c \ll 1$, ($W_0^D : W_1^D : W_2^D = 2 : 3 : 12$). It should be noted that for large macromolecules the extreme narrowing condition will normally not be satisfied. Since the nuclear spin–lattice relaxation rates in the presence and absence of a free radical are given by $(T_1^{xs})^{-1} - (T_1^x)^{-1} = (W_0^D + 2W_1^D + W_2^D + W_0^{Sc})$ and $(T_1^x)^{-1} = W_1^0$, respectively, the leakage factor can be readily measured (or estimated) from the relationship

$$f = \frac{W_0^D + 2W_1^D + W_2^D + W_0^{Sc}}{W_0^D + 2W_1^D + W_2^D + W_0^{Sc} + W_1^0} \tag{6}$$

and

$$f = 1 - \frac{T_1^{xs}}{T_1^x} \tag{7}$$

The electron spin saturation factor (s) is given by

$$s = \frac{S_0 - \bar{S}_z}{S_0} \tag{8}$$

$$\bar{S}_z = \frac{S_0}{1 + \alpha B_{1e}^2 T_1^e T_2^e} \tag{9}$$

where T_1^e and T_2^e are the electron spin–lattice and transverse relaxation times, respectively. Since the microwave power P is proportional to B_{1e}^2, an inverse plot of enhancement $[A]^{-1}$ versus P^{-1} is normally employed experimentally to obtain A_∞, the value of the enhancement for complete saturation, $s = 1$. In addition to the Overhauser effect, time independent interactions are important in studies of solid samples.[80] A solid state effect is an important mechanism in 'rigid' samples containing fixed free radical centers and achieves a maximum for $\omega = \omega_e \pm \omega_n$. This is in contrast to the Overhauser effect where the maximum occurs at $\omega = \omega_e$. Also, a direct and indirect thermal mixing effect can occur when there is a large number of fixed free radical centers such that the ESR line is homogeneously broadened. In the direct thermal mixing effect, a maximum enhancement occurs at $\omega = \omega_e \pm \frac{1}{2}\Delta\omega_n$. The case of time independent DNP interactions is treated in more depth in another article (see ***Dynamic Nuclear Polarization and High-Resolution NMR of Solids***).

To understand the flow DNP experiment, consider a flowing bolus in the low-to-high magnetic field experiment (Figure 10) without DNP enhancement (no microwave irradiation). A silica phase immobilized nitroxide (SPIN) sample is present in the low magnetic field and is similar to the samples previously described by Fyfe.[68] It is apparent that the observed magnetization for a flowing bolus (e.g. benzene) at the high magnetic field detector is dependent on the flow rate. At very low flow rates (or static conditions), the observed NMR signal is dominated by the high magnetic field thermal Boltzmann equilibrated magnetization (M_0^H). However, at sufficiently high flow rates the high magnetic field contribution to the total magnetization decreases dramatically, since the spin–lattice relaxation time (in the absence of the radical) is long relative to the residence time (t_c) in region C. For high flow rates, a significant fraction of the observed signal can result from the low field thermal equilibrated Boltzmann magnetization (M_0^L). That is, the bolus residence time (t_a) in region A is long relative to the significantly shortened spin–lattice relaxation time of the flowing fluid in the presence of the SPIN system. After leaving region A, the bolus is transferred to the high magnetic field detector (region C). For high flow rates, the bolus is transferred via region B in a time that is short relative to the relaxation time in the absence of the radical. Under these conditions, the low field magnetization (M_{xy}^L) will tend to dominate the monitored magnetization at sufficiently high flow rates.[69]

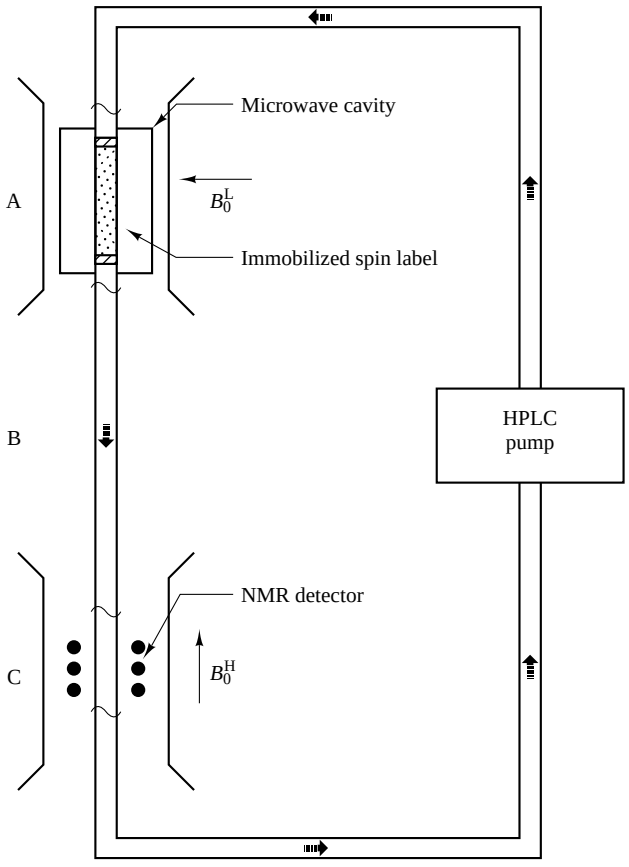

Figure 10 The low magnetic field transfer DNP apparatus. HPLC, high-performance liquid chromatography. (Reprinted by permission from Dorn et al.[69])

If we now consider the flow DNP experiment, a microwave source ($\omega_e/2\pi$ = 9.4 GHz) saturates the electron transition(s) in the low magnetic field B_0^L, and a DNP enhanced flowing bolus is generated. This polarized bolus can then be transferred to the high magnetic field detector. This experiment has the advantage that the polarized bolus is monitored in the high magnetic field in the absence of the radical. Thus, the achievable high field spectral resolution in the chemical shift dimension is only limited by the residual inhomogeneity of the high field magnet and possible flow lifetime broadening. However, even the latter broadening factor can be avoided using a stopped flow transfer DNP experiment.[71]

A model has been reported for the flow transfer DNP experiment[71] which assumes plug flow with the bolus having average residence times τ_a, τ_b, and τ_c in regions A, B, and C, respectively. Under the limiting conditions $\tau_a \gg T_{1a}^x$, $\tau_b \ll T_{1b}^x$ and $\tau_c \ll T_{1c}^x$, the model predicts a maximum enhancement in the low-to-high magnetic field transfer experiment of A/K. It should be noted that the maximum observable enhancement monitored at the high magnet field (without relaxation losses) is attenuated by only the ratio K relative to the corresponding high static field DNP experiment (B_0^H). Since typical values of K are of the order of 10^1–10^2, DNP enhancements can easily exceed the thermal Boltzmann magnetization at the monitoring high magnetic field. This is achievable for favorable flow DNP experiments, since the maximum Overhauser enhancement (A) is 10^3–10^4 for most nuclides [equation (4)].

To date, enhancements for ^{1}H, ^{13}C, and ^{29}Si DNP have been reported using the flow transfer DNP approach. Two different stable radical systems have been employed: (1) a solid–liquid intermolecular transfer (SLIT) experiment utilizing SPIN samples[69,72,73,81,82] or (2) a liquid–liquid intermolecular transfer (L^2IT) experiment in which a stable free radical (e.g. the 2,2,6,6-tetramethyl-1-piperidinyloxy radical, TEMPO) is present in the flowing liquid.[70,71,73]

The SLIT and L^2IT transfer ^{13}C DNP experiments have been used to study the collisional dynamics of fullerene-C_{60} dissolved in deuterated benzene (in the presence of TEMPO) as illustrated in Figure 11.[72] In these experiments the low and high magnetic fields were 0.33 and 14.7 T, respectively (K = 14.4). The ^{13}C DNP spectrum exhibits a negative DNP enhancement for fullerene-C_{60} and the solvent C_6D_6,

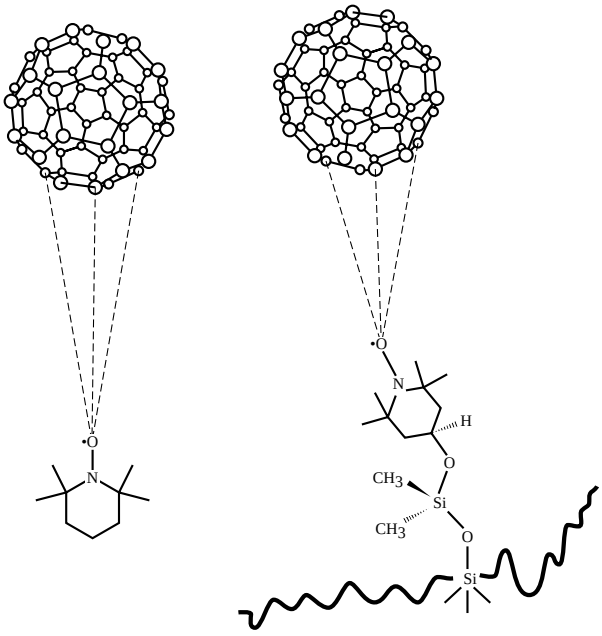

Figure 11 The collisional dynamics of fullerene-C_{60} dissolved in deuterated benzene (in the presence of the free radical TEMPO), as followed by the SLIT and L^2IT transfer ^{13}C DNP experiments

indicating that the electron–nuclear interaction with the free radical (TEMPO) is dipolar dominated in both cases. The ultimate DNP enhancements (A_∞) for fullerene-C_{60} and the solvent (C_6D_6) were -250 ± 20 and -200 ± 20, respectively. In comparison with deuterated benzene (C_6D_6), a further reduction in the ^{13}C DNP enhancement for the larger, more slowly rotating C_{60} molecule might be anticipated because of a further reduction in the dipolar spectral density and/or the presence of a small scalar contribution.[77,78] However, the ultimate ^{13}C DNP enhancement for fullerene-C_{60} was remarkably large, $A_\infty = -250 \pm 20$. This observation in conjunction with the absence of even a minor ^{13}C NMR scalar contact shift suggests that the nuclear–electron time dependent interaction for fullerene-C_{60}/TEMPO is exclusively dominated by the dipolar mechanism. Assuming that a rotationally modulated mechanism dominates the dipolar interaction, the corresponding rotational correlation time (τ_r) was estimated from the expression for exclusive rotational dipolar diffusion:[77,78]

$$\rho_D^r = \frac{1}{1.4 + 0.6[J_D^r(\omega_I)/J_D^r(\omega_e)]} \tag{10}$$

$$J_D^r(\omega) = \frac{1}{2\pi b^6} \frac{\tau_r}{1 + \omega^2 \tau_r^2} \tag{11}$$

where b is the nucleus–electron distance in the complex.

An expression similar to equation (10) has been presented for a dominant translational diffusion mechanism, but the spectral density function $J_D^t(\omega)$ has a different frequency dependence.[83] Using equations (10) and (11), the experimentally measured value for nuclear–electron coupling ($\rho = 0.095$) leads to the value $\tau_r = 65$ ps for the fullerene-C_{60}/TEMPO complex. The presence of a minor scalar component complicates a similar calculation for the C_6D_6/TEMPO system. The rotational correlation time can also be estimated from the Stokes–Einstein equation.[77] Based on the value $\tau_r = 65$ ps, and the viscosity, $\eta \approx 0.65$ cp, a value of $R \simeq 0.46$ nm was predicted, which represents the radius of the complex (fullerene-C_{60}/TEMPO). An alternative expression for exclusive translational diffusion leads to a considerably shorter predicted correlation time than the value obtained from the ^{13}C DNP measurement. However, a model involving a mixture of rotational and translational diffusion contributions cannot be dismissed.[77,78] The results of the flow ^{13}C DNP study suggest very weak momentary transient bond formation during solution collisions of fullerene-C_{60} and TEMPO.

In contrast to the case of fullerene-C_{60} above, selective intermolecular interactions have also been monitored at liquid–liquid and solid–liquid interfaces. To illustrate this point (Figure 12), an L^2IT ^{13}C DNP study[71] of 1-chlorobutane/TEMPO exhibited a strong scalar enhancement ($A_\infty = +460$) for C-1 (to which the chlorine atom is attached) but dipolar enhancements for carbons C-2 (-200), C-3 (-400), and C-4 (-290). In the corresponding SLIT ^{13}C DNP experiment[72] a strong scalar ^{13}C DNP enhancement was also observed at C-1. In contrast, the corresponding ^{1}H DNP SLIT and L^2IT experiments[71] demonstrated only dipolar dominated enhancements for the hydrogens at all four nonequivalent carbons.

Although fullerene-C_{60} and many hydrocarbons exhibit dipolar dominated ^{13}C DNP enhancements at 0.33 T, large scalar ^{13}C DNP enhancements have been observed for chlorinated hydrocarbons (CCl_4, $HCCl_3$, H_2CCl_2). For example, both chloroform and chloroform-*d* exhibit L^2IT ^{13}C DNP

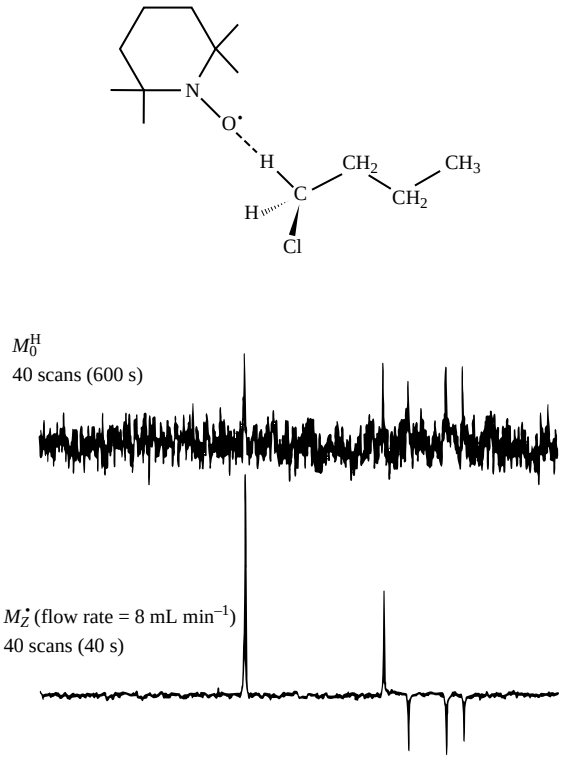

Figure 12 Carbon-13 L^2IT DNP spectrum at 50 MHz for 1-chlorobutane 50% (v/v) in CCl_4/TEMPO (7.9×10^{-2} M). (Reproduced by permission from Dorn et al.[72])

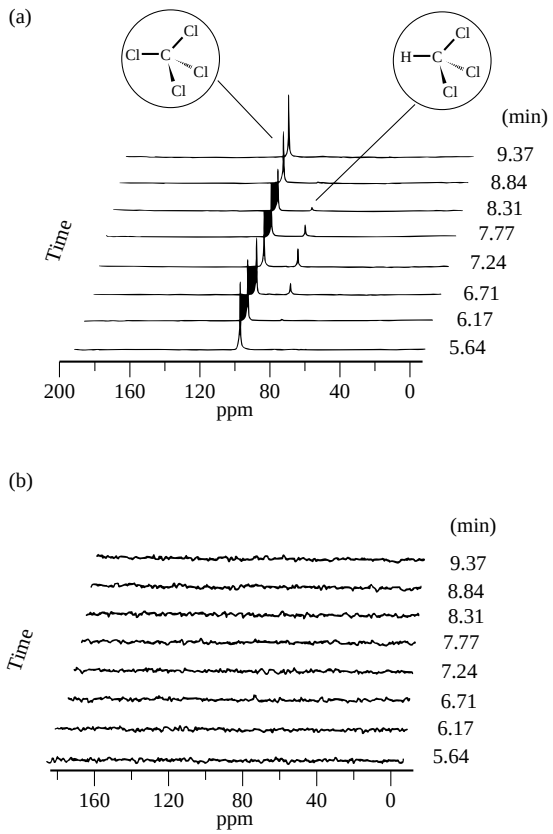

Figure 13 (a) LC–^{13}C DNP spectrum of chloroform (500 μL sample; flow rate, 3.5 mL min^{-1}; number of scans per file, 31; file interval, 31 s; mobile phase, CCl_4). (b) LC–^{13}C NMR spectrum of chloroform under the same conditions as the DNP experiment but without microwave power (B_{1e} = 0)

enhancements (with TEMPO) of +2200 and +2100, respectively, which are close to the scalar limit (A_∞ = +2600) for the ^{13}C nuclide.[71] For the corresponding SLIT experiment with a SPIN sample, ^{13}C DNP enhancement of +760 and +1100, respectively, were reported.[72] It is noteworthy that the SLIT ^{13}C DNP enhancement for chloroform-*d* is over 60 times the ^{13}C NMR thermal Boltzmann magnetization at 4.7 T.

In favorable cases, it is possible to envision NMR applications where practical ^{13}C DNP enhancements could be useful. As one example, direct coupling of liquid chromatography with ^{13}C DNP detection (LC–^{13}C DNP) could help alleviate the sensitivity constraints of LC–^{13}C NMR, as discussed in Section 3.2. Recent work from our laboratory [82] has described directly coupled liquid chromatography with continuous flow SLIT ^{13}C DNP detection (LC–^{13}C DNP). Shown in Figure 13 is the LC–^{13}C DNP profile of a single injected component (chloroform) with carbon tetrachloride as the chromatographic solvent. Although this is a contrived example, no signals were detected in the corresponding flow ^{13}C NMR (no microwave irradiation) experiment. With the SPIN samples used in this study, a ^{13}C DNP enhancement of ~60 has been obtained in comparison with the static thermal ^{13}C NMR Boltzmann magnetization at 4.7 T. Clearly, improvements in higher field superconducting magnet design, instrumentation, and other polarization transfer experiments could provide continued evolution of improvements in NMR signal enhancement into the next century.

5 RELATED ARTICLES

Diffusion: Clinical Utility of MRI Studies; Diffusion and Flow in Fluids; Diffusion Measurements by Magnetic Field Gradient Methods; Diffusion and Perfusion in MRI; Diffusion in Porous Media; Diffusion in Rare Gas Solids; Dynamic Nuclear Polarization and High-Resolution NMR of Solids; Whole Body Magnetic Resonance Angiography.

6 REFERENCES

1. G. Suryan, *Proc. Indian Acad. Sci.* 1951, **33A**, 107.
2. A. I. Zhernovoi and G. D. Latyshev, *NMR in a Flowing Liquid*, Consultants Bureau, New York, 1965.
3. D. W. Jones and T. F. Child, *Adv. Magn. Reson.*, 1976, **8**, 123.
4. J. R. Singer, *Science*, 1972, **175**, 794.
5. K. J. Packer, *Mol. Phys.*, 1969, **17**, 355.
6. E. O. Stejskal, *J. Chem. Phys.* 1965, **43**, 3597.
7. A. N. Garroway, *J. Phys. D: Appl. Phys.*, 1974, **7**, L159.
8. P. A. de Jager, M. A. Hemminga, and A. Sonneveld, *Rev. Sci. Instrum.*, 1978, **49**, 1217.
9. J. Stepišnik, *Progr. Nucl. Magn. Reson. Spectrosc.*, 1985, **17**, 187.
10. A. Caprihan and E. Fukushima, *Phys. Rep.*, 1990, **198**(4), 195.
11. G. C. Chingas, L. Frydman, G. A. Barrall, and J. S. Harwood, in *Magnetic Resonance Microscopy* ed. B. Bluemich and W. Kuhn, VCH, Weinheim, 1992, p. 373.
12. S. A. Altobelli, A. Caprihan, E. Fukushima, and P. D. Majors, in *Magnetic Resonance Microscopy*, ed B. Bluemich and W. Kuhn, VCH, Weinheim, 1992, p. 367.
13. J. J. Grimaldi and B. D. Sykes, *J. Biol. Chem.*, 1975, **250**(5), 1618.
14. C. A. Fyfe, M. Cocivera, and S. W. H. Damji, *Acc. Chem. Res.*, 1978, **11**, 277.
15. R. R. Ernst and W. A. Anderson, *Rev. Sci. Instrum.*, 1966, **37**, 93.
16. J. J. Neil, *Concepts Magn. Reson.*, 1991, **3**(1), 1.
17. C. A. Fyfe, M. Cocivera, S. W. H. Damji, T. A. Hostetter, D. Sproat, and J. O'Brien, *J. Magn. Reson.*, 1976, **23**, 377.
18. J. Bargon, German Patent 2 004973, 1972 (*Chem. Abstr.*, 1972, **76**, 92 940b).
19. Y. Asahi and E. Mizuta, *Talanta*, 1972, **19**, 567.
20. R. O. Kühne, T. Schaffhauser, A. Wokaun, and R. R. Ernst, *J. Magn. Reson.*, 1979, **35**, 39.
21. C. A. Fyfe, M. Cocivera, and S. W. H. Damji, *J. Am. Chem. Soc.*, 1975, **97**, 5707.
22. W. S. Trahanovsky and D. R. Fischer, *J. Am. Chem. Soc.*, 1990, **112**(12), 497.
23. W. S. Trahanovsky, C. H. Chou, D. R. Fischer, and B. C. Gerstein, *J. Am. Chem. Soc.*, 1988, **110**(19), 6579.
24. L. K. Tan and M. Cocivera, *Can. J. Chem.*, 1982, **60**(6), 778.
25. L. K. Tan and M. Cocivera, *Can. J. Chem.*, 1980, **60**(6), 772.
26. M. Cocivera and A. Effio, *J. Org. Chem.*, 1980, **45**(3), 415.
27. S. Funahashi, K. Ishihara, S. Aizawa, T. Sugata, M. Ishii, Y. Inada, and M. Tanaka, *Rev. Sci. Instrum.*, 1993, **64**(1), 130.
28. K. Albert, E. L. Dreher, H. Straub, and A. Rieker, *Magn. Reson. Chem.*, 1987, **25**, 919.
29. M. E. Davis, P. Hathaway, D. Morgan, T. Glass, and H. C. Dorn, *Stud. Surf. Sci. Catal.*, 1987, 38 (Catalysis 1987), 1988, 263.

30. S. I. Selivanov and B. A. Ershov, *Russ. Chem. Rev.*, 1986, **55**, 395.
31. R. Gonzalez-Mendez, D. Wemmer, G. Hahn, N. Wade-Jardetsky, and O. Jardetzky, *Biochim. Biophys. Acta*, 1982, **720**(3), 274.
32. A. M. Wyrwicz, J. C. Schofield, and C. T. Burt, in *Noninvasive Probes in Tissue Metabolism*, ed J. S. Cohen, Wiley, New York, 1982, p. 149.
33. A. A. De Graaf, R. M. Wittig, U. Probst, J. Strohhaecker, S. M. Schoberth, and H. Sahm, *J. Magn. Reson.*, 1992, **98**(3), 654.
34. R. Z. Chen and J. E. Bailey, *Biotechnol. Bioeng.*, 1993, **42**, 215.
35. S. N. Thompson, E. G. Platzer, and R. W. K. Lee, *Magn. Reson. Med.*, 1992, **28**(2), 311.
36. J. J. H. Ackerman, T. H. Grove, G. G. Wong, D. G. Gadian, and G. K. Radda, *Nature*, 1980, **283**, 167.
37. S. M. Eleff, M. D. Schnall, L. Ligetti, M. Osbakken, V. H. Subramanian, B. Chance, and J. S. Leigh, Jr., *Magn. Reson. Med.*, 1988, **7**(4), 412.
38. S. K. Song, R. S. Hotchkiss, I. E. Karl, and J. J. H. Ackerman, *Magn. Reson. Med.*, 1992, **25**(1), 67.
39. K. Albert, G. Kruppa, K. P. Zeller, E. Bayer, and F. Hartmann, *Z. Naturforsch*, 1984, **39C**, 859.
40. H. Santos and D. L. Turner, *J. Magn. Reson.*, 1986, **68**, 345.
41. E. Chiancone, T. Drakenberg, O. Teleman, and S. Forsén, *J. Mol. Biol.*, 1985, **185**(1), 201.
42. N. Watanabe and E. Niki, *Proc. Jpn. Acad., Ser. B.*, 1978, **54**, 194.
43. E. Bayer, K. Albert, M. Nieder, E. Grom, and T. Keller, *J. Chromatogr.*, 1979, **186**, 497.
44. J. Buddrus and H. Herzog, *Org. Magn. Reson.*, 1980, **13**, 153.
45. J. F. Haw, T. E. Glass, D. W. Hausler, E. Motell, and H. C. Dorn, *Anal. Chem.*, 1980, **52**, 1135.
46. H. C. Dorn, *Anal. Chem.*, 1984, **56**, 747A.
47. D. A. Laude, Jr. and C. L. Wilkins, *Trends Anal. Chem.*, 1986, **5**, 230.
48. K. Albert and E. Bayer, *Trends Anal. Chem.*, 1988, **7**, 288.
49. J. F. Haw, T. E. Glass, and H. C. Dorn, *J. Magn. Reson.*, 1982, **49**, 22.
50. L. A. Allen, T. E. Glass, and H. C. Dorn, *Anal. Chem.*, 1988, **60**, 390.
51. D. A. Laude, Jr., R. W. K. Lee, and C. L. Wilkins, *Anal. Chem.*, 1985, **57**, 1464.
52. D. A. Laude, Jr. and C. L. Wilkins, *Anal. Chem.*, 1987, **59**, 546.
53. K. Albert, M. Kunst, E. Bayer, M. Spraul, and W. Bermal, *J. Chromatogr.*, 1989, **463**, 355.
54. K. Albert, M. Kunst, E. Bayer, H. Jan de-Jong, P. Genissel, M. Spraul, and W. Bermel, *Anal. Chem.*, 1989, **61**, 772.
55. M. F. Grenier-Loustalot, P. Grenier, J. Bounoure, M. Grall, and R. Panaras, *Analysis*, 1990, **18**, 200.
56. K. Ute, M. Kashiyama, K. Oka, and K. Hatada, *Makromol. Chem., Rapid Commun.*, 1990, **11**, 31.
57. K. Ute and K. Hatada, *Anal. Sci.*, 1991, **7**, 1629.
58. K. Hatada, K. Ute, T. Kitayama, T. Nishimura, M. Kashiyama, and N. Fujimoto, *Polym. Bull. (Berlin)*, 1990, **23**, 549.
59. K. Hatada, K. Ute, M. Kashiyama, and M. Imanari, *Polym. J. (Tokyo)*, 1990, **22**, 218.
60. L. A. Allen, M. P. Spratt, T. E. Glass, and H. C. Dorn, *Anal. Chem.*, 1988, **60**, 675.
61. S. Forsén and A. Rupprecht, *J. Chem. Phys.*, 1960, **33**, 1888.
62. A. M. J. Mitchell and G. Phillips, *Br. J. Appl. Phys.*, 1956, **7**, 67.
63. M. C. McIvor, *J. Phys. E*, 1969, **2**, 292.
64. D. A. Laude, Jr., R. W. K. Lee, and C. L. Wilkins, *J. Magn. Reson.*, 1984, **60**, 453.
65. D. A. Laude, Jr., R. W. K. Lee, and C. L. Wilkins, *Anal. Chem.*, 1985, **57**, 1281.
66. D. A. Laude, Jr., R. W. K. Lee, and C. L. Wilkins, *Anal. Chem.*, 1985, **57**, 1286.
67. D. A. Laude and C. L. Wilkins, *Macromolecules*, 1986, **19**, 2295.
68. D. Bruck, B. Dudley, C. S. Fyfe, and J. V. Delden, *J. Magn. Reson.*, 1981, **42**, 51.
69. H. C. Dorn, R. Gitti, K. H. Tsai, and T. E. Glass, *Chem. Phys. Lett.*, 1989, **155**, 227.
70. K. H. Tsai, T. E. Glass, and H. C. Dorn, *J. Magn. Reson.*, 1990, **89**, 362.
71. K. H. Tsai and H. C. Dorn, *Appl. Magn. Reson.*, 1990, **1**, 231.
72. H. C. Dorn, T. E. Glass, R. Gitti, and K. H. Tsai, *Appl. Magn. Reson.*, 1991, **2**, 9.
73. H. C. Dorn, J. Gu, D. S. Bethune, R. D. Johnson, and C. S. Yannoni, *Chem. Phys. Lett.*, 1993, **203**, 549.
74. J. L. Motchane, E. Erb, and J. Uebersfeld, *Compt. Rend. Acad. Sci. (Paris)*, 1958, **246**, 1833.
75. R. A. Dwek, R. E. Richards, and D. Taylor, *Annu. Rev. NMR Spectrosc.*, 1969, **2**, 293.
76. N. I. Avdievich, E. G. Bagryanskaya, Yu A. Grishin, and R. Z. Sagdeev, *Chem. Phys. Lett.*, 1989, **155**(2), 141.
77. K. H. Hausser and D. Stehlik, *Adv. Magn. Reson.*, 1968, **3**, 79.
78. W. Müller-Warmuth and K. Meise-Gresch, *Adv. Magn. Reson.*, 1983, **11**, 1.
79. R. D. Bates, *Magn. Reson. Rev.*, 1993, **16**, 237.
80. R. A. Wind, M. J. Duijvestijn, C. Van der Lugt, A. Manenschijn, and J. Vriend, *Progr. Nucl. Magn. Spectrosc.*, 1985, **17**, 33.
81. R. Gitti, C. Wild, C. Tsiao, K. Zimmer, T. E. Glass, and H. C. Dorn, *J. Am. Chem. Soc.*, 1988, **110**, 2294.
82. S. Stevenson and H. C. Dorn, *Anal. Chem.*, 1994, in press.
83. B. Borah and R. D. Bates, *J. Chem. Phys.*, 1981, **74**, 1538.

Biographical Sketch

Harry C. Dorn. *b* 1943. B.S., 1966, University of California, Santa Barbara. Ph.D., 1974, University of California, Davis. Introduced to NMR by G. E. Maciel. Approx. 80 publications. Areas of interest involve spectroscopic studies utilizing NMR, ESR, and DNP.

Liquid Crystalline Samples: Diffusion

Göran Lindblom and Greger Orädd

University of Umeå, Sweden

1	Introduction	1
2	NMR Measurements of Lipid Lateral Diffusion in Oriented Bilayers	1
3	NMR Measurements of Water and Ion Diffusion in Liquid Crystals	4
4	Lipid Lateral Diffusion in Cubic Liquid Crystalline Phases	4
5	Lateral Diffusion in Other Nonlamellar Liquid Crystals	6
6	Related Articles	7
7	References	7

1 INTRODUCTION

The NMR methods involving pulsed magnetic field gradients provide one of the most attractive techniques for studies of molecular transport in lipid membranes and lyotropic liquid crystalline systems. One of the most successful applications of pulsed field gradient (PFG) NMR is found in the field of complex liquids. In particular, this has been an invaluable tool in determining the structures of cubic liquid crystalline phases.[1] Almost two decades ago, the first lateral diffusion coefficient of an amphiphile in a lamellar liquid crystalline phase was measured directly with the PFG NMR method.[2] In recent years, the range of applications of NMR diffusion techniques has been growing rapidly, due to the great improvments in the NMR equipment for diffusion and NMR microscopy.[3] We concentrate here on lyotropic liquid crystalline systems (Figure 1) containing membrane lipids or other amphiphilic molecules.

2 NMR MEASUREMENTS OF LIPID LATERAL DIFFUSION IN ORIENTED BILAYERS

The translational motion of lipids can be measured using the conventional NMR diffusion pulsed field gradient spin echo (PFG-SE) method for anisotropic liquid crystalline systems, if all static proton dipole–dipole interactions can be removed by some mechanical method. For studies of the lateral diffusion of lipids in a lamellar phase the removal of these interactions can be accomplished by a macroscopic alignment of the lamellae between, for example, glass plates.[2,4,5] In lipid bilayers, provided that the translational diffusion rapidly leads to a zero average of all the static, intermolecular dipolar interactions, the dipolar Hamiltonian $\hat{\mathcal{H}}_{\mathrm{D}}$ can be written[6,7]

$$\hat{\mathcal{H}}_{\mathrm{D}} = \sum_{i>j} \sum_{p} F_0^{(2)}(ij) D_{p0}^{(2)}(\Omega) \hat{A}_p^{(2)}(ij) \qquad (1)$$

where

$$F_0^{(2)}(ij) = 2\gamma^2 r_{ij}^3 \overline{D_{00}^{(2)}(\Omega_{ij})} \qquad (2)$$

where γ is the magnetogyric ratio, r_{ij} is the distance between the protons in an intramolecular proton pair ij, Ω_{ij} is the Eulerian angle between the proton–proton vector and the bilayer normal (the so-called 'director'), and $\overline{D_{00}^{(2)}(\Omega_{ij})}$ is a Wigner rotation matrix element.[8] The bar indicates averaging over all the fast motions. Likewise, $D_{p0}^{(2)}(\Omega)$ is a rotation matrix element, and Ω is the Eulerian angle between the bilayer director and the applied magnetic field $\boldsymbol{B}_0$. $\hat{A}_p^{(2)}(ij)$ is a component of an irreducible tensor operator of rank two operating on the nuclear spin coordinates. In a strong magnetic field only the term containing $\hat{A}_0^{(2)}(ij)$ affects the spectrum. $\hat{\mathcal{H}}_{\mathrm{D}}$ for all the protons in the hydrocarbon chain can then be written

$$\hat{\mathcal{H}}_{\mathrm{D}} = \tfrac{1}{2}(3\cos^2\theta - 1) \sum_{i>j} F_0^{(2)}(ij) \hat{A}_0^{(2)}(ij) \qquad (3)$$

From equation (3) it is obvious that if the bilayer is macroscopically aligned and oriented at the so-called magic angle $\theta = 54.7^\circ$, then $\hat{\mathcal{H}}_{\mathrm{D}} = 0$ and the static dipolar couplings are reduced. In the NMR experiment the diffusion is measured in the direction of the magnetic field gradient. For a lipid membrane or a lamellar phase the diffusion coefficient is orientation dependent and two constants D_{L} and $D_{\perp}$ describe the diffusion. D_{L} is the lateral diffusion coefficient for motion parallel with the membrane, and $D_{\perp}$ determines the diffusion perpendicular to the bilayer. The measured diffusion coefficient D for an oriented membrane system is then

$$D = D_{\mathrm{L}} \sin^2\theta + D_{\perp} \cos^2\theta \qquad (4)$$

for a lamellae oriented at the magic angle $\sin^2\theta = \frac{2}{3}$. In lipid bilayers, $D_{\perp}$ should be orders of magnitude smaller than D_{L} and the second term in equation (4) can be neglected.

Early on, this method was used to determine the lateral diffusion coefficient of a phosphatidylcholine lipid in a lamellar phase[2,4] and for potassium oleate[5] (Table 1). One of the most annoying difficulties one was faced with in the first measurements of the lateral diffusion coefficient of lipids was the contribution from water protons to the spin echo signal, which results in a diffusion coefficient for the lipids which is too large. This problem can be solved by a careful exchange of all free protons for deuterium. For example, the lateral diffusion coefficient of a typical amphiphile-like sodium octanoate (C_7COONa) was measured[2] to be equal to $2.1 \times 10^{-10}\,\mathrm{m^2\,s^{-1}}$ at 24 °C.

The lateral diffusion coefficient is also affected[9] by a change in the water content in the lamellar phase (Table 1). It was found that the lateral diffusion of dipalmitoylphosphatidylcholine (DPPC) increased by a factor of 2 for a change in the ^2H_2O content of 15 to 40 wt.%. Wu and Huang[10] have calculated the change in the lateral diffusion as a function of the water content according to the theory of Brownian motion in thin sheets. They found that the dependence of phospholipid diffusion on hydration can be attributed primarily to the change in the bulk water mobility in the multilamellar phase.

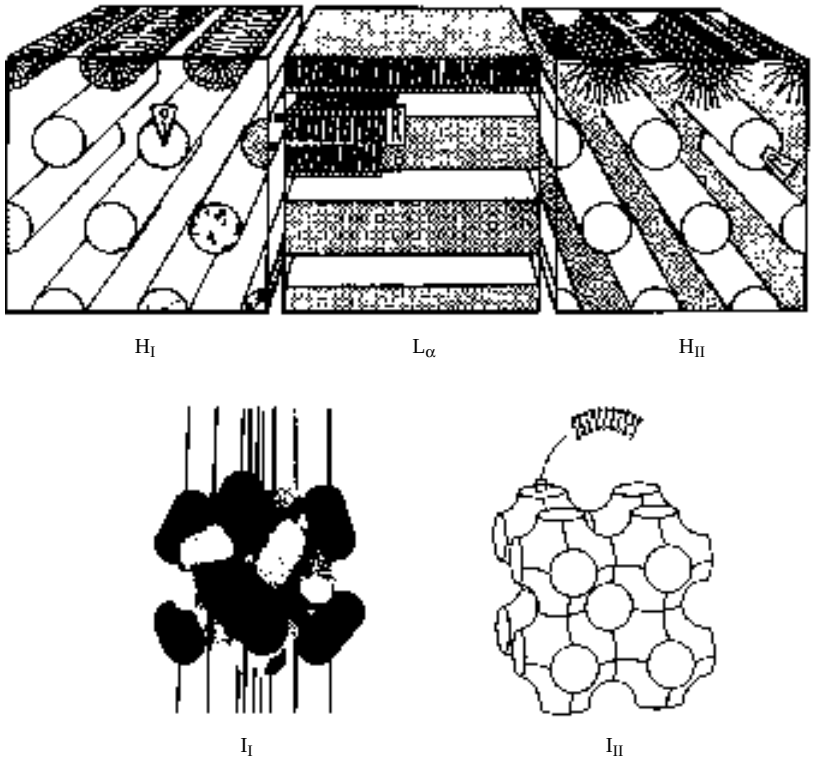

Figure 1 Structure of the most common liquid crystalline phases that membrane lipids can form: (H_I) normal hexagonal phase; (L_α) lamellar phase; and (H_{II}) reversed hexagonal phase.[98] (I_I) A scaled model of a unit cell of a cubic phase structure built up of closed micelles.[83] (I_{II}) Schematic drawing of a bicontinuous cubic phase belonging to the space group $Im3m$[1]

Recently, we reported on the effect of glycerol on the translational and rotational motions in aqueous lipid bilayers.[11] A continuous decrease in the lipid diffusion coefficient was observed upon increasing glycerol contents; thus, at room temperature $D = 12.6 \times 10^{-12}\,m^2\,s^{-1}$ for an aqueous L_α phase, while $D = 1.9 \times 10^{-12}\,m^2\,s^{-1}$ where all the water was displaced by glycerol. It was concluded that glycerol between the lipid bilayers affects the lipid diffusion due to changes in the viscosity in the interbilayer regions. This is also in accordance with the findings of Wu and Huang.[10]

As intuitively expected, the lateral diffusion coefficient depends on the hydrocarbon chain length, but the dependence is rather weak.[2,9] On the other hand, a strong dependence on the translational motion is observed for different polar headgroups of the amphiphiles.[2] Thus, lysophosphatidylcholine (lyso-PC) diffuses somewhat more slowly than the corresponding PC, although the latter has two acyl chains and the lyso compound only one.[12,13] The bulkier headgroup of the lyso-PC molecules most probably plays an important role for the lipid lateral diffusion. In studies[14,15] of the lateral diffusion of the two dominant glucolipids in the bacterium *Acholeplasma laidlawii* it was found that the translational motion of dioleoyldiglucosyldiacylglycerol (DGlcDAG) is about 10 times faster than it is in dioleoyl-PC (DOPC)[16] (Table 1). This difference in the lateral diffusion coefficients can probably be ascribed to differences in the interactions in the polar headgroup region and the packing of the lipids in the bilayer.[2,15] Addition of a monoglucolipid results[14] in a decrease in the lipid lateral diffusion, which has been suggested to be due to hydrogen bonding between the polar headgroups.[15] The theoretical models used in molecular dynamics simulations of the lateral diffusion in lipid bilayers disregard the effect on the polar headgroup, and therefore the calculated diffusion coefficients are much larger than the measured ones. A value of the diffusion coefficient which is about an order of magnitude (or even more) too large is obtained.[17–19] The reason for this discrepancy is that headgroup–headgroup interactions are essential for slowing down the diffusion process.

The effects of cholestrol on lipid membranes have been studied extensively with a number of spectroscopic methods. Cholesterol has been shown to have a condensing effect on many lipids in the lamellar phase, but it was not until recently that the ternary phase diagram of DPPC/cholesterol/water was presented.[20] As the cholesterol content in the lipid bilayer increases, two lamellar phases with different molecular ordering are formed. This unusual behavior has been explained by a theoretical model.[21] The influence of cholesterol on the lipid lateral diffusion in various lamellar liquid crystalline phases has also been investigated (Table 1) by PFG NMR.[9,16] ^{1}H NMR and bandshape simulations of phospholipid/water systems show that the addition of cholesterol to lipid bilayers in the gel phase induces a 'super-Lorentzian' ^{1}H NMR bandshape, which is a result of an enhanced lateral diffusion of the PC molecules.[22] It can be inferred from Table 1 that the cholesterol concentration has a very small effect on the phospholipid diffusion in unsaturated lipid bilayers. This is in accordance with recent molecular dynamics simulations, where it was found that cholesterol does not have any significant effect on the lateral diffusion of the chains.[18] On the other hand, cholesterol has a large influence on the molecular ordering in bilayers.[16,23–25] Thus, cholesterol increases the molecular ordering in a bilayer, but the diffusional motion

Table 1 Lateral Diffusion Coefficients D_L of Some Amphiphiles in Lamellar Phases Aligned between Glass Plates

Lipid system	Composition (wt %)	Temperature (°C)	$D_L \times 10^{11}$ ($m^2\ s^{-1}$)	Reference
Surfactants				
Octylammonium chloride	72	24	33	Lindblom and Wennerström[2]
Water	28			
Aerosol OT	71	24	1.0	Lindblom et al.[62]
Water	29	35	1.7	
Sodium octanoate	22	24	21	Lindblom and Wennerström[2]
Decanol	40			
Water	38			
Lithium perfluorooctanoate	72	25	3	Tiddy[38]
Water	28			
Biological lipids				
Monooleoylglycerol	82	22	1.1	Lindblom et al.[62]
Water	12	35	1.6	
Diglucosyldiacylglycerol (DGlcDAG)	87	45	3.9	Wieslander et al.[14]
Water	13			
Dioleoyl-PC (DOPC)	80	35	0.5	Lindblom et al.[16]
Water	20	45	0.9	
Palmitoyloleoyl-PC (POPC)	80	35	0.6	Lindblom et al.[16]
Water	20			
Dioleoyl-PC	75	35	0.5	Lindblom et al.[16]
Cholesterol	5			
Water	20			
Dioleoyl-PC	70	35	0.5	Ulmius et al.[28]
Sodium cholate	10			
Water	20			
Lysooleoyl-PC	84	26	0.2	Rilfors et al.[13]
Water	16			
Dimyristoyl-PC	75	50	1.2	Wennerström and Lindblom[7]
Water	25			
Dipalmitoyl-PC	85	52	0.6	Kuo and Wade[9]
Water	15			
Dipalmitoyl-PC	75	52	0.9	Kuo and Wade[9]
Water	25			
Dioleoyl-PC	46.2	36	0.3	Rilfors et al.[13]
Dioleoyl-PE	43.8	46	0.4	
Water	10.0	56	0.6	

is unaffected. In a study[13] of the lipid lateral diffusion of a mixture of DOPC, dioleoylphosphatidylethanolamine (DOPE), and water, both lipids were found to have about the same D_L ($5 \times 10^{-12}\ m^2\ s^{-1}$) as DOPC bilayers.[16]

The diffusional motion for powder samples of a liquid crystalline phase have also been measured.[26–28] To reduce the static dipole interactions, a combined multiple pulse homonuclear decoupling and multiple pulse gradient technique[26] has been used to determine the self-diffusion coefficient. By this method the diffusion of DPPC has been studied at 25 °C with 15 wt.% ^2H_2O in the $L_{\beta'}$ gel phase and in the lamellar phase of potassium oleate in 30 wt.% ^2H_2O. The D values obtained in this way are 1.6×10^{-14} and $1.3 \times 10^{-12}\ m^2\ s^{-1}$, respectively. Here the lateral diffusion coefficient is not obtained directly,[29] but is some kind of an average value, since the microcrystallites in the mesophase are randomly oriented. In such a measurement, the diffusion coefficient obtained is too small, compared with the local lateral diffusion. In an early study, Roberts[27] used the stimulated echo to determine the surfactant diffusion in the hexagonal and lamellar phases of potassium laurate/heavy water at 80 °C. Somewhat surprisingly he obtained a similar diffusion coefficient ($D_{lamellar} = 2.4 \times 10^{-10}\ m^2\ s^{-1}$ and $D_{hexagonal} = 2.3 \times 10^{-10}\ m^2\ s^{-1}$) for both phases, although there is a large difference in their structure.

By using pulsed field gradient double quantum spin echo decays the translational diffusion of dichloromethane dissolved in two thermotropic liquid crystals has been studied.[30] Diffusion constants of the solute were determined parallel and perpendicular to the magnetic field.

A method has been presented for simulating ^{31}P NMR spectra from a lipid vesicle dispersion. Experimental spectra are obtained by the use of a DANTE pulse sequence.[31] The

simulation was based on molecules with axially symmetric lineshapes undergoing lateral diffusion on a curved surface. By fitting a set of spectra for which the system is allowed to evolve for a variable time interval after the DANTE excitation, a lateral diffusion coefficient can be calculated from the measured correlation time. Köchy and Bayerl[32] measured ^{2}H quadrupolar transverse relaxation times obtained with the Carr–Purcell–Meiboom-Gill (CPMG) pulse sequence on spherical phospholipid bilayers on a solid support. They took advantage of the fact that the CPMG sequence can progressively filter out contributions to the T_2 relaxation arising from motions, such as lateral diffusion, which are slow on the NMR timescale. For POPC supported bilayers they got $D = 4 \times 10^{-12}\,\mathrm{m^2\ s^{-1}}$ at 30 °C, in good agreement with PFG NMR.[16] An attempt to estimate the lipid lateral diffusion in phospholipid vesicles from ^{13}C spin–spin relaxation was less successful.[33] The authors used a very simple model to describe the spin relaxation, a model which is similar to the so-called 'two-step model'.[34–36] The lateral diffusion coefficient required to fit the values of T_2 is larger by almost two orders of magnitude than the values obtained with PFG NMR.

3 NMR MEASUREMENTS OF WATER AND ION DIFFUSION IN LIQUID CRYSTALS

Most of the investigations of water diffusion in lyotropic liquid crystalline systems have been conducted on powder samples. The intermolecular exchange of protons in the water molecule is rapid on the NMR timescale, and therefore the water signal is relatively sharp even for a nonoriented sample. When the diffusion coefficient is determined for a powder sample with the NMR technique, the resulting echo has contributions from lamellae of all orientations θ, and[29]

$$S(t) = \int_{-1}^{1} \exp\left\{-\frac{2\tau}{T_2(\theta)} - \sin^2\theta\,(\gamma g\delta)^2 D(\Delta - \delta/3)\right\} \mathrm{d}\cos\theta \quad (5)$$

The first measurements of water diffusion coefficients in lamellar phases of a powder sample were performed by Blinc and co-workers.[37] However, the complications described by equation (5) were not considered in their determination of the water diffusion at different temperatures for a sample containing 70% sodium palmitate and 30% water. Assuming that the water molecules in lamellae oriented close to the magic angle make the major contribution to the spin echo, the measured diffusion coefficient should be multiplied[29] by $\frac{3}{2}$ to give $D_\mathrm{L} = 8 \times 10^{-10}\,\mathrm{m^2\ s^{-1}}$. Water diffusion coefficients have, however, also been determined for oriented lamellar phases using both protons[38] and deuterium[39] pulsed field gradient NMR. Callaghan and co-workers[39] found that the diffusion coefficients of ^2H_2O parallel and perpendicular to the bilayer surface are $D_\mathrm{L} = 1.7 \times 10^{-9}$ and $D_\perp = 5 \times 10^{-11}\,\mathrm{m^2\ s^{-1}}$. In this work they also reported the first solid echo PFG ^{2}H NMR experiment performed on a lamellar phase of potassium palmitate and water in the presence of quadrupole splittings.

In the lithium perfluorooctanoate/water system, self-diffusion coefficients are reported for water, lithium and perfluorooctanoate ions in the lamellar and viscous neat phases, as a function of temperature.[38] The difference between diffusion along the water layers and across the perfluorooctanoate bilayers was found to be small for both water and lithium ions. The lithium ion diffusion coefficient was only a factor of 3 larger than that of the perfluorooctanoate amphiphile. The lithium diffusion coefficient has also been determined in a lamellar phase composed of octanoate, water and decanol.[40] It was found that the lithium ion diffusion in this lamellar phase is independent of the composition. This is due to a constant fraction of bound ions in accordance with the ion condensation model previously used to describe the ion binding in lyotropic liquid crystals.[41,42] Recently, the PFG method was applied to estimate of the rates of ionophore-mediated transmembrane exchange of lithium ion in liposomes.[43] There was good agreement between the transmembrane exchange rate estimated from PFG and magnetization transfer ^{7}Li NMR experiments.

Water diffusion coefficients have been measured for powder samples in the two-component system of DPPC and water.[29] The diffusion coefficients were found to be 4–10 times smaller than the translational diffusion coefficient in bulk water, and essentially unaffected by changes in the phase structure.

Some recent investigations of the effect of the mesophase structure on the measured water diffusion coefficients have also been published.[44,47]

4 LIPID LATERAL DIFFUSION IN CUBIC LIQUID CRYSTALLINE PHASES

Lipid translational diffusion coefficients have been determined for a large number of different lyotropic cubic phases (Table 2). There is a great deal of interest in the structure and the properties of membrane lipids, in particular the cubic and reversed hexagonal phases, since these lipid phase structures are believed to be involved in many biologically important membrane processes such as fusion[48–50] and membrane lipid regulation.[1,15,51–53] With X-ray diffraction methods[54–57] the space group of the cubic structure can usually be obtained, but seldom is it possible to distinguish a bicontinuous structure from a structure consisting of closed micellar aggregates. The strength of the PFG NMR method is that it can discriminate between these two structures, since restricted motions in space can be easily observed.[58] The first PFG NMR study of amphiphile diffusion in a cubic phase was carried out by Charvolin and Rigny[59] for a soap system of potassium laurate which formed a cubic phase at 80 °C ($D = 2 \times 10^{-10}\,\mathrm{m^2\ s^{-1}}$). Such a large diffusion coefficient is not compatible with closed aggregates. Conclusions about whether or not a cubic phase consists of closed aggregates are based on a comparison between lipid diffusion coefficients measured by PFG NMR for neigboring phases, with which the cubic phase is in equilibrium.[2,4,60,61]

The apparent diffusion coefficients of cubic and lamellar phases can be qualitatively compared with a simple model.[2,61,62] The restricted lipid diffusion within aggregates building up the cubic lattice can be described by a local diffusion tensor, $\boldsymbol{D}$, where the component representing restricted diffusion in a certain direction is set to zero. The measured diffusion coefficient D is then an average value of the local diffusion tensor:

$$D = \tfrac{1}{3}\overline{\mathrm{Tr}\boldsymbol{D}} \quad (6)$$

where the bar denotes an average over all the sites in a unit cell of the liquid crystal. Depending on how many directions

Table 2 Lipid Diffusion Coefficients D for Some Cubic Liquid Crystalline Phases

Lipid system	Composition (wt.%)	Temperature (°C)	$D10^{11}$ (m^2 s^{-1})	Reference
Aerosol OT	72.4	24	0.36	Lindblom et al.[62]
Water	27.6	35	0.59	
Potassium octanoate	60	24	8.8	Lindblom and Wennerström[2]
Water	40			
Sodium octanoate	39.4	24	<0.1	Lindblom and Wennerström[2]
Octane	4.3			
Water	56.3			
Dodecyltrimethylammonium chloride	84.0	26	0.8	Eriksson et al.[75]
Water	16.0	47	2.0	
Monooleoylglycerol	88	43	1.5	Lindblom et al.[62]
Water	12	57	2.6	
Lysolauroyl-PC	40	29	0.006	Eriksson et al.[12]
Water	60			
Lysooleoyl-PC	79	26	0.14	Eriksson et al.[12]
Water	21			
Dioleoyl-PC	97	60	0.5	Lindblom[97]
Water	3			
Dioleoyl-PC	45	35	0.1	Ulmius et al.[28]
Sodium cholate	30			
Water	25			
Monoglucosyldiacylglycerol (MGlcDAG)	97	35	0.1	Lindblom et al.[15]
Water	3			
Dioleoyl-PC	46.2	66	0.37	Rilfors et al.[13]
Dioleoylphosphatidylethanolamine	43.8	73	0.50	
Water	10.0	83	0.64	
		90	0.78	

are effectively available for the lipid diffusion as measured by PFG NMR, three possibilities can be distinguished:

1. For a cubic phase with closed micelles, the lipid diffusion is restricted in all three directions, all the diagonal elements in the tensor are equal to zero, and D is ideally equal to zero.
2. A cubic structure of connected, long, rod-like aggregates permits lipid diffusion in one direction (along the rod) with the diffusion coefficient $D_{\|}$, and

$$D = \tfrac{1}{3}\overline{\mathrm{Tr}\boldsymbol{D}_{\mathrm{rod}}} = \tfrac{1}{3}D_{\|} \tag{7}$$

3. For a cubic phase with bilayer units, the diffusion $D_{\mathrm{L}}^{\mathrm{cub}}$ can occur in two directions, and

$$D = \tfrac{2}{3}D_{\mathrm{L}}^{\mathrm{cub}} \tag{8}$$

Thus, it can be expected that the aggregate structure in the cubic phase will appreciably influence the magnitude of the measured diffusion coefficients. In particular, PFG NMR provides a convenient method for distinguishing between bicontinuous cubic phases and those having closed aggregates. According to the above equations it should also be possible to obtain a crude estimate of the geometry of the aggregates building up the cubic phase, by comparing diffusion coefficents of lipids in the lamellar and cubic phases. Such a comparison assumes that the local environment of the molecules in the diffusing process is the same in the two phases.

For the comparison of diffusion coefficents of lipids and water in cubic phases, an attractive mathematical model based on a description of the cubic structure by periodic minimal surfaces can be used.[1,63–66] Recently, Anderson and Wennerström[66] have presented numerical results for the geometric obstruction factor of self-diffusion in different bicontinuous, cubic microstructures. The lipid diffusion was modeled as a diffusion of a particle, confined to the polar–apolar dividing surface, with a constant diffusion coefficient D_0. It was proven analytically that the effective diffusion coefficient for a particle diffusing over any minimal surface of cubic symmetry is exactly equal to $\frac{2}{3}D_0$.

4.1 Bicontinuous Cubic Phases

The most widely investigated bicontinuous cubic phases occur in the monooleoylglycerol (MO)/water system. An early X-ray diffraction and PFG NMR investigation of the lipids and water in this system suggested that the cubic phase structure was based on lamellar bilayer units.[62] The simple model described above was applied. The results of the MO system were compared with those of the aerosol OT/water system. The cubic phase of the latter system was suggested to be built up of rod-like aggregates. Using equations (7) and (8), surprisingly good predictions were made of the aggregate shape in the cubic phases.

Table 3 Water and Lipid Diffusion in Cubic Phases of Monooleoylglycerol and Water[72]

^1H_2O[a] (wt.%)	Phase	D_{cub}^{water}/D_0[b]	$D_{cub}^{lipid} \times 10^{12}(m^2s^{-1})$	p_b	n
28.0	*Ia*3*d*	0.201	14.4	0.56	4.3
30.4	*Ia*3*d*	0.237	15.1	0.49	4.2
33.4	*Ia*3*d*/*Pn*3*m*	0.276	1.53	0.41	4.1
36.6	*Pn*3*m*	0.292	15.8	0.39	4.4
39.5	*Pn*3*m*	0.300	1.69	0.38	5.0

[a] 25 °C.
[b] Measured water diffusion coefficient relative to that of pure water (see text).

The cubic phases of several monoglycerides exist over an extended water and temperature region in the phase diagrams.[67] These phases can dissolve substantial amounts of hydrophobic and amphiphilic molecules,[68–71] as well as glycerol.[11] The relationship between the water diffusion coefficient in cubic phases and the MO and water contents has been investigated. The water diffusion coefficient D_{cub}^{water} in a simple two-site model can be written[72]

$$D_{cub}^{water} = p_b D_{cub}^{lipid} + (1 - p_b)\beta D_0 \quad (9)$$

where p_b is the fraction of bound water, D_{cub}^{lipid} is the lipid diffusion coefficient in the cubic phase, β is the obstruction factor for the diffusion of unbound water in the cubic phase, and D_o is the diffusion of bulk water. The association of water obtained from the application of this simple model (Table 3) should be taken as a quantification of the extent to which the surface of the aggregates affects the dynamic properties of water. The diffusion coefficient of water[72] has a discontinuous increase at around 34% water, which harmonizes with the two-phase region between the *Ia*3*d* and *Pn*3*m* cubic structures.[73] The lipid diffusion was found to increase with increasing unsaturation of the acyl chains of the lipid, and it decreases when larger molecules such as cholesterol, gramicidin A, and lysooleoyl-PC are solubilized in the cubic phase. In a cubic liquid crystal of MO, DOPC, and water, the individual lipid diffusion coefficients can be determined simultaneously. The results obtained suggest that when probe techniques are used the choice of the probe itself may influence the measured lipid diffusion coefficient. Recently, we investigated the cubic phase of *N*,*N*-dimethyldodecylammonium oxide (DDAO) having a molar ratio of 97:3 between DDAO and gramicidin and 27 wt.% water. At 25 °C, and taking the diffusion coefficient of water as $D_{water} = 6.3 \times 10^{-11}$ m^2 s^{-1}, the measured diffusion coefficients for the methyl groups of the polar headgroup and the terminal methyl group were 7×10^{-12} m^2 s^{-1}. The latter coefficient should be compared with the coefficient for the diffusion of DDAO in a cubic phase in the absence of gramicidin; the value is 10×10^{-12} m^2 s^{-1}, i.e. gramicidin causes quite a small obstruction effect.

Several membrane lipid–water systems give rise to freeze–fracture replicas of three-dimensional regular arrays of closely packed globular elements, often called 'lipidic particles.'[74] These structural pictures have often been poorly classified, and they have been suggested to show closed lipid aggregates, such as reversed micelles. Investigations of some liquid crystalline phases, giving rise to the freeze–fractured replicas, with X-ray diffraction and PFG NMR indicate that they are: (1) cubic liquid-crystalline phases; and (2), with one exception, bicontinuous cubic phases.[13] There is a rather large accumulation of diffusion coefficients to verify the structure of bicontinuous cubic phases (Table 2).[2,12,14,15,28,53,61,75–80]

4.2 Discontinuous Cubic Phases

Usually these cubic structures are located between the micellar solution and the H_I phase in the phase diagram.[81] X-Ray diffraction showed that this structure belongs to the space group $P43n$ or $Pm3n$. For a long time it was debated whether the structure consists of closed aggregates[12,60,75,82–84] or of a network of connected rod-like micelles with enclosed spherical micelles.[55,85] This debate is now settled,[86,87] and it has been shown conclusively by PFG NMR (Table 2)[83,84,88] that this cubic structure is discontinuous. From NMR lineshapes,[83] spin relaxation,[89,90] and time-resolved quenched fluorescence[84,91] it is concluded that the structure consists of slightly elongated, closed micelles (Figure 1). Recently, a cubic phase consisting of reversed micelles was established.[92] The structure of this phase, which belongs to the space group $Fd3m$, and which is composed of DOPC and dioleoylglycerol or oleic acid and sodium oleate, was recently solved by means of low-resolution crystallography.[93] The structure consists of a complex packing of two types of quasi-spherical reversed micelles. PFG NMR has shown[94] for the cubic phase composed of DOPC and dioleoylglycerol that reversed micelles build up the structure. The diffusion coefficient of DOPC is very small, close to 10^{-13} m^2 s^{-1}, while the diffusion of water and dioleoylglycerol are much more rapid [of the order of 10^{-11} m^2 s^{-1} (Figure 2)]. It was concluded[94] that the reversed micelles contain mainly DOPC and the dioleoylglycerol merely plays the role of a solvent.

5 LATERAL DIFFUSION IN OTHER NONLAMELLAR LIQUID CRYSTALS

The translational diffusion of all three components has been measured in the ternary system DOPC/water/dodecane,[78] where dodecane induces an H_{II} phase. From a comparison between diffusion coefficients, it was concluded that dodecane resides between the water cylinders in the H_{II} phase.

Some lyotropic mesophases, called 'nematics', orient spontaneously in a strong magnetic field. Utilizing ultraviolet (UV) linear dichroism on a solubilized chromophore and PFG NMR on a nematic phase containing potassium dodecanoate, it was shown that this phase is built up of long rod-like micelles.[95,96]

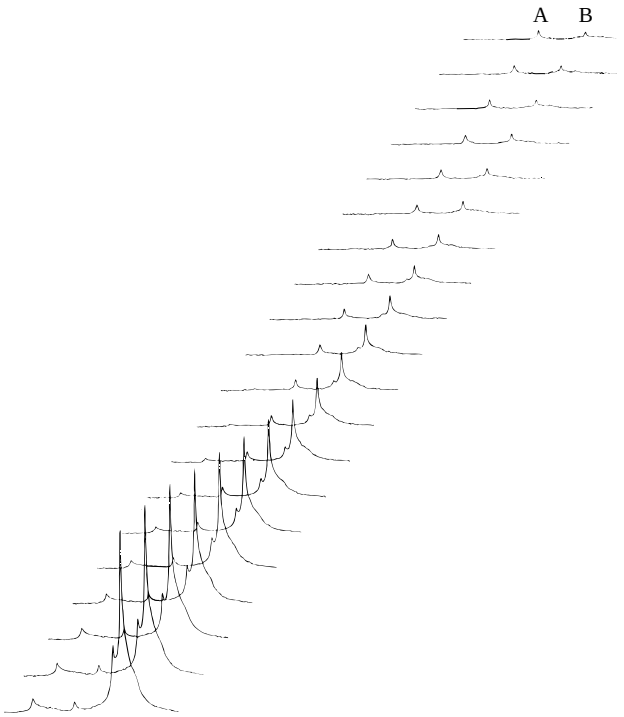

Figure 2 Stacked plot of spectra with increasing strength of the pulsed field gradient in a diffusion experiment performed on the system DOPC/1,2-dioleoylglycerol/^2H_2O (25.44/59.57/14.99) at 42 °C. The two peaks marked in the figure correspond to (A) CH_3 groups of the choline headgroup, and (B) terminal CH_3 groups of DOPC and 1,2-dioleoylglycerol. The diffusion coefficient of A is estimated to be 3×10^{-13} m^2 s^{-1}, while B shows two diffusion coefficients of 0.3×10^{-12} and 15×10^{-12} m^2 s^{-1}

The translational diffusion coefficient of the amphiphile was obtained from an aligned sample oriented at the magic angle. The surfactant diffusion along the rod was found to be $D_L = 5 \times 10^{-11}$ m^2 s^{-1} for potassium laurate and $D_L = 8 \times 10^{-11}$ m^2 s^{-1} for sodium decyl sulfate.[96] These values compare well with the lateral diffusion coefficients for the corresponding lamellar mesophases (Table 1). By means of the relationship $\langle x^2 \rangle = 2Dt$, the length can be estimated to be longer than 2000 nm.

6 RELATED ARTICLES

Amphiphilic Liquid Crystalline Samples: Nuclear Spin Relaxation; Bilayer Membranes: Deuterium and Carbon-13 NMR; Bilayer Membranes: Proton and Fluorine-19 NMR; Diffusion and Flow in Fluids; Diffusion Measurements by Magnetic Field Gradient Methods; Glycolipids; Lipid Polymorphism; Lyotropic Liquid Crystalline Samples; Membrane Lipids of Acholeplasma laidlawii; Phospholipid–Cholesterol Bilayers.

7 REFERENCES

1. G. Lindblom and L. Rilfors, *Biochim. Biophys. Acta*, 1989, **988**, 221.
2. G. Lindblom and H. Wennerström, *Biophys. Chem.*, 1977, **6**, 167.
3. P. T. Callaghan, *Principles of Nuclear Magnetic Resonance Microscopy*, Clarendon, Oxford, 1991.
4. G. Lindblom and H. Wennerström, *Magnetic Resonance of Biological Systems*, St Jovite, Quebec, 1976.
5. S. B. W. Roeder, E. E. Burnell, A.-L. Kuo, and C. G. Wade, *J. Chem. Phys.*, 1976, **64**, 1848.
6. H. Wennerström, *Chem. Phys. Lett.*, 1973, **18**, 41.
7. H. Wennerström and G. Lindblom, *Q. Rev. Biophys.*, 1977, **10**, 67.
8. D. M. Brink and G. R. Satchler, *Angular Momentum*, 3rd edn., Oxford University Press, Oxford, 1993.
9. A. L. Kuo and C. G. Wade, *Biochemistry*, 1979, **18**, 2300.
10. W.-G. Wu and C.-H. Huang, *Lipids*, 1981, **16**, 820.
11. G. Orädd, G. Wikander, G. Lindblom, and L. B.-Å. Johansson, *J. Chem. Soc., Faraday Trans. I*, 1994, **90**, 305.
12. P. O. Eriksson, G. Lindblom, and G. Arvidson, *J. Phys. Chem.*, 1987, **91**, 846.
13. L. Rilfors, P.-O. Eriksson, G. Arvidson, and G. Lindblom, *Biochemistry*, 1986, **25**, 7702.
14. Å. Wieslander, L. Rilfors, L. B.-Å. Johansson, and G. Lindblom, *Biochemistry*, 1981, **20**, 730.
15. G. Lindblom, I. Brentel, M. Sjölund, G. Wikander, and Å. Wieslander, *Biochemistry*, 1986, **25**, 7502.
16. G. Lindblom, L. B.-Å. Johansson, and G. Arvidson, *Biochemistry*, 1981, **20**, 2204.
17. P. van der Ploeg and H. J. C. Berendsen, *Mol. Physiol.*, 1983, **49**, 233.
18. O. Edholm and A. M. Nyberg, *Biophys. J.*, 1992, **63**, 1081.
19. R. M. Venable, Y. H. Zhang, B. J. Hardy, and R. W. Pastor, *Science*, 1993, **262**, 223.
20. M. R. Vist and J. H. Davis, *Biochemistry*, 1990, **29**, 451.
21. J. H. Ipsen, G. Karlström, O. G. Mouritsen, H. W. Wennerström, and M. J. Zuckermann, *Biochim. Biophys. Acta*, 1987, **905**, 162.
22. J. Ulmius, H. Wennerström, G. Lindblom, and G. Arvidson, *Biochim. Biophys. Acta*, 1975, **389**, 197.
23. G. W. Stockton and I. C. P. Smith, *Chem. Phys. Lipids*, 1976, **17**, 251.
24. E. Oldfield, M. Meadows, D. Rice, and R. Jacobs, *Biochemistry*, 1978, **17**, 2727.
25. G. Lindblom, N.-O. Persson, and G. Arvidson, *Adv. Chem. Ser.*, 1976, **152**, 121.
26. M. Silva-Crawford, B. C. Gerstein, A.-L. Kuo, and C. G. Wade, *J. Am. Chem. Soc.*, 1980, **102**, 3728.
27. R. T. Roberts, *Nature (London)*, 1973, **242**, 348.
28. J. Ulmius, G. Lindblom, H. Wennerström, L. B.-Å. Johansson, K. Fontell, O. Söderman, and G. Arvidson, *Biochemistry*, 1982, **21**, 1553.
29. G. Lindblom, H. Wennerström, and G. Arvidson, *Int. J. Quantum Chem.*, 1977, **XII** (Suppl. 2), 153.
30. J. F. Martin, L. S. Selwyn, R. R. Vold, and R. L. Vold, *J. Chem. Phys.*, 1982, **76**, 2632.
31. D. W. Larsen, J. G. Boylan, and B. R. Cole, *J. Phys. Chem.*, 1987, **91**, 5631.
32. T. Köchy and T. M. Bayerl, *Phys. Rev. E*, 1993, **47**, 2109.
33. J. F. Ellena, L. S. Lepore, and D. S. Cafiso, *J. Phys. Chem.*, 1993, **97**, 2952.
34. H. Wennerström, G. Lindblom, and B. Lindman, *Chem. Script.*, 1974, **6**, 97.
35. H. Wennerström, B. Lindman, O. Söderman, T. Drakenberg, and J. B. Rosenholm, *J. Am. Chem. Soc.*, 1979, **101**, 6860.
36. B. Halle and H. Wennerström, *J. Chem. Phys.*, 1981, **75**, 1928.

37. R. Blinc, K. Easwaran, J. Pirs, M. Volfan, and I. Zupancic, *Phys. Rev. Lett.*, 1970, **25**, 1327.
38. G. J. T. Tiddy, *J. Chem. Soc., Faraday Trans. I*, 1977, **73**, 1731.
39. P. T. Callaghan, M. A. Le Gros, and D. N. Pinder, *J. Chem. Phys.*, 1983, **79**, 6372.
40. P. O. Eriksson and G. Lindblom, *Springer Ser. Chem. Phys.*, 1980, **11**, 290.
41. H. Wennerström, B. Lindman, G. Lindblom, and G. J. T. Tiddy, *J. Chem. Soc., Faraday Trans. I*, 1979, **75**, 663.
42. G. Lindblom, L. Rilfors, J. B. Hauksson, I. Brentel, M. Sjölund, and B. Bergenståhl, *Biochemistry*, 1991, **30**, 10938.
43. A. R. Waldeck, A. J. Lennon, B. E. Chapman, and P. W. Kuchel, *J. Chem. Soc., Faraday Trans.*, 1993, **89**, 2807.
44. P. T. Callaghan and O. Söderman, *J. Phys. Chem.*, 1983, **87**, 1737.
45. L. Coppola, C. La Mesa, G. A. Ranieri, and M. Terenzi, *J. Chem. Phys.*, 1993, **98**, 5087.
46. G. Celebre, L. Coppola, and G. A. Ranieri, *J. Chem. Phys.*, 1992, **97**, 7781.
47. J. Chung and J. H. Prestegard, *J. Phys. Chem.*, 1993, **97**, 9837.
48. D. P. Siegel, *Chem. Phys. Lipids*, 1986, **42**, 279.
49. D. P. Siegel, *Biophys. J.*, 1993, **65**, 2124.
50. L. V. Chernomordik, G. B. Melikyan, and Y. A. Chizmadzhev, *Biochim. Biophys. Acta*, 1987, **906**, 309.
51. G. Lindblom, J. Hauksson, L. Rilfors, B. Bergenståhl, Å. Wieslander, and P.-O. Eriksson, *J. Biol. Chem.*, 1993, **268**, 16198.
52. L. Rilfors, Å. Wieslander, and G. Lindblom, in *Subcellular Biochemistry, Mycoplasma Cell Membranes*, eds. S. Rottem and I. Kahane, Plenum, New York, 1993.
53. L. Rilfors, J. Hauksson, and G. Lindblom, *Biochemistry*, 1994, **33**, 6110.
54. V. Luzzati, in *Biological Membranes*, ed. D. Chapman, Academic, New York, 1968.
55. P. Mariani, V. Luzzati, and H. Delacroix, *J. Mol. Biol.*, 1988, **204**, 165.
56. S. M. Gruner, P. R. Cullis, M. J. Hope, and C. P. S. Tilcock, *Ann. Rev. Biophys., Biophys. Chem.*, 1985, **14**, 211.
57. M. W. Tate, E. F. Eikenberry, D. C. Turner, E. Shyamsunder, and S. M. Gruner, *Chem. Phys. Lipids*, 1991, **57**, 147.
58. J. E. Tanner and E. O. Stejskal, *J. Chem. Phys.*, 1968, **49**, 1768.
59. J. Charvolin and P. Rigny, *J. Chem. Phys.*, 1973, **58**, 3999.
60. T. Bull and B. Lindman, *Mol. Cryst. Liquid Cryst.*, 1974, **28**, 155.
61. G. Lindblom, H. Wennerström, G. Arvidson, and B. Lindman, *Biophys. J.*, 1976, **16**, 1287.
62. G. Lindblom, K. Larsson, L. Johansson, K. Fontell, and S. Forsén, *J. Am. Chem. Soc.*, 1979, **101**, 5465.
63. L. E. Scriven, *Nature*, 1976, **263**, 123.
64. D. M. Anderson, S. M. Gruner, and S. Leibler, *Proc. Natl. Acad. Sci. USA*, 1988, **85**, 5364.
65. S. Andersson, S. T. Hyde, K. Larsson, and S. Lidin, *Chem. Rev.*, 1988, **88**, 221.
66. D. M. Anderson and H. Wennerström, *J. Phys. Chem.*, 1990, **94**, 8683.
67. E. S. Lutton, *J. Am. Oil Chem. Soc.*, 1965, **42**, 1068.
68. K. Larsson, K. Gabrielsson, and B. Lundberg, *J. Sci. Food Agric.*, 1978, **29**, 909.
69. B. Ericsson, K. Larsson, and K. Fontell, *Biochim. Biophys. Acta*, 1983, **729**, 23.
70. H. Gutman, G. Arvidson, K. Fontell, and G. Lindblom, in *Surfactants in Solutions*, eds. K. L. Mittal and B. Lindman, Plenum, New York, 1984, Vol. 1, p. 143.
71. B. Ericsson, P. O. Eriksson, J. E. Löfroth, and S. Engstrom, *ACS Symp. Ser.*, 1991, **469**, 251.
72. P. O. Eriksson and G. Lindblom, *Biophys. J.*, 1993, **64**, 129.
73. W. Longley and T. J. McIntosh, *Nature*, 1983, **303**, 612.
74. A. J. Verkleij, C. Mombers, J. Leunissen-Bijvelt, and P. H. J. T. Ververgaert, *Nature*, 1979, **279**, 162.
75. P.-O. Eriksson, A. Khan, and G. Lindblom, *J. Phys. Chem.*, 1982, **86**, 387.
76. L. Rilfors, A. Khan, I. Brentel, Å. Wieslander, and G. Lindblom, *FEBS Lett.*, 1982, **149**, 293.
77. I. Brentel, E. Selstam, and G. Lindblom, *Biochem. Biophys. Acta*, 1985, **812**, 816.
78. M. Sjölund, G. Lindblom, L. Rilfors, and G. Arvidson, *Biophys. J.*, 1987, **52**, 145.
79. J. P. Conroy, C. Hall, C. A. Leng, K. Rendall, G. J. T. Tiddy, J. Walsh, and G. Lindblom, *Prog. Colloid Polym. Sci.*, 1990, **82**, 253.
80. G. Orädd, G. Lindblom, L. B.-Å. Johansson, and G. Wikander, *J. Phys. Chem.*, 1992, **96**, 5170.
81. K. Fontell, *Adv. Colloid Interface Sci.*, 1992, **41**, 127.
82. K. Fontell, K. K. Fox, and E. Hansson, *Mol. Cryst. Liquid Cryst.*, 1985, **1**, 9.
83. P.-O. Eriksson, G. Lindblom, and G. Arvidson, *J. Phys. Chem.*, 1985, **89**, 1050.
84. G. Lindblom, L. B.-Å. Johansson, G. Wikander, P.-O. Eriksson, and G. Arvidson, *Biophys. J.*, 1992, **63**, 723.
85. A. Tardieu and V. Luzzati, *Biochim. Biophys. Acta*, 1970, **219**, 11.
86. R. Vargas, P. Mariani, A. Gulik, and V. Luzzati, *J. Mol. Biol.*, 1992, **225**, 137.
87. H. Delacroix, T. Gulik-Krzywicki, P. Mariani, and V. Luzzati, *J. Mol. Biol.*, 1993, **229**, 526.
88. P.-O. Eriksson, L. Rilfors, G. Lindblom, and G. Arvidson, *Chem. Phys. Lipids*, 1985, **37**, 357.
89. O. Söderman, H. Walderhaug, U. Henriksson, and P. Stilbs, *J. Phys. Chem.*, 1985, **89**, 3693.
90. O. Söderman and U. Henriksson, *J. Chem. Soc., Faraday Trans. I*, 1987, **83**, 1515.
91. L. B.-Å. Johansson and O. Söderman, *J. Phys. Chem.*, 1987, **91**, 5275.
92. J. M. Seddon, E. A. Bartle, and J. Mingins, *J. Phys. Condens. Matter.*, 1990, **2**, 285.
93. V. Luzzati, R. Vargas, A. Gulik, P. Mariani, J. Seddon, and E. Rivas, *Biochemistry*, 1992, **31**, 279.
94. G. Orädd, G. Lindblom, K. Fontell, and H. Ljusberg-Warren, *Biophys. J.*, 1995, **68**, 1856.
95. O. Söderman, G. Lindblom, L. B.-Å. Johansson, and K. Fontell, *Mol. Cryst. Liquid Cryst.*, 1980, **59**,
96. L. B.-Å. Johansson, O. Söderman, K. Fontell, and G. Lindblom, *J. Phys. Chem.*, 1981, **85**, 3694.
97. G. Lindblom, *Acta Chem. Scand. B*, 1981, **35**, 61.
98. L. Rilfors, G. Lindblom, Å. Wieslander, and A. Christiansson, in *Biomembranes*, eds. L. A. Manson and M. Kates, Plenum, New York, 1984, Vol. 12, p. 205.

Biographical Sketch

Göran Lindblom. *b* 1942. M.S., 1969, Ph.D., 1974, Lund, Sweden. Introduced to NMR by S. Forsén, Lund University. Professor in Physical Chemistry, University of Umeå, 1981-present. Approx. 150

publications. Research interests: structure, dynamics and function of biological membranes; physicochemical properties and structure of lyotropic liquid crystals.

Greger Orädd. *b* 1961. M.S. 1989, Ph.D., 1994, Umeå, Sweden. Introduced to NMR by G. Lindblom. Five publications. Research interests: application of NMR diffusion methods to liquid crystals.

Rheo-NMR: A New Window on the Rheology of Complex Fluids

Paul T. Callaghan

Victoria University of Wellington, Wellington, New Zealand

1 Introduction 1
2 Micro-Imaging and NMR Velocimetry 2
3 Applications of Rheo-NMR 4
4 Conclusions 12
5 References 13

1 INTRODUCTION

Over the past decade, NMR has made a significant impact in chemical engineering, where it is being extensively used for the non-invasive study of dispersion and flow in porous media. Now it is finding effective use in the study of the mechanical properties of complex fluids. At the heart of that development is the dual capacity of NMR to provide information at the microscopic level regarding molecular organization and dynamics, and at the macroscopic level regarding the local rate of fluid deformation. It is the combination of the various tools of NMR spectroscopy with those of NMR imaging, and velocimetry that makes this dualism possible.

1.1 Complex Fluids and Rheology

We tend to think of condensed matter as sub-dividing into the two basic phases of solid and liquid. When subjected to a stress a solid will deform by a fixed amount and store energy elastically whereas a liquid flows and dissipates energy continuously in viscous losses. But many interesting materials in their condensed phase possess both solid and liquid-like properties. These include polymer melts and solutions, lyotropic and thermotropic liquid crystals, micellar surfactant phases, colloidal suspensions and emulsions. Most biological fluids, most food materials and many fluids important in industrial processing or engineering applications exhibit such complexity. Complex fluids manifest both an elastic and a viscous response, and they generally possess 'memory', which means that the stress which they exhibit at any moment will depend on their history of prior deformation. They tend to exhibit non-linear mechanical behavior, which means that their mechanical properties may change as the deformation increases, an effect that is generally attributed to molecular reorganization. And they invariably possess a wide range of characteristic time scales, from the rapid (ps to ns) local Brownian motion of small molecules or molecular segments, to the very slow (ms to s) motions associated with the reorganization or reorientation of large molecular assemblies or macromolecules. The study of the mechanical properties of complex fluids is known as 'rheology',[1] a name which derives from the Greek word 'rheo' which means 'to flow'.

Traditionally, rheology was a subject concerned principally with mechanical properties. Recently however attention has focused on trying to determine the molecular basis of complex mechanical properties. If we can better understand this basis then we can better design desirable fluidic properties, we can better process modern materials based on polymers and organized molecular states, we can better produce foods of the right texture, and we can better understand how nature works, for example in the way synovial fluid protects our joints, or in the way a spider can extrude a protein silk whose strength surpasses that of steel.

The interest in the molecular-mechanical link has led to the amalgamation of a number of spectroscopic and rheological techniques in which a flow or deformation cell is incorporated within the spectrometer detection system. Examples include the use of neutron scattering,[2] light scattering,[3] birefringence and dichroism techniques.[4,5] The most recent addition, NMR, has provided a number of new and valuable features. For example, it can be used to study materials which are optically opaque. The imaging capability of NMR means that it can be used to measure local velocity profiles and molecular densities directly. The wide-ranging spectroscopic tools available to NMR also make it possible to measure molecular order and dynamics.

1.2 History of Rheo-NMR

The earliest suggestion of the use of NMR methods to measure rheological properties was by Martins et al., in 1986.[6] These authors pointed out that physically reorienting a sample of a nematic liquid crystal inside the NMR magnet would lead to a slow evolution of the spectrum during subsequent director realignment, interpretation of which could yield information about rotational visco-elasticity. This first type of Rheo-NMR method was later applied by Goncalves et al.,[7] who used proton NMR spectra to monitor the magnetic field reorientation of an initially aligned sample of a nematic polymer liquid crystal, following the sudden physical rotation. By carefully fitting these spectra, rotational (Leslie) viscosities were calculated along with elastic constants associated with defect formation.

In 1990, Nakatani, Polliks and Samulski[8] described a quite different Rheo-NMR experiment in which the proton NMR spectrum of a polymer melt was investigated under shear. They acquired their signal from a 100 kD polydimethylsiloxane sample which was contained in the gap of a cone-and-plate cell located in the NMR electromagnet, and in which the cone was driven to produce a shear rate of $4\,s^{-1}$. In this experiment the proton NMR spectrum broadened under shear and slowly relaxed once shearing ceased. In 1991, another approach to Rheo-NMR was reported by Xia and Callaghan (1991)[9] who showed that NMR microscopy could be used to measure shear-thinning effects in the semi-dilute solution of a high molecular weight polymer, in particular by observing the deviation from Poiseuille flow apparent when

the fluid was pumped through a narrow (700 μm diameter) pipe. Then, in 1994, Grabowski and Schmidt[10] demonstrated the use of the deuterium quadrupole interaction to investigate molecular order in studying the alignment of nematic liquid crystalline directors under shear, finding the equilibrium angle in the competition between the magnetic torque and the shear. This type of experiment proved able to yield the ratio of specific Leslie viscosities to the magnetic anisotropy. A detailed review of the science of Rheo-NMR can be found in a recent chapter[11] in *Reports on Progress in Physics*. Here we will outline the basic principles, and give a few examples.

1.3 Heterogeneity and the Need for Spatial Localization

In rheological measurements a material is subject to deformation and the stress, $\sigma(t)$, is monitored as a function of the time dependent strain, $\gamma(t)$. Such measurements require the deformation of fluid under the influence of relative motion of the fluid with respect to containment surfaces, the source of the externally applied stress. A simple example is that of pipe flow, where a velocity gradient exists between the wall, at which the fluid is stationary, and the center of the pipe, at which the fluid velocity is a maximum. Alternatively, the fluid may be held in a cell whose containment surfaces themselves move, generally in rotation and under the influence of an externally applied torque. Typical geometries used for this purpose are the cone-and-plate cell, the concentric cylindrical Couette cell, and the four roll mill. A feature of all these systems is that the flow is heterogeneous, although in the case of the cone-and-plate, the stress, and hence the velocity gradient may be expected to be uniform. However, even where the stress is uniform, some classes of fluids will exhibit heterogeneous shearing.

One of the great advantages of NMR is that it may be used to image the velocity field within a rheological cell, thus providing non-invasive insight concerning the exact nature of deformational flow. The key to this approach is the use of NMR imaging, and in particular, imaging at microscopic resolution, since the containment cells are often of mm length scale. However, even where velocimetry is not the primary aim of the experiment, and one instead wishes to examine molecular properties via NMR spectroscopy, the heterogeneous nature of many flows dictate that one spatially localizes the acquired spectrum. In consequence the selective excitation or spectroscopic imaging methods of NMR microscopy[12] are demanded. Because of these factors, Rheo-NMR often requires a dual focus on NMR microscopy and NMR spectroscopy, the former giving insight at the mechanical length scale and the latter at the molecular length scale.

2 MICRO-IMAGING AND NMR VELOCIMETRY

2.1 Encoding for Position and Displacement

The basic principles governing NMR microscopy have been described in detail elsewhere.[12] A spin at position **r**, in the presence of a magnetic field gradient, **G**, will experience an additional local spin precession frequency, $\gamma\mathbf{G}.\mathbf{r}$, thus acquiring a phase $\exp(i\mathbf{k}.\mathbf{r})$, **k** being the reciprocal space dimension conjugate to **r** and given by $\gamma\mathbf{G}t$, where t is the evolution time. The nuclear spin density can be reconstructed by acquiring the complete signal over some appropriate volume of **k** space and performing an inverse Fourier transformation, generally, in two dimensions using a plane of spins prepared by a frequency-selective excitation. The high spatial resolution needed for NMR microscopy depends on the use of large polarizing field ($\geq$5 T), small receiver coils of high sensitivity and gradient coils capable of delivering in excess of 20 G cm^{-1}.

In order to image velocity we further encode the signal with a Pulsed Gradient Spin Echo (PGSE) pair.[13,14] These pulses define a second wave vector domain, **q**, and impart a phase shift to the spins which depends directly on the motion of their parent molecules. In particular a spin moving by $\mathbf{R} = \mathbf{r}' - \mathbf{r}$ over the time Δ between the PGSE pulse pair acquires a phase factor $\exp[i\mathbf{q}.\mathbf{R}]$. This contrast factor means that the signal acquired is effectively modulated both in **k**- and **q**-space. Double inverse Fourier transformation of the signal with respect to both **k** and **q** returns the local spin density $\rho(\mathbf{r})$ as well as the function, $\overline{P_s}(\mathbf{R}, \Delta)$, which describes the ensemble distribution of molecular displacements for that location. Image analysis software[14] can be used to automatically process these distributions, using the width to

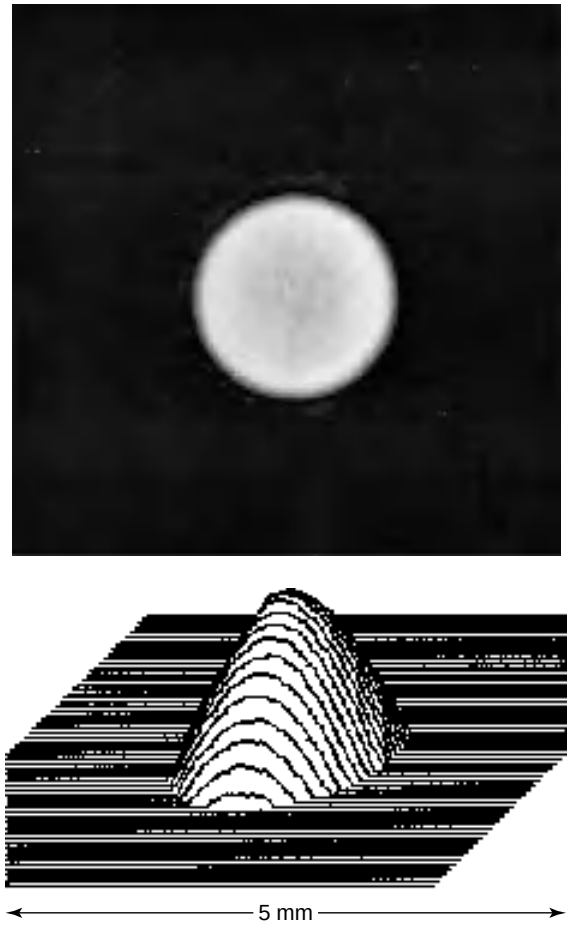

Figure 1 NMR proton density image obtained at 60 MHz from a 1.9 mm ID capillary in which a surfactant solution is flowing. Also shown is a velocity map from the same capillary displayed as a stacked profile plot

estimate the rms Brownian motion $(2D_s\Delta)^{1/2}$ and the mean displacement to estimate the flow. In this manner maps of $D_s(\mathbf{r})$ and $v(\mathbf{r})$ may be constructed. While the method depends on steady state flow conditions in the sample (a typical image will take several minutes to acquire), it does have the advantage of returning accurate and precise velocity maps. The sensitivity of the method is very high, enabling velocity resolution on the order of $10\,\mu m\,s^{-1}$. Figure 1 shows an image of the Poiseuille velocity field for fluid in laminar flow in a capillary.

2.2 Rheo-NMR Devices

Pipe flow methods, while suitable for fluids of low viscosity, have limited use for soft solids or highly viscous liquids where excessive pressure gradients may be needed to maintain the flow. Furthermore pipe flow suffers from the need to provide a sufficient volume of fluid to maintain an inlet reservoir. For viscous materials and for systems where only a small (<1 g) quantity of fluid is available, it is necessary to use containment cells such as the cone-and-plate, cylindrical Couette, four roll mill and bi-axial extension cell. Figure 2 shows examples of such cells which fit within the rf coils of an NMR micro-imaging probehead.[15] All of these deformational flow devices can be driven by a drive shaft which sits in the bore of the magnet and which is turned by a stepper-motor gearbox assembly mounted above the magnet bore.

2.3 Spatially Localized Spectroscopy

In order to acquire an NMR spectrum from a selected region of a sample it is necessary to use one of two methods. In the first, known as spectroscopic imaging, the spectral property is independently encoded in an imaging experiment so that the spectrum can be reconstructed at every position. In the second, known as localized NMR spectroscopy, a frequency-selective RF pulse is applied in the presence of a magnetic field gradient, so that only spins from a desired region of the sample participate in the NMR spectrum. The former approach is comprehensive but time consuming while the latter approach is the most efficient when the region from which the spectrum is desired is known in advance. Such localized spectroscopy is extensively used in biomedical magnetic resonance, where a wide variety of excitation methods are successfully employed.[16,17] One very effective spatial localization method is the composite soft/hard pulse 'selective storage' proposed by Post et al.[18] and first implemented by Aue et al.[19] This so-called 'split-sinc selective storage' consists of a $\pi/2$ non-selective pulse sandwiched between the leading and trailing halves of a $\pi/2$ sinc pulse of opposite phase. The relevant pulse sequence is shown in Figure 3. One of the advantages of this approach is that the desired slice magnetization is stored along the z-axis for later recall, while undesired magnetization is destroyed, thus making the method suitable as a 'front end' on any NMR sequence of interest. One such sequence might be a standard imaging routine (Figure 3a), so that it is possible to inspect and direct the chosen slice as required. Another advantage is the desired spins spend very little time in the transverse plane during the excitation process and thus suffer little T_2 relaxation. The stored z-magnetization is subject only to the much less severe effects of longitudinal relaxation. An example of selective storage used for spectroscopy is shown in Figure 3(b) where a spin echo is used to encode in both the evolution (t_1) and acquisition (t_2) domains.

Figure 4 shows an application[20] of the selective storage sequence shown in Figure 3, in order to deliver magnetization from a selected slice across a cylindrical Couette cell. In the present instance, that magnetization is subsequently spatially encoding to produce the image shown. Having confirmed that this slice is as desired, the same excitation is then used as a precursor to a spectroscopy experiment in which the deuteron quadrupole interaction is measured. This experiment is discussed further in Section 3.3.

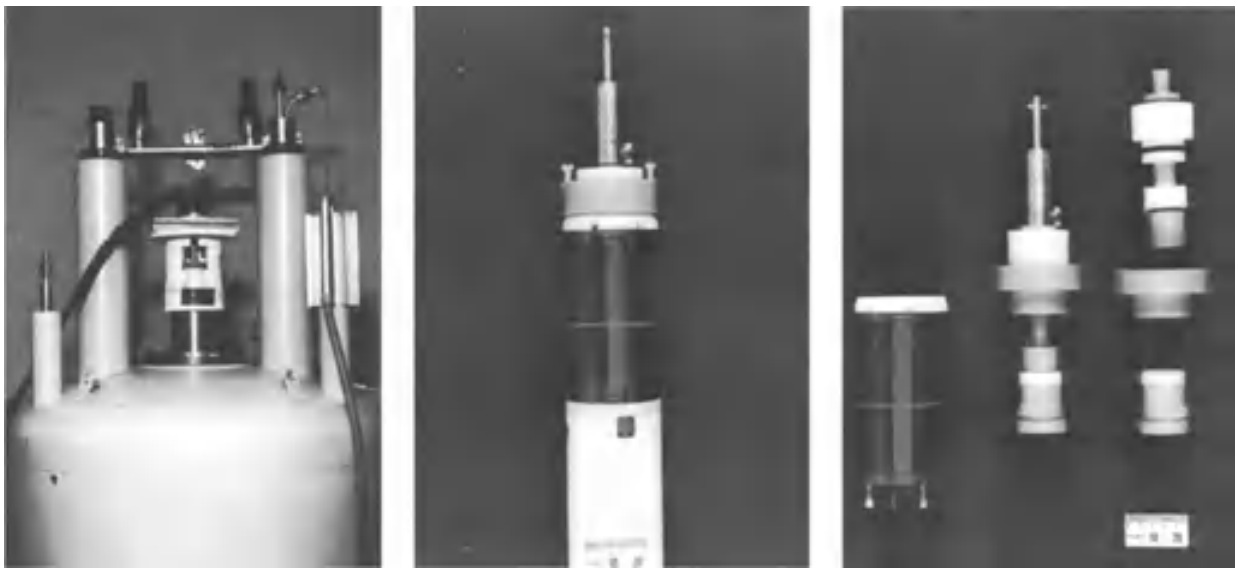

(a) (b) (c) Cone-and-plate assembly

Figure 2 (a) Superconducting standard widebore magnet with motor, driving shaft, (b) microimaging probehead and (c) cone-and-plate, rheometric device

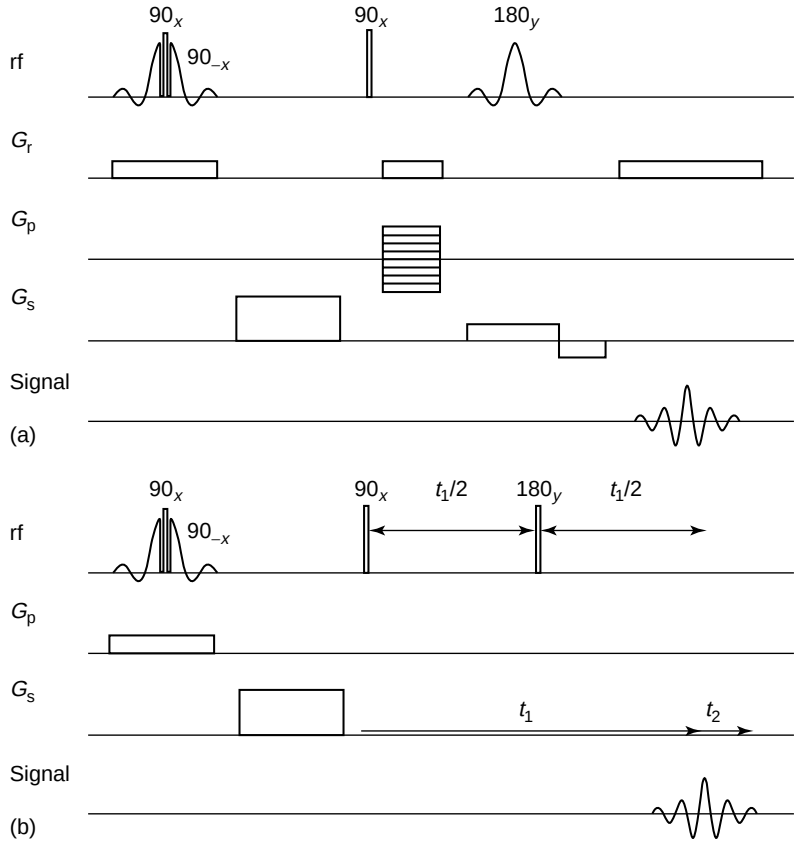

Figure 3 Pulse sequences[20] showing two applications of the selective storage cluster followed by (a) an imaging module and (b) a two-dimensional spectroscopy module. G_p, G_r and G_s are respectively the phase, read and slice gradients. The spoiler gradient shown here is applied along z, however it may equally be applied in any (or all) of the three orthogonal directions following the z-storage

3 APPLICATIONS OF RHEO-NMR

3.1 Heterogeneous Flow and Shear Banding

One important class of rheological measurement concerns the large strain response known as the 'flow curve' for which the stress is measured as a function of the rate of strain, $\dot{\gamma} = \partial\gamma/\partial t$, in a steady state shearing flow. Figure 5(a) shows examples of flow curves for different classes of materials, including Newtonian, shear thinning, shear thickening, and fluids exhibiting a yield stress.[1] The principal rheometric device for such measurement, the small angle cone-and-plate, is shown in Figure 5(b). In this device the stress is almost uniform, varying weakly as $\mathrm{cosec}^4\theta$ between the bottom plate ($\theta = 90°$) and the cone ($\theta = 90° - \alpha$) where α is the cone angle, typically less than 10°. The strain rate $\dot{\gamma} = \partial v_x/\partial y$ is assumed to be highly uniform since both the cone tangential velocity, v_x, and the gap are proportion to the local radius.

One of the most significant contributions of Rheo-NMR has been to show that the uniform shear-rate assumption may be violated in the case of certain classes of fluids in which pathological flow properties are exhibited. Figure 6 shows velocity maps and associated shear-rate maps[21] obtained for the wormlike surfactant system, cetylpyridinium chloride/sodium salicylate in water. While the velocity gradients show no deviation from uniformity at very low shear rates, above a certain critical value $\dot{\gamma}_c$ we observe a dramatic variation in the rate-of-strain across the 6° cone gap in which a very high shear rate band exists at mid-gap (i.e., fixed angle $\theta \approx 90° - \alpha/2$) and independent of radius.

This shear banding phenomena explains the plateau in the flow curve. In the reptation reaction model of Cates,[22] the wormlike micelle system is predicted to exhibit a constitutive behavior as shown schematically in Figure 7 where the region of decreasing stress as the shear rate increases finds its origin in the reduction in entanglements as the worm chains align in the flow. This section of the flow curve is associated with unstable flow. Cates et al.[23] have suggested that because of the instability beyond the shear rate corresponding to the stress maximum, σ_c, in the schematic flow curve, separation of distinct shear bands may occur, in the manner of a first order phase separation. These bands will be associated with the intersections of a coexistence stress tie line with the upper and lower branches of the underlying flow curve and the proportions of each band will be as required to satisfy the average shear rate. That the NMR results are consistent with this picture is clear in Figure 8 where a series of profiles show that as the gap apparent shear rate is increased, the high shear rate band expands in width at approximately constant maximum shear rate rate.

Shear banding effects have apparently been seen in these materials via optical birefringence.[24,25] Birefringence effects are associated with anisotropic molecular alignment[26] and, as a consequence, the flow instability of the wormlike micelles have been associated with the onset of molecular ordering. NMR is also capable of investigating order and alignment

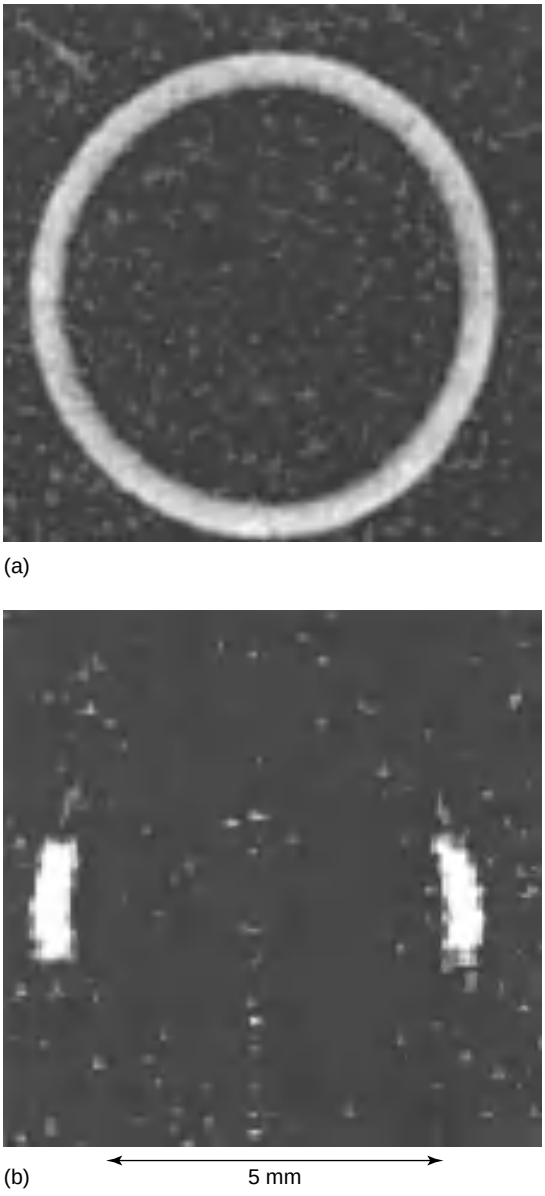

Figure 4 (a) NMR image[36] obtained from protons at 300 MHz of a Couette cell containing the polymer PDMS in the 0.5 mm annular gap and (b) image of the same cell obtained following the selective storage sequence shown in Figure 3(a)

through utilizing inter-nuclear dipole interactions or nuclear quadrupole interactions. It is through the use of such spectroscopic approaches that Rheo-NMR holds the promise of further linking mechanical and molecular properties.

3.2 Nematic Ordering under Shear

By the use of deuteron labeling, it is possible to employ the deuteron quadrupole interaction to measure local order, since this interaction results in a two line NMR spectrum in which the splitting is proportional to the local order parameter, and to the alignment with respect to the magnetic field via the second rank Legendre Polynomial, $P_2(\cos\theta) = (3\cos^2\theta - 1)/2$.

We have used quadrupole interaction spectroscopy, along with spectroscopic imaging, to investigate[27] shear banding in a wormlike micelle system in which birefringence banding had been observed (20% CTAB/D_2O at 41 °C). Figure 9 shows the D_2O ^2H NMR spectrum plotted as a function of radial position across the gap of a cylindrical Couette cell where the magnetic field is aligned with the vorticity axis. At the inner wall, where the stress is highest, a splitting is observed, indicative of a finite quadrupole interaction, while at the outer wall a single peak is observed. This data suggest the formation of a nematic phase at high stress and the transition to an isotropic phase, through a mixed phase region, at the region of low stress. What is particularly interesting about this experiment is that the associated velocity profile shows a banding in the shear rate which does not correlate simply with the local order parameters seen in the ^2H NMR spectra, indicating that the molecular ordering is associated with the monotonically varying stress, rather than the discontinuously varying rate of strain. The example provides valuable new insight regarding the origin of shear banding in systems close to an isotropic/nematic phase transition.

3.3 Shear-induced Director Rotation

Nematic liquid crystals under shear stress experience not only deformational flow but also director reorientation.[28–31] This process involves at least three independent rotational viscosities when describing the linear viscous response. In addition, the shear deformation results in the formation of complex defect structure which are governed by Frank elasticity effects[32] associated with director splay bend and twist. This defect structure is crucial to any understanding of the nonlinear visco-elasticity of liquid crystals. A nice description of the linear viscous response is given by the theoretical treatment of Leslie and Ericksen,[28–31] who derived constitutive relations involving six independent coefficients, μ_n. In this theory the Frank elasticity is ignored. A detailed description of Leslie-Ericksen theory is beyond the scope of this review and can be found elsewhere.[33]

In the context of Rheo-NMR, such nematic systems, which have intrinsic diamagnetic anisotropy, experience in addition a torque due to the magnetic field. Thus any deformation in the director field due to externally applied stress results in a competitive reorientation process. Two types of experiment involving such have been reported. The first is that performed by Martins and co-workers,[6,7] who rapidly rotated a sample of a nematic liquid crystal which had been previously aligned in the magnetic field. In a variety of experiments the subsequent relaxation of the director field back to equilibrium was monitored via the use of both proton and deuterium NMR. In the second type of experiment due to Schmidt and co-workers,[10,34] a nematic system has been continuously sheared in a cone-and-plate cell and the equilibrium direction orientation measured by use of the deuterium quadrupole interaction. The classes of material studied in this manner were thermotropic side-chain liquid crystal polymers, materials which present Leslie viscosities sufficiently large that significant alignment is possible at quite low shear rates, on the order of $1\,s^{-1}$. The rheometer used in these experiments incorporates a bottom plate which is free to rotate against a torsion spring, so that observation of the angular displacement gives a measure of the applied torque, and hence the stress applied to the fluid in the gap. As a consequence this Rheo-NMR device

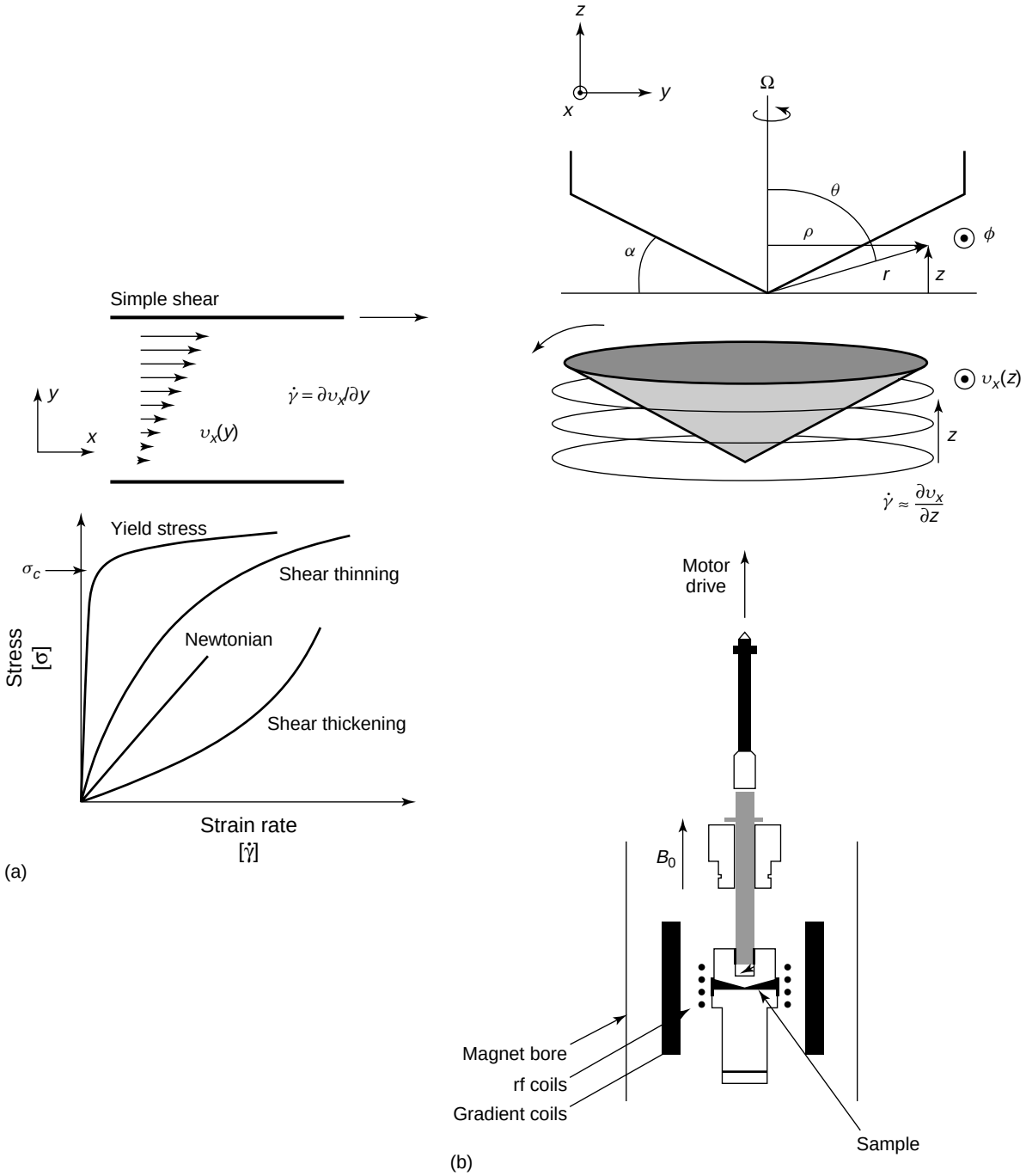

Figure 5 (a) Schematic diagram of simple shear geometry and associated flow curves. (b) Cone-and-plate cell used to produce uniform stress and shear rate conditions along with the cone-and-plate Rheo-NMR device

allows additionally for simultaneous measurement for shear viscosity.

The steady-shear flow behavior of these nematic materials in the presence of a magnetic field, B_0, is nicely described using the Leslie-Ericksen theory. Under a shear rate $\dot{\gamma}$ the director settles at an equilibrium angle to the magnetic field given by[34]

$$\tan\theta = \mp\frac{\chi_a B_0^2}{2\mu_0|\mu_3|\dot{\gamma}} \pm \sqrt{\left(\frac{\chi_a B_0^2}{2\mu_0|\mu_3|\dot{\gamma}}\right)^2 \pm \frac{|\mu_2|}{|\mu_3|}} \qquad (1)$$

where μ_2 and μ_3 are Leslie coefficients, and χ_a is the anisotropic part of the diamagnetic susceptibility tensor. The positive sign in the equation corresponds to a flow aligning ($\mu_2/\mu_3 > 0$) nematic while the negative to a tumbling ($\mu_2/\mu_3 < 0$) nematic. For a flow aligning system a stable angle is found for all shear rates, while for a tumbling nematic, a stable angle exists provided that $\dot{\gamma}$ is sufficiently small that the term inside the square root sign is positive.

Siebert et al. have demonstrated these effects in an experiment on two different nematic systems.[34] The 'flow-aligning' system was a nematic side-chain polysiloxane obtained

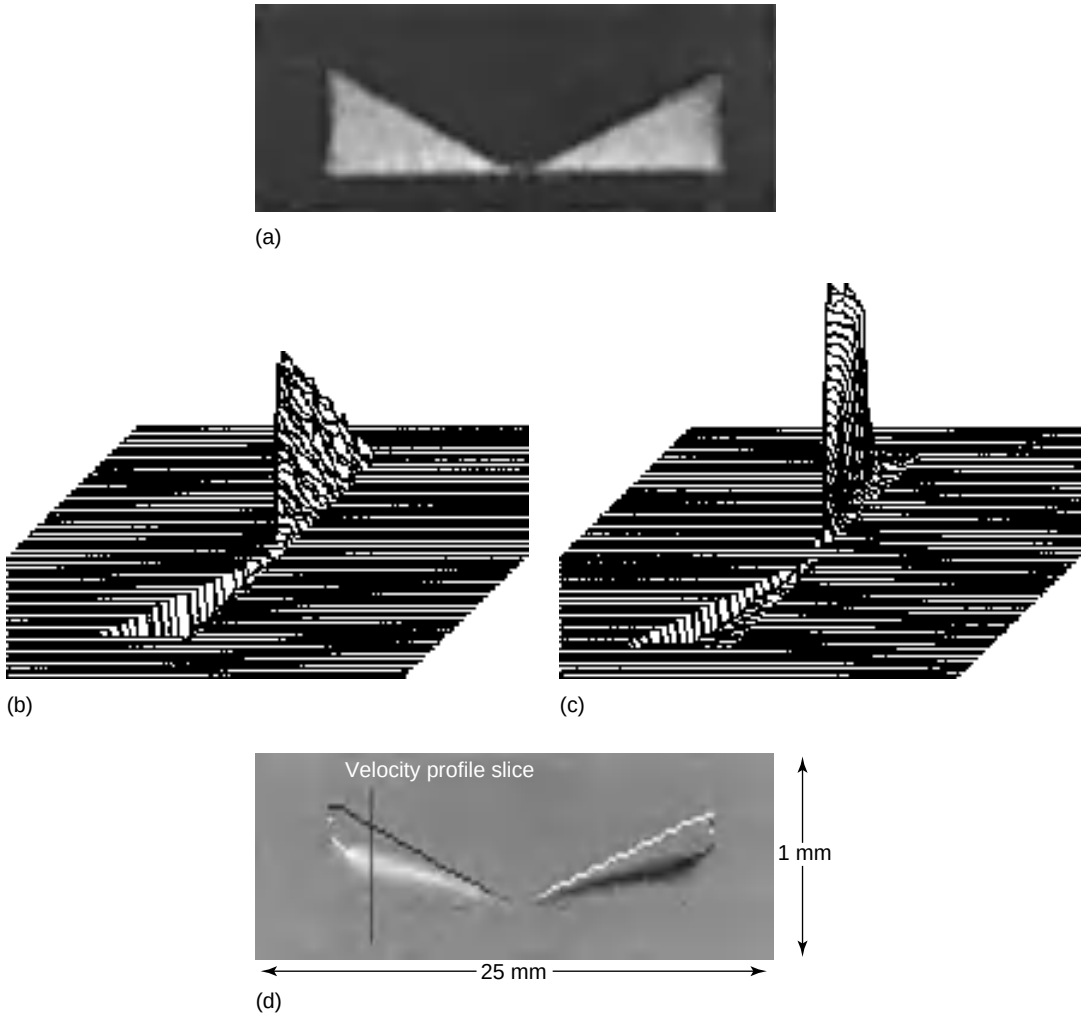

Figure 6 (a) Proton density image obtained at 300 MHz for for cetylpyridinium chloride/NaSal wormlike micelle solution in a 7° cone-and-plate cell (horizontal field of view 25 mm with vertical magnification expanded by a factor of 6). Data taken from Reference[21]. (b) Stacked profile plot showing velocity distribution across the gap at an apparent shear rate of $1.5\,s^{-1}$. (c) As for (b) but for $16\,s^{-1}$. (d) Image of shear rate distribution for cetylpyridinium chloride/NaSal wormlike micelle solution at an apparent shear rate, $\omega/\tan\alpha$ of $16\,s^{-1}$, well beyond the critical shear rate and in an unstable region of the flow curve. Experimental shear rate profiles are taken along a line of approximately fixed radius as shown

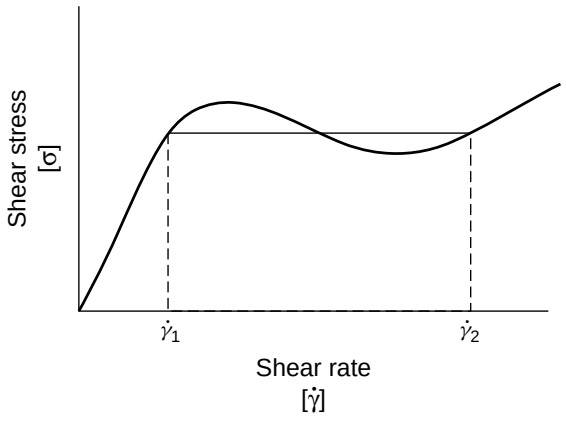

Figure 7 Schematic flow curve for a fluid exhibiting double-valued stress vs rate-of-strain behavior. In the phase separation model for shear banding,[23] $\dot{\gamma}_1$ and $\dot{\gamma}_2$ correspond to coexisting shear rates at a single stress value

by the addition of 2,3,5,6-tetradeuterio-4-methoxyphenyl-4′-butenyloxybezoate to poly(hydrogen methyl siloxane), a material with a glass transition temperature of 4 °C and a clearing point of 97 °C. The experiment was performed at 75 °C and deuterium NMR spectra were acquired at 46 MHz for a range of shear rates. These spectra are used to obtain the angle θ from the quadrupole splitting $\Delta\nu = AP_2(\cos\theta)$, the constant A being determined from the splitting at zero shear. The splittings form an asymptote with increasing shear rate at a θ value of around 70°. This angle, associated as it is with the dominance of mechanical torque over magnetic torque, corresponds to the alignment angle which would occur at all shear rates in the case of zero magnetic field.

The tumbling system was a mixture of 65% (w/w) poly{4-[4-(4-methoxyphenylazo)phenoxl]butylmethacrylate} in 4-trideuterio-methoxybenzoic acid-[4-*n*-hexoxyphenylester]. Corresponding spectra for three different temperatures were obtained in this system and, once again, a shear-rate dependent angle θ was found associated with the competition between

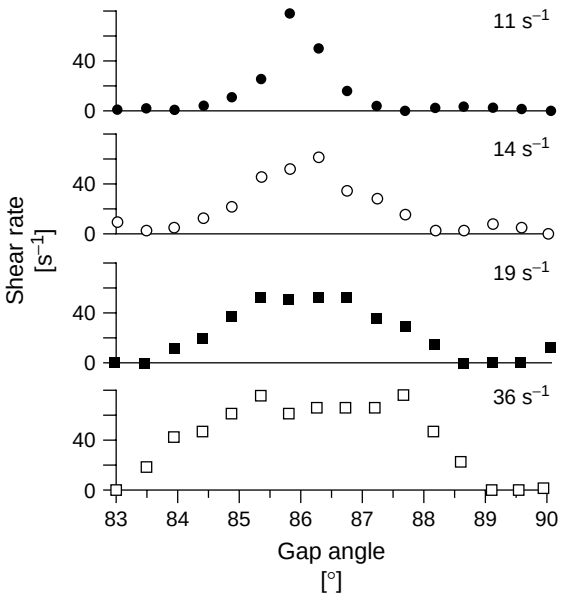

Figure 8 Measured shear rate profiles[21] from for cetylpyridinium chloride/NaSal wormlike micelle solution along a line of approximately fixed radius (as shown in Figure 6) for the 7° cone-and-plate data of Figure 6, for $11\,s^{-1}$, $14\,s^{-1}$, $19\,s^{-1}$ and $36\,s^{-1}$

the magnetic and mechanical torques. At shear rates beyond $\theta \approx 50°$, no splitting could be found, a result consistent with the onset of director tumbling.

Figure 10 shows the respective alignment angles as a function of shear rates along with fits to the data using equation (1). In the case of the two different materials, opposite signs for μ_2 and μ_3 were necessary in order to reproduce the observed curvature of the data, confirming the respective flow aligning and tumbling character of the different polymer liquid crystals.

3.4 Shear-induced Deformation in Polymers

3.4.1 Measurement of Segmental Alignment

Another intriguing correlation between shearing and molecular conformation has been investigated by Rheo-NMR. When a random coil polymer melt is subjected to shear, the polymer chain suffers a bi-axial deformation in which the principal axis of extension has a preferred orientation with respect to the hydrodynamic velocity direction.[26] The geometry is as indicated in Figure 11. As a result of the deformation, the chain entropy is reduced, leading to an increase in the Free Energy, the basis of the elastic response of the polymer melt.

The deformation may be usefully described by means of the averaged segmental alignment tensor[26]

$$S_{\alpha\beta}(t) = \left\langle \int_0^L ds u_\alpha(s,t) u_\beta(s,t) - \frac{1}{3}\delta_{\alpha\beta} \right\rangle \qquad (2)$$

where $\langle \ldots \rangle$ represents the ensemble average and the integral is taken over the curvilinear path of **s** chain segments along the chain length L. In the Doi-Edwards formulation of entangled polymer dynamics[26,35] the stress tensor $\sigma_{\alpha\beta}$ is

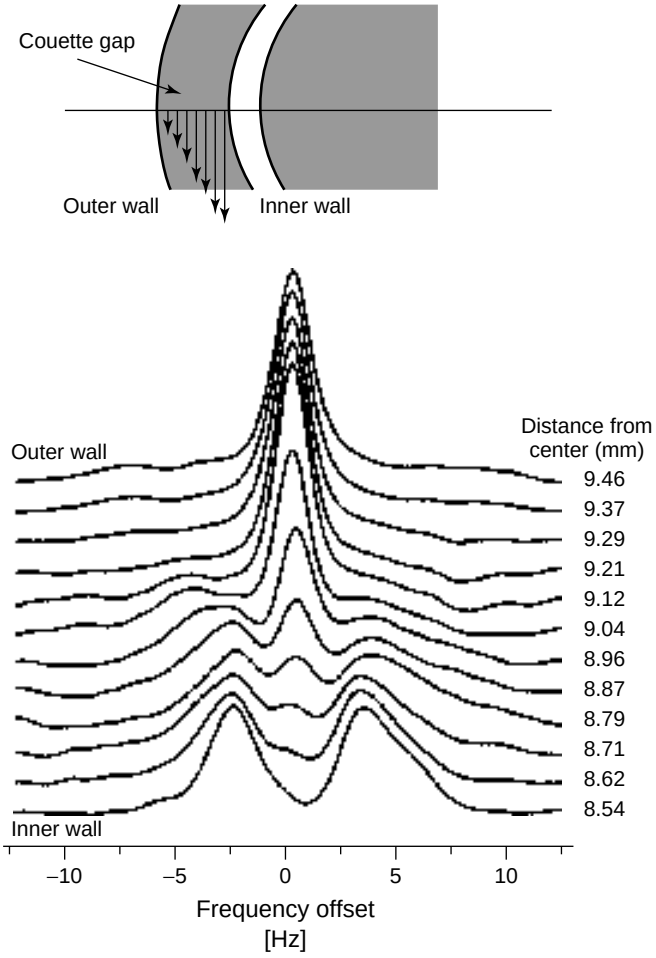

Figure 9 ^{2}H NMR spectra obtained[27] at 46 MHz, from 20% w/w CTAB/D_2O (41 °C) at different positions across the annular gap of a cylindrical Couette cell and at an apparent shear rate of $20\,s^{-1}$. Near the inner wall, where the stress is highest, a quadruple splitting is observed, consistent with an ordered phase, while near the outer wall the single peak of an isotropic phase is seen. In between a mixed phase region exists

shown to be directly proportional to the average alignment tensor $S_{\alpha\beta}$. Where polymer segments are aligned so that $S_{\alpha\beta}$ is non-zero, other physical properties will be anisotropic as well. In particular the dielectric properties which determine the material refractive index will be affected, leading to the optical anisotropy known as birefringence. The correspondence of the stress tensor and the anisotropic part of the refractive index tensor is known as the 'Stress-Optical Law'.

Kilfoil and Callaghan[36] have used deuterium nuclear magnetic resonance to measure the alignment tensor in a high molecular weight polymethylsiloxane (PDMS) melt, employing a small horizontal Couette cell (gap 0.5 mm) in which both the velocity axis element S_{xx} and the gradient element, S_{yy} of the alignment tensor can be projected along the magnetic field. In this work a small benzene probe molecule was placed as a dilute species near a polymer segment whose orientation **u** defines the local director. The tumbling probe molecule undergoes steric interactions with that segment and experience an anisotropic mean orientation. The probe will thus exhibit a scaled down quadrupole splitting associated with that local site

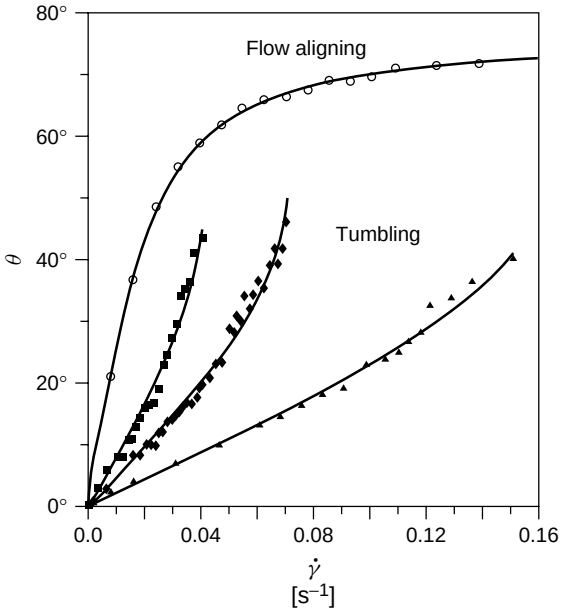

Figure 10 Director orientation, θ as a function of shear rate[34] for both flow aligning (solid squares) and tumbling (open squares 325 K, solid circles, 328 K and open circles 333 K) nematic polymers. (From Ref.[34])

via a 'pseudo-nematic' interaction[5] and samples an ensemble average value for $P_2(\cos\theta)$ as it diffuses over the molecular dimensions.

NMR micro imaging[12] is used to view the PDMS to image the velocity distribution across the gap while the selective-storage localized-spectroscopy method of Figure 3 is used to excite a desired region of the sample for spectroscopy experiments during steady-state shear. Figure 12 shows the measured alignment tensor elements along with fits using the Doi-Edwards model, in which the hierarchy of molecular relaxation times is terminated by the tube disengagement process associated with reptation. Also shown are the selected regions in which either the velocity direction or the velocity gradient (shear axis) is parallel to B_0. The selective excitation pulse sequence which we used has been specially devised to minimize exposure of selected nuclear spins to any relaxation. The best overall fit yields a tube disengagement time of 310 ms, a value which is consistent with the terminal relaxation rate obtained from mechanical measurements. We have also carried out this experiment[36] at fixed shear rate ($\dot\gamma\tau_d = 3.9$), varying the angle ϕ between the velocity direction X and the magnetic field direction through a number of prescribed angles. This was achieved by changing the orientation of the magnetic field gradient used in the precursor selective storage pulse. The angular dependence of the splitting is shown in

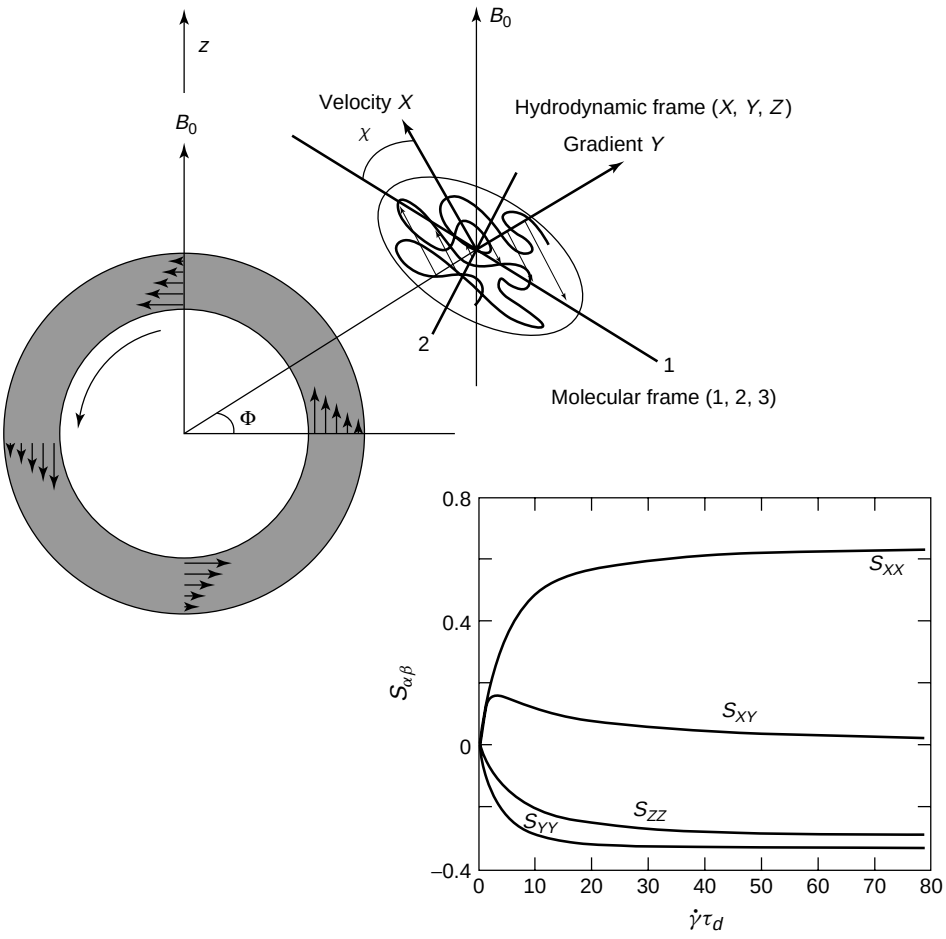

Figure 11 Schematic diagram of 'horizontal Couette cell' in which the vorticity axis is aligned transverse to the magnetic field. The angle between the local velocity direction and the magnetic field is given by ϕ. The angle between the principal axis of the molecular (1, 2, 3) frame and the velocity axis, X, is the so-called extinction angle χ. The lower right inset shows elements of the alignment tensor, $\dot\gamma\tau_d$

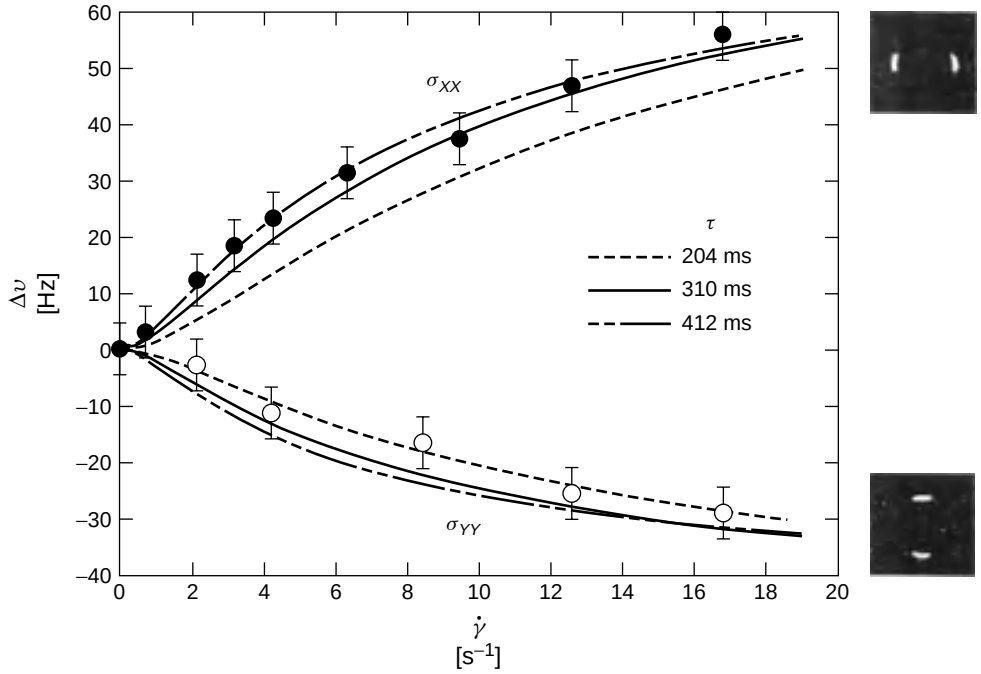

Figure 12 Deuterium quadrupole splittings, $\Delta\upsilon$, versus shear rate, obtained[36] from the spectra derived from a selected region of the horizontal Couette cell in which the velocity direction (solid circles) and gradient direction (open circles) are respectively parallel to the magnetic field. The lines are fits using the Doi-Edwards model in which the absolute splitting (vertical axis) is scaled to yield the pseudonematic order parameter and the horizontal axis is scaled to yield the tube disengagement time, τ_d. The best compromise fit corresponds to $\tau_d = 310$ ms. The images at the right hand side show the regions selected for spectral investigation

Figure 13, along with the curve calculated using Doi-Edwards theory. Again the agreement is excellent, and consistent with the molecular principal axis being aligned at 14.6 degrees to the velocity axis.

3.4.2 T_2 Effects in Entangled Polymers and Gels

Another approach to Rheo-NMR has been demonstrated in a study of relaxation time effects in semi-dilute polymer solutions. Callaghan and Gil[37] used ^{1}H spectroscopy to monitor T_2 relaxation at selected sites on high molecular weight polyacrylamide (PAA) in water, using a cylindrical Couette cell. In this work micro-imaging was employed so that spatially dependent NMR parameters could be imaged across the shearing annulus. Shear banded flow was observed, and a marked reduction in polymer proton T_2 values was found in the high shear region of the flow. Furthermore, the recovery of that T_2 on shear cessation was indicative of slow reorganizational dynamics, on the order of tens to hundreds of seconds. The observed T_2 recovery was found to be multi-exponential and the fast components correlated well with the terminal times measured from the steady state flow curve. Figure 14 shows the correlation of the shear banded flow and the relaxation time reduction while Figure 15 shows the recovery of the proton relaxation rate following shear cessation.

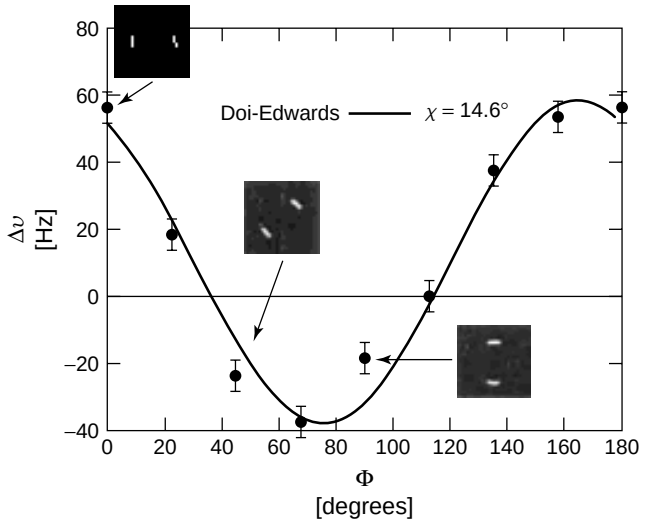

Figure 13 Deuterium quadrupole splittings,[36] $\Delta\upsilon$, versus orientation angle, ϕ, at a fixed Deborah number of $\dot{\gamma}\tau_d = 3.9$. The solid line shows the predictions of the Doi-Edwards model. The images show the selected regions used to obtain $\phi = 0°$, 45° and 90°

The relaxation effects have been interpreted as arising from a deformation of the entanglement tube, such that under strong shear a significant extension occurs along the velocity direction. In consequence, the curvilinear length around tube bends will increase, leading to a slower correlation time for the final orientational motional averaging step, and hence, a faster T_2 relaxation rate.

In another experiment Callaghan and Gil[38] measured proton T_2 relaxation in Carrageen gels under shear and have used changes in relaxation times to gain insight regarding intermolecular interactions responsible for gelation. T_2 relaxation is a particularly easy NMR parameter to measure and may be equally easily used as a contrast in spatially resolved experiments. In consequence

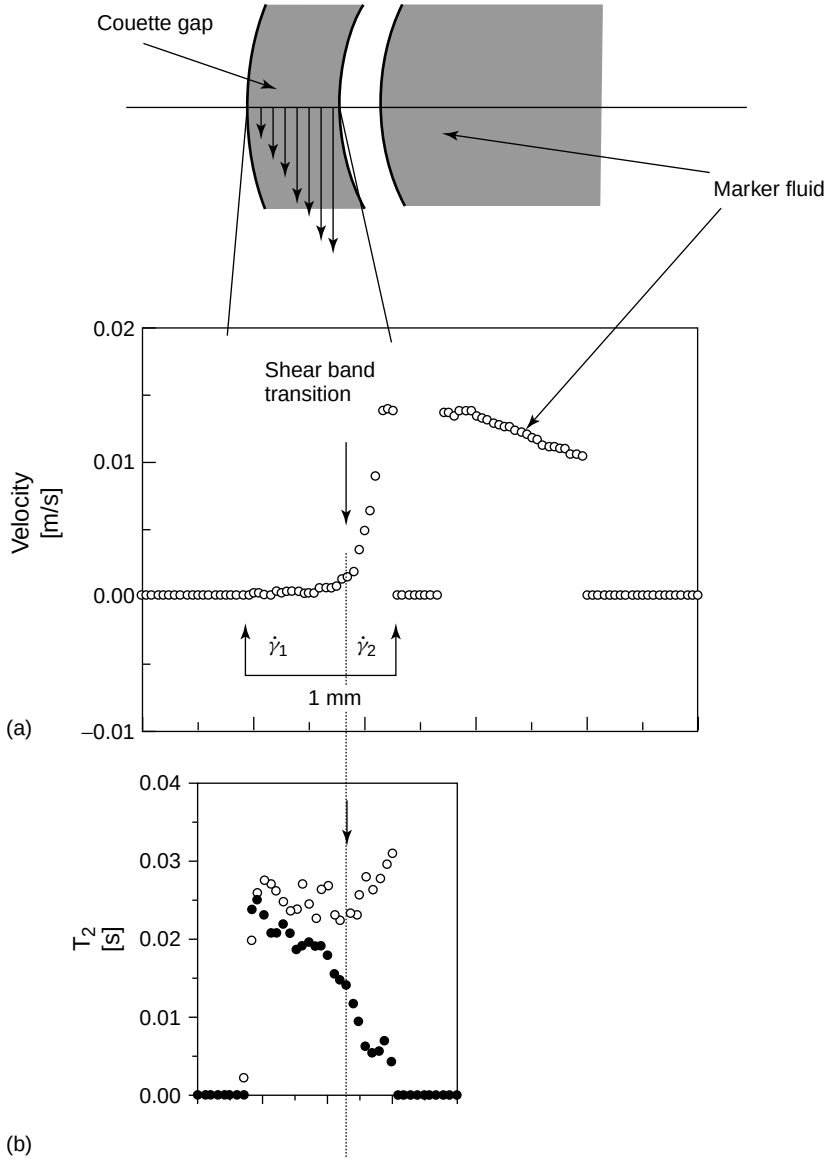

Figure 14 Corresponding velocity and T_2 profiles[37] of PAA/D_2O s a function of radial position across the Couette cell annulus. The velocity profile was obtained at 0.50 Hz. The T_2 profile with open circles is for zero shear and with closed circles for an inner cell rotation speed of 0.5 Hz. The horizontal scales of both velocity and T_2 profiles are identical

the use of T_2 perturbation as a probe of molecular conformational or organizational changes should prove a particularly useful tool in Rheo-NMR studies of complex fluids, and especially for those where changes occur sufficiently slowly that the T_2 change can be observed as a transient.

3.5 Shear-induced Mesophase Structure

The potential for Rheo-NMR studies of shear-induced structure is considerable. One set of systems where NMR is ideally suited is that of lyotropic liquid crystalline phases. A range of cone and plate and cylindrical Couette cell studies have been reported by Lukashek et al.[39,40] and Müller et al.[41] These include cone-and-plate shearing of the hexagonal phase of the amphiphilic oligomer pentaoxyethylene monodecylether ($C_{12}E_5$ in D_2O). Again, deuterium NMR quadrupolar splittings were used to give orientational information. The system appears to behave like a deformable solid, the final state at large strains corresponding to alignment of the hexagonal cylinders along the velocity axis.

For lamellar mesophases, a rich variety of structures is revealed by deuterium NMR studies under shear. For example in lamellar $C_{12}E_4$ shear-aligned, defect-laden lamellae with directors perpendicular to the velocity direction form at low shear rates, but with a transition to spherical multi-lamellar vesicles taking place at higher shear rates. A wide range of lyotropic phases under shear have been studied using neutron scattering and X-ray scattering. NMR provides an opportunity to probe quite different length and time scales in these systems and should prove an important tool in elucidating the effect of deformational flow on molecular organization and dynamics.

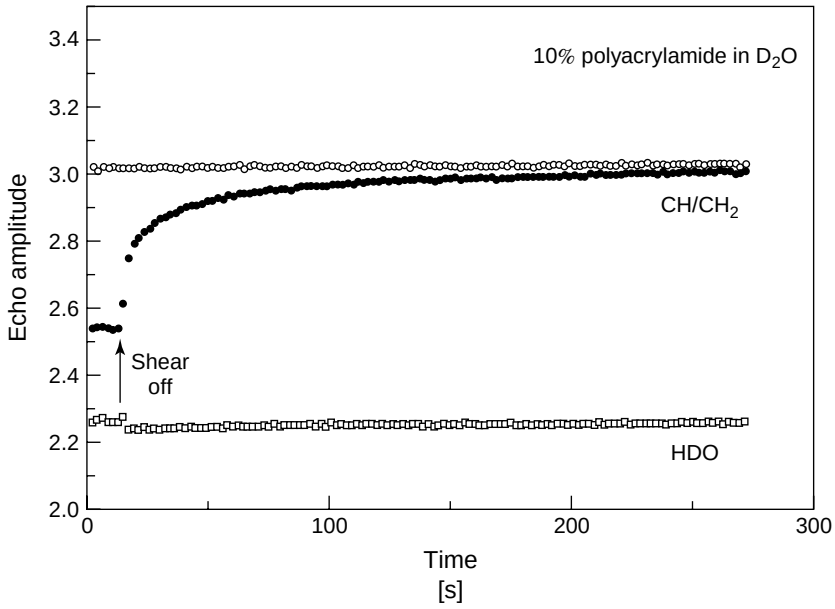

Figure 15 Recovery of the spin echo signal[37] obtained at a fixed delay $2\tau = 10$ ms for the CH/CH_2 region (solid circles) of the 300 MHz proton spectrum in 10% polyacrylamide in D_2O. The open circles show the equilibrium baseline echo intensity obtained some minutes later after full relaxation. The behavior of the water (HDO) peak is shown. This exhibits a much weaker, but observable, transient effect, probably due to baseline effects arising from neighboring polymer proton resonances

3.6 Perturbing Intermolecular Interactions

Central to an understanding of the tertiary structure of biological macromolecules is the role of intermolecular interactions such as hydrogen bonds. Under shearing flow, molecules on differing local streamlines are separated, at a scale-independent rate given by $\dot{\gamma}$. If this rate exceeds the characteristic rate at which intermolecular bonds are naturally broken and reformed, then the tertiary structure is disrupted and the moieties responsible for bond formation will exhibit quite different dynamics than in the bonded state. Thus, Rheo-NMR provides a means of determining which sites on a molecule are responsible for intermolecular binding, by simply comparing high resolution NMR spectra obtained in states of equilibrium and under shear. An example a study of from the synovial fluid polysaccharide, hyaluronin,[42] where ^{13}C spectra have been compared. The one site which shows a significant change is that of the acetamido carbonyl, a moiety which is believed to be responsible for inter-molecular hydrogen bonding.

This last experiment makes clear the very general capability of the Rheo-NMR method. With the exception of the loss of sample space due to the presence of the central cylinder, no sacrifice in signal-to-noise ratio is made in order to carry out NMR under a shearing flow. The use of the cylindrical Couette cell, with all its faces (within the rf coil) machined parallel to the B_0 field means that high spectral resolution is perfectly achievable. Consequently nearly all NMR spectroscopies that are possible in equilibrium, also are also possible under shear and this opens the way for a wide ranging series of NMR studies in which molecular sites responsible for intermolecular interactions are identified and their reaction dynamics determined.

3.7 Extensional Flow

Many important processes involving deformation of soft materials concern extensional flow. An example of an extensional flow cell is shown in Figure 16. The driving unit for this cell is programmed to move the top plug down and stop once the two plugs make contact, or, when a sample is present, when the sample has been deformed completely so as to fill the available volume. This action results in an increasing rate-of-strain, $\dot{\varepsilon}$, as the two cylinders approach one another at velocity v, i.e.,

$$\dot{\varepsilon} = \frac{v}{d_0 - vt} \tag{3}$$

where d_0 is the gap at the time origin, chosen to be the point at which both surfaces come into contact with the material to be deformed. If we take the vertical (compression) axis as z, then the deformation tensor is diagonal and the flow may be ideally described by[26]

$$v_x = \frac{1}{2}\dot{\varepsilon} \quad v_y = \frac{1}{2}\dot{\varepsilon} \quad v_z = -\dot{\varepsilon} \tag{4}$$

The sample generally takes the form of a semi-spherical blob of material. As a result, the final spacing of the plugs is determined by the point at which the material has spread to fill the available plug diameter. This device has been used to study the perturbation experienced in the proton spectrum of a polymer under deformation.[43]

4 CONCLUSIONS

These examples provide a glimpse of possible applications of Nuclear Magnetic Resonance to the study of complex fluid

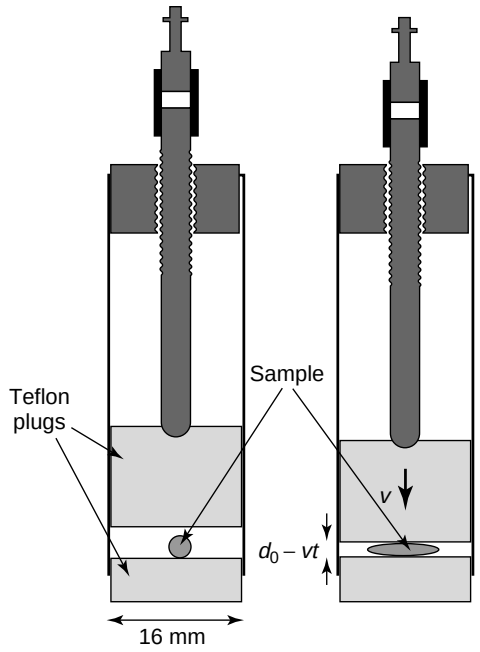

Figure 16 Schematic diagram[43] of extensional flow cell with plug diameter 16 mm

rheology. While this is a very new field of research in which only a handful of groups presently participate, the potential exists for a substantial increase in Rheo-NMR research activity. Systems studied to date include polymer melts and semi-dilute solutions, thermotropic and lyotropic liquid crystals and liquid crystalline polymers, micellar solutions, food materials and colloidal suspensions. Rheo-NMR suffers in a number of respects by comparison with optical methods. NMR is an expensive and complex form of spectroscopy which requires familiarity with the nuclear spin Hamiltonian and the associated effects of spin dynamics. It often suffers from poor signal-to-noise ratios and requires careful tradeoffs in parameter space in order to optimize its effectiveness. Nonetheless NMR offers some unique advantages, including the ability to work with opaque materials, the ability to combine velocimetry with localized spectroscopy, and the ability to access a wide range of molecular properties relating to organization, orientation and dynamics. Rheo-NMR has been able to provide a direct window on a variety of behaviors, including slip, shear-thinning, shear banding, yield stress behavior, nematic director alignment and shear-induced mesophase reorganization. The unique information available with this method suggests that it is likely to become an important tool in elucidating the intriguing rheological behavior of a wide range of complex fluids.

5 REFERENCES

1. H. A. Barnes, J. J. Hutton, and K. Walters, 'An Introduction to Rheology', Elsevier: Amsterdam, 1989.
2. J. Kalus, G. Neubauer, and U. Schemlzer, *Rev. Sci. Instrum.*, 1990, **61**, 3384.
3. R. J. Plano, C. R. Safinya, E. B. Sirota, and L. J. Wenzel, *Rev. Sci. Instrum.*, 1993, **64**, 1309.
4. G. G. Fuller, *Annu. Rev. Fluid. Mech.*, 1990, **22**, 387.
5. G. G. Fuller, 'Optical Rheometry of Complex Fluids', Clarendon Press: Oxford, 1995.
6. A. F. Martins, P. Esnault, and F. Volino, *Phys. Rev. Lett.*, 1986, **57**, 1745.
7. L. N. Goncalves, J. P. Casquilho, J. Figueirinhas, C. Cruz, and A. F. Martins, *Liquid Crystals*, 1993, **14**, 1485.
8. A. I. Nakatani, M. D. Poliks, and E. T. Samulski, *Macromolecules*, 1990, **23**, 2686.
9. Y. Xia and P. T. Callaghan, *Macromolecules*, 1991, **24**, 4777.
10. D. A. Grabowski and C. Schimdt, *Macromolecules*, 1994, **27**, 2632.
11. P. T. Callaghan, *Rep. Prog. Phys.*, 1999, **62**, 599.
12. P. T. Callaghan, 'Principles of Nuclear Magnetic Resonance Microscopy', Oxford University Press: Oxford, 1991.
13. E. O. Stejskal and J. E. Tanner, *J. Chem. Phys.*, 1965, **42**, 288.
14. P. T. Callaghan, C. D. Eccles, and Y. Xia, *J. Phys. E*, 1988, **21**, 820.
15. M. M. Britton, P. T. Callaghan, M. L. Kilfoil, R. W. Mair, and K. Owens, *Appl. Magn. Res.*, 1998, **15**, 287.
16. R. Kimmich and D. Hoepfel, *J. Magn. Reson.*, 1987, **72**, 379.
17. D. M. Doddrell, W. M. Brooks, J. M. Bulsing, J. Field, M. G. Irving, and H. Baddeley, *J. Magn. Reson.*, 1986, **68**, 367.
18. H. Post, D. Ratzel, and P. Brunner, West German Patent, No. P3209263.6, 13 March 1982.
19. W. P. Aue, S. Müller, T. A. Cross, and J. Seelig, *J. Magn. Reson.*, 1984, **56**, 350.
20. M. L. Kilfoil and P. T. Callaghan, *J. Magn. Reson.*, 2000, in press.
21. M. M. Britton and P. T. Callaghan, *Phys. Rev. Lett.*, 1997, **78**, 4930.
22. M. E. Cates, *J. Phys. Chem.*, 1990, **94**, 371.
23. M. E. Cates, T. C. B. McLeish, and G. Marrucci, *Europhys. Lett.*, 1993, **21**, 451.
24. J. P. Decruppe, R. Cressely, R. Makhoufli, and E. Cappelaere, *Colloid Polymer Sci.*, 1995, **273**, 346.
25. R. Makhoufli, J. P. Decruppe, A. Ait-Ali, and R. Cressely, *Europhys. Lett.*, 1995, **32**, 253.
26. M. Doi and S. F. Edwards, 'The Theory of Polymer Dynamics', Oxford University Press: Oxford, 1987.
27. E. Fischer and P. T. Callaghan, *Europhysics Lett.*, 2000, **50**, 803.
28. F. M. Leslie, *Arch. Rat. Mech. Anal.*, 1968, **28**, 265.
29. F. M. Leslie, *Q. J. Appl. Math.*, 1966, **19**, 357.
30. J. L. Ericksen, *Arch. Rat. Mech. Anal.*, 1960, **4**, 231.
31. J. L. Ericksen, *Trans. Soc. Rheol.*, 1961, **5**, 23.
32. F. C. Frank, *Disc. Faraday, Soc.*, 1958, **25**, 19.
33. R. G. Larson, 'Constitutive Equations for Polymer Melts and Solutions', Butterworths: Boston, 1987.
34. H. Siebert, D. A. Grabowski, and C. Schmidt, *Rheologica Acta*, 1997, **36**, 618.
35. M. Doi and S. F. Edwards, *J. Chem. Soc. Faraday Trans. II*, 1978, **74**, 1802 and 1978, **74**, 1818.
36. M. L. Kilfoil and P. T. Callaghan, *Macromolecules*, 2000, **33**, 6828.
37. P. T. Callaghan and A. M. Gil, *Macromolecules*, 2000, **33**, 4116.
38. P. T. Callaghan and A. M. Gil, in 'Magnetic Resonance in Food Systems', ed. G. A. Webb, Royal Society of Chemistry: London, 2000.
39. M. Lukaschek, S. Müller, A. Hansenhindl, D. A. Grabowski, and C. Schmidt, *Colloid Polymer Sci.*, 1996, **274**, 1.
40. M. Lukaschek, D. A. Grabowski, and C. Schmidt, *Langmuir*, 1995, **11**, 3590.
41. S. Müller, P. Fischer, and C. Schmidt, *J. Phys II France*, 1997, **7**, 421.
42. E. Fischer, P. T. Callaghan, F. Heatley, and J. E. Scott, *J. Mol. Struct.*, 2002, **303**, 602–603.
43. P. T. Callaghan and A. M. Gil, *Rheologica Acta*, 1999, **38**, 528.

Biographical Sketch

Paul T. Callaghan received his D. Phil in Physics from Oxford University in 1974, having worked on low temperature studies of hyperfine interactions under the supervision of N. J. Stone. He is Professor of Physics at Massey University, New Zealand and heads a research team working on Pulsed Gradient Spin Echo NMR, and NMR microscopy studies of complex fluid dynamics, and flow and dispersion in porous media. He is Alan MacDiarmid Professor of Physical Science at Victoria University of Wellington, New Zealand. He is author of the book 'Principles of Nuclear Magnetic Resonance Microscopy', published by Oxford University Press and has published around 170 articles in international scientific journals on the subject of nuclear magnetic resonance.

Accuracy Limitations on Internuclear Distances Measured by REDOR

Akira Naito

Yokohama National University, Yokohama, Japan

&

Hazime Saitô

Himeji Institute of Technology, Kamigori, Japan

1	Introduction	1
2	Theoretical Background of the REDOR Experiment	1
3	Rotational Echo Amplitude Calculated by the Density Operator Approach	2
4	Separation of S–I Distances from a S_m–I_n Multiple Spin System	2
5	Tips for Obtaining Accurate Interatomic Distances by REDOR Experiment	4
6	Natural Abundance ^{13}C REDOR Experiment	5
7	Accuracy Limit for REDOR Structure of Peptide and Proteins	6
8	Conclusions	8
9	Related Articles in Volumes 1–8	9
10	References	9

1 INTRODUCTION

In principle, accurate interatomic distances can be evaluated from careful analysis of specific dipolar interactions that were normally sacrificed under the condition of high power decoupling and magic angle spinning (MAS) techniques. A number of methods to recouple a single pair of dipolar interaction among homo and hetero nuclear spin pairs under the magic angle spinning condition have been proposed for determining the interatomic distances.[1–10] These distances have been used as constraints to determine the three-dimensional (3D) structure of peptides and proteins.[11–16] Rotational Echo DOuble Resonance (REDOR) was explored to recouple the relatively weak heteronuclear dipolar interactions under the MAS condition by applying a π pulse synchronously with the rotor period.[8,9] Consequently, the transverse magnetization cannot be refocused completely at the end of the rotor cycle, leading to a reduction of the echo amplitude. The extent of the reduction of the echo amplitude as a function of the number of rotor periods depends on the strength of the heteronuclear dipolar interaction. This method is extensively used to determine the relatively remote interatomic distance of 2–8 Å. When a number of isolated pairs are involved in a REDOR dephasing, the REDOR transformation could be useful in determining interatomic distances because it yields single peaks against distance axis for each heteronuclear coupling strength.[17,18] This approach is, however, not applicable for the case where the observed nuclei in REDOR are coupled with multiple nuclei.

It turned out that determination of accurate interatomic distances ($\pm$0.1 Å) is a prerequisite to arrive at a unique 3D structure of peptides and proteins.[15,16] It is emphasized that the distance measurement by REDOR is the only available means to satisfy this condition among the many kinds of proposed procedures mentioned above in view of the achieved accuracy and precision. Nevertheless, it is important to bear in mind that every possible effort to achieve the distance measurement with ultimate accuracy is essential to any possible applications. This is because any measurement based on the peak-intensity is susceptible to unexpected errors, which are not easy to check. After brief survey, tips to avoid this problem will be discussed in detail.

2 THEORETICAL BACKGROUND OF THE REDOR EXPERIMENT[8]

Transverse magnetization that precesses about the static magnetic field due to the dipolar interaction under the MAS condition moves back to the same direction at every rotor period because the integration of ω_D over one rotor period is zero. Consequently, the rotational echo signals are refocused at every rotor period. When a π pulse is applied to the I nucleus (Figure 1), which is coupled with the S nucleus, in one rotor period, this pulse plays a role to invert the precession direction of the magnetization of the observed S nucleus. Consequently, the magnetization vector of the S nucleus cannot move back to the same direction after one rotor period. Therefore the amplitude of the echo intensity decreases.

The extent of the reduction of the rotational echo amplitude yields the interatomic distances. To evaluate the REDOR echo amplitude theoretically, one has to consider the average precession frequency in the presence of the π pulse at the center of the rotor period over one rotor cycle as follows:

$$\overline{\omega_D(\alpha,\beta)} = \pm\frac{1}{Tr}\left[\int_0^{Tr/2}\omega_D dt - \int_{Tr/2}^{Tr}\omega_D dt\right] = \pm\frac{D}{\pi}\sqrt{2}\sin 2\beta\sin\alpha \quad (1)$$

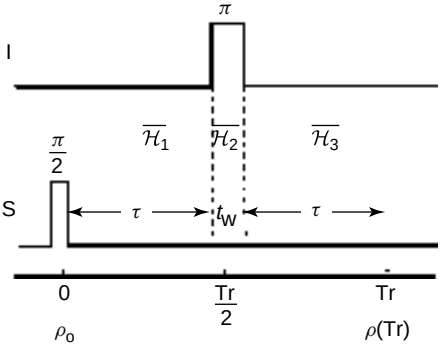

Figure 1 Pulse sequence and timing chart of REDOR experiment

where α is the azimuthal angle and β is the polar angle defined by the internuclear vector with respect to the rotor axis. Therefore, the phase angle, $\Delta\Phi(\alpha, \beta)$ for the Nc rotor cycle can be given by

$$\Delta\Phi(\alpha, \beta) = \overline{\omega_{\mathrm{D}}(\alpha, \beta)}\mathrm{NcTr} \tag{2}$$

where Tr is the rotor period. Finally, the echo amplitude can be obtained by averaging over every orientations as follows

$$S_{\mathrm{f}} = \frac{1}{4\pi}\int_{\alpha}\int_{\beta} cos[\Delta\varphi(\alpha, \beta)]\,\mathrm{d}\alpha \sin\beta\,\mathrm{d}\beta \tag{3}$$

Therefore, the normalized echo difference, $\Delta S/S_{\mathrm{o}}$, can be given by

$$\frac{\Delta S}{S_{\mathrm{o}}} = \frac{S_{\mathrm{o}} - S_{\mathrm{f}}}{S_{\mathrm{o}}} = 1 - S_{\mathrm{f}} \tag{4}$$

Experimentally, REDOR and full echo spectra are acquired for a variety of NcTr values and the respective REDOR (S_{f}) and full echo (S_{o}) amplitudes are evaluated.

3 ROTATIONAL ECHO AMPLITUDE CALCULATED BY THE DENSITY OPERATOR APPROACH[15]

The REDOR echo amplitude can be evaluated more rigorously by using density matrix operators and for the REDOR experiment. The time evolution of density operator, ρ_{o}, under the heteronuclear dipolar interaction during one rotor period, can be considered by taking the pulse length into account. The average Hamiltonian in the rotating frame over one rotor period can be given by

$$\begin{aligned}
\overline{\mathcal{H}} &= \frac{1}{\mathrm{Tr}}\left[\overline{\mathcal{H}_1(t)}\tau + \overline{\mathcal{H}_2(t)}\tau + \overline{\mathcal{H}_3(t)}\tau\right] \\
&= \frac{\mathrm{D}}{4\pi}\Big\{\sin^2\beta[\sin(2\alpha + \omega_{\mathrm{r}}t_{\mathrm{w}}) + \sin(2\alpha - \omega_{\mathrm{r}}t_{\mathrm{w}}) - 2\sin 2\alpha] \\
&\quad - 2\sqrt{2}\sin 2\beta\left[\sin\left(\alpha + \frac{1}{2}\omega_{\mathrm{r}}t_{\mathrm{w}}\right) + \sin\left(\alpha - \frac{1}{2}\omega_{\mathrm{r}}t_{\mathrm{w}}\right) + 2\sin 2\alpha\right] \\
&\quad - \sin^2\beta\,[\sin(2\alpha + \omega_{\mathrm{r}}t_{\mathrm{w}}) + \sin(2\alpha - \omega_{\mathrm{r}}t_{\mathrm{w}})]\,\frac{4\omega_{\mathrm{r}}^2 t_{\mathrm{w}}^2}{4\omega_{\mathrm{r}}^2 t_{\mathrm{w}}^2 - \pi^2} \\
&\quad + \sqrt{2}\sin 2\beta\left[\sin\left(\alpha + \frac{1}{2}\omega_{\mathrm{r}}t_{\mathrm{w}}\right) + \sin\left(\alpha - \frac{1}{2}\omega_{\mathrm{r}}t_{\mathrm{w}}\right)\right] \\
&\quad \times \frac{2\omega_{\mathrm{r}}^2 t_{\mathrm{w}}^2}{\omega_{\mathrm{r}}^2 t_{\mathrm{w}}^2 - \pi^2}\Big\}\hat{I}_Z\hat{S}_Z \\
&\quad + \frac{\mathrm{D}}{4\pi}\Big\{\sin^2\beta[\cos(2\alpha + \omega_{\mathrm{r}}t_{\mathrm{w}}) + \cos(2\alpha - \omega_{\mathrm{r}}t_{\mathrm{w}})] \\
&\quad \times \frac{2\pi\omega_{\mathrm{r}}t_{\mathrm{w}}}{4\omega_{\mathrm{r}}^2 t_{\mathrm{w}}^2 - \pi^2} \\
&\quad - \sqrt{2}\sin 2\beta\left[\cos\left(\alpha + \frac{1}{2}\omega_{\mathrm{r}}t_{\mathrm{w}}\right) + \cos\left(\alpha - \frac{1}{2}\omega_{\mathrm{r}}t_{\mathrm{w}}\right)\right] \\
&\quad \times \frac{2\pi\omega_{\mathrm{r}}t_{\mathrm{w}}}{\omega_{\mathrm{r}}^2 t_{\mathrm{w}}^2 - \pi^2}\Big\}\hat{I}_Z\hat{S}_Y \\
&= a\hat{I}_Z\hat{S}_Z + b\hat{I}_Z\hat{S}_Y
\end{aligned} \tag{5}$$

where ω_{r} is the angular velocity of the rotor and t_{w} is the duration of π pulse. $\overline{\mathcal{H}_1(t)}$, $\overline{\mathcal{H}_2(t)}$, and $\overline{\mathcal{H}_3(t)}$ are the average Hamiltonians corresponding to the period shown in Figure 1. Pulse length, t_{w}, is also considered in the calculations for the analysis of the REDOR results. The density operator, ρ (Tr), at Tr after evolution under the average Hamiltonian can be calculated as

$$\rho(\mathrm{Tr}) = \exp(-i\overline{\mathcal{H}}\mathrm{Tr})\rho_{\mathrm{o}}\exp(i\overline{\mathcal{H}}\mathrm{Tr}) \tag{6}$$

where ρ_{o} is considered to be $\hat{I}y$ after the contact pulse. Then finally the transverse magnetization at Tr can be given by

$$\begin{aligned}
\langle\hat{I}y(\mathrm{Tr})\rangle &= \mathrm{Tr}\{\rho(\mathrm{Tr})\hat{I}y\} \\
&= \cos\left(\frac{1}{2}\sqrt{a^2 + b^2}\mathrm{Tr}\right)
\end{aligned} \tag{7}$$

Echo amplitude in the powder sample can be calculated by averaging over every orientation as follows

$$S_{\mathrm{f}} = \frac{1}{4\pi}\int_{\alpha}\int_{\beta}\langle\hat{I}y(\mathrm{Tr})\rangle\sin\beta\,\mathrm{d}\beta\,\mathrm{d}\alpha \tag{8}$$

Therefore, the normalized echo difference, $\Delta S/S_{\mathrm{o}}$, can be given by equation (4). When the length of t_{w} is zero, equation (7) can be simplified as follows:

$$\langle\hat{I}y(\mathrm{Tr})\rangle = \cos\left(\frac{D}{\pi}\sqrt{2}\sin 2\beta\sin\alpha\mathrm{Tr}\right) \tag{9}$$

In this case, equation (8) is equivalent to equation (3) in the case of $\mathrm{Nc} = 1$.

4 SEPARATION OF S–I DISTANCES FROM A S_m–I_n MULTIPLE SPIN SYSTEM

It should be taken into account that a spin system for a doubly labeled sample should be generally treated as a multiple spin system (S–I_n system) as shown in Figure 2(a) in which S^* is the observed nuclei and the recoupling pulse is applied to the I^* nuclei. The ideal S–I system is available only when the doubly labeled preparation is infinitely diluted with unlabeled preparation. In contrast, uniformly and singly labeled preparations are treated as S_m–I_n and S–I_n systems, respectively (Figure 2b,c), although S^* in the latter is S nuclei of natural abundance. For this reason, it is advisable to utilize a variety of isotopically doubly labeled samples in order to obtain respective interatomic distances, although it is too laborious to make so many kinds of preparations. In fact, we made six kinds of doubly labeled preparations to determine the 3D structure of the pentapeptide, Leu-enkephalin.[16] In addition, it is essential to make certain that all such preparations take the same polymorphic structure, because crystalline peptides or proteins under consideration may take different kinds of polymorphs depending on condition for crystallization, pH, temperature, etc.[15,16] The most convenient way to check this problem is to use the conformation-dependent ^{13}C chemical shifts,

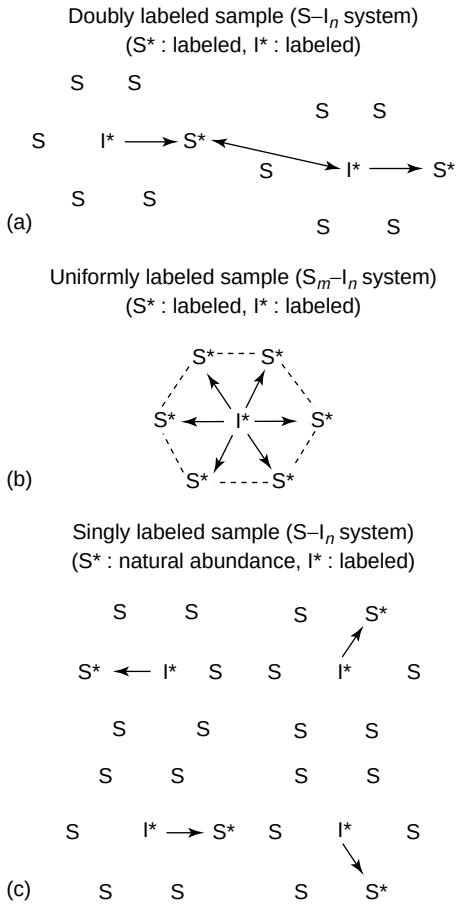

Figure 2 Schematic representation of multiple spin systems for (a) doubly labeled, (b) uniformly labeled and (c) singly labeled samples

which are very sensitive to the presence of such polymorphic structure.[15,16,19]

In this connection, use of a uniformly labeled sample seems to be more attractive both for the sample preparation and also to avoid the problem of polymorphs.[20] This view turned out to be not always true, however, because separation of a particular S–I interaction from S$_m$–I$_n$ spin systems, consisting of many homo- and heteronuclear dipolar and scalar interactions, is not always as straightforward as anticipated. In practice, all of the following conditions should be taken into account to determine the accurate interatomic distances of a particular spin pair from the uniformly labeled samples. First, J coupling among the observed S nuclei should be removed to reduce the phase twist due to the coherent evolution by J coupling, when its magnitude is comparable to the dipolar coupling, as illustrated for uniformly [^{15}N, ^{13}C]-labeled ammonium L-glutamate monohydrate at NcTr = 8 ms (Figure 3).[21,28] This phase twist can be removed by using a shaped pulse as a Z-filter instead of a π pulse at the center position of the REDOR evolution period.[21] Second, the linewidths of individual signals might be broadened due to strong homonuclear dipolar interaction with neighboring S nuclei, which should be eliminated by homonuclear decoupling pulses.[22] Thus, in the case of a uniformly labeled sample, combination of both homonuclear dipolar and scalar decoupling is required to simplify the S$_m$–I$_n$ to S–I$_n$ spin system. Third, relatively shortened transverse relaxation times (T_2), due to residual dipolar interactions, reduce the

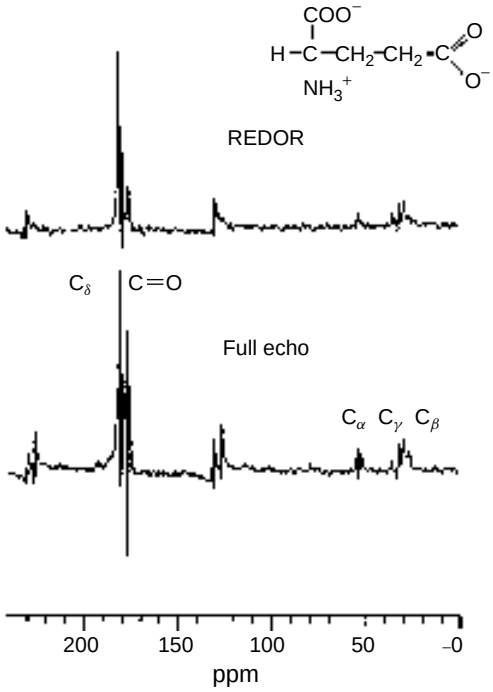

Figure 3 ^{13}C-REDOR and full echo spectra at NcTr = 8 ms for crystalline uniformly labeled ammonium [^{15}N]L-glutamate monohydrate

transverse magnetization during the dipolar recoupling period in REDOR experiments. This makes it difficult to observe the REDOR effect for the nuclei with relatively long internuclear distances, because it is required to measure relatively long evolution times to observe slow dephasing of the REDOR signals. Fourth, REDOR factors against the dipolar evolution time should be analyzed using multiply coupled S–I$_n$ spin systems rather than an isolated two-spin system under the condition of homonuclear decoupling.[23–26] Accordingly, the four kinds of obstacles mentioned above should be removed to determine a set of accurate interatomic distances simultaneously for a uniformly labeled sample.

Gullion et al.[27] proposed a θ-REDOR as an approach to determine the individual interatomic distance in a uniformly labeled sample by dividing S–I$_n$ spin system into 'n' number of isolated S–I two-spin systems. This makes the REDOR analysis simple and allows one to use the REDOR transformation to obtain the dipolar coupling frequencies of individual S–I spin couplings, although this method is not always easy to apply for measurement of a relatively long interatomic distance. Alternatively, homonuclear and scalar interactions are completely removed when natural abundant ^{13}C REDOR experiments were performed.[28] This approach provides an excellent means to determine the interatomic distances for a number of isolated spin pairs simultaneously under condition of high resolution (Figure 2c). Further, it is emphasized that this approach is free from the problem of the above-mentioned shortened T_2 values due to homonuclear ^{13}C spin interactions. However, a multiple coupled spin system, ^{13}C–^{15}N$_n$, has still to be explicitly considered, because the intermolecular dipolar interactions cannot be neglected for a small molecule. In practice, we have recently demonstrated that accurate interatomic distances can be determined by analyzing intramolecular and

intermolecular dipolar contributions based on root mean square deviation (RMSD) between the theoretically and experimentally obtained REDOR factors.[28]

5 TIPS FOR OBTAINING ACCURATE INTERATOMIC DISTANCES BY REDOR EXPERIMENT

It is emphasized that determination of interatomic distances accurate to 0.1 Å is a prerequisite to arrive at a unique solution of the three-dimensional structure of peptides, proteins, etc. A careful evaluation of the following points are the most important steps to obtain reliable interatomic distances by the REDOR experiment, although they have not always been seriously taken into account in a number of papers so far published.

5.1 The Finite Pulse Length and Fluctuation of RF Power

This effect is experimentally observed and calculated using equation (8) as shown in Figure 4. The REDOR parameter, $\Delta S/S_o$, as measured for 20% [1 − ^{13}C, ^{15}N]Gly($r_{CN} = 2.48$ Å) is plotted for the lengths of the ^{15}N π pulse of 13.0 μs for the experiment and 24.6 μs (chosen to satisfy 10% rotor cycle) as a function of NcTr with the calculated lines using the π pulse

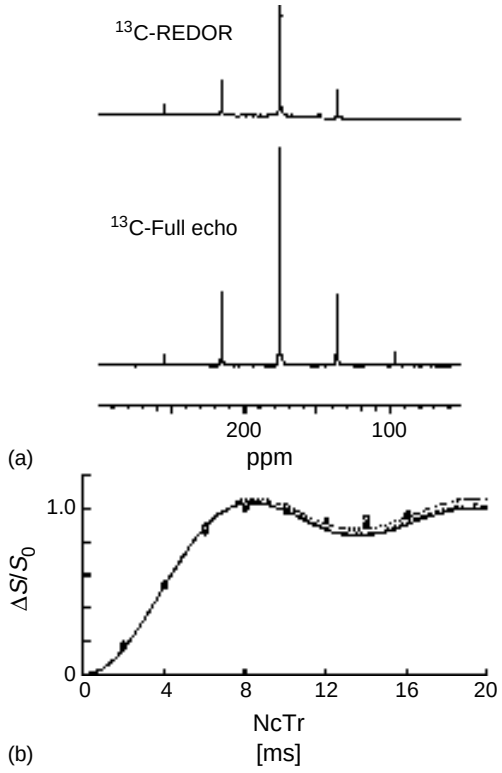

Figure 4 ^{13}C REDOR and full echo spectra of [1-^{13}C, ^{15}N]glycine as recorded by the rotor frequency of 4000 Hz and NcTr of 4 ms (a) and plots of the $\Delta S/S_o$ vs. NcTr (b). Solid and open circles denote the experimental points recorded using a ^{15}N π-pulse of 13.0 and 24.6 μs, respectively. Solid, broken and dotted lines are calculated using the π-pulses of δ, 13.0 and 24.6 μs, respectively, together with the C–N interatomic distance of 2.48 Å[15]

length and finite lengths (13.0 and 24.6 μs) of the π pulse. It turns out, however, that the finite length of the ^{15}N π pulse does not significantly affect the REDOR effect provided that the pulse length is less than 10% of the rotor cycle at the rotor frequency of 4000 Hz. This effect, however, should be seriously taken into account if fast MAS, e.g., 40 kHz is used.

For most spectrometers, it is difficult to be free from fluctuations of RF power during the acquisition of REDOR experiments. It is, therefore, critical that RF power be stabilized. If not, the π pulse will vary in length. Consequently, the REDOR factor is greatly decreased to yield relatively longer interatomic distances. Compensation of instability of such RF power, e.g., by approximate pulse sequence is, therefore, necessary to be free from long term fluctuations of amplifiers. xy-4 and xy-8 pulse sequences have been developed for this purpose. The xy-8 pulse is known to be the best sequence to compensate for the fluctuation of the RF power.[29]

5.2 Contribution from Natural Abundance Nuclei

Since the early stages of the REDOR experiment, contributions from natural abundance nuclei have been seriously considered as a major source of error in the distance measurement.[30] It appears that the observed dipolar interaction can be modified by the presence of such neighboring naturally abundant nuclei. This effect was originally taken into account by simply calculating the $\Delta S/S_o$ value for two isolated pairs and adding proportionally to the natural abundant fraction.[30] Careful analysis of the three-spin system, however, indicates that this sort of simple addition of the fraction of the two-spin system may result in a serious overestimate of the natural abundance effect, to yield shorter distances.[23] The most accurate way to consider the natural abundance effect is, therefore, to treat the whole spin system as a three-spin system by taking into account the neighboring carbons in addition to the labeled pair. In practice, contributions from naturally abundant nuclei can be ignored for ^{13}C REDOR but not for ^{15}N REDOR, because the proportion of naturally abundant ^{13}C nuclei is much higher than that of the ^{15}N nuclei.[23]

5.3 Sample Dilution

^{13}C, ^{15}N-doubly labeled samples are usually used in the REDOR experiment to determine the interatomic distances between the labeled nuclei. More importantly, the dipolar interaction with the labeled ^{15}N nuclei for the neighboring molecules should be taken into account as an additional factor to contribute to the dipolar interaction of the observed pair under consideration. This contribution could be serious when the observed distance is quite remote, because there are many contributions from nearby nuclei. This effect can be completely removed by diluting the labeled sample with a sample of naturally abundant molecules.[23] The sensitivity of the signals, however, has to be sacrificed if one wants to remove the effect completely as the sample must be diluted to 1/49 so that the signal intensity is reduced by a factor roughly 0.02.[11] Instead, it is advised to evaluate the REDOR factors at the infinitely diluted condition by extrapolating the data by stepwise dilution of the sample (i.e., 60%, 30%, etc.) without losing sensitivity, because a linear relationship between the REDOR factor and the dilution is ascertained by a theoretical consideration.[23] Alternatively, the observed plots of $\Delta S/S_o$ values against the

corresponding NcTr values for the sample without dilution can be fitted by a theoretical curve obtained from the dipolar interactions among three-spin systems, although the accuracy is not always improved to the level of the dilution experiment.

5.4 T_2 Effect

The transverse magnetization of the REDOR experiment decays as a function of the ^{1}H decoupling field.[31,32] Under appropriate conditions, molecular motion may interfere with dipolar decoupling. This occurs when molecular motion, if any, exists when the motional frequency is of the same order of magnitude as the decoupling field, and hence the transverse relaxation times (T_2) are significantly shortened. In fact, it was found that the T_2 values of the carbonyl carbons in crystalline Leu-enkephalin are relatively short because of the presence of backbone motion.[33] This is a serious problem for the REDOR experiment, especially for the long distance pairs, because the S/N ratio is significantly deteriorated. In this case, it is required to measure the ^{13}C REDOR signal under a sufficiently strong decoupling field to elongate the transverse relaxation times. It is also useful to perform measurements at low temperature so as to reduce the motional frequency. Note, however, that crystalline phase transitions might be associated together with the freezing of the solvent molecules. This effect has been observed in a variety of enkephalin samples.[34,35]

5.5 RF Inhomogeneity and Confinement of the Sample within RF Coil

In the commercial spectrometer, the rotor is designed to allow the sample volume to be as large as possible in order to gain better sensitivity. Obviously, this arrangement causes H_1 inhomogeneity, which results in a broad distribution of the lengths of the 90° pulses. This problem is serious for the REDOR experiment in which a number of π pulses are applied. As a result, the pulse error can accumulate during the acquisition to give serious error in the measurements of internuclear distances. Particularly, the samples located at the top or bottom part of the sample rotor feel quite a weak RF field. This causes a great reduction of the REDOR factor for a sample that is filled all the way along the sample rotor.[15] This effect should be seriously taken into account prior to experiments with a commercial spectrometer. It is, therefore, strongly recommended to fill the sample only in the central part of the coil just like a multiple pulse experiment to be able to acquire as accurate interatomic distances as possible in the REDOR experiment.

5.6 Standard Sample

All of the considerations mentioned above are essential to achieve accurate interatomic distances. Nevertheless, it is also possible that accuracy may deteriorate even if one of the conditions is not satisfied for every possible measurement. It is therefore advisable to determine the interatomic distances from a standard sample, in order to check that all the conditions are satisfied. More preferentially, use of two standard samples for short and long distances is recommended. In practice, it is recommended to use [1-^{13}C, ^{15}N]glycine as the former standard sample whose C–N interatomic distance is determined as 2.48 Å by a neutron diffraction study, and to check that all the instrumental conditions of a given spectrometer are satisfied prior to every new experiment. As a second standard sample for long distance, it is recommended to use [^{13}C, ^{15}N]*N*-acetyl-Pro-Gly-Phe (Table 1). This crystalline peptide is very stable with relatively long T_2 values, because it does not contain solvent molecules, and the presence of two polymorphic structures is well characterized.[15]

6 NATURAL ABUNDANCE ^{13}C REDOR EXPERIMENT[28]

As mentioned already, it is impossible to obtain meaningful interatomic distances from a uniformly labeled sample as far as the standard REDOR procedure is concerned. Instead, the natural abundance REDOR experiment is more preferable as a means free from both homonuclear dipolar and scalar interactions (Figure 3). This approach provides the interatomic distances for a number of isolated spin pairs simultaneously under high resolution conditions. Further, this approach is free from the problem of the shortened T_2 values due to homonuclear ^{13}C spin interactions. Figure 5 shows the REDOR and full echo spectra of natural abundance ^{13}C nuclei of singly ^{15}N labeled crystalline ammonium [^{15}N]L-glutamate monohydrate (I) at NcTr = 8 ms, in contrast to the twisted spectra from the same sample uniformly labeled (Figure 3). The assignment of peaks to the C_β, $C\gamma$, C_α, C=O and C_δ carbon nuclei, from high to low field, is also shown in Figure 5. The C=O (176.6 ppm) peak was distinguished from the C_δ (179.5 ppm) peak as a peak yielding a stronger REDOR effect as shown in Figure 5. Similarly, the peak at 56.0 ppm was assigned to the C_α carbon nucleus that give the strongest REDOR effect among the three aliphatic ^{13}C peaks. In a similar manner, the peak at 30.5 ppm showed a stronger REDOR effect compared

Table 1 C–N interatomic distances (Å) determined from REDOR experiments as compared with those by X-ray diffraction and MD[15]

Labeled peptides	Experimental			Calculated		
	REDOR	X-Ray		Energy-minimized[a]	MD	
	Orthorhombic	Orthorhombic	Monoclinic[b]		Orthorhombic	Monoclinic
I	3.24 ± 0.05 (3.43 ± 0.05)[c]	3.19	3.76	3.17	3.22 ± 0.10	3.63 ± 0.10
II	3.43 ± 0.05 (3.66 ± 0.05)	3.35	3.21	3.57	3.32 ± 0.10	3.33 ± 0.10
III	4.07 ± 0.05 (4.45 ± 0.05)	3.99	3.91	4.17	3.92 ± 0.10	3.83 ± 0.10

[a]Energy-minimized structure based on REDOR data.
[b]Ref.[36]
[c]Data from Ref.[23] based on fully packed 7.5 mm rotor systems.

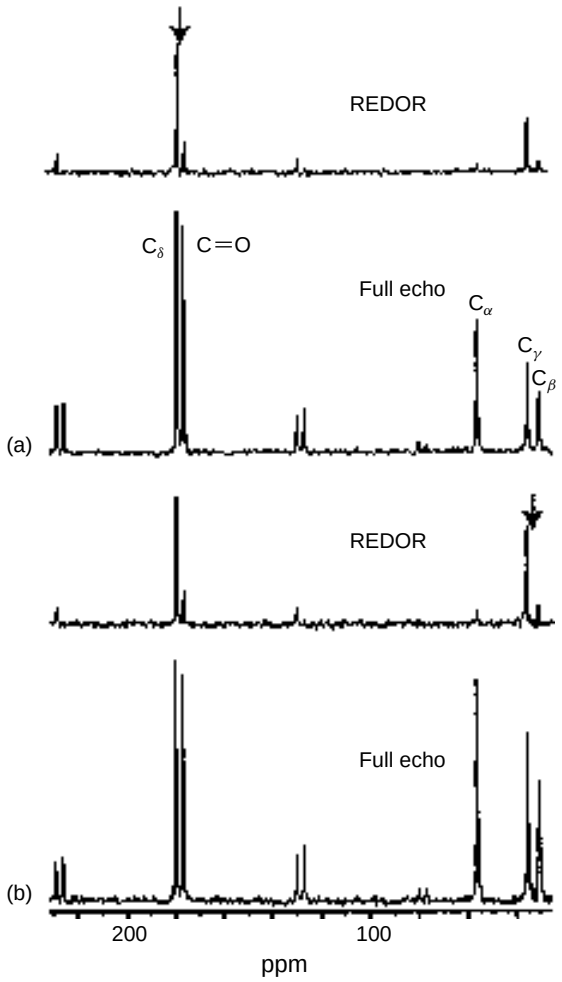

Figure 5 Naturally abundant ^{13}C-REDOR and full echo spectra at NcTr = 8 ms with two different carrier frequencies for crystalline ammonium [^{15}N]L-glutamate monohydrate. Arrows indicate carrier frequency positions at the center of (a) C=O and C_δ resonances; and (b) Cβ and C_γ resonances

with that at 35.2 ppm. Thus, the peaks at 35.2 and 30.5 ppm were assigned to the C_γ and C_β carbon nuclei, respectively.

The interatomic C–N distances between ^{15}N and ^{13}C=O, $^{13}C_\alpha$, $^{13}C_\beta$, $^{13}C_\gamma$, and $^{13}C_\delta$ carbon nuclei were determined with accuracy of 0.15 Å, after experimental conditions were carefully optimized. ^{13}C-REDOR factors for a three-spin system, $(\Delta S/S_o)_{CN1N2}$, and the sum of two isolated two-spin systems, $(\Delta S/S_o)^* = (\Delta S/S_o)_{CN1} + (\Delta S/S_o)_{CN2}$, were further evaluated by the REDOR measurements on isotopically diluted I in a controlled manner. Subsequently, the intramolecular and intermolecular C–N distances were separated by searching the minimum in the contour map of the root mean square deviation (RMSD) between the theoretically and experimentally obtained $(\Delta S/S_o)^*$ values against two interatomic distances, r_{C-N1} and r_{C-N2}. When the intramolecular C–N distance (r_{C-N1}) of the particular carbon nucleus is substantially shorter than the intermolecular distance (r_{C-N2}), C–N distances between the molecule in question and the nearest neighboring molecules can also be obtained, although accuracy is inevitably deteriorated. On the other hand, it was difficult to determine the interatomic distances in the same molecule when the intermolecular dipolar contribution is larger than the intramolecular one as in the case of the C_δ carbon nucleus.

7 ACCURACY LIMIT FOR REDOR STRUCTURE OF PEPTIDE AND PROTEINS

Naito et al.[15] systematically applied this technique to elucidate the three-dimensional structure of *N*-acetyl-Pro-Gly-Phe. They proposed that the carbonyl carbon of the (i-1)th residue and the amino nitrogen of the (i+1)th residue should be labeled with ^{13}C and ^{15}N, respectively. Namely, [1-^{13}C]*N*-acetyl-Pro-[^{15}N]Gly-Phe(I), *N*-acetyl-[1-^{13}C]Pro-Gly-[^{15}N]Phe(II) and [1-^{13}C]*N*-acetyl-Pro-Gly-[^{15}N]Phe(III) were synthesized and the resulting distances were determined to be 3.24 ± 0.05, 3.43 ± 0.05, and 4.07 ± 0.05 Å respectively, utilizing the REDOR factor obtained for the infinitely diluted state to prevent errors from the contributions of the neighboring labeled nuclei. No correction from the contribution of the naturally abundant nuclei turned out to be necessary. Surprisingly, these distances do not agree well with the values obtained from an X-ray diffraction study available when the initial part of this experiment was performed, showing the maximum discrepancy between them to be 0.5 Å.[36] This value seems to be much larger than the expected error as estimated from the precision of the REDOR experiment (±0.05 Å). The reason why the discrepancy is unexpectedly larger was explained by the fact that the crystal (orthorhombic) used for the REDOR experiments is different from that used in the X-ray diffraction study (monoclinic). To check the accuracy of the REDOR experiment, an X-ray diffraction study was performed on the same crystals used for the REDOR experiment. It was found that the distances from the new crystalline polymorph (orthorhombic) agree well between REDOR and X-ray diffraction, within an accuracy of 0.05 Å as shown in Table 1.

Conformational maps based on the possible combinations of the torsion angles of the Pro and Gly residues are calculated on the basis of the distance constraints thus obtained. Further, the difference of the chemical shifts between the C_β and C_γ carbons of the Pro residues $\Delta\beta\gamma$ was used as a constraint to determine the ψ value (−13°).[37] The φ angle of the Pro residue is in many instances restricted to −75° which shows the minimum energy in the residue. Therefore, the torsion angles of the Pro residue are uniquely determined to be (−75°, −28°). Using these torsion angles, conformational maps were again calculated. Finally two pairs of torsion angles were selected as (−112°, 48°) and (−112°, −48°). Minimization by a molecular mechanics calculation yielded the structure of the β-turn I structure, as shown in Figure 6(a). It is found that the three-dimensional structure of this peptide is well reproduced by a molecular dynamics simulation by taking into account all of the intermolecular interactions in the crystals, although a molecular dynamics calculation treating *single* molecular system does not always yield a correct picture as illustrated in Figure 6(b), unless otherwise all the molecules in a unit cell are correctly taken into account.[15,38]

Elucidation of the three dimensional structure of an opioid peptide Leu-enkephalin crystal, Tyr-Gly-Gly-Phe-Leu grown from MeOH/H_2O mixed solvent was performed by the REDOR method alone.[16] This seems to be an additional challenge for this technique to reveal the three-dimensional structure of more complicated systems. Six differently labeled

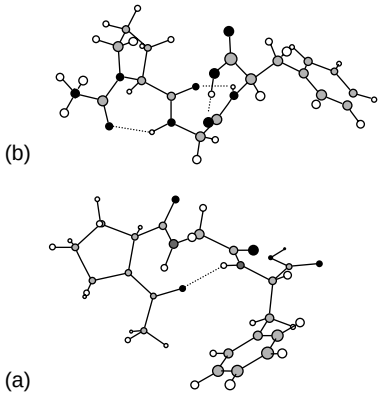

Figure 6 Optimized conformation of *N*-acetyl-Pro-Gly-Phe as obtained by the minimization of energy from the initial form as deduced from the REDOR experiment (a) and a snapshot of the conformation deduced by MD simulation in vacuo (at 100 K) (b)[15]

Leu-enkephaline molecules were synthesized and the resulting interatomic distances (Figure 7a) are accurately determined. It turns out, however, that an extremely careful experiment is required to avoid unexpected crystalline conversion among polymorphs either by dehydration from a tightly sealed rotor or a phase transition occurring at ambient temperature. In principle, pressure under MAS may shift a temperature of phase transition to some extent, because centrifugal force is proportional to the square of the spinning frequency. No significant effect, however, has been noted so far as a sample is spun at relatively low frequency such as 2−4 kHz but care might be taken when rotor is spun at a frequency one order of magnitude high as in 40 kHz.

This may be the reason why final refinement of X-ray diffraction data was abandoned in spite of the pioneering X-ray diffraction data as to the similarity of the tertiary structure between this opioid peptide and morphine.[39] Therefore, it is necessary to check whether the six differently labeled samples are all in the same crystalline polymorph by means of the ^{13}C chemical shifts. Otherwise, meaningless data can be obtained without this precaution. When the distance data are converted to yield the necessary numbers of torsion angles, a unique combination of torsion angles in the corresponding conformational map is determined sequentially as shown in Figure 7(b). It is emphasized that accuracy within 0.1 Å is essential to select unique torsion angles for each amino acid residue. Namely, if the error is larger than 0.41 Å, torsion angles can no longer be selected as shown in Figure 8.

It is also important to point out that the chemical shift data can be used as additional constraints. A three dimensional structure was thus determined as shown in Figure 9. However, this structure is not the same as that previously determined

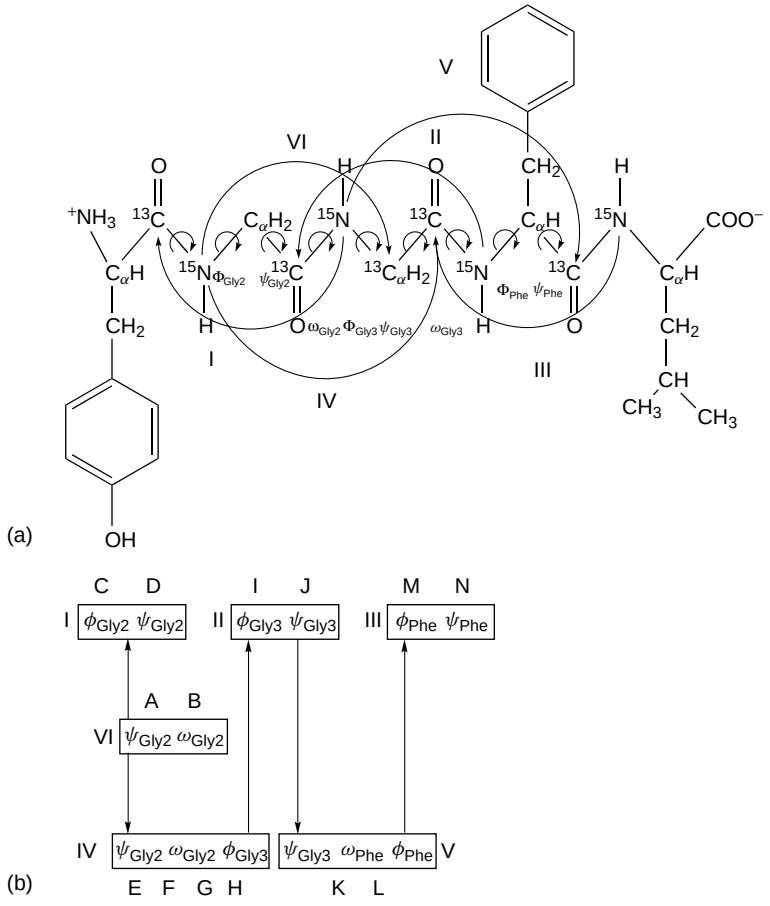

Figure 7 (a) Schematic representation between the sites of a variety of [^{13}C, ^{15}N]-doubly-labeled Leu-enkephalin dehydrates and their related torsion angles. (b) Block diagram to show how respective torsion angles are uniquely determined by the combined examinations of the conformation maps based on the distances of four-bonds apart (I, II, III and VI) and five-bonds apart (IV and V)[16]

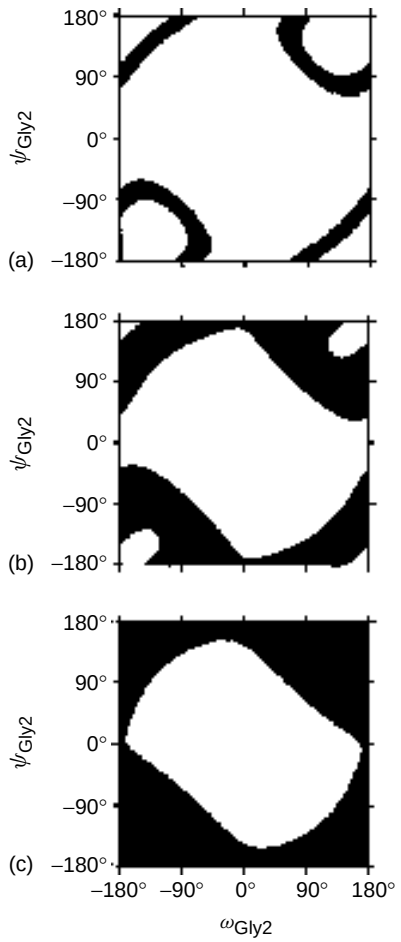

Figure 8 Conformation maps for (Ψ_{Gly2}, ω_{Gly2}) based on the interatomic distance of 4.55 Å with increased experimental errors: (a) ±0.10 Å, (b) ±0.20 Å, and (c) ±0.41 Å[16]

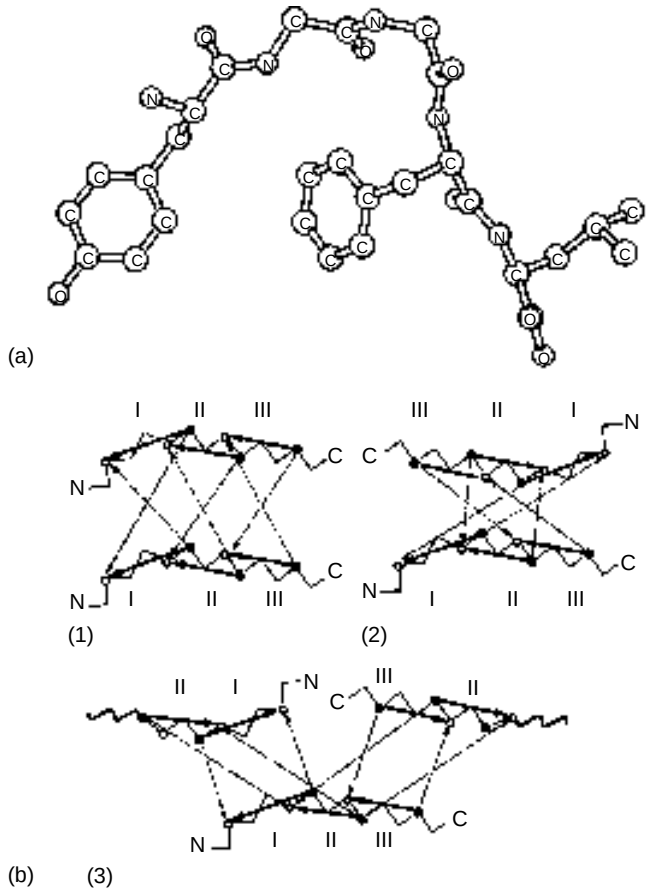

Figure 9 (a) Three-dimensional structure of Leu-enkephalin dihydrate determined uniquely by the successive application of the conformation maps as well as additional constraints of the conformation-dependent ^{13}C chemical shifts. (b) Three kinds of models for putative intermolecular packing as illustrated in the cartoons: (1) interaction through parallel β-sheet form; (2) interaction through an antiparallel β-sheet; and (3) interaction through interaction of three molecules. Solid and dotted arrows correspond with the dipolar interactions between intramolecular and intermolecular $^{13}C-^{15}N$ pairs, respectively[16]

by X-ray diffraction because one is dealing with a crystalline polymorph that is not fully explored. It is possible to figure out the molecular packing in the crystals by looking at the intermolecular dipolar contribution. Since the intermolecular dipolar contributions in I and III are larger than that of II, a β-sheet is formed as one peptide interacts with two peptides as an antiparallel β-sheet as shown in Figure 9(b).

Finally, it should be pointed out that, in order to isolate an S–I spin pair, it is essential to avoid any unnecessary errors from dipolar contributions of neighboring molecules from the overall $S-I_n$ spin system. This is generally encountered for a variety of peptides and the aforementioned dilution procedure turned out to be not required in the case of α-helical polypeptides as far as the measurement of the interatomic distance for $^{15}NH(i)\cdots O = {}^{13}C(i+4)$ is concerned.[40] This is because the interhelical dipolar contribution is found to be negligible in view of the mutual packing of α-helical chains or random mutual orientation between isotopically labeled atoms. Further, it was found that in helical peptides, due to the manner of chain packing, this kind of measurement is feasible to yield 4.5 ± 0.1 Å, without any assumptions, for a variety of transmembrane α-helical peptides in lipid bilayers to mimic a biomembrane at a temperature below liquid crystalline-gel phase transition at which rotation of such peptides about the α-helical axis turns out to be frozen, in spite of the presence of rotational motions of lipid molecules, as viewed from the observation of three principal components of ^{13}C and ^{31}P chemical shift tensors.[41] As is shown in this example, it is essential to ensure that molecular motion is reasonably ceased.

8 CONCLUSIONS

REDOR is one of the most powerful methods to determine accurate interatomic distances after taking into account a number of points in applying the method to a practical sample. Simultaneous measurement of interatomic distances using uniformly labeled samples can only be achieved by removing the homonuclear dipolar and scalar interactions. Alternatively, natural abundance ^{13}C REDOR measurements provide interatomic distances simultaneously free from homonuclear dipolar and scalar interactions. These accurate interatomic distances obtained from REDOR experiments can provide important information on structure and molecular packing of solid peptides and proteins.

9 RELATED ARTICLES IN VOLUMES 1–8

REDOR & TEDOR, Volume 6.

10 REFERENCES

1. D. P. Raleigh, M. H. Levitt, and R. G. Griffin, *Chem. Phys. Lett.*, 1988, **146**, 71.
2. M. H. Levitt, D. P. Raleigh, F. Creuzet, and R. G. Griffin, *J. Chem. Phys.*, 1990, **92**, 6347.
3. R. Tycko and G. Dabbagh, *Chem. Phys. Lett.*, 1990, **173**, 461.
4. B. -Q. Sun, P. R. Costa, D. Kocisko, P. T. Lansbury Jr., and R. G. Griffin, *J. Chem. Phys.*, 1995, **102**, 702.
5. T. Gullion and S. Vega, *Chem. Phys. Lett.*, 1992, **194**, 423.
6. A. E. Bennett, J. H. Ok, R. G. Griffin, and S. Vega, *J. Chem. Phys.*, 1992, **96**, 8624.
7. D. M. Gregory, D. J. Mitchell, J. A. Stringer, S. Kiihne, J. C. Shiels, J. Callahan, M. A. Mehta, and G. P. Drobny, *Chem. Phys. Lett.*, 1995, **246**, 654.
8. T. Gullion and J. Schaefer, *Adv. Magn. Reson.*, 1989, **13**, 57.
9. T. Gullion and J. Schaefer, *J. Magn. Reson.*, 1989, **81**, 196.
10. A. W. Hing, S. Vega, and J. Schaefer, *J. Magn. Reson.*, 1992, **96**, 205.
11. J. R. Garbow and C. A. McWherter, *J. Am. Chem. Soc.*, 1993, **115**, 238.
12. J. R. Garbow, M. Breslav, O. Antohi, and F. Naider, *Biochemistry*, 1994, **33**, 10 094.
13. A. W. Hing, N. Tjandra, P. F. Cottam, J. Schaefer, and C. Ho, *Biochemistry*, 1994, **33**, 8651.
14. R. C. Anderson, T. Gullion, J. M. Joers, M. Shapiro, E. B. Villhauer, and H. P. Weber, *J. Am. Chem. Soc.*, 1995, **117**, 10 546.
15. A. Naito, K. Nishimura, S. Kimura, S. Tuzi, M. Aida, N. Yasuoka, and H. Saitô, *J. Phys. Chem.*, 1996, **100**, 14 995.
16. K. Nishimura, A. Naito, S. Tuzi, H. Saitô, C. Hashimoto, and M. Aida, *J. Phys. Chem. B*, 1998, **102**, 7476.
17. K. T. Mueller, T. P. Jarvie, D. J. Aurentz, and B. W. Roberts, *Chem. Phys. Lett.*, 1995, **242**, 535.
18. T. P. Jarvie, G. T. Went, and K. T. Mueller, *J. Am. Chem. Soc.*, 1996, **118**, 5330.
19. H. Saitô, S. Tuzi, and A. Naito, *Annu. Rep. NMR Spectrosc.*, 1998, **38**, 79.
20. C. A. Michal and L. W. Jelinski, *J. Am Chem. Soc.*, 1997, **119**, 9059.
21. C. P. Jaroniec, B. A. Tounge, C. M. Rienstra, J. Herzfeld, and R. G. Griffin, *J. Am. Chem. Soc.*, 1999, **121**, 100–237.
22. J. Schaefer, *J. Magn. Reson.*, 1999, **137**, 272.
23. A. Naito, K. Nishimura, S. Tuzi, and H. Saitô, *Chem. Phys. Lett.*, 1994, **229**, 506.
24. K. Nishimura, A. Naito, S. Tuzi, and H. Saitô, *J. Phys. Chem. B*, 1999, **103**, 8398.
25. L. M. McDowell, C. A. Klug, D. D. Beusen, and J. Shaefer, *Biochemistry*, 1996, **35**, 5395.
26. J. M. Goetz and J. Schaefer, *J. Magn. Reson.*, 1997, **127**, 147.
27. T. Gullion and C. H. Pennington, *Chem. Phys. Lett.*, 1998, **290**, 88.
28. K. Nishimura, K. Ebisawa, E. Suzuki, H. Saito, and A. Naito, *J. Mol. Struct.*, 2001, **560**, 29.
29. T. Gullion and J. Schaefer, *J. Magn. Reson.*, 1991, **92**, 439.
30. Y. Pan, T. Gullion, and J. Schaefer, *J. Magn. Reson.*, 1990, **90**, 330.
31. D. Suwelack, W. P. Rothwell, and J. S. Waugh, *J. Chem. Phys.*, 1980, **73**, 2559.
32. W. P. Rothwell and J. S. Waugh, *J. Chem. Phys.*, 1981, **74**, 2721.
33. A. Naito, A. Fukutani, M. Uitdehaag, S. Tuzi, and H. Saitô, *J. Mol. Struct.*, 1998, **441**, 231.
34. M. Kamihira, A. Naito, K. Nishimura, S. Tuzi, and H. Saitô, *J. Phys. Chem. A*, 1998, **102**, 2826.
35. M. Kamihira, A. Naito, S. Tuzi, and H. Saitô, *J. Phys. Chem.*, 1999, **103**, 3356.
36. S. K. Brahmachari, T. N. Bhat, V. Sudhakar, M. Vijayan, R. S. Rapaka, R. S. Bhatnagar, and V. S. Aranthanarayanan, *J. Am. Chem. Soc.*, 1981, **103**, 1703.
37. von I. Z. Siemion, T. Wieland, and K. -H. Pook, *Angew. Chem.*, 1975, **87**, 712.
38. M. Aida, A. Naito, and H. Saitô, *J. Mol. Struct. Theochem.*, 1996, **388**, 187.
39. G. D. Smith and T. Blundel, *Science*, 1978, **199**, 1214.
40. S. Kimura, A. Naito, H. Saitô, K. Ogawa, and A. Shoji, *J. Mol. Struct.*, 2001, **157**, 562.
41. S. Kimura, A. Naito, S. Tuzi, and H. Saitô, *J. Mol. Struct.*, 2002, **125**, 602–603.

Biographical Sketches

Akira Naito, *b* 1949. B.Eng., 1973, Nagoya Institute of Technology. Ph.D., 1978, Kyoto University. Post Doctoral Fellow, University of British Columbia, 1978–1984. Assistant Professor, Kyoto University, 1984–1990. Associate Professor, Himeji Institute of Technology, 1990–2001. Professor, Yokohama National University, 2001–present. Approx. 110 publications. Current research specialty: development of solid-state NMR technique and its application to biological systems.

Hazime Saitô, *b* 1937. B.Sc., 1961, Ph.D., 1968, Kyoto University. Research Scientist, Basic Research Laboratories, Toray Industries, Inc., 1963–1975, Section head, Biophysics Division, National Cancer Center Research Institute, Tokyo, 1975–1990. Professor, Himeji Institute of Technology, 1990–present. Approx. 250 publications. Current research specialty: solid state NMR and its application to structural biology with emphasis on membrane proteins.

Adiabatic Polarization-Transfer Methods in MAS Spectroscopy

Matthias Ernst and Beat H. Meier

ETH Zürich, Physical Chemistry, ETH-Hönggerberg, Zürich, Switzerland

1	Introduction	1
2	Theory	3
3	Methods of Heteronuclear Polarization Transfer	5
4	Methods of Homonuclear Polarization Transfer	7
5	Related Articles in this Volume	9
6	Related Articles in Volumes 1–8	10
7	References	10

1 INTRODUCTION

Transfer of spin order is of great importance in magnetic resonance and plays a crucial role in two-dimensional correlation spectroscopy, two-dimensional exchange spectroscopy, and for the sensitivity enhancement of low-γ nuclei. Well-known examples are Hartmann–Hahn cross polarization,[1,2] spin diffusion,[3] INEPT,[4] and NOESY[5] experiments.

All experiments mentioned above are 'sudden' experiments in the sense that they start with the preparation of an initial state characterized by a density operator which corresponds to a non-equilibrium state. Such a non-equilibrium state evolves under the transfer Hamiltonian. The time-evolution of the density operator leads to a transfer of spin order. In an adiabatic experiment, on the other hand, one starts with a density operator that does not evolve under the initial Hamiltonian. The time evolution is initiated by 'slowly' and continuously changing the Hamiltonian in the course of the spin-order transfer such that the density operator follows the Hamiltonian.

A simple example to illustrate the differences between sudden and adiabatic experiments is the inversion of the z-magnetization of a single spin 1/2. The 'sudden' version is a π-pulse applied on-resonance with a pulse duration of $\tau = \pi/\omega_1$. The behavior of the magnetization during the pulse is illustrated in Figure 1(a,c). Critical settings for obtaining perfect inversion are the resonance frequency (which must be 'on-resonance', i.e., $\omega_{\mathrm{rf}} \approx \omega_0$) and the product of pulse length τ and rf-field strength ω_1. The well-known oscillatory behavior of M_z as a function of the pulse length (Figure 1c) is typical for 'sudden' experiments. The adiabatic counterpart of such an inversion pulse is an adiabatic passage through resonance realized by a frequency sweep of the rf-irradiation frequency $\omega_{\mathrm{rf}}(t)$. The behavior is illustrated in Figure 1(b,d). The inversion starts by irradiating the spin system with an irradiation frequency $\omega_{\mathrm{rf}}(0)$ much lower than the resonance frequency ω_0 and ends with a frequency $\omega_{\mathrm{rf}}(\tau)$ much higher than ω_0. The precise shape of the frequency sweep $\omega_{\mathrm{rf}}(t)$ is only important if one is interested in minimizing the pulse length at a certain 'degree of adiabaticity'. The Hamiltonian in the rotating frame (rotating with frequency ω_0 about the static magnetic field) is given by

$$\mathcal{H} = \chi(t) I_z + \omega_1 I_x \tag{1}$$

where $\chi(t) = \omega_{\mathrm{rf}}(t) - \omega_0$ is the off-resonance term. As a function of the time t, the Hamiltonian is rotated from being parallel with I_z to being antiparallel with I_z. As long as the frequency sweep $\omega_{\mathrm{rf}}(t)$ is slow enough (see below) and the sweep range is large enough ($|\omega_{\mathrm{rf}}(0) - \omega_0| \gg |\omega_1|$ and $|\omega_{\mathrm{rf}}(\tau) - \omega_0| \gg |\omega_1|$), the magnetization is inverted irrespective of the exact values of the resonance frequency ω_0, the sweep length τ, and the rf-field strength ω_1. It will become clear in the following, that the polarization transfer experiments of interest are also fully described, for two spin systems, by the simple picture of Figure 1. The polarization transfer will take place in a fictitious spin-1/2 subspace. The only difference to the inversion of z-magnetization will be the labelling of the axes.

In the absence of relaxation, the time evolution of a spin system always conserves the entropy and the total spin order. It is, therefore, in principle reversible and 'adiabatic' in a thermodynamical sense. This is obvious for the simple example of Figure 1 but has also been shown for polarization transfer processes in multi-spin systems for the case of spin diffusion[6,7] and cross polarization.[8,9] In the present context, we use the term adiabatic in a more restricted sense, namely for processes where in addition to the conservation of spin order, the density operator and the instantaneous Hamiltonian commute at all times,[10] i.e.,

$$[\sigma(t), \mathcal{H}(t)] = 0 \tag{2}$$

In this chapter, we will treat the transfer of polarization or longitudinal magnetization between two spins. We start with z-magnetization on a source spin (spin 1) as described by a density operator of the form $\sigma(0) = cI_{1z}$ and measure the amount of polarization on the destination spin (spin 2) after the transfer. The final density operator is of the form $\sigma(\tau) = c'(\tau) I_{2z} + Z(\tau)$ and we can abbreviate the transfer as $I_{1z} \rightarrow I_{2z}$. Here $Z(\tau)$ describes the part of the density operator orthogonal to I_{2z}. We define the polarization P_k of spin k as the expectation value of the operator I_{kz}. The polarization is related to the longitudinal magnetization by $M_{kz} = N_k \hbar \gamma_k P_k$. In general, neither the magnetization nor the polarization of the entire spin system are conserved quantities,[11] but there is an important class of experiments where the sum polarization $\sum_k P_k$ is conserved. Therefore, we will discuss the experiments always in terms of polarization.

Polarization transfer is a special form of the more general term spin-order transfer. Other examples of spin-order transfer include coherence transfer, e.g., $I_{1x} \rightarrow I_{2x}$, and transfer of coherences to two-spin order terms, e.g., $I_{1x} \rightarrow 2I_{1y}I_{2z}$. The distinction between polarization and coherence depends on the frame of reference and is not always unique.

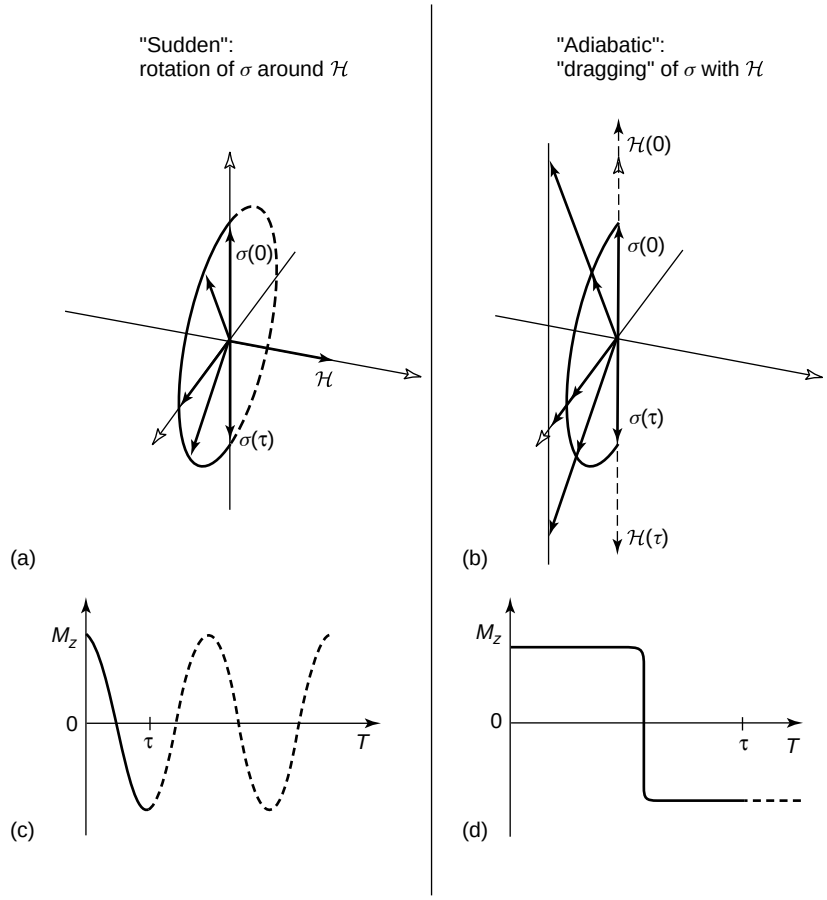

Figure 1 Schematic comparison of (a) sudden and (b) adiabatic inversion of the z-component of the magnetization vector. In the sudden case a π pulse is applied while in the adiabatic case a frequency sweep is shown. The time evolution of the z-magnetization as a function of the pulse duration τ is shown in (c) and (d) for sudden and adiabatic schemes, respectively. For the sudden experiment, the precise choice of τ is crucial to obtain efficient inversion; for adiabatic experiments a variation within rather wide limits does not lead to significant changes in inversion efficiency

Polarization transfer between two spins can often be described by a fictitious spin-1/2 system.[12,13] This is a consequence of the structure of the dipolar-coupling interaction, which has a matrix representation in the product base $|\alpha\alpha\rangle, |\alpha\beta\rangle, |\beta\alpha\rangle, |\beta\beta\rangle$ of the form

$$\frac{1}{2}\begin{bmatrix} \xi^{\Sigma} & 0 & 0 & d^{\Sigma} \\ 0 & \xi^{\Delta} & d^{\Delta} & 0 \\ 0 & d^{\Delta} & \xi^{\Delta} & 0 \\ d^{\Sigma} & 0 & 0 & \xi^{\Sigma} \end{bmatrix} \tag{3}$$

There are no coupling elements between the sum-polarization subspace spanned by $|\alpha\alpha\rangle, |\beta\beta\rangle$ and the difference polarization subspace spanned by $|\alpha\beta\rangle, |\beta\alpha\rangle$. The scalar J-coupling Hamiltonian has the same basic structure. If, besides the dipolar interaction, only a 'Zeeman-type' interaction of the form

$$\frac{1}{2}\begin{bmatrix} \chi^{\Sigma} & 0 & 0 & 0 \\ 0 & \chi^{\Delta} & 0 & 0 \\ 0 & 0 & -\chi^{\Delta} & 0 \\ 0 & 0 & 0 & -\chi^{\Sigma} \end{bmatrix} \tag{4}$$

is present, the total Hamiltonian can be written as the sum of two fictitious spin-1/2 Hamiltonians

$$\mathcal{H} = \mathcal{H}^{\Sigma} \oplus \mathcal{H}^{\Delta} \tag{5}$$

with

$$\mathcal{H}^{\kappa} = \chi^{\kappa} \cdot S_z^{\kappa} + d^{\kappa} \cdot S_x^{\kappa} + \frac{1}{2}\xi^{\kappa} \cdot 1I^{\kappa} \tag{6}$$

where κ stands for either Σ (the double-quantum subspace) or Δ (the zero-quantum subspace) and $1I^{\kappa}$ is the identity operator in the considered subspace. The symbol '$\oplus$' emphasizes that we take the direct sum of the two subspaces of dimension 2×2. Not considering the term proportional to the identity operator which does not influence the evolution of the density operator in the subspace κ, the Hamiltonian

$$\mathcal{H}^{\kappa} = \chi^{\kappa} \cdot S_z^{\kappa} + d^{\kappa} \cdot S_x^{\kappa} \tag{7}$$

has the same form as the one of equation (1) with the dipolar amplitude coupling element d^{κ} taking the role of the rf field in equation (1). The separation into a sum and difference subspace can also be applied to the density operator σ, given that $\sigma(0)$ can be divided according to

$$\sigma = \sigma^{\Sigma} \oplus \sigma^{\Delta} \tag{8}$$

If the density operator contains only terms proportional to I_z, such a separation is always possible according to

$$\sigma = p_1 I_{1z} + p_2 I_{2z} = p^{\Sigma} I_z^{\Sigma} + p^{\Delta} I_z^{\Delta} \tag{9}$$

with $p^{\Sigma} = p_1 + p_2$, $p^{\Delta} = p_1 - p_2$, $I_z^{\Sigma} = 1/2(I_{1z} + I_{2z})$, and $I_z^{\Delta} = 1/2(I_{1z} - I_{2z})$. Obviously, the inversion of the difference polarization $I_z^{\Delta} \rightarrow -I_z^{\Delta}$ is equivalent to a complete polarization transfer, i.e., $I_{1z} \rightarrow I_{2z}$ while the inversion of the sum magnetization $I_z^{\Sigma} \rightarrow -I_z^{\Sigma}$ leads to the polarization transfer $I_{1z} \rightarrow -I_{2z}$.

In polarization transfer schemes based on the dipolar coupling, the value of the effective dipolar coupling constant d^{κ} depends on one or two of the three Euler angles which describe the orientation of the crystallite in the rotor-fixed frame. For a powder sample, the resulting distribution of effective dipolar coupling frequencies does not allow a complete polarization inversion by the equivalent of a 180° pulse with $\tau \cdot d^{\kappa} = \pi$. An optimum choice of the pulse length τ leads to a maximum transfer efficiency for such a 'sudden' experiment of 73% and to an equilibrium value of 50% in an isolated two-spin system. For adiabatic methods, the maximum transfer efficiency is still 100% even in a powder sample. It will be shown below, that adiabatic polarization transfer schemes show a greatly reduced sensitivity to rf-field inhomogeneities compared to their sudden equivalent.

If the adiabaticity is violated during the sweep, the density operator and the Hamiltonian do not commute at all times during the polarization-transfer process ($[\mathcal{H}(t), \sigma(t)] \neq 0$). Under this condition, the density operator starts to precess around the Hamiltonian. Such a precession will be damped by relaxation and possibly rf-field inhomogeneities and lead to a reduction in transfer efficiency.

A number of adiabatic heteronuclear polarization transfer methods have been introduced starting with the ADRF-ARRF scheme for static samples[2,14,15] and the static adiabatic passage through the Hartmann–Hahn matching condition.[16] Adiabatic passage Hartmann–Hahn cross polarization (APHH CP) can also be applied under MAS.[17–21] In these experiments, the amplitude difference of the two applied rf-fields $\omega_{1I}(t) - \omega_{1S}(t)$ is the parameter $\chi(t)$ which is varied in an adiabatic fashion around the Hartmann–Hahn matching condition, i.e., $\chi(t) = \omega_{1I}(t) - \omega_{1S}(t) - f \cdot \omega_r$ with $f = \pm 1, \pm 2$. The variation can also take place around the original Hartmann–Hahn condition with $f = 0$ if the adiabatic transfer is combined with multiple-pulse irradiation.[22]

There is also a number of homonuclear adiabatic polarization transfer schemes under MAS. In adiabatic passage rotational resonance (APRR)[23] the spinning frequency of the MAS rotor $\omega_r(t)$ is varied to obtain a sweep through the rotational resonance condition[24–26] $\Omega_1 - \Omega_2 = n\omega_r$ with $n = \pm 1, \pm 2$ and Ω_k being the isotropic chemical shift of spin k. This leads to the definition $\chi(t) = \Omega_1 - \Omega_2 - n\omega_r(t)$. Adiabatic passage RR was also applied to the central transition of half-integer quadrupolar spins where conventional RR cannot be applied due to the broadening of the resonances by second-order quadrupolar terms.[27] A variation of APRR is the rotational resonance tickling experiment[28–30] where the RR experiment is carried out in a tilted rotating frame and the sweep is accomplished at constant MAS frequency by changing the amplitude of the applied rf-field.

In the adiabatic version of the homonuclear rotary-resonance (HORROR) experiment[31] called dipolar recoupling enhancement through amplitude modulation (DREAM)[32,33] the amplitude of the applied rf-field $\omega_1(t)$ is varied as a function of time to obtain an adiabatic sweep through the HORROR recoupling condition $n \cdot \omega_1 = \omega_r$ with $n = \pm 1, \pm 2$ leading to $\chi(t) = \omega_r - n \cdot \omega_1(t)$. Recently a rf-field-driven dipolar recoupling scheme for half-integer quadrupolar nuclei was introduced[34] which can also be implemented in an adiabatic fashion.

2 THEORY

A spin system which is subject to magic-angle sample spinning (MAS) and to a slow variation of a parameter due to an adiabatic process can be described by a time-dependent Hamiltonian $\mathcal{H}(t, T)$. In this notation, the time-variable t characterizes the fast time dependence due to the MAS and the time-variable T describes the slow time dependence due to the adiabatic variation of a spin-system variable. If we assume that the changes due to T can be neglected over a time period $\tau_r = 2\pi/\omega_r$ then we can define a t-time averaged Hamiltonian

$$\mathcal{H}(T) = \langle \mathcal{H}(T) \rangle_{\tau_r} \tag{10}$$

which no longer depends on the time-variable t and is, therefore, independent of the MAS rotation. There are several ways of carrying out the averaging. The most common descriptions use average Hamiltonian and Floquet theory. The details of this averaging process depend on the specific polarization transfer process under discussion. Different approaches have been used and can be found in the original literature (see below).

For a pair of spins 1/2, the relevant process of the adiabatic polarization transfer can always be described in a subspace κ of the Hamiltonian which is defined by a fictitious spin-1/2 system.[12,13] The T-time dependent system Hamiltonian in this subspace is given by

$$\mathcal{H}^{\kappa}(T) = \chi^{\kappa}(T) \cdot S_z^{\kappa} + |d_{\text{eff}}^{\kappa}| \cdot (\cos(\varphi) S_x^{\kappa} + \sin(\varphi) S_y^{\kappa}) \tag{11}$$

Equation (11) is a trivial generalization of equation (7) caused by the fact that the effective dipolar coupling d_{eff}^{κ} appearing in the context of recoupling experiments is a complex number with absolute value $|d_{\text{eff}}^{\kappa}|$ and the phase $\arg(d_{\text{eff}}^{\kappa}) = \varphi$. The size of $|d_{\text{eff}}^{\kappa}|$ depends on the two Euler angles α and β which describe the rotation from the principal-axis system of the dipolar interaction tensor to the rotor-fixed coordinate system. The third Euler angle γ determines the phase φ but does not influence the magnitude of the coupling, $|d_{\text{eff}}^{\kappa}|$. The phase is simply an integer multiple of γ where the integer depends on the matching condition employed. In a powder sample each crystallite has a different Euler angle γ and, therefore, a different phase φ. The Hamiltonian for each crystallite lies in a different plane spanned by the operators S_z^{κ} and $\cos(\varphi) S_x^{\kappa} + \sin(\varphi) S_y^{\kappa}$. To simplify the theoretical description we can rotate the Hamiltonian by the crystallite-dependent angle φ about $-S_z^{\kappa}$ and recover the simple form of equation (7):

$$\mathcal{H}^{\kappa}(T) = \chi^{\kappa}(T) \cdot S_z^{\kappa} + |d_{\text{eff}}^{\kappa}| \cdot S_x^{\kappa} \tag{12}$$

In the course of the adiabatic polarization transfer the effective chemical-shift term is changed from $\chi(0) = \chi_i$ to $\chi(\tau) = \chi_f$ (where χ_i and χ_f have a different sign) in such a way that the adiabaticity condition

$$a(T) = \frac{\sqrt{\chi^{\kappa}(T)^2 + |d_{\text{eff}}^{\kappa}|^2}}{|\mathrm{d}\Theta^{\kappa}(T)/\mathrm{d}T|} \gg 1 \tag{13}$$

is fulfilled for all times T. Note that the adiabaticity parameter is T-time dependent. Here, the angle $\Theta^\kappa(T) = \arctan(|d^\kappa_{\text{eff}}|/\chi^\kappa(T))$ describes the time-dependent angle between the Hamiltonian and the z-axis. We start at time $T = 0$ with an initial density operator $\sigma^\kappa(0^-) = p^\kappa \cdot S^\kappa_z \approx c \cdot \mathcal{H}^\kappa(0)$ along the z-axis of the subspace κ. If the Hamiltonian $\mathcal{H}^\kappa(0)$ is not parallel with the z-axis, e.g., if the initial offset is not large enough, only the part of the initial density operator that is parallel to the Hamiltonian $\mathcal{H}^\kappa(0)$ has to be taken into account for the further course of the experiment. We denote the density operator just before a projection step at time t by $\sigma^\kappa(t^-)$ and just after the projection step by $\sigma^\kappa(t^+)$. Each projection decreases the spin order because the orthogonal components are assumed to decay irreversibly. After the projection we obtain

$$\sigma^\kappa(0^+) = p^\kappa \cdot \cos(\Theta(0)) S^\kappa_{\text{eff}}(0) \tag{14}$$

where the cosine of the angle $\Theta(0) = \arctan(|d_{\text{eff}}|/\chi^\kappa_i)$ determines the initial loss of polarization due to the projection on the operator $S^\kappa_{\text{eff}}(0)$. This projection is schematically illustrated in Figure 2. The operator

$$S^\kappa_{\text{eff}}(T) = \cos(\Theta(T)) S^\kappa_z + \sin(\Theta(T)) S^\kappa_x \tag{15}$$

stays always parallel to the Hamiltonian. Ideally, the sweep is applied such that $\Theta(0) \approx 0$ and

$$\sigma^\kappa(0^+) \approx p^\kappa \cdot S^\kappa_z \tag{16}$$

If the effective coupling $|d^\kappa_{\text{eff}}|$ is non-zero and equation (13) is fulfilled, the density operator always stays parallel to the Hamiltonian (i.e., along $S^\kappa_{\text{eff}}(T)$) and follows the movement of the Hamiltonian and describes an arc in the plane spanned by S^κ_z and $\cos(\varphi)S^\kappa_z + \sin(\varphi)S^\kappa_y$. For $\varphi = 0$, one obtains the following expression for the density operator during the adiabatic sweep:

$$\sigma^\kappa(T) = p^\kappa \cdot \cos(\Theta_i) S^\kappa_{\text{eff}}(T) \tag{17}$$

Figure 2 shows the trajectory followed by the density operator for a single arbitrary crystallite in the plane spanned by S^κ_z and $\cos(\varphi)S^\kappa_z + \sin(\varphi)S^\kappa_y$ as a function of the time-variable T. For a powder each crystallite follows such a trajectory but due to the variation in the phase φ for the different crystallites the planes are different. At time $T = 0$ the magnetization of all crystallites are aligned along S^κ_z. At the center of the sweep at $\chi^\kappa(T = \tau/2) = 0$ the magnetization is distributed over the plane spanned by S^κ_x and S^κ_y depending on the value of φ. At the end of the sweep at $T = \tau$ the magnetization of all different crystallites is again aligned but now along $-S^\kappa_z$.

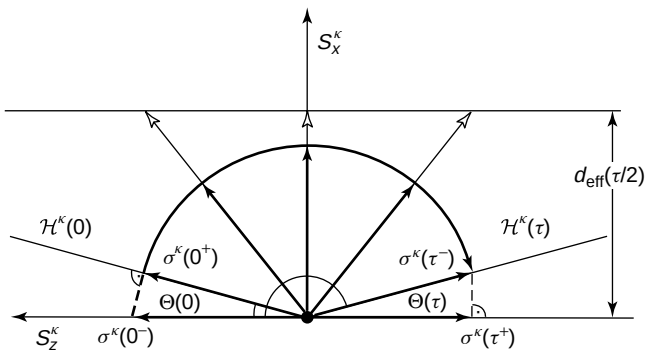

Figure 2 Schematic representation of the adiabatic polarization transfer for a single crystallite orientation in the subspace spanned by S^κ_z and S^κ_x. The initial projection with $\Theta(0)$ the subsequent rotation imposed by the rotation of the Hamiltonian, and the final projection with $\Theta(\tau)$ of the density operator is shown

The density operator at the end of the sweep at $\chi^\kappa(\tau) = \chi^\kappa_f$ is then given by

$$\sigma^\kappa(\tau^-) = p^\kappa \cdot \cos(\Theta(0)) \cdot [\cos(\Theta(\tau)) S^\kappa_z + \sin(\Theta(\tau)) S^\kappa_x] \tag{18}$$

where the angle $\Theta(\tau) = \pi + \arctan(|d^\kappa_{\text{eff}}|/\chi^\kappa_f)$. We have to project the density operator at the end of the sweep onto the z-axis of the subspace κ and obtain the final density operator

$$\sigma^\kappa(\tau^+) = p^\kappa \cdot \cos(\Theta(0)) \cos(\Theta(\tau)) S^\kappa_z \tag{19}$$

For a well-designed experiment, we require that $\Theta(0) \approx 0$ and $\Theta(\tau) \approx \pi$ leading to

$$\sigma^\kappa(\tau^+) \approx -p^\kappa \cdot S^\kappa_z \tag{20}$$

The loss of polarization caused by the two projections at the beginning and the end of the sweep are expressed by the factors $\cos(\Theta(0))$ and $\cos(\Theta(\tau))$ in equation (19), respectively, and can be minimized by starting and ending the adiabatic sweep with initial and final values of the effective chemical shift largely exceeding the value of the effective coupling frequency $|d^\kappa_{\text{eff}}|$.

If the effective coupling $|d^\kappa_{\text{eff}}|$ is zero, the density operator is unchanged by the sweep and we obtain a final density operator $\sigma^\kappa(\tau) \approx \sigma^\kappa(0) = p^\kappa \cdot S^\kappa_z$, assuming that $\Theta(0) \approx 0$ and $\Theta(\tau) \approx \pi$.

In principle, any continuous shape for $\chi^\kappa(T)$ can be used which fulfills equation (13), but to minimize relaxation effects it is advantageous to use a sweep which is as short as possible while still maintaining adiabaticity at all times T. The best shape with respect to adiabaticity is a shape where the angular velocity $\alpha(T) = \mathrm{d}\Theta(T)/\mathrm{d}T$ is proportional to the effective field $\omega_{\text{eff}}(T) = \sqrt{|d^\kappa_{\text{eff}}| + \chi^\kappa(T)^2}$. This requirement is fulfilled for a sweep rate of[35,36]

$$\frac{\mathrm{d}}{\mathrm{d}T}\chi^\kappa(T) \propto \frac{(|d^\kappa_{\text{eff}}|^2 + \chi^\kappa(T)^2)^{3/2}}{|d^\kappa_{\text{eff}}|} \tag{21}$$

Such a function leads to a fast change of $\chi^\kappa(T)$ far from the center of the sweep and a slow change close to the center. To design such a sweep, the sweep has to fulfill the condition $\chi^\kappa(\tau/2) = 0$ which is not possible for all spins in the presence of chemical-shift offsets or rf-field inhomogeneity. A linear sweep of

$$\chi^\kappa(T) = \chi^\kappa_i - \left(\frac{\chi^\kappa_i - \chi^\kappa_f}{\tau} \cdot T\right) \tag{22}$$

is the shape which shows the smallest sensitivity to the value of the system parameters but requires the longest sweep time to remain adiabatic during the entire sweep. In practice, a good compromise is to maintain constant angular velocity during the

sweep for a 'typical' value of the dipolar coupling constant d_{est} which can be implemented by the function

$$\alpha(T) = \frac{\mathrm{d}\Theta(T)}{\mathrm{d}T} = \frac{2}{\tau} \cdot \arctan\left(\frac{\chi_i}{|d_{\text{est}}|}\right) \tag{23}$$

Such a solution leads to the functional form

$$\chi^{\kappa}(T) = |d_{\text{est}}| \cdot \tan\left(\alpha \cdot \left[\frac{\tau}{2} - T\right]\right) \tag{24}$$

for $0 \leq T \leq \tau$ which is more tolerant than the one described by equation (21) to an imprecise estimation of the parameters for the center of the sweep and to the variation of $d_{\text{eff}}(\alpha, \beta, \gamma)$ as a function of the crystallite orientation.

In principle, one can achieve 100% polarization transfer using adiabatic methods compared to a maximum of 73% efficiency using 'sudden' methods. This requires of course, that the polarization transfer process is in the adiabatic limit ($a(T) \gg 1$) for all orientation-dependent effective coupling frequencies $d_{\text{eff}}(\alpha, \beta, \gamma)$. This increased efficiency is due to the fact that the transfer speed of the adiabatic polarization transfer is independent of the Euler angles and of the orientation-dependent size of the effective coupling constant. As was shown earlier, the Euler angle γ only influences the phase in the $S_x^{\kappa} - S_y^{\kappa}$-plane where the trajectory crosses but all trajectories reach the final point at the same point in time (Figure 2b).

3 METHODS OF HETERONUCLEAR POLARIZATION TRANSFER

3.1 Hartmann–Hahn Cross Polarization by Adiabatic Passage

Adiabatic Passage Hartmann–Hahn cross polarization (APHH)[16–21] was designed to combine the advantages of Hartmann–Hahn cross polarization, namely the conservation of the sum polarization, with the advantages of ADRF-ARFF which has a higher transfer efficiency and no critical matching condition. In this experiment the amplitude of one or both of the rf-fields is changed in an adiabatic fashion during the cross-polarization time period (Figure 3) in order to obtain a sweep through the sideband f of the Hartmann–Hahn matching condition $\omega_{1I} - \omega_{1S} = f \cdot \omega_r$.

In the APHH experiment, the sum polarization and σ^{Σ} are constants of the motion and the relevant subspace of the heteronuclear two-spin Hamiltonian is the zero-quantum subspace $\kappa = \Delta$. The Hamiltonian in this subspace has exactly the form of equation (7)

$$\mathcal{H}^{\Delta}(T) = \chi^{\Delta}(T) \cdot S_z^{\Delta} + |d_{f,\text{eff}}| \cdot S_x^{\Delta} \tag{25}$$

with $\chi^{\Delta}(T) = \omega_{1I}(T) - \omega_{1S}(T) - f\omega_r$ where $\omega_{1I}(T)$ and $\omega_{1S}(T)$ are the time-dependent amplitudes of the applied rf fields. The parameter $f = \pm 1, \pm 2$ denotes the sideband of the Hartmann–Hahn matching condition under MAS[37–39] and $d_{f,\text{eff}}$ is the Fourier coefficient of order f of the heteronuclear dipolar coupling. In APHH CP the initial and final value of the amplitude sweep $\chi_i^{\Delta} = \omega_{1I}(0) - \omega_{1S}(0) - f\omega_r$ and $\chi_f^{\Delta} = \omega_{1I}(\tau) - \omega_{1S}(\tau) - f\omega_r$ are limited to about $\pm 1/2\omega_r$

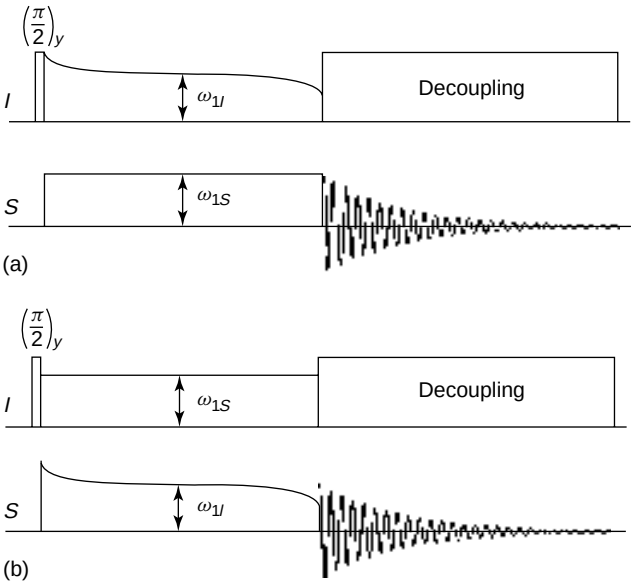

Figure 3 Pulse sequence used for adiabatic cross polarization. The amplitude modulation during the cross-polarization time can be applied either to the proton (a) or to the carbon (b) channel. Cross polarization uses of phase X

in order not to touch one of the other sideband matching conditions. The fictitious spin-1/2 operators in the zero-quantum subspace are defined as $S_z^{\Delta} = 1/2 \cdot (I_z - S_z)$, $S_x^{\Delta} = 1/2 \cdot (S^+I^- + S^-I^+)$, and $S_y^{\Delta} = i/2 \cdot (S^+I^- - S^-I^+)$, where the z-axis (defining I_z and S_z) is chosen along the effective field direction in the rotating frame.[40] Rotating the density operator in the zero-quantum subspace from S_z^{Δ} to $-S_z^{\Delta}$ leads to a complete transfer of magnetization from I_z to S_z because the double-quantum subspace density operator does not evolve during the APHH period of the experiment.

The above description assumes the ideal case of an isolated dipolar-coupled two-spin system where both spins are on-resonance. In the presence of chemical-shift offsets the amplitudes of the rf-fields have to be replaced by the effective fields $\omega_{I,\text{eff}} = \sqrt{(\omega_{1I}(T))^2 + \Omega_I^2}$ and $\omega_{S,\text{eff}} = \sqrt{(\omega_{1S}(T))^2 + \Omega_S^2}$, respectively.[40] In addition, the effective dipolar-coupling frequency $d_{f,\text{eff}}$ becomes weakly time dependent with T.

Adiabatic cross polarization can also be done using the J coupling as a transfer mechanism in liquid[41,42] and solid[43] samples. If we consider the isotropic J-coupling in addition to the dipolar coupling, we can get polarization transfer under MAS for the $f = 0$ matching condition[43] with $d_{0,\text{eff}} = J$. If the system is not isolated but has homonuclear dipolar couplings we can also get polarization transfer for the $f = 0$ and for the $|f| > 2$ matching conditions and the coupling strength of the $f = \pm 1, \pm 2$ matching conditions is modified.

The experimental results of Figure 4 show that adiabatic-passage Hartmann–Hahn cross polarization yields an S-spin signal that is always equal to or larger than the one obtained using Hartmann–Hahn cross polarization with the same contact time. At longer contact times where the transient oscillations[44] are dying out (in the example of Figure 4 for $\tau > 0.4$ ms) a gain of a factor of two in signal is

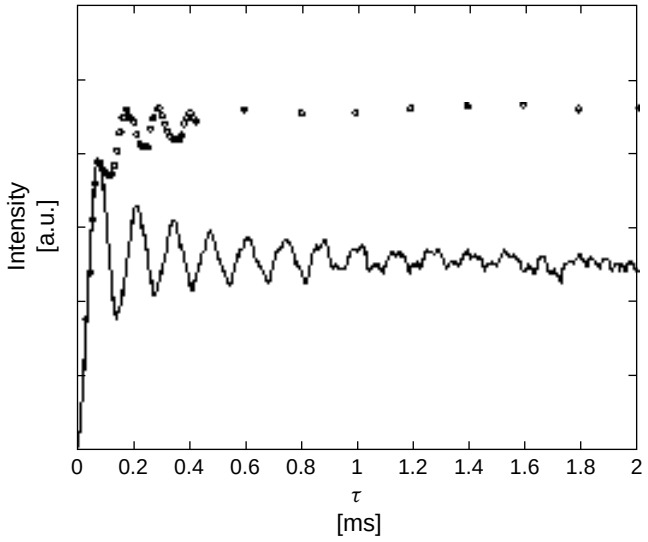

Figure 4 Comparison of the cross-polarized magnetization in Hartmann–Hahn cross polarization (solid line) and adiabatic passage Hartmann–Hahn cross polarization (open circles) measured on a sample of 10% 2-^{13}C-3,3,3-^{2}H-alanine diluted in perdeuterated alanine. The Hartmann–Hahn cross polarization shows the transient oscillations of the one-bond heteronuclear carbon–proton dipolar coupling as a function of the cross-polarization time τ. The adiabatic passage cross polarization is also shown as a function of the total sweep length and leads to a signal which is larger by a factor of almost two. The experiments were carried out at a spinning speed of $\omega_r/2\pi = 22\,\text{kHz}$ using the $f-1$ matching condition and a proton field strength of $\omega_{1I}/2\pi = 108\,\text{kHz}$. (Figure courtesy of René Verel)

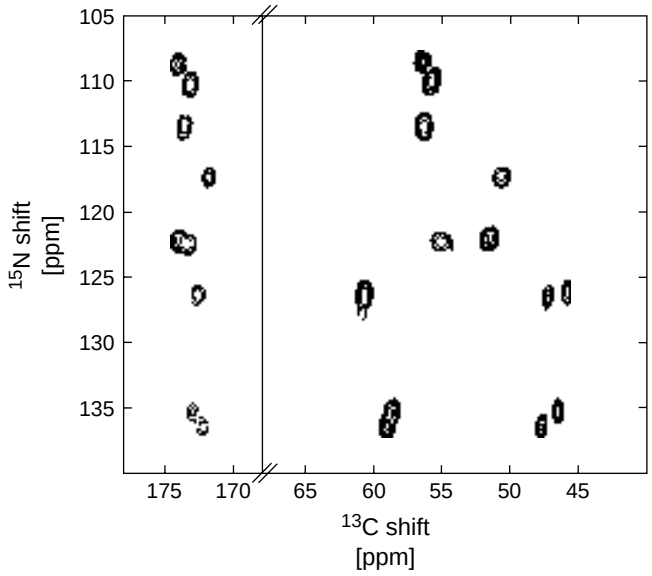

Figure 5 Chemical shift correlation spectrum for a fully ^{13}C, ^{15}N-labelled sample of the cyclic decapeptide antamanide using adiabatic passage Hartmann–Hahn cross polarization. The resulting spectrum correlates each amide nitrogen N_κ with the directly attached carbons: C_α^κ in the same residue and $C'_{\kappa-1}$ in the previous residue. (Figure courtesy of Dr. Andreas Detken)

observed caused by an improved polarization transfer. The theoretical gain of the APHH CP compared to the conventional cross polarization experiment in larger spin systems (IS_n) have been investigated.[21] It was found that APHH CP should always outperforms CP by a factor close to two. For a large system with $n \to \infty$, the theoretical gain is again two[21] although experimentally much lower gains have been found.[17]

A further benefit of the APHH CP experiment is the insensitivity to the matching condition. For small dipolar couplings and fast spinning, the Hartmann–Hahn match is very narrow. It can become quite difficult to match the rf amplitudes and to keep the rf amplitude stable enough over the course of signal accumulation.[45] An example for such a difficult system is ^{13}C–^{15}N cross polarization. For the APHH experiments,[20] these difficulties are greatly reduced because the precise matching condition will be fulfilled at some time during the sweep. The exact position does not play a significant role. Figure 5 shows an example of a heteronuclear ^{13}C–^{15}N correlation experiment where APHH cross polarization between ^{13}C and ^{15}N was used to establish the chemical-shift correlation.[20]

An additional gain in signal intensity can be realized due to the relative insensitivity of APHH cross polarization to rf-field inhomogeneities. Only part of the sample is exactly at the Hartmann–Hahn match of the rf-fields in normal cross polarization. This problem is overcome by APHH cross polarization where all spins go through the matching condition but at different times during the sweep. A similar approach can also be used in 'sudden' experiments by ramping the amplitude

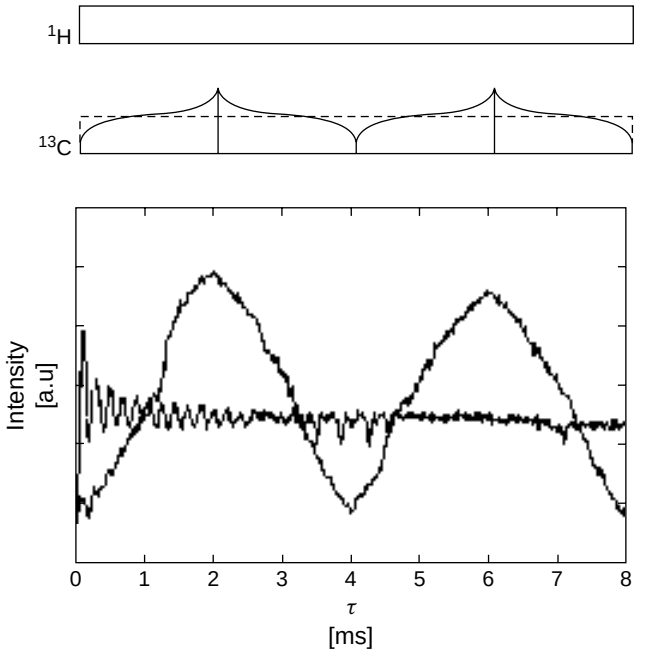

Figure 6 Multiple adiabatic sweeps through the Hartmann–Hahn matching condition allow the reversible transfer of magnetization between protons and carbons. The experiments were carried out using a sample of 10% 2-^{13}C-3,3,3-^{2}H-alanine diluted in perdeuterated alanine. The spinning speed was $\omega_r/(2\pi) = 22\,\text{kHz}$. The $f = -1$ matching condition and a proton field strength of $\omega_{1I}/(2\pi) = 108\,\text{kHz}$ were used. Each of the four adiabatic sweeps had a length of 2 ms. For comparison we also show the intensity of the magnetization which was obtained in the corresponding Hartmann–Hahn cross-polarization experiment as a function of the cross-polarization time. (Figure courtesy of René Verel)

in a CP experiment.[46,47] The ramp CP experiment leads to an equilibrium polarization of ca. 50% in two-spin systems even in the presence of rf-field inhomogeneity but the adiabatic gain of an additional factor of two can only be obtained if the design principles for an adiabatic transfer are employed.

The adiabatic gain can be experimentally verified by an experiment where several adiabatic sweeps are performed sequentially as shown in Figure 6. The behavior during the first sweep is completely equivalent to the one in Figure 5. During the second sweep ($2\,\text{ms} \leq \tau \leq 4\,\text{ms}$) the polarization is transferred back from the ^{13}C spins to the source spin(s), in this case the protons. The whole cycle can be repeated again without noticeable loss of polarization. The polarization in the adiabatic experiments flows back and forth approximately symmetrically around the equilibrium value obtained in a normal CP experiment. The initial jump in the magnetization at $\tau < 1\,\text{ms}$ is due to the initial projection of equation (15).

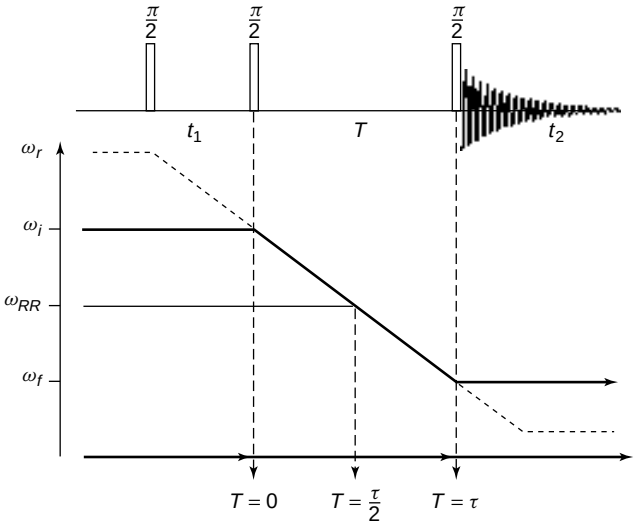

Figure 7 Pulse scheme of the APRR experiment. The pulse scheme follows the basic principle of two-dimensional exchange spectroscopy. The variation of the spinning rate was obtained by using a home-built setup consisting of a parallel arrangement of an air line with a needle valve to control the flow and an air line with a TTL-operated air-valve. This arrangement was placed in parallel with the spinning-speed controller. Upward and downwards spinning-speed ramps were produced by opening or closing the air valve using a user-defined TTL gate from the pulse programmer. Using a 4 mm rotor, a maximum slope of $6000\,\text{s}^{-2}$ was obtained. For higher spinning speeds (>5000 Hz) downward ramps perform better, for low spinning speed upward ramps should be used. If a stable spinning frequency during the t_1 and t_2 periods is not required the linear ramp can be extended (dashed line) to include these time periods. (Figure adapted from Ref.[23])

4 METHODS OF HOMONUCLEAR POLARIZATION TRANSFER

4.1 Adiabatic Passage Rotational Resonance

In the adiabatic passage, rotational-resonance experiment (APRR)[23] the frequency of the rotor is changed during the course of the experiment such that the rotor frequency is swept through the rotational-resonance (RR) condition[24–26] $\Omega_1 - \Omega_2 = n \cdot \omega_r$ in an adiabatic fashion (Figure 7). Such a spinning-frequency sweep can be achieved by suddenly increasing (decreasing) the air pressure on the drive air of the MAS rotor. This can be implemented either by changing

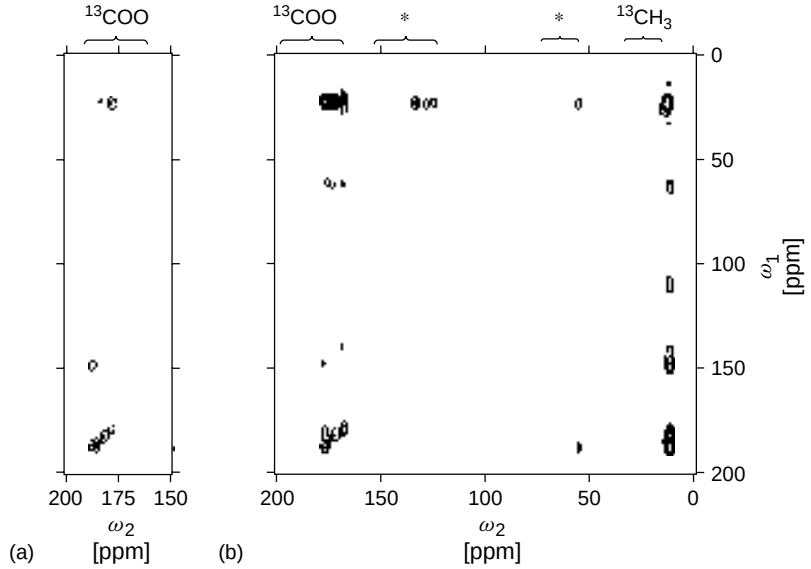

Figure 8 (a) Two-dimensional ^{13}C chemical-shift correlation spectrum of uniformly ^{13}C labelled calcium-acetate monohydrate using RR as a mixing sequence. The strip from the 2D spectrum shows the carboxylic diagonal peaks and the cross peaks to the methyl group region for an experiment recorded at a constant spinning frequency matching the rotational resonance for the spin pair involving the most shielded carboxylic resonance. (b) Two-dimensional ^{13}C chemical-shift correlation spectrum of uniformly ^{13}C labelled calcium-acetate monohydrate using APRR as the mixing sequence. During the mixing time of 40 ms, the spinning frequency was ramped from 1.70 kHz to 1.88 kHz. The APHH passage covered all the $n = 4$ resonances between methyl and carboxylic spins. Four transients were co-added for each of the 256 t_1 increments recorded. The assignment of the resonance lines is given on top of the figure, the chemical shifts are referenced to TMS. Spinning sidebands are denoted by *. (Figure adapted from Ref.[23])

the setting of the spinning-speed controller from the pulse programmer or by using a magnetic valve which opens a bypass high-pressure line.

As the APHH CP experiment, the APRR experiment is a zero-quantum polarization-transfer experiment and the relevant Hamiltonian is the same as for APHH

$$\mathcal{H}^{\Delta}(T) = \chi^{\Delta}(T) \cdot S_z^{\Delta} + |d_{n,\mathrm{eff}}| \cdot S_x^{\Delta} \tag{26}$$

except that $\chi^{\Delta}(T) = \Omega_1 - \Omega_2 - n\omega_r(T)$ where Ω_1 and Ω_2 are the isotropic chemical shifts of the two spins. The effective coupling $d_{n,\mathrm{eff}}$ is given by the Fourier component $n = \pm 1, \pm 2$ of the homonuclear dipolar coupling. Again, a rotation of the density operator from S_z^{Δ} to $-S_z^{\Delta}$ induced by a variation of the MAS frequency, leads to a full transfer of magnetization from spin 1 to spin 2 as the double-quantum subspace is untouched.

In the presence of a non-vanishing chemical-shielding difference tensor the effective coupling frequencies are somewhat modified and higher-order matching conditions with $|n| > 2$ become allowed.

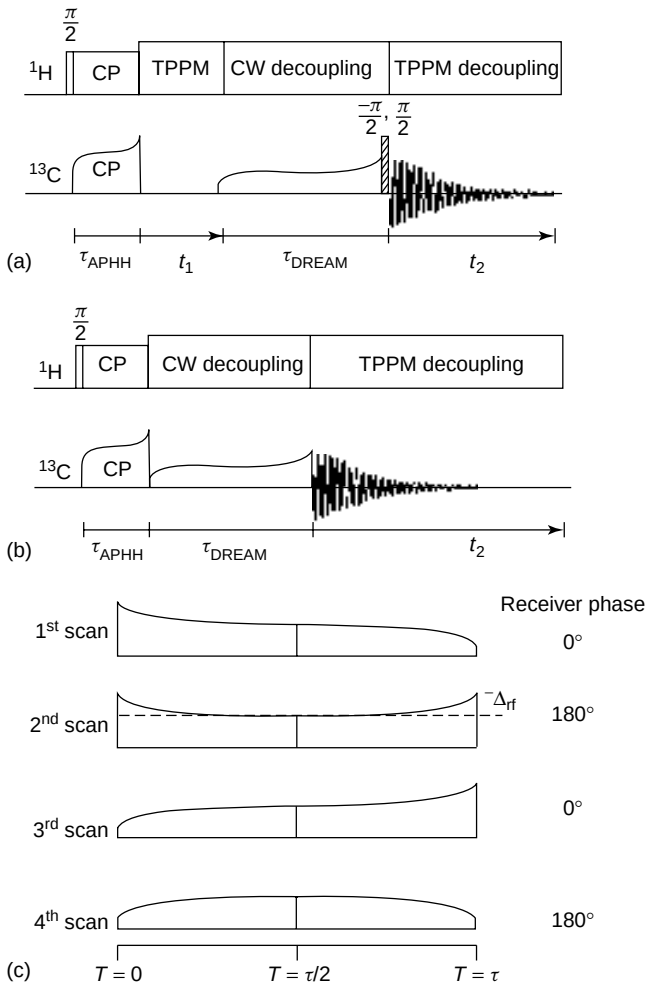

Figure 9 Pulse sequence for (a) the two-dimensional DREAM correlation experiment and (b) the DREAM spin-pair selective experiments. (c) Four different amplitude shapes which can be used in the spin-pair filter experiment and appropriate modification of the receiver phase. (Figure adapted from Ref.[33])

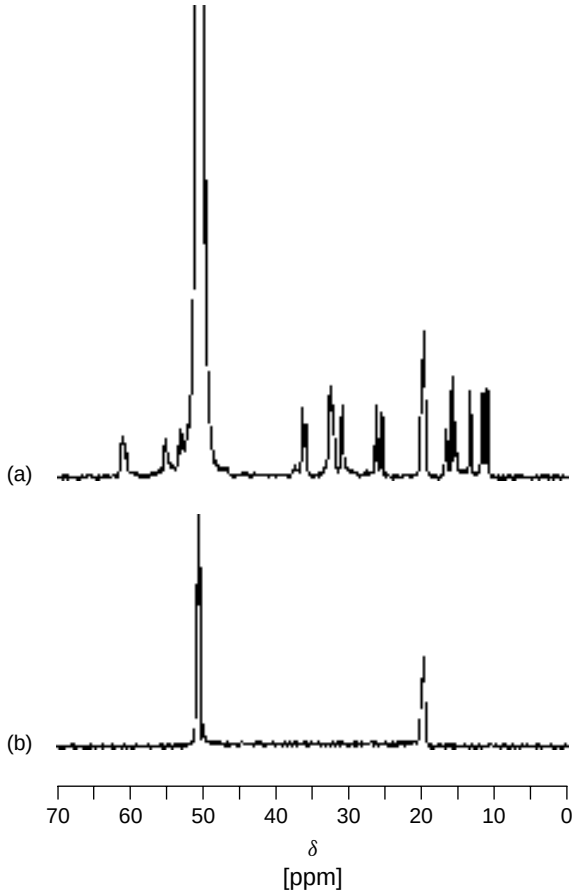

Figure 10 Cross polarization (a) and DREAM SPS (b) spectra of a mixture of 1-$^{13}C_1$-alanine, natural abundance methionine and natural abundance *iso*-leucine. The three substances were mixed in approximately equal weight parts and the sample restricted to the central region of the rotor with a total length of about 3 mm. A total of 3072 scans was co-added for each of the spectra. The spinning frequency was set to $\omega_r/2\pi = 28$ kHz and stabilized within 25 Hz with a spinning speed controller. (Figure adapted from Ref.[32])

One can perform the rotational-resonance experiment also in a tilted frame of reference where the chemical shifts of spins 1 and 2 have to be replaced by the effective fields $\omega_{1,\mathrm{eff}} = \sqrt{(\omega_1(T))^2 + \Omega_1^2}$ and $\omega_{2,\mathrm{eff}} = \sqrt{(\omega_1(T))^2 + \Omega_2^2}$, respectively.[28–30] Instead of a sweep of the spinning frequency ω_r one can change the effective fields as a function of T. The experiment is almost completely equivalent to the spinning-frequency ramp except that the variation of $\chi^{\Delta}(T)$ is now caused by rf-field amplitude changes in full analogy to the APHH experiment.

Figure 8 shows a comparison of a standard RR experiment (Figure 8a) and an APRR experiment (Figure 8b) on a sample of uniformly labelled calcium acetate. The three different resonance lines in the carboxyl region of the spectrum are due to packing effects. The four crystallographically non-equivalent carbonyl carbons give rise to three resolved resonances. The APRR experiment is more broadband and covers all three resolved $^{13}CH_3-{}^{13}COO$ spin pairs while the RR experiment (Figure 8a) leads to transfer for one of these pairs only. Furthermore, APRR shows much higher cross peak intensity. For a fully adiabatic transfer we would expect all intensity to

be in the cross peaks with no intensity left in the diagonal peaks.

Rotational-resonance experiments on the central transition of a pair of dipolar-coupled half-integer quadrupolar spins can be described in full analogy to the rotational resonance experiments in spin-1/2 nuclei if at least one of the two quadrupolar nuclei has a large quadrupolar coupling constant. In half-integer quadrupolar nuclei the central transition is broadened by the second-order quadrupolar shift. Therefore, the conventional rotational-resonance experiment will only allow polarization transfer for a small number of spins which have an averaged chemical-shift difference close to the selected MAS rotation frequency. If we use a sweep through the rotational-resonance condition of all crystallites, then we are able to achieve recoupling for the whole second-order broadened powder pattern and we obtain polarization transfer independent of the crystallite orientation.[27]

4.2 DREAM

In the DREAM experiment[32,33] (Figure 9) a sweep of the rf-field amplitude through the HORROR recoupling condition[31] $2 \cdot \omega_1 = \omega_r$ is used to transfer polarization between homonuclear dipolar-coupled spin pairs. The relevant subspace of the homonuclear dipolar-coupling Hamiltonian is the double-quantum subspace $\kappa = \Sigma$. The Hamiltonian in this subspace is again of the 'standard form' and is given by

$$\mathcal{H}^{\Sigma}(T) = \chi^{\Sigma}(T) S_z^{\Sigma} + |d_{1,\mathrm{eff}}| S_x^{\Sigma} \tag{27}$$

with $\chi^{\Sigma}(T) = 2 \cdot \omega_1(T) - \omega_r$ where $\omega_1(T)$ is the time-dependent rf-field amplitude and $d_{1,\mathrm{eff}}$ is the $f = 1$ Fourier component of the homonuclear dipolar-coupling constant. The fictitious spin-1/2 operators are defined as $S_z^{\Sigma} = (1/2) \cdot (S_{1z} + S_{2z})$, $S_x^{\Sigma} = (1/2) \cdot (S_1^+ S_2^+ + S_1^- S_2^-)$, and $S_y^{\Sigma} = (i/2) \cdot (S_1^+ S_2^+ - S_1^- S_2^-)$ where the z-axis (defining S_{1z} and S_{2z}) is along the applied rf-field. A rotation of the density operator from S_z^{Σ} to $-S_z^{\Sigma}$ leads to a full transfer of polarization from spin 1 to spin 2 assuming that no zero-quantum transitions take place.

The DREAM recoupling sequence has been used as the mixing scheme in two-dimensional correlation experiments (Figure 9a) and in the context of an efficient homonuclear spin-pair filter (Figure 9b) by combining different shapes for the adiabatic sweep. Such a filter is more efficient than a 'sudden' double-quantum filter since not all crystallites need to go through the double-quantum state $S_x^{\Sigma} \cos(\varphi) + S_y^{\Sigma} \sin(\varphi)$ at the same point in time. The different amplitude shapes and their corresponding receiver phase are shown in Figure 9c.

Figure 10 shows an application of the DREAM spin-pair filter to the suppression of natural abundance background signals in a mixture of the amino acids alanine, methionine, and *iso*-leucine. The C_α position of alanine was ^{13}C labelled, all other carbon atoms had natural isotopic abundance. The filtered spectrum (Figure 10b) shows only the alanine C_α,C_β spin-pair resonances, all other resonance are attenuated below the noise level. The efficiency of the selection of the adiabatic spin-pair filter is measured to be 61% from the intensity of the CH_3 resonance. The higher intensity of the (100% labeled) C_α resonance compared to the C_β resonance can be explained by intermolecular $C_\alpha - C_\alpha$ couplings that allow additional spin pairs to pass partially through the filter and is not due to incomplete suppression of isolated spins.

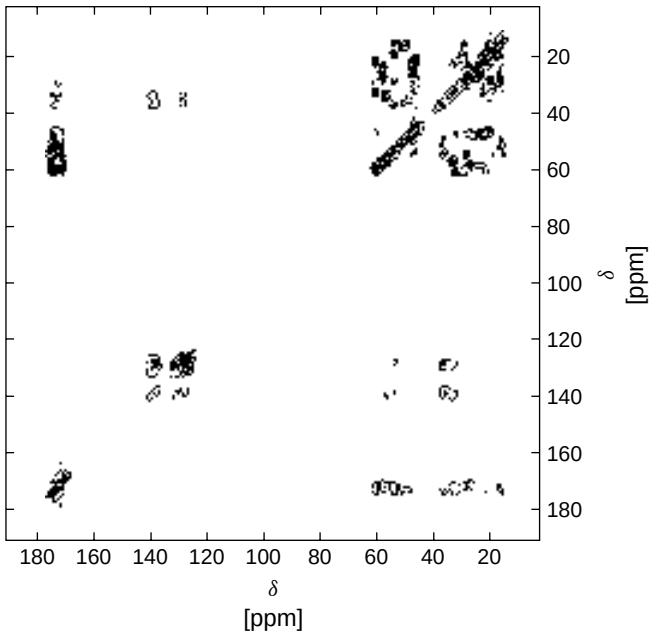

Figure 11 Two-dimensional ^{13}C chemical shift correlation spectrum of the cyclic decapeptide Antamanide using adiabatic DREAM mixing. The spectrum was recorded at a spinning frequency of $\omega_r(2\pi) = 40$ kHz at a proton Larmor frequency of 500 MHz. (Figure courtesy of Aswin Verhoeven)

Figure 11 shows the application of the DREAM sequence as the correlation mechanism in a two-dimensional chemical-shift correlation spectrum. Due to the fact that it is a double-quantum mixing scheme the cross peaks show alternating negative and positive intensities. The spectrum was taken at a MAS frequency of $\omega_r/(2\pi) = 40$ kHz using an rf-field strength at the center of the sweep of $\omega_1/(2\pi) = 20$ kHz. Many dipolar recoupling sequences suffer from the fact that they are more difficult to apply at higher spinning frequencies since the rf-field has to be an integer multiple of the spinning frequency. For DREAM the required rf-field strength is only 1/2 of the spinning frequency which makes the DREAM method very well suited for application at high MAS frequencies. In fact, the method becomes more useful at higher MAS frequencies because the broadbandedness of the DREAM mixing with respect to chemical-shift offsets increases linearly with ω_r. As a rule of thumb, the bandwidth of the sequence is approximately equal to $\pm\omega_r/4$. To cover an entire ^{13}C spectrum on a spectrometer with 400 MHz proton resonance frequency, a spinning frequency of about 35 kHz is required.

5 RELATED ARTICLES IN THIS VOLUME

Three-dimensional Molecular Structures in Uniformly Labelled Solids Determined Using Rotational Resonance in the Tilted Rotating Frame; Magic-angle Spinning Extensions.

6 RELATED ARTICLES IN VOLUMES 1–8

Average Hamiltonian Theory, Volume 2; Cross Polarization in Rotating Solids: Spin-1/2 Nuclei, Volume 3; Cross Polarization in Solids, Volume 3; Floquet Theory, Volume 3; Homonuclear Recoupling Schemes in MAS NMR, Volume 4; Magic Angle Spinning, Volume 5; Rotating Solids, Volume 7.

7 REFERENCES

1. S. R. Hartmann and E. L. Hahn, *Phys. Rev.*, 1962, **128**, 2042.
2. A. Pines, M. G. Gibby, and J. S. Waugh, *J. Chem. Phys.*, 1972, **56**, 1776.
3. N. Bloembergen, *Physica*, 1949, **15**, 386.
4. G. A. Morris and R. Freeman, *J. Am. Chem. Soc.*, 1979, **101**, 760.
5. J. Jeener, B. H. Meier, P. Bachmann, and R. R. Ernst, *J. Chem. Phys.*, 1979, **71**, 4546.
6. S. Zhang, B. H. Meier, and R. R. Ernst, *Phys. Rev. Lett.*, 1992, **69**, 2149.
7. S. M. De Paul, M. Tomaselli, A. Pines, M. Ernst, and B. H. Meier, *J. Chem. Phys.*, 1998, **108**, 826.
8. M. Ernst, B. H. Meier, M. Tomaselli, and A. Pines, *J. Chem. Phys.*, 1998, **108**, 9611.
9. M. Ernst, B. H. Meier, M. Tomaselli, and A. Pines, *Mol. Phys.*, 1998, **95**, 849.
10. A. Abragam, 'The Principles of Nuclear Magnetism', Clarendon Press: Oxford, 1961.
11. S. Zhang, P. Xu, O. W. Sorensen, and R. R. Ernst, *Concepts Magn. Reson.*, 1994, **6**, 275.
12. A. Wokaun and R. R. Ernst, *J. Chem. Phys.*, 1977, **67**, 1752.
13. S. Vega, *J. Chem. Phys.*, 1978, **68**, 5518.
14. A. Pines, in 'First Specialized Colloque Ampere', Krakow: Poland, 1973.
15. M. Mehring, 'Principles of High Resolution NMR in Solids', 2nd edn., Springer: Berlin, 1983.
16. S. Hediger, B. H. Meier, N. D. Kurur, G. Bodenhausen, and R. R. Ernst, *Chem. Phys. Lett.*, 1994, **223**, 283.
17. S. Hediger, B. H. Meier, and R. R. Ernst, *Chem. Phys. Lett.*, 1995, **240**, 449.
18. S. Zhang, C. L. Czekay, and W. T. Ford, *J. Magn. Reson. Ser. A*, 1994, **111**, 87.
19. S. Zhang, *J. Magn. Reson. Ser. A*, 1994, **110**, 73.
20. M. Baldus, D. G. Geurts, S. Hediger, and B. H. Meier, *J. Magn. Reson. Ser. A*, 1996, **118**, 140.
21. P. Hodgkinson and A. Pines, *J. Chem. Phys.*, 1997, **107**, 8742.
22. S. Hediger, P. Signer, M. Tomaselli, R. R. Ernst, and B. H. Meier, *J. Magn. Reson.*, 1997, **125**, 291.
23. R. Verel, M. Baldus, M. Nijman, J. W. M. van Os, and B. H. Meier, *Chem. Phys. Lett.*, 1997, **280**, 31.
24. D. P. Raleigh, A. C. Kolbert, T. G. Oas, M. H. Levitt, and R. G. Griffin, *J. Chem. Soc., Faraday Trans.*, 1988, **84**, 3691.
25. M. G. Colombo, B. H. Meier, and R. R. Ernst, *Chem. Phys. Lett.*, 1988, **146**, 189.
26. M. H. Levitt, D. P. Raleigh, F. Creuzet, and R. G. Griffin, *J. Chem. Phys.*, 1990, **92**, 6347.
27. M. Nijman, M. Ernst, A. P. M. Kentgens, and B. H. Meier, *Mol. Phys.*, 2000, **98**, 161.
28. K. Takegoshi, K. Nomura, and T. Terao, *Chem. Phys. Lett.*, 1995, **232**, 424.
29. K. Takegoshi, K. Nomura, and T. Terao, *J. Magn. Reson.*, 1997, **127**, 206.
30. P. R. Costa, B. Q. Sun, and R. G. Griffin, *J. Am. Chem. Soc.*, 1997, **119**, 10 821.
31. N. C. Nielsen, H. Bildsoe, H. J. Jakobsen, and M. H. Levitt, *J. Chem. Phys.*, 1994, **101**, 1805.
32. R. Verel, M. Baldus, M. Ernst, and B. H. Meier, *Chem. Phys. Lett.*, 1998, **287**, 421.
33. R. Verel, M. Ernst, and B. H. Meier, *J. Magn. Reson.*, 2001, **150**, 81.
34. M. Baldus, D. Rovnyak, and R. G. Griffin, *J. Chem. Phys.*, 2000, **112**, 5902.
35. J. Baum, M. Munowitz, A. N. Garroway, and A. Pines, *J. Chem. Phys.*, 1985, **83**, 2015.
36. C. J. Hardy, W. A. Edelstein, and D. Vatis, *J. Magn. Reson.*, 1986, **66**, 470.
37. R. A. Wind, S. F. Dec, H. Lock, and G. E. Maciel, *J. Magn. Reson.*, 1988, **79**, 136.
38. M. Sardashti and G. E. Maciel, *J. Magn. Reson.*, 1987, **72**, 467.
39. B. H. Meier, *Chem. Phys. Lett.*, 1992, **188**, 201.
40. M. H. Levitt, D. Suter, and R. R. Ernst, *J. Chem. Phys.*, 1986, **84**, 4243.
41. R. D. Bertrand, W. B. Moniz, A. N. Garroway, and G. C. Chingas, *J. Am. Chem. Soc.*, 1978, **100**, 5227.
42. G. C. Chingas, A. N. Garroway, W. B. Monitz, and R. D. Bertrand, *J. Am. Chem. Soc.*, 1980, **102**, 2526.
43. A. Verhoeven, R. Verel, and B. H. Meier, *Chem. Phys. Lett.*, 1997, **266**, 465.
44. L. Muller, A. Kumar, T. Baumann, and R. R. Ernst, *Phys. Rev. Lett.*, 1974, **32**, 1402.
45. E. W. Hagaman, P. C. Ho, L. L. Brown, F. M. Schell, and M. C. Woody, *J. Am. Chem. Soc.*, 1990, **112**, 7445.
46. G. Metz, Xiaoling-Wu, and S. O. Smith, *J. Magn. Reson. Ser. A*, 1994, **110**, 219.
47. G. Metz, M. Ziliox, and S. O. Smith, *Solid State NMR*, 1996, **7**, 155.

Biographical Sketches

Matthias Ernst, *b* 1964. Dipl. Chem., 1988; Dr. sc. nat., 1993, ETH Zürich, Switzerland, with Prof. Richard R. Ernst. Postdoctoral Fellow, University of California at Berkeley, USA, with Prof. Alexander Pines, 1994–1996; Research scientist, University of Nijmegen, The Netherlands, 1996–1998; Research Scientist, ETH Zürich, Switzerland, 1998–present. Research interests include development of new methods for high-resolution solid-state NMR and application of these techniques to materials and biological systems.

Beat H. Meier, *b* 1954. Dipl. Chem., 1978; Dr. sc. nat., 1984, ETH Zürich, Switzerland, with Prof. Richard R. Ernst. Postdoctoral Fellow, 1985–1986, Los Alamos National Laboratory, USA, with Dr. William Earl; Research scientist, 1987–1994, ETH Zürich, Switzerland. Professor of Chemistry, University of Nijmegen, The Netherlands, 1994–1998; Professor of Chemistry, ETH Zürich, Switzerland, 1998–present. Research interests include development of new methods for high-resolution solid-state NMR and application of these techniques to materials and biological systems.

Centerband-Only Detection of Exchange (CODEX): Efficient NMR Analysis of Slow Motions in Solids

Klaus Schmidt-Rohr

Iowa State University, Ames, IA, USA

&

Eduardo R. deAzevedo and Tito J. Bonagamba

Instituto de Física de São Carlos, Universidade de São Paulo, São Carlos, São Paulo, Brazil

1	Introduction	1
2	Exchange NMR Under MAS, and Rotor Synchronization	1
3	Explanation of the CODEX Pulse Sequence	2
4	Analysis and Simulation of CODEX Curves	3
5	Practical Considerations	7
6	Applications of CODEX	8
7	Outlook	8
8	Related Articles in Volumes 1–8	9
9	References	9

1 INTRODUCTION

Solid-state NMR provides some of the most powerful techniques for elucidating details of segmental dynamics in solid materials.[1] Such dynamics have important effects on mechanical and conduction properties of polymers, activity of proteins, stability of pharmaceuticals, transport properties in zeolites, and behavior of amorphous materials near the glass transition.[2–7] While fast dynamics can be characterized to some extent by NMR lineshape analysis and relaxation-time measurements can characterize correlation times over a wide range (see also **Ultraslow Motions in Solids,** Volume 8), the most specific information is obtained in exchange NMR experiments, where relatively slow segmental reorientations with rates of $0.1-10\,000\,s^{-1}$ are observed in terms of changes of orientation-dependent NMR frequencies.[1,8–11] Correlation times and their distributions, reorientation-angle distributions, orientational memory, rate memory, the existence of dynamic heterogeneities, and their size can be characterized by 1D, 2D, 3D, and reduced 4D exchange NMR (see **Polymer Dynamics & Order from Multidimensional Solid State NMR,** Volume 6).[1,12–20] However, the sensitivity and resolution of these traditional exchange-NMR techniques have been limited, since anisotropy-broadened lineshapes or strong sidebands in magic-angle spinning spectra were required. Only by specific isotopic labeling could these limitations be eliminated in part.

The centerband-only detection of exchange (CODEX) NMR technique has overcome these problems, making it possible to observe and characterize slow ($k = 0.1\,s^{-1}$ to $3000\,s^{-1}$) segmental reorientations with the highest available NMR sensitivity and site resolution, in sideband-free magic-angle spinning spectra.[21,22] From short series of one-dimensional macroscopic rotation of the sample (MAS) spectra, the correlation function and correlation time can be determined, and it can be established whether the motion is diffusive or whether it involves jumps between discrete sites, whose number can be measured precisely if all segments are mobile. In addition, motional amplitudes can be estimated, with relatively high sensitivity to small-angle motions. This information is obtained for each site with a resolved line in the sideband-free MAS spectrum.

2 EXCHANGE NMR UNDER MAS, AND ROTOR SYNCHRONIZATION

Figure 1(a) shows the principle of stimulated-echo and exchange-NMR experiments, of which CODEX is an example.[13,16,23–26] After evolution of transverse magnetization during a time t_1, one component of the magnetization is stored along the z-direction during the long mixing time t_m. After a 90° read-out pulse, a stimulated echo forms at $t_2 = t_1$ for segments that did not change frequency during t_m. A pure stimulated echo is obtained by storing the two orthogonal components of the magnetization before t_m in alternate transients and combining their signals after read-out pulses of suitable phase (see Figure 1(a)). In a 2D exchange experiment, the time signal during the period t_2 is observed, and the t_1 period is incremented systematically.

The first exchange NMR experiments to measure reorientations under MAS were performed by Kentgens et al.[27] Their crucial innovation was the introduction of 'rotor synchronization' of the pulse sequence, i.e., making sure that t_m is an integer number of rotation periods, so that the precession of the magnetization resumes at the same rotor orientation where it stopped at the beginning of the mixing time. Otherwise, reorientations of segments relative to the external field occur due to the MAS and overwhelm the more subtle effects of intrinsic segmental reorientations. In later experiments, synchronization with the beginning of the evolution period was also used, in order to achieve pure-phase 2D MAS exchange spectra.[28] Recently introduced one-dimensional versions of the sideband-exchange experiment use similar rotor synchronization.[29,30]

Rotor synchronization for short mixing times can be achieved simply by precise timing of the mixing time. However, for long mixing times, this is not sufficient. For instance, a ±1-Hz deviation from the rotation rate results in a ±36°-deviation in the rotor phase after 100 ms, and complete uncertainty of the rotor phase after $t_m = 1$ s. Therefore, trigger-based active rotor synchronization is necessary. The optical signal of the spinning-speed detector, usually made discrete into 'high' and 'low' states by a Schmitt trigger, is used to start the pulse sequence at a certain rotor orientation, namely at the transition from high to low or low to high. Based on the trigger, one can resume pulsing at the same rotor orientation tens or hundreds of rotations later. In practice, triggering during a pulse such

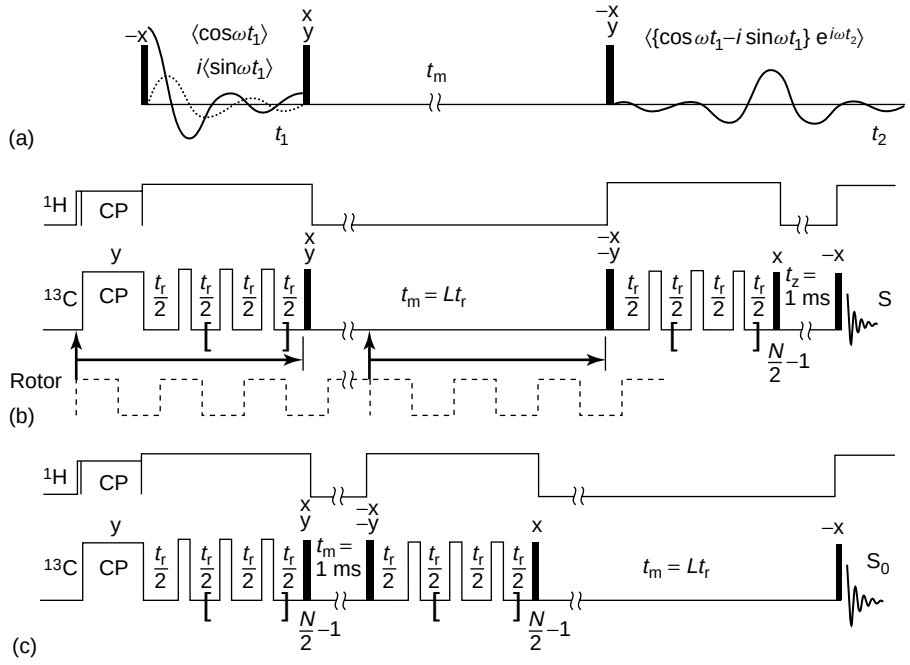

Figure 1 (a) Basic stimulated-echo and exchange-NMR pulse sequence. The fundamental time signals that produce the stimulated echo are indicated. Pointed brackets indicate powder averaging. Cosine and sine components measured with the indicated pulse phases are added in subsequent transients. (b) Basic CODEX pulse sequence and its synchronization with the sample rotation. 90° pulses are shown filled. The series of 180° pulses (short open boxes) during t_1 and t_2 recouple the anisotropic chemical shift, while removing the isotropic shift. The xy-8 phase sequence is used for the 180°-pulse trains. Note the change in the phase of the read-out pulse for the sine-component (+y in (a), −y here); it is required to achieve the correct chemical-shift recoupling. (c) Pulse sequence for obtaining the reference signal S_0, produced by interchanging t_m and t_z in the sequence (b)

as cross polarization should be avoided – in case the trigger signal is absent, the pulse would last indefinitely. To ensure the same rotor orientation at the beginning and end of t_m, the (relatively short) time period between the trigger signal and the start of t_m is reproduced after a trigger signal near the end of t_m. This is indicated by the bold arrows at the bottom of Figure 1(b). Consistent triggering requires the trigger mark on the rotor to be sharp; in practice, a straight pen mark is found to be sufficient.

3 EXPLANATION OF THE CODEX PULSE SEQUENCE

Simply put, CODEX is a stimulated-echo experiment under MAS conditions, with chemical-shift-anisotropy recoupling and intensity referencing in the tradition of REDOR.[31] Figure 1(b) shows the CODEX pulse sequence. After cross-polarization (or single-pulse excitation), the magnetization evolves under the anisotropic chemical shift, recoupled by a series of 180° pulses spaced by $t_r/2$.[22,32] Then, one component of the magnetization is stored for the mixing time t_m, during which motion can occur. The mixing time is a multiple of the rotation period t_r. In successive transients, the phases of the 90°-pulses that bracket the mixing time are changed together by 90°, so that both components, $\cos\Phi_1$ and $\sin\Phi_1$, of the magnetization are retained alternately. If the storage pulse and the read-out pulse always have opposite signs, the sum of two transients yields $\cos\Phi_1 + i\sin\Phi_1$. Except for a scaling factor of 0.5, the signal is effectively the same as if no 90°-pulses and mixing time had been applied, and a rotor echo forms at the end of the second recoupling period ($t_2 = t_1$).

The total phase $\Phi_1 + \Phi_2 = |\Phi_2| - |\Phi_1|$ of the magnetization at the end of the second recoupling period of duration $N/2\ t_r$ is obtained from

$$\Phi_1 = \frac{N}{2}\left(-\int_0^{t_r/2}\omega_1(t)\,\mathrm{d}t + \int_{t_r/2}^{t_r}\omega_1(t)\,\mathrm{d}t\right) = -N\int_0^{t_r/2}\omega_1(t)\,\mathrm{d}t \quad (1a)$$

$$\Phi_2 = \frac{N}{2}\left(\int_0^{t_r/2}\omega_2(t)\,\mathrm{d}t - \int_{t_r/2}^{t_r}\omega_2(t)\,\mathrm{d}t\right) = N\int_0^{t_r/2}\omega_2(t)\,\mathrm{d}t \quad (1b)$$

with the frequencies $\omega_1(t)$ and $\omega_2(t)$ before and after t_m, respectively.[22] In the second step of equation (1a), a standard result of recoupling of inhomogeneous NMR interactions (e.g., chemical shift anisotropy or spin-pair dipolar couplings) was used.[31,32] If $\omega_1(t) = \omega_2(t)$, i.e., if no exchange occurs, equation (1) leads to $\Phi_1 + \Phi_2 = |\Phi_2| - |\Phi_1| = 0$; in other words, the magnetization is refocused in a stimulated echo along its original direction.

At the end of the second recoupling period, the total magnetization is along the original direction that it had during CP. The full magnetization is stored along the z-axis during the period t_z, and subsequently read out for detection. To suppress spinning sidebands during detection, the total suppression of sidebands (TOSS) sequence can be used before detection.[33] Since motion-induced dephasing can break the cylindrical symmetry around the rotor axis required for TOSS, the duration of t_z is incremented in K steps over a full rotation period.[1] This ensures that TOSS suppresses all sidebands except for orders nK (for details see deAzevedo et al.).[22]

In a simple CODEX experiment, the signal intensity S(t_m, $\delta N t_r$) is observed; here we have normalized the time $N t_r$ with the chemical-shift anisotropy parameter δ.[1] To remove effects of T_1 relaxation during t_m and of T_2 relaxation during $N t_r$, a reference spectrum $S_0 = S(0, \delta N t_r)$ is required that has all the same relaxation factors but no motion during t_m. This is achieved by simply interchanging the durations of t_m and t_z, see Figure 1(c). More generally, the requirement is that in the reference experiment t_m is sufficiently short ($t_m = t_r < 1$ ms) while the sum $t_m + t_z$ is the same as in the actual CODEX spectrum. In practice, effects of spectrometer drift are minimized by alternating measurements between CODEX signal S and reference signal S_0 approximately every five minutes. The ratio S(t_m, $\delta N t_r$)/S(0, $\delta N t_r$) can be plotted as a function of t_m or $\delta N t_r$, to characterize the correlation function or the motional geometry, respectively.

Often, it is advantageous to subtract the CODEX spectrum $S = S(t_m, \delta N t_r)$ from the reference spectrum $S_0 = S(0, \delta N t_r)$, to obtain a pure-exchange CODEX spectrum $\Delta S = S_0 - S$. In this difference spectrum, the signals of non-exchanging components are removed from the spectrum. Figure 2(a) shows an example of this procedure for glassy poly(methyl methacrylate), PMMA, measured near ambient temperature. In Figure 2(b), a series of pure-exchange CODEX spectra of PMMA are plotted as a function of the mixing time; they show that some of the sidegroups of this polymer are undergoing large-amplitude motions in the glassy state.[17,34]

The pure-exchange approach can also serve as a useful 'filter' for the signals of slowly-moving groups in a multi-component system.

The normalized pure-exchange CODEX intensity is given by

$$E(t_m, \delta N t_r) = \frac{\Delta S(t_m, \delta N t_r)}{S(0, \delta N t_r)} = \frac{S(0, \delta N t_r) - S(t_m, \delta N t_r)}{S(0, \delta N t_r)} \quad (2)$$

The nomenclature was chosen in analogy to REDOR, where the normalized dephasing provides information on internuclear distances.[31,22]

The t_m-dependence of the pure-exchange CODEX intensity for PMMA and two crystalline model compounds, dimethyl sulfone (DMS) and methylmalonic acid, is plotted in Figure 3(a). The resulting curves correspond to the correlation functions of these dynamics on the millisecond time scale. For DMS, a single-exponential curve is obtained, while PMMA shows some non-exponentiality. Methylmalonic acid shows no exchange except for ^{13}C spin diffusion (see Section 5.1). In Figure 3(b), exchange due to helical jumps in the crystallites of isotactic polypropylene is shown.[28,21]

4 ANALYSIS AND SIMULATION OF CODEX CURVES

4.1 Reorientation-Angle Analysis Based on the Difference Tensor

CODEX can give more information than just the correlation function obtained by recording the intensity as a function of t_m. Through variation of the duration $N t_r$ of the evolution under the recoupled CSA, the amplitude of the reorientations during t_m can be determined. The nuclear spins evolve for N/2 rotor periods with the phase Φ_1 before t_m, and for N/2 rotor periods with the corresponding phase Φ_2 after t_m. The dephasing factor

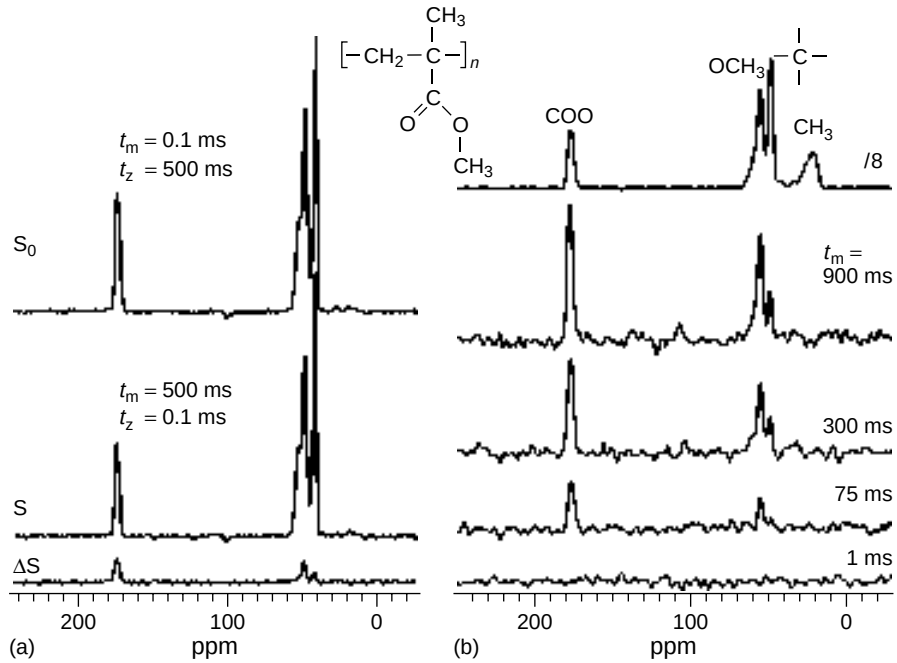

Figure 2 (a) Full reference spectrum S_0, spectrum S after CODEX dephasing and pure-exchange CODEX spectrum $\Delta S = S_0 - S$ of unlabeled PMMA at 300 K, for $t_m = 500$ ms and $N t_r = 800\,\mu$s. The intensity of ΔS is low since only a minority of the sidegroups (35%) are undergoing flips. (b) Series of pure-exchange CODEX spectra of PMMA at 300 K, $\nu_r = 6.5$ kHz, and $N t_r = 615\,\mu$s, as a function of t_m as indicated. For the COO carbon, $\delta N t_r = 8\pi$; for the OCH_3 group, $\delta N t_r = 3.8\pi$. Large-amplitude side-group and smaller-amplitude backbone motions are observed

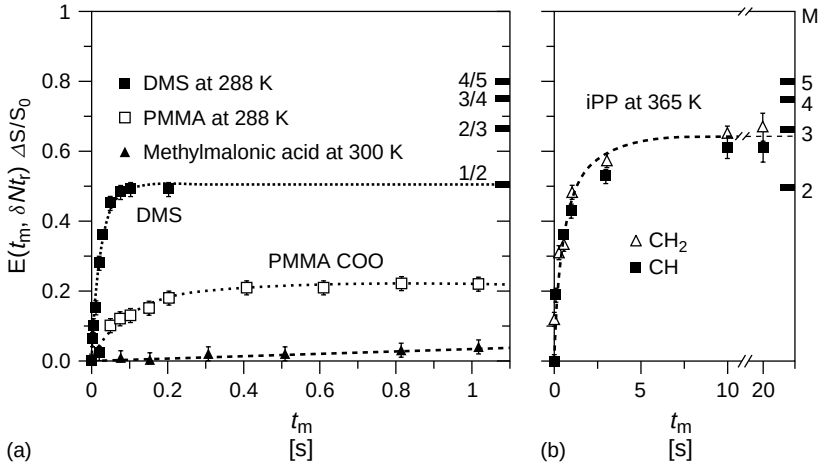

Figure 3 Correlation functions of slow segmental motions obtained from the normalized pure-exchange CODEX intensities $\Delta S/S_0 = E(t_m, \delta N t_r)$ as a function of t_m for (a) COO groups in methylmalonic acid ($T = 300\,K$, $\delta N t_r = 7.6\,\pi$); COO groups in PMMA ($T = 288\,K$, $\delta N t_r = 8\,\pi$); CH_3 groups in DMS ($T = 288\,K$, $\delta N t_r = 12.4\,\pi$); and (b) CH and CH_2 groups in iPP ($T = 365\,K$; $\delta N t_r = 3.6\,\pi$ and $8.5\,\pi$, respectively). On the right, the expected final intensity values for M-site jumps are marked

modulating the amplitude of the signal component detected in the CODEX MAS signal is therefore

$$\frac{S(t_m, \delta N t_r)}{S(0, \delta N t_r)} = \mathrm{Re}\langle \exp(i(\Phi_1 + \Phi_2))\rangle = \langle \cos(|\Phi_2| - |\Phi_1|)\rangle$$
$$= \left\langle \cos\left(N \int_0^{t_r/2} (\omega_2(t) - \omega_1(t))\,\mathrm{d}t \right) \right\rangle \quad (3)$$

The pointed brackets indicate the powder average, which also contains the effect of the correlation time τ_c and mixing time t_m. Note that according to equations (2) and (3), the pure-exchange signal is related directly to the dephasing factor, $E(t_m, \delta N t_r) = 1 - S(t_m, \delta N t_r)/S_0$. In equation (3), the phase $|\Phi_2| - |\Phi_1|$, which depends on $\delta N t_r$ and the reorientation angles (α_R, β_R, γ_R), can be considered as the phase acquired within a time of $N/2\ t_r$ under the action of the chemical-shift difference tensor

$$\overleftrightarrow{\sigma}^{\Delta} = (\overleftrightarrow{\sigma}_2 - \overleftrightarrow{\sigma}_1) \quad (4a)$$

since

$$\omega_2 - \omega_1 = -\gamma B_0 \frac{\vec{B}_0^T}{B_0} (\overleftrightarrow{\sigma}_2 - \overleftrightarrow{\sigma}_1) \frac{\vec{B}_0}{B_0} \quad (4b)$$

The 'width' (principal-value range) $\gamma B_0 N |\sigma_{33}^{\Delta} - \sigma_{11}^{\Delta}|$ of the scaled chemical-shift difference tensor $\gamma B_0 N \overleftrightarrow{\sigma}^{\Delta}$ relative to the spinning speed ω_r determines whether there is significant dephasing due to the anisotropy, i.e., whether the experiment is sensitive to the segmental reorientation. By increasing the number of rotor cycles N, we can enhance the anisotropy to large values $\gamma B_0 N |\sigma_{33}^{\Delta} - \sigma_{11}^{\Delta}| \gg \omega_r$. The useful role of the difference tensor in CODEX simulations will be discussed in Section 4.3 below.

Uniaxial interactions, i.e., with $\eta = 0$, are particularly convenient to treat analytically, because only the unique principal axis needs to be considered. This case is also quite commonly found, e.g., for dipolar couplings in a spin pair or for the ^2H quadrupolar coupling. Therefore, it is instructive to calculate the difference tensor analytically for $\eta = 0$. Due to the uniaxiality, the reorientation is fully characterized by a single reorientation angle β_R between the unique principal axis before and after the mixing time. In the specific case of $\eta = 0$, the principal values of the difference tensor are $\sigma_{22}^{\Delta} = 0$ and the full-width anisotropy $|\sigma_{33}^{\Delta} - \sigma_{11}^{\Delta}|$ of the difference tensor, i.e., the range of possible frequency differences, is[22,35]

$$|\sigma_{33}^{\Delta} - \sigma_{11}^{\Delta}| = |(\sigma_{33} - \sigma_{11}) 2 \sin \beta_R| \quad (5)$$

This represents a strong linear dependence on the reorientation angle for $\beta_R < 45°$, which permits relatively easy detection of small-angle motions. It compares favorably with the more common $(3\cos^2 \beta_R - 1)/2$ angle dependence, which is insensitive to β_R for $\beta_R < 15°$.

Figure 4(a) shows simulated pure-exchange CODEX curves as a function of $\delta N t_r$ for different reorientation angles β_R. The predicted sensitivity to small-angle motions is clearly recognizable. Experimental data points for DMS are also shown. In Figure 4(b), the pure-exchange CODEX intensity $E(\delta N t_r)$ for helical jumps in the crystallites of isotactic polypropylene (iPP) at 365 K and for backbone motion in glassy PMMA at 293 K are shown.[21,28,36] Based on the unitless variable $\delta N t_r$, the motion of iPP is immediately recognized as being of large amplitude, while the methylene groups in the backbone of PMMA reorient by approximately 10°.[22]

For a non-uniaxial interaction, the reorientation of a principal-axes system must be described in terms of three transformation coordinates. As already indicated above, these are usually chosen as the Euler angles α_R, β_R, γ_R between the initial and final PAS orientations. As in the case of $\eta = 0$, calculations of the width of the difference tensor $|\omega_{33}^{\Delta} - \omega_{11}^{\Delta}|$ for general values of η show an initial linear dependence on the reorientation angles β_R and $\varepsilon_R = \alpha_R + \gamma_R$. This can be generally proved by calculating the eigenvalues of the difference tensor for small values of β_R and ε_R.[22]

A simple result is also found for the case of a rotation by an angle β_R' around the n'th principal axis of the interaction tensor $\overleftrightarrow{\sigma}$. Here, $\sigma_{22}^{\Delta} = 0$ and

$$|\sigma_{33}^{\Delta} - \sigma_{11}^{\Delta}| = |(\sigma_{kk} - \sigma_{mm}) 2 \sin \beta_R'| \quad (6)$$

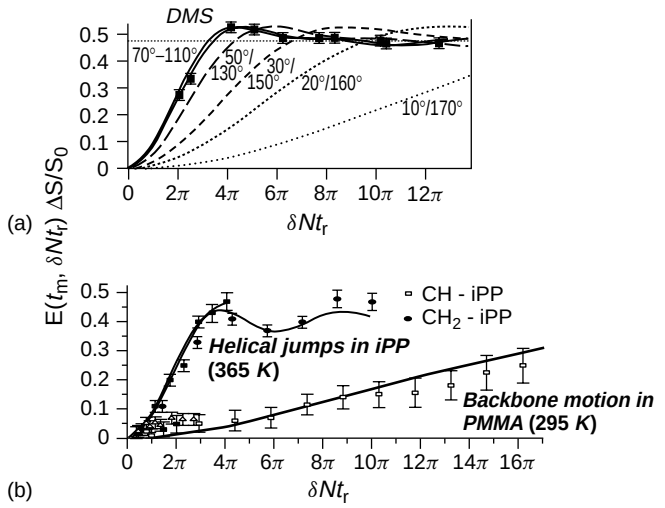

Figure 4 Measurement of the motional amplitude by recording normalized pure-exchange CODEX intensities $\Delta S/S_0 = E(t_m, \delta Nt_r)$ as a function of δNt_r. (a) DMS at 288 K, $t_m = 75$ ms, and $\nu_r = 5.5$ kHz. Also shown are simulations, for $\eta = 0$, of reorientations of the unique principal axis by 10° or 170°, 20° or 160°, 30° or 150°, 50° or 130°, and 70° to 110° (curves in this large-amplitude range are virtually indistinguishable). (b) CODEX intensities $E(t_m, \delta Nt_r)$ as a function of δNt_r for isotactic polypropylene (iPP) at 365 K, $t_m = 1$ s, and for the backbone of glassy PMMA at 293 K, $t_m = 0.5$ s. Comparison with (a) immediately shows that the motions in iPP are of large amplitude, while those of the PMMA backbone are restricted

where n, k, and m label the three principal axes of $\overleftrightarrow{\sigma}$. This is completely analogous to equation (5).

The quantitative analysis of CODEX data requires knowledge of three principal values of the chemical shift tensor, or at least of the chemical-shift anisotropy parameter δ. These values can obtained in a variety of ways. A first estimate can be obtained based on the tabulated CSA principal values of similar chemical groups.[37] Various methods of experimental CSA measurements have been described in the literature.[38–40] The estimation of $|\delta|$ by CSA recoupling under MAS very similar to CODEX has been demonstrated by deAzevedo et al.[22]

In a view traditionally taken in REDOR, rather than considering N as scaling the difference tensor relative to the spinning speed, it is considered that Nt_r is the total time of evolution under the influence of the anisotropic interaction.[32] Then it is found that the dephasing is independent of the spinning speed and only depends on the total time Nt_r.[22] Due to this ω_r-independence, the CODEX pulse sequence works up to very high spinning speeds.

4.2 The Role of the Reorientation-Angle Distribution

In the case of a uniaxial NMR interaction, i.e., $\eta = 0$, the information content of an exchange experiment at a given mixing time t_m can be summarized in terms of the reorientation-angle distribution $R(\beta_R, t_m/\tau_c)$, i.e., the probability density of finding a reorientation angle β_R after a mixing time t_m.[1,14,16,41] Since the correlation time τ_c is the natural reference for t_m, only their ratio, t_m/τ_c, is relevant for the reorientation-angle distribution. The dephasing or pure-exchange intensity CODEX curves are simply $R(\beta_R, t_m/\tau_c)$-weighted superpositions of the CODEX curves $\varepsilon(\delta Nt_r; \beta_R)$ for specific β_R values:[16,42]

$$E(t_m, \delta Nt_r) = \int_0^{90p} R\left(\beta_R, \frac{t_m}{\tau_c}\right) \varepsilon(\delta Nt_r; \beta_R)\, d\beta_R \qquad (7)$$

The integration weighting by $\sin\beta_R$ is contained in $R(\beta_R, t_m/\tau_c)$. The calculation of $\varepsilon(\delta Nt_r; \beta_R)$ is outlined in equation (10) below. Note that while all $\varepsilon(\delta Nt_r; \beta_R)$ have the same shape except for the $\sin\beta_R$ – scaling of their x-axes, their superposition $E(t_m, \delta Nt_r)$ in general has a different shape (to visualize this, consider that similarly the sum of Gaussian bell curves of different widths, even when they have the same center, is not a Gaussian). For a few motional models, the reorientation-angle distributions $R(\beta_R, t_m/\tau_c)$ and corresponding $E(\delta Nt_r; t_m)$ curves are shown in Figure 6. They will be discussed in more detail below.

For non-uniaxial interactions, β_R in this discussion and in equation (7) should be replaced with the full set of reorientation angles $(\alpha_R, \beta_R, \gamma_R)$. For specific motions, other angular variables may be more convenient. For rotations around a given axis, such as the helix axis in helical jumps or the invariant axis in uniaxial rotational diffusion, the angle ψ of rotation around that axis is most convenient.

4.3 Simulation Procedure

For simulations of CODEX curves, each subcurve $\varepsilon(\delta Nt_r; \alpha_R, \beta_R, \gamma_R)$ needed for equation (7) is calculated based on equation (3), using the following steps:

(i) Choose a convenient frame to rotate $\overleftrightarrow{\sigma}_1$ to $\overleftrightarrow{\sigma}_2$. In this frame, $\overleftrightarrow{\sigma}_1$ is expressed by a 3×3 matrix, and the rotation can be performed using Cartesian rotation matrices,

$$\overleftrightarrow{\sigma}_2 = \overleftrightarrow{R}(\alpha_R, \beta_R, \gamma_R)\overleftrightarrow{\sigma}_1\overleftrightarrow{R}^T(\alpha_R, \beta_R, \gamma_R) \qquad (8)$$

or, alternatively, Wigner rotation matrices. The rotation is defined by the Euler angles α_R, β_R, γ_R or by other angles specifying the motion that the segment is supposed to undergo (e.g., the rotation angle around a given axis).

(ii) Calculate the difference tensor (3×3 matrix) $\overleftrightarrow{\sigma}^\Delta = (\overleftrightarrow{\sigma}_2 - \overleftrightarrow{\sigma}_1)$.

(iii) Determine the principal values of $\overleftrightarrow{\sigma}^\Delta$ (i.e., diagonalize $\overleftrightarrow{\sigma}^\Delta$). Calculate its anisotropy parameter δ_Δ and asymmetry parameter η_Δ.

(iv) We can evaluate the integral in equation (3) as follows,

$$\begin{aligned}\int_0^{t_r/2} (\omega_2(t) - \omega_1(t))\, dt &= \int_0^{t_r/2} \omega^\Delta(t)\, dt \\ &= \tilde{S}_1(\delta_\Delta, \eta_\Delta, \alpha_\Delta, \beta_\Delta, \gamma_\Delta)\frac{t_r}{2} \\ &= \delta_\Delta\sqrt{2}\left\{\tfrac{1}{3}\eta_\Delta \sin 2\alpha_\Delta \sin\beta_\Delta \cos\gamma_\Delta \right. \\ &\quad + \tfrac{1}{2}\sin 2\beta_\Delta\left(1 + \tfrac{1}{3}\eta_\Delta \cos 2\alpha_\Delta\right) \\ &\quad \left. \times \sin\gamma_\Delta\right\}\frac{t_r}{2} \qquad (9)\end{aligned}$$

using the Euler angles α_Δ, β_Δ, γ_Δ that specify the orientation of the principal-axes system of the difference

tensor in the rotor-fixed frame. The subcurve $\varepsilon(\delta N t_r; \alpha_R, \beta_R, \gamma_R)$ can now be expressed as

$$\begin{aligned}\varepsilon(\delta N t_r, \alpha_R, \beta_R, \gamma_R) &= 1 - \left\langle \cos\left(N \int_0^{t_r/2} (\omega_2(t) - \omega_1(t))\, dt \right) \right\rangle \\ &= 1 - \left\langle \cos\left[\frac{\tilde{S}(\delta_\Delta, \eta_\Delta, \alpha_\Delta, \beta_\Delta, \gamma_\Delta) N t_r}{2} \right] \right\rangle_{\alpha_\Delta, \beta_\Delta, \gamma_\Delta}\end{aligned} \quad (10)$$

with $\tilde{S}(\delta_\Delta, \eta_\Delta, \alpha_\Delta, \beta_\Delta, \gamma_\Delta)$ as given in equation (9). The pointed brackets represent only the powder average over α_Δ, β_Δ, γ_Δ, i.e., the orientation of the chemical-shift difference tensor. In contrast, in equation (3) the average also included a summation over all reorientation angles. The powder average in equation (10) is calculated numerically.

(v) Go back to (i) to repeat the calculation for a different set of reorientation angles, yielding a different CODEX subcurve.

(vi) Obtain the CODEX curve $E(t_m, \delta N t_r)$ by superimposing the $\varepsilon(\delta N t_r; \alpha_R, \beta_R, \gamma_R)$ subcurves weighted with the reorientation angle distribution $R(\alpha_R, \beta_R, \gamma_R, t_m/\tau_c)$ for the t_m under consideration, according to equation (7).

4.4 Number of Accessible Orientations and Fraction of Mobile Segments

In complex systems such as amorphous polymers, broad distributions of correlation times and motional amplitudes often result in a complex exchange behavior. It is often a good approximation to analyze such situations in terms of a fraction f_m of significantly exchanging segments, and a component $(1 - f_m)$ that does not exchange significantly and therefore can be treated as immobile. The case of a homogeneous system in which all equivalent segments are moving similarly, as is true for most crystals, is obtained by setting $f_m = 1$.

Information about the fraction f_m and the number M of equivalent orientational sites accessible to the mobile segments is obtained from the long-time exchange intensity E_∞. Since a fraction 1/M of the mobile species will reside in the originally selected site, see Figure 5, we have

$$E_\infty = E(t_m \gg \tau_c, \delta N t_r \gg 1) = f_m \left(1 - \frac{1}{M}\right) \quad (11)$$

For $f_m = 1$, the minimum E_∞ is 1/2, obtained for M = 2. For diffusive reorientations of all segments, $M \gg 1$ and $E_\infty \sim 1$; note, however, that for restricted diffusion, very large phases

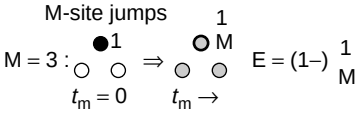

Figure 5 Relation between the final exchange intensity and the number of sites in an M-site jump process. At long times ($t_m \rightarrow \infty$), 1/M of the segments reside in the original site. Thus, the final exchange intensity E_∞ deviates from unity by 1/M

$\delta N t_r$ will be required to reach the final state. Also, if $E_\infty < 1/2$, $f_m < 1$. In fact, equation (11), with M = 2 and $M \rightarrow \infty$, yields rigorous limits for f_m in terms of E_∞:

$$E_\infty < f_m \leq 2E_\infty \quad (12)$$

From E_∞ alone, f_m and M cannot be determined unambiguously. Fortunately, the number of sites M can be measured in a four-time CODEX experiment, which is produced by concatenating two CODEX pulse sequences.[22] In the first CODEX difference experiment with mixing time t_{ma}, the mobile groups are selected; then their exchange behavior, with a final value of 1/M, is characterized selectively in another CODEX MAS section by changing the mixing time t_{mc}. Effects of T_1 relaxation decay can be eliminated by keeping the total z-period $t_{mc} + t_z$ constant. Therefore, no difference is required in the second half of the experiment. The four-time CODEX experiment has close analogies to a reduced four-dimensional (4D) exchange NMR experiment, where the orientation-dependent frequency is probed at four different times.[18] The reduced 4D exchange method, and the closely related four-time exchange experiment have been used to identify the origins of the non-exponential loss of correlation above the glass-transition temperature and to estimate the size of dynamic heterogeneities.[18–20] Four-time CODEX will make such studies much more sensitive and quantitative.

4.5 Jumps vs. Diffusive Motions

A variety of different motional models have been considered in the literature.[1,14] They can be grouped into jump processes and diffusive motions. For instance, symmetric N-site exchange is a common jump process, while isotropic rotational diffusion is the most important example of a diffusive reorientation. Defining distinctions between pure jumps and pure diffusion are seen in the evolutions of their reorientation-angle distributions $R(\beta_R, t_m/\tau_c)$ with time t_m; this behavior can be used in CODEX NMR to identify pure jump motions and diffusive motions. The $R(\beta_R, t_m/\tau_c)$ of four classical motional models and the corresponding CODEX curves $E(\delta N t_r, t_m)$ are shown in Figure 6.

All diffusive motions produce a characteristic change in the shape of $R(\beta_R, t_m/\tau_c)$ with increasing t_m. The sharp peak at $\beta_R = 0°$ gradually broadens and approaches the wide distribution characteristic of the final stage, such as $\sin\beta_R$ for isotropic diffusion. As a result, the shape of the $E(\delta N t_r)$ CODEX curves depends strongly on t_m: For short t_m, the curves rise quite slowly because only small reorientation angles have been reached, while an earlier and faster increase in $E(\delta N t_r)$ (plotted as a function of $\delta N t_r$, with t_m only as a parameter) occurs at long t_m when larger reorientation angles have been attained. These features are clearly visible in Figures 6(c) and 6(d), where isotropic and uniaxial rotational diffusion, respectively, have been simulated.

In contrast, for many pure jump motions the only change in the reorientation-angle distribution is the relative intensity of the reorientation-angle distribution at $\beta_R = 0$ and at $\beta_R \neq 0$. This holds for all two-site jumps, circular three-site jumps, random N-site jumps, and the isotropic random-jump model. As a result, the shape of the $E(\delta N t_r, t_m)$ curves does not change

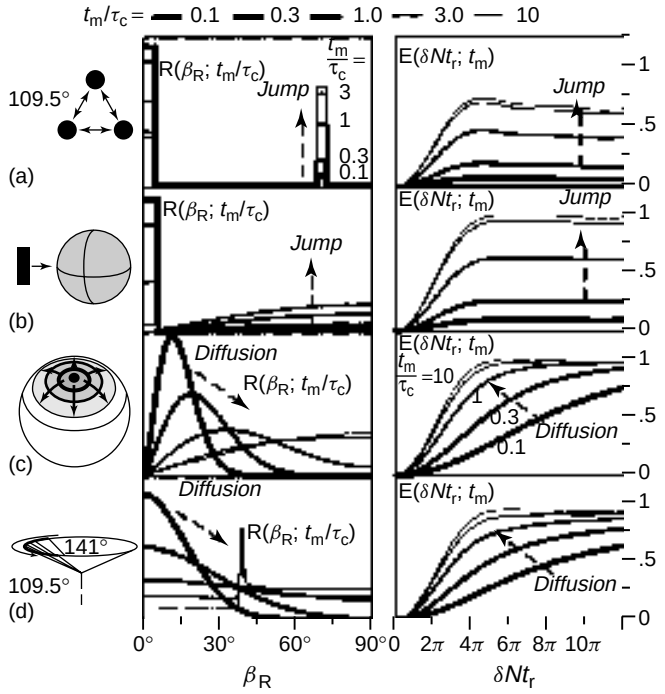

Figure 6 Time evolution of the reorientation-angle distributions $R(\beta_R, t_m/\tau_c)$ for four important motional models, and the corresponding CODEX $E(\delta N t_r, t_m)$ curves (for a uniaxial interaction, $\eta = 0$). As indicated at the top, the line thickness decreases with increasing t_m/τ_c (=0.1, 0.3, 1.0, 3.0, and 10). (a) Three-site jumps, with a 109° (or equivalently 71°) jump angle. (b) Random isotropic jumps. In this model, all orientations are equally likely after the jump. (c) Isotropic rotational diffusion, without amplitude limitation. (d) Uniaxial rotational diffusion on a cone with an apex angle of 141° (or equivalently $2 \cdot 109.5°$). The dashed arrows in the plots indicate the characteristic differences between the t_m/τ_c dependences for jump motions (a,b) and diffusion (c,d)

with t_m. Only its height (y-scale) increases. This is clearly visible in Figures 6(a) and (b).

Helical jumps, where sites along a helical chain are accessed sequentially, do not fall under this category, if the chain forms a 4_n helix (i.e., 4 repeat units in n turns) or more complex helix.[1,27] Nevertheless, their change in reorientation-angle distribution is still characteristically different from that of diffusive motions. The peak at $\beta_R = 0$ does not broaden, and $R(\beta_R, t_m/\tau_c)$ consists only of a few sharp peaks whose relative height changes only slowly. The rise for short t_m will be fast and unchanged, being due to large-angle jumps between neighboring sites; only at long t_m will changes be observed due to the contribution of non-neighboring sites.

Another characteristic aspect of diffusive motions is that the number of sites M is infinite. Thus, at sufficiently large $\delta N t_r$ and t_m, full exchange will be observed. This property is shared with only a very small number of pure jump processes; the isotropic random-jump model, Figure 6(b), is the only prominent example.

However, it should be noted that $M \rightarrow \infty$ is also a property of limited diffusion superimposed on jumps. Such a combined process may still be relatively difficult to distinguish from pure diffusion, in particular if the diffusion has a broad distribution of correlation times.

5 PRACTICAL CONSIDERATIONS

5.1 Spin Exchange by Dipolar Couplings

Segmental dynamics is not the only possible exchange process. Two effects based on dipolar couplings also lead to exchange of anisotropic interactions and intensity changes in the CODEX experiment. The first is relaxation-induced dipolar exchange due to dipolar couplings to heteronuclei, in particular ^{14}N and ^{15}N, that undergo significant longitudinal relaxation during t_m.[43,44] The relaxation removes a heteronuclear coherence term from the density operator and thus reduces the stimulated echo. This effect has been described in detail by Saalwächter and Schmidt-Rohr.[44] Due to the small value of the nitrogen-carbon dipolar coupling, it is a significant problem only for CODEX experiments involving nitrogen-bonded carbon sites with small chemical-shift anisotropies. On the other hand, this relaxation-induced dipolar exchange with recoupling can be exploited to measure internuclear distances between heteronuclei.[44]

The more common second effect is ^{13}C spin diffusion or spin exchange generated by homonuclear dipolar couplings and affected by the ^1H–^{13}C dipolar coupling.[45–48] For ^{13}C in natural abundance, it typically generates 4% exchange intensity within 0.5 s. In isotopically labeled materials, it can occur significantly within 50 ms. Apart from isotopic dilution, the only known procedure for slowing down ^{13}C spin exchange between sites with similar isotropic chemical shifts is to increase the spinning speed. Among the experiments for measuring exchange by segmental reorientation, CODEX is the only one that is compatible with high spinning speeds. We have recently shown that for unprotonated sites, an increase of the spinning speed from 8 to 28 kHz indeed decreases the spin exchange rate by a factor of 3–10.[49] Thus, CODEX under fast MAS can significantly extend the range of correlation times accessible to exchange NMR measurements.

In ^{13}C-enriched proteins, Hong et al. have circumvented the ^{13}C spin diffusion problem by performing a ^{15}N CODEX experiment followed by ^{15}N–^{13}C transfer and ^{13}C detection.[50] The dipolar couplings between the ^{15}N nuclei, which are separated by three bonds and have smaller gyromagnetic ratios, are more than an order of magnitude reduced relative to those of ^{13}C in a uniformly labeled protein.

5.2 Accessible Range of Correlation Times

The rates for which dephasing is observed in CODEX NMR range from ~0.1 to ~5000 s^{-1}. Very slow motions, which require long mixing times, can be studied better by CODEX than by any other NMR technique. The high sensitivity and good dynamic range of CODEX NMR enables detection of the ~10% exchange intensity that arises already within $t_m = 0.1\,\tau_c$, and makes it less sensitive to signal reduction by T_1-relaxation and the increased experiment duration when the mixing time exceeds the recycle delay. Exchange due to ^{13}C spin exchange (see above) which competes with motional exchange, is the main limitation for detecting very slow motions. Even in this aspect, CODEX is often superior. Not only can CODEX under fast MAS slow down spin diffusion among unprotonated carbons but its superior sensitivity also permits a reduction in the isotopic labeling level, or even measurements on ^{13}C in natural abundance.[49] This is

particularly relevant for systems that previously required ^{13}C enrichment for achieving sufficient sensitivity, e.g., benzene undergoing jumps and diffusion in zeolites.[6]

To understand the effect of motions on the 100-μs time scale on CODEX, consider that a clean exchange experiment requires that no motion occurs during the dephasing and rephasing periods Nt_r (i.e., $k < 1000\,s^{-1}$). Nevertheless, even with frequency changes during those periods, some motional dephasing will occur. Its strong dependence on the dephasing time and near independence from the mixing time will identify its high rate.

Finally, motions with rates exceeding the chemical-shift anisotropy significantly will not be detected by CODEX, since the motionally averaged frequencies do not change during the course of the experiment. This will lead to a reduction in E_∞, and care must be taken not to interpret these fast-moving segments as immobile. Fortunately, significant motions with rates exceeding $10\,000\,s^{-1}$ can be detected by other NMR experiments.[9–11,51,52]

5.3 Implementation of the CODEX Pulse Sequence

Due to the simplicity of the CODEX pulse sequence, the implementation of the technique is mostly straightforward. However, since the method relies on measuring signal amplitudes rather than frequency positions, some care should be taken to avoid artifacts. A fixed xy-8 phase sequence is used for the train of 180° pulses that recouple the CSA.[53] Effects of pulse imperfections and T_1 relaxation are minimized or eliminated using the phase cycling given by Reichert et al.[49]

For protonated carbon sites, in particular CH_2 groups, the residual C–H dipolar coupling during the multiple 180° pulses leads to significant dephasing. Fortunately, this does not affect the normalized CODEX data, since the same dephasing occurs in the reference experiment. However, the intensity is degraded. The decoupling is excellent if the ^1H B_1 field strength during the ^{13}C pulses is so high that the duration of a ^{13}C 180° pulse corresponds to a 3*180° pulse length on protons.[54] In order to reduce the ^1H power required to achieve this condition, it can be advantageous to increase the duration of the ^{13}C 180° pulses, i.e., to *reduce* the ^{13}C pulse power.

6 APPLICATIONS OF CODEX

6.1 Dynamics in Complex Glassy Polymers

So far, NMR studies of slow segmental motions of unlabeled polymers in the glassy state have been virtually impossible, due to sensitivity and line-overlap problems. CODEX and its non-spinning analog, 1D PUREX, enable detailed, quantitative studies of these dynamics.[25] The selective observation of exchanging sites in pure-exchange CODEX and 1D PUREX spectra leads to a great increase in resolution and in the dynamic range, which in turn reduces artifacts arising from the often dominant signals of immobile sites.

Examples for the detection of flipping sidegroups in PMMA by CODEX are shown in Figures 2 and 3. The characterization of the motion as a jump process between $M = 2$ sites was confirmed in PMMA by 4-time CODEX.[22] Extending these experiments to a series of glassy poly(*n*-alkyl methacrylates) with COOR sidegroups of various sizes, CODEX has revealed that even some large cyclohexyl sidegroups can flip, but that the flipping fraction is only 9%.[55] Surprisingly, the fraction of flipping sidegroups was found to remain temperature-independent in PMMA with its small methylester sidegroup, while it increases significantly with temperature in polymers with longer sidegroups.[55] In polyphenylene dendrimers, slow dynamics in the highest-generation phenylene rings has been observed by CODEX.[56] Generally, CODEX enables us to study almost any slow dynamic process in polymers and thus learn more about the relation between chain motions and mechanical properties.

6.2 Dynamics in Peptides and Proteins

In biological systems, knowledge of the three-dimensional molecular structure is important, but further insight into the segmental dynamics is also highly valuable. Segmental mobility and function in enzymes are thought to be particularly closely related. Due to the large number of sites that may be distinguished in proteins, the sensitivity and site resolution of CODEX is indispensable for studies of slow motions. Hong and coworkers have introduced ^{13}C-detected ^{15}N CODEX for studies of slow motions in ^{13}C-labeled globular proteins.[50] In a triblock protein hydrogel, the experiments revealed large-amplitude reorientations of the α-helical segments that form the reversible cross-links.[57]

7 OUTLOOK

7.1 Perspective on CODEX, PUREX, and 2D Exchange Spectra

Overall, CODEX is complementary to detailed 2D exchange NMR studies without sample rotation. The CODEX MAS approach makes it easy to identify groups with interesting dynamics, characterize their correlation times, estimate the motional amplitude, obtain information on the mobile fraction and the number of accessible sites, and identify simple jumps or more complex motions. The lineshapes of 1D PUREX spectra, which can be regarded as CODEX without sample rotation, can give valuable hints about the motional geometry.[25] Given enough interest, these sites can then be isotopically labeled by ^2H or ^{13}C to determine the details of the reorientation process by 2D and 3D exchange NMR; the information on the reorientation angle that is contained in 2D exchange patterns is still unparalleled, in particular for distributions of reorientation angles, and for large reorientation angles.[1]

7.2 Summary

Detailed analysis of slow dynamics in complex solids is enabled by centerband-only detection of exchange (CODEX), which combines chemical-shift recoupling by 180°-pulses with exchange NMR. The analysis in terms of the chemical-shift difference tensor explains the surprising sensitivity of the experiment to small-amplitude motions. For uniaxial interactions ($\eta = 0$), this can be expressed by a simple analytical relation. The number of orientational sites accessible to the mobile segments and the fraction of mobile units are reflected in the long-time exchange intensity. Jumps and diffusive motions are distinguishable from the effect of mixing

time on the recoupling-time dependence of their exchange intensity, which reflects the characteristic changes of the reorientation-angle distributions. Pure-exchange CODEX can also be used as a dynamic filter to observe slow-moving groups selectively.

8 RELATED ARTICLES IN VOLUMES 1–8

Brownian Motion & Correlation Times, Volume 2, Chemical Shift Tensor Measurement in Solids, Volume 2, Chemical Shift Tensors, Volume 2, Internal Spin Interactions & Rotations in Solids, Volume 4, Magic Angle Spinning, Volume 5, Multidimensional Spectroscopy: Concepts, Volume 5, Polymer Dynamics & Order from Multidimensional Solid State NMR, Volume 6, Polymer Physics, Volume 6, Protein Dynamics from Solid State NMR, Volume 6, REDOR & TEDOR, Volume 6, Slow & Ultraslow Motions in Biology, Volume 7, Two-Dimensional Methods of Monitoring Exchange, Volume 8, Two-Dimensional Powder Correlation Methods, Volume 8, Ultraslow Motions in Solids, Volume 8.

9 REFERENCES

1. K. Schmidt-Rohr and H. W. Spiess, 'Multidimensional Solid-State NMR and Polymers', Academic Press: London, 1994.
2. T. M. Connor, B. E. Read, and G. Willians, *J. Appl. Chem.*, 1964, **14**, 74.
3. W.-G. Hu and K. Schmidt-Rohr, *Act. Polymer*, 1999.
4. A. G. Palmer, J. Williams, and A. McDermott, *J. Phys. Chem.*, 1996, **100**, 13 293.
5. V. Andronis and G. Zografi, *Pharm. Res.*, 1998, **15**, 835.
6. D. E. Favre, D. J. Schaefer, S. M. Auerbach, and B. F. Chmelka, *Phys. Rev. Lett.*, 1998, **81**, 5852.
7. G. B. McKenna, *Comp. Mater. Sci.*, 1995, **4**, 349.
8. J. Schaefer, R. A. McKay, E. O. Stejskal, and W. T. Dixon, *J. Magn. Reson.*, 1983, **52**, 123.
9. H. W. Spiess, in 'Deuteron NMR – A New Tool for Studying Chain Mobility and Orientation in Polymers', ed H. W. Spiess, Springer: Berlin, 1985, Vol. 66, p. 24.
10. K. Schmidt-Rohr, J. Clauss, and H. W. Spiess, *Macromolecules*, 1992, **25**, 3273.
11. J. Schaefer, M. D. Sefcik, E. O. Stejskal, R. A. McKay, W. T. Dixon, and R. E. Cais, *Macromolecules*, 1984, **17**, 1107.
12. H. W. Spiess, *J. Chem. Phys.*, 1980, **72**, 6755.
13. E. Roessler, *Chem. Phys. Lett.*, 1986, **128**, 330.
14. S. Wefing, S. Kaufmann, and H. W. Spiess, *J. Chem. Phys.*, 1988, **89**, 1234.
15. C. Schmidt, S. Wefing, B. Blumich, and H. W. Spiess, *Chem. Phys. Lett.*, 1986, **130**, 84.
16. S. Wefing and H. W. Spiess, *J. Chem. Phys.*, 1988, **89**, 1219.
17. K. Schmidt-Rohr, A. S. Kulik, H. W. Beckham, A. Ohlemacher, U. Pawelzik, C. Boeffel, and H. W. Spiess, *Macromolecules*, 1994, **27**, 4733.
18. K. Schmidt-Rohr and H. W. Spiess, *Phys. Rev. Lett.*, 1991, **66**, 3020.
19. A. Heuer, M. Wilhelm, H. Zimmermann, and H. W. Spiess, *Phys. Rev. Lett.*, 1995, **75**, 2851.
20. U. Tracht, M. Wilhelm, A. Heuer, H. Feng, K. Schmidt-Rohr, and H. Spiess, *Phys. Rev. Lett.*, 1998, **81**, 2727.
21. E. R. deAzevedo, W.-G. Hu, T. J. Bonagamba, and K. Schmidt-Rohr, *J. Am. Chem. Soc.*, 1999, **121**, 8411.
22. E. R. deAzevedo, W.-G. Hu, T. J. Bonagamba, and K. Schmidt-Rohr, *J. Chem. Phys.*, 2000, **112**, 8988.
23. F. Fujara, S. Wefing, and W. H. Spiess, *J. Chem. Phys.*, 1986, **97**, 2928.
24. B. Geil, F. Fujara, and H. Sillescu, *J. Magn. Reson.*, 1998, **130**, 18.
25. E. R. deAzevedo, T. J. Bonagamba, and K. Schmidt-Rohr, *J. Magn. Reson.*, 2000, **142**, 86.
26. J. Jeener, B. H. Meier, P. Bachmann, and R. R. Ernst, *J. Chem. Phys.*, 1979, **71**, 4546.
27. A. P. M. Kentgens, E. de Boer, and W. S. Veeman, *J. Chem. Phys.*, 1987, **87**, 6859.
28. A. Hagemeyer, K. Schmidt-Rohr, and H. W. Spiess, *Adv. Magn. Reson.*, 1989, **13**, 85.
29. D. Reichert, H. Zimmermann, P. Tekely, R. Poupko, and Z. Luz, *J. Magn. Reson.*, 1997, **125**, 245.
30. V. Gerardy-Montouillout, C. Malveau, P. Tekely, Z. Olender, and Z. Luz, *J. Magn. Reson.*, 1996, **123**, 7.
31. T. Gullion and J. Schaefer, *J. Magn. Reson.*, 1989, **81**, 196.
32. T. Gullion and J. Schaefer, *Adv. Magn. Reson.*, 1989, **13**, 57.
33. W. T. Dixon, *J. Chem. Phys.*, 1982, **77**, 1800.
34. S. C. Kuebler, D. J. Schaefer, and C. Boeffel, *Macromolecules*, 1997, **30**, 6597.
35. T. Terao, H. Miura, and A. Saika, *J. Chem. Phys.*, 1986, **85**, 3816.
36. D. Schaefer, H. W. Spiess, U. W. Suter, and W. W. Fleming, *Macromolecules*, 1990, **23**, 3431.
37. T. M. Duncan, 'A Compilation of Chemical Shift Anisotropies', Farragut: Chicago, 1990.
38. R. Tycko, G. Dabbagh, and P. Mirau, *J. Magn. Reson.*, 1989, **85**, 265.
39. J. Z. Hu, C. Ye, R. J. Pugmire, and D. M. Grant, *J. Magn. Reson.*, 2000, **145**, 230.
40. M. Hong, *J. Am. Chem. Soc.*, 2000, **122**, 3762.
41. C. Schmidt, B. Blümich, and H. W. Spiess, *J. Magn. Reson.*, 1988, **79**, 269.
42. F. Fujara, S. Wefing, and W. F. Kuhs, *J. Chem. Phys.*, 1988, **88**, 6801.
43. J. R. Sachleben, V. Frydman, and L. Frydman, *J. Am. Chem. Soc.*, 1996, **118**, 9786.
44. K. Saalwächter and K. Schmidt-Rohr, *J. Magn. Reson.*, 2000, **145**, 161.
45. C. E. Bronniman, N. M. Szeverenyi, and G. E. Maciel, *J. Chem. Phys.*, 1983, **79**, 3694.
46. H. T. Edzes and J. P. C. Bernards, *J. Am. Chem. Soc.*, 1984, **106**, 1515.
47. D. L. VanderHart, *J. Magn. Reson.*, 1987, **72**, 13.
48. B. H. Meier, *Adv. Magn. Opt. Reson.*, 1994, **18**, 1.
49. D. Reichert, T. J. Bonagamba, and K. Schmidt-Rohr, *J. Magn. Reson.*, 2001, **150**, 1.
50. E. R. deAzevedo, S. B. Kennedy, and M. Hong, *Chem. Phys. Lett.*, 2000, **321**, 43.
51. K. J. McGrath, K. L. Ngai, and C. M. Roland, *Macromolecules*, 1992, **25**, 4911.
52. A. S. Maxwell, I. M. Ward, F. Laupretre, and L. Monnerie, *Polymer*, 1998, **39**, 6835.
53. T. Gullion, D. B. Baker, and M. S. Conradi, *J. Magn. Reson.*, 1990, **89**, 479.
54. Y. Ishii, J. Ashida, and T. Terao, *Chem. Phys. Letters*, 1995, **246**, 439.
55. T. J. Bonagamba, F. Becker-Guedes, E. R. deAzevedo, and K. Schmidt-Rohr, *J. Polymer Sci. B: Phys. Ed.*, 2001, **39**, 2444.
56. M. Wind, U.-M. Wiesler, K. Saalwächter, K. Müllen, and H. W. Spiess, *Angewandte Chemie*, 2001, **13**, 752.
57. S. B. Kennedy, E. R. deAzevedo, W. A. Petka, D. A. Tirrell, T. P. Russell, and M. Hong, *Macromolecules*, 2001, **34**, 8675.

Biographical Sketches

Klaus Schmidt-Rohr, *b* 1967. Diploma (Physics), 1989; Ph.D., 1991, Mainz (Germany), with Prof. H. W. Spiess,

Max-Planck-Institute for Polymer Research. Postdoc with Alex Pines, UC Berkeley, 1993-94. Assistant/Associate Prof., Dept. of Polymer Science & Engineering, UMass–Amherst, 1995–1999. Associate Prof., Dept. of Chemistry, Iowa State University, 2000-present. 1 book & approx. 80 publications on solid-state NMR. Research interests: Development of NMR techniques for studying complex macromolecular solids.

Eduardo Ribeiro de Azevedo, *b* 1974. PhD Phys., 2001, Instituto de Física de São Carlos (IFSC) – Universidade de São Paulo (USP), Brazil, with Prof. Tito José Bonagamba. Visiting Scholar, Polymer Science and Engineering Department, University of Massachusetts, USA, with Prof. Klaus Schmidt-Rohr and Prof. Mei Hong, 1998–1999; Research interests include development or utilization of solid-state NMR methods and their application to study materials.

Tito José Bonagamba, *b* 1960. PhD Phys., 1991, Instituto de Física de São Carlos (IFSC) – Universidade de São Paulo (USP), Brazil, with Prof. H. Panepucci. Professor of Physics, IFSC-USP, 1988-present. Visiting Scientist, Dept. of Polymer Science & Engineering, University of Massachusetts, USA, with Prof. Klaus Schmidt-Rohr, 1998–2000; Visiting Scientist, Ames Laboratory & Dept. of Chemistry, Iowa State University, USA, with Prof. Klaus Schmidt-Rohr, 2000. Research interests include development or utilization of multidimensional solid-state NMR methods and their application to study materials and instrumentation for NMR.

Chemical Shift Tensor Measurement in Solids

Anita M. Orendt
University of Utah, Salt Lake City, UT, USA

1	Introduction	1
2	Magnetic Interactions	1
3	Experimental Considerations	2
4	Samples: Powders versus Single Crystals	3
5	One-Dimensional Powder Techniques	4
6	Two-Dimensional Powder Techniques	6
7	Single Crystal Techniques	12
8	Dipolar Techniques	13
9	Summary	15
10	Related Articles	15
11	References	15

1 INTRODUCTION

There are a number of methods in solid state NMR spectroscopy which can be used to obtain information about the chemical shift tensor. The method of choice is usually a function of the equipment available, the complexity of the sample, the information desired, and the state of the sample at ambient temperatures. This article serves as an overview of the various methods, and deals with the requirements and limitations in terms of both sample and instrumentation for each technique, as well as with the information that can be obtained. A more detailed description for some of these techniques can be found in other portions of the Encyclopedia, as listed in Section 10. It should be noted that no effort is made to include listings of chemical shift tensor data that have been measured. The reader is referred to compilations of this type of data, the most recent being Duncan's book.[1]

Before the description of the methods, a brief introduction concerning the Zeeman interaction, chemical shielding, dipolar coupling, and quadrupolar interactions that must be considered is presented. Again a more detailed discussion concerning these interactions is presented elsewhere in this Encyclopedia or can be obtained from a number of books.[2–5]

2 MAGNETIC INTERACTIONS

2.1 Zeeman Interaction

In the presence of a magnetic field, a nucleus possessing a spin ($I \neq 0$) will be in one of $2I + 1$ energy levels, defined by the magnetic moment of the nucleus and the strength of the static magnetic field, $\boldsymbol{B}_0$. The NMR experiment measures the transitions between these levels. The direction of the applied magnetic field is taken by convention to be along the z direction, and the difference in energy between any two of the allowed states, in frequency units (Hz), can be given as

$$\nu_0 = \gamma_I B_0 / 2\pi \tag{1}$$

This frequency ν_0 is known as the Larmor frequency, and is a function of the field strength and the magnetogyric ratio, γ, of the nucleus.

2.2 Chemical Shielding

The chemical shielding interaction separates the resonance frequencies of nuclei based on their electronic environment. The magnetic field experienced or 'seen' by the nucleus of an atom in a molecule is affected by the electrons that surround that nucleus. The chemical shift tensor is a reflection of this orientation-dependent interaction of the electronic environment of a nucleus with the external magnetic field. In general, a different value of the chemical shift will be observed for a nucleus for each orientation of that molecule in the magnetic field. The dependence of the chemical shift on the molecular orientation will be further elaborated upon in the next section.

In the most general terms this chemical shift interaction is represented by a 3×3 Cartesian matrix,

$$\delta = \begin{bmatrix} \delta_{xx} & \delta_{xy} & \delta_{xz} \\ \delta_{yx} & \delta_{yy} & \delta_{yz} \\ \delta_{zx} & \delta_{zy} & \delta_{zz} \end{bmatrix} \tag{2}$$

The interaction can be decomposed into three parts: the isotropic, the symmetric, and the antisymmetric portions,

$$\delta = \delta_{\text{iso}} + \delta_{\text{sym}} + \delta_{\text{anti}} \tag{3}$$

The isotropic matrix gives the position of the center of the spectrum, while the symmetric matrix defines the lineshape observed. The antisymmetric portion has no observable effect on the lineshape, at the current level of technology and will not be further considered in this work. Often the first two terms are combined and given as

$$\delta = \begin{bmatrix} \delta_{xx} & \delta_{xy} & \delta_{xz} \\ \delta_{xy} & \delta_{yy} & \delta_{yz} \\ \delta_{xz} & \delta_{yz} & \delta_{zz} \end{bmatrix} \tag{4}$$

The resonance frequency that is observed in high-resolution NMR spectroscopy is one-third of the trace of the matrix shown in equation (4), or $\delta_{\text{iso}} = (\delta_{xx} + \delta_{yy} + \delta_{zz})/3$.

There exists some frame in which the matrix in equation (4) is diagonal; in this case the three diagonal elements are known as the principal values of the chemical shift tensor (or tensor components), and are designated as δ_{11}, δ_{22}, and δ_{33}. Convention states that $\delta_{11} \geq \delta_{22} \geq \delta_{33}$, with δ_{11} being in the high-frequency or least shielded direction. The remaining three terms are the Euler angles which define the directions of these principal values in the molecular frame. The axis system in which the symmetric chemical shift matrix is diagonal is known as the principal axis system (PAS).

2.3 Dipolar Coupling

Interactions also exist between magnetic nuclei. The interaction of two spins through space is known as a direct or dipolar coupling. This interaction has a $1/r^3$ dependence on the separation of the two spins and a linear dependence on the γ values of the two spins involved, as shown in equation (5) for the general case of two different spin-$\frac{1}{2}$ nuclei, I and S, e.g., ^{13}C and ^{1}H.

$$D = \frac{\gamma_I \gamma_S \hbar}{r_{IS}^3} \tag{5}$$

The dipolar interaction is also orientation-dependent; in this case the tensor is axially symmetric and has a trace of zero. The fact that the dipolar tensor is traceless means that the dipolar interactions average to zero in high-resolution NMR spectra. The unique component of the dipolar tensor is along the vector connecting the two spins, generally designated as D_{zz} and is equal to $2D$, and the two identical components, D_{xx} and D_{yy}, with the value of $-D$, are in the plane perpendicular to this vector.

In the case of solid state NMR studies of organic compounds, most typically carbon is the nucleus of interest. Only 1.1% of all carbon nuclei are ^{13}C, which is the magnetic isotope of carbon. The remainder of the carbon nuclei have no magnetic moment and as such are nondetectable. For this reason, dipolar couplings between directly bonded carbons only occur in approximately one of every 10 000 pairs. Magnetic isotopes of low natural abundance, such as carbon, are said to be 'rare' or dilute spins. This is also the case for a number of other nuclei, with ^{15}N being a second important case of a rare spin. However, as more than 99% of all hydrogen nuclei are protons (^{1}H) with $I = \frac{1}{2}$, dipolar couplings both between protons and between the rare spins and the protons play an important role in organic compounds. These ^{1}H–^{1}H and ^{1}H–^{13}C dipolar interactions are very large (tens of kHz) and can completely obscure the chemical shift information. Fortunately, these interactions can be removed by a technique known as proton dipolar decoupling, which is the use of irradiation at the proton frequency during the observation period. Decoupling can be used to remove unwanted dipolar interactions in all cases where the rare spin being observed is coupled to an abundant spin system.

There are also several decoupling schemes that remove the dipolar interactions between nuclei of an abundant spin while allowing for the observation of the chemical shift information of that same spin. These techniques are grouped together as multiple pulse decoupling techniques,[6] and are most commonly used when observing ^{1}H or ^{19}F.

Finally, dipolar couplings between two (and occasionally three or more) spins can be used to obtain information about both the orientation of the PAS and the distance between the spins. A molecule can be selectively enriched with two magnetic isotopes to achieve an isolated spin pair; alternatively, compounds can be enriched in one position and the second spin of the dipolar pair can be one of high natural abundance, but uncommon (^{19}F or ^{31}P), or a spin-$\frac{1}{2}$ pair may exist naturally (^{31}P–^{31}P).

2.4 Quadrupolar Effects

For the quadrupolar nuclei, i.e. those with spins ≥ 1, the observed lineshape is typically dominated by the nuclear quadrupole interaction, given for a spin I in equation (6):

$$\boldsymbol{Q} = \frac{eQ}{2I(2I-1)h}\boldsymbol{V} \tag{6}$$

Again the interaction is anisotropic, with the factor eQ being the quadrupole moment and $\boldsymbol{V}$ the electric field gradient (EFG) tensor. The EFG tensor has a PAS just like the chemical shift tensor; the EFG tensor is traceless, and does not appear directly in liquid spectra due to rapid, isotropic molecular tumbling in solution. The quadrupole coupling constant, $\chi = e^2Qq/h$, ranges from 100 kHz to tens of MHz depending on the nuclei (i.e., ^{2}H, ^{14}N, or ^{17}O) and the symmetry about the nuclei.

Due to the fact that quadrupolar coupling terms are usually orders of magnitude larger than the span of the chemical shift values, the lineshapes obtained are typically only fitted using the isotropic chemical shift along with the quadrupolar parameters. Therefore, the principal values of the chemical shift tensor have only been obtained for a small number of quadrupolar nuclei.[1] Due to this lack of reported measurements of the principal values, no further discussion on quadrupolar nuclei will be presented in this article.

When quadrupolar nuclei are coupled to spin-$\frac{1}{2}$ nuclei, there exists a dipolar coupling; this situation will be included in the section on dipolar spectra.

3 EXPERIMENTAL CONSIDERATIONS

3.1 Cross Polarization

The first step in all the experiments that will be discussed is to take the magnetization of the spin of interest from its equilibrium position, aligned with the magnetic field, to the xy plane. This is commonly done using one of two methods: by application of a 90° pulse (also known as a Bloch decay or BD) or by cross polarization (CP).[7]

The experiment of choice is typically CP, in which the signal of the low abundance spin system is enhanced via magnetization transfer from a second magnetic nucleus which has both a higher natural abundance and a higher γ value. Again the most common nucleus used for magnetization transfer is the proton. The CP method has two advantages over BD: there is a signal enhancement of the rare spin by up to a factor of the ratio of the γ value of the high abundance spin to that of the rare, lower γ spin, and the relaxation times, which dictate how fast a repetition rate can be used in the signal averaging process, are typically faster for the more abundant spin.

In the BD experiment, a 90° pulse is used to take the magnetization of the spins directly into the xy plane, followed by an observation period during which the decay of magnetization in this plane as it returns to its equilibrium position along the magnetic field direction is recorded. The BD experiment is used in cases without an abundant spin system, i.e. systems without protons.

In order to obtain signals from only protonated carbons or signals from only nonprotonated carbons, the techniques of short CP or contact times (SCT) and dipolar dephasing (DD) can be used.[8,9] With short contact times (about 40 μs), only carbons with directly bonded protons develop magnetization, resulting in a spectrum containing only signals of these carbons. With DD, time is allowed for magnetization transfer to develop to all carbons, followed by a period during which the magnetization of the strongly coupled spins, i.e. the protonated carbons, is allowed to decay. The magnetization dephasing is much slower for the weakly dipolar-coupled (nonprotonated and mobile methyl carbons) spins. After this dephasing period a normal acquisition shows only signals from these weakly dipolar-coupled carbons.

3.2 Magic Angle Spinning

Magic angle spinning (MAS)[10,11] is a technique used in conjunction with high power decoupling to obtain high-resolution or solution-like spectra from a solid powder sample. With MAS the chemical shift interaction is averaged to its isotropic value and dipolar interactions are removed by rapid rotation of the sample at an angle of 54.7°, the magic angle, with respect to the $\boldsymbol{B}_0$. The average chemical shift δ of a given nucleus in a sample that is rotating about an angle θ with respect to the external magnetic field is given by

$$\begin{aligned}\delta = \delta_{\text{iso}} &+ \tfrac{1}{2}(3\cos^2\theta - 1) \\ &\times \left[\tfrac{1}{2}(3\cos^2\beta - 1)(\delta_{33} - \delta_{\text{iso}})\right. \\ &\left.+\tfrac{1}{2}\cos^2\beta\cos 2\alpha(\delta_{11} - \delta_{22})\right] \qquad (7)\end{aligned}$$

where α and β are two of the three Euler angles which specify the orientation of the PAS in the frame of the spinning system, and the δ quantities are the various elements of the chemical shift tensor. At θ = 54.7°, the term (3 $\cos^2\theta$ − 1) is zero, and the pattern collapses to a single line at the frequency given by the isotropic chemical shift, δ_{iso}, provided that the rotation frequency, ω_{r}, is larger than the width of the powder pattern.

4 SAMPLES: POWDERS VERSUS SINGLE CRYSTALS

4.1 Powder Samples

So-called powder techniques (both one- and two-dimensional) are performed on powdered or microcrystalline samples, or on samples that have molecules in a statistical distribution of all possible orientations with respect to the magnetic field. The principal values of the chemical shift tensor define the spectral lineshape obtained for the case of a decoupled spin-$\frac{1}{2}$ nucleus. The resultant lineshapes as shown in Figure 1 can be used to obtain the principal values of the chemical shift tensor. The change in intensity across the powder pattern can be explained by representing the chemical shift as an ellipsoid centered at the nucleus. The distance from the center to the outside of the ellipsoid represents the magnitude of the chemical shift with the static magnetic field in that direction while the three axes of the ellipsoid are the directions giving rise to the three principal values. While there are only two directions which give rise to each of the three principal values there are multiple directions that give rise to the values between the principal values.

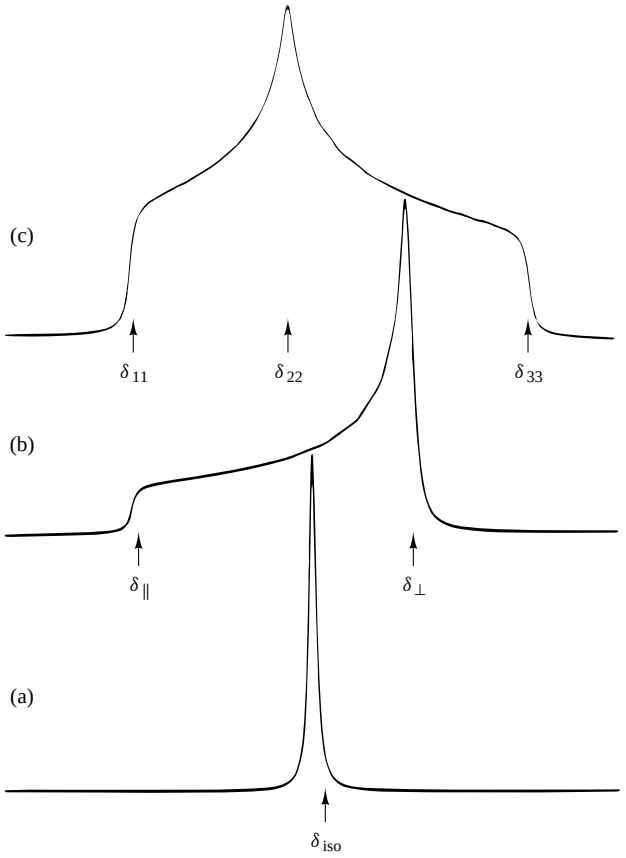

Figure 1 Examples of chemical shift powder patterns for one spin-$\frac{1}{2}$ nucleus: (a) symmetric system, (b) axially symmetric system, and (c) general asymmetric tensor. Arrows indicate the position of the principal values of the chemical shift tensor

For the case of nuclei with highly symmetric electronic environments, for example the carbon in methane, CH_4, the electronic environment does not change as a function of the orientation of the molecule in the magnetic field, and thus the chemical shift is the same in all orientations. This situation occurs when the symmetry at the nucleus is tetrahedral or greater and gives rise to an isotropic chemical shift powder pattern, shown in Figure 1(a), where the three principal values are all equivalent and equal to the value observed in high-resolution NMR spectroscopy. The entire width of the powder pattern is due to residual broadening effects.

The next case is where two of the three principal values are equivalent (known as an axially symmetric tensor) which occurs in cases where there is a threefold symmetry axis through the nucleus, e.g. N of NH_3. The unique principal value lies along the threefold axis and is designated $\delta_{\parallel}$ while the degenerate components are in the plane perpendicular to the axis and are designated $\delta_{\perp}$. These two values can be read from the extremes or breakpoints of the powder pattern, as indicated in Figure 1(b).

The most general case is when the symmetry elements present at the nucleus are all less than threefold, resulting in all three of the principal values being different, as shown in Figure 1(c). In general, only the three principal values of the

chemical shift tensor can be measured from a powder sample. However, in some cases, the symmetry of the molecule at the nuclei of interest can indicate the directions of one or more of the principal values of the tensor (but not which principal value is in that direction). The more the electronic environment varies, the broader the powder pattern.

The techniques that can be used to obtain the principal values of the chemical shift tensor for decoupled spin-$\frac{1}{2}$ nuclei using a powder sample are divided into two broad categories: the one-dimensional (1D) methods, discussed in Section 5, and the two-dimensional (2D) methods, covered in Section 6.

4.2 Single Crystals

In a single crystal there is no longer a distribution of all possible orientations with respect to the external magnetic field as in a powder sample. Instead of seeing broad powder patterns which are independent of the orientation of the powder sample in the magnetic field, the NMR signal from a single crystal placed in a magnetic field is a series of narrow lines, one for each magnetically inequivalent nucleus. When the crystal is rotated, the position of these lines change. The manner in which the position of a given line in the spectrum changes as a function of the crystal orientation in the magnetic field, again for decoupled spin-$\frac{1}{2}$ nuclei, is given by the expression

$$\delta = \delta_{11}\cos^2\alpha\sin^2\beta + \delta_{22}\sin^2\alpha\sin^2\beta + \delta_{33}\cos^2\beta \qquad (8)$$

where α and β are the Euler angles which relate the PAS to the magnetic field direction. Knowing the crystallographic orientation of the single crystal as mounted in the NMR probe, this information can be used to determine the orientation of the PAS in the molecular frame.

Aside from the advantage that the entire chemical shift tensor is determined, a second advantage is that single crystal NMR data are the most precise. The estimated errors in the principal values are in the order of 1 ppm or less, whereas the errors in the powder techniques are generally in the range of 3 ppm or more. Intermolecular interactions and/or structural distortions in crystals can lead to very small shifts in these principal values and/or orientations between two nuclei, and these effects, while immeasurable by powder techniques, can be observed by single crystal NMR.[12]

While this experimental method provides the most information, it is also the method with the most limitations. The most severe limitation is that a relatively large single crystal (several mm in all dimensions) of the compound of interest must be obtained, a feat not always possible. This automatically limits the possibilities to room temperature solids from which single crystals can be grown and transferred into the NMR probe. However, if a suitable crystal can be grown, it is the method of choice.

Single crystal studies have been completed on dilute spin systems, mainly ^{13}C, as well as on abundant spins such as ^{1}H or ^{19}F. For ^{13}C, the cross polarization method in combination with high-power proton decoupling is used; for the abundant spins, multipulse decoupling techniques are necessary.

Just as the powder techniques are divided among 1D and 2D methods, so are the single crystal methods. In Section 7, the experimental techniques for obtaining the chemical shift information from a single crystal will be presented.

5 ONE-DIMENSIONAL POWDER TECHNIQUES

5.1 Static Powder Sample

The simplest, most straightforward experimental method for obtaining the principal values of the chemical shift tensor is to record the spectrum of a static solid sample and measure the principal values from the breakpoints in the powder pattern, as indicated in Figure 1.[2] The sample can be a solid without any molecular reorientation at room temperature, or it can be a sample at a temperature low enough both to take the sample into the solid state and to stop any molecular reorientation. Most typically, the CP technique in conjunction with high-power decoupling is used to obtain the powder pattern of common, low natural-abundance spin-$\frac{1}{2}$ nuclei such as ^{13}C or ^{15}N or a high natural-abundance, but uncommon, nucleus such as ^{31}P. Powder patterns can also be obtained for common, high natural-abundance spin-$\frac{1}{2}$ nuclei (e.g., ^{1}H) with the use of multiple pulse decoupling techniques.

The use of static powder samples has one severe limitation. In molecules containing several nonmagnetically equivalent nuclei, e.g., several different carbons, overlap between the powder patterns can make the determination of the principal values impossible. This is demonstrated by the powder pattern of 1,2,3,6,7,8-hexahydropyrene, given in Figure 2 along with the best fit to the lineshape due to the aromatic carbons. In this case there are three magnetically inequivalent aromatic carbons, with the powder patterns labeled A, B, and C in the decomposed simulation. The portion of the spectral lineshape not fitted is due to the aliphatic carbons.

Even though there have been numerous techniques introduced which help to overcome this limitation concerning sample complexity, the use of a static powder sample is still very common as it is the only technique applicable for certain samples. While variable temperature probes could, in theory, be built to perform many of the experiments that will be discussed below, the majority of the probes that have been built for these techniques can only handle room-temperature solids. On the other hand, it is fairly simple to equip a NMR probe for a static sample with variable temperature capabilities to solidify a liquid and perform a static powder measurement on the sample.

NMR probes have also been constructed to interface with closed cycle cryogenic units, capable of reaching temperatures as low as 4 K.[13,14] This allows the study of not only samples that are liquids or gases at room temperature, but also molecules isolated in an inert environment. Molecules not stable under normal conditions for any reasonable length of time can be generated and quickly deposited on the cold tip of the cryogenic unit, or molecules can be generated photochemically after deposition of a precursor species. For these situations, the only option for obtaining any information on the principal values of the chemical shift tensor is to measure a static powder pattern.

5.2 Variable Angle Sample Spinning

The problem of overlapping tensor patterns can be somewhat alleviated by partially averaging the lineshape by spinning the sample at an angle other than the magic angle, a technique

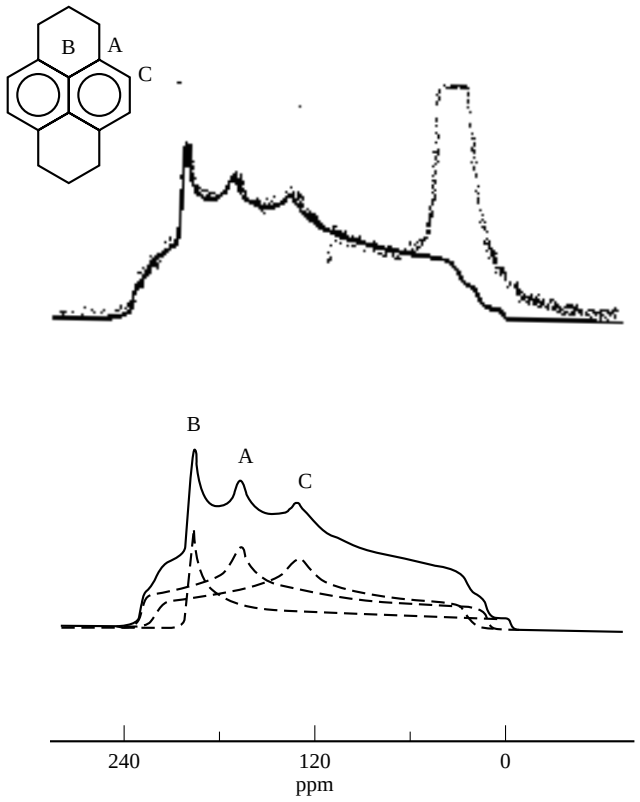

Figure 2 Static powder pattern of 1,2,3,6,7,8-hexahydropyrene with best-fit simulation of the aromatic region. Simulation is decomposed into the three components, where A is the lineshape of the substituted aromatic carbons, B is the pattern of the condensed or bridgehead aromatic carbons, and C is the pattern of the protonated aromatic carbons. (Reproduced by permission of the American Chemical Society from N. K. Sethi, R. J. Pugmire, and D. M. Grant, *Prepr. Am. Chem. Soc., Div. Fuel Chem.*, 1987, **32**, 155)

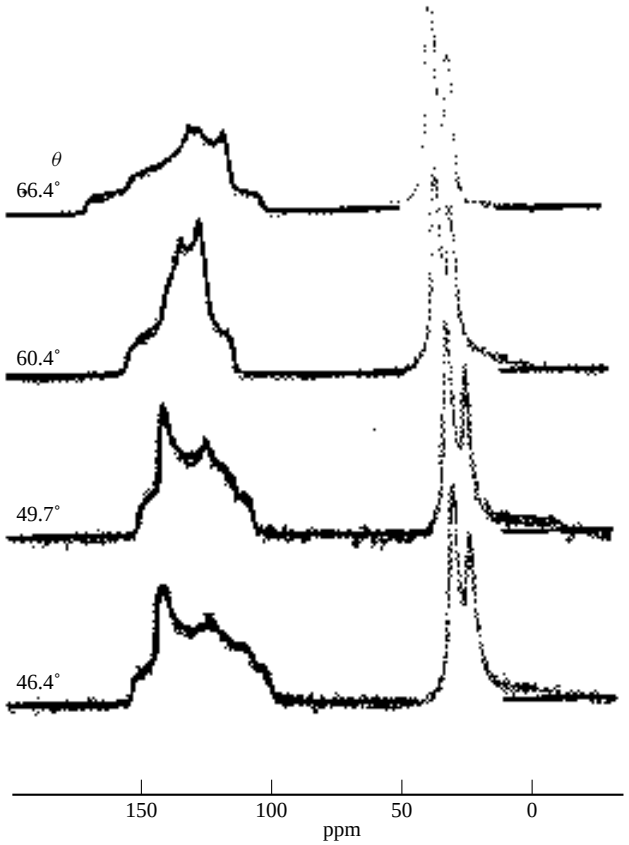

Figure 3 VASS powder patterns of 1,2,3,6,7,8-hexahydropyrene taken at specified angles θ with respect to the static magnetic field direction, along with best fit simulations of the aromatic region. (Reproduced by permission of the American Chemical Society from N. K. Sethi, R. J. Pugmire, and D. M. Grant, *Prepr. Am. Chem. Soc., Div. Fuel Chem.*, 1987, **32**, 155)

known as variable angle sample spinning or VASS.[15,16] As described in Section 3.2, if a sample is spinning at an angle of 54.7° relative to the external magnetic field, and the spinning rate is greater than the width or anisotropy of the pattern, each pattern is collapsed to a relatively narrow line at the isotropic chemical shift, according to the expression in equation (7). If the chosen angle is not the magic angle then the pattern is scaled by the $3\cos^2\theta - 1$ term, where the angle between the spinning axis and the external magnetic field is given as θ. For angles less than the magic angle the pattern is scaled, and for angles greater than the magic angle the pattern is inverted about the isotropic chemical shift as well as scaled. Representative VASS spectra of 1,2,3,6,7,8-hexahydropyrene are shown in Figure 3 for four different angles. It should be noted that the powder pattern for each individual spin is scaled differently, and therefore the resultant patterns are not just scaled versions of one another but are distinctive lineshapes. Experimentally, it has been demonstrated that recording five spectra, one at the magic angle and four at other angles, and simultaneously fitting the four off-angle spectra while locking the isotropic values to those obtained by the magic angle spectrum, gives good results.[17]

One of the major advantages of the VASS technique is that it removes the overlap that is nearly always observed between the δ_{33} component of unsaturated carbons and the aliphatic carbon signals. Also, less time is required to obtain a spectrum with the same signal-to-noise (S/N) ratio as a static powder pattern due to the scaling of the powder pattern. Because a number of different spectra can be recorded and fitted simultaneously, the number of tensors that can be fitted is slightly increased relative to the number of tensors that can be obtained from a static powder pattern.

5.3 Slow Magic Angle Spinning

Another method that can be used to alleviate the problem of overlapping powder patterns is to spin at the magic angle but at speeds less than the width of the patterns, a technique that is known as the Herzfeld–Berger method.[18,19] The resulting spectrum is a series of narrow lines spaced about isotropic chemical shift at integer multiples of the spinning speed for the width of the powder pattern, as shown in Figure 4(b) for the carbons in 1,2,3-trimethoxybenzene. Combining this spectrum with the spectrum taken at a higher speed MAS, shown in Figure 4(a) for 1,2,3-trimethoxybenzene, the center or isotropic chemical shift peaks can be identified, and the various sidebands can then be matched to the proper centerline. The intensities of these spinning sideband (ssb) patterns can

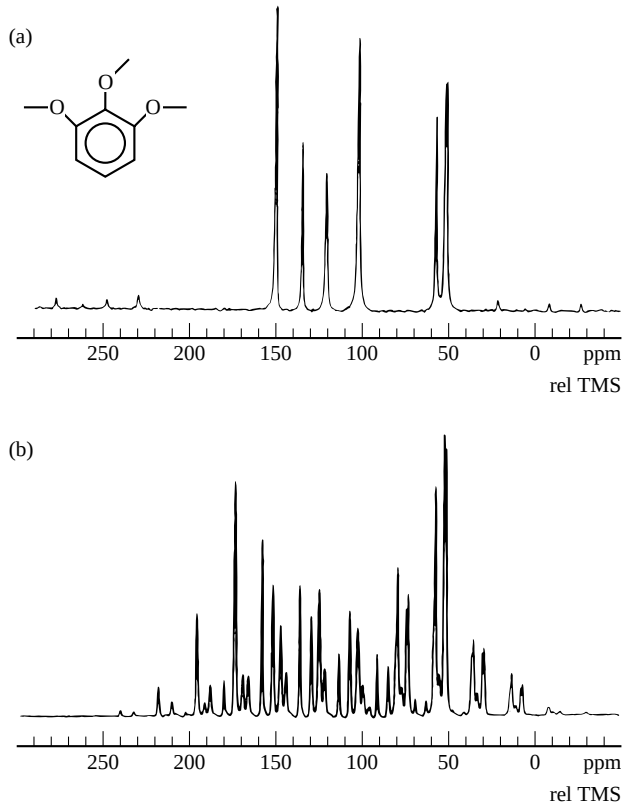

Figure 4 (a) MAS spectrum of 1,2,3-trimethoxybenzene (shown in inset) at a spinning rate of 6.0 kHz. (b) Spinning sideband pattern obtained for 1,2,3-trimethoxybenzene at a spinning rate of 1106 ± 5 Hz

then be analyzed by several methods to yield the principal values of the chemical shift tensor.

This procedure has not been used very widely as it requires a careful measurement of the integrated intensities and the use of a more complex analysis than needed for static patterns, and the errors in the principal values obtained from this technique are typically greater than those from the other methods. Experimentally, it is crucial that the spinning speed be constant (±10 Hz); however, with modern spinning speed controllers this is very feasible. The limitation in the number of magnetically inequivalent spins is determined by the width of the lines; if a compound contains several spins with similar isotropic chemical shifts, overlap can prevent accurate line intensities being obtained.

More recently, the Herzfeld–Berger method has been combined with DANTE pulse sequences[20] to saturate selectively one or more of the ssb patterns to simplify the spectra of complex compounds.[21] After the initial preparation of magnetization by a normal CP sequence, a DANTE sequence centered at the frequency of one of the peaks of the ssb pattern to be destroyed is added. This sequence leaves the magnetization of the other spins unaffected. Several DANTE sequences at different frequencies can be added, with the limitation that the spin–lattice relaxation time (T_1) be of sufficient length that the magnetization for the desired spins does not relax back to thermal equilibrium during the time it takes to apply the saturation sequences.

This concept of producing selective 1D spectra can be considered an alternative to the 2D approach of obtaining all the ssb patterns separated in 2D space, as presented in the section on 2D methods. This same approach is also used in the next section in conjunction with spinning at two different angles.

5.4 Switched Angle Spinning

A one-dimensional version of the 2D switched angle sample spinning (SASS) experiment to be discussed in the next section was introduced in 1990.[22,23] By combining the principles of switched angle spinning with some type of selective irradiation scheme, a spectrum containing only the powder pattern(s) of the selected spin(s) can be obtained. The magnetization of the selected spin is selectively prepared or inverted with the sample spinning at the magic angle using a technique such as the DANTE sequence in the case of Maciel's work[23] or selective soft rf pulses as done by Ashida et al.[22] It is necessary that spinning be conducted at the magic angle in order to be able selectively to irradiate one spin while not affecting the magnetization of the remaining spins. The spinner axis is then changed to a different angle before the detection period, resulting in a scaled powder pattern containing only the signals of the selected spin. There is, however, a limit to how selective a pulse can be; if there are two or more signals closely spaced, it is impossible selectively to irradiate only one of them.

The experiment was undertaken in a 1D manner in the belief that conducting a number of 1D experiments in such a way as to obtain the spectra of all spins may be more time-efficient than conducting a 2D experiment in some cases. This judgment is very dependent on the nature and number of the nuclei in the sample.

6 TWO-DIMENSIONAL POWDER TECHNIQUES

The various 2D techniques that have appeared in the literature are discussed in this section. However, before discussing the specifics of each technique, some comments general to 2D spectroscopy are necessary. First, all 2D spectral techniques can be described in terms of the preparation of a magnetization period, followed by an evolution time, t_1, possibly a mixing time, and then an acquisition time, t_2. The evolution time is increased by a constant time increment between successive spectra in the 2D experiment, and the signal acquired during the acquisition time is a function of both the evolution time and the acquisition time. In all the cases outlined below, the techniques were described for the observation of dilute spin-$\frac{1}{2}$ nuclei, and the preparation period consisted of a normal CP sequence to take the magnetization into the transverse plane. A general 2D pulse sequence, using CP for signal enhancement, is shown in Figure 5.

While these 2D techniques can be divided in a number of ways, in this article the techniques that obtain the isotropic dimension during the evolution time will be discussed first, followed by those which use MAS during the acquisition time to obtain the isotropic information in the second dimension.

As the spectral presentation of the individual powder patterns as ridges in a 2D contour plot, with the projection on the two axes being an isotropic spectrum and a normal powder pattern, is the same in the majority of these techniques, sample spectra are not included for each technique. Instead only one

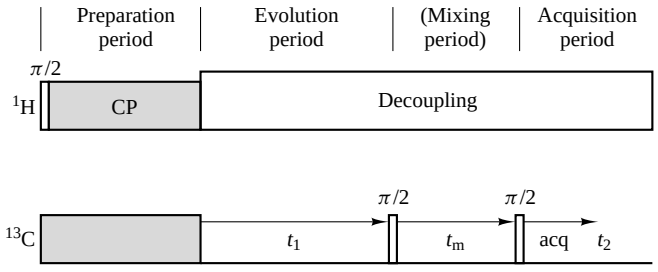

Figure 5 A schematic representation of the times in a general 2D pulse sequence, along with a typical 2D pulse sequence for both the ^{1}H (decoupler) and observe nucleus channels, using CP for the preparation of the magnetization. The pulse sequence shown is the basic 2D chemical exchange scheme. The mixing period is optional

representative spectrum of this type is included. Representative spectra obtained for the 2D methods that present the chemical shift information in a different manner are also included. Also, no information is provided on the details of the phase cycling used in the methods; the reader is referred to the original references for this information.

6.1 Magic Angle Hopping

Magic angle hopping (MAH)[24] was one of the first 2D techniques which provided isotropic chemical shifts, i.e. a normal MAS spectrum in the first dimension, with the individual powder patterns separated in the second dimension. The MAH experiment is carried out with a static sample at the magic angle with respect to the external magnetic field. The sample is successively hopped by 120° about this axis, using a computer-controlled stepping motor such that the sample spends one-third of the evolution time in each of the three orientations. Between these three periods the prepared magnetization is stored along the magnetic field direction with a 90° pulse; the sample is reoriented or hopped, followed by the return of the magnetization to the *xy* plane with a second 90° pulse. The timing of the pulses and the hopping of the sample during the evolution time are shown in Figure 6(a). As there is no spinning of the sample, the isotropic chemical shift dimension has no spinning sidebands.

The major difficulty in this experiment is the requirement of rapidly and accurately reorienting the sample during each scan. The original work reported a hopping time of 150 ms; subsequently, in a paper reporting several modifications to the original experiment,[25] the hopping time was reduced to under 60 ms with the use of a dc servo motor. The shortening of this hopping time is important as the magnetization that is prepared and subsequently stored along the magnetic field by the 90° pulse is decreased by normal $\boldsymbol{T}_1$ relaxation mechanisms. The accuracy in setting the angles is reflected in how complete the averaging process is, and it therefore affects the width of the lines observed in both the isotropic chemical shift spectrum and in the 2D space, placing a limitation of the resolution obtainable.

The reported modifications of the MAH experiment also included a larger sample volume to allow for the measurement of a 2D spectrum in under 24 h, and an increase in the signal collected in each scan by incorporating the last one-third of the evolution time into the acquisition dimension, as discussed in the next technique.

6.2 Magic Angle Turning

One of the most recent 2D techniques for the separation of the overlapping powder patterns was introduced by Gan in 1992[26] and is known as the magic angle turning (MAT) method. Gan's technique is a very simple method which can, in principle, be undertaken on a normal MAS probe without any additional equipment. The MAT method is based on the fact that continuous, very slow, spinning at the magic angle can be used in place of the three discrete 120° hops in the MAH experiment. Instead of mechanically hopping the sample by 120°, Gan proposed that the pulses in the evolution period be separated by a time equal to one-third of the rotor period, as shown in the pulse sequence in Figure 6(b).

A second modification from the previous MAH method is that the acquisition period was started immediately after the last pulse instead of waiting a time period of one-third of the evolution period. This modification of acquiring the complete echo instead of starting the acquisition at the top of the echo increases the signal intensity by nearly a factor of $\sqrt{2}$. A consequence of this modification is that the 2D space is no longer a square but has the powder patterns at an angle defined by $\tan^{-1}(1/3)$, and it must be sheared or rotated by this angle in order to obtain normal projections of the isotropic chemical shift spectrum.

This technique was subsequently refined, and the power of the method demonstrated[27] using a probe designed specifically for the experiment. The probe, designed around a large volume rotor (about 5 cm^3), has a maximum spinning rate of about 200 Hz, and is very stable at spinning rates as low as 22 Hz. Normal commercial MAS probes, on the other hand, are optimized for stable spinning at speeds in the kHz to tens of kHz range and it is usually difficult to maintain stable spinning at very low speeds. The modification of the pulse sequence, designated the triple echo MAT and shown in Figure 6(c), consists of an addition of three echo pulses to Gan's proposed pulse sequence in order to remove phase imperfections and anomalies in the 2D base plane. The lowered spinning speed also simplifies the fitting of the powder patterns obtained as slices of the 2D space, as they are identical to a static powder pattern at these speeds. It was shown that the spectral lineshape is affected at speeds as low as 44 Hz, requiring that the data be fitted instead of being able to read the break points directly from the lineshape. The large volume sample allows for a typical 2D spectrum to be obtained in less than 24 h, making it feasible for this technique to be used on a routine basis.

This paper also demonstrated that the method can be combined with the techniques of SCT to obtain spectra containing signals from only the protonated carbons, and DD for spectra containing only patterns from nonprotonated carbons. A typical 2D spectrum obtained using the triple echo MAT method, along with the individual powder patterns obtained, is shown in Figure 7 for 2,6-dimethoxynaphthalene, which has six inequivalent aromatic carbons.

6.3 5-π Pulse

The 5-π pulse experiment[28] is another method related to the MAT and MAH techniques. In this experiment, as in MAT, the sample is also spinning slowly at the magic angle. However, instead of storing the selected magnetization along

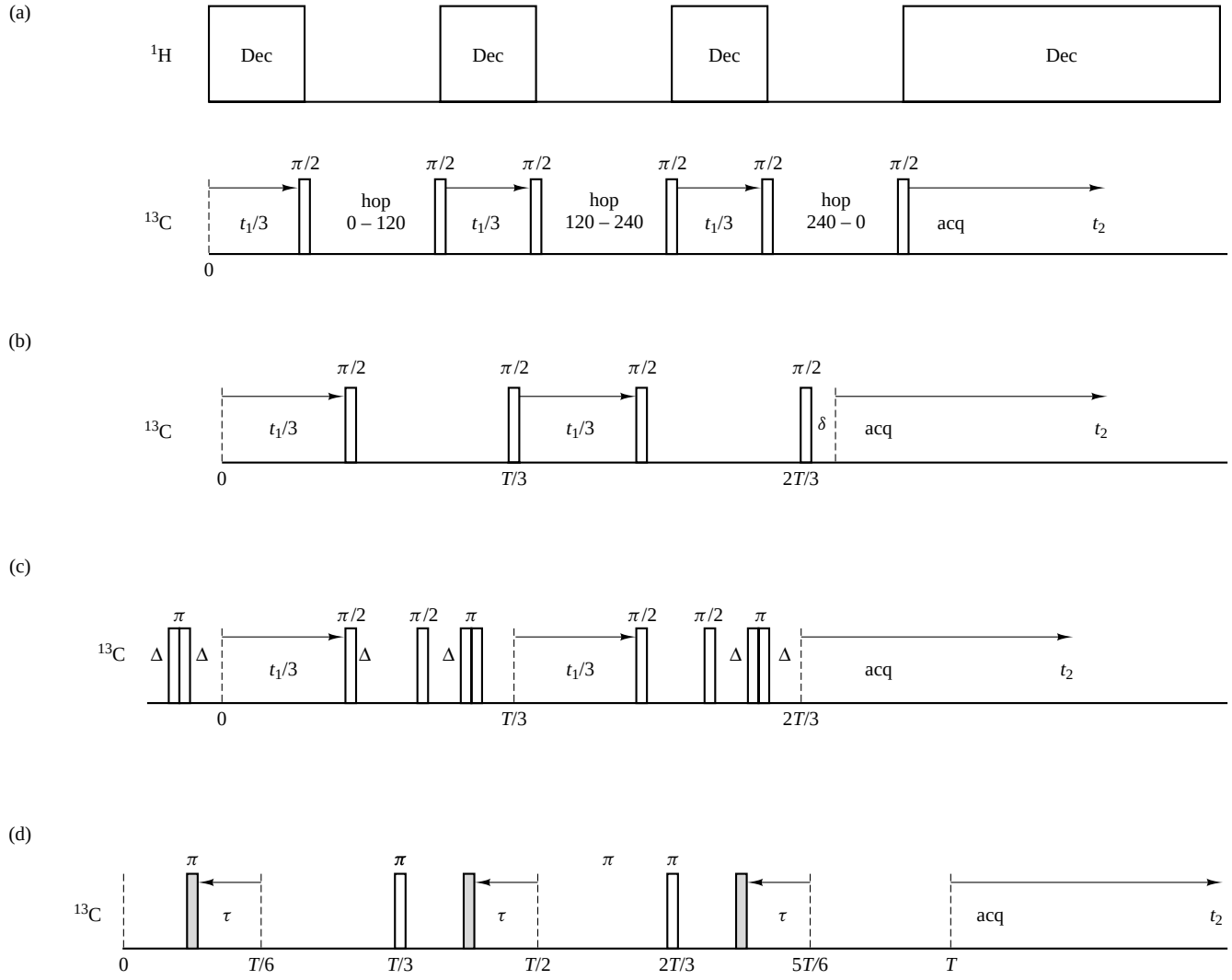

Figure 6 (a) The evolution and acquisition time of the MAH pulse sequence for both the observe and decouple channel. (b) The evolution and acquisition time of the original MAT pulse sequence. (c) The evolution and acquisition time of the triple echo MAT pulse sequence. Δ indicates the echo time. (d) The evolution and acquisition time of the 5-π pulse method. The shaded pulses are the ones which move as a function of the evolution time, τ. For (b)–(d), the decoupler remains on for the entire evolution and acquisition periods. In all cases 0 marks the start of the evolution period, T signifies the length of a rotor period, and a normal CP sequence used to prepare the magnetization

the static field direction during the course of the experiment, the magnetization is kept in the transverse plane and a series of five π pulses are used to achieve the same effect. This method can be thought of as a constant time version of the MAT experiment.

As shown in Figure 6(d), two of the five π pulses are at the fixed times of $T/3$ and $2T/3$ during the evolution period, where T must be an integral number of rotor periods. Each π pulse changes the sign of the phase angle describing the precession of the magnetization up until the application of the pulse. The position of the first, third, and fifth π pulses are set at times $T/6 - \tau$, $T/2 - \tau$, and $5T/6 - \tau$, where τ is the evolution variable which ranges from $-T/6$ to $T/6$. At $\tau = 0$, the five π pulses are evenly spaced at increments of $T/6$, such that the accumulated phase is zero, resulting in the complete suppression of the chemical shift. When $\tau \neq 0$ the pulses are no longer evenly spaced, and the phase accumulation is proportional to $\omega_{iso}\tau$. Thus, the evolution dimension displays an isotropic chemical shift spectrum. The spectrum in the acquisition dimension is either a ssb or a static powder pattern depending on the spinning speed used.

This technique has an advantage over the MAH and MAT experiments in terms of increased sensitivity by avoiding the need to project the magnetization to the longitudinal direction. However, the 5-π pulse method does suffer from a loss of signal at longer evolution times (and therefore lower rotation frequencies) if the T_2 value of the spin is short in comparison to the total time T between the preparation of the magnetization and the start of the acquisition period.

6.4 Stop and Go

In the 2D technique known as stop and go or STAG[29] the sample, at the magic angle with respect to $\boldsymbol{B}_0$, is taken from being stationary during the preparation and evolution of the magnetization to high speed spinning during the acquisition period, as shown in the pulse sequence used in Figure 8(a). The

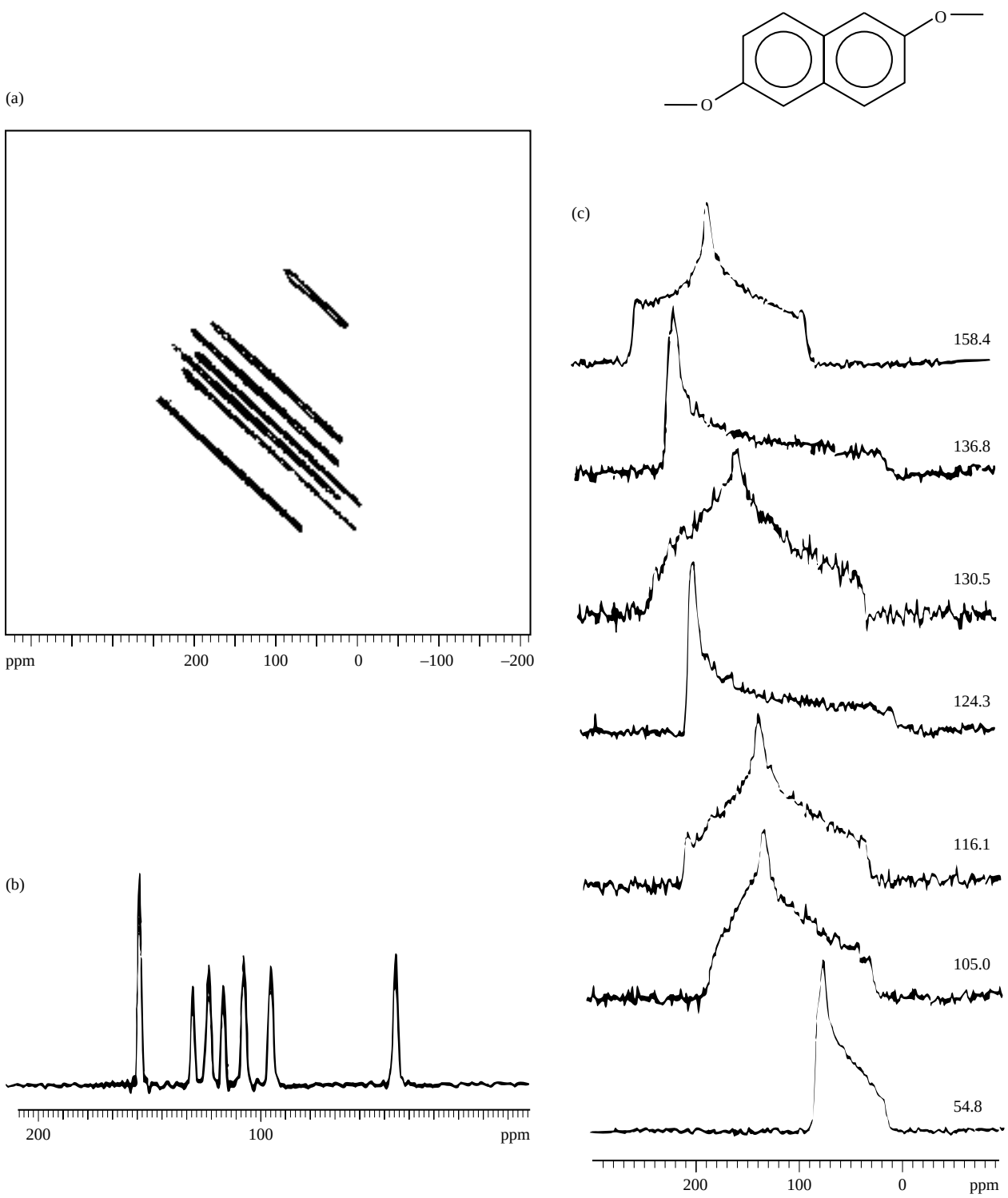

Figure 7 (a) A 2D MAT spectrum of 2,6-dimethoxynaphthalene (shown in inset). (b) The projection in the isotropic chemical shift dimension. (c) The individual powder patterns taken from the 2D spectrum in (a) at the indicated isotropic chemical shifts

air used for spinning is controlled with a solenoid valve that is electronically opened and closed by the pulse programmer controlling the NMR experiment. At the end of the evolution period the magnetization is stored along the magnetic field, in the manner discussed in the previous 2D methods, the air flow is started, and the sample is allowed to come to a relatively high spinning speed. Once the desired spinning speed has been reached, the stored magnetization is returned to the *xy* plane for detection. In the original paper the time required to start the spinner and achieve a spinning speed of 1.7 kHz was in the range of 3–5 s.

The spectra obtained are identical to those of the original MAH spectrum, with the exception that there are now spinning sidebands observed in the spectra as the sample is spinning

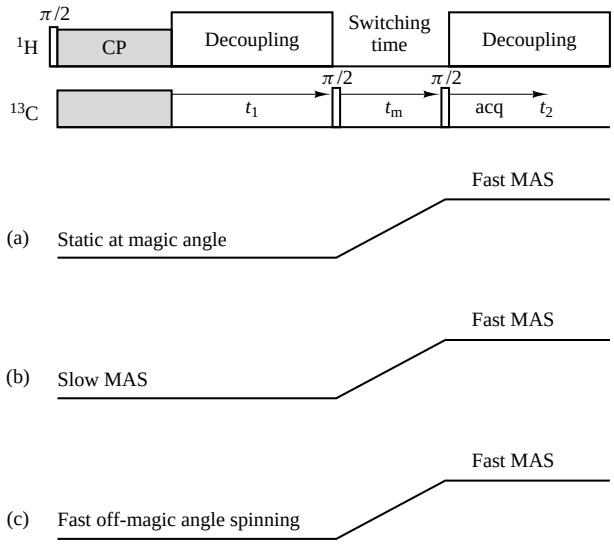

Figure 8 The 2D pulse sequence used in the STAG, S^3, and SAS 2D experiments. A normal CP preparation period was typically used. The $\pi/2$ pulses store the evolved magnetization along the field direction during the switching time and then return it to the transverse plane. (a) For STAG, the sample is stationary during the preparation and evolution periods and is spinning at the magic angle during the acquisition period. (b) In S^3, the spinning speed is increased by a factor of 5–10 during the mixing time. (c) In SAS, the spinning speed remains constant but the spinner axis changes relative to the external magnetic field. The length of time taken to accomplish these changes (the length of the switching period) is discussed in the text

during acquisition. The limitations of this method are also the same; namely this approach is only applicable to spin systems with T_1 relaxation times long compared with the time taken to bring the sample from the static condition to the maximum spinning speed.

6.5 Switched Speed Spinning

The switched speed spinning (S^3)[30] experiment is similar to that of the STAG method except that the spinning speed is only reduced by a factor of ca. 5–10 during the preparation and evolution time of the 2D experiment instead of being completely stopped, and is shown in Figure 8(b). The experiment was performed on an unmodified MAS probe using a commercially available spinning system and the spinner speed was controlled by a system which delivered a flow rate of air proportional to an applied voltage, with the change in this voltage being under the control of the NMR pulse programmer. This results in the anisotropic information being in the form of an ssb pattern instead of a static powder pattern. The fact that the spinning speed is only reduced and not completely stopped should be less demanding on the spinning system.

6.6 Switched Angle Spinning

The next technique has been discussed in the literature under two different names: dynamic angle spinning (DAS) and switched angle spinning (SASS). The method was introduced independently by two different groups shortly after the introduction of the MAH experimental technique.[31,32] This technique also requires reorientation of the sample, however this time a rapidly spinning sample is taken between the magic angle and a second angle during each scan, as shown in Figure 8(c).

In this technique the sample is held at the magic angle during the evolution period of a 2D experimental scheme. The evolved magnetization is then stored along the static magnetic field while the spinning axis is changed from the magic angle to any other angle. Following the angle switch, the stored magnetization is returned to the transverse plane for detection. The second angle used can be any other angle, resulting in patterns that are scaled by the argument $\frac{1}{2}(3\cos^2\theta - 1)$ according to equation (7).

The initial papers on this technique employed switching times on the order of 0.5–2 s. There is now a commercial probe available for SASS measurements with angle switching times on the order of 100 ms, allowing for more widespread use of this method.

Subsequent development of SASS has led to two methods which shorten the time required for the measurement of the chemical shift tensor information. The first involves a technique by which the second dimension, the dimension containing the anisotropic information, can be shortened.[33] In the initial experiment, as in all of the 2D methods discussed, one dimension contains the isotropic chemical shifts and the other contains the separated powder patterns. The projection of the 2D space onto the axis in the second dimension will result in the static powder pattern, as this dimension contains not only the anisotropic information but also the isotropic, i.e. the powder patterns are still offset from each other by the difference in their isotropic chemical shift. However this offset can be removed, resulting in all of the powder patterns being centered at the same frequency. This allows the spectral width in the second dimension to be shortened from that necessary to observe the normal static powder pattern to a spectral width set by the widest of the separated, scaled powder patterns.

The second method introduced to shorten the time necessary to obtain the chemical shift information was the use of the SASS principle in conjunction with selective irradiation or inversion in a 1D experiment,[22,23] as discussed in Section 5.4.

6.7 TOSS–Reverse TOSS

The TOSS (Total Suppression of Spinning Sidebands) sequence was originally introduced by Dixon et al.[34,35] to suppress spinning sidebands in normal MAS spectra, resulting in a spectrum containing only the centerband frequencies. The TOSS sequence consists of a series of four π pulses, applied at precise fractions of a rotor period which allow the intensities of the centerband to add while the magnetization of the sidebands are canceled. This technique improves spectral resolution and simplifies MAS spectra, especially those taken at high fields or at low spinning speeds. However, the price is that information about the anisotropic portion of the chemical shift tensor is lost.

However, the anisotropic information can be restored in a 2D experiment by following a normal TOSS sequence with an evolution time and then applying the 'mirror image' of the TOSS sequence to reverse the averaging before the start of the acquisition period. The TOSS–reverse TOSS pulse sequence[36]

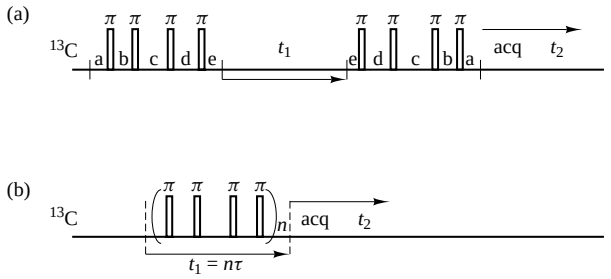

Figure 9 (a) The observe channel portion of 2D pulse sequence used in the TOSS–reverse TOSS technique. The separation between the π pulses is discussed elsewhere.[34–36] (b) The observe channel portion of 2D pulse sequence used in the synchronous application of π pulses with MAS method. The spacing of the four π pulses has been discussed by Tycko et al.[40] The rotor period is equal to τ. The decoupler remains on during the evolution and acquisition times in both sequences

is shown in Figure 9(a). The sample is spun at the magic angle at a relatively slow rotation frequency. During the evolution period, the effect of the TOSS sequence is such that the magnetization is evolving, containing only the isotropic information, without sidebands, while after the reverse TOSS sequence is applied the evolution once again contains the anisotropic information in the form of an ssb pattern. This information is then collected during the acquisition dimension.

6.8 Magic Angle Spinning with Synchronous Application of rf Pulses

The synchronous application of rf pulses during a MAS experiment in order to reconstruct the anisotropic information averaged by the spinning was first introduced by Lippmaa et al.[37] Subsequent improvement[38] led to the application of a train of six π pulses per revolution of the spinner in a 1D experimental format and the adaptation of the method to a 2D experiment utilizing four 2π pulses per rotor cycle to decrease the sensitivity of the experiment to pulse imperfections.[39] However, in none of the above do the breakpoints in the lineshapes correspond directly to the principal values of the chemical shift tensors, and the reported principal values are not in close agreement with those obtained by other techniques.

Tycko et al.[40] modified the basic method to render the intensities of the powder patterns obtained in the 2D space undistorted, making the measured principal values of the tensor more reliable, using a series of four or six π pulses as shown in Figure 9(b). The spacing of the four or six π pulses was chosen such that the isotropic scaling factor was zero.

This method, unlike many of the other 2D methods such as MAH, STAG, and SASS, is not demanding mechanically. Instead, the experiment can be performed on a normal MAS probe on a spectrometer system equipped with the ability to synchronize the application of the pulses with the spinning. However with this method it is more difficult to obtain very accurate principal values, due to the sensitivity of the technique to both the timing and quality of the rf pulses. This technique, along with the TOSS–reverse TOSS and the 5-π pulse method, also does not suffer from the loss of signals from nuclei with shorter T_1 relaxation times.

6.9 Chemical Shift–Chemical Shift Correlation

Chemical shift–chemical shift correlation (CS–CS) spectroscopy[41] is a modification of the 2D exchange NMR experiment,[42] using the basic pulse sequence shown in Figure 5 in which the stationary sample is reoriented by 90° along an axis perpendicular to the external magnetic field during the mixing time of the experiment. The projections in either dimension give the powder pattern of the sample in each of its two orientations relative to the external magnetic field. For a random powder sample, these two projections are identical. The 2D space, however, contains a unique representation of each tensor in the shape of a triangle for an axially symmetric tensor or a hexagon for a general asymmetric tensor, with the position of the corners defined by the principal values of the tensor. These shapes can be understood by considering the case of a single molecule. In the case of an axially symmetric tensor, if the molecule is in a position with respect to the external magnetic field such that its chemical shift is $\delta_{\|}$, then a 90° rotation of this molecule must gave a chemical shift of $\delta_{\perp}$. Likewise, if the signal in the first orientation is at $\delta_{\perp}$, after a 90° rotation it must be either $\delta_{\|}$ or $\delta_{\perp}$, resulting in the triangular pattern observed in the 2D space. For the case of an asymmetric tensor, a 90° rotation from an orientation which has a chemical shift of any one of the three principal values must take the molecule into an orientation that has a chemical shift of either one of the two remaining principal values, creating a hexagonal pattern in the 2D correlation space.

One of the applications of this method is in sorting out the principal values of overlapping powder patterns, as is demonstrated for coronene in Figure 10. Coronene has

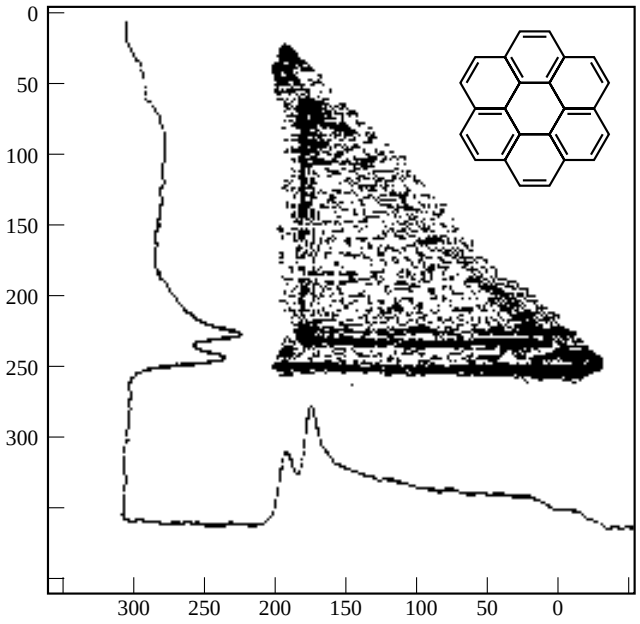

Figure 10 Contour plot of the 2D CS–CS correlation spectrum of coronene (shown in inset)

three magnetically inequivalent sets of carbons. At room temperature the molecule is rotating rapidly about an axis perpendicular to the plane of the molecule, averaging all

the three tensors to axial symmetry. From the normal 1D powder pattern (the projection on either axis) and the isotropic chemical shifts obtained from a MAS spectrum, it is difficult to determine which $\delta_{\parallel}$ and $\delta_{\perp}$ should be paired for the each of the three tensors. The patterns in the 2D space, however, clearly indicate how the six principal values are paired to obtain the three tensors.

6.10 Variable Angle Correlation Spectroscopy

In this experimental approach, known by the acronym VACSY,[43] the approach used to separate the anisotropic information is different from the above techniques. The data are not acquired as a typical 2D data set, i.e., with the evolution time being incremented between individual spectra. Instead, the experiment, performed under the conditions of high-speed spinning, involves collecting a series of VASS spectra taken at different angles. Selected intensities of the signal as a function of time and the spinning angle are then chosen to create a 2D data set for normal 2D FT processing, as shown schematically in Figure 11.

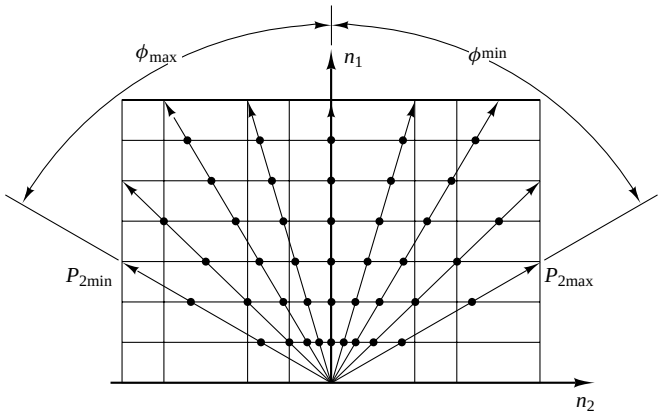

Figure 11 Representation of the strategy employed for obtaining 2D VACSY data. The arrows represent the individual FIDs recorded, each at a different spinning axis angle. The grid of points (n_a,n_i) are the points needed for the 2D FT in the acquisition and evolution dimension. Interpolation between the acquired data points is used to obtain signal intensity at all the grid points that fall inside the wedge formed by the minimum and maximum angles. (Reproduced by permission of the American Institute of Physics from L. Frydman, G. C. Chingas, Y. K. Lee, P. G. Grandinetti, M. A. Eastman, G. A. Barrall, and A. Pines, *J. Chem. Phys.* 1992, **97**, 4800)

The dwell time of the VASS spectra is chosen as the time needed in the isotropic direction for sufficient resolution in this dimension. The dwell time in the acquisition dimension is then a function of the range of angles used, and from this information the spinning angles at which spectra are obtained can be calculated. The intensities at certain points in the grid of (n_a,n_1) points shown in Figure 11 are then obtained, using interpolation as necessary; these intensities are then processed using the normal 2D FT methods. Figure 12 shows plots of the different data processing stages in the procedure of obtaining a 2D isotropic–anisotropic chemical shift spectrum of glycine.

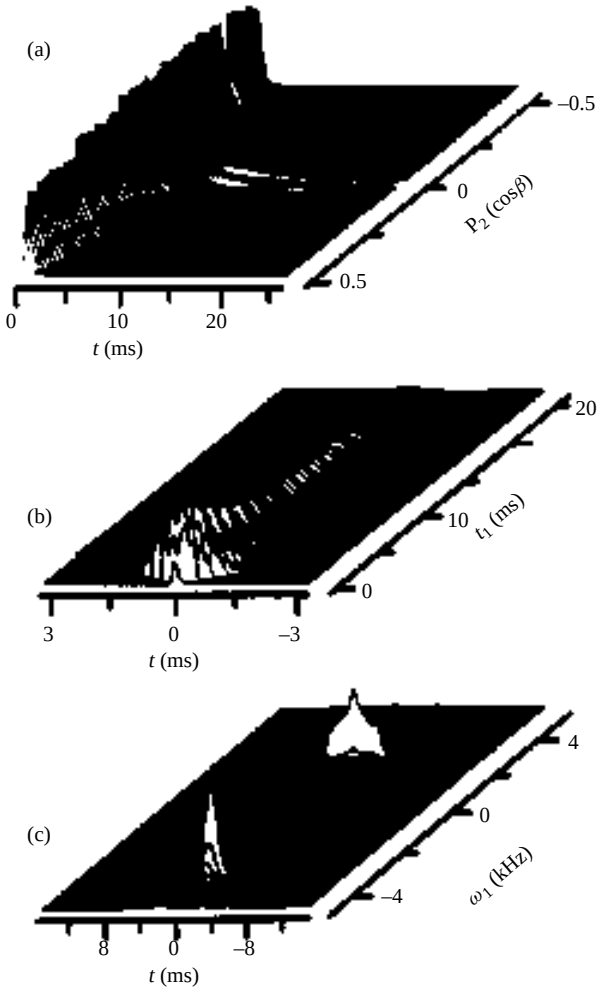

Figure 12 Plots of VACSY data for glycine (H_2NCH_2COOH). (a) Set of 75 FIDs recorded for a grid defined by the dwell time in the isotropic dimension being four times that in the anisotropic dimension. (b) 2D data set after interpolation onto the (n_a,n_i) grid. (c) Spectrum obtained after the 2D FT of data set in (b). (Reproduced by permission of the American Institute of Physics from L. Frydman, G. C. Chingas, Y. K. Lee, P. G. Grandinetti, M. A. Eastman, G. A. Barrall, and A. Pines, *J. Chem. Phys.*, 1992, **97**, 4800)

7 SINGLE CRYSTAL TECHNIQUES

7.1 Crystal Rotation Methods

All the early single crystal studies were undertaken using the 1D crystal rotation method.[2,3] In this method, the crystal is mounted in the probe on a goniometer. A succession of spectra are recorded with the crystal being rotated by a number of degrees between spectra. This rotation is continued until the sample has been rotated by 180°. The step size used depends on the number of lines and how closely they are spaced; a typical step size is on the order of 5–10°. The crystal orientation is then changed by 90° and the process is repeated. Finally the third rotation pattern is obtained for a third axis, perpendicular to the first two rotation axes. A representative rotation pattern of pyrene is shown in Figure 13.

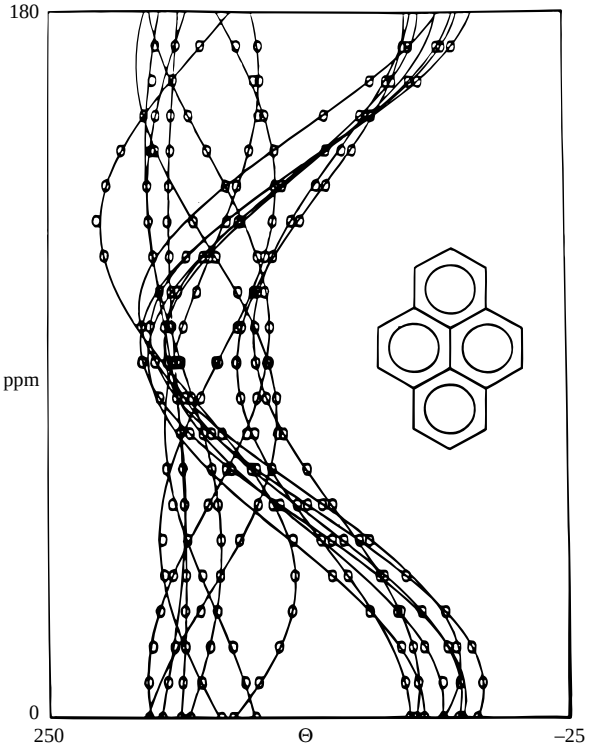

Figure 13 Rotation pattern obtained for one orientation of a single crystal of pyrene (shown in inset). One molecule in the unit cell is sampled nearly in the molecular plane by this rotation; in this case the difference between the in-plane components is small and the lines only move slightly. The other molecule is rotated in and out of the molecular plane and therefore shows a much greater range of chemical shift values as a function of the rotation angle. (Reproduced by permission of the American Chemical Society from C. M. Carter, D. W. Alderman, J. C. Facelli, and D. M. Grant, *J. Am. Chem. Soc.*, 1987, **109**, 2639)

Once the three rotation patterns are obtained, the line positions of each magnetically inequivalent spin must be followed as its position changes from one spectrum to the next, according to the expression given in equation (8). This process can be accomplished in a number of ways, one of which has been to fit the data using a least-squares Simplex fitting routine. Along with the fitting of peaks to different nuclei in one rotation pattern, a connection must be made to the lines in the other two rotation patterns.

Using this method there is a limit to the number of magnetically inequivalent nuclei in the unit cell. As there are more nuclei, the probability that the lines may not all be resolved increases and the large number of line crossings and the crowding often result in rotation patterns that cannot be interpreted, even with small step sizes. This limit has been estimated to be in the range of about 15–20 nuclei and is dependent on the width of the range of chemical shifts for the tensors. As two chemically equivalent nuclei with different orientations in the unit cell will give rise to different chemical shifts, this limitation is very restrictive especially in cases where there is more than one molecule per unit cell.

7.2 2D Crystal Correlation Methods

A 2D technique was introduced in 1985 which allowed for the study of more complex single crystals.[44,45] This method is a modification of the Jeener chemical exchange pulse sequence,[42] with the normal CP sequence for the preparation of the magnetization added. As in the CS–CS method discussed in Section 6.9, the single crystal sample is reoriented during the mixing time of the experiment. This results in a 2D spectrum where the projection onto the axis in one dimension is the spectrum obtained for the first orientation of the crystal, while the projection in the second dimension is the spectrum obtained in the second orientation. In the 2D space there are a number of peaks which correlate a given chemical shift in one dimension (or crystal orientation) with a line position in the second orientation, eliminating the need to determine the best fit in the correlation of the resonance frequencies from one spectrum to the next in a rotation pattern.

In order to obtain all the information contained in a single axis rotation pattern, it has been shown that four 2D correlation spectra are needed. In each of these spectra the two orientations are related by a 45° rotation. The four spectra are taken with the sample between 0° and 45°, 45° and 90°, 90° and 135°, and finally between 135° and 180° (which is 0°). The position of the resonance lines in these four spectra can be connected by placing the four spectra in a square, where the axes corresponding to common crystal position are placed together.

The goniometer used for obtaining rotation patterns is replaced by a device capable of being rotated between two positions using a motor-driven string. The unit has four holes for a lever arm, positioned precisely at 45° increments about the sample. However, the sample must be remounted for each of the three sets of four 2D spectra which are needed for the complete determination of the chemical shift information.

This method was modified in 1989 to include a multiple-axis sample reorientation mechanism[46] to remove the need for remounting the crystal, as this remounting process introduces errors in the data if the three mounted orientations are not exactly perpendicular. This mechanism is designed to move between any pair of six orientations (*X*, *XY*, *Y*, *YZ*, *Z*, and *ZX*) which were selected such that all the information necessary completely to characterize the chemical shift tensor can be obtained. To determine the chemical shift tensor it is necessary to record only six 2D spectra, corresponding to the *X–XY*, *XY–Y*, *Y–YZ*, *YZ–Z*, and *Z–ZX* direction pairs. A representative set of the six 2D spectra is shown in Figure 14 for a single crystal of acenaphthene,[47] which has four molecules per unit cell with two crystallographically unique molecules. The symmetry of the molecule and the crystal combine to give rise to a total of 36 resonances, which can be analyzed to give the 14 unique chemical shift tensors.

In this figure the connectivity of the peaks due to one of the 14 carbons is shown. The spectra shown in Figure 14 were analyzed to obtain all 28 chemical shift tensors, with a standard deviation of 0.52 ppm between the actual peak positions in the 2D spectra and the expected positions based on the best parameters of the chemical shift tensor. To date, the chemical shift tensors have been obtained for crystals containing up to 72 magnetically inequivalent carbons.

8 DIPOLAR TECHNIQUES

Dipolar couplings can be used to assign the orientation of the PAS to the molecular frame for the nuclei coupled, as well

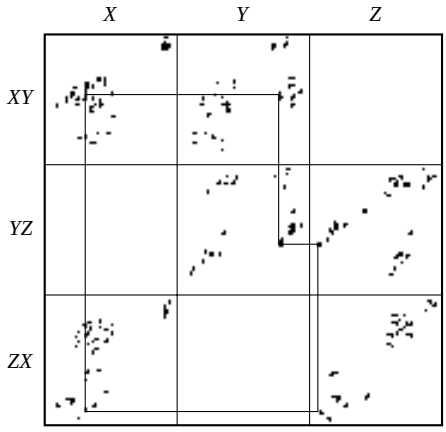

Figure 14 Set of six 2D multiple-axis reorientation spectra obtained for a single crystal of acenaphthene. The connectivity of peaks for one of the 14 magnetically inequivalent carbons is shown. The labels *X, Y, Z, XY, YZ, ZX* refer to the directions discussed in the text (Reprinted with permission from R. J. Iuluicci et al., *J. Am. Chem. Soc.*, **117**, 2336. Copyright (1995) American Chemical Society)

as to provide information on the separation of the two spins. In practice, this technique is used on compounds which have been specifically labeled in two positions, or in compounds in which there is an isolated pair of spin-$\frac{1}{2}$ nuclei, for an example a $^{31}P-^{31}P$ pair. Dipolar couplings also exist between a spin-$\frac{1}{2}$ and a quadrupolar nucleus. The lineshape obtained from a static powder sample containing such a spin pair contains not only the chemical shift information of one (for the case of a heteronuclear dipolar coupling) or both (homonuclear) spins, but also contains information on the orientation of the PAS of the chemical shift tensor with respect to the dipolar vector.

If one were to consider a single molecule in some orientation with respect to the static magnetic field, the chemical shift of a given spin in this molecule specifies the observed line position, that can be designated as ν. If this nucleus were coupled to a second spin, the result would be to see two lines spaced symmetrically about ν, with the separation dependent on D as given by the expression in equation (5) and the position of the dipolar vector. This situation is nicely shown in single crystal studies of compounds containing an isolated spin-$\frac{1}{2}$ pair.

This example can be extended to a spin-$\frac{1}{2}$ pair in a powder sample where the chemical shift of the spins involved is isotropic. In this case the dipolar coupling dominates the lineshape, and a Pake doublet, shown in Figure 15(a), is obtained. The Pake doublet consists of two axially symmetric patterns, with the central peaks being separated by D or $1.5D$ for the cases of heteronuclear and homonuclear spin pairs, respectively.

Now, if the spins have an appreciable anisotropy in their chemical shifts, the lineshape and the analysis of the dipolar pattern is more complicated. A detailed description of the mathematical treatment of the lineshape of dipolar spectra in this case is given in the literature[48] as well as in a recent review article on dipolar coupling.[49] Also, more details can be obtained in other sections of this Encyclopedia. For the purpose of this overview, however, the sensitivity of the lineshape relative to this orientation of the vector between the two spins in the PAS of the chemical shift tensor can be

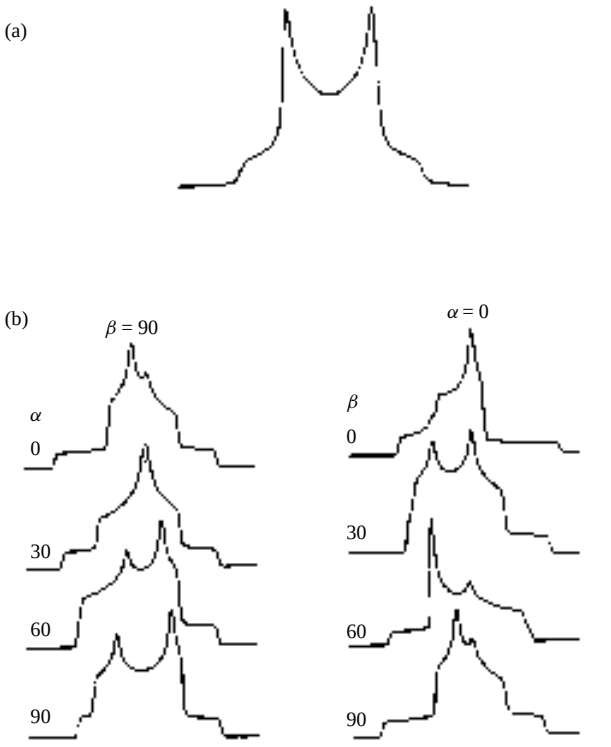

Figure 15 (a) Typical dipolar spectra resulting for the coupling of two spin-$\frac{1}{2}$ nuclei in the absence of any anisotropy in the chemical shift. (b) The dipolar pattern for two spin-$\frac{1}{2}$ nuclei with anisotropy in the chemical shift as a function of the orientation of the internuclear vector with respect to the chemical shift tensor principal axes, where α is the angle between δ_{33} and the dipolar vector, and β the angle between δ_{11} and the projection of the dipolar vector into the plane defined by δ_{11} and δ_{22}. (b) is reproduced by permission of Academic Press from W. P. Powers and R. E. Wayslishen in *Annu. Rep. NMR Spectrosc.*, 1991, **23**, 1

nicely demonstrated with the set of simulated spectra shown in Figure 15(b). The simulations in Figure 15(b) are for the same principal values and dipolar coupling, with only the two angles relating the PAS to the dipolar vector being varied.

As mentioned earlier, a dipolar coupling also exists between a spin-$\frac{1}{2}$ nucleus and a quadrupolar nucleus, and a dipolar spectrum can be obtained by observing the spin-$\frac{1}{2}$ nucleus. The complete chemical shift tensor of the spin-$\frac{1}{2}$ nucleus is obtained, along with the information of the EFG tensor of the quadrupolar nuclei.

Finally, there have been a number of 2D techniques that can be grouped together as separated local field (SLF) techniques, which can provide the chemical shift information in one dimension and information on the dipolar couplings in a second dimension. The SLF technique, first introduced in 1976,[50] can be used to orient the principal values of a rare spin based on the dipolar coupling between that rare spin (S) and an abundant spin (I), typically a ^1H. In SLF, multipulse decoupling is applied during the evolution time of the 2D experiment to decouple all ^1H-H dipolar interactions, leaving the ^1H-X interactions although they are scaled. The initial experiments were applied to single crystals and to oriented samples.

The basic ideas presented by Waugh were extended to unlabeled static powder samples,[51] with the shape of the spectra in the 2D space containing the information on the PAS; however, with powders, the patterns become very complicated if there are even two different dipolar interactions. The SLF technique has also been used with slow magic angle spinning and has been extended to the determination of the complete chemical shift of a nucleus coupled to two other spins,[52,53] as well as to being used to extend some of the 2D powder techniques into 3D techniques to gain the information on the orientation of the PAS.[54]

9 SUMMARY

As stated in the Introduction, the method of choice is primarily dependent on the sample. A single crystal study is the method of choice based solely on the amount of information obtained. The more recent 2D multiple axis reorientation method has opened up the field of single crystal studies to systems approaching 100 inequivalent nuclei. However, the limitation in obtaining a suitable sample, i.e., a large enough crystal of sufficient quality, eliminates this method as a choice for a majority of substances.

If a material is a solid at or near room temperature, but one for which a single crystal cannot be obtained, the method of choice is often determined by the equipment available. If there are more than three or four inequivalent nuclei, the experiment of choice will typically be a 2D method. In the last 12 or so years there has been an explosion of 2D and even a few 3D techniques in solid state NMR designed to obtain chemical shift information. While some of these techniques require specialized probes, several can be undertaken on any modern solid state NMR system equipped with a normal MAS probe, provided that only temperatures near ambient are needed. Though some standard MAS probes are capable of reaching temperatures down to 77 K, attaining very low temperatures at high spinning speeds for long periods of times is not easily or economically achieved.

When the sample of interest is a solid only at very low temperatures, or a sample that is stable only at very low temperatures for any reasonable time period, the choices are limited to the 1D techniques which typically take less time. However, samples that are suitable for study by 1D techniques are only the simpler compounds, i.e. those containing only three or four inequivalent nuclei. There have been efforts to use selective techniques, mainly short contact times, to look at only the protonated nuclei, or dipolar dephasing techniques to observe only the nonprotonated nuclei, but these methods have been shown to be of limited usefulness. The alternative is to use compounds selectively enriched at the nuclei of interest and study only that particular spin.

The lowest temperatures can only be achieved with the use of cryogenic equipment which does not allow for sample spinning, limiting the choice to the study of a static powder sample. It should be mentioned that there are several articles in the literature on MAS probes at temperatures in the region of 4 K, but they do not seem to be used routinely and there are no examples, to the knowledge of the author, on the use of such equipment in the study of molecules which are gases at room temperature. With the use of closed-cycle cryogenic units, it is economically feasible to achieve temperatures as low as 8–10 K on a routine basis. The static sample limits the application of the cryogenic apparatus to studies of very simple cases, or to cases where isotopic labeling has been undertaken. However, this technique is the only method available for the study of reactive species trapped in inert gas matrices, a technique known as matrix isolation. The use of matrix isolation methodology, while very limited in NMR, is more widespread in other forms of spectroscopy.

Finally, for samples where a single crystal study is not possible, but an experimental determination of the PAS orientation is desired, dipolar techniques can be employed. If two dipolar coupled spins exist, or if a sample can be made to contain such a pair using selective enrichment, the orientation of the PAS can be determined for the spins involved. Dipolar spectroscopy has been used at ambient temperatures as well as at cryogenic temperatures.

10 RELATED ARTICLES

Chemical Shift Tensors; Chemical Shift Tensors in Single Crystals; Dipolar and Indirect Coupling Tensors in Solids; Dynamic Angle Spinning; Magic Angle Turning and Hopping; Two-Dimensional Powder Correlation Methods; Variable Angle Sample Spinning.

11 REFERENCES

1. T. M. Duncan, *A Compilation of Chemical Shift Anisotropies*, Farragut Press, Chicago, 1990.
2. M. Mehring, *Principles of High Resolution NMR in Solids*, 2nd edn., Springer-Verlag, New York, 1983.
3. C. A. Fyfe, *Solid State NMR for Chemists*, C.F.C. Press, Guelph, 1983.
4. C. P. Slichter, *Principles of Magnetic Resonance*, 3rd edn., Springer-Verlag, New York, 1992.
5. R. R. Ernst, G. Bodenhausen, and A. Woukan, *Principles of Nuclear Magnetic Resonance in One and Two Dimensions*, Oxford University Press, Oxford, 1990.
6. J. S. Waugh, L. M. Huber, and U. Haeberlen, *Phys. Rev. Lett.*, 1968, **20**, 180.
7. A. Pines, M. G. Gibby, and J. S. Waugh *J. Chem. Phys.*, 1973, **59**, 569.
8. S. J. Opella and M. H. Frey, *J. Am. Chem. Soc.*, 1979, **101**, 5854.
9. L. B. Alemany, D. M. Grant, R. J. Pugmire, T. D. Alger, and K. W. Zilm, *J. Am. Chem. Soc.*, 1983, **105**, 2133.
10. E. R. Andrew and R. G. Eades, *Proc. R. Soc. London*, 1953, **A216**, 398.
11. I. J. Lowe, *Phys. Rev. Lett.*, 1959, **2**, 285.
12. J. C. Facelli and D. M. Grant, *Nature (London)*, 1993, **365**, 325.
13. K. W. Zilm, R. T. Conlin, D. M. Grant, and J. Michl, *J. Am. Chem. Soc.*, 1980, **102**, 6672.
14. J. E. Kohl, M. G. Semack, and D. White, *J. Chem. Phys.*, 1978, **69**, 5378.
15. E. O. Stejskal, J. Schaefer, and R. A. McKay, *J. Magn. Reson.*, 1977, **25**, 569.
16. N. K. Sethi., D. M. Grant, and R. J. Pugmire, *J. Magn. Reson.*, 1987, **71**, 476.
17. N. K. Sethi, R. J. Pugmire, and D. M. Grant, *Prepr. Pap. Am. Chem. Soc., Div. Fuel Chem.*, 1987, **32**, 155.

18. M. M. Maricq and J. S. Waugh, *J. Chem. Phys.*, 1979, **70**, 3300.
19. J. Herzfeld and A. E. Berger, *J. Chem. Phys.*, 1980, **73**, 6021.
20. G. A. Morris and R. Freeman, *J. Magn. Reson.*, 1978, **29**, 433.
21. J. Z. Hu, R. J. Pugmire, A. M. Orendt, D. M. Grant, and C. Ye, *Solid State NMR*, 1992, **1**, 185.
22. J. Ashida, T. Nakai, and T. Terao, *Chem. Phys. Lett.*, 1990, **168**, 523.
23. J. H. Iwamiya, M. F. Davis, and G. E. Maciel, *J. Magn. Reson.*, 1990, **88**, 199.
24. A. Bax, N. M. Szeverenyi, and G. E. Maciel, *J. Magn. Reson.*, 1983, **52**, 147.
25. J. Z. Hu, A. M. Orendt, D. W. Alderman, C. Ye, R. J. Pugmire, and D. M. Grant, *Solid State NMR*, 1993, **2**, 235.
26. Z. Gan, *J. Am. Chem. Soc.*, 1992, **114**, 8307.
27. J. Z. Hu, A. M. Orendt, D. W. Alderman, R. J. Pugmire, C. Ye, and D. M. Grant, *Solid State NMR*, 1994, **3**, 181.
28. J. Z. Hu, D. W. Alderman, C. Ye, R. J. Pugmire, and D. M. Grant, *J. Magn. Reson., Ser. A*, 1993, **105**, 82.
29. R. C. Zeigler, R. A. Wind, and G. E. Maciel, *J. Magn. Reson.*, 1988, **79**, 299.
30. A. C. Kolbert, H. J. M. DeGroot, and R. G. Griffin, *J. Magn. Reson.*, 1989, **85**, 60.
31. A. Bax, N. M. Szeverenyi, and G. E. Maciel, *J. Magn. Reson.*, 1983, **55**, 494.
32. T. Terao, T. Fujii, T. Onodera, and A. Saika, *Chem. Phys. Lett.*, 1984, **107**, 145.
33. T. Nakai and C. A. McDowell, *J. Magn. Reson.*, 1991, **93**, 618.
34. W. T. Dixon, J. Schaefer, M. D. Sefcik, E. O. Stejskal, and R. A. McKay, *J. Magn. Reson.*, 1982, **49**, 341.
35. W. T. Dixon, *J. Chem. Phys.*, 1982, **77**, 1800.
36. A. C. Kolbert and R. G. Griffin, *Chem. Phys. Lett.*, 1990, **166**, 87.
37. E. Lippmaa, M. Alla, and T. Tuherm, *Proc. 19th Congr. AMPERE, Heidelberg, 1976*, p. 113.
38. Y. Yarim-Agaev, P. N. Tutunjian, and J. S. Waugh, *J. Magn. Reson.*, 1982, **47**, 51.
39. A. Bax, N. M. Szeverenyi, and G. E. Maciel, *J. Magn. Reson.*, 1983, **51**, 400.
40. R. Tycko, G. Dabbagh, and P. A. Mirau, *J. Magn. Reson.*, 1989, **85**, 265.
41. C. D. Hughes, M. H. Sherwood, D. W. Alderman, and D. M. Grant, *J. Magn. Reson., Ser. A*, 1993, **102**, 58.
42. J. Jeener, B. H. Meier, P. Buachmann, and R. R. Ernst, *J. Chem. Phys.*, 1979, **71**, 4546.
43. L. Frydman, G. C. Chingas, Y. K. Lee, P. G. Grandinetti, M. A. Eastman, G. A. Barrall, and A. Pines, *J. Chem. Phys.*, 1992, **97**, 4800.
44. C. M. Carter, D. W. Alderman, and D. M. Grant, *J. Magn. Reson.*, 1985, **65**, 183.
45. C. M. Carter, D. W. Alderman, and D. M. Grant, *J. Magn. Reson.*, 1987, **73**, 114.
46. M. H. Sherwood, D. W. Alderman, and D. M. Grant, *J. Magn. Reson.*, 1989, **84**, 466.
47. R. J. Iuliucci, J. C. Facelli, D. W. Alderman, and D. M. Grant, *J. Am. Chem. Soc.*, 1995, **117**, 2336.
48. K. W. Zilm and D. M. Grant, *J. Am. Chem. Soc.*, 1981, **103**, 2913.
49. W. P. Powers and R. E. Wayslishen, *Annu. Rep. NMR Spectrosc.*, 1991, **23**, 1.
50. R. K. Hester, J. L. Ackerman, B. L. Neff, and J. S. Waugh, *Phys. Rev. Lett.*, 1976, **36**, 1081.
51. M. Linder, A. Hohener, and R. R. Ernst, *J. Chem. Phys.*, 1980, **73**, 4959.
52. M. Munowitz, T. -H. Huang, and R. G. Griffin, *J. Chem. Phys.*, 1987, **86**, 4362.
53. C. J. Hartzell, T. K. Pratum, and G. Drobney, *J. Chem. Phys.*, 1987, **87**, 4324.
54. T. Nakai, J. Ashida, and T. Terao, *J. Chem. Phys.*, 1988, **88**, 6049.

Biographical Sketch

Anita M. Orendt. *b* 1958. B.S., 1980, Chemistry, University of Pittsburgh, Ph.D., 1987, Physical Chemistry, University of Utah. Postdoctoral work with Professor David M. Grant, University of Utah, 1987–present. Assistant Professor of Chemistry (half-time), Westminster College of Salt Lake City, 1992–present. Research interests: measurement of chemical shift tensors, applications of solid state NMR at cryogenic temperatures and to matrix isolated species.

Chemical Shift Tensors in Single Crystals

Mark H. Sherwood

IBM Research Division, Almaden Research Center, San Jose, CA, USA

1	Introduction	1
2	Nuclear Shielding and the Chemical Shift Tensor	1
3	The Single Axis Rotation Method	3
4	Single Axis 2D Chemical Shift Tensor Correlation Spectroscopy	4
5	Multiple Axis 2D Chemical Shift Tensor Correlation Spectroscopy	6
6	Assignment Techniques	7
7	Related Articles	8
8	References	8

1 INTRODUCTION

Shortly after its first detection in condensed matter in 1945,[1,2] it became evident that NMR was an extremely sensitive probe of the local electronic environments of magnetic nuclei. Some of the first observations of NMR uncovered a chemical effect on the relative resonance frequencies of identical nuclear isotopes which has come to be known as the chemical shift, and because of this effect NMR has evolved into one of the premier spectroscopic techniques for chemical structure analysis. The primary use of NMR consists of measuring the isotropic chemical shifts of nuclei imbedded in molecules dissolved in solution; however, important information about the anisotropy of this interaction is available from the spectra of solids.[3–5]

Certain characteristics of the anisotropic chemical shift, the principal values of the chemical shift tensor for example, can be obtained from the spectra of powdered samples and, to a lesser extent, from molecules dissolved in liquid crystal solvents. Nevertheless, single crystal samples are preferred, when available, as they allow direct measurements of the complete chemical shift tensor. Single crystals are especially useful for studies of large molecules where the many overlapping powder patterns in traditional one-dimensional (1D) spectra are uninterpretable and where selectively labeling each individual site is impractical. Although progress has been made in extracting principal values from powdered samples of large molecules using two-dimensional (2D) NMR methods,[6] direct measurements of tensor orientations can be made only on single crystals.

This article is written as an introduction to the techniques that are available for measuring chemical shift tensors in single crystals. Although many aspects of the techniques are quite general, the emphasis here will be on measurements of ^{13}C chemical shift tensors in organic systems.

The first measurement of a ^{13}C chemical shift tensor was made in the very early days of ^{13}C NMR by Lauterbur[7] on the carbonate ion of single crystal calcite ($CaCO_3$). This particular sample proved to be ideal because all magnetic nuclei were at low abundance and thus the dipolar broadening was negligible. A few other systems were exploited where similar dilution occurred naturally or was introduced by substitution of ^{2}D for ^{1}H, but progress along these lines was limited. It was only after the introduction of the combined cross polarization and high-power dipolar decoupling techniques[8] that ^{13}C chemical shift tensor measurements became more generally applicable. One of the first demonstrations of these now widely used techniques was in the measurement of ^{13}C chemical shift tensors in single crystal durene (1,2,4,5-tetramethylbenzene).[9]

2 NUCLEAR SHIELDING AND THE CHEMICAL SHIFT TENSOR

The fundamental equation relating the NMR resonance frequency and the magnetic field strength is well known to all students of magnetic resonance

$$\nu_0 = |\gamma/2\pi| B_0 \tag{1}$$

For ^{13}C, this frequency corresponds to 50 MHz in a typical field of 4.7 T.

Due to the electronic circulation set up in a molecule by the applied magnetic field, the effective field experienced by a particular nucleus is not exactly equal to B_0. The electronic 'currents' induce a small shielding field $\boldsymbol{B}_s$ which must be added to $\boldsymbol{B}_0$ to obtain the effective field at the nucleus

$$\boldsymbol{B}_{\text{eff}} = \boldsymbol{B}_0 + \boldsymbol{B}_s \tag{2}$$

This vector addition is shown schematically in Figure 1.

Although $\boldsymbol{B}_s$ is called the shielding field, it does not necessarily oppose $\boldsymbol{B}_0$ and thus deshieldings or paramagnetic shifts are possible. In general, the direction of $\boldsymbol{B}_s$ is not parallel to $\boldsymbol{B}_0$ but the two are related through the shielding tensor which is represented as the 3×3 matrix $\boldsymbol{\sigma}$

$$\boldsymbol{B}_s = -\boldsymbol{\sigma} \cdot \boldsymbol{B}_0 \tag{3}$$

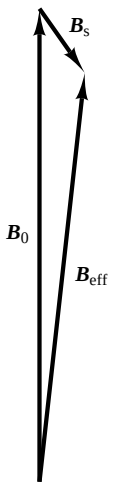

Figure 1 The relationship between the applied field $\boldsymbol{B}_0$, the shielding field $\boldsymbol{B}_s$ and the effective field $\boldsymbol{B}_{\text{eff}}$

The matrix $\boldsymbol{\sigma}$ is usually called a second rank Cartesian tensor although it also contains zeroth and first rank parts as well.

Since B_s is very small compared to B_0, equation (2) can be closely approximated by adding only the component of $\boldsymbol{B}_s$ that is either parallel or antiparallel to $\boldsymbol{B}_0$ to obtain

$$\boldsymbol{B}_{\text{eff}} = \boldsymbol{B}_0 - \frac{\boldsymbol{B}_0}{B_0} \cdot \boldsymbol{\sigma} \cdot \boldsymbol{B}_0 \tag{4}$$

The above approximation is equivalent to *truncation* or restriction to the *secular* terms of the chemical shift Hamiltonian in first-order perturbation theory. It should be pointed out that $\boldsymbol{\sigma}$ can be decomposed into a sum of second rank symmetric and first rank antisymmetric constituents

$$\boldsymbol{\sigma} = \boldsymbol{\sigma}^{\text{S}} + \boldsymbol{\sigma}^{\text{A}} \tag{5}$$

Since $\boldsymbol{\sigma}^{\text{A}}$ leads to components of $\boldsymbol{B}_s$ which are perpendicular to $\boldsymbol{B}_0$, it does not contribute to $\boldsymbol{B}_{\text{eff}}$ in first order and thus its effect on the resonance frequency of the nucleus can be ignored.

The effect of shielding is thus to change the precession frequency of the nucleus from ν_0 to the frequency given by

$$\nu = |\gamma/2\pi| B_{\text{eff}} \tag{6}$$

In practice, the frequency of the bare nucleus is not known, and measurements of the frequency ν are always made relative to a reference frequency ν_{ref}, which for ^{13}C is usually taken as the resonance of liquid tetramethylsilane (TMS). The frequency difference between sample and reference can be written as

$$\nu - \nu_{\text{ref}} = |\gamma/2\pi| \frac{\boldsymbol{B}_0}{B_0} \cdot (\boldsymbol{\sigma}^{\text{S}} - \sigma_{\text{ref}}\mathbf{1}) \cdot \boldsymbol{B}_0 \tag{7}$$

where σ_{ref} is the isotropic chemical shielding constant of the reference compound and $\mathbf{1}$ is the unit matrix. The symmetric difference matrix $(\boldsymbol{\sigma}^{\text{S}} - \sigma_{\text{ref}}\,\mathbf{1})$ is defined as the chemical shift tensor, and is assigned the symbol $\boldsymbol{\delta}$ in order to avoid its confusion with the shielding tensor $\boldsymbol{\sigma}$.

It is customary to report chemical shifts not as frequencies, since these always depend on B_0 which varies from one spectrometer to the next, but as fractions of ν_{ref}. If the chemical shift F is defined as $(\nu - \nu_{\text{ref}})/\nu_{\text{ref}}$, then

$$F = \frac{\boldsymbol{B}_0}{B_0} \cdot \boldsymbol{\delta} \cdot \frac{\boldsymbol{B}_0}{B_0} \tag{8}$$

Equation (8) is the master equation for the chemical shift in a single crystal, as it gives the observed shift in terms of the elements of $\boldsymbol{\delta}$ and the orientation of $\boldsymbol{B}_0$.

For elements with sufficiently low atomic numbers, the chemical shift tensor $\boldsymbol{\delta}$ can be represented in a Cartesian coordinate system as a 3×3 symmetric matrix

$$\boldsymbol{\delta} = \begin{bmatrix} \delta_{xx} & \delta_{xy} & \delta_{zx} \\ \delta_{xy} & \delta_{yy} & \delta_{yz} \\ \delta_{zx} & \delta_{yz} & \delta_{zz} \end{bmatrix} \tag{9}$$

The matrix $\boldsymbol{\delta}$ is called the Cartesian representation of the chemical shift tensor and is completely defined by six independent numbers. It will be seen below that other representations are possible.

The average value of $\boldsymbol{\delta}$ is known as the isotropic chemical shift

$$\delta_{\text{iso}} = \frac{1}{3}(\delta_{xx} + \delta_{yy} + \delta_{zz}) \tag{10}$$

and it is only this part of the chemical shift tensor which can be directly measured in solution samples due to rapid isotropic tumbling of the molecules. The isotropic chemical shift is also called the zeroth rank part of $\boldsymbol{\delta}$ since it transforms as a scalar quantity, i.e., it is invariant under rotation.

A Cartesian tensor can be expressed in a different coordinate system by performing a similarity transformation on the matrix $\boldsymbol{\delta}$

$$\boldsymbol{\delta}' = \mathbf{R}\boldsymbol{\delta}\mathbf{R}^{\text{T}} \tag{11}$$

where $\mathbf{R}$ is a unitary matrix. The element R_{ij} is given by the direction cosine of the ith new coordinate axis with respect to the jth old coordinate axis. For instance, $R_{12} = \cos \gamma_{x'y}$ where $\gamma_{x'y}$ is the angle between the new x axis and the old y axis.

A number of coordinate systems are necessary in single crystal work. The *laboratory frame* is a coordinate system whose z axis lies along the direction of the static magnetic field. Rather than working in the laboratory frame, it is usually more convenient to work in a coordinate system called the *sample frame* whose orientation is fixed with respect to the single crystal sample. The sample frame will always be the coordinate system in which tensors are measured. A third coordinate system is that defined by the symmetry elements of the crystal and this will be called the *crystal frame*. The orientation of the crystal frame relative to the sample frame can usually be found by diffraction methods. For molecules containing high symmetry, it is often useful to define a coordinate system based on molecule symmetry elements called the *molecular frame*. For molecules of low symmetry, coordinate systems can be defined based on the local symmetry of a particular nuclear site and these will be called *local frames*. Finally, there is an important coordinate system known as the *principal axis* system which is unique to each tensor. The principal axis system is discussed below.

The relationships between all of these reference frames, except for that between the sample frame and laboratory frame, are determined by the crystal and molecular structure, and therefore they are not under experimental control. It is clear from equation (11) that once the tensor is known in one of these reference frames, it can be expressed in any of the other frames provided the unitary matrix $\mathbf{R}$ is available.

For any symmetric second rank tensor such as the chemical shift tensor $\boldsymbol{\delta}$, there exists a unitary matrix $\mathbf{S}$ that transforms $\boldsymbol{\delta}$ into a coordinate system in which it is diagonal

$$\mathbf{S}\boldsymbol{\delta}\mathbf{S}^{\text{T}} = \boldsymbol{\Lambda} \tag{12}$$

where $\boldsymbol{\Lambda}$ is a diagonal matrix with elements λ_1, λ_2, and λ_3. This special coordinate system is called the principal axis system and the diagonal tensor elements are called the principal values. Multiplying both sides of equation (12) by $\mathbf{S}^{-1} = \mathbf{S}^{\text{T}}$ yields

$$\boldsymbol{\delta}\mathbf{S}^{\text{T}} = \mathbf{S}^{\text{T}}\boldsymbol{\Lambda} \tag{13}$$

Equation (13) is readily recognized as an algebraic eigenvalue equation and the eigenvalues (principal values) and eigenvectors (principal axes) can be found by solving the secular equation

$$|\boldsymbol{\delta} - \boldsymbol{\Lambda 1}| = \begin{vmatrix} \delta_{xx} - \lambda_1 & \delta_{xy} & \delta_{zx} \\ \delta_{xy} & \delta_{yy} - \lambda_2 & \delta_{yz} \\ \delta_{zx} & \delta_{yz} & \delta_{zz} - \lambda_3 \end{vmatrix} = 0 \qquad (14)$$

A convention for labeling the principal values is generally followed in which they are designated δ_{11}, δ_{22}, and δ_{33} in order of decreasing chemical shift. An alternative to the Cartesian representation of a chemical shift tensor is its representation as three principal values and the three Euler angles that orient the principal axis system with respect to one of the coordinate systems defined above. Other useful representations of the chemical shift tensor are described elsewhere.[10]

Recalling equation (8), the chemical shift F observed when the magnetic field is oriented with direction cosines cos γ_x, cos γ_y, and cos γ_z relative to the sample frame axes can be explicitly written as the quadratic form

$$F = [\cos(\gamma_x)\ \cos(\gamma_y)\ \cos(\gamma_z)] \begin{bmatrix} \delta_{xx} & \delta_{xy} & \delta_{zx} \\ \delta_{xy} & \delta_{yy} & \delta_{yz} \\ \delta_{zx} & \delta_{yz} & \delta_{zz} \end{bmatrix} \begin{bmatrix} \cos(\gamma_x) \\ \cos(\gamma_y) \\ \cos(\gamma_z) \end{bmatrix}$$

$$= \cos^2(\gamma_x)\,\delta_{xx} + \cos^2(\gamma_y)\,\delta_{yy} + \cos^2(\gamma_z)\,\delta_{zz} + 2\cos(\gamma_x)\ \cos,\ (\gamma_y)\delta_{xy} + 2\ \cos(\gamma_y)\ \cos(\gamma_z)\,\delta_{yz} + 2\ \cos(\gamma_z)\ \cos(\gamma_x)\,\delta_{zx} \qquad (15)$$

It is seen from equation (15) that if the chemical shift tensor $\boldsymbol{\delta}$ is known in the sample frame, the chemical shift can be calculated for any orientation of $\boldsymbol{B}_0$. Alternatively, if the chemical shift F is known for six suitably chosen directions of $\boldsymbol{B}_0$, the elements of $\boldsymbol{\delta}$ can be obtained by solving a system of linear equations.

Equation (15) takes on a particularly simple form when expressed in the principal axis system

$$F = \cos^2(\gamma_x)\delta_{11} + \cos^2(\gamma_y)\,\delta_{22} + \cos^2(\gamma_z)\,\delta_{33} \qquad (16)$$

Provided that the reference frequency is chosen such that the three principal values δ_{11}, δ_{22}, and δ_{33} are positive, a connection can be made between equation (16) and the equation of an ellipsoid with semiaxes a, b, and c

$$\frac{x^2}{a^2} + \frac{y^2}{b^2} + \frac{z^2}{c^2} = 1 \qquad (17)$$

The direction cosines of a radius vector $\boldsymbol{r}$ taken from the origin to a point on the surface of the ellipsoid are given by $\cos^2(\gamma_x) = x^2/r^2$, $\cos^2(\gamma_y) = y^2/r^2$, and $\cos^2(\gamma_z) = z^2/r^2$. Substituting these into equation (17) yields

$$\frac{r^2\cos^2(\gamma_x)}{a^2} + \frac{r^2\cos^2(\gamma_y)}{b^2} + \frac{r^2\cos^2(\gamma_z)}{c^2} = 1 \qquad (18)$$

Finally, by making the identities $a^2 = 1/\delta_{11}$, $b^2 = 1/\delta_{22}$, and $c^2 = 1/\delta_{33}$, equation (18) can be rearranged to give

$$\cos^2(\gamma_x)\,\delta_{11} + \cos^2(\gamma_y)\,\delta_{22} + \cos^2(\gamma_z)\,\delta_{33} = \frac{1}{r^2} \qquad (19)$$

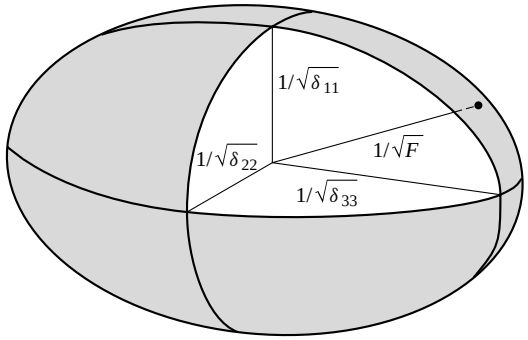

Figure 2 The chemical shift tensor representation ellipsoid

The surface described by equation (19) is called the representation ellipsoid[11] of the chemical shift tensor and is illustrated in Figure 2.

The semiaxes of the ellipsoid are given by $1/\sqrt{\delta_{11}}$, $1/\sqrt{\delta_{22}}$, and $1/\sqrt{\delta_{33}}$. Comparing equation (16) and (19), it is seen that when $\boldsymbol{B}_0$ is oriented along $\boldsymbol{r}$, the length of the radius vector is given by $r = 1/\sqrt{F}$.

The representation ellipsoid thus allows a geometrical interpretation of the chemical shift tensor, and the *mmm* (D_{2h}) symmetry of this object reflects the symmetry of the chemical shift interaction.

In order to understand the effect of crystallographic symmetry on the chemical shift, it is necessary to define some terminology. Nuclear sites related by the rotation or reflection symmetry operations of the space group of the crystal are called *crystallographically equivalent* sites. Those sites that are related by inversion or translation are called *magnetically equivalent* sites. This definition of magnetic equivalence is in contrast to that used in solution NMR where sites related by any symmetry element of the molecule are magnetically equivalent due to the rapid isotropic tumbling of the molecule. As the operations of either inversion or translation do not change the orientation of the representation ellipsoid, a set of magnetically equivalent sites gives rise to a single peak in the spectrum. On the other hand, the representation ellipsoids of crystallographically equivalent sites are oriented differently in the absence of accidental coincidence of the symmetry elements of the representation ellipsoid with those of the space group. Therefore, multiple peaks occur in the spectrum of a single crystal sample when the magnetic field is in a general orientation with respect to a lattice of crystallographically equivalent sites. Two tensors are said to be *congruent* if they are each associated with nuclear sites which are crystallographically equivalent. Congruent tensors have identical principal values, but differ in the orientations of their respective principal axes.

3 THE SINGLE AXIS ROTATION METHOD

In the case of a crystal containing only one set of magnetically equivalent nuclei, the measurement technique is straightforward since the spectrum of such a crystal contains a single peak in any orientation of the field. Six 1D spectra can be obtained with the magnetic field oriented along six different directions. The chemical shift derived from each spectrum, along with the corresponding direction cosines describing

the orientation of the magnetic field, is then substituted into equation (15) to obtain a set of six equations from which the tensor elements are extracted.

The spectrum of a sample containing multiple sets of magnetically equivalent nuclei has a corresponding multiplicity of peaks. In this case the six 1D spectra described above would be useless, since there would be no way to determine which peak in each of the spectra was from a particular set of magnetically equivalent nuclei. One solution to this problem is to acquire many 1D spectra which differ by small angle rotations of the crystal so that the paths of the lines can be traced from one spectrum to the next to form a *rotation pattern*.

Consider a rotation of the crystal about an axis that makes an angle β with the magnetic field $\boldsymbol{B}_0$. The arbitrary sample frame can be oriented such that the x axis is parallel to the rotation axis and the magnetic field $\boldsymbol{B}_0$ lies initially in the xy plane. If the crystal is rotated through an angle α, the direction cosines of the field with respect to the sample frame are given by

$$\cos(\gamma_x) = \cos(\beta) \tag{20}$$

$$\cos(\gamma_y) = \sin(\beta)\cos(\alpha) \tag{21}$$

$$\cos(\gamma_z) = \sin(\beta)\sin(\alpha) \tag{22}$$

It can easily be shown by substituting equations (20)–(22) into equation (15) that the chemical shift F is given by

$$F = A + B\cos(\alpha) + C\sin(\alpha) + D\cos(2\alpha) + E\sin(2\alpha) \tag{23}$$

where

$$A = \tfrac{1}{2}\sin^2(\beta)\,(\delta_{yy} + \delta_{zz}) + \cos^2(\beta)\,\delta_{xx} \tag{24a}$$

$$B = 2\sin(\beta)\cos(\beta)\,\delta_{xy} \tag{24b}$$

$$C = 2\sin(\beta)\cos(\beta)\,\delta_{zx} \tag{24c}$$

$$D = \tfrac{1}{2}\sin^2(\beta)\,(\delta_{yy} - \delta_{zz}) \tag{24d}$$

$$E = \sin^2(\beta)\,\delta_{yz} \tag{24e}$$

From equation (23) it is seen that if the chemical shift is observed at five different angles α, for a given angle β, the coefficients A, B, C, D, and E can be extracted. However, these five coefficients are insufficient to determine fully the six tensor elements and it is apparent that the complete chemical shift tensor cannot be measured from a single rotation pattern.

The most frequently used measurement technique is to obtain three patterns by rotating the crystal about a single axis perpendicular to $\boldsymbol{B}_0$ in the laboratory frame as depicted in Figure 3.

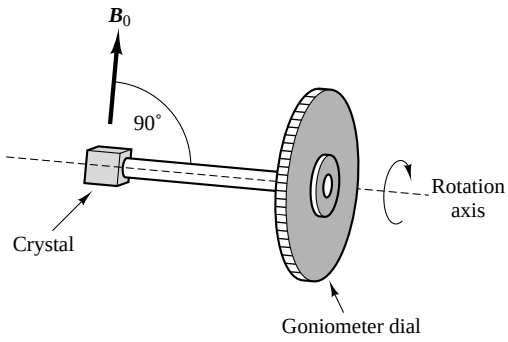

Figure 3 Schematic representation of a simple experimental set-up for obtaining single axis rotation patterns

The three rotation patterns are obtained first with the x, then the y, and finally the z sample frame axis along the rotation direction. The rotation pattern about the x axis is easily obtained from equations (23) and (24) by setting the angle β equal to $\pi/2$

$$F(\alpha_x) = \tfrac{1}{2}(\delta_{yy} + \delta_{zz}) + \tfrac{1}{2}(\delta_{yy} - \delta_{zz})\cos(2\alpha_x) + \delta_{yz}\sin(2\alpha_x) \tag{25}$$

The other two rotation patterns can be found by cyclic permutation of the sample axis labels x, y, and z

$$F(\alpha_y) = \tfrac{1}{2}(\delta_{zz} + \delta_{xx}) + \tfrac{1}{2}(\delta_{zz} - \delta_{xx})\cos(2\alpha_y) + \delta_{zx}\sin(2\alpha_y) \tag{26}$$

$$F(\alpha_z) = \tfrac{1}{2}(\delta_{xx} + \delta_{yy}) + \tfrac{1}{2}(\delta_{xx} - \delta_{yy})\cos(2\alpha_z) + \delta_{xy}\sin(2\alpha_z) \tag{27}$$

Although each rotation pattern is fully determined by measuring the chemical shift at only three different angles, the usual practice is to obtain spectra at many angles by stepping the goniometer from 0° to 180°, and to extract the tensor elements using least-squares methods. This allows a more accurate determination of the tensor and is a necessity if the spectrum of the crystal contains many peaks, since the path of a single peak can be traced only when the crystal is rotated in small angular increments. In order to obtain all six elements of the chemical shift tensor for a particular set of magnetically equivalent nuclei, the path of the corresponding peak must not only be traced within each rotation but must also be traced between rotations. This is accomplished by matching up the rotation patterns at the orientations where they intersect. Figure 4 shows three rotation patterns from which the ^{13}C chemical shift tensors of naphthalene can be obtained.

The rotation method has been successfully applied to many medium-sized molecules;[12] however, it fails when the peaks in the spectra become numerous and crowded since it becomes impossible to trace the paths of individual peaks through the three rotation patterns. Another drawback of the rotation method is the necessity of accurately mounting the crystal three times along the three orthogonal sample axes, but this problem has been overcome using a two-axis goniometer and a unique rf coil as demonstrated by Hauser et al.[13]

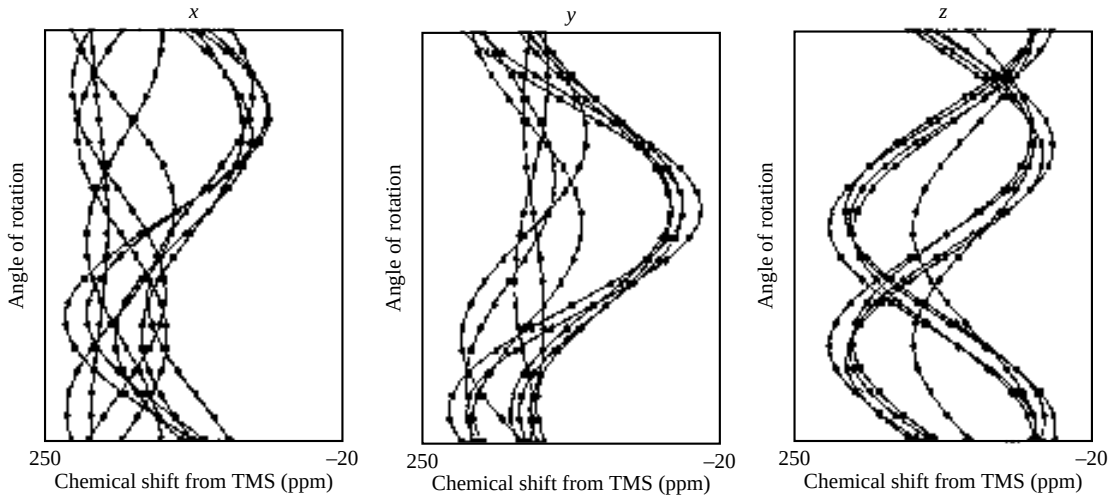

Figure 4 Rotation patterns through 180° about the x, y, and z sample axis sufficient to measure the 10 chemical shift tensors in single crystal naphthalene

4 SINGLE AXIS 2D CHEMICAL SHIFT TENSOR CORRELATION SPECTROSCOPY

The necessity of taking small angular increments in the rotation patterns can be eliminated using a 2D correlation method introduced by Carter et al.[14] This technique obtains 2D spectra in which a peak from a single set of magnetically equivalent nuclei is located by its resonant frequencies at two different orientations of the single crystal. Such spectra are obtained with the modified 2D chemical exchange[15] pulse sequence shown in Figure 5.

The preparation period of this sequence is identical to the usual cross-polarization experiment. During the evolution period, the spins precess at frequencies determined by their chemical shifts at the initial crystal orientation. The evolved magnetization is then stored along the z axis with the pulse labeled b and the crystal is reoriented during the mixing period. At the end of the mixing period, the stored magnetization is rotated back to the transverse plane with the pulse labeled a, and during the detection period the spins precess at frequencies determined by their chemical shifts at the final crystal orientation. An example of a 2D chemical shift tensor correlation spectrum is shown in Figure 6 where all 24 peaks in single crystal sucrose are resolved despite the severe crowding that exists in the corresponding 1D spectra.

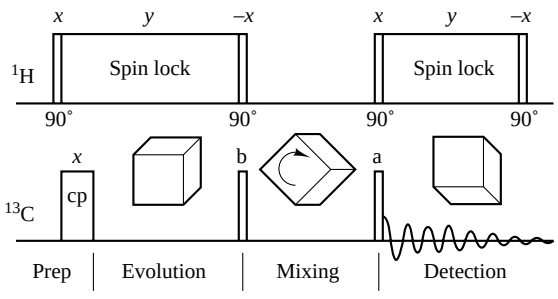

Figure 5 Modified chemical exchange sequence for 2D chemical shift tensor correlation spectroscopy. See text for details. (Reproduced by permission of Academic Press from M. H. Sherwood, D. W. Alderman, and D. M. Grant, *J. Magn. Reson.*, 1989, **84**, 466)

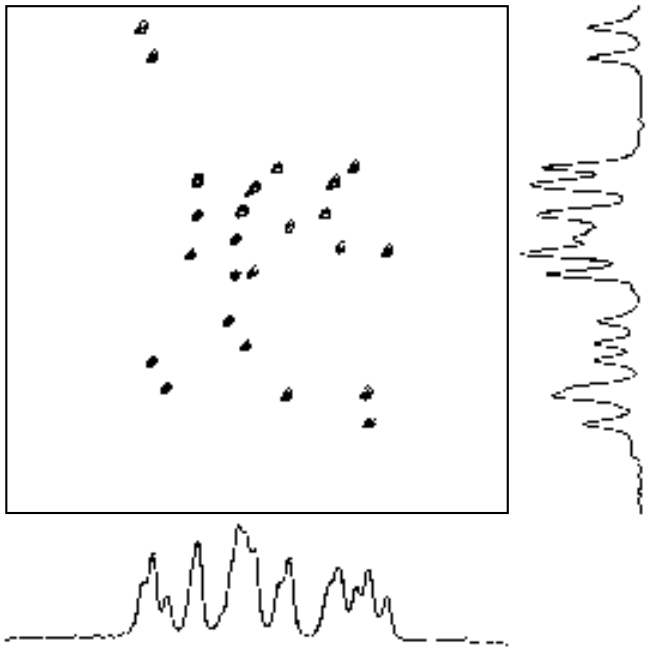

Figure 6 Two-dimensional absorption mode spectrum obtained from sucrose corresponding to a reorientation of $\boldsymbol{B}_0$ by 90° in the sample frame. The plotted spectral width is 5 kHz × 5 kHz (approximately 100 ppm × 100 ppm). The spectrum diagonal runs from upper left (high frequency) to lower right (low frequency). (Adapted by permission of Academic Press from M. H. Sherwood, D. W. Alderman, and D. M. Grant, *J. Magn. Reson.*, 1989, **84**, 466)

It has been shown that the information present in one rotation pattern can be obtained from four 2D spectra taken while stepping the sample from 0° to 45°, 45° to 90°, 90° to 135°, and 135° to 180° (equivalent to 0°).[16] The redundancy in this information permits a powerful square construction which resolves the uncertainties due to peak overlap within each rotation. However, this single axis 2D technique does

not address the problem of joining the three rotation patterns together when there are many overlapping lines in the spectra at the orientations where the patterns intersect. Thus the application of the single axis 2D method is limited to samples where the connections can be made by conventional means. As in the traditional 1D method, it is necessary to mount the sample accurately three times for the single axis 2D measurements.

5 MULTIPLE AXIS 2D CHEMICAL SHIFT TENSOR CORRELATION SPECTROSCOPY

The full power of the 2D technique can be realized by gathering data in such a way that all correlations between required crystal orientations are obtained with a single mounting of the crystal. This is accomplished with a multiple axis sample orienting mechanism which complements the 2D method to form an exceedingly powerful technique for measuring chemical shift tensors in complex single crystals.[17]

As mentioned above, the six independent elements of a chemical shift tensor, in principle, can be determined by measuring the chemical shift with the magnetic field oriented along six suitably chosen directions. Table 1 gives the orientations of six such directions in the sample frame.

Table 1 Six Magnetic Field Directions in the Sample Frame That can be Used to Measure a Chemical Shift Tensor

Magnetic field direction	$\cos(\gamma_X)$	$\cos(\gamma_Y)$	$\cos(\gamma_Z)$	Observed shift
X	1	0	0	F_X
XY	$1\sqrt{2}$	$1/\sqrt{2}$	0	F_{XY}
Y	0	1	0	F_Y
YZ	0	$1/\sqrt{2}$	$1/\sqrt{2}$	F_{YZ}
Z	0	0	1	F_Z
ZX	$1/\sqrt{2}$	0	$1/\sqrt{2}$	F_{ZX}

These directions lie on the surface of a trigonal pyramid and will be referred to here as the pyramidal directions. The observed chemical shifts F_X, F_{XY}, F_Y, F_{YZ}, F_Z, and F_{ZX} are easily calculated from equation (15), yielding the relationships

$$F_X = \delta_{xx} \tag{28a}$$

$$F_{XY} = \delta_{xy} + \delta_{xx}/2 + \delta_{yy}/2 \tag{28b}$$

$$F_Y = \delta_{yy} \tag{28c}$$

$$F_{YZ} = \delta_{yz} + \delta_{yy}/2 + \delta_{zz}/2 \tag{28d}$$

$$F_Z = \delta_{zz} \tag{28e}$$

$$F_{ZX} = \delta_{zx} + \delta_{zz}/2 + \delta_{xx}/2 \tag{28f}$$

which trivally invert to

$$\delta_{xx} = F_X \tag{29a}$$

$$\delta_{xy} = F_{XY} - F_X/2 - F_Y/2 \tag{29b}$$

$$\delta_{yy} = F_Y \tag{29c}$$

$$\delta_{yz} = F_{YZ} - F_Y/2 - F_Z/2 \tag{29d}$$

$$\delta_{zz} = F_Z \tag{29e}$$

$$\delta_{zx} = F_{ZX} - F_Z/2 - F_X/2 \tag{29f}$$

By obtaining the six 2D spectra corresponding to reorientation between the $X–XY$, $XY–Y$, $Y–YZ$, $YZ–Z$, $Z–ZX$, and $ZX–X$ direction pairs, the correlation data are sufficient to determine the complete chemical shift tensors for all of the sets of magnetically equivalent nuclei in the sample. Starting first with the $X–XY$ 2D spectrum, the chemical shifts of the X and XY directions are measured and correlated. Then the observed chemical shifts in the XY direction from the $X–XY$ spectrum are matched with those from the $XY–Y$ spectrum to advance the correlation of the chemical shift to the Y direction, and so forth through YZ, Z, ZX, and back to X. After completion of the full cycle of reorientations, the chemical shift is known for each set of magnetically equivalent nuclei at all six orientations and the tensor elements can be calculated from equations (29a)–(29f). The correlation of chemical shifts around the full cycle forms the closed path depicted in Figure 7(a).

It may be noted that the sense of the reorientation is unimportant. The same frequency information is obtained by reorienting from the X to the XY direction as is obtained by reorienting from XY to X. The only consequence is to interchange the F_1 and F_2 axes of the spectrum.

A powerful criterion, analogous to the square construction described for the single axis 2D approach, allows the correlation of peaks which have identical frequencies at one or more of the six magnetic field directions. It employs reorientations between other pairs of the six measurement directions. The full matrix of 36 possible 2D correlation spectra is shown in Figure 7(b). The 2D spectra that lie along the diagonal of this matrix correspond to trivial correlations between two identical orientations, and are thus of no experimental value. The spectra related by the transpose of this matrix differ only by the sense of the reorientation, and contain the same correlation information. Therefore, only 15 of the 36 possible spectra are necessary to obtain all of the available correlation and frequency information. The spectra matrix construction allows the chemical shifts of a single set of magnetically equivalent nuclei to be traced through all 15 possible 2D correlation spectra simply by connecting the peaks with horizontal and vertical lines as shown in Figure 7(b).

A mechanism which accomplishes the 15 flips has been described in detail elsewhere.[17] Briefly, it consists of an armature into which a glass tube containing the sample is

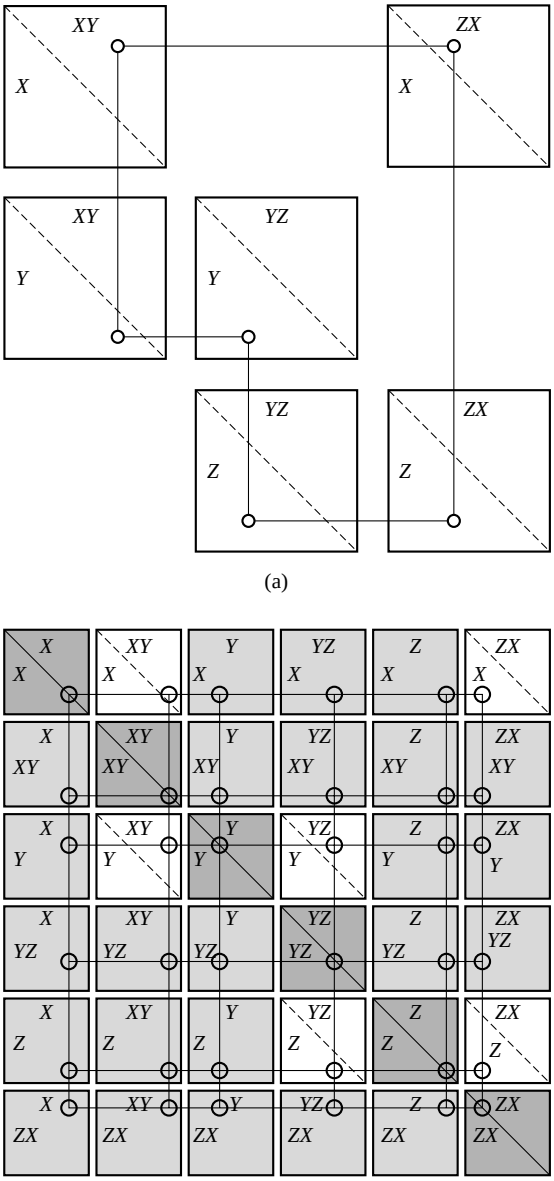

Figure 7 Matrix of 2D spectra. (a) Six 2D spectra corresponding to $XY-X$, $XY-Y$, $YZ-Y$, $YZ-Z$, $ZX-Z$, and $ZX-X$ reorientations. The relationship of the peaks in these spectra is shown for a single set of magnetically equivalent nuclei by the vertical and horizontal connecting lines. Dotted lines indicate the diagonals in the spectra. (b) All 36 possible 2D spectra. The relationship of the peaks in the spectra is shown for a single set of magnetically equivalent nuclei by the vertical and horizontal connecting lines. The six unshaded spectra with dotted diagonals correspond to those of Figure 7(a). The six darkly shaded spectra with solid diagonals are the trivial autocorrelation spectra with the peaks on the diagonals (Reproduced by permission of Academic Press from M. H. Sherwood, D. W. Alderman, and D. M. Grant, *J. Magn. Reson.*, 1989, **84**, 466)

mounted. The armature contains seven accurately drilled holes which define seven rotation axes in the sample frame. A stationary plate attached to the NMR probe contains five axle bearing holes which define five rotation axes in the laboratory frame. The mechanism is assembled by inserting an axle through one of the bearings in the stationary plate and into one of the holes in the armature. By selecting the appropriate combination of bearing and armature hole, each of the 15 possible flips can be performed. The angle of rotation is limited by a precise system of stops. One advantage of this mechanism is that the axis of the tube containing the sample changes by only 19.5° over all assemblies of the mechanism, so that a reasonably good filling factor can be achieved in the rf solenoid.

Although the pyramidal set of directions was used in the original demonstration of multiple axis 2D chemical shift tensor correlation spectroscopy, it should be realized that any set of six directions would suffice if when substituted into equation (15) they yield a system of linearly independent equations for the six chemical shifts. This restriction eliminates any set of directions that completely lie either in a plane or on the surface of a cone.

An important question that arises is how sensitive is the determination of a tensor given a particular set of measurement directions. To address this question, a variance-like figure of merit was developed[18] which quantifies the sensitivity of a given set of measurement directions. This figure of merit was evaluated for a variety of sets of measurement directions including the pyramidal set and the orthogonal rotation set. The most sensitive set of directions was found to be the six apolar directions defined by the vertices of an icosahedron. For this geometry, the figure of merit represents a significant decrease by a factor of 1.0/1.8 from that of the pyramidal directions. Therefore, it is worth considering the icosahedral direction set when designing future mechanisms. It should be noted that there is no further increase in sensitivity upon including more measurement directions than the six icosahedral directions. Another interesting result of this analysis is that the figure of merit for the orthogonal rotations set is only 1.2 times greater than that for the icosahedral directions set. This indicates that the sensitivity of the tensor measurements made using the traditional rotation method is nearly optimal.

The high symmetry of the icosahedron makes possible a very simple mechanism which rotates the crystal about a single laboratory axis inclined at an angle of 64.4° from the field. As can be seen in Figure 8, it will still be necessary to employ three rotation axes in the sample frame as specified by the three vertices labeled a, b, and c. Unfortunately the sample tube axis will reorient by 68.3° in this new mechanism, and a sacrifice in filling factor may be necessary when implementing this geometry.

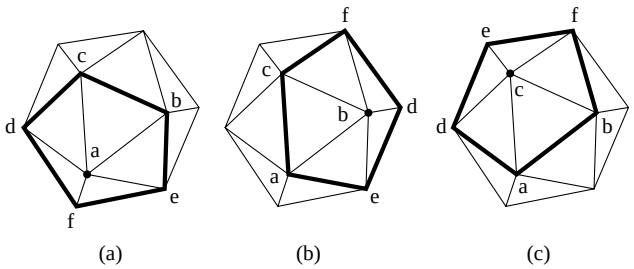

Figure 8 Icosahedra showing the vertex directions which can be aligned along the magnetic field by rotating around the a vertex (a), the b vertex (b), and the c vertex (c) (Reproduced by permission of Academic Press from D. W. Alderman, M. H. Sherwood, and D. M. Grant, *J. Magn. Reson.*, 1990, **86**, 60)

6 ASSIGNMENT TECHNIQUES

Before chemical shift tensors can be rationalized in terms of molecular structure, they must first be assigned to their respective nuclei in the unit cell. This can be a challenging step in the interpretation of the results, since the number of possible assignment permutations increases rapidly for larger molecules. The problem is compounded by the fact that most organic crystals contain two or more magnetically nonequivalent molecules in the unit cell. In order fully to exploit the power of the techniques described above, systematic methods of assignment have been developed based on local symmetry and dipolar spectroscopy. These methods have been described in detail in the literature and therefore will only be described qualitatively here.

Nearly all of the chemical shift tensor assignments made to date are based on the assumption that the symmetry elements of the representation ellipsoid should closely coincide with the actual or approximate local symmetry of its assigned nuclear site. For example, it is well established that the δ_{33} principal values of the ^{13}C chemical shift tensors orient perpendicular to the molecular plane in polycyclic aromatic hydrocarbons.[19] This fact is widely used to assign tensors to a particular molecule when there is more than one molecule in the unit cell. In more complicated molecules lacking any molecular symmetry, the approximate local symmetry established by the directly bonded atoms can be used to make assignments. For small molecules this procedure consists of manually comparing principal axis directions of the measured tensors with the approximate local symmetry elements determined from diffraction data until a reasonable match is found. As the number of measured tensors increases, it becomes more difficult to make all possible comparisons and their qualitative nature makes it difficult to distinguish between closely related assignments. In order to quantify such comparisons, the concept of a distance between two tensors was developed.[10] This distance concept has been combined with linear modeling in order to make possible an automated assignment technique which can explore all possible assignments of a reasonably large set of measured tensors to a corresponding set of chemically similar but magnetically nonequivalent nuclear sites.[10,20]

The orientational dependence of dipolar interactions has also been exploited in order to assign chemical shift tensors to specific nuclei in single crystal samples. Assignments made in this way are quite reliable since dipolar couplings can be calculated with a high degree of accuracy from the positions of the nuclei alone without resorting to molecular electronic theory. In many organic molecular crystals, the positions of all of the carbon and hydrogen nuclei in the unit cell are known from neutron diffraction studies and thus $^{13}C-^{1}H$ separated local field experiments[21,22] can be used in solving the assignment problem.

A simple extension of 2D chemical shift tensor correlation spectroscopy yields a 3D technique which allows detection of $^{13}C-^{1}H$ dipolar couplings for each of the magnetically nonequivalent sets of carbons in the sample.[20] The response of each spin is separated according to its chemical shifts at two different magnetic field orientations and a dipolar spectrum is displayed in the third dimension. This is accomplished by inserting a dipolar evolution period between the end of the mixing time and the beginning of the detection period of the previously described 2D experiment.

7 RELATED ARTICLES

Chemical Shift Tensor Measurement in Solids; Chemical Shift Tensors; Cross Polarization in Solids; Dipolar and Indirect Coupling Tensors in Solids; Multidimensional Spectroscopy: Concepts; Shielding Tensor Calculations; Two-Dimensional Powder Correlation Methods.

8 REFERENCES

1. F. Bloch, W. W. Hansen, and M. Packard, *Phys. Rev.*, 1946, **70**, 474.
2. E. M. Purcell, H. C. Torrey, and R. V. Pound, *Phys. Rev.*, 1946, **69**, 37.
3. M. Mehring, *Principles of High Resolution NMR in Solids*, Springer-Verlag, New York, 1983.
4. U. Haeberlen, *High Resolution NMR in Solids; Selective Averaging*, Academic Press, New York, 1976.
5. T. M. Duncan, *A Compilation of Chemical Shift Anisotropies*, Farragut Press, Chicago, IL, 1990.
6. J. Z. Hu, D. W. Alderman, C. Ye, R. J. Pugmire, and D. M. Grant, *J. Magn. Reson., Ser. A.* 1993, **105**, 82.
7. P. C. Lauterbur, *Phys. Rev. Lett.*, 1958, **1**, 343.
8. A. Pines, M. G. Gibbey, and J. S. Waugh, *J. Chem. Phys.*, 1973, **59**, 569.
9. S. Pausak, A. Pines, and J. S. Waugh, *J. Chem. Phys.*, 1973, **59**, 591.
10. D. W. Alderman, M. H. Sherwood, and D. M. Grant, *J. Magn. Reson. Ser. A.*, 1993, **101**, 188.
11. J. F. Nye, *Physical Properties of Crystals; Their Representation by Tensors and Matrices*, Oxford University Press, New York, 1985.
12. W. S. Veemann, *Prog. NMR Spectrosc.*, 1984, **16**, 193.
13. H. Hauser, C. Radloff, R. R. Ernst, S. Sundell, and I. Pascher, *J. Am. Chem. Soc.*, 1988, **110**, 1054.
14. C. M. Carter, D. W. Alderman, and D. M. Grant, *J. Magn. Reson.*, 1985, **65**, 183.
15. J. Jeener, B. H. Meier, P. Bachman, and R. R. Ernst, *J. Chem. Phys.*, 1979, **71**, 4546.
16. C. M. Carter, D. W. Alderman, and D. M. Grant, *J. Magn. Reson.*, 1987, **73**, 114.
17. M. H. Sherwood, D. W. Alderman, and D. M. Grant, *J. Magn. Reson.*, 1989, **84**, 466.
18. D. W. Alderman, M. H. Sherwood, and D. M. Grant, *J. Magn. Reson.*, 1990, **86**, 60.
19. M. H. Sherwood, J. C. Facelli, D. W. Alderman, and D. M. Grant, *J. Am. Chem. Soc.*, 1991, **113**, 750.
20. M. H. Sherwood, D. W. Alderman, and D. M. Grant, *J. Magn. Reson. Ser. A*, 1993, **104**, 132.
21. M. Mehring, *Principles of High Resolution NMR in Solids*, Springer-Verlag, New York, 1983, Chap. 5.
22. R. R. Ernst, G. Bodenhausen, and A. Wokaun, *Principles of Nuclear Magnetic Resonance in One and Two Dimensions*, Oxford University Press, New York, 1987, pp. 383–396.

Biographical Sketch

Mark H. Sherwood. *b* 1961. B.S., 1983, Colorado State University, where he was introduced to NMR by Gary E. Maciel, Ph.D., 1991, Chemistry, University of Utah, advisor David M. Grant. Visiting scientist, IBM Research Division, Almaden Research Center, 1991–present. Research specialties: carbon-13 and deuteron NMR in solids, NMR imaging at cryogenic temperatures.

Cokes

Marek Pruski

Ames Laboratory and Iowa State University, Ames, IA, USA

1	Introduction	1
2	Relaxation Parameters of Hydrogen and Carbon in Cokes	1
3	Quantitation of Hydrogen and Carbon	2
4	NMR Lineshapes in Cokes	2
5	Structural Parameters of Cokes	4
6	Related Articles	5
7	References	5

1 INTRODUCTION

The advances in NMR over the last three decades have resulted in an increasingly important role that this technique has played in studies of various types of carbonaceous materials. Among these materials are fossil fuels which, due to their impact as a main world energy source, are of primary concern in scientific and engineering research. Of great interest are naturally occurring raw materials, such as coal, crude oil, and oil shales, as well as products of fossil fuel processing. The latter include 'coke', a term used to describe a solid by-product of the petroleum refining process, or a hard, often porous residue left after the destructive distillation (pyrolysis) or liquefaction of coal.

Fossil fuels are known to be enormously heterogeneous and complex materials and no single approach can provide adequate understanding of their structure and best way of utilization. Although the classical chemical methods and some modern analytical techniques (e.g. mass spectroscopy, liquid and gas chromatography, thermogravimetry) have proved useful in characterizing parent materials as well as liquid and gaseous products of coals and petroleum processing, determination of the chemical and physical structure of solid fossil fuels and solid products of fuels processing has not been possible by employing these methods. This need has stimulated application of other spectroscopic techniques including X-ray spectroscopies (X-ray atomic fluorescence and X-ray photoelectron spectroscopy), infrared spectroscopy, optical spectroscopies (laser spark spectroscopy, Raman spectroscopy), ESR spectroscopy, and NMR spectroscopy, which soon came to the forefront of this research. Earlier NMR studies utilized primarily relaxation studies, quantitative analysis of ^{1}H in solids using wideline NMR, and provided quantitative and structural analysis of fossil fuel derived liquids (mainly from coal and petroleum) via liquid state NMR. Since the implementation of high-resolution methods of ^{1}H decoupling, magic angle spinning and CRAMPS, and the methods of enhancing polarization of rare nuclear spins (cross polarization and dynamic nuclear polarization) it became possible to acquire high-resolution spectra of ^{1}H and ^{13}C in a short measuring time.[1]

In spite of different origins, petroleum and coal derived cokes consist primarily of carbon (typically ca. 90% by weight) and hydrogen (below 5%). While smaller concentrations of oxygen, sulfur, nitrogen and various metals (vanadium, nickel, iron) are also present in cokes, it is not surprising that NMR spectroscopy utilizes ^{1}H and ^{13}C nuclei to probe these materials. Below, an overview is given of the fundamental aspects of solid state NMR of ^{1}H and ^{13}C as applied to the studies of carbonaceous solids. The topics include relaxation studies, quantitation, high-resolution methods in ^{13}C and ^{1}H NMR, lineshape analysis, and the relationship between NMR derived data and the chemical structure. Although the utilization of solid state NMR techniques will be shown largely for petroleum derived cokes, most of the approaches described here are also pertinent to fossil fuels, semi-cokes, coal tar pitches, petroleum pitches and other 'bottom-of-the-barrel residues' (see also ***Coal Structure from Solid State NMR*** and ***Fossil Fuels***), as well as for characterization of carbonaceous residues (cokes) from catalyst-controlled reactions.

2 RELAXATION PARAMETERS OF HYDROGEN AND CARBON IN COKES

Measurements of nuclear spin relaxation in solid fossil fuels have been performed in order to provide gross information about local environments and molecular motions, long before modern high-resolution solid state NMR techniques were introduced as an analytical tool. Three relaxation times were commonly measured: (a) T_1, the longitudinal relaxation time characterizing attainment of equilibrium of spin magnetization along a static magnetic field, and generally associated with dipolar fields fluctuating at the Larmor frequency, generated by motion of other magnetically active nuclei and/or unpaired electron spins associated with free radicals; (b) $T_{1\rho}$, the longitudinal relaxation time in the rotating frame characterizing similar motions in the tens of kilohertz frequency range; and (c) T_2, the transverse relaxation time characterizing static spin interactions in solids.

Most of the spin–lattice relaxation studies reported for cokes employed ^{1}H NMR and showed that $T_1{}^{\mathrm{H}}$ and $T_{1\rho}{}^{\mathrm{H}}$ relaxation processes (typical values in the 50–200 ms and 0.3–5 ms range, respectively) depend upon interactions between protons and unpaired electrons (via spin diffusion), while dipolar interactions between protons have a lesser significance. To limit the number of parameters, only a biexponential function is usually used to fit the experimental data although no physical model that justifies such procedure has yet been established. Also, due to the presence of different relaxation mechanisms, and different types of paramagnetic species, a distribution of relaxation parameters is very likely. In such cases the relaxation parameters are the result of a complicated interplay between competing relaxation mechanisms, and spin diffusion may not be effective to identify structural inhomogeneities, even if they existed in cokes. For example, the detailed study of 15 petroleum cokes, produced from pure and mixed residues of various origins, showed that the $T_1{}^{\mathrm{H}}$ and $T_{1\rho}{}^{\mathrm{H}}$ relaxation parameters (including relative fractions of magnetization exhibiting fast and slow relaxation) could not be directly correlated with different structural parameters of cokes as determined by high-resolution methods.[2] In particular, these results did not reveal structural inhomogeneities in cokes in which

aliphatic and aromatic structures dominate. In spite of difficulties with the interpretation of spin lattice processes in cokes, the accurate analysis of $T_1{}^H$ and $T_{1\rho}{}^H$ is often required to characterize quantitatively the cokes via ^{13}C CP MAS experiments.

The proton T_2 relaxation time (or the NMR linewidth), determined under a single pulse excitation, reflects the strength of static $^1H-{}^1H$ dipolar interactions in cokes, and in the absence of molecular motion is a measure of the average internuclear distance in a sample. Unlike coals, which generally exhibit at least two exponential decays, the pyrolyzed cokes show typically a Gaussian decay of transverse magnetization with a single value of T_2 of roughly $20\,\mu$s, indicating homogeneously rigid character of the coke structure, where only hindered motions of functional groups (e.g. CH_3) take place.[2] When molecular motion characterized by correlation time $\tau_c < 10^{-5}$ s is present, e.g. in coals with mobile molecular fragments, solvent swollen coals, pitches above their softening point or during pyrolysis, the increased values of T_2 are a measure of molecular mobility. The measurements of T_2 versus temperature allowed the study, for example, of the glass transition temperature in materials resulting from pyrolysis of petroleum pitches and coal extracts through the mesophase stage to a coke.[3]

3 QUANTITATION OF HYDROGEN AND CARBON

One of the main reasons NMR has become a powerful analytical tool is because for spin-$\frac{1}{2}$ nuclei, such as are ^1H and ^{13}C, the NMR signal may generally be used for quantitative analysis. Using NMR for hydrogen (or carbon) spin counting in cokes implies that: (1) all spins are observed by NMR, (2) the initial (near $t = 0$) time dependence of the FID is known and can be compared with that of a standard, and (3) the physical meaning of all components of the FID is well understood. In single pulse experiments the first few microseconds of the FID are always obscured by the probe ringdown and receiver deadtime, which may result in considerable signal loss in samples with short T_2. This short time behavior of the NMR signal can be determined, and the lost intensity recovered, by using a solid echo excitation sequence, or by applying linear prediction techniques directly to the FID.[2]

Hydrogen is the most sensitive nucleus commonly detected by NMR, but it is also one of the least sensitive when analyzed by chemical methods. In general, NMR offers quick and most reliable measurements of hydrogen concentration in fossil fuel materials, which compare favorably with the results of combustion analysis, Karl–Fisher titration and other techniques. The main possible source of systematic loss of the NMR signal (typically below 10%) is the broadening of the NMR line from dipolar interactions with unpaired electrons present in organic free radicals in cokes. As already mentioned, the analysis of the FID also provides information about molecular mobility.

The quantitative analysis of carbon by single pulse NMR is time consuming due to long ^{13}C relaxation times $T_1{}^C$ and is considered less accurate than chemical analyses. It is mainly used to address the potential quantitation problems in the CP MAS spectra.

4 NMR LINESHAPES IN COKES

The dominant line broadening interactions that affect the NMR lineshapes are chemical shift anisotropy and $^1H-{}^1H$ and/or $^1H-{}^{13}C$ dipolar couplings. However, even if these interactions are eliminated, or reduced, by the high-resolution techniques, the observation of sharp resonances in ^1H and ^{13}C NMR is often precluded by the heterogeneous chemical nature of cokes. The results of high-resolution ^1H and ^{13}C NMR when combined with spin counting, elemental analysis, and other analytical methods, can be used to infer several structural parameters and the 'average' model of a coke.

4.1 ^1H CRAMPS NMR

With values of transverse relaxation times T_2 around $20\,\mu$s, proton linewidths in cokes are ca. 30 kHz, corresponding to 100 ppm at a resonance frequency of 300 MHz. This line broadening results from high abundance and large magnetic moment of ^1H spins, and exceeds the range of proton chemical shifts in hydrocarbons, which is about 15 ppm. Consequently, no information concerning chemical environment of hydrogen can be derived from the NMR spectrum, unless the $^1H-{}^1H$ dipolar interactions are overcome by a suitable NMR technique. However a combination of MAS and homonuclear dipolar decoupling via a multiple pulse sequence (WAHUHA, MREV or BR-24) allows the achievement of quantitative ^1H NMR spectra with linewidths of less than 0.3 ppm in favorable cases [Figure 1(a)]. This technique is referred to as CRAMPS (combined rotation and multiple pulse spectroscopy) (see ***CRAMPS***).[4]

In general, CRAMPS spectra of cokes are less resolved than the spectra of pure crystalline hydrocarbons and some coals; nevertheless, two absorption bands can usually be distinguished, centered at ca. 7 ppm and ca. 2 ppm, and associated with aromatic CH protons, and protons attached to sp^3 carbon atoms, respectively (Figure 1).[2,5] The linewidths corresponding to the two maxima are typically 3–5 ppm [full width at half maximum height (FWHM)], with the inhomogeneous broadening mainly attributed to distribution of chemical shifts. The use of the MREV-8 sequence seems satisfactory for CRAMPS spectroscopy of fossil fuels, as the application of more sophisticated pulse sequences like BR-24 does not lead to increased resolution in these materials. Due to substantial overlap of the aromatic and aliphatic peaks, the spectra are deconvoluted for quantitative analysis by using a superposition of Gaussian lines. The usefulness of the CRAMPS technique becomes apparent when differences in the spectra are viewed as a function of coking conditions, e.g. time or temperature of pyrolysis.[6]

4.2 ^{13}C NMR Techniques: CP MAS and Bloch Decay

^{13}C NMR spectra of cokes, coals and coal-derived products can be measured using conventional single pulse excitation (Bloch decay experiment), or by $^1H-{}^{13}C$ cross polarization, which, combined with high-power ^1H decoupling and MAS, yield spectra with well resolved aromatic and aliphatic carbon bands (Figure 2). Typically, the low-frequency (aliphatic) part of the spectrum consists of a peak located between 10 and

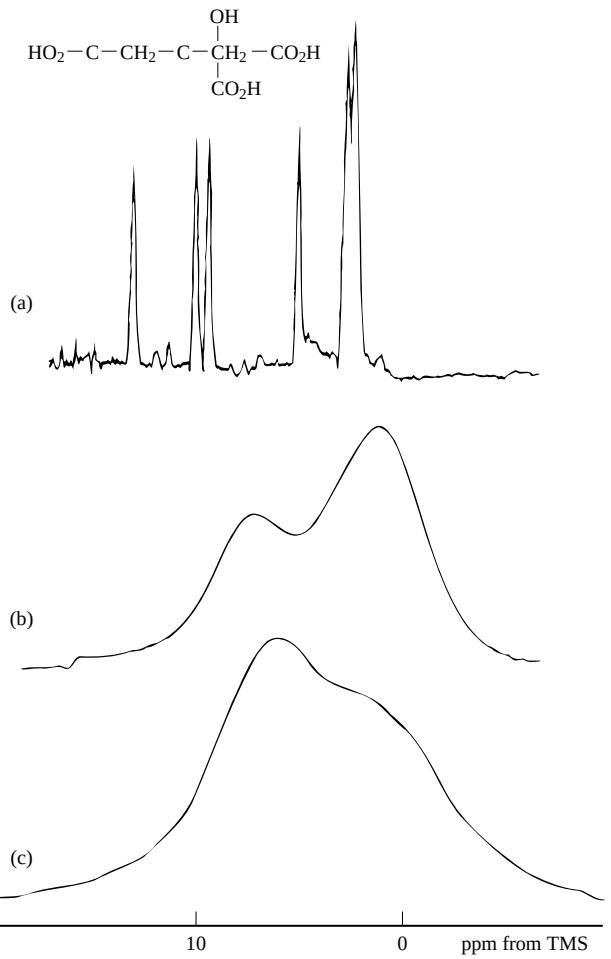

Figure 1 ^{1}H CRAMPS spectra of (a) citric acid, 187 MHz; (b) Pittsburgh No. 8 Argonne Premium Coal, 300 MHz; and (c) petroleum coke produced at Mobil from heavy crude oil, 300 MHz. [Spectrum (a) reproduced by permission of Academic Press from G. E. Maciel, C.E. Bronnimann, and B.L. Hawkins, in 'Advances in Magnetic Resonance: The Waugh Symposium', ed. W.S. Warren, 1990, Vol. 14, p. 125. Spectrum (c) reproduced by permission of Pergamon Press from M. Pruski, D. Michel, and B. C. Gerstein, *Carbon*, 1994, **32**, 31]

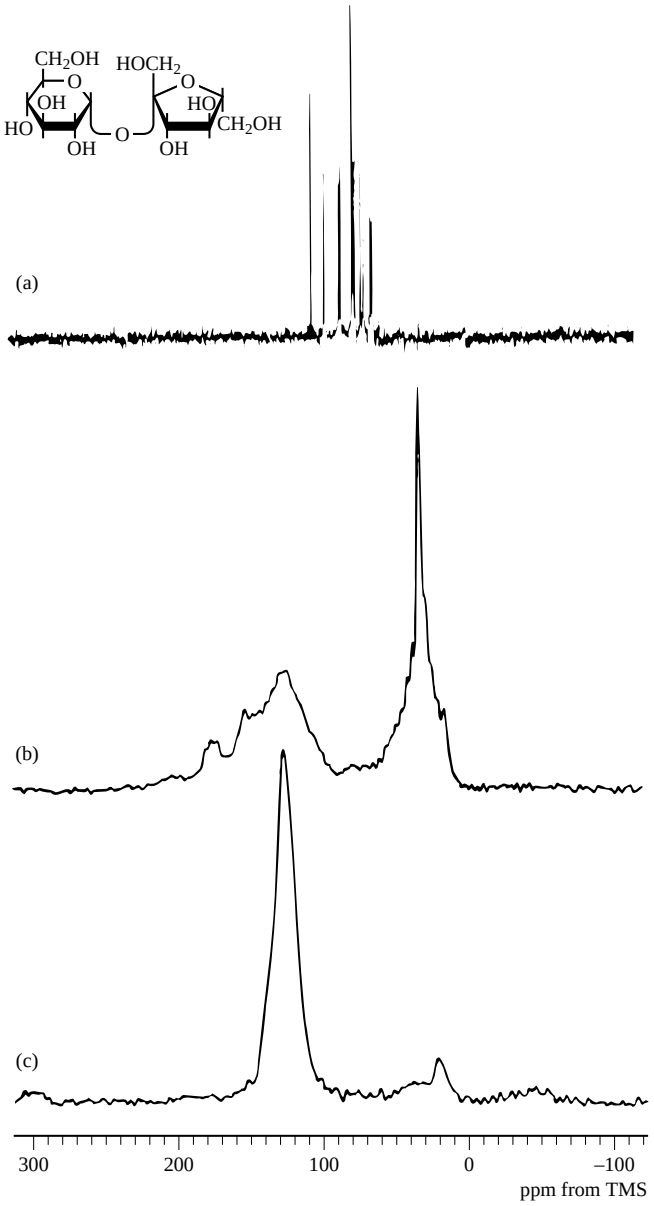

Figure 2 25 MHz ^{13}C CP MAS spectra of (a) sucrose, (b) German brown coal, and (c) petroleum coke produced from heavy crude oil (t_{cp} = 1 ms, spinning speed ν_r = 4.5 kHz)

50 ppm with features that can be assigned to methyl and methylene carbons. The aromatic peak, centered at ca. 130 ppm, is associated mainly with C–H perimeter and nonprotonated aromatic carbons. Although ^{1}H decoupling and MAS substantially reduce the large broadening due to ^{1}H–^{13}C dipolar interaction (ca. 20 kHz) and chemical shift anisotropy (ca. 200 ppm), the ^{13}C spectra of coals and cokes cannot match the liquid-like resolution achieved for many crystalline organic compounds (Figure 2). Again, NMR reflects the chemical complexity of these materials, because the resonances originating from a distribution of chemical environments are superimposed in the spectra.

A variety of sources can limit the accuracy of the intensities measured in these experiments which raised serious concern about the quantitative reliability of ^{13}C NMR methods in the analysis of carbonaceous solids.[7] Several factors that define resolution and quantitative information are general for ^{13}C NMR spectroscopy, e.g. interference of molecular motions with MAS and ^{1}H decoupling, incomplete recovery of carbon magnetization in Bloch decay experiments due to very long $T_1{}^{C}$ relaxation times, and signal loss due to broadening from paramagnetic centers (cokes contain typically ca. 10^{19} unpaired electrons per gram).

Additional difficulties arise when cross polarization is used to enhance the carbon signal.[7–10] The time evolution of carbon magnetization during the CP MAS experiment is a result of a complicated interplay between the spin–lattice relaxation processes in the rotating frame and the cross-polarization processes (described by relaxation time $T_{1\rho}{}^{H}$ and the time constant for cross-polarization process, T_{CH}), which, in turn, are further influenced by sample spinning and sample heterogeneity (see ***Cross Polarization in Rotating Solids: Spin-1/2 Nuclei***). In the simplest case, the time dependence of the ^{13}C magnetization $M_c(t_{CP})$ during the cross polarization contact is given by:

$$M(t_{CP}) = M_0\lambda^{-1}\left[1 - \exp\left(-\lambda\frac{t_{CP}}{T_{CH}}\right)\right] \times \exp\left(-\frac{t_{CP}}{T_{1\rho}^{H}}\right) \quad (1)$$

where M_0 is the carbon equilibrium magnetization, t_{CP} is the cross polarization contact time, and $\lambda = 1 - (T_{CH}/T_{1\rho}{}^{H})$.[11] For quantitative measurements it is required that the build-up of carbon magnetization, determined by T_{CH}, is completed before the loss of proton polarization occurs due to $T_{1\rho}{}^{H}$ relaxation (i.e. hydrogen having short $T_{1\rho}{}^{H}$ values are not contributing to cross polarization, leaving a substantial fraction of carbons 'undetected', unless $T_{CH} << T_{1\rho}{}^{H}$). In general, a wide distribution of T_{CH} times exists in cokes due to different $^{13}C-^{1}H$ distances and internal motion. MAS introduces additional time dependencies to homo- and heteronuclear dipolar Hamiltonians and further complicates the polarization transfer. Since, as described earlier, the $T_{1\rho}{}^{H}$ relaxation processes are also complex in cokes, with substantial fractions of spins having $T_{1\rho}{}^{H}$ values of 500 μs or less,[2] the condition $T_{CH} << T_{1\rho}{}^{H}$ may not be satisfied for those ^{13}C nuclei that are far from the nearest proton, e.g. those that are deeply incorporated in polycondensed aromatic rings.

In spite of the unfavorable cross-polarization dynamics, CP MAS experiments are being successfully applied in the studies of fossil fuels. Most researchers have conceded that, when carefully performed, CP MAS experiments provide quite accurate ^{13}C lineshapes, which in most cases agree well with those obtained from Bloch decay experiments. This assertion seems particularly pertinent for cokes, which by nature are more homogeneous than coals, and a too low carbon spin count in the CP MAS spectra does not necessarily imply an incorrect analysis of carbon functionality. In addition, several CP MAS-based spectral editing techniques have been proposed and applied to carbonaceous solids. The dipolar dephasing experiment has been traditionally used for discriminating between different carbons based on the strength of their dipolar interactions with protons.[12] In coals and cokes, this technique allowed discrimination between aromatic tertiary and aromatic quaternary ring carbons, as well as between aliphatic quaternary and CH_3 carbon atoms and combined CH and CH_2.[12,13] The recently proposed CP MAS sequences that combine depolarization and polarization inversion allow the generation of subspectra representing each of four CH_n (n = 0, 1, 2, 3) subsystems (see ***Spectral Editing Techniques: Hydrocarbon Solids***).[14]

The following experimental conditions and procedures are recommended for obtaining the most reliable CP MAS spectra of solid fossil fuels.[7,9,10]

1. The longitudinal relaxation times T_{1H} and $T_{1\rho}{}^{H}$ should be carefully measured using ^{1}H NMR.
2. Measuring of ^{13}C intensities with variable cross-polarization contact times in the 10 μs to 30 ms range, and fitting the data to equation (1) to obtain the total magnetization $M_c(0)$. Often two components of T_{CH} and $T_{1\rho}{}^{H}$ are necessary to produce a good fit.
3. The use of low MAS frequency (<5 kHz) is useful to avoid the interference of sample spinning with the cross-polarization process. Consequently, the measurements should be performed at low static magnetic fields (<2.5 T) to avoid the spinning sidebands in the spectra and the necessity of spinning sideband suppression. Since the dominant line broadening mechanisms in the CP MAS spectra are heterogeneous, resolution is almost independent on the magnetic field strength.
4. Accurate adjustment of the Hartmann–Hahn match, especially when MAS frequencies of >5 kHz are used.

Finally, the last few years have seen the development of a variety of CP MAS based experiments designed in order to enable efficient cross polarization and evade some of the quantitative distortions in ^{13}C NMR spectra. These techniques include stop-and-go spinning (STAG),[15] magic angle hopping[16] (see ***Magic Angle Turning and Hopping***) and amplitude-modulated cross polarization schemes (AMCP).[17]

While the CP MAS technique is applied in most studies, the Bloch decay experiment has recently become a feasible alternative. With the advent of large MAS rotors, spinning of several cubic centimeters of sample is now possible at 4 kHz, and a reasonable signal-to-noise (S/N) ratio can be achieved in ^{13}C MAS spectra of cokes within a few hours of measuring time, even if the recycle delay of several minutes is required between successive transients.[18] The Bloch decay spectra represent >90% of carbon in many cokes, with the only loss of signal attributed to paramagnetic broadening, and the method is preferable for quantitative studies. As the MAS capabilities continue to improve, Bloch decay may become increasingly used in the future research, leaving CP MAS measurements for quick qualitative surveys, comparative studies, measurements of C–H interactions and spectral editing.

4.3 Other NMR Techniques

The rotating frame dynamic nuclear polarization cross polarization experiment (rf DNP-CP)[19] is an alternative $^{1}H-^{13}C$ polarization scheme which allows nuclear polarization to be enhanced by irradiating the free electrons in a sample. The DNP technique is particularly well suited for solid fossil fuels and substantial carbon signal enhancements have been reported for coals.[19] The DNP experiment requires, however, a source of microwave power and some modifications of the NMR spectrometer (see ***Dynamic Nuclear Polarization and High-Resolution NMR of Solids***).

Variable angle sample spinning (VASS) is another method which partly averages the chemical shift anisotropy while allowing measurements of CSA lineshapes and CSA tensor values (see ***Variable Angle Sample Spinning***). The technique has proved useful in supplementing other types of NMR data to estimate the structure of polycondensed aromatic materials such as some coals and chars.[9]

Also, high temperature in situ NMR has recently embraced fossil fuels and related materials.[20] Several NMR studies were reported in which thermally induced changes in molecular dynamics and chemical shift information during pyrolytic decomposition and formation of solid carbonaceous residues, including coking processes, have been monitored at temperatures as high as 800 K. For these materials, which could be studied above their softening point (e.g. hard coal tar pitch and mesophase pitch prepared from decant oil), ^{1}H and ^{13}C NMR provided highly resolved signals (<1 ppm) that allowed for identification of various structural units.[21]

5 STRUCTURAL PARAMETERS OF COKES

The primary implication of solid state NMR studies of cokes is an enhanced understanding of their chemical

composition. Although the structural information obtained from solid state NMR studies is less detailed than that provided for the feedstocks using liquid state NMR techniques,[22] the parameters measured by ^{1}H and ^{13}C NMR can be used to estimate the 'average' models of these materials.[2,8] The parameters include: hydrogen and carbon concentrations (from quantitative NMR analysis); hydrogen and carbon aromaticities, as obtained from high-resolution NMR of ^{1}H and ^{13}C; fraction of aromatic carbon atoms with directly bonded protons (from ^{13}C NMR with dipolar dephasing); the total H/C mole ratio; and the mole fractions H/C (aromatic) and H/C (aliphatic). Due to their heterogeneity, the validity of 'average' models to describe coals has been questioned by some researchers. However, it is often useful to describe these materials in terms of average properties, as the identification of all individual constituents is very difficult, if not impossible, to accomplish. Also, NMR and elemental analysis show that cokes are more chemically homogeneous, and have low concentrations of heteroatoms, which facilitates structural determination. Two examples of basic structural types present in cokes produced from heavy crude oils by delayed coking at ca. 700 K are shown in Figure 3.[2] These materials may be viewed as high molecular weight conglomerates of polycyclic aromatic, hydrogen deficient structures, formed by covalent bonds or methylene bridges. The structures shown in Figure 3 are typical of cokes, although carbon aromaticities close to 100% were observed for materials produced under more severe coking conditions. Similar structural parameters were also measured for coal liquefaction residues, coal tar pitches, and residual carbons (coke) from thermal decomposition of oil shales.[23] In the last study, a CP MAS technique was used to monitor the decrease of aliphatic carbon peak intensity and formation of polycondensed quaternary carbon at higher temperatures.

For a variety of fossil fuels, solid state NMR spectra can be combined with characterization of feedstocks by liquid state NMR, MRI and high temperature in situ NMR to provide unique identification of structural changes during the entire coking, pyrolysis or liquefaction processes. Such studies allow monitoring of the loss of organic aliphatic matter, while cracking, polymerization and aromatization reactions progress during pyrolysis and the precursors of coke are formed. Following the progress of these reactions has notably improved the understanding of the chemistry of carbonization, and allowed optimization of the technology used in the coking process.

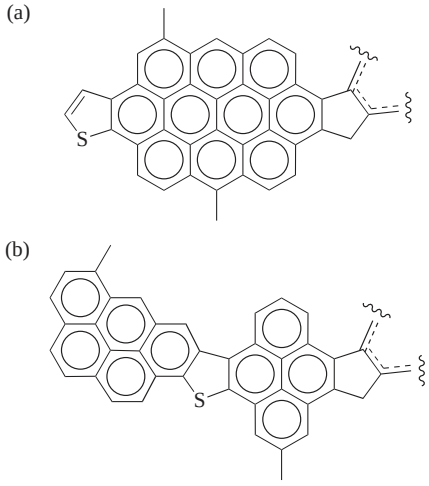

Figure 3 Typical structures of cokes based on structural parameters from solid state NMR of ^{1}H and ^{13}C and elemental analysis. (Reproduced by permission of Pergamon Press from M. Pruski, D. Michel, and B. C. Gerstein, *Carbon*, 1994, **32**, 31)

6 RELATED ARTICLES

Coal Structure from Solid State NMR; CRAMPS; Cross Polarization in Rotating Solids: Spin-1/2 Nuclei; Cross Polarization in Solids; Fossil Fuels; Internal Spin Interactions and Rotations in Solids; Line Narrowing Methods in Solids; Oil Reservoir Rocks Examined by MRI; Wood and Wood Chars.

7 REFERENCES

1. B. C. Gerstein and C. R. Dybowski, *Transient Techniques in NMR of Solids: An Introduction to Theory and Practice*, Academic, New York, 1985.
2. D. Michel, M. Pruski, and B. C. Gerstein, *Carbon*, 1994, **32**, 31; M. Pruski, D. Michel, and B. C. Gerstein, *Carbon*, 1994, **32**, 41.
3. J. S. Hayward, B. Ellis, and B. Rand, *Carbon*, 1988, **26**, 71.
4. B. C. Gerstein, C. Chou, R. G. Pembleton, and R. C. Wilson, *J. Phys. Chem.*, 1977, **81**, 565.
5. G. E. Maciel, C. E. Bronnimann, and B. L. Hawkins, in *Advances in Magnetic Resonance: The Waugh Symposium*, ed. W. S. Warren, Academic, San Diego, 1990, Vol. 14, p. 125.
6. B. C. Gerstein, M. Pruski, and D. Michel, in *Advances in Coal Spectroscopy*, ed. H. L. C. Meuzelaar, Plenum, New York, 1992, Chap. 9
7. R. A. Wind, G. E. Maciel, and R. E. Botto, in *Magnetic Resonance of Carbonaceous Solids* (*Advances in Chemistry Series, Vol. 229*), ed. R. E. Botto and Y. Sanada, American Chemical Society, Washington, 1993, Chap. 1
8. A. M. Orendt, M. S. Solum, N. K. Sethi, R. J. Pugmire, and D. M. Grant, in *Advances in Coal Spectroscopy*, ed. H. L. C. Meuzelaar, Plenum, New York, 1992, Chap. 10
9. C. E. Snape, D. E. Axelson, R. E. Botto, J. J. Delpuech, P. Tekely, B. C. Gerstein, M. Pruski, G. E. Maciel, and M. A. Wilson, *Fuel*, 1989, **68**, 547.
10. M. Pruski, L. dela Rosa, and B. C. Gerstein, *Energy Fuels*, 1990, **4**, 160.
11. M. Mehring, *Principles of High Resolution NMR in Solids*, 2nd edn., Springer, Berlin, 1983, Chap. 4
12. S. J. Opella and M. H. Frey, *J. Am. Chem. Soc.*, 1979, **101**, 5854.
13. P. DuBois Murphy, T. J. Cassady, and B. C. Gerstein, *Fuel*, 1982, **61**, 1233.
14. X. Wu, S. T. Burns, and K. W. Zilm, *J. Magn. Reson., Ser. A*, 1994, **111**, 29.
15. R. C. Zeigler, R. A. Wind, and G. E. Maciel, *J. Magn. Reson.*, 1988, **79**, 299.
16. A. Bax, N. M. Szeverenyi, and G. E. Maciel, *J. Magn. Reson.*, 1983, **52**, 147.
17. S. Hediger, B. H. Meier, and R. R. Ernst, *Chem. Phys. Lett.*, 1993, **213**, 627.
18. G. E. Maciel, C. E. Bronnimann, A. Jurkiewicz, R. A. Wind, and V. H. Pan, *Fuel*, 1991, **68**, 925.

19. R. A. Wind, in *Magnetic Resonance of Carbonaceous Solids* (*Advances in Chemistry Series, Vol. 229*), ed. R. E. Botto and Y. Sanada, American Chemical Society, Washington, 1993, Chap. 10
20. Y. Sanada and L. J. Lynch, in *Magnetic Resonance of Carbonaceous Solids Advances in Chemistry Series, Vol. 229*, ed. R. E. Botto and Y. Sanada, American Chemical Society, Washington, 1993, Chap. 7
21. T. Nishizawa and M. Sakata, *Fuel*, 1991, **70**, 124.
22. See, for example, C. E. Snape, *Fuel* 1983, **62**, 34.
23. J. A. MacPhee, B. N. Nandi, J. A. Ripmeester, and R. E. Hawkins in *Magnetic Resonance, Introduction, Advanced Topics and Applications to Fossil Energy*, ed. L. Petrakis and J. P. Fraissard, Riedel, Dordrecht, 1984, p. 575; F. P. Miknis and G. E. Maciel, *ibid.*, p. 545.

Biographical Sketch

Marek Pruski. *b* 1954. M.S., 1977, Ph.D., 1981, N. Copernicus University (supervisor T. Marszalek), Torun, Poland; Postdoctoral fellow, Ames Laboratory, Iowa State University (with B.C. Gerstein), 1985–88; scientist, Ames Laboratory, Iowa State University, 1988–present. Approx. 50 publications. Current research specialty: solid state NMR and its applications to surface and material sciences.

CRAMPS

Bernard C. Gerstein

Ames Laboratory of Iowa State University, Ames, IA, USA

1	Introduction	1
2	Rotations in Real Space	2
3	Rotations in Spin Space	3
4	Echoes and the Average Hamiltonian	4
5	CRAMPS	6
6	Caveats	7
7	Related Articles	8
8	References	8

1 INTRODUCTION

Combined rotation and multiple pulse spectroscopy (CRAMPS)[1] is one means of using transient techniques in NMR to achieve liquid-like high-resolution NMR spectra of hydrogen and fluorine in solids. Herein will be described the basic ideas leading to the achievement of this resolution. The background required is that obtained by exposure to an undergraduate physical chemistry course, with a smattering of perturbation theory included. There will necessarily be some overlap between the description below, and other articles in this Encyclopedia. Cross references to pertinent subjects are given at the end of the article.

Of all the elements encountered by medical, biological, chemical, and physical scientists, hydrogen is perhaps the most common. The NMR-active nuclide, ^{1}H, is 99.98% abundant, and the magnetic moment is exceeded in magnitude only by the nonnaturally occurring tritium, ^{3}H. ^{1}H was the first nucleus for which NMR was reported.[2,3] Because of the magnitude of its magnetic moment, and its natural abundance, hydrogen is the most easily detected nucleus commonly encountered in NMR. It is routinely used for qualitative and quantitative analysis of organic molecules in the liquid state.

Chemical shifts of hydrogen in organic molecules in solution commonly have a range of about 15 ppm of the resonance frequency. For example, protons in common organic molecules in a spectrometer operating at 500 MHz for ^{1}H will exhibit a chemical shift range of about $15 \times 500 = 7500$ Hz. Scalar couplings to other hydrogen atoms and to carbon atoms are characteristically around 100 Hz. Resolution in commercial liquid state spectrometers is of order of a few tens of hertz, so hydrogen NMR on molecules in the liquid state supplies an easily detectable, well resolved, and sensitive fingerprint for routine analysis.

It was thus initially disappointing that under a single resonant excitation such as was used on liquids, NMR spectra of hydrogen in solids such as ice, or high molecular weight proteins, are broad and featureless. The linewidths are about 15 kHz, an example being given for hydrogen in adipic acid in Figure 1(a).

Exactly those qualities which make ^{1}H such a valuable label for liquid state NMR destroy the resolution of the NMR spectrum of hydrogen in solids. The reasons are physically

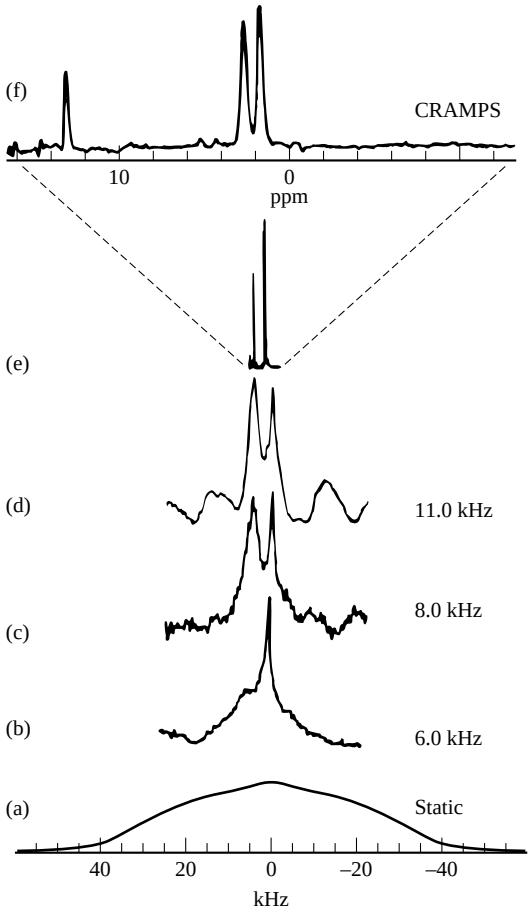

Figure 1 Comparison of NMR spectra taken under: (a) single pulse excitation; (b) MAS at 6 kHz; (c) MAS at 8 kHz; (d) MAS at 11 kHz; (e, f) CRAMPS. (Courtesy of Gary Maciel)

obvious. ^{1}H is a nucleus with relatively high abundance and large magnetic moment. In a static field it behaves as a magnet, producing a magnetic field with the familiar symmetry exhibited by iron filings aligning in the neighborhood of a bar magnet. In the solid state, each hydrogen atom will be exposed not only to the static field of the magnet used for NMR, but also to the sum of the 'dipolar' fields of all other abundantly present protons in the sample. The result is that the resonance frequency of any hydrogen atom in the sample is homogeneously broadened by the effect of the dipolar fields. In addition, there is NMR line broadening in a motionless solid due to the nonspherical symmetry of the surrounding bonding electronic cloud, i.e. due to 'shielding anisotropies'. CRAMPS was developed to attenuate these two major sources of line broadening such that liquid-like NMR spectra of ^{1}H and ^{19}F in solids are achieved in favorable cases.

CRAMPS involves manipulations common to NMR of both liquids and solids. These cause the system under observation to vary in time such that chemical shifts become more resolved. Other interactions, e.g. dc field inhomogeneities in liquids, are averaged to small values. A critical fact here is that all observables depend on variables in both real space (r, θ, ϕ), and spin space (components of spin angular momentum, $\hat{I}_k$, $k = x, y, z$) (see ***Internal Spin Interactions and Rotations in Solids***). The manipulations used selectively to attenuate

internal interactions which cause a loss of resolution therefore include the following:

1. Sample motion in the laboratory makes θ and ϕ time-dependent. For liquids, spinning rates are roughly 100 Hz. Solids are commonly spun 100 times faster.
2. Radiofrequency (rf) pulsing makes the components of the spin angular momentum operators ($\hat{I}_x$, $\hat{I}_y$, and $\hat{I}_z$) time-dependent.

Rotations in real space,[4,5] e.g. magic angle spinning, accomplish what molecular tumbling of molecules in the liquid state does for the shielding anisotropy; namely, it averages the anisotropic shielding to its isotropic, or average, value.

Radiofrequency pulses may be thought of as rotating magnetic moments in 'spin space'. We may therefore think of the combined rotation and multiple pulse technique as using rotations in both 'spin space' and in the real space of the laboratory. As understood early on[6–8] and shown below, rotations in spin space via rf pulses can be arranged to average local dipolar fields, and the resulting NMR line broadening to values smaller than differences in chemical shifts.

An example of the CRAMPS spectrum[9] of hydrogen in adipic acid, $HOOC(CH_2)_4COOH$, is shown in Figure 1(e) and (f). Figure 1(b)–(d) show spectra of the static sample under a single pulse excitation, roughly 40 kHz wide, and the spectrum of the sample under magic angle spinning (see below) at frequencies between 6 and 11 kHz. It can be seen that the resolution between the top and the bottom spectrum has increased under CRAMPS by a factor of roughly 600.

In order to illustrate how the experiment works, we first consider how the physical rotation of solid samples narrows the broadening effect of shielding anisotropies. Then we consider how sequences of rf pulses narrow dipolar broadening.

2 ROTATIONS IN REAL SPACE

The most common motion familiar to the NMR spectroscopist working in liquids is that of simply spinning the NMR tube containing the liquid sample about an axis perpendicular to the static field. This partially averages dc field inhomogeneities over the sample volume and improves resolution. Rotation of a liquid at the magic angle further narrows the lines of liquids (see ***Magnetic Susceptibility and High Resolution NMR of Liquids and Solids***). The manner in which this works might be perhaps understood by a related example. An individual enthusiastic about the game of football, but without much background in mechanics, constructs a sheet metal wind vane, cut into the shape of an American football. The dynamic balance of this particular device is such that instead of pointing to indicate wind direction, it rotates as the wind blows. For rotation too fast for the eye to follow, the football shaped device, being a thin slice the width of the metal when viewed end-on, and a football shaped object when viewed perpendicular to the surface, seems on average to become something smaller than a football, and something larger than a line. On average, it seems that a circular object is seen. Glancing at the wind vane in a high wind, the builder rapidly blinks at this dysfunction of the device. In doing so, the blinking is unwittingly done in concert with the rotation period of the wind vane, and for an instant, instead of the football shaped wind vane, a very narrow line is seen! Each time the eyes were opened, a stroboscopic observation was made of the wind vane viewed head-on.

Following the football analogy, consider the symmetry of the bonding electron cloud about an NMR active ^{13}C in a CO_2 molecule, O=C=O. Clearly this cloud is roughly football shaped. This bonding electron cloud may be thought to circulate in reaction to the imposition of a static magnetic field, producing a 'shielding field'. The details of the circulation, and thus the shielding field, described in terms of a 'shielding ellipsoid' $\boldsymbol{\sigma}$, will be different when the static field is perpendicular to the unique axis of the football than when parallel to it. In fact the shielding field produces an NMR line at $\delta = -90$, i.e. 90 ppm upfield (down frequency; shielded) with respect to ^{13}C in tetramethylsilane (TMS), when the static field is parallel to the unique axis. With the field perpendicular to the unique axis, δ is 245 ppm deshielded with respect to ^{13}C in TMS. In the liquid state, the NMR spectrum of ^{13}C in CO_2 is a narrow line 133 ppm deshielded from TMS. Sufficiently rapid isotropic (random in space) tumbling of the molecule in the liquid results in this football shaped object becoming spherical as viewed by the eye of NMR; the anisotropic shielding is averaged to its isotropic value, which is the average of the three principal axes of the shielding ellipsoid. Note that $133 = (245 + 245 - 90)/3$; the isotropic value of the chemical shift of ^{13}C in CO_2 in the liquid is the average of the values with the dc field along the x, y, and z axes of the shielding ellipsoid.

When the NMR spectrum of carbon dioxide is measured in the powdered, solid state, as dry ice, molecular tumbling is absent. In this case each crystallite contributes an NMR line between 245 ppm and −90 ppm, depending upon the orientation of the shielding ellipsoid in the crystallite to the static field. The total spectrum appears as the 'powder pattern' shown in Figure 2. The weighting of intensity on the high frequency side, corresponding to the static field in the (x, y) plane of the shielding ellipsoid, corresponds to the fact that it is more likely that a given crystallite will have the static field near the (x, y) plane of the shielding ellipsoid than uniquely along the axis of rotation.

The resonance frequency depends on the orientation of the shielding ellipsoid with respect to the static magnetic field, specified by angles θ and ϕ, as shown in Figure 3, and on the asymmetry of the ellipsoid. This asymmetry is uniquely specified by the magnitudes of its three principal axes in ppm

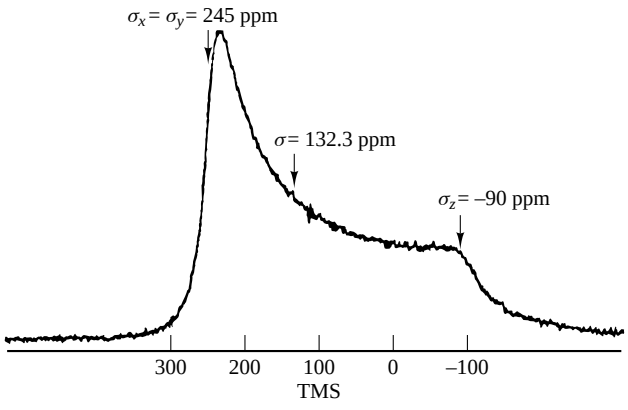

Figure 2 NMR of ^{13}C in powdered solid CO_2. Illustration of shielding anisotropy for an axially symmetric shielding environment. (Courtesy of Anita Orendt)

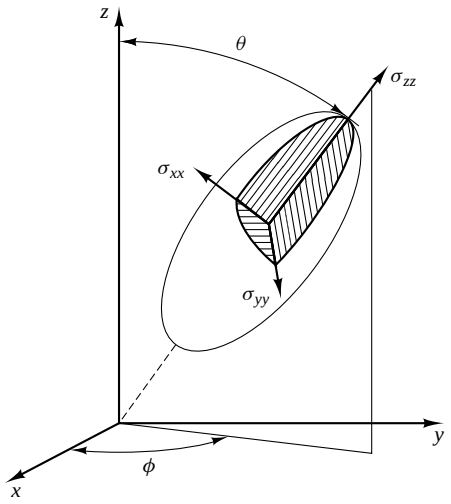

Figure 3 Relationship between the principal axes of the shielding ellipsoid and the laboratory coordinate system; definitions of θ and ϕ

of the resonance frequency, denoted by σ_{xx}, σ_{yy}, and σ_{zz}, or in terms of linear combinations of these which more clearly exhibit the symmetry properties. The combinations are

(a) the average of the magnitudes of the three principal axes, $\sigma_{\rm iso}$, the isotropic shielding, which is that quantity observed in NMR of liquids;
(b) the anisotropy ζ, equal to the difference between σ_{zz} and $\sigma_{\rm iso}$;
(c) the asymmetry η, proportional to the difference in the x and y components.

We note that a similar ellipsoid describes the anisotropy of the dipolar interaction $\boldsymbol{D}$ between two nuclei, but in this case the interaction is axially symmetric, $D_{xx} = D_{yy}$, so the asymmetry for the dipolar interaction is zero.

The resonance frequency of a shielding ellipsoid oriented at θ, ϕ with respect to $\boldsymbol{B}_0$, and with symmetry specified by $\sigma_{\rm iso}$, ζ, and η is given by

$$\omega(\theta, \phi, \sigma_{\rm iso}, \zeta, \eta) = \omega_0\{\sigma_{\rm iso} + \zeta[\tfrac{1}{2}(3\cos^2\theta - 1) + \tfrac{1}{2}\eta \sin 2\theta \cos 2\phi]\} \quad (1)$$

When the sample is set in motion, e.g. by random molecular tumbling, as would take place when the sample is heated to the liquid state, or by sonic agitation of the finely divided solid in a suitable liquid (see ***Ultrasonic Irradiation and NMR***), or by the experimenter about an axis oriented at an angle β to the static field, and at a frequency that is fast compared with the spectral width $\omega_0(\sigma_{xx} - \sigma_{zz})$, it may be shown (see ***Internal Spin Interactions and Rotations in Solids***) that the averaged frequency becomes only a function of the isotropic chemical shift $\sigma_{\rm iso}$, the anisotropy ζ, and the angle β between the spinning axis and the field. This relationship is given by

$$\omega(\omega_0, \beta, \sigma_{\rm iso}, \zeta) = \omega_0[\sigma_{\rm iso} + \tfrac{1}{2}\zeta(3\cos^2\beta - 1)] \quad (2)$$

The terms in η disappear if the sample is spun rapidly enough, or contribute to sidebands if the spinning rate is smaller than the shielding spectral width. Clearly at the 'magic' angle β = arccos $(\frac{1}{3})^{1/2}$, only the isotropic value remains; the spinning has achieved a liquid-like spectrum by averaging the anisotropic information to zero.

It was recognized early on that MAS could also average the dipolar broadening to zero. However, since all nuclei in a sample rich in protons are connected to all others via the through-space dipolar interactions, it is necessary to spin fast compared with the dipolar linewidth to achieve effective narrowing. This means spinning fast compared with 15 kHz, or fast compared with roughly 10^6 rev min^{-1}. Such spinning speeds are not easily achieved, but have been realized in homemade spectrometers with easily machineable polyimide resins,[10] and are also now available in commercial spectrometers making use of high-precision cylindrical ceramic rotors. A comparison of narrowing under ultrafast MAS and the use of CRAMPS has been made,[11] with the conclusion that one would like to have access to both techniques, depending upon the sample. Furthermore, there are spin dynamics containing added information which one may perform using CRAMPS which are not available within the expedient of high speed spinning.

We now consider how manipulating the nuclear spin system with rf pulses averages the dipolar interactions to values smaller than differences in chemical shifts. To do so, we use the background developed in the article ***Echoes in Solids***.

3 ROTATIONS IN SPIN SPACE

All spectroscopy experiments implicitly or explicitly involve solutions of the time dependent Schrödinger equation. We have implicitly invoked one such solution in discussing MAS, above. An understanding of NMR appropriate to the level of this Encyclopedia involves at least a rudimentary knowledge of the solutions of this equation in the density operator formulation. Fortunately there are texts for students at both the entry level[12,13] and advanced levels,[14–16] presenting both these pictures. As a basis for understanding the multiple pulse portion of the CRAMPS experiment, I briefly summarize the results of selective averaging theory on first the shielding interaction, and then the dipolar interaction. Let us start in the rotating frame of the Zeeman interaction, the frame in the real world in which NMR signals are detected after demodulation removes the carrier frequency from the information content of the signal. In the rotating frame, the principal effective magnetic fields which cause a proton to resonate for detection by NMR are: (a) the externally applied rf field, $\boldsymbol{B}_1$, and (b) the sample-supplied, or internal average, of the dipolar fields of all other protons, $\boldsymbol{B}_{\rm D}$. A smaller perturbation is that of the anisotropic shielding field associated with the reaction to electrons in the environment of the hydrogen nucleus of the static external field.

With each field is associated an energy, and a quantum mechanical energy operator $\hat{\mathcal{H}}$. Thus the energy operator in the rotating frame is given by

$$\hat{\mathcal{H}} = \hat{\mathcal{H}}_{\rm rf} + \hat{\mathcal{H}}_{\rm int} \quad (3)$$

where the magnitude of $\hat{\mathcal{H}}_{\rm rf}$ for purposes of solid state experiments is about 5 mT. The magnitude of $\hat{\mathcal{H}}_{\rm int}$ is never greater than a few tenths of a millitesla in the case discussed here—that of homonuclear dipolar coupling. The equation of

motion of the system is then given by the solution to the time dependent Schrödinger equation in the density matrix formulation:

$$i\frac{d\hat{\rho}}{dt} = [\hat{\mathcal{H}}, \hat{\rho}] \tag{4}$$

Here, $\hat{\mathcal{H}}$ is the sum of the rf and internal interactions, as specified in equation (3), $\hat{\rho}$ is the density operator, specified by the wavefunction $|\psi\rangle$, as $|\psi\rangle\langle\psi|$ in Dirac bracket notation. The average values of observables, e.g. $\langle\hat{I}_y(t)\rangle$, the free induction decay detected along the y phase in the rotating frame, are given by

$$\langle\hat{I}_y(t)\rangle = \mathrm{Tr}\,[\hat{\rho}(t)\hat{I}_y] \tag{5}$$

With the interactions separated in magnitude in this manner, it makes sense to treat $\hat{\mathcal{H}}_{\mathrm{int}}$ as a perturbation on $\hat{\mathcal{H}}_{\mathrm{rf}}$. Recall that the transformation to the frame of the Zeeman interaction (the rotating frame) simplifies the description of a nuclear spin in the presence of other interactions; e.g. the oscillating on-resonance rf field becomes static in the rotating frame. Similarly, transformation to the frame of the now largest interaction, the rf field, further simplifies the description of the system. The transformation to the frame of the rf field is accomplished by the relationships

$$\hat{\rho} = \hat{U}_{\mathrm{rf}}\hat{\tilde{\rho}}\hat{U}_{\mathrm{rf}}^{-1} \tag{6}$$

$$i\frac{dU_{\mathrm{rf}}}{dt} = \hat{\mathcal{H}}_{\mathrm{rf}}\hat{U}_{\mathrm{rf}} \tag{7}$$

$$\hat{U}_{\mathrm{rf}}(0,0) \equiv \hat{U}_{\mathrm{rf}}(t=0) = \hat{1} \tag{8}$$

$$\hat{\tilde{\mathcal{H}}}_{\mathrm{int}}(t) = \hat{U}_{\mathrm{rf}}^{-1}(t,0)\hat{\mathcal{H}}_{\mathrm{int}}\hat{U}_{\mathrm{rf}} \tag{9}$$

As mentioned above, the notation $\hat{U}(t, 0)$ is a formal way of saying that the propagator $\hat{U}$ drives the system from time 0 to time t. An explicit operational form of $\hat{U}$ will be given below; for now, accept it as that quantity causing the system to proceed in time, with physical origin in the time-dependent sequence of rf pulses, and the internal interactions as affected by these pulses. The result,

$$i\frac{d\hat{\tilde{\rho}}}{dt} = [\hat{\tilde{\mathcal{H}}}_{\mathrm{int}}, \hat{\tilde{\rho}}] \quad \text{(energy in units of frequency)} \tag{10}$$

is the equation of motion in the frame of the rf field. Now, in the same spirit with which we used the interaction $\hat{\mathcal{H}}$ to transform itself out of the equation of motion [this interaction does not appear in equation (10)] we use the interaction $\hat{\mathcal{H}}_{\mathrm{int}}$ to make another transformation which transforms $\hat{\mathcal{H}}_{\mathrm{int}}$ out of the equation:

$$\hat{\tilde{\rho}} = \hat{U}_{\mathrm{int}}(t,0)\hat{\tilde{\tilde{\rho}}}\hat{U}_{\mathrm{int}}^{-1}(t,0) \tag{11}$$

$$i\frac{d\hat{U}_{\mathrm{int}}}{dt} = \hat{\tilde{\mathcal{H}}}_{\mathrm{int}}\hat{U}_{\mathrm{int}} \tag{12}$$

$$\hat{U}_{\mathrm{int}}(0,0) = 1 \tag{13}$$

Thus $\hat{\rho}$ is replaced by $\hat{\tilde{\rho}}$, $\hat{\tilde{\rho}}$ is replaced by $\hat{\tilde{\tilde{\rho}}}$, $\hat{U}_{\mathrm{rf}}$ is replaced by $\hat{U}_{\mathrm{int}}$, etc. As shown by equation (14), the system in this frame is static; that is,

$$i\frac{d\hat{\tilde{\tilde{\rho}}}}{dt} = [0, \hat{\tilde{\tilde{\rho}}}] = 0 \tag{14}$$

We formally identify this static system with the system at time zero; $\hat{\tilde{\tilde{\rho}}}$ then becomes identical to $\hat{\rho}(0)$. In this perturbation picture, with $\hat{\tilde{\tilde{\mathcal{H}}}}_{\mathrm{int}}$ being a perturbation on $\hat{\mathcal{H}}_{\mathrm{rf}}$, the motion of the system, is then described by

$$\hat{\rho}(t) = \hat{U}_{\mathrm{rf}}(t,0)\hat{U}_{\mathrm{int}}(t,0)\hat{\rho}(0)\hat{U}_{\mathrm{int}}^{-1}(t,0)\hat{U}_{\mathrm{rf}}^{-1}(t,0) \tag{15}$$

4 ECHOES AND THE AVERAGE HAMILTONIAN

Before discussing the operational forms of the propagators $\hat{U}$ explicitly, let us examine equation (15) more closely. It is clear that if both $\hat{U}_{\mathrm{rf}}(t_c,0)$ and $\hat{U}_{\mathrm{int}}(t_c,0)$ are unity at some particular time t_c, then at this special time it appears that the system has simply not changed, i.e. equations (4) and (15) at time t_c tell us that the value of any observable at this time is the value of that observable's operator at time zero; at time t_c, $\hat{\rho}(t_c) = \hat{\rho}(0)$. There is therefore an enormous simplicity in the behavior of the system which the experimenter may accomplish with proper arrangements of rf pulses, since both $\hat{U}_{\mathrm{rf}}$ and $\hat{U}_{\mathrm{int}}$ depend upon $\hat{\mathcal{H}}_{\mathrm{rf}}$—the rf pulses which we supply! The fields (5 MT) generated by the rf pulses are much larger than the 'internal fields' due to dipolar and shielding interactions (<0.3 MT). Therefore, as long as $\hat{U}_{\mathrm{rf}}$ operates for times that are short compared with times in which $\hat{U}_{\mathrm{int}}$ affects the system, its motion is predominantly controlled by $\hat{U}_{\mathrm{rf}}$. Then if the sequence of rf pulses generating $\hat{U}_{\mathrm{rf}}(t_c, 0)$ returns the system to its initial state, $\hat{U}_{\mathrm{rf}}(t_c, 0)$ is formally equal to unity, a result inferred from physics rather than mathematics. Examples of such pulse sequences are easily imagined if the physics is kept clearly in mind. For example, the sequence (τ, 180°_x, 2τ, 180°_x, τ) results in a rotation by 2π about the x axis, leaving the system invariant at cycle time t_c equal to time 4τ. The sequence (τ, 90°_y, τ, 90°_x, 2τ, 90°_{-x}, τ, 90°_{-y}, τ) has phase alternated pairs of pulses which cancel against each other (the y pulse cancels against the $-y$ pulse, and similarly for x) and leaves the system invariant at a cycle time t_c of 6τ. This phase alternated sequence (for each x, a $-x$, and for each y a $-y$) is a variant of the solid echo sequence[17–19] which became famous as the WAHUHA (after John Waugh, Lee Huber, and Ulrich Haeberlen) sequence. Such sequences are said to be cyclic. If these groups of pulses are repeated periodically, they are both cyclic and periodic (see ***Average Hamiltonian Theory***). As long as $\hat{U}_{\mathrm{rf}}(nt_c, 0)$ is the dominant propagator, in the 'windows' between these groups of pulses, the system will behave as if it is not moving in time. The

situation is quite analogous to the observation of the spinning football shaped object by the blinking football fan. If the blinking is done in concert with the rotation at such a time that the object is viewed head-on, i.e. when it appears as a thin line, then only a thin line will be seen at all times *of observation*.

A closer look at equation (15), however, clearly indicates that as time progresses, $\hat{U}_{\text{int}}(nt_c,0)$ begins to affect the motion of the system. Stroboscopic observation as time progresses, in the windows nt_c, will reveal some motion due to $\hat{U}_{\text{int}}(nt_c, 0)$. Now this propagator, $\hat{U}_{\text{int}}(nt_c, 0)$, is determined by $\hat{\tilde{\mathcal{H}}}_{\text{int}}$. The interaction $\hat{\tilde{\mathcal{H}}}_{\text{int}}$ is the sum of $\hat{\tilde{\mathcal{H}}}_{\text{D}}$ and $\hat{\tilde{\mathcal{H}}}_{\text{CS}}$, the dipolar and shielding interactions as manipulated by the rf pulses. If somehow the dipolar interaction (but not the shielding interaction) can be selectively set in motion so that its time average at times nt_c is zero, the remaining information in the windows of the stroboscopic observation will be the shielding. This is exactly what multiple pulse homonuclear decoupling attempts to accomplish. To see how this works, one needs an explicitly operational form for the internal propagator $\hat{U}_{\text{int}}(nt_c, 0)$. The form is illustrated by the spin echo sequence $(\tau, 180^\circ_y, \tau, 180^\circ_y, \tau)$. In the spin echo sequence, we take the internal Hamiltonian to represent any interaction proportional to the operator $\hat{I}_z$: e.g. shielding, resonance offset, static field inhomogeneities, and scalar couplings to unlike nuclei. Homonuclear dipolar coupling, as shown below, is not proportional to $\hat{I}_z$.

When we manipulate $\hat{\tilde{\mathcal{H}}}_{\text{int}}$ by cyclic and periodic sequences of rf pulses (meaning $\hat{U}_{\text{rf}}(t_c, 0)$ is unity) the form of the propagator $\hat{U}_{\text{int}}$ becomes an exponential,[20] with the leading term in the result, stroboscopically observed at cycle times nt_c, given by

$$\begin{aligned}\hat{\rho}(nt_c) &= \hat{U}_{\text{int}}(t_c, 0)\hat{\rho}(0)\hat{U}^{-1}_{\text{int}}(t_c, 0) \\ &= \exp\,(-\mathrm{i}\hat{\bar{\mathcal{H}}}^{(0)}_{\text{int}} nt_c)\ \hat{\rho}(0) \exp\,(\hat{\bar{\mathcal{H}}}^{(0)}_{\text{int}} nt_c)\end{aligned} \tag{16}$$

Here, $\hat{\bar{\mathcal{H}}}^{(0)}_{\text{int}}$, which is equal to the integral over a cycle of the internal Hamiltonian as manipulated in time by the rf pulses,

$$\hat{\bar{\mathcal{H}}}^{(0)}_{\text{int}} = \frac{1}{t_c}\int_0^{t_c} \hat{\tilde{\mathcal{H}}}_{\text{int}}\,\mathrm{d}t \tag{17}$$

may be interpreted as the time average of this manipulated internal Hamiltonian. The manner of manipulation of $\hat{\mathcal{H}}_{\text{int}}$ is given by:

$$\hat{\tilde{\mathcal{H}}}_{\text{int}}(t) = \hat{U}^{-1}_{\text{rf}}(t, 0)\hat{\mathcal{H}}_{\text{int}}\hat{U}_{\text{rf}}(t, 0) \tag{18}$$

$\hat{\tilde{\mathcal{H}}}_{\text{int}}(t)$ is the instantaneous value of the internal Hamiltonian as determined by the rf pulses. $\hat{U}_{\text{rf}}(t, 0)$ is the propagation operator due to the rf pulses from time zero to time t. For n time intervals $\Delta1$, followed by $\Delta2$, ... , followed by Δn, $\hat{U}_{\text{rf}}$ is clearly the propagator during interval $\Delta1$, followed by the propagator over $\Delta2$, ... , as shown by

$$\hat{U}_{\text{rf}}(t, 0) = \hat{U}_{\text{rf}}(\Delta n)\cdots\hat{U}_{\text{rf}}(\Delta1) \tag{19}$$

The inverse of this product of matrix operators is given by

$$\hat{U}^{-1}_{\text{rf}}(t, 0) = \hat{U}^{-1}_{\text{rf}}(\Delta1)\cdots\hat{U}^{-1}_{\text{rf}}(\Delta n) \tag{20}$$

The physical meaning of the exponentials in equation (16) can always be expressed as a product of rotations in spin space acting on components of angular momentum operators. For example, consider the rf pulse sequence with perfect delta function pulses $(\tau, 180^\circ_y, 2\tau, 180^\circ_y, \delta)$ shown in Figure 4. This sequence is used to produce $\hat{\mathcal{H}}_{\text{rf}}$, and thus $\hat{U}_{\text{rf}}$, equal to $\exp\,(-i\int\hat{\mathcal{H}}_{\text{rf}}\,\mathrm{d}t)$, as indicated in Figure 4.

At times $0 < t < \tau$, when the rf Hamiltonian is zero, $\hat{U}_{\text{rf}}(t, 0)$ takes the form $\mathrm{e}^0 = 1$, and in this time interval the value of $\hat{I}_z$ as manipulated by the rf pulse sequence in Figure 4 is given by equation (18). We may physically identify $\hat{U}_{\text{int}}(0 < t < \tau)$ as given in equation (18) with a rotation $\hat{R}$, of unity, performed on $\hat{I}_z$, symbolized by $\hat{R}\hat{I}_z = 1\hat{I}_z$. At time $t = \tau$, the rf Hamiltonian corresponding to the delta function pulse becomes an infinitely fast 180° rotation about the y axis. $\hat{U}_{\text{rf}}(t = \tau) = \exp\,(\mathrm{i}\pi\hat{I}_y)$, and the physical result is a 180°_y rotation $\hat{R}_{180y}$, which sends the operator $\hat{I}_z$ into the operator $-\hat{I}_z$: $\hat{R}_{180y}\hat{I}_z = -\hat{I}_z$. For $\tau < t < 2\tau$ the rf again is zero, and $\hat{U}_{\text{rf}}$ is unity. At $t = 3\tau$, another 180°_y takes place. Under this sequence, therefore, with the spin portion of $\hat{\mathcal{H}}_{\text{int}}$ being proportional to $\hat{I}_z$, and keeping in mind the time ordering dictated by equations (19) and (20), we find the sequence of values of $\hat{I}_z$, the value of $\hat{I}_z$ in the frame of the rf pulses as indicated in Figure 4, and illustrated by the equations

$$0 < t < \tau: \quad \hat{I}_z = \mathrm{e}^{-\mathrm{i}0}\hat{I}_z\mathrm{e}^{\mathrm{i}0} = 1\hat{I}_z1 = 1\hat{I}_z = \hat{I}_z \tag{21a}$$

$$t = \tau: \quad \hat{I}_z = 1\hat{R}_{180y}\hat{I}_z = -\hat{I}_z \tag{21b}$$

$$\tau < t < 2\tau: \quad \hat{I}_z = 1\hat{R}_{180y}1\hat{I}_z = -\hat{I}_z \tag{21c}$$

$$t = 2\tau: \quad \hat{I}_z = 1\hat{R}_{180y}1\hat{R}_{180-y}\hat{I}_z = \hat{I}_z \tag{21d}$$

$$2\tau < t < 3\tau: \quad \hat{I}_z = 1\hat{R}_{180y}1\hat{R}_{180-y}1\hat{I}_z = \hat{I}_z \tag{21e}$$

The familiar result is that at periodic cycle times $4n\tau$, under the spin echo sequence $(\tau, 180^\circ_y, 2\tau, 180^\circ_y, \tau)n$, chemical shifts, and field inhomogeneities, with spin operators $\hat{I}_{zk}$, vanish (but other interactions, such as homonuclear dipolar coupling, do not). This is to say that at cycle times $4n\tau$, with the internal Hamiltonian being proportional to $\hat{I}_z$, $\hat{\bar{\mathcal{H}}}^{(0)}_{\text{int}}$ is zero, as explicitly shown by

$$\hat{\bar{\mathcal{H}}}^{(0)}_{\text{int}}(4n\tau) \approx \frac{1}{4\tau}\int_0^{4\tau}\hat{\mathcal{H}}_{\text{int}}\,\mathrm{d}t = \frac{1}{4\tau}\omega_{\text{CS}}[\hat{I}_z\tau + (-\hat{I}_z)\tau] = 0 \tag{22}$$

Here, ω_{CS} is a product of a constant (γB_{eff}) and the portion of the chemical shift Hamiltonian which is a function of the real space angular variables θ and ϕ considered explicitly earlier when talking about magic angle spinning. We may think of observation at periodic cycle times $t = 4n\tau = nt_c$ as observation in the frame of $\hat{\rho}$.

With the basic ideas outlined above, one may now understand how averaging is accomplished for a more complicated internal interaction than one simply proportional to $\hat{I}_z$. One creates periodic groups of cyclic sequences of

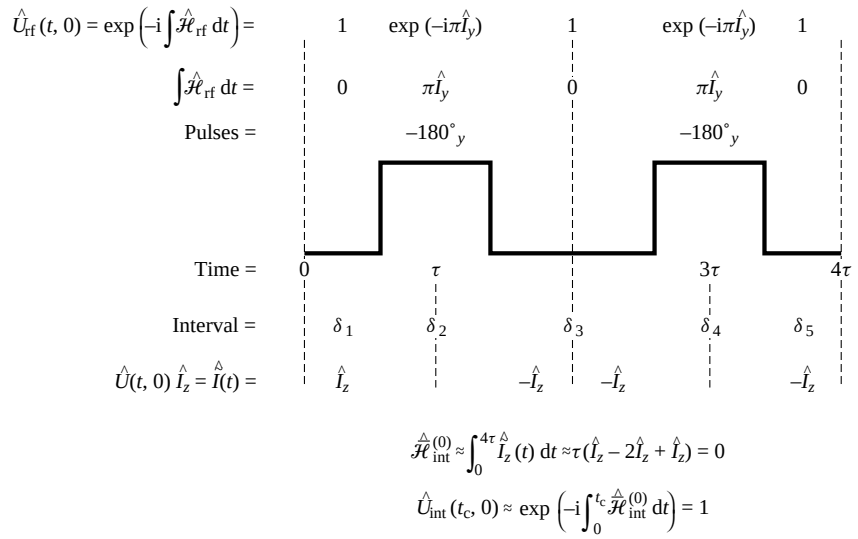

Figure 4 Spin echo sequence (τ, 180°_y, 2τ, 180°_y, τ). Cycle time $t_c = 4\tau$. Also indicated are values of $\hat{\mathcal{H}}_{rf}(t)$, $\hat{U}_{rf}(t, 0)$, $\hat{I}_z(t) = \hat{U}_{rf}{}^{-1}(t, 0)\,\hat{I}_z\hat{U}_{rf}(t, 0)$

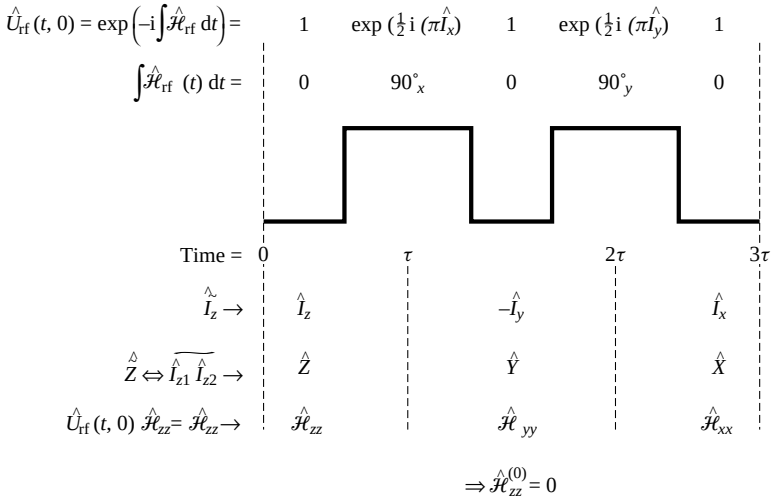

Figure 5 Dipolar echo sequence (τ, 90°_x, τ, 90°_y, τ). Cycle time $t_c = 3\tau$. Also indicated are the values of $\hat{\mathcal{H}}_{rf}(t, 0)$, $\hat{U}_{rf}(t, 0)$, $\hat{I}_z(t)$, $\hat{I}_{z1}\hat{I}_{z2}(t)$, and $\hat{\boldsymbol{I}}_1\cdot\hat{\boldsymbol{I}}_2(t)$

pulses, such that the propagator due to the rf Hamiltonian $\hat{U}_{rf}(nt_c, 0)$ is unity, and such that the internal Hamiltonian in question $\hat{\mathcal{H}}_{int}$ becomes time dependent, i.e. becomes $\hat{\mathcal{H}}_{int}(t)$, and arranges for its time average over a cycle, $(1/t_c)\oint dt\,\hat{\mathcal{H}}_{int}(t)$, to be zero. The resulting modulated echo signal in the time domain, when Fourier transformed, yields a spectrum which reflects all other internal Hamiltonians not averaged to zero by the rf pulses.

5 CRAMPS

Applied to the major broadening interaction in proton or in fluorine containing systems, where ^{1}H or ^{19}F is the only magnetically abundant spin present, the internal interaction between two protons due to dipolar coupling is given by

$$\hat{\mathcal{H}}_{DII} = \omega_D(\theta)(\hat{\boldsymbol{I}}_1 \cdot \hat{\boldsymbol{I}}_2 - 3\hat{I}_{z1}\hat{I}_{z2}) \tag{23}$$

$\omega_D(\theta)$ is the product of a constant and the real space variable θ, the angle between the internuclear vector defining the orientation of the dipole with respect to the external static field. The form need not concern us at this point, except to mention that it must be time-independent. The total dipolar interaction is the sum over all two-body interactions.

Let us denote this two-body interaction by $\hat{\mathcal{H}}_{zz}$, relating to the product of the z components of the two spins in equation (23). Since $\hat{\boldsymbol{I}}_1\cdot\hat{\boldsymbol{I}}_2$ is a scalar product invariant under rotation, pulse sequences will not affect this part of $\hat{\mathcal{H}}_{zz}$. As shown in Figure 5, a 90°_x pulse at time τ rotates the operator $\hat{I}_z$ into the operator $-\hat{I}_y$, via equation (18).

After this 90°_x pulse, therefore, $\hat{\mathcal{H}}_{zz}$ is transformed into $\hat{\mathcal{H}}_{yy}$. A further 90°_y pulse at time 2τ will be seen, using equations (18)–(20), to result in $\hat{\mathcal{H}}_{zz}$ being transformed into $\hat{\mathcal{H}}_{xx}$. Then at a time $t = 3\tau$ the average homonuclear dipolar Hamiltonian [equation (17)] becomes equal to $(\frac{1}{3}\tau)(\hat{\mathcal{H}}_{xx} + \hat{\mathcal{H}}_{yy} + \hat{\mathcal{H}}_{zz})$, which is zero, i.e. the sum $(\hat{\boldsymbol{I}}_1 \cdot \hat{\boldsymbol{I}}_2 - 3\hat{I}_{z1}\hat{I}_{z2}) + (\hat{\boldsymbol{I}}_1 \cdot \hat{\boldsymbol{I}}_2 - 3\hat{I}_{x1}\hat{I}_{x2}) + (\hat{\boldsymbol{I}}_1 \cdot \hat{\boldsymbol{I}}_2 - 3\hat{I}_{y1}\hat{I}_{y2})$ is equal to $3\hat{\boldsymbol{I}}_1 \cdot \hat{\boldsymbol{I}}_2 - 3\hat{\boldsymbol{I}}_1 \cdot \hat{\boldsymbol{I}}_2$. This basic dipolar echo sequence (τ, 90°_x, τ, 90°_y, τ) is not cyclic, since the system is not returned to its initial value at time 3τ. However, as explained above, the phase alternated sequence in which the 90°_x pulse is followed by a 90°_y pulse, then by a 90°_{-y} pulse, and then by a 90°_x pulse is cyclic, and incorporates two dipolar echo experiments. This is the WAHUHA four-pulse sequence. It was first used with stroboscopic observation, as indicated in Figure 6 (see below) to demonstrate that cyclic periodic sequences of rf pulses could lead to averaging of dipolar interactions with resultant detection of much smaller shielding anisotropies. Improved sequences have been developed to remove the loss of resolution associated with experimental artifacts. Two of the best known are the MREV-8 pulse sequence[21] and the BR-24 pulse sequence.[22]

An example of the increase in length of time decay achieved under the BR-24 pulse sequence is shown in Figure 6. Here, the time decay of the magnetization of protons in high density linear polyethylene under the BR-24 sequence, with observation in the first ten windows of the multiple pulse experiment [Figure 6(a)] and a single pulse excitation [Figure 6(b)] are compared. Since the spectral linewidth is proportional to the inverse of the length of the time decay, we see that the resolution under the homonuclear decoupling has been enormously enhanced, the time decay under the BR-24 sequence lasting more than 2 μs, and the decay under a single pulse being over in less than 20 ms. Figure 6(c) shows the Fourier transform of the time decay under the BR-24 sequence, illustrating the shielding anisotropy of protons in high density linear crystalline polyethylene. Combined rotation (MAS) and multiple pulse spectroscopy (CRAMPS) would then collapse the shielding powder pattern to its isotropic value, as shown for adipic acid in Figure 1. Thus combined rotation and multiple pulse spectroscopy, based on the above described ideas, when improved a bit by more complicated pulse sequences to remove loss of resolution due to experimental artifacts, e.g. the the MREV-8 and the BR-24 sequences, is the basic CRAMPS technique today.

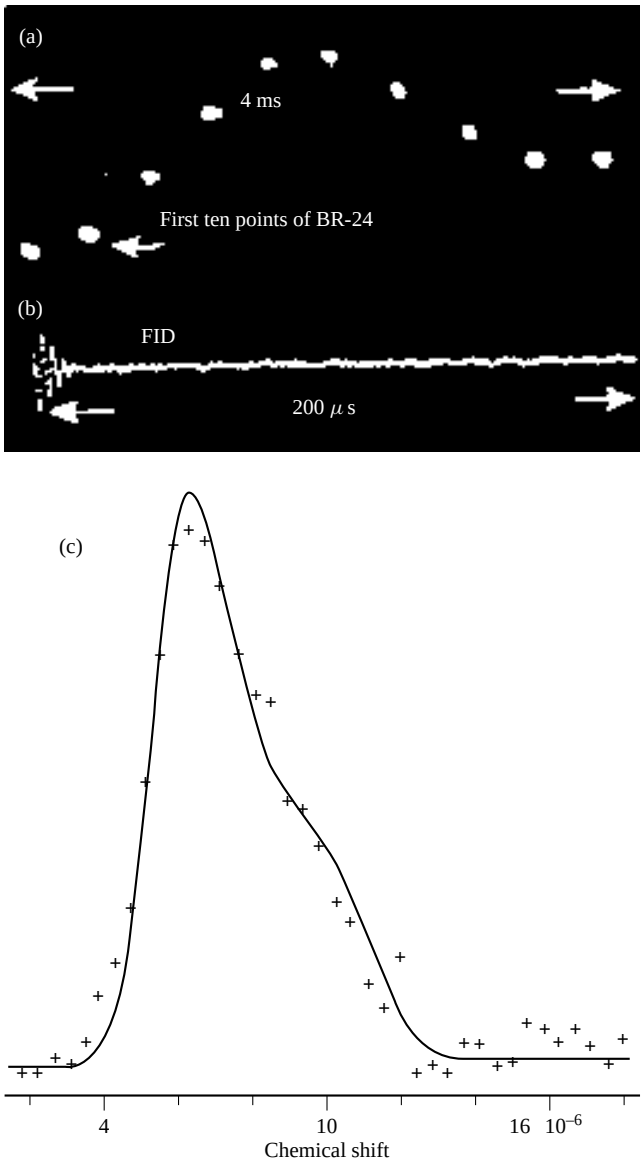

Figure 6 (a) The first ten points of the stroboscopically observed signal of protons in high density linear polyethylene under the BR-24 sequence. (b) FID under a single pulse excitation. Note that the decay under the single pulse excitation is over in roughly 20 μs, whereas the decay under the BR-24 lasts longer than 20 ms. Under MAS, the powder pattern, (c) would collapse to a single line, the isotropic value, obtained in the full CRAMPS experiment, as shown for adipic acid in Figure 1

6 CAVEATS

In the above some implicit assumptions have been made which I will make specific at this point.

1. There exist infinitely fast rf pulses which are '90°' pulses.
2. These rf pulses are in fact much larger than any effects of internal interactions.
3. It is possible to place these pulses sufficiently close together such that the times over which they operate cyclically to bring the system back to its initial state is indeed short compared with dephasing times due to internal interactions.
4. It is possible to observe stroboscopically in the windows between these high-powered pulses.
5. Rotation of the sample does not interfere with the averaging due to spin rotations by the rf pulses.
6. The selective averaging of major broadening interactions (dipolar and shielding anisotropy) does not affect the desired interaction—the isotropic chemical shift.

Each of these assumptions is violated in real experiments to a certain extent:

1. There is no infinitely fast pulse. All rf pulses have a finite width, and have transient phase impurities (the 'phase glitch') associated with them, e.g. a 90°_x pulse will have some transient y phase during the turn-on and turn-off periods. In this multiple pulse experiment with stroboscopic observation of the magnetization, errors in pulse flip angle

and pulse phase rapidly accumulate. For example, a 1° error in flip angle, repeated 1024 times, could result in a 90° pulse becoming a 1114° pulse. To achieve 90° pulses which are sufficiently uniform over the entire sample for this experiment, it is necessary to have an rf coil which is long compared with its diameter. In addition, pulses of a given phase always contain transient phase effects which must be cancelled by use of symmetry adapted pulse sequences. These impurities may be treated theoretically as additional internal interactions which may then be averaged by proper selection of rf pulse sequences.[23]

2. Radiofrequency fields of 5 mT are not infinitely large compared with dipolar fields of ca. 0.3 mT, but are indeed good enough, as shown in Figure 1.
3. With dipolar interactions causing line broadening of 20 kHz, it is necessary that the time over which the dipolar echo sequence operates is short compared with 50 ms.
4. Achieving the 3τ cycle time of the dipolar echo experiment, which is short compared with 50 ms, with a 500 W amplifier, and a receiver recovery time short enough to allow stroboscopic observation of the motion of the system in the observation window lasting 2τ s, is a result of careful engineering of solid state spectrometers; this facility is not generally available in spectrometers used for liquid state NMR, and in some commercially sold spectrometers for high-resolution solid state NMR.
5. Physical rotation of the sample can indeed interfere with the selective averaging performed by the multiple pulse sequences.[24] This interference can produce an extra peak in CRAMPS spectra which is easily recognizable. There are improved pulse sequences being developed which will help reduce this artifact.[25]
6. The multiple pulse sequences which severely attenuate dipolar broadening also generally affect the isotropic shielding by scaling shielding differences. In general, the scaling factor depends upon the sequence used, and the length of the rf pulses compared with the 3τ cycle time of the dipolar echo sequence. Under the MREV-8, sequence for example, the scaling factor is roughly $\frac{1}{2}$, so that a chemical shift difference of 10 ppm, measured at a spectrometer frequency of 100 MHz for ^{1}H, does not translate into 1000 Hz in the observed spectrum, but into 500 Hz. Thus resolution is lost. The scaling factor may be easily determined experimentally.[24]

7 RELATED ARTICLES

Average Hamiltonian Theory; Chemical Shift Tensors in Single Crystals; Echoes in Solids; Internal Spin Interactions and Rotations in Solids; Magic Angle Spinning; Rotating Frame Spin–Lattice Relaxation Off-Resonance; Rotating Solids; Rudimentary NMR: The Classical Picture; Shielding Tensor Calculations; Sideband Analysis in Magic Angle Spinning NMR of Solids; Two-Dimensional Powder Correlation Methods

8 REFERENCES

1. B. C. Gerstein, R. G. Pembleton, R. C. Wilson, and L. M. Ryan, *J. Chem. Phys.*, 1977, **66**, 361.
2. F. Bloch, W. W. Hansen, and M. Packard, *Phys. Rev.*, 1946, **70**, 474.
3. E. M. Purcell, H. C. Torrey, and R. V. Pound, *Phys. Rev.*, 1946, **69**, 37.
4. E. R. Andrew and R. G. Eades, *Proc. R. Soc. Lond., Ser. A*, 1953, **216**, 398.
5. I. Lowe, *Phys. Rev. Lett.*, 1959, **2**, 285.
6. I. J. Lowe, *Bull. Am. Phys. Soc.*, 1957, **2**, 344.
7. P. Mansfield, *Phys. Rev.*, 1965, **137**, A961.
8. J. S. Waugh, L. M. Huber, and U. Haeberlen, *Phys. Rev. Lett.*, 1968, **20**, 180.
9. S. F. Dec, C. E. Bronniman, R. A. Wind, and G. E. Maciel, *J. Magn. Reson.*, 1989, **82**, 454.
10. S. F. Dec and G. Maciel, *J. Magn. Reson.*, 1990, **87**, 153.
11. S. F. Dec, C. E. Bronniman, R. A. Wind, and G. E. Maciel, *J. Magn. Reson.*, 1989, **82**, 454.
12. T. C. Farrar *Introduction to Pulse NMR Spectroscopy*, Farragut, Madison, WI, 1989.
13. B. C. Gerstein and C. R. Dybowski, *Transient Techniques in NMR of Solids; An Introduction to the Theory and Practice*, Academic, Orlando, FL. 1985.
14. M. Mehring, *Principles of High Resolution NMR in Solids*, 2nd edn, Springer, Berlin, 1983.
15. U. Haeberlen, *High Resolution NMR in Solids; Selective Averaging*, Academic, New York, 1976.
16. R. R. Ernst, G. Bodenhausen, and A. Wokaun, *Principles of Nuclear Magnetic Resonance in One and Two Dimensions*, Clarendon, Oxford, 1987.
17. I. J. Lowe, *Bull. Am. Phys. Soc.*, 1957, **2**, 344.
18. P. Mansfield, *Phys. Rev.*, 1965, **137**, A961.
19. J. S. Waugh, L. M. Huber, and U. Haeberlen, *Phys. Rev. Lett.*, 1968, **20**, 180.
20. B. C. Gerstein and C. R. Dybowski, *Transient Techniques in NMR of Solids; An Introduction to the Theory and Practice*, Academic, Orlando, FL, 1985, Chap. 4
21. P. Mansfield, *Phil. Trans. R. Soc. Lond., Ser. A*, 1981, **299**, 479; W.-K. Rhim, D. D. Elleman, and R. W. Vaughan, *J. Chem. Phys.*, 1973, **58**, 1772.
22. D. Burum and W.-K. Rhim, *J. Chem. Phys.*, 1979, **71**, 944.
23. R. R. Ernst, G. Bodenhausen, and A. Wokaun, *Principles of Nuclear Magnetic Resonance in One and Two Dimensions*, Clarendon, Oxford, 1987, Chap. 5
24. B. C. Gerstein and C. R. Dybowski, *Transient Techniques in NMR of Solids; An Introduction to the Theory and Practice*, Academic, Orlando, FL, 1985, Chap. 5
25. J. S. Waugh, Personal communication, MIT, Cambridge, MA, May 1993.

Biographical Sketch

Bernard C. Gerstein. *b* 1932. B.S., 1953, Purdue, USA; Ph.D., 1960, Iowa State. Introduced to NMR by R.W. Vaughan. Faculty in Chemistry, Iowa State University, 1962–present. Approx. 150 publications. Research interests include the theory and practice of learning, and applications of solid state NMR to problems in the physics and chemistry of materials, fossil fuels, and heterogeneous catalysis.

Deuterium NMR in Solids

Lynne S. Batchelder

Cambridge Isotope Laboratories, Inc., Andover, MA, USA

1	Introduction	1
2	The Deuterium Quadrupolar Interaction and the Nuclear Spin Hamiltonian	1
3	Deuterium Powder Lineshapes: Static and Motionally Averaged	3
4	Anisotropic Deuterium Relaxation	5
5	Deuterium Spin Alignment and 2D Exchange Spectroscopy—The Study of Ultraslow Motions in Deuterated Solids	6
6	Other Deuterium NMR Experiments in the Solid State	7
7	Related Articles	8
8	References	8

1 INTRODUCTION

The study of ^{2}H NMR in the solid state offers one method to probe molecular structure and dynamics in solids. This article will describe the details of the method with particular emphasis on the nature of the quadrupolar coupling of the ^{2}H nucleus with a surrounding electric field gradient as well as the ^{2}H NMR spectra and relaxation rates that result from the interaction, particularly in the presence of molecular motion. A few examples will be given to clarify the theoretical explanations given in the text.

The principal utility of studying ^{2}H NMR in solids is the determination of amplitudes and frequencies of molecular motions in crystalline and amorphous solids. The motions are used to explain macroscopic properties of polymers as well as activation barriers in proteins and crystal packing in small molecules. By choosing appropriate instrumental parameters and experimental conditions, motional timescales spanning more than 10 orders of magnitude can be studied. In particular, 1D lineshape studies can reveal information about molecular reorientation with correlation times τ_c such that $10^{-11}\,\text{s} < \tau_c < 10^{-2}\,\text{s}$. Longitudinal relaxation of the ^{2}H nucleus undergoing reorientation is affected when $10^{-7}\,\text{s} < \tau_c < 10^{0}\,\text{s}$. The deuteron spin alignment experiment and the related 2D exchange experiment reveal information about molecular motions occurring on very long timescales, up to $\tau_c \sim 10^2\,\text{s}$. The combination of these techniques makes ^{2}H NMR in solids one of the most versatile methods for examining molecular motion.

While ^{2}H NMR studies of solids offer much promise in molecular dynamics studies, we must consider the following facts. Deuterium is 0.02% naturally abundant, making routine NMR detection really only possible in ^{2}H-enriched molecules. The NMR resonance frequency is 6.5 times lower than the ^{1}H frequency, which also affects the sensitivity. Deuterium has nuclear spin $I = 1$, and therefore possesses a quadrupole moment that defines the nonspherical distribution of nuclear charge. The quadrupole moment interacts with the surrounding electric field gradient, causing a perturbation of the magnetic energy levels of the ^{2}H nucleus. This quadrupolar interaction can broaden the ^{2}H resonance to $\sim$200 kHz, placing certain demands on the NMR instrumentation used to acquire the data. In spite of these difficulties, ^{2}H NMR is used routinely in the study of the molecular structure and dynamics of polymer systems, as well as of proteins, lipids, membranes, liquid crystals, and small molecules.

Fortunately, ^{2}H can be exchanged for ^{1}H in most systems of interest. Deuterated monomers are readily available for use in the synthesis of polymers. Many lipids are available as the perdeuterated analogs; some can be produced with ^{2}H incorporated at specific sites in the molecule. Incorporation of ^{2}H into organisms using deuterated nutrients and D_2O has become a routine method for obtaining deuterated proteins. The use of deuterated amino acids in growth media allows selective incorporation of deuterium as well.

The low magnetogyric ratio of ^{2}H is not a problem at field strengths of $\sim$4.7 T and above. The availability of NMR instrumentation that allows observation of undistorted spectra over a 200 kHz spectral width has been commercially available for many years. The three main requirements are:[1]

1. a transmitter to deliver high-power (1 kW) rf pulses of $\sim 2\,\mu$s to excite sufficiently wide bandwidths;
2. a wideband receiver with low distortion filters over the entire spectral width of 200 kHz; and
3. a high-sensitivity (high-Q) probe with a sufficiently wide bandwidth for the acquisition of distortion-free spectra.

All solid state deuterium NMR pulse sequences are echo sequences due to the wide frequency range of the spectrum. The acquisition of the echo avoids the problem of pulse breakthrough of the FID, leading to severe lineshape distortions. The simplest echo sequence is the two-pulse quadrupolar echo pulse sequence[2] to refocus the magnetization of a deuterium nucleus. This pulse sequence is shown in Figure 1(a).

Acquisition begins at the midpoint of the echo. One can modify this pulse sequence in various ways to measure ^{2}H longitudinal relaxation times in solids, deuteron spin alignment echoes and 2D exchange spectra. These modifications are discussed in subsequent sections of this article.

The interpretation of ^{2}H NMR spectra and relaxation measurements is simplified by the unique properties of the deuterium nucleus. Relaxation is predominantly quadrupolar and allows simplification in dynamic studies of anisotropic molecular motions. To a first approximation, the electronic charge distribution of the ^{2}H atom is spherically symmetric.[3] This results in a well-defined axially symmetric electric field gradient tensor with the principal axis along the C–^{2}H bond.

In the following sections we shall review the ^{2}H Hamiltonian with emphasis on the quadrupolar interaction and the powder lineshapes of polycrystalline samples which result from quadrupolar echo experiments. The methods used to interpret lineshapes, relaxation times and 2D intensity maps are discussed in subsequent sections, which are organized in relation to the correlation times of anisotropic motions which affect their behavior. A final section is included for completeness which discusses ^{2}H magic angle spinning in solids and multipulse quadrupolar echoes.

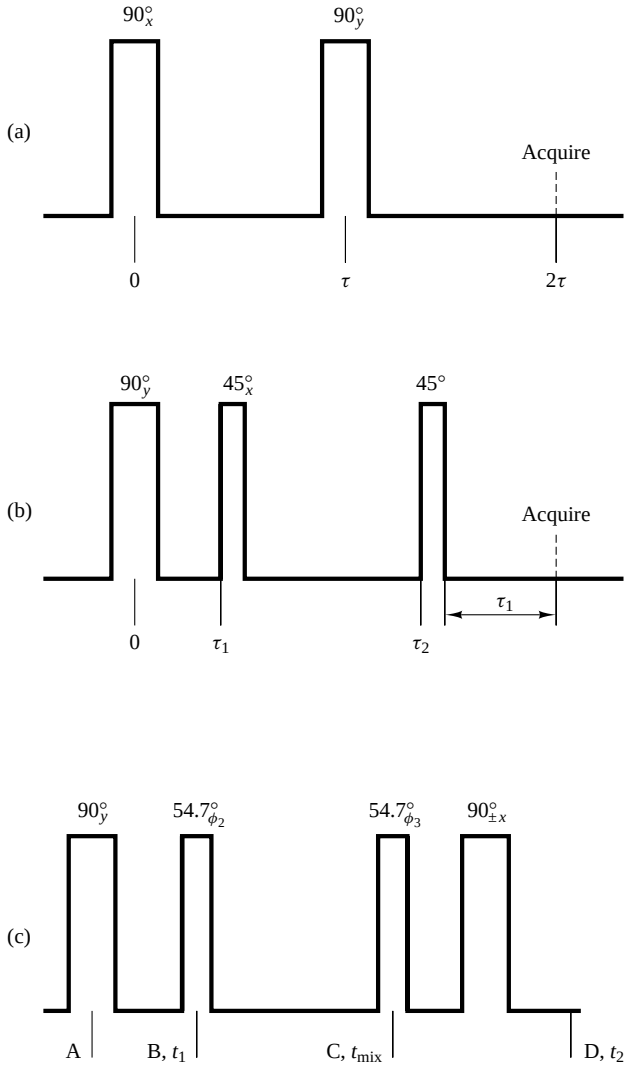

Figure 1 Pulse sequence diagrams for (a) quadrupolar echo pulse sequence[2], (b) ^{2}H spin alignment experiment[17] and (c) 2D exchange experiment.[18–24] In (c) the phase of the second and third pulses is set to y for measuring the stimulated echo and set to x for measuring the spin alignment echo (see text)

2 THE DEUTERIUM QUADRUPOLAR INTERACTION AND THE NUCLEAR SPIN HAMILTONIAN

In order for a nucleus to have a nonspherical charge distribution, its spin must be 1 or greater. Such nuclei, like deuterium with $I = 1$, possess an electric quadrupole moment. The quadrupole moment is a measure of the difference in nuclear charge distribution between the components parallel and perpendicular to z. As a nuclear magnetic moment interacts with an external magnetic field, the electric quadrupole moment interacts with an external electric field gradient. Electrical effects on the energy required to reorient the nucleus are limited to electric field gradients that interact with the ^{2}H quadrupole moment. Since the electron density of the deuterium atom is spherical to a first approximation, the electric field gradient at a deuterium nucleus is due entirely to the electric charge from proximal atoms.

The coupling energy, E, of a nonspherical ^{2}H nuclear charge distribution, $\rho_n(\boldsymbol{r}_n)$, with an electric field gradient arising from the surrounding electronic charges, $\rho_e(\boldsymbol{r}_e)$, can be described classically by[4]

$$E = \iint \frac{\rho_n(\boldsymbol{r}_n)\rho_e(\boldsymbol{r}_e)\,\mathrm{d}^3r_n\,\mathrm{d}^3r_e}{|\boldsymbol{r}_n - \boldsymbol{r}_e|} \tag{1}$$

By expanding $1/|\boldsymbol{r}_n - \boldsymbol{r}_e|$ in terms of the spherical harmonics and replacing the classical charge distributions by quantum mechanical operators[4] the interaction energy becomes

$$E = \langle\hat{\mathcal{H}}\rangle = \sum_{l,m} e\frac{4\pi}{2l+1}\left\{\sum_{i=1}^{N} e_i R_i^l Y_l^m(\Theta_i, \Phi_i)\right\} \times \left\{\sum_{i=1}^{n} r_i^{-(l+1)} Y_l^m(\theta_i, \phi_i)\right\} \tag{2}$$

where E is the expectation value of the Hamiltonian $\hat{\mathcal{H}}$; $-e$ is the charge of the electron; R_i, Θ_i and Φ_i are the nuclear coordinates; r_i, θ_i and ϕ_i are the electron coordinates; and $Y_1^m(\Theta_i, \Phi_i)$ and $Y_1^m(\theta_i, \phi_i)$ are the spherical harmonics of the nucleus and electrons, respectively.

Both the nuclear operator, $\{\Sigma_{i=1}^{N} e_i R_l^i Y_m^l(\Theta_i, \Phi_i)\}$ and the electronic operator, $\{\Sigma_{i=1}^{n} r_i^{-(l+1)} Y_l^m(\theta_i, \phi_i)\}$ are second-rank tensors.[4]

By application of the Wigner–Eckhardt theorem and substitution of the Clebsch–Gordan coefficients[5] for the nuclear operator, and by rewriting the components of the electronic tensor in the same way, the quadrupole Hamiltonian takes the following form:

$$\hat{\mathcal{H}}_Q = -\frac{1}{6}\sum_{\alpha}\sum_{\beta}\left\{\frac{\partial^2 V(x, y, z)}{\partial\alpha\,\partial\beta}\right\} Q_{\alpha\beta} \tag{3}$$

where $\alpha,\beta = x, y, z$,

$$\hat{Q}_{\alpha\beta} = eQ\left\{\tfrac{3}{2}[\hat{I}_\alpha\hat{I}_\beta + \hat{I}_\beta\hat{I}_\alpha] - \delta_{\alpha\beta}\hat{\boldsymbol{I}}^2\right\} \tag{4}$$

Q is the classical quadrupole moment, defined by

$$eQ = \int \rho_n(3z_n^2 - r_n^2)\,\mathrm{d}\tau_n \tag{5}$$

$\hat{\boldsymbol{I}}$ is the total deuterium angular momentum operator, and $V(x, y, z)$ is the potential produced at (x, y, z) by exterior charges.

The tensor $V_{\alpha\beta} = [\partial^2 V(x, y, z)/\partial\alpha\,\partial\beta]$ is symmetric in x, y, z and traceless ($\nabla^2 V = 0$). Therefore, it can be diagonalized by choosing a suitable set of principal axes,[6] and the deuterium quadrupolar Hamiltonian may be simplified to give

$$\hat{\mathcal{H}}_Q = \frac{eQ}{4}[V_{zz}(3\hat{I}_z^2 - \hat{\boldsymbol{I}}^2) + (V_{xx} - V_{yy})(\hat{I}_x^2 - \hat{I}_y^2)] \tag{6}$$

Only two parameters are necessary to characterize the gradients of the potential: the field gradient, eq, and the asymmetry parameter, η, defined as

$$eq = V_{zz} \tag{7}$$

$$\eta = \frac{|V_{xx} - V_{yy}|}{V_{zz}} \tag{8}$$

The asymmetry parameter measures the departure from cylindrical symmetry of the nuclear charge distribution. For axial symmetry ($V_{xx} = V_{yy}$)

$$\hat{\mathcal{H}}_{\mathrm{Q}} = \frac{eQ}{4}[3\hat{I}_z^2 - \hat{I}^2] \tag{9}$$

and the coupling energies are

$$E(^2\mathrm{H}) = \langle \hat{\mathcal{H}}_{\mathrm{Q}} \rangle = \frac{e^2qQ}{4}[3m^2 - 2] \tag{10}$$

where m is the eigenvalue of $\hat{I}_z$, $I(I + 1) = 2$ is the eigenvalue of $\hat{\boldsymbol{I}}^2$, and $e^2qQ = \chi h$ is called the quadrupole coupling constant.

The quadrupolar energy of a ^{2}H nucleus can be estimated if one assumes an electronic charge distribution for V. Referring to Gerstein and Dybowski,[7] the calculation of the quadrupolar energy for a deuterium nucleus is found from $E = eQ|V|/6$ where $e = 4.08 \times 10^{-20}$ esu, $Q = 2.8 \times 10^{-27}$ cm^2 and $|V| = 8.9 \times 10^{42}\,\mathrm{s^{-1}\,cm^{-2}\ esu^{-1}}$ for a ^{2}H nucleus next to an electron that is 1 Bohr radius away and opposite a positively charged ion also 1 Bohr radius away. The quadrupolar energy is calculated to be 3.1×10^5 Hz. The quadrupolar coupling constant is proportional to the energy.

For a ^{2}H nucleus in an applied magnetic field the general form of the Hamiltonian takes the form of the sum of two terms, the Zeeman term and the quadrupolar term:

$$\hbar\hat{\mathcal{H}}(^2\mathrm{H}) = \hbar\hat{\mathcal{H}}_{\mathrm{Z}} + \hbar\hat{\mathcal{H}}_{\mathrm{Q}} \tag{11}$$

The other energy terms which may affect the total Hamiltonian include the chemical shift, dipolar, and spin–spin coupling interactions. Although the magnitude of the ^{2}H quadrupolar moment is small (2.8×10^{-27} cm^2) compared with other quadrupolar nuclei, the quadrupolar energy term dominates in the solid state, and the other contributions can be neglected in the ^{2}H spin Hamiltonian. (In liquids this is not the case since isotropic reorientation causes the $\hat{\mathcal{H}}_{\mathrm{Q}}$ to vanish). However, the quadrupolar interaction is still dominated by the larger Zeeman interaction ($\hat{\mathcal{H}}_{\mathrm{Q}} \ll \hat{\mathcal{H}}_{\mathrm{Z}}$) at the field strengths typical for this experiment.

A ^{2}H nucleus, due to its nuclear spin $I = 1$, has three energy states denoted by $m = -1, 0, +1$. In an external magnetic field in the absence of perturbations the allowed transitions between the Zeeman energy levels $E_{m_{+1}}, E_{m_0}, E_{m_{-1}}$ lead to degenerate frequencies $\hbar\omega_+ = \hbar\omega_-$. The quadrupolar term $\hbar\hat{\mathcal{H}}_{\mathrm{Q}}$ is given by equation (6), which becomes, in the presence of a large external magnetic field,[6]

$$\hbar\hat{\mathcal{H}}_{\mathrm{Q}} = \frac{\chi h}{8}[(3\cos^2\theta - 1) + \eta\sin^2\theta\cos 2\phi] \tag{12}$$

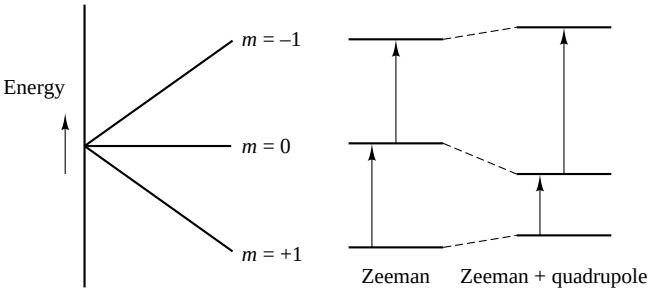

Figure 2 Energy level diagram for the ^{2}H nuclear magnetic energy levels showing the perturbation caused by the quadrupole moment

where θ and ϕ are the polar and azimuthal angles relating the principal axis system of the electric field gradient to the external field. For axial symmetry ($\eta = 0$), the total energies are described by

$$E_m = -\gamma\hbar H_0 m + \frac{\chi h}{8}(3\cos^2\theta - 1)[3m^2 - 2] \tag{13}$$

The effect of the anisotropic quadrupolar interaction is to remove the degeneracy of the Zeeman levels in the solid state. The two allowed transitions result in a pair of frequencies for each chemically inequivalent deuteron (Figure 2). The separation of the resonance frequencies depends on the angle between the external magnetic field and the z axis of the electric field gradient tensor. From equation (13), $\Delta\nu_q = 3\chi(3\cos^2\theta - 1)/4$.

Single crystal studies of deuterated molecules have been used to determine quadrupole coupling constants and relate them to molecular structure.[4] However, the dynamic information obtained from single crystals is limited, and therefore the study of ^{2}H NMR powder patterns of polycrystalline and amorphous solids has been more widely used.

3 DEUTERIUM POWDER LINESHAPES: STATIC AND MOTIONALLY AVERAGED

Solid state NMR spectra of single crystals provide valuable information but are impractical or very difficult to obtain for many systems. Additionally, these studies completely ignore amorphous solids. For these reasons it is often desirable to study polycrystalline and amorphous samples to understand their macroscopic behavior. The NMR spectra of spin-$\frac{1}{2}$ nuclei of most polycrystalline solids obtained with no line-narrowing techniques are generally broad, featureless resonances.[7] In contrast, the ^{2}H powder spectra of deuterated solids possess a wealth of information with characteristic lineshapes that contain information about molecular reorientation amplitudes and frequencies. In this section the equations which describe the resulting lineshapes will be developed.

In most cases the deuterium quadrupolar interaction of a carbon–deuterium bond is cylindrically symmetric, with its principal axis lying along the bond axis.[3] For this reason we shall concentrate on axially symmetric interactions to develop the equations for the powder lineshapes. We shall see that an axially symmetric lineshape for a static or slowly reorienting moiety can become axially asymmetric in the presence of more

rapid molecular motion. The reader is referred to Haeberlen[8] and Mehring[9] for equations describing axially asymmetric ($\eta > 0$) lineshapes.

3.1 Static or Slow Molecular Motion

A ^{2}H NMR spectrum of a single crystal will show two discrete resonances where the separation in frequency is related to the angle between the principal axis of the quadrupolar tensor and the laboratory frame. In a polycrystalline or amorphous solid, a random distribution of orientation of crystallites occurs where each orientation has equal probability. For deuterated molecules which do not experience reorientation other than librational motion or where the reorientation rate ($1/\tau_c$) of some well-defined motion is less than the quadrupolar coupling frequency, χ, the ^{2}H powder pattern is described by an axially symmetric tensor. For deuterium in solids one can describe the distribution by an equation relating the angular-dependent frequency to principal axis systems of the quadrupolar interaction and the laboratory frame:[8]

$$\omega_{zz} = \omega_{11}\cos^2\alpha\sin^2\beta + \omega_{22}\sin^2\alpha\sin^2\beta + \omega_{33}\cos^2\beta \quad (14)$$

For axial symmetry ($\omega_{11} = \omega_{22} = \omega$, $\omega_{33} = \omega$) equation (14) becomes

$$\omega_{zz} = (\omega_{||} - \omega_{\perp})\cos^2\beta + \omega_{\perp} \quad (15)$$

β is the angle between the z axis of the laboratory frame and the z axis of the quadrupolar tensor. $\omega_{\perp}$ is the NMR frequency of those crystallites where the C–D bond axis (and the z-axis of the electric field gradient) is perpendicular to the external magnetic field. Similarly, $\omega_{||}$ corresponds to the frequency where the C–D bond is parallel to the external field.

In a polycrystalline sample the resonance lineshape will be the sum of all the discrete lines and will account for all possible orientations. In order to determine the lineshape it is necessary to calculate the intensity of the resonance lines at each orientation. The intensity, $I(\omega)$, when integrated over a certain frequency interval, $\omega_a \ldots \omega_b$, is proportional to the probability of the orientation. $I(\omega)$ can be determined by calculating the area between the curves $\omega = \omega_a$ and $\omega = \omega_b$ on a sphere where the distribution of axially symmetric field gradient tensors is constant:[8,9]

$$\int_{\omega_a}^{\omega_b} I(\omega)\,\mathrm{d}\omega = c \iint_{\substack{\text{between curves}\\ \omega=\omega_a \text{ and } \omega=\omega_b}} \sin\theta\,\mathrm{d}\theta\,\mathrm{d}\phi \quad (16)$$

Using the normalized frequency $\omega = (\Delta/2)(3\cos^2\theta - 1)$, the intensity function becomes[9,10]

$$I(\omega) = \frac{1}{\sqrt{3}\Delta}\frac{1}{\sqrt{(2\omega/\Delta)+1}} \quad (17)$$

where $\Delta = \chi$ and ω is defined as $-\Delta/2 < \omega < \Delta$ for one deuterium transition and $-\Delta < \omega < \Delta/2$ for the second deuterium transition.

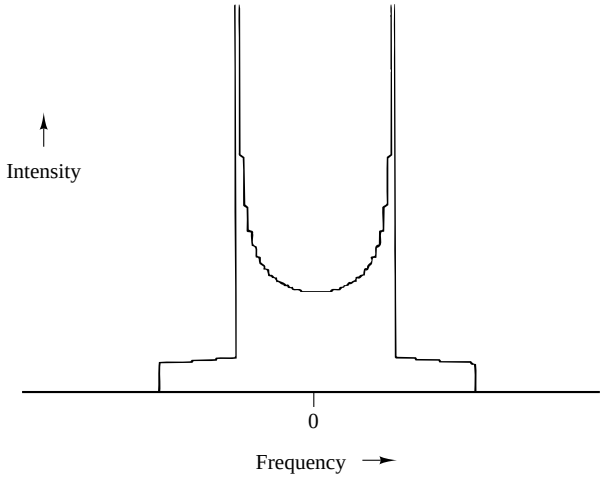

Figure 3 Theoretical ^{2}H powder lineshape for a deuteron surrounded by an axially symmetric field gradient. The powder pattern is the sum of the two resonances due to the two allowed transitions of the deuterium nucleus

Equation (17) describes the lineshape for one-half of the deuterium powder pattern. The other half is the mirror image of equation (17) with the center of symmetry at $\omega = 0$. The entire theoretical lineshape for a static C–D bond is plotted in Figure 3.

From Section 2, where the quadrupole interaction energy was calculated to be about 300 kHz, we see that the frequency difference of the perpendicular singularities of the powder pattern is related to the quadrupole coupling constant as $\Delta\omega = 3\pi\chi$. The observed ^{2}H powder pattern will be line broadened due to the lifetime broadening of the individual frequency components.

For axially asymmetric ($\eta > 0$) quadrupolar tensors, the lineshape becomes

$$f(\omega) = \frac{K(m)}{\pi\sqrt{(\omega-\omega_{11})}\sqrt{(\omega_{33}-\omega_{22})}} \quad \text{for } \omega_{33} > \omega \geq \omega_{22} \quad (18)$$

where $m = (\omega_{22} - \omega_{11})(\omega_{33} - \omega)/(\omega_{33} - \omega_{22})(\omega - \omega_{11})$ and

$$f(\omega) = \frac{K(m)}{\pi\sqrt{(\omega_{33}-\omega)}\sqrt{(\omega_{22}-\omega_{11})}} \quad \text{for } \omega_{22} > \omega \geq \omega_{11} \quad (19)$$

where $m = (\omega - \omega_{11})(\omega_{33} - \omega_{22})/(\omega_{33} - \omega)(\omega_{22} - \omega_{11})$.

In both cases, $K(m) = \int_0^{\pi/2} \mathrm{d}\phi[1 - m^2\sin^2\phi]^{-1/2}$.

The reader is referred to Haeberlen[8] and Spiess[10] for a more complete description and analysis of powder lineshapes, including that for an axially asymmetric ($\eta > 0$) quadrupolar tensor.

3.2 Motional Averaging of the ^{2}H Powder Lineshape

In solids, molecular reorientation can occur at rates as high as 10^{12} s^{-1} at temperatures between 100 and 500 K. Methyl groups are examples for molecular systems which undergo rapid reorientation. Relaxation rates and second moments are affected by the molecular motion, as are ^{2}H powder lineshapes.

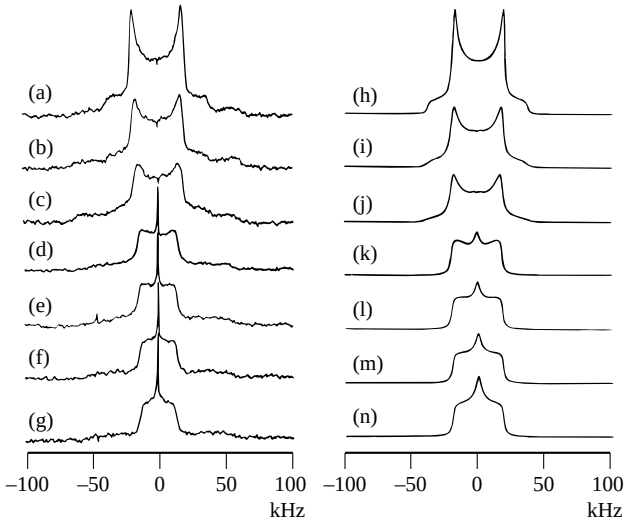

Figure 4 Experimental (a)–(g) and calculated (h)–(n) ^{2}H NMR spectra of leucine-d_{10}-labeled collagen.[10] The experimental spectra were acquired at the following temperatures: (a) −85 °C, (b) −43 °C, (c) −18 °C, (d) −6 °C, (e) +1 °C, (f) +15 °C and (g) +30 °C. The theoretical spectra were calculated using a two-site jump model with the following reorientation rates: (h) $<6 \times 10^3$ (rad s^{-1}), (i) 1.9×10^4 (rad s^{-1}), (j) 3.1×10^4 (rad s^{-1}), (k) 3.7×10^5 (rad s^{-1}), (1) 6.3×10^5 (rad s^{-1}), (m) 8.7×10^5 (rad s^{-1}), and (n) 1.2×10^6 (rad s^{-1})

If the molecule is undergoing reorientation on a timescale of the order of the quadrupolar interaction or faster, the observed frequencies will be averaged, and the resulting lineshape can be analyzed to determine the rate of motion for a given motional model. One can use this analysis to differentiate between fast diffusion and discrete jump motion.[11] This is illustrated in Figure 4 for a collagen sample that is labeled with deuterated leucine (leucine-d_{10}). At low temperatures the lineshape is the expected static axially symmetric powder pattern. As the temperature is increased, the lineshape becomes distorted due to two-site jump motion of the leucine side chain. The equation for the motionally averaged frequency depends on the model used to describe the motion. In fact, many models can be used to describe the same frequency dependence. If one has additional information about the possible motional models, then an estimate of the timescale of motions can be made and related back to the macroscopic properties of the sample.

The lineshape changes are related to the angle through which the C–D bond is reorienting by the relationship[8]

$$\Delta_n = \frac{3\chi}{4}(3\cos^2\gamma - 1) \tag{20}$$

where γ is the angle between the bond vector and the rotation axis.

Rapid reorientation occurs when $1/\tau_c \gg \chi$.

The most lineshape distortion takes place when the reorientation rate $(1/\tau_c)$ is of the order of the quadrupole coupling. In those cases the lineshape can be described by[8]

$$I(\omega) = \frac{\kappa(\omega_1 - \omega_2)^2}{4(\omega_1 - \omega)^2(\omega_2 - \omega)^2 + \kappa^2(\omega + \omega^2 - 2\omega)^2} \tag{21}$$

where κ is the reorientation rate expressed in radians per second. A complete discussion of the motionally averaged lineshape is given by Haeberlen.[8]

4 ANISOTROPIC DEUTERIUM RELAXATION

For deuterium, the spin relaxation is dominated by the quadrupolar interaction, and we need only consider this when interpreting relaxation times. As the lineshapes of deuterium powder spectra yield information about rates of motion for different reorientation models, the deuterium relaxation times also are a source of useful information about models of motion and correlation times. The observed relaxation times can be described by equations relating the reorientation to the spectral density functions involved.

4.1 Longitudinal Relaxation, T_1

The general expression for the spin–lattice relaxation of deuterium is[12]

$$\frac{1}{T_1} = \frac{\omega_Q^2}{3}[J_1^Q(\omega_1) + 4J_2^Q(2\omega_1)] \tag{22}$$

where $\omega_Q = 3\chi/4$.

The spectral density functions are described by[11]

$$J_m^Q(\omega) = 2\int_0^\infty C_m^Q(t)\,\cos(\omega t)\,\mathrm{d}t \tag{23}$$

where $C_m^Q(t)$ is the autocorrelation function that describes the orientation dependence of the quadrupolar tensor as

$$C_m^Q(t) = \langle R_{2m}^{Q*}(0) R_{2m}^Q(t)\rangle/(\rho_{20}^Q)^2 \tag{24}$$

where angular brackets $\langle\ \rangle$ denote the ensemble average, and $R_{2m}^Q(t)$ and ρ_{20}^Q are elements of the irreducible quadrupole tensor in the laboratory frame and principal axis system, respectively.

The correlation functions for various models of motion have been evaluated by Torchia and Szabo.[12] In particular, by measuring deuterium spin–lattice relaxation times of deuterated methyl groups one can differentiate between free diffusion and three-site jump models of a methyl group undergoing rapid reorientation. For three-site jump motion in the extreme narrowing limit

$$\frac{1}{T_1} = \frac{4\omega_Q^2\tau}{9}(1 + \cos^2\theta) \tag{25}$$

where θ is the angle between the molecular axis system and the external magnetic field. For free diffusion

$$\frac{1}{T_1} = \frac{8\omega_Q^2\tau_1}{27} \tag{26}$$

where there is no θ dependence. In other words, the T_1 shows an orientation dependence for discrete three-site jump

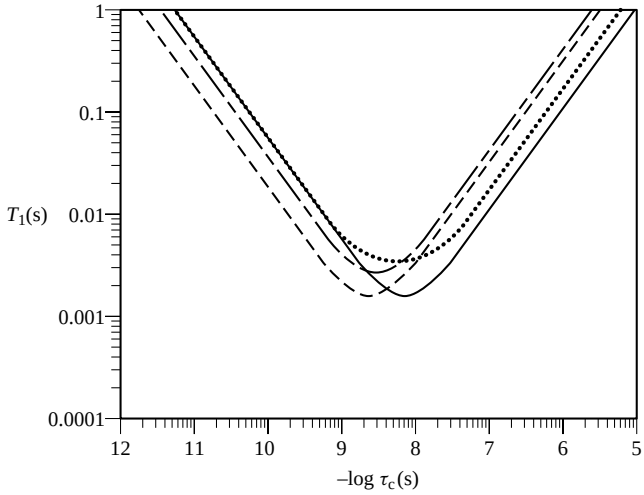

Figure 5 Theoretical behavior of ^{2}H T_1 at 38.45 MHz, plotted as a function of correlation time, $\omega_Q/2\pi$ = 128.2 s^{-1}. Three-site jumps: t_c = jump rate/3; $\theta = 0^\circ$ (- - -) and $\theta = 90^\circ$ (- — -). Free diffusion: $t_c = t_1$ = 1/diffusion constant; $\theta = 0^\circ$ (—) and $\theta = 90^\circ$ (. . .)

motion but no angular dependence results when the C–D bond undergoes free diffusion (Figure 5).

The equations describing the two orientation-dependent T_1s for two orientations (parallel and perpendicular) are listed below.[13]

For three-site jumps the equations are

$$\frac{1}{T_1} = \frac{8\omega_Q^2}{81}\left(\frac{\tau_c}{1+\omega^2\tau_c^2} + \frac{8\tau_c}{1+4\omega^2\tau_c^2}\right), \quad \theta = 0^\circ \qquad (27)$$

$$\frac{1}{T_1} = \frac{12\omega_Q^2}{81}\left(\frac{\tau_c}{1+\omega^2\tau_c^2} + \frac{2\tau_c}{1+4\omega^2\tau_c^2}\right), \quad \theta = 90^\circ \qquad (28)$$

Free diffusion is described by

$$\frac{1}{T_1} = \frac{8\omega_Q^2}{81}\left(\frac{\tau_1}{1+\omega^2\tau_1^2} + \frac{8\tau_2}{1+\omega^2\tau_2^2}\right), \quad \theta = 0^\circ \qquad (29)$$

$$\frac{1}{T_1} = \frac{4\omega_Q^2}{81}\left(\frac{\tau_1}{1+\omega^2\tau_1^2} + \frac{2\tau_2}{1+\omega^2\tau_2^2} + \frac{4\tau_1}{1+4\omega^2\tau_1^2} + \frac{2\tau_2}{1+4\omega^2\tau_2^2}\right), \theta = 90^\circ \qquad (30)$$

4.2 Transverse Relaxation–Anisotropic Deuterium, T_2

Where the reorientation rate of a deuterated molecule is of the order of the quadrupole coupling frequency, the deuterium lineshape is affected by the delays in the pulse sequence.[14] The effect includes intensity losses which are not uniform but frequency dependent across the spectrum. This is due to the anisotropic T_2 which is manifest when the exchange rate or reorientation rate is comparable to the size of the quadrupolar interaction. The effect becomes more pronounced as the delay between the pulses increases. The T_2 can be determined by measuring the echo amplitude as a function of t_1, the pulse sequence delay time. In the fast exchange limit and where $t_c \ll t_1$ the equation for the echo amplitude becomes[15]

$$K(2t_1) = \exp(-2t_1/T_2) \qquad (31)$$

When $t_c \sim \nu_q$, severe distortions and intensity losses result. Using this method one can also distinguish between motional models since the echo distortion varies with different reorientation. The equations dealing with this effect are given by Vega.[15] A very complete treatment of the intensity losses is described by Hirschinger et al.[16] and Shadt et al.[17]

5 DEUTERIUM SPIN ALIGNMENT AND 2D EXCHANGE SPECTROSCOPY—THE STUDY OF ULTRASLOW MOTIONS IN DEUTERATED SOLIDS

The two previous sections have dealt with the quadrupolar echo pulse sequence and its utility in determining and interpreting lineshapes for deuterated moieties undergoing medium to fast molecular motions. The lower limit to motions which can be studied using this technique is determined by $1/T_2$*. In deuterated polymers and other solids, this value is usually about a few hundred microseconds. In order to study ultraslow molecular motions which occur on a timescale slower than $1/T_2$*, one must choose one of two different experiments. The first technique is the deuterium spin alignment method,[18–20] which gives accurate information about motions which occur at rates up to a few hundred per second. This experiment uses a three-pulse sequence to generate a spin alignment echo. The echo amplitude decreases as the delay time between the first two pulses increases. The pulse sequence is shown in Figure 1(b). Deuterium spin alignment with three rf pulses leads to a stimulated echo, the amplitude of which is affected by molecular motion. The exchange rate can be determined from the decay of the echo height as a function of t_2. However, one cannot discriminate between motional models using this technique. The 2D exchange experiment (discussed below) allows one to make that observation.

A more recent technique was developed to give not only information about the rates of molecular motion but also the model for motion as well. This technique combines the spin alignment method with 2D NMR spectroscopy to yield a 2D exchange method for deuterium in the solid state.[21–25] The pulse sequence required for deuterium 2D exchange spectroscopy is a four-pulse sequence with a mixing period during which frequencies may be exchanged if the mixing time is greater than the correlation time of the motion. The reader is referred to other articles in the Encyclopedia as well as to Ernst et al.[26] for a complete detailed explanation of 2D NMR spectroscopy.

One can detect frequency changes accurately if the mixing time is greater than the evolution time and less than T_1.[22] This experiment allows the study of motions with rates from 10^{-3} to 100 s. If one has anisotropic coupling with axial symmetry

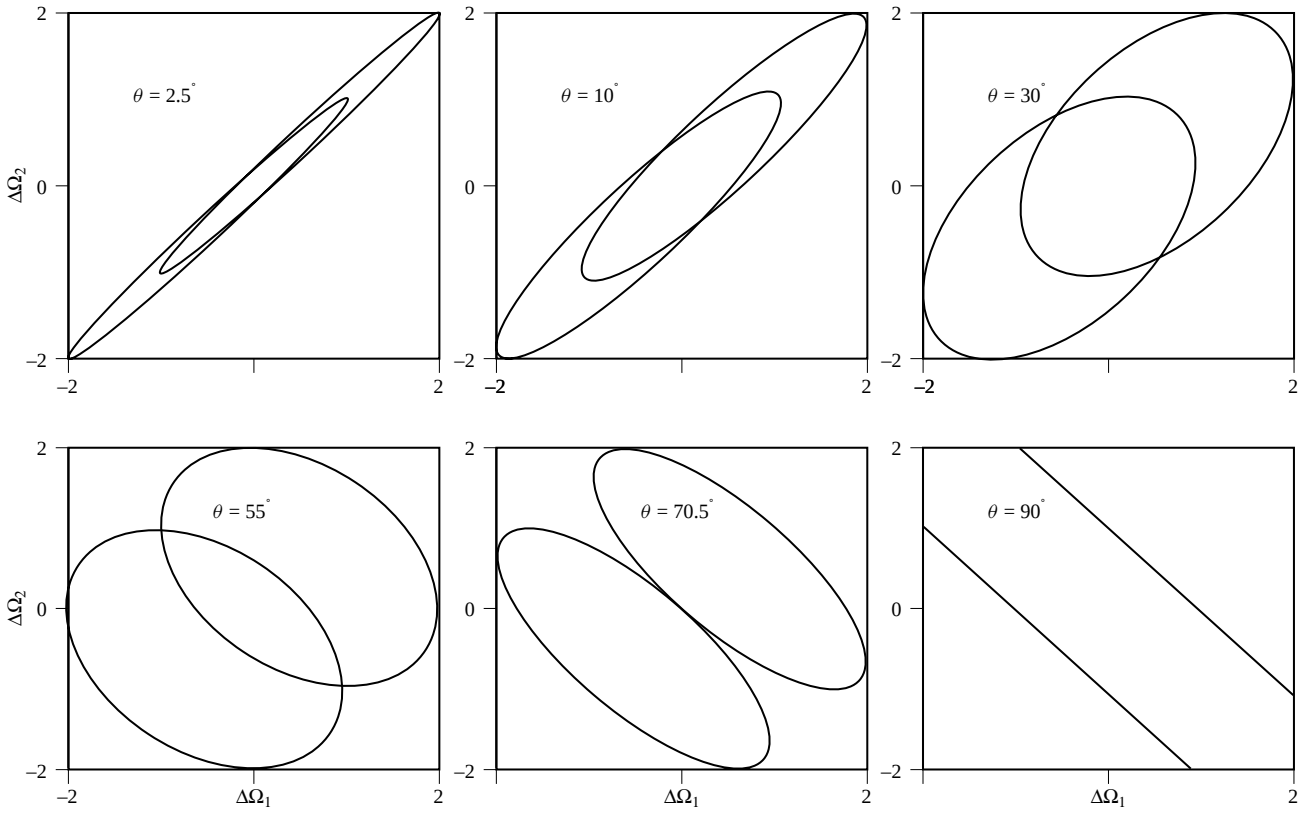

Figure 6 Intensity patterns for ^{2}H 2D exchange powder spectra with an axially symmetric quadrupole coupling tensor undergoing various reorientation angles, θ

(C–^{2}H), 2D exchange allows model-free determination of the angle through which a deuterated group rotates during the mixing period. The pulse sequence is shown in Figure 1(c).

A brief description of the unique aspects of the pulse sequence used for the deuterium 2D exchange experiment is presented here. The mixing time should be greater than t_c. The phase alternation of the pulse sequence gives rise to two types of echo; the spin alignment echo and the stimulated echo. Appropriate data processing of the two echo signals results in a pure absorption mode spectrum. The 2D map of the ^{2}H exchange frequencies results in a combination of autocorrelation signals and cross-correlation signals. The autocorrelation signal is the deuterium powder lineshape along the diagonal. The cross-correlation signals depend on the type of motion as well as the amplitude of the motion. The echoes are modulated according to the frequency of the molecular motion that occurs during the mixing period. These modulations lead to off-diagonal intensity in the form of ellipses. One ellipse will be observed for each deuterium transition and for each jump angle represented in the motional model. Therefore, one can determine the number of discrete sites of the reorientation. In the presence of N-site discrete reorientation, the 2D map will have ridges and straight lines which are parallel to the frequency axes. In other words the 2D exchange experiment discriminates between continuous diffusion and discrete jump motion as well as between two-site and four-site jump motion. One can describe the intensity map as an ellipse for each of the two allowed deuterium transitions. The amplitude of the motion is determined from the tangent of the ratio of the semiaxes of the ellipse. A tetrahedral jump model or four-site hop gives rise to two ellipses for each transition, and a continuous diffusion motion will broaden the ridges of the ellipse with a corresponding decrease in intensity.

The equations describing the ellipses of the deuterium 2D exchange experiment are as follows:[22]

$$\Omega_1 - \Omega_0 = \pm\tfrac{1}{2}\Delta(3\cos^2\theta - 1) = \pm\tfrac{1}{4}\Delta[1 + 3\cos(2\theta)] \quad (32)$$

and

$$\begin{aligned}\Omega_2 - \Omega_0 &= \pm\tfrac{1}{2}\Delta[3\cos^2(\theta \pm \theta_s) - 1] \\ &= \pm\tfrac{1}{4}\Delta\{1 + 3\cos[2(\theta \pm \theta_s)]\}\end{aligned} \quad (33)$$

Figure 6 shows a theoretical 2D map of a methyl group undergoing a two-site jump for a variety of angles. Such 2D studies allow the correlation of properties at different times and can separate different properties.

6 OTHER DEUTERIUM NMR EXPERIMENTS IN THE SOLID STATE

It is worth mentioning here some other solid state deuterium NMR experiments used in structure and dynamics studies of polymers and other solids. Although not as widely used as the quadrupolar echo experiment or the 2D exchange method, these experiments are valuable for certain classes of compounds and areas of study.

6.1 Deuterium MAS in Solids[27, 28]

By combining magic angle sample spinning and the deuterium quadrupolar echo experiment one can measure quadrupole coupling constants and asymmetry parameters of nonequivalent deuterons with overlapping powder patterns. The addition of sample spinning also improves the resolution and sensitivity considerably so that one may consider studying unenriched samples. The theory has been developed for static as well as dynamic systems, and the experiment extends the possible dynamic range to study very slow and very fast motions.

6.2 Multiple Pulse Quadrupolar Echoes[28]

When studying fast or slow motions in deuterated species, one must consider the effects of dipolar coupling, or the resulting lineshapes can be misinterpreted as being due to intermediate exchange processes. Using a four-pulse (MW-4) multipulse sequence[29] combined with the quadrupole echo pulse sequence one can distinguish between the intermediate exchange regime and heteronuclear dipolar dephasing. The measurement of the dipolar coupling between protons and deuterons is allowed using this experiment.

6.3 Combined 2D Exchange and Magic Angle Spinning[30]

A recent experiment that combines magic angle spinning with the 2D exchange pulse sequence provides some interesting intensity maps of deuterated species if no exchange is taking place. In these types of system, if the rotor period is synchronous with the mixing time no cross peaks result (the ridge pattern is lost) and there is a comparable gain in sensitivity. There have been reports of 2D spectra acquired for deuterium in natural abundance using this experiment.[30]

7 RELATED ARTICLES

Glycolipids; Inorganic Solids; Internal Spin Interactions and Rotations in Solids; Liquid Crystalline Samples: Deuterium NMR; Protein Dynamics from Solid State NMR; Quadrupolar Interactions; Quadrupolar Nuclei in Solids; ORelaxation of Quadrupolar Nuclei Measured via Multiple Quantum Filtration; Solid Biopolymers; Solid State Probe Design; Two-Dimensional Powder Correlation Methods; Ultraslow Motions in Solids.

8 REFERENCES

1. R. J. Wittebort, S. E. Woehler, and C. H. Bradley, *J. Magn. Reson.*, 1986, **67**, 143.
2. J. H. Davis, K. R. Jeffrey, M. Bloom, M. I. Valic, and T. P. Higgs, *Chem. Phys. Lett.*, 1976, **42**, 390.
3. M. Mokarram and J. L. Ragle, *J. Chem. Phys.*, 1973, **36**, 2770.
4. A. A. Abragam, *Nuclear Magnetism*, Oxford, 1961.
5. A. R. Edmonds, *Angular Momentum in Quantum Mechanics*, Princeton University Press, Princeton, 1960.
6. C. P. Slichter, *Principles of Magnetic Resonance*, 2nd edn., Springer-Verlag, New York, 1978.
7. B. C. Gerstein and C. R. Dybowski, *Transient Techniques in NMR of Solids; An Introduction to the Theory and Practice*, Academic Press, Orlando, 1985.
8. U. Haeberlen, *High Resolution NMR in Solids Selective Averaging*, Academic Press, New York, 1976.
9. M. Mehring, *Principles of High Resolution NMR in Solids*, 2nd edn., Springer-Verlag, New York, 1983.
10. H. W. Spiess, *Basic Principles and Progress*, Springer-Verlag, New York, 1978.
11. L. S. Batchelder, C. E. Sullivan, L. W. Jelinski, and D. A. Torchia, *Proc. Natl. Acad. Sci. USA*, 1982, **79**, 386.
12. D. A. Torchia and A. Szabo, *J. Magn. Reson.*, 1982, **49**, 107.
13. L. S. Batchelder, C. H. Niu, and D. A. Torchia, *J. Am. Chem. Soc.*, 1983, **105**(8), 2228.
14. R. J. Wittebort, E. T. Olejniczak, and R. G. Griffin, *J. Chem. Phys.*, 1987, **86**(10), 5411.
15. A. J. Vega, *J. Magn. Reson.*, 1985, **65**, 252.
16. J. Hirschinger, H. Miura, K. H. Gardner, and A. D. English, *Macromolecules*, 1990, **23**, 2153.
17. R. J. Schadt, E. J. Cain, and A. D. English, *J. Phys. Chem.*, 1993, **97**, 8387.
18. H. W. Spiess, *J. Chem Phys.*, 1980, **72**, 6755.
19. M. Lausch and H. W. Spiess, *J. Chem Phys.*, 1980, **71**, 182.
20. M. Lausch and H. W. Spiess, *J. Magn. Reson.*, 1983, **54**, 466.
21. C. Schmidt, S. Wefing, B. Blumich, and H. W. Spiess, *Chem. Phys. Lett.*, 1986, **130**(1.2), 84.
22. C. Schmidt, B. Blumich, and H. W. Spiess, *J. Magn. Reson.*, 1988, **79**, 269.
23. S. Wefing and H. W. Spiess, *J. Chem. Phys.*, 1988, **89**(3), 1219.
24. S. Wefing, S. Kaufmann, and H. W. Spiess, *J. Chem. Phys.* 1988, **89**(3), 1234.
25. S. Kaufmann, S. Wefing, D. Schaefer, and H. W. Spiess, *J. Chem. Phys.*, 1990, **93**(1), 197.
26. R. R. Ernst, G. Bodenhausen, and A. Wokaun, *Principles of Nuclear Magnetic Resonance in One and Two Dimensions*, Oxford University Press, Oxford, 1987.
27. J. G. Kristensen, H. Bildsoe, H. J. Jakobsen, and N. C. Nielsen, *J. Magn. Reson.*, 1992, **100**, 437.
28. R. J. Schadt, R. Y. Dong, E. Gunther, and B. Blumich, *J. Magn. Reson.*, 1992, **96**, 393.
29. M. L. H. Gruwel, *Chem. Phys. Lett.*, 1992, **191**(6), 621.
30. D. Reichert, Z. Olender, R. Poupko, H. Zimmermann, and Z. Luz, *J. Chem. Phys.*, 1993, **98**(10), 7699.

Biographical Sketch

Lynne S. Batchelder. *b* 1953. B.S. 1975 Tufts University, USA, M.S. and Ph.D., 1978, University of Massachusetts, USA. Introduced to NMR by J. L. Ragle while at the University of Massachusetts. Senior research scientist, Varian Associates, USA, 1982–89. Technical Services Manager, Cambridge Isotope Laboratories, Inc., USA, 1992–present. Interests include NMR instrumentation, isotope labeling and protein structure.

Dipolar and Indirect Coupling Tensors in Solids

Roderick E. Wasylishen

Dalhousie University, Halifax, Nova Scotia, Canada

1	Introduction	1
2	Direct Dipolar Coupling	2
3	Indirect Spin–Spin Coupling	4
4	Summary	10
5	Related Articles	10
6	References	10

1 INTRODUCTION

Nuclei which possess the property of spin also have an associated nuclear magnetic moment. It is the interaction between these nuclear magnetic moments and a strong applied magnetic field $\boldsymbol{B}_0$ which forms the basis of the NMR experiment. This interaction, known as the Zeeman interaction, is always the most important spin interaction for spin-$\frac{1}{2}$ nuclei. In addition to the externally applied magnetic field, nuclei may also experience much smaller internal magnetic fields. For example, the field-induced motion of electrons generates small magnetic fields which modify the applied magnetic field and result in the phenomenon known as nuclear magnetic shielding or chemical shielding. In addition, neighboring nuclear spins may also create small magnetic fields which modify the applied magnetic field. There are two fundamental mechanisms by which one nuclear magnetic moment may interact with another: the *direct* magnetic dipole–dipole interaction and the *indirect* spin–spin interaction. The magnitude of the direct dipolar interaction is directly proportional to the inverse cube of the separation between two spins, while the indirect interaction does not depend on distance in any simple way since it is a two-stage process mediated by the intervening electrons. Because the mechanism of indirect spin–spin coupling involves electrons, this parameter depends on the detailed electronic structure of a molecule. Both the direct and indirect coupling interactions are bilinear in the nuclear spin operators (see below). In principle, the direct dipolar and indirect spin–spin interactions couple every spin of the sample with all others.

Most early NMR investigations were ^{1}H NMR studies, because of the relatively large magnetic moment of ^{1}H (hence its high inherent sensitivity to NMR detection), its large natural abundance (99.985%), and its ubiquitous presence in chemical compounds. The direct dipolar interaction has special significance in these studies since proton–proton direct dipolar interactions are largely responsible for the general appearance of ^{1}H NMR spectra of solid materials. Furthermore, the ^{1}H–^{1}H dipolar interaction provided the first important application of NMR in chemistry. Specifically, Pake[1] used the ^{1}H–^{1}H direct dipolar interaction to determine the H–H separation of water molecules in gypsum ($CaSO_4.2H_2O$): $r_{H-H} = 0.158$ nm.

The indirect spin–spin coupling interaction was first observed as magnetic field-independent splittings in the NMR spectra of solution samples.[2–4] In solution, the direct dipolar interaction averages to zero because of the rapid random tumbling motion of molecules. The first indirect spin–spin coupling constant J was reported by Proctor and Yu in 1951.[2] It involved the indirect spin–spin coupling between the antimony and fluorine nuclei of the SbF_6 anion in an aqueous solution of $NaSbF_6$; $J(^{121}Sb, ^{19}F)$ = 1.9 kHz. Shortly after this report, Gutowsky and co-workers reported the observation of $J(^{31}P, ^{19}F)$ in $P(O)Cl_2F$ (1.2 kHz), $P(O)ClF_2$ (1.1 kHz), and $CH_3(O)PF_2$ (1.3 kHz).[3] The first ^{1}H–^{1}H electron-mediated spin–spin couplings were reported in the same year by Hahn and Maxwell.[4] They studied the frequency modulation of ^{1}H NMR spin echoes arising from molecules with chemically nonequivalent hydrogen nuclei. For dichloroacetaldehyde ($CHCl_2CHO$), two distinct modulation frequencies were observed on the ^{1}H spin echo envelope: one corresponding to the difference in ^{1}H chemical shifts, and a second, much smaller frequency J which was independent of the applied magnetic field [$^3J(^1H, ^1H) = 0.7$ Hz]. On the basis of their measurements, Hahn and Maxwell proposed that the Hamiltonian describing electron coupled spin interactions in isotropic fluids should be of the form $J_{N,N'}\boldsymbol{I}_N \cdot \boldsymbol{I}_{N'}$. However, for a pair of coupled spins residing in a molecule which is not rapidly tumbling in an isotropic fluid, Ramsey[5] later pointed out that the energy of interaction $E_{N,N'}$ depends on the orientation of the spin pair in the applied magnetic field. In general, the energy of interaction is given by

$$E_{N,N'} = h\boldsymbol{I}_N \cdot \boldsymbol{J}_{N,N'} \cdot \boldsymbol{I}_{N'} + hJ_{N,N'}\boldsymbol{I}_N \cdot \boldsymbol{I}_{N'} \qquad (1)$$

where $\boldsymbol{J}_{N,N'}$ is a second rank tensor whose trace is zero and $J_{N,N'}$ is the isotropic indirect spin–spin coupling constant.

In solid samples, splittings arising from indirect spin–spin coupling were not observed until 1967.[6] In the solid state, the magnitude of direct dipolar interactions among magnetically abundant spins, such as ^{1}H or ^{19}F, precluded the measurement of much smaller indirect spin–spin interactions. However, by spinning samples rapidly about an axis inclined at 54° 44′ with respect to the applied magnetic field, broadening due to anisotropic chemical shielding and direct dipolar interactions can be largely removed. Using this technique, known as magic angle spinning (MAS), Andrew et al.[6] observed splittings due to $J(^{75}As, ^{19}F)$ of 905 Hz, and $J(^{121}Sb, ^{19}F)$ of 1820 Hz in the ^{19}F NMR spectra of solid $KAsF_6$ and $KSbF_6$, respectively. From the ^{19}F NMR linewidths observed in nonspinning samples of these salts, the authors were able to conclude that the hexafluoroarsenate and hexafluoroantimonate anions are dynamically disordered. Rapid jumps of the MF_6 octahedra about their symmetry axes average *intra*molecular dipolar interactions to zero. Subsequently, VanderHart et al.[7] studied the ^{19}F and ^{31}P NMR lineshapes of static samples of polycrystalline $BaFPO_3$ where the directly bonded ^{19}F and ^{31}P nuclei are coupled by both the direct dipolar and the indirect spin–spin coupling interactions. The authors indicated that with an accurate value of the ^{19}F–^{31}P separation r_{FP}, one could calculate the contribution that the direct dipolar interaction makes to the overall ^{19}F or ^{31}P NMR lineshape and, in principle, determine the anisotropy in the indirect spin–spin coupling, a parameter which is usually inaccessible.

The objective of this article is to present an introductory discussion of how spin–spin coupling interactions are described

and how they manifest themselves in the NMR spectra of diamagnetic systems, particularly in NMR studies of solids. The discussion will focus on the indirect spin–spin coupling tensor $\boldsymbol{J}$, since detailed discussions of the direct dipolar interaction can be found in several textbooks on NMR.[8–11] For pedagogical reasons, it is most convenient to focus the discussion on simple two-spin systems.

2 DIRECT DIPOLAR COUPLING

A nucleus with nonzero total spin angular momentum $\hbar\boldsymbol{I}$ also possesses a magnetic moment $\boldsymbol{\mu}$. The magnetic moment and angular momentum vectors are related by the magnetogyric ratio γ, a unique constant for any given isotope:

$$\boldsymbol{\mu} = \gamma\hbar\boldsymbol{I} \tag{2}$$

It is useful to consider the total static magnetic field emanating from a magnetic dipole. At a point P, the static field depends on the distance r and the angle θ between the magnetic dipole and P; the z component of the local field is $\gamma r^{-3}\hbar\,(3\cos^2\theta - 1)\,(\mu_0/4\pi)$. With $\theta = 0^\circ$, the local field 0.1 nm from a proton is 5.64 mT, several orders of magnitude less than the magnitude of typical external fields employed in NMR experiments.

From classical electrodynamics, the energy of interaction E between two magnetic dipoles, $\boldsymbol{\mu}_1$ and $\boldsymbol{\mu}_2$, separated by a distance r may be written as

$$E = [(\boldsymbol{\mu}_1 \cdot \boldsymbol{\mu}_2)r^{-3} - 3(\boldsymbol{\mu}_1 \cdot \boldsymbol{r})(\boldsymbol{\mu}_2 \cdot \boldsymbol{r})r^{-5}](\mu_0/4\pi) \tag{3}$$

where μ_0 is the permeability constant, $\mu_0 = 4\pi \times 10^{-7}$ kg m s^{-2} A^{-2}. If the two dipoles $\boldsymbol{\mu}_1$ and $\boldsymbol{\mu}_2$ have the same orientation with respect to $\boldsymbol{r}$ then equation (3)becomes:

$$E = (\boldsymbol{\mu}_1 \cdot \boldsymbol{\mu}_2)r^{-3}(1 - 3\cos^2\theta)(\mu_0/4\pi) \tag{4}$$

where θ is the angle between the direction of the two magnetic dipoles and the vector $\boldsymbol{r}$ which separates them.

In NMR studies, one is generally concerned with nuclear magnetic moments. Consider two nuclei (1 and 2) separated by a distance r in a magnetic field (Figure 1). The quantum mechanical Hamiltonian describing the direct dipolar interaction, $\hat{\mathcal{H}}_{\mathrm{DD}}$, is constructed by replacing the vectors $\boldsymbol{\mu}_1$ and $\boldsymbol{\mu}_2$ in equation (3) by their corresponding operators, $\gamma_1\hbar\hat{\boldsymbol{I}}_1$ and $\gamma_2\hbar\hat{\boldsymbol{I}}_2$:

$$\hat{\mathcal{H}}_{\mathrm{DD}} = \gamma_1\gamma_2\hbar^2[(\hat{\boldsymbol{I}}_1 \cdot \hat{\boldsymbol{I}}_2)r^{-3} - 3(\hat{\boldsymbol{I}}_1 \cdot \boldsymbol{r})(\hat{\boldsymbol{I}}_2 \cdot \boldsymbol{r})r^{-5}](\mu_0/4\pi) \tag{5}$$

where γ_i is the magnetogyric ratio of nucleus i (in rad s^{-1} T^{-1}), $\hat{\boldsymbol{I}}_i$ is the nuclear spin angular momentum operator, and $\boldsymbol{r}$ is the internuclear vector. In an NMR experiment, the direction of the magnetic moments is defined by the direction of the applied magnetic field $\boldsymbol{B}_0$.

If one expands the scalar products in equation (5),

$$\hat{\boldsymbol{I}}_1 \cdot \hat{\boldsymbol{I}}_2 = \hat{I}_{1x}\hat{I}_{2x} + \hat{I}_{1y}\hat{I}_{2y} + \hat{I}_{1z}\hat{I}_{2z} \tag{6}$$

$$\hat{\boldsymbol{I}}_1 \cdot \boldsymbol{r} = \hat{I}_{1x}x + \hat{I}_{1y}y + \hat{I}_{1z}z \tag{7}$$

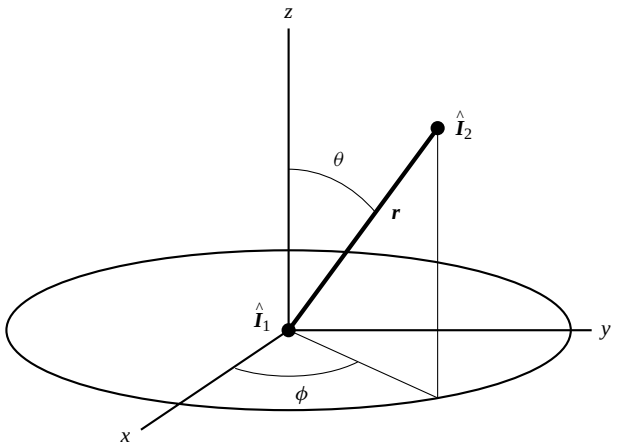

Figure 1 Coordinate system used to describe the coupling of two spins $\hat{\boldsymbol{I}}_1$ and $\hat{\boldsymbol{I}}_2$ separated by a distance r. A strong applied magnetic field lies along the z axis

$$\hat{\boldsymbol{I}}_2 \cdot \boldsymbol{r} = \hat{I}_{2x}x + \hat{I}_{2y}y + \hat{I}_{2z}z \tag{8}$$

the direct dipolar Hamiltonian may be expanded and rewritten as

$$\begin{aligned}\hat{\mathcal{H}}_{\mathrm{DD}} = \gamma_1\gamma_2\hbar^2 r^{-5}[&\hat{I}_{1x}\hat{I}_{2x}(r^2 - 3x^2) + \hat{I}_{1y}\hat{I}_{2y}(r^2 - 3y^2)\\ &+\hat{I}_{1z}\hat{I}_{2z}(r^2 - 3z^2) - (\hat{I}_{1x}\hat{I}_{2y} + \hat{I}_{1y}\hat{I}_{2x})3xy\\ &-(\hat{I}_{1y}\hat{I}_{2z} + \hat{I}_{1z}\hat{I}_{2y})3yz - (\hat{I}_{1z}\hat{I}_{2x} + \hat{I}_{1x}\hat{I}_{2z})3zx]\\ &\times(\mu_0/4\pi)\end{aligned} \tag{9}$$

This equation can be expressed in matrix form:

$$\hat{\mathcal{H}}_{\mathrm{DD}} = hR\left\{[\hat{I}_{1x} \quad \hat{I}_{1y} \quad \hat{I}_{1z}]\right.$$
$$\left.\begin{bmatrix} (r^2 - 3x^2)/r^2 & -3xy/r^2 & -3xz/r^2 \\ -3xy/r^2 & (r^2 - 3y^2)/r^2 & -3yz/r^2 \\ -3xz/r^2 & -3yz/r^2 & (r^2 - 3z^2)/r^2 \end{bmatrix} \begin{bmatrix} \hat{I}_{2x} \\ \hat{I}_{2y} \\ \hat{I}_{2z} \end{bmatrix}\right\} \tag{10}$$

where R is defined as the direct dipolar coupling constant,

$$R = \gamma_1\gamma_2 r^{-3}(\hbar/2\pi)(\mu_0/4\pi) \tag{11}$$

Equation (10) can be abbreviated as

$$\hat{\mathcal{H}}_{\mathrm{DD}} = hR(\hat{\boldsymbol{I}}_1 \cdot \boldsymbol{D} \cdot \hat{\boldsymbol{I}}_2) \tag{12}$$

where $\boldsymbol{D}$; is the direct dipolar tensor.

It is easy to see that if the internuclear vector $\boldsymbol{r}$, lies along the z axis, then the dipolar tensor becomes diagonal:

$$\boldsymbol{D} = \begin{bmatrix} 1 & 0 & 0 \\ 0 & 1 & 0 \\ 0 & 0 & -2 \end{bmatrix} \tag{13}$$

This is the so-called principal axis system (PAS) of the dipolar tensor. Note that the principal components of the dipolar tensor

are axially symmetric, i.e. $D_{11} = D_{22}$. From equation (10) it is also obvious that the dipolar tensor is symmetric (i.e. $D_{\alpha\beta} = D_{\beta\alpha}$). Finally, it is also clear that the trace of the dipolar tensor is zero. This result indicates that the direct dipolar interaction does not influence the positions of peaks in liquid phase NMR spectra. It can also be shown that for isolated spin pairs in solid samples the time averaged expectation value of $\hat{\mathcal{H}}_{\mathrm{DD}}$ is zero under conditions of MAS.[12] The sample must be spun rapidly with respect to the direct dipolar coupling constant R.

In order to discuss the NMR spectrum of two dipolar coupled spins in the solid state, it is convenient to transform equation (5) from Cartesian coordinates to spherical polar coordinates. This is readily accomplished by setting: $x = r \sin\theta \cos\phi$, $y = r \sin\theta \sin\phi$, $z = r \cos\theta$ and expressing $\hat{I}_x$ and $\hat{I}_y$ in terms of the raising and lowering operators $\hat{I}^+$ and $\hat{I}^-$, respectively:

$$\hat{\boldsymbol{I}}^+ = \hat{I}_x + \mathrm{i}\hat{I}_y, \quad \hat{\boldsymbol{I}}^- = \hat{I}_x - i, \hat{I}_y \tag{14}$$

Spin functions used to describe a nuclear spin state are eigenfunctions of the Zeeman Hamiltonian; they are often denoted by $|\, I,\, m\rangle$, where I is the nuclear spin quantum number and m is the z component of the spin angular momentum in units of $\hbar$ (i.e. $\hat{I}_z \mid I,\, m\rangle = m|I,\, m\rangle$). The spin quantum number m may take on values of $-I, -I+1, \ldots, +I$. Thus, for spin-$\frac{1}{2}$ nuclei there are only two states $|\, \frac{1}{2}, \frac{1}{2}\rangle$ and $|\, \frac{1}{2}, -\frac{1}{2}\rangle$, which are generally denoted by $|\, \alpha\rangle$ and $|\, \beta\rangle$, respectively: $\hat{I}_z \mid \alpha\rangle = \frac{1}{2}|\alpha\rangle$ and $\hat{I}_z|\beta\rangle = -\frac{1}{2}|\beta\rangle$, while $\hat{I}^+|\alpha\rangle = 0$, $\hat{I}^+|\beta\rangle = |\alpha\rangle$, $\hat{I}^-|\alpha\rangle = |\beta\rangle$ and $\hat{I}^-|\beta\rangle = 0$. Further details concerning the quantum mechanics of angular momentum can be found elsewhere.[8–11,13,14]

In spherical polar coordinates, the dipolar Hamiltonian can be expressed in terms of the so-called dipolar alphabet:

$$\hat{\mathcal{H}}_{\mathrm{DD}} = hR(\hat{A} + \hat{B} + \hat{C} + \hat{D} + \hat{E} + \hat{F}) \tag{15}$$

Each of the terms $\hat{A}$ to $\hat{F}$ contains spin operators and a spatial term generally involving both θ and ϕ. Each term alters the spin functions used to describe a spin pair in a characteristic way. Explicit expressions for the terms $\hat{A}$ to $\hat{F}$ are given in several NMR textbooks.[8–11]

To describe the NMR spectrum of a pair of equivalent homonuclear spins in a strong magnetic field, it is only necessary to consider the terms $\hat{A}$ and $\hat{F}$:

$$\hat{A} = -\hat{I}_{1z}\hat{I}_{2z}(3\cos^2\theta - 1) \tag{16}$$

$$\hat{B} = \tfrac{1}{4}[\hat{\boldsymbol{I}}_1^+ \cdot \hat{\boldsymbol{I}}_2^- + \hat{\boldsymbol{I}}_1^- \cdot \hat{\boldsymbol{I}}_2^+](3\cos^2\theta - 1) \tag{17}$$

Clearly, the $\hat{A}$ term does not alter the simple product spin functions $|\, \alpha\alpha\rangle$, $|\, \alpha\beta\rangle$, $|\, \beta\alpha\rangle$, and $|\, \beta\beta\rangle$ (e.g. $\hat{I}_{1z}\hat{I}_{2z}|\alpha\beta\rangle = (\frac{1}{2})(-\frac{1}{2})|\alpha\beta\rangle$). On the other hand, the $\hat{B}$ term contains the 'flip-flop' operator $\hat{I}_1^+\hat{I}_2^- + \hat{I}_1^-\hat{I}_2^+$, which alters the spin functions $|\, \alpha\beta\rangle$ to $|\, \beta\alpha\rangle$, and vice versa. For a pair of magnetically equivalent spins which are dipolar coupled in a strong applied magnetic field $\boldsymbol{B}_0$, the appropriate Hamiltonian operator is

$$\hat{\mathcal{H}} = \hat{\mathcal{H}}_{\mathrm{Z}} + \hat{\mathcal{H}}_{\mathrm{DD}} \tag{18}$$

where $\hat{\mathcal{H}}_{\mathrm{Z}} = -\nu_0 h(\hat{I}_{1z} + \hat{I}_{2z}$, and $\nu_0 = \gamma B_0/2\pi$. To describe such a spin system, it is convenient to use the following basis functions:

$$|t_1\rangle = |\alpha\alpha\rangle \tag{19a}$$

$$|t_0\rangle = 2^{-1/2}(|\alpha\beta\rangle + |\beta\alpha\rangle)$$

$$|s\rangle = 2^{-1/2}(|\alpha\beta\rangle - |\beta\alpha\rangle) \tag{19b}$$

$$|t_{-1}\rangle = |\beta\beta\rangle \tag{19c}$$

Using these basis functions, the total matrix of the truncated dipolar Hamiltonian operator is diagonal. The resulting eigenvalues of $\hat{\mathcal{H}}$ (in frequency units) are:

$$|t_1\rangle: \quad -\nu_0 - \tfrac{1}{4}R(3\cos^2\theta - 1) \tag{20a}$$

$$|t_0\rangle: \quad \tfrac{1}{2}R(3\cos^2\theta - 1) \tag{20b}$$

$$|t_{-1}\rangle: \quad \nu_0 - \tfrac{1}{4}R(3\cos^2\theta - 1) \tag{20c}$$

$$|s\rangle: \quad 0 \tag{20d}$$

where θ is the angle between the dipolar vector and the applied magnetic field $\boldsymbol{B}_0$. Transitions involving the antisymmetric $|\, s\rangle$ level are symmetry-forbidden; therefore only two transitions, $\nu_0 \pm \frac{3}{4}R(3\cos^2\theta - 1)$, are allowed.

For any general orientation of a spin pair in an applied magnetic field, the two peaks are separated by $(\frac{3}{2})R(3\cos^2\theta - 1)$. Spectra from an isolated homonuclear spin pair in a hypothetical single crystal and powder sample are shown in Figure 2. The powder spectrum, known as a Pake powder pattern, is obtained by considering all orientations of the dipolar vector in $\boldsymbol{B}_0$ ($0^\circ \le \theta \le 180^\circ$; $0^\circ \le \phi \le 360^\circ$). The separation between the discontinuities, $(\frac{3}{2})R$, corresponds to $\theta = 90^\circ$ while the shoulders are separated by $3R$, which corresponds to the $\theta = 0^\circ$ orientation.

For a pair of unlike spins A and X, where the two spins have different magnetogyric ratios but both are spin $\frac{1}{2}$, it is only necessary to consider the A term of $\hat{\mathcal{H}}_{\mathrm{DD}}$ since this is the only term in the dipolar alphabet which commutes with $\hat{\mathcal{H}}_{\mathrm{Z}}$. The A-spin NMR spectrum consists of two peaks at $\nu_{\mathrm{A}} \pm (\frac{1}{2})R(3\cos^2\theta - 1)$, where $\nu_{\mathrm{A}} = \gamma_{\mathrm{A}}B_0/2\pi$; the X-spin spectrum will be identical, except for the fact that it is centered about ν_{X} instead of ν_{A}. For unlike spins, the separation between the discontinuities in the A-spin or X-spin Pake powder pattern is R. If the X spin is a quadrupolar nucleus, calculation of the A-spin NMR spectrum may be more difficult, particularly if the high-field approximation is not applicable [i.e. $\hat{\mathcal{H}}_{\mathrm{Z}}(X) \approx \hat{\mathcal{H}}_{\mathrm{Q}}(X)$]. An instructive example of this problem was provided by Stoll et al.[15] who discussed the ^{13}C NMR spectra of the $^{13}\mathrm{C} - {}^{14}\mathrm{N}$ spin pair in a single crystal of $K_2Pt(CN)_4Br_{0.3}{\cdot}3H_2O$.

In practice, the chemical shielding interaction is orientation dependent, and thus it will also influence the detailed NMR lineshape. For protons, anisotropic chemical shielding generally causes a minor perturbation on the Pake doublet powder pattern, since it will be several orders of magnitude smaller than the direct dipolar interaction. However, for most other nuclei, the anisotropic chemical shielding (in frequency units) may be comparable to or greater than the dipolar interactions with adjacent nuclei. Under such conditions the

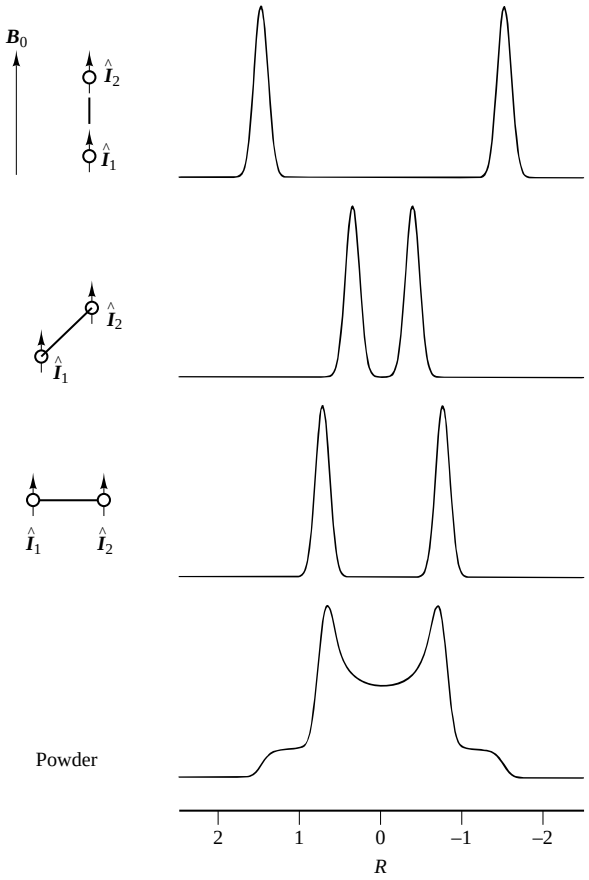

Figure 2 Calculated NMR spectra for two equivalent spins $\hat{\boldsymbol{I}}_1$ and $\hat{\boldsymbol{I}}_2$ which interact with one another by the direct dipolar interaction. From top to bottom: calculated spectra for three orientations of the internuclear vector in the applied magnetic field $\boldsymbol{B}_0$, θ = 0°, 45°, 90°, respectively. The bottom spectrum is the Pake powder pattern which results from a sum of spectra of individual crystallites which are randomly distributed in the sample. The calculated spectra have been convoluted with a Gaussian function to simulate weak dipolar interactions with more remote nuclei

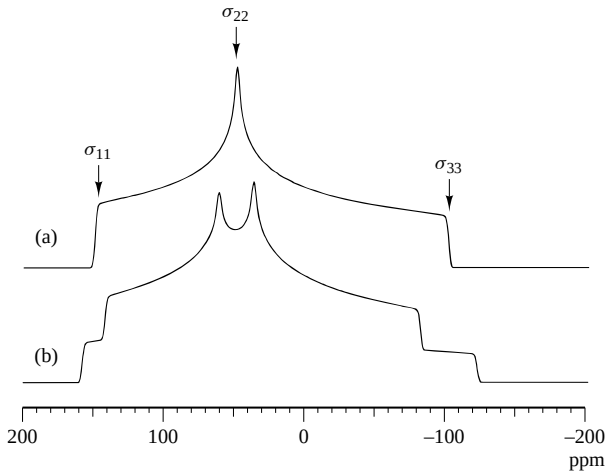

Figure 3 (a) A typical spin-$\frac{1}{2}$ NMR powder pattern of an isolated spin with anisotropic chemical shielding. The principal components of the chemical shielding tensor are easily identified from the powder pattern by the shoulders at σ_{11} and at σ_{33} and the discontinuity at σ_{22}. (b) Same as (a), but the influence of direct dipolar coupling with an adjacent spin-$\frac{1}{2}$ nucleus is illustrated. The direct dipolar interaction causes an apparent splitting of the chemical shielding powder pattern

Table 1 Typical Direct and Indirect Spin–Spin Coupling Constants Involving Carbon

X	Compound	R [a](Hz)	$J(\mathrm{M},^{13}\mathrm{C})_{\mathrm{iso}}$ (Hz)	$K(\mathrm{M,C})_{\mathrm{iso}}$ [b]
^{13}C	$C(CH_3)_4$ [c]	2080	37	4.9
^{29}Si	$Si(CH_3)_4$ [c]	−920	−50	8.4
^{73}Ge	$Ge(CH_3)_4$ [c]	−140	−19	17.7
^{119}Sn	$Sn(CH_3)_4$ [c]	−1090	−340	30.1
^{207}Pb	$Pb(CH_3)_4$ [c]	590	250	39.9
^{113}Cd	$Cd(CH_3)_2$ [d]	−740	−513	76.3
^{199}Hg	$Hg(CH_3)_2$ [e]	660	690	127
^{199}Hg	$Hg(CH_3)(NO_3)$ [e]	660	1800	331

[a]Approximate values. [b]$K_{\mathrm{N,N'}} = 4\pi^2 J_{\mathrm{N,N'}}/h\gamma_{\mathrm{N}}\gamma_{\mathrm{N'}}$ (units 10^{20} N A^{-2} m^{-3}). [c]Dalling and Gutowsky.[57] [d]Dreeskamp and Hildenbrand.[58] [e]Jokisaari et al.[59]

'A'-spin NMR spectrum of an AX-spin system in a static powder sample will consist of $2I$ + 1 overlapping powder patterns, where I is the spin quantum number of X (Figure 3). One can often obtain valuable information concerning the orientation of chemical shielding tensors by analyzing dipolar chemical shift NMR spectra.[14,16–18]

Typical values of the direct dipolar coupling constant involving directly bonded spin pairs range from a few hundred hertz to several kilohertz. For example, for the directly bonded ^{13}C–^{15}N spin pair in the amide fragment of a peptide, $R \approx 1.3$ kHz; for the directly bonded ^{13}C–^{1}H spin pair in a typical organic compound, $R \approx 23$ kHz. Further examples of direct dipolar coupling constants involving carbon are given in Table 1.

Much recent research is being focused on recoupling of dipolar interactions in high-resolution MAS experiments, e.g. the rotational resonance and rotational echo double resonance (REDOR) techniques.[19–21] The objective of these experiments is to determine internuclear separations from small dipolar coupling constants. In fact, as will be outlined in Section 3.2, these experiments yield only an effective dipolar coupling constant which is dependent on the anisotropy in the indirect coupling as well as the direct dipolar coupling constant R.

As an aside, it is important to indicate that anisotropic molecular vibrations can result in a subtle vibrationally induced asymmetry of the dipolar coupling tensor; this will be most important when the direct dipolar coupling involves a hydrogen nucleus.[22,23]

The discussion presented here can be extended to more complex spin systems. For example, Van Hecke et al.[24] studied the ^{1}H and ^{19}F NMR spectra of the bifluoride ion in a single crystal of KHF_2. In addition, systems containing the $^{13}CH_2$ fragment have attracted considerable attention.[25–27]

3 INDIRECT SPIN–SPIN COUPLING

As mentioned in Section 1, indirect spin–spin coupling is a two-stage process. One can imagine the spin at one nucleus perturbing the electrons in its vicinity. The resulting

perturbation is transferred via the electronic framework of the molecule to electrons in the vicinity of the second nucleus. The distinctive ways in which a nuclear moment perturbs the surrounding electrons is known as a mechanism for indirect spin–spin coupling (see below). The total indirect spin–spin coupling constant J is a sum of the contributions arising from each mechanism. Clearly, the contribution that each coupling mechanism makes to J is directly proportional to the product of the nuclear magnetic moments of the two coupled nuclei. The sign of indirect spin–spin coupling constants can be either positive or negative. If the indirect spin–spin coupling interaction stabilizes the antiparallel arrangement of the nuclear spins, then the indirect spin–spin coupling is positive. The magnitudes of isotropic indirect spin–spin coupling constants are readily measured in solution NMR studies. Values as small as 0.10 Hz are routinely measured. Isotropic values rarely exceed 30 kHz; however, a ^{199}Hg,^{199}Hg indirect spin–spin coupling constant of 139.6 kHz has been reported for the Hg_3^{2+} ion.[28] Typical values of one-bond indirect spin–spin coupling constants involving carbon, $^1J(\mathrm{M},^{13}\mathrm{C})_{\mathrm{iso}}$, are given in Table 1. The literature on isotropic indirect spin–spin coupling constants is extensive.[29] Over the past 45 years many important relationships between spin–spin coupling constants J_{iso} and molecular structure have been established. On the other hand $\boldsymbol{J}$ tensors are difficult to characterize experimentally. Furthermore, reliable quantum mechanical calculations of $\boldsymbol{J}$ tensors or their corresponding isotropic values are a challenge.[30] Here, the properties of the $\boldsymbol{J}$ tensor are outlined. This is followed by a discussion of how the $\boldsymbol{J}$ tensor can be experimentally characterized from solid state NMR measurements.

3.1 Nature of $\boldsymbol{J}$ Coupling Tensors

The Hamiltonian describing the indirect spin–spin coupling of two spins, $\boldsymbol{I}_1$ and $\boldsymbol{I}_2$, may be expressed as

$$\hat{\mathcal{H}}_J = h\hat{\boldsymbol{I}}_1 \cdot \boldsymbol{J} \cdot \hat{\boldsymbol{I}}_2 \tag{21}$$

where $\boldsymbol{J}$ is the indirect spin–spin coupling tensor. The $\boldsymbol{J}$ tensor is a second rank tensor which is described by nine matrix elements in a Cartesian coordinate system. For example, in a particular molecular fixed axis system, the $\boldsymbol{J}$ tensor might be represented by the matrix:

$$\boldsymbol{J} = \begin{bmatrix} J_{aa} & J_{ab} & J_{ac} \\ J_{ba} & J_{bb} & J_{bc} \\ J_{ca} & J_{cb} & J_{cc} \end{bmatrix} \tag{22}$$

In contrast to the direct dipolar tensor, the $\boldsymbol{J}$ tensor has a nonvanishing trace.

A general second-rank tensor can be decomposed into a sum of irreducible tensors of rank l = 0, 1, 2.[31,32] Thus the indirect spin–spin coupling tensor can be written as

$$\boldsymbol{J} = \boldsymbol{J}^{(0)} + \boldsymbol{J}^{(1)} + \boldsymbol{J}^{(2)} \tag{23}$$

In equation (23) the l = 0 tensor is the isotropic part of the tensor,

$$\boldsymbol{J}^{(0)} = (\tfrac{1}{3}\ \mathrm{Tr}\ \boldsymbol{J})\boldsymbol{1} = J_{\mathrm{iso}}\boldsymbol{1} \tag{24}$$

where $\mathrm{Tr}\ \boldsymbol{J} = (J_{aa} + J_{bb} + J_{cc})$ and $\boldsymbol{1}$ is the unit tensor with diagonal components equal to 1 and all off-diagonal elements zero. The second term in equation (23), l = 1, is the antisymmetric part of the tensor,

$$\boldsymbol{J}^{(1)} = \tfrac{1}{2}(\boldsymbol{J} - \boldsymbol{J}^{\mathrm{t}}) \tag{25}$$

where $\boldsymbol{J}^{\mathrm{t}}$ is the transpose of $\boldsymbol{J}$. The transpose of a 3 × 3 matrix is obtained by replacing the first column by the first row, the second column by the second row, and the third column by the third row. Since the diagonal elements of $\boldsymbol{J}$ and $\boldsymbol{J}^{\mathrm{t}}$ are identical, the diagonal elements of the antisymmetric tensor are zero. The third term in equation (23), l = 2, is the symmetric part of the tensor, defined as

$$\boldsymbol{J}^{(2)} = \tfrac{1}{2}(\boldsymbol{J} + \boldsymbol{J}^{\mathrm{t}}) - J_{\mathrm{iso}}\boldsymbol{1} \tag{26}$$

Although the trace of the symmetric part is zero, the diagonal elements are, in general, not zero.

To a very good approximation, only tensors with l = 0 and l = 2 affect the general appearance of an NMR spectrum.[32] That is, even though the antisymmetric components of a particular $\boldsymbol{J}$ tensor may be non zero, these components do not perturb the observed spectrum in first order. In fact, the existence of antisymmetric components in any indirect spin–spin coupling tensor has never been demonstrated experimentally.[33]

For each symmetric $\boldsymbol{J}$ tensor ($\boldsymbol{J}^{(0)} + \boldsymbol{J}^{(2)}$), there exists a principal axis system for which the matrix $\boldsymbol{J}^{(2)}$ is diagonal. The diagonal elements, denoted by J_{xx}, J_{yy}, and J_{zz}, are called the principal elements, with the convention:

$$|J_{zz}| \geq |J_{xx}| \geq |J_{yy}| \tag{27}$$

The principal axis system of the $\boldsymbol{J}$ tensor is often fixed by the molecular symmetry. For a linear molecule there are only two components, $J_{\parallel}$ and $J_{\perp}$, describing the coupling of the nuclear spin components parallel and perpendicular to the internuclear axis, respectively. Similarly, there are only two non-zero components of the symmetric $\boldsymbol{J}$ tensor for a pair of nuclei sitting on the highest order symmetry axis of molecules in the point groups D_{nd}, D_{nh}, C_{nh}, C_{nv}, and S_n, with $n \geq 3$. The number of independent components in the $\boldsymbol{J}$ tensor for other group symmetries has been tabulated by Buckingham et al.[33] and by Robert and Wiesenfeld.[34]

In describing the orientation dependence of NMR parameters, it is often useful to define the anisotropy of the parameter. This provides a measure of the maximum orientation dependence of that particular parameter. The anisotropy of the indirect spin–spin coupling tensor is usually defined as

$$\Delta J = J_{zz} - \tfrac{1}{2}(J_{xx} + J_{yy}) \equiv \tfrac{3}{2}(J_{zz} - J_{\mathrm{iso}}) \tag{28}$$

In the case of axial symmetry, equation (28) simplifies to

$$\Delta J = J_{\parallel} - J_{\perp} \tag{29}$$

In such cases it is straightforward to show that

$$\boldsymbol{J} = \begin{bmatrix} J_{\perp} & 0 & 0 \\ 0 & J_{\perp} & 0 \\ 0 & 0 & J_{\parallel} \end{bmatrix} = J_{\mathrm{iso}}\boldsymbol{1} + \begin{bmatrix} -\Delta J/3 & 0 & 0 \\ 0 & -\Delta J/3 & 0 \\ 0 & 0 & 2\Delta J/3 \end{bmatrix} \tag{30}$$

Under these conditions the Hamiltonian equation (21), becomes

$$\hat{\mathcal{H}}_{\boldsymbol{J}} = hJ_{\rm iso}\hat{\boldsymbol{I}}_1 \cdot \hat{\boldsymbol{I}}_2 + h\hat{\boldsymbol{I}}_1 \cdot \boldsymbol{J}' \cdot \hat{\boldsymbol{I}}_2 \tag{31}$$

where $\boldsymbol{J}'$ is the traceless '$\Delta\boldsymbol{J}$' tensor which is of the same form as the dipolar tensor [equation (13)]. Since the trace of $\boldsymbol{J}'$ is zero, it is clear that the anisotropy in the principal components of $\boldsymbol{J}$ has no influence on the NMR spectra of isotropic fluids. In principle, ΔJ could provide a mechanism for spin–lattice relaxation, but this mechanism has never been identified as being important.[35]

Ramsey's theory[5] serves as the basis for most theoretical discussions of indirect spin–spin coupling tensors. Following Ramsey, the nonrelativistic Hamiltonian describing nuclear spin, electron spin interactions can be represented by

$$\hat{\mathcal{H}} = \hat{\mathcal{H}}^{(1a)} + \hat{\mathcal{H}}^{(1b)} + \hat{\mathcal{H}}^{(2)} + \hat{\mathcal{H}}^{(3)} \tag{32}$$

The first two terms are the so-called orbital diamagnetic (OD) and orbital paramagnetic (OP) terms which account for the interaction between the nuclear magnetic moments and the orbital motion of the electrons. The third term, $\hat{\mathcal{H}}^{(2)}$, accounts for the spin-dipolar (SD) interactions between the nuclear and electronic magnetic moments. The last term, $\hat{\mathcal{H}}^{(3)}$, accounts for the interaction of the nucleus and the electron spin at the nucleus; this interaction is known as the Fermi contact (FC) interaction. Using these interactions, various approaches, generally based on second-order perturbation theory, are used to calculate indirect nuclear spin–spin coupling tensors. Five separate terms contribute to the overall $\boldsymbol{J}$ tensor:

$$\boldsymbol{J} = \boldsymbol{J}^{(1a)} + \boldsymbol{J}^{(1b)} + \boldsymbol{J}^{(2)} + \boldsymbol{J}^{(3)} + \boldsymbol{J}^{(4)} \tag{33}$$

The orbital diamagnetic contribution $\boldsymbol{J}^{(1a)}$ involves only the ground electronic state of the system. The other four terms involve the following combination of interactions: OP–OP, SD–SD, FC–FC, and FC–SD. The OP term has matrix elements between the ground state and excited singlet states while the SD and FC interactions have matrix elements between the ground state and excited triplet states. The FC–FC contribution to the $\boldsymbol{J}$ tensor is completely isotropic. In contrast, the FC–SD cross term does not contribute to the isotropic value of the spin–spin coupling tensor, but only to its anisotropy, thus the trace of the tensor arising from this term is zero. The other two terms contribute to both the isotropic and anisotropic portion of the total $\boldsymbol{J}$ tensor.

Explicit expressions for each of the five terms in equation (33) are given in several standard NMR texts and review articles.[29,36] It should be mentioned that the theory of Ramsey is a nonrelativistic theory which assumes that orbital and spin angular momenta are L–S coupled. Pyykkö[37] has developed a relativistic analogue of Ramsey's theory based on j–j coupling. Undoubtedly, relativistic effects will be important for indirect spin–spin coupling constants involving nuclei beyond the second row. Furthermore, it has been found that consideration of relativistic effects in extended Hückel calculations tends to increase the calculated anisotropy of spin–spin coupling tensors.[38]

In equation (33), each term is of the form $\gamma_N\gamma_{N'}h\boldsymbol{K}_{N,N'}/4\pi^2$, where $\boldsymbol{K}_{N,N'}$ is called the reduced indirect spin–spin coupling tensor involving nuclei N and N'. The reduced coupling tensor is independent of the magnitude of the nuclear magnetic moments and, therefore, it is useful in comparing indirect spin–spin coupling tensors involving different spin pairs. Note that $\boldsymbol{J}_{N,N'}$ has units of Hz (s^{-1}) and $\boldsymbol{K}_{N,N'}$ has units of N A^{-2} m^{-3} (or, equivalently, T^2 J^{-1}).[39] The isotropic indirect spin–spin coupling constants involving carbon in Table 1 have also been expressed as reduced coupling constants. As one descends the group 14 elements, M, of the Periodic Table in the series $M(CH_3)_4$, $\boldsymbol{K}$(M,C) increases with atomic number Z_M. Similarly, in the series X_3MPR_3, where M is a group 13 element, $\boldsymbol{K}$(M,P) increases as follows: $\approx 10 \times 10^{20}$ N A^{-2} m^{-3} (M = B), $\approx 20 \times 10^{20}$ (Al), $\approx 65 \times 10^{20}$ (M = Ga), and $\approx 100 \times 10^{20}$ (M = In).[40] Qualitatively, these trends can be rationalized by considering only the Fermi contact mechanism; however, there is evidence that the tensor, $\boldsymbol{K}$(In,P), in $Br_3InP[4\text{-}(CH_3O)\text{-}C_6H_4]_3$ is anisotropic, implying that mechanisms other than the Fermi contact contribute to this particular $\boldsymbol{J}$ tensor.[40]

3.2 Measurement of $\boldsymbol{J}$ Coupling Tensors

Using NMR spectroscopy, $\boldsymbol{J}$ tensors can be characterized by studying the spectra of single crystals,[41–43] solid powder samples,[44–47] or samples oriented in liquid crystalline solvents.[48,49] In isotropic fluids, only the isotropic indirect spin–spin coupling constant (a scalar) is measured. For simple molecules in the gas phase ΔJ can, in principle, be measured using molecular beam magnetic resonance techniques.[50] So far, the latter technique has only been successfully applied to thallium fluoride.[51] In this case, $J(^{205}\text{Tl}, {}^{19}\text{F})_{\rm iso} = -13.3 \pm 0.7$ kHz and $\Delta J(^{205}\text{Tl}, {}^{19}\text{F}) = 11.1 \pm 0.7$ kHz. Below, the NMR spectra of a simple heteronuclear two-spin system residing in a rigid solid will be discussed. Particular emphasis is placed on describing how the NMR spectra depend on ΔJ.

Consider a pair of heteronuclear spins A and X, also denoted by '1' and '2', respectively, which are coupled to one another via direct and indirect spin–spin interactions in a strong applied magnetic field. Furthermore, if the $\boldsymbol{J}$ tensor is axially symmetric and coincident with the direct dipolar tensor, $J_\parallel$ and $J_\perp$ correspond to orientations where the internuclear vector is parallel and perpendicular, respectively, to the applied magnetic field. Under these conditions the appropriate nuclear spin Hamiltonian for the A spin is:

$$\hat{\mathcal{H}} = \hat{\mathcal{H}}_{\rm Z} + \hat{\mathcal{H}}_{\rm CS} + \hat{\mathcal{H}}_{\rm DD} + \hat{\mathcal{H}}_J \tag{34}$$

where $\hat{\mathcal{H}}_{\rm CS}$ accounts for the anisotropic chemical shielding. For now it is assumed that the chemical shielding is independent of the orientation of the molecule in the applied magnetic field. Both $\hat{\mathcal{H}}_{\rm DD}$ and $\hat{\mathcal{H}}_J$ are of the same form. As already indicated

$$\hat{\mathcal{H}}_{\rm DD} = hR\hat{\boldsymbol{I}}_1 \cdot \boldsymbol{D} \cdot \hat{\boldsymbol{I}}_2 = -hR\hat{I}_{1z}\hat{I}_{2z}(3\cos^2\theta - 1) \tag{35}$$

Similarly, equation (31) becomes

$$\hat{\mathcal{H}}_J = h\hat{\boldsymbol{I}}_1 \cdot \boldsymbol{J} \cdot \hat{\boldsymbol{I}}_2 = hJ_{\rm iso}\hat{I}_{1z}\hat{I}_{2z} + h(\Delta J/3)\hat{I}_{1z}\hat{I}_{2z} \times (3\cos^2\theta - 1) \tag{36}$$

Using the basic product functions for an AX spin system consisting of two spin-$\frac{1}{2}$ nuclei, it is straightforward to calculate the four energy levels. The A spectrum results from two allowed transitions at:

$$\nu = \nu_A - m_X J_{iso} + m_X[R - (\Delta J/3)](3\cos^2\theta - 1) \quad (37)$$

where $m_X = +\frac{1}{2}$ or $-\frac{1}{2}$. The two A peaks are separated by

$$\Delta\nu = J_{iso} - [R - (\Delta J/3)](3\cos^2\theta - 1) \quad (38)$$

Often, the term $R - (\Delta J/3)$ in equations (37) and (38) is called the effective dipolar coupling constant R_{eff}; thus,

$$\Delta\nu = J_{iso} - R_{eff}(3\cos^2\theta - 1) \quad (39)$$

The splittings, $\Delta\nu$, that would be observed as the A–X bond axis, $\boldsymbol{r}_{AX}$, in a single crystal is rotated about an axis perpendicular to $\boldsymbol{B}_0$ are shown in Figure 4. Several important points emerge from equations (37)–(39) and Figure 4:

1. For a single crystal sample, equation (39) also applies if the chemical shielding is anisotropic.
2. From Figure 4 it is apparent that the maximum *variation* in the splitting of the A peaks is $3R_{eff}$. Experimentally, one cannot separately determine R and ΔJ; only R_{eff} can be measured. If a value for the internuclear separation r_{AX} can be determined independently by diffraction techniques, R can be calculated from equation (11), and ΔJ can be obtained from the experimental value of R_{eff}.
3. The relative sign of J_{iso} and R_{eff} can be deduced from single crystal measurements. If J_{iso} and R_{eff} have the same sign, the maximum splitting will be $|J_{iso}| + |R_{eff}|$, while the minimum splitting will be $|J_{iso}| - 2|R_{eff}|$. On the other hand, if J_{iso} and R_{eff} have opposite signs, the maximum splitting will be $|J_{iso}| + 2|R_{eff}|$ and the minimum splitting will be $|J_{iso}| - |R_{eff}|$.

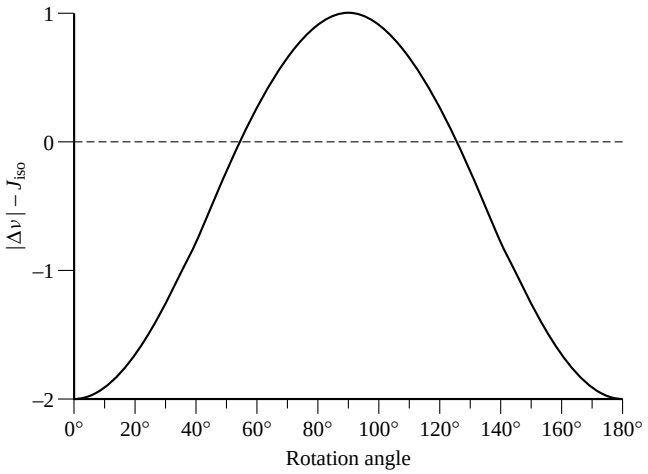

Figure 4 Separation between the two allowed A spin transitions for an AX spin system in a single crystal as a function of the orientation in the applied magnetic field $\boldsymbol{B}_0$. Splittings are given in units of R_{eff}. The rotation axis is perpendicular to $\boldsymbol{B}_0$ and the rotation angle θ is defined as the angle between $\boldsymbol{r}_{AX}$ and $\boldsymbol{B}_0$

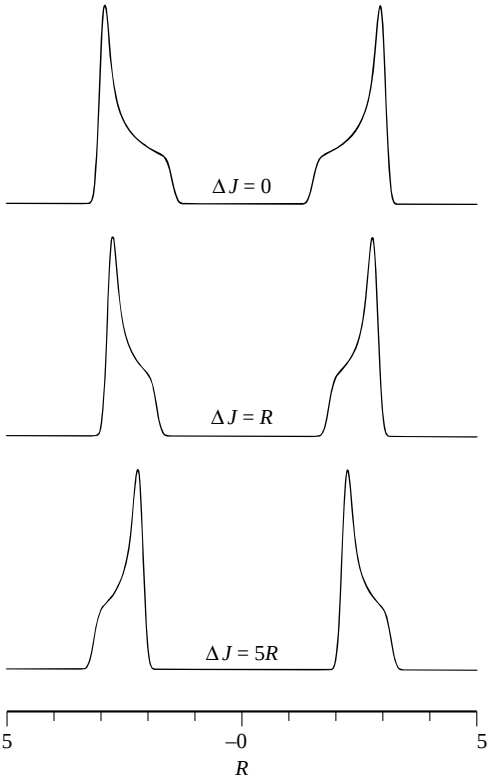

Figure 5 The effect of ΔJ on the A-spin NMR spectrum of a powder sample containing a heteronuclear AX spin pair. In each case $J_{iso} = 5R$. With $\Delta J = 3R$, each subspectrum collapses into an isotropic peak

In the case of a powder sample, the A spectrum consists of two subspectra corresponding to $m_X = +\frac{1}{2}$ and $m_X = -\frac{1}{2}$. Each subspectrum is one-half of a conventional Pake powder pattern (Figure 5). The isotropic frequencies of the two subspectra are separated by J_{iso}. (Note that if $J_{iso} = 0$, conventional Pake powder patterns would be observed except for the case where $\Delta J = 3R$.)

In calculating the spectra shown in Figure 5, the chemical shielding is assumed to be isotropic (i.e. independent of orientation). In order to calculate the A-spin NMR powder lineshape, allowing for the possibility of anisotropic chemical shielding, it is convenient to define the orientation of the internuclear vector in the PAS of the chemical shielding tensor (Figure 6). In this case one can show that the frequency of the A-spin transitions are given by:

$$\nu_m(\theta,\phi) = \nu_L - \nu_{CS} - m_X\nu_D - m_X J_{iso} \quad (40)$$

$$\nu_L = \gamma_A B_0/2\pi \quad (41)$$

$$\nu_{CS} = \left(\frac{\gamma_A B_0}{2\pi}\right)(\sigma_{11}\sin^2\theta\cos^2\phi + \sigma_{22}\sin^2\theta\sin^2\phi + \sigma_{33}\cos^2\theta) \quad (42)$$

$$\nu_D = R_{eff}\{1 - 3[\sin\beta\sin\theta\cos(\phi - \alpha) + \cos\beta\cos\theta]^2\} \quad (43)$$

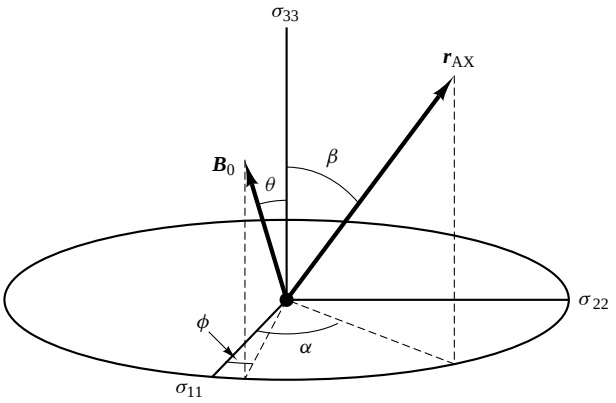

Figure 6 The orientation of an internuclear vector $\boldsymbol{r}_{AX}$ in the principal axis system (PAS) of the A-spin shielding tensor. The angles θ and ϕ define the orientation of $\boldsymbol{B}_0$ in the PAS of the shielding tensor

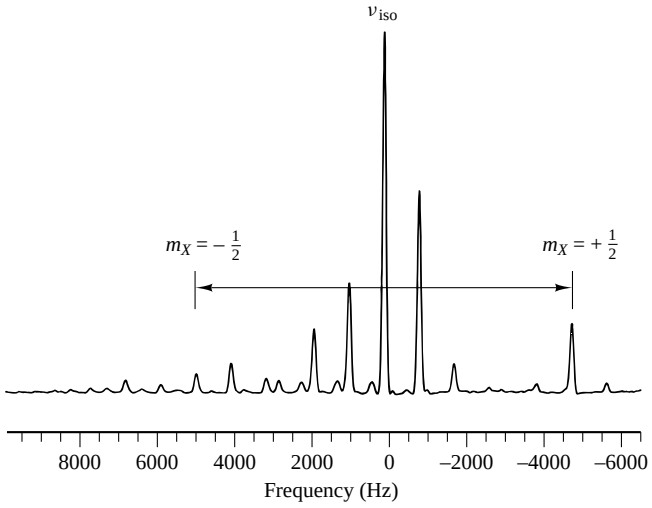

Figure 7 The ^{31}P NMR spectrum of a powder sample of [HgP(*o*-tolyl)$_3$(NO$_3$)$_2$]$_2$ obtained with relatively slow magic angle sample spinning (ν_r = 892 Hz). The spectrum was obtained with high-power ^{1}H decoupling and cross polarization in an applied magnetic field of 4.7 T, corresponding to a ^{31}P NMR Larmor frequency of 81.0 MHz. Frequencies are given with respect to the isotropic ^{31}P NMR peak of solid $NH_4H_2PO_4$. The horizontal arrow indicates the separation between the isotropic peak positions of the ^{199}Hg satellite peaks (J_{iso} = 9660 Hz). Note that the spinning sidebands of the high-frequency satellite peak, $m_{Hg-199} = -\frac{1}{2}$, extend over a much larger range than do those of the low-frequency satellite corresponding to $m_{Hg-199} = \frac{1}{2}$

where the principal components of the chemical shielding tensor σ_{11}, σ_{22}, and σ_{33} are defined such that $\sigma_{11} \leq \sigma_{22} \leq \sigma_{33}$. All angles are defined in Figure 6. In deriving equations (40)–(43), it is assumed that the $\boldsymbol{J}$ tensor is axially symmetric and that the $\boldsymbol{J}$ and $\boldsymbol{D}$ tensors are coincident. Even with these assumptions, the A-spin NMR powder spectrum may prove difficult to analyze.[18]

From the above discussion, it should be clear that if one is interested in characterizing a particular $\boldsymbol{J}$ tensor using solid state NMR techniques, single crystal NMR studies are desirable. Unfortunately, few studies have been reported to date.[41–43] Such studies are generally tedious, require relatively large single crystals (e.g. sides of 1 mm or greater), and the results of an X-ray or neutron diffraction investigation. In some cases, values of ΔJ can be obtained from the analysis of NMR powder spectra which arise from isolated spin pairs.[44–47] For example, for a series of mercury phosphine complexes values of $\Delta J(^{199}\text{Hg}, ^{31}\text{P})$ of the order of 5 kHz have been estimated from the analysis of static ^{31}P NMR spectra.[46,47] Below, the general procedure used to analyze such spectra is outlined.

The ^{31}P CP MAS spectrum of one of these complexes, [HgP(*o*-tolyl)$_3$(NO$_3$)$_2$]$_2$, is shown in Figure 7. The natural abundance of ^{199}Hg is 16.84% ($I = \frac{1}{2}$), therefore the ^{31}P NMR spectrum of the molecules containing the ^{199}Hg–^{31}P spin pair is a doublet with separation $J(^{199}\text{Hg},^{31}\text{P})_{iso}$ = 9660 Hz. The sign of this indirect spin–spin coupling constant is assumed to be positive on the basis of double resonance NMR experiments carried out on related molecules in solution. The only other naturally occurring isotope of mercury with nonzero spin is ^{201}Hg ($I = \frac{3}{2}$; natural abundance 13.22%), but the ^{31}P NMR spectrum of the ^{201}Hg–^{31}P spin pair is very broad and difficult to observe at room temperature. Molecules containing other naturally occurring isotopes of mercury give rise to a single isotropic peak, since the mercury nuclei of these isotopes have $I = 0$. In order to obtain R_{eff}, it is most advantageous to obtain a ^{31}P NMR spectrum of a static powder sample (Figure 8). Again, the intense central feature in the ^{31}P NMR spectrum corresponds to molecules where mercury nuclei have a spin $I = 0$.

Analysis of this central lineshape provides the principal components of the phosphorus shielding tensor, information required to analyze the subspectra arising from the ^{199}Hg–^{31}P spin pairs. In this case, the phosphorus shielding tensor is

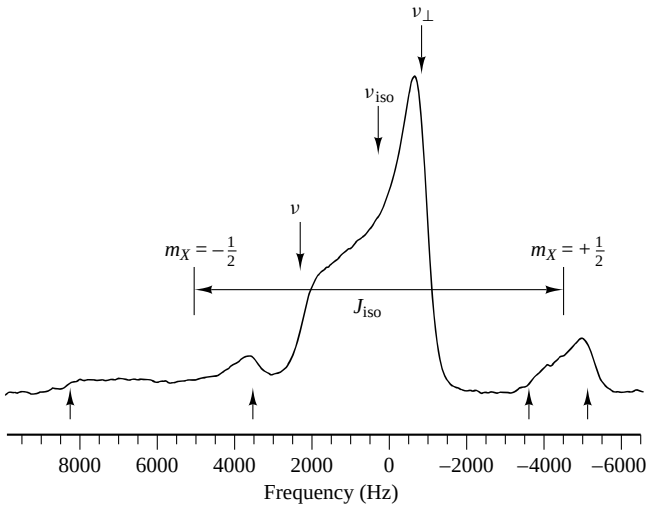

Figure 8 The ^{31}P NMR spectrum of a static powder sample of [HgP(*o*-tolyl)$_3$(NO$_3$)$_2$]$_2$ obtained at 81.0 MHz

approximately axially symmetric with the unique component along the Hg–P bond axis. Inspection of the spectrum shown in Figure 8 indicates that the high-frequency subspectrum corresponding to $m_{Hg-199} = -\frac{1}{2}$ is stretched (breadth ≈4.75 kHz), while the low-frequency subspectrum corresponding to $m_{Hg-199} = \frac{1}{2}$ is squeezed (breadth ≈1.45 kHz) relative to the intense central powder pattern [$(\nu_\parallel - \nu_\perp) \approx 3.10$ kHz]. In this particular case it is straightforward to show that the

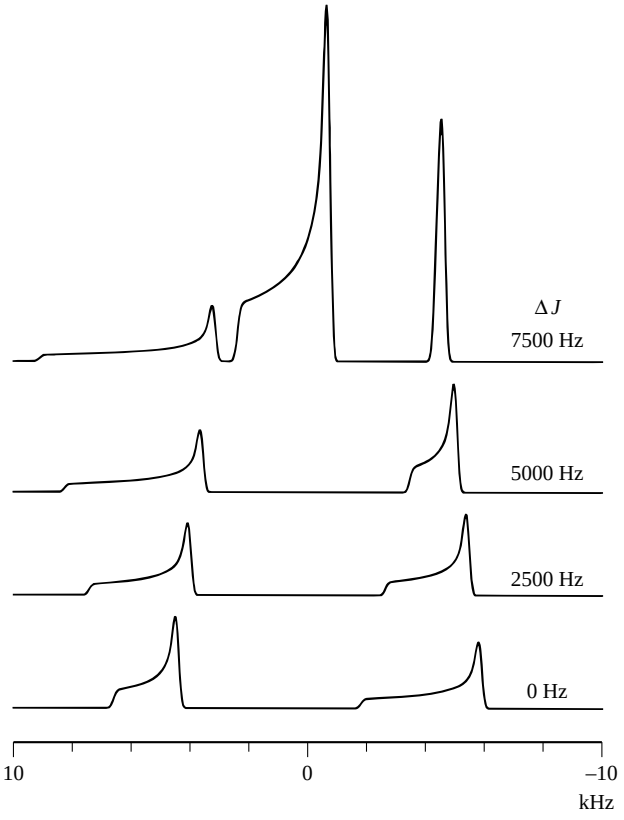

Figure 9 Calculated ^{31}P NMR powder spectra of [HgP(*o*-tolyl)$_3$(NO$_3$)$_2$]$_2$ as a function of ΔJ. The direct dipolar coupling constant, R = 0.64 kHz, and ($\nu_{\parallel} - \nu_{\perp}$) $\approx$ 3.10 kHz were held constant in each calculation. The central uncoupled ^{31}P NMR spectrum is only shown in the top spectrum; its intensity has been suppressed to emphasize the variations in the satellite subspectra as a function of ΔJ

breadth of each subspectrum is given by

$$\Delta\nu_{\pm m(Hg-199)} = (\nu_{\parallel} - \nu_{\perp}) \pm 3m_{Hg-199}R_{eff} \qquad (44)$$

Solving equation (44), one obtains R_{eff} = −1.10 kHz. From the known values of r_{Hg-P} in closely related compounds, R = 0.64 kHz; thus (ΔJ/3) = 1.74 kHz and ΔJ = 5.2 kHz. Note that if the relative signs of R_{eff} and J_{iso} were not known, another acceptable solution would be R_{eff} = + 1.10 kHz, hence ΔJ = −1.38 kHz. The sensitivity of the ^{31}P NMR spectrum of [HgP(*o*-tolyl)$_3$(NO$_3$)$_2$]$_2$ to ΔJ is illustrated in Figure 9. A complete single crystal ^{31}P NMR study of a closely related compound, HgP(cyclohexyl)$_3$(NO$_3$)$_2$, has recently been completed.[52] A typical rotation pattern is shown in Figure 10. Analysis indicates that R_{eff} = −1.07 kHz, leading to comparable values of ΔJ(^{199}Hg,^{31}P).[52] The results of these studies are significant in that they indicate that mechanisms other than the Fermi contact contribute to the $\boldsymbol{J}$(^{199}Hg, ^{31}P) tensor.

For AX spin systems in powder samples, one can also obtain R_{eff} from slow spinning MAS or variable angle spinning NMR studies; however, the errors tend to be large. Therefore, unless R_{eff} is significantly different than R, any estimate of ΔJ may be meaningless.

If a spin-$\frac{1}{2}$ nucleus is coupled to a neighboring quadrupolar nucleus, the spin-$\frac{1}{2}$ MAS NMR lineshape will often exhibit

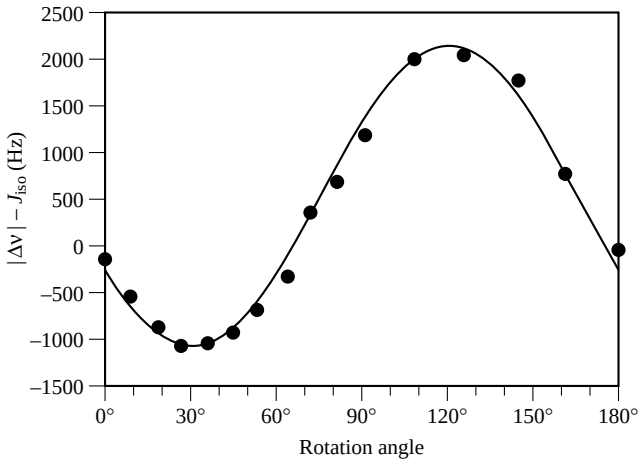

Figure 10 Plot of $\Delta\nu - J$(^{199}Hg,^{31}P)$_{iso}$ versus the rotation angle for a single crystal of HgP(cyclohexyl)$_3$(NO$_3$)$_2$. In this case the rotation axis is approximately perpendicular to the vector $\boldsymbol{r}_{Hg-P}$ so that the maximum observed variation in frequency (3.21 kHz) is approximately $3R_{eff}$

residual 'dipolar splittings' due to coupling with the quadrupolar nucleus.[53] In such cases the magic angle is no longer 'magic' because of the breakdown of the high-field approximation. Qualitatively, the Zeeman states of the quadrupolar nuclei are perturbed by the quadrupolar interaction. Thus, the detailed spin-$\frac{1}{2}$ MAS NMR lineshape depends on R_{eff}, $\boldsymbol{B}_0$, the nuclear quadrupolar coupling constant, and the orientation of the EFG tensor at the quadrupolar nucleus with respect to R_{AX}. Unless information concerning the EFG tensor at the quadrupolar nucleus is available from independent NMR or NQR studies, analysis of the spin-$\frac{1}{2}$ MAS NMR spectrum will be problematic.

Information concerning ΔJ is also available from NMR studies of solute molecules partially ordered in liquid crystalline solvents; however, again one can only determine $\boldsymbol{R}_{AX}$. In fact, from such experiments one measures a parameter which is related to $-S_{zz}[R - (\Delta J/3)]$, where S_{zz} is an order parameter, typically of the order of 0.1. In addition, it is necessary to make vibrational corrections and consider solute–liquid crystal solvent interactions. In spite of these problems, reliable values of ΔJ appear to be available for several compounds. For example, for methyl fluoride, ΔJ(^{19}F,^{13}C) = 404 ± 31 Hz, and thus ΔJ(^{19}F,^{13}C)/J(^{19}F,^{13}C)$_{iso}$ = −2.5 ± 0.2;[54] for dimethylmercury, ΔJ(^{199}Hg,^{13}C) = 855 ± 14 Hz, and thus ΔJ(^{199}Hg,^{13}C)/ J(^{199}Hg,^{13}C)$_{iso}$ = 1.25 ± 0.02.[55]

As mentioned in Section 2, several NMR experiments have been developed to recouple the direct dipolar interaction under conditions of MAS. Although such experiments actually measure R_{eff}, and not R, it is probably reasonable to assume that (ΔJ/3) $\ll R$, if the coupled nuclei are both first row elements (e.g. ^{13}C and ^{15}N), where J_{iso} is probably at least an order of magnitude less than R. Clearly, reliable theoretical calculations could be of value in assessing the validity of this assumption for any given spin pair.

Finally, it is of interest to mention that, several years ago, Andrew and Farnell[56] investigated the effect of magic angle sample spinning on each of the irreducible tensors which describe the indirect spin–spin coupling tensor [equation (23)]. Of course, MAS does not influence the term $J\mathbf{1}$; also, the traceless symmetric components do not influence

the MAS spectrum. However, for a homonuclear spin pair, they found that MAS will not necessarily result in a complete averaging of the antisymmetric components of the **J** tensor [i.e. components of $\boldsymbol{J}^{(1)}$ in equation (23)]. The contribution of the antisymmetric components was predicted to be most important when the chemical shift difference between the two coupled spins was very small. Further discussions of the possibility of measuring antisymmetric components of the **J** tensor are given in the excellent review by Robert and Wiesenfeld.[34] As already mentioned, the antisymmetric components of any indirect spin–spin coupling tensor have not been experimentally characterized.

4 SUMMARY

From the experimental point of view, it is clear that the mathematical properties of the anisotropic indirect **J** tensor are analogous to those of the direct dipolar tensor. As a result, it is impossible to measure separately the anisotropic **J** tensor and the direct dipolar tensor. Fortunately, for isolated spin pairs in rigid solid samples, the direct dipolar tensor can always be calculated if structural data are available. The most reliable procedure for characterizing **J** tensors in the solid state involves single crystal NMR experiments. For solid powder samples the determination of ΔJ is often problematic. The reliability of a powder analysis will always be greatest when: (i) the spin pair of interest lies along a symmetry axis, (ii) J_{iso} is large enough so that the individual subspectra are well resolved, and (iii) R is small or at least comparable to $\Delta J/3$. With the availability of higher sensitivity NMR hardware and advanced single crystal NMR experiments one can hope that more reliable experimental data will become available. In the future, one can also anticipate significant advances in computational techniques, particularly for relatively small molecules involving atoms of the first two rows of the Periodic Table. Unfortunately, these are the systems where it is most difficult to obtain reliable experimental data concerning the anisotropy in the **J** tensor. In any case, it is clear that in order to formulate meaningful models relating J couplings to molecular structure, a better understanding of the **J** tensor is essential. Obviously, any information that indicates which mechanisms are or are not operative is critically important in leading to a better understanding of J coupling phenomena.

5 RELATED ARTICLES

Anisotropy of Shielding and Coupling in Liquid Crystalline Solutions; CRAMPS; Electron–Nuclear Multiple Resonance Spectroscopy; Indirect Coupling: Semiempirical Calculations; Indirect Coupling: Theory and Applications in Organic Chemistry; Internal Spin Interactions and Rotations in Solids; Magic Angle Spinning; REDOR and TEDOR; Rotating Solids.

6 REFERENCES

1. G. E. Pake, *J. Chem. Phys.*, 1948, **16**, 327.
2. W. G. Proctor and F. C. Yu, *Phys. Rev.*, 1951, **81**, 20.
3. H. S. Gutowsky and D. W. McCall, *Phys. Rev.*, 1951, **82**, 748.
4. E. L. Hahn and D. E. Maxwell, *Phys. Rev.*, 1951, **84**, 1246.
5. N. F. Ramsey, *Phys. Rev.*, 1953, **91**, 303.
6. E. R. Andrew, L. F. Farnell, and T. D. Gledhill, *Phys. Rev. Lett.*, 1967, **19**, 6.
7. D. L. VanderHart, H. S. Gutowsky, and T. C. Farrar, *J. Chem. Phys.*, 1969, **50**, 1058.
8. M. Mehring, *High Resolution NMR in Solids*, 2nd edn, Springer, Berlin, 1983.
9. B. C. Gerstein and C. R. Dybowski, *Transient Techniques in NMR of Solids*, Academic, Orlando, Fl., 1985.
10. R. K. Harris, *Nuclear Magnetic Resonance Spectroscopy*, Longman, Burnt Mill, 1986.
11. C. P. Slichter, *Principles of Magnetic Resonance*, 3rd edn, Springer, Berlin, 1989.
12. E. R. Andrew, *Progr. NMR Spectrosc.*, 1971, **8**, 1.
13. P. L. Corio, *Structure of High-Resolution NMR Spectra*, Academic, New York, 1966.
14. M. Munowitz, *Coherence and NMR*, Wiley, New York, 1988.
15. M. E. Stoll, R. W. Vaughan, R. B. Saillant, and T. Cole, *J. Chem. Phys.*, 1974, **61**, 2896.
16. K. W. Zilm and D. M. Grant, *J. Am. Chem. Soc.*, 1981, **103**, 2913.
17. R. K. Harris, K. J. Packer, and A. M. Thayer, *J. Magn. Reson.*, 1985, **62**, 284.
18. K. Eichele and R. E. Wasylishen, *J. Magn. Reson., Ser A*, 1994, **106**, 46, and references therein.
19. M. H. Levitt, D. P. Raleigh, F. Creuzet, and R. G. Griffin, *J. Chem. Phys.*, 1990, **92**, 6347.
20. T. Gullion and J. Schaefer, *Adv. Magn. Reson.*, 1989, **13**, 57.
21. J. M. Griffiths and R. G. Griffin, *Anal. Chim. Acta*, 1993, **283**, 1081.
22. T. Nakai, J. Ashida, and T. Terao, *Mol. Phys.*, 1989, **67**, 839.
23. J. M. Millar, A. M. Thayer, D. B. Zax, and A. Pines, *J. Am. Chem. Soc.*, 1986, **108**, 5113.
24. P. Van Hecke, H. W. Spiess, U. Haeberlen, and S. Haussühl, *J. Magn. Reson.*, 1976, **22**, 93 (see also p. 103).
25. T. Terao, H. Miura, and A. Saika, *J. Chem. Phys.*, 1986, **85**, 3816.
26. A. J. Kim, M. I. Altbach, and L. G. Butler, *J. Am. Chem. Soc.*, 1991, **113**, 4831.
27. K. Schmidt-Rohr, M. Wihelm, A. Johansson, and H. W. Spiess, *Magn. Reson. Chem.*, 1993, **31**, 352.
28. R. J. Gillespie, P. Granger, K. R. Morgan, and G. J. Schrobilgen, *Inorg. Chem.*, 1984, **23**, 887.
29. C. J. Jameson, in *Multinuclear NMR*, ed. J. Mason, Plenum, New York, 1987, Chap. 4, pp. 89–131.
30. R. H. Contreras and J. C. Facelli, *Ann. Rep. NMR Spectrosc.*, 1993, **27**, 255.
31. R. F. Schneider, *J. Chem. Phys.*, 1968, **48**, 4905.
32. H. W. Spiess, *NMR, Basic Principles Prog.*, 1978, **15**, 55.
33. A. D. Buckingham, P. Pyykkö, J. B. Robert, and L. Wiesenfeld, *Mol. Phys.*, 1982, **46**, 177.
34. J. B. Robert and L. Wiesenfeld, *Phys. Rep.*, 1982, **86**, 363.
35. J. S. Blicharski, *Z. Naturforsch., Teil a*, 1972, **27**, 1355.
36. J. Kowalewski and A. Laaksonen, in *Theoretical Models in Chemical Bonding*, Part 3, ed. Z. B. Maksić, Springer, Berlin, 1991, p. 387.
37. P. Pyykkö, *Chem. Phys.*, 1977, **22**, 289.
38. A. Viste, M. Hotokka, L. Laaksonen, and P. Pyykkö, *Chem. Phys.*, 1982, **72**, 225.

39. W. T. Raynes, *Magn. Reson. Chem.*, 1992, **30**, 686.
40. R. E. Wasylishen, K. C. Wright, K. Eichele, and T. S. Cameron, *Inorg. Chem.*, 1994, **33**, 407.
41. A. Nolle, *Z. Phys. B*, 1979, **34**, 175.
42. P. N. Tutunjian and J. S. Waugh, *J. Chem. Phys.*, 1982, **76**, 1223; *J. Magn. Reson.*, 1982, **49**, 155.
43. K. Eichele, G. Wu, R. E. Wasylishen, and J. F. Britten, *J. Phys. Chem.*, 1995, **99**, 1030.
44. D. L. VanderHart and H. S. Gutowsky, *J. Chem. Phys.*, 1968, **49**, 261.
45. U. Haubenreisser, U. Sternberg, and A.-R. Grimmer, *Mol. Phys.*, 1987, **60**, 151.
46. G. H. Penner, W. P. Power, and R. E. Wasylishen, *Can. J. Chem.*, 1988, **66**, 1821.
47. W. P. Power, M. D. Lumsden, and R. E. Wasylishen, *J. Am. Chem. Soc.* 1991, **113**, 8257.
48. J. W. Emsley and J. C. Lindon, *NMR Spectroscopy Using Liquid Crystal Solvents*, Pergamon, Oxford, 1975.
49. J. Lounila and J. Jokisaari, *Prog. NMR Spectrosc.*, 1982, **15**, 249.
50. N. F. Ramsey, *Molecular Beams*, Oxford University Press, Oxford, 1956.
51. R. von Boeckh, G. Gräff, and R. Ley, *Z. Phys.*, 1964, **179**, 285.
52. M. D. Lumsden, K. Eichele, R. E. Wasylishen, T. S. Cameron, and J. F. Britten, *J. Am. Chem. Soc.*, 1994, **116**; 11129.
53. R. K. Harris and A. C. Olivieri, *Prog. NMR Spectrosc.*, 1992, **24**, 435.
54. J. Jokisaari, Y. Hiltunen, and J. Lounila, *J. Chem. Phys.*, 1986, **85**, 3198.
55. A. Pulkkinen, Y. Hiltunen, and J. Jokisaari, *Liq. Cryst.*, 1988, **3**, 737.
56. E. R. Andrew and L. F. Farnell, *Mol. Phys.*, 1968, **15**, 157.
57. D. K. Dalling and H. S. Gutowsky, *J. Chem. Phys.*, 1971, **55**, 4959.
58. H. Dreeskamp and K. Hildenbrand, *Z. Naturforsch., Teil a*, 1968, **23**, 940.
59. J. Jokisaari, K. Räisänen, J. Kuonanoja, P. Pyykkö, and L. Lajunen, *Mol. Phys.*, 1980, **39**, 715.

Acknowledgments

I wish to thank Dr. Klaus Eichele and Michael D. Lumsden for their assistance in preparing the figures for this contribution. Also, I wish to thank Klaus, Mike, Gang Wu, and Professor Aatto Laaksonen for many helpful comments. Our research has been generously supported by NSERC of Canada.

Biographical Sketch

Roderick Wasylishen. *b* 1944. B.Sc., 1968, Waterloo, Ph.D., 1972, Manitoba. Introduced to NMR by Terry Gough at the University of Waterloo and Ted Schaefer at the University of Manitoba. NRC of Canada PDF at the National Institutes of Health, Bethesda, Maryland with Ted Becker. 1972–74. Department of Chemistry, University of Winnipeg, 1974–82; Dalhousie University, 1982–present. Approx. 180 publications. Current research specialty: NMR studies of solids, chemical shielding, spin–spin coupling, EFG tensors, NMR lineshapes, NMR relaxation.

Dipolar Spectroscopy: Transient Nutations and Other Techniques

Mario Engelsberg

Universidade Federal de Pernambuco, Recife, Pernambuco, Brazil

1	Introduction	1
2	Dipolar Spectroscopy of Isolated Pairs	1
3	Suppression of other Broadening Interactions	2
4	Dipolar Spectra	4
5	Related Articles	5
6	References	5

1 INTRODUCTION

The application of dipolar spectroscopy as a structural tool in solids can be realized with the help of transient nutations and other similar techniques. The main objective is to take advantage of the unambiguous geometric and dynamical interpretation of purely homonuclear dipolar spectra involving a small number of interacting spins. Thus, the requirements to be met not only involve the removal of broadening caused, for example, by shielding interactions and static field inhomogeneities, but also that homonuclear dipolar couplings remain either unchanged or are affected in a easily accountable way.

Dipolar spectroscopy in solids using transient nutations was pioneered by Yannoni and Kendrick[1] as a method for obtaining structural information in systems where the lack of some degree of long-range order excludes the use of diffraction techniques. The method, which involves enrichment of an isotopically rare spin-$\frac{1}{2}$ nucleus at two selected molecular positions, followed by dilution of the pairs either in the unenriched material or in a matrix, is ideally suited for structural studies in amorphous solids, reaction intermediates, catalysts, etc.

Transient nutation is just one of the available strategies for dipolar spectroscopy in solids. The suppression of inhomogeneous broadening can also be achieved by employing a train of properly chosen rf pulses. Of the possible pulse sequences, the venerable Carr–Purcell sequence[2] and its variations, with some additions and corrections, has also been shown[3] to be quite effective as a structural tool in disordered solids, giving some advantage in overall spectral resolution.

2 DIPOLAR SPECTROSCOPY OF ISOLATED PAIRS

In order to extract useful geometrical and dynamical information in disordered solids from the homonuclear magnetic dipole–dipole interaction, it is required that the spectra contain sharp and well-defined features, even when the dipoles are randomly oriented. This can be achieved, for example, by creating small clusters of mutually interacting dipoles through isotopic enrichment and matrix isolation or dilution. The simplest strategy is to attempt to approximate a regime of isolated pairs.

For a pair of identical nuclear spins $\boldsymbol{I}_1$ and $\boldsymbol{I}_2$ and magnetogyric constant γ in a strong magnetic field $B_0 = \omega_0/\gamma$ along the z axis, the secular[4] Hamiltonian $\hat{\mathcal{H}}_{12}$ involving Zeeman and dipolar interactions can be written as

$$\hat{\mathcal{H}}_{12} = -\hbar\omega_0(\hat{I}_{z1} + \hat{I}_{z2}) + A_{12}(\hat{\boldsymbol{I}}_1 \cdot \hat{\boldsymbol{I}}_2 - 3\hat{I}_{z1}\hat{I}_{z2}) \qquad (1)$$

where

$$A_{12} = \hbar^2\gamma^2(3\cos^2\theta_{12} - 1)/2r_{12}^3 = \hbar^2\gamma^2 P_2(\cos\theta_{12})/r_{12}^3 \quad (2)$$

$P_2(\cos\theta_{12})$ in equation (2) denotes a second-order Legendre polynomial, $\boldsymbol{r}_{12}$ represents the internuclear vector, and θ_{12} is the angle between $\boldsymbol{r}_{12}$ and $\boldsymbol{B}_0$.

The eigenfunctions and eigenvalues of $\hat{\mathcal{H}}_{12}$ for spin-$\frac{1}{2}$ nuclei can be verified from equation (1) to be the triplet states $|t_+\rangle = |+\ +\rangle$, $|t_-\rangle = |-\ \ -\ \rangle$ and $|t_0\rangle = (|+-\rangle + |-+\rangle)/\sqrt{2}$, with energies $E_{t+} = \hbar\omega_0 + A_{12}/2$, $E_{t-} = -\hbar\omega_0 + A_{12}/2$, and $E_{t0} = -A_{12}$, respectively, and the singlet state $|t_0\rangle = (|+-\rangle - |-+\rangle)/\sqrt{2}$ with energy $E_{s0} = 0$. Since the latter is not connected to the triplet states by a rf magnetic field, the spectrum consists of only two lines, the famous Pake[5] doublet, with a frequency separation given by:

$$\begin{aligned}\delta\nu_{\mathrm{p}} &= 3\hbar\gamma^2(3\cos^2\theta_{12} - 1)/4\pi r_{12}^3 \\ &= 3\hbar\gamma^2 P_2(\cos\theta_{12})/2\pi r_{12}^3 \end{aligned} \qquad (3)$$

Most important as a structural tool in systems lacking long-range order is the spectrum of randomly oriented isolated pairs of spin-$\frac{1}{2}$ nuclei. It can be obtained from equation (3) under the assumption of vectors $\boldsymbol{r}/r$ uniformly distributed on a unit sphere. The spectral weight in the frequency interval $\mathrm{d}\nu$ is then proportional to the solid angle $2\pi\ \sin\theta\ \mathrm{d}\theta$ and to $1/(\mathrm{d}\nu/\mathrm{d}\theta)$, where $\nu - \nu_0 = \pm\delta\nu_p/2$ [equation (3)] are the positions of the two members of the Pake doublet relative to the Larmor frequency $\nu_0 = (\gamma/2\pi)B_0$. Thus, the frequency spectrum for randomly oriented[5] isolated pairs can be seen to be proportional to $1/|\cos\theta|$ and, consequently, to display singularities for $\theta = \pi/2$ corresponding to $\nu - \nu_0 = \pm 3\hbar\gamma^2/8\pi r_{12}{}^3 = \pm\Delta_{\mathrm{p}}/2$.

Not only can useful geometrical information be obtained from a spectrum of isolated pairs (Figure 1), but also a description of the dynamics. If the internuclear vector $\boldsymbol{r}_{12}$ is assumed to execute a hindered rotational motion reorienting about a fixed direction in space by random jumps between several positions, the changes in the spectrum shown in Figure 1 can be accurately predicted from the postulated dynamical model for the motion.[6] Moreover, if the reorientation rate is fast compared with $\delta\nu_{\mathrm{p}}$ [equation (3)], a simple average of $P_2(\cos\theta_{12})$ can be performed in order to determine the changes in the spectrum corresponding to this fast motional regime. If the fixed polar angle of $\boldsymbol{B}_0$ relative to the reorientation axis is denoted by Γ, and the constant angle between $\boldsymbol{r}_{12}$ and the reorientation axis is denoted by ψ_{12}, the addition theorem for spherical harmonics

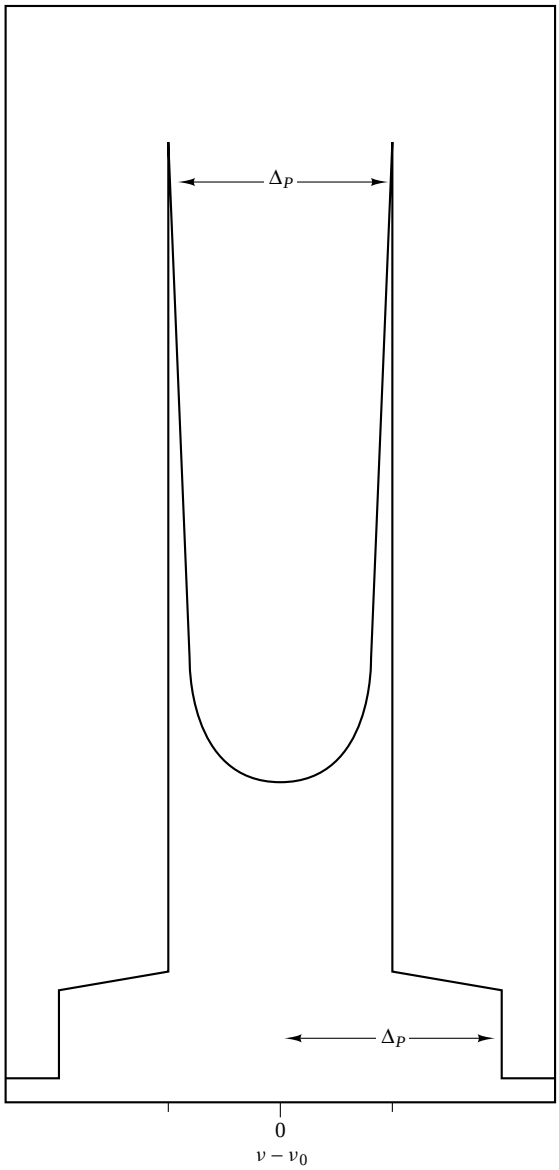

Figure 1 Spectrum of randomly oriented isolated pairs of dipolar-coupled spin-$\frac{1}{2}$ nuclei. The frequency separation between the singularities in the distribution of Pake doublets has the value $\Delta_p = 3\gamma^2\hbar/4\pi r_{12}^3$

can be used to perform the average $\langle P_2(\cos\ \theta_{12})\rangle$ over the time-dependent azimuthal angle associated with $\boldsymbol{r}_{12}$, yielding[7]

$$\langle P_2(\cos\theta_{12})\rangle = P_2(\cos\Gamma)(3\cos^2\psi_{12} - 1)/2 \qquad (4)$$

Equation (4) is valid in the fast motion limit, for hindered rotation between positions of three-fold or higher symmetry, regardless of the details of the motion.

One concludes from equations (3) and (4) that the spectrum corresponding to random directions of the reorientation axis remains identical to the rigid case (Figure 1), but its width can be seen from equation (4) to be reduced by the factor $(3\cos^2\psi_{12} - 1)/2$.

3 SUPPRESSION OF OTHER BROADENING INTERACTIONS

In order to use dipolar spectra of isolated pairs as a structural tool, one needs to suppress other couplings. For spin-$\frac{1}{2}$ nuclei, heteronuclear dipole–dipole interactions, broadening by anisotropic chemical shifts or Knight shifts, and susceptibility broadening in small metallic particles, are among the most frequently found interactions that can mask the spectrum of dipole–dipole coupled isolated pairs.

3.1 Coherent Averaging

As a first step, the choice of an appropriate sequence of pulses for suppressing these couplings without affecting the homonuclear dipolar interactions is worth examining within the framework of average Hamiltonian theory.[8] For δ function excitation pulses, the evolution of the density operator in the rotating frame in the limit of closely spaced pulses has been shown to be governed, after many cycles, by an average Hamiltonian:

$$\bar{\hat{\mathcal{H}}} = (1/T)\sum_{k=1}^{n}\hat{\mathcal{H}}_{nk}\tau_k \qquad (5)$$

where τ_k represents the time interval between the kth and the $(k + 1)$th pulse in a cycle consisting of n pulses with period $T = \sum_{k=1}^{n}\tau_k$. The $\hat{\mathcal{H}}_{nk}$ values in equation (5) can be controlled by the experimenter by a suitable choice of pulses, adequate to the particular internal interactions present.

For the Carr–Purcell sequence, one has $n = 2$ and $\tau_1 = \tau_2 = 2\tau$. Representing the π pulses by the spin rotation operators $\hat{P}_1 = \hat{P}_2 = \exp(-i\pi\hat{I}_y)$ it can be shown[8] that the average Hamiltonian reduces to:

$$\bar{\hat{\mathcal{H}}} = \tfrac{1}{2}(\hat{\mathcal{H}} + \hat{P}_2\hat{\mathcal{H}}\hat{P}_2^{-1}) \qquad (6)$$

which satisfies the requirements for dipolar spectroscopy. Terms in $\hat{\mathcal{H}}$ corresponding to various types of shifts have the general form:

$$\hat{\mathcal{H}}_S = \sum_i \Delta\sigma_i\hat{I}_{zi} \qquad (7)$$

where, for the case of secular chemical shifts, the shielding anisotropy $\Delta\sigma_i$ terms depend upon the orientation of the principal axes of the shielding tensor[8] at the ith site relative to $\boldsymbol{B}_0$. From equation (7) it is clear that $\bar{\hat{\mathcal{H}}}_S = 0$, since the π pulses represented by $\hat{P}_2$ in the second term of the equation simply change the sign of $\hat{\mathcal{H}}_S$. On the other hand, the homonuclear dipolar interaction [equation (1)], being bilinear in the individual spin operators, remains unaffected.

Although the secular heteronuclear interaction is also linear in the individual $\hat{I}_{zi}$ operators and can also be suppressed by the Carr–Purcell sequence and its variations, it is generally more convenient in practice to use strong rf irradiation at the Larmor frequency of these spins for an effective decoupling from the resonant nuclei.

Other pulse sequences also satisfy the requirements for dipolar spectroscopy. For example, several variations of the Carr–Purcell sequence have been proposed in order to compensate for the cumulative error caused by imperfect π pulses. In the Carr–Purcell–Meiboom–Gill (CPMG) sequence[9] this is achieved by a 90° shift between the phase of the π pulses and the phase of the preparation pulse. Other compensated sequences, which have been proposed[10] with a similar aim, involve cycles for 4, 8, or 16 π pulses.

3.2 Transient Nutations

A different approach is needed in order to examine the applicability of transient nutation as a tool for dipolar spectroscopy. This approach permits, at the same time, an evaluation of the effect of π pulses of finite width on dipolar spectra obtained using the CPMG sequence. In the laboratory frame, the total Hamiltonian $\hat{\mathcal{H}}$ includes, in addition to the Zeeman interaction $\hat{\mathcal{H}}_Z$, an interaction with a time-dependent rf field at resonance which may be amplitude modulated by pulses. It also includes a distribution of shifts [equation (7)] and the secular homonuclear dipole–dipole couplings $\hat{\mathcal{H}}_d$:

$$\hat{\mathcal{H}} = -\hbar\omega_0\hat{I}_z - 2\hbar\omega_1(t)\hat{I}_x\cos\omega_0 t - 2t\omega_1(t)I_x\cos\omega_0 t + \sum_i \Delta\sigma_i\hat{I}_{zi} + \hat{\mathcal{H}}_d \tag{8}$$

where, from equations (1) and (2),

$$\hat{\mathcal{H}}_d = \sum_{i\rangle j} A_{ij}(\hat{\boldsymbol{I}}_i\cdot\hat{\boldsymbol{I}}_j - 3\hat{I}_{zi}\hat{I}_{zj}) \tag{9}$$

In the transient nutation experiment, an oscillating rf field of constant amplitude $2\omega_1/\gamma$ is applied suddenly along the x axis of the laboratory frame starting from equilibrium. The ensuing transient precession about the effective field in the rotating frame is then recorded, either point by point after an rf field of variable duration or by sampling through appropriately chosen receiver windows, and Fourier transformed. For simplicity, the conditions for decoupling of the nonresonant spins are assumed to hold, and consequently heteronuclear dipolar interactions have not been included in $\hat{\mathcal{H}}$.

One is interested in the evolution of the density operator $\hat{\rho}'$, in a rotating tilted frame,[11] where one of the two rotating components of the oscillating magnetic field is stationary along the z axis. The transformed density operator $\hat{\rho}'$ can be obtained from the laboratory frame operator $\hat{\rho}$ through the transformation $\hat{\rho}' = \hat{P}\hat{R}\hat{\rho}\hat{R}^{-1}\hat{P}^{-1}$ where

$$\hat{P} = \exp(i\pi\hat{I}_y/2); \quad \hat{R} = \exp(i\omega_0 t\hat{I}_z) \tag{10}$$

Starting from the time evolution of the density operator in the laboratory frame, the evolution of $\hat{\rho}'$ can be shown[11] to be governed by an effective Hamiltonian

$$\hat{\mathcal{H}}'_e = \hat{P}\hat{R}\hat{\mathcal{H}}_e\hat{R}^{-1}\hat{P}^{-1} \tag{11}$$

where $\hat{\mathcal{H}}_e = \hat{\mathcal{H}} - \hat{\mathcal{H}}_Z$, and $\hat{\mathcal{H}}_Z = -\hbar\omega_0\hat{I}_z$ denotes the Zeeman interaction.

Since the secular interactions in $\hat{\mathcal{H}}$ [equations (8) and (9)] commute with $\hat{R}$, the calculation of $\hat{\mathcal{H}}'_e$ from equations (10) and (11) is simplified. Neglecting terms oscillating at frequency $2\omega_0$, the effective Hamiltonian in the rotating tilted frame reduces to

$$\hat{\mathcal{H}}'_e = -\hbar\omega_1\hat{I}_z + \sum_{i\rangle j} A_{ij}(\hat{\boldsymbol{I}}_i\cdot\hat{\boldsymbol{I}}_j - 3\hat{I}_{xi}\hat{I}_{xj}) - \sum_i \Delta\sigma_i\hat{I}_{xi} \tag{12}$$

Furthermore, if the amplitude of the rotating magnetic field ω_1/γ is large compared to the strength of the internal fields, and the system is initially in a state described by an equilibrium density operator $\hat{\rho}(0) = \text{const} \times \hat{I}_z$ in the laboratory frame [and hence by $\hat{\rho}'(0) = -\text{const} \times \hat{I}_x$ in the rotating tilted frame], the *decay* of the transient nutation signal is governed by the terms in equation (13) which commute with $\hat{I}_z$. It is therefore convenient to write, with the help of raising and lowering operators, the last two terms in equation (12) as a purely secular part, obeying the selection rule[4] $\Delta(m_i + m_j) = 0$, plus nonsecular terms satisfying $\Delta(m_i + m_j) \neq 0$. This leads to:

$$\hat{\mathcal{H}}'_e = -\hbar\omega_1\hat{I}_z - \frac{1}{2}\hat{\mathcal{H}}_d - \frac{3}{4}\sum_{i\rangle j} A_{ij}(\hat{I}_{i+}\hat{I}_{j+} + \hat{I}_{i-}\hat{I}_{j-}) - \frac{1}{2}\sum_i \Delta\sigma_i(\hat{I}_{i+} + \hat{I}_{i-}) \tag{13}$$

Equation (13) shows that the transient nutation signal satisfies the requirements for dipolar spectroscopy. Since the last two terms have become nonsecular and do not contribute to the decay, inhomogeneous broadening caused by resonance shifts is suppressed, although an inhomogeneous rf field may still cause broadening.[12] In addition, the strength of the secular dipolar term in equation (14) is one-half the value of the dipolar interaction in the laboratory frame[13] [equation (9)]. Hence the width of the spectrum of isolated pairs shown in Figure 1 is expected to be half the value calculated from equation (3).

3.3 CPMG Sequence with Finite Pulse Widths

The system is prepared by an initial $\pi/2$ pulse and evolves during a time interval τ. A train of π pulses of width t_w, separated by intervals 2τ, and phase shifted by 90° with respect to the initial $\pi/2$ pulse is then applied. The signal amplitudes at the echo maxima are further recorded as a function of time, and Fourier transformed to obtain the frequency spectrum.

Since for the CPMG case, $\omega_1(t)$ in equation (8) represents a periodic function of period $T = 2\tau + t_w$ consisting of rectangular pulses with amplitudes $\omega_{1a} = \pi/t_w$, the steps leading from equation (8) to equation (13) yield an effective Hamiltonian identical to $\hat{\mathcal{H}}'_e$ [equation (13)], but with a time-dependent term $\hbar\omega_1(t)\hat{I}_z$. Moreover, since one is observing the evolution stroboscopically, it is convenient to transform $\hat{\mathcal{H}}'_e$ to a 'toggling frame' where the precession about externally

applied fields, either static or time-dependent, is removed. This is achieved by the transformation[11]

$$\hat{\rho}'_{\rm et}(t) = \exp[-{\rm i}\phi(t)\hat{I}_z/2]\,\hat{\rho}'_{\rm e}(t)\exp[{\rm i}\phi(t)\hat{I}_z/2)] \qquad (14)$$

where:

$$\phi(t) = 2\int_0^t \omega_1(t')\,{\rm d}t' \qquad (15)$$

The evolution of $\hat{\rho}'_{\rm et}(t)$, given by equations (14) and (15), is governed by the effective Hamiltonian

$$\hat{\mathcal{H}}'_{\rm et} = -\frac{1}{2}\hat{\mathcal{H}}_{\rm d} - \frac{3}{4}\sum_{i\rangle j} A_{ij}\{\hat{I}_{i+}\hat{I}_{j+}\exp[{\rm i}\phi(t)] + {\rm c.c.}\}$$
$$-\frac{1}{2}\sum_i \Delta\sigma_i\{\hat{I}_{i+}\exp[-{\rm i}\phi(t)/2] + {\rm c.c.}\} \qquad (16)$$

where c.c. denotes the Hermitian conjugate of the operators within the braces.

As pointed out by Waugh and Wang,[11] only the zero-frequency components of the time-dependent terms in equation (16) can contribute to the observed decay, because the time-dependent parts correspond to frequencies much higher than A_{ij} and $\Delta\sigma_i$ if $1/(t_{\rm w} + 2\tau)$ is sufficiently large. For the periodic functions in equation (16), which involve sine and cosine functions of $\phi(t)$ and $\phi(t)/2$, the zero-frequency components can be obtained graphically in a relatively simple manner by calculating the corresponding averages over one period. Assuming the first π pulse at time from τ from the origin and a sequence of perfect rectangular π pulses of width $t_{\rm w}$, the zero-frequency component of exp $[\pm{\rm i}\phi(t)/2]$ can be seen to vanish leading to a suppression of shifts in equation (16). On the other hand, the dc component of exp $[{\rm i}\phi(t)]$, denoted by $\mathcal{L}$, is given by[3]

$$\mathcal{L} = \frac{1}{T}\int_0^T \cos\phi(t')\,{\rm d}t' = 1 - D \qquad (17)$$

where $T = 2\tau + t_{\rm w}$ is the period, and $D = 2\tau/T$ denotes the duty factor of the sequence of π pulses.

In order to evaluate the effect of π pulses of finite width upon the spectrum of isolated pairs (Figure 1), one can diagonalize the static part of $\hat{\mathcal{H}}'_{\rm et}$ [equation (16)] given by

$$\hat{\mathcal{H}}'_{\rm et} = -\tfrac{1}{2}A_{12}(\hat{\boldsymbol{I}}_1\cdot\hat{\boldsymbol{I}}_2 - 3\hat{I}_{z1}\hat{I}_{z2}) - \tfrac{3}{4}A_{12}(\hat{I}_{1+}\hat{I}_{2+}\mathcal{L}$$
$$+\hat{I}_{1-}\hat{I}_{2-}\mathcal{L}^*) \qquad (18)$$

For spin-$\frac{1}{2}$ nuclei, an adequate basis is composed of the singlet and triplet states introduced earlier in connection with equations (1) and (2). The states $|t_0\rangle$ and $|s_0\rangle$ are still eigenfunctions of $\hat{\mathcal{H}}'_{\rm et}$, whereas two appropriate linear combinations of $|t_+\rangle$ and $|t_-\rangle$ constitute the other two eigenstates.

The quantity of interest in the CPMG experiment is proportional to ${\rm Tr}\,(\hat{\rho}'_{\rm et}(t)\hat{I}_{\rm z})$ and can be explicitly computed[3] from the known eigenvalues and eigenvectors yielding a spectrum of two lines for a given orientation of $\boldsymbol{B}_0$. The frequency separation Δ between the lines for $\theta_{12} = \pi/2$, corresponding to the singularities in the spectrum of randomly oriented pairs (Figure 1) is governed by the second term in equation (18), since the first term commutes with $\hat{\rho}'_{\rm et}(0) = {\rm const}\times\hat{I}_z$ and does not cause any decay. It can be shown[3] that Δ is given by

$$\Delta = 3\gamma^2\hbar(1-D)/4\pi\boldsymbol{r}_{12}^3 \qquad (19)$$

4 DIPOLAR SPECTRA

Figure 2 shows a ^{13}C spectrum of polycrystalline acetic acid at T = 80 K; there is a very close correspondence with the theoretical spectrum shown in Figure 1. The sample contains 4% doubly ^{13}C-labeled acetic acid dissolved in ^{13}C-depleted acetic acid. A modified CPMG sequence with 2τ = 86.4 μs and $t_{\rm w}$ = 9.6 μs, including proton decoupling and cross polarization,[14] was employed. A central peak partially caused by spin locking[7] in the average rf field is omitted for clarity.

Dipolar spectra obtained by employing transient nutations generally display poorer resolution than do those obtained with CPMG sequences, because of the reduction in spectral range by a factor of 2 [equation (13)]. Good resolution is especially important when pairs with more than one interatomic distance are involved.[15] On the other hand, for the CPMG sequence, the splitting Δ(Figure 2) depends on the duty factor, but

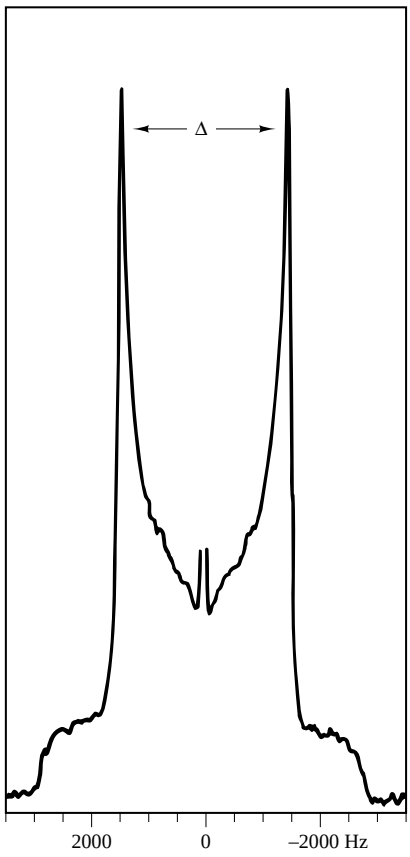

Figure 2 ^{13}C spectrum of polycrystalline acetic acid at T = 80 K. The sample contains 4% doubly ^{13}C-labeled acetic acid dissolved in ^{13}C-depleted acetic acid. A modified CPMG sequence with pulse separation 2τ = 86.4 μs and pulse width t_ω = 9.6 μs was employed (Reproduced by permission from M. Engelsberg and C. S. Yannoni, *J. Magn. Reson.*, 1990, **88**, 393)

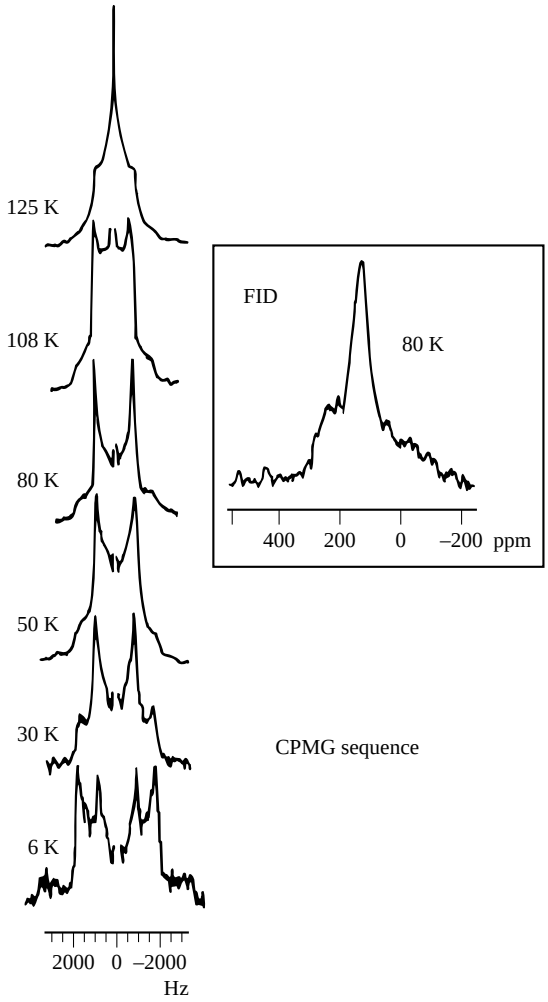

Figure 3 ^{13}C dipolar spectra of benzene (1,2-$^{13}C_2$) chemisorbed on Pt/η-Al_2O_3 obtained by a modified CPMG sequence at various temperatures. The narrow central peak, partially due to spin locking, has been omitted for clarity in all spectra, except the one at 125 K. (Inset) Conventional (FT of FID) proton-decoupled spectrum in the same system at T = 80 K, with shifts measured with respect to a TMS reference (Reproduced by permission from M. Engelsberg, C. S. Yannoni, M. A. Jacintha, C. Dybowski, and R. E. de Souza, *J. Phys. Chem.*, 1994, **98**, 2397. © 1994 American Chemical Society)

the variation has been shown experimentally[3] to agree with the linear dependence predicted by equation (19). Thus a simple correction permits accurate measurement of interatomic distances.[3]

One example of dipolar spectroscopy which helps to illustrate its applicability is provided by the study of benzene chemisorbed on an η-alumina-supported platinum catalyst.[6] The inset in Figure 3 shows a conventional proton-decoupled ^{13}C spectrum of benzene (ν_0 = 15 MHz), doubly labeled in *ortho* positions, chemisorbed on Pt/η–Al_2O_3 at T = 80 K, obtained by FT of the FID. Also shown in Figure 3 are spectra of the same system at various temperatures obtained from a modified CPMG sequence, where the suppression of inhomogeneous broadening uncovers a rich variety of geometrical and dynamical information. The four peaks at the lowest temperature correspond to benzene molecules at different sites, not to different bond lengths.[6,16] For some sites the molecules are rapidly reorienting about the hexad axis,[17] corresponding to $\psi_{12} = \pi/2$ in equation (4), while for others this reorientation rate is small. This explains the difference of a factor of 2 in the splittings of the two inner peaks compared with the outer peaks. At temperatures above 80 K, the spectra can be simulated[6] assuming that the axis of hindered rotation no longer remains perpendicular to the plane of the molecule.

Other examples[15,18,19] of dipolar spectra in a variety of systems further illustrate the usefulness of the techniques described in Section 3 for probing the structure and dynamics of solids.

5 RELATED ARTICLES

Average Hamiltonian Theory; Echoes in Solids; Homonuclear Recoupling Schemes in MAS NMR; Internal Spin Interactions and Rotations in Solids; Nutation Spectroscopy of Quadrupolar Nuclei.

6 REFERENCES

1. C. S. Yannoni and R. D. Kendrick, *J. Chem. Phys.*, 1981, **74**, 747.
2. H. Y. Carr and E. M. Purcell, *Phys. Rev.*, 1954, **94**, 630.
3. M. Engelsberg and C. S. Yannoni, *J. Magn. Reson.*, 1990, **88**, 393.
4. A. Abragam, *The Principles of Nuclear Magnetism*, Oxford University Press, London, 1961, Chap. 4
5. G. E. Pake, *J. Chem. Phys.*, 1948, **16**, 327.
6. M. Engelsberg, C. S. Yannoni, M. A. Jacintha, C. Dybowski, and R. E. de Souza, *J. Phys. Chem.*, 1994, **98**, 2397.
7. C. P. Slichter, *Principles of Magnetic Resonance*, 2nd edn., Springer, Berlin, 1980, Chaps. 3 and 6.
8. J. S. Waugh, C. H. Wang, L. M. Huber, and R. L. Vold, *Phys. Rev.*, 1968, **48**, 662.
9. S. Meiboom and D. Gill, *Rev. Sci. Instrum.*, 1958, **29**, 688.
10. T. Gullion, D. B. Baker, and M. S. Conradi, *J. Magn. Reson.*, 1990, **89**, 479.
11. J. S. Waugh and C. H. Wang, *Phys. Rev.*, 1967, **162**, 209.
12. D. Horne, R. D. Kendrick, and C. S. Yannoni, *J. Magn. Reson.*, 1980, **38**, 493.
13. D. Barnaal and I. J. Lowe, *Phys. Rev. Lett.*, 1963, **11**, 258.
14. A. Pines, M. G. Gibby, and J. S. Waugh, *J. Chem. Phys.*, 1973, **59**, 569.
15. C. S. Yannoni and T. C. Clarke, *Phys. Rev. Lett.*, 1983, **51**, 1191.
16. M. Engelsberg, C. S. Yannoni, M. A. Jacintha, and C. Dybowski, *J. Am. Chem. Soc.*, 1992, **114**, 8319.
17. E. R. Andrews and R. G. Eades, *Proc. R. Soc. Lond., Ser A*, 1953, **218**, 537.
18. J. F. M. Post, B. W. Cook, S. R. Dowd, I. J. Lowe, and C. Ho, *Biochemistry*, 1984, **23**, 6138.
19. C. S. Yannoni, P. P. Bernier, D. S. Bethune, G. Meijer, and J. R. Salem, *J. Am. Chem. Soc.*, 1991, **113**, 3190.

Biographical Sketch

Mario Engelsberg. *b* 1939. Lic. Física 1966, Universidad de Buenos Aires, Argentina. Ph.D. (Physics), Washington University (St. Louis)

(supervisor R. E. Norberg), 1971. Postdoctoral work, University of Pittsburgh (with I. J. Lowe). Professor of Physics, Universidade Federal de Pernambuco, Recife, Brazil, 1974–present. Approx. 55 publications in applications of solid state NMR to physics and chemistry of materials and in NMR imaging at very low magnetic fields.

Double Rotation

Yue Wu

University of North Carolina, Chapel Hill, NC, USA

1	Introduction	1
2	Averaging of the Quadrupole Interaction under DOR	1
3	Principles of the DOR Probe Design	5
4	Sideband Suppression by Synchronization	7
5	CP Double Rotation	8
6	Related Articles	9
7	References	9

1 INTRODUCTION

Double rotation (DOR) is a technique of fast sample rotation. It was designed primarily for obtaining high-resolution NMR spectra of half-integer quadrupolar nuclei in solids along with the technique of dynamic angle spinning (DAS).[1–3] This article describes briefly the theory and the experimental implementation of DOR.

One of the major problems of NMR spectroscopy in solids is its inferior resolution compared to that in liquids. In a powder or polycrystalline sample the random distribution of crystallite orientations with respect to the external magnetic field often causes line broadening through the angular dependence of spin interactions including the chemical shift anisotropy (CSA). In addition, line broadening may also arise from spin–spin interactions even in a single crystal. As a result, resonance lines associated with crystallographically inequivalent sites often overlap with each other, resulting in a loss of important structural information. In contrast, NMR spectra in liquids are of high resolution. Since molecules in liquids experience a rapid isotropic tumbling, only the scalar part of spin interactions such as the isotropic chemical shift is recorded in an NMR spectrum. The angular dependence, for instance, is averaged out by rapid molecular tumbling at a rate much faster than the timescale of the involved spin interactions. It is intriguing, as demonstrated by the magic angle spinning (MAS) technique[4,5] which rotates the entire sample rapidly along a single axis inclined at 54.74° with respect to the external magnetic field, that a uniform sample motion can accomplish line-narrowing effects in solids that are similar to the effects of rapid isotropic molecular tumbling in liquids. The reason for this 'magic' effect is based on the symmetry of the spin interactions.[6]

MAS is very effective in removing broadening mechanisms such as CSA and dipole–dipole interactions.[4,5,7,8] High-resolution MAS spectra of various nuclei, including ^{13}C, ^{29}Si, ^{31}P, and ^{1}H, provide valuable information in the study of solid materials. It turns out that the 'magic' of MAS is much less effective for half-integer quadrupolar nuclei such as ^{27}Al, ^{17}O, ^{11}B, and ^{23}Na. In general, quadrupole interactions are very strong in solids with a noncubic local environment. Typically the line broadening generated by the angular dependence of quadrupole interactions in a strong static external magnetic field is large compared with shielding anisotropies. In general, only the $\frac{1}{2} \leftrightarrow -\frac{1}{2}$ central transition can be readily observed because the central transition is broadened only by the second-order perturbation of quadrupole interactions to the Zeeman interaction. In many solids, even this second-order effect of quadrupole interactions contributes significantly to the line broadening. This has been a major obstacle for solid state NMR of half-integer quadrupolar nuclei in various materials, including molecular sieves, zeolites, and minerals. Since the angular dependence of the second-order quadrupole interaction has a different symmetry than the first-order effect,[6] it is not surprising that the simple trajectory of MAS cannot replace the motion of isotropic tumbling. Figure 1(a) shows the static spectrum of the spin $I = \frac{3}{2}$ nucleus ^{23}Na in a sample containing a mixture of sodium sulfate and sodium oxalate with a molar ratio of 2:1. All spectra shown here were recorded on 400 MHz NMR spectrometers. Both sodium sulfate and sodium oxalate contain a single sodium site. The two inequivalent sodium sites are obviously not resolved in the static spectrum. Under MAS the linewidth is reduced somewhat, as shown in Figure 1(b). The resolution, however, is still too low to distiguish unambiguously the two inequivalent sodium sites. One may think that isotropic tumbling is the only solution for removing the broadening due to the second-order quadrupole interactions. Fortunately, this is not the case. Solutions employing simple mechanical motions exist, including DOR and DAS.

In a DOR NMR experiment the sample is spun rapidly inside a sample-containing small inner rotor which is embedded inside a large outer rotor.[9,10] Under the DOR condition the inner rotor spins along an axis which is inclined at an angle $\beta_1 = 30.56°$ with respect to the spinning axis of the outer rotor; simultaneously, the outer rotor spins along an axis which is set at an angle $\beta_2 = 54.74°$ with respect to the external magnetic field $\boldsymbol{B}_0$. This is illustrated in Figure 2(a). The effect of DOR is demonstrated clearly in Figure 1(c) with the inner rotor spinning at about 5 kHz and the outer rotor spinning at 970 Hz. The two inequivalent sodium sites in the mixture of sodium sulfate and sodium oxalate are completely resolved under DOR with a residual linewidth of 80 Hz. In addition to the two centerbands, which are expanded in Figure 1(d), the DOR spectrum also contains spinning sidebands because of the limited spinning speeds of the inner and outer rotors. The intensity ratio of the two components in Figure 1(c) agrees with the 2:1 molar ratio of the sodium sulfate versus sodium oxalate in this mixture.

2 AVERAGING OF THE QUADRUPOLE INTERACTION UNDER DOR

2.1 The Trajectory of DOR

In order to understand the time dependence of the Hamiltonian under DOR, the motion of the sample has to be described precisely. This is accomplished through three sets of Euler angles relating the orientation of the external magnetic field $\boldsymbol{B}_0$ to a coordinate frame associated with a crystallite. The first set of Euler angles $(0, \beta_2, \omega_R t)$ corresponds to a rotation which rotates the laboratory (LAB) coordinate frame (X, Y, Z) into coincidence with the coordinate frame

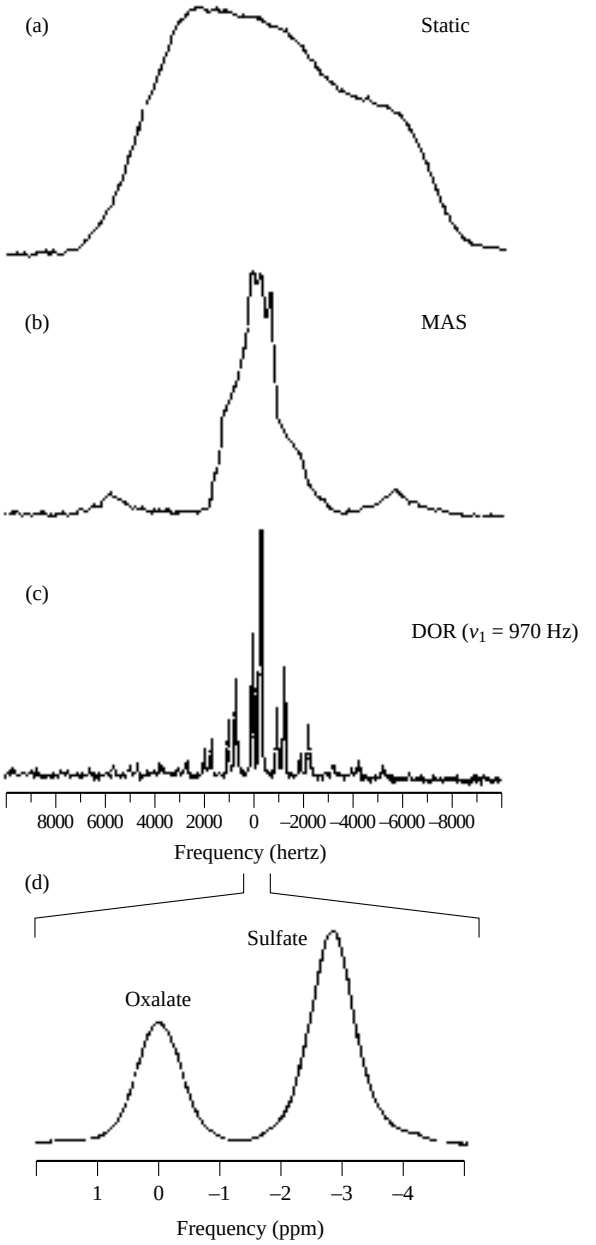

Figure 1 NMR spectra of ^{23}Na central transition in a 2:1 polycrystalline mixture of sodium sulfate and sodium oxalate. (a) Static spectrum, and (b) MAS spectrum with a rotor spinning speed of 5.7 kHz. (c) DOR spectrum with the outer rotor spinning at 970 Hz clearly revealing the two-line structure. (d) An expanded version of (c) showing the centerband peaks originating from the two components of the mixture

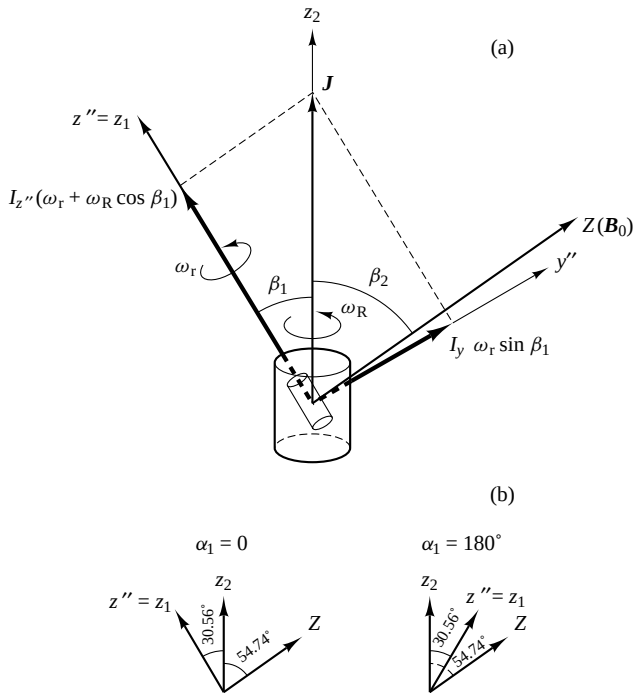

Figure 2 (a) The basic elements of a DOR NMR probe. The spinning axis of the outer rotor is at an angle of 54.74° with respect to $\boldsymbol{B}_0$, and the spinning axis of the inner rotor is set at an angle of 30.56° with respect to the outer rotor axis. By adjusting the ratio of moments of inertia $I_{y''}/I_{z''}$, the addition of the two vector components of the angular momentum along the inner rotor axis z'' and the y'' axis can be made to point along the outer rotor axis z_2, so that spinning the outer rotor will not affect the orientation of the total angular momentum of the inner rotor. (b) Illustration of the $\alpha_1 = 0$ and $\alpha_1 = 180^\circ$ positions

(x_2, y_2, z_2) associated with the outer rotor. The Z and z_2 axes are along the external static magnetic field $\boldsymbol{B}_0$ and the spinning axis of the outer rotor, respectively, and ω_R is the angular velocity of the outer rotor. Here, both the first and the third Euler angles can be chosen as zero at time $t = 0$ because both the orientations of the (X, Y) and the (x_2, y_2) axes can be defined arbitrarily at time $t = 0$. The angle β_2 is the angle between the external static magnetic field $\boldsymbol{B}_0$ and the spinning axis of the outer rotor. As explained later, the exact value of β_2, which can be set experimentally, is crucial. The second set of Euler angles $(\alpha_1, \beta_1, \omega_r t)$ describes a rotation which rotates the outer rotor coordinate frame (x_2, y_2, z_2) into coincidence with the coordinate frame (x_1, y_1, z_1) associated with the inner rotor. The z_1 axis is along the spinning axis of the inner rotor and ω_r is the angular velocity of the inner rotor. Note that the angle α_1 cannot be set arbitrarily to zero because the only remaining degree of freedom, namely the choice of the orientations of the (x_1, y_1) axes, has been used to set the third Euler angle $\omega_r t$ to be zero at time $t = 0$. When $\alpha_1 = 0$ or 180°, the inner rotor axis at $t = 0$ is in the plane defined by the spinning axis of the outer rotor and the magnetic field $\boldsymbol{B}_0$, as shown in Figure 2(b). The angle α_1 is an operationally well-defined angle which can be correlated with the timing of the rf excitation pulse through synchronization by an optical sensor. The third set of Euler angles $(\alpha^i, \beta^i, \gamma^i)$ describes a rotation which rotates the coordinate frame (x_1, y_1, z_1) into coincidence with the coordinate frame (x^i, y^i, z^i) which is associated with a particular crystallite of the sample.

2.2 The Quadrupole Interaction

The Hamiltonian of the quadrupole interaction can be expressed as[7,8,11]

$$\hat{\mathcal{H}}_Q = \frac{eQq_{zz}}{2I(2I-1)} \sum_{m=-2}^{2} (-1)^m V^{(2,-m)} \hat{T}^{(2,m)} \qquad (1)$$

where e is the electronic charge, Q is the quadrupole moment of the nucleus, I is the spin quantum number, q_{zz} is one of the principal components ($|q_{zz}| \geq |q_{yy}| \geq |q_{xx}|$) of the Cartesian electric-field-gradient (EFG) tensor in the principal axis system (PAS), and $\hat{T}^{(2,m)}$ and $V^{(2,m)}$ are irreducible second-rank tensors. $T^{(2,m)}$ are spin operators given by

$$\left.\begin{aligned} \hat{T}^{(2,0)} &= \tfrac{1}{\sqrt{6}}(3\hat{I}_z^2 - \hat{I}^2), \\ \hat{T}^{(2,\pm1)} &= \tfrac{1}{\sqrt{2}}(\hat{I}_{\pm1}\hat{I}_z + \hat{I}_z\hat{I}_{\pm1}),\ \hat{T}^{(2,\pm2)} = \hat{I}_{\pm1}^2 \end{aligned}\right\} \quad (2)$$

where $\hat{I}_{\pm1} = \mp(\hat{I}_x \pm \mathrm{i}\hat{I}_y)/\sqrt{2}$, and $\hat{I}_x$, $\hat{I}_y$, and $\hat{I}_z$ are components of the spin angular momentum operator $\hat{\boldsymbol{I}}$. $V^{(2,m)}$, which relate only to spatial parameters, can be expressed as[12]

$$V^{(2,m)} = \sum_{m'=-2}^{2} D^{(2)}_{m',m}(\alpha, \beta, \gamma)\rho^{(2,m')} \quad (3)$$

where $D^{(2)}_{m',m}$ are the Wigner rotation matrices, (α, β, γ) are Euler angles describing a rotation which brings the PAS frame of the EFG tensor into coincidence with the LAB frame, and $\rho^{(2,m')}$ are components of the reduced EFG tensor (the EFG tensor scaled by $1/q_{zz}$) in the PAS of the EFG tensor, given by

$$\rho^{(2,0)} = \sqrt{\tfrac{3}{2}}, \quad \rho^{(2,\pm1)} = 0, \quad \rho^{(2,\pm2)} = \tfrac{1}{2}\eta \quad (4)$$

where η is the asymmetry parameter of the EFG tensor, defined as $\eta = (q_{xx} - q_{yy})/q_{zz}$. Notice that the angles (β, α) are in fact the polar angles of the orientation of the external static magnetic field $\boldsymbol{B}_0$ with respect to the PAS of the EFG tensor.

For NMR experiments in a high external magnetic field the Zeeman interaction $\hat{\mathcal{H}}_Z$ dominates, and the quadrupole interaction $\hat{\mathcal{H}}_Q$ can be treated as a perturbation. Since the Zeeman eigenstates $|m\rangle = |-I\rangle,.|-I+1\rangle, \ldots, |I\rangle$ are nondegenerate, perturbation calculations can be carried out easily. The first-order perturbation is given by

$$\Delta E_m^{(1)} = \langle m|\hat{\mathcal{H}}_Q|m\rangle = \frac{[3m^2 - I(I+1)]h\chi}{2\sqrt{6}I(2I-1)}V^{2,0} \quad (5)$$

where $\chi = eq_{zz}Q/h \equiv e^2qQ/h$ is the nuclear quadrupole constant and h is the Planck constant. It is evident from equation (3) that $V^{(2,0)}$ depends on the orientation of the crystallite. Thus, the effect of this first-order perturbation will cause line broadening in a powder sample. It is clear, however, that the resonance frequency of the central transition $\nu(\frac{1}{2} \leftrightarrow -\frac{1}{2}) = \nu_L + (\Delta E^{(1)}_{-1/2} - \Delta E^{(1)}_{1/2})/h = \nu_L$, where ν_L represents the Larmor frequency, is not affected by the quadrupole interaction to the first order. This is the reason why the resonance of the $\frac{1}{2} \leftrightarrow -\frac{1}{2}$ central transition is much narrower than the resonances of the satellite transitions such as the $\frac{3}{2} \leftrightarrow \frac{1}{2}$ transition.

The effect of the quadrupole interaction on the $\frac{1}{2} \leftrightarrow -\frac{1}{2}$ central transition has to be evaluated by the second-order perturbation, which is given by

$$\Delta E_m^{(2)} = \sum_{\substack{m'=-I \\ m'\neq m}}^{I} \frac{|\langle m|\hat{\mathcal{H}}_Q|m'\rangle|^2}{E_m^{(0)} - E_{m'}^{(0)}} \quad (6)$$

where $E_m^{(0)}$ is the unperturbed energy eigenvalue of the Zeeman eigenstate $|m\rangle$. This second-order perturbation of the quadrupole interaction can be evaluated easily using equations (1) and (6). The resulting resonance frequency shift $\Delta\nu(\frac{1}{2} \leftrightarrow -\frac{1}{2}) = (\Delta E^{(2)}_{-1/2} - \Delta E^{(2)}_{1/2})/h$ for the central transition can be expressed as

$$\Delta\nu(\tfrac{1}{2} \leftrightarrow -\tfrac{1}{2}) = \frac{-\chi^2}{[2I(2I-1)]^2\nu_L} \times [I(I+1) - \tfrac{3}{4}](2|V^{(2,1)}|^2 - |V^{(2,2)}|^2) \quad (7)$$

using the fact that $|V^{(2,2)}|^2 = |V^{(2,-2)}|^2$, $|V^{(2,1)}|^2 = |V^{(2,-1)}|^2$, and the properties of the spin operators. The term $|V^{(2,2)}|^2$ can be written as

$$|V^{(2,2)}|^2 = \sum_{m,m'=-2,0,2} D^{(2)}_{m',2}(\alpha, \beta, \gamma)D^{*(2)}_{m,2}(\alpha, \beta, \gamma)\rho^{(2,m')}\rho^{(2,m)} \quad (8)$$

Terms with m or $m' = \pm 1$ vanish in equation (8) because $\rho^{(2,\pm1)} = 0$. From the property $D^{*(2)}_{m,m'} = (-1)^{m-m'}D^{(2)}_{-m,-m'} = D^{(2)}_{-m,-m'}$ for even m and m', equation (8) can be modified as

$$|V^{(2,2)}|^2 = \sum_{m,m'=-2,0,2} D^{(2)}_{m',2}(\alpha, \beta, \gamma)D^{(2)}_{-m,-2}(\alpha, \beta, \gamma) \times \rho^{(2,m')}\rho^{(2,m)} \quad (9)$$

According to the coupling rule,[12] the product $D^{(2)}_{m',2}D^{(2)}_{-m,-2}$ can be expressed as

$$D^{(2)}_{m',2}D^{(2)}_{-m,-2} = \sum_{l=0}^{4} c(2\,2\,l;\ m'-m)c(2\,2\,l;\ 2\ -2)D^{(l)}_{m'-m,0} \quad (10)$$

where $c(l_1\ l_2\ l;\ m_1\ m_2)$ are the Clebsch–Gordan coefficients. In fact, only terms with $l = 0, 2, 4$ in equation (10) will contribute in equation (9) because[12] $c(l_1l_2l; m_1m_2) = (-1)^{l_1+l_2+l}c(l_2l_1l; m_2m_1)$ and $l_1 = l_2 = 2$ will make $l = 1$ and $l = 3$ terms disappear from equation (9). Similarly, it can be shown that

$$|V^{(2,1)}|^2 = -\sum_{m,m'=-2,0,2} D^{(2)}_{m',1}(\alpha, \beta, \gamma)D^{(2)}_{-m,-1}(\alpha, \beta, \gamma) \times \rho^{(2,m')}\rho^{(2,m)} \quad (11)$$

where the product $D^{(2)}_{m',1}D^{(2)}_{-m,-1}$ can be expressed as

$$D^{(2)}_{m',1}D^{(2)}_{-m,-1} = \sum_{l=0,2,4} c(2\,2\,l;\ m'-m) \times c(2\,2\,l;\ 1\ -1)D^{(l)}_{m'-m,0} \quad (12)$$

Table 1 Values of the Coefficient $a_{l,m}$ for Different l and m

	$m = 0$	$m = \pm 2$	$m = \pm 4$
$l = 0$	$-\frac{3}{10}\left(1+\frac{\eta^2}{3}\right)$		
$l = 2$	$-\frac{6}{7}\left(1-\frac{\eta^2}{3}\right)$	$\frac{2\sqrt{6}}{7}\eta$	
$l = 4$	$\frac{81}{70}\left(1+\frac{\eta^2}{18}\right)$	$\frac{27}{14\sqrt{10}}\eta$	$\frac{9}{4\sqrt{70}}\eta^2$

The matrices $D^{(l)}_{m'-m,0}(\alpha, \beta, \gamma)$ in equations (10) and (12) are related to the spherical harmonics as[12]

$$D^{(l)}_{m'-m,0}(\alpha, \beta, \gamma) = \sqrt{\frac{4\pi}{2l+1}} Y^*_{l,m'-m}(\beta, \alpha) = \sqrt{\frac{4\pi}{2l+1}} (-1)^{m'-m} Y_{l,m-m'}(\beta, \alpha) \quad (13)$$

Thus, the resonance frequency shift $\Delta\nu(\frac{1}{2} \leftrightarrow -\frac{1}{2})$ caused by the second-order effect of the quadrupole interaction can be expressed as a linear combination of spherical harmonics,[2]

$$\Delta\nu(\tfrac{1}{2} \leftrightarrow -\tfrac{1}{2}) = \frac{\chi^2}{[2I(2I-1)]^2\nu_L}\left(I(I+1)-\frac{3}{4}\right) \times \sum_{l=0,2,4}\sum_{\substack{m=-l \\ \text{even}}}^{l} a_{l,m}\sqrt{\frac{4\pi}{2l+1}} Y_{l,m}(\beta, \alpha) \quad (14)$$

where the coefficients $a_{l,m}$ are listed in Table 1. The line broadening comes from the fact that the orientation (β, α) associated with each crystallite distributes randomly in a powder sample. Since $Y_{0,0}(\beta, \alpha) = 1/\sqrt{4\pi}$, the $l = 0$ term in equation (14) contributes to $\Delta\nu(\frac{1}{2} \leftrightarrow -\frac{1}{2})$ a quantity

$$\Delta\nu^{(2)}_{iso} = -\frac{3}{10}\frac{\chi^2[I(I+1)-\frac{3}{4}]}{\nu_L[2I(2I-1)]^2}(1+\tfrac{1}{3}\eta^2) \quad (15)$$

which is independent of the polar angles (β, α). $\Delta\nu^{(2)}_{iso}$ is called the isotropic second-order quadrupolar shift. This isotropic shift always exists even under sample spinning or the tumbling motion unless the rate of motion is much faster than the Larmor frequency.

2.3 The Effect of DOR

The sample motion under DOR renders the Hamiltonian time-dependent through the changes of the polar angles (β, α) of the external magnetic field with respect to the PAS system of the EFG tensor. Since the adjacent energy levels (nondegenerate) under the static condition are separated from each other approximately by $h\nu_L$, and the quadrupole interaction only adds a small correction, the time dependence of the Hamiltonian under DOR can be considered to be adiabatic given that the spinning rates (typically a few kilohertz) of the double rotor are much smaller than ν_L. This time dependence can be incorporated in $\Delta\nu(\frac{1}{2} \leftrightarrow -\frac{1}{2})$ through the following transformation of the spherical harmonics:[12]

$$Y_{l,m}(\Theta, \Phi) = \sum_{m'=-l}^{l} Y_{l,m'}(\theta, \phi) D^{(l)}_{m',m}(\alpha', \beta', \gamma') \quad (16)$$

where (θ, ϕ) are the polar angles of a vector in the old coordinate frame, (Θ, Φ) are the polar angles of the same vector in the new coordinate frame, and $(\alpha', \beta', \gamma')$ are the Euler angles of a rotation which brings the old coordinate frame into coincidence with the new coordinate frame. Applying this transformation three times, LAB → outer rotor →inner rotor → PAS, the spherical harmonics $Y_{l,m}(\beta, \alpha)$ in equation (14) can be expressed as

$$Y_{l,m}(\beta, \alpha) = \sum_{m',m'',n=-l}^{l} D^{(l)}_{m',m}(\alpha^i, \beta^i, \gamma^i) D^{(l)}_{m'',m'}(\alpha_1, \beta_1, \omega_r t) \times D^{(l)}_{n,m''}(0, \beta_2, \omega_R t) Y_{l,n}(0, 0) \quad (17)$$

The factors $D^{(l)}_{m',m}(\alpha^i, \beta^i, \gamma^i)$ cause line broadening because of the random distribution of the Euler angles $(\alpha^i, \beta^i, \gamma^i)$ in a powder sample.

Since $Y_{l,n}(0,0)=0$ for $n \neq 0$ and $Y_{l,0}(0, 0) = \sqrt{(2l+1)/4\pi}$, equation (17) can be reduced to

$$Y_{l,m}(\beta, \alpha) = \sum_{m',m''=-l}^{l} \sqrt{\frac{(2l+1)}{4\pi}} \times D^{(l)}_{m',m}(\alpha^i, \beta^i, \gamma^i) d^{(l)}_{m'',m'}(\beta_1) d^{(l)}_{0,m''}(\beta_2) \times \exp[-i(m'\omega_r + m''\omega_R)t] \exp(-im''\alpha_1) \quad (18)$$

where $d^{(l)}_{m',m}$ are the reduced Wigner rotation matrices. Assuming that $m'\omega_r + m''\omega_R \neq 0$ for all pairs of m' and m'' in equation (18) unless $m' = m'' = 0$, for instance by choosing $\omega_r > 5\omega_R$, then the only term remaining in equation (18) after time averaging is (the secular term)

$$Y_{l,m}(\beta, \alpha) = \sqrt{\frac{(2l+1)}{4\pi}} D^{(l)}_{0,m}(\alpha^i, \beta^i, \gamma^i) d^{(l)}_{0,0}(\beta_1) d^{(l)}_{0,0}(\beta_2) \quad (19)$$

This term depends on the angles β^i and γ^i. For $l = 2$ and $l = 4$ this anisotropic effect can be completely eliminated by choosing the angles β_1 and β_2 such that both

$$d^{(2)}_{0,0}(\beta_1) d^{(2)}_{0,0}(\beta_2) = P_2(\cos\beta_1) P_2(\cos\beta_2) = 0 \quad (20a)$$

and

$$d^{(4)}_{0,0}(\beta_1) d^{(4)}_{0,0}(\beta_2) = P_4(\cos\beta_1) P_4(\cos\beta_2) = 0 \quad (20b)$$

where $P_2(\cos\varphi) \equiv (3\cos^2\varphi - 1)/2$ and $P_4(\cos\varphi) \equiv (35\cos^4\varphi - 30\cos^2\varphi + 3)/8$ are the second and fourth Legendre polynomials. The solutions for equations (20a) and (20b) are $\beta_1 = 54.74^\circ$ and $\beta_2 = 30.56^\circ$ or $\beta_1 = 54.74^\circ$ and $\beta_2 = 70.12^\circ$.

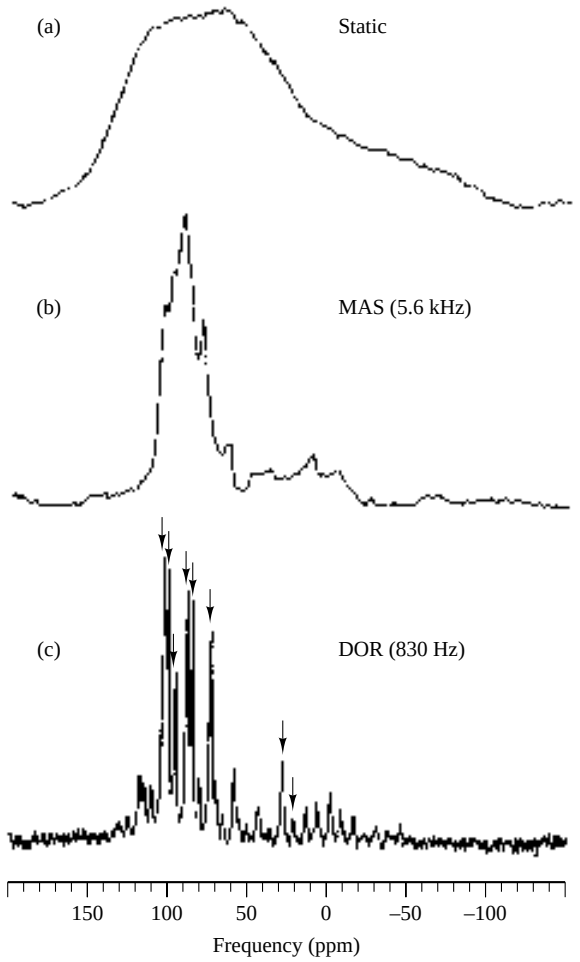

Figure 3 NMR spectra of ^{17}O central transition in polycrystalline $CaSiO_3$ wollastonite. (a) Static spectrum, and (b) MAS spectrum with a rotor speed of 5.6 kHz. (c) DOR spectrum with outer rotor spinning at 830 Hz. Lines arising from eight resolved oxygen sites are indicated by arrows; other peaks are spinning sidebands. The chemical shift reference is ^{17}O in water

Dramatic effects of line narrowing by DOR have been demonstrated for many half-integer quadrupolar nuclei. For instance, the ^{17}O spectrum of the mineral wollastonite can be improved significantly by DOR. Figure 3(a) and (b) show the static and MAS ^{17}O spectra of wollastonite, respectively. Clearly, the nine crystallographically distinct sites in wollastonite are far from being resolved under MAS. The resolution is enhanced substantially under DOR, as shown in Figure 3(c) where eight resonance peaks can be clearly identified. Peaks which are not indicated by arrows in Figure 3(c) are spinning sidebands. In order to obtain a clean spectrum with minimal sideband intensity, fast spinning speeds of the inner and outer rotors are required.

3 PRINCIPLES OF THE DOR PROBE DESIGN

The basic elements of a DOR probe[9,10] are illustrated in Figure 2. The large outer rotor is set at the magic angle of 54.74° with respect to the static magnetic field. The rf coil is wound around the outer rotor. The air bearing and drive system for the outer rotor is similar to the conventional MAS system as shown in Figure 4(a). The outer rotor, represented by the shaded area in Figure 4(a), is centered by two pins (part 9), supported by the air bearing (part 6), and driven by air jets (part 7). As expected, the internal structure of the outer rotor is far more complicated than a regular MAS spinner. As shown in Figure 4(b), it contains the entire air bearing and drive system for the inner rotor which spins along an axis set at an angle of 30.56° with respect to the outer rotor axis. The inner rotor (part 1) is also centered by two pins (part 5) mounted on two small caps (part 15). The air bearing (part 3) and drive (part 4) for the inner rotor are mounted inside the body of the outer rotor. The air for the bearing and drive of the inner rotor is fed through two cylinders (part 10) which fit inside the two pockets (part 10′) on the outer rotor with a very small clearance. The minimal clearance allows the outer rotor to spin freely without significant leakage of air.

It is well known that a spinning object, like the inner rotor, has a tendency to maintain its spinning orientation unless a torque is exerted on it. Under DOR the spinning orientation of the inner rotor changes direction rapidly. Thus, a torque has to be provided to the inner rotor by the bearing system which only has a limited load capacity. This extra burden imposed by the torque may cause a 'crash' of the inner rotor spinning. Fortunately, nature provides a self-adjusting mechanism which can reduce the torque to a tolerably small value under DOR.

A perfectly balanced inner rotor requires not only axial symmetry with respect to the rotation axis of the inner rotor but also mirror symmetry with respect to the plane which is perpendicular to the rotation axis of the inner rotor and contains the cross-point of the inner and outer rotor rotation axes. The equation governing this motion is

$$\boldsymbol{\tau} = \frac{\mathrm{d}\boldsymbol{J}}{\mathrm{d}t} \tag{21}$$

where $\boldsymbol{J}$ is the angular momentum of the inner rotor and τ is the torque applied to the inner rotor through the bearing. The angular momentum can be expressed in terms of the angular velocity ($\omega_{x'}$, $\omega_{y''}$, and $\omega_{z''}$)

$$\boldsymbol{J} = \boldsymbol{i} I_{x''}\omega_{x''} + \boldsymbol{J} I_{y''}\omega_{y''} + \boldsymbol{k} I_{z''}\omega_{z''} \tag{22}$$

where $\boldsymbol{i}$, $\boldsymbol{j}$, and $\boldsymbol{k}$ are the unit vectors of the PAS (x'', y'', z'') of the moment of inertia tensor of the inner rotor with principal values $I_{x''}$, $I_{y''}$, and $I_{z''}$. For a cylindrical inner rotor, z'' is chosen to be along the rotation axis of the inner rotor, y'' is in the plane containing the rotation axes of both the inner and the outer rotors, and $I_{x''} = I_{y''}$. There are two contributions to the inner rotor angular velocity $\omega_{z''}$, the angular velocity ω_r originating from the inner rotor rotation around its own axis and the angular velocity $\omega_R \cos \beta_1$ imposed by the rotation of the outer rotor as illustrated in Figure 2(a). The only contribution to $\omega_{y''}$, $\omega_R \sin \beta_1$, comes from the rotation of the outer rotor, whereas $\omega_{x''} = 0$. The total angular momentum $\boldsymbol{J}$ is the vector sum of the two components $I_{z''}(\omega_r + \omega_R \cos \beta_1)\boldsymbol{k}$ and $I_{y''}\omega_R \sin \beta_1 \boldsymbol{j}$. It is clear that if this vector sum $\boldsymbol{J}$ is along the rotation axis of the outer rotor, the total angular momentum will become time-independent; thus, no torque is involved in the motion of the inner rotor. This torque-free condition can

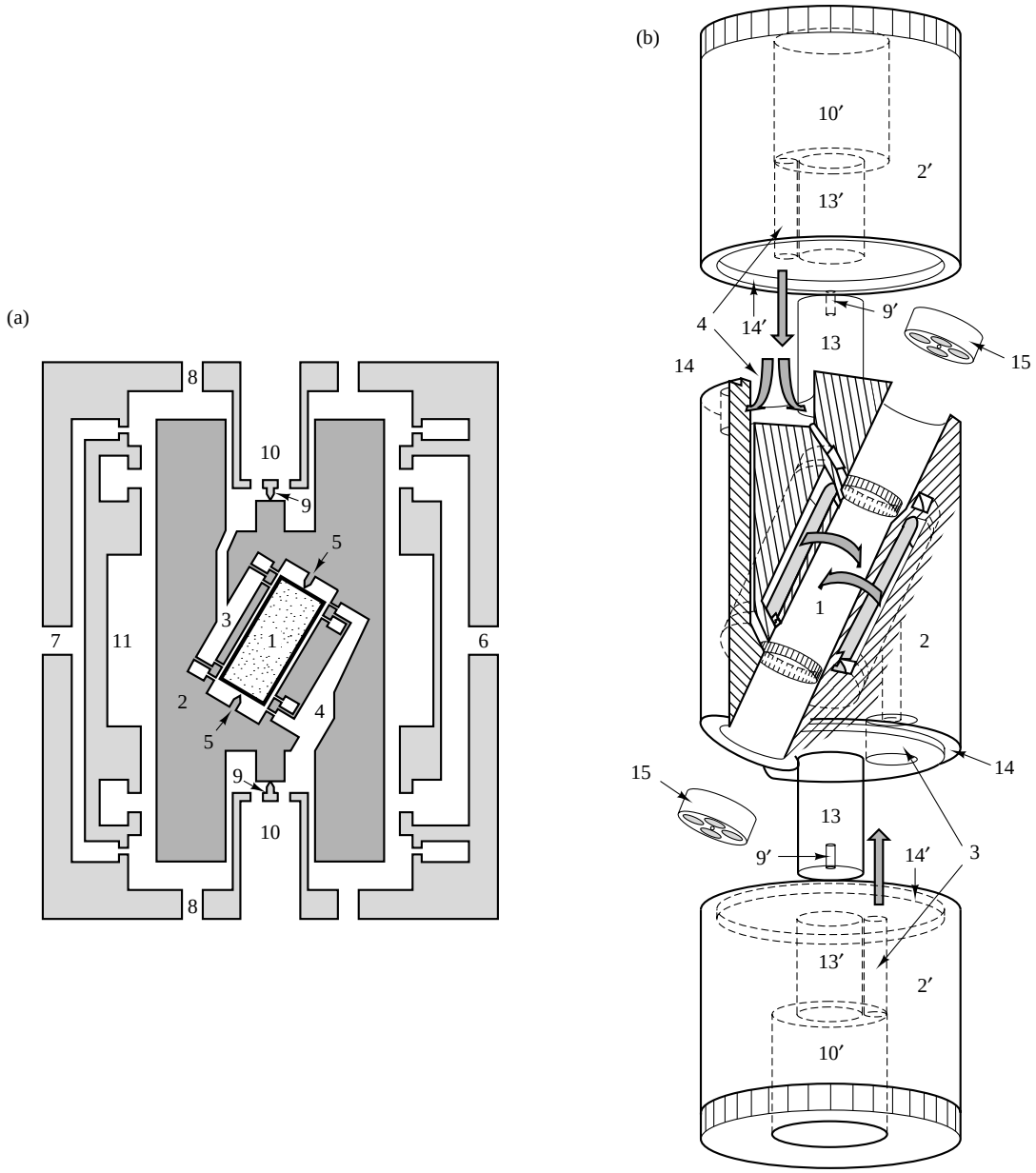

Figure 4 A double-rotor probe design. (a) DOR probe. (b) Details of the double rotor. The numbers, which apply both to (a) and (b), indicate 1, inner rotor with flutes at both ends; 2 and 2′, building blocks of the double rotor held together by the axles 13 with matching counterparts 13′, and the step-shoulder 14 with matching counterparts 14′; 3 and 4, air channels and holes for the bearing and drive system of the inner rotor; 5, pins to hold the inner rotor in place; 6 and 7, the bearing and drive system for the outer rotor; 8, air exhaust holes for the outer rotor; 9, pins to hold the outer rotor in place; 10, air passage for the inner rotor which fits into the pocket 10′ with minimal clearance; 11, space for the rf coil; 15, caps holding the inner rotor in place and allowing air escape for the inner rotor system

be realized if

$$\tan\beta_1 = \frac{I_{y''}\omega_R \sin\beta_1}{I_{z''}(\omega_r + \omega_R \cos\beta_1)} \tag{23}$$

or

$$\frac{\omega_r}{\omega_R} = \cos\beta_1 \left(\frac{I_{y''}}{I_{z''}} - 1\right) \tag{24}$$

The ratio $I_{y''}/I_{z''}$ is determined by the shape of the inner rotor. Consequently, the ratio ω_r/ω_R corresponding to the torque-free condition is also determined by the spinner design. The typical value of the ratio ω_r/ω_R is around 5–6 with the inner rotor spinning at about 5 kHz and the outer rotor spinning at 1 kHz. In practice, there is no need to adjust the spinning speeds of the inner and outer rotors manually to satisfy the torque-free condition because a self-adjusting mechanism is in place.[10] To operate the double rotor, the inner rotor is first brought to a high speed. Then the outer rotor speed is slowly increased. Initially, the ratio ω_r/ω_R is too high for the torque-free condition. Consequently, a torque is generated, and the friction on the inner rotor generated by this torque slows down the spinning of the inner rotor. As a result, the ratio ω_r/ω_R is reduced, thus the torque and friction also decrease. Finally,

the system stabilizes the inner rotor spinning speed at a ω_r/ω_R ratio close to the torque-free condition. As the outer rotor speed increases, the inner rotor speed increases as well to maintain the torque-free condition.

4 SIDEBAND SUPPRESSION BY SYNCHRONIZATION

Since the spinning speeds of the inner and outer rotors are limited by the current technology, the DOR spectrum often consists of a large number of intense sidebands along with the centerband, as can be seen clearly in Figure 3(c). These sidebands may cause severe problems in practical applications. For instance, the sidebands associated with one lattice site may overlap with the centerband associated with another crystallographically inequivalent site. Such interference makes the recognition of crystallographically inequivalent sites difficult. In principle, the centerband can be distinguished from the sideband by changing the spinning speed of the outer rotor, because the resonance frequency of the centerband does not vary with the change of the spinning speed whereas the sideband does. However, this method is ineffective when the residual linewidth as a result of the random distribution of local environment becomes comparable to the spinning speed of the outer rotor. Therefore, the suppression of spinning sidebands is very important for practical applications.

To simplify the problem, consider the case where the spinning rate of the inner rotor is infinite. Under this condition, equation (18) can be reduced to

$$Y_{l,m}(\beta,\alpha) = \sum_{m''=0}^{l} \sqrt{\frac{(2l+1)}{4\pi}} \times D^{(l)}_{0,m}(\alpha^i,\beta^i,\gamma^i) d^{(l)}_{m'',0}(\beta_1) d^{(l)}_{0,m''}(\beta_2) \times 2\cos[m''(\omega_R t+\alpha_1)] \quad (25)$$

The $m'' = 0$ term in equation (25) is zero under the DOR condition. As mentioned earlier, the effect of motion under DOR can be treated as an adiabatic process. Thus, the evolution of the NMR signal $s(t)$ associated with the central transition can be described by

$$s(t) \propto \exp[i\varphi(t)] \quad (26)$$

The accumulated phase $\varphi(t)$, according to equation (25), can be calculated by[13,14]

$$\varphi(t) = \omega_0 t + \int_0^t dt' \sum_{m=1}^{4} a_m \cos[m(\alpha_1 + \omega_R t)] \quad (27)$$

where ω_0 is the angular isotropic resonance frequency including the Larmor frequency and the isotropic second-order quadrupolar shift, and the time $t = 0$ corresponds to the timing of the rf excitation pulse. The detailed expressions of the coefficients a_m have no bearing on our following discussion. The expression of equation (27) is quite simple for the case of $\alpha_1 = 0$ or $\alpha_1 = 180^\circ$, which can be selected by synchronizing the rf excitation pulse with the position of the rotor. The accumulated phase $\varphi(t)$ is[13]

$$\varphi(t) = \omega_0 t + \xi_{even} \pm \xi_{odd} \quad (28)$$

where the upper and lower signs correspond to the $\alpha_1 = 0$ and $\alpha_1 = 180^\circ$ cases, respectively, and

$$\xi_{even} = \frac{a_2}{2\omega_R}\sin(2\omega_R t) + \frac{a_4}{4\omega_R}\sin(4\omega_R t) \quad (29a)$$

$$\xi_{odd} = \frac{a_1}{\omega_R}\sin(\omega_R t) + \frac{a_3}{3\omega_R}\sin(3\omega_R t) \quad (29b)$$

The real part (the X channel) of the signal is given by

$$\cos\varphi(t) = \cos(\omega_0 t)(\cos\xi_{even}\cos\xi_{odd} \mp \sin\xi_{even}\sin\xi_{odd}) - \sin(\omega_0 t)(\sin\xi_{even}\cos\xi_{odd} \pm \cos\xi_{even}\sin\xi_{odd}) \quad (30)$$

It can be shown that the above expression of $\cos\varphi(t)$ can be expanded in the following form:[13,14]

$$\cos\varphi(t) = \sum_{k=-\infty}^{\infty} \{A_{2k}\cos[(\omega_0 + 2k\omega_R)t] \pm B_{2k+1}\cos[(\omega_0 + (2k+1)\omega_R)t]\} \quad (31)$$

where A_{2k} and B_{2k+1} are coefficients which are independent of time t. This expression of $\cos\varphi(t)$ can be derived by using the series expansion for the functions $\cos(z\sin\theta)$, $\sin(z\sin\theta)$, $\cos(z\cos\theta)$, and $\sin(z\cos\theta)$. For instance,

$$\cos(z\sin\theta) = J_0(z) + 2\sum_{k=1}^{\infty} J_{2k}(z)\cos(2k\theta) \quad (32)$$

where the coefficients J_0 and J_{2k} are the Bessel functions. Based on these expansions, it can be shown that the terms $\cos\xi_{even}\cos\xi_{odd}$ and $\sin\xi_{even}\cos\xi_{odd}$ in equation (30) contribute only to the terms $A_{2k}\cos[(\omega_0 + 2k\omega_R)t]$ in equation (31); these terms represent the centerband and the even-numbered rotational sidebands. Similarly, it can be shown that the terms $\sin\xi_{even}\sin\xi_{odd}$ and $\cos\xi_{even}\sin\xi_{odd}$ in equation (30) contribute only to the terms $B_{2k+1}\cos[(\omega_0 + (2k+1)\omega_R)t]$ in equation (31); these terms represent the odd-numbered rotational sidebands. Therefore, the centerband and the even-numbered sidebands do not change when α_1 changes from 0 to 180° whereas the odd-numbered sidebands change sign. Thus, the odd-numbered sidebands can be cancelled completely by alternating the acquisition between $\alpha_1 = 0$ and $\alpha_1 = 180^\circ$ using synchronization. It is also clear from equation (31) that the real part of the signal is in the pure absorptive phase. Similar arguments can be applied to the imaginary part (the Y channel) of the signal, and it is in the pure dispersive phase. Figure 5 shows the unsynchronized ^{23}Na DOR spectra and the corresponding synchronized spectra in sodium oxalate for two different outer rotor speeds, 604 and 800 Hz. Indeed, addition of the spectra obtained at $\alpha_1 = 0$ and $\alpha_1 = 180^\circ$ eliminates the odd-numbered sidebands. The sideband pattern can be simulated using values of $\chi = 2.43$ MHz and $\eta = 0.77$, assuming that the sidebands arise mainly from the

second-order quadrupole interaction. In general, however, the DOR sideband pattern also contains contributions of other interactions such as CSA.

5 CP DOUBLE ROTATION

The technique CP MAS has become one of the most important techniques in solid state NMR.[15] High sensitivity or selectivity based on the proximity between two kinds of nuclei (e.g. ^{13}C and ^{1}H) is provided by the CP process, whereas high resolution is achieved by MAS and decoupling. Although CP MAS can be useful for half-integer quadrupolar nuclei, its application is restricted by the limited resolution of MAS. Therefore, it is a natural step to combine CP with DOR, which will provide the proximity information with high resolution.

In a CP experiment involving spin-$\frac{1}{2}$ nuclei (e.g. ^{1}H) and the observing half-integer quadrupolar nuclei S, a transverse magnetization of the I spins is first created by a 90° pulse. This is followed by simultaneously turning on resonant rf fields for both I and S nuclei over a time duration τ_c (the contact time). It is well known that the transverse magnetization of the I spins can be transferred efficiently to the magnetization of the S spins through the spin–spin interaction under the Hartmann–Hahn condition.[16,17] For half-integer quadrupolar nuclei with quadrupole interactions much larger than the interaction of the rf field with the S spin, the Hartmann–Hahn condition can be formulated as[18,19]

$$\omega_{1I} = (S + \tfrac{1}{2})\omega_{1S} \tag{33}$$

where S is the spin quantum number for the S nuclei and $\omega_{1\mathrm{I}}$ and $\omega_{1\mathrm{S}}$ are the rf amplitudes associated with the I and S nuclei, respectively.

Since the spin–spin interaction decreases rapidly as the distance between two spins increases, CP provides useful information on the proximity between the I and S nuclei. The fact that CP DOR can provide such proximity information with high resolution makes this technique very useful in the study of materials.[20] This point is illustrated by the application of CP DOR in $AlPO_4$-11, an aluminophosphate molecular sieve with linear channels. There are five phosphorus and five aluminum crystallographically distinct sites[21] with a 1:1:1:1:1 ratio in $AlPO_4$-11. Figure 6(a) shows a proton-decoupled ^{27}Al DOR spectrum with an outer rotor spinning speed ν_L = 725 Hz. All five resonance lines including an octahedral peak at −19.6 ppm are revealed by DOR. The four tetrahedral peaks are at 43.8, 39.8, 38.2, and 28.0 ppm, respectively. Other peaks in the spectrum are spinning sidebands. Figure 6(b) shows a proton-decoupled CP DOR spectrum with ν_L = 725 Hz and a contact time τ_c = 300 μs. The proton nutation frequency (5 kHz) is matched to the nutation frequency of the ^{27}Al central transition. No signal is observable under the mismatched condition. The octahedral aluminum sites are formed by chemisorption of two adsorbed water molecules. Therefore, it has a stronger coupling with the protons than the tetrahedral sites do. It is of interest that the tetrahedral peak at 28.0 ppm shows up only weakly in the CP DOR spectrum, indicating that the corresponding site is avoided by adsorbed water molecules.

The technique of DOR is not only effective for eliminating the second-order quadrupolar broadening, but also for

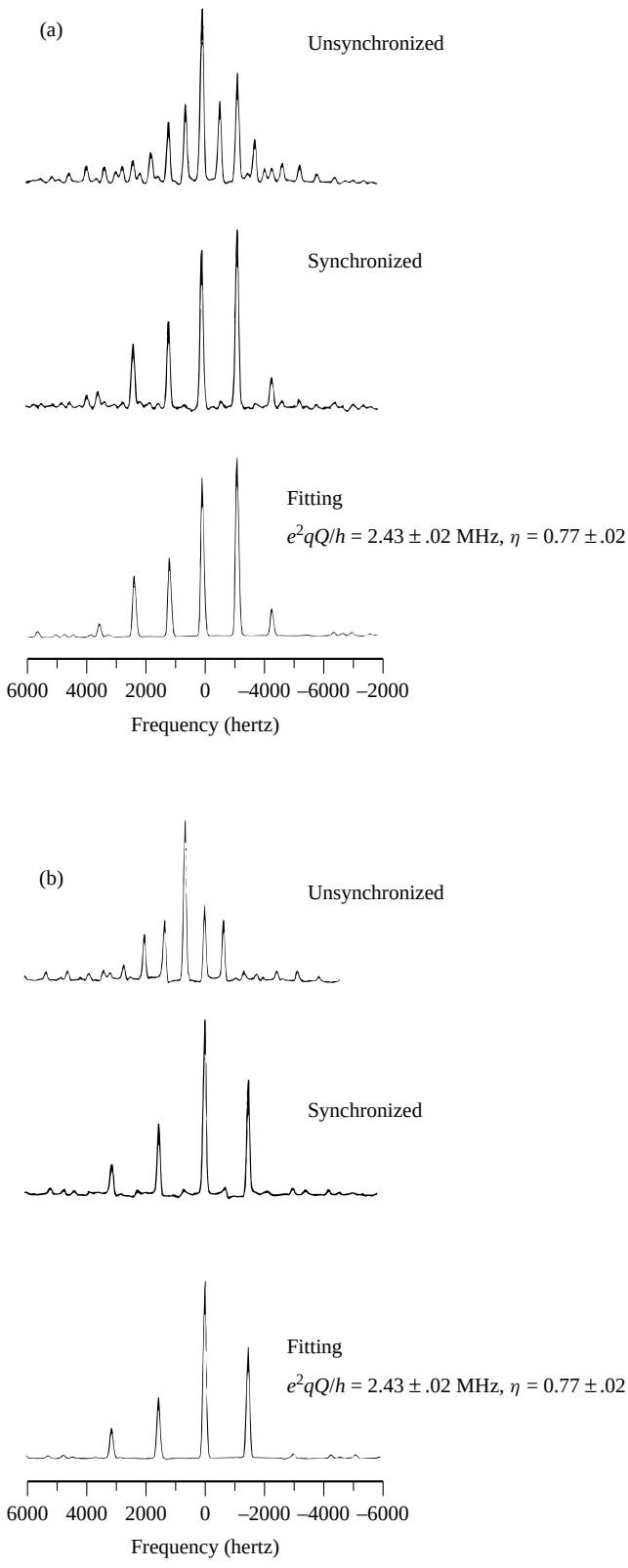

Figure 5 The effects of synchronizing the outer rotor at angles α_1 = 0 and α_1 = 180° with rf pulses on the DOR spectra of ^{23}Na in polycrystalline sodium oxalate. (a) Unsynchronized and synchronized spectra with the outer rotor spinning at 604 Hz. A computer simulation is also shown with χ = 2.43 MHz and η = 0.77. (b) Similar spectra obtained with the outer rotor spinning at 800 Hz. The computer simulation uses the same parameters as in (a)

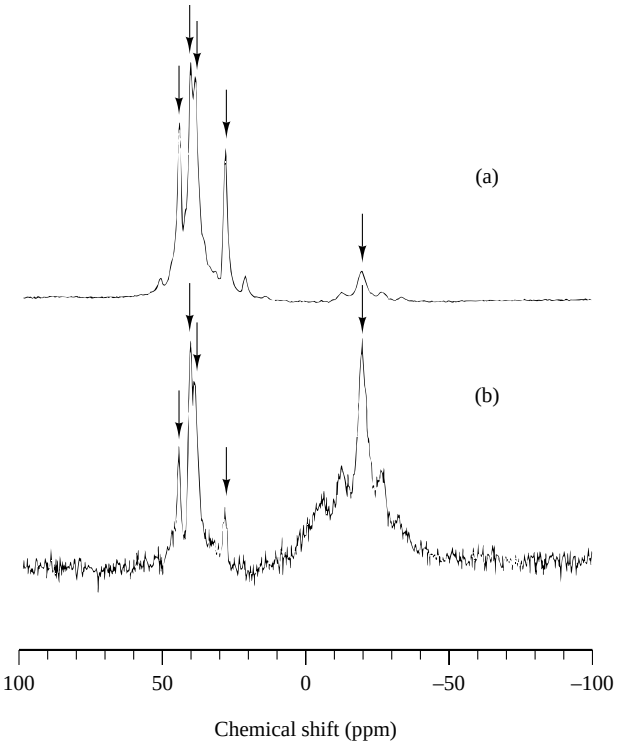

Figure 6 (a) Aluminum-27 DOR spectrum of $AlPO_4$-11 with the outer rotor spinning at 725 Hz with proton decoupling; (b) CP DOR spectrum with the outer rotor spinning at 725 Hz with proton decoupling and a contact time of 300 μs. The ^{27}Al signal in dilute aqueous $Al(NO_3)_3$ solution was used as the chemical shift reference

removing dipole–dipole interactions.[22] This feature is very important for observations of abundant nuclei with high gyromagnetic ratios such as ^{27}Al, ^{23}Na, and ^{11}B. Since its first experimental demonstration in 1988[1] examples of useful applications include DOR NMR studies of minerals,[3,23] molecular sieves,[20,22,24,25] and zeolites.[26,27] This list is incomplete by far, and is still growing.

6 RELATED ARTICLES

Dynamic Angle Spinning; High Speed MAS of Half-Integer Quadrupolar Nuclei in Solids; Internal Spin Interactions and Rotations in Solids; Line Narrowing Methods in Solids; Magic Angle Spinning; Molecular Sieves: Crystalline Systems; Quadrupolar Interactions; Quadrupolar Nuclei in Solids.

7 REFERENCES

1. A. Samoson, E. Lippmaa, and A. Pines, *Mol. Phys.*, 1988, **65**, 1013.
2. A. Llor and J. Virlet, *Chem. Phys. Lett.*, 1988, **152**, 248.
3. B. F. Chmelka, K. T. Mueller, A. Pines, J. Stebbins, Y. Wu, and J. Z. Zwanziger, *Nature*, 1989, **339**, 42.
4. E. R. Andrew, A. Bradbury, and R. G. Eades, *Arch. Sci.*, 1958, **11**, 223.
5. I. J. Lowe, *Phys. Rev. Lett.*, 1959, **2**, 285.
6. A. Samoson, B. Q. Sun, and A. Pines, in *Pulsed Magnetic Resonance: NMR, ESR, and Optics*, ed. D. M. S. Bagguley, Clarendon Press, Oxford, 1992.
7. M. Mehring, *Principles of High Resolution NMR in Solids*, 2nd edn., Springer-Verlag, Berlin, 1983.
8. U. Haeberlen, *High Resolution NMR in Solids; Selective Averaging*, Academic Press, New York, 1976.
9. A. Samoson and A. Pines, *Rev. Sci. Instrum.*, 1989, **60**, 3239.
10. Y. Wu, B. Q. Sun, A. Pines, A. Samoson, and E. Lippmaa, *J. Magn. Reson.*, 1990, **89**, 297.
11. M. H. Cohen and F. Reif, in *Solid State Physics*, ed. F. Seitz and D. Turnbull, Academic Press, New York, 1957, Vol. 5.
12. M. E. Rose, *Elementary Theory of Angular Momentum*, Wiley, New York, 1961.
13. A. Samoson and E. Lippmaa, *J. Magn. Reson.*, 1989, **84**, 410.
14. B. Q. Sun, J. H. Baltisberger, Y. Wu, A. Samoson, and A. Pines, *Solid State Nucl. Magn. Reson.*, 1992, **1**, 267.
15. J. Schaefer, E. O. Stejskal, and R. R. Buchdal, *Macromolecules*, 1977, **10**, 384.
16. S. R. Hartmann and E. L. Hahn, *Phys. Rev.*, 1964, **128**, 2042.
17. A. Pines, M. G. Gibby, and J. S. Waugh, *J. Chem. Phys.*, 1973, **59**, 569.
18. C. S. Blackwell and R. L. Patton, *J. Phys. Chem.*, 1984, **88**, 6135.
19. A. Vega, *Solid State Nucl. Magn. Reson.*, 1992, **1**, 17.
20. Y. Wu, D. Lewis, J. S. Frye, A. R. Palmer, and R. A. Wind, *J. Magn. Reson.*, 1992, **100**, 425.
21. P. J. Barrie, M. E. Smith, and J. Klinowski, *Chem. Phys. Lett.*, 1991, **180**, 6.
22. Y. Wu, Z-y Peng, Z. Olejniczak, B. Q. Sun, and A. Pines, *J. Magn. Reson. A*, 1993, **102**, 29.
23. K. T. Mueller, Y. Wu, B. F. Chmelka, J. Stebbins, and A. Pines, *J. Am. Chem. Soc.*, 1991, **113**, 32.
24. Y. Wu, B. F. Chmelka, A. Pines, M. Davis, P. Grobet, and P. Jacobs, *Nature*, 1990, **346**, 550.
25. R. Jelinek, B. F. Chmelka, Y. Wu, A. Pines, P. J. Barrie, and J. Klinowski, *J. Am. Chem. Soc.*, 1991, **113**, 4097.
26. G. J. Ray and A. Samoson, *Zeolites*, 1993, **13**, 410.
27. G. W. Haddix, M. Narayana, W. D. Gillespie, M. B. Georgellis, and Y. Wu, *J. Am. Chem. Soc.*, 1994, **116**, 672.

Biographical Sketch

Yue Wu. *b* 1959. B.S., 1983, Ph.D., 1987, University of Leuven, Belgium. Introduced to NMR by A. Pines at the University of California at Berkeley. Faculty in the Department of Physics and Astronomy, University of North Carolina at Chapel Hill, 1991–present. Research interests: the development of solid state NMR techniques and the application of NMR in the study of quasicrystals, nanocrystals, zeolites and molecular sieves, and high-temperature polymers.

Double-Quantum NMR Spectroscopy of Dipolar Coupled Spins Under Fast Magic-Angle Spinning

Hans Wolfgang Spiess

Max-Planck-Institut für Polymerforschung, Mainz, Germany

1 Introduction 1
2 High Resolution Solid State NMR 1
3 Applications 5
4 Conclusions and Outlook 12
5 Related Articles in this Volume 14
6 Related Articles in Volumes 1–8 14
7 References 14

1 INTRODUCTION

Double-quantum (DQ) NMR spectroscopy of dipolar coupled spins in solids under fast magic angle spinning (MAS) is new a tool, by use of which topics of general interest in materials science and bioscience can be addressed. For instance, in advanced synthetic as well as in biological systems self assembly of carefully chosen building blocks is of central importance.[1–4] Hydrogen bonding and aromatic π-π interactions are key features of supramolecular chemistry.[5] Despite being highly ordered on a local scale, such systems often do not crystallize. Therefore, their structures cannot be determined by conventional X-ray crystallography or neutron scattering. Alternatives are needed which should provide structural and dynamic information, preferably requiring only small amounts of as-synthesized samples, without the need for isotopic labeling. High resolution solid state ^{1}H-NMR can meet these requirements,[6–8] provided that sufficiently selective information can be extracted from the corresponding spectra.

Since 1994 we have systematically pursued the development of solid state ^{1}H NMR for that purpose by combining fast MAS[9] and DQ NMR spectroscopy,[10] which makes use of the homonuclear dipole–dipole coupling between protons.[11,12] The spectral resolution can be increased by use of similar methods exploiting heteronuclear ^{1}H–^{13}C dipole–dipole couplings.[13] These techniques take advantage of the significant simplification of the multispin dipolar coupled network under fast MAS, where two-spin correlations predominate,[14] and have provided new insight in

- hydrogen bonded structures in the solid state[15]
- columnar stacking and molecular dynamics of discotics[16]
- chain order and translational motion in polymer melts[17]
- chain organization on surfaces.[18]

This review briefly outlines these new approaches for studying supramolecular organization and demonstrate their advantages with specific examples.

2 HIGH RESOLUTION SOLID STATE NMR

Various aspects of solid state NMR are subjects of other articles in this Encyclopedia. For a full treatment of earlier work including multidimensional techniques, we refer to our extended monograph.[19]

2.1 Magic Angle Spinning

A particularly important recent advance in solid state NMR is fast MAS with rotor frequencies $\omega_R > 2\pi \cdot 25\,\text{kHz}$[9] up to $2\pi \cdot 50\,\text{kHz}$ as described by Samoson (see **Magic-angle Spinning Extensions**).[20] For most organic solids, the strongest ^{1}H–^{1}H dipole–dipole coupling, e.g., in CH_2 groups with a proton–proton distance of 0.18 nm are of the order of $\omega_D \approx 2\pi \cdot 20.6\,\text{kHz}$. Thus, the condition $\omega_R \geq \omega_D$ can be met even for the strongest dipole–dipole couplings. Since in most cases the remaining spins are further away, the corresponding remote couplings can effectively be 'spun out'

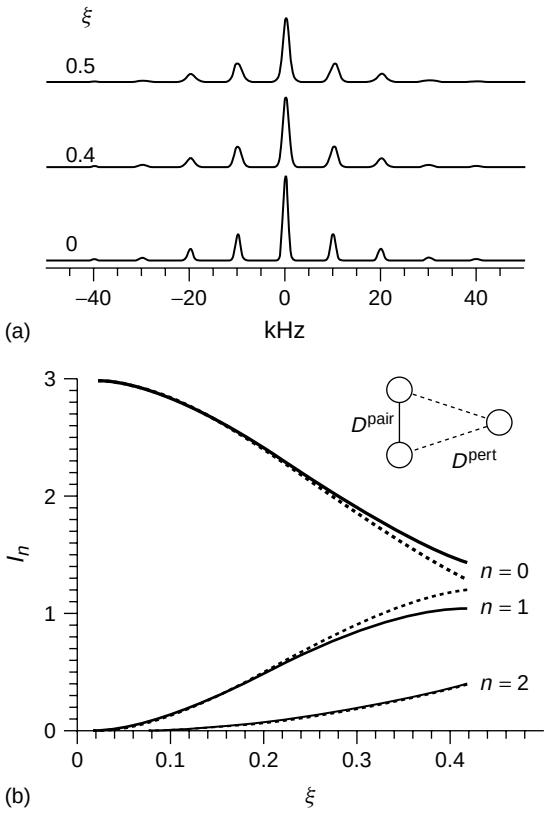

Figure 1 (a) Simulated MAS NMR spectra f or a spin-pair subject to a perturbing spin in an isosceles triangle arrangement for various ratios ξ of the perturbing dipole–dipole coupling ω_D^{pert} to the rotor frequency ω_R. (b) Centreband ($n = 0$) and sideband ($n = 1$, 2) intensities in MAS spectra for the three-spin system in (a) as function of ξ. Solid lines, two- and three-spin correlations; dotted lines, only two-spin correlations.[21] (Reproduced by permission of Academic Press)

and only the strongest couplings, originating from the shortest distances, are retained. This simple picture is indeed borne out in an elaborate theoretical treatment of multi-spin systems under fast MAS, combining Floquet theory and perturbation theory.[14] The higher-spin contributions are found to scale with increasing powers of the inverse rotor frequency and become less and less important at higher and higher ω_R.

As an example, Figure 1(a) shows MAS NMR spectra for a spin-pair subject to a perturbing spin in an isosceles triangle arrangement for various ratios ξ of the perturbing dipole–dipole coupling ω_D^{pert} to the rotor frequency ω_R.[21] Sideband patterns are observed, from which the dominant dipole–dipole coupling D^{pair} can be determined straightforwardly as indicated in Figure 1(b). The simulated center and sideband intensities, calculated from simply adding the contributions of pair correlations are very good approximations for the full treatment including three-spin correlations. The linewidths, however, significantly increase with ξ as the dominant term there involves three-spin correlations. Thus, the strongest dipole–dipole couplings can simply be determined from one-dimensional (1D) MAS sideband patterns.

2.2 Homonuclear Double-Quantum Coherences

In order to obtain a structure, the weaker remote dipole–dipole couplings, relating protons of different chemical entities are particularly informative. They can now be determined by DQ MAS NMR spectroscopy.[11,12] The basic experimental scheme, a specific pulse sequence and a coherence pathway diagram,[22] are shown in Figure 2(a): firstly, a double-quantum coherence (DQC) is excited, which subsequently evolves during an incremented time period t_1. Afterwards, the DQC is converted into observable single-quantum coherence (SQC), which is detected in the acquisition period. Pure absorption mode 2D spectra are ensured by generating amplitude modulated signals in t_1 through proper selection of symmetric pathways.[19,22] During excitation and reconversion the *homonuclear* dipole–dipole interaction is recoupled. Numerous ways for achieving this have been developed, as described by Levitt (see **Symmetry-Based Pulse Sequences in Magic-Angle Spinning Solid-State NMR**)[23] (see also Ref.[24])

The nature of the corresponding 2D spectra is illustrated in Figure 2(b,c). Here we consider two kinds of pairs of spins, labeled 1 and 2, with different chemical shifts. The excitation of DQ coherence is based on the dipole–dipole coupling between the two spins involved. Thus, if the two kinds of groups are separated (Figure 2(b)), DQ signals can only occur at $2\omega_1$ and $2\omega_2$ along the DQ dimension, i.e., on the diagonal of a 2D plot with proper frequency scaling. These signals reflect the dipolar couplings within the respective groups. Note that distinct from the INADEQUATE experiment in isotropic liquids based on the isotropic scalar

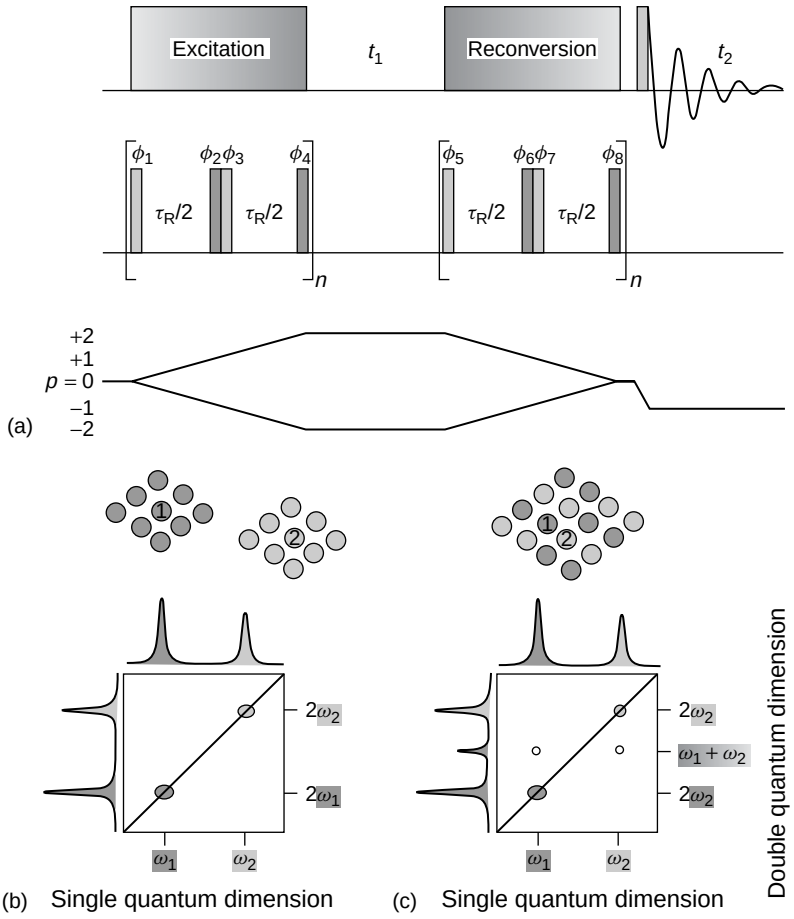

Figure 2 (a) Pulse sequence and coherence transfer pathway of a homonuclear DQ MAS experiment, all pulses have 90° flip angles. (b) Scheme of DQ MAS NMR spectrum for separated spin pairs, (c) for spin pairs in spatial proximity

couplings,[22] the intragroup coherences occur despite the fact that the isotropic chemical shifts of the two spins are equal. This reflects the fact that in solids the DQ coherence is generated by the anisotropic dipole–dipole coupling. If the groups are intermixed (Figure 2(c)), DQ coherences between spins of different groups can also be excited. They occur at the sum-frequency $\omega_1 + \omega_2$ in the DQ dimension and can be detected at both frequencies ω_1 and ω_2 in the single quantum dimension. Thus, such a pair of lines in the 2D-NMR spectrum directly maps the spatial proximity between group 1 and group 2. For short excitation times the intensities of the DQ signals are proportional to D_{ij}^2 where D_{ij} describes the dipole–dipole coupling between the two spins involved.

Spectra as discussed in the previous section are obtained in a *rotor-synchronized fashion*, i.e., the t_1 increment is set equal to the rotor period τ_R and yield distance constraints for the dipolar coupled nuclei. More accurate values for dipole–dipole couplings may be obtained from build-up curves of DQC, which for isolated spin pairs, such as doubly labeled ^{13}C–^{13}C, exhibit an oscillatory behavior.[25] Strongly coupled ^1H–^1H systems, however, quickly develop multi-spin character and the oscillations are damped out. Nevertheless, even there the initial build-up is dominated by DQCs and can quantitatively be analyzed.[26,27]

The dipole–dipole coupling constants as well as the geometry of dipolar coupled clusters as, e.g., in triple- or quadruple hydrogen bonds, can much better be elucidated if DQ *spinning sidebands* are generated by choosing a t_1 time increment well below τ_R.[11,12] Examples calculated for an isolated spin pair are plotted in Figure 3 as a function of $D_{ij}\tau_{exc}$. Note that these sidebands occur despite the fact that the DQC for an isolated spin-pair does not evolve during the evolution time t_1. Instead, the *reconversion* is *rotor encoded* because the dipole–dipole Hamiltonian modulated by MAS differs at the beginning of excitation and reconversion. This mechanism is termed *reconversion rotor encoding* (RRE) and occurs whenever the Hamiltonians involved have an amplitude modulation on the rotor phase, which is also the case in MQ MAS experiments on quadrupolar nuclei.[28,29] The two cases have been compared in detail.[30] In actual applications, the rotor frequency ω_R and the excitation time τ_{exc} will be chosen to generate up to third

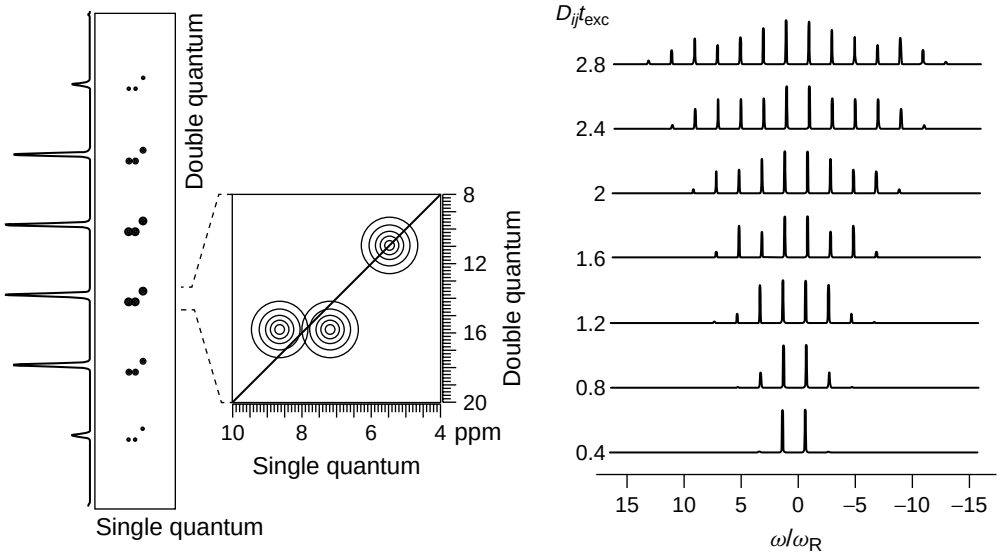

Figure 3 DQ spinning sideband patterns calculated for increasing values of the product of the dipolar coupling and the excitation time

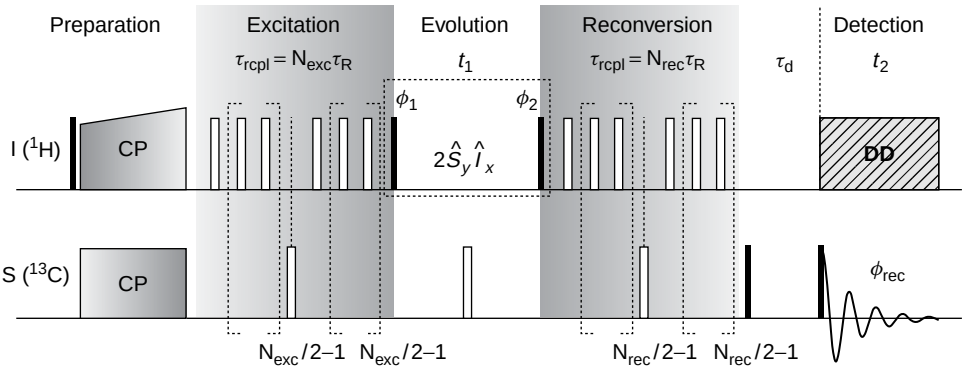

Figure 4 Pulse sequence for heteronuclear ^1H–^{13}C correlation experiments based on combining the concepts of REDOR and HMQC. For details see Ref.[38] Solid and open bars indicate 90° and 180° pulses, respectively. (Reproduced by permission of American Institute of Physics)

order sidebands in order to achieve sufficient signal-to-noise ratios, yet avoid multi-spin effects, which lead to *evolution rotor modulation* (ERM).[30] Notably, multi-spin effects give rise to additional (even-order) sidebands and can, therefore, be easily identified.

2.3 Heteronuclear Multiple-Quantum Coherences

Two-dimensional ^{1}H DQ MAS experiments as described in Section 2.2 still suffer from the limited spectral resolution in solid state ^{1}H NMR. Therefore, heteronuclear methods involving ^{13}C or ^{15}N offer significant advantages for obtaining more specific distance constraints. Indeed, if combined with homonuclear ^{1}H–^{1}H decoupling by rotor synchronized multiple pulse sequences[31] or frequency switched Lee-Goldburg experiments,[32] remarkable resolution has been achieved in model compounds[33] as well as biologically relevant systems.[34] Once specific ^{1}H–^{13}C spin pairs are identified, precise measurement of their dipole–dipole couplings via spinning sidebands also offers a new and efficient way to study molecular dynamics in analogy to ^{2}H-NMR experiments,[19] yet without the need for elaborate isotope labeling. Rotational-echo double-resonance (REDOR)[35,36] currently is most popular for determining heteronuclear dipole–dipole couplings in solids. It is based on a particularly simple approach of *recoupling*, i.e., the application of equally spaced π-pulses twice per rotor period on one of the isotopes. When applied under fast MAS in order to efficiently reduce the homonuclear dipole–dipole coupling, REDOR can be combined with multiple-quantum spectroscopy in a whole class of dipolar heteronuclear multiple spin correlation (DIP-HMSC) experiments[37,38] which are more selective than determining distance constraints via cross polarization and spin diffusion experiments.[39,40] The basic pulse sequence for a ^{1}H–^{13}C heteronuclear multiple-quantum correlation (HMQC) experiment is depicted in Figure 4. As in homonuclear DQ-NMR, the first half of the REDOR recoupling is identified as the excitation period, and the second as the reconversion period. In between, HMQC evolution occurs during t_1. The ^{13}C chemical shift is fully refocused by π-pulses during excitation, evolution and reconversion.

Similar to the homonuclear case, Section 2.2, precise values for heteronuclear dipole–dipole couplings can be determined via sideband patterns, which are generated through rotor encoding (RRE) as well as evolution (ERM). Consequently, the sideband patterns for an isolated heteronuclear spin pair, plotted as a function of the excitation time in Figure 5(a), exhibit the same features as in the homonuclear case (Figure 3). Again, in actual experiments the excitation times are chosen short enough such that a limited number of sidebands is created and multi-spin effects are minimized for C–H groups. The unavoidable three-spin coherences in rigid CH_2 groups, in fact, lead to efficient dephasing.[37,38] This can be used for spectral simplification, but also offers an easy way to distinguish mobile methylene groups from rigid ones.

DQ sideband patterns also offer new ways to study the rate and the geometry of rotational motions,[16,38] where the site selectivity is particularly high for heteronuclear DQ coherences. In Figure 5(b) simulated sideband patterns are plotted for the C–H group which is a sensitive probe of phenylene rotation, often met in practice.[19] At low temperatures one would expect small-angle librations. With increasing temperatures the angular excursions will increase until full rotation might be reached. The resulting motionally averaged dipolar couplings are readily calculated via the internet by use of our NMR-WEBLAB.[41] As shown in Figure 5(b), the sideband patterns show a marked dependence of the flip angle α. A recent experimental example is provided by the restricted phenylene motion in polyphenylene dendrimers,[42] a new type of nanomaterials.[1]

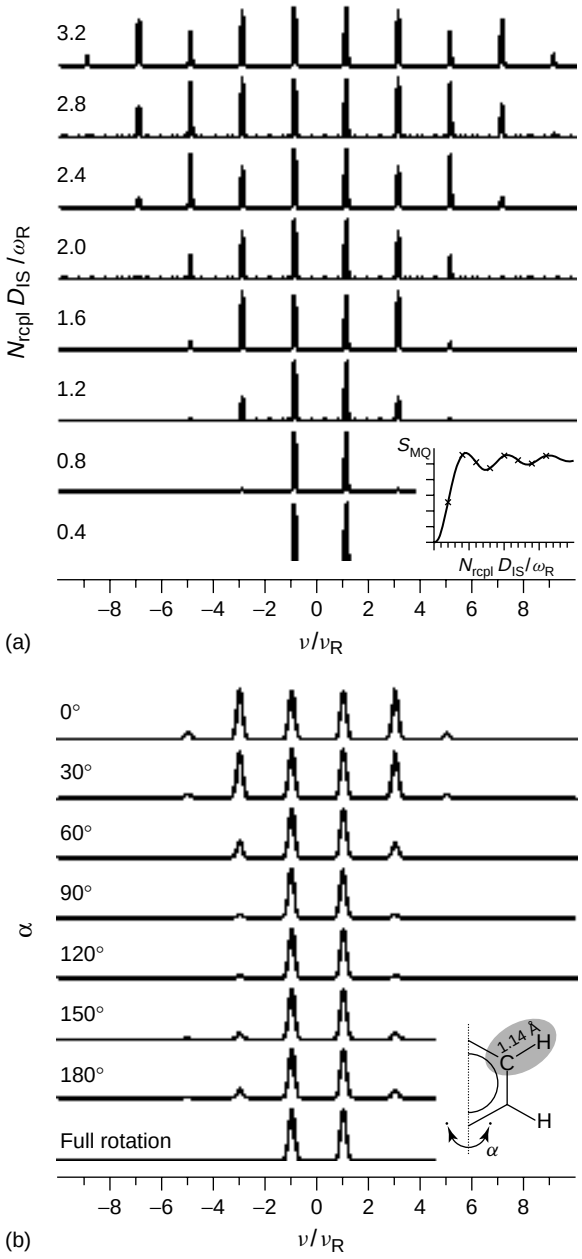

Figure 5 (a) Calculated HMQ spinning sideband patterns for a single IS spin pair for increasing values of the ratio of the product of the dipolar coupling strength D_{IS} multiplied by the number of pump cycles N_{rcpl} and the rotor frequency ω_R. For details see.[38] (b) Calculated heteronuclear DQ MAS NMR spinning sideband patterns for rotating phenylene groups and different flip angles α as indicated ($N_{rcpl}D_{IS}/\omega_R = 1.67$). (Reproduced by permission of American Institute of Physics)

3 APPLICATIONS

3.1 Spin Counting

The classic application of MQ NMR in solids as pioneered by A. Pines in the early 1980s is spin counting.[43] He showed that it is possible to excite homonuclear MQCs comprising more than 100 spins, by exploiting the through-space dipole–dipole coupling. With this technique it was possible, for instance, to prove the existence of small clusters of proton spins on the surface of silica catalyst supports.[44] In fact, the growth of MQCs in a spin cluster as depicted in Figure 6(a) can be described by a statistical model. The intensities of the coherence orders follow a Gaussian distribution, the width of which increases with excitation time. Such behavior indicates that the build-up of homonuclear MQCs amongst strongly coupled spins occurs via a random walk. The different pathways indicated in Figure 6(a) result from the non-localized and, therefore, non-selective growth of the spin-cluster. As demonstrated in Figure 6(c), this behavior is also found under MAS conditions, provided efficient recoupling is achieved.[27]

Distinct from that, MQCs in the I-spin subspace of a heteronuclear IS NMR experiment are excited via the dipole–dipole coupling of all these spins to a single S spin. For this selected site the multitude of surrounding I spins creates

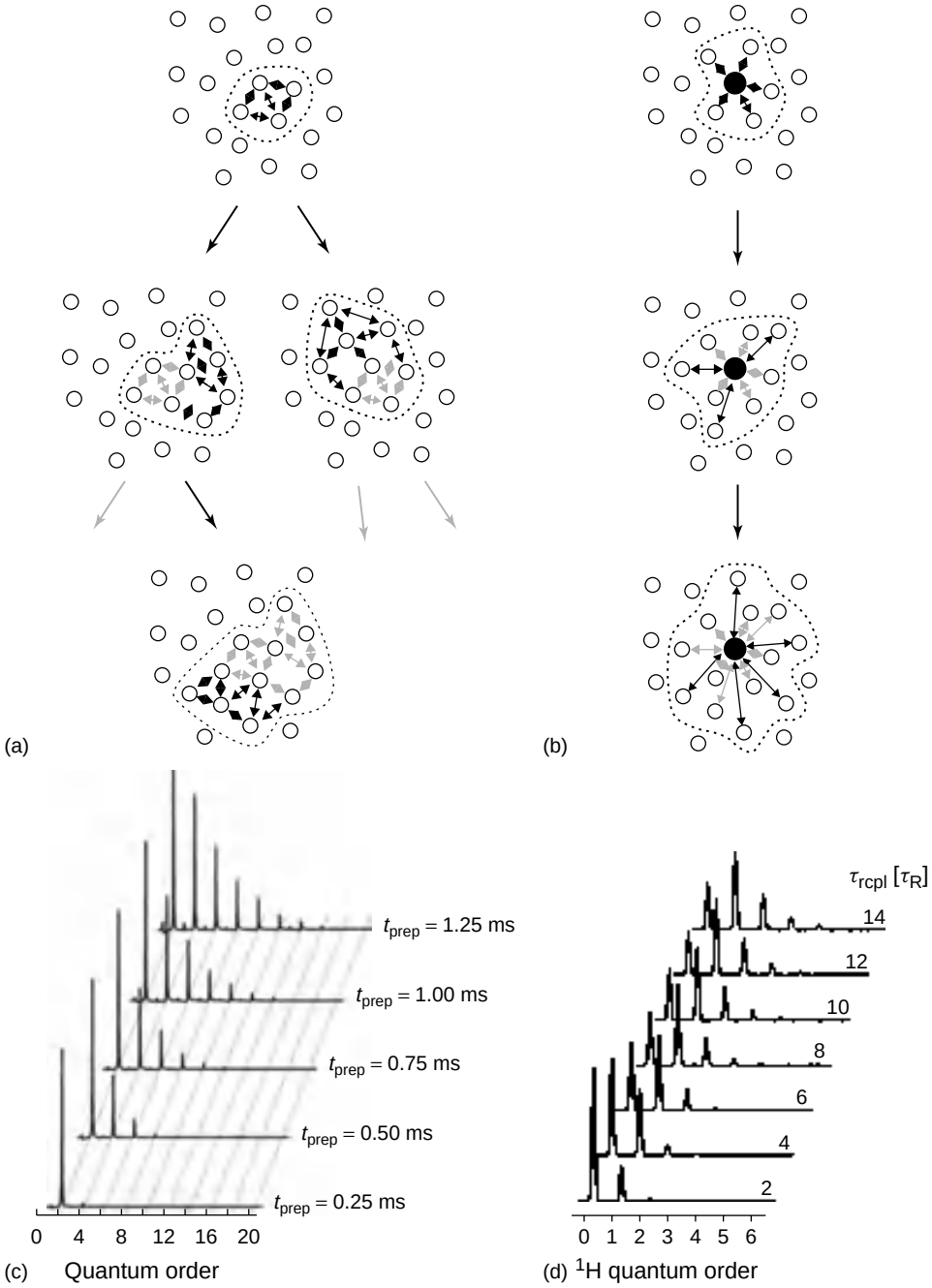

Figure 6 Growth of spin clusters as probed in homonuclear (a) and heteronuclear (b) MQ NMR experiments. Experimental examples for adamantane (^{1}H···^{1}H homonuclear, (c)), for details see Ref.[27] and L-alanine (^{1}H···^{13}C heteronuclear, (d)), for details see Ref.[38] (Reproduced by permission of American Institute of Physics, (a), (b), (d) and Academic Press, (c))

a local field. The number of proton (I) spins incorporated in the HMQ can only grow by including remote spins with sufficient couplings to the S spin [Figure 6(b)]. Thus, build-up of higher spin coherences will converge with time. As shown in Figure 6(d), higher order MQCs are indeed observed for the carboxyl carbon in uniformly ^{13}C labeled L-alanine,[38] but the intensity distribution obviously is not Gaussian. Thus, heteronuclear spin counting indeed probes a selected local environment and therefore is anticipated as a new tool for structural investigations.

3.2 Structure

3.2.1 Hydrogen Bonding

Protons in hydrogen bonded structures exhibit ^1H chemical shifts well away from the aliphatic peaks. Therefore, high resolution ^1H solid state NMR is ideally suited for investigating such systems as noted early on.[45] Moreover, correlations between the ^1H isotropic chemical shifts and the hydrogen-bond strength specified by O···H or O···O distances from single-crystal analyses have been established.[46] The first example of the new kind of information about proton–proton distance constraints available from solid state DQ MAS NMR was the investigation of the unusual hydrogen bonded structures in benzoxazine dimers.[15] These dimers are of interest as model compounds for a new class of phenolic materials, the polybenzoxazines prepared by Ishida and coworkers.[47] These systems combine several favorable properties, such as near-zero shrinkage on polymerization as well as low water absorption, which are attributed to their favorable hydrogen-bonding.

Figure 7(a) shows the superimposed ^1H MAS NMR spectra of both the methyl (solid line) and ethyl (dashed line)

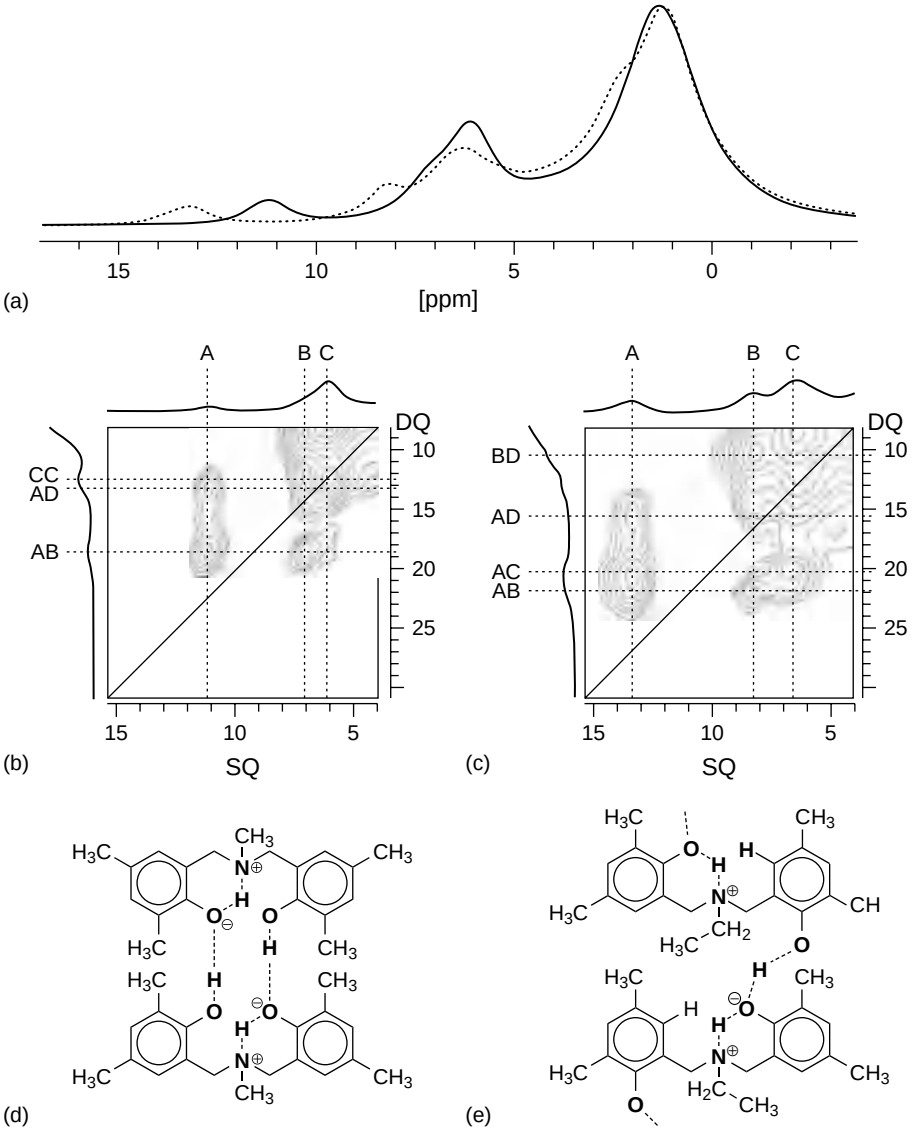

Figure 7 (a) ^1H MAS NMR spectra of benzoxazine dimers at 500 MHz. Solid line, methyl derivative; dotted line, ethyl derivative. (b), (c) Low field region of the ^1H DQ MAS NMR spectrum of the methyl and ethyl derivative, respectively. (d), (e) Schematic arrangement of the methyl dimers into pairs (d) and the ethyl dimers into extended chains (e). For details see Ref.[15] (Reproduced by permission of American Chemical Society)

derivative. The spectra differ markedly in the low-field region, which gives a first hint towards different hydrogen bond arrangements in the two cases. The differences are even more marked in the ^{1}H DQ MAS NMR spectra, whose low-field regions are displayed in Figures 7(b) and 7(c). The labels (A, B, C, and D) refer to the SQ resonances of the hydrogen bonded, aromatic, and aliphatic protons, respectively. The peaks in the DQ spectrum indicate proximities of protons within about 0.35 nm[15] and are labeled accordingly as AB, AC, etc. The most striking differences between the methyl- and ethyl-dimer spectra are the strong aromatic auto peak (CC) and only weak intensity (AC) indicating a DQC between a O···H···N and an aromatic proton for the methyl-dimer, while the situation is reversed for the ethyl-derivative. As discussed in detail elsewhere,[15] this indicates pair formation from two dimers, Figure 7(d) in the methyl-derivative, and extended hydrogen bonded chains, Figure 7(e) for the ethyl-dimers. These structural differences have meanwhile been confirmed by X-ray diffraction.

Another example of elucidating complex hydrogen bonded structures is provided by our study of supramolecular polymers[48] coupled via quadrupole bonds in 2-ureido-4-pyrimidone units, where keto- and enol tautomers in the solid state could clearly be distinguished by DQ MAS NMR.[49] DQ spinning sideband patterns have also been used to locate the protons in bilirubin, a compound of considerable medical importance. It is a product of the metabolism of hemoglobin from red blood cells. Due to an unusually strong intramolecular hydrogen bonding arrangement, bilirubin itself is insoluble in water and can only be removed from the body after being conjugated enzymatically with glucuronic acid.[50] Inefficient removal of bilirubin from the body manifests itself as jaundice. Solid state NMR now has provided proton−proton distances with an accuracy of ±0.002 nm in this important system.[51]

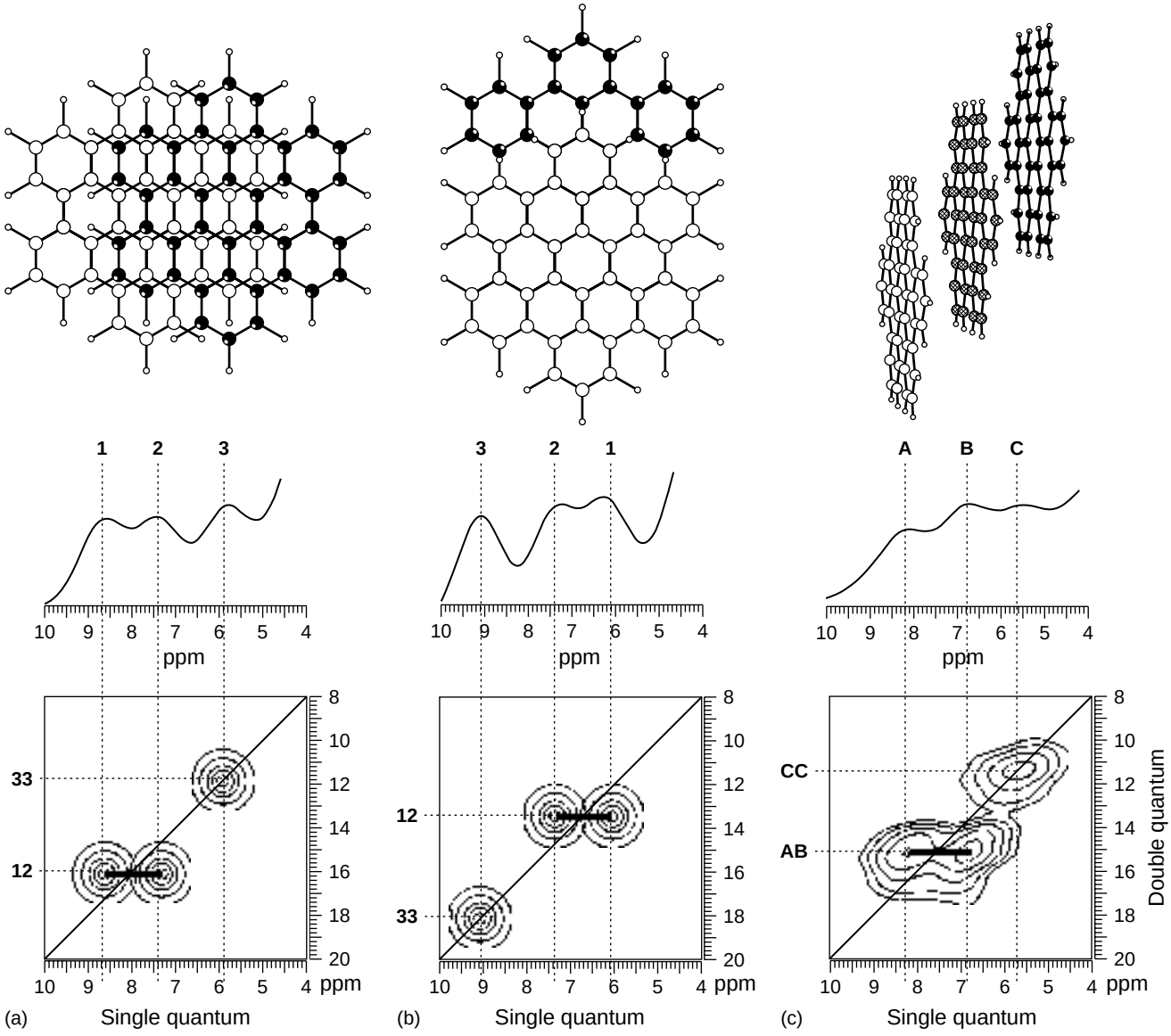

Figure 8 Calculated ^{1}H MAS NMR spectra and schematic ^{1}H DQ MAS NMR spectra for different arrangements of HBC discs, staggered in different directions (a, b). Experimental ^{1}H spectra of HBC–C_{12} together with staggered arrangement (c). For details see Ref.[54] (Reproduced by permission of American Chemical Society)

3.2.2 Aromatic π-π Interactions in Columnar Structures and Guest-Host Complexes

In addition to hydrogen-bonding, the ^{1}H chemical shifts are very sensitive to ring currents associated with π-electrons in aromatic moieties.[52] While in solution, the isotropic molecular tumbling removes most of the π-shifts, in the solid state the protons are exposed to the π-electrons of nearby aromatic moieties, be they intra- or intermolecular. The latter information is particularly valuable for elucidating supramolecular structures.[2,5] A clear-cut example is provided by the columnar stacking of substituted hexa-*peri*-hexabenzocoronene (henceforth referred to as HBC). Opposed to solution or the liquid crystalline phase, where the discs tumble isotropically or rotate rapidly around the column axis, in the solid three distinct aromatic lines are observed in the aromatic region of the ^{1}H-NMR spectrum[16] (Figure 8). The DQ-spectrum exhibits a strong CC auto and two AB cross peaks, which implies the presence of only two types of pairs of aromatic protons, H_A-H_B, H_C-H_C. For quantitative analysis, advanced quantum chemical calculations of NMR chemical shifts are needed.[53] They show that staggered arrangements of the HBC moieties indeed give rise to π-shifts of several ppm.[54] The assignment, which of the chemically shifted protons form pairs is achieved by DQ-NMR and is essential to determine the type of staggering. In a herringbone-structure which corresponds to that of unsubstituted HBC (Figure 8(a)) none of the carbons are aligned, whereas in structure (b) half of the carbons are located directly above or below a carbon of the adjacent layer resembling the packing in graphite. The latter (Figure 8(b)) could clearly be excluded, because it does not match the experimental 2D NMR pattern (Figure 8(c)). The pattern in Figure 8(a), however, agrees well with the experimental one. This proves the specific packing arrangement hypothesized earlier,[16] that this alkylsubstituted system adopts the structure of unsubstituted HBC itself. Through-space π-shifts are remarkably long-range, with an aromatic ring at a distance of 0.7 nm still exerting a measurable influence. Thus, in the final simulation, three HBC moieties had to be taken into account (Figure 8(c)).

The combination of ^{1}H DQ MAS-NMR with advanced ab initio quantum chemical calculations also proved essential for elucidating the structure of a supramolecular guest-host complex. The receptor shown in Figure 9(a) belongs to the family of molecules termed molecular tweezers due to their concave–convex topology and ability to selectively form complexes with electron-deficient compounds.[55] An X-ray crystal structure is available for this system, offering an opportunity to check the reliability of the spectroscopic approach.[56] Figure 9(b) presents a rotor-synchronized ^{1}H DQ MAS spectrum of the complex (Figure 9(a)). Despite the high field (700 MHz) used, the spectral resolution for the many aromatic protons is unsatisfactory. The different sites can much better be distinguished in a heteronuclear correlation spectrum (Figure 9(c)) which was recorded with the REPT-HSQC experiment.[37] The two overlapping ^{13}C lines at 128.7 and 129.6 ppm are assigned to the guest CH groups (5a and 5b), which are well separated by 3.6 ppm in the ^{1}H-dimension. This demonstrates that the π-shifts are much more significant for the protons than they are for the carbons.[54,56] In the present case, the binding of the electron-deficient 1,4-dicyanobenzene guest in the complex is such that the symmetry of the molecular tweezer is broken (Figure 9(a)) and the two adjacent guest protons experience the π-shifts due to the host to largely different degrees. Moreover, the end pair of aromatic protons are directed into the ring current of the naphthalene unit of the next host, which explains the π-shifted 4 ar^{II} resonance.[56] Thus both, the guest–host complexation, as well as the packing of the "loaded" tweezers within the supramolecular solid can be probed by solid state NMR and quantified by ab initio calculation.

3.2.3 Surface Studies

The high sensitivity of ^{1}H NMR makes it possible to study defect sites and molecules adsorbed at surfaces in a straightforward way.[44] Two examples are discussed. The first concerns a ^{1}H-MQ MAS NMR study of defect sites in a zeolite.[57] As in supramolecular systems, the structures of defects are difficult to study in these industrially important microporous solids,[58] because the defects are usually not ordered in the crystallographic sense and, therefore, are not easily amenable to analysis by diffraction methods. Figure 10(a) shows the 2D ^{1}H DQ MAS NMR spectrum of an as-made all silica ZSM-12 zeolite.[57] The signal at 10 ppm in the SQ dimension is due to a DQC generated by the cluster of silanol protons of the defect site. The observation of a strong centreband in the ^{1}H DQ MAS spinning sideband pattern (Figure 10(b)) proves that at least three silanol groups are engaged in hydrogen bonding within the defect site. These results have important implications concerning the nucleation mechanism of high-quality zeolites, as they provide new information on the structure of charge-compensating units in the zeolite colloidal precursors.

In another example ^{1}H DQ MAS NMR recently has also provided new insight in the packing of polyelectrolyte multilayers (PEMs) on silica colloids.[18] These systems, generated by alternate adsorption of anionic and cationic polymers are being explored for numerous applications ranging from photonics to enzyme encapsulation.[59,60] Fast MAS NMR at high fields (700 MHz) of such systems is able to distinguish, e.g., water adsorbed at the surface from that in the PEM and the silanol groups. Two-dimensional ^{1}H DQ MAS NMR, however, is needed to probe the organization of the polyelectrolytes within the multilayers. The DQ spectra (Figure 10) exhibit cross-peaks between the aromatic protons of the poly(styrene sulfonate) (PSS) polyanion and the poly(diallyldimethyl-ammonium) (PDADMAC) polycation in both, the bulk complex and the multilayers. These findings[18] are consistent with conclusions based on less direct experimental probes that these polyelectrolyte multilayers are structurally very similar to the corresponding bulk complexes.[61]

3.3 Dynamics

3.3.1 Axial Motion of Discs in Columnar Liquid Crystals

A unique strength of solid state NMR is its ability to probe molecular dynamics over many orders of magnitude with site selectivity and specific geometric sensitivity.[19,62] High resolution DQ MAS of dipolar coupled spins has further broadened our tools in this area. This is illustrated by a few examples. Consider as a particularly simple case the rotation of the discs around the column axis in discotic liquid crystals.[63]

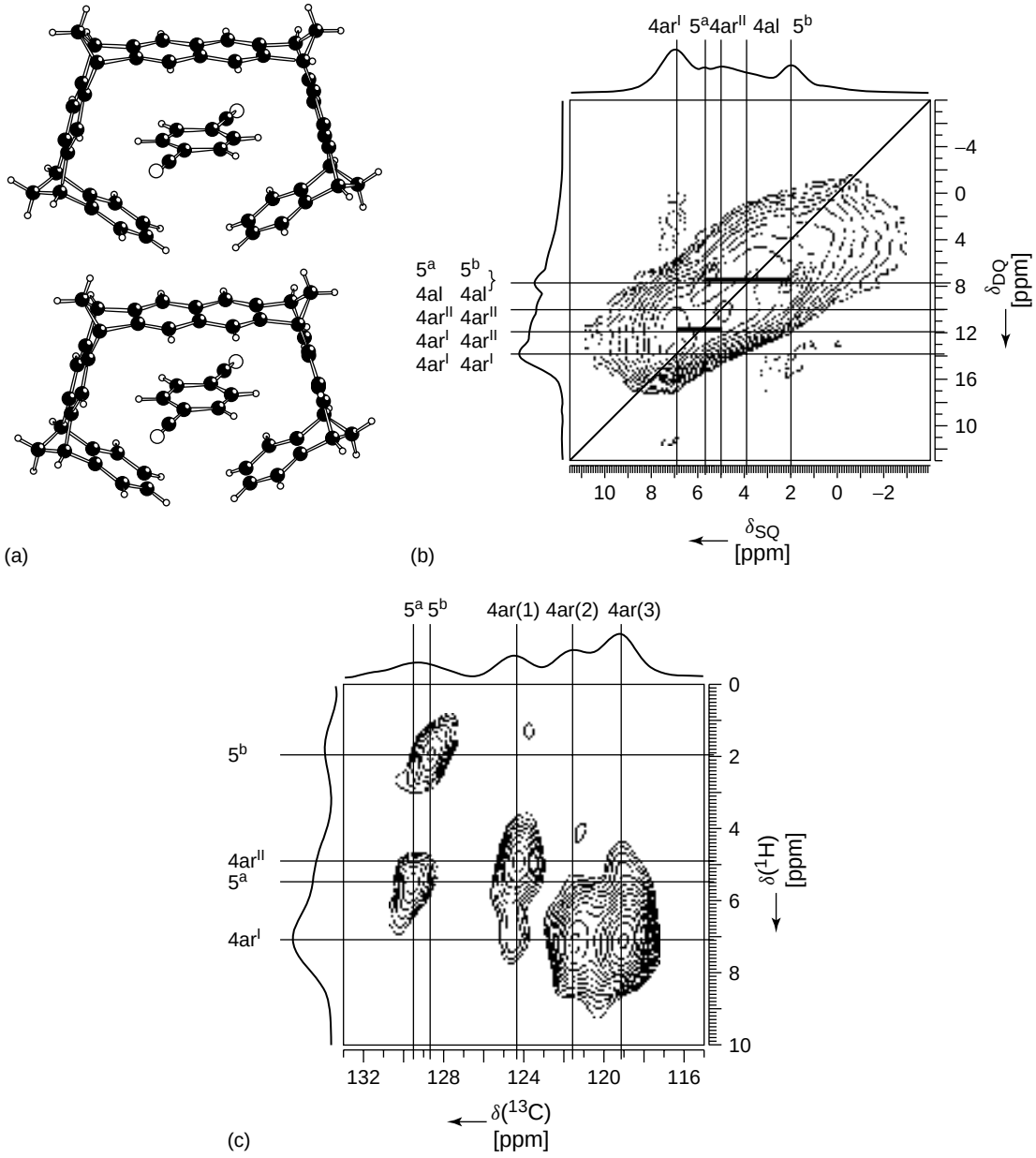

Figure 9 (a) Solid state packing of a molecular tweezer. (b) ^{1}H DQ MAS NMR spectrum at 700 MHz, and (c) ^{1}H–^{13}C HSQS MAS NMR correlation spectrum, for details see Ref.[56]

In the past, studying this motional process required ^{2}H NMR of selectively labeled systems, which was indeed done for HBC.[64] The effort seemed justified in view of the favorable properties of these systems, i.e., extremely stable mesophase and record charge carrier mobility along the column axis.[65] This tedious approach can now be circumvented. Figure 12 presents ^{1}H DQ MAS spinning sidebands of HBC-C_{12}, containing C_{12} alkyl chains, in (a) the crystalline and (b) the LC phases.[16] The aromatic protons are grouped as well separated pairs and, thus, an analysis within the spin-pair approximation is appropriate. As is evident from the insets on the right of Figure 12 the DQ-spinning sideband patterns are very sensitive to the strength of the dipolar coupling, which can be determined with high accuracy to yield values of (15 ± 0.9) kHz and (6 ± 0.5) kHz in the solid and the LC phase, respectively. The reduction factor due the axial motion of the discs is thus 0.4 corresponding to an order parameter of 0.8, remembering that for a completely regular column the H–H vectors would be at right angles to the column axis and the reduction factor would be 0.5.[19] The reduced order parameter indicates additional out-of-plane motion in addition to the axial rotation.

The limited order of these systems also shows up in the X-ray diffraction pattern displayed in Figure 13(a). The order can be increased by inserting phenylene units between the core and the alkyl chains (HBC-PhC_{12}),[66] as is evident from the sharper X-ray reflections in Figure 13(b). In ^{1}H NMR, however, we cannot resolve the core and the exophenyl moieties. This can be achieved by heteronuclear ^{1}H–^{13}C DQ NMR applying REPT-HMQC techniques.[37] Indeed, analysis of the sideband patterns for the C–H groups (Figure 13, lower part) yields core

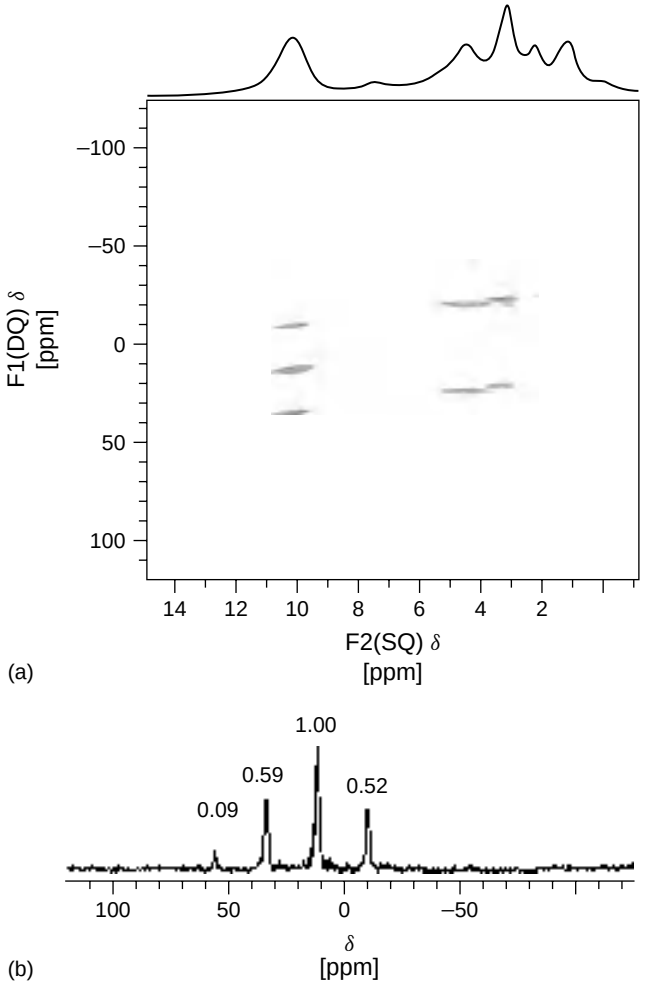

Figure 10 (a) ^{1}H DQ MAS NMR spectrum (500 MHz) of an all silica ZSM zeolite. (b) Sideband pattern for the hydrogen bonded protons, for details see Ref.[57] (Reproduced by permission of American Chemical Society)

order parameters of 0.78 ± 0.09 and 0.93 ± 0.09 for HBC-C_{12} and HBC-PhC_{12}, respectively, indicating less out-of-plane mesogen mobility in the latter. The ease with which this information is obtained with 10 mg of as-synthesized samples made it possible to report such findings together with the synthesis of these new materials.[66]

3.3.2 Slow Motions from Double-Quantum Exchange NMR

Multidimensional exchange NMR spectroscopy provides unique information about the time scale as well as the geometry of slow molecular motions,[19] latest developments are described by Schmidt-Rohr (see **Centerband-Only Detection of Exchange (CODEX): Efficient NMR Analysis of Slow Motions in Solids**).[67] Extending DQ NMR spectroscopy into that area, therefore, represented a special challenge. Recently, such a homonuclear DQ-DQ exchange experiment has been designed[68] by combining two DQ experiments as depicted in Figure 14(a). The dipole−dipole coupling between two distinct spins is used to generate a DQ coherence, and the orientation dependent coupling is measured by means of the DQ-MAS sideband pattern before and after a mixing time. In a reduced three-dimensional experiment, the two DQ-sideband patterns are correlated, resulting in a DQ-DQ sideband pattern which is sensitive to the reorientation angle. By referencing the DQ-DQ time signal, the information content of the pattern is divided into the sidebands and the centreband, with the former reflecting only the moieties which have undergone a reorientation changing the dipole−dipole coupling, and the latter predominantly containing contributions from moieties which retained their dipole−dipole coupling because they remained in, or returned to, their initial position. Hence a single sideband pattern provides access to the reorientation angle and the relative number of sites characteristic of the motional process. As a first example, Figure 14(b) displays calculated (black) and experimental (gray) ^{13}C–^{13}C DQ MAS sideband patterns for the crystalline phase of doubly labeled poly(ethylene). The exchange spectra reflect the 180° flip motion due to the slow α-process of this material, yielding a C–C reorientation angle of $70 \pm 5°$ in accord with 2D dipolar exchange NMR experiments on the same sample under static conditions.[69] One of the advantages of the MAS technique is its ability to probe the chain motion also in the non-crystalline regions, which is particularly important in view of the reviewed interest in the crystallization process of semicrystalline polymers[70] and the relation of the α-process to ultradrawability of such polymers.[71]

3.3.3 Chain Order and Translational Motion in Polymer Melts

High resolution DQ MAS NMR also offers new possibilities to probe dynamic processes involving considerably longer length scales. Figure 15 displays the ^{1}H DQ MAS NMR spectrum of 1.4 poly(butadiene) (PB) in the melt. The rapid segmental motion largely averages intra- and intermolecular dipole−dipole couplings, such that narrow lines result. Despite of that, strong auto- and cross-DQ peaks are observed, from which residual dipole−dipole couplings between the different protons can be determined.[17] They result from the fact that the chain motion in an entangled melt is not completely isotropic on intermediate length- and timescales. Numerous ways have been designed to probe the resulting dynamic order parameters by NMR.[72] ^{1}H DQ MAS NMR is the only way which can clearly distinguish *intra-* and *intergroup* couplings, and therefore determine order parameters for vectors directed *along* the chain, which were found to be considerably higher than anticipated.[17]

In order to quantify our findings, the measured order parameters are analyzed in terms of the celebrated reptation model of chain motion, formulated by De Gennes[73] and Doi and Edwards.[74] As depicted in Figure 16(a) the reptation model considers single chains subject to spatial restrictions due to entanglements, which are considered to act effectively like a tube through which the selected chain reptates. Four separate length- and timescales are distinguished (Figure 16(a)). In the different regimes different scaling laws for the mean-square displacement of chain segment due to *translational* motion are predicted, which also show up in the correlation function $C_R(t)$ probed by the residual dipole−dipole couplings, Figure 16(b). Here, the crossover from regime II ($t^{-1/4}$) to regime III ($t^{-1/2}$) is most indicative of reptation.[17,75,76] This crossover is indeed observed in polymer melts as shown for

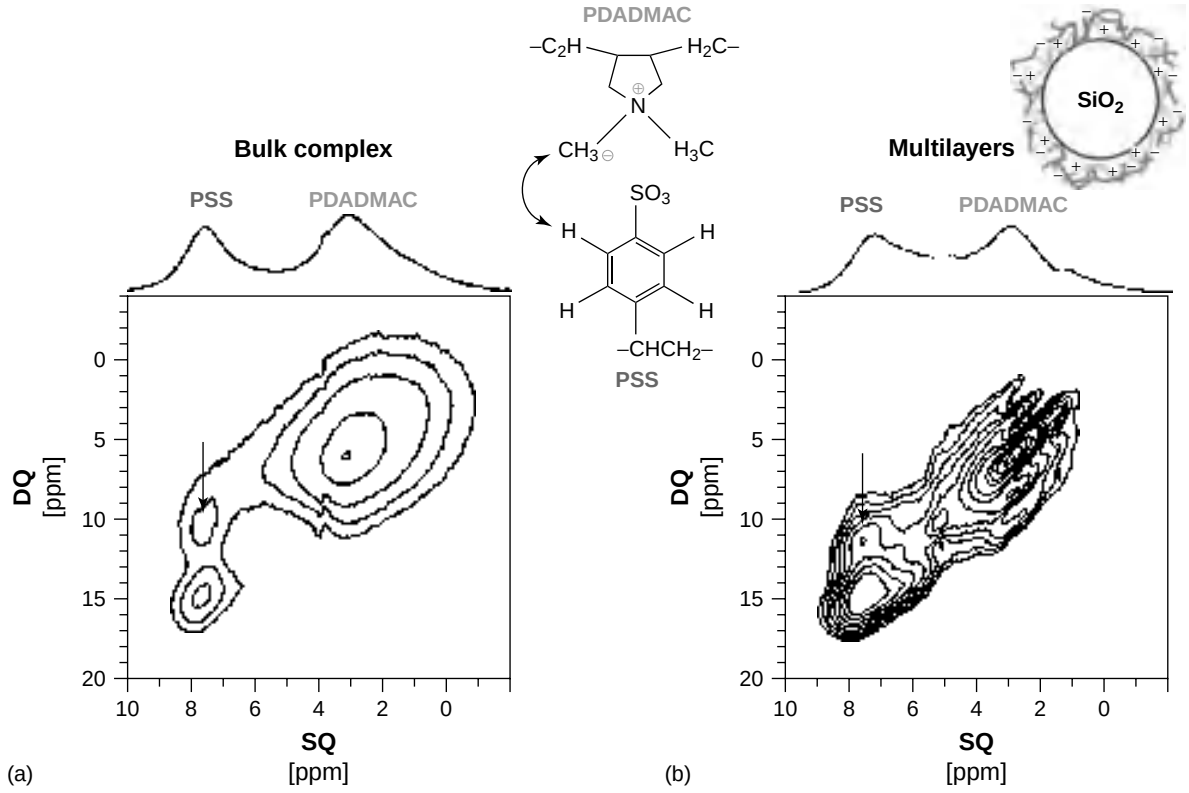

Figure 11 ^{1}H DQ MAS NMR spectra (700 MHz) for a PSS/PDADMAC polyelectrolyte complex (a) and polyelectrolyte multilayer on a silica surface (b). For details see Ref.[18]

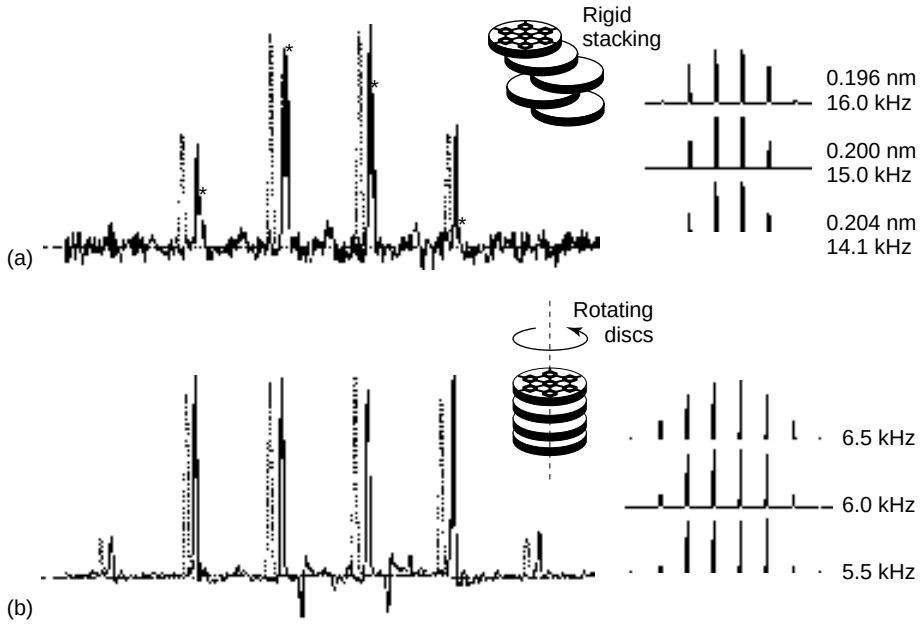

Figure 12 ^{1}H–^{1}H DQ spinning sideband patterns of HBC–C_{12} in the solid state (a) and in the columnar liquid crystalline phase (b), where the discs rotate around the column axis as indicated. For details see Ref.[16] (Reproduced by permission of American Chemical Society)

PB in Figure 16(c),[17,76] which forces us to conclude that the characteristic length scale for the residual dipole–dipole couplings is indeed the entanglement length, i.e., nanometers.[73,74] Thus, DQ NMR emerges as a simple alternative to neutron scattering for probing the chain organization of polymers.[77] Further insight was provided through a recent study,[76] where the effect of restricting the chain motion by anchoring one or both chain ends in polystyrene (PS)-PB blockcopolymers

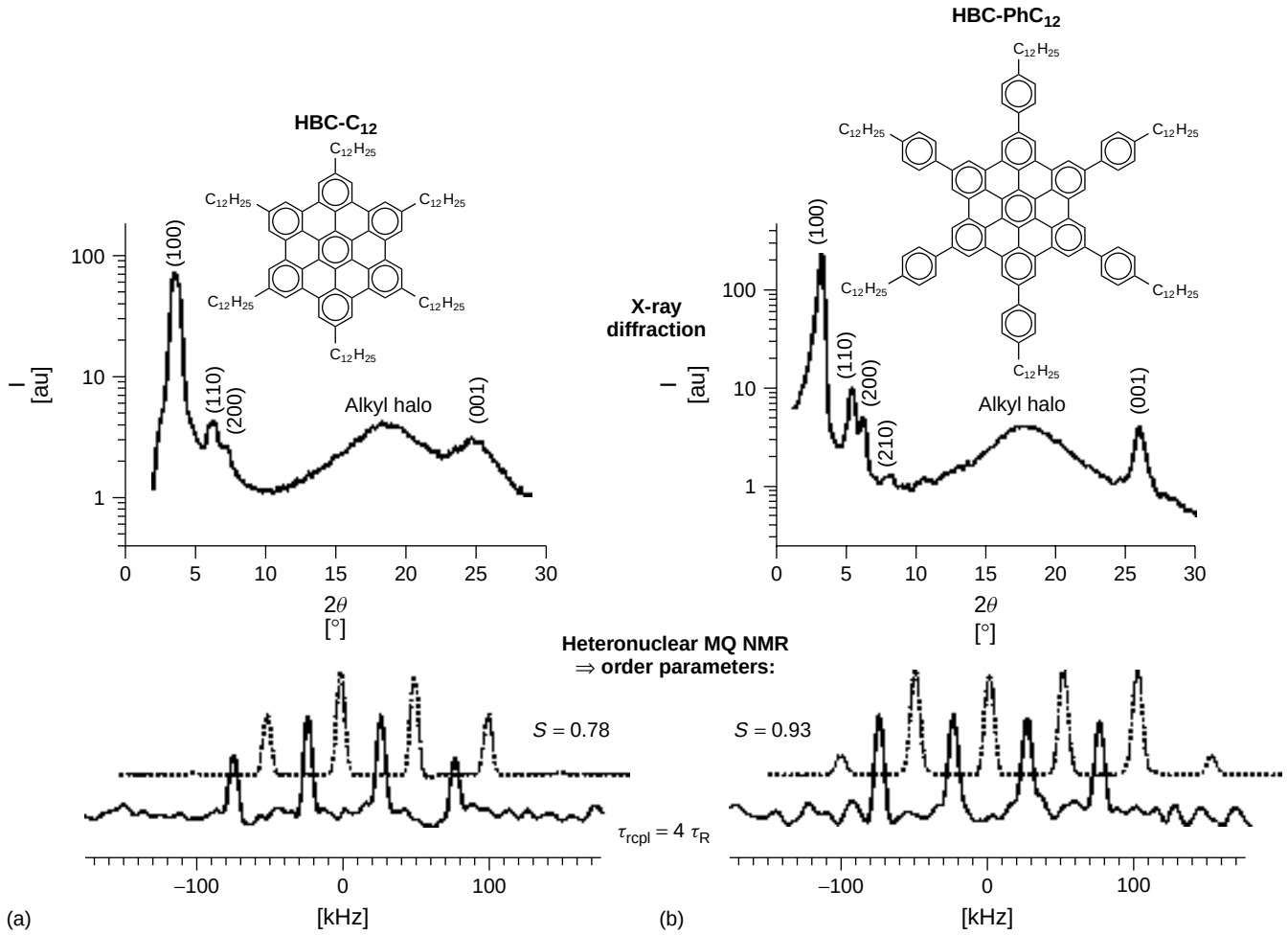

Figure 13 Comparison of powder wide angle X-ray patterns (a) and heteronuclear ^{1}H–^{13}C DQ spinning sideband patterns (b) of HBC–C_{12} (a) and HBC-PhC_{12} (b). For details see Ref.[66]

was investigated (Figure 16(c)). Not only did the chain motion slow down, the order parameters were found to increase drastically in these systems, where the polymer melt is confined to lamellae of a few tens of nm. These observations lead us to conclude that amorphous polymers are, in fact, structured in terms of nanodomains,[76] which is also consistent with new views of polymer crystallization from the melt.[70]

4 CONCLUSIONS AND OUTLOOK

Only a few years after the first DQ MAS spectra of strongly dipolar coupled solids have been recorded[11] this type of spectroscopy has emerged as a powerful tool for structural and dynamical elucidation of complex systems. This overview has focused on applications in soft matter research, i.e., on supramolecular organic systems, where spectra are recorded on small amounts (10–15 mg) of as-synthesized samples and the results are obtained overnight; but the methodology can be applied in general. For instance, high resolution DQ MAS NMR spectroscopy of isotopically labeled systems of biological interest yields torsional angles in peptides[78,79] and thus important information about the chain conformation. The sensitivity of ^{1}H chemical shifts to ring current in aromatic systems has been exploited in determining the packing of porphyrines.[34] The full information about distances and the relative orientation of specific moieties is available from DQ-NMR spectroscopy on static samples of specifically labeled materials[80] and has provided important information about the chain conformation and packing of synthetic macromolecules.[81] Last, but not least, DQ MAS NMR spectroscopy has provided hitherto inaccessible information about the connectivity of building blocks and medium range order of inorganic glasses.[82,83]

The development of the technique is far from complete. Major advances are expected in the years to come. For instance, selection of coherence pathways by pulsed field gradients, well-established in high-resolution NMR in liquids, has recently been demonstrated in rotating solids.[84,85] Likewise, inverse detection and heteronuclear editing has been realized in MAS NMR in both, synthetic polymers and biopolymers.[86,87] Indeed, an increase of the signal to noise ratio by a factor of 10 has been achieved for ^{15}N by such an approach.[49] Thus solid state NMR is envisaged to become as valuable a tool for the supramolecular chemist as solution state NMR is for the synthetic chemist today.

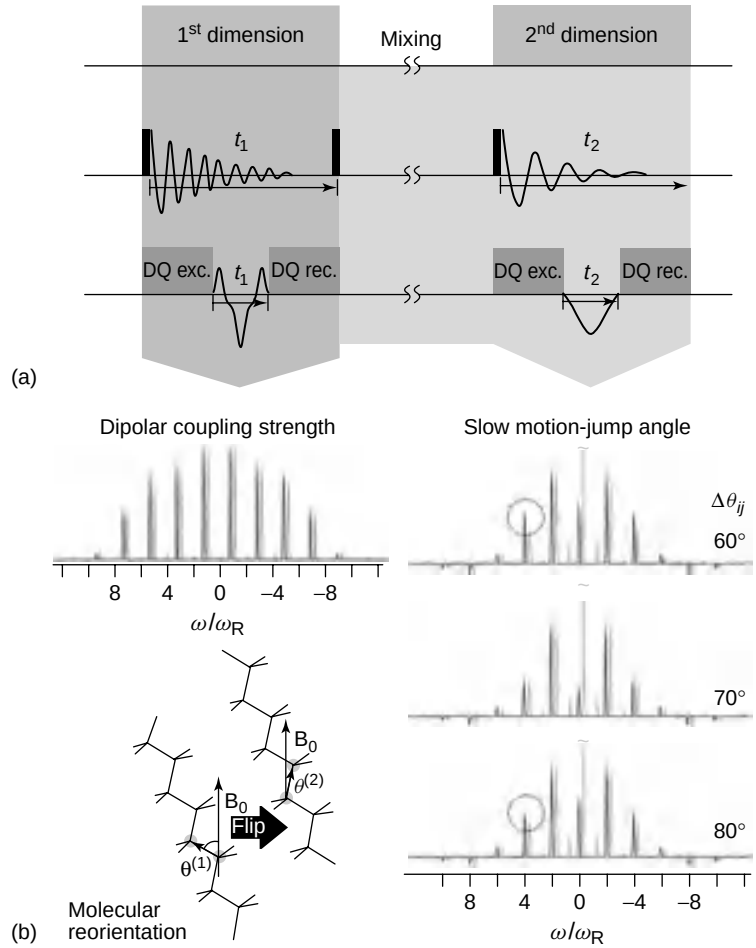

Figure 14 (a) Schematic representation of DQ exchange experiments for elucidation of slow molecular dynamics, lower trace compared to a conventional exchange experiment, middle trace.[19] (b) Calculated (black) and observed (gray) ^{13}C–^{13}C DQ MAS NMR sideband pattern of crystalline poly(ethylene) yielding the dipolar coupling strength and DQ-DQ exchange sideband patterns for different jump angles. For details see Ref.[68] (Reproduced by permission of Academic Press)

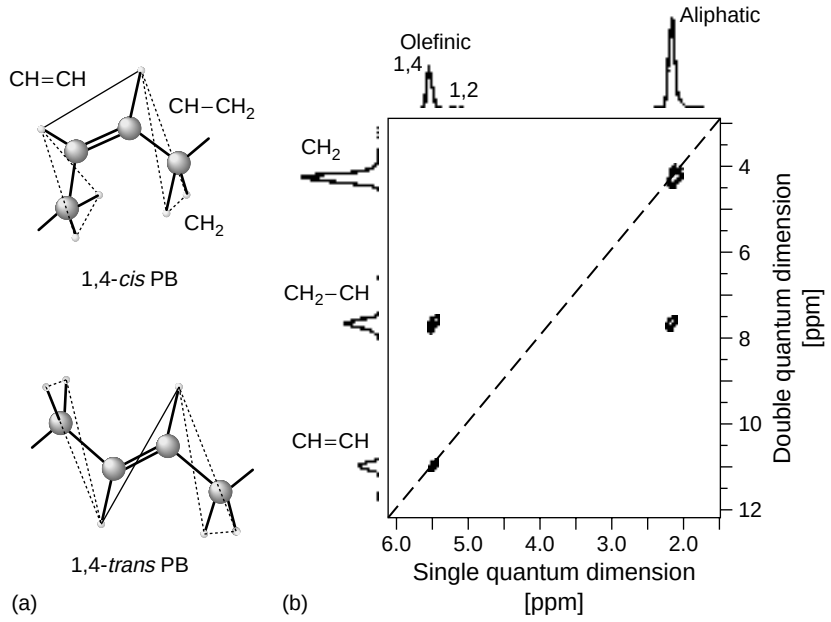

Figure 15 (a) Spin pair dipolar couplings in *cis* and *trans* polybutadiene (PB) units. (b) ^1H DQ MAS NMR spectrum (500 MHz) of a PB melt well above T_g. For details see Ref.[17] (Reproduced by permission of American Physical Society)

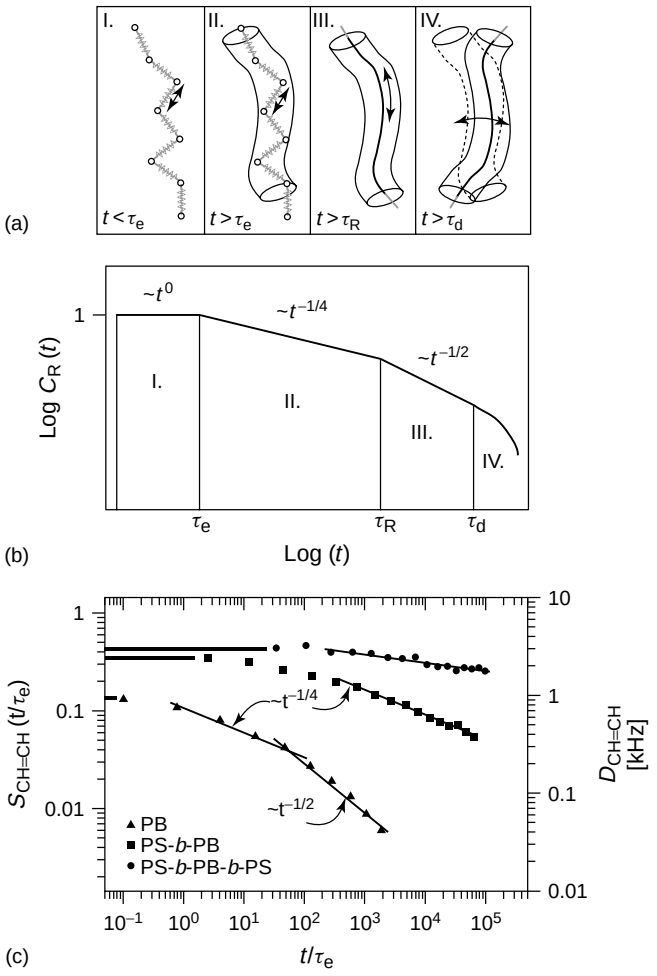

Figure 16 (a) Illustration of the different dynamic regimes considered in the reptation model. (b) Scaling behavior of the correlation function $C_R(t)$ available through ^{1}H DQ MAS NMR in the different dynamic regimes shown in (a). (c) Experimental dipolar couplings for PB and polystyrene-PB diblock (PS-PB) and triblock (PS-PB-PS) copolymers. For details see Ref.[76] (Reproduced by permission of American Chemical Society)

5 RELATED ARTICLES IN THIS VOLUME

Adiabatic Polarization-Transfer Methods in MAS Spectroscopy; Centerband-Only Detection of Exchange (CODEX): Efficient NMR Analysis of Slow Motions in Solids; Dynamics of Hydrogen Transfer in Liquids and Solids; Magic-angle Spinning Extensions; Symmetry-Based Pulse Sequences in Magic-Angle Spinning Solid-State NMR; Spinning Sideband Analysis for Spin-1/2 Nuclei; Structural and Dynamic Characterization of Soft Polymers by Solid State NMR and Field Gradient NMR; Supramolecular Chemistry; Through-Bond Experiments in Solids.

6 RELATED ARTICLES IN VOLUMES 1–8

CRAMPS, Volume 3; Cross Polarization in Rotating Solids: Spin-1/2 Nuclei, Volume 3; Double Quantum Coherence, Volume 3; Floquet Theory, Volume 3; HETCOR in Organic Solids, Volume 4; High Speed MAS of Half-Integer Quadrupolar Nuclei in Solids, Volume 4; Homonuclear Recoupling Schemes in MAS NMR, Volume 4; Hydrogen Bonding, Volume 4; Magic Angle Spinning, Volume 5; Multidimensional Spectroscopy: Concepts, Volume 5; Multiple Quantum Coherence in Spin-1/2 Dipolar Coupled Solids, Volume 5; Multiple Quantum Coherences in Extended Dipolar Coupled Spin Networks, Volume 5; Multiple Quantum NMR in Solids, Volume 5; Polymer Dynamics & Order from Multidimensional Solid State NMR, Volume 6; Polymer Physics, Volume 6; REDOR & TEDOR, Volume 6; Rotating Solids, Volume 7; Shielding: Overview of Theoretical Methods, Volume 7; Sideband Analysis in Magic Angle Spinning NMR of Solids, Volume 7.

7 REFERENCES

1. 'Encyclopedia of Materials: Science and Technology', Pergamon: Amsterdam, 2001.
2. J. M. Lehn, 'Supramolecular Chemistry', Wiley-VCH: Weinheim, 1995.
3. K. Müllen and G. Wegner, eds 'The Oligomer Approach', Wiley-VCH: Weinheim, 1998.
4. G. A. Jeffrey and W. Saenger, 'Hydrogen Bonding in Biological Structures', Springer-Verlag: New York, 1991.
5. J. L. Atwood, J. E. D. Davies, D. D. MacNiol, and F. Vögtle eds, 'Comprehensive Supramolecular Chemistry', Elsevier: Oxford, 1996.
6. M. Mehring, 'Principles of High Resolution NMR in Solids', Springer: Berlin, 1983.
7. R. E. Taylor, R. G. Pmbleton, L. M. Ryan, and B. C. Gerstein, *J. Chem. Phys.*, 1979, **71**, 4541.
8. G. Scheler, U. Haubenreisser, and H. Rosenberger, *J. Magn. Reson.*, 1981, **44**, 134.
9. H. J. Jakobsen, in 'Encyclopedia of Nuclear Magnetic Resonance', eds D. M. Grant and R. K. Harris, Wiley: Chichester, 1996, Vol. 1, p. 398.
10. M. Munowitz and A. Pines, *Adv. Chem. Phys.*, 1987, **66**, 1.
11. H. Geen, J. J. Titman, J. Gottwald, and H. W. Spiess, *Chem. Phys. Lett.*, 1994, **227**, 79.
12. J. Gottwald, D. E. Demco, R. Graf R, and H. W. Spiess, *Chem. Phys. Lett.*, 1995, **243**, 314.
13. W. Sommer, J. Gottwald, D. E. Demco, and H. W. Spiess, *J. Magn. Reson.*, 1995, **A 113**, 131.
14. C. Filip, S. Hafner, I. Schnell, D. E. Demco, and H. W. Spiess, *J. Chem. Phys.*, 1999, **110**, 423.
15. I. Schnell, S. P. Brown, H. Y. Low, H. Ishida, and H. W. Spiess, *J. Am. Chem. Soc.*, 1998, **120**, 11 784.
16. S. P. Brown, I. Schnell, J. D. Brand, K. Müllen, and H. W. Spiess, *J. Am. Chem. Soc.*, 1999, **121**, 6712.
17. R. Graf, A. Heuer, and H. W. Spiess, *Phys. Rev. Lett.*, 1998, **80**, 5738.
18. L. N. J. Rodriguez, S. De Paul, C. J. Barrett, L. Reven, and H. W. Spiess, *Adv. Mater.*, 2000, **12**, 1934.
19. K. Schmidt-Rohr K. and H. W. Spiess, 'Multidimensional Solid State NMR and Polymers', Academic Press: New York, 1994.
20. A. Samoson, 'Encyclopedia of Nuclear Magnetic Resonance', eds D. M. Grant and R. K. Harris, Wiley: Chichester, 2002, Vol. 9.
21. I. Schnell, I. and H. W. Spiess, *J. Magn. Reson.*, 2001, **151**, 153.
22. R. R. Ernst, G. Bodenhausen, and A. Wokaun, 'Principles of Nuclear Magnetic Resonance in One and Two Dimensions', Clarendon Press: Oxford, 1987.
23. M. H. Levitt, 'Encyclopedia of Nuclear Magnetic Resonance', eds D. M. Grant and R. K. Harris, Wiley: Chichester, 2002, Vol. 9.

24. A. Brinkmann, M. Edén, and M. H. Levitt, *J. Chem. Phys.*, 2000, **112**, 8539.
25. R. Graf, D. E. Demco, J. Gottwald, S. Hafner, and H. W. Spiess, *J. Chem. Phys.*, 1997, **138**, 167.
26. R. Graf, D. E. Demco, S. Hafner, and H. W. Spiess, *Solid State NMR*, 1998, **12**, 139.
27. H. Geen, R. Graf, A. S. Heindrichs, B. S. Hickman, I. Schnell, H. W. Spiess, and J. J. Titman, *J. Magn. Reson.*, 1999, **125**, 224.
28. L. Frydman and J. S. Harwood, *J. Am. Chem. Soc.*, 1995, **20**, 11 784.
29. C. Fernandez and J. P. Amoureux, *Chem. Phys. Lett.*, 1995, **242**, 449.
30. U. Friedrich, I. Schnell, S. P. Brown, A. Lupulescu, D. E. Demco, and H. W. Spiess, *Mol. Phys.*, 1998, **95**, 1209.
31. S. Hafner and H. W. Spiess, *Concepts Magn. Reson.*, 1998, **10**, 99.
32. A. Bielecki, A. C. Kolbert, H. J. M. de Groot, R. G. Griffin, and M. H. Levitt, *Adv. Magn. Reson.*, 1990, **14**, 111.
33. A. Lesage, L. Duma, D. Sakellariou, and L. Emsley, *J. Am. Chem. Soc.*, 2001, **123**, 5747.
34. B.-J. van Rossum, D. B. Steensgaard, F. M. Mulder, G. J. Boender, K. Schaffner, A. R. Holzwarth, and H. J. M. de Groot, *Biochemistry*, 2001, **40**, 1587.
35. T. Gullion and J. Schaefer, *Adv. Magn. Reson.*, 1989, **13**, 57.
36. T. Gullion, *Magn. Reson. Rev.*, 1997, **17**, 83.
37. K. Saalwächter, R. Graf, and H. W. Spiess, *J. Magn. Reson.*, 1999, **140**, 471.
38. K. Saalwächter and H. W. Spiess, *J. Chem. Phys.*, 2001, **114**, 5707.
39. B. van Rossum, H. Förster, and H. J. M. de Groot *J. Magn. Reson.*, 1996, **124**, 516.
40. M. Baldus and B. H. Meier, *J. Magn. Reson.*, 1997, **128**, 172.
41. V. Macho, L. Brombacher, and H. W. Spiess, *Appl. Magn. Reson.*, 2001, **20**, 405.
42. M. Wind, U.-M. Wiesler, K. Saalwächter, K. Müllen, and H. W. Spiess, *Adv. Mater.*, 2001, **13**, 752.
43. J. Baum, M. Munowitz, A. N. Garroway, and A. Pines, *J. Chem. Phys.*, 1985, **83**, 2105.
44. S. J. Hwang, D. O. Uner, T. S. King, M. Pruski, and B. C. Gerstein, *J. Phys. Chem.*, 1995, **99**, 3697.
45. U. Haeberlen, 'Advances in Magnetic Resonance Suppl.1', Academic Press: San Diego, CA, 1976.
46. R. K. Harris, in 'Encyclopedia of Nuclear Magnetic Resonance', eds D. M. Grant and R. K. Harris, Wiley: Chichester, 1996, Vol. 5, p. 3314.
47. H. Ishida and H. Y. Low, *Macromolecules*, 1997, **30**, 1099.
48. R. P. Sijbesma, F. H. Beijer, L. Brunsveld, B. J. B. Folmer, J. H. K. K. Hirschberg, R. F. M. Lange, J. K. L. Lowe, and E. W. Meijer, *Science*, 1997, **278**, 1601.
49. I. Schnell, B. Langer, S. H. M. Söntjens, M. H. P. van Genderen, and H. W. Spiess, *J. Magn. Reson.*, 2001, **150**, 57.
50. J. R. Chowdhury, A. S. Wolkoff, N. R. Chowdhury, I. M. Arias in 'The Metabolic and Molecular Bases of Inherited Diseases', eds C. R. Scriver, A. L. Beaudet, W. S. Sly, and D. Valle, McGraw-Hill: New York, 1995, Vol. II, pp. 2161–2208.
51. S. P. Brown, X. X. Zhu, K. Saalwächter, and H. W. Spiess, *J. Am. Chem. Soc.*, 2001, **123**, 4275.
52. P. Lazzeretti, *Prog. NMR Spectrosc.*, 2000, **36**, 1.
53. A. C. de Dios, *Prog. NMR Spectrosc.*, 1996, **29**, 229.
54. C. Ochsenfeld, S. P. Brown, I. Schnell, J. Gauss, and H. W. Spiess, *J. Am. Chem. Soc.*, 2001, **123**, 2597.
55. F.-G. Klärner, U. Burkert, M. Kamieth, R. Boese, and J. Benet-Buchholz, *Chem. Eur. J.*, 1999, **5**, 1700.
56. S. P. Brown, T. Schaller, U. P. Seelbach, F. Koziol, C. Ochsenfeld, F.-G. Klärner, and H. W. Spiess, *Angew. Chem. Int. Ed. Engl.*, 2001, **40**, 717.
57. D. F. Shantz, J. Schmedt auf der Günne, H. Koller, and R. F. Lobo, *J. Am. Chem. Soc.*, 2000, **122**, 6659.
58. H. van Beckum, E. M. Flanigen, and J. C. Jansen, 'Introduction to Zeolite Science and Practice', Elsevier: Amsterdam, 1991.
59. G. Decher, *Science*, 1997, **277**, 1232.
60. F. Caruso and H. Möhwald, *J. Am. Chem. Soc.*, 1999, **121**, 6039.
61. S. T. Dubas and J. B. Schlenoff, *Macromolecules*, 1999, **32**, 8153.
62. H. W. Spiess, *Ber. Bunsenges. Phys. Chem.*, 1997, **101**, 153.
63. D. Demus, J. W. Goodby, G. W. Gray, H. W. Spiess, and V. Vill, eds 'Handbook of Liquid Crystals', Wiley-VCH: Weinheim, 1998.
64. P. Herwig, C. W. Kayser, K. Müllen, and H. W. Spiess, *Adv. Mater.*, 1996, **8**, 510.
65. A. M. van de Craats, J. M. Warman, A. Fechtenkötter, J. D. Brand, M. A. Harbison, and K. Müllen, *Adv. Mater.*, 1999, **11**, 1469.
66. A. Fechtenkötter, K. Saalwächter, M. A. Harbison, K. Müllen, and H. W. Spiess, *Angew. Chem. Int. Ed. Engl.*, 1999, **38**, 3039.
67. K. Schmidt-Rohr, 'Encyclopedia of Nuclear Magnetic Resonance', eds D. M. Grant and R. K. Harris, Wiley: Chichester, 2002, Vol. 9.
68. I. Schnell, A. Watts, and H. W. Spiess, *J. Magn. Reson.*, 2001, **149**, 90.
69. W.-G. Hu, C. Boeffel, and K. Schmidt-Rohr, *Macromolecules*, 1999, **32**, 1619.
70. G. Hauser, J. Schmidtke, and G. Strobl, *Macromolecules*, 1998, **31**, 6250.
71. W.-G. Hu and K. Schmidt-Rohr, *Acta Polym.*, 1999, **50**, 271.
72. J. P. Cohen-Addad, *Prog. NMR Spectrosc.*, 1993, **25**,1.
73. P. G. de Gennes, *J. Chem. Phys.*, 1971, **55**, 572.
74. M. Doi and S. F. Edwards, 'The Theory of Polymer Dynamics', Clarendon Press: Oxford, 1986.
75. R. C. Ball, P. T. Callaghan, E. T. Samulski, *J. Chem. Phys.*, 1997, **106**, 7352.
76. T. Dollase, R. Graf, A. Heuer, and H. W. Spiess *Macromolecules*, 2001, **33**, 298.
77. D. Richter, *Physica B*, 2000, **276–278**, 22.
78. M. Hong, J. D. Gross, and R. G. Griffin, *J. Phys. Chem.*, 1997, **B101**, 5869.
79. X. Feng, P. J. E. Verdegem, Y. K. Lee, D. Sandstrom, M. Eden, P. Bovee Gueurts, W. J. de Grip, J. Lugtenburg, H. J. M. de Groot, and M. H. Levitt, *J. Am. Chem. Soc.*, 1997, **119**, 6853.
80. K. Schmidt-Rohr, *Macromolecules*, 1996, **29**, 3375.
81. K. Schmidt-Rohr, W. Hu, and N. Zumbulyadis, *Science*, 1998, **280**, 714.
82. M. Feike, C. Jäger, and H. W. Spiess, *J. Non-Cryst. Solids*, 1998, **223**, 200.
83. K. Glock, O. Hirsch, P. Rehak, B. Thomas, and C. Jäger, *J. Non-Cryst. Solids*, 1998, **234**, 113.
84. T. Fritzhanns, S. Hafner, D. E. Demco, H. W. Spiess, and F. Laukien, *J. Magn. Reson.*, 1998, **134**, 355.
85. T. Fritzhanns, D. E. Demco, S. Hafner, and H. W. Spiess, *Mol. Phys.*, 1999, **97**, 931.
86. Y. Ishii and R. Tycko, *J. Magn. Reson.*, 2000, **142**, 199.
87. Y. Ishii, J. P. Yesinowski, and R. Tycko, *J. Am. Chem. Soc.*, 2001, **123**, 2921.

Biographical Sketch

Hans Wolfgang Spiess, *b* 1942. Ph.D., 1968, Physical Chemistry, University of Frankfurt, Germany. Research associate, Florida State University, 1968–1970; Max-Planck Institute, Heidelberg with K. H. Hausser, 1970–1975; University of Mainz, 1975–1978. Professor at University of Mainz, 1978–1980, University of Munster, 1981–1982, University of Bayreuth, 1983–1984. Director, Max-Planck-Institut for Polymer Research, Mainz since 1984. Approx. 350 publications and a monograph on multidimensional solid-state NMR and polymers. Current research interests: solid state NMR and its applications in polymer science and supramolecular systems.

Dynamic Angle Spinning

Philip J. Grandinetti

The Ohio State University, Columbus, OH, USA

1	Introduction	1
2	Basic Principles of Dynamic Angle Spinning	1
3	Implementation of Dynamic Angle Spinning	5
4	Applications of DAS	7
5	Related Articles	8
6	References	8

1 INTRODUCTION

Dynamic angle spinning (DAS) is a two-dimensional NMR experiment designed for removing multiple-rank anisotropic broadenings in solid state NMR. It is a technique that has proven useful for obtaining the high-resolution isotropic solid state NMR spectra of the central transition of half-integer quadrupolar nuclei broadened to second order (see also ***Quadrupolar Nuclei in Solids***). This narrowing is accomplished by using the angle of the sample rotation axis as a dynamic variable in a two-dimensional experiment.

It has long been understood that the second-order anisotropic broadenings of the central transition of half-integer nuclei simply cannot be removed with magic angle or variable angle spinning,[1] and it was even thought that no spatial averaging solution existed. In 1988 new averaging approaches that solve this problem were disclosed by both the Pines group and the Virlet group at the 9th European Experimental NMR conference in Bad-Aussee. In subsequent publications by both groups[2,3] the underlying theory for removing second- and higher-order broadenings was presented, and two new experimental techniques emerged for removing second-order broadenings: double rotation (DOR) (see also ***Double Rotation*** and dynamic angle spinning (DAS), both first achieved experimentally at Berkeley.[2,4,5] DAS combines the ideas of switched rotation axis[6,7] and discrete averaging experiments[8] to remove the second-order broadenings of the central transition of half-integer nuclei.

In this article the basic principles behind DAS are discussed along with a description of how DAS is implemented and some illustrative examples of its use.

2 BASIC PRINCIPLES OF DYNAMIC ANGLE SPINNING

In NMR the Zeeman interaction is normally the dominant nuclear spin interaction, and the NMR transition frequency can be expanded in a perturbation series,[9]

$$\Omega(\theta,\phi) = \Omega^{(0)} + \Omega^{(1)}(\theta,\phi) + \Omega^{(2)}(\theta,\phi) + \cdots \qquad (1)$$

with the Zeeman interaction as the zeroth-order term

$$\Omega^{(0)} = -\gamma B_0 \qquad (2)$$

where γ is the nuclear gyromagnetic ratio and B_0 is the external magnetic field strength. The higher order terms in equation (1) are due to internal spin interactions (e.g. chemical shift, quadrupolar coupling, etc.). These interactions are second rank by nature and thus the higher order terms can be expanded in limited spherical harmonic series

$$\Omega^{(1)}(\theta,\phi) = \Omega^{(1)}_{\rm iso} + \sum_{k=-2}^{2} c^{(1)}_{2,k} Y_{2,k}(\theta,\phi) \qquad (3)$$

$$\Omega^{(2)}(\theta,\phi) = \Omega^{(2)}_{\rm iso} + \sum_{k=-2}^{2} c^{(2)}_{2,k} Y_{2,k}(\theta,\phi) + \sum_{k=-4}^{4} c^{(2)}_{4,k} Y_{4,k}(\theta,\phi) \qquad (4)$$

where (θ,ϕ) are the angles between the external magnetic field direction and the principal axis system of the internal spin interactions. The terms $\Omega_{\rm iso}{}^{(n)}$ and the coefficients $c_{L,k}{}^{(n)}$ are listed in Tables 1 and 2 for the chemical shift and quadrupolar interactions.

In a liquid sample the random and rapid molecular reorientations average the NMR transition frequency over all values of θ and ϕ. This incoherent averaging over the full sphere removes all anisotropic broadenings and only the isotropic NMR frequencies are observed. This can be easily seen by averaging equations (3) and (4) over the sphere.

To obtain an isotropic spectrum from a solid sample, it is not necessary to average over all points on the entire sphere.[10] When the anisotropy in the NMR transition frequency is completely described by second-rank spherical harmonics, as in equation (3), the anisotropy can be coherently averaged away by reorientating the sample so that the external magnetic field is directed along only the three vertices on the face of an octahedron as shown in Figure 1(a). This is often the case with spin-$\frac{1}{2}$ nuclei. The discrete reorientation of the sample along these vertices is realized in a magic angle hopping (MAH)[8] experiment, (see also ***Magic Angle Turning and Hopping***) and the continuous rotation on a cone[10] with apex angle of 54.74° which passes through the vertices of the octahedron, is realized in a magic angle spinning (MAS)[11,12] experiment (see also ***Magic Angle Spinning***).

For NMR transition frequencies with higher than first-order terms, octahedral symmetry may not be sufficient for obtaining an isotropic spectrum. For example, if the quadrupolar coupling is sufficiently large that the second-order term is required to describe the spectrum, then the size of the first-order broadening can be on the order of many MHz; thus it can be virtually impossible to obtain the complete NMR spectrum of a quadrupolar nucleus in a polycrystalline sample, since the bandwidth of conventional NMR spectrometers is typically only a few hundred kHz. Fortunately, for half-integer spin quadrupolar nuclei, the central $m = \frac{1}{2} \rightarrow -\frac{1}{2}$ transition is unaffected by the first-order quadrupolar term and in many cases is broadened only by the second-order term of

Table 1 Isotropic Frequency Shifts and Spherical Harmonic Coefficients for the $m \rightarrow m-1$ Transition of Spin I from First-Order Perturbation Theory for Chemical Shift and Quadrupolar Interactions[a]

	Chemical shift	Quadrupolar
$\Omega_{\mathrm{iso}}^{(1)}$	$\sigma \gamma B_0$	0
$c_{2,0}^{(1)}$	$\sqrt{\frac{4\pi}{5}} \cdot \gamma B_0(\sigma_{ZZ} - \sigma)$	$\sqrt{\frac{9}{5}} \cdot \frac{\pi^{3/2}\chi}{I(2I-1)}(2m-1)$
$c_{2,\pm 2}^{(1)}$	$\sqrt{\frac{2\pi}{15}} \cdot \gamma B_0(\sigma_{YY} - \sigma_{XX})$	$\sqrt{\frac{3}{10}} \cdot \frac{\pi^{3/2}\chi\eta}{I(2I-1)}(2m-1)$

[a] σ_{XX}, σ_{YY}, σ_{ZZ} are the principal components of the chemical shift tensor, χ is e^2qQ/h, and η is the quadrupolar asymmetry parameter.

Table 2 Isotropic Frequency Shifts and Spherical Harmonic Coefficients for the $m \rightarrow m-1$ Transition of Spin I from Second-Order Perturbation Theory for the Quadrupolar Interaction[a]

$\Omega_{\mathrm{iso}}^{(2)}$	$-\frac{3}{10}\frac{\pi^2\chi^2}{I^2(2I-1)^2\gamma B_0}\left(\frac{\eta^2}{3}+1\right)[I(I+1)-9m(m-1)-3]$
$c_{2,0}^{(2)}$	$\sqrt{\frac{36}{245}}\frac{\pi^{5/2}\chi^2}{I^2(2I-1)^2\gamma B_0}\left(\frac{\eta^2}{3}-1\right)[2I(I+1)-9m(m-1)-15/4]$
$c_{2,\pm 2}^{(2)}$	$\sqrt{\frac{24}{245}}\frac{\pi^{5/2}\chi^2\eta}{I^2(2I-1)^2\gamma B_0}[2I(I+1)-9m(m-1)-15/4]$
$c_{4,0}^{(2)}$	$\frac{3}{35}\frac{\pi^{5/2}\chi^2}{I^2(2I-1)^2\gamma B_0}\left(\frac{\eta^2}{18}+1\right)[9I(I+1)-51m(m-1)-39/2]$
$c_{4,\pm 2}^{(2)}$	$\frac{1}{\sqrt{490}}\frac{\pi^{5/2}\chi^2\eta}{I^2(2I-1)^2\gamma B_0}[9I(I+1)-51m(m-1)-39/2]$
$c_{4,\pm 4}^{(2)}$	$\frac{1}{\sqrt{1260}}\frac{\pi^{5/2}\chi^2\eta^2}{I^2(2I-1)^2\gamma B_0}[9I(I+1)-51m(m-1)-39/2]$

[a] χ is e^2qQ/h and π is the quadrupolar asymmetry parameter.

equation (4), which can be on the order of a few kHz. Unfortunately, while the second-rank spherical harmonics in equation (4) are removed using octahedral symmetry, the fourth-rank spherical harmonics are not. Therefore, to average away completely the anisotropy in this case a better approximation to the sphere is required. This can be done by reorientating the sample so that the external magnetic field is directed along the six vertices on the icosahedron as shown in Figure 1(b) or in Figure 1(c). The discrete reorientation of the sample along these vertices is realized in a dynamic angle hopping (DAH)[13] experiment and the continuous rotation on two cones[10] with apex angles of 0° and 63.43° or 37.38° and 79.19°, which pass through the icosahedral vertices, is realized in a dynamic angle spinning (DAS)[3–5,10,14–21] experiment.

A DAS reorientation trajectory is implemented as a two-dimensional NMR experiment which correlates a spin's resonance frequency while spinning at one angle with its frequency while spinning at a second angle. In DAS the sample is spun about a single axis for the first evolution period and then hopped to a second angle for the second evolution period as shown in Figure 2(a). Two rf pulses are used to quench the evolution during the time required to hop.

When spinning about a single axis equations (3) and (4) are averaged to

$$\overline{\Omega^{(1)}}(\beta,\theta',\phi') = \Omega_{\mathrm{iso}}^{(1)} + P_2(\cos\beta)\sum_{m=-2}^{2} c_{2,m}^{(1)} Y_{2,m}(\theta',\phi') \quad (5)$$

$$\overline{\Omega^{(2)}}(\beta,\theta',\phi') = \Omega_{\mathrm{iso}}^{(2)} + P_2(\cos\beta)\sum_{m=-2}^{2} c_{2,m}^{(2)} Y_{2,m}(\theta',\phi') + P_4(\cos\beta)\sum_{m=-4}^{4} c_{4,m}^{(2)} Y_{4,m}(\theta',\phi') \quad (6)$$

where β is the angle between the spinner axis and the magnetic field, $P_n(\cos\theta)$ are Legendre polynomials, and (θ',ϕ') are the angles between the spinner axis and the principal axis system of the internal spin interactions. If the two rotor axis angles in a DAS experiment are chosen so that for all the spins the anisotropic frequency at the first angle is mirrored about the isotropic frequency when spinning at the second angle, then

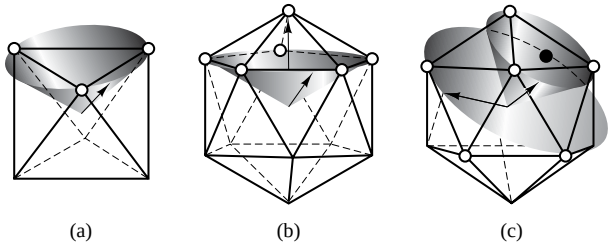

Figure 1 (a) Octahedral symmetry can be implemented with a single continuous trajectory in cases where tensors of rank 2 are to be eliminated. (b,c) Icosahedral symmetry can be implemented with just two continuous trajectories in cases where tensors of rank 2 and 4 are to be eliminated. Time spent along one particular trajectory is proportional to the number of vertices. In (b) the two spinning axes are $\beta_1 = 0^\circ$ and $\beta_2 = 63.43^\circ$, and the ratio of times spinning at the two angles is 1:5. In (c) the angles are $\beta_1 = 37.38^\circ$ and $\beta_2 = 79.19^\circ$, and the ratio of times spinning at the two angles is 1:1. (Adapted by permission of Elsevier Science Publishers from B. Q. Sun, J. H. Baltisberger, Y. Wu, A. Samoson, and A. Pines, 'Solid State NMR', 1992, **1**, 267, and by permission of Clarendon Press from Samoson et al.)

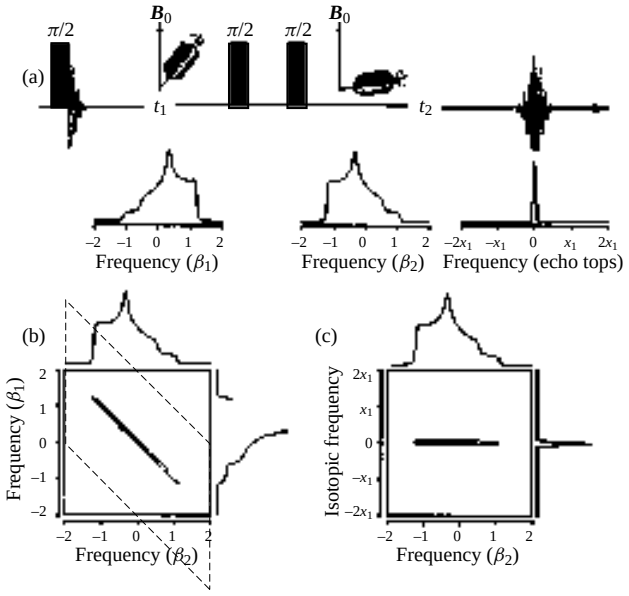

Figure 2 (a) Simplest implementation of 2D DAS pulse sequence. (b) 2D variable angle spinning correlation spectrum obtained from the sequence in (a). (c) 2D DAS spectrum obtained from (b) after applying the shearing transformation as described in the text

all decay of the signal in t_1 due to the anisotropic broadening is refocused into an echo during t_2. For systems broadened up to second order this mirror image condition is fulfilled when the angle pair (β_1,β_2) satisfies the conditions

$$x_1 P_2(\cos\beta_1) + x_2 P_2(\cos\beta_2) = 0 \tag{7}$$

$$x_1 P_4(\cos\beta_1) + x_2 P_4(\cos\beta_2) = 0 \tag{8}$$

and

$$x_1 + x_2 = 1 \tag{9}$$

The DAS echo forms at a time $(x_2/x_1)t_1$ during t_2 evolution. By collecting the intensity of the echo tops as a function of t_1/x_1 and Fourier transforming this interferogram, the isotropic DAS spectrum is obtained. By collecting all the data in t_2 as a function of t_1, and performing a 2D Fourier transform, a spectrum as shown in Figure 2(b) is obtained. This 2D spectrum correlates the NMR spectrum obtained while spinning at β_1 with the NMR spectrum obtained while spinning at β_2. If the angle pair (β_1,β_2) satisfies equations (7)–(9), then the 2D correlation for each site will be isotropic and linear and given by:

$$\omega_2 = \frac{1}{x_2}(\Omega_{\text{iso}} - x_1\omega_1) \tag{10}$$

There is a continuous set of angle pairs that exist which provide this isotropic 2D correlation, including the angle pairs $(0^\circ,63.43^\circ)$ where $x_1/x_2 = 5$ and $(37.38^\circ, 79.19^\circ)$ where $x_1/x_2 = 1$. Equations (7)–(9) may be solved analytically for the angle pairs (β_1,β_2) in terms of x_1 and x_2:

$$\beta_1 = \cos^{-1}\frac{\sqrt{1+\sqrt{\frac{4x_2}{5x_1}}}}{3} \tag{11}$$

$$\beta_2 = \cos^{-1}\frac{\sqrt{1-\sqrt{\frac{4x_1}{5x_2}}}}{3} \tag{12}$$

where $0.8 \leq x_2/x_1 \leq 5$. Of course, the order of the angle pair may be reversed with a corresponding reversal of the fractional time spent at each angle.

The 2D spectrum of Figure 2(b) can be transformed with a shearing transformation to obtain the 2D DAS spectrum shown in Figure 2(c), which correlates the isotropic resonance of a site with its anisotropic lineshape. Shearing transformations are well known in NMR.[22] In DAS the 2D spectrum is sheared by an angle θ_S, given by

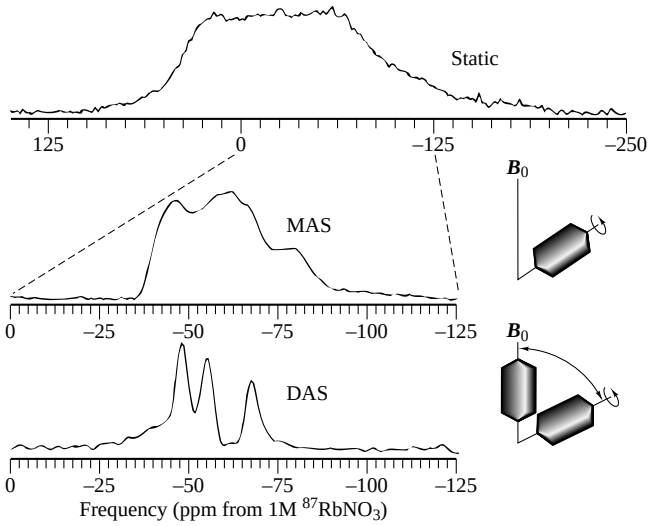

Figure 3 Static, MAS, and DAS ^{87}Rb NMR spectra of polycrystalline $RbNO_3$

$$\theta_S = \tan^{-1}\left(\frac{x_2}{x_1}\right) \tag{13}$$

followed by a scaling of the ω_1 axis by x_1. The shearing transformation may be implemented by applying a t_1-dependent first-order phase correction:

$$S'(t_1', \omega_2') = \mathrm{e}^{\mathrm{i}\phi(t_1,\omega_2)} S(t_1, \omega_2) \tag{14}$$

where

$$\phi(t_1, \omega_2) = \left(\frac{x_2}{x_1}\right)\omega_2 t_1 \tag{15}$$

before the final Fourier transform with respect to t'_1. This correction removes the tilting in $S(\omega_1,\omega_2)$, transforming it into $S'(\omega'_1,\omega'_2)$, so that an isotropic spectrum may be obtained from a projection onto the ω'_1 axis.

Figure 3 depicts the static, MAS, and DAS spectra of polycrystalline $RbNO_3$. $RbNO_3$ contains three inequivalent Rb sites in its unit cell. While the MAS provides considerable narrowing of the static spectrum by removing the second-rank spherical harmonic orientational broadenings, it still contains scaled fourth-rank orientational broadenings. With DAS, both second- and fourth-rank orientational broadenings are removed and the three inequivalent Rb sites can be resolved.

Because DAS is a two-dimensional experiment it is more time consuming than MAS; however, DAS does provide a means of separating the anisotropic lineshapes correlated to the isotropic frequency of each resolved site. For example, Figure 4 depicts the 2D DAS spectrum of $RbNO_3$. Since the isotropic resonances of all three inequivalent Rb sites can be resolved, cross sections correlated to each isotropic frequency provide the separated anisotropic lineshape for each site. These separated lineshapes can be analyzed to obtain the quadrupolar coupling parameters associated with each resonance. This information can be useful in providing structural information. For example, in the case of $RbNO_3$, a simple point charge calculation of the electric field gradients at each Rb site in the unit cell gives quadrupolar asymmetry parameters of approximately 0.9, 0.6, and 0.3. On this basis, the three resonances in the 2D DAS spectrum can be assigned to the three sites in the unit cell as shown in Figure 4. This approach can also be extended to amorphous solids where a continuous set of overlapping anisotropic lineshapes can also be separated according to correlated isotropic frequencies and used to quantify continuous structural distributions.

An interesting consequence of the shearing transformation in DAS is that the spinning sidebands can appear at nonintegral multiples of the spinning speed in the isotropic dimension. A schematic example of the behavior of spinning sidebands after a shearing transformation is shown in Figure 5 for the two cases θ_s = 45° and θ_s = 38.7°. The frequency axes in Figure 5(a) are in units of Ω_R, the actual spinning speed. The example in Figure 5(b) is the familiar situation in 2D echo spectroscopy, where the dephasing and refocusing times are equal (e.g. 2D J spectroscopy). In this example even though the spectrum is sheared, the sidebands remain aligned such that a projection onto the ω'_1 axis contains only sidebands at integer multiples of $0.5\Omega_R$. In contrast, the example in Figure 5(c), where x_1 = 0.44 and x_2 = 0.56, describes a 2D echo experiment with unequal dephasing and refocusing times. In this situation the spinning sidebands are not aligned in ω'_1, and consequently a projection onto ω'_1 yields a fairly complicated sideband pattern.

Simulated and experimental isotropic projections from the ^{87}Rb DAS of $RbClO_4$, demonstrating the sideband behavior for various pairs of DAS angles, are shown in Figure 6. In each isotropic 1D DAS spectrum the spinning sidebands appear at integral multiples of $x_1\Omega_R$ and $x_2\Omega_R$ and also at the sum and difference frequencies of the integral multiples of $x_1\Omega_R$ and $x_2\Omega_R$. The angle pair (37.78°, 79.19°) has an advantage that $x_1\Omega_R = x_2\Omega_R = 0.5\Omega_R$ and a simple side band spacing of $0.5\Omega_R$ is obtained. Of particular interest is the fact that the 1D DAS spectrum for the (0°,63.43°) angle pair contains only spinning sidebands at multiples of $x_2\Omega_R = 0.83\Omega_R$. The spinning sidebands at $x_1\Omega_R = 0.17\Omega_R$ do not exist and thus the (0°,63.43°) angle pair provides the highest effective spinning speed when removing first- and second-order broadenings with DAS.

The (0°,63.43°) angle pair offers other advantages, in particular for cross polarization (CP) experiments (see also ***Cross Polarization in Rotating Solids: Spin-1/2 Nuclei***). Vega[23,24] has shown that it may be difficult or even impossible to obtain efficient CP transfer of all sites in a multisite system when spinning at the magic angle. This problem can

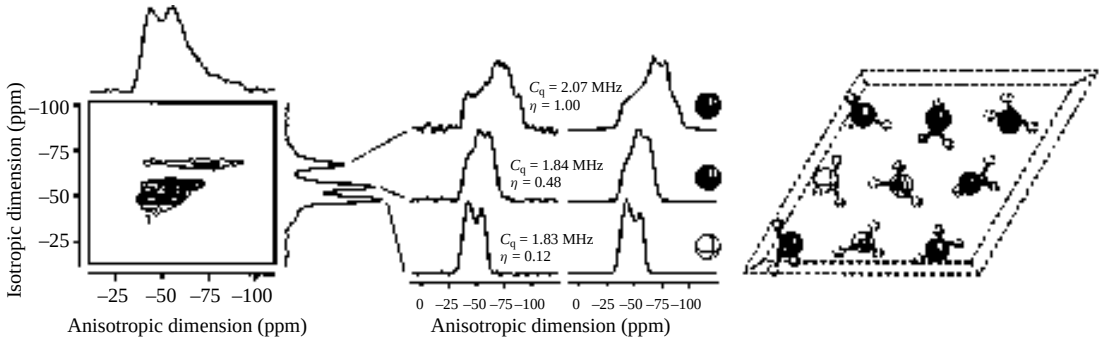

Figure 4 On the left is the two-dimensional ^{87}Rb DAS NMR spectrum of $RbNO_3$ at 4.2 T. Cross sections from this spectrum provide the separated one-dimensional anisotropic lineshapes for each ^{87}Rb site. These lineshapes can be fitted to obtain the quadrupolar coupling parameters for each site. In this case each resonance could be assigned to a Rb site in the unit cell (shown on the right) by comparing the electric field gradients obtained from the measured quadrupolar coupling constants with the electric field gradient at each Rb site obtained from a simple point charge model calculation (see text). (Adapted by permission of Academic Press from Grandinetti et al.[20]

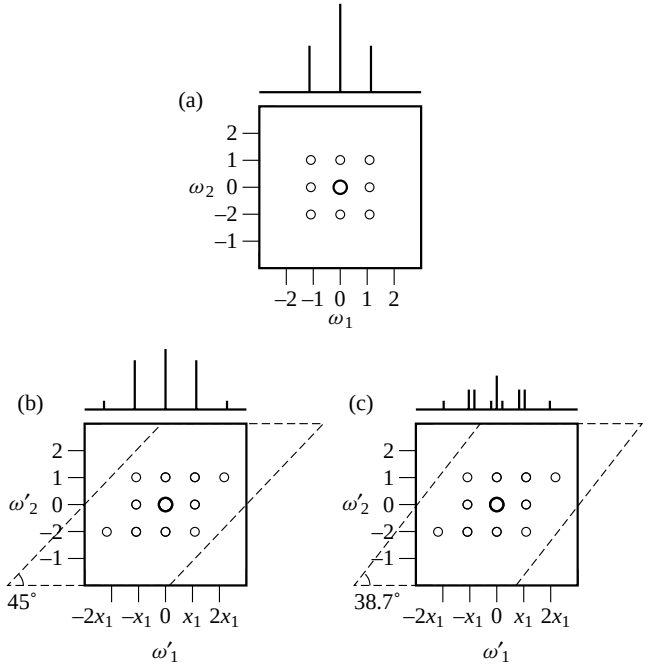

Figure 5 Schematic examples of the effects of the shearing transformation on sideband positions in DAS. (a) Unsheared 2D spectrum. (b) Sheared 2D spectrum obtained from the two-dimensional spectrum in (a) by a shearing transformation employing a shearing angle of 45° and a scaling of the ω_1 by $x_1 = 0.5$. In this case the spinning sidebands in the 2D spectrum are aligned with respect to ω'_1 so that a projection onto the ω'_1 axis only contains spinning sidebands separated by integer multiples of $0.5\Omega_R$. (c) Sheared 2D spectrum obtained from the 2D spectrum in (a) by a shearing transformation employing a shearing angle of 38.7° and a scaling of the ω_1 by $x_1 = 0.56$. In this case the spinning sidebands in the 2D spectrum are not aligned with respect to ω'_1 so that a projection onto the ω'_1 axis contains spinning sidebands that are separated by multiples of and also sum and difference frequencies of $x_1\Omega_R = 0.56\Omega_R$ and $x_2\Omega_R = 0.44\Omega_R$. (Reproduced by permission of Academic Press from P. J. Grandinetti, Y. K. Lee, J. H. Baltisberger, B. Q. Sun, and A. Pines, *J. Magn. Reson.*, 1993, **102**, 71)

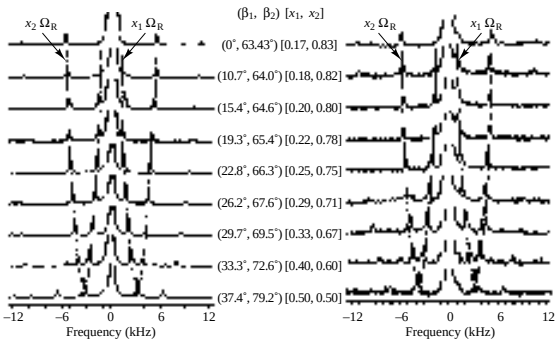

Figure 6 Simulated and experimental 1D DAS spectra of $^{87}RbClO_4$ for various rotor angle pairs (β_1,β_2) and fractions $[x_1,x_2]$. All spectra were obtained with a rotor frequency of $\Omega_R = 6.4$ kHz. The quadrupolar coupling parameters of $RbClO_4$ used in the simulations are C_q = 3.2 MHz and $\eta = 0.1$. (Adapted by permission of Academic Press from P. J. Grandinetti, Y. K. Lee, J. H. Baltisberger, B. Q. Sun, and A. Pines, *J. Magn. Reson.*, 1993, **102**, 71)

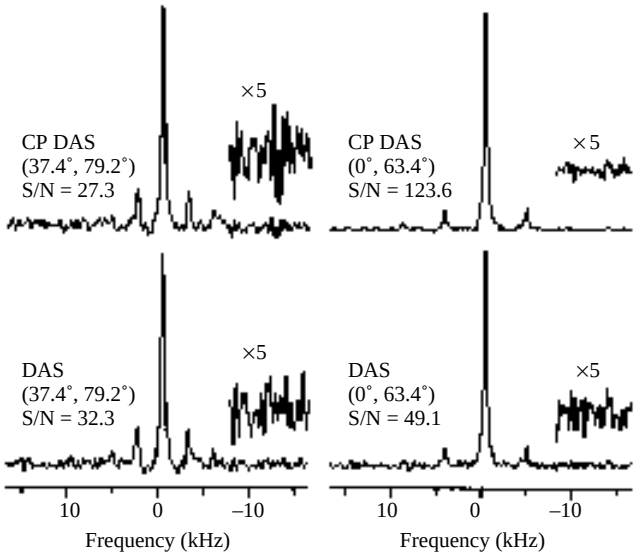

Figure 7 DAS and CP DAS spectra of sodium pyruvate acquired using the DAS angle pairs (37.38°,79.19°) and (0°,63.43°). With (0°,63.43°) an improvement of 2.5 in S/N ratio is observed with CP compared with the spectrum taken without CP. In addition, the CP DAS experiment using (0°,63.43°) has an S/N ratio over 4.5-times that of the CP DAS experiment using (37.38°,79.19°). (Reproduced by permission of Taylor & Francis Ltd. from Baltisberger et al.[25])

be eliminated in a DAS experiment by exploiting the time independence of the spin eigenvalues when spinning at 0° (parallel) to the external magnetic field. By performing the CP step while spinning at 0° the full static CP intensity can be recovered.[25] In Figure 7, the decoupled DAS and CP DAS spectra of sodium pyruvate for the (37.38°,79.19°) and (0°,63.43°) angle pairs illustrate the significant increases in signal-to-noise ratio (S/N) that can be obtained with the (0°,63.43°) angle pair.

From Tables 1 and 2 it is clear that the isotropic frequency shifts of both the first-order chemical shift and the second-order quadrupolar shift have different dependences on the external magnetic field strength. These different dependences can be exploited as a means of separating the isotropic chemical and quadrupolar shifts. In Figure 8(a) the isotropic ^{87}Rb DAS spectra of $RbNO_3$ measured at four different magnetic fields are depicted. As shown in Figure 8(b), the isotropic resonance frequency in ppm for each site is a linear function of $1/B_0{}^2$ with the isotropic chemical shift given by the intercept and the second-order quadrupolar shift given by the slope.[16]

3 IMPLEMENTATION OF DYNAMIC ANGLE SPINNING

Four variants of the DAS pulse sequence are depicted in Figure 9. The simplest implementation is shown in Figure 9(a). In this sequence, DAS can be viewed as a 2D exchange experiment with a rotor reorientation during the mixing time and, as in the 2D exchange experiment, an amplitude-modulated response in t_1 makes it possible to obtain pure-absorption-mode 2D spectra using the hypercomplex or TPPI (time proportional phase increment) approach to 2D data acquisition. The hypercomplex data acquired with this sequence are Fourier-transformed and phase-corrected in a manner similar to that described elsewhere,[22] with the only

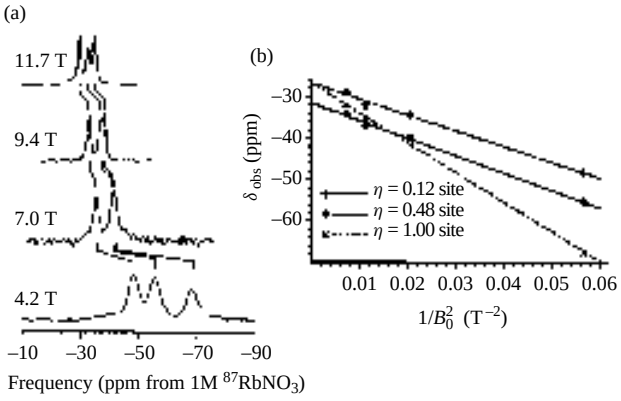

Figure 8 (a) ^{87}Rb DAS spectra of $RbNO_3$ collected at (a) 11.7 T, 9.4 T, 7.0 T, and 4.2 T. (b) Isotropic shifts of $^{87}RbNO_3$ plotted versus $1/\boldsymbol{B}_0{}^2$ and fitted using a linear least-squares routine. The intercepts and slopes are used to calculate the values of $\delta_{iso}{}^{(CS)}$ (ppm) and $C_q(1 + \eta^2/3)^{1/2}$ (MHz), respectively. (Reproduced by permission of Academic Press from Baltisberger et al.[16])

difference being the shearing transformation described by equations (14) and (15).

equations (14) and (15). When there is an inhomogeneous broadening associated with the isotropic DAS dimension, both pathways shown in Figure 9(b) can be acquired using the hypercomplex approach for an additional 2 increase in signal-to-noise ratio. This often occurs when DAS is applied to materials in which there is a continuous distribution of atomic environments resulting in a continuous distribution of second-order quadrupolar and isotropic chemical shifts.

Mueller et al.[18] pointed out that extracting the quadrupolar coupling parameters from the anisotropic DAS dimension can be difficult when additional chemical and dipolar anisotropies are present. Chemical shift and dipolar anisotropic broadenings can be removed when spinning at 54.74°, leaving only quadrupolar anisotropic broadening; 54.74°, unfortunately, is not a solution of equations (11) and (12). The solution of Mueller et al.[18] was to incorporate a second rotor reorientation into the DAS sequence so that the final angle for detection is the magic angle. This approach and its shifted echo variant are shown in Figures 9(c) and 9(d). With the evolution times defined in Figures 9(c) and 9(d) a shearing transformation is not necessary to obtain the isotropic/anisotropic 2D DAS spectrum; however, for the shifted echo experiment the phase correction of equation (16) is still required.

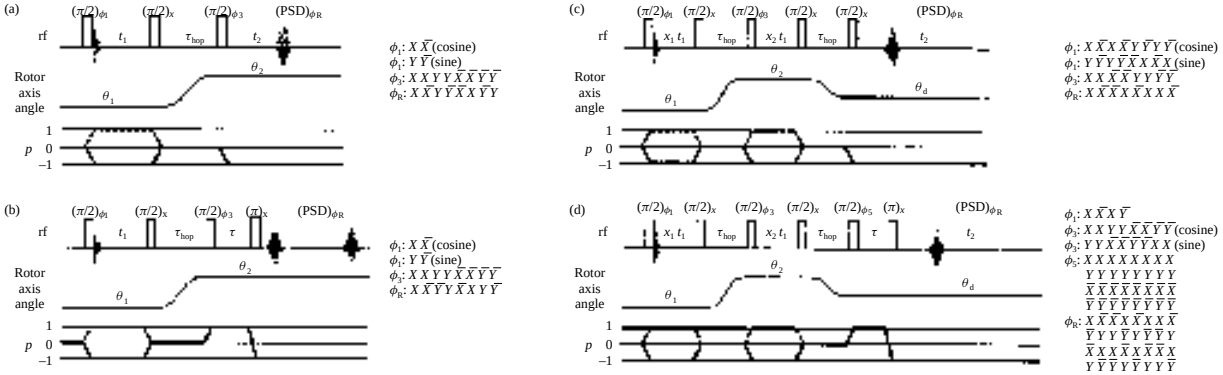

Figure 9 Pulse sequences, coherence transfer pathways, and minimal phase cycles for (a) dynamic angle spinning, (b) shifted echo dynamic angle spinning, (c) MAS-detected dynamic angle spinning, and (d) MAS-detected shifted echo dynamic angle spinning

In Figure 9(b), a different approach is taken that provides pure absorption-mode lineshapes in addition to a 2 increase in the signal-to-noise ratio. In this approach, the coherence-transfer echoes, which are formed because of the inhomogeneous broadenings intrinsic to the DAS experiment, are time-shifted by an amount τ with a π pulse to obtain whole echo acquisition in t_2, and thus a pure absorption mode 2D spectrum. The length of τ is a multiple of the rotor period, and typically large enough so that the echo in t_2 begins at zero. Only the $p = 0 \rightarrow -1 \rightarrow 0 \rightarrow 1 \rightarrow -1$ pathway is selected in this case. The complex 2D data acquired with this sequence are processed in the same fashion as conventional phase-modulated 2D data, with the only difference being a τ-dependent first-order phase correction of

$$\phi(\tau, \omega) = \omega_2 \tau \qquad (16)$$

to remove the phase modulation because of the time-shifted echo, in addition to the shearing transformation described by

Using rotor-synchronized π pulses it is possible to eliminate all sidebands in a DAS experiment using the DAH-180 sequence of Gann et al.,[13] shown in Figure 10. Under this pulse sequence all evolution at 63.43° that does not contribute to t_1 evolution is refocused by spending equal time as +1 and −1 coherences, while all t_1 evolution occurs only as −1 coherences. This sequence has the advantage that the intensities of the suppressed sidebands are completely transferred to the centerband, unlike other sideband suppression techniques such as TOSS.[26] In contrast to the DAS sequences in Figure 9, the DAH-180 sequence has a trade-off between sensitivity and resolution. DAH-180 is a constant time experiment, so in order to increase the resolution a larger constant time is required which then leads to increased intensity losses via T_2 relaxation processes.

There are a few limitations of the DAS technique, most notably being its current inability to refocus homonuclear dipolar broadenings. This is a consequence of the storage pulses which fail to store higher than first-rank coherences.

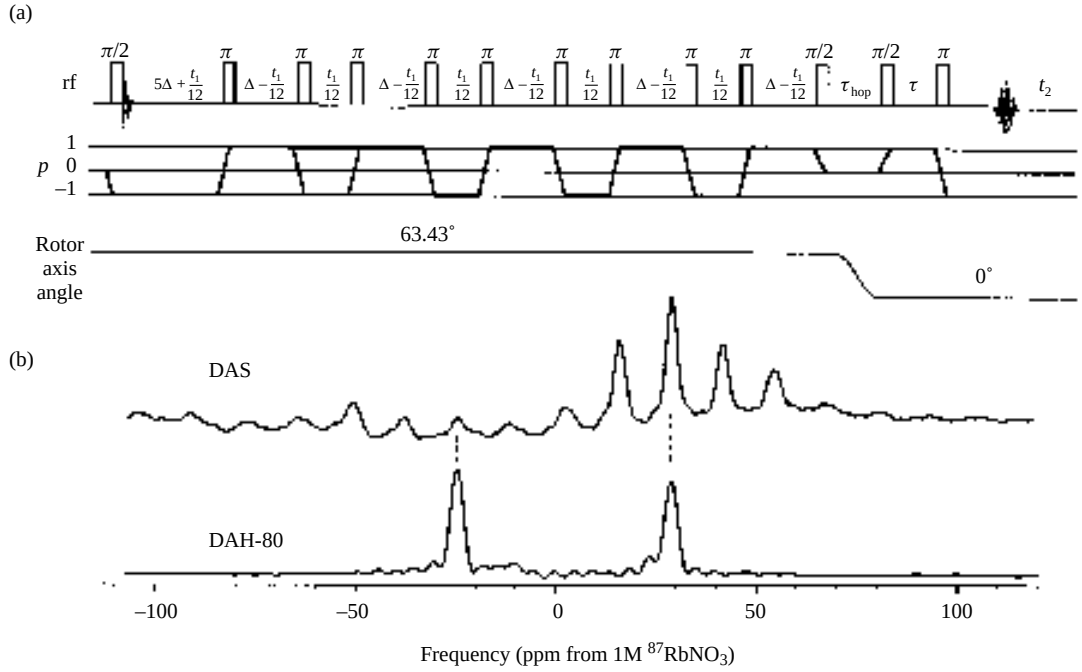

Figure 10 (a) DAH-180 pulse sequence which produces sideband-free dynamic angle spinning spectra. The experiment is performed over N rotor cycles with a rotor period of τ_r. $\Delta = N\tau_r/10$. (b) Comparison of the ^{87}Rb spectra of Rb_2SO_4 taken at 9.4 T at a spinning frequency of 1.8 kHz using DAS (with side bands) and using DAH-180 (sideband-free). (Reproduced by permission of Elsevier Science Publishers from Gann et al.[13])

These broadenings are largest with abundant nuclei with high gyromagnetic ratios (e.g. ^{27}Al, ^{11}B, ...). Baltisberger et al.[25] have shown that homonuclear broadenings will be a function of the DAS angle pair and the (0°,63.43°) angle pair produces spectra with the minimum broadenings; however, it does not eliminate it. For certain nuclei it is possible to eliminate the homonuclear dipolar broadenings using the isotopic depletion approach of Youngman and Zwanziger.[27] By enriching glassy B_2O_3 to 97% in ^{10}B, they obtained increased resolution by eliminating the ^{11}B dipolar broadenings from the ^{11}B DAS spectrum.

Another limitation arises from the finite time required to hop the rotor axis between the DAS angle pairs. When the spin–lattice relaxation time T_1 is on the order or less than the hop time ($T_1 \leq \tau_{hop}$) there will be significant losses in signal intensity. For this reason integrated intensities in DAS may not accurately reflect the site populations.

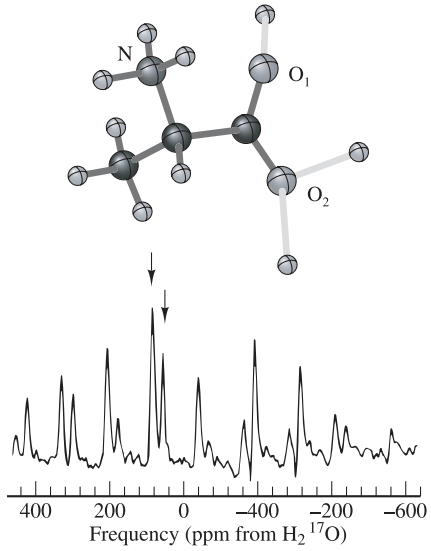

Figure 11 (Top) The structure of L-alanine showing the differences in hydrogen bonding on the two oxygen sites. (Bottom) Isotropic ^{17}O (0°,63.43°) CP DAS spectrum of L-alanine at 7.04 T with the two resolved centerbands for the two sites marked with arrows. (Adapted by permission of the International Society of Magnetic Resonance from S. L. Gann, et al.[28])

4 APPLICATIONS OF DAS

Since its development DAS has been successfully applied to a number of multisite crystalline compounds. Mueller and coworkers[14,15] have applied ^{17}O DAS to a number of crystalline silicates, resolving inequivalent bridging (Si–O–Si) and nonbridging (Si–O–M) oxygens. Baltisberger et al.[16] have applied ^{87}Rb DAS to a number of crystalline inorganic rubidium salts and obtained isotropic spectra along with correlated anisotropic spectra from which quadrupolar coupling parameters could be obtained. Gann et al.[28] obtained the spectrum shown in Figure 11 where they could resolve the two crystallographically distinct oxygen sites of L-alanine in a (0°,63.43°) CP DAS experiment.

Farnan et al.[29] showed that DAS is particularly advantageous when applied to amorphous samples (see also ***Amorphous Materials***) where a continuous structural distribution results in a continuous distribution of anisotropic lineshapes. In the 2D DAS spectrum these anisotropic lineshapes can be separated according to their isotropic frequencies, analyzed, and then used to help map the isotropic lineshape into structural

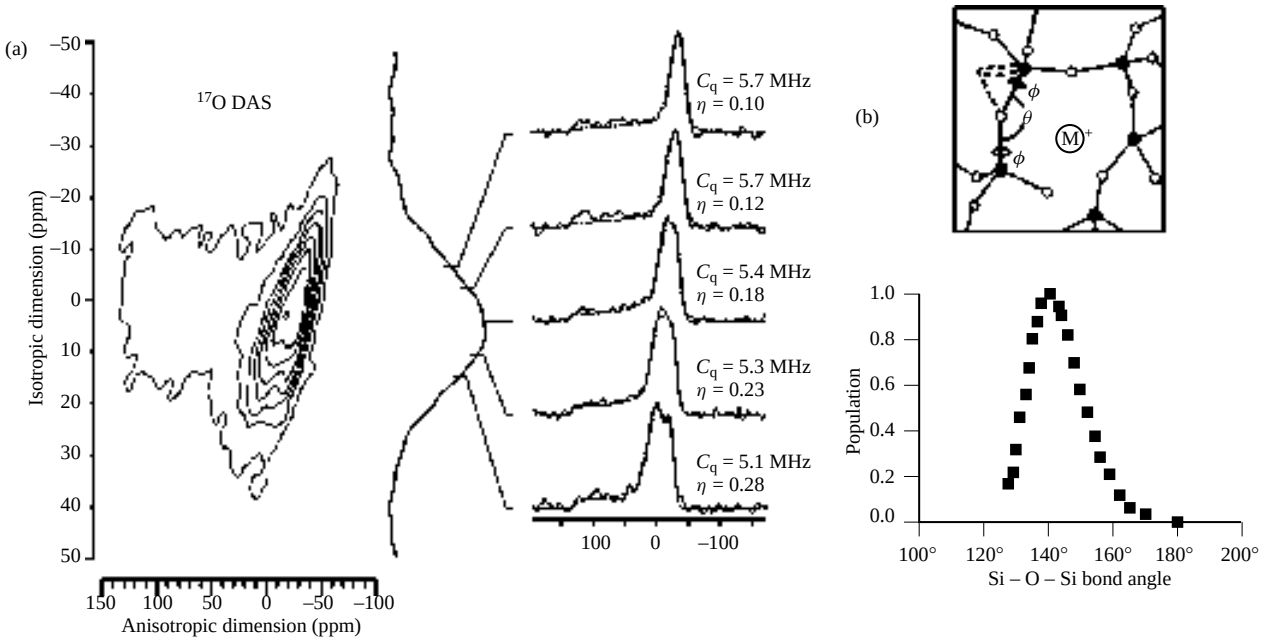

Figure 12 (a) ^{17}O 2D DAS spectrum of the bridging oxygen (Si–O–Si) resonances in $K_2Si_4O_9$ glass, shown together with the isotropic lineshape, and selected anisotropic cross sections correlated to specific frequencies in the isotropic lineshape. Because the glass contains a continuous distribution of Si–O–Si bond angles, and the ^{17}O isotropic frequency varies continuously with Si–O–Si bond angle, the bridging oxygen isotropic linewidth in the glass is ∼ 25-times wider than a bridging oxygen resonance in a crystalline silicate. Since the ^{17}O anisotropic lineshapes for each Si–O–Si angle are separated in a 2D DAS spectrum, the separated anisotropic lineshapes can be fitted to obtain the isotropic lineshape as a function of the quadrupolar coupling parameters. With the help of experimental as well as ab initio based correlations between quadrupolar coupling parameters and the Si–O–Si bond angles, the isotropic lineshape can then be mapped into the Si–O–Si bond angle distribution for the glass. (b) The Si–O–Si bond angle distribution in $K_2Si_4O_9$ glass derived from its ^{17}O DAS spectra. (Adapted by permission of MacMillan Magazines Ltd. from Farnan, et al.[29])

distributions. Figure 12(a) depicts a 2D ^{17}O DAS spectrum of the bridging oxygen (Si–O–Si) resonances in $K_2Si_4O_9$ glass. In this case the Si–O–Si bond angle distribution in Figure 12(b) was derived from the 2D DAS spectrum.

5 RELATED ARTICLES

Amorphous Materials; Double Rotation; Line Narrowing Methods in Solids; Magic Angle Spinning; Magic Angle Turning and Hopping; Multidimensional Spectroscopy: Concepts; Quadrupolar Interactions; Quadrupolar Nuclei in Glasses; Quadrupolar Nuclei in Solids; Sideband Analysis in Magic Angle Spinning NMR of Solids; Variable Angle Sample Spinning.

6 REFERENCES

1. S. Ganapathy, S. Schramm, and E. Oldfield, *J. Chem. Phys.*, 1982, **77**, 4360
2. A. Samoson, E. Lippmaa, and A. Pines, *Mol. Phys.*, 1988, **65**, 1013.
3. A. Llor and J. Virlet, *Chem. Phys. Lett.*, 1988, **152**, 248.
4. B. F. Chmelka, K. T. Mueller, A. Pines, J. Stebbins, Y. Wu, and J. W. Zwanziger, *Nature (London)*, 1989, **339**, 42.
5. K. T. Mueller, B. Q. Sun, G. C. Chingas, J. W. Zwanziger, T. Terao, and A. Pines, *J. Magn. Reson.*, 1990, **86**, 470.
6. T. Terao, T. Fujii, T. Onodera, and A. Saika, *Chem. Phys. Lett.*, 1984, **107**, 145.
7. A. Bax, N. M. Szeverenyi, and G. E. Maciel, *J. Magn. Reson.*, 1983, **55**, 494.
8. A. Bax, N. M. Szeverenyi, and G. E. Maciel, *J. Magn. Reson.*, 1983, **52**, 147.
9. M. Goldman, P. J. Grandinetti, A. Llor, Z. Olejniczak, J. R. Sachleben, and J. W. Zwanziger, *J. Chem. Phys.*, 1992, **97**, 8947.
10. A. Samoson, B. Q. Sun, and A. Pines, in *Pulsed Magnetic Resonance: NMR, ESR, and Optics — A Recognition of E. L. Hahn*, ed. D. M. S. Bagguley, Clarendon Press, Oxford, UK, 1992.
11. E. R. Andrew, A. Bradbury, and R. G. Eades, *Nature (London)*, 1958, **182**, 1659.
12. I. J. Lowe, *Phys. Rev. Lett.*, 1959, **2**, 285.
13. S. L. Gann, J. H. Baltisberger, and A. Pines, *Chem. Phys. Lett.*, 1993, **210**, 405.
14. K. T. Mueller, Y. Wu, B. F. Chmelka, J. Stebbins, and A. Pines, *J. Am. Chem. Soc.*, 1991, **113**, 32.
15. K. T. Mueller, J. H. Baltisberger, E. W. Wooten, and A. Pines, *J. Phys. Chem.*, 1992, **96**, 7001.
16. J. H. Baltisberger, S. L. Gann, E. W. Wooten, T. H. Chang, K. T. Mueller, and A. Pines, *J. Am. Chem. Soc.*, 1992, **114**, 7489.
17. M. A. Eastman, P. J. Grandinetti, Y. K. Lee, and A. Pines, *J. Magn. Reson.*, 1992, **98**, 333.
18. K. T. Mueller, E. W. Wooten, and A. Pines, *J. Magn. Reson.*, 1990, **92**, 620.
19. K. T. Mueller, G. C. Chingas, and A. Pines, *Rev. Sci. Instrum.*, 1991, **62**, 1445.
20. P. J. Grandinetti, J. H. Baltisberger, A. Llor, Y. K. Lee, U. Werner, M. A. Eastman, and A. Pines, *J. Magn. Reson., Ser. A*, 1993, **103**, 72.

21. P. J. Grandinetti, Y. K. Lee, J. H. Baltisberger, B. Q. Sun, and A. Pines, *J. Magn. Reson., Ser. A*, 1993, **102**, 195.
22. R. R. Ernst, G. Bodenhausen, and A. Wokaun, *Principles of Nuclear Magnetic Resonance in One and Two Dimensions*, Oxford University Press, Oxford, UK, 1987.
23. A. J. Vega, *J. Magn. Reson.*, 1992, **96**, 50.
24. A. J. Vega, *Solid State NMR*, 1992, **1**, 17.
25. J. H. Baltisberger, S. L. Gann, P. J. Grandinetti, and A. Pines, *Mol. Phys.*, 1994, **81**, 1109.
26. W. T. Dixon, *J. Chem. Phys.*, 1982, **77**, 1800.
27. R. E. Youngman and J. W. Zwanziger, *J. Non-Cryst. Solids*, 1994, **168**, 293.
28. S. L. Gann, J. H. Baltisberger, E. W. Wooten, H. Zimmerman, and A. Pines, *Bull. Magn. Reson.*, 1994, **16**, 68.
29. I. Farnan, P. J. Grandinetti, J. H. Baltisberger, J. F. Stebbins, U. Werner, M. A. Eastman, and A. Pines, *Nature (London)*, 1992, **358**, 31.

Biographical Sketch

Philip J. Grandinetti. *b* 1960. B.S., 1982, M.S., 1984, Chemistry, West Virginia University, USA (with Nar S. Dalal), Ph.D., 1988, Physical Chemistry, University of Illinois, USA (with Jiri Jonas). Postdoctoral fellow, 1989–93, University of California, Berkeley, USA (with Alex Pines). Faculty in Chemistry, Ohio State University, 1993–present. Approx. 20 publications. Current research interests: applications of solid state NMR to materials research.

Dynamic Nuclear Polarization and High-Resolution NMR of Solids

Robert A. Wind

Battelle/Pacific Northwest Laboratories, Richland, WA, USA

1	Introduction	1
2	Theory	1
3	Applications of DNP NMR	4
4	Summary, Conclusions, and Perspectives	8
5	Related Articles	9
6	References	9

1 INTRODUCTION

In solids containing both magnetic nuclei and unpaired electrons, polarization transfer can be obtained between the electron and nuclear spin systems by irradiating at or near the electron Larmor frequency. The result is an enhanced nuclear polarization and, henceforth, an enhanced NMR signal. This effect is called dynamic nuclear polarization (DNP).

Several mechanisms can be responsible for the DNP phenomenon. In 1953, Overhauser predicted that in metals the NMR signal could be enlarged by saturating the resonance line of the conducting electrons: the Overhauser effect.[1] Carver and Slichter[2] showed experimentally in metallic lithium that Overhauser's revolutionary concept was correct.

Later on, Abragam and Proctor[3] and, independently, Jeffries[4] and Erb et al.[5] found the occurrence of a DNP effect in solids containing fixed, mutually more or less isolated, unpaired electrons: the solid state effect. Finally, a third DNP effect has also been observed: the thermal mixing effect, which is present when the concentration of (fixed) unpaired electrons is so high that the mutual dipolar interactions between the electrons become comparable to the other interactions between the electrons and their surroundings. Provotorov[6] showed that in that case the electron spin system can be characterized by two polarizations: one associated with the population distribution over the Zeeman levels and one associated with the population distribution over the internal local magnetic fields which the electrons are experiencing. These polarizations may change if off-resonance irradiation is applied. Abragam and Borghini[7] used the results of Provotorov and showed that when the polarization associated with the local fields is changed, the nuclear polarization changes as well, due to a coupling between these two polarizations induced by the irradiating microwave field: the indirect thermal mixing effect. Goldman[8] remarked that this coupling could be present also in the absence of microwave irradiation, and its significance for DNP was shown by Buishvili:[9] the direct thermal mixing effect. The thermal mixing effects become especially important when the nuclear Larmor frequency is comparable to or smaller than the ESR line width.

In principle large NMR signal enhancements can be obtained via DNP, maximal of the order of the ratio of the gyromagnetic ratios of the electrons and the nuclei. For example, for protons this would result in an enhancement factor of 660, and for ^{13}C nuclei this factor would be as large as 2600. In the earlier days of DNP this aspect was mainly used and applied for the production of polarized targets used in high-energy physics or to study magnetic ordering in the μK region. However, during the past 15 years new applications have emerged as well. This has been achieved by combining DNP with modern solid state NMR techniques such as cross polarization (CP), magic angle spinning (MAS), and two-dimensional NMR spectroscopy. As a result, more detailed information about structures and dynamics of materials amenable to DNP NMR could be obtained than would have been possible without DNP.

DNP NMR spectroscopy can be applied successfully in a large variety of solid materials such as those in which the unpaired electrons occur naturally, e.g., in the form of dangling bonds, materials in which bond ruptures have occurred, e.g., resulting from pyrolysis or ionizing radiation, materials containing paramagnetic impurities, and materials doped with a suitable paramagnetic agent. In this paper several applications of DNP NMR spectroscopy in solid materials research will be given following a brief description of the DNP phenomenon. Finally, some future aspects of the technique will be discussed.

2 THEORY

Extensive reviews of the different DNP effects have been given elsewhere.[10–14] Here we shall confine ourselves to a short treatment of the main features of DNP. We shall restrict ourselves to discussing only the Overhauser and the solid state effects. Hence we shall neglect the thermal mixing effects The main reasons for this omission are that in many cases the Overhauser and solid state effects dominate, and that the overall features of the thermal mixing effects are not much different from that of the solid state effect. Moreover, the thermal mixing effects require a rather lengthy derivation, which is beyond the scope of this article.

As is necessary in the description of any NMR experiment, we have to start with the Hamiltonian. For an electron–nuclear spin system the relevant Hamiltonian is given by

$$\hat{\mathcal{H}} = -\omega_e \hat{S}_z - \omega_n \hat{I}_z + \hat{\mathcal{H}}_{ee} + \hat{\mathcal{H}}_{en} + \hat{\mathcal{H}}_{nn} \qquad (1)$$

The first two terms are the Zeeman interactions of the electrons and nuclei, respectively, where $\hat{S}_z = \sum_{j=1}^{N_e} \hat{S}_z^j$ are the electron spin operators and $\hat{I}_z = \sum_{i=1}^{N_n} \hat{I}_z^i$ are the nuclear spin operators. The term N_e is the number of unpaired electrons and N_n is the number of nuclei. Furthermore, in equation (1), $\omega_e = \gamma_e B_0$ and $\omega_n = \gamma_n B_0$, where γ_e and γ_n are the magnetogyric ratios of the electrons and nuclei, respectively, and B_0 is the external magnetic field strength. Finally, $\hat{\mathcal{H}}_{ee}$, $\hat{\mathcal{H}}_{en}$, and $\hat{\mathcal{H}}_{nn}$ denote the spin–spin interactions between the electrons, between the electrons and the nuclei, and between the nuclei, respectively. For DNP, the most

important term in equation (1) is the so-called hyperfine interaction term $\hat{\mathcal{H}}_{\mathrm{en}}$. In general, this term consists of two parts, the scalar interaction term $\hat{\mathcal{H}}^{\mathrm{s}}_{\mathrm{en}}$ and the dipolar term $\hat{\mathcal{H}}^{\mathrm{d}}_{\mathrm{en}}$. The scalar interaction arises from a finite electron spin density at the nuclear sites, either directly from the unpaired electron itself or mediated by bonding electrons polarized by the unpaired electrons.

Before describing the DNP phenomenon we first consider the energy level scheme of electron–nuclear spin pairs. For simplicity we restrict ourselves to nuclear spin-$\frac{1}{2}$ systems, with positive γ_{n} values. The result is then the simple four-energy-level scheme given in Figure 1. Also given are the nuclear and electron quantum numbers, m_{n} and m_{e}, respectively (for the electrons the highest energy state corresponds to $m_{\mathrm{e}} = +\frac{1}{2}$, because γ_{e} is negative), and as usual we denote a state in which, for example, $m_{\mathrm{n}} = +\frac{1}{2}$ and $m_{\mathrm{e}} = -\frac{1}{2}$ by the notation $|+-\rangle$. Finally, the amount of nuclei in each state is denoted by $N_{\mathrm{n}1}, N_{\mathrm{n}2}$, etc. Then, defining $N_{\mathrm{n}}^{+} = N_{\mathrm{n}2} + N_{\mathrm{n}4}$ and $N_{\mathrm{n}}^{-} = N_{\mathrm{n}1} + N_{\mathrm{n}3}$ as the total amounts of nuclei in the + and − states, respectively, we can define the nuclear polarization, P_{n}, as

$$P_{\mathrm{n}} = \frac{N_{\mathrm{n}}^{+} - N_{\mathrm{n}}^{-}}{N_{\mathrm{n}}^{+} + N_{\mathrm{n}}^{-}} = \frac{N_{\mathrm{n}}^{+} - N_{\mathrm{n}}^{-}}{N_{\mathrm{n}}} = \frac{\Delta N_{12} + \Delta N_{34}}{N_{\mathrm{n}}} \qquad (2)$$

In Figure 1 the situation of thermal equilibrium is depicted, where the population distribution is governed by the Boltzmann distribution corresponding to the lattice temperature. Then P_{n} is defined as P_{n}^{0}. Similar expressions can be given for the electron polarization, P_{e}, and its thermal equilibrium value, P_{e}^{0}. It can easily be derived that in the high-temperature approximation, where $h\omega_{\mathrm{e}}/kT_{\mathrm{L}}$, $h\omega_{\mathrm{n}}/kT_{\mathrm{L}} \ll 1$, P_{n}^{0} and P_{e}^{0} are given by

$$P_{\mathrm{n}}^{0} = \frac{1}{2}\,\omega_{\mathrm{n}}\hbar(kT_{\mathrm{L}})^{-1} \quad \text{and} \quad P_{\mathrm{e}}^{0} = \frac{1}{2}\omega_{\mathrm{e}}\hbar(kT_{\mathrm{L}})^{-1} \qquad (3)$$

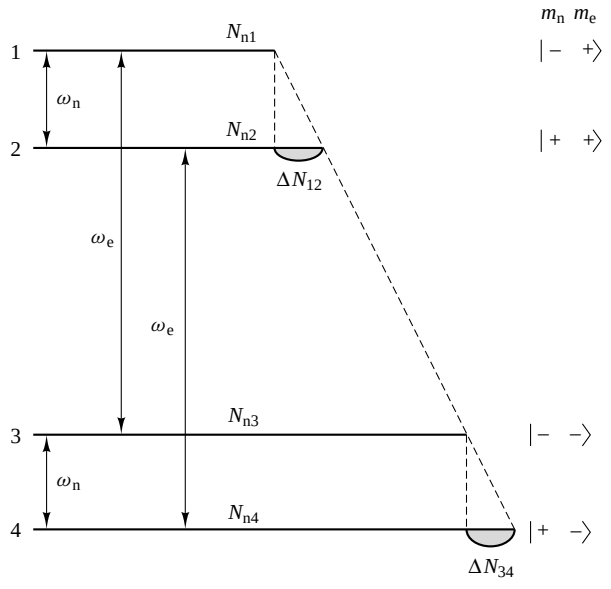

Figure 1 The Zeeman energy level scheme of electron–nuclear spin pairs. The population distribution over the energy levels depicts the thermal equilibrium situation

where T_{L} is the lattice temperature. It follows from equation (3) that the thermal equilibrium polarization of the electrons is a factor $\gamma_{\mathrm{e}}/\gamma_{\mathrm{n}}$ larger than that of the nuclei. It is this difference in polarization that is used in DNP, which we shall now consider.

2.1 The Overhauser Effect

The Overhauser effect occurs when $\hat{\mathcal{H}}_{\mathrm{en}}$ is time-dependent on a timescale of the order ω_{e}^{-1}. Then $\hat{\mathcal{H}}_{\mathrm{en}}(t)$ causes relaxation transitions between the various levels depicted in Figure 1, which, when combined with an irradiation at the electron Larmor frequency, results in a change in the nuclear polarization.

In order to illustrate this, we assume that the scalar interaction term, $\hat{\mathcal{H}}^{\mathrm{s}}_{\mathrm{en}}$, dominates. It can be shown that $\hat{\mathcal{H}}^{\mathrm{s}}_{\mathrm{en}}$ causes a relaxation transition between the $|+-\rangle$ and $|-+\rangle$ states of the electron–nuclear system, hence between the levels 1 and 4 in Figure 1. We shall call this relaxation rate W^{s}_{14}, which is given by $W^{\mathrm{s}}_{14} = \frac{1}{2}\overline{a_{ij}^{2}}\,\boldsymbol{J}(\omega_{\mathrm{e}} + \omega_{\mathrm{n}}, \tau_{\mathrm{c}})$; $\boldsymbol{J}(\omega, \tau_{\mathrm{c}})$ is the spectral density function characterizing the time dependence, $\overline{a_{ij}^{2}}$ is the time-averaged value of a_{ij}^{2}, where a_{ij} denotes the strength of the scalar interaction. As with all relaxation transitions, after some population distortion $W_{14}{}^{\mathrm{s}}$ restores the Boltzmann distribution between the energy levels connected by W^{s}_{14}, hence between levels 1 and 4. Now suppose that we are irradiating with a microwave field of amplitude B_1 and a frequency ω close to ω_{e}. This means that we are irradiating between the electron Zeeman levels 1 and 3 respectively 2 and 4 with an induced transition probability $W/2 = (\pi/2)\gamma_{\mathrm{e}}^{2}B_1^{2}g(\omega - \omega_{\mathrm{e}})$, where $g(\omega)$ is the normalized lineshape function of the ESR line.

Suppose also that W is large enough to saturate the ESR line completely. Then in the stationary situation, the population distribution over the various levels becomes as given in Figure 2. Due to the saturating irradiation the population of level 1 becomes equal to that of level 3, and the population of level 2 becomes equal to that of level 4. Due to the relaxation transition, W^{s}_{14}, the Boltzmann distribution exists between the levels 1 and 4. As a result, the population differences between the nuclear Zeeman levels 1 and 2 respectively 3 and 4 is increased: the nuclear polarization is (positively) enhanced. The enhancement curve, which is the Overhauser enhancement factor as a function of the irradiation frequency ω, reflects the (saturated) ESR line, and is symmetrical about ω_{e} for symmetrical ESR lines. The enhancement becomes maximal for $\omega = \omega_{\mathrm{e}}$. An Overhauser effect also occurs when the (time-dependent) dipolar electron–nuclear interactions, $\hat{\mathcal{H}}^{\mathrm{d}}_{\mathrm{en}}$, dominate. It can be shown that $\hat{\mathcal{H}}^{\mathrm{d}}_{\mathrm{en}}$ causes relaxation transitions between all four energy levels, so that the result becomes more complicated. However, it can be shown that often the relaxation transition between the levels 2 and 3 dominates, and the reader can easily convince himself that in this situation the nuclear polarization enhancement becomes negative.

The question arises under which circumstances we can expect to observe an Overhauser effect. As already stated above, a time-dependence in $\hat{\mathcal{H}}_{\mathrm{en}}$ is needed with a correlation time of the order of $(\omega_{\mathrm{e}} \pm \omega_{\mathrm{n}})^{-1} \simeq \omega_{\mathrm{e}}{}^{-1}$, which in practice means that τ_{c} has to be of the order 10^{-11} to 10^{-12} s. In

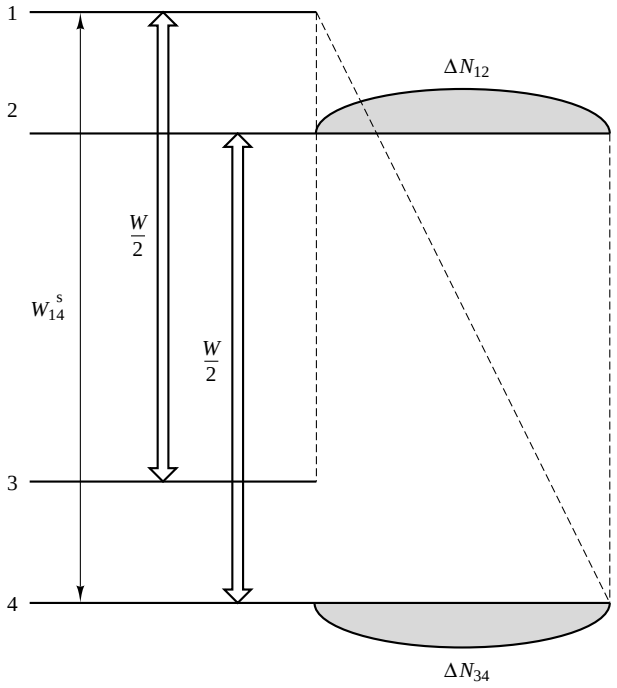

Figure 2 The Overhauser effect due to the scalar electron–nuclear interactions. The population distribution over the energy levels depicts the stationary situation

solids, the molecular motions are almost never that fast, so that an Overhauser effect due to this type of motion is highly unlikely. However, other processes may occur in solids that do provide the required time dependence: (1) in conductors or semiconductors, the conducting electrons move very rapidly through the lattice, rendering the spatial coordinates in $\hat{\mathcal{H}}_{\text{en}}$ time-dependent on a fast scale (this explains the success of observing an Overhauser effect in metals[2]); (2) in solids with large amounts of unpaired electrons and/or with electrons with a delocalized electron density distribution, strong electron–electron spin exchange interaction may occur.[15] These interactions, which arise from electrostatic Coulomb interactions, cause a time-dependence in the electron spin operator $\hat{S}$ occurring in $\hat{\mathcal{H}}_{\text{en}}$, and hence in $\hat{\mathcal{H}}_{\text{en}}$ itself. Also this time-dependence can be fast enough to fulfill the requirements for the Overhauser effect.[10] An example is the Overhauser effect observed in graphite and other solids containing large aromatic clusters.

2.2 The Solid State Effect

The solid state effect occurs in solids with fixed paramagnetic centers and with electron–nuclear interactions that are time-independent or only slowly time-dependent, with correlation times typically larger than about 10^{-5} s. The presence of $\hat{\mathcal{H}}_{\text{en}}$ means that there exist, beside the external B_0 field, static local magnetic fields in the sample, partly oriented perpendicular to B_0. It is well known from second-order perturbation theory that the result of such interactions is that the electron–nuclear states can no longer be described by the pure product functions given in Figure 1, but become mixed with other states. The admixture coefficient depends on the energy

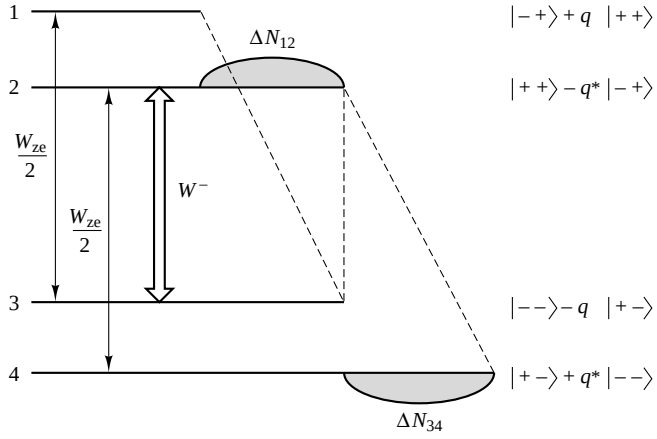

Figure 3 The solid state effect due to the forbidden transition W^-. The population distribution over the energy levels depicts the stationary situation

difference between the levels corresponding to the states and increases with decreasing energy differences. Hence, in highest order, the mixture occurs between the states corresponding to the levels 1 and 2 respectively 3 and 4. The result is given in Figure 3, where q (and its complex conjugate q^*) denotes the admixture coefficient. It should be emphasized that q is small, typically of the order 10^{-3} to 10^{-4}. Nevertheless, these small admixtures have as an important consequence that irradiation with a frequency $\omega_e - \omega_n$ or $\omega_e + \omega_n$ leads to a nonzero transition probability between the levels 2 and 3 respectively 1 and 4.

In order to understand this we consider the effect of irradiating with a frequency $\omega_e - \omega_n$. If the eigenstates were not mixed nothing would happen, because the matrix element $\langle -- |\hat{\mathcal{H}}_{\text{rf}}| ++\rangle$ is zero as the Hamiltonian $\hat{\mathcal{H}}_{\text{rf}}$ representing the rf irradiation is proportional to single spin operators. However, if the eigenstates are mixed, a small but nonzero transition probability is obtained because now nonzero matrix elements such as $-q\langle +- |\hat{\mathcal{H}}_{\text{rf}}| ++\rangle$ occur. This is called the 'forbidden' transition, W^-. Similar results are obtained for irradiation at $\omega_e + \omega_n$, giving rise to a 'forbidden' transition W^+. The quantities W^+ and W^- are given by

$$W^{\pm} = 2|q|^2 \pi \gamma_e^2 \boldsymbol{B}_1^2 g(\omega_e - \omega \pm \omega_n) \qquad (4)$$

The effect of irradiating at $\omega_e - \omega_n$ on the nuclear polarization is depicted in Figure 3. Here we have also incorporated the effect of the electron Zeeman relaxation rate, W_{Ze}. Then, in the stationary situation, W_{Ze} maintains the Boltzmann distribution between the electron Zeeman levels 1 and 3 with respect to 2 and 4, whereas W^- equalizes the populations of levels 2 and 3. The result is a positive enhancement of the nuclear polarization P_n: the solid state effect. In a similar way it can be shown that irradiation at $\omega_e + \omega_n$ leads to a negative enhancement of P_n. For symmetrical ESR lines the solid state enhancement curve, which is the enhancement factor as a function of the irradiation frequency ω, is antisymmetrical about ω_e. The enhancement becomes maximal for $\omega = \omega_e \pm \omega_n$.

In Figure 4 examples are given of enhancement curves due to the various DNP effects, including the effects of thermal mixing. As mentioned before we will not treat thermal mixing in any detail. Here we confine ourselves to remarking that,

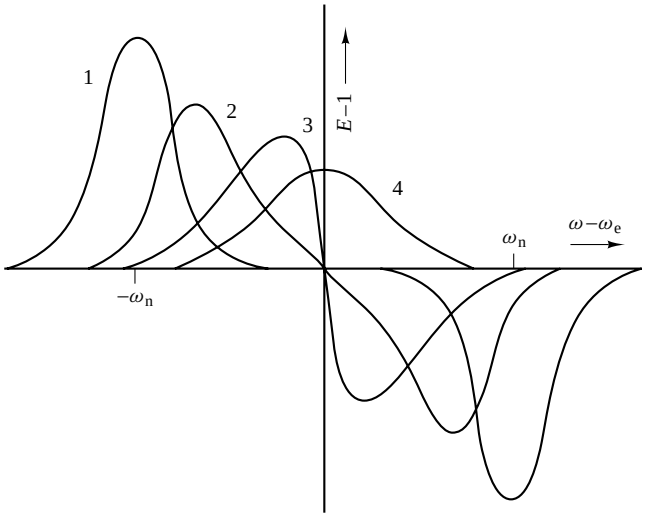

Figure 4 The enhancement curves of the various DNP effects: curve 1, solid state effect; curve 2, indirect thermal mixing effect; curve 3, direct thermal mixing effect; curve 4, Overhauser effect. Reproduced by permission of Marcel Dekker, Inc., from R. A. Wind, in 'Modern NMR Techniques and Their Application in Chemistry', eds. A. I. Popov and K. Hallenga, 1991, p. 125

like the enhancement curve due to the solid state effect, the thermal mixing enhancement curves are antisymmetrical about ω_e for symmetrical ESR lines. The direct effect of thermal mixing becomes maximal when the offset frequency, $\omega - \omega_e$, is comparable to the ESR linewidth, whereas indirect thermal mixing gives a maximal enhancement for offset frequencies between those for which the direct thermal effect and the solid state effect become maximal.

2.3 Enhancement Factors

As already mentioned in the Introduction, in theory large DNP enhancement factors can be expected, of the order of γ_e/γ_n. However, in practice, several factors can limit the magnitude of the enhancement factor which is actually obtained. We shall illustrate this for enhancements by the Overhauser and solid state DNP effects (for a more general treatment the reader is referred elsewhere[13,14,16,17]). For the Overhauser effect, we have already remarked that DNP enhancement can be positive or negative, depending on whether the scalar or the dipolar electron–nuclear interactions dominate. As a consequence, as in general both types of interactions are present, the enhancement is reduced and can become almost zero in unfavorable cases.

In the solid state effect, irradiation with a frequency ω can lead simultaneously to both forbidden transition probabilities W^- and W^+. This is especially the case when the ESR linewidth is comparable to the ω_n, see Figure 5 (in fact, as is shown in the figure, irradiation can result in both the allowed transition probability, W, and the forbidden transition probabilities W^- and W^+). As W^- and W^+ result in enhancements of opposite sign, the result is a decreased solid state enhancement, the so-called unresolved solid state effect. This can occur especially for low γ_n nuclei, for which ω_n is small. (However, it can be shown[13,14] that in these cases the enhancements due to thermal mixing increase, so that

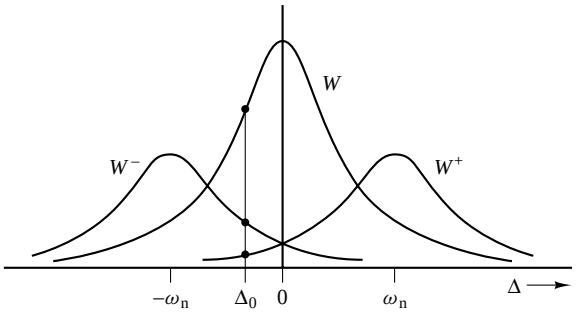

Figure 5 The allowed and forbidden transition probabilities as a function of the offset frequency $\Delta = \omega - \omega_e$. Irradiation at Δ_0 simultaneously leads to W, W^-, and W^+

the overall enhancement can still be large.) Other parameters that determine the enhancements are the amount of unpaired electrons, N_e, which has to be relatively large; the ESR linewidth, which should be small; the electron spin–lattice relaxation rate, W_{ze}, which should be large; the amplitude of the microwave field, B_1, which should be large; the external magnetic field, B_0, which should be small in order to obtain appreciable forbidden transition rates (this is only important for the solid state effect); the nuclear Zeeman relaxation rate, which should be small; and the correlation time τ_c characterizing the time dependence in $\hat{\mathcal{H}}_{en}$. As has already been mentioned, if $\tau_c \approx \omega_e \approx 10^{-11}$ to 10^{-12} s, the Overhauser effect dominates, whereas the solid state effect is observed when $\tau_c \geq 10^{-5}$ s. For τ_c values between these limits, both effects are small; if electron–nuclear interactions exist with different time constants, both effects might be present. We shall encounter this situation later.

The author and others[14,16,17] have given expressions for the different enhancement factors, from which the enhancements can be calculated if the various parameters mentioned above are known. For instance, for abundant-spin systems with large γ_n values and fixed paramagnetic centers, appreciable solid state enhancement factors (a factor 10 or more) can be expected under the following conditions: $N_e \geq 10^{24}\,m^{-3}$; ESR linewidth ≤ 1 mT; ${W_{ze}}^{-1}$ of the order of μ s; $B_1 \geq 0.03$ mT; $B_0 = 1.4$ T; nuclear Zeeman relaxation time ≥ 1 s. For rare-spin systems with small γ_n values, the enhancement factors are often at least an order of magnitude larger, which is mainly due to larger Zeeman relaxation times and an increased importance of the direct thermal mixing effect.[14]

It should be kept in mind, however, that these parameters are not independent of each other, and that large enhancements have been observed under completely different conditions. For instance, in natural diamonds a large ^{13}C enhancement factor of 200 is observed[14] despite the small value of N_e ($\simeq 10^{22}\,m^{-3}$). The reason is the large carbon Zeeman relaxation time ($\simeq 2000$ s) occurring in this material.

3 APPLICATIONS OF DNP NMR

Both the DNP enhancement curves and the DNP-enhanced NMR spectra can be used to obtain detailed and often unique information about the chemical and physical properties of solid materials, and representative illustrations of such applications will be given in this section. All experiments that will be

described have been performed in an external field of 1.4 T, corresponding to an electron Larmor frequency of 40 GHz and nuclear Larmor frequencies of 60 MHz for protons, 15 MHz for ^{13}C nuclei, and 12 MHz for ^{29}Si nuclei. Elaborate descriptions of the experimental setups, including the probes have been given.[18,19] All measurements were performed at room temperature.

3.1 The DNP Enhancement Curves

The symmetrical or antisymmetrical character of the DNP curve makes it possible to determine whether the electron–nuclear interactions are time-dependent, time-independent, or whether both types of interactions are present. This is illustrated in Figure 6, where are given the enhancement curves for ^{1}H and ^{13}C using DNP for a low-volatile bituminous coal. The ^{1}H DNP curve, Figure 6(a), contains both a symmetric and antisymmetric contribution, presumably because part of the electrons undergo rapid spin-exchange interactions whereas other electrons behave as fixed paramagnetic centers. The ^{13}C curve, Figure 6(b), is antisymmetric within experimental error, probably due to the much larger enhancements resulting from the static electron–carbon interactions, which overshadow the relatively small Overhauser enhancement. The occurrence of both the Overhauser and solid state effect in the ^{1}H DNP curves has been observed in a large variety of coals of different rank,[20] as well as in cellulose heat-treated in the temperature range 250–1000 °C.[21] It was found that for heating temperatures above 275 °C unpaired electrons were formed as a result of band ruptures and a DNP effect was observed. In the lower temperature range, up to ca. 450 °C, the solid state and thermal mixing effects dominate, whereas, between 450 °C and 700 °C, it is mainly an Overhauser effect which is observed (above 700 °C no DNP effect may be measured because the ESR line becomes very broad). However, the DNP enhancement curves indicate that an Overhauser effect also exists in the low temperature range, and that the solid state and thermal mixing effects are present for heating temperatures up to 500 °C. This is attributed to the small amounts of unpaired electrons undergoing rapid spin-exchange interactions at low temperatures, and behaving as fixed centers at the higher temperatures, respectively. In fact, it could be shown that the DNP curves could be used to detect fractions of electrons smaller than 1% either behaving as fixed centers or submitted to exchange interactions.

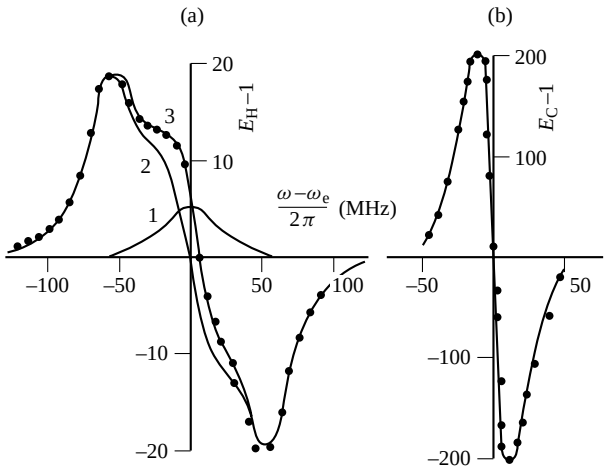

Figure 6 DNP enhancement curves obtained in a low-volatile bituminous coal. (a) ^{1}H DNP curves: curve 1, symmetric part; curve 2, antisymmetric part; curve 3, overall enhancement; dots, experimental. (b) ^{13}C DNP curve. Reproduced by permission of the American Chemical Society from R. A. Wind, R. H. Lewis, H. Lock, and G. E. Maciel, in 'Magnetic Resonance in Carbonaceous Solids', eds. R. E. Botto and Y. Sanada, ACS Ser. No. 229, 1993, p. 45

3.2 DNP and High-Resolution NMR in Solids

The increase in the NMR signal due to DNP can be used to reduce measuring times or to measure relatively small amounts of compounds. This ability is especially important for NMR spectroscopy on rare-spin species where, in the absence of DNP, long measuring times, several hours or more, are required in order to obtain an acceptable signal-to-noise ratio. In this section we shall give examples of such DNP NMR experiments.

In solids containing, besides unpaired electrons, both abundant spins and rare spins, the rare-spin polarization can be enhanced via DNP in two ways. (1) *Indirectly*, by first enhancing the abundant-spin polarization followed by a polarization exchange between the abundant and rare spins via cross polarization (CP). This is called the DNP CP (or DNP CP MAS when magic angle spinning is applied as well) experiment. In those cases where both the abundant spins and the electrons are homogeneously distributed in the sample, the spin diffusion among the abundant nuclei is generally strong enough to establish a single, average, polarization enhancement for all abundant nuclei, resulting, after CP, in an enhanced, undistorted, NMR spectrum of the rare nuclear spins. (In compounds where the electrons and/or the abundant nuclei are not homogeneously distributed, a distribution in DNP enhancements may also occur. As we shall see later, this effect can be used selectively to study interfaces and surfaces.) (2) The rare-spin polarization can also be enhanced *directly* via a polarization exchange between the electrons and the rare nuclei. This experiment, in which the rare-spin NMR signal is observed via a standard 90° rf pulse, will be called the DNP SP (MAS) experiment (SP = single pulse). Of course, in materials such as ceramics and diamonds, which do not contain abundant spins, DNP SP is the only possible technique. As the spin diffusion between rare spins is small, a distribution of enhancement factors often exists in the DNP SP experiment with larger enhancements for the nuclei in the vicinity of the unpaired electrons.[14] This has the disadvantage that distortions can occur in the DNP SP NMR spectra, but has the (potentially powerful) advantage that this experiment makes it possible selectively to probe structures and dynamics near the unpaired electrons.

It should be noted that in solids containing both rare and abundant nuclear spins, even in a DNP SP experiment the rare spin polarization can also be enhanced indirectly via a polarization exchange with the abundant spins. This has been called the three-spin effect.[22] This phenomenon is observed in cases that the rare-spin Zeeman relaxation is dominated by the interactions between the rare and abundant nuclear spins. Hence this effect is more likely to occur for rare nuclei remote from the unpaired electrons, where the electron–nuclear

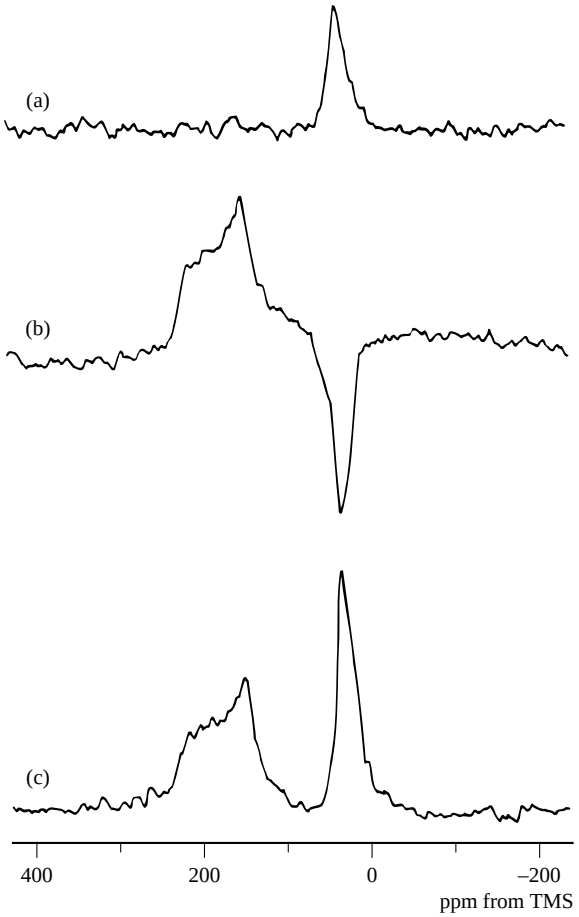

Figure 7 ^{13}C NMR spectra of a composite of *trans*-polyacetylene and polyethylene. (a): Result of an SP experiment; (b) and (c): Results of a DNP SP experiment without (b) and with (c) proton saturation. Reproduced by permission of the Academic Press from G. G. Maresch, R. D. Kendrick, C. S. Yannoni, and M. E. Galvin, *J. Magn. Reson.*, 1989, **82**, 41

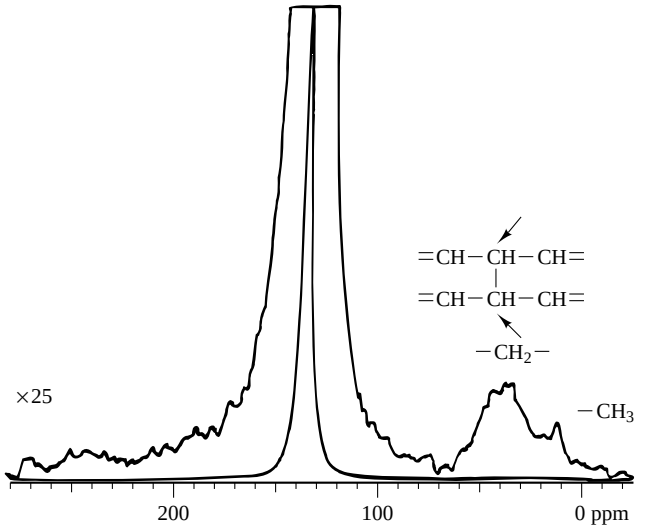

Figure 8 ^{13}C spectrum of *trans*-polyacetylene, obtained via ^{1}H–^{13}C DNP CP MAS NMR. The main line at 135 ppm is due to the ^{13}C nuclei inside the $(CH)_x$ chains; structural defects responsible for the other lines are indicated in the figure

interactions become weak. The three-spin effect arises from the nuclear Overhauser effect (NOE). This is similar to the Overhauser effect described in Section 2. The only differences are that NOE is caused by nuclear–nuclear interactions instead of electron–nuclear interactions, and that NOE is due to dipolar interactions only. It follows from Section 2 that NOE leads to a positive polarization enhancement of the rare-spin polarization if the abundant spin polarization is decreased via saturation (assuming that the gyromagnetic ratio of the nuclei is positive). However, if the abundant spin polarization is, for example, positively enlarged via DNP, the NOE enhancement of the rare spins becomes negative. Consequently, in a rare-spin DNP SP experiment, a positive direct enhancement from the electrons can be counteracted by a negative NOE enhancement. The three-spin effect is illustrated in Figure 7 where ^{13}C spectra are shown of a polymer consisting of small islands of *trans*-polyacetylene (PA) embedded in a matrix of polyethylene (PE). In *trans*-polyacetylene, $(CH)_x$, unpaired electrons (the so-called solitons) are present, presumably arising from bond-alternation domain walls.[23] These solitons move rapidly over the chains at least part of the time, giving rise to an Overhauser effect.[14,24] It follows that for the ^{13}C line around 20 ppm, which is due to the PE carbons which are for the major part remote from the solitons in the PA chains, the NOE effect leads to a negative enhancement in a DNP SP experiment without proton saturation. However, the ^{13}C line around 200 ppm is due to the carbons in the PA chains. Here the soliton–carbon interactions are so strong that the NOE effect is not observed. The three-spin effect can be avoided by partially saturating the abundant-spin polarization to such an extent that the polarization remains at its thermal equilibrium value.

We shall now consider applications of the DNP CP MAS and DNP SP MAS experiments.

3.2.1 Increase in Sensitivity

The increase in sensitivity due to DNP can result in dramatic decreases in the measuring time of an experiment. This can be used, for instance, for a fast (of the order of minutes) characterization of coal,[20] ceramics,[25] and diamonds,[14] to perform two-dimensional experiments in a relatively short time[24] (in this latter case, a two-dimensional experiment is reported for PA which would have required a measuring time of 165 years without DNP!), or to detect small amounts of molecules. An example of the latter application is shown in Figure 8 where the (natural abundance) ^{13}C DNP CP MAS spectrum of *trans*-polyacetylene is shown. Despite the fact that the amount of material was small (8 mg), the ^{1}H enhancement was so large (27-times in this experiment), that a ^{13}C spectrum with an excellent signal-to-noise ratio was obtained in a relatively short time.[26] In fact, it can be determined that the small narrow line at 13 ppm, which is due to the methyl end groups of the polyacetylene chains, represents only 0.5% of the total amount of carbons, or 3×10^{16} ^{13}C nuclei.

3.2.2 Structures and Dynamics Near the Unpaired Electrons

An example of the type of local information that can be obtained via DNP is shown in Figure 9. In this figure, ^{13}C spectra are shown of *trans*-polyacetylene obtained after a few

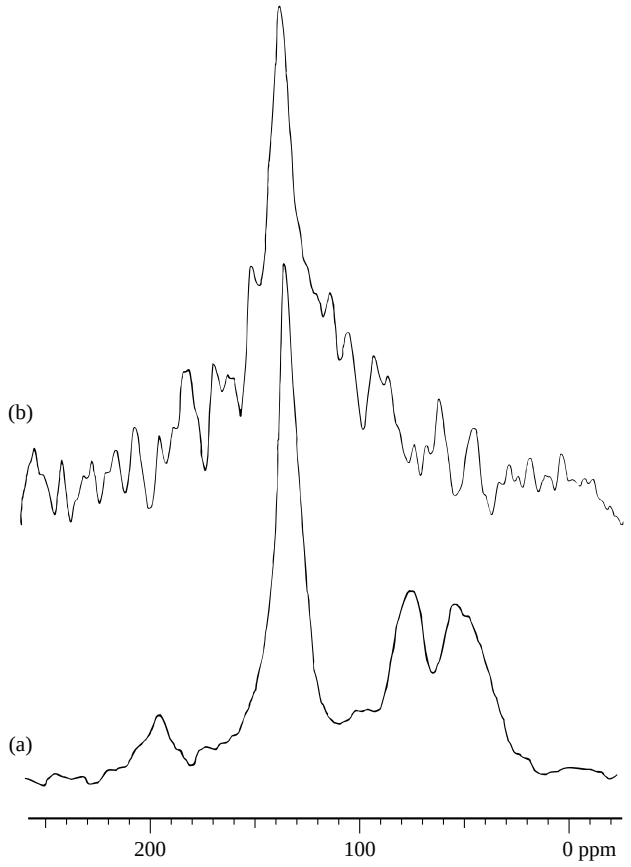

Figure 9 ^{13}C spectra of *trans*-polyacetylene, exposed to air for 4 months, obtained via (a) DNP CP MAS NMR and (b) DNP SP MAS NMR

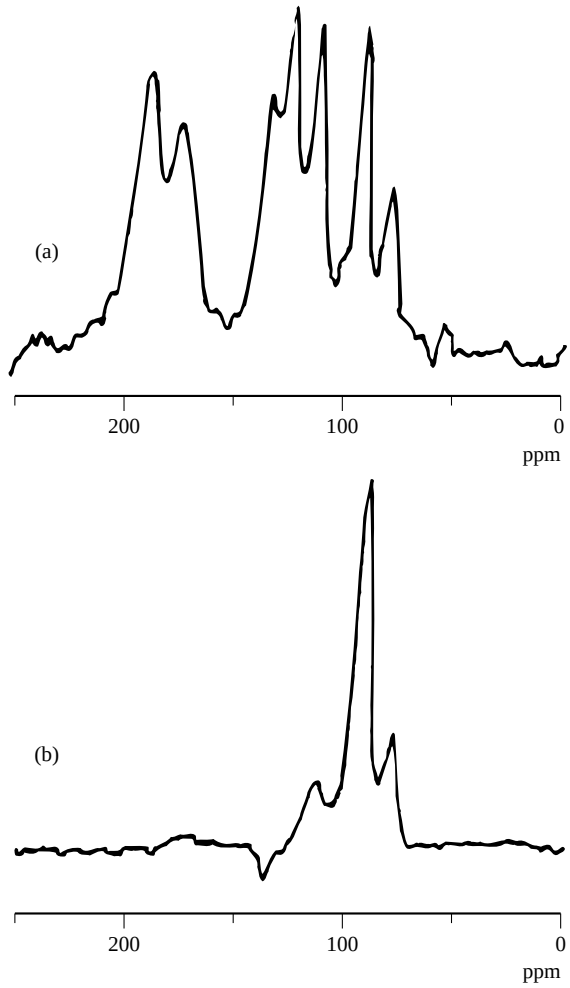

Figure 10 ^{13}C spectra of (fluoranthenyl)$_2PF_6$, obtained via (a) DNP CP MAS NMR and (b) DNP SP MAS NMR. Reproduced by permission of Marcel Dekker, Inc., from R. A. Wind, in 'Modern NMR Techniques and Their Application in Chemistry', eds. A. I. Popov and K. Hallenga, 1991, p. 125

months of exposure of the sample to air. Figure 9(a) shows the result of a DNP CP MAS experiment on ^{13}C. Compared with Figure 8, it follows that extra lines are observed due to the formation of ethene oxide groups, oxygen bridges, hydroxyl groups, and carbonyl groups.[27] Figure 9(b) shows the spectrum obtained via a ^{13}C DNP SP MAS experiment. We observe here that only the carbons in the $(CH)_x$ chains are detected. Hence in the latter experiment mainly the carbons in the chains below the surface are observed. These are not affected by exposure to the air.

Another type of local information that can be obtained via DNP SP MAS is the spin-density distribution of the unpaired electrons over the molecules.[26] An example of this possibility is the organic conductor (fluoranthenyl)$_2PF_6$. At room temperature this material behaves as a one-dimensional metal where the conduction electrons move more or less freely along paths parallel to the molecular stacks.[28] The electron mobility is so large that only an Overhauser effect is observed in this sample.[29] The average enhancement for ^1H is positive. This means that the dominating electron–proton hyperfine interaction is scalar. As a consequence, the overall enhancement of the DNP CP MAS spectrum of ^{13}C is positive as well, and Figure 10(a) shows the result of such an experiment. However, completely different results are obtained in the DNP SP MAS experiment on ^{13}C, shown in Figure 10(b). Here some lines are enhanced positively, indicative of a dominant electron–carbon scalar interaction, and one line is enhanced negatively due to a dominating electron–carbon dipolar interaction, whereas for the other lines the two DNP effects eliminate one another, resulting in a negligibly small enhancement. This phenomenon is due to the distribution of the electron density over the fluoranthenyl molecules, which is different at the different sites of the carbons, resulting in different ratios of the electron–carbon scalar and dipolar interactions. Hence, experiments utilizing DNP SP MAS can be used to determine the electron density distribution over the sites of the chemically different carbons.

Another application of DNP NMR in conductors is the determination of Knight shifts.[29] The Knight shift is proportional to the polarization of the conducting electrons. Hence, by saturating the ESR line, not only a signal enhancement due to DNP is obtained, but the Knight shift is suppressed as well. It has been shown[29] that for (fluoranthenyl)$_2PF_6$ the Knight shifts in the various carbon lines could be separated from the 'ordinary' chemical shift.

3.2.3 Interfaces and Surfaces

An example of an interfacial study with DNP NMR is an investigation of an immiscible mixture of polycarbonate

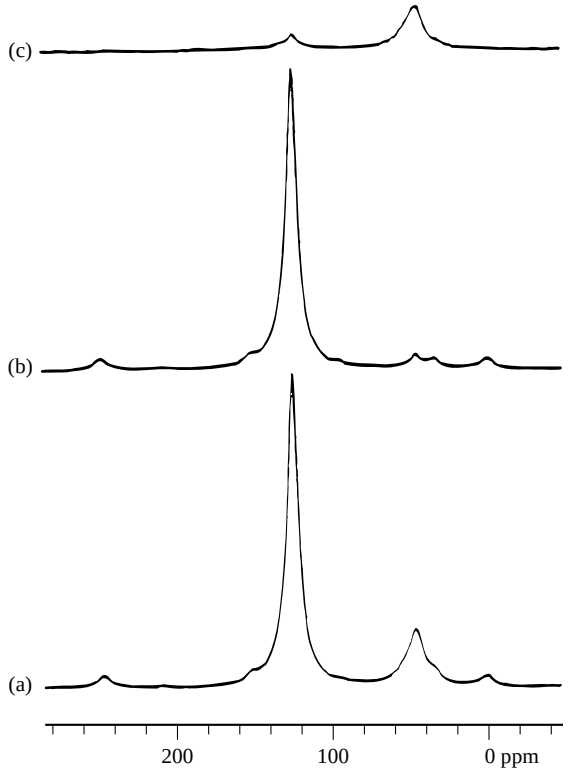

Figure 11 ^{13}C CP MAS NMR spectra of polycarbonate/polystyrene blends (a) with and (b) without ^{1}H DNP. The difference spectrum (c) has two features: the intensity around 40 ppm is due to the sp^3-hybridized carbons in PS whereas the intensity around 120 ppm arises from the carbons in the PC chains at the interface. Reproduced by permission of the American Society from M. Afeworki, R. A. McKay, and J. Schaefer, *Macromolecules*, 1992, **25**, 4084

(PC) and polystyrene (PS).[19,30] The samples consisted of thin film blends in which the polystyrene was doped with the stable radical BDPA [1,3-bis(diphenylene)-2-phenylallyl]. The interfacial region of PC could then be studied by measuring the DNP enhancement of protons via $^{1}H-^{13}C$ DNP CP MAS NMR. Figure 11 shows the results of such a measurement, carried out on a blend consisting of PC, which is labeled at the 3 and 3′ ring positions with 99 atom% ^{13}C, and PS, which is ^{13}C-depleted in all phenyl ring carbons. In this way, interferences between the NMR resonances of the aromatic carbons of the two polymers, which are partially overlapping, were avoided, and the peak observed at 120 ppm was almost exclusively due to the ^{13}C-labeled sites in PC. As the unpaired electrons in BDPA behave as fixed paramagnetic centers, the DNP enhancement of ^{1}H is mainly due to the solid state effect. Figure 11(a) and (b) show the $^{1}H-^{13}C$ CP MAS spectra obtained with and without ^{1}H DNP, respectively. It follows that the protons in PS, which are close to the unpaired electrons, are enhanced to the greatest extent (a factor of 20) and that there is also a small but noticeable enhancement for the protons in PC. This can be seen more clearly in Figure 11(c) where the differential spectrum is given. It has been shown[30a] that the proton polarization in PC is enhanced due to direct polarization transfer from these protons to the electrons, and that the signal of ^{13}C in PC observed in the differential spectrum arises from a 60 Å region from the PC/PS boundary which is 2% of the PC film thickness. Moreover, the

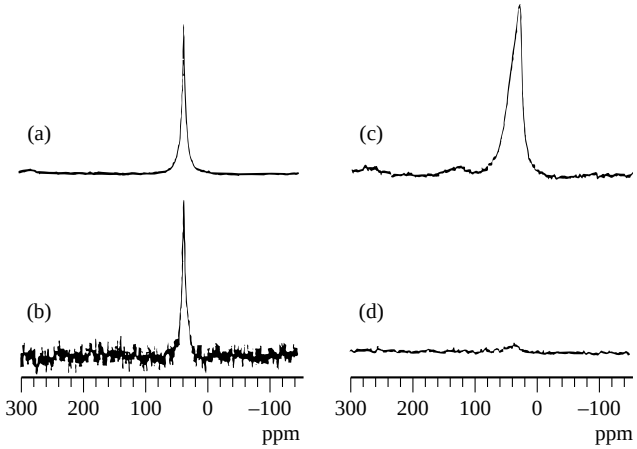

Figure 12 ^{13}C spectra of a 14% ^{13}C-enriched CVD diamond film, obtained via (a) DNP SP MAS NMR, (b) SP MAS NMR, (c) $^{1}H-^{13}C$ DNP CP MAS NMR, and (d) $^{1}H-^{13}C$ CP MAS NMR. Reproduced by permission of the American Institute of Physics from H. Lock, R. A. Wind, and G. E. Maciel, *J. Chem. Phys.*, 1993, **99**, 3363

authors were able to show that the interfacial aromatic carbons in PC have less motion than that of the bulk-PC aromatic carbons. This was attributed to restricted interchain motions resulting from a more dense packing for the PC chains near the PS barrier.

An example of a surface that can be studied via DNP NMR is provided by an investigation of chemical vapor deposited (CVD) diamond films.[31] Figure 12 shows ^{13}C spectra of a 14% ^{13}C enriched diamond film prepared by microwave-plasma-assisted CVD, using CH_4 and H_2 as feed gases.[31b] During the formation of the diamond films, unpaired electrons occur in the form of dangling bonds, which can be used for DNP measurements. Figure 12(a) and (b) show the results of ^{13}C DNP SP MAS NMR and SP MAS NMR, respectively, illustrating the increase in sensitivity due to DNP (the ^{13}C DNP enhancement factor is 50). Figure 12(c) and (d) show ^{13}C spectra obtained via $^{1}H-^{13}C$ DNP CP MAS and CP MAS NMR. A small percentage of protons (<0.1 atom %) is present at the intergrain boundaries of the diamond, and DNP can be used to enhance the proton signal (the enhancement factor is 25). It follows from Figure 12(c) that the hydrogenated diamond surfaces give rise to new resonances in the carbon spectrum (it was shown that the broad resonance at around 45 ppm actually consists of two lines), and the chemical shifts corresponding to these lines have been used to investigate the possibilities of different ‘diamondoids’, hydrogen-bearing carbon structures, occurring at the surfaces.[31b]

4 SUMMARY, CONCLUSIONS, AND PERSPECTIVES

High-resolution NMR combined with microwave-induced DNP has resulted in new areas of rare-spin NMR studies in solids. In many materials large DNP enhancement factors have been observed, which made possible NMR experiments which could not have been performed without DNP. The maximum proton enhancement that has been measured in a probe capable of MAS was 60, carbon enhancements of a few hundred were no exception, and in a ceramic fiber a silicon

enhancement factor 1000 was reported.[25] Although the DNP enhancements were not so large in some other materials, it should be kept in mind that even smaller enhancements can be very useful as they cause a reduction in the measuring time proportional to the square of the enhancement. Besides increasing the NMR sensitivity, DNP can also be used for other purposes such as the study of the structures and dynamics near the unpaired electrons, the detection of small amounts of electrons undergoing strong exchange interactions or behaving as fixed centers, the determination of the mobility and the spin-density distribution of conducting electrons, the study of surfaces and interfaces, the determination of Knight shifts, and DNP-enhanced imaging.[32] Finally, DNP NMR has been applied in a large variety of solid materials, such as doped polymers, coal, pyrolyzed materials, amorphous silica, organic conductors, semiconductors, natural and artificial diamonds, polymer composites, and ceramics.

However, it should be noted that many other possibilities for utilizing DNP NMR still remain to be explored:

1. Other types of radicals such as ions, nitroxide radicals, or radicals resulting from ionizing radiation.
2. Other materials; for example, experiments have already been started to explore the potential of DNP in zeolites, catalysts, and biomaterials.
3. High-resolution DNP NMR on quadrupolar nuclei.
4. High-resolution DNP NMR at different temperatures.
5. High-resolution DNP NMR at different pressures.
6. Combination of DNP with other high-resolution solid NMR techniques such as CRAMPS, fast MAS, DAS, DOR.
7. Combination of high-resolution NMR with different DNP techniques, which have been developed to increase the DNP enhancement factors and to improve the polarization transfer rates. Examples of these new techniques are the NOVEL (Nuclear spin Orientation Via Electron spin Locking) experiment,[33] which is an electron–nuclear analog of the CP experiment, and which provides fast polarization transfer (μs); the integrated solid effect (ISE),[34] where DNP is combined with adiabatic rapid passage through the ESR line, resulting in increased enhancement factors; DNP in the nuclear rotating frame,[35] which reduces the polarization transfer time by several orders of magnitude and which can be used to avoid distortion in the CP spectra resulting from rotating frame relaxation effects; DNP in higher external magnetic fields,[36] which might improve the resolution of the NMR spectra, and nuclear polarization enhancement using light irradiation. Examples of the latter techniques are microwave-induced optical nuclear polarization (MIONP),[37] optically polarized xenon and other rare gases, which can be used to study surfaces[38] and optical nuclear polarization (ONP).[39] Large enhancements have been obtained; for example, by applying the ISE technique in a naphthalene crystal doped with pentacene, in which the triplet state is highly polarized by photo-excitation, a DNP enhancement factor of the naphthalene protons of 5500 has been found.[40]

It can be expected that this and the other new methodologies and applications will further enhance the applicability of solid state NMR, and that many exciting new results will emerge in the near future.

5 RELATED ARTICLES

Cross Polarization in Rotating Solids: Spin-1/2 Nuclei; Cross Polarization in Solids; Electron–Nuclear Hyperfine Interactions; Electron–Nuclear Multiple Resonance Spectroscopy; Magic Angle Spinning; Nuclear Overhauser Effect; Optically Enhanced Magnetic Resonance.

6 REFERENCES

1. A. W. Overhauser, *Phys. Rev.*, 1953, **92**, 411.
2. T. R. Carver and C. P. Slichter, *Phys. Rev.*, 1953, **92**, 212.
3. A. Abragam and W. G. Proctor, *C. R. Acad. Sci.*, 1958, **246**, 2253.
4. C. D. Jeffries, *Phys. Rev.*, 1957, **106**, 164.
5. E. Erb, J. L. Motchane, and J. Uebersfeld, *C. R. Acad. Sci.*, 1958, **246**, 2121.
6. B. N. Provotorov, *Sov. Phys. JETP*, 1962, **14**, 1126.
7. A. Abragam and M. Borghini, in *Progress in Low Temperature Physics*, ed. C. J. Gorter, North-Holland Publishing Co., Amsterdam, 1964, Vol. 4, Chap. 8
8. M. Goldman, *Phys. Rev.*, 1965, **138**, A1675.
9. L. L. Buishvili, *Sov. Phys. JETP*, 1966, **22**, 1277.
10. A. Abragam, *The Principles of Nuclear Magnetism*, Clarendon Press, Oxford, 1961.
11. K. H. Hausser and D. Stehlik, in *Advances in Magnetic Resonance*, ed. J. S. Waugh, Academic Press, New York, 1968, Vol. 3, p. 79.
12. M. Goldman, *Spin Temperature and NMR in Solids*, Clarendon Press, Oxford, 1970.
13. A. Abragam and M. Goldman, *Nuclear Magnetism: Order and Disorder*, Clarendon Press, Oxford, 1982.
14. R. A. Wind, M. J. Duijvestijn, C. van der Lugt, A. Manenschijn, and J. Vriend, *Prog. NMR Spectrosc.*, 1985, **17**, 33.
15. N. W. Ashcroft and N. D. Mermin, *Solid State Physics*, Saunders College, Philadelphia, PA, 1976, Chap. 32
16. M. J. Duijvestijn, R. A. Wind, and J. Smidt, *Physica*, 1986, **138B**, 147.
17. R. A. Wind, R. H. Lewis, H. Lock, and G. E. Maciel, in *Magnetic Resonance of Carbonaceous Solids*, eds. R. E. Botto and Y. Sanada, *ACS Ser. No. 229*, 1993, 45.
18. R. A. Wind, F. E. Anthonio, M. J. Duijvestijn, J. Smidt, J. Trommel, and G. M. C. de Vette, *J. Magn. Reson.*, 1983, **52**, 424.
19. M. Afeworki, R. A. McKay, and J. Schaefer, *Macromolecules*, 1992, **25**, 4084.
20. R. A. Wind, M. J. Duijvestijn, C. van der Lugt, J. Smidt, and H. Vriend, *Fuel*, 1987, **66**, 876.
21. R. A. Wind, L. Li, G. E. Maciel, and J. B. Wooten, *Appl. Magn. Reson.*, 1993, **54**, 161.
22. G. G. Maresch, R. D. Kendrick, C. S. Yannoni, and M. E. Galvin, *J. Magn. Reson.*, 1989, **82**, 41.
23. W. P. Su, J. R. Schrieffer, and A. J. Heeger, *Phys. Rev. Lett.*, 1978, **42**, 1698.
24. M. J. Duijvestijn, A. Manenschijn, J. Smidt, and R. A. Wind, *J. Magn. Reson.*, 1985, **64**, 461.
25. R. H. Lewis, R. A. Wind, and G. E. Maciel, *J. Mater. Res.*, 1993, **8**, 649.
26. R. A. Wind, in *Modern NMR Techniques and Their Application in Chemistry*, eds. A. I. Popov and K. Hallenga, Marcel Dekker, Inc., New York, 1991, p. 125.
27. R. A. Wind, M. J. Duijvestijn, and J. Vriend, *Solid State Commun.*, 1985, **56**, 713.

28. M. Mehring and J. Spengler, *Phys Rev. Lett.*, 1984, **53**, 2441.
29. (a) W. Stocklein, C. S. Yannoni, H. Seidel, and D. Singel, *Chem. Phys. Lett.*, 1987, **141**, 277; (b) R. A. Wind, H. Lock, and M. Mehring, *Chem. Phys. Lett.*, 1987, **141**, 283.
30. (a) M. Afeworki and J. Schaefer, *Macromolecules*, 1992, **25**, 4092; (b) M. Afeworki and J. Schaefer, *Macromolecules*, 1992, **25**, 4097; (c) M. Afeworki, S. Vega, and J. Schaefer, *Macromolecules*, 1992, **25**, 4100.
31. (a) H. Lock, G. E. Maciel, and C. E. Johnson, *J. Mater. Res.*, 1992, **7**, 2791; (b) H. Lock, R. A. Wind, and G. E. Maciel, *J. Chem. Phys.*, 1993, **99**, 3363.
32. G. E. Maciel and M. F. Davis, *J. Magn. Reson.*, 1985, **64**, 356.
33. A. Henstra, P. Dirksen, J. Schmidt, and W. Th. Wenckebach, *J. Magn. Reson.*, 1988, **77**, 389.
34. A. Henstra, P. Dirksen and W. Th. Wenckebach, *Phys. Lett. A*, 1988, **134**, 134.
35. R. A. Wind and H. Lock, *Adv. Magn. and Opt. Reson.*, 1990, **15**, 51.
36. S. Un, T. Prisner, R. T. Weber, M. J. Seaman, K. W. Fishbein, A. E. Dermott, D. J. Singel, and R. G. Griffin, *Chem. Phys. Lett.*, 1992, **189**, 54.
37. (a) H. Brunner, R. H. Fritsch, and K. H. Hausser, *Z. Naturforsch.*, 1987, **42a**, 1456; (b) P. Dirksen, A. Henstra, and W. Th. Wenckebach, *J. Magn. Reson.*, 1990, **86**, 549.
38. (a) Z. Wu, W. Happer, M. Kitano, and J. Daniels, *Phys. Rev. A*, 1990, **42**, 2774; (b) D. Raftery, L. Reven, H. Long, A. Pines, P. Tang, and J. A. Reimer, *J. Phys. Chem.*, 1993, **97**, 1649.
39. (a) D. Stehlik and H.-M. Vieth, in *Pulsed Magnetic Resonance: NMR, ESR and Optics*, ed. D. M. S. Bagguley, Clarendon Press, Oxford, UK, 1992, p. 446; (b) S. K. Buratto, D. N. Shykind, and D. P. Weitekamp, *Phys. Rev. B*, 1991, **44**, 9035.
40. A. Henstra, T.-S. Lin, J. Schmidt, and W. Th. Wenckebach, *Chem. Phys. Lett.*, 1990, **165**, 6.

Biographical Sketch

R. A. Wind. *b* 1942. B.S., 1966, Ph.D., 1972, Delft, The Netherlands Introduced to NMR by J. Smidt. Faculty in Delft University of Technology, 1972–85; Senior research scientist, Colorado State University, 1985–90; Director of Research and Development, Chemagnetics/Otsuka Electronics, 1990–93; Senior staff scientist, Battelle/PNL, 1993–present. Approx. 90 publications. Current research specialties: NMR/DNP NMR and its applications in liquids and solids chemistry.

Echoes in Solids

Bernard C. Gerstein

Ames Laboratory of Iowa State University, Ames, Iowa, USA

1	Introduction	1
2	Basic Ideas	1
3	Time-Dependent Quantum Mechanics of the Spin Echo	1
4	Rotations in Spin Space: Selective Averaging	2
5	The Average Hamiltonian and Echoes	3
6	The Modulated Spin Echo	4
7	The Dipolar Echo and the First-Order Quadrupolar Echo	5
8	Transient Nutations: A Variant	5
9	Multiple Quantum Coherence	5
10	Related Articles	6
11	References	6

1 INTRODUCTION

When a person stands at the edge of a deep canyon and sharply shouts their own name, it may happen that this name, somewhat distorted, and not as loud, will come back to them after a second or so. This return of the initial signal we call an echo. We think of the opposite wall of the canyon reflecting the signal back toward us. In the jargon of NMR, we could say that a sharp signal was broadcast, something is there to 'reflect' this signal, and a somewhat attenuated and distorted response, an 'echo' of the original, is detected at a later time. There is a sense in which we might say that time has been reversed in this experience—except that, for exact time reversal, we might expect that the name would return to us spoken backwards.

One use of echoes in materials science is that in nondestructive testing on metals by sharp sonic signals. Here, a transducer is used to broadcast a pulse of sound into the solid, and the echo, received back by a detector, is used to infer voids, cracks, or general faults in the material. In this case, the echo received from the initial pulse of sound is modulated by the information from macroscopic defects in the solid, and this modulation is unwound to infer the nature of the defect. This case is almost an exact analog of the 'modulated spin echo' first reported by Hahn and Maxwell.[1] In this article, we provide an introduction to the subject of echoes in the study of solids by NMR, with specific attention to those echoes produced by the rotations of internal interactions by the radiofrequency field, $\boldsymbol{B}_1$. We can call these 'spin echoes'. As is discussed in ***Rotating Solids*** there are also echoes produced by physical rotations of the sample, e.g., by 'magic angle spinning'. We call these 'spun echoes'. In this article, we pay specific attention to the case of 'spin echoes' in solids, and their production and detection under radiofrequency excitations.

2 BASIC IDEAS

A spin echo[2] in NMR is quite analogous to that produced when calling one's name in a canyon. A transient transverse magnetization is created, something is done to cause this magnetization to be 'reflected' backwards, and, at a later time, this magnetization transient, somewhat attenuated, flashes back into our detector. We can then repeat the event that refocused the magnetization, and again we shall see an echo. If we are able to watch the signal on the detector, let us say an oscilloscope screen that is exhibiting the memory of a digitizer, from the moment of the broadcast of the initial signal to the return of the echo, and we repeat the refocusing event five times, we might see a signal such as that shown in Figure 1.

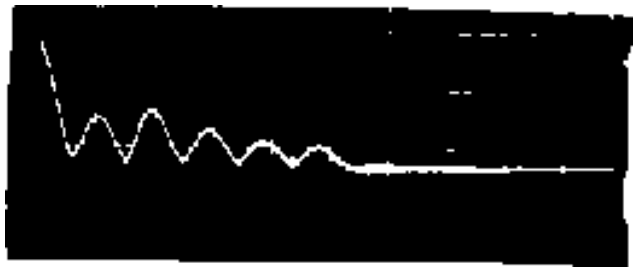

Figure 1 Magnetization amplitude $I(t)$ versus time t. Left, initial decay after a 90° pulse. Five echoes follow five 180° refocusing pulses

This signal is in fact a series of spin echoes when the nucleus in question is ^{1}H in water; the sequence used to produce this effect is the Carr–Purcell[3] version of the Hahn spin echo sequence. The system is prepared with the magnetization along the y direction in the rotating frame by a $90°_x$ pulse, and then a series of 180° pulses, switched in phase by 90° from the preparation pulse (which is to say, along the y axis in the rotating frame), are used to produce the echoes: we designate the sequence by the shorthand notation $90°_x$, τ, $(180°_y, 2\tau) \times 5$.

The signal shown in Figure 1 is observed with the reference phase adjusted for detection along the y axis in the rotating frame. It has a number of interesting features. First, we see a hint of the transient 90° pulse at the beginning, on the left of the figure, as the few points from the baseline up. Second, we see the free induction decay after this pulse. Then, we see a hint of the 180° pulse, and subsequently a signal 'refocusing' back up, reaching an echo maximum, and then decaying back down. This situation is repeated four more times. If we look just at the echo envelope, i.e., the maximum at the beginning of the FID, and the succeeding maxima of the echoes, we see that this envelope roughly describes something looking like an exponential decay. However, in the case shown, there is clearly an oscillation in the envelope—a modulation of the echoes. The spin echo experiment and the modulation of the echo envelope are the subjects here. Finally, we see that the envelope of the echo lasts longer than the FID itself; i.e., if we denote the decay constant for the FID by T_2*, and the decay constant for the echo envelope by T_2 then we see that the effective decay time of the FID, T_2, has been lengthened compared with T_2* by the sequence of 180° refocusing pulses. A classical picture of the initial excitation and the 180° refocusing is shown in Figure 2 for a single refocusing pulse.

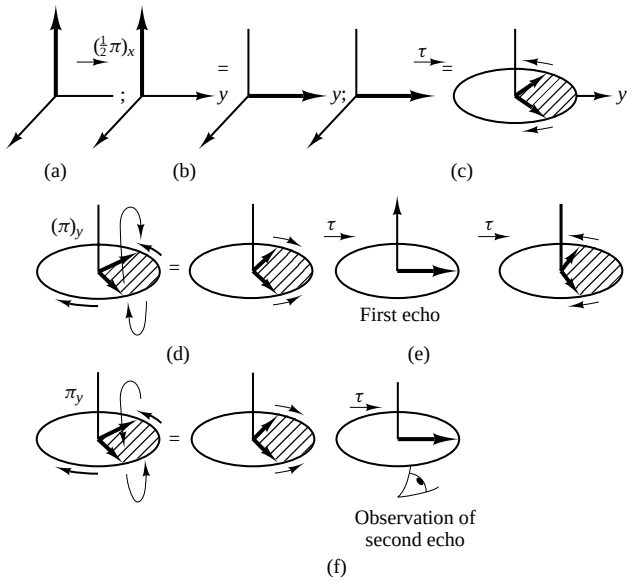

Figure 2 Classical picture of the spin echo: top, polarization, and 90° pulse, followed by dephasing on resonance. Bottom, 180° refocusing pulses, followed by rephasing

3 TIME-DEPENDENT QUANTUM MECHANICS OF THE SPIN ECHO

To place our discussion in perspective, it is necessary to recognize explicitly what has been implicit in the above introduction, namely, that there are two fundamental facts about NMR.

1. A nucleus with a magnetic moment proportional to a constant γ, will resonate at an angular frequency ω in a static magnetic field $\boldsymbol{B}$ given by $\omega = \gamma B$. The sensitivity to detection is proportional to γ, and to the natural abundance of the nucleus in question.
2. Hidden in fundamental fact 1 is the time-dependent mechanics tersely summarized in the following equations:

$$\mathrm{i}\frac{\mathrm{d}\hat{\rho}}{\mathrm{d}t} = [\hat{\mathcal{H}}, \hat{\rho}] \quad \text{(energies in units of radial frequency)} \tag{1}$$

$$\langle \hat{I}_y(t) \rangle = \mathrm{Tr}\, \hat{\rho}(t)\hat{I}_y \tag{2}$$

$$\hat{\rho}(t) = \hat{U}(t, 0)\hat{\rho}(0)\hat{U}^{-1}(t, 0) \tag{3}$$

Equation (1) is the time-dependent Schrödinger equation, expressed in density matrix formalism.[4] equation (2) shows how the solution of equation (1) is used to obtain the time dependence of observables, e.g., the time decay of the magnetization of a nuclear spin system under a resonant excitation. In equation (2) detection is made along the y axis of the rotating frame. The Fourier transform of the time decay is the NMR spectrum. Implicit in equation (2) is the fact that we are using matrix representations to describe our system. Tr $\hat{A}$ denotes the trace, or sum of the diagonal elements, of the matrix representing the operator $\hat{A}$. Equation (3) indicates the formal solution of equation (1). The absolutely critical term here is the propagator $\hat{U}(t,0)$, which drives the ensemble of magnetically resonant nuclei under study from time zero to time t (quite a lovely introduction to the subject of propagators in quantum mechanics is given by Mattuck[5]). It is exactly an understanding of how the experimenter controls $\hat{U}(t,0)$ that makes NMR such a powerful technique for probing the properties of inert and living matter.

4 ROTATIONS IN SPIN SPACE: SELECTIVE AVERAGING

All spectroscopy experiments implicitly or explicitly involve solutions of the time-dependent Schrödinger equation. An understanding of NMR involves at least a rudimentary knowledge of the solutions of this equation in the density operator formulation. Fortunately, there are texts for students at both the entry level[6,7] and advanced levels[8–10] presenting both of these pictures. Abragam's monumental 1961 monograph 'Principles of Nuclear Magnetism'[11] is still a standard reference in the field, with gems yet to be mined so long after its publication.

As a basis for understanding the spin echo experiment, we tersely summarize the results of selective averaging theory on first the result of the spin echo sequence upon an ensemble of spins $\frac{1}{2}$ in a solid, e.g., protons in solid gypsum, $CaSO_4.2H_2O$. Here, the principal internal interactions are, in decreasing order of magnitude,

1. anisotropic shielding;
2. the homonuclear dipolar interaction.

We start in the rotating frame of the Zeeman interaction, the frame in the laboratory in which NMR signals are detected after demodulation removes the carrier frequency from the information content of the signal. In the rotating frame, the principal effective magnetic fields that cause a spin-$\frac{1}{2}$ nucleus such as a proton to resonate for detection by NMR are

1. The externally applied radiofrequency field $\boldsymbol{B}_1$, which is constant in the rotating frame on resonance, with, e.g., an interaction Hamiltonian for a pulse along the phase x being

$$\hat{\mathcal{H}}_1 = -\gamma B_1 \hat{I}_x = -\omega_1 \hat{I}_x \tag{4}$$

2. The sample-supplied, or internal, average of the fields associated with all other internal interactions. For non-spin-$\frac{1}{2}$ nuclei, the major interaction is the electric field gradient, which perturbs the energy levels of quadrupolar nuclei. For concentrated spin-$\frac{1}{2}$ nuclei such as ^{1}H and ^{19}F, the major fields are the dipolar fields of all other protons or fluorine nuclei, $\boldsymbol{B}_\mathrm{D}$, in which a proton or fluorine will precess with a frequency

$$\omega_\mathrm{D} = \gamma B_\mathrm{D} \tag{5}$$

A smaller perturbation is the anisotropic shielding field associated with the reaction of electrons in the environment of the nucleus under observation to the externally imposed static field. With each field is associated an energy and a quantum mechanical energy operator $\hat{\mathcal{H}}$. Thus the energy operator in the rotating frame is given by

$$\hat{\mathcal{H}} = \hat{\mathcal{H}}_\mathrm{rf} + \hat{\mathcal{H}}_\mathrm{int} \tag{6}$$

where the magnitude of $\hat{\mathcal{H}}_{\rm rf}$ for purposes of solid state experiments is about 5 mT. The magnitude of $\hat{\mathcal{H}}_{\rm int}$ is never greater than a few tenths of a millitesla in the case discussed here. The equation of motion of the system is then given by the solution to equation (1) with $\hat{\mathcal{H}}$ being the sum of the rf and internal interactions, as specified in equation (6). The average values of observables, e.g., $\langle \hat{I}_y(t) \rangle$, the free induction decay detected along the y phase in the rotating frame, are given by equation (2).

With the interactions separated in magnitude in this manner, it makes sense to treat $\hat{\mathcal{H}}_{\rm int}$ as a perturbation of $\hat{\mathcal{H}}_{\rm rf}$. Recall that the transformation to the frame of the Zeeman interaction (the rotating frame) simplifies the description of a nuclear spin in the presence of other interactions: for example, the oscillating on-resonance rf field becomes static in the rotating frame. Similarly, transformation to the frame of the now largest interaction $\hat{\mathcal{H}}$ further simplifies the description of the system. The transformation to the frame of the rf is accomplished by the following relations:

$$\hat{\rho} = \hat{U}_{\rm rf} \tilde{\hat{\rho}} \hat{U}_{\rm rf}^{-1} \tag{7}$$

$$\mathrm{i} \frac{\mathrm{d}\hat{U}_{\rm rf}}{\mathrm{d}t} = \hat{\mathcal{H}}_{\rm rf} \hat{U}_{\rm rf} \tag{8}$$

$$\hat{U}_{\rm rf}(0,0) \equiv \hat{U}_{\rm rf}(t=0) = \hat{1} \tag{9}$$

$$\tilde{\hat{\mathcal{H}}}(t) = \hat{U}_{\rm rf}^{-1}(t,0) \hat{\mathcal{H}} \hat{U}_{\rm rf}(t,0) \tag{10}$$

As mentioned above, the notation $\hat{U}(t,0)$ is a formal way of saying that the propagator, $\hat{U}$, drives the system from time 0 to time t. An explicit operational form of $\hat{U}$ will be given below; for now, accept it as that quantity causing the system to proceed in time, with physical origin in the time-dependent sequence of rf pulses and the internal interactions as affected by these pulses. The result,

$$\frac{\mathrm{i}\mathrm{d}\tilde{\hat{\rho}}}{\mathrm{d}t} = [\tilde{\hat{\mathcal{H}}}_{\rm int}, \tilde{\hat{\rho}}\,] \tag{11}$$

where $\tilde{\hat{\mathcal{H}}}_{\rm int}$ is given by equation (10), is that the motion of the system in the new frame, the frame of the rf field, now no longer explicitly contains the rf interaction (recall that transforming to the frame of the Zeeman field removed that interaction from the description of the system).

We next make a second transformation to the frame of $\hat{\mathcal{H}}_{\rm int}$, simply reproducing equations (7)–(10) with the appropriate change in symbols:

$$\tilde{\hat{\rho}} = \hat{U}_{\rm int}(t,0) \tilde{\tilde{\hat{\rho}}} \hat{U}_{\rm int}^{-1}(t,0) \tag{12}$$

$$\frac{\mathrm{i}\mathrm{d}\hat{U}_{\rm int}}{\mathrm{d}t} = \tilde{\hat{\mathcal{H}}}_{\rm int} \hat{U}_{\rm int} \tag{13}$$

$$\hat{U}_{\rm int}(0,0) = \hat{1} \tag{14}$$

Thus $\hat{\rho}$ is replaced by $\tilde{\hat{\rho}}$, $\tilde{\hat{\rho}}$ is replaced by $\tilde{\tilde{\hat{\rho}}}$, $\hat{U}_{\rm rf}$ is replaced by $\hat{U}_{\rm int}$, etc. The system in this frame is static:

$$\mathrm{i} \frac{\mathrm{d}\tilde{\tilde{\hat{\rho}}}}{\mathrm{d}t} = [0, \tilde{\tilde{\hat{\rho}}}\,] = 0 \tag{15}$$

We formally identify this static system with the system at time zero; $\hat{\rho}$ then becomes identical to $\hat{\rho}(0)$. In this perturbation picture, with $\hat{\mathcal{H}}_{\rm int}$ being a perturbation of $\hat{\mathcal{H}}_{\rm rf}$, the motion of the system is described by

$$\hat{\rho}(t) = \hat{U}_{\rm rf}(t,0) \hat{U}_{\rm int}(t,0) \hat{\rho}(0) \hat{U}_{\rm int}^{-1}(t,0) \hat{U}_{\rm rf}^{-1}(t,0) \tag{16}$$

5 THE AVERAGE HAMILTONIAN AND ECHOES

Before becoming explicit about the operational forms of the propagators $\hat{U}$, let us examine equation (16) more closely. It is clear that if both $\hat{U}_{\rm rf}(t_{\rm c},0)$ and $\hat{U}_{\rm int}(t_{\rm c},0)$ are unity at some particular time $t_{\rm c}$ then, at this special time, it appears that the system has simply not changed, i.e., equations (2) and (16) at time $t_{\rm c}$, tell us that the value of any observable at this time is the value of that operator at time zero; at time $t_{\rm c}$, $\hat{\rho}(t_{\rm c}) = \hat{\rho}(0)$. There is therefore an enormous simplicity in the behavior of the system, which the experimenter may accomplish with proper arrangements of sufficiently powerful rf pulses, since both $\hat{U}_{\rm rf}$ and $\hat{U}_{\rm int}$ depend upon $\hat{\mathcal{H}}_{z\rm rf}$, the rf pulses that we supply! The fields (5 mT) generated by the rf pulses are much larger than the 'internal fields' due to dipolar interactions and shielding (<0.3 mT) (but not, in general, electric field gradients on quadrupolar nuclei). That is to say, the initial broadcast of our excitation is 'sharp', as in the name-calling event described at the beginning of this article. In that case, if we had called our name slowly and softly compared with the background noise of the wind sighing through the trees, and the calls of the eagle circling below, we would not have received back an echo response to our call. In more mathematically explicit terms, as long as $\hat{U}_{\rm rf}$ operates for times short compared with times in which $\hat{U}_{\rm int}$ affects the system, its motion is predominantly controlled by $\hat{U}_{\rm rf}$. Then, if the sequence of rf pulses generating $\hat{U}_{\rm rf}(t_{\rm c},0)$ returns the system to its initial state, $\hat{U}_{\rm rf}(t_{\rm c},0)$ is formally equal to unity—a result inferred from physics rather than mathematics. Examples of such pulse sequences are easily imagined if the physics is kept clearly in mind. One example is the sequence $(t,\ 180^\circ_y,\ \tau,\ 180^\circ_y,\ \tau)$ which results in a rotation by 2π about the y axis, leaving the system invariant at a cycle time $t_{\rm c} = 3\tau$. The sequence $(\tau,\ 90^\circ_x,\ \tau,\ 90^\circ_y,\ 2\tau,\ 90^\circ_{-y},\ \tau,\ 90^\circ_{-x},\ \tau)$ has pairs of pulses that cancel each other (the y pulse cancels the $-y$ pulse, and similarly for x) and leave the system invariant at a cycle time $t_{\rm c} = 6\tau$. Such sequences are said to be *cyclic*. If these groups of pulses are repeated periodically, they are both cyclic and *periodic*. As long as $\hat{U}_{\rm rf}(nt_{\rm c},0)$ is the dominant propagator, in the 'windows' between these groups of pulses, the system will behave as if it is not moving in time. The behavior of the system becomes refocused at these 'echo times' $nt_{\rm c}$.

We have here a situation analogous to that which we might imagine if we had been able to use a strobe light to watch the glitter and dynamic flowing that was a performance by the late Janice Joplin. To see her perform at her most intense,

belting out a song like 'Try (Just a Little Bit Harder)', was to experience a visual sensation of watching mercury boiling. Under a strobe, however, we might have been able to recognize that her motions, which were rhythmatic with the beat of the music, viewed in the windows of time periodic with these motions, would make her appear to us to be almost not moving. However, since she was not just an automaton repeating a periodic motion in sync with the strobe, we should see that nuances that were lost without the strobe now become visible. She would appear to move very slowly, in analogy to a modulated spin echo (see below). We might say that her motion appears to vary quite slowly relative to her motion when seen in the absence of a strobe. The rapid motion that we should see without a strobe has been selectively averaged to zero. In this circumstance, we are able to see details of much slower motion that we might have missed had we viewed her doing her full routine—which could be quite rapid and stunning.

6 THE MODULATED SPIN ECHO

With the performance of Janice Joplin viewed in a strobe light kept in mind, let us take a close look at equation (16). We see here that as time progresses, $\hat{U}_{\rm int}(nt_{\rm c},0)$ begins to affect the motion of the system. If the propagator $\hat{U}_{\rm rf}(t,0)$ dominates the situation at short times, meaning that the magnitude of $\hat{\mathcal{H}}_{\rm rf}$ is much larger than the magnitude of $\hat{\mathcal{H}}_{\rm int}$, then, as time progresses, observation in the windows $nt_{\rm c}$ will reveal some motion due to $\hat{U}_{\rm int}(nt_{\rm c},0)$. Now this propagator, $\hat{U}_{\rm int}(nt_{\rm c},0)$, is determined by $\hat{\mathcal{H}}_{\rm int}$. The interaction $\hat{\mathcal{H}}_{\rm int}$ in the case considered is the sum of $\hat{\mathcal{H}}_{\rm D}$ and $\hat{\mathcal{H}}_{\rm CS}$, the dipolar and shielding interactions as manipulated by the rf pulses. If somehow the dipolar interaction (but not the shielding interaction) can be selectively set in motion so that its time average at times $nt_{\rm c}$ is zero, the remaining information in the windows of the stroboscopic observation will be the shielding. The nuances of a Joplin performance become visible if the rapid periodic motion in time with the rhythm is selectively averaged out of our vision by using a strobe. This is exactly what multiple pulse homonuclear decoupling attempts to accomplish. To see how this works, one needs an explicit operational form for the internal propagator $\hat{U}_{\rm int}(nt_{\rm c},0)$. The form is illustrated with the spin echo sequence, (τ, 180°_y, τ, 180°_y, τ). In the sequence, we take the internal Hamiltonian to represent any interaction proportional to the operator $\hat{I}_z$, e.g., shielding, resonance offset, static field inhomogeneities, and scalar couplings to unlike nuclei. Homonuclear dipolar coupling, as shown below, is not simply proportional to $\hat{I}_z$.

When we manipulate $\hat{\mathcal{H}}_{\rm int}$ by cyclic and periodic sequences of rf pulses [$\hat{U}_{\rm rf}(nt_{\rm c},\ 0) = 1$] the form of the propagator $\hat{U}_{\rm int}$ becomes an exponential (see Chapter 4 of Gerstein and Dybowski[6]), with the leading term in the result, observed at cycle times $nt_{\rm c}$, given by

$$\begin{aligned}\hat{\rho}(nt_{\rm c}) &= \hat{U}_{\rm int}(nt_{\rm c})\hat{\rho}(0)\hat{U}_{\rm int}^{-1}(nt_{\rm c},0)\\ &= \exp(-{\rm i}\hat{\bar{\mathcal{H}}}_{\rm int}^{(0)})\,\hat{\rho}(0)\,\exp({\rm i}\hat{\bar{\mathcal{H}}}_{\rm int}^{(0)})\end{aligned} \tag{17}$$

Here, $\hat{\bar{\mathcal{H}}}_{\rm int}^{(0)}$ is equal to the integral over a cycle of the internal Hamiltonian as manipulated in time by the rf pulses:

$$\hat{\bar{\mathcal{H}}}_{\rm int}^{(0)} = \frac{1}{t_{\rm c}}\int_0^{t_{\rm c}} \hat{\tilde{\mathcal{H}}}_{\rm int}(t)\,{\rm d}t \tag{18}$$

This time average of the internal Hamiltonian, as manipulated by the rf pulses, may be interpreted as an average internal Hamiltonian. If this time average is zero, then, for a cyclic, periodic sequence, both $\hat{U}_{\rm rf}(nt_{\rm c})$ and $\hat{U}_{\rm int}(nt_{\rm c})$ will be unity, and at times $nt_{\rm c}$ the system will behave as if there is nothing driving it; it will 'echo' its initial state in time.

The manner of manipulation of $\hat{\tilde{\mathcal{H}}}_{\rm int}$ is as follows:

$$\hat{\tilde{\mathcal{H}}}(t) = \hat{U}_{\rm rf}^{-1}(t,0)\hat{x}_{\rm int}\hat{U}_{\rm rf}(t,0) \tag{19}$$

$\hat{\tilde{\mathcal{H}}}_{\rm int}(t)$ is the *instantaneous* value of the internal Hamiltonian as determined by the rf pulses. $\hat{U}_{\rm rf}(t,0)$ is the propagator due to the rf pulses from time zero to time t. For n time intervals δ_1, followed by δ_2, ... , followed by δ_n, $\hat{U}_{\rm rf}$ is clearly the propagator during interval δ_1, followed by the propagator during δ_2, ... :

$$\hat{U}_{\rm rf}(t,0) = \hat{U}_{\rm rf}(\delta_n)\cdots\hat{U}_{\rm rf}(\delta_1) \tag{20}$$

The inverse of this product of matrix operators is given by

$$\hat{U}_{\rm rf}^{-1}(t,0) = \hat{U}_{\rm rf}^{-1}(\delta_1)\hat{U}_{\rm rf}^{-1}(\delta_2)\cdots\hat{U}_{\rm rf}^{-1}(\delta_n) \tag{21}$$

The physical meaning of the exponentials in equation (17) can be seen from the fact that they can always be expressed as a product of rotations in spin space acting on components of angular momentum operators. For example, consider the rf pulse sequence with perfect delta-function pulses (τ, 180°_y, 2τ, 180°_y, τ), shown in Figure 3.

This sequence is used to produce $\hat{\mathcal{H}}_{\rm rf}$, and thus $\hat{U}_{\rm rf}$, equal to $\exp(-i\int_0^t \hat{\tilde{\mathcal{H}}}{\rm d}t)$, as indicated in Figure 3. At times $0 < t < \tau$ when the rf Hamiltonian is zero, $\hat{U}_{\rm rf}(t,0)$ takes the form $e^0 = 1$, and in this time interval the value of $\hat{I}_z$ as manipulated by the rf pulse sequence in Figure 3 is given by equation (19). We may physically identify $\hat{U}_{\rm int}(0 < t < \tau)$ as given in equation (19) with a rotation $\hat{R}$ of unity, performed on $\hat{I}_z$, symbolized by $\hat{R}\hat{I}_z = 1\cdot\hat{I}_z$. At time $t = \tau$, the rf Hamiltonian corresponds to an infinitely fast rotation about the y axis of 180°. $\hat{U}_{\rm rf}(t = \tau) = \exp(i\pi\hat{I}_y)$, and the physical result is a 180°_y rotation, $\hat{R}_{180y}$, which sends the operator $\hat{I}_z$ into the operator $-\hat{I}_z$. For $\tau < t < 2\tau$ the rf again is zero, and $\hat{U}_{\rm rf}$ is unity. At $t = 3\tau$, another 180°_y takes place. Under this sequence, therefore, with the spin portion of $\hat{\mathcal{H}}_{\rm int}$ being proportional to $\hat{I}_z$, and keeping in mind the time ordering dictated by equations (20) and (21), we find the sequence of values of $\hat{I}_z$ in the frame of the rf pulses (see Figure 3)

$$0 < t < \tau:\quad \hat{I}_z \to {\rm e}^{-0}\hat{I}_z{\rm e}^0 = 1\cdot\hat{I}_z\cdot 1 = 1\cdot\hat{I}_z = \hat{I}_z \tag{22a}$$

$$t = \tau:\quad \hat{I}_z \to 1\cdot\hat{R}_{180y}\hat{I}_z = -\hat{I}_z \tag{22b}$$

$$\tau < t < 3\tau:\quad \hat{I}_z \to 1\cdot\hat{R}_{180y}\cdot 1\cdot\hat{I}_z = -\hat{I}_z \tag{22c}$$

$$3\tau < t \le 4\tau:\quad \hat{I}_z \to -\hat{I}_z \tag{22d}$$

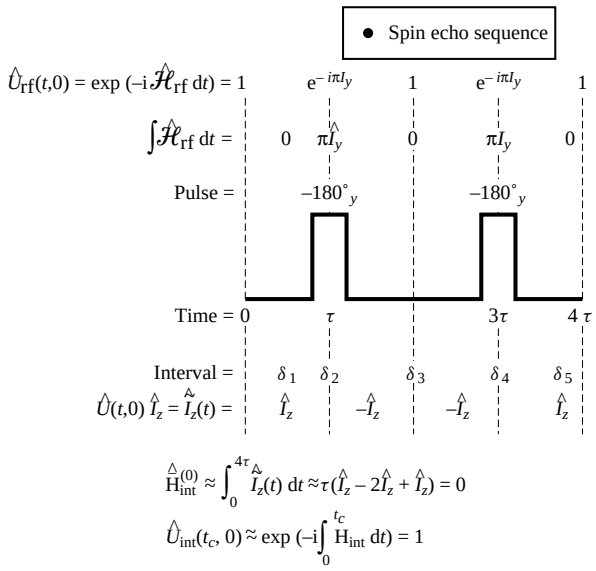

Figure 3 Spin echo sequence, illustrating the pulses (square waves), the propagator associated with the pulses, $\hat{U}_{rf}(t,0)$, and the average Hamiltonian associated with an internal interaction proportional to $\hat{I}_z$

The familiar result is that at periodic cycle times $4n\tau$, under the spin echo sequence $(\tau,\ 180^\circ_y,\ 2\tau,\ 180^\circ_y) \times n$, chemical shifts and field inhomogeneities, with spin operators $\hat{I}_{zk}$, vanish, but other interactions, such as homonuclear dipolar coupling, do not. That is to say, at cycle times $4n\tau$, with the internal Hamiltonian being proportional to $\hat{I}_z$, $\hat{\tilde{\mathcal{H}}}^{(0)}_{int}$ is zero:

$$\begin{aligned}\hat{\tilde{\mathcal{H}}}^{0}_{int} &\propto \int_0^{4\tau} dt\ \hat{U}_{rf}^{-1}(t)\hat{\mathcal{H}}_{cs}\hat{U}_{rf}(t) \\ &= 2\omega_{cs}[\hat{I}_z\tau + (-\hat{I}_z)\tau] = 0 \end{aligned} \tag{23}$$

Here ω_{CS} is a product of a constant (ΔB_{eff}) and the part of the chemical shift Hamiltonian that is a function of the real space angular variables θ and ϕ. We may think of observation at periodic cycle times $t = 4n\tau = nt_c$ as observation in the frame of $\hat{\rho}$.

7 THE DIPOLAR ECHO AND THE FIRST-ORDER QUADRUPOLAR ECHO

The above are the basic ideas behind the use of rf pulses to produce echoes in solids. With these ideas, it is possible to see how rf sequences may be tailored to average to zero a specific interaction, and leave other interactions for observation. Two other interactions that immediately come to mind are the homonuclear dipolar interaction and the first-order quadrupolar interaction. Both of these have interactions that are bilinear in spin operators (***Internal Spin Interactions and Rotations in Solids***). For example, the first-order quadrupolar interaction scales as

$$\hat{\mathcal{H}}_Q \propto \hat{I}^2 - 3\hat{I}_z^2 \tag{24}$$

and the two-body homonuclear dipolar interaction scales as

$$\hat{\mathcal{H}}_{DII} \propto \hat{\boldsymbol{I}}_1 \cdot \hat{\boldsymbol{I}}_2 - 3\hat{I}_{z1}\hat{I}_{z2} \tag{25}$$

A sequence that averages both of these interactions to zero at cycle time 3τ is $(\tau,\ 90^\circ_x, \tau, 90^\circ_y,\ \tau)$. The mechanics may be worked out by the reader, or one can refer to ***CRAMPS*** for an example of how this works. We must remind ourselves here that the condition for the production of an echo is that the initial signal be 'sharp' enough, and the reflecting wall 'hard' enough. This translates to the physical fact already alluded to that the magnitude of $\hat{\mathcal{H}}_{rf}$ must be larger than the magnitudes of the internal Hamiltonians being attacked by the rf. While this can be made generally true for dipolar interactions, it is not generally so for quadrupolar interactions, where in general the magnitude of $\hat{\mathcal{H}}_{rf}$ will be of the order of or smaller than $\hat{\mathcal{H}}_Q$. A case where the rf field is sufficiently larger than the quadrupolar interaction is that of aluminum metal, and Mehring has used this sequence to average the first-order quadrupolar interaction in this system to zero (see page 80 of Mehring[8]). These sequences are further discussed in ***CRAMPS***.

8 TRANSIENT NUTATIONS: A VARIANT

An interesting variant of an echo in a solid, meaning an internal Hamiltonian has been averaged to zero at the echo time, is that of the transient nutation[12] experiment, in which the spins of an ensemble of dipolar coupled spin-$\frac{1}{2}$ nuclei are 'nutated' (spun around) the x axis in the rotating frame by a strong rf field in the x phase. The field is turned off at intervals, and the magnetization along the y axis sampled, in a closely analogous way to a multiple pulse experiment, where the magnetization is sampled in the windows of the experiment where some internal Hamiltonian is averaged to zero. In this case, the dipolar Hamiltonian may be written as

$$\begin{aligned}\hat{\mathcal{H}}_D/\omega \equiv \hat{\mathcal{H}}_{zz} &= \hat{\boldsymbol{I}}_1 \cdot \hat{\boldsymbol{I}}_2 - 3\hat{I}_{z1}\hat{I}_{z2} \\ &\equiv -\tfrac{1}{2}(\hat{\boldsymbol{I}}_1 \cdot \hat{\boldsymbol{I}}_2 - 3\hat{I}_{x1}\hat{I}_{x2}) \\ &\quad +\tfrac{3}{2}(\hat{I}_{y1}\hat{I}_{y2} + 3\hat{I}_{z1}\hat{I}_{z2}) \\ &\equiv -\tfrac{1}{2}\hat{\mathcal{H}}_{xx} + \tfrac{3}{2}(\hat{I}_{y1}\hat{I}_{y2} + 3\hat{I}_{z1}\hat{I}_{z2}) \end{aligned} \tag{26}$$

The terms in $\hat{\mathcal{H}}_{xx}$, commuting with $\hat{I}_x$, the dominant interaction from the rf in the rotating frame, are secular. The other terms are nonsecular, do not commute with the major Hamiltonian, and therefore oscillate themselves out of sight. Under this sequence, therefore, the dipolar Hamiltonian is scaled by a factor of $\frac{1}{2}$, the chemical shift is averaged to zero, and for systems in which the shielding anisotropy is of order of magnitude of the dipolar interaction, e.g., $^{13}C-^{13}C$ pairs in which both shielding anisotropy and homonuclear dipolar coupling are about 3 kHz at fields of roughly 2.3 T, the dipolar coupling can be clearly dug out from under the combined dipolar shielding signal.

9 MULTIPLE QUANTUM COHERENCE

Further, with a bit of imagination, one can see that it might not be desirable to average a given interaction to zero, but to manipulate it in order to obtain information hitherto not available, e.g., counting of the number of spins in a small cluster. This subject is discussed in ***Multiple Quantum Coherence Imaging***, ***Multiple Quantum Coherence in Spin-1/2 Dipolar Coupled Solids*** and ***Multiple Quantum Coherences in Extended Dipolar Coupled Spin Networks***

10 RELATED ARTICLES

Average Hamiltonian Theory; CRAMPS; Dipolar Spectroscopy: Transient Nutations and Other Techniques; Echo-Planar Imaging; Internal Spin Interactions and Rotations in Solids; Line Narrowing Methods in Solids; Multiple Quantum Coherence Imaging; Multiple Quantum Coherence in Spin-1/2 Dipolar Coupled Solids; Multiple Quantum NMR in Solids; Rotating Solids; Quadrupolar Nuclei in Solids; Rotating Solids; Ultrasonic Irradiation and NMR.

11 REFERENCES

1. E. L. Hahn and D. E. Maxwell, *Phys. Rev.*, 1951, **82**, 748.
2. E. L. Hahn, *Phys. Rev.*, 1950, **80**, 580.
3. H. Y. Carr and E. M. Purcell, *Phys. Rev.*, 1954, **94**, 630.
4. T. C. Farrar and J. E. Harriman, *Density Matrix Formalism and its Applications in NMR Theory*, Farragut Press, Madison, WI, 1992.
5. R. D. Mattuck, *A Guide to Feynman Diagrams and the Many Body Problem*, 2nd edn., McGraw-Hill, New York, 1976, (reprinted by Dover, New York, 1992).
6. B. C. Gerstein and C. R. Dybowski, *Transient Techniques in NMR of Solids; An Introduction to the Theory and Practice*, Academic Press, Orlando, 1985.
7. M. Goldman, *Quantum Description of High-Resolution NMR in Liquids*, Oxford University Press, Oxford, 1988.
8. M. Mehring, *Principles of High Resolution NMR in Solids*, 2nd edn., Springer-Verlag, Berlin, 1983.
9. U. Haeberlen, *High Resolution NMR in Solids: Selective Averaging*, Academic Press, New York, 1976.
10. R. R. Ernst, G. Bodenhausen, and A. Wokaun, *Principles of Nuclear Magnetic Resonance in One and Two Dimensions*, Clarendon Press, Oxford, 1987.
11. A. Abragam, *Principles of Nuclear Magnetism*, Oxford University Press, Oxford, 1961.
12. C. S. Yannoni and R. D. Kendrick, *J. Chem. Phys.*, 1981, **74**, 747.

Biographical Sketch

Bernard C. Gerstein. *b* 1932. B.S. Purdue, 1953, Ph.D., 1960, Iowa State University, USA. Introduced to NMR by R. W. Vaughan. Faculty in Chemistry Iowa State University, 1962–present. Approximately 150 publications, with H. F. Franzen the text 'Rudimentary Thermodynamics', and with C. R. Dybowski, the book 'Transient Techniques in NMR of Solids; An Introduction to the Theory and Practice'. Research interests include the applications of solid state NMR to problems in the physics and chemistry of materials, fossil fuels, and heterogeneous catalysis.

Fullerenes and Related Molecules as Studied by Solid State NMR

Anita M. Orendt

Center for High Performance Computing, University of Utah, Salt Lake City, UT, USA

1	Introduction	1
2	History of Fullerene Discovery	1
3	Studies on Pure C_{60}	1
4	Studies on Pure C_{70}	3
5	Studies on Pure Higher Fullerenes	4
6	Studies on Nanotubes	4
7	Studies on the Intercalation Complexes of Fullerenes	5
8	Concluding Remarks	6
9	References	7

1 INTRODUCTION

The fullerenes, which by definition are polyhedral, closed cages of n carbons having twelve pentagonal and $(n/2 - 10)$ hexagonal faces, have been proposed to be important constituents of soots and interstellar dust. In addition to the more common single-walled closed cage compounds such as C_{60} and C_{70}, multiple-walled cage structures are also known, with onion-like structures of up to twenty concentric layers having been demonstrated to exist. Among the related compounds are nanotubes, or elongated fullerenes; single-walled and multi-walled, capped or open-ended varieties exist. There also exist endohedral or *incar*-fullerenes that have atoms or small molecules trapped inside the cages. In addition, there are intercalation complexes of fullerenes with atoms or molecules held in the interstitial crystal sites. The intercalation complexes with alkali metal atoms have attracted much attention, especially A_3C_{60} species with A=K, Rb, or Cs, as they are superconductors with transition temperatures, T_c, above 30 K. Several books and reviews on the chemistry and physics of fullerenes are given in the references[1–5] to provide further information on this interesting class of compounds.

Solid state nuclear magnetic resonance, NMR, studies beyond simple MAS spectra (magic angle spinning) on this class of compounds have been mainly limited to studies on C_{60}, C_{70}, and intercalation complexes of C_{60}, mainly due to the sample requirements of solid state NMR. These studies have provided insight into the structure, phase transitions, dynamics, and electronic properties of these compounds. There has been one solid state NMR study of the dynamics of C_{76} as well as a recent study on nanotubes. This article will focus on these studies by solid state NMR and the information they have provided.

2 HISTORY OF FULLERENE DISCOVERY

Until relatively recently it was an accepted fact that pure carbon existed in one of two allotropic forms: graphite and diamond, both having extended structures, the first with sp^2-hybridized carbons and the second with sp^3-hybridized carbons. This changed in 1984 when the first spectroscopic evidence of a molecular form of carbon was published.[6]

A mass spectrum of laser vaporized graphite published by researchers at Exxon showed the existence of a number of carbon clusters with the maximum intensity being C_{60}. About a year later Harold Kroto's group at Sussex University in the UK found conditions where C_{60} was produced nearly exclusively.[7]

Richard Smalley of Rice University proposed the familiar truncated icosahedral or soccer ball structure for C_{60}, shown in Figure 1a, and the name buckminsterfullerene. This was not the first time such a structure had been suggested, however, as there had been a number of theoretical studies on the structure, stability, and properties of this C_{60} structure prior to 1984.[8–10]

The next advance in the study of C_{60} came in 1990 when Krätschmer, Fostiropoulos, and Huffman developed a method to make macroscopic quantities of C_{60} and obtained infrared, IR, and X-ray powder diffraction spectra that supported the predicted structure.[11] The subsequent work on the isolation and purification of C_{60} also led to the isolation of the first of the higher fullerenes, C_{70}, shown in Figure 1b, in which a band of ten carbons is added around the equator of the C_{60} structure. The confirmation of the C_{60} and C_{70} structures followed shortly thereafter, with ^{13}C solution NMR unambiguously confirming the proposed structure of both compounds. C_{60} showed the expected single line at 143 ppm for all 60 carbons while C_{70}, with D_{5h} symmetry, showed five lines between 130 and 150 ppm in a 10 : 20 : 10 : 20 : 10 ratio as expected.[12] The assignment of these resonances to the five groups of carbon atoms, labeled C_a through C_e in Figure 1b, was confirmed by a solution ^{13}C INADEQUATE spectrum (Incredible Natural Abundance DoublE QUantum Transfer Experiment).[13] Continuing work led to the isolation of a number of other fullerenes, both smaller and larger than the dominant C_{60} compound.

Richard Smalley and Robert Curl Jr. from Rice University in Houston, Texas along with Harold Kroto from Sussex University in England were awarded the 1996 Nobel Prize in Chemistry for their work on the discovery of fullerenes.

3 STUDIES ON PURE C_{60}

Before going into details on the NMR studies of pure C_{60}, some information on the crystal habitat is necessary. At room temperature C_{60} is known to exist as an orientationally disordered face-centered cubic (fcc) structure. There is a phase transition, observed by both differential scanning calorimetry and x-ray powder diffraction, at about 250 K to a simple cubic (sc) with orientational order.

Solid state NMR provided the first measure of the bond lengths of C_{60} through the $^{13}C–^{13}C$ dipolar coupling in

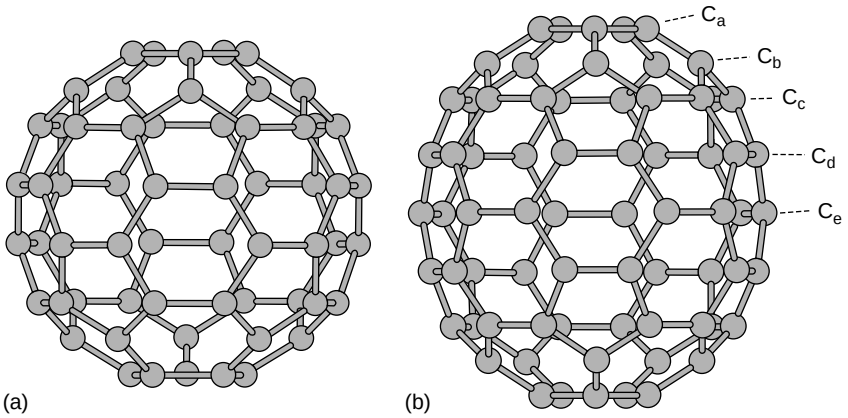

Figure 1 Structures of (a) C_{60} and (b) C_{70}. In C_{70}, carbons are labeled C_a–C_e, based on their chemical shifts

partially enriched C_{60}.[14] This was accomplished using the Carr-Purcell Meiboom-Gill pulse sequence, which selectively removes the chemical shift anistropy, CSA, while retaining the dipolar coupling. The measurement indicated that there were two different bond lengths, 1.45 Å and 1.40 Å, in a 2 : 1 ratio, consistent with the proposed structure. This result can be compared with a subsequent gas phase electron diffraction measurement of 1.458 Å for a bond joining two six-membered rings and 1.401 Å for the bond joining the five- and six-membered rings.[15] Similar distances have also been obtained by low temperature single crystal x-ray diffraction and by low temperature powder neutron diffraction.

In addition to the structural studies, work has been completed on the dynamics of C_{60}.[16,17] The static ^{13}C NMR powder patterns obtained as a function of temperature are shown in Figure 2. At room temperature a narrow line indicative of rapid, isotropic rotation is obtained. As the temperature is lowered a broad feature appears in the spectrum. Below 100 K the static spectrum is dominated with the broad anisotropic powder pattern characteristic of a molecule that is stationary on the NMR timescale, meaning that the correlation time for isotropic reorientation is large compared to the inverse of the static linewidth. There is no evidence of the 250 K phase transition from either the static or MAS spectrum. There is sometimes a small percentage of the material that is still motionally averaged as evidenced by the sharp peak superimposed on the broad CSA pattern. The intensity of this feature is a function of the purity of the sample and is believed to be due to molecules having low energy barriers to reorientation when they are near structural defects in the crystal structure due to the presence of impurities.

Additional information is obtained by looking at the T_1 relaxation times, generally obtained by saturation recovery methods, as a function of temperature, as shown in Figure 3.[17] In T_1 measurements a phase transition can be manifested as a discontinuity in the curve of T_1 versus temperature. This is the case in C_{60}. The T_1 data were fit to a model of going from essentially unhindered, rapid isotropic motion in the high temperature fcc phase to a reorientation restricted to jumping between symmetry related orientations in the low temperature sc form. Further analysis of the temperature dependence of the motion, using the fact that the dominant relaxation mechanism is the CSA, provided an activation barrier to rotation of about 5.9 J/mol in the fcc phase and from 17 to 25 J/mol in the sc form.

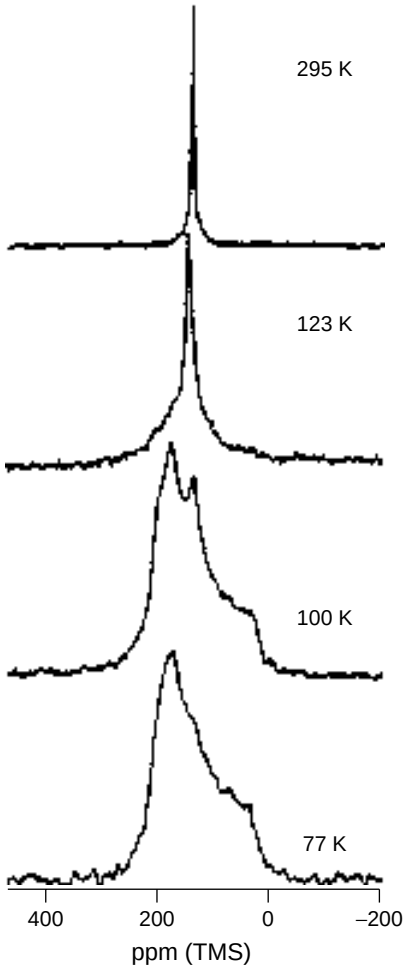

Figure 2 Static solid state ^{13}C NMR spectrum of C_{60} as a function of temperature. The spectra change from a lineshape indicative of rapid isotropic motion at 295 K to one of no molecular motion on the NMR timescale at 77 K. (Reproduced by permission of the American Chemical Society from Ref.[16])

The low temperature powder pattern also gives the principal components of the chemical shift tensor, which can be used to provide insight into the electronic structure. These have been measured to be 220, 186, and 40 ppm[16] (or 213, 182,

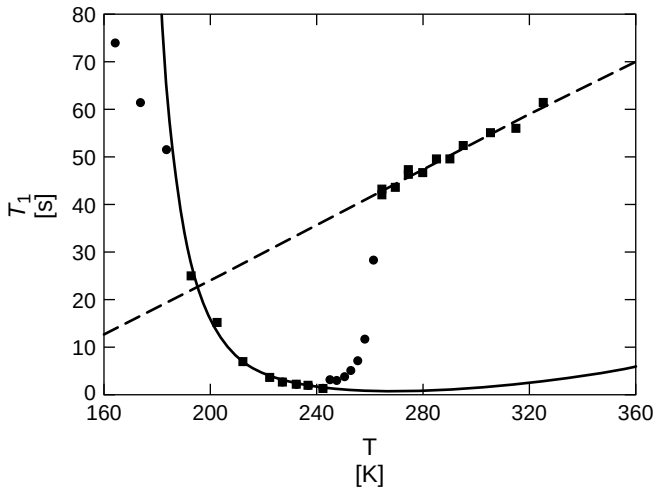

Figure 3 The temperature dependence of the ^{13}C T_1 relaxation time of solid C_{60} at a field strength of 9.39 T. The 260 K phase transition is responsible for the discontinuity in the curve. Squares are T_1 values obtained from a single exponential fit of the T_1 saturation recovery data; circles are the average of the two T_1 values obtained from a double exponential fitting. The solid line is the fit of the data for the sc phase between 193 and 243 K, based on a model of relaxation dominated by the CSA. The dashed line is the fit of the data above 263 K for the sample in the fcc phase. (Reproduced by permission of the American Physical Society from Ref.[17])

and 33 ppm).[17] These numbers are typical aromatic chemical shift tensor numbers with the δ_{33} component showing the characteristic shift to a higher value expected due to the strain of the five-membered rings. The principal values are similar to the values for the five-membered ring carbons in other aromatic systems, such as corannulene[18] (224, 177, and 6 ppm), acenaphthene[19] (213, 195, and 13 ppm), and pyracene[20] (202, 192, and 24 ppm). In contrast, the δ_{33} components for bridgehead carbons in six-membered ring compounds are usually less than 0 ppm, and in the case of coronene it is measured at −38 ppm for the innermost carbon.[18]

4 STUDIES ON PURE C_{70}

There are three solid state NMR studies, all published in 1993, that have measured the relaxation data, MAS spectra, and/or the static powder pattern as a function of temperature on samples of greater than 98% pure C_{70}.[21–23] While the basic dynamic interpretation of the spectra are consistent between these three reports, there are significant differences.

C_{70} has three known phases.[24] Above 330 K it exists in either an fcc or a hexagonal closed packed (hcp) structure with complete rotational disorder, similar to the room temperature phase of C_{60}. Between about 280 and 330 K the crystal structure is rhombohedral with the long axis directed essentially along the [111] crystal axis; rotational disorder exists perpendicular to this axis. A molecular dynamics simulation predicted that the motion in this phase is not pure uniaxial rotation about the long axis, but includes a precession of the long axis about this crystal axis.[25] Below 280 K the structure becomes monoclinic with orientational ordering; however, no details are known about the molecular orientation. It has also been determined that in order to obtain the equilibrium low temperature ordered phase, the crystal must be cooled extremely slowly (e.g., over a matter of many hours) from the high temperature phase through the lower temperature transition. If cooled quickly, as in sublimation, the two high temperature phases with their rotational freedom have been shown to persist until very low temperatures, even down to 10 K. Therefore, careful treatment of the sample is necessary to ensure knowledge of its phase.

NMR provides some evidence of the phase transitions. Upon increasing the temperature of a sample that has first been cooled slowly from 300 to 50 K, the MAS spectra as a function of temperature showed a small shift in the isotropic positions of several of the resonances at approximately 273 K and 323 K, consistent with the known phase transition temperatures.[24] The T_1 temperature dependence in one study[22] showed a deviation from the expected curve at about 280 K; in the other study[23] the T_1 measurements did not show any significant discontinuities at this phase transition temperatures.

There have been two static 1D NMR measurements as a function of temperature. In the first, by Blinc et al.,[21] the static lineshape was measured as a function of temperature from 450 to 50 K at a ^{13}C frequency of 67.89 MHz. There were two increases in the width of the static pattern as the temperature was lowered: from about 1 kHz above 300 K to nearly 3 kHz below 200 K with the full static linewidth of about 12 kHz being reached below 100 K. The spectra of the rhombohedral phase between 270 and 120 K were fit according to ordering of the sample along [111] crystallographic axis and the onset of uniaxial rotation with precession. Those between 120 and 50 K were fit as a gradual slowing of the uniaxial rotation, with the lowest temperature lineshape simulated as the overlap of five axially symmetric tensors. The lineshapes of these intermediate temperature spectra, however, were not the expected overlap of five axially symmetric patterns, and are not consistent, both in terms of spectral features and linewidths, with the experimental results of the other two studies. Maniwa et al.[22] also measured the 1D static powder pattern as a function of temperature between 340 and 77 K at a ^{13}C frequency of 65.5 MHz. From a single tensor fit of the 77 K spectrum the principal values were estimated to be 225, 200, and 25 ppm, values similar to those of C_{60}. The spectra at intermediate temperatures were simulated as five overlapping axially symmetric tensors using the above measured static principal values, adjusted to axial symmetry for the rotation about the long axis, and assuming the δ_{33} component is oriented perpendicular to the carbon cage. Therefore, the same tensor is averaged by a different angle, as the angle between the long axis and the δ_{33} component is different for each of the five inequivalent positions. There were no values for the measured anisotropy reported. The simulation was similar to the experiment, as can be seen in Figure 4, and differences were accounted for by the fact that the predicted precession of the long axis, which would lead to a further narrowing of the axially symmetric tensor, was not included in the simulation.

Tycko et al.[23] studied C_{70} with a slow spinning sideband intensity analysis between 320 and 230 K, a 2D MAS/CSA correlation experiment at 233 K, and a static 1D measurement

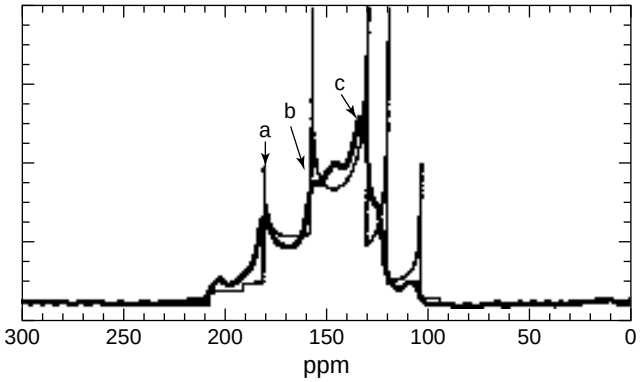

Figure 4 Observed (thick line) and simulated (thin line) ^{13}C static spectrum of C_{70} at 295 K at a frequency of 65.5 MHz. The simulation assumes five overlapping axially symmetric shift tensors based on static tensor components of 225, 200, 20 ppm, and angles of 38, 51, 78, 66, and 78° between the rotation axis and the δ_{33} component for carbons C_a–C_e, respectively. (Reproduced by permission of the Physical Society of Japan from Ref.[22])

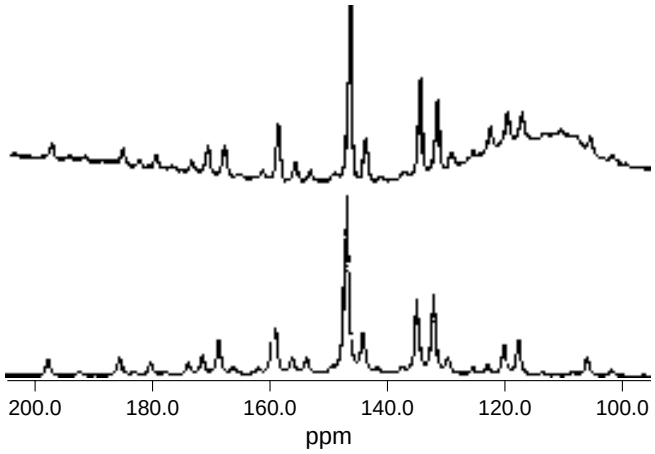

Figure 5 Slow spinning ^{13}C MAS NMR spectrum of C_{70} at 283 K and a spin rate of 1.2 KHz along with the simulated spectra using spinning sideband intensities from a Herzfeld-Berger analysis and information from a 2D MAS/CSA experiment. (Reproduced by permission of the American Institute of Physics from Ref.[23])

at 50 K. The 2D MAS/CSA experiment separates the individual powder patterns based in the 2D space by the isotropic chemical shift values. A representative spinning sideband pattern at 283 K, along with its simulation based on both a Herzfeld-Berger spinning sideband intensity analysis[26] and the values from the 2D experiment, are shown in Figure 5. From these simulations, the anisotropy (defined as $\Delta\sigma = \sigma_\perp - \sigma_\parallel$) of the five tensors at 230 K were reported as 162, 27, −42, −72, and −77 ppm for carbons C_a–C_e, respectively. In all cases the spectra are axially symmetric, indicative of the uniaxial rotation expected at this temperature. Based on a full anisotropy of 200 ppm for a static sample taken from the 50 K static pattern, the authors showed that the scaling of the anisotropy is consistent with that expected for uniaxial rotation about the long axis assuming the δ_{33} component is normal to the cage.

In summary, the variations in the ^{13}C NMR lineshape as a function of temperature from a sample of pure C_{70} are rich in information about the motional characteristics of the three known phases. The NMR studies give a consistent picture of the molecular motion first changing from anisotropic rotation to uniaxial rotation about the long axis, with a slight precession. This is followed by the transformation into the low temperature phase in which there is no molecular motion. However, the principal values of the five inequivalent carbons of C_{70} have not yet been obtained. Accurate tensor components for these five carbons should be obtainable from a 2D spectrum in which the CSA of individual carbons is separated by their isotropic values, provided that the experiment is performed below 100 K and that care is taken in the sample cooling procedure.

5 STUDIES ON PURE HIGHER FULLERENES

There is much less information, from any source, on the structure and dynamics of the larger fullerenes. For C_{76}, a single solid state NMR study exists.[27] The C_{76} molecule has a chiral D_2 structure calculated to have three distinct molecular axes of lengths 8.75, 7.50 and 6.54 Å. Solution NMR shows nineteen resonances in the range of 130–150 ppm. The solid state NMR lineshape gives evidence that at room temperature C_{76} also undergoes rapid, isotropic motion at room temperature, but as it is cooled there is no evidence of going first to uniaxial rotation as in C_{70}. Instead, the spectra indicate a relatively sharp transition between anisotropic rotation and a static molecule between approximately 170 and 135 K. The T_1 temperature dependence also showed a slight discontinuity in the range of 170 K; this may be evidence of a still unknown phase transition.

6 STUDIES ON NANOTUBES

Due to recent advancements in the procedures to make and purify nanotubes, samples of sufficient size and uniformity are now becoming available for study. The single walled nanotube (SWNT) structures can be thought of as a tube made from a single layer graphite sheet that has been rolled to form a tube; the ends can be open or closed with a semi-fullerene cap. Nanotubes are characterized by their diameters and their helicity, which is a measure of how the hexagons wind around the surface. Several representative structures of capped nanotubes with different helicities are given in Figure 6. Nanotubes can exhibit either semiconducting or metallic electronic properties depending on these two properties. The SWNT also self assemble into larger structures known as bundles or ropes; the manner of this assembly is also believed to affect the properties of the nanotube.

The first solid state NMR study of the CSA and T_1 relaxation behavior of a SWNT has very recently appeared in the literature.[28] Due to the manner of production of these structures, it is very important to either purify the samples to remove traces of paramagnetic metal catalysts that lead to extensive broadening of the powder pattern or to perform the synthesis with alternative catalysts. The reported static and MAS spectra of a SWNT sample with a diameter of 0.85 nm are given in Figure 7. The MAS has a single resolved peak at 124 ppm with a full width at half height of about

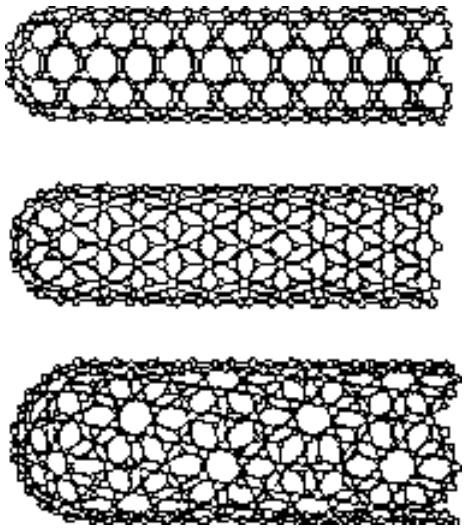

Figure 6 Sample structures of nanotubes of different diameters and helicity. (Reproduced by permission of Imperial College Press from Ref.[2], p. 33)

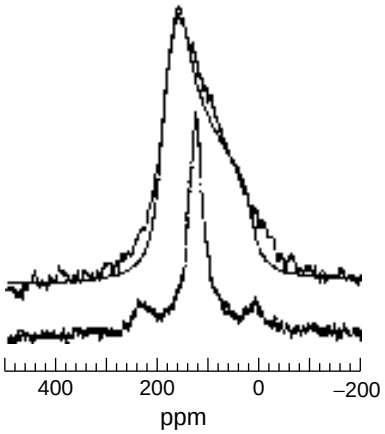

Figure 7 The static and MAS (at a spin rate of 11.7 KHz) solid state ^{13}C spectra of a nanotube of average diameter 0.85 nm. A fit of the static powder pattern to a single tensor is also shown. (Reproduced by permission of the American Association for the Advancement of Science from Ref.[28])

30 ppm; fitting the room temperature static pattern as a single tensor yielded the tensor principal values of 195, 160 and 17 ppm. These principal values again show the expected increase in the δ_{33} component associated with the strain of the non-planar environment. The T_1 relaxation behavior of this sample was best fit to a double exponential function with the slower relaxation component being attributed to tubes with metallic characteristics and the longer component due to tubes exhibiting semi-conducting behavior. However, both components showed the linear relationships with temperature expected for the Korringa relaxation (see discussion in next section) through the conducting electron band of metallic samples.

Further NMR studies on nanotubes should now follow as homogenous samples are becoming available in large enough quantities, allowing for a better understanding of the properties of these materials.

7 STUDIES ON THE INTERCALATION COMPLEXES OF FULLERENES

There are many examples of intercalation complexes of C_{60}. In the room temperature fcc structure of C_{60} there are two tetrahedral sites and one octahedral site per molecule with estimated radii of 1.1 and 2.1 Å, respectively. Both sites are large enough to hold most atoms and even small molecules.

The most widely studied group of intercalation complexes is the alkali fullerides, A_xC_{60}, ionic solids comprised of A^+ and C_{60}^{x-} ions. The $x = 1, 3, 4$, and 6 species have been isolated and characterized. Electronically, the lowest unoccupied molecular orbital (LUMO) of the parent C_{60} is triply degenerate. Therefore, both the neutral species with an empty LUMO and the C_{60}^{6-} ion with a full LUMO should be, and are, insulators. The others, with a partially full conduction band, are expected to have metallic behavior. However, no clear evidence of metallic behavior has been found in either the A_1 or A_4 species. The A_3 species have been shown to be conductors and superconductors,[29] with transition temperatures (T_c's) measured to be above 30 K.[30] These are among the highest T_c's known with the exception of the so-called "room temperature" copper oxide superconductors which have temperatures of about 150 K. For this reason the A_3C_{60} fullerides have attracted the most attention. A brief summary of the solid state NMR of A_3C_{60} follows; a more comprehensive treatment of the alkali fullerides, including details of the mechanisms of superconductivity, is referenced.[31]

Before going into details about the NMR results on these compounds, two effects of the conduction band on the NMR must be discussed. The first is the Knight shift, which is a shift in the resonance frequency observed in metals due to the hyperfine coupling of the nucleus to the conducting band electrons.[32] The measured resonance frequency is the sum of the chemical shift and the Knight shift. This electron-nuclear coupling also dominates the T_1 relaxation in these compounds. The linear relationship observed between the T_1 relaxation time and temperature in conducting systems is quantified by the Korringa[33] relationship, and is often reported as a plot of $(1/T_1T)$ versus T. Neither of these effects is observed in the superconducting state, leading to observable changes at T_c in plots of the temperature dependence of both the shift and the T_1 relaxation time.

The fcc structure of K_3C_{60}, as well as the other A_3C_{60} structures, is shown in Figure 8.[34] The most significant difference between this structure and that of pure C_{60} is that the C_{60} entities are no longer orientationally disordered, but are oriented with a hexagonal face directed towards the tetrahedral site, maximizing its size. A series of spectra of the A_3C_{60} compounds are shown in Figure 9. In the NMR of the alkali metal atoms, differentiation of the atoms in the tetrahedral and octahedral sites, as well as a splitting of the tetrahedral peak, is observed. The two tetrahedral peaks are believed to be due to crystal distortions and the splittings can be removed by going to higher temperatures. Diffraction studies have not shown any evidence of this distortion. The measured ^{13}C spectra show the effect of decreased motional freedom of the C_{60} ion as the size of the alkali metal increases (radii of the alkali ions are: K^+ 1.33 Å, Rb^+ 1.48 Å, Cs^+ 1.67 Å). In addition, the observed Knight shift is relatively small, with

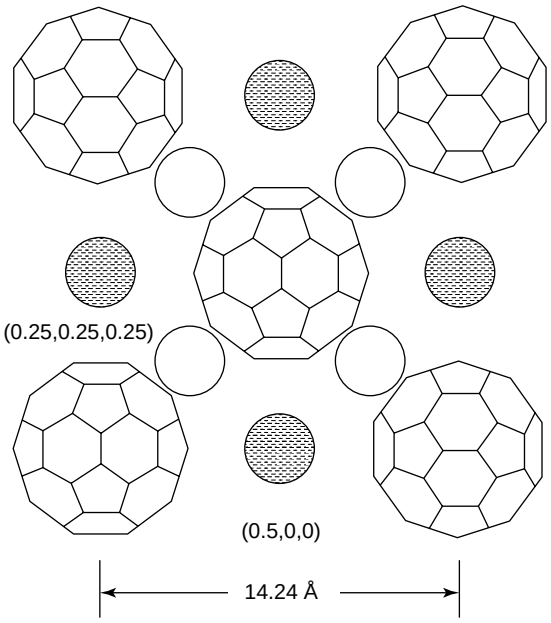

Figure 8 Structure of K_3C_{60} alkali fulleride. The open and hatched spheres represent the potassium at the tetrahedral and octahedral sites, respectively. (Reproduced by permission of the Nature Publishing Group from Ref.[34])

the sum of the Knight shift and any change in the chemical shift from neutral C_{60} being only 30–50 ppm. Most calculations of the expected Knight shift in these compounds are much larger. The temperature dependence of both the total shift (Knight and chemical) and the T_1 relaxation time are shown in Figure 10 for the case of Rb_2CsC_{60}, which has a T_c of about 30 K. All the plots show the expected changes at this temperature. Tycko et al.[35] has used the value of T_1T in the normal conducting state to make a rough estimation of the density of electronic states at the Fermi level (about 20 eV^{-1} per C_{60} ion). The Arrhenius behavior of the T_1 in the superconducting state was also used to obtain a measure of the electronic energy gap ($3T_c$ for K_3C_{60} and $4T_c$ for Rb_3C_{60}).

The above shows the important information on the structure and electronic properties of the alkali fullerides solid state NMR has provided. However, many questions about the structure and electronic properties remain unanswered. Also, contradictions in the experimental data still exist, and must be reconciled before the electronic behavior of this class of compounds can be understood.

8 CONCLUDING REMARKS

Solid state NMR has been shown to be a powerful tool in the study of the structure, phase transitions, dynamics, and electronic properties of the C_{60}, C_{70}, and several intercalation complexes of C_{60} and should continue to contribute to the study of these materials in the future. There still exist unresolved issues in the study of the alkali fullerides that solid state NMR can address. Higher fullerenes and nanotubes samples of sufficient size and purity (and uniformity in the case of nanotubes) are just now beginning to become available, and more solid state NMR studies probing into the structure and properties of these materials should follow. In addition, solution ^{3}He NMR studies of the endohedral or *incar*-fullerenes He@C_{60} and He@C_{70}, have shown how the helium atom can be used as a magnetic probe of the fullerene cage.[36] Variable temperature, solid state

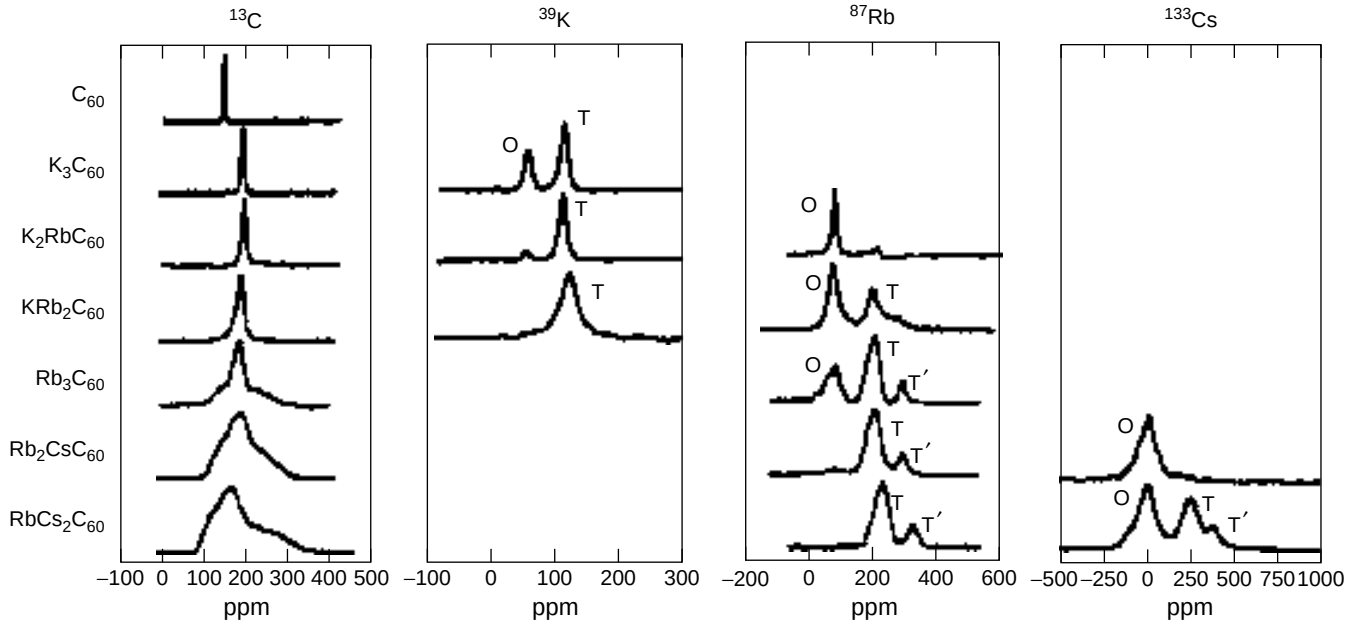

Figure 9 Static room temperature ^{13}C (referenced to TMS), ^{39}K, ^{87}Rb, and ^{133}Cs (all referenced to the free alkali ions) spectra for a series of A_3C_{60} compounds. Features of interest are the presence of multiple tetrahedral environments for the larger Rb and Cs ions, the anisotropy indicative of the lack of C_{60} rotation with the Cs ions, and the absence of a large Knight shift between C_{60} and any of the alkali fullerides. (Reproduced by permission of the American Physical Society from Ref.[31])

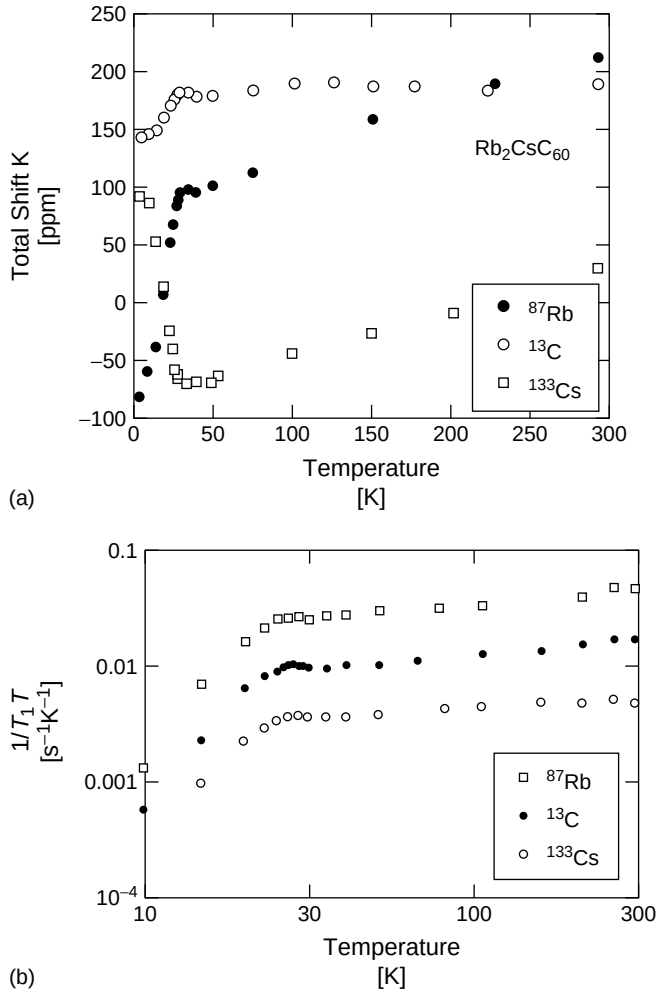

Figure 10 Knight shift (a) and T_1 (b) behavior as a function of temperature observed for Rb_2CsC_{60}, (T_c of about 30 K). All data is taken at a field strength of 8.8 T. The shifts for Rb in the figure are the center of mass of the two tetrahedral site resonances. The increasing chemical shift for Cs is believed to be due to a negative electron-nuclear hyperfine coupling. ((a) Reproduced by permission of the American Physical Society from Ref.[31]; and (b) Reproduced by permission of the American Physical Society from Ref.[37])

^{3}He NMR studies on these compounds should be of great interest.

9 REFERENCES

1. K. M. Kadish and R. S. Ruoff eds, 'Fullerenes Chemistry, Physics and Technology', Wiley-Interscience: New York, 2000.
2. R. Taylor, 'Lecture Notes on Fullerene Chemistry: A Handbook for Chemists', Imperial College Press: London, 1999.
3. H. Kuzmany, J. Fink, M. Mehring, and S. Roth eds, 'Physics and Chemistry of Fullerenes and Derivatives', World Scientific Publishing Co. Pte. Ltd.: New Jersey, 1995.
4. K. Prassides ed, 'Physics and Chemistry of the Fullerenes', NATO ASI Ser C., Vol. 443, Kluwer Academic Publishers: Boston, 1994.
5. G. S. Hammond and V. J. Kuck eds, 'Fullerenes: Synthesis, Properties, and Chemistry of Large Carbon Clusters', ACS Symposium Series 481, American Chemical Society: Washington, DC, 1992.
6. E. A. Rohlfing, D. M. Cox, and A. Kaldor, *J. Chem. Phys.*, 1984, **81**, 3322.
7. H. W. Kroto, J. R. Heath, S. C. O'Brien, R. F. Curl, and R. E. Smalley, *Nature*, 1985, **318**, 162.
8. E. Osawa, *Kagaku*, 1970, **25**, 854.
9. D. A. Bochvar and E. G. Gal'pern, *Proc. Acad. Sci., USSR*, 1973, **209**, 610.
10. R. A. Davidson, *Theor. Chim. Acta*, 1981, **58**, 193.
11. W. Krätschmer, L. D. Lamb, K. Fostiropoulos, and D. Huffman, *Nature*, 1990, **347**, 354.
12. R. Taylor, J. P. Hare, A. K. Abdul-Sada, and H. W. Kroto, *Chem. Commun.*, 1990, 1423.
13. R. D. Johnson, G. Meijer, J. R. Salem, and D. S. Bethune, *J. Am. Chem. Soc.*, 1991, **113**, 3619.
14. C. S. Yannoni, P. P. Bernier, D. S. Bethune, G. Meijer, and J. R. Salem, *J. Am. Chem. Soc.*, 1991, **113**, 3190.
15. K. Hedberg, L. Hedberg, D. S. Bethune, C. A. Brown, H. C. Dorn, R. D. Johnson, and M. deVries, *Science*, 1991, **254**, 410.
16. C. S. Yannoni, R. D. Johnson, G. Meijer, D. S. Bethune, and J. R. Salem, *J. Phys. Chem.*, 1991, **95**, 9.
17. R. Tycko, G. Dabbagh, R. M. Fleming, R. C. Haddon, A. V. Makhija, and S. M. Zahurak, *Phys. Rev. Lett.*, 1991, **67**, 1886.
18. A. M. Orendt, J. C. Facelli, S. Bai, A. Rai, M. Gossett, L. T. Scott, J. Boerio-Goates, R. J. Pugmire, and D. M. Grant, *J. Phys. Chem. A.*, 2000, **104**, 149.
19. R. J. Iuliucci, J. C. Facelli, D. W. Alderman, and D. M. Grant, *J. Am. Chem. Soc.*, 1995, **117**, 2336.
20. A. M. Orendt, N. K. Sethi, J. C. Facelli, W. J. Horton, R. J. Pugmire, and D. M. Grant, *J. Am. Chem. Soc.*, 1992, **114**, 2832.
21. R. Blinc, J. Dolinsek, J. Seliger, and D. Arcon, *Solid State Commun.*, 1993, **88**, 9.
22. Y. Maniwa, A. Ohi, K. Mizoguchi, K. Kume, K. Kikuchi, K. Saito, I. Ikemoto, S. Suzuki, and Y. Achiba, *J. Phys. Soc. Jpn.*, 1993, **62**, 1131.
23. R. Tycko, G. Dabbagh, G. B. M. Vaughan, P. A. Heiney, R. M. Strongin, M. A. Cichy, and A. B. Smith III, *J. Chem. Phys.*, 1993, **99**, 7554.
24. G. B. M. Vaughan, P. A. Heiney, D. E. Cox, J. E. Fischer, A. R. McGhie, A. L. Smith, R. M. Strongin, M. A. Cichy, and A. B. Smith III, *Chem. Phys.*, 1993, **178**, 599.
25. M. Sprik, A. L. Cheng, and M. L. Klein, *Phys. Rev. Lett.*, 1992, **69**, 1660.
26. J. Herzfeld and A. Berger, *J. Chem. Phys.*, 1980, **73**, 6021.
27. Y. Maniwa, K. Kume, K. Kikuchi, K. Saito, I. Ikemoto, S. Suzuki, and Y. Achiba, *Phys. Rev. B*, 1996, **53**, 14196.
28. X.-P. Tang, A. Kleinhammes, H. Shimoda, L. Fleming, K. Y. Bennoune, S. Sinha, C. Bower, O. Zhou, and Y. Wu, *Science*, 2000, **288**, 492.
29. A. F. Hebard, M. J. Rosseinsky, R. C. Haddon, D. W. Murphy, S. H. Glarum, T. T. M. Palstra, P. Ramirez, and A. R. Kortan, *Nature*, 1991, **350**, 600.
30. T. T. M. Palstra, O. Zhou, Y. Iwasa, P. E. Sulewski, R. M. Fleming, and B. R. Zegarski, *Solid State Commun.*, 1995, **93**, 327.
31. C. H. Pennington and V. A. Stenger, *Rev. Mod. Phys.*, 1996, **68**, 855.
32. W. D. Knight and S. Kobayashi, in 'Encyclopedia of Nuclear Magnetic Resonance', eds D. M. Grant and R. K. Harris, John Wiley & Sons: Chichester, 1996, Vol. 4, p. 2672.
33. C. P. Slichter, 'Principles of Magnetic Resonance', 3rd edition, Springer-Verlag: New York, 1992, page 151–157.
34. P. W. Stephens, L. Mihaly, P. L. Lee, R. L. Whetten, S.-M. Huang, R. Kaner, R. Deiderich, and K. Holczer, *Nature*, 1991, **351**, 632.

35. R. Tycko, G. Dabbagh, M. J. Rosseinsky, D. W. Murphy, A. P. Ramirez, and R. M. Fleming, *Phys. Rev. Lett.*, 1992, **68**, 1912.
36. M. Saunders, H. A. Jimenez-Vazquez, R. J. Cross, S. Mroczkowski, D. I. Freedburg, and F. A. L. Anet, *Nature*, 1994, **367**, 256.
37. V. A. Stenger, C. H. Pennington, D. R. Buffinger, and R. P. Ziebarth, *Phys. Rev. Lett.*, 1995, **74**, 1649.

Biographical Sketch

Anita M. Orendt, *b* 1958. B. S. 1980, Chemistry, University of Pittsburgh; Ph. D., 1987, Physical Chemistry, University of Utah. Postdoctoral work with Professor David M. Grant, University of Utah, 1987–1999. Assistant Professor of Chemistry (half-time), Westminster College of Salt Lake City, 1992–1994. Staff Scientist for Molecular Sciences, Center for High Performance Computing, University of Utah, 1999–present. Approximately 40 publications on measurement of chemical shift tensors. Research Interests: measurement and calculations of chemical shift tensors, especially in polycyclic aromatic hydrocarbons and in strained systems.

HETCOR in Organic Solids

Douglas P. Burum

Bruker Instruments, Inc., Billerica, MA, USA

1	Introduction	1
2	Methods for Obtaining Heteronuclear Correlation in Solids	1
3	Theory of Solids HETCOR	2
4	Experimental Considerations	4
5	Typical Results	5
6	Modified Versions of Solids HETCOR	5
7	Conclusions	6
8	Related Articles	6
9	References	6

1 INTRODUCTION

During the past few years, multidimensional experiments — 2D, 3D, etc.—have come into widespread use in high-resolution (liquid state) NMR (see ***Multidimensional Spectroscopy: Concepts***). Perhaps the most obvious advantage of this class of experiments is the possibility of correlating various spectral features. For example, COSY can be used to correlate chemically shifted peaks on the basis of *J* couplings (see ***COSY Two-Dimensional Experiments*** and ***COSY Spectra: Quantitative Analysis***), NOESY on the basis of the NOE effect (see ***NOESY***) and HETCOR on the basis of heteronuclear *J* couplings (see ***Heteronuclear Shift Correlation Spectroscopy***). A second important advantage is the ability to deconvolute overlapping resonance peaks by spreading them out in several dimensions. This can be of tremendous importance when studying very large molecules such as proteins.

A smaller number of multidimensional experiments—almost all of them 2D—have been introduced for the analysis of rigid solids. Examples include separated local field,[1] 2D chemical exchange,[2] and wideline separation spectroscopy (WISE).[3] In this article, solids HETCOR[4] is discussed. Solids HETCOR provides *het*eronuclear *cor*relations based on direct, 'through-space' interactions (dipole-dipole coupling; see ***Internal Spin Interactions and Rotations in Solids***). Since it can remove the overlap between adjacent resonances, solids HETCOR is also possibly the most powerful method available for accurate determination of proton chemical shifts in organic solids.

In addition, solids HETCOR is not especially difficult to implement. Generally speaking, almost any spectrometer capable of performing CP MAS (see ***Cross Polarization in Solids***, ***Magic Angle Spinning***, ***Rotating Solids*** and ***Cross Polarization in Rotating Solids: Spin-1/2 Nuclei***), 2D NMR and CRAMPS (see ***CRAMPS***) can be readily configured to perform solids HETCOR. In general, solids HETCOR can be applied to the correlation of any two nuclear species, so long as it is possible to transfer magnetization from one species to the other. In order to simplify the discussion, however, HETCOR will be discussed in this article in reference to the correlation of ^{1}H and ^{13}C chemical shifts.

2 METHODS FOR OBTAINING HETERONUCLEAR CORRELATION IN SOLIDS

As with any 2D experiment, solids HETCOR is composed of four basic parts—preparation, evolution, mixing and detection. Proton magnetization is created during the preparation period, and then the ^{1}H spins are allowed to precess at a rate determined by their chemical shifts. This is followed by a mixing period, during which polarization is transferred from the ^{1}H spins to nearby ^{13}C spins, and finally a detection period during which the ^{13}C FID is recorded. Typically, the sample is rotated at the magic angle throughout the entire experiment (see ***Magic Angle Spinning***; ***Rotating Solids***).

The preparation and detection parts of the HETCOR experiment are straightforward. The preparation consists of a single 90° pulse on the protons, and the detection part consists of ^{13}C signal detection during CW ^{1}H decoupling, exactly as in a standard CP MAS experiment. On the other hand, the evolution and mixing periods tend to be somewhat complicated, due to the need to suppress ^{1}H–^{1}H homonuclear dipolar coupling and ^{1}H–^{13}C heteronuclear dipolar coupling.

One approach is to spin the sample very rapidly at the magic angle, so that all dipolar coupling is suppressed.[5] If this can be accomplished, pulse sequences typical of high resolution 2D NMR can then be applied. Unfortunately, this is only practical for highly mobile solids, such as lipids, membranes and suspensions. Nevertheless, it can be a very powerful technique for these classes of materials.

In the so-called WISE experiment,[3] the ^{1}H–^{1}H dipolar coupling is allowed to be active during the evolution period. The WISE evolution period is just a time incremented delay immediately following the preparation 90° ^{1}H pulse, and the result is a 2D spectrum that correlates ^{13}C chemical shifts with ^{1}H–^{1}H dipolar broadened powder patterns. An example of a WISE spectrum is given in Figure 1.

In order to correlate ^{1}H chemical shifts with ^{13}C chemical shifts in rigid solids, some sort of multiple pulse technique must be employed to suppress dipole interactions during the evolution and mixing periods. During the ^{1}H evolution, both the ^{1}H–^{1}H homonuclear dipolar interaction and the ^{1}H–^{13}C heteronuclear dipolar interaction must be suppressed. The most commonly suggested methods include 'windowed' CRAMPS pulse sequences such as MREV-8 with simultaneous CW decoupling of the ^{13}C spins[6,7] and windowless multiple pulse sequences applied to both the ^{1}H and ^{13}C spins simultaneously.[8] Of these, the most successful method appears to be the simultaneous application of BB-24 to the ^{1}H spins and BLEW-24 to the ^{13}C spins.[4] It is interesting to note that a 48 pulse version of this pulse sequence, based on BLEW-48, has been tried, but without any improvement of the resulting spectrum.[9]

During the mixing time, the ^{1}H–^{1}H homonuclear dipolar coupling must be suppressed in order to avoid loss of correlation specificity due to homonuclear spin diffusion. However, the ^{1}H–^{13}C heteronuclear dipolar coupling must be retained to allow cross polarization (see ***Cross Polarization in Solids***). A number of methods have been suggested to accomplish this, including Hartmann–Hahn cross polarization applied with a very brief cross-polarization time,[6,7] Hartmann–Hahn cross polarization using CRAMPS line-narrowing sequences such as MREV-8 applied simultaneously to the ^{1}H and ^{13}C spins,[7] transfer of magnetization via multiple quantum states

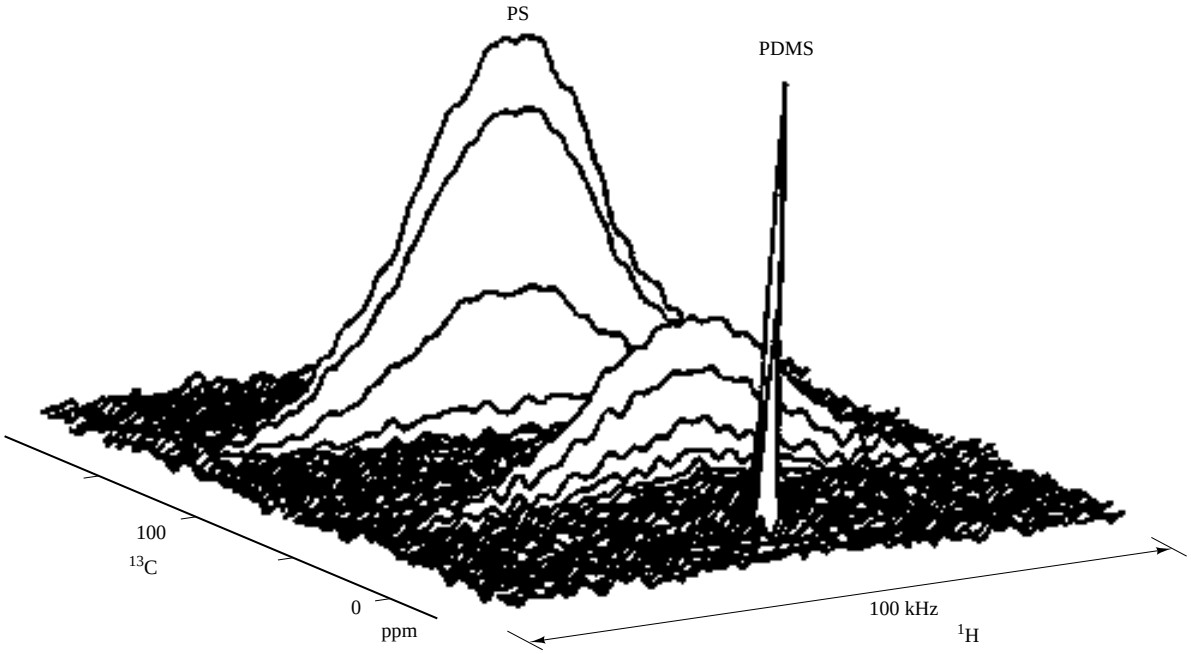

Figure 1 WISE spectrum of polystyrene block copolymer with poly(dimethylsiloxane) (PS-b-PDMS) (50:50 mol%). The reduced linewidth in the ^{1}H dimension indicates the much higher mobility of the PDMS, which does not induce significant mobility in the PS. (Reproduced by permission of Schmidt-Rohr et al.[3])

using ^{1}H CRAMPS followed by simultaneous ^{1}H and ^{13}C 90° pulses[7] and Hartmann–Hahn cross polarization using frequency switched Lee–Goldberg irradiation.[4] The most successful method appears to be cross polarization by simultaneous application of the windowless isotropic mixing (WIM) pulse sequence to the ^{1}H and ^{13}C spins[8].

3 THEORY OF SOLIDS HETCOR

The basic solids HETCOR pulse sequence is shown in its most common form in Figure 2. In order to understand the effectiveness of the BLEW-24/BB-24 combination in suppressing the heteronuclear dipolar interaction, it is useful to apply average Hamiltonian theory (see ***Average Hamiltonian Theory***), and to consider the effect on the average Hamiltonian when 90° rf pulses are applied simultaneously to both the proton and carbon spins. The secular part of the heteronuclear dipolar Hamiltonian can be expressed as

$$\hat{\mathcal{H}}_{\mathrm{D}}^{(Z)} = \sum_{i,j} A_{i,j} \hat{I}_{i,z} \hat{S}_{j,z} \tag{1}$$

If the rf amplitudes are adjusted such that the Hartmann–Hahn condition is satisfied, the proton and carbon 90° pulse

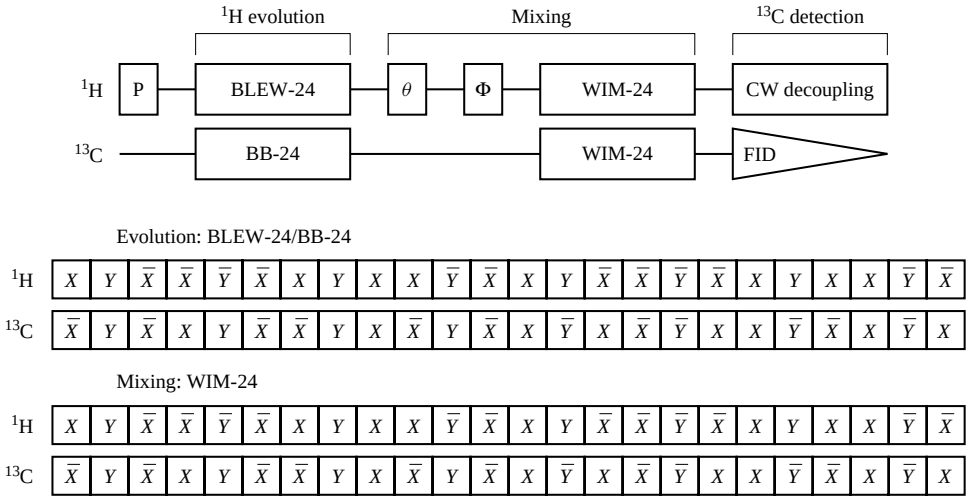

Figure 2 Basic solids HETCOR pulse sequence. In its most common form, the fully windowless BLEW-24 sequence is applied to the ^{1}H spins and the fully windowless BB-24 sequence is applied to the ^{13}C spins during the evolution period, and the fully windowless WIM-24 sequence is applied simultaneously to both spin systems during the mixing period

widths will be equal. During the simultaneous pulse, the dipolar Hamiltonian in the toggling reference frame becomes time dependent. Assuming that the rf phases for both protons and carbons lie along the Y axes in the doubly rotating frame, this time-dependent Hamiltonian can be expressed as

$$\hat{\tilde{\mathcal{H}}}_{\mathrm{D}}^{(Z)}(t) = \hat{\mathcal{H}}_{\mathrm{D}}^{(Z)} \cos^2 \Omega + \hat{\mathcal{H}}_{\mathrm{D}}^{(X)} \sin^2 \Omega + \hat{\mathcal{H}}_{\mathrm{D}}^{(ZX)} \sin 2\Omega \quad (2)$$

where Ω varies from zero to 90° during the pulse, and the cross term may be written

$$\hat{\mathcal{H}}_{\mathrm{D}}^{(ZX)} = \sum_{i,j} \tfrac{1}{2} A_{i,j} (\hat{I}_Z \hat{S}_X + \hat{I}_X \hat{S}_Z) \quad (3)$$

By simple integration on time, the zeroth-order average heteronuclear dipolar Hamiltonian for this individual, simultaneous pulse is then given by

$$\hat{\tilde{\mathcal{H}}}_{\mathrm{D}}^{(0)} = \tfrac{1}{2}\hat{\mathcal{H}}_{\mathrm{D}}^{(Z)} + \tfrac{1}{2}\hat{\mathcal{H}}_{\mathrm{D}}^{(X)} + \frac{2}{\pi}\hat{\mathcal{H}}_{\mathrm{D}}^{(ZX)} \quad (4)$$

Table 1 Phase Cycling During the Heteronuclear Correlation Experiment[a,b,c,d]

Scan	1	2	3	4	5	6	7	8
P	X	−X	X	−X	X	−X	X	−X
^{13}C WIM-24[e]	X	X	−Y	−Y	−X	−X	Y	Y
Receiver	X	−X	−Y	Y	−X	X	Y	−Y

[a]For all scans, θ = X, ϕ = 63°(−Y).
[b]All pulses except ϕ are 90° pulses.
[c]The overall ^{1}H phase of the initial pulse P, the BLEW-24 evolution period and the first mixing pulse θ are incremented by 90° after each experiment in order to obtain phase sensitive spectra by the TPPI method.
[d]Reprinted by permission of Burum et al.[4]
[e]^{13}C WIM-24 refers to the overall phase shift of the WIM-24 sequence applied to the ^{13}C nuclei.

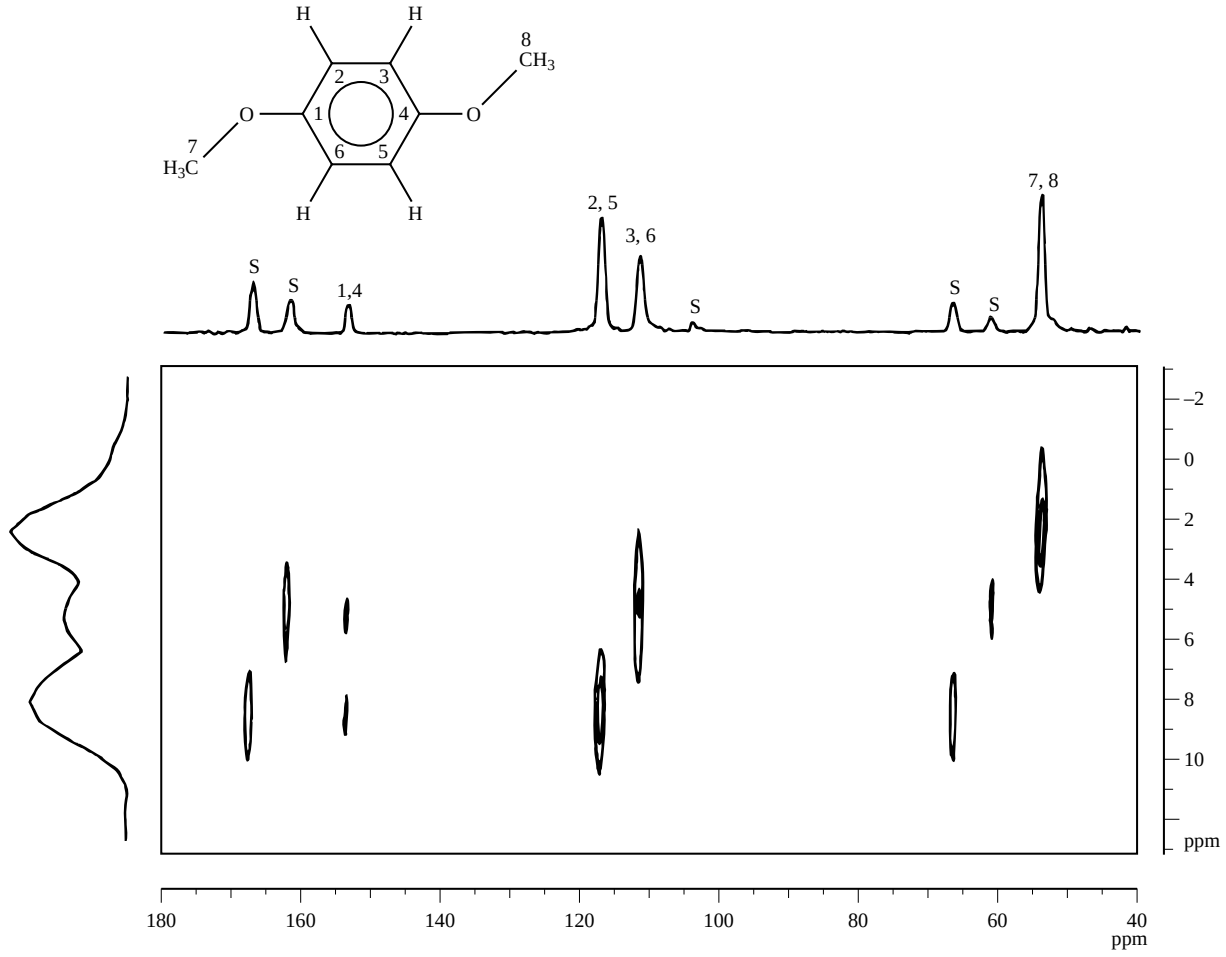

Figure 3 Solids HETCOR spectrum of *p*-dimethoxybenzene. The spectra shown above and to the left are projections of the 2D data, and are similar to what could be expected from 1D CRAMPS (^{1}H) and CP MAS (^{13}C). (Reproduced by permission of Burum et al.[4])

The BLEW-24/BB-24 sequence is entirely composed of simultaneous pulses of this type. Therefore, the zeroth-order average Hamiltonian for the sequence as a whole is simply a sum of terms of the form given in equation (4). If the terms are listed in order, one finds that the 'pure' terms cancel for each 6-pulse group, and the 'mixed' terms cancel over each 12-pulse group. The first 12 pulses of BB-24 therefore form a unit for which all zeroth-order dipolar terms vanish. By reflecting this subcycle to form BB-24, all the first-order terms are caused to vanish as well due to symmetry.

A similar analysis can be applied to WIM-24, with the result that the chemical shifts and homonuclear dipolar couplings of both the ^{1}H and ^{13}C spins vanish, and the zeroth-order average Hamiltonian for the heteronuclear dipolar coupling is given by the isotropic expression

$$\tilde{\hat{\mathcal{H}}}_{\mathrm{D}}^{(0)} = \tfrac{1}{3}[\hat{\mathcal{H}}_{\mathrm{D}}^{(X)} + \hat{\mathcal{H}}_{\mathrm{D}}^{(Y)} + \hat{\mathcal{H}}_{\mathrm{D}}^{(Z)}] \qquad (5)$$

4 EXPERIMENTAL CONSIDERATIONS

Phase cycling according to the scheme given in Table 1 is typically added to the basic experiment shown in Figure 2 to suppress potential artifacts. The 180° phase alternation of the initial $\pi/2$ pulse P is an implementation of the well-known 'spin temperature alternation' method for eliminating receiver dead time effects. The cycling of the overall ^{13}C WIM-24 phase is used to eliminate any quadrature images which might otherwise result from an improperly balanced receiver.

In order to obtain purely absorptive, phase sensitive 2D spectra, time proportional phase incrementation (TPPI)[10] can be introduced. For example, the overall ^{1}H phase of the first half of the experiment, including the first pulse, the entire evolution period and the first mixing pulse, may be advanced by 90° after each experiment.

Typical experimental conditions for solids HETCOR include a MAS spinning speed of approximately 4000 Hz, rf levels adjusted to obtain a 90° pulse on both the ^{1}H and ^{13}C channels of between 4.0 and 4.5 μs, and cross polarization using 1 or 2 WIM cycles. Optimum experimental performance may be obtained by carefully adjusting both the ^{1}H and ^{13}C rf channels of the spectrometer according to standard CRAMPS tune-up procedures[11,12] for perfect phase and flip angle and minimum phase transient. However, this is often not necessary in order to obtain good quality spectra, since the result of nonideal tuning is primarily seen in artifacts that lie either on the axes or along the center line in the ^{1}H dimension.

In order to avoid center line artifacts without degrading ^{13}C resolution, it is useful to switch the ^{1}H rf frequency during the pulse sequence, such that it lies to one side of the ^{1}H

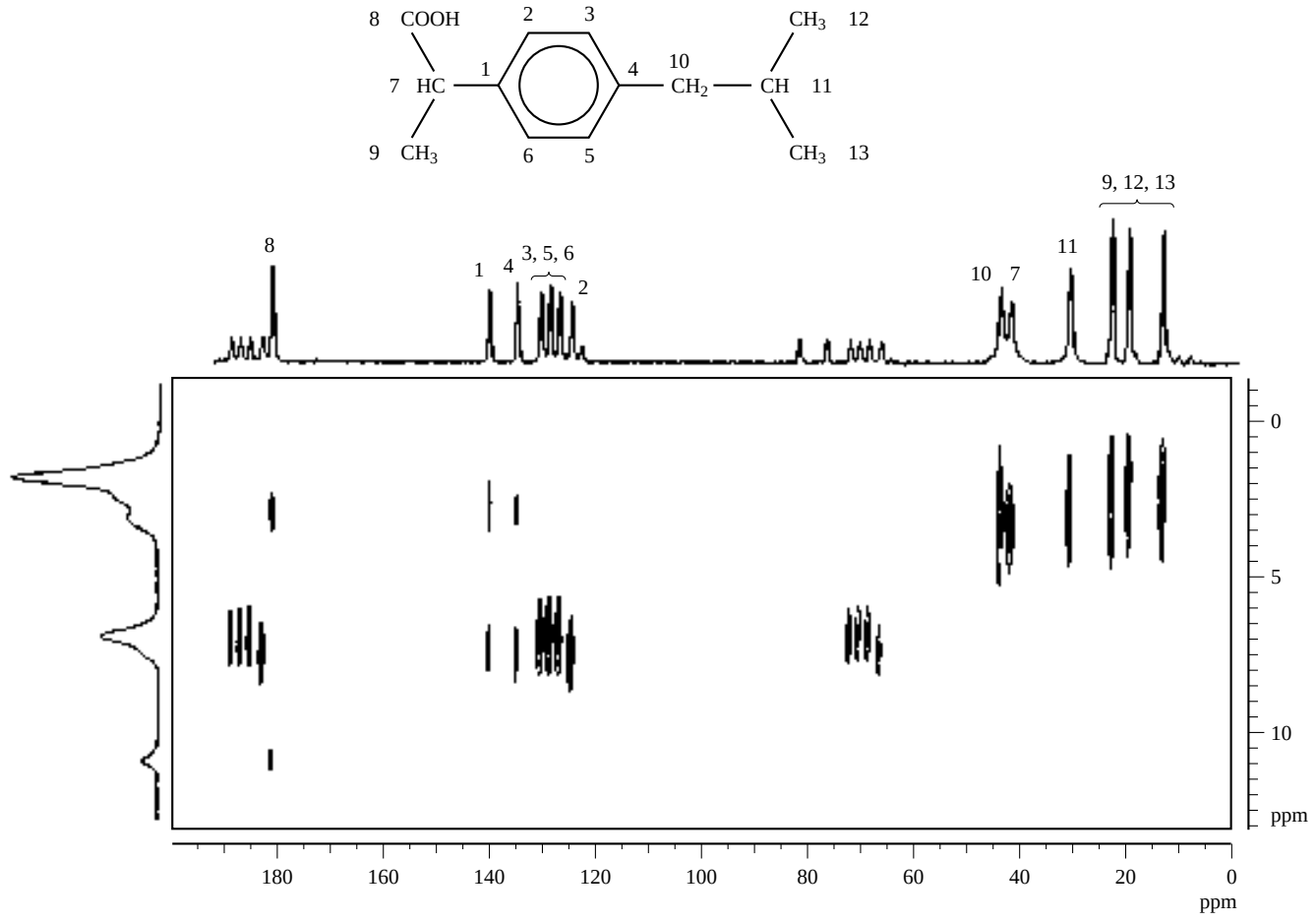

Figure 4 Solids HETCOR spectrum of ibuprofen. Note the long-range coupling information provided for nonprotonated carbons. Note also the precise proton chemical shift information available, due to the deconvolution of resonance overlaps in the carbon dimension. The 1D spectra above and to the left of the 2D spectrum are the ^{13}C CP MAS spectrum and the ^{1}H BR-24 CRAMPS spectrum of the same compound

spectrum during the preparation and evolution periods, but then is switched to the center of the ^{1}H spectrum during the mixing and detection periods.

5 TYPICAL RESULTS

A typical solids HETCOR spectrum of a small organic molecule, *p*-dimethoxybenzene, is shown in Figure 3. Not only do correlations from directly bonded $^{1}H–^{13}C$ pairs appear, but also couplings between nonprotonated carbons and more distant protons. This type of long-range correlation is also present in the solids HETCOR spectrum of ibuprofen shown in Figure 4. Both spectra illustrate the very powerful resolving power for ^{1}H chemical shifts using this method, where separate ^{1}H chemical shift values can be obtained for each line in the spectrum. In this figure, a standard ^{13}C CP MAS spectrum and a BR-24 CRAMPS spectrum have been presented in place of the usual projections. It is clear from the BR-24 ^{1}H spectrum that full deconvolution of the lines within the aromatic and aliphatic regions is not possible using CRAMPS alone.

A typical solids HETCOR spectrum of a polymer, PPO [poly(2,6-dimethyl-*p*-phenylene oxide)], is shown in Figure 5. Long range couplings between nonprotonated carbon spins and their nearest-neighbor protons have been used in this case to reveal information about the polymer chain conformation.[13] In general, useful solids HETCOR spectra can be obtained from most organic solids for which a well resolved ^{13}C CP MAS spectrum can be measured.

As a general rule, correlation peaks for directly bonded $^{13}C–^{1}H$ pairs are always visible in solids HETCOR experiments, and peaks for nonprotonated ^{13}C spins separated by two bonds from one or more ^{1}H spins are also normally present. Although the interaction is 'through space', not 'through bond', the two bond rule for long range correlations seems to be a good general guideline. When a ^{13}C spin is directly bonded to a proton, there is an interference effect that greatly reduces the interaction between that carbon and other, more distant protons. Therefore, only one strong peak is normally obtained from protonated carbons. Nonprotonated carbons, on the other hand, are often coupled to more than one proton with roughly equal strengths, in which case more than one peak can be obtained for the same carbon. Thus, nonprotonated carbons often provide some of the best structural information from solids HETCOR.

6 MODIFIED VERSIONS OF SOLIDS HETCOR

The BLEW-24/BB-24 version of solids HETCOR was introduced in 1991. Since then, a few modifications have been proposed for specific applications. In one modification,

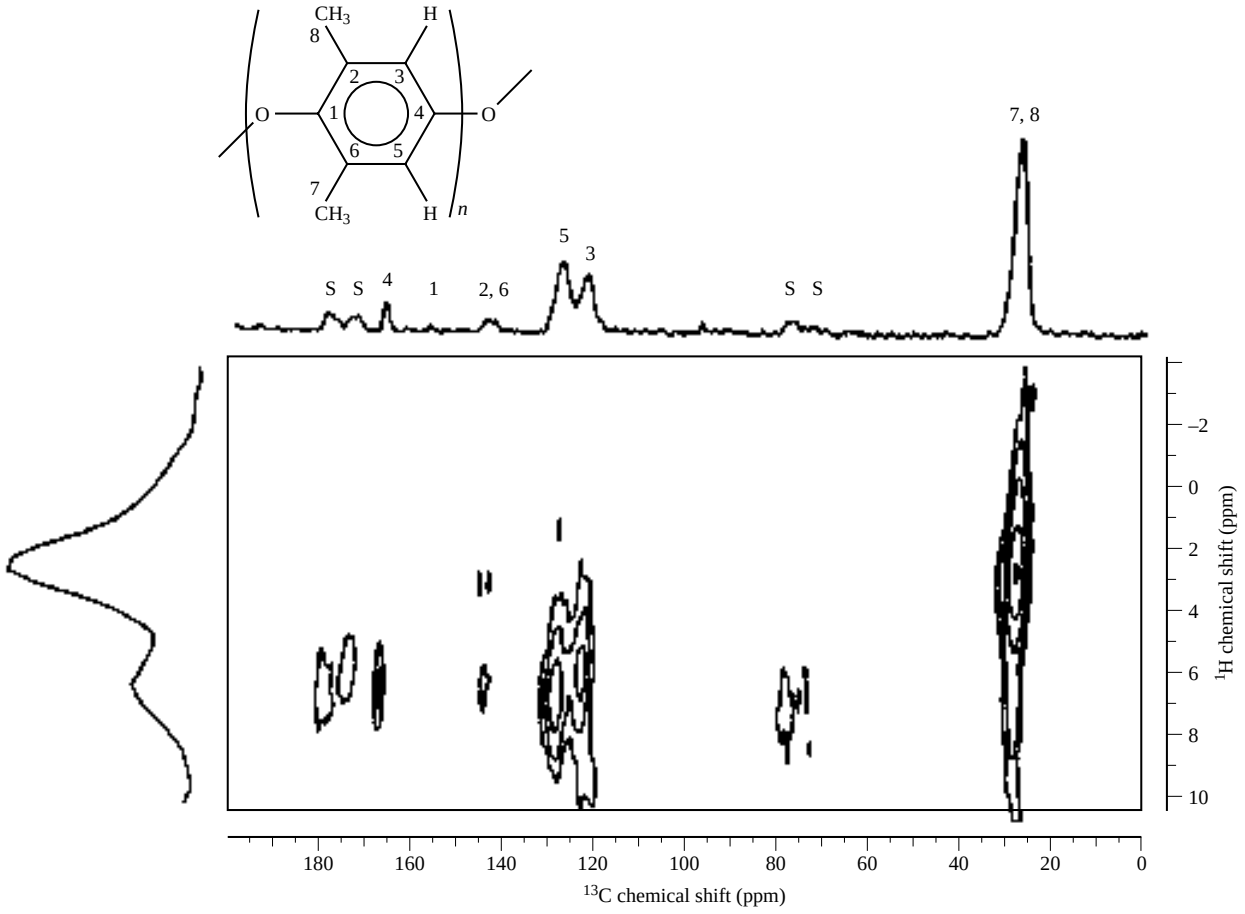

Figure 5 Solids HETCOR spectrum of poly(2,6-dimethyl-*p*-phenylene oxide) (PPO). Long range couplings from this spectrum have been used to reveal information about the polymer chain conformation. (Reprinted by permission of Burum et al.[4])

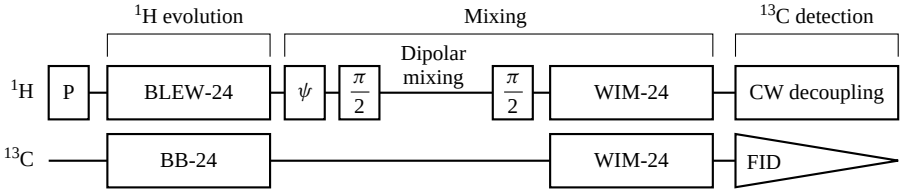

Figure 6 Solids HETCOR pulse sequence with additional ^{1}H spin diffusion mixing time

introduced by Li et al.,[14] a short delay is added between the evolution and mixing times as shown in Figure 6 to allow limited nuclear spin diffusion among the protons. This approach can be used to bypass the interference effect mentioned above and obtain correlations between protonated carbons and more distant protons. Using this technique, Li et al. were able to obtain evidence of polymer blending.

In another modified version of solids HETCOR proposed by Bronnimann et al.,[15] the mixing time is extended to enhance signals from weak, long range couplings. Normally, the mixing time in solids HETCOR is limited to a fraction of a rotor period because the cross-polarization process during WIM is reversed by the magic angle spinning. In the experiment suggested by Bronnimann et al., one or two simultaneous ^{1}H and ^{13}C WIM cycles are applied during the first portion of the rotor period, and then the ^{13}C magnetization is stored along the Z axis while WIM is applied only to the ^{1}H spins for the remainder of the rotor period. The sequence is then repeated for several additional rotor cycles, giving an effective cross-polarization period that is much longer than normal. This technique tends to be limited to samples with weakly coupled protons, since magnetization from protons with strong homonuclear dipolar coupling is difficult to maintain for long times during WIM irradiation. Nevertheless, Bronnimann et al. were able to obtain interesting results for ^{1}H–^{31}P correlation in bone using this method.

7 CONCLUSIONS

The BLEW-24/BB-24 version of solids HETCOR is relatively easy to implement, and can provide useful data for a wide variety of experimental samples. Typically, any sample for which well resolved ^{13}C CP MAS spectra can be obtained will be a good candidate for solids HETCOR. Heteronuclear correlations, obtained primarily from nonprotonated carbons, can provide useful information for structure determination and peak assignments. Deconvolution of the ^{1}H resonances in the carbon dimension allows ^{1}H chemical shifts to be determined to an accuracy unequalled by any other technique. Modified experiments have been proposed that can extend the method to detect longer range correlations, and it can be expected that more enhancements, including 3D techniques, will be forthcoming in the future.

8 RELATED ARTICLES

CRAMPS; Cross Polarization in Solids; Dipolar and Indirect Coupling Tensors in Solids; Heteronuclear Shift Correlation Spectroscopy; Internal Spin Interactions and Rotations in Solids; Magic Angle Spinning; Multidimensional Spectroscopy: Concepts.

9 REFERENCES

1. A. C. Kolbert, M. H. Levitt, and R. G. Griffin, *J. Magn. Reson.*, 1989, **85**, 42.
2. H. W. Spiess, *Chem. Rev.*, 1991, **91**, 1321.
3. K. Schmidt-Rohr, J. Clauss, and H. W. Spiess, *Macromolecules*, 1992, **25**, 3273.
4. D. P. Burum and A. Bielecki, *J. Magn. Reson.*, 1991, **94**, 645.
5. C. W. B. Lee and R. G. Griffin, *Biophys. J.*, 1989, **55**, 355.
6. P. Caravatti, G. Bodenhausen, and R. R. Ernst, *Chem. Phys. Lett.*, 1982, **89**, 363.
7. E. Roberts, S. Vega, and R. Griffin, *J. Am. Chem. Soc.*, 1984, **106**, 2506.
8. P. Caravatti, L. Braunschweiler, and R. R. Ernst, *Chem. Phys. Lett.*, 1983, **100**, 305.
9. C. E. Bronnimann, C. F. Ridenour, D. R. Kinney, and G. E. Maciel, *J. Magn. Reson.*, 1992, **97**, 522.
10. R. R. Ernst, G. Bodenhausen, and A. Wokaun, *Principles of Nuclear Magnetic Resonance in One and Two Dimensions*, Clarendon Press, Oxford, 1987, p. 340.
11. U. Haubenreisser and B. Schnabel, *J. Magn. Reson.*, 1979, **35**, 175.
12. D. P. Burum, M. Linder, and R. R. Ernst, *J. Magn. Reson.*, 1981, **43**, 463.
13. A. Bielecki, D. P. Burum, D. M. Rice, and F. E. Karasz, *Macromolecules*, 1991, **24**, 4820.
14. S. Li, D. M. Rice, and F. E. Karasz, *Macromolecules*, 1994, **27**, 2211.
15. C. E. Bronnimann, private communication.

Biographical Sketch

D. P. Burum. *b* 1952. B. S., Harvey Mudd College, 1974; Ph.D., California Institute of Technology (advisor R. W. Vaughan), 1979. Postdoctoral Assistant under R. R. Ernst 1979–80. Joined Bruker Instruments as an applications specialist in solid state NMR in 1982. Currently Bruker USA national product manager for analytical NMR. Approx. 25 publications. Research interests center around development of coherent averaging pulse techniques, including CRAMPS, two-dimensional HETCOR, spectral editing, etc.

Heteronuclear Decoupling in Solids

A. K. Khitrin and B. M. Fung

University of Oklahoma, Norman, OK, USA

&

G. McGeorge

Bristol-Myers Squibb, New Brunswick, NJ, USA

1 Introduction 1
2 Physical Picture of Decoupling 2
3 TPPM and Other Decoupling Sequences for Solids 3
4 Discussion 6
5 Related Articles in Volumes 1–8 8
6 References 8

1 INTRODUCTION

Sensitivity and resolution are two of the major factors for the success of various classes of NMR experiments. Increased resolution allows one to be more confident of the results of spectral analyses, which may be highly important for the analysis of polymorphism in organic systems, for example. The peak area of a given resonance is a constant under given experimental conditions and improved resolution increases the peak height, which correspondingly also increases sensitivity. A factor of two reduction in linewidth produces an associated four-fold reduction in collection time to obtain the same signal to noise ratio under identical collection conditions. Degraded resolution may also distort principal shielding values determined from static powder patterns.[1]

The mechanisms which impact resolution are numerous, and vary depending upon whether one is dealing with rigid or mobile materials. In this article we will be following the development of resolution enhancement within crystalline solids and to a lesser extent liquid-crystals. Conformational variability, isotropic and anisotropic magnetic susceptibility, shielding anisotropy, dipolar interactions with heteronuclei, and motional modulation all impact the absolute linewidth of a system and were discussed by VanderHart et al.[2]

1.1 Historical Perspective of Decoupling

Over the years it has been possible to perform complicated coherent manipulations on nuclear spin systems using modern NMR spectrometers, so that undesirable line-broadening interactions can be effectively "turned off," while interactions carrying useful information remain intact or only scaled. One of the most important ways to perform decoupling, or average such interactions, is to apply an external radio-frequency (rf) field. The earliest implementation of this idea was proposed by Bloch for heteronuclear decoupling[3] of dipolar interactions. Here one type of nucleus is irradiated with a continuous wave (CW) rf field to average out scalar or dipolar interactions between nuclei of different types. The application of broadband noise decoupling by Ernst,[4] in addition to the earlier introduction of the Fourier transform technique[5,6] led to the fast development of ^{13}C NMR spectroscopy.

We will be considering systems of two spin species, abundant nuclei I and rare nuclei S. The problem of concern is how to decouple rare nuclei from abundant ones by completely averaging all interactions between S and I, allowing one to sensitively probe various S spin properties. The concentration of rare nuclei is supposed to be so small that all interactions between spins S can be neglected. In liquids, anisotropic interactions, such as direct dipole-dipole interactions, are averaged by fast molecular motions. The only interactions of practical importance that survive the time-averaging process are isotropic chemical shifts and scalar spin-spin interactions, or J-couplings. Though the latter may add very useful information to the NMR spectra of liquids, the homonuclear J-couplings between spins I are usually too small to produce a noticeable effect on heteronuclear decoupling. Neglecting these interactions creates a crucial simplification for the analysis, since the problem is reduced to the dynamics of only two spins, one spin S coupled to another spin I. When spin I is irradiated at exact resonance by a CW rf field of sufficient strength, ideal decoupling can be achieved. However, the presence of different chemical shifts does not allow the resonance condition to be satisfied simultaneously for all I spins, making it necessary to use more complicated broadband decoupling schemes without applying excessive decoupler power. A general theoretical analysis was given by Waugh,[7] who showed that decoupling will be effective over a certain bandwidth if the net precessional angle of a spin I is insensitive to offsets within this bandwidth. Later, an extension of this theory to systems of arbitrary spins I was made.[8] Experimentally, very efficient broadband decoupling sequences for liquids, such as MLEV-16,[9] WALTZ-16,[10] GARP,[11] and adiabatic frequency sweep[12] have been introduced and are widely used now. The development of the broadband decoupling techniques for liquids is described in Volume 3[13] (see **Decoupling Methods,** Volume 3).

1.2 Decoupling for Solids and Liquid Crystals

Although our analysis will be quite general, we will consider ^{1}H as the abundant (I) and ^{13}C as the rare nuclei (S), which is the most common case in studies of organic solids. Unlike liquids, one must consider extended networks of interactions within solids and liquid crystals. Of most importance to us are the dipolar couplings arising from the abundant I nuclei. Their range is about 100 kHz for solids and 10 kHz for liquid crystals. However, it is not just the strength of the dipolar interactions that makes these systems completely different from liquids, but the complicated concerted dynamics of a large number of spins that cannot be accurately described by analytical methods or by computer simulations. At present, computers can handle less than a dozen coupled spins 1/2, which is not enough to model a three-dimensional solid structure. Analytical approaches, such

as the average Hamiltonian theory of Waugh,[14] provide a description in terms of a small parameter ε, which is a ratio of the magnitude of the interaction (in frequency units) and the frequency with which this interaction is modulated in order to achieve averaging. The perturbative theoretical approaches give results in the form of series expansions in ε. At $\varepsilon \ll 1$ the first non-vanishing term of such an expansion can be considered as an effective, or average Hamiltonian. In practice, if this condition could be met, there would be no problem with good decoupling in solids with a CW rf decoupling field. However, experimentalists are usually limited by the strength of the rf field ($\gamma B_2/2\pi$) to about 100 kHz, and it is desirable to get good decoupling when $\varepsilon \sim 1$. Moreover, even if the average Hamiltonian could be calculated with high accuracy, it is not easier to calculate spin dynamics with this Hamiltonian than with initial dipolar interactions. Therefore, at best, such average Hamiltonians could be used only for qualitative estimates. Even with these drawbacks, the average Hamiltonian theory remains the best analytical tool that supports a design of homo- and heteronuclear decoupling sequences.

For liquid crystals, the order parameter is very sensitive to rf heating[15] and it is necessary to use relatively low decoupling power ($\gamma B_2/2\pi \leq 20$ kHz). Therefore, many broadband decoupling sequences have been developed for the study of ^{13}C NMR of liquid crystals.[16–19] At the same time, CW irradiation with high power (50–100 kHz) had remained the main method for decoupling in solids for many years, even though several decoupling sequences for solids had been proposed.[1,20] These new methods were not universally utilized and it was the advent of the two-pulse phase modulation (TPPM) scheme[21] by Bennett et al., which brought significant attention to alternate decoupling schemes for solid-state NMR experiments. With this sequence it was now possible to simply and routinely decouple better than with CW irradiation. The interest brought around with this sequence sparked a resurgence of articles discussing factors that impact decoupling,[22] enhanced theories or models of decoupling, new decoupling schemes[23–29] and applications utilizing these alternate schemes.[30,31]

This may have also been a result of the fact that hardware developments were proceeding exceedingly fast. More high field spectrometers were in operation ($\geq$9.4 Tesla), MAS spinners were reaching 24 kHz and can now exceed 45 kHz and decoupler fields could exceed a nutation frequency, $\nu_1 \geq$ 200 kHz. These hardware considerations alone necessitated a better understanding of decoupling mechanisms. Vander-Hart and Campbell[22] extensively described the variations in ^{13}C CW-decoupled linewidths as a function of decoupler frequency, amplitude and MAS frequency. In particular they showed that, because of the existence of proton chemical shift anisotropy, the amplitude for maintaining a fixed resolution (in ppm) at different B_0, and a fixed MAS frequency, is proportional to $\sqrt{B_0}$. Thus higher fields require even higher levels of CW decoupling. This is the requirement successfully circumvented by using the 'second-averaging' strategies like TPPM discussed later.

2 PHYSICAL PICTURE OF DECOUPLING

One way to consider the problem of decoupling in solids is to analyze the dynamics of the ^{13}C spin in the presence of the time-dependent field $h(t)$ created by the surrounding protons

$$h(t) = \sum_{j>0} b_{0j} I_{jZ}(t) \tag{1}$$

where the index 0 is reserved for a single ^{13}C nucleus, b_{ij} is the dipolar interaction constant, and I_{jZ} is the z-component of the spin of the proton j. The time dependence of the z-components of the proton spins reflects an effect of the homonuclear proton–proton interaction and rf decoupling sequence. The lineshape of ^{13}C peaks are determined by the dephasing of the ^{13}C spin in the local dipolar fields created by surrounding protons. If, as in the case of liquids, there is practically no interactions between protons, a simple train of 180° pulses for protons would periodically change the sign of $h(t)$. This would lead to complete refocusing of the ^{13}C magnetization and, therefore, to ideal decoupling. However, internal dynamics of the proton spins (flip-flops) along with the time dependence arising from shielding anisotropy creates additional time dependence of $h(t)$, making this simple decoupling scheme ineffective.

When the number of neighboring protons is large, the static distribution of the local fields is close to Gaussian. Then, the Anderson-Weiss theory[32,33] can be applied to analyze this problem, and the ^{13}C FID signal $G(t)$ can be expressed in terms of the time autocorrelation function for the local field $G(t) = \langle h(t)h(0)\rangle$, where $h(t)$ is given by equation (1). In dimensionless units, when $\langle h^2(0)\rangle = 1$, the FID signal is

$$G(t) = \exp\left[-\int_0^t (t-\tau)g(\tau)\,\mathrm{d}\tau\right] \tag{2}$$

The goal of decoupling is to extend the decay time of $G(t)$ as much as possible, but the problem is that there is no good recipe for calculating the autocorrelation function $g(\tau)$. Nevertheless, by assuming a simple model form of this function, one can qualitatively analyze the situation and come to the following conclusion:[25] the decoupling efficiency of a direct modulation of $h(t)$ by rf irradiation of protons is higher than that resulting from coherent averaging of the dipolar interactions. This leads to a practical consideration for building efficient decoupling sequences for solids: one should use conditions near the CW irradiation mode, which gives the fastest modulation rate at a given rf power, and should use only a small fraction of the available rf power for additional averaging.

The second way to consider the decoupling problem is to try to analyze the average Hamiltonian. As it was mentioned above, there is little hope that at $\varepsilon \sim 1$ a quantitative description can be obtained, but this approach can reveal some useful qualitative trends. We will start with the Hamiltonian in the rotating frame for the ^{1}H (I) and ^{13}C (S) spins expressed in angular frequency units

$$H = H_{\mathrm{rf}} + \sum_{j>0} \delta_j I_{jZ} + H_{IS} + H_{II} \tag{3}$$

H_{rf} is the interaction of the spin system with the rf decoupling pulses, δ_j is the resonance frequency of the jth proton relative to the decoupler frequency, H_{IS} is the dipole–dipole interactions between ^{13}C spin and surrounding protons:

$$H_{IS} = \sum_{j>0} 2b_{0j}\, S_{0Z}\, I_{jZ} \tag{4}$$

H_{II} is the dipole–dipole interaction between the proton spins

$$H_{II} = \sum_{i>j>0} b_{ij}(2I_{iZ}I_{jZ} - I_{iX}I_{jX} - I_{iY}I_{jY}) \quad (5)$$

The chemical shift terms of the S spins and the $I-I$ and $I-S$ scalar couplings are omitted for the sake of simplicity.

Since the system is supposed to be irradiated only near the resonance frequency of the abundant spins I, the only term of the Hamiltonian that contains the spin operator for the rare spin S and, therefore, directly affects its dynamics is H_{IS}. It describes the interaction of the ^{13}C spin with the local field $h(t)$. For a CW decoupling field, the term $H_{\rm rf}$ in equation (3) is equal to $-\omega_{\rm rf}I_x$, where $\omega_{\rm rf}$ is the amplitude of the rf decoupling field (its on-resonance circular polarized component).

To consider the effect of modulation on decoupling, it is convenient to use a new tilted frame. This frame is established by rotations about the y-axis in each of the proton spin subspaces at angles $\theta_j = \text{arctg}\,(\delta_j/\omega_{\rm rf})$ (Figure 1). In this frame each of the proton spins experiences an action of the effective field $\omega_j = (\delta_j^2 + \omega_{\rm rf}^2)^{1/2}$ directed along the new x-axis. H_{IS} is partially averaged by the effective fields, and the non-averaged part of the heteronuclear interactions, $H_{IS}^{(1)}$, is determined by a projection of the z-component of the proton spin onto ω_j or new x-axis. Then, the average Hamiltonian in the tilted frame can be rewritten as

$$H^{(1)} = -\sum_{j>0} \omega_j I_j + H_{IS}^{(1)} + H_{II} \quad (6)$$

where

$$H_{IS}^{(1)} = \sum_{j>0} 2b_{0j} \sin\theta_j S_{0Z} I_{jX} \quad (7)$$

The effective field also produces some averaging effect on H_{II}. For example, in the limit of high $\omega_{\rm rf}$ its secular part becomes $-(1/2)\ H_X$, where H_X has the same form as H_{II} with x and z indices exchanged. However, a more detailed description of the homonuclear interactions is difficult because of the large number of protons involved.

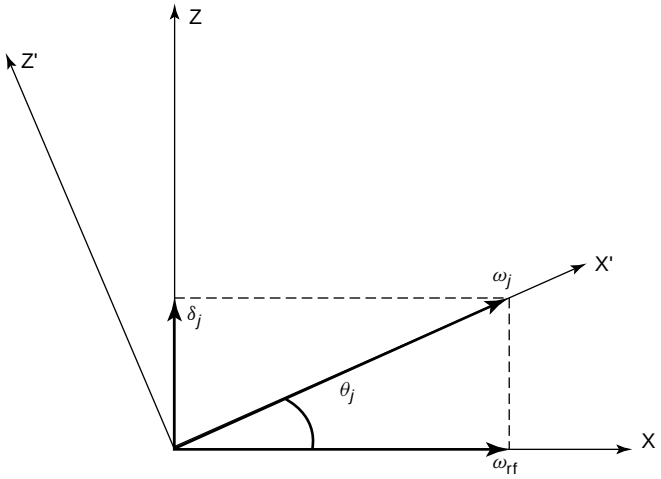

Figure 1 The tilted frame. (Reproduced from Ref.[25] by permission of the American Physical Society)

The residual heteronuclear interaction [equation (6)] can be further suppressed by averaging the x-components of the proton spins in the tilted frame. Since all the protons have the same y-axis direction in this frame, it is possible to arrange a resonance in the rotating frame that will flip the x-components of the proton spins by applying a time-dependent field in the y-direction. A simple way to do this is to periodically modulate the phase of the applied rf field. If the amplitude of the phase modulation is small, $\phi(t) \ll 1$, the effect is equivalent to an extra field which is perpendicular to the effective fields. Then, the Hamiltonian (equation (6)) changes to

$$H^{(1)} = -\omega_j I_j - \omega_{\rm rf}\phi(t) I_Y + H_{IS}^{(1)} + H_{II} \quad (8)$$

Using this analysis, one can see that the TPPM decoupling sequence[21] has an effect of second averaging, where a stepwise phase modulation makes the first and strongest harmonic of $\phi(t)$ to be in resonance with the effective fields.[19,21,23] To confirm this idea, a study of the performance of the TPPM decoupling sequence for a liquid sample as a function of the decoupler frequency offset was made.[25] The results showed that good decoupling (second averaging) is achieved when the resonance condition in the rotating frame is exactly matched.

As in the case of $H_{\rm IS}$, the averaging of $H_{IS}^{(1)}$ is complicated by distribution of the resonance frequencies ω_j in the rotating frame. One of the sources is the dispersion of the proton resonance frequencies (chemical shifts and associated anisotropies) in the laboratory frame. Another source of the ω_j distribution is the inhomogeneity of the rf field. Because the field induced by the phase-modulation should be large enough to excite the whole spectrum in the rotating frame, its amplitude should not be less than the rf inhomogeneity of the probe. In some sense, the proton dipolar field is also a source of such a distribution. The analysis described above suggests that it is possible to improve the decoupling by arranging an efficient averaging of the longitudinal (with respect to the effective fields) components of the proton spins for a relatively broad range of the effective fields. More broadband excitation in the rotating frame and, therefore, better decoupling can be achieved by using several forms of modulation of the rf field. These sequences will now be discussed.

3 TPPM AND OTHER DECOUPLING SEQUENCES FOR SOLIDS

3.1 TPPM

Introduction of the TPPM heteronuclear decoupling sequence[21] resulted in significant improvement of resolution in CPMAS experiments on a routine basis. The experimental scheme is shown in Figure 2, whereby, after the standard cross-polarization (CP) period, the protons are irradiated by a sequence of consecutive pulses of duration τ_p, and with phases alternating between the two values $-\phi/2$ and $\phi/2$. With experimental optimization, the flip angle corresponding to τ_p is usually slightly less than π, and the modulation angle ϕ is in the range $10-50°$.

Since it is extremely difficult to analyze the corresponding spin dynamics, especially in the presence of MAS, a computer simulation for a simple model, CH_2 group, was

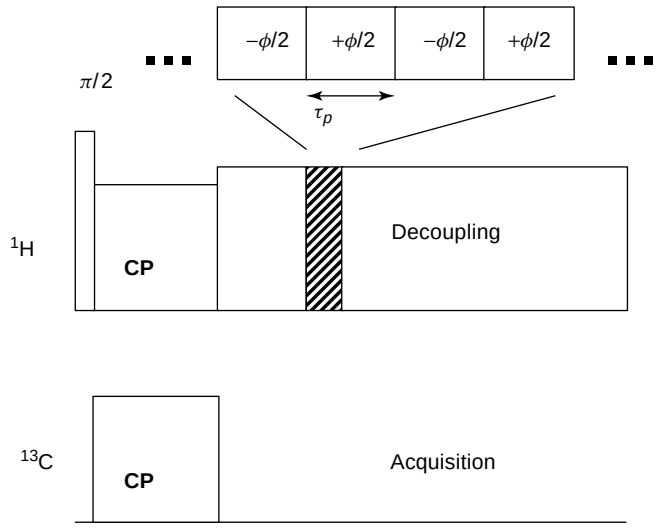

Figure 2 Scheme of the CPMAS experiment with the TPPM decoupling sequence

performed.[21] Though it could not give a quantitative description of real systems, the results of simulations confirmed some of the experimental observations: the optimal phase-modulation angle decreases with higher spinning speeds and the relative improvement over CW irradiation increases as the rf power is increased.

Another simple theoretical model, which allows the simulation of spin dynamics for TPPM and other phase-modulated sequences has been proposed.[28] The model consists of the pair of spins, S and I, with the I-spin coupled to a thermal I-spin bath. A spin-diffusion superoperator describes the coupling to this bath. The strong points of this model are that (1) the corresponding spin-diffusion rate constant can be independently measured in an experiment and (2) the calculation complexity is significantly reduced since the large number of protons in the system can be treated as an averaged diffusion coefficient. Therefore, this approach has a potential of providing a semi-quantitative description. Its application to simulate the performance of the TPPM sequence for the whole two-dimensional map of parameters τ_p and ϕ gave good agreement with experimental measurements.

Examples of the enhanced decoupling by TPPM are commonplace in the literature for ^{13}C, with a few examples being observed for other heteronuclei. Figure 3 shows an example of applying TPPM to a natural abundance ^{15}N sample of creatinine hemisuflate [no 1, no as] obtained from Aldrich. In this particular case TPPM removed the necessity of determining the exact proton resonance frequency, as a direct consequence of the increased bandwidth which allows one to decouple all protons effectively. This may be highly important for nitrogen since the associated protons can possess high variability in their chemical shifts.

3.2 TPFM and FMPM

Gan and Ernst introduced a set of modifications of the TPPM sequence.[23] The modified sequences used a two-pulse frequency modulation (TPFM) scheme, instead of the phase modulation of TPPM, and combinations of frequency and phase modulation (FMPM). If the x-axis of the rotating frame is directed along the main decoupling rf field, the phase modulation effectively creates a time dependent field in the y-direction of the rotating frame. The frequency modulation creates a time dependent field in the z-direction. A comparison between TPFM and TPPM showed that they have the same performance, i.e., the important factor is the presence of an additional perpendicular field, regardless of its direction, which can create a secondary precessional direction in the effective field. Moreover, the FMPM sequence can result in circularly polarized additional fields. It was experimentally demonstrated[23] that only one of the two possible circular polarizations (FMPM-left and FMPM-right), which is in resonance with the main decoupling rf field, improves the performance compared to CW decoupling. These experiments supported the idea that the basic mechanism of the improved performance of the TPPM is the secondary precession in the rotating frame.[21] Circular polarization, for the same efficiency of the resonance, uses only one half of the modulation amplitude. It can be good for the decoupling efficiency, since the optimal modulation phase for the TPPM is a compromise between the favorable effect of a large modulation angle and the constraint that ϕ should be a small angle.[21] Unfortunately, this possible advantage of using circular polarized modulation, compared to TPPM, was not demonstrated experimentally.

3.3 WISP-N

In addition to frequency modulation, one has at one's disposal the capability of modulating the amplitude of the decoupler field. Geen and co-workers recently demonstrated the feasibility of this approach,[26] where improved decoupling was observed in comparison to CW by utilizing a cosine amplitude-modulated waveform which was rotor synchronized. The decoupling was only comparable to TPPM at spinning rates $\leq$8 kHz, at which point TPPM showed significant advantage. This was counter-intuitive when compared to what was expected for these WISP-N (wideband-shaped modulation functions) pulse trains. This sequence was developed for the high-spinning regime whereby the homonuclear $I-I$ coupling is reduced to the point that the effective coupling is less than the applied rf field strength. In reality this is a very difficult task to accomplish, but with probe technology advancing as rapidly as it has been over the last few years it is anticipated that it will be a very important sequence.

3.4 CN_n^v and RN_n^v

An alternative and very promising approach to designing the decoupling sequences for fast spinning rates was proposed by Levitt and co-workers,[24,27] where it is essential to consider the rotational aspects of the Hamiltonians arising from MAS. It makes use of symmetry considerations to analyze corresponding average Hamiltonians. From all possible decoupling sequences, only those belonging to a definite class of symmetry are taken into consideration. It limits possible types of sequences, but allows one to take advantage of elegant theorems which can be used to predict the elimination of many average Hamiltonian terms. Two classes of these symmetric sequences for heteronuclear decoupling were denoted as CN_n^v and RN_n^v.

A supercycle of such sequence consists of N cycles C. The cycle C can be arbitrary, except that, in the absence of

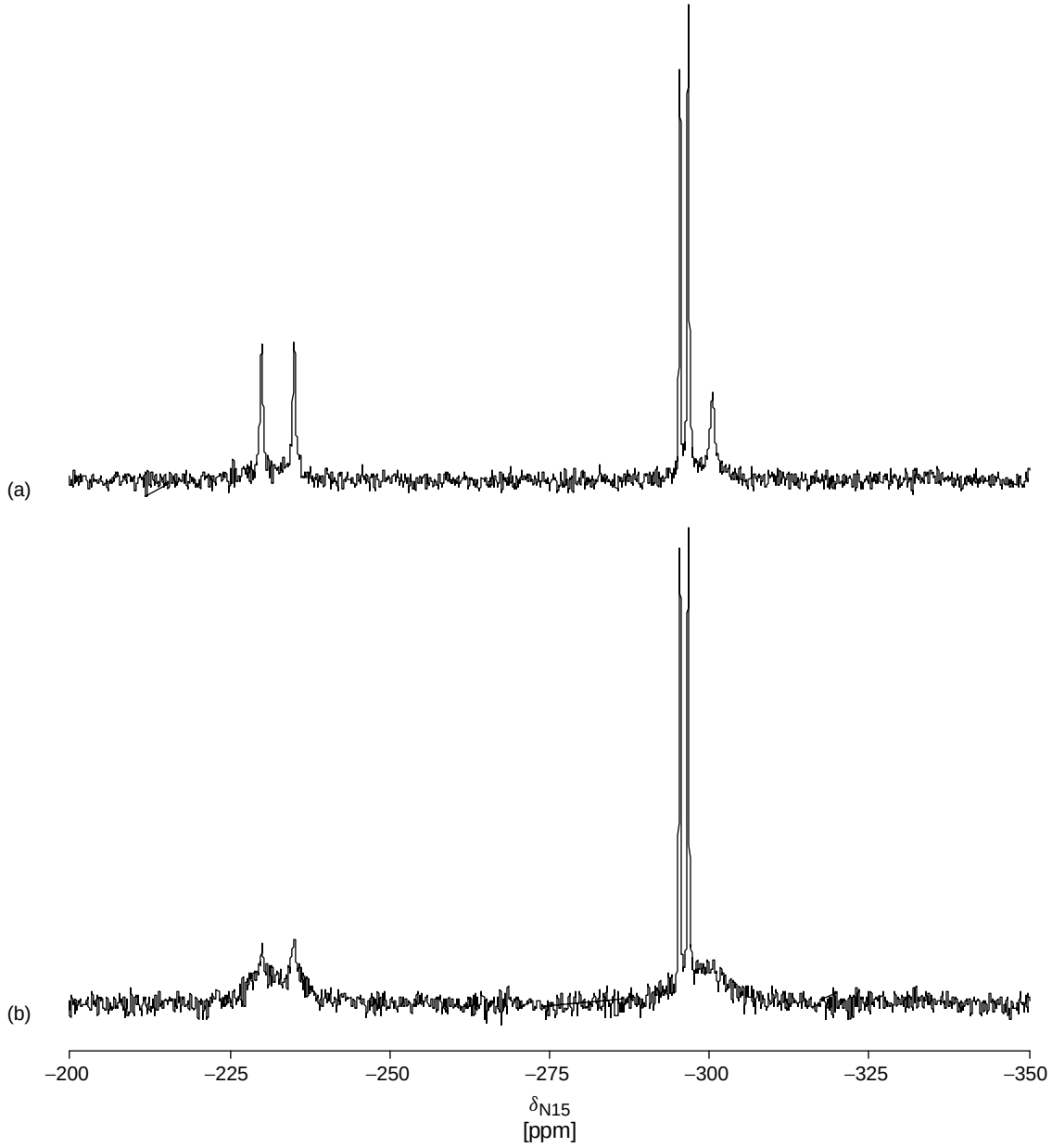

Figure 3 Natural abundance ^{15}N CMPAS spectra of creatinine hemisulfate with (a) TPPM and (b) CW decoupling. Spectra were collected on a Chemagnetics CMX400 spectrometer, 4 kHz spinning speed, a recycle delay of 120 s, a contact time of 3 ms, 63 kHz ^{1}H decoupling rf field, and for (a) a TPPM pulse duration of 8 μs and phase change of 18° total deviation

other interactions, it returns the irradiated spin to its initial state. The phase for each successive cycle C is incremented stepwise and makes ν complete turns during the supercycle, while at the same time, the rotor makes n complete turns. Hence a supercycle of symmetry CN_n^ν is given by

$$CN_n^\nu = (C^0)_{\phi 0}(C^0)_{\phi 1} \ldots (C^0)_{\phi N-1} \tag{9}$$

where $\phi_q = 2\pi q \nu / N$.

The second class of sequence symmetries, RN_n^ν, consists of a pulse sequence element R which rotates the spin by π around the x-axis, followed by a pulse element R′ in which all rf phases are reversed in sign. Then, these R and R′ elements are combined together in a rotor synchronized fashion according to

$$RN_n^\nu = (R)_\phi (R)_{-\phi} (R)_\phi (R)_{-\phi} \ldots (R)_\phi (R)_{-\phi} \tag{10}$$

where $\phi = \pi \nu / N$. There are $N/2$ RR′ pulses spanning n rotor periods.

This sequence resembles TPPM in that the symmetry is reflective in nature; however, it is much more constrictive in the pulse phase and duration values available. Hence, TPPM in general falls out of this theoretical description. For the reported experimental results[27] at 13 kHz MAS and 78 kHz rf decoupling field, these new sequences were essentially equivalent to TPPM. Nevertheless, it is very possible that for higher spinning rates the symmetry-based approach could be

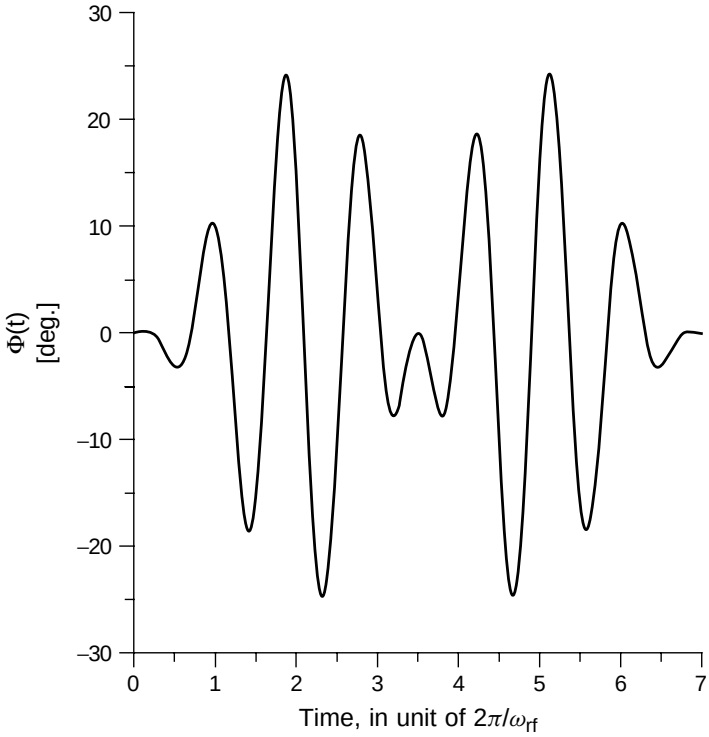

Figure 4 Phase-modulation function for the sequence CPM 4–7. (Reproduced from Ref.[23] by permission of the American Physical Society)

the most powerful tool for searching for efficient heteronuclear decoupling schemes for solids.

3.5 SPINAL and CPM $m - n$

More recently, it has been shown that continuous modulation of the phase of the rf field in a more complicated way also improves the decoupling.[19,25] The premise of this approach is to arrange an efficient averaging of the longitudinal components (with respect to the effective field) of the proton spins. In principle, this can be achieved by applying an infinite set of equally spaced harmonics of the field which is perpendicular to the effective field in the rotating frame.[25] A computer simulation showed that efficient and fast averaging in the interval between any two neighboring harmonics happens when the amplitudes (in frequency units) of the linearly polarized harmonics are equal to the separation between the harmonics. In practice, only a few harmonics need to be used because the harmonics with frequencies too far from any resonance in the effective field produce no effect on spin dynamics.

Based on the above consideration, a class of new heteronuclear decoupling sequences, abbreviated as CPM $m - n$ (cosine phase modulation) was introduced.[25] In any of these sequences the phase modulation function $\Phi(t)$ is a sum of m harmonics (cosine terms) with the frequency interval between them equal to $1/n$ units of ω_{rf}. The period of such a sequence is $2\pi n/\omega_{\mathrm{rf}}$. A requirement that the angle $\Phi(t)$ should remain small gives a limitation in the number of harmonics and the frequency interval between them. The amplitude of each cosine term in $\Phi(t)$ should be equal to $1/n$. An example of $\Phi(t)$ for the CPM 4–7 sequence is:

$$\Phi(t) = \left(\frac{1}{7}\right)\left\{-\cos\left(\omega_{\mathrm{rf}}\left(\frac{6}{7}\right)t\right) + \cos(\omega_{\mathrm{rf}}t) + \cos\left(\omega_{\mathrm{rf}}\left(\frac{8}{7}\right)t\right) - \cos\left(\omega_{\mathrm{rf}}\left(\frac{9}{7}\right)t\right)\right\} \qquad (11)$$

Here, π phase shifts are used for the two outer harmonics to decrease the maximum modulus of $\Phi(t)$ without affecting the averaging in the main interval $\omega_{\mathrm{rf}} < \omega < (8/7)\omega_{\mathrm{rf}}$. This phase-modulation function is shown in Figure 4. For practical implementation, the phase is changed in small steps at constant intervals.

As an illustration of the performance of this sequence, the ^{13}C CP/MAS spectrum of polycrystalline L-tyrosine hydrochloride monohydrate is shown in Figure 5. The results of applying CW decoupling, TPPM, and SPINAL-64 sequences are also shown in the same figure for comparison. SPINAL-64 is a decoupling sequence specifically designed for liquid crystals.[19] It produces a multi-frequency excitation in the rotating frame, though in a less regular manner, and its performance for solids is almost as good as that of CPM 4–7. Other multiharmonic CPM $m - n$ sequences with $1 < m < n < 8$ also showed better decoupling than TPPM.[25]

3.6 Amplitude Modulation

In addition to the phase modulation schemes, amplitude modulations have also been proposed,[26] but the improvement over TPPM do not seem to be as pronounced.

4 DISCUSSION

In the analysis given in the previous sections, the effect of magic-angle spinning (MAS) of the sample was not considered. It is clear that the spinning rate has a significant

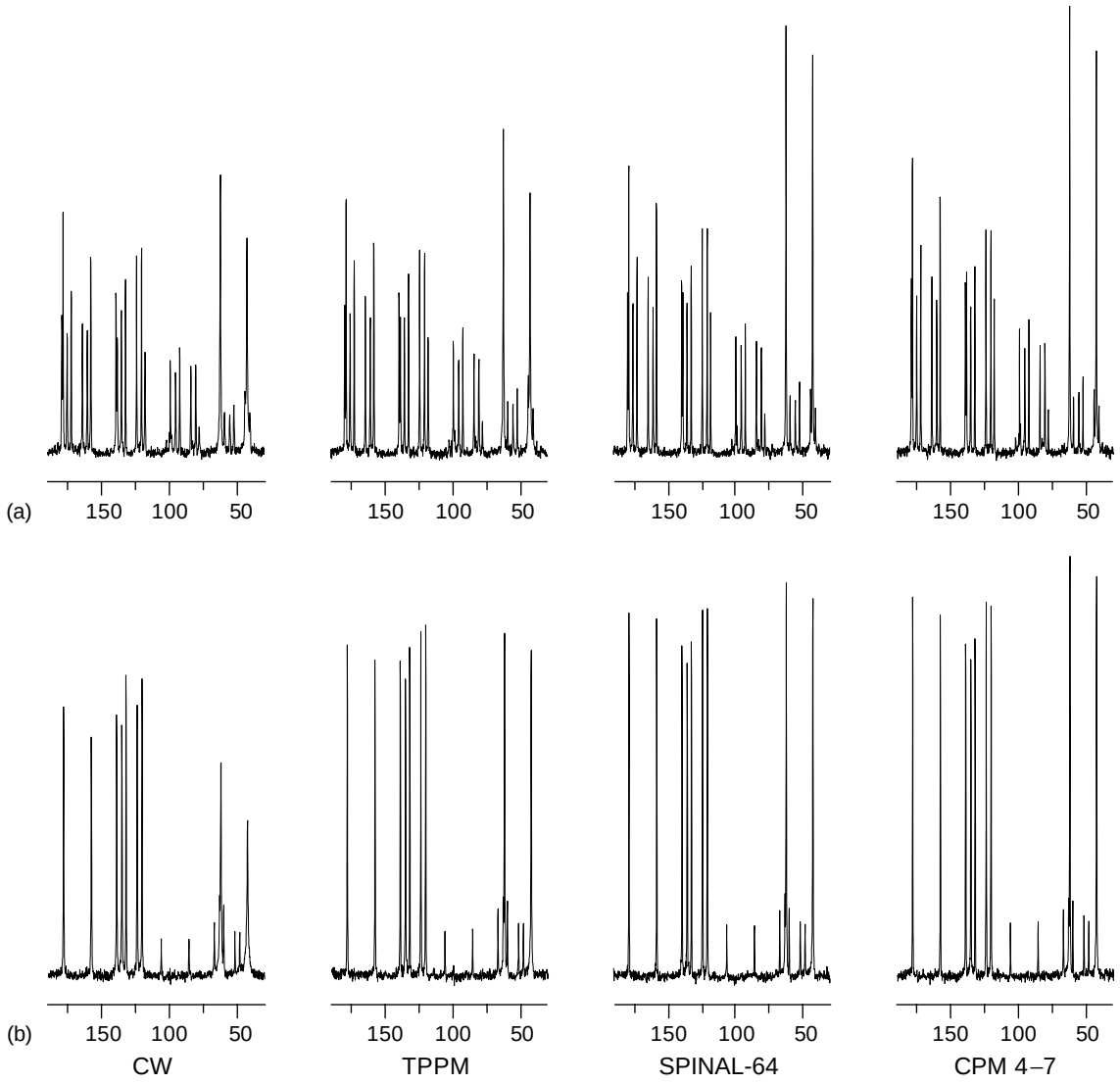

Figure 5 Carbon-13 CPMAS spectra of L-tyrosine hydrochloride monohydrate with various decoupling sequences at ^{1}H decoupling rf field of 75 kHz and spinning rates of (a) 4.0 kHz and (b) 7.2 kHz. Spectra were collected on a Varian UNITY/INOVA-400 spectrometer

influence on the relative performance of different decoupling sequences. For a study carried out at moderate spinning rates (4–7 kHz), it was found that the improvement of the CPM $m-n$ sequences over TPPM decreases as the spinning rate increases (Figure 5).[25] More recently, the effect of spinning rate (ω_r) on the efficiency of decoupling has been studied.[34,35] Although one might expect that the efficiency would generally increase with the decoupling power $\omega_{\rm rf}$, the change is actually not so simple at high spinning rates. For CW decoupling, the efficiency increases with $\omega_{\rm rf}/\omega_r$ in an oscillating way, so that for very fast spinning higher decoupling power could actually be less effective.[34,35] Quantitatively, it was found that the efficiency shows minima for $\omega_{\rm rf}/\omega_r = 1, 2, 3, \ldots$,[34,35] and it was suggested that for spinning frequencies larger than 40 kHz, $\omega_{\rm rf}/\omega_r \approx 1/4$ is most suitable for low-power CW decoupling.[34] For phase-modulated decoupling at a fixed spinning rate, the increase in the decoupling efficiency with $\omega_{\rm rf}$ is faster for CPM $m-n$ and SPINAL-64 than for TPPM. However, there exists a minimum value of $\omega_{\rm rf}$ for CPM $m-n$ and SPINAL-64 to perform better than TPPM, and this minimum value becomes larger for higher spinning rates.[35]

When $\omega_{\rm rf}$ is much larger than ω_r, the change of the Hamiltonian caused by sample rotation can be considered as adiabatic for averaging of the zero-order heteronuclear interactions H_{IS}. However, this is not necessarily true for averaging of $H_{IS}^{(1)}$, since the second averaging occurs at a slower time scale. A possible rotary resonance can spoil this second averaging and such a resonance should be avoided. It is hard to predict which of the discussed sequences will be the best under any particular experimental condition, but a variety of them allows the experimenter to find the one with the best performance for their class of system. It is possible that, for better decoupling at higher spinning rates, the sequences should be rotor-synchronized. In this case, the symmetry-based approach[27] could be very useful for designing efficient decoupling sequences.

Spinning rate is only one of many important factors that affect relative performance of decoupling sequences. Some other hardware parameters and characteristics of the sample,

such as amplitude of the decoupling rf field and its inhomogeneity, width of the proton spectrum and its spin diffusion properties, are also very important. A variety of experimental situations makes it unlikely that the "universal" best decoupling sequence can be found. Traditionally, sequences of pulses with fixed amplitudes and phases are used in NMR experiments. They are simpler for programming and for theoretical analysis. On the other hand, continuous phase modulation is used in the multiharmonic heteronuclear decoupling sequences for broadband decoupling and in a recently published efficient homonuclear dipolar decoupling sequence.[36] In both cases computer simulation was used to optimize the parameters. However, as it was mentioned above, the computer simulation cannot be very realistic and quantitative for solids. Considering all these factors, one can envision that future designs of decoupling sequences may contain a number of undetermined parameters which can be optimized for each sample under a particular experimental situation in the same way as autoshimming for liquid samples.

5 RELATED ARTICLES IN VOLUMES 1–8

Average Hamiltonian Theory, Volume 2; Decoupling Methods, Volume 3; Double Resonance, Volume 3; Echoes in Solids, Volume 3; HETCOR in Organic Solids, Volume 4; Spin Diffusion in Solids, Volume 7.

6 REFERENCES

1. D. Suter, A. Pines, J. H. Lee, and G. Drobny, *Chem. Phys. Lett.*, 1988, **144**, 324.
2. D. L. VanderHart, W. L. Earl, and A. N. Garroway, *J. Magn. Reson.*, 1981, **44**, 361.
3. F. Bloch, *Phys. Rev.*, 1954, **93**, 944.
4. R. R. Ernst, *J. Chem. Phys.*, 1966, **45**, 3845.
5. R. R. Ernst and W. A. Anderson, *Rev. Sci. Instrum.*, 1966, **37**, 93; R. R. Ernst, *Adv. Magn. Reson.*, 1966, **2**, 1.
6. I. J. Lowe and R. E. Norberg, *Phys. Rev.*, 1957, **107**, 46.
7. J. S. Waugh, *J. Magn. Reson.*, 1982, **50**, 30.
8. D. Suter, K. V. Schenker, and A. Pines, *J. Magn. Reson.*, 1987, **73**, 90.
9. M. H. Levitt, R. Freeman, and T. A. Frenkiel, *Adv. Magn. Reson.*, 1983, **11**, 47.
10. A. J. Shaka, J. Keeler, and R. Freeman, *J. Magn. Reson.*, 1983, **53**, 313.
11. A. J. Shaka, P. B. Barker, and R. Freeman, *J. Magn. Reson.*, 1985, **64**, 547; A. J. Shaka and J. Keeler, *Prog. NMR Spectrosc.*, 1987, **19**, 47.
12. E. Kupce and R. Freeman, *J. Magn. Reson.*, 1996 **A118**, 299; R. Fu and G. Bodenhausen, *J. Magn. Reson.*, 1996, **A119**, 129.
13. A. J. Shaka, in 'Encyclopedia of NMR', eds D. M. Grant and R. K. Harris, Wiley: Chichester, 1996, p. 1558.
14. U. Haeberlen and J. S. Waugh, *Phys. Rev.*, 1968, **175**, 453; J. S. Waugh, in 'Encyclopedia of NMR', eds D. M. Grant and R. K. Harris, Wiley: Chichester, 1996.
15. B. M. Fung, *J. Magn. Reson.*, 1990, **86**, 160.
16. K. V. Schenker, D. Suter, and A. Pines, *J. Magn. Reson.*, 1987, **73**, 99.
17. D. Sandström and M. H. Levitt, *J. Am. Chem. Soc.*, 1996, **118**, 6966.
18. Y. Yu and B. M. Fung, *J. Magn. Reson.*, 1998, **130**, 317.
19. B. M. Fung, A. K. Khitrin, and K. Ermolaev, *J. Magn. Reson.*, 2000, **142**, 97.
20. P. Tekely, P. Palmas, and D. Canet, *J. Magn. Reson.*, 1994, **A107**, 129.
21. A. E. Bennett, C. M. Rienstra, M. Auger, K. V. Lakshmi, and R. G. Griffin, *J. Chem. Phys.*, 1995, **103**, 6951.
22. D. L. VanderHart and G. C. Campbell, *J. Magn. Reson.*, 1998, **134**, 88.
23. Z. Gan and R. R. Ernst, *Solid State Nucl. Magn. Reson.*, 1997, **8**, 153.
24. M. Eden and M. H. Levitt, *J. Chem. Phys.*, 1999, **111**, 1511.
25. A. K. Khitrin and B. M. Fung, *J. Chem. Phys.*, 2000, **112**, 2392.
26. H. Geen, A. S. D. Heindrichs, J. J. Titman, M. Ernst, and B. H. Meier, *J. Phys. B*, 2000, **33**, 3377.
27. M. Carravetta, M. Eden, X. Zhao, A. Brinkmann, and M. Levitt, *Chem. Phys. Lett.*, 2000, **321**, 205.
28. M. Ernst, H. Zimmermann, and B. H. Meier, *Chem. Phys. Lett.*, 2000, **317**, 581.
29. K. Takegoshi, J. Mizokami, and T. Terao, *Chem. Phys. Lett.*, 2001, **341**, 540.
30. G. McGeorge, D. W. Alderman, and D. M. Grant, *J. Magn. Reson.*, 1999, **137**, 138.
31. D. J. Mitchell and J. N. S. Evans, *Chem. Phys. Lett.*, 1998, **292**, 656.
32. P. W. Anderson and P. R. Weiss, *Rev. Mod. Phys.*, 1953, **25**, 269.
33. A. Abragam, 'The Principles of Nuclear Magnetism', Oxford University Press: Oxford, 1961.
34. M. Ernst, A. Samoson, and B. H. Meier, *Chem. Phys. Lett.*, 2001, **348**, 293–302.
35. A. K. Khitrin, T. Fujiwara, and H. Akutsu, to be published.
36. D. Sakellariou, A. Lesage, P. Hodgkinson, and L. Emsley, *Chem. Phys. Lett.*, 2000, **319**, 253.

High Speed MAS of Half-Integer Quadrupolar Nuclei in Solids

Hans J. Jakobsen

University of Aarhus, Aarhus C, Denmark

1 Introduction 1
2 Hamiltonian for Quadrupolar Nuclei in MAS NMR 2
3 Applications of High-Speed MAS NMR to Quadrupolar Nuclei 4
4 Other Sample Rotation Techniques 8
5 Related Articles 9
6 References 9

1 INTRODUCTION

Recourse to the NMR periodic table of spin isotopes reveals that about 75% of these nuclei possess a spin $I > \frac{1}{2}$, i.e., the spin isotopes known as the quadrupolar nuclei. Most quadrupolar nuclei (approximately 90%) have half-integer spin ($I = \frac{3}{2}, \frac{5}{2}, \frac{7}{2}, \ldots$), and it is therefore not surprising that by far the largest number of solid state NMR studies of quadrupolar nuclei have involved half-integer spins, maybe with the exception of ^{2}H ($I = 1$). Magic angle spinning (MAS) NMR of quadrupolar nuclei made its breakthrough in the early 1980s, first of all thanks to the exploratory ^{27}Al and ^{23}Na MAS investigations by Müller et al.,[1] Oldfield et al.,[2] and Samoson and Lippmaa.[3] Perhaps the best known MAS NMR spectrum for a half-integer quadrupolar nucleus is that of ^{79}Br in a KBr sample, which is used by almost every MAS NMR spectroscopist for adjustment of the magic angle.[4] Since that time, MAS NMR studies of $I = \frac{3}{2}, \frac{5}{2}, \frac{7}{2}, \ldots$ quadrupolar nuclei have constituted an increasingly important tool in solid state chemistry and materials research. In particular, ^{23}Na ($I = \frac{3}{2}$) and ^{27}Al ($I = \frac{5}{2}$) MAS NMR have played a significant role in studies of minerals, zeolites, catalysts, cements, and ceramics as evidenced by the numerous investigations in these fields.

For most half-integer quadrupolar nuclei (e.g., ^{23}Na and ^{27}Al), the quadrupolar coupling interaction is the predominant mechanism leading to strong line broadening in the solid state NMR spectra of powders. For a few other less commonly studied nuclei (e.g., ^{51}V, ^{59}Co, ^{85}Rb, ^{87}Rb, and ^{133}Cs), additional line broadening from chemical shielding anisotropy (CSA) becomes important, and may influence the appearance of their spectra.[5] The line broadening of the individual transitions ($I \leftrightarrow I - 1, \ldots, +\frac{1}{2} \leftrightarrow -\frac{1}{2}, \ldots, -I + 1 \leftrightarrow -I$) from the quadrupolar interaction can be quantified in terms of the quadrupolar coupling constant $\chi = e^2qQ/h$ (i.e., the magnitude of the interaction) and the asymmetry parameter η ($0 \leq \eta \leq 1$), which characterizes the symmetry of the electric field gradients around the nucleus. For example, for an axially symmetric electric field gradient tensor ($\eta = 0$), the *satellite* transitions (i.e., transitions other than $m = \frac{1}{2} \leftrightarrow m = -\frac{1}{2}$) give rise to characteristic quadrupolar splittings

$$\nu_Q = \frac{\chi}{4I(2I-1)}(6|m| - 3) \quad (1)$$

between the 'horns' for the different symmetric $\pm m \leftrightarrow \pm (m - 1)$ transitions. From equation (1), it also follows that the maximum width of the spectrum for a spin-I quadrupolar nucleus, given approximately by $2\nu_Q$ for $|m| = I$, equals $3\chi/2I$.[6] Therefore, for the complete spectrum of all transitions not to extend beyond a spectral width of, for example, 2 MHz it is required that $\chi \leq 2$ MHz for $I = \frac{3}{2}$ and $\chi \leq 3.3$ MHz for $I = \frac{5}{2}$, i.e. rather small quadrupolar couplings. On the other hand, the *central* ($+\frac{1}{2}, -\frac{1}{2}$) transition, which is not affected by the first-order quadrupolar splitting, has a much smaller linewidth than any satellite transition. Thus, this has been the most commonly observed transition in static and MAS NMR studies of half-integer quadrupolar nuclei.

The line-narrowing effect of MAS will split the satellite transitions into numerous spinning sidebands (ssbs; cf. the ^{79}Br MAS spectrum of KBr[4]) and *reduce* the width for the central transition by a factor of about 2.5–3 as compared with the static spectrum. Provided the spinning speed ($\nu_r = \omega_r/2\pi$) is larger than the CSA and dipolar interactions, MAS will greatly improve both resolution and sensitivity (S/N ratio) for the observed spectrum. In high-field NMR, the quadrupolar interaction is much smaller than the Zeeman splitting, and can be described by average Hamiltonian theory in the secular approximation.[6,7] In this approximation, the central transition is perturbed only to second order by the quadrupolar interaction (see below).[6,7] For polycrystalline powders, this leads to a characteristic lineshape, which is unaffected (or cannot be further narrowed) by increasing ν_r beyond the width of the lineshape.[8] Provided ν_r is larger than this width, χ, η, and δ (the isotropic chemical shift) can easily be determined with good accuracy by computer fitting of the observed lineshape.[6] As an example of the characteristic lineshapes that may be observed for the central transition at sufficiently high spinning speeds, Figure 1 shows a series of computer simulations for a spin $I = \frac{5}{2}$ nucleus (e.g., ^{27}Al) using χ = 5.0 MHz, ν_L = 104.2 MHz, and various η values ($0 \leq \eta \leq 1$). For comparison, the corresponding lineshapes for the static case are also shown. It should be noted that the total width of the MAS lineshape between the outermost shoulders/edges increases only slightly on increasing η, whereas the positions of the singularities, shoulders, and edges depend strongly on η. Furthermore, the widths of the lineshapes are proportional to χ^2 and inversely proportional to the Larmor frequency $\nu_L = \omega_L/2\pi$, i.e. to the magnetic field strength for a particular nucleus (see below).

From the above considerations one may draw the following qualitative conclusions.

1. For small quadrupolar couplings, the second-order contribution may be too small for the lineshape of the central transition to be resolved in the MAS spectrum. This would prevent determination of χ and η from this transition, which is usually the case for $\chi/[4I(2I - 1)]$ 75 kHz at ν_L = 100 MHz, i.e., χ 0.9 MHz for ^{23}Na and χ 3.0 MHz for ^{27}Al at 9.4 T. In such cases, the manifold of ssbs for the satellite transitions may be taken into full advantage, since it has been shown that accurate χ and η values may

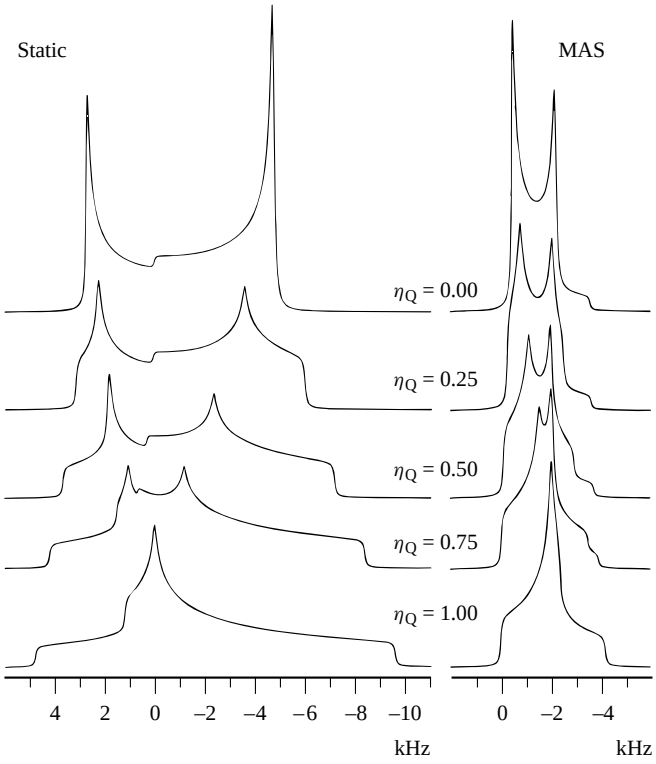

Figure 1 Simulated static (left) and MAS (right) lineshapes for the central transition of a spin $I = \frac{5}{2}$ nucleus for various values of η and assuming $\nu_r = \infty$. All simulated spectra employed χ = 5.0 MHz, ν_L = 104.2 MHz (i.e., ^{27}Al at 9.4 T), and a Lorentzian line broadening of 100 Hz

be determined from computer fitting of the ssb intensity pattern observed on modern spectrometers equipped with fast receivers.[6,9]

2. For much larger χ values than discussed in (1), the manifold of ssbs for the satellite transition may extend far beyond the maximum spectral width of the spectrometer and appear with heavily reduced intensities as compared with (1). In such cases, χ and η are most conveniently determined by computer fitting of the second-order quadrupolar lineshape observed for the central transition. Obviously, the availability of the maximum magnetic field strength and spinning speed will set the limit for the maximum χ value that can readily be determined for each nuclei by MAS NMR. This will be discussed further below.
3. For cases of intermediate χ values between (1) and (2), it may be possible to determine χ and η from computer analysis of both the manifold ssbs (1) and the lineshape for the central transition (2). In such cases, it turns out that the more accurate values are obtained from analysis of the ssb pattern (2).

Since the methods (1)–(3) outlined above for determination of χ and η all involve computer fitting of lineshapes and/or intensities from experimental MAS spectra, this puts high demands on the quality of the MAS probes, especially on the spinning performance. Thus, for the sample spinner systems the following requirements are important:

(a) the highest possible spinning frequency ν_r for the largest possible sample volume of the rotor; ν_r values up to about 24 kHz have been achieved for small cylindrical (3.5 mm outer diameter) rotors during recent years (see ***Jakobsen, Hans J.: A Retrospect on the Development of High-Speed Sample Spinners for Solids since 1980*** and ***Doty, F. David: A Random Walk Toward High-Speed Sample Spinning***);
(b) long term stability in ν_r ($\Delta\nu_r$ within a few hertz) at any spinning speed for a particular rotor size; this can be achieved by stabilizing the air-drive pressure mechanically (however, computer controlled rotor-speed stabilizers with $\Delta\nu_r$ 1 Hz are also available);
(c) adjustability and long term stability of the magic angle (54.736°) to within about 0.001°; this is of special importance when second-order lineshapes for the ssbs of the satellite transitions are subjected to computer simulations.

During the past decade, our laboratory has been intensively engaged in design/construction of spinner assemblies and CP MAS probes with special emphasis on fulfilling the requirements for studies of quadrupolar nuclei.[10–12] In particular, the recent progress and positive development around real supersonic spinning systems (see ***Jakobsen, Hans J.: A Retrospect on the Development of High-Speed Sample Spinners for Solids since 1980***) will have further impact on quadrupolar nuclei.

2 HAMILTONIAN FOR QUADRUPOLAR NUCLEI IN MAS NMR

The underlying theory and development of a software package for simulation/fitting of MAS NMR spectra to different approximations under different experimental conditions have been described in detail in recent papers from our laboratory.[5,6,9] In this description, the general Hamiltonian for a quadrupolar nucleus in a strong magnetic field $\boldsymbol{B}_0$ and subjected to an rf field $\boldsymbol{B}_1$,

$$\hat{\mathcal{H}} = \hat{\mathcal{H}}_Z + \hat{\mathcal{H}}_Q + \hat{\mathcal{H}}_{CSA} + \hat{\mathcal{H}}_{DD} + \hat{\mathcal{H}}_{rf} \tag{2}$$

is approximated by the second-order average Hamiltonian for a Larmor period,

$$\hat{\tilde{\mathcal{H}}}(t) = \hat{\tilde{\mathcal{H}}}_Q^{(1)}(t) + \hat{\tilde{\mathcal{H}}}_Q^{(2)}(t) + \hat{\tilde{\mathcal{H}}}_{rf}(t) \tag{3}$$

where the Zeeman interaction representation (high-field NMR, $\hat{\mathcal{H}}_Z \gg \hat{\mathcal{H}}_Q$) is employed and $\hat{\mathcal{H}}_{CSA} + \hat{\mathcal{H}}_{DD}$ have been neglected (this is acceptable for most quadrupolar nuclei under MAS conditions).

Under MAS and in the second-order approximation, the first- and second-order terms of the quadrupolar interaction take the forms

$$\hat{\tilde{\mathcal{H}}}_Q^{(1)}(t) = \omega_Q^{(1)}(t)[3\hat{I}_z^2 - I(I+1)] \tag{4}$$

$$\hat{\tilde{\mathcal{H}}}_Q^{(2)}(t) = \omega_Q^{(21)}(t)[-8\hat{I}_z^2 + 4I(I+1) - 1]\hat{I}_z + \omega_Q^{(22)}(t)[-2\hat{I}_z^2 + 2I(I+1) - 1]\hat{I}_z \tag{5}$$

where the factors $\omega_{\mathrm{Q}}^{(1)}(t)$ and $\omega_{\mathrm{Q}}^{(2q)}(t)$ are time-dependent because of MAS, and are given by

$$\omega_{\mathrm{Q}}^{(1)}(t) = \frac{2\pi\chi}{4I(2I-1)} \times \sum_{n=1}^{2}[P_n^{(0)}\cos(n\gamma + n\omega_{\mathrm{r}}t) + R_n^{(0)}\sin(n\gamma + n\omega_{\mathrm{r}}t)] \quad (6)$$

$$\omega_{\mathrm{Q}}^{(2q)}(t) = \frac{1}{2\omega_{\mathrm{L}}}\left(\frac{2\pi\chi}{4I(2I-1)}\right)^2 \times \left\{C^{(q)} + \sum_{n=1}^{4}[P_n^{(q)}\cos(n\gamma + n\omega_{\mathrm{r}}t) + R_n^{(q)}\sin(n\gamma + n\omega_{\mathrm{r}}t)]\right\} \quad (7)$$

The time-independent coefficients $C^{(q)}$, $P_n^{(q)}$, and $R_n^{(q)}$ are functions of the asymmetry parameter η ($0 \le \eta \le 1$) and the Euler angles α and β; expressions for these coefficients are given in Table 1 of Skibsted et al.[6] The Euler angles (α,β,γ) relate the principal axis frame of the quadrupolar coupling tensor to the rotor fixed frame, and are defined according to the conventions of Spiess.[13] Finally, for on-resonance excitation (X phase), the rf term is given by

$$\hat{\tilde{\mathcal{H}}}_{\mathrm{rf}} = \gamma B_1 \hat{I}_x \quad (8)$$

and for an infinitely short (ideal) rf pulse, the expression for the total FID for a quadrupolar nucleus in a powder undergoing MAS has been derived:[6]

$$s(t) = \sum_{\alpha\beta\gamma}\sum_{m} p_m \exp[\mathrm{i}\Phi_m(\alpha,\beta,\gamma;t)] \quad (9)$$

From equations (4)–(7), we note that the first- and second-order terms for the quadrupolar interaction can be written as

$$\hat{\tilde{\mathcal{H}}}_{\mathrm{Q}}^{(1)}(t) + \hat{\tilde{\mathcal{H}}}_{\mathrm{Q}}^{(2)}(t) = [\hat{\tilde{\mathcal{H}}}_{\mathrm{Q}}^{(1)}(t)]_{\text{time-dependent}} + [\hat{\tilde{\mathcal{H}}}_{\mathrm{Q}}^{(2)}(t)]_{\text{time-dependent}} + [\hat{\tilde{\mathcal{H}}}_{\mathrm{Q}}^{(2)}(t)]_{\text{time-independent}} \quad (10)$$

since the two coefficients $C^{(1)}$ and $C^{(2)}$ in equation (7) are time-independent, i.e., independent of the spinning frequency. These time-independent second-order terms describe small frequency shifts depending on the Euler angles α and β, whereas the time-dependent second-order terms describe the distribution of intensity from the individual crystallites over the ssbs. It is the combination of these two second-order effects that introduces a unique lineshape not only for the central transition (and any possible ssbs) but also a unique and different lineshape for each ssb of the satellite transitions.

As mentioned above, we see from equations (6) and (7) that the first-order contribution $\hat{\tilde{\mathcal{H}}}_{\mathrm{Q}}^{(1)}(t)$, which determines the width of the satellite transitions, is proportional to χ, while the second-order contributions are proportional to χ^2 and inversely proportional to ν_{L}.

2.1 Central Transition

The central ($+\frac{1}{2}$, $-\frac{1}{2}$) transition for half-integer quadrupolar nuclei has the largest transition probability,[6,14] and is independent of the quadrupolar interaction to first order [$\hat{\mathcal{H}}_{\mathrm{Q}}^{(1)}(t)$]. Therefore, it has the largest intensity and exhibits the most narrow spectral width of all transitions for a powder. However, provided χ is large enough, the linewidth will broaden and eventually give rise to the unique lineshape discussed above, because of the contribution from $\hat{\mathcal{H}}_{\mathrm{Q}}^{(2)}(t)$. In addition to the ratio χ^2/ν_{L} for a particular I spin, the experimental observation of a well-defined second-order lineshape is very much dependent on the presence of other line-broadening mechanisms such as relaxation, crystallinity, a distribution of χ and η values within the powder, or paramagnetic impurities. Provided ν_{r} is greater than the width of the central transition, the ssbs from this transition are usually small. In such cases, there are only negligible differences between the lineshape of the observed centerband and the simulated (optimized) lineshape employing only the time-independent terms $C^{(1)}$ and $C^{(2)}$ of equation (7), i.e., simulations assuming infinite ν_{r} and displayed in Figure 1. Calculations in this approximation reduce to an expression that is equivalent to that originally derived by Samoson et al.[8] These authors also produced graphs for the positions of the singularities (relative to the isotropic chemical shift)[8] for the lineshapes (Figure 1). Good estimates of χ, η, and δ may be derived from these graphs for an observed spectrum (e.g., for starting parameters in a computer fitting of the experimental lineshape). When ν_{r} becomes similar to or smaller than the width of the central transition, decent simulations for comparison with the experimental spectra can only be performed by including all terms of equation (7) (both time-independent and time-dependent). This makes the simulations/fitting more difficult and time-consuming. Obviously, a straightforward determination of large χ values from MAS NMR of the central transition becomes very much dependent on the maximum spinning speed for the MAS probe employed, combined with the available magnetic field strength[15] (see below).

2.2 Satellite Transitions

As opposed to the central transition, the appearance of the satellite transitions in MAS NMR first of all reflects the first-order [$\hat{\mathcal{H}}_{\mathrm{Q}}^{(1)}(t)$] quadrupolar interaction. The MAS NMR spectrum of these transitions consists of a manifold of ssbs with a maximum width approximately equal to $3\chi/2I$. The shape of the envelope for this symmetrical ssb pattern reflects the value of η.[6,9] On modern spectrometers with maximum spectral widths of 2–4 MHz, the observation of this ssb pattern constitutes a very accurate method for the determination of small χ values (4 MHz). The effect of the second-order [$\hat{\mathcal{H}}_{\mathrm{Q}}^{(2)}(t)$] interaction is to introduce a unique

lineshape or (if unresolved) line broadening for each ssb. This lineshape (or broadening) differs for each ssb throughout the spectrum, and the shape of the nth sideband from the centerband also varies, depending upon ν_r. However, since the ratio of the second-order to first-order coefficients is proportional to $\chi/[4I(2I - 1)\nu_L]$ [equations (6) and (7)], and usually small (of order 10^{-3} for $\chi < 4$ MHz and $\nu_L \approx 100$ MHz, i.e., ^{23}Na and ^{27}Al at 9.4 T), the effect of the second-order terms on the integrated intensities for each ssb can be neglected. This is illustrated in Figure 2, which shows simulations of the ssb manifold for the satellite transitions of a spin $I = \frac{3}{2}$ nucleus with χ = 2.0 MHz, η = 0.0, and ν_L = 105.8 MHz (^{23}Na and 9.4 T) based on equation (9) with an infinite short (ideal) rf pulse. The simulation in Figure 2(a), which includes $\omega_Q^{(1)}(t)$ and all terms of $\omega_Q^{(2q)}(t)$, shows different peak heights for the symmetrical ($\pm n$th) ssbs because of the lineshape for the individual ssbs induced by the time-dependent terms of $\omega_Q^{(2q)}(t)$. Examples of the lineshapes are apparent from the expansions in Figure 2(a). The simulation in Figure 2(b) uses $\omega_Q^{(1)}(t)$ and only the time-dependent terms of $\omega_Q^{(2q)}(t)$ (i.e., no lineshape but 'true' intensities for the ssbs), while the calculated spectrum in Figure 2(c) is based on the first-order terms $[\omega_Q^{(1)}(t)]$ only. Comparison of the spectra in Figures 2(b) and 2(c) demonstrates that the first-order terms alone yield an excellent approximation for the ssb intensities. Thus, employing integrated intensities for each ssb in the experimental spectrum, it is unnecessary to include any second-order terms for determination of even quite large χ values by fitting of simulated to experimentally integrated ssb intensities. This not only greatly reduces computing time, but is also quite fortunate, since often the lineshapes of the ssbs are unresolved or distorted compared with the real MAS lineshape because of different line-broadening mechanism, small variations in spinning speed, or slight misadjustment of the magic angle. In particular, it should be noted that an incorrect setting of the magic angle (off by 0.01° or less) can have a dramatic effect on the lineshape of the ssbs[16] as opposed to the effect on the lineshape for the central transition. Finally, it should be mentioned that in certain cases it may be of interest to perform the full simulations as in Figure 2(a) for comparison of experimental and simulated second-order lineshapes for the ssbs. Examples of the different types of simulated ssb patterns for comparison with experimental spectra may be found in Skibsted et al.[6,9,17]

In view of the large spectral widths (megahertz range) generally required for the observation of all ssbs for the satellite transitions, it is expected that the assumption of ideal rf excitation and detection used in the simulations above (e.g., Figure 2) does not hold for the experimental ssb intensities. The reason is that maximum achievable rf field strengths are usually in the range $\gamma B_1/2\pi \approx 50-100$ kHz and that MAS probes are usually high-Q probes ($Q \approx 200$). However, as is apparent from our first simulations employing ideal rf excitation of experimental MAS satellite spectra,[9] the effects of nonideal rf pulse excitation are not as serious as would have been expected based on earlier experiences of nonuniform rf excitation in static solid state NMR. The reason is that pulse imperfections (i.e., both phase and intensity errors) experienced by a particular crystallite and pulse perfections for another crystallite are transmitted to a large part of ssbs across the spectrum because of the time dependence of the quadrupolar interaction due to the sample rotation during acquisition. Our later work[6] has evaluated the impact of nonuniform rf excitation on the first-order ssb intensities in MAS NMR of satellite transitions and also the effect of the Q factor of the probe during detection. Both effects tend to reduce the ssb intensities in the outer wings of the spectrum, and have been incorporated into the simulation software. For simulations including these effects and their excellent agreement with experimental ssb intensities, the reader is referred to the figures in Skibsted et al.[6] (in particular Figures 2 and 6). From these results, it may be summarized that the main experimental implications to reduce phase and intensity errors are

1. on-resonance rf conditions for the center of the spectrum;
2. $\gamma B_1/2\pi \geq 40$ kHz;
3. a small pulse length (τ_p 1 μs), ensuring that $\tau_p \ll (1/\nu_r)$ and that the spectrum can be phased to positive absorption across the full spectral width ($1/\Delta$t) using a linear phase correction of $-360° \times \tau_p/(2\ \Delta$t).

It should be noted that the discrepancy between the ideal and finite pulse spectra increases markedly on increasing τ_p, which is partly ascribed to transfer of magnetization into multiple quantum coherences.[18] On the other hand, at least simulations indicate that the spectra are less sensitive to increases in the rf field strength in the normal range of 40 kHz $\leq \gamma B_1/2\pi \leq$ 100 kHz. Finally, it is our experience that the observation of a perfect symmetry of the ssb intensities for the satellite transitions around the center of the spectrum can be quite sensitive to the complete probe tuning circuitry (including filters, cable lengths, and the MAS probe itself). For example, changing lengths of the coaxial cables may slightly influence and can be used to improve the symmetry of the ssb intensities for the satellite transitions at different nuclear resonance frequencies.

3 APPLICATIONS OF HIGH-SPEED MAS NMR TO QUADRUPOLAR NUCLEI

From the theoretical considerations and aspects discussed above, it is obvious that stable and high speed spinning performance for the MAS probe constitute a most important entity of the complete spectrometer system in determinations of quadrupolar coupling parameters employing MAS NMR. In addition these probe properties also play a decisive role in many applications of MAS NMR to quadrupolar nuclei in inorganic chemistry, geology, and materials research. In this section, we shall consider selected examples of the applications of high-speed MAS NMR; those of a straightforward, routine nature will be presented first, and will be followed by some examples of determination of large χ values.

3.1 Clay Minerals

The mixed-layer illite/smectite clay minerals constitute an important class of minerals that have been studied intensively by ^{27}Al MAS NMR since the early days of this technique. These minerals exhibit two central transitions in their ^{27}Al MAS NMR spectra: one each for octahedrally and tetrahedrally coordinated aluminum, Al(VI) and Al(IV); respectively. Generally, these studies aimed at a determination

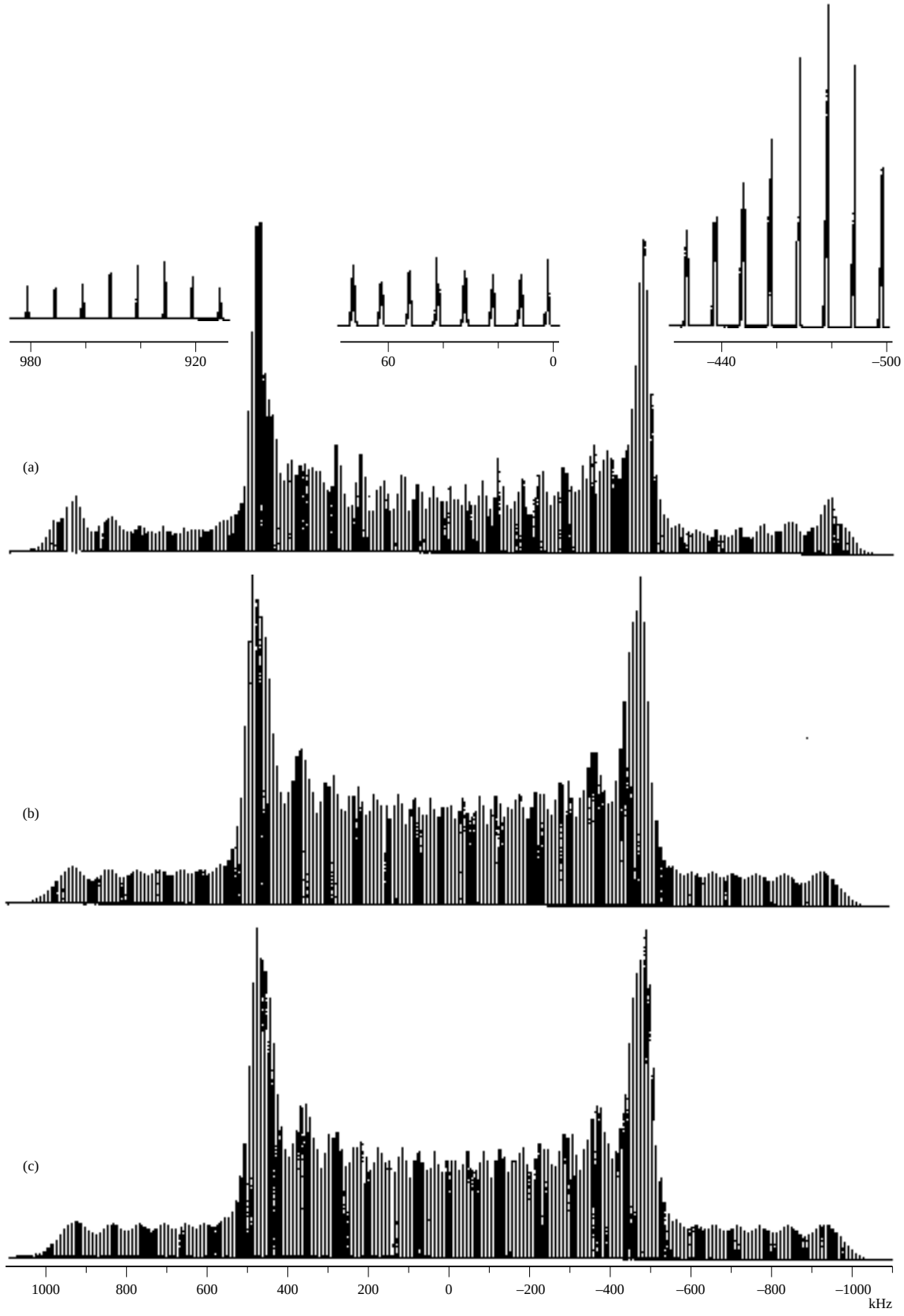

Figure 2 Simulated MAS NMR spectra of the satellite transitions for a spin $I = \frac{3}{2}$ nucleus using χ = 2.0 MHz, η = 0.0, ν_r = 10 kHz, and ν_L = 105.8 MHz (^{23}Na at 9.4 T). The calculations include (a) $\omega_Q^{(1)}(t)$ and all terms for $\omega_Q^{(2q)}(t)$, (b) $\omega_Q^{(1)}(t)$ and the time-dependent terms of $\omega_Q^{(2q)}(t)$, and (c) $\omega_Q^{(1)}(t)$ only. The second-order lineshape of the individual ssbs in (a), caused by the time-independent terms of $\omega_Q^{(2q)}(t)$, is clarified in the expansions

of the Al(IV)/Al(VI) ratios of the samples. However, the early determinations were severely hampered by the large number of ssbs for the central transitions (and therefore overlapping resonances) in the region of interest (0−70 ppm) because of the maximum $\nu_r \approx 4$ kHz employed prior to 1987. Furthermore, the intensities of these ssbs increase markedly with increasing content of paramagnetic impurities (especially Fe) of the samples.[19,20] The advent of high-speed spinning ($\nu_r \approx 10$ kHz) caused a dramatic improvement in the simplicity for the spectra since the ssbs could now be significantly suppressed,[21] and most importantly can be placed outside the region for the two centerband signals, even at the highest magnetic field strengths employed today. Provided the sample is excited by proper rf field strength and pulse length (i.e., a short and 'hard' pulse with flip angle $<15^\circ$),[3] the resulting spectra allow quantitative assessment of the Al(IV)/Al(VI) ratios in a simple and accurate manner. Such determinations have been of particular interest in examining clays sampled from a depth of about 4000 m in the oilfields of the North Sea.[21]

3.2 Ultrastable Y Zeolites

Ultrastable Y (USY) zeolites represent an important class of catalytic materials, which are usually prepared by hydrothermal dealumination of Y zeolites with a framework Si/Al ratio of about 2.5. The structural changes accompanying this treatment have been intensively studied by ^{29}Si and ^{27}Al MAS NMR. ^{29}Si MAS NMR shows that the framework Si/Al ratio, F(Si/Al), a quantity strongly related to the degree of stabilization and catalytic properties, increases as a function of steaming temperature and time. On the other hand, the total bulk Si/Al ratio, as measured by X-ray fluorescence (XRF), remains virtually constant, even for highly dealuminated samples. Therefore, large quantities of nonframework aluminum (NFA) must be present in USY zeolites, and numerous studies have employed ^{27}Al MAS NMR in attempts to characterize and quantify the Al species in these materials.[22] ^{27}Al MAS NMR spectra of USY zeolites are generally described as consisting of three signals: one at approximately 60 ppm, assigned to framework aluminum (FA), and one each at about 30 and 0 ppm attributed to NFA. In addition, the spectra exhibit a very broad hump below the three more distinct resonances—a feature that is especially pronounced in spectra of highly dealuminated samples. Quantification of the three ^{27}Al resonances in terms of the NFA% of the total Al content has consistently given too low values for the Al^{NFA}/Al^{total} % in all attempts of such determinations. This led to the concept of 'NMR-invisible Al', which flourished in the literature for some time and has been associated in particular with NFA sites having large quadrupolar interactions.

It was not until recently, when we applied high-speed spinning, $\nu_r \approx 18$ kHz, to USY zeolites in a study at 9.4 T,[22] that good consistency between the quantitative results (Al^{NFA}/Al^{total} %) obtained by ^{27}Al MAS NMR and a combination of other methods (XRF and ^{29}Si MAS NMR) could be achieved. The effect of high-speed spinning on the ^{27}Al MAS NMR spectra of strongly dealuminated USY zeolites is to increase the intensities of all three resonances (0, 30, and 60 ppm) by different percentages. This intensity increase occurs at the expense of the broad hump, which is completely eliminated ('spun out') only for $\nu_r \approx 18$ kHz at 9.4 T (see Figure 3 of Kellberg et al.[22]). Thus, the results of high-speed spinning show that the NFA residing within the hump contributes to all three narrow resonances. This is consistent with a ^{27} Al−{^{1}H} cross polarization MAS study of the same zeolites, which shows that the NFA in USY zeolites consists of Al species possessing all three types of Al coordination: Al(IV), Al(V), and Al(VI). Further details on the nature of the NFA can be found in Kellberg et al.[22] Thus, this technique appears a prerequisite and the most straightforward method for obtaining quantitative results of the different Al species in these catalysts.

3.3 Determination of 'Large' χ Values from the Central Transition at High Spinning Speeds

Perhaps the most important implication of high-speed spinning involves the determination of 'large' quadrupolar coupling constants χ from simulations of 'undistorted' second-order lineshapes for the central transition of half-integer quadrupolar nuclei. In this sense of the word, 'undistorted' means that ν_r is sufficiently large to place the first-order ssbs for the central transition just outside the region for the centerband. In such cases, the analysis/simulation of the experimental spectrum in terms of χ, η, and δ is usually straightforward. At lower spinning speeds, the central transition splits into complicated lineshapes, which are generally unamenable to spectral simulation and quantification—at least if χ and η are unknown. Obviously, a high-performance, high-speed spinning probe can be an economical alternative to a high-field spectrometer in such studies.[15] In general, the condition for the observation of a distortionless centerband for a spin-I half-integer quadrupolar nucleus can be expressed as[15]

$$\chi^2(1+\tfrac{1}{6}\eta)^2 \lesssim \frac{112\nu_L\nu_r I^2(2I-1)}{9(I+\tfrac{3}{2})} \qquad (11)$$

Thus, employing ν_r = 20 kHz and the highest magnetic field strength presently available (17.6 T), undistorted lineshapes for the central transition may be observed in ^{23}Na ($I = \frac{3}{2}$, ν_L = 198.4 MHz) and ^{27}Al ($I = \frac{5}{2}$, ν_L = 195.4 MHz) MAS NMR for χ values up to 7.8 and 15.8 MHz, respectively (assuming an intermediate value of η = 0.60).

As an illustrative example of the advantages of high-speed spinning in MAS NMR of quadrupolar nuclei at intermediate magnetic field strengths, we reinvestigated the ^{27}Al MAS NMR spectrum of $3CaO{\cdot}Al_2O_3$ (C_3A) at 7.1 and 9.4 T for ν_r up to 19 kHz.[15] An earlier reported ^{27}Al MAS spectrum of C_3A, recorded at 11.7 T and $\nu_r \approx 7$ kHz, showed a poorly resolved and distorted spectrum for the central transition.[23] However, this spectrum was analyzed in terms of just one set of quadrupolar coupling parameters,[23] despite the fact that the unit cell of C_3A contains two nonequivalent AlO_4 groups according to XRD. In the early days (1987), with a maximum spinning speed $\nu_r \approx 10$ kHz for our MAS probes, we recorded the ^{27}Al MAS spectrum of C_3A [Figure 3(a)] at 7.1 T, using ν_r = 8.0 kHz. At that time, this spectrum was far too distorted and complex for us to analyze. Following our development of a high-speed 4 mm rotor system,[12] we later recorded the 18−19 kHz ^{27}Al spectra shown in Figures 3(c) and 3(e) (on-

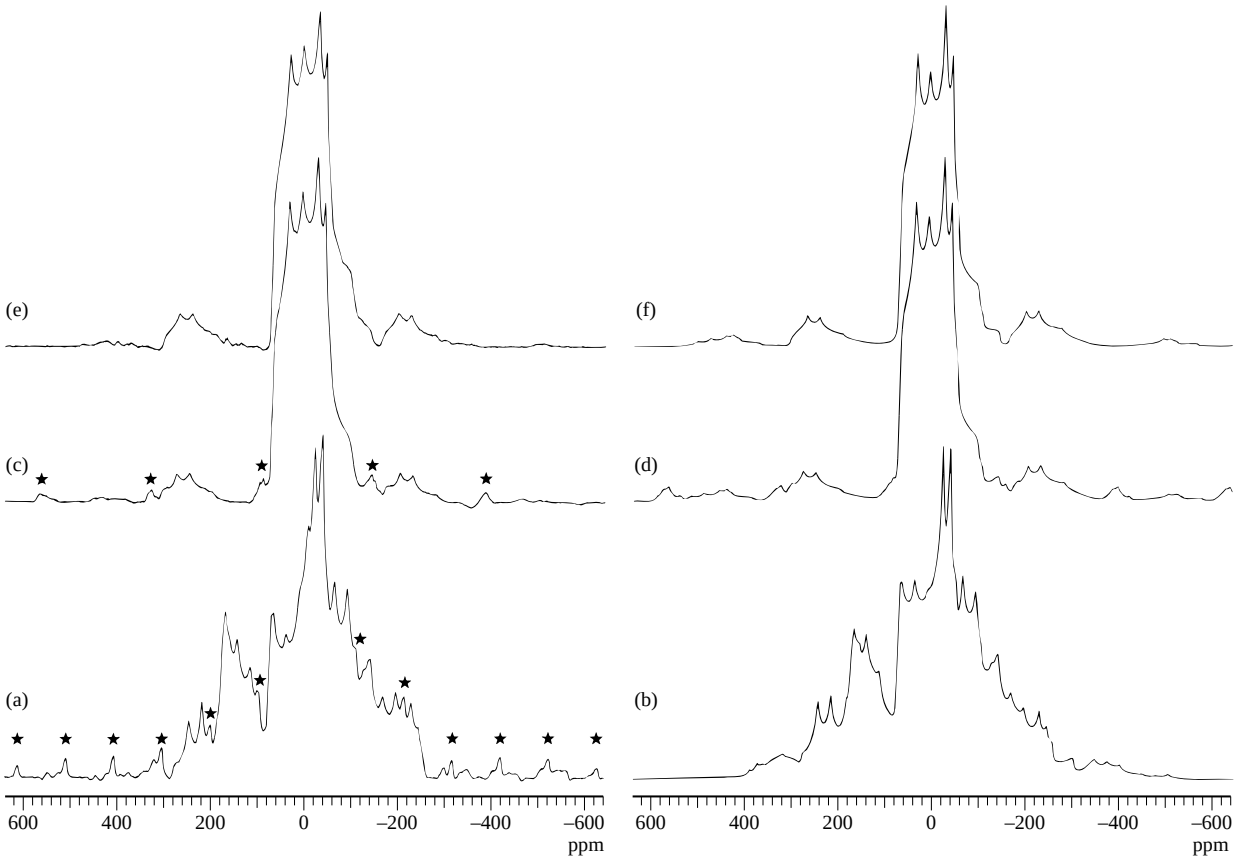

Figure 3 Experimental (a), (c), (e) and simulated (b), (d), (f) 78.2 MHz (7.1 T) ^{27}Al MAS NMR spectra of the central transition (including spinning sidebands) for C_3A obtained at different spinning speeds. For (a) and (b), ν_r = 8.0 kHz, with the spectrum in (a) recorded in 1987 using a 7 mm rotor. For (c) and (d), ν_r = 18.7 kHz (4 mm rotor), where resonances from the $(\pm\frac{3}{2}, \pm\frac{1}{2})$ satellite transitions have been included in the simulated spectrum (d). For (e) and (f), ν_r = 18.2 kHz, obtained under a slightly off-MAS (about 0.2°) condition to suppress resonances from the $(\pm\frac{3}{2}, \pm\frac{1}{2})$ satellite transitions; these transitions are not included in the simulation (f). The parameters used for the simulated spectra are given in Skibsted et al.[15] Positions of spinning sidebands and centerbands for the satellite transitions in the experimental spectra are indicated by asterisks (*)

and slightly off-angle, respectively). These spectra are easily analyzed in terms of two sets of χ, η, and δ values, as shown by the simulated spectra in Figures 3(d) and (f), which result from addition of two second-order lineshapes in a 1:1 ratio.[15] With these parameters at hand, the simulated spectrum for ν_r = 8.0 kHz in Figure 3(b) shows an excellent agreement with the originally recorded 'low-speed' spectrum in Figure 3(a).

Other research groups have similarly taken advantage of the combination of especially high magnetic field strengths with high-speed spinning for determination of 'large' χ values from observed second-order lineshapes of the central transition in ^{27}Al MAS NMR.[24–26] Examples include the extensively studied mineral andalusite, which has been investigated at 11.7 T employing ν_r = 15 kHz[24] and 18.4 kHz,[25] respectively, and at 14.1 T for ν_r = 14.8–19.5 kHz.[26]

Another aspect of high-speed spinning in MAS NMR for the central transition(s) may be found in the important area of quantitative analysis. Examples include accurate determinations of (i) the relative number of multiple sites within the asymmetric unit of synthetic or natural minerals[16,27] and (ii) the composition/identification of individual phases in phase mixtures.[17] Such analysis may be greatly assisted by the information that can be gained from the observation of the ssb pattern for the satellite transitions.[16,17,27]

3.4 Exactly On- and Slightly Off-MAS NMR of the Satellite Transitions

As pointed out and demonstrated for our first probe design with $\nu_r \approx 15$ kHz,[11] the possibility of high-speed spinning is important not only for the observation of the central transition but especially also in MAS NMR of the satellite transitions. The obvious reason is the increased sensitivity with which the individual ssbs for these transitions can be observed by increasing ν_r. Maybe just as important is the ability to adjust the magic angle accurately, because the correct second-order MAS lineshape (if observable) for each ssb is extremely dependent on an exact setting of the magic angle (see above). Thus, we have designed an adjustment device that allows very fine increments and stability in the angle adjustment.[28] Furthermore, ^{23}Na MAS NMR of the satellite transitions for $NaNO_3$ was proposed as a much more sensitive sample, as compared with ^{79}Br MAS NMR of KBr,[4] for accurately setting the magic angle.[28] In the ^{23}Na MAS NMR spectrum of $NaNO_3$, no second-order lineshapes are observed for the ssbs[6,9] and the linewidth of the individual ssbs can be narrowed down to between 0.7 and 0.8 ppm at the magic angle. Actually, the linewidth varies slightly throughout the ssbs of the manifold; the narrowest ssbs (approx. 0.7 ppm) are observed for

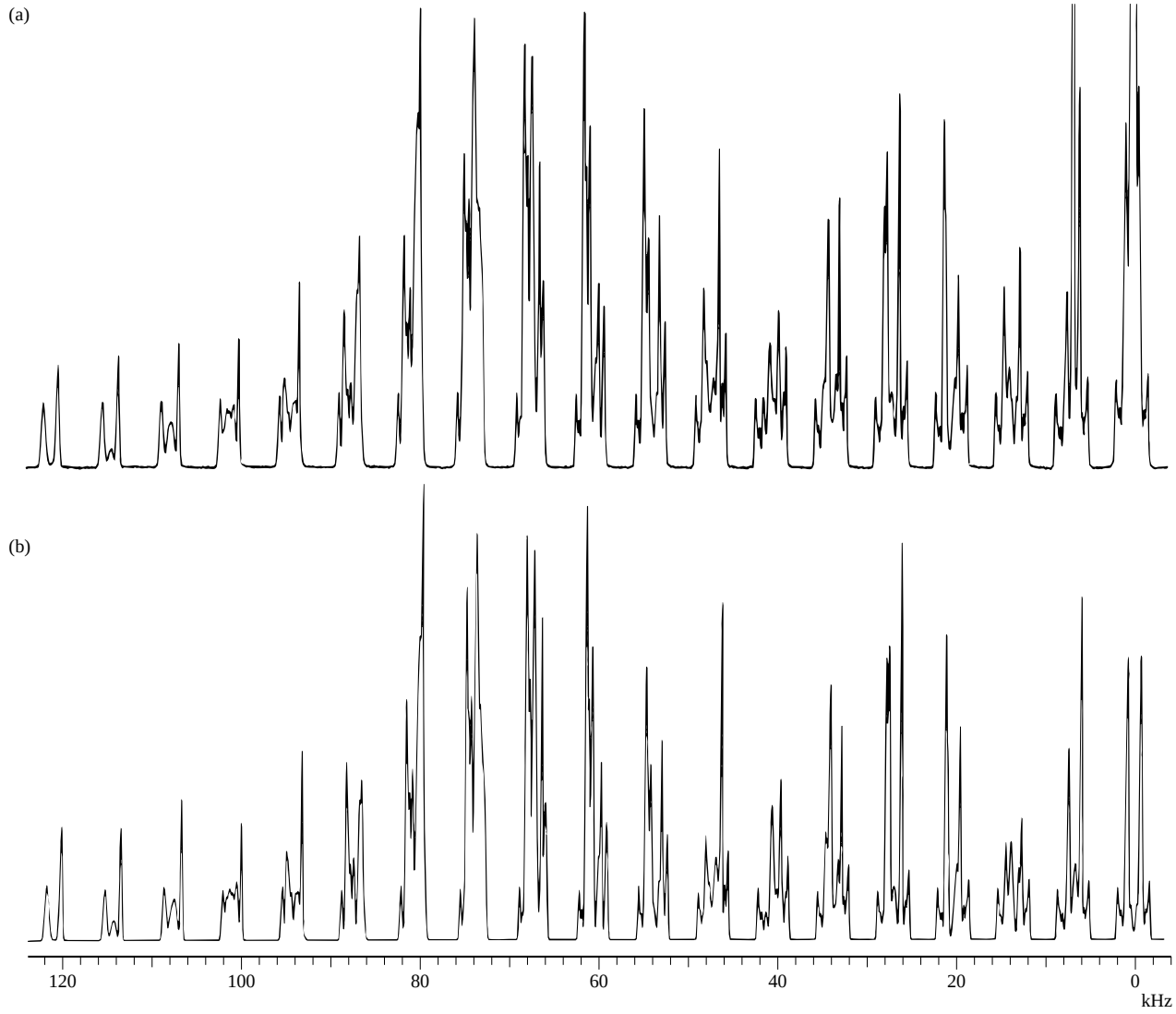

Figure 4 Expansion of part of the complex spinning sideband lineshapes observed for the ^{23}Na satellite transitions in $NaNO_3$ using slightly off MAS ($\Delta\theta = -0.44^\circ$) at 105.8 MHz (9.4 T): (a) experimental spectrum; (b) simulated spectrum calculated using ν_r = 6730 Hz, $\Delta\theta = -0.44^\circ$, χ = 337 kHz, and η = 0.0. Distortions from the central transition and its first few ssbs are observed near 0 kHz

the two 'horns' about ±80 kHz from the center of the spectrum, whereas the broader ssbs (approx. 0.8 ppm) and the most sensitive to angle adjustment are found close to the central transition. Using these linewidths as a probe, it is our experience that the magic angle can be adjusted to better than 0.001°. Slightly off-MAS (i.e., with variable angle spinning VAS), the individual ssbs start splitting into complex lineshapes. For example, for an offset $\Delta\theta = -0.44^\circ$ in the angle adjustment, the very broad and complex lineshapes observed for the ssbs are shown for some of these as the expansion in Figure 4(a). These lineshapes depend on χ, η (χ = 337 kHz, η = 0.00 for $NaNO_3$[6,9]), ν_r, and the offset $\Delta\theta$, and can be simulated based on the first-order Hamiltonian alone, employing the correct angle for the spinning axis ($54.736^\circ + \Delta\theta$), as shown in Figure 4(b). Note that the width of the ssb lineshapes mainly reflects the degree of offset $\Delta\theta$, while the lineshapes themselves are determined by χ and η for the sample.

The observation and simulation of the slightly off MAS ^{23}Na NMR spectrum of $NaNO_3$ in Figure 4 suggest an alternative method for the determination of χ and η that can be useful in certain situations. For 'small' χ values that do not give rise to an observable second-order lineshape for the central transition, χ and η are usually determined from analysis of the manifold of ssbs observed on large spectral widths (1–4 MHz), as discussed earlier. However, if a spectrometer with a fast receiver is not available, the observation of a limited number of ssbs (e.g., employing a 100 kHz spectral width) slightly off-MAS may allow determination of χ and η from lineshape analysis as illustrated in Figure 4.

4 OTHER SAMPLE ROTATION TECHNIQUES

In addition to the development and straightforward applications of high speed MAS for half-integer quadrupolar nuclei, the past decade has also witnessed the appearance and applications of several other sample rotation techniques for studies of such nuclei. These methods include double rotation (DOR)

(see ***Double Rotation***) dynamic angle spinning (DAS) (see ***Dynamic Angle Spinning***) (MAS) nutation NMR (see ***Nutation Spectroscopy of Quadrupolar Nuclei***) and variable angle spinning (VAS) (see ***Variable Angle Sample Spinning***). DOR NMR (see ***Double Rotation***) especially appears a very promising method, particularly when combined with high speed MAS, in studies of multiple sites leading to overlapping MAS lineshapes for the central transitions.

5 RELATED ARTICLES

Average Hamiltonian Theory; Double Rotation; Dynamic Angle Spinning; Geological Applications; Inorganic Solids; Magic Angle Spinning; Multiple Quantum NMR in Solids; Quadrupolar Interactions; Quadrupolar Nuclei in Solids; Variable Angle Sample Spinning.

6 REFERENCES

1. D. Müller, W. Gessner, H.-J. Behrens, and G. Scheler, *Chem. Phys. Lett.*, 1981, **79**, 59.
2. M. D. Meadows, K. A. Smith, R. A. Kinsey, T. M. Rothgeb, R. P. Skarjune, and E. Oldfield, *Proc. Natl. Acad. Sci. USA*, 1982, **79**, 1351.
3. A. Samoson and E. Lippmaa, *Phys. Rev. B*, 1983, **28**, 6567.
4. J. S. Frye and G. E. Maciel, *J. Magn. Reson.*, 1982, **48**, 125.
5. J. Skibsted, N. C. Nielsen, H. Bildsøe, and H. J. Jakobsen, *Chem. Phys. Lett.*, 1992, **188**, 405.
6. J. Skibsted, N. C. Nielsen, H. Bildsøe, and H. J. Jakobsen, *J. Magn. Reson.*, 1991, **95**, 88.
7. M. M. Maricq and J. S. Waugh, *J. Chem. Phys.*, 1979, **70**, 3300.
8. A. Samoson, E. Kundla, and E. Lippmaa, *J. Magn. Reson.*, 1982, **49**, 350.
9. H. J. Jakobsen, J. Skibsted, H. Bildsøe, and N. C. Nielsen, *J. Magn. Reson.*, 1989, **85**, 173.
10. V. Langer, P. Daugaard, and H. J. Jakobsen, *J. Magn. Reson.*, 1986, **70**, 472; US Patent 4 739 270, April 19, 1988.
11. H. J. Jakobsen, P. Daugaard, and V. Langer, *J. Magn. Reson.*, 1988, **76**, 162.
12. P. Daugaard, V. Langer, and H. J. Jakobsen, *Design of a high-speed 4, 5, 7, and 12 mm spinner system in zirconia ceramics for MAS/VAS NMR of solids, Poster WP 20, 31st Experimental NMR Conference, Asilomar, CA, April 1–5, 1990*.
13. H. W. Spiess, in *NMR Basic Principles and Progress*, eds. P. Diehl, E. Fluck, and E. Kosfeld, Springer-Verlag, Berlin, 1978, Vol. 15, p. 55.
14. A. Samoson, *Chem. Phys. Lett.*, 1985, **119**, 29.
15. J. Skibsted, H. Bildsøe, and H. J. Jakobsen, *J. Magn. Reson.*, 1991, **92**, 669.
16. J. Skibsted, E. Henderson, and H. J. Jakobsen, *Inorg. Chem.*, 1993, **32**, 1013.
17. J. Skibsted and H. J. Jakobsen, *Solid State Nucl. Magn. Reson.*, 1994, **3**, 29.
18. N. C. Nielsen, H. Bildsøe, and H. J. Jakobsen, *Chem. Phys. Lett.*, 1992, **191**, 205.
19. B. A. Goodman and J. W. Stucki, *Clay Miner.*, 1984, **19**, 663.
20. E. Oldfield, R. A. Kinsey, K. A. Smith, J. A. Nichols, and R. J. Kirkpatrick, *J. Magn. Reson.*, 1983, **51**, 3215.
21. H. J. Jakobsen, H. Jacobsen, and H. Lindgreen, *Fuel*, 1988, **67**, 727.
22. L. Kellberg, M. Linsten, and H. J. Jakobsen, *Chem. Phys. Lett.*, 1991, **182**, 120, and references cited therein.
23. D. Müller, W. Gessner, A. Samoson, E. Lippmaa, and G. Scheler, *Polyhedron*, 1986, **5**, 779.
24. L. B. Alemany, H. K. C. Timken, and I. D. Johnson, *J. Magn. Reson.*, 1988, **80**, 427.
25. L. B. Alemany, D. Massiot, B. L. Sheriff, M. E. Smith, and F. Taulelle, *Chem. Phys. Lett.*, 1991, **177**, 301.
26. S. F. Dec, J. J. Fitzgerald, J. S. Frye, M. P. Shatlock, and G. E. Maciel, *J. Magn. Reson.*, 1991, **93**, 403.
27. D. Massiot, C. Bessada, J. P. Coutures, and F. Taulelle, *J. Magn. Reson.*, 1990, **90**, 231.
28. H. J. Jakobsen, V. Langer, P. Daugaard, and H. Bildsøe, *A device and method for magic angle adjustment with millidegree accuracy using MAS of quadrupolar nuclei, Poster WP 19, 31st Experimental NMR Conference, Asilomar, CA, April 1–5, 1990*.

Biographical Sketch

Hans J. Jakobsen. *b* 1940. B.S., 1961, Ph.D., University of Aarhus, 1964. Introduced to NMR by K. Schaumburg, 1962. Faculty in Dept. of Chemistry, Univ. of Aarhus 1964–present. Approximately 135 publications. Research interests include the practice and theory of high-resolution solid state NMR with applications to chemistry and materials research.

Homonuclear Recoupling Schemes in MAS NMR

Janet M. Griffiths, Andrew E. Bennett and Robert G. Griffin

Massachusetts Institute of Technology, Cambridge, MA, USA

1	Introduction	1
2	Dipolar Hamiltonian Under Magic Angle Spinning	1
3	Rotor-Driven Homonuclear Recoupling	2
4	Homonuclear Recoupling Via Spin Echoes	3
5	Direct Recoupling Sequences: DRAMA and USEME	4
6	Emerging Techniques	4
7	Concluding Remarks	4
8	Related Articles	5
9	References	5

1 INTRODUCTION

Beginning in 1988, a number of developments have taken place in the design of NMR pulse sequences suitable for reintroducing homonuclear dipole–dipole couplings to magic angle spinning (MAS) experiments. These sequences utilize the direct coupling between nuclear magnetic dipoles to measure internuclear distances, thereby providing important constraints for the determination of molecular structure.[1] The motivation for utilizing solid state NMR stems from its ability to access polycrystalline and amorphous systems, including those with high molecular mass. Often, these systems are not amenable to study by crystallography or multidimensional solution NMR. The NMR methods described here offer resolution comparable with X-ray crystallography (0.005 to 0.02 nm for distances of $\leq$0.5 nm) and have been employed to investigate the structure of biomolecules and polymeric materials.[2,3]

In relatively rare circumstances, internuclear distance measurements can be made directly from well-resolved splittings in powder spectra.[4] A more common situation is for the shielding anisotropy and the multiplicity of homonuclear and heteronuclear couplings to obscure the splittings associated with coupled spins. It is therefore necessary to improve the spectral resolution using MAS, which attenuates these interactions, and to reintroduce the homonuclear dipolar couplings using a selectively engineered pulse sequence. Until quite recently, few MAS recoupling experiments had been proposed, in part due to the complexity of the theoretical analysis, which requires consideration of the time-dependent spin interactions during MAS. The complications arise because of the noncommutation of the flip-flop term of the homonuclear dipolar Hamiltonian with the chemical shift interactions.

This article describes several homonuclear MAS recoupling schemes. Rotational resonance (R^2)[5,6] relies on the mechanical motion of the sample rotor to recouple the spin system, while dipolar recovery at the magic angle (DRAMA),[7,8] unified spin echo and magic echo (USEME),[9,10] simple excitation for the dephasing of rotational echo amplitudes (SEDRA),[11] and rf-driven recoupling (RFDR),[12,13] employ multiple pulse sequences to interfere with the spatial averaging imposed by MAS. The coupled spin systems which are currently addressed with these schemes are comprised of 'magnetically dilute' spin$-\frac{1}{2}$ pairs, such as ^{13}C–^{13}C, ^{15}N–^{15}N, or ^{31}P–^{31}P. Typical ^{13}C dipolar strengths are $\sim$2 kHz for directly bonded spin pairs, and decrease to $<$50 Hz for distances $\sim$0.4 to 0.6 nm, which are of interest in structural problems. Owing to the small magnitude of these couplings, and also due to the low natural abundance of some nuclei (e.g. 1.1% for ^{13}C and 0.33% for ^{15}N), samples are prepared with selective or uniform labeling, and dipolar couplings are measured within the high-resolution environment afforded by MAS.

2 DIPOLAR HAMILTONIAN UNDER MAGIC ANGLE SPINNING

The dipolar Hamiltonian describes the coupling of nuclear magnetic moments in a high magnetic field, and can be expressed in the general form

$$\mathcal{H}_{\mathrm{D}}(t) = \sum_{i<j} \omega_{ij}^{\mathrm{D}}(t)[3I_{zi}I_{zj} - \boldsymbol{I}_i \cdot \boldsymbol{I}_j] \qquad (1)$$

Equation (1) is composed of two parts, the bilinear 'A' term, $2I_{zi}I_{zj}$, and the flip-flop 'B' term $-\frac{1}{2}[I_{-1}I_{+2} + I_{+1}I_{-2}]$. The coefficients, $\omega_{ij}^{\mathrm{D}}(t)$, are directly proportional to the magnitude of the dipole–dipole interaction between nuclei i and j according to equation (2), where r_{ij} is the internuclear distance, γ_i and γ_j are the gyromagnetic ratios of the two nuclei, and $\theta_{ij}(t)$ is the time-dependent angle between the static magnetic field and the internuclear vector:

$$\omega_{ij}^{\mathrm{D}}(t) = \frac{\mu_0}{4\pi}\frac{\gamma_i\gamma_j}{r_{ij}^3}\left(\frac{1-3\cos^2\theta_{ij}(t)}{2}\right) \qquad (2)$$

When the rotor axis is oriented at the magic angle, all terms of equation (2) become time-dependent.

For 'unlike' spins (i.e. possessing different γs), the flip-flop term in equation (1) is truncated, and the heteronuclear dipolar Hamiltonian reduces to the 'A' contribution. For 'like' spins, the flip-flop term is usually truncated when the difference in isotropic chemical shifts, $\Delta\omega = \omega_1 - \omega_2$, between the spins is relatively large compared with the dipole coupling, and the resulting Hamiltonian is similar to the heteronuclear case. This situation is frequently encountered for ^{13}C and ^{15}N spins. For ^{1}H pairs, the more common situation is $|\mathcal{H}_{\mathrm{D}}| \gg \Delta\omega$, and both terms in equation (1) are significant.

MAS imparts a time dependence to the chemical shift and dipolar coupling terms in the Hamiltonian. The chemical shift Hamiltonian ($\mathcal{H}_{\mathrm{CS}}$) consists of a time-independent isotropic contribution and oscillating terms due to the shielding anistropy, and it is efficiently averaged by MAS even if the rotation frequency, ω_{r} is less than the magnitude of $|\mathcal{H}_{\mathrm{CS}}|$, resulting in sharp spectral lines. The consequent MAS spectrum is comprised of a centerband at ω_{i}, flanked by a set of rotational sidebands spaced at integer multiples of ω_{r}. The 'inhomogeneous' dynamics of $\mathcal{H}_{\mathrm{CS}}$ arises from the fact that it is self-commuting at different times.[14] The heteronuclear coupling term is also inhomogeneous, and dipolar terms between weakly coupled spins are strongly attenuated at typical

MAS spinning speeds (3–12 kHz). In contrast, the homonuclear dipolar coupling behaves homogeneously in that sharp sidebands are not formed unless the rotation rate exceeds the coupling strength, $\omega_r \gg |\mathcal{H}_D|$. Under most conditions, the chemical shift difference also leads to truncation of the flip-flop term.

3 ROTOR-DRIVEN HOMONUCLEAR RECOUPLING

For homonuclear spin pairs, the energy mismatch created by the isotropic chemical shift difference limits the efficiency of magnetization exchange via the dipolar flip-flop term. An exception occurs when the sample rotation frequency satisfies the rotational resonance (R^2) condition, $\Delta\omega = n\omega_r$, where n is a small integer.[15] At R^2, the macroscopic sample spinning frequency matches the energy difference between two chemically shifted spins, and the dipolar flip-flop term again becomes significant. The reintroduction of the dipolar coupling permits energy to exchange between the spins at an enhanced rate which is governed by the coupling strength, and furthermore, induces spectral line broadening and splittings that are particularly prominent for strongly coupled spins.

In 1988, Raleigh et al. rediscovered the R^2 phenomenon and recognized that it could be exploited to measure weak homonuclear couplings.[5,6] The basis of this technique is a careful matching of spinning rate to the chemical shift difference ($\Delta\omega = n\omega_r$) and the detection of magnetization exchange between spin pairs. Figure 1 shows the pulse sequence used for measuring the distance between two chemically shifted spins I_{z1} and I_{z2}. A nonequilibrium population is established by inverting one of the resonance lines, and longitudinal exchange of the magnetization between coupled spins occurs during the mixing time, τ_m. The free induction decay signal is recorded for a number of discrete mixing times, and a plot of the difference polarization $\frac{1}{2}(I_{z1} - I_{z2})$ is compared with a numerical simulation of the exchange for the estimated dipolar coupling strength.

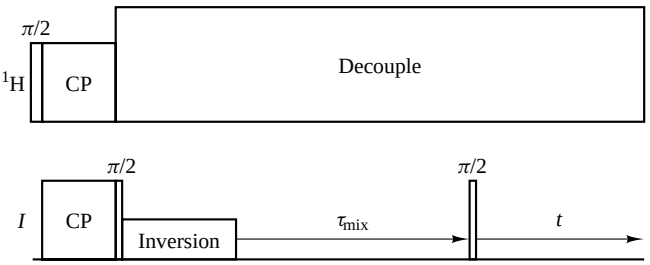

Figure 1 The R^2 pulse sequence. Initial transverse magnetization, generated with cross polarization, is placed along the z axis using a $\pi/2$ pulse. A population imbalance is created by inverting one resonance peak using a weak, selective pulse or DANTE sequence. Rotor-driven magnetization exchange takes place between coupled spins if the sample spinning rate is adjusted to match the difference in isotropic chemical shifts ($\Delta\omega_{iso} = n\omega_r$). After a variable mixing period, τ_m, a second ($\pi/2$) pulse returns the magnetization to the transverse plane and the remaining difference in signal intensities, $\frac{1}{2}(I_{z1} - I_{z2})$, is recorded as a free induction decay signal. A magnetization exchange curve is generated by recording this quantity for a number of discrete mixing times, usually between 0–30 ms. Strong proton decoupling reduces dephasing by abundant protons and helps to maintain a sharp R^2 condition

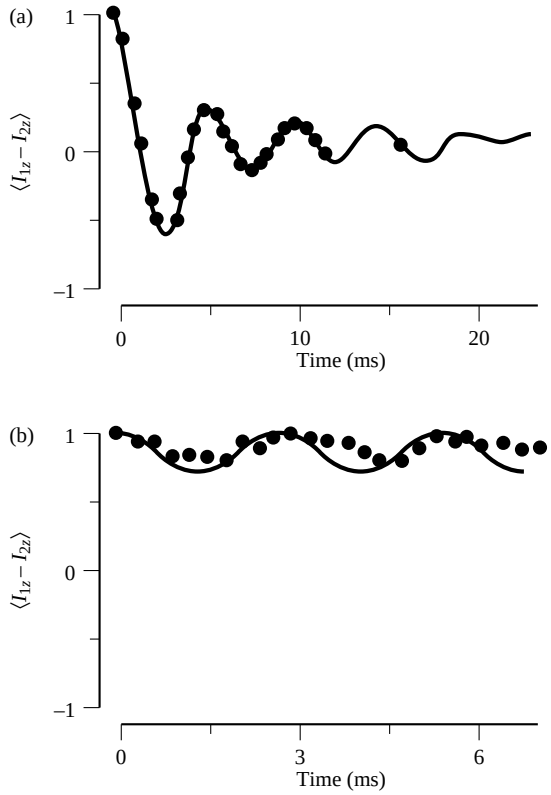

Figure 2 (a) Experimental (•) and simulated (–) magnetization exchange curve for double-^{13}C-labeled zinc acetate $Zn^{+2}(CH_3COO^-)_2.2H_2O$ recorded at the $n = 3R^2$ condition ($\omega_r/2\pi$ = 4.38 kHz). Experimental points represent the difference magnetization $\frac{1}{2}(I_{z1} - I_{z2})$ normalized to $\tau_m = 0$. (b) The magnetization exchange curve recorded at $\omega_r/2\pi$ = 4.26 kHz, corresponding to an off-R^2 condition. Simulation parameters for zinc acetate are found in Levitt et al.[6]

A demonstration of magnetization exchange at the $n = 3$ condition is shown in Figure 2(a) for 1,2-^{13}C-labeled zinc acetate $Zn^{2+}(CH_3COO^-)_2.2H_2O$, where oscillatory decay of the difference magnetization arises from exchange between these strongly coupled spins. A numerical simulation of the magnetization curve is also shown and corresponds to an internuclear distance of 0.151 ± 0.002 nm. Figure 2(b) shows the difference polarization recorded at a sample rotation rate which is set 120 Hz away from the $n = 3R^2$ condition. Model compound studies have demonstrated that internuclear distances ≤0.6 nm to a resolution of ±0.005 to ±0.02 nm are accessible via the R^2 method.

The theoretical aspects of magnetization exchange at the R^2 condition are treated in a number of works using Average Hamiltonian theory[6,16,17] and Floquet theory.[17–19] A fictitious field approach, wherein magnetization exchange is described within a $\{|2\rangle,|3\rangle\}$ subspace, provides a geometric description of resonant magnetization exchange.[6,13] The Floquet analysis leads to an expression for the effective Hamiltonian at sample rotation rates close to the R^2 condition $\Delta\omega \approx n\omega_r$ and which is valid for synchronous acquisition of the data:

$$\bar{\mathcal{H}}_{eff} = \tfrac{1}{2}(\Delta\omega - n\omega_r)[I_{z1} - I_{z2}] + \tfrac{1}{2}|\omega_{eff}^{D}(n)|[I_{+1}I_{-2} + I_{-1}I_{+2}] \quad (3)$$

The first term in equation (3) represents the offset from the R^2 condition. In general, the effective dipolar frequency $|\omega_{\text{eff}}^{\text{D}}(N)|$ appearing in the second term depends on both the coupling and the shielding anisotropies. However, in the case of small shielding anisotropy, it reduces to the magnitude of the nth Fourier coefficient $|\omega_n^{\text{D}}(\alpha, \beta)|$ of the time-dependent prefactor in equation (3), where (α, β) denote the orientation of the internuclear vector in a frame rotating with the rotor.

The exact time course of magnetization exchange at R^2 is determined by the magnitude of the homonuclear dipolar coupling, the principal values of the I_{z1} and I_{z2} chemical shift tensors, the relative orientations of the chemical shift and dipolar tensors, and the isotropic J coupling of the spin pair. Magnetization exchange rates are insensitive to molecular orientations for the $n = 1$ condition for a typical application, but have a stronger dependence for higher resonance orders.[20] In some circumstances, this sensitivity can be exploited to yield additional structural information, in the form of tensor orientations, from MAS spectra.

The R^2 analysis also requires an estimation of the zero quantum relaxation time, T_2^{ZQ} which is associated with the zero quantum coherence $(I_{x1}I_{y2} - I_{y1}I_{x2})$. Kubo and McDowell have shown that it can be approximated by the individual single quantum relaxation rates, T_2.[19] An estimate of $(T_2^{\text{ZQ}})^{-1}$ is therefore found by summing the inverse linewidths of resonance peaks (measured at an off-R^2 condition) after correction for magnet inhomogeneity. The zero quantum relaxation pathway competes with magnetization exchange at R^2 and is most significant when couplings are weak or resonance peaks are broad. Under these circumstances, the exchange processes is damped, and the magnetization exchange decays monotonically.

The R^2 technique has been applied to a variety of biological solid state systems. Examples include the investigation of the mechanism of inactivation in a ^{31}P-labeled enzyme bound inhibitor,[21] establishing the folding motif of membrane-bound peptides,[22] measuring retinal-to-protein distances in the 26 kDa integral membrane protein bacteriorhodopsin,[23,24] and describing the amide bond geometry of a fragment of the β-amyloid protein associated with Alzheimer's disease.[25]

4 HOMONUCLEAR RECOUPLING VIA SPIN ECHOES

RFDR (rf-driven dipolar recoupling) and SEDRA (simple excitation for the dephasing of rotational echo amplitudes) are two related approaches employing spin echoes to reintroduce homonuclear dipolar couplings to MAS spectra. In both experiments, recoupling is accomplished via the modulation of the dipolar Hamiltonian by the difference in chemical shifts between the coupled spins. Both schemes lead to an efficient reintroduction of the homonuclear dipolar interaction across a broad range of chemical shift differences and MAS spinning speeds.

The SEDRA experiment is based on the observation of transverse echo dephasing during a rotor-synchronized π pulse train. Dephasing due to shielding anisotropy and heteronuclear interactions is refocussed after each pair of spin echo π pulses, while a net dephasing arises from the homonuclear dipolar flip-flop term. A train of rotor-synchronized π pulses is also used

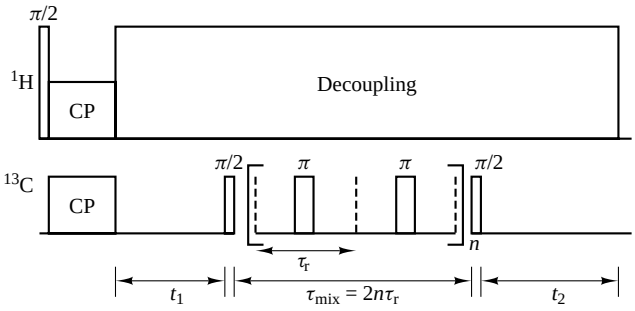

Figure 3 The RFDR pulse scheme for 2D homonuclear correlation spectroscopy. Following cross polarization to create transverse S spin magnetization (shown here for ^{13}C), spins evolve according to their chemical shifts during t_1. A nonselective $\pi/2$ pulse places the magnetization of one spin along the z axis. During a variable mixing time, τ_{m}, single π pulses (one per rotor period, τ_{r}) drive longitudinal magnetization exchange between coupled spins. A second nonselective $\pi/2$ pulse returns the magnetization to the transverse plane and S spin magnetization is recorded. The SEDRA sequence involves monitoring the dephasing with the same MAS spin echo sequence. Reprinted from Bennett et al.[12]

for RFDR, but the exchange of longitudinal magnetization among dipolar coupled spins is detected instead. Figure 3 shows a diagram of the RFDR pulse sequence. In the one-dimensional (1D) version, an inversion pulse is employed, and magnetization exchange between coupled spins is reported by the time course of the difference polarization. A 2D version of the experiment utilizes a t_1 evolution period, and the resulting chemical shift correlation spectra show cross peaks between dipole coupled sites.

The spin dynamics of the spin echo recoupling sequence can be approximated with average Hamiltonian theory[12] or Floquet theory.[11] The zeroth order result (neglecting shielding anisotropy) for a spin echo cycle of one π pulse per rotor period is an effective Hamiltonian containing only a dipolar flip-flop term:

$$\bar{\mathcal{H}}_{\text{eff}}^{(0)} = \tfrac{1}{2}\bar{\omega}_{\text{eff}}^{\text{D}}[I_{+1}I_{-2} + I_{+2}I_{-1}] \tag{4}$$

The dipolar frequency, $\bar{\omega}_{\text{eff}}^{\text{D}}$ depends on the spinning speed ω_{r} and $\Delta\omega$ as follows:

$$\bar{\omega}_{\text{eff}}^{\text{D}} = \frac{2}{\pi}\sum_{n=1,2}\text{Re}\{\omega_n^{\text{D}}(\alpha,\beta)\}\frac{\frac{\Delta\omega}{\omega_{\text{r}}}}{\left(\frac{\Delta\omega}{\omega_{\text{r}}}\right)^2 - n^2} \times(-1)^{n-1}\sin\left(n\pi\frac{\Delta\omega}{\omega_{\text{r}}}\right) \tag{5}$$

The dipolar frequency has maxima at the rotational resonance conditions, but significant recoupling is achieved over a broader range. The pulse sequence is particularly effective in recoupling under the condition $\omega_{\text{r}} \leq \Delta\omega \leq 2\omega_{\text{r}}$.

Simulation of the magnetization exchange during RFDR (monitored by 2D cross-peak intensities or 1D exchange curves) and dephasing during SEDRA experiments requires the measurement or reasonable estimation of relaxation parameters, and all relevant chemical shift and dipolar tensors parameters and orientations, as in the case of R^2.

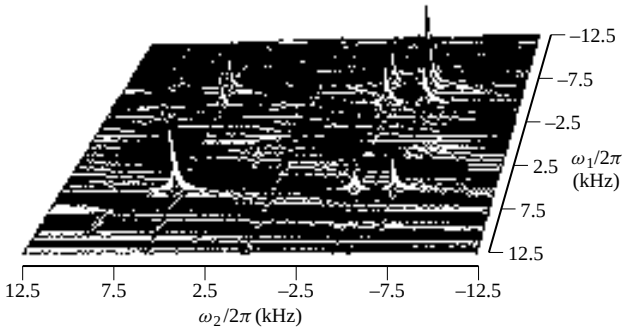

Figure 4 A stack plot of the 2D RFDR magnitude spectrum of uniformly ^{13}C-labeled alanine recorded with τ_m = 8.6 ms and $\omega_r/2\pi$ = 3.72 kHz. Cross peaks demonstrate the dipolar coupled spins. In this example, cross peaks from directly bonded ^{13}C nuclei appear in $\leq$ 2 ms. Reprinted from Bennett et al.[12]

SEDRA and RFDR are 'broadband' recoupling schemes that offer some important advantages over the R^2 technique in situations where spectral lines are inhomogeneously broadened, or when it is not feasible to match the rotation rate dictated by the R^2 condition. The RFDR technique and the recently introduced *t*-SEDRA experiment[26], are suitable for 2D homonuclear dipolar correlation spectroscopy, and may be used to map couplings between more than two coupled spins, if the exchange of magnetization between all coupled spins is traced. A demonstration of the 2D RFDR correlation experiment is given in Figure 4, for uniformly ^{13}C-labeled alanine, where cross peaks between all coupled ^{13}C sites are prominent after a mixing time of 8.6 ms. A similar 2D approach was adopted to examine the geometry of two conformers in the membrane protein bacteriorhodopsin.[27]

5 DIRECT RECOUPLING SEQUENCES: DRAMA AND USEME

A direct reintroduction of the homonuclear coupling is accomplished with rotor synchronized $\pi/2$ pulses in the DRAMA (dipolar recovery at the magic angle) experiment. This scheme, shown in Figure 5, relies on the interference between the RF modulation of the dipolar spin operators and the oscillations imposed on them by MAS. Chemical shift interactions are removed to zeroth order through the use of π pulses. The recoupling effect in DRAMA does not require the existence of chemical shift differences between the spins. However, it is most efficient when the chemical shift anisotropies and resonance offsets are small compared with ω_r since these interactions complicate the spin dynamics and lead to a loss of magnetization.

The effective Hamiltonian can be obtained with Floquet theory[28] or average Hamiltonian theory.[7,8] The latter analysis, equation (6) yields a nonzero dipolar term:

$$\bar{\mathcal{H}}^{(0)}_{\text{eff}} = \frac{4}{\pi}\text{Re}\left\{\omega^{\text{D}}_{n=1}(\alpha,\beta)\right\}\bar{\omega}^{\text{D}}_{\text{eff}}(I_{z1}I_{z2} - I_{y1}I_{y2}) \qquad (6)$$

DRAMA has also been extended to include double quantum filtering, which restricts the detected NMR signal to resonances from coupled spin pairs and therefore simplifies the spectra of

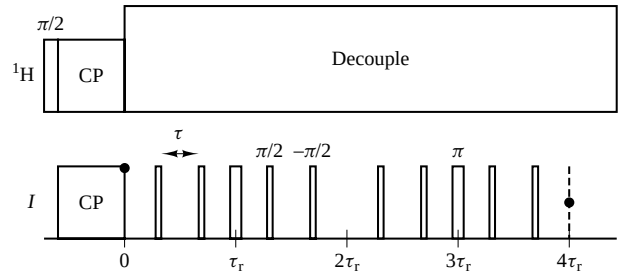

Figure 5 The DRAMA pulse sequence. The pulse cycle, consisting of 4 τ_r is comprised of a pair of $\pi/2$ pulses with alternating phase **X**, **X**, and two π pulses which are also alternated by **X**, $\bar{\mathbf{X}}$. The $\pi/2$ pulses interfere with dipolar refocussing by MAS

complex molecules.[8] This approach has been used to enhance selectively the signal of ^{13}C sites within a $\sim$0.5 nm radius of a selectively labeled site in an undecapeptide of molecular mass 1100.

Direct recoupling of the dipolar interaction is also achieved with a continuous rf field applied during the second half of each rotor cycle. This approach, called USEME (unified spin echo and magic echo) utilizes the partial cancellation of rotational echo refocussing via a combined spin echo and magic echo sequence to yields a scaled homonuclear coupling.[9,10]

6 EMERGING TECHNIQUES

Improvements in the efficiency of homonuclear recoupling schemes remains an important goal. Several recently introduced homonuclear recoupling sequences hold the promise of compensating for the complications introduced by large chemical shift differences in DRAMA-type experiments.[29,30] The MELODRAMA (melding of spin locking and DRAMA) method reintroduces the dipolar coupling in a spin-locking interaction frame by utilizing 90° rotor-synchronized phase shifts.[31] The recoupling effect is relatively insensitive to chemical shift and anisotropy, rendering the method suitable for 2D correlation spectroscopy. The double quantum filtering experiment called HORROR (homonuclear rotary resonance), utilizes a rotary resonance condition between the sample rotation frequency and the rf field to provide efficient double quantum transfer between coupled spin pairs.[32] A novel approach to homonuclear recoupling that combines angle switching and phase shifted π and $\pi/2$ pulses was recently reported by Tycko.[33] This experiment, called NASDY (normal angle spinning dipolar spectroscopy) takes advantage of the static contribution to the dipolar coupling by recovering this contribution at a sample rotation angle other than the magic angle.

7 CONCLUDING REMARKS

Solid state NMR experiments that restore dipolar couplings to MAS spectra are becoming increasingly important for investigating the molecular structure of polycrystalline and amorphous materials. These experiments provide geometric information by measuring precise distance measurements and establishing spatial connectivities. Selectivity is also offered

through the choice of nucleus and specific labeling scheme. Potential applications include distinguishing between various protein folding patterns, determining the bonding arrangements of molecules absorbed on surfaces, mapping the interface between two materials or phases such as polymer blends, and elucidating active site geometries in biomolecules.

A number of important challenges remain in the development of homonuclear recoupling schemes; these include improvements in sensitivity for the detection of weak couplings and extension of these methods to multiple spin environments in a manner analogous to multidimensional solution NMR. Such developments will vastly improve the efficiency of gathering structural information via solid state NMR.

8 RELATED ARTICLES

Average Hamiltonian Theory; Dipolar and Indirect Coupling Tensors in Solids; Magic Angle Spinning; REDOR and TEDOR; Rotational Resonance in Biology; Sideband Analysis in Magic Angle Spinning NMR of Solids.

9 REFERENCES

1. R. R. Ernst, G. Bodenhausen, and A. Wokaun, *Principles of Nuclear Magnetic Resonance in One and Two Dimensions*, Oxford University Press, Oxford, 1987.
2. J. M. Griffiths and R. G. Griffin, *Anal. Chim. Acta*, 1993. **283**, 1081.
3. A. E. Bennett, R. G. Griffin and S. Vega, in *NMR Basic Principles and Progress*, ed. B. Blümich, Springer-Verlag, Berlin, 1994, Vol. 32, p. 1.
4. G. E. Pake, *J. Chem. Phys.*, 1948 **16**, 327.
5. D. P. Raleigh, M. H. Levitt, and R. G. Griffin, *Chem. Phys. Lett.*, 1988, **146**, 71.
6. M. H. Levitt, D. P. Raleigh, F. Cruezet, and R. G. Griffin, *J. Chem. Phys.*, 1990, **92**, 6347.
7. R. Tycko and G. Dabbagh, *Chem. Phys. Lett.*, 1990, **173**, 461.
8. R. Tycko and S. O. Smith, *J. Chem. Phys.*, 1993, **98**, 932.
9. A. Ramamoorthy, T. Fujiwara and N. Nagayama, *J. Magn. Reson., Ser. A*, 1993, **104**, 366.
10. T. Fujiwara, A. Ramamoorthy, K. Nagayama, K. Hioka, and T. Fujito, *Chem. Phys. Lett.*, 1993, **212**, 81.
11. T. Gullion and S. Vega, *Chem. Phys. Lett.*, 1992, **194**, 423.
12. A. E. Bennett, J. H. Ok, and R. G. Griffin, *J. Chem. Phys.*, 1992, **96**, 8634.
13. D. K. Sodickson, M. H. Levitt, S. Vega, and R. G. Griffin, *J. Chem. Phys.*, 1993, **98**, 6742.
14. M. M. Maricq and J. S. Waugh, *J. Chem. Phys.*, 1979, **70**, 3300.
15. E. R. Andrew, A. Bradbury, R. G. Eades and V. T. Wynn, *Phys. Lett.*, 1963, **4**, 99.
16. Z. H. Gan and D. M. Grant, *Mol. Phys.*, 1989, **67**, 1419.
17. T. Nakai and C. A. McDowell, *Mol. Phys.*, 1992, **77**, 569.
18. A. Schmidt and S. Vega, *J. Chem. Phys.*, 1992, **4**, 2655.
19. A. Kubo and C. A. McDowell, *J. Chem. Soc., Faraday Trans.*, 1988, **84**, 3713.
20. F. Creuzet, D. P. Raleigh, M. H. Levitt, and R. G. Griffin, submitted 1994.
21. A. E. McDermott, F. Creuzet, R. G. Griffin, L. E. Zawadzke, Q. Ye, and C. T. Walsh, *Biochemistry*, 1990, **29**, 5767.
22. O. B. Peerson, S. Yoshimura, H. Hojo, S. Aimoto, and S. O. Smith, *J. Am. Chem. Soc.*, 1992, **114**, 4332.
23. L. M. Thompson, A. E. McDermott, J. Raap, C. M. van den Wielen, J. Lugtenburg, J. Herzfeld, and R. G. Griffin, *Biochemistry*, 1992, **31**, 7931.
24. K. V. Lakshmi, M. Auger, J. Raap, J. Lugtenburg, R. G. Griffin, and J. Herzfeld, *J. Am. Chem. Soc.*, 1993, **115**, 8515.
25. R. G. S. Spencer, K. J. Halverson, M. Auger, A. E. McDermott, R. Griffin, and P. T. Lansbury Jr., *Biochemistry*, 1991, **30**, 10 382.
26. O. Weintraub, S. Vega, C. Hoelger and H. H. Limbach, submitted, 1994.
27. J. M. Griffiths, K. V. Lakshmi, A. E. Bennett, J. Rapp, J. Lugtenburg, J. Herzfeld, and R. G. Griffin, *J. Am. Chem. Soc.*, 1994, **116**, 10 178.
28. O. Weintraub, and S. Vega, *J. Magn. Reson., Ser. A*, 1993, **105**, 245.
29. C. A. Klug, W. Zhu, M. E. Merritt and J. Schaefer, *J. Magn. Reson., Ser. A*, 1994, **109**, 134.
30. J. Callahan and G. Drobny, *Poster presentation at the Experimental Nuclear Magnetic Resonance Conference, CA, Asilomar, April 10-15, 1994*.
31. B. Sun, P. R. Costa, D. Kocisko, P. T. Lansbury, Jr., and R. G. Griffin, *J. Chem. Phys.*, 1995, **102**, 702.
32. N. C. Nielson, H. Bildsoe, H. J. Jakobsen, and M. H. Levitt, *Poster presentation at the Experimental Nuclear Magnetic Resonance Conference*, Asilomar, CA, April 10–15, 1994.
33. R. Tycko, *J. Am. Chem. Soc.*, 1994, **116**, 2217.

Acknowledgments

The authors acknowledge the support of the National Institutes of Health (GM-23403, GM-23289, GM-25505 and RR-00995). We wish to acknowledge P. R. Costa, F. Creuzet, M. H. Levitt, A. E. McDermott, D. P. Raleigh, D. K. Sodickson, B. Q. Sun, and S. Vega for stimulating discussions and for their contributions to the development of these NMR techniques.

Biographical Sketches

Janet M. Griffiths. *b* 1963. B.Sc. University of Cincinnati (Chemical Engineering), 1985; Ph.D., University of California, Berkeley (Chemical Engineering), 1992. American Cancer Society postdoctoral fellow, Department of Chemistry & Francis Bitter National Magnet Laboratory, Massachusetts Institute of Technology, 1992–1995. Research interests; the development and application of NMR techniques to investigate the structure of heterogeneous systems including catalytic surfaces and membrane proteins.

Andrew E. Bennett. *b* 1964. B.A., Wesleyan University (Chemistry), 1986; M.S., University of California, Berkeley (Physical Chemistry), 1990; Ph.D., Department of Chemistry & Francis Bitter National Magnet Laboratory, Massachusetts Institute of Technology, 1995. Research interest; the development of new methods for the measurement of dipolar couplings in solids.

Robert G. Griffin. *b* 1942. B.S., University of Arkansas, 1964; Ph.D., Washington University (St. Louis), 1969; postdoctoral fellow, Department of Chemistry, MIT 1969–72. Staff member Francis Bitter National Magnet Laboratory, MIT, 1972–1989; Professor of Chemistry, MIT 1989–current; Director, Francis Bitter National Magnet Laboratory, 1992–current. Approximately 190 publications. Research interests: development of new methods for performing high resolution NMR experiments in solids, high frequency EPR, and applications of these techniques to problems in biological, chemical, and physical systems.

Line Narrowing Methods in Solids

Joseph Virlet

CEA Saclay, Service de Chimie Moléculaire, Gif-sur-Yvette, France

1	Introduction	1
2	Line Narrowing	3
3	Sample Motion: Magic Angle Spinning	6
4	Spin Motions: Decoupling and Averaging out the Broadening Due to the Dipolar Interactions	9
5	Two Useful Methods for Half-Integer Spins: CP MAS and CRAMPS. Averaging Out Both Anisotropic Chemical Shifts and Dipolar Broadening	10
6	Sample Motion Again: DAS and DOR	11
7	Mistuning and Recoupling: Limits to Resolution, and Tools for Structural Studies	14
8	Other Approaches to Line Narrowing in Solids	16
9	MQ-MAS, A New Efficient Line Narrowing Method for Quadrupolar Nuclei	17
10	Conclusions	18
11	Related Articles	18
12	References	18

1 INTRODUCTION

The aim of this article is to give an overview of the principles and the experimental aspects of the different techniques (magic angle spinning, CP MAS, CRAMPS, DAS, DOR, etc.) that have been introduced in order to obtain high-resolution NMR spectra in solids.

The theoretical and experimental details will be found in the related articles (listed at the end of this article) devoted to each particular line-narrowing method. This article will describe, using as little mathematics as possible, the common underlying principles of all the line-narrowing methods in solids, how line narrowing can be performed, the main limitations to line narrowing, and how the mistuning or resonance effects that may result in a residual linewidth can be used in order to obtain more structural information on materials under study.

As well as some good introductory chapters in textbooks on NMR,[1–4] there are a number of books fully devoted to different aspects of high-resolution NMR in solids.[5–9] A review of trends in the subject can be found in the proceedings of the 'John Waugh Symposium'.[10]

1.1 A Short History of Line-Narrowing Methods in Solids

In nonviscous liquids, the NMR lineshapes are naturally narrow (with the exception of some quadrupolar nuclei). This is due to molecular motions (Brownian motion), which average out all the possible sources of broadening. This has allowed the enormous development of high-resolution NMR. However, in solid samples, and especially in powdered solids, the lines remain broad. However, beginning in 1958, experimental methods have been devised that, like Brownian motion in liquids, make the interactions time-dependent, and provide high-resolution NMR spectra of solids. This has been achieved by rotating the sample or the spins: these are the line-narrowing techniques. Although the resolution that can be achieved in solids is not as high as in liquids, it is nowadays about three orders of magnitude better than in a static sample.

The first line-narrowing experiments were, in 1958, the magic angle spinning experiments by E. R. Andrew[11] and I. Lowe[12] and others. Successful averaging was achieved for the chemical shift anisotropy, for heteronuclear dipolar coupling, and for homonuclear dipolar interaction when it was not too high (e.g. between ^{31}P nuclei or between ^{19}F nuclei when the linewidth is reduced by molecular motions).

Spinning at the magic angle fast enough to average out the dipolar interaction between abundant spins like protons in an organic solid was (and remains today) unachievable. Therefore attention focused on spins with high gyromagnetic factor: ^{1}H and ^{19}F. The challenge was first to average out the homonuclear dipolar interaction, without cancelling the chemical shift. Most of the early work was done on fluorine, which has a greater spread of chemical shifts. Solid echo experiments showed that it was possible to extend by one echo, and then (1966) by multiple echoes,[13] the transverse magnetization lifetime, thus averaging out the homonuclear dipolar interaction. When calculating the effect of multiple echoes, the periodic (or 'cyclic') structure of the multipulse leads to large simplifications. John Waugh realized an important property of this modulation: for averaging out an interaction, a coherent modulation of frequency Ω is more efficient than a random fluctuation of correlation time $\tau = 1/\Omega$. This was the concept of coherent averaging. It made more accessible the modulation speed required for line narrowing. Pulsed and continuous magic angle irradiations were introduced, and then, in 1968, the WAHUHA multipulses.[14] A key to the development of those methods was the introduction of the average Hamiltonian. The calculation of the exact value of the average Hamiltonian uses a perturbation expansion. The expressions for the successive terms were obtained using the Magnus expansion. Symmetry properties of the multipulse irradiation were also used systematically to cancel these higher order terms due to all the experimental imperfections of the irradiations. This led to the compensated MREV-8 multipulse sequence.

Later, in 1972, another method of line narrowing in solids was devised by Pines et al.[15] The addressed nuclei were diluted nuclei with spin-$\frac{1}{2}$, like ^{13}C at natural abundance (1.1%), in organic solids. Their homonuclear dipolar interaction is very low (about 50 Hz). The broadening due to the heteronuclear dipolar coupling with protons was averaged out by decoupling, that is, by strong irradiation at the proton frequency. The low natural signal of ^{13}C was enhanced by cross polarization with the abundant protons.

In these experiments, as well as in the WAHUHA experiments, the chemical shift anisotropy of ^{19}F, ^{13}C, etc. was preserved (with scaling), as well as the isotropic chemical shift. This allowed many nice experiments on simple compounds. However, when more than a few different spin species were present, unless using monocrystals, overlapping powder lineshapes could not be easily disentangled. This precluded wide use of these methods.

Some years later, in 1977, Schaeffer published the first spectra of ^{13}C in organic solids and polymers with proton decoupling, magic angle spinning, and cross polarization.[16] This is the CP MAS method, which is now widely used. Here, only the isotropic chemical shifts of ^{13}C were preserved, free from any anisotropic broadening. Well-resolved spectra were obtained, looking very similar to high-resolution spectra in liquids. Along the same lines and in the same year, a combination of magic angle spinning and multipulse (WAHUHA, MREV-8, etc.) irradiation allowed Gerstein[17] to obtain high-resolution NMR spectra of ^{1}H. This is the CRAMPS experiment. A huge number of results have been obtained in the fields of organic chemistry and polymers using ^{13}C CP MAS. On the other hand, CRAMPS—more tricky and demanding for the spectrometer and the experimentalist—has had a more restricted use.

In zero field, because there is no magnetic field and therefore no reference direction, the spectra are free from anisotropic broadening. Transient measurements of zero field NMR, with the sample shuttling between high and zero field, were first obtained in 1985. A very difficult but an elegant approach was also proposed and demonstrated experimentally for obtaining zero field NMR spectra in high field.

All these methods were restricted to spin-$\frac{1}{2}$.

Achieving high-resolution NMR of the allowed transitions of half-integer quadrupolar nuclei with a large quadrupolar interaction was for a long time considered as impossible. In 1988, the principle of two closely related methods, for line narrowing of quadrupolar nuclei—DAS and DOR—was found and announced independently by Llor and Virlet in Saclay and the Pines group in Berkeley. Experimental results were obtained in Berkeley in agreement with the theoretical previsions.

High-resolution solid state NMR of integer quadrupolar nuclei may be obtained by indirect (^{2}H, ^{14}N) or direct (^{14}N: overtone spectroscopy) detection of multiple quantum transitions. However, such complex methods still require further development, and, in any case, are not widely used for application purposes. For instance, in ^{14}N overtone spectroscopy, one needs to implement together DAS (or DOR) and the excitation and observation of a forbidden transition. Besides, in quadrupolar systems in rotating samples, coherence transfer becomes a very intricate process.

Very recently, a new line narrowing method for quadrupolar nuclei, called MQ-MAS, has been introduced recently by L. Frydman.[83] The sample is simply rotating at magic angle. Unlike DAS and DOR, there is no reorientation of the spinning axis of the sample. This extra motion is replaced by some pulses which result in coherence transfer 'forth and back' and evolution 'within' some 'forbidden' multiple quantum transitions. This method is at least as efficient[83–85] as DAS and DOR and can be settled easily on any solid state NMR spectrometer, without the need of sophisticated DAS and DOR probes.

Since the early days of the line-narrowing story, it has been realized that the anisotropic interactions that are wiped out in order to improve resolution nevertheless contain very useful structural information. Therefore, the last part of the line-narrowing saga is to devise ways, such as rotational resonances, for reintroducing and measuring those anisotropic terms, selectively for each spin species resolved by line narrowing. Typical of such methods are dipolar dephasing, separated field spectroscopy and all its variants, TEDOR, and REDOR, or rotational resonance. Thus one-dimensional spectra may be obtained (often called edited spectra), of spins selected according to the strength of the anisotropic interaction they withstand. Alternately, one may manage the experiments so that these anisotropic interactions may appear in one dimension of two-dimensional spectra, with the isotropic chemical shifts in the second dimension. The 1D edited spectra may be viewed as slices of these 2D spectra.

1.2 Some Definitions

As usual in NMR, we shall talk about the magnetic field $\boldsymbol{B}_0$ instead of the more correct magnetic induction field $\boldsymbol{B}_0$.

In the context of dipolar decoupling and of cross-polarization, 'dilue and low γ' nuclei like ^{13}C or ^{29}Si are called 'rare spins' by contrast with the 'abundant and high γ' spins like ^{1}H or ^{19}F which are called 'abundant spins'. The exact situation depends on the relative strength of the different (S–S, I–I and I–S) dipolar interactions. Follow A. Pines and M. Mehring, here and later, we call I the 'abundant spins' and S the 'rare spins'. What is told about protons, ^{1}H, or about carbons, ^{13}C, may generally be extended to 'I spins' and 'S spins'.

1.2.1 'Internal Interactions'

(See ***Chemical Shift Tensors***; ***Dipolar and Indirect Coupling Tensors in Solids***; ***Internal Spin Interactions and Rotations in Solids***; ***Quadrupolar Interactions***; ***Quadrupolar Nuclei in Solids***.)

In NMR, the positions of the lines are slightly shifted from the Larmor frequency $\omega_0 = 2\pi\nu_0 = \gamma B_0$ of the spin under observation by the interactions of the spins with their surroundings. These 'internal' interactions are the chemical shielding, the dipolar magnetic coupling, the quadrupolar interaction, and the indirect J coupling. With the exception of the quadrupolar interaction, the shifts due to these interactions are always much smaller than the Larmor frequency. These interactions bring structural and/or dynamical information about the molecule or the material. They are, by essence, anisotropic. The shifts of the lines induced by these interactions are therefore dependent on the orientation of the chemical bonds, or of the crystallographic site, etc., that is, macroscopically, of the sample with respect to the magnetic field.

1.2.2 A Typical Pulse NMR Experiment

In the following, unless otherwise stated, we shall refer implicitly to a typical NMR experiment.

1. It begins with the preparation of a transverse magnetization of spins S. This may be
   (a). a $\frac{1}{2}\pi$ pulse that rotates the longitudinal equilibrium magnetization (aligned along the magnetic field $\boldsymbol{B}_0$) into the transverse plane (perpendicular to $\boldsymbol{B}_0$);
   (b). a cross polarization (see ***Cross Polarization in Rotating Solids: Spin-1/2 Nuclei***; ***Cross Polarization in Solids*** and Sections 5.1.1 and 7.2.2 below) between abundant spins I (typically ^{1}H) and rare spins S (typically ^{13}C).

2. This is followed by a precession of the transverse magnetization of spins S in the transverse plane, at a frequency $\omega = \omega_0 + \omega_{\text{int}}$ close to its Larmor frequency ω_0, shifted from ω_0 by ω_{int}. This precessing magnetization induces a signal, which is acquired and Fourier transformed. During the precession time, the interactions are made time-dependent in order to average out their anisotropic part, which in powders causes line broadening. When the spins can be considered as evolving independently, the observed signal is

$$\begin{aligned} S(t) &= S(0)\exp\left\{-\mathrm{i}\left[\omega_0 + \int_0^t \omega_{\text{int}}(\tau)\,\mathrm{d}\tau\right]t\right\} \\ &= S(0)\exp\{-\mathrm{i}[\omega_0 + \varphi_{\text{int}}(t)]t\} \end{aligned} \tag{1}$$

where $\omega_{\text{int}}(t)$ is the time-dependent frequency shift due to the interactions. This assumption of an independent evolution of each spin S is exact when the only interactions of the spin S with its surroundings are the chemical shielding, a quadrupolar interaction, or a dipolar coupling (say, heteronuclear) with different spin species. 'Different' means that the difference in frequencies ω is greater than the 'size' (see Section 2.2) of that dipolar coupling. Such a spin system has been called *inhomogeneous*. If there is a strong dipolar coupling between like spins, one must generally study the evolution of the whole coupled spin system, which is called *homogeneous*.

2 LINE NARROWING

2.1 Line Narrowing in Nature

(See ***Brownian Motion and Correlation Times***.)

High-resolution NMR in solids was for long time thought to be unachievable. Only a single broad line is usually observed. However, it was observed very early that, even in solids, sufficiently fast molecular motions or chemical exchange result in some line narrowing. One of the first and more famous examples is the jump reorientation of the benzene molecule about its C_6 axis, which, as its speed increases with temperature, reduces the second moment of the ^{1}H NMR line from $10^{-7}\,\mathrm{T}^2$ below 90 K to $2 \times 10^{-8}\,\mathrm{T}^2$ above 120 K.

In liquids, the NMR lines are sharp because molecular motions are so fast and so isotropic that they average out the interactions that broaden the lines in solids.

Is it possible to achieve line narrowing artificially, by rotating the sample or the spins, in order to get resolved spectra in solids as in liquids? The answer is 'Yes'.

2.2 Average Value of a Time-Dependent Interaction

What do 'so fast' and 'averaged out' mean? Let us give an initial definition, to be refined later. Let us consider an interaction $D = D_{\text{iso}} + D_{\text{an}}[\Omega(t)]$ whose anisotropic part D_{an} is time dependent. We shall often refer to the 'size' or the 'strength' of an interaction. By this, we mean 'the absolute value of the shift' ω_{int} induced by that interaction, that is, the maximum frequency of evolution of the spins under the effect of that interaction. If that interaction is time-dependent or orientation-dependent, a safe size is the maximum of the absolute value:

$$\text{size}[D(\Omega(t))] = \max_{\Omega} |D(\Omega(t))| \tag{2}$$

Let us consider an interaction $D = D_{\text{iso}} + D_{\text{an}}(\Omega(\text{t}))$ whose anisotropic part D_{an} is time-dependent. Let ω_{an} (in Hz) be the size of D_{an}. The motion is said to be *fast* if during the characteristic time $\tau_{\text{a}} = 2\pi/\omega_{\text{a}}$, a molecule spans a very high number of orientations Ω_{i} and positions ($\text{N} \approx 1/\omega_{\text{an}}\tau_{\text{c}}$). The *average value* of these anisotropic terms may be defined as

$$\bar{D} = \sum_{i=1}^{N} \tau_i D(\Omega_i) \Big/ \sum_{i=1}^{N} \tau_i \tag{3}$$

where τ_i is the time spent in each orientation. If N is very high, the sums can be replaced by integrals. Let $w(\Omega)$ be the probability of the orientation Ω; then

$$\begin{aligned} \bar{D}_{\text{an}} &\approx \frac{1}{t_2 - t_1}\int_{t_1}^{t_2} w(\Omega(t))D_{\text{an}}(\Omega(t))\,\mathrm{d}t \\ &= \int_{\Omega} w(\Omega)D_{\text{an}}(\Omega)\,\mathrm{d}\Omega \Big/ \int_{\Omega} w(\Omega)\,\mathrm{d}\Omega \end{aligned} \tag{4}$$

In an isotropic liquid, these orientations are evenly distributed, $w(\Omega) = 1$, so that, owing to the symmetry properties of the interactions,

$$\bar{D} = \bar{D}_{\text{iso}} + \bar{D}_{\text{an}} \approx \frac{1}{4\pi}\int_{\Omega} D(\Omega)\,\mathrm{d}\Omega = D_{\text{iso}} \tag{5}$$

In isotropic nonviscous liquids, the anisotropic part of the interactions is averaged out to zero: only their isotropic part is observed. In NMR, one obtains a 'resolved' spectrum, with thin lines whose positions depend only on the isotropic part (the trace of the tensors).

2.3 Lattice Motions and Spin Motions

Each interaction is described by an internal Hamiltonian $\hat{\mathcal{H}}_{\text{int}}$, which is the product of two tensor operators, $\hat{F}$ and $\hat{J}$, respectively dependent on the orientations of the sample and of the spins with respect to the magnetic field $\boldsymbol{B}_0$ (see ***Internal Spin Interactions and Rotations in Solids***)

$$\hat{\mathcal{H}}_{\text{int}} = \sum_q \hat{F}_q \hat{J}_q \tag{6}$$

In nature, it is usually the lattice part $\hat{F}$ that is time-dependent, owing to molecular motions. The time dependence of the spin part is observed more rarely—for instance, when a proton is coupled to a rapidly relaxing quadrupolar nucleus like ^{129}I.

Artificial line narrowing uses the time dependence of the lattice part (sample rotation) and/or of the spin part (irradiation).

2.4 Artificial Line Narrowing

Artificially, time dependence may be induced in the Hamiltonian $\hat{\mathcal{H}}$ either through the lattice terms $\hat{F}_q$, by a mechanical motion (most often a rotation) of the sample, or

through the spin terms $\hat{J}_q$, by an irradiation of the spins:

$$\hat{\mathcal{H}}(t) = \sum_q \hat{F}_q(t)\hat{J}_q(t) \tag{7}$$

The key feature that makes the experiment possible is that, in order to average out the anisotropic interactions, one does not need to sample as many orientations as occur in liquids with Brownian motion. A small number of well-chosen orientations is most often sufficient, $N = 3$, for instance, for the chemical shift anisotropy. This has been known for a long time: interactions are very effectively averaged in solids by jump rotational motions by finite angles (e.g., $2\pi/6$ in solid benzene).

2.5 Mechanical Rotation or Spin Irradiation

(See ***Probe Design and Construction***; ***Solid State Probe Design***.)

In order to average out an interaction, these orientations are to be sampled in a time shorter than the 'size' ω_{an} of the interaction. The speed of the mechanical rotations is limited (at present to about 23 kHz for a rotor diameter of about 4 mm) by the speed of the sound in the propeller gas, or by the mechanical strength of the rotor materials. On the other hand, the speed of the spin motions is limited by the intensity of the radiofrequency field: for a given sample size, a first limitation is the power of the amplifiers; if the sample size can be reduced or the amplifier power increased, the ultimate limit comes from arcing within the probe.

Radiofrequency fields as high as 400 kHz [pulse duration $\tau(\frac{1}{2}\pi, {}^1\mathrm{H}) \approx 0.6\,\mu\mathrm{s}$] have been used. However, 60–100 kHz is more typical. The lack of inertia of the spins thus allows faster reorientations, and also sudden changes of the speed or orientation of the rotation axis. This flexibility is used to compensate for the residual broadening proceeding from the nonideality of real experiments.

At this stage, it is also important to note that for spins $\frac{1}{2}$ it is impossible by mere spin irradiation to average out the anisotropic part of an interaction without averaging at the same time its isotropic part. Such a result requires motion of the sample. For instance, saving the isotropic part of the chemical shielding when averaging out its anisotropy is achieved by magic angle spinning. Similarly, if a quadrupolar second-order broadening has to be eliminated, DAS or DOR (see Section 6) or MQ-MAS (see Section 9) methods are required.

However, if an interaction has to completely suppressed, irradiation may be sufficient: refocusing by a π pulse for chemical shielding, homonuclear or heteronuclear decoupling for dipolar interaction, etc.

2.6 Average Hamiltonian

(See ***Average Hamiltonian Theory***.)

Deeper insight into the averaging process has led to the average Hamiltonian concept. Let a spin system evolve from time t_1 to t_2 under the effect of a time-dependent Hamiltonian $\hat{\mathcal{H}}(t)$. Under some conditions to be specified below, at time t_2 the state of the spin system is the same as that which would be obtained under the effect of a constant Hamiltonian, the 'average Hamiltonian' $\bar{\hat{\mathcal{H}}}$, acting during the same time $t_2 - t_1$.

At any time, the expectation value $\langle\hat{A}\rangle$ of an observable $\hat{A}$ (e.g. $\hat{A} = \hat{I}_{x,y}$, the transverse magnetization) is given by

$$\langle\hat{A}(t)\rangle = \mathrm{Tr}\{\hat{A}\hat{\rho}(t)\} \tag{8}$$

The trace of the operator $\hat{O}$ is the sum of the diagonal elements of the matrix representation of the operator $\hat{O}$

$$Tr\{O\} = \sum_n \langle n|O|n\rangle \tag{8a}$$

The evolution of the density matrix $\hat{\rho}(t)$ is described by the Liouville equation

$$\frac{\mathrm{d}\hat{\rho}(t)}{\mathrm{d}t} = -\mathrm{i}[\hat{\mathcal{H}}(t), \hat{\rho}(t)] \tag{9}$$

whose solution is

$$\hat{\rho}(t) = \hat{U}^{-1}(0,t)\hat{\rho}(0)\hat{U}(0,t) \tag{10}$$

If the Hamiltonian is time-independent, the evolution operator is, immediately,

$$\hat{U}(t_1, t_2) = \exp[-\mathrm{i}\hat{\mathcal{H}}(t_2 - t_1)] \tag{11}$$

If the Hamiltonian is time-dependent, the situation is more intricate. Let first consider a time-dependent Hamiltonian that takes the discrete values $\hat{\mathcal{H}}_1, \hat{\mathcal{H}}_2, \hat{\mathcal{H}}_3, \ldots, \hat{\mathcal{H}}_i, \ldots$ during the successive intervals $\tau_1, \tau_2, \ldots \tau_i, \ldots$; $t_2 - t_1 = \sum_k \tau_k$. The evolution operator $\hat{U}(t_1, t_2)$ is

$$\begin{aligned}\hat{U}(t_1, t_2) &= \exp(-\mathrm{i}\hat{\mathcal{H}}_1\tau_1)\exp(-\mathrm{i}\hat{\mathcal{H}}_2\tau_2)\cdots\exp(-\mathrm{i}\hat{\mathcal{H}}_k\tau_k)\cdots \\ &= {}^{T}\prod_k \exp(-\mathrm{i}\hat{\mathcal{H}}_k\tau_k)\end{aligned} \tag{12}$$

where ${}^{T}\Pi$ means that the product is 'time-ordered'.

2.6.1 *The Interaction 'Commutes with Itself'*

The calculation of the evolution operator $\hat{U}(0, t)$ is easy if (as, for instance, for the chemical shielding in a rotating sample) the Hamiltonian at any two different times t_1 and t_2 commutes with itself; that is,

$$[\hat{\mathcal{H}}(t_1), \hat{\mathcal{H}}(t_2)] = \hat{\mathcal{H}}(t_1)\cdot\hat{\mathcal{H}}(t_2) - \hat{\mathcal{H}}(t_2)\cdot\hat{\mathcal{H}}(t_1) = 0 \tag{13}$$

for all t_1, t_2. This means that the effect of the interaction on the spin system at time t_2 is dependent on its previous value at time t_1.

One gets immediately and exactly

$$\hat{U}(t_1, t_2) = \exp[-\mathrm{i}\bar{\hat{\mathcal{H}}}_{12}(t_2 - t_1)] \tag{14}$$

The spin system appears to evolve during the time interval $t_c = t_2 - t_1 = \sum_k \tau_k$ under the effect of the *average Hamiltonian*

$$\tilde{\hat{\mathcal{H}}}_{12} = \frac{1}{t_2 - t_1} \sum_k \hat{\mathcal{H}}_k \tau_k \tag{15}$$

This is exact, without any approximation. Extension to a continuous time dependence of the Hamiltonian is straightforward:

$$\tilde{\hat{\mathcal{H}}}_{12} = \frac{1}{t_2 - t_1} \int_{t_1}^{t_2} \hat{\mathcal{H}}(\tau)\, \mathrm{d}\tau \tag{16}$$

2.6.2 The Interaction Does Not Commute with Itself

If the Hamiltonian at any two different times t_1, t_2 does not commute with itself (as, for instance, in the cases of a rotating sample, more than two spins with mutual dipolar coupling, or two spins with a mutual dipolar coupling and different chemical shielding tensors at least partially overlapping), that is,

$$[\hat{\mathcal{H}}(t_1), \hat{\mathcal{H}}(t_2)] \neq 0 \tag{17}$$

then it is no longer permissible to permute the order of the terms in the product of the exponential operators. The order of the different factors in the product expansion of the evolution operator must be taken into account very carefully (this is also true for a continuous time variation of the Hamiltonian):

$$U(t_1, t_2) = (1 - \mathrm{i}\hat{\mathcal{H}}_1 \tau_1 + \ldots)(1 - \mathrm{i}\hat{\mathcal{H}}_2 \tau_2 + \ldots) \cdots \times (1 - \mathrm{i}\hat{\mathcal{H}}_k \tau_k + \ldots) \cdots \tag{18}$$

2.6.2.1 The 'Zeroth-Order Average Hamiltonian'—a Simple Case. The expressions in equations (15) and (16) for the average Hamiltonian remains valid only to first order, that is, if the time modulation of the Hamiltonian is so fast that

$$\hat{\mathcal{H}}_k \tau_k \ll 1, \quad \sum_k \hat{\mathcal{H}}_k \tau_k \ll 1 \tag{19}$$

If these conditions are fulfilled, one may write $\hat{U}(t) \approx 1 - \mathrm{i} \sum_k \hat{\mathcal{H}}_k \tau_k + \ldots$, and, under the same conditions,

$$\hat{U}(t_1, t_2) \approx \exp\left(- \mathrm{i} \sum_k \hat{\mathcal{H}}_k \tau_k \right) \approx \exp(-\mathrm{i}\tilde{\hat{\mathcal{H}}}^{(0)} t_\mathrm{e}) \tag{20}$$

so that the spin system appears, as above, to evolve during t_c under the effect of a zeroth-order average Hamiltonian $\tilde{\hat{\mathcal{H}}}^{(0)} = \sum_k \hat{\mathcal{H}}_k \tau_k / t_\mathrm{c}$. However, unlike the former case this simple expression is valid only at first order—that is, for very short evolution times.

2.6.2.2 Higher Order Average Hamiltonian. If the conditions in equation (19) are not fulfilled, higher order terms like $\hat{\mathcal{H}}_k \hat{\mathcal{H}}_l \tau_k \tau_l$ must be taken into account in the development of the average Hamiltonian. These terms lead to a departure from full averaging in the ideal experiment designed so that $\tilde{\hat{\mathcal{H}}}^{(0)} = 0$. These extra terms give the residual linewidth. John Waugh and his co-workers have shown that the Magnus expansion of the exponential evolution operator is a very powerful method to obtain expressions for and symmetry properties of these extra terms. These higher order terms are expressed as averages of commutators of the Hamiltonian at different times $(\hat{\mathcal{H}}_k \hat{\mathcal{H}}_l - \hat{\mathcal{H}}_l \hat{\mathcal{H}}_k) \tau_k \tau_l$, etc. The convergence properties of the Magnus expansion have been widely discussed.[18,19]

2.6.3 Periodic Hamiltonian

A simplification occurs if, as in line narrowing experiments, the Hamiltonian is periodic, of period T:

$$\hat{\mathcal{H}}(t + T) = \hat{\mathcal{H}}(t) \tag{21}$$

Here, it is clear that

$$\hat{U}(0, nT) = [\hat{U}(0, T)]^n = \exp[-\mathrm{i}n(\tilde{\hat{\mathcal{H}}})_{0,T}] \tag{22}$$

where $(\tilde{\hat{\mathcal{H}}})_{0,T}$ is the average Hamiltonian over the time interval $nT \leq t \leq (n + 1)T$. If it is zero then $\hat{U}(nT,(n + 1)T) = 1$. The spin system will recover its initial state, $\hat{\rho}(nT) = \hat{\rho}(0)$, at times $t = nT$. Rotational echoes appear at times $t = nT$. Sampling stroboscopically at these times makes the spin system evolve as if there were no longer a broadening interaction: line narrowing is achieved.

In any case, for a periodic Hamiltonian, the full evolution of the system is known if one knows its evolution over one period T: $\tau \leq t \leq T + \tau$. The line narrowing efficiency may be determined accurately by calculating the average Hamiltonian over one period T. If the fundamental frequency of modulation $2\pi/T$ is greater than the 'size' of the anisotropic interactions then the zeroth-order average Hamiltonian will be a good approximation.

If the evolution time is not an integer number of periods, the evolution for the residual fraction of period must be calculated separately. Thus the time evolution from $t = 0$ to any time $nT + \tau$ is

$$\hat{U}(0, nT + \tau) = \exp[-\mathrm{i}n(\tilde{\hat{\mathcal{H}}})_{0,T}] U(0, \tau) = U(0, \tau) \exp[-\mathrm{i}n(\tilde{\hat{\mathcal{H}}})_{\tau,\tau+T}] \tag{23}$$

This allows the calculation of the signal between the rotational echoes at times $t = nT$. It is important to note that shifting the time interval by a fraction of a period will not always give the same average Hamiltonian: $(\tilde{\hat{\mathcal{H}}})_{\tau,\tau+T}$, the average Hamiltonian over the time interval $nT + \tau \leq t \leq (n + 1)T + \tau$, is generally not equal to $(\tilde{\hat{\mathcal{H}}})_{0,T}$. Measuring the signal not only at the tops of the rotational echoes but also between these echoes leads to a rotational sideband pattern whose spectral width is inversely proportional, in the time domain, to the width of the rotational echoes. For instance, spins with a very large quadrupolar interaction may show hundreds of sidebands, and extremely sharp rotational echoes.

For calculating the effects of a periodic time dependence of the Hamiltonian, there is now a trend toward using Floquet theory.[19]

2.7 Symmetry

2.7.1 How to Describe Rotations: Wigner Matrices and Legendre Polynomials

In order to make clear, in a systematic way, the behavior of the anisotropic interactions under reorientations, the best

way is to expand the lattice part $\hat{F}$ of the Hamiltonian in an orthogonal basis of Wigner matrices, and the corresponding spin part $\hat{J}$ in a basis of the T_l^m tensor spin operators (see ***Dipolar and Indirect Coupling Tensors in Solids***; ***Internal Spin Interactions and Rotations in Solids***)

$$\hat{\mathcal{H}} = \sum_q \hat{F}_q \hat{J}_q = \sum_l \sum_{m=-l}^{l} \hat{T}_l^{-m} A_l^m D_l^{m0}(\Phi_c, \Theta_c, 0) \quad (24)$$

The A_l^m are the components of the lattice tensors $\hat{F}_q$. The polar angles Φ_c and θ_c give the direction of the magnetic field $\boldsymbol{B}_0$ in the principal axis system of the interaction lattice tensor. Φ_c and θ_c are different for each crystallite in a powder. It is also possible to write

$$\hat{\mathcal{H}} = \sum_q \hat{F}_q \hat{J}_q = \sum_l \sum_{m,m'=-l}^{l} T_l^{-m} A_l^m D_l^{mm'}(\alpha, \beta, \gamma) D_l^{m'0}(\varphi, \vartheta, 0) \quad (25)$$

Here θ and φ are the polar angles of the direction of the magnetic field in a unique frame fixed with respect to the whole sample, whereas α, β, and γ are, for each site and each crystallite, the Euler angles of the rotation that bring the principal axes of the local tensor $\hat{F}_q$ into that macroscopic sample frame. In a powder sample, the angles α, β, and γ depend on the orientation of the crystallites in a reference frame fixed with respect to the whole sample. The Wigner matrices are

$$D_l^{m'm}(\alpha, \beta, \gamma) = \mathrm{e}^{-\mathrm{i}m'\alpha} d_l^{m'm}(\beta) \mathrm{e}^{-\mathrm{i}m\gamma} \quad (26)$$

with $d_l^{m'm}(\beta)$ the reduced Wigner matrices. The $d_l^{m'm}(\beta)$ are polynomials in $\sin^p \beta \cos^q \beta$ of maximum degree $p + q \leq l$. An equivalent expansion is frequently used in a basis of Legendre polynomials $P_l^m(\cos\beta)$. In particular,

$$d_l^{00}(\beta) = P_l^0(\cos\beta) = P_l(\cos\beta) \quad (27)$$

These two orthogonal bases differ only by normalization constants and phase factors (± 1), depending on authors and their conventions.

2.7.2 Selective Averaging

(See ***Average Hamiltonian Theory***.)

Let $\hat{\mathcal{R}}_L(\theta, \xi)$ be the operator of rotation through an angle ξ about the axis of the sample (which is tilted θ away from the magnetic field direction). Under the effect of $\hat{\mathcal{R}}_L(\theta, \xi)$, a term of order l will transform in the subspace l, so that equation (25) becomes

$$\begin{aligned}\hat{\mathcal{R}}_L(\theta, \xi)\hat{\mathcal{H}} &= \sum_l \sum_{m,m'=-l}^{l} T_l^{-m} A_l^m D_l^{mm'}(\alpha, \beta, \gamma) D_l^{m'0} \\ &\quad \times(\varphi + \xi, \vartheta, 0) \\ &= \sum_l \sum_{m,m'=-l}^{l} T_l^{-m} A_l^m D_l^{mm'}(\alpha, \beta, \gamma) \\ &\quad \times \mathrm{e}^{-\mathrm{i}m'\xi} D_l^{m'0}(\varphi, \vartheta, 0) \end{aligned} \quad (28)$$

The $\hat{T}_l^m$ spin tensors have, with respect to rotation in the spin space, a rotational behavior similar to that of the Wigner matrices in the lattice space.

It is possible to find a rotation or a set of successive rotations that average out the term of a given order l and not the others. For instance, if the sample spends equal periods of time in each of $N \geq l + 1$ orientations related by $\xi_k = 2k\pi/N$, $k = 1, \ldots, N$, rotations, it is clear that the average value is zero for any term with $m \neq 0$, so that the average value due to the lattice motion is

$$\frac{1}{N} \sum_{k=1}^{N} \mathcal{R}_L(\theta, 2k\pi/N)\hat{\mathcal{H}} = \sum_l \left[\sum_{m=-l}^{l} T_l^{-m} A_l^m D_l^{m0}(\alpha, \beta, \gamma) \right] P_l(\cos\theta) \quad (29)$$

For any $l \neq 0$, there is at least one value θ_l such that $P_l(\theta_l) = 0$. For $l' \neq l$, one has always $P_{l'}(\theta_l) \neq 0$. As jump reorientations are difficult to achieve, a continuous rotation about the axis is preferred. The $m \neq 0$ terms are then periodic. These $m \neq 0$ terms give rise to rotational sidebands, which vanish when the frequency of rotation is greater than the 'size' of the anisotropic interaction.

Thus, the lattice part of the chemical shift interaction has $l = 0$ (isotropic) and $l = 2$ (anisotropic) terms. The anisotropy of the chemical shift can be averaged out and its isotropic part preserved. This is almost trivial, because the isotropic term is invariant under any rotation. On the other hand, the lattice part of the dipolar interactions has only $l = 2$ anisotropic terms: averaging out these anisotropic terms averages out the whole dipolar interaction.

In spin space, the chemical shift interaction behaves as an $l = 1$ tensor, whereas the homonuclear dipolar interaction behaves as an $l = 2$ tensor. Therefore, one can, by an appropriate rotation in spin space (induced by appropriate rf pulses or irradiation), average out the homonuclear dipolar interaction, without averaging the chemical shift completely (it is only scaled down). This is *selective averaging*.

Averaging the anisotropic part of an interaction that has $l = 0,2,4$ tensor terms will require a more subtle motion than that which averages out only either the $l = 2$ or the $l = 4$ terms.

3 SAMPLE MOTION: MAGIC ANGLE SPINNING

(See ***Magic Angle Spinning***; ***Magic Angle Turning and Hopping***.)

3.1 The Magic Angle

It is easy to show that for the main interactions (chemical shielding, dipolar coupling, and quadrupolar interaction at first order), the above expansion of the lattice part contains only terms with $l = 0$ and $l = 2$. The condition

$$d_2^{00}(\theta) = \tfrac{1}{2}(3\cos^2\theta - 1) = 0 \quad (30)$$

leads to $\cos\theta = \sqrt{\frac{1}{3}}$, that is $\theta = 54^\circ\ 44'$. Spinning the sample about an axis tilted by that angle away from the direction of the magnetic field B_0 averages out the $l = 2$ terms. This is the *magic angle*. If the rotation axis is not exactly tilted at the magic angle then lines (and each of their rotational sidebands, if the spinning speed is not high enough) remain broadened: their shape is that of the static spectrum, scaled by the factor $\frac{1}{2}(3\cos^2\theta - 1)$.

3.2 Magic Angle Hopping

Averaging the chemical shielding anisotropy has been performed by jumping for equal time periods $\frac{1}{3}\tau$ between three orientations related by 120° rotations about an axis tilted 54° 44′ away from the magnetic field direction.

This experiment is very interesting from a conceptual point of view. Hopping is used in the DAS experiment (see Section 6). In the hopping experiment is set up so that the rotation speed appears infinite. It is free from any sidebands (see Section 3.4.2), whatever the spread of the anisotropic interactions. However, it is very time-consuming. It also requires accurate angular positioning, which is very difficult to achieve when fast switching is also required.

The experiment begins with a pulse (or a cross polarization) that rotates the magnetization in the transverse plane. At the end of the third period, the amplitude $A(\tau)$ of the transverse magnetization is recorded. The experiment is repeated for different values of the period τ.

As sudden reorientations cannot be achieved, the system evolution has to be frozen during the reorientations. This can be performed in the following ways.

1. The magnetization can be stored along the magnetic field $\boldsymbol{B}_0$ before the reorientation by a $(\frac{1}{2}\pi)_\varphi$ pulse, and recalled in the transverse plane after the reorientation by a $(-\frac{1}{2}\pi)_\varphi$ pulse. The experiment has to be performed twice for each reorientation (because one can store either the x component or the y component of the transverse magnetization); that is, four times if there are three orientations to be sampled. This requires only that the reorientation time, during which the magnetization has to be stored, is shorter than the longitudinal relaxation time T_1.
2. An irradiation of the form $(\tau_x - \tau_{\bar{x}} -)_n$ can be used. The x component of the transverse magnetization, which is in phase with the rf field, is spin locked; the y component of the transverse magnetization, which is in quadrature with the rf, undergoes repetitively equal and opposite rotations about the rf field, which cancel each other. If the rf field is much greater than the chemical shielding (and if there are no other interactions such as quadrupolar or dipolar interactions that may induce failure of the 'freezing' efficiency of this irradiation), the transverse magnetization at the end of the irradiation is the same as at the beginning. Here the reorientation time must be shorter than the relaxation time in the rotating frame $T_{1\rho}$.

3.3 Magic Angle Spinning

The principle of line narrowing was discovered and the first averaging experiments performed in 1958–1959 by Andrew[11] and Lowe,[12] using a continuous rotation about an axis tilted 54°44′ away from the magnetic field. This remains nowadays the most used method; it is known as magic angle spinning (MAS).[20]

Inside the coil of the NMR probe (see ***Solid State Probe Design***), the rotation of the sample, sustained on air bearings, is driven by air jets. The early experiments used two types of turbines.

1. In the 'mushroom' type[21] used by Andrew[11] in the pioneering experiments, the bearing is of conical shape; the air comes through holes that are not perpendicular to the plane tangent to the cone; this provides both bearing and drive. Such a design is quite easy to construct. However, it does not allow simultaneous optimization of the drive efficiency and the stability of the rotor.
2. Lowe used cylindrical spinners, supported by two Nylon needle axes, and driven by an air jet.[12]

Nowadays, most spinners are cylindrical, with two air bearings and with separate air input holes for bearings and drive.[22] Spinners with cylindrical bearings and conical drive are sometimes used, for instance for rotating sealed samples or for low-temperature operation. Metal parts are avoided for the stator and especially the rotor, which is made of a nonconducting material (like any sample container, it must be transparent to rf fields and must not generate Foucault currents when rotated in the magnetic field).

3.4 Magic Angle and Spin $\frac{1}{2}$: Averaging the Chemical Shift Anisotropy

For an isolated spin $S = \frac{1}{2}$, the only interaction is the chemical shielding. Spinning at the magic angle yields a central sharp line, centered at the isotropic chemical shift ω_i.

3.4.1 Rotational Sidebands

(See ***Sideband Analysis in Magic Angle Spinning NMR of Solids***.)

If the rotational speed ω_{rot} is not high enough compared with the 'size' of the interaction ω_a then sidebands appear, $\pm n\omega_{rot}$ apart from the central one, over a frequency range of about ω_a.[23] As the chemical shielding commutes with itself at different times, the lines (central one and sidebands) are narrow, whatever the spinning speed. The outline of the sidebands can be easily analyzed, and provides the chemical shift anisotropy (CSA) and asymmetry.

3.4.2 Sideband Suppression: Scaling, TOSS, and 'deTOSS'

Simultaneous rf irradiation and MAS allow simplification of the spectrum: the sidebands may be eliminated either by a 'scaling'[24] irradiation that compresses the apparent 'size' of the shielding interaction, or by using the TOSS (total suppression of sidebands) sequence, which wipes out the sidebands of the spectrum without changing the size of the shielding.[25] TOSS spectra are not quantitative: under the TOSS effect, the intensity of the sidebands vanishes without being wholly collected in the centerband. In the TOSS experiment, a series of four π pulses with a determined spacing, applied before the acquisition and during the first period of rotation,

sets the initial condition of the spin system so that no sidebands appear during acquisition. Improved new sideband suppression pulse sequences have been devised.

In a very nice 2D experiment, after a TOSS sequence and an evolution period under the TOSS conditions (resulting in no sidebands), a reversed TOSS pulse sequence is applied, before acquisition.[26] A 2D spectrum is obtained with isotropic chemical shift in one dimension and the full comb of sidebands in the second dimension.

3.5 Magic Angle and Quadrupolar Nuclei

Magic angle spinning is a very efficient line narrowing tool for spin $S = \frac{1}{2}$ like ^{1}H and ^{13}C. These two spins are therefore very efficient local probes for high-resolution NMR studies of organic compounds such as polymers, and proteins in the solid state. Inorganic materials also contain spin-$\frac{1}{2}$ nuclei such as ^{29}Si and ^{31}P. The former is used extensively for NMR studies of inorganic materials. However, most useful nuclei in inorganic compounds are quadrupolar with spin $S > \frac{1}{2}$. Is MAS efficient for line narrowing of quadrupolar nuclei? The answer is 'very often, no'.

3.5.1 Quadrupolar Nuclei: The Static Spectrum

(See ***Quadrupolar Nuclei in Solids***.)

An isolated quadrupolar nucleus is subjected to two interactions: chemical shielding and quadrupolar interaction. The latter is most often much stronger than the former. The static NMR spectrum of a quadrupolar nucleus (see ***Quadrupolar Interactions***) of spin S contains $2S$ lines corresponding to transitions $m - 1 \leftrightarrow m$; $-\mathrm{S} + 1 \leq m \leq S$. The shift of these lines is at first order, and if the asymmetry of the quadrupolar tensor is zero, $\frac{1}{2}\nu_{\mathrm{Q}}(m - \frac{1}{2})(3\cos^2\theta_{\mathrm{Q}} - 1)$, where ν_{Q} is the quadrupolar frequency and θ_{Q} the angle of the principal axis of the quadrupolar tensor with the magnetic field. This shift depends on the orientation according to the same law as the chemical shift anisotropy and the dipolar interaction. In a powder sample, the spectrum of an integer spin (S = 1, 2, 3, ...) is a superposition of $2S$ broad overlapping powder patterns. For half-integer quadrupolar nuclei ($S = \frac{3}{2}, \frac{5}{2}, \ldots$), the central line $-\frac{1}{2} \leftrightarrow \frac{1}{2}$, is unshifted, at this first order. If the quadrupolar interaction ν_{Q} is not much smaller than the Larmor frequency ν_0, there is a second order shift for all the lines, proportional to ν_{Q}^2/ν_0. Therefore, in a powder sample, that central line remains sharp, with a much higher amplitude than the $2S - 1$ broad overlapping powder patterns of the outer lines. If there is no dispersion of the size of the quadrupolar interaction, the outer lines display sharp singularities. If not, they appear as a very wide Gaussian-like line at the base of the sharp central line, if any. If the signal-to-noise ratio is low and/or the quadupolar interaction large, this broad line may disappear in the noise or be blurred in the spectrometer baseline distortion, so that only the central line is observed. This occurs frequently. In any case, the signal amplitude of the signal of a half-integer quadrupolar nucleus is generally much higher than that of an integer one, other things being equal.

3.5.2 MAS of Quadrupolar Nuclei

(See ***High Speed MAS of Half-Integer Quadrupolar Nuclei in Solids***.)

3.5.2.1 Small Quadrupolar Interactions: MAS is Efficient.

When spinning a sample at the magic angle, what is observed is similar to the case of chemical shielding anisotropy. Let the quadrupolar interaction be the dominant one—greater than the chemical shift anisotropy or the dipolar interaction. The position of the central line is due only to the isotropic chemical shift. The outer line powder patterns split into combs of sidebands, which are shifted by an integer multiple of the spinning frequency. This has been observed for integer spins, for instance ^{2}H (S = 1),[27] as well as for half-integer spins. This is useful. It should be noted, however, that this is true only if the quadrupolar interaction is sufficiently small. Analysis of the contour of the comb of sidebands allows determination of the size and asymmetry of the quadrupolar tensor, or its distribution. This last case is frequently observed in cubic crystals such as KBr, where the quadrupolar interaction is due only to strains in the crystal. The splitting of the outer lines into that comb of sidebands is also a way to disclose them when blurred in the baseline in the static powder pattern.

As the quadrupolar interaction is often very strong, magic angle spinning makes the width and therefore the amplitude of the sidebands very sensitive to any departure from the magic angle—much more than for chemical shielding. Extracting the chemical shift from the positions of the outer transitions therefore requires very accurate tuning and stability of the rotation axis orientation. This excessive sensitivity may be turned into an advantage: looking at the intensity of the sidebands, or, directly on the free induction decay, at the amplitude and number of the rotational echoes, is one of the best ways to set the probe exactly at the magic angle.

If the chemical shift anisotropy is not smaller than the spinning frequency, the central line acquires sidebands, whereas the outer-line sidebands may suffer some change in amplitude. In favorable cases this allows one to get the chemical shielding tensor together with the quadrupolar one, and also their relative orientation.

3.5.2.2 Strong Quadrupolar Interaction: MAS is Inefficient.

When the quadrupolar interaction is large, that is, no longer much smaller than the Larmor frequency, the number of sidebands in the comb increases. As many as hundreds of sidebands can be observed for ^{27}Al, for instance. More worryingly the central line and all the sidebands are shifted and widened by second-order quadrupolar interactions. (This shift is the same for all the sidebands of the $m \leftrightarrow m - 1$ and $-m \leftrightarrow -m + 1$ transitions. Adversely, the shape and broadening are different for all the sidebands, even of one given transition.) There is no longer any spectral resolution. This broadening is due to the second-order quadrupolar interaction, whose size is proportional to ν_{Q}^2/ν_0. When the magnetic field $\boldsymbol{B}_0$ increases, the shielding increases, whereas this second-order quadrupolar broadening decreases: the resolution goes as B_0^2. However, a high enough field is not always available.[28] It has also been found experimentally that line narrowing cannot be achieved by either magic angle spinning or variable angle spinning ('VAS') (it is reduced by at most a factor of about 4). This can easily be understood theoretically: MAS is ineffective, even at infinite speed. New methods (DAS and DOR) have been devised for this complex situation (see Section 6). Nevertheless, simulation and exploitation of MAS and VAS spectra of quadrupolar nuclei are the subject of intense activity.[29]

3.6 Magic Angle and Heteronuclear Dipolar Coupling

3.6.1 Spin $\frac{1}{2}$ Coupled to Other Spins $\frac{1}{2}$

The heteronuclear dipolar coupling between two spins $\frac{1}{2}$ of different species (a ^{13}C and a ^{1}H for instance) commutes with itself at any time. With respect to sample motion, it behaves exactly like the shielding interaction. It is averaged out by magic angle spinning, if fast enough. If not, there is a comb of sidebands. Note that if there are also I–I dipolar interactions, averaging out the I–S dipolar interaction requires a spinning speed higher not only than the I–S dipolar interaction, but also than the I–I dipolar interaction. However, in organic solids, the ^{13}C–^{1}H and ^{1}H–^{1}H interactions are usually so strong that the spinning rate is not high enough. Such a strong heteronuclear interaction can be fully averaged out only by decoupling (see Section 4.2).

3.6.2 Spin $\frac{1}{2}$ Coupled to a Quadrupolar Nucleus

The dipolar coupling with a quadrupolar nucleus, even of low γ, is not averaged out by MAS. Indeed, the quantization axis of the quadrupolar nucleus is no longer along the magnetic field $\boldsymbol{B}_0$, and changes when the electric field gradient rotates with the crystallite. The dipolar coupling between the spin $\frac{1}{2}$ and the quadrupolar nucleus no longer behaves as a second-order tensor: it involves higher order terms[30,31] (see Section 6.1).

3.7 Magic Angle and Homonuclear Dipolar Interaction

(See ***Rotating Solids*** and Sections 4.3 and 6.1 below.)

In a spinning sample, the homonuclear dipolar coupling does not commute with itself. The evolution of the spin system can only be calculated analytically, by a perturbation expansion when the rotational speed is much greater than the strength of the dipolar interaction. Otherwise, a numerical approach must be used. This is possible if a few spins only are involved. The dipolar lineshape splits into sidebands, whose width decreases as the spinning speed increases. Their intensity varies as $1/\omega_{\mathrm{rot}}^2$. For strong ^{1}H–^{1}H dipolar interactions in rigid organic solids, line narrowing cannot be achieved routinely at the highest spinning speeds now available (see Sections 3.7 and 5.2.1).

3.7.1 The Rotating Homonuclear Pair

It might be thought that a single pair of spins in mutual dipolar coupling would be tractable. This is true if there is only a homonuclear dipolar interaction, or if the chemical shift tensors of the two spins have axial symmetry about the direction of the internuclear vector. In that case, the total Hamiltonian always commute with itself, and the calculation goes as above for the CSA.

Now let two spins have the same Larmor frequency, a mutual dipolar coupling, and each a different anisotropic chemical shift. The effect of the sample rotation on such a homonuclear spin pair cannot be calculated so easily. For a static sample, the lineshape already depends on 12 parameters [the 3 components of each shielding tensor, the 3 Euler angles (α, β, γ) defining their mutual orientation, the distance $|\boldsymbol{r}|$ between the two spins, and the orientation, (θ, φ) of the internuclear vector $\boldsymbol{r}$]. Rotating the sample makes the situation even worse. Depending on the sample orientation, the spins may change from 'like' to 'unlike'. This means that the ratio ρ of the dipolar coupling to the difference in chemical shift changes from $\rho > 1$ to $\rho < 1$. Any perturbation expansion valid at one time t_1 may no longer be valid at another time t_2. In contrast with the case of a spin subjected to an anisotropic chemical shielding or a heteronuclear dipolar interaction, the time evolution and the resulting spectrum cannot be calculated analytically. This problem has been addressed by two different main approaches.[32]

4 SPIN MOTIONS: DECOUPLING AND AVERAGING OUT THE BROADENING DUE TO THE DIPOLAR INTERACTIONS

4.1 Spin Dilution Effect on Dipolar Interaction

The strength of the homonuclear dipolar coupling is easily reduced by spin dilution. This occurs naturally for ^{13}C, whose isotopic abundance is 1.1%. In organic solids, the ^{13}C–^{13}C homonuclear dipolar coupling is only about 50 Hz, that is 1 ppm at 7 T. Such a small residual coupling is easily averaged out by MAS. The situation is similar for ^{29}Si–^{29}Si dipolar coupling [higher isotopic abundance (4%), but lower γ, and often larger Si–Si distances]. In the context of dipolar decoupling and of cross-polarization, 'dilute and low γ' nuclei like ^{13}C or ^{29}Si are called 'rare spins' by contrast with the 'abundant and high γ' spins like ^{1}H or ^{19}F which are called 'abundant spins'. The exact situation, that is the relative strengths of the different (S–S, I–I and I–S) dipolar interactions, following A. Pines and M. Mehring, here and later we call I the 'abundant spins' and S the 'rare spins'. What is told about protons ^{1}H or about carbons ^{13}C may generally be extended to 'I spins' and 'S spins'.

4.2 Heteronuclear Decoupling

A heteronuclear dipolar coupling with spins of another species (e.g., ^{1}H if one is observing ^{13}C) is averaged out by *decoupling*, that is, by a continuous irradiation of these (here ^{1}H) nuclei, at their resonance frequency.[7,8] As for sample rotation (see Section 3.6.1) the intensity of the rf field must not only be higher than the I–S dipolar interaction, but also high than the I–I dipolar interaction. The efficiency of that decoupling is much less dependent on the 'offset' from the resonance frequency than in liquids (following a $\cos^2\theta$ law instead of a $\cos\theta$ law). Decoupling sequences, made up of trains of composite pulses, like COMARO-2[33] or ALPHA-3,[34] have been designed for liquid crystals or rigid solids, which are less sensitive to the 'offset' or to the effects of the quadrupolar interactions. They become very useful for slightly paramagnetic solids,[35] and presumably also for decoupling ^{19}F in organic fluorides.

4.3 Homonuclear Decoupling

When the dipolar coupling is homonuclear, the situation is more complex: a simple irradiation of the spins will average

out both the shielding and the dipolar interaction. The key lies in the different behaviors of these two interactions with respect to spin rotations: shielding anisotropy behaves as a first-order tensor, and homonuclear dipolar interaction as a second-order tensor (see Section 2.7.2).

4.3.1 Magic Angle Irradiation

Here too, as above (see Section 3) when averaging by lattice motion, it is sufficient that the Hamiltonian take, during equal time intervals, three values related by 120° rotations about the [111] direction in the spin space (the [001] direction is that of the magnetic field $\boldsymbol{B}_0$). (Here, one must work in the 'good' reference frame, namely, the 'toggling frame'.[36]) This can be achieved by three 120° reorientations about the [111] direction: this leads to the Lee–Goldburg experiments,[14,37] which are conceptually the simplest. The 120° rotations are achieved by '120° pulses' ($\omega_1\tau_{\text{pulse}} = \frac{2}{3}\pi$) of intensity ω_1, at magic angle in the rotating frame: $\Delta\omega$, the offset from resonance of the rf field, is such that $\Delta\omega/\omega_1 = \tan\theta_{\text{m}} = \sqrt{2}(\theta_{\text{m}} = 54°\,44')$. As for magic angle spinning, continuous irradiation can be used as well. To first order, the homonuclear dipolar coupling is wiped out, whereas the shielding (isotropic and anisotropic parts) is scaled by a factor $\sqrt{\frac{1}{3}}$. Higher order error terms (rf field inhomogeneity, etc.) can be compensated by reversing periodically the phase and the offset of the rf field. Before fast frequency switching became available, one had to switch a continuous 'offset field' $\Delta B_0 = \Delta\omega/\gamma$. This was not very practical, so that other kinds of magic angle irradiation (WAHUHA, etc.; see Section 4.3.2) were preferred. Nowadays, fast frequency switching has become possible, and this kind of experiment may undergo a renewal of interest.[38]

4.3.2 Multipulse Trains: WAHUHA, MREV-8, BR-24, etc.

(See ***Average Hamiltonian Theory***.)

A few later, similar results were obtained with on-resonance 90° pulses about the directions $X, Y, -X, -Y$ of the rotating frame. This led to the development of the multipulse train called WAHUHA, then later to MREV-8 and BR-24.[7,8,14] To first order, the average Hamiltonian is zero over the elementary cycle, of duration t_{c}, involving four pulses. Higher order terms due to rf field inhomogeneity, finite width of the pulses, errors and instabilities of the amplitude and phases of the pulses, rf field inhomogeneity, and frequency offsets have been discussed in great detail.

As for the lattice reorientations, careful examination of the symmetry properties of the Hamiltonian and of the sequences allowed, by periodic repetition of the elementary pulse cycle with appropriate permutation of the phase of the pulses, successive cancelation of these higher order 'error terms'. This has led to the sequences MREV-8, BR-24, BR-52, etc.[39,40] A compromise has to be found between lengthening the sequence and compensating for higher error terms. The most used sequence is MREV-8, followed by BR-24.

The observation of the NMR signal may be done stroboscopically, either in one shot, once during each elementary cycle t_{c} of a single multipulse train, in any of the two longest intervals between the pulses (the 'long windows'), or point by point, at the end of the multipulse train evolution time whose length is incremented after each acquisition. At constant cycle time, by lengthening the pulse length, it is possible to reduce to zero the 'short windows' and keep only the 'long windows' between the pulses for signal observation. It is also possible to suppress all the windows: this leads to continuous irradiation, with cyclic phase modulation (there are six pulses of equal duration within each elementary cycle). These are the 'semi-windowless' or 'windowless' (BLEW-12 and BLEW-48) sequences.[41,42] Windowless sequences gives the greater decoupling efficiency for a given rf power.

4.3.2.1 Tuning. As these sequences require very accurate tuning of the widths, amplitudes, phases, and spacing of the pulses, very efficient tuning sequences have been devised. Small errors are amplified by their cumulative effect along a multipulse train. Each sequence is designed to be sensitive selectively to one or a few errors only. Tuning protocols using a set of such sequences have been established.[43,44]

4.3.2.2 New Sequences?. Based on a different approach, the TREV-8[45] sequences are also attractive. Although their efficiency and sensitivity to departures from the ideal condition are in some situations better than those of the classical sequences of the MREV-8 type, they are not yet widely used; neither are the closely related trains of solid echoes,[46] which have been more extensively discussed theoretically as well as experimentally. Only recently, has the efficiency of TREV-8 been seriously tested by experiments. This kind of sequence might be attractive for solid imaging. Automatic design of new sequences by computer optimization has been tried.[47]

5 TWO USEFUL METHODS FOR HALF-INTEGER SPINS: CP MAS AND CRAMPS. AVERAGING OUT BOTH ANISOTROPIC CHEMICAL SHIFTS AND DIPOLAR BROADENING

5.1 CP MAS

(See ***Cross Polarization in Rotating Solids: Spin-1/2 Nuclei***.)

In order to obtain resolved spectra of diluted spin-$\frac{1}{2}$ (the 'rare spins') like ^{13}C at natural isotopic abundance, in strongly protonated solids, one uses magic angle spinning to wipe out the anisotropic part of the chemical shift of the 'rare spins' (and their small homonuclear dipolar coupling) and, during acquisition, a strong heteronuclear decoupling, in order to eliminate the broadening due to the coupling with the protons.

5.1.1 Sensitivity Enhancement: Cross Polarization

Usually, one takes advantage of the coupling of the low-γ rare S spins (e.g., ^{13}C) with the abundant high-γ I spins (e.g. ^{1}H) in order to enhance the carbon signal by cross polarization with the protons. Cross polarization occurs as a result of a recoupling process (see Section 7.2.2). The signal intensity is increased by a factor γ_I/γ_S, (about 4 for ^{1}H/^{13}C). As a consequence, one has to wait between two experiments for the return to equilibrium, no longer of S (^{13}C), but now of I (^{1}H). As $T_1(^{1}\text{H})$ is usually quite a bit shorter than $T_1(^{13}\text{C})$, this allows faster repetition of the signal acquisition. The repetition rate may be increased further if one uses a 'flip-back' pulse[48] that returns the remaining spin locked proton

magnetization back to along the magnetic field $\boldsymbol{B}_0$, reducing the time necessary to come back close to the equilibrium state.

5.1.2 Resolution and Sensitivity

The resolution of the CP MAS experiment for spins $\frac{1}{2}$ has been discussed thoroughly.[7,49] The decoupling irradiation must be at resonance, its amplitude being greater than the strength of the I–S and I–I dipolar coupling.

In disordered materials (amorphous solids and glasses) the main limitation to resolution originates in the sample itself—it is the dispersion of the chemical shifts due to the differences in environment. In liquids, the environment of a molecule fluctuates, and only its average value is observed; this is known as the intermolecular or the solvent contribution to the chemical shift. In solids, this effect broadens the lines. It cannot be fully suppressed by spinning the sample.

Another fundamental limitation is due to the magnetic susceptibility of the sample. Owing to the granular form of a sample, and to the irregular shape of each grain, the demagnetizing field inside each grain of the sample is neither constant in a grain nor isotropic. Even if the anisotropic part of the demagnetizing field is averaged out by MAS, the dispersion of its isotropic part remains and broadens the lines. Attempts have been made to avoid these effects by filling the intergranular space with a liquid of the same magnetic susceptibility as the grains. This can work only if the magnetic susceptibility is isotropic.

A later study has also disclosed a shift and a broadening due to a second-order effect of the dipolar interaction, which varies as B_0^{-2}: about 0.7 ppm for ^{13}C at 1.4 T in polyethylene.[50] Even at 7 T, the effect (about 0.03 ppm, i.e., 2 Hz) is not quite negligible. This second-order shift contains tensorial terms of order higher than 2 that cannot be eliminated by MAS.

5.2 CRAMPS

(See ***CRAMPS***.)

To measure the isotropic chemical shifts of abundant spins in a solid, one needs at the same time an MREV-8 type decoupling to remove both the broadening of the homonuclear dipolar interaction and the magic angle spinning, in order to eliminate the anisotropic part of the chemical shift: this is the CRAMPS experiment.[7,51,52]

5.2.1 CRAMPS or High-Speed MAS?

In order to average out the very strong ^{1}H-^{1}H dipolar interaction in rigid inorganic solids, a MAS rotation of 40–50 kHz would be needed. This is exemplified by the results obtained at a rotation speed of 23 kHz, close to the maximum presently available:[53] at rotational speeds routinely available, good spectra can be obtained only for systems with large proton dilution. Therefore, for rigid organic solids, CRAMPS is needed. A typical resolution of CRAMPS is 0.5 ppm, which has to be compared with the spread of chemical shift of protons of about 10 ppm. There is an excellent review of CRAMPS, especially about its experimental aspects.[52]

For ^{19}F, the size of the homonuclear dipolar couplings is at most 40% of that for ^{1}H. As the chemical shift spread is much greater for ^{19}F than for ^{1}H, the line narrowing efficiency is not required to be so high for ^{19}F, in order to get resolved spectra.[54] Further, if the chemical shift anisotropy is much greater than the dipolar coupling, the fluorines whose chemical shift tensors have different principal values and/or different orientation in the lattice become inequivalent: the 'flip–flop' terms of the dipolar interaction become nonsecular—they are 'quenched'. The ^{19}F–^{19}F dipolar coupling behaves as a heteronuclear one. Such a Hamiltonian commutes with itself at any time. The spectrum splits immediately into a set of sidebands whose width at first order no longer depends on the speed of rotation. These sidebands are usually thin—exactly as for a chemical shift interaction of dilute spins.

In other solids where all fluorines are equivalent (e.g., CaF_2), a substantial width of 2 kHz may remain when spinning at 16 kHz. CRAMPS is needed for such inorganic fluorides when the dipolar coupling is dominant. Care must be exercised, because CRAMPS is efficient for only small offsets, typically $\pm$5 kHz with a BR-24 sequence with $\tau = \pm 3\,\mu$s, $\pm$16 ppm for ^{19}F (or ^{1}H) at 7 T, whereas the chemical shift spreads of the mono- or difluorides (e.g., NaF and CaF_2) extend over 100 ppm. It has been proposed to extend the spectral width by reducing the duration of the elementary cycle of the multipulse sequence, using a 'semiwindowless' or a 'windowless' sequence and acquiring the signal, point by point, at the end of the irradiation, as a function of the number N of elementary cycles (N = 0, 1, 2, 3, ...).[55]

Note also that in the intermediate case where the chemical shift anisotropy is of the same order of magnitude as the dipolar coupling (e.g.,[54] SnF_4), the line narrowing brought by MAS is less efficient than for other homologous compounds where the dipolar coupling is dominant. This is due to the existence in the lattice part of the expression of the eigenvalues of the Hamiltonian of tensorial terms of order higher than 2, with a sufficient weight, which 'resist' MAS (as well as MREV-8).

5.2.2 A Warning

Cumulative errors due to mistuning in the phase and timing makes the multipulse sequences prone to artifacts. In addition, detecting the signal in short windows between pulses leads to signal distortion and baseline artifacts. Interference effects between the pulse irradiation and the sample rotation are a further source of artifacts.[56] The CRAMPS experiments must therefore be performed very carefully, and are not reliable without sufficient knowledge of the physics of spin dynamics. The new generation of fully digitally controlled NMR spectrometers is expected to improve that situation.

6 SAMPLE MOTION AGAIN: DAS AND DOR

(see ***Double Rotation***; ***Dynamic Angle Spinning***.)

6.1 When MAS No Longer Works: The 'Very Anisotropic Interactions'

As mentioned in Section 3.5.2, MAS is inefficient in fully averaging the second-order quadrupolar broadening. There

are some other cases where MAS does not work (and never would—even at infinite speed). Some are of practical importance, such as the dipolar coupling between ^{13}C and ^{14}N. This is also the case for second-order dipolar coupling,[50] etc. These interactions are called 'very anisotropic'. Their common characteristic will be shown to be that their lattice part contains tensorial terms $P_l^m(\cos\theta)$ of order l greater than 2, or equivalently terms $\cos^p\theta\,\sin^q\theta$, with $p + q > 2$.

We shall consider here the line narrowing of the central $\frac{1}{2} \leftrightarrow -\frac{1}{2}$ transition of a half-integer quadrupolar nucleus. For such nuclei, since one is interested only in the frequency of the sharp and intense central $\frac{1}{2} \leftrightarrow -\frac{1}{2}$ transition, one makes the assumption that the transition behaves as an isolated spin-$\frac{1}{2}$. This assumption is a classical one, and it works. It neglects any population transfer between the two $\frac{1}{2}$ and $-\frac{1}{2}$ levels and the other levels. (This requires only that the radiofrequency pulse is of low amplitude as compared with the quadrupolar interaction: $\omega_{rf} \ll \omega_Q$, and, for rotating samples, the pulse duration is shorter than the period of rotation $\tau_{pulse} \leq \tau_{rot}$.) The way in which the frequency of that transition depends on the orientation of the sample is well known (see ***Quadrupolar Nuclei in Solids***). With this simplifying assumption, the Hamiltonian of that 'fictitious' spin-$\frac{1}{2}$ is

$$\hat{\mathcal{H}} = f(\Omega(t))\hat{S}_z \tag{31}$$

It commutes with itself at any time. The average Hamiltonian is therefore easy to calculate. It is a scalar function of lattice orientation, multiplied by a linear spin operator. It cannot be suppressed by any spin irradiation without averaging together with the chemical shift, including its isotropic part. For an isolated half-integer spin $f(\Omega(t)) = \nu_Q^{(2)}(\Omega(t)) + \nu_0(\sigma_{iso} + \Delta\sigma(\Omega(t)))$. Whereas the chemical shift anisotropy $\Delta\sigma(\Omega(t))$ is averaged out by magic angle spinning, the quadrupolar second order shift $\nu_Q^{(2)}(\Omega(t))$ cannot be so.

6.2 A Solution: DAS and DOR

The solution was found almost at the same time and independently in Saclay[57] and at Berkeley.[58–60] It was shown that motions of the sample can be devised that average out the very anisotropic interactions. The simplest of these motions involves a rapid rotation of the sample around an axis whose orientation is made time-dependent: this may be either by a toggling of the axis direction between two or more orientations (dynamic angle spinning, DAS) or by a continuous precession motion of that axis (double rotation, DOR). Experimental results have been obtained in Berkeley with both methods, confirming the validity of the theoretical predictions. Second-order broadening of the $\frac{1}{2} \leftrightarrow -\frac{1}{2}$ transition of ^{23}Na or ^{17}O has been reduced by more than one order of magnitude.[60,61]

6.3 Towards the Solution: A Careful Analysis of the Rotational Behavior of the Interactions

The principles of the DAS and DOR experiments are well explained in the original publications.[57,59,61] The solution was found by a simple but careful analysis of the behavior of the isotropic interactions under the effect of rotations in lattice space.

The second-order quadrupolar shift depends on the size of the quadrupolar interaction ν_Q and its asymmetry η and on the Larmor frequency ν_0. It contains terms of up to fourth degree in $\cos\Theta_c$. Careful examination shows that, for a spinning sample, it can be expanded as

$$\nu_Q^{(2)} = \frac{(\nu_Q)^2}{\nu_0} \sum_{l=0,2,4} \sum_{m=-l}^{l} (A_Q^{(2)})_l^m D_l^{m0}(\Phi_c, \Theta_c, 0) \tag{32}$$

If the sample is spun fast enough about an axis whose orientation is θ, the average value of the interaction is

$$\nu_Q^{(2)}(\Omega(t) = B_0^0 + \sum_{l-2.4} B_l^0(\alpha, \beta, \gamma) P_l(cos(\theta)) \tag{33}$$

with

$$\begin{aligned} B_l^0(\alpha, \beta, \gamma) &= \left(\sum_{m'=-l}^{l} (A_l^{m'} D_l^{m'0}(\alpha, \beta, \gamma) \right) \\ &= \sum_{m'=-l}^{l} (A_Q^{(2)})_l^{m'} D_l^{m'0}(\alpha, \beta, \gamma) \end{aligned} \tag{34}$$

whereas the time-dependent terms give sidebands.

Tilting the rotation axis of the sample at the magic angle $\theta = 54^\circ\,44'$, as in MAS, cancels the term $P_2(\cos\theta)$: unfortunately, this does not cancel the $P_4(\cos\theta)$ term. Alternately tilting the rotation axis at either of the two angles $30^\circ\,31'$ or $70^\circ\,07'$ which cancels the $P_4(\cos\theta)$ term, does not cancel the $P_2(\cos\theta)$ term. Thus, line narrowing cannot be performed by rotation about a single fixed axis. This explains why MAS and VAS are inefficient.

Assume now that the sample is spinning about an axis tilted by angles $\theta_1, \theta_2, \theta_3, \ldots, \theta_n$ during successive time intervals $\tau_1, \tau_2, \tau_3, \ldots, \tau_n$, switching suddenly from one orientation to the next one. Line narrowing will be achieved if the total dephasing due to the anisotropic terms is zero whatever are α, β, γ

$$\begin{aligned} \Phi(\alpha, \beta, \gamma) = \sum_{k=1}^{n} \tau_k [& B_2^0(\alpha, \beta, \gamma) P_2(\cos\vartheta_k) \\ & + B_4^0(\alpha, \beta, \gamma) P_4(\cos\theta_k)] = 0 \end{aligned} \tag{35}$$

Is this possible? One of the keys to the principle of the experiment is that the relative weight $B_2^0(\alpha, \beta, \gamma)/B_4^0(\alpha, \beta, \gamma)$ of these two contributions $P_2(\theta_k)$ and $P_4(\theta_k)$ is dependent on the crystallite orientation (α,β,γ). Therefore the total dephasing Φ cancels for any crystallite only if the following two equations are fulfilled simultaneously

$$\sum_{k=1}^{n} \tau_k P_2(\cos\theta_k) = 0, \quad \sum_{k=1}^{n} \tau_k P_4(\cos\theta_k) = 0 \tag{36}$$

or, for continuous reorientation,

$$\begin{aligned} \int_{t_1}^{t_2} P_2(\cos\theta(t))\,dt = 0 \\ \int_{t_1}^{t_2} P_4(\cos\theta(t))\,dt = 0 \end{aligned} \tag{37}$$

This makes $\overline{v_Q^{(2)}(\Omega(t))}^{DAS} = B_0^0$ independent of the lattice orientation. Line narrowing is achieved.

6.4 DAS and DOR

First, let a sample take six orientations Ω_i, whose five $\Omega_1, \ldots, \Omega_5$ are obtained by tilting the sample away from the former orientation Ω_0 by an angle $\theta = \arccos\sqrt{\frac{1}{5}} = 63^\circ 25'$ about five axes, lying in the plane perpendicular to the magnetic field $\boldsymbol{B}_0$, and $\frac{2}{5}k\pi$ apart from each other. Equation (36) is fulfilled: the second-order quadrupolar broadening will be averaged out. To the best of our knowledge, this experiment has never been performed.

6.4.1 DAS

On practical grounds, since reorientation times are not negligible compared with relaxation times, discrete rotational jumps are to be avoided as much as possible. This leads one to prefer sample motions involving a continuous rotation of the sample about an axis, as in MAS. What is new here is that, in order to wipe out anisotropic terms of tensorial order greater than 2, this rotation axis must reorient itself during the experiment: this reorientation may be a discrete jump as in DAS or a continuous reorientation as in DOR. In the former implementation of DAS, the rotation axis toggles between two orientations: $37^\circ\ 22'$ and $79^\circ\ 11'$ away from the magnetic field $\boldsymbol{B}_0$. The transverse magnetization is allowed to evolve for equal times ($\tau_2 = k\tau_1$; $k = 1$) in each one of these two orientations. Equation (36) is fulfilled. These evolution times are defined as the intervals between the $\frac{1}{2}\pi$ pulses that bring the magnetization into the transverse plane of the rotating frame and restore the magnetization along the direction of the magnetic field.

As switching the axis orientation from θ_1 to θ_2 cannot be done suddenly, the evolution of the transverse magnetization must be 'frozen' during the switching time (about 10–30 ms). Usually, in DAS experiments, this is done by flipping back the magnetization from the transverse plane to the direction of the magnetic field (see Section 3.2). Along the magnetic field, the magnetization is a quasi-invariant—as long as the time delays are shorter than the longitudinal relaxation time. As explained above, the experiment must be repeated twice, storing first the x component, then the y component of the transverse magnetization. The results of the two experiments are conveniently added together in the computer memory, in order to restore the complex evolution of the magnetization in the transverse plane. For a detailed description of the DAS experiment see ***Dynamic Angle Spinning***.

6.4.2 DOR

In DAS, the rotation axis is moving in a plane. A smoother motion may be achieved by allowing the axis to move out of one plane. The required averaging is obtained, for instance, if the sample is spinning at an angular speed ω_{int} about an axis which is itself moving at an anglular speed ω_{ext} on cone of aperture $2\theta_{\text{in}}$, whose axis is tilted θ_{ext} away from the magnetic field B_0. In that case, the average second order quadrupolar interaction is

$$\overline{v_Q^{(2)}(\Omega(t))}^{DOR} = B_0^0 + \sum_{l=2.4} B_l^0(\alpha, \beta, \gamma) \times P_l(\cos\theta_{\text{in}})\, P_l(\cos\theta_{\text{ext}}) \qquad (38)$$

whereas the time-dependent terms give sidebands at $n\omega_{\text{in}} + m\omega_{\text{ext}}$. Line narrowing is achieved by taking $\theta_{\text{in}} = \vartheta'_4 = 30^\circ 33'$ and $\theta_{\text{ext}} = \vartheta_2 = 54^\circ 44'$ which makes $P_4(\cos\theta_{\text{in}}) = 0$ and $P_2(\cos\theta_{\text{ext}}) = 0$ so that $\overline{v_Q^{(2)}(\Omega(t))}^{DOR} = B_0^0$. This solution gives the best filling factor and orthogonality of the rf field and B_0 field, resulting in the best NMR sensitivity. The other solutions [$\vartheta_{\text{in}} = \vartheta''_4 = 72^\circ 19'$; $\vartheta_{\text{ext}} = \vartheta_2$] or [$\vartheta_{\text{in}} = \vartheta_2$; $\vartheta_{\text{ext}} = (\vartheta'_4$ or $\vartheta''_4)$] are not as efficient. They are not used.

6.4.3 A Warning: The Isotropic Second-Order Shift—A Limit to Resolution for DAS and DOR

The anisotropic chemical shift is, evidently, averaged out by DAS and DOR. The dispersion of chemical shifts is the same as for MAS.

The second-order quadrupolar shift involves, besides the anisotropic components that are averaged out by DAS and DOR, an isotropic term independent of the orientation. This has two consequences.

1. The shift of each line is the sum of the second-order quadrupolar isotropic shift and the isotropic chemical shift, and not the chemical shift alone.
2. This isotropic term is proportional to the square of the quadrupolar interaction, ν_{Q}^2. Dispersion of the values of the quadrupolar interaction leads to broadening, which is not averaged out by DAS and DOR. In crystalline materials, this dispersion and therefore the residual linewidth are small, so that DAS and DOR can enhance the resolution by one or two orders of magnitude compared with MAS alone. In amorphous, glassy, and disordered materials, the quadrupolar interaction has a wide dispersion: it may happen that DAS and DOR can not give any improvement over MAS.

6.4.4 DAS or DOR?

DAS experiments are well suited for dilute or low gyromagnetic ratio γ nuclei, like ^{17}O. For high-γ abundant nuclei like ^{23}Na, the homonuclear dipolar coupling means that the spins no longer evolve independently. It is then expected that dephasing no longer accumulates independently for each spin species, nor can it be refocused as simply as in the ideal DAS experiment; furthermore, spin diffusion can occur during the switching time of the axis and mix the 'stored magnetization' of each spin species: this also prevents such good refocusing.

If the orientation of the rotation axis of the outer rotor is $54^\circ\ 44'$ (the magic angle) away from the magnetic field $\boldsymbol{B}_0$, as in MAS, DOR is able to average out the dipolar interaction at least partly. This allows better line narrowing.

In DAS, the relaxation time T_1 must be longer than the switching time, whose minimum achieved (and achievable?) value is nowadays about 20 ms. In DOR, the relaxation times must be longer than the rotation period of the outer rotor, nowadays about 1 ms. DOR allows the study of nuclei with faster relaxation times.

One advantage of DAS is that it allows one to put the coil close to the sample rotor, and therefore provides a good filling factor. However, the signal must be acquired point by point. In the present design of the DOR probes, the coil is wound around the external rotor, inside of which is the inner rotor. The inner rotor fills the coil, with a low filling factor. This lowers the sensitivity. However, a DOR spectrum can be obtained in one scan.

As for MAS, sidebands are observed. Their calculation, although straightforward, is very lengthy. Typical rotation speeds are, for DAS, 5–10 kHz and for DOR, 5 kHz for the inner rotor and 1 kHz for the outer one. As a consequence, sidebands are spaced more widely in DAS than in DOR. Perfect synchronization of the two rotations in DOR, or of the rotation and the pulses in DAS, is not absolutely necessary. In some cases, it allows improved spectral resolution by suppressing some rotation sidebands.

The relative efficiency of the two methods DAS and DOR may be checked with the experimental results obtained at Berkeley[58–60,62,63] on ^{23}Na and ^{17}O. A striking example is the spectrum of ^{17}O in wollastonite, $CaSiO_3$,[64] where DAS and DOR have allowed resolution of the nine different lines expected from the crystallographic structure.

The practical interest of these methods is such that a few years after their invention, DAS and DOR probes (see ***Solid State Probe Design***) were commercially available. However, these probes are very complex. Their development has not reached the level of maturity of MAS probes. Two detailed descriptions have been published for DOR probes,[62] in which the dynamic equilibrium of these nested rotors is discussed in detail. A more concise description of a DAS probe has also been published.[63]

At present, once a DOR rotor has been equilibrated and is spinning (this may be a challenge—as with the former MAS spinners), signal acquisition is straightforward. It may be easier to spin a DAS rotor; however, more care must be exercised in the calibration (accuracy and reproducibility) of the two angles, in achieving a fast angle switching, and also in performing the acquisition and proceeding the signal.

7 MISTUNING AND RECOUPLING: LIMITS TO RESOLUTION, AND TOOLS FOR STRUCTURAL STUDIES

The anisotropic parts of the interactions may appear in the spectra as an unwanted residual linewidth, or as a limitation on resolution due to imperfections or as artifacts in the experiments. These may also be reintroduced deliberately, in a controlled way, in order to measure them by a suitable modification of the experiments. Indeed, the anisotropic parts of the interactions contain much structural information. If they must be eliminated in order to obtain highly resolved spectra, where spins in different local environments are distinguished by their isotropic chemical shifts, it would still be useful, once resolution has been achieved, to measure these interactions for each spin species.

This evolution under anisotropic interactions can occur during the acquisition time: the lines are broadened by these anisotropic terms. It can also occur during the preparation time or during an evolution time between the preparation and the acquisition:

(a) if that time is fixed, one gets a 1D spectrum, with a selection of the spin species observed, according to the anisotropic interactions that they see;

(b) if that time is varied, one may get a 2D spectrum, with, in one dimension, the isotropic chemical shift, which allows identification of the different spin species, and in the second dimension, the anisotropic interaction, measured for each spin species.

The 1D spectra may be viewed as slices in the 2D spectrum.

7.1 Mistuning

Line broadening may be induced in many ways: it occurs if the rotation axis orientation, the frequency of irradiation (offsets), or the Hartmann–Hahn match are not perfectly tuned. It may also occur if the speed of sample rotation or the irradiation amplitude are not high enough. These are *mistuning* effects. It may also occur, even if each parameter is tuned at its convenient value, if, by chance, the frequencies of two time modulations are equal. These are *resonance* effects (see Section 7.2).

7.1.1 Measurement of Shielding Anisotropy

(See ***Two-Dimensional Powder Correlation Methods***.)

In MAS, if the speed is not high enough, a comb of rotational sidebands appears. This may be considered undesirable. However, its shape does allow measurement of the chemical shift anisotropy or the quadrupolar interaction. Switched-speed MAS experiments have been devised and performed that provide 2D spectra with only the isotropic chemical shift (one line per spin species) in one dimension, and a set of sidebands in the other.

Otherwise, in MAS, if the axis is not tilted exactly at the magic angle, each sideband will exhibit the static powder pattern, scaled by a factor $\frac{1}{2}(3\cos^2\theta - 1)$. This is a limit on resolution. It may be done deliberately as a way to measure the chemical shift anisotropy for each spin species: mistuning the angle θ from the magic angle allows one to adjust that scaling factor. In a 1D experiment, the powder pattern of each spin species can be made apparent, scaled without overlapping as it is in a static sample. A 2D switched-angle MAS experiment has been devised in which sample rotation occurs away from the magic angle during the evolution time, and then, after switching, at the magic angle during acquisition. This provides the resolved isotropic spectrum in one dimension, and the static powder pattern for each spin species in the second dimension.

7.1.2 Strong Heteronuclear Dipolar Interactions: Measuring and Editing

7.1.2.1 Editing. (See ***Spectral Editing Techniques: Hydrocarbon Solids***.)

Even with optimum line narrowing, the spectra may be overcrowded. 'Editing' of the spectra ensures that the lines of only some nuclei have significant intensity. For carbons, selection is usually made according to the strength of the carbon–proton heteronuclear coupling. It must be noted that, in contrast with liquids, where editing uses the scalar indirect coupling (which is usually invariant, whatever the motional state of a molecule), the dipolar interaction, on which spectral

editing methods in organic solids rely, has no isotropic invariant part and is strongly dependent on the rate and symmetry of the molecular motions: a motion may affect a CH and a CH_2 group differently. In solids, spectral editing sequences may have to be carefully tuned for each sample and each motional state of a sample.

In CP MAS, if the proton decoupling irradiation is not of sufficient intensity, or not at the proton resonance frequency, the decoupling efficiency is reduced. The broadening is higher, the higher the dipolar coupling of the rare spins with the abundant ones. This may be a limit on resolution, or a way to distinguish, in a 1D spectrum, which carbons are close to protons and which are not.

In CP MAS, the closer the carbon is to protons and the greater the number of these protons, the faster is the increase in carbon polarization. A too short cross polarization time will thus distort the relative amplitudes of different species of carbons. However, this can be used for selectively enhancing the signal of those carbons close to protons.

In CP MAS, if the decoupling of the protons does not begin immediately after the cross polarization, the carbons evolve under the effect of their dipolar coupling with the protons. It is currently said that they 'dephase'. As this dipolar coupling varies from carbon to carbon in the sample, the whole carbon magnetization is destroyed by interference. Adjusting the delay allows one to see all the carbons, or only those far from any protons. This is usually called 'dipolar dephasing'.

7.1.2.2 Measuring the Heteronuclear Dipolar Interaction. (See ***Two-Dimensional Powder Correlation Methods***.)

If the protons are themselves strongly coupled together by dipolar interactions, one cannot think about 'the protons coupled to one carbon'. The carbon evolution not only reflects the $^{13}C-^{1}H$ coupling, which may easily be analyzed into structural data—it also depends on the mutual $^{1}H-^{1}H$ coupling between protons, which blurs the structural information. A solution is to average out, selectively by an MREV-8 type multipulse, the $^{1}H-^{1}H$ dipolar interaction. The $^{1}H-^{1}H$ dipolar interaction, averaged out, no longer damps the $^{13}C-^{1}H$ dipolar interaction. This procedure can formally be applied after the preparation time, during the evolution time, before acquisition in the presence of decoupling of the heteronuclear coupling: this is separated local field spectroscopy (SLF).[65] It may also be applied during the cross polarization time, using a magic angle irradiation for cross polarization.[66] SLF, first performed on static samples, has also been implemented on spinning samples.[67]

7.2 Simultaneous Synchronous Motions: Recoupling and Rotational Resonance

7.2.1 Resonances

In all of the experiments described above, an anisotropic interaction has been made observable by 'mistuning' the line-narrowing experiment during the acquisition, or during some evolution time before acquisition. Another more subtle manifestation of the anisotropic terms may occur, even if the sample spinning and/or irradiation are tuned for perfect averaging. Let two processes make an anisotropic interaction time-dependent. If the frequencies (or some of their multiples) are equal, resonance effects occur that make parts of these anisotropic interactions again time-independent, so that they manifest themselves in the spectra. This is quite obvious. Consider two periodic functions of same the frequency and same phase:

$$A(t) = A_0 \cos \omega t, \quad B(t) = B_0 \cos \omega t \tag{38}$$

Each has a zero average value. However, their product will have a nonzero average value:

$$A(t)B(t) = \frac{1}{2} A_0 B_0 (1 + \cos 2\omega t) \tag{39}$$

In line-narrowing experiments, there are many time-modulation frequencies that may come into resonance with each other: for example, the sample spinning frequency, the amplitude of an irradiation, the cycle time of a multipulse irradiation, and the difference in chemical shift between two spin species. These lead to subtle, and sometime strong, limitations on resolution. However, this may be used to reintroduce, deliberately, at some definite time in the experiment, some anisotropic interaction in order to measure it.

7.2.2 Cross Polarization

The most striking example of recoupling is cross polarization. In the doubly rotating tilted frame, where the X axis is along the magnetic field $\boldsymbol{B}_0$, the $\hat{I}_X \hat{S}_X$ part of the $I-S$ dipolar interaction is made time-dependent by two simultaneous irradiations, at the Larmor frequencies of the I and S spins. Each irradiation makes that term periodically time-dependent with frequency $\omega_{1I} = \gamma_I B_{1I}$ or $\omega_{1S} = \gamma_S B_{1S}$. If the amplitudes ω_{1I} and ω_{1S} of the irradiations are equal (this is the Hartmann–Hahn condition), the $\hat{I}_X \hat{S}_X$ term becomes time-independent and can induce a very fast flip–flop exchange of polarization between I and S spins.

7.2.2.1 Cross Polarization of a Spinning Sample. (See ***Cross Polarization in Rotating Solids: Spin-1/2 Nuclei***.)

If the sample is spun as in CP MAS, the situation becomes more intricate: the $I-S$ dipolar interaction becomes modulated by the rotation of the sample: giving a third time dependence! In organic solids, the $^{13}C-^{1}H$ dipolar coupling within a CH or CH_2 group is much stronger than the 5 kHz spinning speeds ω_{rot} available in the earlier CP MAS experiments. In that case, in a first approximation, the modulation due to sample spinning may be neglected. The cross polarization behaves roughly as expected for a static sample. However, it was observed that for adamantane or for quaternary carbons, cross polarization did not occur at the Hartmann–Hahn condition $\omega_{\text{rf}}^I = \omega_{\text{rf}}^S$, but also when the two rf intensities differ by $n = \pm 1, \pm 2$ times the spinning speed: $\omega_{\text{rf}}^I = \omega_{\text{rf}}^S + n\omega_{\text{rot}}$. The cross polarization has a sideband structure. This situation becomes almost a rule for ^{29}Si. In most inorganic compounds, Si is not directly bound to ^{1}H: the $^{29}Si-^{1}H$ dipolar interaction is much smaller than the $^{13}C-^{1}H$ coupling in CH_n groups in organic solids. For ^{29}Si, cross polarization always has that sideband structure. This is quite troublesome: for $n = 0$, the time-independent part of the dipolar coupling may be small; for $n \neq 0$, owing to the rf field inhomogeneity, the Hartmann–Hahn condition cannot be fulfilled over the whole sample. Further, the smaller the dipolar interaction, the more restricted is the range of amplitude of the rf irradiation or the offset from the Larmor frequency, which

fulfills the Hartmann–Hahn condition. This problem has been addressed recently by amplitude or phase modulation of the rf amplitude at the sample rotation frequency. This restores a time-independent $I-S$ dipolar interaction and makes the cross polarization more efficient.

7.2.3 Line Broadening by Molecular Motions

(See ***Brownian Motion and Correlation Times***.)

Assume that some anisotropic interaction, of size ω_{an}, is made time-dependent by a random molecular motion whose correlation time is τ_c, and also by the line-narrowing experiment, whose characteristic frequency is ω_{exp}. This may be, in MAS, the speed of rotation ω_r, or in CP MAS, the intensity ω_{rf} of the decoupling field (i.e., the angular velocity of rotation of protons about it) or, in CRAMPS, $2\pi/t_c$, where t_c is the elementary cycle of the multipulse. As in a static sample, this may also be the difference in chemical shift between two spin species. If the inverse correlation time ${\tau_c}^{-1}$ is close to the characteristic frequency ω_{exp}, $\omega_{exp}\tau_c \approx 1$, then the line narrowing becomes inefficient. The order of magnitude of the residual linewidth is

$$\Delta\nu_{res} = \omega_{an}^2 \frac{\tau_c}{1+\omega_{exp}^2\tau_c^2} \tag{40}$$

This line broadening is a limit on resolution. It may also be used as a source of information on molecular motions.

7.2.4 Multipulse Artifact Lines

(See ***Rotating Solids***.)

If the period of rotation of the sample or its multiples is equal to the cycle time (or its multiples) of a multipulse interaction (e.g., CRAMPS), artifact lines, or in some cases broadening, may occur.[56] However, such effects are not always troublesome, and have been turned into useful methods.

7.2.5 Measurement of the Small Interactions

(See ***Homonuclear Recoupling Schemes in MAS NMR***; ***REDOR and TEDOR***; ***Rotating Solids***.)

If the dipolar couplings are small, they are fully averaged out by MAS. This occurs for $^{13}C-^{13}C$ homonuclear dipolar coupling or for $^{15}N-^{13}C$ or $^{15}N-^{31}P$ heteronuclear dipolar couplings. For structural studies, internuclear distances greater than typically 250 pm are important.

These couplings may again be made efficient by resonance: the sample rotation is made equal to the difference in chemical shifts between the two carbons. This is *rotational resonance*,[71] which was observed very early on.[72] It results in a broadening of each line as a powder pattern, whose analysis gives the dipolar interactions. However, if the dipolar coupling is too small, the width of that powder pattern is blurred in the residual broadening due to other sources. The size of the recoupled dipolar interactions can still be measured by looking at their effect on longitudinal magnetization spin exchange.[71,73]

The use of some judiciously chosen pulses (pairs of $\frac{1}{2}\pi$ pulses—DRAMA,[74]—or one or several π pulses—SEDRA,[75] DICSY, and RFDR[76]) applied during each sample rotation period also compensates for a part of the averaging out of the dipolar coupling by sample spinning, and allows one to measure small homonuclear (e.g., $^{13}C-^{13}C$) dipolar couplings, in 1D or 2D experiments.

For heteronuclear couplings, adjusting the rf amplitude $\omega_{rf}(^{15}N)$ so that it matches the speed of rotation (or its multiples) has allowed measurement of the $^{15}N-^{31}P$ dipolar coupling.[31,77] Similar, but more complex experiments, involving a quadrupolar nucleus, have allowed probing of $^{15}N-^{13}C$ distances.[78] The use of π pulses to prevent the averaging effect of MAS has been employed in the REDOR and TEDOR experiments devised for probing the distances between rare spins such as $^{15}N-^{13}C$[79] to 500 pm, with a 10 pm precision.

8 OTHER APPROACHES TO LINE NARROWING IN SOLIDS

8.1 Zero Field NMR and Zero Field NMR in High Field

(See ***Zero Field NMR***.)

It has been mentioned that the source of anisotropy, which in a powder makes the different crystallites inequivalent, is the magnetic field $\boldsymbol{B}_0$. Suppressing $\boldsymbol{B}_0$ removes the orientation dependence of the eigenvalue frequencies of the spin system. An orientation dependence of the transition amplitudes remains, induced by the presence of the coils of the NMR probe. This has been known for a long time for nuclear quadrupole resonance (NQR). For spins $\frac{1}{2}$, the zero field dipolar spectrum may be obtained by an indirect detection method:

1. polarization of the sample in high field inside the magnet;
2. shuttling of the sample to zero field outside the magnet;
3. sudden switching to zero field;
4. evolution in zero field (eventually in the presence of some irradiation);
5. sudden transition to nonzero field;
6. shuttling back to high field;
7. measurement of the NMR signal as a function of the time spent in zero field.

This was called 'zero field NMR'.[80] Another very nice experiment is 'zero field NMR in high field', where, by a recoupling experiment involving sample rotation and spin irradiation, a dipolar spectrum free from any orientation dependence, similar to the zero field spectrum, has been obtained for ^1H and for ^{13}C, without moving the sample out of the magnetic field.[81]

These very skilful experiments have not yet gained wide application: they are experimentally tricky and are subject to signal loss due to zero field relaxation induced by slow motions. Further, a zero field dipolar spectrum is more difficult to analyze than a high-field one.

8.2 Multiple Quantum Spectroscopy

(See ***Multiple Quantum NMR in Solids***; ***Overtone Spectroscopy of Quadrupolar Nuclei***.)

For quadrupolar nuclei, a less widely explored class of methods involves multiple quantum forbidden transitions, which, at first order, are free from quadrupolar broadening. These may be and have been detected indirectly (^2H, ^{14}N) or

directly (^{14}N overtone spectroscopy). However, the multiple quantum lines remain subjected to second-order broadening. DAS may, in principle, remove this broadening. We are not aware of a successful implementation of such an experiment. Along the same direction, it has been shown by Amoureux[82] that in the very particular case of spins $\frac{3}{2}$, the second-order quadrupolar broadening of the forbidden $\frac{3}{2} \leftrightarrow -\frac{3}{2}$ transition can be averaged out by spinning the sample at an axis tilted 30° 33′ (or 70° 07′) away from the magnetic field $\boldsymbol{B}_0$, without changing this orientation. Unfortunately, at this angle, the CSA is not averaged out.

9 MQ-MAS, A NEW EFFICIENT LINE NARROWING METHOD FOR QUADRUPOLAR NUCLEI

(*See* ***Multiple Quantum NMR in Solids***; ***Phase Cycling***.)

Since the initial writing of this article, a new line narrowing method for quadrupolar nuclei, called MQ-MAS, has been introduced recently by L. Frydman.[83] Since then, results using an improved coherence transfer method have been obtained.[84,85] The resolution obtained by MQ-MAS is as at least as good as that obtained with DAS or DOR.[83–85] MQ-DAS is much easier.

In some respects, MQ-DAS is very similar to the DAS experiment (see Section 6). In DAS and MQ-MAS, the sample is spinning. As in DAS, MQ-MAS involves two evolution times such that the dephasing induced during the first evolution period by some anisotropic interactions is exactly compensated during the second period. However, in DAS the orientation of the spinning axis of the sample is switched in between. Here, in MQ-MAS, the sample is always spinning at the magic angle, but a switch (a transfer) is performed between two different coherence states of the quadrupolar spin. A motion of the sample has been replaced by a motion in spin space. For an $S = 3/2$ spin, the spin system is allowed to evolve first for a time t_1 in the $-3/2 \leftrightarrow 3/2$ three quantum transverse coherences (called $I_{x,y}^{1-4}$) then for a time t_2 in the $-1/2 \leftrightarrow 1/2$ one quantum transverse coherences (called $I_{x,y}^{2-3}$). As in DAS, an echo is observed at time, $t_2 = kt_1$, whose amplitude is no longer damped by the anisotropic second-order quadrupolar interaction. For MQ-MAS and an $S = 3/2$ spin, $k = 7/9$. That amplitude is free from any decay due to first-order or second-order quadrupolar broadening, as well as chemical shift anisotropy. As in DAS, Fourier transformation of the $S(t_1, t_2)$ signal leads to a 2D spectrum, with the isotropic shifts (chemical shift and isotropic second order quadrupolar shift) in the t_1 dimension, isotropic and [4th rank $P_4(\cos\vartheta)$ terms] anisotropic interactions in the second t_2 dimension.

How does MQ-MAS work? It may be realised that the total dephasing due to the anisotropic terms for any transition M $\leftrightarrow$ M′ can be written

$$\omega_{M,M'}(\alpha,\beta,\gamma,\theta) = \sum_{l=0,2,4} C_l^{interaction}(M,M') \times P_l(\cos\vartheta) B_l^0(\alpha,\beta,\gamma)$$

where $C_l^{interaction}(M, M')$ is the matrix element of a spin operator, dependent on the interaction and on the transition M $\leftrightarrow$ M′; $P_l(\cos\vartheta)$ depends on the orientation of the spinning axis and $B_l^0(\alpha, \beta, \gamma)$ depends on the crystallite orientation α, β, γ only for $l = 2, 4$. Within a transition $M \leftrightarrow M'$ the $C_l^{interaction}(M, M')$ is a constant which for DAS and DOR (see Section 6) was implicitly included in the coefficients $B_l^0(\alpha, \beta, \gamma)$.

Line narrowing is achieved if the total dephasing due to the anisotropic terms $B_l^0(\alpha, \beta, \gamma)$ and $B_l^0(\alpha, \beta, \gamma)$ is zero

$$\Phi(\alpha,\beta,\gamma) = \sum_{l=2,4}\sum_{k=1}^{n} \tau_k (C_l^{interaction}(M_k, M_k') B_l^0 \times (\alpha,\beta,\gamma) P_l(\cos\vartheta_k)) = 0$$

that is for DAS (see Section 6) if

$$(\tau_1 P_2(\cos\vartheta_1) + \tau_2 P_2(\cos\vartheta_2)) = 0;$$
$$(\tau_1 P_4(\cos\vartheta_1) + \tau_2 P_4(\cos\vartheta_2)) = 0$$

and for MQ-MAS if,

$$P_2(\cos\vartheta) = 0$$
$$(\tau_1 C_4^{interaction}(3/2, -3/2) + \tau_2 C_4^{interaction}(1/2, -1/2)) = 0$$

Thus, in MQ-MAS, the $-3/2 \leftrightarrow 3/2$ symmetric coherence is, like the $-1/2 \leftrightarrow 1/2$ one, free from first order quadrupolar broadening ($C_l^{Q,1}(M, -M) = 0$). The $P_2(\cos\vartheta)$ anisotropic terms (second order quadrupolar broadening, CSA, ...) are averaged out by the magic angle spinning, as usual. The second order quadrupole $P_4(\cos\vartheta)$ anisotropic terms are cancelled by a coherence transfer echo, instead of a 'spinning axis orientation switch' echo. Here, unlike the DAS or DOR experiment, one does not remains cosily within the 'allowed $-1/2 \leftrightarrow 1/2$ transition'. Within the restricted space of the $-1/2 \leftrightarrow 1/2$ transition, it was impossible by mere rf irradiation to average out an anisotropic term without wiping out at the same time all the isotropic terms so that an extra motion is required: this led to DAS and DOR. Here, using coherence transfer 'to' and 'from' forbidden multiquantum coherences, and evolution 'within' those coherences has made selective averaging possible.

Coherence transfer to 'forbidden transitions' in quadrupolar nuclei is sometimes thought difficult. In fact, it is easy, and known from a long time[1] to occur, for instance in quadrupolar echoes. In powder samples, as required for MQ-MAS, coherence transfer can easily be performed using short pulses.[84–86] Starting from the equilibrium magnetization, transfer to the $-3/2 \leftrightarrow 3/2$ symmetric coherence is obtained by short rf pulse of length $\tau \cong \pi_{liquid}/\omega_{rf}$. The transfer efficiency is maximum not for those crystallites whose quadrupolar coupling C_Q null ($C_Q \cong 0$) as usually for the excitation of a transverse magnetization, but for those whose C_Q is of the same magnitude as the rf field, ($C_Q \approx \omega_{rf}$). Transfer back from the $-3/2 \leftrightarrow 3/2$ coherence to the $-1/2 \leftrightarrow 1/2$ coherence is maximised for $\tau \cong \pi_{liquid}/\omega_{rf}(2S + 1)$ and $C_Q \approx \omega_{rf}$. As, in quadrupolar nuclei, such short pulses result always to transfer to several coherences, selection of the required ones is performed by phase cycling of the pulses.

MQ-MAS is a very attractive method. Some advantages are:

1. Coherence transfer can be performed much faster than spinning axis reorientation. In DAS, switching of the spinning axis required about ∼20 msec, whereas coherence transfer is a motion in spin space requires only some short rf pulses (several μsec).
2. Motion in the spin coherence states gives 'extra degrees of freedom'[84] and will allow many new different line narrowing or recoupling experiments to be devised in the future.
3. In contrast to DAS and DOR which required highly sophisticated probes, MQ-MAS can be settled easily on any solid state NMR spectrometer, and in the near future, routinely.

10 CONCLUSIONS

Line narrowing in solids is, together with multidimensional NMR in liquids and NMR imaging, one of the domains where important developments have arisen during the last 30 years. To be expected in next few years are some refinements of line-narrowing methods and new developments of the 'mistuning' and 'recoupling' methods for acquiring the structural information carried by the anisotropic terms.

11 RELATED ARTICLES

Anisotropy of Shielding and Coupling in Liquid Crystalline Solutions; Average Hamiltonian Theory; Brownian Motion and Correlation Times; CRAMPS; Cross Polarization in Rotating Solids: Spin-1/2 Nuclei; Cross Polarization in Solids; Deuterium NMR in Solids; Dipolar and Indirect Coupling Tensors in Solids; Double Resonance; Double Rotation; Dynamic Angle Spinning; Geometric Phases; High Speed MAS of Half-Integer Quadrupolar Nuclei in Solids; Homonuclear Recoupling Schemes in MAS NMR; Internal Spin Interactions and Rotations in Solids; Magic Angle Spinning; Magic Angle Turning and Hopping; Multiple Quantum NMR in Solids; Probe Design and Construction; Quadrupolar Interactions; Quadrupolar Nuclei in Solids; REDOR and TEDOR; Rotating Solids; Sideband Analysis in Magic Angle Spinning NMR of Solids; Silicon-29 NMR; Spectral Editing Techniques: Hydrocarbon Solids; Two-Dimensional Powder Correlation Methods; Variable Angle Sample Spinning; Zero Field NMR.

12 REFERENCES

1. A. Abragam and M. Goldman, *Nuclear Magnetism: Order and Disorder*, Clarendon Press, Oxford, 1982, Chaps. I and II.
2. C. P. Slichter, *Principles of Magnetic Resonance*, 3rd edn., Springer-Verlag, Berlin, 1990.
3. M. Munowitz, *Coherence and NMR*, Wiley, New York, 1988.
4. R. K. Harris, *Nuclear Magnetic Resonance Spectroscopy*, Longman, Harlow, UK, 1986.
5. C. Fyfe, *Solid State NMR for Chemists*, CFC Press, Guelph, Ontario, 1983.
6. G. Engelhart and D. Michel, *High Resolution Solid State NMR of Silicon and Zeolites*, Wiley, New York, 1987.
7. U. Haeberlen, *High Resolution NMR in Solids: Selective Averaging*, Academic Press, New York, 1976.
8. M. Mehring, *The Principle of High Resolution NMR in Solids*, Springer-Verlag, Berlin, 1983.
9. B. C. Gerstein and C. R. Dybowski, *Transient Techniques in NMR of Solids*, Academic Press, New York, 1985.
10. S. Warren (ed.), *Advances in Magnetic Resonance*, Academic Press, San Diego, 1989 and 1990, Vols. 13 and 14.
11. E. R. Andrew, A. Bradbury, and R. G. Eades, *Nature (London)*, 1958, **182**, 1659; 1959, **183**, 1802.
12. I. Lowe, *Phys. Rev. Lett.*, 1959, **2**, 285.
13. E. D. Ostroff and J. S. Waugh, *Phys. Rev. Lett.*, 1966, **16**, 688; P. Mansfield and D. Ware, *Phys. Lett.*, 1966, **22**, 133.
14. J. S. Waugh, L. M. Huber, and U. Haeberlen, *Phys. Lett.*, 1968, **20**, 180; U. Haeberlen and J. S. Waugh., *Phys. Rev.*, 1968, **175**, 453.
15. A. Pines, M. G. Gibby, and J. S. Waugh, *J. Chem. Phys.*, 1972, **56**, 1776.
16. J. Schaefer, E. O. Stejskal, and R. Buchdahl, *Macromolecules*, 1977, **10**, 384.
17. B. C. Gerstein, R. G. Pembelton, R. C. Wilson, and L. M. Ryan, *J. Chem. Phys.*, 1977, **66**, 362.
18. M. Goldman, A. Llor, Z. Olejniczcak, P. Grandinetti, and J. Zwanziger, *J. Chem. Phys.*, 1992, **97**, 8947.
19. Y. Zur, M. H. Levitt, and S. Vega, *J. Chem. Phys.*, 1983, **78**, 5293; M. M. Maricq, in *Advances in Magnetic Resonance*, ed. S. Warren, Academic Press, San Diego, 1990, Vol. 14, p. 151.
20. E. R. Andrew, in *Progress in NMR Spectroscopy*, eds. J. W. Emsley, J. Feeney, and L. H. Sutcliffe, Pergamon, Oxford, 1971, Vol. 8, p. 1.
21. E. Henriot and E. Huguenard, *C. R. Hebd. Séances Acad. Sci.*, 1925, **180**, 1389; J. W. Beams, *Rev. Sci. Instrum.*, 1930, **1**, 667.
22. F. D. Doty and P. D. Ellis, *Rev. Sci. Instrum.*, 1981, **52**, 1868.
23. M. M. Maricq and J. Waugh, *J. Chem. Phys.*, 1979, **70**, 3300; J. Herzfeld and A. E. Berger, *J. Chem. Phys.*, 1980, **73**, 6021.
24. J. D. Ellet and J. S. Waugh, *J. Chem. Phys.*, 1971, **55**, 53; W. P. Aue, D. P. Burum, and R. R. Ernst, *J. Magn. Reson.*, 1980, **38**, 375.
25. W. T. Dixon, J. Schaefer, M. D. Sefifcik, E. O. Stejskal, and R. A. McKay, *J. Magn. Reson.*, 1982, **49**, 341; D. P. Rayleigh, A. C. Kolbert, and R. G. Griffin, *J. Magn. Reson.*, 1990, **89**, 1.
26. A. C. Kolbert and R. G. Griffin, *Chem. Phys. Lett.*, 1990, **166**, 87.
27. J. L. Ackerman, R. Eckman, and A. Pines, *Chem. Phys.*, 1979, **42**, 423.
28. S. F. Dec and G. Maciel, *J. Magn. Reson.*, 1990, **87**, 133.
29. S. Ganapathy, S. Schramm, and E. Oldfield, *J. Chem. Phys.*, 1982, **77**, 4360; S. F. Dec and G. E. Maciel, *J. Magn. Reson.*, 1990, **87**, 133; W. P. Power, R. E. Wasilylishen, S. Mooiobrek, A. Pettit, and W. Danchura, *J. Phys. Chem.*, 1990, **94**, 591; J. T. Cheng, J. C. Edwards, and P. D. Ellis, *J. Phys. Chem.*, 1990, **94**, 553 (equation (9) of this reference must be corrected); N. K. Seth, D. W. Alderman, and D. M. Grant, *Mol. Phys.*, 1990, **71**, 217; F. Lebfevre, J. P. Amoureux, C. Fernandez, and E. G. Derouane, *J. Chem. Phys.*, 1987, **86**, 6070.
30. A. Naito, S. Ganapathy, and C. A. McDowell, *J. Magn. Reson.*, 1967, **48**, 367; *J. Chem. Phys.*, 1981, **77**, 5393; J. G. Hexem, M. H. Frey, and S. J. Opella, *J. Chem. Phys.*, 1982, **77**, 3847; A. C. Olivieri, L. Frydman, and L. E. Diaz, *J. Magn. Reson.*, 1987, **75**, 50.
31. Z. Gan and D. M. Grant, *J. Magn. Reson.*, 1990, **90**, 522.
32. M. H. Levvitt, D. P. Raleigh, F. Creuzet, and R. G. Griffin, *J. Chem. Phys.*, 1990, **92**, 6347; A. Kubo and C. A. McDowell, *J.*

Chem. Phys., 1990, **92**, 7156; A. Schmidt and S. Vega, *J. Chem. Phys.*, 1992, **96**, 2655.

33. K. V. Scheinker, D. Suter, and A. Pines, *J. Magn. Reson.*, 1987, **73**, 99; D. Suter, A. Pines, J. H. Lee, and G. Drobny, *Chem. Phys. Lett.*, 1988, **144**, 324.
34. D. S. L. Mui, B. M. Fung, I. R. Bonnell, and E. L. Enwall, *J. Magn. Reson.*, 1985, **64**, 124.
35. T. K. Pratum, *J. Magn. Reson.*, 1990, **88**, 384.
36. U. Haeberlen, *High Resolution NMR in Solids: Selective Averaging*, Academic Press, New York, 1976, pp. 58–59.
37. M. Lee and W. Goldburg, *Phys. Rev. A*, 1965, **140**, 1261; M. Mehring and J. S. Waugh, *Phys. Rev. B*, 1972, **5**, 3459.
38. A. Bielecki, A. C. Kolbert, H. J. M. de Grool, R. G. Griffin, and M. H. Levitt, in *Advances in Magnetic Resonance*, ed. S. Warren, Academic Press, San Diego, 1990, Vol. 14, p. 111.
39. P. Mansfield and U. Haeberlen, *Z. Naturforsch. A*, 1973, **28**, 1081.
40. W. K. Rhim, D. D. Elleman, and R. W. Waughan, *J. Chem. Phys.*, 1973, **59**, 3740; W. K. Rhim, D. D. Elleman, L. B. Schreiber, and R. W. Waughan, *J. Chem. Phys.*, 1974, **60**, 4595; D. P. Burum and W. K. Rhim, *J. Chem. Phys.*, 1979, **71**, 944.
41. M. Mehring, *Rev. Sci. Instrum.*, 1973, **44**, 64.
42. D. P. Burum, M. Linder, and R. R. Ernst, *J. Magn. Reson.*, 1981, **44**, 173.
43. D. Burum, M. Linder, and R. R. Ernst, *J. Magn. Reson.*, 1981, **43**, 463.
44. A. J. Shaka, D. N. Shykind, G. C. Chingas, and A. Pines, *J. Magn. Reson.*, 1988, **80**, 96.
45. K. Takegoshi and C. A. McDowel, *Chem. Phys. Lett.*, 1985, **116**, 100.
46. W. K. Rhim, A. Pines, and J. S. Waugh, *Phys. Rev. B*, 1971, **3**, 684; A. Pines, W. K. Rhim, and J. S. Waugh, *J. Magn. Reson.*, 1972, **6**, 457.
47. H. Liu, J. Glaser, and G. P. Drobny, *J. Chem. Phys.*, 1990, **93**, 7543.
48. J. Tegenfeldt and U. Haerbelen, *J. Magn. Reson.*, 1979, **36**, 453.
49. W. L. Earl and D. L. Van der Hart, *J. Magn. Reson.*, 1982, **48**, 35.
50. D. Van Der Hart, *J. Chem. Phys.*, 1985, **84**, 1196.
51. B. Gerstein, *Phil. Trans. R. Soc. Lond. Ser. A*, 1981, **299**, 521.
52. G. E. Maciel, in *Advances in Magnetic Resonance*, ed. S. Warren, Academic Press, San Diego, 1990, Vol. 14, p. 125.
53. S. F. Dec, R. A. Wind, G. E. Maciel, and F. E. Anthonio, *J. Magn. Reson.*, 1986, **70**, 355; S. F. Dec, C. E. Bronnimann, R. A. Wind, and G. E. Maciel, *J. Magn. Reson.*, 1989, **82**, 854.
54. A. T. Kreinbrink, C. D. Savasky, J. W. Pyrz, D. G. A. Nelson, and S. Honkonen, *J. Magn. Reson.*, 1990, **88**, 267.
55. P. Jackson, *J. Magn. Reson.*, 1990, **90**, 391.
56. E. T. Olejniczak, S. Vega, and R. G. Griffin, *J. Chem. Phys.*, 1984, **81**, 4804.
57. A. Llor and J. Virlet, in *Proceedings of 9th EENC, Bad Aussee, Austria, May 1988*; A. Llor and J. Virlet, *Chem. Phys. Lett.*, 1988, **152**, 248.
58. G. C. Chingas, C. J. Lee, E. Lipmaa, K. T. Mueller, A. Pines, A. Samoson, B. Q. Sun, B. Q. Suter, and T. Terao, in *Proceedings of 24th Congress Ampère, Poznan, Poland, August 1988*.
59. A. Samoson, E. Lipmaa, and A. Pines, *Mol. Phys.*, 1988, **65**, 1013.
60. B. F. Chemkla, K. T. Mueller, A. Pines, A. Samoson, B. Q. Sun, D. Suter, and T. Terao, *Nature (London)*, 1988, **339**, 42.
61. K. T. Mueller, B. Q. Sun, G. C. Chingas, J. W. Zwanziger, T. Terao, and A. Pines, *J. Magn. Reson.*, 1990, **86**, 470.
62. A. Samoson and A. Pines, *Rev. Sci. Instrum.*, 1989, **52**, 1868; Y. Wu, B. Q. Sun, A. Pines, A. Samoson, and E. Lipmaa, *J. Magn. Reson.*, 1990, **89**, 297.
63. K. T. Mueller, B. Q. Sun, G. C. Chingas, J. W. Zwanziger, T. Terao, and A. Pines, *J. Magn. Reson.*, 1990, **86**, 470.
64. K. T. Mueller, Y. Wu, B. F. Chemkla, J. Stobbins, and A. Pines, *J. Am. Chem. Soc.*, 1991, **113**, 32.
65. E. F. Rybaczewsky, B. L. Neff, J. S. Waugh, and J. S. Sherfinsky, *J. Chem. Phys.*, 1977, **67**, 1231.
66. R. K. Hester, J. L. Ackerman, V. R. Cross, and J. S. Waugh, *Phys. Rev. Lett.*, 1975, **34**, 993.
67. G. G. Webb and K. W. Zilm, *J. Am. Chem. Soc.*, 1989, **111**, 2455.
68. D. E. Demco, J. Tegenfeldt, and J. S. Waugh, *Phys. Rev. B*, 1975, **11**, 4133.
69. M. H. Levitt, D. Suter, and R. R. Ernst, *J. Chem. Phys.*, 1986, **84**, 4243.
70. L. Muller, A. Kumar, T. Baumann, and R. R. Ernst, *Phys. Rev. Lett.*, 1974, **32**, 1402.
71. D. P. Raleigh, M. H. Levitt, and R. G. Griffin, *Chem. Phys. Lett.*, 1988, **146**, 71; M. H. Levitt, D. P. Raleigh, F. Creuzet, and R. G. Griffin, *J. Chem. Phys.*, 1990, **92**, 6347.
72. E. R. Andrew, A. Bradbury, R. G. Eades, and V. T. Wynn, *Phys. Lett.*, 1963, **4**, 99.
73. N. C. Nielsen, F. Creuzet, and R. G. Griffin, *J. Magn. Reson. Ser. A*, 1993, **103**, 245.
74. R. Tycko and G. Dabbagh, *Chem. Phys. Lett.*, 1990, **173**, 461; R. Tycko and S. O. Smith, *J. Chem. Phys.*, 1993, **98**, 932.
75. T. Gullion and S. Vega, *Chem. Phys. Lett.*, 1992, **194**, 423.
76. J. H. Ok, R. G. S. Spencer, A. E. Benett, and R. G. Griffin, *Chem. Phys. Lett.*, 1992, **197**, 389; A. E. Benett, J. H. Ok, and R. G. Griffin, *J. Chem. Phys.*, 1992, **96**, 8624.
77. T. G. Oas, R. G. Griffin, and M. H. Levitt, *J. Chem. Phys.*, 1988, **89**, 692; M. H. Levitt, T. G. Oas, and R. G. Griffin, *Isr. J. Chem.*, 1988, **28**, 271.
78. C. P. Grey, W. S. Veeman, and A. J. Vega, *J. Chem. Phys.*, 1993, **98**, 7711.
79. G. R. Marshall, D. D. Bensen, K. Kocielek, M. T. Leplawy, Y. Pan, and J. Schaefer, *J. Am. Chem. Soc.*, 1990, **112**, 963; V. Bork, T. Guillon, A. Hing, and J. Schaefer, *J. Magn. Reson.*, 1990, **88**, 523; Y. Pan, T. Guillon, and J. Schaefer, *J. Magn. Reson.*, 1990, **90**, 3330; T. Guillon and J. Schaefer, in *Advances in Magnetic Resonance*, ed. S. Warren, Academic Press, San Diego, 1989, Vol. 13, p. 57.
80. D. B. Zax, A. Bielecki, K. W. Zilm, A. Pines, and D. P. Weitekamp, *J. Chem. Phys.*, 1985, **83**, 4877; A. Llor and J. Virlet, *J. Chim. Phys.*, 1987, **84**, 1257; A. Llor, Z. Olejniczak, J. Sachleben, and A. Pines, *Phys. Rev. Lett.*, 1991, **67**, 1989; A. Llor, Z. Olejniczak, and A. Pines, *J. Chem. Phys.*, 1995, **103**, 3966; 1995, **103**, 3982.
81. R. Tycko, *J. Magn. Reson.*, 1987, **75**, 193; *Phys. Rev. Lett.*, 1988, **60**, 2734; *J. Chem. Phys.*, 1990, 5776; R. Tycko, G. Dabbagh, J. C. Duchamp, and K. W. Zilm, *J. Magn. Reson.*, 1990, **89**, 205.
82. J. P. Amoureux, *Solid State Nucl. Magn. Res.*, 1993, **2**, 83.
83. L. Frydman and J. S. Hartwood, *J. Am. Chem. Soc.*, 1995, **117**, 5367.
84. D. Massiot, B. Touzo, D. Trumeau, J. P. Coutures, J. Virlet, P. Florian, and P. J. Grandinetti, *Solid State NMR*, in press.
85. C. Fernadez and J. P. Amoureux, *Solid State NMR*, in press; *Chem. Phys. Lett.*, in press.
86. S. Vega and Y. Naor, *J. Chem. Phys.*, 1981, **75**, 75.

Biographical Sketch

Joseph Virlet. *b* 1940. Docteur ès Sciences 1971. Introduced to NMR by P. Rigny and M. Goldman. Approx. 50 publications. Research interest: solid state NMR and its applications: molecular crystals, plastic crystals, molecular motions and group theory, ultraslow motions, dipolar order, double resonance, high-resolution NMR in solids, DAS and DOR methods, NMR in silicates and cements.

Low-γ Nuclei in Solid Samples

Mark E. Smith

University of Warwick, Coventry, UK

1 Introduction 1
2 Experimental Difficulties 1
3 Experimental Techniques for Observation of Low-γ Nuclei 4
4 Applications of Low-γ Nuclei 7
5 Related Articles in this Volume 13
6 Related Articles in Volumes 1–8 13
7 References 13

1 INTRODUCTION

NMR is used as an experimental probe for problems ranging from biomedical imaging and chemistry to the physics of materials such as high temperature superconductors. Almost every element has an NMR-active isotope so in principle NMR could be used as an experimental probe that effectively covers the entire periodic table. However, if a survey is carried out of NMR and MRI studies that appear in the contemporary literature relatively few nuclei make up a bulk of the reports. Protons are the most studied nucleus for the simple reason that this nearly 100% abundant nucleus, with one of the largest nuclear magnetic moments, produces high NMR sensitivity. ^{19}F and ^{31}P are other commonly studied spin-1/2 nuclei because of their high NMR sensitivity. Other spin-1/2 nuclei with NMR data frequently reported, although not themselves intrinsically sensitive, often occur in conjunction with sensitive nuclei so that polarization transfer techniques can be used to improve sensitivity. ^{13}C and ^{15}N fall into this category and are much studied because of their importance to organic chemistry. NMR studies of inorganic materials have become increasingly important and nuclei such as ^{29}Si and ^{27}Al are now more widely reported. These are illustrations of the types of nuclei that are now commonly studied by NMR in the solid state. However liquid state studies make up the vast majority of NMR work with very many fewer solid state NMR reports. Even in liquids, as multinuclear studies become more common with reports available from most NMR-active nuclei, a group of nuclei termed low-γ are significantly under-represented because their small gyromagnetic ratios give rise to small magnetic moments. The term 'low-γ' is somewhat arbitrary but a useful working definition is provided by the commercial probe manufacturers since their standard magic angle spinning (MAS) probes usually tune down to ^{15}N. This is a pragmatic view since ^{15}N is very important for the studies of mainly organic problems, and there is relatively little demand for nuclei with smaller magnetic moments. Hence for the purposes of this contribution nuclei with smaller magnetic moments than ^{15}N will be taken as low-γ. For a spectrometer equipped with a 9.4 T magnet (corresponding to a ^{1}H resonance frequency of 400 MHz) such nuclei resonate below 40 MHz.

Although liquid state NMR reports from low-γ nuclei appear, it should be remembered that the information about these nuclei is often not from direct excitation and observation but indirectly using polarization transfer techniques such as INEPT and DEPT, and/or inverse detection methods. Many of these approaches are not available in solids meaning that often direct detection is the only real option. Consequently solid state NMR studies of low-γ nuclei are extremely sparse. This lack of studies is not a reflection of the potential applications that exist for these nuclei. For example titanium would be very useful for examining structural problems in a range of technologically significant ceramics, and several metals (e.g., magnesium, potassium, zinc) form important centers in metalloproteins that play a central role in enzyme activity. Direct observation of low-γ nuclei is difficult for several reasons which include low sensitivity, quadrupole effects, relaxation times and corruption of the early parts of the FID. This article will examine in detail the physical background to these difficulties and outline approaches that help alleviate them. Illustrations of the applications of these nuclei will be given but for a more detailed discussion of applications see reference [1]. In setting up experiments, especially for low-γ nuclei with a quadrupole moment, it is often useful to know a compound that will reliably provide a signal and some suggestions are given here.

2 EXPERIMENTAL DIFFICULTIES

2.1 Sensitivity

Signal generation in an NMR experiment can be explained in terms of a classical description of the magnetization.[2,3] When a sample is placed in a static magnetic field (B_o) the degeneracy of the nuclear spin states is lifted, and for a spin I, $2I + 1$ equally spaced energy levels form (spaced by ΔE). Nuclei populate these energy levels with a probability given by a Boltzmann factor which is proportional to $\exp(-\Delta E/kT)$ where k is Boltzmann's constant and T is the absolute temperature. The energy of a particular state is given by $\mu.B_o$, where $\mu = \gamma\hbar I$, leads to an energy of $\gamma\hbar B_o m_z$, as B_o is taken to define the z direction. Hence the energy separation between adjacent levels is $\gamma\hbar B_o$. ΔE is relatively small compared to the thermal energy (kT). This small energy difference is one of the fundamental problems of NMR since via the Boltzmann factor the population difference which is the source of the NMR signal is very small relative to the total number of nuclei in the sample making NMR a relatively insensitive technique. For example at 9.4 T at room temperature for ^{1}H only 6 in 10^5 of the protons contribute to the net NMR signal. Compare this to ^{89}Y, a low-γ spin-1/2 nucleus, where this fraction has fallen to 3 in 10^6. This population difference gives rise to the bulk magnetization per unit volume (M_o) which is given by Curie's Law

$$M_o = \frac{N\gamma^2 B_o \hbar^2 I(I+1)}{3kT} \quad (1)$$

where N is the total number of NMR-active nuclei of the type being considered per unit volume which means that the natural abundance of the NMR-active isotope is of central importance to the sensitivity. The magnetization depends on several parameters. It is proportional to B_o, from the Boltzmann factor. It is also proportional to γ^2 comprising γ from the Boltzmann factor and γ from the magnetic moment. Comparing the ratio of M_o for ^{1}H and ^{89}Y assuming all things other than γ being equal gives ~414 illustrating how strong this factor is.

In NMR experiments this equilibrium magnetization is rotated coherently by rf pulses giving a maximum signal when the magnetization becomes transverse to the z-direction which follows a 90° pulse. The transverse magnetization then precesses at a rate proportional to γB_o through the torque exerted by the B_o field of $\underset{\sim}{M}_o \times \underset{\sim}{B}_o$. Through Faraday's Law of electromagnetic induction the induced voltage is proportional to rate of change ($\propto \gamma B_o$) of magnetization ($\propto \gamma^2 B_o$) to produce an induced signal[4] S given by

$$S = \frac{N V_c \gamma^3 B_o^2 \hbar^2 I(I+1)}{3kT} \qquad (2)$$

where V_c is the volume of the sample. For low-γ nuclei induced voltages are typically ~μV and are significantly lower compared to nuclei with larger magnetic moments. The influence of these factors in determining the signal intensity can be seen by comparing the intrinsic sensitivity (per magnetic nucleus) of ^{13}C which is 133 times greater than ^{89}Y (this assumes that the sensitivity is proportional to γ^3 as in equation (2) which is generally accepted although some analysis has shown that the variation is proportional to $\gamma^{5/2}$). So that even though ^{89}Y is 100% naturally abundant compared to only 1.1% for ^{13}C, the γ-factor results in ^{89}Y displaying a relative sensitivity of only 69.6% of ^{13}C. Hence one of the most obvious points for low-γ nuclei is that their relative receptivity is for the most part worse than ^{13}C (Tables 1 and 2) which is itself often regarded as an insensitive nucleus.

Equation (2) indicates the other factors that can be used, as for all nuclei, to enhance signal intensity. A larger sample can be used (increases V_c), the experiment can be carried out at lower temperature and at higher applied magnetic field. Also if the natural abundance of an isotope is low then isotopic enrichment will help with sensitivity. Papers should be read carefully as solid state NMR reports of low-γ nuclei often use enriched samples, making the experiment much more tractable than at natural abundance. The most significant change in experimental technology relevant to low-γ nuclei is the wider availability of higher magnetic fields (i.e., ≥11.7 T).

Table 1 Some NMR properties of some low-γ spin-1/2 nuclei

Isotope	Natural abundance (%)	ν_o at 9.4 T (MHz)	Relative receptivity[a]
^{57}Fe	2.19	12.952	4.2×10^{-3}
^{89}Y	100	19.668	0.696
^{103}Rh	100	12.689	0.180
^{107}Ag	51.82	16.192	0.197
^{109}Ag	48.18	18.614	0.279
^{169}Tm	100	33.070	3.216
^{183}W	14.40	16.647	0.061

[a]Relative receptivity, the receptivity[3] given $\gamma^3 C I(I+1)$ relative to ^{13}C.

Signal increases with applied magnetic field, with detailed analysis indicating that this increase is proportional to field as $B_0^{3/2} - B_0^{7/4}$. The detail is not important, it is the fact that the sensitivity rises rapidly with field that makes the NMR study of low-γ nuclei in solids much more feasible than even just a few years ago. Magnetic materials can overcome the sensitivity problem by taking the approach of increasing the magnetic field to an extreme. The hyperfine field in a magnetic material can be enormous (e.g., for ^{163}Dy in the pure metal at 1.4 K it is 572.9 T, see Ref.[5] and references therein) so that the consequent increase in signal effectively removes the sensitivity problem, although these large internal fields introduce problems of their own, for example often causing linebroadening.

2.2 Relaxation Effects

One of the most common approaches to improve signal to noise (S/N) is to add together successive transients. Taking n transients improves S/N by $\sqrt{n}$ compared to a single transient.[6] This increase in S/N assumes that the magnetization is fully relaxed between successive transients which is determined by T_1. Relaxation can also present a significant problem for low-γ nuclei as well. The relaxation rate can be thought of as being determined by the product of the magnitude of the interaction and the amount of motion at frequencies related to the Larmor frequencies (which is termed the spectral density). Even if two differing nuclei have the same motion then the low-γ nucleus will have weaker relaxation as the interaction will be smaller. Low-γ nuclei can have extremely long relaxation times, for example in rigid inorganic solids ^{89}Y ($I = 1/2$) T_1 values of 4 h in Y_2O_3 and 6.6 h in Y_2O_2S have been recorded. Many of the low-γ nuclei are quadrupolar so in solution quadrupolar relaxation is the dominant mechanism, and can even cause significant line broadening. It is often naively assumed relaxation will be rapid in solids. Whilst the interaction may be large this does not necessarily produce rapid relaxation since in rigid solids there is very limited modulation to produce relaxation. For low-γ quadrupole nuclei relaxation times can be extremely variable, and one must be careful not to saturate the magnetization.

Long relaxation times exacerbate the sensitivity problems of low-γ nuclei. Solid state NMR studies of low-γ nuclei are noticeably biased to systems where relaxation is reduced through either significantly increased interactions and/or motion. A class of materials where relaxation is significantly enhanced is those containing conduction electrons and NMR for all the metallic elements listed in Tables 1 and 2 has been reported. Conduction electrons reducing relaxation times also help ^{89}Y NMR studies of yttrium hydrides and yttrium-containing high temperature superconductors. Solid state NMR studies of silver have also been biased to systems where relaxation is reduced through motion of the silver ion. Relaxation is also enhanced in materials that contain paramagnetic ions and NMR studies of such materials appear (although often there is the additional complication of a very broad NMR line). Electronic relaxation can be exploited by paramagnetically doping diamagnetic solids, with an example being ^{89}Y in ceramics. In undoped ceramics values of T_1 of hours have been determined but adding ~70 μmol g^{-1} of Europium ions reduces this to <1 s. Europium was found to be the paramagnetic ion that is

Table 2 Some NMR Properties of some Low-γ Quadrupolar Nuclei

Isotope	Spin	Natural abundance (%)	ν_o at 9.4 T (MHz)	Relative receptivity[a]	Quad. moment (fm^2)	Quadrupole broadening factor[b]	Sternheimer antishielding factor (γ_∞)[c]	Suggested solid set-up compound
^{14}N	1	99.63	28.912	2.841	2.04		−6.7	NH_4Cl
^{25}Mg	5/2	10.13	24.504	0.397	19.94	8.60	−4.1	MgO
^{33}S	3/2	0.76	30.724	0.040	−6.78	3.30	−52.2	$NH_4Al(SO_4)_2{\cdot}12H_2O$
^{35}Cl	3/2	75.53	39.236	8.091	−8.17	3.75	−42.0	KCl
^{37}Cl	3/2	24.47	32.660	1.514	−6.46	2.80	−42.0	KCl
^{39}K	3/2	93.10	18.688	1.079	5.85	4.20	−21.8	KCl
^{43}Ca	7/2	0.14	26.952	9.1×10^{-3}	−4.90	1.39×10^{-1}	−18.8	CaO
^{47}Ti	5/2	7.28	22.584	0.224	30.2	21.40	−9.0	$SrTiO_3$
^{49}Ti	7/2	5.51	22.592	0.225	24.7	6.08	−9.0	$SrTiO_3$
^{53}Cr	3/2	9.55	22.604	0.196	−15	21.9	−6.6	–
^{61}Ni	3/2	1.19	35.796	0.092	16.2	16.18		–
^{67}Zn	5/2	4.11	25.072	0.173	15.0	4.76	−21.9	Cubic ZnS
^{73}Ge	9/2	7.76	13.992	0.095	−19.6	3.36	−8.7	–
^{87}Sr	9/2	7.02	17.396	0.164	33.5	7.91	−47.8	$SrTiO_3$
^{91}Zr	5/2	11.23	37.319	1.549	−17.6	6.02	−26.6	$BaZrO_3$
^{95}Mo	5/2	15.72	26.168	0.751	−2.2	0.98	−20[9]	$Mo(CO)_6$
^{97}Mo	5/2	9.46	26.716	0.481	25.5	12.88	−20[9]	$Mo(CO)_6$
^{99}Ru	5/2	12.72	18.456	0.213	7.9	1.80		–
^{101}Ru	5/2	17.07	20.684	0.402	45.7	53.75		–

[a]Relative receptivity, the receptivity[3] given $\gamma^3 C I(I+1)$ relative to ^{13}C adjusted for quadrupolar nuclei by the fractional contribution of the central transition.
[b]Quadrupole broadening factor, the second-order quadrupolar broadening of the central transition which is proportional to $Q^2(I(I+1) - (3/4))^2 / \gamma(2I(2I-1))^2$ and has been normalized to ^{27}Al.
[c]Sternheimer antishielding factor is given where meaningful calculations have been carried for ions with closed shell structure, e.g., Al^{3+}, Cl^-. Where possible given for a lattice, and if not for free ions. For full references to primary literature, see Ref.[1]

most efficient at enhancing relaxation whilst not significantly broadening the spectrum.

2.3 Quadrupole Effects

Most low-γ nuclei possess a quadrupole moment, so that quadrupolar effects will influence NMR spectra. All apart from ^{14}N ($I = 1$) are non-integer spins. For ^{14}N both single quantum transitions are first-order broadened so the magnetization is spread over a range of $2\nu_Q(= 6\chi I2)$, which is typically ~MHz so will give rise to broad lines. Non-integer spin quadrupole nuclei have a central $(-1/2, 1/2)$ transition which experiences no first-order broadening but the satellite transitions are broadened to first-order.[7,8] This differential broadening of central and satellite transitions means that it is observation of the central transition that is usually favored in solid state NMR. Second-order quadrupolar broadening is proportional to ν_Q^2/ν_0, and it is the inverse dependence on ν_0 that, with all other things being equal, means that the low Larmor frequency, which is a consequence of the low-γ, will cause a broader central transition compared to cases for nuclei with larger magnetic moments where χ is the same. This broadening also exacerbates the problems of sensitivity. Since second-order broadening decreases with increasing field, higher fields bring about gains of sensitivity for quadrupolar nuclei proportional to $B_0^{11/4}$.

2.4 Corruption of the Start of the FID

In a conventional pulsed FT NMR experiment the simplest most direct approach is to apply a single pulse followed by acquisition of the FID, which is then Fourier transformed to produce the spectrum. Some potential pitfalls are experimental effects which corrupt the start of the time domain signal, which can be usefully split into deadtime and probe ringing. Deadtime is a general term used to describe effects that mean the spectrometer system is unable to record the NMR signal. Deadtime comes from several sources but the two principal ones are (i) the probe and (ii) other electronic spectrometer components, including filters, preamplifier, receiver and even the cables. The pulses applied to the probe, which is essentially a tuned rf circuit, are usually rectangular (i.e., have very rapid rise and fall times compared to the duration of the pulse). However, the time at which the voltage in the circuit actually falls to zero depends on a time constant which is determined by the circuit. A convenient parameter to describe the time constant is the quality factor Q, which is defined as the Larmor frequency (ν_0)/full width half maximum of the tuning curve of the probe circuit (i.e., a plot of impedance versus frequency), which also equals $2\pi\nu_0 L/R$, where L is the effective inductance and R is the resistance of the probe circuit.[6] The deadtime is the time constant of the exponential decay at the probehead and is given by

$$t_{\text{dead}} = \frac{Q}{\pi\nu_0} \tag{3}$$

So for a Q of 100 (which is often a conservative estimate for many probes) at 20 MHz this is 1.6 μs. Hence the voltage will be too large in the coil for the sensitive receiver to be able to record the tiny NMR signal for ~10 μs and this represents the best possible case. From equation (3) the situation could be improved by reducing Q. Unfortunately this is at best only

a partial answer as reducing Q decreases the sensitivity of the probehead which is also one of the factors required to improve chances of observing low-γ nuclei. Decreasing Q will also reduce the rf field at the probehead (for a given power) increasing the 90° pulse length. When broad lines are being observed to get the most uniform irradiation over a broad range, a short 90° pulse length is necessary.[6] The effect of the loss of the start of the FID ($f(t)$) can be considered most easily by writing down an idealized time domain representation of the FID as

$$D(t) \times f(t) \tag{4}$$

where $D(t) = 0$, $0 \leq t \leq t_{\text{dead}}$ and $D(t) = 1$, $t \geq t_{\text{dead}}$.

Fourier transforming this gives the FT of the FID (i.e., the expected spectrum) convoluted with $\sin c(\omega - \omega_o)t$ with the latter manifest as a large rolling of the baseline.[6] The practical situation is often more complex than this analytic function and an example is shown in Figure 1 for an ^{89}Y resonance. In this case the resonance can still be clearly defined but if the resonance were much broader the lineshape would be significantly distorted and it would be difficult to know what the true lineshape is.

Working at higher frequency decreases t_{dead}. However, practice often shows that the advantage in removing distortion by working at higher frequency is not as marked as might be anticipated, usually because the start of the FID is corrupted by ringing. Ringing is an all-embracing term to describe effects that induce FID-like voltages in the coil. Typical sources of this effect are the electromagnetic effects of the pulse interacting with the surroundings (e.g., the probe body) so that either mechanical and/or re-radiation effects occur. Acousto-mechanical effects can also occur in the coil that can continue after the pulse is turned off producing a short-lived pseudo-FID. The overall efficiency (E_c) of this process is given by

$$E_c = \frac{k_1 B_0^2}{d\nu_s \left(1 + \dfrac{k_2 e^2 \nu_0^2}{\nu_s^4}\right)} \tag{5}$$

where k_1 and k_2 are constants, e is the coil resistivity, d is the bulk density and ν_s is the acoustic wave velocity. Equation (5) shows that at constant B_0 the situation is worse at lower frequency, and at constant frequency it is worse at higher B_0. These short-lived voltages can look like broad resonances or baseline distortion. Careful probe design can reduce ringing effects and a lot of work has gone into reducing these effects and it has been extensively reviewed by Gerothanassis.[9]

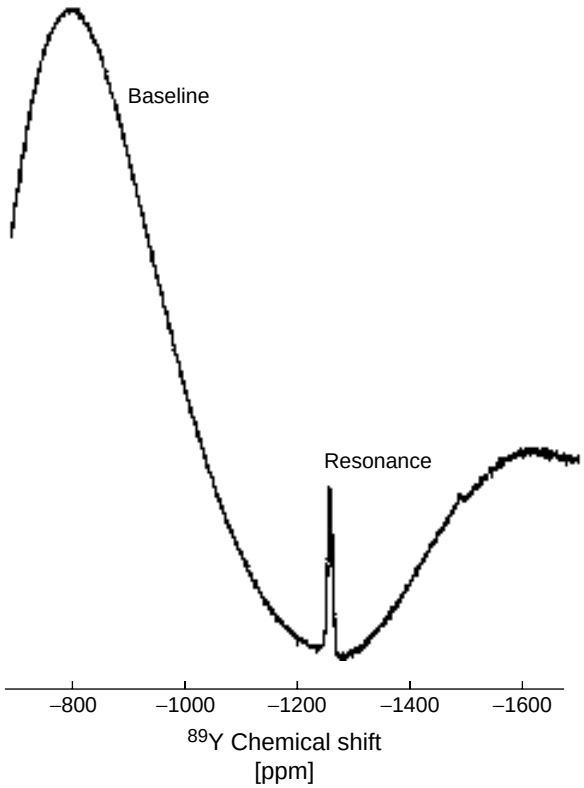

Figure 1 ^{89}Y NMR spectrum from a static powder recorded at a frequency of 17.7 MHz showing baseline roll effects from corruption of the initial part of the FID

3 EXPERIMENTAL TECHNIQUES FOR OBSERVATION OF LOW-γ NUCLEI

The usual techniques for observing NMR signals from solids are in principle available for low-γ nuclei, which includes static experiments, MAS, advanced techniques (such as DAS and DOR) and 2D methods. In all cases the problem with sensitivity makes the experiment more difficult than for nuclei with larger magnetic moments.

3.1 Static Methods

The normal considerations of using sufficiently short pulses to fully excite lines, especially broad ones, are necessary. For a pulse of length T_p the power spectrum ($P(\nu)$) is

$$P(\nu) = \frac{A \sin^2 \pi T_p(\nu_0 - \nu)}{(\nu_0 - \nu)^2} \tag{6}$$

The pulse should be short enough so that the central flat region of this irradiation profile covers the entire spectrum. Sensitivity demands that the maximum signal per pulse is obtained so that a 90° pulse should be applied. As the tip angle of the magnetization is $\theta = \gamma B_1 T_p$, to produce short T_p values even for $\theta = 90°$ as γ goes down requires B_1 to be increased. This can be achieved by using a smaller coil but this reduces sensitivity as the sample volume decreases. Hence the only way that coils with sufficient volume to produce good sensitivity can be used is to apply brute force. So a high power transmitter, i.e., at least 1 kW, should be available for routine observation of low-γ nuclei.

Ringing and deadtime effects that distort lineshapes can be overcome by moving the effective time zero point outside the deadtime by using an echo sequence. Most echo methods apply two pulses $\theta_1 - \tau - \theta_2$. Many variations of pulse lengths will produce an echo with (90°, 90°) and (90°, 180°) the most popular combinations, although when uniformity of irradiation is required the pulses are often sub-90° and sensitivity is consequently sacrificed. Typically an echo is then formed at τ after the second pulse and this is the new origin of the time domain. Pulse sequences have also been developed to

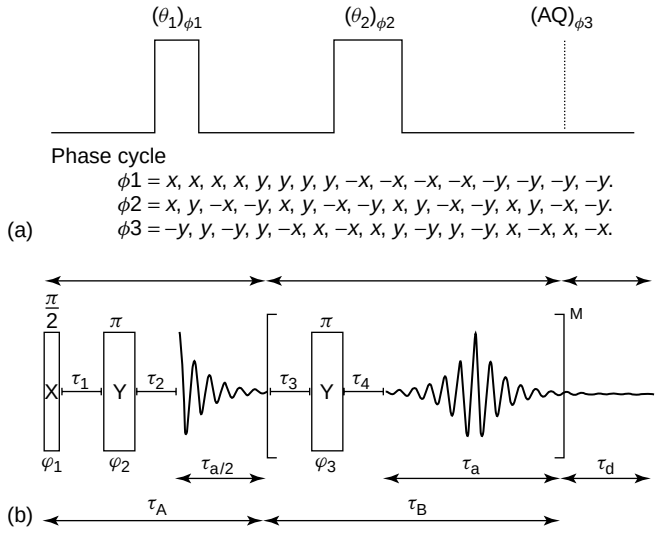

Figure 2 (a) Spin-echo with extended phase cycling as proposed by Kunwar et al., *J. Magn. Reson.*, 1986, **69**, 124 and (b) the QCPMG sequence of Larsen et al., *J. Am. Chem. Soc.*, 2000, **122**, 7080

help cancel deadtime and ringing effects usually based on the principle that the signal and artifacts show different responses to the pulses so that phase cycling can be used to cancel out the artifacts. A practically very useful sequence shown is in Figure 2(a) which combines formation of a spin-echo with phase cycling to produce quadrature detection, as well as canceling direct magnetization and ringing effects. As the echo moves the $t = 0$ position outside the region where detection occurs, a sufficient data sampling rate should be used so that the effective $t = 0$ position is well defined. If T_2 is sufficiently short that an echo time can be used such that the whole echo can be recorded without an unacceptably large loss of signal there is no need to accurately define the new $t = 0$ position. FT of the whole echo is then effectively integration over $\pm\infty$ producing a signal-to-noise $\sqrt{2}$ larger than that obtained by FT from the echo maximum.[10] The spectrum can be formed by using a magnitude calculation which removes phasing errors and gives a pure absorption lineshape. The spectrum can also be phased as usual but the first-order phase correction is large. Another recent approach which appears to give significant advantage to cancel ringing is to modulate the phase of the pulse $\pm x$.

Rather than using a single echo it has recently been suggested that a train of refocusing π-pulses (that are selective on the central transition) similar in form to the Carr–Purcell–Meiboom–Gill (CPMG) sequence [Figure 2(b)] could have significant advantages. The π-pulses refocus the quadrupolar induced dephasing. Hence the refocused magnetization only decays relatively slowly compared to the timescale of the decay of an individual echo. A whole string of echoes are recorded and the whole echo train is Fourier transformed to give a series of sharp bands that follow closely the static lineshape. This provides significant signal enhancement as the intensity from the powder lineshape is concentrated into a series of sharp bands. This is especially true if T_1 is long compared to the timescale of the echo train. For example if T_1 required the recycle time to be 16 s but 60 echoes could be collected without significant magnetization decay, using single echoes would take ~30 min compared to a few milliseconds as an echo train. The interpulse delays (τ_a in the diagram) determine the frequency spacing of the sharp lines that make up the spectrum. The delays need to be adjusted so that baseline artifacts are minimized, give significant improvement in S/N but also to provide enough lines to accurately define the powder lineshape so that it can be simulated. Splitting the spectra into a series of narrow bands also has advantages that low intensity second sites can be observed, and even if baseline artifacts are not completely removed because the baseline can be observed, functions can be used to correct any residual problems.

Direct excitation via pulses cannot efficiently excite and record resonances once they become broader than ~200 kHz.[11] A philosophy that can be adopted is to record a broad line as a series of narrow-banded experiments that can be combined to produce the broad resonance. Various methods have been proposed to achieve this. A relatively weak rf pulse can be used to form a spin-echo and the on-resonance magnetization can be recorded which forms one data point. The system is then retuned to a new frequency and the process repeated which maps out the lineshape point by point. This is an extremely laborious process but lineshapes are accurately recorded as shown in Figure 3 for the titanium signal from $Y_2Ti_2O_7$ where the lineshape is 250 kHz wide. In Figure 3 the pulse echo experiment is shown for comparison. In the direct experiment (Figure 3(a)) the singularities of the powder lineshape can be readily seen but bandwidth effects (excitation and response) result in the center of the spectrum having much enhanced intensity distorting the lineshape. The frequency stepped lineshape (Figure 3(c)) much more closely reproduces the expected lineshape (Figure 3(b)). A variant of this approach is to leave the system tuned to constant frequency and vary the applied magnetic field.[8,11] This was a very common approach in the early days of NMR but with the preeminence of superconducting magnets it is unusual to change the field. However examples now exist where spectroscopic NMR systems have a controlled sweep coil that alters the main magnetic field. Control of the sweep coil is integrated with the pulse programmer and the whole lineshape can automatically be mapped out as illustrated by ^{27}Al where lines as broad as 3.5 MHz have been accurately recorded. Although no reports from low-γ exist using this approach, it is ideal for the study of low-γ nuclei as it is a narrow-banded experiment, so that large sample volumes can be used which helps sensitivity.

These static experiments which step the frequency or field while producing accurate lineshapes are relatively time inefficient experiments as at any particular instant only a small fraction of the spins are being excited. The time efficiency can be improved by slowly rotating the sample (~1 rpm) which brings different crystallites into resonance. This approach termed rotisserie has been shown to lead to large savings in the time necessary to produce ^{14}N spectra from ceramics.[12] The modulation of the echo amplitude produced by the rotation itself contains information about the interaction and has been used in an experiment termed steamer.

3.2 Magic Angle Spinning

The most common approach used in solid state NMR spectroscopy is MAS to remove the anisotropic broadening and so improve spectral resolution which is as much an advantage for low-γ nuclei as it is for other nuclei. There has been a push

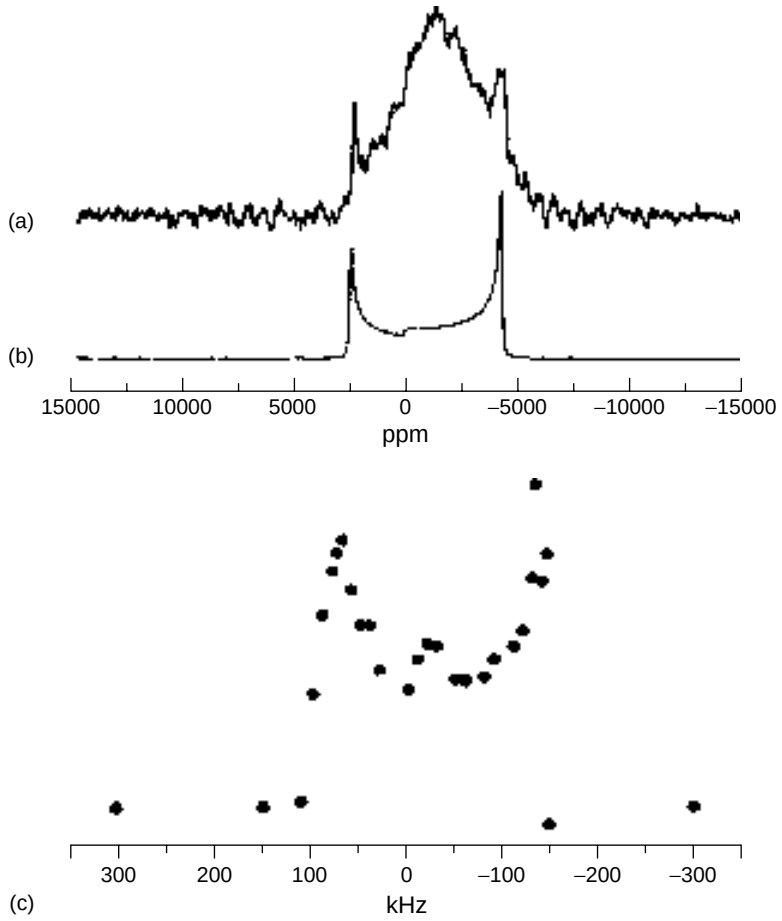

Figure 3 Static ^{49}Ti NMR spectra at 33.80 MHz of $Y_2Ti_2O_7$ showing (a) the pulsed echo spectrum, (b) a simulation and (c) the stepped frequency experiment

over the last few years in observing nuclei such as ^{23}Na and ^{27}Al for ever higher spinning speeds to narrow ever larger ν_Q and this has been achieved by using smaller diameter rotors. The advantages produced by the availability of higher spinning speeds would also be true for low-γ nuclei. However because sensitivity is such an important consideration, spinning speed is often not the primary consideration for low-γ nuclei. Even modest spinning speeds can be helpful and ^{43}Ca spectra were obtained from a series of compounds using a 14 mm diameter rotor spinning at 2 kHz. The whole range of rotor diameters should be available with probably 7–9.5 mm being optimum. Again ringing/deadtime affect MAS NMR spectra so that MAS can be combined with echo experiments as discussed above to remove these. The only minor amendment is that the echo spacing needs to be related to the time modulation introduced by the spinning process, with the echo spacing an integer number of rotor cycles.

In MAS it is important to set the angle accurately. If the probes have a wide tuning range then the traditional nuclei (^{23}Na, ^{27}Al, ^{79,81}Br) can still be used for setting the angle. If these are not available, alternatives have been suggested which use the satellite transition technique. These nuclei include ^{85}Rb in RbCl and ^{39}K in KBr. Alternative nuclei include ^{14}N in compounds where the resonance can be narrowed into a set of sidebands over a range that is not too limited. The molybdenum resonance of $Mo(CO)_6$ has also been suggested as an ideal candidate for angle setting as it provides a strong signal with sidebands whose widths are sensitive to angle but they can be observed a long way from the magic angle.

An interesting variant of the MAS experiment is a technique for modulating the phase of sidebands according to their order by a series of pulses. This 2D experiment separates the centerband and sidebands in the second dimension even if they strongly overlap in the normal spectrum. This approach has been used for higher-γ nuclei.[13] There would be the disadvantage of sensitivity for low-γ nuclei but it may be a way of overcoming the larger second-order quadrupolar widths often encountered.

3.3 Cross-polarization

Signal enhancement by transfer of polarization from a sensitive nucleus such as protons to a less sensitive nucleus is a common enhancement scheme for nuclei such as carbon in materials where the magnetization source is plentiful.[2,3] Again the same approach is in principle applicable to low-γ nuclei and has been used in organometallic materials where protons are plentiful for ^{89}Y and ^{109}Ag.[14] CP from protons can potentially provide significant enhancement which could be as much as 20 for ^{89}Y. CP between such nuclei does pose an important problem in that for the heteronuclear dipole terms to be energy conserving and allow magnetization transfer to

proceed, the Hartman–Hahn condition has to be maintained between protons (H) and a low-γ nucleus x, $\gamma_H B_{1H} = \gamma_x B_{1x}$. The large difference in the gyromagnetic ratios means that the transmitter on the x-side has to supply significant power levels which may, because of slow CP dynamics, have to be applied for several tens of ms. This means that the probe and preamplifier electronics need to be robust. Modern sequences such as time-averaged precession and off resonance effects have somewhat improved the situation but it is still a consideration. CP to such nuclei also needs careful selection of the set-up compounds for optimization of the system and this has been considered in detail.[14]

3.4 Advanced Line Narrowing Techniques

In the last decade or so there has been a whole series of innovative approaches to improve the spectral resolution from non-integer spin quadrupole nuclei that are broadened by residual second-order quadrupole effects.[8] Spinning around a single axis cannot simultaneously remove both first-order and second-order effects. Hence more complex time dependencies are applied with techniques such as DAS and DOR. In principle these can be applied equally well to low-γ nuclei. However in both cases sensitivity is a limiting factor. DAS can provide a good filling factor in the probe but it is a 2D technique so is a time consuming experiment. Although smaller DOR probes are becoming available, the philosophy of a rotor within a rotor means the filling factor is typically low which is a problem when sensitivity is an important factor. The more recently introduced multiple quantum (MQ) technique is also a 2D technique. To excite the multiple quantum transitions requires that high rf fields are applied and this introduces more stringent power requirements (as for CP) for low-γ nuclei. Also the high power requirements mean that small diameter MAS probes are favored for MQ experiments but this again introduces the sensitivity problem. In all these experiments the sensitivity problems, either because of the 2D nature of the experiments or the filling factor mean that the applications of these techniques to low-γ nuclei are extremely sparse. The only two applications known to the author are ^{25}Mg MQ MAS in samples enriched to 90–99%. Another MQ experiment is the double quantum excitation that has been applied to ^{14}N in overtone spectroscopy.[15] In these systems where there is significant quadrupole interaction the $(-1 \leftrightarrow 1)$ transition becomes weakly allowed. The overtone spectra are significantly narrower than the normal static first-order quadrupole broadened lineshapes (by a factor of $6\nu_o/\chi$) but they still have structure which can be used to deduce the magnitude of the interaction.

4 APPLICATIONS OF LOW-γ NUCLEI

Some examples of the application of low-γ nuclei will now be examined. There will be a concentration on insulating, diamagnetic solid materials, although some illustrations from metals and magnetic materials will also be given. For more detailed discussions of NMR of metals and magnetic materials the relevant sections of this encyclopedia can be referred to as well as some of the textbooks in this area (e.g., Refs.[5,6]). For a detailed set of references to applications of low-γ nuclei see Ref.[1] This section is not intended to be comprehensive but gives some examples of the most promising NMR work that has been recently performed on low-γ nuclei. Other low-γ nuclei exist but are not included here either because there are very few or no solid state NMR reports (e.g., ^{21}Ne, ^{83}Kr, ^{105}Pd, ^{177}Hf, ^{189}Os, ^{197}Au and ^{235}U) or there are alternative isotopes with more favorable parameters (e.g., ^{85}Rb, ^{131}Xe, ^{135}Ba and ^{201}Hg) although NMR reports of the low-γ nuclei exist.

4.1 Spin-1/2 Nuclei

4.1.1 Yttrium-89

^{89}Y NMR data has been reported for a range of materials. There is strong overlap between the shift ranges of different YO_n species so that unambiguous assignment on the basis of shift alone is unwise. Nitrogen substitution for oxygen as a nearest neighbor produces the expected positive shift. In oxide-based materials values of chemical shift anisotropy (CSA) have been measured in the range 102–161 ppm. Y_2O_3 is an important additive for densifying silicon nitride based ceramics with the yttrium segregating as a secondary grain boundary phase and therefore only constituting a relatively small volume fraction. However ^{89}Y NMR was able to identify these secondary phases when paramagnetic ions were added to shorten T_1 which can easily be hours for ^{89}Y. One of the most intriguing applications has been the use of ^{89}Y in paramagnetically doped materials to probe the atomic ordering in solid solution. For example, the ^{89}Y NMR spectra of $Y_{2-y}Ln_yM_2O_7$ (Ln = lanthanide) shows additional resonances as Ln is added [Figure 4], attributed to $Y(OY)_{6-x}(OLn)_x$ as x changes altering the hyperfine field at the central yttrium of some sites. The peak (A) associated with $x = 0$ shows a significantly longer relaxation time. These observations have proved highly useful for understanding the distribution of paramagnetic centers in laser and phosphor materials such as Y_2O_3, Y_2O_2S and $Y_3Al_5O_{12}$.

Other applications of ^{89}Y include monitoring changes in the location and motion of hydrogen in yttrium hydrides. By far the greatest use of ^{89}Y NMR has been as a probe of the high temperature ceramic superconductors related to $YBa_2Cu_3O_7$ and $YBa_2Cu_4O_8$. In these materials the yttrium ion resides between the CuO_2 planes that are believed to be central to the superconductivity of these materials. Theoretical attempts to understand the electronic behavior are strongly constrained by the NMR determined Knight shift which is a measure of spin susceptibility at different atomic sites. A wide range of structural substitutions is possible in these materials with most physical interest in those on the copper planes and chain sites. Substitution into the planes has little effect on structure, whereas that into the chains drives the structure tetragonal. These structural effects are reflected directly in the isotropic shift of ^{89}Y. The underlying complexity of the spin dynamics can make interpretation of the NMR interactions and relaxation difficult. This has spawned some extremely elegant NMR work such as looking at $^{16/18}$O isotope effects on the ^{89}Y NMR. These ceramics are usually type-II superconductors so that there is variation of the internal local fields because of the vortex flux lattice. ^{89}Y NMR measurements have provided information about the distribution of the internal fields and of the flux lattice motion.

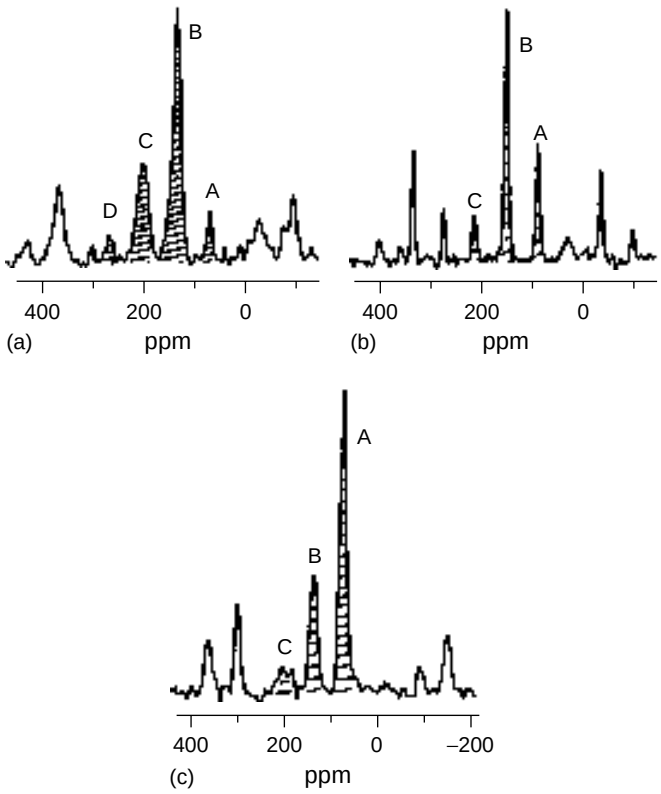

Figure 4 ^{89}Y MAS NMR spectra recorded at 17.64 MHz of (a) $Y_{1.7}Nd_{0.3}Ti_2O_7$ collected with a 1 s recycle time, and $Y_{1.9}Pr_{0.1}Ti_2O_7$ collected with (b) 1 s and (c) 45 s recycle times. (Reproduced with permission of the copyright owner from C. P. Grey et al. *J. Am. Chem. Soc.*, 1990, **112**, 4670)

4.1.2 Silver-107, -109

The limited range of solid state NMR data from silver has revealed, as expected for a heavy metal, a wide chemical shift range of ~1500 ppm (excluding Knight shift effects) and in asymmetric environments significant CSA although the number of accurate measurements is very limited. In silver thiolates values of CSA were found to be in the range 570–2120 ppm. The high local symmetry and simple chemistry of silver halides has meant these are the most studied compounds by silver NMR. AgI is of central importance to a number of technologically significant fast ion conducting phases and shows several polytypes which cover an isotropic chemical shift range of ~100 ppm. Silver can be very mobile in solids even at room temperature and this often leads to averaged NMR spectra and the changes of spectra with temperature are seen in phases such as $Rb{\cdot}KAg_4I_5$ and $Ag_xCu_{1-x}I$. Studies of silver-containing glasses such as $AgI{\cdot}Ag_2O{\cdot}B_2O_3$ and $2AgI{\cdot}xAg_2MoO_4$ have followed phase separation and crystallization. Comparison of glassy and crystalline phases based on $AgPO_3$ showed differences of 90 ppm which has been ascribed to changes in the silver coordination between the two states. Formation of silver particles within zeolite cages has also been followed by NMR with the silver initially deposited as $AgNO_3$ which was subsequently reduced to the metal. The bulk of solid state NMR studies have used ^{109}Ag simply because of its 42% better sensitivity than ^{107}Ag.

4.1.3 Tungsten-183

Very few solid state NMR spectra exist from ^{183}W. The few studies that have been carried out reflect its very low sensitivity and have reported extremely long values of T_1. Since tungsten is a heavy metal CSA spreads out the intensity over a large frequency range in all but the most symmetric environments. Crystallography indicates that the alkali tungstates and $W(CO)_6$ are highly symmetric and an MAS linewidth as low as 6 Hz was recorded for $W(CO)_6$. To optimize ^{1}H–^{183}W CP experiments $(NH_4)_2WS_4$ has been suggested as a good set-up compound. The very few papers reporting ^{183}W solid state NMR indicate that it is still a difficult nucleus to study.

4.1.4 Other Spin-1/2 Nuclei

Table 1 contains some other spin-1/2 nuclei. There are no NMR reports of these nuclei from insulating, diamagnetic solids as their S/N in typically applied magnetic fields is so poor. Iron is an important constituent of many magnetic materials. In materials where the internal field can be typically 20–30 T the greatly improved signal at this very high magnetic field means that NMR reports exist.[5] NMR reports of rhodium have been from the element itself and metallic alloys.

4.2 Quadrupolar Nuclei

4.2.1 Nitrogen-14

All transitions are first-order quadrupolar broadened for ^{14}N so that all the intensity is spread over $\sim 2\nu_Q$ which can be very demanding on the spectrometer. The values of χ for nitrogen have been determined to be in the range 0–8 MHz with typical values 3–4 MHz. The number of solid state NMR studies of ^{14}N has been very limited even though it is 99.63% abundant. The importance of nitrogen in many fields of science and technology means that nitrogen NMR of solids could be widely applied. ^{14}N studies have shown relaxation times typically in the range 10–1000 s. Much of the work carried out on solids has been on static samples but as the first-order quadrupole interaction is inhomogeneous the effect of MAS should be to split up the resonance into narrow spinning sidebands even at modest spinning speeds. Since faster, more stable and controllable spinning has become available over recent years MAS is now a much more viable alternative. In crystalline compounds a set of sharp spinning sidebands form in MAS spectra which is shown in Figure 5 for AlN. Applying MAS improves S/N and procedures for using variable spinning speeds allow the centerband to be identified. The broad spectra demand very accurate angle setting for efficient narrowing. If the angle is slightly mis-set then lineshapes are produced which can be used to deduce the interaction provided that the offset angle is known. Studies employing ^{14}N have included those looking at the internal motion of nitrogen-containing organic phases and tetraalkylammonium salts. Single crystal rotation studies of ammonium and nitrate-containing materials have been reported, with careful analysis of the rotation pattern showing that although first-order quadrupolar broadening dominates, CSA makes a significant contribution. MAS NMR spectra have been reported from ceramic phases such as AlN and BN,

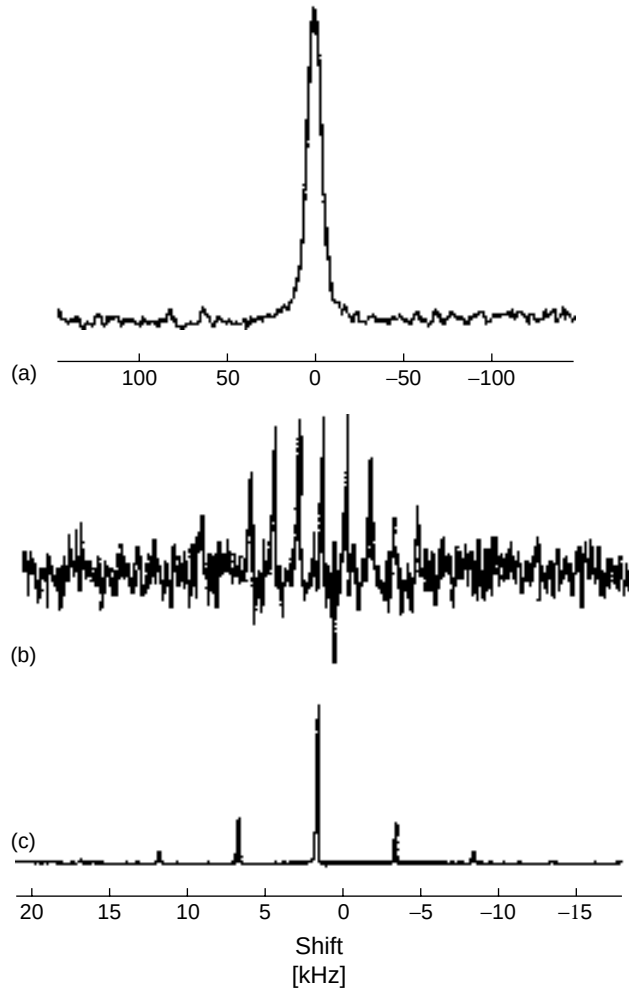

Figure 5 ^{14}N NMR spectra recorded at 28.9 MHz of AlN (a) static and using MAS at (b) 1.5 kHz and (c) 5 kHz. (Reproduced with permission of the copyright owner from T. J. Bastow et al., *Solid State NMR*, 1998, **10**, 241)

with NB_3 and NB_4 environments showing a shift difference of ~70 ppm.

4.2.2 Magnesium-25

Magnesium is important in many fields such as cellular biochemistry and earth sciences. The total shift range observed in inorganic materials is only ~125 ppm. Studies have shown that the shift between MgO_6 and MgO_4 is only ~25–40 ppm. As ^{25}Mg is a low frequency quadrupolar nucleus and in many compounds the linewidths are much larger than this shift difference, unambiguously identifying the local environment is difficult. Heating MgO over the temperature range room temperature to 1300 °C showed only a 2 ppm variation in the isotropic position. In nanocrystalline MgO as the particle size varied from 3 to 35 nm the linewidth decreased from 2 kHz to 450 Hz and the peak position increased from 18 to 25.3 ppm. χ in magnesium-containing silicates is typically 2–3.2 MHz. High temperature studies have shown that the motion of magnesium in silicates is strongly coupled to the motion of the network. On melting the change in chemical shift indicates that the average coordination of magnesium increases in the melt with octahedral coordination preferred. Thermal decomposition of magnesium-containing minerals is a technologically important process and examples studied by ^{25}Mg NMR include magnesite, dolomite, hydrotalcite and synthetic hectorite. MgO like Y_2O_3 is an important densifying additive for silicon nitride based ceramics and the phases formed in this process have been followed by NMR. One of the most impressive applications of ^{25}Mg solid state NMR is to biochemically important Mg^{2+}-binding complexes which included the first observation of an asymmetric magnesium center with five nearest neighbor (nn) oxygens and one nn nitrogen. Magnesium NMR data has also been reported from magnesium and related metallic alloys. Work hardening of magnesium introduces a distribution of electric field gradients which smears out the first-order broadened satellites. Other ^{25}Mg reports have included the dilute alloy Mg-(6%Al) and the intermetallic phase $Mg_{17}Al_{12}$ with three signals observed in the latter whose intensities agree with the crystallographic site distribution.

4.2.3 Sulfur-33

Many applications could be envisaged for ^{33}S yet the number of NMR studies is extremely sparse reflecting how difficult it is to observe a low-γ quadrupolar nucleus with a natural abundance of only 0.76%. Early NMR observations of ^{33}S included the magnetic materials α-MnS and EuS. The most commonly reported ^{33}S resonance is from ZnS, where the cubic and hexagonal forms have been compared. There is an isotropic chemical shift difference between these polymorphs of only ~3 ppm but the hexagonal form has a broader static lineshape with both second-order quadrupolar and CSA contributing. There have been two major studies of ^{33}S resonances from solid inorganic materials and the main conclusion was that sulfates covered a very small shift range at 320–338 ppm with χ of 0.53–2.3 MHz. Sulfides covered a much broader shift range of −347 to 291 ppm with narrower resonances reflecting the smaller χ in these more ionic environments. The relative shifts of the different sulfides can be explained in terms of bond-electronegativity arguments. The advantages of high magnetic fields and MAS to study low-γ nuclei were illustrated by a comparison of a static experiment at 4.7 T compared to an MAS experiment at 14.1 T using ~0.1 of the sample. The former required ~40 times longer averaging to obtain a comparable S/N. The limited range of χ so far determined for ^{33}S suggests that quadrupolar broadening may not be as bad as anticipated on the basis of the Sternheimer antishielding factor, and could encourage wider investigations, especially in enriched samples.

4.2.4 Chlorine-35, -37

The two chlorine isotopes have similar magnetic moments with Larmor frequencies differing by ~20%. Although ^{37}Cl has only 75% of the second-order quadrupolar broadening compared to ^{35}Cl the greater natural abundance of ^{35}Cl results in a receptivity 5.34 times greater than ^{37}Cl, so that ^{35}Cl is usually favored for NMR study. Chlorine exhibits a very wide range of χ. In materials where strong covalent bonding is present values of χ as high as 80 MHz are not uncommon, which are inaccessible to standard NMR techniques. Alkali and ammonium chlorides produce very narrow MAS lines

and comparison of the two isotopes and studies at different magnetic fields show that quadrupole effects are absent. In perchlorates the symmetric ClO_4^- environments means relatively small χ are encountered (<3 MHz). The shift range of chlorine is large as perchlorates are shifted by ~1000 ppm from the chloride region. With the two isotopes internal checks on the simulation parameters can be carried out since χ should be in the ratio 1.269 for the two isotopes. Chlorine NMR data has been reported from phase changes for several organic perchlorate and chloride phases. Other ^{35}Cl NMR studies have been from inorganic phases including the storage phosphor BaFCl and the encapsulation of metal clusters in sodalite cages which also contain chlorine. Mixed metal layer hydroxides such as hydrotalcite and hydrocalunite are important because of their anion exchange properties and ^{35}Cl NMR has shown that these two materials are very different.

4.2.5 Potassium-39

Static NMR spectra from model crystalline inorganic potassium salts often show well defined quadrupolar lineshapes with sharp singularities from which the quadrupolar parameters can usually be deduced with χ typically in the range 1–2 MHz. Even in samples containing two sites there is usually a sufficient number of distinct features so that the parameters for each site can be deduced [Figure 6]. CSA usually only makes a small contribution to the static linewidth with a single crystal rotation pattern of KNO_3 showing that the tensor components cover a range of only 18 ppm. The potassium halides gave relatively narrow lines and cover a shift range of ~37 ppm. Static spectra from potassium-containing montmorillonite showed that when the sample is wet there are two superimposed potassium signals, with the narrower line attributed to exchangeable potassium, since hydration increases the mobility of this potassium species. As the samples went through a series of wetting-drying cycles the ratio of the exchangeable to fixed potassium decreased in line with agronomical studies. The relatively small χ values determined for ^{39}K means that with the high magnetic fields now available only modest MAS rates are necessary. Two of the few MAS studies for ^{39}K have been of the temperature dependence of the shift in the cubic and tetragonal polymorphs of KO_2 and of changes in the susceptibility of $KNiF_3$ over the range 180–450 K. Some of the more unusual reports of ^{39}K include the biomolecule K.monensin with $\chi \sim 3.2$ MHz, and in electrides and alkalides where potassium can be both positively and negatively charged with the relative shifts between these species explained in terms of the different electron configurations of the ions. The largest number of ^{39}K solid state NMR reports in recent years has been from K_3C_{60} and related phases, with signals observed from tetrahedrally and octahedrally coordinated sites. Exchange between different sites and interaction with cation vacancies have been elucidated. The similar temperature dependence of all the ^{39}K resonances and the ^{13}C signal indicate that these samples have a uniform Pauli susceptibility.

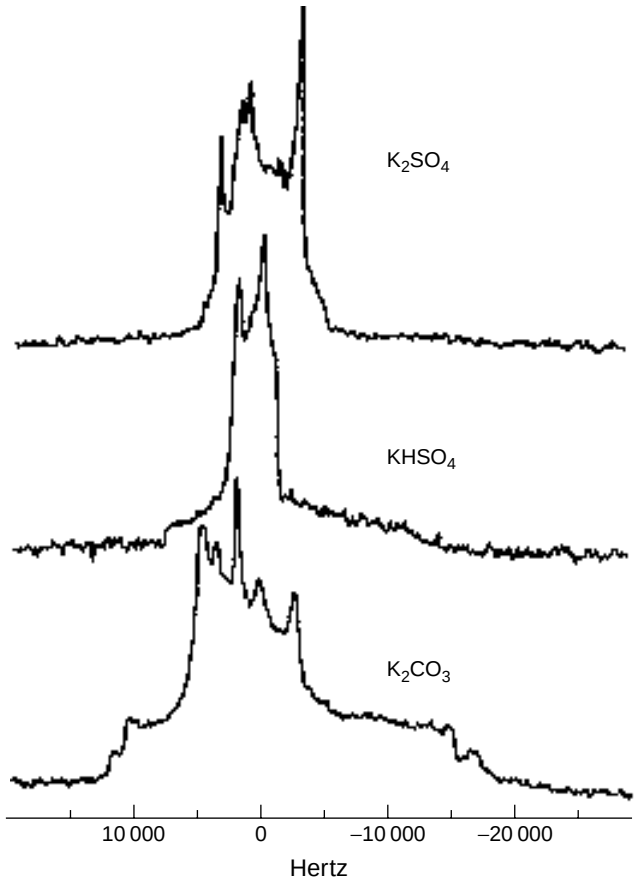

Figure 6 ^{39}K static NMR central transition lineshapes from three compounds containing two crystallographically distinct potassium sites recorded at 18.67 MHz. (Reproduced with permission of the copyright owner from T. J. Bastow, *J. Chem. Soc. Faraday Trans.*, 1991, **87**, 2453)

4.2.6 Calcium-43

The very low natural abundance of ^{43}Ca of 0.14% means that most studies to date have employed schemes to enhance the signal and/or used significant isotopic enrichment. The interest in high temperature ceramic superconductors that contain calcium has encouraged studies that parallel those of ^{89}Y. The ^{43}Ca NMR parameters were used to monitor the spin susceptibility and the magnetic field distribution caused by the vortex flux lattice. Calcium silicates are important phases in cement and concrete chemistry, and a series of ^{43}Ca-enriched samples have been studied. In some sol-gel produced samples the ^{43}Ca resonance is relatively broad and featureless but was observed to narrow on aging for 6 months which was attributed to ordering within the gel. The relatively ionic nature of the Ca–O bond should result in relatively small χ so that modest MAS rates could be usefully employed. The low sensitivity can then be improved by using large volume rotors, >9.5 mm with 14 mm preferred, spinning at a few kHz. By adopting this approach acceptable S/N can be typically achieved within ~1 day. A series of silicates, carbonates and sulfates revealed a shift range of ~160 ppm. The polymorphs of $CaCO_3$, aragonite and calcite give very different ^{43}Ca MAS NMR spectra with calcite showing a second-order quadrupolar lineshape whereas the MAS line of aragonite has no discernible quadrupolar features. Very few quadrupolar parameters have been reported for ^{43}Ca but examples include calcite where $\chi = 1.40$ MHz and $\eta = 0$, and $CaAl_4O_7$ where $\chi = 3.5$ MHz and $\eta = 0$.

4.2.7 Titanium-47, -49

The main experimental difficulty with titanium NMR is that both isotopes have moderately large quadrupole moments (Q) in the ratio $^{49}Q/^{47}Q = 0.8179$. It is usually the second-order quadrupolar broadened central $(1/2, -1/2)$ transition that is observed where the relative broadening is $\Delta\nu^{47}/\Delta\nu^{49} \sim 3.522$. A quirk of titanium NMR is that the isotopes have extremely similar values of γ. At 9.4 T the resonance frequencies only differ by ~6 kHz. The typical width of the resonances observed means that most spectra consist of completely overlapped resonances from the two isotopes. TiO_2 is a technologically important material in its own right and the three polymorphs, anatase, brookite and rutile, all consist of TiO_6 units but with differing connectivities, orientations and distortions of the local environment which means their isotropic chemical shifts differ by ~200 ppm and χ by a factor of three. In sol-gel produced TiO_2 initially some narrow titanium resonances are obtained which on heating show structure which can be simulated to quantify the anatase/rutile ratio. This approach has been further extended to titania nanoparticles where it was shown that there is accurate agreement between the ratio of the different phases as determined by NMR and X-ray diffraction. The sample in Figure 7 crystallized at ~700 °C, and between 700 and 850 °C rutile grows at the expense of anatase. NMR has a distinct advantage over XRD for detecting small quantities of anatase as the relatively narrow resonance shows up well in the NMR spectrum. $BaTiO_3$ with its important piezoelectric and ferroelectric properties has resulted in extensive NMR studies including single crystal work, and although quadrupolar effects dominate the rotation pattern of the centerband, CSA makes a noticeable contribution of ~40 ppm. It is likely that simulating static NMR powder spectra from titanium will need to take into account CSA effects. In $ATiO_3$ materials the A cation has been shown to have an influence on the ^{47,49}Ti NMR spectra. For a range of perovskite- and ilmenite-structured phases although χ

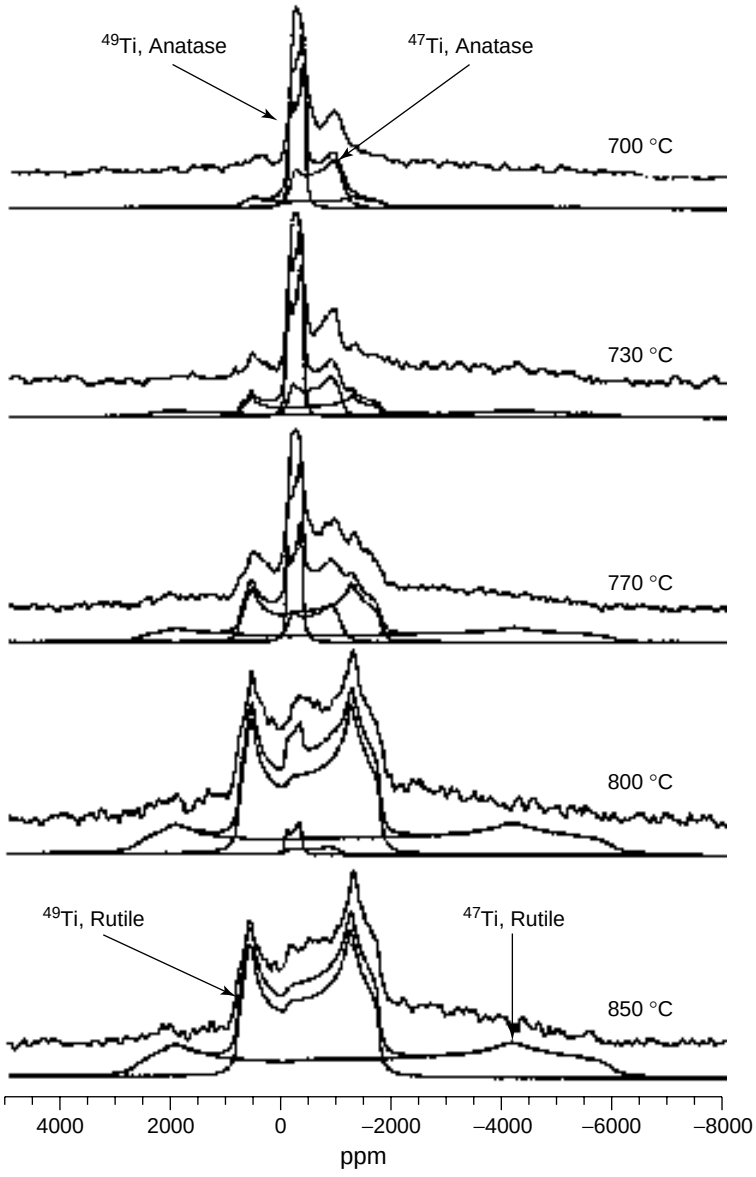

Figure 7 Static ^{47,49}Ti NMR spectra recorded at 33.81 MHz from nanocrystalline TiO_2 with varying anatase/rutile content. (Reproduced with permission of the copyright holder from C. Gervais et al., *Chem. Mat.*, 2001, **13**, 466)

increases with increasing site distortion the correlation is not strong. However within each structural group there is a good correlation of δ_{iso} with the mean Ti-O bondlength. As yet the amount of NMR data from titanium is too small to say whether or not TiO_4, TiO_5 and TiO_6 can be distinguished on the basis of NMR parameters. NMR studies from metallic compounds have included Ti itself and alloys such as TiAg, $TiAl_3$, TiB_2, TiH_2 and the solid solution $TiC_{1-x}N_x$. Titanium is one of the most promising low-γ nuclei for immediate investigation by solid state NMR at high applied magnetic field.

4.2.8 Zinc-67

Solid state ^{67}Zn NMR data has been obtained from zinc metal allowing the temperature variation of both the Knight shift and χ to be determined. The most common ^{67}Zn NMR reports have been from the zinc chalcogenide series. For ZnS the MAS spectrum constrains the quadrupolar parameters by removing CSA effects, and then the static spectrum can be simulated to give the CSA tensor components with $\delta_{11} = 380 \pm 2$ ppm and $\delta_{22} = \delta_{33} = 358 \pm 2$ ppm. ZnO has been studied by a variety of NMR methods because of the practical interest in this material. Heavily doped ZnO (e.g., 0.03–3 at% aluminium and gallium) is a transparent conductor and linear variations of shift with dopant concentration have been observed. In all simulations to date from non-cubic materials it appears that both quadrupolar and CSA effects have to be taken into account. This has been confirmed by a careful single crystal study of zinc acetate which showed that although the CSA is relatively small it is still significant and if not accounted for would alter the value of χ deduced. Zinc acetate and its hydrate make good model compounds since on hydration the zinc coordination increases from 4 to 6 with a large change in δ_{iso} of 260 ppm. Zinc is an important center in metalloproteins. In model compounds as the local coordination changes from ZnN_4 to ZnS_4 δ_{iso} changes by 68 ppm. The QCPMG approach has been employed to provide much improved S/N. In $Zn(OOCH)_2.2H_2O$ the two inequivalent sites could be readily seen using this approach even though δ_{iso} only differ by 10 ppm. χ differ by more than 50% between these two sites. The QCPMG approach has allowed for the first time zinc with mixed nearest neighbor environments to be observed. The very high magnetic fields and modern approaches now available open up some exciting possibilities for ^{67}Zn NMR of solids.

4.2.9 Zirconium-91

The first solid state NMR report from ^{91}Zr appears to have been for the cubic metal $ZrZn_2$. Other reports of Knight shifts from metallic systems include ZrC_2, ZrC, ZrH_2, ZrV_2, $ZrMo_2$, ZrCo and Al_3Zr (Figure 8(b)). Some alloys show subsidiary minor peaks which are thought to be associated with structural defects. The first NMR measurement of ^{91}Zr from an insulating phase was a single crystal rotation pattern of $ZrSiO_4$. Apart from locally symmetric compounds such as $CaZrO_3$, some metal zirconium phosphates and alkali zirconium fluorides where χ is typically <2 MHz, the values of χ can be high, around 20 MHz. Such large values pose problems for direct pulse excitation/detection at even moderately high magnetic fields. Many of the resonances that appear in the literature have been recorded by frequency stepped techniques which

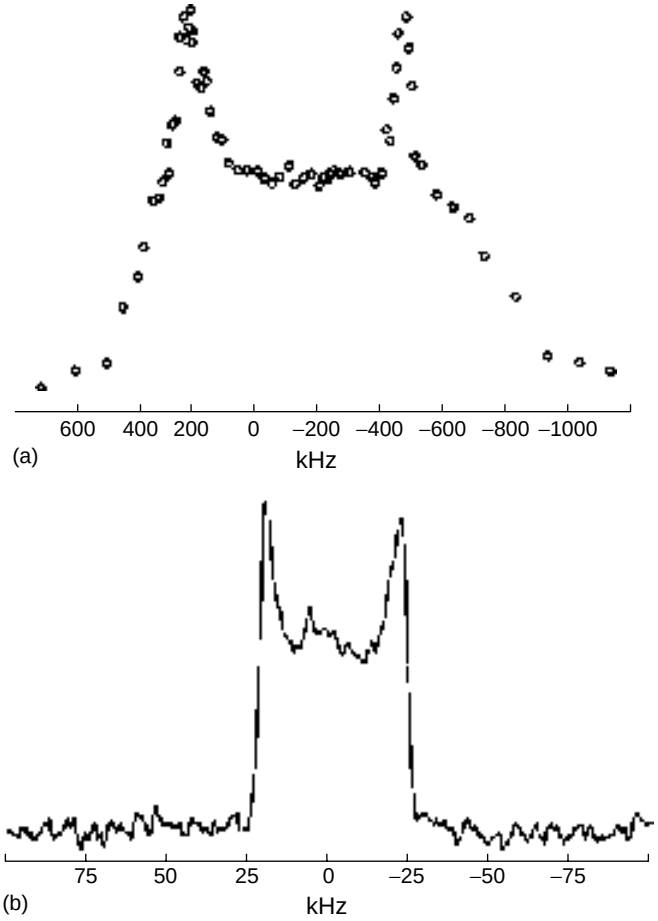

Figure 8 ^{91}Zr NMR spectra recorded at 37.21 MHz from (a) ZrF_4 using a frequency stepped echo (Reproduced with permission of the copyright owner from T. J. Bastow, *Z. Naturforsch. A*, 1994, **49**, 320) and (b) Al_3Zr using a direct echo (Reproduced with permission from the copyright owner from T. J. Bastow et al., *Phys. Rev. B*, 1998, **58**, 2988)

makes collecting such spectra somewhat laborious. This is exemplified by ZrF_4 where $\chi = 53.7$ MHz so that at 9.4 T the central transition itself extends over ~1.5 MHz (Figure 8(a)). ZrO_2 is an important high toughness structural ceramic, as well as a functional ceramic as the electrolyte in solid oxide fuel cells. Often small amounts of secondary, stabilizing oxide are added which results in complex phase mixtures. There are four polymorphs of ZrO_2 and the NMR data on these has revealed only small differences in δ_{iso} (~10 ppm) whereas there is significant variation in the quadrupolar parameters, making χ a much better discriminator of these phases.

4.2.10 Molybdenum-95, -97

The resonance frequency of the two molybdenum isotopes differs by only ~2%. ^{95}Mo is the preferred nucleus for NMR observation because of its higher sensitivity and 13.1 times smaller second-order quadrupolar broadening. In alkali molybdates typically $\chi \sim 0$ whereas with increasing structural distortion χ rapidly increases. Recent work has shown that in simulating static powder patterns of the central transition there are significant contributions from both quadrupole ($\chi = 1.15$ MHz, $\eta = 0.82$ for $Na_2MoO_4{\cdot}2H_2O$) and CSA (a span

of ~200 ppm) interactions. Molybdenum containing materials are often used in catalytic applications as a surface species, and it is important to be able to distinguish MoO_4 and MoO_6. Much of the work from the early 1990s was somewhat inconclusive as to whether the coordination of molybdenum could unambiguously be distinguished, and although more recent evidence suggests that the NMR data can distinguish these the range of parameters from each environment needs to be accurately established. The implication of the early work was that tetrahedral species tended to give narrower lines than octahedral sites, although this is not always true. The importance of $Mo(CO)_6$ in the surface chemistry of molybdenum is illustrated by there being at least six NMR reports of it, including a single crystal study. All the transitions can be observed as the total spectrum covers only ~70 kHz which has allowed all the NMR parameters to be deduced, and the $^1J(^{95}Mo,^{13}C)$ has been observed in the MAS spectra. Other ^{95}Mo solid state NMR studies have included the molybdenum chalcogenides, $MoSi_2$ and Mo_2C using the central and satellite transitions to deduce the interactions. In a series of glasses $(AgI)_y[(AgO)_x(MoO_3)_{1-x}]_{1-y}$ ^{95}Mo NMR showed that at $x = 0.5$ only isolated MoO_4^{2-} existed whereas at lower x there were also octahedral molybdate units present.

4.2.11 Other Low-γ Quadrupole Nuclei

Narrow ^{87}Sr NMR resonances occur in cubic compounds such as SrO, SrS and $SrTiO_3$. The use of the QCPMG sequence greatly improved sensitivity allowing observation of good ^{87}Sr lineshapes from non-cubic materials $Sr(NO_3)_2$ and $SrMoO_4$.

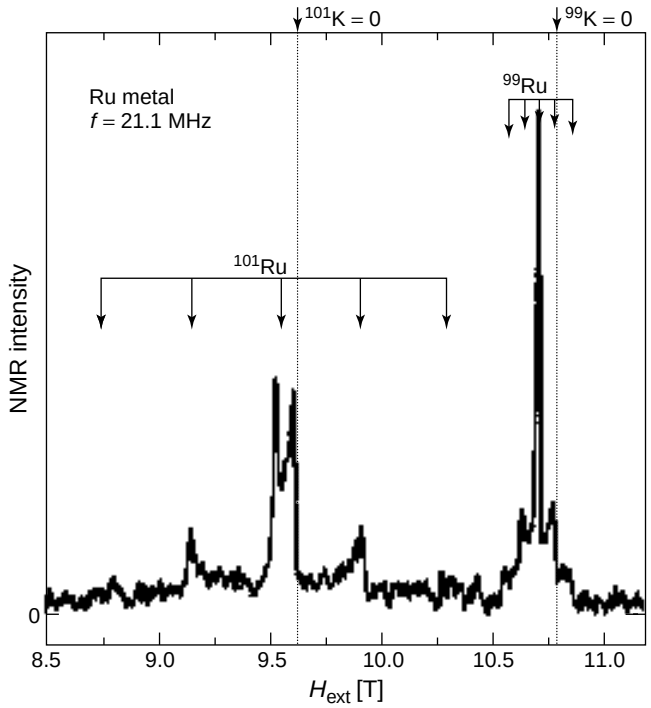

Figure 9 Spin echo field sweep spectra of ^{99}Ru and ^{101}Ru from hexagonal ruthenium metal recorded at 21.1 MHz. (Reproduced with permission of the copyright owner from H. Mukuda et al., *Phys. Rev. B*, 1999, **60**, 12 279)

Modulation of the ^{53}Cr NMR echo formed in the ferromagnets $CdCr_2S_4$ and $CuCrSe_4$ provided information about the hyperfine fields. ^{61}Ni NMR spectra from an almost equiatomic alloy $Ni_{49.6}Al_{50.4}$ gave a shift of 1220 ppm. Germanium is an extremely rarely reported nucleus by NMR but in single crystals of germanium with differing isotopic compositions lattice distortions were observed to produce quadrupole effects in the lineshape. ^{99}Ru and ^{101}Ru NMR have been compared from a series of compounds that include RuO_2, $SrRuO_3$, $CaRuO_3$ and Sr_2RuO_4. From the element itself both isotopes were observed in a swept frequency experiment (Figure 9) as their resonant frequencies only differ by ~11% but the markedly different quadrupolar moments (a factor of 5.8) are immediately apparent from their effects on the spectra.

5 RELATED ARTICLES IN THIS VOLUME

MQMAS Advances; Multiple-quantum Magic-angle Spinning Experiments on Half-integer Nuclei: Fundamentals.

6 RELATED ARTICLES IN VOLUMES 1–8

Ceramics, Volume 2; Chemical Shift Tensor Measurement in Solids, Volume 2; Cross Polarization in Solids, Volume 3; Double Rotation, Volume 3; Dynamic Angle Spinning, Volume 3; Echoes in Solids, Volume 3; High Speed MAS of Half-Integer Quadrupolar Nuclei in Solids, Volume 4; Inorganic Solids, Volume 4; Knight Shift, Volume 4; Line Narrowing Methods in Solids, Volume 4; Magic Angle Spinning, Volume 5; Probe Design & Construction, Volume 6; Probes for Special Purposes, Volume 6; Quadrupolar Interactions, Volume 6; Quadrupolar Nuclei in Solids, Volume 6; Radiofrequency Pulses: Response of Nuclear Spins, Volume 6; Sensitivity of the NMR Experiment, Volume 7; Solid State Probe Design, Volume 7; Spectrometers: A General Overview, Volume 7; Wide Lines for Nonquadrupolar Nuclei, Volume 8.

7 REFERENCES

1. M. E. Smith, *Annu. Rep. NMR Spectrosc.*, 2001, **43**, 121.
2. B. C. Gerstein and C. Dybowski, 'Transient Techniques in NMR of Solids', Academic Press: New York, 1985.
3. R. K. Harris, 'NMR Spectroscopy', Pitman: London, 1984.
4. D. I. Hoult, *Concepts Magn. Reson.*, 1989, **1**, 1.
5. A. P. Guimaraes, 'Magnetism and Magnetic Resonance in Solids', John Wiley and Sons: New York, 1998.
6. E. Fukushima and S. B. W. Roeder, 'Experimental Pulse NMR', Addison-Wesley: Reading, MA, 1981.
7. M. H. Cohen and F. Reif, *Solid State Phys.*, 1957, **5**, 321.
8. M. E. Smith and E. R. H. van Eck, *Prog. NMR Spectrosc.*, 1999, **34**, 159.
9. I. P. Geronthanassis, *Prog. NMR Spectrosc.*, 1987, **19**, 267.
10. P. T. Callaghan, 'Principles of NMR Microscopy', Clarendon Press: Oxford, 1991.
11. M. E. Smith and J. H. Strange, *Meas. Sci. Technol.*, 1996, **7**, 449.
12. J. P. Yesinowski, in 'Solid State NMR Spectroscopy of Inorganic Materials', ed. J. J. Fitzgerald, ACS Symp. Ser. No. 717, Amer. Chem. Soc.: Washington, DC, 1999, p 359.
13. D. Massiot, V. Montouillout, F. Fayon, P. Florian, and C. Bessada, *Chem. Phys. Lett.*, 1997, **272**, 295.

14. A. Sebald, *NMR Basic Principles Prog.*, 1994, **31**, 92.
15. R. Tycko and S. J. Opella, *J. Chem. Phys.*, 1987, **86**, 1761.

Biographical Sketch

Mark E. Smith, *b* 1963. B.Sc. 1984 Cambridge, Ph.D. 1988 Warwick. Solid state NMR has been the main research technique used. Has held positions at Bruker Analytische Messtechnik, Rheinstetten, CSIRO Division of Materials Science, Melbourne, lecturer in physics then reader in solid state NMR at the University of Kent and is currently reader in physics at the University of Warwick. Has published approximately 120 papers and book chapters. Research interests are developing a multinuclear magnetic resonance approach to studying solid materials with the main aim to better understand structural and atomic disorder in inorganic solids and thus to broaden the applications of solid state NMR as a characterization technique in materials physics.

Magic Angle Spinning

E. Raymond Andrew

University of Florida, Gainesville, FL, USA

1	Introduction	1
2	Magic Angle Spinning and Dipolar Interactions	1
3	Magic Angle Spinning and Anisotropic Shift Interactions	3
4	Magic Angle Spinning and Anisotropic Interactions	5
5	Magic Angle Spinning and Indirect Spin–Spin Interactions	5
6	Magic Angle Spinning and Nuclear Quadrupole Interactions	6
7	Macroscopic and Microscopic Motions	6
8	Factors affecting Resolution	7
9	Spinners	8
10	Double Spinners	8
11	Magic Angle Spinning and Other Techniques	9
12	Magic Angle Spinning and NMR Imaging of Solids	9
13	Related Articles	10
14	References	10

1 INTRODUCTION

Magic angle spinning, often abbreviated as MAS, is a procedure which enables high-resolution NMR spectra to be obtained from solid materials. The procedure consists of rotating the solid specimen about an axis inclined at the angle $54^\circ 44'$ to the direction of the magnetic field of the NMR magnet. This angle is $\cos^{-1}(1/\sqrt{3})$, and it is shown later that sufficiently rapid rotation about this particular axis removes most broadening interactions from the NMR spectrum leaving only fine structures of the type which are found in NMR spectra of liquids. The method may be applied to all kinds of solid materials, ionic solids, molecular solids, polymers, semiconductors, metals, alloys; the solid material may be polycrystalline, monocrystalline, or amorphous. The method is also used in the NMR imaging of solid heterogeneous materials.

Magic angle spinning may be used on its own, and may also be successfully combined with other line-narrowing techniques. It may be combined with multiple pulse methods (CRAMPS) to obtain high-resolution NMR spectra, especially of hydrogen and fluorine nuclei, from solids. The combination of magic angle spinning with cross-polarization methods has been fruitful in enabling high-resolution NMR spectra to be obtained from ^{13}C and other nuclei of low abundance. Magic angle spinning has also been used in combination with multiple quantum NMR spectroscopy.

Magic angle spinning is now a standard feature of NMR spectroscopy of solid materials and modern commercial NMR spectrometers provide facilities for this technique. Very fast rotation is needed and rotation speeds of 25 kHz are now achieved. The broadening of spectra by second order quadrupolar interactions requires spinning about other magic axes and thus calls for rotation about two axes simultaneously or sequentially.

We now turn to a more detailed consideration of the subject.

One of the most striking and characteristic features of nuclear magnetic resonance is that the spectra for solids are so very much broader than those for liquids. An excellent example is provided by water whose proton NMR linewidth at room temperature is about 0.1 Hz, while for ice at low temperatures it is about 10^5 Hz, six orders of magnitude broader. The well-understood origin of this substantial difference in behavior lies in the static anisotropic interactions to which the nuclei in the solid are subject. In mobile fluids the rapid isotropic motions of the nuclei average the anisotropic interactions and effectively remove them from the spectrum. As a consequence, a rich high-resolution NMR spectrum is often revealed that is of great value in the structural and dynamical analysis of molecules and NMR is now a standard spectroscopic technique in all chemical laboratories.

At first sight it might therefore seem that applications of high-resolution NMR spectroscopy would be inevitably confined to liquid specimens. Such a restriction would be a serious limitation since there are enormous numbers of solid materials which cannot be examined in the liquid state either because they will not dissolve in any suitable solvent, or do not melt without decomposition, or significantly change their structure in the liquid state. Consequently, there has been great interest in pursuing ways in which high-resolution NMR spectra may also be obtained from solid specimens.

First of all we note that a solid does not present a completely rigid atomic architecture. Often in the solid state there is sufficient motion of the nuclei to narrow the NMR spectra substantially and sometimes the spectrum is sufficiently narrowed to resolve a high-resolution NMR spectrum. An example is the ^{31}P NMR spectrum from polycrystalline P_4S_3 at 420 K, which is 26 K below its melting point.[1] An AB_3 type spectrum is resolved, a doublet arising from the three basal nuclei in the molecule and a quartet coming from the apical nuclei. The J coupling constant and the chemical shift separation were determined.

Although in more general cases sufficient motion is not present in solids to narrow the NMR lines, we may try to emulate Nature by imposing a motion on the nuclei. This was first done by rapidly spinning the solid specimen by Andrew, Bradbury, and Eades[2–4] and independently by Lowe.[5]

The anisotropic nuclear interactions which are of interest in solid state NMR spectroscopy are the following:

1. Direct magnetic dipolar interactions:
   (a) homonuclear;
   (b) heteronuclear
2. Indirect electron coupled interactions:
   (a) homonuclear;
   (b) heteronuclear
3. Electric quadrupolar interactions (for nuclei with spin $I > \frac{1}{2}$)
4. Electron shielding interactions (chemical shift, Knight shift)

Each of these interactions gives rise to NMR spectral broadening which it is desirable to remove. Consideration will therefore now be given to the effect of MAS on each of them.[6]

2 MAGIC ANGLE SPINNING AND DIPOLAR INTERACTIONS

We begin by examining the effect of rapid specimen rotation on nuclear magnetic dipolar interactions since they are always present in some degree and were historically the first to be considered and removed; moreover this gives a good insight into the operation of the method.

The truncated dipolar interaction Hamiltonian, for all nuclear pairs i, j in a solid, both like and unlike, is

$$\mathcal{H}_{\mathrm{d}} = \sum_{i<j} \tfrac{1}{2}\gamma_i\gamma_j\hbar^2 \boldsymbol{r}_{ij}^{-3}(\boldsymbol{I}_i\cdot\boldsymbol{I}_j - 3I_{iz}I_{jz})(3\cos^2\theta_{ij} - 1) \quad (1)$$

where γ_i, γ_j are the nuclear gyromagnetic ratios, $\boldsymbol{r}_{ij}$ is the internuclear displacement, and θ_{ij} is the angle between $\boldsymbol{r}_{ij}$ and the Zeeman magnetic field $\boldsymbol{B}_0$, which is directed along the z axis in the laboratory frame. The NMR spectrum is in principle calculated by treating $\mathcal{H}_{\mathrm{d}}$ as a perturbation on the Zeeman term $\mathcal{H}_z$, where

$$\mathcal{H}_{\mathrm{d}} = -\sum_i \gamma_i\hbar\boldsymbol{I}_i\cdot\boldsymbol{B}_0 \quad (2)$$

Since the isotropic average $\overline{\cos^2\theta_{ij}} = \frac{1}{3}$, it follows from equation (1) that the isotropic average of the dipolar Hamiltonian, $\mathcal{H}_{\mathrm{d}} = 0$, and rapid isotropic motion in fluids therefore eliminates the dipolar interaction from the NMR spectrum, yielding very sharp spectral lines.

If a solid specimen, whether monocrystalline, polycrystalline, or amorphous, is rotated uniformly with angular velocity ω_{r} about an axis inclined to $\boldsymbol{B}_0$ at angle β, every internuclear vector $\boldsymbol{r}_{ij}$ in the solid describes a motion illustrated in Figure 1. The angle θ_{ij} becomes time-dependent and the factor $(3\cos^2\theta_{ij} - 1)$ in equation (1) runs through a range of values that may be positive or negative. Its average value may be made zero by a judicious choice of β.

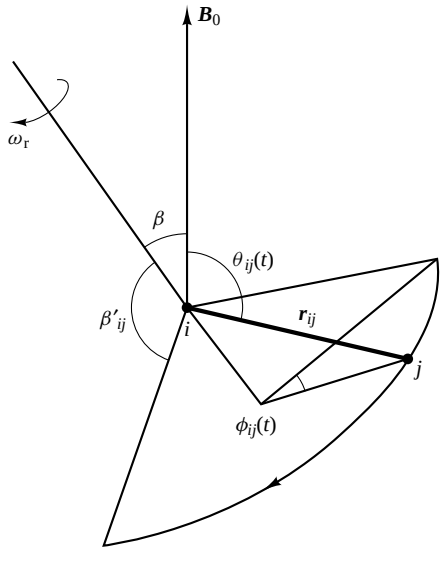

Figure 1 Diagram illustrating the motion of a typical internuclear vector $\boldsymbol{r}_{ij}$ when a solid is rotated with angular velocity ω_{r} about an axis inclined at an angle β to $\boldsymbol{B}_0$

Expressing $\cos\theta_{ij}$ in terms of the other angles in the system

$$\cos\theta_{ij} = \cos\beta\cos\beta'_{ij} + \sin\beta\sin\beta'_{ij}\cos(\omega_{\mathrm{r}}t + \phi_{\mathrm{o}ij}) \quad (3)$$

we find, after rearrangement, that

$$\begin{aligned}\mathcal{H}_{\mathrm{d}}(t) = \sum_{i<j} \tfrac{1}{2}\gamma_i\gamma_j\hbar^2\boldsymbol{r}_{ij}^{-3}(\boldsymbol{I}_i\cdot\boldsymbol{I}_j - 3I_{iz}I_{jz}) \\ \times\{\tfrac{1}{2}(3\cos^2\beta - 1)(3\cos^2\beta'_{ij} - 1) \\ +\tfrac{3}{2}\sin 2\beta\sin 2\beta'_{ij}\cos(\omega_{\mathrm{r}}t + \phi_{\mathrm{o}ij}) \\ +\tfrac{3}{2}\sin^2\beta\sin^2\beta'_{ij}\cos 2(\omega_{\mathrm{r}}t + \phi_{\mathrm{o}ij})\}\end{aligned} \quad (4)$$

Note that the first term in the curly bracket is constant, while the second and third terms are periodic with zero mean value. It is convenient to divide $\mathcal{H}_{\mathrm{d}}(t)$ into two terms, its mean value $\bar{\mathcal{H}}_{\mathrm{d}}$ and the remainder, which is periodic with zero mean value:

$$\mathcal{H}_{\mathrm{d}}(t) = \bar{\mathcal{H}}_{\mathrm{d}} + (\mathcal{H}_{\mathrm{d}} - \bar{\mathcal{H}}_{\mathrm{d}}) \quad (5)$$

The first term on the right hand side is constant and gives a reduced dipolar interaction and the narrowed spectrum, while the second term, which is periodic in ω_{r} and $2\omega_{\mathrm{r}}$, gives rise to rotational sidebands at multiples of ω_{r}. We note that in the special case of $\beta = \frac{1}{2}\pi$, that since $\sin 2\beta = 0$, only even-order sidebands are found. We see therefore from the first line of equation (4) that

$$\begin{aligned}\bar{\mathcal{H}}_{\mathrm{d}} = \tfrac{1}{2}(3\cos^2\beta - 1)\sum_{i<j}\tfrac{1}{2}\gamma_i\gamma_j\hbar^2\boldsymbol{r}_{ij}^{-3} \\ \times(\boldsymbol{I}_i\cdot\boldsymbol{I}_j - 3I_{iz}I_{jz})(3\cos^2\beta'_{ij} - 1)\end{aligned} \quad (6)$$

If we now compare equations (1) and (6), we see that for polycrystalline and amorphous materials the spectrum retains an identical shape, but is reduced in width by the scale factor

$$F(\beta) = |\tfrac{1}{2}(3\cos^2\beta - 1)| \quad (7)$$

The second moment of the narrowed spectrum is reduced by $F^2(\beta)$. On the other hand, one can show that the second moment of the whole spectrum, including sidebands, is unchanged, expressing the invariance of the second moment of the whole spectrum.[2,7–9]

Let us note some particular values of $F(\beta)$:

For $\beta = 0$, $F(\beta) = 1$
For $\beta = \frac{1}{2}\pi$, $F(\beta) = \frac{1}{2}$
For $\beta = \cos^{-1}(1/\sqrt{3}) = 54°44'$, $F(\beta) = 0$

Thus rotation about $\boldsymbol{B}_0$ has no effect as one expects, rotation about an axis normal to $\boldsymbol{B}_0$ halves the spectral width, while rotation about an axis making the special angle $54°44'$ should reduce the dipolar broadening to zero. At the Ampère Congress in Pisa in 1960, where we presented some of our results, the late Professor C. J. Gorter of Leiden referred to the apparently 'magic' properties of this special angle which led us to refer to it as the 'magic angle' thereafter.

These predictions were found to be borne out experimentally. It was realized that in a successful demonstration the rate of rotation must be at least comparable with the NMR

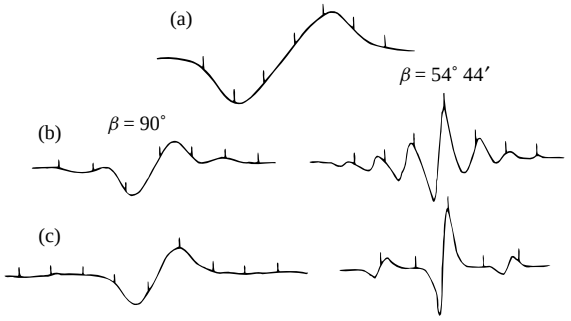

Figure 2 The effect of rapid rotation of a solid on its dipolar-broadened spectrum. ^{23}Na NMR derivative spectra of monocrystalline sodium chloride. Markers are at 800 Hz intervals. (a) Static crystal; (b), (c) recordings with the crystal spinning at 800 and 1600 Hz, respectively. The left-hand pair of recordings was obtained with the rotation axis perpendicular to the magnetic field. The right-hand pair was obtained with the rotation axis inclined at the magic angle of 54°44′ to $\boldsymbol{B}_0$ (Andrew, Bradbury, and Eades[2,3])

linewidth and that the NMR linewidth of the static material must therefore not be too large. The first experiments of Andrew et al.[2,3,6] therefore avoided proton or fluorine NMR and instead used ^{23}Na NMR in sodium chloride whose static linewidth was about 2 kHz. A single crystal was used to prevent any quadrupolar broadening due to strains or other defects in this cubic crystal. The second moment from the static crystal agreed within experimental error with the value of $0.55G^2$ calculated from the theory of Van Vleck.[9] When the crystal was first rotated[2] about an axis perpendicular to $\boldsymbol{B}_0$ ($\beta = \frac{1}{2}\pi$), the spectrum was indeed halved in width with sidebands appearing at $2\omega_r$, as illustrated in Figure 2. Then by rotating the crystal at the magic angle ($\beta = 54^\circ 44'$), the central line did indeed narrow[3,6] very sharply with spinning sidebands appearing at multiples of ω_r, also shown in Figure 2. These spectra were obtained before the days of Fourier transform NMR spectrometers for solids and appear as derivative spectra as was customary from wideline NMR spectrometers at that time.

The variations of the width of the central spectrum followed the reduction factor $F(\beta)$ of equation (7) quite well, as shown in Figure 3. The linewidth at the magic angle was 200 Hz,

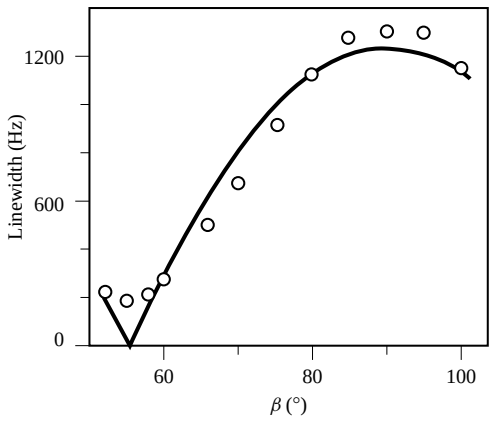

Figure 3 Variation of linewidth of the ^{23}Na NMR spectrum of a rotating crystal of sodium chloride with the angle β. The full line is the theoretical curve give by equation (7); the circles are the experimental observations (Andrew, Bradbury, and Eades[3])

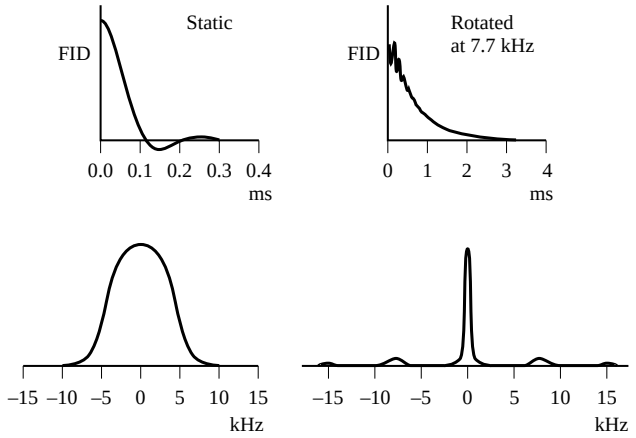

Figure 4 Aluminum-27 free induction decays (a) and Fourier transformed NMR spectra (b) of polycrystalline aluminum. The left-hand diagrams refer to the static specimen; the right-hand diagrams refer to the specimen spinning about the magic axis at 7.7 kHz. Two rotation sidebands are seen on either side of the narrowed central line (Andrew, Hinshaw, and Tiffen[10,11])

largely determined by field inhomogeneity of the wideline NMR magnet; magic angle linewidths of a few Hz have since been obtained by using high-resolution NMR magnets. Early verification of these ideas was independently obtained by Lowe,[5] who used a crystal of calcium fluoride and a sample of polytetrafluoroethylene.

A good example of the removal of dipolar broadening by MAS using pulsed NMR techniques is provided by the ^{27}Al NMR spectrum of polycrystalline aluminum metal.[10,11] As illustrated in Figure 4, the spectrum of the static material is about 10 kHz wide. Magic angle spinning at 7.7 kHz reduced this width to about 400 Hz. This enabled the isotropic Knight shift to be measured with very much improved precision, yielding a value of $1640 \pm 1 \times 10^{-6}$ relative to $AlCl_3$ solution at 298 K. A similar improvement in the precision of measurement of isotropic Knight shifts was obtained for ^{63}Cu and ^{65}Cu in polycrystalline copper metal.[12]

3 MAGIC ANGLE SPINNING AND ANISOTROPIC SHIFT INTERACTIONS

The electron shielding or chemical shift interaction of a nucleus in a nonmetallic solid may be written

$$\mathcal{H}_s = \gamma\hbar(\boldsymbol{I} \cdot \boldsymbol{\sigma} \cdot \boldsymbol{B}_0) \tag{8}$$

where $\boldsymbol{\sigma}$ is the chemical shift tensor of the nucleus. In metals the shift interaction is conventionally defined with opposite sign

$$\mathcal{H}_s = -\gamma\hbar(\boldsymbol{I} \cdot \boldsymbol{K} \cdot \boldsymbol{B}_0) \tag{9}$$

where $\boldsymbol{K}$ is the Knight shift tensor of the nucleus. Apart from this difference of sign, the behavior of $\boldsymbol{\sigma}$ and $\boldsymbol{K}$ is the same in the sections which follow.

We note that $\boldsymbol{\sigma}$ and $\boldsymbol{K}$ are second-rank tensors, but unlike the dipolar interaction tensor, which is a traceless,

axially symmetric tensor, $\boldsymbol{\sigma}$ and $\boldsymbol{K}$ are not traceless, are not necessarily axially symmetric, and may not even necessarily be symmetric.[13] However any antisymmetric components have negligible effects on the spectrum[14,15] and will be neglected.

Since the components of the shift tensor are in practice small compared with unity, we need only retain σ_{zz} and rewrite equation (8) as

$$\mathcal{H}_s = \gamma \hbar I \sigma_{zz} B_0 \tag{10}$$

If the principal values of $\boldsymbol{\sigma}$ are σ_p (p = 1, 2, 3) and the direction cosines of its principal axes with respect to $\boldsymbol{B}_0$ are λ_p, then

$$\sigma_{zz} = \sum_p \lambda_p^2 \sigma_p \tag{11}$$

Since the isotropic average of each λ_p^2 is $\frac{1}{3}$, the average value of σ_{zz} in an ordinary isotropic fluid is

$$\bar{\sigma}_{zz} = \tfrac{1}{3} \operatorname{tr} \boldsymbol{\sigma} = \sigma \tag{12}$$

where σ is the scalar chemical shift encountered in the high-resolution NMR spectra of fluids.

When a rigid array of nuclei in a solid is rotated with angular velocity ω_r about an axis inclined at angle β to $\boldsymbol{B}_0$ and at angles χ_p to the principal axes of $\boldsymbol{\sigma}$, we have [cf. equation (3)]:

$$\lambda_p = \cos\beta \cos\chi_p + \sin\beta \sin\chi_p \cos(\omega_r t + \psi_p) \tag{13}$$

From equations (10), (11), and (13) we see that a time dependence is imposed on $\mathcal{H}_s$, and as with the dipolar interaction we may decompose $\mathcal{H}_s$ into its mean value $\bar{\mathcal{H}}_s$ and terms periodic in ω_r which generate spinning sidebands. Substituting equation (13) into equation (11) and taking the time average, we find for each nucleus

$$\bar{\sigma}_{zz} = \tfrac{3}{2}\sigma \sin^2\beta + \tfrac{1}{2}(3\cos^2\beta - 1) \sum_p \sigma_p \cos^2\chi_p \tag{14}$$

Consequently when β is the magic angle $\cos^{-1}(1/\sqrt{3})$, we see that $\bar{\sigma}_{zz}$ reduces to the scalar isotropic value σ and the shift anisotropy is removed from the NMR spectrum for every nucleus in the specimen whatever the degree of anisotropy or asymmetry of its shift tensor and whatever the orientation of its principal axes, a result derived by Andrew and Wynn.[16]

The time-averaged shift given in equation (14) may be reexpressed in terms of the anisotropy parameter $\delta = \sigma_3 - \sigma$ and the asymmetry parameter $\eta = (\sigma_2 - \sigma_1)/\delta$ of each nucleus.[6] Substituting these parameters in equation (14) and rearranging, we get

$$\bar{\sigma}_{zz} = \sigma + \tfrac{1}{2}(3\cos^2\beta - 1)\delta\{\tfrac{1}{2}(3\cos^2\theta' - 1) + \tfrac{1}{2}\eta \sin^2\theta' \cos 2\phi'\} \tag{15}$$

where θ' and ϕ' are spherical polar angles relating the specimen rotation axis to the principal axes of the shift tensor ($\chi_3 = \theta'$; $\cos\chi_2 = \sin\theta' \cos\phi'$; $\cos\chi_1 = \sin\theta' \sin\phi'$). Expressed in this form we see in a direct manner how the ubiquitous Legendre factor $\frac{1}{2}(3\cos^2\beta - 1)$ controls the shift anisotropy in the time-averaged Hamiltonian $\bar{\mathcal{H}}_s$ for every nucleus in the specimen.

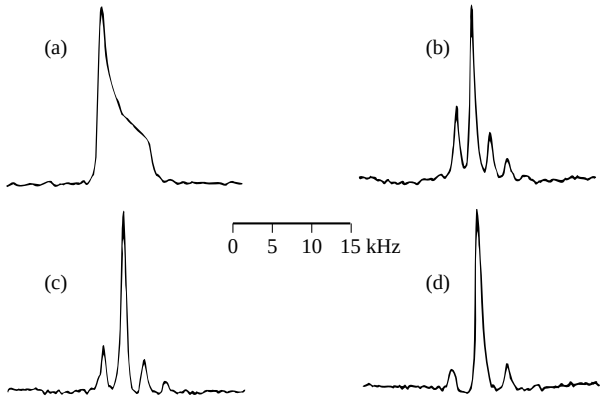

Figure 5 The removal of shift anisotropy by magic angle spinning. ^{111}Cd NMR spectra of polycrystalline cadmium metal, (a) static and rotating about the magic axis at (b) 2.1, (c) 2.6 and (d) 3.6 kHz (Andrew, Hinshaw, and Tiffen[11])

An early clear experimental example of the removal of shift anisotropy by MAS is provided by cadmium, a metal with a hexagonal crystal structure. The ^{111}Cd NMR spectra of polycrystalline specimen of cadmium metal[17] are shown in Figure 5. The spectrum for the static material shows the asymmetric profile characteristic of an axially symmetric shift tensor. Dipolar broadening is small in this material on account of the low isotopic abundance (12%) of both magnetic isotopes and their low nuclear moments ($-$ 0.6 nuclear magnetons); the Knight shift anisotropy is therefore the dominant source of NMR broadening in cadmium powder in a field of 1.4 T. Also shown in Figure 5 are spectra for three magic angle spinning rates. It is seen that magic angle spinning removes the anisotropy and it enables the isotropic Knight shift to be obtained with precision[17] ($4321 \pm 7 \times 10^{-6}$ ppm for ^{111}Cd, $4324 \pm 7 \times 10^{-6}$ ppm for ^{113}Cd relative to cadmium nitrate solution).

We may notice a new feature in Figure 5. Unlike the dipolar broadened spectra, where the rotation rate must be comparable with the linewidth to obtain substantial narrowing, here we see that the line breaks up almost immediately into an array of satellites each of narrow breadth. The essential difference is that here, with shift anisotropy, the spectrum is inhomogeneously broadened. Each element of the spectrum of the static specimen arises from crystallites of a particular orientation, each with a small intrinsic width. The situation is closely analogous to the NMR line from a liquid broadened by an inhomogeneous magnetic field; each volume element in the sample constitutes its own portion of the spectrum. The intrinsic width of the spectrum may then be recovered from the decay of the spin echo envelope. Analogous rotational echoes have been observed[17,18] and the decay envelope of such echoes gives the intrinsic width of each shifted spin packet.

Many chemically-shifted fine structures have been resolved in the NMR spectra of polycrystalline solids using MAS. An early example was provided by solid phosphorus pentachloride[19] which yielded two well-resolved ^{31}P lines, reduced to 10 Hz breadth by fast magic angle spinning, arising from the differently shielded PCl_4^+ and PCl_6^- ions of which the solid is composed, and this enabled interesting cross-relaxation effects to be examined.[20–22]

4 MAGIC ANGLE SPINNING AND ANISOTROPIC INTERACTIONS

In the two previous sections we have shown from first principles that fast specimen rotation about an axis inclined at angle β to $\boldsymbol{B}_0$ introduces a factor $\frac{1}{2}(3\cos^2\beta - 1)$ into the time-averaged Hamiltonian representing the dipolar interaction and also into that representing the anisotropic shift interaction. In fact this is quite a general result. Similar calculations from first principles show that the same factor appears in the time-averaged Hamiltonian representing the anisotropic electron-coupled spin–spin interactions[14] and in that representing first-order electric quadrupole interaction,[23] showing that MAS should therefore remove all these symmetric second-rank tensor interactions. This suggests that all these interactions could be treated in a common formalism.

The various interactions may be written:

$$\mathcal{H}_{\mathrm{d}} = \sum_{i<j} (\boldsymbol{I}_i \cdot \boldsymbol{D}_{ij} \cdot \boldsymbol{I}_j) \quad \text{direct dipolar interaction} \tag{16}$$

$$\mathcal{H}_J = h \textstyle\sum_{i<j} (\boldsymbol{I}_i \cdot \boldsymbol{J}_{ij} \cdot \boldsymbol{I}_j) \quad \text{indirect electron-coupled interaction} \tag{17}$$

$$\mathcal{H}_{\mathrm{s}} = \hbar \textstyle\sum_{i<j} \gamma_i (\boldsymbol{I}_i \cdot \boldsymbol{\sigma}_i \cdot \boldsymbol{B}_0) \quad \text{electron shielding, nonmetals} \tag{18}$$

$$\mathcal{H}_{\mathrm{s}} = -\hbar \textstyle\sum_{i<j} \gamma_i (\boldsymbol{I}_i \cdot \boldsymbol{K}_i \cdot \boldsymbol{B}_0) \quad \text{electron shielding, metals} \tag{19}$$

$$\mathcal{H}_{\mathrm{Q}} = \textstyle\sum_i \frac{eQ_i}{6I_i(2I_i-1)} (\boldsymbol{I}_i \cdot \boldsymbol{V}_i \cdot \boldsymbol{I}_i) \quad \text{electric quadrupolar interaction} \tag{20}$$

Equation (16) is an alternative version of equation (1), where $\boldsymbol{D}_{ij}$ is the truncated dipolar interaction tensor between nuclei i and j. In equation (17) $\boldsymbol{J}_{ij}$ is the electron-coupled spin–spin interaction tensor between nuclei i and j. In equation (20) eQ_i is the electron quadrupole moment of nucleus i and $\boldsymbol{V}_i$ is the electric field gradient tensor at its site.

The quantities $\boldsymbol{D}_{ij}$, $\boldsymbol{J}_{ij}$, $\boldsymbol{\sigma}_i$, $\boldsymbol{K}_i$, and $\boldsymbol{V}_i$ are all second-rank tensors. The quantity $\boldsymbol{D}_{ij}$ is axially symmetric and traceless; $\boldsymbol{V}_i$ is symmetric and traceless; the other three are not restricted. We shall however continue to neglect any antisymmetric component of tensors $\boldsymbol{\sigma}_i$, $\boldsymbol{K}_i$, and $\boldsymbol{J}_{ij}$, and we can render them all traceless by the simple expedient of subtracting their constant isotropic trace. Thus

$$\boldsymbol{J} = J\boldsymbol{1} + \boldsymbol{J}^*, \quad \text{where } J = \tfrac{1}{3}\,\mathrm{tr}\,\boldsymbol{J} \tag{21}$$

$$\boldsymbol{\sigma} = \sigma\boldsymbol{1} + \boldsymbol{\sigma}^*, \quad \text{where } \sigma = \tfrac{1}{3}\,\mathrm{tr}\,\boldsymbol{\sigma} \tag{22}$$

$$\boldsymbol{K} = K\boldsymbol{1} + \boldsymbol{K}^*, \quad \text{where } K = \tfrac{1}{3}\,\mathrm{tr}\,\boldsymbol{K} \tag{23}$$

In these expressions $\boldsymbol{1}$ is the unit tensor, J, σ and K are the isotropic coupling constants and shifts encountered in isotropic liquids. The tensors $\boldsymbol{J}^*$, $\boldsymbol{\sigma}^*$, and $\boldsymbol{K}^*$ are all traceless symmetric tensors representing the anisotropic properties of these interactions.

These five second-rank tensor interactions represented by equations (16)–(23) all have a common structure and, as Haeberlen[15] has shown, they may be cast in a common form in terms of their irreducible tensor operators:

$$\mathcal{H}_\lambda = C^\lambda \sum_l \sum_{m=-l}^{l} (-1)^m R^\lambda_{l,-m} T^\lambda_{l,m} \tag{24}$$

in which C^λ are constants specific to each interaction, the terms $R^\lambda_{l,-m}$ are angular functions in coordinate space and the terms $T^\lambda_{l,m}$ are spin products. Since we are dealing with traceless symmetric second-rank tensors, the only terms $R^\lambda_{l,-m}$ in equation (24) which are nonzero are those with $l = 2$ and $m = 0, \pm 2$.

We now need to express the tensor components $R^\lambda_{l,-m}$ for each nucleus or pair of nuclei in the laboratory frame in terms of its components in a convenient crystal frame of reference rotating in the laboratory frame. Next these components in the crystal frame need to be expressed in terms of the invariant principal values of the tensor in its principal axis frame. These two transformations are readily accomplished using the Wigner rotation matrices $\mathcal{D}^l_{m'm}(\alpha, \beta, \gamma)$, where α, β, γ are the Euler angles relating the frames of reference. The number of terms in this double transformation is severely limited since in calculating the spectra we are restricted to terms in the Hamiltonian which are secular, $m = 0$. In the transformation from the crystal frame to the laboratory frame we are left with Wigner rotation matrices of the form $\mathcal{D}^2_{m'0}(0, \beta, \omega_{\mathrm{r}}t)$; as before β is the angle between the spinning axis and $\boldsymbol{H}_0$. Noting that those Wigner matrices with factors $e^{\pm i\omega_{\mathrm{r}}t}$, $e^{\pm 2i\omega_{\mathrm{r}}t}$ average to zero under sufficiently fast rotation, we find only one nonzero rotation matrix is left, namely

$$\mathcal{D}^2_{00}(0, \beta, \omega_{\mathrm{r}}t) = \tfrac{1}{2}(3\cos^2\beta - 1) \tag{25}$$

Thus all terms in the averaged Hamiltonian $\bar{\mathcal{H}}_\lambda$, for all five traceless tensor interactions, contain this factor, equation (25). When β is the magic angle $\cos^{-1}(1/\sqrt{3}) = 54°44'$ all these anisotropic interactions therefore vanish under fast rotation. We are then left with the isotropic shift interactions and the isotropic J couplings [the scalar terms in equations (21), (22) and (23)] as in liquids, and high-resolution NMR spectra are recorded from solid specimens with MAS just as in ordinary liquid specimens.

5 MAGIC ANGLE SPINNING AND INDIRECT SPIN–SPIN INTERACTIONS

The removal of anisotropic broadening interactions by magic angle spinning frequently reveals fine structure previously obscured; a good example is the demonstration of spin multiplets in solids. In Figure 6 the ^{19}F NMR spectrum of polycrystalline hexafluoroarsenate $KAsF_6$ is shown.[24] The spectrum from the static material is about 15 kHz wide. Magic

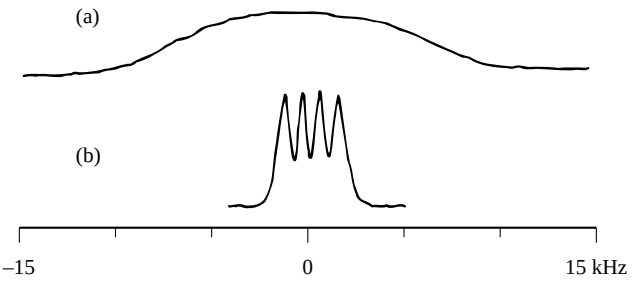

Figure 6 A spin multiplet resolved in the solid state by magic angle spinning. ^{19}F NMR spectra of polycrystalline $KAsF_6$. (a) Static specimen; (b) specimen spinning at 5.5 kHz, displaying quartet structure due to J coupling between ^{19}F and ^{75}As nuclei (Andrew, Farnell, and Gledhill[24])

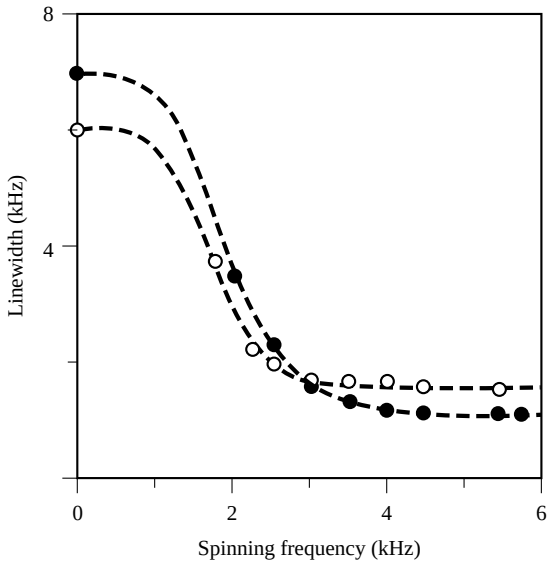

Figure 7 NMR linewidths for copper metal as a function of spinning frequency: •, ^{63}Cu; ○, ^{65}Cu (Andrew, Carolan, and Randall[26]). The rotationally invariant linewidths above 4 kHz arise from the Ruderman–Kittel interaction

angle spinning at 5.5 kHz substantially removed the anisotropic sources of broadening (D, J^*, σ^*) and resolved a spin quartet with an isotropic coupling constant J of 905 Hz. The quartet arises from the coupling of the ^{19}F nuclei with the 100% abundant ^{75}As nucleus in the octahedral AsF_6^- ions in the solid. This was in fact the first spin multiplet to be resolved in the NMR spectrum of a solid (Andrew, Farnell, and Gledhill[24,25]).

Electron-coupled nuclear spin interactions are also encountered in metals and in particular are manifested in the narrowed spectra of copper. As shown in Figure 7 magic angle spinning substantially reduces the ^{63}Cu and ^{65}Cu linewidths, but for spinning rates above 3 kHz a constant limiting linewidth is reached which is evidently due to a rotationally invariant interaction.[26,27] By comparing the second moments of the residual lines and noting that they are in the inverse ratio of the abundances of the two copper isotopes, it was possible to show that the residual breadths were due to the Ruderman–Kittel electron-coupled nuclear interactions. A value of $J = 230 \pm 10$ Hz was extracted for the nearest-neighbor coupling constants in reasonable agreement with theory and consistent with the value for silver.[28]

6 MAGIC ANGLE SPINNING AND NUCLEAR QUADRUPOLE INTERACTIONS

It was shown in Section 4 that fast magic angle spinning should also average the quadrupolar Hamiltonian $\mathcal{H}_Q$ to a small value. This is not such an easy interaction to put to an experimental test since quadrupolar interactions in noncubic environments tend to be large. Even when they are less than the Zeeman interaction, first-order perturbation theory is often not a sufficient approximation and second-order contributions need consideration, as will be described later in Section 10.

However, an unequivocal test was carried out by Tzalmona and Andrew[29] using two noncubic cesium salts, Cs_2SO_4 and Cs_2CO_3. The cesium nucleus ^{133}Cs, which has 100% abundance and spin-$\frac{7}{2}$, has an unusually small electric quadrupole moment, -3×10^{-27} cm^2. Consequently the quadrupole broadening in these salts was of order of 10^3 Hz and first-order theory suffices to describe it. Moreover since the nearest-neighbor separation of the cesium atoms is about 0.4 nm, and there are no other abundant magnetic nuclei in the solids, the dipolar contribution to the linewidth is an order of magnitude smaller than the quadrupolar contribution. MAS at 3 kHz reduced the NMR linewidth by a factor of 18 in the sulfate and by a factor of 7 in the carbonate.

Later a striking demonstration of the removal of first-order quadrupole broadening was provided[30] with ^{2}H NMR. The weak quadrupole moment of the deuteron, 2.7×10^{-27} cm^2, enabled a narrowing of three orders of magnitude to be obtained with MAS at 4 kHz.

7 MACROSCOPIC AND MICROSCOPIC MOTIONS

If an NMR spectrum is already partially narrowed by molecular motion within a solid it is of practical interest to enquire whether magic angle spinning will remove the remaining breadth. Two different situations may be distinguished[31] with different answers to the question which has been posed. The first may be called ‘fast restricted motion’ and the second ‘slow and moderate isotropic motion’.

In the first category of fast restricted motion, molecules or groups in the solid may for example reorient rapidly and randomly about one defined molecular axis leading to a reduced plateau value of the second moment. In such a case when the solid specimen is rotated about the magic axis, the average interaction Hamiltonian must be found by taking the time average over both macroscopic and microscopic motions, and it is found[31] that the anisotropic interactions all average to zero. This conclusion is borne out by experiment, for example, in polytetrafluoroethylene. The ^{19}F NMR spectrum at room temperature is already narrowed to about 30% of its low-temperature rigid structure width and MAS removes the remaining breadth associated with other degrees of molecular freedom.[5] In such cases the microscopic molecular motion makes the task of macroscopic narrowing easier, since the rate

of rotation need only be comparable with the already reduced linewidth.

In the second situation of slow or moderate isotropic motion, substantial spectral narrowing has been achieved by *isotropic* molecular rotation and diffusion. All degrees of freedom of the molecules have been mobilized, but the rate of motion, though fast enough to narrow the spectrum substantially, is not fast enough to give the really sharp lines characteristic of mobile liquids. Let us consider some typical orders of magnitude. Suppose we have a solid whose rigid lattice NMR linewidth is 10^4 Hz. Internal isotropic motion with a correlation frequency of 10^6 Hz would narrow the spectrum to an observed width of 10^2 Hz. In this situation macroscopic spinning at 10^2 Hz will have no effect on the residual linewidth, nor even spinning at 10^4 Hz. The frequency of magic angle spinning will have to be greater than that of the internal motion, 10^6 Hz in our example, to produce further narrowing of the line and such a fast rotation rate is impossible to achieve. With this class of material internal microscopic molecular motion is a hindrance and not a help in securing very narrow lines.

There are intermediate situations between these two extreme types of behavior, particularly in polymers, and this enables information to be obtained about internal motions present.

8 FACTORS AFFECTING RESOLUTION

There are a large number of factors which determine the ultimate width of the NMR lines in spectra obtained with magic angle spinning. These are discussed in turn.

8.1 Instrumental Factors

Inhomogeneity of the Laboratory Magnetic Field $\boldsymbol{B}_0$: This is always an important factor in high-resolution NMR spectroscopy of all kinds. Clearly the most uniform magnetic field possible should always be employed. Specimen rotation itself removes residual inhomogeneities in planes normal to the rotation axis.

Imperfect Adjustment to the Magic Angle: This assumes greater importance the greater the degree of narrowing achieved. If the angle β deviates from the magic value $54^\circ 44'$ by a small angle ϵ, the residual linewidth will be $\sqrt{2}\epsilon$ of the original width as one sees directly from equations (7) and (25). For a reduction of 100 times, ϵ must therefore be less than half a degree; for a reduction of 1000 times, ϵ must be less than $2.5'$.

Angular Instability: It follows from the previous paragraph that the spinner axis must remain in adjustment and must not wander, wobble, or nutate significantly from its correct orientation.

Insufficiently Fast Spinning: In general the faster the specimen is spun the narrower the lines become, provided there is no rotationally invariant residual broadening. Theory suggests the line should narrow as ω_r^{-2}, though experiment bears this out only approximately.[32,33]

Bulk Susceptibility Effects: For an ellipsoidal sample of homogeneous material with isotropic magnetic susceptibility in a uniform magnetic field, the field within the sample is also uniform. For a polycrystalline sample of irregular particles of possibly anisotropic susceptibility, with voids in between, the field will not be uniform with the sample.[34] The effects of voids can be reduced by compaction.

8.2 Residual Interactions

Residual Dipolar and Pseudodipolar Interactions: This is related to the situation of insufficiently fast spinning mentioned above. Dipolar interactions between like nuclei with different orientations of shift tensor are not completely averaged.

Chemical Shift Distributions: This reflects a fundamental difference between the solid and liquid states. There can be a small distribution of isotropic shifts throughout the specimen for nominally equivalent nuclei, arising from small variations of environment and physical defects. In solution any similar small variations of shift will be removed by dynamic averaging by the molecules. In solids the molecules generally remain in their particular environment. Such distributions generate a residual linewidth proportional to $\boldsymbol{B}_0$.

Intermolecular J Couplings: This also reflects a fundamental difference between the solid and liquid states. Since in the solid state molecules continue to have the same environment, there can be static intermolecular J couplings; in the liquid state molecular motion removes their effect. A distribution of small J couplings will generate a field-independent residual breadth.

Ruderman–Kittel Interactions: This applies to conductors and was discussed in Section 5.

Anisotropic Tensor Interactions: The $\boldsymbol{J}$ tensor is not necessarily symmetric, i.e., it is not necessarily equal to its transpose. However we have so far neglected any antisymmetric component on the grounds that its effect on the NMR spectrum should be small. Nevertheless when very narrow lines are achieved, the contribution of these components should be remembered since magic angle spinning does not remove them.[14]

Quadrupole Effects: In addition to second-order quadrupole interactions discussed in Section 6, another interesting effect has been noted in ^{13}C high-resolution NMR spectra in solids. When the ^{13}C atom is bonded to ^{14}N ($I = 1$) it is observed that the dipolar coupling between the two nuclei is not entirely removed by magic angle spinning, often leaving an asymmetric doublet.[35] The relatively strong quadrupole interaction of ^{14}N with the electric field gradient at its site competes with the Zeeman interaction for the alignment of the ^{14}N spins and modifies the angular dependence of its dipolar interaction with other spins. With ^{15}N ($I = \frac{1}{2}$) this source of broadening is absent in the ^{13}C spectra, thus confirming the correct identification of its origin. Although limiting the resolution obtainable with ^{13}C nuclei bonded to nitrogen, this interaction does assist in the assignment of such lines in the spectrum.

Multipole Effects: Nuclei with $I \geq \frac{3}{2}$ may have a magnetic octupole moment and in several cases nuclear octupole interactions have been established. Nuclei with $I \geq 2$ may have an electric hexadecapole moment, and in general a nucleus with $I = \frac{n}{2}$ may have a 2^n moment (magnetic for n odd, electric for n even). Such interactions have not been significant in solids beyond $n = 2$. Nevertheless it may be pointed out that higher order multipole interactions involve tensor products of higher rank whose transformations involve higher-order spherical harmonics, and $54^\circ 44'$ will not be the appropriate magic rotation angle to average them to zero.

8.3 Motional and Relaxation Effects

Spin–Lattice Relaxation: Nuclear spin–lattice relaxation is always a source of spectral broadening contributing a width of order $(\pi T_1)^{-1}$, where T_1 is the nuclear spin–lattice relaxation time.

Cross Relaxation: If the spinning frequency is exactly equal to the frequency separation between two chemically-shifted lines (or a submultiple of that frequency), mutual spin exchanges can take place between the two systems of nuclei.[20] This promotes spin–lattice relaxation and also generates a resonant rotational line broadening which amounted to 50 Hz in solid phosphorus pentachloride.[21]

Slow Internal Motions: This was discussed in Section 7.

9 SPINNERS

A variety of spinner configurations have been used. An early type which was used with success for many years[2,36] is shown in Figure 8 and illustrates many features common to all spinners. It is based on a type introduced by Henriot and Huguenard[37,38] and developed by Beams,[39,40] and was recognized as convenient for NMR work since it was compact and, having a gas bearing, was capable of very high frequencies of rotation. It was necessary for NMR purposes to make the rotors of nonmetallic materials for use in a magnetic field, to incorporate a specimen chamber into the rotor, and to adapt the system for use in an NMR spectrometer probe.

The turbine is driven by compressed gas which emerges through inclined jets machined in the stator and impinges on the conical underside of the rotor which is provided with a set of flutes. The rotor is thus supported on a gas bearing and rotates with little frictional resistance. The specimen is on top of the rotor and is an integral part of the rotor construction; it spins freely within the radiofrequency coil of the NMR spectrometer with a good filling factor. The rotors spin with very constant speed about an axis inclined at any angle to the vertical, even upside down. Some spinners consist of a cylindrical body containing the specimen and have a conical gas bearing at each end. Others have plane gas bearings at the ends and are driven by gas jets impinging on flutes cut in the cylindrical surface.

It was found that at high gas pressures the rotation frequency reached a limiting value[36] when the peripheral velocity approached the velocity of sound in the gas. Compressed air or nitrogen may be used to drive the rotors, but higher speeds were obtainable using compressed helium gas since the velocity of sound in helium is 2.7-times higher than in air. With a 19 mm diameter rotor of the type shown in Figure 8 driven by compressed helium, rotation frequencies of 15 kHz were achieved. The latest cylindrical spinners of 5 mm diameter have reached rotation frequencies of 21 kHz, while those of 3.5 mm have reached 27 kHz. (I am grateful to Dr David Doty of Doty Scientific, Columbia, SC, for this information.)

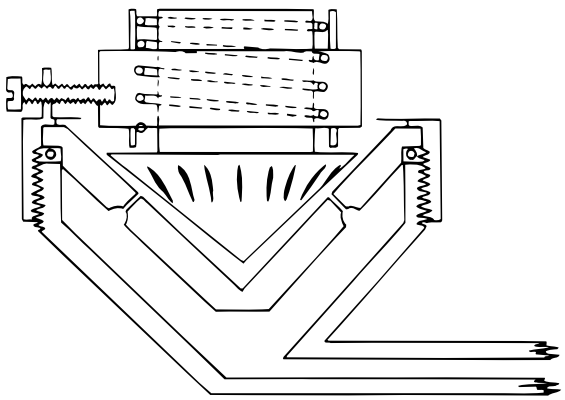

Figure 8 Turbine assembly for magic angle spinning (Andrew et al.[36])

At a rotation frequency of 10 kHz (600 000 rev min^{-1}) the peripheral velocity of a 19 mm diameter rotor is 600 m s^{-1} (2000 km h^{-1}), and the peripheral acceleration is $4 \times 10^6 g$. The rotors must therefore be made of strong material. Strong polymers such as Nylon have been used and also silicon nitride and glass fiber and carbon fiber reinforced materials.

The ideal magic angle spinner will rotate at high speeds with great stability for long periods of time. The specimen within the rotor must occupy the radiofrequency coil with high filling factor. The ideal spinner assembly should contain no nuclei of the species whose NMR is being recorded. It should ideally be possible to change specimens rapidly as in high-resolution NMR of liquids and without having to dismantle the probe assembly in order to do so. There should be a precise fine adjustment to the magic angle. It should moreover be possible to vary the temperature of the specimen over a wide range. Naturally all these desirable attributes are not easy to realize simultaneously. Some rotor systems concentrate on optimization of a particular aspect such as very high rotation frequency, or excellent stability, or ready interchangeability of specimens.

10 DOUBLE SPINNERS

For nuclei with an electric quadrupole moment ($I > \frac{1}{2}$) in a noncubic environment, the NMR spectrum is broadened by quadrupole interactions which can be quite sizeable. In such a case the spectrum is not adequately characterized by first-order perturbation theory alone but needs also at least second-order perturbation theory to describe it. First-order perturbations are proportional to the second rank Legendre polynomial P_2 and as we saw in Sections 2, 3, and 4, magic angle spinning can remove this when the angle β between the spinner axis and the magnetic field satisfies:

$$P_2(\cos\beta) = \tfrac{1}{2}(3\cos^2\beta - 1) = 0 \qquad \beta = 54^\circ 44' \quad (26)$$

This is the magic angle we have been concerned with throughout this article so far.

Removal of first-order quadrupole broadening can leave significant second-order broadening which limits the attainment of high-resolution NMR spectra from solids. Second-order perturbations are proportional to the fourth rank Legendre polynomial P_4 and can be removed by causing β to satisfy:

$$P_4(\cos\beta) = \tfrac{1}{8}(35\cos^4\beta - 30\cos^2\beta + 3) = 0 \quad (27)$$

This equation has two solutions

$$\beta = 30^\circ 34' \quad \text{and} \quad 70^\circ 7' \quad (28)$$

which give rise to two new second-order magic angles.

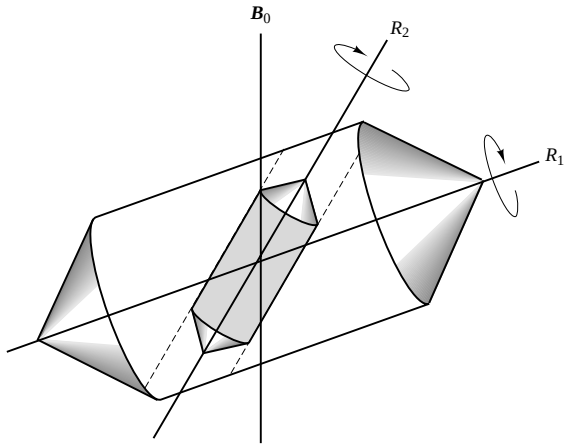

Figure 9 Schematic diagram of a double spinner (Samoson, Lippmaa, and Pines[41]). The solid sample is placed within the inner rotor which spins within the larger rotor. The angle between R_1 and the magnetic field is the customary magic angle of 54°44′. The angle between R_1 and R_2 is the secondary magic angle of 30°34′

Removal of both first- and second-order broadening can therefore be achieved by spinning the specimen about two axes simultaneously, the specimen being enclosed in a small rotor spinning rapidly within a larger rotor spinning more slowly, as shown in Figure 9. This double spinner pioneered by Samoson, Lippmaa, and Pines[41] has achieved substantial first- and second-order quadrupole narrowing using magic angles of 54°44′ and 30°34′ and spinning frequencies of 2000 Hz for the inner rotor and 400 Hz for the outer rotor. This technique has been called *double rotation* or DOR and can lead to the removal of all first- and second-order sources of broadening in the NMR spectra of solids.[42] Rotation frequencies of 7000 Hz (inner) and 1600 Hz (outer) have now been achieved for 0.1 mL samples. (I am grateful to Dr David Doty of Doty Scientific, Columbia, SC, for this information.)

Instead of spinning the specimen about two axes simultaneously, the specimen may be spun about two axes sequentially, so chosen that the time average of both Legendre polynomials is zero. This alternative technique is called *dynamic angle spinning* or DAS.[42]

11 MAGIC ANGLE SPINNING AND OTHER TECHNIQUES

Magic angle spinning by itself can frequently provide high-resolution NMR spectra from solid specimens. A good example is provided by the zeolites where magic angle spinning enables a ^{29}Si NMR spectrum to be recorded with five well-resolved lines.[43] These correspond to the silicon atoms coordinated to 0, 1, 2, 3, 4 other silicons, enabling the structures of aluminosilicate networks to be determined.

However for proton NMR spectroscopy of polycrystalline and amorphous solids, the spectra can be 30–100 kHz wide and spinners do not rotate fast enough to narrow homogeneously broadened spectra of this width. On the other hand, multiple pulse sequences can substantially narrow such spectra, but they do not remove all sources of broadening. In such cases the two techniques can be profitably combined to obtain more highly resolved spectra than either technique can achieve separately.

11.1 Magic Angle Spinning and Multiple Pulse NMR

First of all we should note that whereas magic angle spinning removes all anisotropic sources of broadening which can be represented by second-rank symmetric tensor interactions (Section 4), provided the specimen is rotated fast enough, multiple pulse NMR does not remove broadening due to heteronuclear interactions (dipolar $\boldsymbol{D}$ and indirect $\boldsymbol{J}$*), nor does it remove broadening due to anisotropic chemical shifts in polycrystalline and amorphous materials. The heteronuclear interactions can in principle be removed by spin decoupling, but there still remains the broadening due to chemical shift anisotropy. For protons this may be typically several kHz, depending on the operating NMR frequency. It is clear therefore that magic angle spinning can remove residual sources of anisotropic broadening that multiple pulse irradiation cannot remove.

This combination of techniques is sometimes referred to as CRAMPS,[44] or Combined Rotation And Multiple Pulse Spectroscopy (qv).

11.2 Magic Angle Spinning and Cross-Polarization NMR

Highly resolved ^{13}C NMR spectra may be obtained from solid specimens using magic angle spinning with cross-polarization double resonance methods.[45–47] The double resonance procedure decouples the strong proton heteronuclear dipolar interactions and heteronuclear J couplings and, by using the Hartmann–Hahn condition, provides enhancement of the weak ^{13}C NMR signal by proton polarization transfer. Consequently the residual spectral width of several kHz arises mainly from the anisotropic ^{13}C chemical shifts in polycrystalline and amorphous specimens and the weak homonuclear ^{13}C dipolar interactions. Both of these interactions are readily removed by magic angle spinning.

This technique is often abbreviated CP MAS or Cross Polarization with Magic Angle Spinning. It has been successfully applied to ^{13}C, ^{15}N, ^{29}Si, and ^{31}P NMR spectroscopy of solid specimens.

11.3 Magic Angle Spinning and Double Quantum NMR

In double quantum NMR spectroscopy for nuclei with I = 1 such as ^{2}H, the Δm = 2 transitions are independent of quadrupole broadening in first order and have a narrow intrinsic width of order 1 kHz. Magic angle spinning can then easily remove this broadening and yield a narrow resonance line.[48]

12 MAGIC ANGLE SPINNING AND NMR IMAGING OF SOLIDS

NMR imaging of structured solid materials is more difficult to achieve than the NMR imaging of liquid or liquid-like materials such as living systems. This is because the inherent NMR spectral breadth of a solid is very much greater than

that of a liquid by typically 10^3- to 10^4-times. If each picture element (pixel) in the image is to be resolved from its adjacent pixels, the applied magnetic field gradients which provide spatial encoding must be larger than for liquid-like systems by the same factor of 10^3–10^4. This leads to the need for very large magnetic field gradients for imaging solid structures, which are difficult to achieve. One method of avoiding this difficulty is to narrow the NMR linewidth of the solid by magic angle spinning. If the NMR linewidth of a solid specimen is reduced by several orders of magnitude to a liquid-like breadth, then conventional magnetic field gradients of the magnitude customarily encountered in the MRI of living systems can then be used.

If the solid object to be imaged is not too large, it can be placed in a MAS rotor and spun at the magic angle in the usual way. There is however the complication that the structure we wish to determine and display as an image is now rotating relative to the laboratory. It is therefore also necessary to rotate the field gradients in synchronism with the rotor. Such a rotating field gradient can be generated by an orthogonal set of coils fed in quadrature; synchronism may readily be achieved optically, electrically, or acoustically. In this way NMR images have been generated of structured solids while in the rotating frame of the spinner.[49]

13 RELATED ARTICLES

Average Hamiltonian Theory; Chemical Shift Tensors; CRAMPS; Cross Polarization in Rotating Solids: Spin-1/2 Nuclei; Dipolar and Indirect Coupling Tensors in Solids; Double Rotation; Dynamic Angle Spinning; High Speed MAS of Half-Integer Quadrupolar Nuclei in Solids; Imaging Techniques for Solids and Quasi-Solids; Indirect Coupling: Semiempirical Calculations; Internal Spin Interactions and Rotations in Solids; Knight Shift; Line Narrowing Methods in Solids; Magic Angle Turning and Hopping; Quadrupolar Interactions; Quadrupolar Nuclei in Solids; Rotating Solids; Sideband Analysis in Magic Angle Spinning NMR of Solids.

14 REFERENCES

1. E. R. Andrew, W. S. Hinshaw, and A. Jasinski, *Chem. Phys. Lett.*, 1974, **24**, 399.
2. E. R. Andrew, A. Bradbury, and R. G. Eades, *Nature (London)*, 1958, **182**, 1659.
3. E. R. Andrew, A. Bradbury, and R. G. Eades, *Nature (London)*, 1959, **183**, 1802.
4. E. R. Andrew, *Arch. Sci. Genève*, 1959, **12**, 103 (fasc. spéc.).
5. I. J. Lowe, *Phys. Rev. Lett.*, 1959, **2**, 285.
6. E. R. Andrew, *Philos. Trans. R. Soc. London, Ser. A*, 1981, **299**, 505.
7. E. R. Andrew and R. A. Newing, *Proc. Phys. Soc.*, 1958, **72**, 959.
8. E. R. Andrew and G. J. Jenks, *Proc. Phys. Soc.*, 1962, **80**, 663.
9. J. H. Van Vleck, *Phys. Rev.*, 1948, **74**, 1168.
10. E. R. Andrew, W. S. Hinshaw, and R. S. Tiffen, *Phys. Lett. A*, 1973, **46**, 57.
11. E. R. Andrew, W. S. Hinshaw, and R. S. Tiffen, *J. Magn. Reson.*, 1974, **15**, 191.
12. E. R. Andrew, J. L. Carolan, and P. J. Randall, *Phys. Lett. A*, 1971, **35**, 435.
13. A. D. Buckingham and S. M. Malm, *Mol. Phys.*, 1971, **22**, 1127.
14. E. R. Andrew and L. F. Farnell, *Mol. Phys.*, 1968, **15**, 157.
15. U. Haeberlen, *High Resolution NMR in Solids: Advances in Magnetic Resonance*, Suppl. 1, Academic Press, New York, 1976.
16. E. R. Andrew and V. T. Wynn, *Proc. R. Soc. London, Ser. A*, 1966, **291**, 257.
17. M. Maricq and J. S. Waugh, *Chem. Phys. Lett.*, 1977, **47**, 327.
18. M. Maricq and J. S. Waugh, *J. Chem. Phys.*, 1979, **70**, 3300.
19. E. R. Andrew, A. Bradbury, R. G. Eades, and G. J. Jenks, *Nature (London)*, 1960, **188**, 1096.
20. E. R. Andrew, A. Bradbury, R. G. Eades, and V. T. Wynn, *Phys. Lett.*, 1963, **4**, 99.
21. E. R. Andrew, S. Clough, L. F. Farnell, T. D. Gledhill, and I. Roberts, *Phys. Lett.*, 1966, **21**, 505.
22. E. R. Andrew, W. Vennart, G. Bonnard, R. M. Croiset, M. Demarcq, and E. Mathieu, *Chem. Phys. Lett.*, 1976, **43**, 317.
23. A. C. Cunningham and S. M. Day, *Phys. Rev.*, 1966, **152**, 287.
24. E. R. Andrew, L. F. Farnell, and T. D. Gledhill, *Phys. Rev. Lett.*, 1967, **19**, 6.
25. E. R. Andrew, M. Firth, A. Jasinski, and P. J. Randall, *Phys. Lett. A*, 1970, **31**, 446.
26. E. R. Andrew, J. L. Carolan, and P. J. Randall, *Phys. Lett. A*, 1971, **37**, 125.
27. E. R. Andrew, in *Proc. 17th Congr. Ampère*, ed. V. Hovi, North-Holland, Amsterdam, 1973, p. 18.
28. E. R. Andrew and W. S. Hinshaw, *Phys. Lett. A*, 1973, **43**, 113.
29. A. Tzalmona and E. R. Andrew, in *Magnetic Resonance and Related Phenomena*, eds. P. S. Allen, E. R. Andrew, and C. A. Bates, North-Holland, Amsterdam, 1975, p. 241.
30. J. L. Ackerman, R. Eckman, and A. Pines, *Chem. Phys.*, 1979, **42**, 423.
31. E. R. Andrew and A. Jasinski, *J. Phys. C*, 1971, **4**, 391.
32. S. Clough and K. W. Gray, *Proc. Phys. Soc.*, 1962, **79**, 457.
33. H. Kessemeier and R. E. Norberg, *Phys. Rev.*, 1967, **155**, 321.
34. A. N. Garroway, D. L. Vanderhart, and W. L. Earl, *Philos. Trans. R. Soc. London, Ser. A*, 1981, **299**, 609.
35. C. J. Groombridge, R. K. Harris, K. J. Packer, B. J. Say, and S. F. Tanner, *J. Chem. Soc., Chem. Commun.*, 1980, 174.
36. E. R. Andrew, L. F. Farnell, M. Firth, T. D. Gledhill, and I. Roberts, *J. Magn. Reson.*, 1969, **1**, 27.
37. E. Henriot and E. Huguenard, *C.R. Acad. Sci. Paris*, 1925, **180**, 1389.
38. E. Henriot and E. Huguenard, *J. Phys. Radium*, 1927, **8**, 433.
39. J. W. Beams, *Rev. Sci. Instrum.*, 1930, **1**, 667.
40. J. W. Beams, *J. Appl. Phys.*, 1937, **8**, 795.
41. A. Samoson, E. Lippmaa, and A. Pines, *Mol. Phys.*, 1988, **65**, 1013.
42. B. Q. Sun, J. H. Baltisberger, Y. Wu, A. Samoson, and A. Pines, *Solid State NMR*, 1992, **1**, 267.
43. J. M. Thomas and J. Klinowski, *Adv. Catal.*, 1985, **33**, 199.
44. B. C. Gerstein, R. G. Pembleton, R. C. Wilson, and L. M. Ryan, *J. Chem. Phys.*, 1977, **66**, 361.
45. A. Pines, M. G. Gibby, and J. S. Waugh, *Chem. Phys. Lett.*, 1972, **15**, 373.
46. J. Schaefer and E. O. Stejskal, *J. Am. Chem. Soc.*, 1976, **98**, 1031.
47. E. Lippmaa, M. Alla, and T. Tuherm, in *Proc. 19th Congr. AMPERE, Heidelberg, 1976*, p. 113.

48. R. Eckman, L. Müller, and A. Pines, *Chem. Phys. Lett.*, 1980, **74**, 376.
49. D. G. Cory, J. W. M. van Os, and W. S. Veeman, *J. Magn. Reson.*, 1988, **76**, 543.

Biographical Sketch

E. Raymond Andrew. *b*. 1921. B.A. (Physics), M.A. Ph.D., Sc.D., Cambridge University, UK, Hon. D.Sc. Turku, Poznan, Leipzig, FRSE and FRS. Postdoctoral Fellow, Harvard with E. M. Purcell. Lecturer, St. Andrews University, Scotland. Professor of Physics, University of Wales, Bangor. Professor and Dean of Science, Nottingham University, England. Currently Research Professor, University of Florida, USA. President, Groupement AMPERE, 1974–80. President, ISMAR, 1983–86. Editor, *Magnetic Resonance in Medicine*, 1983–91. Approx. 330 publications. Research interests: NMR in condensed matter, NMR imaging, MR in medicine.

Magic Angle Turning and Hopping

Jian Zhi Hu

University of Utah, Salt Lake City, UT, USA, and Wuhan Institute of Physics, Chinese Academy of Sciences, China

and

Wei Wang and Ronald J. Pugmire

University of Utah, Salt Lake City, UT, USA

1	Introduction	1
2	Simple Theory	1
3	Experimental Results	6
4	Conclusions	7
5	Related Articles	7
6	References	8

1 INTRODUCTION

It is well known that, in a solid, the chemical shift of a nucleus is a function of molecular orientation with respect to the external magnetic field. This phenomenon is described as the chemical shift anisotropy (CSA) and is directly related to the local electronic structure of the nucleus. The principal values of the CSA as well as their orientation in the molecular frame can be obtained through a single crystal study (see ***Chemical Shift Tensors in Single Crystals***.). However, for the majority of compounds, the difficulties associated with growing a single crystal of sufficient size limits the application of current single crystal methods. In a powder sample the orientation information is lost because of the random distribution of the crystallites. However, the principal values which are very useful in characterizing the structure of a molecule are still available in the powder pattern obtained from a stationary or slowly spinning sample when the molecule has few enough unique nuclei that the spectrum can be interpreted. Unfortunately, the overlap of several broad powder patterns often prevents the spectral separation necessary for individual identification and measurement.

In an effort to address this problem of spectral overlap, many 2D techniques have been developed to obtain a 2D spectrum with an isotropic shift projection along one dimension and a stationary or slow-spinning sideband powder pattern along the other (see ***Chemical Shift Tensors***). One of the first techniques developed was the magic angle hopping (MAH) experiment of Bax et al.[1] By successively 'hopping' the sample 120° about an axis at the magic angle, an isotropic shift dimension is obtained since the average of the resonance frequencies at the three orthogonal positions is the isotropic shift.

An analog of the MAH experiment employing continuous slow rotation of the sample has recently been demonstrated by Gan.[2] Gan's elegant technique uses pulses spaced at one-third of the rotor period to obtain the isotropic shift evolution. We call Gan's experimental technique the magic angle turning (MAT) experiment because of the very slow rotation involved. Significant improvements in the experimental details have been made to optimize these two experiments.[3–6]

In this article, a simple theory is given to describe the MAH experiment and the most recent version of the MAT experiments, together with typical experimental results included to show the basic principles and the power of these two related methods.

2 SIMPLE THEORY

It is known[7] that the average of the chemical shifts along three mutually perpendicular directions corresponds to the isotropic chemical shift ω_{iso}, i.e., $\omega_{iso} = (\omega_x + \omega_y + \omega_z)/3$, where ω_x, ω_y, ω_z represent the chemical shifts when the external field is along the corresponding direction denoted by the subscripts. The basis of the MAH and MAT experiments is derived from the fact that the exchange of these three mutually perpendicular axes can be realized by rotating the sample 120° about an axis inclined at the magic angle from the external field. In the following discussion, the MAH method is explained in detail to show how the isotropic chemical shift dimension is synthesized and how the 2D amplitude-modulated hypercomplex FID data sets, which give pure absorption phase spectra, are formed.

The basic principle of the MAH experiment can be best explained with the model pulse sequence of Figure 1(a). Enhanced ^{13}C transverse magnetization is created by the traditional cross polarization (CP) from protons and at the end of the CP period the magnetization is released at $t = 0$ to precess for a time $t_b/3$ through an angle $\omega_x t_b/3$ for a specific crystallite, where ω_x is the angular frequency when the x axis of the crystallite is along the external magnetic field and t_b is the evolution time. One component of the transverse magnetization is then projected onto and preserved along the longitudinal axis by the 90° projection pulse labeled p_1. The phase of the projection pulse selects either the $\cos(\omega_x t_b/3)$ or $\sin(\omega_x t_b/3)$ transverse components. A rapid 120° sample rotation about the magic angle axis reorients the crystallite so that its y axis is along the magnetic field direction during the period L, while at the same time the orthogonal component of the magnetization is purged by transverse relaxation. A 90° pulse brings the stored longitudinal magnetization back onto the transverse plane and the magnetization then precesses through another angle $\omega_y t_b/3$ before being projected again by the 90° pulse p_2, whose phase selects either the $\cos(\omega_y t_b/3)$ or $\sin(\omega_y t_b/3)$ components. Another 120° sample rotation is then performed, aligning the z axis of the crystallite along the magnetic field, followed by a 90° pulse which brings the stored longitudinal magnetization back to the transverse plane where it precesses through a third angle $\omega_z t_b/3$ before being projected again by the 90° pulse p_3, whose phase selects either the $\cos(\omega_z t_b/3)$ or $\sin(\omega_z t_b/3)$ components. A 90° read pulse with phase x is applied followed by data acquisition for a time t_a. The magnetization being acquired precesses again with the frequency ω_z whose amplitude is modulated by a multiplication of the components given by the three evolution segments. Finally, the sequence is followed by a reverse 240° sample rotation which brings the rotor back to its starting position.

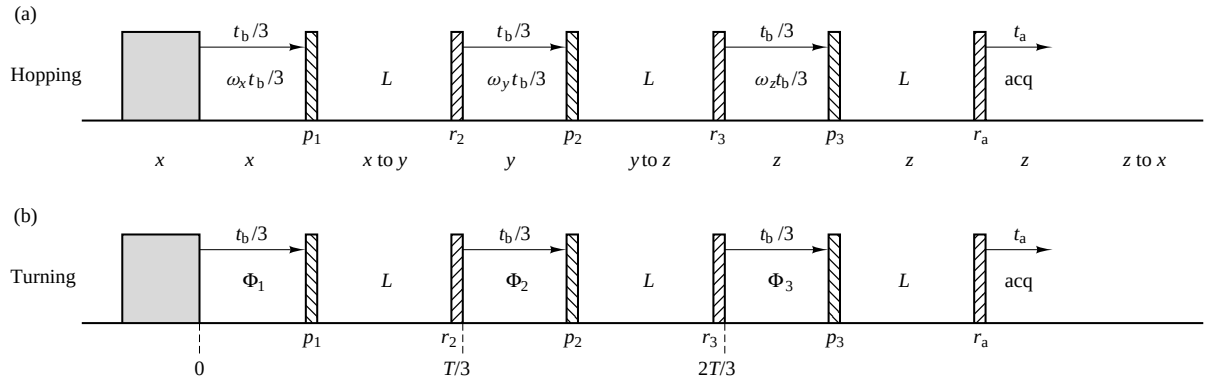

Figure 1 (a) The pulse sequence for the magic angle hopping (MAH) experiment, where L represent the longitudinal magnetization. The quantities x, y, and z refer to the position of a crystallite relative to the magnetic field as the sample is hopped around the magic angle. The phase table is given in Hu et al.[3] (b) The pulse sequence for the prototype magic angle turning (MAT) experiment, where T is an integer number of rotor periods (except a multiple of three rotor periods) and L represents the time between the projection pulses, p, and the read pulses, r, during which the magnetization is along the longitudinal axis. In both figures the proton decoupler is turned off during the period L. The phase table is given in Hu et al.[4]

The amplitude of each FID is a product of the three amplitude factors selected by the phases of the three projection pulses. Equations (1)–(8) define the eight combinations which describe the FID of the resulting magnetization:

$$F_1(t_b, t_a) = \cos(\omega_x t_b/3)\cos(\omega_y t_b/3)\cos(\omega_z t_b/3)\exp(i\omega_z t_a) \quad (1)$$

$$F_2(t_b, t_a) = -\sin(\omega_x t_b/3)\sin(\omega_y t_b/3)\cos(\omega_z t_b/3)\exp(i\omega_z t_a) \quad (2)$$

$$F_3(t_b, t_a) = -\sin(\omega_x t_b/3)\cos(\omega_y t_b/3)\sin(\omega_z t_b/3)\exp(i\omega_z t_a) \quad (3)$$

$$F_4(t_b, t_a) = -\cos(\omega_x t_b/3)\sin(\omega_y t_b/3)\sin(\omega_z t_b/3)\exp(i\omega_z t_a) \quad (4)$$

$$F_5(t_b, t_a) = \sin(\omega_x t_b/3)\cos(\omega_y t_b/3)\cos(\omega_z t_b/3)\exp(i\omega_z t_a) \quad (5)$$

$$F_6(t_b, t_a) = \cos(\omega_x t_b/3)\sin(\omega_y t_b/3)\cos(\omega_z t_b/3)\exp(i\omega_z t_a) \quad (6)$$

$$F_7(t_b, t_a) = \cos(\omega_x t_b/3)\cos(\omega_y t_b/3)\sin(\omega_z t_b/3)\exp(i\omega_z t_a) \quad (7)$$

$$F_8(t_b, t_a) = -\sin(\omega_x t_b/3)\sin(\omega_y t_b/3)\sin(\omega_z t_b/3)\exp(i\omega_z t_a) \quad (8)$$

The corresponding phase of the projection pulses, p_1, p_2, and p_3, are listed in Table 1. These equations can be combined using the three angle formulas to give

$$F_1(t_b, t_a) + F_2(t_b, t_a) + F_3(t_b, t_a) + F_4(t_b, t_a) = \cos(\omega_x t_b/3 + \omega_y t_b/3 + \omega_z t_b/3)\exp(i\omega_z t_a) \quad (9)$$

and

$$F_5(t_b, t_a) + F_6(t_b, t_a) + F_7(t_b, t_a) + F_8(t_b, t_a) = \sin(\omega_x t_b/3 + \omega_y t_b/3 + \omega_z t_b/3)\exp(i\omega_z t_a) \quad (10)$$

Remembering that

$$\omega_{iso} t_b = (\omega_x + \omega_y + \omega_z) t_b/3 \quad (11)$$

introduction of a second independent imaginary unit j into equation (11) and adding equations (9) and (10) creates a

Table 1 The Basic Phase Table for the Model Pulse Sequences in Figures 1 and 2[a]

nt	1	2	3	4	5	6	7	8	9	10	11	12	13	14	15	16
p_0	$+x$	$+x$	$+x$	$+x$	$-x$	$-x$	$-x$	$-x$	$+x$	$+x$	$+x$	$+x$	$-x$	$-x$	$-x$	$-x$
p_1	$+y$	$+x$	$+x$	$+y$	$+y$	$+x$	$+x$	$+y$	$+x$	$+y$	$+y$	$+x$	$+x$	$+y$	$+y$	$+x$
p_2	$+y$	$+x$	$+y$	$+x$	$+y$	$+x$	$+y$	$+x$	$+y$	$+x$	$+y$	$+x$	$+y$	$+x$	$+y$	$+x$
p_3	$+y$	$+y$	$+x$	$+x$	$+y$	$+y$	$+x$	$+x$	$+y$	$+y$	$+x$	$+x$	$+y$	$+y$	$+x$	$+x$
R	$+x$	$-x$	$-x$	$-x$	$-x$	$+x$	$+x$	$+x$	$-x$	$-x$	$-x$	$+x$	$+x$	$+x$	$+x$	$-x$
M	M_1	M_2	M_3	M_4	M_1	M_2	M_3	M_4	M_5	M_6	M_7	M_8	M_5	M_6	M_7	M_8

[a] R represents the phase for the receiver and M the magnetization being acquired [see equations (1)–(8)];
[b] nt is the transition number.

2D amplitude-modulated hypercomplex FID $F(t_b,t_a)$[8] for each specific crystallite:

$$F(t_b, t_a) = \exp(j\omega_{iso}t_b)\exp(i\omega_z t_a) \quad (12)$$

The acquired FID is simply a powder average of equation (12). Because equation (11) is satisfied for any crystallite orientation, the powder average of the first term in equation (12) remains the same, while the powder average of the second term in equation (12) gives the FID representing a stationary powder pattern. Hence, the evolution dimension is completely separated from the acquisition dimension. The evolution frequency is given simply by the isotropic chemical shift so that the projection of the 2D spectrum onto the evolution dimension axis resembles a MAS spectrum. The stationary powder patterns, which contain the principal value information, are along the acquisition dimension.

A disadvantage of this model MAH pulse sequence is that the transverse magnetization must be projected onto the longitudinal axis three times, with each projection losing a portion of the total magnetization. Improvements in the pulse sequence used for the original MAH experiment have been demonstrated[3] wherein the transverse magnetization is projected only twice, the last one-third of the evolution period is incorporated into the acquisition period, and a conventional echo sequence τ, 180°, τ is inserted between the last read pulse and the start of the data acquisition. These modifications of the model MAH pulse sequence provide an increase in signal-to-noise ratio (S/N) of approximately a factor of $\sqrt{2}$. The improved quality of the base plane associated with these experimental modifications is significant.[3] The revised experiment also incorporates the hypercomplex FID for the evolution dimension according to the two angle formulas by selecting the phase of the projection pulses. The signal intensity from a particular carbon lies along a line defined by $F_b = F_{iso} - (\frac{1}{3})F_a$, where F_{iso} is the isotropic frequency of the carbon. The 2D spectrum obtained in this manner and plotted in a square has the bands inclined relative to the acquisition dimension axis at an angle $\arctan[w_a/(3w_b)]$, where w_b and w_a are the evolution (F_b) and acquisition (F_a) spectral widths, respectively. In order to obtain a 2D spectrum whose projection along one axis gives the isotropic shift spectrum, these data must be sheared through the inclined angle.

The analog of the MAH pulse sequence for the prototype MAT experiment is given in Figure 1(b). A detailed description of the MAT sequence, which was originally proposed by Gan,[2] and subsequent modifications have been given by Hu et al.[4–6] By comparing Figure 1(a) with Figure 1(b), it is clear that these two sequences are similar in timing. Instead of using a series of fast hopping steps, the experiment employs a continuous slow rotation of the sample with pulses spaced at one-third of the rotor period in order to obtain the isotropic shift evolution. The principle involved in the prototype MAT experiment can thus be understood in the following way. For any value of evolution time t_b, the rotation of a specific crystallite about the magic angle axis spans three angles relative to each other by 120° around the circle of rotation during the three evolution segments specified in Figure 1(b). For any given crystallite position in one segment, additional corresponding positions are obtained in the other two rotor segments which are separated by 120°. These three crystallite positions are mutually perpendicular to each other in space. The average of their frequencies is the isotropic chemical shift. Thus, the total phase accumulation at the end of the evolution period is simply

$$\Phi_1 + \Phi_2 + \Phi_3 = \int_0^{t_b} \omega_{iso}\,dt = \omega_{iso}t_b \quad (13)$$

The 2D spectrum obtained in this manner presents a completely sideband-free isotropic chemical shift projection along one axis, with spinning sideband powder patterns projected along the second axis.

The data set produced by the prototype MAT and triple echo MAT experiments have been used to study a number of materials ranging from model compounds to coals.[4,9] The triple echo data must be sheared in order to produce a data set with the evolution and acquisition dimensions properly displayed along the F_b and F_a dimensions. The triple echo spectra have minor spectral artifacts which become evident when one simulates the entire 2D dataset.[6]

A powerful variation of the MAT experiment is called the PHase cORrected MAT (PHORMAT) method which overcomes a number of limitations of previous MAT implementations.[6] The new experiment produces spectra which project a spinning sideband-free isotropic shift spectrum onto the evolution axis without the need for spectral shearing. Echo pulses are incorporated into the pulse sequence in such a way that the magnetization refocuses exactly, despite the modulation of the chemical shift by the rotation of the sample. The resultant spectra are free of artifacts and can be fitted with simulations to extract the principal values of chemical shift tensors with high precision.[6]

The PHORMAT method employs the two pulse sequences shown in Figure 2. The sequences work to convert phase modulation to amplitude modulation, creating the equivalents of positive and negative evolution times by placing 180° echo pulses either before or after the three accumulation periods. FIDs corresponding to positive evolution times are obtained from the + pulse sequence in Figure 2. By selecting the phase of the projection pulses p_1 and p_2, four + pulse sequence FIDs are obtained which are amplitude-modulated by the cosines and sines of the precession angles $(-\alpha_1 + \beta_1 + \Phi_1)$ and $(-\alpha_2 + \beta_2 + \Phi_2)$ which accumulate during the first and second sections of the evolution period. Phase modulation by the precession angle $(-\alpha_3 + \beta_3 + \Phi_3)$ accumulates during the third section of the evolution period. The individual FIDs are thus

$$F_{CC}^{+} = \cos(-\alpha_1^{+} + \beta_1^{+} + \Phi_1^{+})\cos(-\alpha_2^{+} + \beta_2^{+} + \Phi_2^{+}) \times \exp[i(-\alpha_3^{+} + \beta_3^{+} + \Phi_3^{+})]F_a(t_a) \quad (14a)$$

$$F_{CS}^{+} = \cos(-\alpha_1^{+} + \beta_1^{+} + \Phi_1^{+})\sin(-\alpha_2^{+} + \beta_2^{+} + \Phi_2^{+}) \times \exp[i(-\alpha_3^{+} + \beta_3^{+} + \Phi_3^{+})]F_a(t_a) \quad (14b)$$

$$F_{SC}^{+} = \sin(-\alpha_1^{+} + \beta_1^{+} + \Phi_1^{+})\cos(-\alpha_2^{+} + \beta_2^{+} + \Phi_2^{+}) \times \exp[i(-\alpha_3^{+} + \beta_3^{+} + \Phi_3^{+})]F_a(t_a) \quad (14c)$$

and

$$F_{SS}^{+} = \sin(-\alpha_1^{+} + \beta_1^{+} + \Phi_1^{+})\sin(-\alpha_2^{+} + \beta_2^{+} + \Phi_2^{+}) \times \exp[i(-\alpha_3^{+} + \beta_3^{+} + \Phi_3^{+})]F_a(t_a) \quad (14d)$$

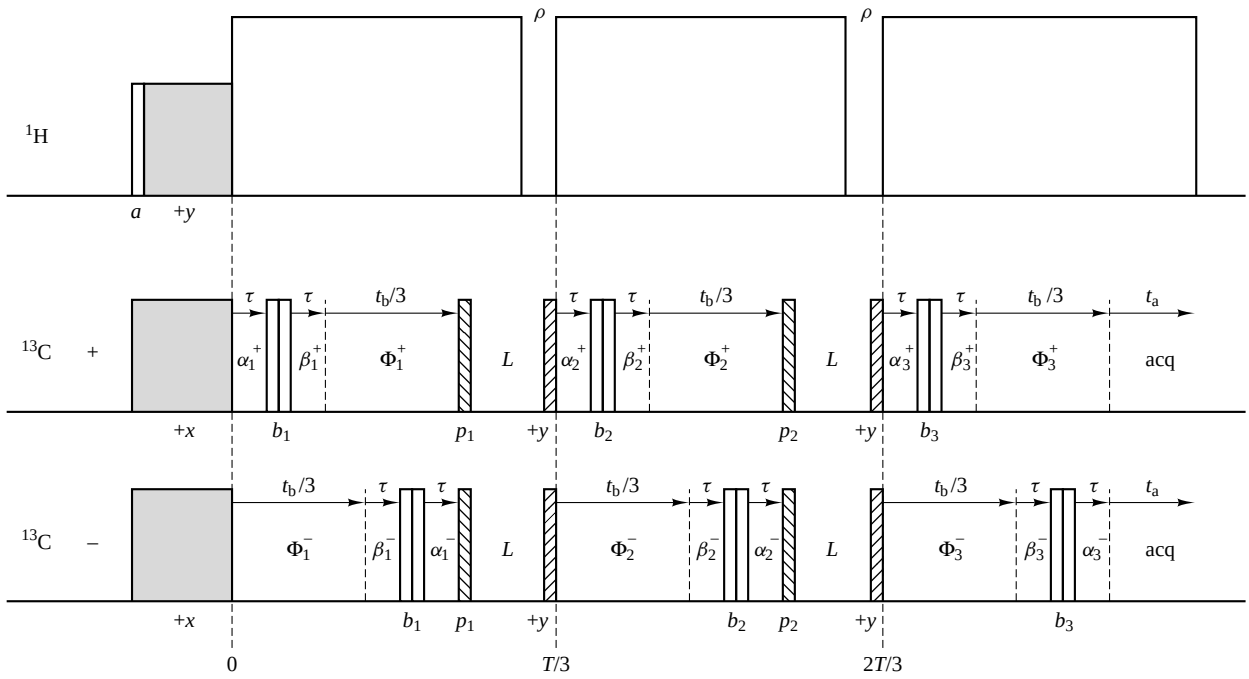

Figure 2 Pulse sequences of the PHORMAT experiment

Again, $F_a(t_a)$ is the acquisition FID which would follow a single 90° pulse. These four FIDs can be combined as

$$F^+ = F^+_{CC} - F^+_{SS} + iF^+_{CS} + iF^+_{SC} \tag{15}$$

where multiplication by $i = \sqrt{-1}$ means a 90° phase shift of the acquisition dimension FID. It can be shown[6] that this combination yields simply

$$F^+ = \{\cos(\omega_{iso} t_b) + i\sin(\omega_{iso} t_b)\} F_a(t_a) \tag{16}$$

FIDs corresponding to negative evolution times are obtained from the − pulse sequence in Figure 2 which interchanges the order of the evolution time and the echo sequences. These FIDs are

$$F^-_{CC} = \cos(+\alpha_1^- - \beta_1^- - \Phi_1^-)\cos(+\alpha_2^- - \beta_2^- - \Phi_2^-) \times \exp[i(+\alpha_3^- - \beta_3^- - \Phi_3^-)] F_a(t_a) \tag{17a}$$

$$F^-_{CS} = \cos(+\alpha_1^- - \beta_1^- - \Phi_1^-)\sin(+\alpha_2^- - \beta_2^- - \Phi_2^-) \times \exp[i(+\alpha_3^- - \beta_3^- - \Phi_3^-)] F_a(t_a) \tag{17b}$$

$$F^-_{SC} = \sin(+\alpha_1^- - \beta_1^- - \Phi_1^-)\cos(+\alpha_2^- - \beta_2^- - \Phi_2^-) \times \exp[i(+\alpha_3^- - \beta_3^- - \Phi_3^-)] F_a(t_a) \tag{17c}$$

and

$$F^-_{SS} = \sin(+\alpha_1^- - \beta_1^- - \Phi_1^-)\sin(+\alpha_2^- - \beta_2^- - \Phi_2^-) \times \exp[i(+\alpha_3^- - \beta_3^- - \Phi_3^-)] F_a(t_a) \tag{17d}$$

These FIDs are similarly combined as

$$F^- = F^-_{CC} - F^-_{SS} + iF^-_{CS} + iF^-_{SC} \tag{18}$$

giving

$$F^- = \{\cos(\omega_{iso} t_b) - i\sin(\omega_{iso} t_b)\} F_a(t_a) \tag{19}$$

The composite FIDs F^+ and F^- are then combined to form the real and imaginary parts of a hypercomplex 2D FID

$$F_R = \cos(\omega_{iso} t_b) F_a(t_a) = +\tfrac{1}{2}(F^+ + F^-) \tag{20a}$$

and

$$F_I = \sin(\omega_{iso} t_b) F_a(t_a) = -\tfrac{i}{2}(F^+ - F^-) \tag{20b}$$

Again using the second imaginary unit $j = \sqrt{-1}$ for the evolution dimension, the 2D hypercomplex FID can be written

$$F = F_R + jF_I = \exp(j\omega_{iso} t_b) F_a(t_a) \tag{21}$$

This 2D FID transforms to an absorption–absorption phased 2D spectrum that projects an isotropic shift spectrum with no spinning sidebands onto the evolution dimension axis.

Equation (21) has been derived in the absence of relaxation. The effect of transverse relaxation during the evolution time can be included by writing

$$F = \exp(-6\tau/T_2)\exp(-t_b/T_2)\exp(j\omega_{iso} t_b) F_a(t_a) \tag{22}$$

The $\exp(-t_b/T_2)$ term gives the evolution dimension linewidth. The term $\exp(-6\tau/T_2)$ attenuates the response by a factor which depends on T_2, which may differ for the various spins in the molecule. The delay τ, which allows time for receiver recovery and probe ringdown, can be made short enough that this attenuation has a minimal effect on the signal-to-noise (S/N) ratio for all but the shortest values of T_2. When accurate spin counts are required, corrections for this attenuation

can be made for each spin by using the values of T_2 determined from the analysis of each spin's evolution dimension linewidth.

The eight FIDs are always used in the combinations in equations (15) and (18). The pulse phase cycles which produce these composite FIDs are given in Table 1. The phase cycles for the + and − sequences are identical. Phase cycling the 90° projection pulses p_1 and p_2 suppresses baseplane artifacts from longitudinal relaxation during the two periods labeled L in Figure 2. Phase cycling the initial proton 90° pulse inverts the spin temperature. The phase cycling of the 180° pulses b_1, b_2, and b_3 further suppresses baseplane artifacts. The phases of the proton and carbon spin locking pulses and the 90° carbon tipping pulses are fixed.

Both PHORMAT pulse sequences include two periods, labeled L in Figure 2, during which one component of the magnetization is stored along the longitudinal axis and the other component is purged by transverse relaxation. The decoupling is interrupted for a constant time ρ at the end of these periods to ensure effective purging. Turning the decoupler off for the entire L period is avoided because the decoupler duty cycle would then change as t_b is incremented, and the resultant variable heating could detune the probe.

Any variation in the rotor frequency experienced during the PHORMAT experiment will degrade the resolution if the pulse sequences employ fixed times to approximate one-third of the rotor period. Two contrasting strategies exist for maintaining the resolution. The pulse sequences can remain fixed and the rotor frequency stabilized with a feedback system to control the airflow. Alternatively, the rotor frequency can be allowed to vary over a restricted range, and the pulse sequences synchronized to one-third the actual rotor period.

The PHORMAT experiment combines all of the desirable features of the prototype MAT[4,6] and the 5-π MAT experiments:[5] (i) spinning sidebands are absent from the evolution dimension at any rotor frequency; (ii) a pure absorption–absorption phased spectrum without phase-twist is produced; (iii) the evolution dimension displays the pure isotropic shift spectrum, avoiding the need for spectral shearing and using the evolution dimension spectral width efficiently; (iv) the cancellation of the phase accumulations during the echo sequences is exact because all three 180° pulses are included in the evolution period; (v) the minimum number of projection pulses is required, improving the signal-to-noise ratio; (vi) there is at least a time τ between the last transmitter pulse and the acquisition, allowing time for probe ringdown and receiver recovery; and (vii) the experiment approximately preserves the integrated volumes of the peaks when τ is short, thus enabling quantitative spin counting.

The PHORMAT experiment obtains the isotropic shift spectrum in the evolution dimension, with the attendant disadvantage that isotropic resolution is obtained at the expense of experimental time. However, on the other hand, the experiment obtains the principal values directly from the acquisition dimension, which displays the unperturbed

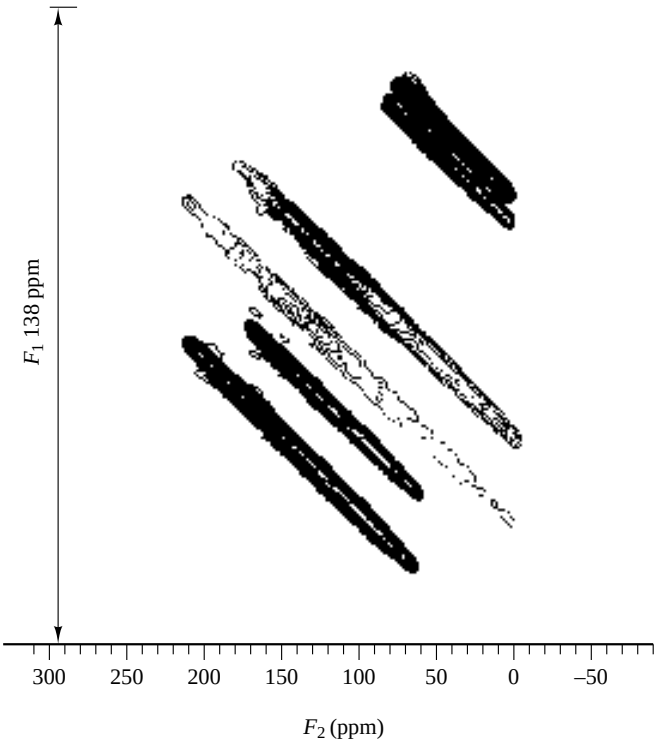

Figure 3 The contour plot 2D MAH spectrum of 1,2,3-trimethoxybenzene. The experiment was performed on a Bruker CXP-200 spectrometer with a ^{13}C frequency of 50.304 MHz. Approximately 4 g of the sample were used for the experiment. With the hopping mechanism used, 60 ms were required for each 120° sample hop. This spectrum was obtained with the following experimental conditions: an echo delay time Δ of 200 μs, a contact time of 4 ms, a recycle delay of 8 s, an acquisition dwell time of 48 μs, and a t_1 increment of 144 μs. A 2D spectrum was obtained with the isotropic chemical shift axis inclined at an angle of 45° to the F_2 axis. The dataset contained 32 t_1 values. Data were acquired for 128 scans in the real data set and 128 scans in the imaginary data set for a total measuring time of about 19 h. The decoupler offset was set such that a 34 kHz decoupling field was centered at a frequency corresponding to the center of the aromatic ^1H chemical shift range in the compound to optimize the lineshape of the protonated aromatic carbons. No line broadening was applied in either dimension

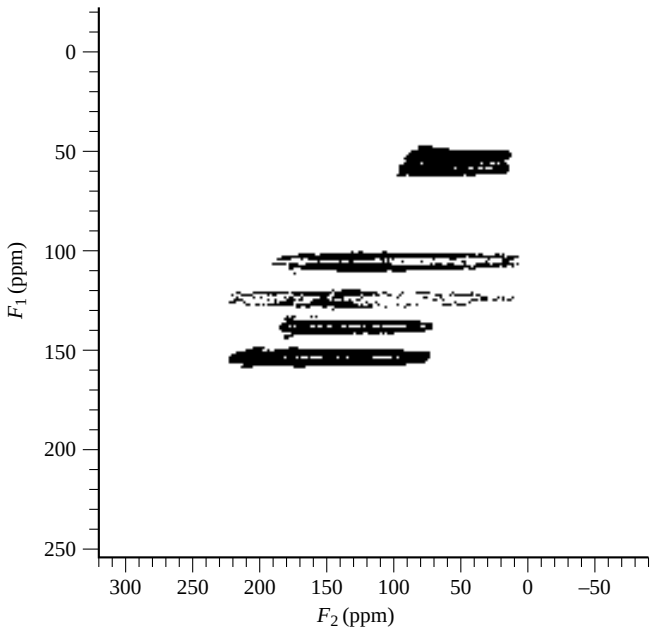

Figure 4 The 45° sheared spectrum of Figure 3

spectrum of a slowly rotating sample with no scaling factors subject to errors from pulse imperfections.

3 EXPERIMENTAL RESULTS

The 2D contour plot spectrum given in Figure 3 for 1,2,3-trimethoxybenzene (TMB) was produced by the MAH experiment using the pulse sequence described by Hu et al.[3] Shearing the data in Figure 3 by 45° produces a 2D contour plot with the isotropic shift lying along the F_b axis, shown in Figure 4, while the anisotropic information is preserved along the F_a axis. The isotropic chemical shift spectrum shown in Figure 5 was obtained by projecting the data shown in Figure 4 onto the F_b axis. Spectral slices corresponding to each isotropic chemical shift were extracted, giving the powder patterns shown in Figure 6. The tensor components obtained by manually picking the breakpoint in these slices are in good agreement with those obtained from a single crystal study[10] and are given in Table 2. However, due to the mechanical difficulties in accurately setting the magic angle as well as precisely accomplishing each 120° sample hop, the resolution achieved with this experiment in the isotropic chemical shift dimension was limited to approximately 5 ppm. The MAH experiment was not capable of resolving methyl groups M_1 and M_3 whose isotropic shifts differed by 1 ppm. Fortunately, these difficulties associated with the MAH experiment are successfully circumvented by the MAT experiments since the magic angle can be set precisely experimentally and a constant slow spinning rate can be easily achieved with a homebuilt large rotor system. The enhanced resolution obtained on TMB with the triple echo MAT experiment (which successfully resolved the methyl groups M_1 and M_3) has been previously demonstrated.[4] The principal values of the chemical shift tensor were obtained by directly measuring the shifts of the peaks and the breakpoints at the halfheight positions.

The enhanced quality of the PHORMAT experiment is illustrated in the 2D contour plot of 1,2,3-TMB in Figure 7 obtained by using the pulse sequence of Figure 2. The isotropic chemical shift projection was obtained in the same way as previously described for the MAH and prototype MAT experiments. The resolution of methyl groups M_1 and M_2 achieved in TMB can be observed in the 2D contour plot and the projection of the isotropic shifts onto the evolution dimension demonstrates line separation nearly to the baseline for these two carbons. Even so, the presence of Gibb's wiggles, due to premature truncation in the evolution dimension, indicates that higher resolution would be available from this sample if sufficient time increments were employed

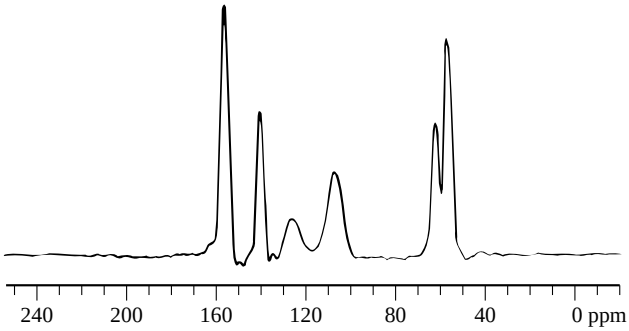

Figure 5 The isotropic chemical shift projection spectrum of Figure 4

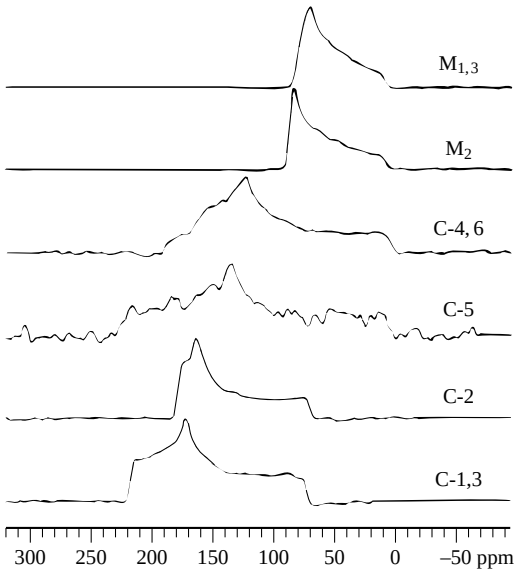

Figure 6 The powder pattern of each individual carbon in TMB obtained by the MAH experiment

Table 2 The Principal Values of ^{13}C Chemical Shift Tensors in 1,2,3-Trimethoxybenzene Obtained by the MAH[a] and the PHORMAT Experiments

Assignments	δ_{11}	δ_{22}	δ_{33}	$\delta_{average}$
M_1	81[81](83)	70[70](71)	10[10](9)	54[54](54)
M_2	86[87](88)	81[83](83)	10[10](10)	59[60](60)
M_3	82[81](82)	69[70](70)	14[10](13)	55[54](55)
C-1	218[217](218)	173[172](172)	73[73](73)	154[154](154)
C-3	218[217](217)	173[172](172)	73[73](72)	154[154](153)
C-2	180[179](179)	165[164](164)	73[71](71)	139[138](138)
C-4	190[188](187)	125[122](123)	7[6](7)	107[105](106)
C-6	190[188](186)	125[122](121)	7[6](8)	107[105](105)
C-5	223[b][225](227)	134[138](136)	11[9](10)	123[124](124)

[a]The data in brackets are from the MAH experiment[3] and the data in parentheses are from a single crystal study.[10] The remainder of the data are from the PHORMAT experiment. The data for MAH and PHORMAT experiments are referenced to TMS with an estimated error of less than ±2 ppm.

[b]Due to the low S/N for C-5 the value for δ_{11} was obtained from the isotropic shift and the other two break-point values for δ_{22} and δ_{33}.

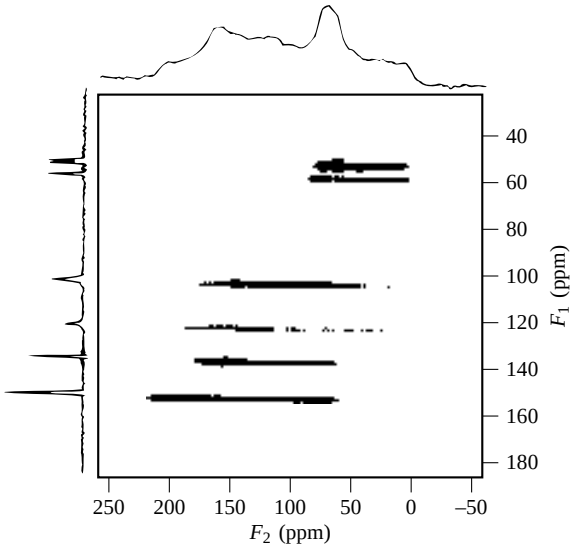

Figure 7 Contour plot of the PHORMAT spectrum of 1,2,3-trimethoxybenzene (TMB). The lowest contour level and the contour interval are 5% of the maximum peak height. Only one-half of the acquisition dimension spectral width is shown. The experiment was performed on a Varian VXR-200 NMR spectrometer with a ^{13}C frequency of 50.309 MHz. Approximately 5 g of sample were used for the experiment. This spectrum was obtained with the following experimental conditions: sample spinning rate 30 Hz with rotor synchronization, an echo delay time (τ in the pulse sequence diagram) 60 μs, a contact time of 4 ms, a recycle delay of 8 s, an acquisition dwell time of 40 μs, a t_1 increment of 120 μs. The decoupler interruption time was 250 μs. The data set contained 218 t_1 values. Data were acquired for 32 scans in the real data set and 32 scans in the imaginary data set for a total measuring time of 3 d. The decoupler offset was set such that a decoupling field (approximately 48 kHz) was centered in the middle of the aromatic ^{1}H chemical shift range in the compound. No line broadening was applied in the evolution dimension, but there was a 2 ppm line broadening on the acquisition dimension. The isotropic chemical shift spectrum is projected onto the left side of the 2D contour. The presence of Gibb's wiggle indicates more resolution is attainable by acquiring with more t_1 increments

in the experimental parameters. In the MAT experiments one obtains approximately the same resolution as that achieved in a traditional CP MAS spectrum. Projection of the overlapping powder patterns onto the acquisition dimension illustrates how hopeless it would be to try to interpret the data if one were constrained to work in only one dimension.

The resolution obtained in the 2D contour plot of TMB is sufficient to distinguish the minor difference between the δ_{33} components of M_1 and M_3. The CSA principal values obtained by simulating the 1D spectral slices taken at the isotropic shift values are listed in Table 2. In a separate study of methyl α-D-glucopyranoside, two lines with isotropic shift separation of 0.7 ppm were successfully resolved[6] and the precision of the principal values was within an rms average distance of only 0.57 ppm when compared with values obtained from a careful single crystal study. Selected individual powder patterns obtained with the PHORMAT sequence are displayed in Figure 8. The high resolution of the MAT experiments and the ability of the technique for sorting overlapping tensors with the same isotropic chemical shift value has been demonstrated in 2,3-dimethylnaphthalene[4] as well as in such

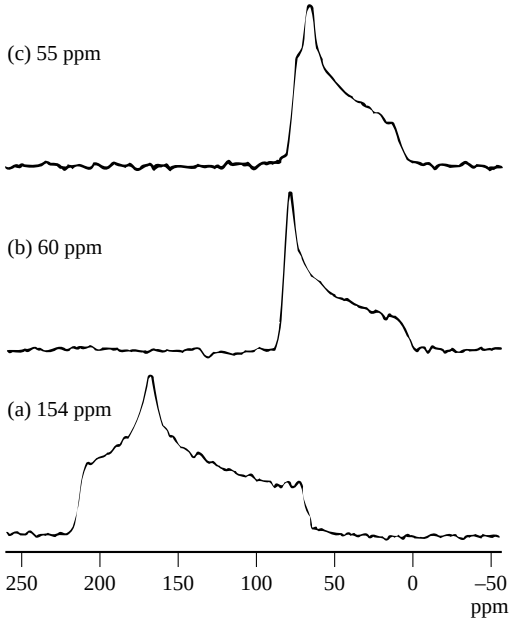

Figure 8 The powder patterns of three selected carbons in TMB at indicated isotropic chemical shifts: (a) 154 ppm slice; (b) 60 ppm slice; and (c) 55 ppm slice

complex materials as a naphthalene-derived pitch and a series of coals.[9]

4 CONCLUSIONS

The data presented in this paper demonstrate that the magic angle hopping and magic angle turning experiments can be used to obtain ^{13}C principal values in a powdered solid by separating tensor powder patterns according to their isotropic shifts. The chemical shift principal value data obtained from the PHORMAT experiment has been found to approximate closely the values obtained from single crystal experiments. The major problems associated with obtaining MAS spectra at high fields, the very high spinning speeds required to suppress or separate sidebands, and the consequent difficulty in uniformly polarizing all spins are eliminated by the MAH and MAT experiments. Large sample volume systems have been used to enhance the sensitivity of these experiments and a typical 2D measurement can be obtained in a reasonable (e.g. 1–2 d) amount of time. Because of the simplicity in accurately setting the magic angle, a particular advantage of MAT experiments over MAH is found in the high-resolution feature of the experiments. In the isotropic chemical shift dimension, the spectral resolution of the MAT experiments is approximately the same as that of a traditional CP MAS experiment. The PHORMAT experiment produces 2D spectra with flat baseplanes and the absence of other troublesome artifacts which permits ready simulation of the entire 2D data set.

5 RELATED ARTICLES

Chemical Shift Tensor Measurement in Solids; Chemical Shift Tensors; Chemical Shift Tensors in Single Crystals; Coal Structure from Solid State NMR.

6 REFERENCES

1. A. Bax, N. M. Szeverenyi, and G. E. Maciel, *J. Magn. Reson.*, 1983, **52**, 147.
2. Z. Gan, *J. Am. Chem. Soc*., 1992, **114**, 8307.
3. J. Z. Hu, A. M. Orendt, D. W. Alderman, C. Ye, R. J. Pugmire, and D. M. Grant, *Solid State NMR*, 1993, **2**, 235.
4. J. Z. Hu, A. M. Orendt, D. W. Alderman, R. J. Pugmire, C. Ye, and D. M. Grant, *Solid State NMR*, 1994, **3**, 181.
5. J. Z. Hu, D. W. Alderman, C. Ye, R. J. Pugmire, and D. M. Grant, *J. Magn. Reson. Ser. A*, 1993, **105**, 82.
6. J. Z. Hu, W. Wang, F. Liu, M. S. Solum, D. W. Alderman, and R. J. Pugmire, *J. Magn. Reson., Ser. A*, 1995, **113**, 210.
7. M. M. Maricq and J. S. Waugh, *J. Chem. Phys*., 1979, **70**, 3300.
8. R. R. Ernst, G. Bodenhausen, and A. Wokaun, *Principles of Nuclear Magnetic Resonance in One and Two Dimensions*, Clarendon Press, Oxford, 1987.
9. J. Z. Hu, M. S. Solum, D. W. Alderman, R. J. Pugmire, C. Ye, and D. M. Grant, *Energy Fuels*, 1995, **9**, 717.
10. C. M. Carter, J. C. Facelli, D. W. Alderman, and D. M. Grant, *J. Chem. Soc., Faraday Trans. 1*, 1988, **84**, 3673.

Biographical Sketches

Jian Zhi Hu. *b* 1962. B.S., 1983, M.S., 1986, University of Lanzhou, Ph.D., 1994, joint training between Wuhan Institute of Physics and the University of Utah. Assistant professor, Wuhan Institute of Physics, 1988–present, where he was introduced to NMR by Chaohui Ye; currently undertaking postdoctoral work at the University of Utah. Approximately 20 publications. Research interests solid state NMR.

Wei Wang. *b* 1962. B.S., 1984, Tsinghua University, Ph.D., 1993, University of Illinois at Urbana-Champaign. Trained in EPR by R. Linn Belford. Postdoctoral, University of Utah, 1993–1995, where he was introduced to NMR by David M. Grant and Ronald J. Pugmire. Approximately 10 publications. Research interests: applications of magnetic resonance in solid state chemistry.

Ronald J. Pugmire. *b* 1937. B.S., 1959, Idaho State College, Ph.D., 1966, Chemistry, University of Utah, USA, where he was introduced to NMR by David M. Grant. Postdoctoral research, University of Utah, 1966–68. Faculty in Chemical and Fuels Engineering, and Associate Vice President for Research, University of Utah, 1968–present. Approximately 155 publications. Research specialties: carbon-13 NMR, chemical shielding in liquids and solids, coal chemistry and applications of NMR spectroscopy in coal science.

Magic-angle Spinning Extensions

A. Samoson

National Institute of Chemical Physics and Biophysics, Tallinn, Estonia

1 Introduction 1
2 Principles of High Speed Rotation 1
3 Practical Considerations 2
4 Applications Specific to High Speeds 3
5 Conclusions 5
6 References 5

1 INTRODUCTION

Fast mechanical rotation is used in diverse situations, ranging from the gentle breeze of a dental drill, spinning at 5–7 kHz, to the roar of aircraft jet turbines with 500 m s^{-1} tip speeds. Rotation frequencies of 23 kHz have been achieved with microfabricated single crystal silicon turbines, representing a level of fast developing microelectromechanical systems.[1] The ultimate example was recently demonstrated by rotating a single molecule:[2] Cl_2 was polarized by a strong electrical field, oscillating at a frequency of 370 THz. Despite rapid alternation of the electric field polarity, the molecule lines up with the axis of the field. The alignment energy of 50 meV is actually about one million times larger than the proton Zeeman energy in a 11.7 T magnet. The axis of the oscillation of the electric field was then made to rotate by combining frequency modulated circularly polarized laser beams. The molecule followed adiabatically up to 4.1 THz, at this point two atoms dissociated.

Several branches of spectroscopy benefit from fast rotation. A high peripheral speed can be used to provoke Doppler shifts in gamma spectroscopy.[3] Line narrowing due to a wavefunction phase summation at three different sample positions was demonstrated in ESR.[4] However, due to exceptionally low transition energies and long relaxation rates, the most beneficial application of the fast rotation has been in NMR.

The magnetic field, used in NMR as a generator of the spin energy levels, has one inherent drawback: the axial nature. If nonoriented solid samples are studied, the observable signal sums up from all spectral transition frequencies determined by the orientation of the field direction in atomic coordinates, instead of a single scalar value required for the best resolution. The field orientation dependency can be suppressed by fast mechanical reorientation of the sample. One particular field trajectory has proven specially efficient. It is described by a rotation at an angle, derived from a root of a second order Legendre polynomial. The rotation angle is equal to the angle between the body diagonal of the cube and one of its edges and the trajectory of the magnetic field can be regarded as an infinite collection of three orthogonal spatial directions. The intuitive explanation of the averaging effect can thus be related to a cubic approximation of SO_3 symmetry which would perfectly annihilate the original axial nature of the magnetic field. Next (and so far only) regular distributions of field directions follow octahedral symmetry. This can be shown to remove 15 interactions including rank 29 as the highest,[5] if the interactions are classified by symmetry properties of the Legendre polynomials. The key to a scalar measurement process is the speed of the magnetic field reorientation. If the time constant is short compared to the nuclear relaxation and dephasing processes, the scalar value emerges from the spectra. Although a rotation as slow as few hundred revolutions per second (Hertz) may show an effect on the spectra, lines may still be broadened or flanked by sidebands. Higher speeds are usually advantageous and offer more experimental flexibility.

The experimental history of high resolution NMR in solids has thus been a quest for higher spinning speeds. Principally two different rotor designs have been used. First experiments used a conical rotor design, exploiting Bernoulli forces to hold the rotor in the coil.[6] Better stability and higher speeds have been achieved by a double gas bearing system, pioneered by the group of Lippmaa in Tallinn.[7] The design principles are relatively well mastered by now and several implementations have claimed a rotor surface speed exceeding that of the speed of sound in air. However, practical applications are limited to sub-sonic speeds by the dependable strength of the rotor material. The presence of the magnetic field limits the choice of materials to nonconductive ceramics or polymer compounds.

2 PRINCIPLES OF HIGH SPEED ROTATION

The design and successful exploitation of MAS equipment is based on a careful consideration of the stress acting on the rotor wall. The most important equation in high-speed technology of hollow rotors was given by Chree in 1891 and it relates peripheral speed, V, with the ratio of the working strength, T, to the density of the rotor wall material ρ_r[8]

$$V^2 = \frac{T}{\rho_r} \tag{1}$$

For the filled rotors the total force, directed towards the rotor wall, can be evaluated using an analogy with a pressurized vessel (Figure 1).

Each particle with a mass dm, rotating at an angular velocity ω at a distance r from the axis of rotation, is pulled towards the periphery with the force

$$dF = dm\omega^2 r \tag{2}$$

As seen from Figure 1, the mass of the particle with density ρ can be expressed as

$$dm = r \sin\alpha \, dr h \rho \tag{3}$$

where h is a measure of the length of the rotor. Integration over the full radius of the rotor gives

$$F = \int_0^R dF = \frac{1}{3} R^2 \omega^2 \sin\alpha h \rho \tag{4}$$

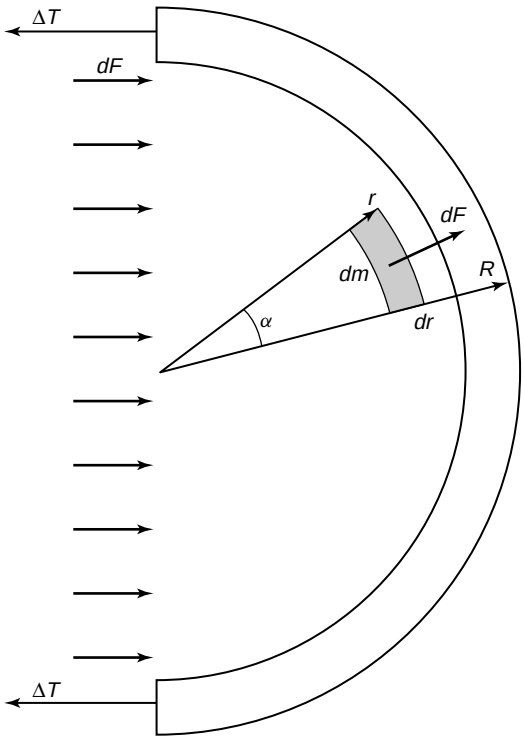

Figure 1 Evaluation of the stress force, acting on the rotor wall

The ratio of the force to surface gives a pressure on the wall of the rotor of

$$P = \frac{1}{3}R^2\omega^2\rho \tag{5}$$

The effective cross section, subject to a uniform pressure, can be trivially expressed as

$$S = 2Rh \tag{6}$$

The total force, acting on a semicylindrical rotor element, should be counterbalanced by a wall strength

$$PS = 2\Delta hT \tag{7}$$

where T represents the tensile strength of the material. From this the basic expression follows immediately

$$\nu = \frac{1}{\pi D}\sqrt{\frac{3T\Delta'}{\rho}} \tag{8}$$

where Δ' is a relative wall thickness.

Although this expression does not take into account the mass of the rotor wall, essential conclusions can be made readily. A convenient measure is a product of the rotor diameter and speed (mm × kHz or m × Hz). This, along with the sample density, gives the load on the rotor wall. The maximum load is determined by the wall thickness and tensile strength.

The support for high speed rotors is provided typically by gas lubricated bearings. The reason is not only the low friction, but also a certain freedom for self-balancing. This freedom is given by the gap of the order of few tens of micrometers between the bearing surface and the rotor. The principle of self-balancing was established by De Laval in 1889. According to this principle, rotors spin about the principal axis of inertia rather than the axis of symmetry after passing critical frequencies. The critical frequencies are determined by the stiffness of the bearing and the mass of the rotor and are typically of the order of a few kilohertz for high speed rotors. A brief reduction of the bearing gas pressure lowers the stiffness and may promote passing of the resonance region during the rotor startup. Many details about construction of turbines with gas driven rotors can be found in a seminal paper by Doty and Ellis.[9]

3 PRACTICAL CONSIDERATIONS

Obviously, the most straightforward way to increase the top speed that is still sustainable by the rotor is to reduce the rotor diameter. A further improvement can be brought about by a careful selection of the rotor material, due to the inverse square root dependency on the tensile strength. For polymers, the tensile strength is determined by a limit of spatial expansion. A relatively low Young's modulus of most polymers prevent them from reaching high speeds, since rotor expansion is sufficient to quench a lubrication of the gas bearing. Better performance can be expected from more rigid ceramics, despite their brittleness. For nonductile ceramics the tensile strength is set by a fracture limit. A rigorous estimation of the critical rotation frequency, associated with material disintegration, is complicated for technical ceramic materials. An unrealistically detailed picture of microscopic processes is required. The mechanical properties of two frequently used compounds, zirconia and silicon nitride, depend sensitively on their preparation history. Both are typically powder sintered, resulting in quite inhomogeneous structure. They are characterized by an average grain size, the grain size distribution and adhesion quality. Zirconia derives its strength from a martensic phase transformation. At a room temperature, zirconia is stable in its monoclinic crystal phase. With special processing, parts of the material can be made to retain a high-temperature tetragonal phase, which is 3–5% more compact.[10] If this partially stabilized zirconia (PSZ) is subjected to a mechanical load, cracks eventually start to form. High stresses around the crack tip trigger the expansive phase transformation to low density form, squeezing further crack propagation.

Various (semi)macroscopic parameters are used to estimate the mechanical properties of the ceramic materials. The most widespread property, fracture toughness, requires a knowledge of critical flaw size and gives only an indirect estimate for the rupture limit.[11] More pertinent flexural strength is estimated usually from bending tests. The three point bending test characterizes a material only over a relatively small volume; four point bending data are more representative. Overall volume performance is further characterized by a Weibull modulus, m. For NMR rotors, where material strength over the entire specimen is important, $m = 30$ can be considered to provide a reasonable confidence for the strength values. Comparing data from different ceramic providers suggest that tensile strengths of 500–800 MPa can be expected for a well prepared material. This value may change with thermal chocking and continuous stress, especially for zirconia. The strength reduces also with

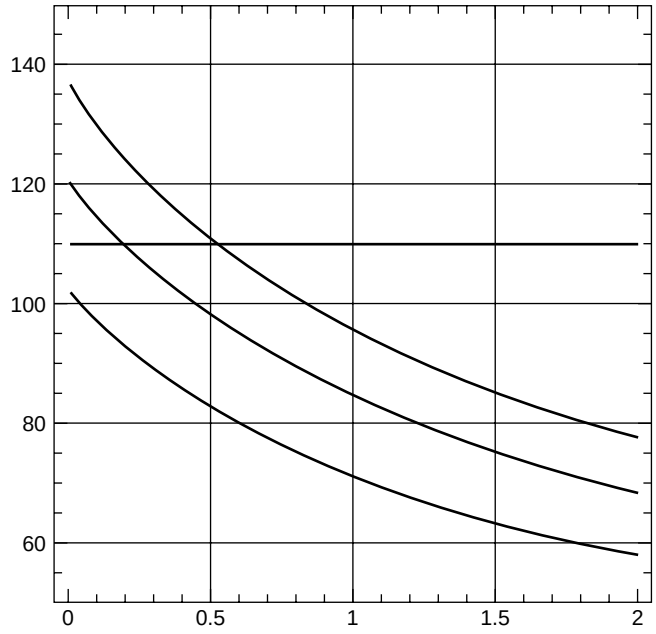

Figure 2 Dependence of the critical speed–diameter product on the ratio of sample density to rotor density. Three plots are given for different relative (i.e., divided by density) tensile strengths 900/6, 700/6 and 500/6 MPa cm^3 g^{-1}, for a wall thickness $\Delta = 0:2$. Horizontal line shows the speed of sound at the rotor surface

an increase of temperature, noticeably already by a few hundred degrees. More involved calculations, which also account for the rotor wall weight, are presented graphically in Figure 2. A bold line marks the speed of sound in air at the surface of the rotor. For a reasonably broad range of sample densities, 100 mm kHz appears as a limit for high-strength materials. Indeed, practical realizations are in agreement with this estimate. In 1997, 2.5-mm rotors, specified up to 33–35 kHz, became commercially available.[12] Speeds of up to 50 kHz with rotors of about 2 mm diameter were demonstrated in 1999 in an academic laboratory (National Institute of Chemical Physics and Biophysics, Tallinn, Estonia).[13] It is instructive to compare these values with the ultimate molecular rotor, as described in the introduction. Considering internuclear distance 0.26 nm at the breaking point, ca. 1000 mm kHz as a product of the maximum rotation speed and diameter can be evaluated. This is merely an order of magnitude more than achieved with the macroscopic MAS rotor.

Several artifacts accompany the high speed experiments. The sample is subjected to a stress gradient, ranging from 0 to about 10^6 g at the periphery. This may for example broaden lines of quadrupole nuclei due to piezoelectric effects. Another potential complication may be the sample heating. Friction with the surrounding atmosphere becomes quite noticeable at high speeds. As brought to the attention of the NMR community in Ref.[14] the surface temperature heats up as a quadratic function of the speed.[15] The isotropic shift of Pb in lead nitrate is a convenient thermometer for solid state NMR.[16] Deduced temperatures, measured up to speeds 40 kHz,[13] indeed follow closely the quadratic speed dependency (Figure 3). The upper data point was deliberately limited to 40 kHz in view of the exceptionally high density (4.53) of lead nitrate. Extrapolation to 50 kHz, and using a conversion factor 0.753 ppm degree^{-1}

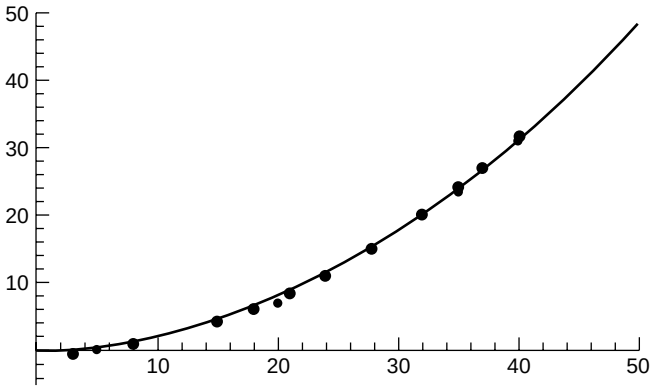

Figure 3 Dependence of 207 $Pb(NO_3)_2$ temperature on the rotation speed (kHz)

predicts about a 66° increase in the rotor temperature over ambient.

The problems listed above are present for any size of rotor, reaching critical frequency of the mechanical failure. Specific for the small rotors is a loss of the signal due to a reduced amount of the sample. On the other hand, smaller resonance coils provide higher rf fields.

4 APPLICATIONS SPECIFIC TO HIGH SPEEDS

As explained above, reliable speed range can most efficiently be increased with reduction of the rotor diameter. Disregarding a trivial case of economy with expensive isotope-labelled or otherways limited samples, this is generally considered in NMR to be a disadvantage. For a majority of routine applications, spinning at 10–15 kHz gives adequate spectral quality. The problem associated with the reduction of the number of resonating nuclei is gradually alleviated by advances in magnet technology. Moreover, proliferation of the high-field magnets naturally demands faster spinning to keep in par with increased anisotropy and spectral expansion. There are also a number of special experimental situations, where the quality or even the feasibility of the measurements depend on the speed of rotation.[17]

Of the many nuclear recoupling methods, adiabatic two spin coherence generation, based on avoided level crossings (DREAM),[18] is remarkably insensitive to specific parameters of (inter)nuclear interactions. The key mechanism of nuclear dipolar recoupling, the so-called HORROR condition,[19] is only efficient when sample rotation frequency is exactly two times larger than the locking rf field amplitude. To be broadbanded enough to cover a typical carbon-13 spectrum, the rf amplitude should be comparable to (or larger than) the spectral width of carbon at the magnetic field applied. An example of the speed dependency is illustrated in Figure 4. The DREAM-filtered double quantum spectra of antamanide, cyclic decapeptide, have been recorded under otherwise identical conditions at two speeds, 20 and 40 kHz. Drastic differences can be observed in the aliphatic region of the spectra.

The rotation speed increase can be useful in the spectroscopy of quadrupole nuclei. A single quantum second-order linewidth features a definite value under the magic angle spinning conditions. For very strong quadrupole coupling constants, high speeds are required to separate the centerband

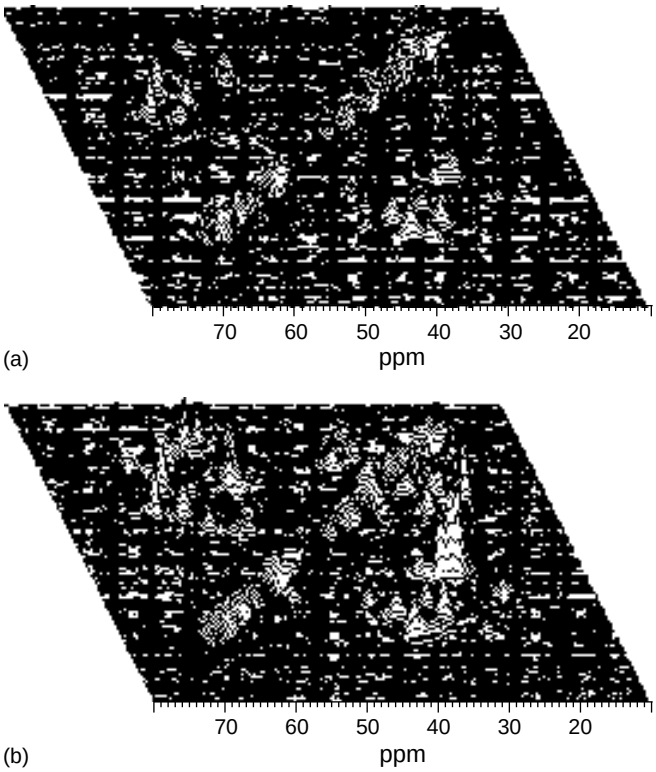

Figure 4 A comparison of 20 and 40 kHz ^{13}C DREAM spectra of antamanide. High speed spectra also exhibit some negative peaks due to the second polarization transfer during adiabatic passage. Spectra were acquired by A. Verhoeven and R. Verel, B. Meier NMR group, ETH Zürich

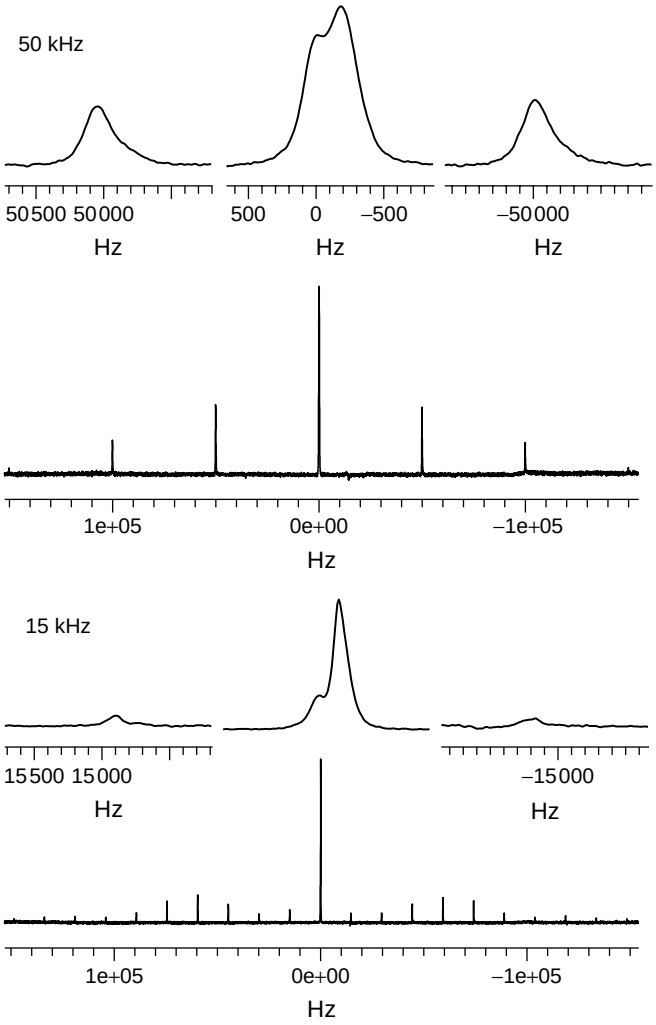

Figure 5 ^{23}Na spectra of $NaNO_3$ at 53 MHz. Expanded plots show centerbands and respective first sidebands, formed by the overlapping $(3/2 \rightarrow 1/2, -1/2 \rightarrow -3/2)$ satellite transitions of the spin 3/2 nucleus. The sideband pattern in the low speed spectrum indicates a shape of the first order quadrupole broadening of the satellite transitions. At the high speed, the centerband of the satellite transition has an intensity, comparable to that of the central transition. The two peaks are shifted due to the second quadrupolar effect

from sidebands.[20] Even more crucial is the rotation speed for registration of the satellite transitions, which are subject to a relatively strong first order quadrupole interaction.[21] The satellite transitions have a different isotropic position, and particularly in the case of spin 5/2 are also less affected by effects of the electric field dispersion.[22] This makes the satellite transition spectroscopy a valuable complementary method for high-resolution work. The gain of the satellite transition intensity as a function of the rotation speed is illustrated in Figure 5.

Perhaps the most intriguing high speed application is the possibility of suppressing homonuclear dipolar interactions. Homonuclear dipolar linebroadening in a rigid system of hydrogen atoms may exceed 50 kHz. Under magic angle spinning, the residual linewidth is only a weak function of spinning speed, decreasing linearly with first power of the speed. Multipulse sequences[23] have been developed to refocus dipolar dephasing periodically. This refocussing has been demonstrated to work also in combination with a slow sample rotation.[24] For rigid systems the multipulse approach can offer resolution of a few tenths of ppm. In the case of plastic crystals and the presence of fast molecular motion, the multipulse approach becomes principally less effective. It may also be technically difficult to retain stability over a sufficiently long measurement period. Figure 6 presents ^{1}H MAS only spectra of camphor, where J-coupling becomes visible at 50 kHz. Moving to the higher fields, fast rotation starts to provide informative spectra also for rigid systems, as shown in Figure 7. The relative resolution grows proportionally with the field strength, since residual linebroadening retains its absolute value which depends mostly on the rotation speed. Both advantages combined bring a virtually quadratic improvement in resolution. However, a subtle deviation from this trend can already be observed in higher field spectra (831 MHz). Although the resolution is better, the absolute linewidth is clearly larger than at 500 MHz. Here a natural, susceptibility induced broadening starts to compete with the residual dipolar linewidth and no further substantial resolution enhancement is possible.[25] The case of high speeds as a method of improving resolution may actually turn out to be the only alternative for measurements at high fields, because several experimental parameters start to complicate the application of the multi-pulse sequences. First, it is technically more demanding to generate the required rf field strength. Secondly, the multi-pulse sequences inherently lose efficiency with

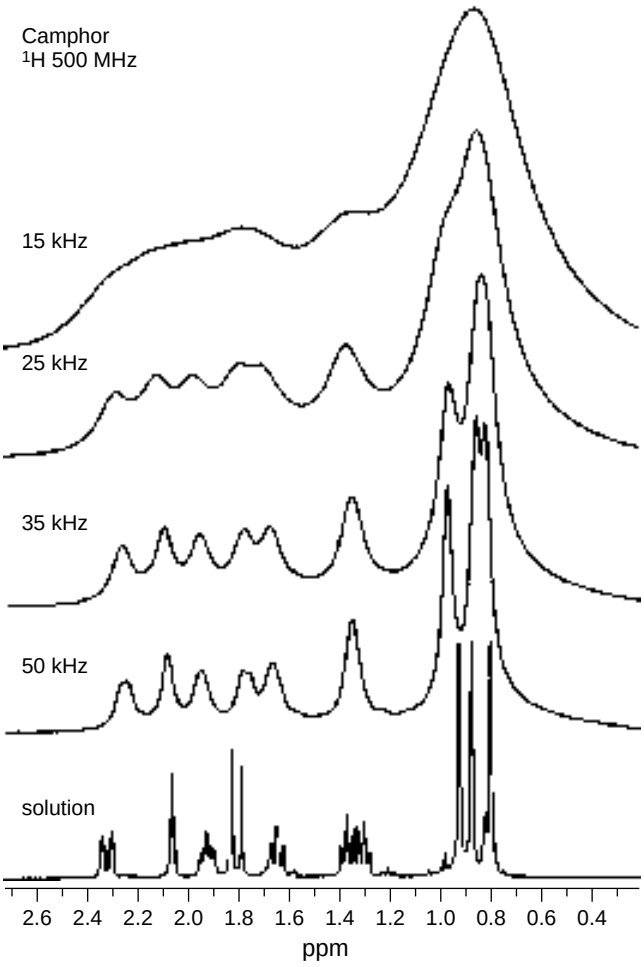

Figure 6 ^{1}H spectra of camphor. Lines are relatively narrow due to a molecular rotation. Nevertheless, faster rotation brings a substantial resolution enhancement, revealing finally J splitting of the two lines in the 1.8 and 2.3-ppm regions

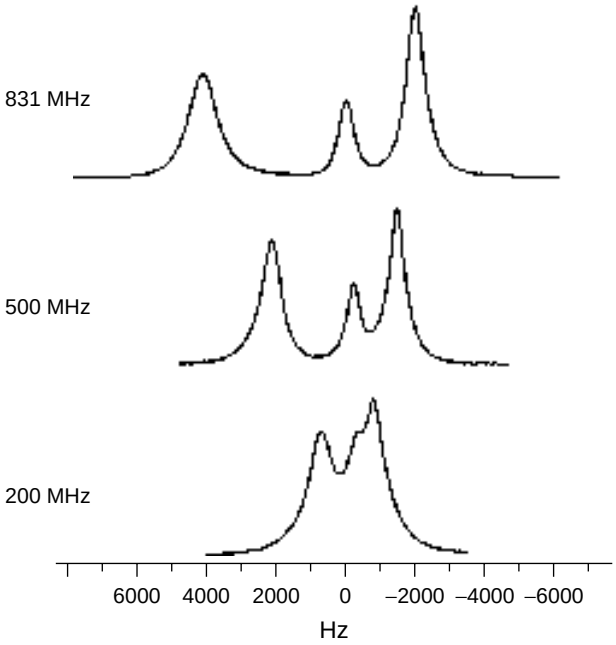

Figure 7 ^{1}H spectra of alanine at 200, 500 and 831 MHz. Sample rotation at 45 kHz. The 831 MHz spectrum was recorded at NHMFL

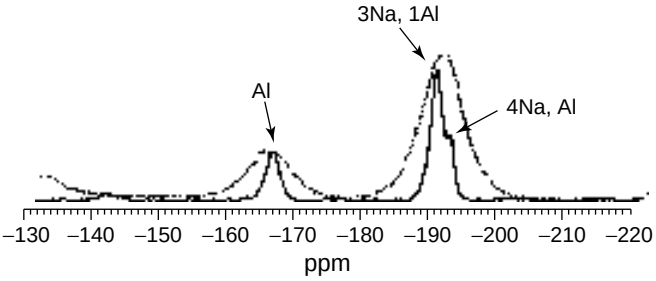

Figure 8 ^{19}F spectra of the mineral Chiolite $Na_5Al_3F_{14}$. A combined effect of the field (19.6 vs. 8.5 T) and rotation speed (40 vs 20 kHz) confirms the existence of three different coordination environments, as indicated, with intensity ratio of 2 : 4 : 1. Spectra were recorded by L. S. Du, SUNY Stony Brook

expansion of the spectral width. This is particularly true for the spectroscopy of ^{19}F. A qualitative improvement can be observed when both high field and rotation speed are combined, as seen in Figure 8.[26] For several experimental situations, resolution enhancement under MAS may be not only a matter of convenience, but imperative in order to free the pulse space for specific tasks. For example in the case of inverse detection experiments, the homonuclear proton system needs to remain decoupled, while being selectively cross-polarized by nitrogen.[27] High rotation speeds also allow exchange of averaging order in decoupling experiments.[28] A very low amplitude proton rf field is then needed for well-resolved carbon spectra.

5 CONCLUSIONS

Material strength of the rotor presents a major constraint in determining the performance range of MAS. A product of rotor diameter and highest speed form a material constant, set currently to about 100 mm kH. Practical and reliable values remain about 10–20% below that, as a tribute to the statistical nature of the mechanical properties of ceramics used for the rotors. Development of the sub 2-mm rotors has allowed speeds of 50 kHz to be reached. The most immediate benefits that arise from fast MAS are likely to be found in the spectroscopy of high-gamma and quadrupole nuclei. The extended range of possible rotation frequencies provides more exibility in choosing various matching conditions with either rf field amplitudes or spectral positions of different atomic sites. This feature may significantly facilitate atomic topology studies.

6 REFERENCES

1. L. G. Frechette, S. A. Jacobson, K. S. Breuer, F. F. Ehrich, R. Ghodssi, R. Khanna, C. W. Wong, X. Zhang, M. A. Schmidt, and A. H. Epstein, 'Solid State Sensor and Actuator Workshop', Hilton Head Island, SC, June 4–8, 2000.
2. D. M. Villeneuve, S. A. Aseyev, P. Dietrich, M. Spanner, M. Yu. Ivanov, and P. B. Corkum, *Phys. Rev. Lett.*, 2000, **85**, 542.
3. K. Treml and H. Langho, *Z. Phys.*, 1976, **B25**, 123.

4. M. Hubrich, C. Bauer, and H. W. Spiess, *Chem. Phys. Lett.*, 1997, **273**, 259.
5. A. Samoson, B. Sun, and A. Pines, 'New Angles in Motional Averaging, Pulsed Magnetic Resonance: NMR, ESR, and Optics', Clarendon: Oxford, 1992.
6. E. R. Andrew, A. Bradbury, and R. G. Eades, *Nature*, 1958, **182**, 1659.
7. E. Lippmaa, M. Alla, A. Salumäe, and T. Tuherm, U.S. Patent 4254373, 1981.
8. C. Chree, *Proc. Cambridge Phil. Soc.*, 1981, **7**, 201.
9. F. D. Doty and P. D. Ellis, *Rev. Sci. Instrum.*, 1981, **52**, 1868.
10. R. C. Garvie, R. H. Hannink, and R. T. Pascoe, *Nature*, 1975, **258**, 703.
11. R. G. Munro and S. W. Freiman, *J. Am. Ceram. Soc.*, 1999, **82**, 2246.
12. 'Bruker Analytik GmbH', Rheinstetten-4, Germany.
13. A. Samoson and T. Tuherm, 'The Alpine Conference on Solid-State NMR', Chamonix-Mont Blanc, France, Sept. 1999, p. T3; A. Samoson, 41st ENC, Asilomar, April 2000, p. 59; A. Samoson, T. Tuherm, and J. Past, *J. Magn. Reson.*, 2001, **149**, 264.
14. T. Mildner, H. Ernst, and D. Freude, *Solid-State NMR*, 1995, **5**, 269.
15. D. Geropp, *Ing.-Arch.*, 1969, **38**, 195.
16. A. Bielecki and D. P. Burum, *J. Magn. Reson.*, 1995, **A116**, 215.
17. P. Hartmann, J. W. Zwanziger, and C. Jäger, *Solid State NMR*, 2000, **16**, 189.
18. R. Verel, M. Baldus, M. Ernst, and B. Meier, *Chem. Phys. Lett.*, 1998, **287**, 421.
19. N. Nielsen, H. Bildsoe, H. Jakobsen, and M. Levitt, *J. Chem. Phys.*, 1994, **101**, 1805.
20. A. Samoson, E. Kundla, and E. Lippmaa, *J. Magn. Reson.*, 1982, **49**, 350.
21. A. Samoson, *Chem. Phys. Lett.*, 1985, **119**, 29.
22. E. Lippmaa, A. Samoson, and M. Magi, *J. Am. Chem. Soc.*, 1986, **108**, 1730.
23. J. S. Waugh, L. Huber, and U. Haeberlen, *Phys. Rev. Lett.*, 1968, **20**, 180.
24. B. Schnabel, U. Haubenreisser, G. Scheler, and R. Müller, in 'Proceedings of the 19th Congress Ampere, Heidelberg', 1976, 441; B. C. Gerstein, R. G. Pembleton, R. C. Wilson, and L. M. Ryan, *J. Chem. Phys.*, 1977, **66**, 361.
25. A. Samoson, T. Tuherm, and Z. Gan, *Solid-State NMR*, 2001, **20**, 130.
26. L. S. Du, A. Samoson, T. Tuherm, and C. P. Grey, *Chem. Mat.*, 2000, **12**(12), 3611.
27. Y. Ishii, R. Tycko, *J. Magn. Reson.*, 2000, **142**, 199.
28. M. Ernst, A. Samoson, and B. H. Meier, *Chem. Phys. Lett.*, 2001, **348**, 293.

Acknowledgements

Material presented in this overview is partly of original nature. Underlying work was supported by the Estonian Science Foundation and several extramural grants (University of Leipzig, NHMFL in Tallahassee, ETH Zürich, SUNY Stony Brook).

Biographical Sketch

Ago Samoson, *b* 1955. Ph.D., 1984, Solid State Physics, Institute of Chemical Physics and Biophysics, and Institute of Physics, Estonia. Research associate of various degrees, National Institute of Chemical Physics and Biophysics, Tallinn, Estonia, 1978–1987, 1989–1990, 1995–; Visiting Scholar, University of California, Berkeley 1987–1989, Applications Scientist, Bruker Analytische Messtechnik, Rheinstetten, Germany, 1991–1992; Visiting Scientist, University of Uppsala, Sweden, 1993–1994. Approx. 50 publications. Current research interests: (applications of) solid state NMR, development of instrumentation.

Magic-angle Turning Spectra of Solids Involving 5π-pulse Sequences

David M. Grant

University of Utah, Salt Lake City, UT, USA

1 Introduction 1
2 The Classical Banded-Matrix Secular Treatment of Slow Turning Spectra 1
3 The 5π-Pulse Experiment 7
4 TIGER Processing of Two-Dimensional NMR Spectra 9
5 The FIREMAT Variant of the 5π-PULSE Experiment 11
6 The 2D-PASS Form of a 5π-Pulse Experiment 12
7 Comparison of 5π-Pulse Type of Experiments 15
8 References 17

1 INTRODUCTION

The initial publication of the *Encyclopedia of Nuclear Magnetic Resonance* contains a description of several slow magic angle turning (MAT) experiments[1,2] that have as their antecedent the magic angle hopping (MAH) experiment of Bax, Szvereneyi and Maciel.[3] The MAT articles are based on the seminal work of Gan[4] and several subsequent developments that improve the spectral quality. Pulse breakthrough may distort MAT spectra, and the distortion can be minimized with three echo refocusing π-pulses.[5] Time reversal symmetry in the phase corrected MAT (PHORMAT) enhancement,[6] eliminates the need for computer shearing of a skewed spectrum arising from the use of combined amplitude and phase modulation in the original MAT experiment. The PHORMAT approach gives a high-quality hypercomplex 2D spectrum with the isotropic shifts along the evolution axis and tensor bands in the acquisition dimension. Unfortunately, PHORMAT suffers, as do all amplitude modulated MAT experiments, from the use of flip back pulses that are costly in the signal-to-noise (S/N) ratio. The 5π-PULSE/MAT experiment[7] directly improves this situation by leaving the magnetization totally in the *xy*-plane during the entire evolution period.

Before discussing the phase-modulated 5π-pulse experiments with emphasis on the two most popular variants, basic principles of sample rotation are discussed in Section 2 with a classical formulation of appropriate Bloch equations. A banded-matrix secular equation[8] is used for characterizing the spinning-sideband amplitudes common to magic angle rotating samples. The approach also processes rotational sideband data to yield principal-shift frequencies. This *classical* method is a numerically efficient alternative to Floquet theory[9] and/or the Bessel functions solutions used by Hertzfeld and Berger.[10] The banded matrix method, in concert with a SIMPLEX minimization procedure, converges rapidly to the principal-shift values used in fitting the time-dependent free induction decays (FID). The fit of time-dependent FID data is considerably more precise than the fit of single peak intensities.

The 5π-PULSE/MAT experiment[7] is discussed in Section 3. It provides a basis for constructing a two-dimensional FID in which the spectrum is transformed into isotropic shifts along the evolution axis and individual tensor bands along the acquisition axis. Two important variants of 5π-PULSE/MAT, i.e., the five π replicated magic angle turning (FIREMAT)[11] and the 2D phase adjusted spinning sidebands (2D-PASS),[12,13] improve the S/N and yield higher quality spectral resolution in a more time-efficient manner. In a matter of hours, either of these two methods provides 2D spectra on molecules containing 50 or more carbon atoms. The FIREMAT variant is a direct extension of the original 5π-PULSE/MAT technique, whereas the related 2D-PASS approach evolved more from the PASS sideband manipulation experiments of Dixon.[14] Otherwise, both FIREMAT and 2D-PASS share a common starting point at the zero evolution time, $t_e = 0$ and may be explained with the same theoretical machinery.

A useful development in data processing, the technique for importing greater evolution resolution[15] (TIGER) treated in Section 4, may be used to enhance MAT methods. TIGER with MAT data enhances simultaneously the resolution and S/N in the evolution dimension. In contrast to Fourier transform (FT) methods, TIGER is a convolution technique that contracts one of the dimensions of the 2D FIDs of MAT by importing resolution from an associated 1D guide spectrum. TIGER yields a 1D acquisition FID for each nuclear spin that is immediately suited for banded-matrix processing and generally increases the efficiency of data collection by reducing the number of evolution increments, especially in smaller molecules.

FIREMAT (Section 5) includes TIGER but also involves a method for replicating periodic blocks of acquisition FIDs. These replicated blocks of evolution data enhance the resolution and time efficiency of FIREMAT. The creative 2D-PASS (Section 6) approach separates, by sideband order, the magnetization in the evolution dimension. In Section 7, the results of 5π-PULSE (with and without TIGER), FIREMAT, and 2D-PASS (with both FT and fast FT) are compared, and their respective sensitivities and time efficiencies briefly discussed.

2 THE CLASSICAL BANDED-MATRIX SECULAR TREATMENT OF SLOW TURNING SPECTRA

2.1 Bloch's Equation of Motion

Bloch's equation, ignoring relaxation, is given by

$$\frac{\mathrm{d}\vec{\mu}_\nu}{\mathrm{d}t} = \vec{\mu}_\nu \times \gamma_\nu \vec{B}_0 = -\vec{\Omega}_\nu \times \vec{\mu}_\nu \qquad (2.1)$$

where $\vec{\mu}_\nu$ is the magnetic moment of the spin ν, and $\vec{\Omega}_\nu = \gamma_\nu \vec{B}_0 = -\omega_\nu(\mathrm{LAB})$ is an angular precession velocity that is

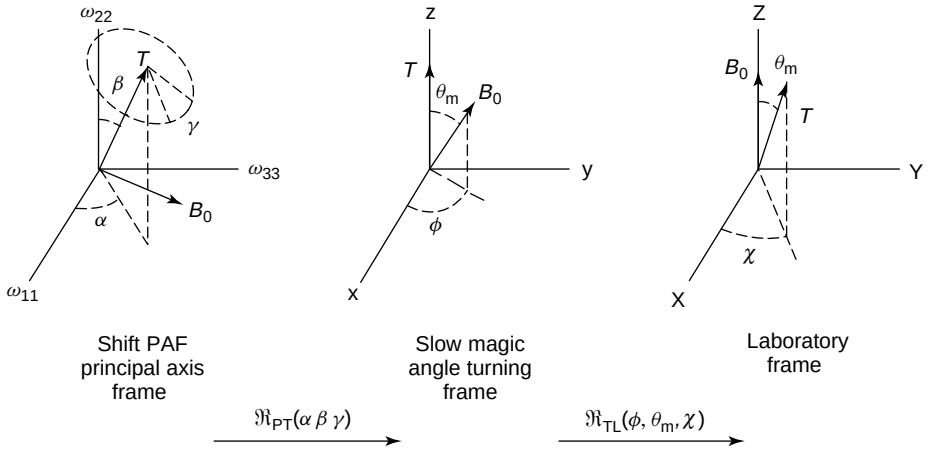

Figure 1 The principal shift axis, turning and laboratory frames for sample rotation

co-linear with $\vec{B}_0$. The Zeeman approximation locks the νth spin to the strong $\vec{B}_0$ lying along the Z-axis in the laboratory or Zeeman frame. Utilizing equation (2.1) in the detection plane yields two differential equations for the counter-rotating vectors:

$$\frac{\mathrm{d}\mu_{\nu+}}{\mathrm{d}t} = -i\omega_\nu(\mathrm{LAB})\mu_{\nu+}, \quad \frac{\mathrm{d}\mu_{\nu-}}{\mathrm{d}t} = +i\omega_\nu(\mathrm{LAB})\mu_{\nu-} \quad (2.2)$$

The irreducible representations of the magnetic moment, $\mu_{\nu\pm}$, in the xy plane are

$$\mu_{\nu\pm} = \mu_{\nu x} \pm i\mu_{\nu y} \quad (2.3)$$

In the absence of a sign for γ_ν, component $\mu_{\nu+}$ is selected arbitrarily as the preferred form for the following development. It is an equally simple matter to use $\mu_{\nu-}$.

2.2 Transformations Between Relevant Chemical Shift Frames

The three frames, given in Figure 1, are necessary to describe the spin precession in a rotating sample. They are the principal axis frames, the slow turning axis frame and the laboratory frame with the turning axis at the magic angle relative to the magnetic field.

An equation for ω_ν(LAB) in the laboratory frame may be given in terms of the zeroth and 2nd rank irreducible shift frequencies,[16] $\omega_0^{(0)}(\mathsf{LAB})$ and $\omega_0^{(2)}(\mathbf{LAB})$, respectively:

$$\omega_\nu(\mathrm{LAB}) = \frac{1}{\sqrt{3}}\omega_0^{(0)}(\mathsf{LAB}) + \sqrt{\frac{2}{3}}\omega_0^{(2)}(\mathsf{LAB}) \quad (2.4)$$

The spin label, ν, is ignored for the moment to reduce the complexity of the expressions. The zero-rank frequency, $\omega_0^{(0)}(\mathsf{LAB}) = \omega_0^{(0)}(\mathrm{PAF}) = \sqrt{3}\omega_{\mathrm{iso}}$, is rotationally invariant in all frames. Only the $m = 0$ projection, $\omega_0^{(2)}(\mathbf{LAB})$, is relevant under the Zeeman approximation for the $l = 2$ second-order irreducible spherical frequencies given in the LAB frame. The transformations between various reference frames using Wigner rotational matrix terms yield the following:

$$\begin{aligned}\omega_0^{(2)}(\mathsf{LAB}) &= \sum_{n=-2}^{+2} \mathbf{D}_{o,n}^{(2)^*}(\phi, \theta, \chi)_{\mathrm{TL}}\omega_n^{(2)}(\mathsf{TURN}) \\ &= \sum_{n=-2}^{+2}\sum_{m=-2}^{+2} \mathbf{D}_{o,n}^{(2)^*}(\phi, \theta, \chi)_{\mathrm{TL}}\mathbf{D}_{n,m}^{(2)^*}(\alpha, \beta, \gamma)_{\mathrm{PT}}\omega_m^{(2)}(\mathsf{PAF})\end{aligned} \quad (2.5)$$

where $\omega_{\pm1}^{(2)}(\mathsf{PAF}) = 0$. Typical Euler angle sets, $(\alpha\beta\gamma)$ and $(\phi\theta\chi)$, are used for the (PAF $\rightarrow$ TURN) and (TURN $\rightarrow$ LAB) transformations denoted in Figure 1 as PT and TL, respectively. Zare[17] discusses the molecular to laboratory expansion, given by equation (2.5), in terms of rotational matrix components, $\mathbf{D}_{n,m}^{(\ell)^*}(\alpha, \beta, \gamma)_{\mathrm{PT}}$. It is critical that the correct matrix be used for the forward and reverse transformations between the laboratory and molecular frames. The Wigner rotation matrix that transforms irreducible-shift frequencies from the (LAB $\rightarrow$ TURN) or (TURN $\rightarrow$ PAF) has matrix elements defined by Zare:[18]

$$\mathbf{D}_{m,n}^{(\ell)}(\alpha, \beta, \gamma)_{\mathrm{TP}} = e^{-im\alpha}d_{m,n}^{(\ell)}(\beta)e^{-in\gamma} \quad (2.6)$$

The reverse rotational transformation from the PAF, fixed in the molecular frame, to the laboratory TURN frame is accomplished with a rotation matrix that is the inverse of equation (2.6), i.e., the complex conjugate of its transpose. Hence, the $\mathbf{D}_{n,m}^{(\ell)^*}(\alpha, \beta, \gamma)_{\mathrm{PT}}$ terms in equation (2.5) are given by

$$\mathbf{D}_{n,m}^{(\ell)^*}(\alpha, \beta, \gamma)_{\mathrm{PT}} = \mathbf{D}_{m,n}^{(\ell)^{-1}}(\alpha, \beta, \gamma)_{\mathrm{TP}} = e^{in\gamma}d_{n,m}^{(\ell)}(\beta)e^{im\alpha} \quad (2.7)$$

Note in equation (2.5) the row and column indices conform and specify a matrix multiplication without violating the commutation rules of rotational operators. Differences in conventions have made this topic somewhat perplexing in the literature. Thus, for the convenience of the reader the form of the Wigner rotation matrix, $\mathbf{D}^{(2)^*}(\alpha, \beta, \gamma)_{\mathrm{PT}}$, used herein is provided as follows:

$$\mathbf{D}^{(2)^*}(\alpha,\beta,\gamma)_{\mathrm{PT}} =$$

$$\begin{bmatrix}
\frac{1}{4}e^{-2i\gamma}(1+\cos\beta)^2e^{-2i\alpha} & \frac{1}{2}e^{-2i\gamma}\sin\beta(1+\cos\beta)e^{-i\alpha} & \sqrt{\frac{3}{8}}e^{-2i\gamma}\sin^2\beta & -\frac{1}{2}e^{-2i\gamma}\sin\beta(\cos\beta-1)e^{i\alpha} & \frac{1}{4}e^{-2i\gamma}(1-\cos\beta)^2e^{2i\alpha} & -2\\
-\frac{1}{2}e^{-i\gamma}\sin\beta(1+\cos\beta)e^{-2i\alpha} & \frac{1}{2}e^{-i\gamma}(2\cos\beta-1)(1+\cos\beta)e^{-i\alpha} & \sqrt{\frac{3}{2}}e^{-i\gamma}\cos\beta\sin\beta & \frac{1}{2}e^{-i\gamma}(2\cos\beta+1)(1-\cos\beta)e^{i\alpha} & -\frac{1}{2}e^{-i\gamma}\sin\beta(\cos\beta-1)e^{2i\alpha} & -1\\
\sqrt{\frac{3}{8}}\sin^2\beta e^{-2i\alpha} & -\sqrt{\frac{3}{2}}\cos\beta\sin\beta e^{-i\alpha} & \frac{1}{2}(3\cos^2\beta-1) & \sqrt{\frac{3}{2}}\cos\beta\sin\beta e^{i\alpha} & \sqrt{\frac{3}{8}}\sin^2\beta e^{2i\alpha} & 0\\
\frac{1}{2}e^{i\gamma}\sin\beta(\cos\beta-1)e^{-2i\alpha} & \frac{1}{2}e^{i\gamma}(2\cos\beta+1)(1-\cos\beta)e^{-i\alpha} & -\sqrt{\frac{3}{2}}e^{i\gamma}\cos\beta\sin\beta & \frac{1}{2}e^{i\gamma}(2\cos\beta-1)(1+\cos\beta)e^{i\alpha} & \frac{1}{2}e^{i\gamma}\sin\beta(1+\cos\beta)e^{2i\alpha} & +1\\
\frac{1}{4}e^{2i\gamma}(1-\cos\beta)^2e^{-2i\alpha} & \frac{1}{2}e^{2i\gamma}\sin\beta(\cos\beta-1)e^{-i\alpha} & \sqrt{\frac{3}{8}}e^{2i\gamma}\sin^2\beta & -\frac{1}{2}e^{2i\gamma}\sin\beta(1+\cos\beta)e^{i\alpha} & \frac{1}{4}e^{2i\gamma}(1+\cos\beta)^2e^{2i\alpha} & +2\\
-2 & -1 & 0 & +1 & +2 & n
\end{bmatrix} \quad M \tag{2.8}$$

The combination of equations (2.4) and (2.5) gives the following frequency expression in the laboratory frame, $\omega(\mathbf{LAB})$, for the various spins,

$$\omega(\mathrm{LAB}) = \frac{1}{\sqrt{3}}\omega_0^{(0)}(\mathsf{PAF}) + \sqrt{\frac{2}{3}}\sum_{n=-2}^{+2}\sum_{m=-2}^{+2}\mathbf{D}_{o,n}^{(2)^*}(\phi,\theta,\chi)_{\mathrm{TL}}\mathbf{D}_{n,m}^{(2)^*}(\alpha,\beta,\gamma)_{\mathrm{PT}}\omega_m^{(2)}(\mathsf{PAF}) \tag{2.9}$$

The alternative, but equivalent, similarity transformations use the standard directional-cosine matrix[19]

$$\mathbf{R}(\alpha,\beta,\gamma)_{\mathrm{PT}} = \begin{bmatrix} \cos\alpha\cos\beta\cos\gamma - \sin\alpha\sin\gamma & \sin\alpha\cos\beta\cos\gamma + \cos\alpha\sin\gamma & -\sin\beta\cos\gamma \\ -\cos\alpha\cos\beta\sin\gamma - \sin\alpha\cos\gamma & -\sin\alpha\cos\beta\sin\gamma + \cos\alpha\cos\gamma & \sin\beta\sin\gamma \\ \cos\alpha\sin\beta & \sin\alpha\sin\beta & \cos\beta \end{bmatrix}$$

to convert the chemical-shift tensor from the PAF into the turning frame and subsequently to the laboratory frames as follows:

$$\begin{aligned} T_{\mathrm{TURN}} &= \mathbf{R}(\alpha,\beta,\gamma)_{\mathrm{PT}}\cdot T_{\mathrm{PAF}}\cdot\mathbf{R}^{-1}(\alpha,\beta,\gamma)_{\mathrm{PT}} \\ T_{\mathrm{LAB}} &= \mathbf{R}(\phi,\theta,\chi)_{\mathrm{TL}}\cdot T_{\mathrm{TURN}}\cdot\mathbf{R}^{-1}(\phi,\theta,\chi)_{\mathrm{TL}} \\ &= \mathbf{R}(\phi,\theta,\chi)_{\mathrm{TL}}\cdot\mathbf{R}(\alpha,\beta,\gamma)_{\mathrm{PT}}\cdot T_{\mathrm{PAF}} \\ &\quad\cdot\mathbf{R}^{-1}(\alpha,\beta,\gamma)_{\mathrm{PT}}\cdot\mathbf{R}^{-1}(\phi,\theta,\chi)_{\mathrm{TL}} \end{aligned} \tag{2.10}$$

$\mathbf{R}^{-1}(\alpha,\beta,\gamma)_{\mathrm{PT}}$ is the transpose of the unitary matrix, $\mathbf{R}(\alpha,\beta,\gamma)_{\mathrm{PT}}$. Application of equation (2.10) yields the same expression for $\omega(\mathsf{LAB})$ (i.e., the [3,3] term in T_{LAB}) as obtained for the Wigner rotation transformations given in equation (2.9) when equation (2.8) is employed.

2.3 Irreducible-Spherical Shift Frequencies and Appropriate Rotational Transformations

The definition of irreducible-spherical shift frequencies[16] in any molecular frame is as follows:

$$\begin{aligned} \omega_0^{(0)}(\mathrm{mol}) &= \frac{1}{\sqrt{3}}[\omega_{zz}+\omega_{xx}+\omega_{yy}] = \sqrt{3}\omega_{\mathrm{iso}} \\ \omega_0^{(2)}(\mathrm{mol}) &= \sqrt{\frac{2}{3}}\left[\omega_{zz}-\frac{1}{2}(\omega_{xx}+\omega_{yy})\right] = \sqrt{\frac{3}{2}}[\omega_{zz}-\omega_{\mathrm{iso}}] \\ \omega_{\pm1}^{(2)}(\mathrm{mol}) &= \frac{1}{2}[\mp(\omega_{xz}+\omega_{zx}) - i(\omega_{yz}+\omega_{zy})] \\ \omega_{\pm2}^{(2)}(\mathrm{mol}) &= \frac{1}{2}[(\omega_{xx}-\omega_{yy}) \pm i(\omega_{xy}+\omega_{yx})] \end{aligned} \tag{2.11}$$

These irreducible frequencies in radians per second express the symmetrical portion of the chemical shift tensor. Division by 2π converts equation (2.11) from radians per second to cps or Hz. In the PAF tensor only diagonal elements exist and equation (2.11) reduces to the zero-rank isotropic frequency and three ($m = -2, 0, 2$) of the five second-rank frequencies, respectively, as follows:

$$\omega_0^{(0)}(\mathsf{PAF}) = \sqrt{3}\omega_{\mathrm{iso}} \tag{2.12}$$

with the second-rank frequencies given in vector form, i.e.,

$$\overline{\omega}^{(2)} = \begin{bmatrix} \omega_{-2}^{(2)}(\mathsf{PAF}) \\ \omega_{-1}^{(2)}(\mathsf{PAF}) \\ \omega_0^{(2)}(\mathsf{PAF}) \\ \omega_1^{(2)}(\mathsf{PAF}) \\ \omega_2^{(2)}(\mathsf{PAF}) \end{bmatrix} = \begin{bmatrix} \frac{1}{2}\omega_{\mathrm{span}} \\ 0 \\ \sqrt{\frac{2}{3}}\omega_{\mathrm{acent}} \\ 0 \\ \frac{1}{2}\omega_{\mathrm{span}} \end{bmatrix} \tag{2.13}$$

where $\omega_{\mathrm{iso}} = (1/3)(\omega_{11}+\omega_{22}+\omega_{33})$, $\omega_{\mathrm{acent}} = \omega_{22} - (1/2)(\omega_{11}+\omega_{33})$ and $\omega_{\mathrm{span}} = (\omega_{11}-\omega_{33})$. The notations iso, acent, and span are used for isotropic, acentricity, and span, respectively. Note that the ω_{zz} direction is best identified with the ω_{22} principal frequency and the ω_{xx} and ω_{yy} terms with ω_{11} and ω_{33} principal frequencies, respectively. The ω_{11}, ω_{22} and ω_{33} are the principal chemical shift frequencies. In Mason's[20] convention for symmetry combination of tensor terms, iso and span are the same as used herein, but acent, equal to the product of Mason's skew times the span, is preferred in this work. These proposed simple irreducible forms are very useful with Wigner rotation matrices because they exhibit the symmetry features of irreducible tensors while skew and the traditional asymmetry parameter are ratios of irreducible forms.

It is convenient to evaluate the relevant part of the rotational matrix RTL using values of the Euler angles: $\phi, \theta = \theta_m, \chi = 0$. The selection of χ equal to zero, while arbitrary, expresses the cylindrical symmetry of the $\vec{B}_0$ magnetic field in the laboratory frame. Thus,

$$\mathbf{D}_{0,0}^{(2)^*}(\phi,\theta_m,\chi)_{\mathrm{TL}} = d_{0,0}^{(2)}(\theta_m) = \frac{1}{2}(3\cos^2\theta_m - 1) = 0$$

$$\begin{aligned}
\mathbf{D}^{(2)^*}_{0,\pm1}(\phi,\theta_m,\chi)_{\mathrm{TL}} &= d^{(2)}_{0,\pm1}(\theta_m)e^{\pm i\phi} \\
&= \pm\sqrt{\frac{3}{2}}\sin\theta_m\cos\theta_m e^{\pm i\phi} = \pm\sqrt{\frac{1}{3}}e^{\pm i\phi} \\
\mathbf{D}^{(2)^*}_{0,\pm2}(\phi,\theta_m,\chi)_{\mathrm{TL}} &= d^{(2)}_{0,\pm2}(\theta_m)e^{\pm 2i\phi} \\
&= \sqrt{\frac{3}{8}}\sin^2\theta_m e^{\pm 2i\phi} = \sqrt{\frac{1}{6}}e^{\pm 2i\phi} \qquad (2.14)
\end{aligned}$$

Here, $\cos^2\theta_m = 1/3$ and $\sin^2\theta_m = 2/3$. The transformation matrix from the TURN frame to LAB frame now is limited to the row vector,

$$\mathbf{D}^{(2)^*}_{0,n(-2,-1,0,+1,+2)}(\phi,\theta,\chi)_{\mathrm{TL}} = \left[\sqrt{\frac{1}{6}}e^{-2i\phi} \quad -\sqrt{\frac{1}{3}}e^{-i\phi} \quad 0 \quad +\sqrt{\frac{1}{3}}e^{i\phi} \quad \sqrt{\frac{1}{6}}e^{+2i\phi}\right] \qquad (2.15)$$

Note that χ drops out of equation (2.15) because of the cylindrical symmetry in the magnetic field. While the generalized $\mathbf{D}^{(2)^*}(\phi,\theta,\chi)_{\mathrm{TL}}$ Wigner rotation matrix is a 5×5 matrix, only the middle row of the matrix, $\mathbf{D}^{(2)^*}_{0,n(-2,-1,0,+1,+2)}(\phi,\theta,\chi)_{\mathrm{TL}}$, is relevant to the angular precession frequency in the Zeeman approximation. This simplification in the mathematics arises whenever $\vec{B}_0$, the static magnetic field, dominates all other interactions and defines the Z-axis as the relevant laboratory direction for the angular precession frequency, $\omega_\nu(\mathrm{LAB})$.

The summations in equation (2.9) over n and m express a $(1\times5)\cdot(5\times5)\cdot(5\times1)$ matrix multiplication of the matrices contained in equations (2.15), (2.8), and (2.13). Thus,

$$\begin{aligned}
\omega_\nu(\mathrm{LAB}) = \omega_{\mathrm{iso}} &+ \sqrt{\frac{2}{3}}\left[\sqrt{\frac{1}{6}}e^{-2i\phi} \quad -\sqrt{\frac{1}{3}}e^{-i\phi} \quad 0 \quad +\sqrt{\frac{1}{3}}e^{i\phi} \quad \sqrt{\frac{1}{6}}e^{+2i\phi}\right]\cdot \qquad (2.16)\\
&\begin{bmatrix}
\frac{1}{4}e^{-2i\gamma}(1+\cos\beta)^2e^{-2i\alpha} & (\cdots) & \sqrt{\frac{3}{8}}e^{-2i\gamma}\sin^2\beta & (\cdots) & \frac{1}{4}e^{-2i\gamma}(1-\cos\beta)^2e^{2i\alpha}\\
-\frac{1}{2}e^{-i\gamma}\sin\beta(1+\cos\beta)e^{-2i\alpha} & (\cdots) & \sqrt{\frac{3}{2}}e^{-i\gamma}\cos\beta\sin\beta & (\cdots) & -\frac{1}{2}e^{-i\gamma}\sin\beta(\cos\beta-1)e^{2i\alpha}\\
(\cdots) & (\cdots) & (\cdots) & (\cdots) & (\cdots)\\
\frac{1}{2}e^{i\gamma}\sin\beta(\cos\beta-1)e^{-2i\alpha} & (\cdots) & -\sqrt{\frac{3}{2}}e^{i\gamma}\cos\beta\sin\beta & (\cdots) & \frac{1}{2}e^{i\gamma}\sin\beta(1+\cos\beta)e^{2i\alpha}\\
\frac{1}{4}e^{2i\gamma}(1-\cos\beta)^2e^{-2i\alpha} & (\cdots) & \sqrt{\frac{3}{8}}e^{2i\gamma}\sin^2\beta & (\cdots) & \frac{1}{4}e^{2i\gamma}(1+\cos\beta)^2e^{2i\alpha}
\end{bmatrix}\cdot
\begin{bmatrix}
\frac{1}{2}\omega_{\mathrm{span}}\\ 0\\ \sqrt{\frac{2}{3}}\omega_{\mathrm{acent}}\\ 0\\ \frac{1}{2}\omega_{\mathrm{span}}
\end{bmatrix}
\end{aligned}$$

The null terms arising in the two outer vectors greatly simplifies the result of multiplying the three matrices (a vector, a square matrix, and a vector) found in equation (2.16). Thirteen of the 25 terms in the 5×5 matrix are nonvanishing, but they become irrelevant due to the null terms in the TL transformation and in the PAF irreducible principal-frequency vector.

2.4 Precession Frequency Dependency on Transformation Angles

Consideration of the first matrix multiplication in equation (2.16) makes it immediately obvious that the overall transformation depends only on the sum of $(\phi+\gamma)$. Therefore, it is possible to subsume ϕ and γ into a single angle identified with the mechanical rotation of the sample.[21] Apportioning $(\phi+\gamma)$ into pre-pulse and post-pulse periods divides the angle into useful time-independent and time-dependent components. A sudden approximation at zero-time, $t=0$, is invoked for the B_1 pulse that nutates the magnetic spin into the xy-observing plane. The $(\phi+\gamma)$ angle therefore divides into an orientational lattice angle, γ_o, and a time-dependent angular term, $\gamma_t = \omega_r t$, where the mechanical rotational frequency is given by ω_r. Thus,

$$(\phi+\gamma) = \gamma_o + \gamma_t = \gamma_o + \omega_r t \qquad (2.17)$$

The spin identity of unique nuclei now is reintroduced with the index ν. Equations (2.16) and (2.17) render $\omega_\nu(\mathrm{LAB})$ in the following compacted form,[22]

$$\omega_\nu(\mathrm{LAB}) = \sum_{n=-2}^{2} W_{\nu,n}(\alpha,\beta)e^{ni\gamma_o}e^{ni\omega_r t} \qquad (2.18)$$

The phase factor, $e^{ni\gamma_o}$, depends on the lattice angle, γ_o, and on the second-rank projection index, n. The explicit form of the $W_{\nu,n}(\alpha,\beta)$ terms, obtained from the matrix multiplications in equation (2.16), depends on the irreducible shift-frequency parameters, $(\omega_{\mathrm{iso}},\omega_{\mathrm{acent}},\omega_{\mathrm{span}})$, for each ν spin as follows:

$$\begin{aligned}
W_2(\alpha,\beta) &= \frac{1}{24}[(1+\cos\beta)^2e^{i2\alpha} + (1-\cos\beta)^2e^{-i2\alpha}]\omega_{\mathrm{span}} \\
&\quad + \frac{1}{6}[\sin^2\beta]\omega_{\mathrm{acent}} \\
W_1(\alpha,\beta) &= \frac{\sqrt{2}}{12}[\sin\beta(1+\cos\beta)e^{i2\alpha} + \sin\beta(\cos\beta-1)e^{-i2\alpha}]\omega_{\mathrm{span}} \\
&\quad - \frac{\sqrt{2}}{3}[\sin\beta\cos\beta]\omega_{\mathrm{acent}} \\
W_o &= \omega_{\mathrm{iso}} \\
W_{-1}(\alpha,\beta) &= \frac{\sqrt{2}}{12}[\sin\beta(\cos\beta-1)e^{i2\alpha} + \sin\beta(1+\cos\beta)e^{-i2\alpha}]\omega_{\mathrm{span}} \\
&\quad - \frac{\sqrt{2}}{3}[\sin\beta\cos\beta]\omega_{\mathrm{acent}} \\
W_{-2}(\alpha,\beta) &= \frac{1}{24}[(1-\cos\beta)^2e^{i2\alpha} + (1+\cos\beta)^2e^{-i2\alpha}]\omega_{\mathrm{span}} \\
&\quad + \frac{1}{6}[\sin^2\beta]\omega_{\mathrm{acent}} \qquad (2.19)
\end{aligned}$$

Note that the zero-rank shift frequency, $\omega_0^{(0)}(\mathsf{LAB})$, provides the expression for W_0, whereas $\omega_0^{(2)}(\mathsf{LAB})$ relates to W_{-2}, W_2, W_{-1} and W_1. Substituting equation (2.18) into equation (2.2) and using the μ_+ form, as indicated earlier, gives the following Bloch equation:

$$\frac{\mathrm{d}\mu_\nu(\alpha,\beta,\gamma_o|t)}{\mathrm{d}t} = -i\sum_{n=-2}^{2} W_{\nu,n}(\alpha,\beta,)e^{in\gamma_o}e^{in\omega_r t}\mu_\nu(\alpha,\beta,\gamma_o|t) \tag{2.20}$$

2.5 Powder Averaging of Bloch's Equation of Motion in MAT Experiments

The orientation of all equivalent nuclei in a single crystal, as a function of time, is represented by $(\alpha,\beta,\gamma_o|t)$. Thus, the magnetization of nuclei in microcrystalline powders with identical spatial-orientations is given by the designation $\mu(\alpha,\beta,\gamma_o|t)$. Maricq and Waugh[23] observed in single crystals, with only one molecular orientation, that phase variations appear in the spectral sidebands relative to the center-band phase. These phase variations relate to $e^{in\gamma_o}$, providing the rf observing pulses are synchronized with the angular positions of the rotating sample.

In a microcrystalline sample, the phase factor $e^{in\gamma_o}$, must be powder averaged, thereby resulting in some loss of phase specificity. When equation (2.18) is powder averaged over the γ_o angle, $\mu(\alpha,\beta,\gamma_o|t)$ is converted into an ensemble magnetization, $m_\nu(\alpha,\beta|t)$. This $m_\nu(\alpha,\beta|t)$ ensemble consists of the ν spins in those crystallites with a common turning axis, which is described by α and β in the PAF. Members of this subset distribute uniformly over the different values of γ_o. Consequently, equation (2.20) becomes

$$\frac{\mathrm{d}m_\nu(\alpha,\beta|t)}{\mathrm{d}t} = -i\sum_{n=-2}^{2} W_{\nu,n}(\alpha,\beta)\overline{e^{in\gamma_o}}e^{in\omega_r t}m_\nu(\alpha,\beta|t) \tag{2.21}$$

2.5.1 Powder Average over γ_o

Focus now turns to the average phase factor, $\overline{e^{in\gamma_o}}$, and its ensemble $m_\nu(\alpha,\beta|t)$. In an elegant proof, Levitt[24] exhibited that the phase factors for the center-band and sidebands were all equal in rotating micro-crystalline powders. Levitt's treatment assumes three constraints. (i) All spins in the $\mu_\nu(\alpha,\beta,\gamma_o|t)$ subset experience the same *average* Hamiltonian. (ii) The sample rotation takes the sub-ensemble of spins, $\mu_\nu(\alpha,\beta,\gamma_o|t)$, related to the turning axis through a periodic cycle of resonance frequencies. (iii) The orientations of these $\mu(\alpha,\beta,\gamma_o|t)$ crystallites experience a uniform distribution over γ_o. Postulate (i) defines the subset of spins belonging to the α,β turning axis. The periodic character of $e^{in\gamma_o}$ satisfies (ii). Finally, (iii) specifies an essential feature of a random powder to give uniform mathematical averaging of the phase factor around the rotational path. The uniform angular probability leads to the following expression:

$$\int_0^{2\pi} P(\gamma_o)d\gamma_o = P(\gamma_o)\int_0^{2\pi} d\gamma_o = 1 \tag{2.22}$$

hence $P(\gamma_o) = 1/2\pi$.

If one integrates $e^{in\gamma_o}$ from a to $a+2\pi$, expressions for the average phase factor are obtained as follows:

$$\begin{aligned}\overline{\exp(in\gamma_o)} &= \exp\left(inP(\gamma_o)\int_a^{a+2\pi}\gamma_o d\gamma_o\right) = \exp\left(\frac{in}{4\pi}[\gamma_o^2]_a^{a+2\pi}\right)\\ &= \exp(in(\pi+a)) = [\exp(i(\pi+a))]^n = (\pm1)^n\end{aligned} \tag{2.23}$$

The averaged factors reference the phase of the sidebands to the corresponding center-band identified with the zero rank W_o. The selection of a specific crystallite by the parameter a is totally arbitrary. Thus it is convenient to choose real values for a (e.g., $a=\pi$ or $a=0$) to give the final term in equation (2.23). For $n=+2$ or -2 the phase factor is always unity, but when $n=+1$ or -1 then the arbitrariness of odd rank projections creeps into the phase factor. Zare has treated this feature at some length.[25] The ensemble average of γ_o, given in equation (2.23), is now complete. It is easily shown below that use of either $+1$ or -1 for $\overline{e^{in\gamma_o}}$ will not alter the results of this treatment. In keeping with traditional practices,[26] the negative sign for $(\pm1)^n$ is arbitrarily selected for this development. Equation (2.18) then becomes

$$\begin{aligned}\omega_\nu(\mathrm{LAB}) &= \sum_{n=-2}^{2}(-1)^n W_{\nu,n}(\alpha,\beta)e^{in\omega_r t}\\ &\equiv \sum_{n=-2}^{2}(-1)^n W_{\nu,n}(\alpha,\beta)e^{in\gamma_t}\end{aligned} \tag{2.24}$$

and equation (2.21) yields

$$\frac{\mathrm{d}m_\nu(\alpha,\beta|t)}{\mathrm{d}t} = -i\sum_{n=-2}^{2}(-1)^n W_{\nu,n}(\alpha,\beta)e^{in\omega_r t}m_\nu(\alpha,\beta|t) \tag{2.25}$$

2.5.2 Solution of the Bloch equation for the m_ν $(\alpha,\beta|\mathrm{t})$ Subsystem of Spins

The $e^{in\omega_r t}$ term makes equation (2.25) quite intractable; consequently, an infinite Fourier expansion is used for $m_\nu(\alpha,\beta|t)$ to provide a numerical solution for equation (2.25):

$$m_\nu(\alpha,\beta|t) = A\sum_{k=-\infty}^{+\infty} a_{\nu,k}(\alpha,\beta)e^{-i(\omega_{\nu,\mathrm{iso}}+k\omega_r)t} \tag{2.26}$$

where A includes arbitrary spectral phase factors, $e^{-\rho}$, and scaling constants such as m_0. The $a_{\nu,k}(\alpha,\beta)$ are expansion coefficients for the α,β designated subsystem. Inserting equation (2.26) into equation (2.25) gives the following expressions:

$$\begin{aligned}\frac{\mathrm{d}m_\nu(\alpha,\beta|t)}{\mathrm{d}t} &= -iA\sum_{k=-\infty}^{+\infty}(\omega_{\nu,\mathrm{iso}}+k\omega_r)a_{\nu,k}(\alpha,\beta)e^{-i(\omega_{\nu,\mathrm{iso}}+k\omega_r)t}\\ &\equiv -iA\sum_{k=-\infty}^{+\infty}\sum_{n=-2}^{2}(-1)^n W_{\nu,n}(\alpha,\beta)\\ &\quad\times e^{in\omega_r t}a_{\nu,k}(\alpha,\beta)e^{-i(\omega_{\nu,\mathrm{iso}}+k\omega_r)t}\end{aligned} \tag{2.27}$$

Equation (2.27) may be simplified by dropping $dm_\nu(\alpha, \beta|t)/dt$, clearing the common factors, $-iAe^{i\omega_{\nu,\mathrm{iso}}t}$, and rearranging and collecting the remaining terms to obtain the following:

$$\sum_{k=-\infty}^{+\infty} \sum_{n=-2}^{2} \left\{ \begin{array}{c} (\omega_{\nu,\mathrm{iso}} + k\omega_r) a_{\nu,k}(\alpha, \beta) e^{-ik\omega_r t} - \\ (-1)^n W_{\nu,n}(\alpha, \beta) a_{\nu,k}(\alpha, \beta) e^{-i(k-n)\omega_r t} \end{array} \right\} = 0 \quad (2.28)$$

Equation (2.28) is multiplied by $e^{i\lambda\omega_r t}$ and integrated over time. The Kronecker delta is used to exploit the orthogonal character of the Fourier expansion terms to give

$$\sum_{k=-\infty}^{+\infty} \sum_{n=-2}^{2} \left\{ \begin{array}{c} (\omega_{\nu,\mathrm{iso}} + k\omega_r) a_{\nu,k}(\alpha, \beta) \delta_{k,\lambda} - \\ (-1)^n W_{\nu,n}(\alpha, \beta) a_{\nu,k}(\alpha, \beta) \delta_{k-n,\lambda} \end{array} \right\} = 0 \quad (2.29)$$

Equation (2.29) may be placed into a compacted expression by enforcing the various $\delta_{k,\lambda}$ terms, expanding the n index explicitly, and temporarily ignoring the α, β and ν designations to reduce complexity. This gives the following set of constrained equations:

$$\sum_{\lambda=-\infty}^{+\infty} \{W_2 a_{\lambda+2} - W_1 a_{\lambda+1} + \lambda\omega_r a_\lambda - W_{-1} a_{\lambda-1} + W_{-2} a_{\lambda-2}\} = 0 \quad (2.30)$$

Each set of five terms in $n = -2, \ldots, +2$ for a constant value of λ becomes linearly independent expressions, and a summation over λ converts equation (2.30) into the following set of simultaneous equations:

$$\begin{array}{ccccccc} & & \cdots & & \cdots & \cdots \\ W_{-2}a_{-4} & -W_{-1}a_{-3} & -2\omega_r a_{-2} & -W_1 a_{-1} & +W_2 a_0 & = 0 & \lambda = -2 \\ W_{-2}a_{-3} & -W_{-1}a_{-2} & -\omega_r a_{-1} & -W_1 a_0 & +W_2 a_1 & = 0 & \lambda = -1 \\ W_{-2}a_{-2} & -W_{-1}a_{-1} & +0 & -W_1 a_1 & +W_2 a_2 & = 0, & \text{for } \lambda = 0 \\ W_{-2}a_{-1} & -W_{-1}a_0 & +\omega_r a_1 & -W_1 a_2 & +W_2 a_3 & = 0 & \lambda = 1 \\ W_{-2}a_0 & -W_{-1}a_1 & +2\omega_r a_2 & -W_1 a_3 & +W_2 a_4 & = 0 & \lambda = 2 \\ & & \cdots & & \cdots & \cdots \end{array} \quad (2.31)$$

The compacted notation for the W_n and a_λ is used for convenience, but it must be remembered that W_n and a_λ terms both include ν and the $\alpha\beta$ axis designations. By converting equation (2.31) into a matrix product, this set of simultaneous equations gives the typical secular equation as follows:

$$\begin{bmatrix} \cdots & \cdots & \cdots & \cdots & & & & & \\ W_{-2} & -W_{-1} & -2\omega_r & -W_1 & W_2 & 0 & 0 & 0 & 0 \\ 0 & W_{-2} & -W_{-1} & -\omega_r & -W_1 & W_2 & 0 & 0 & 0 \\ 0 & 0 & W_{-2} & -W_{-1} & 0 & -W_1 & W_2 & 0 & 0 \\ 0 & 0 & 0 & W_{-2} & -W_{-1} & \omega_r & -W_1 & W_2 & 0 \\ 0 & 0 & 0 & 0 & W_{-2} & -W_{-1} & 2\omega_r & -W_1 & W_2 \\ & & & & & \cdots & \cdots & \cdots & \cdots \end{bmatrix} \times \begin{bmatrix} \cdots \\ a_{-2} \\ a_{-1} \\ a_{0^-} \\ a_1 \\ a_2 \\ \cdots \end{bmatrix} = 0 \quad (2.32)$$

Diagonalization of the banded matrix with the Gaussian elimination procedure yields values for the $a_{\nu,\lambda}(\alpha\beta)$ eigenvectors that encode the $W_{\nu,n}(\alpha, \beta)$ information for the νth spin. Recall from equation (2.19) that $W_{\nu,n}(\alpha, \beta)$ contains the acent and span irreducible spectral parameters and the α, β Euler angles that prescribe the geometric orientation α, β of the turning axis relative to the PAF. The infinite expansion in λ converges quite rapidly once λ times the interval between spinning sidebands exceeds the span of the tensor band. As k and λ are both arbitrary indices in equation (2.29), the solution for $a_{\nu,\lambda}(\alpha\beta)$ from equation (2.32) converts equation (2.26) into

$$m_\nu(\alpha, \beta|t) = A \sum_{\lambda=-\infty}^{+\infty} a_{\nu,\lambda}(\alpha, \beta) e^{-i(\omega_{\nu,\mathrm{iso}} + \lambda\omega_r)t} \quad (2.33)$$

2.5.3 *Powder Averaging over α and β*

A final powder average over the α, β turning axes still is needed to compare the results with the acquisition FID. This step is accomplished by solving equation (2.32) for each member of the complete set of spherical surface points defined by α, β. One then must sum $m_\nu(\alpha, \beta|t)$ over all α, β rotation axes to define $M_\nu(t)$, the acquisition FID, of the νth spin as follows:

$$M_\nu(t) = \sum_{\alpha\beta} w_{\alpha\beta} \cdot m_\nu(\alpha\beta|t) \quad (2.34)$$

The weighting factor, $w_{\alpha\beta}$, for the α, β mechanical turning vector prescribes the fraction of spherical surface area assigned to each α, β rotational axis. Thus, $w_{\alpha\beta}$ are essential to weight the fractional contributions of a surface summation over $a_{\nu,\lambda}(\alpha\beta)$.

The powder averaging is straightforward as long as one is moving in the forward direction, where known chemical-shift values simulate a rotational pattern. This process involves merely selecting a representative and distributed number of surface points over which the numerical mapping can faithfully convert the shift values into adequate spectral response functions. Such ensemble averaging over α, β affects only the $W_{n=\pm1,\pm2}$ terms in equation (2.32). Accordingly, the $a_{\nu,\lambda}(\alpha\beta)$ values for each subset of spins, properly weighted and designated by α, β are stored in a summation register to give the ensemble average for $M_\nu(t)$.

Among the first numerical approaches used in such problems was the POWDER method by Alderman et al.[27] This method utilizes an octahedral face embedded into one of the PAF octants prescribed by the chemical shift tensor. The equilateral triangular face is readily subdivided to yield the number of points required for convergence. These points also have a specific factor that weights the fraction of surface points subtended in the solid angle of the incremental triangular segment. A numerical method by Lebedev,[28] and used by Eden and Levitt,[29] is based on a mathematical procedure for averaging physical properties over the surface of a sphere. The machinery, involving spherical-harmonic expansions of the spherical surface, requires the utilization of defined surface points along with appropriate weighting factors. The Utah laboratory has found that the Lebedev method converges rapidly and its sophistication makes it slightly more precise than the POWDER method for the same number of α, β points. However, increasing the number of spherical surface points to achieve more precision in the Lebedev convergence can become somewhat laborious if the set is not

readily available. Conversely, altering the number of surface points is easily achieved in the POWDER method.[27] A number of other numerical schemes[28] have been used to powder-average α, β surface points, but our laboratory has had experience only with POWDER and the Lebedev approach.

A slightly more challenging problem is the extraction of chemical shift parameters from the rotational bands found for a new nuclear rotational pattern. In this reverse approach, one uses successive iterations, guided by the simplex method, to converge on the best set of tensor-shift parameters to fit the rotational patterns. Initial shift parameters are selected and used with equation (2.32) to obtain an initial set of $a_{\nu,\lambda}(\alpha\beta)$. These initial FID values are compared with the experimental FID values, and simplex fitting varies the shift parameters until satisfactory convergence is reached between the experimental and computed results. In subsequent iterations, the set of $a_{\nu,\lambda}(\alpha\beta)$ must be re-scaled by properly weighting with $w_{\alpha\beta}$. As the Gaussian elimination procedure for diagonalizing a banded matrix is efficient, this iterative numerical method for powder averaging α, β orientations achieves convergence with remarkably efficiency even with a modest PC computer.

3 THE 5π-PULSE EXPERIMENT[7]

Figure 2 presents the basic sequence for the 5π-PULSE experiment subdivided into the evolution and acquisition regimes. During the rotor period, T, five π or 180° pulses modulate the developing phases of the magnetization, Φ_j, in the evolution regime. Figure 2 summarizes the respective evolution details rendered in time variables (T, t_e), or in phase angles $(2\pi, \Phi_{j=1,\ldots,6})$.

A mixture of γ_t in radians and degrees will be used for clarity and/or compaction of the notation. This use should be clear even if slightly inconsistent. Note the phase modulation in the evolution dimension at T is only dependent on the isotropic shifts of the various nuclear spins.

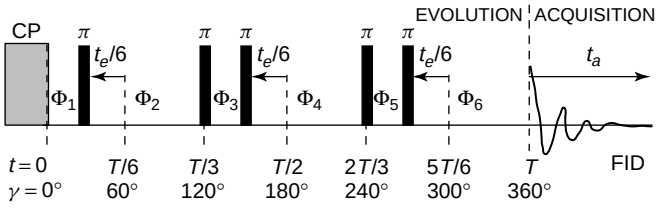

Figure 2 Carbon channel pulse sequence for the 5π-PULSE experiment. (Adapted from Ref.[7] with permission)

3.1 Magnetization in the 5π-PULSE Experiment

A standard 2D FID for a multinuclear subsystem of spins has the following general form:

$$m_\nu(t_e, t_a) = \sum_{\nu=1}^{N_\nu} m_o(\nu) \cdot g_\nu(t_e) \cdot f_\nu(t_a) \tag{3.1}$$

The sum over the index ν includes the different nuclei in the sample. $m_o(\nu)$ is the initial magnetization of the νth spin. The time-dependent function, $f_\nu(t_a)$, expresses the contribution from the νth FID. These functions are digitized and converted into frequency space using FT methods. At $t = T$ the phase accumulation during the evolution period for the νth nucleus is

$$g_\nu(t_e) = e^{-R_\nu(T)} e^{i\Phi_\nu(t_e)} \tag{3.2}$$

The term, $e^{i\Phi_\nu(t_e)}$, is a periodic phase-angle accumulation factor characterized by the angle, $\Phi_\nu(t_e)$. Equal pulse offsets, given in Figure 2 for the 1st, 3rd and 5th π pulses, are defined by the evolution time, t_e, on which $\Phi_\nu(t_e)$ depends. The five π pulses are equally spaced at $t_e = 0$, leaving the phase accumulation, for this specific evolution time, refocused and unaltered at time T. Combining equations (3.1) and (3.2) yields

$$m_\nu(t_e, t_a) = m_o(\nu) e^{-R_\nu(T)} e^{i\Phi_\nu(t_e)} f_\nu(t_a) \tag{3.3}$$

The relaxation term, $e^{-R_\nu(T)}$, in equations (3.2) and (3.3) decreases $m_o(\nu)$ to an effective magnetization value, $m_o(\nu)e^{-R_\nu(T)}$, that obtains when the acquisition FID begins. This decrease results from spin-spin relaxation with an effective rate given by

$$R_\nu(T) = l\left(\frac{T}{T_{L_\nu}}\right) + h\left(\frac{T}{T_{G_\nu}}\right)^2 \tag{3.4}$$

The relaxation constants, T_{L_ν} and T_{G_ν}, are the respective Lorentzian and Gaussian relaxation times typically used in solid-state studies, and mixing coefficients are l and h.

3.2 The Relationship between Phase Accumulation and the 5π-Pulse Scheme

An analysis of the phase angles in Figure 2 supplies the phase factors associated with the evolution dimension of the 2D spectrum. Table 1 summarizes the accumulation of angular phase due to rotation in the MAT experiment and to the π reflections on $m_\nu(\alpha, \beta|t)$ found in equation (2.33). The five π pulses are specified in Figure 2.

In this development, the B_1 field lies along the original $m_o(\nu)$ axis, but any other presumption would only produce

Table 1

jth phase	Developing phase accumulation	
	At the beginning of the jth period	At the end of the jth period
1	0	ϕ_1
2	$-\phi_1$	$\phi_2 - \phi_1$
3	$\phi_1 - \phi_2$	$(\phi_1 + \phi_3) - \phi_2$
4	$\phi_2 - (\phi_1 + \phi_3)$	$(\phi_2 + \phi_4) - (\phi_1 + \phi_3)$
5	$(\phi_1 + \phi_3) - (\phi_2 + \phi_4)$	$(\phi_1 + \phi_3 + \phi_5) - (\phi_2 + \phi_4)$
6	$(\phi_2 + \phi_4) - (\phi_1 + \phi_3 + \phi_5)$	$(\phi_2 + \phi_4 + \phi_6) - (\phi_1 + \phi_3 + \phi_5)$

an arbitrary phase shift that ultimately fails to affect the conclusions. At the end of the evolution period, i.e., $t = T$, the phase-angle accumulation becomes

$$\Phi_\nu(t_e) = (\Phi_2 + \Phi_4 + \Phi_6) - (\Phi_1 + \Phi_3 + \Phi_5) \tag{3.5}$$

The six phase periods, Φ_j, develop according to the following integrals along the γ_t path:

$$\Phi_j = \int_{t(j-1)}^{t(j)} \omega_\nu(\mathrm{LAB}|t)\,\mathrm{d}t = \frac{T}{2\pi}\int_{\gamma(j-1)}^{\gamma(j)} \omega_\nu(\mathrm{LAB}|\gamma_t)\,\mathrm{d}\gamma_t \tag{3.6}$$

where $\omega_\nu(\mathrm{LAB}|t)$ and $\omega_\nu(\mathrm{LAB}|\gamma_t)$ are the relevant t or γ_t forms of equation (2.24) for the νth spin. The two forms of integrals in equation (3.6) relate by a conformal change of variables from time to a rotational angle given by

$$\gamma_t = \omega_r t \quad \text{and} \quad \mathrm{d}t = \frac{\mathrm{d}\gamma_t}{\omega_r} = \frac{T}{2\pi}\,\mathrm{d}\gamma_t \tag{3.7}$$

The constraints imposed by equation (3.7) upon equation (3.6) and by the information and conventions in Figure 2 specify the specific phase-angle expressions as follows:

$$\begin{aligned}
\Phi_1 &= \frac{T}{2\pi}\int_0^{\frac{\pi}{3}-\frac{\pi}{3}t_e/T} \omega_\nu(\mathrm{LAB}|\gamma_t)\,\mathrm{d}\gamma_t \\
\Phi_2 &= \frac{T}{2\pi}\int_{\frac{\pi}{3}-\frac{\pi}{3}t_e/T}^{\frac{2\pi}{3}} \omega_\nu(\mathrm{LAB}|\gamma_t)\,\mathrm{d}\gamma_t \\
\Phi_3 &= \frac{T}{2\pi}\int_{\frac{2\pi}{3}}^{\pi-\frac{\pi}{3}t_e/T} \omega_\nu(\mathrm{LAB}|\gamma_t)\,\mathrm{d}\gamma_t \\
\Phi_4 &= \frac{T}{2\pi}\int_{\pi-\frac{\pi}{3}t_e/T}^{\frac{4\pi}{3}} \omega_\nu(\mathrm{LAB}|\gamma_t)\,\mathrm{d}\gamma_t \\
\Phi_5 &= \frac{T}{2\pi}\int_{\frac{4\pi}{3}}^{\frac{5\pi}{3}-\frac{\pi}{3}t_e/T} \omega_\nu(\mathrm{LAB}|\gamma_t)\,\mathrm{d}\gamma_t \\
\Phi_6 &= \frac{T}{2\pi}\int_{\frac{5\pi}{3}-\frac{\pi}{3}t_e/T}^{2\pi} \omega_\nu(\mathrm{LAB}|\gamma_t)\,\mathrm{d}\gamma_t
\end{aligned} \tag{3.8}$$

The $\omega_\nu(\mathrm{LAB}|\gamma_t)$ frequency response function in the laboratory frame, taken from equation (2.24), is modified to separate the zero-rank from the second-rank terms, as follows:

$$\begin{aligned}
\omega_\nu(\mathrm{LAB}|\gamma_t) &= \sum_{n=-2}^{2} (-1)^n W_{\nu,n}(\alpha,\beta)e^{in\gamma_t} \\
&= W_{\nu,o} + \sum_{n=\pm1,\pm2} (-1)^n W_{\nu,n}(\alpha,\beta)e^{in\gamma_t}
\end{aligned} \tag{3.9}$$

The $\omega_\nu(\mathrm{LAB}|\gamma_t)$ in equation (3.9) is divided into its two parts (i.e., the zero-rank rotationally invariant term, $W_{\nu,o}$, and four second-rank terms given by the summation of n over ±1 and ±2).

3.2.1 The Zero-Rank Term

The phase associated with the zero-rank term, $W_{\nu,o} = \omega_{\mathrm{iso}}$, of equation (3.9) when substituted into equation (3.8) and in turn into equation (3.5) yields the following:

$$\begin{aligned}
&\Phi_\nu(t_e) \\
&= \frac{T\omega_{\mathrm{iso}}}{2\pi}\left\{\begin{aligned}
&-\int_0^{\frac{\pi}{3}-\frac{\pi}{3}t_e/T}\mathrm{d}\gamma_t + \int_{\frac{\pi}{3}-\frac{\pi}{3}t_e/T}^{\frac{2\pi}{3}}\mathrm{d}\gamma_t - \int_{\frac{2\pi}{3}}^{\pi-\frac{\pi}{3}t_e/T}\mathrm{d}\gamma_t \\
&+\int_{\pi-\frac{\pi}{3}t_e/T}^{\frac{4\pi}{3}}\mathrm{d}\gamma_t - \int_{\frac{4\pi}{3}}^{\frac{5\pi}{3}-\frac{\pi}{3}t_e/T}\mathrm{d}\gamma_t + \int_{\frac{5\pi}{3}-\frac{\pi}{3}t_e/T}^{2\pi}\mathrm{d}\gamma_t
\end{aligned}\right\} \\
&= \frac{T\omega_{\mathrm{iso}}}{2\pi}\left\{2\left(-\tfrac{\pi}{3}+\tfrac{2\pi}{3}-\pi+\tfrac{4\pi}{3}-\tfrac{5\pi}{3}\right)+2\pi+2\pi\frac{t_e}{T}\right\} \\
&= \omega_{\mathrm{iso}}t_e
\end{aligned} \tag{3.10}$$

This form may now be substituted into equation (3.2) as discussed below.

3.2.2 The Second-rank Terms

Attention is now directed to the second-rank terms (i.e., $n = \pm1,\ \pm2$) of equation (3.9). These components vanish under the symmetry of equation (3.5). It is sufficient to show that any one of the generic terms is zero for all four second-rank terms to vanish. Thus, equations (3.5), (3.6) and any of the $n \neq 0$ components of equation (3.9) gives

$$\begin{aligned}
\Phi_{\nu,n}(t_e) &= \frac{T(-1)^n W_{\nu,n}(\alpha,\beta)}{2\pi} \\
&\times\left\{\begin{aligned}
&-\int_0^{\frac{\pi}{3}-\frac{\pi}{3}t_e/T} e^{in\gamma_t}\,\mathrm{d}\gamma_t + \int_{\frac{\pi}{3}-\frac{\pi}{3}t_e/T}^{\frac{2\pi}{3}} e^{in\gamma_t}\,\mathrm{d}\gamma_t \\
&-\int_{\frac{2\pi}{3}}^{\pi-\frac{\pi}{3}t_e/T} e^{in\gamma_t}\,\mathrm{d}\gamma_t + \int_{\pi-\frac{\pi}{3}t_e/T}^{\frac{4\pi}{3}} e^{in\gamma_t}\,\mathrm{d}\gamma_t \\
&-\int_{\frac{4\pi}{3}}^{\frac{5\pi}{3}-\frac{\pi}{3}t_e/T} e^{in\gamma_t}\,\mathrm{d}\gamma_t + \int_{\frac{5\pi}{3}-\frac{\pi}{3}t_e/T}^{2\pi} e^{in\gamma_t}\,\mathrm{d}\gamma_t
\end{aligned}\right\}
\end{aligned} \tag{3.11}$$

Upon integrating, one obtains

$$\begin{aligned}
\Phi_{\nu,n}(t_e) &= \frac{T(-1)^n W_{\nu,n}(\alpha,\beta)}{2\pi i n} \\
&\times\left\{\begin{aligned}
&2(+e^{in120^\circ}+e^{in240^\circ})+e^{in0^\circ}+e^{in360^\circ} \\
&+2(e^{in60^\circ}+e^{in180^\circ}+e^{in300^\circ})e^{in60^\circ t_e/T}
\end{aligned}\right\} = 0
\end{aligned} \tag{3.12}$$

Hence, the symmetry of the 5π-pulse sequence results in nullifying the four second-rank terms and in turn suppressing each of the sideband terms. This pulse scheme leaves the 2D spectrum to develop along the evolution direction under the influence of only the isotropic shifts.

3.3 The 2D FIREMAT FID Magnetization

The evolution FID for the νth nucleus is given by substituting equation (3.10) into equation (3.2),

$$g_\nu(t_e) = e^{-R_\nu(T)}e^{i\omega_{\nu,\mathrm{iso}}t_e} \tag{3.13}$$

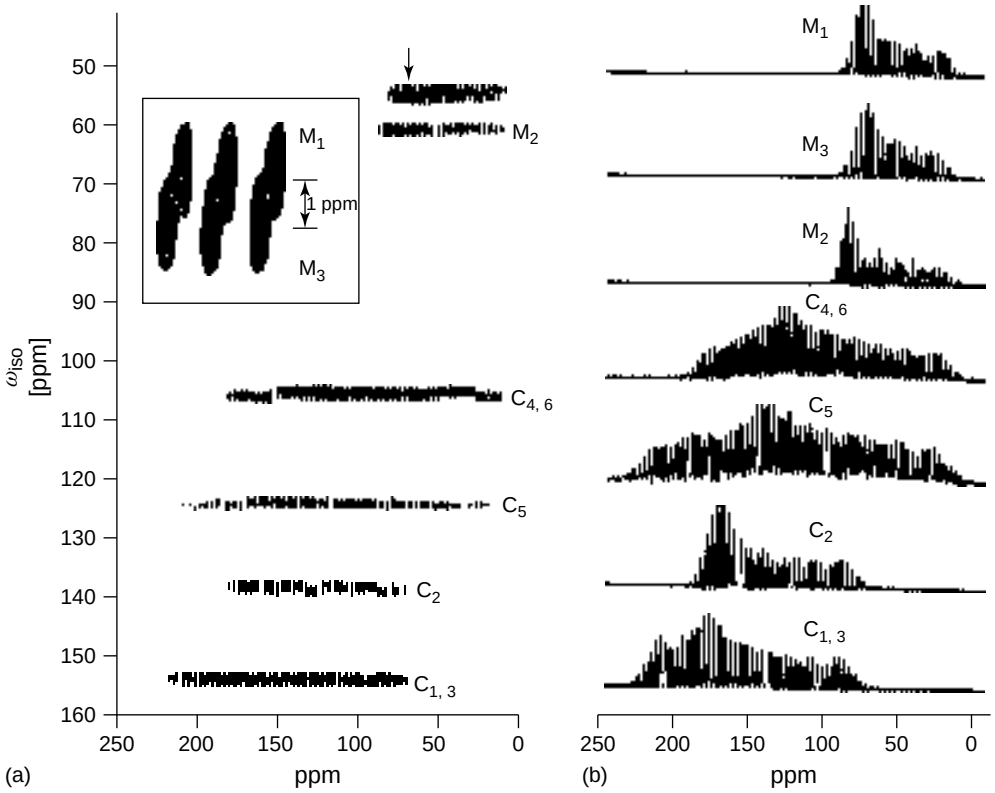

Figure 3 (a) A contour plot of the 5π-PULSE spectrum of 1,2,3-trimethoxybenzene, and (b) the corresponding ω_{iso} slices through the contour plot. The insert in (a) is a blow-up of a portion in the 1 and 3 methyl patterns to indicate the resolution between M_1 and M_3. (Reproduced from Ref.[7] with permission)

which when substituted into equation (3.1) yields an expression for the 2D FID.

$$m_\nu(t_e, t_a) = \sum_{\nu=1}^{N_\nu} m_o(\nu) e^{-R_\nu(T)} e^{i\omega_{\nu,\mathrm{iso}} \cdot t_e} f_\nu(t_a) \qquad (3.14)$$

Equation (3.14) is now in the standard mathematical form of a typical 2D FID with the acquisition FIDs separated linearly from the isotropic FID. The 2D FT of equation (3.14) yields a high-quality 2D spectrum in the frequency domain of solid 1,2,3-trimethoxybenzene (see Figure 3). Both the contour plot and corresponding slices through the different carbon-tensor bands exhibit representative data from the 5π-PULSE experiment.

3.3.1 The Individual Spin FIDs in the Acquisition Dimension

The acquisition FID, $f_\nu(t_a)$, is sampled rapidly and extends for a sufficient period for the νth nucleus to yield adequate spectral range and resolution in this dimension. In Figure 3(b) the spinning sideband patterns for the νth nucleus are separated by their isotropic shifts. A trade-off exists between decreasing the magnetization at T (i.e., $t_a = 0$) due to spin relaxation and the need for t_e to be sufficiently long to yield an evolution spectrum of adequate resolution.

4 TIGER PROCESSING OF TWO-DIMENSIONAL NMR SPECTRA

The rather significant compromises, made between S/N and resolution in solid NMR spectra, impact the accuracy of determining spectral parameters in solid NMR experiments. All Fourier methods experience such difficulties, of course, but solid spectra are particularly sensitive to this trade-off because of relatively rapid spin-spin relaxation in solids compared with liquids. Shortening the length of the evolution sampling periods minimizes loss of magnetization from such relaxation effects and increases the time efficiency of the experiment. Unfortunately, the resolution of the experiment is adversely affected. Early MAT solid-state experiments suffered from detrimental flip back pulses that significantly attenuate the magnetization in the xy plane, but the 5π-PULSE method avoids this problem of flip back pulses in the traditional MAT suite of experiments. However, as implied in Section 3 this method still requires relatively extensive evolution data-tables to achieve high resolution.

The so-called TIGER procedure[15] offers a way to extract high-resolution data from an otherwise truncated evolution data. Conversely, use of more but shorter t_e time increments increases the spectral width and thereby diminishes the incidence of aliasing in the evolution dimension. Such compromises in the t_a dimension are avoided because of the size of the acquisition FID data tables. In the process of achieving this objective with TIGER, the workers at the Utah NMR laboratory rediscovered two important papers by Manassen, Navon, and Moonen,[30,31] in which an extensive mathematical basis for TIGER is given. The minor differences between TIGER and the work of Manassen et al.[30,31] primarily reflect the different spectroscopic capabilities common in spectrometers extant at the two different publication times (separated by a decade). Specialists will want to study the complete

mathematical treatments of TIGER contained in these three relevant references.[15,30,31] TIGER is a general multidimensional method that has potential for enhancing a number of NMR applications, but the space and focus of this article precludes treatments that go beyond how TIGER works in MAT experiments.

4.1 Matrix Form of the FID Expression

Equation (3.14) may be formulated in standard matrix notation by first casting this equation in a form that reflects the digitized arrays encountered in data collection methods. This is done by expressing $t_e = (n_e - 1)\tau_e$ and $t_a = (n_a - 1)\tau_a$, where τ_e and τ_a are the incremental sampling periods in the respective evolution[32] and acquisition dimensions. The integer 1 is subtracted from digitization indices, n_e and n_a, to allow t_e and t_a to assume zero values. Thus, the digitizing indices, $n_e = 1, \ldots, N_e$ and $n_a = 1, \ldots, N_a$, are associated with N_e and N_a that are respectively the total number of evolution and acquisition increments. The νth spin index is n_ν. The digitized matrices appear as follows:

$$\mathbf{M}(n_e, n_a)_{N_e \text{ by } N_a} = \mathbf{G}(n_e, \nu)_{N_e \text{ by } N_\nu} \cdot \mathbf{F}(\nu, n_a)_{N_\nu \text{ by } N_a} \quad (4.1)$$

where

$$\mathbf{G}(n_e, \nu) = m_o(n_\nu) e^{-R_\nu(T)} e^{i(n_e-1)\omega_{\nu,\text{iso}}\tau_e} \quad (4.2)$$

$$\mathbf{F}(\nu, n_a) = f_\nu([n_a - 1]\tau_a) \quad (4.3)$$

The matrix multiplication in equation (4.1) represents the sum over ν in equation (3.14). In addition, the matrix dimensions, given in equation (4.1), assist in their physical interpretation as a row labeled by ν in $\mathbf{F}(\nu, n_a)$ contains the acquisition contribution to the FID for the νth spin. Likewise, the ν column in $\mathbf{G}(n_e, \nu)$ specifies the corresponding evolution FID component for the νth spin. While the individual $\mathbf{G}(n_e, \nu)$ and $\mathbf{F}(\nu, n_a)$ components are not directly measurable in the 5π-PULSE experiment, the 2D digitized components represented by $\mathbf{M}(n_e, n_a)$ are obtained directly in 2D 5π-PULSE experiments.

Manipulating equation (4.1) allows the extraction of $\mathbf{F}(\nu, n_a)$ from $\mathbf{M}(n_e, n_a)$. Multiplying both sides of equation (4.1) by the complex transpose, $\tilde{\mathbf{G}}^*(\nu, n_e)$, yields

$$\tilde{\mathbf{G}}^*(\nu, n_e)_{N_\nu \text{ by } N_e} \cdot \mathbf{M}(n_e, n_a)_{N_e \text{ by } N_a} = \{\tilde{\mathbf{G}}^*(\nu, n_e) \cdot \mathbf{G}(n_e, \nu)\}_{N_\nu \text{ by } N_\nu} \cdot \mathbf{F}(\nu, n_a)_{N_\nu \text{ by } N_a} \quad (4.4)$$

The inverse square matrix $\{\tilde{\mathbf{G}}^*(\nu, n_e) \cdot \mathbf{G}(n_e, \nu)\}^{-1}$, converts equation (4.4) into equation (4.5) and provides the desired $\mathbf{F}(\nu, n_a)$:

$$\mathbf{F}(\nu, n_a)_{N_\nu \text{ by } N_a} = \{\tilde{\mathbf{G}}^*(\nu, n_e) \cdot \mathbf{G}(n_e, \nu)\}^{-1}_{N_\nu \text{ by } N_\nu} \cdot \tilde{\mathbf{G}}^*(\nu, n_e)_{N_\nu \text{ by } N_e} \cdot \mathbf{M}(n_e, n_a)_{N_e \text{ by } N_a} \quad (4.5)$$

Both sides of equation (4.5) generate matrices that are of identical dimensions, N_ν by N_a. Hence, corresponding ν rows identify directly with each other. These $\mathbf{F}(\nu, n_a)$ vectors provide a separated and digitized FID for each of the νth spins. Hamilton[33] and Graybill[34] describe this matrix process as a way to perform a linear regression or a linear least-squares fit in general, and in particular for the FID of each individual spin in this application. Redundant data, when available, actually improve the mathematical analysis.

The mathematical developments linking equations (4.1) and (4.5) presumes a number of constraints on the equations to render the matrix procedures viable. It is essential that $N_e \geq N_\nu$. The index N_e is the total number of evolution increments and N_ν is the number of different nuclear spins. When $N_e < N_\nu$, the evolution data are insufficient to complete the matrix operations for all nuclear spins (i.e., $\nu = 1, \ldots, N_\nu$) and the process fails. If $N_e > N_\nu$, redundancy exists in the evolution data, and the matrix manipulations provide an even better regression or least-squares fit of the data. Should $N_e = N_\nu$, the operations yield solutions for the $\mathbf{F}$ vectors but without the statistical benefit of redundant data. Redundancy reduces the errors in a least-squares analysis. A final constraint on the mathematical manipulations requires the existence of a so-called guide spectrum expressed by $\mathbf{G}(n_e, \nu)$. Further details appear in Section 4.2.

This contraction of the 2D digitized FID data to individual nuclear 1D FIDs, is definitely not an FT procedure. Instead, the process involves more of a convolution method based on linear regression principles used in matrix least-squares computations.

4.2 Fitting the Guide Spectrum

The digitized guide spectra, contained in the $\mathbf{G}(n_e, \nu)$ matrix, starts with a typical isotropic spectrum such as obtained from a MAS high-speed spinning spectrum. Each isotropic peak is simulated and the corresponding digitized vector is placed into the νth row of the associated $\tilde{\mathbf{G}}^*(\nu, n_e)$ matrix to give

$$\tilde{\mathbf{G}}^*(\nu, N_e) = [\tilde{g}^*(\nu, 1) \cdots \tilde{g}^*(\nu, n_e) \cdots \tilde{g}^*(\nu, N_e)] \quad (4.6)$$

The individual digitized $\tilde{g}^*(\nu, n_e)$ value is the n_e element of the $\tilde{\mathbf{G}}^*(\nu, N_e)$ vector for the νth spin, and standard matrix methods give $\mathbf{G}(N_e, \nu)$ from the associated matrix, $\tilde{\mathbf{G}}^*(\nu, N_e)$.

Fitting a high-resolution isotropic spectrum (e.g., a MAS spectrum) to $\tilde{\mathbf{G}}^*(\nu, N_e)$ or $\mathbf{G}(N_e, \nu)$ becomes a crucial step in modeling FIDs such as described in equation (4.6). The fitting procedure adjusts the isotropic spectral frequencies and line shapes with a SIMPLEX algorithm until a satisfactory spectral fit is achieved. The isotropic frequencies follow directly from the independent guide spectrum and the line shapes are simulated using both Lorentzian and Gaussian relaxation processes in accordance with equation (3.4).

4.3 Illustration of the TIGER Method

The most instructive drawing in the literature[15] for the TIGER procedure uses as an example the PHORMAT spectrum (a rotational, but dense sideband spectrum) of 1,2,3-trimethoxybenzene (see Figure 4). The TIGER method is general and an additional application of TIGER will be provided as an example of a FIREMAT spectrum in Section 5. Figure 4 provides a graphic illustration on how the isotropic guide spectrum is decomposed into the individual νth columns of the $\mathbf{G}(N_e, \nu)$ matrix and then used with the 2D FID data to obtain the acquisition FIDs that exhibit the shift-tensor information. In this example, the number of evolution increments was only

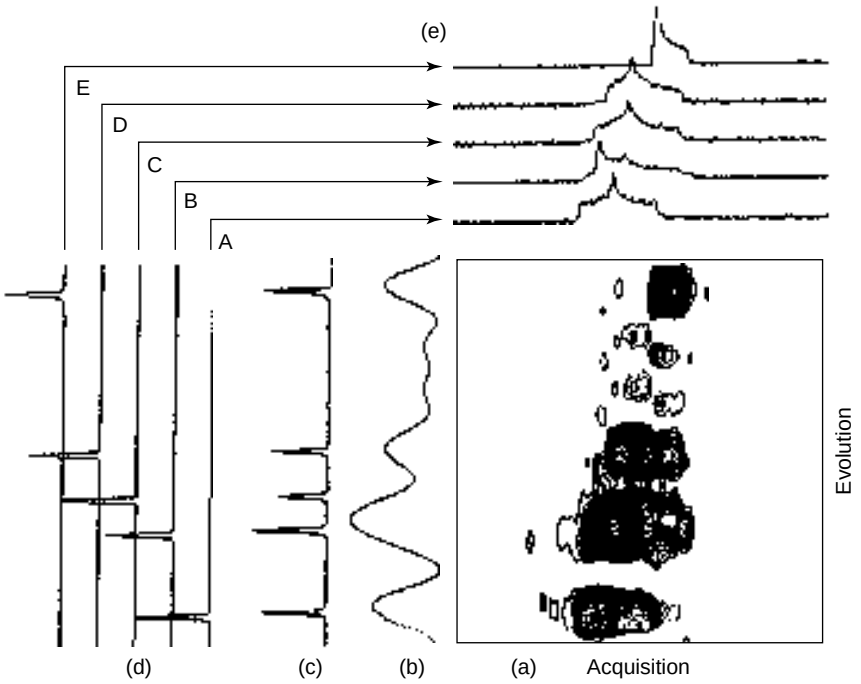

Figure 4 TIGER processing of a 2D solid spectrum of 2,6-dimethoxynaphthalene. (a) Typical 2D FT results obtained for the sparse eight evolution increments. (b) The projection of the 2D-frequency spectrum onto the evolution dimension illustrates the very broad lines in this dimension. (c) A sharp CP/MAS isotropic guide spectrum. (d) Individually simulated peaks of the CP/MAS spectrum provide the information for populating the **G** matrix. The simulated peaks involve a regression fit of both the frequency and shapes of the individual lines in the guide spectrum. (e) The de-convoluted individual ν shift-tensor bands. (Reproduced from Ref.[15] with permission)

eight, a number barely more than the six different nuclei in 2,6-dimethoxynaphthalene. This figure illustrates the unusual resolving power of the technique without a high evolution sampling rate that is costly in time. The narrow isotropic line widths imported into the evolution frequency dimension are at least an order of magnitude narrower than the corresponding line widths from a truncated FT of the 2D FID data. While the greater resolution of TIGER data is beneficial because of its discriminating abilities, the sharper line patterns also improve the S/N in the frequency domain.

Figure 4 includes one case of accidental degeneracy in peak B that is readily observable as two tensors in the B spectral band. Note importing the very narrow guide spectrum has the same effect of converting the broad peaks, shown in (b), into sharp frequency responses shown in Figure 4(c) for shift-tensor bands. This high resolution affects the accuracy with which spectral parameters can be determined. The increase in spectral definition and sensitivity is a hallmark of a TIGER processed spectrum.

5 THE FIREMAT VARIANT OF THE 5π-PULSE EXPERIMENT

The FIREMAT extension to the 5π-PULSE experiment uses the same evolution pulse scheme and TIGER processing method as the parent experiment. This new method also employs the pseudo 2D sideband suppression (P2DSS) replication strategy of Gan[35] to expand the data in the evolution dimension. By replicating information collected in the acquisition dimension and placing these data into the evolution dimension, the resolution is enhanced considerably along the isotropic shift axis. Whereas P2DSS collects data only at the rotor's echo position (i.e., 0, T, $2T$, etc.), FIREMAT replicates echoing data blocks found at all digitized increments. This allows one to decrease the number of evolution increments below the number of different nuclei that influences the TIGER method.

5.1 The P2DSS Method[35] and Replication of Refocused Spectral Data

The data replication scheme of P2DSS is given in Figure 5. The periodic features of MAT create rotational echoes in both dimensions and allow the data reorganization depicted in Figure 5. The echoes in both dimensions allow isotropic data tables to be populated solely from acquisition magnetization detected at multiples of T.

One may use the 1D string of evolution data along $t_a = 0$ to create a FID for the isotropic dimension. A Fourier transform from time to frequency space yields isotropic spectra that mimic a CP/MAS spectrum except for artifacts introduced by the discontinuous relaxation parameters, represented by the step functions along the right edge of Figure 5. Simulations indicate that sinc-type functions, resulting from these discontinuities, can introduce significant artifacts into the frequency spectrum whenever $T_2 \approx T$. Fortunately, the discontinuities smooth out when $T_2 > T$ and leave the baseline relatively unaffected as indicated in Figure 6.

5.2 The FIREMAT Method with Full Replication of Refocused Spectral Data

The FIREMAT variant[11] expands upon the P2DSS approach and digitizes throughout the whole rotor period in accordance with Figure 7. The magnetization experiences rotational

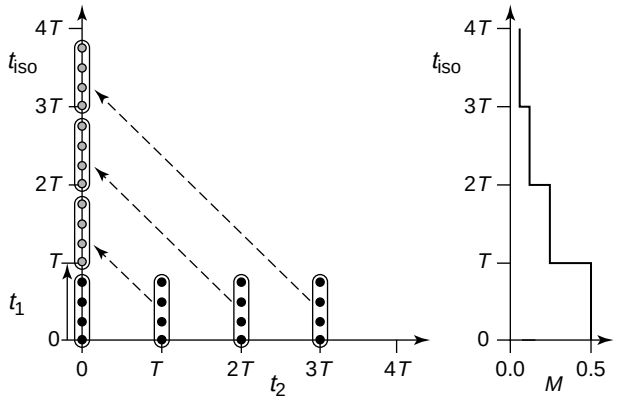

Figure 5 Graphical example of Gan's P2DSS Replication Scheme. The 2D FID is sampled in the acquisition dimension only at the echo position of the rotor. The solid circles represent the actual data. The open circles are replicated data obtained from the measured data and transported as shown in the figure. The right-hand side of the figure schematically represents the attenuation of the echo intensity due to relaxation during one rotation. (Reproduced from Ref.[11] with permission)

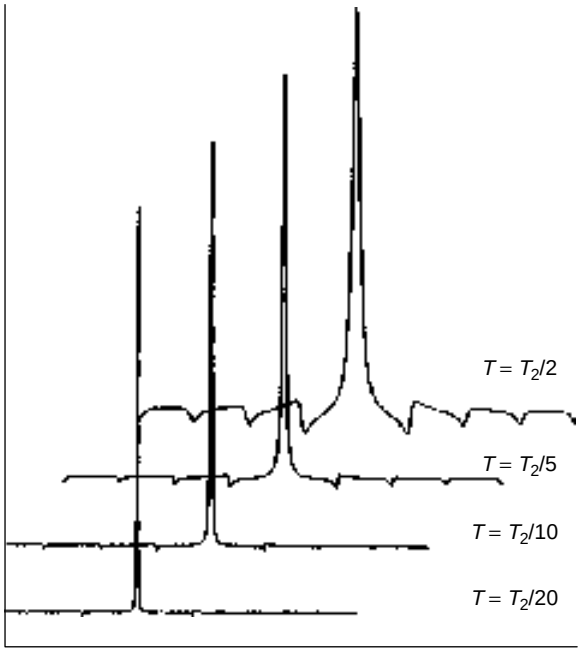

Figure 6 Sync-type artifacts are due to stepped relaxation discontinuities in the evolution data, but TIGER ameliorates this problem by minimizing the distortions. Note that, unlike true sidebands, the artifacts are dispersive and opposite in phase on each side of the spectral line. (Adapted from Ref.[11] with permission)

echoes at $t_a = T, 2T, \ldots, nT$, and, with repeated replication, a fully populated 2D evolution array may be obtained from the acquisition data-table. An $N_e \times N_a$ array bounds the size of this 2D data set, except as truncated by the replication process. The right border of Figure 7 again represents the discontinuous relaxation that may introduce spectral artifacts such as found in Figure 6.

Note the 1D string of FIREMAT data points along $t_a = 0$ constitutes the same 1D data used by Gan[35] to obtain

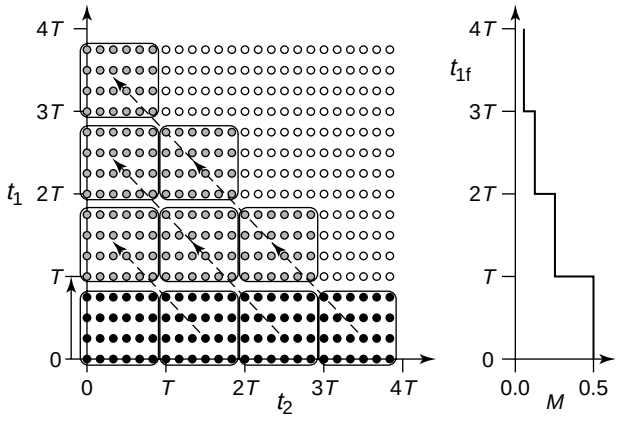

Figure 7 Graphical example of the FIREMAT replication scheme. Solid and open circles are actual and replicated data points of the type shown in Figure 5. The discontinuous relaxation intensities are again represented on the right-hand side of the figure. Data at the rotational echo positions and all intermediate positions populates a full 2D FT data table. (Reproduced from Ref.[11] with permission)

his P2DSS. While Gan's isotropic spectrum is more of an idiosyncratic construct of a CP/MAS spectrum, it becomes a special kind of 1D guide spectrum in the FIREMAT procedure. The guide, when constituted in this manner, arises directly from the 2D data and thus mitigates artifacts arising from irregularities in the replication step. The irregularities include discontinuous relaxation, correlation effects from repeated use of the same data, and possible abnormalities due to the manner in which the replicated blocks are truncated. Comparisons between single crystal and FIREMAT data fail to reveal significant replication errors.

5.3 FIREMAT Spectra of Erythromycin-A

Figure 8 illustrates the use of the FIREMAT method to obtain a spectrum on the medicinal, erythromycin-A, containing 36 different carbon atoms. The spectral quality and power of this 2D solid state technique is obvious and the time to acquire the data was only 19 h. The large numbers of carbons in erythromycin-A prevent the data from being presented conveniently in a single figure. Thus, the two remaining sp^2 carbons and a structure for erythromycin-A are given independently in Figure 8. Benefit is derived by aliasing the two sp^2 carbons into open spectral regions as the evolution timing increments can be decreased and the time-efficiency enhanced.

6 THE 2D-PASS FORM OF A 5π-PULSE EXPERIMENT

Antzutkin et al.[12] first proposed 2D-PASS by combining strategies used in PASS by Dixon[14] and in those underlying the 5π-PULSE experiment. In the evolution dimension, the 2D-PASS method separates, by spinning sideband order, the 2D FID. As the evolution dimension merely orders the sidebands by rank, this does not affect the high-resolution spectra found in the 2D-PASS approach[12] because all critical information is contained in the extensive acquisition FID. The original 1D-PASS, also a rotating solids experiment, uses only 4-π pulses

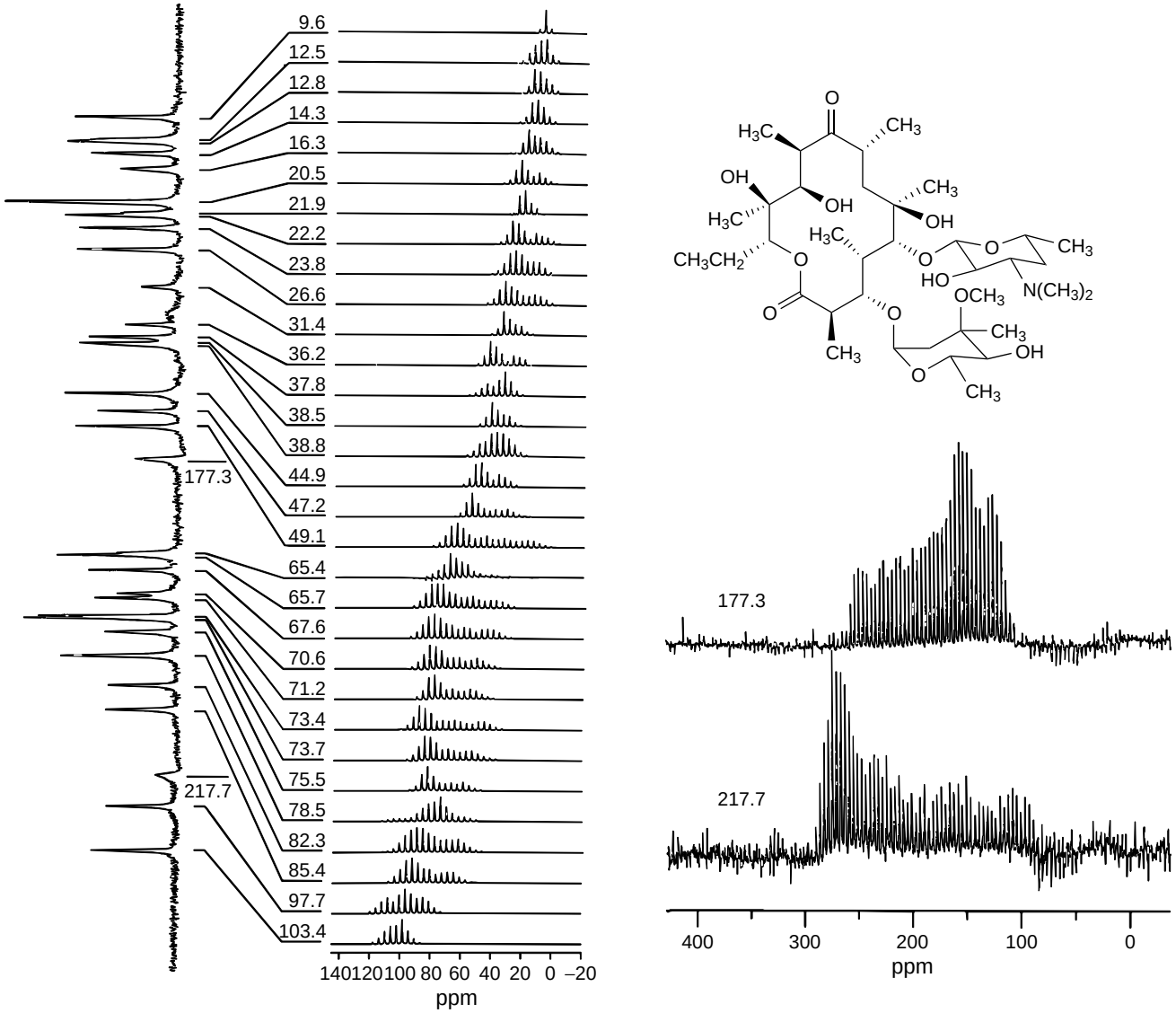

Figure 8 FIREMAT spectra of Erythromycin A Dihydrate shown from left to right for isotropic shifts and spinning sidebands of (a) sp^3 and (b) sp^2 carbons, respectively. (Reproduced from Ref.[11] with permission)

to phase adjust the spinning sidebands. However, if the original PASS approach[14] is adapted to a 2D 4π-PASS scheme, it would involve a variable-duration preparation period thereby introducing nonuniform relaxation. The fifth π-pulse included in 2D-PASS by Antzutkin et al.[12] refocuses the magnetization at a constant evolution period, T, and avoids variable spin relaxation perturbations that would otherwise deteriorate the 2D spectral quality.

6.1 The Postulated Pitch Angle

The 2D-PASS method utilizes a postulated variable pitch angle, Θ_e, or evolution time, t_e, defined in several different ways as follows:

$$\Theta_e = \omega_r t_e = 2\pi \frac{t_e}{T} = 2\pi \frac{n_e - 1}{N_e} \tag{6.1}$$

where ω_r is the slow-turning angular velocity and T is the period of the sample revolution.[36] The Θ_e and t_e have been formulated with linearly displaced evolution increments. The increment index is n_e, and the total number of evolution increments is N_e. To designate the $t_e = 0$ choice for the first increment, the integer 1 is again subtracted from n_e. Unfortunately, values for t_e are not programmed directly into the spectrometer's computer. A mathematical relation, however, relates the five π-pulses in the t_k timing sequence to the postulated Θ_e. Further, each of the five π-pulses is characterized by a time, t_k, or timing angle, θ_k, related to one another as follows: $t_k/T = \theta_k/2\pi$. This so-called pitch angle, Θ_e, is an important mathematical construct, designed to create a proper Fourier frequency conjugate that transforms the FIDs into separated rank-ordered sidebands. Hence,

$$m_v(t_e, t_a) = m_o(v)\Omega(t_e)F(t_a) \tag{6.2}$$

where the evolution phase factor, $\Omega(t_e)$ is given as

$$\Omega(t_e) = e^{-R(T)} e^{im\omega_r t_e} = e^{-R(T)} e^{im\Theta_e} \tag{6.3}$$

$F(t_a)$ is the acquisition FID separated by spinning sideband order. The formulation of Θ_e, in terms of the timing sequence of the π-pulses given by t_k, is represented graphically in Figure 9. This creative construction of Θ_e preserves the symmetry of the sideband information, while conforming to the standard 2D FID format for $m_\nu(t_e, t_a)$ given in equation (6.2).

6.2 The Relationships between the Pitch Angle and Timing Sequence

The connection between the evolution pitch angle, Θ_e, and the five timing angles, $\theta_{k=1,\ldots,5}$, follows the same mathematical machinery with slightly different notations from that used in Section 3.2. (Note $\theta_{k=0} = 0$ and $\theta_{k=6} = 2\pi$). This allows a direct comparison of the 5π-PULSE and 2D-PASS methods. It should be emphasized, however, that the expressions used herein are equivalent to the quintessential equations (28) and (29) of Antzutkin et al.[12] Using a common formalism enables one to appreciate the subtle differences and similarities between the 5π-PULSE and the 2D-PASS methods. The following equations are reproduced for convenience:

$$\Phi_\nu(t_e) = (\Phi_2 + \Phi_4 + \Phi_6) - (\Phi_1 + \Phi_3 + \Phi_5) \tag{3.5}$$

$$\Phi_j = \int_{t(j-1)}^{t(j)} \omega_\nu(\mathrm{LAB}|t)\,\mathrm{d}t = \frac{T}{2\pi}\int_{\gamma(j-1)}^{\gamma(j)} \omega_\nu(\mathrm{LAB}|\gamma_t)\,\mathrm{d}\gamma_t \tag{3.6}$$

$$\omega_\nu(\mathrm{LAB}) = \sum_{n=-2}^{2} (-1)^n W_{\nu,n}(\alpha,\beta)e^{in\gamma_t} = W_{\nu,o} + \sum_{n=\pm1,\pm2} (-1)^n W_{\nu,n}(\alpha,\beta)e^{in\gamma_t} \tag{3.9}$$

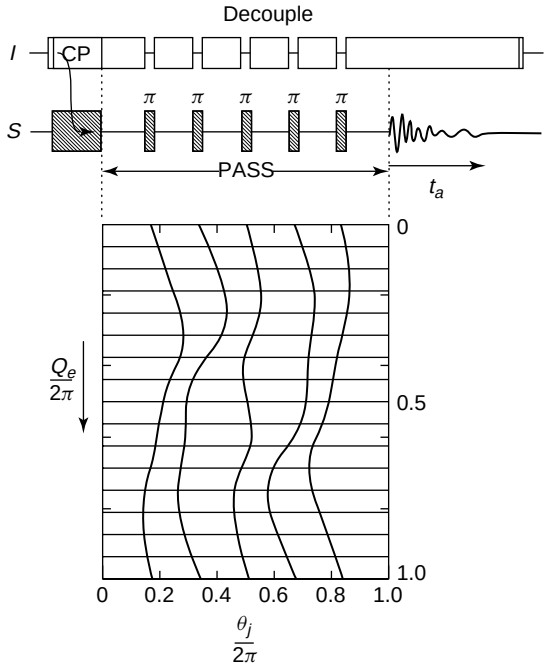

Figure 9 The pitch angle, Θ_e, plotted versues the phase displacements, $\theta_{j=1,\ldots,5}$, of the five π-pulses needed to refocus different sideband orders in the 2D PASS approach. (Adapted from Ref.[12] with permission)

The integral limits in 2D-PASS are specified by $\gamma(j) = \theta_j$. The total phase accumulation up to the time, t_e, for the nucleus ν is indicated by $\Phi_\nu(t_e)$, and the six corresponding sub-period phase accumulations by $\Phi_{j=1,\ldots,6}$ designated by the index j. These phase accumulations, illustrated explicitly in Figure 2 and implied in Figure 9, hold for each independent nucleus, ν. The zero-rank, $W_{\nu,n=o} = \omega_{\nu,\mathrm{iso}}$, and the second-rank, $W_{\nu,n=\pm1,\pm2}(\alpha,\beta)$, frequency terms are given explicitly in equation (2.19).

The imposed boundary conditions on the timing sequence differ between the 5π-PULSE and 2D-PASS experiments. In Section 3.2 it was noted that the 5π-PULSE timing sequence preserves the $\omega_{\nu,\mathrm{iso}}$ terms, but the remaining four second-rank terms, $W_{\nu,n=\pm1,\pm2}(\alpha,\beta)$, average to zero. It now is shown how 2D-PASS suppresses by design the $\omega_{\nu,\mathrm{iso}}$ terms while implementing a spectral feature based on the four $W_{\nu,n=\pm1,\pm2}(\alpha,\beta)$ terms.

6.2.1 The Zero-rank Term

By analogy to the 5π-PULSE development in Section 3.2.1, $\Phi_\nu(\Theta_e)$ may also be expressed for the zero-rank term in $\Phi_{j=1,\ldots,6}$ as follows:

$$\Phi_{\nu,n=o}(\Theta_e) = \omega_{\nu,\mathrm{iso}}\frac{T}{2\pi}\left[\left(\int_{\theta_1}^{\theta_2}\mathrm{d}\gamma_t + \int_{\theta_3}^{\theta_4}\mathrm{d}\gamma_t + \int_{\theta_5}^{2\pi}\mathrm{d}\gamma_t\right) - \left(\int_0^{\theta_1}\mathrm{d}\gamma_t + \int_{\theta_2}^{\theta_3}\mathrm{d}\gamma_t + \int_{\theta_4}^{\theta_5}\mathrm{d}\gamma_t\right)\right] \tag{6.4}$$

Integrating equation (6.4) yields the following expressions:

$$\Phi_{\nu,n=o}(\Theta_e) = \omega_{\nu,\mathrm{iso}}\frac{T}{2\pi}[-2(\theta_1 - \theta_2 + \theta_3 - \theta_4 + \theta_5) + 2\pi] = 0 \tag{6.5}$$

where $\Phi_{\nu,o}(\Theta_e)$ has been suppressed by setting it equal to zero. From equation (6.5) it becomes a simple matter to suppress the $\omega_{\nu,\mathrm{iso}}$ by forcing the linear combination of time angles to vanish. Hence, this null condition is used to form one of five constraints in the construction of Θ_e, and is expressed as

$$\pi - (\theta_1 - \theta_2 + \theta_3 - \theta_4 + \theta_5) = 0 \text{ or } t_1 - t_2 + t_3 - t_4 + t_5 = \frac{1}{2}T \tag{6.6}$$

The equivalent expression in time follows from $\theta_\kappa = 2\pi(t_\kappa/T)$.

6.2.2 The Second-rank Terms

Attention is now turned to the second-rank terms. As before, it is sufficient to integrate only one of the $n = \pm1, \pm2$ terms. Following the logic of Section 3.2.2, the n-labeled second-rank terms becomes

$$\Phi_\nu(\Theta_e) = (-1)^n W_{\nu,n}(\alpha,\beta) \times \frac{T}{2\pi}\left[\left(\int_{\theta_1}^{\theta_2} e^{in\gamma_t}\mathrm{d}\gamma_t + \int_{\theta_3}^{\theta_4} e^{in\gamma_t}\mathrm{d}\gamma_t + \int_{\theta_5}^{2\pi} e^{in\gamma_t}\mathrm{d}\gamma_t\right) - \left(\int_0^{\theta_1} e^{in\gamma_t}\mathrm{d}\gamma_t + \int_{\theta_2}^{\theta_3} e^{in\gamma_t}\mathrm{d}\gamma_t + \int_{\theta_4}^{\theta_5} e^{in\gamma_t}\mathrm{d}\gamma_t\right)\right] \tag{6.7}$$

Table 2 Timings for 2D-PASS Experiment Shown in Figure 9 (taken from Ref.[12])

Evolution increment	Pitch angle $\frac{\Theta_e}{2\pi} = \frac{n_e - 1}{N_e}$	$\frac{\theta_1}{2\pi}$	$\frac{\theta_2}{2\pi}$	$\frac{\theta_3}{2\pi}$	$\frac{\theta_4}{2\pi}$	$\frac{\theta_5}{2\pi}$
1	0.00000	0.16667	0.33333	0.50000	0.66667	0.83333
2	0.06250	0.18989	0.36501	0.52042	0.69657	0.85127
3	0.12500	0.21668	0.39542	0.53812	0.72177	0.86239
4	0.18750	0.24453	0.42002	0.54898	0.73845	0.86496
5	0.25000	0.26915	0.43011	0.54584	0.74192	0.85703
6	0.31250	0.28147	0.41078	0.52131	0.73135	0.83935
7	0.37500	0.26731	0.35926	0.49092	0.71890	0.81992
8	0.43750	0.23472	0.31159	0.48618	0.71464	0.80533
9	0.50000	0.20979	0.29022	0.50000	0.70979	0.79022
10	0.56250	0.19467	0.28536	0.51382	0.68841	0.76528
11	0.62500	0.18008	0.28110	0.50908	0.64074	0.73269
12	0.68750	0.16065	0.26865	0.47870	0.58922	0.71853
13	0.75000	0.14297	0.25808	0.45416	0.56990	0.73085
14	0.81250	0.13504	0.26155	0.45102	0.57998	0.75547
15	0.87500	0.13761	0.27823	0.46188	0.60458	0.78333
16	0.93750	0.14874	0.30343	0.47958	0.63499	0.81011

Evaluating the integrals in equation (6.7) gives the following:

$$\Phi_{\nu,n}(\Theta_e) = W_{\nu,n}(\alpha, \beta)\frac{(-1)^n T}{in2\pi} \times [e^0 + e^{2\pi} + 2(-e^{in\theta_1} + e^{in\theta_2} - e^{in\theta_3} + e^{in\theta_4} - e^{in\theta_5})] \tag{6.8}$$

Using definitions given in equations (6.3) and (3.9), the total phase accumulation, $\Phi_\nu(t_e)$, for the postulated pitch angle is given by

$$\Phi_{\nu,n}(\Theta_e) = (-1)^p W_{\nu,n}\frac{T}{2\pi}\int_0^{\Theta_e} e^{in\gamma_t}\,\mathrm{d}\gamma_t = -W_{\nu,n}\frac{T}{in2\pi}(e^{in\Theta_e} - 1) \tag{6.9}$$

Note $(-1)^p$ provides the alternating phase coherency of successive π-pulses (in this case $p = 5$).

Combining equations (6.8) and (6.9) and eliminating common factors yields

$$e^{in\Theta_e} + 1 + 2(-e^{in\theta_1} + e^{in\theta_2} - e^{in\theta_3} + e^{in\theta_4} - e^{in\theta_5}) = 0 \tag{6.10}$$

Five simultaneous equations were obtained from equations (6.6) and (6.10) from which five θ_k values are found for a given value of Θ_e. The four equations ($n = \pm 1, \pm 2$) embodied in equation (6.9) are best separated[12] into $n = 1, 2$ and into real and imaginary components to calculate values for four of the five θ_k constraints that yield each set of $\Theta_e = 2\pi(n_{e-1}/N_e)$ evolution increments. Antzutkin et al.[12] include a simultaneous equation sub-routine (Mathematica[37]) in their appendix for calculating the five $\theta_k/2\pi$ values that are used to construct Θ_e. Typical timing values are given in Table 2 for the 16 incremented pitch angles in the 2D-PASS experiment.

6.3 2D-PASS Spectra of Ampicillin

The 2D-PASS spectra (both contour and peak plots) for ampicillin[13] are presented in Figure 10. Note how the data combine in such a way that the evolution dimension contains only rank-ordered sidebands, whereas the acquisition-dimension portrays both isotropic and shift tensor information of each sideband component. Computer shearing of the 2D spectral data provides the same rotational sideband pattern for a given nucleus, as found in the FIREMAT spectrum given in Figure 8. Considerable benefits in spectral resolution derive from the larger acquisition data tables in 2D-PASS. These advantages mirror the improvements in the FIREMAT spectra due to data replication.

7 COMPARISON OF 5π-PULSE TYPE OF EXPERIMENTS

7.1 Qualitative Comparison of FIREMAT and 2D-PASS Methods

A careful comparison of Figures 2 and 9, at $t_e = 0$, indicates that 2D-PASS and FIREMAT, along with its predecessor 5π-PULSE, should all give equivalent spectral responses at $t_e = 0$. This similarity in the time-zero magnetization for FIREMAT and 2D-PASS suggests, to a first approximation, that these experiments should have comparable S/N. This conclusion has been verified when a constant number of evolution increments is used in both FIREMAT and 2D-PASS data on the same compound.[38] Further, the error propagation in the fit of principal shift values revealed no statistically significant difference, providing proper allowance is made for the greater implementation of automation in the FIREMAT data analysis.

FIREMAT includes automated subroutines for the TIGER and Banded-Matrix-SIMPLEX processing of FIDs in the time domain. Considerably more data in regression fits usually enhance the spectral quality. Hence, the extracted shift parameters are improved considerably by time domain fitting of the FIDs. The sensitivity of spectral parameters from 2D-PASS data would also probably benefit from time-domain fitting of the FIDs. The Herzfeld–Berger method[10] is often used to extract the 2D-PASS shift parameters from peak-height measurements that unfortunately fail to take advantage of the increased data found in a time domain FID.

Except for $t_e = 0$, the 2D-PASS and FIREMAT methods diverge in their treatment of the evolution dimension, and a number of differences may affect the time efficiency of the relative experiments. These differences primarily deal with the use of

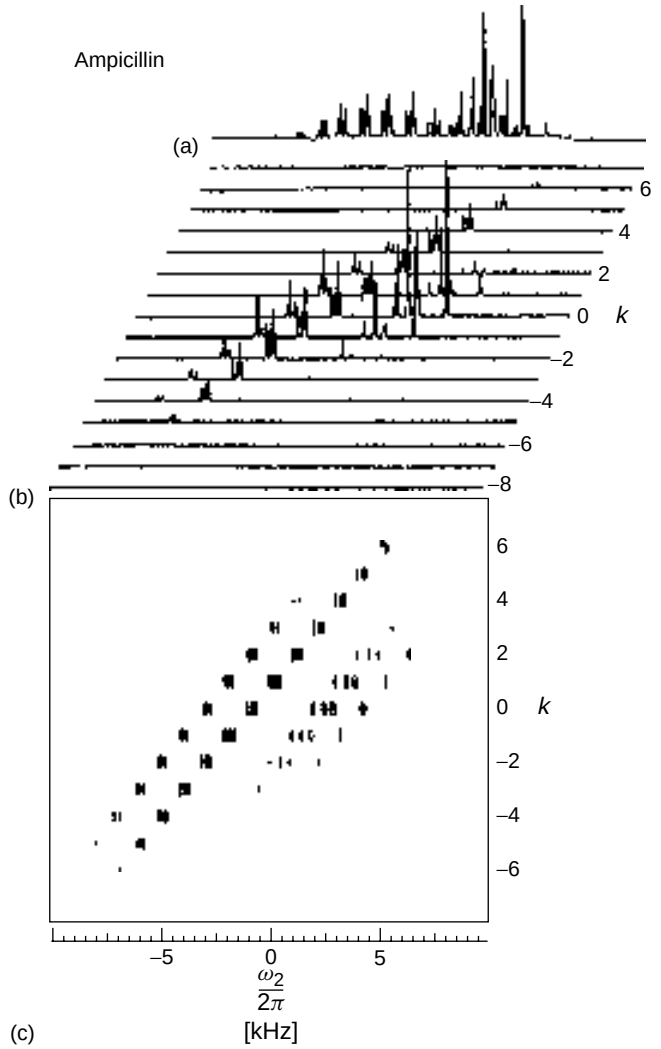

Figure 10 2D-PASS of ampicillin. (Reproduced from Ref.[13] with permission)

TIGER and with spectral aliasing in the evolution dimension that may or may not be important depending upon the molecular size and spectral complexity. The spectroscopist's control over these factors is limited to the selection of the turning frequency, $1/T$, and sampling rate, $1/\tau_e$, whether one uses an actual (FIREMAT) or an effective (2D-PASS) value for τ_e, which is the incremental sampling period. Discounting differences in aliasing and the benefits and/or disadvantages of TIGER, the two methods are otherwise essentially the same except for the visual presentation of the spectral results in frequency space.

7.2 Turning Rates, ω_r, Turning Period, T, and Minimum Span, ω_{span}, of the Shift Tensor

At least three spinning bands (the center and a minimum of two sidebands) for each unique nucleus must be collected in order to determine three principal shift-tensor frequencies and/or the corresponding three irreducible shift frequencies: ω_{iso}, ω_{acent}, and ω_{span}. When the turning rate exceeds a value somewhere between $\omega_{span}/3$ (for axially symmetric tensors) to $\omega_{span}/2$ (for centro-symmetric tensors), the number of spinning bands could be less than three. In this instance, it is impossible to determine chemical shift principal values from such a rotation pattern. ω_{span}^{min} is defined as the minimal spectral width for the narrowest tensor, which establishes the maximum rotation rate that will allow all tensors in the sample to be determined simultaneously. The situation of an axially symmetric shift tensor is more restrictive because ω_{iso} is no longer found at the mid-point of the band. In this situation the factor of 1/3 should be used to specify the maximum turning rate, ω_r^{max}, or minimum turning period, T^{min}. Under these constraints the various quantities are related by

$$\omega_r^{max} = \left(\frac{2\pi}{T^{min}}\right) \leq \left(\frac{\omega_{span}^{min}}{3}\right) \text{ or } T^{min} \geq \left(\frac{6\pi}{\omega_{span}^{min}}\right) \qquad (7.1)$$

Consider a typical methyl chemical-shift ω_{span} of 1500 Hz obtained from a 15 ppm ω_{span} in a 400 MHz proton instrument (i.e., 100 MHz for ^{13}C). This value in equation (7.1) requires that the maximum turning rate, $\omega_r^{max}/2\pi$, be 500 Hz or less in order to observe at least three sidebands. Slower turning rates further increase the number of sidebands that are beneficial to the precision of the extracted principal shift values.

7.3 Spectral Evolution Resolution, ω_{res}^{evol}, Spin-spin Relaxation, T_2, Evolution Periods, T

Standard FT relationships affecting resolution also govern in the solid state experiments encountered in this article. Thus, the evolution resolution, ω_{res}^{evol}, is limited by the spin-spin relaxation time, T_2, in accordance with

$$\omega_{res}^{evol} \cong \left(\frac{1}{T_2}\right) \geq \frac{2\pi}{T^{min}} \text{ or } T^{min} \geq 2\pi T_2 \cong \left(\frac{2\pi}{\omega_{res}^{evol}}\right) \qquad (7.2)$$

When $1/T_2$ is greater than $2\pi/T^{min}$, the relaxation broadens the rotational sidebands beyond the ω_{span}^{min} of the tensor and it becomes impossible to characterize such tensor bands. Hence, as a practical matter, ω_{span}^{min} is specified by the narrowest shift tensor whose principal values can be measured from the spinning bands. When one or more of the narrower shift tensors is not distinguishable from spherically symmetric tensors due to relaxation limitations, the anisotropic features of the tensor are lost. Careful attention must be given to this problem because both relaxation and rapid rotations that are too fast will exhibit spherical tensor properties. Relaxation in most bio-organic solids, which tend to exhibit considerable internal motion, usually does not limit the anisotropic tensor information for many bio-molecules. Turning the sample too rapidly need not be a problem as this situation is under the control of the spectroscopist.

7.4 Evolution Spectral Widths and the Sampling Rates

To monitor a spectral width in the evolution dimension and avoid aliasing, the evolution sampling-rate, $1/\tau_e$, must be greater than the evolution spectral width, ω_{SW}^{evol}, properly converted into Hz. This condition is expressed by

$$\frac{1}{\tau_e} \geq \left(\frac{\omega_{SW}^{evol}}{2\pi}\right) \qquad (7.3)$$

For the 5π-PULSE experiment, $\omega_{SW}^{evol} = \omega_{isoW}^{evol}$, the overall width of the isotropic spectrum. Aliasing or resolution in the evolution dimension for 2D-PASS is not of concern. The only issue in 2D-PASS becomes one of the total number of sidebands required to cover the largest tensor band, while maintaining at least three tensor sidebands for the narrowest tensor (see below).

7.5 The Parent 5π-PULSE Experiment

It is a simple matter to calculate a minimal number of evolution increments, $N_e = T/\tau_e$, by multiplying equations (7.1) by (7.3). The inequality is still valid providing the 5π-PULSE experiment is not limited by relaxation as indicated in equation (7.2). In this limit, the following expression is obtained:

$$N_e(5\pi\text{-Pulse}) = \frac{T^{min}}{\tau_e} \geq \left(\frac{3 \cdot \omega_{isoW}^{evol}}{\omega_{span}^{min}}\right) \tag{7.4}$$

Further, the required number of evolution increments depends on the number of nuclear spins that must be differentiated with the FID or with TIGER. This expression is given as follows:

$$N_e(5\pi\text{-Pulse}) \geq N_\nu \tag{7.5}$$

Assuming possible values of $\omega_{isoW}^{evol} \approx 150$ ppm and $\omega_{span}^{min} \approx 10$ ppm, the number of evolution increments, in the absence of relaxation constraints, would exceed 45 irrespective of the molecular size. Greater efficiency could be realized if ω_{isoW}^{evol} were smaller or if ω_{span}^{min} were to be larger. For example, the more favorable case where $\omega_{isoW}^{evol} \approx 80$ ppm and $\omega_{span}^{min} \approx 20$ ppm, would require only 12 increments. One can also escape some of the time inefficiencies if a modest amount of aliasing can be tolerated, especially in relatively small molecules where aliasing may be readily identified. Line broadening due to truncating the FID unduly will limit the S/N ratio and the effective resolution of the frequency domain.

7.6 The Parent 5π-PULSE Experiment with TIGER

The introduction of TIGER processing usually leaves the rotational lines narrower and enhances the S/N. The information from the guide spectrum can be used to optimize resolution and avoid aliasing. Sharper lines from the guide spectrum also yield higher peak intensities with a favorable impact on the S/N in the frequency domain. TIGER is especially powerful when the isotropic width and the minimum span are very similar. In this case, very narrow lines obtain with N_e barely larger than N_ν as found in Figure 4. Nonetheless, the TIGER formalism still requires that the minimum number of evolution increments be equal to or greater than the number of nuclear spins in order to obtain the matrix inverse required.[39] This situation is quite critical when molecular size increases to 50–100 carbon-13 nuclei for relevant bio-molecules, and one must conform to the expression in equation (7.5). Further, the creation of a suitable guide spectrum is much more difficult when overlapping isotropic peaks found in larger molecules introduces accidental degeneracy into the spectrum.

7.7 The FIREMAT Variant of 5π-PULSE

In the absences of a relaxation limitation, the replication provides efficiency for FIREMAT that no longer depends on number of nuclear spins. The replication scheme used in this method contains sufficient N_e to eliminate the constraint on N_ν. The evolution time sampling rate, $1/\tau_e$, still governs aliasing in the evolution dimension and the second term of equation (7.5) still obtains:

$$N_e(\text{FIREMAT}) \geq \left(\frac{3 \cdot \omega_{isoW}^{evol}}{\omega_{span}^{min}}\right) \tag{7.6}$$

7.8 The 2D-PASS Alternative to 5π-PULSE

The number of sidebands in 2D-PASS needed to span the widest tensor band determines N_e(2D-PASS). The minimal number of sidebands is readily calculated by enforcing at least three sidebands for the narrowest tensor and noting the corresponding impact on the number of sidebands in the widest tensor. Hence, the constraint for 2D-PASS yields the following:

$$N_e(\text{2D-PASS}) \geq \left(\frac{3 \cdot \omega_{SW}^{max}}{\omega_{span}^{min}}\right) \tag{7.7}$$

where ω_{SW}^{max} is the maximum width of the spectrum, including all of the rank-ordered side bands. To optimize the use of Fast-FT methods with 2D-PASS, it becomes necessary to increase the number of evolution increments to the next higher power of 2 above N_e(2D-PASS) given in equation (7.7). One of the benefits claimed for 2D-PASS is that standard 2D FT methods may be used to secure a frequency domain spectrum. TIGER, it may be argued, benefits the FIREMAT approach.

7.9 Comparison of 2D-PASS and FIREMAT

Abandoning the alleged advantages of using Fast FT methods or TIGER, equations (7.6) and (7.7) identify the factors that primarily differentiate the two methods. As ω_{SW}^{max} and ω_{isoW}^{evol} are very similar, one is left with the conclusion that the two approaches are comparable. There are instances when the maximum spectral span is larger than the spread of isotropic shifts and vice versa. Hence, the two methods are each preferred under different circumstances. The differences that the author's laboratory has found, deal primarily with the efficiencies of fitting time domain FIDs or peak heights in the frequency domain. Use of TIGER can produce enhanced S/N in the frequency domain and favors peak-height fitting. Time domain fitting of FIDs would equalize this advantage. Thus, both FIREMAT and 2D-PASS are sufficiently similar that personal experience likely becomes the dominant factor in choosing between the two approaches. However, both methods have proven sufficiently successful with moderately large biomolecules to attest to the arrival of 2D solid state methods in chemical studies.

8 REFERENCES

1. A. M. Orendt, in 'Encyclopedia of Nuclear Magnetic Resonance', eds D. M. Grant and R. K. Harris, John Wiley & Sons: Chichester, 1996, Vol. 2, p. 1282.

2. J. Zh. Hu, W. Wang, and R. J. Pugmire, in 'Encyclopedia of Nuclear Magnetic Resonance', eds D. M. Grant and R. K. Harris, John Wiley & Sons: Chichester, 1996, Vol. 5, p. 2914.
3. A. Bax, N. M. Szvereneyi, and G. E. Maciel, *J. Magn. Reson.*, 1983, **52**, 147.
4. Z. Gan, *J. Am. Chem. Soc.*, 1992, **114**, 8307.
5. J. Zh. Hu, A. M. Orendt, D. W. Alderman, R. J. Pugmire, C. Ye, and D. M. Grant, *Solid State NMR*, 1994, **3**, 181.
6. J. Zh. Hu, W. Wang, F. Liu, M. S. Solum, D. W. Alderman, R. J. Pugmire, and D. M. Grant, *J. Magn. Reson. A*, 1994, **113**, 210.
7. J. Zh. Hu, D. W. Alderman, C. Ye, R. J. Pugmire, and D. M. Grant, *J. Magn. Reson. A*, 1993, **105**, 82.
8. N. K. Sethi, D. W. Alderman, and D. M. Grant, *Mol. Phys.*, 1990, **71**, 217.
9. S. Vega, in 'Encyclopedia of Nuclear Magnetic Resonance', eds D. M. Grant and R. K. Harris, John Wiley & Sons: Chichester, 1996, Vol. 3, p. 2011.
10. J. Herzfeld and A. E. Berger, *J. Chem. Phys.*, 1980, **73**, 6021.
11. D. W. Alderman, G. McGeorge, J. Zh. Hu, R. J. Pugmire, and D. M. Grant, *Mol. Phys.*, 1998, **95**, 1113.
12. O. N. Antzutkin, S. C. Shekar, and M. H. Levitt, *J. Magn. Reson.*, 1995, **115**, 7.
13. O. N. Antzutkin, Y. K. Lee, and M. H. Levitt, *J. Magn. Reson.*, 1998, **135**, 144.
14. W. T. Dixon, *J. Magn. Reson.*, 1981, **44**, 220; *J. Chem. Phys.*, 1982, **77**, 1800.
15. G. McGeorge, J. Zh. Hu, C. L. Mayne, D. W. Alderman, R. J. Pugmire, and D. M. Grant, *J. Magn. Reson.*, 1997, **129**, 134.
16. D. M. Grant, in 'Encyclopedia of Nuclear Magnetic Resonance', eds D. M. Grant and R. K. Harris, John Wiley & Sons: Chichester, 1996, Vol. 2, p. 1305.
17. R. N. Zare, 'Angular Momentum', John Wiley & Sons: New York, 1988, pp. 177–180. Zare closes his discussion of conventions, "by considering the always vexing problem of relating spherical tensor components defined in space-fixed and molecule-fixed frames".
18. R. N. Zare, 'Angular Momentum', John Wiley & Sons: New York, 1988, p. 85.
19. R. N. Zare, 'Angular Momentum', John Wiley & Sons: New York, 1988, p. 81.
20. J. Mason, *Solid State NMR*, 1993, **2**, 285.
21. M. Mehring, 'High Resolution NMR in Solids', 2nd edition, Springer: New York, 1983. Mehring provides an equivalent transformation from frame P to L using two spherical harmonic expansions. This approach is comparable to the two Wigner rotation matrix transformations used in this work as only four variable rotational angles are needed in either formalism.
22. Maple 6, © Waterloo Maple Inc. Automatic mathematical software is used to derive the expression in equation (2.15). Agreements between the Wigner rotation matrix and the similarity transformations mutually confirm the validity of the derivations.
23. M. M. Maricq and J. S. Waugh, *J. Chem. Phys.*, 1979, **70**, 3300. These workers found experimentally that sidebands exhibit different phases relative to the center band in rotating single crystals. Conversely, it had been known for some time that spinning side bands on powder microcrystalline materials have identical phase factors.
24. M. H. Levitt, *J. Magn. Reson.*, 1989, **82**, 427.
25. R. N. Zare, 'Angular Momentum', John Wiley & Sons: New York, 1988, note 5, page 18. "In my first encounter with phase conventions I took the attitude, 'Why should I bother because after all, the phase is arbitrary?' .... This is the first of many instances where care must be exercised in the choice of phase, a most vexing aspect of angular momentum theory. Finally, a warning should be made to the uninitiated that phase conventions must be checked in going from one literature reference to another ...". The reader is referred to Zare's profundity on this subject, much of which had to be omitted.
26. E. U. Condon and G. H. Shortley, 'Theory of Atomic Spectra', Cambridge University Press, 1935; paperback 1963.
27. D. W. Alderman, M. S. Solum, and D. M. Grant, *J. Chem. Phys.*, 1986, **84**, 3717.
28. V. I. Lebedev, *Zh. Vychisl. Mat. Fiz.*, 1975, **15**, 48; 1976, **16**, 193; *Sibirsk. Mat. Zh.*, 1977, **18**, 132; *Sov. Phys.-Dokl.*, 1992, **45**, 587.
29. M. Eden and M. H. Levitt, *J. Magn. Reson.*, 1998, **132**, 220.
30. Y. Manassen, G. Navon, and C. T. W. Moonen, *J. Magn. Reson.*, 1987, **72**, 551.
31. Y. Manassen and G. Navon, *J. Magn. Reson.*, 1988, **79**, 291.
32. To be precise, the TIGER method does not require that the t_e increments be equal as required by FT methods. However, the replication scheme employed in the FIREMAT application in this article is best served with equal increments. Further information on unequal t_e intervals is treated in the literature.
33. W. C. Hamilton, 'Statistics in Physical Science', Ronald Press, New York, 1964.
34. F. A. Graybill, 'Theory and Application of the Linear Model', Wadsworth and Brooks/Cole: Pacific Grove, 1976.
35. Zh. Gan, *J. Magn. Reson. A.*, 1994, **109**, 253.
36. The development of the topic in terms of angle or time is immaterial, because the angular velocity, ω_r, is constant and converts the two quantities directly into each other.
37. S. Wolfram, 'Mathematica: A System for Doing Mathematics by Computer', Addison-Wesley: Reading, MA, 1988.
38. J. Zh. Hu, F. Guenneau, C. M. V. Taylor, D. W. Alderman, R. J. Pugmire, and D. M. Grant, 'Comparison between FIREMAT and 2D-PASS, unpublished.
39. See discussion of equations (2.41) to (4.5) in section 4.1.

Acknowledgements

Today's diverse scientific endeavors seldom allow one to point to a single overpowering contribution. The author has attempted to provide a rather extensive list of citations that underlie the anthology of this topic. All of these contributions have been significant, but many other essential sources also warrant commendation. During the preparation of this article, the author was supported by the National Institutes of Health (grant GM 08521-41) and by the Department of Energy (grant DE-FG03-94ER14452).

Biographical Sketch

David M. Grant, *b* 1931. B.S., 1954, Ph.D., 1957, Chemistry, University of Utah, USA. Positions: DuPont Instructor, University of Illinois, 1957–1958, introduced to NMR by Herb Gutowsky and Martin Karplus. Faculty in Chemistry, University of Utah since 1958, presently Distinguished Professor. Awards and Recognitions: 1969 Calif. Section Gold Medal (ACS); 1973 Utah ACS Section Award; 1973–1974; Sherman Fairchild Distinguished Scholar, Cal. Inst. Tech.; 1987 Univ. of Utah Rosenblatt Prize; 1991 ACS Award in Petroleum Chem.; 1992 Utah Governor's Medal for Science; 1995 Vaughan Prize; 1998, Treasurer, ISMAR. Current research specialties: methods and theoretical foundations of carbon-13 NMR, coupled spin relaxation and molecular motions, chemical shifts in liquids and solids with emphasis on carbon-13 shift tensors and their origins in electronic and molecular structure. About 400 Scientific Publications.

Magnetic Susceptibility and High Resolution NMR of Liquids and Solids

David L. Vander Hart
National Institute of Standards and Technology, Gaithersburg, MD, USA

1	Introduction	1
2	Physical Origins of Susceptibility, Definitions, and Equations	1
3	Magnetic Susceptibility Effects in the High-Resolution NMR of Liquids	2
4	Magnetic Susceptibility Effects in Solid State NMR	4
5	Miscellaneous Considerations	7
6	Related Articles	8
7	References	8

1 INTRODUCTION

The principal aspects of high-resolution (HR) NMR which are influenced by magnetic susceptibility (MS) effects in nonconducting materials are spectral resolution and the accurate measurement of chemical shift. Also, with the wide application of NMR to imaging, particularly the imaging of heterogeneously structured materials, MS effects can influence the quality and interpretation of the images obtained. It is also possible to obtain MS information about materials using high-resolution NMR techniques. In this presentation, the physical origins of susceptibility in nonconducting materials are sketched, a few basic equations are given, the tensorial nature of susceptibility is pointed out, and a number of practical considerations are offered including the influence of sample spinning, particularly at the magic angle. Only diamagnetic and paramagnetic susceptibility are considered; ferromagnetism and antiferromagnetism are not discussed. Finally, a few comments are included regarding the use of high-resolution NMR to measure MS values, both molecular MS and the MS of condensed phases.

2 PHYSICAL ORIGINS OF SUSCEPTIBILITY, DEFINITIONS, AND EQUATIONS

In classical electromagnetism, the magnetic induction $\boldsymbol{B}$ and the magnetic field strength $\boldsymbol{H}$ inside a medium, are related by the equation

$$\boldsymbol{B} = \mu_0(\boldsymbol{H} + \boldsymbol{M}) \tag{1}$$

where $\boldsymbol{M}$ is the magnetization or magnetic moment per unit volume. Quantities appearing in equation (1) are in rationalized SI units where $\boldsymbol{H}$ and $\boldsymbol{M}$ are expressed in A m^{-1} and $\boldsymbol{B}$ has the units of tesla. Quantities given in bold-face type are either vectors or tensors. The permeability of free space, μ_0, takes the value $4\pi \times 10^{-7}$ T m A^{-1} (Bennett et al. have published a useful reference paper[1] delineating appropriate conversions from cgs to SI units for quantities related to magnetism.) For isotropic nonferromagnetic materials,

$$\boldsymbol{M} = \kappa \boldsymbol{H} = (d/M)\kappa_{\mathrm{M}}\boldsymbol{H} \tag{2}$$

where κ and κ_{M} are respectively called the rationalized volume and molar magnetic susceptibilities, d is the density in kg m^{-3} and M is the molar mass in kg mol^{-1}. (κ is equivalent to the quantity $4\pi\chi_{\mathrm{v}}$ in the cgs system, where χ_{v} is the volume MS; κ and χ_{v} are both dimensionless. The relationship between κ_{mole}, having units of m^3 mol^{-1}, and χ_{M} in the cgs system, having units of cm^3 mol^{-1}, is that numerically $4\pi\chi_{\mathrm{M}} = 10^6\,\kappa_{\mathrm{mole}}$.) MS is a bulk property of materials. Thus, MS is associated with an ensemble of molecules and is not intended to describe the details of the response to an external field over molecular distances. At the same time, individual molecules possess molecular susceptibility tensors.[2,3] Moreover, for nonconducting materials, the uniformity of κ_{M} for solid, liquid, and gaseous forms of the same material implies that bulk MS values probably derive from summed molecular magnetic susceptibilities.[3,4] Indeed, the molecular theory of diamagnetism is described in terms of molecular wavefunctions.

2.1 Diamagnetic and Paramagnetic Susceptibility

The two kinds of MS considered are diamagnetic and paramagnetic. Diamagnetic susceptibility is a generalized response to the magnetic field of the orbiting paired electrons in a sample.[2] This response is most often negative in sign and usually weak,[5] i.e. $\kappa \approx -10^{-5}$. Owing to the fact that the diamagnetic susceptibility arises from the reaction of electrons in their orbitals to the presence of the magnetic field, this quantity is usually quite independent of temperature. There are generally two terms contributing to the diamagnetic susceptibility,[2]

$$\kappa_{\mathrm{mole}} = -\frac{Ne^2\mu_0}{4m}\sum_i \overline{x_i^2 + y_i^2} + \frac{Ne^2\mu_0}{2m^2}\sum_{n(\neq 0)}\frac{|(0|\hat{L}_z|n)|^2}{E_n - E_0} \tag{3}$$

where N is Avogadro's number, e is the charge on the electron in coulombs, m is the mass of the electron in kg, i is an index over all electrons in the molecule, and n is an index over all excited electronic states of corresponding energies E_n (in joules) in the molecule. The first term is an average over all of the electrons in the ground state, where the z direction lies along $\boldsymbol{H}$. The size of this term is usually associated with the ability of the electrons, especially the outer electrons, to circulate freely in planes perpendicular to $\boldsymbol{H}$. The second term involves the mixing of ground and excited electron states by the angular momentum operator $\hat{L}_z$. The first term is negative and the second term is positive but usually smaller than the first; hence the sum is usually negative.

Paramagnetic susceptibility most often arises from unpaired electrons whose net polarizations in the magnetic field yield an MS which is positive in sign and somewhat larger than

the diamagnetic contribution. The latter is still there but is usually masked by the paramagnetic contribution. The electronic polarization which gives rise to the paramagnetic contribution is temperature-dependent and the paramagnetic susceptibility reflects that. For example, suppose a molecule of molar mass M has unpaired electrons, then, according to Langevin,[6]

$$\kappa_{\text{mole}} = N\mu^2\mu_0/3kT \tag{4}$$

where μ is the magnetic moment of the unpaired spins on the molecule; μ, in J T^{-1}, is given by

$$\mu = 2\beta[S(S+1)]^{1/2} \tag{5}$$

where S is the total spin which is equal to half the number of unpaired spins and β is the Bohr magneton in units of J T^{-1}. Substituting equation (5) into equation (3) gives

$$\begin{aligned}\kappa_{\text{mole}} &= 4N\mu_0\beta^2 S(S+1)/3kT \\ &= [6.286 \times 10^{-6} S(S+1)/T]\,\text{m}^3\,\text{mol}^{-1}\end{aligned} \tag{6}$$

Paramagnetic susceptibilities are usually larger than diamagnetic susceptibilities; ratios of 10 to 100 are not uncommon. Molecular oxygen has unpaired electrons and a relatively small molar mass; its presence in dissolved form can be a measurable perturbation on the measurement of diamagnetic susceptibility.[7]

2.2 Tensorial Character of Magnetic Susceptibility

In principle, the molecular MS and the bulk MS in solids is anisotropic,[2,3,8] giving rise to a *tensorial* interaction, i.e. the general definition of $\boldsymbol{M}$ in equation (2) is

$$\boldsymbol{M} = \boldsymbol{\kappa}\cdot\boldsymbol{H} \tag{7}$$

where $\boldsymbol{\kappa}$ is a tensor. Thus, $\boldsymbol{M}$ may, in principle, depart from the direction of $\boldsymbol{H}$. Anisotropic bulk MS (ABMS) is most often associated with the crystalline state of matter in contrast with the glassy or liquid states of matter where isotropic bulk MS (IBMS) is most commonly found. For diamagnetic crystals, ABMS can arise because both the magnetic susceptibility of each molecule is anisotropic and the molecules in the unit cell preserve a net orientation of their different susceptibility axes. A common molecular source of ABMS in organic compounds is the aromatic ring.[3,8,9] Ring currents, which are induced by the magnetic field when there is some projection of the normal to the ring along the magnetic field, offer a significant contribution to the MS tensor. If an aromatic compound has a crystal habit where the ring normals have a net projection along some axis, then there is a high probability that such a crystal will display ABMS. Graphite, as an extreme example, has a very large anisotropy[10] because of its dense planar fused-ring structure.

For paramagnetic materials, the existence of an anisotropic electron $\boldsymbol{g}$ tensor, for example, can give rise to ABMS since net electron polarization then becomes a function of orientation. The $\boldsymbol{g}$ tensor can become very anisotropic, particularly for certain transition metal compounds where crystal field splittings and electron spin–orbit couplings both play a role in determining the anisotropy of $\boldsymbol{g}$.[11] For example, the electrons in high-spin iron in the heme group have $g_{\parallel}$ close to the free-electron value of 2, whereas $g_{\perp}$ is about 6. As will be seen, there is considerable difference in the NMR resolution one obtains with magic angle spinning (MAS) if ABMS, rather than IBMS, is present.

2.3 Relationship Between Sample Shape and Uniform Internal Fields

For many NMR experiments, a uniform internal magnetic field is desired (uniform on a scale significantly larger than the molecular scale) so that interactions on the molecular scale can be exposed. In principle, one can make the external field very homogeneous, but the introduction of a material with finite MS into this homogeneous field generally modifies the field, both outside and inside the material. Thus, one is interested in how sample shape influences the field internal to the material and what shapes will give rise to a uniform internal field when the body is placed in a uniform external field.

For a body described by a single MS tensor, the general ellipsoid is the only finite body shape which, in the presence of a uniform external field, gives rise to a uniform internal field.[12] Cylinders of infinite length and spheres are ellipsoids of rotation; high-resolution NMR samples often approximate these shapes. It is possible, in principle, that if an ellipsoid, probably a single crystal, has an ABMS tensor whose principal axes do not coincide with the axes of the ellipsoid, that the direction of the uniform internal field will not coincide with the direction of the external field. However, for diamagnetic and paramagnetic materials, deviations from the external field direction will be negligible.

At this point we will separately consider MS effects in high-resolution liquid NMR and in solid state NMR. In liquid state NMR the measurement of chemical shifts can often be made very accurately; moreover, resolution is of primary importance. Also, most materials associated with the high-resolution experiment, including the sample, possess IBMS. In contrast, for solid state NMR, the so-called 'high-resolution' techniques generally achieve resolution which is, at best, an order of magnitude worse than in the liquid state and, more typically, two or more orders of magnitude worse. Thus, for solids, one is less concerned with the influence of MS on accurate chemical shift measurements. At the same time, in the solid state, MS effects can influence the measurement of chemical shifts in ways that do not happen for liquids. Of probably greater interest is the role which MS plays in determining resolution in the solid state. The added possibility that samples have ABMS also increases the complexity of dealing with MS, since strategies for reducing IBMS broadening only work partially when ABMS is present.

3 MAGNETIC SUSCEPTIBILITY EFFECTS IN THE HIGH-RESOLUTION NMR OF LIQUIDS

3.1 Resolution

For spectroscopic NMR applications, one generally desires the best resolution possible. MS considerations have dictated

several items in the standard practice of high-resolution NMR. Usually, sample tubes are cylindrical and are ideally filled with liquid which extends both above and below the rf coil so as to approximate an ellipsoid, thereby promoting internal field uniformity in the region of the coil. When sample volume is limited, one often uses a spherical sample tube, again approximating an ellipsoid, although the stem attached to the sphere is a significant perturbation on the uniformity of the field inside the sphere.

Sample spinning is a second way of dealing with MS effects to improve resolution, although a primary motivation for sample spinning is that it averages out inhomogeneities in the static field perpendicular to the spinning axis. Variations in the wall thickness of the NMR tube and/or a lack of concentricity cause the magnetic field to be warped in the sample region since the magnetic susceptibility of the glass is usually different from the liquid. Spinning about the tube axis helps to average these effects to smaller values. This averaging is more effective in the iron magnet geometry, where $\boldsymbol{H} \perp \boldsymbol{s}$ ($\boldsymbol{s}$ is the unit vector in the spinning-axis direction), than it is in the usual superconducting-magnet geometry where $\boldsymbol{H} \parallel \boldsymbol{s}$. This difference comes about because only in the former case does the orientation of $\boldsymbol{H}$, with respect to the vectors connecting the liquid and the tube imperfections, become modulated by spinning.

Discontinuities of MS within the sample also degrade resolution. Air bubbles, precipitates, etc. in a sample are all undesirable. Even a spherical air bubble creates a large perturbation since, in general, an ellipsoid of one susceptibility inside of an ellipsoid of a different susceptibility will result in nonuniform fields inside of both ellipsoids, even though the external field was originally uniform.

Finally, MS effects dictate certain things about probe construction. Aside from electromagnetic interferences, the asymmetric disposition of the probe elements (electronic components, mechanical supports, etc.) perturb the field lines on a distance scale comparable with the size of the object. The strategies for minimizing degradation of resolution include (a) maintaining sufficient distance between the elements and the sample so that the perturbations at the sample change slowly enough, spatially, that shim-coil compensation is possible, (b) distributing perturbing elements symmetrically, and (c) attempting to match the MS of the probe elements to that of air. The method for achieving the latter is usually to combine some paramagnetic character with the diamagnetic character of a material. For example, a substantial improvement in resolution has been demonstrated[13] by replacing a copper rf coil with one having an MS much closer to that of air. A minor drawback to this approach of MS matching is that the paramagnetic contribution will be temperature-dependent.

3.2 Chemical Shift Measurements

The NMR resonance frequency observed in a liquid for a magnetic nucleus at a given chemical site on a molecule is often a very well-defined frequency, especially for a spin-$\frac{1}{2}$ nucleus. In general, one uses measured frequencies to deduce something about the molecule, about a chemical site in the molecule, or about how a site is influenced by its immediate intermolecular interactions (e.g. hydrogen bonding, solvation shells, etc.) Of less interest are those influences on the chemical shift which derive from mean fields averaged over many molecules. The MS effects fall into this latter category. The resonance frequency ω_0 ($= 2\pi\nu_0$) for a given nucleus, ignoring spin couplings, is given by the Larmor relationship,

$$\omega_0 = \gamma \mu_0 H_{\mathrm{n}} \tag{8}$$

where H_{n} is the magnetic field strength seen by the nucleus and γ is the gyromagnetic ratio of the observed nucleus in units of rad T^{-1}. Zimmerman and Foster[12] took the approach that $\boldsymbol{H}_{\mathrm{n}}$ is the vector sum of five parallel vector fields,

$$\boldsymbol{H}_n = \boldsymbol{H}_0 + \boldsymbol{h}_1 + \boldsymbol{h}_2 + \boldsymbol{h}_3 + \boldsymbol{h}_4 \tag{9}$$

where $\boldsymbol{H}_0$ is the applied external field, $\boldsymbol{h}_1$ is the demagnetizing field, proportional to the susceptibility, arising from the shape of the sample, $\boldsymbol{h}_2$ is the contribution due to magnetization external to the Lorentz sphere,[14,15] $\boldsymbol{h}_3$ is the field associated with local intermolecular interactions, e.g. hydrogen bonding, and $\boldsymbol{h}_4$ is the field arising from intramolecular contributions, e.g. the response to the magnetic field of electrons, particularly those surrounding the nucleus observed, plus the influence of molecular conformation, etc. It is the quantity ($\boldsymbol{h}_3$ + $\boldsymbol{h}_4$) which one seeks to measure and interpret via the chemical shift measurements. For liquid samples of IBMS, having overall ellipsoidal shapes and placed into a uniform field $\boldsymbol{H}_0$,

$$\boldsymbol{h}_1 = -\alpha\kappa \boldsymbol{H}_0 \tag{10}$$

where α is the demagnetizing factor tabulated for the general ellipsoid by Osborne.[16] This factor depends on the axis ratios of the ellipsoid and the direction of the magnetic field with respect to these axes. Values of α for certain ellipsoids are as follows: 0 for $\boldsymbol{H}_0$ parallel to the axis of a long cylinder and $\frac{1}{2}$ perpendicular to the same cylinder, $\frac{1}{3}$ for a sphere, and 1 for $\boldsymbol{H}_0$ perpendicular to the plane of a thin disk. The field ($\boldsymbol{H}_0$ + $\boldsymbol{h}_1$) is considered to be the average magnetic field internal to the liquid. It is thus, perhaps, not so obvious why the field $\boldsymbol{h}_2$ must be added to this mean internal field in order to take proper account of the mean internal field seen at the nucleus.[14,15] The quantity $\boldsymbol{h}_2$ arises, in a sense, from the consideration that the mean internal field ($\boldsymbol{H}_0$ + $\boldsymbol{h}_1$) is the mean field *after* the liquid has been magnetized. Since the molecule containing the nucleus in question is also in an induced-magnetism state, it is fair to ask whether the mean effective field which magnetized a given volume is not slightly different from the final mean field. The suggestion then is that the mean field seen by the nucleus is this slightly different field. To address this problem, one considers the fictitious removal of a very small sphere of magnetized liquid surrounding a molecule. Removal is especially fictitious because one 'freezes' in the field lines prior to the removal of the sphere so that the sphere is uniformly magnetized and the magnetic field lines in the liquid near the hole are also unperturbed.[15] When one considers this problem in this so-called Lorentz sphere, one finds that the compensating field $\boldsymbol{h}_2$ is given by

$$\boldsymbol{h}_2 = (1/3)\boldsymbol{M} = (1/3)\kappa \boldsymbol{H}_0 \tag{11}$$

Therefore, the MS-corrected field $\boldsymbol{H}_{\mathrm{c}}$ seen by the molecule in its average local environment is[12]

$$\boldsymbol{H}_c = \boldsymbol{H}_0 + \boldsymbol{h}_1 + \boldsymbol{h}_2 = \boldsymbol{H}_0\{1 + [(1/3) - \alpha]\kappa\} \tag{12}$$

For a spherical liquid sample, $\boldsymbol{H}_c$ is $\boldsymbol{H}_0$; for long cylindrical spinning samples,[12,17]

$$\boldsymbol{H}_c = \boldsymbol{H}_0[1 + (1/6)(3\cos^2\beta - 1)\kappa] \tag{13}$$

where β is the angle between $\boldsymbol{H}_0$ and the spinning axis vector, $\boldsymbol{s}$. equation (13) indicates that the susceptibility corrections are very different for $\boldsymbol{H}_0$ perpendicular or parallel to $\boldsymbol{s}$; moreover, if $\boldsymbol{s}$ assumes the magic angle, β_M = arccos $(3^{-1/2})$, then the susceptibility term vanishes[17] and $\boldsymbol{H}_c = \boldsymbol{H}_0$.

A usual method of making a referenced chemical shift measurement in high-resolution NMR is to mix an internal chemical shift standard with a test liquid. This works quite well in that both kinds of molecules experience the same perturbations from MS, assuming the mixture to be a true solution. On occasion, however, chemicals are not compatible or contamination is an important issue. Then one often uses a concentric tube arrangement with one liquid in the central tube and the other in the annular space. It does not matter, from the point of view of the MS corrections to be applied, which of the spaces is occupied by the reference so long as tubes are spun. (Static concentric tubes with $\boldsymbol{H}_0$ perpendicular to the tube axis, generate a substantial distribution of internal fields over the two sample regions.[12]) Moreover, equation (13) is used to determine $\boldsymbol{H}_c$ in both liquid regions.

Recognize that the convention for chemical shift, δ, is that shifts to higher resonance frequency imply more *positive* δ values. (Note that this sign convention is also consistent with Knight shifts[18] as well as the more conventionally used chemical shift scales for protons, ^{13}C nuclei, etc.) If one measures the apparent chemical shift difference $\Delta\delta_{obs}$ (= $\delta - \delta_{ref}$) between two resonances originating from each of the sample regions, then for the iron-core magnet geometry with $\boldsymbol{H}_0 \perp \boldsymbol{s}$, the susceptibility-corrected shift $\Delta\delta_{corr}$ is given by

$$\Delta\delta_{corr} = \Delta\delta_{obs} - (1/6)(\kappa^{ref} - \kappa) \tag{14}$$

and for the superconducting geometry with $\boldsymbol{H}_0 \parallel \boldsymbol{s}$

$$\Delta\delta_{corr} = \Delta\delta_{obs} + (1/3)(\kappa^{ref} - \kappa) \tag{15}$$

where κ^{ref} is the MS of the reference liquid and κ is the MS of the test-sample liquid.

Application of equations (14) and (15) is not always convenient when one of the MS values is not known. This situation arises often for mixtures as well as neat liquids. It is possible to estimate κ, if one knows the composition and density of a material, using Pascal's constants.[3,8,19,20] This method assumes additivity relationships for the contributions from the various atoms. Corrections which depend on the nature of the bonding are also included. For known mixtures whose individual κ values are known, a molar-volume additivity assumption works quite well[21] for estimating κ for the mixture:

$$\kappa_{mixt} = \phi_1\kappa_1 + \phi_2\kappa_2 \tag{16}$$

where ϕ_1 and ϕ_2 are respectively the volume fractions of components 1 and 2.

4 MAGNETIC SUSCEPTIBILITY EFFECTS IN SOLID STATE NMR

4.1 Influence on Resolution

Solid particles come in all shapes and sizes. Particles can be crystalline, semicrystalline (e.g. polymers), amorphous or glassy materials, or even rubbery liquid-like materials. Generally, solid particles do not naturally occur as ellipsoids with ideal shape factors. This section offers a framework for estimating the spread of internal magnetic fields inside of an arbitrary particle; also an estimate of broadening in a powder sample is given. In addition, the question is raised as to what can be done, if anything, to reduce the susceptibility broadening in an NMR spectrum. The short answer is that magic angle sample spinning (MAS) will fully average to zero broadening from IBMS for particles of any shape, but when ABMS is present, MAS will result in incomplete averaging. In general, one must use single crystals of an ellipsoidal shape to eliminate ABMS broadening.

Given a particle, characterized by a single MS tensor and of a general shape, introduced into a uniform magnetic field, one can calculate the distribution of internal magnetic fields due to particle shape in the following way.[17] About any given point in the particle, where one wishes to calculate the internal field, define a primary sphere which is the largest sphere that remains within the particle. Subdivide the remaining regions of the particle into i spherical volumes, V_i, choosing the spheres of different sizes so as to account for all of the remaining particle volume. According to equation (7), the magnetic field induces a magnetic moment per unit volume in the particle; thus, each of these spheres represents a magnetic moment $\boldsymbol{\mu_i}$ given by

$$\boldsymbol{\mu}_i = V_i\boldsymbol{\kappa}\cdot\boldsymbol{H} \tag{17}$$

and the projection along $\boldsymbol{H}$ of the dipolar field $\boldsymbol{h}_i$ due to $\boldsymbol{\mu}_i$, evaluated at the center of the primary spheres will be

$$h_i = (\mu_i/r_i^3)(3\cos^2\theta_i - 1) \tag{18}$$

where, in polar coordinates centered at the origin of the primary sphere, r_i is the distance to the center of V_i and θ_i is the angle between the field direction and the line connecting the centers of the primary and the ith spheres. The sample-shape-dependent contribution to the field dispersion at the center of the primary sphere is the sum of the h_i values since the contribution from the first sphere does not contribute to the dispersion. A similar calculation can be performed at all points in the particle in order to obtain the distribution of internal fields for an arbitrary particle shape. We begin by discussing broadening for particles possessing IBMS.

4.1.1 Samples with Isotropic Magnetic Susceptibility

Drain[22] estimated the MS broadening of NMR lines in powder samples having IBMS by considering the broadening due to the shape of each particle and due to the packing of the particles. The contribution from shape was calculated by assuming that the particles were isolated prolate or oblate ellipsoids with axial ratios of 2 or 0.5, respectively. A

uniform distribution of ellipsoid orientations in the field [leading to a distribution of α values in equation (10)] gives rise to lineshapes which are asymmetric, resembling powder lineshapes for axially symmetric chemical shift tensors.[23] Drain estimated the interparticle contribution to MS broadening by using the dipole approximation to calculate the distribution within a spherical particle due to spherical cubic-close-packed arrays of neighboring particles. The result was that comparable broadening arose from sample shape and from neighbor distributions. The full width, in Hz, of the resulting resonance was about $\kappa\nu_0/4$, where it is assumed that either air or vacuum surrounds each particle. This corresponds to about 2 ppm for the typical organic material. Obviously, a significant improvement in resolution could be obtained if a liquid with a matching susceptibility were introduced into the sample chamber.[24] Then, MS broadening would be reduced to about $\Delta\kappa\nu_0/4$ where $\Delta\kappa$ is the difference in κ between the particles and the liquid. Note that Drain's estimate of line broadening assumes that the overall shape of the powder sample does not deviate strongly from an ellipsoid; if it does, there is an additional MS broadening due to overall sample shape. Another way to eliminate MS broadening in solid materials with IBMS is to melt-cast or melt-crystallize them into ellipsoidal shapes. In the absence of voids, MS broadening then ought to be very small.

One can also average to zero the broadening from IBMS effects by using MAS.[17] The dipolar form of equation (18) suggests that the angular averages of all $\boldsymbol{h}_i$ will vanish with MAS. Hence, the average dispersion will also vanish. The efficacy of MAS has also been demonstrated for samples containing liquids together with solids, such as glass beads.[17] These authors reported linewidths for the liquid-component nuclei consistent with expectations involving the rotational averages of equation (18), namely, that spinning samples with $\boldsymbol{s} \perp \boldsymbol{H}$ simply reduced the static-sample linewidth by a factor of two, whereas MAS eliminated the MS broadening when the diffusion length of the molecules in the liquid over a rotor period was small in comparison to the bead diameter. The success of eliminating MS broadening from solid state spectra is very vividly seen in the MAS ^{13}C spectrum of a cubic material such as adamantane where, in the presence of MAS, broadening due to other sources is also minimal and observed linewidths approach those expected from the inhomogeneities of the applied field.[25]

4.1.2 Samples with Anisotropic Bulk Magnetic Susceptibility

We turn now to the more complicated case of ABMS where κ is a tensor, rather than a scalar, and this tensor has principal values κ_1, κ_2, and κ_3, given in order of decreasing magnitude. In the sense that the ABMS tensor can formally be separated into an isotropic part, characterized by the mean of the principal values, and an anisotropic part, characterized by deviations from the mean, the behavior of the isotropic part will be the same as discussed above. It is only the anisotropic part which will require further consideration.

As an example of ABMS, let us consider the aromatic ring which is the most common source of diamagnetic ABMS in organic systems. Aromatic molecules typically have anisotropic molecular magnetic susceptibilities;[3] thus, their crystalline counterparts often possess ABMS as well. It is useful to think of the aromatic ring itself as an analog of ABMS in solids since, in liquid state NMR, the aromatic ring gives rise to the familiar ring current shifts.[26] These shifts are illustrated in Figure 1 where an aromatic ring is drawn and atoms A1 and A2 are placed outside of the ring, A1 along the hexad axis and A2 in the plane of the ring. If there is isotropic tumbling in a liquid containing an aromatic ring, and if the atoms A1 and A2 maintain their position with respect to this ring, then the resonance of A1 will shift to higher field and the resonance of A2 will shift to lower field. Even though the influence of the ring current on the atoms A1 and A2, at any fixed orientation, can be described as a dipolar interaction, isotropic reorientation does not average this interaction to zero because the *strength of the dipole moment is a function of orientation*. Only for a dipole moment of *fixed* magnitude, will the average dipolar field at all surrounding points vanish upon isotropic tumbling. The sign of the ring current shift at a given point in space usually takes the sign of the dipolar field when the induced moment on the ring is strongest, i.e. when $\boldsymbol{H}$ is parallel to the hexad axis.

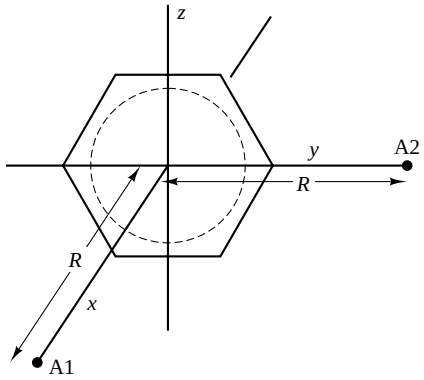

Figure 1 Geometry illustrating, at atoms A1 and A2, ring current shifts arising from the induced circulation of electrons in the π orbitals of the benzene ring. The C_6 axis of the ring, i.e. the direction of the maximum induced dipole, lies along x, and A1 is situated on x. Atom A2 lies along y. If, during isotropic tumbling or MAS, atoms A1 and A2 maintain their orientation with respect to the benzene ring, then A1 will experience an average reduction in its local field. This change in field is opposite in sign and twice the magnitude seen at A2. The interaction between the ring and the atoms is a dipolar interaction, but shifts arise because of the orientation dependence of the induced dipole. In glassy materials, aromatic rings give rise to a spread of frequencies for nearby atoms. In the presence of MAS, crystals possessing ABMS produce analogous shifts. Replace the benzene ring by a crystal with an axially symmetric κ tensor oriented along x. Similar shifts will occur for atoms in surrounding regions over distances comparable to the crystal size

For ABMS in solids, one might think of replacing the aromatic ring in Figure 1 with, say, a spherical single crystal which possesses ABMS. At some distance outside of this sphere, a change in the orientation of $\boldsymbol{H}$ with respect to the ABMS tensor of the sphere will create a change in the strength of the induced magnetic moment of the spherical crystal. This change will alter the strength of the dipolar fields emanating from this sphere. Hence, the isotropic average of the sphere's dipolar field at all external points will not, in general, vanish.

From the foregoing discussion we may draw qualitative conclusions about ABMS line broadening *in the presence of MAS*, given that MAS was effective in eliminating line broadening when only IBMS is present:

1. An isolated ellipsoidal single crystal will have no ABMS broadening since the field inside of the ellipsoid is uniform for all orientations.
2. A spherical hole inside of a sphere with ABMS will cause broadening.
3. A nonellipsoidally shaped single crystal with ABMS will cause ABMS broadening unless κ is axially symmetric and its unique axis lies along the spinning axis.
4. In a powder sample where each particle is a single crystal, ABMS broadening arises from both particle shape and from interparticle perturbations.
5. Densification via, say, melt crystallization, of a polycrystalline sample possessing ABMS increases ABMS broadening.
6. Dilution of ABMS crystallites with a material having IBMS reduces the interparticle contribution to ABMS broadening for resonances associated with these crystallites but creates ABMS broadening for resonances in the material with IBMS. The efficacy of such dilution depends rather strongly on having ABMS particles which are themselves single crystals, i.e. diluting polycrystalline ABMS particles is not very effective.

An empirical estimate of ABMS line broadening is based on MAS linewidth data[27] for hexamethylbenzene, a substance having an axially symmetric MS tensor. In a melt crystallized (densely polycrystalline) sample, ABMS line broadening yielded a full width at a halfheight of 0.93 ppm which, for hexamethylbenzene is a linewidth, in Hz, of $0.18\Delta\kappa\nu_0$ where $\Delta\kappa = \kappa_{\parallel} - \kappa_{\perp}$. In the work just referred to, points 3, 5, and 6 listed above were also demonstrated and a very crude calculation of interparticle broadening was attempted.

In the absence of MAS, ABMS line broadening is, of course, also eliminated for a *static* single crystal in the form of an ellipsoid.

4.2 Influence of Magnetic Susceptibility on Chemical Shift Measurements

4.2.1 Referencing the Anisotropic Chemical Shift

In the discussion which follows, the assumption is made that one wishes to determine the isotropic or anisotropic chemical shift values, relative to some reference material, *to a precision exceeding the magnitude of potential susceptibility corrections*. In many cases, the precision of the determination is such that one cannot justify a preoccupation with MS corrections. For example, MS issues are important in the measurement of chemical shifts for protons in organic materials because of the usually small range (8–10 ppm) of proton chemical shifts. In comparison, MS corrections for ^{13}C shifts are less important; yet MS effects can be seen because of the relatively high resolution achievable on observing dilute spin-$\frac{1}{2}$ nuclei such as ^{13}C. In paramagnetic materials or certain inorganic materials with larger susceptibilities, a consideration of the impact of MS on chemical shift is also in order.

One way to measure a chemical shift tensor is to rotate a single crystal in a magnetic field about orthogonal axes. This allows one to map the chemical shift and, by correlating these shifts with other measurements, e.g. X-ray, one can relate these shifts to directions in the molecules. Since each determination of a resonance position is undertaken using a static sample, shape effects for the crystal come into play. Obviously, the narrowest lines will be for ellipsoids. If one does not wish to make shape-dependent MS corrections at each orientation, then a sphere should be employed. If the spherical crystal has IBMS, then the chemical shift anisotropy measured will be correct. If the crystal has ABMS, then one knows that $\boldsymbol{M}$ in equation (7) has a magnitude that is a function of orientation. Yet, according to the foregoing discussion on susceptibility corrections in liquids, where equation (9) was used, if the contribution from the Lorentz sphere is included, then $(\boldsymbol{h}_1 + \boldsymbol{h}_2) = 0$ for a sphere, i.e. there should be no correction term which depends on κ at any orientation. Yet, Spiess et al.,[28] in a very careful study of ferrocene, observed small deviations from an axially symmetric shielding tensor for the protons of ferrocene in a spherical single crystal. They attributed these deviations to ABMS effects, arguing that motional averaging of the ferrocene rings and crystal symmetry combine to predict an axially symmetric shift tensor. If ABMS effects persist in a single-crystal sphere, then the appropriateness of the Lorentz correction $\boldsymbol{h}_2$ is questioned. Since the observed deviations were small, there may be alternative explanations. Nevertheless, it still seems that when the magnitude of the potential susceptibility corrections is a significant fraction of the apparent chemical shift anisotropy, the most reasonable recipe for determining true chemical shift anisotropies in materials with ABMS is to use a spherical single crystal and make no MS corrections.

4.2.2 Referencing the Isotropic Chemical Shift

The question arises as to effective strategies for referencing *isotropic* chemical shifts in solids. For solids with IBMS, an effective approach is to utilize MAS with a sample geometry such that an unknown material surrounds a central glass capillary containing a primary liquid reference, such as tetramethylsilane (TMS) for ^{13}C or ^{1}H nuclei. It does not matter whether the walls of the glass have uneven thickness or whether the spinning creates bubbles in the liquid. The main precaution, related to $\boldsymbol{B}_0$ homogeneity, is to distribute the liquid over the same axial range of the rotor that the sample occupies. The chemical shift measured between reference and solid needs no correction for MS, although there can be some other solid state contributions to the apparent chemical shift, e.g. from second-order dipolar effects.[29,30] Once the chemical shift of a suitable solid is measured in the way outlined above, that solid can be used as a secondary shift standard. For materials with IBMS, unknown and standard can be mixed in any fashion, utilizing MAS, and the measured shift differences will need no further MS correction.

The geometry for referencing the chemical shift in samples with ABMS is a more complicated problem. An approximate method is to employ MAS on a sample in which a liquid reference in a capillary is surrounded by a powder sample of the ABMS material, where the grain size of the powder is much smaller than the wall thickness of the capillary, and the particles in the powder have no preferred orientation. In this case the signal from the powder will have substantial ABMS broadening; yet, to the liquid in the capillary, the powder will look like a material with IBMS. Therefore, within the approximation that ABMS broadening in the powder is symmetric, one will get a chemical shift difference which is correct. Symmetric broadening is not necessarily

expected since broadening arises from effective dipolar interactions which typically have asymmetric, powder-average field distributions associated with them. Also, in contrast to the IBMS case, for arbitrary powder samples having ABMS, it is not required that the mean resonance position, i.e. that position about which the first moment of the resonance intensity vanishes, is without influence from ABMS. Qualitatively, one expects ABMS-induced powder-average shifts to be closely related to the existence of regular and highly asymmetric shapes for the individual powder particles.

This author is unaware of any geometry for a sample, whereby an unknown material with ABMS, *in the form of a single crystal of some shape*, can be combined with a chemical shift reference material possessing IBMS in such a way that differences in the isotropic values of unknown and reference chemical shifts can be measured reliably without a prior knowledge of the orientation of the ABMS tensor in that material. The complicated nature of chemical shift referencing has been demonstrated for a polymer film possessing ABMS.[25] In the presence of MAS, variations in shifts of about 1.5 ppm were observed between ^{13}C nuclei in TMS, contained in a central capillary tube, and ^{13}C nuclei in the oriented polymer film. These differences arose when the orientation of the unique axis of the ABMS tensor was changed from parallel to the rotor axis to perpendicular to the cylindrical walls of the rotor.

If one presumes that the Lorentz sphere correction applies to all diamagnetic and paramagnetic solids, then for a spherical single crystal possessing ABMS as well as for a spherical liquid sample, the field seen by the nucleus is just the external field $\boldsymbol{H}_0$. Hence, a true chemical shift difference, in the absence of ABMS broadening, could be measured by sequential substitution of such samples. Of course, the use of MAS for the single crystal or the employment of rotation patterns would be required in order to identify the isotropic chemical shift; moreover, for the liquid sample, the influence of the container wall will be present and this is also most easily dispensed with using MAS.

5 MISCELLANEOUS CONSIDERATIONS

5.1 Influence on Multidimensional NMR

The development of 'high-resolution' techniques in solids has enabled spectroscopists to design multidimensional NMR strategies for solids. When the chemical shifts of one nucleus form the basis for one of the NMR dimensions, then it is possible that MS effects can appear. The author has seen such effects using proton multiple pulse techniques combined with MAS. The dipolar fields arising from either IBMS or ABMS in a glassy or semicrystalline solid can be distributed in a way which is not highly correlated with the anisotropic chemical shift tensors on the molecules. The net influence of MS is to create a distribution of effective chemical shift tensors. For a given chemical site, effective tensors throughout the sample have dispersions of principal values but the same isotropic average for IBMS. For ABMS, a dispersion of isotropic shifts also exists. Thus, in a proton 2D experiment, for example, where MS effects can be a modest fraction of the chemical shift range or of chemical shift anisotropies, one tends to create spatially based as well as chemically based correlations of polarization as one increments the time for chemical shift evolution. As usual in NMR, this can be a nuisance as well as a source of information.

5.2 Use of NMR to Measure Unknown Magnetic Susceptibilities

From the foregoing discussions, it is clear that if one has two liquids in the concentric-tube geometry and utilizes MAS, any chemical shift difference associated with the two liquids will need no MS correction. A second measurement with either $\boldsymbol{s} \perp \boldsymbol{H}_0$ or $\boldsymbol{s} \parallel \boldsymbol{H}_0$ will yield the susceptibility difference between two liquids [equations (14) and (15)]. Provided the MS is known for one of the liquids, this measurement will yield the MS of the unknown liquid. One could forego the magic angle measurement above and simply use chemical shift data employing internal standards. However, any contribution to the shift arising, for example, from a change in intermolecular associations would produce an error in the susceptibility determination. Another approach[31] to measuring diamagnetic susceptibilities in liquids involves measuring a chemical shift difference from sequential experiments for some nucleus belonging to a liquid for which κ is desired. First the measurement is made for the neat liquid; then the measurement is repeated for that liquid suspended as a separate phase, in spherical droplets, in another immiscible liquid for which κ is known. This method gave reported κ values to within a few per cent of literature values.

It is also possible to estimate paramagnetic susceptibilities using NMR signals. Feher and Knight[32] in 1955 used two capillaries, filled with water, and oriented them inside of a tube filled with Mn_2O_3 powder. One capillary was parallel and one perpendicular to $\boldsymbol{B}_0$. The tube axis was in the remaining orthogonal direction. The difference in resonance frequency between the two tubes of water allowed them to estimate κ to within 6% of the listed value. Other variants of this experiment using different geometries have also been employed. For example, Li et al. measured the shift of the proton resonance in a sphere of water when that sphere was sequentially placed in a powder of an unknown and then in a powder of a reference material.[33] It is also possible to estimate the MS of a paramagnetic substance by simultaneously measuring, using concentric-tube geometry, the shift difference for a nucleus in a reference material in two solutions. One solution is the reference dissolved in a pure solvent; the other solution is the same but augmented by a known amount of paramagnetic material.[34,35]

5.3 Measurement of Anisotropic Molecular Magnetic Susceptibilities

A molecule possessing anisotropic molecular magnetic susceptibility experiences a weak alignment in a magnetic field. Its order parameter is proportional[36,37] to $\Delta\kappa H^2/kT$, where $\Delta\kappa$ is the anisotropy in the molecular magnetic susceptibility tensor. The first evidence for this alignment[36] was observed at 9.3 T in solutions of multiring aromatic compounds where deuteron resonances were split by less than 1 Hz. Subsequently, several halomethanes were examined[37] at

14.35 T, again revealing deuteron splittings of a few tenths of a Hz. The precision of these measurements is not high, but clearly the precision ought to improve rapidly as one moves to higher fields. Deuterons are ideal nuclei for observing this alignment since their natural linewidths in low viscosity liquids are quite narrow; yet, the quadrupolar interaction responsible for the splitting is conveniently large. A significant increase in the quadrupolar interaction would make the linewidths unacceptably broad for detecting small splittings.

5.4 A Basic Strategy for Suppressing MS Effects in Magnetic Resonance Imaging

One often wishes to image the density of a liquid, like water, in the vicinity of solid (e.g. bones) or rarified (e.g. as occurs for lungs[38]) phases (see ***Lung and Mediastinum: A Discussion of the Relevant NMR Physics***.). Corresponding abrupt changes in MS have the effect of modifying resonance frequencies in a local manner.[39] To the extent that the resonance frequency of a nucleus determines its spatial position in an imaging application, where field gradients are applied, the MS shift will create an undesirable apparent 'spatial shift'. A strategy[40,41] for minimizing such shifts involves creating imaging sequences where chemical shifts and MS-induced shifts are refocused but gradient pulses are applied during the dephasing and rephasing times in such a way that the resonance offsets due to these external gradients do not refocus. The result is that the 'spatial shifts' arising from MS effects get scaled approximately by the ratio of the local gradient field strength to the static field strength; hence the spatial shift becomes negligible in most materials.

6 RELATED ARTICLES

Chemical Shift Tensor Measurement in Solids; Chemical Shift Tensors in Single Crystals; Diffusion in Porous Media; Lung and Mediastinum MRI; Magnetic Field Induced Alignment of Molecules; Oil Reservoir Rocks Examined by MRI; Probe Design and Construction; Probes for High Resolution; Susceptibility and Diffusion Effects in NMR Microscopy; Susceptibility Effects in Whole Body Experiments.

7 REFERENCES

1. L. H. Bennett, C. H. Page, and L. J. Swartzendruber, *J. Res. Nat. Bur. Stand.*, 1978, **83**, 9.
2. J. H. Van Vleck, *Electric and Magnetic Susceptibilities*, Oxford University Press, Oxford, UK, 1932.
3. W. H. Flygare, *Chem. Rev.*, 1974, **74**, 653.
4. R. K. Reber and G. F. Boeker, *J. Chem. Phys.*, 1947, **15**, 508.
5. *Handbook of Chemistry and Physics*, 73rd edn., ed. D. R. Lide, CRC Press, Boca Raton, FL, 1992, Sect. 9.
6. P. Langevin, *Ann. Chim. Phys.*, 1905, **5**, 70; *J. Phys.*, 1905, **4**, 678.
7. B. C. Eggleston, D. F. Evans, and R. E. Richards, *J. Chem. Soc.*, 1954, 941.
8. J. A. Pople, W. G. Schneider, and H. J. Bernstein, *High Resolution Nuclear Magnetic Resonance*, McGraw-Hill, New York, 1959, Chaps. 2 and 4.
9. L. Pauling, *J. Chem. Phys.*, 1936, **4**, 673.
10. K. S. Krishnan, *Nature (London)*, 1934, **133**, 174.
11. J. E. Wertz and J. R. Bolton, *Electron Spin Resonance, Elementary Theory and Applications*, McGraw-Hill, New York, 1972.
12. J. R. Zimmerman and M. R. Foster, *J. Phys. Chem.*, 1957, **61**, 282.
13. L. F. Fuks, F. S. C. Huang, C. M. Carter, W. A. Edelstein, and P. B. Roemer, *J. Magn. Reson.*, 1992, **100**, 229.
14. M. A. Lorentz, *The Theory of Electrons*, Dover, New York, 1952.
15. R. P. Feynman, R. B. Leighton, and M. Sands, *The Feynman Lectures on Physics*, Addison-Wesley, Reading, MA, 1964, Vol. II, Chaps. 10, 11, 34.
16. J. A. Osborne, *Phys. Rev.*, 1945, **67**, 351.
17. D. Doskočilová, D. D. Tao, and B. Schneider, *Czech. J. Phys. B*, 1975, **25**, 202.
18. C. P. Slichter, *Principles of Magnetic Resonance*, Springer-Verlag, Berlin, 1978, Chap. 4
19. P. Pascal, *Chemie generale*, Masson et Cie, Paris, 1949.
20. C. K. Ingold, *Structure and Mechanism in Organic Chemistry*, Cornell University Press, Ithaca, NY, 1953.
21. W. R. Angus and D. V. Tilston, *Trans. Faraday Soc.*, 1947, **43**, 221.
22. L. E. Drain, *Proc. Phys. Soc.*, 1962, **80**, 1380.
23. N. Bloembergen and J. A. Rowland, *Acta Metall.*, 1953, **1**, 731.
24. M. E. Stoll and T. J. Majors, *J. Magn. Reson.*, 1982, **46**, 283.
25. W. L. Earl and D. L. VanderHart, *J. Magn. Reson.*, 1982, **48**, 35.
26. J. S. Waugh and R. W. Fessenden, *J. Am. Chem. Soc.*, 1957, **79**, 846.
27. D. L. VanderHart, W. L. Earl, and A. N. Garroway, *J. Magn. Reson.*, 1981, **44**, 361.
28. H. W. Spiess, H. Zimmermann, and U. Haeberlen, *Chem. Phys.*, 1976, **12**, 123.
29. D. L. VanderHart, *J. Chem. Phys.*, 1986, **84**, 1196.
30. M. P. Augustine, K. W. Zilm, and D. B. Zax, *J. Chem. Phys.*, 1993, **98**, 9432.
31. J. Homer and H. K. Al-Daffaee, *J. Chem. Soc., Faraday Trans. 2*, 1985, **81**, 803.
32. G. Feher and W. D. Knight, *Rev. Sci. Instrum.*, 1955, **26**, 293.
33. J. Li, M. E. Lashier, G. L. Schrader, and B. C. Gerstein, *Appl. Catal.*, 1991, **73**, 83.
34. D. F. Evans, *J. Chem. Soc.*, 1959, 2003.
35. S. K. Sur, *J. Magn. Reson.*, 1989, **82**, 169.
36. J. A. B. Lohman and C. MacLean, *Chem. Phys.*, 1978, **35**, 269.
37. A. A. Bothner-By, J. Dadok, P. K. Mishra, and P. C. M. Van Zijl, *J. Am. Chem. Soc.*, 1987, **109**, 4180.
38. D. C. Ailion, T. A. Case, D. D. Blatter, A. H. Morris, A. G. Cutillo, C. H. Durney, and S. A. Johnson, *Bull. Magn. Reson.*, 1984, **6**, 130.
39. T. A. Case, C. H. Durney, D. C. Ailion, A. G. Cutillo, and A. H. Morris, *J. Magn. Reson.*, 1987, **73**, 304.
40. P. Bendel, *IEEE Trans. Med. Imag.*, 1985, **MI-4**, 114.
41. J. B. Miller and A. N. Garroway, *J. Magn. Reson.*, 1986, **67**, 575.

Acknowledgments

The author wishes to acknowledge the assistance of L. H. Bennett, L. J. Swartzendruber, J. F. Douglas, A. N. Garroway, G. Eaton, J. Carolan, and A. Vega in the preparation of this manuscript.

Biographical Sketch

David L. VanderHart. *b* 1941. B.A., 1963, Ph.D., 1968, Physical Chemistry, University of Illinois, supervisor, H. S. Gutowsky. Postdoctoral work with W. H. Flygare (molecular Zeeman effect), 1968–69. Polymers Division, National Institute of Standards and Technology, Gaithersburg, MD, USA, 1969–present. Approx. 70 publications. Current research specialty: solid state NMR of polymers with an emphasis on obtaining morphological information.

MQMAS Advances

Jean-Paul Amoureux

Université de Lille, Villeneuve d'Ascq, France

&

Marek Pruski

Iowa State University, Ames, IA, USA

1	Introduction	1
2	Theoretical Background	3
3	Detection of Pure-phase Spectra	4
4	Processing and Interpretation of MQMAS Spectra	9
5	Measurements of Dipolar Connectivities	17
6	Sensitivity Enhancement via CPMG Method	23
7	Conclusion	24
8	Related Articles in this Volume	24
9	Related Articles in Volumes 1–8	24
10	References	24

1 INTRODUCTION

NMR's ability to probe the structure of materials strongly depends upon the availability of high-resolution spectra, which serve as fingerprints of the physico-chemical surroundings of the studied nuclei. In powdered solids, the nuclear spins experience various anisotropic interactions, which broaden their spectra and render NMR more difficult for structural determinations. For spin-1/2 nuclei these interactions include dipole-dipole coupling between spins, chemical shift anisotropy (CSA), indirect spin–spin coupling and interaction with unpaired electrons.[1] The resolution and sensitivity gaps between liquid and solid state NMR began to decrease in the 1960s and 1970s with the introduction of radio frequency (RF) decoupling, magic angle spinning (MAS) and cross polarization (CP) methods.[2–5] These developments, in concert with the continuing advances in NMR hardware and software allowed for increasingly precise measurement of the spin interactions in solid samples, including the isotropic chemical shifts of spin-1/2 nuclei.

Until recently, however, these techniques could not overcome the line broadening in NMR spectra of the quadrupolar nuclei with spin greater than 1/2. This broadening arises from the coupling of the non-spherical charge distribution of such nuclei with the gradient of the electric field created by the surrounding electrons. The quadrupolar broadening is 'more anisotropic' than the first order interactions (CSA and dipolar coupling), in the sense that it contains higher order orientational terms of significant magnitude. Thus, more complex motions of the sample, or of the spin magnetization, are needed in order to achieve the highest possible resolution.[6–8] This article will focus on some of the concepts and experiments associated with the acquisition of isotropic solid state spectra of the quadrupolar nuclei by combining the multiple quantum (MQ) NMR with MAS.[8,9] In the last years MQMAS has revolutionized solid state NMR of the so-called half-integer quadrupolar spins. The most prominent nuclei that are amenable to this technique include ^{11}B (S = 3/2), ^{17}O (S = 5/2), ^{23}Na (S = 3/2) and ^{27}Al (S = 5/2).

The theory necessary for understanding of the quadrupolar interaction has been described before in numerous textbooks, monographs and reviews.[1,10–13] We first note that the size of the quadrupolar interaction can be described by the quadrupolar frequency ν_Q, which is proportional to the quadrupole moment Q of a nucleus and the electric field gradient (EFG). Depending upon the size of Q and the local electronic environment, the values of ν_Q can range from zero to several hundred of MHz. In NMR, we generally consider the strong field case, $\nu_0 > \nu_Q$, where ν_0 is the Larmor frequency in the static field $\mathbf{B}_0$. In this approximation, the first- and second-order quadrupolar energies can be easily calculated using the perturbation theory. For half-integer spins, the first-order quadrupolar effect on the satellite transition frequencies ($m - 1 \leftrightarrow m$, $m \neq 1/2$) is of the order of ν_Q. Thus, in a powdered sample, the NMR spectrum is spread over a frequency range that for most nuclei exceeds the range of chemical shifts and the bandwidth of the spectrometer under pulse excitation. However, the central transition ($-1/2 \leftrightarrow 1/2$) is not affected to first order. In the absence of additional line broadenings from chemical shift and/or dipolar interaction, the width of the powder spectrum for the central transition is determined only by the second order quadrupolar terms. Since this contribution is typically 10^2 to 10^3 times smaller than ν_Q, the central transition yields a narrower and more intense spectrum, which is the subject of most studies on half-integer quadrupolar nuclei. We note that in this approximation the width of the central transition spectrum is inversely proportional to the magnitude of magnetic field $\mathbf{B}_0$.

The detection of broad quadrupolar lineshapes can rarely be accomplished with single pulse excitation because of the loss of magnetization within the dead time of the receiver. This necessitates the use of multi-pulse excitation, with the two-pulse spin-echo sequences being the most common.[14,15] In case of sufficiently broad lines, the acquisition of spectra can be accomplished by scanning the frequency, or the magnetic field $\mathbf{B}_0$, and via point by point acquisition of the echo intensity.[16] While the static, spin-echo experiments continue to be used in the case of strong quadrupolar interactions, most studies of quadrupolar nuclei in the last two decades utilized the line-narrowing effect of spinning the sample under MAS or variable angle (VASS) conditions.[17,18] MAS eliminates the first order broadening completely and reduces the quadrupolar contribution to the central transition line width by a factor of approximately three. Consequently, the experimental strategies applied in the MAS experiments depend on the size of quadrupolar coupling. For ν_Qs not exceeding few hundred kHz, it is often possible to observe the whole spectrum, which appears as a wide manifold of spinning sidebands. The spacing between sidebands is equal to the spinning speed ν_R, whereas their individual widths and shapes are governed both by ν_R and the second order quadrupolar interaction. The width

and the shape of the entire manifold allow one to determine ν_Q and the asymmetry parameter of the EFG tensor η_Q.[17,19] The accuracy of such measurements strongly depends on the uniformity of the RF excitation, precise setting of the magic angle, probe bandwidth and tuning of the spectrometer. For large values of ν_Q, the spinning sidebands for the satellite transitions are often distorted, overlapping and embedded in background noise. Consequently, it becomes advantageous to use the MAS lineshape corresponding to the central transition for determination of the NMR parameters. While this strategy often relies upon the availability of high magnetic fields and high spinning speeds, trustworthy values of ν_Q, η_Q and the isotropic chemical shift δ_{CS} can be obtained from the computer simulations of the observed lineshapes.[20] In favorable cases, several distinct resonances can be fully characterized in a single MAS spectrum.

Several other strategies have been developed for improving the resolution of quadrupolar NMR spectra. These include static and MAS two-dimensional (2D) nutation experiments that utilize the correlation between the quadrupolar parameters and the precession frequencies induced by RF pulses of different lengths and intensities.[21–23] For moderate values of ν_Q not exceeding 1 MHz, SATRAS (satellite transition spectroscopy) can be used to determine the quadrupole and chemical shift parameters.[24,25] The problem of overlapping spinning sidebands in the MAS spectra of quadrupolar nuclei can be overcome using the recently proposed QPASS (quadrupolar phase alternated sideband suppression) sequence.[26] Finally, several techniques combined with MAS have been developed that allow for studies of dipolar interactions between the quadrupolar and spin-1/2 nuclei. These include the CP experiment, REDOR (rotational echo double resonance), TEDOR (transferred echo double resonance), TRAPDOR (transfer of populations double resonance) and REAPDOR (rotational echo adiabatic passage double resonance).[27–35]

As mentioned above, the second order quadrupolar interaction is not averaged to zero by MAS alone. However, remarkable developments have been made recently in this area of solid state NMR. The theoretical foundations and two different experimental realizations of complete spatial averaging of the second order broadening of the central transition were published in the late 1980s by the groups of Pines and Virlet.[6,7,36] It was shown that such spatial averaging requires mechanical rotation of the sample around an axis that has time dependent orientations. In the one-dimensional DOR (double rotation) experiment, the sample is spun in a small inner rotor, which is rotating inside an outer rotor.[6] The rotation axis of the outer rotor is set at the magic angle ($\chi_m = 54.74°$ with respect to $\mathbf{B}_0$), while the rotation axis of the inner rotor moves continuously on a cone of an aperture of 61.12°. In contrast with DOR, the DAS (dynamic angle spinning) technique uses two discrete rotational orientations (commonly tilted 37.38° and 79.19° away from $\mathbf{B}_0$) and correlates the corresponding resonance frequencies in a 2D experiment.[7] In general, DOR results in better averaging of the dipolar interactions and allows for studying of samples with fast relaxation times. DAS, on the other hand, provides a better filling factor and separates the anisotropic lineshapes associated with each isotropic resonance. The line narrowing abilities of DOR and DAS are best demonstrated in crystalline materials, where resolution enhancement by one or two orders of magnitude has been reported.[37] Most recently, it has been proposed and demonstrated by Frydman et al. that the line narrowing of the central transition can be obtained without changing the orientation of the spinning axis, as long as the motion of this axis in space is replaced by changing the coherence state of the observed spins.[8,9] This experiment is referred to as multiple quantum magic angle spinning (MQMAS) NMR. Similar to DAS, MQMAS is a two-dimensional method, which correlates the phase evolutions of the MQ and single quantum (1Q) coherences and allows for observation of a purely isotropic echo. The change of the coherence state of half-integer quadrupolar spins can be effectively accomplished by strong RF irradiation.[38,39] The MQMAS method precludes most of the shortcomings of DOR (presence of closely spaced spinning sidebands) and DAS (loss of magnetization during the reorientation of the spinner axis) and, being technically straightforward, has found enthusiastic approval in the NMR community. The resolution enhancement that this technique can provide is demonstrated in Figure 1, which compares static, MAS and MQMAS spectra of ^{87}Rb in well-crystallized $LiRbSO_4$.[40] The observed line width in $LiRbSO_4$ changed from approximately 400 ppm in a static spectrum to 150 ppm under MAS and 1.5 ppm in MQMAS. Hundreds of applications of this technique in the studies of catalysts, glasses and other amorphous and crystalline inorganic solids have been published.

In the six years since its inception, a great body of work has been reported that extended the efficiency and the analytical capabilities of the MQMAS method. Extensive

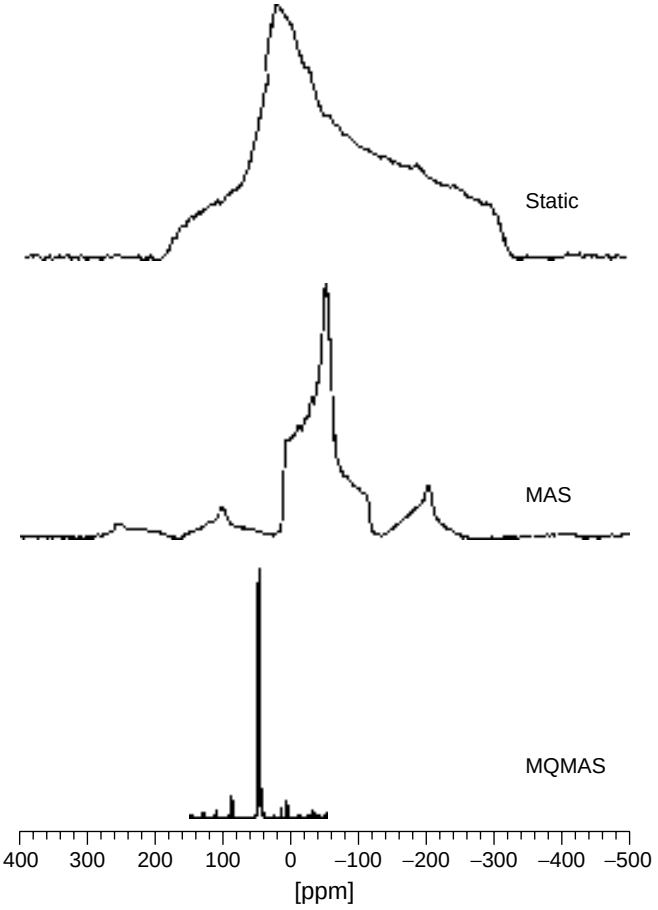

Figure 1 Static, MAS and MQMAS (isotropic projection) spectra of ^{87}Rb in polycrystalline $LiRbSO_4$ taken at 130.88 MHz

theoretical background and explanation of spin manipulations involved in MQMAS, including excitation, conversion and selection of transfer pathways for MQ coherences, is given by L. Frydman (see **Multiple-quantum Magic-angle Spinning Experiments on Half-integer Nuclei: Fundamentals**). In this article, only a brief description of the fundamental principles of the MQMAS experiment is presented. Subsequently, we review the schemes for detection of pure-phase spectra, the data processing methods (including referencing, quantitative analysis and interpretation of MQMAS spectra) and the MQMAS-based double resonance experiments.

2 THEORETICAL BACKGROUND

We consider an ensemble of nuclei with half-integer spin quantum number $S > 1/2$ in a strong magnetic field. There are $2S + 1$ Zeeman energy levels associated with such spins that can be labeled with their magnetic quantum number m. The existence of a non-vanishing (m, m′) element in the density matrix shows that there is a p-quantum coherent superposition of the states $|m\rangle$ and $|m'\rangle$ with multiplicity defined by $p = m - m'$. Thus, the diagonal elements of the density matrix (m, m), which represent the relative populations of the Zeeman states $|m\rangle$, correspond to zero-quantum coherences. It can be shown that these are the only coherences present in the density matrix of a system at thermal equilibrium. Under the conditions normally encountered in NMR the reduced density matrix can be used, which describes the relative deviations from a completely uniform distribution. The reduced density matrix at thermal equilibrium is proportional to S_z (the z component of the total spin angular momentum operator S).

In the frame of the Zeeman interaction, i.e., the 'rotating frame', the secular second order Hamiltonian governing the S spin system can be written as

$$H = H_{Q1} + H_{Q2} + [\nu_0\Delta\delta + m_I J + F(\alpha_s, \beta_s)]S_z \quad (1)$$

where

$$H_{Q1} = \overline{\nu}_Q(\alpha_s, \beta_s, \eta_Q)[S_z^2 - S^2/3] \quad (2)$$

$$H_{Q2} = -\frac{\nu_Q^2}{2\nu_0}[V_1V_{-1}(4S^2 - 8S_z^2 - 1) + V_2V_{-2}(2S^2 - 2S_z^2 - 1)]S_z$$
$$= B(\alpha_s, \beta_s, \eta_Q)S_z + D(\alpha_s, \beta_s, \eta_Q)S_z^3 \quad (3)$$

with

$$\overline{\nu}_Q(\alpha_s, \beta_s, \eta_Q) = 1.5\nu_Q[3\cos^2\beta_s - 1 + \eta_Q\sin^2\beta_s\cos 2\alpha_s] \quad (4)$$

and

$$\nu_Q = \frac{e^2qQ}{4S(2S-1)h} = \frac{C_Q}{4S(2S-1)} \quad (5)$$

In the above equations H_{Q1} and H_{Q2} represent the first and second order perturbation terms for the quadrupole interaction, $\Delta\delta$ is the resonance offset (in ppm), J is the scalar coupling constant between spin S and another spin I with magnetic number m_I, eq is the largest principal axis value of the EFG tensor, C_Q is the quadrupole coupling constant, while ν_0 and h have their usual meaning. The last term in equation (1) accounts for CSA, the anisotropy of J coupling and heteronuclear dipolar couplings, $\overline{\nu}_Q$ is the quadrupole splitting, and V_1, V_{-1}, V_2 and V_{-2} are the eigenvalues of the quadrupolar tensor in the laboratory frame. The orientation dependencies of F, $\overline{\nu}_Q$, V_1, V_{-1}, V_2 and V_{-2} can be described in terms of two polar angles α_s and β_s orienting the direction of $\mathbf{B}_0$ in the principal axis system (PAS) of the EFG tensor. Implicit in F is the dependence of the non-quadrupolar anisotropic interactions on their orientation with respect to the quadrupolar tensor, which can be described using additional sets of Euler angles.

The MQ transitions are induced using RF pulses. Following these excitations, coherences freely precess during the evolution periods. We first consider the free evolution of phase Φ^{stat} associated with the coherence (m, m′) in a single crystallite within a static sample under the Hamiltonian H described in equation (1). In the absence of RF magnetic field and relaxation processes this evolution can be written as

$$\Phi^{stat}(m, m') = [\overline{\nu}_Q(m + m') + \nu_0\Delta\delta + m_I J + F(\alpha_s, \beta_s)$$
$$+ B(\alpha_s, \beta_s, \eta_Q) + D(\alpha_s, \beta_s, \eta_Q)$$
$$\times (m^2 + mm' + m'^2)](m - m')t \quad (6)$$

It is clear that none of the internal Hamiltonians in equation (1) has an effect on the zero-quantum coherences (m, m). In nuclei with moderate or large ν_Q values, the first term in equation (6) is dominant. As a result, all non-diagonal elements ($m \neq \pm m'$) are quickly dephased, which prevents their further detection. For the anti-symmetric p-quantum coherences (p/2, −p/2), the evolution phase can be written as

$$\Phi^{stat}(p/2, -p/2) = \left\{p[\nu_0\Delta\delta + m_I J + F(\alpha_s, \beta_s)] + \sum_{k=0,2,4} A_k^Q(\alpha_s, \beta_s, \eta_Q)C_k(S, p)\right\}t \quad (7)$$

Explicit expressions for $A_k^Q(\alpha_s, \beta_s, \eta_Q)$ and $C_k(S, p)$ can be found in Amoureux.[41]

Under high-speed sample spinning at an angle χ with respect to $\mathbf{B}_0$, the evolution phase changes to

$$\Phi^{\chi}(p/2, -p/2) = \{p[\nu_0\Delta\delta + m_I J] + A_0^Q(\eta_Q)C_0(S, p)$$
$$+ [pF(\alpha_R, \beta_R) + A_2^Q(\alpha_R, \beta_R, \eta_Q)C_2(S, p)]P_2(\cos\chi)$$
$$+ A_4^Q(\alpha_R, \beta_R, \eta_Q)C_4(S, p)P_4(\cos\chi)\}t \quad (8)$$

where the polar angles α_R, β_R describe the orientation of the rotor axis with respect to the EFG tensor, and equation (9) shows the second and fourth order Legendre polynomials

$$P_2(\cos\chi) = \frac{1}{2}(3\cos^2\chi - 1)$$
$$P_4(\cos\chi) = \frac{1}{8}(35\cos^4\chi - 30\cos^2\chi + 3) \quad (9)$$

Equation (8) illustrates the challenge associated with observing high resolution spectra of half-integer quadrupolar spins: in a standard, single pulse experiment with a fixed rotation axis, the anisotropic broadening cannot be completely removed because no value of χ can simultaneously satisfy the condition $P_2(\cos\chi) = P_4(\cos\chi) = 0$. Consequently, the efficient line

narrowing methods must utilize more complex motions of the sample, or the spin magnetization. MQMAS technique achieves high resolution by involving both spatial and spin manipulations of the broadening interactions.[8] Under fast MAS rotation ($\chi_m = 54.74°$), the simplified evolution phase can be written as

$$\Phi^{MAS}(\frac{p}{2}, -\frac{p}{2}) = \{p[\nu_0\Delta\delta + m_I J] + A_0^Q(\eta_Q)C_0(S, p) + A_4^Q(\alpha_R, \beta_R, \eta_Q)C_4(S, p)P_4(\cos\chi_m)\}t \quad (10)$$

The remaining anisotropic broadening originates from the last term in equation (10), which is scaled with respect to a static case, but not eliminated by MAS alone. The unconventional aspect of the MQMAS approach is that the selective averaging of second-order quadrupolar broadening is completed by forcing the spin system to evolve outside of the 'allowed' central transition coherence, i.e., by transferring it into the multiple quantum coherences ($\mp p/2$, $\pm p/2$) with $p > 1$. After letting the spins evolve during time t_1, the spin system is transferred back to the ($-1/2$, $1/2$) coherence and allowed to freely evolve again during time t_2. The evolution phases in t_1 and t_2 are then correlated in a 2D experiment. The isotropic echo is observed as shown in equation (11), where R(S, p) is

$$t_{2e} = -[C_4(S, p)/C_4(S, -1)]t_1 = R(S, p)t_1 \quad (11)$$

$$R(S, p) = \frac{p[36S(S+1) - 17p^2 - 10]}{36S(S+1) - 27} \quad (12)$$

As the sign of $C_4(S, p)$ is reversed when changing that of p, it is always possible to obtain a positive ratio for R(S, p), which leads to a detectable echo at positive time t_{2e}. This echo signal corresponds to the selection of $p < 0$ for $|p| = 2S$ and $p > 0$ for $|p| < 2S$. Therefore, the echo pathway for spin $S = 3/2$ nuclei can be described using the notation $0 \rightarrow p = -3 \rightarrow -1$. Correspondingly, the correlation of $p = 3$ and $p = -1$ coherences ($0 \rightarrow 3 \rightarrow -1$ pathway) represents the so-called antiecho pathway, where the anisotropic quadrupolar broadening refocuses at negative values of the acquisition time t_2. The concept of antiecho will be later used in describing the experiments that allow for the acquisition of pure absorption spectra (Section 3).

A 2D Fourier transformation of the time domain signal provides a correlation spectrum, which consists of narrow resonance bands with ridges extended along the direction given by

$$F_1 = R(S, p)F_2 \quad (13)$$

where F_2 and F_1 represent frequencies in the single and multiple quantum dimensions, respectively. It is convenient to apply a shearing transformation in order to align these ridges with the F_2 direction. The shearing process transforms F_1 into a new isotropic dimension, which will be denoted F_{ISO} (see Section 4.2).

The basic MQMAS experiment consists of four steps:

(i) RF excitation of MQ coherences
(ii) evolution of these coherences under the internal Hamiltonian H during time t_1

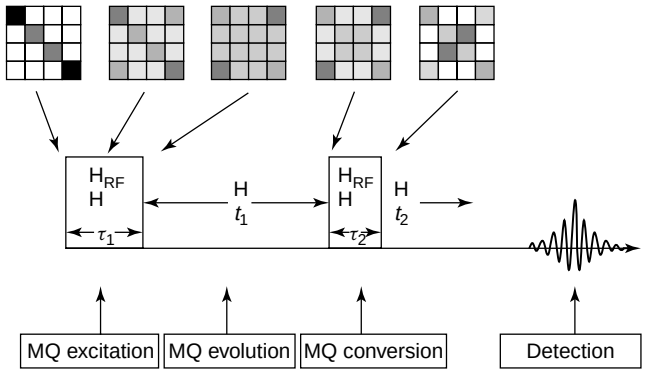

Figure 2 Schematic diagram of the original MQMAS experiment.[8] Time evolution of the reduced density matrix of spin-3/2 nuclei is also shown, with darker squares representing the increased amount of (m, m′) coherence

(iii) reconversion of the MQ coherences into the observable single quantum coherence, again using suitable RF sequence, and
(iv) detection of the signal as a function of time t_2.[8]

The pulse sequence used in the original MQMAS experiment contains two strong continuous wave (CW) RF pulses of duration τ_i and phase ϕ_i, used for preparation (MQ excitation) and mixing (MQ $\rightarrow -1$Q conversion): $H_1(\tau_1)_{\phi 1} - t_1 - H_2(\tau_2)_{\phi 2} - t_2$, as shown in Figure 2. The role of the excitation pulse (or sequence) is to create the largest possible amount of p-quantum coherence along the anti-diagonal of the density matrix (($\pm p/2$, $\mp p/2$), $3 \leq |p| \leq 2S$), as shown schematically on top of the figure for $S = 3/2$. The dephasing that this coherence acquires during the evolution time t_1 is then selectively transferred to the observable -1Q central transition by the second pulse (or sequence) where it refocuses according to equation (11).

Considerable research effort targeted two main weaknesses of MQMAS, namely the limited efficiency of excitation and reconversion, and sensitivity to the magnitude of C_Q. The efficiency could be significantly increased by using the highest possible RF magnetic field ν_{RF} (the so-called hard pulses), fast amplitude modulation (FAM), double frequency sweeps (DFS), rotary resonance excitation and rotation-induced adiabatic coherence transfer method (RIACT).[42–47] FAM, DFS and RIACT are least sensitive to C_Q and thus extend the range of quadrupolar couplings that are accessible to MQMAS to larger values. The most commonly used coherence pathways and acquisition schemes include the split-t_1 scheme with shifted (whole) echo and the z-filter method.[48–51] Several studies were reported that reviewed these schemes and evaluated their performance using standard samples.[40,52,53] At present, it appears that the split-t_1 whole echo scheme with FAM conversion could become a method of choice in MQMAS NMR, as it combines high efficiency with quantitative accuracy and is easy to implement in standard NMR spectrometers.

3 DETECTION OF PURE-PHASE SPECTRA

In general, the time domain signal corresponding to a single resonance in a given crystallite is given by a phase-modulated

function

$$s(t_1, t_2) = s_p \exp(2\pi i \nu_p t_1) \exp(2\pi i \nu_{-1} t_2) \exp[-(\lambda_p t_1 + \lambda_1 t_2)] \quad (14)$$

where s_p represents the amplitude of signal derived via the $0 \rightarrow p \rightarrow -1$ pathway, ν_p and ν_{-1} are the resonance frequencies of the symmetric coherences in p-quantum (p/2, −p/2) and single quantum (−1/2, 1/2) dimensions, and λ's represent the respective transverse relaxation rates (note that $\lambda_p = \lambda_{-p}$). Phase modulation of the detected signal is invariably encountered in 2D spectroscopy while using a single coherence transfer pathway.[54] A complex 2D Fourier transformation of $s(t_1, t_2)$ yields the frequency spectrum

$$S(F_1, F_2) = s_p[a(F_1, \nu_p) + id(F_1, \nu_p)][a(F_2, \nu_{-1}) + id(F_2, \nu_{-1})] \quad (15)$$

where $a(F_i, \nu_j)$ and $d(F_i, \nu_j)$, with i = 1,2 and j = p, −1, are the absorptive (real) and dispersive (imaginary) parts of the spectrum along the multiple and single quantum dimensions

$$a(F_i, \nu_j) = \frac{\lambda_j}{\lambda_j^2 + (F_i - \nu_j)^2}$$

$$d(F_i, \nu_j) = \frac{F_i - \nu_j}{\lambda_j^2 + (F_i - \nu_j)^2} \quad (16)$$

The absorptive and dispersive components are superimposed in equation (15), giving rise to phase-twisted lineshapes. This problem cannot be avoided simply by the adjustment of the phase sensitive detector. Although such a procedure allows the selection of the real part of $S(F_1, F_2)$

$$S^R(F_1, F_2) = s_p[a(F_1, \nu_p)a(F_2, \nu_{-1}) - d(F_1, \nu_p)d(F_2, \nu_{-1})] \quad (17)$$

the absorptive and dispersive components remain mixed in the spectrum. Such mixed-phase spectra were observed in the first MQMAS experiments that used the selection of a single coherence pathway, sometimes referred to as simple echo or simple antiecho (see Figure 3a). This is a major shortcoming, especially in cases where the observation of undistorted lineshapes in the anisotropic dimension is of significant interest or when two resonances are located in close proximity in a 2D spectrum (compare spectrum (a) with a properly acquired and phased spectrum (b) in Figure 3). The basic concepts of phase separation were first developed to facilitate the analysis of 2D correlation spectra in solutions.[54] Since the inception of MQMAS, several strategies for the collection and processing of the data have been proposed, which in essence allow for the 2D phase-adjustment. These strategies can be classified into two categories, based on the appearance of the maximum echo signal in the first row (i.e., $t_1 = 0$) of the 2D data set. The first involves a phase modulated procedure in which the maximum signal (echo) is delayed to $t_{2e} > 0$ by applying one or several $\pm 1Q \rightarrow \mp 1Q$ Hahn echoes.[14] The second category includes amplitude modulated experiments in which $t_{2e} = 0$ for $t_1 = 0$. The performance of various approaches has been thoroughly examined and compared by Brown and Wimperis.[52] We will review these methods briefly in Sections 3.1 and 3.2. Sections 3.3 and 3.4 will describe the methods that allow determination of the sign

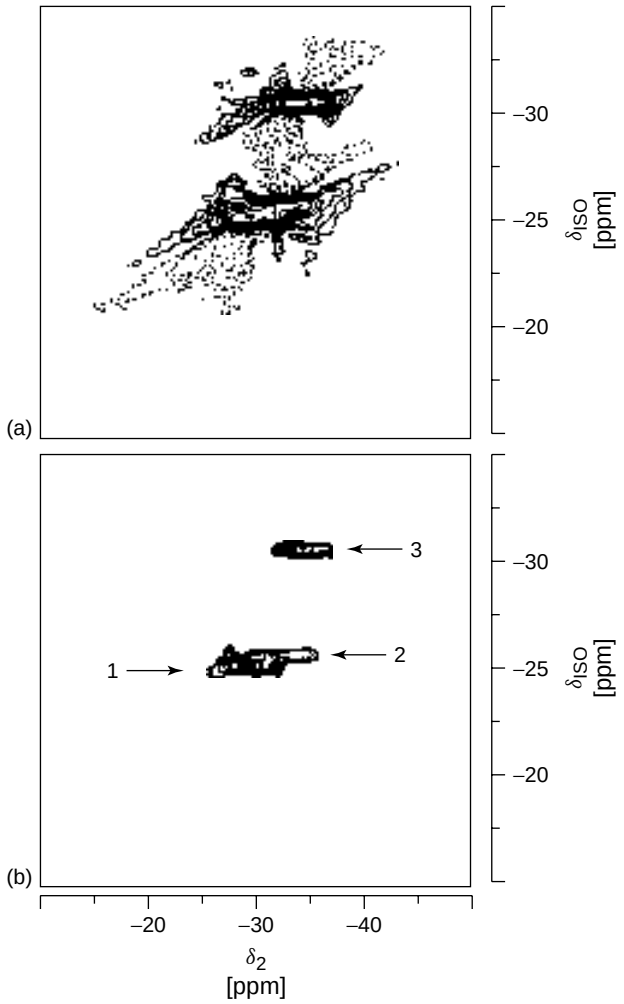

Figure 3 Sheared 3QMAS spectra measured for ^{87}Rb in $RbNO_3$. The following experimental conditions were used: $\nu_0 = 196.4$ MHz, $\nu_{RF} = 70$ kHz, $\nu_R = 10$ kHz. Positive and negative levels are represented on the contour plots by solid and dashed lines, respectively. Spectrum (a) results from acquisition of an echo coherence transfer pathway ($0 \rightarrow -3 \rightarrow -1$). When both echo and antiecho pathways ($0 \rightarrow \pm 3 \rightarrow -1$) are properly used, see spectrum (b), the dispersive parts disappear and all three Rb species present in this compound can be distinguished

of frequency in the F_1 dimension for experiments involving amplitude modulation.

3.1 Phase Modulation during t_1; Shifted Echo and Antiecho

The method of shifting the echo (and/or antiecho) eliminates the dispersive components from the spectrum by utilizing the symmetry properties of the time domain signals and their complex Fourier transforms. The complex Fourier transform of the two halves of a suitably phased symmetrical NMR echo is real. Each half yields the absorption components with the same phase and the dispersion components with opposite phases, which thus cancel. In MQMAS, the shifted echo (antiecho) approach relies upon the introduction of a refocusing π pulse at the end of the pulse sequence in order to delay the formation of an echo (antiecho) in the t_2 domain by a time interval τ.[50,52]

The time domain signals, the pulse sequence and the corresponding coherence transfer pathways for these experiments are schematically shown in Figure 4. As mentioned earlier, the 2D data set that results from the use of a single coherence pathway exhibits phase modulation. In such case, the 2D time-domain signal can be written as shown in equations (18) and (19)

$$s(t_1, t_2, \tau) = s_p \exp(2\pi i \nu_p t_1) \exp(2\pi i \nu_1 \tau) \exp(2\pi i \nu_{-1} t_2) \times \exp[-(\lambda_p t_1 + \lambda_1 \tau + \lambda_1 t_2)] \quad (18)$$

Since $\nu_1 = -\nu_{-1}$,

$$s(t_1, t_2, \tau) = s(t_1, t_2, 0) \exp[-(2\pi i \nu_{-1} + \lambda_1)\tau] \quad (19)$$

In the time domain, the signal first appears at $t_2 < \tau + t_{2e}$, where t_{2e} is given by equation (11) for echo and antiecho. The signal then rises until reaching a maximum at $t_2 = \tau + t_{2e}$, and decays to zero at $t_2 > \tau + t_{2e}$. The echo and antiecho signals (Figures 4a and 4b) shift forward and backward, respectively, as the time t_1 increases. It is important that the delay time τ be long enough to avoid truncation of the signal at any value of t_1. In this case, the shifted echo and shifted antiecho methods are referred to as whole echo experiments.[50] Clearly, the delay τ has to be longer in the case of the shifted antiecho, which can result in noticeable loss of signal due to transverse relaxation. A complex 2D Fourier transformation of $s(t_1, t_2, \tau)$, followed by a first-order phase correction of $2\pi \nu_{-1} \tau$ in the F_2 dimension, yields a spectrum described by

$$S(F_1, F_2) = 2s_p[a(F_1, \nu_p) + id(F_1, \nu_p)]a(F_2, \nu_{-1}) \exp(-2\lambda_1 \tau) \quad (20)$$

Hence, a pure phase spectrum is obtained in spite of the fact that the time domain signal given by equation (18) is phase modulated. The signal to noise (S/N) ratio is multiplied by $\sqrt{2}\exp(-2\lambda_1\tau)$, compared to the standard (non-shifted) method, and thus can be increased when the transverse losses are minor. An added advantage here is that phase modulation in itself yields sign discrimination in the F_1 domain. It is important to note that the success of these techniques in obtaining pure-phase spectra relies upon the ability of obtaining a symmetric function in the time domain for each value of t_1. Thus, it is essential that inhomogeneous second order quadrupolar broadening dominates the homogeneous effect due to, for example, the homonuclear dipolar interaction (see also Section 4.3). However, there appears to be no difference in resolution between the techniques leading to the shifted echo or antiecho.[52]

While the above method utilizes sequences for acquisition of signals via the echo or antiecho pathways in separate experiments, the shifted echo and shifted antiecho can be detected simultaneously (Figure 4c). By using the schemes that yield equal intensities of these two signals, an amplitude modulated spectrum can be obtained as described in the next section.[50]

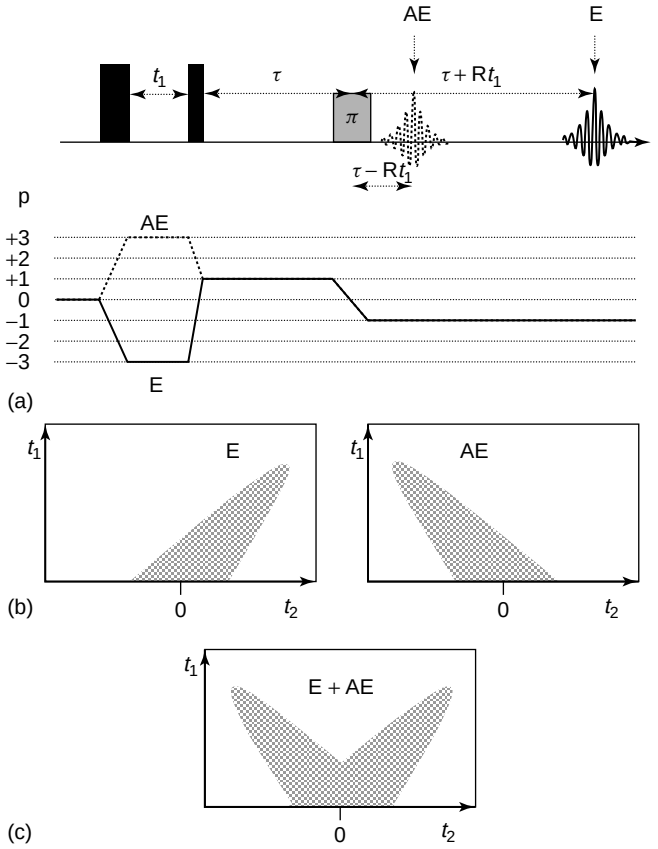

Figure 4 (a) Pulse sequence and coherence transfer pathways for the whole echo (antiecho) experiments, with $S = 3/2$ nuclei. Nonselective (hard) and selective (soft) pulses are represented by black and gray rectangles, respectively. (b) Time domain signals for shifted echo (E) and shifted antiecho (AE) phase modulated experiments. The signal is observed after the third pulse at $t_{2e} = \tau + Rt_1$ for the echo and at $t_{2e} = \tau - Rt_1$ for the antiecho. (c) Similar representation of the whole echo experiment in which shifted echo and shifted antiecho signals are acquired simultaneously

3.2 Amplitude Modulation during t_1; Z-filter Method

A frequently used approach for phase separation is to produce a time domain signal with amplitude modulation. In MQMAS this can be easily accomplished by using a linear combination of the signals from echo and antiecho coherence pathways. In general, this signal can be written as

$$s(t_1, t_2) = [s_p \exp(2\pi i \nu_p t_1) + s_{-p} \exp(2\pi i \nu_{-p} t_1)] \times \exp(2\pi i \nu_{-1} - \lambda_1) t_2 \exp(-\lambda_p t_1) \quad (21)$$

where $\nu_p = -\nu_{-p}$. When $s_p = s_{-p}$, the evolution during t_1 can be described by a cosine amplitude-modulated function

$$s(t_1, t_2) = 2s_p \cos(2\pi \nu_p t_1) \exp(2\pi i \nu_{-1} t_2) \exp[-(\lambda_1 t_2 + \lambda_p t_1)] \quad (22)$$

A 2D Fourier transform of this signal (complex in t_2 and complex in t_1 of the real part of $S(t_1, F_2)$) yields the spectrum $S(F_1, F_2)$ with a purely absorptive real part

$$S(F_1, F_2) = s_p\{[a(F_1, \nu_p) + a(F_1, -\nu_p)] + i[d(F_1, \nu_p) - d(F_1, -\nu_p)]\}a(F_2, \nu_{-1}) \quad (23)$$

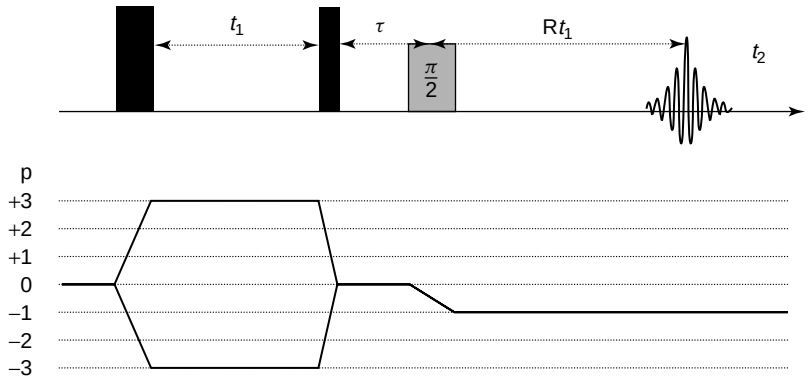

Figure 5 Pulse sequence and coherence transfer pathway for z-filter MQMAS

Note that the same purely absorptive real part can also be obtained by a 2D Fourier transform that is complex in t_2 and real (cosine) in t_1

$$S(F_1, F_2) = s_p[a(F_1, \nu_p) + a(F_1, -\nu_p)][a(F_2, \nu_{-1}) + id(F_2, \nu_{-1})] \quad (24)$$

When $s_p = -s_{-p}$, the evolution during t_1 becomes a sine amplitude-modulated function

$$s(t_1, t_2) = 2is_p \sin(2\pi\nu_p t_1) \exp(2\pi i\nu_{-1} t_2) \exp[-(\lambda_1 t_2 + \lambda_p t_1)] \quad (25)$$

and the same purely absorptive spectrum can be obtained in similar ways.

Although the acquisition of signals from the coherence transfer pathways leading to echo and antiecho can be done in two consecutive experiments, e.g., by proper selection of $0 \rightarrow +p \rightarrow -1$ and $0 \rightarrow -p \rightarrow -1$ pathways, it is more suitable to acquire these signals simultaneously.[42] For spin-3/2 nuclei, by choosing the length of the conversion pulse such that the corresponding flip-angle is approximately 90° and by using a 6-phase cycling scheme, one can acquire a single, sine amplitude-modulated free induction decay (FID) from these two pathways. The equalization $s_p = -s_{-p}$ does not merely reflect an average over the powdered sample, but occurs for each crystallite regardless of its orientation, at least for moderate values of H_{Q2}. It has been shown, that such acquisition can be also applied in concert with RIACT method.[47,55] In this technique, the efficiencies of both pathways $0 \rightarrow \pm 3 \rightarrow -1$ are essentially the same when a sufficiently large RF magnetic field is used.

However, the simultaneous balancing of the echo and antiecho intensities in 3QMAS becomes increasingly difficult for higher spin quantum numbers. Under no conditions can the echo and antiecho intensities be equalized for all individual crystallites, and only a powder-averaged matching of intensities is possible when $S > 3/2$. Although this matching can be obtained with relatively good efficiency, the resulting spectra invariably exhibit a dispersive phase. The difficulties are further increased for MQ experiments of higher order, where this equalization procedure causes a significant loss of signal.

The shortcomings of the above method can be quite easily overcome by using a so-called 'z-filter'.[48,51] This approach to eliminate phase distortions has been used earlier in 1D and 2D liquid state NMR and in DAS experiments.[54,56] The implementation of the z-filter into the 3QMAS experiment utilizing two hard pulses and the corresponding coherence transfer pathways are shown in Figure 5.[51] The z-filter consists of a short delay τ during which all magnetizations are stored along $\mathbf{B}_0$ (z-axis of the laboratory frame) as zero quantum coherences, and then transferred back to the observable single quantum coherences using a 'soft' pulse with selective $\pi/2$ flip angle. Thus, the sequence utilizes the $(0 \rightarrow \pm p \rightarrow 0 \rightarrow -1)$ coherence pathway, which results in the contributions of the echoes and anti-echoes being completely symmetric in terms of coherence transfers during the first and second hard pulses. Consequently, the efficiencies of both pathways are equal for all crystallites, leading to cosine amplitude-modulation of the 2D signal (Figure 6). An added advantage of this method is that it is robust and easy to optimize. The first pulse is adjusted to generate the maximum amount of the desired MQ coherences, and the second pulse maximizes their transfer to the zero quantum level. The delay τ must be long enough to eliminate the 'undesired' coherences that may be present due to incomplete MQ filtering, and short enough to prevent the line broadening and signal loss due to homogeneous dipolar effects and chemical exchange processes. A delay equivalent to few rotor periods is usually a good trade-off. This delay can be extended and used as a mixing time in the measurement of relative orientation of quadrupole tensors in well crystallized compounds.[57] The choice of a suitable ν_{RF} level for the soft z-filter pulse is also a compromise, in this case between selectivity and completeness of irradiation of the central transition. This is illustrated in Figure 7, which shows the relative intensities of z-filter MQMAS signals as a function of ν_{RF} applied to generate the soft pulse. This figure shows that although only a part of the signal is generated at very low values of ν_{RF} (i.e., when ν_{RF} is smaller than the MAS line width divided by $(S + 1/2)$), the use of very high strength of RF field diminishes the signal due to excitation of the undesired coherences. Setting ν_{RF} at 10–20 kHz is usually a good choice for the selective pulses in these types of experiments.

The amplitude modulated signals can be also obtained by simultaneous acquisition of the shifted echo and shifted antiecho signals, as shown schematically in Figure 4c.[50] A complete amplitude modulation is only observed when the contributions of the shifted echo and shifted antiecho are equal and, as was the case in the phase modulated whole echo experiments, when the inhomogeneous broadening dominates the lineshape. However, even when the contributions from

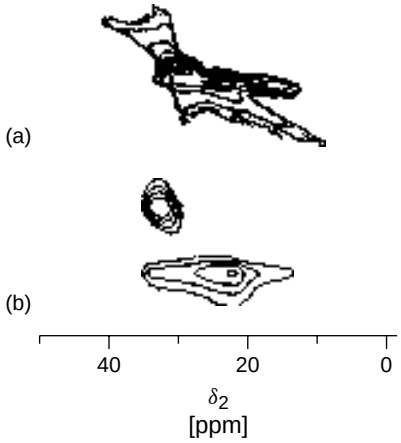

Figure 6 Two matching sections of ^{27}Al 3QMAS spectra in $AlPO_4$-14 recorded using two hard RF pulses: (a) phase modulated spectrum obtained without the z-filter (pathway $0 \rightarrow \pm 3 \rightarrow -1$) and (b) amplitude modulated spectrum measured using the z-filter (pathway $0 \rightarrow \pm 3 \rightarrow 0 \rightarrow -1$)

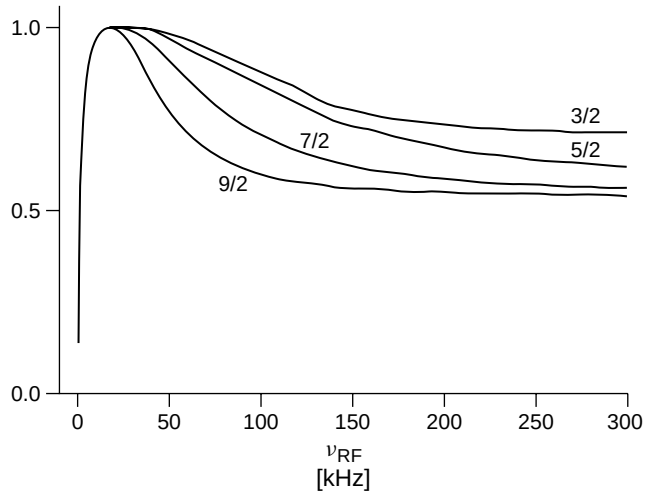

Figure 7 Evolution of the signal detected with the standard z-filter MQMAS experiment, as a function of ν_{RF} for the soft pulse. The following assumptions were made: the length of the soft pulse (in μs) is equal to $250\,000/(S + 1/2)\nu_{RF}$, the hard pulses use $\nu_{RF} = 300$ kHz, the irradiation is made on resonance at $\nu_o = 100$ MHz, $\nu_R = 15$ kHz and $\eta_Q = 0$. The full MAS line width is 19.3 kHz and the C_Q values are 6, 12.2, 18.8, and 25.5 MHz for $S = 3/2$, 5/2, 7/2 and 9/2, respectively. All curves are normalized to the maximum intensity value obtained with $\nu_{RF} = 20$ kHz

these two pathways are not equal, the 2D Fourier transform performed as described earlier in this section yields pure phase lineshapes.

The disadvantage of amplitude-modulated methods is that the resulting spectrum, described by equations (23) and (24), is fully symmetric with respect to $F_1 = 0$, i.e., the signals appearing at $F_1 = \nu_p$ and $F_1 = -\nu_p$ are indistinguishable. Thus, folding of frequencies in F_1 domain occurs in the 2D spectra obtained with such methods of acquisition. In principle, the problem of foldover can be avoided by locating the carrier frequency to one side of all spectral lines. Since this simple method causes loss of signal due to off-resonance irradiation and is often inconvenient, the so-called time-proportional phase increments (TPPI) approach or the hypercomplex data acquisition is often used to restore sign discrimination in F_1.

3.3 TPPI

In TPPI,[58] the phase ϕ^{prep} of the RF preparation pulse (or sequence) is incremented linearly with t_1

$$\phi^{prep} = \frac{\pi t_1}{2p\Delta t_1} \tag{26}$$

where Δt_1 is the time increment in t_1. The amplitude-modulated time domain signal, equation (22), then becomes

$$\begin{aligned} s(t_1, t_2) &= 2s_p \cos\left[2\pi\left(\nu_p t_1 + \frac{p\phi^{prep}}{2\pi}\right)\right] \\ &\quad \times \exp(2\pi i \nu_{-1} t_2) \exp[-(\lambda_1 t_2 + \lambda_p t_1)] \\ &= 2s_p \cos\left[2\pi\left(\nu_p + \frac{1}{4\Delta t_1}\right) t_1\right] \\ &\quad \times \exp(2\pi i \nu_{-1} t_2) \exp[-(\lambda_1 t_2 + \lambda_p t_1)] \end{aligned} \tag{27}$$

After Fourier transformation, the spectrum is as described by equations (23) and (24). Its real part is purely absorptive and equal to

$$\begin{aligned} S^R(F_1, F_2) = s_p \Bigg[& a\left(F_1, \nu_p + \frac{1}{4\Delta t_1}\right) \\ & + a\left(F_1, -\nu_p - \frac{1}{4\Delta t_1}\right)\Bigg] a(F_2, \nu_{-1}) \end{aligned} \tag{28}$$

i.e., the resulting spectrum is shifted along F_1 by $+1/4\Delta t_1$ for ν_p and by $-1/4\Delta t_1$ for its folded resonance. Thus, it becomes possible to place the carrier frequency in the center of the spectral region and discriminate between positive and negative offsets as if the signal were acquired in quadrature mode. It is advisable to decrease Δt_1 (increase the Nyquist frequency) by a factor of two with respect to an experiment done without TPPI, in order to avoid the frequency foldover between $a(F_1, \nu_p)$ and $a(F_1, -\nu_p)$.

3.4 Hypercomplex Data Acquisition (States Method)

The hypercomplex approach, also known as the States method, relies upon acquisition of signals from two complementary experiments, which provide the distinction of real and imaginary parts in t_1 in the same way as the classical quadrature detection does in t_2.[59] Both echo and antiecho signals in MQMAS are acquired simultaneously in this method. For each increment in t_1, two time domain signals s_X and s_Y are created and measured with the phases ϕ^{prep} of the preparation sequence equal to 0 and $\pi/2p$, respectively (see equations (29) and (30)).[50]

$$\begin{aligned} s_X(t_1, t_2) &= 2s_p \cos(2\pi \nu_p t_1) \exp(2\pi i \nu_{-1} t_2) \\ &\quad \times \exp[-(\lambda_1 t_2 + \lambda_p t_1)] \end{aligned} \tag{29}$$

$$\begin{aligned} s_Y(t_1, t_2) &= 2s_p \cos(2\pi \nu_p t_1 + p\phi^{prep}) \exp(2\pi i \nu_{-1} t_2) \\ &\quad \times \exp[-(\lambda_1 t_2 + \lambda_p t_1)] \\ &= -2s_p \sin(2\pi \nu_p t_1) \exp(2\pi i \nu_{-1} t_2) \\ &\quad \times \exp[-(\lambda_1 t_2 + \lambda_p t_1)] \end{aligned} \tag{30}$$

We assume here that the echo and antiecho contribute equally to the observed signal, i.e., that the condition $s_p = s_{-p}$ holds for s_X and s_Y. This can be accomplished using the methods described in Section 3.2. The complex Fourier transformation in t_2 yields equations (31) and (32)

$$s_X(t_1, F_2) = 2s_p \cos(2\pi \nu_p t_1)[a(F_2, \nu_{-1}) + id(F_2, \nu_{-1})] \exp(-\lambda_p t_1) \quad (31)$$

$$s_Y(t_1, F_2) = -2s_p \sin(2\pi \nu_p t_1)[a(F_2, \nu_{-1}) + id(F_2, \nu_{-1})] \exp(-\lambda_p t_1) \quad (32)$$

The real parts of s_X and s_Y are then combined to produce a new complex signal

$$s(t_1, F_2) = s_X^R(t_1, F_2) - is_Y^R(t_1, F_2) = 2s_p a(F_2, \nu_{-1}) \times \exp(2\pi i \nu_p t_1) \exp(-\lambda_p t_1) \quad (33)$$

A complex Fourier transformation of $s(t_1, F_2)$ with respect to t_1 then produces, for the real part, a pure-phase spectrum

$$S(F_1, F_2) = 2s_p a(F_2, \nu_{-1})[a(F_1, \nu_p) + id(F_1, \nu_p)] \quad (34)$$

with a single resonance located at $(F_1, F_2) = (\nu_p, \nu_{-1})$.

The TPPI and hypercomplex methods result in the same S/N ratio per unit of experimental time. However, the hypercomplex method allows for separating of the echo and antiecho signals according to

$$s_E(t_1, t_2) = s_X(t_1, t_2) - is_Y(t_1, t_2)$$
$$s_A(t_1, t_2) = s_X(t_1, t_2) + is_Y(t_1, t_2) \quad (35)$$

which can be independently processed (e.g., apodized).

4 PROCESSING AND INTERPRETATION OF MQMAS SPECTRA

One of the primary benefits of MQMAS is that it allows for separation and measurement of the isotropic chemical and quadrupolar-induced shifts by analyzing a single 2D spectrum.[9] However, proper assignment of the resonance shifts along the F_1 and F_2 dimensions in such an analysis is not immediately obvious. In this section, we examine the distribution of resonances in MQMAS spectra and discuss the interpretation of resonance shifts that result from processing the data with and without the shearing transformation.

4.1 Unsheared Spectrum

A typical MQMAS spectrum, resulting from a standard 2D Fourier transformation of a temporal data set obtained with the methods described in the previous sections, consists of several extended bands similar to those depicted in Figure 8a. Analysis and interpretation of such an unsheared spectrum is facilitated by introducing the chemical shift (CS) axis, the anisotropic (A) axis and the quadrupolar induced shift (QIS) axis. In a hypothetical spectrum with negligible quadrupolar interactions, the resonances would be sharp and located on the CS axis at $-p\nu_0\Delta\delta$ and $\nu_0\Delta\delta$ in the multiple and single quantum dimensions, respectively. The slope of the CS axis

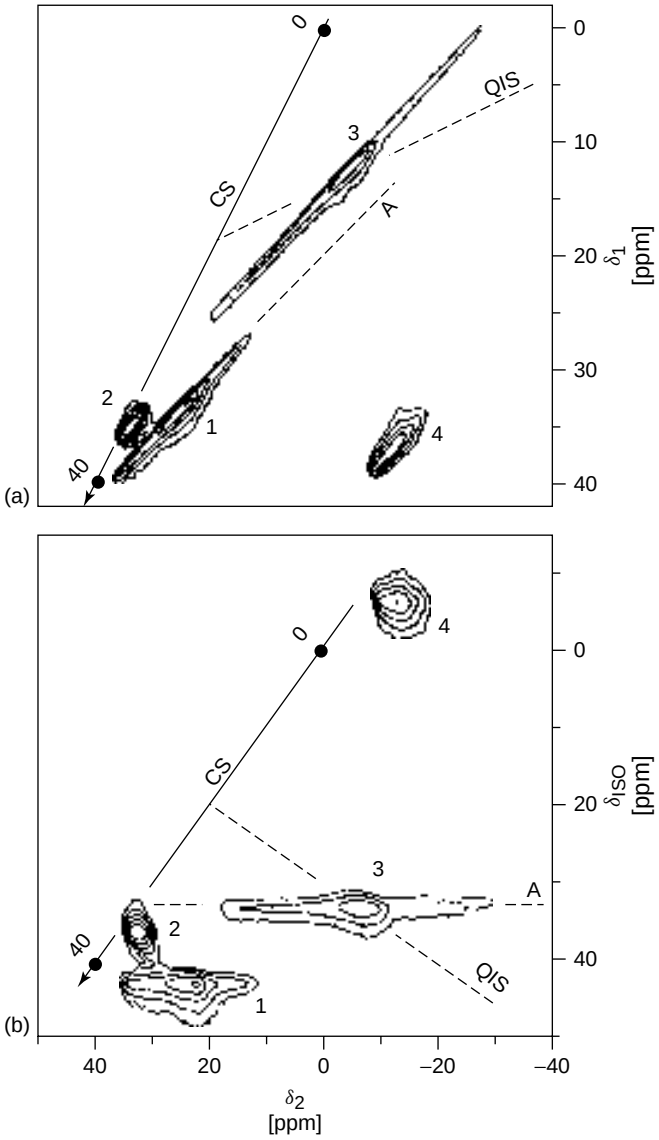

Figure 8 (a) Unsheared and (b) sheared 3QMAS spectra of ^{27}Al in $AlPO_4$-14 acquired at $\nu_0 = 104.2$ MHz using the z-filter sequence with rotor synchronization, $\nu_R = 14.5$ kHz, and $\nu_{RF} = 200$ kHz. The CS, A and QIS axes are plotted, as described in the text. Two tetrahedral sites (1 and 2), one fivefold coordinated site (3) and one sixfold coordinated site (4) are resolved, in agreement with crystallographic data. Note that resonance 4 is folded over in (a) due to the limited spectral width in rotor-synchronized spectra

is either $-p$ when resonances are expressed in Hz or 1 when ppm scales are used instead (vide infra). The A axis is defined by the orientation of anisotropic ridges in MQMAS spectra (see equation (13)) and has a slope R(S, p) given by equation (12). In the MQMAS experiment, which detects only species with a non-zero quadrupolar interaction, the center of gravity of a given resonance is displaced from the CS axis, in both dimensions, by the quadrupolar-induced shift. Assuming that the efficiency of MQMAS is constant for all crystallite orientations, this shift [see equation (10)] can be expressed (in Hz) as

$$\nu_{QIS}(S, p) = A_0^Q(\eta_Q)C_0(S, p) \quad (36)$$

The direction in which this displacement occurs defines the QIS axis, which has a slope ξ given by

$$\xi(S, p) = \frac{\nu_{QIS}(S, p)}{\nu_{QIS}(S, -1)} = \frac{-p[4S(S+1) - 3p^2]}{[4S(S+1) - 3]} \quad (37)$$

Since for a given pair (S, p) the quadrupolar induced shifts have a unique sign, all observed resonances (except for the spinning sidebands) must appear on the same side of the CS axis, as seen in Figure 8. The factors R and ξ have been given in Amoureux and Fernandez for all experimentally accessible values of S and p.[60] With the help of these parameters, both the chemical shift and quadrupolar parameters can be extracted from the unsheared spectra in a straightforward manner. The isotropic chemical shift of a given resonance is simply found by projecting its center of gravity on the CS axis along the QIS direction. Similarly, the displacement of this resonance from the CS axis measured along F_1 and F_2 and given (in Hz) by

$$\nu_{QIS}(S, p) = \frac{3p}{10\nu_0} \frac{[4S(S+1) - 3p^2]}{[4S(2S-1)]^2} P_Q^2 \quad (38)$$

can be used to evaluate the second-order quadrupolar effect parameter P_Q

$$P_Q = C_Q \sqrt{1 + \eta_Q^2/3} \quad (39)$$

From equation (39), the quadrupolar coupling constant C_Q can be determined accurately, provided the asymmetry parameter η_Q is known, e.g., from simulation of MAS lineshape.

4.2 Shearing Transformation; Referencing of MQMAS Spectra

MQMAS spectra can be most conveniently analyzed by applying a shearing transformation, which places the A axis parallel to the F_2 axis (Figure 8b) and creates a new dimension labeled F_{ISO} (or δ_{ISO}). The direct advantage of such an approach is that the orthogonal projection of MQMAS spectrum onto the F_{ISO} axis does not include the anisotropic quadrupolar and chemical shift contributions. A similar projection onto the F_2 axis yields the pQ-filtered anisotropic MAS powder pattern. This pattern should not be generally used for the accurate determination of C_Q and η_Q due to the distortions of the observed intensities, which can be severe for large values of C_Q. In addition, for a given value of C_Q these distortions increase with increasing |p| (Figure 9a). More reliable values of C_Q and η_Q can be obtained from the simulation of the MAS spectra acquired using a short RF pulse.

In the sheared spectrum, the frequency F_{ISO} can be conveniently expressed as a linear combination of F_1 and F_2

$$F_{ISO} = F_1 + RF_2 \quad (40)$$

where R is given by equation (12). This convention allows for direct determination of the sample rotation rate from the sheared spectrum when it is plotted in Hz.[60] In order to introduce the referencing in ppm, let us first consider a single resonance that is not affected by the quadrupole interaction, located at coordinates $(-p\nu_0\Delta\delta,\ \nu_0\Delta\delta)$ on the CS axis of an unsheared spectrum. After the shearing transformation, its coordinate F_{ISO} in the isotropic dimension is given in

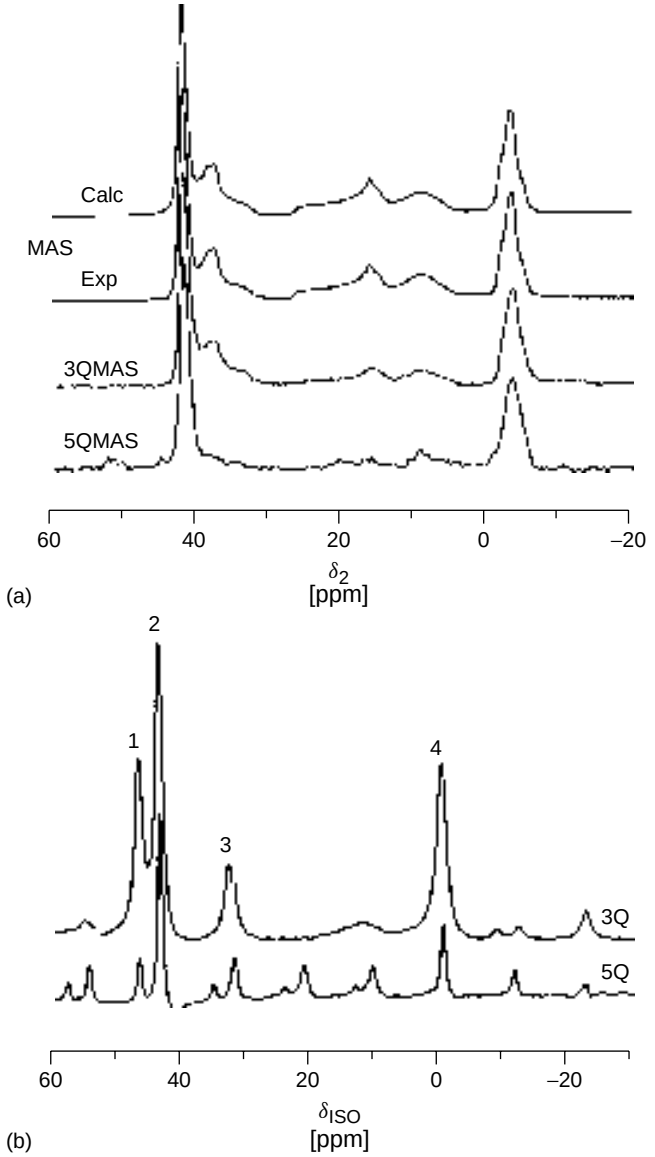

Figure 9 ^{27}Al NMR spectra of $AlPO_4$-14 obtained at 156.4 MHz: (a) simulated and experimental MAS spectrum obtained using a $\pi/12$ flip angle, compared with the anisotropic projections of 3QMAS and 5QMAS spectra; (b) isotropic projections of ^{27}Al MQMAS spectra. The isotropic resonances are labeled following Figure 8, the remaining peaks represent spinning sidebands

$$F_{ISO} = (R - p)\nu_0\Delta\delta \quad (41)$$

The ppm scales δ_1, δ_2 and δ_{ISO} use the apparent Larmor frequencies, which are equal to ν_0, $-p\nu_0$, and $(R - p)\nu_0$ along F_2, F_1 and F_{ISO}, respectively. In the absence of the quadrupole interaction, this convention results in the shifts being identical and equal to $\Delta\delta$ along the three axes.

We have seen above (equation (38)), that the quadrupole interaction shifts the resonance away from the CS axis in both dimensions. In an unsheared spectrum, this shift can be

expressed in ppm as equation (42) with equation (43)

$$\delta_{\mathrm{QIS}}(\mathrm{S,\,p}) = -\frac{\nu_{\mathrm{QIS}}(\mathrm{S,\,p})}{\mathrm{p}\nu_0}10^6 = -\frac{3}{10}\frac{[4\mathrm{S}(\mathrm{S}+1)-3\mathrm{p}^2]}{[4\mathrm{S}(2\mathrm{S}-1)]^2}\frac{\mathrm{P_Q^2}}{\nu_0^2}10^6 = \mathrm{k}_{|\mathrm{p}|}\mathrm{P_Q^2} \quad (42)$$

$$\mathrm{k}_{|\mathrm{p}|} = -\frac{3}{10}\frac{[4\mathrm{S}(\mathrm{S}+1)-3\mathrm{p}^2]}{[4\mathrm{S}(2\mathrm{S}-1)\nu_0]^2}10^6 \quad (43)$$

Clearly, $\delta_{\mathrm{QIS}}(\mathrm{S,\,p})$ is always negative along the δ_2 dimension ($\mathrm{k}_1 < 0$), but can be positive or negative along δ_1, depending on S and |p|. After the shearing transformation, the quadrupolar-induced shift in the $\mathrm{F_{ISO}}$ dimension becomes always positive and independent of p

$$\delta_{\mathrm{QIS,ISO}} = \frac{\nu_{\mathrm{QIS,ISO}}(\mathrm{S,\,p})}{(\mathrm{R}-\mathrm{p})\nu_0}10^6 = -\frac{10}{17}\delta_{\mathrm{QIS}}(\mathrm{S},-1) = -\frac{10}{17}\mathrm{k}_1\mathrm{P_Q^2} \quad (44)$$

Thus, the QIS direction in the 2D sheared spectrum expressed in ppm has a constant slope of $-10/17$, regardless of the values of S and p. Since the CS axis of such a spectrum has a constant slope of 1, the MQMAS sheared spectra displayed using these ppm scales are independent of p for a given spin system. To illustrate this point, the isotropic projections of 3QMAS and 5QMAS spectra of ^{27}Al in aluminophosphate $AlPO_4$-14 are compared in Figure 9b.[61]

Finally, it is interesting to note that MQMAS can be also useful in determination of the indirect scalar spin–spin coupling.[62] Indeed, while the J values are often small with the common quadrupolar nuclei, the J dephasing is proportional to p in the multiple quantum dimension [equation (10)] thus increasing the corresponding splitting in this dimension. Along the isotropic axis of the sheared spectrum, this splitting becomes independent of p when expressed in ppm

$$\delta_{\mathrm{ISO}} = \Delta\delta + \delta_{\mathrm{QIS,ISO}} + 10^6\mathrm{m_I}\mathrm{J}/\nu_0 \quad (45)$$

and therefore should preferentially be observed in 3QMAS for best sensitivity. Thus, in well crystallized samples, the presence of scalar coupling multiplets can be detected by recording the MQMAS spectra at different fields.

It should be noted that the above referencing scheme is directly applicable to the spectra obtained using satellite transitions and magic angle spinning (STMAS) NMR.[63] Again, the QIS slope of $-10/17$ is observed provided that the appropriate values of R are used. The apparent Larmor frequencies used to calculate the normalized shifts along the δ_{ISO} axis [see equation (41)] are half of those calculated for 3QMAS.

4.3 Split-t_1 Method

The split-t_1 method of data acquisition relies upon the splitting of time t_1 into single and multiple quantum evolution periods in proportion to the ratio R(S, p).[48] By doing so, the fourth-order anisotropic term given in equation (10) can be always refocused at the end of the t_1 period. After 2D Fourier transformation, the inhomogeneously broadened ridges appear parallel to the F_2 axis, which eliminates the need for the shearing transformation. As is shown below, the split-t_1 method has been combined with the whole echo experiment to provide a very efficient scheme for MQMAS. Another advantage of an echo being stationary within the acquisition period is that the time domain signal is easier to apodize by using t_1-independent weighting functions. This split-t_1 mode of data acquisition can be conveniently used in MQMAS-based heteronuclear correlation spectroscopy (MQ-HETCOR) experiments and in the Carr–Purcell–Meiboom–Gill (CPMG) MQMAS experiments (see Sections 5.1 and 6).

In the split-t_1 amplitude modulated methods, for each crystallite, the echo and antiecho coherence pathways must contribute to the processed signal with equal amplitude in order to obtain a pure absorption lineshape (see Section 3.2). For spin-3/2 nuclei, this can be achieved by using the coherence transfer pathway with the z-filter, $0 \rightarrow \pm3 \rightarrow \pm1 \rightarrow 0 \rightarrow -1$, as shown in Figure 10a.[52,64] The efficiency of this four-pulse method can be improved by using FAM, DFS or RIACT methods for the ±3Q to ±1Q conversion.[43–45,47,55,65,66] This scheme

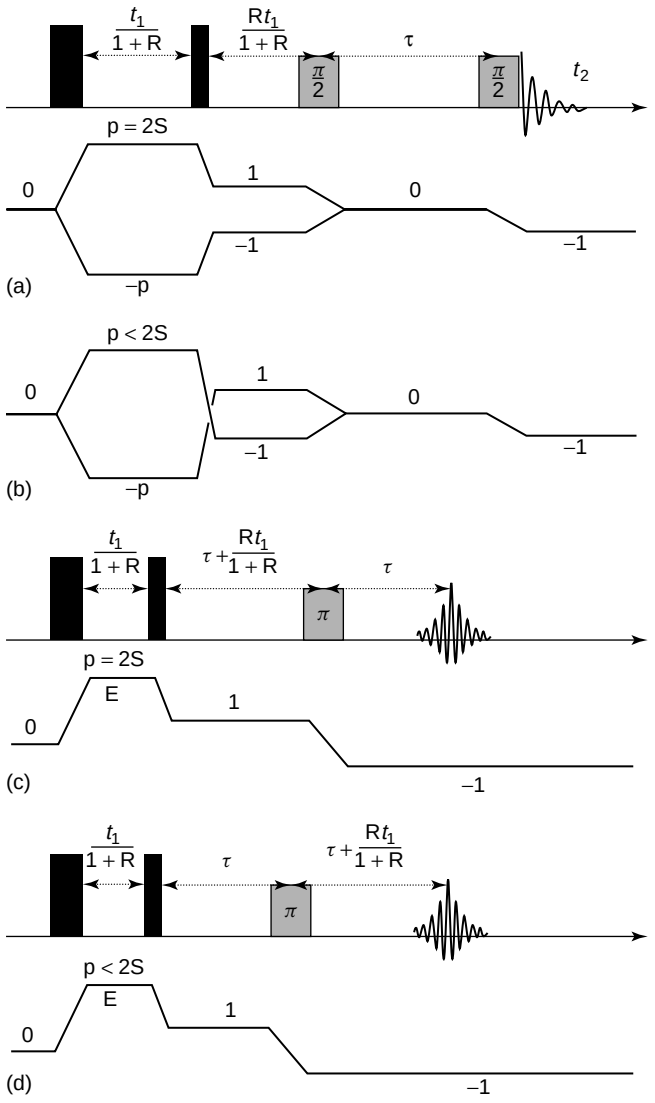

Figure 10 (a) Amplitude modulated split-t_1 pulse sequence and coherence pathway for $\mathrm{p} = 2\mathrm{S}$. For $\mathrm{p} < 2\mathrm{S}$, the experiment can be performed using the same pulse sequence and the coherence pathway as shown in figure (b). (c) and (d) Phase modulated split-t_1 pulse sequences and coherence pathways for $\mathrm{p} = 2\mathrm{S}$ and $\mathrm{p} < 2\mathrm{S}$

can easily be extended to 5-, 7-, and 9 QMAS experiments with spin-5/2, -7/2 and -9/2 nuclei. The symmetric split-t_1 pathways $0 \rightarrow \pm 3 \rightarrow \mp 1 \rightarrow 0 \rightarrow -1$ were also proposed for 3QMAS experiments with spins $S > 3/2$ (see Figure 10b). However, such experiments are relatively inefficient, as they involve the coherence change of $|\Delta p| = 4$ during $\pm 3 \rightarrow \mp 1$ conversion.

The split-t_1 method can be also used in phase modulated (shifted echo) experiments, which generate pure phase spectra through the acquisition of the whole echo. The coherence pathway displayed in Figure 10c ($0 \rightarrow 3 \rightarrow 1 \rightarrow -1$), uses $|\Delta p| = 2$ and requires a short spin echo interval.[52] For spin-3/2 systems in which the loss of magnetization due to T_2 effects is not significant, this MQMAS scheme has been recommended as the most efficient, especially when used with the FAM or DFS conversion.[40,52] This scheme works equally well in 5-, 7- and 9 QMAS experiments for spins 5/2, 7/2 and 9/2, respectively. For the MQMAS experiments with $|p| < 2S$, this scheme can be modified, as shown in Figure 10d. The referencing of split-t_1 spectra can be performed using the same method as described in Section 4.2.

4.4 Resolution of MQMAS Spectra

The timing of the echo formation, as described by equation (11), is independent on the size of quadrupolar and CSA interactions, the orientation of crystallites, and the experimental conditions (ν_{RF} and ν_R). Thus, isotropic resolution should be consistently achieved by the MQMAS method, at least in the absence of strong dipolar broadening. The isotropic line width has been analyzed in several 3QMAS spectra of $RbNO_3$ and $LiRbSO_4$, which were obtained using various schemes for coherence transfer with CW nutation, RIACT and FAM pulses.[40] $LiRbSO_4$ was particularly useful in these tests due to exceptionally narrow line observed in this compound (see Figure 1). Indeed, no significant changes in resolution were observed while switching between different coherence transfer schemes, ν_{RF} frequencies and conversion methods.

However, several authors have reported an enhancement of resolution upon increasing the MQ order p from three to five (and seven) both in crystalline and amorphous samples (see Figure 9b and Figure 11).[61,67,68] It should be noted that due to the presence of p-dependent scaling factors (see Section 4.2), non-uniform RF excitation, dipolar effects, and spinning

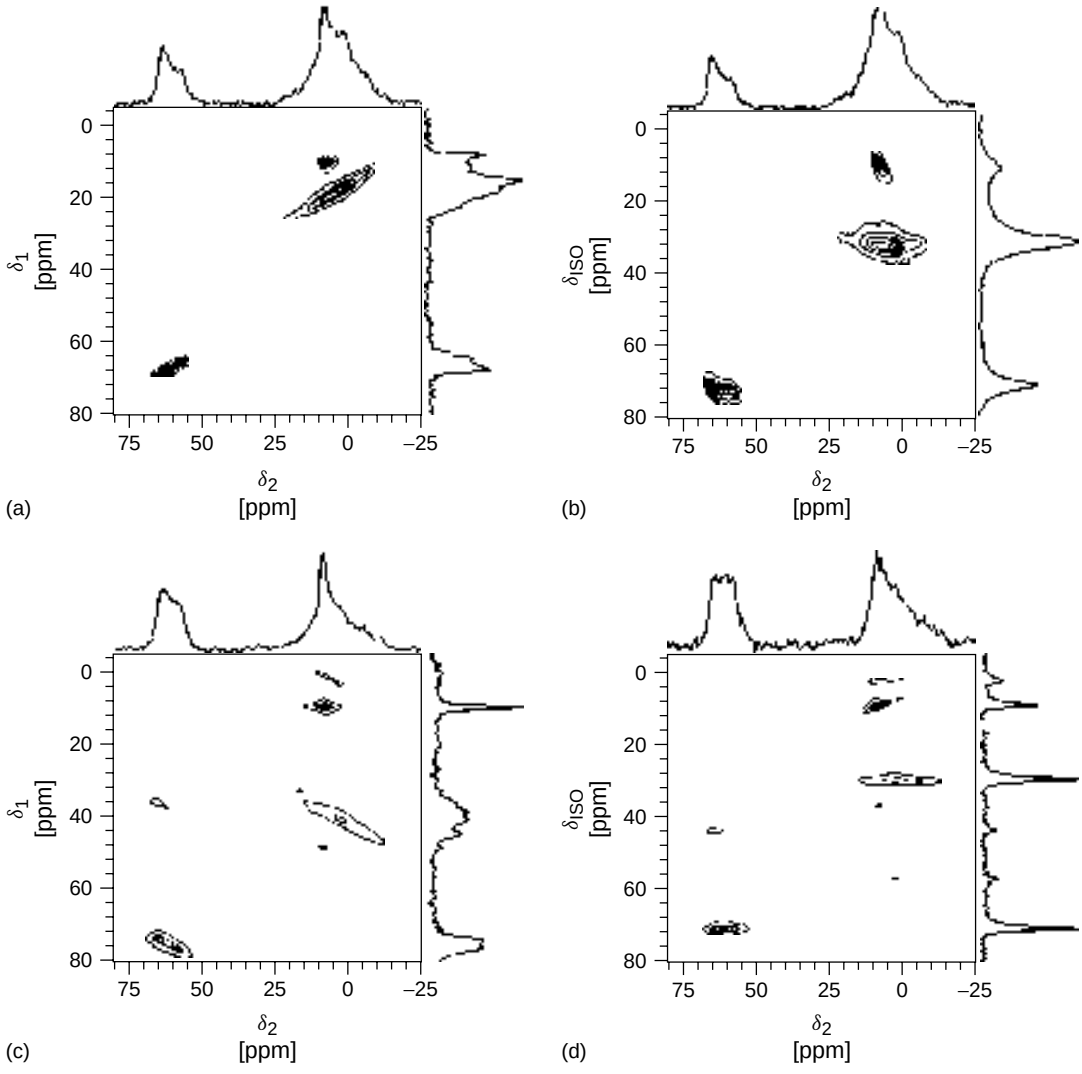

Figure 11 ^{27}Al MQMAS spectra of $SrAl_{12}O_{19}$: (a) unsheared 3QMAS, (b) sheared 3QMAS, (c) unsheared 5QMAS, and (d) sheared 5QMAS. Note the different appearance of spectral features in the Figures (a) and (c) due to the relocation of A and QIS axes

sidebands, a comparison between MQMAS experiments of different order is not straightforward. The improvement of resolution between 3QMAS and higher-order MQMAS spectra cannot be easily determined from the line width in ppm (which is arbitrary), or from the line width in Hz (due to different scaling factors involved). Instead, the dispersion of shifts relative to the observed line width along the isotropic dimension should be used when comparing these experiments.

However, it has also been noticed that this increase in the apparent resolution is not uniform among different spin systems. Recent investigations have attributed these effects to the interplay between inhomogeneous and homogeneous contributions to the isotropic line width.[67,68] In the case of well-crystallized samples, the inhomogeneous contributions may be due to inhomogeneity of the static magnetic field, changes in magnetic susceptibility, incomplete heteronuclear decoupling and second-order quadrupolar-dipolar couplings.[69,70] Since the Hamiltonians associated with these interactions are linear in S_z, under the p-quantum evolution the corresponding inhomogeneous broadening scales in the same way as the dispersion of isotropic shifts. Consequently, no apparent increase in resolution should be observed in higher-order MQMAS spectra.[60,68] The homogeneous contribution, however, is not expected to increase with p.[68] Therefore, in crystalline samples with strong homogeneous contribution to the line broadening, considerable enhancement of the isotropic resolution may be observed by moving to higher-order MQMAS schemes. This enhancement is less evident in amorphous samples, where the distribution of isotropic shifts dominates the spectra. In such cases, the more sensitive 3QMAS experiments are recommended.

Interestingly, the presence of dipolar interactions may have an opposite effect on the resolution. Since in a static sample the dipolar dephasing is proportional to p [F term in equation (7)], MAS averaging becomes less efficient in higher order multiple quantum experiments.[71] In the presence of strong dipolar interactions, continuous wave decoupling may be insufficient during t_1, and composite decoupling may be necessary to obtain a well resolved spectrum.[72,73] In the majority of applications, however, the most practical way to achieve efficient homo- and hetero-nuclear decoupling in MQMAS experiments is to use the highest possible spinning speed. The added advantage of using high spinning speed is the increased spectral width along F_1 in the experiments performed with rotor synchronization. The rotor-synchronized spectra have improved S/N ratio, although their spectral width is limited along the F1 dimension.[74]

Finally, the resolution enhancement in MQMAS can be also due to the narrowing in the MQMAS efficiency curves that is observed for higher values of p. Therefore, for each species, the relative intensities of various parts of the 2D spectra may become distorted in such a way that they appear narrower when |p| increases, especially in highly disordered samples with wide distributions of quadrupolar and/or chemical shift parameters. Most likely, this effect is negligible when using transfer methods that are less sensitive to the quadrupole splitting (FAM, DFS, or RIACT).

4.5 Quantification of MQMAS Intensities

The great advantage of MQMAS over the standard MAS experiment is the high resolution that it provides. However, MQMAS skews the spectral intensities, due to the strong dependence of the multiple quantum excitation and conversion on the quadrupole splitting $\overline{\nu}_Q$, which, in turn, is a function of C_Q, η_Q and the crystallite orientation [see equations (4) and (5)]. The resulting spectra are not quantitative in the isotropic dimension and have distorted lineshapes in the MAS dimension. Examples of such effects are shown in Figures 9 and 11. In order to minimize these distortions it is always advisable to use the aforementioned FAM, DFS and RIACT schemes for excitation and conversion. We now describe additional strategies to retrieve quantitative intensities from the MQMAS spectra.

One of these strategies relies upon combining the information given by MQMAS and MAS. In short, MQMAS can be used to obtain highly resolved spectra and to determine the isotropic chemical shifts and the quadrupolar parameters for different sites. This provides a starting set of parameters for simulation of the MAS spectra in order to obtain accurate intensities. Special care must be taken to assure the quantitative accuracy of the MAS spectra by using short RF pulses (small tip angles) for excitation. We note that this method is suitable for analysis of spectra that are not significantly broadened due to dipolar interactions and/or distribution of chemical shift and quadrupolar parameters.

Secondly, quantitative information can be obtained by calculating the theoretical powder-averaged efficiency curves for MQMAS experiments as a function of P_Q. The efficiency curves for 3QMAS and 5QMAS experiments performed using an RF magnetic field of 70 kHz are depicted in Figure 12.[61] Since the parameter P_Q can be easily derived from analysis of the first moment of the MQMAS spectrum, these curves can be used to offset the quantitative distortions. Indeed, in case of $AlPO_4$-14 this method yielded correct concentrations of various aluminum species.[61] This technique is suitable for

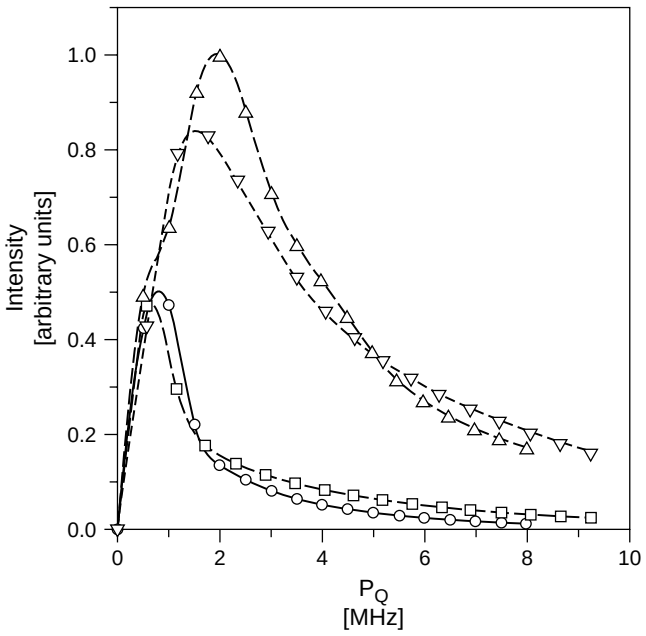

Figure 12 Relative intensities of 3QMAS (dashed lines) and 5QMAS (solid lines) spectra versus P_Q, calculated for $\nu_{RF} = 70$ kHz (Δ, O: $\eta_Q = 0$, ∇ : $\eta_Q = 1$)

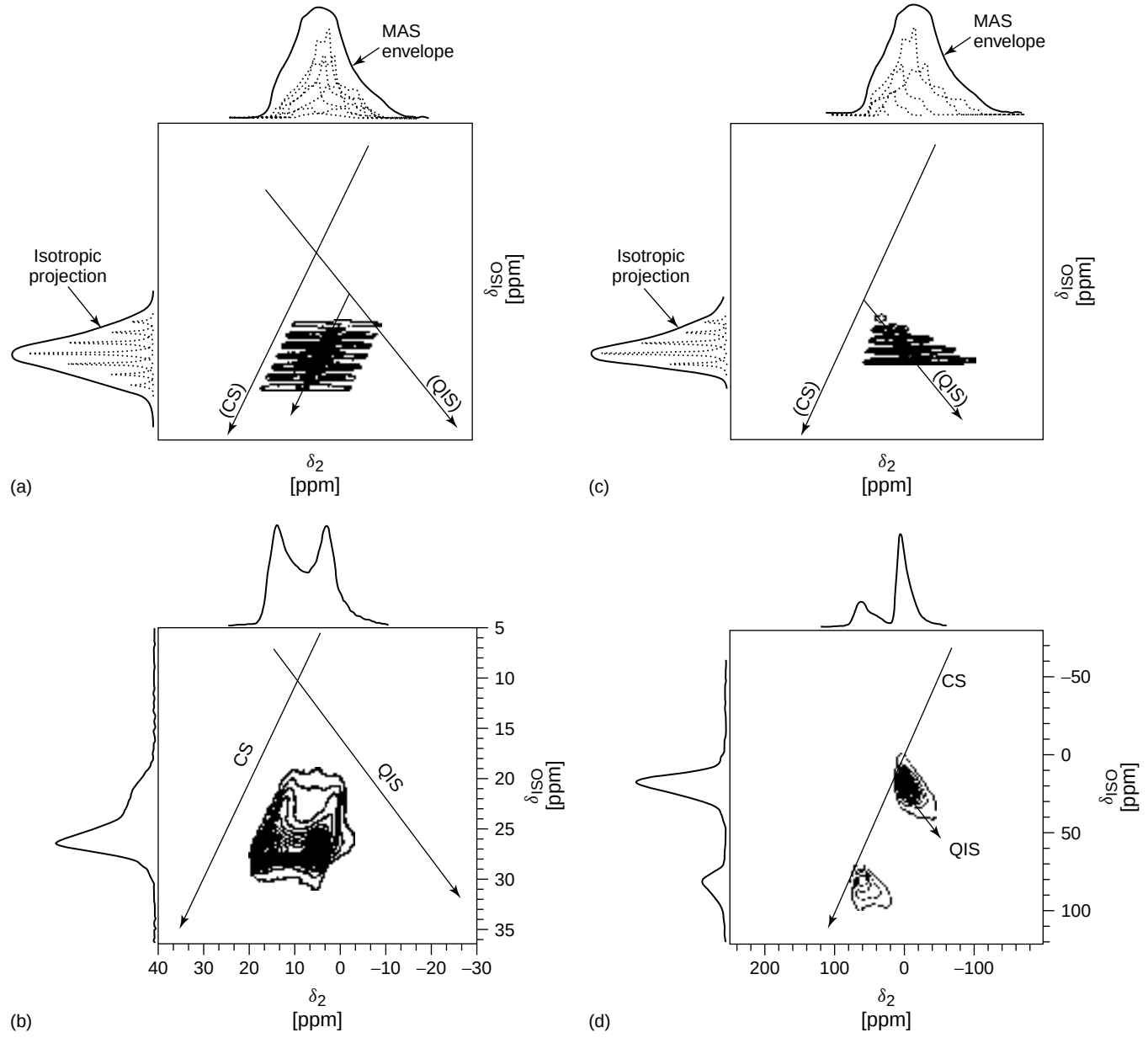

Figure 13 Schematic representations of a Gaussian distribution of (a) δcs and (c) P_Q. The individual slices add up to form the isotropic and anisotropic projections of the 2D spectra. (b) and (d) show the experimental examples of such distributions found in amorphous B_2O_3 and γ-alumina, respectively

the analysis of spectra with substantial broadening, e.g., due to amorphous nature of the sample.

4.6 Analysis of Distribution of Quadrupolar and Chemical Shift Parameters

Many samples of interest in chemistry and materials science do not have a well-organized structure with long range order. In such systems, the resonances cannot be described with a unique set of quadrupolar and chemical shift parameters. Instead, the distributions of these parameters must be considered to properly interpret the spectra. However, the numerical analysis of MQMAS spectra can provide a complete quantitative determination of the distribution of the isotropic chemical shifts δ_{CS} and the quadrupolar parameters (P_Q or C_Q and η_Q). In partly disordered or amorphous materials, this information can be used to assess the degree of disorder and can be further utilized to evaluate other properties, such as inter-nuclei distances or bond angle distributions. For example, ^{27}Al distributions can be interpreted using relationship between δ_{CS} and the T–O–T angle, or between C_Q and the O–T–O angle, where t = Al, Si. In the same way, the distribution of ^{17}O parameters can be used to analyze the Si–O–Si and Al–O–Si angles.[75–78]

To illustrate how these distributions are manifested in the MQMAS spectrum, let us first consider a single site that is characterized by a unique set of parameters δ_{CS}, C_Q and η_Q. Let us further assume that the residual line broadening due to dipolar interactions with other spins can be ignored. This leads to a second-order quadrupolar pattern with a well-defined

lineshape in an MAS spectrum and a narrow pattern in the corresponding MQMAS spectrum. In the sheared MQMAS spectrum, the center of gravity of this pattern is given by

$$\delta_2^{\mathrm{g}} = \delta_{\mathrm{CS}} + \mathrm{k}_{|1|}\mathrm{P}_{\mathrm{Q}}^2 \tag{46}$$

$$\delta_{\mathrm{ISO}}^{\mathrm{g}} = \delta_{\mathrm{CS}} - \frac{10}{17}\mathrm{k}_{|1|}\mathrm{P}_{\mathrm{Q}}^2 \tag{47}$$

where $\mathrm{k}_{|1|}$ is given by equation (43) and $\mathrm{P_Q}$ is given by equation (39). As explained in Section 4.2, any changes of δ_{CS} or $\mathrm{P_Q}$ cause shifts of the spectrum along the CS or QIS directions, respectively. Consequently, a distribution of these parameters broadens the observed 2D patterns. The numerically generated illustrations of the spectral changes due to the distribution of chemical shift and $\mathrm{P_Q}$ are shown in Figures 13a and 13c, respectively. The corresponding examples of experimental distributions are shown in Figures 13b and 13d. We note that a Gaussian distribution of chemical shifts results in a Gaussian broadening along the isotropic and anisotropic projections. However, since the intensities and widths of the individual spectra depend on the quadrupolar parameters, an asymmetrical broadening of the projections occurs in the case of a Gaussian distribution of $\mathrm{P_Q}$. In most practical applications, the distributions of δ_{CS} and $\mathrm{P_Q}$ are encountered simultaneously, which makes the spectral analysis more complex. Nevertheless, these distributions can be separated because the directions of CS and QIS axes differ by approximately 75°.

The sheared MQMAS spectrum $\mathrm{S_e}$ measured experimentally is described by an integral of the individual two-dimensional MQMAS spectra over all possible combinations of chemical shift and quadrupolar parameters

$$\mathrm{S_e}(\delta_2, \delta_{\mathrm{ISO}}) = \int_{-\infty}^{+\infty} \mathrm{d}\delta_{\mathrm{CS}} \int_0^{+\infty} \mathrm{dC_Q} \int_0^1 \mathrm{S_c}(\delta_2, \delta_{\mathrm{ISO}}; \delta_{\mathrm{CS}}, \mathrm{C_Q}, \eta_{\mathrm{Q}}) \times \Pi(\delta_{\mathrm{CS}}, \mathrm{C_Q}, \eta_{\mathrm{Q}})\mathrm{d}\eta_{\mathrm{Q}} \tag{48}$$

In equation (48), $\mathrm{S_c}$ is the calculated MQMAS spectrum corresponding to a single set of lineshape parameters δ_{CS}, $\mathrm{C_Q}$ and η_{Q}, based on the evolution of the spin density matrix during the entire MQMAS experiment. The probability function $\Pi(\delta_{\mathrm{CS}}, \mathrm{C_Q}, \eta_{\mathrm{Q}})$ characterizes the distribution of δ_{CS}, $\mathrm{C_Q}$ and η_{Q}. The propagation of the density matrix results from the first ($\mathrm{H_{Q1}}$) and second ($\mathrm{H_{Q2}}$) order quadrupole interactions, as well as the RF Hamiltonians during the pulses. As a result of sample spinning, all these interactions are rendered time-dependent, which requires the use of sophisticated routines, such as MQSIM, PULSAR, SIMPSON, or GAMMA.[55,60,79,80]

Two different strategies can be used for solving equation (48) to obtain $\Pi(\delta_{\mathrm{CS}}, \mathrm{C_Q}, \eta_{\mathrm{Q}})$. The so-called direct method relies upon iterative fit of $\Pi(\delta_{\mathrm{CS}}, \mathrm{C_Q}, \eta_{\mathrm{Q}})$ using, e.g., linear least square procedure to minimize the deviation between the experimental and simulated spectra. The second method directly computes the distribution from the experimental MQMAS spectrum by performing the so-called inversion of the 2D spectrum.[81]

In the direct method, it is assumed that the chemical shift and quadrupolar parameters are statistically independent, i.e.,

$$\Pi(\delta_{\mathrm{CS}}, \mathrm{C_Q}, \eta_{\mathrm{Q}}) = \Pi_{\mathrm{CS}}(\delta_{\mathrm{CS}})\Pi_{\mathrm{Q}}(\mathrm{C_Q}, \eta_{\mathrm{Q}}) \tag{49}$$

It is further assumed that the distribution of δ_{CS} may be described by a Gaussian distribution

$$\Pi_{\mathrm{CS}}(\delta_{\mathrm{CS}}) = \frac{1}{\sqrt{2\pi}\sigma_{\mathrm{CS}}} \exp\left[-\frac{(\delta_{\mathrm{CS}} - \langle\delta_{\mathrm{CS}}\rangle)^2}{2\sigma_{\mathrm{CS}}^2}\right] \tag{50}$$

where σ_{CS} is the variance of the chemical shift distribution around its average value $\langle\delta_{\mathrm{CS}}\rangle$. This assumption is applicable to various distributed systems (e.g., glasses), in which bond angles are randomly distributed around an average value, and for which a linear correlation exists between the bond angles and the isotropic chemical shifts of nuclei involved in these bonds.[75]

When considering the quadrupole interaction, it has been shown that the distributions of $\mathrm{C_Q}$ and η_{Q} can be fitted by a two dimensional probability function[82]

$$\Pi_{\mathrm{Q}}(\mathrm{C_Q}, \eta_{\mathrm{Q}}) = \frac{\mathrm{C_Q^4}\eta_{\mathrm{Q}}}{\sqrt{2\pi}\sigma_{\mathrm{Q}}^5}\left(1 - \frac{\eta_{\mathrm{Q}}^9}{9}\right) \exp\left[-\frac{\mathrm{C_Q^2}\left(1 + \frac{\eta_{\mathrm{Q}}^2}{3}\right)}{2\sigma_{\mathrm{Q}}^2}\right] \tag{51}$$

In this model, the quadrupolar probability function only depends on a single parameter σ_{Q}, and the marginal distribution profiles are given by[82]

$$\Pi_{\mathrm{Q}}(\mathrm{C_Q}) = \int_0^1 \Pi_{\mathrm{Q}}(\mathrm{C_Q}, \eta_{\mathrm{Q}})\mathrm{d}\eta_{\mathrm{Q}} \tag{52a}$$

$$\Pi_{\mathrm{Q}}(\eta_{\mathrm{Q}}) = \int_0^{\infty} \Pi_{\mathrm{Q}}(\mathrm{C_Q}, \eta_{\mathrm{Q}})\mathrm{dC_Q} \tag{52b}$$

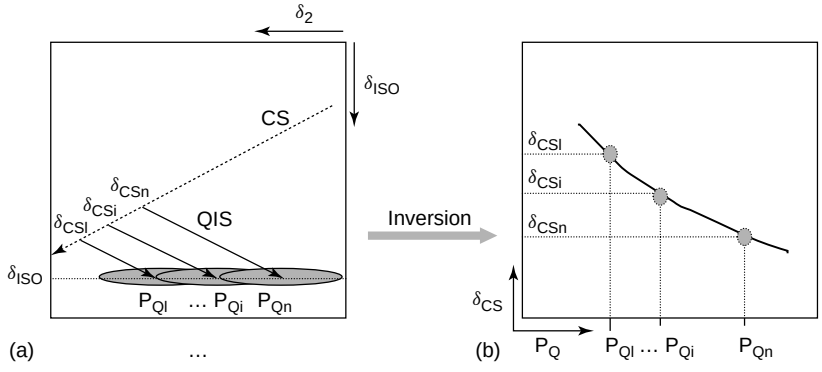

Figure 14 (a) Schematic representation of an experimental slice at position δ_{ISO}, composed of narrow bands defined by a large number of sets (δ_{CSi}, $\mathrm{P_{Qi}}$) that fulfill equation (47). (b) Representation of the quadrupolar parameter $\mathrm{P_{Qi}}$ versus the chemical shift δ_{CSi}. Each isotropic slice on the spectrum (a) provides, after inversion, a specific curve in this 2D representation

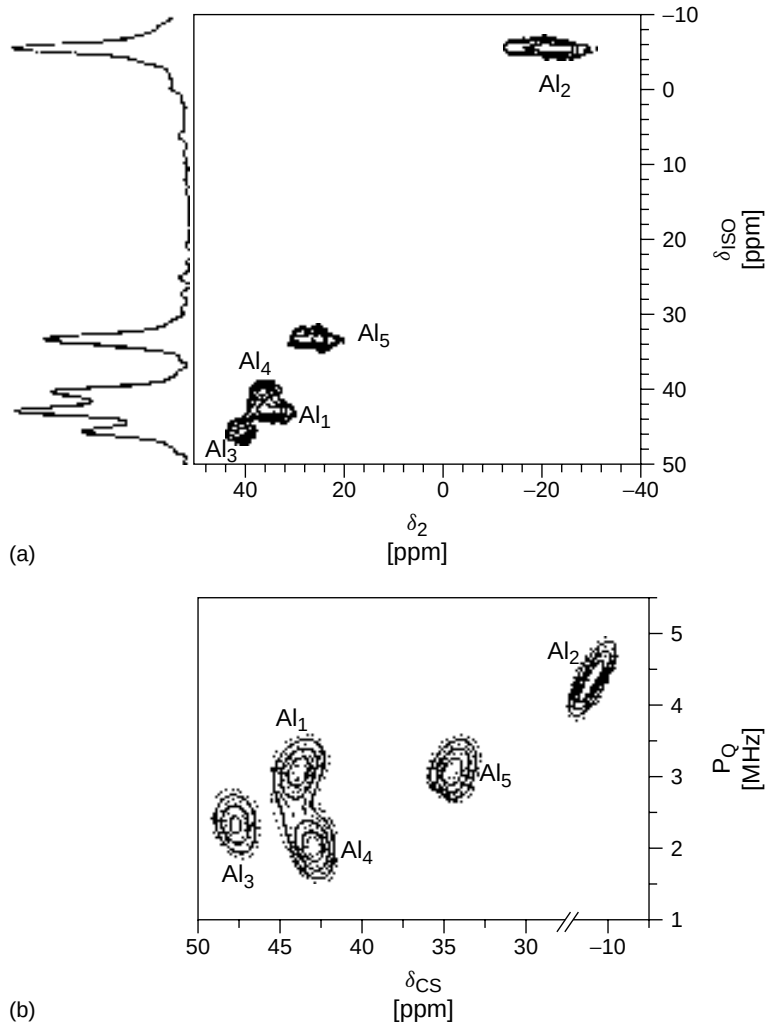

Figure 15 (a) ^{27}Al 3QMAS spectrum of the calcined and fully rehydrated $AlPO_4$-11.[85] The spectrum was acquired at $\nu_0 = 104.2$ MHz using ^{1}H decoupling, $\nu_R = 14$ kHz and $\nu_{RF} = 300$ kHz. (b) Distributions of δ_{CS} and P_Q obtained from the inversion of spectrum (a)

The average values $\langle C_Q \rangle$ and $\langle \eta_Q \rangle$ can be easily obtained from these equations (52). Thus only three parameters ($\langle \delta_{CS} \rangle$, σ_{CS}, σ_Q) are used to fit the MQMAS spectrum when using the direct method.

In the inverse method, the simulations can be simplified by assuming that the spectra are governed by a distribution of chemical shift and second order quadrupolar parameter P_Q, thus reducing the number of unknown functions to two. In cases when an approximate value of η_Q is unknown, a value of η_Q of approximately 0.5 is used in order to calculate S_c for a given value of P_Q. In a distributed resonance, a slice located at δ_{ISO} in the sheared spectrum results from a superposition of all one-dimensional MQ-filtered spectra that satisfy the condition given by equation (47) for δ_{CS} and P_Q. Thus, the two-dimensional integral of equation (48) can be reduced to a single integral with respect to P_Q

$$S_e(\delta_2)_{\delta_{ISO}} = \int_0^\infty S_c(\delta_2; \delta_{CS}(P_Q), P_Q)\Pi(\delta_{CS}(P_Q), P_Q)dP_Q \quad (53)$$

with δ_{CS} given by equation (47). Solving equation (53) to obtain $\Pi(\delta_{CS}(P_Q), P_Q)$ corresponds to inversion of the 2D spectrum. The solution can be drawn for different slices δ_{ISO} of the 2D spectrum. For each slice, the distribution function Π is evaluated versus the P_Q parameter, and for each P_Q value the corresponding δ_{CS} value is determined from equation (47). This corresponds to the determination of a particular curve in the complete two-dimensional parameter space (see Figure 14). The superposition of the curves obtained for all slices yields the final two-dimensional distribution function $\Pi(\delta_{CS}, P_Q)$. As previously noticed, solving this integral equation is not straightforward and requires the use of regularization methods.[81,83,84]

The inversion method was initially applied to analyze the 3QMAS spectra of ^{27}Al in crystalline aluminophosphate $AlPO_4$-11.[85] The 3QMAS spectrum of a crystalline aluminophosphate $AlPO_4$-11 is displayed in Figure 15a, which shows the five crystallographic sites resolved by this technique. The distribution analysis based on this spectrum leads to the canonical representation displayed in Figure 15b. As expected, the intensities of the five Al species are equal and the average values of δ_{CS} and P_Q agree very well with the literature data. A study that compares the quality of the direct and inverse approaches is yet to be reported.

5 MEASUREMENTS OF DIPOLAR CONNECTIVITIES

As a rule, the development of new high-resolution methods in NMR inspires progress in measurements of interactions between the observed nuclei and their neighbors. Such measurements provide means for analyzing the intermediate range ordering in these spin systems. The development of DOR, DAS and MQMAS offered no exception. Several methods that measure the dipolar connectivities between quadrupolar and spin-1/2 nuclei under high-resolution followed the inception of these techniques. Most of these methods utilize indirect excitation via cross polarization for spectral editing of the DOR and MQMAS spectra or for the DAS-based and MQMAS-based HETCOR experiments.[86–91] As the spin dynamics of the CP transfer that involves quadrupolar nuclei is very complex, CP-based methods may suffer from quantitative uncertainties. However, analysis of internuclear interactions between spin-1/2 and quadrupolar nuclei can also be made by reintroducing the heteronuclear dipolar dephasing between these spins using RF pulses that are synchronized with the MAS rotor. One of such methods, REDOR, capable of measurement of dipolar interactions and internuclear distances, has been combined with MQMAS.[30,31,92,93] An attempt has been also made to replace cross polarization with the coherence transfer via TEDOR.[94]

5.1 Cross Polarization and MQMAS

The dipolar coupling between two spins can be used to indirectly produce nuclear magnetization of the observed spins via CP transfer from another spin system. The standard spin-1/2 → spin-1/2 CP experiments are usually performed between abundant and rare spins to enhance the nuclear magnetization of the latter.[95] The polarization transfer in such systems is well understood, and obtaining quantitative spectra

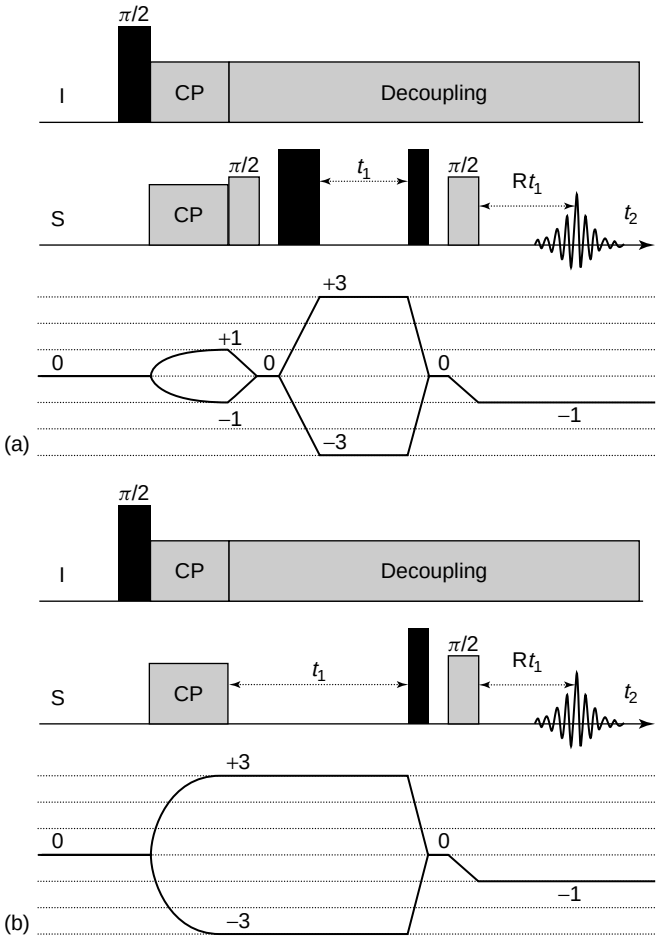

Figure 16 Pulse sequences and coherence transfer pathways for (a) 1QCP-3QMAS and (b) 3QCP-3QMAS experiments with z-filter. The phase cycling used in these experiments must include spin temperature inversion, to avoid direct observation of spins S

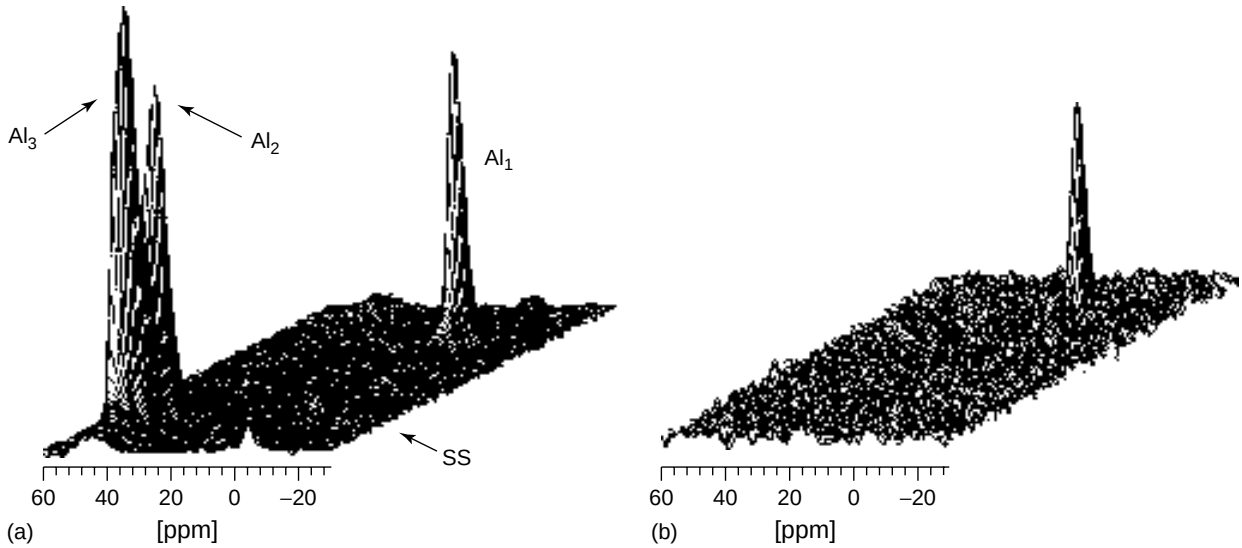

Figure 17 2D NMR spectra of ^{27}Al in $AlPO_4$-CHA obtained using (a) 3QMAS and (b) $^{19}F \rightarrow {}^{27}Al$ 1QCP-3QMAS.[87] The experiment was performed using $\nu_0 = 104.2$ MHz, $\nu_R = 20$ kHz, CP contact time of 0.3 ms and ν_{RF}^S field strengths of approximately 250 kHz, 20 kHz and 5 kHz during hard pulses, soft pulses and CP transfer, respectively. ^{19}F decoupling was applied during evolution and acquisition times using $\nu_{RF}^I \approx 80$ kHz. SS denotes the spinning sideboard

is relatively easy. For reasons to be discussed later, CP between spin-1/2 and quadrupolar nuclei does not generally lead to enhanced sensitivity. However, it is of interest as method for spectral editing. When appropriate line narrowing methods are applied to both spins, the CP transfer can be further employed to obtain high-resolution HETCOR spectra.

It has been shown that the use of cross polarization can be coupled with the MQMAS experiment. The 1QCP-MQMAS experiment shown in Figure 16a, transfers the magnetization of spins I into the ± 1Q central transition of spins S. The resulting single quantum coherence is converted into a population inversion between the states with $m = \pm 1/2$ by a selective $\pi/2$ pulse. After a short delay, a standard MQMAS is performed, e.g., using the scheme with z-filter.[85,87] More direct approaches, relying on polarization transfer to multiple quantum coherences (MQCP-MQMAS), have been successfully implemented by several authors.[96–99] The possibility of CP transfer directly to MQ coherences has been demonstrated earlier for $^{1}H \rightarrow {}^{23}Na$ system under static conditions.[100] One of the pulse sequences and coherence transfer schemes proposed for the MQCP-MQMAS experiment is shown in Figure 16b.[99] Theoretical analysis of multiple quantum cross polarization of quadrupolar nuclei has been reported under static and MAS conditions.[97,98,100]

The 1QCP-3QMAS experiment has been carried out between ^{19}F and ^{27}Al nuclei in fluorinated triclinic chabazite-like $AlPO_4$ aluminophosphate, which contains one octahedral site Al_1 coordinated to fluorine, and two sites labeled Al_2 and Al_3 representing aluminum in AlO_4 tetrahedra. The octahedral aluminum site Al_1 that is bonded to fluorine can be easily distinguished by this method (Figure 17).[87] A $^{1}H \rightarrow {}^{27}Al$ 1QCP-3QMAS experiment was applied for probing the interaction of water with the framework aluminum of fully rehydrated $AlPO_4$-11 aluminophosphate, where it allowed for distinguishing the Al sites that are most and least susceptible to hydration.[85] Such distinction would not be possible without the separation of ^{27}Al resonances under high-resolution conditions. Figure 18 shows the 5QMAS and 5QCP-5QMAS spectra of ^{45}Sc ($S = 7/2$) in scandium sulfate pentahydrate, where CP to all sites is observed.[99] The 3QMAS experiments did not allow for complete resolution of sites 1 and 2. Cross polarization to seven quantum coherences has been also demonstrated for the same sample (not shown). It has been noted that the matching parameters differed for different coherence orders and should be determined separately in each experiment.

The first high-resolution HETCOR NMR spectroscopy involving quadrupolar nuclei used DAS to average the second-order quadrupolar interaction.[89] Experimental schemes of Figure 16 can be easily modified to achieve a 3D high-resolution HETCOR-MQMAS experiment by inserting an additional evolution period between the initial ($\pi/2$) pulse on spins I and the CP transfer. However, due to unfavorable relaxation rates such experiments would require very long acquisition times. Therefore, it is advantageous to use the 2D MQMAS-HETCOR schemes shown in Figure 19, which utilize the $S \rightarrow I$ polarization transfer from fast relaxing quadrupolar nuclei.[90] The experiment can be designed for $S = 3/2$ (Figure 19a) or $S > 3/2$ (Figure 19b), and is performed by spin-locking the isotropic echo that forms at time Rt_1 after the second pulse, followed by CP transfer and acquisition of spins I signal in the t_2 domain.

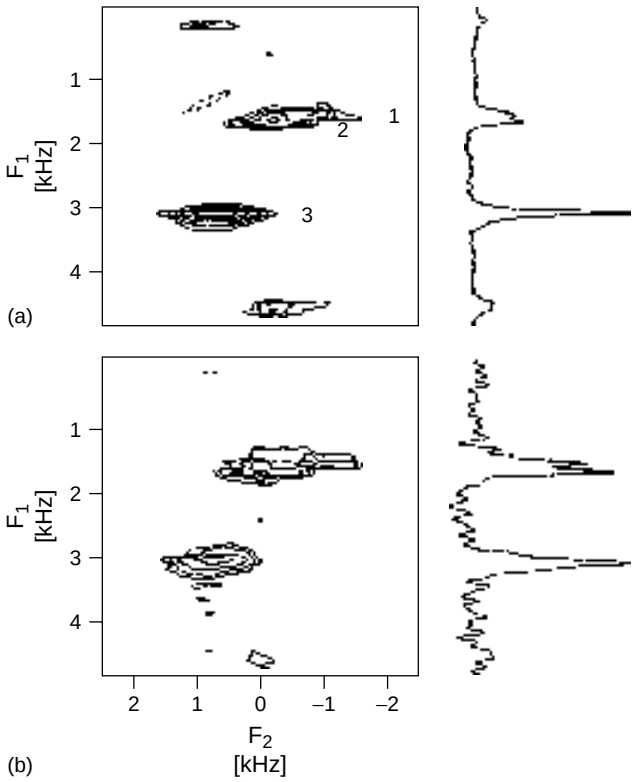

Figure 18 2D NMR spectra of ^{45}Sc in $Sc_2(SO_4)_3 \cdot 5H_2O$ obtained using (a) 5QMAS and (b) $^{1}H \rightarrow {}^{45}Sc$ 5QCP-5QMAS.[99] The experiment was performed at $\nu_0 = 97.2$ MHz with $\nu_R = 6.5$ kHz. The CP transfer used $\nu_{RF}^{S} \approx 100$ kHz, $\nu_{RF}^{I} \approx 50$ kHz and a contact time of 1 ms. ^{1}H decoupling was applied during evolution and acquisition times

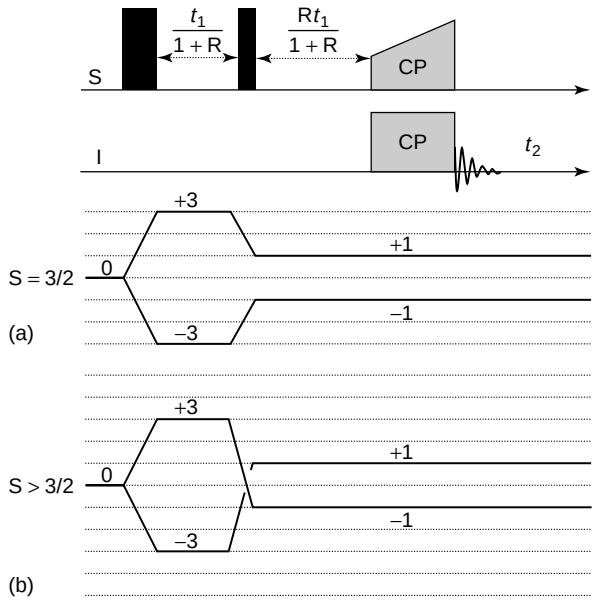

Figure 19 Pulse sequence and coherence transfer pathways used in 3QMAS-HETCOR experiment for (a) $S = 3/2$ and (b) $S > 3/2$

The 3QMAS-HETCOR method has been first used to obtain the spectrum shown in Figure 20a, which correlates the isotropic resonances of ^{23}Na and ^{31}P in $Na_3P_3O_9$.[90] Figure 20b

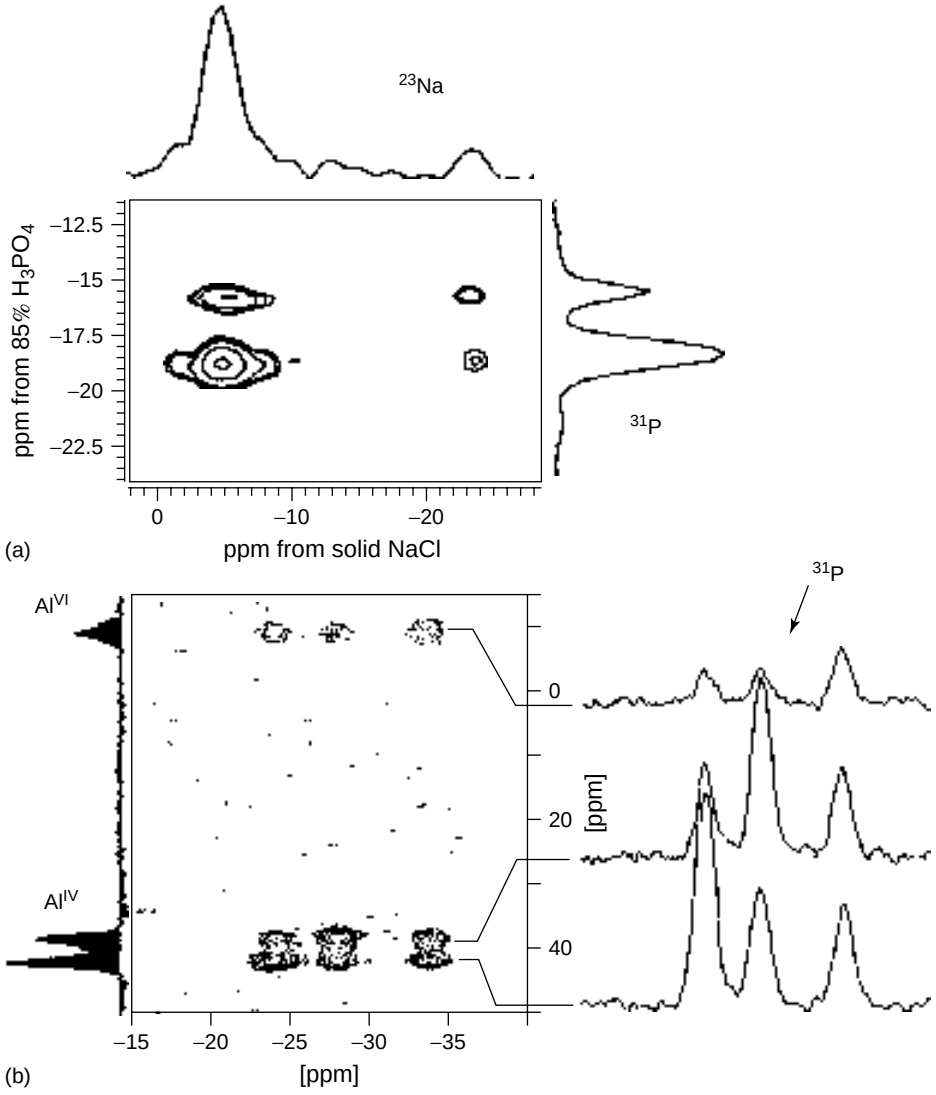

Figure 20 (a) $^{23}Na \rightarrow {}^{31}P$ 3QMAS-HETCOR spectrum of $Na_3P_3O_9$.[90] (b) $^{27}Al \rightarrow {}^{31}P$ HETCOR spectrum of VPI-5[91]

depicts the $^{27}Al \rightarrow {}^{31}P$ 3QMAS-HETCOR spectrum of the large-pore aluminophosphate molecular sieve VPI-5 in a fully hydrated state.[91] In both spectra, significant increase of resolution has been achieved with respect to a standard (CPMAS) version of the HETCOR experiment.

5.2 MQMAS with TEDOR and REDOR

The application of CP transfer to half-integer quadrupolar nuclei is difficult due to the complicated spin dynamics involved in both the spin locking and the cross polarization processes under MAS. These dynamics are strongly anisotropic with respect to crystallite orientation and depend on the relative size of the quadrupole frequency ν_Q, the amplitudes of the RF magnetic field applied to the I and S spins (ν^I_{RF} and ν^S_{RF}), the spinning speed ν_R and the resonance offsets $\delta\nu_{0I}$ and $\delta\nu_{0S}$. Significant progress in understanding of these processes has been made recently due to several excellent contributions.[28,29,86,96–99] Some of the challenges involved in such experiments are briefly reviewed below.

The Hartmann-Hahn matching condition for CP requires that $\nu^I_{RF} = \nu_{nut}$, where ν_{nut} is one of the nutation frequencies associated with the cross polarized coherence of the S spin.[101] In case of static CP between spin-1/2 nuclei and the single quantum central transition coherence of quadrupolar nuclei under on-resonance irradiation, this translates to

$$\nu^I_{RF} = \nu^S_{RF}, \quad |\overline{\nu}_Q| \ll \nu^S_{RF} \tag{54}$$

$$\nu^I_{RF} = (S + 1/2)\nu^S_{RF}, \quad |\overline{\nu}_Q| \gg \nu^S_{RF} \tag{55}$$

where $\overline{\nu}_Q$ is given by equation (4).[29]

The Hartmann-Hahn condition for CP of the (±3/2, ∓3/2) 3Q transitions cannot be well defined in a polycrystalline sample, as it depends on the crystallite orientation

$$\nu^I_{RF} = A_{nut}(\nu^S_{RF})^3/(\overline{\nu}_Q)^2, \quad |\overline{\nu}_Q| \gg \nu^S_{RF} \tag{56}$$

where, again, the conditions $\nu_R = \delta\nu_{0I} = \delta\nu_{0S} = 0$ are assumed, and $A_{nut} = 1.5$, 6, 15, and 30 for $S = 3/2$, 5/2, 7/2 and 9/2, respectively.[99,100]

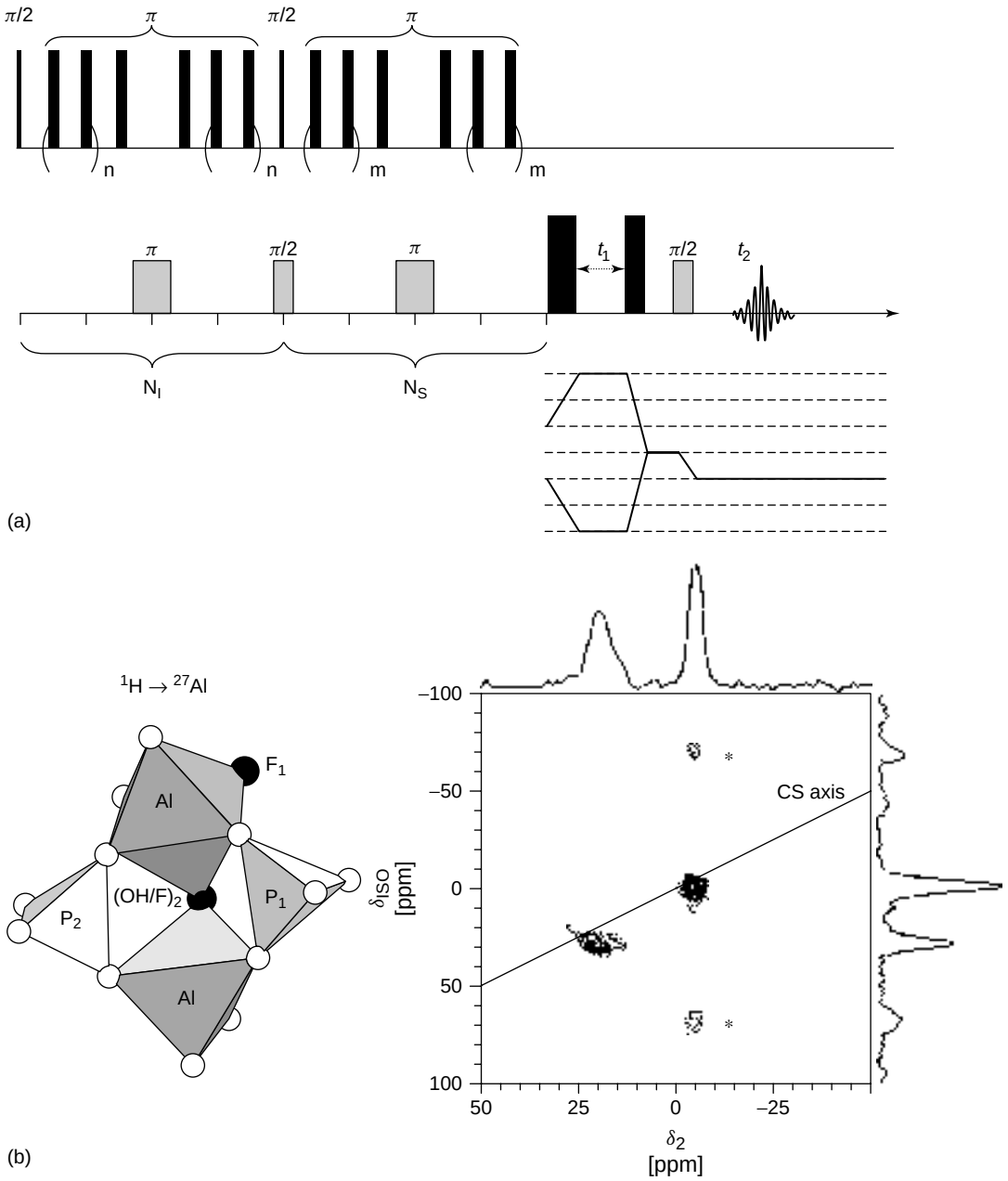

Figure 21 (a) Pulse sequence and coherence transfer pathways used in TEDOR-3QMAS experiment. (b) $^{1}H \rightarrow {}^{27}Al$ TEDOR-3QMAS spectrum of aluminophosphate $AlPO_4$-CJ2

Sample spinning makes $\overline{\nu}_Q$ time dependent and thus complicates both spin locking and polarization transfer.[28,29] The effect of MAS can be described by using the parameter $\alpha_{ad} = (\nu_{RF}^S)^2/\nu_Q\nu_R$ that is related to the speed with which $\overline{\nu}_Q$ crosses zero during sample spinning.[28] It has been shown that efficient spin-locking can be maintained when $\alpha_{ad} \ll 1$ (sudden passage) or when $\alpha_{ad} \gg 1$ (adiabatic passage), whereas the intermediate case $\alpha_{ad} \cong 1$ results in a loss of the spin-locked state. In addition, rotational modulation of the I–S dipolar interaction has profound effect on the CP process itself.[29,102]

The sudden regime ($\alpha_{ad} \ll 1$) implies the use of low RF magnetic fields, such that $\nu_{RF}^S \ll |\overline{\nu}_Q|$ for most crystallites. Under such conditions, the polarization is transferred predominantly to the single quantum central transition coherence of the S spins. The corresponding Hartmann-Hahn matching condition is

$$\nu_{RF}^I = \pm\left(S + \frac{1}{2}\right)\nu_{RF}^S \pm n\nu_R, \quad n = 1, 2 \tag{57}$$

Optimization of the Hartmann-Hahn match becomes very ambiguous in this regime due to the extreme sensitivity to off-resonance effects. Inhomogeneities of the RF magnetic field in doubly tuned probes further complicate the situation. As a result, the absence of a resonance in the CP spectrum should not be used as evidence for the lack of $I \leftrightarrow S$ connectivity without some careful experimentation.

The spin dynamics under adiabatic passage condition ($\alpha_{ad} \gg 1$) is also complex. Experimentally, this regime can be

approached by reducing the spinning speed and/or increasing the strength of RF field. Since there are significant benefits of using the highest available ν_R in MQMAS, we consider only the latter option.[74,103] Under typical conditions of $\nu_R \geq 10$ kHz and $\nu_Q = 1$ MHz, this translates to ν_{RF}^S being much greater than 100 kHz. In this case, the condition $|\overline{\nu}_Q| \gg \nu_{RF}^S$ is no longer satisfied for most of the crystallites and the nutation behavior of the S spins varies strongly with changing orientation. Consequently, no simple Hartmann-Hahn formula can be derived for 1Q and MQCP transfers. Numerical simulations show that such CP transfer is not strongly affected by the interference from ν_R, $\delta\nu_{0I}$ and $\delta\nu_{0S}$, but depends on the quadrupolar parameters, the dipolar coupling D between I and S, and the RF magnetic fields ν_{RF}^I and ν_{RF}^S.[96–99] In general, 1QCP transfer with strong RF fields ($\alpha_{ad} \gg 1$), is less efficient than with weak RF fields ($\alpha_{ad} \ll 1$), except for samples with relatively low values of C_Q and large dipolar couplings. Under fast MAS, there is a striking similarity between the 1Q, 3Q and 5Q intensities obtained with each set of C_Q and D values. A detailed analysis shows that two processes are involved here: a slow CP transfer (with the time constant of the order of 1/D) to all (p/2, −p/2) coherences followed by equilibration of these coherences via a RIACT-like mechanism, which generates fast $1Q \leftrightarrow 3Q \leftrightarrow 5Q$ transfers (with the time constant of $\sim 1/4\nu_R$) in cross polarized nuclei.

The quantitative uncertainties associated with the complex dynamics of spin-locking and CP transfer could be avoided by using TEDOR NMR. This technique has been successfully used in the studies of HETCOR spectra and dipolar couplings in spin systems involving spin-1/2 and quadrupolar nuclei under MAS.[31,32] In the TEDOR method, the magnetization is transferred in a way that is similar to an INEPT experiment in liquids. The dipolar interaction between spins I and S, which is refocused every rotor period in the standard MAS experiments, can be reintroduced by using properly spaced rotor-synchronized RF pulses. It has recently been shown that TEDOR can be used in concert with MQMAS by replacing the Hartmann-Hahn CP transfer in the scheme of Figure 16a, as shown in Figure 21a.[94] The TEDOR pulses must be selective for the central transition of S spins, and thus of weak amplitude. The TEDOR-MQMAS method has been tested on borax and $AlPO_4$−CJ2 aluminophosphate, where $^1H \rightarrow {}^{11}B$, $^1H \rightarrow {}^{27}Al$ and $^{19}F \rightarrow {}^{27}Al$ spectra were acquired (see Figure 21b). A reverse experiment, similar to that used in the MQMAS-HETCOR scheme can be also considered. According to the numerical simulations, TEDOR-MQMAS appears to be less sensitive to off-resonance effects than CP-MQMAS. However the applicability of this technique to nuclei with strong quadrupole interactions has yet to be tried.

Another version of an approach without the use of CP has been proposed, which combines the high-resolution capabilities of MQMAS with the direct determination of hetero-nuclear dipolar couplings via REDOR. Figure 22 shows the schematic diagrams of two MQ-REDOR experiments, referred to as MQ-t_1-REDOR and MQ-t_2-REDOR. The MQ-t_2-REDOR technique (Figure 22a), employs two strong and two selective RF pulses at the Larmor frequency ν_{0S} with phases cycled to select the $0 \rightarrow \pm p \rightarrow 0 \rightarrow +1 \rightarrow -1$ coherence pathway.[92] When spaced by an integer number of rotor periods nt_R, the selective pulses create two windows in which the sequences of π pulses can be applied to the spin-1/2 nuclei. Similar to the standard REDOR experiment, the role of the π pulses is to prevent MAS from refocusing the dephasing due to the dipolar interaction between spins I and S.[30]

The spectral editing capabilities of MQ-t_2-REDOR method are illustrated in Figure 23, which shows several ^{27}Al NMR spectra of $AlPO_4$-CHA aluminophosphate (see also Figure 17).[92] The tetrahedral sites Al_2 and Al_3 are not well resolved by MAS alone (spectrum (a)), but are easily distinguished by using the MQMAS method (spectrum (b)). The so-called REDOR difference spectra, obtained by subtracting the MQMAS spectra obtained without and with the dephasing pulses are shown in Figures 23c−d. As expected, only the resonance from fluorinated site (Al_1) remains strong in the spectrum of Figure 23c. However, the capabilities of the MQ-t_2-REDOR method extend beyond spectral editing. By changing the number of rotor cycles, one can measure the REDOR curves for all three Al species and estimate their distances from the nearest fluorine.[30] The results (see Figure 24) are in good agreement with the results inferred from synchrotron radiation experiments. The MQ-t_1-REDOR experiment (see Figure 22b), employs the REDOR sequence during multiple rather than single quantum evolution.[93] Because the dipolar effect is enhanced by a factor of p during the p-quantum evolution (see F term in equation (7)), this technique has potential for improved sensitivity toward weak dipolar interactions. Indeed, the results of Figure 24 show

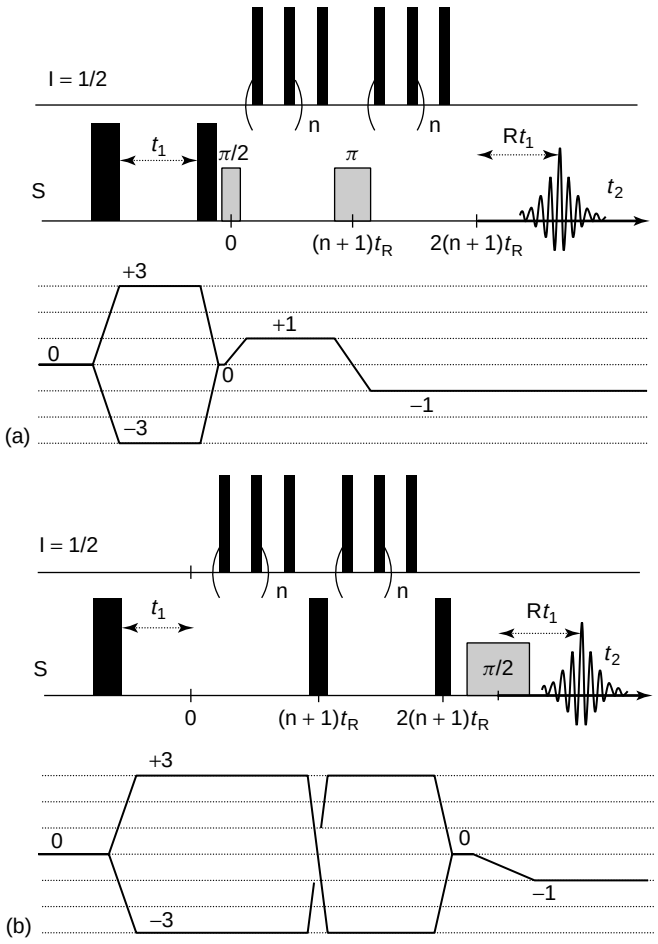

Figure 22 Pulse sequences and coherence transfer pathways used in (a) MQ-t_2-REDOR and (b) MQ-t_1-REDOR experiments

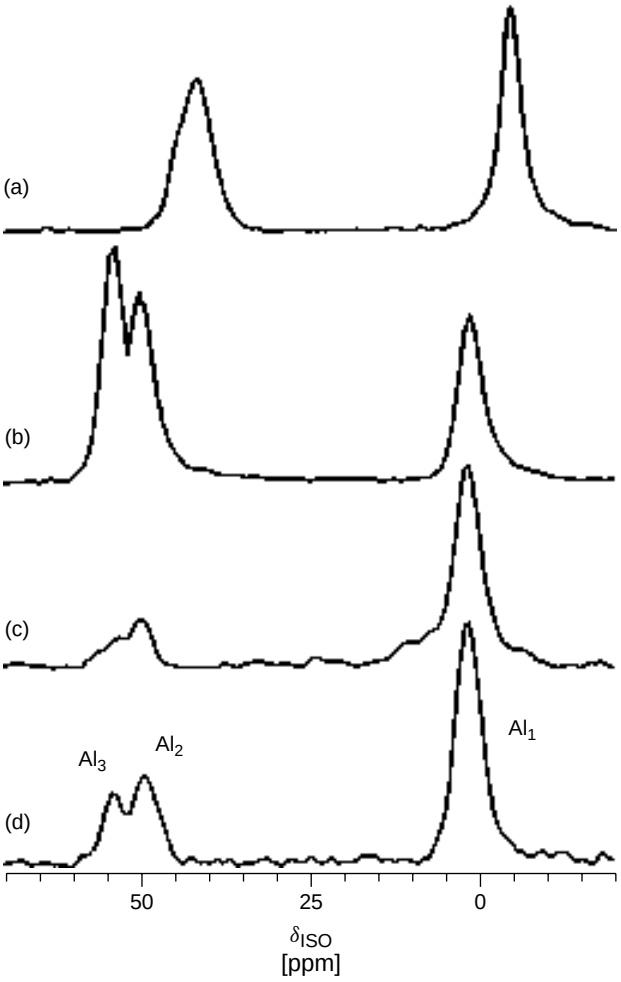

Figure 23 ^{27}Al NMR spectra of fluorinated $AlPO_4$-CHA aluminophosphate: (a) MAS, (b) 3QMAS, (c) 3Q-t_2-REDOR difference for $n = 5$, and (d) 3Q-t_2-REDOR difference for $n = 29$

that in $AlPO_4$-CHA the apparent size of ^{19}F-^{27}Al coupling measured using 3Q-t_1-REDOR was higher by a factor of 3 when compared with the data obtained with 3Q-t_2-REDOR.[93]

Although the concept of dipolar recoupling during MQ evolution is attractive, the 3Q-t_1-REDOR experiment has potential limitations. First, the more complex coherence pathway employed by this method causes a loss of sensitivity of approximately 2–8, depending on the C_Q and S spin values. Another potential drawback of both MQ-REDOR experiments stems from non-uniform response of the quadrupolar spins to the RF pulses used in the MQMAS experiment. One may expect the effect that the orientational anisotropy of MQ excitation has on the MQ-t_1-REDOR curves to be enhanced, especially in samples with significant C_Q values. However, both experimental and theoretical results show that the experiment is surprisingly robust. Indeed, the initial slope of the REDOR curve is nearly independent of C_Q for small or moderate quadrupolar interactions, and the quality of the fit improves markedly when the strength of RF field is increased, even for large C_Q values.[93] REDOR recoupling during triple quantum evolution has been recently used to determine the relative orientations of the quadrupolar and dipolar principal axis systems.[104] In this

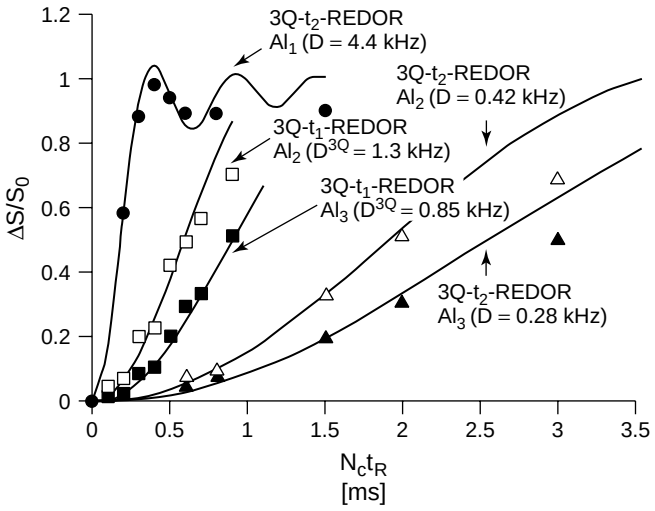

Figure 24 Experimental and simulated MQ-t_1-REDOR and MQ-t_2-REDOR curves for $ALPO_4$-CHA.[93] The values of dipolar coupling D between ^{19}F and ^{27}Al corresponding to the simulated curves are given in parentheses

experiment, the REDOR recoupling immediately follows the excitation of 3Q coherences. After the $\pm 3Q \rightarrow \mp 3Q$ inversion, a $\pi/2$ pulse is applied to spins I to create a mixture of heteronuclear 2Q and 4Q coherences, which are subsequently allowed to precess during evolution period t_1. The t_1 period is followed by a similar REDOR recoupling period to recover the 3Q coherences, which are then converted into the observable – 1Q coherence. The resulting spectrum exhibits patterns of spinning sidebands along the MQ dimension, which depend on the dipolar coupling, the quadrupolar parameters and the relative orientation of the quadrupolar and dipolar PAS.

Another experiment, referred to as MQMAS with dipolar dephasing (DD-MQMAS) is shown in Figure 25. It uses the standard z-filtered MQMAS scheme for spins S, while the dipolar recoupling with spins I is accomplished using a series of π pulses applied synchronously with the rotor frequency to the I spins during the multiple quantum evolution.[105] The simple $0 \rightarrow \pm p \rightarrow 0 \rightarrow -1$ coherence pathway that is used here results in line broadening, but allows for fast,

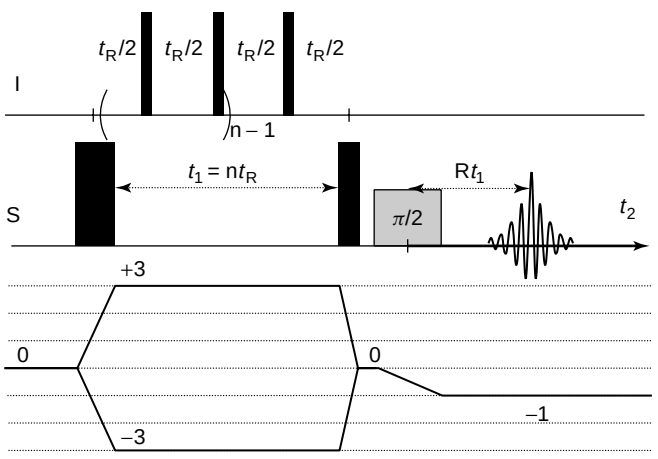

Figure 25 DD-MQMAS experiment: pulse sequence and coherence transfer pathway

yet only semi-quantitative, determination of the internuclear connectivities in well crystallized compounds.

6 SENSITIVITY ENHANCEMENT VIA CPMG METHOD

Advances in manipulating the MQ coherences considerably improved the sensitivity of the MQMAS experiment. Additional gain in the S/N ratio can be accomplished by applying a CPMG train of rotor-synchronized, selective π pulses during the acquisition of data in t_2.[106–108] The resulting CPMG-MQMAS spectrum is split into periodic combs of spin-echo sidebands that spread along the anisotropic dimension. Since the integrated spectral intensity is not affected by this procedure, the apparent S/N ratio for individual spikes can be significantly enhanced. The gain in S/N ratio is governed by periodicity τ_a of the CPMG train and the homogeneous spin–spin relaxation time T_2. The truncation effects require that τ_a exceeds the net dephasing time of transverse magnetization T_2^*, which determines the maximum gain available by this method.

An example of the experimental scheme for CPMG-MQMAS experiment with spin-3/2 nuclei, based on the split-t_1 method, is shown in Figure 26.[108] In this experiment the excitation of MQ coherences and their reconversion to the single quantum coherence is achieved following the usual rules. The CPMG sequence uses selective π pulses of the same strength of RF field as the soft pulse in the z-filter method. The phase cycling of each sequence follows the standard procedures, and the phases of the CPMG train are adjusted according to the Meiboom-Gill scheme. The sequence in Figure 26 utilizes contributions from the echo and antiecho coherence pathways, which leads to cosine modulated FIDs. Approaches suitable for spin-5/2 nuclei have been also proposed.[109]

The appearance of CPMG spectrum is determined by the sampling conditions: smaller separation τ_a between the echoes in time domain increases the S/N ratio in frequency domain at the expense of anisotropic line shape, which is determined by a reduced number of sidebands. Although the spin-echo sidebands are regularly spaced with respect to the carrier frequency, the sideband manifolds corresponding to different sites are usually well separated along the isotropic dimension. This is manifested in Figure 27, which shows a series of

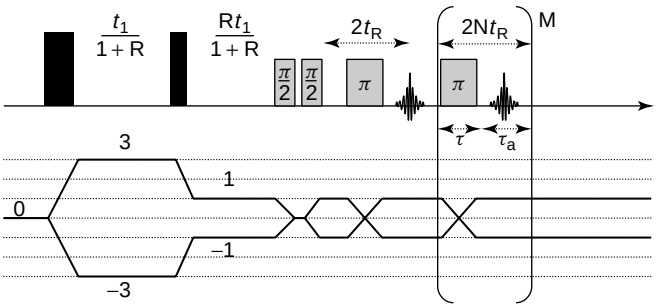

Figure 26 CPMG-3QMAS pulse sequence and coherence transfer pathway for spin-3/2 nuclei.[108] The part of the sequence shown in parenthesis is rotor-synchronized according to $2Nt_R = \tau + \tau_a$, where τ is the duration of the selective π pulse (including the transient effects) and τ_a is the echo sampling period

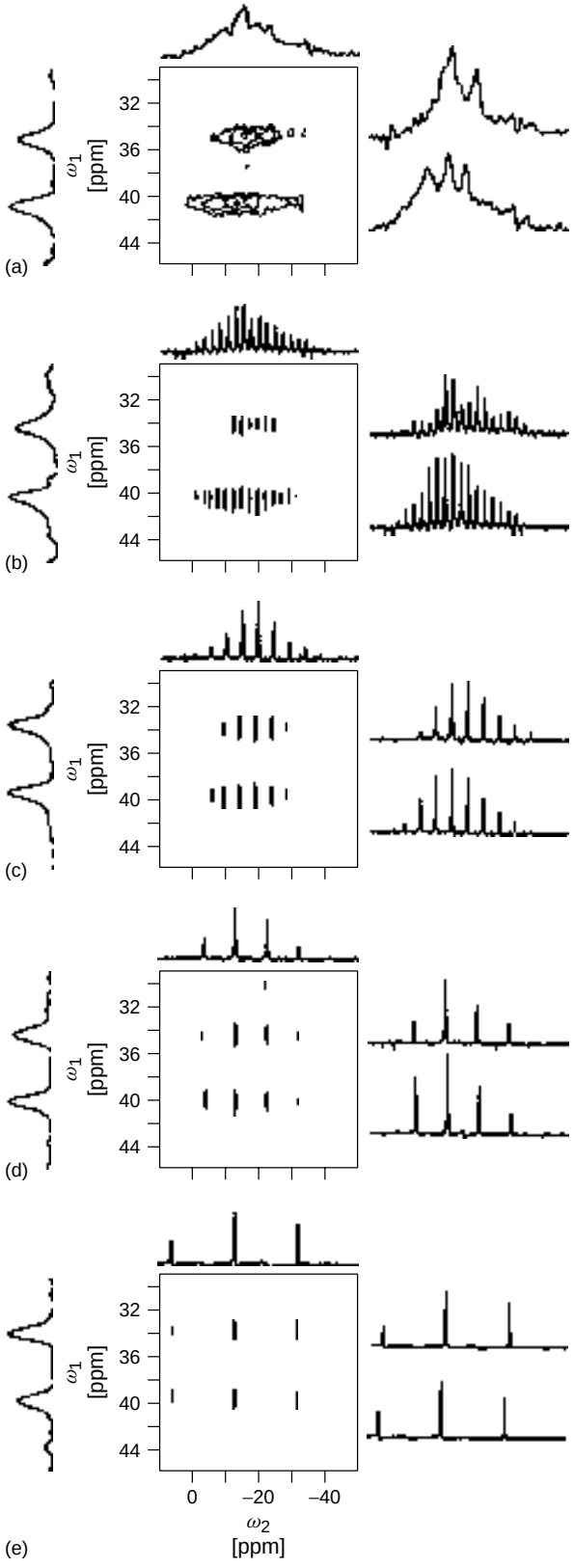

Figure 27 ^{23}Na MQMAS (a) and CPMG-MQMAS (b–e) spectra of an equimolar mixture of Na_2SO_4 and $Na_2C_2O_4$ recorded at $\nu_0 =$ 105.8 MHz using ν_R rates between 10 and 11 kHz and $\nu_{RF} = 58$ kHz for all pulses.[108] All CPMG-MQMAS spectra used $\tau = 150\,\mu$s and the following values of τ_a and M: (b) 4 ms, 9; (c) 2 ms, 19; (d) 1 ms, 39, and (e) 0.5 ms, 80

^{23}Na MQMAS and CPMG-3QMAS spectra of an equimolar mixture of Na_2SO_4 and $Na_2C_2O_4$.[108] Although each spectrum has been recorded with the same number of scans, spectra b-e corresponded to S/N gain factors of 5, 8, 12 and 20, respectively.

It has been shown that accurate parameters for quadrupole and chemical shift interactions can be extracted from the CPMG-MQMAS spectra via numerical simulation that accounts for the time-modulation of quadrupolar interaction in the course of RF pulses.[110] In addition, several methods for the numerical treatment of the CPMG spectra have been proposed, which further improve the S/N ratio and allow for full recovery of the echo envelope. These include modification of the sideband envelope through echo shifting, reconstruction of the full spectrum by superimposing the echoes, and various schemes for noise filtering via apodization.[109] Additional improvement of the numerical analysis is possible by the use of data processing techniques that are alternative to discrete Fourier transform. Recently, a simple processing technique, referred to as ANAFOR, has been proposed based on the least squares method used in linear prediction and the TIGER routines.[111,112] These methods allow for precise determination of intensities in truncated multidimensional spectra based on outside information about the line shape parameters. ANAFOR can be especially useful in the CPMG-MQMAS experiments, where the positions of sidebands are known in advance and other line shape parameters can be obtained using, e.g., one-dimensional methods. By using truncated time-domain data sets, ANAFOR offered further significant gain in sensitivity. For example, this method has been applied to ^{1}H-^{27}Al MQ-t_2-REDOR measurements in $AlPO_4$-ZON where the experimental time has been decreased by a factor of six.[111]

7 CONCLUSION

Since its development, MQMAS has matured to become a powerful investigative tool that benefits various areas of chemistry and materials science. Many research groups have applied this method to the studies of catalytic materials, glasses, numerous other crystalline and amorphous inorganic compounds and even biological samples. A wide-ranging description of these applications would warrant a separate review.

In spite of recent advances, the MQMAS method itself continues to evolve. Most of the recent effort targets the improvement of sensitivity, which may offer new perspectives for high resolution studies of inherently challenging nuclei, such as ^{17}O. New types of correlation schemes are being considered in order to increase the sensitivity and/or resolution. For example, the recently proposed schemes that use two different MQ coherences during t_1 may have the potential of improved resolution over the standard MQMAS experiment.[113] Also recently, a technique referred to as satellite transition MAS (STMAS) has been proposed, which provides isotropic spectra of half-integer quadrupolar nuclei by correlating the evolution of single quantum inner-satellite transitions in t_1 with that observed during t_2 for the $(-1/2,1/2)$ central transition (see 'Satellite Transition NMR Spectroscopy of Half-Integer Quadrupolar Nuclei under Magic Angle Spinning').[63] This is also the case for the CESAME (central satellite MAS experiment) which has been proposed most recently.[114]

8 RELATED ARTICLES IN THIS VOLUME

Adiabatic Polarization-Transfer Methods in MAS Spectroscopy; Multiple-quantum Magic-angle Spinning Experiments on Half-integer Nuclei: Fundamentals; Satellite Transition NMR Spectroscopy of Half-Integer Quadrupolar Nuclei under Magic-Angle Spinning.

9 RELATED ARTICLES IN VOLUMES 1–8

Cross Polarization in Solids, Volume 3; Double Rotation, Volume 3; Dynamic Angle Spinning, Volume 3; Line Narrowing Methods in Solids, Volume 4; Multidimensional Spectroscopy: Concepts, Volume 5; Quadrupolar Interactions, Volume 6; Quadrupolar Nuclei in Solids, Volume 6.

10 REFERENCES

1. A. Abragam, 'Principles of Nuclear Magnetism', Oxford University Press: London, 1961.
2. E. R. Andrew, A. Bradbury, and R. G. Eades, *Nature*, 1958, **182**, 1659.
3. J. S. Waugh, L. M. Huber, and U. Haeberlen, *Phys. Lett.*, 1968, **20**, 180.
4. A. Pines, M. G. Gibby, and J. S. Waugh, *J. Chem. Phys.*, 1972, **56**, 1776.
5. B. C. Gerstein, R. G. Pembelton, R. C. Wilson, and L. M. Ryan, *J. Chem. Phys.*, 1977, **66**, 362.
6. A. Samoson, E. Lipmaa, and A. Pines, *Mol. Phys.*, 1988, **65**, 1013.
7. K. T. Mueller, B. Q. Sun, G. C. Chingas, J. W. Zwanziger, T. Terao, and A. Pines, *J. Magn. Reson.*, 1990, **86**, 470.
8. L. Frydman and J. S. Harwood, *J. Am. Chem. Soc.*, 1995, **117**, 5367.
9. A. Medek, J. S. Harwood, and L. Frydman, *J. Am. Chem. Soc.*, 1995, **117**, 12 779.
10. C. P. Slichter, 'Principles of Magnetic Resonance', 3rd edn., Springer-Verlag: Berlin, 1990.
11. M. H. Cohen and F. Rief, in 'Solid State Physics', eds F. Seitz and D. Turnbull, Academic Press: New York, 1958, Vol. 5, p. 321.
12. D. Freude and J. Haase, in 'NMR Basic Principles and Progress', eds P. Diehl, E. Fluck, and R. Kosfeld, Springer-Verlag: Berlin, 1993, Vol. 29, p. 1.
13. A. Vega, in 'Encyclopedia of Magnetic Resonance', eds D. M. Grant and R. K. Harris, John Wiley & Sons: Chichester, Vol. 6, p. 3869, 1996.
14. E. L. Hahn, *Phys. Rev.*, 1950, **80**, 580.
15. E. Oldfield, H. K. C. Timken, B. Montez, and R. Ramachandran, *Nature*, 1985, **318**, 163.
16. T. Bastow, *Solid State NMR*, 1994, **3**, 17.
17. H. J. Jakobsen, in 'Encyclopedia of Magnetic Resonance', eds D. M. Grant and R. K. Harris, John Wiley & Sons: Chichester, 1996, Vol. 4, p. 2370.
18. S. Ganapathy, S. Schramm, and E. Oldfield, *J. Chem. Phys.*, 1982, **77**, 4360.
19. J. Skibsted, N. C. Nielsen, H. Bildsoe, and H. J. Jakobsen, *J. Magn. Reson.*, 1991, **95**, 88.

20. E. Kundla, A. Samoson, and E. Lipmaa, *Chem. Phys. Lett.*, 1981, **83**, 229.
21. A. Samoson and E. Lipmaa, *J. Magn. Reson.*, 1988, **79**, 255.
22. N. C. Nielsen, H. Bildsoe, and H. J. Jakobsen, *J. Magn. Reson.*, 1992, **97**, 149.
23. A. P. M. Kentgens, *J. Magn. Reson.*, 1993, **A104**, 302.
24. A. Samoson, *Chem. Phys. Lett.*, 1985, **119**, 29.
25. C. Jager, *J. Magn. Reson.*, 1992, **99**, 353.
26. D. Massiot, V. Montouillout, F. Fayon, P. Florian, and C. Bessada, *Chem. Phys. Lett.*, 1997, **272**, 295.
27. C. S. Blackwell and R. L. Patton, *J. Phys. Chem.*, 1984, **88**, 6135.
28. A. J. Vega, *J. Magn. Reson.*, 1992, **96**, 50.
29. A. J. Vega, *Solid State NMR*, 1992, **1**, 17.
30. T. Gullion and J. Schaefer, *J. Magn. Reson.*, 1989, **81**, 196.
31. A. W. Hing, S. Vega, and J. Schaefer, *J. Magn. Reson.*, 1992, **96**, 205.
32. C. A. Fyfe, K. T. Mueller, H. Grodney, and K. C. Wong-Moon, *Chem. Phys. Lett.*, 1992, **199**, 198.
33. E. R. H. van Eck, R. Jansen, W. E. J. R. Maas, and W. S. Veeman, *Chem. Phys. Lett.*, 1990, **174**, 428.
34. C. P. Grey and A. J. Vega, *J. Am. Chem. Soc.*, 1995, **117**, 8232.
35. T. Gullion, *J. Magn. Reson.*, 1995, **A117**, 326.
36. A. Llor and J. Virlet, *Chem. Phys. Lett.*, 1988, **152**, 248.
37. K. T. Mueller, Y. Wu, B. F. Chmelka, J. Stebbins, and A. Pines, *J. Am. Chem. Soc.*, 1991, **113**, 32.
38. S. Vega and Y. Naor, *J. Chem. Phys.*, 1981, **75**, 75.
39. N. C. Nielsen, H. Bildsoe, and H. J. Jakobsen, *Chem. Phys. Lett.*, 1992, **191**, 205.
40. M. Pruski, J. W. Wiench, and J.-P. Amoureux, *J. Magn. Reson.*, 2000, **147**, 286.
41. J.-P. Amoureux, *Solid State NMR*, 1993, **2**, 83.
42. J.-P. Amoureux, C. Fernandez, and L. Frydman, *Chem. Phys. Lett.*, 1996, **259**, 347.
43. P. K. Madhu, A. Goldbourt, L. Frydman, and S. Vega, *Chem. Phys. Lett.*, 1999, **307**, 41.
44. P. K. Madhu, A. Goldbourt, L. Frydman, and S. Vega; *J. Chem. Phys.*, 2000, **112**, 2377.
45. A. P. M. Kentgens and R. Verhagen, *Chem. Phys. Lett.*, 1999, **300**, 435.
46. T. Vosegaard, P. Florian, D. Massiot, and P. J. Grandinetti, *J. Chem. Phys.*, 2001, **114**, 4618.
47. G. Wu, D. Rovnyak, and R. G. Griffin, *J. Am. Chem. Soc.*, **118**, 9326, 1996.
48. S. P. Brown, S. J. Heyes, and S. Wimperis, *J. Magn. Reson.*, 1996, **A119**, 280.
49. P. J. Grandinetti, J. H. Baltisberger, A. Llor, Y. K. Lee, U. Werner, M. A. Eastman, and A. Pines, *J. Magn. Reson.*, 1993, **A103**, 72.
50. D. Massiot, B. Touzo, D. Trumeau, J. P. Coutures, J. Virlet, P. Florian, and P. J. Grandinetti, *Solid State NMR*, 1996, **6**, 73.
51. J.-P. Amoureux, C. Fernandez, and S. Steuernagel, *J. Magn. Reson.*, 1996, **A123**, 116.
52. S. P. Brown and S. Wimperis, *J. Magn. Reson.*, 1997, **128**, 42.
53. T. Vosegaard, P. Florian, P. J. Grandinetti, and D. Massiot, *J. Magn. Reson.*, 2000, **143**, 217.
54. R. R. Ernst, G. Bodenhausen, and A. Wokaun, 'Principles of Nuclear Magnetic Resonance in One and Two Dimensions', Clarendon: Oxford, 1987.
55. T. Charpentier, Ph.D. Thesis, University of Paris XI, France, 1998.
56. K. T. Mueller, E. W. Wooten, and A. Pines, *J. Magn. Reson.*, 1991, **92**, 620.
57. N. G. Dowell, S. E. Ashbrook, J. McManus, and S. Wimperis, *J. Am. Chem. Soc.*, 2001, **123**, 8135.
58. A. Bax, R. Freeman, and S. P. Kempsell, *J. Magn. Reson.*, 1980, **41**, 349.
59. D. J. States, R. A. Haberkorn, and D. J. Ruben, *J. Magn. Reson.*, 1982, **48**, 286.
60. J.-P. Amoureux and C. Fernandez, *Solid State NMR*, 1998, **10**, 211.
61. C. Fernandez, J.-P. Amoureux, J. M. Chezeau, L. Delmotte, and H. Kessler, *Microporous Materials*, 1996, **6**, 331.
62. G. Wu, S. Kroeker, R. E. Wasylishen, and R. G. Griffin, *J. Magn. Reson.*, 1997, **A124**, 237.
63. Z. Gan, *J. Am. Chem. Soc.*, 2000, **122**, 3242.
64. S. P. Brown and S. Wimperis, *J. Magn. Reson.*, 1997, **124**, 279.
65. D. Iuga, H. Schafer, R. Verhagen, and A. P. M. Kentgens, *J. Magn. Reson.*, 2000, **147**, 192.
66. K. H. Lim and C. P. Grey, *Solid State NMR*, 1998, **13**, 101.
67. S. H. Wang, Z. Xu, J. H. Baltisberger, L. M. Bull, J. F. Stebbins, and A. Pines, *Solid State NMR*, 1997, **8**, 1.
68. K. J. Pike, R. P. Malde, S. E. Ashbrook, J. McManus, and S. Wimperis, *Solid State NMR*, 2000, **16**, 203.
69. J. McManus, R. Kemp-Harper, and S. Wimperis, *Chem. Phys. Lett.*, 1999, **311**, 292.
70. S. Wi and L. Frydman, *J. Chem. Phys.*, 2000, **112**, 3248.
71. M. Hanaya and R. K. Harris, *Solid State NMR*, 1997, **8**, 147.
72. V. Lacassagne, P. Florian, V. Montouillout, C. Gervais, F. Babonneau, and D. Massiot, *Magn. Reson. Chem.*, 1998, **36**, 956.
73. A. E. Bennett, C. M. Rienstra, M. Auger, K. V. Lakshmi, and R. G. Griffin, *J. Chem. Phys.*, 1995, **103**, 6951.
74. D. Massiot, *J. Magn. Reson.*, 1996, **A122**, 240.
75. J. L. Baltisberger, Z. Xu, J. F. Stebbins, S. H. Wang, and A. Pines, *J. Am. Chem. Soc.*, 1996, **118**, 7209.
76. H. Hunger and T. Horvath, *J. Am. Chem. Soc.*, 1996, **118**, 12 302.
77. H. Maekawa, P. Florian, D. Massiot, H. Kiyono, and M. Nakamura, *J. Phys. Chem.*, 1996, **100**, 5525.
78. U. T. Pingel, J.-P. Amoureux, T. Anupold, F. Bauer, H. Ernst, C. Fernandez, D. Freude, and A. Samoson, *Chem. Phys. Lett.*, 1998, **294**, 345.
79. M. Bak, J. T. Rasmussen, and N. C. Nielsen, *J. Magn. Reson.*, 2000, **147**, 296.
80. S. A. Smith, T. O. Levante, B. H. Meier, and R. R. Ernst, *J. Magn. Reson.*, 1994, **106**, 75.
81. J. Zwanziger, *Solid State NMR*, 1994, **3**, 219.
82. G. Czjzek, J. Fink, F. Gotz, H. Schmidt, J. M. D. Coey, J. P. Rebouillat, and A. Lienard, *Phys. Rev.*, 1981, **B23**, 2513.
83. F. Angeli, T. Charpentier, P. Faucon, and J. C. Petit, *J. Phys. Chem.*, 1999, **B103**, 10 356.
84. F. Angeli, J. M. Delaye, T. Charpentier, J. C. Petit, D. Ghaleb, and P. Faucon, *J. Non-Cryst. Solids*, 2000, **276**, 132.
85. C. Fernandez, L. Delevoye, J.-P. Amoureux, D. P. Lang, and M. Pruski, *J. Am. Chem. Soc.*, 1997, **119**, 6858.
86. W. Sun, J. T. Stephen, L. D. Porter, and Y. Wu, *J. Magn. Reson.*, 1995, **A116**, 181.
87. M. Pruski, D. P. Lang, C. Fernandez, and J.-P. Amoureux, *Solid State NMR*, 1997, **7**, 327.
88. S. E. Ashbrook, S. P. Brown, and S. Wimperis, *Chem. Phys. Lett.*, 1998, **288**, 509.
89. T. P. Jarvie, R. M. Wenslow, and K. T. Mueller, *J. Am. Chem. Soc.*, 1995, **117**, 570.
90. S. H. Wang, S. M. De Paul, and L. M. Bull, *J. Magn. Reson.*, 1997, **125**, 364.
91. C. Fernandez, C. Morais, and M. Pruski, *Solid State NMR*, 2002, **21**, 61.
92. C. Fernandez, D. P. Lang, J.-P. Amoureux, and M. Pruski, *J. Am. Chem. Soc.*, 1998, **120**, 2672.
93. M. Pruski, A. Bailly, D. P. Lang, J.-P. Amoureux, and C. Fernandez, *Chem. Phys. Lett.*, 1999, **307**, 35.
94. J.-P. Amoureux and M. Pruski, in preparation.
95. A. Pines, M. G. Gibby, and J. S. Waugh, *J. Chem. Phys.*, 1973, **59**, 569.
96. D. Rovnyak, M. Baldus, and R. G. Griffin, *J. Magn. Reson.*, 2000, **142**, 145.
97. K. H. Lim and C. P. Grey, *J. Chem. Phys.*, 2000, **112**, 7490.
98. S. E. Ashbrook and S. Wimperis, *Mol. Phys.*, 2000, **98**, 1.

99. S. E. Ashbrook and S. Wimperis, *J. Magn. Reson*, 2000, **147**, 238.
100. S. Vega, *Phys. Rev.*, 1981, **23**, 3152.
101. S. R. Hartmann and E. L. Hahn, *Phys. Rev.*, 1962, **128**, 2042.
102. E. O. Stjeskal, J. Schaefer, and J. S. Waugh, *J. Magn. Reson.*, 1977, **28**, 105.
103. J.-P. Amoureux, M. Pruski, D. P. Lang, and C. Fernandez, *J. Magn. Reson.*, 1998, **131**, 170.
104. A. Lupulescu, S. P. Brown, and H. W. Spiess, in preparation.
105. M. Pruski, C. Fernandez, D. Lang, J.-P. Amoureux, *Catalysis Today*, 1999, **49**, 401.
106. H. Y. Carr and E. M. Purcell, *Phys. Rev.*, 1954, **94**, 630.
107. S. Meiboom and D. Gill, *Rev. Sci. Inst.*, 1958, **29**, 688.
108. T. Vosegaard, F. H. Larsen, H. J. Jakobsen, P. D. Ellis, and N. C. Nielsen, *J. Am. Chem. Soc.*, 1997, **119**, 9055.
109. R. Lefort, J. W. Wiench, M. Pruski, and J.-P. Amoureux, *J. Chem. Phys.*, 2002, **116**, 2493.
110. F. H. Larsen and N. C. Nielsen, *J. Phys. Chem. A*, 1999, **103**, 10 825.
111. P. Bodart, J.-P. Amoureux, and F. Taulelle, *Solid State NMR*, 2002, **21**, 1.
112. G. McGeorge, J. Z. Hu, C. Mayne, D. W. Alderman, R. J. Pugmire, and D. M. Grant, *J. Magn. Reson.*, 1997, **129**, 134.
113. A. Jerschow, J. W. Logan, and A. Pines, *J. Magn. Reson.*, 2001, **149**, 268.
114. J.-P. Amoureux, C. Morais, J. Trebosc, J. Rocha, and C. Fernandez, *J. Am. Chem. Soc.*, submitted.

Biographical Sketches

Jean-Paul Amoureux, *b* 1946. Eng., 1970, Paris, Ph.D., 1976, University of Lille, France. Approx. 140 publications. His interest in solid state NMR started in 1985, after assuming a position of professor in the Laboratoire de Dynamique et Structure des Materiaux Moleculaires (CNRS) at the University of Lille. Current research includes the development of new solid state NMR methods with emphasis on half-integer quadrupolar nuclei.

Marek Pruski, *b* 1954. M.S., 1977, Ph.D., 1981, N. Copernicus University, Torun, Poland. Introduced to NMR in 1982 at the N. Copernicus University and Universität Leipzig. Postdoctoral fellow at the Iowa State University (with B. C. Gerstein), 1985–88, scientist and head of solid state NMR group, Ames Laboratory, Iowa State University 1988–present. Approx. 90 publications. Current research specialty: solid state NMR and its applications to surface and material sciences, high resolution methods for half-integer quadrupolar nuclei.

Multiple Quantum Coherence in Spin-1/2 Dipolar Coupled Solids

Bernard C. Gerstein

Ames Laboratory of US DOE & Iowa State University, Ames, IA, USA

1	Introduction	1
2	Single Quantum Coherence	2
3	Coherent Averaging	3
4	Development of Multiple Quantum Coherence: Use of a Double Quantum Propagator	4
5	Detection of Multiple Quantum Coherence	6
6	A Single Quantum Propagator	9
7	Related Articles	11
8	References	11

1 INTRODUCTION

Think for a moment about the area of the North American continent known as the 'Great Plains'. In the twenty thousand years before the coming of the Europeans to this area, the thirty millions of original peoples were able to see herds of antelope, and of native bison, so multitudinous that it took hours for a running herd to pass. There grew the native prairie grasses that sustained them, such as the Big Bluestem, Little Bluestem, and Indian Coneflower used by the indigenous peoples for medicinal purposes, and only recently found to be of medicinal use to the descendants of the descendants of the first Europeans. One of the stunning sights that these newcomers recorded in their arrival to the center of this 'New World' was the effect of the wind on the seas of prairie grasses, since replaced by corn and soybeans, which moved like 'waves of the sea'—seemingly endlessly abundant then, but since almost become extinct. Where had lived the peoples whose names themselves had the music of the prairies associated with them—the 'Illinois', 'Sioux', 'Ojibway', 'Menominee', 'Pawnee', 'Mesquakie' ... —were Katherine Lee Bates's (author of the song 'America the Beautiful') 'amber waves of grain', each stem coherently moving in concert with millions of others to produce the effect of being on an immense ocean, through which sailed the 'prairie schooner covered wagons' of those seeking more living room.

Now consider that sight, so vast and continuous that it drove some of the early invaders to madness with time. Here were countless billions of single, almost identical stems, enough to be called by Gibbs an 'ensemble' of those elegantly beautiful flora. The effect of waves of an ocean was produced by these two-meter high plants waving in phase with each other under the excitation of a wind, with wavelength long compared with the separation between the individual stems, and powerful enough to cause millions of them to move in concert so they appear to be a single body. In this example, we are given some hint of what the word 'coherence' can mean: the movement, in phase, in both time and space, of an ensemble of identical systems, such that vast portions of them can be detected being in a state which describes a macroscopic entity.

In magnetic resonance, we produce a coherence in phase among individual spins in an ensemble by excitation with a radiofrequency having a wavelength enormous compared with the separation between individual nuclear spins. We generally detect such coherence of an ensemble of spins waving in the static field of our magnet via the voltage induced by a sufficiently large number in an inductor such that a signal is detectable above the Johnson noise (but see ***Optically Enhanced Magnetic Resonance***). Since the inductor is a dipole producer, and a dipole detector, i.e., a detector of coherence associated with transitions between states differing in spin quantum number by a single quantum, we can only directly detect *single* quantum coherence ($\Delta k = 1$) of such an ensemble.

In the present discussion, we want to elucidate the meaning of multiple quantum coherence in the special case of dipolar coupled spin-$\frac{1}{2}$ systems, and to illustrate how the experiment is accomplished to produce and detect such a phenomenon. To do so, it is necessary to first amplify the meaning of 'coherence'. Then we shall proceed to discuss the production of multiple quantum coherence, and finally the means used for detection. To begin, we use the familiar example of the ideas behind the development and detection of single quantum coherence in spin-$\frac{1}{2}$ systems. Then the concepts used to produce *multiple* quantum coherence ($\Delta k \geq 2$) in ensembles of dipolar coupled spin-$\frac{1}{2}$ systems are developed. Thought experiments are used to illustrate conversion of populations ($\Delta k = 0$) into multiple quantum coherence with the use of coherent averaging to produce a multiple quantum propagator (quite a lovely introduction to the subject of propagators in quantum mechanics is given by Mattuck[1]). Propagators that develop multiple quantum coherence in steps of single and double quanta are discussed and illustrated. Experimental details concerning the manipulations necessary to perform the experiments are given. Experimental results using a single quantum propagator are shown for adamantane, and for a liquid crystal containing isolated clusters of 21 protons. The aim of this work is to present, in an easily understandable manner, and perhaps with a fresh perspective, the ideas behind the creation and detection of multiple quantum coherence in ensembles of homonuclear dipolar coupled spin-$\frac{1}{2}$ systems. To this end, both theoretical ideas and experimental details will be presented so that readers will have the background to perform such experiments on their own instruments, given the appropriate phase shifting capabilities.

Before beginning to discuss the specifics of coherence, and its production and detection, we note that spin counting by multiple quantum coherence is one of a variety of possible two-dimensional NMR experiments[2–4] that first began to appear in the mid 1970s and have since been extensively reviewed.[5–9] In the specific case of using multiple quantum coherence (MQC) to enumerate numbers of strongly coupled spins in ensembles of coupled clusters of protons in solids,[10,11] the initial work developed multiple quantum coherence in steps of two quanta, such that values of MQC, k, of 0, 2, 4, 6, ... , or (depending on the state of the system prepared before the use of multiple pulse techniques to produce MQC) 1, 3, 5, ... , might be detected. Later work (see below) resulted in the use of pulse sequences that developed MQC in steps of one quantum, such that values of $k = 0, 1, 2, \ldots$ could be detected.

In liquids, the coupling mechanism used to produce multiple quantum coherence is the two-body scalar or J coupling. The secular portion of the spin space part of this interaction is $\hat{I}_z\hat{S}_z$ for the heteronuclear case. In solids, the case to be discussed here, the interaction is the two-body homonuclear dipolar coupling between spin-$\frac{1}{2}$ systems, e.g., among protons in a solid. The secular portion of the 'spin space' part of this interaction is $\hat{\boldsymbol{I}}_1\cdot\hat{\boldsymbol{I}}_2 - 3\hat{I}_{z1}\hat{I}_{z2}$. The pulse sequences used to develop MQC in the latter case will therefore differ from those used for the former, in the same sense that the dipolar echo sequence (τ, $90_x{}^\circ$, τ, $90_y{}^\circ$, τ) (see ***CRAMPS***) differs from the spin echo sequence (τ, $180_x{}^\circ$, τ) (see ***Echoes in Solids***). However, the extension of the present description to heteronuclear dipolar coupling and to scalar coupling should be obvious, with the techniques used to generate and detect MQC being more easily achieved than in the present case.

2 SINGLE QUANTUM COHERENCE

We first ask: 'What do we observe in an NMR experiment?' The answer is always a transverse component of spin angular momentum. With phase detection along y in the rotating frame, what is observed is

$$\text{FID} \sim \langle \hat{I}_y(t)\rangle = \text{Tr}\{\hat{\rho}(t)\hat{I}_y\} \tag{1}$$

From this formalism, it is immediately obvious that we are invoking the use of the quantum statistical method, in that the density operator $\hat{\rho}$ must be used to describe the phenomena discussed here.[12] Statistical thermodynamics enters when we consider that the ensemble in question is prepared in some equilibrium state before observation, i.e., we expose an ensemble of nuclear spins I in a field until equilibrium is achieved under the Zeeman interaction $\hat{\mathcal{H}}$, and

$$\hat{\rho}(0) \equiv \hat{\rho}^{\text{equilibrium}} = \frac{1}{Z}\exp\left(-\frac{\hat{\mathcal{H}}}{k_\text{B}T}\right) \sim \sum_k \hat{I}_{zk}$$
$$k = 1, 2, \ldots \tag{2}$$

is the operator form of $\hat{\rho}$. Z is the ensemble partition function and k_B Boltzmann's constant.

The FID, whose time dependence is given by $\hat{\rho}(t)$, and whose phase is specified in this case by the operator $\hat{I}_y$, is driven by the presence of time-independent Hamiltonians $\hat{\mathcal{H}}$ as follows:

$$\hat{\rho}(t) = \exp(-\text{i}\hat{\mathcal{H}}t)\,\hat{\rho}(0)\exp(\text{i}\hat{\mathcal{H}}t) \tag{3}$$

The spectrum is obtained by Fourier transformation of the FID. We remind ourselves of the quantum mechanics involved in this statement with a short review.

We consider an ensemble of weakly interacting identical systems, each described by a set of single particle stationary states $|m_a\rangle$, which are eigenstates of the z component of nuclear spin angular momentum such that $\hat{I}_z|m_a\rangle = a|m_a\rangle$. These identical systems for purposes of the present discussion might be 'isolated' nuclear spins (e.g., ^{13}C nuclei at a natural abundance of 1.1% decoupled from other nuclei via strong rf decoupling), or isolated pairs of nuclear spins (e.g., pairs of protons in partially hydrated calcium sulfate, $CaSO_4{\cdot}xH_2O$, with $x < 2$), or many (of order 10^{23}) protons in strongly dipolar coupled solids. If a system consists of more than a single spin-$\frac{1}{2}$ nucleus then the stationary states describing the system can be arranged into linear combinations of products of single particle states, which we denote by $|M_a\rangle$, which are eigenfunctions of the square of the total spin angular momentum operator, $\hat{I}^2$, and of the z component of the angular momentum, $\hat{I}_z$.

Two of these many body states, $|M_a\rangle$, $|M_b\rangle$, differ by $k = a - b$ in the z component of the angular momentum. Further, the state of each system can in general be a time-dependent superposition of these stationary states:

$$|\Psi(t)\rangle = \sum_j c_j(t)|M_j\rangle \tag{4}$$

where the phase factor of the jth stationary state, $\text{e}^{\text{i}\phi_j}$ has been implicitly included in the time-dependent amplitude $c_j(t)$.

For example, in ensembles that consist of coupled pairs of spin-$\frac{1}{2}$ nuclei, each with stationary states α and β, where the coupling interaction is small compared with the Zeeman interaction, the normalized stationary states of the coupled systems, which can be arranged to be eigenfunctions of the square of the total spin operator, $\hat{I}^2$, and of the z component of spin, $\hat{I}_z$, are $|\alpha(1)\rangle|\alpha(2)\rangle$, $\sqrt{\frac{1}{2}}[|\alpha(1)\rangle|\beta(2)\rangle \pm |\beta(1)\rangle|\alpha(2)\rangle]$ and $|\beta(1)\rangle|\beta(2)\rangle$, which are the four two-particle functions describing the triplet and singlet spin states. Two coupled spins can have maximum total spin quantum number $I = 1$, and z component $-I < \langle\hat{I}_z\rangle < I$ in steps of unity. Three coupled spins can have maximum total spin quantum number $I = \frac{3}{2}$, etc.

We remember that the statistical probability of finding any system in stationary state $|M_s\rangle$ is

$$P_s = \overline{c_s^*(t)c_s(t)} = \overline{c_s(t)c_s^*(t)} \tag{5}$$

where the overbars mean an ensemble average. The operator $\hat{\rho}$ is defined by the ensemble average of the product $\hat{\rho} = |\psi\rangle\langle\psi|$ such that the i,jth matrix element is

$$\rho_{kj} = \overline{\langle k|\Psi\rangle\langle\Psi|\ j\rangle} = \overline{c_k c_j^*} \tag{6}$$

A nonvanishing value of ρ_{ss} therefore represents a population of the state $|M_s\rangle$. An observable signal in NMR means a nonvanishing value of $\rho_{s,s+1}$. This means that in the ensemble of systems being observed, there is a *phase coherence* associated with system states $|M_s\rangle$ and $|M_{s+1}\rangle$. We designate this a single quantum coherence. This is to say that we observe a decaying oscillation resulting from an ensemble in which the time-dependent state responsible for the behavior of each system is a superposition of two states differing from each other by a single quantum, *and having the same phase*. What does this mean? With the basis set for a spin-$\frac{1}{2}$ system being $|\alpha\rangle$ and $|\beta\rangle$, and for the kth basis state $|k\rangle$, the amplitude factor being $C_k = |C_k|\text{e}^{\text{i}\phi_k}$, an individual spin-$\frac{1}{2}$ system will have single particle wavefunction $|\psi\rangle = |C_\alpha|\text{e}^{\text{i}\gamma}|\alpha\rangle + |C_\beta|\text{e}^{\text{i}\phi}|\beta\rangle$. Here γ and ϕ are the phases of the single particle basis set functions, and the C_k will in general be time-dependent. A

very special kth single particle wavefunction in which the phase δ_k on the two basis functions is the same,

$$|\psi_k\rangle = e^{i\delta_k}\sqrt{\tfrac{1}{2}}(|\alpha_k\rangle + i|\beta_k\rangle) \tag{7}$$

is a *phase coherent superposition* of the two states that differ by $k = 1$ in the z component of the angular momentum. This system can be prepared by starting at time equal to zero with a single particle wavefunction $e^{i\delta_k}|\alpha\rangle$, and turning on an rf pulse, *operating on a timescale short compared with any dephasing tendency of the ensemble*, which rotates the z magnetization associated with the state $|\alpha\rangle$ by 90°, and converts it into the transverse magnetization described by the above superposition. *For this special combination*, $\langle\psi_k|\hat{I}_{yk}|\psi_k\rangle = \frac{1}{2}$. In an ensemble of spin-$\frac{1}{2}$ noninteracting systems represented by such a phase coherent superposition, $|\psi_{tot}\rangle = \Pi_k|\psi_k\rangle$, and for such an ensemble we find the ensemble average to be

$$\begin{aligned}\langle\hat{I}_y\rangle &= \langle\psi|\hat{I}_y|\psi\rangle \\ &= \frac{1}{N}\prod_k e^{-i\delta_k}\sqrt{\tfrac{1}{2}}(\langle\alpha_k| - i\langle\beta_k|)\Big(\sum_{k'}\hat{I}_{yk'}\Big)e^{i\delta_k} \\ &\quad\times\sqrt{\tfrac{1}{2}}(|\alpha_k\rangle + i|\beta_k\rangle) \\ &= \tfrac{1}{2}\end{aligned} \tag{8}$$

because the phase factors cancel! Another way of saying this is that

$$\rho_{\alpha\beta} = \frac{1}{N}\sum_k |C_{\alpha k}|e^{i\gamma_k}|C_{\beta k}|e^{i\phi_k} \equiv \overline{C_\alpha C_\beta} \neq 0 \tag{9}$$

Note that, in general, if γ and ϕ are not zero then the above sum is a superposition of sines and cosines that will average to zero—the random phase case.

The creation of multiple quantum coherence is equivalent to causing ρ to evolve in such a manner that $\rho_{rs} \neq 0$, and in the following discussion, we shall see how this inequality is achieved.

3 COHERENT AVERAGING

We next remind ourselves of the results of coherent averaging theory as applied to the spin portion of internal Hamiltonians.[13] We first note that a nuclear spin Hamiltonian may, in general, be expressed as the product of a constant characteristic of the interaction in question, and of 'spin space' operators. For example, for the heteronuclear dipolar interaction between spins $\hat{\boldsymbol{I}}$ and $\hat{\boldsymbol{S}}$, the constant is $\gamma_I\gamma_S/r_{IS}^3$, the 'real space' portion is $1 - 3\cos^2\theta$, and the 'spin space' portion is $\hat{I}_z\hat{S}_z$. It is assumed that the real space portions of the internal Hamiltonians are constant in the experiments under consideration, i.e., there is no molecular motion or experimenter-supplied sample spinning.

When we manipulate $\hat{\mathcal{H}}_{int}$ by rf pulse sequences that are cyclic [the ensemble is returned to its initial state after a cycle of rf pulses, meaning that the propagator $\hat{U}_{rf}(t_c,0)$ associated with the pulse train from time zero to time t_c is unity at cycle times t_c (and integer multiples of these times)] and periodic, the leading term in the result, observed at cycle times nt_c is

$$\hat{\rho}(nt_c) = \exp(-i\tilde{\hat{\mathcal{H}}}^{(0)}nt_c)\hat{\rho}(0)\exp(i\tilde{\hat{\mathcal{H}}}^{(0)}nt_c) \tag{10}$$

where $\tilde{\hat{\mathcal{H}}}^{(0)}$ is the time average of a static internal Hamiltonian made time-dependent by the rf pulses:

$$\tilde{\hat{\mathcal{H}}}^{(0)}_{int} = \frac{1}{t_c}\int_0^{t_c} dt\,\hat{\tilde{\mathcal{H}}}_{int}(t) \tag{11}$$

$\hat{\tilde{\mathcal{H}}}_{int}(t)$ is the instantaneous value of the internal Hamiltonian as determined by the rf pulses:

$$\hat{\tilde{\mathcal{H}}}_{int}(t) = \hat{U}^{\dagger}_{rf}(t,0)\hat{\mathcal{H}}_{int}\hat{U}_{rf}(t,0) \tag{12}$$

$\hat{U}_{rf}(t,0)$ is the propagation operator due to the rf pulses from time zero to time t. For n time intervals δ_1, followed by δ_2, followed by $\ldots$, δ_n, $\hat{U}_{rf}$ may be expressed as the product

$$\hat{U}_{rf}(t,0) = \hat{U}_{rf}(\delta_n)\cdots\hat{U}_{rf}(\delta_1) \tag{13}$$

whereby

$$\hat{U}^{-1}_{rf}(t,0) = \hat{U}^{-1}_{rf}(\delta_1)\cdots\hat{U}^{-1}_{rf}(\delta_n) \tag{14}$$

Equation (12) can always be expressed as a product of rotations in spin space acting on components of angular momentum operators. For example, if the rf pulse sequence $(\tau, 180_{y^\circ}, \tau)$ with perfect delta function rf pulses produces $\hat{U}_{rf}$, then at times $0 \le t \le \tau$, when the rf Hamiltonian is zero, $U_{rf}(t,0)$ takes the form $e^0 = 1$, and in this time interval, $\hat{\tilde{I}}_z = e^0\hat{I}_z e^0 = 1\cdot\hat{I}_z\cdot 1$, which we may formally identify as a rotation $\hat{R}$ of unity, performed on $\hat{I}_z$, symbolized by $\hat{R}\hat{I}_z = 1\cdot\hat{I}_z$. At time $t = \tau$, the rf Hamiltonian corresponds to an infinitely sharp 180° rotation about the y axis. $\hat{U}_{rf}(t = \tau) = \exp(i\pi\hat{I}_y)$, and the physical result is a 180_{y° rotation $\hat{R}_{180y}$. For $\tau < t < 2\tau$, the rf again is zero, and $\hat{U}_{rf}$ is unity. Under this sequence, therefore, with the spin portion of $\hat{\mathcal{H}}_{int}$ being proportional to $\hat{I}_z$, keeping in mind the time ordering dictated by equations (12) and (14), we find

$$0 \le t < \tau: \quad \hat{\tilde{I}}_z = 1\cdot\hat{I}_z = \hat{I}_z \tag{15a}$$

$$t = \tau: \quad \hat{\tilde{I}}_z = 1\cdot\hat{R}_{180y}\hat{I}_z = -\hat{I}_z \tag{15b}$$

$$\tau < t \le 2\tau: \quad \hat{\tilde{I}}_z = 1\cdot\hat{R}_{180y}\cdot 1\cdot\hat{I}_z = -\hat{I}_z \tag{15c}$$

The familiar result is that at cycle times $2n\tau$, under the spin echo sequence $(\tau, 180^\circ, \tau)^n$, chemical shifts and field inhomogeneities, with spin operators $\hat{I}_{zk}$, vanish (but other interactions, such as homonuclear dipolar coupling, do not). This is to say that at cycle times $2n\tau$, with the internal Hamiltonian being proportional to $\hat{I}_z$, that $\tilde{\hat{\mathcal{H}}}^{(0)}_{int}$ is zero, i.e.,

$$\begin{aligned}\tilde{\hat{\mathcal{H}}}^{(0)}_{cs} &\sim \int_0^{2n\tau} dt\,\hat{U}^{-1}_{rf}(t)\hat{\tilde{\mathcal{H}}}_{cs}\hat{U}_{rf}(t) \\ &= \omega_{cs}[\hat{I}_z\tau + (-\hat{I}_z)\tau] = 0\end{aligned} \tag{16}$$

where ω_{cs} is a product of a constant and the real space portion of the chemical shift Hamiltonian.

Another, perhaps less familiar, result is that under homonuclear dipolar decoupling sequences [τ, $90_{x}{}^{\circ}$, τ, $90_{y}{}^{\circ}$, τ], homonuclear dipolar terms vanish, but chemical shifts are scaled. Consider the dipolar echo sequence [τ, $90_{x}{}^{\circ}$, τ, $90_{y}{}^{\circ}$, 2τ, $90_{y}{}^{\circ}$, τ, $90_{x}{}^{\circ}$, τ]. Using equations (12)–(14), we find for ideal delta function rf pulses, the following values of $\hat{\tilde{I}}_z(t)$:

$$0 \le t < \tau: \quad \hat{\tilde{I}}_z = 1 \cdot \hat{I}_z = \hat{I}_z \tag{17a}$$

$$t = \tau: \quad \hat{\tilde{I}}_z \to 1 \cdot \hat{R}_{90x}\hat{I}_z = -\hat{I}_y \tag{17b}$$

$$\tau < t < 2\tau: \quad \hat{\tilde{I}}_z = 1 \cdot \hat{R}_{90x} \cdot 1\hat{I}_z = -\hat{I}_y \tag{17c}$$

$$t = 2\tau: \quad \hat{\tilde{I}}_z \to 1 \cdot \hat{R}_{90x} \cdot 1 \cdot \hat{R}_{90y}\hat{I}_z = -\hat{I}_x \tag{17d}$$

etc., from which we may immediately infer that, the scalar product $\hat{\boldsymbol{I}}_1 \cdot \hat{\boldsymbol{I}}_2$ being invariant to rotation, the time dependence of the operator $\hat{\tilde{\mathcal{H}}}_{zz} = (\hat{\boldsymbol{I}}_1 \cdot \hat{\boldsymbol{I}}_2 - 3\hat{I}_{z1} < \hat{I}_{z2})$ is as follows:

$$0 \le t < \tau: \quad \hat{\tilde{\mathcal{H}}}_{zz} = \hat{\mathcal{H}}_{tt} \tag{17e}$$

$$t = \tau: \quad \hat{I}_{z1}\hat{I}_{z2} \to \hat{I}_{y1}\hat{I}_{y2}, \quad \text{so} \quad \hat{\tilde{\mathcal{H}}}_{zz} \to \hat{\mathcal{H}}_{yy} \tag{17f}$$

etc. Then the two-body average homonuclear dipolar Hamiltonian is

$$\begin{aligned}\hat{\tilde{\mathcal{H}}}_{\mathrm{DII}}^{(0)} = \frac{\omega_{\mathrm{D}}}{6\tau}[&\tau(\hat{\boldsymbol{I}}_1 \cdot \hat{\boldsymbol{I}}_2 - 3\hat{I}_{z1}\hat{I}_{z2}) + \tau(\hat{\boldsymbol{I}}_1 \cdot \hat{\boldsymbol{I}}_2 - 3\hat{I}_{y1}\hat{I}_{y2}) \\ &+2\tau(\hat{\boldsymbol{I}}_1 \cdot \hat{\boldsymbol{I}}_2 - 3\hat{I}_{x1}\hat{I}_{x2}) + \tau(\hat{\boldsymbol{I}}_1 \cdot \hat{\boldsymbol{I}}_2 - 3\hat{I}_{y1}\hat{I}_{y2}) \\ &+\tau(\boldsymbol{I}_1 \cdot \boldsymbol{I}_2 - 3I_{z1}I_{z2})] \\ \equiv \tfrac{1}{3}\omega_{\mathrm{D}}&(\hat{\mathcal{H}}_{zz} + \hat{\mathcal{H}}_{yy} + \hat{\mathcal{H}}_{xx}) = 0\end{aligned} \tag{18}$$

where ω_{D} is a product of a constant and the real space portion of the space–spin product dipolar Hamiltonian.

An important result just seen is that the sum

$$(\hat{\mathcal{H}}_{xx} + \hat{\mathcal{H}}_{yy} + \hat{\mathcal{H}}_{zz})\tau = \sum_k \hat{\mathcal{H}}_{kk} = 0 \tag{19}$$

for two spins $\boldsymbol{I}_1$ and $\boldsymbol{I}_2$. *In both of the above cases*, the average Hamiltonian for a specific interaction is made to vanish, leaving remaining interactions to be observed. *However*, it is possible to manipulate certain internal interactions such that the average Hamiltonian is not zero, but something else that we want.

4 DEVELOPMENT OF MULTIPLE QUANTUM COHERENCE: USE OF A DOUBLE QUANTUM PROPAGATOR

What do we want as an average Hamiltonian in order to develop multiple quantum coherence? The answer is an average Hamiltonian that allows the density operator at zero time $\hat{\rho}(0)$ to evolve in such a manner that $\hat{\rho}_{1,1\pm k} \neq 0$, where k is the order of the multiple quantum coherence.

The process, then, is to manipulate some internal Hamiltonian with cyclic, periodic rf pulses such that at cycle times nt_{c}, we have an average Hamiltonian that allows a zero-time equilibrium density operator,

$$\hat{\rho}(0) \equiv \hat{\rho}_{\mathrm{eq}} \sim \sum_i \hat{I}_{zi}, \quad i = 1, 2, \ldots \tag{20}$$

containing only diagonal terms representing populations in the Zeeman basis set, to develop MQC, i.e., to develop in such a manner that $\hat{\rho}_{i,i\pm k} \neq 0$, for $1 \le k < \infty$. Since we can only detect single quantum coherence (SQC) with NMR, we note in advance that once produced, the MQC must be reduced to SQC *in a manner* that *reflects the* MQC *therein contained* in order to be detected.

Examples of terms in the density operator that exhibit SQC might be single spin terms $\hat{I}_i^+$ and $\hat{I}_i^-$, or two-spin products of the form $\hat{I}_1^+\hat{I}_{z2}$. Double quantum coherence is represented by two-spin product terms in the density operator such as $\sum_{ij}(\hat{I}_i^+\hat{I}_j^+ + \hat{I}_i^-\hat{I}_j^-)$. Triple quantum coherence would be represented by three-spin products such as $\hat{I}_j^+\hat{I}_k^+\hat{I}_m^+$.

We can understand how this process works by example. An ensemble of spin-$\frac{1}{2}$ systems (e.g., protons in solid adamantane) is allowed to come to equilibrium in a static field for a time that is long compared with T_1. Then

$$\hat{\rho}(0) \sim \sum_i \hat{I}_{zi} \tag{21}$$

The sum is over all spins in the sample. Under the influence of an average Hamiltonian, produced by coherent averaging in spin space, as discussed for the cases of the spin echo and the dipolar echo, this ensemble is allowed to evolve over time. The formal time evolution formula may be expressed in terms of the product

$$f(\hat{A}, \hat{B}) = \mathrm{e}^{\hat{A}}\hat{B}\,\mathrm{e}^{-\hat{A}} \tag{22}$$

where $\hat{A}$ and $\hat{B}$ are operators.

It may be shown (equation (4.19) in Gerstein and Dybowski[13]) that an equivalent form of this product is

$$\begin{aligned}\mathrm{e}^{\hat{A}} - \hat{B}\,\mathrm{e}^{-\hat{A}} = \hat{B} + [\hat{A}, \hat{B}] + [\hat{A}, [\hat{A}, \hat{B}]]/2! \\ +[\hat{A}, [\hat{A}, [\hat{A}, \hat{B}]]]/3! + \ldots\end{aligned} \tag{23}$$

i.e.,

$$\hat{\rho}(nt_{\mathrm{c}}) \sim \exp(-\mathrm{i}\hat{\tilde{\mathcal{H}}}nt_{\mathrm{c}}) \sum_i \hat{I}_{zi} \exp(\mathrm{i}\hat{\tilde{\mathcal{H}}}nt_{\mathrm{c}}) \tag{24}$$

and

$$\begin{aligned}\rho(nt_{\mathrm{c}}) = \sum_i \hat{I}_{zi} + \left[-\mathrm{i}nt_{\mathrm{c}}\hat{\tilde{\mathcal{H}}}, \sum_i \hat{I}_{zi} \right] \\ +\left[-\mathrm{i}nt_{\mathrm{c}}\hat{\tilde{\mathcal{H}}}, \left[-\mathrm{i}nt_{\mathrm{c}}\hat{\tilde{\mathcal{H}}}, \sum_i \hat{I}_{zi} \right] \right] \Big/ 2! + \cdots\end{aligned} \tag{25}$$

The leading term $\sum_i \hat{I}_{zi}$ represents populations. The following terms must then be arranged so as to evolve single and higher quantum coherences.

In order to understand how to choose an average Hamiltonian that will produce multiple quantum coherence in the time-developed density operator $\hat{\rho}(t)$ as given by equation (25), it is necessary to look at the commutation rules for angular momentum operators. We know that

$$[\hat{I}_{k1}, \hat{I}_{k2}] = [\hat{I}_{k1}, \hat{I}_{k1}] = 0, \quad k = x, y, z \tag{26a}$$

$$[\hat{I}_z, \hat{I}^{\pm}] = \pm\hat{I}^{\pm} \tag{26b}$$

$$[\hat{I}^{\pm}, \hat{I}^{+}] = \pm 2\hat{I}_z \tag{26c}$$

$$[\hat{I}^{\pm}, \hat{I}^{\pm}] = 0 \tag{26d}$$

Given the form of $\hat{\rho}_{\mathrm{eq}} \equiv \hat{\rho}(0) \sim \sum_i \hat{I}_{zi}$, equations (24) and (26a)–(26d) immediately tell us that we want $\tilde{\hat{\mathcal{H}}}$ to contain terms such as $\hat{I}_i^+$. Since we are using the internal homonuclear dipolar coupling Hamiltonian $\hat{\mathcal{H}}_{zz}$ as that which is to be manipulated in order to develop the multiple quantum coherence according to equation (27), we realize that we shall always be dealing with products between spins 1 and 2 containing terms such as $\hat{I}_{m1}\hat{I}_{m2}$, with $m = x, y, z$.

To begin to think about how rotations in spin space affect the two-body homonuclear dipolar Hamiltonian $\hat{\mathcal{H}}_{zz}$, it is useful to remember[13] that the effect of a rotation of the mth component of angular momentum, $\hat{I}_m$ by the operation

$$\begin{aligned}\hat{R}_j(\theta)\hat{I}_m &= \exp(\mathrm{i}\theta\hat{I}_j)\hat{I}_m \exp(-\mathrm{i}\theta\hat{I}_j) \\ &= \hat{I}_m \cos(\theta\epsilon_{jmp}) - \hat{I}_p \sin(\theta\epsilon_{jmp})\end{aligned} \tag{27}$$

where ϵ_{jmp} is zero if any two of j, m, and p are the same, unity if j, m, and p represent some cyclic order of x, y, and z, and -1 if the order is anticyclic. Then a result found after some algebra is that a rotation of the two-body Hamiltonian for spins 1 and 2, $\hat{\mathcal{H}}_{zz}$, by ξ about the y axis, followed by a rotation by ϕ about the z axis, yields

$$\begin{aligned}\hat{R}_z(\phi)\hat{R}_y(\xi)\hat{\mathcal{H}}_{zz} = {} & \tfrac{1}{2}\omega_{\mathrm{D}}(3\cos^2\xi - 1)\hat{\mathcal{H}}_{zz} \\ & -\tfrac{3}{2}\omega_{\mathrm{D}}(\hat{I}_{z1}\hat{I}_2^+ + \hat{I}_1^+\hat{I}_{z2})\mathrm{e}^{-\mathrm{i}\phi}\sin\xi\cos\xi \\ & +\tfrac{3}{2}\omega_{\mathrm{D}}(\hat{I}_1^+\hat{I}_2^+\mathrm{e}^{2\mathrm{i}\phi} + \hat{I}_1^-\hat{I}_2^-\mathrm{e}^{-2\mathrm{i}\phi}) \\ & \times \sin^2\xi\end{aligned} \tag{28}$$

The interesting result shown by equation (28) is that a general rotation of $\hat{\mathcal{H}}_{zz}$ in spin space yields a propagator (the exponential of the rotated Hamiltonian) containing populations ($\hat{\mathcal{H}}_{zz}$), single quantum terms ($\hat{I}_1^{\pm}\hat{I}_{z2}$) and double quantum terms ($\hat{I}_1^{\pm}\hat{I}_2^{\pm}$). As a special case of this result, we illustrate the formation of a two-quantum propagator under a particularly simple periodic and cyclic sequence.[11] This is the sequence (τ, 90°_x 4τ, $90^\circ_{\bar{x}}$, τ), which we shall denote by x, $\bar{x}$. We assume ideal delta function pulses. Under this sequence, the operator $\tilde{\hat{I}}_z(t)$ is as follows:

$$0 \le t < \tau: \quad \tilde{\hat{I}}_z = 1 \cdot \hat{I}_z = \hat{I}_z \tag{29a}$$

$$t = \tau: \quad \tilde{\hat{I}}_z = \hat{R}_{90x}\hat{I}_z = -\hat{I}_y \tag{29b}$$

$$\tau < t < 5\tau: \quad \tilde{\hat{I}}_z = -\hat{I}_y \tag{29c}$$

$$t = 5\tau: \quad \tilde{\hat{I}}_z = \hat{R}_{90x} \cdot 1 \cdot \hat{R}_{90x}\hat{I}_z = \hat{I}_z \tag{29d}$$

$$5\tau < t \le 6\tau: \quad \tilde{\hat{I}}_z = \hat{I}_z \tag{29e}$$

Then, for example, in the time interval $0 \le t < \tau$, $\tilde{\hat{\mathcal{H}}}_{zz} = \hat{\mathcal{H}}_{zz}$ [see equation (12)]. From an observation of the values of $\tilde{\hat{I}}_z(t)$, and the recognition that $\hat{\mathcal{H}}_{kk}$ contains the product $\tilde{\hat{I}}_k\tilde{\hat{I}}_k$ with $k = x, y, z$, it is possible to infer the values of $\tilde{\hat{\mathcal{H}}}_{zz}(t)$, immediately, and thus to calculate the average Hamiltonian corresponding to $\hat{\mathcal{H}}_{zz}$ to zeroth order:

$$\tilde{\hat{\mathcal{H}}}zz^{(0)} = \frac{1}{6\tau}\int_0^{6\tau} \mathrm{d}t\, \tilde{\hat{\mathcal{H}}}_{zz} = \tfrac{1}{3}(\hat{\mathcal{H}}_{zz} + 2\hat{\mathcal{H}}_{yy}) \tag{30}$$

With the identity $\sum_k \hat{\mathcal{H}}_{kk} = 0$, we find that, under the above sequence,

$$\tilde{\hat{\mathcal{H}}}_{zz}^{(0)} \simeq (\hat{\mathcal{H}}_{xx}\hat{\mathcal{H}}_{yy} + 2\hat{\mathcal{H}}_{yy}) = \hat{\mathcal{H}}_{yy} - \hat{\mathcal{H}}_{xx} \tag{31}$$

The reader will want to verify that under the sequence y, $\bar{y} \equiv (\tau, 90^\circ_y, 4\tau, 90^\circ_{\bar{y}}, \tau)$ the average homonuclear dipolar Hamiltonian is the negative of that found in equation (31), i.e. is proportional to $\hat{\mathcal{H}}_{xx} - \hat{\mathcal{H}}_{yy}$. Thus this sequence can be used to produce an average Hamiltonian that will act to reverse, in time, the effect of the average of the average Hamiltonian $\hat{\mathcal{H}}_{yy} - \hat{\mathcal{H}}_{xx}$ that was used to produce the MQC. As will be seen, this reconversion is performed in such a manner that the information content associated with the MQC is not lost. The means of doing so (see below) is to phase-shift the two quantum excitation sequence x, $\bar{x}$ with respect to the two quantum reconversion sequence y, $\bar{y}$ in steps of $2\pi/k_{\max}$, where $k_{\max}$ is the highest order of MQC to be observed.

With $\hat{I}^{\pm} = \hat{I}_x \pm \mathrm{i}\hat{I}_y$, we find that the average two-body homonuclear dipolar Hamiltonian under the two quantum excitation sequence x, $\bar{x}$ is proportional to

$$\hat{I}_1^+\hat{I}_2^+ + \hat{I}_1^-\hat{I}_2^- \tag{32}$$

for the pair of spins $\boldsymbol{I}_1$ and $\boldsymbol{I}_2$.

Now consider how this sequence can be used to develop multiple quantum coherence for an ensemble of *pairs* of dipolar coupled spins $\boldsymbol{I}_1$ and $\boldsymbol{I}_2$. We might anticipate in advance that for this simple case, using a two quantum propagator, all that will be seen are populations, and two quantum coherence. Under this sequence, repeated for n cycle times, $\tau_{\mathrm{c}} = 6\tau$, the time dependence of the density matrix becomes

$$\hat{\rho}(nt_{\mathrm{c}}) = \hat{U}_{2\mathrm{Q}}\hat{\rho}(0)\hat{U}_{2\mathrm{Q}}^{-1} \tag{33}$$

where $\hat{U}_{2\mathrm{Q}}$ is, to zeroth order,

$$\hat{U}_{2\mathrm{Q}} = \exp[-\tfrac{1}{2}\mathrm{i}nt_{\mathrm{c}}\omega_{\mathrm{D}}(\hat{I}_1^+\hat{I}_2^+ + \hat{I}_1^-\hat{I}_2^-)] \tag{34}$$

Then, with $\theta = \frac{1}{2}nt_{\mathrm{c}}\omega_{\mathrm{D}}$, equations (24) and (25) yield

$$\begin{aligned}\hat{\rho}(nt_{\mathrm{c}}) &\simeq \hat{I}_{z1} + \hat{I}_{z2} + \mathrm{i}\theta[\hat{I}_1^+\hat{I}_2^+ + \hat{I}_1^-\hat{I}_2^-, \hat{I}_{z1} + \hat{I}_{z2}] \\ &\quad + (i\theta)^2[\hat{I}_1^+\hat{I}_2^+ + \hat{I}_1^-\hat{I}_2^-, [\hat{I}_1^+\hat{I}_2^+ + \hat{I}_1^-\hat{I}_2^-, \hat{I}_{z1} + \hat{I}_{z2}]]/2! + \ldots \\ &= \hat{I}_{z1} + \hat{I}_{z2} - 2\mathrm{i}\theta(\hat{I}_1^+\hat{I}_2^+ + \hat{I}_1^-\hat{I}_2^-)\end{aligned} \tag{35}$$

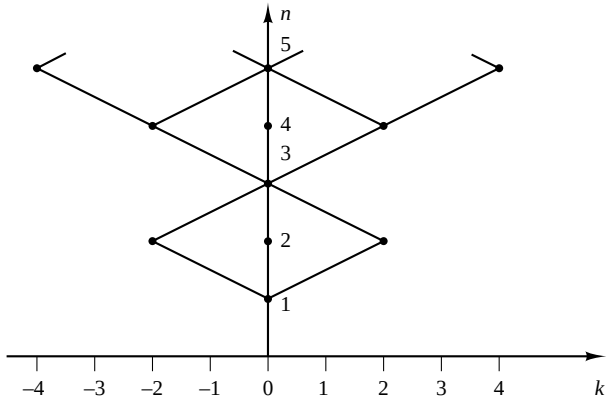

Figure 1 Selection rule for an n-spin operator after excitation with a double quantum propagator. The allowed values are $k = \pm 2, \pm 6, \ldots$, for n even, and $k = 0, \pm 4, \pm 8, \ldots$, for n odd

Only the first two terms in the series represented by equations (24) and (25) are nonzero. The remaining terms vanish. Only populations and double quantum coherence remains. At values of θ near zero, i.e., at times nt_c that are small compared with the inverse of the dipolar linewidth ω_D^{-1}, there exist only populations. As nt_c becomes of the order of the dipolar linewidth, two quantum coherence makes its appearance. No more than two quantum coherence is ever seen, regardless of how long the system is allowed to evolve, as one would physically expect from an ensemble consisting of coupled pairs of spins $\frac{1}{2}$. The reader will want to verify that for this representation of $\hat{\rho}(nt_c)$ only the terms ρ_{11}, ρ_{22}, ρ_{33}, ρ_{13}, and ρ_{31} are nonzero within the triplet basis set $|I, I_z\rangle$:

$$|m\rangle = |3\rangle = |1, 1\rangle = |\alpha\alpha\rangle \tag{36a}$$

$$|m-1\rangle = |2\rangle = |1, 0\rangle = \sqrt{\tfrac{1}{2}}|\alpha\beta + \beta\alpha\rangle \tag{36b}$$

$$|m-2\rangle = |1\rangle = |1, -1\rangle = |\beta\beta\rangle \tag{36c}$$

by performing the calculations $\langle m|\hat{\rho}(nt_c)|m-k\rangle$.

The results just calculated for an ensemble of dipolar coupled spin-$\frac{1}{2}$ pairs indicate that, under the propagator $\hat{U}_{2Q}$ developed by the sequence $(\tau, 90^\circ_x, 4\tau, 90^\circ_{\bar{x}}, \tau)$, the selection rules are such that populations and double quantum coherence is observed for an ensemble of pairs of dipolar coupled spins $\frac{1}{2}$. More generally, these selection rules for ensembles of n coupled spins may be exhibited by the diagram shown in Figure 1. This diagram states that, under this sequence, double quantum coherence will be exhibited by ensembles of 2, 4, 6, ... coupled spins, four quantum coherence will be exhibited by ensembles of 5, 7, 9, ... coupled spins, etc.

5 DETECTION OF MULTIPLE QUANTUM COHERENCE

We must now consider more closely what was meant by the past statement that the MQC, once produced, must be transferred to SQC in a manner that reflects the MQC previously produced. As a thought experiment to begin the process, recall the inversion–recovery experiment for measuring T_1. In this case, the system is prepared in a state of nonequilibrium populations by an inverting 180° pulse. After a time τ, during which the system is allowed to evolve under 'T_1 processes', these populations are converted into SQC using a 90° pulse. The initial intensity of the decay after the 'readout' 90° pulse is used, as a function of τ, to calculate T_1. A similar reasoning applies to detecting MQC. The MQC is developed as a function of multiples of the production sequence cycle time t_c. This development is only observable if it is converted into SQC. During the development, therefore, the MQC is manipulated in such a manner that, when converted back into SQC, the information content of the MQC is contained in the initial intensity of the SQC which is detected.

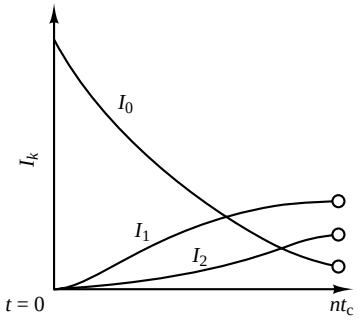

Figure 2 Time evolution of the order of n quantum coherence using a single quantum propagator. The intensity of (I_0) decreases as spin pairs begin to couple to develop the higher order of MQC and build up their intensity (I_1 and I_2)

To form a picture of how this works, it is useful to think about how the different orders of n quantum coherence evolve with time. As indicated in the example in equation (35), the higher orders of MQC develop as $\theta \approx nt_c\omega_{Dij}$ increases for the i,jth pair of spins. Therefore, it seems reasonable that the evolution of, e.g., populations, SQC, and two-quantum coherence (DQC) might look as shown in Figure 2. I_0 represents populations, I_1 the intensity of single quantum coherence, I_2 the intensity of DQC, etc. Initially, one starts with populations. As spin pairs begin to couple to form higher orders of n quantum coherence, there is a net loss in populations, and a build up [in the particular example for which the calculation using equation (35) was made], first of DQC, the second term in the expansion of the evolution of $\hat{\rho}$, and then of higher orders of MQC as time increases. In the example shown in Figure 2, we assume that we are allowed to build MQC in steps of single quanta, and we shall later provide a single quantum propagator $\hat{U}_{1Q}$ that allows this development to be performed.

Given the development of MQC shown in Figure 2, caused by the single quantum propagator U_{1Q}, it is simple to conceive how one reverses the process to convert back to an observable SQC. One simply causes the system to evolve under the propagator $\hat{U}_{1Q}^{-1}$. Since $\hat{U}_{1Q}$ will be of the form $\exp(-i\tilde{\hat{\mathcal{H}}}nt_c)$, with $\tilde{\hat{\mathcal{H}}}$ being an average Hamiltonian created by manipulating the homonuclear dipolar interaction, time reversal is achieved by manipulating the homonuclear dipolar Hamiltonian such that from time nt_c to $2nt_c$ the average Hamiltonian is $-\tilde{\hat{\mathcal{H}}}$. In the case of the two quantum propagator, we have seen that the sequence $(\frac{1}{4}\tau, 90^\circ_x, \tau, 90^\circ_{\bar{x}}, \frac{1}{4}\tau)$ produces the average Hamiltonian proportional to $\hat{\mathcal{H}}_{yy} - \hat{\mathcal{H}}_{xx}$. We have pointed out that the sequence $(\frac{1}{4}\tau, 90^\circ_y, \tau, 90^\circ_{\bar{y}}, \frac{1}{4}\tau)$ results in

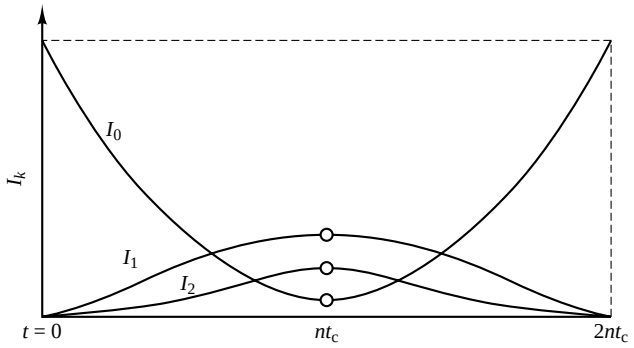

Figure 3 The MQC for higher orders are first created over a time period nt_c, and then collected this MQC back into ZQC at the time $2nt_c$ by using the negative of the average Hamiltonian. Aside from relaxation, the preparation ($0 \leq t < nt_c$) and mixing period ($nt_c \leq t < 2nt_c$) exactly mirror each other. This diagram illustrates the statement of the cyclic properties of $\hat{U}_{rf}$. At the end of $2nt_c$, I_0 ($t = 0$) = $I_0(t = 2nt_c)$

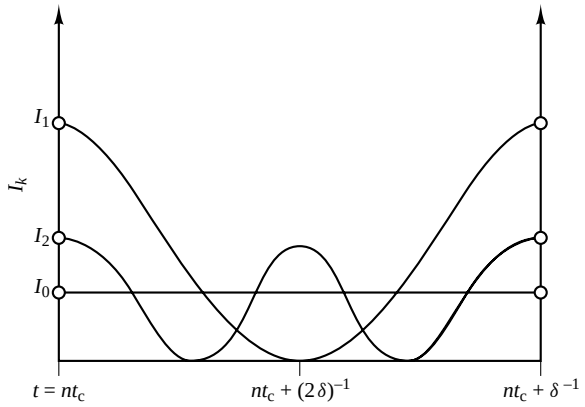

Figure 4 The behavior of ZQC, SQC, and DQC with a frequency offset δ (in Hz), after the preparation period nt_c. The n quantum coherence has the property of the cosine function, $I_n \propto \cos(n\delta/\text{Hz})$. See equation (42)

the average homonuclear dipolar Hamiltonian $\hat{\mathcal{H}}_{xx} - \hat{\mathcal{H}}_{yy} \equiv -(\hat{\mathcal{H}}_{yy} - \hat{\mathcal{H}}_{xx})$. Thus, the application of the sequence

$$(\tfrac{1}{4}\tau, 90^\circ_x, \tau, 90^\circ_x, \tfrac{1}{4}\tau)n, (\tfrac{1}{4}\tau, 90^\circ_y, \tau, 90^\circ_y, \tfrac{1}{4}\tau)n$$

would first create the MQC over a time of n cycle times t_c, and then, by time reversal accomplished by using the negative of the average Hamiltonian during the preparation period, 'collect' this MQC back into zero quantum coherence (ZQC) at time $2nt_c$. The process might be visualized as indicated in Figure 3.

At this point, however, there is no information content in the ZQC shown in Figure 3 at time $2nt_c$ that would be indicative of the MQC created during the times nt_c.

Therefore, as a second thought experiment, dictated by the knowledge that different orders of MQC (see below) oscillate at multiples of the SQC under a frequency offset, let us assume that after the production period nt_c, a frequency offset δ (in Hz) is imposed upon the experiment. Then the behavior of ZQC, SQC, and DQC might appear as indicated in Figure 4. The ZQC does not oscillate under an offset. The SQC will oscillate with period δ^{-1}. The DQC will oscillate with period $(2\delta)^{-1}$, etc.

Now suppose that the evolution time for MQC under the offset δ were set to be $(2\delta)^{-1}$. Then at that time I_1 would be zero, I_0 would retain its value at time $t = nt_c$, and I_2 would have oscillated to its value at time $(2\delta)^{-1}$, the period of its oscillation. Therefore, if the reconversion from nonvanishing off-diagonal elements of the density operator back to populations represented by diagonal elements were initiated at time $nt_c + (2\delta)^{-1}$, in the absence of an offset, the value of I_0 at time $2nt_c + (2\delta)^{-1}$ would contain *no contribution* from the SQC. The SQC monitored as the value of the initial intensity of the FID after a 90° pulse at time $nt_c + (2\delta)^{-1}$ would therefore be lower than that in the absence of an offset. One way of visualizing this result is shown in Figure 5, where different symbols are used to trace the imagined evolution of MQC back into populations after time $nt_c + (2\delta)^{-1}$. The symbol I_n, $n \geq 1$, means the n quantum coherence. The symbol I_n^0 means the contribution of the n quantum coherence developed at time $nt_c + (2\delta)^{-1}$ back into populations. The net

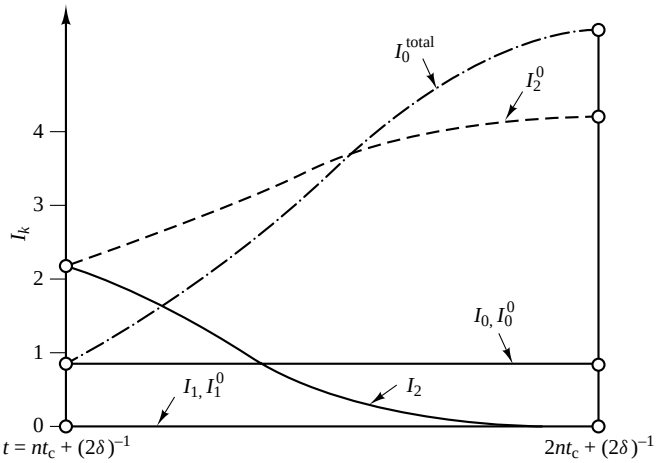

Figure 5 The behavior of the MQC at the evolution time $(2\delta)^{-1}$. $I0/k$ is the development of ZQC with k quantum coherence as its parent

magnetization associated with population differences, observed as the initial intensity of the FID after a 'readout' pulse converting population differences into SQC, is labeled I_0^{tot}. Clearly, I_0^{tot} will oscillate with time under a frequency offset during the evolution period, and this oscillation provides the means of detecting MQC therein contained, as indicated more analytically below.

The scheme of production and reconversion of MQC corresponding to the time development shown in Figure 3, i.e., in the absence of an offset, meaning in the absence of an evolution period, is indicated in Figure 6; a single quantum propagator acts on the ensemble of coupled spins from time zero to time nt_c, and the inverse of that propagator acts for an equal period of time afterwards. The ZQC at time $2nt_c$ is converted into observable SQC by a 90° 'readout' pulse, and is represented by the initial value of the FID. In the absence of irreversibility, the initial amplitude of the FID detected at time $2nt_c$ will be the same as that detected at time zero after a 'readout' 90° pulse. The equality of these two amplitudes, incidentally, is one means of detecting one's ability to perform time reversal effectively, which is a measure of the perfection of the pulse sequences used.

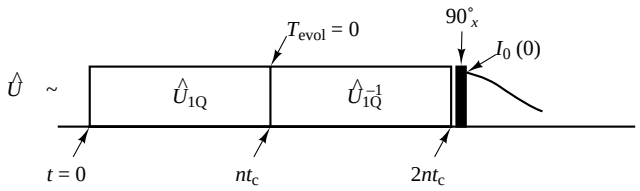

Figure 6 The scheme of a two-dimensional NMR pulse sequence, composed of preparation, evolution, mixing and detection periods, is adapted to develop multiple quantum coherence. The evolution period is set at zero

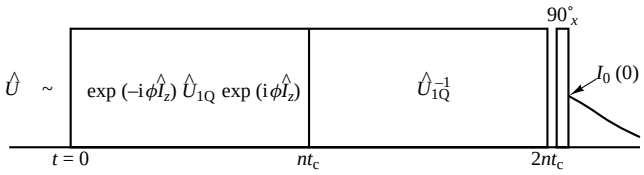

Figure 7 The arrangement of pulse sequence and the way of phase shifting during the multiple quantum experiment. The phases only of the pulses in the preparation period are shifted at the same time with the aid of a digital phase shifter, while the phases of the pulses in the mixing period remain unchanged

The imposition of a frequency offset δ during the evolution period, to detect MQC at the end of the mixing period, is not without its problems. One problem is that there is irreversible time evolution of the ensemble during the evolution period due to T_2 processes. A means of avoiding this problem is to realize that imposition of a phase shift[14] ϕ *during the preparation period* $0 \leq t < nt_c$ is formally equivalent to imposition to a frequency offset, and causes the same oscillations of the various orders of MQC as would be observed under a frequency offset. The effect of a phase increment during the preparation period on the detected signal intensity at the end of the mixing period is now considered. In the absence of an evolution period, the initial intensity of the FID detected at the end of the mixing period $t = 2nt_c$ is

$$\langle \hat{I}_z(t = 2nt_c)\rangle = \mathrm{Tr}\{\hat{\rho}(t = 2nt_c)\hat{I}_z\} \tag{37}$$

But

$$\hat{\rho}(2nt_c) = \hat{U}_{1Q}^{-1}\hat{U}_{1Q}\hat{I}_z\hat{U}_{1Q}^{-1}\hat{U}_{1Q} = \langle \hat{I}_z(t = 0)\rangle \tag{38}$$

in the absence of irreversibility due to imperfections, and interactions other than homonuclear dipolar coupling. Looking more carefully at the combination of equations (37) and (38), and leaving the subscript off the propagators $\hat{U}$ for simplicity, we find that

$$\begin{aligned}
\langle \hat{I}_z(t = 2nt_c)\rangle &= \mathrm{Tr}\{\hat{U}^{-1}\hat{U}\hat{I}_z\hat{U}^{-1}\hat{U}\hat{I}_z\} \\
&= \mathrm{Tr}\{\hat{U}\hat{I}_z\hat{U}^{-1}\hat{U}\hat{I}_z\hat{U}^{-1}\} \\
&= \sum_r \langle r|\hat{U}\hat{I}_z\hat{U}^{-1}\hat{U}\hat{I}_z\hat{U}^{-1}|r\rangle \\
&= \sum_{r,s} \langle r|\hat{U}\hat{I}_z\hat{U}^{-1}|s\rangle\langle s|\hat{U}\hat{I}_z\hat{U}^{-1}|r\rangle \\
&= \sum_{r,s} |\langle r|\hat{U}\hat{I}_z\hat{U}^{-1}|s\rangle|^2
\end{aligned} \tag{39}$$

Equation (39) has an interesting interpretation. The quantity $\hat{U}(nt_c,0)\hat{I}_z\hat{U}^{-1}(nt_c,0)$ measures how much multiple quantum coherence has been developed under the propagator $\hat{U}$. The quantity $\langle r|\hat{U}\hat{I}_z\hat{U}^{-1}|s\rangle$ measures the k quantum coherence, where $k = r - s$, as described earlier, and as will be again illustrated shortly. The term $|\langle r|\hat{U}\hat{I}_z\hat{U}^{-1}|s\rangle|^2$ is the intensity of the k quantum coherence. Thus the quantity detected as the SQC by a proper 'readout' pulse at time $t = 2nt_c$ is the result of producing multiple quantum coherence under a propagator $\hat{U}$ acting for a time $t = nt_c$, and converting this coherence back into populations via the inverse propagator $\hat{U}^{-1}$ during an equal time nt_c.

Now we need to ask: 'What is the effect of a phase change ϕ imposed on all of the pulses during the preparation period, but not on the pulses during the mixing period, at the total evolution time $t = 2nt_c$?' In this experiment, the 'evolution period' identified as the time between the preparation and mixing periods, is zero. A phase change ϕ is effected by physically rotating all excitation pulses during the preparation period by ϕ. This means that a 180°_x pulse, for example, becomes $180^\circ_{x+\phi}$, and a $180^\circ_{\bar{x}}$ pulse becomes $180^\circ_{\bar{x}+\phi}$, etc. The operator form of $\hat{U}$ rotated by ϕ is just $\hat{U}_\phi = \exp(-i\phi)\hat{I}_z\hat{U}\exp(i\phi\hat{I}_z)$. The experimental arrangement is indicated in Figure 7.

The expectation value of $\hat{I}_z$ detected at times $t = 2nt_c$ will be dependent upon ϕ, as follows:

$$\begin{aligned}
\langle \hat{I}_z(\phi, 2nt_c)\rangle &= \mathrm{Tr}\{\hat{U}(2nt_c, 0)\hat{\rho}(0)\hat{U}^{-1}(2nt_c, 0)\hat{I}_z\} \\
&= \mathrm{Tr}\{\hat{U}_{\phi=0}^{-1}(2nt_c, nt_c)\hat{U}_\phi(nt_c, 0)\hat{I}_z\hat{U}_\phi^{-1}(nt_c, 0) \\
&\quad \times \hat{U}_{\phi=0}(2nt_c, nt_c)\hat{I}_z\} \\
&\equiv \mathrm{Tr}\{\hat{U}_0^{-1}\hat{U}_\phi\hat{I}_z\hat{U}_\phi^{-1}\hat{U}_0\hat{I}_z\} \\
&= \sum_{r,s} \langle r|\exp(-i\phi\hat{I}_z)\hat{U}\exp(i\phi\hat{I}_z)\hat{I}_z \\
&\quad \times \exp(-i\phi\hat{I}_z)U^{-1}\exp(i\phi\hat{I}_z)|s\rangle\langle s|\hat{U}\hat{I}_z\hat{U}^{-1}|r\rangle \\
&= \sum_{k=r-s} \mathrm{e}^{-ik\phi}|\langle r|\hat{U}\hat{I}_z\hat{U}^{-1}|s\rangle|^2
\end{aligned} \tag{40}$$

We have noted that the quantity $\hat{U}\hat{I}_z\hat{U}^{-1}$ represents the time development of $\hat{I}_z$ under the propagator $\hat{U}$, in this case a propagator developing MQC. Nonzero values of $\langle r|\hat{U}\hat{I}_z\hat{U}^{-1}|s\rangle$ indicate nonzero values of $r - s = k$ quantum coherence $|\langle r|\hat{U}\hat{I}_z\hat{U}^{-1}|s\rangle|^2$ is the intensity of the k quantum coherence.

The result,

$$\langle \hat{I}_z(\phi, 2nt_c)\rangle = \sum_{k=-\infty}^{\infty} \mathrm{e}^{-ik\phi}|\langle r|U I_z U^{-1}|s\rangle|^2 \tag{41}$$

may be compared with the value of the free precession decay of a system containing an ensemble of spins oscillating with intensities A_n at frequencies ω_n with some phase ϕ_n with respect to the phase of detection, chosen to be y for the present example:

$$G(t) = \langle \hat{I}_y(t)\rangle = \sum_n A_n \cos(\omega_n t + \phi_n) \tag{42}$$

The FT to the frequency domain reveals the frequency content of $G(t)$ which, with appropriate phase correction, becomes the frequency spectrum $G(\omega) = F^{-}G(t)$. By direct analogy, the result (equation (41)) is the superposition in the phase domain $G(\phi)$ of oscillations with intensities $A_k = \langle r|\hat{U}\hat{I}_z\hat{U}^{-1}|s\rangle|^2$, and oscillations in the ϕ domain specified by k:

$$G(\phi) = \sum_k A_k \cos(k\phi + \delta_k) \tag{43}$$

The ϕ dependence is experimentally mapped by incrementing the phase of all pulses during the preparation period by $\Delta\phi$, in a series of m experiments at fixed preparation and mixing periods nt_c, and observing the initial value of the FID following a 90° sampling pulse immediately after $t = 2nt_c$. In practice the signal-to-noise ratio is increased if the entire on-resonant decay is integrated from a period after the receiver has recovered from the overload of the 90° pulse until no further signal is present. For strongly dipolar coupled systems with a properly operating solid state spectrometer operating at, say, 220 MHz for protons, this means a dead time of about 3 μs, and an integration period of less than 1 μs.

The k dependence of $G(\phi)$ is determined from the ϕ FT. Though it is not obvious from the above discussion, $G(\phi)$ is symmetric in k, so only the cosine transform is needed:

$$G(k) = \frac{1}{\sqrt{2\pi}} \int_0^\infty \mathrm{d}\phi\, G(\phi) \cos k\phi \tag{44}$$

Therefore, both positive and negative coherences are detected simultaneously. One need use $k_{\max}$ phase shifts $\delta\phi_i$,

$$0 \leq \delta\phi_i \leq \pi \tag{45}$$

in steps $\Delta\phi = \pi/k_{\max}$ to obtain all of the information necessary for the production of a multiple quantum spectrum $G(k)$ versus k, via Fourier transformation of the oscillatory signal $G(\phi)$ collected from the initial values of the FIDs after the multiple quantum production and collection sequences (i.e., after the preparation and mixing periods). This is to say that to see a multiple quantum spectrum $G(k)$ versus k, with k extending to $k_{\max}$, one carries out $n = k_{\max} + 1$ experiments with phase shifts $\Delta\phi_1 = 0$, $\Delta\phi_2 = \pi/k_{\max}$, $\Delta\phi_3 = 2\pi/k_{\max}$, ... ,$\Delta\phi_n = \pi$. In the absence of irreversibility, the value of $G(\phi)$ versus ϕ is symmetric about $\phi = \pi$. Therefore the values of $G(\phi)$ in the range $\pi < \phi \leq 2\pi$ are obtained from the data in the range $0 \leq \phi \leq \pi$; i.e. $G(2\pi) = G(0)$, $G(2\pi - \pi/k_{\max}) = G(\pi/k_{\max})$, etc. A suitably large number (e.g., 100) of periods of $G(\phi)$ versus ϕ are then stored as an array that can be apodized by the function $e^{-a\phi}$ and Fourier transformed on ϕ to produce the multiple quantum spectrum $G(k)$ versus k. This spectrum will show peaks differing by units of 2 quanta each if a two quantum propagator is used, or in steps of one quantum each if a single quantum (see below) is used.

The selection rules for exciting single quantum coherence are shown in Figure 8. With the system prepared only as polarization ($\boldsymbol{I}_z \neq 0$), two coupled spins ($n = 2$) will contribute single quantum coherence and zero quantum coherence, three coupled spins will contribute zero and double quantum coherence, etc.

An example of experimental data obtained for $G(\phi)$, with $0 \leq \phi \leq 2\pi$, using a single quantum propagator on adamantane,

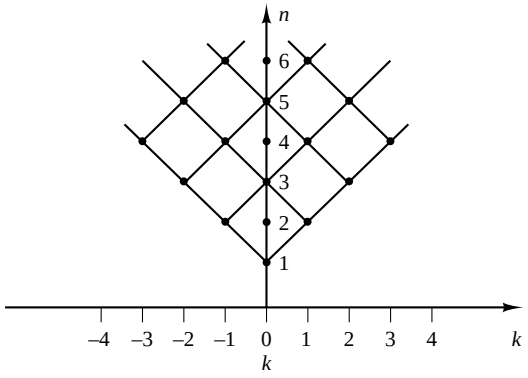

Figure 8 Selection rules for the single quantum propagator used in this work

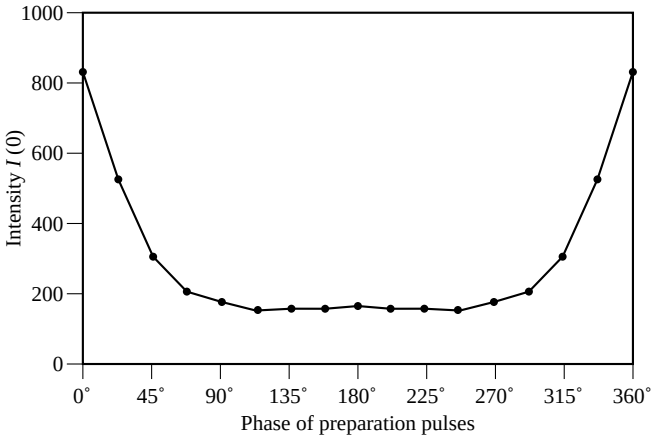

Figure 9 The intensity changes with the phase increment ($\Delta\phi = 22.5°$) of the preparation pulses, plotted in the phase domain (adamantane). The FID of each phase is transformed to frequency domain, and each point on the plot is obtained by integrating the whole spectrum area, normally from −50 kHz to 50 kHz

with phase increments chosen so as to see $k_{\max} = 8$ and with 312 μs of excitation time, is shown in Figure 9. These points repeated 128 times to fit to 2K size, and tapered by an appropriate apodization function, are shown in Figure 10. The baseline decay represents populations, so it may be subtracted from the oscillations shown in Figure 10 using a baseline adjustment technique before performing the transform on ϕ to yield the multiple quantum spectrum shown in Figure 11. Note that the zero quantum peak is not present in this spectrum.

We now discuss the development of multiple quantum coherence using a single quantum propagator.

6 A SINGLE QUANTUM PROPAGATOR

The development of MQC under pulse sequences resulting in a single quantum propagator for dipolar coupled spin-$\frac{1}{2}$ systems was first reported and discussed by Suter et al.[15] in 1987. The sequence that we have used to produce the data shown in Figures 9–11 was developed by M. Goldman,[16] and is essentially identical to that published in 1988 by the Pines group.[17]

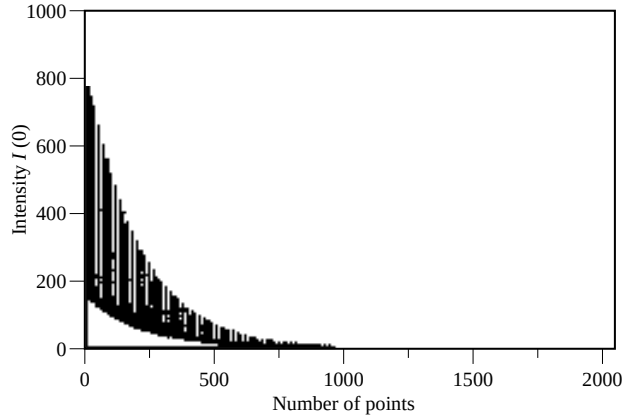

Figure 10 An extension of data point and tapering are performed to generate a data set in the phase domain. Figure 9 was repeated until the number of data points was 2K, and then tapered by using an appropriate apodization function

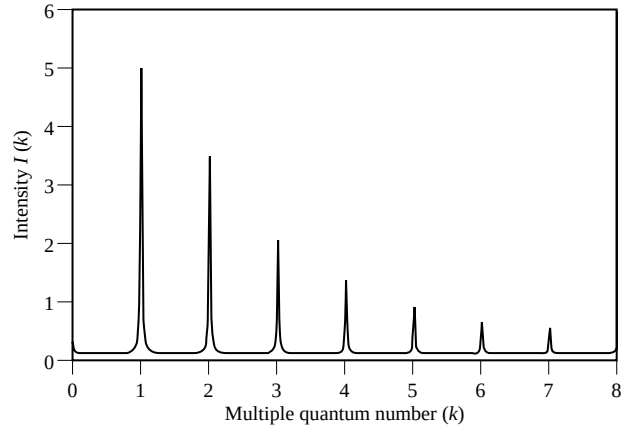

Figure 11 The Fourier transformed spectrum, from phase domain to multiple quantum number domain. The intensity distribution over the multiple quantum number $k = 8$ can be seen. The preparation time was 260 μs. The highest number of quanta $k_{\max}$ is not seen, due to the increment of the phase used

This sequence is shown in Figure 12. Important to understanding how this sequence works is an understanding of the development of internal Hamiltonians during finite pulses, an example of which is in Chapter 5, Section V of Pines[8] for the case of the 'flip-flop' phase tuning sequence (τ, 90°_x, τ, $90^\circ_{\bar{x}}$, τ). Applied to the sequence of Figure 12, the calculation proceeds as follows: consider the time interval $0 \le t < \frac{1}{4}\tau$. Immediately after a perfect delta function rotation by 45°_x at $t = 0$, $\hat{\tilde{\mathcal{H}}}_{zz}$ will be

$$\hat{R}_x(45^\circ)\hat{\mathcal{H}}_{zz} = \tfrac{1}{2}(\hat{\mathcal{H}}_{zz} + \hat{\mathcal{H}}_{yy}) - \tfrac{3}{2}(\hat{I}_{z1}\hat{I}_{y2} + \hat{I}_{y1}\hat{I}_{z2}) \quad (46)$$

The contribution to $\hat{\tilde{\mathcal{H}}}^{(0)}_{zz}$ for this period will then be

$$\frac{1}{t_c}\int_0^{\tau/4} \hat{\tilde{\mathcal{H}}}_{zz}\,\mathrm{d}t = \frac{1}{t_c}\frac{\tau}{8}[\hat{\mathcal{H}}_{zz} + \hat{\mathcal{H}}_{yy} - 3(\hat{I}_{z1}\hat{I}_{y2} + \hat{I}_{y1}\hat{I}_{z2})] \quad (47)$$

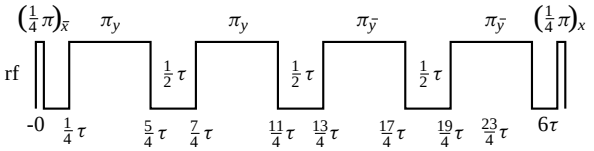

Figure 12 Pulse sequence for the single quantum propagator developed by Goldman,[16] and used in this work

During the period $\frac{1}{4}\tau \le t < \frac{5}{4}\tau$,

$$\begin{aligned}\hat{\tilde{\mathcal{H}}}_{zz}(t) &= \hat{R}_{45x}\hat{R}_{\xi y}\hat{\mathcal{H}}_{zz} \\ &= \hat{R}_{45x}\{\hat{\boldsymbol{I}}_1\cdot\hat{\boldsymbol{I}}_2 - 3[\hat{I}_{z1}\hat{I}_{z2}\cos^2\xi + \hat{I}_{x1}\hat{I}_{x2}\sin^2\xi \\ &\quad +(\hat{I}_{z1}\hat{I}_{x2} + \hat{I}_{x1}\hat{I}_{z2})\sin\xi\cos\xi]\} \\ &= \hat{\boldsymbol{I}}_1\cdot\hat{\boldsymbol{I}}_2 - \tfrac{3}{2}\{(\hat{z}_1\hat{z}_2 + \hat{y}_1\hat{y}_2 + \hat{z}_1\hat{y}_2 + \hat{y}_1\hat{z}_2)\cos^2\xi \\ &\quad +2\hat{x}_1\hat{x}_2\sin^2\xi \\ &\quad +\sqrt{2}[(\hat{z}_1 + \hat{y}_1)\hat{x}_2 + \hat{x}_1(\hat{z}_2 + \hat{y}_2)]\sin\xi\cos\xi\} \quad (48)\end{aligned}$$

where $\hat{z}_1\hat{z}_2$ is now used to designate $\hat{I}_{z1}\hat{I}_{z2}$, etc., to ease the notation.

During the period $\frac{1}{4}\tau < t < \frac{5}{4}\tau$, the flip angle ξ varies from zero to 180°. In the interval $\frac{1}{4}\tau < t \le \frac{5}{4}\tau$, the contribution of $\hat{\tilde{\mathcal{H}}}_{zz}$ to $\hat{\mathcal{H}}^{(0)}_{zz}$ can be calculated by assuming the flip angle ξ to be linear in t, so $\xi = \pi(t - \frac{1}{4}\tau)/\tau$, and $\mathrm{d}t = \tau\,\mathrm{d}\xi/\pi$. Then, in the period $\frac{1}{4}\tau \le t < \frac{5}{4}\tau$, or $0 \le \xi < \pi$, the contribution to $\hat{\mathcal{H}}^{(0)}_{zz}$ is

$$\begin{aligned}\hat{\tilde{\mathcal{H}}}_{zz(0)} &= \frac{1}{t_c}\int \hat{\tilde{\mathcal{H}}}_{zz}(t)\,\mathrm{d}t \\ &= \frac{1}{t_c}\left\{\tau\hat{\boldsymbol{I}}_1\cdot\hat{\boldsymbol{I}}_2 - 3[(\hat{z}_1\hat{z}_2 + \hat{y}_1\hat{y}_2 + \hat{z}_1\hat{y}_2 + \hat{y}_1\hat{z}_2)]\right. \\ &\quad \times\frac{\tau}{2\pi}\int_0^\pi \cos^2\xi\,\mathrm{d}\xi + \hat{x}_1\hat{x}_2\frac{\tau}{\pi}\int_0^\pi \sin^2\xi\,\mathrm{d}\xi \\ &\quad \left.+[(\hat{z}_1 + \hat{y}_1)\hat{x}_2 + \hat{x}_1(\hat{z}_2 + \hat{y}_2)]\frac{\tau}{\pi\sqrt{2}}\int_0^\pi \sin\xi\cos\xi\,\mathrm{d}\xi\right\} \\ &= \frac{\tau}{2t_c}[\tfrac{1}{2}(\hat{\mathcal{H}}_{zz} + \hat{\mathcal{H}}_{yy}) + \hat{\mathcal{H}}_{xx} - \tfrac{3}{2}(\hat{z}_1\hat{y}_2 + \hat{y}_1\hat{z}_2)] \quad (49)\end{aligned}$$

In the period immediately following $t = \frac{5}{4}\tau$, and before any other pulses are applied,

$$\hat{\tilde{\mathcal{H}}}_{zz} = \tfrac{1}{2}[\hat{\mathcal{H}}_{zz} + \hat{\mathcal{H}}_{yy} - 3(\hat{y}_1\hat{z}_2 + \hat{z}_1\hat{y}_2)] \quad (50)$$

Proceeding in this manner, it may be verified that the sequence shown in Figure 12, with cycle time $t_c = 6\tau$, yields the following values for the average Hamiltonian associated with the homonuclear dipolar coupling Hamiltonian $\hat{\mathcal{H}}_{zz}$ and the chemical shift $\hat{\mathcal{H}}_{cs} = \sum_{zz}\hat{I}_z$:

$$\begin{aligned}\hat{\tilde{\mathcal{H}}}_{zz} &= -(\hat{I}_{z1}\hat{I}_{y2} + \hat{I}_{y1}\hat{I}_{z2}) \\ &= -(\hat{I}_{z1}\hat{I}_2^+ - \hat{I}_{z1}\hat{I}_2 + \hat{I}_1^+\hat{I}_{z2} - \hat{I}_1^-\hat{I}_{z2})/2\mathrm{i} \quad (51)\end{aligned}$$

a pure single quantum operator, and $\hat{\tilde{\mathcal{H}}}_{cs}(0) = 0$.

7 RELATED ARTICLES

Average Hamiltonian Theory; CRAMPS; Double Quantum Coherence; Echoes in Solids; Optically Enhanced Magnetic Resonance.

8 REFERENCES

1. R. D. Mattuck, *A Guide to Feynman Diagrams in the Many Body Problem*, 2nd edn., McGraw-Hill, New York, 1976 (reprinted by Dover, New York, 1992).
2. H. Tanaka, T. Terao, and T. Hashi, *J. Phys. Soc. Jpn.*, 1975, **39**, 378.
3. H. Tanaka and T. Hashi, *J. Phys. Soc. Jpn.*, 1974, **39**, 1139.
4. W. P. Aue, E. Bertholdi, and R. R. Ernst, *J. Chem. Phys.*, 1976, **64**, 2229.
5. G. Bodenhausen, in *Progress in Nuclear Magnetic Resonance Spectroscopy*, eds. J. W. Emsley, J. Feeney, and L. H. Sutcliffe, Pergamon Press, Oxford, 1983, Vol. 14, p. 137.
6. D. Weitekamp, in *Advances in Magnetic Resonance*, ed. J. S. Waugh, Academic Press, New York, 1983, Vol. 11, p. 111.
7. M. Munowitz and A. Pines, in *Advances in Chemical Physics*, ed. I. Prigogine, Wiley, New York, 1987, Vol. 66, p. 1.
8. A. Pines, in *Proceedings of the 100th Fermi School on Physics, Varenna, 1986*, ed. B. Maraviglia, North-Holland, Amsterdam, 1988.
9. G. Drobny, *Annu. Rev. Phys. Chem.*, 1985, **262**, 451.
10. Y. S. Yen and A. Pines, *J. Chem. Phys.*, 1983, **78**, 3579.
11. J. Baum, M. Munowitz, A. N. Garroway, and A. Pines, *J. Chem. Phys.*, 1983, **83**, 2015.
12. M. Goldman *Quantum Description of High Resolution NMR in Liquids*, Oxford University Press, Oxford, 1988, Section 2.5.
13. B. C. Gerstein and C. R. Dybowski, *Transient Techniques in NMR of Solids: an Introduction to the Theory and Practice*, Academic Press, San Diego, 1985, Chapters 4 and 5.
14. S. Emid, *Physica B*, 1985, **128**, 79.
15. D. Suter, S. B. Liu, J. Baum, and A. Pines, *Chem. Phys.*, 1987, **114**, 103.
16. M. Goldman, personal discussions during the RMN Summer School organized by J. Virlet, 1987, Les Houches, France.
17. D. N. Shykind, J. Baum, S.-B. Liu, and A. Pines, *J. Magn. Reson*, 1988, **76**, 149.

Biographical Sketch

Bernard C. Gerstein. *b* 1932. B.S., 1953, Purdue, USA; Ph.D., 1960, Iowa State. Introduced to NMR by R. W. Vaughan. Faculty in Chemistry, Iowa State University, 1962–present. Approx. 150 publications. Research interests include the theory and practice of learning, and applications of solid state NMR to problems in the physics and chemistry of materials, fossil fuels, and heterogeneous catalysis.

Multiple Quantum NMR in Solids

Karen K. Gleason

Massachusetts Institute of Technology, Cambridge, MA, USA

1	Introduction	1
2	MQ Coherence Intensities	1
3	MQ Excitation by $\hat{\mathcal{H}}_{yx}$	2
4	Measuring MQ Intensities	3
5	Small Dipole Coupled Networks	4
6	Large Dipole Coupled Networks	5
7	Dimensionality of a Nuclear Spin Distribution	6
8	Relaxation and Effect of Molecular Motion	8
9	Related Articles	9
10	References	9

1 INTRODUCTION

Multiple quantum (MQ) NMR can provide unique insight into the distribution and motion of nuclei in solids. In this article, we consider multiple quantum coherences associated with homonuclear dipolar coupling among spin-$\frac{1}{2}$ nuclei in solids. Therefore, we consider nuclei with high natural isotopic abundance and a high gyromagnetic ratio. ^{1}H MQ NMR has been applied to study organic solids,[1–3] amorphous semiconductors,[4–7] and adsorbates on catalysts[8–14] and chromatography columns.[15] In addition, ^{19}F MQ NMR has been used to study bulk salts,[16] photosensitive salt/polymer mixtures,[17–19] and bulk polymers.[20] MQ NMR of ^{31}P in solids has also been demonstrated.[21] Several review articles and textbook chapters on MQ NMR experiments and their applications are available.[21–29]

The rate of MQ coherence development depends on the strength and time dependence of each pairwise homonuclear dipolar coupling as well as the number of such pairs. For a network of N equivalent nuclei, the second moment M_2 of the distribution of all the pairwise homonuclear dipole couplings can be related to the geometry of the spin distribution through the van Vleck equation:[30]

$$M_2 = \tfrac{3}{4}\gamma^4\hbar^2 \frac{I(I+1)}{2} \sum_{i<j}^{N-1} \frac{(1-3\cos^2\theta_{ij})^2}{r_{ij}^6} \qquad (1)$$

Thus, many combinations of internuclear distances r_{ij} and the total number of pairs in the summation $N-1$ can give rise to identical M_2. Using MQ NMR, the number and distribution of dipolar couplings can be investigated independently, thus allowing the distribution of nuclei in a solid to be explored.

Observation of MQ coherence development in solids is accomplished interferometrically via a two-dimensional NMR technique.[1,29] By incrementing the MQ preparation time τ, the presence of finite clusters of nuclei can be distinguished from nuclear distributions which are homogeneous on the 1–2 nm length scale of this experiment.[2,3] Coherences arising from a cluster of nuclei will saturate with increasing MQ excitation time, because no additional nuclei are available for correlation in the surrounding region. In contrast, the number of nuclei coupled together in a large homogeneous dipole network will increase monotonically with time until relaxation occurs.

Furthermore, a simple scaling exists for the growth of MQ coherences among many bulk materials.[16,31] This behavior allows homogeneous three-dimensional distributions of nuclei to be differentiated from one- and two-dimensional distributions.[31–33] Identification of two-dimensional distributions is particularly valuable for determining whether a given nuclear species, such as ^{1}H, ^{19}F, or ^{31}P, is segregated at a surface,[31,34] such as a grain boundary in a polycrystalline material. A model which expands the density matrices in terms of average product operators allows these differences to be evaluated numerically.[31]

More complex distributions of nuclei can also be analyzed using MQ NMR. For example, both isolated salt molecules and large aggregates of salt have been observed simultaneously within polymeric matrices.[17–19] Finally, MQ NMR and its relaxation may serve as a valuable probe of molecular reorientation in solids which modulate the dipolar coupling network at frequencies in the kilohertz range.[20,35,36]

2 MQ COHERENCE INTENSITIES

Analysis of MQ intensities is the underlying principle for using MQ NMR as a 'spin-counting' technique, allowing the number of dipole coupled nuclei in a isolated cluster to be determined.[3] Although only two possible states, α and β, exist for an individual spin-$\frac{1}{2}$ nucleus, when N of these nuclei are dipole coupled there are 2^N possible product states. Thus, a $2^N \times 2^N$ density matrix is required to represent fully the time development of MQ coherence intensity among N dipolar coupled spin-$\frac{1}{2}$ nuclei. A schematic representation of ρ for $N = 3$ is shown in Figure 1, where the indices of the matrix are the eight possible product states. Diagonal elements can be used to calculate the populations of the product states, while the off-diagonal elements indicate the MQ coherences between two different states.

The MQ coherence order, n, is equal to the difference in m_z between the two states. Since the z component of angular momentum m_z of an individual spin state is $\pm\frac{1}{2}$, m_z for the product states ranges from $-N/2$ to $+N/2$. Thus, MQ orders can be positive, negative, or zero, provided that $|n| \leq N$. This limitation provides a very elegant way of determining the number of dipole coupled spins in a spatially isolated cluster. However, there is only one way to achieve such an $n = N$ coherence, making it statistically difficult to observe intensity in highest MQ order for large N. Fortunately, the number of density matrix elements Z_n for lower order coherences ($|n| < N$) also depends on the number of coupled nuclei:

$$Z_n = \sum_{i<j} \delta_{[(m_{zi}-m_{zj}),n]} = \binom{2N}{N-|n|} \qquad (2)$$

In this equation, Z_0 includes both off-diagonal elements with $n = 0$, representing true zero quantum coherence (0Q), and diagonal elements representing self-correlation among the

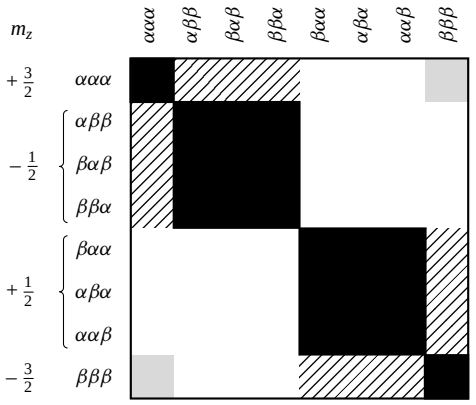

Figure 1 Schematic representation of ρ for $N = 3$. The 2^3 product states are sorted by m_z so that elements corresponding to even MQ coherences ($n = 0$, black; $|n| = 2$, striped) appear in the upper left and lower right quadrants. The remaining elements correspond to odd MQ orders ($|n| = 1$, white; $|n| = 3$, grey)

states, as no difference is resolved between these two types of element by most MQ experiments.

Each element in Figure 1 is shaded according to the absolute value of its corresponding MQ order. Note that the first $4^N/2$ indices in Figure 1 represent the states with $m_z = (N - k)$, where k is an integer. Thus, elements corresponding to even order MQ coherences will appear only in the upper left and lower right quadrants of the density matrix. The remainder of the elements in the upper right and lower left quadrants correspond to odd order MQ coherences. If only even order MQ coherences are excited, this density matrix will be block diagonal with only $4^N/2 = 32$ possible nonzero elements. For $N = 3$, the number of elements contributing to the even orders will be $Z_0 = 20$ and $(Z_2 + Z_{-2}) = 12$.

At equilibrium, the density matrix is proportional to I_z. Thus, only the diagonal elements are nonzero. As MQ excitation begins, intensity develops in density matrix elements of low MQ order. Longer excitation times are required for growth of high-order MQ coherences. The n quantum intensity at any time τ after MQ excitation is begun $I_n(\tau)$, contains contributions from all Z_n density matrix elements comprising that order:[37]

$$I_n(\tau) = \sum_{i<j} \delta_{[(m_{zi}-m_{zj}),n]} |\rho_{ij}(\tau)|^2 \tag{3}$$

Thus, calculation of MQ dynamics requires following the time evolution of the density matrix under the influence of the Hamiltonian corresponding to the MQ excitation sequence during the experiment.

The Liouville von Neumann equation of motion can be used to calculate $\hat{\rho}(\tau)$ explicitly:

$$\frac{\mathrm{d}\hat{\rho}(\tau)}{\mathrm{d}\tau} = \mathrm{i}[\hat{\rho}(\tau), \tilde{\hat{\mathcal{H}}}] \tag{4}$$

where $\hat{\mathcal{H}}$ is the Hamiltonian applied to the system for a duration τ in order to develop MQ coherences. If average Hamiltonian theory can be applied, the solution of equation (4) is

$$\hat{\rho}(\tau) = \exp(-\mathrm{i}\tilde{\hat{\mathcal{H}}}\tau)\rho(0)\exp(\mathrm{i}\tilde{\hat{\mathcal{H}}}\tau) \tag{5}$$

For small numbers of spins ($N \leq 9$), the development of $I_n(\tau)$ has been calculated explicitly using equations (3) and (5).[32,37,38]

However, tracking the time development of the 4^N density matrix elements is a large task for any significant number of coupled spins. For $N = 95$, the number of density matrix elements exceeds the number of hydrogen atoms in the Earth's sun! Thus for a large N, statistical limit behavior is often assumed, in which all MQ coherences have equal probability, allowing the magnitude of all density matrix elements to become equal at long excitation times.

The assumption of a statistical limit[37] greatly simplifies the analysis of MQ coherence intensities since the intensity of an n quantum coherence depends only on the number of elements of that order Z_n:

$$I_n = \frac{C Z_n}{4^N} \tag{6a}$$

The inverse of the constant C represents the fraction of density matrix elements where nonzero intensity could be excited. This fraction depends upon the selectivity of the Hamiltonian applied to the system. When nonselective excitation is used, all MQ orders are excited and $C = 1$. However, selective MQ excitation is often used. For instance, if only even MQ orders are excited, $C = 2$. Since equation (2) shows that Z_n is a function of n and N only, the distribution of $I_n(\tau)$ allows N to be determined. When $N \geq 6$, the right-hand side of equation (6a) can be approximated by a Gaussian distribution:

$$I_n \simeq \frac{C}{\sqrt{N\pi}} \exp(-n^2/N) \tag{6b}$$

Equations (6a) and (6b) are valid for all positive, negative and zero integer values of n, and are normalized such that

$$\sum_{n=-\infty}^{\infty} I_n = 1 \tag{7}$$

In addition, note that the MQ intensity distribution is symmetric, $I_n = I_{-n}$, and that I_0 contains both populations and true 0Q coherences. Furthermore, higher order coherences are statistically more difficult to achieve than lower order coherences. As will be shown below, I_0 tends to deviate more from the predicted values than the positive orders; only the latter are generally utilized to determine N. Statistical limit behavior is often a poor assumption for very small groups of spins, due to presence of symmetry forbidden transitions.

3 MQ EXCITATION BY $\hat{\mathcal{H}}_{yx}$

One of the most desirable Hamiltonians for exciting MQ coherences in solids is $\hat{\mathcal{H}}_{yx}$:

$$\tilde{\hat{\mathcal{H}}}_{yx} = -\frac{1}{2}\sum_{i<j} R_{ij}(\hat{I}_{i+}\hat{I}_{j+} + \hat{I}_{i-}\hat{I}_{j-}) \tag{8}$$

Other Hamiltonians such as $\hat{\mathcal{H}}_{zx}$ have been used for exciting MQ coherences. However, higher orders develop more quickly under $\hat{\mathcal{H}}_{yx}$,[38] maximizing the number of spins that can be correlated before relaxation effects become significant.

The bilinear raising and lowering operators $\hat{I}_{+i}\hat{I}_{+j}$, and $\hat{I}_{-i}\hat{I}_{-j}$ allow only even-order MQ coherence intensity to evolve when $\hat{\mathcal{H}}_{yx}$ is utilized in conjunction with an equilibrium initial density matrix $\rho(0)$ that is proportional to $\hat{I}_z$. When only half of all possible orders are excited, the intensity of each is twice that of a nonselective experiment [equation (6)]. The increased intensity is particularly important for detecting high-order coherences, which are statistically less likely than lower order coherences. Odd order and nonselective excitation using $\hat{\mathcal{H}}_{yx}$ results when prepulses create an initial density matrix proportional to the single quantum operator $\hat{I}_x$ or it can be made nonselective if $\rho(0)$ is a mixture of $\hat{I}_z$ and $\hat{I}_x$, respectively.[40]

For spin counting applications it is important to note that the selection rules for $\hat{\mathcal{H}}_{yx}$ from an initial density matrix proportional to $\hat{I}_z$ result in the inability to create $n = N$ quantum coherence. Obviously, N quantum coherence cannot be developed when N is odd. More surprisingly, N quantum coherence cannot be achieved among $N = 4k$ dipole coupled spins, where k is a positive integer.[40] Thus, four quantum coherence cannot develop among an isolated cluster of four coupled nuclei. While these limitations appear problematic, the ability to achieve N quantum coherence via other MQ propagators can be even more restrictive. For instance, under $\hat{\mathcal{H}}_{zx}$ the N quantum order can never be achieved when starting from the equilibrium density matrix. The restrictions on creating N quantum coherence are only significant for size determination among very small clusters of nuclei. In larger dipole coupled networks, the signal-to-noise ratio of the highest order MQ coherence is generally below the detection limit, rendering the ability to achieve this coherence insignificant.

To carry out the MQ experiment in the laboratory, the phase ϕ of $\hat{\mathcal{H}}_{yx}$ is generally varied.[1,2] One or more repetitions of the eight-pulse cycle shown below have been used to create $\hat{\mathcal{H}}_{yx}(\phi)$:

$$(\Delta/2) - 90^\circ_\phi - (\Delta') - 90^\circ_\phi - (\Delta) - 90^\circ_\phi - (\Delta') - 90^\circ_\phi - (\Delta) - 90^\circ_{\phi+180^\circ} - (\Delta') - 90^\circ_{\phi+180^\circ} - (\Delta) - 90^\circ_{\phi+180^\circ} - (\Delta') - 90^\circ_{\phi+180^\circ} - (\Delta/2)$$

where $\phi = 0^\circ$ corresponds to an x pulse. The relationships between the delays is $\Delta' = 2\Delta + t_p$, where t_p is the pulse length. The average Hamiltonian, $\tilde{\hat{\mathcal{H}}}_{yx}(\phi)$ is then

$$\tilde{\hat{\mathcal{H}}}_{yx}(\phi) = -\frac{1}{2}\sum_{i<j} R_{ij}[\hat{I}_{i+}\hat{I}_{j+}\exp(2i\phi) + \hat{I}_{i-}\hat{I}_{j-}\exp(-2i\phi)] \quad (9)$$

Considering $0^\circ \le \phi < 360^\circ$, $\tilde{\hat{\mathcal{H}}}_{yx}(\phi) = \hat{\mathcal{H}}_{yx}$ at $\phi = 0^\circ$ or 180° and $\tilde{\hat{\mathcal{H}}}_{yx}(\phi) = -\hat{\mathcal{H}}_{yx}$ at $\phi = 90^\circ$ or 180°. During the mixing period, the value of ϕ is fixed at 90°, corresponding to $-\hat{\mathcal{H}}_{yx}$.

In the presence of heteronuclear couplings, the $\hat{\mathcal{H}}_{yx}$ sequence can be used to examine the distribution of I spins without irradiation of the S spin frequency or reduction of the $I-S$ couplings by isotopic exchange.[16] This is particularly important when both ^{19}F and ^{1}H are present in the sample of interest.

As in any multiple pulse NMR experiment, deviations from perfect delta pulses, finite pulse cycle times with respect to the inverse frequences of the interactions in the sample, and off-resonance effects can lead to undesirable effects.[42] The sensitivity to chemical shift offset has recently been exploited to measure the correlation length of the chemical shift shielding tensor in polycrystalline solids.[43] This increased sensitivity of higher order coherences to magnetic field gradients has also been exploited to enhance the spatial resolution of NMR imaging of solids.[44] In the future, excitation using shaped rf pulses has the potential for improving experimental implementation of the MQ experiment.[45] In practice, rectangular pulses with $t_p \le 3\,\mu$s and eight-pulse cycle times t_c, of $30-72\,\mu$s are generally employed, and the experiment is carried out on resonance.

4 MEASURING MQ INTENSITIES

Although MQ coherences have sometimes been detected directly by CW NMR,[22] MQ coherences cannot be detected directly by FT NMR. Since MQ intensities are nonlinear under CW experiments, two-dimensional NMR experiments are currently employed for this purpose. Only an overview of the required experimental procedure is provided below. Additional descriptions can be found in Yen and Pines,[1] Baum et al.,[2] Baum and Pines,[3] and Gleason.[21]

As in most two-dimensional NMR experiments, there are four distinct periods: preparation, evolution, mixing, and detection. During the preparation period, of length τ and phase ϕ, MQ coherences are excited as a result of homonuclear dipole couplings, and nonzero intensity is developed in the off-diagonal elements of the density matrix [equation (9)]. However, no observable magnetization from these elements can be detected experimentally. These coherences evolve during t_1, the evolution period time. The mixing period of length τ (identical to the preparation period length) and phase $\phi = 90^\circ$, converts MQ coherences in the off-diagonal elements back into diagonal elements, corresponding to z magnetization. Finally, the detection period is used to create observable signal $S(\phi, \tau)$.

In order to resolve the various n quantum coherences, the phase of the preparation period ϕ is changed from 0 to 360° in increments of $\Delta\phi$, while the preparation period length, the mixing period length, and the phase of mixing period are held fixed. Fourier transformation of this series of $S(\phi,\tau)$ at constant τ with respect to ϕ yields the intensities of the n quantum orders $I_n(\tau)$. At least $2n$ phase shifts must be performed when detectable n quantum intensity is present. Fewer phase shifts will alias high-order coherence intensity to lower values of n. Most commonly, $\Delta\phi$ is set at 5.6° or 2.8°, allowing detection of $|n| \le 16$ and 32, respectively.

In order to determine the local distribution of nuclei within a sample, $I_n(\tau)$ is measured for a series of τ. Generally,

$\tau = n_c t_c$ which corresponds to changing the integer number of repetitions n_c, of the basis eight-pulse MQ subcycle for $\hat{\mathcal{H}}_{yx}$. In a given sample, longer τ values correspond to probing the dipolar network over increasing distances.

The length of the evolution period t_1 can also be incremented, allowing MQ coherences to evolve under the internal Hamiltonian of the spin system, yielding the n quantum coherence lineshapes.[1] However, for many applications, only the integrated intensity of the coherence is required. Thus, the evolution period time t_1 is often set to zero,[5,46] maximizing the final signal intensity and significantly decreasing acquisition time. This also eliminates the effects of couplings linear in $\hat{I}_z$ such as chemical shift and heteronuclear dipole coupling during the evolution period.

When $t_1 = 0$ and relaxation effects are neglected, the density matrices at times 0 and 2τ are identical when $\phi = 0^\circ$ or 180°, so called 'time reversal'. At other ϕ some transverse magnetization will also be present at the end of the mixing period and the magnitude of z magnetization will be reduced. Thus, prior to the detection period, a delay which is long compared to T_2 but short compared to T_1 allows for decay of any transverse magnetization transients. Then, a $\pi/2$ pulse can be applied to detect $S(\phi,\tau)$. Spin locking with periodic sampling can be employed during the detection period to enhance the signal-to-noise ratio of $S(\phi,\tau)$.

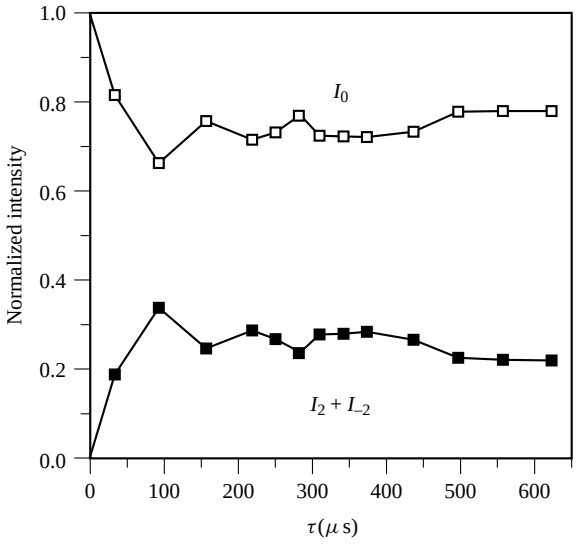

Figure 2 The ^{19}F zero quantum and +2 and −2 quantum intensities from an even-selective experiment on 2 wt.% NH_4+$CF_3SO_3^-$ in poly(*p*-hydroxystyrene). The salt is well dispersed in the polymer, and thus its CF_3 group behaves as expected for $N = 3$. Oscillations are distinct at early τ and destructive interference leads to steady-state values at long τ. (Reproduced by permission of the American Chemical Society from Limb et al.[19]

5 SMALL DIPOLE COUPLED NETWORKS

Even when the number of dipole coupled spins is small, the dynamics of MQ coherence growth can become quite complicated. The simplest possible system to consider is isolated pairs ($N = 2$) of spin-$\frac{1}{2}$ nuclei with identical internuclear separations and orientations with respect to the external magnetic field. Thus, all intrapair dipole coupling constants R are identical and much stronger than any interpair coupling. Then, even order selective excitation by $\hat{\mathcal{H}}_{yx}$ allows only the zero quantum and ± 2 quantum intensity to develop as given by the analytical solution to equation (5):

$$I_2(\tau) = I_{-2}(\tau) = \tfrac{1}{2}[1 - I_0(\tau)] = \tfrac{1}{2}[1 - \cos(R\tau)] \quad (10)$$

In the absence of relaxation, the oscillatory exchange of MQ coherence intensity between the orders will continue indefinitely.[38]

In a macroscopic NMR sample, such as a single crystal or a liquid crystal, identical orientations of internuclear vectors with respect to the external magnetic field can occur. By contrast, polycrystalline powders are the most commonly used samples for MQ NMR. Even for isolated pairs with identical internuclear spacings, the angular dependence of the dipolar coupling interaction leads to destructive interference among the characteristic frequencies which contribute to the MQ intensity development, leading to steady state values of I_n at long τ.

The appearance of oscillations which are damped at long times is characteristic of the powder average of a small number of coupled spins.[41] Figure 2 shows the ^{19}F MQ coherence development for sodium triflate salt ($NH_4^+CF_3SO_3$) well dispersed in polyhydroxystyrene.[19] Only the $n = 0$, 2, and −2 quantum orders have nonzero intensity under the even-selective MQ excitation employed. This is the same behavior expected for an isolated network of three dipole coupled ^{19}F nuclei, where only even MQ orders with $|n| \leq 3$ develop. This result indicates that the average spacing between the salt anions is large, allowing its CF_3 group to act as an isolated $N = 3$ cluster. Note that this configuration can be represented by the density matrix shown in Figure 1. Furthermore, the development of ± 2 quantum coherence intensity indicates that the time average of the intraion dipole couplings is nonzero. Thus, the triflate anion is not reorienting rapidly and isotropically within the polymeric matrix.

Clear oscillations in the MQ intensities are initially observed in Figure 2, while steady state is approached at $\tau >$ 500 ms. The observed long time values are 0.78 for the zero quantum coherence and 0.22 for the sum of the +2 and −2 quantum coherences. These values differ significantly from the predictions of equation (6a), utilizing $N = 3$ and $C = 2$, of 0.625 and 0.375, respectively. This difference shows that the statistical limit has not been achieved, a problem that was anticipated for very small numbers of coupled spins due the presence of symmetry disallowed MQ transitions. Thus, it is desirable to determine N for very small networks by detecting the highest order coherence present, rather than by assuming that the statistical limit holds.

For larger groups of spins, good agreement with the statistical limit behavior has been found. The liquid crystal, *p*-hexyl-*p*′-cyanobiphenyl ($C_{19}H_{21}N$) is a finite cluster of dipole coupled spins, since translation and anisotropic rotation serve to destroy intermolecular dipole couplings, while intramolecular dipole couplings maintain nonzero values. As expected, the positive order MQ coherences grow with τ until all the protons on the liquid crystal molecule are coupled on the experimental timescale. No further increase occurs as the preparation time increases further. The distribution of the steady state MQ intensities is well described by equation (6b)

with $N = 20 \pm 1$. This result is in excellent agreement with the known structural formula.[3]

Thus, MQ NMR gives quantitative information on the number of nuclei in a limited network of dipole, when the structure is unknown. For instance, the size of small hydrogenated defects in amorphous semiconductors has been determined.[4–7] The clustering of molecules inside zeolites[9,11–14] and the distribution of molecules on catalysts[8,10,29] and on chromatographic supports[15] have also been investigated using the MQ spin counting technique.

6 LARGE DIPOLE COUPLED NETWORKS

Although the MQ dynamics of spin systems for which the dipole coupling network extends beyond the typical 1–2 nm length scale of a MQ NMR experiment are nearly impossible to calculate exactly, similar development of $I_n(\tau)$ is observed in many samples. Figure 3 shows the development of positive even-order MQ coherence intensity for CaF_2 powder for increasing τ created from integral multiple repeats of t_c between 30 and 60 μs. The smooth MQ development in Figure 3 is a result of the distribution of dipole coupling present in this polycrystalline sample. Significant oscillations in $I_n(\tau)$ can be seen in a single crystal CaF_2 with its (111) direction oriented perpendicular to the applied magnetic field (Figure 4). For this configuration, all internuclear vectors to the nearest ^{19}F neighbors are at either 54.7°, the magic angle, or (54.7 + 180)°. Thus, all four dipole couplings between nearest neighbors are zero for this configuration. The strongest couplings in this system are actually between next nearest neighbors. The lack of angular dispersion and relative weak dipole couplings lead to only slow damping of the oscillation of the MQ coherences which arises from the even weaker dipolar coupling to neighbors in other shells. The small dipolar couplings in the (111) oriented crystal also lead to slower growth of positive MQ intensities than is observed for the powdered CaF_2 sample.

The observed distributions of $I_n(\tau)$ for polycrystalline powders are often described empirically as a Gaussian distribution, as can be seen in Figure 5 for powdered CaF_2 and GaP, where the solid lines are given by equation (7). The slow development of MQ coherence intensity in GaP allows the comparison to be made for low $N(\tau)$ while CaF_2 provides information at higher $N(\tau)$ values. This description is convenient, as the single parameter $N(\tau)$ can be used to describe an entire MQ spectrum.[2] However, the interpretation of $N(\tau)$ via equation [6,7]6 is not straightforward, since the number of coupled spins is ill defined in this situation. Materials with the highest dipolar couplings also display the fastest growth of $N(\tau)$. Thus $N(\tau)$ has been considered as a parameter that is dependent on the size, structure, and motion of the dipolar coupling network.

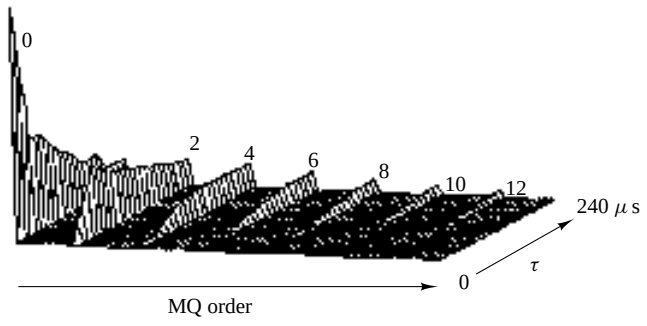

Figure 3 Even-order selective ^{19}F MQ spectra of a polycrystalline powder of CaF_2. As τ increases, high-order coherence intensities grow monotonically

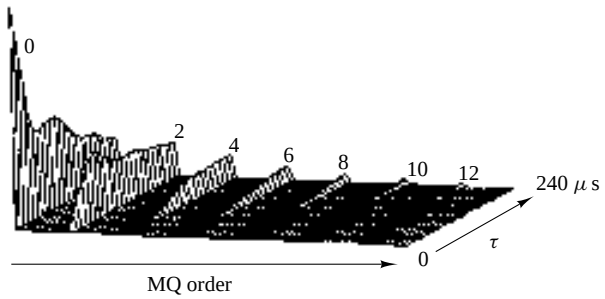

Figure 4 Even-order selective ^{19}F MQ spectra of a single crystal of CaF_2 oriented with its (111) direction along the external magnetic field. The lack of angular orientation distribution, as compared to the powder (Figure 3), leads to oscillatory growth of the zero and two quantum coherences, while the smaller magnitude of the dipole couplings in this sample leads to slower higher order coherence growth

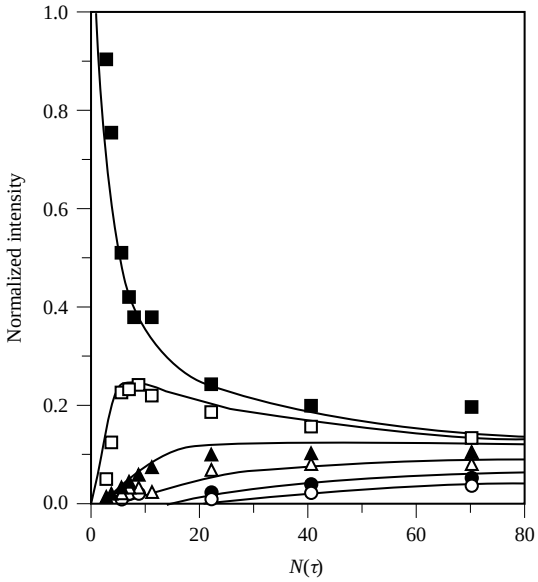

Figure 5 Gaussian distribution (——) and experimentally measured intensities versus $N(\tau)$ for two large dipole coupled networks, $Ca^{19}F_2$ (squares) and $Ga^{31}P$ (other symbols), showing reasonable agreement for $N(\tau) < 70$: (■) I_0, (□) I_2, (▲) I_4, (△) I_6, (●) I_8, (○) I_{10}

Non-Gaussian behavior of the distribution of positive MQ orders for infinite spin systems at long τ has been noted, usually becoming significant when $N(\tau)$ is greater than about 70. In addition, a least-squares fit to equation (6) underpredicts the intensity of the nonzero orders while overpredicting the zero quantum intensity. This may indicate relaxation of intensity in the off-diagonal density matrix elements back to diagonal elements. These effects are not seen in the 21-spin system, liquid crystal *p*-hexyl-*p*′-cyanobiphenyl ($C_{19}H_{21}N$), experiments at similar τ, and thus cumulative pulse errors cannot be the sole cause of the deviation. Experimentally,

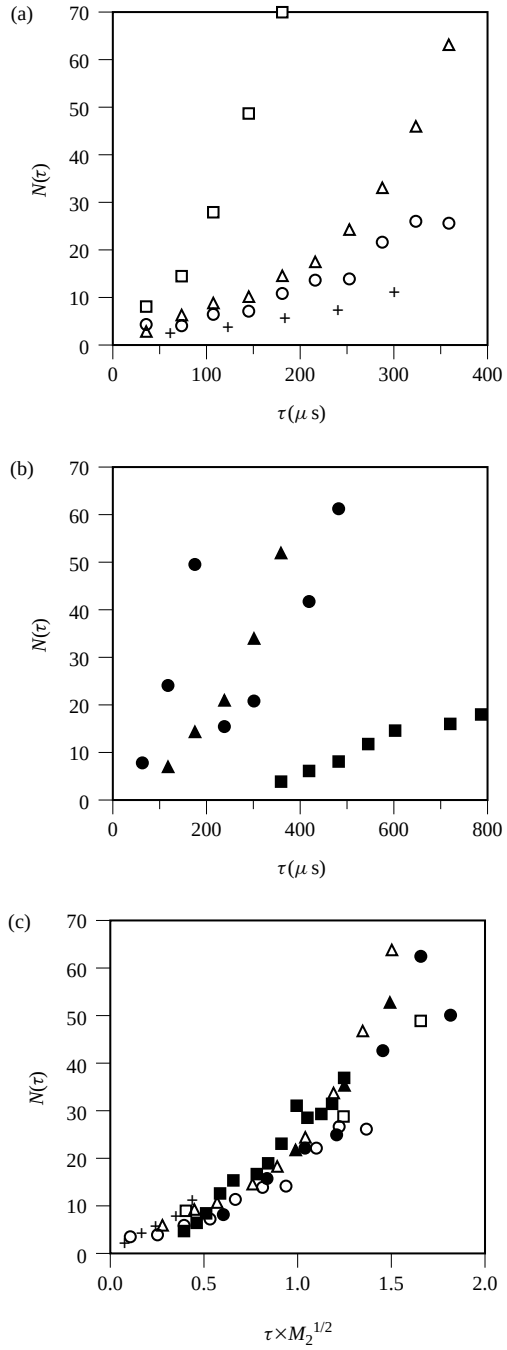

Figure 6 Effective number of correlated nuclei, $N(\tau)$ as function of τ for three-dimensional distributions (a): (□) CaH_2 (^{1}H),[31] (△) adamantane (^{1}H),[31] (○) sodium bicarbonate (^{1}H),[31] (+) Ga P (^{31}P).[21] (b) All ^{19}F:[16] (+) CaF_2, (▲) $NaAsF_6$, (●) CsF, (■) $(C_6F_5)_3SAsF_6$. (c) A universal MQ growth curve is seen for all the samples in (a) and (b), when a nondimensional time axis is created by multiplying τ by $M_2^{1/2}$ (equation (1))

the zero quantum intensity deviates from Gaussian behavior at the smallest number of correlated spins, making it a strong indicator of the onset of relaxation effects.

However, as shown in Figure 6(a) and 6(b) for $N(\tau) < 70$, $N(\tau)$ does grow as the MQ excitation time τ increases. This development of $N(\tau)$ can be described by a universal growth curve when a dimensionless MQ excitation time is created by multiplying τ by $M_2^{\frac{1}{2}}$.[18,21,31] The result of this scaling is shown in Figure 6(c), where $M_2^{\frac{1}{2}}$ has been calculated from equation (1) using the known crystal structures of the materials. The solids represented in Figure 6 fall into one of two catagories. In both categories the dipolar field at each nucleus in a three-dimensional crystal lattice is equivalent and time independent on the MQ timescale. For the first class of materials, no translation or rotation occurs on the NMR timescale. Examples of this category include Ca^1H_2, $Ca^{19}F_2$, and $Ga^{31}P$. In the second class, rapid isotropic rotation exists in the absence of translation, allowing only intermolecular dipole couplings to survive. Examples of such behavior are ^{1}H in adamantane or ^{19}F in salts containing hexafluoroarsenate anions (AsF_6^-). For this second category, the high concentration of NMR active nuclei with relatively low dipole couplings allows larger numbers of spins to be correlated before relaxation effects become significant.

The MQ dynamics of many molecular solids do not follow the universal growth curve, since these solids possess a variety of short internuclear spacings and motion which is neither fast nor isotropic. Sometimes, lowering the sample temperature can eliminate such undesirable motion. In addition, some nuclear distributions are inherently nonuniform, and non-Gaussian intensity distributions are observed even at short τ. For example, both isolated salt molecules and salt aggregates can exist within the same salt/polymer mixture.[17,19] The fraction of each environment can be quantitated by treating the observed MQ spectra as a linear combination of the two MQ intensity distributions. Treatment of MQ coherence growth from nuclei within tightly coupled clusters in addition to slower intercluster growth has also been used to analyze proton distributions in amorphous hydrogenated semiconductors[4–7] and to characterize the distribution of molecules absorbed in zeolites.[11,12]

7 DIMENSIONALITY OF A NUCLEAR SPIN DISTRIBUTION

Certain deviations from the MQ universal behavior [Figure 6(c)] for large dipole coupled networks cannot be accounted for by the presence of molecular motion. Such deviations may indicate that the nuclear distribution is not three dimensional. Hydrogen existing on the surface of a treated natural diamond powder is an example of a two-dimensional distribution.[31] For the diamond powder, the $N(\tau)$ versus τ curve exhibits a concave upward shape, unlike $N(\tau)$ for the 21-spin liquid crystal, which saturates at large preparation times. Thus, the diamond powder represents a large dipole coupled network. However, its MQ growth does not follow the universal scaling behavior of the three-dimensional model compounds. Even greater deviation from the universal curve was found for the initial MQ growth among protons in hydroxyapatite which provides a pseudo-one-dimensional distribution of spin-$\frac{1}{2}$ nuclei.[33]

To predict the influence of dimensionality on the rate of MQ coherence in large dipolar networks, a solution to equation (4) is required. For this purpose $\hat{\rho}(\tau)$ is expanded in terms of product operators, as an alternative to tracking the time development of each of the 4^N individual elements.[41] These product operators are formed from the multiplication

of individual spin operators ($\hat{I}_{iz}$, $\hat{I}_{i+}$ or $\hat{I}_{i-}$) from M of the N nuclei in the dipole network. For example, $\hat{I}_{5z}\hat{I}_{6-}\hat{I}_{7+}\hat{I}_{8z}$, represents $M = 4$ possible product operators when $N \geq 8$.

Two simplifications[31] allow $\hat{\rho}(\tau)$ to be approximated by an expansion requiring only N coefficients:

$$\hat{\rho}(\tau) \approx \sum_{M=1}^{N} C_M(\tau)\hat{P}_M \tag{11}$$

Here, $\hat{P}_M$ is a time independent average product operator, representing all the possible product operators containing M spins. Thus, the time evolution of the MQ coherence and multiplicity of all possible product operators with respect to M is contained in the coefficients $C_M(\tau)$.

When $\hat{\rho}(0) = \hat{I}_z$, only $C_1(0)$ has nonzero intensity. Intensity develops in C_M for $M > 1$ with increasing τ through the commutator obtained when equation (11) is substituted into equation (4) under excitation by $\hat{\mathcal{H}}_{yx}$:

$$\sum_M \left(\frac{\mathrm{d}C_M}{\mathrm{d}\tau}\hat{P}_M\right) = \frac{-\mathrm{i}}{4}\sum_M C_M\left\{\sum_i^N\sum_{i\neq j}^N R_{ij}[\hat{P}_M, (\hat{I}_{i+}\hat{I}_{j+}\hat{I}_{i-}\hat{I}_{j-})]\right\} \tag{12}$$

This summation represents only N coupled differential equations, thus significantly reducing the volume of calculation required compared to the exact solution. Information on the order of the MQ coherences has been averaged away. However, approximating the effective spin correlation size $N(\tau)$ as the center of mass of the distribution of C_M over M allows the results of the average product operator model to be compared directly with experimental measurements of $N(\tau)$.[31]

To emphasize that the rate of MQ coherence development through equation (12) is strongly dependent on the geometry of the dipole coupled network, only two values of R_{ij} will be considered. All nearest neighbor dipole couplings are taken to be equal to the root-mean-square value over the powder average for the nearest neighbor separation, and all R_{ij} for all non-neighboring nuclei are set equal to zero. This is a stepwise approximation to the true decay in the magnitude of dipole coupling constants with internuclear distance cubed.

Because R_{ij} is nonzero only for nearest neighbors, only product operators representing M spins occupying a contiguous region of space will contribute to the average product operator $\hat{P}_M$. For simplicity, lines, squares, and cubes are the shapes assumed to be associated with $\hat{P}_M$ for nuclei distributed uniformly over one-, two-, and three-dimensional lattices, respectively. A schematic drawing of P_9 for a two-dimensional (surface) distribution of nuclei is shown in Figure 7. In order to compute MQ dynamics, the commutator in equation (11) must be evaluated. Only adjacent i,j spin pairs need to be considered because only these have nonzero values of R_{ij}. Thus, the larger the number of nearest neighbors, the greater the possibilities for high-order MQ development. As shown in Figure 7, the spin pair i,j and the M spins comprising $\hat{P}_M$ will have zero, one, or two of their spins in common; these cases correspond to pairs external to, at the surface of, or internal to $\hat{P}_M$, respectively. The commutator for external pairs is identically zero, resulting in no change in the size of the MQ coherence. Products of $M + 1$ and $M - 1$ spin operators result from commutators involving surface and internal pairs, respectively.

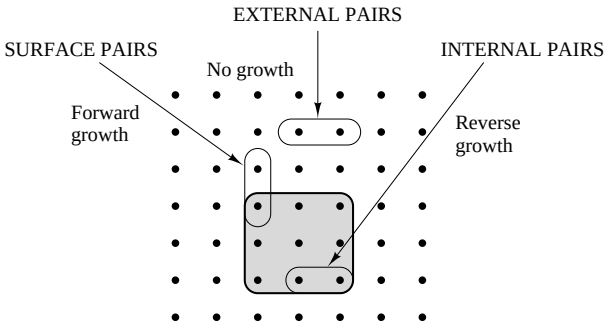

Figure 7 Schematic drawing of $\hat{P}_M$, the average product operator for nine spins on a two-dimensional square lattice. Surface pairs lead to forward MQ growth, while internal pairs reduce the coherence size. Faster MQ coherence growth rates are anticipated as the dimensionality of the lattice increases, since the ratio of surface pairs to internal pairs increases

The $\hat{P}_{M+1}$ operators represent forward growth of the MQ coherence size, while the $\hat{P}_{M-1}$ operators correspond to reverse growth, allowing equation (12) to be simplified to

$$\sum_M (\mathrm{d}C_M/\mathrm{d}\tau)\hat{P}_M = \frac{-\mathrm{i}}{4}\sum_M C_M \times (W^{\mathrm{f}}_{M+1}\hat{P}_{M+1} + W^{\mathrm{r}}_{M-1}\hat{P}_{M-1}) \tag{13}$$

Note that the $\Delta M = \pm 1$ selection rule for product operator evolution under $\hat{\mathcal{H}}_{yx}$ is evident from this equation. The forward and reverse growth rate coefficients W^{f}_M and W^{r}_M depend on the number of pairs at the surface of and internal to $\hat{P}_M$. Since the surface-to-volume ratio for $\hat{P}_M$ depends on its dimensionality, higher MQ growth rates are anticipated for homogeneous distributions of nuclei of increasing dimensionality.

Thus, using average product operators, an N-spin system can be represented by a set of N simultaneous differential equations, allowing the MQ dynamics of large numbers of spins, arranged in varying morphologies, to be easily simulated. Figure 8 shows the growth of $N(\tau)$ predicted by the average product operator model using only nearest neighbor couplings of 1.0 kHz. The analytical formulae used to calculate W^{f}_M and W^{r}_M in equation (13) are given in Levy and Gleason.[31] The three curves were obtained by considering 2500 nuclei arranged uniformly on linear, square, or cubic lattices. As expected, the three-dimensional configuration of nuclei yields the fastest MQ growth. The linear geometry yields slow linear growth of $N(\tau)$. The model can be used to simulate the MQ dynamics of various types of spin distribution and has been extended to nuclear distributions having more than one characteristic nearest neighbor dipole coupling.[31]

The model and experimental data can be compared by scaling the time axis in Figure 7. The experimental data for CaH_2 and for hydrogenated diamond powder given in Figure 9 are in good agreement with the computer simulations of MQ coherence growth for two- and three-dimensional nuclear distributions based on the average product operator

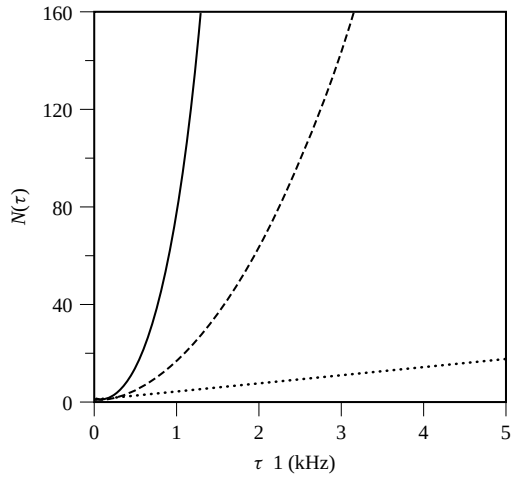

Figure 8 Values of $N(\tau)$ predicted by the average product operator model for spin-$\frac{1}{2}$ nuclei evenly spaced on a line, square lattice, or cubic lattice. In each case, the nearest neighbor dipole coupling was fixed at 1 kHz. The most rapid growth of $N(\tau)$ results for the cubic lattice which has the largest number of nearest neighbors, while the linear arrangement, with the lowest number of nearest neighbors, yields the slowest development of $N(\tau)$. (Reproduced by permission of NMR Concepts from Gleason[21]

model with only one adjustable parameter. In addition, the initial MQ growth of the pseudo-one-dimensional distribution of protons in hydroxyapatite has been found to agree with the slow, nearly linear growth predicted by the results of the product operator calculation for the one-dimensional distribution of nuclei.[33]

8 RELAXATION AND EFFECT OF MOLECULAR MOTION

MQ relaxation rates have been considered in detail by Ernst in terms of the Redfield formalism.[35] The zero quantum and

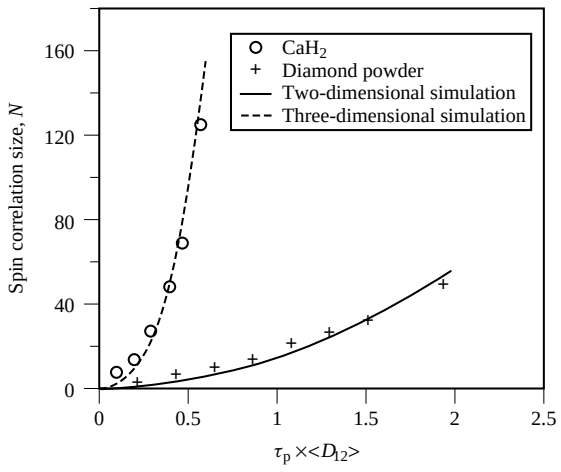

Figure 9 Comparison of MQ dynamics predicted by average operator theory and experimental data for infinite two- and three-dimensional systems. (Reproduced by permission of the American Chemical Society from Levy and Gleason[30]

$n \geq 2$ MQ relaxation rates provide information on the spectral densities of autocorrelation and cross-correlation functions which is not obtainable from the more traditionally measured single quantum relaxation rates. Since the sensitivity to static magnetic field inhomogeneity is proportional to the MQ order, this effect can be problematic when measuring higher order MQ relaxation rates. However, zero quantum relaxation rates have the desirable property of not being influenced by such gradients. This exact theoretical treatment of MQ relaxation has been applied to the external paramagnetic relaxation of two spin-$\frac{1}{2}$ nuclei in a liquid[35] and of an oriented CH_3 group in a liquid crystal.[36] However, application of this exact theory becomes increasingly difficult as the size of the coupled spin-$\frac{1}{2}$ network increases and when the results must be averaged over many possible orientations. Thus, although general considerations have been addressed,[23,28] the measurement and quantitive analysis of MQ relaxation in polycrystalline solids have been limited to date.

Empirically it has been observed that the total signal present in the detection period after MQ excitation of a rigid solid decreases with τ, often becoming negligible for $\tau > 1$ ms. The largest number of spins correlated is thus generally limited to between 100 and 1000, corresponding to a 1–2 nm length scale in a bulk three-dimensional solid. In addition, models for the growth of MQ coherence are difficult to validate because spin correlation data are generally only available for relatively very short τ.

Additional effects are observed when molecular motion modulates the dipolar couplings in solids through variations in internuclear distances and/or the orientation of the internuclear vectors with respect to the applied magnetic field.[20] When the timescale for motion is comparable to τ, complete time reversal of the preparation period is not achievable during the mixing period. Thus, the fraction of magnetization which is actually refocused by the MQ experiment f_{MQ} will generally be < 1. However, efficient refocusing can occur if the frequency of the molecular motion and the MQ experiment are matched correctly. Since τ is generally between 30 μs and 1 ms, motions with frequencies between 1 and 33 kHz can be probed. Since MQ coherences can involve anywhere from 2 to >100 nuclei, the correlated motion for atomic groups of various sizes can be probed, rather than tracking the motion of a single site.

As temperature is monotonically increased and the MQ preparation time is fixed, the frequency of motion can take on several of these special refocusing frequencies, interspersed by defocusing frequencies. Thus, a series of oscillations in f_{MQ} with temperature is expected. In addition to identifying the frequency of motion, the shapes of these oscillations are signatures of the underlying mechanism of molecular motion, e.g. multisite hops versus continuous rotations. Only motions which restore the relative positions of the nuclei after the MQ experiment will cause refocusing. Motions, such as translational diffusion, which do not restore the initial configuration of the nuclei will not produce refocusing under any condition.

Figure 10 shows the temperature dependent ^{19}F f_{MQ} for two polytetrafluoroethylene samples of different crystallinity.[19] Each line indicates a fixed value of the MQ preparation period τ. The overall decrease in f_{MQ} with increasing τ indicates that relaxation is not associated with molecular motion. However, at each fixed τ, oscillations in f_{MQ} can be seen. Oscillations in

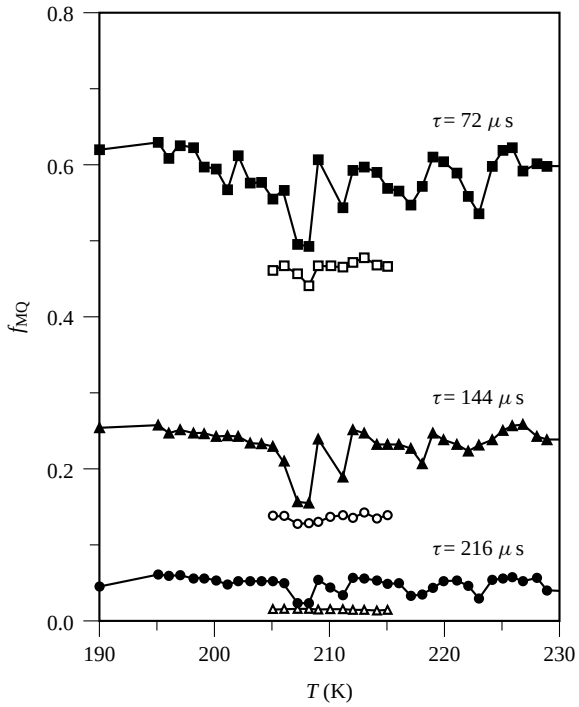

Figure 10 The fraction of refocused magnetization, f_{MQ} at three different values of τ as a function of temperature for *as*-polymerized (■, ▲, ●, ——) and melt-crystallized (□, ○, △, ------) polytetrafluoroethylene. Oscillations are seen only in the *as*-polymerized polymer, corresponding to the motion of a point defect

f_{MQ} are observed from 208 to 230 K for the 98% crystalline sample, while this ratio is constant over the same temperature range for the 64% crystalline sample. These oscillations may be associated with paracrystalline defects found only in the first sample. Thus, the MQ refocusing experiment is able to differentiate clearly between polymer samples which have different thermal histories. The sharpness of the MQ refocusing features and their variations in magnitude, shape, and sign with temperature are signatures of the molecular level details of the underlying dynamics which produce them.

9 RELATED ARTICLES

Amorphous Silicon Alloys; Average Hamiltonian Theory; Diamond Thin Films; Double Quantum Coherence; Liquid Crystals: General Considerations; Molecular Sieves: Crystalline Systems; Multiple Quantum Coherence in Spin-1/2 Dipolar Coupled Solids; Multiple Quantum Coherences in Extended Dipolar Coupled Spin Networks; Multiple Quantum Spectroscopy in Liquid Crystalline Solvents; Multiple Quantum Spectroscopy of Liquid Samples; Polymer Dynamics and Order from Multidimensional Solid State NMR.

10 REFERENCES

1. Y.-S. Yen and A. Pines, *J. Chem. Phys.*, 1983, **78**, 3579.
2. J. Baum, M. Munowitz, A. N. Garroway, and A. Pines, *J. Chem. Phys.*, 1985, **83**, 2015.
3. J. Baum and A. Pines, *J. Am. Chem. Soc.*, 1986, **108**, 7447.
4. J. Baum, K. K. Gleason, A. Pines, A. N. Garroway, and J. A. Reimer, *Phys. Rev. Lett.*, 1986, **56**, 1377.
5. K. K. Gleason, M. A. Petrich, and J. A. Reimer, *Phys. Rev. B*, 1987, **36**, 3259.
6. M. A. Petrich, K. K. Gleason, and J. A. Reimer, *Phys. Rev. B*, 1987, **36**, 9722.
7. S. Mitra, K. K. Gleason, H. Jia, and J. S. Shinar, *Phys. Rev. B*, 1993, **48**, 2175.
8. P.-K. Wang, C. P. Slichter, and J. H. Sinfelt, *Phys. Rev. Lett.*, 1984, **53**, 82.
9. R. Ryoo, S. B. Liu, L. C. de Menoval, K. Takegushi, B. Chmelka, M. Tresoshe, and A. Pines, *J. Phys. Chem.*, 1987, **91**, 6575.
10. S. J. Hwang, T. S. King, and B. C. Gerstein, *Catal. Lett.*, 1991, **8**, 367.
11. B. F. Chmelka, J. G. Pearson, S. B. Liu, R. Ryoo, L. C. de Menorval, and A. Pines, *J. Phys. Chem.*, 1991, **95**, 303.
12. J. G. Pearson, B. F. Chmelka, D. N. Shykind, and A. Pines, *J. Phys. Chem.*, 1992, **96**, 8517.
13. S. B. Hong, H. M. Cho, and M. E. Davis, *J. Phys. Chem.*, 1993, **97**, 1622.
14. S. B. Hong, H. M. Cho, and M. E. Davis, *J. Phys. Chem.*, 1993, **97**, 1629.
15. W. V. Gerasimowicz, A. N. Garroway, J. B. Miller, and L. C. Sander, *J. Phys. Chem.*, 1992, **96**, 3658.
16. B. E. Scruggs and K. K. Gleason, *J. Magn. Reson.*, 1992, **99**, 149.
17. B. E. Scruggs and K. K. Gleason, *Macromolecules*, 1992, **25**, 1864.
18. B. E. Scruggs and K. K. Gleason, *J. Magn. Reson.*, 1992, **99**, 149.
19. S. J. Limb, B. E. Scruggs, and K. K. Gleason, *Macromolecules*, 1993, **26**, 3750.
20. D. A. Lathrop and K. K. Gleason, *Macromolecules*, 1993, **26**, 4652.
21. K. K. Gleason, *Concepts Magn. Reson.*, 1993, **5**, 199.
22. G. Bodenhausen, *Prog. NMR Spectrosc.*, 1981, **14**, 137.
23. D. P. Weitekamp, *Adv. Magn. Reson.*, 1983, **11**, 111.
24. M. Munowitz and A. Pines, *Science*, 1986, **233**, 525.
25. S. Lacelle, *Adv. Magn. Opt. Reson.*, 1991, **16**, 173.
26. M. Mehring, *Principles of High Resolution NMR in Solids*, Springer, Berlin, 1983, pp. 233–259.
27. M. Munowitz, *Coherence and NMR*, Wiley, New York, 1988, pp. 123–124, 200–218.
28. T. J. Norwood, *Prog. Nucl. Magn. Reson. Spectrosc.*, 1992, **24**, 295.
29. B. C. Gerstein, M. Pruski, and S. J. Hwang, *Bull. Magn. Reson.*, 1993, **15**, 211.
30. A. Abragam, *The Principles of Nuclear Magnetism* Clarendon, Oxford, 1961.
31. D. H. Levy and K. K. Gleason, *J. Phys. Chem.*, 1992, **96**, 8125.
32. B. E. Scruggs and K. K. Gleason, *Chem. Phys.*, 1992, **166**, 367.
33. G. Cho and J. P. Yesinowski, *Chem. Phys. Lett.*, 1993, **205**, 1.
34. B. E. Scruggs and K. K. Gleason, *J. Phys. Chem.*, 1993, **97**, 9187.
35. A. Wokaun and R. R. Ernst, *Mol. Phys.*, 1978, **36**, 317.
36. J. Tang and A. Pines, *J. Chem. Phys.*, 1980, **72**, 3290.
37. J. B. Murdock, W. S. Warren, D. P. Weitekamp, and A. Pines, *J. Magn. Reson.*, 1984, **60**, 205.
38. M. Munowitz, *Mol. Phys.*, 1990, **71**, 959.
39. D. Suter, S. B. Liu, J. Baum, and A. Pines, *Chem. Phys.*, 1987, **114**, 103.

40. Y. Ba and W. S. Veeman, *Isr. J. Chem.*, 1992, **32**, 173.
41. M. Munowitz, A. Pines, and M. Mehring, *J. Chem. Phys.*, 1987, **86**, 3172.
42. B. C. Gerstein and C. R. Dybowski, *Transient Techniques in NMR of Solids*, Academic, Orlando, 1985, Chap. 5
43. L. M. Moran and J. P. Yesinowski, *Chem. Phys. Lett.*, 1994, **222**, 363.
44. A. N. Garroway, J. Baum, M. G. Munowitz, and A. Pines, *J. Magn. Reson.*, 1984, **60**, 337.
45. C. J. Lee, N. Murali, and N. S. Warren, *Adv. Magn. Reson.*, 1990, **14**, 241.
46. S. Emid, *Physica B*, 1985, **128**, 79.

Biographical Sketch

Karen K. Gleason. *b* 1960. B.S., 1982, M.S., 1982, MIT; Ph.D., University of California, Berkeley, 1987. Introduced to NMR by J.A. Reimer. Faculty, Chemical Engineering, MIT, 1987–present. Approx. 50 publications. Research interests: application of NMR to thin films and interfaces, particularly for detecting low concentrations of hydrogen, and development of multiple quantum NMR spectroscopy.

Nutation Spectroscopy of Quadrupolar Nuclei

Bernard C. Gerstein

Ames Laboratory of Iowa State University, Des Moines, IA, USA

1	Introduction	1
2	General Considerations: Hamiltonians	1
3	The Nutation Spectrum	3
4	Experimental Considerations	3
5	Phasing of the Spectra	4
6	Line Broadening	4
7	Effect of Recycle Delay	4
8	An Example: ^{45}Sc in $Sc_2(SO_4)_3$	4
9	Related Articles	4
10	References	4

1 INTRODUCTION

As pointed out in the article ***Rudimentary NMR: The Classical Picture***, the natural motion of a magnetic moment in a field is a precession, or nutation, of the moment $\boldsymbol{M} = \gamma \boldsymbol{I}$ about the field $\boldsymbol{B}$ with nutation frequency $\omega = \gamma B$. It is this nutation in the rotating frame of the Zeeman interaction, as applied to the NMR spectra of nuclei with quadrupolar moments $I \geq 1$ that is the subject of this discussion. The main difference between the case discussed here and NMR of spin-$\frac{1}{2}$ nuclei is that in general the condition $\hat{\mathcal{H}}_{\rm rf} > \hat{\mathcal{H}}_{\rm int}$ is not met, so the condition for assuming that the rf pulses take place in an infinitely short time compared with the effects of internal Hamiltonians is violated.

In this case, we must consider the time development of the system when both the quadrupolar Hamiltonian and the rf Hamiltonian are of the same order of magnitude, or even when $\hat{\mathcal{H}}_{\rm Q} > \hat{\mathcal{H}}_{\rm rf}$. It was realized[1] that even in this case quite useful information could be extracted if the experiment was made into a two-dimensional situation, where the system evolves in time under $\hat{\mathcal{H}}_{\rm rf} + \hat{\mathcal{H}}_{\rm Q}$ for a time t_1, and then evolves under just $\hat{\mathcal{H}}^{\rm Q}$ for a time period t_2. The double Fourier transform on both times then yields the nutation spectrum, e.g. in Figure 1, from which may be inferred the number of different chemical species in the sample under investigation, and the relative values of the quadrupole versus the rf interactions, as discussed below.

2 GENERAL CONSIDERATIONS: HAMILTONIANS

As discussed by Mehring in ***Internal Spin Interactions and Rotations in Solids***, the form of the rf Hamiltonian for, e.g. a pulse with x phase, is

$$\hat{\mathcal{H}}_{\rm rf} = -\omega_1 \hat{I}_x \equiv -\omega_{\rm rf} \hat{I}_x \tag{1}$$

The pertinent Hamiltonian for a static sample during the evolution period under the influence of an rf pulse turned on for a time t_1, with x phase and a quadrupolar interaction not small compared with the pulse strength Ω_1, including and offset from resonance is

$$\begin{aligned}\hat{\mathcal{H}}^1(t_1) &= [\hat{\mathcal{H}}_{\rm off} + \hat{\mathcal{H}}_{\rm rf} + \hat{\mathcal{H}}^1_{\rm Q}] \\ &= \delta \hat{I}_z - \omega_1 \hat{I}_x + \omega^*_{\rm Q}[3\hat{\boldsymbol{I}}^2 - I(I+1)]\end{aligned} \tag{2}$$

where $\omega_{\rm Q}{}^* = \omega_{\rm Q}(3\cos^2\theta - 1 + \eta \sin^2\theta \cos 2\phi)$, and $\omega_{\rm Q} = 2\pi e^2 qQ/8hI(I+1) \equiv 2\pi\chi/8I(I+1)$, and θ, ϕ are the polar angles orienting the electric field gradient (EFG) tensor with respect to the static field axis, taken to be the z axis in the laboratory, and η is the asymmetry of the EFG tensor. Dipolar interactions and nonsecular quadrupolar interactions (second-order terms) have been neglected.

After the rf pulse, assumed to be strong compared with the magnitude of the shielding Hamiltonian, the system evolves for time t_2 under shielding, chemical shift, and the nonsecular quadrupolar terms (taking into account only the central $\frac{1}{2}-\frac{1}{2}$ transition),

$$\hat{\mathcal{H}}^2(t_2) = \hat{\mathcal{H}}_{\rm Z} + \hat{\mathcal{H}}_{\rm CS} + \hat{\mathcal{H}}^2_{\rm Q} \tag{3}$$

where Z stands for Zeeman, CS is chemical shift, and the superior 2 means the nonsecular second-order terms which have the major effect on the central transition. Using the density matrix formalism,[2] with the equilibrium density operator in the high temperature form, in the frame of detection of the signal which is the rotating frame (the Zeeman interaction disappears from the description), the evolution during time t_1 is

$$\hat{\rho}(t_1) = \exp\{-{\rm i}\hat{\mathcal{H}}_1 t_1\}\hat{\rho}\exp\{{\rm i}\hat{\mathcal{H}}_1 t_1\} \tag{4}$$

While the Zeeman states $|I, m\rangle$ are not exact eigenfunctions of the first- and second-order quadrupolar Hamiltonians, their linear combinations will be and can be found by diagonalization of the total Hamiltonian. If $\mathbf{T}$ is the orthogonal transformation which diagonalizes the Hamiltonian, then we may express the density operator at time t_1 in matrix form as

$$\boldsymbol{\rho}(t_1) = \mathbf{T}\cdot\exp\{-{\rm i}\mathbf{D}t_1\}\mathbf{T}^+\boldsymbol{\rho}(0)\mathbf{T}\exp\{{\rm i}\mathbf{D}t_1\}\mathbf{T}^+ \tag{5}$$

$\mathbf{D}$ represents the diagonalized matrix of the Hamiltonian $\hat{\mathcal{H}}^1$ with eigenvalues

$$E_j = \sum_p T^*_{pj} H^1_{pq} T_{qj} \tag{6}$$

and eigenfunctions

$$|j\rangle = \sum_k T^*_{kj}|I, m_k\rangle \tag{7}$$

Assuming that only coherence between states $|\frac{1}{2}\rangle$ and $|-\frac{1}{2}\rangle$ is detected during time t_2, so only the elements $\rho_{1/2,-1/2}$ need

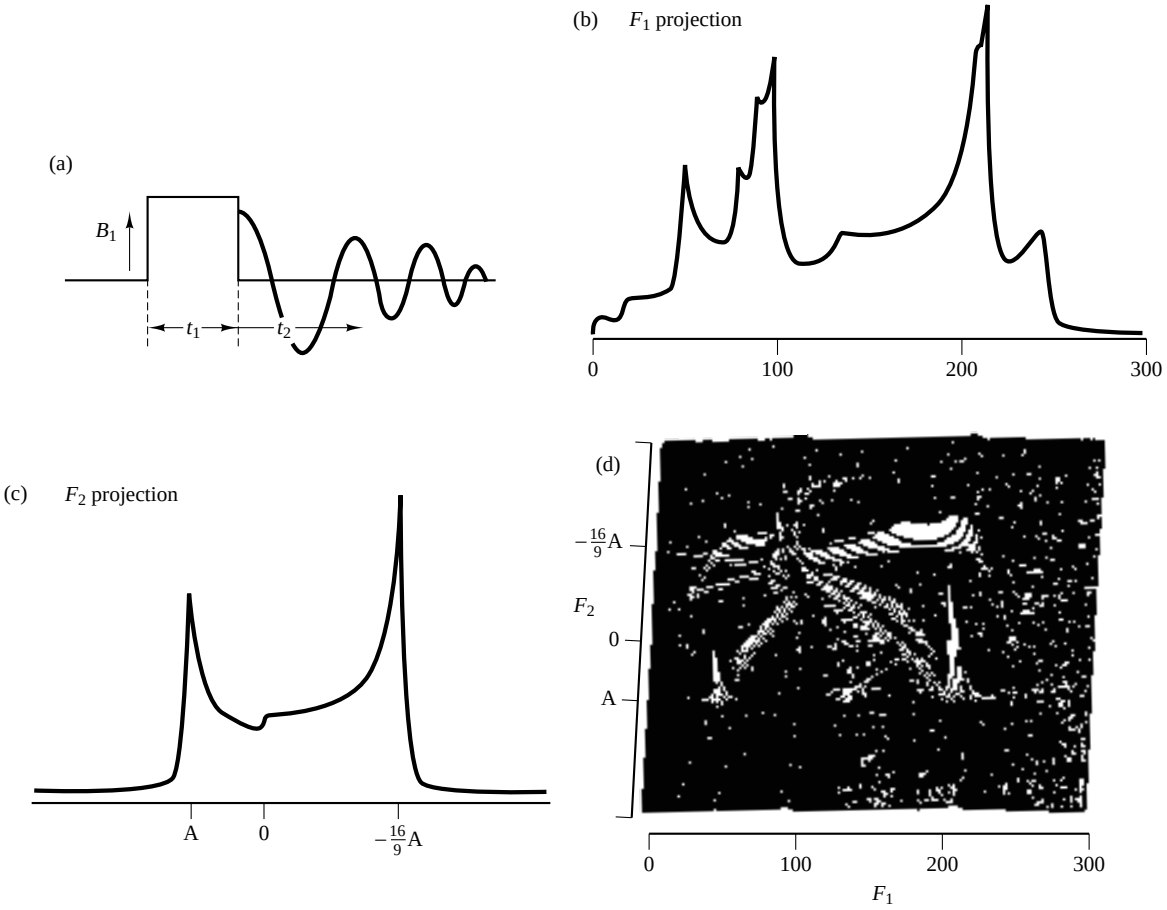

Figure 1 (a) Pulse scheme of the experiment; a free induction decay is acquired during t_2 as a function of the pulse length t_1. Subsequent Fourier transformation of the signals obtained yields a typical 2D powder pattern as shown in (d). This spectrum was calculated for $I = \frac{5}{2}$ with a ratio $\omega_Q/\omega_{rf} = 0.45$ and $\eta = 0$. The F_2 projection of this pattern (c) gives the second-order quadrupole powder pattern, and the F_1 projection (b) is a characteristic nutation spectrum for the ratio ω_Q/ω_{rf}

be evaluated, the signal from the central transition $S(t_1, t_2)$ can then be evaluated as follows:

$$S(t_1, t_2) = \mathrm{Tr}\{\hat{\rho}(t_1, t_2)(\hat{I}_x + \mathrm{i}\hat{I}_y)\} \propto \hat{\rho}(t_1)_{1/2,-1/2} \exp\{-\mathrm{i}\omega_2 t_2\}$$
$$= \sum_{k,j} (R_{-1/2,1/2})_{k,j} \exp\{\mathrm{i}\omega_{k,j} t_1\} \exp\{-\mathrm{i}\omega_2 t_2\} \quad (8)$$

Here, ω_2 represents the Larmor precession of the spins during the time t_2 and ω_{kj} is the transition frequency in the rotating frame between states $|k\rangle$ and $|j\rangle$. The coefficients $(R_{-1/2,1/2})_{kj}$ represent the contributions from coherence between states $|k\rangle$ and $|j\rangle$ in the rotating frame during t_1 to the $\frac{1}{2}$, $-\frac{1}{2}$ coherence detected during t_2:

$$(R_{-\frac{1}{2},\frac{1}{2}})_{k,j} = T_{\frac{1}{2},k} T^*_{-\frac{1}{2},j} \sum_m T^*_{m,k} T_{m,j} \rho(0)_{m,m} \quad (9)$$

The states of an isolated spin-$\frac{7}{2}$ in the presence of magnetic field B, with quadrupole coupling constant $2\pi\chi = 1$ MHz and asymmetry $\eta = 0$, are shown in Figure 2.

In summary, during time t_1 the system develops in time with eigenfunctions and eigenvalues which depend upon the ratio of ω^*_Q and ω_{rf}. The coherences between these levels, with frequency ω_{kj}, develop during time t_1 and contribute to the coherence detected between the state $|\frac{1}{2}\rangle$, $|-\frac{1}{2}\rangle$ detected during time t_2. Therefore, a 2D Fourier transform of the acquired signal will give a characteristic powder pattern [Figure 1(d)], with projection on the F_2 axis shown in Figure 1(c) being the normal powder pattern of the $\frac{1}{2}-\frac{1}{2}$ transition associated with

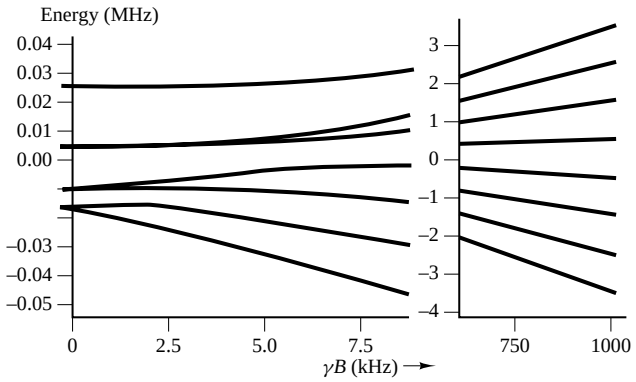

Figure 2 Energy diagram of an isolated spin $I = \frac{7}{2}$ in the presence of a magnetic field B with quadrupole parameters $e^2qQ/h = 1$ MHz and $\eta = 0$. On the left is the low field situation $\mathcal{H}_Z < \mathcal{H}_Q$ and on the right is the situation $\mathcal{H}_Z \gg \mathcal{H}_Q$, where $\mathcal{H}_Q$ appears to be negligible

shielding anisotropy and second-order quadrupole broadening. Projection onto the F_1 axis [Figure 1(b)] gives the nutation spectrum which depends upon the quadrupole parameters χ and η, the spin quantum number I, and the rf field strength ω_1, and is independent of chemical shift.

3 THE NUTATION SPECTRUM

As an example, the calculated nutation spectra as a function of ω_Q/ω_{rf} is shown in Figure 3.

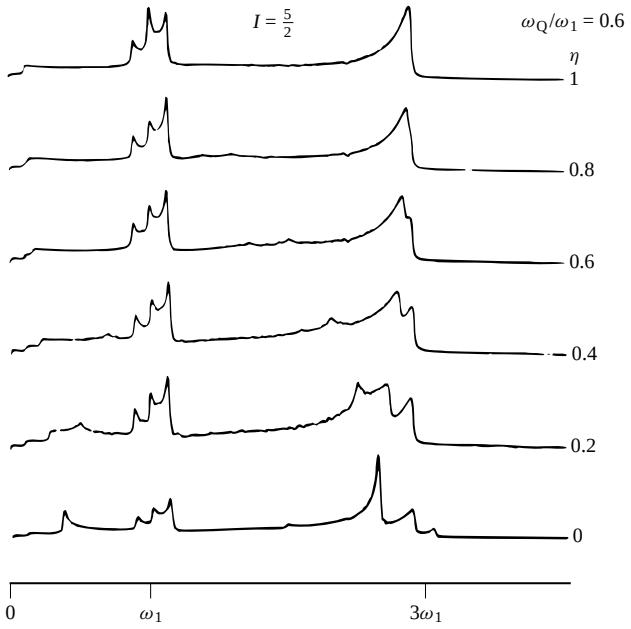

Figure 3 Calculated nutation spectra as a function of ω_Q/ω_{rf} ($\eta = 0$)

When there is only one site for the species under study, a 1D nutation spectrum suffices to characterize this species. When nuclei of a given spin are present in more than a single environment, it is advantageous to study the entire 2D powder pattern.

4 EXPERIMENTAL CONSIDERATIONS

To obtain experimental nutation spectra which can be compared with the calculated spectra, it is important to keep several experimental conditions in mind.

The first of these is the resonance offset. Thus, when the system is irradiated on-resonance ($\omega = \omega_0$) then the matrix of H_1 in equation (10) becomes symmetric with respect to both diagonals of the matrix. As a result of this

$$\left.\begin{aligned} (R_{-1/2,1/2})_{i,j} &= -(R_{-1/2,1/2})_{j,i}, \quad i \neq j \\ &\text{and} \\ (R_{-1/2,1/2})_{i,j} &= 0, \qquad\qquad i = j \end{aligned}\right\} \tag{10}$$

Substitution in equation (8) shows that the signal then becomes

$$S(t_1, t_2) = \sum_{i<j} (R_{-1/2,1/2})_{i,j} \sin\{\omega_{ij} t_1\} \exp\{-i\omega_2 t_2\} \tag{11}$$

The amplitude of the signal detected during t_2 is sine-modulated, which allows us to obtain pure absorption spectra. The presence of an off-resonance term in B_1 lowers the symmetry of its matrix and the modulation now becomes a phase modulation, which cannot be changed to amplitude modulation by phase cycling. Thus there will be dispersive contributions to the lineshapes which can easily distort powder patterns.

Another effect of off-resonance irradiation is the appearance of a dispersive line at $\omega_1 = 0$. This is due to the magnetization component along the $\boldsymbol{B}_{eff}$ field in the rotating frame which does not evolve during t_1. Both effects of off-resonance irradiation can even be observed for spins with $I = \frac{1}{2}$ for which the signal in such a case can be written as:

$$\begin{aligned} S(t_1, t_2) \sim [&A(1 - \cos(\omega_{eff} t_1) + iB \sin(\omega_{eff} t_1)] \\ &\times \exp\{-i\omega_2 t_2\} \end{aligned} \tag{12}$$

where $A = \omega_{rf}\Delta\omega/2(\omega_{rf}^2 + \Delta\omega^2)$ and $B = \omega_{rf}/2\sqrt{(\omega_{rf}^2 + \Delta\omega^2)}$. When $\Delta\omega = \omega - \omega_0 \neq 0$, then $A \neq 0$ and thus a constant and a $\cos(\omega_{eff} t_1)$ term is introduced, causing respectively the $\omega_1 = 0$ signal and the phase modulation. To avoid complications it is clearly recommendable to irradiate on-resonance, i.e. with the excitation frequency ω equal to the Larmor frequency γB_0. That on-resonance in this case does not mean equal to the $\frac{1}{2}$, $-\frac{1}{2}$ transition frequency is shown by the following magic angle spinning (MAS) experiment. Here the Larmor frequency lies outside the quadrupole lineshape and Figure 4 shows the nutation spectra of $NaNO_2$ ($e^2qQ/h = 1.1$ MHz, $\eta = 0.1$) as a function of the excitation frequency. In this case we are in the extreme situation $\omega_Q \gg \omega_{rf}$ and MAS does not influence the nutation spectrum. It is clear that the line at $\omega_1 = 0$ increases relative to the line at $2\omega_{rf}$. The line at $\omega_1 = 0$ is

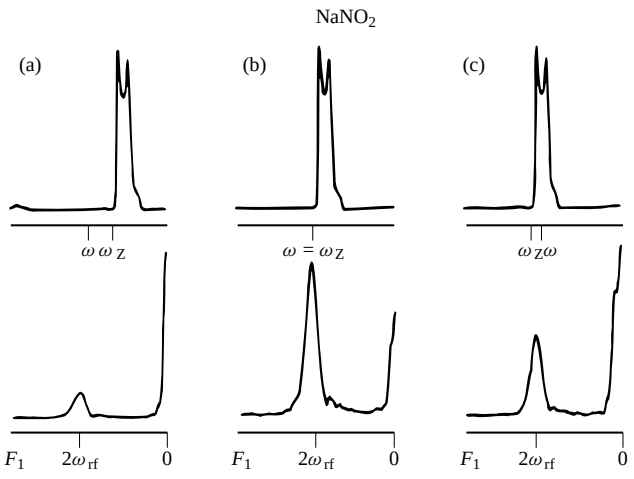

Figure 4 MAS spectra of $NaNO_2$ together with their nutation spectra as a function of the excitation frequency ω. (a) Off-resonance irradiation; in the nutation spectrum we see a large line at $\omega_1 = 0$. (b) Irradiation close to the Larmor frequency (outside the powder pattern) gives the best nutation spectrum. (c) With the carrier frequency equal to the average $\frac{1}{2}$, $-\frac{1}{2}$ transition frequency (in the middle of the powder pattern), the line at $\omega_1 = 0$ increases again

minimal when we irradiate outside the powder pattern near the Larmor frequency. An easy method to reduce the line at $\omega_1 = 0$ is to subtract the last (longest t_1 value) experiment in the 2D experiment from all the previous experiments. When enough t_1 experiments are performed, the quadrupolar modulation has damped out, and the only signal emerging after a long rf pulse is that of the magnetization causing the zero frequency signal in the F_1 direction. Because the magnetization component along $\boldsymbol{B}_{\text{eff}}$ has the same magnitude in every experiment (assuming no relaxation), subtraction of the last experiment reduces its influence on the spectrum.

5 PHASING OF THE SPECTRA

It is important to obtain pure absorption spectra when one wants to obtain 2D powder patterns which can be analyzed in a straightforward way. Because we want no dispersion signals to appear in the spectrum, it is not possible to perform an absolute value calculation. Therefore, the spectra have to be phased manually. As we have seen in the preceding paragraph, off-resonance irradiation introduces phase modulation and thus dispersive lineshapes are introduced in the spectra. This makes it very difficult to phase the spectra properly. This is so difficult because when phasing a 2D spectrum one has to set the phase correction on one slice (row or column) of the spectrum and it is not possible to inspect the effect of such a phase correction on the total spectrum. It would be desirable to have a program that shows the phase corrections of the whole spectrum directly on the display. As modern NMR spectrometers are equipped with minicomputers using array processors, it should be possible to do so because nutation spectra are generally of small size.

When one is only interested in the 1D nutation spectrum (the F_1 projection) of a sample, there is a way to avoid phasing the whole 2D spectrum. In this case we can take the first point of every FID emerging directly after the pulse of length t_1. If we arrange these points as a function of t_1, we have the amplitude modulation of the detected t_2 signal as a 1D interferogram. A straightforward 1D Fourier transform of this interferogram will give us the nutation spectrum which can be phased easily.

6 LINE BROADENING

An important cause of line broadening in the F_1 dimension is the inhomogeneity of the rf magnetic field. The effect of rf inhomogeneity cannot simply be described with a Lorentzian broadening $\exp(-t_1/\tau_1)$ because a spread in ω_{rf} will also cause a spread in the ratio $\omega_{\text{Q}}/\omega_{\text{rf}}$, and will thus change the whole nutation spectrum. Furthermore the lineshapes due to rf inhomogeneity will not be Lorentzian but asymmetric. Only in the extreme case $\omega_{\text{rf}} \gg \omega_{\text{Q}}$ do we get a line at nutation frequency ω_{rf} with a linewidth directly determined by the rf inhomogeneity. In the other extreme case $\omega_{\text{rf}} \ll \omega_{\text{Q}}$, there will be a line at $(I + \frac{1}{2})\omega_{\text{rf}}$, so the linewidth will be $(I + \frac{1}{2})\gamma$-times the rf inhomogeneity. It is therefore important to use a probe with an accurately formed rf coil to reduce rf inhomogeneity as much as possible, and care should be taken that the whole sample is in the coil.

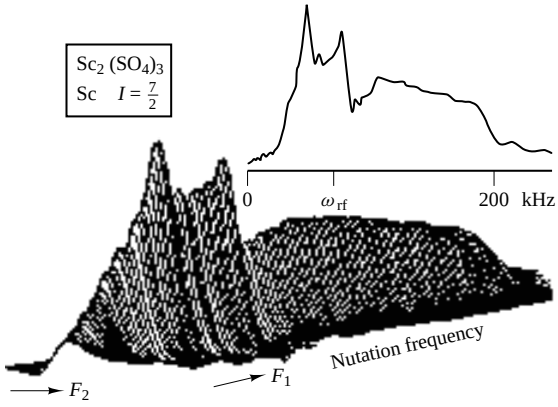

Figure 5 Two-dimensional nutation spectrum of ^{45}Sc in $Sc_2(SO_4)_3$ recorded on a Bruker WM-500 instrument, together with its F_1 projection (256 t_1 increments of 1.5 μs with a 70 kHz rf field)

7 EFFECT OF RECYCLE DELAY

Another important experimental aspect in the nutation experiment is that one has to ensure that the recycle delay or relaxation delay is long enough for the system to return to equilibrium before the next pulse arrives. If the recycle delay is short with respect to T_1 then the build up of magnetization along the z axis is incomplete. This will distort the pure sine amplitude modulation of the FID. Fourier transformation of a distorted sin $\omega_1 t$ wave will give a line at frequency ω_1 plus a number of harmonics at $2\omega_1$, $3\omega_1$, ... The number and amplitude of these harmonics depend on the distortion of the sine wave, and they can easily be mistaken for components with a large quadrupole frequency.

8 AN EXAMPLE: ^{45}Sc IN $Sc_2(SO_4)_3$

An example is the ^{45}Sc ($I = \frac{7}{2}$) nutation spectrum of $Sc_2(SO_4)_3$ (Figure 5). The spectrum of the central transition measured at 121.5 MHz is 2.6 kHz wide and shows no structure; MAS narrows the spectrum to 600 Hz. The MAS spectrum recorded at 43.8 MHz does show some structure from which it becomes clear that there must be sites with different quadrupole parameters but the same chemical shift. The 2D nutation spectrum is well structured. Comparing its projection to our set of calculated spectra reveals that the major constituent has $e^2qQ/h \sim 2$ MHz with a low asymmetry parameter ($\eta \sim 0.2$).

9 RELATED ARTICLES

Inorganic Solids; Internal Spin Interactions and Rotations in Solids; Quadrupolar Interactions; Quadrupolar Nuclei in Glasses; Quadrupolar Nuclei in Solids.

10 REFERENCES

1. E. Kundla, A. Samoson, and E. Lippmaa, *Chem. Phys. Lett.*, 1981, **83**, 229.

2. T. Farrar and J. E. Harriman, *Density Matrix Theory and its Applications in NMR Spectroscopy*, The Farragut Press, Madison, WI, 1992.

Acknowledgments

Most of the material in this treatment came from the Ph.D. Thesis of A. P. M. Kentgens, under the direction of Wiebren Veeman at The Katholieke Universiteit te Nijmegen, The Netherlands, with the permission of Wiebren Veeman.

Biographical Sketch

Bernard C. Gerstein. *b* 1932. B.S., 1953, Purdue, USA; Ph.D., 1960, Iowa State University. Introduced to NMR by R. W. Vaughan. Faculty in Chemistry, Iowa State University, 1962–present. Approx. 150 publications. Research interests include the theory and practice of learning, and applications of solid state NMR to problems in the physics and chemistry of materials, fossil fuels, and heterogeneous catalysis.

Overtone Spectroscopy of Quadrupolar Nuclei

Robert Tycko

National Institutes of Health, Bethesda, MD, USA

1	Introduction	1
2	Theory	1
3	Experiments	2
4	Conclusions	4
5	Related Articles	5
6	References	5

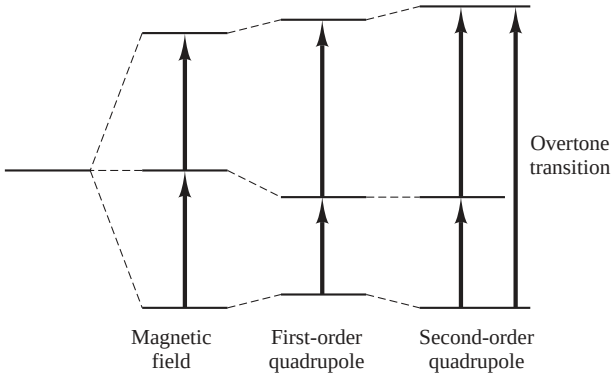

Figure 1 Spin energy levels for a spin-1 nucleus. The splitting of the energy levels due to a strong magnetic field and the first-order and second-order perturbations of the energy levels due to a quadrupole coupling are shown. (Adapted by permission of the American Chemical Society from R. Tycko and S. J. Opella, *J. Am. Chem. Soc.*, 1986, **108**, 3531)

1 INTRODUCTION

In the context of NMR, 'overtone spectroscopy' refers to the direct excitation of nuclear spin transitions and coherences and the direct detection of NMR signals at frequencies that are nearly multiples of the Larmor frequency ν_0. Overtone spectroscopy depends on the excitation and detection of 'forbidden' transitions, i.e. transitions that cannot be excited or detected directly in the limit of very strong external dc magnetic fields but that become excitable or detectable directly when the interactions of nuclear spins with the dc field are not very much stronger than the internal nuclear spin couplings. Recent interest in overtone spectroscopy grew out of the work of Bloom and LeGros,[1] who showed that overtone transitions have sufficient intensity in practice to be of experimental utility. Subsequent work[2,3] showed that overtone spectroscopy has real advantages when applied to solid state NMR measurements of integer-spin nuclei with large quadrupole couplings. Since ^{14}N is the most important nucleus of this type from the standpoint of chemistry and biochemistry, recent work has focused on ^{14}N overtone NMR.

Overtone spectroscopy should be distinguished from multiple quantum spectroscopy. In multiple quantum spectroscopy, one typically applies rf pulses with a carrier frequency close to ν_0 in order to excite nuclear spin coherences with oscillation frequencies that are nearly multiples of ν_0. The oscillation of these coherences is then detected indirectly through its effect on the single quantum signals near ν_0. In overtone spectroscopy, the rf carrier frequency is about equal to the oscillation frequency of the coherences, and the oscillation of the coherences is detected directly. Conceptually speaking, overtone spectroscopy can be thought of as a single photon spectroscopy, while multiple quantum spectroscopy can be thought of as a multiple photon spectroscopy. In some cases, the same coherences may be excited and detected either by overtone NMR or by multiple quantum NMR. As a general rule, overtone methods are probably more effective than multiple quantum methods when the nuclear quadrupole splittings exceed 1 MHz.

Figure 1 shows a spin energy level diagram for a spin-1 nucleus such as ^{14}N. A spin-1 nucleus has three possible eigenstates. In the absence of all spin interactions, the three states are degenerate. The interaction with an external dc field produces three equally spaced energy levels and two allowed, single quantum transitions at frequency ν_0. A nuclear quadrupole coupling that is weaker than the interaction with the external field perturbs the energy levels. To first order, a quadrupole coupling with coupling constant ν_Q shifts the middle ($m = 0$) level relative to the upper and lower ($m = \pm 1$) levels by an amount $\nu_Q^{(1)}$ proportional to ν_Q. This produces the first-order quadrupole splitting, with single quantum transitions at $\nu_0 \pm \nu_Q^{(1)}$. To second order, the quadrupole coupling additionally shifts the upper and lower levels by amounts $\pm\nu_Q^{(2)}$ proportional to ν_Q^2/ν_0. This is the second-order quadrupole shift. The single quantum transitions are then at $\nu_0 \pm \nu_Q^{(1)} + \nu_Q^{(2)}$. In addition, the overtone transition at frequency $2\nu_0 + 2\nu_Q^{(2)}$ becomes weakly allowed, producing signals and nutation frequencies proportional to ν_Q/ν_0 in pulsed NMR experiments. Although the overtone signals are intrinsically weaker than the allowed single quantum (or 'fundamental') signals, the fact that the overtone spectrum spans a frequency range that is narrower than the single quantum spectrum by a factor of the order of ν_Q/ν_0 makes measurement of the overtone signals substantially more tractable, especially in polycrystalline and noncrystalline solids (where the resonance lines are inhomogeneously broadened powder patterns) and in single crystals with several inequivalent sites. Thus, particularly in ^{14}N NMR, overtone spectroscopy allows NMR signals to be obtained and nuclear relaxation rates to be measured in systems where NMR experiments would otherwise be extremely difficult or impossible. Overtone spectra also contain structural information that is absent in single quantum spectroscopy, through the dependence of the overtone transition moment on the molecular or crystal orientation and on the direction of the applied rf field.

Overtone NMR spectroscopy of spin-1 nuclei is analogous to earlier 'half-field' electron paramagnetic resonance (EPR) studies of triplet states,[4,5] with the nuclear quadrupole coupling taking the place of the electronic spin–spin coupling or zero field splitting. Calculations of lineshapes and transition probabilities carried out for half-field EPR[6,7] are therefore applicable to overtone NMR of spin-1 nuclei.

2 THEORY

A detailed description of the theory and the implementation of overtone spectroscopy has been given by Tycko and Opella.[3] The essential theoretical points follow from consideration of the spin Hamiltonian $\hat{\mathcal{H}}$ for a quadrupolar nucleus with spin $\hat{S}$:

$$\hat{\mathcal{H}} = \hat{\mathcal{H}}_{\mathrm{S}} + \hat{\mathcal{H}}_{\mathrm{rf}} \tag{1}$$

$$\hat{\mathcal{H}}_{\mathrm{S}} = -h\nu_0\hat{S}_z + h\nu_{\mathrm{Q}}[3\hat{S}^2_{z'} - \hat{S}^2 + \eta(\hat{S}^2_{x'} - \hat{S}^2_{y'})] \tag{2}$$

$$\hat{\mathcal{H}}_{\mathrm{rf}} = 2\hbar\gamma_S B_1(\hat{S}_x\cos\theta + \hat{S}_z\sin\theta)\cos(2\pi\nu t + \phi) \tag{3}$$

$\hat{\mathcal{H}}_{\mathrm{S}}$ includes the interaction with the external dc field along z (the Zeeman interaction) and the quadrupole coupling. The principal axes of the quadrupole coupling tensor are $x'y'z'$. ν_{Q} is defined as $(e^2qQ)/[4S(2S-1)]$. $\hat{\mathcal{H}}_{\mathrm{rf}}$ is the interaction with an rf field with amplitude $\boldsymbol{B}_1$, frequency ν, phase ϕ, and direction in the xz plane at angle θ to x. γ_S is the nuclear gyromagnetic ratio. In the limit $\nu_0 \gg \nu_{\mathrm{Q}}$, the eigenstates of $\hat{\mathcal{H}}_{\mathrm{S}}$ are simply the eigenstates of S_z, i.e. $\{|m\rangle\}$. When this limit does not apply, but $\nu_0 > \nu_{\mathrm{Q}}$, the eigenstates are $\{|\psi_m\rangle\}$, given by

$$|\psi_m\rangle = |m\rangle + \sum_{m'\neq m} C_{mm'}|m'\rangle \tag{4}$$

If the laboratory axes (xyz) and quadrupole principal axes ($x'y'z'$) are related by Euler angles α, β, and γ, the coefficients $C_{mm'}$ are given to first order in ν_{Q}/ν_0 by

$$\begin{aligned} C_{mm'} = \frac{\nu_{\mathrm{Q}}}{2(m'-m)\nu_0}\{&-\delta_{m',\,m+1}[S(S+1) \\ &-m(m+1)]^{\frac{1}{2}}(2m+1)F(\alpha,\beta,\gamma) - \delta_{m',\,m-1} \\ &\times[S(S+1)-m(m-1)]^{\frac{1}{2}}(2m-1)F^*(\alpha,\beta,\gamma) \\ &+\delta_{m',\,m+2}\{[S(S+1)-m(m+1)][S(S+1) \\ &-(m+1)(m+2)]\}^{\frac{1}{2}}G(\alpha,\beta,\gamma) \\ &+\delta_{m',\,m-2}\{[S(S+1)-m(m-1)][S(S+1) \\ &-(m-1)(m-2)]\}^{\frac{1}{2}}G^*(\alpha,\beta,\gamma)\} \end{aligned} \tag{5a}$$

$$\begin{aligned} F(\alpha,\beta,\gamma) = e^{i\gamma}[&3\sin\beta\cos\beta - \eta(\cos 2\alpha\sin\beta\cos\beta \\ &+ i\sin 2\alpha\sin\beta)] \end{aligned} \tag{5b}$$

$$\begin{aligned} G(\alpha,\beta,\gamma) = e^{2i\gamma}\Bigg\{&\frac{3}{2}\sin^2\beta \\ &+\eta\left[\frac{1}{2}\cos 2\alpha(1+\cos^2\beta) + i\sin 2\alpha\cos\beta\right]\Bigg\} \end{aligned} \tag{5c}$$

To second order in ν_{Q}/ν_0, the energy E_m of the state $|\psi_m\rangle$ is

$$\begin{aligned} E_m = h\nu_0\Bigg\{&-m + \frac{\nu_{\mathrm{Q}}}{2\nu_0}[3m^2 - S(S+1)][(3\cos^2\beta - 1) \\ &+\eta\cos 2\alpha\sin^2\beta] + \sum_{m'\neq m}(m'-m)|C_{mm'}|^2\Bigg\} \end{aligned} \tag{6}$$

The orientation-dependent frequency of the overtone transition in a spin-1 nucleus is then

$$\nu_{1,\,-1}(\alpha,\beta,\gamma) = 2\nu_0 + \frac{\nu_{\mathrm{Q}}^2}{\nu_0}(|F(\alpha,\beta,\gamma)|^2 + |G(\alpha,\beta,\gamma)|^2) \tag{7}$$

and the orientation-dependent transition moment is

$$\begin{aligned} M_{1,\,-1}(\alpha,\beta,\gamma) &\equiv \langle\psi_1|S_x\cos\theta + S_z\sin|\psi_{-1}\rangle \\ &= \frac{\nu_{\mathrm{Q}}}{\nu_0}[\sin\theta F(\alpha,\beta,\gamma) + \cos\theta G(\alpha,\beta,\gamma)] \end{aligned} \tag{8}$$

The nutation frequency (i.e. the inverse of the 2π pulse length) for excitation of the overtone transition is given by $\gamma_S B_1|M_{1,-1}|/\pi$. The overtone signal amplitude is proportional to $|\rho_{1,-1}M_{1,-1}|$, where $|\rho_{1,-1}|$ is the amplitude of the overtone coherence excited by rf pulses. Thus, equation (8) displays the unusual features of overtone spectroscopy that the nutation frequency depends on the orientation of the quadrupole tensor principal axis system, that overtone transitions can be excited by rf fields applied parallel to the external dc field ($\theta = \pi/2$), and that signals can be detected by rf solenoid coils wound parallel to the dc field. Overtone powder pattern lineshapes in polycrystalline and noncrystalline solids are determined by the orientation-dependent overtone frequency in equation (7) weighted by an orientation-dependent function related to $M_{1,-1}$. The precise details of the weighting function depend on the excitation method. In the linear (i.e. small flip-angle pulse) regime, the weighting function is $|M_{1,-1}|^2$. Equation (8) shows that the weighting function, and hence the observed lineshape, depends on θ.

Since the coefficients $C_{mm'}$ are nonzero only for $|m - m'| = 1$ or 2, only the first ($\nu \approx 2\nu_0$) and second ($\nu \approx 3\nu_0$) overtone transitions have transition moments proportional to ν_{Q}/ν_0, and only the first overtone transition has a transition moment proportional to ν_{Q}/ν_0 when $\theta = \pi/2$. Higher overtone transitions are weaker, with transition moments proportional to higher powers of ν_{Q}/ν_0.

3 EXPERIMENTS

3.1 Detection of ^{14}N Overtone Transitions by CW NMR

Creel et al.[8] have reported the detection of the ^{14}N spectrum of hexamethylenetetramine by CW NMR methods in fields up to 2.2 T, where ν_0 = 6.6 MHz. The quadrupole coupling frequency $\nu_{\mathrm{Q}} = (e^2qQ)/4h$ is roughly 1.1 MHz in hexamethylenetetramine. Although the fields in these experiments were low by modern standards, they were high enough that the highest frequency ^{14}N signals can be considered to be overtones of the lower frequency signals.

3.2 Indirect Detection of ^{14}N Overtone Transitions

Blinc et al.[9] measured the ^{14}N NMR spectrum of triglycine sulfate by means of the Hartmann–Hahn double resonance, indirect detection technique.[10] Working in a 0.42 T field, they determined the ^{14}N resonant frequencies by observing proton NMR signals following an adiabatic demagnetization–adiabatic remagnetization cycle, with rf irradiation of the ^{14}N nuclei during a delay period between the demagnetization and remagnetization steps. In such an experiment, the proton NMR signals are destroyed or attenuated whenever the rf frequency is close to a ^{14}N resonance. In the work of Blinc et al., three resonances were observed for a single ^{14}N site, but the dc field was so low that it would be improper to call one resonance an overtone of the others. Essentially the same method was later applied to overtone spectroscopy at considerably higher fields by Tycko and Opella and by Garroway and Miller.[11] Related experiments, but involving double quantum rather than overtone excitation, were carried out by Schnur et al.[12] The indirect detection method is a comparatively simple way to locate overtone resonances in organic compounds, with high sensitivity (in favorable cases, on a single transient) but with low resolution. Figure 2 shows double resonance rf pulse sequences for the indirect detection of overtone signals.

3.3 Direct Detection of ^{14}N Overtone Signals Following Double Quantum Excitation

Bloom and LeGros[1] showed that the ^{14}N overtone signals from a single crystal of $NaNO_2$, with ν_Q = 1.4 MHz, could be detected directly with adequate sensitivity in a 5.4 T field

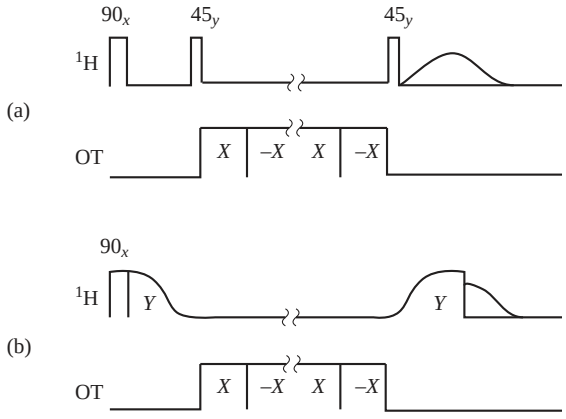

Figure 2 Sequences of rf pulses applied to proton (^{1}H) spins and to an overtone (OT) transition for the indirect detection of overtone transitions in organic solids. (a) Proton dipolar order is created by a two pulse Jeener–Broekaert sequence. A train of OT pulses, with alternating rf phases, destroys part of the dipolar order when the OT carrier frequency is close to a nuclear resonance. Proton NMR signals, proportional to the remaining dipolar order, are detected after the final proton pulse. In a typical application, one scans the OT carrier frequency and looks for a reduction in the proton signal at the OT resonance. (b) Same procedure as (a), but with dipolar order created by adiabatic demagnetization in the rotating frame (ADRF) and proton signals detected after adiabatic remagnetization in the rotating frame (ARRF). A signal enhancement by a factor of 4 over the Jeener–Broekaert method is possible

(ν_0 = 16.6 MHz). In the experiments of Bloom and LeGros, rf pulses were not applied at the overtone resonant frequency. Instead, the overtone coherence was excited by the double quantum excitation technique of Vega and Pines,[13] in which a rf pulse at frequency $\nu_0 + \nu_Q^{(2)}$, with amplitude less than ν_Q/γ_S, is applied for a time about equal to $3\pi\nu_Q/2(\gamma_S B_1)^2$. Thus, signals were detected at twice the frequency of the applied pulses. So far, this method of exciting overtone transitions has been of interest primarily from the standpoint of pure spectroscopy. Excitation near the overtone resonant frequency itself has proven to be a more practical approach.

3.4 Direct Detection and Direct Excitation of ^{14}N Overtone Transitions

Tycko and Opella[2,3] carried out a series of experiments that demonstrated the feasibility of the direct excitation and direct detection of ^{14}N overtone spectra in single crystal and polycrystalline organic solids. They showed that overtone coherences could be excited both by direct pulsed excitation of the overtone transition and by cross polarization from proton magnetization. They demonstrated the high resolution inherent in overtone spectroscopy when high-power proton decoupling is employed (overtone resonances in single crystals subject to small strains and small degrees of disorder are broadened by second-order rather than first-order quadrupole effects). They showed that quadrupole coupling constants and asymmetry parameters could be determined from overtone lineshapes of polycrystalline samples and that the powder pattern lineshapes depend on the direction of the rf coil used for excitation and detection. They also demonstrated two-dimensional overtone nutation spectroscopy, for measuring overtone nutation frequencies, and two-dimensional overtone separated-local-field spectroscopy, for measuring ^{14}N–^{1}H dipole–dipole couplings. Radiofrequency pulse sequences for the acquisition of one-dimensional ^{14}N overtone spectra of organic solids are shown in Figure 3. Examples of one-dimensional ^{14}N overtone spectra are shown in Figures 4 and 5.

Tycko and Opella[3] have discussed the comparative sensitivities of ^{14}N overtone spectroscopy and single quantum spectroscopy. Because of the reduced spectral widths and linewidths in typical overtone spectra, overtone spectroscopy has sensitivity at least comparable to that of single quantum spectroscopy despite the weakly allowed nature of overtone transitions.

Tycko and Opella[3] have also carried out preliminary experimental investigations of the effects of rapid sample spinning on ^{14}N overtone spectra of polycrystalline solids. They found that spinning about a single axis changed, but did not narrow, the overtone powder pattern lineshape. Takegoshi and Hikichi[14] performed calculations of overtone lineshapes under sample spinning that supported the experimental results. They have also discussed the use of double rotation (DOR) and dynamic angle spinning (DAS) methods as a means of narrowing the second-order quadrupole shift powder patterns observed in ^{14}N overtone spectroscopy.[14] Although this approach to line narrowing has not been demonstrated in experiments, it may turn out to be a valuable one. In principle, either the DOR or the DAS technique, or some suitable variant of these techniques, may allow one to obtain resolved ^{14}N

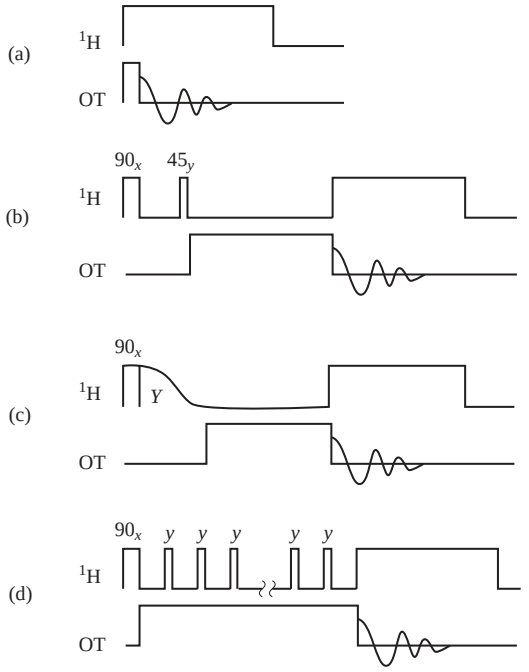

Figure 3 Pulse sequences for the direct detection of overtone spectra in organic solids. (a) Direct excitation of overtone coherences with a single OT pulse. High-power proton decoupling is applied during the acquisition of the overtone signals. (b) A Jeener–Broekaert sequence is used to create proton dipolar order. Overtone coherences are generated by cross polarization from dipolar order. (c) Adiabatic demagnetization in the rotating frame is used to create proton dipolar order. Overtone coherences are generated by cross polarization from dipolar order. (d) Overtone coherences are generated by cross polarization from transverse proton magnetization, prepared by pulsed spin locking. Pulsed, rather than continuous, spin locking reduces the effective proton rf field, allowing a Hartmann–Hahn match to be achieved despite the relatively weak effective OT rf field (due to the weakly allowed nature of the overtone transitions). (Adapted by permission of the American Institute of Physics from Tycko and Opella, *J. Chem. Phys.*, 1987, **86**, 1761)

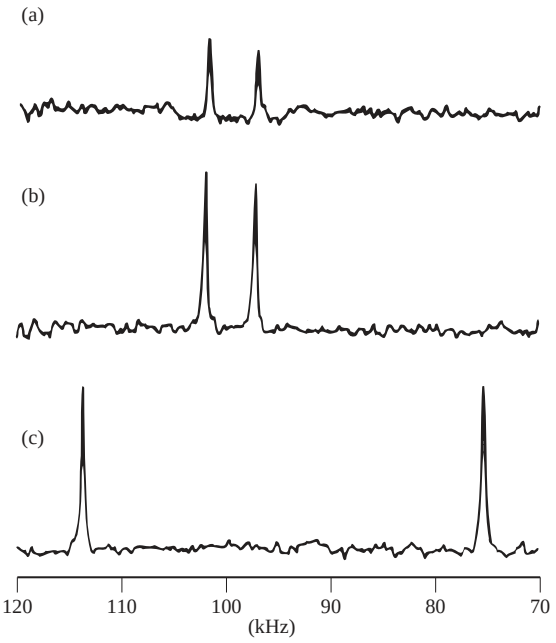

Figure 4 ^{14}N overtone NMR spectra of a 50 mg single crystal of *N*-acetyl-D,L-valine, obtained at 5.89 T ($2\nu_0$ = 36.118 MHz). The two lines result from the two magnetically inequivalent molecules in the unit cell. All spectra result from the acquisition of 1024 transients. (a) Direct excitation, using the pulse sequence in Figure 3(a). (b) Cross polarization, using the pulse sequence in Figure 3(b). (c) Cross polarization, using the pulse sequence in Figure 3(b), after an arbitrary 10° rotation of the crystal. The change in the overtone resonant frequencies is due to the orientation dependence of the second-order quadrupole shifts. (Adapted by permission of the American Chemical Society from Tycko and Opella, *J. Am. Chem. Soc.*, 1968, **108**, 3531)

overtone NMR lines from chemically inequivalent nitrogen sites in a complex polycrystalline solid (i.e. a polycrystalline peptide or oligonucleotide). The resonant frequencies in such an experiment would be determined by the isotropic parts of the chemical shift and the second-order quadrupole shift. In addition, one expects a small contribution to the overtone lineshapes from a spinning sample due to Berry's phase, as observed in pure NQR spectra of spinning samples.[15] The effects of Berry's phase, which arise because the nuclear spin eigenstates are functions of orientation when the quadrupole coupling is large, are expected to be of the order of $|C_{mm'}|^2\nu_R$, where ν_R is the sample spinning frequency, which is less than 100 Hz for typical experimental conditions.

Takegoshi and Hikichi[16] have also carried out a rotation study of a single crystal of L-alanine to determine the ^{14}N quadrupole coupling constant and asymmetry parameter in this compound. The observed angular dependences of the overtone frequency and intensity were well described by the expressions derived by perturbation theory.

Ramanathan and Opella[17] have investigated the effects of irradiation of ^{14}N overtone resonances on the ^{13}C NMR spectrum of a single crystal of *N*-acetyl-D,L-valine. The ^{13}C NMR lineshapes at 3.52 T are asymmetric triplets for carbon atoms that are coupled to ^{14}N nuclei in this crystal, with asymmetry due to the large ^{14}N quadrupole coupling (ν_Q = 0.8 MHz). Irradiation of the ^{14}N overtone resonances caused the triplet ^{13}C lineshapes to collapse into unresolved doublets. Ramanathan and Opella showed that this 'overtone decoupling' could be carried out selectively, allowing particular ^{14}N overtone resonances to be correlated with particular ^{13}C resonances. Selective overtone decoupling may be useful in the assignment of resonances in single crystal NMR studies.

4 CONCLUSIONS

Overtone spectroscopy is a useful addition to the techniques of solid state NMR. The reduced spectral widths and linewidths of ^{14}N overtone spectra compared with traditional single quantum spectra clearly make overtone spectroscopy the preferred means of applying ^{14}N NMR to the study of many classes of solids. In many cases, overtone spectroscopy is the only practical way to observe ^{14}N NMR signals. At the very least, this allows measurements of spin relaxation rates and approximate quadrupole coupling constants to be performed. Such measurements can probe the chemical, structural, dynamical, and electronic properties of solids.

Extensions of overtone spectroscopy to NMR of nuclei with spins greater than one are possible, but have not yet been

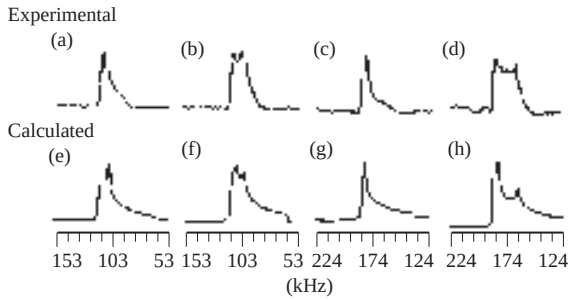

Figure 5 Experimental (a–d) and (e–h) calculated ^{14}N overtone NMR spectra of *N*-acetyl-D,L-valine powder, obtained at 5.89 T (a,b,e,f) and 3.54 T (c,d,g,h) with the pulse sequence in Figure 3(c). The rf solenoid coil used for excitation and detection of overtone signals is perpendicular to the external magnetic field in (a), (c), (e), and (g), and parallel to the external magnetic field in (b), (d), (f), and (h). Each experimental spectrum is the result of approximately 20 000 transients on a 200 mg sample. In the calculations, signal contributions from the various possible molecular orientations are weighted by $|M_{1,-1}|$ (see text), and effects of the ^{14}N chemical shift anisotropy are included. (Adapted by permission of the American Institute of Physics from Tycko and Opella, *J. Chem. Phys.*, 1987, **86**, 1761)

investigated in detail. For most quadrupolar nuclei, with non-integer spins, the 'central transition' (i.e. the $m = \frac{1}{2} \leftrightarrow m = -\frac{1}{2}$ transition) is already unaffected by first-order quadrupole splittings and is fully allowed. The arguments in favor of overtone spectroscopy are therefore less compelling. Nonetheless, one expects the observation of overtone signals in conjunction with single quantum signals to afford spectral simplification, contribute to the determination of quadrupole coupling parameters, and facilitate the assignment of resonances. The measurement of overtone relaxation rates may also add to the information available from relaxation measurements on the central transition.

5 RELATED ARTICLES

Cross Polarization in Solids; Double Rotation; Dynamic Angle Spinning; Geometric Phases; Quadrupolar Nuclei in Glasses; Quadrupolar Nuclei in Solids.

6 REFERENCES

1. M. Bloom and M. A. LeGros, *Can. J. Phys.*, 1982, **64**, 1522.
2. R. Tycko and S. J. Opella, *J. Am. Chem. Soc.*, 1986, **108**, 3531.
3. R. Tycko and S. J. Opella, *J. Chem. Phys.*, 1987, **86**, 1761.
4. J. H. van der Waals and M. S. deGroot, *Mol. Phys.*, 1959, **2**, 333.
5. M. S. deGroot and J. H. van der Waals, *Mol. Phys.*, 1960, **3**, 190.
6. P. Kottis and R. Lefebvre, *J. Chem. Phys.*, 1963, **39**, 393.
7. P. Kottis and R. Lefebvre, *J. Chem. Phys.*, 1964, **41**, 379.
8. R. B. Creel, E. D. von Meerwall, and R. G. Barnes, *Chem. Phys. Lett.*, 1977, **49**, 501.
9. R. Blinc, M. Mali, R. Osredkar, A. Prelesnik, I. Zupancic, and L. Ehrenberg, *J. Chem. Phys.*, 1971, **55**, 4843.
10. S. R. Hartmann and E. L. Hahn, *Phys. Rev.*, 1962, **128**, 2042.
11. A. N. Garroway and J. B. Miller, *J. Magn. Reson.*, 1989, **82**, 591.
12. G. Schnur, R. Kimmich, and F. Winter, *J. Magn. Reson.*, 1986, **66**, 295.
13. S. Vega and A. Pines, *J. Chem. Phys.*, 1977, **66**, 5624.
14. K. Takegoshi and K. Hikichi, *Chem. Phys. Lett.*, 1992, **194**, 359.
15. R. Tycko, *Phys. Rev. Lett.*, 1987, **58**, 2281.
16. K. Takegoshi and K. Hikichi, *Chem. Phys. Lett.*, 1993, **206**, 450.
17. K. V. Ramanathan and S. J. Opella, *J. Magn. Reson.*, 1988, **78**, 367.

Biographical Sketch

Robert Tycko. *b* 1959. A.B., 1980, Princeton University; Ph.D., 1984, University of California at Berkeley. Postdoctoral fellow, University of Pennsylvania, 1984–86. Member of the Technical Staff, AT&T Bell Laboratories, Murray Hill, NJ, 1986–94. Investigator, National Institutes of Health, Bethesda, MD, 1994–present. Approx. 50 publications on magnetic resonance. Research specialties: fundamental principles of magnetic resonance spectroscopy, development of new NMR techniques, characterization of the structural, dynamical, and electronic properties of chemical systems, materials, and biochemical systems.

Polysaccharide Solid State NMR

Hazime Saitô

Himeji Institute of Technology, Kamigori, Hyogo, Japan

1	Introduction	1
2	Conformation-Dependent ^{13}C Chemical Shifts	1
3	Secondary Structure of Gel-Forming Polysaccharides	1
4	Dynamic Aspects of Polysaccharide Gels	4
5	Concluding Remarks	5
6	Related Article	5
7	References	5

1 INTRODUCTION

A variety of polysaccharides are known to play essential roles as the structural components in the cell walls of plant and microorganisms, in insect cuticles, as storage polysaccharides, as matrix components in animal fluids and connective tissues, and as molecular signals for biological recognition. These functions are strongly related to their respective secondary structures, taking in the solid, gel, or solution states. Nevertheless, it is not easy to reveal the secondary structures of these polysaccharides either in the solid or in solution, as compared with those of globular proteins or nucleic acids which have been extensively studied by X-ray diffraction or multidimensional NMR spectroscopy. This is mainly because the crystallization of polysaccharides for an X-ray diffraction study is extremely difficult and the number of interresidual nuclear Overhauser enhancements in solution NMR is not sufficient for the purpose of model building. Moreover, it should be emphasized that the secondary structures of polysaccharides are generally very heterogeneous, especially in the gel state in which several different kinds of domain are simultaneously present.

Conformational elucidation by solid state NMR spectroscopy as a means for in situ structural analysis is especially important for a number of polysaccharides, because they are in many instances not soluble in mild solvent systems (such as aqueous solution) and other spectroscopic means for this purpose are virtually unavailable. It should be anticipated that solubilization in either alkaline or DMSO solution can usually be associated with a conformational change. In addition, too much reliance should not be laid on a secondary structure as deduced by fiber X-ray diffraction studies, because any physical treatment to improve the crystallinity (such as thermal treatment) may cause a conformational change. There remains an ambiguity about secondary structure owing to the limited number of diffraction data available. In this respect solid state NMR is invaluable as a complement to fiber X-ray diffraction as well as a means to gain insight into the dynamic aspects of polysaccharides, especially in relation to a study of gel networks.

2 CONFORMATION-DEPENDENT ^{13}C CHEMICAL SHIFTS

We have previously shown that the ^{13}C chemical shifts of a variety of molecular systems, including polypeptides and proteins, carbohydrates and polysaccharides, ionophores, etc., vary by as much as 8 ppm depending on their conformations.[1,2] In principle, such a conformation-dependent change in polysaccharides is observable either in the solid state or in solution when rapid conformational isomerism about the glycosidic linkages is frozen. However, there are a limited number of examples which exhibit the existence of conformation-dependent ^{13}C chemical shifts: ^{13}C chemical shifts recorded in solution are generally identical, within experimental error, to those observed in the solid state, as in higher molecular weight (1 → 3)-β-D-glucans and α-cycloamylose. The situation arose when rapid rotational motion about the glycosidic linkages was frozen (even in solution) due to the formation of cross-links or to the presence of cyclic structures for the (1 → 3)-β-D-glucans and α-cycloamylose, respectively.

The existence of conformation-dependent ^{13}C chemical shifts, however, is more clearly visualized by an examination of the ^{13}C chemical shifts of solid polysaccharides which have a variety of polymorphs. It is also useful to examine the ^{13}C NMR spectra of crystalline cycloamyloses enclosing a variety of guest molecules, because detailed conformational data for such complexes are available from single crystal X-ray diffraction studies. We previously demonstrated that the C-1 and C-4 ^{13}C chemical shifts of crystalline cycloamyloses enclosing various types of guest molecules could be well related to a set of torsion angles about the glycosidic linkages (ϕ, ψ).[3] Later, similar but slightly different relationships[4,5] were proposed. Therefore, conformational elucidation by means of solid state NMR is feasible on the basis of the concept of conformation-dependent ^{13}C chemical shifts.[1,2]

3 SECONDARY STRUCTURE OF GEL-FORMING POLYSACCHARIDES

It is well recognized that cross-links of polysaccharide gels are formed via several degrees of molecular association of the ordered polysaccharide chains. It is thus important to obtain the detailed in situ secondary structure of various polymorphs of polysaccharides by solid state NMR as reference data useful for conformational studies of gel samples.

3.1 (1 → 3)-β-D-Glucans

As an illustrative example, we first demonstrate comparative ^{13}C NMR studies on linear and branched (1 → 3)-β-D-glucans isolated from bacteria and reserve polysaccharide, and fungi (edible mushrooms), respectively.[6,7] Curdlan [(**1**), Figure 1], a bacterial linear (1 → 3)-β-D-glucan from *Alcaligenes faecalis* (Wako Pure Chemicals, Osaka, Japan) is able to form a firm elastic gel when its aqueous suspension is heated at a temperature above 54 °C. On the other hand, several branched glucans such as lentinan (Ajinomoto Co. Japan), schizophyllan (Taito, Japan), etc. (**2**) from various types of mushrooms are able to form gels of a rather brittle type at higher

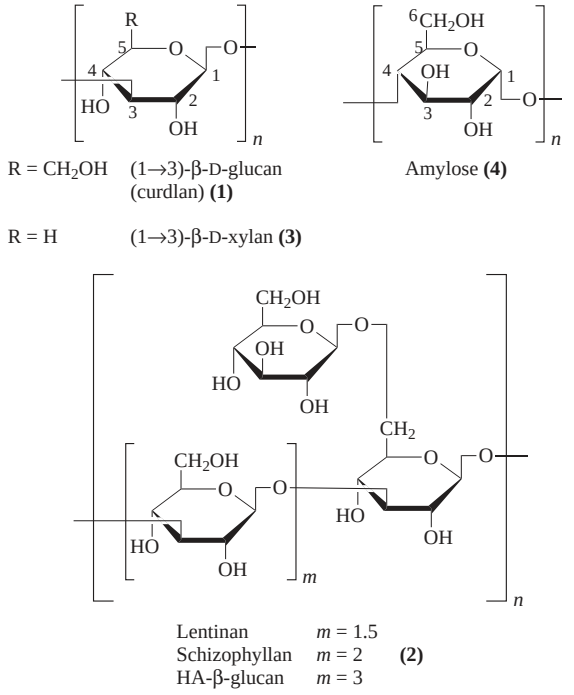

Figure 1 Primary structures of a variety of polysaccharides

concentrations (>10%). Such a difference in macroscopic texture of these gel samples is closely related to a different architecture of the network structure between the two types of gels, as will be discussed later in more detail. In fact, rather sharp ^{13}C NMR signals (about 40% of the total NMR spectrum) are visible from curdlan gel using conventional liquid state NMR with broadband decoupling.[8] The C-1 and C-3 ^{13}C chemical shifts from the elastic gel were displaced to high frequency by 2.8 and 3.2 ppm, respectively, as compared with those of a lower molecular weight glucan with a random coil conformation. As pointed out in the previous section, such a conformation-dependent ^{13}C chemical shift of (1 → 3)-β-D-glucans arises from the fact that the rotational motions of the polysaccharide backbone about the glycosidic linkages are frozen due to the formation of an ordered helical conformation. The polysaccharide chain in this case must be a *single* helical species in spite of the existence of a triple helical model, based on fiber X-ray diffraction studies,[9,10] because the molecular chain is found to be rather flexible, as demonstrated by relaxation parameters such as the spin–lattice relaxation times and the NOE.[6] In contrast, all of the ^{13}C NMR signals of the branched glucans were found to be completely suppressed in the gel state as recorded on a traditional solution state NMR spectrometer.[11] This finding implies that the molecular conformations of these two types of polysaccharides are different from each other. It is essential for this reason to examine the solid state ^{13}C NMR spectra of various types of polymorphs in (1 → 3)-β-D-glucans for use as reference data.

Figure 2 illustrates the ^{13}C NMR spectrum of a hydrated sample of curdlan (b) obtained by placing it in a desiccator at 96% relative humidity for 8 h compared with that of the anhydrous powder as received from the manufacturer (a)[12] and annealed curdlan[13] prepared by heating an aqueous suspension at 150 °C followed by slow cooling (c). It is noteworthy

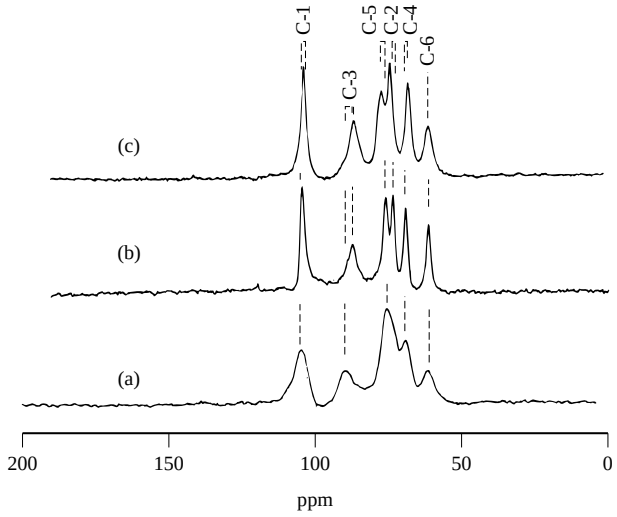

Figure 2 ^{13}C CP MAS NMR spectra of curdlan in the solid state: (a) anhydrous; (b) hydrated; and (c) annealed[12]

that the ^{13}C NMR linewidths of the hydrated sample are considerably narrowed in comparison to those of the anhydrous sample and are comparable to those of the annealed curdlan [Figure 2(c)]. The C-3 ^{13}C chemical shift of curdlan hydrate is displaced to low frequency by 2.5 ppm with respect to that of the anhydrous state. Distinction between the hydrated and annealed curdlan is straightforward by means of the C-5 chemical shifts (75.8 ppm and 77.5 ppm for the former and latter, respectively) and the peak separation between the C-5 and C-2 signals (2.0 and 3.2 ppm, respectively). Lyophilized curdlan from DMSO solution gave rise to narrower spectra but the peak positions were exactly the same as those for the anhydrous sample.[14] Annealed curdlan may be related straightforwardly to the triple-helix form on the basis of its powder X-ray diffraction by reference to previous fiber diffraction data.[9,10]

Hydrated curdlan gave rise to ^{13}C NMR signals which were identical to those observed in the gel state. Hence, this form was ascribed to the flexible single helix already mentioned. Consistent with this view, a recent fiber X-ray diffraction[15] study showed the presence of a 6/1 single helix conformation for the curdlan gel prepared by heating an aqueous suspension at 70 °C for 10 min, although Fulton and Atkins previously ascribed a similar diffraction pattern to a 7/1 triple helix conformation.[16] It is surprising that the C-1 and C-3 chemical shifts of the single helical curdlan hydrate are very similar to those of the triple helical annealed curdlan, although distinction between the two forms is possible from the C-2 and C-5 peaks. This is because the two pairs of the torsion angles about the glycosidic linkages (ϕ, ψ) are very similar, as revealed by X-ray diffraction studies.[10,15] The anhydrous form, on the other hand, is ascribed to a single-chain form whose torsion angles vary to some extent from those of the single helix form owing to loss of hydrated water molecules (which are essential for stability in the single helix conformation). In a similar manner, DMSO molecules in the single-chain form are complexed with the polysaccharide chains (ca. 0.5 DMSO molecules per residue)[14] and may play an important role for the conformational stabilization, although they are readily replaced by water molecules on hydration

to yield the single helix form.[12,14] This situation is very similar to the case of DMSO molecules complexed with V-amylose, which are very easily replaced by water molecules by hydration, leading to the conversion to the B- form, as will be described later.

Linear (1 → 3)-β-D-glucans of low molecular weight oligomers such as laminariheptaose and acid-degraded curdlan with a degree of polymerisation (*DP*) of 14 can adopt neither the single helix nor triple helix form, as judged from the characteristic ^{13}C signals.[12,13,17] Interestingly, glucans of either short-chain (*DP* < 14) or longer-chain species are incapable of forming triple helices by lyophilization from aqueous solution. Laminaran from *Laminaria* species (*DP* 39) turned out to be able to exist in the triple helix form by lyophilization from aqueous solution, although this polysaccharide adopts a random coil form in aqueous solution.[13] In contrast, triple helix conformations were achieved when high molecular weight branched (1 → 3)-β-D-glucans such as schizophyllan or HA-β-glucan were lyophilized from their aqueous solution, although the single-chain form was available from an aqueous solution of lentinan.[17] It is now clear that the obvious preponderance of the single helix conformation for the linear (1 → 3)-β-D-glucans of high molecular weight arises mainly from insufficient hydration. Once this molecule is completely dissolved in an aqueous solution at a temperature above 150 °C, it is able to refold to yield the triple helical conformation when cooled slowly to ambient temperature.[13] It is thus expected that such a conversion is inefficient when heated samples are cooled rapidly (at most 50%).[13] It is noteworthy that conversion of the single helix to the triple helix by annealing at 150 °C is accompanied by fragmentation of the polymer chain due to thermal degradation from an initial *DP* of 3930 to a final *DP* of 110.[18] Such an annealing is not necessary in the case of the branched glucans, because these molecules are well hydrated in aqueous media at ambient temperature. It appears that rather weak intermolecular association of the branched glucan (as compared with that of the linear glucan) arises from the presence of a pendant glucose moiety (Figure 1) for every two or three glucose residues. This is the reason why the branched (1 → 3)-β-D-glucans and laminaran have a preponderance of the triple helix over the single helix conformations.

In general, several types of polysaccharides including (1 → 3)-β-D-glucans can acquire the double or triple stranded form as the most energetically stable, as expected from a molecular mechanics calculation.[19] Nevertheless, any given polysaccharide sample does not always take the energetically most stable conformation, because of different sample histories. Distinction between the single and multiple helical chains, however, is not always straightforward to obtain by X-ray diffraction, because distinguishing multiple stranded coaxial helices and nested single helices is one of the most difficult problems encountered in interpreting fiber diffraction data.[20] It should be emphasized that this problem is readily solved by examination of the conversion diagram of these polysaccharides after a series of physical treatments, as summarized in Figure 3. The present approach can be further extended to any types of polysaccharide. In fact, a very similar conversion diagram was recently obtained for (1 → 3)-β-D-xylan (**3**), which is also found to acquire the three above-mentioned types of conformation, as may be expected from its structural similarity with (1 → 3)-β-D-glucans.[21] The

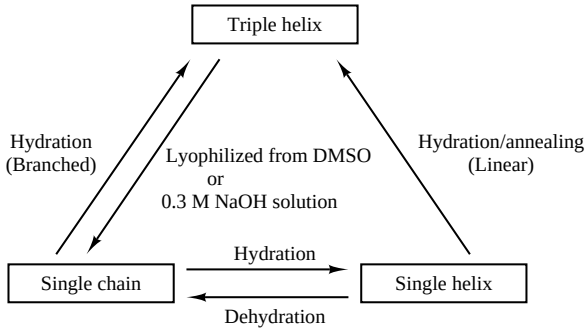

Figure 3 Conversion diagram for (1 → 3)-β-D-glucans by various physical treatments (based on Saitô et al.[12,13])

triple helical conformation was initially proposed for (1 → 3)-β-D-xylan[22] and then adopted for (1 → 3)-β-D-glucan, because the C-6 hydroxymethyl group of the latter is located outside the helical chains. It turned out that the triple helix conformation of the former is more stable than that of the latter because of the greater hydrophobic character in the polymer chain and it cannot be readily converted to the single chain form even if dissolved in DMSO. This type of conversion was made possible by dissolution of the sample in aqueous zinc chloride solution in place of the more common DMSO solution.[21]

3.2 Amylose and Starch

Amylose (**4**) has a common feature with (1 → 3)-β-D-glucans as viewed from the presence of the single helical conformation, which is stabilized by DMSO molecules, and also from its gel-forming ability. Amylose and starch are known to have the following four kinds of polymorphs: V-, A-, B-, and C-forms.[23,24] The V form exists as a complex with a variety of small organic molecules and has a left-handed single helical conformation. The A- and B-forms are found in cereal and tuber starches, respectively, and can be distinguished by the splittings of the C-1 peaks as triplet and doublet peaks, respectively.[25–27] In contrast, V-amylose gives rise to single lines.[28] The C-4 peak of V-amylose is particularly displaced to high frequency by ca. 4–5 ppm from that of the B form. These amylose polymorphs can also be mutually interconverted by a series of physical treatments in a similar manner to (1 → 3)-β-D-glucan, as demonstrated for amylose of low molecular weight (*DP* 17, Figure 4).[29] Obviously, anhydrous amylose lyophilized from a DMSO solution [Figure 4(b)] gave rise to a spectral pattern of the V form. The anhydrous powder as received, however, has an amorphous structure distorted from the B form, as judged from the broad envelope of the ^{13}C NMR signal in the C-1 region and the absence of the C-4 peak at 81 ppm [Figure 4(a)]. Furthermore, hydration of the anhydrous powder or V-amylose resulted in conversion to the B-amylose as judged from the ^{13}C NMR spectra [Figure 4(c)]. It is interesting that such conversion occurs efficiently for amylose of either low (*DP* 17) or high (*DP* 1000) molecular weight but was incomplete for amylose of intermediate molecular weight (*DP* 100).[29]

The secondary structure of the B form was initially considered to be the single helical conformation,[30] since the conversion of the V- to the B-form amylose takes place on humidification.[31] Later, however, the structure was refined as

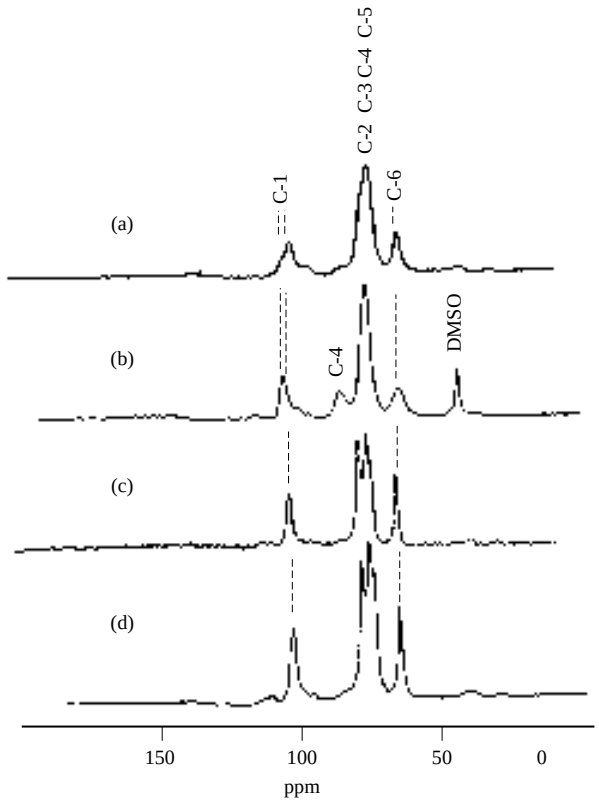

Figure 4 ^{13}C CP MAS NMR spectra of low molecular weight amylose (*DP* 17): (a) anhydrous powder; (b) anhydrous lyophilized sample from DMSO solution; (c) hydrated amylose power; and (d) hydrated iodine complex[29]

a right-handed double helix in an antiparallel fashion.[32] The handedness of the double helix form, however, was recently revised as a left-handed double helix.[33] Nevertheless, it is hardly likely that simple humidification of amylose by placing it in a desiccator at a relative humidity of 96% causes such a drastic conformational change. In this connection, it is crucially important to clarify whether the secondary structure of B-amylose is a left-handed single helix as suggested from solid state NMR or a left-handed double helix as suggested from fiber X-ray diffraction study.

It was expected that ^{2}H NMR spectra of ^2H_2O or DMSO-d_6 complexed to amylose by forming the B- or V-form would be split into a doublet pattern, with the separation of peaks being about 100–200 kHz and 40 kHz (with C_3 rotation of the methyl group), respectively, if they are tightly bound to the polymer chains (static). It emerged, however, that only a singlet was visible as a result of rapid isotropic averaging of the quadrupole interaction in the solid state, with correlation times on the order of 10^{-6} s. The correlation times of isotropic tumbling of ^2H_2O and DMSO-d_6 as estimated from ^{2}H spin–lattice relaxation times are found to be in the vicinity of the T_1 minimum and on the high-temperature side of the T_1 minimum, respectively.[29]

4 DYNAMIC ASPECTS OF POLYSACCHARIDE GELS

Network structures of gel samples should be highly heterogeneous from the conformational and dynamic point of view. Any single NMR measurement, however, does not give rise to such information, because the correlation times of the molecular motions may be broadly distributed from the liquid- to solid-like domains. We have already demonstrated that ^{13}C NMR signals from the liquid-like domains are easily visible with a conventional solution state spectrometer but those of the solid-like domains are not.[5,6] It is therefore necessary to record NMR signals from these solid-like domains in order to gain some insight into the gel structure and dynamics. It is accordingly a major advantage of the NMR approach that it is able to select a particular domain from a variety of motionally different domains.

We have recorded ^{13}C NMR spectra of curdlan gels (Figure 5) by various methods including broadband decoupling for the liquid-like domain as discussed above (b), high-power dipolar decoupling with magic angle spinning (MAS) for intermediate domains between the liquid- and solid-like domains (c), and cross-polarization magic angle spinning (CP MAS) for the solid-like domains (d), and have compared these with the ^{13}C NMR spectrum of hydrated curdlan (a).[34] Such comparison indicated that the single helix form is dominant for all of the motionally different domains of an elastic curdlan gel, although a low intensity peak arising from the contribution from the triple helix is visible in the solid-like domains as shown by the arrowed peak in the CP MAS NMR spectrum. It is worthwhile to relate here the present view of the gel structure with the data for gel strength as a function of heating temperature:[35] the gel strength is almost the same at temperatures between 60–80 °C (low-set gel) and thereafter increases with heating temperature together with the development of turbidity and shrinkage of the gel (high-set gel). The first step of gelation thus corresponds to the formation of pseudo cross-links by hydrophobic association of

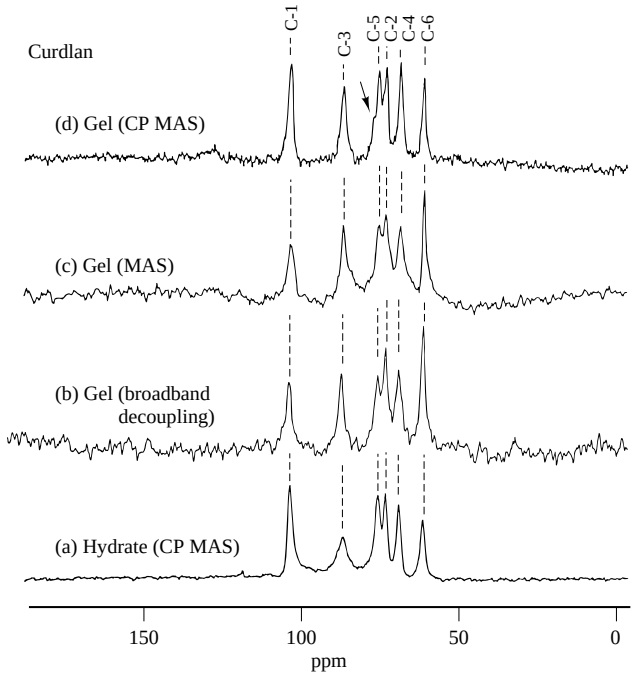

Figure 5 ^{13}C NMR spectra of curdlan gel (b–d) and curdlan hydrate (a) recorded by various types of NMR measurements: (a) and (d) by CP MAS; (b) by broadband decoupling; and (c) by MAS experiments[34]

the single helical chain. The increased gel strength in the high-set gel is well explained in terms of an increased proportion of the triple helical conformation.[5,6]

On the other hand, we found that ^{13}C NMR spectra of branched glucans such as lentinan, schizophyllan, and HA-β-glucan exhibited characteristic peaks of the triple helix conformation.[34] As pointed out, such a preponderance of the triple helix forms resulted in the complete absence of the peaks from the liquid-like domains.[5,6] In this connection, Yanaki and co-workers[36] showed that the triple helical chain of (1 → 3)-β-D-glucans is stiffer than that of native collagen, as manifested from the measurements of persistent chain length for schizophyllan (2000 ± 300 Å). This means that the resulting slow tumbling motion of the stiff rod-like triple helices is not sufficient to average out the dipolar or chemical shift anisotropy interactions in the gel state. Thus, it follows that the major gelation mechanism for the branched (1 → 3)-β-D-glucans proceeds from partial association of the triple helical chains. It appears that the absence of the flexible molecular chain is consistent with the property of a brittle gel. Here we point out that the linear and branched (1 → 3)-β-D-glucans so far discussed are involved in a variety of host-defence biological responses such as antitumor activity, activation of the coagulation system of horseshoe crab amebocyte lysate (LAL), etc. It is interesting that such biological response is initiated by recognition of the molecular chains of the single helical conformations.[18,37,38]

Gidley[39] showed that amylose gel exhibits two kinds of ^{13}C NMR signals: B type signals from motionally restricted regions as recorded by the CP MAS technique and signals identical to those found in aqueous solution. Obviously the latter signals can be ascribed to the presence of a mobile region (liquid-like domain) in the network whose conformation is random coil. The former peaks are naturally ascribed to the solid-like domain with cross-links, either consisting of double helical junction zones,[39] or aggregated regions of the single helical chains[29] as discussed in the previous section. To date, two different views have been presented for the gelation mechanism of amylose: Miles et al.[40] have suggested that gels are formed upon cooling molecularly entangled solutions as a result of phase separation of the polymer-rich phase, whereas Wu and Sarko[33] proposed that gelation occurs through cross-linking by double helical junction zones. Recently, we measured the ^{13}C spin−lattice relaxation times of the liquid- and solid-like domains of starch gel by means of dipolar decoupled single pulse MAS and CP MAS, respectively.[41] It turned out that the T_1 of the C-6 carbon is 0.16 s and 2.1 s for the former and latter, respectively. It appears that such a long T_1 for the latter as compared with that of other types of swollen gels (<0.5 s) arises mainly from motionally restricted crystalline portions consisting of aggregated molecular species such as single helical chains. In any case, it is crucially important to distinguish single helical chains from double helical chains by means of solid state NMR spectroscopy.

5 CONCLUDING REMARKS

It has been demonstrated that the solid state NMR approach is a very powerful means of clarifying conformational features of a variety of polysaccharides in an empirical manner based on the concept of the conformation-dependent displacements of ^{13}C chemical shifts. Careful examination of an NMR-based conversion diagram by a series of physical treatments has proved to be a very useful means for the distinction of single-chain/multiple helices. The application of a modern methodology is urgently required to determine the secondary structure in a nonempirical manner, such as rotational echo double resonance or rotational resonance as currently being applied to a variety of peptides or proteins in the solid state.

6 RELATED ARTICLES

Solid Biopolymers.

7 REFERENCES

1. H. Saitô, *Magn. Reson. Chem.*, 1986, **24**, 835.
2. H. Saitô and I. Ando, *Annu. Rep. NMR Spectrosc.*, 1989, **21**, 209.
3. H. Saitô, G. Izumi, T. Mamizuka, S. Suzuki, and R. Tabeta, *J. Chem. Soc., Chem. Commun.*, 1982, 1386.
4. J. A. Ripmeester, *J. Inclusion Phenom.*, 1985, **4**, 179.
5. R. G. Veregin, C. A. Fyfe, R. H. Marchessault, and M. G. Taylor, *Carbohydr. Res.*, 1987, **160**, 41.
6. H. Saitô, *ACS Symp. Ser.*, 1981, **150**, 125.
7. H. Saitô, *ACS Symp. Ser.*, 1992, **489**, 296.
8. H. Saitô, T. Ohki, and T. Sasaki, *Biochemistry*, 1977, **16**, 908.
9. R. H. Marchessault, Y. Deslandes, K. Ogawa, and P. R. Sundarajan, *Can. J. Chem.*, 1977, **55**, 300.
10. C. T. Chuah, A. Sarko, Y. Deslandes, and R. H. Marchessault, *Macromolecules*, 1983, **16**, 1375.
11. H. Saitô, T. Ohki, and T. Sasaki, *Carbohydr. Res.*, 1979, **74**, 227.
12. H. Saitô, M. Yokoi, and Y. Yoshioka, *Macromolecules*, 1989, **22**, 3892.
13. H. Saitô, R. Tabeta, M. Yokoi, and T. Erata, *Bull. Chem. Soc. Jpn.*, 1987, **60**, 4259.
14. H. Saitô and M. Yokoi, *Bull. Chem. Soc. Jpn.*, 1989, **62**, 392.
15. K. Okuyama, A. Otsubo, Y. Fukuzawa, M. Ozawa, T. Harada, and N. Kasai, *J. Carbohyr. Chem.*, 1991, **10**, 645.
16. W. S. Fulton and E. D. T. Atkins, *ACS Symp. Ser.*, 1980, **141**, 385.
17. H. Saitô, R. Tabeta, T. Sasaki, and Y. Yoshioka, *Bull. Chem. Soc. Jpn.*, 1986, **59**, 2093.
18. Y. Yoshioka, N. Uehara, and H. Saitô, *Chem. Pharm. Bull.*, 1992, **40**, 1221.
19. T. L. Bluhm and A. Sarko, *Can. J. Chem.*, 1977, **55**, 293.
20. T. A. Foord and E. D. T. Atkins, *Biopolymers*, 1987, **28**, 1345.
21. H. Saitô, J. Yamada, Y. Yoshioka, Y. Shibata and T. Erata, *Biopolymers*, 1991, **31**, 933.
22. E. D. T. Atkins, K. D. Parker, and R. D. Preston, *Proc. R. Soc. London, Ser. B.*, 1969, **173**, 209.
23. A. Sarko and P. Zugenmaier, *ACS Symp. Ser.*, 1980, **141**, 459.
24. D. French, *Starch: Chemistry and Technology*, ed. R. L. Whistler and E. D. Pascal, 2nd edn., Academic Press, New York, 1984, p. 183.
25. R. P. Veregin, C. A. Fyfe, R. H. Marchessault, and M. G. Taylor, *Macromolecules*, 1986, **19**, 1030.
26. M. J. Gidley and S. M. Bociek, *J. Am. Chem. Soc.*, 1985, **107**, 7040.
27. F. Horii, H. Yamamoto, A. Hirai, and R. Kitamaru, *Carbohydr. Res.*, 1987, **160**, 29.

28. H. Saitô and R. Tabeta, *Chem. Lett.*, 1981, 713.
29. H. Saitô, J. Yamada, T. Yukumoto, H. Yajima, and R. Endo, *Bull. Chem. Soc. Jpn.*, 1991, **64**, 3528.
30. J. B. Blackwell, A. Sarko, and R. H. Marchessault, *J. Mol. Biol.*, 1969, **42**, 379.
31. F. R. Senti and L. P. Witnauer, *J. Am. Chem. Soc.*, 1948, **70**, 1438.
32. H. C. H. Wu and A. Sarko, *Carbohydr. Res.*, 1978, **61**, 7.
33. A. Imberty and S. Perez, *Biopolymers*, 1988, **27**, 1205.
34. H. Saitô, Y. Yoshioka, M. Yokoi, and J. Yamada, *Biopolymers*, 1990, **29**, 1689.
35. T. Harada, *ACS Symp. Ser.*, 1977, **45**, 265.
36. T. Yanaki, T. Norisue, and H. Fujita, *Macromolecules*, 1980, **13**, 1462.
37. H. Saitô, Y. Yoshioka, N. Uehara, J. Aketagawa, S. Tanaka, and Y. Shibata, *Carbohydr. Res.*, 1991, **217**, 181.
38. J. Aketagawa, S. Tanaka, H. Tamura, Y. Shibata, and H. Saito, *J. Biochem (Tokyo)*, 1993, **113**, 683.
39. M. J. Gidley, *Macromolecules*, 1989, **22**, 351.
40. M. J. Miles, V. J. Morris, and S. G. Ring, *Carbohydr. Res.*, 1985, **135**, 257.
41. H. Saitô, H. Shimizu, T. Sakagami, A. Tuzi, and A. Naito, in *Magnetic Resonance in Food Science*, ed. P. S. Bolton, I. Delgadillo, A. M. Gil, and G. A. Webb, Royal Society of Chemistry, London, 1995, p. 257.

Biographical Sketch

Hazime Saitô. *b* 1937. B.S., 1961, Ph.D., 1968 (supervisor Teijiro Yonezawa), applied chemistry, Kyoto University, Japan. Postdoctoral work at The National Research Council, Canada (with Ian C. P. Smith). Research chemist, Toray Industries, 1963–75, section head, Biophysics Division, National Cancer Center Research Institute, Tokyo, 1975–90, Professor, Himeji Institute of Technology, 1990–present. Approx. 200 publications. Current research specialty: solid state NMR and its application to biophysical chemistry/structural biology.

Polysaccharides and Complex Oligosaccharides

C. Allen Bush

University of Maryland, Baltimore County, Baltimore, MD, USA

1	Introduction	1
2	Covalent Structure Determination	1
3	Conformation and Dynamics	3
4	Related Articles	5
5	References	5

1 INTRODUCTION

Complex oligosaccharides and polysaccharides are composed of a wide variety of different monosaccharides in different linkages. They are not involved as energy sources in metabolism but should be considered rather as 'informational macromolecules' encoding information which is generally important in intercellular communication. The information which they store is decoded by interaction with specific binding proteins known as lectins.[1] The cell surface oligosaccharides of membrane glycoproteins and glycolipids have been implicated in such important biological functions as inflammation[2] and cellular differentiation.[3] The cell surface polysaccharides of bacteria, including lipopolysaccharides, capsular polysaccharides, and other cell wall polysaccharides are implicated in bacterial adhesion and coaggregation.[4,5] Two different aspects of the structure are important to an understanding of the biology of these interactions. First, one must determine the covalent chemical structure of complex oligosaccharides and polysaccharides including the absolute configuration of the constituent monosaccharides. Secondly, one must also determine their three-dimensional folding and their conformation. If they do not adopt a single conformation but rather exist in multiple conformations which exchange, then one must also determine the dynamics of the conformational exchange. This knowledge will make a major contribution to our understanding the interactions of complex oligosaccharides with lectins. High-resolution NMR spectroscopy has been important in all three facets of the structure of complex oligosaccharides and polysaccharides.

2 COVALENT STRUCTURE DETERMINATION

Determination of the covalent structure of a complex oligosaccharide or polysaccharide is not so simple as determination of a peptide sequence or of a nucleotide sequence. With the possibility of two sugar ring forms (furanoside or pyranoside) and of two anomeric forms (α and β) as well as multiple linkage positions, much more detailed information is required for a description of the structure of a complex oligosaccharide which often includes branching. At present there is no single established method for structure determination and many different methods involving enzymatic digestion, chemical degradation, and methylation analysis are used for various problems. The catalog of available *endo*- and *exo*-glycosidases is inadequate and the outcome of chemical reactions involving sugars is notoriously unpredictable. These facts contribute to the attractiveness of instrumental methods such as mass spectrometry and NMR spectroscopy which require minimal chemistry.

2.1 Proton NMR Spectroscopy

The first major contribution of high-resolution ^{1}H NMR spectroscopy to this problem was the structural reporter group method which became useful with the introduction of high-field superconducting spectrometers operating at 360 MHz. An oligosaccharide or polysaccharide in the quantity range of 100 nmol to 1 μmol is dissolved in D_2O and a ^{1}H spectrum is recorded with chemical shifts referred to DSS.[6,7] In this method, which was first used in glycopeptides and was later extended to glycolipids in DMSO solution, certain well-resolved resonances can often be recognized in one-dimensional spectra. For example the anomeric region at ca. 4.4–5.4 ppm usually contains resonances of anomeric protons most of which are isolated (see ***Carbohydrates and Glycoconjugates***). Accurately measured values of the chemical shift can be combined with the multiplet splitting to characterize the oligosaccharide or polysaccharide. Other structural reporter resonances which contribute to the fingerprint include methyl doublets near 1.3–1.5 ppm typical of 6-deoxyhexoses and methyl singlets around 2.0 ppm characteristic of *N*- or *O*-acetyl methyl groups. Methylene resonances of 3-deoxy sugars can be found between 1.8 and 2.3 ppm. But many overlapping resonances of the methine protons between 3.5 and 4.0 ppm are unresolved and contribute minimal information. The chemical shifts and multiplet structures of the isolated structural reporter resonances can be used to characterize the oligosaccharide or polysaccharide, since no two distinct structures have ever been found to have the same NMR spectrum.

Although the structural reporter method has been used primarily for *N*-linked glycopeptides and glycolipids, it can be used on any oligosaccharide or polysaccharide for which a reference library of closely related structures is available (see ***Carbohydrates and Glycoconjugates***). The method has also been used extensively for the oligosaccharide alditols isolated from the alkaline borohydride degradation of mucin glycoproteins.[8–10] In polysaccharides with a repeating subunit, only the structural reporter resonances of the repeat unit are observed and the spectrum resembles that of an oligosaccharide without a reducing terminal. The method works well in any system of closely related bacterial polysaccharides.[11] Although the structural reporter method has been generally associated with ^{1}H NMR spectroscopy, a very similar approach has been used in the ^{13}C NMR of bacterial polysaccharides as will be described below. The structural reporter method for ^{1}H spectra is fast (~30 min) requiring less spectrometer time than other NMR methods and is comparatively sensitive yielding at least some information on samples as small as 20–100 nmol.

A complete assignment of all the proton signals is more difficult, but it provides much more information

on the structure of a polysaccharide for which there are no available spectra for closely similar compounds. A complete assignment of the ^{1}H spectrum can in principle be established by spin correlation since each sugar ring forms a chain of scalar coupled spins. While correlation by scalar coupling was originally done by spin decoupling, usually by difference methods, two-dimensional methods such as COSY are generally preferred for modern instrumentation. The experiment is usually performed in a phase-sensitive mode with a double quantum filter.[11,12] Spin correlation is started at the anomeric proton resonance or at some other structural reporter resonance such as a methyl doublet of a 6-deoxyhexose. Correlation through the entire spin system by COSY can be augmented by 2D HOHAHA or TOCSY which is especially valuable for resonances which are close in chemical shift, giving rise to COSY cross peaks close to the diagonal.[13] From these 2D COSY and TOCSY spectra, one can extract the homonuclear coupling constants which are very useful in assigning the stereochemistry of the sugar pyranoside residue. Two vicinally coupled protons which are axial make a dihedral angle of 180° implying a large coupling constant which is observed in practice to range from 7–11 Hz, whereas any coupling involving equatorial protons exhibits a small *gauche* coupling constant ranging in practice from 0.5–3 Hz (see ***Vicinal Coupling Constants and Conformation of Biomolecules***). Hence these data reveal whether substituents are axial or equatorial, providing the anomeric configuration of the glycosidic linkage as well as the identity of the sugar residue. The identities of the monosaccharides are then to be confirmed by carbohydrate analysis by a method such as HPLC.

Two common difficulties arise which may prevent the above scheme from providing a successful assignment of the ^{1}H spectrum. The first problem is strong coupling which is all too common in the crowded 3.4–4.4 ppm region of the carbohydrate spectrum. It arises when the chemical shifts of two resonances which are coupled are separated by an amount which is not large compared with the coupling constant. Homonuclear two-dimensional TOCSY or HOHAHA spectroscopy can be used to obtain cross peaks which are well removed from the diagonal in many cases. But if the difference in chemical shift is less than twice the coupling constant, the multiplet shape cannot be extracted interfering with the assignment of stereochemistry by homonuclear coupling, ^3J(H,H). In this case, heteronuclear NMR methods involving ^{13}C resolution are required, as will be discussed below. A second problem in spin correlation about the ring arises for very small values of ^3J(H,H) associated with some *gauche* protons.

NOESY correlations can often be used to correlate such *gauche* protons since they are close in space. A hybrid homonuclear method combining TOCSY with ROESY or NOESY may be useful in such cases and long-range heteronuclear coupling correlation can also be useful as will be described below (see ***Carbohydrates and Glycoconjugates***).

Although the scheme outlined above for spin correlation can be used to assign all proton resonances in a ring and to identify the sugar residues and their anomeric configuration, it does not provide the sequence of residues or their linkage and branching. For this purpose, homonuclear spin correlation is not informative and correlation through space by NOESY can be employed. The anomeric proton of one residue is often close to the aglycone proton directly across the glycosidic linkage, giving rise to NOESY cross peaks which identify the linkage.[13,14] Unfortunately this proximity depends on the conformation of the glycosidic linkage and many exceptions are observed in which a large NOE is seen between the anomeric proton resonance and that of the proton adjacent to the linkage position. This situation arises most often when the adjacent proton is equatorial.[11,13] Although the NOESY data can be useful for the assignment of oligosaccharide sequences, the information on the linkage position is not definitive unless the conformation is known, which is usually not the case for a completely new polysaccharide of unknown structure. Thus the linkage position must be confirmed by some other type of data, such as methylation analysis or long-range heteronuclear correlation to be described below.

Observation of NOESY in oligosaccharides and polysaccharides is complicated by difficulties arising from a dependence on the rotational correlation time. NOE is positive for small molecules and negative for larger ones such as proteins and DNA duplexes.[15] (See ***Nuclear Overhauser Effect***.) For intermediate sized molecules having a rotational correlation time τ_c approximately equal to the reciprocal of the spectrometer frequency ω, the NOE disappears altogether. This is approximately the case for a tetrasaccharide at 500 MHz. One solution to this problem is to change the viscosity of the solution, and thus the τ_c, by changing the sample probe temperature[16] or the viscosity of the solvent by the addition of a viscous cosolvent such as DMSO.[17,18] If it is not desirable to alter the solvent conditions, one can resort to NOE in the rotating frame for which NOEs are positive for all rotational correlation times (see ***ROESY*** and ***Carbohydrates and Glycoconjugates***.) One difficulty with this experiment, which is known as ROESY, is that one must be careful to account for magnetization transfer by the HOHAHA mechanism which leads to cross peaks of the opposite sign and which may cancel ROESY peaks.

The observation of a NOE in polysaccharides is usually straightforward since it is commonly large and negative. Wide variations in flexibility are observed among polysaccharides depending strongly on the linkages. Thus wide variations of linewidth are observed, but generally the NOE is negative.[11] The dynamics of the internal motion in polysaccharides is a complex topic which will be addressed below.

2.2 Carbon-13 NMR Spectroscopy

The ^{13}C spectra of carbohydrates generally show much better chemical shift dispersion than do the ^{1}H spectra. In D_2O solution referenced to DSS, the anomeric signals are dispersed between 95 and 110 ppm and methyl carbon resonances are observed at 15–25 ppm. Since the signals corresponding to the methine carbon atoms of the sugar ring are spread over a much wider spectral region (between 55 and 85 ppm) than are the corresponding signals in the ^{1}H spectrum, there is only a moderate amount of overlap of the signals even at the low fields typical of iron core magnet NMR spectrometers (20–25 MHz carbon ^{13}C frequency). With the introduction of Fourier transform ^{13}C spectroscopy in the 1970s, the spectra of many carbohydrates were recorded, revealing both the promise and some of the difficulties with this type of spectroscopy. A major problem arises from the low sensitivity associated with the direct observation of ^{13}C in natural abundance, especially

with low magnetic field strength spectrometers. Although the requirement for sample sizes of 20–50 μmol severely limited applications to oligosaccharides from eukaryotic glycopeptides and glycolipids, bacterial polysaccharides are often available in such quantities and spectra were reported for a number of bacterial polysaccharides such as the *O*-antigen chains of lipopolysaccharides (LPS), capsular polysaccharides, and other bacterial cell wall polysaccharides.[19–21] A second problem with these early studies of ^{13}C NMR spectra of carbohydrates was the lack of a simple method for the rigorous assignment of ^{13}C signals analogous to the ^3J(H,H) correlation method described above for the assignment of ^{1}H spectra. In the absence of a correlation method, the only data upon which to base resonance assignments were ^{13}C chemical shifts and extensive sets of rules for 'glycosylation shifts' were developed.[22,23] Recently more sophisticated computer-based schemes for this type of correlation have been developed for complex oligosaccharides.[24–26] Although the large chemical shift dispersion of ^{13}C spectra leads to well-resolved spectra, the large effects complicate any rational scheme for assignment based on regular differences in chemical shifts. This situation has led to many revisions of the spectral assignments of the ^{13}C spectra of complex carbohydrates as more rigorous correlation-based methods for assignment were introduced. These methods include specific ^{13}C incorporation by chemical synthesis,[27] DEPT methods which count the protons bonded to a particular carbon atom,[28] or comparison of chemical shifts in D_2O and H_2O solution (DIS).[29] In spite of the difficulties in obtaining reliable ^{13}C resonance assignments in these early ^{13}C studies, the data proved to be immensely useful in studies of bacterial polysaccharide structure.[19,20]

Major advances in ^{13}C NMR spectroscopy of polysaccharides have resulted from the more common use of correlation methods which follow chemical bonds. Rigorous assignment of the ^{13}C spectrum can be derived from the ^{1}H assignment by one-bond C–H coupling correlation. While such a correlation is not very practical for ^{13}C detection in macromolecules, the recent introduction of inverse detection or ^{1}H-detected ^{13}C spectroscopy has greatly increased the utility of this approach. Not only is the sensitivity of ^{1}H-detected ^{13}C spectra greatly improved, but it also gives the ^{1}H spectrum the higher resolution of the detected dimension where it is most needed. In a convenient implementation called HMQC[30] the rather crowded ^{1}H spectrum is resolved in the F_1 dimension by the excellent dispersion of the ^{13}C dimension. This spreads out the resonances that would otherwise overlap in the ^{1}H spectrum and also provides a scheme for the assignment of the ^{13}C resonances once a rigorous assignment of the ^{1}H spectrum is derived from homonuclear spin correlation as described above.[31] Another advantage of HMQC arises in the case of strongly coupled ^{1}H resonances, which are often resolved by the difference in ^{13}C chemical shift. The large value of ^1J(C,H) (~140 Hz) removes the strong coupling for natural abundance samples in which there is only one ^{13}C atom in the average sugar ring.[11] In the absence of strong coupling, the correct homonuclear multiplet shape can be deduced as required for the assignment of the stereochemistry of the pyranoside ring and identification of the sugar. With hybrid methods such as coupled HMQC–COSY, one can assign the correct multiplet shape and chemical shift even in cases for which the ^{1}H resonances exactly overlap.[32] The combination of ^{1}H homonuclear correlation and ^{1}H-detected ^{13}C correlation enables a complete assignment of both spectra for complex carbohydrates which are available in quantities of about 1 μmol. This is reasonable for bacterial polysaccharides, but may not be suitable for glycopeptides or glycolipids from eukaryotes which are often not available in such large quantities.

Another important extension of these heteronuclear methods is long-range correlation of ^{1}H with ^{13}C over two and three bonds by the method popularly known as HMBC.[33] The pulse sequence is similar to that used for HMQC but it involves longer delays to allow antiphase magnetization to develop over the smaller coupling. In this experiment, there is a reduction in sensitivity due to the long delays (30–50 ms) which are required and if T_2 is not much longer than the delays, substantial signal is lost. Particularly for polysaccharide samples with wide lines, this experiment is less sensitive than HMQC and can require as much as 10 μmol of sample depending on the linewidth. HMBC spectra provide valuable confirmation of ^{1}H and ^{13}C resonance assignments through correlation within the sugar ring, and also complete assignments for cases in which vicinal homonuclear coupling constants are too small to provide correlation.[11] But the main function of HMBC spectra is correlation across the glycosidic linkage.[31] This allows assignment of the glycosidic linkage in a rigorous way which follows the chemical bonds. This method has found a number of recent applications for determining glycosidic linkages in bacterial polysaccharides.[11] In favorable cases, this information can take the place of data from methylation analysis and a complete structure of a polysaccharide can be determined essentially by NMR methods with very little ancillary data.

3 CONFORMATION AND DYNAMICS

The question of the three-dimensional conformation of complex oligosaccharides and polysaccharides is distinct from the primary or covalent structure. A truly detailed understanding of the conformation and dynamics requires contributions from a number of techniques, but at the present time data from NMR spectroscopy have made the most significant contributions to the solution of this problem. Computer molecular modeling is generally essential to the satisfactory interpretation of the experimental NMR data.[34] It seems likely that contributions from other experimental biophysical methods such as X-ray crystallography and fluorescence spectroscopy can be expected to increase as the importance of oligosaccharide–lectin interactions becomes more apparent.[35]

An early contribution of NMR data to oligosaccharide conformation was the homonuclear ^3J(H,H) values which are especially useful for determining the puckering of the pyranoside rings of sugars. Since the six-membered pyranoside rings generally assume defined chairs, their ^3J(H,H) values are either large (7–11 Hz) for coupling between axial protons or small (0–3 Hz) for coupling involving equatorial protons, as is described above in connection with the assignment of ring stereochemistry. For furanosides, the pucker is much more complicated, with the five-membered rings adopting envelope conformations in rapid exchange. Measurements of ^3J(H,H) for furanosides have been useful in determining the relative contributions from the various envelope conformations which are important in DNA and RNA conformation.[36]

(See ***Vicinal Coupling Constants and Conformation of Biomolecules***.) A combination of empirical and ab initio calculations has been used to model the furanoside rings and to fit the ^3J(H,H) data to the model.

For oligosaccharides composed of relatively rigid pyranoside rings, the glycosidic dihedral angles describe the conformation and dynamics of the polysaccharide.[37] Homonuclear coupling data are uninformative regarding the relative conformation of the rings with respect to each other and much more information on oligosaccharide and polysaccharide conformation has been derived from ^{1}H NOE data which report on distances through space.[15] (See ***Nuclear Overhauser Effect***.) The strategy is similar to that used in the determination of protein structure in solution by NMR methods which relies heavily on computer modeling methods for an interpretation of the NMR data (See ***Structures of Larger Proteins, Protein-Ligand, and Protein-DNA Complexes by Multi-Dimensional Heteronuclear NMR***). The earliest studies of oligosaccharide conformation were performed on chemically synthesized models of blood group oligosaccharides in which steady-state NOEs were interpreted qualitatively.[38] Models were built with a simple empirical energy function and the NOE data were interpreted qualitatively to confirm these models. This method has also been used in bacterial polysaccharides.[39,40]

A more quantitative method for incorporating the NOE data into molecular modeling schemes follows methods often used in the interpretation of NMR data of proteins in which experimental distance constraints are derived from the NOE data. The distance constraints, which are most commonly derived from the 'isolated spin pair approximation', are treated as pseudo energy terms in the modeling to force a conformation which is consistent with the experimental NOE data (see ***Structures of Larger Proteins, Protein-Ligand, and Protein-DNA Complexes by Multi-Dimensional Heteronuclear NMR***). Choe et al.[41] have used NOE constraints to study the core oligosaccharide of the glycosamino glycans and Scarsdale et al.[42] have described an application to gangliosides. Homans and Forster[43] have also outlined a detailed method for restrained molecular dynamics for oligosaccharides.

A slightly different approach to the quantitative evaluation of NOE data for modeling of oligosaccharides is spin matrix analysis. In this method a molecular model is built and interactions among all the ^{1}H spins are treated to include three spin effects and spin diffusion (see ***Protein Structures: Relaxation Matrix Refinement***). The model is then adjusted to determine whether any conformation can be found for which all the simulated NOE data agree with experiment. This method was first introduced by Brisson and Carver[44] for steady-state NOE in glycopeptides. The matrix method for oligosaccharides was later extended to transient two-dimensional NOESY data which are technically more convenient.[45] The spin matrix method has been adapted to include quantitative interpretation of rotating frame or ROESY data.[46]

An inherent problem with both methods outlined above for the quantitative interpretation of NOE data for oligosaccharides is that they ignore internal motion. The matrix method begins with the assumption of a simple isotropically rotating rigid model and the restrained molecular modeling methods are generally assumed to converge to a single conformation. Careful analysis of the results of either method can be used to test for consistency of a single rigid model with the experimental data, but it is difficult to incorporate internal motion into a quantitative NOESY calculation. The question of the flexibility of complex oligosaccharides is important and remains somewhat controversial.[47,48] Certainly, the relatively narrow lines observed in NMR spectra of polysaccharides (2–15 Hz) having molecular weights as high as 100 kDa suggest that there must be some type of flexibility. One possible interpretation is that certain types of oligosaccharides, such as the blood group epitopes, do assume relatively rigid conformations, while other sugar linkages are flexible, providing structural 'hinges'.[34,48]

One approach to the interpretation of NOE in the presence of internal motion is to assume that the molecular modeling results are correct, assign statistical weights to the minimum energy conformations, and then calculate average NOE. Under the assumption that the rate of conformational exchange is fast compared with T_1 but slow compared with the overall τ_c of the oligosaccharide, one may average the values of the spin matrix elements and then solve the problem.[45,48] Unfortunately it is not known whether this assumption about the kinetics of conformational exchange is correct.

The uncertainty about the details of the conformational dynamics of polysaccharides suggests that additional types of experimental information are needed. The interpretation of NOESY data for a system with internal motion can be quite complex since motion can modulate not only the orientation of ^{1}H–^{1}H vectors but also the distances between protons. It has been recognized for many years that heteronuclear coupling ^3J(C,H) values could be used to correlate with dihedral angles (see ***Vicinal Coupling Constants and Conformation of Biomolecules***). Interpretation of coupling data such as ^3J(C,H) in an oligosaccharide with internal motion is much simpler than NOE since the motion is almost certainly fast compared with the timescale of the interaction (ms). But it has proven to be technically very difficult to measure these coupling constants for macromolecules with ^{13}C in natural abundance. Data were first reported from 1D ^{13}C spectra and ^{1}H spectra of oligosaccharides synthesized with specific ^{13}C enrichment.[27] More recently, long-range heteronuclear coupling constants have been measured in natural abundance by ^{13}C-detected ^{1}H spin echo methods.[49] But the low sensitivity of ^{13}C-detected methods presents a serious limitation and this method requires a resolved ^{1}H spectrum which is a rarity in complex carbohydrates. The improved sensitivity of ^{1}H detection, which has been described above for long-range ^{13}C–^{1}H correlation, provides a method for encoding values of ^3J(C,H).[50] Several one-dimensional versions of ^{1}H-detected ^3J(C,H) have been demonstrated in disaccharides and trisaccharides by Poppe and van Halbeek.[51] In spite of the improved sensitivity, cancellation of the antiphase components of heteronuclear doublets hampers accurate measurements for macromolecules. When the linewidths are comparable to the values of the coupling constants (1–8 Hz), the latter cannot be accurately measured due to antiphase cancellation. In the ECOSY method of Montelione et al.,[52] large one-bond coupling to resolve the long-range coupling removes the problem of overlap making it possible to measure accurately coupling constants much smaller than the linewidth.[53] (See ***Coupling Constants Determined by ECOSY***.) This approach has been used in carbohydrates in natural abundance with ^{13}C selective filters,[54] and in polysaccharides with uniform ^{13}C enrichment.[55]

The question of internal motion in complex polysaccharides can also be addressed by spin relaxation methods in which $J(\omega)$, the spectral density, is sampled at a number of different frequencies to measure the different types of motion which contribute to nuclear relaxation. Measurements of different relaxation rates, T_1, T_2, $T_{1\rho}$, and NOE of ^{15}N or ^{13}C can be combined in order to provide this information.

4 RELATED ARTICLES

Carbohydrates and Glycoconjugates; Coupling Constants Determined by ECOSY; Glycolipids; NOESY; Nuclear Overhauser Effect; Polysaccharide Solid State NMR; ROESY; Structures of Larger Proteins, Protein-Ligand, and Protein-DNA Complexes by Multi-Dimensional Heteronuclear NMR; Vicinal Coupling Constants and Conformation of Biomolecules.

5 REFERENCES

1. K. Drickamer, *J. Biol. Chem.*, 1988, **263**, 9557.
2. A. Varki, *Curr. Opin. Cell Biol.*, 1992, **4**, 257.
3. T. Feizi, *Curr. Opin. Struct. Biol.*, 1991, **1**, 766.
4. I. Ofek and R. J. Doyle, *Bacterial Adhesion to Cells and Tissues*, Chapman & Hall, New York, 1993.
5. P. E. Kolenbrander, N. Ganeshkumar, F. J. Cassels, and C. V. Hughes, *FASEB J.*, 1993, **7**, 406.
6. J. F. G. Vliegenthart, H. van Halbeek, and L. Dorland, *Pure Appl. Chem.*, 1981, **53**, 45.
7. J. F. G. Vliegenthart, L. Dorland, and H. van Halbeek, *Adv. Carbohydr. Chem. Biochem.*, 1983, **41**, 209.
8. A. Klein, C. Carnoy, G. Lambin, P. Roussel, J. A. van Kuik, P. de Waard, and J. F. G. Vliegenthart, *Eur. J. Biochem.*, 1991, **198**, 151.
9. J. A. van Kuik, P. de Waard, J. F. G. Vliegenthart, A. Klein, C. Carnoy, G. Lambin, and P. Roussel, *Eur. J. Biochem.*, 1991, **198**, 169.
10. G. Strecker, J. M. Wieruszeski, O. Cuvillier, J. C. Michalski, and J. Montreuil, *Biochimie*, 1992, **74**, 39.
11. C. Abeygunawardana and C. A. Bush, *Adv. Biophys. Chem.*, 1993, **3**, 199.
12. J. Dabrowski, *Methods Enzymol.*, 1989, **179**, 122.
13. C. A. Bush, *Bull. Magn. Reson.*, 1988, **10**, 73.
14. T. A. W. Koerner, Jr., J. H. Prestegard, P. C. Demou, and R. K. Yu, *Biochemistry*, 1983, **22**, 2687.
15. D. Neuhaus and M. Williamson, *The Nuclear Overhauser Effect in Structural and Conformational Analysis*, VCH Publishers, New Yorka, 1989.
16. B. N. N. Rao, V. K. Dua, and C. A. Bush, *Biopolymers*, 1985, **24**, 2207.
17. H. Kovacs, S. Bagley, and J. Kowalewski, *J. Magn. Reson.*, 1989, **85**, 530.
18. P. Cagas and C. A. Bush, *Biopolymers*, 1992, **32**, 277.
19. P. A. J. Gorin, *Adv. Carbohydr. Chem. Biochem.*, 1981, **38**, 113.
20. H. J. Jennings, *Adv. Carbohydr. Chem. Biochem.*, 1983, **41**, 155.
21. P. K. Agrawal, *Phytochemistry*, 1992, **31**, 3307.
22. A. Allerhand and E. Berman, *J. Am. Chem. Soc.*, 1984, **106**, 2400.
23. A. Allerhand and E. Berman, *J. Am. Chem. Soc.*, 1984, **106**, 2412.
24. P. E. Jansson, L. Kenne, and G. Widmalm, *J. Chem. Inf. Comput. Sci.*, 1991, **31**, 508.
25. P. E. Jansson, L. Kenne, and G. Widmalm, *Anal. Biochem.*, 1991, **199**, 11.
26. G. M. Lipkind, A. S. Shashkov, N. E. Nifantev, and N. K. Kochetkov, *Carbohydr. Res.*, 1992, **237**, 11.
27. R. Barker and A. S. Serianni, *Acc. Chem. Res.*, 1986, **19**, 307.
28. D. M. Doddrell, D. T. Pegg, and M. R. Bendall, *J. Magn. Reson.*, 1982, **48**, 323.
29. P. E. Pfeffer, K. M. Valentine, and F. W. Parrish, *J. Am. Chem. Soc.*, 1979, **101**, 1265.
30. A. Bax, R. H. Griffey, and B. L. Hawkins, *J. Magn. Reson.*, 1983, **55**, 301.
31. R. A. Byrd, W. Egan, M. F. Summers, and A. Bax, *Carbohydr. Res.*, 1987, **166**, 47.
32. C. Abeygunawardana, C. A. Bush, and J. O. Cisar, *Biochemistry*, 1991, **30**, 8568.
33. A. Bax and M. F. Summers, *J. Am. Chem. Soc.*, 1986, **108**, 2093.
34. C. A. Bush, *Curr. Opin. Struct. Biol.*, 1992, **2**, 655.
35. K. G. Rice, P. Wu, L. Brand, and Y. C. Lee, *Curr. Opin. Struct. Biol.*, 1993, **3**, 669.
36. J. Raap, J. H. Van Boom, H. C. Van Lieshout, and C. A. G. Haasnoot, *J. Am. Chem. Soc.*, 1988, **110**, 2736.
37. J. W. Brady, *Adv. Biophys. Chem.*, 1990, **1**, 155.
38. T. H. Thogersen, R. U. Lemieux, K. Bock, and B. Meyer, *Can. J. Chem.*, 1982, **60**, 44.
39. T. Peters, J.-R. Brisson, and D. R. Bundle, *Can. J. Chem.*, 1990, **68**, 979.
40. K. Bock, H. Lönn, and T. Peters, *Carbohydr. Res.*, 1990, **198**, 375.
41. B.-Y. Choe, G. C. Ekborg, L. Rodén, S. C. Harvey, and N. R. Krishna, *J. Am. Chem. Soc.*, 1991, **113**, 3743.
42. J. N. Scarsdale, P. Ram, J. H. Prestegard, and R. K. Yu, *J. Comput. Chem.*, 1988, **9**, 133.
43. S. W. Homans and M. Forster, *Glycobiology*, 1992, **2**, 143.
44. J. R. Brisson and J. P. Carver, *Biochemistry*, 1983, **22**, 1362.
45. C. A. Bush, *Methods Enzymol.*, 1994, **240**, 446.
46. R. Bazzo, C. J. Edge, M. R. Wormald, T. W. Rademacher, and R. A. Dweck, *Chem. Phys. Lett.*, 1990, **174**, 313.
47. J. P. Carver, *Curr. Opin. Struct. Biol.*, 1991, **1**, 716.
48. C. A. Bush and P. Cagas, *Adv. Biophys. Chem.*, 1992, **2**, 149.
49. C. Morat, F. R. Taravel, and M. R. Vignon, *Magn. Reson. Chem.*, 1988, **26**, 264.
50. T. J. Norwood, J. Boyd, N. Soffe, and I. D. Campbell, *J. Am. Chem. Soc.*, 1990, **112**, 9638.
51. L. Poppe and H. van Halbeek, *J. Magn. Reson.*, 1991, **93**, 214.
52. G. T. Montelione, M. E. Winkler, P. Rauenbuehler, and G. Wagner, *J. Magn. Reson.*, 1989, **82**, 198.
53. C. Biamonte, C. B. Rios, B. A. Lyons, and G. T. Montelione, *Adv. Biophys. Chem.*, 1994, **4**, in press.
54. L. Poppe, W. S. York, and H. van Halbeek, *J. Biomol. NMR*, 1993, **3**, 81.
55. R. Gitti, G. Lond, and C. A. Bush, *Biopolymers*, 1994, **34**, 1327.

Acknowledgments

Research supported by NIH Grant GM 31449.

Biographical Sketch

C. Allen Bush. *b* 1938. B.A., 1961, Cornell University, Ph.D., 1965, University of California, Berkeley. Faculty, Illinois Institute of Technology, 1968–89. Currently Professor of Biochemistry, University of Maryland, Baltimore County. Approx. 100 publications. Research interests: structural chemistry of complex carbohydrates by NMR, computer modeling, circular dichroism and HPLC.

Protein Dynamics from Solid State NMR

Stanley J. Opella

University of Pennsylvania, Philadelphia, PA, USA

1	Introduction	1
2	Solid State NMR Spectroscopy	1
3	Backbone Sites in Proteins	2
4	Aromatic Side Chains	2
5	Aliphatic Side Chains	3
6	Summary	4
7	Related Articles	4
8	References	5

1 INTRODUCTION

Solid state NMR spectroscopy is one of the premier methods for characterizing protein dynamics. It is used primarily to describe the intramolecular motions of proteins that are immobilized as part of supramolecular structures in solution, such as membrane or virus particles, or in crystalline samples. Although many different experiments and calculations reflect the internal motions in proteins, it is generally quite difficult to extract detailed information about these motions. By contrast, the effects of motional averaging on the lineshapes of solid state NMR spectra are so clear cut that their analysis has provided a very large proportion of the definitive information currently available about protein dynamics.

Spectral parameters from the nuclear spin interactions operative in both solution NMR and solid state NMR experiments are strongly affected by motion; however solid state NMR experiments have the advantages of avoiding the influences of overall reorientation and analyzing the effects of motional averaging on powder pattern lineshapes. Since the proteins themselves are immobilized by their environments, motion associated with specific backbone or side-chain sites can be readily identified. For the most part, solid state NMR studies of molecular dynamics rely on the analysis of powder patterns by comparing the experimental lineshapes with those calculated for static sites affected by specific models of motional averaging, although relaxation parameters can be analyzed in combination with the lineshapes to determine the actual frequencies of the motions. These studies typically require isotopic labeling of the protein with ^{2}H, ^{13}C, or ^{15}N.

An important benefit of solid state NMR studies is that the structure and dynamics of proteins can be considered in concert. Both orientation and distance measurements are feasible with solid state NMR experiments, and these results can be used to determine the three-dimensional structures of proteins. Of course, the results of the NMR dynamics studies are complementary to the structural information also derived from X-ray crystallography and solution NMR spectroscopy. The backbone and side-chain motions of individual residues are of considerable interest because they have a profound effect on the properties and functions of proteins, especially the structural and membrane proteins where solid state NMR spectroscopy finds its greatest applicability.

2 SOLID STATE NMR SPECTROSCOPY

The precise nature of the influence of molecular motion on spectral parameters, especially powder pattern lineshapes, depends on the spin interactions that are present at the site of interest, the frequencies, amplitudes, and directions of local and global motions, and experimental parameters such as the frequencies of the resonances and the amplitudes and timings of the irradiations. There is a comprehensive review on the subject of NMR studies of dynamics and it provides the necessary physical and mathematical detail for understanding the roles of motion in solid state NMR spectroscopy.[1] There are also reviews on the applications of solid state NMR spectroscopy to protein dynamics.[2,3]

The solid state NMR approach to studying molecular dynamics that is most successful relies on the fundamental concept of dilute spins to provide the necessary isolation of the spin interactions. The spin-$\frac{1}{2}$ nuclei of ^{13}C and ^{15}N are available in isotopically enriched sites in proteins. Although these spins interact strongly with the abundant ^{1}H spins, which can usually be decoupled with strong enough irradiation, they do not interact among themselves; therefore, the spectral parameters available for the analysis of motional averaging are heteronuclear dipolar couplings and chemical shift anisotropy. Deuterium with spin 1 is widely used in solid state NMR studies of molecular dynamics because its lineshapes are dominated by the effects of the nuclear quadrupole interaction, and ^{2}H labeling can be placed in backbone and side-chain sites.

In polycrystalline or unoriented samples, where the proteins do not undergo rapid overall reorientation, powder pattern lineshapes like those in Figure 1 are obtained.[2] The absence of motion in a molecular site must always be defined with respect to a frequency determined by the observed spectral parameter from the dominant spin interactions. Static powder pattern lineshapes are calculated from the principal values of the tensor that describes the spin interaction by taking into account the probability density of all orientations of the tensor with respect to the applied magnetic field. The frequency breadth of a powder pattern reflects the total spectral range for the resonance frequencies possible for the spin interactions at a particular site, since all possible angles are present in a powder. It is this breadth that determines the lower limit for the frequencies of motions that can influence the powder pattern lineshape.

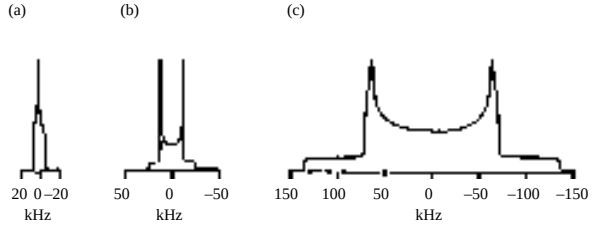

Figure 1 Calculated static powder patterns for an aromatic carbon site. (a) ^{13}C chemical shift anisotropy. (b) ^{13}C–^{1}H heteronuclear dipolar coupling. (c) ^{2}H quadrupolar coupling. (Reproduced by permission from Opella.[2])

Figure 1 presents calculated powder patterns for three spin interactions that can be arranged to be present through isotopic labeling at an aromatic carbon site with a bonded hydrogen. The ^{13}C chemical shift powder pattern from an aromatic carbon is clearly nonaxially symmetric; the $^{13}C-^{1}H$ dipolar powder pattern is axially symmetric; and the ^{2}H quadrupolar powder pattern is nearly axially symmetric. These spectra are displayed on a constant frequency scale in Figure 1 to demonstrate the range of frequencies to which the different spectral parameters are sensitive. For example, the chemical shift powder pattern is averaged by motions substantially slower than those required to average the heteronuclear dipolar and quadrupole powder patterns.

In addition to the frequencies of the motions, the lineshapes are affected by their amplitudes, directions, and other characteristics. In order to understand the influences of these factors, specific models of motions must be considered because of the intimate relationships among molecular sites, spin interactions, and the motions. There are substantial differences between how slow, large amplitude motions and rapid, small amplitude motions affect lineshapes; examples of both are seen in proteins.

3 BACKBONE SITES IN PROTEINS

The initial step in the investigation of a protein is to find out if the entire polypeptide chain is immobile. This information, by itself, is highly suggestive about general aspects of the architecture of the protein, since mobile residues do not participate in the secondary structure of the protein. This is particularly relevant for membrane proteins which characteristically have mobile loops and termini and rigid, structured helical regions. Backbone dynamics are characterized most directly by observing powder pattern lineshapes from labeled sites in unoriented samples and comparing their shape and breadth with those from rigid polycrystalline samples. Residues that undergo large-amplitude motions more often than the frequency breadth of the powder pattern are readily recognized because they have narrow resonance lines at the average, isotropic frequency. The spectra in Figure 2 demonstrate that it is possible to observe narrow, isotropic resonance intensity from the mobile sites superimposed on the broad powder pattern lineshape from the structured sites in a membrane protein.[4] The narrow resonance intensity arises from the mobile sites near the N- and C-termini, although most of the residues of the membrane-bound form of the protein are rigidly held in structured helical regions of the protein.

As shown in Figure 2, ^{15}N-labeled protein samples are very useful in describing the dynamics of proteins. However since the amide tensor in the backbone sites is nearly axially symmetric with the parallel component along the helical axis, it is necessary to observe powder patterns from other sites in order to establish if rotation about an axis coincident with transmembrane helices in the bilayer is occurring. The indole nitrogen of tryptophan side chains is ideal for this, enabling this site to be used to monitor the global motion of the protein since the bulky, asymmetric side chain is rigidly held within the framework of the protein. The results for the membrane-bound form of fd coat protein are shown in Figure 3.[5] The data from ^{15}N-labeled gramicidin in bilayers are quite different;

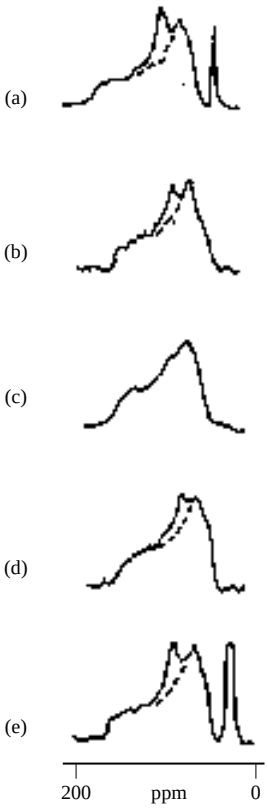

Figure 2 Experimental solid state ^{15}N NMR spectra of the membrane-bound form of fd coat protein in lipid bilayers. (a) Uniformly ^{15}N labeled. (b) Selectively [^{15}N]glycine-labeled (four residues). (c) Selectively [^{15}N]leucine-labeled (two residues). (d) Selectively [^{15}N]Phe-labeled (three residues). (e) Selectively [^{15}N]lysine-labeled (five residues). (Reproduced by permission from Bogusky et al.[4])

although at low temperatures the peptide is immobile, it rapidly rotates at higher temperatures in bilayers.[6] Experiments with other nuclei have confirmed these same results for gramicidin.[7] Global molecular reorientation about a single axis has also been observed for Pf1 virus particles[8] and bacteriorhodopsin in bilayers.[9] In addition to the global motions and large-amplitude local motions, it is possible to use solid state NMR to describe smaller fluctuations through relaxation measurements.[10]

The backbone dynamics of several membrane proteins have been analyzed in detail by solid state NMR experiments.[12–15] Dynamics studies of bacteriorhodopsin in particular have utilized spectra from both backbone and side-chain sites to monitor the motions of the backbone.[16–19] Deuterium NMR spectra of many labeled sites show narrow isotropic resonance intensity superimposed on broad powder patterns,[20] which is typically the case for membrane proteins. The results have been interpreted in terms of structural models of bacteriorhodopsin where the mobile residues are most likely associated with the mobile C-terminus or interhelical loops.[21,22]

4 AROMATIC SIDE CHAINS

The motions of the aromatic amino acid side chains have received a great deal of attention in all studies of

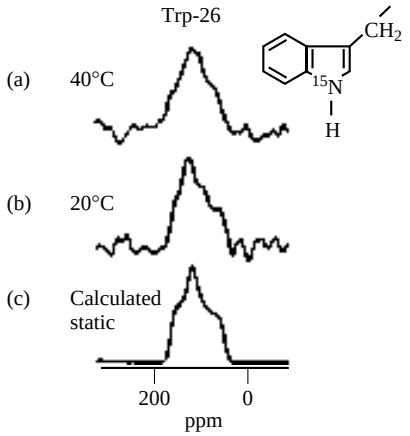

Figure 3 ^{15}N solid state NMR spectra of specifically indole-labeled Trp fd coat protein in lipid bilayers. (Reproduced by permission from Leo et al.[11])

protein dynamics. Not only are these residues important to the structure of the molecules, but also their bulk suggests that their individual motions must influence a substantial number of other residues. Phenylalanine and tyrosine rings have C_2 symmetry and an obvious path for internal motion, the $C^{\beta}-C^{\gamma}$ bond axis. In principle, there are two limiting cases for reorientation of the rings around this axis: (1) jumps (or ring flips) between two indistinguishable sites, where the residence times are long compared with the transit times; and (2) diffusional rotation, where the rings are continuously moving about the bond axis. While all of the spin interactions present in the ring can be used in these studies, the vast majority of work has utilized ^{2}H quadrupole powder patterns to provide the experimental data.[18,23–25] The calculated powder patterns shown in Figure 4 vary strongly with the types of motion.

fd is a filamentous bacteriophage consisting of about 3000 copies of its major coat protein surrounding its DNA. The virus and its coat protein are immobile on all NMR timescales analyzed. The coat protein is small, with two tyrosine residues. The lineshape of the ^{2}H NMR spectrum of [^{2}H]tyrosine (Tyr)-labeled fd virus is very similar in appearance to that calculated for the flip-averaged rings sites.[23] The protein has three phenylalanine (Phe) residues and the ^{2}H NMR spectrum of [^{2}H]Phe-labeled fd is a superposition of two different powder patterns. The inner pattern is from the δ and ϵ bonds undergoing rapid 180° ring flips; the lineshape is very similar to those observed for the Tyr-labeled sample and calculated for the flip-averaged static spectrum. The C–D bonds of the Phe rings contribute the outer discontinuities as a static powder pattern, because these deuterons are unaffected by reorientation about the $C^{\beta}-C^{\gamma}$ bond axis.[24] The lineshape of the [^{2}H]Phe-labeled ^{2}H NMR spectrum demonstrates that these rings also flip rapidly. The observed frequencies in the powder patterns are reduced slightly from those anticipated for a rigid ring only undergoing flips, indicating the presence of some small-amplitude motions. The ^{2}H NMR powder pattern from the single tryptophan (Trp) residue shows its side chain to be tightly constrained within the protein.

Solid state NMR studies on peptides and proteins lead to some general conclusions about the dynamics of aromatic side chains. In the cases examined Trp rings are rigid on NMR

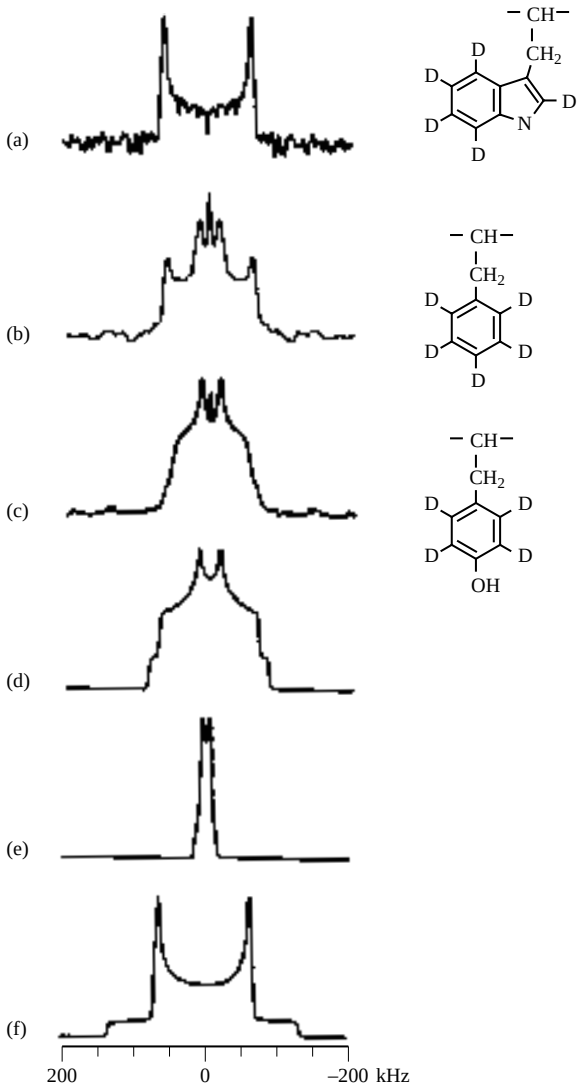

Figure 4 Solid state ^{2}H NMR spectra. (a), (b), and (c) are experimental spectra from selectively ^{2}H-labeled aromatic residues in fd bacteriophage. (d), (e), and (f) are calculated spectra for rigid C–D bonds subject to defined motional averaging. (a) Experimental spectrum from the one labeled tryptophan. (b) Experimental spectrum from the three labeled phenylalanines. (c) Experimental spectrum from the two labeled tyrosines. (d) Calculated spectrum for a C–D bond undergoing two-site hops on an aromatic ring. (e) Calculated spectrum for a C–D bond undergoing diffusional rotation on an aromatic ring. (Reproduced by permission from Gall et al.[23])

timescales, whereas many Tyr and Phe rings undergo two-site 180° hop motions. The aromatic side chains undergo both large-amplitude jump motions and small-amplitude librations in a well-defined manner. The conclusion based on the solid state NMR data is that the proteins in these side chains are both highly ordered and very mobile.

5 ALIPHATIC SIDE CHAINS

Most of the attention in solid state NMR studies of aliphatic side chains in proteins has been focused on CD_3-labeled sites. Both lineshapes and relaxation parameters can

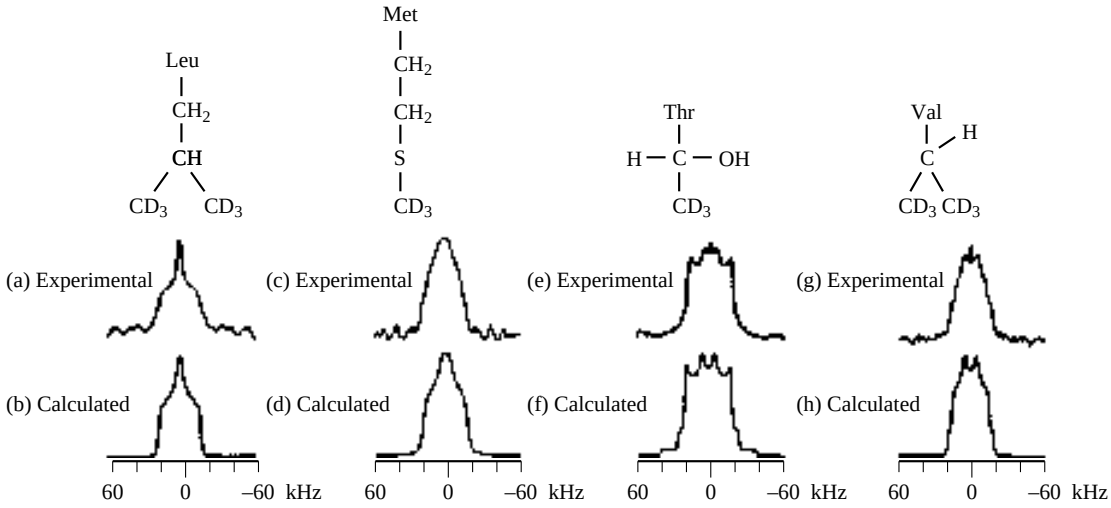

Figure 5 Comparison of experimental and calculated spectra for selectively CD_3-labeled fd virus samples. Leu = leucine, Met = methionine, Thr = threonine, Val = valine. (Reproduced by permission from Colnago et al.[5])

be analyzed. At temperatures of interest for proteins the lineshapes of deuterated methyl groups are axially symmetric powder patterns that are significantly reduced in breadth from a static pattern.[26,27] Since jumps between three or more equivalent sites and diffusional rotation affect powder pattern lineshapes in the same way, the characteristic features of the spectra are indicative of only the angles of intramolecular motion. The facile reorientation of CD_3 groups about their C_3 axis has been extensively studied in crystalline amino acids and peptides, as well as proteins.[5,11,17,19,28,29] It is relatively easy to place deuterated methyl groups in desired locations through synthesis or biosynthetic incorporation, and they have favorable properties for analysis.

The effects of the motional averaging on methyl groups have been observed in ^2H NMR experiments in many different amino acid side chains in peptides and proteins.[5,11] Figure 5 compares calculated ^2H NMR powder patterns characteristic of the methyl group motions actually observed in proteins. All methyl groups undergo rapid reorientation about the C_3 symmetry axis. In addition, many aliphatic side chains undergo rapid jump motions about tetrahedral or near-tetrahedral carbon sites. The deuterium powder pattern lineshapes resulting from two-site jump motions on top of the C_3 axis methyl group reorientation can be calculated by standard methods as two-site 'fast-exchange' processes consisting of jumps betwen two equally populated positions. This was first demonstrated for leucine residues in collagen,[29] and subsequently in a variety of proteins. Of course, large-amplitude motions that occur in all directions result in isotropic averaging of the powder pattern lineshapes to single line resonances that occur at the central frequency for the interaction. Because of the limitations imposed by the side chains, the C–D groups can undergo isotropic reorientation only if the backbone at those residues undergoes isotropic reorientation.

6 SUMMARY

The methods for solid state NMR studies of protein dynamics are well developed, especially with regard to the observation and analysis of motionally averaged powder pattern lineshapes of unoriented or polycrystalline samples. In large part, the success of the applications depends on the placement of isotopic labels in selected locations.

The main conclusion from solid state NMR studies of proteins is that their dynamics fall into three distinct categories. Sites that do not have large-amplitude motions, which occur frequently compared with the timescale of the spectral parameter measured, are categorized as 'rigid' or 'immobile', even if they have small-amplitude rapid motions that result in slight reductions of the parameters compared with static values. Some sites, especially in side chains, undergo large-amplitude jumps between several conformations with residence times that are long compared with the transit times between conformations. In addition, there are mobile sites that undergo rapid reorientation in many directions that are, by definition, unstructured.

Relaxation measurements can provide quantitative information about rates of motion. However, there are many variables that influence the interpretation of these results, and this limits the certainty of the conclusions about the amplitudes and directions of motions. Indeed, there is a tendency to reduce the detail by resorting to an order parameter analysis in order to increase the reliability of the interpretations. Optical and other methods of studying dynamics have even less detail and certainty.

Solid state NMR spectroscopy gives definitive descriptions of the most important backbone and side-chain motions of proteins. The combination of detail concerning the directions, amplitudes, and types of motions with the reliability of lineshape analysis makes this a very powerful approach for the analysis of the time-dependent behavior of proteins.

7 RELATED ARTICLES

Polymer Dynamics and Order from Multidimensional Solid State NMR; Protein Dynamics from NMR Relaxation.

8 REFERENCES

1. H. W. Spiess, *NMR Basic Principles Progr.*, 1982, **15**, 55.
2. S. J. Opella, *Methods Enzymol.*, 1986, **131**, 327.
3. D. A. Torchia, *Annu. Rev. Biophys. Bioeng.*, 1984, **13**, 125.
4. M. J. Bogusky, G. C. Leo, and S. J. Opella, *Proteins Struct. Funct. Genet.*, 1988, **4**, 123.
5. L. A. Colnago, K. G. Valentine, and S. J. Opella, *Biochemistry*, 1987, **26**, 847.
6. H. Hu, K.-C. Lee, and T. A. Cross, *Biochemistry*, 1993, **32**, 7035.
7. R. E. Koeppe, II, J. A. Killian, and D. V. Greathouse, *Biophys. J.*, 1994, **66**, 14.
8. P. Tsang and S. J. Opella, *Biopolymers*, 1986, **25**, 1859.
9. B. A. Lewis, G. S. Harbison, J. Herzfeld, and R. G. Griffin, *Biochemistry*, 1985, **24**, 4671.
10. H. B. R. Cole and D. A. Torchia, *Chem. Phys.*, 1991, **158**, 271.
11. G. C. Leo, L. A. Colnago, K. G. Valentine, and S. J. Opella, *Biochemistry*, 1987, **26**, 854.
12. T. A. Cross and S. J. Opella, *J. Mol. Biol.*, 1985, **182**, 367.
13. S. J. Opella, Y. Kim, and P. McDonnell, *Methods Enzymol.*, 1994, **239**, 536.
14. K.-J. Shon, Y. Kim, L. A. Colnago, and S. J. Opella, *Science*, 1991, **252**, 1303.
15. P. A. McDonnell, K. Shon, Y. Kim, and S. J. Opella, *J. Mol. Biol.*, 1993, **233**, 447.
16. D. M. Rice, A. Blume, J. Herzfeld, R. J. Wittebort, T. H. Huang, S. K. Das Gupta, and R. G. Griffin, *Biomol. Stereodyn.*, 1981, **11**, 255.
17. R. A. Kinsey, A. Kintanar, M.-D. Tsai, R. L. Smith, N. James, and E. Oldfield, *J. Biol. Chem.*, 1981, **256**, 4146.
18. R. A. Kinsey, A. Kintanar, and E. Oldfield, *J. Biol. Chem.*, 1981, **256**, 9028.
19. M. A. Keniry, A. Kintanar, R. L. Smith, H. S. Gutowsky, and E. Oldfield, *Biochemistry*, 1984, **23**, 288.
20. M. A. Keniry, H. S. Gutowsky, and E. Oldfield, *Nature (London)*, 1984, **307**, 383.
21. J. Herzfeld, C. M. Mulliken, D. J. Siminovitch, and R. G. Griffin, *Biophys. J.*, 1987, **52**, 855.
22. J. L. Bowers and E. Oldfield, *Biochemistry*, 1988, **27**, 5156.
23. C. M. Gall, T. A. Cross, J. A. DiVerdi, and S. J. Opella, *Proc. Natl. Acad. Sci. USA*, 1982, **79**, 101.
24. C. M. Gall, J. A. DiVerdi, and S. J. Opella, *J. Am. Chem. Soc.*, 1981, **103**, 5039.
25. D. M. Rice, R. J. Wittebort, R. G. Griffin, E. Meirovitch, E. R. Stimson, Y. C. Meinwald, J. H. Freed, and H. A. Scheraga, *J. Am. Chem. Soc.*, 1981, **103**, 7707.
26. L. S. Batchelder, C. H. Nin, and D. A. Torchia, *J. Am. Chem. Soc.*, 1983, **105**, 2228.
27. K. Beshah, E. T. Olejniczak, and R. G. Griffin, *J. Chem. Phys.*, 1987, **86**, 4730.
28. L. W. Jelinski and D. A. Torchia, *J. Mol. Biol.*, 1980, **138**, 255.
29. L. W. Jelinski, C. E. Sullivan, and D. A. Torchia, *Nature (London)*, 1980, **284**, 531.

Acknowledgments

This research performed at the University of Pennsylvania was supported by grants GM24266, GM29754, and AI20770 from the National Institutes of Health.

Biographical Sketch

Stanley J. Opella. *b* 1947. B.S., Chemistry, University of Kentucky (undergraduate research with S. L. Smith), 1969. Ph.D., Chemistry, Stanford University (with O. Jardetzky and H. McDonnell), 1974. Postdoctoral fellow, Massachusetts Institute of Technology (with J. S. Waugh), 1975–76. Currently Professor of Chemistry at the University of Pennsylvania. Approx. 125 publications. Research interests: development and application of NMR spectroscopy for the study of proteins, especially protein structure determination by solid state NMR spectroscopy.

Proton Chemical Shift Measurements in Biological Solids

Ann McDermott
Columbia University, New York, NY, USA

and

Cynthia F. Ridenour
Otsuka Electronics, Inc., Fort Collins, CO, USA

1 Introduction 1
2 Approaches to Narrowing Proton Resonances 1
3 Information From the Lineshape 2
4 Hydrogen Bonding: Chemical Shift and Hydrogen Exchange 2
5 2D Correlation with Carbon 3
6 Conclusions 4
7 Related Articles 4
8 References 4

1 INTRODUCTION

There are strong motivations for pursuing solid state NMR of protons, namely the inherently good sensitivity and the possibilities for study of hydrogen bonding via chemical shifts. Despite its enormous potential, solid state NMR of protons in biomolecules has had surprisingly few applications in comparison with other high-resolution NMR methods for studying biological macromolecules. In this article we discuss experimental solutions to the problem of spectral resolution and the analysis of spectra for chemical information. Although essentially all of the successful measurements of chemical shift and shift anisotropy were obtained on simple crystalline solids we also discuss possible future applications in structural biology.

2 APPROACHES TO NARROWING PROTON RESONANCES

Producing narrow proton linewidths is the most significant challenge to solid state proton NMR. For the case of a typical rigid organic solid, ^{1}H NMR spectra obtained without sample spinning or with moderate speed sample spinning show very broad lines, on the order of a few tens of kilohertz. Narrowing of these lines by the technique of combined rotation and multiple pulse spectroscopy, CRAMPS,[1–4] or by dilution of the protons[5–7] has been demonstrated in crystalline small molecules. These methods have provided the means to study hydrogen bonding and proton exchange in solids, but practically no high-resolution solid state ^{1}H NMR applications to macromolecules have been reported. In contrast to rigid organic solids, solids with high molecular mobility such as lipids and membrane structures often provide well-resolved ^{1}H NMR simply by Bloch decay acquisition with slow magic angle spinning.[8–11]

The CRAMPS method is the most common experimental approach to achieving high-resolution ^{1}H spectra of materials in the solid state. It has been used in interesting applications of chemical analysis,[12–15] and probably has the most potential for general studies of amorphous biological solids. Proton NMR linewidths obtained by CRAMPS or magnetic dilution can be as low as 0.2 ppm, which could be sufficient to separate the typical functional groups found in a protein but of course would never be adequate for site-specific assignments of even a small peptide. Highly crystalline compounds typically produce the narrowest lines, while compounds with some amorphous character produce somewhat broader lines.[14] Macroscopic susceptibility due to the shape of the microcrystal presumably contributes to the linewidth, and specific anisotropic bulk susceptibility effects in aromatic systems have been discussed.[14]

An alternative method that has been little pursued to date is the detection of deuterons during magic angle spinning (MAS). With this approach resolution comparable to that of CRAMPS or dilution can often be obtained without special effort,[16,17] and spectral overlap can be avoided by utilizing selective labeling. Considerable spectral intensity is squandered into spinning sidebands, so application of methods to fold the sidebands together is important. On the other hand, the quadrupolar constants and dynamic information normally obtained from static ^{2}H NMR can be derived from the sideband patterns in these spectra. Several reports of cross polarization between deuterium and protons have appeared.[16,18]

In the following discussion we will focus more on CRAMPS than the other two approaches because of the much larger existing literature and the far fewer complications with sample preparation. We illustrate the typical appearance of CRAMPS spectra of simple organic biological solids with a series of CRAMPS spectra of amino acids and dipeptides in Figure 1; some of these samples have also been characterized by measurement of dilute protons[6] or by spinning ^{2}H spectra.[17] It is apparent from Figure 1 that the linewidths are significantly below 1 ppm in every case and the spectra allow resolution

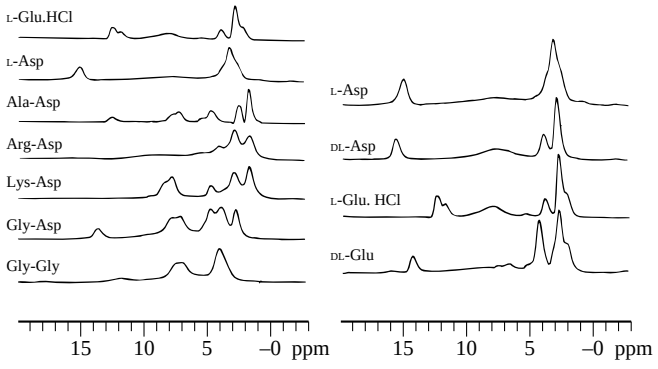

Figure 1 The 200 MHz BR-24 spectra of crystalline amino acids (as indicated). Pulse length was 1.3 μs with a τ value of 2.3–3.0 μs and spinning speeds of 1.0–1.5 kHz. Sixteen transients were accumulated. Glu = glutamic acid, Asp = aspartic acid, Ala = alanine, Arg = arginine, Lys = lysine, Gly = glycine

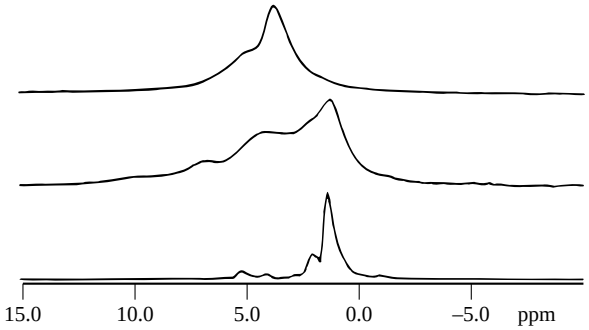

Figure 2 Typical CRAMPS spectra of biological molecules, measured at 187 MHz with the BR-24 pulse sequence.[19] Top: amylopectin; middle: γ-globulin; bottom: coconut oil. Spectra were acquired with MAS spinning speed of 1–2 kHz, pulse width = 1.0–1.2 μs, τ = 3.0 μs, repetition time 1.7 s

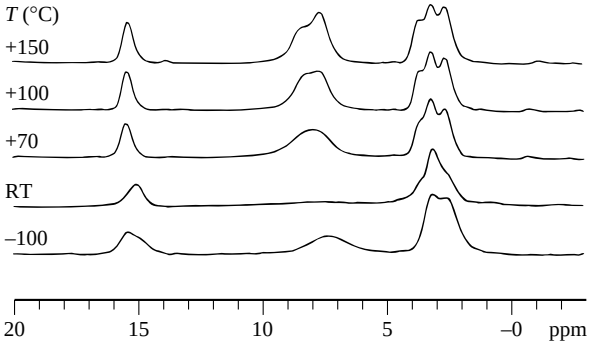

Figure 3 The 200 MHz BR-24 spectrum of l-aspartic acid at various temperatures. Note that the amine resonance at 7.7 ppm disappears near room temperature (RT) due to the microsecond correlation time for the amine's threefold hopping rate. This behavior is quite common for amine groups although the critical temperature is variable

of one chemical classification from another. For aliphatic or aromatic protons the chemical shifts are comparable to those known from solution state experiments, that is −1 to 2 ppm for methyl groups, 1–3 ppm for methylene, 3–5 ppm for methine, and 6–8 ppm for aromatic protons. Unlike solution spectroscopy, in solid state experiments observing acid and other exchangeable protons is possible, and in particular for the case of carboxylic acids the range in typical shifts is quite a lot broader than the linewidths. The amine and many of the other N–H functionalities are often around 7–8 ppm, while imidazole protons and structural water protons and carboxylic acids can be found at a broad range of shift values depending on hydrogen bonding, with strongly hydrogen-bonded groups being significantly deshielded (10–20 ppm). The chemical shifts and lineshapes for resonances in hydrogen bonding groups are discussed in detail in the following sections.

Typical ^{1}H CRAMPS spectra of other biological materials are also exhibited in Figure 2.[19] The carbohydrate spectrum (top) is dominated by methine and hydroxyl protons. The protein spectrum (middle) shows contributions from methyl, methylene, methine, amine, and other groups but is largely unresolved. A methylene resonance at 1.3 ppm dominates the lipid spectrum (bottom). As noted above, MAS-only spectra of lipids provide good ^{1}H resolution. Proton linewidths of lipids and highly mobile materials are often narrower in MAS-only spectra than in CRAMPS spectra[19] due to pulse imperfections in the multiple pulse sequence.

3 INFORMATION FROM THE LINESHAPE

All three detection methods show certain potentially confusing effects that deserve special comment. As has been reported previously[1,20] dynamic processes can interfere with the CRAMPS detection of groups undergoing motion if the correlation times are comparable to the pulse width, the multiple pulse cycle time, or to the sample spinning speed. This effect is often seen at room temperature in the form of missing amine resonances. Amine groups enact a three-site hopping motion on the microsecond timescale near room temperature since they have activated barriers in the range of 30 kJ mol^{-1}. This motion has been previously characterized by wideline ^{1}H T_1 measurements[21] but not by lineshape methods. Such amine lines that are broad or undetected near room temperature are readily detected at temperatures above 70 °C or below −100 °C in typical cases. Figure 3 shows variable temperature ^{1}H CRAMPS spectra of L-aspartic acid in which the amine line at 7.7 ppm illustrates this effect. Other effects on the lineshapes as a function of temperature are often observed, and analysis of these lineshapes by explicit simulation would be informative but has not yet been accomplished. Other than the amine rotation, common local motions in proteins rarely result in loss of signal because the rates are not on the microsecond timescale near room temperature. The ^{2}H MAS spectra exhibit lineshape and intensity effects for amines in a comparable temperature range: here the sampling rate of data collection is usually in the submegahertz range so again motions in the microsecond range interfere with detection. Proton spectra of magnetically diluted (deuterated) samples detected using Bloch decay during MAS would presumably show lineshape effects due to much slower motions, approximately on the millisecond timescale. Hence detection of sharp spectra due to the amine peaks is usually straightforward by ^{1}H MAS spectra. In all three methods interpretation of line intensities is quite unreliable because of all of these lineshape effects and/or the uncertainties involved in the extent of chemical incorporation of deuterium.

Protons that are directly bound to nitrogens often exhibit a lineshape that is obviously affected by the incomplete averaging of dipolar coupling to the ^{14}N resulting from the fact that the strongly quadrupolar ^{14}N is not in the high-field limit. These effects are most clear in lower field spectra[22] and can be seen in the 200 MHz high-temperature CRAMPS spectrum of aspartic acid (Figure 3) but also have been seen in well-resolved high field spectra.[5] They offer the possibility of characterization of the bonding geometry and the quadrupole parameters for the nitrogen from the ^{1}H lineshapes[22] as has been done for ^{13}C lineshapes for ^{13}C^{14}N pairs.[23–26]

4 HYDROGEN BONDING: CHEMICAL SHIFT AND HYDROGEN EXCHANGE

For protons that participate in hydrogen bonding, there are well-known correlations between the shielding of the ^{1}H isotropic chemical shift, the ^{1}H shielding anisotropy, the ^{2}H coupling constant, and hydrogen bonding distances[1,27–29] for

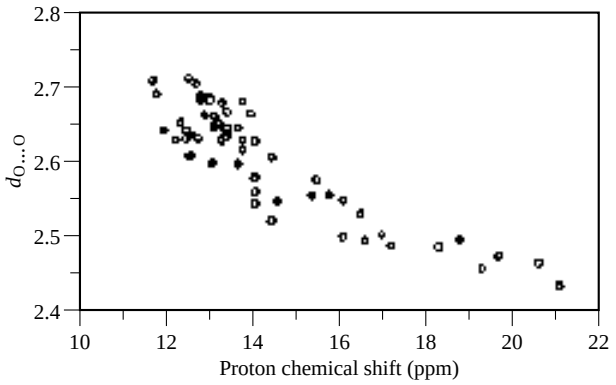

Figure 4 The ^{1}H chemical shifts of the amino acids in Figure 1 plotted against their O ... O distances as indicated by crystallography. Filled circles show proton chemical shifts derived from our data, as shown in Figure 1; crystal structures for these compounds can be found in Rao,[40] Eggleston and Hodgson,[41–43] Derissen et al.,[44] Bhat and Vijayan,[45] Sequeira et al.,[46] and Hamilton and Parthasarathy.[47] The open circles are from previous measurements in Harris et al.[1]

small crystalline compounds. Quantification of hydrogen bonding is of great interest for studies in structural biology because of the role in recognition and conformational preferences. Solid state NMR could potentially be far more sensitive to details of hydrogen bonding and ionization states than crystallography. The chemical shifts for the acid protons for carboxyl groups in amino acids (shown in Figure 1) correlate with hydrogen-bonding length and this plot is shown in Figure 4 in filled circles. In comparison with previous measurements[1] which are entered here as open circles, our data encompass a rather restricted range because of the limited scope of compounds that are both relevant as model systems for proteins and sufficiently characterized. Clearly there is some scatter in the data but there is also a general trend that reproduces previous correlations.

Anisotropy of the proton shielding has been reported in a variety of solids with very simple structures; a thorough compilation and reviews are available.[30–32] Many of these values were obtained from static multiple pulse measurements on either single crystals or powders or from rotation plots of the deuterium signal of a single crystal. The shielding anisotropy, $|\Delta\sigma| = |(\sigma_\perp - \sigma_\parallel)|$, is quite narrow (about 4–7 ppm) for alkyl or aromatic protons (except for methyl groups which are 1–2 ppm), but for some ionizable protons the anisotropy is more pronounced, with values of approximately 17 ppm for amides and 16–30 ppm for acids, alcohols, and water, but only about 5 ppm for amines. A detailed analysis of tensor values and orientations would presumably be useful in studying nonbonded interactions but is probably not possible in biological solids in the near future. Many complications affect the CSA measurements by CRAMPS, such as residual homonuclear and heteronuclear dipolar interactions, molecular motion, and chemical shift scaling. Magnetically dilute protons in organic solids give rise to spinning sidebands during low-speed MAS, and when the percentage of hydrogens that are replaced with deuterons is approximately 99% or larger these sidebands appear to be dominated by CSA effects (A. McDermott, unpublished).

A point of specific interest in solid state studies of hydrogen bonding is the fact that hydrogen bonds can have profound effects upon reactivity in biological catalysis. For example, acid–base chemistry or proton mobility in the solid state is presumably strongly affected by local nonbonded interactions, a point which is relevant in many enzyme mechanisms. The geometric preferences of hydrogen bonds and the specific control of reactivity can be probed in the solid state studies since particular networks are arrested on an experimentally accessible timescale. Protons that participate in typical thermally driven and near-reversible exchange processes in proteins are found on the 'ionizable' hydrogen bonded groups such as carboxyl, imidazole, water, amine, alcohol, and guanidinium. The typical exchange timescales of microseconds to hours are presumably sensitive to the specific hydrogen-bonding geometry in a way that might be predicted by ab initio[33] or semiempirical methods. A systematic study of chemical exchange processes as a function of geometry in structurally characterized solids by NMR would help to clarify the theory of proton exchange.

Recent advances in ^{1}H NMR of deuterated simple model compounds for proteins show that such measurements of exchange processes are possible. Variable temperature two-dimensional (2D) methods applied to one example of a low symmetry hydrogen-bonded network of carboxylic acids and crystallographic water molecules demonstrated unambiguously that a proton is transferred between water and a carboxyl group[6] in an activated process with a barrier of 37 kJ mol^{-1}. Additional measurements will be necessary for the purpose of creating a database that correlates rates of exchange with structural features.

5 2D CORRELATION WITH CARBON

The more ambitious goal of utilizing ^{1}H NMR for detailed structural analyses of amorphous solid materials or complex solid state macromolecules is not practical without addressing the problem of resolution of one ^{1}H resonance from the others of the same chemical functional group. The approach taken by solution NMR spectroscopy to correlate the ^{1}H resonance with nearby or attached heteronuclei is applicable in solids as well. The ^{15}N or ^{13}C NMR spectra in the solid state are considerably broader than solution spectra but nonetheless often allow distinction of a handful of selectively labeled residues. Two important classes of 2D H–X experiments for solid state NMR of H–X pairs are dipolar chemical shift correlation methods or 'DIPSHIFT'[34] for determination of the bond distance to a great accuracy in a spin pair and heteronuclear correlation methods or 'HETCOR',[35–37] which maps the chemical shifts of the X nucleus to nearby protons via the dipolar coupling. The latter is clearly the experiment of choice when more than one proton connected with the heteronucleus of interest should be resolved and rather approximate distance information will suffice. Our recent work with HETCOR and modified versions of the pulse sequence demonstrate the observation of longer H–X distances including C–O ... H hydrogen bonds which appear as weak cross peaks. Rotor-synchronized transfer sequences have been used to increase the range of H–X distances probed by this method.[38] As an example, the HETCOR spectrum of alanyl aspartic acid is shown in Figure 5. In particular the ^{1}H–^{13}C correlation peaks between the carboxyl groups around 170 ppm in the ^{13}C dimension and the acid proton near 12.5 ppm in the

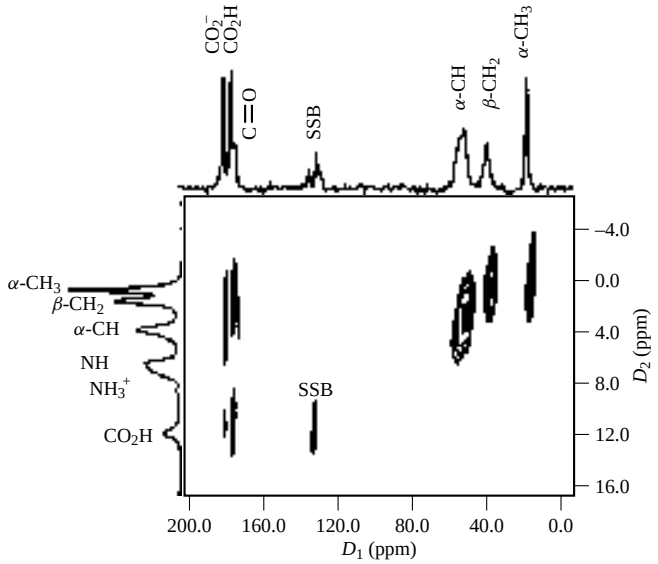

Figure 5 Rotor-synchronized HETCOR spectrum of alanyl aspartic acid at 200 MHz and room temperature. Magnetization transfer was accomplished by 2.5 WIM-24 cycles per rotor period during four sequential rotor periods. The 90° pulse lengths were 3.2 μs for both channels. Experimental repetition time was 1.7 s. Data matrix was 80 × 512 points zero-filled to 512 × 512 with 20 Hz linebroadening in D_2 and a Kaiser window applied to D_1. SSB = spinning sidebands

^{1}H dimension are indirectly connected pairs; several of the ^{13}C resonances show more than one ^{1}H cross peak.

Since essentially all of the resolution in the HETCOR experiment comes from the heteronuclear dimension, it is probably worthwhile to reiterate the virtues of such a 2D experiment in comparison with a one-dimensional (1D) heteronuclear measurement. Although detailed information about hydrogen bonding is available from heteronuclear NMR, the information from the ^{1}H shifts is often independent of that obtained from the heteronuclear shift. A case in point is the carboxylate group: the ^{1}H shift depends on the interaction of the detected acid proton with the nearest hydrogen bond acceptor, while σ_{22} of the ^{13}C shift depends on the distance between the carboxyl oxygen, which acts as a hydrogen bond acceptor, and the nearest proton.[39] The 2D HETCOR experiment provides the possibility of identifying the chemical nature of the hydrogen bonding partners to a carbon-containing functional group, even if the partners are water molecules. In a more practical light, we have found the HETCOR experiment to be quite useful in determining or confirming ^{13}C assignments for larger peptides and pharmaceuticals. As for disadvantages, obviously the time investment in such an experiment is enormously greater than that necessary for a 1D heteronuclear experiment. In the 2D spectra interpretation of the proton dimension is subject to similar complications as the CRAMPS experiment. In particular the intensities of the lines depend strongly on the presence or absence of mid-kHz motions.

Some of these issues are well illustrated with the spectrum of natural abundance alanyl aspartic acid. The three carbonyl-type carbons are readily identified by the HETCOR spectrum with one being a protonated carboxyl, one being deprotonated but hydrogen bonded to the protonated carbonyl, and the third being an amide carbonyl with no cross peak to the acid proton. A strong hydrogen bond between the two carboxyl groups is indicated by both the deshielded acid proton (14 ppm) that was detected in the HETCOR spectrum and the σ_{22} value for the deprotonated carboxyl group (184 ppm) that was determined in 1D low-spinning CP MAS sideband analysis. Moreover the assignment of both the ^{13}C and ^{1}H dimensions can be verified by comparison of the ^{1}H shifts in the cross peaks of the carbonyl resonances with those in the methylene/methine region. From such a comparison one could have identified, for example, that the protonated carboxyl is alpha to a methylene while the deprotonated carboxyl is alpha to a methine. The fact that good sensitivity was obtained for a naturally abundant dipeptide implies that moderate-sized proteins can be studied by this approach if they are selectively labeled.

6 CONCLUSIONS

The long-established relationships between proton shift and hydrogen-bonding distances were confirmed in the more restricted data base of amino acids and peptides. Utilization of these 1D CRAMPS methods for proteins is unlikely because of the 0.3–1 ppm linewidths. These measurements might be of use in more complex solids if the spectrum is separated into two dimensions using correlations to attached heteronuclei in the HETCOR experiment. Demonstrations of HETCOR spectra on small peptides with naturally abundant ^{13}C demonstrate the requisite sensitivity for biological work and indicate the potential for measuring hydrogen bonding parameters and confirming assignments.

7 RELATED ARTICLES

HETCOR in Organic Solids; Hydrogen Bonding; Line Narrowing Methods in Solids; Magic Angle Spinning Carbon-13 Lineshapes: Effect of Nitrogen-14.

8 REFERENCES

1. R. K. Harris, P. Jackson, L. H. Merwin, B. J. Say, and G. Hagele, *J. Chem. Soc., Faraday Trans. 1*, 1988, **84**, 3649.
2. B. C. Gerstein, R. G. Pembleton, R. C. Wilson, and L. M. Ryan, *J. Chem. Phys.*, 1977, **66**, 361.
3. D. P. Burum and W. K. Rhim, *J. Chem. Phys.*, 1979, **71**, 944.
4. B. C. Gerstein, *Philos. Trans. R. Soc. London, Ser. A*, 1981, **299**, 521.
5. A. E. McDermott, F. J. Creuzet, A. C. Kolbert, and R. G. Griffin, *J. Magn. Reson.*, 1992, **98**, 408.
6. L. Zheng, K. Fishbein, R. Griffin, and J. Herzfeld, *J. Am. Chem. Soc.*, 1993, **115**, 6254.
7. J. Yesinowski, H. Eckart, and G. Rossman, *J. Am. Chem. Soc.*, 1988, **110**, 1367.
8. S. Un, Ph.D. Dissertation, University of California, Berkeley, 1987.
9. C. Lee and R. G. Griffin, *Biophys. J.*, 1989, **55**, 355.
10. J. Forbes, C. Husted, and E. Oldfield *J. Am. Chem. Soc.*, 1988, **110**, 1059.
11. V. Rutar, *J. Agric. Food Chem.*, 1989, **37**, 67.

12. G. Maciel, C. Bronniman, and B. Hawkins, *Adv. Magn. Reson.*, 1990, **14**, 125.
13. C. E. Bronnimann, R. C. Zeigler, and G. E. Maciel, *J. Am. Chem. Soc.*, 1988, **110**, 2023.
14. C. E. Bronnimann, B. L. Hawkins, M. Zhang, and G. E. Maciel, *Anal. Chem.*, 1988, **60**, 1743.
15. P.-J. Chu, M. J. Potrzebowski, Y. Gao, and A. I. Scott, *J. Am. Chem. Soc.*, 1990, **112**, 881.
16. L. Muller, *Chem. Phys.*, 1981, **61**, 235.
17. L. Zheng, Ph.D. Dissertation, Brandeis University, Waltham, MA, 1993.
18. A. J. Kim and L. G. Butler, *J. Magn. Reson.*, 1992, **99**, 292.
19. C. F. Ridenour, Ph.D. Dissertation, Colorado State University, Fort Collins, CO, 1992.
20. U. Haeberlin and J. Waugh, *Phys. Rev.*, 1969, **185**, 420.
21. E. R. Andrew, *Mol. Phys.*, 1976, **31**, 1479.
22. A. Naito, A. Root, and C. A. McDowell, *J. Phys. Chem.*, 1991, **95**, 3578.
23. A. C. Olivieri, L. Frydman, and L. E. Diaz, *J. Magn. Reson.*, 1987, **75**, 50.
24. J. W. Diesveld, E. M. Menger, H. T. Edjes, and W. S. Veeman, *J. Am. Chem. Soc.*, 1980, **102**, 7935.
25. J. G. Hexem, M. Frey, and S. J. Opella, *J. Chem. Phys.*, 1982, **77**, 3847.
26. N. Zumbulyadis, P. M. Henrichs, and R. H. Young, *J. Chem. Phys.*, 1981, **75**, 1603.
27. B. Berglund and R. W. Vaughan, *J. Chem. Phys.*, 1980, **73**, 2037.
28. G. A. Jeffrey and Y. Yeon, *Acta Crystallogr., Sect. B*, 1986, **42**, 410.
29. M. C. Etter and G. M. Vojta, *J. Magn. Reson.*, 1991, **93**, 609.
30. T. M. Duncan, *A Compilation of Chemical Shift Anisotropies*, Farragut Press, Chicago, 1990, pp. H-1–H-12.
31. U. Haeberlin, *High Resolution NMR in Solids; Selective Averaging*, Academic Press, New York, 1976.
32. M. Mehring, *Principles of High Resolution NMR in Solids*, 2nd edn., Springer, New York, 1983.
33. K. Luth and S. Scheiner, *Int. J. Quantum Chem., Quantum Chem. Symp.*, 1992, **26**, 817.
34. M. G. Munowitz and R. G. Griffin, *J. Chem. Phys.*, 1982, **76**, 2848.
35. P. Caravatti, G. Bodenhausen, and R. R. Ernst, *Chem. Phys. Lett.*, 1982, **89**, 363.
36. J. E. Roberts, S. Vega, and R. G. Griffin, *J. Am. Chem. Soc.*, 1984, **106**, 2506.
37. D. P. Burum and A. Bieleski *J. Magn. Reson.*, 1991, **94**, 645.
38. C. E. Bronnimann, R. A. Santos, and R. A. Wind, *J. Magn. Reson.*, 1994, **105**, 183.
39. Z. Gu and A. McDermott, *J. Am. Chem. Soc.*, 1993, **115**, 4282.
40. S. T. Rao, *Acta Crystallogr., Sect. B*, 1973, **29**, 1718.
41. D. S. Eggleston and D. J. Hodgson, *Int. J. Peptide Protein Res.*, 1985, **25**, 242.
42. D. S. Eggleston and D. J. Hodgson, *Int. J. Peptide Protein Res.*, 1983, **21**, 288.
43. D. S. Eggleston and D. J. Hodgson, *Int. J. Peptide Protein Res.*, 1982, **19**, 206.
44. J. L. Derissen, H. J. Endeman, and A. F. Peerdman, *Acta Crystallogr., Sect. B*, 1968, **24**, 1349.
45. T. N. Bhat and M. Vijayan, *Acta Crystallogr., Sect. B*, 1976, **32**, 891.
46. A. Sequeira, H. Rajagopal, and R. Chidambaram, *Acta Crystallogr., Sect. B*, 1972, **28**, 2514.
47. T. F. W. C. Hamilton and R. Parthasarathy, *Acta Crystallogr., Sect. B*, 1972, **28**, 2083.

Biographical Sketches

Ann McDermott. *b* 1960. B.S., 1981, Harvey Mudd College; Ph.D., 1987, University of California, Berkeley, with Professor Ken Sauer and Dr. Melvin Klein; postdoctoral research, 1988–1990, MIT and Francis Bitter National Magnet Laboratory with Professor Robert Griffin, postdoctoral research 1990–1991, Université Catholique de Louvain, Institute for Clinical Pathology, Tropical Diseases Unit; Assistant Professor of Chemistry, Columbia University, 1991–present.

Cynthia F. Ridenour. *b* 1962. B.A., 1984, University of Colorado, Boulder; Ph.D., 1992, Colorado State University, with Professor Gary E. Maciel, applications scientist, Otsuka Electronics (USA), Inc., 1992–present.

Quadrupolar Nuclei in Liquid Samples

Pierre Laszlo
Université de Liège, Liège, Belgium and Ecole Polytechnique, 91128, Palaiseau, France

1	Introduction	1
2	Microdynamics From Deuterons	2
3	Organolithium Compounds: Electronic Structure, Geometry, and Degree of Aggregation	2
4	Nitrogen-14	3
5	Oxygen-17	4
6	The Sodium Anion	4
7	Coordination of Aluminum-27	5
8	Microenvironment of the Chloride Ion	6
9	How Does Cobalt-59 Relax in Octahedral Complexes?	7
10	A Note on the Sternheimer Antishielding Factor	8
11	Conclusions	8
12	Related Articles	8
13	References	8

1 INTRODUCTION

Nuclei with a spin quantum number equal to or greater than unity have an electric quadrupole moment Q, prolate or oblate. The quadrupolar coupling is the interaction between such an electric quadrupole—stemming from the nonspherical distribution of the proton charges within the nucleus—and the electric field gradient due to the rest of the molecule. This field arises entirely from charges external to the nucleus: the other nuclei and the electrons both contribute. Thus, the electrostatic field gradient (EFG) is a traceless tensor. In its principal axis system (α,β,γ), it is represented by two observables, for example,

$$eq = V_{\alpha\alpha}, \quad \eta = \frac{V_{\beta\beta} - V_{\gamma\gamma}}{V_{\alpha\alpha}} \tag{1}$$

The axes are chosen so as to rank the components of the EFG in the alphabetical sequence $|V_{\alpha\alpha}| > |V_{\beta\beta}| > |V_{\gamma\gamma}|$. η is called the asymmetry parameter, and $\chi = e^2qQ/h$ is known as the quadrupolar coupling constant. In general, quadrupolar coupling constants range between a few tens of kilohertz and a few megahertz.

A majority of the nuclides in the Periodic Table are quadrupolar. Yet, so far, the historical development of NMR has given a privileged position to spin-$\frac{1}{2}$ nuclei such as ^{1}H, ^{13}C, ^{15}N, ^{19}F, ^{29}Si, ^{31}P, and ^{131}Xe. The objective reasons are the very high sensitivity of protons, the fact that the composition of organic molecules is predominantly carbon, hydrogen, oxygen, and nitrogen, and the ease with which both scalar and dipolar couplings can be used to provide rich structural information. The former reveal coupling patterns (multiplets) uniquely diagnostic of the number and type of neighboring nuclei, and thus indicate the local connectivity. The latter, as manifested especially through nuclear Overhauser effects, gives complementary information about internuclear distances.

The efficiency of quadrupolar relaxation makes it, in general, rather difficult to extract these two types of structural information from the magnetic resonance of a quadrupolar nucleus. One should perhaps add to these objective reasons the innate conservatism of chemists—and indeed of paradigmatic science in general.

Yet quadrupolar nuclei have themselves so much to give to their observer. Even though chemists have tended to neglect it, the quadrupolar coupling constant holds comparable intrinsic interest to the electric dipole moment. It is one of the few measures we have of the electronic distribution in molecules, which in turn determines so many of their ground state properties, and can also be astutely used to make predictions of reactivity.

As is well known, any NMR relaxation mechanism gives a relaxation rate proportional to the square of the relevant interaction energy, multiplied by a spectral density. In the extreme narrowing limit, the spectral density at zero frequency is a correlation time, as defined from the appropriate correlation function. With the quadrupolar interaction energy into the megahertz range, this means that its fluctuations on a picosecond timescale, i.e., one characteristic of reorientation of organic molecules in solution, will be readily amenable to measurement. The attendant relaxation rates will be of the order of a few hertz. Thus, another major application of quadrupolar NMR is to the study of dynamics and microdynamics.

It is impossible within the space available here to give a thorough overview of the field. Probably, even a list of references for the past decade would more than fill the available space. Thus, a decision has been made not even to attempt comprehensiveness—because this would actually lead to its very opposite, superficiality. This is the reason why we have opted for a personal selection.

What are the main characteristics of this selection? It will emphasize contributions to science rather than technology. Good science is something like a convolution product between an important problem, a good idea to solve it, and an adequate technique—probably in that order. This review will also attempt to lay the groundwork for future historians by backtracking to the original seminal contributions. Scientists tend to downplay their predecessors in order to put their own contributions in the best possible light—sometimes even at the extent of mutilating their bibliography of highly relevant references. Perhaps, the length of time that this reviewer has invested in NMR will give a more balanced overview.

Yet another characteristic is the limitation to isotropic environments. This is apparently a severe limitation drastically curtailing applications of quadrupolar NMR: the transitions being made degenerate, the spectra are apparently devoid of the quadrupolar interaction, in the form of an observed splitting. Nevertheless, as already stated, even though there may be a single resonance to record, its relaxation behavior is determined by the magnitude of the quadrupolar interaction. Hence, while other articles are devoted to quadrupolar nuclei in the presence of local order, as in solids or liquid crystals (see ***Liquid Crystals: General Considerations***), this review confines itself to quadrupolar nuclei in isotropic media.

Two more constraints on this article should be mentioned briefly. Obviously, the author's own work will not be mentioned. More cruel yet is the taboo on individual areas that could have had their natural niche within this review—such as the lovely ^{43}Ca study of calciproteins by the Lund group—but which are covered elsewhere in the Encyclopedia.

2 MICRODYNAMICS FROM DEUTERONS

Deuterium is rather easy to substitute for hydrogen in organic molecules. Such a move is attractive for NMR studies. Since scalar couplings are reduced by the ratio of the gyromagnetic ratios, the spectrum is simplified—and the chemical shifts in ppm to first approximation remain the same. Furthermore, replacement of a proton with a deuteron makes interpretation of relaxation measurements much simpler. In the absence of electronic relaxation by paramagnetic species, deuteron relaxation is exclusively quadrupolar.

The electrostatic field gradient at deuterium arises from imperfect (but near-perfect) cancellation of nuclear and electronic contributions. Accordingly, the quadrupolar coupling constant χ associated with a carbon–deuterium C–^{2}H bond usually has values of about 160–180 kHz, depending upon carbon hybridization and substitution.[1] Deuterium quadrupolar coupling constants have been obtained from ab initio SCF calculations. These yield coupling constants accurate to about 5% (10 kHz). A plot of the calculated versus the experimental values has unit slope, a standard deviation of 10 kHz and a correlation coefficient of 0.989 for 24 data points. The confidence limits (P = 0.95) of the slope and the intercept include 1 and 0, respectively. Examination of the calculated values reveals an empirical proportionality to one another of the electronic and nuclear parts of the quadrupolar coupling constant. This observation is turned into a model that yields electrostatic field gradients at deuterium, q, of equal quality to the SCF calculations.[2]

The history of chemistry shows an empirical law not unlike Haeckel's Law ('ontogeny recapitulates phylogeny'), namely, whatever organic chemistry has achieved, organometallic chemistry strives to emulate. An instance is the quadrupolar coupling constant of deuterium in metal hydrides. It ranges from 55 to 158 kHz, as obtained from T_1 relaxation data in solution, and provides useful information on the ionicity of the metal–deuterium bond.[3]

After this aside, we return to deuterium-labeled organic molecules. Under extreme narrowing conditions, the longitudinal and transverse relaxation rates are equal and given by $R_{1,2} = \frac{3}{2}\pi^2\chi^2(1 + \frac{1}{3}\eta^2)\tau_c$, where η is the asymmetry parameter, which vanishes only when the C–D bond is coaxial, with a threefold or higher molecular symmetry axis. Thus, longitudinal relaxation times in the range of 17 ms to 17 s are measured under these conditions. Knowledge of both the quadrupolar coupling constant χ and the asymmetry parameter η, combined with measurement of the relaxation rates, thus yields the effective reorientational correlation time τ_c. For instance, methylenephenanthrene tumbles about in deuteriochloroform solution with τ_c = 13.6 ps. The anisotropy of the reorientation can be probed simply by monitoring C–D bonds variously located with respect to the inertial axes around which the molecule rotates: the fastest reorientational motion is associated with the highest symmetry axis.

Whenever the C–D bond, instead of being attached to a rigid skeleton, is part of a rotor, at least two correlation times are needed for the description of its motion: τ_i for the internal rotation and τ_M for the overall motion. For instance, a $-CH_2D$ group in an isotropically reorienting molecule corresponds to

$$\tau_\chi = 0.11\tau_M + 0.89(\tau_M^{-1} + \tau_i^{-1}) \qquad (2)$$

A number of substituted aromatic molecules have been examined in this way.[4]

Consider now a molecule A that incorporates the telltale C–D bond and that is involved in a dynamic equilibrium process A + B = AB. Let us denote by k_a and k_d the rate constants for association and dissociation. Since the system bears its own internal clocks ('To choose time is to save time'—Francis Bacon[5]), with τ_f and τ_g the correlation times of the free A molecule and of the complex AB, it becomes possible to measure k_a and k_d.[6] Brevard and Lehn achieved such a truly lovely application. They studied the charge-transfer complexes between trinitrobenzene as the electron acceptor and fluorene, methylfluorene, and methylenephenanthrene as the electron donors. The results showed that each of the CT complexes amounted to a collision complex.[7] During the last two decades, there have been numerous applications of deuterium nuclear relaxation to organic and biomolecules.[8]

To give but one example of the sophistication that has been achieved, a study has examined the intercalates formed by dimethyl sulfoxide in the interstitial space of a kaolinite clay, using DMSO-d_6. The results show the coexistence of two DMSO sites. In one of these sites, with χ = 67 kHz, the methyl group rotors hop through angular steps of 140°. In the other site, with χ = 59 kHz, the methyl groups hop through 110°. The former is a site in which one methyl group is anchored in a hexagonal hole within the honeycombed silicate layer, and the DMSO molecule is able to rotate around this sulfur–carbon axis. The latter has the DMSO pyramid with its symmetry plane, through the S–O bond and bisecting the C–S–C angle, orthogonal to the parallel layers of the clay.[9]

3 ORGANOLITHIUM COMPOUNDS: ELECTRONIC STRUCTURE, GEOMETRY, AND DEGREE OF AGGREGATION

The two lithium nuclides are ^{6}Li and ^{7}Li, with natural abundances of 7.42% and 92.58%, respectively. The spin quantum numbers are 1 and $\frac{3}{2}$, respectively. Nevertheless, ^{6}Li has a tiny quadrupole moment of -0.0008×10^{-28} m^2 making it an honorary spin-$\frac{1}{2}$ nucleus.[10]

An elegant use of the two isotopes is Jackman's study of the structure of phenyllithium in diethyl ether–cyclohexane (1:2) and in tetramethylethylenediamine (TMEDA)–cyclohexane (1:9) stable solutions. The idea stems from the contrasted abilities of the two lithium nuclides at dipole–dipole relaxation. Lithium-7 has 70% of the ^{1}H effectiveness while ^{6}Li has only 8%.[11,12] In the solid state, the diethyl ether solvate is a tetramer by X-ray evidence. Hence, if this cubic tetramer endures in solution, it should undergo isotropic reorientation. Describing its motion with a single correlation time is thus legitimate. This correlation time is obtained independently from the T_1 of C-4,

which arises from exclusive dipolar relaxation by the proton attached 110.7 pm away. The difference in relaxation rate R_1 of the neighboring ^{13}C nucleus at C-1 with the two lithium isotopes provides the carbon–lithium distance, with excellent accuracy. Use of [2,3,5,6-$^2H_4$]phenyllithium eliminates contributions to T_1 of C-1 from the *ortho* protons. It is necessary to measure T_1 values at 2.35 T to make relaxation by chemical shift anisotropy negligible. In this manner, the Li–C-1 distance is measured as 227 ± 5 pm in diethyl ether–cyclohexane (tetramer) and as 218.8 ± 2.2 pm in TMEDA–cyclohexane (dimer). Confirmation of the two oligomers comes from monitoring relaxation of H-2 by its two adjacent lithium nuclei in both the dimer and the tetramer. The observed values are 262 ± 2 pm in ether–cyclohexane, uniquely consistent with the tetrameric structure.[13]

Brown pioneered the use of lithium NMR to elucidate structures of alkyllithiums. The first lithium NMR showed ethyllithium to consist of a single hexameric species,[14] bound strongly enough for the exchange rate constant to be less than $10\,s^{-1}$.[15] In 1965, Lucken showed the quadrupolar coupling constant in methyllithium to be smaller than 16 kHz.[16] Brown translated the absence of $^6Li–^7Li$ scalar coupling in the methyllithium tetramer into a negligible metal–metal bond order.[17] A group at Dow Chemical made the first observation of $^7Li–^{13}C$ scalar coupling in methyllithium,[18] in various solvents.[19] The finding of a statistical distribution in ^{13}C-enriched methyllithium was consistent only with a cubic tetramer in which each lithium had three adjacent methyl groups, in accord with the local environment hypothesis of Seitz and Brown,[20] which had enabled Brown not only to confirm a cubic tetrameric structure in solution but also to measure an activation energy of approximately 100 kJ mol^{-1} for dissociation.[21,22] Subsequent work showed that the degree of oligomerization of alkyllithiums is solvent-dependent, *n*-butyllithium going from the tetramer in ether to the hexamer in hydrocarbon solutions,[23] and that, furthermore, the bonding changes from an ion pair to a covalent carbon–lithium bond as a function of the solvent.[24] Several alkyllithium compounds are converted by small amounts of bases from hexamers to solvated tetramers.[25]

The stylistic feature characteristic of the school of Brown is the use of scalar couplings to ^6Li as structural evidence. Lithium diisopropylamide (LDA) generates kinetic enolates from carbonyls. Its use in organic synthesis has become widespread in recent years.[26] The solution structure of lithium enolates is therefore of central importance. It determines their solubility, the effect of cosolvents, and addition to aldehydes and acid chlorides. Mixed aggregates determine the diastereo- and enantioselectivities.[27,28] X-ray structures in the solid state do not necessarily extend to solution structures, and the latter determine the chemistry. Hence NMR has unique value in ascertaining those. A pioneering study is that by Grutzner of the solution in tetrahydrofuran of the simplest enolate, namely, that from acetaldehyde. Carbon-13 relaxation rates indicate aggregation—the cluster is significantly bigger than a THF molecule. These data also indicate anisotropic reorientation, with fast (slow) rotation of the C-1–H (C-2–H) dipole. With an effective radius of 580 pm, the aggregated species is identified as the cubic $(CH_2{=}CHOLi)_4$ tetramer. It includes lithiums with a quadrupolar coupling constant of 65 kHz. The enolate rotates more rapidly about its C–O axis than the aggregate reorients in solution.[29] Such cubic tetramers are involved in highly selective formation of such products as result from alkylation of the lithium enolate of norbonenone, whose structure[30] was established at the same time as others of the same ilk.[31]

The solution structure of lithium isopropylcyclohexylamide (LICA) was characterized by Collum at Cornell, as an equimolar mixture of the *cis* and *trans* lithium-bridged dimers: $^6Li–^{15}N$ double labeling[32–34] shows N–Li–N and Li–N–Li connectivity. LDA exists also as the cyclic dimer. In THF solution, each lithium is coordinated to the two amide nitrogens and to a single THF. This conclusion results unambiguously from ^6Li detection of ^{15}N homonuclear zero quantum coherence[35]—the technique devised by Müller[36] and Bodenhausen and Ruben.[37] As hexamethylphosphoric triamide (HMPA) is added, HMPA sequentially displaces each of the two THF solvates in the dimer, as proved by both $^6Li–^{15}N$ and $^6Li–^{31}P$ coupling patterns.[38] Mixed dimers can form in the presence of other enolates; for instance, one LDA is replaced in the cyclic dimer by one pinacolate, as shown by the ^6Li coupled to a single ^{15}N.[39] In hydrocarbon (hexane) solution, LDA exists as an equilibrium mixture of at least three cyclic oligomers.[40]

It is worth making explicit the above statement about the virtue of inverse-detected ^{15}N homonuclear zero quantum spectroscopy, and reproduce here Collum's explanation. It provides a rigorous distinction of D_{2h} cyclic dimers from D_{nh} higher oligomers. In the ^{15}N zero quantum experiment, homonuclear ^{15}N two-spin coherence is prepared from the two ^{15}N spins neighboring a ^6Li atom in a $^6Li–^{15}N$ doubly labeled lithium dialkylamide cyclic oligomer. During the evolution period, the zero quantum coherence will evolve under scalar coupling only to ^6Li spins that couple to one, but not both, ^{15}N spins. For a lithium amide dimer, all ^6Li spins coupled to ^{15}N spins involved in the two-spin coherence couple to both ^{15}N spins. Consequently, the coupling pattern will be a singlet along the f_1 dimension of the 2D spectrum. In higher cyclic oligomers, there exist two ^6Li spins that couple to one, but not both, ^{15}N spins. The zero quantum coherence will develop scalar coupling to the two nonshared ^6Li spins, resulting in a 1:2:3:2:1 pattern along the f_1 dimension. As a result of a refocusing delay employed prior to detection, all oligomers will show a 1:2:1 pattern along the f_2 dimension.[41]

4 NITROGEN-14

With an isotopic abundance of 99.7% and a spin quantum number I of unity, ^{14}N suffers from a low gyromagnetic ratio and from long longitudinal relaxation times (see ***Nitrogen NMR***). Its relaxation is dominated by the quadrupolar mechanism—even in the most unfavorable situations. The tiny ammonium ion NH_4^+ relaxes exclusively by the quadrupolar mechanism, despite the zero electrostatic field gradient at nitrogen in the full T_d symmetry.[42] Even in the paramagnetic hexacyanide complexes of chromium, manganese, and iron, the ^{14}N linewidths are determined solely by quadrupolar relaxation.[43] Resonances are usually very broad, with linewidths greater than 500 Hz. Bypassing these experimental difficulties calls either for astute experiments or for a cop-out. Many have chosen the latter, resorting to ^{15}N enrichment, in particular for investigating biomolecules such as proteins

and nucleic acids. Nevertheless, there have been a few studies of the ^{14}N chemical shift in relation to structure. For instance, the extent of $d_\pi - p_\pi$ bonding has been determined in *N*-trimethylsilylaminoboranes[44] and in trimethylsilylamines.[45] Likewise, σ and π contributions from fluorine are sorted out in fluoronitrogen cations.[46] The nitrogen chemical shift gives a rather direct estimate of the atomic charge.[47] But there have been some rather smart solutions to circumvent the ^{14}N limitations. Indirect measurement of ^{14}N relaxation rates is feasible through attached protons in amino groups by measurement of the ^{1}H longitudinal rate in the rotating frame. In this manner, ^{14}N relaxation has been studied in a variety of biomolecules, such as nucleotide bases.[48,49] Another elegant experiment—also indirect and also taking advantage of the sensitivity of ^{1}H NMR—is observation of ^{14}N double quantum (DQ) coherence in isotropic solution. The usual recipe with two $\frac{1}{2}\pi$ pulses on the *S* spins (^{14}N) during the preparation sequence fails. Augmentation of this sequence by spin tickling of *I* spins ($I = \frac{1}{2}$) mixes *S*-spin DQ coherence into the *S*-spin magnetization.[50] An alternative solution is to excite and detect the *S* DQ coherence by using only the *I* magnetization and applying single hard pulses at both *I* and *S* frequencies. This is an example of heteronuclear coherence transfer taking advantage of the signal enhancement accruing from using only proton magnetization for both the initial and the final conditions. The method was tested on ammonium nitrate 8 M (!) in water acidified to pH 1 to slow down proton exchange. The DQ ^{14}N coherence is observed, with a splitting $2J = 105$ Hz. The multiplet resonance is a quintet with a vanishing central line. Using the composite particle method and replacing the two $I = 1$ spins with four $I = \frac{1}{2}$ spins and evaluating the matrix elements does indeed give the line amplitudes for the five transitions $m^I = \pm 2, \pm 1$, and 0: this last one has zero amplitude.[51] Determination of the quadrupolar coupling constant and of the asymmetry parameter for ^{15}N even approximately and for some general category such as cyano group, nitro group, or secondary amine, would seem to demand recourse to a method such as microwave spectroscopy, or NMR in a single crystal, or even pure quadrupole resonance. A smart manner of obtaining these required parameters in the liquid state is applicable to polar groups: alignment by a strong external electric field. Thus, the principal components of the quadrupolar coupling tensors were determined in the ^{14}N NMR of nitrobenzene.[52]

Nitrogen-14 NMR gives a handle onto relaxation, especially of highly symmetrical nitrogen-containing solutes having a vanishingly small electrostatic field gradient at nitrogen. The azide anion N_3^- shows a strong dependence of the T_1 values for both nitrogen types upon concentration. The ratio T_1(end)/T_1(central) is 0.25, reflecting a ratio of the corresponding χ values of 0.50.[53] The transverse relaxation rates for the azide ion nitrogens are extremely sensitive to the presence of an associating counterion. Observed values in aqueous solution are 500 Hz with Zn(II), 1000 Hz with Cd(II), 5×10^6 Hz with Cu(II), 2.5×10^6 Hz with Mn(II), and 6×10^5 Hz with Fe(III).[54] In an early piece of work, as handsome as it turned out to be useful, Pople had calculated the lineshapes for a spin $I = 1$ (^{14}N) resonance scalar-coupled with a spin $I = \frac{1}{2}$ (^{1}H) for various values of the ^{14}N relaxation rate. In this manner, one may obtain the ^{14}N relaxation rate indirectly from the proton resonance lineshape.[55] More than 30 years later, the method is still very useful. For instance, the ^{14}N linewidth in methyl-substituted ammonium ions increases from less than 0.2 Hz in NH_4^+ to 32.1, 80.7, and 96.4 Hz with the successive introduction of one, two, and three methyl groups; the activation energy for molecular reorientation remains relatively invariant at about 10.6 kJ mol^{-1}.[56]

5 OXYGEN-17

Townes and Dailey pioneered the interpretation of quadrupolar coupling constants to analyze chemical bonding. They did it on bonds involving halogens.[57] Brown made use of similar tactics to gain insight into the details of the carbonyl group, using ^{17}O NMR. A representative carbonyl has the α, β, and γ axes of the quadrupolar interaction tensor (see Section 1) oriented along the carbon–oxygen internuclear axis, perpendicular to the carbonyl plane, and in that plane, respectively. In 28 carbonyl-containing compounds, Cheng and Brown found a π population ranging from 1.366 for *p*-benzoquinone to 1.742 for sodium bicarbonate. The less polarizable σ bond has a narrower range, as expected. The formal electronic charge on oxygen is rather large, of the order of one electron.[58,59] Following the pioneering work of Kintzinger,[60,61] numerous authors have obtained chemical shifts and quadrupolar coupling constants in organic molecules.[62] Likewise, after Lauterwein gave a similar impulse for applications to biomolecules,[63,64] these have thrived, and have presently reached studies of hemoglobin and myoglobin.[65] Also, ^{17}O NMR is a nice biochemical labeling technique.[66] Organometallic applications have developed in parallel, to the structures of species such as metal carbonyls[67] and oxo–peroxo complexes,[68] and to mechanistic studies.[69] With the new techniques of dynamic angle spinning and double rotation,[70] ^{17}O NMR has penetrated into the solid state, and is helping to elucidate the structure of silicates.[71]

To end this section, we single out studies of molecular microdynamics based on ^{17}O relaxation to a large extent. They include, of course, water, for which the isotropic motional model was shown to be an adequate description in the picosecond timescale.[72] The motion of tetrahedral oxo anions is a natural for the technique,[73] and correlation times in heavy water at 28 °C are 0.80 ps for perchlorate, 2.8 ps for sulfate, and 14–16 ps for phosphate, reduced to 0.73 ps (perchlorate) and 1.1 ps (sulfate) in methanol-d_4.[74]

6 THE SODIUM ANION

The preamble to this story took place in London, at the Royal Institution in 1808, when Humphry Davy, after he had isolated sodium and potassium, heated the latter in ammonia and obtained potassamide.[75,76] Weyl proceeded to study the blue solutions formed when alkali metals dissolve in dry ammonia.[77] Mendeleev pointed out the quantitative resemblance between the alkali metals and the halogens.[78] Thus, alkali metal anions ought to be capable of existence. In the early 1960s, Dye used optical spectra in support of the postulated existence of alkali metal anions when the alkali metals are dissolved in primary amines and in some polyethers.[79]

In 1974, Ceraso and Dye obtained a ^{23}Na NMR spectrum with distinct, well-separated resonances for the cryptated

sodium cation and the sodium anion, after they had co-dissolved metallic sodium and the [2.2.2]cryptand in an organic solvent, ethylamine. The signal of the sodium anion is found 63 ppm to low frequency of the aqueous sodium chloride reference, and is solvent-independent when measured in THF, methylamine, and ethylamine.[80,81] Clearly, Dye had been following very carefully the new developments in polyether and cryptate chemistry, and realized the versatility of their utilizations.

The NMR spectrum published in 1974 truly demonstrated the structure of the sodium anion, Na^-. The paramagnetic part of the shielding constant of the sodium nucleus in the sodium cation arises from the introduction of orbital angular momentum by interaction of the filled outer p shell with electron pairs from neighboring solvent donor molecules.[82] The sodium anion, with a more diffuse electronic distribution, and with only a weaker interaction with external electronic pairs, should have much less of a paramagnetic shift. The two spin-paired electrons in the 3s orbital shield the 2p electrons from the influence of the solvent. Indeed, its chemical shift, with reference to external saturated aqueous NaCl, is invariant at -57 to -63 ppm[83,84] and the same within experimental error as that of -63.8 ppm calculated for the isolated anion in a gas.[85] Thus, the system studied consisted of Na^+C222.Na^-, where C222 denotes the cryptand.

Edwards's group in Cambridge then showed that it was not mandatory to hide away the sodium cation in a crown ether or cryptand in order to dismutate sodium metal into the +1 and -1 oxidation states. When they dissolved sodium in anhydrous hexamethylphosphoric triamide (HMPA), they recorded the ^{23}Na spectrum of the naked anion at -62 ppm with a linewidth of 10 Hz.[86] They were unable to observe any resonance from the sodium cation, presumably because of its extreme width in the paramagnetic (solvated electrons) solution. The Cambridge group proceeded to make a similar series of observations in 12-crown-4[87] and in various amide solutions, *N*,*N*-diethylacetamide, *N*,*N*-di-*n*-propylacetamide, *N*,*N*-dimethylpropanamide, and tetramethylurea: the chemical shift of the sodide ion is both solvent- and temperature-independent, at -62.3 ± 0.3 ppm. The linewidth is very narrow, 8–13 Hz from 233 to 200 K, in contrast to Na^+, for which the linewidth trebles in going from 279 to 250 K, in diethylacetamide solution.[88] Again, Edwards and co-workers were unable to detect the signals of the solvated cations. Direct measurements of the longitudinal relaxation rate for Na^- in solutions containing an alkali countercation in 12-crown-4 showed independence with respect to the nature of the alkali counterion. Relaxation occurs by a predominant, although rather inefficient, quadrupolar relaxation mechanism via the reorientational–vibrational motion of the surrounding 12-crown-4 molecules in the liquid. Furthermore, solvation of the sodium anion by the crown ether is very weak: there is neither a preferential orientation of the crown ether nor a clearly identifiable first solvation shell around the sodide anion. An RMS value of 0.03 MHz is deduced for the quadrupolar coupling constant χ in 12-crown-4 solutions: Na^- is a gas-like entity in solution.[89,90]

The ^{23}Na NMR of both Na^+C222 and Na^- in polycrystalline Na^+C222.Na^- was monitored from the $(+\frac{1}{2}, -\frac{1}{2})$ transition, as a function of the Larmor frequency (at 4.7, 8.5, and 11.7 T): second-order perturbation theory gives the shift of this central transition with frequency as

$$\nu - \nu_L = -\chi^2[I(I+1) - \tfrac{3}{4}](1 + \tfrac{1}{3}\eta^2)/30\nu_L \qquad (3)$$

where ν_L is the Larmor frequency and η the asymmetry parameter. For the cryptated sodium cation, the authors determined χ = 1.2 MHz and an isotropic chemical shift of -6.5 ppm, essentially the same as that for Na^+C222 in solution in various solvents. The quadrupolar contribution to the static linewidth of the complexed cation in Na^+C222.Na^- is 320 Hz whereas the observed linewidth is 3700 ± 300 Hz—a difference ascribable to dipolar couplings with the protons in the methylene groups of the [2.2.2] cryptand. Conversely, the sodium anion has a quadrupolar coupling constant χ of 0.26 MHz and a calculated (van Vleck expression) dipolar broadening from $^1H\cdots Na^-$ interactions of 2860 Hz in excellent agreement with the observed linewidth of 2800 Hz.[91] More recently, Dye has provided a more accurate determination of the quadrupolar coupling constant for the sodium anion from a single crystal ^{23}Na NMR study of the same Na^+C222.Na^- system. Values for χ of 1.268 and 0.1763 MHz were determined for Na^+ and Na^-, respectively. Isotropic chemical shifts of -5.5 and -61.8 ppm were obtained for the cation and the anion, respectively.[92] At the time of writing (December 1993), Dye is studying mixed systems such as $Cs^+(18C6)_2Na^-$, in which the ^{23}Na chemical shift of about -61 ppm is diagnostic of the sodium anion.[93]

7 COORDINATION OF ALUMINUM-27

Many applications reflect the natural state of aluminum, which constitutes 9% of the Earth's crust. They concern aluminates and aluminosilicates. In the latter category, it is not so much layered clays (phyllosilicates), but rather microporous aluminosilicates, zeolites, that have been extensively studied as industrially important catalysts. Especially since the discovery of the Mobil process for conversion of methanol into gasoline on the HZSM-5 zeolites, there has been a flurry of high-resolution ^{27}Al NMR studies of these solids. Nevertheless, the field of ^{27}Al NMR is wider. At the time when Delpuech wrote his useful review, most data pertained to tetra- or hexacoordinate compounds.[94] A fuller picture can now be given. Benn pointed out that the chemical shift characterized organoaluminum compounds in classes, depending on coordination of the metal. Tricoordinate aluminum has a chemical shift of about 250 ppm, tetracoordinate aluminum about 150 ppm, pentacoordinate aluminum about 120 ppm, and hexacoordinate aluminum 0 ppm with respect to an external reference of $Al(acac)_3$.[95] A word is in order here about the ^{27}Al reference. Usually, the hexaaquoaluminum(III) cation, $[Al(H_2O)_6]^{3+}$, is chosen.[96] It is sensitive to second-sphere effects.[97] Another candidate, with the merit of better invariance to solvation and concentration, is the AlH_4^- anion, with δ = 101 ppm with respect to the aluminum(III) hydrate.[98] A caveat on the use of ^{27}Al NMR for characterization of organometallics was issued.[99] Distinction between tricoordinate and tetracoordinate aluminum in alkylaluminum phenoxides was made.[100] In the gauge-independent decomposition,[101] the diamagnetic part of the shielding constant is invariant within a few ppm. Variations arise from the paramagnetic contribution, itself dominated by

the HOMO–LUMO gap. Low-valent aluminum compounds have been made in recent years. The chemical shift of aluminum(I) compounds has been studied experimentally and theoretically.[102] The latter are SCF calculations[103–105] using the gauge-including atomic orbital (GIAO) method.[106] The surprise is that, rather than settling into a niche of their own next to the others for aluminum(III) compounds, aluminum(I) compounds are anarchists, roaming through the whole range of ^{27}Al chemical shifts. The calculated values include one of the most shielded (AlCp, −170 ppm) and one of the most deshielded (AlSi(t-Bu)$_3$, 854 ppm). The actual, quite different, chemical shifts, are −111 and 64.5 ppm, respectively. They point to the existence of AlCp as the tetramer Al_4Cp_4 and to the importance of solvation effects in determining the chemical shift of AlSi(t-Bu)$_3$. The calculations confirm the correlation between the calculated shielding constants and the HOMO–LUMO energy gap.

A seminal finding for solid state studies of aluminosilicates has been the sensitivity of the ^{27}Al chemical shift to the composition of the second coordination sphere. Thus, studies of aluminosilicate solutions showing that the chemical shift for Si–O–Al units depended on the structural unit (Q^0, Q^1, Q^2, or Q^3) with incremental changes[107] launched this very active field. Aluminum-27 NMR can serve to characterize synthetic and natural zeolites.[108] Owing to the strong industrial interest already referred to, increased technical sophistication was brought to bear on structural studies of zeolites. Klinowski in Cambridge resorted to quadrupolar nutation ^{27}Al NMR to study isomorphous substitutions in the zeolite Y framework.[109] Already in 1988, one could start reading reviews of MAS studies in zeolites.[110] The advantages of very high fields $\boldsymbol{B}_0$ and ultrafast spinning became clear,[111] and were applied to samples such as USY zeolites[112] or dealuminate Y zeolite.[113] Another big experimental breakthrough was the development of double rotation and of dynamic angle spinning to average out both the first- and second-order anisotropic broadenings in solids. In this manner, it has been possible to characterize both tetrahedral environments and heavily distorted pentacoordinate aluminum in zeolites of the $AlPO_4$-21 and $AlPO_4$-25 types.[114] The ^{27}Al longitudinal relaxation was related to the organic molecules and exchangeable cations present within the channels and supercages of the zeolites.[115] A fine multinuclear study paid attention to satellite transitions,[116] which have been receiving increased attention.[117] The analytical aspects were not neglected, and quantitation of aluminum in zeolites was perfected.[118] A study was made of β-zeolites in relation to their catalytic prowess.[119] Of course, the acidic HZSM-5 received star treatment.[120] Aluminophosphate zeolites[121] such as VPI-5[122] and $AlPO_4$-11[123,124] were also studied. Aluminum-27 NMR was the test used to distinguish between various models of ionic solvation.[125] The quadrupolar coupling constant was determined for aqueous Al(III) in solutions of perchloric acid.[126] Other aluminosilicates got the studies that they deserved. The mechanism of kaolinite dehydroxylation was scrutinized,[127] and likewise its thermal transformation[128] and activated layered aluminosilicates were examined.[129] Adsorption of chlorine on γ-alumina was monitored.[130] Cross polarization focused on surface aluminum atoms on alumina.[131] Iron-bearing montmorillonites—outstanding catalysts for quite a few organic reactions—were examined.[132] A related study examined Friedel–Crafts catalysts formed by adsorption of divalent fluorides on the K-10 montmorillonite, a partly amorphized 2:1 clay used as a cracking catalyst in the petrochemical industry.[133] The structure of pumice was examined.[134] In the bio-inorganic realm, aluminum porphyrins were studied.[135] Dimerization of tricoordinate aluminum(III) Lewis acids such as trimethylaluminum deserved some attention.[136] Preferential solvation of aluminum(III) perchlorate in binary mixtures of urea and DMF was studied.[137]

8 MICROENVIRONMENT OF THE CHLORIDE ION

Chlorine-35 NMR was given an early and outstanding review, which continues to be extremely valuable.[138] We shall focus here on a few more recent contributions that in various guises examine the immediate environment of the chloride anion, probed by ^{35}Cl NMR. An interesting question is that of the proximity of the countercation, in the presence of a complexant that encapsulates this cation. Thus, the ^{35}Cl linewidths were determined for the KCl–18-crown-6 complex in various solvents. The chloride anion exists in acetonitrile in a completely dissociated state, approximating the proverbial and elusive 'naked anion'. The ^{35}Cl linewidth due to the Cl-ion-paired with the crown ether is 90 ± 20 Hz in aqueous solutions. The contact ion pair is that in which Cl^- and K^+ are nearest neighbors. It would have a significantly greater linewidth, of about 550 Hz. Thus, because the crown ether grabs the potassium cation with a pseudoequatorial arrangement of its coordinated oxygens, while the apical positions are occupied by water molecules, the chloride anion is unable to coordinate the potassium cation. What is observed instead is a loose, solvent-separated ion pair.[139] Another interesting question is competition between two different counterions. For instance, lithium chloride and lithium perchlorate were studied in acetone solution in the presence of various phosphates. The ^{35}Cl linewidth is monitored as a function of concentration. It shoots up in the presence of triphenyl phosphate $O{=}P(OC_6H_5)_3$. The observation is consistent only with dissymmetric penetration of the perchlorate anion coordination shell by the Li–O–P fragment, with this particular phosphate only.[140] Conceptually similar experiments can be carried out in yet more exotic environments. Sodalites are aluminosilicates with a nanoporous structure that makes them of interest in quantum electronics, nonlinear optics, information storage and processing, and so on. A recent study focused on sodalite semiconductors. The chloride anions are distributed within the cavities of $Na_{8-n-p}Ag_nX_{2-p}$ lattices. Narrow ^{35}Cl resonances are, nevertheless, observed. They stem from the presence of highly symmetrical species. A sharp peak at −122 ppm (0.1 M NaCl external reference) is ascribed to Na_4Cl tetrahedra encapsulated within the sodalite cavities. A substantially low-frequency-shifted peak at −310 ppm in the fully Ag^+-exchanged system corresponds likewise to encapsulated Ag_4Cl clusters. These symmetrical environments around the halide anion give rise to narrow resonances in the ^{35}Cl MAS spectra.[141]

Hydrophobic effects leading to asymmetric solvation and/or aggregation have been reported by many authors. Let us start with water–dimethyl sulfoxide binary mixtures. The relaxation rates at intermediate solvent compositions are higher than those in either pure solvent by more than one order of magnitude. This pronounced deviation from ideality contrasts with that of

the chemical shift: the ^{35}Cl chemical shift varies linearly with composition.[142,143] Useful applications from such observations need not resort to sophisticated analyses. Even at an empirical level, they can be turned into extremely useful consequences. A case at hand is the study by the Martins in Nantes of chloride ion reactivity. They examined the variation in the transverse relaxation of ^{35}Cl as a function of temperature for 13 chloride salts in acetonitrile solutions. When two ammonium species, such as tetrabutyl- and benzyltributylammonium chlorides, are mixed at a fixed concentration, the ^{35}Cl linewidths do not vary linearly between the values characteristic of each species. A broadening occurs, and the maximum linewidth is reached at equimolar concentrations of the two salts. From its magnitude, both types of ammonium cations must coexist in the chloride ion coordination shell. Likewise, the ^{35}Cl linewidth is very sensitive to the presence of phenols in the solution, and depends in a simple way on the pK_a of the phenol added. This behavior makes it feasible to define a linewidth $\Delta\nu^0_{\frac{1}{2}}$ characteristic of the chloride anion in various organic salts. This parameter, with an observed range of 45–450 Hz, appears to measure the reactivity of the chloride anion as displayed in reactions under phase transfer catalysis, or in the catalytic phosgenation of phenol.[144]

Paradoxically, we have kept for the end of this section the apparently much simpler behavior of a chloride salt in aqueous solution. Consider magnesium chloride. The limiting behavior at infinite dilution has been described with a so-called dynamically oriented solvation model, specifying both the structure and the internal dynamics of the hydration spheres of Mg^{2+} and Cl^-. The ^{35}Cl relaxation rate gives a value of 0.43 for water–water correlation effects, i.e., the influence of water from outer hydration layers on the hydration water molecules.[145] Turning to chloride ion relaxation for $MgCl_2$ at finite concentrations, this shows contributions from ion–ion interaction, ion-hydration water, and in-bulk water. At low salt concentrations, below 1 M, the main contribution (75%) arises from bulk water. With increasing $MgCl_2$ concentration, the contribution from the magnesium hydration water molecules becomes more important, and at 5.5 M is responsible in turn for about 75% of the total ion–water contribution. This is very likely due to encounter between the chloride anions and the hexaaquomagnesium(II) cations, with temporary distortion of the hydration shell during the encounter.[146]

9 HOW DOES COBALT-59 RELAX IN OCTAHEDRAL COMPLEXES?

Cobalt-59 NMR has the attraction of 100% isotopic abundance, high sensitivity, and an enormous range of chemical shifts. In hexacoordinate octahedral cobalt(III) complexes, the chemical shifts are correlated to electronic excitation energies, owing to magnetic-field-induced mixing of the $^1T_{1g}$ excited state with the $^1A_{1g}$ ground state, leading to a paramagnetic contribution to the ^{59}Co shielding. A quadrupolar mechanism appears to serve as the dominant mode of relaxation in cobalt(III) complexes devoid of full octahedral symmetry. Indeed, linewidths become very large in the presence of permanent electrostatic field gradients at cobalt.[147] The quadrupolar coupling constant has a value of 2.7 MHz in $[Co(NH_3)_6]^{3+}$, is multiplied about 20-fold on replacement of one ammonia by one water ligand (inner sphere perturbation),[148] but increases only slightly to 3.5 MHz in the $[Co(NH_3)_6]^{3+}$–ClO_4^- ion pair (outer sphere perturbation).[149]

The question remains of the origin of the linewidth in fully symmetric octahedral cobalt(III) complexes. Spin–rotation relaxation has been invoked. For hexamminecobalt(III), $[Co(NH_3)_6]^{3+}$, the longitudinal relaxation rate extrapolated to infinite dilution shows a temperature invariance suggestive of operation of a spin–rotation mechanism with the opposite temperature dependence to that of quadrupolar relaxation. The results were consistent with a quadrupolar coupling constant of about 3 MHz and a spin–rotation coupling constant of 72 kHz.[149] Scalar relaxation of the second kind[150] is another potential contributor. Take the same example of hexamminecobalt: the cobalt nucleus is scalar-coupled to the ^{14}N nucleus, which relaxes efficiently by a nucleus–electric quadrupole mechanism. Such an interaction makes the transverse ^{59}Co relaxation rate proportional to the product of the square of the interaction energy J and the correlation time τ_N descriptive of reorientation of the nitrogen spin. Thus, differences between T_1 and T_2 in some CoN_6 complexes have been ascribed to unresolved scalar couplings with nitrogen, of the order of magnitude of 50 Hz.[151,152] And, of course, there is the problem of explaining the intervention of quadrupolar relaxation in a complex with strict O_h symmetry, in which the electrostatic field gradient at the central nucleus has to vanish. The origin of the fluctuating EFG must be found either in instantaneous distortions with respect to the ideal O_h geometry or in deviations from this perfect symmetry due, for instance, to the proximity of a counterion. When, indeed, a charged anion was placed in the outer sphere of $[Co(en)_3]^{3+}$ and $[Co(pn)_3]^{3+}$ complexes, its contribution was reported as insignificant.[151] The remaining explanation—that of excitation of the vibrational modes of the octahedron[153]—was scrutinized in the case of tris(tropolonato)cobalt(III), and appears as a likely candidate.[152]

Potassium hexacyanocobaltate(III) $K_3Co(CN)_6$ was examined by monitoring the relaxation rates of all the nuclei in the anion. Although the ^{59}Co relaxation rate decreases with increasing temperature, the slope is half that for ^{13}C. Again, this uncoupling of ^{59}Co relaxation from rotational reorientation is suggestive of modulation of the EFG by solvent-assisted molecular vibrations.[154]

In order to proceed further the ^{59}Co chemical shift and its relationship to the linewidth enters as another piece of evidence. The context is Deverell's electronic distortion theory.[155,156] The valence atomic orbitals distort upon each collision with a solvent molecule. A paramagnetic contribution to shielding σ_p stems from injection of electrons into atomic orbitals with the appropriate symmetry. This also sets up a fluctuating electrostatic field gradient at the nucleus monitored. The relaxation rate R_1 is predicted to be proportional to the product of the reorientational correlation time with the square of a term $\sigma_p\ \Delta E$, where ΔE is the average electron excitation energy. Thus, the square root of the linewidth is predicted to be proportional to the chemical shift. After normalization to unit viscosity, the ^{23}Na linewidths for a series of sodium cation solvates[157] and for sodium cryptates[158] obey this prediction with impressive discipline. In like manner, three octahedral cobalt(III) complexes were studied in a number of solvents: $Co(en)_3Cl_3$ and *cis*- and *trans*-$Co(en)_2(N_3)_2NO_3$. Attempts to correlate linewidths and viscosity-normalized linewidths with

the solvent electric dipole moment failed to provide convincing support for the Hertz electrostatic model.[159–162] The square root of the viscosity-normalized linewidths, after correction for scalar relaxation of the second kind [a 45 Hz contribution to the linewidth for $Co(en)_3Cl_3$], produces excellent linear correlations with the ^{59}Co chemical shift.[163] A related study examined cobalt(III) porphyrin complexes—cobalt(III) is an excellent isomorphous substituent for iron(III), and ^{59}Co NMR is more amenable than ^{57}Fe NMR. The contribution of scalar relaxation of the second kind amounted to about 5% of the excess linewidth only. Arbitrary subtraction from the linewidth of a 100 Hz increment led to a quite decent linear relationship between the square root of the linewidth and the chemical shift.[164] This makes for an incisive tool, as an example will show. Two types of cobalt(III) tetraphenylporphyrin complexes are studied: unhindered or hindered, the latter bearing *ortho*-chloro or methyl substituents sterically interfering with the *meso* phenyl rings. A corrected linewidth F is defined by subtraction of a 81 Hz contribution for relaxation by scalar coupling, and by normalization to unit viscosity. Then $F^{1/2}$ correlates handsomely with the chemical shift only if the electrostatic field gradient q changes sign for the hindered complexes compared with the unhindered ones. This is a unique piece of information. It means that the electron density in the hindered complexes migrates from the axial d orbitals d_{xz}, d_{yz}, and d_{z^2} to the equatorial d orbitals $d_{x^2-y^2}$ and d_{xy}. This amounts, for the molecule as a whole, to a build-up of σ electron density at the expense of π electron density, due to steric inhibition of resonance.[165] Once again, quadrupolar NMR shows its mettle in matters of electronic distribution!

10 A NOTE ON THE STERNHEIMER ANTISHIELDING FACTOR

This is a magnifying factor that increases the effective interaction between an electrostatic field gradient q at the nucleus, and the quadrupole moment of the nucleus Q.[166–168] The reason is that the mere presence of an electrostatic quadrupole (the nucleus) distorts (slightly) the spherical electronic distribution around it, consisting of the core electrons. There is a radial part in which electrons close to the positive (negative) poles of the quadrupole are pulled in (out). There is an angular part in which s electrons acquire a d-orbital-like polarization: these distortions are conveniently referred to as, for example, 2s $\rightarrow$ d excitations. Shielding corresponds to values of the Sternheimer factor γ between 0 and 1, and antishielding corresponds to negative values of γ. Access to γ is, in general, by calculation. For instance, while the sodium cation has a Sternheimer γ of -5.073 computed at the Hartree–Fock level, the sodium anion has values of -14.98 and -15.69, depending on the method used for incorporating electron correlation.[169]

The problem is more severe yet: which value to choose from those available in the literature? For instance, in the series of halide anions, the spread between the lowest and the highest value of γ is a factor of about 2.[170–172]

11 CONCLUSIONS

In closing, this reviewer begs to be allowed the privilege of editorializing—of expressing a few sincere opinions, and submitting a few concluding observations. At the risk of belaboring the obvious, we cannot help stating that quadrupolar nuclei, at the time of writing, remain outside the mainstream of NMR studies. There are objective reasons: experimental difficulty first and foremost. For instance, ^{57}Fe is a rather discouraging nucleus, in spite of the importance of iron as an element. However, now that indirect methods of detection—we did mention earlier the example of ^{14}N—are becoming routine, we may hope for more and more forays into the quadrupolar jungle.

It became clear while preparing this survey that there are shockingly few studies of molecular electronic distributions from NMR of quadrupolar nuclei. The weak explanation is the need for determination of the full shielding tensor and of the full quadrupolar interaction tensor from high-resolution solid state studies. But here again technical solutions exist. One must conclude that the main problem is the sociological (or psychological?) issue of the necessary collaboration between theoreticians and experimentalists.

Relaxation studies are another underdeveloped area. Scientists shy away from it for a basic reason: they are being confronted with only one observable, namely the linewidth or the transverse relaxation rate. And this single observable is determined by the product of at least two parameters: the correlation time and the quadrupolar coupling constant. The obvious solution is to get at the correlation time (or the spectral density) with other nuclei—which a number of people have done, to splendid avail unfailingly.

Quite a few very handsome physicochemical studies have addressed themselves to ionic relaxation, in order to probe solutions of electrolytes. In that area, electrostatic models have been perhaps unduly popular. They have served as a red rag, to lure physical chemists into their intricacies, their (too) large number of (in fact) adjustable parameters. The relevance of electrostatic models to the systems studied from hindsight does not strike one as self-evident.

My last point is that the science-historical law asserting that the real advances to significant progress are contributed by outsiders to a field is once again vindicated. Brilliant work by Jean-Marie Lehn (^2H, ^{14}N), Jim Dye (^{23}Na), and Ted Brown ($^{6,7}Li$, ^{17}O) has thus been at the forefront of both chemical science and NMR science.

12 RELATED ARTICLES

Liquid Crystals: General Considerations; Nitrogen NMR.

13 REFERENCES

1. C. Brevard and J.-P. Kintzinger, in *NMR and the Periodic Table*, ed. R. K. Harris and B. E. Mann, Academic Press, New York, 1978, Chap. 5
2. H. Huber, *J. Chem. Phys.*, 1985, **83**, 4591.
3. D. Nietlispach, V. I. Bakhmutov, and H. Berke, *J. Am. Chem. Soc.*, 1993, **115**, 9191.
4. C. Brevard, J.-P. Kintzinger, and J.-M. Lehn, *Tetrahedron*, 1972, **28**, 2447.
5. Francis Bacon, *Of Dispatch*.

6. P. Laszlo, in *Progress in Nuclear Magnetic Resonance Spectroscopy*, ed. J. W. Emsley, J. Feeney, and L. H. Sutcliffe, Pergamon Press, Oxford, 1979, Vol. 13, p. 257.
7. C. Brevard and J.-M. Lehn, *J. Am. Chem. Soc.*, 1970, **92**, 4987.
8. H. H. Mantsch, H. Saitô, and I. C. P. Smith, in *Progress in Nuclear Magnetic Resonance Spectroscopy*, ed. J. W. Emsley, J. Feeney, and L. H. Sutcliffe, Pergamon Press, Oxford, 1977, Vol. 11, p. 211.
9. M. J. Duer and J. Rocha, *J. Magn. Reson.*, 1992, **98**, 524.
10. H. Günther, D. Moskau, P. Bast, and D. Schmalz, *Angew. Chem., Int. Ed. Engl.*, 1987, **26**, 1212.
11. L. M. Jackman and J. C. Trewella, *J. Am. Chem. Soc.*, 1976, **98**, 5712.
12. L. M. Jackman and J. C. Trewella, *J. Am. Chem. Soc.*, 1979, **101**, 6428.
13. L. M. Jackman and L. M. Scarmoutzos, *J. Am. Chem. Soc.*, 1984, **106**, 4627.
14. T. L. Brown, D. W. Dickerhoof, and D. A. Bafus, *J. Am. Chem. Soc.*, 1962, **84**, 1371.
15. T. L. Brown and J. A. Ladd, *J. Organomet. Chem.*, 1964, **2**, 373.
16. E. A. C. Lucken, *J. Organomet. Chem.*, 1965, **4**, 252.
17. T. L. Brown, L. M. Seitz, and B. Y. Kimura, *J. Am. Chem. Soc.*, 1968, **90**, 3245.
18. L. D. McKeever, R. Waack, M. A. Doran, and E. B. Baker, *J. Am. Chem. Soc.*, 1968, **90**, 3244.
19. L. D. McKeever, R. Waack, M. A. Doran, and E. B. Baker, *J. Am. Chem. Soc.*, 1969, **91**, 1057.
20. L. M. Seitz and T. L. Brown, *J. Am. Chem. Soc.*, 1966, **88**, 2174.
21. T. L. Brown, *Acc. Chem. Res.*, 1968, **1**, 23.
22. T. L. Brown, *Pure Appl. Chem.*, 1970, **23**, 447.
23. L. D. McKeever and R. Waack, *J. Chem. Soc., Chem. Commun.*, 1969, 750.
24. R. Waack, L. D. McKeever, and M. A. Doran, *J. Chem. Soc., Chem. Commun.*, 1969, 117.
25. H. L. Lewis and T. L. Brown, *J. Am. Chem. Soc.*, 1970, **92**, 4664.
26. K. Smith, *Chem. Brit.*, 1982, **13**, 29.
27. R. Amstutz, W. B. Schweizer, D. Seebach, and J. D. Dunitz, *Helv. Chim. Acta*, 1981, **64**, 2617.
28. D. Seebach, R. Amstutz, and J. D. Dunitz, *Helv. Chim. Acta*, 1981, **64**, 2622.
29. J. Q. Wen and J. B. Grutzner, *J. Org. Chem.*, 1986, **51**, 4220.
30. J. H. Horner, M. Vera, and J. B. Grutzner, *J. Org. Chem.*, 1986, **51**, 4212.
31. D. Hoell, J. Lex, and K. Müllen, *J. Am. Chem. Soc.*, 1986, **108**, 5983.
32. L. M. Jackman and L. M. Scarmoutzos, *J. Am. Chem. Soc.*, 1987, **109**, 5348.
33. L. M. Jackman, L. M. Scarmoutzos, and W. Porter, *J. Am. Chem. Soc.*, 1987, **109**, 6524.
34. N. Kallman and D. B. Collum, *J. Am. Chem. Soc.*, 1987, **109**, 7466.
35. J. H. Gilchrist and D. B. Collum, *J. Am. Chem. Soc.*, 1992, **114**, 794.
36. L. Müller, *J. Am. Chem. Soc.*, 1979, **101**, 4481.
37. G. Bodenhausen and D. J. Ruben, *Chem. Phys. Lett.*, 1980, **69**, 185.
38. F. E. Romesberg, J. H. Gilchrist, A. T. Harrison, D. J. Fuller, and D. B. Collum, *J. Am. Chem. Soc.*, 1991, **113**, 5751.
39. A. S. Galiano-Roth, Y.-J. Kim, J. H. Gilchrist, A. T. Harrison, D. J. Fuller, and D. B. Collum, *J. Am. Chem. Soc.*, 1991, **113**, 5053.
40. Y.-J. Kim, M. P. Bernstein, A. S. G. Roth, F. E. Romesberg, P. G. Williard, D. J. Fuller, A. T. Harrison, and D. B. Collum, *J. Org. Chem.*, 1991, **56**, 4435.
41. D. B. Collum, *Acc. Chem. Res.*, 1993, **26**, 227.
42. J. Mason, *Chem. Rev.*, 1981, **81**, 205.
43. M. Shporer, G. Ron, A. Loewenstein, and G. Navon, *Inorg. Chem.*, 1965, **4**, 358.
44. H. Nöth, W. Tinhof, and B. Wrackmeyer, *Chem. Ber.*, 1974, **107**, 518.
45. K. Barlos, G. Hübler, H. Nöth, P. Wanninger, N. Wiberg, and B. Wrackmeyer, *J. Magn. Reson.*, 1978, **31**, 363.
46. J. Mason and K. O. Christe, *Inorg. Chem.*, 1983, **22**, 1849.
47. M. Comeau, M.-T. Béraldin, E. C. Vauthier, and S. Fliszar, *Can. J. Chem.*, 1985, **63**, 3226.
48. M. E. Moseley and P. Stilbs, *Can. J. Chem.*, 1978, **56**, 1302.
49. M. E. Moseley and P. Stilbs, *Can. J. Chem.*, 1979, **57**, 1075.
50. V. W. Miner and J. H. Prestegard, *J. Am. Chem. Soc.*, 1981, **103**, 5979.
51. Y. S. Yen and D. P. Weitekamp, *J. Magn. Reson.*, 1982, **47**, 476.
52. T. M. Plantenga, H. Bulsink, F. J. deKanter, and C. Maclean, *Chem. Phys.*, 1982, **65**, 71.
53. A. Loewenstein, *J. Magn. Reson.*, 1982, **49**, 332.
54. T. Raj and R. G. Bryant, *J. Magn. Reson.*, 1979, **34**, 537.
55. J. Pople, *Mol. Phys.*, 1958, **1**, 168.
56. J. D. Halliday, P. E. Bindner, and S. Padamshi, *Can. J. Chem.*, 1985, **63**, 2975.
57. C. H. Townes and B. P. Dailey, *J. Chem. Phys.*, 1949, **17**, 782.
58. T. L. Brown and C. P. Cheng, *Symp. Faraday Soc.*, 1978, **13**, 75.
59. C. P. Cheng and T. L. Brown, *J. Am. Chem. Soc.*, 1980, **102**, 6418.
60. C. Delseth and J.-P. Kintzinger, *Helv. Chim. Acta*, 1982, **65**, 2273.
61. J.-P. Kintzinger, in *NMR of Newly Accessible Nuclei*, ed. P. Laszlo, Academic Press, New York, 1983, Vol. 2, Chap. 4
62. D. W. Boykin, ed., *^{17}O NMR Spectroscopy in Organic Chemistry*, CRC Press, Boca Raton, FL, 1991.
63. I. P. Gerothanassis, R. Hunston, and J. Lauterwein, *Helv. Chim. Acta*, 1982, **65**, 1764.
64. I. P. Gerothanassis, R. Hunston, and J. Lauterwein, *Helv. Chim. Acta*, 1982, **65**, 1774.
65. E. Oldfield, H. C. Lee, C. Coretsopoulos, F. Adebodun, K. D. Park, S. Yang, J. Chung, and B. Phillips, *J. Am. Chem. Soc.*, 1991, **113**, 8680.
66. A. Marker and A. B. Roy, *Biochim. Biophys. Acta*, 1983, **742**, 446.
67. R. T. C. Brownlee and B. P. Shehan, *J. Magn. Reson.*, 1986, **66**, 503.
68. M. Postel, C. Brevard, H. Arzoumanian, and J. G. Riess, *J. Am. Chem. Soc.*, 1983, **105**, 4922.
69. S. Aygen, H. Hanssum, and R. van Eldik, *Inorg. Chem.*, 1985, **24**, 2853.
70. E. W. Wooten, K. T. Mueller, and A. Pines, *Acc. Chem. Res.*, 1992, **25**, 209.
71. K. T. Mueller, Y. Wu, B. F. Chmelka, J. Stebbins, and A. Pines, *J. Am. Chem. Soc.*, 1991, **113**, 32.
72. J. R. C. van der Maarel, D. Lankhorst, J. de Bleijser, and J. C. Leyte, *Chem. Phys. Lett.*, 1985, **122**, 541.

73. Y. Masuda, M. Sano, and H. Yamatera, *J. Chem. Soc., Faraday Trans. 1*, 1985, **81**, 127.
74. Y. Masuda, M. Sano, and H. Yamatera, *J. Phys. Chem.*, 1985, **89**, 3086.
75. T. E. Thorpe, *Humphry Davy: Poet and Philosopher*, Cassell, London, 1896, p. 129.
76. Sir H. Hartley, *Humphry Davy*, EP Publishing, East Ardsley, 1972, Chap. 6
77. W. Weyl, *Ann. Phys. (Leipzig)*, 1864, **121**, 601.
78. D. I. Mendeleev, *The Principles of Chemistry*, 3rd edn., Longman, London, 1905.
79. R. R. Dewald and J. L. Dye, *J. Phys. Chem.*, 1964, **68**, 1321.
80. J. M. Ceraso and J. L. Dye, *J. Chem. Phys.*, 1974, **61**, 1585.
81. J. L. Dye, C. W. Andrews, and J. M. Ceraso, *J. Phys. Chem.*, 1975, **79**, 3076.
82. P. Laszlo, *Angew. Chem., Int. Ed. Engl.*, 1978, **17**, 254.
83. J. L. Dye and M. G. DeBacker, *Annu. Rev. Phys. Chem.*, 1987, **38**, 271.
84. A. Ellaboudy, M. L. Tinkham, B. VanEck, J. L. Dye, and P. B. Smith, *J. Phys. Chem.*, 1984, **88**, 3852.
85. G. Malli and S. Fraga, *Theor. Chim. Acta*, 1966, **5**, 275.
86. P. P. Edwards, S. C. Guy, D. M. Holton, and W. McFarlane, *J. Chem. Soc., Chem. Commun.*, 1981, 1185.
87. D. M. Holton, P. P. Edwards, D. C. Johnson, C. J. Page, W. McFarlane, and B. Wood, *J. Chem. Soc., Chem. Commun.*, 1984, 740.
88. D. M. Holton, P. P. Edwards, D. C. Johnson, C. J. Page, W. McFarlane, and B. Wood, *J. Am. Chem. Soc.*, 1985, **107**, 6499.
89. D. M. Holton, A. Ellaboudy, N. C. Pyper, and P. P. Edwards, *J. Chem. Phys.*, 1986, **84**, 1089.
90. N. C. Pyper and P. P. Edwards, *J. Am. Chem. Soc.*, 1986, **108**, 78.
91. A. Ellaboudy and J. L. Dye, *J. Magn. Reson.*, 1986, **66**, 491.
92. J. Kim and J. L. Dye, *J. Phys. Chem.*, 1990, **94**, 5399.
93. R. H. Huang, J. L. Eglin, S. Z. Huang, L. E. H. McMills, and J. L. Dye, *J. Am. Chem. Soc.*, 1993, **115**, 9542.
94. J.-J. Delpuech, in *NMR of Newly Accessible Nuclei*, ed. P. Laszlo, Academic Press, New York, 1983, Vol. 2, Chap. 6
95. R. Benn, A. Rufinska, H. Lehmkuhl, E. Janssen, and C. Krüger, *Angew. Chem., Int. Ed. Engl.*, 1983, **22**, 779.
96. R. Benn and A. Rufinska, *Angew. Chem., Int. Ed. Engl.*, 1986, **25**, 861.
97. J. W. Akitt and J. M. Elders, *J. Magn. Reson.*, 1985, **63**, 587.
98. H. Nöth, *Z. Naturforsch. B*, 1980, **35**, 119.
99. R. Benn, A. Rufinska, E. Janssen, and H. Lehmkuhl, *Organometallics*, 1986, **5**, 825.
100. R. Benn, E. Janssen, H. Lehmkuhl, A. Rufinska, K. Angermund, P. Betz, R. Goddard, and C. Kruger, *J. Organomet. Chem.*, 1991, **411**, 37.
101. R. Ditchfield, *Mol. Phys.*, 1974, **27**, 789.
102. J. Gauss, U. Schneider, R. Ahlrichs, C. Dohmeier, and H. Schnöckel, *J. Am. Chem. Soc.*, 1993, **115**, 2402.
103. J. Almlöf, K. Faegri, and K. Korsell, *J. Comput. Chem.*, 1982, **3**, 385.
104. D. Cremer and J. Gauss, *J. Comput. Chem.*, 1986, **7**, 274.
105. M. Häser and R. Ahlrichs, *J. Comput. Chem.*, 1989, **10**, 104.
106. M. Häser, R. Ahlrichs, H. P. Baron, P. Weis, and H. Horn, *Theor. Chim. Acta*, 1992, **83**, 455.
107. D. Mueller, D. Hoebbel, and W. Gessner, *Chem. Phys. Lett.*, 1981, **84**, 25.
108. J. B. Nagy, Z. Gabelica, G. Debras, E. G. Derouane, J. P. Gilson, and P. A. Jacobs, *Zeolites*, 1984, **4**, 133.
109. P. P. Man and J. Klinowski, *Chem. Phys. Lett.*, 1988, **147**, 581.
110. P. S. Iyer, J. Scherzer, and Z. C. Mester, *ACS Symposium Series 368*, American Chemical Society, Washington, DC, 1988, p. 48.
111. L. B. Alemany, H. K. C. Timken, and I. D. Johnson, *J. Magn. Reson.*, 1988, **80**, 427.
112. L. Kellberg, M. Linsten, and H. J. Jakobsen, *Chem. Phys. Lett.*, 1991, **182**, 120.
113. J. Rocha, S. W. Carr, and J. Klinowski, in *Abstracts of Papers, 202nd National Meeting of the American Chemical Society, American Chemical Society, Washington, DC, 1991*, p. 6.
114. R. Jelinek, B. F. Chmelka, Y. Wu, P. J. Grandinetti, A. Pines, P. J. Barrie, and J. Klinowski, *J. Am. Chem. Soc.*, 1991, **113**, 4097.
115. J. Haase, H. Pfeifer, W. Oehme, and J. Klinowski, *J. Chem. Soc., Chem. Commun.*, 1988, 1142.
116. N. C. Nielsen, H. Bildsoe, H. J. Jakobsen, and P. Norby, *Zeolites*, 1991, **11**, 622.
117. C. Jager, *J. Magn. Reson.*, 1992, **99**, 353.
118. P. P. Man and J. Klinowski, *J. Chem. Soc., Chem. Commun.*, 1988, 1291.
119. J. Perezpariente, J. Sanz, V. Fornes, and A. Corma, *J. Catal.*, 1990, **124**, 217.
120. R. H. Meinhold and D. M. Bibby, *Zeolites*, 1990, **10**, 74.
121. R. Jelinek, B. F. Chmelka, Y. Wu, M. E. Davis, J. G. Ulan, R. Gronsky, and A. Pines, *Catal. Lett.*, 1992, **15**, 65.
122. Y. Wu, B. F. Chmelka, A. Pines, M. E. Davis, P. J. Grobet, and P. A. Jacobs, *Nature (London)*, 1990, **346**, 550.
123. P. J. Barrie, M. E. Smith, and J. Klinowski, *Chem. Phys. Lett.*, 1991, **180**, 6.
124. S. Prabakar, K. J. Rao, and C. N. R. Rao, *Mater. Res. Bull.*, 1991, 805.
125. J. B. Sloan, S. A. Cannon, E. C. Delionback, and J. J. Dechter, *Inorg. Chem.*, 1985, **24**, 883.
126. J. M. Garrison and A. L. Crumbliss, *Inorg. Chem.*, 1988, **27**, 3058.
127. R. C. T. Slade and T. W. Davies, *Coll. Surf.*, 1989, **36**, 119.
128. J. Rocha and J. Klinowski, *Phys. Chem. Miner.*, 1990, **17**, 179.
129. B. Y. Kornilovich and A. T. Pilipenko, *Inorg. Mater.*, 1989, **25**, 693.
130. M. C. Rohner, V. K. Sharma, and W. Richarz, *Can. J. Chem. Eng.*, 1989, **67**, 513.
131. H. D. Morris and P. D. Ellis, *J. Am. Chem. Soc.*, 1989, **111**, 6045.
132. H. D. Morris, S. Bank, and P. D. Ellis, *J. Phys. Chem.*, 1990, **94**, 3121.
133. F. M. Asseid, J. M. Miller, and J. H. Clark, *Can. J. Chem.*, 1992, **70**, 2398.
134. A. M. Venezia, M. A. Floriano, G. Deganello, and A. Rossi, *Surf. Interf. Anal.*, 1992, **18**, 532.
135. J. M. Desimone, M. Staengle, J. S. Riffle, and J. E. McGrath, in *Abstracts of Papers, 199th National Meeting of the American Chemical Society, American Chemical Society, Washington, DC, 1990*, p. 375.
136. Z. Cerny, J. Fusek, O. Kriz, S. Hermanek, M. Solc, and B. Casensky, *J. Organomet. Chem.*, 1990, **386**, 157.
137. A. Fratiello, V. Kubo-Anderson, S. Azimi, C. Fowler, E. Marinez, R. Perrigan, S. Shayegan, and B. Yao, *Magn. Reson. Chem.*, 1992, **30**, 280.

138. B. Lindman and S. Forsén, *Chlorine, Bromine and Iodine NMR. Physico-Chemical and Biological Applications*, Springer-Verlag, Berlin, 1976.
139. T. Sugawara, M. Yudasaka, Y. Yokoyama, T. Fujiyama, and H. Iwamura, *J. Phys. Chem.*, 1982, **86**, 2705.
140. J. J. C. van Lier, L. J. M. van de Ven, J. W. de Haan, and H. M. Buck, *J. Phys. Chem.*, 1983, **87**, 3501.
141. R. Jelinek, A. Stein, and G. A. Ozin, *J. Am. Chem. Soc.*, 1993, **115**, 2390.
142. M. Yudasaka, T. Sugawara, H. Iwamura, and T. Fujiyama, *Bull. Chem. Soc. Jpn.*, 1982, **55**, 311.
143. B. Lindman, in *NMR of Newly Accessible Nuclei*, ed. P. Laszlo, Academic Press, New York, 1983, Vol. 1, p. 233.
144. G. Remaud, G. J. Martin, and M. L. Martin, *J. Phys. Chem.*, 1985, **89**, 2082.
145. R. P. W. J. Struis, J. de Bleijser, and J. C. Leyte, *J. Phys. Chem.*, 1989, **93**, 7932.
146. R. P. W. J. Struis, J. de Bleijser, and J. C. Leyte, *J. Phys. Chem.*, 1989, **93**, 7943.
147. P. Laszlo, in *Cobalt-59*, ed P. Laszlo, Academic Press, New York, 1983, Vol. 2, Chap. 9
148. H. Hartmann and H. Sillescu, *Theor. Chim. Acta*, 1964, **2**, 371.
149. R. B. Jordan, *J. Magn. Reson.*, 1980, **38**, 267.
150. A. Abragam, *Principles of Nuclear Magnetism*, Clarendon Press, Oxford, 1961, p. 309.
151. K. Rose and R. G. Bryant, *J. Magn. Reson.*, 1979, **35**, 223.
152. D. M. Doddrell et al., *Aust. J. Chem.*, 1979, **32**, 1219.
153. K. A. Valiev, *Soviet Phys. JETP*, 1960, **37**, 77.
154. V. P. Chacko and R. G. Bryant, *J. Magn. Reson.*, 1984, **57**, 79.
155. C. Deverell, *Mol. Phys.*, 1969, **16**, 491.
156. C. Deverell, in *Progress in Nuclear Magnetic Resonance Spectroscopy*, ed. J. W. Emsley, J. Feeney, and L. H. Sutcliffe, Pergamon Press, Oxford, 1969, Vol. 4, p. 235.
157. A. Delville, C. Detellier, A. Gerstmans, and P. Laszlo, *J. Magn. Reson.*, 1981, **42**, 14.
158. J.-P. Kintzinger and J.-M. Lehn, *J. Am. Chem. Soc.*, 1974, **96**, 3313.
159. H. G. Hertz, *Ber. Bunsenges. Phys. Chem.*, 1973, **77**, 531.
160. H. G. Hertz, *Ber. Bunsenges. Phys. Chem.*, 1973, **77**, 688.
161. H. G. Hertz, M. Holz, G. Keller, H. Versmold, and C. Yoon, *Ber. Bunsenges. Phys. Chem.*, 1974, **78**, 493.
162. C. A. Melendres and H. G. Hertz, *J. Chem. Phys.*, 1974, **61**, 4156.
163. K. K. W. Ho, W. Y. Choy, C. Yu-Xin, and S. C. F. Au-Yeung, *J. Magn. Reson.*, submitted.
164. K. I. Hagen, C. M. Schwab, J. O. Edwards, J. G. Jones, R. G. Lawler, and D. A. Sweigart, *J. Am. Chem. Soc.*, 1988, **110**, 7024.
165. H. Bang, J. O. Edwards, J. Kim, R. G. Lawler, K. Reynolds, W. J. Ryan, and D. A. Sweigart, *J. Am. Chem. Soc.*, 1992, **114**, 2843.
166. R. Sternheimer, *Phys. Rev.*, 1950, **80**, 102.
167. R. M. Sternheimer, *Phys. Rev.*, 1966, **146**, 140.
168. R. M. Sternheimer, *Z. Naturforsch. A*, 1986, **41**, 24.
169. D. M. Holton, A. Ellaboudy, N. C. Pyper, and P. P. Edwards, *J. Chem. Phys.*, 1986, **84**, 1089.
170. E. A. C. Lucken, *Nuclear Quadrupole Coupling Constants*, Academic Press, London, 1969.
171. K. D. Sen and P. T. Narasimhan, *Advances in Nuclear Quadrupole Resonance*, ed. Smith Heyden, London, 1974, Vol. 1.
172. P. C. Schmidt, K. D. Sen, T. P. Das, and A. Weiss, *Phys. Rev. B*, 1980, **22**, 4167.

Biographical Sketch

Pierre Laszlo. *b* 1938; B.S., 1961, D.Sc., 1965, Sorbonne, Paris. Research Associate, Princeton University, 1962–63. Assistant professor, Princeton University, 1966–70. Professor of chemistry, University of Liège, 1970–present. Professor of chemistry, École polytechnique, 1986–present. Over 200 publications, 14 books. With a gut repugnance for mere data collection, takes price in extracting good quantitative information about hidden variables. Will chew on a phenomenon and lay it aside with isolation of the predominant factor. Benchmark date is 1974, first foray into sodium NMR. His heroes include Anatole Abragam, Frank Anet, Richard Ernst and Ray Freeman, Erwin Hahn, Jean Jeener, Paul Lauterbur, Alex Pines, John Pople, John Waugh, and Don Woessner

Quantum Tunneling Spectroscopy

Stan Clough

Department of Physics, University of Nottingham, Nottingham, UK

1	Introduction	1
2	The Rotational Spectrum of a Triangular Rotor	1
3	Fundamental Considerations	3
4	Experiments and Techniques	3
5	Related Articles	4
6	References	4

1 INTRODUCTION

Low-temperature molecular tunneling spectroscopy is of interest for four reasons: it continues into the quantum domain the study of molecular motion, it provides an outstanding example of a classical to quantum transition, it extends NMR and spin thermodynamics into the adjacent domain of coherent molecular dynamics, and finally it clarifies historical conceptual problems concerning particle indistinguishability and the topology of rotation space. The main results have recently been surveyed.[1]

The rotations of hindered symmetrical groups like CH_3 and NH_4 in solids persist to helium temperatures where the motion of hindered triangular rotors like CH_3 is characterized by a discrete frequency, the tunnel frequency ω_t, derived from the overlap of ground state librational oscillator wavefunctions localized in adjacent wells of a three-well potential. A typical low-temperature CH_3 spectrum consists of three frequencies: $\pm\omega_t$ and 0. The quantum motion of tetrahedral rotors like NH_4 and ND_4 is more complicated,[2] with several tunnel frequencies associated with rotation about the different symmetry axes. The structured spectrum changes with increasing temperature towards a Lorentzian peak with a halfwidth $1/\tau_c$, where τ_c is an orientational correlation time. This spectrum is explained by a quasi-classical hopping model. The transition, which has been studied by both magnetic resonance and neutron scattering,[3] is illustrated in Figure 1.

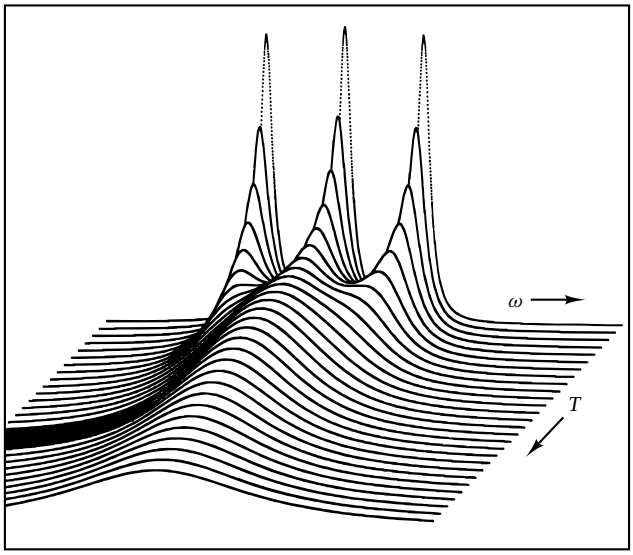

Figure 1 The rotational spectrum of a hindered CH_3 group changes from three frequencies $\pm\omega_t$ and 0 at low temperature to a Lorentzian spectrum of rotational hopping motion at high temperature. The figure is a model with a single temperature-dependent parameter that gives a good representation of observations in many materials. The temperature and frequency scales depend on the height of the hindering barrier

2 THE ROTATIONAL SPECTRUM OF A TRIANGULAR ROTOR

2.1 Stationary States

Low-temperature states have well-defined wavenumbers k. The change from well-defined orientation at high temperatures is similar to the change from hopping conduction to band conduction of polarons and excitons. Like these phenomena, molecular rotation is modeled by a particle in a periodic potential with an orientation coordinate ϕ and a hindering potential $V\cos 3\phi$. Special features are due to the finite extent, 2π, of the rotational coordinate space. For stationary states, we assume a cyclic boundary condition $\psi(\phi + 2\pi) = \psi(\phi)$ and the Hamiltonian

$$\hat{\mathcal{H}} = -\frac{\hbar^2}{2I}\frac{\partial^2}{\partial\phi^2} - V\cos 3\phi \qquad (1)$$

whose eigenvalues for the lowest band are

$$\hbar\omega(k) = -\tfrac{2}{3}\hbar\omega_t \cos\tfrac{2}{3}\pi k \qquad (2)$$

The eigenfunctions are Bloch waves with k lying between $\frac{3}{2}$ and $-\frac{3}{2}$. The boundary condition selects $k = \pm 1$ or 0. The energies are thus $-\frac{2}{3}\hbar\omega_t$ and $\frac{1}{3}\hbar\omega_t$, the latter being doubly degenerate. The three frequencies derived from the energy differences are $\pm\omega_t$ and 0, the low-temperature spectrum.

2.2 Excitations and Dynamics

When dynamical interaction with the environment is included, the space ϕ is open and may be envisaged as a helix upon which wavepackets rotate.[4] A wavepacket confined to one turn of the helix is single-valued within a range 2π and is formed by superposing two of the eigenfunctions of equation (1). Two nodes separated by 2π form the leading and trailing edges of the wavepacket. Three elemental wavepackets rotate with the angular velocities $\pm\omega_t$ and 0. Generation of wavepackets from the stationary states and their subsequent evolution in time can be compared with a 90° pulse and subsequent free induction decay in NMR. The rotation is observable, because it modulates spin-dependent interactions so that molecular rotation and NMR are intimately linked. Thermal excitation results in a transfer of angular momentum, which changes the average wavenumber, $k_a = \pm\frac{1}{2}$ or 0 to

$k_a + \sigma$, $\hbar d\sigma/dt$ being the torque. The general rotation frequency derived from equation (2) is

$$\omega_{k_a,\sigma} = (\tfrac{3}{4})^{-1/2}\omega_t \sin[\tfrac{2}{3}\pi(\sigma + k_a)] \quad (3)$$

A distribution of σ explains the broad rotational spectra of Figure 1. Relaxation to stationary states with integer k causes σ to approach zero as the temperature falls.

A wavepacket only has large amplitudes in the potential wells, and can be represented by three complex amplitudes. The three elementary wavepackets can be superposed by adding their amplitudes to form a more general wavepacket whose evolution involves all three frequencies $\omega_{k_a,\sigma}$. This complex wavepacket rotates and oscillates in shape. At low temperature, the frequency 0 is the rotation frequency and the frequencies $\pm\omega_t$ are shape oscillations. Thus the rotor comes to orientational rest, but continues its internal oscillations. This character changes smoothly into one of rotation as σ grows in absolute value. When $\sigma = \frac{3}{4}$, the complex wavepacket rotates clockwise, moving smoothly through each of the three wells in turn. To accomplish the passage between wells, the shape of the wavepacket oscillates in sympathy with the rotation. The coherent evolution of wavepackets for $\sigma = 0$ and $\sigma = \frac{3}{4}$ is compared in Figure 2.

2.3 Combined Spin and Rotational Dynamics

As an alternative to a reference frame in which the lattice is stationary, it is useful to use a frame in which the wavepacket is stationary. In this frame, σ appears as a vector potential in the angular momentum operator and the wavenumbers remain integers. Observables are the same whichever frame is used. The vector potential can be incorporated into a spin Hamiltonian to combine quantum rotation and spin dynamics. In the case of a methyl group,

$$\hat{\mathcal{H}} = \hat{\mathcal{H}}_Z + \hat{\mathcal{H}}_{DD} + \hat{\mathcal{H}}_R \quad (4)$$

$$\hat{\mathcal{H}}_R = -\tfrac{1}{3}\hbar\omega_t(\hat{R}\, e^{i2\pi\sigma/3} + \hat{R}^{-1}e^{-i2\pi\sigma/3}) \quad (5)$$

where $\hat{\mathcal{H}}_Z, \hat{\mathcal{H}}_{DD}$, and $\hat{\mathcal{H}}_R$ are the Zeeman, dipole–dipole, and rotation Hamiltonians. The basis functions are the eight product spin states of three protons at the three lattice sites. These states can be regarded as shorthand for Slater determinants. The operator $\hat{R}$ cyclically permutes the three spin states round the lattice sites. Rotation clockwise through $\frac{2}{3}\pi$ introduces the phase change $\frac{2}{3}\pi\sigma$ and rotation anticlockwise the reverse phase change. Changes in σ arise owing to collisions between one of the methyl protons and a neighboring atom. This formalism can be extended to tetrahedral molecules.

A spin state is propagated by equation (4). The new feature compared with ordinary spin dynamics is inertia. Whereas the precession frequency of a spin depends only on the instantaneous magnetic field, the rotation frequency of a methyl group depends on the previous dynamical history. The evolution involves two coupled equations: the time-dependent Schrödinger equation and the differential equation for σ. For thermal excitations, some stochastic assumption concerning $d\sigma/dt$ must be made. Another torque is due to the angular dependence of the dipole–dipole energy. This can be obtained by rotating the state slightly using $\lambda\hat{R}$, where λ is small, and finding the rate of change of dipolar energy. The change in the dipole–dipole energy due to rotation, familiar at high temperatures, has a low-temperature counterpart in which molecular rotation changes owing to the angular dependence of the dipole–dipole energy.

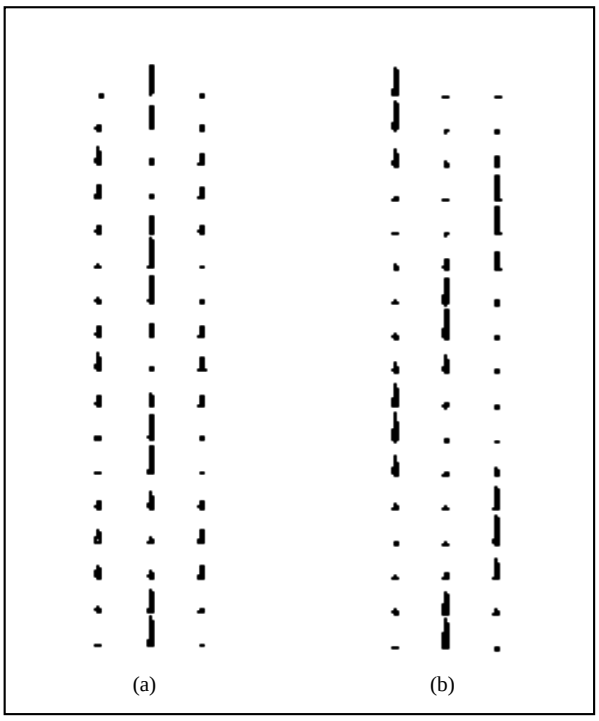

Figure 2 A methyl group wavepacket is described by three intensities in three potential wells on a circle. At low temperature (a), the wavepacket oscillates in shape without rotating. A rotational impulse changes the motion to one of coherent rotation (b), the correlated shape oscillations now assisting the passage from well to well

2.4 The Quantum-to-Classical Transition

The temperature dependence of the rotational spectrum is remarkably similar for all materials except for the scaling of temperature with barrier height. The host lattice serves as a heat bath, destroying coherence and exerting a fluctuating torque. The notable feature is that the outer (shape oscillation) peaks of the low-temperature rotational spectrum move inward with increasing temperature. There have been many theories of this,[3] which can be divided (see Section 3) into those that attribute the reduction to properties of the host lattice and those that regard it as an essential feature of the quantum-to-classical transition. The latter view is that the wavepacket shape oscillations slow down to meet the rising rotation rate in order to play their new role of assisting rotation, while fluctuations in the rotation rate broaden the spectrum. The simplest idea[4] is that the slowing can be described as a spectral averaging process. Orientational hopping is assumed to be accompanied by hopping in k-space. In this way, increasing localization in space is compensated by delocalization in k-space. The frequencies of the low-temperature spectrum are assumed to hop between $\pm\omega_t$ and 0 owing to k modulation,

while each is also subject to random phase modulation due to the changes in orientation. The spectrum is obtained by summing the elements of a matrix $\mathbf{M}^{-1}$, where

$$\mathbf{M}=\begin{bmatrix} \mathrm{i}(\omega_t-\omega)-2\rho-\delta & \rho & \rho \\ \rho & \mathrm{i}(-\omega_t-\omega)-2\rho-\delta & \rho \\ \rho & \rho & -\mathrm{i}\omega-2\rho-\delta \end{bmatrix} \quad (6)$$

Here ρ represents the rate of k hopping and δ the rate of orientational hopping. Both are identified with $1/\tau_c$. At low temperatures, $1/\tau_c \ll \omega_t$, and the frequencies and halfwidths $3/\tau_c$ of the three peaks are obtained from the diagonal elements of equation (6). At high temperatures, ω_t may be neglected. The spectrum is centered at $\omega = 0$, and the halfwidth is $1/\tau_c$. The classical hopping model is thus extended to the quantum regime. Figure 1 is calculated in this way. The parameter $1/\tau_c$ typically obeys an Arrhenius law, and can be roughly equated with a thermal average of the bandwidths of occupied excited librational states. The temperature dependence of the rotational spectrum is thus obtainable from the tunneling frequency without adjustable parameters.

3 FUNDAMENTAL CONSIDERATIONS

3.1 Indistinguishability

Particle indistinguishability has a crucial role in the theory. According to an argument from early quantum theory,[5] the hindering potential for symmetric molecules must be invariant to the interchange of the space and spin coordinates of the protons. For a methyl group, this means a threefold symmetry,[6] which prevents excitation of wavepackets and is inconsistent with the high-temperature hopping model. Though the symmetry constraint correctly identifies the stationary states of a hindered methyl group by excluding nonintegral k, it is incompatible with wavepacket dynamics. The reason is that wavepackets and stationary states have different topologies. Consider the evolution from one to the other. A superposition of two similar wavepackets $\psi(\omega t)$ and $\psi(\omega t - \gamma)\exp(\frac{1}{2}\mathrm{i}\gamma)$ is a stationary state if $\gamma = (2n + 1)\pi$. As a stationary state is approached, the helical space–time path of the wavepacket broadens, and turns of the helix overlap. The number n of rotations in a time $2\pi/\omega$ becomes ambiguous. Destructive interference between paths of different n restricts k to integral values. When the coordinate ωt disappears, the labels that in wavepacket states refer to nonidentical proton trajectories refer to identical indistinguishable particles. The symmetry constraints with antisymmetrization ensure that the phase is continuous and the Pauli principle is satisfied. Excitations restore the helical space–time topology and the proton trajectories. The constraints no longer strictly apply, but quantum behavior results while wavepackets imperfectly reflect the topology of neighboring stationary states.

3.2 The Topology of Rotation Space

The identification of labels with particles also leads to the identification of molecular rotation with the symmetry operation of permutation. This is only possible if the rotation space ϕ is closed. Symmetry-constrained theories consequently allow only integral wavenumbers and limit dynamics to transitions that conserve the wavenumber. This makes them completely different from other transport theories, and gives rise to the view that rotation is fundamentally different from translation. The unconstrained theory of Section 2 has affinities with superconductivity, SQUIDs and quantum transport phenomena in general, besides linking with the hopping model of transport.

4 EXPERIMENTS AND TECHNIQUES

The first effect of tunneling rotation to be observed was that motionally narrowed NMR lines of methyl-containing compounds often fail to broaden when the temperature is reduced to 4 K. With falling temperature, the frequency of components of the dipole–dipole interaction converge on $\pm\omega_t$, as in Figure 1, giving rise to discrete sidebands of the NMR spectrum. The total second moment of the NMR spectrum is conserved, so the sidebands are very weak if the tunnel frequency is large. The failure to broaden demonstrates that $\omega_t/2\pi$ exceeds a few tens of kilohertz. ESR studies of free radicals containing rotating methyl groups in the fragment $C-CH_3$ display more detail. At high temperature, the hyperfine spectrum is a 1 : 3 : 3 : 1 quartet, indicating equal interaction of the electron spin with the three protons. When the temperature is reduced, the spectrum changes to a seven-line pattern 1 : 1 : 1 : 2 : 1 : 1 : 1 with half the spacing of the quartet, the two inner peaks of the quartet having split into 1 : 1 : 1 triplets.[6] The splitting is due to two of the three methyl states with magnetic quantum number $\frac{1}{2}$ forming stationary wavepackets—one in the orientation that minimizes the hyperfine energy and one in the orientation that maximizes it. The energy difference is the separation of the outer members of the triplet. The central member of the triplet has $k = 0$. The collapse of the outer members of each triplet on to the central member is due to the two wavepackets hopping between the two orientations and averaging the orientationally dependent energy. As the rate of rotation increases, the tunnel frequency falls to join it, as in Figure 1. The effect is that all three members of the triplet are involved in the motional averaging process. This is observed through the fact that the central member of the triplet does not remain narrow, while the outer pair merges with it.

The main ESR transitions correspond to flips of the electron spin, while the nuclear quantum number m remains unchanged. Transitions in which m also changes give rise to weak sideband transitions, which enable the tunnel frequency to be measured with precision. The detection of such transitions, their approximate location having been previously deduced by ENDOR, marked the true beginning of tunneling spectroscopy, the motional spectrum being clearly separate from the pure magnetic transitions. Similar tunneling sidebands of NMR spectra open a frequency window in the region of 200 kHz, rather than the 100 MHz range of ESR. Level crossing or tunnel resonance techniques[7] greatly aid the detection of weak sideband transitions and extend the range of accessible tunnel frequencies. A magnetic field is chosen such that the molecular tunnel frequency is equal to a Larmor frequency—either the electron Larmor frequency for free radicals or the nuclear Larmor frequency in ordinary materials. At these internal resonances, transfer of energy between magnetic and rotational

energy occurs through a resonant relaxation process. Energy is exchanged between a Zeeman reservoir and a tunneling reservoir, each of which relaxes to the lattice by its own relaxation process. The ideas of spin thermodynamics are extended, and the process provides an extremely sensitive way of detecting tunnel frequencies. It requires the ability to vary the magnetic field. This is done either by changing the NMR measurement frequency or by using field cycling. There are two versions of the technique. In one, the sample is doped with paramagnetic impurities, often by γ irradiation, and the tunnel frequency is tuned to the electron Larmor frequency. In the other, the tunnel frequency is tuned to the nuclear Larmor frequency. Together, these cover the range from a few megahertz to 50 GHz. With paramagnetic impurities, what is observed is a dynamic polarization effect at the magnetic field of the internal resonance. Energy is transferred between the electron Zeeman and tunneling reservoirs when there is a small mismatch in their frequencies, the energy balance being made up by the nuclear Zeeman system, which is heated or cooled according to the sign of the mismatch.

The direct observation of tunneling sideband transitions is generally difficult, because they must be driven with a field that is nonuniform across the molecule. It is the dipole–dipole interaction, mixed into the magnetic states, that drives the transitions. This effect is naturally stronger at low fields. Low-field dipole–dipole driven NMR has consequently proved to be a powerful way of studying tunneling. Either a true low field[8] using field cycling or a low effective field in the rotating frame[9] may be employed, and both have given good results. They cover the frequency range from 60 kHz to 1 MHz, and thus link with tunnel resonance methods to provide a spectroscopy covering six decades of frequency. An example of a low-field spectrum is shown in Figure 3. Double resonance techniques can be employed to increase population differences and enhance transitions. The next frontier to still lower frequencies has recently been breached by the use of the Lee–Golburg method of line narrowing. Low-field Fourier transform tunnel spectroscopy is conducted slightly off-resonance in the rotating frame.[10] Another recent development in low-field spectroscopy is the use of SQUID detection.[11] It seems likely that developments in the future will come from the increasing exploitation of NMR time domain techniques to interchange magnetic and rotational order, using the spins to monitor the coherent tunneling motion.

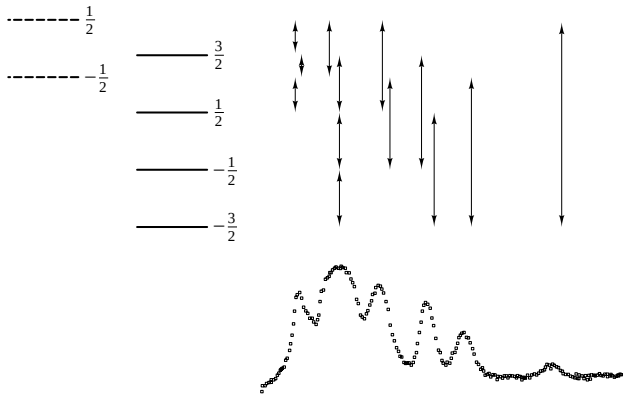

Figure 3 The low-field dipole–dipole driven NMR spectrum of dimethylmalonic acid obtained at 4.2 K. The proton Larmor frequency is 210 kHz and the tunnel frequency that splits $m = \frac{1}{2}$ and $-\frac{1}{2}$ levels is 330 kHz

There are many other phenomena associated with tunneling rotation that a brief review cannot cover, but two observations connected with nearly free rotors should be mentioned. The Haupt effect[12] is a spectacular nuclear dynamic polarization effect that occurs when the temperature of 4-methylpyridine is changed at fairly low temperatures as the slow evolution in the rotational states of the nearly free methyl group drives a large change in the dipole–dipole temperature. The second effect[13] is the optical observation of fractional quantization of the rotation of nonequilateral triangles of nitrogen atoms in molecular beams. Molecular quantum rotation covers a very wide range of phenomena. Because of its dynamical simplicity, it very clearly exhibits features that are common to all quantum systems.

5 RELATED ARTICLES

Brownian Motion and Correlation Times; Field Cycling Experiments; Geometric Phases; Low Spin Temperature NMR; Ortho–Para Hydrogen at Low Temperature; Quantum Exchange; SQUIDs.

6 REFERENCES

1. A. J. Horsewill, *Spectrochim. Acta, Part A*, 1992, **48**, 379.
2. Z. T. Lalowicz, U. Werner, and W. Muller-Warmuth, *Z. Naturforsch. A*, 1988, **43**, 219.
3. A. Heidemann, M. Prager, and M. Monkenbusch, *Z. Phys. B, Condensed Matter*, 1989, **76**, 77.
4. S. Clough, A. J. Horsewill, A. M. Alsanoosi, M. J. Barlow, and M. R. Johnson, *Chem. Phys. Lett.*, 1993, **211**, 637.
5. P. A. M. Dirac, *The Principles of Quantum Mechanics*, 2nd edn., Oxford, University Press, Oxford, 1935, Chap. 10
6. J. H. Freed, *J. Chem. Phys.*, 1965, **43**, 1710.
7. H. Glattli, A. Sentz, and M. Eisenkremer, *Phys. Rev. Lett.*, 1972, **28**, 871.
8. S. Clough, A. J. Horsewill, P. J. McDonald, and F. O. Zelaya, *Phys. Rev. Lett.*, 1985, **55**, 1794.
9. D. W. Nicoll and M. M. Pintar, *Phys. Rev. B*, 1981, **23**, 1064.
10. A. Z. Danyanovich, J. Peternelj, and M. M. Pintar, *Physica B*, 1994, **202**, 273.
11. C. Connor, J. Chang, and A. Pines, *Rev. Sci. Instrum.*, 1990, **61**, 1059.
12. J. Haupt, *Z. Naturforsch. A*, 1968, **23**, 208.
13. G. Delacretaz, E. R. Grant, R. L. Whetten, L. Woste, and J. W. Zwanziger, *Phys. Rev. Lett.*, 1986, **56**, 2598.

Biographical Sketch

Stan Clough. *b* 1932. B.Sc., 1952, Ph.D., 1963, Bangor, Wales. Industrial scientist 1952–59. Started ESR and NMR at ICI. Faculty member, Bangor, 1959–63; Nottingham, 1963–present. Approx. 150 papers. Research specialties: use of ESR, ENDOR, NMR and neutron scattering to develop molecular tunneling spectroscopy, study the quantum-to-classical transition, and extend the concepts and techniques of coherent NMR spectroscopy to particle dynamics.

REDOR and TEDOR

Jacob Schaefer

Department of Chemistry, Washington University, St. Louis, MO, USA

1	Refocusing and Dephasing	1
2	REDOR Dephasing for Recrystallized Labeled Alanines	1
3	Long-Range Couplings and the Natural-Abundance Background	3
4	Coherence Transfer and Selectivity	5
5	Combination Experiments and Synchronous Detection	6
6	Related Articles	7
7	References	7

1 REFOCUSING AND DEPHASING

Rotational echo double resonance (REDOR) NMR is a new analytical spectroscopic technique for solids spinning at the magic angle which has been developed during the last 6 years.[1] REDOR provides a direct measure of heteronuclear dipolar coupling between isolated pairs of labeled nuclei. In a solid with a $^{13}C-^{15}N$ labeled pair, for example, the ^{13}C rotational echoes that form each rotor period following a $^{1}H-^{13}C$ cross polarization transfer can be prevented from reaching full intensity by insertion of a ^{15}N π pulse each half rotor period (Figure 1). The ^{15}N pulse in the middle of the evolution period is replaced by a ^{13}C pulse so that isotropic carbon chemical shifts are in phase at the beginning of data acquisition. The REDOR difference (the difference between a ^{13}C NMR spectrum obtained under these conditions and one obtained with no ^{15}N π pulses) has a strong dependence on the $^{13}C-^{15}N$ dipolar coupling and hence the $^{13}C-^{15}N$ internuclear distance.[2] REDOR is described as double resonance even though three radiofrequencies (typically ^{1}H, ^{13}C, and ^{15}N) are used because the protons are removed from the important evolution part of the experiment by resonant decoupling. The dephasing of magnetization in REDOR arises from a local dipolar $^{13}C-^{15}N$ field gradient and involves no polarization transfer. REDOR has no dependence on ^{13}C or ^{15}N chemical shift tensors and does not require resolution of a $^{13}C-^{15}N$ coupling in the chemical shift dimension.[2]

The evolution of observable S-spin magnetization for a single crystallite on resonance under magic angle spinning and an $I-S$ dipolar coupling is shown in Figure 2 (left). Each dot represents the result of evolution for an equal fraction of a rotor period, with a minor homogeneous decay superimposed for display purposes. At the beginning of the rotor cycle, the magnetization is the observable, $\langle\hat{S}_x\rangle$. Under sample rotation and $I-S$ dipolar coupling, the observable magnetization is transformed into nonobservable bilinear coherence, $\langle\hat{I}_z\hat{S}_y\rangle$, and then back into $\langle\hat{S}_x\rangle$. By the end of the rotor cycle the full observable magnetization has been recovered. For a collection of crystallites in a powder, individual phase accumulations (the product of resonance frequency and time) vary in size and sign depending on crystallite orientation in the magnetic field. This causes phase interference during the rotor cycle and an apparent decay of the observable signal for the powder. Nevertheless, because the magnetization from each crystallite refocuses completely, the dephasing for the powder is also refocused into a full rotational echo at the end of the rotor cycle.

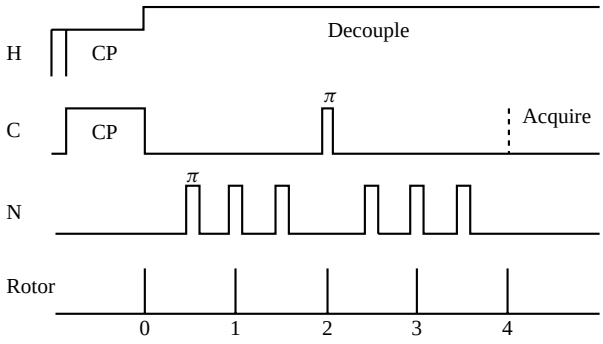

Figure 1 Pulse sequence for a version of REDOR ^{13}C NMR. Two equally spaced, ^{15}N 180° pulses per rotor period result in the dephasing of transverse carbon magnetization produced by a cross-polarization (CP) transfer from dipolar-coupled protons. Carbon–nitrogen dipolar coupling determines the extent of dephasing. A ^{13}C 180° pulse replaces the ^{15}N pulse in the middle of the dephasing period and refocuses isotropic ^{13}C chemical shift differences at the beginning of data acquisition. After the CP transfer, resonant decoupling removes the protons from the experiment. The illustration is for four rotor cycles

However, even for a single crystallite, the refocusing is incomplete in the presence of dephasing I-spin π pulses (Figure 2, right). Evolution for the crystallite is identical to that shown at the left of the figure between times '1' and '2'. The I-spin inverting π pulse, which ends at time '3', changes the sign of $\langle\hat{I}_z\hat{S}_y\rangle$. This process is repeated under the second I-spin π pulse which ends at time '5'. At the end of the rotor cycle (time '6'), the transformation of bilinear coherence created during the rotor cycle into observable magnetization is incomplete. For a powder, a rotational echo of diminished intensity is observed. The extent of the diminution depends on the $I-S$ coupling. The diminution is maximum for two dephasing pulses and is independent of their exact placement so long as the pulse spacing is one-half of the rotor period.[2]

2 REDOR DEPHASING FOR RECRYSTALLIZED LABELED ALANINES

The results of a REDOR experiment performed using the pulse sequence of Figure 1 on an equimolar, recrystallized mixture of L-[2-^{13}C,^{15}N]alanine and L-[1-^{13}C]alanine are shown in Figure 3.[3] The full echo ^{13}C NMR spectrum (S_0) after two rotor cycles with no dephasing is at the bottom of the Figure, and the REDOR difference ($\Delta S = S_0 - S$, where S is the spectrum with dephasing) as a function of the number of rotor cycles, is shown at the top of the Figure. The 900 Hz intramolecular $^{13}C-^{15}N$ coupling results in a sizeable ΔS for the methine carbon atom after only two rotor cycles; this ΔS reaches a maximum after four rotor cycles, and then oscillates in amplitude. The average 100 Hz intermolecular coupling produces a small carboxyl carbon atom ΔS after two rotor cycles, which increases monotonically with dephasing time.

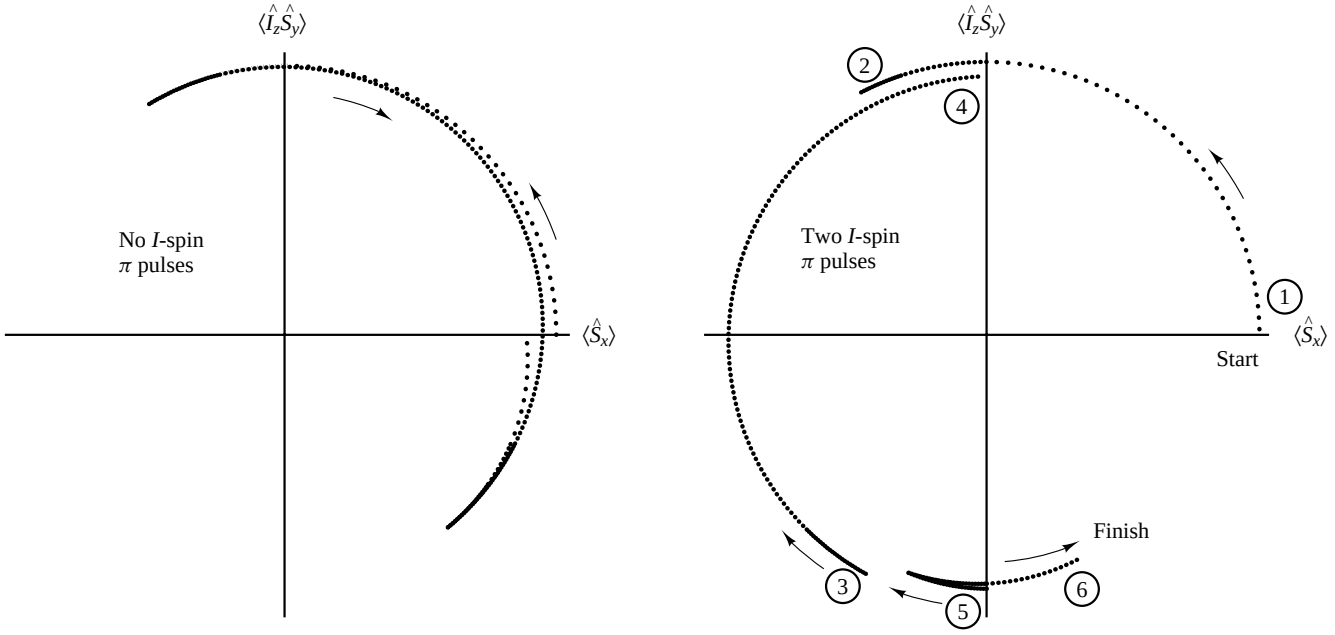

Figure 2 Schematic diagram of the evolution of the IS density matrix for a single crystal under magic angle spinning and $I-S$ dipolar coupling during a REDOR pulse sequence with no dephasing pulses (left) and with dephasing pulses (right)

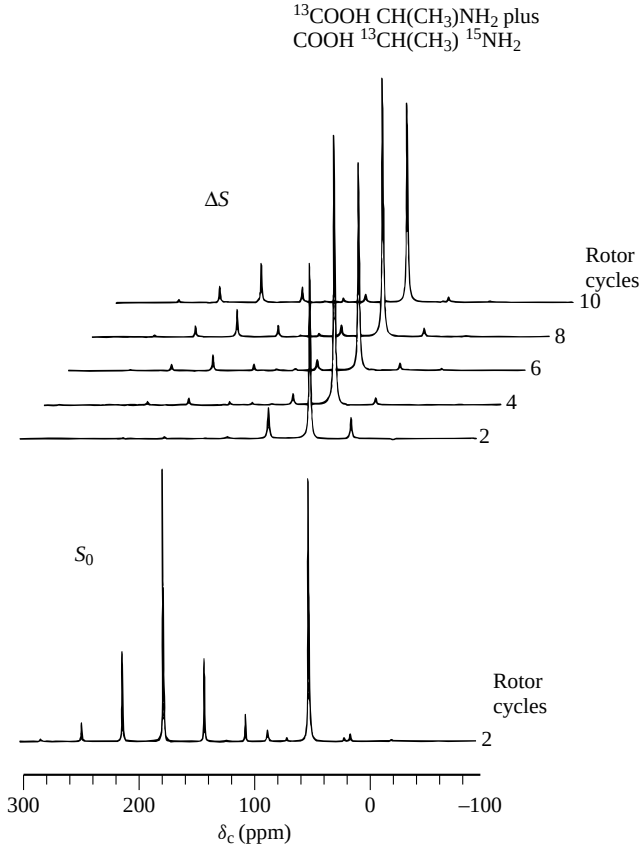

Figure 3 The 50.3-MHz REDOR ^{13}C NMR spectra of an equimolar, recrystallized mixture of L-[2-^{13}C,^{15}N]alanine and L-[1-^{13}C]alanine, as a function of the number of rotor cycles. A full echo spectrum (S_0) after two rotor cycles is shown at the bottom of the Figure and REDOR difference spectra (ΔS) at the top. Magic angle spinning was at 2702 Hz

The $\Delta S/S_0$ ratios for both carbon atoms have the same dependence on the dimensionless parameter, λ_D (Figure 4, solid circles and squares). The theoretical dependence (Figure 4, solid line) was calculated by performing an isotropic powder average over the dephasing for individual crystallites (Figure 2, right). Thus, the angular dependence of the dipolar interaction is suppressed. The resulting universal dephasing behavior needs to be calculated only once for all heteronuclear spin-1/2 pairs. (REDOR applications also include quadrupolar nuclei like ^{2}H, with either direct observation of deuterium or indirect observation through REDOR dephasing. Calculation of the theoretical $\Delta S/S_0$ behavior is slightly more complicated.)[4]

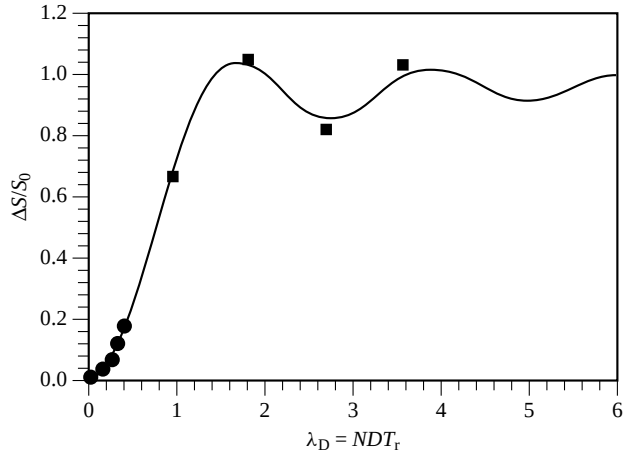

Figure 4 Observed dependence of $\Delta S/S_0$ on the universal parameter, λ_D, for the ^{13}C–^{15}N double-labeled alanine mixture of Figure 3. (N is the number of rotor cycles with dephasing, D is the dipolar coupling constant, and T_r is the rotor period)

A few experimental values of $\Delta S/S_0$ determine λ_D, which then establishes D since the total dephasing time (the product of the number of rotor cycles of dephasing and the rotor period) is known. Because $D = \gamma_I\gamma_S h/2\pi r^3_{IS}$, the observed dephasing can be translated into an internuclear distance directly. If $\Delta S/S_0$ and hence D are known experimentally to 10%, the distance is known with 2% accuracy. Weak dipolar couplings associated with large internuclear distances can be effectively amplified in REDOR by simply allowing the rotor to go around. The only practical problem is holding the echo train together. This depends on the technical difficulty of completely decoupling the protons, which may require low temperatures to suppress kHz regime molecular motions.[5] Translating dipolar couplings into distances in the presence of large-amplitude motions involves specifying a model for the motion.[6]

3 LONG-RANGE COUPLINGS AND THE NATURAL-ABUNDANCE BACKGROUND

In the early applications of REDOR to C–N distance determinations in peptides, relatively few dephasing pulses were used so that sometimes large natural-abundance corrections were necessary.[7] More recently, increased dephasing has been possible as a result of the development of phase routing schemes[8] (Figure 5) that eliminate the dependence of REDOR determinations on frequency offsets and pulse imperfections.[9]

For example, the ^{13}C signal for the label in the nine-residue emerimicin fragment, Ac-Phe-[1-^{13}C]MeA$_2$-MeA-MeA-Val-[^{15}N]Gly$_6$-Leu-MeA-MeA-*O*-Bzl, where Ac = acetyl, Phe = phenylalanine, MeA = methylalanine, Val = valine, Gly = glycine, Leu = leucine, Bzl = benzyl is not resolved from that of natural-abundance peptide carbonyl carbon atoms, which make a constant 7.7% contribution to the full echo signal, S_0. This correction can either be measured in a separate experiment on a natural-abundance sample, or calculated from the known structure.[10] In addition, the natural-abundance ^{13}C carbonyls of Val$_5$ and Gly$_6$ are, respectively, one and two bonds away from the ^{15}N label and so will make a contribution to ΔS that reaches a maximum value of 2% by about N_c = 16. The other natural-abundance carbonyl ^{13}C atoms are all farther away from the ^{15}N label than is the carbonyl label at MeA$_2$. Thus, for $N_c > 32$, the observed ΔS is dominated by the coupling of the ^{15}N–^{13}C labels and additional natural-abundance corrections are unimportant. By N_c = 96, $\Delta S/S_0$ is greater than 0.7 (Figure 6), consistent with a D value of 40 Hz, corresponding to a C–N distance of 4.2 ± 0.1 Å. The distance by X-ray analysis[11] is 4.16 Å. The natural-abundance correction to D is less than 2 Hz when N_c = 96, which means that less than a 0.05-Å correction for the C–N distance is required. The agreement between X-ray and REDOR determinations of the [1-^{13}C]MeA$_2$–[^{15}N]Gly$_6$ distance for this calibration sample for N_c = 8 to N_c = 112

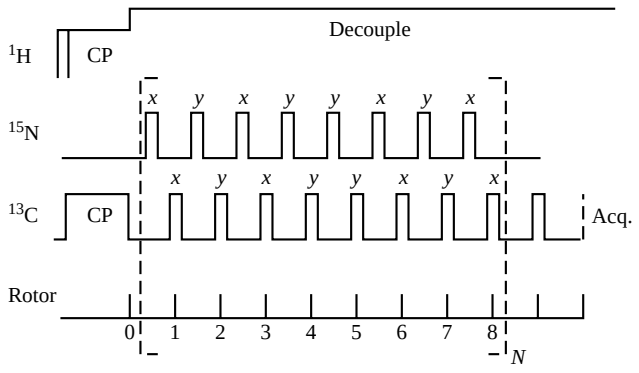

Figure 5 REDOR pulse sequence with dephasing π pulses on both the nitrogen and carbon channels. The pulses are applied using an *xy*-8 phase cycling scheme to eliminate offset effects and pulse imperfections. Signal acquisition begins two rotor cycles after the completion of a full 8*N* rotor cycles of dephasing. CP = cross polarization. Acq = acquisition

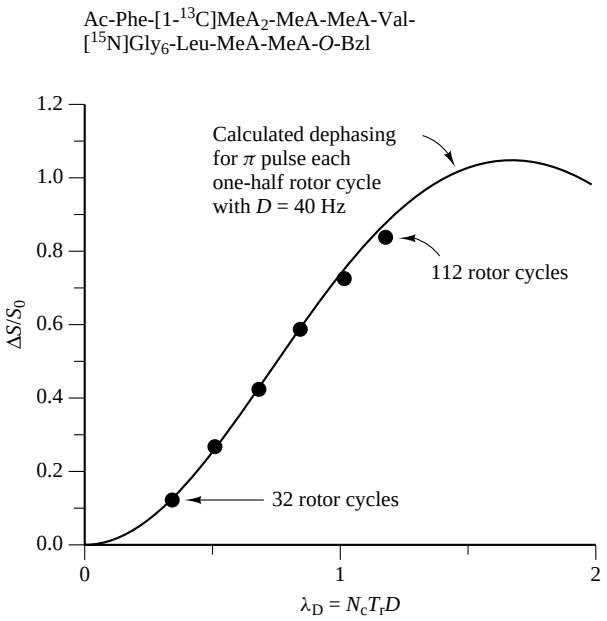

Figure 6 Observed dependence of $\Delta S/S_0$ on the universal parameter, λ_D, for a ^{13}C–^{15}N double-labeled fragment of emerimicin. The pulse sequence of Figure 5 was used. The experimental results (solid circles) are in agreement with calculation (solid line) assuming a ^{13}C–^{15}N dipolar coupling of 40 Hz corresponding to a C–N distance of 4.1 ± 0.1 Å. The natural-abundance correction to $\Delta S/S_0$ at N_c = 8 is 50% and at N_c = 100 is 4%

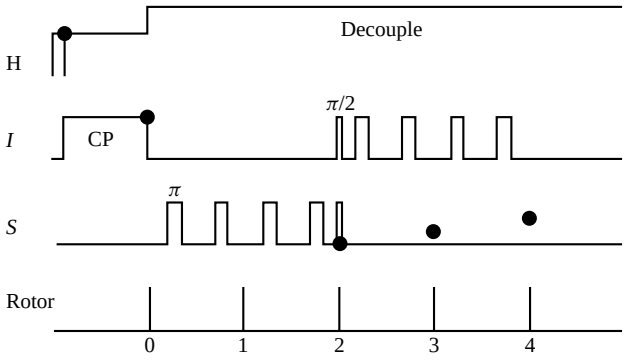

Figure 7 Pulse sequence for TEDOR *I*–*S* NMR. Following a cross-polarization (CP) transfer from abundant protons to generate initial *I*-spin magnetization, the effect of the protons is removed by resonant decoupling. The π pulses are shown separated by one-half rotor periods. The coherence transfer is achieved by simultaneous $\pi/2$ pulses in the middle of the evolution period. The solid circles represent observable magnetization

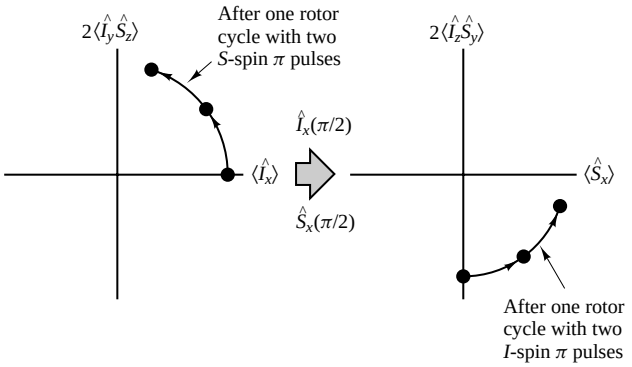

Figure 8 Schematic diagram of the evolution of the density matrix for a powder during the TEDOR pulse sequence of Figure 7 before the coherence transfer pulses (left) and after the application of the transfer pulses (right). The phase angle between $\langle\hat{I}_x\rangle$ and $\langle\hat{I}_y\hat{S}_z\rangle$ for each rotor cycle is indicated by the solid circles and is calculated using the technique illustrated in Figure 2 (right) together with a powder average. The effect of the 90° pulses is to permute I and S subscript indices

confirms that with the compensation of the *xy*-8 phase cycling scheme, hundreds of dephasing pulses can be used with no significant accumulation of error for a REDOR difference.[10] A few, accurate long range distance determinations are often sufficient to establish unambiguously the local conformation of a peptide or protein.[12]

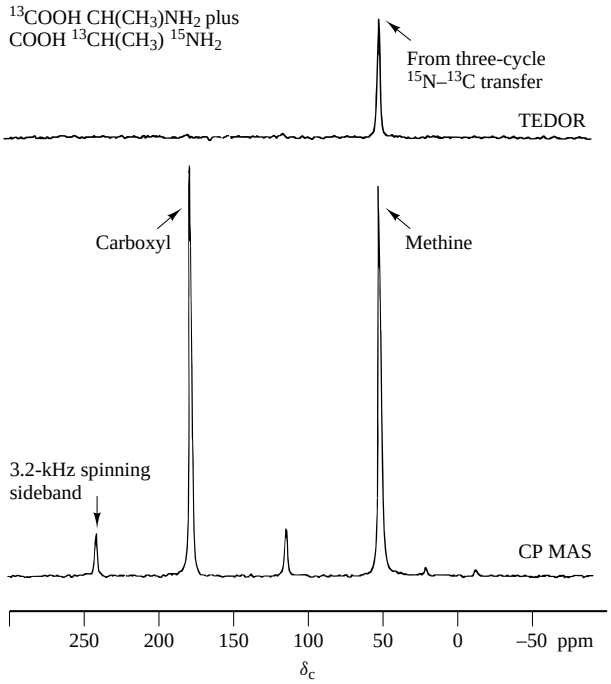

Figure 9 Transferred-echo double-resonance (top) and cross-polarization, magic angle spinning (CP MAS, bottom) ^{13}C NMR spectra of a recrystallized equimolar mixture of L-[2-^{13}C,^{15}N]alanine and L-[1-^{13}C]alanine. The TEDOR spectrum was obtained using three rotor cycles each of dephasing and refocusing. This is insufficient to generate significant carboxyl-carbon magnetization because the average intermolecular C–N dipolar coupling is weak

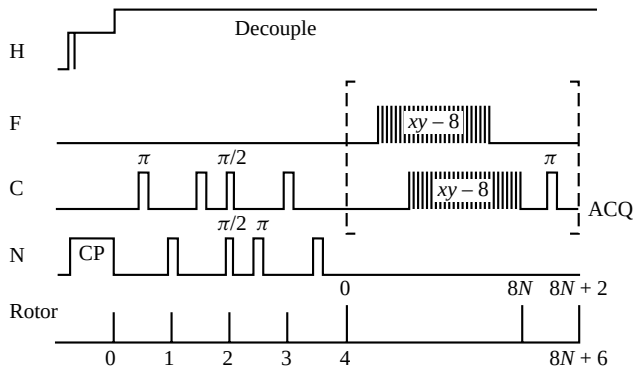

Figure 10 Pulse sequence for TEDOR combined with REDOR. The TEDOR part of the experiment (which for this illustration extends over the first four rotor cycles following the H–N cross polarization transfer) selects ^{13}C magnetization by a coherence transfer from ^{15}N. The REDOR part of the experiment (broken brackets) immediately follows the TEDOR preparation and measures dipolar coupling of the selected ^{13}C to ^{19}F. REDOR dephasing is performed using the phase-routing scheme illustrated in Figure 5. Two rotor cycles are added to the sequence so that the start of data acquisition is not coincident with a pulse

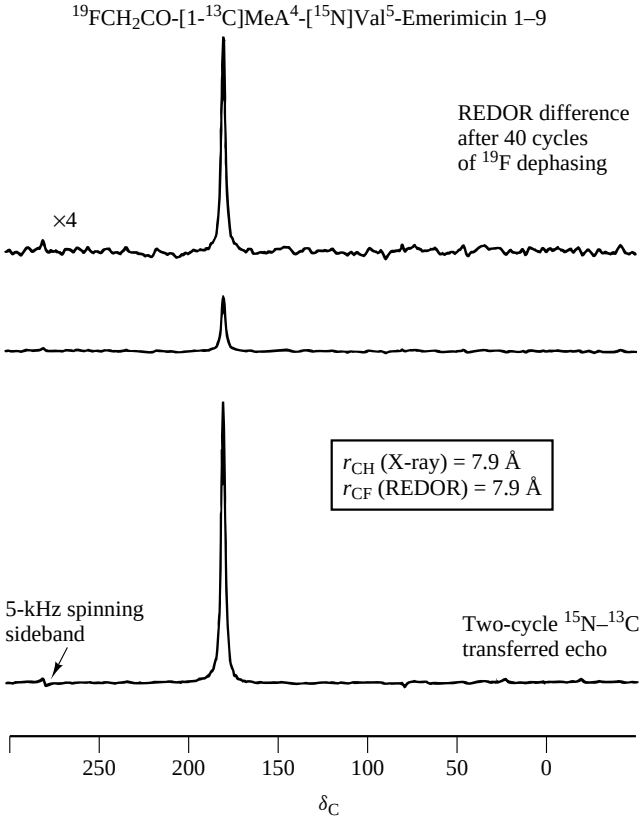

Figure 11 TEDOR–REDOR ^{13}C NMR spectra of a ^{19}F, ^{13}C, ^{15}N-labeled emerimicin (see Figure 6). The TEDOR spectrum (bottom) was obtained using an N–C coherence transfer as illustrated in Figure 7. The TEDOR–REDOR difference spectrum (the difference between TEDOR spectra with and without dephasing REDOR pulses) is shown at the top of the Figure. This spectrum was obtained by ^{19}F dephasing of the ^{15}N-TEDOR-selected ^{13}C magnetization over 40 rotor cycles

Background corrections for ^{13}C-observe ^{15}N-dephase REDOR are relatively simple to calculate because the ^{15}N natural abundance is low and γ_N is small. A measured value involves a separate sample with no ^{15}N label. The minor, observed $\Delta S/S_0$ for the single-labeled sample is then usually just subtracted from that for the double-labeled sample.[3] The correction is more involved for ^{13}C–^{31}P and ^{13}C–^{19}F pairs. For example, a ^{19}F-observe ^{13}C-dephase REDOR experiment designed to measure the dipolar coupling for a labeled ^{19}F–^{13}C pair separated by 10 Å must take into account the sizeable number of natural-abundance ^{13}C atoms within dephasing range of the ^{19}F. One way[13] to interpret the observed $\Delta S/S_0$ is to generate a model lattice with 1% randomly distributed ^{13}C. If all ^{13}C–^{13}C coupling is ignored, the ^{19}F-observed, ^{13}C-dephase REDOR ΔS can be interpreted in terms of a collection of independent, ^{19}F(label)-^{13}C(label)-^{13}C(natural abundance), three-spin clusters, whose dipolar-tensor orientations are known from the lattice parameters.

4 COHERENCE TRANSFER AND SELECTIVITY

Sometimes a natural-abundance background cannot be measured or calculated easily. In this situation, the dipolar-coupled spins can be selected from among the background of uncoupled spins by a coherence transfer from one spin of the heteronuclear pair to the other. The pulse sequence for this selection is shown in Figure 7. Transverse magnetization is first established in the I-spin system by a cross-polarization transfer from abundant protons. The dephasing of I-spin magnetization by dipolar-coupled S spins through rotor-synchronized S-spin π pulses leads to a bilinear coherence (Figure 8, left) that is transferred by an I,S pair of $\pi/2$ pulses (Figure 8, shaded arrow). These pulses occur together at the completion of a rotor cycle (Figure 7) and interchange the indices of the bilinear coherence. Finally, the transferred bilinear coherence is transformed into observable S-spin transverse magnetization by rotor-synchronized I-spin π pulses (Figure 8, right). The entire procedure is called transferred echo double resonance (TEDOR).[14] TEDOR is a rotor-synchronized solid state experiment which is based on some of the same coherence transfer principles as the INEPT solution state experiment.

The results of a TEDOR experiment using the pulse sequence of Figure 7 performed on the mixed double-labeled alanine sample discussed above are shown in Figure 9. Proton polarization is first transferred to nitrogen atoms. Then three rotor cycles are used to create bilinear ^{15}N–^{13}C coherence, and three more rotor cycles to produce observable methine carbon atom magnetization following the coherence transfer. The TEDOR theoretical transfer efficiency[14] is 50% compared with the observed 35% (Figure 9). Because TEDOR is not a difference experiment, TEDOR has the same theoretical sensitivity as REDOR. No sizeable carboxyl

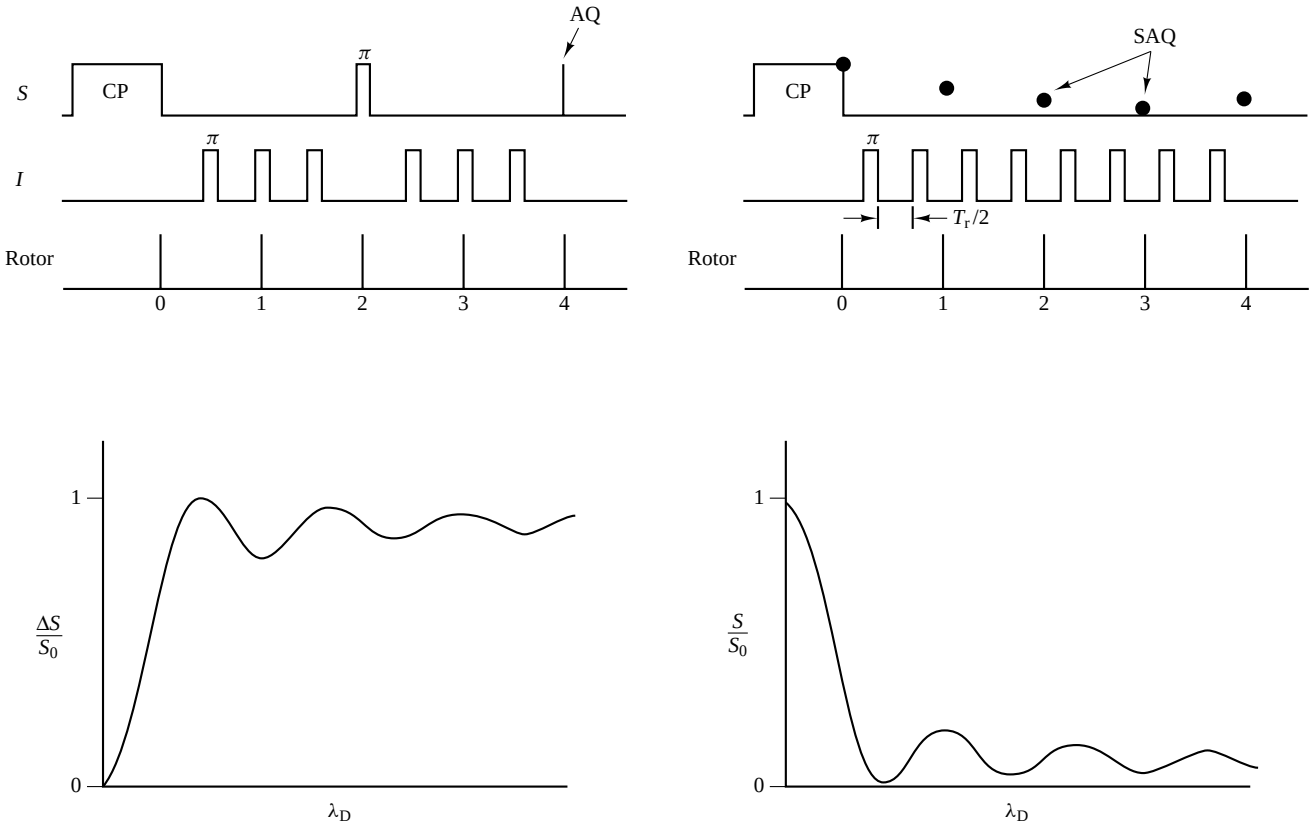

Figure 12 Two schemes for REDOR. (Left) Acquisition of a time domain signal follows evolution during which dephasing pulses diminish observable magnetization and create nonobservable $I-S$ bilinear coherence. This scheme is suitable for multiline spectra and a separate $\Delta S/S_0$ is measured for each line in the spectrum. The dependence on λ_D is determined by varying the number of rotor cycles. (Right) Synchronous detection of a time domain signal during evolution is suitable for a single-line spectrum. The observed S/S_0 is $1 - (\Delta S/S_0)$. AQ = acquisition; SAQ = synchronous acquisition

carbon magnetization is observed in Figure 9 because the short evolution time was insufficient for the weak intermolecular $^{15}N-^{13}C$ coupling to create significant bilinear coherence. If there had been a collection of nitrogen atoms all with comparable strong, couplings to carbon atoms, the TEDOR coherence transfer could still have been made selective by alternating the sign of the starting nitrogen magnetization for just one type of ^{15}N by DANTE inversion of the selected nitrogen atom signal every other scan.[15] The sign of the transferred bilinear coherence would then alternate, as would that of the observed carbon atom magnetization corresponding to the selected $^{15}N-^{13}C$ coupling. Data routing could then discriminate between carbon signals.

5 COMBINATION EXPERIMENTS AND SYNCHRONOUS DETECTION

TEDOR can be used alone or in combination to make highly selective TEDOR–TEDOR and TEDOR–REDOR experiments.[16] The pulse sequence for the latter is illustrated in Figure 10. A TEDOR sequence is tailored to select the carbonyl carbon atom signal of residue 4 of a ^{19}F, ^{13}C, ^{15}N triple-labeled emerimicin fragment (Figure 11). The $^{15}N-^{13}C$ selected magnetization is then dephased by REDOR ^{19}F π pulses resulting in the determination of a selected 8-Å C–F distance. This combination experiment involves four radiofrequencies in the same sequence which is possible using transmission-line probe technology.[17] The tuning elements in these probes are outside the magnet in a large, shielded box with isolation of all radiofrequencies, making high power on four channels practical.[18]

The observed signal in the TEDOR–REDOR experiment can be detected either as part of a two-dimensional experiment in which full S and S_0 spectra are obtained by normal acquisition starting with a rotor cycle (Figure 12, left), or synchronously with one sampling per rotor cycle (Figure 12, right). The former is used for complicated spectra with more than one resonance even after selection by TEDOR. The latter is used for the simple, one-line spectra that usually result from a TEDOR preparation. Synchronous detection[2] has the sensitivity advantage of generating the entire REDOR dephasing pattern in real time. The dipolar evolution dimension can be mapped by variation of the number of rotor cycles,[1] or variation of the position of the dephasing pulse within the rotor period.[2] The latter has a constant total dipolar evolution time which eliminates the echo-train lifetime from the analysis. In both of these two-dimensional methods, spins which contribute to the S-spin signal but have no $I-S$ coupling (a common situation for a natural-abundance background) do not interfere with the determination of the $I-S$ interaction.[16] Such spins produce a constant offset in the dipolar time domain and so a zero-frequency spike in the dipolar frequency domain. The $I-S$ coupling is determined by the width of the dipolar spectrum.[2]

Even an efficient TEDOR transfer does not result in observable magnetization associated with an isotropic powder. Thus, some crystallite orientations are discriminated against depending on the orientation of the *IS* and *SX* dipolar tensors in an $I-S-X$ three-spin TEDOR–REDOR experiment. Nevertheless, following an efficient $I-S$ TEDOR transfer, the *initial* S-observe, X-dephase REDOR behavior depends only on the size of the dipolar tensors and not on their orientation (Figure 13). Thus, interpretation of the 20% dephasing (Figure 14) in a TEDOR–REDOR experiment on the triple-labeled peptide of Figure 11 does not require knowledge of $^{15}N-^{13}C-^{19}F$ geometry in order to extract a C–F distance.[16] This will be the situation for most long-range distance determinations in general, simply because little dephasing is observed and determination of the dipolar coupling is based on the initial S/S_0 behavior. However, for systems with stronger couplings, Fourier transforms of the TEDOR–REDOR dipolar evolution offer the opportunity to establish geometry by comparisons with theoretical dipolar lineshapes (Figure 15).

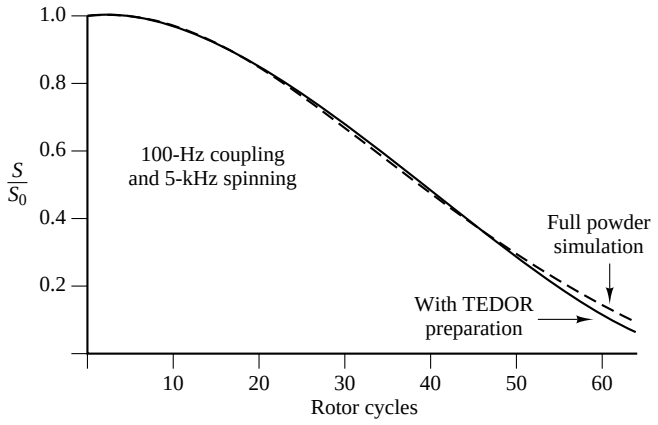

Figure 13 Simulation of X-spin REDOR dephasing of $I-S$ TEDOR-selected S-spin magnetization (solid line). The simulation assumed an $I-S$ coherence transfer after two rotor cycles of dephasing, followed by two rotor cycles of transformation of coherence into observable S-spin magnetization (see Figure 7). For $S/S_0 > 0.5$, the simulation is almost independent of orientation of $I-S$ and $S-X$ dipolar tensors (results not shown) and closely matches that for a full isotropic powder (dotted line). All simulations were performed assuming that the $I-S$ coupling was 1.2 kHz, the $S-X$ coupling was 100 Hz, and the magic angle spinning was 5 kHz

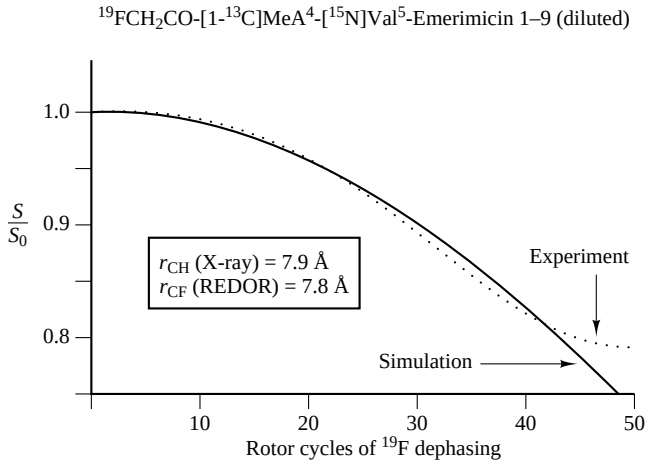

Figure 14 Synchronously sampled time domain ^{13}C signal of a ^{19}F, ^{15}N, ^{13}C-triple-labeled emerimicin diluted by natural-abundance peptide. The ^{15}N TEDOR-selected ^{13}C signal is sampled once each rotor period either with (S) or without (S_0) ^{19}F dephasing pulses. Magic angle spinning was at 5 kHz

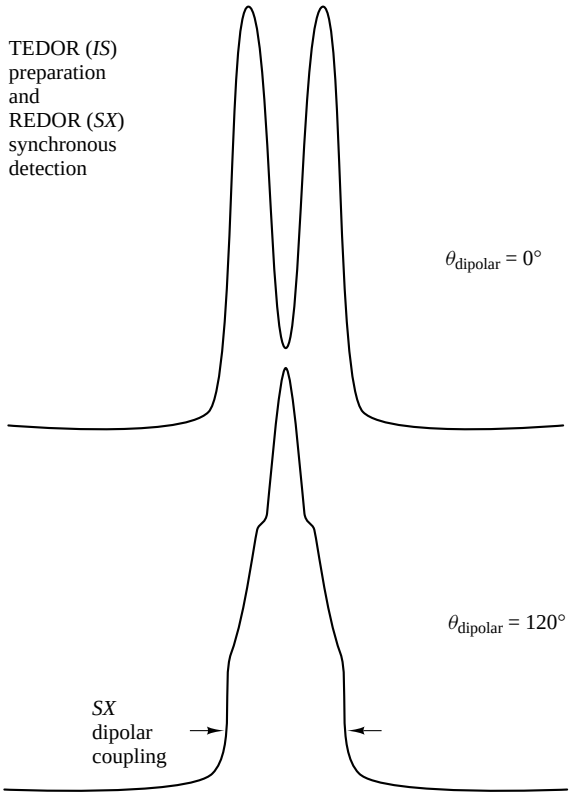

Figure 15 Dipolar spectra obtained by Fourier transforms of time domain simulations performed as described in the caption to Figure 13. The widths of both dipolar spectra are determined by the 100-Hz $S-X$ coupling. Details of the lineshape are determined by orientation of $I-S$ and $S-X$ dipolar tensors

6 RELATED ARTICLES

Cross Polarization in Solids; Electron– Nuclear Multiple Resonance Spectroscopy; INEPT; Magic Angle Spinning; Rotating Solids; Selective Excitation in MRI and MR Spectroscopy.

7 REFERENCES

1. T. Gullion and J. Schaefer, *J. Magn. Reson.*, 1989, **81**, 196.
2. T. Gullion and J. Schaefer, *Adv. Magn. Reson.*, 1989, **13**, 55.
3. Y. Pan, T. Gullion, and J. Schaefer, *J. Magn. Reson.*, 1990, **90**, 330.
4. A. Schmidt, R. A. McKay, and J. Schaefer, *J. Magn. Reson.*, 1992, **96**, 644.
5. B. A. Lewis, G. S. Harbison, J. Herzfeld, and R. G. Griffin, *Biochemistry*, 1985, **24**, 4671.
6. J. Schaefer, E. O. Stejskal, R. A. McKay, and W. T. Dixon, *Macromolecules*, 1984, **17**, 1479.
7. G. R. Marshall, D. D. Beusen, K. Kociolek, A. S. Redlinski, M. T. Leplawy, Y. Pan, and J. Schaefer, *J. Am. Chem. Soc.*, 1990, **112**, 963.
8. T. Gullion, D. B. Baker, and M. S. Conradi, *J. Magn. Reson.*, 1990, **89**, 479.
9. T. Gullion and J. Schaefer, *J. Magn. Reson.*, 1991, **92**, 439.
10. A. W. Hing, N. Tjandra, P. F. Cottam, J. Schaefer, and C. Ho, *Biochemistry*, 1994, **33**, 8651.
11. G. R. Marshall, E. E. Hodgkin, D. A. Langs, G. D. Smith, J. Zabrocki, and M. T. Leplawy, *Proc. Natl. Acad. Sci. U.S.A.*, 1990, **87**, 487.
12. A. M. Christensen and J. Schaefer, *Biochemistry*, 1993, **32**, 2868.
13. L. M. McDowell, C. A. Klug, D. D. Beusen, and J. Schaefer, *Biochemistry*, submitted.
14. A. W. Hing, S. Vega, and J. Schaefer, *J. Magn. Reson.*, 1992, **96**, 205.
15. D. D. Mueller, A. Schmidt, K. L. Papan, R. A. McKay, and J. Schaefer, 1995, **34**, 5597.
16. S. M. Holl, G. R. Marshall, D. D. Beusen, K. Kociolek, A. S. Redlinski, M. T. Leplawy, R. A. McKay, S. Vega, and J. Schaefer, *J. Am. Chem. Soc.*, 1992, **114**, 4830.
17. S. M. Holl, R. A. McKay, T. Gullion, and J. Schaefer, *J. Magn. Reson.*, 1990, **89**, 620.
18. R. A. McKay, US Patent 4446431, 1994.

Acknowledgments

This work was supported by NIH grant GM-40634.

Biographical Sketch

Jacob Schaefer, *b* 1938. B.S., 1960, Ph.D., 1964, physical chemistry, University of Minnesota, USA. Research scientist at Monsanto Company, St. Louis, 1964–1986; collaborated with E. O. Stejskal in 1976 to combine cross polarization with magic angle spinning. Faculty in Chemistry, Washington University in St. Louis, 1986–present. Approx. 200 publications. Research specialty: development of techniques for the NMR of polymeric and biological solids.

Reorientation in Crystalline Solids: Propeller-Like R_3M Species

Jörg Kümmerlen and Angelika Sebald
Universität Bayreuth, Bayreuth, Germany

1 Introduction 1
2 Some Illustrative Examples of R_3M Reorientation in the Solid State as Viewed by High-Resolution Solid State NMR Techniques 2
3 Some Concluding Remarks 5
4 Related Articles 6
5 References 6

1 INTRODUCTION

Ever since the pioneering investigations on the anisotropic reorientation of solid benzene by Andrew and Eades,[1] NMR spectroscopy has proved to be a valuable tool for the elucidation of various types of nonrigidities and fluxional behavior of molecules in both the solid and solution state: the following years have seen an ever-increasing importance of NMR methods for the detection and quantification of dynamic solid state processes. In line with the instrumental development of NMR from wideline methods to include high-resolution solid state techniques, a whole range of techniques, sensitive to a large range of correlation times τ_c, and each typical for the respective experimental approach, are available nowadays.

More traditional NMR methods for the investigation of solid state dynamics utilize spin–lattice relaxation[2,3] in either the laboratory frame (T_1) or in the rotating frame ($T_{1\rho}$), and the calculation of second moments.[4] These techniques have been extremely important and are still popular. Multiple pulse techniques[5] have further made the timescale of chemical shielding anisotropy available; examples for the application of such techniques are the molecular dynamics of solid C_6F_{12},[5] the reorientation of P_4,[3] and $Fe(CO)_5$.[6] Coherent averaging of anisotropic spin interactions by magic angle spinning (MAS) and high-power decoupling, in combination with cross-polarization (CP) techniques[7] in order to overcome inherent sensitivity problems for low-γ and/or low natural abundance nuclei, has also opened up new possibilities for the investigation of dynamic solid state processes by means of NMR: adaptation of solution state-type NMR experiments such as lineshape analysis of exchange-broadened spectra or one- and two-dimensional (1D, 2D) magnetization transfer experiments,[8] have become accessible for the solid state.

One prime target for the investigation of solid state dynamics has recently been the area of organic polymers[9–12] where 2D ^{13}C exchange spectroscopy (EXSY) and 1D and 2D ^2H NMR of selectively deuterated compounds are the methods of choice. The research field of organometallic chemistry has so far been fairly reluctant to use high-resolution solid state NMR techniques for the elucidation of molecular dynamics. Where activation parameters have been determined at all, this was mostly done by considering ^1H spin–lattice relaxation.[13] Anisotropic $2\pi/n$ reorientation of aromatic ligands (n denotes the n-fold axis of the idealized geometry of the ligand) π-bonded to transition metals and CO chemical exchange in carbonyl–transition metal complexes are fairly well documented,[13] while processes such as diene jumps[14] are much less common.

Activation energies E_a of the $2\pi/n$ jump reorientation of such aromatic ligands are generally fairly uniform and quite similar in solution and in the solid state. For instance, E_a for η^5-$C_5H_5TM(CO)_3$ (TM = transition metal) is in the range 7–10 kJ mol^{-1}, E_a for η^6-$C_6H_6TM(CO)_3$ is approximately 15–27 kJ mol^{-1}. The $2\pi/5$ and $2\pi/6$ reorientation of the analogous permethylated ligands C_5Me_5 and C_6Me_6 (Me = methyl), respectively, in such complexes do not show significantly higher activation energies. The $2\pi/n$ jump reorientation of such 'disk-like' aromatic ligands is sterically not very demanding, which explains the experimental finding of fairly uniform and low activation energies for such processes. In contrast, CO exchange in transition metal–carbonyl complexes is far more sterically demanding and much more dependent on the actual crystal structure, so that activation energies for CO exchange in solid transition metal complexes are far less uniform and, in general, exceed 50 kJ mol^{-1}.[13]

In contrast to the uniform dynamic behavior found for the $2\pi/n$ reorientation of π-bonded aromatic ligands in transition metal complexes, no such uniform dynamic behavior is to be expected for the $2\pi/3$ reorientation of R_3M species, simply because a great variety of such species in an even greater variety of chemical and structural environments exists. R_3M species such as CH_3, BH_3, or NH_3 groups will usually show very fast $2\pi/3$ reorientation, depending on the steric constraints of their molecular environment. At very low temperatures, $2\pi/3$ reorientation of such small R_3M moieties is a tunneling process,[15] and at still fairly low temperatures the onset of thermally activated $2\pi/3$ reorientation is observed.[16] Rates of reorientation of such small R_3M species do correlate with the steric and electronic requirements of their molecular environment and are generally strongly temperature-dependent: the activation characteristics of thermally activated $2\pi/3$ reorientation, e.g. the internal reorientation of Me groups, normally catapult into a very fast regime at or near room temperature.

Even for much bulkier species R_3M, such as CF_3,[2,5] CMe_3,[17] $SiMe_3$,[18] NMe_3,[19] and PMe_3,[20] an enormous spread of $2\pi/3$ jump rates and activation energies is to be expected for this thermally activated process owing to the great variety of molecular and crystal structures which can accommodate this process, in addition to the rich chemistry of compounds containing Me_3M groups. For M = C, Si, N, and P, M will usually be in a more or less distorted tetrahedral coordination. An even greater variation of $2\pi/3$ jump rates and activation energies can be predicted for species Me_3M where M denotes a metal such as Sn or Pb: for R_3M = Me_3Sn, Me_3Pb, both fourfold tetrahedral or fivefold trigonal-bipyramidal coordination of M = Sn, Pb are found in the solid state.

From the above it is obvious that $2\pi/3$ reorientation is a common solid state dynamic process, involving R_3M species all over the Periodic Table of the elements. Schematically we may describe this process as is shown in Scheme 1, regardless of whether $R_{A,B,C}$ are crystallographically equivalent or

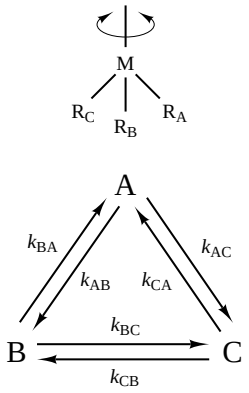

Scheme 1

not. Clearly, the dynamic properties of chemically different propellers R_3M will vary greatly and, thus, will challenge the unique potential of solid state NMR to provide the appropriate window of observation for an enormous range of correlation times.

We should also address the question why one should be interested to learn about $2\pi/3$ reorientation of R_3M species in crystalline solids. For small R_3M species such as CH_3, naturally, the quantum chemical low-temperature behavior and the gradual take-over by thermal activation are of major theoretical importance. For bulky species R_3M, with $R \neq H$, thermally activated R_3M reorientation is the focus of attention: the single crystal X-ray structures of many compounds containing R_3M fragments are known. However, X-ray crystallography cannot normally detect this random $2\pi/3$ jump process so that necessarily the static picture of such compounds obtained by diffraction methods is somewhat incomplete. The geometric, static picture from X-ray diffraction, in turn, provides important information about the potential barriers (van der Waals interactions) for the $2\pi/3$ reorientation monitored by NMR. We may, thus, expect to learn more about the subtle interplay of packing in the crystal versus the steric requirements of anisotropic R_3M reorientation. However, we cannot expect to be able to definitely separate cause and effect in this interplay.

The following practical examples are taken from a group of reorienting species Me_3M which are (i) at least, in part, fragments of molecules of known single crystal X-ray structure and (ii) accessible to high-resolution solid state NMR methods for the determination of their dynamic R_3M properties.

2 SOME ILLUSTRATIVE EXAMPLES OF R_3M REORIENTATION IN THE SOLID STATE AS VIEWED BY HIGH-RESOLUTION SOLID STATE NMR TECHNIQUES

Even if—with one exception—all the following examples have been borrowed from organotin and organolead chemistry (R_3M = Me_3Sn and Me_3Pb), we do not wish to highlight a particular branch of chemistry. The examples were chosen because the entire range of very slow to very fast reorientation is represented here by one group of reasonably closely related chemicals and, in particular, because depending on the ligands X in solid Me_3SnX or Me_3PbX, the three regimes of reorientation—fast, intermediate, slow—as discussed in Sections 2.1–2.3 are accessible at or near room temperature and, thus, can be investigated conveniently by using standard CP MAS equipment.

2.1 Fast R_3M Reorientation: Rates of the Order of 10^4 Hz

Let us consider particles CH_3 and/or Me_3M, and jump rates for the mutual exchange in these particles of the same order of magnitude as the applied B_1 field strength. Under these conditions destructive interference between coherent averaging of the $^1H-^{13}C$ dipolar interaction (high-power ^1H decoupling) and incoherent averaging due to the (random) jump processes occurs, resulting in enhanced transverse relaxation of the observed ^{13}C magnetization and, thus, temperature-dependent ^{13}C linewidths. Rothwell and Waugh[16] have theoretically and experimentally investigated this T_2 effect as a versatile tool to characterize motional processes in solids. Following Rothwell and Waugh,[16] the inverse T_2 relaxation time can be written as:

$$\frac{1}{T_2} = \frac{4\gamma_I^2\gamma_S^2\hbar^2}{15r^6} I(I+1)\left(\frac{\tau_c}{1+\omega_1^2\tau_c^2}\right) \qquad (1)$$

and three regimes can be distinguished: a so-called long correlation limit ($\omega_1\tau_c \gg 1$), where the S spin linewidth (here ^{13}C) is dependent on τ_c *and* ω_1, an intermediate regime ($\omega_1\tau_c \approx 1$) of maximum line-broadening, and a short correlation regime ($\omega_1\tau_c \ll 1$) where the S spin linewidth is independent of ω_1 but dependent on τ_c.

This type of line-broadening mechanism is illustrated in Figure 1, depicting the ^{13}C CP MAS spectra of hexamethylethane as a function of temperature.[16] In the temperature

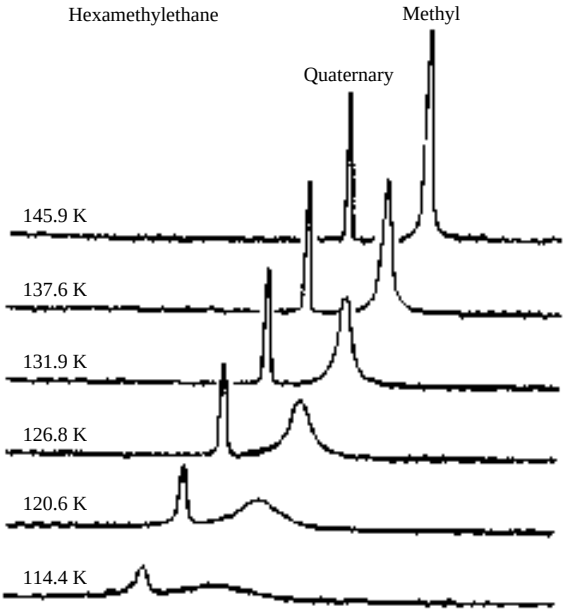

Figure 1 ^{13}C CP MAS spectra of solid hexamethylethane, Me_3C-CMe_3, illustrating the combined effect of internal methyl group plus Me_3C reorientation in the temperature range T = 114.4–145.9 K. (Reproduced with permission of the American Institute of Physics from Rothwell and Waugh[16])

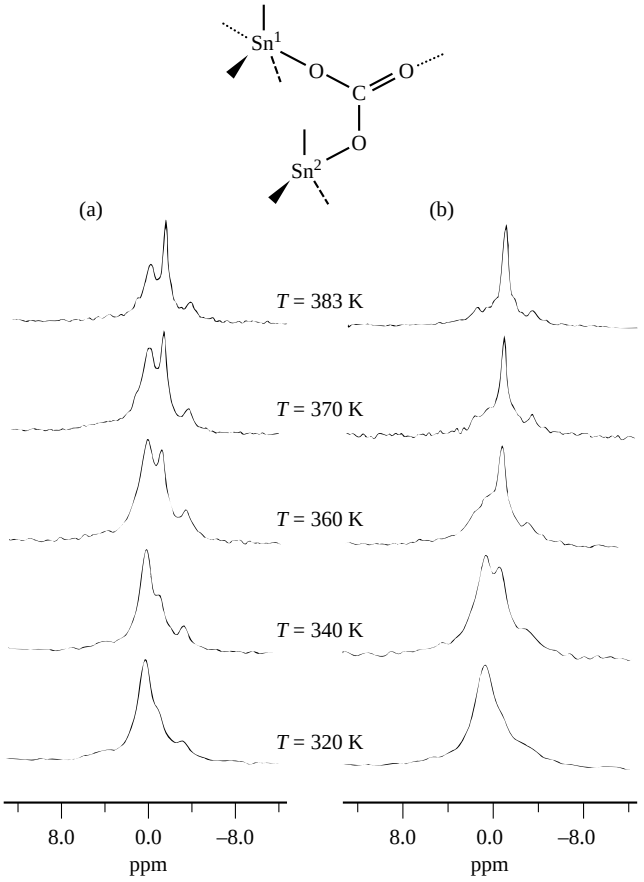

Figure 2 Methyl region of 75.5 MHz ^{13}C CP MAS spectra of polymeric crystalline $(Me_3Sn)_2CO_3$ in the temperature range T = 320–383 K for two different decoupling field strengths ω_1 (a) 4.5×10^5 and (b) 1.96×10^5 rad s^{-1}. Note that the faster reorienting trigonal-bipyramidal Me_3Sn^1 group ($\delta^{13}C \approx -1$ ppm) is in the short correlation limit over this T = 320–383 K range, while the tetrahedral Me_3Sn^2 group ($\delta^{13}C \approx 1$ ppm) is in the long correlation limit for this temperature range and, thus, shows a dependence of the ^{13}C linewidths on both T and ω_1. The linewidth of the ^{13}C resonance of the Me_3Sn^1 group depends on the temperature but is independent of ω_1. (Reproduced by permission of John Wiley & Sons, Ltd, from Kümmerlen and Sebald[21])

range 114.4–145.9 K, Me_3C-CMe_3 shows appropriate correlation times to allow simultaneous Me and Me_3C reorientation to be monitored by this T_2-related method.

A useful correlation time regime for the extraction of the kinetic parameters of R_3M reorientation by this method for the reorientation of R_3M = $SnMe_3$ in solid $(Me_3Sn)_2CO_3$ is reached at higher temperatures.[21] Figure 2 illustrates the ^{13}C CP MAS spectra of $(Me_3Sn)_2CO_3$ in the temperature range T = 320–383 K. Solid $(Me_3Sn)_2CO_3$ contains two different Me_3Sn moieties (one trigonal-bipyramidal Me_3Sn^1 unit, one tetrahedral Me_3Sn^2 group) per molecular unit; in this temperature range Me_3Sn^1 is in the short correlation limit while Me_3Sn^2 is in the long correlation limit.[21]

This method, as developed by Rothwell and Waugh,[16] is a truly versatile tool: it does not depend on the chemical inequivalence of exchanging sites (see below), it operates by using two easily adjustable experimental parameters (ω_1, T), it will be relevant for a great number of solid organic and organometallic compounds at or near room temperature, and is by no means restricted to the $I-S$ combination $^1H-^{13}C$. In our view, it should clearly contribute to the development of an attitude which no longer 'considers the prospect of broadening due to incomplete removal of the dipolar interaction an evil'.[16]

2.2 Intermediate R_3M Reorientation Rates: 1D Exchange broadening Regime

Intuitively, one may be tempted to assume that in solids at ambient temperatures somewhat slower reorientational R_3M processes (depending on the nature of R and M, $R_3M \neq CH_3$) with jump rates in the range approximately 10^1-10^3 Hz are as common as are the faster R_3M reorientation processes discussed in Section 2.1. If we wish to obtain kinetic data in this intermediate range 10^1-10^3 Hz, straightforward 1D variable temperature CP MAS spectroscopy, focused on the ligands R, in conjunction with lineshape analysis of the exchange broadened spectra often provides the appropriate NMR tool.

In order for this tool to be useful, the R_3M species under consideration must fulfill several conditions. The ligands R must be crystallographically inequivalent and give rise to separate isotropic resonances for the different sites involved in the exchange process at low temperatures. The accessible range of correlation times is then further defined by the external magnetic field strength B_0 (defining the separation of resonances on the chemical shift scale in Hz) plus the available CP MAS temperature range. Of course, a change of B_0 corresponds to a fictitious change in temperature and, thus, can be used to extend the range of accessible jump rates for this method. The accessible CP MAS temperature range must cover the entire range from 'rigid on the 1D chemical shift scale' through 'coalescence' to 'fast on the 1D chemical shift scale' to allow for lineshape simulations. If, furthermore, the condition is fulfilled that the ligands R give rise to isotropic resonances under suitable CP MAS conditions (the so-called fast spinning regime), then well-established methods[2,3] to simulate three-site exchange broadened spectra to obtain kinetic data can be absorbed directly from existing procedures[22–24] originally designed for solution state NMR purposes. Of course, lineshape simulation of variable temperature exchange-broadened CP MAS spectra is not a model-free procedure but depends on the components Π_{jk} of the matrix describing the exchange process:[2]

$$\frac{d}{dt}M_j(t) = i\omega_j M_j(t) - \frac{1}{T_{2j}}M_j(t) + \sum_k \Pi_{jk}M_k(t) \quad (2)$$

For solid state CP MAS purposes, lineshape simulations should only be used if sufficient independent evidence exists that no further causes but the R_3M three-site exchange can be responsible for lineshape changes as a function of temperature. For instance, single crystal X-ray crystallography and/or the variable temperature NMR properties of the remainder of the R_3M-containing molecule are helpful sources of information.

One type of reorienting R_3M species which often falls into the appropriate regime of reorientation rates near room temperature, allowing kinetic data to be obtained from variable temperature ^{13}C CP MAS plus lineshape analysis, are Me_3Sn groups in solid trimethyltin compounds.[25–28] Two such examples are illustrated in Figures 3 and 4.

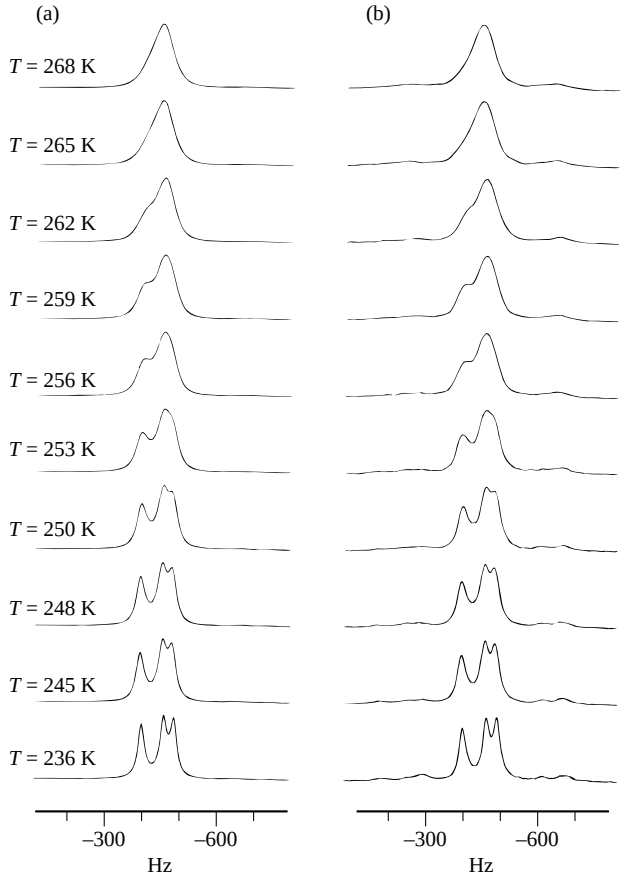

Figure 3 Methyl region of 75.5 MHz ^{13}C CP MAS spectra of $Me_3Sn{-}C{\equiv}C{-}SnMe_3$ in the temperature range T = 236–268 K; (a) simulation assuming three-site exchange due to Me_3Sn reorientation, (b) experimental spectra. (Reproduced with permission from Kümmerlen et al.,[27] copyright 1994 American Chemical Society)

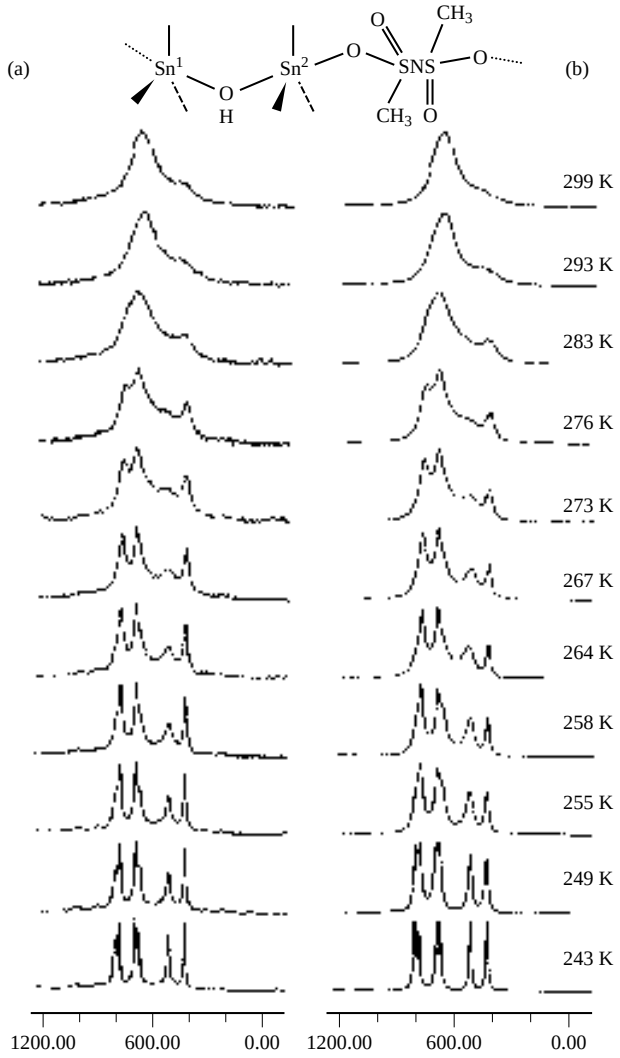

Figure 4 Me_3Sn methyl region of 75.5 MHz ^{13}C CP MAS spectra of polymeric crystalline $[Me_3SnN(SO_2Me)_2{\cdot}Me_3SnOH]$ in the temperature range T = 243–299 K; (a) experimental spectra, (b) simulation; scales for (a) and (b) are in Hz. This compound contains two different Me_3Sn propellers per molecular unit which display different jump rates and activation energies for this process over the entire temperature range investigated (T = 200–299 K). See also Figure 6 for comparison. (Reproduced with permission from Kümmerlen and Sebald,[25] copyright 1993 American Chemical Society)

The methyl region of the ^{13}C CP MAS spectra of $Me_3Sn{-}C{\equiv}C{-}SnMe_3$[27] in the temperature range T = 236–268 K and corresponding simulations are shown in Figure 3. Solid $Me_3Sn{-}C{\equiv}C{-}SnMe_3$ contains two symmetry-equivalent Me_3Sn groups which at room temperature are in their respective fast exchange regime of Me_3Sn reorientation on the 1D ^{13}C CP MAS scale. At T = 236 K and below, three ^{13}C resonances corresponding to three inequivalent methyl groups per Me_3Sn group are clearly resolved (see also Figure 5 on $Me_3Pb{-}C{\equiv}C{-}PbMe_3$ for comparison). An Arrhenius plot of Me_3Sn jump rates as a function of temperature yields an activation energy E_a = 45.8 ± 2.4 kJ mol^{-1} for Me_3Sn reorientation in solid $Me_3Sn{-}C{\equiv}C{-}SnMe_3$.[27]

Figure 4 illustrates a slightly more complicated case, Me_3Sn reorientation in solid $[Me_3SnN(SO_2Me)_2{\cdot}Me_3SnOH]$ as characterized by variable temperature ^{13}C CP MAS.[25,26] This compound is a crystalline polymer, containing two crystallographically inequivalent trigonal-bipyramidal Me_3SnO_2 groups per molecular unit. From inspection of Figure 4 it is clear that over the entire temperature range Me_3Sn^1 and Me_3Sn^2 show different jump rates. Accordingly, different activation energies are obtained as well, E_a = 38.6 and 44.8 kJ mol^{-1}.

The examples shown in Figures 3 and 4 represent R_3M propellers which are truly 'convenient' from an experimental CP MAS point of view: moderate temperatures suffice to obtain all necessary data points. The limits of thermal stability for slower reorienting Me_3M species, or the inaccessibility of sufficiently low temperatures under CP MAS conditions in the case of faster Me_3M reorientation, can severely handicap the practical usefulness of this 1D variable temperature ^{13}C CP MAS plus lineshape analysis approach.

2.3 Slow R_3M Reorientation: 2D Exchange Spectroscopy

Under conditions where the Me_3M rate of reorientation is/becomes significantly smaller than the chemical shift differences between the ^{13}C resonances of the inequivalent methyl groups, the lineshape of these ^{13}C methyl resonances

is unaffected by the reorientational process and kinetic information can no longer be obtained from 1D ^{13}C CP MAS. At this point 2D ^{13}C exchange spectroscopy (2D EXSY) steps in, as (long) mixing times τ_m in the pulse sequence CP-t_1-$\pi/2$-τ_m-$\pi/2$-t_2[22] can accommodate the situation of slow Me_3M reorientation fairly well; in principle, useful possible durations of τ_m are only limited by the eventual onset of T_1 relaxation. This 2D EXSY solid state experiment is analogous to solution state 2D EXSY—only the ^{13}C preparation pulse is replaced by the cross-polarisation sequence for solid state applications. Not only does 2D EXSY extend the range of accessible jump rates towards slow reorientation, but also in those cases where 1D ^{13}C CP MAS *is* informative because the exchange-broadened ^{13}C regime is accessible, additional 2D EXSY experiments usually help to obtain better, more extensive data sets to determine activation energies from jump rates.

In contrast to the analysis of exchange broadened 1D ^{13}C CP MAS spectra, where kinetic information can only be extracted from simulations based on an explicit kinetic model of the dynamic process, 2D EXSY spectra let us directly unravel the kinetic network, model-free, by simple integration of relative off-diagonal intensities as a function of temperature and τ_m. For rather simple systems such as reorienting Me_3M species, where either the number of simultaneously present different jump rates is small or the spread of jump rates is limited, mixing times τ_m can usually be chosen to be short enough so that quantification of the dynamic process can be carried out within the limits of the initial rate approximation.[22] ^{13}C 2D EXSY is particularly convenient for cases such as Me_3M reorientation owing to the fact that methyl ^{13}C resonances will usually be in the fast spinning regime, not giving rise to spinning sidebands even with fairly moderate spinning frequencies ν_{rot}.

Finally, we will consider two examples of Me_3M reorientation as seen by ^{13}C 2D EXSY. Our first example is Me_3Pb reorientation in $Me_3Pb{-}C{\equiv}C{-}PbMe_3$.[27] The room temperature ^{13}C 2D EXSY experiment depicted in Figure 5 shows that

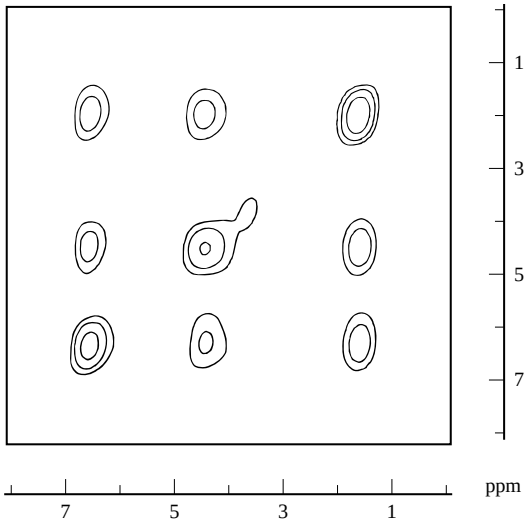

Figure 5 Methyl region of 75.5 MHz ^{13}C CP MAS EXSY of $Me_3Pb{-}C{\equiv}C{-}PbMe_3$ at T = 298 K, mixing time τ_m = 600 ms, ν_{rot} = 3.5 kHz; corresponding to an Me_3Pb reorientation rate κ = 0.3 Hz. (Reproduced with permission from Kümmerlen et al.,[27] copyright 1994 American Chemical Socieity)

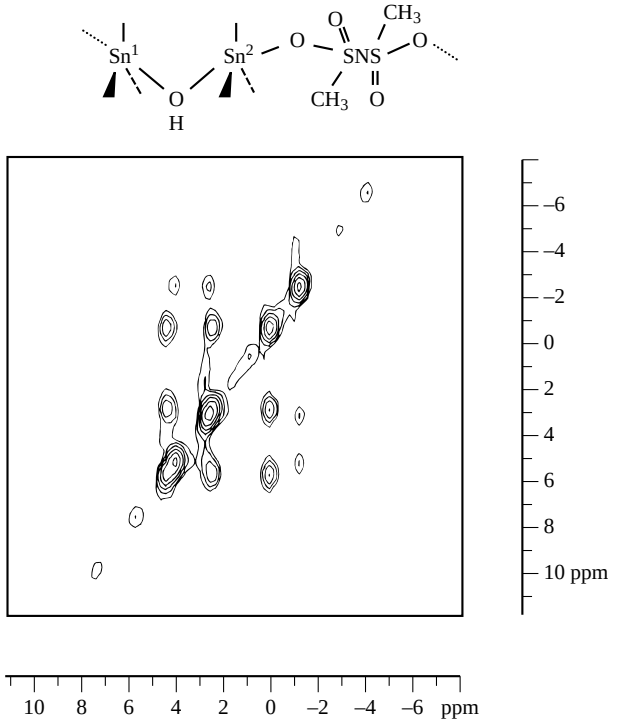

Figure 6 Me_3Sn methyl region of 75.5 MHz ^{13}C CP MAS EXSY of $[Me_3SnN(SO_2Me)_2{\cdot}Me_3SnOH]$ at T = 220 K, mixing time τ_m = 500 ms, ν_{rot} = 2.2 kHz. Note the differing off-diagonal intensities for the two different Me_3Sn propellers in this compound, due to differing rates of reorientation for Me_3Sn^1 and Me_3Sn^2. See also Figure 4 for comparison. (Reproduced with permission from Kümmerlen and Sebald,[25] copyright 1993 American Chemical Socieity)

$Me_3Pb{-}C{\equiv}C{-}PbMe_3$ is in a slow exchange regime on the 1D ^{13}C chemical shift scale at T = 298 K—in contrast to the analogous tin compound, $Me_3Sn{-}C{\equiv}C{-}SnMe_3$ (see Figure 3). In addition, ^{13}C 2D EXSY proves that the three methyl groups in this Me_3Pb unit *are* indeed inequivalent: exchange peaks between all diagonal resonances occur. Also the ^{13}C 2D EXSY experiment on $[Me_3SnN(SO_2Me)_2{\cdot}Me_3SnOH]$[25] in Figure 6 serves for assignment purposes: first of all, it is easily seen from the different off-diagonal intensities that Me_3Sn^1 and Me_3Sn^2 in this compound do show different rates of Me_3Sn reorientation as was also obvious from variable temperature 1D ^{13}C CP MAS (see Figure 4 for comparison). Second, 2D EXSY in this case also proves which methyl ^{13}C resonances belong together in Me_3Sn^1 and Me_3Sn^2, respectively.

3 SOME CONCLUDING REMARKS

We hope to have demonstrated that—beyond the specific dynamic properties of Me_3Sn or Me_3Pb groups in the solid state—high-resolution solid state NMR investigations concerned with the dynamic properties of solid organic and organometallic compounds have an important role to play for a deeper understanding of the principles governing the overall structure of a crystalline solid. The task of bulky reorienting R_3M groups is to act as a sensitive probe of their intra- and intermolecular environment and its influence on the dynamic properties of R_3M. From a practical point of view,

better quantitative knowledge of the solid state dynamics of organic and organometallic compounds should help to prevent frustration with routine ^{13}C CP MAS applications in this field of chemistry.

4 RELATED ARTICLES

Brownian Motion and Correlation Times; Chemical Exchange Effects on Spectra; Cross Polarization in Rotating Solids: Spin-1/2 Nuclei; NOESY; Polymer Dynamics and Order from Multidimensional Solid State NMR; Two-Dimensional Methods of Monitoring Exchange.

5 REFERENCES

1. (a) E. R. Andrew, *J. Chem. Phys.*, 1950, **18**, 607; (b) E. R. Andrew and R. G. Eades, *Proc. R. Soc. London, Ser. A*, 1953, **218**, 517.
2. M. Mehring, *Principles of High Resolution NMR in Solids*, Springer Verlag, Berlin, 1983.
3. H. W. Spiess, in *NMR—Basic Principles and Progress*, eds. P. Diehl, E. Fluck, and R. Kosfeld, Springer Verlag, Berlin, 1978, Vol. 15, p. 59.
4. C. P. Slichter, *Principles of Magnetic Resonance*, Springer Verlag, Berlin/Heidelberg/New York, 1978
5. U. Haeberlen, *Adv. Magn. Reson.*, 1976, Suppl. 1.
6. H. W. Spiess, R. Grosescu, and U. Haeberlen, *Chem. Phys.*, 1974, **6**, 226.
7. A. Pines, M. G. Gibby, and J. S. Waugh, *J. Chem. Phys.*, 1972, **56**, 1776.
8. J. Jeener, B. H. Meier, P. Bachmann, and R. R. Ernst, *J. Chem. Phys.*, 1979, **71**, 4546.
9. B. Blümich and H. W. Spiess, *Angew. Chem.*, 1988, **100**, 1716; *Angew. Chem., Int. Ed. Engl.*, 1988, **27**, 1655.
10. H. W. Spiess, *Chem. Rev.*, 1991, **91**, 1321.
11. A. Hagemeyer, K. Schmidt-Rohr, and H. W. Spiess, *Adv. Magn. Reson.*, 1989, **13**, 85.
12. C. Schmidt, B. Blümich, and H. W. Spiess, *J. Magn. Reson.*, 1988, **79**, 269.
13. D. Braga, *Chem. Rev.*, 1992, **92**, 633.
14. (a) R. Benn, H. Grondey, R. Nolte, and G. Erker, *Organometallics*, 1988, **7**, 777; (b) R. Benn, H. Grondey, G. Erker, R. Aul, and N. Reiner, *Organometallics*, 1990, **9**, 2493.
15. B. Black, G. Majer, and A. Pines, *Chem. Phys. Lett.*, 1993, **201**, 550 and references therein.
16. W. P. Rothwell and J. S. Waugh, *J. Chem. Phys.*, 1981, **74**, 2721.
17. F. G. Riddell, S. Arumugam, K. D. M. Harris, M. Rogerson, and J. H. Strange, *J. Am. Chem. Soc.*, 1993, **115**, 1881.
18. (a) A. E. Aliev, K. D. M. Harris, and D. C. Apperley, *J. Chem. Soc., Chem. Commun.*, 1993, 251; (b) G. H. Penner and J. M. Polson, *J. Chem. Soc., Dalton Trans.*, 1993, 803.
19. Y. N. Chihara, N. Nakamura, and H. Chihara, *Can. J. Chem.*, 1988, **66**, 1848.
20. S. J. Heyes, M. L. H. Green, and C. D. Dobson, *Inorg. Chem.*, 1991, **30**, 1930.
21. J. Kümmerlen and A. Sebald, *Magn. Reson. Chem.*, 1994, **32**, 173.
22. R. R. Ernst, G. Bodenhausen, and A. Wokaun, *Principles of Nuclear Magnetic Resonance in One and Two Dimensions*, Oxford Science Publishers, Oxford, UK, 1991.
23. J. Sandström, *Dynamic NMR Spectroscopy*, Academic Press, London/New York, 1982.
24. G. Binsch and H. Kessler, *Angew. Chem.*, 1980, **92**, 445.
25. J. Kümmerlen and A. Sebald, *J. Am. Chem. Soc.*, 1993, **115**, 1134.
26. J. Kümmerlen, I. Lange, W. Milius, A. Sebald, and A. Blaschette, *Organometallics*, 1993, **12**, 3541.
27. J. Kümmerlen, A. Sebald, and E. Sendermann, *Organometallics*, 1994, **13**, 802.
28. R. K. Harris, M. M. Sünnetcioglu, and R. D. Fischer, *Spectrochim. Acta*, 1994, **50A**, 2069.

Acknowledgments

Generous support of our work by the Deutsche Forschungsgemeinschaft and the Fonds der Chemischen Industrie is gratefully acknowledged.

Biographical Sketch

Angelika Sebald. *b* 1955. Dipl. Chem., 1979, Ph.D., 1983, Universität München. University of Durham, UK, 1985–87; Universität Bayreuth, 1987–present; Habilitation, 1990; since 1991 Heisenberg fellowship (DFG). Approx. 90 publications. Research interests: applications of solid state NMR techniques to problems in inorganic and organometallic chemistry.

Jörg Kümmerlen. *b* 1962. Dipl. Chem., 1990, Ph.D. 1993, Universität Bayreuth. ETH Zürich, 1993–94; University of Nijmegen, 1994–95; Universität Bayreuth, 1995–present. Approx. 20 publications. Research interests include: applications of solid state NMR techniques to dynamic processes in solids and biopolymers.

Rotating Solids

Robert G. Griffin

Massachusetts Institute of Technology, Cambridge, MA, USA

1	Introduction	1
2	Early History	1
3	Hamiltonians, Rotational Echoes, and Spectra	2
4	Multiple Pulse NMR in Rotating Solids	5
5	Multidimensional MAS Experiments	7
6	Related Articles	10
7	References	10

1 INTRODUCTION

In the late 1960s and early 1970s, a number of experiments were developed that were aimed at performing 'high-resolution NMR in solids'. In general, these techniques are classified into two general categories:

1. multiple pulse (MP) experiments, aimed at attenuating the homonuclear dipolar couplings in strongly coupled spin systems typically found in protonated solids;
2. dilute spin double resonance/cross-polarization (CP) experiments, which detect signals from magnetically dilute nuclei such as ^{13}C and ^{15}N in the presence of strong dipolar decoupling.

However, in both cases, the resulting spectra consisted of powder patterns due to shift anisotropies, or rather broad lines in spectra of single crystals. Thus, while the resolution of solid state spectra was much improved, it was still not comparable to that observed in liquids.

This situation changed dramatically with the marriage of magic angle spinning (MAS), a 'partially successful' mechanical rotation technique also developed to attenuate dipolar couplings in solids, with CP and/or MP to yield a new class of hybrid solid state techniques. In these cases, homo- or heteronuclear decoupling removes the dipolar interactions, and MAS narrows the shift anisotropy. The resulting spectra exhibit resolution comparable to that observed in liquids, and, as a consequence, these techniques are currently widely utilized in a variety of forms to examine problems in biology, chemistry, physics, materials science, and a number of engineering disciplines.

The subject of this article is the early developments that led to these MAS techniques, and advances in MAS that have occurred in the last 15 years or so. We focus primarily on the spectra of dilute $I = \frac{1}{2}$ spins in 1D and 2D experiments, with a brief interlude where we consider the possibility of reintroducing the dipolar coupling of the dilute spins to ^{1}H (so-called DIPSHIFT experiments), since this was the initial MAS 'recoupling technique'. More recent advances in the area of homonuclear and heteronuclear recoupling (rotational resonance, DRAMA, RFDR, REDOR, TEDOR, etc.) are considered in other articles.

2 EARLY HISTORY

The initial MAS NMR experiments were performed in the late 1950s,[1,2] and were aimed at attenuating homonuclear dipolar interactions in NMR spectra of solids, thereby revealing the underlying chemical shifts and scalar spin couplings. The approach was successful in cases where the dipolar couplings $|\hat{\mathcal{H}}_{\rm d}|$ were not too large, and therefore the spinning rate $\omega_{\rm r}/2\pi$ satisfied the condition $\omega_{\rm r}/2\pi > |\hat{\mathcal{H}}_{\rm d}|$. Early results obtained on ^{23}Na in NaCl, on ^{31}P in PCl_5, and on ^{19}F in $KAsF_6$ demonstrated line narrowing, and resolution of chemical shifts and J couplings, respectively.[3,4] However, in the 1960s, NMR spectrometers utilized iron magnets and continuous wave (CW) observation techniques, and this in turn constrained researchers to observe primarily ^{1}H and ^{19}F, which generally yield spectra with dipolar breadths of 25–50 kHz. Since available spinning speeds were in the range of 5–10 kHz, the spectra could not in general be narrowed, a result connected with the fact that $\hat{\mathcal{H}}_{\rm d}$ is a *homogeneous* interaction.[5] For this reason, for most of the 1960s and early 1970s, MAS was viewed as an interesting but not very useful technique.

During this period, several developments occurred that eventually led to a renaissance in MAS. First, in 1968, J. S. Waugh and co-workers introduced MP techniques for attenuating homonuclear dipolar couplings in solids.[6] Since the cycle of four pulses in a WAHUHA experiment could be applied rapidly compared with the size of $|\hat{\mathcal{H}}_{\rm d}|$, this technique, and its subsequent refinements,[7–9] have been more successful than MAS in removing homonuclear dipolar couplings. In 1972, a second, very versatile approach to high resolution in solids emerged from Waugh's laboratory. At that time, FT spectroscopy[10,11] was developing as the preferred method of recording solution spectra, and reports describing spectra of less abundant nuclei (^{13}C, ^{15}N, etc.) were beginning to appear. It seemed reasonable that ^{13}C and ^{15}N spectra should also be observed in solids, and an approach for accomplishing this involving a Hartmann–Hahn[12] cross polarization and decoupling[13,14] was described by Pines et al.[15] While both MP and CP were very interesting developments, they both yielded spectra consisting of powder patterns or required single crystals; therefore, much of the high-resolution NMR community was unimpressed with the promise of the solid state NMR.

It was appreciated by at least a few individuals that an approach to narrowing these powder spectra was to incorporate MAS into the experiment.[16] Specifically, any second-rank tensor—dipolar, chemical shift, quadrupole, Knight shift, and indirect dipolar couplings—is narrowed by MAS. Ultimately, this led to the Schaefer and Stejskal[17] experiment, which demonstrated that high-resolution, 'liquid-like' spectra of solids could be obtained by combining dilute spin double resonance—cross polarization and decoupling—and MAS into what is now referred to as a CP MAS experiment. Later, Gerstein and co-workers[18] performed similar experiments with MP and MAS, a technique now referred to as CRAMPS (combined rotation at the magic angle and multiple pulse).

Initially, CP MAS experiments were performed at a ^{13}C frequency of about 22.6 MHz, and therefore a typical 150–200 ppm ^{13}C shift tensor was 3.75–5.00 kHz wide, and near the regime $\omega_{\rm r}/2\pi > \Delta\sigma$. Conventional wisdom dictated that line narrowing by MAS would not occur unless this condition was satisfied; therefore, spinning experiments should

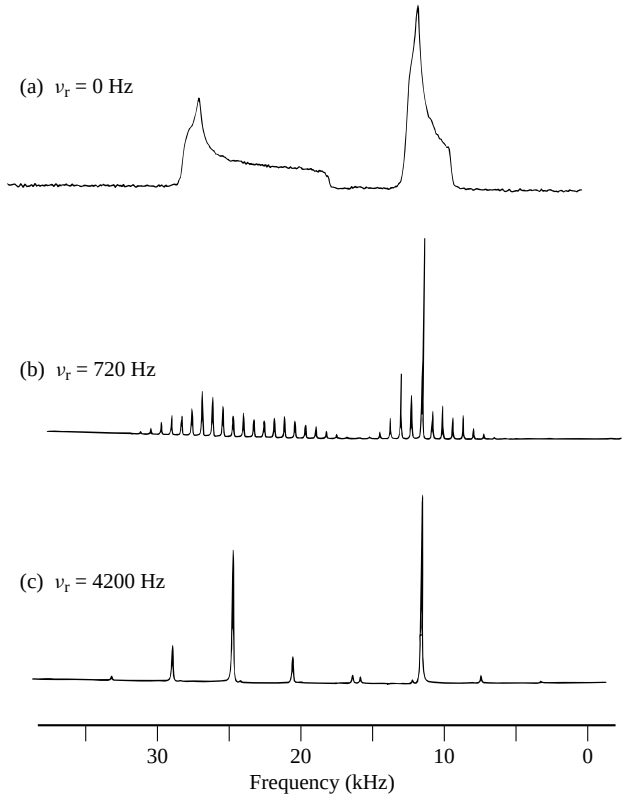

Figure 1 Static (a) and MAS (b, c) ^{13}C spectra of zinc acetate, showing the effect of MAS on chemical shift anisotropic powder patterns. The spectra were obtained with a standard CP sequence. The rotational sidebands observed in (b) and (c) are spaced at the spinning frequency. The breadths of the powder patterns are 10.2 and 3.2 kHz, respectively, for the $-CO_2^-$ and $-CH_3$ resonances. Note that the sidebands for the methyl pattern are completely attenuated at $\omega_r/2\pi$ = 4.2 kHz

be performed at low fields, and not in the superconducting solenoids that were becoming the standard polarizing field for NMR spectrometers. However, the results of performing MAS in the slow spinning regime, $\omega_r/2\pi < \Delta$, where Δ is the size of the interaction of interest, were already in the literature. In 1974, Andrew et al.[19] showed that the Knight shift observed in Cd metal narrows into a sharp centerband and sidebands when the spinning rate is less than the breadth of the pattern. Subsequently, several other groups[20–23] observed the same behavior for shift anisotropy powder patterns of ^1H decoupled spectra of $I = \frac{1}{2}$ nuclei: ^{13}C, ^{31}P, etc. Some examples of the type of spectra observed are shown in Figure 1, where ^1H-decoupled ^{13}C spectra of zinc acetate. H_2O (ZnAc) are illustrated as a function of spinning speed.

The CO_2^- and $-CH_3$ powder lineshapes are about 10.2 and 3.2 kHz wide, respectively, and evolve to a sharp centerband and sets of sidebands at spinning speeds of 4.2 kHz. These types of spectra are now routinely observed in the spectra of $I = \frac{1}{2}$ nuclei, and have brought solid state NMR into the realm of high resolution. Specifically, resolved centerbands and sidebands are observed for each magnetically inequivalent nucleus, and therefore MAS spectra can be used in much the same fashion as their high-resolution counterparts observed in solution. The remainder of this article will consider the shape of these spectra (i.e., the sideband intensities), new ways of utilizing and manipulating sidebands, and multidimensional experiments.

3 HAMILTONIANS, ROTATIONAL ECHOES, AND SPECTRA

3.1 MAS Hamiltonian

The generalized laboratory frame Hamiltonian for a nuclear spin interaction is

$$\hat{\mathcal{H}} = C\hbar \sum_{l=0,2} \sum_{m=-1}^{1} (-1^m) \hat{R}_{l-m} \hat{T}_{lm} \tag{1}$$

where C is a collection of constants, and $\hat{R}$ and $\hat{T}$ are second-rank tensor operators containing the spatial and spin dependences of the coupling, respectively.[24] In a principal axis system (PAS), the tensor $\boldsymbol{R}$ representing $\hat{R}$ is diagonal, with principal values R_{ii} ($i = x,y,z$). These lead to an isotropic component

$$R = \tfrac{1}{3}(R_{xx} + R_{yy} + R_{zz}) \tag{2}$$

an anisotropy

$$\delta = R_{zz} - R \tag{3}$$

and an asymmetry

$$\eta = \frac{R_{xx} - R_{yy}}{\delta} \tag{4}$$

with the diagonal elements ordered so that

$$|R_{zz} - R| \rangle |R_{xx} - R| \rangle |R_{yy} - R| \tag{5}$$

The mechanical system under consideration consists of a rotor inclined at an angle θ relative to the external field $\boldsymbol{B}_0$ and spinning at ω_r. The laboratory frame with $z \| \boldsymbol{B}_0$ is related to the PAS of a specific coupling tensor $\boldsymbol{R}$ by two sets of Euler angles. The first transformation takes the laboratory into the rotor frame with Euler angles (θ_m, $-\omega_r t$), and the second maps the rotor frame onto the PAS of the coupling tensor. Using the definitions above and some algebra, we obtain a compact form for the MAS Hamiltonian. Specifically, for the chemical shift $\hat{T}_{00} = \hat{I}_z B_0$ and $\hat{T}_{20} = \sqrt{\frac{2}{3}} \hat{I}_z B_0$, we obtain

$$\begin{aligned} \hat{\mathcal{H}}(t) &= \omega(t) \hat{I}_z \\ &= -\Delta\omega \hat{I}_z - \omega_1 [g_1 \cos(\omega_r t + \varphi_1) + g_2 \cos(2\omega_r t \\ &\quad + \varphi_2)] \hat{I}_z \end{aligned} \tag{6}$$

in which

$$\Delta\omega = \omega_1^0 + \omega_{off} = \tfrac{1}{3}\omega_0(\sigma_{11} + \sigma_{22} + \sigma_{33}) + \omega_{off} \tag{7}$$

$$\omega_1 = \omega_0(\sigma_{33} - \tfrac{1}{3}\mathrm{Tr}\boldsymbol{\sigma}) = \omega_0\sigma_{33} - \omega_1^0 \tag{8}$$

g_1 and g_2 depend on the Euler angles β and γ,

$$g_1 = \tfrac{1}{2}(\tfrac{1}{2}\sin 2\theta \sin\beta) \times[(\eta\cos 2\gamma + 3)^2\cos^2\beta + \eta^2\sin^2 2\gamma]^{1/2} \quad (9a)$$

$$g_2 = \tfrac{1}{2}(\tfrac{1}{2}\sin^2\theta_m)\{[\tfrac{3}{2}\sin^2\beta - \tfrac{1}{2}\eta\cos 2\gamma(1+\cos^2\beta)]^2 + \eta^2\cos^2\beta\sin^2 2\gamma\}^{1/2} \quad (9b)$$

The phase factors ϕ_1 and ϕ_2 are given by

$$\varphi_1 = \alpha + \varphi_1 \quad (10a)$$

$$\varphi_2 = 2\alpha + \varphi_2 \quad (10b)$$

where

$$\tan\varphi_1 = \eta\frac{\sin 2\gamma}{\eta\cos 2\gamma + 3}\cos\beta \quad (11a)$$

$$\tan\varphi_1 = \eta\frac{\cos\beta\sin 2\gamma}{\frac{3}{2}\sin^2\beta - \frac{1}{2}\eta\cos 2\gamma(1+\cos^2\beta)} \quad (11b)$$

for axially symmetric tensors $\eta = 0$ and

$$\varphi_1 = \alpha, \quad \varphi_2 = 2\alpha, \quad (12)$$

Similar expressions can be derived for the heteronuclear dipolar Hamiltonian with $\hat{T}_{00} = 0$ and $\hat{T}_{20} \approx \hat{I}_z\hat{S}_z$ [in equation (1)]. Note that a term proportional to $3\cos^2\theta_m - 1$ must be added to equation (6) when the spinning is off the magic angle. Recently, a new approach for expressing the anisotropy of NMR Hamiltonians has been suggested involving the span $\Omega = \sigma_{33} - \sigma_{11}$ and skew $k = (\sigma_{11} + \sigma_{33} - 2\sigma_{22})/(\sigma_{33} - \sigma_{11})$ of the interaction. These definitions are discussed in ***Sideband Analysis in Magic Angle Spinning NMR of Solids***.

3.2 Rotational Echoes

The spectra in Figure 1 result from the fact that the chemical shift interaction is *inhomogeneous*, a term used by Portis[25] to denote that a 'hole could be burned' into spectral patterns. In the absence of motion, continuous irradiation of one part of a powder pattern with a narrow frequency signal will saturate that part of the spectrum, and, because of the absence of coupling among the spins, that saturation will not diffuse through the spectral lineshape. In contrast, if the line is homogenously broadened, for instance, if a homonuclear dipolar coupling determines the lineshape, then irradiation at a narrow band of frequencies will diffuse through the spin reservoir and lead to saturation of the entire spectrum. Thus, solid state spectra can be decoupled with single frequency irradiation, whereas liquids require wideband (noise or composite pulse[26,27]) decoupling.[5] Another approach to this statement is to consider the average Hamiltonian $\langle\bar{\hat{\mathcal{H}}}\rangle$ for an MAS experiment:[22,24]

$$\langle\bar{\hat{\mathcal{H}}}\rangle = \sum_{\mu=0}^{\infty}\bar{\hat{\mathcal{H}}}^{(\mu)} \quad (13)$$

where the first two terms are

$$\bar{\hat{\mathcal{H}}}^{(0)} = \frac{\omega_r}{2\pi}\int_0^{2\pi/\omega_r}\hat{\mathcal{H}}(t')\,dt' \quad (14a)$$

$$\bar{\hat{\mathcal{H}}}^{(1)} = \frac{i\omega_r}{4\pi}\int_0^{2\pi/\omega_r}\int_0^{t''}[\hat{\mathcal{H}}_0(t'),\hat{\mathcal{H}}(t'')\,dt'\,dt'' \quad (14b)$$

Because of the oscillatory nature of the MAS chemical shift Hamiltonian [see equation (6)], the time-dependent terms vanish, and the zeroth-order term $\bar{\hat{\mathcal{H}}}^{(0)}$ is equal to the isotropic shift. Physically, this tells us that the system returns to its initial state after each revolution of the spinner. In general, the higher order correction terms like equation (14b) will be nonzero, and when $|\bar{\hat{\mathcal{H}}}|\tau_c\rangle 1$ (where τ_c is the cycle time), these terms interfere with the line narrowing. In the case of the 'homogeneous' homonuclear dipolar coupling, $\bar{\hat{\mathcal{H}}}^{(1)}$ is of substantial size, because the coupling between i and j does not commute with that between i and k, or j and k, etc. However, for the chemical shift, the commutator in equation (14b) vanishes, as do those in higher-order correction terms. For this reason, the chemical shift powder patterns are resolved into sideband patterns even in the slow spinning regime $\omega_r/2\pi < \delta$.

Finally, it should be mentioned that the heteronuclear dipolar and first-order quadrupolar couplings are also inhomogeneous, as is an isolated dipolar-coupled pair of like spins, and all of these cases will yield sideband spectra similar to those in Figure 1.[5] However, when a homonuclear dipolar coupling is present, in addition to two or more spins with noncoaxial chemical shift tensors, the result is a homogeneous interaction that will not narrow completely. Some interesting examples of this last case are discussed below.

The average Hamiltonian describes the state of the system modulo the rotor period, but it says nothing about the evolution during the rotor cycle. In fact, what occurs for slow spinning is that the signal is recovered after each rotation as an echo, and for systems with reasonable decay times, a train of echoes is observed. The vanishing of $\bar{\hat{\mathcal{H}}}^{(0)}$ means that each echo will have the same shape, an example being shown in Figure 2(a). The Fourier transform of this train yields a centerband/sideband spectrum similar to those illustrated in Figure 1. The linewidths of the centerband and sidebands are determined by the decay time of the entire echo train, while the shape of the sideband envelope is governed by the shape of the rotational echoes.[5]

Our intuitive understanding of the behavior of single spins in liquids is enhanced by the use of vector pictures, which are very useful for depicting FIDs, Hahn spin echoes, and a number of other phenomena. Similarily, vector pictures provide insight into formation of rotational echoes and other phenomena associated with MAS. In Figure 3, we illustrate spin packet trajectories for two crystallites under MAS for a rotor period, and we have shrunk the length of the vector during the rotor period to clearly show its path. The magnetization trajectories are shown for three cases: before a π pulse is applied [(a) and (b)], after a single π pulse [(c) and (d)], and after two π pulses [(e) and (f)]. In all cases, the motion is τ_r-periodic, so that vectors return to their initial positions after a rotor period. We shall return to a discussion of this figure when we consider echoes. It has been shown[28] that a powder average of these spin packets leads to formation of

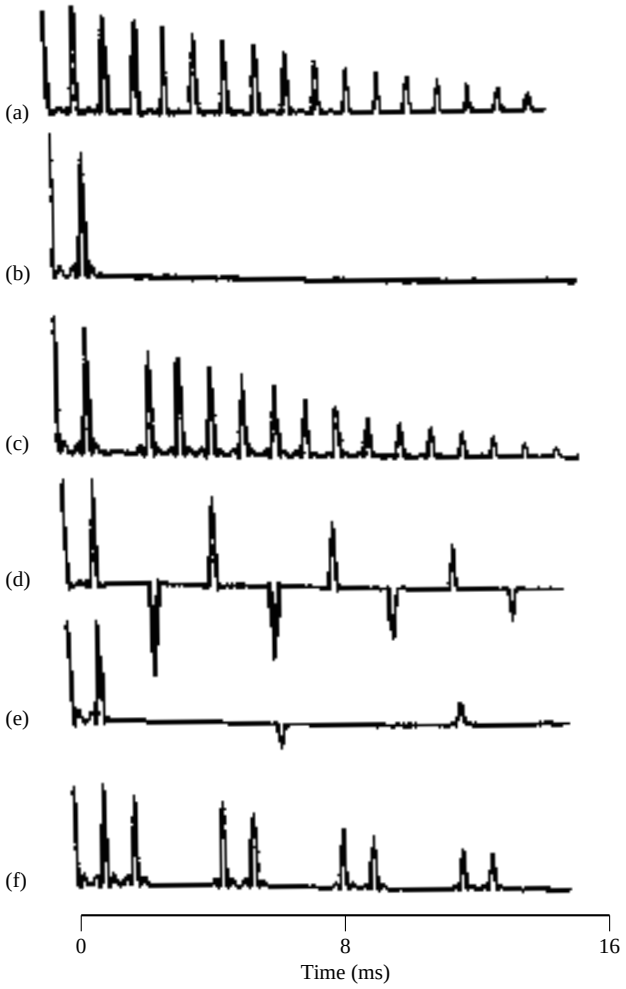

Figure 2 Rotational echo trains measured on a sample of [1-^{13}C]-glycine spinning at $\omega_r/2\pi$ = 1.03 kHz. The rf carrier frequency coincided with the isotropic chemical shift: (a) a train of unperturbed rotational echoes; (b) a single π pulse inserted at $\frac{3}{2}\tau_r$ results in the disappearance of the echo train; (c) two π pulses inserted at $\frac{3}{2}\tau_r$ and $\frac{5}{2}\tau_r$ result in the disappearance and reappearance of the echo train at $3\tau_r$; (d) multiple applications of $(-\pi_x-\tau_r-\pi_y-\text{echo})$ lead to the train with alternate echoes inverted; (e) echo train with $\tau_c = \frac{3}{5}\tau_r$ and alternating phases (0° and 90°) of the pulses; an inverted echo is recovered after $2n\tau_r = 6$ echoes and the intervening application of $2m\tau_r = 10$ π pulses; (f) echo train with $\tau_c = 2\tau_r$

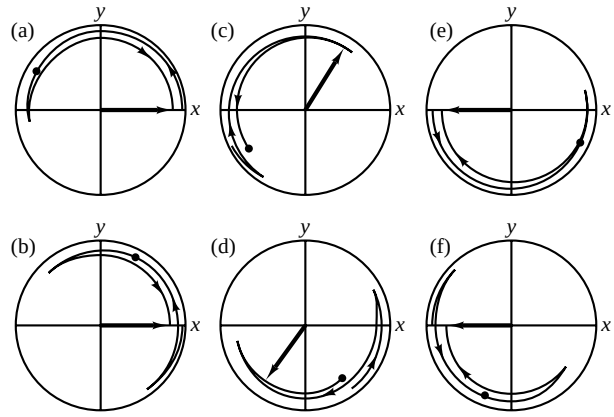

Figure 3 Spin packet trajectories in the rotating frame, showing the effect of π pulses on rotational echo formation. All calculations used $\omega_r/2\pi$ = 2.0 kHz, δ = 5.0 kHz, η = 0, and β = 60°. The position of the magnetization vector at $\frac{1}{2}\tau_r$ is represented by a dot, while the position of the vector at the end of the next rotor period is represented by a long arrow. The direction of motion of the vectors is indicated by arrowheads. The length of the vector was shrunk over time in order to make the paths clearer. (a) α = 60°: evolution from 0 to τ_r. (b) α = 20°: evolution from 0 to τ_r. (c) α = 60°: evolution from $\frac{1}{2}\tau_r$ to $\frac{3}{2}\tau_r$ after the first π pulse of phase 0° was applied at $\frac{1}{2}\tau_r$; a second π pulse of phase 90° was applied at $\frac{3}{2}\tau_r$. (d) α = 20°: same as in (c). (e) α = 60°: evolution from $2\tau_r$ to $3\tau_r$ after the application of the second π pulse of phase 90° at $\frac{3}{2}\tau_r$. (f) α = 20°: same as in (e)

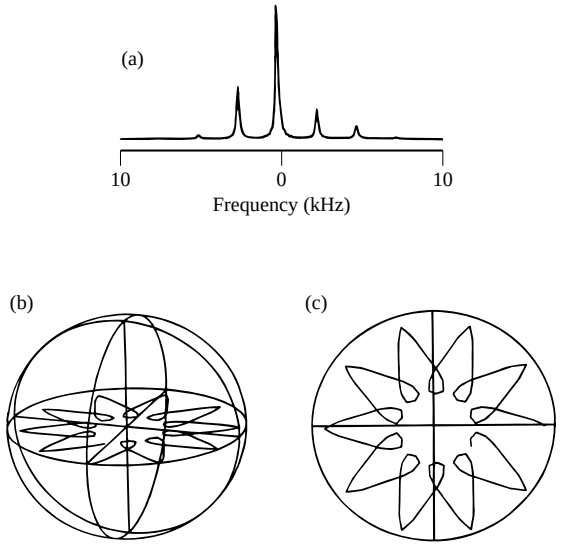

Figure 4 (a) MAS spectrum for δ = 5.4 kHz, η = 0 and spinning at $\omega_r/2\pi$ = 2.0 kHz, 200 Hz off resonance. (b, c) The magnetization path corresponding to the MAS spectrum shown in (a) and its (x, y) projection. The petals in the rosette pattern correspond to the formation of rotational echoes

the 'rosette pattern' illustrated in Figure 4. Here we show the path of the magnetization in a MAS experiment for a sample with δ = 5.4 kHz, η = 0, and $\omega_r/2\pi$ = 2.0 kHz, with a resonance offset of 200 Hz, and nine rotational echoes are apparent.

3.3 Spectra

There have now been many interesting applications utilizing these MAS spectra in biology, chemistry, physics, and materials science. These include studies of chemical exchange and other dynamic phenomena in solids, as well as studies of structure. In order to illustrate the explosive growth of MAS NMR in structural investigations, we present an illustration of the size of molecular system, which is often a limiting parameter in many magnetic resonance studies, that can be approached with this technique. Figure 5 shows spectra of a double ^{13}C-labeled membrane protein, [14-^{13}C]retinal-[ε-^{13}C]Lys-bacteriorhodopsin (bR), which has not been crystallized and which cannot be effectively studied with solution NMR techniques because of its size and aggregation. The top trace in the figure contains lines due to both the label and the natural abundance background, while the middle

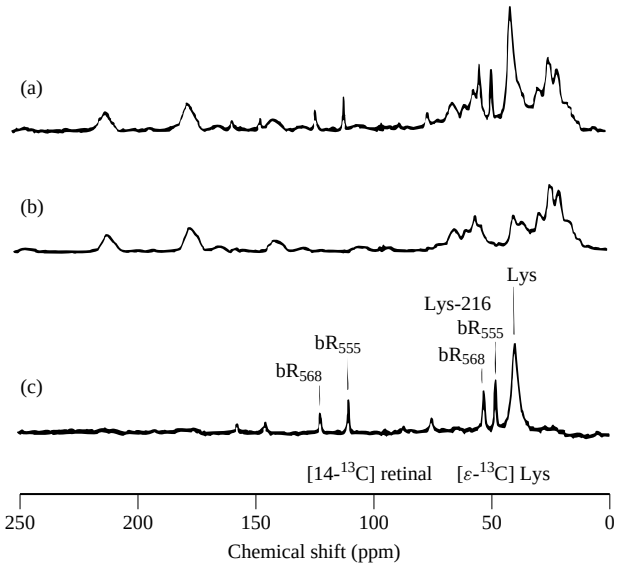

Figure 5 ^{13}C MAS spectra of dark-adapted bR collected at −80 °C with a sample spinning speed of 2.8 kHz: (a) [14-^{13}C]retinal-[ε-^{13}C]Lys-bR; (b) unlabeled bR; (c) the difference spectrum obtained upon subtraction of (b) from (a). The signals at 40, 48 and 53 ppm are due to the [ε-^{13}C]Lys label, and the signals in the 100−130 ppm range arise from the [14-^{13}C]retinal marker resonances. Rotational sidebands are observed 35 ppm upfield and downfield of the centerbands

trace shows only the natural abundance spectrum. The bottom trace illustrates the difference spectrum exhibiting only the ^{13}C labels. Dark-adapted bR contains a 60 : 40 mixture of 13-*cis*- and all-*trans*-retinal (referred to as bR_{555} and bR_{568}, respectively, where the numbers indicate the wavelengths of their absorption maxima). Therefore, there are two retinal and two Lys lines in the spectrum, together with a line due to six lysines not involved in the Schiff base linkage. bR has a molecular weight of 26.6 kDa, and the membrane is about 75 wt% protein, leading to an effective MW ≈ 35.5 kDa. Together, the two retinal and Lys Schiff baselines represent a single ^{13}C, and thus for the bR_{568} resonances, we are observing about 40% of a single ^{13}C, corresponding to a single ^{13}C in a protein of MW ≈ 88 kDa. Further, it is possible with recoupling techniques (rotational resonance and RFDR) to measure the distance between the retinal and lysine labels, and to determine the conformation about the retinal C=N bond in both bR_{555} and bR_{568}. Because of its ability to address protein problems of this size, MAS NMR will undoubtably continue to find applications in many different areas.

4 MULTIPLE PULSE NMR IN ROTATING SOLIDS

In this section, we describe the effects of MP trains on MAS spectra. We first consider the effects of single and multiple π pulse trains on rotational echoes, since these effects are important in designing other experiments. This is followed by a discussion of the TOSS and scaling experiments, which are used to manipulate sidebands in MAS spectra. Several features of these experiments, including intensity losses and rotor frequency lines, will emerge from the discussion. Finally, we describe the hybrid, TOSS/scaling experiment, which combines desirable features of each approach.

4.1 π Pulses and Rotational Echoes

The simplest multiple pulse (≥2 pulses) experiment possible is the addition of π pulse(s) following excitation (cross polarization or a 90° pulse) analogous to a Carr−Purcell experiment in liquids. Experimental results showing the effects of π pulses during a rotor period are shown in Figure 2(b)−(f).

In Figure 2(b), a π_x pulse is applied at the middle of a rotor period, in this case $\frac{3}{2}\tau_r$, and the signal vanishes. This effect is readily understood by examining the single crystallite magnetization trajectories shown in Figure 3, where we have plotted the path for before [(a) and (b)] and after [(c) and (d)] the π_x pulse for two crystallite orientations: α = 60°, β = 60° (a) and α = 20°, β = 60° (b). Following excitation, both vectors lie along the x axis, evolve on the trajectories shown, and return to the origin after each rotor period, resulting in the formation of an echo. The application of a π_x pulse in the middle of a rotor period (corresponding to the position of the dot on the trajectory) results in a reflection of the trajectory about the x axis of the rotating frame. Thus, while the pulse does not affect the periodicity of the crystallite's magnetization path, it does reorient each vector in a way that alters their phase relationship, and the signal disappears. A second π_x pulse at $\frac{5}{2}\tau_r$, again when the vector position is at the 'dot', restores the phase relation among the crystallites, and the echo train reappears [Figure 2(c)].

Another parameter of importance in echo phenomena is the relative phase of the rf pulses. In Figure 2(d), we show that the echo train may be inverted—in this case, multiple times from positive to negative to positive, etc.—by employing a 90° phase shift in the second of the two rf pulses. Specifically, instead of using $-\pi_x\tau_r\pi_x-$ for the refocusing, we use $-\pi_x\tau_r\pi_y-$. Thus, the initial 'scrambling' of the phases accomplished by the π_x pulse is reversed by a π_y pulse, but the refocusing occurs along the $\bar{x}$ rather than the x direction. This is easily understood by comparing Figures 3(c) and (d) with Figures 3(e) and (f), where the application of the π_y pulse results in refocusing along $\bar{x}$. Each new application of the $-\pi_x\tau_r\pi_y-$ sequence again reverses the sign of the subsequent echo, as shown in Figure 2(d).

As is discussed elsewhere,[29] there are many other combinations of π pulses that will yield echo trains, and the general conditions for echo formation in these trains have been studied. Specifically, for

$$\tau_c = \frac{n}{m}\tau_r \tag{15}$$

where τ_c is the cycle time, τ_r the rotor period, and n and m are integers, refocusing will occur only for odd m; after $2m$ π pulses, echo formation will occur at $2n\tau_r$. Some results using this formula are shown in Figure 2(e) for $\tau_c = \frac{3}{5}\tau_r$ (a string of ten π pulses yields an echo at $6\tau_r$) and Figure 2(f), where $\tau_c = 2\tau_r$.

4.2 TOSS and Chemical Shift Scaling

The sidebands in a MAS spectrum, which reflect the anisotropic chemical shift, contain information that can be invaluable in understanding molecular and electronic structure.[30,31] Nevertheless, in analytical applications of MAS,

the isotropic shift is the focus of attention, a fact that has provided the impetus to develop techniques to eliminate or attenuate sidebands. To date, there have been two approaches to the problem: the TOSS experiment, due originally to Dixon,[32] and its subsequent variations,[33–35] and scaling, due to Aue et al.[36,37] The methods are based on fundamentally different physical principles, and each has its advantages and disadvantages.

The original four π pulse version of the TOSS pulse sequence is illustrated in Figure 6, and some experimental spectra obtained from [1-^{13}C]glycine are shown in Figure 7. The top two spectra were taken at $\omega_r/2\pi$ = 3.20 kHz with MAS (a) and TOSS (b), and the TOSS experiment clearly suppresses the rotational sidebands. The physical basis for TOSS is spin packet alignment—the preparation pulses result in a situation where the centerbands have the same amplitude and phase, and therefore add constructively. In contrast, the sidebands have different phases, add destructively, and are canceled when a powder average is performed. There is, however, a problem with this process, which is evident in Figure 7. First, the spectral intensity that resides in the sidebands is not transferred to the centerband by the alignment process. More specifically, when TOSS was first proposed, it appeared that the behavior illustrated in the top half of Figure 7 would always prevail. However, it was soon noticed that substantial intensity losses occur when the tensor is large or when the spinning speed low—i.e., when $\delta/(\omega_r/2\pi) \gg 1$.[38] The spectra in the bottom half of Figure 7 dramatically illustrate this point, in that the centerband inverts when $\delta/(\omega_r/2\pi) \approx 8$. Calculations and experimental data show that for an $\eta = 0$ tensor, the centerband intensity is positive when $\delta/(\omega_r/2\pi) \leq 6$; however, for larger values of this parameter, the intensity approaches zero, and becomes negative for $\delta/(\omega_r/2\pi) > 8$. Thus, TOSS centerband intensities cannot be employed to 'count spins' in the same fashion as normal NMR spectra, and the signal-to-noise ratio of the experiment is decreased substantially. In addition, since the pulse sequence is spread over 1–4 rotor periods, TOSS is difficult to apply to samples with broad NMR lines. Finally, with weak rf fields, the pulses sometimes overlap.

Despite these limitations, the idea suggested by Dixon is an important addition to the repertoire of MAS experiments, and its features have been explored extensively. Equations for the timing of the pulses have been presented,[28,35,39] and have been solved analytically by Lang[40] and more recently by Levitt and co-workers.[34,41] New timings[42] and sequences have been explored, including the SELTICS sequence with continuous rf burst,[33] which suspends the chemical shift evolution. In addition, TOSS has been employed to examine

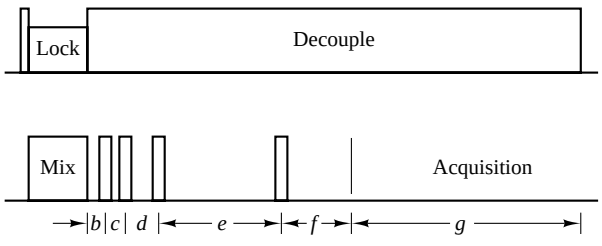

Figure 6 TOSS pulse sequence used to suppress rotational sidebands. The locations of the pulses and the initiation of sampling over two rotor periods are (in fractions of a rotor period) b = 0.1763, c = 0.6289, d = 0.8617, d = 1.2060, e = 1.6485, f = 1.8170, and g = 1.9326

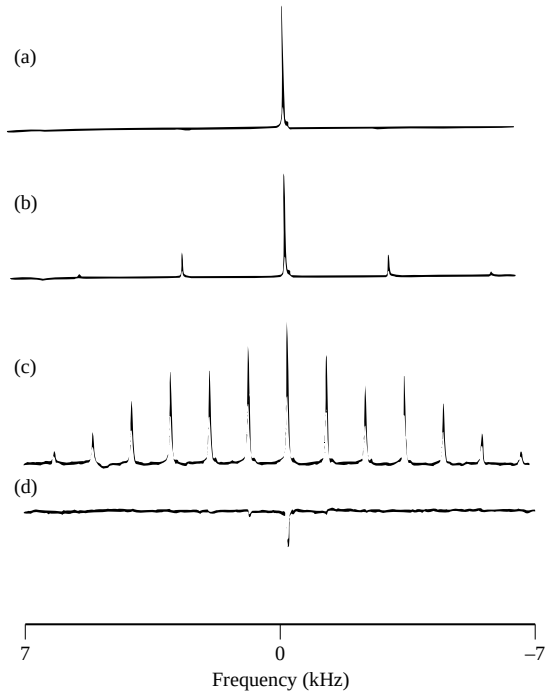

Figure 7 Experimental MAS and TOSS spectra of [1-^{13}C]glycine: (a) MAS at $\omega_r/2\pi$ = 3.2 kHz; (b) TOSS at $\omega_r/2\pi$ = 3.2 kHz; (c) MAS at $\omega_r/2\pi$ = 1.2 kHz; (d) TOSS at $\omega_r/2\pi$ 1.2 kHz. The same phase correction was employed for all spectra. Note that the sideband intensity was not transferred to the centerband in (b) and that the centerband inverts when $\Delta\sigma/(\omega_r/2\pi) > 4.5$, as shown in (d)

chemical exchange,[43–45] and can be usefully incorporated into 2D experiments to separate isotropic and anisotropic chemical shifts.[29]

The second approach to attenuating sidebands involves incorporation of a MP experiment into a MAS experiment to reduce the effect size of the shift anisotropy. If the scale factor q is sufficiently small then $q\ \Delta\sigma/\nu_r < 1$, and the spectrum will be dominated by centerbands. This is based on the well-known fact that all multiple pulse trains scale certain interactions to varying degrees. For example, WAHUHA and MREV-8, etc.[6,7] scale $\hat{\mathcal{H}}_d^{I-I}$ to zero and the chemical shift by 0.57 and 0.47, respectively. The first experiment explicitly designed to scale chemical shifts was that of Ellett and Waugh.[46] More recently, Aue et al.[47,48] developed improved scaling sequences, and used them to scale ^{13}C–^{1}H J couplings.

By itself, scaling will not reduce the sidebands in a MAS spectrum to zero, and therefore it is advantageous to combine scaling with TOSS in a hybrid experiment. The timings for the TOSS sequence must be adjusted to account for the scaling sequence,[49] but the result is a substantial increase in the signal strength of lines associated with large anisotropies. This is illustrated in Figure 8, where we show the MAS, TOSS, and TOSS/scaling spectra of alanine. A comparison of Figures 8(a) and (b) shows that, while TOSS does suppress sidebands, it does little to enhance the $-CO_2^-$ centerband intensity. However, as shown in Figure 8(c), the presence of a scaling sequence distills the intensity of the $-CO_2^-$ sidebands into the centerband so that the three lines are of approximately equal intensity, as expected. In the process, the intensity of

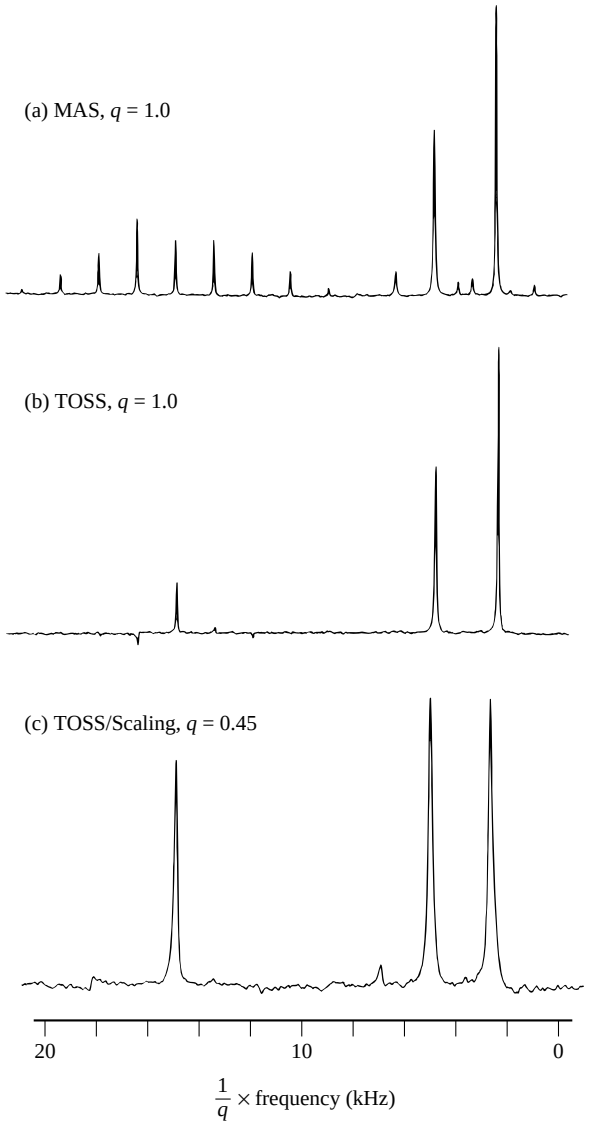

Figure 8 79.9 MHz ^{13}C spectra of natural abundance Ala obtained at $\omega_r/2\pi$ = 1.5 kHz. (a) MAS spectrum showing the numerous sidebands arising from the $-CO_2^-$ group and the narrow centerbands from the $-CH_3$ and α-CH carbons. (b) TOSS spectrum illustrating the attenuation of the sidebands and the loss of intensity that occurs for the $-CO_2^-$ centerband—i.e., it should be of equal intensity to the other lines in the spectrum. (c) TOSS/Scaling spectrum demonstrating that the signal intensity present in the rotational sidebands may be transferred to the centerband. The noise in the baseline has increased owing to the greater bandwidth used for the integrate-and-hold circuit that sampled the magnetization

the $-CO_2^-$ centerband increases by a factor of approximately five.

4.3 Rotor Frequency Lines and Powder Lineshapes

In a multiple pulse experiment, a factor responsible for limiting resolution is the (lack of) perfection of the pulse train. In fact, the development of pulse sequences that compensate for pulse errors has been a major industry in NMR. The effects of pulse errors also appear in MAS multiple pulse experiments—but in an unexpected manner. In many practical cases, a scaling or CRAMPS experiment with a scale factor of 0.5 will move the intensity to the centerbands, which are then readily identifiable. In addition, however, extra lines appear in the spectra at 0, $\pm n\omega_r/2\pi$, etc., which are referred to as *rotor frequency lines*.[28,36,37] These lines are also observed in ^1H CRAMPS spectra and appear and disappear as the resonance offset is changed.[36,37,50]

A theoretical explanation of these phenomena[28,50] is rather lengthy and involved. Physically, the origin of rotor lines is the presence of small pulse errors, which create components perpendicular to the average Hamiltonian and lead to a significant alteration in the paths of the magnetization vectors. For example, if a small (about 2%) pulse error is included in the calculation—the scaling is performed with 270°_x, $265^\circ_{\bar{x}}$ pulses rather than $270^\circ_{x(\bar{x})}$ pulses—then rotor frequency lines at 0 and $\pm n\omega_r/2\pi$ appear in the spectra. Concurrently, the intensity is reduced, since the signal goes into the rotor line rather than the real spectrum.

Finally, it should be mentioned that scaling, MREV-8, and other multiple pulse experiments function well as long as the cycle times of the experiments satisfy the condition $\tau_c < \tau_r$. In practice, this means there are three or more pulse cycles per rotor period. With fewer cycles, $\tau_c \approx \tau_r$ and a number of interesting phenomena occur. For example, when $2\tau_c = \tau_r$, powder patterns rather than sharp lines appear in the spectra, albeit in distorted forms.[20,36,37,51,52]

5 MULTIDIMENSIONAL MAS EXPERIMENTS

In this section, we review some of the early and simplest multidimensional MAS experiments employed for resolving and correlating various interactions in solid state NMR spectra. Our discussion will focus primarily on 2D experiments for

1. separation of isotropic and anisotropic chemical shifts;
2. separation of the heteronuclear dipolar interaction and chemical shifts;
3. heteronuclear chemical shift correlation spectroscopy;
4. 2D chemical exchange experiments.

This is currently a rapidly expanding area, and correlation experiments involving other homonuclear and heteronuclear dipolar interactions are discussed in ***Homonuclear Recoupling Schemes in MAS NMR*** and ***REDOR and TEDOR***.

5.1 Isotropic and Anisotropic Chemical Shifts

As discussed above, MAS NMR spectra sometimes display large numbers of sidebands, which degrade the resolution. Restoration of the resolution provided the impetus for the development of the TOSS, Scaling, and TOSS/Scaling experiments. However, since these experiments discard two-thirds of the information available in the spectra, it is useful to consider methods to restore these data. This problem was originally addressed with a 2D experiment with isotropic chemical shifts on one axis and isotropic and anisotropic on the second.[37] In order to extract the isotropic spectrum, the magnetization was sampled synchronously with the rotation in the $\omega_1/2\pi$ dimension, yielding the isotropic spectrum, and sampled without restriction in $\omega_2/2\pi$, which will contain both isotropic and anisotropic shifts. The difficulty

with synchronous sampling is the limited bandwidth in the $\omega_1/2\pi$ dimension (typically $\pm 2-4$ kHz), which is too small to accommodate the dispersion of isotropic ^{13}C shifts at superconducting fields (about 20 kHz). Therefore, the spectra will be aliased in this dimension, and, for example, lines from the $-CH_3$, $-CH_2-$ region of the spectrum will appear in the aromatic/carboxyl region. However, the $\omega_2/2\pi$ dimension contains *redundant* information—namely, both the isotropic and anisotropic shifts—and, for this reason, this sort of problem will not generally occur. Nevertheless, in certain situations, the 2D spectrum will not be completely resolved—in particular, when two resonances, δ_i and δ_j, satisfy the following two conditions: (i) $\delta_i - \delta_j = n\omega_r/2\pi$ and (ii) their shift anisotropies are sufficiently large that their sideband patterns overlap. Because the isotropic shifts are separated by $n\omega_r/2\pi$, they occur at the same frequency in $\omega_1/2\pi$, and their sideband patterns are then overlapped. However, by incorporating chemical shift scaling into the t_1 dimension, it is possible to circumvent this problem and to affect a complete resolution of the spectrum.[37]

A second solution to this problem is the TOSSOT experiment,[29] whose pulse sequence is shown in Figure 9, and will be recognized as forward and reverse TOSS. Initially, the TOSS sequence prepares magnetization to yield a t_1 period of isotropic evolution, while the time-reversed TOSS restores the anisotropic spectrum during t_2. The physical basis for the experiment is that the spin packet alignment resulting from TOSS can be restored at any time subsequent to its preparation by a mirror image sequence. However, TOSS must be initiated at the peak of a rotor echo to perform sideband suppression. Thus, in the present scheme, it is not possible to initiate TOSS at an arbitrary time in a rotor period. In addition, the TOSSOT scheme does show significant resonance offset effects, so care must be exercised in extracting anisotropies. Nevertheless, the experiment functions well in performing a 2D separation of isotropic shifts in $\omega_1/2\pi$ and isotropic plus anisotropic in $\omega_2/2\pi$. A 2D resolved spectrum of Tyr · HCl taken at $\omega_r/2\pi$ = 1.7 kHz illustrating the technique is shown in Figure 10. Note the substantial sideband manifolds present for the aromatic lines, which are clearly separated by their isotropic chemical shift. These lines are strongly overlapped in the 1D projection shown at the top.

The TOSSOT experiment has recently been employed by Geen and Bodenhausen[43,44] in studies of chemical exchange and in observation of isotropic chemical shifts.

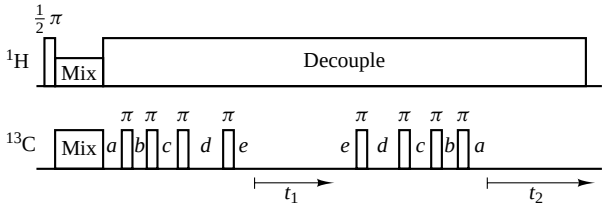

Figure 9 TOSSOT (TOSS/reverse TOSS) pulse sequence for 2D resolution of isotropic and anisotropic chemical shifts. The interpulse delays measured from the centers of the π pulses were (in fractions of a rotor period) a = 0.1226, b = 0.0773, c = 0.2236, d = 1.0433, and e = 0.7744

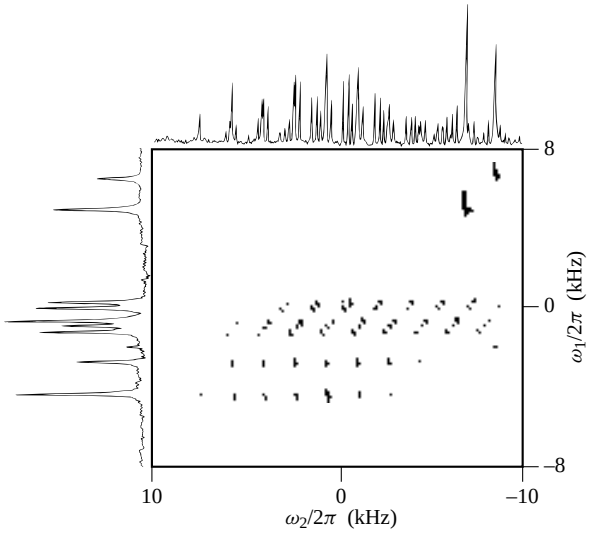

Figure 10 2D resolved ^{13}C TOSSOT spectrum of Tyr · HCl, $\omega_r/2\pi$ = 1.7 kHz. The normal MAS spectrum is given at the top and the ω_1 projection on the left. Slices in ω_1 with negative intensity were phase-reversed in the ω_1 projection. The ^{13}C pulse length was 8.0 s

5.2 Heteronuclear Dipolar and Chemical Shift

The heteronuclear dipolar coupling, like the chemical shift, is an inhomogeneous interaction, and will therefore yield sharp sidebands in a MAS experiment. Thus, if homonuclear couplings can be suppressed with an MP train, it is possible to separate the heteronuclear dipolar interaction and the chemical shift in a 2D correlation experiment. The Hamiltonian for this system is conveniently written as

$$\hat{\mathcal{H}} = a(\Omega,t)\hat{S}_z + b(\Omega,t)\hat{I}_z\hat{S}_z + c(\Omega,t)\sum_{i,j}(\hat{\boldsymbol{I}}_i \cdot \hat{\boldsymbol{I}}_j - 3\hat{I}_{iz}\hat{I}_{jz}) \qquad (16)$$

where we have collected the angular and temporal dependence in the coefficients $a(\Omega,t)$, $b(\Omega,t)$, and $c(\Omega,t)$. There are several pulse sequences that can be used to affect the desired separation, two of which are shown in Figure 11. The magnetization is prepared by cross polarization, and during t_1, the $a(\Omega,t)$ and $c(\Omega,t)$ terms are removed from equation (16) by application of a refocusing pulse and MREV-8, respectively. What remains during t_1 is the heteronuclear $\hat{I}_z\hat{S}_z$. During t_2, ^{1}H decoupling is applied, removing the $b(\Omega,t)$ and $c(\Omega,t)$ terms and leaving the chemical shift term $\hat{S}_z$. In addition, spectra are often recorded in the regime $\omega_r/2\pi < \Delta\sigma$, so we initiate sampling at the peak of a rotational echo to ensure the proper phase relationship among the sidebands in the chemical shift domain; t_1 thus runs from 0 to $N\tau_r$, and sampling commences at $2N\tau_r$.

The 2D dipolar/chemical shift (DIPSHIFT) spectra obtained from this experiment consist of a matrix of sidebands spaced at $\omega_r/2\pi$ in each dimension, which display two unusual features illustrated in Figure 12. The dipolar slices corresponding to chemical shift sidebands are asymmetric, and inverted sidebands are present in some of the slices. The origin of this effect has been discussed elsewhere,[53] and is due to the weighting of symmetric dipolar slices by the chemical shift,

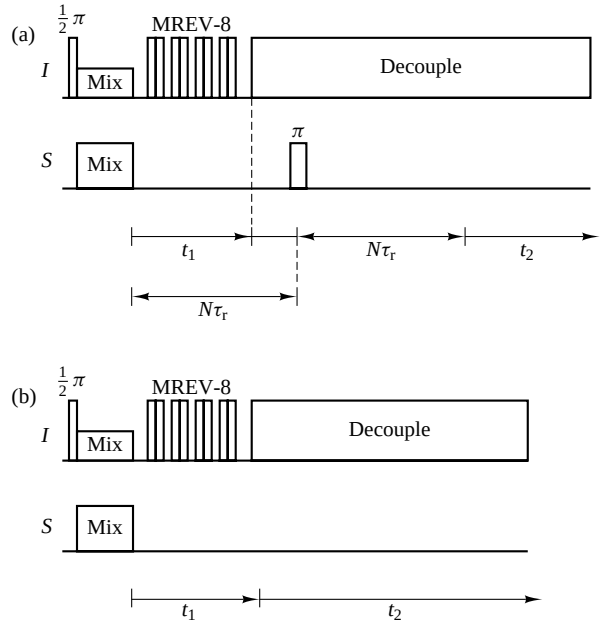

Figure 11 Pulse sequences for 2D dipolar–chemical shift spectroscopy. (a) The constant time experiment with a rotor synchronized π pulse to refocus isotropic chemical shifts at $N\tau_r$. Acquisition commences at $2N\tau_r$. (b) Simplified experiment where a shearing transformation is required to align the sideband manifolds

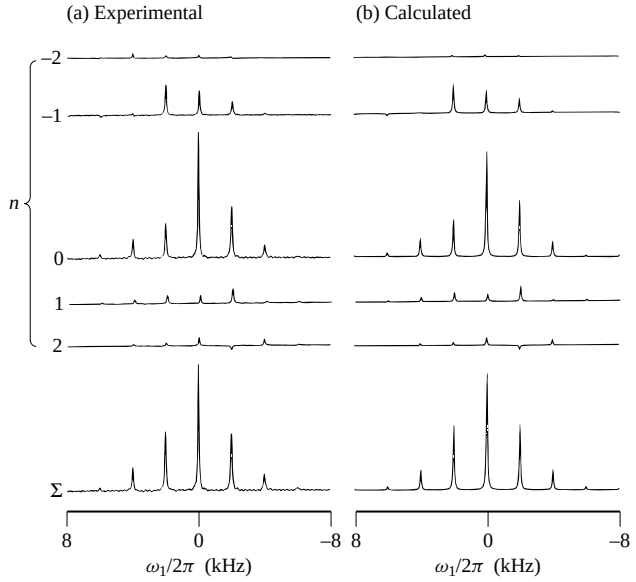

Figure 12 2D dipolar chemical shift spectra of ^{15}N-acetyl-DL-valine (NAV) $\omega_r/2\pi$ = 2.000 kHz. Slices were taken on points corresponding to sideband frequencies in ω_2. (a) Spectrum from the experiment of Figure 11 after shearing. (b) Simulation using the chemical shift tensor, the N–H bond length, and the nutual orientation of the chemical shift and dipolar tensors of NAV; σ_{11} = −64.7 ppm, σ_{22} = −39.7 ppm, σ_{33} = 104.4 ppm and r_{NH} = 105 pm. Polar angles of the NH bond in the principal axis system of the N shielding tensor are (θ, ϕ) = (22°, 0°). The multiple pulse scaling factor was κ = 0.480

leading to asymmetric and inverted sidebands. The dipolar slices corresponding to four sidebands and a centerband for the ^{15}N–^{1}H DIPSHIFT spectrum obtained from *N*-acetyl-DL-valine is shown in Figure 12, and the asymmetric intensities in the dipolar slices and inverted sidebands are apparent. When a full powder average is performed—i.e., when the dipolar and chemical shift spectra are projected onto the $\omega_1/2\pi$ and $\omega_2/2\pi$ axes, respectively—these two features disappear, as shown in Figure 12. The experimental spectrum and simulation of Figure 12 agree extremely well, and yield r_{NH} = 104.9 ± 0.3 pm and an angle between the σ_{33} element of the tensor and the NH direction of 22° in agreement with single crystal studies. Differences in tensor orientation as small as 5° lead to sideband intensities that are perceptively different.

The salient feature of the DIPSHIFT experiment is that it can locate protons in polycrystalline or amorphous solids. This cannot be done accurately with X-rays, and instead requires a neutron diffractometer and large single crystals. Furthermore, the NMR experiment is relatively easy to perform, and can yield proton-rare spin bond distances with a precision of better than 0.5% and relative orientations of tensors to less than 5°. This has been studied in an experimental comparison of neutron and NMR data,[54] and the NMR bond distances are consistently about 3.5 pm longer than the diffraction results owing to different vibrational averaging.[55] Otherwise, there is an excellent correlation between the two techniques, indicating that DIPSHIFT-type experiments can be used to obtain structural data on polycrystalline samples.

There have been a number of other versions and applications of DIPSHIFT experiments. For example, the sequence shown in Figure 11(b) yields the same spectra as Figure 11(a), but with improved signal-to-noise, since there is only a delay of t_1 prior to sampling. However, the slices in the chemical shift dimension must be corrected with a shearing transformation.[56]

In addition, sequences with scaling and double windows[57,58] have been described, as have measurements of bond distances in DNA[59] and studies of dynamics of aromatic rings in polymers.[60]

5.3 Heteronuclear Correlation Spectra

Another 2D experiment that is extremely useful in solution NMR is heteronuclear correlation spectroscopy,[61] where, for example, the ^{13}C spectrum is used to increase dispersion of the ^{1}H spectrum. Since resolution in the ^{1}H spectra of solids is relatively poor, it could possibly be improved with such a technique. The basic sequence for correlation spectroscopy has a preparation period consisting of a 90° pulse on ^{1}H, and during the evolution, a multiple pulse train is applied to ^{1}H while decoupling ^{13}C; thus, only ^{1}H chemical shifts persist. This is followed by a mixing period and detection of ^{13}C in the presence of ^{1}H decoupling. During the mixing period, several schemes can be employed to transfer coherence between the spin reservoirs. Some possibilities considered by Roberts et al.[62] were normal cross polarization, single pulse transfers, and pulse transfers involving MREV-8, while Caravatti et al.[63] proposed an interesting windowless isotropic mixing sequence (WIM) for this purpose. The optimal mixing technique depends somewhat on the sample being studied. For molecules like adamantane and *cis*-polybutadiene, the pulse transfer schemes work well, whereas for rigid solids the simultaneous MREV-8 cycles or the WIM sequence are preferable because of their selectivity. Burum and Bielecki[64] have further improved these schemes,

focusing on the homonuclear and heteronuclear decoupling during the evolution period.

5.4 Dynamic Processes in Solids

Over the last decade, several groups have employed MAS in 2D exchange experiments for solids.[65–68] Typically, these experiments have involved studies of intramolecular proton transfer processes or the dynamics of motion of aromatic rings or polymers.[45] In the fast spinning limit ($\Delta\sigma/\nu_r < 1$), the solid state experiment is a simple modification of Jeener's classic three-pulse sequence,[39] except that the first $\frac{1}{2}\pi$ pulse in Jeener's sequence is typically replaced by cross polarization, and ^{1}H decoupling is applied during t_1 and t_2. In the opposite high-field limit, where the 1D spectrum exhibits sidebands ($\Delta\sigma/\nu_r > 1$), the 2D spectrum will be complicated by 'self-cross peaks' between every sideband in a sideband family, even if that resonance is not undergoing exchange. Veeman and co-workers[66] demonstrated that an exchange spectrum may be observed when $\Delta\sigma/\nu_r > 1$, provided that the mixing period is synchronized with the rotor period.

Clearly, isotropic evolution during t_1 (or t_2) will eliminate self-cross peaks, and the exchanging signals will not be dispersed over sidebands in either dimension. In early experiments, this was accomplished by working at low fields or by inserting chemical shift scaling into t_1, which focused the intensity into the centerband. Thus, proton transfer in tropolone[65] and slow aromatic ring flips occurring with a time constant of about 4 s in *p*-nitroanisole were examined.[67] More recently, a variety of slow motions in polymers have been studied,[45] as well as intermolecular exchange processes involving proton transfers in oxalic acid dihydrate between the COOHs and H_2Os of hydration.[69] 2D ^{1}H spectra (obtained from ^{2}H-labeled samples to eliminate ^{1}H dipole broadening) showing cross peaks due to this exchange process are shown in Figure 13. The exchange has a rate constant of about $55\,s^{-1}$ at 17 °C and $E_a \approx 35.6\,kJ\,mol^{-1}$. The 2D experiment is also extremely useful in elucidating complicated exchange networks in solids, as shown by spectra of the complex of oxalic acid and ammonium hydrogen oxalate hydrate.[69]

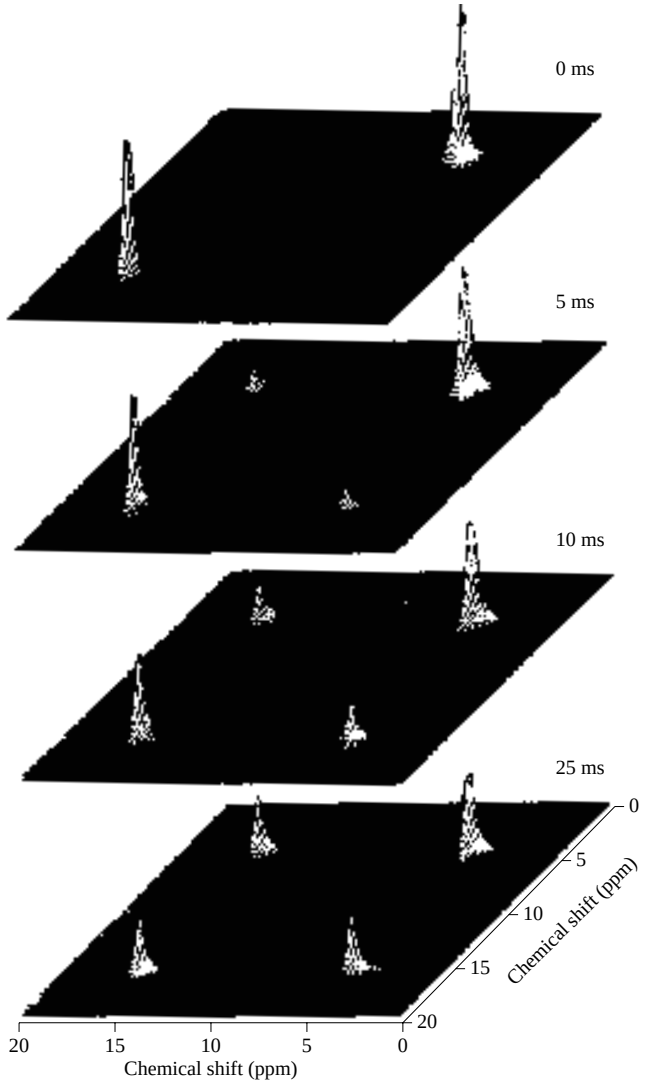

Figure 13 2D 400 MHz ^{1}H spectra of oxalic acid dihydrate (90% ^{2}H-labeled) obtained with the Jeener three-pulse (NOESY) sequences. Note the cross peaks due to proton transfer between the −COOH and H_2O moieties

6 RELATED ARTICLES

Average Hamiltonian Theory; CRAMPS; Double Rotation; Dynamic Angle Spinning; High Speed MAS of Half-Integer Quadrupolar Nuclei in Solids; Homonuclear Recoupling Schemes in MAS NMR; Magic Angle Spinning; Magic Angle Turning and Hopping; Probe Design and Construction; REDOR and TEDOR; Sideband Analysis in Magic Angle Spinning NMR of Solids.

7 REFERENCES

1. I. J. Lowe, *Phys. Rev. Lett.*, 1959, **2**, 285.
2. E. R. Andrew, A. Bradbury, and R. G. Eades, *Nature (London)*, 1958, **182**, 1659.
3. E. R. Andrew, L. F. Farnell, and T. D. Gledhill, *Phys. Rev. Lett.*, 1967, **19**, 6.
4. E. R. Andrew, M. Firth, A. Jasinski, and P. J. Randall, *Phys. Lett. A*, 1970, **31**, 446.
5. M. M. Maricq, and J. S. Waugh, *J. Chem. Phys.*, 1979, **70**, 3300.
6. J. S. Waugh, L. M. Huber, and U. Haeberlen, *Phys. Rev. Lett.*, 1968, **20**, 180.
7. P. Mansfield, *J. Phys. C*, 1971, **4**, 1444.
8. D. P. Burum and W.-K. Rhim, *J. Chem. Phys.*, 1979, **71**, 944.
9. D. P. Burum, M. Linder, and R. R. Ernst, *J. Magn. Reson.*, 1981, **44**, 173.
10. I. J. Lowe and R. E. Noreberg, *Phys. Rev.*, 1957, **107**, 46.
11. R. R. Ernst and W. Anderson, *Rev. Sci. Instrum.*, 1966, **37**, 93.
12. S. Hartmann and E. L. Hahn, *Phys. Rev.*, 1962, **128**, 2092.
13. L. Sarles and R. Cotts, *Phys. Rev.*, 1958, **111**, 853.
14. F. Bloch, *Phys. Rev.*, 1958, **111**, 841.
15. A. Pines, M. G. Gibby, and J. S. Waugh, *J. Chem. Phys.*, 1973, **59**, 569.
16. U. Haeberlen and J. S. Waugh, *Phys. Rev.*, 1968, **175**, 453.
17. J. Schaefer and E. O. Stejskal, *J. Am. Chem. Soc.*, 1976, **98**, 1031.

18. B. C. Gerstein, R. G. Pembleton, R. C. Wilson, and L. M. Ryan, *J. Chem. Phys.*, 1971, **66**, 361.
19. E. R. Andrew, W. S. Hinshaw, and R. S. Teffin, *J. Magn. Reson.*, 1974, **15**, 191.
20. E. Lippmaa, E. Alla, and T. Tuherm, in *Proceedings of 19th Ampère Congress, Heidelberg, 1976*, p. 113.
21. E. O. Stejskal and J. Schaefer, *J. Magn. Reson.*, 1977, **25**, 569.
22. M. M. Maricq and J. S. Waugh, *Chem. Phys. Lett.*, 1977, **47**, 327.
23. R. A. Haberkorn, *J. Am. Chem. Soc.*, 1978, **100**, 1296.
24. U. Haeberlen, *High Resolution NMR in Solids: Selective Averaging. Advances in Magnetic Resonance, Supplement No. 1*, Academic Press, New York, 1976.
25. A. Portis, *Phys. Rev.*, 1953, **91**, 1071.
26. M. H. Levitt, in *Progress in Nuclear Magnetic Resonance Spectroscopy*, ed. J. W. Emsley, J. Feeney, and L. H. Sutcliffe, Pergamon Press, Oxford, 1986, Vol. 18, p. 61.
27. J. S. Waugh, *J. Magn. Reson.*, 1982, **50**, 30.
28. E. T. Olejniczak, S. Vega, and R. G. Griffin, *J. Chem. Phys.*, 1984, **81**, 4804.
29. A. C. Kolbert and R. G. Griffin, *Chem. Phys. Lett.*, 1990, **166**, 87.
30. G. S. Harbison, S. O. Smith, J. A. Pardoen, J. M. L. Courtin, J. Lugtenburg, J. Herzfeld, R. A. Mathies, and R. G. Griffin, *Biochemistry*, 1985, **24**, 6955.
31. J. Hu, J. Herzfeld, and R. G. Griffin, *Proc. Natl. Acad. Sci. USA*, in press.
32. W. T. Dixon, *J. Chem. Phys.*, 1982, **77**, 1800.
33. J. Hong and G. S. Harbison, *J. Magn. Reson., Ser. A*, 1993, **105**, 128.
34. Z. Song, O. N. Antzutkin, X. Feng, and M. H. Levitt, *Solid State NMR*, 1993, **2**, 143.
35. D. P. Raleigh, E. T. Olejniejak, and R. G. Griffin, *J. Chem. Phys.*, 1988, **89**, 1333.
36. W. P. Aue, D. J. Ruben, and R. G. Griffin, *J. Magn. Reson.*, 1982, **46**, 354.
37. W. P. Aue, D. J. Ruben, and R. G. Griffin, *J. Chem. Phys.*, 1984, **80**, 8302.
38. D. P. Raleigh, E. T. Olejniczak, S. Vega, and R. G. Griffin, *J. Magn. Reson.*, 1986, **106**, 8302.
39. D. P. Raleigh, E. T. Olejniczak, S. Vega, and R. G. Griffin, *J. Magn. Reson.*, 1987, **72**, 238.
40. S. S. Lang, *J. Magn. Reson.*, 1993, **104**, 345.
41. O. N. Antzukin, Z. Song, X. Feng, and M. H. Levitt, *J. Chem. Phys.*, 1994, **100**, 130.
42. N. C. Nielsen, H. Bildsoe, and H. J. Jakobsen, *J. Magn. Reson.*, 1988, **80**, 149.
43. H. Geen and G. Bodenhausen, *J. Chem. Phys.*, 1992, **97**, 2928.
44. H. Geen and G. Bodenhausen, *J. Am. Chem. Soc.*, 1993, **115**, 1529.
45. A. Hagemeyer, Schmitt-Rhom, and H. W. Spiess, in *Advances in Magnetic Resonance*, ed. J. S. Waugh, Academic Press, New York, 1989, vol. 13, p. 85.
46. J. D. Ellett, Jr. and J. S. Waugh, *J. Chem. Phys.*, 1969, **51**, 2851.
47. W. P. Aue and R. R. Ernst, *J. Magn. Reson.*, 1978, **31**, 533.
48. W. P. Aue, D. P. Burum, and R. R. Ernst, *J. Magn. Reson.*, 1980, **38**, 375.
49. D. P. Raleigh, E. T. Olejniejak, and R. G. Griffin, *J. Magn. Res.*, 1991, **93**, 472.
50. S. Vega, E. T. Olejniczak, and R. G. Griffin, *J. Chem. Phys.*, 1984, **80**, 4832.
51. A. Bax, N. Szeverenyi, and G. E. Maciel, *J. Magn. Reson.*, 1983, **51**, 400.
52. Y. Yarmin-Agaev, P. N. Tutunjian, and J. S. Waugh, *J. Magn. Reson.*, 1982, **47**, 51.
53. M. G. Munowitz and R. G. Griffin, *J. Chem. Phys.*, 1982, **76**, 2848.
54. J. E. Roberts, G. S. Harbison, M. G. Munowitz, J. Herzfeld, and R. G. Griffin, *J. Am. Chem. Soc.*, 1987, **109**, 4163.
55. E. R. Henry and A. Szabo, *J. Chem. Phys.*, 1985, **82**, 4753.
56. A. C. Kolbert, M. H. Levitt, and R. G. Griffin, *J. Magn. Reson.*, 1989, **85**, 42.
57. M. G. Munowitz, W. P. Aue, and R. G. Griffin, *J. Chem. Phys.*, 1982, **77**, 1686.
58. M. G. Munowitz and R. G. Griffin, *J. Chem. Phys.*, 1983, **78**, 613.
59. J. A. Diverdi and S. J. Opella, *J. Am. Chem. Soc.*, 1982, **104**, 1761.
60. J. Schaefer, E. O. Stejskal, R. A. McKay, and W. T. Dixon, *Macromolecules*, 1986, **17**, 1479.
61. G. Bodenhausen and R. Freeman, *J. Magn. Reson.*, 1977, **28**, 471.
62. J. E. Roberts, S. Vega, and R. G. Griffin *J. Am. Chem. Soc.*, 1984, **106**, 2506.
63. P. Caravatti, L. Braunschweiler, and R. R. Ernst, *Chem. Phys. Lett.*, 1983, **100**, 305.
64. D. P. Burum and A. Bielecki, *J. Magn. Reson.*, 1991, **95**, 184.
65. N. M. Szeveranyi, M. J. Sullivan, and G. E. Maciel, *J. Magn. Reson.*, 1982, **47**, 462.
66. A. F. De Jong, A. P. M. Kentgens, and W. S. Veeman, *Chem. Phys. Lett.*, 1984, **109**, 337.
67. G. S. Harbison, D. P. Raleigh, J. Herzfeld, and R. G. Griffin, *J. Magn. Reson.*, 1985, **64**, 284.
68. J. Jeener, B. H. Meier, P. Bachmann, and R. R. Ernst, *J. Chem. Phys.*, 1979, **71**, 4546.
69. L. Zheng, K. W. Fishbein, R. G. Griffin, and J. Herzfeld, *J. Am. Chem. Soc.*, 1993, **115**, 6245.

Biographical Sketch

Robert G. Griffin. *b* 1942. B.S., 1964, University of Arkansas, USA, Ph.D., 1969, Washington University, St. Louis. Postdoctoral Fellow, Department of Chemistry, MIT 1969–72. Staff member, Francis Bitter National Magnet Laboratory, MIT, 1972–1989. Professor of Chemistry, MIT, 1989–present. Director, Francis Bitter National Magnet Laboratory, 1992 – present. Approx. 190 publications. Research interest include development of new methods for performing high-resolution NMR experiments in solids, high-frequency DNP and EPR, and applications of these techniques to problems in biological, chemical, and physical systems.

Satellite Transition NMR Spectroscopy of Half-Integer Quadrupolar Nuclei under Magic-Angle Spinning

Zhehong Gan

Center of Interdisciplinary Magnetic Resonance (CIMAR), National High Magnetic Field Laboratory (NHMFL), Tallahassee, FL, USA

1 Introduction 1
2 Quadrupolar Effects 2
3 1D Satellite Transition Magic-Angle Spinning Spectra 3
4 2D Satellite Transition Magic-Angle Spinning Experiment 6
5 Conclusions 9
6 References 9

1 INTRODUCTION

Most of the magnetically active nuclei in the Periodic Table possess spins with $S > 1/2$ that are known as quadrupolar nuclei because of the quadrupolar moment of nuclei interacting with surrounding electric field gradient.[1] Quadrupolar interactions, typically in the order of MHz, often dominate over other spin interactions such as dipolar coupling and chemical shift anisotropy and make NMR spectra of powder samples very broad. When the quadrupolar splitting is small compared to the Zeeman energy differences, perturbation theory may be used to express the quadrupolar coupling Hamiltonian to first order.[1]

$$H_Q^{(1)} = \frac{c_q}{4S(2S-1)}(3S_z^2 - S^2)\left(\frac{3\cos^2\beta - 1}{2} - \frac{\eta}{2}\sin^2\beta\cos 2\alpha\right) \quad (1)$$

The S_z^2 dependence immediately leads to a vanished first-order effect to the single-quantum $m_z = -1/2 \leftrightarrow 1/2$ transition of half-integer quadrupolar nuclei. Absence of a first-order effect reduces the central transition line width to the order of kHz. Magic-angle sample spinning narrows the central transition line further by suppressing chemical shift anisotropy and dipolar interactions. The improvement on spectral resolution has made NMR spectroscopy of half-integer quadrupolar nuclei a powerful tool for structural characterization of a variety of solid materials despite of the large quadrupolar interactions.[2–5]

There are multiple transitions among the $2S + 1$ energy-level manifolds of spins with $S > 1/2$. This article focuses on pairs of single-quantum transitions on two sides of the central transition known as satellite transitions. Satellite transitions are affected by quadrupolar interaction to first order and their static NMR spectra are usually very broad. It is not surprising that there are fewer NMR studies on satellite transitions than on central transitions. However, the advent of magic-angle spinning technology has made the acquisition of satellite transition spectra easier than ever.[6–9] Fast sample spinning can average the first-order quadrupolar effect to zero with spinning axis precisely at the magic-angle, yielding sharp resonance lines and spinning sidebands.[7–9] Perhaps the best-known satellite transition spectrum is that of KBr. The small quadrupolar coupling from lattice distortion of the nominally cubic KBr ($\sim$100 kHz) makes the ^{79}Br satellite transitions easily detectable. The sensitivity of satellite transition spinning sidebands on magic-angle setting and the convenience of the Larmor frequency very close to ^{13}C have made KBr an ideal sample for magic-angle calibration.[10]

For large quadrupolar couplings, spinning sidebands in MAS satellite transition spectra are broadened by the second-order quadrupolar effect similar to central transition peaks.[7,9] Averaging the second-order quadrupolar effect has been a long-standing issue in high-resolution NMR of half-integer quadrupolar nuclei. Unlike dipolar coupling and chemical shift anisotropy, the second-order effect contains high-rank anisotropic terms that cannot be averaged by MAS.[4,5] Residual second-order effects broaden resonance lines and may prevent resolution among nonequivalent sites. Observing satellite transitions can be advantageous in better spectral resolution over the commonly observed central transition. Samoson has discovered that the second-order effect to $\pm 3/2 \leftrightarrow \pm 1/2$ satellite transitions is 24/7 times smaller than the central transition for $S = 5/2$ spins and the relative position between satellite and central transition peaks can be used to separate the contribution from the isotropic second-order quadrupolar shift for chemical shift measurements.[6] Results at high magnetic fields and with fast spinning speed have clearly demonstrated these advantages.[9] Jakobsen et al. have studied the intensities of satellite transition spinning sidebands for measuring quadrupolar coupling parameters in analogy to the analysis of chemical shift spinning sidebands by Maricq and Waugh and by Herzfeld and Berger.[11,12] Satellite transitions are directly affected by the first-order quadrupolar interactions and the spinning sideband analysis is mostly suitable for small quadrupolar couplings with powder patterns up to 1 MHz wide.[7] Satellite transitions also play an important role in spin dynamics of central transitions such as in nutation and spin-lock experiments. The central transition matrix element of spin operator S_x equals to $(S + 1/2)$ therefore the nutation frequency of the central transition is $(S + 1/2)$ times faster than a $S = 1/2$ spin with the assumption of an isolated two-level system for the central transition. The presence of satellite transitions causes the central transition coherence to nutate at multiple frequencies that can affect the excitation and the quantitative nature of central transition spectra.[13] Spin-lock is important in cross-polarization and coherence transfer and can be easily achieved by a continuous-wave RF field for $S = 1/2$ spins. For half-integer quadrupolar nuclei, however, the presence of satellite transitions makes spin-lock of central transitions a non-trivial matter under magic-angle spinning.

The central transition coherence can leak through satellite transitions during repeated zero-crossings induced by the sample rotation.[14]

The second-order quadrupolar effect remains even under MAS and broadens resonance lines. Although high magnetic fields can reduce the second-order effect, ideally it is the best to average all anisotropic terms for so-called isotropic NMR spectra. This goal was first achieved by double rotation (DOR). The first rotation at the magic-angle averages the $l = 2$ anisotropic terms and the second rotation inside the MAS rotor at an angle that $P_4(\cos 30.56^\circ) = 0$ averages the residual high-rank $l = 4$ anisotropic terms.[15] A two-dimensional experiment with flipping spinning axis, namely dynamic angle spinning (DAS), was also proposed to refocus the signal decay caused by the anisotropic second-order effect.[16] Both DOR and DAS techniques lead to isotropic NMR spectra of half-integer quadrupolar nuclei; nevertheless the implementation of non-fixed axes sample spinning is technically difficult.[17,18] The invention of multiple-quantum magic-angle spinning (MQMAS) by Frydman et al. opened a new avenue toward isotropic NMR spectra.[19,20] Correlation between $-m_q/2 \leftrightarrow m_q/2$ multiple-quantum and central transitions refocuses the signal decay caused by the second-order effect and results in isotropic spectra. Transition-correlated experiments can be performed with commercially available MAS probes and it has gained a widespread use. However, low sensitivities and the poor quantitative nature of the MQ experiment remain as the major obstacles to its applications and a number of excitation and conversion schemes have been developed to improve the efficiencies of manipulating MQ coherence.[21–32] Recently, a different approach was proposed to dramatically improve the efficiency of transition-correlated experiments.[33] The satellite transition magic-angle spinning (STMAS) experiment correlates single-quantum satellite transitions that can be directly excited and efficiently converted to central transitions.[34] The high efficiencies of the satellite transition experiment have been demonstrated. It has also been shown that accurate magic-angle setting and stable sample spinning are required to average out the first-order quadrupolar interactions to satellite transitions for generating isotropic NMR spectra of half-integer quadrupolar nuclei.[34]

The scope of this article focuses on recent developments on satellite transition NMR spectroscopy particularly the STMAS experiment. The first half presents the theory of satellite transition NMR. The second-order quadrupolar effect to satellite transitions is expanded in rotation matrix elements. The expansion and the comparison with central transitions reveal important features of satellite transition NMR spectra. These features are demonstrated experimentally with model samples of various spins. The second half describes the STMAS experiment. The principle of the experiment to obtain isotropic NMR spectra is explained and the excitation and conversion of satellite transitions are studied. The experiment is demonstrated with various pulse sequences and model samples and the strict requirements on magic-angle setting and sample spinning stability are discussed.

2 QUADRUPOLAR EFFECTS

When the Zeeman splitting is sufficiently large compared to the effect of electric field gradients, the magnetization quantum number $m_z = S, S-1, \ldots, -S$ may be used to describe

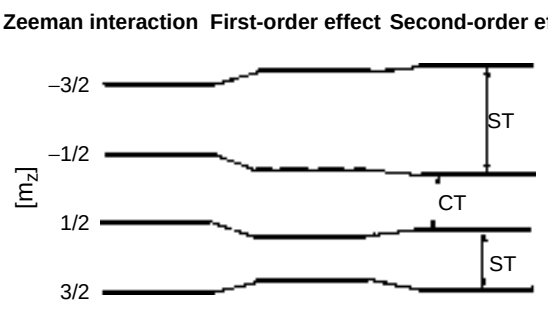

Figure 1 Energy level diagram of a $S = 3/2$ spin

the system to the first order. The energy levels of a nuclear spin S are split into a $2S + 1$ manifold separated by Larmor frequency. The first-order quadrupolar interaction shifts the energy levels by $\omega_q\ [3m_z^2 - S(S+1)]$ and has no effect on $-m_z \leftrightarrow m_z$ transition (see Figure 1). For half-integer spins, the $-1/2 \leftrightarrow 1/2$ central transition is a single-quantum transition that can be observed directly. For integer spins, all single-quantum transitions are affected by the first-order quadrupolar interaction and double-quantum transitions may have a vanished first-order effect. High-resolution double-quantum spectroscopy has been explored with indirect detection for ^{2}H nuclei and with overtone detection for ^{14}N nuclei.[35–37] The topics on integer-spins can be found in these references and will not be discussed further here. A number of review articles are also recommended for general aspect of central transition NMR and early works on satellite transition spectroscopy.[38–41]

The second-order quadrupolar effect is derived using Average Hamiltonian theory.[42] The full quadrupolar Hamiltonian can be expressed in terms of irreducible second-rank spin operators

$$H_Q = \omega_q \sum_{m=-2}^{2} (-1)^m Q_{2,-m} T_{2,m}, \quad \omega_q = \frac{2\pi e^2 q_{zz} Q}{2S(2S-1)h} \tag{2}$$

$$T_{2,0} = \frac{(3S_z^2 - S^2)}{\sqrt{6}}$$

$$T_{2,\pm 1} = \frac{\mp(S_\pm S_z + S_z S_\pm)}{2} \tag{3}$$

$$T_{2,\pm 2} = \frac{S_\pm^2}{2}, \quad S_\pm = S_x \pm i S_y$$

The quadrupolar coupling tensor components $Q_{2,m}$ can be obtained from the components in the principal axis system (PAS) frame through a rotation to the laboratory frame (α, β, γ)

$$Q_{2,m} = \sum_{m'=-2}^{2} \rho_{2,m'} D^2_{m',m}(\alpha, \beta, \gamma) \tag{4}$$

$$\rho_{2,0} = \sqrt{\frac{3}{2}}, \quad \rho_{2,\pm 1} = 0, \quad \rho_{2,\pm 2} = -\frac{\eta}{2} \tag{5}$$

$\eta = (q_{yy} - q_{xx})/q_{zz}$ is the asymmetry factor of the EFG tensor. The $T_{2,0}$ term in the quadrupolar Hamiltonian commutes with Zeeman interaction and affects the transitions in the first-order.

The second-order effect can be obtained by applying Average Hamiltonian theory in the NMR rotating frame:[43]

$$H_Q^{(2)} = -\left\{ Q_{2,-1}Q_{2,1}[T_{2,-1}, T_{2,1}] + \frac{Q_{2,-2}Q_{2,2}[T_{2,-2}, T_{2,2}]}{2} \right\} \frac{\omega_q^2}{\omega_0} \quad (6)$$

where $\omega_0 = -\gamma B_0$ is Larmor frequency. The commutators in the second-order Hamiltonian can be derived explicitly

$$[T_{2,-1}, T_{2,1}] = -\left(4S^2 - 8S_z^2 - 1\right) S_z / 2$$
$$[T_{2,-2}, T_{2,2}] = -\left(2S^2 - 2S_z^2 - 1\right) S_z \quad (7)$$

and the product of spatial parameters

$$Q_{2,-m}Q_{2,m} = \sum_{m',m''=-2}^{2} \rho_{2,m'}\rho_{2,m''} D^2_{m',m}(\alpha,\beta,\gamma) \times D^2_{m'',-m}(\alpha,\beta,\gamma) \quad (8)$$

can be expanded using the Clebsch-Gordon series[44,45]

$$D^2_{m',m} D^2_{m'',-m} = \sum_{l=0}^{4} \sum_{m'+m''=-l}^{l} c(22l, m'm'') \times c(22l, m-m) D^l_{m'+m'',0} \quad (9)$$

Equations (6)–(9) lead to the second-order quadrupolar Hamiltonian expanded in rotation matrix elements

$$H_Q^{(2)} = \frac{\omega_q^2}{\omega_0} \sum_{l=0,2,4} C_l(S, S_z) \sum_{m=-l}^{l} a^{(2)}_{l,m} D^l_{m,0}(\alpha,\beta,\gamma) \quad (10)$$

$$C_l(S, S_z) = c(22l; 1-1)\left(4S^2 - 8S_z^2 - 1\right) S_z + c(22l; 2-2)\left(2S^2 - 2S_z^2 - 1\right) S_z \quad (11)$$

$$a^{(2)}_{l,m} = \sum_{m'+m''=m} c(22l; m'm'')\rho_{2,m'}\rho_{2,m''} / 2 \quad (12)$$

The expansion coefficients $a^{(2)}_{l,m}$ vanish for $l = 1$ and 3 because of the relation $c(l_1l_2l; m_1m_2) = (-1)^{l_1+l_2+l} c(l_2l_1l; m_2m_1)$ of Clebsch-Gordon coefficients.[43,44] Thus, the second-order quadrupolar Hamiltonian contains an $l = 0$ isotropic term, the $l = 2$ terms and the high-rank $l = 4$ anisotropic terms.

The shift to transition frequencies by the second-order effect can be calculated from the expectation values of the $C_l(S, S_z)$ in $H_Q^{(2)}$. For central transitions $m_z = -1/2 \leftrightarrow 1/2$

$$\omega_{CT} = \sum_{l=0,2,4} C_l(\alpha,\beta,\gamma)$$

$$C_l = \frac{\omega_q^2[S(S+1) - 3/4]}{\omega_0} \sum_{m=-l}^{l} c_{l,m} D^l_{m,0}(\alpha,\beta,\gamma) \quad (13)$$

$$c_{l,m} = -[2c(22l; 1-1) + c(22l; 2-2)] \times \sum_{m'+m''=m} c(22l; m'm'')\rho_{2,m'}\rho_{2,m''} \quad (14)$$

Table 1 Expansion Coefficients c_{lm} of the Second-Order Quadrupolar Effect to Central Transitions

	$m = 0$	$m = \pm 2$	$m = \pm 4$
$l = 0$	$\frac{3}{10}\left(1 + \frac{\eta^2}{3}\right)$		
$l = 2$	$\frac{6}{7}\left(1 - \frac{\eta^2}{3}\right)$	$\frac{2\sqrt{6}}{7}\eta$	
$l = 4$	$-\frac{81}{70}\left(1 + \frac{\eta^2}{18}\right)$	$\frac{27\sqrt{10}}{140}\eta$	$-\frac{9\sqrt{70}}{280}\eta^2$

The explicit expressions of $c_{l,m}$ are listed in Table 1.

The second-order quadrupolar Hamiltonian in equation (10) implies that the second-order effect varies among transitions only through the expectation values of $C_l(S, S_z)$. For $m_S - 1/2 \leftrightarrow m_S + 1/2$ satellite transition, the frequency shift from the second-order effect can be expressed in terms of the expansion coefficients of the central transitions and corresponding scaling factors

$$\omega_{ST} = \sum_{l=0,2,4} R^l_{S,m_S} C_l(\alpha,\beta,\gamma) \quad (15)$$

$$R^l_{S,m_S} = 1 - \frac{12m_s^2[4c(22l; 1-1) + c(22l; 2-2)]}{[4S(S+1) - 3] \cdot [2c(22l; 1-1) + c(22l; 2-2)]} \quad (16)$$

The explicit expressions of the scaling factors for $l = 0$, 2 and 4 are

$$R^0_{S,m_S} = 1 - \frac{36m_s^2}{4S(S+1) - 3}, \quad l = 0 \quad (17)$$
$$R^2_{S,m_S} = 1 - \frac{18m_s^2}{4S(S+1) - 3}, \quad l = 2$$
$$R^4_{S,m_S} = 1 - \frac{68m_s^2}{3[4S(S+1) - 3]}, \quad l = 4$$

Table 2 lists the scaling factors for all satellite transitions with spins S up to 9/2.

3 1D SATELLITE TRANSITION MAGIC-ANGLE SPINNING SPECTRA

The previous section derived the first and second-order quadrupolar effect to central and satellite transitions. For

Table 2 Scaling Factors of Expansion Coefficients between Satellite and Central Transitions

		$l = 0$	$l = 2$	$l = 4$
$S = 3/2$,	$m_S = \pm 1$	−2	−1/2	−8/9
$S = 5/2$,	$m_S = \pm 1$	−1/8	7/16	7/24
	$m_S = \pm 2$	−7/2	−5/4	−11/6
$S = 7/2$,	$m_S = \pm 1$	2/5	7/10	28/45
	$m_S = \pm 2$	−7/5	−1/5	−23/45
	$m_S = \pm 3$	−22/5	−17/10	−12/5
$S = 9/2$,	$m_S = \pm 1$	5/8	13/16	55/72
	$m_S = \pm 2$	−1/2	1/4	1/18
	$m_S = \pm 3$	−19/8	−11/16	−9/8
	$m_S = \pm 4$	−5	−2	−50/18

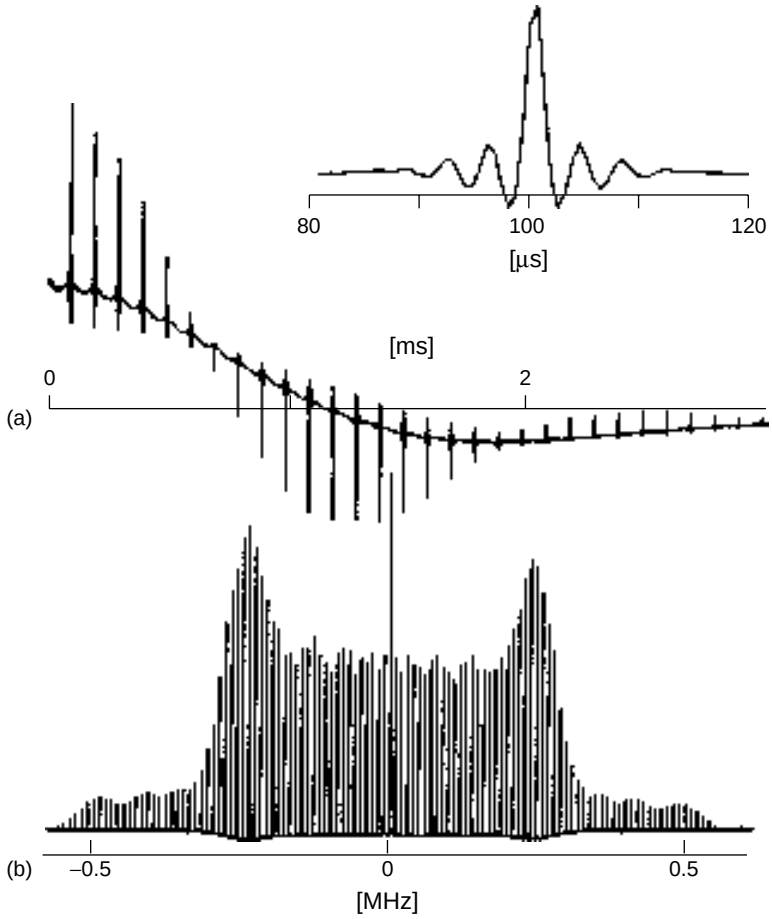

Figure 2 ^{23}Na free-induction-decay (a) and MAS spectrum (b) of $NaNO_2$ with 10 kHz spinning frequency. The insert shows the expansion to one of the rotational echoes

samples spinning at the magic-angle, the quadrupolar effects are modulated by the sample rotation. The expansion of quadrupolar effects in rotation matrix elements is advantageous because the rotation from the PAS frame to laboratory frame can be expressed as

$$D^l_{m',m}(\alpha,\beta,\gamma) = \sum_{m''=-l}^{l} D^l_{m'',m}(-\omega_r t, -\theta_M, 0) D^l_{m',m''}(\alpha_r,\beta_r,\gamma_r) = \sum_{m''=-l}^{l} d^l_{m'',m}(\theta_M) e^{im''\omega_r t} D^l_{m',m''}(\alpha_r,\beta_r,\gamma_r) \quad (18)$$

where $(\alpha_r, \beta_r, \gamma_r)$ is the rotation from the PAS frame to the rotor frame and $(-\omega_r t, -\theta_M, 0)$ describes the sample rotation with frequency ω_r and angle θ_M. Under fast sample spinning, various expansion terms of quadrupolar effects are scaled accordingly by $d^l_{0,0}(\theta_M) = P_l(\cos\theta_M)$. With the spinning axis at the magic-angle, the first-order quadrupolar effect and the $l = 2$ terms of the second-order effect are averaged. The high-rank $l = 4$ terms, however, still remain under MAS and the anisotropic second-order effect, scaled by $P_4(\cos\theta_M)$, broadens both central and satellite lines.

With finite spinning frequencies, modulation of the large first-order quadrupolar interaction yields rotational echoes in the time-domain signals and spinning sidebands in the frequency-domain spectra. Figure 2 shows a train of rotational echoes and an array of spinning sidebands as a result of averaging the first-order quadrupolar effect with spinning frequencies much lower than the quadrupolar coupling constant. The complete average of the large first-order effect occurs very briefly at the exact rotor cycles. The matching of evolution time to rotor cycles and the setting of magic-angle are the most important factors in averaging the first-order quadrupolar interactions.

The intensities of spinning sidebands show a line shape very similar to the static powder pattern. The first-order quadrupolar effect shifts satellite transition frequencies and splits the $\pm m_S - 1/2 \leftrightarrow \pm m_S + 1/2$ pair as

$$\Delta\nu^{(1)}_{m_S} = \frac{3 m_S c_q}{S(2S-1)}\left(\frac{3\cos^2\beta - 1}{2} - \frac{\eta}{2}\sin^2\beta\cos 2\alpha\right) \quad (19)$$

The maximum splitting occurs at $\beta = 0$ and leads to the full width of the powder pattern $3c_q/S(2S-1)$ for the inner pair of satellite transitions. The width increases linearly with $|m_S|$ for outer pairs of satellite transitions.

The second-order quadrupolar effect is responsible for the line shape of both central and satellite peaks under MAS. Among the expansion terms, the isotropic term $l = 0$ merely shifts the resonance frequency from the isotropic chemical shift and causes no additional line broadening. For the central

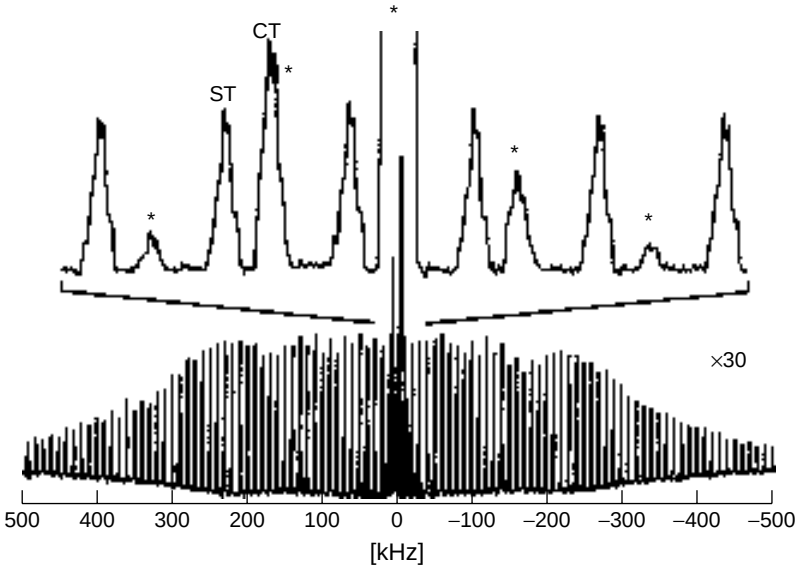

Figure 3 Satellite transition spectra of Na_2SO_4 under 10 kHz MAS

transition, the isotropic second-order quadrupolar shift is upfield (note the negative sign in $\omega_0 = -\gamma B_0$)

$$\omega_{CT}^0 = \frac{3[S(S+1) - 3/4]\omega_q^2}{10\omega_0}\left(1 + \frac{\eta^2}{3}\right) \qquad (20)$$

The terms $l = 2$ are averaged by MAS and the terms $l = 4$ become the only remaining anisotropic terms that broaden resonance lines. Because all transitions are shifted by the same anisotropic terms, $C_4(\alpha, \beta, \gamma)$, different only by the scaling factor R^4_{S,m_S}, the line shape for satellite transitions should be the same as the central transition except only the relative width determined by the scaling factors R^4_{S,m_S}. A negative R^4_{S,m_S} represents a reversed line shape.

The scaling factors R^4_{S,m_S} with explicit values listed in Table 2 are important when comparing spectral features between satellite and central transitions. Figure 3 shows the satellite transition spectra of Na_2SO_4 with spinning axis carefully calibrated to the magic-angle. The line shape of the satellite transition spinning sidebands is close to a mirror image of the central transition peak, in agreement with the scaling factor $R^4_{S,\pm1} = -8/9$ for the $S = 3/2$ spin.

Figure 4 displays the ^{27}Al satellite and central transition spectra of $9Al_2O_3 + 2B_2O_3$, a model system for spins $S = 5/2$. The sample has four non-equivalent ^{27}Al sites with quadrupolar coupling constants ranging from 6–9 MHz and the central transition lines are partially overlapped due to the line broadening by the second-order quadrupolar effects. The comparison between satellite and central transition spectra shows much narrower line width for satellite transition lines because the scaling factor of inner satellite transitions over the central transition is less than 30% ($R^4_{5/2,\pm1} = 7/24$). The outer satellite transitions in comparison are nearly twice as broad as the central transitions, $R^4_{5/2,\pm2} = -11/6$. Most of the outer satellite transition intensities are immersed in the baseline because of the broad line width and the poor excitation of outer satellite transitions. Only the relatively narrow Al_{VI} site shows a visible outer satellite transition peak. Checking

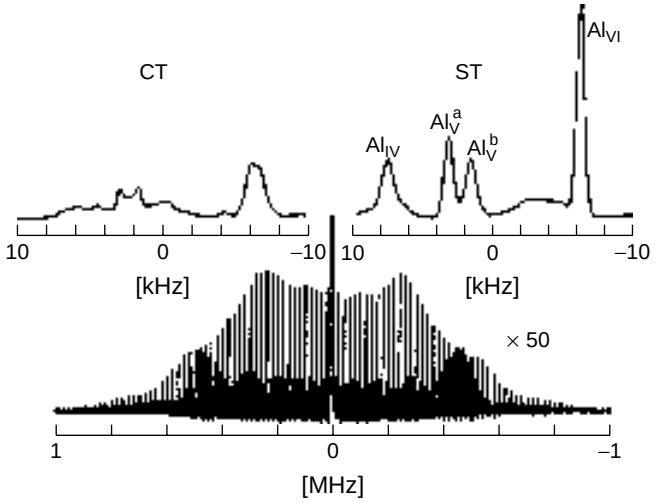

Figure 4 ^{27}Al MAS (20 kHz) spectrum of $9Al_2O_3 + 2B_2O_3$. The two inserts show the central (CT) and the satellite (ST) transition spectra within 20 kHz spectral window

through Table 2, it is interesting to find that the $\pm5/2 \leftrightarrow \pm3/2$ satellite transitions of $S = 9/2$ spins have a second-order effect 18 times smaller than the central transition that could provide much higher resolution.

The isotropic $l = 0$ term contributes no additional line broadening; however, it can change the relative peak position and affect the resolution among nonequivalent sites. In amorphous or disordered systems, the isotropic terms can become a factor in the line width. Distribution on quadrupolar couplings leads to a spread of the isotropic second-order quadrupolar shift to broaden spectral lines. For $S = 5/2$ spins, the isotropic second-order shift to the inner pair ($m_S = \pm1$) satellite transitions is 8 times smaller than the central transition and is expected to causes less line broadening by the mentioned mechanism in disordered systems.[6] In any case, satellite transition spectra compliment central transition spectra to find the best spectral resolution.

4 2D SATELLITE TRANSITION MAGIC-ANGLE SPINNING EXPERIMENT

The two-dimensional satellite transition MAS experiment correlates satellite (ω_1) with central (ω_2) transitions under magic-angle spinning.[33] The timing of the evolution period t_1 is synchronized with the rotor cycles such that the first-order quadrupolar effects to the satellite transitions are averaged by sample spinning precisely at the magic-angle. The resonance frequencies along the two dimensions are contributions from the isotropic chemical shift, the isotropic and the anisotropic $l = 4$ second-order effects

$$\omega_1 = \omega_\delta + R^0_{S,m_S}\,\omega^0_{CT} + R^4_{S,m_S}\,C_4(\Omega_r)\,P_4(\cos\theta_M)$$
$$\omega_2 = \omega_\delta + \omega^0_{CT} + C_4(\Omega_r)\,P_4(\cos\theta_M) \qquad (21)$$

For powder samples, superposition over Ω_r yields a ridge-shaped peak in the 2D STMAS spectra. The peak centers at $(\omega_\delta + \omega^0_{CT} R^0_{S,m_S}, \omega_\delta + \omega^0_{CT})$ and tilts at slope R^4_{S,m_S}. A shear of the 2D spectrum along ω_1 can make the peak parallel with the ω_2 axis and a projection to the ω_1 axis yields an isotropic peak at the position

$$\omega_{iso} = (1 - R^4_{S,m_S})\omega_\delta + (R^0_{S,m_S} - R^4_{S,m_S})\omega^0_{CT} \qquad (22)$$

In the time-domain, the signal from the correlation between satellite and central transitions can be written as

$$S(t_1, t_2) = \sum_{p_1,p_2=\pm1}\sum_{\Omega_r} E_{p_1}(\Omega_r)C_{p_1,p_2}(\Omega_r) \times e^{ip_1[\omega_\delta + R^0_{S,m_S}\omega^0_{CT} + R^4_{S,m_S}C_4(\Omega_r)]t_1} e^{ip_2[\omega_\delta + \omega^0_{CT} + C_4(\Omega_r)]t_2} \qquad (23)$$

where the factors $E_{p_1}(\Omega_r)$ and $C_{p_1,p_2}(\Omega_r)$ represent the excitation and coherence transfer of satellite transitions; p_1, $p_2 = \pm1$ are coherence orders of the single-quantum satellite and central transitions during the t_1 and t_2 periods, respectively. Superposition over Ω_r causes the signal to decay rapidly except at $t_2 = -(p_2/p_1)R^4_{S,m_S}t_1$ where coherence transfer echoes are formed. For coherence orders with $R^4_{S,m_S}p_2/p_1 > 0$, the echoes are outside the $t_1, t_2 > 0$ quadrant of the 2D time coordinate and are known as antiechoes.[45] For coherence orders with $R^4_{S,m_S}p_2/p_1 < 0$, coherence transfer echoes occur inside the $t_1, t_2 > 0$ quadrant and can be acquired directly. The signal intensities along the echo ridge $t_2 = -(p_2/p_1)R^4_{S,m_S}t_1$ oscillate at the frequency $\omega_{iso} = (1 - R^4_{S,m_S})\omega_\delta + (R^0_{S,m_S} - R^4_{S,m_S})\omega^0_{CT}$, the same expression as equation (22), and yield an isotropic NMR spectrum with a Fourier transformation.

Excitation and conversion of satellite transition coherence are critical to the efficiency of the 2D STMAS experiment. Satellite transitions are single-quantum transitions that can be excited directly. Short and strong pulses can cover the large frequency offsets caused by the first-order quadrupolar effect on the satellite transition. In Figure 4, the satellite and central transition spectra are plotted on the same intensity scale and the relative intensities indicate the efficiency of satellite transition excitation. Although individual spinning sidebands that span more than 1 MHz wide are low, the total spectral intensities from all spinning sidebands are actually higher than the CT peaks. The ratio between ST and CT intensities approaches the value $Tr(S_x^{ST}S_x) : Tr(S_x^{CT}S_x) = 16 : 9$ for the $S = 5/2$ spin assuming a uniformly excited coherence $\sigma = S_x$.

A single mixing pulse can transfer satellite transition coherence directly to central transitions. Figure 5 displays simulations and experimental results of the coherence transfer. The simulations show that the transfer is in-phase, i.e., $S_x^{(ST)} \rightarrow S_x^{(CT)}$ and $S_y^{(ST)} \rightarrow S_y^{(CT)}$ regardless of the pulse phase. Out-phase pulses, e.g., S_y pulse for $S_x^{(ST)} \rightarrow S_x^{(CT)}$ transfer, are more efficient than in-phase pulses. Simulations also show that a 180° phase shift to RF pulses has no effect on the single-pulse coherence transfer. These results suggest that a phase cycle $+x, +y, -x, -y$ to the mixing pulse balances the difference on transfer amplitude between in-phase and out-phase pulses and consequently selects the $p = -1 \rightarrow -1$ coherence transfer pathway. This pathway generates coherence transfer echoes for negative $R^4_{S,m}$ such as $S = 3/2$ spins ($R^4_{3/2,\pm1} = -8/9$) but yields coherence transfer antiechoes for spins with positive $R^4_{S,m}$. A selective π-pulse to the central transition prior to signal acquisition can convert the coherence transfer antiechoes to echoes for isotropic spectra of $S = 5/2$ spins and other spins with negative $R^4_{S,m}$. The simulations for $S = 5/2$ spins show much higher transfer amplitudes from inner satellite transitions than from outer satellite transitions. This difference can be interpreted qualitatively as the follows. Mixing of spin states by a RF pulse can be described as $|i\rangle \rightarrow \sum_j p_{ij}|j\rangle$ with $p_{ii} \rightarrow 1$ and $p_{i\neq j} \rightarrow \varepsilon$ for short pulses. For satellite transitions that share energy levels with central transition, e.g., $|1/2\rangle\langle 3/2|$, the coherence transfer $|1/2\rangle\langle 3/2| \rightarrow |1/2\rangle\langle -1/2|$ is in the order of ε. The transfer becomes second-order ε^2 for any transitions not sharing energy levels with the targeted transition. In Figure 5, the experimental optimization illustrates the high efficiency of the single-pulse mixing of inner satellite transition coherence. The optimized peak height from coherence transfer is close to 50% of peak height in the conventional central transition spectrum acquired under the same experimental conditions.

A pair of mixing-pulses sandwiched with a z-filter can also be used for the coherence transfer. The first mixing-pulse transfers satellite transition coherence to the polarization of central transitions. The second mixing-pulse flips the stored polarization for detection after the z-filter. The pulse sequence with two-pulse mixing is identical to the sequence used for 2D exchange experiments and selects both $p_1 = \pm1$ coherence-orders during the evolution period. Half of the transferred coherence contributes to the coherence transfer echoes and the other half goes to the anti-echoes. The two-pulse mixing has an advantage of pure-absorptive line shape irrespective to the signs of $R^4_{S,m}$.[33,34]

Figure 6 shows the 2D STMAS spectra of a mixed sample of Na_2SO_4 and $Na_2C_2O_4$. The correlation of satellite and central transitions yields ridge-shaped peaks that clearly resolve the overlap between two components. The peaks tilt at the slope $R^4_{3/2,\pm1} = -8/9$. A shear of the 2D spectrum corrects the tilt and results in an *isotropic* versus *anisotropic* spectrum where the projection to the isotropic-dimension shows two resolved isotropic peaks. The pulse sequence with two-pulse mixing is the same as the sequence used for 2D exchange experiments and the peak along the diagonal resulting from the central transition to central transition (CT-CT) peak is not affected by the frequency offset of satellite transitions. Thus, the relative intensities between diagonal and cross peaks

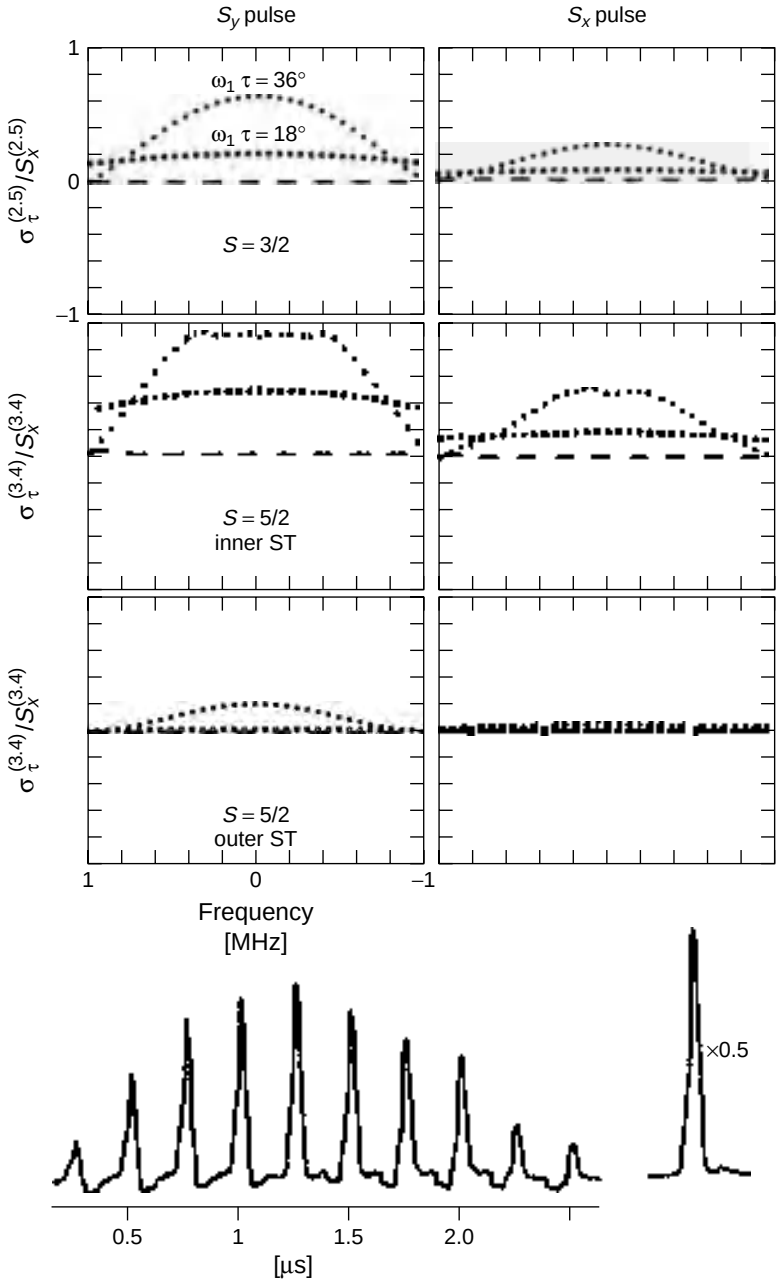

Figure 5 Coherence transfer from satellite to central transition by a single mixing pulse with RF field strength $\omega_1/2\pi = 100\,\text{kHz}$ and pulse length $\omega_1\tau = 18°$ (circles) and 36° (stars). The coherence transfer was calculated as a function of satellite transition frequency of an $S = 3/2$ and an $S = 5/2$ spins including both inner and outer satellite transitions. The two columns show the transfer by out-phase (left) and in-phase (right) pulses relative to the satellite transition coherence $S_x^{(ST)}$. The array of spectra in the bottom shows the optimization for the mixing pulse length with $\omega_1/2\pi = 60\,\text{kHz}$ for Na_2SO_4 along with a conventional central transition spectrum acquired under the same experimental conditions

are good indicators to measure the efficiencies experimentally. The two-pulse mixing yields ST-CT peaks about 30% of the diagonal peak. When the diagonal peak is compared with the ST-CT peaks (see Figure 5) obtained by the one-pulse mixing sequence under the same experimental conditions the ratio rises to nearly 80%.

Figure 7 illustrates the 2D STMAS spectrum of $9Al_2O_3 + 2B_2O_3$ for $S = 5/2$ spins. The spectrum was obtained with one-pulse mixing and a selective π-pulse before the data acquisition. The spin-echo sequence converts coherence transfer anti-echoes to echoes. The resulting spectrum is similar to $S = 3/2$ spins except that the ridge-shape peaks tilt at the opposite direction because of the sign change to the scaling factor $R^4_{5/2,\pm1} = 7/24$.

Magic-angle setting is the most critical factor in satellite transition NMR experiments. Deviations of the spinning axis from magic-angle reintroduce the first-order quadrupolar effects. Residual first-order effects can distort the satellite transition line shape and cause line broadening in 2D STMAS spectra. The line broadening can be estimated by the full width

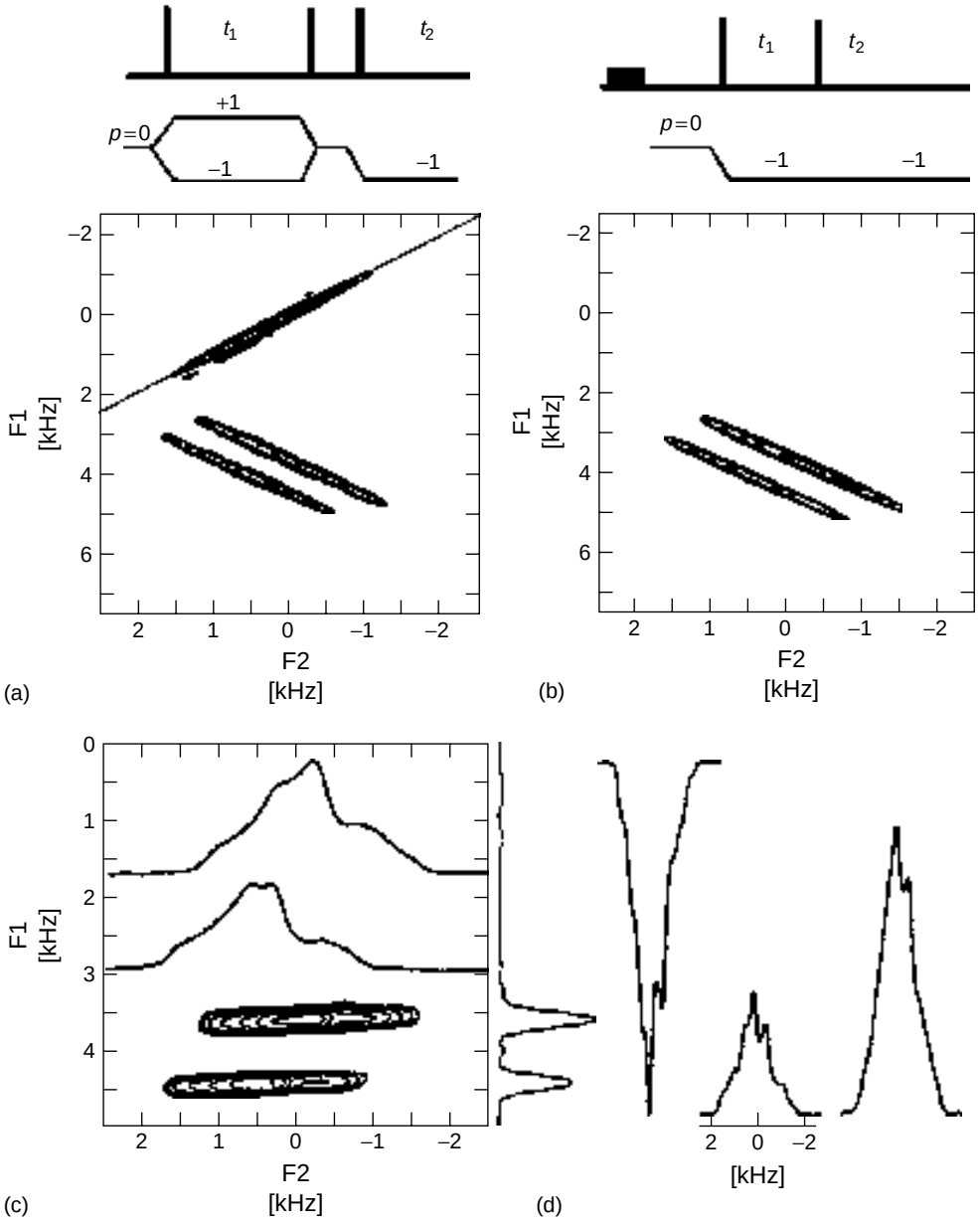

Figure 6 2D ^{23}Na STMAS spectra of a mixture of Na_2SO_4 and $Na_2C_2O_4$ acquired with (a) two-pulse mixing and (b) one-pulse mixing. The spectrum in (c) is obtained by a spectral tilt of (b) to correct the slope of ridge-shaped peaks. The projection to the isotropic dimension and the line shape along the anisotropic dimension are also plotted. The three projections in (d), from left to right, are obtained from the diagonal peak in (a) along the thin line, the cross peaks in (a), and the cross peaks in (b). The pulse sequence in (a) is identical to the sequence used for 2D exchange experiments. The phase cycle for the one-pulse mixing in (b) can be found in the text and the soft pulse is used for presaturation of the central transitions

of satellite transition powder pattern, $3c_q/S(2S-1)$, and the scaling factor $P_2(\cos\theta_S)$ by MAS

$$\Delta\nu_1 = \frac{3c_q}{S(2S-1)} P_2(\cos\theta_S) \tag{24}$$

A scaling factor $< 10^{-4}$ (0.004° in magic-angle setting) is required to reduce typical quadrupolar interactions from a few MHz to less than a few hundred Hz. Stable sample spinning is also critical to synchronize the evolution time with the rotor cycles for complete average of the first-order quadrupolar effect. A drift $\Delta\nu_r$ on spinning frequency causes a mismatch $t_1\Delta\nu_r/\nu_r$ to the synchronization condition. The mismatch at $t_1 \approx T_2^*$ should be small compared the width of the satellite transition rotational echoes Δt_1 (see Figure 1)

$$\Delta\nu_r < \nu_r \cdot \Delta t_1/T_2^* \tag{25}$$

With typical values $\nu_r \approx 10\,\text{kHz}$, $1/T_2^* \approx 300\,\text{Hz}$ and $\Delta t_1 \approx 1\,\mu s$, the stability on spinning frequency required for the STMAS experiment can be estimated about $\pm 3\,\text{Hz}$.

Finally, a comparison between MQMAS and STMAS experiments is summarized as follows. Both experiments correlate transitions of half-integer quadrupolar nuclei to obtain

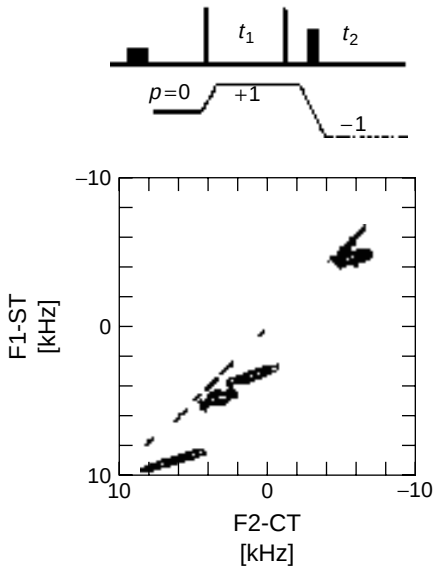

Figure 7 2D STMAS pulse sequence and spectrum of $9Al_2O_3 + 2B_2O_3$ with 20 kHz MAS. The pulse sequence uses a single pulse for mixing and the central transition selective π-pulse after the mixing generates coherence transfer echoes for $S = 5/2$ spins. The soft pulse in the beginning presaturates central transition coherence

isotropic NMR spectra under MAS. The satellite transition experiment requires accurate magic-angle setting and stable sample spinning to average out the first-order quadrupolar interactions whereas the multiple-quantum experiment correlates two transitions, both with vanished first-order effect. The excitation and the conversion of the single-quantum satellite transitions are much more efficient than that of multiple-quantum transitions. The relatively higher efficiencies allow rapid acquisition of high-resolution isotropic NMR spectra of half-integer quadrupolar nuclei (note the spectra in Figures 6 and 7 were acquired in just a few minutes).

5 CONCLUSIONS

Theoretical analysis and experimental results display the attractive features and technical requirements of satellite transition MAS NMR spectroscopy. Correlation between satellite and central transitions yields isotropic NMR spectra of half-integer quadrupolar nuclei. The transition-correlated experiment takes the advantage of efficient excitation and conversion of single-quantum satellite transitions for high-resolution NMR spectra of half-integer quadrupolar nuclei. In order to average out large first-order quadrupolar interactions, satellite transition experiment requires accurate setting of magic-angle and stable sample spinning.

6 REFERENCES

1. A. Abragam, 'Principles of Nuclear Magnetism', Clarendon Press: Oxford, 1961.
2. G. E. Maciel, *Science*, 1984, **226**, 282.
3. E. Oldfield and R. J. Kirkpatrick, *Science*, 1985, **227**, 1537.
4. E. Kundla, A. Samoson, and E. Lippmaa, *Chem. Phys. Lett.*, 1981, **83**, 229.
5. S. Ganapathy, S. Schramm, and E. Oldfield, *J. Chem. Phys.*, 1982, **77**, 4360.
6. A. Samoson, *Chem. Phys. Lett.*, 1985, **119**, 29.
7. H.J. Jakobsen, J. Skibsted, H. Bildsoe, and N.C. Nielsen, *J. Magn. Reson.*, 1989, **85**, 173.
8. L. B. Almany, D. Massiot, B. L. Sherriff, M. E. Smith, and F. Taullele, *Chem. Phys. Lett.*, 1991, **177**, 301.
9. C. Jäger, *J. Magn. Reson.*, 1992, **99**, 353.
10. J. S. Frye and G. E. Maciel, *J. Magn. Reson.*, 1982, **48**, 125.
11. M. Maricq and J. S. Waugh, *J. Chem. Phys.*, 1979, **70**, 3300.
12. J. Herzfeld and A. Berger, *J. Chem. Phys.*, 1980, **73**, 6021.
13. A. Samoson and E. Lippmaa, *J. Magn. Reson.*, 1988, **79**, 255.
14. A. Vega, *J. Magn. Reson.*, 1992, **96**, 50.
15. A. Samoson, E. Lippmaa, and A. Pines, *Mol. Phys.*, 1988, **65**, 1013.
16. A. Llor and J. Virlet, *J. Chem. Phys. Lett.*, 1988, **152**, 248.
17. B. F. Chmelka, K. T. Mueller, A. Pines, J. Stebbins, Y. Wu, and J. W. Zwanziger, *Nature*, 1989, **339**, 42.
18. K. T. Mueller, B. Q. Sun, G. C. Chingas, J. W. Zwanziger, T. Terao, and A. Pines, *J. Magn. Reson.*, 1990, **86**, 470.
19. L. Frydman and J. S. Harwood, *J. Am. Chem. Soc.*, 1995, **117**, 5367.
20. A. Medek, J. S. Harwood, and L. Frydman, *J. Am. Chem. Soc.*, 1995, **117**, 12 779.
21. C. Fernandez and J. P. Amoureux, *Chem. Phys. Lett.*, 1995, **242**, 449.
22. G. Wu, D. Rovnyank, B. Q. Sun, and R. G. Griffin, *Chem. Phys. Lett.*, 1996, **249**, 210.
23. G. Wu, D. Rovnyank, and R. G. Griffin, *J. Am. Chem. Soc.*, 1996, **118**, 9326.
24. D. Massiot, B. Tonzo, D. Trumean, J. P. Coutures, J. Virlet, P. Florian, and P. J. Grandinetti, *Solid State NMR*, 1996, **6**, 73.
25. M. J. Duer and C. Stourton, *J. Magn. Reson.*, 1997, **124**, 189.
26. C. Fernandez and P. J. Amoureux, *Solid State NMR*, 1998, **10**, 211.
27. J. P. Amoureux, C. Fernandez, and S. Steuernagel, *J. Magn. Reson. A*, 1996, **119**, 280.
28. S. P. Brown, S. J. Heyes, and S. Wimperis, *J. Magn. Reson. A*, 1996, **119**, 280.
29. D. Massiot, *J. Magn. Reson. A*, 1996, **122**, 240.
30. S. Ding and C. A. McDowell, *Chem. Phys. Lett.*, 1997, **270**, 81.
31. L. Marinelli, A. Medek, and L. Frydman, *J. Magn. Reson.*, 1998, **132**, 88.
32. S. Ding and C. A. McDowell, *J. Magn. Reson.*, 1998, **135**, 61.
33. Z. Gan, *J. Am. Chem. Soc.*, 2000, **122**, 324.
34. Z. Gan, *J. Chem. Phys.*, 2001, **114**, 10 845.
35. S. Vega, T. W. Shattuck, and A. Pines, *Phys. Rev. Lett.*, 1976, **37**, 43.
36. R. Tycko and S. J. Opella, *J. Am. Chem. Soc.*, 1986, **108**, 3551.
37. R. Tycko and S. J. Opella, *J. Phys. Chem.*, 1987, **86**, 1761.
38. M. Smith and E.R.H. van Eck, *Prog. NMR Spectrosc.*, 1999, **34**, 159.
39. J. Zwanziger and B. F. Chmelka, 'NMR Basic Principles and Progress', Springer-Verlag: Berlin, 1994, Vol. 31, p 202.
40. C. Jaeger, 'NMR Basic Principles and Progress', Springer-Verlag: Berlin, 1994, Vol. 31, p 135.
41. H. J. Jokobsen, in 'Encyclopedia of NMR', eds D. M. Grant and R. K. Harris, Wiley: Chichester, 1996.
42. M. Goldman, P. J. Grandinetti, A. Llor, Z. Olejniczak, J. R. Sachleben, and J. W. Zwanziger, *J. Chem. Phys.*, 1992, **97**, 8947.
43. J. J. Sukurai, 'Modern Quantum Mechanics', Addison-Wesley: New York, 1994.
44. M. E. Rose, 'Elementary Theory of Angular Momentum', Wiley: New York, 1951.
45. R. R. Ernst, G. Bodenhausen, and A. Wokaun, 'Principles of Nuclear Magnetic Resonance in One and Two Dimensions', Clarendon Press: Oxford, 1987.

Biographical Sketch

Zhehong Gan, *b* 1964. Ph.D. 1990, Chemical Physics, University of Utah (supervisor David M. Grant). NMR Spectroscopist, University of Illinois at Champaign-Urbana, 1990–93; Research Associate with R. R. Ernst, Eidgenössische Technische Hochschule (ETH), Switzerland, 1994–1998; Scientist, National High Magnetic Field Laboratory, USA, 1998–present. Approx. 40 publications. Current research interests: solid state NMR methodology and theory.

Sideband Analysis in Magic Angle Spinning NMR of Solids

Judith Herzfeld and Xiaobing Chen
Brandeis University, Waltham, MA, USA

1	Introduction	1
2	Moments	2
3	Sideband Ratios	5
4	Simulations	6
5	Complications	7
6	Related Articles	7
7	References	7

1 INTRODUCTION

In general, the effective magnetic field at a nucleus depends on the orientation of the molecule in the applied field. In the simplest case of a dilute spin-$\frac{1}{2}$ system, the orientation dependence is due to the anisotropy of the chemical shielding. Typically, the electron density in a molecule is highly anisotropic, with accumulations along the bond axes between neighboring nuclei. This leads to complicated electron currents which depend on the direction of the applied magnetic field relative to the bond axes. At experimentally accessible applied field strengths, where only the first-order effects on the electrons are observed, the chemical shielding is most generally expressed in linear algebraic terms as a second-rank tensor with elements ${}^{A}\sigma_{ij}$ which specify the magnitude of the ith element of the induced magnetic field vector at nucleus A when the applied magnetic field is along direction j. In most cases, the asymmetry of the tensor is not measurable[1–3] and the effective chemical shielding tensor is the symmetric tensor equal to half of the sum of the exact tensor and its transpose. This symmetric tensor has a principal axis system in which it is diagonal and three principal values (conventionally $\sigma_{11} \leq \sigma_{22} \leq \sigma_{33}$) corresponding to the chemical shielding along the three principal axes. Detailed information about the electron distribution around the nucleus is thus summarized in six chemical shielding parameters (the six elements of the symmetric tensor, or the three principal values and the three Euler angles for the principal axis system). For this reason chemical shielding tensors have attracted considerable experimental and theoretical interest.[4,5]

All six chemical shielding parameters can be measured if a single crystal of sufficient size is available which allows the molecules to be studied in at least six appropriately chosen orientations relative to the applied field.[6] In powder samples, all molecular orientations are represented at the same time, with corresponding chemical shifts. The result is a broad signal with a characteristic shape known as a powder pattern [see, for example, Figure 1]. Although all orientational information has been lost, the three principal values of the shielding tensor, which specify the maximum, minimum, and most common

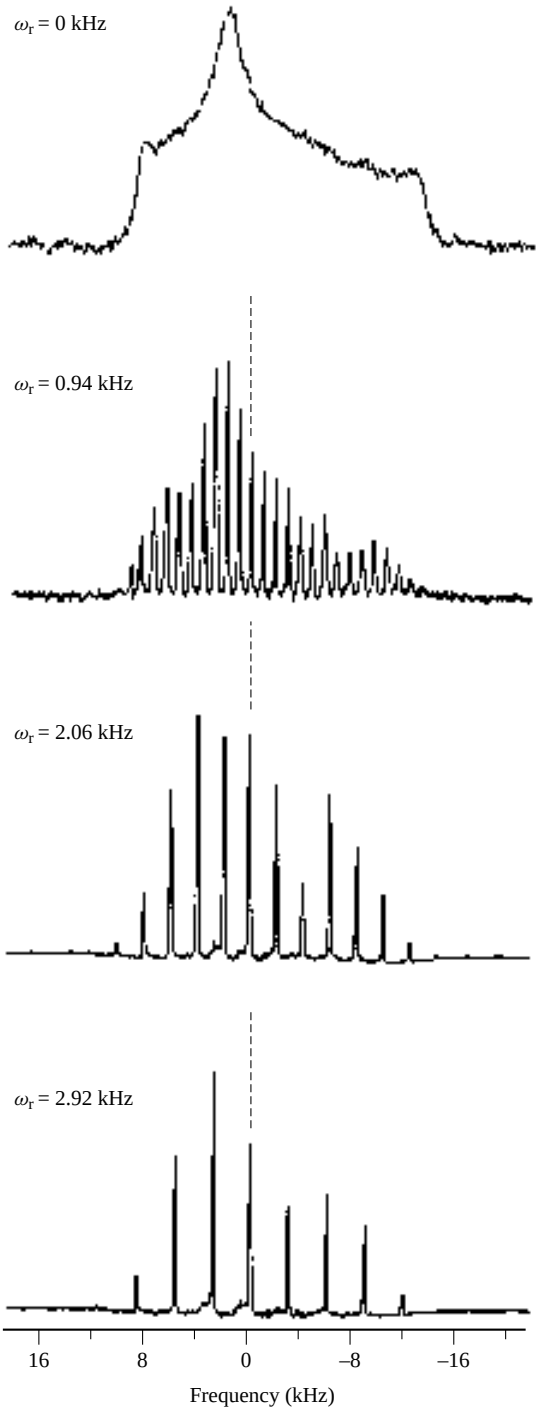

Figure 1 Proton decoupled ^{31}P spectra, at 119.05 MHz, of barium diethyl phosphate spinning at the magic angle[20]

chemical shifts, are apparent in the discontinuities of the powder pattern.[7] This is the most straightforward way to measure the three principal values of the shielding tensor. However, in many samples (notably biological ones) the discontinuities of the powder pattern may be obscured by overlap of multiple powder patterns and by poor signal-to-noise ratio due to the dispersal of the signal intensity over the breadth of the powder pattern. Two-dimensional (2D) correlation spectroscopy on reoriented samples can be used to sort overlapped powder patterns,[8] but the signal-to-noise

ratio is further deteriorated by the dispersal of signal intensity over 2D powder patterns.

Motional averaging reduces the effective range of chemical shielding, thereby improving both resolution and signal-to-noise ratio. In the limit of rapid isotropic tumbling, all of the signal is found at the average of the principal values of the chemical shielding (i.e. one-third of the trace of the tensor which is invariant to rotation). This isotropically averaged signal is observed for molecules in solution unless they are so large that the rotational diffusion is too slow. When the natural motion is not sufficiently fast or isotropic, the isotropic average of the chemical shift (or any second-rank tensor, such as the dipolar interaction) can be produced mechanically by spinning sufficiently rapidly about an axis tilted at the 'magic angle', $\cos^{-1}(\frac{1}{3}) = 54^\circ 44'$, relative to the direction of the applied field.[9,10]

While rapid magic angle spinning (MAS) provides high-resolution spectra of solid, dilute spin-$\frac{1}{2}$ systems, all information about the chemical shielding anisotropy (and hence the underlying anisotropy of the electron density) is lost. Use of rotor-synchronized rf pulses to prevent averaging in a second evolution period yields 2D spectra with powder patterns in the second dimension positioned at the isotropic chemical shift in the first dimension.[11] Similar results can be obtained by purely mechanical means, using 'magic angle hopping'[12] or 'stop-and-go spinning'.[13] This use of a second dimension to separate powder patterns that overlap in one dimension allows direct determination of the principal values of the chemical shift. However, the experiments are relatively demanding and do not address the signal-to-noise problem of powder patterns.

Anisotropic information can also be recovered by MAS at rates that are too small to average the chemical shielding anisotropy completely.[14] Spinning a crystallite at a frequency ω_r in the laboratory frame of reference, results in an applied field that swings around a cone with a frequency ω_r in the crystallite frame of reference [see equation (1) in Herzfeld and Berger[15]]. The chemical shielding of spins in the crystallite therefore oscillates around the isotropic value during the rotor period. The corresponding modulation of the Larmor precession produces a free induction decay for each crystallite with frequency components at integral multiples of ω_r above and below the isotropic value [see equation (21) in Herzfeld and Berger[15]]. The magnitudes and phases of these components will depend on the differences between the three principal values of the chemical shielding and on the initial orientation of the crystallite (given by three Euler angles). However, for a 'carousel'[16] of crystallites with orientations related by a uniform distribution of rotations around the rotor axis (corresponding to integration over the Euler angle γ in Herzfeld and Berger[15]), out-of-phase contributions cancel to produce a pure absorption NMR spectrum, consisting of a band at the isotropic frequency (the centerband) flanked by sidebands spaced at the spinning frequency with magnitudes depending on the values of the other two Euler angles and the differences between the principal values of the chemical shielding [see equation (24) in Herzfeld and Berger[15]]. It follows that the spectrum of a powder sample, representing contributions from the full range of the other two Euler angles, is also purely absorptive (see also Levitt,[16] Maricq and Waugh,[17] and Gullion and Conradi[18]) and that the magnitudes of the sidebands in the MAS powder spectrum will depend on the differences between the three principal values of the chemical shielding. The span, $\Omega = \sigma_{33} - \sigma_{11}$, and the skew, $\kappa = (\sigma_{11} + \sigma_{33} - 2\sigma_{22})/(\sigma_{33} - \sigma_{11})$,[19] can therefore be derived from the sideband intensities, while the isotropic average, $\sigma_{iso} = (\sigma_{11} + \sigma_{22} + \sigma_{33})/3$, is given by the position of the centerband. Analysis of slow MAS spectra thus presents an opportunity to determine experimentally all three principal values of the chemical shift without sacrificing resolution or signal-to-noise ratio.

Fortunately, the assignment of band order in slow MAS spectra is straightforward because the position of the centerband is independent of spinning speed and the associated sidebands are all spaced at the spinning frequency. Unfortunately, however, the dependence of the sideband intensities on the principal values of the chemical shielding is complicated, as illustrated by the example in Figure 1. Two approaches have been taken to extract the span and skew from the sideband intensities. Maricq and Waugh[21] have made use of the relatively simple dependence of the second and third moments of the sideband pattern on the span and skew. On the other hand, Herzfeld and Berger[15] have focused on the practical benefits of working with the ratios of the sideband intensities. We review both of these methods.

2 MOMENTS

Using I_N to represent the intensity of the Nth sideband (the signal at the frequency $N\omega_r$ above the isotropic frequency), the kth moment of a slow MAS spectrum is given by

$$M_k = \omega_r^k \sum_N N^k I_N \Big/ \sum_N I_N \tag{1}$$

Maricq and Waugh[21] found that the span and skew can be derived from the second and third moments according to the equations

$$\Omega = (1/2)\delta(3 - \eta) \tag{2}$$

and

$$\kappa = (3/2)\delta(1 + \eta)/\Omega \tag{3}$$

where δ is given by

$$8\delta^3 - 30M_2\delta - 35M_3 = 0 \tag{4}$$

and η is given by

$$\eta^2 = [15(M_2/\delta^2) - 3] = [1 - (35/2)(M_3/\delta^3)] \tag{5}$$

Equations (4) and (5) have three solutions for δ, each with two solutions for η. These six solutions correspond to the six permutations of the three principal values of the chemical shielding.

The accuracy of this method of sideband analysis clearly depends critically on the accuracy of the determination of the two moments. In practice, this requires that all the sidebands be resolved from other contributions to the spectrum. In addition, the sensitivity of the moments to the intensities of the higher order sidebands necessitates accurate measurement

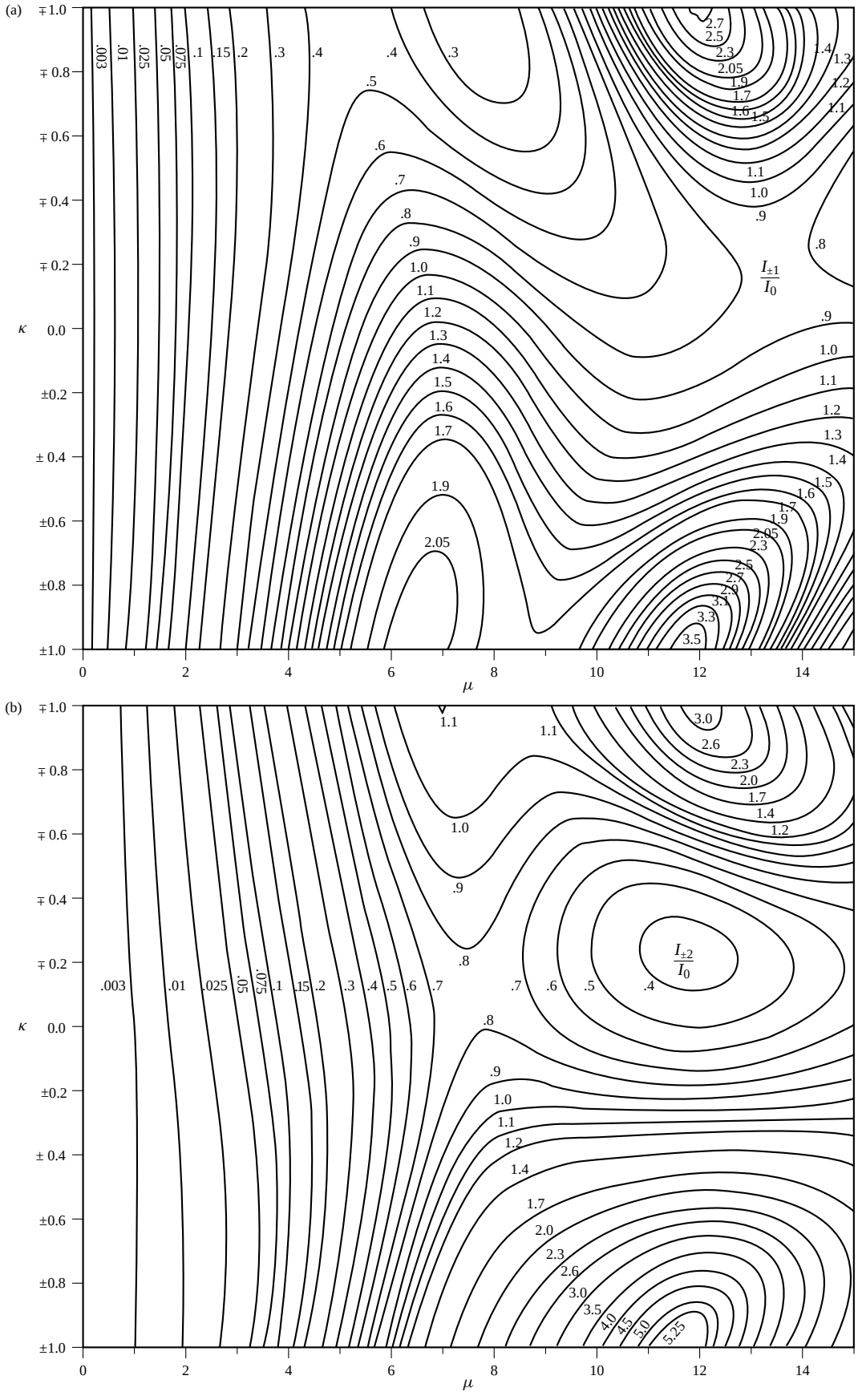
(a)
(b)
$\frac{I_{\pm 1}}{I_0}$
$\frac{I_{\pm 2}}{I_0}$
κ
μ
∓1.0
∓ 0.8
∓ 0.6
∓ 0.4
∓ 0.2
0.0
±0.2
± 0.4
±0.6
±0.8
±1.0
0
2
4
6
8
10
12
14

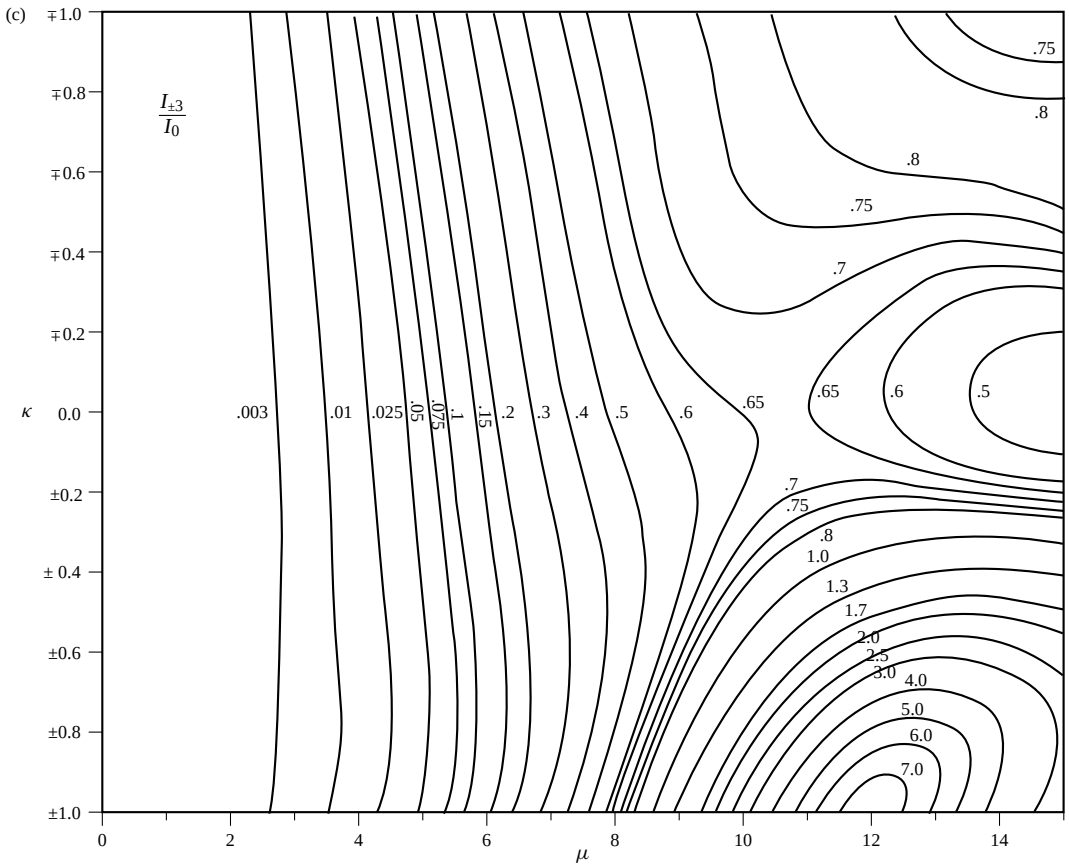
(c)
$\frac{I_{\pm 3}}{I_0}$
κ
μ
∓1.0
∓0.8
∓0.6
∓0.4
∓0.2
0.0
±0.2
± 0.4
±0.6
±0.8
±1.0
0
2
4
6
8
10
12
14
.003
.01
.025
.05
.075
.1
.15
.2
.3
.4
.5
.6
.65
.7
.75
.8
1.0
1.3
1.7
2.0
2.5
3.0
4.0
5.0
6.0
7.0

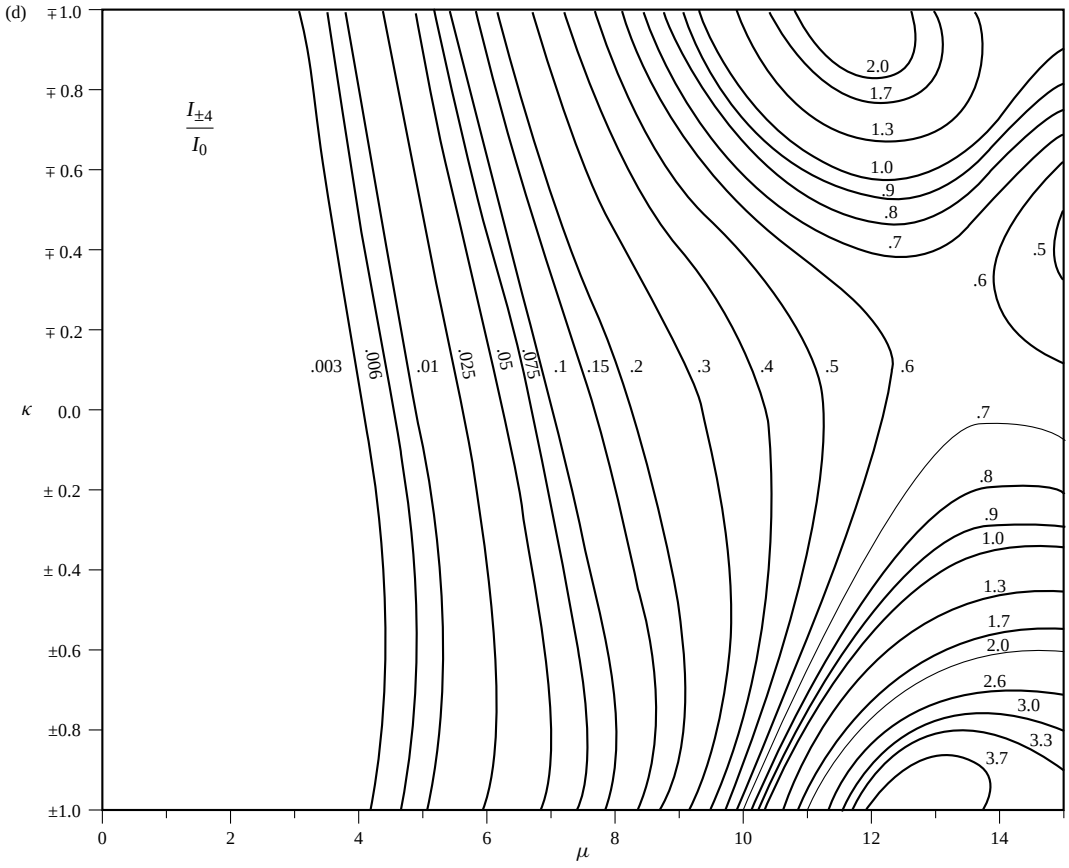
(d)
$\frac{I_{\pm 4}}{I_0}$
κ
μ
∓1.0
∓ 0.8
∓ 0.6
∓ 0.4
∓ 0.2
0.0
± 0.2
± 0.4
±0.6
±0.8
±1.0
0
2
4
6
8
10
12
14
.003
.006
.01
.025
.05
.075
.1
.15
.2
.3
.4
.5
.6
.7
.8
.9
1.0
1.3
1.7
2.0
2.6
3.0
3.3
3.7

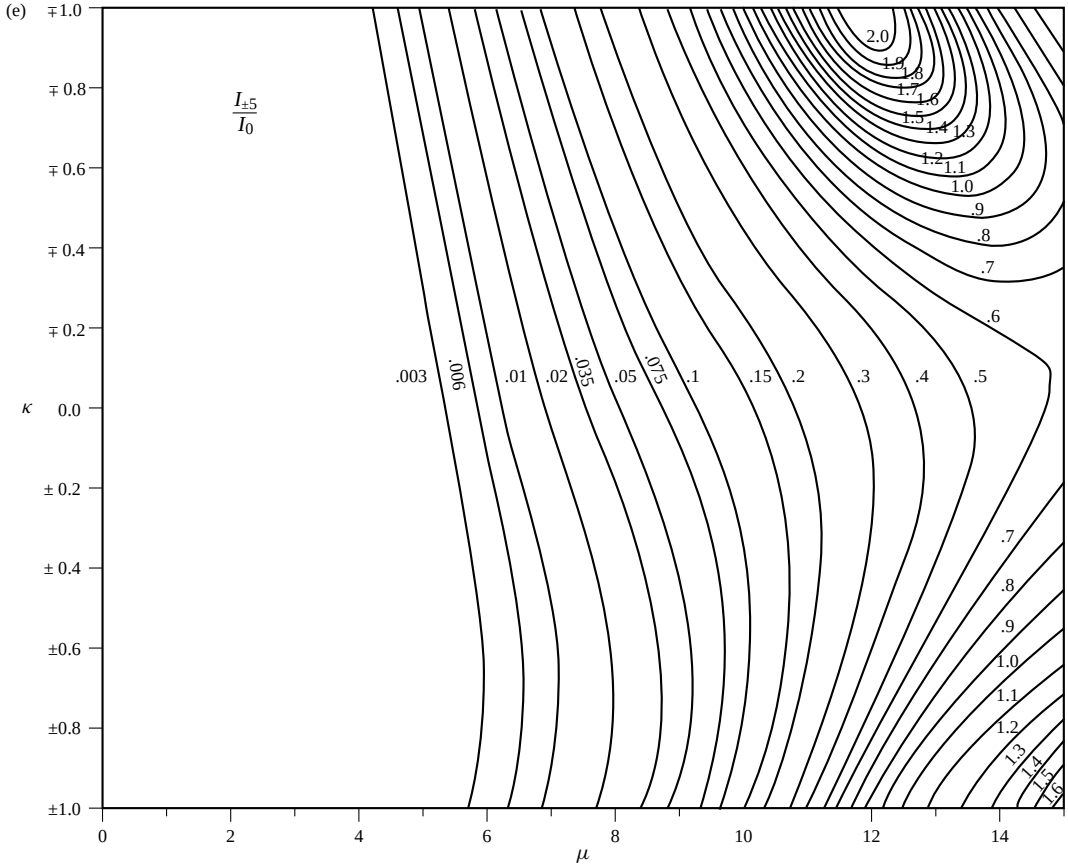

Figure 2 Contour plots of I_N/I_0 for values of N as indicated in (a)–(e).[15] This half strip corresponds to the convention $\sigma_{11} \leq \sigma_{22} \leq \sigma_{33}$. The five other permutations of the principal values correspond to the half strip for $\mu < 0$ and the four quadrants above and below the half strips

of weak signals that may be obscured by noise. The effects of inaccuracies in the measurement of higher order sidebands have been considered by Clayden et al.[22] in applications to slow MAS ^{31}P spectra of sodium dihydrogen orthophosphate, with a nonaxial shielding tensor, and triphenylphosphine oxide, with an axial shielding tensor. It was found that omitting sidebands of only 1% of the intensity of the most intense sideband was enough to produce significant variability in the derived principal values of the shielding. M_3 is the more vulnerable to inaccuracy than M_2 and examination of equations (4) and (5) shows that if $|M_3| > (\frac{2}{35})(5M_2)^{\frac{3}{2}}$ there is only one real solution for δ and no real values for η. This is a particular problem in the case of near axial tensors, for which $|M_3|$ is especially large compared with M_2 and η^2 tends toward zero. Inaccuracies in this regime easily lead to imaginary values of η. (See for example the case of triphenylphosphine oxide in Herzfeld et al.[20]) In general, moment analysis demands superb signal-to-noise ratio, especially for near axial tensors.

3 SIDEBAND RATIOS

Reliance on high-order sidebands, or any particularly inconvenient sidebands, can be avoided by using a search procedure to find those values of the span and skew that provide the best match to the intensities of the relatively accessible sidebands alone. In this process it is necessary to use ratios of sideband intensities for normalization.[15] Usually the centerband is one of the relatively strong sidebands and so it is convenient to use that for normalization. This places a special burden on accurate measurement of the intensity of the centerband and if this is not convenient other ratios can be used instead (see, for example, Fenzke et al.[23]). In the search for the best fit of the available intensity ratios, it is computationally demanding to calculate sideband intensities directly for every change in span and skew [e.g., using equations (24) and (33) Herzfeld and Berger,[15] for example]. Excellent accuracy can be obtained with much improved speed by bicubic spline interpolation between values calculated on a grid of points in the parameter space.[15] Such a grid of values is available for the intensities of the N = 0, ±1, ±2, ±3, ±4, ±5 bands, for values of the scaled span $\mu = (\gamma B/\omega_r)\ \Omega$ (where γ is the gyromagnetic ratio of the nucleus and B is the strength of the applied field) from 0 to 15,[15] and can be extended to larger spans[24] and higher orders,[23] as necessary.

In order to make good use of sideband intensity ratios, it is helpful to examine their dependence on the span and the skew graphically. Figure 2 shows contour plots for the intensity ratios $I_{\pm N}/I_0$, for N = 1 to 5. These graphs have several uses. First, they can be used to estimate graphically the span and skew for a particular set of experimental intensity ratios by locating the intersections of the corresponding contours. An example is shown in Figure 3 for barium diethyl phosphate. The graphical estimate of span and skew may suffice for some

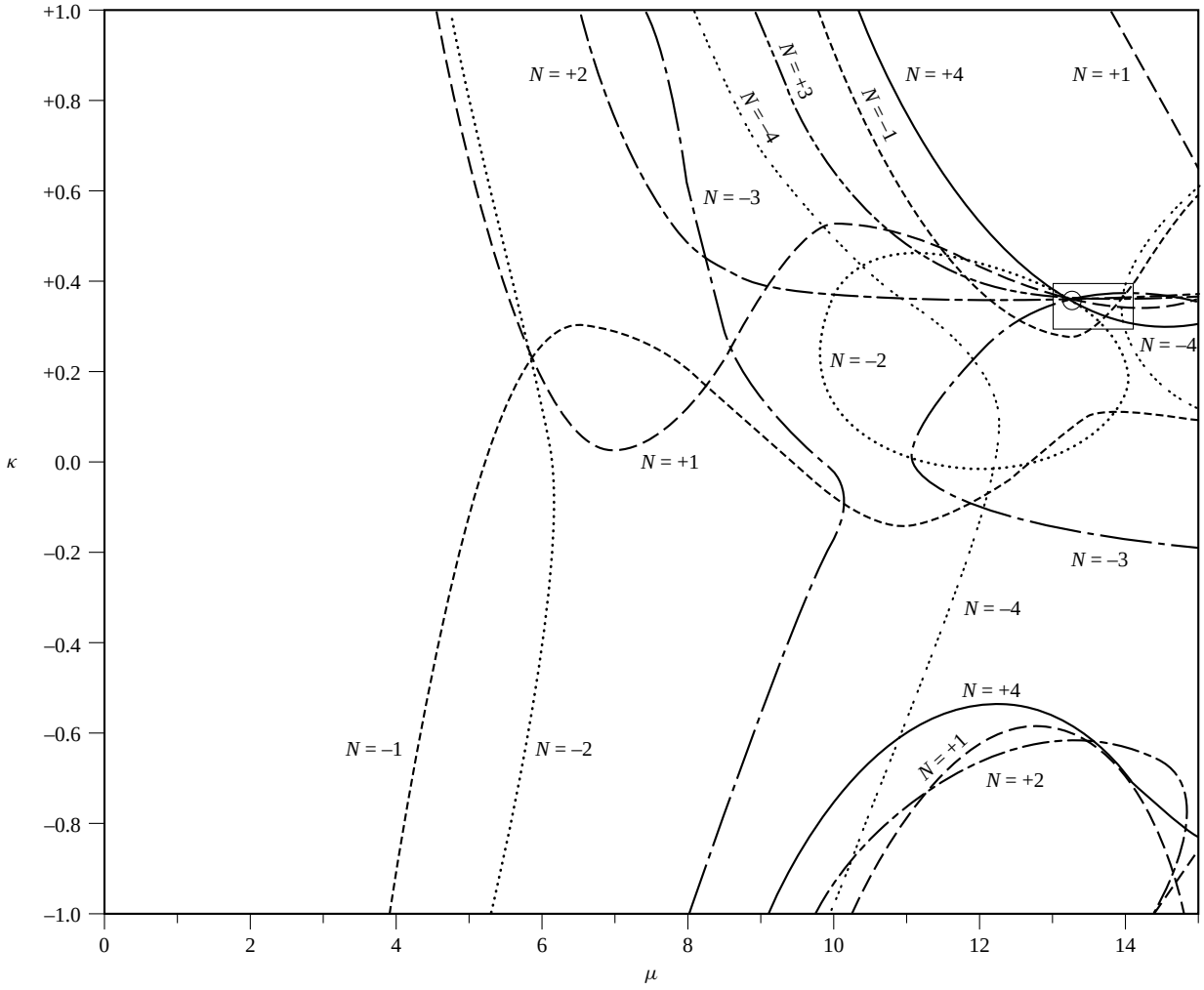

Figure 3 Graphical analysis of sideband intensity ratios I_N/I_0 from a ^{31}P spectrum, at 119.05 MHz, of barium diethyl phosphate spinning at 1.705 kHz.[15] Notice that the contours for $N > 0$ appear as they do in Figure 2, while the contours for $N < 0$ appear flipped over. This is necessary to superimpose corresponding values of κ. The estimated values of the scaled span, μ, and the skew, κ, are indicated with two different estimates of uncertainty by the circle and rectangle at $\mu \approx 13$ and $\kappa \approx 0.4$

purposes (see, for example, graphical ^{31}P results for sodium dihydrogen orthophosphate and triphenylphosphine oxide in Tables 1 and 3 of Clayden et al.[22]) or may be used as the starting point of a numerical fitting procedure for greater refinement.

The graphs in Figure 2 can also be used to design experiments. For example, it is clear that the intensity ratios are insensitive to the skew (as indicated by nearly vertical contours) for small values of μ. Thus a sufficiently low spinning speed must be chosen for μ to be large enough to obtain information about the skew. For near axial tensors (κ tending toward ± 1), the graphs show that μ must be even larger to obtain spectra sensitive to the skew. This difficulty has been noted by Clayden et al. for the nearly axially symmetric ^{31}P tensor of triphenylphosphine oxide, as compared with the nonaxial ^{31}P tensor of sodium dihydrogen orthophosphate (see Figures 3 and 8 of Clayden et al.[22]). Nevertheless, in both cases, graphical analysis of sideband ratios gives reasonably good estimates for the principal values of the chemical shielding, in contrast to the results of moment analysis (see Tables 1 and 3 of Clayden et al.[22]). For small spans, the spinning speed may need to be impractically low to obtain informative values of μ. However, for such narrow tensors, the skew is not of great practical interest because the three principal values are so similar.

4 SIMULATIONS

The reliability of the above methods depends on the extraction of accurate intensities for individual bands in slow MAS spectra. If the centerbands are well resolved, then overlap of sidebands with centerbands can be avoided by careful choices of spinning speeds or, for busier spectra, by a 2D experiment that sorts sidebands according to their isotropic chemical shifts.[25,26] However for spectra with overlapping centerbands or poor signal-to-noise ratio, extraction of accurate band intensities is not possible. In these cases, a more suitable approach is a direct least-squares fit of the full spectrum.[22] A relatively rapid scheme for such a fit was developed by deGroot et al.[27] Spectra are simulated for trial parameters by convolving a simple lineshape with sideband

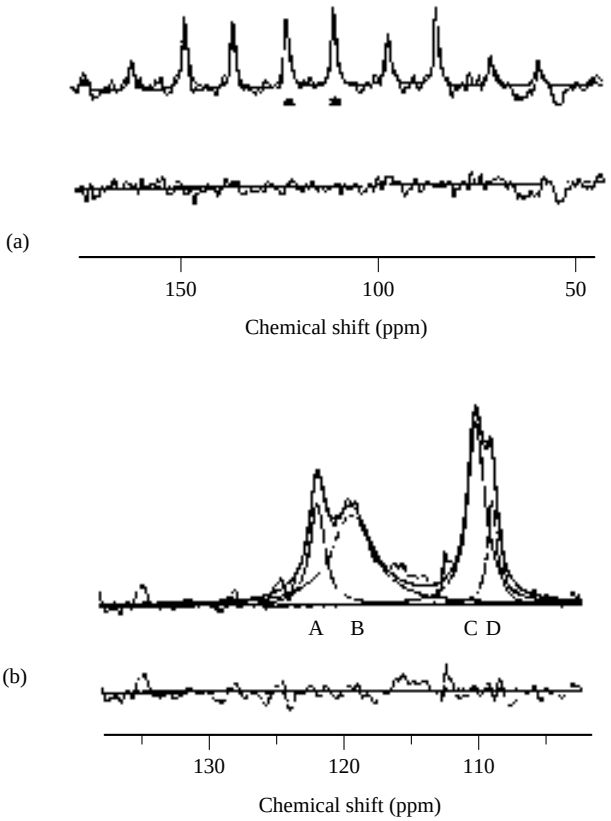

Figure 4 Carbon-13 MAS difference spectra and simulations for 14-^{13}C-retinal-labeled bacteriorhodopsin at (a) neutral pH with spinning speed 2.0 kHz[27] and (b) at low pH with spinning speed 3.0 kHz.[28] Chemical shifts are relative to TMS. The centerband is marked for each species by an asterisk or a letter. The least-squares simulations are represented by smooth lines. For the overlapped signals at low pH, the components that constitute the fit are also shown. Below each spectrum the residues are shown

intensities calculated by interpolation between stored values on a grid of points in span–skew space (from Herzfeld and Berger[15]). These calculated bands are positioned on a polynomial background according to the isotropic shifts and spinning speed. Least-squares iteration of the parameter search is pursued until the residuals reach the noise level. Figure 4 shows the results of such fits for a sample of 14-^{13}C-retinal-labeled bacteriorhodopsin at neutral pH and at low pH. At neutral pH, there are two species and their signals are fully resolved. In this case, the virtue of the fit is in the objective treatment of the noise. At low pH, four species are present, with some overlap of centerbands. In this case, the fit is essential for treating overlap, as well as noise.

5 COMPLICATIONS

Errors in sideband analysis may arise from noise in the spectrum or from mistaken theoretical assumptions. For analyses using moments or sideband ratios, the most straightforward means of assessing noise-limited accuracy is to repeat the analysis for variations of the measured sideband intensities over the range of values consistent with the noise.[29] This is preferable to arbitrary cut-offs in the acceptable overall deviations between theory and experiment.[23,29] For simulations, more rigorous sensitivity analysis is possible. In this case, it is convenient to choose a nonlinear least-squares fitting package that includes built-in statistical error estimation.[27]

The fundamental theoretical assumption made in the usual sideband analysis is that the chemical shielding is the only source of anisotropy. This is appropriate for a dilute spin-$\frac{1}{2}$ system with proton decoupling. However, cross polarization is an important tool in solid state NMR. In MAS experiments with cross polarization, Jeschke and Grossmann[30] reported systematic deviations between simulated and the experimental sidebands. They point out that the normal assumption that the magnetization of spins is independent of molecular orientation may be invalid for cross-polarized spins due to: (i) Hartmann–Hahn mismatch anisotropy, (ii) for short contact times, anisotropic orientation of the heteronuclear pair axis, and (iii) for long contact times, anisotropic relaxation in the rotating frame.

Other sources of anisotropy are also of interest. Spin-$\frac{1}{2}$ systems with heteronuclear dipolar interactions still behave inhomogeneously and various strategies of sideband analysis can be used to determine the strength of the dipolar interaction and the orientation of the heteronuclear axis relative to the principal axes of the chemical shielding.[21,31,32] Sideband analysis is also useful for systems with weak quadrupolar interactions.[21,33] However, systems with homonuclear dipolar interactions or strong quadrupolar interactions do not behave inhomogeneously and do not lend themselves to sideband analysis.[21,34,35]

6 RELATED ARTICLES

Anisotropy of Shielding and Coupling in Liquid Crystalline Solutions; Carbon and Nitrogen Chemical Shifts of Solid State Enzymes; Carbon-13 Spectral Simulation; Chemical Shift Tensor Measurement in Solids; Chemical Shift Tensors; Chemical Shift Tensors in Single Crystals; Dipolar and Indirect Coupling Tensors in Solids; Line Narrowing Methods in Solids; Magic Angle Spinning; Magic Angle Turning and Hopping; Proton Chemical Shift Measurements in Biological Solids; Rotating Solids; Variable Angle Sample Spinning.

7 REFERENCES

1. R. G. Griffin, J. D. Ellett, M. Mehring, J. G. Bulitt, and J. S. Waugh, *J. Chem. Phys.*, 1972, **57**, 2147.
2. F. K. Kneubühl, *Phys. Kondens. Mater.*, 1963, **1**, 410.
3. U. Haeberlen, *High Resolution NMR in Solids: Selective Averaging, Advances in Magnetic Resonance*, Suppl. 1, ed. J. S. Waugh, Academic Press, New York, 1976, p. 31.
4. M. Mehring, *High Resolution NMR in Solids*, 2nd edn., Springer, New York, 1983.
5. J. A. Tossell (ed.), *Nuclear Magnetic Shieldings and Molecular Structure*, Kluwer Academic, Dordrecht, 1993.
6. W. S. Veeman, *Prog. NMR Spectrosc.*, 1984, **16**, 193.
7. N. Bloembergen and J. A. Rowland, *Acta Metall.*, 1953, **1**, 731.
8. C. D. Hughes, M. H. Sherwood, D. W. Alderman, and D. M. Grant, *J. Magn. Reson. A*, 1993, **102**, 58.

9. E. R. Andrew and R. G. Eades, *Proc. R. Soc. London, Ser. A*, 1953, **216**, 398.
10. I. L. Lowe, *Phys. Rev. Lett.*, 1959, **2**, 285.
11. R. Tycko, G. Dabbagh, and P. A. Mirau, *J. Magn. Reson.*, 1989, **85**, 265.
12. A. Bax, N. M. Szeverenyi, and G. E. Maciel, *J. Magn. Reson.*, 1983, **52**, 147.
13. R. G. Ziegler, R. A. Wind, and G. E. Maciel, *J. Magn. Reson.*, 1988, **79**, 299.
14. E. O. Stejskal, J. Schaefer, and R. A. McKay, *J. Magn. Reson.*, 1977, **25**, 569.
15. J. Herzfeld and A. E. Berger, *J. Chem. Phys.*, 1980, **73**, 6021.
16. M. H. Levitt, *J. Magn. Reson.*, 1989, **82**, 427.
17. M. Maricq and J. S. Waugh, *Chem. Phys. Lett.*, 1977, **47**, 327.
18. T. Gullion and M. S. Conradi, *J. Magn. Reson.*, 1990, **86**, 39.
19. J. Mason, *Solid State Nucl. Magn. Reson.*, 1993, **2**, 285.
20. J. Herzfeld, A. Roufosse, R. A. Haberkorn, R. G. Griffin, and M. J. Glimcher, *Philos. Trans. R. Soc. London, Ser. B*, 1980, **289**, 459.
21. M. Maricq and J. S. Waugh, *J. Chem. Phys.*, 1979, **70**, 3300.
22. N. J. Clayden, C. M. Dobson, L. Y. Lian, and D. J. Smith, *J. Magn. Reson.*, 1986, **69**, 476.
23. D. Fenzke, B. Macb, and H. Pfeifer, *J. Magn. Reson.*, 1990, **88**, 172.
24. C. J. Groombridge, *Magn. Reson. Chem.*, 1993, **31**, 380.
25. A. C. Kolbert and R. G. Griffin, *Chem. Phys. Lett.*, 1990, **166**, 87.
26. D. P. Raleigh, E. T. Olejniczak, and R. G. Griffin, *J. Magn. Reson.*, 1991, **93**, 472.
27. H. J. M. deGroot, S. O. Smith, A. C. Kolbert, J. M. L. Courtin, C. Winkel, J. Lugtenburg, J. Herzfeld, and R. G. Griffin, *J. Magn. Reson.*, 1991, **91**, 30.
28. H. J. M. deGroot, S. O. Smith, J. Courtin, E. van den Berg, C. Winkel, J. Lugtenburg, R. G. Griffin, and J. Herzfeld, *Biochemistry*, 1990, **29**, 6873.
29. G. E. Hawkes, K. D. Sales, L. Y. Lian, and R. Gobetto, *Proc. R. Soc. London, Ser. A*, 1980, **424**, 93.
30. G. Jeschke and G. Grossmann, *J. Magn. Reson. A*, 1993, **103**, 323.
31. J. Herzfeld, J. E. Roberts, and R. G. Griffin, *J. Chem. Phys.*, 1987, **86**, 2.
32. P. J. Chu, R. R. Carvajal, and J. H. Lunsford, *Chem. Phys. Lett.*, 1990, **175**, 407.
33. T. H. Walter, L. Reven, and E. Oldfield, *J. Phys. Chem.*, 1989, **93**, 1320.
34. S. Hayashi, and K. Hayamizu, *Chem. Phys. Lett.*, 1991, **157**, 381.
35. A. Kubo and C. A. McDowell, *J. Chem. Phys.*, 1990, **92**, 7156.

Biographical Sketches

Xiaobing Chen. *b* 1967. B.E., 1990, Tsinghua University, China; M.A., 1992, Brandeis University. Currently Ph.D. candidate at Harvard University.

Judith Herzfeld. *b* 1948. A. B. 1967, Barnard College, Columbia University, Ph.D., 1972, Massachusetts Institute of Technology, USA, M. P. P., 1973, John F. Kennedy School of Government, Harvard University. Faculty in Chemistry, Amherst College, USA, 1973–74, Faculty in Physiology and Biophysics, Harvard Medical School, 1975–85, Faculty in Chemistry, Brandeis University, 1985–present. Currently Professor of Biophysical Chemistry. Approx. 115 publications. Research specialties: solid state NMR studies of the structure and function of membrane proteins, statistical mechanical studies of entropically driven long-range order in crowded solutions of self-assembling amphiphiles.

Silicon-29 NMR of Solid Silicates

Günter Engelhardt

University of Stuttgart, Stuttgart, Germany

1	Introduction	1
2	Silicate Structure Types	1
3	Experimental NMR Techniques	2
4	General Features of the Spectra and Spectral Parameters	3
5	Survey of Information on Silicate Structure Available from the Spectra	5
6	Applications	9
7	Related Articles	9
8	References	9

1 INTRODUCTION

Though static ^{29}Si CW NMR spectra of quartz, cristobalite, amorphous silica, and silicate glasses were measured as early as 1956,[1] it was more than 20 years before the first systematic study of solid silicates by ^{29}Si MAS FT NMR spectroscopy was accomplished.[2] Subsequently, the application of this method has grown rapidly and is now a powerful tool in the structural characterization of a wide range of silicate materials. The development is closely related to the great progress made in the 1980s in the instrumentation and methods for the registration of solid state ^{29}Si NMR spectra and their detailed interpretation. Nowadays, high magnetic field strengths and a wide selection of experimental NMR techniques, such as MAS, high-power dipolar decoupling, cross polarization (CP), two-dimensional experiments, and variable temperature measurements, are available on modern solid state NMR spectrometers. Moreover, it was shown even in the initial work on ^{29}Si MAS NMR of silicates and related materials, and has been further confirmed in numerous subsequent studies, that the ^{29}Si chemical shift is most sensitive to the chemical and structural surroundings of the silicon atoms. Chemically and/or crystallographically inequivalent Si sites can thus be detected by distinct resonances in the spectra. Moreover, empirical and theoretical relations have been established between the ^{29}Si chemical shift and the kind, number, and structural arrangement of the nearest and second-nearest neighbor atoms of the silicon atom. Silicon-29 MAS NMR can thus provide detailed information on the local structure around the silicon atoms and is, therefore, a valuable complement to X-ray or neutron diffraction techniques which monitor the periodic long-range order of crystalline materials.

Silicon-29 MAS NMR can also be successfully applied to amorphous or highly disordered solids, the study of which by X-ray diffraction (XRD) techniques is notoriously difficult. It should be emphasized, however, that, at least for crystalline materials, the combination of ^{29}Si NMR and XRD results is often a prerequisite for the reliable interpretation of the NMR spectra and, also, particularly appropriate for a more complete and detailed description of the structure.

Numerous papers have been published on the application of solid state ^{29}Si NMR to a wide range of crystalline and amorphous silicates and aluminosilicates, and the progress in the field has recently been summarized in several review articles.[3–5] In addition, a comprehensive review of the fundamentals and applications of ^{29}Si NMR to silicates considering the literature up to 1986 has been presented in a book.[6] Extensive compilations of ^{29}Si chemical shift data of silicates are given, for example, in Stebbins[4] and Engelhardt and Michel.[6]

In this article a concise review is given of ^{29}Si NMR spectroscopy of silicates with emphasis on the application of solid state MAS NMR techniques to powder samples. In particular, the characteristic features of the ^{29}Si MAS NMR spectra and the related information on structure and composition of silicates are considered from a general point of view and illustrated by selected examples. However, no detailed discussion on specific classes of silicate materials, such as zeolites, minerals, glasses, and amorphous silica, is presented since other articles in the Encyclopedia are devoted to these subjects (see, e.g. ***Molecular Sieves: Crystalline Systems***; ***Geological Applications***; ***Amorphous Materials***; ***Silica Surfaces: Characterization***). To facilitate the subsequent discussions, Section 2 gives a brief introduction to the general structure of silicates and aluminosilicates and the notation used for their description. Section 3 summarizes the pertinent techniques in solid state NMR of ^{29}Si. The general features of the ^{29}Si MAS NMR spectra and their intrinsic parameters are discussed in Section 4, followed, in Section 5 by a survey of the specific information available from ^{29}Si NMR on structure and composition of silicates and aluminosilicates. Finally, applications of ^{29}Si NMR to selected subjects are summarized in Section 6.

2 SILICATE STRUCTURE TYPES

The basic structural units of the silicate framework are SiO_4 tetrahedra which link together in a great variety of ways by sharing the oxygen atoms at their vertices. The resulting configurations can be classified by their topology:[7] SiO_4 tetrahedra may exist as isolated monomeric anions (nesosilicates), or may be connected by sharing one or two oxygen atoms forming dimeric and trimeric structures (sorosilicates), rings (cyclosilicates), or infinite chains (inosilicates). Single rings and chains may be put together to build up double rings or multiple chains, respectively, and, by linking an infinite number of chains, two-dimensional single layers (layer- or phyllosilicates) are formed. Connection of two or more tetrahedral layers results in the formation of double layers and finally infinite three-dimensional frameworks (tectosilicates). The number of oxygen atoms *not* shared by a second silicon atom ('nonbridging oxygens') determines the negative charge of the complex anionic silicate network, which is balanced by the positive charge of cations located within the interstices of the structure.

Aluminosilicates may be thought of as being formed from silicates by isomorphous replacement of SiO_4 with AlO_4 tetrahedra. The extra charge introduced by the negatively charged AlO_4 tetrahedra must be balanced by additional cations elsewhere in the structure. The distribution of Si and

Al atoms on the tetrahedral sites of the framework may be ordered or disordered and is, in general, governed by Loewenstein's rule,[8] which suggests that AlO_4 tetrahedra in aluminosilicate networks do not share oxygen atoms ('AlOAl avoidance principle').

Crystalline silicates and aluminosilicates play an important role as rock-forming minerals and as synthetic materials of great industrial and scientific interest. There is also a wide range of disordered or noncrystalline systems, such as amorphous silicates and silicas, gels, and glasses, the structure of which also consists of joined SiO_4 (and possibly AlO_4) tetrahedra, but lacking in any distinct long range order or lattice periodicity. A few silicate structures are known which contain sixfold coordinated silicon, i.e. SiO_6 octahedra (e.g. stichovite, thaumasite), and fivefold coordinated SiO_5 has recently been observed in quenched high-pressure silicate glasses and crystalline $CaSiO_3$ samples.[9]

For the presentation of the structure of building units or silicate anions in the following, the commonly used Q^n notation is adopted.[6] In this notation, Q represents a silicon atom bonded to four oxygen atoms forming a tetrahedron. The superscript n indicates the connectivity, i.e. the number of other Q units attached to the SiO_4 tetrahedron in question. Thus, Q^0 denotes the monomer orthosilicate anion SiO_4^{4-}, Q^1 end groups of chains, Q^2 middle groups in chains or rings, Q^3 chain branching sites, and Q^4 three-dimensionally cross-linked groups. A subscript denotes the number of equal Q^n units present in the corresponding silicate anion species. For aluminosilicates the number of AlO_4 tetrahedra bound to the central silicon of a Q^n unit is given in parentheses, e.g. $Q^n(m\mathrm{Al})$ means a SiO_4 group connected via oxygen bridges to m Al and $n - m$ other Si atoms, where $n = 0{-}4$ and $m \leq n$. In framework aluminosilicates, which are built up exclusively from $Q^4(m\mathrm{Al})$ units, the designation $\mathrm{Si}(n\mathrm{Al})$ is also used. The constitution of the basic Q^n, $\mathrm{Si}(n\mathrm{Al})$, and $Q^3(m\mathrm{Al})$ units is also depicted in Figures 5, 6, and 8 shown in a later section (Section 5.3).

To avoid confusion it should be noted that the general term 'silicate' is often used in this article in its broadest sense, i.e. it may include both silicates (only Si on tetrahedral sites) *and* aluminosilicates (Si and Al on tetrahedral sites).

3 EXPERIMENTAL NMR TECHNIQUES

Although single crystal (see ***Chemical Shift Tensors in Single Crystals***) or static powder ^{29}Si NMR can provide valuable information on local bonding and symmetry in silicates, these techniques have only been applied sparingly. Complete single crystal studies are time consuming and require, at least for work with ^{29}Si in its natural abundance (4.7%), relatively large crystals (usually about 5 mm in diameter), which are normally not available. Static powder studies yield direct information on the anisotropy of the ^{29}Si chemical shift but suffer from broad and often overlapping resonances and also need long measuring times.

The main reason for line broadening in the ^{29}Si NMR spectra of solid silicates is, in general, shielding anisotropy which can be fully averaged by the MAS technique (see ***Magic Angle Spinning***). Therefore, the overwhelming majority of solid state ^{29}Si NMR studies of silicates have been performed using MAS of powder samples. The chemical shift anisotropy for ^{29}Si in silicates is generally less than 100 ppm. Thus, narrow isotropic lineshapes without or with only weak spinning sidebands can be observed at magnetic field strengths $\boldsymbol{B}_0$ up to 9.4 T by MAS applying spinning frequencies of about 4–6 kHz. Such spinning rates are easily attainable by standard MAS probes with rotors of 7 mm diameter and, if necessary, even spinning rates up to 15 kHz and more can be achieved if smaller rotors (4 mm diameter) are used. Moreover, residual spinning sidebands may be removed by special sideband suppression techniques. If the orientational information available from chemical shift anisotropy data is of particular interest, the three components of the shielding tensor can be retrieved from the detailed analysis of MAS sideband patterns (see ***Sideband Analysis in Magic Angle Spinning NMR of Solids***) registered at moderate spinning rates. The MAS technique also averages weak heteronuclear dipolar interactions to distant protons or to other NMR-active nuclei, e.g. ^{27}Al in aluminosilicates. Stronger dipolar couplings of ^{29}Si to nearby protons can be removed by *high-power proton decoupling*.

In addition to MAS and dipolar decoupling, which by the line-narrowing effect result in a considerable improvement of the signal-to-noise ratio of the spectra, the intensities of the ^{29}Si NMR peaks may be substantially enhanced by use of the ^{1}H–^{29}Si CP technique, (see ***Cross Polarization in Solids*** and ***Cross Polarization in Rotating Solids: Spin-1/2 Nuclei***), provided that ^{1}H nuclei capable of polarization transfer to ^{29}Si are present in the sample. In silicates and related materials the most likely candidates for CP are protons of SiOH groups, but under certain conditions also protons of water or organic molecules adsorbed onto porous materials, or functional groups bonded at the silicates surface may give effective CP enhancements. Another advantage of the CP technique is that significantly shorter repetition times for spectral accumulation can be applied since the magnetization recovery of the protons is governed by the longitudinal relaxation time $T_{1\mathrm{H}}$ rather than $T_{1\mathrm{Si}}$, the former being generally much shorter. Beside the gain in sensitivity, ^{29}Si CP MAS NMR spectra may provide valuable information on specific proton–silicon coordinations, e.g. on SiOH groups or more distant Si$\cdots$H interactions (see Section 5.7). However, because the CP efficiency is determined by the cross-relaxation rate ${T_{\mathrm{HSi}}}^{-1}$ which depends strongly on the Si$\cdots$H distance (${T_{\mathrm{HSi}}}^{-1} \propto {r_{\mathrm{HSi}}}^{-6}$), the resulting intensity enhancement in the CP MAS spectra may be rather different for distinct Si sites. Therefore, ^{29}Si CP MAS NMR spectra of silicates are not always quantitatively reliable in the sense of single pulse MAS spectra. For quantitative information from ^{29}Si CP NMR spectra, detailed studies of the CP characteristics by contact time variation and relaxation measurements (T_{HSi}, $T_{1\rho\mathrm{H}}$) are required.

Substantial gains in sensitivity and resolution are further achieved by application of high magnetic field strength $\boldsymbol{B}_0$. It is thus generally advantageous to measure ^{29}Si MAS NMR spectra of silicates at high field, e.g. at $B_0 \geq 7$ T, corresponding to resonance frequencies of ν_0 (^{29}Si) $\geq$ 59.6 MHz.

Structural transformations and dynamic processes in solid silicates and their melts can be profitably studied by ^{29}Si MAS NMR experiments at varying temperatures. In principle, variable temperature MAS NMR measurements in the range of about -100 to $+200\,^\circ$C can be performed with most commercially available MAS probes by cooling or heating the sample via the flowing gas stream used for sample spinning.

However, extension of the range of temperatures applicable in MAS NMR experiments remains a technical challenge. Nevertheless, sample temperatures of up to 600–700 °C have been achieved in special designs of gas- or laser-heated MAS probes. Even higher temperatures have been reached in static NMR experiments, and temperatures up to 1250 °C have been applied to static ^{29}Si NMR investigations of solid and molten silicates.[10]

Two-dimensional (2D) NMR techniques are well established in solution studies but have found only limited use so far in solids. There have been, however, several successful studies on the connectivity patterns of tetrahedral Si sites in microporous silica polymorphs with a complex framework structure (see Fyfe et al.[11] and references therein) and glasses[12] using the well-known COSY or INADEQUATE pulse sequences. In these studies scalar coupling interactions in the ^{29}Si–O–^{29}Si connections are used to establish the three-dimensional (3D) connectivities of the silicate framework. In addition, a 2D ^{1}H–^{29}Si CP MAS NMR heteronuclear correlation experiment has been proposed which provides specific information on SiOH groups at the silicate surface.[13] In general, ^{29}Si isotopic enrichment of the samples considerably reduces the measuring times, but 2D ^{29}Si MAS NMR spectra have also been obtained from natural abundance materials, making the method quite generally applicable.

4 GENERAL FEATURES OF THE SPECTRA AND SPECTRAL PARAMETERS

4.1 From Liquids to Solids

Liquid state high-resolution ^{29}Si NMR has been used extensively to study the structure and quantitative distribution of silicate anions present in aqueous silicate solutions of a great variety of compositions (for a review see Chapter III of Engelhardt and Michel[6]). In general, sharp lines appear in the solution spectra, the chemical shifts of which depend sensitively on the specific structural surrounding of the SiO_4 tetrahedra. Characteristic chemical shift ranges were observed for the different Q^n units, and about 20 distinct silicate anion types containing up to 10 silicon atoms could be positively identified by detailed considerations of the shift effects owing to next-nearest and second-nearest Q^n connections, chain length, cyclization, and, in particular, of scalar spin–spin couplings in ^{29}Si isotopically enriched silicate solutions.[14] In addition, the incorporation of aluminum into silicate anions has been proved in highly alkaline, diluted, aluminosilicate solutions.[6,15]

Clearly, this potential of ^{29}Si NMR to provide detailed information on the silicate structure should be extremely useful if it could also be applied to solid silicates. However, line broadening in solids prevents resolution of distinct signals for structurally different Si sites in the spectra if conventional NMR techniques are used. Therefore, application of MAS and possibly dipolar decoupling is required to narrow the lines, as considered in the preceding section. Although the high resolution of liquid state NMR spectra is normally not attained in solid silicates, well-separated narrow resonances are observed in the ^{29}Si MAS NMR spectra of highly crystalline materials. Moreover, the spectra of solid silicates are often much simpler than those of silicate solutions since the variety and complexity of silicate anion types is normally greatly reduced in the crystalline solid. A striking example is shown in Figure 1 by the ^{29}Si NMR spectra of a crystalline sodium silicate hydrate and its liquid melt which corresponds to the solution of the same composition.[16] While the crystalline sample exhibits a single line of the monomeric Q^0 unit, the liquid shows a number of resonances representing different silicate anions. On the other hand, specific solid state effects may cause additional line splittings or line shifts not present in the solution spectra, which can provide valuable information on subtle details of the solid structure. This is demonstrated in Figure 2 by the ^{29}Si MAS NMR spectrum of the trimethylsilyl ester of cubic octamer silicate 'Q_8M_8' (M denotes the trimethylsilyl group). The spectrum of Q_8M_8 in benzene solution (not shown) exhibits two sharp lines at +12.4 ppm for the silicon in the M group and at −108.6 ppm for the silicon in the Q group, indicating a highly symmetric structure of the Q_8M_8 molecule in solution. In the crystalline solid, the resonances are split into three (δ = 11.76, 11.70, 11.50 ppm) and four (δ = −108.34, −108.62, −109.33, −109.68 ppm) components, respectively, owing to a slight asymmetric deformation of the Q_8 cube in the crystal lattice (resulting in four inequivalent pairs of Q sites) and nonequivalent orientations of the M groups, in full agreement with the X-ray structure.[17] Note also the excellent resolution

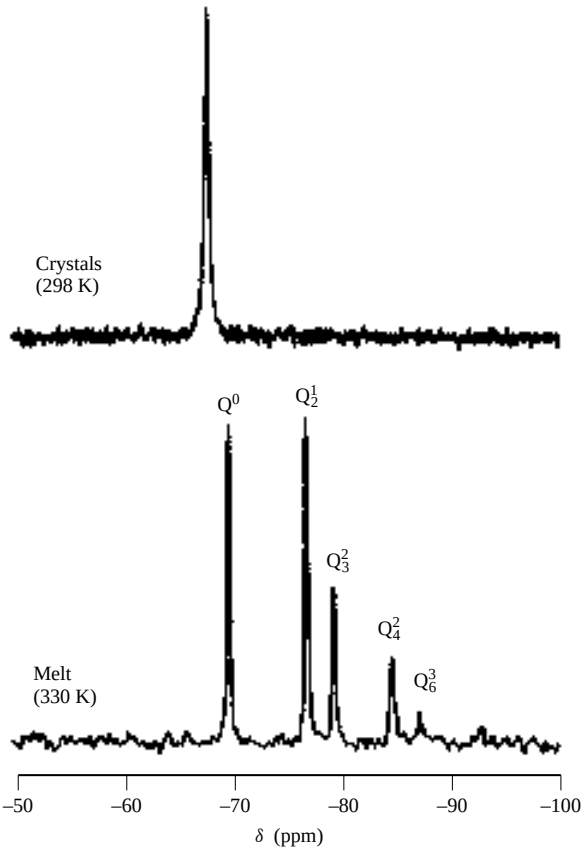

Figure 1 ^{29}Si MAS NMR spectra of crystalline sodium silicate hydrate of composition $Na_2H_2SiO_4{\cdot}8H_2O$ and its melt. The line assignment to monomer (Q^0), dimer (Q1/2), cyclotrimer (Q2/3), cyclotetramer (Q2/4), and prismatic hexamer (Q3/6) silicate anions is indicated in the spectrum of the melt.

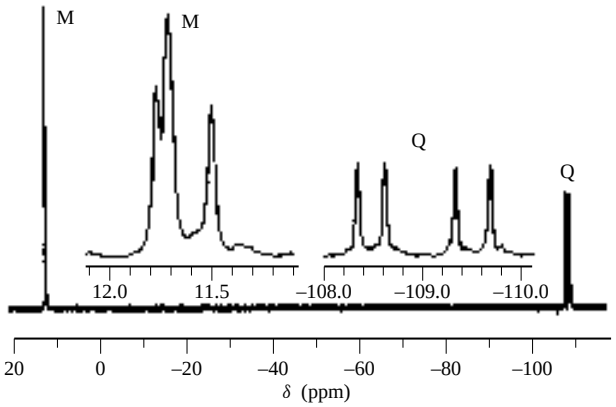

Figure 2 ^{29}Si CP MAS NMR spectrum of crystalline Q_8M_8 (the cubic octamer silicic acid trimethylsilyl ester, $[Si_8O_{20}][Si(CH_3)_3]_8$). The inserts are expanded regions of the M and Q signals.

achieved permitting the clear separation of two lines with a chemical shift difference of only 0.06 ppm in this spectrum. Owing to the sharp lines, the large dispersion of the M and Q resonances, the well-defined line splittings, and the dynamics of the CP processes, crystalline Q_8M_8 powder is particularly well suited for checking the spectrometer resolution, setting the Hartmann–Hahn match for CP experiments, and for use as a secondary chemical shift reference.

Although, as shown above, characteristic differences may appear between liquid and solid state spectra, it is important to note that the general relationships between spectral characteristics and structure deduced from the ^{29}Si NMR spectra of silicate solutions also hold for solid silicates and may, therefore, provide a first guideline for the interpretation of the solid state spectra.

4.2 Spectral Parameters

The individual peaks of a ^{29}Si NMR spectrum are characterized by three main parameters, which can be readily extracted from the spectrum: the chemical shift, δ, the intensity, I, and the linewidth, $\Delta\nu_{1/2}$. These parameters are closely related to the structure of the sample being investigated and are preferentially used in structural ^{29}Si NMR studies of silicates. Some general relationships between the NMR parameters and structural features of silicates will be considered below.

4.2.1 Chemical Shift

Most of the structural information that can be derived from ^{29}Si NMR spectra of silicates arises from the chemical shifts. Since δ is dependent on the electronic environment of the ^{29}Si nucleus, it is closely related to the type, position, and bonding characteristics of the surrounding atoms. For silicate structures and related systems, many empirical relationships between δ and structural features have been established, and, at least in part, substantiated by theoretical considerations (see below). In particular, a shift of approximately 10 ppm to lower frequency is generally observed for each newly formed SiOSi connection in a given Q^n environment, while each replacement of silicon with aluminum in a $Q^n(m\text{Al})$ environment induces a shift contribution of about 5 ppm to higher frequency. Consequently, the central Si atoms of the $Q^n(m\text{Al})$ units are more shielded with increasing connectivity, n, and decreasing number of Al atoms, m.

Besides the chemical environment, δ further depends on the particular geometry around the Si atom in question. Linear correlations have been established between δ and the mean SiOT (T = Si, Al) bond angles, α, nonbonded Si–Si distances, d_{SiSi}, Si–O bond lengths, d_{SiO}, and, for cubic structures, lattice parameters, a_0, all derived from the X-ray structures of a large number of framework silicates and aluminosilicates. The correlations indicate low-frequency shifts of δ with decreasing d_{SiO} and increasing α, d_{SiSi}, and a_0.

These dependences could be rationalized by a simple theoretical model (see Engelhardt[18] and references therein) combining quantum chemical calculations with the general shielding theory. In short, the model shows that shielding increases almost linearly with the (positive) net atomic charge, q_{Si}, at the silicon atom, which itself rises with the number of SiOT bridges, n, and decreases with the number of Al atoms, m, of the $Q^n(m\text{Al})$ environments. This result from the theoretical model is in full agreement with the experimental observations considered above. The q_{Si} value further depends on the degree of s hybridization, ρ, of the oxygen bond orbitals in the four O–Si bonds defining the SiO_4 tetrahedron. Since ρ is related to the SiOT bond angle, α, by $\rho = \cos\alpha/(\cos\alpha - 1)$, and reciprocal to d_{SiO}, the observed correlation with larger shielding at increasing α and decreasing d_{SiO} is confirmed by the theoretical model.

A simple relationship has further been derived between δ and the structures of a large number of silicate minerals and ^{29}Si chemical shifts, which is based on the magnetic susceptibility anisotropy of the bonds to second-nearest neighbors modified by the bond valence and the angle at the bridging oxygen.[19]

Finally, it should be noted that δ is further extremely sensitive to the coordination number of the silicon atom. Large, low-frequency shifts are observed in going from four- to five- to sixfold silicon coordination by oxygen (see below).

4.2.2 Line Intensity

In general, the integrated intensities of the peaks observed in a ^{29}Si NMR spectrum are directly related to the number of corresponding silicon atoms present in the sample. Thus, from relative peak intensities the quantitative proportions of the various structurally distinct Si sites can be determined. However, in order to obtain reliable signal intensities, the pulse repetition times and pulse width (flip angle) used in the spectral registration must be carefully selected to avoid saturation due to insufficient spin relaxation between the pulses. The relaxation times T_1 of ^{29}Si in silicates may be rather long in certain cases (up to several thousand seconds) and may differ for different Si sites in the sample. In such cases the pulse timing must be adjusted with regard to the longest T_1. As mentioned above, the signal intensities of CP spectra are often not quantitatively reliable owing to different CP efficiencies of Si in structurally distinct surroundings.

4.2.3 Linewidth

Provided that instrumental factors, such as inhomogeneity of the $\boldsymbol{B}_0$ field and missetting of the magic angle or rotor

instabilities, can be excluded, the most likely contributing factors to the linewidth in ^{29}Si MAS NMR spectra of silicates are (i) dispersion of chemical shifts due to structural disorder, distortion, or amorphization of the silicate framework, (ii) residual dipolar interactions of the ^{29}Si nucleus with ^{1}H, ^{27}Al, or other NMR active nuclei, and (iii) the presence of paramagnetic impurities.

Line broadening by chemical shift dispersion is a very common occurrence in the spectra and is very often the limiting factor for the linewidth. Chemical shift dispersion occurs owing to slightly different environments around nominally equivalent $Q^n(m\,Al)$-type silicon atoms characterized by small distortions of bond angles and bond lengths. The latter may be created by lattice imperfections, crystallographic inequivalence, or local distributions of second-nearest and further tetrahedral neighboring atoms, but also by localized cations or other nonframework constituents. Hence, very broad resonances ($\Delta\nu_{1/2} \approx 10-20$ ppm) are observed for highly disordered systems, such as amorphous or glassy materials, while narrow peaks ($\Delta\nu_{1/2} \approx 0.1-3$ ppm) appear in the ^{29}Si MAS NMR spectra for highly crystalline, perfectly ordered silicates. Insufficient MAS averaging of dipolar interactions with protons of water of hydration or hydroxyl groups can be overcome by high-power proton decoupling. Line broadenings due to dipolar interactions between ^{29}Si and the quadrupolar ^{27}Al nuclei in aluminosilicates may be significant for direct Si–O–Al pairings but are essentially eliminated at $\boldsymbol{B}_0$ field strengths of 4.7 T or higher. Paramagnetic centers (e.g. heavy metal cations) present in the sample as impurities or constituent parts of the structure can give rise to severe line broadening or may even render the spectrum undetectable, as, for example, observed for samples of olivine with different Fe^{2+} contents.[20]

5 SURVEY OF INFORMATION ON SILICATE STRUCTURE AVAILABLE FROM THE SPECTRA

In this section the information on local structure and chemical composition that can be derived from the ^{29}Si NMR spectra of solid silicates will be summarized from a general point of view. Unless otherwise stated the following considerations refer to ^{29}Si MAS NMR spectra of microcrystalline samples recorded at high magnetic field strengths and under optimum conditions for maximum spectral resolution and reliable line intensities.

5.1 Number and Population of Si Sites in Nonequivalent Environments

The most direct and rather fundamental information which follows immediately from the number of distinct resonances observed in the ^{29}Si MAS NMR spectra is the number of chemically and/or crystallographically inequivalent Si sites present in the silicate sample. Moreover, from the normalized peak intensities, the relative populations of the various sites can be determined. The number of inequivalent sites that can be distinguished in the spectra depends on the relationship between spectral resolution (linewidth) and chemical shift difference between the distinct resonances. As mentioned above, for highly crystalline samples with well-ordered structures, usually very narrow lines are observed, and subtle differences in the structural surrounding of the corresponding Si sites may be detected. Figure 3 shows the ^{29}Si MAS NMR spectrum of highly crystalline tricalcium silicate, Ca_3SiO_5, a major constituent of Portland cement. The X-ray structure of Ca_3SiO_5 reveals the presence of nine crystallographically distinct Si sites in isolated SiO_4^{4-} tetrahedra (Q^0). In full agreement with this structure, the spectrum exhibits seven clearly resolved lines, two of them with double intensities, for the nine Q^0 environments in the narrow range of -69 to -75 ppm.[21] In contrast, amorphous, glassy or ill-crystallized samples with highly disordered structures show, in general, broad and overlapping resonances rendering the interpretation of the spectra difficult. However, if sensible assumptions can be made on line positions and lineshapes, the spectra may be analyzed by decomposition and line fitting procedures.

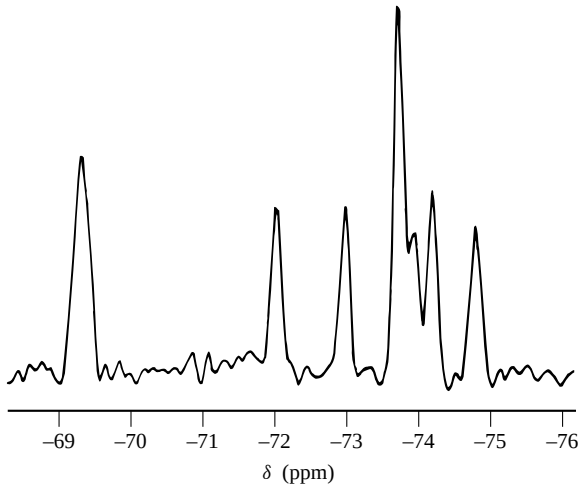

Figure 3 ^{29}Si MAS NMR spectrum of tricalcium silicate, Ca_3SiO_5. (Reproduced by permission of the American Chemical Society from Mägi et al.[21]).

5.2 Coordination Number of Si

The vast majority of silicates contain fourfold coordinated silicon but a number of structures with six-coordinated Si are also known. Silicon-29 MAS NMR can clearly distinguish between the different Si coordination numbers owing to large differences in the ^{29}Si chemical shifts. While δ values between -60 and -120 ppm are typical of four-coordinated SiO_4 in silicates,[6] the resonances of octahedral SiO_6 coordinations, as observed e.g. in thaumasite, stishovite,[22] $MgSiO_3$-rich garnets, perovskites, and other high-pressure silicate minerals[23] appear in the range between -170 and -220 ppm. The clear distinction between four- and six-coordinated Si is demonstrated in Figure 4 by the ^{29}Si MAS NMR spectrum of a high-pressure $MgSiO_3$ sample which exhibits several resonances that could be attributed to the SiO_4 and SiO_6 environments of distinct silicate phases present in this material.[23] Silicon-29 NMR has also revealed the presence of five-coordinated SiO_5 in silicate materials. Weak resonances at about -150 ppm have recently been attributed to SiO_5 in quenched high-pressure alkali silicate glasses and crystalline $CaSiO_3$ samples.[9]

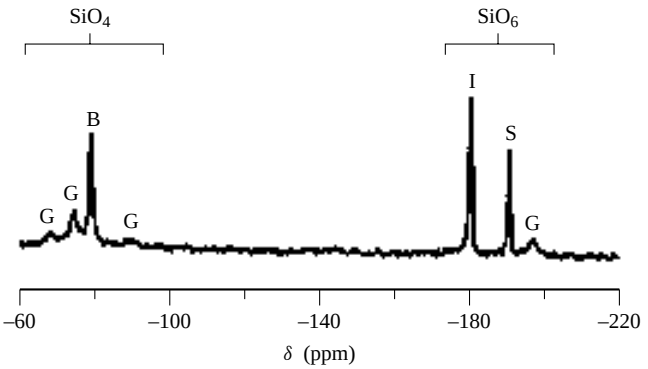

Figure 4 ^{29}Si MAS NMR spectrum of a high-pressure $MgSiO_3$ phase showing resonances of four- and six-coordinated silicon in garnet (G), β-$MgSiO_3$ (B), ilmenite (I), and stishovite (S). (Reproduced by permission of the American Association for the Advancement of Science from Stebbins and Kanzaki[23]).

5.3 Local Chemical Environment of SiO_4 Tetrahedra

It was shown in Section 4.2.1 that the ^{29}Si chemical shifts of SiO_4 tetrahedra in silicates depend sensitively on type and structural arrangement of the second nearest neighbor atoms at the silicon atom. There are, in particular, two characteristic features which affect the ^{29}Si chemical shift of a SiO_4 group: characteristic shifts to lower frequency are observed with increasing number of SiOT bridges (T = Si, Al) formed by the SiO_4 tetrahedron (SiO_4 connectivity), and typical shifts to higher frequencies follow from the replacement of Si with Al in the second coordination sphere of the central silicon (degree of tetrahedral Al substitution). Similar effects have been observed for substitution of tetrahedral Ga in gallosilicates.[6]

A large number of aluminum-free silicates of different degree of SiO_4 connectivity, i.e. neso-, soro-, cyclo-, ino-, and layer silicates and silica polymorphs, have been studied by ^{29}Si MAS NMR, and the resulting ranges of δ for the five Q^n environments are displayed in Figure 5. The increasing shielding with higher degree of SiO_4 connectivity, n, is obvious. However, with the exception of the Q^4 units, the Q^n

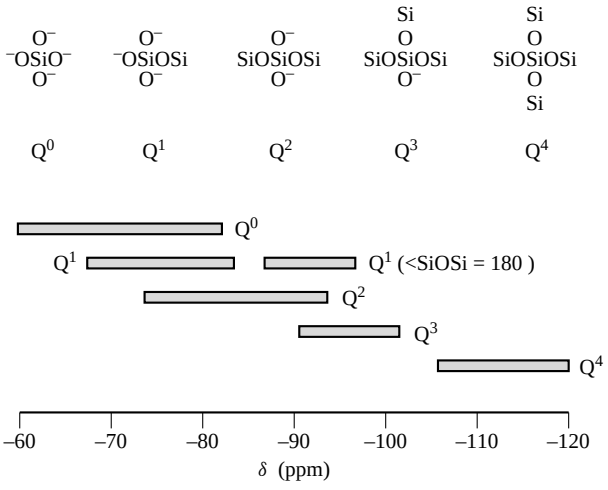

Figure 5 Ranges of ^{29}Si chemical shifts of $Si(O^-)_{4-n}(OSi)_n$ coordinations (Q^n) in silicates. (Reproduced by permission of Springer-Verlag from Engelhardt and Koller[5]).

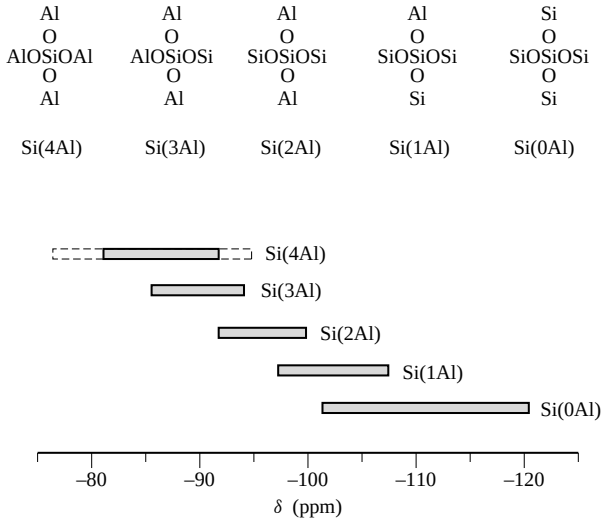

Figure 6 Ranges of ^{29}Si chemical shifts of $Si(OSi)_{4-n}(OAl)_n$ coordinations [Si(nAl)] in tectoaluminosilicates. The dotted lines for Si(4Al) designate the particularly large range observed for 1:1 aluminosilicate sodalites with different cage fillings.[18] (Reproduced by permission of Springer-Verlag from Engelhardt and Koller[5]).

shift ranges overlap significantly and a simple correlation of δ and Q^n type for a silicate of unknown structure is likely to be risky. Nevertheless, δ may be used as a guide to the Q^n units present, especially if other shift contributions originating from, e.g., cation effects or different geometry are considered.[21]

The characteristic ranges of shift for the five Si(nAl) (or Q^4(mAl) environments in framework aluminosilicates shown in Figure 6 have been established from a large body of shift data measured in various types of tectoaluminosilicates, silica polymorphs, and, in particular, zeolites. Only Q^4-type silicons are present in framework silicates but, as in the case of Q^n, the ranges of δ for the Q^4(mAl) units overlap. Nevertheless, the assignment of the usually well-separated lines to the corresponding Si(nAl) units is, in general, feasible. As an example, Figure 7 shows the MAS NMR spectrum of ^{29}Si in a microporous framework aluminosilicate with an Si/Al atomic ratio of 2.2, i.e. zeolite ZK-5. Five well-resolved resonances are observed which can easily be attributed to the five distinct Si(nAl) environments by the chemical shifts. Spectra of this type are quite typical for aluminosilicates and do not depend very much on the particular framework structure, at least if no crystallographically inequivalent Si sites are present in the structure. With decreasing Al content (i.e. increasing Si/Al ratio) the intensities shift from the high-frequency lines for Si(nAl) with higher n to those of the low-frequency Si(nAl) lines with lower n, and vice versa, i.e., single-line spectra were observed for Si/Al = 1, i.e. Si(4Al), and for Si/Al = ∞ (SiO_2), i.e. Si(0Al).

Finally, the typical ranges of δ for the four different Q^3(mAl) tetrahedral units in layer aluminosilicates are displayed in Figure 8. Similar to the tectoaluminosilicates, multiple resonances observed for a certain layer silicate can usually be attributed to the distinct Q^3(mAl) units, despite the overlap of the δ ranges. Besides the aluminum atoms incorporated in the tetrahedral silicate layer, further aluminum may be present in the octahedral sheet which, however, induces comparatively small effects on δ.

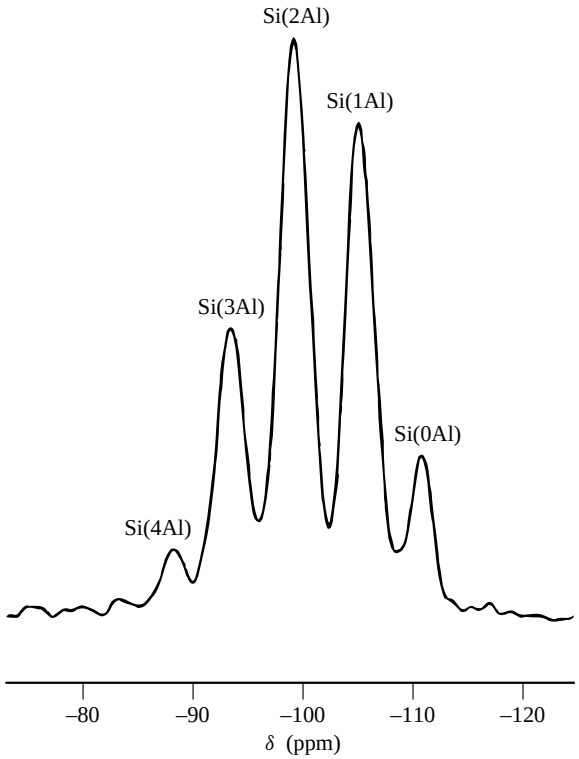

Figure 7 ^{29}Si MAS NMR spectrum of zeolite ZK-5, a microporous tectoaluminosilicate of Si/Al = 2.2. The line assignments to the five distinct Si(nAl) coordinations are indicated.

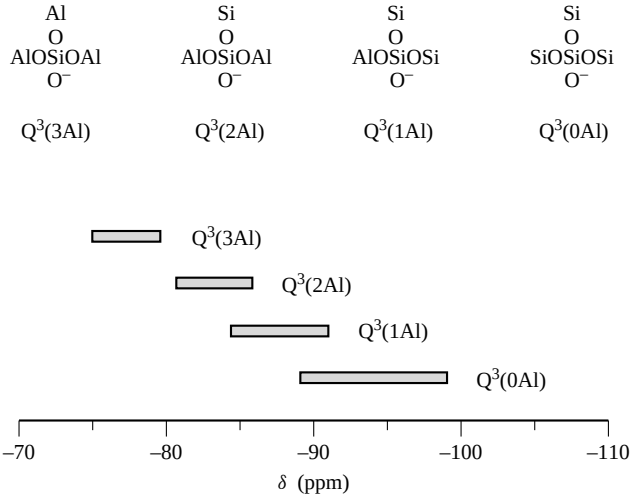

Figure 8 Ranges of ^{29}Si chemical shifts of Si(OH)(OSi)$_{3-m}$(OAl)$_m$ coordinations [Q^3(mAl)] in layer aluminosilicates. (Reproduced by permission of Springer-Verlag from Engelhardt and Koller[5]).

5.4 Atomic Ratio of Si/Al in the Aluminosilicate Framework

Provided that the NMR spectrum of ^{29}Si in an aluminosilicate is correctly interpreted in terms of the different Q^n(mAl) units, the atomic ratio of tetrahedral Si and Al in the structure can be calculated from the peak intensities according to the equation

$$\mathrm{Si/Al} = \sum_{m=0}^{n} I_{n,m} / \sum_{m=0}^{n} (m/n) I_{n,m} \qquad (1)$$

where $I_{n,m}$ are the intensities of the Q^n(mAl) peaks and summation is from $m = 0$ to $m = n$, i.e., from 0 to 3 in layer aluminosilicates and from 0 to 4 in framework aluminosilicates.[6] The above equation is independent of the specific structure of the aluminosilicate and includes the aluminum which is substitutionally incorporated into the tetrahedral framework, but excludes any nonframework aluminum frequently present, e.g. in layer aluminosilicates and in chemically or thermally treated zeolites. If the total Si/Al ratio of such samples is known from the overall chemical composition, the proportion of nonframework Al can readily be determined.

5.5 Ordering of Si and Al in the Aluminosilicate Framework

For the general case of a random distribution of Si and Al atoms on the tetrahedral sites of an aluminosilicate framework of Si/Al atomic ratio $1/p$, the probabilities of the occurrence of the various Q^n(mAl) configurations can be calculated by the binomial probability distribution

$$P_{n,m} = \frac{n!}{m!(n-m)!} p^m (1-p)^{n-m} \qquad (2)$$

It is obvious that the Si, Al distribution cannot be random if the relative Q^n(mAl) intensities measured in the ^{29}Si NMR spectrum of a certain aluminosilicate are significantly different from the calculated probabilities. If, however, the calculated populations and observed intensities are similar, then both ordering and disorder are possible. Hence ^{29}Si NMR can disprove random substitution of Si and Al but cannot prove it.

Specific information about the topological Si, Al distribution can be derived by comparing the relative Q^n(mAl) populations obtained from ^{29}Si NMR peak intensities with model-generated populations. The latter may be derived, e.g. from ordering schemes which are constructed by distributing the respective number of Si and Al atoms on the T sites of a certain repeating unit of the structure. It should be noted, however, that NMR monitors the averaged local environments of the Si atoms throughout the framework and the whole sample volume, which do not, therefore, necessarily imply any simple long-range ordering. Nevertheless, specific Si, Al distributions or, less specifically, the degree of dispersion of Al atoms over the framework has been deduced from the ^{29}Si MAS NMR spectra of a number of zeolites and layer aluminosilicates with different tetrahedral Si/Al ratios. A review of the strategies and methods applied is given in Chapter V of Engelhardt and Michel.[6] For recent applications see, for example, Herrero.[24]

5.6 Crystallographically Inequivalent Si Sites

The broad shift ranges observed for the distinct Q^n and Q^n(mAl) environments (see Figures 5, 6, and 8) indicate

the influence of different bonding geometries around the Si atom on δ, as already discussed in Section 4.2.1. Distinct resonances may thus be observed in the ^{29}Si MAS NMR spectra for Si atoms residing in chemically equivalent $Q^n(m\mathrm{Al})$ environments but occupying crystallographically nonequivalent sites which differ in SiOT bond angles and/or SiO bond lengths. Pertinent examples are the splittings of the Q^3 and M lines in the spectrum of Q_8M_8 (Figure 2), the seven Q^0 lines observed in Ca_3SiO_5 (Figure 3), and the appearance of several resonances in the ^{29}Si MAS NMR spectra of a variety of silica polymorphs and high-silica zeolites,[6] e.g. the 20 lines observed for the 24 crystallographically inequivalent Q^4 sites in the monoclinic form of silicalite.[25] The number and, from line intensities, the relative occupancies of crystallographically distinct Si sites can thus be obtained from the spectra and may be directly related to the results of diffraction experiments. Moreover, for framework silicates the mean SiOT bond angles, α, of the different Si sites can be estimated from δ by applying the quantitative correlations between δ and α considered in Section 4.2.1. These correlations reveal that δ changes by about 0.6 ppm for a 1° change in α. Since, for highly crystalline materials, a peak-to-peak resolution of 0.1 ppm can be achieved in the ^{29}Si MAS NMR spectra, differences in the mean bond angles of about 0.2° may be detected. If the mean bond angles are known from X-ray structure refinements, δ can be calculated which may be helpful in the correct assignment of multiline spectra,[18] as, for example, in the case of the above-mentioned silicalite.[26]

5.7 Characterization of SiOH Groups in Silicate Materials

It was shown in Section 3 that application of the CP technique selectively enhances the signal intensity of Si nuclei near protons and that the enhancement factor depends on the Si···H distance and the CP contact time applied. At short contact times, intense lines of SiOH (e.g. in Q^3 or Q^2 structural groups) are observed, while the signals of Si nuclei with larger Si···H distances (e.g. Q^4 adjacent to Q^3) are strongly reduced or do not appear (e.g. Q^4 surrounded only by other Q^4 groups) in the CP MAS spectra. An even more detailed discrimination of the different Si environments can be achieved by application of CP with variable contact times.[27] However, as mentioned in Section 3, CP MAS spectra are not always quantitatively reliable. But once the linewidth and position of less abundant species have been determined from the CP MAS spectrum, this information may be used for the quantitation of weak and overlapping lines in the single-pulse MAS spectrum by line fitting procedures.

5.8 Si–O–Si Framework Connectivities

The direct determination of bonding connectivities between the various crystallographically inequivalent SiO_4 sites of a 3D silicate framework has recently become feasible by application of 2D ^{29}Si MAS NMR experiments such as COSY and INADEQUATE[11] (see Section 3). The latter experiment has been proved to be particularly useful since only double quantum coherence signals, i.e. only signals due to ^{29}Si nuclei coupled via scalar spin interactions in the ^{29}Si–O–^{29}Si connection are observed in the 2D plot. This

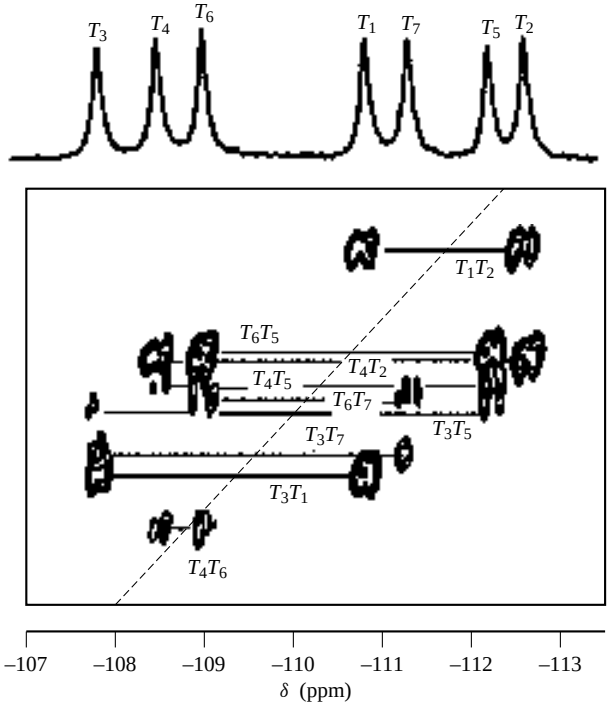

Figure 9 Contour plot of the 2D ^{29}Si MAS INADEQUATE experiment on high-silica zeolite ZSM-12 with the 1D MAS NMR spectrum shown above. The T site assignments and TOT connectivities are indicated in the spectra. (Reproduced by permission of the American Chemical Society from Fyfe et al.[11]).

is demonstrated in Figure 9 by the 2D INADEQUATE ^{29}Si MAS NMR spectrum of high-silica zeolite ZSM-12.[11] The F_2 dimension is the normal ^{29}Si chemical shift scale while the F_1 domain represents the double quantum frequencies of the resonances. Connected signals occur equally spaced on either side of the diagonal of the plot at the same frequencies in F_2 as the corresponding lines from the simple one-dimensional (1D) experiment. The ZSM-12 structure has seven crystallographically distinct Si sites with equal occupancies in the unit cell which are reflected by the seven lines of equal intensity in the 1D MAS NMR spectrum shown above the 2D plot of Figure 9. All of the nine connectivities expected for the known ZSM-12 structure are observed in the 2D spectrum. The lines may be assigned unambiguously from the expected connectivities by trial and error, but a partial assignment from other data may also be used as a starting point. Such information may be gained, for example, from the expected intensity distribution of the lines, the above-mentioned correlations between δ and SiOSi bond angles, or from different relaxation behavior of particular sites. Other than INADEQUATE, 2D plots from COSY experiments have the normal ^{29}Si chemical shift scale in both F_1 and F_2 and the connectivities appear by cross peaks. However, large intensities along the diagonal occur which may obscur cross peaks close to the diagonal.

So far, 2D ^{29}Si NMR experiments have been mostly applied to high-silica zeolite materials with known structures, and additional details of some of the structures have been revealed. In the case of unknown structures, 2D experiments will make it possible to select between different structural models and to prove or disprove proposed structures or crystallographic space

groups as, for example, shown recently for the low-temperature form of zeolite ZSM-11 and for zeolite ZSM-23.[28]

Silicon-29 COSY MAS NMR spectroscopy has also been applied to ^{29}Si isotopically enriched sodium silicate glasses and sodium phosphosilicate glasses.[12] The cross peaks observed in the COSY spectra of sodium silicate glasses suggest that a substantial portion of the Q^2 and Q^3 as well as Q^3 and Q^4 silicate sites in the glass are interconnected on a nearest neighbor level. In contrast, no cross peaks were observed for the sodium phosphosilicate glass, implying that the Q^4 and six-coordinate silicate sites present in this glass are not linked directly together.

6 APPLICATIONS

Important fields of application of solid state ^{29}Si NMR in the various branches of silicate science are listed below. For more detailed information on these topics the reader is referred to the related articles in the Encyclopedia and the selected reviews or research papers from the recent literature cited in parentheses.

1. Zeolites and related microporous materials (see ***Molecular Sieves: Crystalline Systems***; ***Microporous Materials and Xenon-129 NMR***, and Fyfe et al.,[11] Klinowski,[29] Engelhardt[30]).
2. Mineralogy and geochemistry (see ***Geological Applications*** and Kirkpatrick,[3] Stebbins,[4] Wilson,[31] Stebbins[32]).
3. Silicate and aluminosilicate glasses (see ***Amorphous Materials*** and Kirkpatrick,[3] Grimmer,[33] Dupree,[34] Eckert[35]).
4. Amorphous silica (see ***Silica Surfaces: Characterization*** and Leonardelli et al.,[27] Pfleiderer et al.,[36] Legrand et al.,[37] Chuang et al.[38]).
5. Cements (see Hjorth et al.,[39] Kirkpatrick and Jong,[40] Tong et al.,[41] Grimmer[42]).
6. Phyllosilicates and their transformations (see Kinsey et al.,[43] Weiss et al.,[44] Lambert et al.,[45] Herrero et al.[46]).

7 RELATED ARTICLES

Amorphous Materials; Cross Polarization in Rotating Solids: Spin-1/2 Nuclei; Geological Applications; Magic Angle Spinning; Molecular Sieves: Crystalline Systems; Silica Surfaces: Characterization; Silicon-29 NMR.

8 REFERENCES

1. G. R. Holzman, P. C. Lauterbur, J. H. Anderson, and W. Koth, *J. Chem. Phys.*, 1956, **25**, 172.
2. E. Lippmaa, M. Mägi, A. Samoson, G. Engelhardt, and A.-R. Grimmer, *J. Am. Chem. Soc.*, 1980, **102**, 4889.
3. R. J. Kirkpatrick, in *Spectroscopic Methods in Mineralogy and Geology*, ed. F. C. Hawthorne, Mineralogical Society of America, Washington, DC, 1988, p. 341 (*Rev. Mineral.*, 18)
4. J. F. Stebbins, in *Handbook of Physical Constants*, ed. T. H. Ahrens, American Geophysical Union, Washington, DC, 1993.
5. G. Engelhardt and H. Koller, *NMR Basic Principles Prog.*, 1994, **31**, 1.
6. G. Engelhardt and D. Michel, *High-Resolution Solid-State NMR of Silicates and Zeolites*, Wiley, Chichester, 1987.
7. F. Liebau, *Structural Chemistry of Silicates—Structure, Bonding, and Classification*, Springer, Berlin, 1985.
8. W. Loewenstein, *Am. Mineral.*, 1954, **39**, 92.
9. J. F. Stebbins, *Nature (London)*, 1991, **351**, 638.
10. I. Farnan and J. Stebbins, *J. Am. Chem. Soc.*, 1990, **112**, 32.
11. C. A. Fyfe, Y. Feng, H. Grondey, G. T. Kokotailo, and H. Gies, *Chem. Rev.*, 1991, **91**, 1525.
12. C. T. G. Knight, R. J. Kirkpatrick, and E. Oldfield, *J. Non-Cryst. Solids*, 1990, **116**, 140.
13. A. J. Vega, *J. Am. Chem. Soc.*, 1988, **110**, 1049.
14. R. K. Harris and C. T. G. Knight, *J. Chem. Soc., Faraday Trans. 2*, 1983, **79**, 1539.
15. R. F. Mortlock, A. T. Bell, and C. J. Radke, *J. Phys. Chem.*, 1991, **95**, 7847.
16. H. Koller, G. Engelhardt, and J. Felsche, *Z. Anorg. Allg. Chem.*, 1995, **621**, 301.
17. G. Engelhardt, D. Zeigan, D. Hoebbel, A. Samoson, and E. Lippmaa, *Z. Chem. (Leipzig)*, 1982, **22**, 314.
18. G. Engelhardt, *Stud. Surf. Sci. Catal.*, 1989, **52**, 151.
19. B. L. Sheriff, H. D. Grundy, and J. S. Hartman, *Eur. J. Mineral.*, 1991, **3**, 751.
20. A.-R. Grimmer, F. v. Lampe, M. Mägi, and E. Lippmaa, *Z. Chem. (Leipzig)*, 1983, **23**, 343.
21. M. Mägi, E. Lippmaa, A. Samoson, G. Engelhardt, and A.-R. Grimmer, *J. Phys. Chem.*, 1984, **88**, 1518.
22. A.-R. Grimmer, F. v. Lampe, and M. Mägi, *Chem. Phys. Lett.* 1986, **132**, 549.
23. J. F. Stebbins and M. Kanzaki, *Science*, 1991, **251**, 294.
24. C. P. Herrero, *J. Phys. Chem.*, 1991, **95**, 3282.
25. C. A. Fyfe, H. Strobl, G. T. Kokotailo, G. J. Kennedy, and G. E. Barlow, *J. Am. Chem. Soc.*, 1988, **110**, 3373.
26. G. Engelhardt and H. van Koningsveld, *Zeolites*, 1990, **10**, 650.
27. S. Leonardelli, L. Facchini, C. Fretigny, P. Tougne, and A. P. Legrand, *J. Am. Chem. Soc.*, 1992, **114**, 6412.
28. C. A. Fyfe, H. Grondey, Y. Feng, G. T. Kokotailo, S. Ernst, and J. Weitkamp, *Zeolites*, 1992, **12**, 50.
29. J. Klinowski, *Chem. Rev.*, 1991, **91**, 1459.
30. G. Engelhardt, *Stud. Surf. Sci. Catal.*, 1991, **58**, 285.
31. M. A. Wilson, *NMR Techniques and Applications in Geochemistry and Soil Chemistry*, Pergamon Press, Oxford, 1987.
32. J. F. Stebbins, in *Spectroscopic Methods in Mineralogy and Geology*, ed. F. C. Hawthorne, Mineralogical Society of America, Washington DC, 1988, p. 405 (*Rev. Mineral.*, 18).
33. A.-R. Grimmer, *Exp. Tech. Phys.*, 1988, **36**, 81.
34. R. Dupree, *Exp. Tech. Phys.*, 1988, **36**, 315.
35. H. Eckert, *Prog. NMR Spectrosc.*, 1992, **24**, 159.
36. B. Pfleiderer, K. Albert, E. Bayer, L. van de Ven, J. de Haan, and C. Cramers, *J. Phys. Chem.*, 1990, **94**, 4189.
37. A. P. Legrand, H. Taibi, H. Hommel, P. Tougne, and S. Leonardelli, *J. Non-Cryst. Solids*, 1993, **115**, 122.
38. I.-S. Chuang, D. R. Kinney, C. E. Bronnimann, R. C. Zeigler, and G. E. Maciel, *J. Phys. Chem.*, 1992, **96**, 4027.
39. J. Hjorth, J. Skibstedt, and H. J. Jacobsen, *Chem. Concr. Res.*, 1988, **18**, 789.
40. R. J. Kirkpatrick and C. D. Jong, in *Application of NMR to Cement Chemistry*, eds. A.-R. Grimmer and P. Colombet, Gordon & Breach, London, 1994, p. 55.
41. Y. Tong, H. Du, and L. Fei, *Cem. Concr. Res.*, 1990, **20**, 986.

42. A.-R. Grimmer, in *Application of NMR to Cement Chemistry*, eds. A.-R. Grimmer and P. Colombet, Gordon & Breach, London, 1994, p. 113.
43. R. A. Kinsey, R. J. Kirkpatrick, J. Hower, K. A. Smith, and E. Oldfield, *Am. Mineral.*, 1985, **70**, 537.
44. C. A. Weiss, S. P. Altaner, and R. J. Kirkpatrick, *Am. Mineral.*, 1987, **72**, 935.
45. J. F. Lambert, W. S. Millman, and J. J. Fripiat, *J. Am. Chem. Soc.*, 1989, **111**, 3517.
46. C. P. Herrero, J. Sanz, and J. M. Serratosa, *J. Phys. Chem.*, 1989, **93**, 4311.

Biographical Sketch

Günter Engelhardt. *b* 1936. Dipl.-Chem., 1960. Dr.rer.nat., 1963, Technical University of Dresden, East Germany (supervisor Heinrich Kriegsmann), Dr. habil., 1969, Humboldt University Berlin, East Germany. Central Institute of Physical Chemistry, Academy of Sciences of the GDR, Berlin-Adlershof, East Germany, 1963–86. Faculty of Chemistry, University of Konstanz, West Germany, 1987–92. Institute of Chemical Technology I, University of Stuttgart, Germany, 1992–present. Approx. 180 publications, and, with D. Michel, the book High-Resolution Solid-State NMR of Silicates and Zeolites. Current research specialty: multinuclear solid state MR and its application to zeolite catalysts and other inorganic materials.

Spectral Editing Techniques: Hydrocarbon Solids

Kurt W. Zilm

Yale University, New Haven, CT, USA

1	Introduction	1
2	Background on Spectral Editing of Liquids	1
3	Challenges Posed by Solids	1
4	Experimental Considerations and Caveats	5
5	Summary	6
6	Related Articles	6
7	References	6

1 INTRODUCTION

Spectral editing techniques in NMR in general are methods that aid the spectroscopist in assigning or simplifying complex high-resolution spectra. Most approaches to spectral editing have been developed in the context of NMR of ^{13}C where the emphasis has been on separating ^{13}C resonances on the basis of their multiplicity, i.e. the number of directly attached ^{1}Hs. This type of information, when combined with the analysis of ^{13}C chemical shifts, is very often sufficient for determining the chemical structure of rather complex organic molecules. As such, spectral editing of solution NMR finds wide application in industry for the structural characterization of polymers, drugs, and petroleum based products. Development of similar methods which are applicable to solid samples has been motivated by a large number of important applications to geochemical and material science.

This article deals with spectral editing approaches developed specifically for high-resolution solid state NMR of ^{13}C. Many different strategies have been applied to this problem, and the space provided here unfortunately does not permit covering every aspect of this subfield. Most of the relevant literature is cited in two recent papers,[1,2] and the interested reader may find more extensive citations contained therein.

2 BACKGROUND ON SPECTRAL EDITING OF LIQUIDS

The high information content of ^{13}C NMR spectra of liquids is well known. It follows directly from the large dispersion of the ^{13}C chemical shift and the remarkably tight correlation of ^{13}C chemical shifts with structure. The beautiful stick-spectrum simplicity of ^{13}C spectra is made possible by ^{1}H decoupling and the low natural abundance of ^{13}C which eliminates complications from ^{13}C–^{13}C J couplings. Their information content is greatly increased if the multiplicity of the ^{13}C resonances can be determined.

Editing techniques for ^{13}C NMR of liquids rely on the fairly narrow range of values for $^{1}J(^{13}\mathrm{C},^{1}\mathrm{H})$. This permits one to devise pulse sequences in which the evolution of the ^{13}C magnetization can be made to depend principally upon the number n of directly attached ^{1}Hs in CH_n groups. The attached proton test (APT) is the simplest example. In its most basic form, a $\pi/2$, τ, π, τ, acquire echo sequence is applied to the ^{13}C with ^{1}H decoupling during acquisition. A π pulse is also applied to the ^{1}Hs after the first τ, resulting in J modulation of the ^{13}C spin echo. During the 2τ evolution period the dephasings of the ^{13}C chemical shifts are refocused, while those due to $^{1}J(^{13}\mathrm{C},^{1}\mathrm{H})$ accumulate. Setting τ to $\frac{1}{2}J$ produces a spectrum in which the CH_3 and CH_1 resonances are inverted, while the CH_2 and CH_0 resonances are absorptive.

For complex ^{13}C spectra, more powerful methods are required, but all rely upon J couplings in some manner. In editing protocols based on INEPT, J modulation is used to label the ^{1}H magnetization which is then transferred to the ^{13}C (see ***INEPT***). The various CH_n groups can be amplitude modulated in distinct ways depending upon the length of the time evolution due to J coupling. On this basis schemes can be devised in which linear combinations of a few different experiments produce CH_3-only, CH_2-only, CH_1-only, and CH_0-only spectra. Techniques utilizing DEPT provide some improvement in selectivity, as the differentiation of CH_n groups depends upon a pulse flip angle rather than a period τ of free evolution under $^{1}J(^{13}\mathrm{C},^{1}\mathrm{H})$. Especially clean separation of CH_n subspectra has been achieved using multiple quantum coherence among the J-coupled spins. This *s*ubspectral *e*diting using a *mu*ltiple-quantum *t*rap (SEMUT) has the advantage of being relatively insensitive to the value of $^{1}J(^{13}\mathrm{C},^{1}\mathrm{H})$.

3 CHALLENGES POSED BY SOLIDS

As discussed elsewhere in the Encyclopedia, obtaining high-resolution ^{13}C spectra of organic solids requires both magic angle spinning (MAS) and high-power decoupling of the protons. These techniques are usually combined with cross polarization (CP) in a CP MAS experiment. The need to remove broadening associated with chemical shift anisotropy and ^{13}C–^{1}H dipolar couplings presents a new set of problems in the design of methods for spectral editing. Over the last 20 years of development in high-resolution NMR of solids three basic strategies have been applied to this problem. The first has been to design pulse sequences which produce J-modulated signals in solids, and thereby directly adapt the techniques just discussed to solids. The others use ^{13}C–^{1}H dipolar couplings as the basis for selection of CH_n. Some of these methods use the relative strengths of dipolar couplings or rates of CP to differentiate ^{13}C signals of different multiplicities. Others rely upon the establishment of quasi-equilibrium states in the CP process and thus differentiate the ^{13}C multiplicities on the basis of the ratio of the inverse rotating frame spin temperature of the ^{13}C to that for its directly bonded protons.

3.1 *J* Modulation in Solids

Observing resolved $^{1}J(^{13}\mathrm{C},^{1}\mathrm{H})$-coupled multiplets in CP MAS ^{13}C spectra of solids is made difficult by the strong

$^1H-^1H$ and $^1H-^{13}C$ dipolar couplings. In the absence of strong on-resonance ^1H decoupling, CP MAS spectra of typical rigid samples are broad and relatively featureless. The $^1H-^{13}C$ dipolar broadening is by itself inhomogeneous, and should therefore be suppressed by MAS. However the spin-exchange mediated by the $^1H-^1H$ dipolar couplings is faster than typical rates of MAS. Therefore the spin states of ^1H can change several times during a MAS cycle, and the average of the $^1H-^{13}C$ dipolar interaction is then no longer zero. In a simplified picture one can consider this to be a lifetime broadening of the ^{13}C resonances due to the short lifetime of the spin states of the directly attached protons. Terao and co-workers[3] first demonstrated that suppression of the $^1H-^1H$ dipolar couplings could make it possible to observe $^1J(^{13}C,^1H)$-coupled multiplets in solids. In their work, ^1H decoupling at the magic angle in the rotating frame was first used. Subsequently a number of homonuclear sequences such as MREV-8 have been applied as homonuclear multiple pulse decoupling (MPD) for this purpose. For systems such as plastic crystals where molecular motion has already appreciably averaged the dipolar couplings, MPD produces CP MAS spectra with well-resolved $^1J(^{13}C,^1H)$ coupled multiplets. The couplings observed are reduced by the scaling factor appropriate to the particular MPD sequence used.

This approach has been extended to editing schemes that most resemble those used in liquids. The basic approach is to insert MPD sequences in the periods of free evolution under $^1J(^{13}C,^1H)$. APT-type spectra of motionally narrowed solids have been acquired in this fashion, but in the general case the MPD does not produce sufficient narrowing of the proton NMR spectra to permit sustained J modulation. Terao and co-workers[4] have investigated the limitations of this approach most extensively for rigid solids. One sequence they have successfully used in producing J modulation for rigid solids consists of CP followed by a J-modulated rotor synchronized echo. During the first half of the echo, magnetization of the ^{13}C nuclei evolves under proton homonuclear decoupling. This period, t_1, is adjusted to be equal to one rotor cycle. Over the course of the rotor period J modulation accumulates, but any modulation by the $^{13}C-^1H$ dipolar coupling and the ^{13}C CSA is refocused. After the π pulse, high-power dipolar decoupling is applied for another period t_1. This second interval refocuses the isotropic chemical shift and effects of any bulk susceptibility broadening that accumulated during the first t_1 period. FIDs taken as a function of t_1 then are largely only modulated by $^1J(^{13}C,^1H)$. In this manner a 2D heteronuclear J-resolved spectrum can be obtained with multiplets in the ω_1 dimension. However this approach still does not yield clean multiplets. For instance, the outer lines in quartets for CH_3 groups are very much broader than the central pair, and they are barely resolved.

At the moment, J modulation based editing techniques for solids will remain useful only for systems with significant motional narrowing. Advances in the efficiency of homonuclear decoupling, especially under conditions of MAS, are needed before such techniques can become widely applicable. Problems also remain in combining these homonuclear decoupling requirements with the typical hardware used for CP MAS NMR. While the approach has been proven in principle, development of generally applicable methods for solids along these lines remains a challenge for the future.

3.2 Dipolar Dephasing and Related Schemes

The most generally applicable editing techniques for solids take advantage of the strong dipolar couplings inherent in solids, rather than treating them as a nuisance to be eliminated. The simplest approach to spectral editing in CP MAS NMR of organic solids is the venerable technique[5] of dipolar dephasing (DD) or interrupted decoupling. After CP, the ^1H decoupler is turned off for $\sim 50\,\mu s$. This is a sufficient time for the $^{13}C-^1H$ dipolar coupling to dephase the transverse magnetization for any ^{13}C with a directly bonded ^1H, as long as the dipolar coupling is not motionally averaged. Therefore the lines for rigid CH_1 and CH_2 groups are effectively suppressed. Rapid rotation of CH_3 groups at room temperature leads to different behavior for these protonated carbons. This rotation renders the three $^{13}C-^1H$ dipolar couplings equal, and reduces them to one-third of their static value. Depending upon the spin state of the protons, the ^{13}C in a CH_3 group can experience one of two possible dipolar fields. Whenever the three protons are in the same state ($\alpha\alpha\alpha$ or $\beta\beta\beta$), the three couplings reinforce one another, and the ^{13}C experiences the field of a single full $^{13}C-^1H$ dipolar coupling. However, three-quarters of the time the ^1Hs are in a state such as $\alpha\alpha\beta$ or $\beta\beta\alpha$. In this instance the fields due to two of the couplings will exactly cancel. The net dipolar field then is usually only one-third of a single $^{13}C-^1H$ dipolar coupling, and this is similar to that often experienced through nonbonded contacts by a CH_0. Thus, in most instances, methyl groups at room temperature behave like nonprotonated carbons under dipolar dephasing. The DD spectrum then consists of slightly attenuated resonances for just the CH_0 and CH_3 groups. Comparison with a fully polarized CP MAS spectrum provides a simple qualitative method for categorizing resonances as either CH_3 + CH_0 or CH_2 + CH_1. In many instances, a simple CP MAS spectrum can be fully assigned using this approach in combination with information from linewidth or chemical shifts.

Several approaches have been taken to improve on the basic DD technique. In some instances the dephasing interval leads to an unacceptable linear phase correction due to the delayed acquisition. A π pulse may be inserted in the interrupted decoupling interval to alleviate this to some degree. However, as first pointed out by Munowitz and Griffin,[6] the π pulse should be applied only after a full rotor period to ensure that both the isotropic and anisotropic portions of the ^{13}C chemical shift are refocused. Other groups have investigated the spin dynamics of the DD experiment with the desire to separate CH_n resonances more completely or quantitatively.[7] The approach has been to fit the dephasing of the ^{13}C resonances as a function of the dephasing time, τ_D, to some type of model dephasing function. Since it can be argued the different CH_n groups may have characteristic dephasing characteristics, this approach would seem to have some validity. In this manner one can then extrapolate back in dephasing time to recover the initial intensities of the CH_3 and CH_0 resonances.

The best way to view the DD experiment is actually as a low-resolution 1D version of separated local field (SLF) spectroscopy under MAS conditions. During τ_D the ^{13}C FID is dominated by the $^{13}C-^1H$ dipolar couplings, and is damped by the $^1H-^1H$ dipolar interactions. An isolated CH_1 group then has a decay profile that is essentially a damped Pake doublet FID, that for a CH_2, i.e. a Pake 'triplet'. Since the local structure of isolated CH_n groups of a given n does not

vary appreciably in organic solids, these decays would be quite characteristic were it not for the $^1H-^1H$ dipolar couplings. This complication can be removed by applying MPD during the dephasing interval. In this manner the number of dipolar couplings is determined from a spectral pattern, i.e. sideband intensities, rather than from a less structure-specific average dephasing rate.

The first proposal for this type of MAS SLF spectroscopy was by Munowitz and Griffin[6] as a means of measuring C–H distances. Webb and the author[8] later investigated using the spinning sideband patterns characteristic of the different CH_n groups for spectral editing. The proposed 2D experiment consists of CP followed by MPD (usually MREV-8) for t_1 to produce dipolar evolution in the first frequency dimension. This is followed by a $\pi/2(\phi_i)$, τ, $\pi/2(x)$ sequence to selectively project the ^{13}C magnetization onto one axis of the rotating frame. The period, τ, is a few hundred μs and is used to dephase magnetization not placed along z by the $\pi/2(\phi_i)$ pulse. Following the $\pi/2(x)$ pulse, the normal dipolar decoupled ^{13}C FID is acquired during time period t_2. Cycling the phase ϕ_i in a time proportional phase incrementation scheme avoids the need to acquire a quadrature data set in t_1. The sideband patterns generated this way in the ω_1 dimension retain both dipolar and CSA effects. However, at low-to-moderate field strengths the patterns are so dominated by the $^{13}C-^1H$ dipolar couplings that they can still be easily deconvolved into their CH_n components. Since CH_2 groups have two dipolar couplings, they have nearly twice as many sidebands, and are readily distinguished from CH_1 groups by this technique. Decomposition of complex CP MAS spectra with many overlapping lines has been demonstrated using this approach. At higher fields the same deconvolution methods can be applied using Munowitz and Griffin's rotor-synchronized sequence to eliminate the complications due to CSA. The requirement for delaying acquisition to several rotor periods after the initial CP interval, however, can result in substantial losses in sensitivity. A further simplification has been proposed by Sethi.[9] Since the temporal evolution during t_1 in the MAS SLF experiments is well understood, only a few special times t_1 need be acquired. Using this approach Sethi has introduced 1D editing schemes that also can be used to separate CH_1 and CH_2 resonances.

3.3 Schemes Using CP Dynamics

The previous methods rely upon the relative strengths of $^{13}C-^1H$ dipolar couplings or the different numbers of dipolar couplings to discriminate between different CH_n groups. The dipolar couplings are used essentially to dephase or modulate the ^{13}C resonances in a predictable manner. Another strategy is to use the ways in which these differences in the dipolar coupling network result in differences in the CP dynamics between the CH_n groups.

The simplest description of the CP process considers the transfer as a first-order kinetic process with a time constant T_{CH}. However, it is well known that this description is only qualitatively correct, and only phenomenologically describes the long-time behavior ($t \gg T_2$). At short CP times the Hartmann–Hahn transfer is dominated by the details of the dipolar coupling network between a ^{13}C and its directly bonded ^1Hs. In single crystals, one even observes transient oscillations in the polarization transfer. For powdered samples under moderate MAS, the transient effect manifests itself as a rapid initial period of CP transfer in which the ^{13}C and its attached ^1Hs come into a quasi-equilibrium. Spin diffusion to the more distant protons transports polarization more slowly to these ^1Hs coupled to the ^{13}C. This slower process determines the rate at which the ^{13}C reaches its final fully polarized state. In the quasi-equilibrium state, the initially unpolarized ^{13}C nuclei share the polarization equally with their directly attached protons. CH_1 and CH_2 groups then polarize to one-half and two-thirds of their full intensity, respectively, on the short timescale. Because of their motionally averaged dipolar field, CH_3 groups behave similarly to nonprotonated carbons. Both the CH_0 and CH_3 groups then polarize more slowly, with the polarization bottleneck to full enhancement usually being the rate of $^1H-^1H$ spin diffusion. As long as the transfer of transient polarization among the closely coupled spins is faster than the $^1H-^1H$ spin diffusion and direct transfer from more distant protons, it can be put to good use in spectral editing schemes.

One particularly useful approach for distinguishing the signals of $CH_1 + CH_2$ from those of $CH_0 + CH_3$ based on the previous ideas is the depolarization (DEP) technique.[10] After a several ms CP interval, the spin locked ^1H magnetization is allowed to dephase by turning off the ^1H rf for several hundred μs, while keeping the ^{13}C spin locked. Turning the ^1H rf back on reestablishes the CP contact, and the ^{13}C magnetization can be used to repolarize the depolarized ^1Hs. If the phase of the ^1H rf is switched 90° every 25–50 μs over a total period of a few hundred μs, there will be no net buildup in the ^1H magnetization, only a net drain from the ^{13}C. Since only the $CH_1 + CH_2$ carbons polarize on this timescale, their signals are fully depleted after the depolarization, while the $CH_0 + CH_3$ signals are attenuated only slightly. The resulting DEP spectrum is much like a DD spectrum. However since the ^{13}C are spin locked until the depolarization is finished, there are no problems with linear phase errors as in DD.

Polarization inversion (PI) can also be used in a similar fashion.[11] In this technique the ^{13}C are first fully polarized by CP, and the phase of the rf in the ^1H channel suddenly inverted. Since the ^1H spin temperature has now been inverted, the ^{13}C will try to follow. Those ^{13}C with strong $^{13}C-^1H$ dipolar couplings first quickly depolarize, and then repolarize in the opposite direction. Since the zero crossings for CH_1 and CH_2 groups are different, they can be used in some instances to distinguish resonances. Nulling of resonances in this manner has also been referred to as cross depolarization[12] (CPD). A further variant adds a final short polarization period onto the CPD sequence.[13] The depolarization and repolarization periods in this cross-depolarization–repolarization technique (CPDR) can be adjusted so as simultaneously to null the CH_1 and CH_2 groups. This is not in general possible with the cross-depolarization interval alone.

Sangill et al.[2] have presented a thorough study of the use of CPD and CPDR in spectral editing. Their analysis focused on using optimized combinations of CPD and CPDR spectra to produce CH_n-only spectra, $n = 0–3$, while maintaining good sensitivity. By paying careful attention to the CP dynamics, they were able successfully to separate complex CP MAS spectra into their CH_n subspectral components.

Burum and Bielecki[14] have introduced a particularly clever method based on CP dynamics for selectively detecting CH_2

groups in CP MAS NMR. Their method, WIMSE (*w*indowless *i*sotropic *m*ixing for *s*pectral *e*diting), starts with a CP interval under a multiple pulse cycle which eliminates the $^1H-^1H$ dipolar couplings during the CP step while maintaining the $^{13}C-^1H$ couplings. Over a MAS rotor period under these conditions, no net polarization is transferred to ^{13}C nuclei in CH groups. Instead, whatever magnetization is transferred at the start of the rotor cycle 'echoes' back from the ^{13}C to the ^1H at the end. However, the presence of two dipolar couplings in a CH_2 group defeats this 'rotational polarization echo' effect. The resulting spectrum then consists solely of the CH_2 component in a complex CP MAS spectrum. CH_3 and CH_0 lines do not appear as their CP rates are too slow.

3.4 Techniques Using Quasi-Equilibrium States

Another successful method based on differences in CP dynamics between the different CH_n groups is the solid state attached proton test, or SSAPT method. Initially the ^{13}C are fully polarized using a 2–3 ms CP interval. Immediately following this, a short PI period is applied, typically on the order of 50 μs. At the beginning of the PI time the ^{13}C and their directly attached ^1Hs are equally polarized. Upon reversal of the phase in the ^1H spin locking rf, this equilibrium is broken, and the spins try to reequilibrate. Since the CH_3 and CH_0 groups polarize slowly, they are relatively unaffected by this short PI interval. The CH_2 and CH_1 groups, on the other hand, have sufficient time to reach a quasi-equilibrium state through a rapid transient CP transfer. In the case of the CH_1 group, the ^{13}C and the ^1H have equal but opposite polarizations at the start of the PI. During the short PI time these magnetizations cancel, and the signal for the CH_1 carbons is very effectively nulled. The ^{13}C nuclei in the CH_2 groups carry 1 unit of polarization as opposed to the -2 units in the ^1Hs at the beginning of the PI interval. This results in -1 unit of total polarization to be shared among the three spins in the quasi-equilibrium state. At the end of the PI period, the CH_2 signal is then inverted with an intensity of $-\frac{1}{3}$ of its fully polarized signal. The SSAPT spectrum then has CH_3 + CH_0 signals nearly fully polarized and positive, CH signals nulled, and CH_2 signals inverted at one-third intensity. In many instances this provides a very straightforward means of separating the contributions from the different CH_n groups to a ^{13}C CP MAS spectrum.[15,16]

This approach has been extended to a complete spectral editing protocol by Wu, Burns, and the author.[1] Since the establishment of the quasi-equilibrium state depends upon the ratio of the inverse rotating frame spin temperatures of the ^{13}C and its directly bonded ^1Hs, this technique is less sensitive to the CP rates. In this sense it is a relatively robust editing procedure.

The complete spectral editing procedure due to Wu et al. uses four basic experiments (see Figure 1). One begins by acquiring a CH_2-only spectrum. The sequence used starts with a short CP contact which polarizes the CH and CH_2 groups to their quasi-equilibrium intensities of $\frac{1}{2}$ and $\frac{2}{3}$ respectively. This is followed by a short PI interval of roughly the same length. During PI the CH signals null, as does any small CH_3 or CH_0 polarization built up during the CP step. The CH_2 ^{13}C magnetization goes to $-\frac{1}{3}$ of its initial value, resulting in a spectrum with $-\frac{2}{9}$ the intensity for these carbons. This

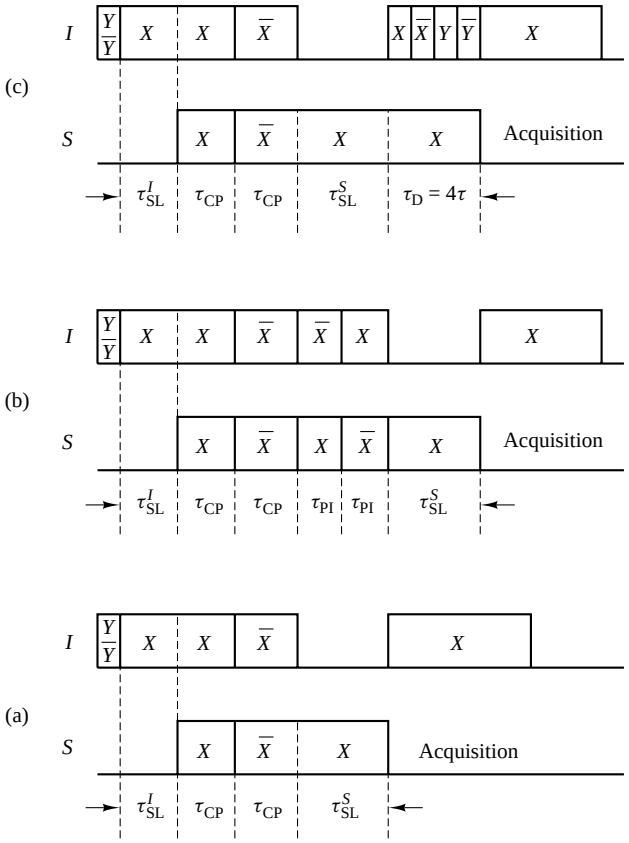

Figure 1 Sequences used in the editing protocol of Wu et al. All employ simultaneous phase inversion to alleviate problems with Hartmann–Hahn mismatches. (a) CP sequence. The additional spin locking delay τ_{SL}^S is used to make the total ^{13}C spin locking time the same in all of the sequences. (b) SCPPI sequence used to acquire CH_2-only spectra. (c) Depolarization sequence. The time τ_{SL}^I is added in these sequences mainly to minimize distortions from ^1H rotating frame relaxation

short CP polarization inversion (SCPPI) spectrum then has contributions from only the CH_2 groups.

The second experiment is a short contact CP (SCP). This will have intensity principally from the CH and CH_2 carbons. Another short CP spectrum with a depolarization interval is also acquired (SCPD). The SCPD spectrum can be used to subtract out the contamination of the SCP data from CH_3 and CH_0 groups. Unfortunately the CH_3 and CH_0 carbons have sufficiently different CP dynamics that they are differentially attenuated, and this subtraction alone is insufficient. In most instances, however, the shift ranges for CH_3 and CH_0 groups are adequately separated so that a dividing line on the ^{13}C chemical shift scale can be chosen to separate these groups. Different weighting factors can then be applied to the upfield (CH_3) and downfield (CH_0) regions for this purpose. The result of this procedure is a relatively clean CH-only spectrum.

To acquire semiquantitatively correct CH_0 and CH_3 spectra, a long CP depolarization spectrum is acquired (LCPD). This spectrum is again split into CH_0 and CH_3 regions, and each part corrected for the differential signal loss of the two types of groups in the depolarization step.

The cleanest and most quantitative results are obtained with this method if the intensity factors for spectral decomposition are determined experimentally on a known model system.

Table 1 Typical Intensities for CH_n Resonances in Pulse Sequences Used for Spectral Editing

	CH_n			
Experiment	CH_0	CH_1	CH_2	CH_3
LCP	100	100	100	100
SCP	10.5	57.5	68	22.6
SCPPI	0	0	−22	0
SCPD	7.2	0	0	10.4
LCPD	82.5	0	0	57.5

Using the set of sequences shown in Figure 1, the intensity matrix in Table 1 is found to be typical. LCP is used to denote a standard (long) CP experiment which is used as the 100% intensity reference.

As the entries demonstrate, the CH and CH_2 group intensities in the SCPPI and SCP experiments are quite close to those expected from the quasi-equilibrium description of the CP dynamics.

Figure 2 compares the four spectra acquired in the editing protocol for cholesteryl acetate to the normal CP MAS spectrum. In the solid state there are two molecules in the unit cell producing a doubling of the lines. Furthermore, changes in conformation lead to significant shifts in many resonances. Using the intensity matrix in Table 1, the CH_n, $n = 0-3$, only spectra can be reconstructed from these data. The results of this data manipulation are shown in Figure 3, clearly demonstrating the simplifications made possible by this spectral editing approach. As a check on this editing protocol, one may sum the CH_n subspectra to produce a synthetic CP MAS spectrum. This is compared with the normal CP MAS spectrum in Figure 4, along with the difference of the two. The small differences observed indicate the reliability of the approach used.

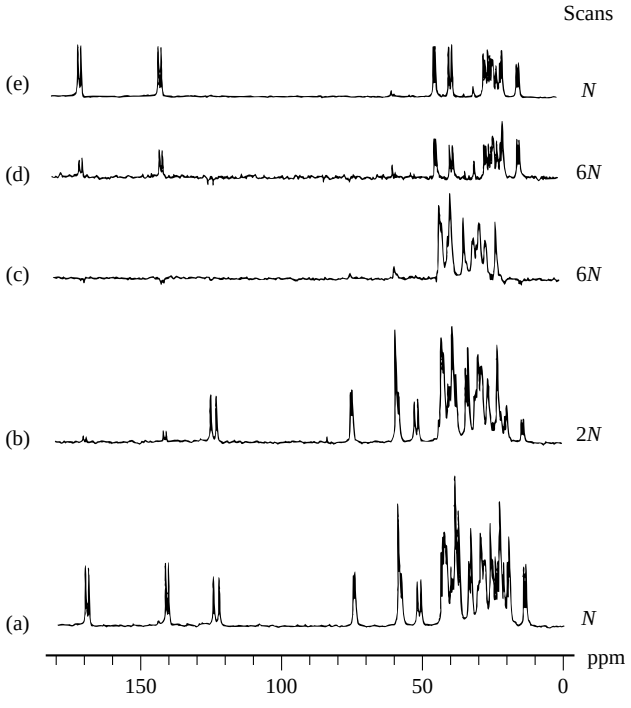

Figure 2 Data from a spectral editing experiment on cholesteryl acetate. (a) Normal CP spectrum for comparison. (b) SCP spectrum. (c) SCPPI spectrum. (d) SCPD spectrum. (e) LCPD spectrum. In practice larger numbers of scans are acquired for the lower signal-to-noise experiments as indicated in the figure

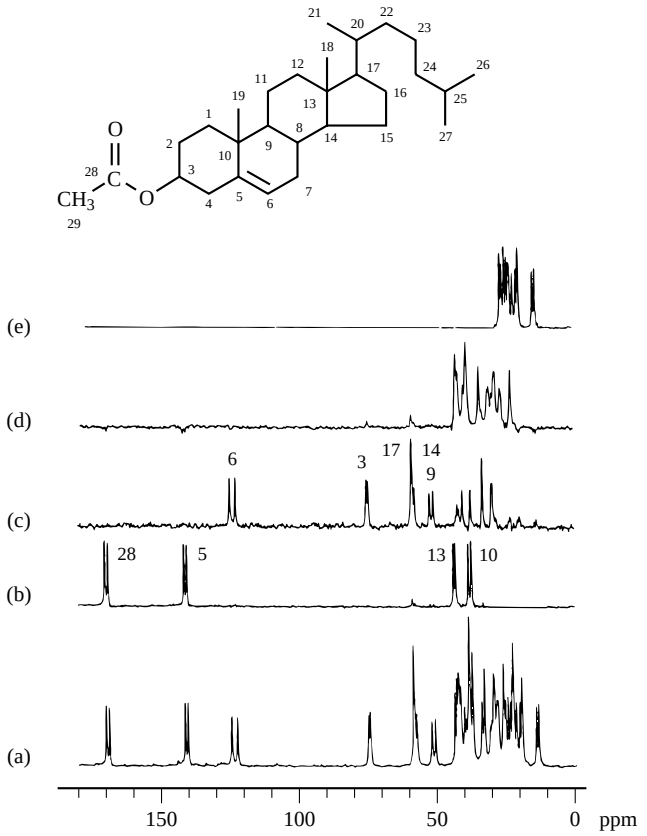

Figure 3 Subspectra constructed from the data in Figure 2. (a) Normal CP MAS spectrum again for comparison. (b) CH_0-only. (c) CH_1-only. (d) CH_2-only. (e) CH_3-only. Some of the assignments made possible by the editing technique are given in the inset

4 EXPERIMENTAL CONSIDERATIONS AND CAVEATS

Except for the simplest approaches to spectral editing in solids, one must pay some extra attention to the experimental setup. In particular, very high MAS spin rates and rf inhomogeneity can adversely affect the CP dynamics relied upon in most methods. The sharpening of the Hartmann–Hahn condition, and the need to match typically on a sideband condition, $\omega_1 = \omega_2 + \omega_r$, makes a homogeneous rf field more important than in a standard CP MAS experiment. Good experimental practice requires stable rf levels, restricting the sample to well within the rf coil, and a stable spin rate. For experiments utilizing short CP, PI, or depolarization periods, additional modifications that make the matching condition less sensitive are needed. Our group has found the simultaneous phase inversion method[1,14,15] easy to incorporate in editing schemes. The pulse sequences in Figure 1 utilize this approach to make the results much less sensitive to how well the matching condition is set and maintained throughout the experiment.

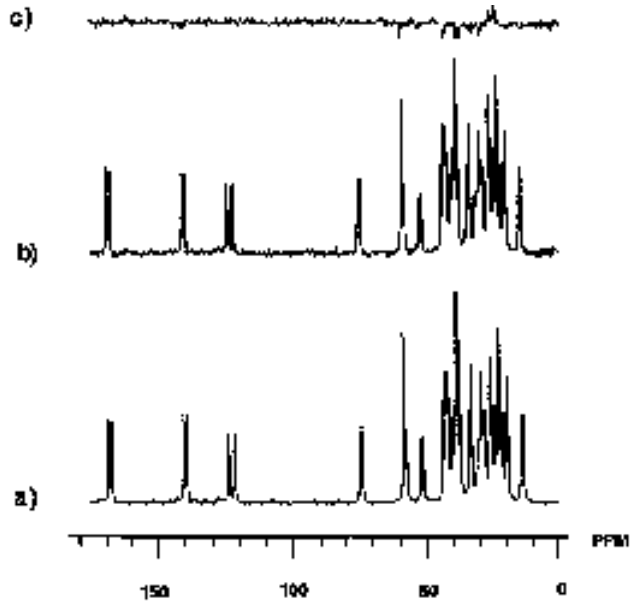

Figure 4 Comparison of the (a) normal CP MAS spectrum and (b) the synthetic one produced by direct summation of the subspectra in Figure 3(b)–(e). (c) The difference between the normal and synthetic CP MAS spectra

When spectra are to be combined in an editing procedure, it is also important to consider rf heating, droop in the rf levels, and $T_{1\rho}$ relaxation. Whenever possible, it is a good practice then to keep the rf fields on for comparable periods of time in the different experiments to be combined. The sequences in Figure 1 have been constructed to take these additional complications into account. Table 2 gives the set of delays in reference to Figure 1 that have been found to give optimal performance in editing applications on rigid solids at moderate fields and MAS rates. These parameters have been used and tested in applications to many coals and polymers as well as on model systems.

Methods which employ homonuclear decoupling sequences require additional care in spectrometer alignment. For these methods one must more carefully adjust all rf levels, and pay especial attention to rf homogeneity. In practice one must follow the same procedures as used to prepare for a ^{1}H CRAMPS experiment. Similar complications from the interaction of the MAS and the MPD also occur as found in CRAMPS.

The majority of the methods that have been discussed here rely on differences in the dipolar coupling networks found between the various CH_n groups. These are washed out when there is significant motional averaging, and as such all of these methods have limitations. On the other hand, such motional narrowing has many signatures which are easy to recognize, and provides another means of discriminating between resonances in a complex spectrum. When very fast MAS rates are employed, the spin dynamics also change.[17] Most methods presented here work best at low to moderate MAS rates (5 kHz or below). Additional complications can arise at high fields because of the CSA spinning sidebands. Since different molecular orientations with respect to the rotor contribute more intensity to some sidebands than others, the inhomogeneous nature of the CP dynamics can be accentuated. Under many editing schemes the center and sidebands can then behave differently, complicating analysis. In the light of these difficulties, most applications to complex systems have employed low field operation ($B_0 < 4$ T). Additional work is needed to delineate how high-field and high-speed MAS operation can be accommodated with the majority of these methods.

Table 2 Delay Parameters for Spectral Editing

	Delay (μs)				
Experiment	$\tau_{SL}{}^I$	$2\tau_{CP}$	$2\tau_{PI}$	$\tau_{SL}{}^S$	τ_D
LCP	140	1500	0	400	0
SCP	1600	40	0	400	0
SCPPI	1600	40	35	365	0
SCPD	1600	40	0	300	100
LCPD	140	1500	0	300	100

5 SUMMARY

At present there are many methods available for distinguishing CH_3 + CH_0 groups from CH and CH_2 centers in CP MAS spectra. A number of reliable approaches for separating CH and CH_2 groups have also appeared, and some of these have been combined in complete spectral editing protocols which separate resonances by multiplicity. These methods have many applications in organic geochemistry and polymer science. Further advances are required before most of these techniques can be combined with operation at the highest available field strengths and spin rates.

6 RELATED ARTICLES

CRAMPS; Cross Polarization in Rotating Solids: Spin-1/2 Nuclei; Cross Polarization in Solids; Fossil Fuels; Heteronuclear Assignment Techniques; INEPT; Magic Angle Spinning; Quantitative Measurements; Rotating Solids; Solid State Probe Design; Spin Echo Spectroscopy of Liquid Samples.

7 REFERENCES

1. X. Wu, S. T. Burns, and K. W. Zilm, *J. Magn. Reson. Ser. A*, 1994, **107**, in press.
2. R. Sangill, N. Rastrup-Andersen, H. Bildsøe, H. J. Jakobsen, and N. C. Neilsen, *J. Magn. Reson. Ser. A*, 1994, **107**, 67.
3. T. Terao, H. Miura, and A. Saika, *J. Chem. Phys.*, 1981, **75**, 1573.
4. H. Miura, T. Terao, and A. Saika, *J. Chem. Phys.*, 1986, **85**, 2458.
5. M. Alla and E. Lippmaa, *Chem. Phys. Lett.*, 1976, **37**, 260.
6. M. G. Munowitz and R. G. Griffin, *J. Chem. Phys.*, 1982, **76**, 2848.
7. L. B. Alemany, D. M. Grant, R. J. Pugmire, T. D. Alger, and K. W. Zilm, *J. Am. Chem. Soc.*, 1983, **105**, 2133.
8. G. W. Webb and K. W. Zilm, *J. Am. Chem. Soc.*, 1989, **111**, 2455.
9. N. K. Sethi, *J. Magn. Reson.*, 1991, **93**, 265.

10. X. Wu, S. Zhang, and X. Wu, *Chem Phys. Lett.*, 1989, **162**, 321.
11. X. Wu, S. Zhang, and X. Wu, *J. Magn. Reson.*, 1988, **77**, 343.
12. M. T. Melchior, *22nd Exp. NMR Conf., Asilomar, CA, March 1991*, poster B-29.
13. J. S. Hartman and J. A. Ripmeester, *Chem. Phys. Lett.*, 1990, **168**, 219.
14. D. P. Burum and A. Bielecki, *J. Magn. Reson.*, 1991, **95**, 184.
15. X. Wu and K. W. Zilm, *J. Magn. Reson., Ser. A*, 1993, **104**, 119.
16. X. Wu and K. W. Zilm, *J. Magn. Reson., Ser. A*, 1993, **102**, 205.
17. X. Wu and K. W. Zilm, *J. Magn. Reson., Ser. A*, 1993, **104**, 154.

Acknowledgments

I wish to acknowledge the especially important contributions of two of my colleagues in this field. The first is Dr Gretchen Webb, my first graduate student, who was instrumental in working out 2D MAS SLF methods for editing, as well as developing much of the hardware that still makes these experiments work so well in our laboratory. The second is Dr Xiaoling Wu, my long-time associate, collaborator, and friend. It is because of Xiaoling's experimental acumen and theoretical insight that our laboratory has been able to contribute so successfully to the development of spectral editing methods for solids.

Biographical Sketch

Kurt W. Zilm. *b* 1955. B.S., 1976, Ph.D., 1981, University of Utah. Introduced to NMR by D. M. Grant. Faculty in Chemistry Yale University, 1983–present. Approx. 80 publications. Research interests: theory and development of NMR techniques for solving problems of chemical interest, studies of transition metal polyhydrides, supported metal catalysts, matrix-isolated organic intermediates and metal clusters, applications of optical pumping in gas phase NMR, tunneling in NMR, dipolar demagnetizing field effects in NMR and development of new solids NMR techniques for structural studies in polymers and organic geochemistry.

Spin Diffusion in Solids

T. T. Peter Cheung

Phillips Petroleum Company, Bartlesville, OK, USA

1	Introduction	1
2	Effects of Spin Diffusion on Nuclear Spin Relaxation	2
3	Studies of Polymer Morphology by Proton Spin Diffusion	4
4	Related Articles	6
5	References	6

1 INTRODUCTION

Spin diffusion is a phenomenon in which spin information, or more specifically the spin magnetization, at one location of a substance is transported to other locations. In solids, where the translations of the spin-bearing atoms are highly restricted, the transport of spin information is mediated by spin–spin interactions. In the following, this transport phenomenon and its effects on NMR will be described. Historically, spin diffusion was considered a nuisance, because it tends to average out useful spin information that reflects the spatial heterogeneity of a solid. As will be described below, with an understanding of spin diffusion and appropriate NMR pulse sequences, one can actually extract spatial information about disordered solids such as polymers by following how the local magnetization is transported by spin diffusion.

Consider an isolated pair of identical spins $\frac{1}{2}$, $\boldsymbol{I}_1$ and $\boldsymbol{I}_2$, in a strong external magnetic field. They are coupled to each other by an exchange interaction $\lambda\hat{\boldsymbol{I}}_1 \cdot \hat{\boldsymbol{I}}_2$. If the system is initially in the spin state $|\uparrow\ \downarrow\rangle$, the spins will evolve under the influence of the exchange interaction to the $|\downarrow\ \uparrow\rangle$ state in which there are opposite flips in the 'directions' of the two spins. The total wavefunction of the system can be expressed as

$$\varphi(t) = c_1(t)|\uparrow\downarrow\rangle + c_2(t)|\downarrow\uparrow\rangle \tag{1}$$

By solving the time-dependent Schrödinger equation, the probability that the system remains in $|\uparrow\ \downarrow\rangle$ is

$$|c_1(t)|^2 = \cos^2[(\lambda/\hbar)t] \tag{2}$$

and the probability that it evolves to $|\downarrow\ \uparrow\rangle$ is

$$|c_2(t)|^2 = 1 - \cos^2[(\lambda/\hbar)t] \tag{3}$$

Therefore, the exchange interaction leads to a cyclic transfer of spin information, which, in this case, is the magnetization of spin $\boldsymbol{I}_1$, represented by $|c_1(t)|^2 - |c_2(t)|^2$, from spin $\boldsymbol{I}_1$ to spin $\boldsymbol{I}_2$, and then back to spin $\boldsymbol{I}_1$ again, with a frequency of $\lambda/\hbar$.

In solids, nuclear spins like ^{1}H are strongly coupled by dipole–dipole interactions, the secular part of which has the form

$$\hat{\mathcal{H}}_{\mathrm{d}}^0 = \frac{1}{4}\sum_i \sum_j \frac{(3\cos^2\theta_{ij} - 1)\hbar^2\gamma^2}{r_{ij}^3}(\hat{\boldsymbol{I}}_i \cdot \hat{\boldsymbol{I}}_j - 3\hat{I}_{iz}\hat{I}_{jz}) \tag{4}$$

where θ_{ij} is the angle between the direction of the external magnetic field and the vector joining the spin $\boldsymbol{I}_i$ at location $\boldsymbol{r}_i$ and the spin $\boldsymbol{I}_j$ at $\boldsymbol{r}_j$, and $\boldsymbol{r}_{ij} = |\boldsymbol{r}_i - \boldsymbol{r}_j|$. The exchange term $\hat{\boldsymbol{I}}_i \cdot \hat{\boldsymbol{I}}_j$ in equation (4) allows the exchange of magnetization between two coupled spins $\boldsymbol{I}_i$ and $\boldsymbol{I}_j$. Because of the r_{ij}^{-3} dependence, the interaction can be restricted to nearest-neighbor spins. If the spins $\boldsymbol{I}_1$ and $\boldsymbol{I}_2$ mentioned earlier are a part of the solid and interact with many other spins $\boldsymbol{I}_i$ of the same kind, it becomes very likely that before the magnetization from spin $\boldsymbol{I}_2$ returns to the spin $\boldsymbol{I}_1$, it will spread to other spins coupled to spin $\boldsymbol{I}_2$. This transfer of magnetization will continue to spins at farther distances from spin $\boldsymbol{I}_1$ in a manner very similar to that of the random walk. Hence the term 'spin diffusion' was coined.[1,2]

The spin diffusion equation can be formally derived from the dipole–dipole Hamiltonian in equation (4) using linearized projection operator techniques.[3] However, it is much easier to understand in terms of the rate equation for the *local* magnetization $m(\boldsymbol{r}_i,t)$, which is defined as the thermal average of $\hat{I}_{iz}$ at time t:

$$\frac{\partial m(\boldsymbol{r}_i, t)}{\partial t} = \sum_j{}' W(\boldsymbol{r}_i, \boldsymbol{r}_j)[m(\boldsymbol{r}_j, t) - m(\boldsymbol{r}_i, t)] \tag{5}$$

This equation is an expression of linear response theory stating that the rate of change of the local magnetization at site $\boldsymbol{r}_i$ has a linear (i.e., first-order) dependence on the differences in the local magnetization between site $\boldsymbol{r}_i$ and its nearest-neighbor sites $\boldsymbol{r}_j$. $W(\boldsymbol{r}_i,\boldsymbol{r}_j)$ is the rate of the spin flip–flop induced by the dipole–dipole interaction between spins $\boldsymbol{I}_i$ and $\boldsymbol{I}_j$, and is of the order of the spin–spin relaxation rate $(T_2)^{-1}$. The prime on the summation above indicates that the summation over j is restricted to nearest neighbors of the spin $\boldsymbol{I}_i$. In the simple case where the nuclear spins are arranged in a cubic array, the summation along the x axis can be expressed as

$$a^2 W(\boldsymbol{r}_i, \boldsymbol{r}_i + a\boldsymbol{i}) \frac{\left(\frac{m(\boldsymbol{r}_i + a\boldsymbol{i}, t) - m(\boldsymbol{r}_i, t)}{a}\right) - \left(\frac{m(\boldsymbol{r}_i, t) - m(\boldsymbol{r}_i - a\boldsymbol{i}, t)}{a}\right)}{a} \tag{6}$$

where $\boldsymbol{i}$ is the unit vector along the x axis and a is the lattice constant. In the continuum limit, this reduces to

$$a^2 W(\boldsymbol{r}, \boldsymbol{r} + a\boldsymbol{i}) \frac{\partial^2 m(\boldsymbol{r}, t)}{\partial x^2} \tag{7}$$

Similar expressions can be obtained for the sums along the y and z directions. Neglecting the anisotropy of $W(\boldsymbol{r},\boldsymbol{r} + a\boldsymbol{i})$ or replacing it with W, the average over the three directions, the rate equation becomes the diffusion equation

$$\frac{\partial m(\boldsymbol{r}, t)}{\partial t} = D\nabla^2 m(\boldsymbol{r}, t), \quad \text{with} \quad D = a^2 W \tag{8}$$

Because the nonsecular part of the dipole–dipole interaction as well as other magnetic interactions that we have not considered can lead to spin–lattice relaxation of the nuclear magnetization, one should also include a relaxation term $-m(\boldsymbol{r},t)/T_1(\boldsymbol{r})$ on the right-hand side of the spin diffusion equation when the spin relaxation rate is comparable to the diffusion rate.

Using the Fermi golden rule, the spin flip rate W can be expressed as

$$W \approx |\hat{H}_{\mathrm{d}}^0|^2 f(\omega_i - \omega_j) \tag{9}$$

where ω_i and ω_j are the Larmor frequencies of the spins $\boldsymbol{I}_i$ and $\boldsymbol{I}_j$, and $f(\omega)$ is the lineshape function of the spin pair due to

the action of all the other spins. It has a width of order T_2^{-1} and decays rapidly to zero with increasing ω. The difference in the Larmor frequencies $(\omega_i - \omega_j)$ represents the amount of energy required to flip the two spins in opposite directions. The implication of equation (9) is that the rate of the spin flip is fastest; thus, the spin diffusion is most efficient when the spins have the same Larmor frequency, i.e., when the process is energy-conserving. If the difference in the Larmor frequencies is much larger than T_2^{-1} then the spin flip stops and the spin diffusion is quenched.

Equation (8) holds not only in the laboratory frame but also in the rotating frame, provided that the spin locking field is much larger than the dipolar interactions. For simplicity, we shall not distinguish between spin diffusion in these two frames unless the circumstance requires it and we shall adopt the notation T_{L} for the spin–lattice relaxation time in either frame.

Spin diffusion plays an important role in the understanding of spin–lattice relaxation phenomena in solids when spin relaxation can occur mainly at few isolated locations. For instance, at very low temperatures, spin relaxation in polymers with long molecular chains takes place mainly at the end groups, where motions are still possible. Paramagnetic impurities in crystalline materials also act as relaxation centers for the nuclear spins because of the rapid fluctuations of the electronic spin moments. The relaxation of the total magnetization

$$M(t) = \int_V m(\boldsymbol{r}, t)\, \mathrm{d}^3 r \tag{10}$$

where V is the sample volume, depends on both the relaxation rate at these centers and the rate at which the local magnetization is transported to these centers by spin diffusion.

The question of how well spin diffusion can be utilized to extract information about a system depends largely on one's ability to solve the diffusion equation according to appropriate sets of initial and boundary conditions. The methods of solving the spin diffusion equation are very similar to those used in heat conduction, and there are a number of excellent texts[4,5] treating the latter in great detail. There is one fundamental fact about the diffusion process that should be borne in mind, namely, spin information will travel a distance l in a time $t \approx l^2/D$. In other words, a spin will know what happens to another spin a distance l away in a time t. The consequence is that a spatial inhomogeneity in the local magnetization with a characteristic length l will disappear in a time $t \approx l^2/D$. Let us put this another way: the inhomogeneity will not occur if it requires a time much longer than l^2/D to develop. A good example is the spin–lattice relaxation of protons in solid polymers at ambient temperature. In semicrystalline polymers[6] there are at least two different intrinsic T_1s associated with the crystalline and amorphous phases because of the difference in segmental motions of the polymer chains. However, typically, one observes only a single decay in the total magnetization $M(t)$, with a ${T_1}^{-1}$ being the weighed average of the intrinsic ${T_1}^{-1}$ of each phase. The reason is that the intrinsic T_1s are much longer than the time it takes spin diffusion to occur across the domains of each phase; any inhomogeneity that would have been developed in the magnetization due to the different intrinsic T_1s is averaged out by the spin diffusion.

On the other hand, by using appropriate NMR pulse sequences, one can create a nonuniform magnetization in a solid with a characteristic length l on a timescale much shorter than l^2/D. Then the transfer of the magnetization by spin diffusion can be observed by NMR. Very often, the nonuniform magnetization that can be created reflects the spatial heterogeneity of the solid itself. Therefore, spin diffusion provides an useful means to study the spatial properties of disordered materials. We shall discuss more of this later.

2 EFFECTS OF SPIN DIFFUSION ON NUCLEAR SPIN RELAXATION

2.1 Spin–Lattice Relaxation by Paramagnetic Impurities

Spin diffusion in solids was first discovered[1] in spin–lattice relaxation experiments with crystalline substances, like CaF_2, doped with paramagnetic impurities. The dipolar coupling between the electronic spin of the paramagnetic center and the nuclear spin leads to spin–lattice relaxation at the nuclear site with a rate[2]

$$\frac{1}{T_1(r)} = \frac{C}{r^6} \tag{11}$$

where r is the distance between the nuclear and electronic spins. It turned out that the experimental relaxation time was several orders of magnitude shorter[1,2] than that calculated from equation (11). It was realized that, while the nuclear spins in the vicinity of the paramagnetic site relaxed very rapidly, those at a distance did not because of the r^{-6} dependence in the relaxation rate. In order for the whole spin system to relax, spin diffusion must have transported the magnetization to the vicinity of the paramagnetic sites. The time evolution of the local magnetization due to a single impurity is given by

$$\frac{\partial m(\boldsymbol{r}, t)}{\partial t} = D\nabla^2 m(\boldsymbol{r}, t) - \frac{C}{r^6}[m(\boldsymbol{r}, t) - m_0] \tag{12}$$

where m_0 is the thermal equilibrium value of $m(\boldsymbol{r},t)$. There is a critical radius b_0 around the impurity, inside which the local magnetic field due to the electronic spin is so large that the Larmor frequencies of the nuclei there will be very different from those in the bulk of the solid, and they will escape detection. Furthermore, the large gradient in the Larmor frequency essentially quenches the spin diffusion within the critical radius b_0, because the spin flips in the diffusion process are no longer energy-conserving.

Equation (12) can be solved either by numerical methods[7] or by using the steady state approximation $\partial m(\boldsymbol{r},t)/\partial t = 0$. To solve the steady-state equation,[8–10] the following assumptions are usually made:

1. there is a 'pseudopotential' radius

$$b = 0.7(C/D)^{1/4} \tag{13}$$

   around an impurity, inside which the nuclear spins relax so rapidly that the local magnetization is always at the equilibrium value;
2. the concentration ρ of the impurities is sufficiently low that the average distance $2R$ between them is much larger than b;
3. the pseudopotential radius b is larger than the critical radius b_0.

These assumptions can be summarized as

$$R \gg b \rangle b_0, \quad \text{with} \quad \rho^{-1} = \tfrac{4}{3}\pi R^3 \tag{14}$$

By matching the boundary condition at b, the steady-state solution yields

$$1/T_1 = 4\pi\rho b D \tag{15a}$$

for $M(t)$. Equation (15a) agrees qualitatively with experimental data.[2] The fact that the spin–lattice relaxation depends on C as well as the diffusion coefficient D indicates that spin diffusion plays an important role in the process, but it is not the rate-determining step.

A $1/T_1$ similar to that in equation (15a) can also be obtained by an order-of-magnitude argument. It may serve to illustrate the role of spin diffusion without using complicated mathematics. As indicated in equation (11), the spin–lattice relaxation of a nuclear spin due to a paramagnetic impurity decreases very rapidly with increasing distance between them. Therefore, when the concentration of impurities is low, the spin relaxation times of the majority of the nuclear spins are much longer than the diffusion time between them, except for those within a radius b_d from the impurity. This radius b_d is determined by the condition that the spin diffusion time for the distance from the impurity to the radius b_d be of the order of $(C/b_\mathrm{d}^6)^{-1}$. That is, $b_\mathrm{d}^2/D \approx b_\mathrm{d}^6/C$. This yields $b_\mathrm{d} \approx (C/D)^{\frac{1}{4}} \approx b$. Because of the condition in equation (14), the number of nuclei inside the radius b_d is much smaller than that in the bulk, and can be neglected. In the limit of rapid diffusion, the spin–lattice relaxation rate of $M(t)$ is given by the weighed average of $1/T_1(r)$ in equation (11) for the nuclei outside radius b_d:

$$\begin{aligned}\frac{1}{T_1} &\approx \frac{\int_{b_\mathrm{d}}^{R} Cr^{-6} 4\pi r^2 \,\mathrm{d}r}{\int_{b_\mathrm{d}}^{R} 4\pi r^2 \,\mathrm{d}r} \\ &\approx \rho \tfrac{4}{3}\pi (C/b_\mathrm{d}^3) \\ &\approx \rho b D\end{aligned} \tag{15b}$$

where b_d has been replaced by b and a numerical factor of the order of unity has been neglected. Since $T_1 \approx (R^2/D)R/b$ in equation (15b), it is much longer than R^2/D, the time it takes spin diffusion to transverse a distance R. Therefore, the rapid diffusion approximation is indeed valid.

2.2 Proton Spin Relaxation via End Groups in Polymers

At low temperatures, spin–lattice relaxation of polymers occurs mainly at the end groups of the polymer chains, since the motions of the backbones of the polymers are 'frozen' out. End groups like methyl groups retain considerable motions even at very low temperatures, and act as sinks that relax the whole spin system by means of spin diffusion. Spin–lattice relaxation in solid n-alkanes[11] is a classic example of how spin relaxation is affected by the spin diffusion process. Here the role of spin diffusion can be followed mathematically, because the diffusion is essentially one-dimensional along the chain axis. Taking the center of the chain as the origin of the x axis and using the symmetry requirement $\partial m(x,t)/\partial x|_0 = 0$, the solution for $m(x,t)$ is

$$m(x,t) = \sum_{n=0}^{\infty} A_n \cos p_n x \exp(-D p_n^2 t) \tag{16}$$

For an alkane molecule of length L with N carbon atoms, the lattice constant a is roughly L/N. The boundary condition is

$$D\frac{\partial m(x,t)}{\partial x}\bigg|_{x=L/2} = -\frac{am(x,t)}{T_\mathrm{e}}\bigg|_{x=L/2} \tag{17}$$

which equates the flux of the magnetization to the methyl group to the rate $1/T_\mathrm{e}$ by which the magnetization is relaxed by the rotation of the methyl group. This leads to the equation

$$\tfrac{1}{2}Lp_n \tan \tfrac{1}{2}Lp_n = \frac{La}{2DT_\mathrm{e}} \tag{18}$$

which relates p_n to the length of the chain, the diffusion coefficient, and the relaxation rate at the end group.

In the limit of rapid spin diffusion, i.e., $DT_\mathrm{e} \gg L^2$, we have

$$p_n^2 = \frac{2}{NDT_\mathrm{e}} \tag{19}$$

Since all the terms in the sum in equation (16) have the same time constant, the spin–lattice relaxation rate of $M(t)$ is

$$\begin{aligned}T_\mathrm{L}^{-1} &= Dp_n^2 \\ &= (2/N)(T_\mathrm{e})^{-1}\end{aligned} \tag{20}$$

which is the weighed average of the relaxation rate at the end groups. The factor of 2 is due to the fact that there are two methyl groups in each alkane molecule.

On the other hand, in the opposite limit of $DT_\mathrm{e} \ll L^2$, where now the spin diffusion is the rate limiting step, one has instead

$$p_n \approx (2n+1)\pi/L \tag{21}$$

Because of the n dependence of p_n, only the first term in the sum in equation (16) is important, and the spin–lattice relaxation rate becomes

$$T_\mathrm{L}^{-1} = D(\pi/aN)^2 \tag{22}$$

It is independent of T_e! One important difference between the spin–lattice relaxation rates in the fast and slow diffusion limits is their dependence on the size of the molecules. The former is proportional to N^{-1}, while the latter has a N^{-2} dependence. Experimentally, the spin–lattice relaxation rate in the rotating frame $T_{1\rho}^{-1}$ of n-alkanes[11] at $-190\,^\circ$C was found to have an $N^{-1.7}$ dependence. This indicates that the spin–lattice relaxation in the rotating frame is governed, to a large extent, by how fast the local magnetization is transported by spin diffusion to the end groups.

2.3 Proton Spin Relaxation in Semicrystalline Polymers in the Rotating Frame

The above discussion can be extended to ^{1}H spin relaxation in semicrystalline polymers at ambient temperature. The polymers consist of domains of crystalline and amorphous phases. Owing to different backbone motions available at ambient temperature, each phase has a different intrinsic T_1 and $T_{1\rho}$. Since the proton spin–spin interactions may be different, different spin diffusion coefficients can also be assigned to the two phases. Because the T_1s are typically

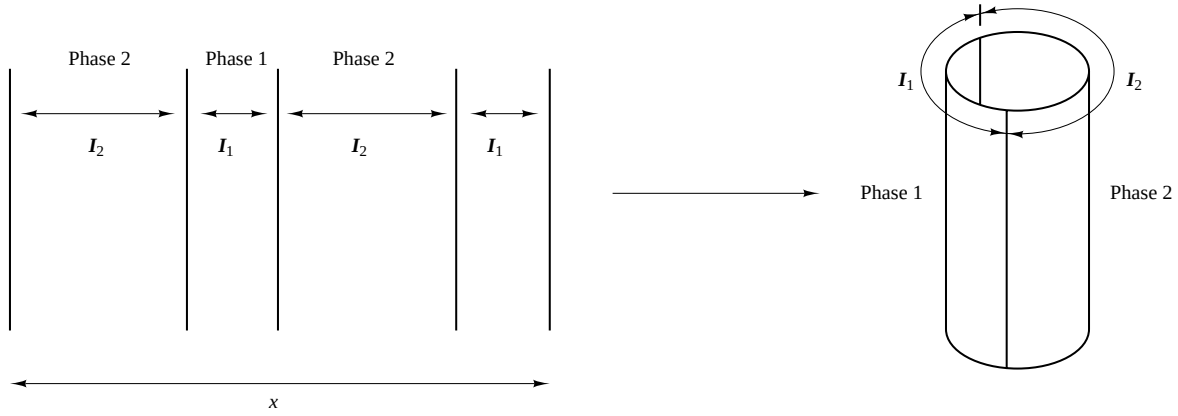

Figure 1 A two-phase, one-dimensional model of spin diffusion in a polymer. The multiple domain arrangement on the left is reduced to a two-domain system with a cyclic boundary condition

much longer than the spin diffusion time across a domain, only a simple exponential decay is observed in the total magnetization, with T_1^{-1} being the weighed average of the intrinsic T_1^{-1}s. However, the $T_{1\rho}$s are found to be sufficiently short that the spatial averaging by spin diffusion is not complete, and multiple component decay can be observed.[6,12,13] To treat the effects of spin diffusion on $T_{1\rho}$ in the general case would require solving the diffusion equation numerically. To simplify the matter, the following approximations are often made.

1. The domains have the form of parallel layers. The spin diffusion is one-dimensional perpendicular to the layers.
2. Only one domain of each of the crystalline and amorphous phases is considered. They are arranged in such a way that they are joined to each other at both ends.

This arrangement is depicted in Figure 1. Pairs of diffusion coefficients D_1 and D_2, intrinsic relaxation times $T_{1\rho}(1)$ and $T_{1\rho}(2)$, and thicknesses l_1 and l_2 are assigned to the amorphous and crystalline layers, respectively.

To see how the spin diffusion affects the spin relaxation times, let us consider the case in which the spin relaxation time $T_{1\rho}(1)$ of the amorphous phase is short and satisfies the condition $T_{1\rho}(1) \ll T_{1\rho}(2)$, l_1^2/D_1 and l_2^2/D_2. This amounts to treating the amorphous phase as a sink that relaxes the magnetization of the crystalline phase via spin diffusion. At the same time, the magnetization in the crystalline phase is also relaxed by the direct coupling to the lattice, with a rate $1/T_{1\rho}(2)$. Define the center of the crystalline layer as the origin of the x axis. The spin diffusion equation in the crystalline region is

$$\frac{\partial m(x,t)}{\partial t} = D_2 \frac{\partial^2}{\partial x^2} m(x,t) - \frac{m(x,t)}{T_{1\rho}(2)} \quad \text{for} \quad -\tfrac{1}{2}l_2 < x < \tfrac{1}{2}l_2 \qquad (23)$$

The substitution

$$m(x,t) \equiv \exp[-t/T_{1\rho}(2)]\, m^*(x,t) \qquad (24)$$

reduces equation (23) to the one-dimensional diffusion equation for $m^*(x,t)$, but now without the decay term. The solution of $m^*(x,t)$ has the same form as that on the right-hand side of equation (16). The condition $T_{1\rho}(1) \ll T_{1\rho}(2)$ and l_1^2/D_1 indicates that the magnetization relaxes uniformly across the amorphous domain, which leads to the same boundary condition for $m^*(x,t)$ as that in equation (17) except that T_e is replaced by $T_{1\rho}(1)$ and L by l_2. The diffusion problem is therefore reduced to that of the spin relaxation via the end groups described earlier. Furthermore, because $T_{1\rho}(1)$ is much shorter than l_2^2/D_2, the coefficient p_n is given by the diffusion limiting solution in equation (21). With equation (24), one finds that the relaxation time constants of the multiple component decay of the total magnetization are $T_{1\rho}(1)$ and the $T_{1\rho}(2,n)$s, where

$$\frac{1}{T_{1\rho}(2,n)} = \frac{1}{T_{1\rho}(2)} + \frac{D_2(2n+1)^2\pi^2}{l_2^2} \qquad (25)$$

with $n = 0, \ldots, \infty$. The relative intensities of the decay components associated with each $T_{1\rho}(2,n)$ are directly proportional to $(2n+1)^{-2}$. If $T_{1\rho}(2)$ is much longer than l_2^2/D_2 then only the $T_{1\rho}(2,n=0)$ term is important, and the number of components in the decay is reduced to two: one with a time constant $[1/T_{1\rho}(2) + D_2\pi^2/l_2^2]^{-1}$ and the other with $T_{1\rho}(1)$. It is important to realize that when more than one $T_{1\rho}(2,n)$ contribute to the decay of $M(t)$, the intensities of these components in the decay have no direct relationship to the number of nuclei contributing to them.

The dependence of $T_{1\rho}(2,n)$ on l_2 suggests that the domain size in polymers may be extracted indirectly from the proton spin relaxation measurements. In the general case, one may solve the diffusion equation numerically and fit the results to the experimental data.[12,13] In the special case where $T_{1\rho}(1) \ll T_{1\rho}(2)$, l_1^2/D_1 and l_2^2/D_2, the data are simply fitted with a multiple component decay with the time constants given by equation (25). $T_{1\rho}(1)$, $T_{1\rho}(2)$, and l_2 are usually treated as the adjustable parameters.[14]

3 STUDIES OF POLYMER MORPHOLOGY BY PROTON SPIN DIFFUSION

Information about domain size can be obtained directly using the Goldman–Shen method.[15] This is based on the idea that with appropriate NMR pulse sequences, nonuniform magnetization associated with the spatial inhomogeneity of a solid can be created on a timescale much shorter than that of the spin diffusion. By monitoring the return of the magnetization to the uniform state by spin diffusion, the sizes of the spatial inhomogeneities can be deduced. As the most

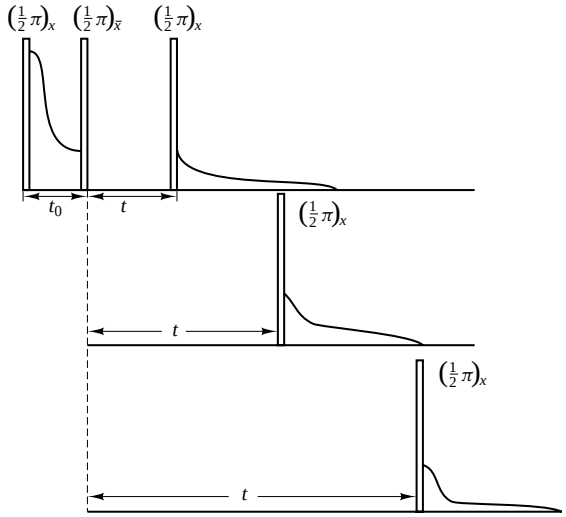

Figure 2 The Goldman–Shen NMR pulse sequence. The magnetization in the crystalline phase is randomized in a time t_0. The transfer of magnetization by spin diffusion from the amorphous domain to the crystalline one occurs during the time t

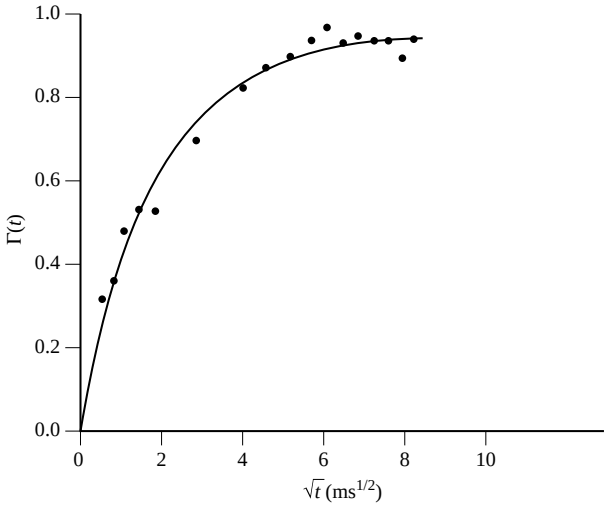

Figure 3 The recovery of the magnetization $\Gamma(t)$ in the crystalline phase of a polypropylene film as a function of the diffusion time t. The experimental data are represented by the solid circles. The theoretical fit according to equations (30) and (31) is given by the solid line

abundant and strongly coupled spin in polymers, ^{1}H is usually the nucleus of choice for such studies.

The original Goldman–Shen pulse sequence $[(\frac{1}{2}\pi)_x - t_0 - (\frac{1}{2}\pi)_x - t - (\frac{1}{2}\pi)_x]$ was first applied to homopolymers with rigid and mobile phases.[16–18] We shall use semicrystalline polymers as an example for our discussion. To a large extent, the free induction decay (FID) of semicrystalline polymers consists of two components associated with the crystalline (rigid) and amorphous (mobile) phases. The spin–spin relaxation time T_2 of the crystalline domain is usually shorter than that of the amorphous domain. By decomposing the FID with curve fitting techniques, one determines the fraction of the total proton magnetization in each phase. The Goldman–Shen pulse sequence shown in Figure 2 exploits this difference. After the initial $(\frac{1}{2}\pi)_x$ pulse, one waits for a fixed time t_0 during which the total magnetization of the crystalline phase M_2 is allowed to decay to zero while there is still sufficient magnetization left in the amorphous phase. The second pulse returns the remaining magnetization M_1 in the amorphous phase to the direction of the external magnetic field. The magnetization in the amorphous phase is allowed to diffuse back to the crystalline phase for a variable time t. By decomposing the FID observed after the third pulse, one determines the amount of magnetization that has been transferred back to the crystalline phase. The spin diffusion period t should be shorter than the T_1 of the system, so that the return of the magnetization to the crystalline phase is due to spin diffusion and not because of spin–lattice relaxation. The sizes of domain structures suitable for spin diffusion studies are those which the spin diffusion can transverse in a time of the order of T_1. For a typical T_1 of the order of 0.1 s and ^{1}H spin diffusion coefficient of $6 \times 10^{-12}\,\mathrm{cm^2\ s^{-1}}$, they are about 8 nm.

The recovery of the magnetization in the crystalline phase is defined as

$$\Gamma(t) = \frac{M_2(t)}{M_2(t \to \infty)} = 1 - \frac{M_1(t) - M_1(t \to \infty)}{M_1(t=0) - M_1(t \to \infty)} \tag{26}$$

An example of $\Gamma(t)$ for polypropylene film is shown in Figure 3. To extract spatial information from $\Gamma(t)$, one needs to solve the diffusion equation according to the initial and boundary conditions appropriate to the problem. In general, solutions can be obtained only by numerical methods,[19] even for the simplest polymer models. Fortunately, analytical solutions are available if one assumes either (i) that the diffusion coefficient is the same for both the amorphous and crystalline phases or (ii) that the diffusion coefficient of the crystalline phase is much shorter than that of the amorphous phase.

The solution to the first case is described in detail by Cheury and Gerstein.[18] We shall present a simplified account here. Again, we consider the model given in Figure 1. Let the center of the amorphous domain be the origin of the x axis. The amorphous domain occupies the region $-\frac{1}{2}l_1 < x < \frac{1}{2}l_1$, while the crystalline domain extends from $-\frac{1}{2}l_1$ to $-\frac{1}{2}(l_1 + l_2)$ and from $\frac{1}{2}l_1$ to $\frac{1}{2}(l_1 + l_2)$. For simplicity, we shall assume that l_2 is much larger than l_1, which is appropriate when the polymer has a high degree of crystallinity. With the initial conditions

$$m(x, t=0) = \begin{cases} 1 & \text{for } x \in \text{amorphous phase} \\ 0 & \text{for } x \in \text{crystalline phase} \end{cases} \tag{27}$$

and the boundary condition

$$\left.\frac{\partial m(x,t)}{\partial x}\right|_{x=\pm(l_1+l_2)/2} = 0 \tag{28}$$

one obtains

$$\begin{aligned} \psi(t) &\equiv \int_{-l_1/2}^{l_1/2} [m(x,t) - m(x, t \to \infty)]\,\mathrm{d}x \\ &= \frac{8}{l_1 + l_2} \sum_{n=1}^{\infty} \frac{\sin^2(\frac{1}{2}p_n l_1)}{p_n^2} \exp(-D p_n^2 t), \quad \text{with} \quad p_n = \frac{2\pi n}{l_1 + l_2} \\ &\approx l_1 \left\{ 1 - \int_0^t \mathrm{d}\tau \left(\frac{D}{\pi l_1^2 \tau}\right)^{1/2} \left[1 - \exp\left(-\frac{l_1^2}{4D\tau}\right)\right]\right\} \\ &\qquad \text{for} \quad l_1 \ll l_2 \end{aligned} \tag{29}$$

For a single layer of the amorphous and crystalline phase, $\Gamma(t) = 1 - \psi(t)/\psi(0)$. This expression for $\Gamma(t)$ is applicable to oriented polymers with lamellar domains. However, if the distribution of the domains is isotropic, spin diffusion in each of the directions (whether along the x, y, or z axis) is equivalent. The general form of $\Gamma(t)$, taking this into account, is

$$\Gamma(t) = 1 - [\psi(t)/\psi(0)]^3 \tag{30}$$

In semicrystalline polymers, there is always a distribution of the width of the domains. The result in equation (29) amounts to assuming a delta function for the distribution of l_1. On the other hand, averaging equation (29) over a Poisson distribution $(1/\langle l_1\rangle)\exp(-l_1/\langle l_1\rangle)$ for l_1, where $\langle l_1\rangle$ is the average l_1, $\psi(t)/\psi(0)$ becomes

$$\frac{\psi(t)}{\psi(0)} = \exp\left(\frac{Dt}{\langle l_1\rangle^2}\right)\operatorname{erfc}\left(\sqrt{\frac{Dt}{\langle l_1\rangle^2}}\right) \tag{31}$$

where erfc is the complementary error function. Regardless of the form of the distribution of l_1, the short-time behavior of $\Gamma(t)$ depends only on $\langle l_1\rangle$, the average value of l_1. This can be seen by expanding equation (29) in the limit of small t and substituting the result into equation (30):

$$\Gamma(t) = \frac{6}{\sqrt{\pi}}\left(\frac{Dt}{\langle l_1\rangle^2}\right)^{1/2} \quad \text{for} \quad t \ll \frac{\langle l_1\rangle^2}{D} \tag{32}$$

In Figure 3, equation (30) with $\psi(t)/\psi(0)$ given by equation (31) is fitted to the data for the polypropylene film. For $D = 6.75 \times 10^{-12}\,\mathrm{cm^2\ s^{-1}}$, a value of $\langle l_1\rangle = 4.9\,\mathrm{nm}$ is obtained from the fit.

In block copolymers[13] and polymer blends,[6] one sometimes encounters two polymers with very different T_2s. The approximation of a single spin diffusion coefficient is clearly invalid. In this case, one may consider the two-domain model in Figure 1 in the limits

$$D_1 \ll D_2, \quad l_1 \ll l_2 \tag{33}$$

where subscripts 1 and 2 represent the phases with long and short T_2, respectively. We shall refer to these as the slow and fast diffusion domains. With the conditions in equation (33), the spin diffusion in the slow domain is again reduced to the diffusion limiting case of what we have discussed for spin relaxation via end groups. With the initial condition that there is only magnetization in the slow diffusion region, one obtains

$$\begin{aligned}\frac{\psi(t)}{\psi(0)} &= \sum_{n=0}\frac{8}{(2n+1)^2\pi^2}\exp\left[-D_1\left(\frac{2n+1}{l_1}\right)^2\pi^2 t\right] \\ &\approx 1 - \frac{4}{\sqrt{\pi}}\left(\frac{D_1 t}{l_1^2}\right)^{1/2} \quad \text{for} \quad t \ll l_1^2/D_1\end{aligned} \tag{34}$$

The recovery of the magnetization in the fast diffusion domain (assuming isotropic distribution of the domains and spin diffusion in three directions) becomes

$$\Gamma(t) = \frac{12}{\sqrt{\pi}}\left(\frac{D_1 t}{l_1^2}\right)^{1/2} \quad \text{for} \quad t \ll l_1^2/D_1 \tag{35}$$

which should be compared with equation (32). As a function of $\sqrt{t}$, the slope of $\Gamma(t)$ in equation (35) is twice as large as that in equation (32). [The short-time ($t \ll {l_1}^2/D_1$) result in equation (34) is slightly different from that in equation (17) of Cheung and Gerstein.[18] The latter is based on the transfer of magnetization from the slow diffusion domain to the fast diffusion one at only one interface between the domains. However, the transfer in the two-domain model in Figure 1 occurs at two interfaces. The result is that the slope of $\Gamma(t)$ as a function of $\sqrt{t}$ in equation (35) is twice as large as that obtained from equation (17) of Cheung and Gerstein.[18]] We can summarize the results in both equations (32) and (35) by the following statement. In the Goldman–Shen experiment, the *initial* return of the magnetization to the domain, which has been depleted of magnetization, increases linearly with $\sqrt{t}$, and the slope is proportional to $(D/l^2)^{\frac{1}{2}}$, with D and l being the spin diffusion coefficient and the size of the domain from which the magnetization emanates.

Several modifications of the Goldman–Shen pulse sequence have been proposed. Two of the significant ones are

1. the use of multiple pulse techniques[19,20] to suppress spin diffusion during the creation of the nonuniform magnetization (i.e., in the time window t_0) and to enhance the ^{1}H spectral resolution at the detection period;[21]
2. identification of domains with ^{13}C NMR after ^{1}H–^{13}C cross polarization.[22–24]

The latter is used in the detection period, and is particularly suitable for polymer blends[25] consisting of two polymers with very different structures.

4 RELATED ARTICLES

Dynamic NMR in Liquid Crystalline Solvents; Electron–Nuclear Multiple Resonance Spectroscopy; Rotating Frame Spin–Lattice Relaxation Off-Resonance.

5 REFERENCES

1. N. Bloembergen, *Physica*, 1949, **15**, 386.
2. A. A. Abragam, *The Principles of Nuclear Magnetism*, Clarendon Press, Oxford, 1961.
3. T. T. P. Cheung, *Phys. Rev. B*, 1981, **23**, 1404.
4. J. Crank, *The Mathematics of Diffusion*, Clarendon Press, Oxford, 1975.
5. H. S. Carslaw and J. C. Jaeger, *Conduction of Heat in Solids*, Clarendon Press, Oxford, 1959.
6. V. J. McBrierty and D. C. Douglass, *J. Polym. Sci., Macromol. Rev.*, 1981, **16**, 295; *Phys. Rep.*, 1980, **63**, 63, and references therein.
7. J. I. Kaplan, *Phys. Rev. B*, 1971, **3**, 604.
8. G. R. Khutsishvili, *Proc. Inst. Phys. Acad. Sci. Georgia (USSR)*, 1956, **4**, 3.
9. P. G. de Gennes, *J. Phys. Chem. Solids*, 1958, **7**, 345.
10. H. E. Rorschach Jr., *Physica*, 1964, **30**, 38.
11. D. C. Douglass and G. P. Jones, *Phys. Rev.*, 1966, **45**, 956.
12. K. J. Packer, J. M. Pope, R. R. Young, and M. E. A. Cudby, *J. Polym. Sci., Polym. Phys. Ed.*, 1984, **22**, 589.
13. H. Tanaka and T. Nishi, *Phys. Rev. B*, 1986, **33**, 32.
14. K. J. Packer, I. J. F. Poplett, M. J. Taylor, M. E. Vickers, A. K. Whittaker, and K. P. J. Williams, *Makromol. Chem. Macromol. Symp.*, 1990, **34**, 161.
15. M. Goldman and L. Shen, *Phys. Rev.*, 1966, **144**, 321.
16. R. A. Assink, *Macromolecules*, 1978, **11**, 1233.

17. K-L. Li, A. A. Jones, P. T. Inglefield, and A. D. English, *Macromolecules*, 1989, **22**, 4198.
18. T. T. P. Cheung and B. C. Gerstein, *J. Appl. Phys.* 1981, **52**, 5517.
19. J. R. Havens and D. L. VanderHart, *Macromolecules*, 1985, **18**, 1663.
20. K. Schmidt-Rohr, J. Clauss, B. Blumich, and H. W. Spiess, *Magn. Reson. Chem.*, 1990, **28**, S3.
21. T. T. P. Cheung, B. C. Gerstein, L. M. Ryan, R. E. Taylor, and C. Dybowski, *J. Chem. Phys.*, 1980, **73**, 6059.
22. N. Zumbulyadis, *J. Magn. Reson.*, 1983, **53**, 486.
23. R. H. Newman, *Chem. Phys. Lett.*, 1991, **180**, 301.
24. S. Zhang, B. H. Meier, and R. R. Ernst, *Solid State Nucl. Magn. Reson.*, 1992, **1**, 313.
25. D. L. VanderHart, *Makromol. Chem., Macromol. Symp.*, 1990, **34**, 125.

Biographical Sketch

T. T. Peter Cheung. *b* 1952. B.S., 1974, Rockhurst College; Ph.D., 1978, Princeton University. Postdoctoral Fellow, Washington University, 1979; Postdoctoral Fellow, Iowa State University, 1980. Senior research chemist, Phillips Petroleum Company, 1981–present. Approx. 40 publications. Research interests include stochastic processes in disordered solids, statistical theory of condensation, ^{129}Xe NMR, X-ray photoelectron spectroscopy of alloys, and applied catalysis.

Spinning Sideband Analysis for Spin-1/2 Nuclei

Robin K. Harris

Department of Chemistry, University of Durham, South Road, Durham, UK

&

Alejandro C. Olivieri

Universidad Nacional de Rosario, Rosario, Argentina

1	Introduction	1
2	Theory	1
3	Retrieval of Tensor Parameters	3
4	Error Analysis	4
5	Interplay of Tensors	5
6	Related Articles in this Volume	9
7	Related Articles in Volumes 1–8	9
8	References	9

1 INTRODUCTION

In the ideal situation for applying NMR spectroscopy, a homogeneous solution is placed inside a homogeneous external magnetic field, leading to single and narrow resonances for each non-equivalent NMR-active nucleus contained in the sample. However, this paradise is almost never reached. Whenever the sample is a liquid crystal, a solid or a slowly reorienting macromolecule, and/or when the magnetic field is not perfectly homogenous within the sample, usually unwanted spinning sidebands appear, flanking the relevant peaks at integral multiples of the sample spinning frequency. The presence of sidebands causes two main problems: (1) a decrease in the height of the central peak, since the overall signal intensity is distributed among the components of the sideband manifold, and (2) a possibility of sidebands overlapping with other interesting peaks, thereby complicating the spectral analysis.

However, sidebands usually contain useful information. The intensity distribution varies according to the sample spinning speed and to the changes of the chemical shift and/or relevant dipolar interactions and/or quadrupolar interactions across the sample. Particularly interesting are the effects observed in high-resolution magic-angle spinning (MAS) NMR spectroscopy, which is the standard technique to analyze powdered solid samples. Suitable analysis of the intensities may allow the characterization of the shielding and/or dipolar and/or quadrupolar tensor(s) affecting the studied nucleus. This explains why a considerable effort has been devoted to the theoretical calculation of sideband intensities, to the development of methods capable of extracting such information, and to their use for many different nuclei and for a variety of chemical systems.

In the present review, methods for retrieval of the principal components of the relevant tensors from MAS NMR spectroscopic data are revisited, along with suitable analysis of the experimental errors affecting them. Also, a range of applications for structural and dynamic problems is briefly covered. The article builds on the paper by Herzfeld[1] (see **Sideband Analysis in Magic Angle Spinning NMR of Solids,** Volume 7, which was relatively short, though it contained the plots for the graphical method). We will not, herein, describe spinning-sideband analysis for quadrupolar nuclei or for two-dimensional experiments or for situations of rotational resonance. The article will also be restricted to sample-spinning about the magic angle (i.e., VAS or variable angle spinning situations will not be treated). However, cases where dipolar interactions with quadrupolar nuclei affect spinning sidebands for spin-1/2 nuclei will be discussed.

2 THEORY

2.1 The Approach of Maricq and Waugh[2]

We commence with a discussion of the simplest situation, where only shielding is under consideration. The shielding tensor $\boldsymbol{\sigma}$ is of second-rank, with principal components defined in the principal axis system (PAS) as σ_{11}, σ_{22} and σ_{33}. These components are labeled in such a way that

$$|\sigma_{33} - \sigma_{\text{iso}}| \geq |\sigma_{11} - \sigma_{\text{iso}}| \geq |\sigma_{22} - \sigma_{\text{iso}}| \tag{1}$$

where $\sigma_{\text{iso}} = (\sigma_{11} + \sigma_{22} + \sigma_{33})/3$ is the isotropic chemical shift. In the σ scale, more positive values correspond to lower resonance frequencies, i.e., increased shielding (notice that $\sigma - \sigma_{\text{ref}} = -\delta$).

It is customary to define the parameters $\Delta\sigma$ (shielding anisotropy) and η (asymmetry parameter) in order to characterize the $\boldsymbol{\sigma}$ tensor as

$$\Delta\sigma = \sigma_{33} - (\sigma_{11} + \sigma_{22})/2 \tag{2}$$

$$\eta = (\sigma_{22} - \sigma_{11})/(\sigma_{33} - \sigma_{\text{iso}}) \tag{3}$$

Sideband intensities in MAS NMR have been calculated by a number of methods. A general review of numerical simulation of solid-state NMR experiments, including those for rotating samples, has appeared.[3] We present here a brief derivation of Maricq and Waugh's equations,[2] and show how intensities can be conveniently calculated from the latter, in order to introduce computer programs for retrieving the tensor components.

For a single nucleus within a static microcrystalline sample, the shielding Hamiltonian is given in the high-field case by

$$\hbar^{-1}\widehat{\mathcal{H}} = -\omega_0\sigma_{zz}\widehat{I}_z \tag{4}$$

where ω_0 is the resonance frequency in angular units and σ_{zz} is the appropriate component of the $\boldsymbol{\sigma}$ tensor relating the spin component I_z and the magnetic field $\boldsymbol{B}_0$ (assumed to point

along the z axis). The required σ_{zz} component is obtained from the diagonal $\boldsymbol{\sigma}$ tensor (as defined in its PAS)

$$\boldsymbol{\sigma} = \begin{pmatrix} \sigma_{11} & 0 & 0 \\ 0 & \sigma_{22} & 0 \\ 0 & 0 & \sigma_{33} \end{pmatrix} \tag{5}$$

In order to obtain σ_{zz} in a MAS experiment, the tensor $\boldsymbol{\sigma}$ is subjected to the following transformations: (1) from its PAS to the MAS frame (where the z axis coincides with the spinning axis), and (2) from the latter frame to the laboratory (LAB) frame (where the z axis is coincident with $\boldsymbol{B}_0$). The latter rotations are accomplished by using the following sets of Euler angles: (α, β, γ) for the first rotation, and $(\psi, \xi, 0)$ for the second. Now $\psi = \alpha_o + \omega_r t$, where ω_r is the sample spinning frequency, and ξ is the angle between $\boldsymbol{B}_0$ and the spinning axis, i.e., $\xi = 54.7°$ for the magic-angle situation (Figure 1)*. Therefore

$$\begin{aligned} \boldsymbol{\sigma}(\text{MAS}) &= \boldsymbol{R}_z(\gamma)\boldsymbol{R}_x(\beta)\boldsymbol{R}_z(\alpha)\boldsymbol{\sigma}(\text{PAS})\boldsymbol{R}_z^{-1}(\alpha)\boldsymbol{R}_x^{-1}(\beta)\boldsymbol{R}_z^{-1}(\gamma) \\ \boldsymbol{\sigma}(\text{LAB}) &= \boldsymbol{R}_x(\xi)\boldsymbol{R}_z(\psi)\boldsymbol{\sigma}(\text{MAS})\boldsymbol{R}_z^{-1}(\psi)\boldsymbol{R}_x^{-1}(\xi) \end{aligned} \tag{6}$$

where $\boldsymbol{R}$ are generalized rotation matrixes, the rotation axes are denoted as subscripts, and the rotation angles are in parentheses.

The result is

$$\begin{aligned} \sigma_{zz} = \sigma_{\text{iso}} + \frac{2}{3}\left[\frac{\cos 2\psi'}{2}(\sigma'_{22} - \sigma'_{11}) + \sin 2\psi'\ \sigma'_{12}\right] \\ + \frac{2\sqrt{2}}{3}(\sigma'_{13}\sin\psi' + \sigma'_{23}\cos\psi') \end{aligned} \tag{7}$$

where

$$\psi' = \psi + \gamma$$

$$\sigma'_{22} = (\sigma_{11}\sin^2\alpha + \sigma_{22}\cos^2\alpha)\cos^2\beta + \sigma_{33}\sin^2\beta \tag{8}$$

$$\sigma'_{11} = \sigma_{11}\cos^2\alpha + \sigma_{22}\sin^2\alpha \tag{9}$$

$$\sigma'_{12} = (\sigma_{11} - \sigma_{22})\sin\alpha\cos\alpha\cos\beta \tag{10}$$

$$\sigma'_{13} = (\sigma_{11} - \sigma_{22})\sin\alpha\cos\alpha\sin\beta \tag{11}$$

$$\sigma'_{23} = (\sigma_{11}\sin^2\alpha + \sigma_{22}\cos^2\alpha)\sin\beta\cos\beta - \sigma_{33}\sin\beta\cos\beta \tag{12}$$

Notice from equation (7) that σ_{zz} is time dependent, and oscillates with frequencies 0, $\omega_r t$ and $2\omega_r t$ ($\psi = \omega_r t$). Hence the shielding becomes time-dependent. Since the relevant Hamiltonian $\widehat{\mathcal{H}}$ commutes with itself at all times, the propagator $U(t)$ of the spin system is given by $U(t) = \exp[i\hbar^{-1}\int_0^t \widehat{\mathcal{H}}(t)\,dt$. Therefore, the time-dependent FID can be written as[1,2]

$$f(t) = f_0 \exp[i\theta(t)] \tag{13}$$

where

$$\theta(t) = \int_0^t \omega_0\sigma_{zz}(t)\,dt \tag{14}$$

* An alternative but equivalent approach is the use of Wigner rotation formulae. For a discussion, see B.C. Gerstein and C.R. Dybowski, 'Transient Techniques in NMR of Solids', Academic Press, 1985.

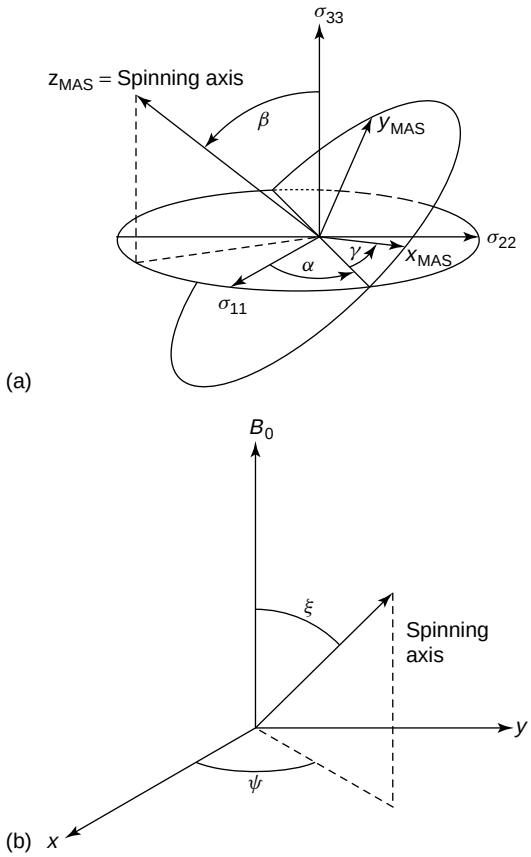

Figure 1 (a) mutual relationship between the magic-angle spinning frame (MAS) and the frame defined by the principal components of the shielding tensor. (b) orientation of the spinning axis with respect to the external magnetic field

Integrating equation (14) for a MAS cycle yields[1]

$$\begin{aligned} \theta(t) = \omega_0 \Bigg\{ \sigma_{\text{iso}} t + \frac{1}{3\omega_r}\left[\frac{\sin 2\psi'}{2}(\sigma'_{22} - \sigma'_{11}) - \cos 2\psi'\ \sigma'_{12}\right] \\ + \frac{2\sqrt{2}}{3\omega_r}(\sigma'_{23}\sin\psi' - \sigma'_{13}\cos\psi') - \\ - \frac{1}{3\omega_r}\left[\frac{\sin 2\gamma}{2}(\sigma'_{22} - \sigma'_{11}) - \cos 2\gamma\ \sigma'_{12}\right] \\ + \frac{2\sqrt{2}}{3\omega_r}(\sigma'_{23}\sin\gamma - \sigma'_{13}\cos\gamma)\Bigg\} \end{aligned} \tag{15}$$

Frequency information can be gathered from equations (13–15) by applying a Fourier transformation. Since $\theta(t)$ is periodic (with period $2\pi/\omega_r$), the observed spectrum will consist of peaks centred at $(\omega_0\sigma_{\text{iso}} + k\omega_r)$, where k is an integer (positive or negative). The corresponding Fourier coefficients provide the amplitudes F_k of the frequency components, and are given by:

$$\begin{aligned} F_k = \frac{1}{2\pi}\int_0^{2\pi} \exp\left[i\,(k\psi + A_2\sin 2\psi + B_2\cos 2\psi\right. \\ \left. + A_1\sin\psi + B_1\cos\psi)\right]\,d\psi \end{aligned} \tag{16}$$

$$A_1 = 2\sqrt{2}\omega_0\sigma'_{23}/(3\omega_r) \tag{17}$$

$$A_2 = \omega_0(\sigma'_{22} - \sigma'_{11})/(6\omega_r) \tag{18}$$

$$B_1 = -2\sqrt{2}\omega_0\sigma'_{13}/(3\omega_r) \quad (19)$$

$$B_2 = -\omega_0\sigma'_{12}/(3\omega_r) \quad (20)$$

The peak intensities are obtained from the squared modulus $|F_k|$.[1] However, it should be noticed that the above discussion corresponds to a single nucleus whose σ tensor is oriented in the LAB frame according to the angles (α, β, γ). For a microcrystalline sample, therefore, the peak intensities are given by the following powder average[1]

$$I_k = \frac{1}{4\pi}\int_0^{\pi}\int_0^{2\pi} |F_k|^2 d\alpha \ \sin\beta \ d\beta \quad (21)$$

An approximate method of calculation based on the above equations has been discussed, which uses a series expansion, and does not require the computation of integrals such as those in equation (21).[4] This method is accurate for values of $\omega_0\Delta\sigma/\omega_r$ up to ca. 3. However, better accuracy is obtained by employing computer-based approaches to calculate each sideband at a time, using equation (21), while an alternative method consists of calculating the FID [equation (13)] and then performing a computer Fourier transformation. In the latter approach, the Fourier transform contains the intensities of all sidebands at the same time. Spinning sideband manifolds arising from paramagnetic shift anisotropy can be similarly calculated.[5] When overlapping peaks occur, it may be useful to apply maximum entropy deconvolution before spinning sideband intensities are calculated, in order to isolate different sideband manifolds which would otherwise be unresolvable,[6] though in principle direct fitting of the complete sidebands, including their shapes, may be better.

The range of applicability of the above equations should be mentioned. As explained above, equation (21) applies to cases where the spin Hamiltonian commutes with itself at all times. These include, besides the case of a single non-interacting nucleus, other situations such as: (1) nuclei subjected to heteronuclear dipolar or indirect coupling interactions and (2) nuclei under homonuclear AX-type dipolar or indirect interactions (see below). Conversely, the above approach is no longer applicable when strongly coupled homonuclear interactions occur.

2.2 Other Approaches

When homonuclear interactions occur, and provided the coupled pairs of nuclei are isolated, one can apply Floquet theory, average Hamiltonian theory or a numerical evaluation of the spin density matrix in order to calculate the sideband intensities.[7–13] An interesting example is provided by the ^{31}P,^{31}P coupling in a phosphole tetramer and in an *ortho* diphosphino benzene derivative, where information concerning the orientations of the phosphorus chemical shift tensors and the sign of $J(^{31}\text{P},^{31}\text{P})$ have been deduced.[9]

Another area where the above theory cannot be applied is when chemical exchange takes place in the intermediate regime (i.e., when the exchange rates are comparable to the difference in frequency between the exchanging $\boldsymbol{\sigma}$ tensors). Here again a Liouville treatment of the exchange, together with Floquet theory, can successfully account for the sideband intensities.[14–16] However, it should be noticed that, for rapidly exchanging systems, the equations of Maricq and Waugh[2] can be confidently applied by considering the nuclei under the influence of an effective tensor $\boldsymbol{\sigma}_{\text{eff}}$ given by a population-weighted average of the contributing $\boldsymbol{\sigma}$ tensors. Pertinent examples of this latter situation are illustrated by the fast solid-state proton transfer taking place between individual phosphate units in the dihydrogen phosphates,[17] in the phosphoric acid:urea adduct[18] and in the complexes formed by phenols and a phosphine oxide.[19]

For homonuclear coupling interactions which are extended to the whole sample, none of the above methods can be applied. Two such cases are worth of mention: (1) the effect of ^{1}H,^{1}H dipolar coupling on ^{1}H spinning sideband intensities of hexamethylbenzene, which has been related to M_n dipolar moments ($n = 2, 4, 6$ and 8),[20] and (2) dipolar ^{31}P,^{31}P coupling in MH_2PO_4 phosphates ($M = K^+$, Rb^+ and NH_4^+), accounted for by assuming that the ^{31}P nuclei are acting as if they were non-equivalent, and that the coupling extends to only a nearest neighbor sphere.[21,22]

3 RETRIEVAL OF TENSOR PARAMETERS

In this Section we review the methods which are usually employed for retrieving tensor parameters from sideband intensities when the equations of Maricq and Waugh[1] apply, again using the notation for a simple shielding case. This is also relevant to cases where intensities are not solely determined by the shielding tensor $\boldsymbol{\sigma}$, but also by effective tensors resulting from the interplay of the latter with other relevant interactions (see below).

Several approaches have been described in the literature in order to retrieve shielding tensor parameters from sideband intensities. One of them is Maricq and Waugh's method of moments,[2] in which the computation of the second and third moments M_2 and M_3 respectively allows the parameters $\Delta\sigma$ and η to be obtained by solving the following system of equations

$$8(\Delta\sigma)^3 - 30M_2(\Delta\sigma) - 35M_3 = 0 \quad (23)$$

$$\eta^2 = 1 - 35M_3/2(\Delta\sigma)^3 \quad (24)$$

where $M_n = \omega_r^n \sum k^n I_k / \sum I_k$. Equations (23) and (24) have three solutions for $\Delta\sigma$, and each of them, in turn, provides two solutions for η. The six pairs of values of $\Delta\sigma$, η correspond to the six possible permutations of the three principal components of the $\boldsymbol{\sigma}$ tensor. Due to the presence of the factor k^n in the definition of the nth moment, the accuracy of applying the above method depends critically on the intensities of outer sidebands, which are usually small and therefore are the most affected by experimental noise.

To avoid the latter problems, Herzfeld and Berger devised a graphical method based on a relatively small set of accessible sideband intensities.[1] Specifically, they generated plots of the intensity ratios I_k/I_0 ($k \neq 0$) as a function of two parameters, μ and ρ, which conveniently replace $\Delta\sigma$ and η

$$\mu = \omega_0\Delta\sigma(1 + \eta/3)/\omega_r \quad (25)$$

$$\rho = \pm(1 - \eta)/(1 + \eta/3) \quad (26)$$

Since the plots are based on ratios of intensities rather than on absolute values of I_k, the latter need not be normalized.

Only ratios involving experimentally accessible values of I_k are considered. The method is based on localizing the values of μ and ρ for which the experimental intensity ratios closely match the theoretical ones.[1] Additionally, a qualitative view of the errors in estimating the retrieved parameters can be obtained by comparing the shielding tensors calculated from different values of k. Neither the moments method nor the graphical method of Herzfeld and Berger are now greatly used.

The generalized use of computers in the chemical laboratory has led to convenient computer-based methods for obtaining shielding parameters (or 'paramagnetic shift anisotropies'[5]), mainly based on iterative methods.[23–26] Figure 2 shows an example.[27,28] In such cases one starts from a given set of initial parameter guesses (these can be the Herzfeld-Berger parameters μ and ρ, or directly $\Delta\sigma$ and η), and refines them iteratively, using standard routines for non-linear parameter estimation. Simplex or Newton-Gauss methods are used to minimize the standard deviation s_{fit} (or, alternatively, χ^2)

$$s_{\text{fit}} = \left\{ \frac{[I_k(\text{calc}) - I_k(\text{exp})]^2}{(n-2)} \right\}^{\frac{1}{2}} \tag{28}$$

where n is the number of experimentally accessible sidebands.

Computer-based methods which use the full sideband manifold are considered to be the most reliable ones. However, the choice of the optimum number of sidebands to obtain for fitting (i.e., the decision as to the best value of ω_r) is a matter for discussion.[29] The software packages from the Varian and Bruker manufacturers now contain programs for spinning sideband analysis. A ^{119}Sn example[30] of ssb fitting using the STARS program[31] is shown in Figure 3.

The use of Floquet theory for calculating spinning sideband manifolds has been reviewed.[32] A further method, described by Fenzke et al.,[33] generates a series of computer files from equation (22) for values of μ, ρ in the ranges (0,20) and (−1,1) respectively, containing the theoretical sideband intensities, with k ranging from −10 to 10 (this may constitute a drawback of the method, although one may produce files for a larger ranges of μ, ρ and k). From a measured set of experimental intensities, a statistical error indicator $\varepsilon = 1 - [\Sigma I_k(\text{calc}) I_k(\text{exp})]^2 / \Sigma I_k^2(\text{calc}) \Sigma I_k^2(\text{exp})$ is computed, and a computer search is made for the values of μ and ρ which lead to its minimum value. A plot of this error indicator as a function of μ, ρ in the vicinity of the minimum provides an estimation of the experimental errors. Figure 4 gives such a three-dimensional plot of ε as a function of μ and ρ for the case of the [^{2}H$_7$]-urea/phosphoric acid adduct.[18] The projection of the plot onto the μ, ρ plane (Figure 4b) gives a qualitative view of the fitting errors.

4 ERROR ANALYSIS

Two sources of errors should be considered in retrieving shielding parameters from MAS sideband intensities: (1) experimental errors leading to observed sideband intensities which deviate from those theoretically expected, and (2) computer-fitting errors, which depend on the characteristics of the minimization procedure, and also on the shielding parameters themselves.

A number of publications have considered several experimental factors affecting the accuracy in the derived parameters.[24,25,30,33,34] When using cross-polarization methods, for example, variations of the polarization efficiency with the orientation within the sample may be a source of error. This error stems from the anisotropy of the Hartmann-Hahn mismatch.[25] To overcome this problem, use of a modified pulse

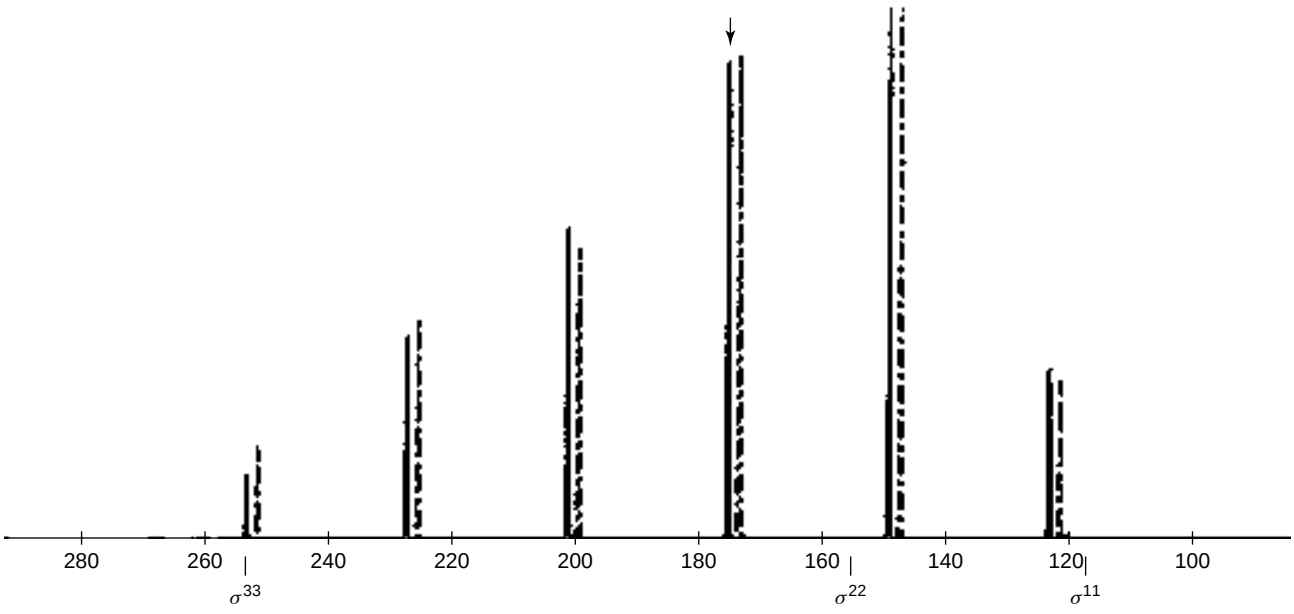

Figure 2 Example of the iterative fitting of a ^{13}C spinning sideband manifold, obtained at a spin rate of 1.3 kHz using an in-house computer program.[28] The C22 band of Form II of cortisone acetate is illustrated.[27] The vertical arrow indicates the centerband. The solid line (to which the shift scale refers) represents the experimental spectrum, while the dashed line (arbitrarily offset) is as computer-fitted with the parameters $\zeta = -78$ ppm, $\eta = 0.49$. (Note: (a) these values differ slightly from those in Table 2 of Ref.[27] and (b) Figure 2 of Ref.[27] incorrectly refers to C5 rather than C22.) (Reproduced by permission from E. A. Christopher, R. K. Harris and R. A. Fletton, *Solid State NMR*, 1992, **1**, 93)

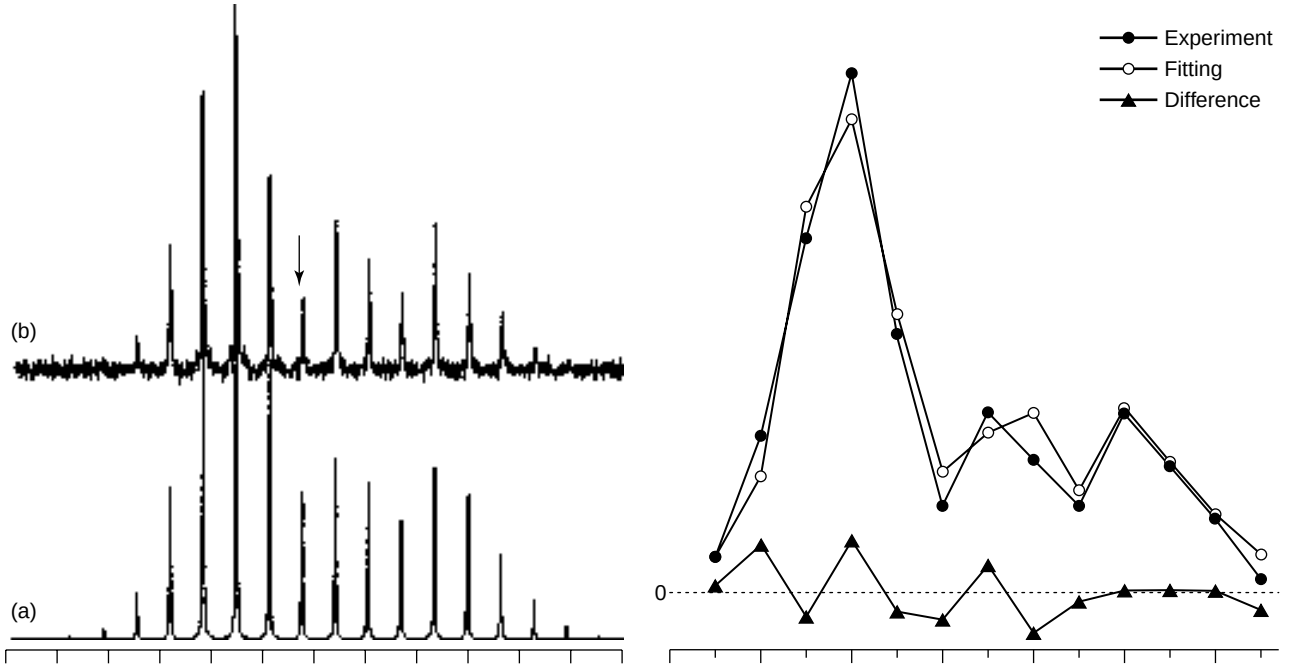

Figure 3 (a) Computed-fitted and (b) experimental (111.9 MHz) ^{119}Sn-{^{1}H} spinning sideband patterns for tin sulfate. The parameters obtained by the use of the Varian STARS program are $\zeta = 553$ ppm, $\eta = 0.14$. The rotation rate was 9.0 kHz. The fitting is carried out with a constant linewidth, so the peak-heights of (a) and (b) do not necessarily match well. The integrals and the differences between experimental and simulated values are plotted to the right, the horizontal dashed line being at zero level

sequence called multiple-contact isotropic cross-polarization (MCICP) has been proposed, together with an empirical intensity correction function.[25] On the other hand, for single-pulse excitation (direct polarization), an important factor is the variation in the degree of polarization of the nuclei over the full frequency range of the spectrum, as a result of the finite duration of the pulse used in the excitation process.[31,34] This latter problem becomes serious for heavy nuclei such as ^{199}Hg, for which shielding anisotropies of thousands of ppm may occur. Attempts have been made to correct for these deviations by utilizing the theoretical RF field amplitude as a function of frequency.

The estimation of fitting errors has been discussed several times,[24–26,35,36] and in special detail in a recent publication.[37] Once the best-fit parameters and the standard deviation s_{fit} (equation (28)) are obtained by the program, one may estimate the errors in $\Delta\sigma$ and η by computing the so-called marginal standard deviations

$$s_{\text{marg}}(i) = s_{\text{fit}}[(B^{-1})_{\text{ii}}]^{1/2} \tag{29}$$

where B is a covariance matrix defined as $B_{\text{ij}} = \sum \left[dI_k(\text{calc})/di\right]\left[dI_k(\text{calc})/dj\right]$, and i,j are refined parameters. Additionally, the following ratio of variances is useful in assessing whether the parameters are properly defined by the experimental intensities

$$R_{\text{i}} = \frac{(B^{-1})_{\text{ii}}}{(B_{\text{ii}})^{-1}} \tag{30}$$

Another recent article[29] has considered the accuracy of tensor parameters measured using solid-state NMR and has used a similar approach. Comparison to the static limit shows that the determination of the anisotropy is more reliable in spinning experiments than in static ones, and an optimum number of sidebands has been found for which the estimation of the anisotropy is the most accurate. However, an analogous analysis for the asymmetry parameter shows it to be consistently more reliably determined from a static spectrum.

In fact, it has been pointed out several times[28,36–38] that the uncertainty in asymmetry values derived from ssb analysis is very high when the magnitude is low. Indeed, it becomes difficult to distinguish axial symmetry from non-axial cases when $\eta < 0.2$. The comparison of R_{i} with critical values of F from standard statistical tables allows one to determine if the parameters have been adequately modelled.[37] However, though the parameters may appear to be well defined, the standard errors in η may be too high to draw definite conclusions regarding axiality. This problem is highlighted when the value of the ratio $\omega_0\Delta\sigma/\omega_{\text{r}}$ is sufficiently small.[37]

Questions of errors and correlations between parameters have also been discussed by Skibsted et al.[39] They have illustrated contour plots of rms deviations between experimental and simulated intensities for the spinning sidebands in the ^{133}Cs MAS spectrum of $CsVO_3$, but the emphasis in their work is on the interplay of shielding and quadrupolar tensors.

5 INTERPLAY OF TENSORS

In many cases, more than one type of tensor will affect static NMR bandshapes and hence spinning sideband manifolds. The matter is relatively simple when only inhomogeneous interactions are involved since these can be considered to contribute independently to the Hamiltonian. It is instructive to consider the simplest situation involving three such tensors,

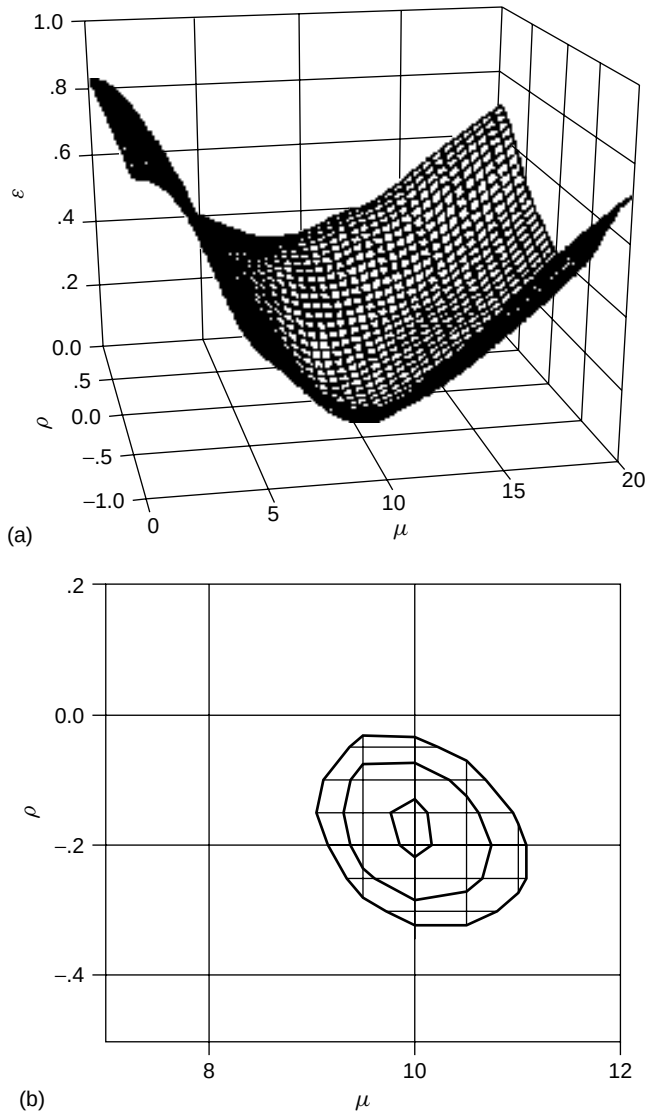

Figure 4 Minimization graphs relevant to ^{31}P spinning sideband analysis for the ($^2H_7$)-urea phosphoric acid adduct[18]: (a) Plot of ε as a function of μ, ρ. (b) Projection of the plot onto the μ, ρ plane for a closer inspection of the minimum

namely shielding, dipolar coupling and indirect ('scalar') coupling. The influence of a sufficiently large isotropic indirect coupling constant is necessary in order to give resolvable subspectra of spinning sideband manifolds (see below), which allows spectral analysis to proceed. In this section a common alternative definition of anisotropy to that given in equation (2) will be used, namely

$$\zeta = \sigma_{33} - \sigma_{\text{iso}} \tag{31}$$

It is clear that the two definitions are equivalent, with $\Delta\sigma = 3\zeta/2$.

5.1 Interplay of σ, D and J[40–43]

The simplest case, which illustrates the essential features, occurs for isolated heteronuclear two-spin (AX) systems with $I_A = I_X = 1/2$, in which axial symmetry prevails, so that asymmetry in $\boldsymbol{\sigma}$ and $\boldsymbol{J}$ can be ignored. All three tensors for, say, the A spins, are co-axial (with the major principal axis along the internuclear A, X distance, r_{AX}), and the anisotropy in $\boldsymbol{J}$ has exactly the same form as the dipolar coupling, $\boldsymbol{D}$, so that an effective parameter D' may be defined as

$$D' = D - \frac{\Delta J}{3} \tag{32}$$

where D is the dipolar coupling constant in frequency units, $(\mu_o/4\pi)\gamma_A\gamma_X\hbar/2\pi r_{AX}^3$, and ΔJ is the anisotropy in $\boldsymbol{J}$ (see **Dipolar & Indirect Coupling Tensors in Solids,** Volume 3; **Indirect Nuclear Spin–Spin Coupling Tensors**) expressed as $J_\parallel - J_\perp$. Note that this implies that there is no NMR experimental method which is able to separate D and ΔJ. The discussion will proceed under the assumption that γ_A and γ_X are both positive, but the results can be readily adjusted if this is not the case. The NMR Hamiltonian may be written as

$$\begin{aligned} h^{-1}\widehat{\mathcal{H}} = &-\nu_A^o\left[1 - \left\{\sigma_A^{iso} + \frac{1}{2}\zeta_A\ (3\cos^2\theta - 1)\right\}\right]\widehat{I}_{zA} \\ &- \nu_X^o\left[1 - \left\{\sigma_X^{iso} + \frac{1}{2}\zeta_X\ (3\cos^2\theta - 1)\right\}\right]\widehat{I}_{zX} \\ &+ J_{AX}^{iso}\widehat{I}_{zA}\widehat{I}_{zX} - D'(3\cos^2\theta - 1)\widehat{I}_{zA}\widehat{I}_{zX} \end{aligned} \tag{33}$$

where $\nu_o^A = \gamma_A B_o/2\pi$ and $\nu_o^X = \gamma_X B_o/2\pi$ are the A and X Larmor frequencies in the absence of shielding, σ_A^{iso} and σ_X^{iso} are the isotropic A and X shielding constants, ζ_A and ζ_X are the shielding anisotropies expressed as $\sigma_A^\parallel - \sigma_A^{iso}$ and $\sigma_X^\parallel - \sigma_X^{iso}$, respectively, J_{AX} is the isotropic (A, X) coupling constant and θ is the angle between $\boldsymbol{r}_{AX}$ and $\boldsymbol{B}_o$. The transitions of the A nucleus are therefore described by

$$\begin{aligned} \nu_A = &\nu_A^o\left[1 - \left\{\sigma_A^{iso} + \frac{1}{2}\zeta_A\ (3\cos^2\theta - 1\right\}\right] \\ &- J_{AX}m_X + D'(3\cos^2\theta - 1)m_X \end{aligned} \tag{34}$$

where m_X is the appropriate spin component quantum number for the X spin. This equation reduces to

$$\nu_A = \nu_A^{iso} - \frac{1}{2}\nu_A^o\zeta_A^{eff}(3\cos^2\theta - 1) - J_{AX}m_X \tag{35}$$

where ζ_A^{eff} is an effective tensor anisotropy given by

$$\zeta_A^{eff} = \zeta_A - \frac{2D'm_X}{\nu_A^o} \tag{36}$$

The A transitions therefore form two sub-spectra ($m_X = \pm\frac{1}{2}$), in one of which the shielding and dipolar tensors reinforce one another whereas in the other they partially cancel

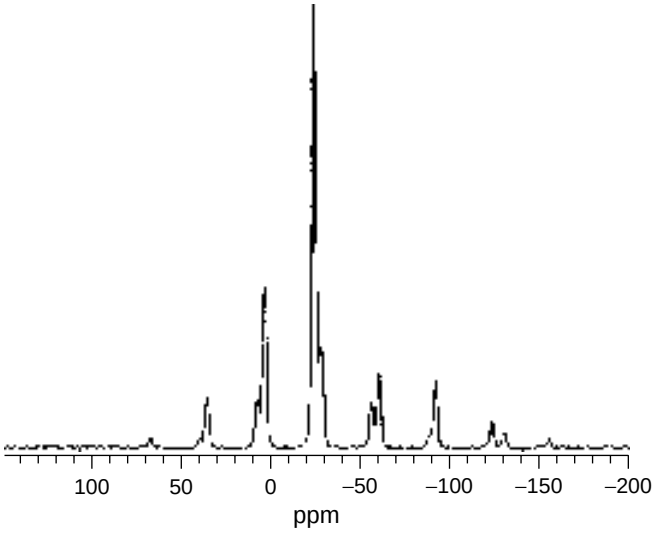

Figure 5 Proton-decoupled ^{19}F CPMAS NMR spectrum of $(Ph_2FPNMe)_2$ at 188 MHz, and spin rate 6 kHz showing the difference in centerband intensities of the two doublet components, arising from the 'squeezing' and 'stretching' of the relevant subspectra. (Figure adapted from that in R. K. Harris and L. A. Crowe, *J.C.S. Dalton*, 1999, 4315, with permission)

each other. Thus one static powder subspectrum is 'stretched' whereas in the other is 'squeezed'.

Under slow MAS conditions, the influence of the angle-dependent term $3\cos^2\theta - 1$ is translated into a distribution of intensities among the relevant spinning sidebands, which extend over a larger frequency range for the 'stretched' subspectrum than for the 'squeezed' subspectrum. The isotropic coupling serves to resolve the subspectra, enabling the spinning sideband manifolds to be analysed separately, thus yielding the two values of ζ_A^{eff}. One consequence is that the centerbands of the two components, split by J_{AX}, have different intensities (see Figure 5).[44] The magnitudes of ζ_A, D' and J_{AX} are readily obtained by the analysis. Since the sign of ζ_A will normally be obvious (and can be obtained separately by spinning sideband analysis of an A spectrum obtained with X-decoupling) sign information on J_{AX} and D' are obtained, albeit with some ambiguity. Only the relative signs of D' and J_{AX} are determined, the rule being as follows: If the high-frequency spinning sideband manifold has the larger magnitude of ζ_A^{eff}, then (i) for positive ζ_A, D' and J_{AX} have the same sign, whereas (ii) for negative ζ_A, D' and J_{AX} have opposite signs. The inverse is true if the larger magnitude of ζ_A^{eff} belongs to the low-frequency subspectrum. If r_{AX} is known (e.g., from diffraction studies), D can be calculated, so ΔJ can be derived, though with an ambiguity unless the sign of J_{AX} is known. On the other hand, if the relative magnitudes of D and $\Delta J/3$ can be assumed, the absolute sign of J_{AX} can be determined.[40,42]

The extension to a linear AX_2 case is straightforward. There will now be three spinning sideband manifolds in the A spectrum, with effective tensor anisotropies given by

$$\zeta_A^{eff} = \zeta_A - \left(\frac{2D'}{\nu_o^A}\right)\sum m_X \qquad (37)$$

where $\sum m_X = 1, 0$ or -1, associated with centerbands at $\nu_A^{iso} - J_{AX}\sum m_X$. The central sideband manifold gives ζ_A directly, because it is independent of D'. Clearly this is an advantage, particularly if A-{X} spectra cannot be obtained because of spectrometer limitations.

Zilm and Grant[45] derived expressions for heteronuclear two-spin (AX) solid-state spectra of static samples, and these have been adapted for MAS cases and further discussed by Harris et al.[40] and Haubenreisser et al.[41] The theory involved can form the basis of a computer program involving the Euler angles between the tensor axes. This has been done by Cherryman and Harris[43] for the AX and AX_2 cases, though still under the assumptions that $\boldsymbol{J}$ is axially symmetric and co-axial with $\boldsymbol{D}$. These authors analysed the spectra to triple-fit the coupled and A-{X} decoupled spectra of the AX case (see Figure 6) simultaneously (and correspondingly for the three subspectra of the AX_2 case). Triple fitting can also be carried out for spectra with satellite peaks arising from isotopic mixtures, e.g., for ^{19}F spectra influenced by coupling to ^{119}Sn[42,45] or for ^{31}P spectra of compounds exhibiting ^{31}P, ^{195}Pt coupling.[46] Recently, errors in the simultaneous fit of shielding tensor components and in the Euler angles which fix the orientation of the tensor in the molecular frame have been discussed, and clues have been given concerning the experimental variables to be set in order to obtain the desired accuracy in the orientation angles.[47]

Cases involving homonuclear coupling (dipolar and indirect) together with shielding are more complex and have been mentioned briefly above, references 9 and 10 supplying ideal cases.

Practical application of the above theory has been made for the two-spin (^{13}C, ^{31}P) case,[40,41] for the two-spin (^{119}Sn,

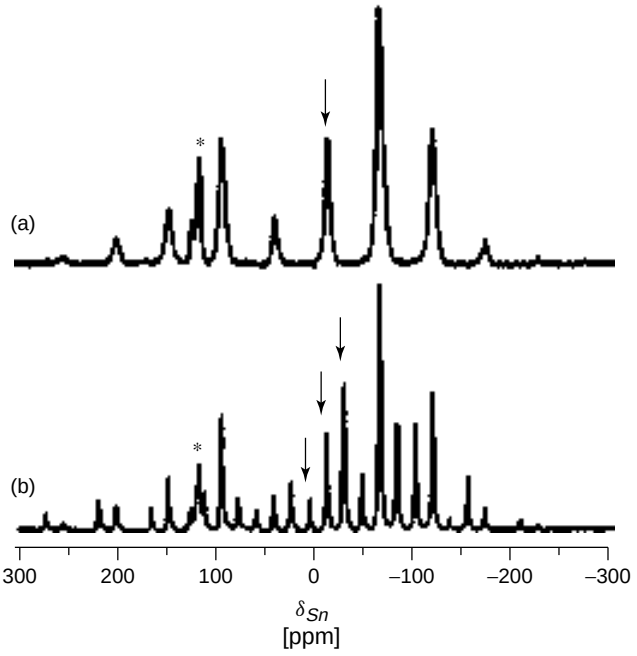

Figure 6 Proton-decoupled ^{119}Sn CPMAS NMR spectra of $^{n}Bu_3SnF$ at 74.6 MHz and spin rate 4 kHz. (a) Triple-resonance case (i.e., ^{19}F-decoupled). (b) Spectra with fluorine coupling effects to show the three subspectra. Triple-fit procedures for the spinning sideband patterns shown in (b) give tensor information which, for the shielding interaction, are consistent with those derived from (a). (Reproduced by permission from J. C. Cherryman and R. K. Harris, *J. Magn. Reson.*, 1997, **128**, 21)

^{19}F) situation,[43] and for (^{119}Sn, ^{19}F) AX_2 spectra.[42,43] The lack of observable differences in intensity distribution between spinning sideband manifolds of subspectra arising from (^{195}Pt, ^{31}P) indirect coupling has been taken[48] as evidence that ^{195}Pt shielding anisotropy dominates over dipolar coupling in *cis*-$PtMe_2(PPh_3)_2$.

5.2 Interplay of σ, D and q[49–51]

For spin-1/2 nuclei coupled to quadrupolar spins, second-order effects occur because the influence of the quadrupolar interaction is transferred to the spin-1/2 by the coupling (see **Magic Angle Spinning Carbon-13 Lineshapes: Effect of Nitrogen-14,** Volume 5; **Magic Angle Spinning: Effects of Quadrupolar Nuclei on Spin-1/2 Spectra,** Volume 5). This has two effects: (i) it alters the multiplet splittings which would otherwise be equal to $|J_{AX}|$, and (ii) it causes each multiplet peak to be a powder pattern (see Ref.[52] for a review). Such complications do not affect the spinning sideband analysis described above as long as the multiplet components are clearly resolved (and provided integrals rather than peak heights are used as intensities since the powder patterns vary in shape). Thus, similar principles to those of the above Section can be invoked for AX cases in which dipolar coupling is between the observed spin-1/2 and a single quadrupolar nucleus. Equation (35) can still be used, but now m_X takes $2I + 1$ possible values ($m_X = I, I-1, I-2 \ldots . -I$), resulting in $2I+1$ subspectra. Clearly spinning sideband analysis becomes more accurate since the number of parameters involved is the same as for two spin-1/2 nuclei. Such spectra have been examined[49] for (^{31}P, ^{55}Mn), (^{31}P, ^{59}Co) and (^{31}P, ^{93}Nb) spin systems (Figure 7).

However, this simple situation is seldom true for ^{13}C spectra involving (^{13}C, ^{14}N) spin pairs, since in this case the relevant isotropic indirect coupling constants are generally small, even negligible. The powder patterns for the subspectra involving $m_N = \pm 1$ overlap, giving a 2 : 1 or 1 : 2 appearance to the spectrum in the limit of fast spinning. However, the powder bandshapes will vary over the spinning sideband manifold,[50] so that in the simplest situation,

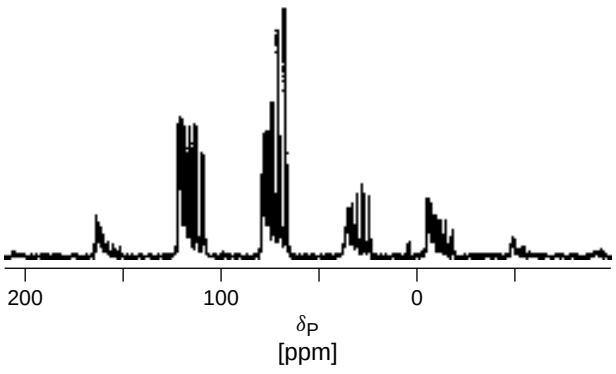

Figure 7 Phosphorus-31 direct polarization spectrum of $Mn_2(CO)_9PPh_3$ at 121.4 MHz showing the differences in spinning sideband intensities for the subspectra from the multiplet components (arising from ^{55}Mn, ^{31}P coupling) because of the interplay between the shielding, quadrupolar and indirect coupling tensors. (Reproduced by permission from R. Gobetto, R. K. Harris and D. C. Apperley, *J. Magn. Reson.*, 1992, **96**, 119)

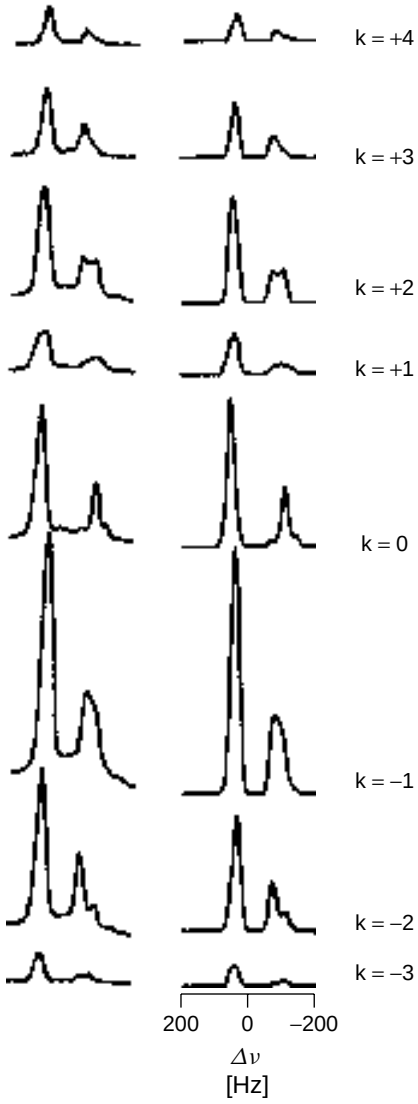

Figure 8 Centerband and sidebands for the high-frequency cyanide ^{13}C CPMAS signals of ($\{(CH_3)_3Pb\}_4Ru(CN)_6$) at 75.4 MHz. Left: experimental bandshapes (rotation rate 4.3 kHz). Right: computer simulation. (Reproduced by permission from N. A. Davies, R. K. Harris and A. C. Olivieri, *Mol. Phys.*, 1996, **87**, 669)

i.e., when $\boldsymbol{\sigma}$, $\boldsymbol{D}$ and $\boldsymbol{q}$ are axially symmetric and co-axial, the angle β between their unique axes and the spinning axis becomes an important variable. The theory has been discussed by Davies et al.[50] and applied (using a perturbation approach) to the cyanide carbon signals of a coordination polymer, $[\{(CH_3)_3Pb\}_4Ru(CN)_4]_\infty$ (see Figure 8). The shape of the centerband at infinite spinning speed is dominated by the intensities of the major singularities at $\beta = 54.7°$ and 90°. As the rotation rate is lowered, the former loses intensity in comparison to the latter. The splitting of the centerband therefore apparently increases as the rotation speed decreases (see Figure 9). There are concomitant changes in the shapes of the spinning sidebands. Their patterns and their intensities can be simulated using standard theory,[53] and therefore information on ζ_C, D_{CN} (in principle, D') and q obtained. Off-MAS ^{13}C spinning sideband manifolds for the cyanide signal of CH_3CN have also been simulated,[51] and used together

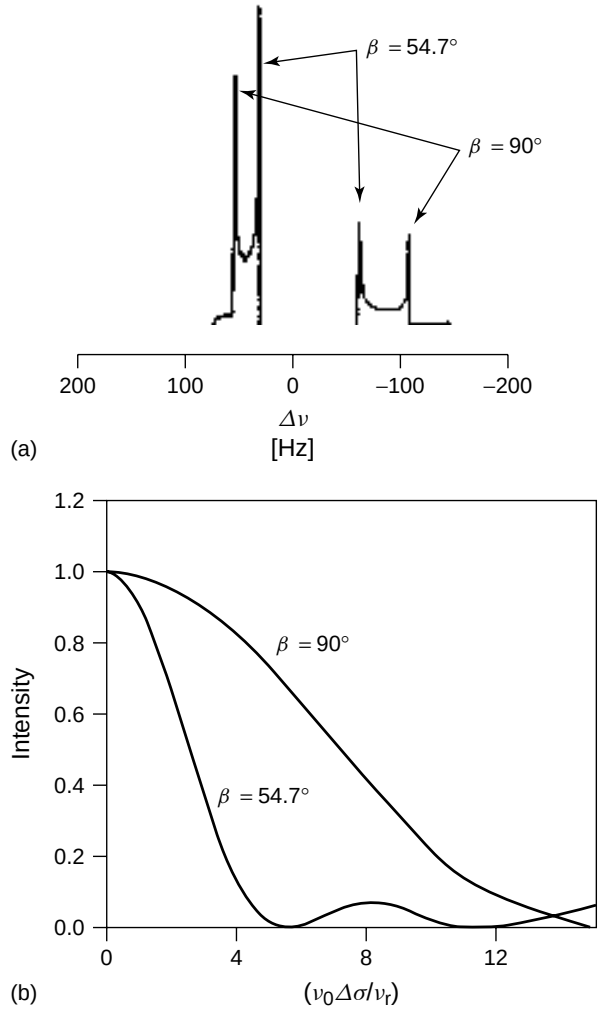

Figure 9 (a) calculated bandshape for an asymmetric 2 : 1 splitting produced by residual second-order ^{13}C, ^{14}N dipolar coupling. The peaks associated with the orientations $\beta = 90°$ and 54.7° (where β is the angle made by the unique axes of the co-axial tensors $\boldsymbol{\sigma}$, D and q with the spinning axis) are indicated by arrows. (b) calculated (normalized) centerband intensities for crystallites with $\beta = 90°$ and 54.7° as a function of the ratio between the shielding anisotropy (expressed in Hz) and the spinning frequency. (Reproduced by permission from N. A. Davies, R. K. Harris and A. C. Olivieri, *Mol. Phys*., 1996, **87**, 669)

with other NMR spectra to yield detailed data on $\boldsymbol{\sigma}$, $\boldsymbol{D}$ and $\boldsymbol{q}$.

Ding and McDowell[54] have pointed out the limitations of most calculations of spectra involving coupling between spin-1/2 and quadrupolar nuclei. They give a general and exact description of the problem within the framework of the density matrix, including the spinning sidebands in a natural manner. They apply the theory to ^{13}C spectra of $KPt(CN)_4.3H_2O$, including the ^{195}Pt satellites, and show that the complex spectra are fitted extremely well at different spinning rates, yielding the relevant parameters. A density matrix approach has also been used by Amoureux et al.[55] to produce a general computer program, PULSAR, to simulate a wide range of NMR situations involving interplay of different tensors, including the Euler angles between their axes.

6 RELATED ARTICLES IN THIS VOLUME

Magic-angle Spinning Extensions; Satellite Transition NMR Spectroscopy of Half-Integer Quadrupolar Nuclei under Magic-Angle Spinning.

7 RELATED ARTICLES IN VOLUMES 1–8

Chemical Shift Tensor Measurement in Solids, Volume 2; Dynamic Angle Spinning, Volume 3; High Speed MAS of Half-Integer Quadrupolar Nuclei in Solids, Volume 4; Magic Angle Spinning, Volume 5; Sideband Analysis in Magic Angle Spinning NMR of Solids, Volume 7; Variable Angle Sample Spinning, Volume 8.

8 REFERENCES

1. J. Herzfeld and A. E. Berger, *J. Chem. Phys.*, 1980, **73**, 6021.
2. M. M. Maricq and J. S. Waugh, *J. Chem. Phys.*, 1979, **70**, 3300.
3. P. Hodgkinson and L. Emsley, *Prog. NMR Spectrosc.*, 2000, **36**, 201.
4. B. Q. Sun and E. A. Pines, *Appl. Magn. Reson.*, 1993, **5**, 43.
5. A. R. Brough, C. P. Grey, and C. M. Dobson, *J. Am. Chem. Soc.*, 1993, **115**, 7318.
6. J. Hjorth, J. Skibsted, and H. J. Jakobsen, in 'Methodology and Applications of Inversion within Geophysics, Astronomy, Geodesy and Physics', Proceedings of the Interdisciplinary Inversion Workshop II, ed K. Mosegaard, Copenhagen, 1993.
7. N. K. Sethi, D. W. Alderman, and D. M. Grant, *Mol. Phys.*, 1990, **71**, 217.
8. A. Schmidt and S. Vega, *Isr. J. Chem.*, 1992, **32**, 215.
9. G. Wu, B. Sun, R. E. Wasylishen, and R. G. Griffin, *J. Magn. Reson.*, 1997, **124**, 366.
10. R. Challoner, T. Nakai, and C. A. McDowell, *J. Chem. Phys.*, 1991, **94**, 7038.
11. R. Challoner, C. A. McDowell, M. Yoshifuji, K. Toyota, and J. A. Tossell, *J. Magn. Reson. Ser. A*, 1993, **104**, 258.
12. G. Wu, R. E. Wasylishen, and R. D. Curtis, *Can. J. Chem.*, 1992, **70**, 863; G. Wu and R. E. Wasylishen, *Inorg. Chem.*, 1992, **31**, 145; *J. Chem. Phys.*, 1993, **99**, 6321.
13. A. Kubo and C. A. McDowell, *J. Chem. Phys.*, 1990, **92**, 7156.
14. A. Schmidt, S. O. Smith, D. P. Rayleigh, J. E. Roberts, R. G. Griffin, and S. Vega, *J. Chem. Phys.*, 1986, **85**, 4248.
15. A. Schmidt and S. Vega, *J. Chem. Phys.*, 1987, **87**, 6895.
16. M. J. Duer and M. H. Levitt, *Solid State NMR*, 1992, **1**, 211.
17. A. C. Olivieri, C. M. Lagier, D. C. Apperley, and R. K. Harris, *Solid State NMR.*, 1992, **1**, 205.
18. C. M. Lagier, D. C. Apperley, U. Scheler, A. C. Olivieri, and R. K. Harris, *J. Chem. Soc. Faraday Trans.*, 1996, **92**, 5047.
19. C. M. Lagier, A. C. Olivieri, and R. K. Harris, *J. Chem. Soc. Perkin Trans.*, 1998, **2**, 1791.
20. Y. Shen, T. Wu, and Y. Yang, *Chem. Phys. Lett.*, 1995, **242**, 83.
21. K. Eichele and R. E. Wasylishen, *J. Phys. Chem.*, 1994, **98**, 3108.
22. C. M. Lagier and A. C. Olivieri, *J. Magn. Reson.*, 1997, **126**, 138.
23. J. R. Ascenso and R. K. Harris, unpublished (1985) (first referred to in the open literature in R. K. Harris and A. Sebald, *J. Organomet. Chem.*, 1987, **331**, C9); L. H. Merwin, Ph.D. Thesis, University of Durham, 1987 (reported in the open literature in R. K. Harris, L. H. Merwin, and G. Hägele, *J. Chem. Soc. Faraday Trans. I*, 1989, **85**, 1409).
24. H. J. M. de Groot, S. O. Smith, A. C. Kolbert, J. M. L. Courtin, C. Winkel, J. Lugtenburg, J. Herzfeld, and R. G. Griffin, *J. Magn. Reson.*, 1991, **91**, 30.

25. G. Jeschke and G. Grossmann, *J. Magn. Reson. Ser. A*, 1993, **103**, 323.
26. N. J. Clayden, C. M. Dobson, L.-Y. Lian, and D. J. Smith, *J. Magn. Reson.*, 1986, **69**, 476.
27. E. A. Christopher, R. K. Harris, and R. A. Fletton, *Solid State NMR*, 1992, **1**, 93.
28. L. H. Merwin, Ph.D. Thesis, University of Durham, 1987; H.-P. Bai, Ph.D. Thesis, University of Durham, 1991.
29. P. Hodgkinson and L. Emsley, *J. Chem. Phys.*, 1997, **107**, 4808.
30. R. K. Harris, D. C. Apperley, P. Avalle, and P. Amornsakchai, unpublished work.
31. Varian Incorporated, NMR Systems STARS software.
32. A. D. Bain and R. S. Dumont, *Concepts Magn. Reson.*, 2001, **13**, 159.
33. D. Fenzke, B. Maess, and H. Pfeiffer, *J. Magn. Reson.*, 1990, **88**, 172.
34. G. A. Bowmaker, R. K. Harris, and S.-W. Oh, *Coord. Chem. Rev.*, 1998, **167**, 49.
35. G. E. Hawkes, K. D. Sales, L. Y. Lian, and E. R. Gobetto, *Proc. R. Soc. Lond. A*, 1989, **424**, 93.
36. P. D. Ellis and H. Bildsøe, referred to in H. Jakobsen, P. D. Ellis, R. R. Inners, and C. F. Jensen, *J. Am. Chem. Soc.*, 1982, **104**, 7442.
37. A. C. Olivieri, *J. Magn. Reson. Ser. A*, 1996, **123**, 207.
38. R. K. Harris, P. Jackson, L. H. Merwin, B. J. Say, and G. Hägele, *J. Chem. Soc. Faraday Trans. 1*, 1988, **84**, 3649.
39. J. Skibsted, T. Vosegaard, H. Bildsøe, and H. J. Jakobsen, *J. Phys. Chem.*, 1996, **100**, 14 872.
40. R. K. Harris, K. J. Packer, and A. M. Thayer, *J. Magn. Reson.*, 1985, **62**, 284.
41. U. Haubenreisser, U. Sternberg, and A.-R. Grimmer, *Mol. Phys.*, 1987, **60**, 151.
42. H. Bai and R. K. Harris, *J. Magn. Reson.*, 1992, **96**, 24.
43. J. C. Cherryman and R. K. Harris, *J. Magn. Reson.*, 1997, **128**, 21.
44. R. K. Harris and L. A. Crowe, *J.C.S. Dalton*, 1999, 4315.
45. K. W. Zilm and D. M. Grant, *J. Am. Chem. Soc.*, 1981, **103**, 2913.
46. L. A. Crowe, Ph.D. Thesis, University of Durham, 1999; L. A. Crowe, K. B. Dillon, R. K. Harris, J. A. K. Howard, and M. D. Roden, to be published.
47. A. C. Olivieri, *Solid State NMR*, **11**, 1998, 181.
48. R. K. Harris, P. Reams, and K. J. Packer, *J. Mol. Struct.*, 1986, **141**, 13.
49. R. Gobetto, R. K. Harris, and D. C. Apperley, *J. Magn. Reson.*, 1992, **96**, 119.
50. N. A. Davies, R. K. Harris, and A. C. Olivieri, *Mol. Phys.*, 1996, **87**, 669.
51. J. Sepa, R. J. Gorte, B. H. Suits, and D. White, *Chem. Phys. Lett.*, 1996, **252**, 281.
52. R. K. Harris and A. C. Olivieri, *Prog. NMR Spectrosc.*, 1992, **24**, 435.
53. A. C. Olivieri, *Solid State NMR*, 1997, **10**, 19.
54. S. Ding and C. A. McDowell, *J. Chem. Phys.*, 1997, **107**, 7762.
55. J. P. Amoureux, C. Fernandez, and Y. Dumazy, *J. Chem. Phys.*, 1995, **92**, 1939.

Biographical Sketches

Robin K. Harris, *b* 1936. B.A. (Nat. Sci.), Ph.D. (supervisor Norman Sheppard), Sc.D., University of Cambridge, UK. Postdoctoral work at Mellon Institute, Pittsburgh, PA (with Aksel Bothner-By). Successively lecturer, senior lecturer, and professor, University of East Anglia, UK. Currently Professor of Chemistry, University of Durham, UK. Secretary-General of ISMAR, 1986-92. Approx. 460 publications. Current research specialty: solid-state NMR and its applications in materials chemistry.

Alejandro C. Olivieri, *b* 1958. B.Sc. (Catholic University, Argentina), Ph.D. (supervisor Manuel G. Sierra), National University of Rosario, Argentina. Postdoctoral work at the University of Illinois at Urbana-Champaign, USA (with Iain Paul and David Curtin). Successively Associate Professor and currently Full Professor, Department of Analytical Chemistry, National University of Rosario, Argentina. Approx. 100 publications. Current research interests: NMR and its applications to organic and analytical chemistry.

Symmetry-Based Pulse Sequences in Magic-Angle Spinning Solid-State NMR

Malcolm H. Levitt

Chemistry Department, Southampton University, Southampton, UK

1 Introduction 1
2 Homonuclear Sequences 2
3 Heteronuclear Sequences 19
4 Applications 20
5 Conclusions 29
6 References 29

1 INTRODUCTION

Much modern solid-state NMR technology is based on two physical manipulations: (i) rotation of the sample in space, usually at a fixed frequency around a fixed axis, but sometimes using more complicated trajectories; and (ii) rotation of the nuclear spin polarizations using applied rf fields.

Magic-angle spinning was first demonstrated independently by Andrew and Lowe[1,2] in 1959. These researchers demonstrated a noticeable narrowing effect on the NMR spectra of abundant spins in solids when the sample was rotated at several kHz around an axis tilted by the angle $\arctan\sqrt{2} = 54.74^\circ$ with respect to the main magnetic field (see **Magic Angle Spinning,** Volume 5). However, the magic-angle spinning (MAS) method was not employed much at first because it was thought to be ineffective unless the spinning frequency greatly exceeded the size of the anisotropic nuclear spin interactions – a condition difficult to satisfy except for a limited number of samples. The situation changed at the end of the 1970s, when it was found that magic-angle spinning dramatically narrowed the proton-decoupled NMR peaks of isolated ^{13}C spins in organic solids.[3] The ^{13}C peaks split up into narrow 'spinning sidebands', even though the spinning frequency was much smaller than the chemical shift anisotropy (CSA). MAS, in combination with Hartmann–Hahn cross-polarization and heteronuclear decoupling, became a standard method for examining the NMR spectra of rare spin species such as ^{13}C and ^{15}N in solids.[4] Commercial NMR companies began to offer MAS equipment as options for their spectrometers, allowing an explosion of applications.

The use of nuclear spin rotations by applied rf fields developed in parallel. The basic technique of *hetero*nuclear decoupling was already introduced by Bloch,[5] and advanced rapidly in the context of solution NMR with the introduction of noise modulation[6] and composite pulse decoupling[7–9] (see **Decoupling Methods,** Volume 3). In solid-state NMR, on the other hand, heteronuclear decoupling methodology stagnated until the introduction of the two-pulse phase modulation (TPPM) by Griffin and co-workers.[10] The methodology of *homo*nuclear dipolar decoupling in solids received more attention from the start. This process started with the use of magic-angle off-resonance irradiation by Lee and Golburg[11] and continued with the pulse methods of Waugh, Huber and Haeberlen,[12,13] Mansfield,[14] Rhim and Vaughan,[15] Burum and co-workers[16] and many others (see **Average Hamiltonian Theory,** Volume 2). Advances in digital electronics made possible new approaches, such as the frequency-switched Lee–Goldburg (FSLG) method.[17] These methodological developments were accompanied by important theoretical advances such as the average Hamiltonian theory and its variants.[13,14,18]

For much of this period, the spatial and spin manipulations were treated separately. For example, the principles of homonuclear decoupling by applied rf fields were developed explicitly for static samples – the rotation of the sample during the rf pulse sequence, in the case of MAS, was regarded as a minor additional perturbation. Similarly, the principles of echo formation by sample rotation generally neglected the duration of applied rf pulses. This conceptual separation was made possible by an experimental separation of timescales. Routinely-available spinning frequencies were much smaller than routinely-available nutation frequencies under applied rf fields. This situation was not fundamentally changed even when the 'combined rotation and multiple pulse sequence' (CRAMPS) methods were introduced[19,20] (see **CRAMPS,** Volume 3). At the rather low spinning frequencies used initially, it was a reasonable approximation to ignore the MAS rotation during the rf pulse sequence. The enhanced narrowing effect of CRAMPS could be treated roughly by tacking the MAS rotation onto the end of a static average Hamiltonian calculation.

At the beginning of the 1980s, two developments highlighted the fact that rf pulse sequences and sample rotation could combine in unexpected and powerful ways. In the extraordinary sideband suppression and separation schemes of Dixon,[21,22] carefully-timed sequences of strong π pulses were applied to the rotating sample in order to manipulate the spinning sideband patterns generated by the subsequent free-induction decay. Around the same time, Waugh and co-workers applied a repetitive pulse train synchronous with the sample rotation, and showed that the averaging effect of the magic-angle rotation on the chemical shift anisotropy could be suppressed.[23] This would now be called a 'CSA recoupling' experiment.

The term 'recoupling' was first used in the *heteronuclear* context, when it was shown that the application of a continuous rf field to one spin species may restore the effect of the heteronuclear dipolar interaction to a second spin species, by counteracting the averaging effect of the magic-angle rotation.[24,25] This requires selection of the rf amplitude so that the magic-angle rotation frequency is a small integer multiple of the nutation frequency under the rf field, a condition termed 'rotary resonance'. It was also pointed out that the same effect could be produced by applying two strong 180° pulses every rotational cycle to one of the spin species.[25] This idea was developed independently by Schaefer et al., leading to the highly-successful rotational echo double resonance (REDOR) method[26,27] (see **REDOR & TEDOR,**

Volume 6). As discussed below, the REDOR scheme fits into the symmetry theory of rotor-synchronized pulse sequences (in the modern notation defined below, the symmetry of the usual version of REDOR is $R4_2^1$).

The next important advances were made by Tycko and co-workers.[28,29] It was shown that rotor-synchronized pulse sequences, in combination with sample rotation about a non-magic-angle axis, could be used to emulate a zero-field NMR experiment (see **Zero Field NMR,** Volume 8). In the context of the present article, it is important to note that Tycko used symmetry relationships to simplify the task of pulse sequence design. In the modern notation defined below, one would describe Tycko's 'zero-field in high-field' pulse schemes as having the symmetry $C5_1^1$.

The second development made by Tycko's group also had a wide impact. The dipolar recoupling at the magic angle (DRAMA) scheme[30–32] initiated the field of *homonuclear* dipolar recoupling in solids (see **Homonuclear Recoupling Schemes in MAS NMR,** Volume 4). DRAMA is a rather simple pulse sequence of strong 90° pulses separated by intervals and is not particularly robust. A partially successful attempt was made to improve it using symmetry-based arguments.[32] A popular alternative is the radio-frequency driven recoupling (RFDR) scheme of Griffin and co-workers, which is based on strong 180° pulses.[33,34] As discussed below, part of the success of RFDR may now be understood in terms of its symmetry properties (in modern notation, the symmetry of the usual version of RFDR is $R4_4^1$).

A different approach to dipolar recoupling was introduced with the double-quantum homonuclear rotary resonance (2Q-HORROR) method.[35] This was a development of the heteronuclear rotary resonance method, exploiting the additional resonance conditions associated with double-quantum transitions in homonuclear spin systems. The HORROR method showed for the first time that it is possible to achieve highly efficient 2Q excitation in a powder sample, in part by a tighter control of the orientation-dependence of the recoupled Hamiltonian. The appropriate property has come to be called "γ-encoding", and will be discussed below.

HORROR is only feasible for coupled spins with small chemical shift differences. It required a fresh theoretical approach to extend this method to more general systems while retaining the γ-encoded 2Q recoupling property. This effort lead to the C7 pulse scheme and its variants,[36–42] which are capable of efficient broadband double-quantum recoupling. In modern notation, these schemes have the symmetry $C7_2^1$. These methods were applied to a variety of problems, including the measurement of molecular torsional angles in a membrane protein.[43,44]

As well as being practically successful, the theory behind C7 was very powerful, and could be used for a variety of problems. A further extension of the symmetry theory led to a pallette of symmetries suitable for γ-encoded double-quantum recoupling, including methods which are applicable at high spinning frequencies.[39] The symmetry theorems were also used to treat the problem of heteronuclear decoupling in MAS solids, generating schemes competitive with the TPPM modulation method.[41,45]

In a related development, Spiess and co-workers showed that CRAMPS may be implemented at high MAS spinning frequencies by synchronizing the rf cycles with the sample rotation.[46,47] In modern notation, these schemes have the symmetry $C3_1^0$ and $C4_1^0$.

Schemes such as C7 are based on repeated radio-frequency cycles, shifted in phase and synchronized with the sample rotation. Each cycle is designed to return the nuclear spins to their initial states, if other spin interactions are ignored, i.e., each cycle provides a rotation through 0°, 360°, or 720°, etc. Although effective for double-quantum excitation, this construction scheme is too restrictive when applied to many other recoupling problems. A set of new symmetries were therefore developed, based on 180° rotation elements.[41] These symmetries, called R-symmetries, suggest many new classes of pulse sequence, and also help explain the operation of many existing schemes. As discussed below, many of the successful methods invented in the past, such as RFDR, REDOR, and TPPM conform to the R-symmetries. This is probably not a coincidence.

The invention of R-symmetries was anticipated by the through bond spectroscopy (TOBSY) method of Baldus and Meier.[48–52] These authors also used symmetry arguments to design their pulse sequences, which have the modern symmetry notation $R6_1^0$ and $R8_1^0$.

The discovery of the R-symmetries is still too recent to assess their full significance. Some of the promising recent applications are discussed below.

2 HOMONUCLEAR SEQUENCES

2.1 Spin Interactions

The symmetry-based approach to the design of rotor-synchronized pulse sequences exploits the rotational properties of the nuclear spin interactions. In general, each spin interaction may be expressed as a product of three terms, expressing the transformation properties of the interaction with respect to rotations of the molecular framework ('space'), rotations of the nuclear spin polarizations ('spin') and rotations of the external magnetic field. These rotational properties may be summarized in terms of the three *rotational ranks* which define each nuclear spin interaction. The set of rotational ranks forms the *rotational signature* of a nuclear spin interaction. The rotational signatures are summarized for the most important homonuclear interactions of spin-1/2 in Table 1.

As may be seen from Table 1, the significant nuclear spin interactions all have ranks 0, 1 or 2. For example, those interactions which are invariant to a particular type of rotation are assigned rank zero. Interactions which have the rotational symmetry of a p-orbital in atomic theory are assigned rank 1. Interactions which have the rotational symmetry of a d-orbital in atomic theory are assigned rank 2.

Consider, for example, the homonuclear dipolar interaction between nuclear spins. This has rank 2 with respect to both

Table 1 Rotational signatures of homonuclear spin interactions in diamagnetic systems of spin-1/2

Interaction	Space rank, l	Spin rank, λ	Field rank
Isotropic chemical shift	0	1	1
Chemical shift anisotropy	2	1	1
J-coupling	0	0	0
Dipole–dipole coupling	2	2	0

spatial and spin rotations, indicating, for example, that a rotation of the molecular framework by 180° does not change the interaction strength, while a rotation through 90° changes the sign of the interaction.

The chemical shift anisotropy interaction is more complicated, since it is a three-body interaction, involving the nuclear spins, the electronic environment and the external magnetic field. It has ranks 2, 1 and 1 with respect to molecular rotations, spin rotations, and external field rotations, respectively. This interaction changes sign if the nuclear spins are rotated by 180°, with the molecules and the field held fixed. The CSA interaction also changes sign if the external field is rotated through 180°, while the spin polarizations and the molecular environment are held fixed. The CSA interaction does not change sign, on the other hand, if the molecules are rotated through 180°, while the spins and the field are held fixed.

Many NMR textbooks conflate the 'spin' part and the 'field' part into one compound term, often called, confusingly, the 'spin part' of the interaction. This practice obscures the rotational properties and is best avoided.

There are also minor interactions such as the antisymmetric part of the chemical shift tensor (space, spin, field ranks of 1, 1 and 1), and the J-coupling anisotropy (space, spin, field ranks of 2, 2 and 0), which are omitted here for simplicity.

The spherical ranks listed in Table 1 are defined as follows: An irreducible spherical tensor of rank l has $2l + 1$ components, with a component index m running from $-l$ to $+l$ in integer steps. A rotation interconverts these $2l + 1$ components according to the transformation equation:

$$R(\Omega)T_{\lambda m}R(\Omega)^{\dagger} = \sum_{m'=-l}^{+l} T_{\lambda m'}D^{l}_{m'm}(\Omega) \qquad (1)$$

Here $R(\Omega)$ are rotation operators and $D^{l}_{m'm}(\Omega)$ is an element of the $(2l + 1)$-dimensional Wigner matrix. The symbol Ω indicates a triplet of Euler angles $\Omega = \{\alpha, \beta, \gamma\}$ defining a general three-dimensional rotation. Irreducible spherical tensors, Wigner matrices and Euler angles are discussed thoroughly in the literature.[4] A particularly useful compilation is given in Ref.[53] The article **Internal Spin Interactions & Rotations in Solids,** Volume 4, summarizes many key results.

The Wigner elements have the following form:

$$D^{l}_{m'm}(\Omega) = \exp\{-\mathrm{i}m'\alpha\}d^{l}_{m'm}(\beta)\exp\{-\mathrm{i}m\gamma\} \qquad (2)$$

where $d^{l}_{m'm}(\beta)$ is called a reduced Wigner matrix element.

Although the detailed form of the Wigner matrices and the spherical tensors depends on the rank, and the approach appears to be mathematically complicated at first sight, the transformation properties are always the same, which permits a universal approach to pulse sequence theory.

2.2 Reference Frames

The discussion of spin interactions in rotating solids is facilitated by defining a set of reference frames (Figure 1).

2.2.1 The Principal Axis Frame P^{Λ}

The *principal axis frame* P^{Λ} provides the simplest form of the spin interaction Λ. For example, consider the through-space dipole–dipole interaction (DD interaction) between two spins j and k. The z-axis of the principal axis frame P^{jk} is oriented along the vector joining the spins j and k. In this frame, the spherical tensor components with $m = \pm 1$ and $m = \pm 2$ vanish, leaving only the $m = 0$ component. For the CSA interaction of spin j, the $m = \pm 1$ components vanish in the principal axis frame P^{j}, while the $m = 0$ and $m = \pm 2$ components remain finite.

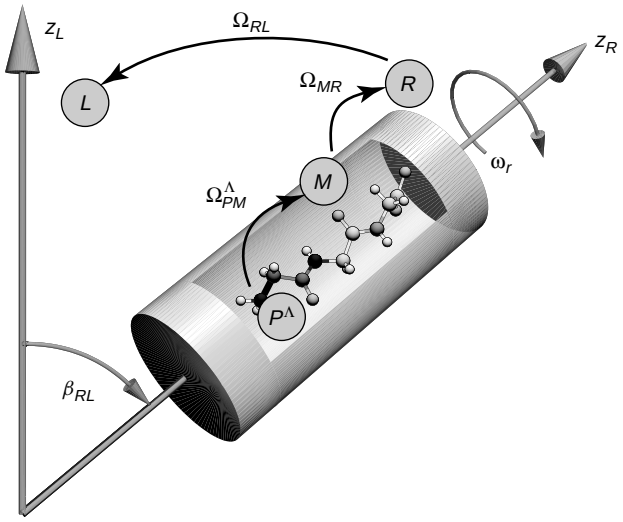

Figure 1 Definition of the reference frames in magic-angle spinning NMR experiments. (Adapted from Ref.[82])

In general, there are many different spin interactions, and each one has a different principal axis frame P^{Λ}.

2.2.2 The Molecular Frame M

The molecular reference frame M is fixed with respect to the molecular structure. It is usual to transform all of the different spin interactions into the common reference frame M before further manipulations are imposed.

A principal axis frame P^{Λ} is related to the molecular frame M by a set of three Euler angles, denoted $\Omega^{\Lambda}_{PM} = \{\alpha^{\Lambda}_{PM}, \beta^{\Lambda}_{PM}, \gamma^{\Lambda}_{PM}\}$. These Euler angles define the relative orientation of the frames P^{Λ} and M. In general, there are several spin interactions, each with a different set of Euler angles Ω^{Λ}_{PM}, specifying its orientation with respect to the common molecular frame M.

2.2.3 The Rotor Frame R

In a spinning solid, the orientation of the molecules with respect to the rotating sample holder ('rotor') is of great importance. The rotor-fixed frame R is defined such that its z-axis is along the rotational axis. The Euler angles $\Omega_{MR} = \{\alpha_{MR}, \beta_{MR}, \gamma_{MR}\}$ define the relative orientation of the molecular reference frame and the rotor frame.

If the sample were a single crystal, with only one molecule in the asymmetric unit of the crystal structure, then all molecules in the sample would have the same set of Euler angles Ω_{MR}. In practice, the sample usually has an orientational distribution of some kind, and in the extreme case of a disordered sample such as a powder, the Euler angles Ω_{MR} are distributed randomly. In such cases, the results of experiments must be analyzed by integrating spin dynamical calculations

over all possible values of the Euler angles Ω_{MR}. This is called powder averaging.

The Euler angle γ_{MR} has special significance in the theory of rotating solids. Molecules which have the same values of α_{MR} and β_{MR} but different values of γ_{MR} are related by a rotation around the rotor axis. This implies that the mechanical rotation of the sample causes such molecules to pass through the same cycle of laboratory frame orientations, but with a mutual time shift. This concept has been called a *carousel*,[54] since the riders on a playground carousel follow the same circular path, but are shifted with respect to each other in time.

In some samples, it is convenient to include one or more reference frames intermediate between M and R. For example, in crystalline solids, it is common to define a crystal-fixed reference frame C, and a set of Euler angles $\Omega_{MC} = \{\alpha_{MC}, \beta_{MC}, \gamma_{MC}\}$ defining the orientations of the molecules with respect to the crystal axes. If there is more than one more molecule in the crystal unit cell, then several sets of Euler angles Ω_{MC} are needed. The orientation of the crystal with respect to the rotor is defined through the Euler angles Ω_{CR}. In ordered samples such as fibres, on the other hand, it is useful to define a fibre director axis system D. The Euler angles Ω_{MD} relate the molecular axis system M to the fibre director system D, and a further set of Euler angles Ω_{DR} relate the fibre director to the rotor axis. By factorizing the problem in this way, it is possible to define independent orientation distributions for the molecules with respect to the fibre, and for the fibres with respect to the rotor. An example of this approach is found in Refs.[55,56] If the sample is a powder, these intermediate axis systems are unnecessary, and they will be omitted in the following discussion.

2.2.4 The Laboratory Frame L

The laboratory frame is chosen so that its z-axis is along the external magnetic field. The relative orientation of the sample holder and the field are defined by the Euler angles $\Omega_{RL} = \{\alpha_{RL}, \beta_{RL}, \gamma_{RL}\}$.

In magic-angle spinning NMR, the sample rotates at a fixed angular frequency ω_r about a fixed axis, subtending the magic angle $\theta_{\text{magic}} = \arctan\sqrt{2}$ with respect to the magnetic field. In these circumstances, the relevant Euler angles are given by

$$\begin{aligned} \alpha_{RL} &= \alpha^0_{RL} - \omega_r t \\ \beta_{RL} &= \theta_{\text{magic}} = \arctan\sqrt{2} \\ \gamma_{RL} &= \text{arbitrary} \end{aligned} \tag{3}$$

Here α^0_{RL} defines the orientation of the rotor at time point $t = 0$, which is rigorously defined as the start of signal acquisition (to be consistent with the normal definition of the Fourier transform, which involves an integral from $t = 0$ to $t = \infty$). If the rotation of the sample is not synchronized with the pulse sequence, the angle α^0_{RL} varies randomly from transient to transient. If necessary, the rotation of the sample may be synchronized optically with the pulse sequence, so as to obtain reproducible and controllable values of α^0_{RL}. This is usually unnecessary in powder samples.

The negative sign in the expression for α_{RL} is consistent with the usual definition of the Euler angles[53] and leads to a right-handed rotation of the sample in the case that ω_r is positive.

The second Euler angle β_{RL} is the angle between the rotor axis and the field. For exact magic-angle spinning it is exactly equal to θ_{magic}, but for other experiments, such as off-axis spinning, variable-axis spinning, or "zero-field in high-field" experiments, the angle β_{RL} may take other values. In the rest of this article, exact MAS is assumed.

In double rotation or dynamical angle spinning experiments,[57–59] the time-dependence of the Euler angles Ω_{RL} is more complicated (see **Double Rotation,** Volume 3). I ignore such possibilities here (double rotation may be handled neatly by introducing an 'outer rotor' frame as an intermediate between R and L).

2.3 Frame Transformations

The following 'chain rule' for the Wigner matrices greatly facilitates the transformations of spin interactions between the different frames:

$$D^l(\Omega_{AB})D^l(\Omega_{BC}) = D^l(\Omega_{AC}) \tag{4}$$

For example, a given spin interaction Λ may be transformed from its principal axis frame into the laboratory frame using equation (1) and the following chain:

$$D^l(\Omega^{\Lambda}_{PM})D^l(\Omega_{MR})D^l(\Omega_{RL}) = D^l(\Omega^{\Lambda}_{PL}) \tag{5}$$

Note the pattern of the subscripts. This notation greatly facilitates the task of concatenating multiple frame transformations.

2.4 Rf Euler Angles

The mathematics of spherical tensor rotations may also be applied to the rotations of the nuclear spin polarizations by resonant rf fields. In general, a sequence of resonant rf fields induces a time-dependent rotation of the resonant spins, which may be expressed as follows:

$$U_{\text{rf}}(t, t^0) = \exp\{-\text{i}\alpha_{\text{rf}}(t)I_z\}\exp\{-\text{i}\beta_{\text{rf}}(t)I_y\}\exp\{-\text{i}\gamma_{\text{rf}}(t)I_z\} \tag{6}$$

Here U_{rf} is the propagator under the applied rf fields, starting from the initial point of the pulse sequence, denoted t^0, up to an arbitrary time t, and $\{I_x, I_y, I_z\}$ are the total angular momentum operators of the resonant spin species. In general, the propagator may be determined by integrating the Schrödinger equation:

$$\frac{\text{d}}{\text{d}t}U_{\text{rf}}(t, t^0) = -\text{i}\mathcal{H}_{\text{rf}}(t)U_{\text{rf}}(t, t^0) \tag{7}$$

under the boundary condition $U_{\text{rf}}(t^0, t^0) = \mathbf{1}$. The operator $\mathcal{H}_{\text{rf}}$ is the spin Hamiltonian for the interaction with the rf field, and depends on the amplitude, phase and frequency of the applied rf field in the usual way.

In general, the rf Euler angles $\Omega_{\text{rf}} = \{\alpha_{\text{rf}}, \beta_{\text{rf}}, \gamma_{\text{rf}}\}$ do not have an *obvious* relationship with the applied rf pulse sequence. Nevertheless, these angles provide a convenient way of defining the symmetry properties of the spins under rf irradiation, and it is always possible to derive the Euler angle

trajectory from a given pulse sequence. Furthermore, it also possible to discover the pulse sequence that provides a desired trajectory of rf Euler angles.

2.5 Rotational Components

The mechanical rotation of the sample induces a time-dependent trajectory of the Euler angles $\Omega_{RL} = \{\alpha_{RL}, \beta_{RL}, \gamma_{RL}\}$, while the rf pulse sequence induces a time-dependent trajectory of the Euler angles $\Omega_{\mathrm{rf}} = \{\alpha_{\mathrm{rf}}, \beta_{\mathrm{rf}}, \gamma_{\mathrm{rf}}\}$. Suppose that a certain spin interaction has space rank l and spin rank λ. According to equation (1), the spatial rotation induces a mixing of the $(2l + 1)$ space components with $m = -l, -l + 1 \cdots + l$. Similarly, in the interaction frame of the rf field (see **Average Hamiltonian Theory,** Volume 2), the spin rotations induce a mixing of the $(2\lambda + 1)$ spin components with $\mu = -\lambda, -\lambda + 1 \cdots + \lambda$.

In the presence of sample rotation and resonant rf fields, each spin interactions may therefore be regarded as a superposition of $(2l + 1) \times (2\lambda + 1)$ components, characterized by quantum numbers m and μ:

$$\mathcal{H}^{\Lambda} = \sum_{m=-l}^{+l} \sum_{\mu=-\lambda}^{+\lambda} \mathcal{H}^{\Lambda}_{lm\lambda\mu} \tag{8}$$

In the case of exact magic-angle spinning, the components with $l = 2$ and $m = 0$ vanish, due to the following property of the magic angle:

$$d^2_{00}(\theta_{\mathrm{magic}}) = 0 \tag{9}$$

Explicit expressions for the components $\mathcal{H}^{\Lambda}_{lm\lambda\mu}$ may be found in Refs.[45,60]

A summary of the spin interaction components, in the case of exact magic-angle spinning, is given in Table 2.

2.6 Symmetry Classes

The space and spin trajectories may be synchronized so as to generate an average Hamiltonian containing desired combinations of quantum numbers $\{l, m, \lambda, \mu\}$ while other combinations are suppressed.

This is done by setting up periodic symmetry relationships between the mechanical and rf rotations. Consider two arbitrary time points, separated by an interval $n\tau_r/N$, where n and N are integers, and $\tau_r = |2\pi/\omega_r|$ is the rotational period of the sample. From equation (3), the continuous rotation of the sample imposes the following relationship on the spatial Euler angles:

$$\begin{aligned} \alpha_{RL}\left(t + \frac{n\tau_r}{N}\right) &= \alpha_{RL}(t) - \frac{2\pi n}{N} \\ \beta_{RL}\left(t + \frac{n\tau_r}{N}\right) &= \beta_{RL}(t) \end{aligned} \tag{10}$$

The rf pulse sequence imposes similar-looking rules on the rf Euler angles (equation (6)).

In the case of CN^{ν}_{n} sequences, the following Euler angle symmetry is imposed:

$$\begin{aligned} \beta_{\mathrm{rf}}\left(t + \frac{n\tau_r}{N}\right) &= \beta_{\mathrm{rf}}(t) \\ \gamma_{\mathrm{rf}}\left(t + \frac{n\tau_r}{N}\right) &= \gamma_{\mathrm{rf}}(t) - \frac{2\pi\nu}{N} \end{aligned} \tag{11}$$

where ν is an integer, possibly different from n.

In the case of RN^{ν}_{n} sequences, the Euler angle symmetry is slightly different:

$$\begin{aligned} \beta_{\mathrm{rf}}\left(t + \frac{n\tau_r}{N}\right) &= \beta_{\mathrm{rf}}(t) \pm \pi \\ \gamma_{\mathrm{rf}}\left(t + \frac{n\tau_r}{N}\right) &= \gamma_{\mathrm{rf}}(t) - \frac{2\pi\nu}{N} \end{aligned} \tag{12}$$

These symmetries apply to arbitrary time points within the pulse sequence.

The symbol CN^{ν}_{n} and RN^{ν}_{n} is called the *symmetry class* of the rotor-synchronized pulse sequence. The integers N, n and ν are called the *symmetry numbers* of the pulse sequence. As will be seen, the symmetry class defines a set of *selection rules* for the average Hamiltonian, which may be used to manipulate the recoupling and decoupling properties of the pulse sequence.

2.7 Rotor-Synchronized Pulse Sequences

The symmetries in equations (11) and (12) only refer to two Euler angles; the behavior of the third Euler angle α_{rf} is left completely free. This freedom implies that there are many inequivalent ways of implementing equations (11) and (12). Some simple possibilities are described below.

2.7.1 CN^{ν}_{n} Sequences

The CN^{ν}_{n} Euler angle symmetries [equations (10) and (11)] are generated by rotor-synchronized pulse schemes of the general form shown in Figure 2. The idea is that n rotational periods of the sample are subdivided into N equal intervals. Each interval contains a radio frequency pulse sequence which is a *cycle*, i.e., it induces a rotation of the nuclear spins through an integer multiple of 360° (including zero). The radio-frequency phases of subsequent cycles are shifted with respect to each other by the angle $2\pi\nu/N$, causing a repeated incrementation (or decrementation) of the radio-frequency phase as one proceeds through the sequence. The integers n and ν may therefore be interpreted as space and spin *winding numbers*.[39] The sample rotates bodily through n full rotations, in the same time that it takes the radio-frequency phases to

Table 2 Components of homonuclear spin interactions in the interaction frame of an applied rf field, in the case of exact magic-angle spinning

Interaction	Space rank, l	Space components, m	Spin rank, λ	Spin components, μ
Isotropic chemical shift	0	0	1	$\{-1, 0, 1\}$
Chemical shift anisotropy	2	$\{-2, -1, 1, 2\}$	1	$\{-1, 0, 1\}$
J-coupling	0	0	0	0
Dipole–dipole coupling	2	$\{-2, -1, 1, 2\}$	0	$\{-2, -1, 0, 1, 2\}$

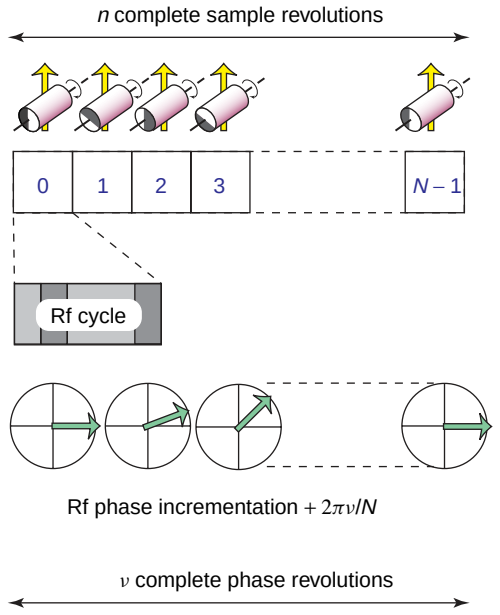

Figure 2 Construction of CN_n^{ν} sequences

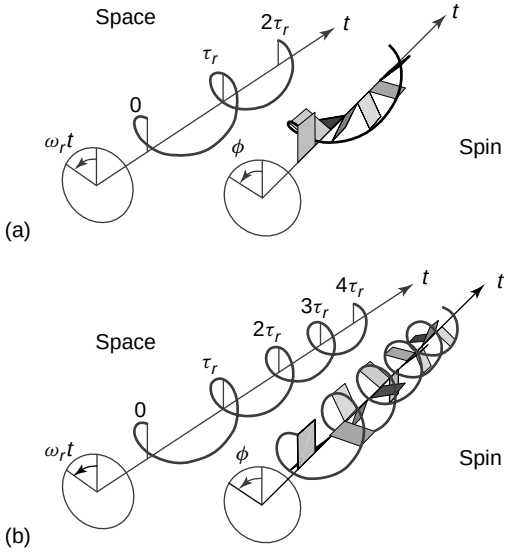

Figure 3 Visualization of the symmetry numbers for (a) $C7_2^1$ sequences, and (b) $C14_4^5$ sequences. The left-hand helices represent the spatial rotation of the sample as a function of time. The right-hand helices depict the modulation of the rf phase as a function of time. n spatial rotations are completed in the same time as ν spin rotations. The rf phase is modulated in N discrete steps, depicted by the planes in the right-hand diagrams. (Adapted from Ref.[39])

advance through ν full rotations, in N equal steps. This idea is conveyed for the cases of $C7_2^1$ and $C14_4^5$ in Figure 3.

These symmetry properties are independent of the internal structure of the rf cycles, providing that each cycle accomplishes a final rotation through an integer multiple of 360°.

For a proof that sequences with this structure generate the Euler angle symmetry given in equation (11), see Ref.[60]

For the sake of concreteness, consider a $C7_2^1$ sequence based upon the cyclic element $\mathcal{C} = 270_0 180_{180} 90_0$, where ξ_ϕ indicates a rectangular, resonant rf pulse with flip angle ξ and phase ϕ, and the angles are written in degrees. The full $C7_2^1$ sequence is as follows:

$$270_0 180_{180} 90_0 270_{51.43} 180_{231.43} 90_{51.43} 270_{102.86} 180_{282.86} 90_{102.86} -$$
$$270_{154.29} 180_{334.29} 90_{154.29} 270_{205.71} 180_{25.71} 90_{205.71} -$$
$$270_{257.14} 180_{77.14} 90_{257.14} 270_{308.57} 180_{128.57} 90_{308.57} \quad (13)$$

where the pulses are contiguous (no gaps in between). The rf field amplitude is chosen so that the entire sequence of 21 pulses fits exactly into two complete rotational periods of the sample. This requires that the spin nutation frequency in the rf field is exactly seven times the sample spinning frequency. The sequence in equation (13) is called POST-C7.[37]

2.7.2 RN_n^{ν} Sequences

A construction scheme for generating sequences with the Euler angle symmetries in equations (10) and (12) involves the following steps:

1. Select a sequence of rf pulses which rotates the nuclear spins through 180° about the x-axis. Call this element $\mathcal{R}$.
2. Change the *signs* of all rf phases within the element $\mathcal{R}$. Call this phase-inverted element $\mathcal{R}'$.
3. Select the rf amplitude so that N elements $\mathcal{R}$ occupy exactly the same time interval as n rotational periods of the sample. The number of elements N must be even in the case of RN_n^{ν} symmetry.
4. The RN_n^{ν} sequence consists of $N/2$ *pairs* of elements $\mathcal{R}_\phi \mathcal{R}_{-\phi}$, where ϕ is an overall phase shift, equal to $\phi = \pi\nu/N$ radians.

A simplified diagram of this procedure is shown in Figure 4 (step 2 above is omitted for simplicity). This looks similar to the set-up for a CN_n^{ν} sequence, but with the two differences that each element provides a 180° rotation, rather than a cycle, and that the rf phase is alternated between two values, rather than being incremented.

For a proof that sequences with this structure generate the Euler angle symmetry given in equation (12), see Ref.[60]

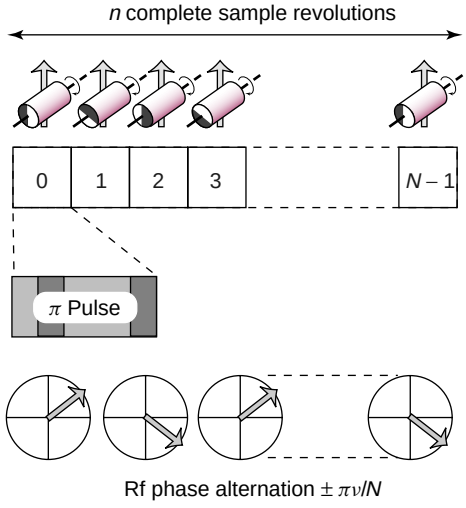

Figure 4 Construction of RN_n^{ν} sequences

As a concrete example, suppose that one would like to build a $R18_2^9$ sequence on the composite pulse $90_0 90_{90} 90_0$, which is known to have favorable homonuclear decoupling properties.[61] The first step is to establish whether this element induces a 180° rotation about the x-axis. This may be tested by rotating the three spin angular momentum operators, as follows:

$$\begin{aligned} I_x &\xrightarrow{90_0} I_x \xrightarrow{90_{90}} -I_z \xrightarrow{90_0} I_y \\ I_y &\xrightarrow{90_0} I_z \xrightarrow{90_{90}} I_x \xrightarrow{90_0} I_x \\ I_z &\xrightarrow{90_0} -I_y \xrightarrow{90_{90}} -I_y \xrightarrow{90_0} -I_z \end{aligned} \tag{14}$$

From this it may be seen that the $90_0 90_{90} 90_0$ sequence does transform I_z into $-I_z$, which is an appropriate property for a 180° rotation about the x-axis, but that it also exchanges the operators I_x and I_y, which is not appropriate. A little consideration leads to the conclusion that the $90_0 90_{90} 90_0$ sequence implements a rotation by 180° about an axis which is intermediate between the x-axis and the y-axis, i.e., phase shifted by 45°. This may also be proved by rotation operator algebra.[62]

This defect may be remedied by phase shifting the whole sequence by −45°. This leads to the element

$$\mathcal{R} = 90_{-45} 90_{45} 90_{-45} \tag{15}$$

which now implements the correct rotation. Changing the sign of all phases leads to

$$\mathcal{R}' = 90_{45} 90_{-45} 90_{45} \tag{16}$$

The desired $R18_2^9$ sequence requires additional phase shifts of $\phi = \pm\pi \times 9/18$ radians, or ±90°. The appropriate elements are therefore

$$\mathcal{R}_\phi = 90_{45} 90_{135} 90_{45} \tag{17}$$

and

$$\mathcal{R}'_{-\phi} = 90_{-45} 90_{-135} 90_{-45} \tag{18}$$

The full $R18_2^9$ sequence has the following structure:

$$R18_2^9(\text{version 1}) = \{90_{45} 90_{135} 90_{45} 90_{-45} 90_{-135} 90_{-45}\}^9 \tag{19}$$

where nine repetitions of the bracketed elements occupy exactly two rotational periods of the sample. If the phases are restricted to the interval 0–360°, we get

$$R18_2^9(\text{version 1}) = \{90_{45} 90_{135} 90_{45} 90_{315} 90_{225} 90_{315}\}^9 \tag{20}$$

If the element $\mathcal{R}$ contains no internal phase shifts, or when it only contains 180° phase shifts, then the conversion of $\mathcal{R}$ into $\mathcal{R}'$ may be ignored. For example, if a single 180_0 is used for the element $\mathcal{R}$, then the $R18_2^9$ sequence is as follows:

$$R18_2^9(\text{version 2}) = \{180_{90} 180_{270}\}^9 \tag{21}$$

where nine repetitions of the bracketed elements occupy exactly two rotational periods of the sample.

Although the construction principles of the RN_n^ν sequences appear to be quite complicated, the end result is sometimes very simple.

2.8 Effective Hamiltonian

In many circumstances, the behavior of the nuclear spins under a pulse sequence may be described using the theory described in **Average Hamiltonian Theory,** Volume 2. Suppose that the pulse sequence starts at time point t^0 and lasts until time point $t^0 + \tau$. Suppose also that the period of the pulse sequence is given by $T = n\tau_r$, where n is the space winding number. The propagator for the pulse sequence between the time points t^0 and $t^0 + \tau$ is written as

$$U(t^0 + \tau, t^0) \cong U_{\text{rf}}(t^0 + \tau, t^0) \exp\{-\text{i}\overline{\mathcal{H}}(t^0)\tau\} \tag{22}$$

where U_{rf} is the propagator for the rf field alone (equation (6)), $\overline{\mathcal{H}}(t^0)$ is the *effective Hamiltonian* of the internal spin interactions, for a pulse sequence starting at point t^0.

In a rotating sample, the effective Hamiltonian depends upon the starting time point t^0, since the orientation of the sample constantly changes.

The effective Hamiltonian may be approximated using the Magnus expansion:

$$\overline{\mathcal{H}}(t^0) \cong \overline{\mathcal{H}}^{(1)}(t^0) + \overline{\mathcal{H}}^{(2)}(t^0) + \cdots \tag{23}$$

where the first two terms are given by

$$\begin{aligned} \overline{\mathcal{H}}^{(1)}(t^0) &= T^{-1} \int_{t^0}^{t^0+T} \mathrm{d}t\, \mathcal{H}_{\text{int}}(t) \\ \overline{\mathcal{H}}^{(2)}(t^0) &= (2\text{i}T)^{-1} \int_{t^0}^{t^0+T} \mathrm{d}t_2 \int_{t^0}^{t_2} \mathrm{d}t_1 [\mathcal{H}_{\text{int}}(t_2), \mathcal{H}_{\text{int}}(t_1)] \end{aligned} \tag{24}$$

Here $\mathcal{H}_{\text{int}}$ is the internal spin Hamiltonian, expressed in the interaction frame of the rf field. This equation employs a consistent numbering system for the Magnus expansion terms, in which the kth Magnus term is proportional to a product of k Hamiltonians. Much literature uses a more awkward numbering, in which the indices start at zero.

The term $\overline{\mathcal{H}}^{(1)}$ is called the *average Hamiltonian*. The term $\overline{\mathcal{H}}^{(2)}$ is called the *second-order correction* to the average Hamiltonian, and so on.

If the internal spin Hamiltonian is small compared to the period T of the pulse sequence, then the average Hamiltonian expansion may be terminated after the first or second term.

Note that equation (22) represents the propagator over an arbitrary interval τ, while the average Hamiltonian terms in equation (24) involve integrals over the full period of the pulse sequence. This useful approximation allows results derived for entire periodic pulse sequences to be extended, with caution, to non-integral numbers of rf cycles. We have generally found this approximation to work well for the symmetry-based sequences.

2.9 First-Order Selection Rules

The interaction frame spin Hamiltonian is a sum of many rotational components, as in equation (8). The average Hamiltonian may therefore be written

$$\overline{\mathcal{H}}^{(1)}(t^0) = \sum_{lm\lambda\mu} \overline{\mathcal{H}}^{(1)}_{lm\lambda\mu}(t^0) \tag{25}$$

where

$$\overline{\mathcal{H}}^{(1)}_{lm\lambda\mu}(t^0) = T^{-1} \int_{t^0}^{t^0+T} \mathrm{d}t\, \mathcal{H}_{lm\lambda\mu}(t) \tag{26}$$

Each of these components is modulated by the spatial rotation of the sample, and the rotations of the spin polarizations induced by the rf field. If the pulse sequence is a member of the CN_n^ν or RN_n^ν symmetry classes, then the synchronized modulations possess the symmetry properties summarized in equations (10)–(12).

In Refs.[45,60] it is shown that these symmetry properties lead to *selection rules* on the average Hamiltonian terms:

2.9.1 Selection Rules for CN_n^ν Sequences

For CN_n^ν sequences, the following selection rule applies:

$$\overline{\mathcal{H}}^{(1)}_{lm\lambda\mu} = 0 \quad \text{if } mn - \mu\nu \neq NZ \tag{27}$$

where Z is any integer, including zero.

2.9.2 Selection Rules for RN_n^ν Sequences

For RN_n^ν sequences, the following selection rule applies:

$$\overline{\mathcal{H}}^{(1)}_{lm\lambda\mu} = 0 \quad \text{if } mn - \mu\nu \neq \frac{N}{2} Z_\lambda \tag{28}$$

Here Z_λ is any integer with the same *parity* as the spin rank λ. If λ is even, then Z_λ takes the values $0, \pm 2, \pm 4, \ldots$. If λ is odd, then Z_λ takes the values $\pm 1, \pm 3, \pm 5, \ldots$.

Equations (27) and (28) are the central results of symmetry-based pulse sequence theory. These two simple equations have wide consequences.

As a first example, consider a pulse sequence with symmetry $C7_2^1$. Let us examine the fate of double-quantum dipole–dipole terms with quantum numbers $\{l, m, \lambda, \mu\} = \{2, 1, 2, 2\}$. Equation (27) states that the average Hamiltonian of this term vanishes if the quantity $mn - \mu\nu$ is not equal to an integer multiple of N. Substituting in the values $m = 1$, $n = 2$, $\mu = 2$ and $\nu = 1$ we obtain $mn - \mu\nu = (1 \times 2) - (2 \times 1) = 0$. This is an integer multiple of $N = 7$, so the term $\{l, m, \lambda, \mu\} = \{2, 1, 2, 2\}$ is *symmetry allowed*. One cannot be sure whether this term actually exists without further calculation, but at least symmetry does not exclude it. Consider now the chemical shift anisotropy term with quantum numbers $\{l, m, \lambda, \mu\} = \{2, -2, 1, 1\}$. The expression $mn - \mu\nu$ evaluates to the value $mn - \mu\nu = ((-2) \times 2) - (1 \times 1) = -5$. This is not an integer multiple of 7, so this term is *symmetry forbidden* in the first-order average Hamiltonian.

Now consider the fate of the same two terms under the symmetry $R18_1^7$, using the rule in equation (28). The homonuclear dipole–dipole terms have a spin rank $\lambda = 2$, which is even. Equation (28) implies that a dipole–dipole term is symmetry-forbidden unless $mn - \mu\nu$ is equal to an even multiple of 9. For the term $\{l, m, \lambda, \mu\} = \{2, 1, 2, 2\}$, the expression $mn - \mu\nu$ evaluates to $(1 \times 1) - (2 \times 7) = -13$. This is not an even multiple of 9, so the term $\{2, 1, 2, 2\}$ is forbidden under the symmetry $R18_1^7$. For the chemical shift anisotropy term $\{l, m, \lambda, \mu\} = \{2, -2, 1, 1\}$, on the other hand, the expression $mn - \mu\nu$ evaluates to the value $mn - \mu\nu = ((-2) \times 1) - (1 \times 7) = -9$. This is an odd multiple of 9, and since the spin rank λ is also odd, this term is symmetry-allowed.

2.10 Space-Spin Selection Diagrams

The consequences of equations (27) and (28) are conveniently evaluated using *space-spin selection diagrams* (SSS diagrams). Two examples are given in Figure 5 and 6.

The branching lines in these diagrams show the possible values of $mn - \mu\nu$ for the particular class of spin interaction, split up into the 'space' part mn and the 'spin' part $\mu\nu$. The number of branches depends on the type of spin interaction, according to Table 2, while the spacing between the branches depends on the symmetry numbers n and ν. The right-hand side of each diagram shows a barrier containing holes spaced by the symmetry number N. Those pathways that are *blocked* by the barrier represent values of $mn - \mu\nu$ which *do* satisfy the inequalities in equations (27) and (28), and represent components that are symmetry-forbidden. Those pathways that *pass* through the holes in the barrier represent values of $mn - \mu\nu$ which *do not* satisfy the inequalities in equations (27) and (28), indicating components that are symmetry-allowed. The SSS diagrams allow the consequences of the inequalities in equations (27) and (28) to be visualized clearly.

The positions of the holes depend on the symmetry class. For the CN_n^ν class of symmetries, the holes in the barrier occur at levels $0, \pm N, \pm 2N, \ldots$. For the RN_n^ν class of symmetries, the positions of the holes depends on whether the spin rank λ is even or odd. For even ranks, the holes occur at levels $0, \pm N, \pm 2N, \ldots$, as in the case of CN_n^ν symmetries. For odd ranks, on the other hand, the holes occur at levels $\pm N/2, \pm 3N/2, \ldots$, where $N/2$ is an integer, since N is even.

2.10.1 SSS Diagrams for $C7_2^1$ Symmetry

The behavior of the chemical shift anisotropy (CSA) terms under $C7_2^1$ symmetry is shown in Figure 5(a). There are four branches in the space part, corresponding to the $m = \{-2, -1, 1, 2\}$ components indicated in Table 2. For clarity, only the branches with $m \leq 0$ are shown: the branches with negative m are mirror images. The $m = 0$ component vanishes in the case of exact magic-angle spinning. The 'space' branches are spaced vertically by two units, according to the winding number $n = 2$. Each of these branches splits into three spin components, with indices $\mu = \{-1, 0, 1\}$, and spaced vertically by one unit, according to the winding number $\nu = 1$. Since the value of N is 7, the barrier on the right contains holes at levels $0, \pm 7, \pm 14, \ldots$. There are no CSA pathways which pass through these holes, indicating that the average Hamiltonian contains no CSA terms. The SSS diagram shows immediately that the pulse sequence is compensated for the effects of CSA, to first order.

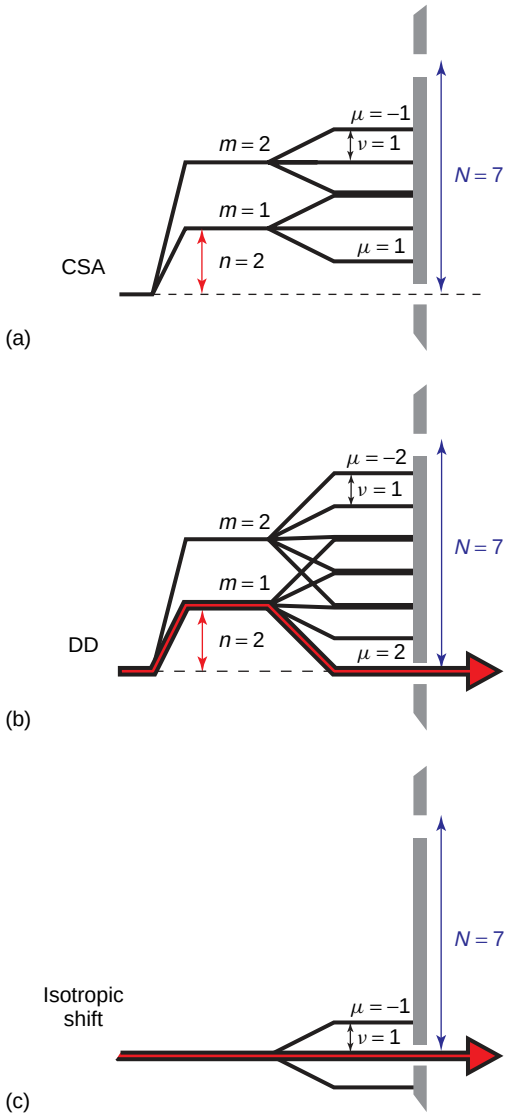

Figure 5 Space-spin selection diagram for $C7_2^1$ symmetry, omitting components with $m < 0$. (a) Behavior of the CSA terms. All terms are symmetry-forbidden. (b) Behavior of the homonuclear DD coupling terms. The component $\{l, m, \lambda, \mu\} = \{2, 1, 2, 2\}$ is symmetry-allowed. (c) Behavior of the isotropic chemical shift terms. The component $\{l, m, \lambda, \mu\} = \{0, 0, 1, 0\}$ is symmetry-allowed

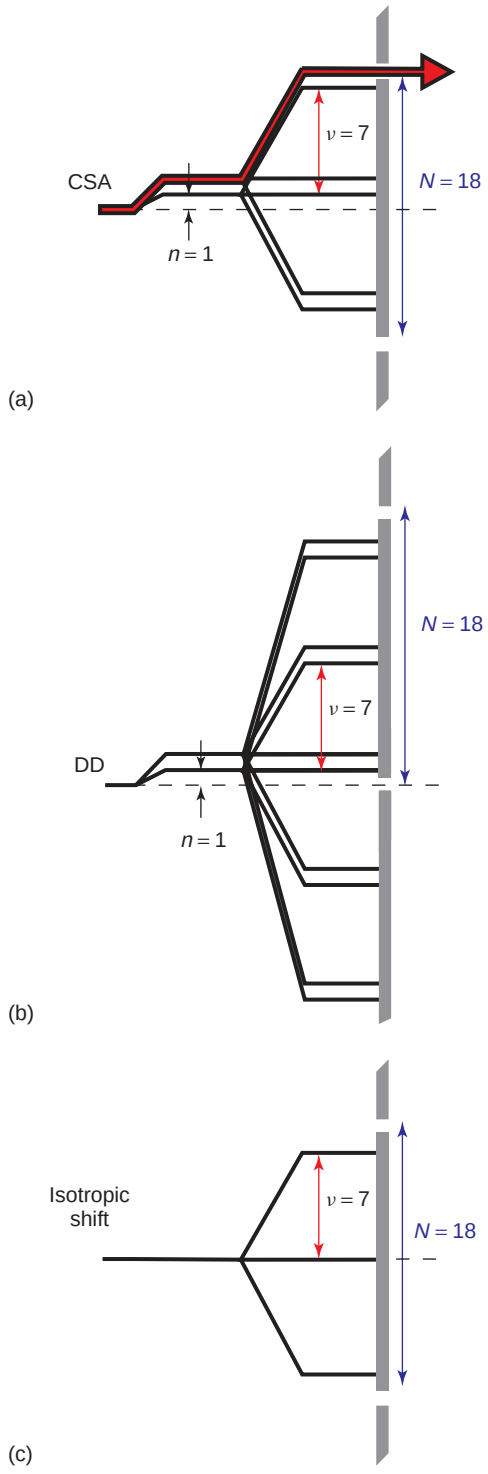

Figure 6 Space-spin selection diagram for $R18_1^7$ symmetry, omitting components with $m < 0$. (a) Behavior of the CSA terms. The component $\{l, m, \lambda, \mu\} = \{2, 2, 1, -1\}$ is symmetry-allowed. (b) Behavior of the homonuclear DD coupling terms. All components are symmetry-forbidden. (c) Behavior of the isotropic chemical shift terms. All components are symmetry-forbidden. Note that the positions of the holes change, depending on whether the spin rank λ is odd or even

The behavior of the dipole–dipole coupling (DD) terms under $C7_2^1$ symmetry is shown in Figure 5(b). Here too there are four branches in the space part, corresponding to the $m = \{-2, -1, 1, 2\}$ components in Table 2. Only the branches with non-negative m are shown, for the sake of clarity. Each of the space branches splits into five spin branches, with indices $\mu = \{-2, -1, 0, 1, 2\}$. As may be seen, the branch with $\{l, m, \lambda, \mu\} = \{2, 1, 2, 2\}$ passes through a hole in the barrier, indicating that this component is symmetry-allowed. The mirror-image branch with $\{l, m, \lambda, \mu\} = \{2, -1, 2, -2\}$ is also symmetry-allowed (not shown).

Since all the CSA terms are symmetry-forbidden, and the only symmetry-allowed DD terms have quantum numbers $\mu = \pm 2$, sequences with the symmetry $C7_2^1$ behave as *CSA-compensated double-quantum recoupling sequences*.

Now consider the SSS diagram for isotropic chemical shift terms, shown in Figure 5(c). Since the space and spin ranks are $l = 0$ and $\lambda = 1$, there is one space component, with $m = 0$,

and three spin components, with $\mu = \{-1, 0, 1\}$. The SSS diagram shows that the isotropic shift component $\{l, m, \lambda, \mu\} = \{0, 0, 1, 0\}$ is symmetry-allowed under $C7_2^1$ symmetry. This implies that $C7_2^1$ sequences are vulnerable to isotropic chemical shifts, unless additional precautions are taken. We return to this issue later.

2.10.2 SSS Diagrams for $R18_1^7$ Symmetry

The behavior of the CSA terms under $R18_1^7$ symmetry is shown in Figure 6(a). The left-hand side shows the two space branches with $m = 1$ and 2. The $m = 0$ component vanishes in the case of exact magic-angle spinning. The space branches are spaced vertically by 1 unit, according to the winding number $n = 1$. Each branch splits into three spin components, with indices $\mu = \{-1, 0, 1\}$, and spaced vertically by 7 units, according to the winding number $\nu = 7$. Since the spin rank λ of the CSA terms is equal to 1, which is an odd number, the barrier on the right contains holes at odd multiples of $N/2$, which is equal to 9 in this case. The holes in the barrier are therefore at levels $\pm 9, \pm 27, \ldots$. As may be seen, the CSA term $\{l, m, \lambda, \mu\} = \{2, 2, 1, -1\}$ passes through a hole, which indicates that $R18_1^7$ symmetry is a *CSA recoupling sequence*.

The behavior of the DD terms under $R18_1^7$ symmetry is shown in Figure 6(b). The space branches with $m = 1$ and 2 split into five spin components, with indices $\mu = \{-2, -1, 0, 1, 2\}$. In the case of DD couplings, the spin rank λ is equal to 2, which is an even number. As a result, the barrier on the right contains holes at even multiples of 9, i.e., $0, \pm 18, \pm 36, \ldots$. As may be seen, the barrier blocks all of the DD terms. This indicates that sequences with $R18_1^7$ symmetry are insensitive to homonuclear dipole–dipole couplings, to first order.

The behavior of the isotropic chemical shift terms under $R18_1^7$ symmetry is shown in Figure 6(c). None of the three components with $m = 0$ and $\mu = \{-1, 0, 1\}$ pass through the barrier. This indicates that sequences with $R18_1^7$ symmetry are insensitive to isotropic chemical shifts, to first order.

One may conclude that $R18_1^7$ sequences accomplish recoupling of the CSA interactions, compensated to first order for homonuclear DD couplings and isotropic chemical shifts.

2.11 Higher-Order Selection Rules

In many cases, the first-order Magnus term (the average Hamiltonian) is not a sufficiently good approximation to the effective Hamiltonian of a pulse sequence. Although the higher-order correction terms $\overline{\mathcal{H}}^{(2)}, \overline{\mathcal{H}}^{(3)}, \ldots$ are more complicated than the first-order terms, they are also subject to selection rules in the case of pulse sequence symmetry.

By analogy with equation (25), the second-order term $\overline{\mathcal{H}}^{(2)}$ may be written as a superposition of many rotational components:

$$\overline{\mathcal{H}}^{(2)}(t^0) = \sum_{l_2 m_2 \lambda_2 \mu_2} \sum_{l_1 m_1 \lambda_1 \mu_1} \overline{\mathcal{H}}^{(2)}_{l_2 m_2 \lambda_2 \mu_2, l_1 m_1 \lambda_1 \mu_1}(t^0) \tag{29}$$

where each component is given by

$$\overline{\mathcal{H}}^{(2)}_{l_2 m_2 \lambda_2 \mu_2, l_1 m_1 \lambda_1 \mu_1}(t^0) = (2\mathrm{i}T)^{-1} \int_{t^0}^{t^0+T} \mathrm{d}t_2 \int_{t^0}^{t_2} \mathrm{d}t_1 [\mathcal{H}_{l_2 m_2 \lambda_2 \mu_2}(t_2), \mathcal{H}_{l_1 m_1 \lambda_1 \mu_1}(t_1)] \tag{30}$$

The horrifying complexity is moderated by the following selection rules:

For CN_n^ν sequences, the following selection rule applies:

$$\overline{\mathcal{H}}^{(2)}_{l_2 m_2 \lambda_2 \mu_2, l_1 m_1 \lambda_1 \mu_1} = 0 \text{ if } \begin{cases} m_2 n - \mu_2 \nu \neq NZ \\ \text{AND} \\ m_1 n - \mu_1 \nu \neq NZ \\ \text{AND} \\ (m_2 + m_1) n - (\mu_2 + \mu_1) \nu \neq NZ \end{cases} \tag{31}$$

where Z is any integer, including zero.

For RN_n^ν sequences, the following selection rule applies:

$$\overline{\mathcal{H}}^{(2)}_{l_2 m_2 \lambda_2 \mu_2, l_1 m_1 \lambda_1 \mu_1} = 0 \text{ if } \begin{cases} m_2 n - \mu_2 \nu \neq \dfrac{N}{2} Z_{\lambda_2} \\ \text{AND} \\ m_1 n - \mu_1 \nu \neq \dfrac{N}{2} Z_{\lambda_1} \\ \text{AND} \\ (m_2 + m_1) n - (\mu_2 + \mu_1) \nu \neq \dfrac{N}{2} Z_{\lambda_2 + \lambda_1} \end{cases} \tag{32}$$

where Z_{λ_2} is an integer with the same parity as λ_2, Z_{λ_1} is an integer with the same parity as λ_1, and $Z_{\lambda_2+\lambda_1}$ is an integer with the same parity as $\lambda_2 + \lambda_1$.

These selection rules are proved in Refs.[45,60]

Although the second-order selection rules do not usually allow the elimination of all undesirable terms, they do greatly reduce the labor required to evaluate the terms. For example, in general, there are 208 components to the $\overline{\mathcal{H}}^{(2)}$ term involving commutators of dipole–dipole coupling and CSA interactions. In the presence of a $R14_2^6$ sequence, only 16 of these are symmetry-allowed.

The R-sequence selection rule equation (32) is more restrictive than that for C-sequences equation (31). As a result, R-sequences tend to have smaller numbers of higher-order terms than C-sequences, which often translates into improved performance.

The second-order selection rules allow a straightforward count of the number of symmetry-allowed terms of a particular type. Higher-order term counts may be used to get a feel for the qualitative performance of a particular symmetry, without performing detailed calculations.[41,45] However, this rather crude criterion should not be relied on completely.

It is possible to extend these second-order selection rules to arbitrarily high orders.[45]

2.12 Scaling Factors

The selection rules provide information on which terms are symmetry-forbidden. However, they provide no information on the magnitude of the symmetry-allowed terms.

In general, the form of a symmetry-allowed first-order term is as follows:

$$\overline{\mathcal{H}}^{\Lambda}_{lm\lambda\mu}(t^0) = \kappa_{lm\lambda\mu} [A^{\Lambda}_{lm}]^R \exp\{-\mathrm{i}m(\alpha^0_{RL} - \omega_r t^0)\} T^{\Lambda}_{\lambda\mu} \tag{33}$$

where $[A^{lm}_{\Lambda}]^R$ is a component of the spatial tensor of interaction Λ, expressed in the rotor-fixed frame R, and $T^{\Lambda}_{\lambda\mu}$ is a component of the spin tensor of interaction Λ, expressed in the laboratory frame. The factor $\kappa_{lm\lambda\mu}$ is called the *scaling factor* of the pulse sequence, and depends upon the symmetry class, as well as the detailed structure of the basic element upon which the pulse sequence is built.

The scaling factor may be a complex number. Its magnitude is always less than one, which indicates that the suppression of unwanted terms is always accompanied by a reduction in the magnitude of the symmetry-allowed terms.

2.12.1 Scaling Factor Formulae

General formulae for the scaling factors are given in Ref.[60] In the case of CN_n^ν sequences, the scaling factor for a symmetry-allowed term $\{l, m, \lambda, \mu\}$ is given by

$$\kappa_{lm\lambda\mu} = \tau^{-1} d^l_{m0}(\beta_{RL}) \int_0^\tau \mathrm{d}t\, d^\lambda_{\mu 0}(-\beta_{\mathrm{rf}}(t)) \exp\{\mathrm{i}(\mu\gamma_{\mathrm{rf}}(t) + m\omega_r t)\} \quad (34)$$

where $\tau = n\tau_r/N$ is the duration of a basic element $\mathcal{C}$, $\tau_r = |2\pi/\omega_r|$ is a rotor period, and $\beta_{\mathrm{rf}}(t)$ and $\gamma_{\mathrm{rf}}(t)$ are rf Euler angles [equation (6)]. The basic element C is assumed to extend from time $t = 0$ to $t = \tau$.

In the case of RN_n^ν sequences, the scaling factor is given by

$$\kappa_{lm\lambda\mu} = \tau^{-1} d^l_{m0}(\beta_{RL}) \times \int_0^\tau \mathrm{d}t\, d^\lambda_{\mu 0}(-\beta_{\mathrm{rf}}(t)) \exp\{\mathrm{i}(\mu\gamma_{\mathrm{rf}}(t) - \mu\frac{\pi\nu}{N} + m\omega_r t)\} \quad (35)$$

There is an extra complex factor in this case, since the first element of a RN_n^ν sequence is not the same as the basic element.

The scaling factor is calculated most readily if the basic elements of the pulse sequence do not contain any rf phase shifts, or if the phase shifts are integer multiples of 180°. This is the case of *amplitude-modulated* basic elements. For example, $\mathcal{C} = 270_0 180_{180} 90_0$ is an amplitude-modulated basic element, while $\mathcal{R} = 90_{-45} 90_{45} 90_{-45}$ is a *phase-modulated* basic element. In the case of amplitude-modulated basic elements, the rf Euler angles are given by

$$\beta_{\mathrm{rf}}(t) = \int_0^t \mathrm{d}t' \omega_{\mathrm{nut}}(t')$$
$$\gamma_{\mathrm{rf}}(t) = \pi/2 \quad (36)$$

where ω_{nut} is the amplitude of the rf field, expressed as a nutation frequency (180° phase shifts may be taken into account by reversing the sign of ω_{nut}).

The calculation of the scaling factor is more difficult if the basic element is phase modulated. General formulae are given in Ref.[60] Andreas Brinkmann has written a *Mathematica*[63] program which provides the scaling factors of general sequences of rectangular pulses. The program is available on the web (*http://www.soton.ac.uk/~mhl*).

2.12.2 Physical Interpretation

The formulae for the scaling factor, equations (34) and (35) contain three factors. The first term, $d^l_{m0}(\beta_{RL})$ is purely spatial, and concerns the transformation of spatial rank-l tensors by the physical rotation of the sample. This term depends on the tilt of the rotation axis with respect to the magnetic field. The second term $d^\lambda_{\mu 0}(-\beta_{\mathrm{rf}}(t))$ corresponds to the time-dependent transformation of rank-λ spin operators by the rf field. The third term (the complex exponential factor) takes into account the physical rotation of the sample within the duration of each pulse sequence element. The formula for the R-sequence scaling factor, equation (35), contains a further phase factor, which arises because the first element of a R-sequence is phase shifted with respect to the basic element $\mathcal{R}$.

In general, it is desirable that the magnitude of $\kappa_{lm\lambda\mu}$ is as large as possible. It helps if one develops a physical feel of how $\kappa_{lm\lambda\mu}$ is generated.

In most cases, the angle β_{RL} is equal to the magic angle, so that the first term $d^l_{m0}(\beta_{RL})$ is not open to manipulation (an exception is provided by the 'zero-field in high-field' pulse sequences, where the choice of the spinning angle is an important element of the pulse sequence design).

In many cases, the symmetry number N is much larger than n. In this case, the duration of each element is much less than a rotor period, and it is possible to ignore the rotation of the sample during the individual rf elements, as a first approximation. This corresponds to the neglect of the $m\omega_r t$ terms in equations (34) and (35). This is called the quasi-static approximation.

In the quasi-static limit, only the rf rotations affect the accumulating time average of $T_{\lambda\mu}$ spin operators. For example, consider the problem of double-quantum recoupling. The relevant Wigner element in this case is $d^2_{20}(\beta_{\mathrm{rf}})$, which is proportional to $\sin^2(\beta_{\mathrm{rf}})$. This term is always positive, and is maximized at $\beta_{\mathrm{rf}} = 90°$ and $\beta_{\mathrm{rf}} = 270°$. It follows that the main contributions to the scaling factor are obtained when the Euler angle β_{rf} is close to the values 90° or 270°. At the same time, the Euler angle γ_{rf} should be kept fixed. As shown in equation (36), this may be ensured by using an amplitude-modulated basic element.

The simplest cyclic element is $\mathcal{C} = 360_0$. The rotation under this pulse takes the Euler angle β_{rf} linearly from 0 to 360°. Double-quantum excitation is accomplished near the 'hot spots' at $\beta_{\mathrm{rf}} = 90°$ and $\beta_{\mathrm{rf}} = 270°$. No double-quantum excitation is achieved, on the other hand, at the 'cold spots' $\beta_{\mathrm{rf}} = 0$ and $\beta_{\mathrm{rf}} = 180°$. The element $\mathcal{C} = 360_0$ spends equal time near the 'hot' and 'cold' spots. Nevertheless, the appropriate Wigner element is always positive, so the scaling factor is satisfactory ($|\kappa_{2122}| = 0.157$ for the case of $C7_2^1$ symmetry).

The scaling factor may be improved by turning the rf field off near the 'hot spots' $\beta_{\mathrm{rf}} = 90°$ and $\beta_{\mathrm{rf}} = 270°$, allowing the double-quantum operators more time to accumulate. An example of this technique is given by the sequence

$$\mathcal{C} = 90_0 - \tau_\omega - 180_0 - \tau_\omega - 90_0 \quad (37)$$

where the 'window' duration τ_ω is selected so that the overall element occupies an interval $\tau = n\tau_r/N$. In the limit of infinitely strong and short pulses, the element in equation (37) provides a greatly improved scaling factor of $|\kappa_{2122}| = 0.308$ for the case of $C7_2^1$ symmetry. Although the scaling factor may be increased by introducing windows, this method has not been used very often, perhaps because the strong rf pulses make the problem of proton decoupling more acute (see below).

In practice, it is common to use elements which are locally compensated for rf inhomogeneity. This improves the robustness of the pulse sequence to rf amplitude deviations. The original version of the C7 pulse sequence used the locally-compensated element $\mathcal{C} = 360_0 360_{180}$ in a $C7_2^1$ symmetry

scheme.[36] In this case, each of the double-quantum 'hot spots' at $\beta_{\rm rf} = 90°$ and $\beta_{\rm rf} = 270°$ are traversed twice during each element. The scaling factor of $|\kappa_{2122}| = 0.155$ is almost the same as for the simple element $\mathcal{C} = 360_0$, which has $|\kappa_{2122}| = 0.157$. The values are slightly different because of the rotation of the sample during the rf element.

In the quasi-static limit, the efficiency of double-quantum recoupling is greatly reduced if the Euler angle $\gamma_{\rm rf}$ is allowed to vary. For example, the scaling factor for the phase-modulated element $\mathcal{C} = 360_0360_{120}360_{240}$ is given by $|\kappa_{2122}| = 0.047$ in the case of $C7_2^1$ symmetry.

If the values of N and n are comparable, the quasi-static approximation breaks down. In this case, it is necessary to think much more carefully about how the physical rotation of the sample and the spin rotations combine. Amplitude-modulated elements are no longer optimal as far as the scaling factor is concerned. For example, consider the symmetry $C7_5^1$, which provides similar selection rules to $C7_2^1$ (except that the $\{l, m, \lambda, \mu\} = \{2, \pm1, 2, \mp2\}$ terms are selected, rather than $\{2, \pm1, 2, \pm2\}$). In the case of $C7_5^1$ symmetry, the scaling factor for the allowed term $\{l, m, \lambda, \mu\} = \{2, 1, 2, -2\}$ is given by $|\kappa_{212-2}| = 0.064$ for the amplitude-modulated standard element $\mathcal{C} = 360_0360_{180}$. This low scaling factor is due to the considerable rotation of the sample during the $\mathcal{C}$ element, leading to a strong variation of the $\omega_r t$ term in equation (34).[39,40] The scaling factor may be greatly improved by using the phase-modulated element $\mathcal{C} = 360_0360_{120}360_{240}$. For the case of $C7_5^1$ symmetry, one obtains the value $|\kappa_{212-2}| = 0.144$.[39] The improvement in scaling factor arises because the modulations of the Euler angle $\gamma_{\rm rf}$ due to the rf phase shifts compensate the modulation of the $\omega_r t$ term, to a good approximation. Note that the phase shifts must be performed in the correct sense: The scaling factor for the element $\mathcal{C} = 360_0360_{240}360_{120}$, in the case of $C7_5^1$ symmetry, is only $|\kappa_{212-2}| = 0.044$.

In some cases, pulse sequences work even if the scaling factor is very small. For example, the most commonly-used version of the RFDR pulse sequence[33,34] employs XY phase cycling and conforms to $R4_4^1$ symmetry. This symmetry is appropriate for zero-quantum DD recoupling, since it allows the homonuclear DD terms $\{l, m, \lambda, \mu\} = \{2, \pm1, 2, 0\}$ and $\{2, \pm2, 2, 0\}$, while suppressing other DD terms and all chemical shift terms. However, the first reports of this pulse sequence used an $\mathcal{R}$ element consisting of a strong 180° pulse followed by a 'window' in which the rf field is turned off. This is a puzzling choice of basic element, since the scaling factors for all symmetry-allowed DD terms vanish if the rf pulses are infinitely short. In fact, this pulse sequence reasonably well because the rf pulses always have a finite duration, so that the scaling factor is small but finite. In addition, J-couplings and higher-order effects play a role. Recent implementations of RFDR take a more sophisticated approach.[64,65]

2.12.3 Vanishing Scaling Factors

In many cases, the scaling factors for some symmetry-allowed terms are deliberately set to zero. For example, the symmetry $C7_2^1$ allows the isotropic chemical shift term $\{l, m, \lambda, \mu\} = \{0, 0, 1, 0\}$. Pulse sequences with this symmetry are therefore vulnerable to isotropic shift variations. The basic elements $\mathcal{C} = 360_0$, 360_0360_{180} and $90_0360_{180}270_0$ set the scaling factor κ_{0010} to zero, compensating these pulse sequences for isotropic chemical shifts or resonance offset effects. R-symmetries such as $R14_2^6$ do not need this precaution, since all isotropic chemical shift terms are symmetry-forbidden in this case.

Another example is provided by the MELODRAMA sequence for homonuclear dipolar recoupling.[66] Some versions of this sequence are based on $C4_1^1$ symmetry. In these cases, the isotropic shift term $\{l, m, \lambda, \mu\} = \{0, 0, 1, 0\}$ is symmetry-allowed, but may be suppressed by using basic elements of the form $\mathcal{C} = (360k)_0$, where k is an integer. Other versions of the MELODRAMA sequence[66] have $R4_1^1$ symmetry, which suppresses all isotropic shift terms without extra precautions. None of these symmetries, however, remove all of the CSA terms.

The recently-described C-REDOR sequences[67] are remarkable examples of how the basic element may be designed so as to destroy undesirable symmetry-allowed terms. The main variants of C-REDOR sequences are based upon $C3_3^1$ and $C7_7^1$ symmetry. These symmetries allow CSA terms of the form $\{l, m, \lambda, \mu\} = \{2, \pm2, 1, 0\}$ and $\{2, \pm1, 1, 0\}$, the isotropic shift term $\{0, 0, 1, 0\}$, and also the homonuclear DD coupling terms $\{2, \pm2, 2, 0\}$ and $\{2, \pm1, 2, 0\}$. However, by choosing a basic element $\mathcal{C} = 90_0360_{180}270_0$, the scaling factors of all terms vanish, except for those belonging to the CSA terms $\{2, \pm1, 1, 0\}$. These sequences may therefore be used to selectively recouple CSA terms while suppressing the isotropic chemical shifts and homonuclear DD couplings. C-REDOR has been applied to the selective recoupling of heteronuclear DD interactions,[67] which behave in the same way as the CSA terms, if the rf field is resonant with only one spin species (see below).

The vanishing scaling factors of certain terms under specific pulse sequences is probably due to additional symmetries. This is a promising area for further theory.

2.13 Orientation Dependence

In most cases, the magnitudes of the recoupled spin interactions depend on the orientation of the molecular reference frame with respect to the rotor. The only exceptions are when isotropic spin interactions such as the J-coupling or the isotropic chemical shift are selected, or in the special case of 'zero-field in high-field' experiments.[28,29]

The orientation-dependence of the recoupled spin interactions creates both problems and opportunities. A powerful feature of the symmetry theory is that it allows the form of the orientation-dependence to be manipulated qualitatively by choosing certain combinations of symmetry numbers.

The recoupled spin Hamiltonian in equation (33) is proportional to the spatial tensor component in the rotor-fixed frame, defined through the transformation chain

$$[A_{lm}^{\Lambda}]^R = \sum_{m'',m'} [A_{lm''}^{\Lambda}]^P \, D^l_{m''m'}(\Omega_{PM}^{\Lambda}) D^l_{m'm}(\Omega_{MR}) \qquad (38)$$

Here $[A_{lm}^{\Lambda}]^P$ are components of the spatial tensor, expressed in its own principal axis frame. The expression in equation (38) depends on the three Euler angles $\Omega_{MR} = \{\alpha_{MR}, \beta_{MR}, \gamma_{MR}\}$ defining the orientation of the molecular reference frame with respect to the rotor frame. In general, the recoupled spin Hamiltonian is anisotropic, and depends upon all three orientational Euler angles.

2.13.1 γ-Encoding

Suppose that a particular set of quantum numbers $\{l, m, \lambda, \mu\}$ is symmetry-allowed in the average Hamiltonian. The spatial Wigner element has the following form:

$$D^{l}_{m'm}(\Omega_{MR}) = \exp\{-\mathrm{i}m'\alpha_{MR}\} d^{l}_{m'm}(\beta_{MR}) \exp\{-\mathrm{i}m\gamma_{MR}\} \quad (39)$$

This may be combined with equation (33) to show how a single recoupled term depends upon the Euler angle γ_{MR}, the time point t^0 at which the symmetry-based pulse sequence starts, and the rotor Euler angle α^0_{RL} at the time point $t = 0$:

$$\overline{\mathcal{H}}^{\Lambda}_{lm\lambda\mu}(\gamma_{MR}, t^0, \alpha^0_{RL}) = \overline{\mathcal{H}}^{\Lambda}_{lm\lambda\mu}(0, 0, 0) \times \exp\{-\mathrm{i}m(\gamma_{MR} + \alpha^0_{RL} - \omega_r t^0)\} \quad (40)$$

The three parameters γ_{MR}, t^0 and α^0_{RL} may be included in a single complex phase factor.

It follows that only the *phase*, and not the *magnitude*, of the single term $\overline{\mathcal{H}}^{\Lambda}_{lm\lambda\mu}$ depends on the orientational Euler angle γ_{MR}. This property is termed *γ-encoding* of the recoupled term $\overline{\mathcal{H}}^{\Lambda}_{lm\lambda\mu}$.

In general, there are several symmetry-allowed terms $\overline{\mathcal{H}}^{\Lambda}_{lm\lambda\mu}$ with the same value of l, λ and μ but different values of m. Each of these terms contains the same spin operator $T^{\Lambda}_{\lambda\mu}$, but with a different spatial coefficient. These multiple coefficients interfere in a complicated way. As a result, the *complete* recoupled spin Hamiltonian is usually not γ-encoded.

It is possible to maintain γ-encoding of the entire recoupled Hamiltonian, by imposing a *one-to-one correspondence* between the symmetry-allowed spatial quantum numbers $\{l, m\}$ and the symmetry-allowed spin quantum numbers $\{\lambda, \mu\}$. This prevents the interference of terms with the same value of μ but different values of m.

For example, consider the symmetry $C6^1_2$. This leads to double-quantum recoupling of the DD terms, with suppression of all CSA terms to first order. The symmetry-allowed DD terms have the quantum numbers $\{2, -2, 2, 2\}$, $\{2, -1, 2, -2\}$, $\{2, 1, 2, 2\}$ and $\{2, 2, 2, -2\}$. The average Hamiltonian is *not* γ-encoded, since each spin term $\mu = 2$ is associated with two spatial components, $m = -2$ and $m = 1$.

If the symmetry number N is increased from 6 to 7, the symmetry $C7^1_2$ is generated, which only allows the DD terms $\{2, -1, 2, -2\}$ and $\{2, 1, 2, 2\}$. Since each spin component is now associated with only a single spatial component, the recoupled spin Hamiltonian is γ-encoded. Some of the success of the C7 pulse sequence and its variants may be attributed to the γ-encoding of the average Hamiltonian. For example, the theoretical maximum efficiency of double-quantum filtering experiments is usually increased by around 20% by using a γ-encoded pulse sequence.[36] In addition, γ-encoded pulse sequences enjoy much greater freedom in the relative timing of the pulse sequence and the sample rotation (see below).

The orientation-dependence of γ-encoded and non-γ-encoded sequences are contrasted in Figure 7. For γ-encoded sequences, the magnitude of the recoupled Hamiltonian is cylindrically symmetrical around the sample rotation axis.

2.13.2 Non-γ-Encoded Sequences

Although γ-encoding is generally a positive feature, it does have some disadvantages. As explained above, γ-encoding is generally imposed by eliminating some components of the average Hamiltonian. This enhanced selectivity is generally accompanied by a reduction in the overall magnitude of the recoupled Hamiltonian. In some cases, for example in long-range distance measurements, this is a disadvantage, since the recoupled interactions compete with relaxation and other loss processes. As a result, non-γ-encoded pulse sequences are sometimes preferable if the largest possible recoupled Hamiltonian is required, and its orientation-dependence is of lesser importance.

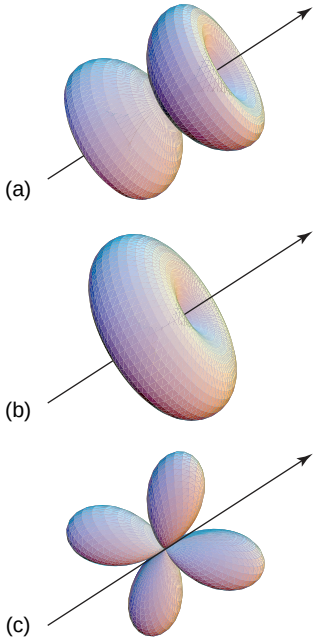

Figure 7 Polar plots showing the orientation-dependence of different dipolar recoupling sequences with respect to the magic-angle rotation axis (solid arrow). The direction of the external field is vertical. In each case, the magnitude of the recoupled Hamiltonian for a given orientation of the internuclear vector is proportional to the distance from the origin to the surface, in the direction of the vector. (a) γ-encoded recoupling of $m = \pm 1$ terms; (b) γ-encoded recoupling of $m = \pm 2$ terms; (c) non-γ-encoded recoupling

The complicated orientation-dependence of non-γ-encoded sequences may also be put to good use. Spiess and co-workers[68,69] have shown that the orientation-dependence generates characteristic signal modulations in certain two-dimensional experiments. These modulations may be matched with simulations in order to obtain structural information such as internuclear distances. In these applications, the recoupling pulse sequence must *not* be γ-encoded.

A further disadvantage of γ-encoding is that the construction of compensated supercycles is more difficult.

Some recoupled Hamiltonians *cannot* be γ-encoded within the framework of the symmetry theory described here. For example, consider the problem of zero-quantum recoupling in the presence of MAS. Since the selection rules are invariant to an overall sign change, it is not possible to allow terms of the form $\{l, m, \lambda, \mu\} = \{2, m, 2, 0\}$ without also allowing terms of the form $\{2, -m, 2, 0\}$. Since the $\mu = 0$ term is associated with two spatial terms $\pm m$, the resulting Hamiltonian is not γ-encoded. If desired, a γ-encoded zero-quantum DD Hamiltonian may be generated by rotational resonance,[70–72] which

is based on different principles (see **Rotational Resonance in Biology,** Volume 7).

2.13.3 β-Dependence

Consider the γ-encoded recoupling of dipole–dipole interactions between two spins j and k. Since the DD interaction is symmetrical, the tensor components $[A_{2m}^{jk}]^P$, written in the principal axis system of the DD interaction, vanish for the case $m \neq 0$. From equation (33), the recoupled DD interaction between spins j and k has the form

$$\overline{\mathcal{H}}_{2m2\mu}^{jk}(t^0) = \kappa_{2m2\mu}[A_{20}^{jk}]^P d_{0m}^2(\beta_{PR}^{jk}) \times \exp\{-\mathrm{i}m(\gamma_{PR}^{jk} + \alpha_{RL}^0 - \omega_r t^0)\}T_{2\mu}^{jk} \qquad (41)$$

Here β_{PR}^{jk} and γ_{PR}^{jk} are Euler angles relating the principal axis frame of the DD interaction to the rotor-fixed frame. For example, β_{PR}^{jk} is the angle subtended by the internuclear $j \rightarrow k$ vector and the rotation axis of the sample.

If the sequence implements γ-encoded recoupling, then equation (41) contains the entire orientation-dependence of the $T_{2\mu}^{jk}$ spin operator. As may be seen, the magnitude of the recoupled Hamiltonian depends on β_{PR}^{jk} according to the reduced Wigner function $d_{0m}^2(\beta_{PR}^{jk})$.

The relevant functions have the following form:

$$d_{00}^2(\beta) = \frac{1}{2}(3\cos^2\beta - 1)$$

$$d_{0\pm1}^2(\beta) = \pm\sqrt{\frac{3}{8}}\sin 2\beta$$

$$d_{0\pm2}^2(\beta) = \sqrt{\frac{3}{8}}\sin^2\beta \qquad (42)$$

The type of orientation-dependence may be selected by choosing the m-value of the symmetry-allowed component.

For example, consider the double-quantum recoupling sequences with symmetry $C7_2^1$. As discussed above, this symmetry implements γ-encoded recoupling with selection of the $\{l, m, \lambda, \mu\} = \{2, 1, 2, 2\}$ and $\{2, -1, 2, -2\}$ terms. Since the $m = \pm 1$ terms are symmetry-allowed, the magnitude of the recoupled Hamiltonian is proportional to $d_{01}^2(\beta_{PR}^{jk})$, and hence depends upon orientation according to the function $\sin(2\beta_{PR}^{jk})$. The recoupling effect is maximized at the angles $\beta_{PR}^{jk} = 45°$ and 135°, and vanishes at the orientations $\beta_{PR}^{jk} = 0$ or 180° (internuclear vector along the spinning axis) and also $\beta_{PR}^{jk} = 90°$ (internuclear vector perpendicular to the spinning axis). A sketch of the orientation dependence of the $C7_2^1$ recoupled Hamiltonian is shown in Figure 7(a).

The symmetry $C8_3^1$, on the other hand, implements γ-encoded double-quantum recoupling with selection of the terms $\{l, m, \lambda, \mu\} = \{2, -2, 2, 2\}$ and $\{2, 2, 2, -2\}$. In this case, the magnitude of the recoupled Hamiltonian is proportional to $d_{02}^2(\beta_{PR}^{jk})$, and hence depends upon orientation according to the function $\sin^2(\beta_{PR}^{jk})$. In this case, the recoupling effect is maximized at the angle $\beta_{PR}^{jk} = \pi/2$ (internuclear vector perpendicular to the spinning axis) and vanishes for the angles $\beta_{PR}^{jk} = 0$ and π (internuclear vector parallel to the spinning axis). A sketch of the orientation dependence of the $C8_3^1$ recoupled Hamiltonian is shown in Figure 7(b).

These orientation-dependences may be exploited in the magic-angle spinning of oriented materials.[55,56,73–75] Glaubitz has proposed a series of different recoupling experiments, in order to deduce the angles subtended by internuclear vectors and the spinning axis with a minimum of ambiguity.[75] This should enhance the molecular structural information which may be obtained from the magic-angle spinning NMR of oriented samples.

The symmetry-aided manipulation of orientation-dependence may also be useful in the NMR of disordered samples such as powders. It is possible to gain information on the relative orientation of pairs of interactions by correlating them with each other using multiple-dimensional NMR methods.[43,44,76–81] It should be possible to enhance the information content of such experiments, and resolve ambiguities, by using combinations of recoupling symmetries applied in different time intervals of a multidimensional experiment. At the moment, such experiments are still in the planning stage.

2.14 Phase-Time Relationships

The spin tensors transform in the following way when rotated about the z-axis:

$$\exp\{-\mathrm{i}\phi I_z\}T_{\lambda\mu}^{\Lambda}\exp\{-\mathrm{i}\phi I_z\} = T_{\lambda\mu}^{\Lambda}\exp\{-\mathrm{i}\mu\phi\} \qquad (43)$$

This equation may be combined with equation (40) to obtain the dependence of a recoupled Hamiltonian term on the orientational angles γ_{MR} and α_{RL}^0, the rf phase ϕ, and the initial time point t^0:

$$\overline{\mathcal{H}}_{lm\lambda\mu}^{\Lambda}(\gamma_{MR}, t^0, \alpha_{RL}^0, \phi) = \overline{\mathcal{H}}_{lm\lambda\mu}^{\Lambda}(0,0,0,0) \times \exp\{-\mathrm{i}[m(\gamma_{MR} + \alpha_{RL}^0 - \omega_r t^0) + \mu\phi]\} \qquad (44)$$

As discussed in Ref.[82], this relationship may be used to remove the dependence of the recoupled Hamiltonian on the initial time point t^0. The desired effect is achieved for the case $\mu \neq 0$ by shifting the overall rf phase according to the formula:

$$\phi = \frac{m}{\mu}\omega_r t^0 \qquad (45)$$

If this is done, then the average Hamiltonian term $\overline{\mathcal{H}}_{lm\lambda\mu}^{\Lambda}$ is independent of the initial time point t^0 at which the pulse sequence starts. Equation (45) is called a *phase-time relationship*.

In general, the recoupled Hamiltonian contains many symmetry-allowed terms, which may have different ratios of m and μ. If that is the case, then the formula in equation (45) cannot be implemented simultaneously for all of them, and it is impossible to compensate the full recoupled Hamiltonian for a change in the timing by a shift in the rf phase. This is clearly the case if the sequence is not γ-encoded.

If the sequence is γ-encoded, and if all the symmetry-allowed terms have the same ratio m/μ, then the pulse sequence may be applied at arbitrary time points in a pulse sequence, providing the overall rf phase is adjusted according to equation (45). This is an important practical principle of γ-encoded recoupling sequences, which has been applied in many different experimental contexts.[39,60,79,82–84]

A typical application is two-dimensional double-quantum spectroscopy. The pulse sequence consists of a preparation period, which may consist of a CN_n^ν recoupling sequence, followed by a variable evolution interval t_1, followed by a mixing interval, which might be a second CN_n^ν sequence, followed by signal detection.

In solution NMR, it is possible to vary the evolution interval t_1 in arbitrarily small steps, in order to obtain a sufficiently large spectral bandwidth in the double-quantum dimension. This is because the operation of the preparation and mixing sequences is independent of the times at which they are applied.

In magic-angle-spinning solid-state NMR, on the other hand, the situation is completely different, since the rotation of the sample modulates the spin Hamiltonian during the pulse sequence. In general, the average Hamiltonian generated by the second recoupling sequence depends on the time at which it is applied, and hence on the interval t_1. As a result, multi-dimensional experiments often display strong periodic modulations in the indirectly-detected dimension, which are due to the rotation of the sample during t_1 (see **Double-Quantum NMR Spectroscopy of Dipolar Coupled Spins Under Fast Magic-Angle Spinning**). It is easy to misinterpret these modulations as being due to the evolution of coherences in the interval t_1.

If the sequence is not γ-encoded, the only way to avoid these orientational modulations is to restrict t_1 to be integer multiples of a rotor period, so that the sample has the same orientation at the beginning and end of the evolution interval. However, this is a very strong restriction which in many cases greatly cramps the spectral width.

However, if the sequence is γ-encoded, and if all symmetry-allowed terms have the same ratio m/μ, then it is possible to vary the evolution interval completely freely by coupling the rf phase to the timing, according to the phase-time relationship equation (45). This allows multiple-quantum spectroscopy with an arbitrarily large bandwidth in the indirectly-detected dimension. Examples, including explicit formulae for the radio-frequency phases, are given in Refs.[39,60,79,82–84]

2.15 Incomplete Cycles

As mentioned before, the average Hamiltonian theory is strictly valid only for integer multiples of complete CN_n^ν or RN_n^ν cycles, i.e., complete multiples of n rotor periods. However, in most cases, the theory seems to work very well even when the full cycles are not completed. This allows a further degree of freedom in experimental design, since it becomes possible to adjust the recoupling intervals in relatively fine time steps.

This is an important advantage in experiments which aim to measure the magnitude of recoupled interactions. A fine time resolution of the recoupling interval is often a prerequisite for obtaining a result of the desired accuracy. Fine time resolution also makes it easier to maximize signal strength in multiple-quantum-filtering experiments.

There is an important complication associated with the use of incomplete recoupling cycles. In general, the pulse sequence propagator under a recoupling sequence is the product of two terms (equation (22)). The first term is the propagator for the rf field under the pulse sequence, while the second term concerns the average Hamiltonian of the internal spin interactions, which is subject to the selection rules discussed above. In the case of *complete* CN_n^ν or RN_n^ν sequences, the first term may be omitted, since the complete sequence behaves as a cycle, with an rf propagator proportional to the unity operator. However, this is not always the case for *incomplete* pulse sequences.

The CN_n^ν sequences present few problems in this respect, since the rf propagator for an incomplete CN_n^ν sequence is still proportional to the unity operator, providing that integer numbers of $\mathcal{C}$ elements are completed. As a result, only the average Hamiltonian must be taken into account for integer multiples of $\mathcal{C}$ elements.

Matters are more complicated for RN_n^ν sequences. If q elements $\mathcal{R}$ are completed, the rf propagator is given by

$$U_{\mathrm{rf}}(t^0 + q\tau_{\mathcal{R}}, t^0) = \exp\{-\mathrm{i}2q\phi I_z\}\exp\{-\mathrm{i}q\pi I_x\} \qquad (46)$$

where I_x and I_z is the longitudinal angular momentum operator of the irradiated spins, and the phase ϕ is given ideally by $\phi = \pi\nu/N$. The duration of each element is $\tau_{\mathcal{R}} = n\tau_r/N$, where τ_r is a rotor cycle.

In the case of even q, the rf propagator leads to an additional z-rotation of the spin operators, which must be taken into account by a compensatory rf phase shift of subsequent rf pulses. This phase shift must be added to the phase shifts imposed by the phase-time relationships, described above, as well as any phase shifts required in the phase cycling procedure, used to select NMR signals passing through certain orders of spin coherence.

In the case of odd q, there is a rotation of the spins by an odd multiple of π about the x-axis, as well as the phase rotation by $2q\phi$. The additional x-rotation may be taken into account by changing the *sign* of subsequent rf phases.

The overall implementation of these multiple phase shifts and phase inversions is quite complex. Refs.[39,60,79,82–84] give some practical examples with explicit formulae for the rf phases.

If these phase factors are taken into account correctly, it is possible to achieve fine time resolution of both the duration of the recoupling sequences and the intervals between them. In many cases, this is a decisive practical advantage.

2.16 Supercycles

In many cases, the performance of the recoupling sequences is enhanced by *supercycling*, which means repetition of the sequence with some variation of the rf phase shifts or the order of the pulse sequence elements.

The effect of supercycling is well understood on the level of the first-order average Hamiltonian. The higher order effects of supercycling, on the other hand, are currently not well researched, despite their importance. Some of the results sketched below should be regarded as preliminary. Refs.[39,60] contain some relevant theory.

Most of the supercycles used so far fall into the categories summarized below:

2.16.1 180° Phase Shift Supercycles

If a complete CN_n^ν or RN_n^ν sequence is repeated with a 180° phase shift, we get a two-step supercycle denoted $[\mathcal{S}]_0[\mathcal{S}]_{180}$.

Here $[\mathcal{S}]_\phi$ indicates an overall phase shift of all elements in the sequence $\mathcal{S}$ by the angle ϕ.

This supercycle cancels all components with odd values of μ in the first-order average Hamiltonian. The supercycle therefore implements an additional selection rule which is superimposed on the CN_n^ν or RN_n^ν selection rules.

For example, the symmetry $C5_2^1$ implements γ-encoded double-quantum homonuclear recoupling, with selection of the $\{l, m, \lambda, \mu\} = \{2, \pm1, 2, \pm2\}$ terms, similar to $C7_2^1$. However, $C5_2^1$ symmetry also allows CSA terms with quantum numbers $\{2, \pm2, 1, \mp1\}$ and single-quantum DD terms with quantum numbers $\{2, \pm2, 2, \mp1\}$. These undesirable terms all have odd values of μ and may be suppressed by building a supercycle of the form $[C5_2^1]_0[C5_2^1]_{180}$. The resulting sequence is called SPC5.[40] It has the same first-order average Hamiltonian properties as $C7_2^1$ but lower rf field requirements.[40] There are other ways of achieving the same result.[39]

Supercycles of the form $[\mathcal{S}]_0[\mathcal{S}]_{180}$ may be used whenever the desired components of the first-order average Hamiltonian have even values of μ. Even when this supercycle does not add to the selectivity of the first-order average Hamiltonian, it tends to reduce higher-order terms. For example, the CSA compensation of RN_n^ν sequences for homonuclear double-quantum recoupling is improved by using supercycles of the form $[RN_n^\nu]_0[RN_n^\nu]_{180}$.[85]

2.16.2 120° Phase Shift Supercycles

A higher degree of coherence order selectivity is implemented by using three-step phase cycles of the form $[\mathcal{S}]_0[\mathcal{S}]_{120}[\mathcal{S}]_{240}$. Supercycles of this type suppress all terms in the average Hamiltonian in which μ is not an integer multiple of 3. Since all spin interactions have μ values between 2 and -2, this supercycle $[\mathcal{S}]_0[\mathcal{S}]_{120}[\mathcal{S}]_{240}$ selects the $\mu = 0$ components in the average Hamiltonian, suppressing single-quantum and double-quantum terms.

This type of supercycle is useful for stabilizing zero-quantum recoupling sequences such as $R4_4^1$.[65]

2.16.3 Phase Inversion Supercycles

A different effect is achieved by supercycles of the form $\mathcal{SS}'$, where $\mathcal{S}'$ indicates the sign reversal of all rf phase shifts in the sequence $\mathcal{S}$. For example, if $\mathcal{S}$ consists of a $RN_n^{-\nu}$ sequence based on the elements $\mathcal{R} = 90_{-45}90_{45}90_{-45}$ and $\mathcal{R}' = 90_{45}90_{-45}90_{45}$, then $\mathcal{S}'$ consists of a RN_n^ν sequence based on the elements $\mathcal{R} = 90_{45}90_{-45}90_{45}$ and $\mathcal{R}' = 90_{-45}90_{45}90_{-45}$.

This type of supercycle replaces first-order average Hamiltonian terms of the form $aT_{\lambda\mu} + a^*T_{\lambda-\mu}$ by the expression $Re\{a\}(T_{\lambda\mu} + T_{\lambda-\mu})$. The effect is to convert the phase modulation of the average Hamiltonian into an amplitude modulation.

This type of supercycle cannot be used for γ-encoded sequences, but has been used with advantage for zero-quantum recoupling sequences, which cannot be γ-encoded.[65] It is used in many popular implementations of REDOR[26,27] and RFDR.[33,34]

2.16.4 Combined Phase Inversion and 180° Pulse Insertion Supercycles

It is possible to combine phase inversion with the insertion of strong 180° pulses, leading to supercycles of the form $\mathcal{S}\Pi_0\mathcal{S}'\Pi_{180}$, where Π_ϕ indicates the insertion of a strong, short, 180° pulse of phase ϕ.

If the inserted 180° pulses are ideal and infinitely short, this supercycle maintains the γ-encoding of the average Hamiltonian and also deletes average Hamiltonian terms with odd values of the spin rank λ. This type of supercycle is particularly useful for improving the chemical shift compensation of a pulse sequence.

Tycko used this type of supercycle to compensate 'zero-field in high-field' experiments for chemical shifts.[28,29]

In practice, 180° pulse insertion supercycles are awkward to implement, especially at high spinning frequencies, because the finite duration of real 180° pulses disturbs the timing of the other pulse sequence elements, breaking the pulse sequence symmetry.

2.16.5 Combined Phase Inversion and Cyclic Permutation Supercycles

A similar effect to the insertion of strong 180° pulses is achieved by *cyclically permuting* a 180° pulse sequence element. For example, the cyclic permutation of a 180° element $\mathcal{R}$ of the phase-inverted cycle $\mathcal{S}'$ may be denoted $\mathcal{R}^{-1}\mathcal{S}'\mathcal{R}$, where the notation $\mathcal{R}^{-1}\mathcal{S}'$ indicates the deletion of the element $\mathcal{R}$ from the beginning of the sequence $\mathcal{S}'$.

For example, consider a $C14_4^5$ sequence based on the simple element $\mathcal{C} = 360_0$, i.e.,

$$\mathcal{S} = 360_0360_{128.57}360_{257.14}360_{25.71}360_{154.29}360_{282.86}360_{51.43}- 360_{180}360_{308.57}360_{77.14}360_{205.71}360_{334.29}360_{102.86}360_{231.43} \quad (47)$$

spanning four rotational periods. The phase inverted cycle $\mathcal{S}'$ is as follows:

$$\mathcal{S}' = 360_0360_{231.43}360_{102.86}360_{334.29}360_{205.71}360_{77.14}360_{308.57}- 360_{180}360_{51.43}360_{282.86}360_{154.29}360_{25.71}360_{257.14}360_{128.57} \quad (48)$$

The sequence $\mathcal{R}^{-1}\mathcal{S}'\mathcal{R}$ derived by cyclically-permuting the element $\mathcal{R} = 180_0$ of $\mathcal{S}'$ is therefore

$$\mathcal{R}^{-1}\mathcal{S}'\mathcal{R} = 180_0360_{231.43}360_{102.86}360_{334.29}360_{205.71}360_{77.14}360_{308.57}- 360_{180}360_{51.43}360_{282.86}360_{154.29}360_{25.71}360_{257.14}- 360_{128.57}180_0 \quad (49)$$

This type of supercycle has almost the same effect as the combined phase inversion/180° pulse insertion supercycle discussed above. At the same time there is no need to apply very strong rf pulses. The timing complications associated with the inevitably finite duration of "strong" pulses are also avoided.

The cyclic permutation of an element creates a shift in the timing of the second sequence, disturbing the symmetry. In the case of γ-encoded pulse sequences, the timing shift may be compensated by modifying the rf phase of the second cycle, according to the phase-time relationship (equation (45)). This leads to the modified supercycle $[\mathcal{S}]_0[\mathcal{R}^{-1}\mathcal{S}'\mathcal{R}]_\delta$, where the overall phase shift δ is given by

$$\delta = -\frac{m}{\mu}\omega_r\tau_\mathcal{R} \quad (50)$$

Here $\tau_{\mathcal{R}}$ is the duration of the cyclically permuted element $\mathcal{R}$, and m/μ is the ratio of space and spin quantum numbers selected by the γ-encoded CN_n^ν sequence.

In the case of equation (49), the symmetry $C14_4^5$ selects the rotational components $\{l, m, \lambda, \mu\} = \{2, \pm 1, 2, \mp 2\}$, and the permuted element has a duration $\tau_{\mathcal{P}} = 2\tau_r/7$. The phase correction is therefore $\delta = \pi/7 = 25.71°$. The supercycle is

$$\begin{aligned}[\mathcal{S}]_0[\mathcal{R}^{-1}\mathcal{S}'\mathcal{R}]_\delta = {} & 360_0 360_{128.57} 360_{257.14} - \\ & 360_{25.71} 360_{154.29} 360_{282.86} 360_{51.43} 360_{180} - \\ & 360_{308.57} 360_{77.14} 360_{205.71} 360_{334.29} 360_{102.86} - \\ & 360_{231.43} 180_{25.71} 360_{257.14} 360_{128.57} 360_0 - \\ & 360_{231.43} 360_{102.86} 360_{334.29} 360_{205.71} - \\ & 360_{77.14} 360_{308.57} 360_{180} 360_{51.43} 360_{282.86} - \\ & 360_{154.29} 180_{25.71} \end{aligned} \tag{51}$$

This comprises one half of the SC14 sequence.[39]

This type of supercycle has beneficial effects on the CSA compensation of recoupling sequences, without destroying the γ-encoding.

2.16.6 Additional Supercycles

It is possible to construct supercycles by using consecutive CN_n^ν sequences based upon different basic elements $\mathcal{C}$. For example, Rienstra et al.[38] concatenated a $C7_2^1$ sequence based upon the basic cycle $\mathcal{C}_a = 360_0 360_{180}$ with a second $C7_2^1$ sequence based upon a different basic cycle $\mathcal{C}_b = 180_0 360_{180} 180_0$. Some higher-order error terms of the individual cycles cancel out in the mixed supercycle $C7_2^1(a)C7_2^1(b)$.

More complex supercycles may be created by superimposing the basic supercycle types, and by transposing, mixing, and permuting the elements. For example, the full SC14 supercycle[39] is

$$[[\mathcal{S}]_0[\mathcal{R}^{-1}\mathcal{S}'\mathcal{R}]_\delta]_0[[\mathcal{S}]_0[\mathcal{R}^{-1}\mathcal{S}'\mathcal{R}]_\delta]_{180} \tag{52}$$

where $\mathcal{S}$ is a $C14_4^5$ sequence using the basic element $\mathcal{C} = 360_0$, the element $\mathcal{R} = 180_0$ is cyclically permuted, and $\delta = 25.71°$. The CMR7 sequence[38] employs a particularly complicated supercycle structure.

At the moment, an empirical approach to supercycle construction prevails, since a complete higher-order theory has not yet been developed.

Supercycling should be implemented with care. In many cases, the supercycles are unnecessary, and readily harm the pulse sequence performance if they are used incorrectly.

2.17 Rf Imperfections

In practice, all rf pulse sequences are subject to various types of instrumental imperfection. Some typical imperfections of practical importance are:

1. Spatial inhomogeneity in the *amplitude* of the rf field over the sample volume;
2. Spatial inhomogeneity in the *direction* of the rf field over the sample volume, which translates into a phase modulation of the rf field as the sample rotates;[25,86,87]
3. Transients in the rf field upon changes in the driving field amplitude or phase, caused by the limited frequency bandwidth of the probe;[85,88]
4. Instability or droop in the rf field applied to the probe;
5. Errors in the values of rf phase shifts;
6. Phase instability of the rf field.

Many of these imperfections have been investigated rather thoroughly, and some fit well into the framework of the symmetry theory. In particular, rf amplitude inhomogeneity may be included by using a set of interaction frame Hamiltonian terms with the quantum numbers $l = 0$, $m = 0$, $\lambda^{\text{eff}} = Z_g$ and $\mu = \{-1, 0, +1\}$. Here λ^{eff} is the 'effective spin rank' of the rf inhomogeneity terms and Z_g is any *even* integer ('*g*' stands for *gerade*, which means 'even' in German).

It is surprising that the 'effective spin rank' λ^{eff} of the rf inhomogeneity terms is *even*, since the rf spin Hamiltonian actually contains rank 1 spin operators. This is because the rf inhomogeneity terms depend on the phase of the rf field, even before transformation into the interaction frame. As a result, these terms behave differently to the others.[89]

The rf inhomogeneity terms may be inserted into the selection rules and space-spin selection diagrams in the usual way. For example, it is easy to see that the rf inhomogeneity term $\{l, m, \lambda^{\text{eff}}, \mu\} = \{0, 0, Z_g, 0\}$ is symmetry-allowed under $C7_2^1$ and $R18_1^7$ sequences, while the terms $\{0, 0, Z_g, \pm 1\}$ are symmetry-forbidden. In order to achieve first-order rf compensation, one must therefore set the scaling factors for the symmetry allowed $\{0, 0, Z_g, 0\}$ terms to zero. This may be done by using amplitude-modulated basic elements $\mathcal{C}$ or $\mathcal{R}$. It follows that symmetries such as $C7_2^1$ and $R18_1^7$ have first-order compensation for rf inhomogeneity if they are based on amplitude-modulated elements.

In practice, higher-order terms are very important in determining the robustness of a pulse sequence with respect to rf amplitude deviations. These terms may be analyzed by using the selection rules equations (31) and (32). In many cases, it is simpler to use crude geometric arguments as a guideline.[39] For example, although the symmetry $C7_2^1$ is compensated for rf amplitude errors to first order (in the case of amplitude-modulated basic elements), geometrical arguments show that the second-order rf error terms are large.[39] As a result, $C7_2^1$ sequences must usually be based on elements which have a built-in rf error compensation, such as the original element $\mathcal{C} = 360_0 360_{180}$,[36] or the "POST" element $\mathcal{C} = 90_0 360_{180} 270_0$.[37] In Ref.[39] it is shown by geometrical arguments that the symmetry $C14_4^5$ has a higher degree of intrinsic rf error compensation, and that it is therefore feasible to use this symmetry together with the uncompensated basic element $\mathcal{C} = 360_0$. This provides a two-fold reduction in the rf field requirements for a given spinning frequency.

The effect of rf transients has also been analyzed.[85] A combination of electronic simulations and experimental measurements has led to the development of a simple analytical model for the transient behavior of the rf field at the sample. This model was used for accurate spin dynamical simulations during symmetry-based sequences, including the transient probe response. The effect of transients is minor, at least in the cases examined so far.

There is one common spectrometer imperfection which is a cause for real concern. In many contexts, the RN_n^ν class of

pulse sequences is extremely sensitive to the precise value of the rf phase shift. As described above, RN_n^ν sequences are composed of elements with the alternating phase values $\pm\pi\nu/N$. Even small deviations from this precise phase shift value may be disastrous.[85] A phase shift accuracy of $\pm 0.1^\circ$ or better is necessary for many applications of RN_n^ν sequences. In particularly demanding applications, such as long-range distance measurements, the phase shift accuracy should be an order of magnitude better still. Such extreme accuracy stretches current rf hardware. At the moment, only direct digital synthesis (DDS) of the rf wave produces sufficiently reliable and accurate phase shifts. Unfortunately, not all commercial spectrometers are equipped with such devices.

The extreme phase-shift sensitivity of RN_n^ν sequences may be understood using equation (46). This equation shows that a complete RN_n^ν sequence rotates resonant spins about the z-axis through the angle $2N\phi$. Since the value of the phase shift is ideally $\phi = \pi\nu/N$, the overall rotation angle generated by one RN_n^ν sequence is ideally $\Phi = 2\pi\nu$ radians. This is an integer multiple of 360°, and so has no effect on the spin system. If a set of K consecutive RN_n^ν sequences are applied, the overall rotation is through an angle $\Phi = 2\pi\nu K$, which also has no effect. However, if the value of ϕ is in error by a small angle Δ, then the overall rotation over K cycles is in excess by the angle $2NK\Delta$. For example, in the case of a $R14_2^6$ sequence, a phase deviation of only $\Delta = 0.1^\circ$ leads to an accumulating error of 2.8° per complete RN_n^ν sequence. Since a typical short-range pulse sequence employs around five complete sequences, the accumulated error rotation is about 14°. This is enough to degrade the double-quantum filtering efficiency significantly, especially since the double-quantum coherences are twice as sensitive as single-quantum coherences to phase shift errors. In a long-range application where around 50 complete sequences are used, the 0.1° phase shift error is disastrous.

CN_n^ν sequences are much less sensitive to phase shift errors, since there are no *accumulating* rotations in this case.

The extreme phase shift sensitivity of RN_n^ν sequences may be removed by using the supercycle $\mathcal{SS}'$. However, this method is only applicable to non-γ-encoded sequences. Work is under way towards a more general solution of this serious practical problem.

2.18 Selection of Sequences

Although the symmetry theory provides a sound framework for the search for suitable pulse sequences, this framework still allows enormous freedom. In order to develop a pulse sequence for a specific task, one must:

- Identify the space-spin components $\{l, m, \lambda, \mu\}$ which must be selected, and those that must be suppressed;
- Identify the set of suitable CN_n^ν or RN_n^ν symmetries;
- Identify the desired range of MAS frequencies;
- Identify a suitable basic element ($\mathcal{C}$ in the case of CN_n^ν symmetry, or $\mathcal{R}$ in the case of RN_n^ν symmetry);
- Identify a suitable supercycle, if required.

For each problem, there are usually a large number of feasible symmetries, and within each symmetry, there is an infinity of possible basic elements.

This great freedom is both a strength and a disadvantage: It is a strength because it allows one to design a sequence tailored to the specific requirements of the experiment; it is a disadvantage because there are too many possibilities for a complete search.

The first two steps are easy: The application itself defines the desired and undesired space-spin components, and it is a straightforward task to identify the set of appropriate symmetries. This may be done manually using space-spin selection diagrams, or by using a Mathematica program[63] developed for this purpose (available at *http://www.soton.ac.uk/∼mhl*).

The next stage is to choose the symmetry class and the basic element. Here one must pay attention to the following factors:

- The scaling factor for a given basic element $\mathcal{C}$ (or $\mathcal{R}$) under the symmetry class CN_n^ν (or RN_n^ν) should be reasonably high.
- The required rf field depends on the basic element and also the symmetry class (more specifically, the ratio of N to n). If the pulse sequence is intended to be broadband, it is usually desirable that the nutation frequency under the rf field should be as large as possible without being impractically large (see the subject of heteronuclear decoupling, discussed below).
- A rough guide to the relative performance of different symmetries is available by counting the number of symmetry-allowed higher-order terms, using the selection rules in equations (31) and (32).
- It is sometimes unnecessary for the pulse sequence symmetry to suppress all of the undesired rotational components. Undesired components may also be suppressed by using a basic element which provides a zero scaling factor for the undesired rotational components. Supercycling may also be used to suppress the undesired symmetry-allowed components. These strategies are used in the SPC5[40] and C-REDOR[67] schemes.

Previous experience in designing composite pulses[7–9,61,62] has been useful for guiding the choice of $\mathcal{C}$ and $\mathcal{R}$ elements (see **Composite Pulses,** Volume 2). For example, the composite pulse 360_0360_{180} is known to be a robust rf cycle with good rf amplitude compensation and reasonably broadband behavior with respect to isotropic chemical shifts. Its chemical shift performance may be enhanced considerably by cyclically-permuting a 90_0 pulse, leading to $\mathcal{C} = 90_0360_{180}270_0$. This 'permutationally offset-stabilized' (POST) element is a stalwart of liquid-state broadband decoupling experiments,[7–9] and was used in the design of the POST-C7 sequence.[37] Similarly, the element $\mathcal{R} = 90_0270_{180}$ is known as an offset-compensated 180° composite pulse,[7–9,61,62] and often proves to be a good choice in the context of RN_n^ν sequences.[41,60]

More recently, semi-automated computer searches have been used to identify suitable sequences. For example, Brinkmann[60] developed a combinatorial approach in which a large number of combinations of feasible symmetries, basic elements, and supercycle schemes are tested numerically by simulation under a variety of test situations.

The future may see a move towards more sophisticated basic elements, employing smoothly modulated pulse shapes rather than rectangular pulses. A full flowering of this field may require further improvements in the speed and flexibility of the electronic hardware.

3 HETERONUCLEAR SEQUENCES

In practice, most samples contain several nuclear spin species. The selection rules and design principles may be extended to the case of heteronuclear spin interactions.

3.1 Heteronuclear Spin Interactions

Suppose that the rotating sample contains two interacting spin species, denoted I and S, which are subjected to resonant rf fields at the corresponding nuclear Larmor frequencies. The nuclear spin interactions may be classified in terms of their spherical ranks under spatial (molecular) rotations, rotations of the I-spin polarizations by rf fields, rotations of the S-spin polarizations by rf fields, and rotations of the external magnetic field. The corresponding classification scheme is shown in Table 3. As may be seen, all interactions, with the exception of the homonuclear J-couplings, have different rotational properties. The symmetry theory of homonuclear rotor-synchronized pulse sequences is extended to the heteronuclear case by employing two different sets of spin quantum numbers.

In the presence of rf fields on both spin species I and S, the interaction frame Hamiltonian may be described as a superposition of many rotational components:

$$\mathcal{H}^{\Lambda} = \sum_{m=-l}^{+l} \sum_{\mu_I=-\lambda_I}^{+\lambda_I} \sum_{\mu_S=-\lambda_S}^{+\lambda_S} \mathcal{H}^{\Lambda}_{lm\lambda_I\mu_I\lambda_S\mu_S} \tag{53}$$

as listed in Table 4.

The fundamental design task in heteronuclear spin systems is to design pulse sequence symmetries which select a small number of combinations of these terms, while suppressing others.

Table 3 Rotational signatures of interactions in heteronuclear systems

Interaction	Space rank, l	I-Spin rank, λ_I	S-Spin rank, λ_S	Field rank
I-Spin isotropic shift	0	1	0	1
I-Spin CSA	2	1	0	1
I-Spin J-coupling	0	0	0	0
I-Spin DD-coupling	2	2	0	0
S-Spin isotropic shift	0	0	1	1
S-Spin CSA	2	0	1	1
S-Spin J-coupling	0	0	0	0
S-Spin DD-coupling	2	0	2	0
IS J-coupling	0	1	1	0
IS DD-coupling	2	1	1	0

3.2 Strong Heteronuclear Decoupling

A common method for heteronuclear decoupling at the same time as homonuclear recoupling involves the application of a CN_n^{ν} or RN_n^{ν} sequence on one channel while a strong resonant rf field is applied to the second channel. If the rf field is strong enough, this suppresses the heteronuclear spin interactions, so that the two spin species are *decoupled* from each other.

If the strong resonant irradiation is on the I-spin channel, the appropriate selection rules are:
Case of $CN_n^{\nu_S}$ sequences with I-spin decoupling:

$$\overline{\mathcal{H}}^{(1)}_{lm\lambda_I\mu_I\lambda_S\mu_S} = 0 \quad \text{if} \quad mn - \mu\nu_S \neq NZ \quad \text{or if } \lambda_I = 1 \tag{54}$$

Case of $RN_n^{\nu_S}$ sequences with I-spin decoupling:

$$\overline{\mathcal{H}}^{(1)}_{lm\lambda_I\mu_I\lambda_S\mu_S} = 0 \quad \text{if } mn - \mu\nu_S \neq \frac{N}{2}Z_{\lambda_S} \quad \text{or if } \lambda_I = 1 \tag{55}$$

Empirically, it is found that effective heteronuclear decoupling requires a relatively large ratio of the nutation frequencies of the spins under their corresponding rf fields, i.e., if the decoupling irradiation is applied to the I-spins, while a recoupling sequence is applied to the S-spins, the ratio of nutation frequencies should be at least $|\omega^I_{\text{nut}}/\omega^S_{\text{nut}}| > \sim 3$.[38]

In the absence of S-spin irradiation, two-pulse phase modulation (TPPM) of the decoupler field usually enhances the quality of the decoupling.[10] This does not usually appear to be the case when an rf field is also applied to the S-spins. Under some circumstances, however, the decoupling quality may be improved by placing the I-spin rf field well off-resonance, so as to approach or satisfy the Lee–Goldburg condition.[11] These effects are of great practical importance but are not fully understood.

Since many of the applications of the symmetry-based sequences are in isotopically-labelled organic solids, good heteronuclear decoupling is of great importance. The need for a very strong decoupler field is a strong constraint on the applications of these pulse sequences, since typical NMR probes cannot tolerate simultaneous resonant rf fields on two irradiation channels for very long. A typical practical limit corresponds to nutation frequencies of around 100 kHz

Table 4 Components of I and S-spin interactions in the interaction frame of two resonant rf fields, in the case of exact magic-angle spinning

Interaction	Space rank, l	Space components, m	I-Spin rank, λ_I	I-Spin components, μ_I	S-Spin rank, λ_S	S-Spin components, μ_S
I-Spin isotropic shift	0	0	1	$\{-1, 0, 1\}$	0	0
I-Spin CSA	2	$\{-2, -1, 1, 2\}$	1	$\{-1, 0, 1\}$	0	0
I-Spin J-coupling	0	0	0	0	0	0
I-Spin DD-coupling	2	$\{-2, -1, 1, 2\}$	2	$\{-2, -1, 0, 1, 2\}$	0	0
S-Spin isotropic shift	0	0	0	0	1	$\{-1, 0, 1\}$
S-Spin CSA	2	$\{-2, -1, 1, 2\}$	0	0	1	$\{-1, 0, 1\}$
S-Spin J-coupling	0	0	0	0	0	0
S-Spin DD-coupling	2	$\{-2, -1, 1, 2\}$	0	0	2	$\{-2, -1, 0, 1, 2\}$
IS J-coupling	0	0	1	$\{-1, 0, 1\}$	1	$\{-1, 0, 1\}$
IS DD-coupling	2	$\{-2, -1, 1, 2\}$	1	$\{-1, 0, 1\}$	1	$\{-1, 0, 1\}$

for the I-spin channel and around 50 kHz for the S-spin channel, applied for intervals of up to around 20 ms. Since the symmetry-based sequences require a fixed ratio of the nutation frequency to the spinning frequency, the limitation in the tolerable rf power restricts the operational spinning frequency. For example, the C7 pulse sequence is typically limited to spinning frequencies of 7 kHz or less.[36]

3.3 Single-Channel Sequences

If the rf field is only applied to one spin species, the opportunities for symmetry selection are restricted. For example, if rf fields are applied at the I-spin Larmor frequency, but not at the S-spin Larmor frequency, the S-spin quantum number is restricted to $\mu_S = 0$. In effect, only the first 5 columns in Table 4 are relevant. Under these circumstances, the rotational properties of the I-spin CSA and that of the IS DD coupling are indistinguishable: Both have $l = 2$ and $\lambda_I = 1$. Similarly, the I-spin isotropic shift and that of the IS J-coupling both have $l = 0$ and $\lambda_I = 1$.

The selection rules for symmetry-based pulse sequences with rf irradiation on the I-spin channel are:
Case of $CN_n^{\nu_I}$ sequences with no S-spin rf fields:

$$\overline{\mathcal{H}}^{(1)}_{lm\lambda_I\mu_I\lambda_S\mu_S} = 0 \quad \text{if } mn - \mu\nu_I \neq NZ \tag{56}$$

Case of $RN_n^{\nu_I}$ sequences with no S-spin rf fields:

$$\overline{\mathcal{H}}^{(1)}_{lm\lambda_I\mu_I\lambda_S\mu_S} = 0 \quad \text{if } mn - \mu\nu_I \neq \frac{N}{2}Z_{\lambda_I} \tag{57}$$

Here Z_{λ_I} is any integer with the same parity as the spin rank λ_I. These are the same as equations (27) and (28). The S-spin quantum numbers λ_S and μ_S are irrelevant.

It follows that if the rf irradiation is restricted to one channel, the same pulse sequences recouple the heteronuclear DD interactions and the CSA interactions of the resonant spins.

3.4 Dual Pulse Sequences

If rf fields are applied at the Larmor frequencies of both spin species, there are many more opportunities for symmetry selection. As described in Ref.[60] four different symmetry classes may be envisaged, denoted $CN_n^{\nu_I,\nu_S}$, $CRN_n^{\nu_I,\nu_S}$, $RCN_n^{\nu_I,\nu_S}$ and $RN_n^{\nu_I,\nu_S}$ Figure 8. The basic elements may be different on the two channels, although they must have the same duration $n\tau_r/N$. The phase shift scheme for the I-spin irradiation follows the usual construction rule for C-sequences (in the case of $CN_n^{\nu_I,\nu_S}$ or $CRN_n^{\nu_I,\nu_S}$), or for R-sequences (in the case of $RCN_n^{\nu_I,\nu_S}$ or $RN_n^{\nu_I,\nu_S}$), and depends on the symmetry numbers N, n and ν_I. Similarly, the phase shift scheme for the S-spin irradiation follows the construction rule for C-sequences (in the case of $CN_n^{\nu_I,\nu_S}$ or $RCN_n^{\nu_I,\nu_S}$), or for R-sequences (in the case of $CRN_n^{\nu_I,\nu_S}$ or $RN_n^{\nu_I,\nu_S}$), and depends on the symmetry numbers N, n and ν_S.

The selection rules for dual sequences may be derived by extension of the single-channel case, and are given by the following expressions:[60]

Case of $CN_n^{\nu_I,\nu_S}$ sequences:

$$\overline{\mathcal{H}}^{(1)}_{lm\lambda_I\mu_I\lambda_S\mu_S} = 0 \quad \text{if } mn - \mu_I\nu_I - \mu_S\nu_S \neq NZ \tag{58}$$

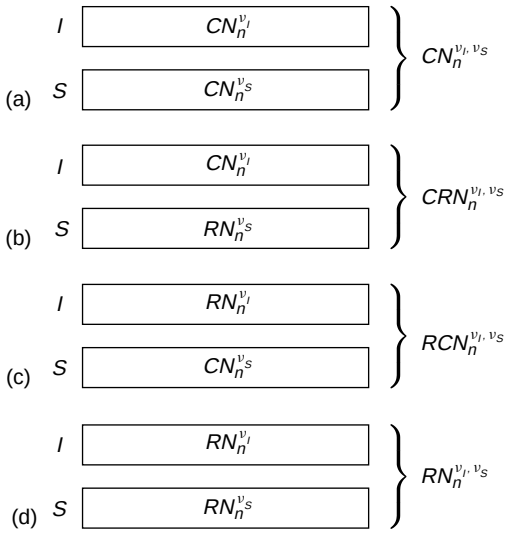

Figure 8 Naming convention for 2-channel heteronuclear pulse sequences

Case of $RCN_n^{\nu_I,\nu_S}$ sequences:

$$\overline{\mathcal{H}}^{(1)}_{lm\lambda_I\mu_I\lambda_S\mu_S} = 0 \quad \text{if } mn - \mu_I\nu_I - \mu_S\nu_S \neq \frac{N}{2}Z_{\lambda_I} \tag{59}$$

Case of $CRN_n^{\nu_I,\nu_S}$ sequences:

$$\overline{\mathcal{H}}^{(1)}_{lm\lambda_I\mu_I\lambda_S\mu_S} = 0 \quad \text{if } mn - \mu_I\nu_I - \mu_S\nu_S \neq \frac{N}{2}Z_{\lambda_S} \tag{60}$$

Case of $RN_n^{\nu_I,\nu_S}$ sequences:

$$\overline{\mathcal{H}}^{(1)}_{lm\lambda_I\mu_I\lambda_S\mu_S} = 0 \quad \text{if } mn - \mu_I\nu_I - \mu_S\nu_S \neq \frac{N}{2}Z_{\lambda_I+\lambda_S} \tag{61}$$

The consequences of these selection rules may be explored by extended space-spin selection diagrams, as described in Ref.[60] Expressions for the higher-order selection rules, and the dual-channel scaling factors, are also available.[60]

The dual-channel selection rules enable the design of pulse sequences which select interactions on the basis of their full rotational properties, as detailed in Table 4. For example, the symmetry $CR14_3^{2,2}$ suppresses all average Hamiltonian terms except those with the quantum numbers $\{l, m, \lambda_I, \mu_I, \lambda_S, \mu_S\} = \{0, 0, 0, 0, 0, 0\}$ and $\{2, \mp1, 1, \pm1, 1, \pm1\}$. This symmetry therefore enables γ-encoded double-quantum heteronuclear recoupling, with suppression of all homonuclear DD couplings, all chemical shift terms, and all heteronuclear J-couplings.[60]

In principle, the selection rules (equations (58)–(61)) permit the rational design of homonuclear recoupling sequences with simultaneous heteronuclear decoupling. In principle, this approach could avoid the severe power requirements of the strong heteronuclear decoupling method (see above). However, no dual sequences with significant advantages over conventional decoupling methods have been found yet.

4 APPLICATIONS

This section presents a brief summary of some of the published applications of the symmetry theory sketched above.

Sets of symmetry solutions appropriate for a number of different recoupling and decoupling problems are provided. The field is developing rapidly and these descriptions are by no means exhaustive.

4.1 Double-Quantum Homonuclear Recoupling

Double-quantum homonuclear recoupling has a number of important practical applications, including (see **Homonuclear Recoupling Schemes in MAS NMR,** Volume 4 and **Low-γ Nuclei in Solid Samples**):

- Passing signals through double-quantum coherences allows the suppression of signals from isolated spins-1/2. This is particularly useful, for example, in the spectroscopy of multiply-^{13}C-labelled macromolecules, since the 'background' signals from naturally-occurring isolated ^{13}C nuclei are suppressed, allowing the selective observation of the labelled spin clusters.[31,36,43,44]
- Double-quantum spectroscopy, and double-quantum filtered correlation spectroscopy, are useful for peak assignments.
- Double-quantum coherences are sensitive to the correlations between local magnetic fields. Double-quantum NMR allows the relative orientations of different spin interactions to be determined, and hence the estimation of interbond angles and torsional angles.[43,44,76–81,90,91]
- Double-quantum recoupling provides a route to the excitation of higher coherence orders.[81,92–94]

Double-quantum homonuclear decoupling sequences may be classified according to whether or not they provide a γ-encoded recoupled Hamiltonian.

4.1.1 γ-Encoded Double-Quantum Recoupling

Many CN_n^ν symmetries provide γ-encoded double-quantum recoupling. As described above, γ-encoding simplifies the orientation-dependence of the recoupling, improving the clarity of the dipolar oscillations and the efficiency of the double-quantum excitation, and improving the time resolution.

Some of the symmetries achieving γ-encoded double-quantum recoupling selectively recouple the $m = \pm 1$ terms (Table 5), while others recouple the $m = \pm 2$ terms (Table 6). In general, the former are more efficient. The isotropic chemical shift terms are symmetry-allowed so the scaling factors of these terms must be set to zero by a suitable choice of the basic element $\mathcal{C}$. Table 5 includes the symmetry $C7_2^1$, which was initially demonstrated with the basic element $\mathcal{C} = 360_0360_{180}$.[36] The 'POST' element $\mathcal{C} = 90_0360_{180}270_0$ is more robust with respect to chemical shift offsets and is now favored.[37] The symmetry $C14_4^5$ allows operation at high spinning frequencies, if it is stabilized by the use of supercycles.[39] A variant of $C7_2^1$ employing a complex supercycle structure has been described.[38] Sequences with the symmetry $C5_2^1$ have also been used, in conjunction with a two-step supercycle to remove the components $\mu = \pm 1$.[40]

The $C7_2^1$ sequences have already been applied to 'real' systems, such as membrane proteins. For example, $C7_2^1$ sequences were applied to a $^{13}C_2$-labelled sample of the photoreceptor protein bovine rhodopsin, allowing selective observation of the labelled sites with suppression of the background signals

Table 5 A set of CN_n^ν symmetries for γ-encoded homonuclear double-quantum recoupling, with selection of $\{l, m, \lambda, \mu\} = \{2, \pm 1, 2, \pm 2\}$ or $\{2, \pm 1, 2, \mp 2\}$ terms, and suppression of all CSA terms. The isotropic shift term $\{0, 0, 1, 0\}$ and the homonuclear J-coupling $\{0, 0, 0, 0\}$ are also symmetry-allowed. All inequivalent solutions in the range $N \leq 20, n \leq 10$ and $\nu \leq 10$ are shown

$C7_1^3$	$C9_1^4$	$C11_1^5$	$C13_1^6$	$C15_1^7$	$C17_1^8$
$C19_1^9$	$C7_2^1$	$C8_2^1$	$C8_2^3$	$C9_2^1$	$C10_2^1$
$C11_2^1$	$C12_2^1$	$C12_2^5$	$C13_2^1$	$C14_2^1$	$C15_2^1$
$C16_2^1$	$C16_2^7$	$C17_2^1$	$C18_2^1$	$C19_2^1$	$C20_2^1$
$C20_2^9$	$C7_3^2$	$C11_3^4$	$C13_3^5$	$C17_3^7$	$C19_3^8$
$C7_4^2$	$C9_4^2$	$C10_4^3$	$C11_4^2$	$C13_4^2$	$C14_4^5$
$C15_4^2$	$C17_4^2$	$C18_4^7$	$C19_4^2$	$C7_5^1$	$C9_5^2$
$C11_5^3$	$C13_5^4$	$C17_5^6$	$C19_5^7$	$C7_6^3$	$C8_6^1$
$C8_6^3$	$C10_6^3$	$C11_6^3$	$C13_6^3$	$C14_6^3$	$C16_6^3$
$C16_6^5$	$C17_6^3$	$C19_6^3$	$C20_6^3$	$C20_6^7$	$C9_7^1$
$C11_7^2$	$C13_7^3$	$C15_7^4$	$C17_7^5$	$C19_7^6$	$C7_8^3$
$C9_8^4$	$C10_8^1$	$C11_8^4$	$C13_8^4$	$C14_8^3$	$C15_8^4$
$C17_8^4$	$C18_8^5$	$C19_8^4$	$C7_9^1$	$C11_9^1$	$C13_9^2$
$C17_9^4$	$C19_9^5$	$C7_{10}^2$	$C8_{10}^1$	$C8_{10}^3$	$C9_{10}^4$
$C11_{10}^5$	$C12_{10}^1$	$C12_{10}^5$	$C13_{10}^5$	$C14_{10}^5$	$C16_{10}^3$
$C16_{10}^5$	$C17_{10}^5$	$C18_{10}^5$	$C19_{10}^5$		

Table 6 A set of CN_n^ν symmetries for γ-encoded homonuclear double-quantum recoupling, with selection of $\{l, m, \lambda, \mu\} = \{2, \pm 2, 2, \pm 2\}$ or $\{2, \pm 2, 2, \mp 2\}$ terms, and suppression of all CSA terms. The isotropic shift term $\{0, 0, 1, 0\}$ and the homonuclear J-coupling $\{0, 0, 0, 0\}$ are also symmetry-allowed. All inequivalent solutions in the range $N \leq 20, n \leq 10$ and $\nu \leq 10$ are shown

$C8_1^3$	$C10_1^4$	$C12_1^5$	$C14_1^6$	$C16_1^7$	$C18_1^8$
$C20_1^9$	$C10_2^3$	$C14_2^5$	$C18_2^7$	$C8_3^1$	$C10_3^2$
$C14_3^4$	$C16_3^5$	$C20_3^7$	$C10_4^1$	$C14_4^3$	$C18_4^5$
$C8_5^1$	$C12_5^1$	$C14_5^2$	$C16_5^3$	$C18_5^4$	$C10_6^1$
$C14_6^1$	$C8_7^3$	$C10_7^2$	$C12_7^1$	$C16_7^1$	$C18_7^2$
$C20_7^3$	$C10_8^3$	$C14_8^1$	$C18_8^1$	$C8_9^3$	$C10_9^4$
$C14_9^2$	$C16_9^1$	$C20_9^1$	$C14_{10}^3$	$C18_{10}^1$	

(see **Bacteriorhodopsin & Rhodopsin,** Volume 2). The evolution of the $^{13}C_2$ double-quantum coherences in the presence of local fields from the neighboring protons allowed determination of a H–C–C–H torsional angle in the retinylidene chromophore.[43] A conformational change could be detected in a trapped photointermediate.[44] The same experiment has also been demonstrated on carbohydrates.[77,78] The experiment may be extended to allow the determination of ^{15}N–^{13}C–^{13}C–^{15}N torsional angles in peptides and proteins.[79–81]

If double-quantum recoupling sequences are applied to single-quantum coherences in clusters of more than two spins, triple-quantum coherences are developed.[92] These triple-quantum coherences may also be used for torsional angle investigations.[81] The double-quantum recoupled spin dynamics in three-spin-1/2 clusters have been investigated by two-dimensional spectroscopy.[39] High orders of coherence have been excited by applying $C7_2^1$ sequences to abundant protons.[93] The relaxation of zero-quantum coherence has been studied by using a $C7_2^1$ sequence to excite double-quantum coherence,

followed by a coherence transfer into zero-quantum coherence using a selective pulse pair.[83]

$C7_2^1$ sequences have also been applied to glasses,[95–98] zeolites,[99] inorganic phosphates,[100–102] proteins[103] and drug molecules.[104]

Figure 9 shows a two-dimensional double-quantum ^{13}C spectrum of [U−^{13}C]-L-tyrosine, obtained using the SC14 pulse sequence at a spinning frequency of 20 kHz.[39] The utility of such spectra for peak assignment is obvious.

There are also a large number of RN_n^ν symmetries suitable for γ-encoded double-quantum recoupling. A set of symmetries which selectively recouple the $m = \pm 1$ terms are listed in Table 7. All of these symmetries suppress the isotropic chemical shift terms, and many of them are particularly robust with respect to chemical shift anisotropies. The symmetries $R14_2^6$ and $R22_4^9$ with $\mathcal{R} = 90_{180}270_0$ have been mainly used so far.[41,85] Measurement of the excitation dynamics of the double-quantum coherences allows the accurate estimation of ^{13}C–^{13}C bond lengths and medium-range distances in $^{13}C_2$-labelled systems, even in the presence of large CSA interactions.[85]

As discussed above, the orientation-dependence of the recoupling under the $m = \pm 1$ sequences (Tables 5 and 7) is different from that under the $m = \pm 2$ sequences (Table 6). This is expected to improve the information content of the NMR spectroscopy of rotating oriented samples.[75] Preliminary results have been obtained.[105]

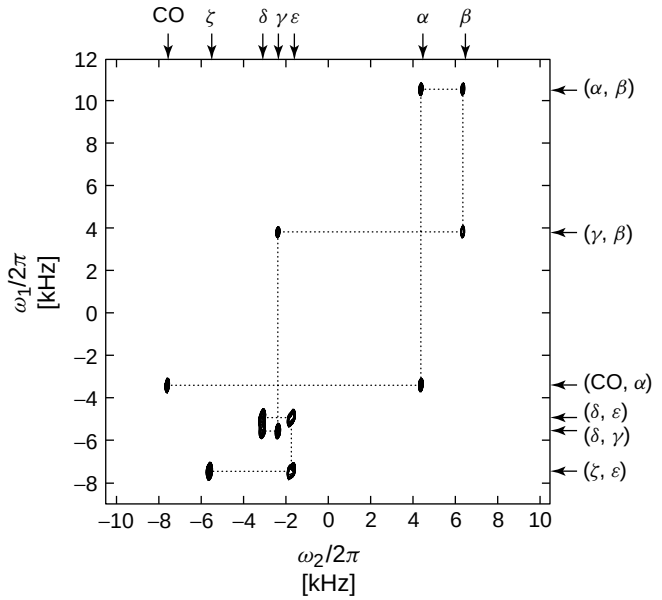

Figure 9 Two-dimensional double-quantum spectrum of [U−^{13}C]-L-tyrosine, obtained at a field of 9.4 T and a spinning frequency of 20 kHz, using the SC14 pulse sequence. The dashed lines are guides for the eye. (Adapted from Ref.[39])

Table 7 A set of RN_n^ν symmetries for γ-encoded homonuclear double-quantum recoupling, with selection of $\{l, m, \lambda, \mu\} = \{2, \pm 1, 2, \pm 2\}$ or $\{2, \pm 1, 2, \mp 2\}$ terms, and suppression of all isotropic shift and CSA terms. The homonuclear J-coupling $\{0, 0, 0, 0\}$ is also symmetry-allowed. All inequivalent solutions in the range $N \leq 20, n, \leq 10$ and $\nu \leq 10$ are shown

$R12_2^1$	$R12_2^5$	$R14_2^1$	$R14_2^6$
$R16_2^1$	$R16_2^7$	$R18_2^1$	$R18_2^8$
$R20_2^1$	$R20_2^9$	$R14_4^2$	$R14_4^5$
$R18_4^2$	$R18_4^7$		

4.1.2 *Non-γ-Encoded Double-Quantum Recoupling*

It is also possible to implement 2Q homonuclear recoupling without γ-encoding. An example is the back-to-back (BABA) recoupling sequence[102,106–108] which is given by

$$90_0 - \tau - 90_{180}90_{90} - \tau - 90_{270} \tag{62}$$

The rf pulses are assumed to be strong and short and the delay τ is adjusted so that the complete sequence lasts one rotor period. This sequence corresponds to the first two elements of a $C4_2^1$ sequence, using the basic element $\mathcal{C} = 90_0 - \tau - 90_{180}$. The $C4_2^1$ symmetry implements double-quantum recoupling, but also allows many unwanted terms, such as the isotropic chemical shift term $\{l, m, \lambda, \mu\} = \{0, 0, 1, 0\}$, CSA terms of the form $\{l, m, \lambda, \mu\} = \{2, \pm 2, 1, 0\}$, and zero-quantum DD terms of the form $\{l, m, \lambda, \mu\} = \{2, \pm 2, 2, 0\}$. However, the scaling factors for all of these terms vanish if the rf pulses are made infinitely short. In this limit, the only symmetry-allowed terms in the first-order average Hamiltonian are of the form $\{l, m, \lambda, \mu\} = \{2, \pm 1, 2, \pm 2\}$ and $\{2, \pm 1, 2, \mp 2\}$. In the limit of very strong rf fields, BABA therefore implements non-γ-encoded homonuclear DD recoupling with compensation for chemical shifts. Although the lack of γ-encoding has disadvantages, the same property allows the robustness of the sequence to be enhanced by constructing a $\mathcal{SS}'$ supercycle, i.e.,

$$\begin{aligned} &90_0 - \tau - 90_{180}90_{90} - \tau - 90_{270}90_0 - \tau - 90_{180} \\ &90_{270} - \tau - 90_{90} \end{aligned} \tag{63}$$

In addition, the absence of γ-encoding causes orientationally-induced modulations in 2D experiments, which may be analyzed in order to estimate internuclear distances.[68,69] The

Table 8 A set of CN_n^ν symmetries for non-γ-encoded homonuclear double-quantum recoupling. The symmetries $C6_2^1$ and $C6_8^1$ suppress all CSA terms and all homonuclear DD terms except $\{l, m, \lambda, \mu\} = \{2, \pm 2, 2, \mp 2\}$ and $\{2, \pm 1, 2, \pm 2\}$. The symmetries $C6_4^1$ and $C6_{10}^1$ suppress all CSA terms and all homonuclear DD terms except $\{l, m, \lambda, \mu\} = \{2, \pm 2, 2, \pm 2\}$ and $\{2, \pm 1, 2, \mp 2\}$. The isotropic shift term $\{0, 0, 1, 0\}$ and the homonuclear J-coupling $\{0, 0, 0, 0\}$ are symmetry-allowed. All inequivalent solutions in the range $N \leq 20, n \leq 10$ and $\nu \leq 10$ are shown

$C6_2^1$	$C6_4^1$	$C6_8^1$	$C6_{10}^1$

supercycled version of BABA has been applied to a variety of systems including phosphate networks[106,107] and glasses.[108]

There are several C-symmetries which provide non-γ-encoded 2Q recoupling with suppression of all CSA terms, even in the case of finite rf fields (see Table 8). The isotropic chemical shift terms are readily suppressed by an appropriate choice of the basic element. These C-sequences may provide an alternative to BABA in the case of limited rf field strength.

4.2 Zero-Quantum Homonuclear Recoupling

The radio-frequency-driven recoupling (RFDR) pulse sequence is widely used to transfer longitudinal magnetization between dipolar coupled spin sites in the solid state (see **Homonuclear Recoupling Schemes in MAS NMR,** Volume 4). The most common application is as the mixing interval in a two-dimensional experiment. If the J-couplings are neglected, the 2D spectrum displays cross peaks which indicate the spatial proximity of spin sites.

The most popular version of RFDR employs the so-called XY8 phase scheme.[33,34] This corresponds to a sequence of strong 180° pulses, spaced at intervals of one rotor period, with rf phases of $\{0, 90, 0, 90, 90, 0, 90, 0\}$. This corresponds to a $\mathcal{SS}'$ supercycle of a $R4_4^1$ sequence, with an overall 45° phase shift. This is indeed an appropriate symmetry for zero-quantum homonuclear recoupling, as may be seen from the list of solutions in Table 9. Symmetries such as $R4_4^1$ select terms of the form $\{l, m, \lambda, \mu\} = \{2, \pm1, 2, 0\}$ and $\{2, \pm2, 2, 0\}$. The recoupling is not γ-encoded, which harms its efficiency in a non-oriented sample, but the lack of γ-encoding permits the use of the stabilizing supercycle $\mathcal{SS}'$.

Table 9 A set of RN_n^ν symmetries for recoupling of the $\{l, m, \lambda, \mu\} = \{2, \pm2, 2, 0\}$ and $\{2, \pm1, 2, 0\}$ terms with suppression of all other homonuclear DD terms, CSA terms and isotropic shift terms. The homonuclear J-coupling $\{0, 0, 0, 0\}$ is symmetry-allowed. All inequivalent solutions in the range $N \leq 40, n \leq 10$ and $\nu \leq 20$ are shown

$R4_4^1$	$R6_6^1$	$R6_6^2$	$R4_8^1$
$R8_8^1$	$R8_8^3$	$R10_{10}^1$	$R10_{10}^2$
$R10_{10}^3$	$R10_{10}^4$		

The curious aspect of RFDR is that the scaling factor for the symmetry-allowed terms tends to zero in the limit of a strong rf field. Indeed, simulations show that the only reason RFDR works is because of the finite duration of practical rf pulses, interference from chemical shifts,[34] and the significant effect of J-couplings (which may even be dominant in some circumstances). Ishii[64] has given a symmetry-based analysis of RFDR with finite rf pulses, and proposed the use of symmetries such as $R4_4^1$ and $R6_6^1$. Brinkmann and Schmedt auf der Günne[65] have demonstrated additional symmetries and explored the use of more complex $\mathcal{R}$ elements in order to allow operation at high spinning frequencies. One recommended sequence involves the supercycle $[\mathcal{SS}']_0[\mathcal{SS}']_{120}[\mathcal{SS}']_{240}$ where $\mathcal{S}$ is a $R6_6^2$ sequence using the

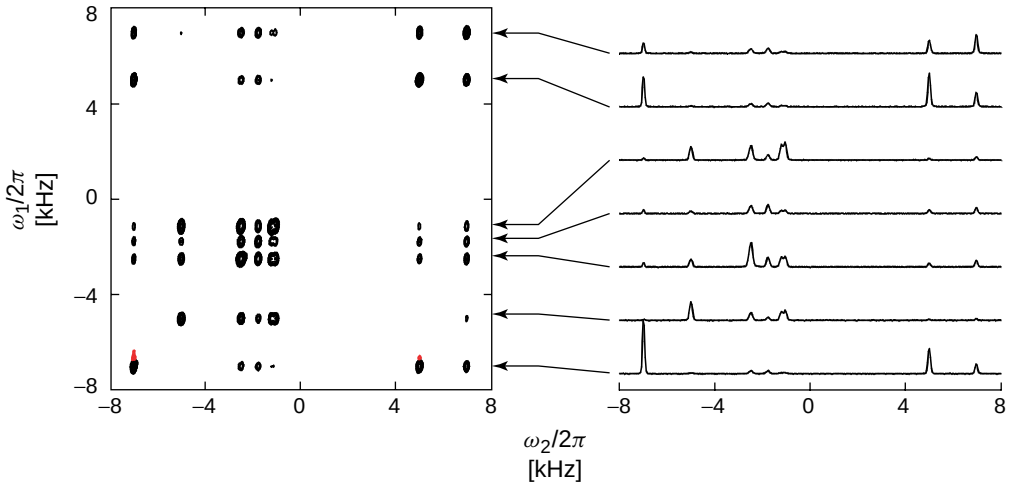

Figure 10 Two-dimensional correlation spectrum of [U−^{13}C]-L-tyrosine, obtained at a field of 9.4 T and a spinning frequency of 23 kHz, using a supercycled $R6_6^2$ pulse sequence, with a mixing interval of 9.9 ms. (Adapted from Ref.[65])

Table 10 A set of RN_n^ν symmetries for γ-encoded recoupling of the $\{l, m, \lambda, \mu\} = \{2, \pm2, 2, \pm1\}$ or $\{2, \pm2, 2, \mp1\}$ components of the homonuclear DD couplings with suppression of all other homonuclear DD terms, CSA terms and isotropic shift terms. The homonuclear J-coupling $\{0, 0, 0, 0\}$ is symmetry-allowed. All inequivalent solutions in the range $N \leq 20, n \leq 10$ and $\nu \leq 10$ are shown

$R10_1^2$	$R12_1^2$	$R14_1^2$	$R16_1^2$	$R18_1^2$	$R20_1^2$	$R14_2^4$	$R18_2^4$	$R10_3^4$	$R14_3^6$
$R16_3^6$	$R20_3^6$	$R14_4^8$	$R18_4^8$	$R12_5^{10}$	$R14_5^{10}$	$R16_5^{10}$	$R18_5^{10}$	$R14_6^{12}$	$R20_6^{12}$
$R10_7^4$	$R12_7^2$	$R16_7^{14}$	$R18_7^{14}$	$R20_7^{14}$	$R14_8^2$	$R18_8^{16}$	$R10_9^2$	$R14_9^4$	$R16_9^2$
$R20_9^{18}$	$R14_{10}^6$	$R18_{10}^2$							

Table 11 A set of CN_n^ν symmetries for selection of homonuclear J-couplings $\{l, m, \lambda, \mu\} = \{0, 0, 0, 0\}$ with suppression of all homonuclear DD couplings and CSA terms. Some isotropic shift terms are also symmetry-allowed. All inequivalent solutions in the range $N \leq 20, n \leq 10$ and $\nu \leq 10$ are shown

$C3_1^0$	$C4_1^0$	$C5_1^0$	$C6_1^0$	$C6_1^3$	$C7_1^0$	$C8_1^0$	$C8_1^4$	$C9_1^0$	$C9_1^3$
$C10_1^0$	$C10_1^3$	$C10_1^5$	$C11_1^0$	$C11_1^3$	$C11_1^4$	$C12_1^0$	$C12_1^3$	$C12_1^4$	$C12_1^6$
$C13_1^0$	$C13_1^3$	$C13_1^4$	$C13_1^5$	$C14_1^0$	$C14_1^3$	$C14_1^4$	$C14_1^5$	$C14_1^7$	$C15_1^0$
$C15_1^3$	$C15_1^4$	$C15_1^5$	$C15_1^6$	$C16_1^0$	$C16_1^3$	$C16_1^4$	$C16_1^5$	$C16_1^6$	$C16_1^8$
$C17_1^0$	$C17_1^3$	$C17_1^4$	$C17_1^5$	$C17_1^6$	$C17_1^7$	$C18_1^0$	$C18_1^3$	$C18_1^4$	$C18_1^5$
$C18_1^6$	$C18_1^7$	$C18_1^9$	$C19_1^0$	$C19_1^3$	$C19_1^4$	$C19_1^5$	$C19_1^6$	$C19_1^7$	$C19_1^8$
$C20_1^0$	$C20_1^3$	$C20_1^4$	$C20_1^5$	$C20_1^6$	$C20_1^7$	$C20_1^8$	$C20_1^{10}$	$C3_2^0$	$C5_2^0$
$C6_2^3$	$C7_2^0$	$C9_2^0$	$C9_2^3$	$C10_2^5$	$C11_2^0$	$C11_2^3$	$C11_2^5$	$C12_2^3$	$C13_2^0$
$C13_2^3$	$C13_2^5$	$C13_2^6$	$C14_2^3$	$C14_2^7$	$C15_2^0$	$C15_2^3$	$C15_2^5$	$C15_2^6$	$C15_2^7$
$C16_2^3$	$C16_2^5$	$C17_2^0$	$C17_2^3$	$C17_2^5$	$C17_2^6$	$C17_2^7$	$C17_2^8$	$C18_2^3$	$C18_2^5$
$C18_2^9$	$C19_2^0$	$C19_2^3$	$C19_2^5$	$C19_2^6$	$C19_2^7$	$C19_2^8$	$C19_2^9$	$C20_2^3$	$C20_2^5$
$C20_2^7$	$C4_3^0$	$C5_3^0$	$C7_3^0$	$C8_3^0$	$C8_3^4$	$C9_3^1$	$C9_3^2$	$C9_3^4$	$C10_3^0$
$C10_3^1$	$C10_3^5$	$C11_3^0$	$C11_3^1$	$C11_3^2$	$C12_3^1$	$C12_3^2$	$C12_3^4$	$C12_3^5$	$C13_3^0$
$C13_3^1$	$C13_3^2$	$C13_3^4$	$C14_3^0$	$C14_3^1$	$C14_3^2$	$C14_3^5$	$C14_3^7$	$C15_3^1$	$C15_3^2$
$C15_3^4$	$C15_3^5$	$C15_3^7$	$C16_3^0$	$C16_3^1$	$C16_3^2$	$C16_3^4$	$C16_3^7$	$C16_3^8$	$C17_3^0$
$C17_3^1$	$C17_3^2$	$C17_3^4$	$C17_3^5$	$C17_3^8$	$C18_3^1$	$C18_3^2$	$C18_3^4$	$C18_3^5$	$C18_3^7$
$C18_3^8$	$C19_3^0$	$C19_3^1$	$C19_3^2$	$C19_3^4$	$C19_3^5$	$C19_3^7$	$C19_3^9$	$C20_3^0$	$C20_3^1$
$C20_3^2$	$C20_3^4$	$C20_3^5$	$C20_3^8$	$C20_3^9$	$C20_3^{10}$	$C3_4^0$	$C5_4^0$	$C6_4^3$	$C7_4^0$
$C9_4^0$	$C9_4^3$	$C10_4^5$	$C11_4^0$	$C11_4^1$	$C11_4^5$	$C12_4^1$	$C12_4^3$	$C12_4^5$	$C13_4^0$
$C13_4^1$	$C13_4^3$	$C13_4^6$	$C14_4^1$	$C14_4^7$	$C15_4^0$	$C15_4^1$	$C15_4^3$	$C15_4^5$	$C15_4^6$
$C16_4^1$	$C16_4^3$	$C16_4^5$	$C16_4^7$	$C17_4^0$	$C17_4^1$	$C17_4^3$	$C17_4^5$	$C17_4^6$	$C17_4^7$
$C18_4^1$	$C18_4^3$	$C18_4^9$	$C19_4^0$	$C19_4^1$	$C19_4^3$	$C19_4^5$	$C19_4^6$	$C19_4^7$	$C19_4^9$
$C20_4^1$	$C20_4^3$	$C20_4^5$	$C20_4^7$	$C20_4^9$	$C3_5^0$	$C4_5^0$	$C6_5^0$	$C6_5^3$	$C7_5^0$
$C8_5^0$	$C8_5^4$	$C9_5^0$	$C9_5^3$	$C11_5^0$	$C11_5^2$	$C11_5^4$	$C12_5^0$	$C12_5^3$	$C12_5^4$
$C12_5^6$	$C13_5^0$	$C13_5^1$	$C13_5^2$	$C13_5^6$	$C14_5^0$	$C14_5^1$	$C14_5^3$	$C14_5^6$	$C14_5^7$
$C15_5^1$	$C15_5^2$	$C15_5^3$	$C15_5^4$	$C15_5^6$	$C15_5^7$	$C16_5^0$	$C16_5^1$	$C16_5^2$	$C16_5^4$
$C16_5^7$	$C16_5^8$	$C17_5^0$	$C17_5^1$	$C17_5^2$	$C17_5^3$	$C17_5^4$	$C17_5^8$	$C18_5^0$	$C18_5^1$
$C18_5^2$	$C18_5^3$	$C18_5^6$	$C18_5^7$	$C18_5^9$	$C19_5^0$	$C19_5^1$	$C19_5^2$	$C19_5^3$	$C19_5^4$
$C19_5^6$	$C19_5^8$	$C20_5^1$	$C20_5^2$	$C20_5^3$	$C20_5^4$	$C20_5^6$	$C20_5^7$	$C20_5^8$	$C20_5^9$
$C5_6^0$	$C7_6^0$	$C9_6^1$	$C9_6^2$	$C9_6^4$	$C10_6^5$	$C11_6^0$	$C11_6^2$	$C11_6^4$	$C13_6^0$
$C13_6^2$	$C13_6^4$	$C13_6^5$	$C14_6^5$	$C14_6^7$	$C15_6^1$	$C15_6^2$	$C15_6^4$	$C15_6^5$	$C15_6^7$
$C16_6^1$	$C16_6^7$	$C17_6^0$	$C17_6^1$	$C17_6^2$	$C17_6^4$	$C17_6^7$	$C17_6^8$	$C18_6^1$	$C18_6^5$
$C18_6^7$	$C19_6^0$	$C19_6^1$	$C19_6^2$	$C19_6^4$	$C19_6^5$	$C19_6^8$	$C19_6^9$	$C20_6^1$	$C20_6^5$
$C20_6^9$	$C3_7^0$	$C4_7^0$	$C5_7^0$	$C6_7^0$	$C6_7^3$	$C8_7^0$	$C8_7^4$	$C9_7^0$	$C9_7^3$
$C10_7^0$	$C10_7^1$	$C10_7^5$	$C11_7^0$	$C11_7^1$	$C11_7^5$	$C12_7^0$	$C12_7^3$	$C12_7^4$	$C12_7^6$
$C13_7^0$	$C13_7^2$	$C13_7^4$	$C13_7^5$	$C15_7^0$	$C15_7^2$	$C15_7^3$	$C15_7^5$	$C15_7^6$	$C16_7^0$
$C16_7^3$	$C16_7^4$	$C16_7^5$	$C16_7^6$	$C16_7^8$	$C17_7^0$	$C17_7^1$	$C17_7^2$	$C17_7^4$	$C17_7^6$
$C17_7^8$	$C18_7^0$	$C18_7^1$	$C18_7^3$	$C18_7^5$	$C18_7^6$	$C18_7^8$	$C18_7^9$	$C19_7^0$	$C19_7^1$
$C19_7^2$	$C19_7^3$	$C19_7^4$	$C19_7^8$	$C19_7^9$	$C20_7^0$	$C20_7^1$	$C20_7^2$	$C20_7^4$	$C20_7^5$
$C20_7^8$	$C20_7^9$	$C20_7^{10}$	$C3_8^0$	$C5_8^0$	$C6_8^3$	$C7_8^0$	$C9_8^0$	$C9_8^3$	$C10_8^5$
$C11_8^0$	$C11_8^1$	$C11_8^2$	$C12_8^1$	$C12_8^3$	$C12_8^5$	$C13_8^0$	$C13_8^1$	$C13_8^2$	$C13_8^6$
$C14_8^5$	$C14_8^7$	$C15_8^0$	$C15_8^2$	$C15_8^3$	$C15_8^5$	$C15_8^6$	$C17_8^0$	$C17_8^2$	$C17_8^3$
$C17_8^5$	$C17_8^6$	$C17_8^7$	$C18_8^3$	$C18_8^7$	$C18_8^9$	$C19_8^0$	$C19_8^1$	$C19_8^2$	$C19_8^5$
$C19_8^6$	$C19_8^7$	$C19_8^9$	$C20_8^1$	$C20_8^3$	$C20_8^5$	$C20_8^7$	$C20_8^9$	$C4_9^0$	$C5_9^0$
$C7_9^0$	$C8_9^0$	$C8_9^4$	$C10_9^0$	$C10_9^3$	$C10_9^5$	$C11_9^0$	$C11_9^3$	$C11_9^5$	$C12_9^1$
$C12_9^2$	$C12_9^4$	$C12_9^5$	$C13_9^0$	$C13_9^1$	$C13_9^3$	$C13_9^6$	$C14_9^0$	$C14_9^1$	$C14_9^3$
$C14_9^6$	$C14_9^7$	$C15_9^1$	$C15_9^2$	$C15_9^4$	$C15_9^5$	$C15_9^7$	$C16_9^0$	$C16_9^3$	$C16_9^4$

(*continued overleaf*)

Table 11 (*Continued*)

$C16_9^5$	$C16_9^6$	$C16_9^8$	$C17_9^0$	$C17_9^2$	$C17_9^3$	$C17_9^5$	$C17_9^6$	$C17_9^7$	$C19_9^0$
$C19_9^2$	$C19_9^3$	$C19_9^4$	$C19_9^6$	$C19_9^7$	$C19_9^8$	$C20_9^0$	$C20_9^3$	$C20_9^4$	$C20_9^5$
$C20_9^6$	$C20_9^7$	$C20_9^8$	$C20_9^{10}$	$C3_{10}^0$	$C6_{10}^8$	$C7_{10}^0$	$C9_{10}^0$	$C9_{10}^3$	$C11_{10}^0$
$C11_{10}^3$	$C11_{10}^4$	$C12_{10}^3$	$C13_{10}^0$	$C13_{10}^1$	$C13_{10}^2$	$C13_{10}^4$	$C14_{10}^1$	$C14_{10}^7$	$C15_{10}^1$
$C15_{10}^2$	$C15_{10}^3$	$C15_{10}^4$	$C15_{10}^6$	$C15_{10}^7$	$C16_{10}^1$	$C16_{10}^7$	$C17_{10}^0$	$C17_{10}^1$	$C17_{10}^2$
$C17_{10}^4$	$C17_{10}^6$	$C17_{10}^8$	$C18_{10}^3$	$C18_{10}^7$	$C18_{10}^9$	$C19_{10}^0$	$C19_{10}^2$	$C19_{10}^3$	$C19_{10}^4$
$C19_{10}^6$	$C19_{10}^7$	$C19_{10}^8$							

Table 12 A set of RN_n^ν symmetries for selection of homonuclear J-couplings $\{l, m, \lambda, \mu\} = \{0, 0, 0, 0\}$ with suppression of all homonuclear DD couplings, CSA terms and isotropic shift terms. All inequivalent solutions in the range $N \leq 20, n \leq 10$ and $\nu \leq 10$ are shown

$R6_1^0$	$R8_1^0$	$R10_1^0$	$R12_1^0$	$R12_1^3$	$R14_1^0$	$R14_1^3$	$R14_1^4$	$R16_1^0$	$R16_1^3$
$R16_1^4$	$R16_1^5$	$R18_1^0$	$R18_1^3$	$R18_1^4$	$R18_1^5$	$R18_1^6$	$R20_1^0$	$R20_1^3$	$R20_1^4$
$R20_1^5$	$R20_1^6$	$R20_1^7$	$R6_2^0$	$R10_2^0$	$R12_2^3$	$R14_2^0$	$R16_2^3$	$R16_2^5$	$R18_2^0$
$R18_2^3$	$R18_2^6$	$R20_2^3$	$R20_2^5$	$R20_2^7$	$R8_3^0$	$R10_3^0$	$R14_3^0$	$R14_3^2$	$R14_3^5$
$R16_3^0$	$R16_3^1$	$R16_3^4$	$R16_3^7$	$R18_3^1$	$R18_3^2$	$R18_3^4$	$R18_3^5$	$R18_3^7$	$R18_3^8$
$R20_3^0$	$R20_3^1$	$R20_3^2$	$R20_3^5$	$R20_3^8$	$R20_3^9$	$R6_4^0$	$R10_4^0$	$R12_4^1$	$R12_4^3$
$R12_4^5$	$R14_4^0$	$R18_4^0$	$R18_4^3$	$R18_4^6$	$R20_4^1$	$R20_4^3$	$R20_4^5$	$R20_4^7$	$R20_4^9$
$R6_5^0$	$R8_5^0$	$R12_5^0$	$R12_5^3$	$R14_5^0$	$R14_5^1$	$R14_5^6$	$R16_5^0$	$R16_5^1$	$R16_5^4$
$R16_5^7$	$R18_5^0$	$R18_5^2$	$R18_5^3$	$R18_5^6$	$R18_5^7$				

Table 13 A set of CN_n^ν symmetries for selection of isotropic chemical shift terms. All CSA terms and homonuclear DD coupling terms are suppressed. The homonuclear J-coupling $\{0, 0, 0, 0\}$ is symmetry-allowed. All inequivalent solutions in the range $N \leq 20, n \leq 10$ and $\nu \leq 10$ are shown

$C3_1^0$	$C4_1^0$	$C5_1^0$	$C6_1^0$	$C6_1^3$	$C7_1^0$	$C8_1^0$	$C8_1^4$	$C9_1^0$	$C9_1^3$
$C10_1^0$	$C10_1^3$	$C10_1^5$	$C11_1^3$	$C11_1^4$	$C12_1^3$	$C12_1^4$	$C12_1^6$	$C13_1^3$	$C13_1^4$
$C13_1^5$	$C14_1^3$	$C14_1^4$	$C14_1^5$	$C14_1^7$	$C15_1^3$	$C15_1^4$	$C15_1^5$	$C15_1^6$	$C16_1^3$
$C16_1^4$	$C16_1^5$	$C16_1^6$	$C16_1^8$	$C17_1^3$	$C17_1^4$	$C17_1^5$	$C17_1^6$	$C17_1^7$	$C18_1^3$
$C18_1^4$	$C18_1^5$	$C18_1^6$	$C18_1^7$	$C18_1^9$	$C19_1^3$	$C19_1^4$	$C19_1^5$	$C19_1^6$	$C19_1^7$
$C19_1^8$	$C20_1^3$	$C20_1^4$	$C20_1^5$	$C20_1^6$	$C20_1^7$	$C20_1^8$	$C20_1^{10}$	$C3_2^0$	$C5_2^0$
$C6_2^3$	$C7_2^0$	$C9_2^0$	$C9_2^3$	$C10_2^5$	$C11_2^3$	$C11_2^5$	$C12_2^3$	$C13_2^3$	$C13_2^5$
$C13_2^6$	$C14_2^3$	$C14_2^7$	$C15_2^3$	$C15_2^5$	$C15_2^6$	$C15_2^7$	$C16_2^3$	$C16_2^5$	$C17_2^3$
$C17_2^5$	$C17_2^6$	$C17_2^7$	$C17_2^8$	$C18_2^3$	$C18_2^5$	$C18_2^9$	$C19_2^3$	$C19_2^5$	$C19_2^6$
$C19_2^7$	$C19_2^8$	$C19_2^9$	$C20_2^3$	$C20_2^5$	$C20_2^7$	$C4_3^0$	$C5_3^0$	$C7_3^0$	$C8_3^0$
$C8_3^4$	$C9_3^1$	$C9_3^2$	$C9_3^4$	$C10_3^0$	$C10_3^1$	$C10_3^5$	$C11_3^1$	$C11_3^2$	$C12_3^1$
$C12_3^2$	$C12_3^4$	$C12_3^5$	$C13_3^1$	$C13_3^2$	$C13_3^4$	$C14_3^1$	$C14_3^2$	$C14_3^5$	$C14_3^7$
$C15_3^1$	$C15_3^2$	$C15_3^4$	$C15_3^5$	$C15_3^7$	$C16_3^1$	$C16_3^2$	$C16_3^4$	$C16_3^7$	$C16_3^8$
$C17_3^1$	$C17_3^2$	$C17_3^4$	$C17_3^5$	$C17_3^8$	$C18_3^1$	$C18_3^2$	$C18_3^4$	$C18_3^5$	$C18_3^7$
$C18_3^8$	$C19_3^1$	$C19_3^2$	$C19_3^4$	$C19_3^5$	$C19_3^7$	$C19_3^9$	$C20_3^1$	$C20_3^2$	$C20_3^4$
$C20_3^5$	$C20_3^8$	$C20_3^9$	$C20_3^{10}$	$C3_4^0$	$C5_4^0$	$C6_4^3$	$C7_4^0$	$C9_4^0$	$C9_4^3$
$C10_4^5$	$C11_4^1$	$C11_4^5$	$C12_4^1$	$C12_4^3$	$C12_4^5$	$C13_4^1$	$C13_4^3$	$C13_4^6$	$C14_4^1$
$C14_4^7$	$C15_4^1$	$C15_4^3$	$C15_4^5$	$C15_4^6$	$C16_4^1$	$C16_4^3$	$C16_4^5$	$C16_4^7$	$C17_4^1$
$C17_4^3$	$C17_4^5$	$C17_4^6$	$C17_4^7$	$C18_4^1$	$C18_4^3$	$C18_4^9$	$C19_4^1$	$C19_4^3$	$C19_4^5$
$C19_4^6$	$C19_4^7$	$C19_4^9$	$C20_4^1$	$C20_4^3$	$C20_4^5$	$C20_4^7$	$C20_4^9$	$C3_5^0$	$C4_5^0$
$C6_5^0$	$C6_5^3$	$C7_5^0$	$C8_5^0$	$C8_5^4$	$C9_5^0$	$C9_5^3$	$C11_5^2$	$C11_5^4$	$C12_5^3$
$C12_5^4$	$C12_5^6$	$C13_5^1$	$C13_5^2$	$C13_5^6$	$C14_5^1$	$C14_5^3$	$C14_5^6$	$C14_5^7$	$C15_5^1$
$C15_5^2$	$C15_5^3$	$C15_5^4$	$C15_5^6$	$C15_5^7$	$C16_5^1$	$C16_5^2$	$C16_5^4$	$C16_5^7$	$C16_5^8$
$C17_5^1$	$C17_5^2$	$C17_5^3$	$C17_5^4$	$C17_5^8$	$C18_5^1$	$C18_5^2$	$C18_5^3$	$C18_5^6$	$C18_5^7$
$C18_5^9$	$C19_5^1$	$C19_5^2$	$C19_5^3$	$C19_5^4$	$C19_5^6$	$C19_5^8$	$C20_5^1$	$C20_5^2$	$C20_5^3$

Table 13 (*Continued*)

$C20_5^4$	$C20_5^6$	$C20_5^7$	$C20_5^8$	$C20_5^9$	$C5_6^0$	$C7_6^0$	$C9_6^1$	$C9_6^2$	$C9_6^4$
$C10_6^5$	$C11_6^2$	$C11_6^4$	$C13_6^2$	$C13_6^4$	$C13_6^5$	$C14_6^5$	$C14_6^7$	$C15_6^1$	$C15_6^2$
$C15_6^4$	$C15_6^5$	$C15_6^7$	$C16_6^1$	$C16_6^7$	$C17_6^1$	$C17_6^2$	$C17_6^4$	$C17_6^7$	$C17_6^8$
$C18_6^1$	$C18_6^5$	$C18_6^7$	$C19_6^1$	$C19_6^2$	$C19_6^4$	$C19_6^5$	$C19_6^8$	$C19_6^9$	$C20_6^1$
$C20_6^5$	$C20_6^9$	$C3_7^0$	$C4_7^0$	$C5_7^0$	$C6_7^0$	$C6_7^3$	$C8_7^0$	$C8_7^4$	$C9_7^0$
$C9_7^3$	$C10_7^0$	$C10_7^1$	$C10_7^5$	$C11_7^1$	$C11_7^5$	$C12_7^3$	$C12_7^4$	$C12_7^6$	$C13_7^2$
$C13_7^4$	$C13_7^5$	$C15_7^2$	$C15_7^3$	$C15_7^5$	$C15_7^6$	$C16_7^3$	$C16_7^4$	$C16_7^5$	$C16_7^6$
$C16_7^8$	$C17_7^1$	$C17_7^2$	$C17_7^4$	$C17_7^6$	$C17_7^8$	$C18_7^1$	$C18_7^3$	$C18_7^5$	$C18_7^6$
$C18_7^8$	$C18_7^9$	$C19_7^1$	$C19_7^2$	$C19_7^3$	$C19_7^4$	$C19_7^8$	$C19_7^9$	$C20_7^1$	$C20_7^2$
$C20_7^4$	$C20_7^5$	$C20_7^8$	$C20_7^9$	$C20_7^{10}$	$C3_8^0$	$C5_8^0$	$C6_8^3$	$C7_8^0$	$C9_8^0$
$C9_8^3$	$C10_8^5$	$C11_8^1$	$C11_8^2$	$C12_8^1$	$C12_8^3$	$C12_8^5$	$C13_8^1$	$C13_8^2$	$C13_8^6$
$C14_8^5$	$C14_8^7$	$C15_8^2$	$C15_8^3$	$C15_8^5$	$C15_8^6$	$C17_8^2$	$C17_8^3$	$C17_8^5$	$C17_8^6$
$C17_8^7$	$C18_8^3$	$C18_8^7$	$C18_8^9$	$C19_8^1$	$C19_8^2$	$C19_8^5$	$C19_8^6$	$C19_8^7$	$C19_8^9$
$C20_8^1$	$C20_8^3$	$C20_8^5$	$C20_8^7$	$C20_8^9$	$C4_9^0$	$C5_9^0$	$C7_9^0$	$C8_9^0$	$C8_9^4$
$C10_9^0$	$C10_9^3$	$C10_9^5$	$C11_9^3$	$C11_9^5$	$C12_9^1$	$C12_9^2$	$C12_9^4$	$C12_9^5$	$C13_9^1$
$C13_9^3$	$C13_9^6$	$C14_9^1$	$C14_9^3$	$C14_9^6$	$C14_9^7$	$C15_9^1$	$C15_9^2$	$C15_9^4$	$C15_9^5$
$C15_9^7$	$C16_9^3$	$C16_9^4$	$C16_9^5$	$C16_9^6$	$C16_9^8$	$C17_9^2$	$C17_9^3$	$C17_9^5$	$C17_9^6$
$C17_9^7$	$C19_9^2$	$C19_9^3$	$C19_9^4$	$C19_9^6$	$C19_9^7$	$C19_9^8$	$C20_9^3$	$C20_9^4$	$C20_9^5$
$C20_9^6$	$C20_9^7$	$C20_9^8$	$C20_9^{10}$	$C3_{10}^0$	$C6_{10}^3$	$C7_{10}^0$	$C9_{10}^0$	$C9_{10}^3$	$C11_{10}^3$
$C11_{10}^4$	$C12_{10}^3$	$C13_{10}^1$	$C13_{10}^2$	$C13_{10}^4$	$C14_{10}^1$	$C14_{10}^7$	$C15_{10}^1$	$C15_{10}^2$	$C15_{10}^3$
$C15_{10}^4$	$C15_{10}^6$	$C15_{10}^7$	$C16_{10}^1$	$C16_{10}^7$	$C17_{10}^1$	$C17_{10}^2$	$C17_{10}^4$	$C17_{10}^6$	$C17_{10}^8$
$C18_{10}^3$	$C18_{10}^7$	$C18_{10}^9$	$C19_{10}^2$	$C19_{10}^3$	$C19_{10}^4$	$C19_{10}^6$	$C19_{10}^7$	$C19_{10}^8$	

Table 14 A set of RN_n^ν symmetries for selection of isotropic chemical shift terms. In all cases, the terms $\{l, m, \lambda, \mu\} = \{0, 0, 1, \pm 1\}$ are selected. All CSA terms and homonuclear DD coupling terms are suppressed. The homonuclear J-coupling $\{0, 0, 0, 0\}$ is symmetry-allowed. All inequivalent solutions in the range $N \leq 20, n \leq 10$ and $\nu \leq 10$ are shown

$R6_1^3$	$R8_1^4$	$R10_1^5$	$R12_1^6$	$R14_1^7$	$R16_1^8$	$R18_1^9$	$R20_1^{10}$
$R6_2^3$	$R10_2^5$	$R14_2^7$	$R18_2^9$	$R8_3^4$	$R10_3^5$	$R14_3^7$	$R16_3^8$
$R20_3^{10}$	$R6_4^3$	$R10_4^5$	$R14_4^7$	$R18_4^9$	$R6_5^3$	$R8_5^4$	$R12_5^6$
$R14_5^7$	$R16_5^8$	$R18_5^9$					

Table 15 A set of RN_n^ν symmetries for γ-encoded recoupling of CSA interactions, with selection of $\{l, m, \lambda, \mu\} = \{2, \pm 2, 1, \pm 1\}$ or $\{2, \pm 2, 1, \mp 1\}$ terms, and suppression of isotropic shift and homonuclear DD terms. The homonuclear J-coupling $\{0, 0, 0, 0\}$ is also symmetry-allowed. The same solutions implement γ-encoded heteronuclear recoupling if they are applied to only one spin species. All inequivalent solutions in the range $N \leq 20, n \leq 10$ and $\nu \leq 10$ are shown

$R10_1^3$	$R12_1^4$	$R14_1^5$	$R16_1^6$	$R18_1^7$	$R20_1^8$	$R14_2^3$	$R18_2^5$	$R10_3^1$	$R14_3^1$
$R16_3^2$	$R20_3^4$	$R14_4^1$	$R18_4^1$	$R12_5^4$	$R14_5^3$	$R16_5^2$	$R18_5^1$	$R14_6^5$	$R10_7^1$
$R12_7^4$	$R16_7^6$	$R18_7^5$	$R20_7^4$	$R14_8^5$	$R18_8^7$	$R10_9^3$	$R14_9^3$	$R16_9^6$	$R20_9^8$
$R14_{10}^1$	$R18_{10}^7$								

Table 16 A set of RN_n^ν symmetries for non-γ-encoded zero-quantum recoupling of CSA interactions, with selection of $\{l, m, \lambda, \mu\} = \{2, \pm 2, 1, 0\}$ terms, and suppression of all isotropic shift and homonuclear DD terms. The homonuclear J-coupling $\{0, 0, 0, 0\}$ is also symmetry-allowed. The same solutions implement zero-quantum heteronuclear recoupling if they are applied to only one spin species. All inequivalent solutions in the range $N \leq 20, n \leq 10$ and $\nu \leq 10$ are shown

$R12_3^1$	$R12_3^2$	$R12_3^4$	$R12_3^5$	$R16_4^1$	$R16_4^3$	$R16_4^5$	$R16_4^7$	$R20_5^1$	$R20_5^2$
$R20_5^3$	$R20_5^4$	$R20_5^6$	$R20_5^7$	$R20_5^8$	$R20_5^9$	$R12_9^1$	$R12_9^2$	$R12_9^4$	$R12_9^5$

element $\mathcal{R} = 90_{180}270_0$. An experimental correlation spectrum of [U–^{13}C]-L-tyrosine at a spinning frequency of 20 kHz is shown in Figure 10.

4.3 Homonuclear Single-Quantum Recoupling

Table 10 shows a set of symmetries for recoupling the $\mu = \pm 1$ components of the homonuclear DD interaction. These symmetries are expected to be useful in multiple-quantum spin counting experiments.[93,94,109,110]

4.4 Selection of J-Couplings

Compilations of symmetries appropriate for the selection of homonuclear J-couplings $\{l, m, \lambda, \mu\} = \{0, 0, 0, 0\}$ with suppression of homonuclear DD couplings and chemical shift anisotropies are given in Tables 11 and 12. The RN_n^ν symmetries in Table 12 also suppress isotropic chemical shift terms. For the CN_n^ν symmetries in Table 11, on the other hand, the scaling factors for the isotropic shift terms must be set to zero by an appropriate choice of $\mathcal{C}$.

These symmetries may be used in through-bond correlation spectroscopy (TOBSY) experiments.[48–52] The pulse sequence is used as the mixing interval in a two-dimensional experiment; The transfer of longitudinal magnetization generates cross peaks in the 2D spectrum, indicating spin sites with finite mutual J-couplings (see **Through-Bond Experiments in Solids**).

The original pulse sequences of this kind, suggested by Baldus and Meier[48–52] have symmetries $R6_1^0$ and $R8_1^0$. Two groups[50,51] have proposed a new range of pulse sequence, operational at higher spinning frequencies, which employ symmetries such as $C9_3^1$, $C9_6^1$ and others included in Table 11. Chan has demonstrated a $R30_6^{14}$ sequence which also has good performance at high spinning frequency.[52]

4.5 Selection of Isotropic Chemical Shifts

High-resolution isotropic shift spectra may be obtained in solids if all DD couplings and CSA terms are suppressed. In principle, this may be done by sufficiently rapid sample spinning. However, in practice, the required spinning frequencies are usually impractical. A well-designed rf pulse sequence may assist the spatial averaging, leading to acceptable resolution at practical spinning frequencies. The most common applications of such CRAMPS methods are in the high-resolution ^{1}H NMR of organic powdered solids (see **Line Narrowing Methods in Solids,** Volume 4).

Tables 13 and 14 show symmetry solutions for fast-spinning CRAMPS. All these symmetries suppress the homonuclear DD couplings and the CSA interactions, while allowing some isotropic shift terms. In this application it is particularly important that the scaling factors for the isotropic shift terms are as large as possible. This requires careful design of the element $\mathcal{C}$.

Spiess and co-workers employed $C3_1^0$ and $C4_1^0$ symmetries in fast-spinning CRAMPS experiments, using the known WHH4 cycles[12,13] as the basic element $\mathcal{C}$.[46,47] Recently, Madhu and Zhao demonstrated the use of $R18_2^9$ symmetry.[111] Figure 11 shows an experimental ^{1}H spectrum obtained at a spinning frequency of 20 kHz with a $R18_2^9$ sequence

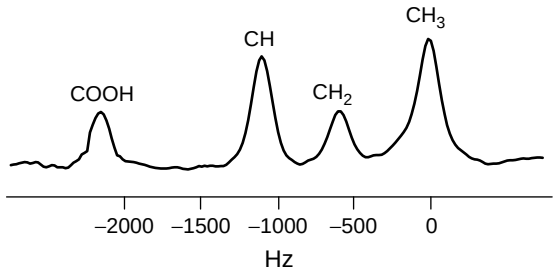

Figure 11 ^{1}H spectrum of monoethylfumarate, obtained at a field of 9.4 T and a spinning frequency of 20 kHz with a $R18_2^9$ sequence. After correcting for the pulse sequence scaling factor, the linewidths of all four peaks are given by approximately 0.9 ppm. (Adapted from Ref.[111])

constructed from basic elements $\mathcal{R} = 90_{-45}90_{45}90_{-45}$. Note the use of a phase-modulated basic element, in order to enhance the local averaging of the strong homonuclear interactions.

4.6 CSA Recoupling

Table 15 shows a set of symmetries leading to γ-encoded recoupling of CSA interactions, with suppression of isotropic chemical shifts and homonuclear DD couplings. The recoupled average Hamiltonian is transverse, i.e., it has the form $I_x \cos\phi + I_y \sin\phi$.

These sequences could be useful for measuring the CSA principal values of individual sites in coupled spin clusters.

Table 16 shows a set of symmetries leading to recoupling of the zero-quantum ($\mu = 0$) part of the CSA interaction, with suppression of isotropic chemical shifts and homonuclear DD couplings. In this case, the recoupling is not γ-encoded, and the recoupled average Hamiltonian is longitudinal, i.e., proportional to the operator I_z.

4.7 γ-Encoded Heteronuclear Recoupling

The solutions in Table 15 may also be used for the selective γ-encoded recoupling of heteronuclear DD interactions. If these sequences are applied repetitively at the Larmor frequency of one spin species, while the NMR signals from a coupled spin species are observed, the resulting spectrum displays a splitting, due to the recoupled heteronuclear interactions. Since the recoupling is γ-encoded, the splittings are prominent, even in orientationally-disordered systems such as powders.

Zhao has demonstrated the measurement of ^{13}C–^{1}H and ^{15}N–^{1}H DD couplings, using sequences with $R18_1^7$ and $R18_2^5$ symmetries.[112,113] An experimental example is shown in Figure 12. The figure shows the individual ^{15}N spectra of the two different NH groups in the imidazole ring of L-histidine hydrochloride monohydrate, obtained in a 2D experiment in which a $R18_2^5$ sequence is applied at the ^{1}H Larmor frequency.[113] There is a visible difference in the two splittings, which corresponds to a 4 pm difference in the two NH bond lengths. This difference is attributed to an intermolecular hydrogen bond formed by one of the NH groups. This result shows the potential of recoupling experiments for investigating the details of intermolecular interactions and other bonding

Table 17 A set of $CRN_n^{\nu_I,\nu_S}$ symmetries for γ-encoded double-quantum heteronuclear recoupling, with suppression of all CSA terms, isotropic chemical shift terms, homonuclear DD terms, and heteronuclear J-couplings. All symmetries recouple terms of the form $\{l, m, \lambda_I, \mu_I, \lambda_S, \mu_S\} = \{2, \mp 1, 1, \pm 1, 1, \pm 1\}$ The homonuclear J-couplings $\{0, 0, 0, 0, 0, 0\}$ are symmetry-allowed. All in-equivalent solutions in the range $N \leq 20, n \leq 9$ and $N/n \leq 7$ are shown

$CR14_3^{2,2}$	$CR14_3^{-5,-5}$	$CR16_3^{1,4}$	$CR16_3^{-4,-7}$	$CR18_3^{-1,7}$	$CR18_3^{1,5}$
$CR18_3^{-2,8}$	$CR18_3^{2,4}$	$CR18_3^{-4,-8}$	$CR18_3^{-5,-7}$	$CR20_3^{-1,8}$	$CR20_3^{-2,9}$
$CR20_3^{2,5}$	$CR20_3^{-5,-8}$	$CR20_4^{-1,7}$	$CR20_4^{1,5}$	$CR20_4^{-3,9}$	$CR20_4^{3,3}$
$CR20_4^{-5,-9}$	$CR20_4^{-7,-7}$	$CR14_5^{1,1}$	$CR14_5^{-6,-6}$	$CR16_5^{-1,4}$	$CR16_5^{-4,7}$
$CR18_5^{-2,6}$	$CR18_5^{2,2}$	$CR18_5^{-3,7}$	$CR18_5^{-7,-7}$	$CR16_6^{1,1}$	$CR16_6^{-7,-7}$
$CR20_6^{-1,5}$	$CR20_6^{-5,9}$	$CR16_7^{-3,4}$	$CR16_7^{-4,5}$	$CR18_7^{-1,3}$	$CR18_7^{1,1}$
$CR18_7^{-6,8}$	$CR18_7^{-8,-8}$	$CR20_7^{1,2}$	$CR20_7^{-2,5}$	$CR20_7^{-5,8}$	$CR20_7^{-8,-9}$
$CR20_8^{-1,3}$	$CR20_8^{1,1}$	$CR20_8^{-3,5}$	$CR20_8^{-5,7}$	$CR20_8^{-7,9}$	$CR20_8^{-9,-9}$
$CR14_9^{-1,-1}$	$CR14_9^{6,6}$	$CR16_9^{3,-4}$	$CR16_9^{4,-5}$	$CR20_9^{-3,4}$	$CR20_9^{-4,5}$
$CR20_9^{-5,6}$	$CR20_9^{-6,7}$				

Table 18 A set of $RN_n^{\nu_I,\nu_S}$ symmetries for γ-encoded double-quantum heteronuclear recoupling, with suppression of all CSA terms, isotropic chemical shift terms and homonuclear DD terms. All symmetries recouple terms of the form $\{l, m, \lambda_I, \mu_I, \lambda_S, \mu_S\} = \{2, \mp 1, 1, \pm 1, 1, \pm 1\}$ The homonuclear J-couplings $\{0, 0, 0, 0, 0, 0\}$ and heteronuclear J-coupling $\{0, 0, 1, 0, 1, 0\}$ are symmetry-allowed. All inequivalent solutions in the range $N \leq 20, n \leq 9$ and $N/n \leq 7$ are shown

$R14_3^{2,-5}$	$R16_3^{1,-4}$	$R16_3^{4,-7}$	$R18_3^{-1,-2}$	$R18_3^{1,-4}$	$R18_3^{2,-5}$
$R18_3^{4,-7}$	$R18_3^{5,-8}$	$R18_3^{7,8}$	$R20_3^{-1,-2}$	$R20_3^{2,-5}$	$R20_3^{5,-8}$
$R20_3^{8,9}$	$R20_4^{-1,-3}$	$R20_4^{1,-5}$	$R20_4^{3,-7}$	$R20_4^{5,-9}$	$R20_4^{7,9}$
$R14_5^{1,-6}$	$R16_5^{-1,-4}$	$R16_5^{4,7}$	$R18_5^{-2,-3}$	$R18_5^{2,-7}$	$R18_5^{6,7}$
$R16_6^{1,-7}$	$R20_6^{-1,-5}$	$R20_6^{5,9}$	$R16_7^{-3,-4}$	$R16_7^{4,5}$	$R18_7^{-1,-6}$
$R18_7^{1,-8}$	$R18_7^{3,8}$	$R20_7^{1,-8}$	$R20_7^{-2,-5}$	$R20_7^{2,-9}$	$R20_7^{5,8}$
$R20_8^{-1,-7}$	$R20_8^{1,-9}$	$R20_8^{-3,-5}$	$R20_8^{3,9}$	$R20_8^{5,7}$	$R14_9^{1,-6}$
$R16_9^{3,4}$	$R16_9^{-4,-5}$	$R20_9^{-3,-6}$	$R20_9^{-4,-5}$	$R20_9^{4,7}$	$R20_9^{5,6}$

perturbations, in systems that are unsuitable for crystallography or solution NMR.

The symmetry $C5_1^1$ has also been used for γ-encoded heteronuclear recoupling, although it does not fully suppress the homonuclear DD terms.[114–116] The performance of $C5_1^1$ is acceptable if it is used together with a basic element $\mathcal{C}$ with good local averaging properties for the homonuclear DD interactions. The frequency-switched Lee–Goldburg (FSLG)[17] and MREV[14,15] sequences have both been used.[114–116] Nevertheless, one expects some interference from the homonuclear DD couplings in the $C5_1^1$-based methods.

4.8 Non-γ-Encoded Heteronuclear Recoupling

The symmetries in Table 16 lead to zero-quantum recoupling of heteronuclear DD interactions, with suppression of chemical shift terms and homonuclear DD couplings. The recoupled heteronuclear interactions are proportional to the operator product $I_z S_z$.

If the RN_n^ν sequence is applied to the I-spin species, the S-spin NMR signals display a splitting which may be used to estimate the magnitude of the heteronuclear DD coupling. Since the recoupling is not γ-encoded, the splittings are relatively obscure in a powder sample.

Although the CSA interactions of resonant spins are recoupled at the same time as the heteronuclear DD interactions, the influence of the recoupled CSA terms is often minor, since the terms commute. In the single-quantum case of Table 15, on the other hand, the two recoupled interactions do not necessarily commute, and may interfere with each other in a complex way. The solutions in Table 15 are therefore only suitable for the heteronuclear recoupling of spins with small CSA interactions, while the solutions in Table 16 are more generally applicable.

The symmetries in Table 16 may be regarded as extensions of the REDOR pulse sequence.[26,27] Unlike REDOR, they implement homonuclear dipolar decoupling of the irradiated spin species, and should be applicable to systems with homonuclear dipolar interactions.

REDOR itself consists of two 180° pulses per rotor period, and therefore belongs to the symmetry class $RN_{N/2}^\nu$. The most common implementation of REDOR follows the XY8 phase scheme, which corresponds to the supercycle $\mathcal{SS}'$ of the symmetry $R4_2^1$. This symmetry implements selection of the $\{l, m, \lambda, \mu\} = \{2, \pm 1, 1, 0\}$ terms, just as the solutions in Table 16. However, the $R4_2^1$ symmetry also allows homonuclear DD terms of the form $\{2, \pm 2, 2, 0\}$, $\{2, \pm 1, 2, \pm 2\}$ and $\{2, \pm 1, 2, \mp 2\}$. These recoupled homonuclear DD interactions interfere with the operation of REDOR in non-dilute spin systems, a defect which should be reduced by the symmetries in Table 16.

Chan has discovered a different way of suppressing the homonuclear DD interactions in the REDOR method.[67] The

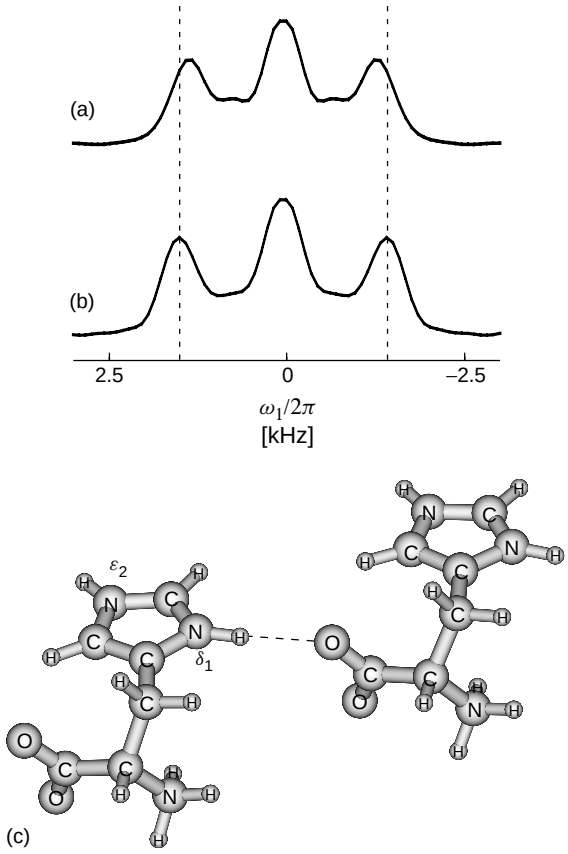

Figure 12 (a) Experimental ^{15}N spectrum of the δ_1 nitrogen site of [U$-^{13}$C,^{15}N]-L-histidinium hydrochloride monohydrate, obtained by a 2D experiment in the presence of $R18_2^5$ irradiation of the protons, at a magnetic field of 9.4 T and a spinning frequency of 20 kHz. The three-peak structure is due to the recoupled heteronuclear interaction between the ^{15}N and the directly-bonded ^{1}H. (b) Experimental ^{15}N spectrum of the ε_2 nitrogen site. Note that the splitting is slightly larger than in plot (a). These spectra show that the δ_1 NH bond is about 4 pm longer than the ε_2 NH bond. This elongation is attributed to the existence of an intermolecular hydrogen bond (see crystal structure in (c)). (Adapted from Ref.[113])

C-REDOR sequences are based upon the symmetries $C3_3^1$ and $C7_7^1$. These symmetries allow heteronuclear DD terms of the form $\{l, m, \lambda, \mu\} = \{2, \pm1, 1, 0\}$ and $\{2, \pm2, 1, 0\}$, and also the isotropic chemical shift term $\{0, 0, 1, 0\}$ and homonuclear DD terms of the form $\{2, \pm1, 2, 0\}$ and $\{2, \pm2, 2, 0\}$. This does not seem very promising since most of these terms are undesirable. However, by using the POST element $\mathcal{C} = 90_0360_{180}270_0$, the scaling factors for all of the symmetry-allowed terms with the exception of $\{2, \pm1, 1, 0\}$ and $\{0, 0, 0, 0\}$ may be made to vanish. The result is a REDOR-like average Hamiltonian with suppression of homonuclear DD couplings. This has been demonstrated experimentally.[67]

4.9 Double-Quantum Heteronuclear Recoupling by Dual Pulse Sequences

It is also possible to recouple heteronuclear interactions by applying synchronized rf irradiation to both spin species. This procedure allows γ-encoded recoupling of the heteronuclear interactions with the suppression of CSA interference.

The 'dual' selection rules in equations (58)–(61) may be used to generate the symmetry solutions. Sets of symmetries suitable for γ-encoded double-quantum heteronuclear recoupling are shown in Table 17 and 18. All of these symmetries recouple the terms of the form $\{l, m, \lambda_I, \mu_I, \lambda_S, \mu_S\} = \{2, \mp1, 1, \pm1, 1, \pm1\}$ with suppression of all isotropic chemical shift, homonuclear DD coupling and CSA terms. In the case of the $CRN_n^{\nu_I,\nu_S}$ symmetries in Table 17, the heteronuclear J-couplings are also suppressed.

Brinkmann[60] has shown that these symmetries may be used for the generation of heteronuclear multiple-quantum coherences, for the measurement of heteronuclear coupling constants, and for implementing magnetization transfer between spin species. For example, a sequence with the symmetry $R24_9^{5,10}$ has been used to obtain a heteronuclear multiple-quantum spectrum of a labelled amino acid.[60]

4.10 Heteronuclear Decoupling

The two-pulse phase modulation (TPPM) decoupling method[10] may also be understood qualitatively using the symmetry theory. The TPPM modulation scheme corresponds to a RN_n^ν sequence with a large ratio of N to n, although exact synchronization with the sample rotation does not appear to be important in this case. Edén has shown[41,45] that in many cases, a similar decoupling quality to TPPM may be achieved with exactly synchronized CN_n^ν and RN_n^ν sequences, and that the decoupling quality correlates reasonably well with higher-order term counts obtained by applying the rules in equations (31) and (32). In addition, there is evidence that the quality of heteronuclear decoupling is enhanced by implementing homonuclear *recoupling* at the same time, using symmetries such as $R24_2^1$.[41] This actually happens inadvertently in many implementations of TPPM. This observation is consistent with the well-known effect of 'self-decoupling', where strong homonuclear couplings within one spin species can narrow the peaks of a second, coupled, spin species.[4] (See **Heteronuclear Decoupling in Solids**.)

5 CONCLUSIONS

The symmetry theory sketched here is still in its infancy, although it is already clear that it provides much insight into the operation of many existing pulse sequences, as well as many new experimental possibilities. There remain many theoretical problems, such as the treatment of higher-order terms, and many practical problems, such as the phase-shift sensitivity of the RN_n^ν sequences. It is hoped that this summary will encourage many other research groups to explore the subject.

6 REFERENCES

1. E. R. Andrew, A. Bradbury, and R. G. Eades, *Nature*, 1959, **183**, 1802.
2. I. J. Lowe, *Phys. Rev. Lett.*, 1959, **2**, 285.
3. E. O. Stejskal, J. Schaefer, and J. S. Waugh, *J. Magn. Reson.*, 1977, **28**, 105.
4. M. Mehring, 'High Resolution NMR in Solids', 2nd edn., Springer: Berlin, 1982.

5. A. Abragam, 'The Principles of Nuclear Magnetism', Clarendon Press: Oxford, 1961.
6. R. R. Ernst, *J. Chem. Phys.*, 1966, **45**, 3845.
7. M. H. Levitt and R. Freeman, *J. Magn. Reson.*, 1981, **43**, 502.
8. J. S. Waugh, *J. Magn. Reson.*, 1982, **49**, 517.
9. M. H. Levitt, R. Freeman, and T. A. Frenkiel, *Adv. Magn. Reson.*, 1983, **11**, 47.
10. A. E. Bennett, C. M. Rienstra, M. Auger, K. V. Lakshmi, and R. G. Griffin, *J. Chem. Phys.*, 1995, **103**, 1.
11. M. Lee and W. I. Goldburg, *Phys. Rev. A*, 1965, **140**, 1261.
12. J. S. Waugh, M. L. Huber, and U. Haeberlen, *Phys. Rev. Lett.*, 1968, **20**, 180.
13. U. Haeberlen and J. S. Waugh, *Phys. Rev.*, 1968, **175**, 453.
14. P. Mansfield, *J. Phys. C*, 1971, **4**, 1444.
15. W. K. Rhim, D. D. Elleman, L. B. Schreiber, and R. W. Vaughan, *J. Chem. Phys.*, 1974, **60**, 4595.
16. D. P. Burum, M. Linder, and R. R. Ernst, *J. Magn. Reson.*, 1981, **44**, 173.
17. A. Bielecki, A. C. Kolbert, and M. H. Levitt, *Chem. Phys. Lett.*, 1989, **155**, 341.
18. M. Hohwy and N. C. Nielsen, *J. Chem. Phys.*, 1997, **106**, 1.
19. B. C. Gerstein, R. G. Pembleton, R. D. Wilson, and L. J. Ryan, *J. Chem. Phys.*, 1977, **66**, 361.
20. G. E. Maciel, C. E. Bronnimann, and B. Hawkins, *Adv. Magn. Reson.*, 1990, **14**, 125.
21. W. T. Dixon, *J. Chem. Phys.*, 1982, **77**, 1800.
22. O. N. Antzutkin, Z. Song, X. Feng, and M. H. Levitt, *J. Chem. Phys.*, 1994, **100**, 130.
23. Y. Yarim-Agaev, P. N. Tutunjian, and J. S. Waugh, *J. Magn. Reson.*, 1982, **47**, 51.
24. T. G. Oas, R. G. Griffin, and M. H. Levitt, *J. Chem. Phys.*, 1988, **89**, 692.
25. M. H. Levitt, T. G. Oas, and R. G. Griffin, *Isr. J. Chem.*, 1988, **28**, 271.
26. T. Gullion and J. Schaefer, *J. Magn. Reson.*, 1989, **81**, 196–200.
27. T. Gullion and J. Schaefer, *Adv. Magn. Reson.*, 1989, **13**, 57.
28. R. Tycko, *Phys. Rev. Lett.*, 1988, **60**, 2734.
29. R. Tycko, *J. Chem. Phys.*, 1990, **92**, 5776.
30. R. Tycko and G. Dabbagh, *Chem. Phys. Lett.*, 1990, **173**, 461.
31. R. Tycko and G. Dabbagh, *J. Am. Chem. Soc.*, 1991, **113**, 9444.
32. R. Tycko and S. O. Smith, *J. Chem. Phys.*, 1993, **98**, 932.
33. A. E. Bennett, J. H. Ok, R. G. Griffin, and S. Vega, *J. Chem. Phys.*, 1992, **96**, 8624.
34. D. K. Sodickson, M. H. Levitt, S. Vega, and R. G. Griffin, *J. Chem. Phys.*, 1993, **98**, 6742.
35. N. C. Nielsen, H. Bildsøe, H. J. Jakobsen, and M. H. Levitt, *J. Chem. Phys.*, 1994, **101**, 1805.
36. Y. K. Lee, N. D. Kurur, M. Helmle, O. G. Johannessen, N. C. Nielsen, and M. H. Levitt, *Chem. Phys. Lett.*, 1995, **242**, 304.
37. M. Hohwy, H. J. Jakobsen, M. Edén, M. H. Levitt, and N. C. Nielsen, *J. Chem. Phys.*, 1998, **108**, 2686.
38. C. M. Rienstra, M. E. Hatcher, L. J. Mueller, B. Sun, S. W. Fesik, and R. G. Griffin, *J. Am. Chem. Soc.*, 1998, **120**, 10 602–10 612.
39. A. Brinkmann, M. Edén, and M. H. Levitt, *J. Chem. Phys.*, 2000, **112**, 8539–8554.
40. M. Hohwy, C. M. Rienstra, C. P. Jaroniec, and R. G. Griffin, *J. Chem. Phys.*, 1999, **110**, 7983–7992.
41. M. Carravetta, M. Edén, X. Zhao, A. Brinkmann, and M. H. Levitt, *Chem. Phys. Lett.*, 2000, **321**, 205–215.
42. A. Brinkmann, M. Carravetta, X. Zhao, M. Edén, J. Schmedt auf der Günne, and M. H. Levitt, in 'Perspectives on Solid State NMR in Biology', eds S. Kühne and H. J. M. de Groot, Kluwer: Dordrecht, 2001.
43. X. Feng, P. J. E. Verdegem, Y. K. Lee, D. Sandström, M. Edén, P. Bovee-Geurts, W. J. de Grip, J. Lugtenburg, H. J. M. de Groot, and M. H. Levitt, *J. Am. Chem. Soc.*, 1997, **119**, 6853–6857.
44. X. Feng, P. J. E. Verdegem, M. Edén, D. Sandström, Y. K. Lee, P. Bovee-Geurts, W. J. de Grip, J. Lugtenburg, H. J. M. de Groot, and M. H. Levitt, *J. Biomol. NMR*, 2000, **16**, 1–8.
45. M. Edén and M. H. Levitt, *J. Chem. Phys.*, 1999, **111**, 1511–1519.
46. D. E. Demco, S. Hafner, and H. W. Spiess, *J. Magn. Reson. A*, 1995, **116**, 36.
47. S. Hafner and H. W. Spiess, *J. Magn. Reson. A*, 1996, **121**, 160.
48. M. Baldus and B. H. Meier, *J. Magn. Reson. A*, 1996, **121**, 65.
49. M. Baldus, R. J. Iulicci, and B. H. Meier, *J. Am. Chem. Soc.*, 1997, **119**, 1121–1124.
50. E. H. Hardy, R. Verel, and B. H. Meier, *J. Magn. Reson.*, 2001, **148**, 459–464.
51. A. S. D. Heindrichs, H. Geen, C. Giordani, and J. J. Titman, *Chem. Phys. Lett.*, 2001, **335**, 89–96.
52. J. C. C. Chan and G. Brunklaus, in press.
53. D. A. Varshalovich, A. N. Moskalev, and V. K. Kheronskii, 'Quantum Theory of Angular Momentum', World Scientific: Singapore, 1988.
54. M. H. Levitt, *J. Magn. Reson.*, 1989, **82**, 427.
55. Z. Song, O. N. Antzutkin, Y. K. Lee, S. C. Shekar, A. Ruppre-cht, and M. H. Levitt, *Biophys. J.*, 1997, **73**, 1539.
56. L. van Dam and M. H. Levitt, *J. Mol. Biol.*, 2000, **304**, 541–560.
57. A. Samoson, E. Lippmaa, and A. Pines, *Mol. Phys.*, 1988, **65**, 1013.
58. A. Llor and J. Virlet, *Chem. Phys. Lett.*, 1988, **152**, 248.
59. B. F. Chmelka and A. Pines, *Science*, 1989, **246**, 71.
60. A. Brinkmann and M. H. Levitt, *J. Chem. Phys.*, 2001, **115**, 357–384.
61. M. H. Levitt, *Prog. NMR Spectrosc.*, 1986, **18**, 61.
62. M. H. Levitt and R. Freeman, *J. Magn. Reson.*, 1981, **43**, 65.
63. S. Wolfram, 'Mathematica: A System for Doing Mathematics by Computer', Addison-Wesley: New York, 1991.
64. Y. Ishii, *J. Chem. Phys.*, 2001, **114**, 8473–8483.
65. A. Brinkmann, J. Schmedt auf der Günne, and M. H. Levitt, to be published.
66. B. -Q. Sun, P. R. Costa, D. Kocisko, P. T. Lansbury, and R. G. Griffin, *J. Chem. Phys.*, 1995, **102**, 702.
67. J. C. C. Chan, *Chem. Phys. Lett.*, 2001, **335**, 289–297.
68. H. Geen, J. J. Titman, J. Gottwald, and H. W. Spiess, *J. Magn. Reson. A*, 1995, **114**, 264.
69. R. Graf, D. E. Demco, S. Hafner, and H. W. Spiess, *Solid State Nucl. Magn. Reson.*, 1998, **12**, 139.
70. D. P. Raleigh, M. H. Levitt, and R. G. Griffin, *Chem. Phys. Lett.*, 1988, **146**, 71.
71. M. H. Levitt, D. P. Raleigh, F. Creuzet, and R. G. Griffin, *J. Chem. Phys.*, 1990, **92**, 6347.
72. M. Helmle, Y. K. Lee, P. J. E. Verdegem, X. Feng, T. Karlsson, J. Lugtenburg, H. J. M. de Groot, and M. H. Levitt, *J. Magn. Reson.*, 1999, **140**, 379–403.
73. G. S. Harbison and H. W. Spiess, *Chem. Phys. Lett.*, 1986, **124**, 128.
74. P. Tang, C. -L. Juang, and G. S. Harbison, *Science*, 1990, **249**, 70.
75. C. Glaubitz and A. Watts, *J. Magn. Reson.*, 1998, **130**, 305.
76. X. Feng, Y. K. Lee, D. Sandström, M. Edén, H. Maisel, A. Sebald, and M. H. Levitt, *Chem. Phys. Lett.*, 1996, **257**, 314.
77. S. Ravindranathan, X. Feng, T. Karlsson, G. Widmalm, and M. H. Levitt, *J. Am. Chem. Soc.*, 2000, **122**, 1102–1115.
78. S. Ravindranathan, T. Karlsson, K. Lycknert, G. Widmalm, and M. H. Levitt, *J. Magn. Reson.*, 2001, **151**, 136–141.
79. X. Feng, M. Edén, A. Brinkmann, H. Luthman, L. Eriksson, A. Gräslund, O. N. Antzutkin, and M. H. Levitt, *J. Am. Chem. Soc.*, 1997, **119**, 12 006–12 007.
80. P. R. Costa, J. D. Gross, M. Hong, and R. G. Griffin, *Chem. Phys. Lett.*, 1997, **280**, 95–103.
81. M. Edén, A. Brinkmann, H. Luthman, L. Eriksson, and M. H. Levitt, *J. Magn. Reson.*, 2000, **144**, 266–279.

82. A. Brinkmann, Ph.D. thesis, Stockholm University, 2001.
83. T. Karlsson, A. Brinkmann, P. J. E. Verdegem, J. Lugtenburg, and M. H. Levitt, *Solid State Nucl. Magn. Reson.*, 1999, **14**, 43–58.
84. M. Hong, *J. Magn. Reson.*, 1999, **136**, 86–91.
85. M. Carravetta, M. Edén, O. G. Johannessen, H. Luthman, P. J. E. Verdegem, J. Lugtenburg, A. Sebald, and M. H. Levitt, *J. Am. Chem. Soc.*, 2001, **123**, 10 628–10 638.
86. M. Goldman, V. Fleury, and M. Guron, *J. Magn. Reson. A*, 1996, **118**, 11.
87. P. Tekely and M. Goldman, *J. Magn. Reson.*, 2001, **148**, 135–141.
88. M. Mehring and J. S. Waugh, *Rev. Sci. Instrum.*, 1972, **43**, 649.
89. M. Carravetta, M. H. Levitt, and A. Brinkmann, to be published.
90. K. Schmidt-Rohr, *J. Am. Chem. Soc.*, 1996, **118**, 7601.
91. D. M. Gregory, M. A. Mehta, J. C. Shiels, and G. P. Drobny, *J. Chem. Phys.*, 1997, **107**, 28.
92. M. Edén and M. H. Levitt, *Chem. Phys. Lett.*, 1998, **293**, 173.
93. H. Geen, R. Graf, A. S. D. Heinrichs, B. S. Hickman, I. Schnell, H. W. Spiess, and J. J. Titman, *J. Magn. Reson.*, 1999, **138**, 167.
94. O. N. Antzutkin and R. Tycko, *J. Chem. Phys.*, 1999, **110**, 2749.
95. R. Witter, P. Hartmann, J. Vogel, and C. Jager, *Solid State Nucl. Magn. Reson.*, 1998, **13**, 189–200.
96. F. Fayon, C. Bessada, J. P. Coutures, and D. Massiot, *Inorg. Chem.*, 1999, **38**, 5212–5218.
97. A. Le Sauze, L. Montagne, G. Palavit, F. Fayon, and R. Marchand, *J. Non-Cryst. Solids*, 2000, **263**, 139–145.
98. D. Fayon, D. Massiot, K. Suzuya, and D. L. Price, *J. Non-Cryst. Solids*, 2001, **283**, 88–94.
99. D. F. Schantz, J. Schmedt auf der Günne, H. Koller, and R. F. Lobo, *J. Am. Chem. Soc.*, 2000, **122**, 6659–6663.
100. W. A. Dollase, M. Feike, H. Förster, T. Schaller, I. Schnell, A. Sebald, and S. Steuernagel, *J. Am. Chem. Soc.*, 1997, **119**, 3807.
101. X. Helluy, C. Marichal, and A. Sebald, *J. Phys. Chem. B*, 2000, **104**, 2836–2845.
102. W. Sommer, J. Gottwald, D. E. Demco, and H. W. Spiess, *J. Magn. Reson. A*, 1995, **113**, 131–134.
103. A. N. Appleyard, R. B. Herbert, P. J. F. Henderson, A. Watts, and P. J. R. Spooner, *Biochim. Biophys. Acta*, 2000, **1509**, 55–64.
104. D. A. Middleton, C. S. Le Du., X. Peng, D. G. Reid, and D. Saunders, *J. Am. Chem. Soc.*, 2000, **122**, 1161–1170.
105. C. Glaubitz, M. Carravetta, M. Edén, and M. H. Levitt, in 'Perspectives on Solid State NMR in Biology', eds S. Kühne and H. J. M. de Groot, Kluwer: Dordrecht, 2001.
106. M. Feike, D. E. Demco, R. Graf, J. Gottwald, S. Hafner, and H. W. Spiess, *J. Magn. Reson. A*, 1996, **122**, 214.
107. M. Feike, R. Graf, I. Schnell, C. Jäger, and H. W. Spiess, *J. Am. Chem. Soc.*, 1996, **118**, 9631.
108. R. Witter, P. Hartmann, J. Vogel, and C. Jäger, *Solid State Nucl. Magn. Reson.*, 1998, **13**, 189.
109. M. G. Munowitz and A. Pines, *Science*, 1986, **233**, 501.
110. D. Suter, S. B. Liu, J. Baum, and A. Pines, *Chem. Phys.*, 1987, **114**, 103–109.
111. P. K. Madhu, X. Zhao, and M. H. Levitt, *Chem. Phys. Lett.*, 2001, **346**, 142–148.
112. X. Zhao, M. Edén, and M. H. Levitt, *Chem. Phys. Lett.*, 2001, **342**, 353–361.
113. X. Zhao, J. L. Sudmeier, W. W. Bachovchin, and M. H. Levitt, *J. Am. Chem. Soc.*, in press.
114. J. D. Gross, P. R. Costa, and R. G. Griffin, *J. Chem. Phys.*, 1998, **108**, 7286–7293.
115. M. Hohwy, C. P. Jaroniec, B. Reif, C. M. Rienstra, and R. G. Griffin, *J. Am. Chem. Soc.*, 2000, **122**, 3218–3219.
116. B. Reif, M. Hohwy, C. P. Jaroniec, C. M. Rienstra, and R. G. Griffin, *J. Magn. Reson.*, 2000, **145**, 132–141.

Acknowledgements

I would like to thank my research group in Stockholm for helping develop and test these concepts, and for providing experimental results for this review, especially: Young Lee, Oleg Antzutkin, Mattias Edén, Andreas Brinkmann, Marina Carravetta, Xin Zhao, and P. K. Madhu. I would also like to thank Beat Meier, Jerry Chan, Hans Spiess and Yoshitaka Ishii for supplying results prior to publication.

Biographical Sketch

Malcolm Harris Levitt, *b* 1957. D. Phil. 1981, University of Oxford, England. Research associate, Weizmann Institute, Israel, 1981–1982, with S. Vega; ETH-Zürich, Switzerland, 1982–1986, with R. R. Ernst; Princeton University, USA, 1986, with W. S. Warren. Research Scientist at the Francis Bitter National Magnet Laboratory, Cambridge, MA, USA 1986–1990. Royal Society Research Fellow at the Interdisciplinary Research Centre for Superconductivity, Cambridge, England, 1990–1991. Lecturer at the Physical Chemistry Division, University of Stockholm, Sweden, 1992–1997. Professor in NMR Methodology, Physical Chemistry Division, University of Stockholm, Sweden, 1997–2001. Professor in Physical Chemistry, Southampton University, England, from 2001. Approx 120 publications. Current research interests: methodology and theory of NMR and its applications, especially to biological materials.

Three-dimensional Molecular Structures in Uniformly Labelled Solids Determined Using Rotational Resonance in the Tilted Rotating Frame

K. Takegoshi and Takehiko Terao

Department of Chemistry, Graduate School of Science, Kyoto University, Kyoto, Japan

1 Introduction 1
2 Theory 1
3 Method 2
4 Application to Glycylisoleucine 4
5 Concluding Remarks 10
6 References 10

1 INTRODUCTION

While solution NMR methods have been successfully applied for elucidating three dimensional (3D) structures of molecules including proteins (see **Biological Macromolecules: Structure Determination in Solution,** Volume 2), solid-state NMR has not attained such a stage. This review demonstrates the state of the art of structural determination of a whole molecule by solid state NMR, which should be complementary to solution NMR and irreplaceable for insoluble systems. In NMR of solids, measurements of dipolar interactions provide direct information on geometrical structures; they are most conveniently made under magic angle spinning (MAS) (see **Magic Angle Spinning,** Volume 5) with hidden potential of determining more than one distance using a single sample. However, most of the methods developed so far are of non-selective measurements of dipolar couplings, by which it is difficult to deduce quantitative structural information when more than two spins are involved. Hence, only one specific internuclear distance or dihedral angle is commonly determined by selectively isotope-labeling a particular pair of atoms. Then, many doubly-labeled samples must be prepared, if one tries to determine the 3D structure composed of sizable atoms by such non-selective approaches. On the other hand, if a specific dipolar interaction in a multiply or uniformly labeled system can selectively be recoupled, all the structural parameters necessary to determine the 3D structure can be obtained one by one using a single sample, significantly saving labor for sample preparation.

To achieve frequency-selective recoupling, it is required to remove all dipolar couplings at once, and recouple a specific pair. Using MAS, one can remove all the dipolar couplings together with chemical shift anisotropies under proton decoupling, and therefore the remaining problem is to achieve selective recoupling under MAS fast enough to remove all the other dipolar interactions simultaneously. For homonuclear dipolar interactions, rotational resonance (R^2)[1–8] has been developed as a simple selective recoupling method, and in fact, has been applied to biologically interesting molecules.[9] In the R^2 method, selection of a pair of spins is made by adjusting an integral multiple of the MAS frequency ν_R to the difference of the chemical shifts of the two spins. Therefore, R^2 is frequency-difference selective, and if more than one spin pair with the same separation exists, they are simultaneously recoupled. Further, when the chemical shift difference for the two spins is relatively small, the MAS frequency must be lowered, leading to imperfect decoupling of the other dipolar interactions.

Selective recoupling among homonuclear spins can also be achieved in a tilted rotating frame.[10] Under rf irradiation, the Zeeman interaction for a spin system can be written in a tilted rotating frame (X, Y, Z) as

$$\frac{\mathcal{H}}{\text{Hz}} = \sum_i \nu_{ei} \hat{I}_{Zi} \tag{1}$$

while the conventional Zeeman interaction in the rotating frame (x, y, z) is written as

$$\mathcal{H} = \sum_i \Delta\nu_i \hat{I}_{zi} \tag{2}$$

where ν_e denotes the effective field and $\Delta\nu$ is the resonance offset. By comparing these two equations, it may be expected that the R^2 condition in the rotating frame:

$$|\Delta\nu_1 - \Delta\nu_2| = n\nu_R \tag{3}$$

would be modified in the tilted rotating frame as

$$|\nu_{e1} - \nu_{e2}| = n\nu_R \tag{4}$$

In fact, this is one of the recoupling conditions in the tilted rotating frame. There are additional recoupling conditions, namely, $\nu_{e1} + \nu_{e2} = n\nu_R$ and $\nu_{eX} = n\nu_R$ ($X = I$ or S), as derived in the following section. These conditions are referred to as the R2TR (rotational resonance in the tilted rotating frame) conditions. There are three adjustable parameters to achieve one of the R2TR conditions, namely, the intensity ν_1 and the frequency ν of the rf irradiation and the MAS frequency ν_R. This diversity makes it possible to find an R2TR condition even for a pair of spins with a small chemical shift difference without relaxing the fast MAS condition necessary for decoupling all other dipolar couplings. Further, it should be pointed out here that, while R^2 is frequency-difference selective, R2TR is frequency selective. Hence, a particular dipolar coupling can be recoupled by properly choosing the experimental parameters even when more than two lines have equal chemical-shift differences.

2 THEORY

First, we briefly touch upon rotational resonance recoupling. A dipolar-coupled homonuclear two-spin $I - S$ system in a

rotating powdered sample is considered. For simplicity, the chemical shift anisotropies (CSAs) are neglected. The total spin Hamiltonian can be written as

$$\mathcal{H} = \Delta\nu_I \hat{I}_z + \Delta\nu_S \hat{S}_z + \mathcal{H}_D(t) \tag{5}$$

where $\mathcal{H}_D(t)$ is the homonuclear dipolar interaction

$$\mathcal{H}_D(t) = D(t)\left\{\hat{I}_z\hat{S}_z - \frac{1}{4}(\hat{I}_+\hat{S}_- + \hat{I}_-\hat{S}_+)\right\} \tag{6}$$

with the spatial part modulated by MAS

$$D(t) = \sum_{n=\pm1,\pm2} \nu_{Dn} \exp(in\nu_R t) \tag{7}$$

Here, ν_{Dn} is a function of the internuclear distance and the polar angles defining the direction of the $I-S$ vector in a rotor-fixed frame. $\mathcal{H}_D(t)$ is transferred into the frame of the Zeeman interaction by using the unitary operator

$$U(t) = \exp(i\Delta\nu_I \hat{I}_z t)\exp(i\Delta\nu_S \hat{S}_z t) \tag{8}$$

as

$$\begin{aligned}\widetilde{\mathcal{H}_D}(t) &= U(t)\mathcal{H}_D(t)U^{-1}(t)\\ &= \sum_{n=\pm1,\pm2} \nu_{Dn}\Big[\hat{I}_z\hat{S}_z\exp(in\nu_R t)\\ &\quad -\frac{1}{4}(\hat{I}_+\hat{S}_- + \hat{I}_-\hat{S}_+)\exp\{i(n\nu_R - \Delta)\}\Big]\end{aligned} \tag{9}$$

where Δ is the difference of the isotropic chemical shift: $\Delta = \nu_I - \nu_S$. This equation shows that the rotational resonance recoupling occurs at $\Delta = n\nu_R$ with $n = \pm1, \pm2$. If one takes account of the chemical shift anisotropies, one can prove that recoupling occurs even under higher-order ($|n| > 2$) conditions.[4]

Second, we examine the effect of continuous wave rf irradiation along the x-axis of the rotating frame for the two-spin system. The total Hamiltonian

$$\mathcal{H} = \Delta\nu_I \hat{I}_z + \Delta\nu_S \hat{S}_z + \nu_1(\hat{I}_x + \hat{S}_x) + \mathcal{H}_D(t) \tag{10}$$

is transformed into the tilted rotating frame (X, Y, Z) by the unitary transformation of

$$U_{TR} = \exp(i\beta_I \hat{I}_y)\exp(i\beta_S \hat{S}_y) \tag{11}$$

where β_X denotes the angle between the z-axis of the rotating frame (i.e., the direction of the static field) and the Z-axis of the tilted rotating frame (i.e., the direction of the effective field) for the X spin. The total spin Hamiltonian in the tilted rotating frame can be given by

$$\begin{aligned}\mathcal{H}^{TR} &= U_{TR}\mathcal{H}U_{TR}^{-1}\\ &= \nu_{eI}\hat{I}_Z + \nu_{eS}\hat{S}_Z + U_{TR}\mathcal{H}_D(t)U_{TR}^{-1}\end{aligned} \tag{12}$$

where ν_{eX} denotes the strength of the effective field for the X spin. This is further transferred into the interaction frame using the following unitary operator

$$U_{\text{eff}}(t) = \exp(i\nu_{eI}\hat{I}_Z t)\exp(i\nu_{eS}\hat{S}_Z t) \tag{13}$$

and the result is

$$\begin{aligned}\mathcal{H}_D^*(t) &= U_{\text{eff}}(t)U_{TR}\mathcal{H}_D(t)U_{TR}^{-1}U_{\text{eff}}^{-1}(t)\\ &= \sum_{n=\pm1,\pm2}\nu_{Dn}[A\hat{I}_Z\hat{S}_Z\exp(-in\nu_R t)\\ &\quad + B[\hat{I}_+\hat{S}_-\exp\{i(n\nu_R + \Delta_{\text{eff}})t\}\\ &\quad + \hat{I}_-\hat{S}_+\exp\{i(n\nu_R - \Delta_{\text{eff}})t\}]\\ &\quad + R[\hat{I}_Z\hat{S}_+\exp\{i(n\nu_R + \nu_{eS})t\}\\ &\quad + \hat{I}_Z\hat{S}_-\exp\{i(n\nu_R - \nu_{eS})t\}]\\ &\quad + S[\hat{I}_+\hat{S}_Z\exp\{i(n\nu_R + \nu_{eI})t\}\\ &\quad + \hat{I}_-\hat{S}_Z\exp\{i(n\nu_R - \nu_{eI})t\}]\\ &\quad + Q[\hat{I}_+\hat{S}_+\exp\{i(n\nu_R + \Sigma_{\text{eff}})t\}\\ &\quad + \hat{I}_-\hat{S}_-\exp\{i(n\nu_R - \Sigma_{\text{eff}})t\}]]\end{aligned} \tag{14}$$

where the coefficients A, B, R, S, and Q are functions of the angle β_X, whose explicit forms are found in Ref.[11]. It can be shown that the spatial part of $\mathcal{H}_D^*(t)$ is modulated by MAS with the spinning frequency ν_R and $2\nu_R$, while the spin part is modulated by the effective field with the frequencies of $\Sigma_{\text{eff}} = \nu_{eI} + \nu_{eS}$, $\Delta_{\text{eff}} = \nu_{eI} - \nu_{eS}$, ν_{eI}, and ν_{eS}. When any of the conditions Σ_{eff}, Δ_{eff}, ν_{eI}, or $\nu_{eS} = m\nu_R$ ($m = \pm1$ or ±2) is met, the time dependence of the spatial part and the spin part in $\mathcal{H}_D^*(t)$ is partially canceled with each other to give a static dipolar interaction $\overline{\mathcal{H}_D}^*$.

3 METHOD

Determination of the 3D structure of a multiply labeled molecule can be accomplished by obtaining all bond lengths, bond angles, and dihedral angles. For a peptide, however, one may use typical bond lengths and angles because they differ only slightly among peptides, and the peptide 3D structure can be constructed by determining dihedral angles.

Figure 1 illustrates the strategy. For a multiply $^{13}C/^{15}N$ labeled peptide, all dipolar interactions are removed uniformly by fast MAS and proton decoupling. Then, a specific three-bonds distant pair of spins is selectively recoupled by applying an rf field satisfying a proper R2TR condition. The time development of the magnetization of either of the paired spins is measured, from which the corresponding dihedral angle is deduced. This procedure is repeated for other spin pairs, until all the dihedral angles are determined.

The pulse sequence for the selective recoupling experiments is shown in Figure 2(a). During the recoupling period (t_m), the rf field satisfying a R2TR condition $\nu_{eI} + \nu_{eS} = \nu_R$ is applied to one of the paired spins concerned. This rf field also functions for spin-locking the magnetization. Then, the t_m dependence of the spin-locked magnetization is monitored after removing the possible small y component of the magnetization by applying a 90°_X pulse. The t_m dependence of the magnetization is also affected by $T_{1\rho}$ relaxation. Measuring $T_{1\rho}$ under the same irradiation condition but with a slightly ($\sim$500 Hz) different spinning frequency so as not to satisfy the DQ R2TR condition, we can remove the relaxation effect from the t_m dependence by multiplying it by $\exp(t_m/T_{1\rho})$.

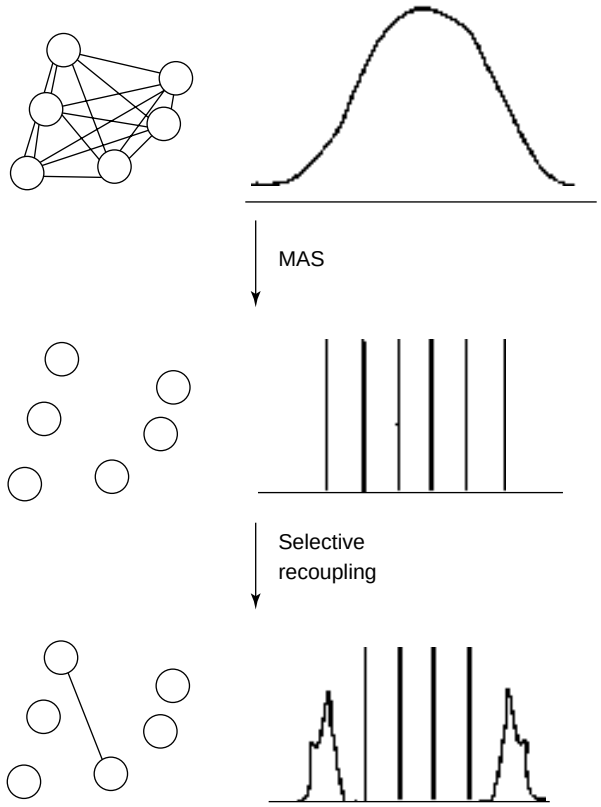

Figure 1 Schematic illustration of uniform decoupling by MAS and selective recoupling

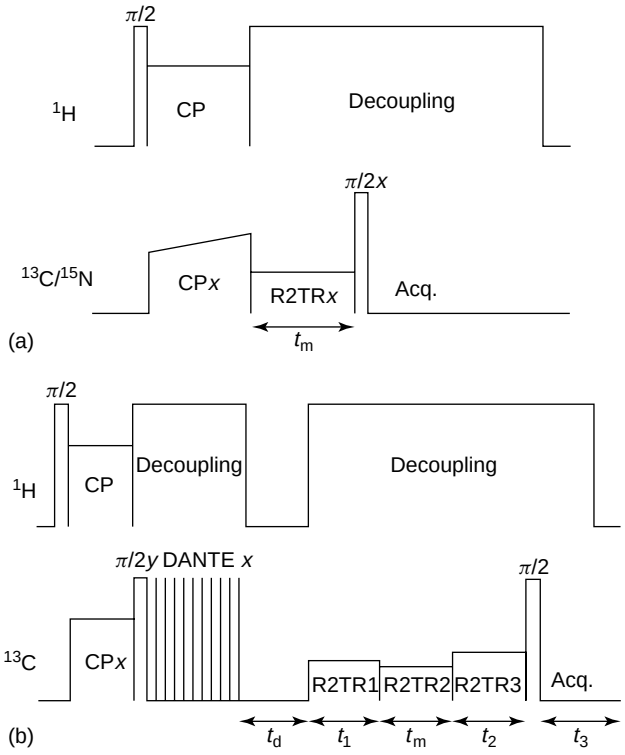

Figure 2 Pulse sequences to determine dihedral angles. (a) Dipolar recoupling experiment. After CP, a rf field satisfying a DQ condition for a particular pair of ^{13}C spins is applied on resonance to one of the spins for a recoupling time t_m. Then, the transverse magnetization of the spin is observed as a function of t_m. (b) 2D dipolar correlation experiment. After CP, the C magnetization in a four ^{13}C spin (A–B–C–D) system is suppressed by a DANTE pulse train. The A–B and the C–D dipolar interactions are selectively recovered in the t_1 and t_2 periods, respectively. These dipolar powder patterns are correlated by transferring magnetization from A or B to C or D in the mixing period. The AB/CD dipolar correlation spectrum is obtained by observing the C magnetization in the detection period t_3. (Reproduced from Nomura et al.[13] with kind permission from Kluwer Academic Publishers)

The other conditions of ZQ, SQ, and DQ ($n > 1$) are not suitable for the present experiments for the following reasons. First, to satisfy a ZQ condition, the chemical shift difference between a specific pair of spins must be larger than ν_R. However, chemical shift differences of ^{13}C or ^{15}N spin pairs at a common magnetic-field intensity are not so large as to satisfy a ZQ condition for ν_R fast enough to completely decouple the other dipolar couplings. Second, under a SQ condition, both chemical shift anisotropies (CSAs) of the relevant carbons are dominantly recovered, obscuring the effect of dipolar recoupling. Last, a DQ condition with $n > 1$, which requires a large rf-field intensity for ν_R fast enough to decouple the other dipolar couplings, lowers the selectivity of recoupling.

The influence of intermolecular dipolar couplings on the dipolar recoupling experiments was reduced by diluting a uniformly labeled sample (10%) with natural abundance material (90%). In the recoupling-time dependence experiments for the 10% uniformly labeled sample, 10% of the signal intensity at $t_m = 0$ was subtracted from the intensity observed at each recoupling time t_m, because it was found that the magnetization of the natural abundance material is kept almost constant during t_m.

An alternative approach to determine a dihedral angle is to measure mutual orientations of two or more anisotropic spin interactions. In the R2TR method, one can easily and quickly switch the dipolar interaction to be recoupled from one to another by changing ν and ν_1 under a constant spinning speed contrary to the normal R^2 method. This makes it possible to realize a 2D experiment which correlates the AB and CD dipolar powder patterns in an A–B–C–D ^{13}C spin system. Figure 2(b) shows the pulse sequence for the 2D dipolar correlation experiment. After cross polarization (CP), the C magnetization is suppressed by a selective 90° (DANTE) pulse followed by a dephasing period (t_d). In the first evolution period (t_1) the AB dipolar interaction is selectively recoupled, in the mixing period the A or B magnetization is selectively transferred to the C or D spin, and in the second evolution period (t_2) the C magnetization evolves under the selectively recoupled CD dipolar interaction. The AB/CD dipolar correlated 2D powder pattern is selectively obtained by observing the C spin in the detection period (t_3).

Recoupling may take place even in off-R2TR conditions to some extent, making the selectivity incomplete. The incompleteness of selectivity can be taken into account by including several spins into simulations in addition to the relevant two spins. To examine selectivity, we studied magnetization transfer in uniformly ^{13}C labeled L-alanine.[11] Figure 3(a) shows the ^{13}C 2D exchange NMR spectrum observed without applying any ^{13}C rf field during a mixing time of 4 ms under a MAS frequency of 5718 Hz. No conventional R^2 effects were observed at this spinning speed. The spectrum in Figure 3(b)

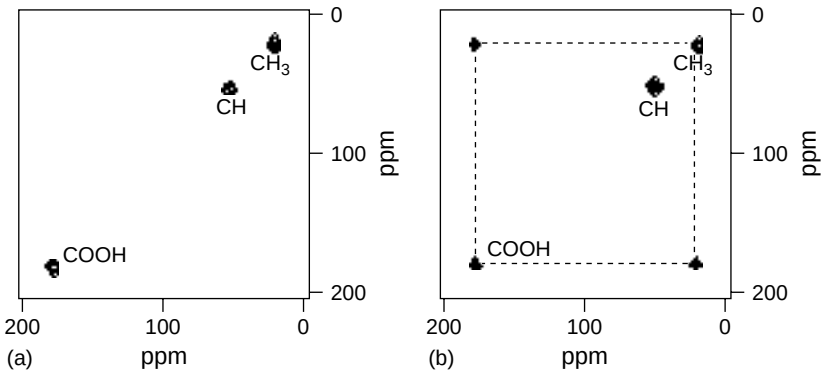

Figure 3 ^{13}C 2D exchange NMR spectra of uniformly ^{13}C labeled L-alanine. It was observed (a) without and (b) with applying a ^{13}C rf field during a mixing time of 4 ms under the MAS frequency of 5718 Hz. The rf field with the intensity of 4 kHz was applied at 296.7 ppm for the spectrum (b) to satisfy a R2TR condition $\Delta_{\text{eff}} = 2\nu_{\text{R}}$ for the carboxyl and the methyl carbons

was obtained at the same spinning speed while applying an rf field with the intensity of 4 kHz during the same mixing time to satisfy the ZQ R2TR condition $\Delta_{\text{eff}} = 2\nu_{\text{R}}$ for the carboxyl and methyl ^{13}C spins. Cross peaks appear between the carboxyl and methyl carbons, but no cross peaks can be seen between the carboxyl and methine carbons or between the methine and methyl carbons. This result confirms that the dipolar interaction between the carboxyl and the methyl carbons can be selectively recovered by the R2TR experiment, in spite of the fact that the recoupled dipolar coupling is below one fourth the other couplings. The stronger couplings remain completely decoupled by MAS.

Figure 4 shows the observed and the calculated mixing-time dependence of the individual ^{13}C magnetizations after saturation of the methyl carbon signal. The initial rapid oscillation of the carboxyl ^{13}C magnetization can be ascribed to the spinning sidebands in the tilted rotating frame,[11] which is damped quickly within a few milliseconds due to rf-field inhomogeneity. Hence, in the following, this oscillation in the simulation was damped to the same extent as the experimental data. Except for this initial oscillation and slight decay due to relaxation, the sum of the ^{13}C magnetizations of the carboxyl and the methyl carbons, $M_{0I} + M_{0S}$, is shown to be conserved. Further, the observed and the calculated curves for the methine carbon in Figure 4(b) again shows that the polarization transfer occurs selectively between the carboxyl and the methyl carbons, and further that a mixing time of 5 ms is enough for the polarization transfer between two carbons separated by 0.25 nm.

Further, to examine how large the chemical shift difference between non-relevant spins should be to achieve high selectivity, several isotropic chemical-shift values were assumed for the methine carbon, keeping its chemical shift anisotropy constant. Figure 5 shows the calculated mixing-time dependence of the methine ^{13}C magnetization for four chemical shift differences between the methyl and the methine carbons: 0, 500, 1000, and 2340 Hz. From Figure 5, it can be concluded that the chemical shift difference should be larger than 1000 Hz for selective transfer, leading to the following practical criteria of spins being added in simulations: For the selective recoupling experiment of A and D in a A–B–C–D ^{13}C system with observing the D magnetization, not only all the four spins, but also the following ^{13}C spin(s), if any: ^{13}C directly bonded to D (A), and ^{13}C within about 0.25 nm from D (A) with the ν_{e} difference between the ^{13}C and A (D) less than 1000 Hz.

4 APPLICATION TO GLYCYLISOLEUCINE

In the following, the complete 3D structure of a glycylisoleucine (Gly-Ile) molecule by R2TR is determined using a powder sample of uniformly ^{13}C,^{15}N-labeled Gly-Ile molecules, including all the positions of carbons, nitrogens, and oxygens in both main and side chains.[12,13] The 3D structure of a Gly-Ile molecule is obtained by measuring the six dihedral angles shown in Figure 6. In this study, ψ_{G}, ω_{G}, ϕ_{I}, χ_{I1}, and χ_{I2} are defined as dihedral angles N_{G}–$\text{C}^{\alpha}_{\text{G}}$–$\text{C}'_{\text{G}}$–$\text{N}_{\text{I}}$, $\text{C}^{\alpha}_{\text{G}}$–$\text{C}'_{\text{G}}$–$\text{N}_{\text{I}}$–$\text{C}^{\alpha}_{\text{I}}$, C'_{G}–N_{I}–$\text{C}^{\alpha}_{\text{I}}$–$\text{C}'_{\text{I}}$, C'_{I}–$\text{C}^{\alpha}_{\text{I}}$–$\text{C}^{\beta}_{\text{I}}$–$\text{C}^{\gamma 1}_{\text{I}}$, and $\text{C}^{\alpha}_{\text{I}}$–$\text{C}^{\beta}_{\text{I}}$–$\text{C}^{\gamma 1}_{\text{I}}$–$\text{C}^{\delta}_{\text{I}}$, respectively, by taking zero degrees for the *cis* conformation. ψ_{I} is defined as the angle between the N_{I}–$\text{C}^{\alpha}_{\text{I}}$ bond and the O^{1}_{I}–C'_{I}–O^{2}_{I} plane, being between 0 and 180°. ψ_{G}, ω_{G}, ϕ_{I}, and χ_{I1} were determined by performing the R2TR dipolar recouping experiment for a proper three or four-bonds distant spin pair, and χ_{I2} by a 2D dipolar correlation experiment because of the reason mentioned later, assuming the typical bond lengths and angles shown in Figure 6. The planar configuration of the peptide plane was also assumed.

Although the CSA interaction was neglected in Theory for simplicity, it does contribute to the results, and should thus be included into numerical calculations. Especially, the contribution of the CSA tensors for carbonyl carbons and amide nitrogens in the main chain are important owing to their large anisotropies (see **Chemical Shift Tensors,** Volume 2). However, the CSA tensors for carbonyl carbons are not very different from peptide to peptide. Hence, the mean values of δ and η for the carbonyl carbon tensors reported for some peptides are adopted (Table 1). For the directions of the principal axes, it is generally observed that the σ_{33} axis is perpendicular to the sp^2 plane.[14] On the other hand, the σ_{22} axis may make a small angle with the C=O bond direction. For C'_{G}, the σ_{33} axis is assumed to be perpendicular to the sp^2 plane and the σ_{22} axis makes the angle of 4.5° with the C'_{G}–O_{G} bond toward the C'_{G}–$\text{C}^{\alpha}_{\text{G}}$ bond.[15] For C'_{I}, the σ_{33} axis is perpendicular to the sp^2 plane and the σ_{11} axis is along the $\text{C}^{\alpha}_{\text{I}}$–$\text{C}'_{\text{I}}$ bond. The δ and η values for N_{I} and N_{G} were

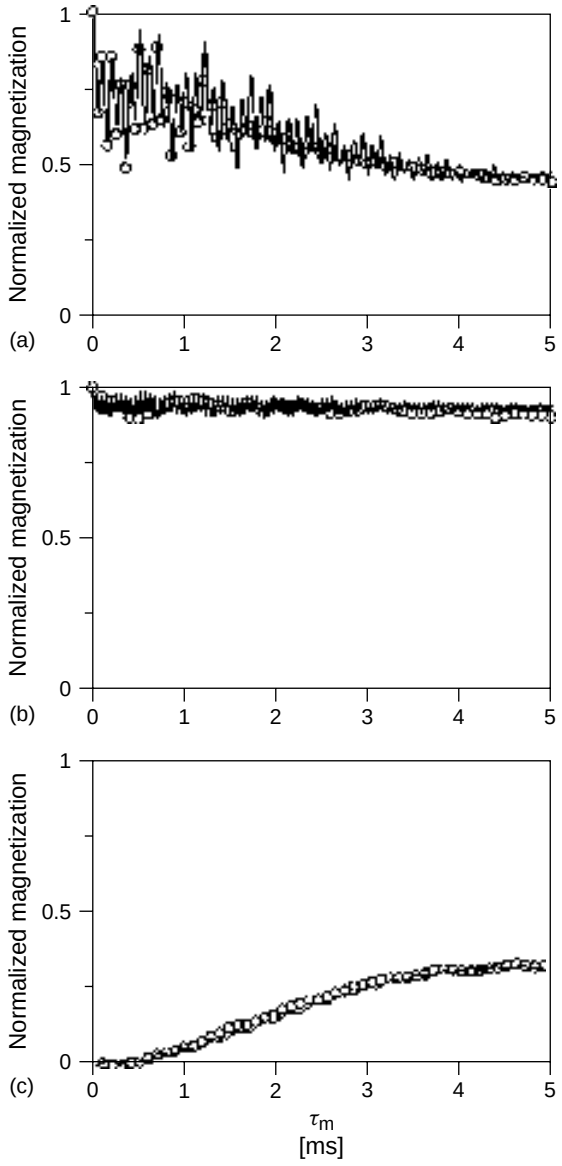

Figure 4 Experimental (○) and simulated (−) mixing-time dependence of the normalized magnetizations of (a) the carboxyl, (b) the methine, and (c) the methyl carbons under the condition $\Delta_{eff} = 2\nu_R$ satisfied between the carboxyl and the methyl carbons after saturation of the methyl carbon signal. The experiments were performed with the same parameters as described in the caption of Figure 3, excluding the initial magnetization for the methyl carbon. (Reproduced from Takegoshi et al.[11] with kind permission from Academic Press)

determined from spinning side bands observed at a low speed. The σ_{22} axis for N_I is assumed to be perpendicular to the peptide plane and the σ_{11} axis is along the N–C=O bond.[16] For N_G, the σ_{33} direction is along the N_G–C_G^α bond direction and the σ_{11} axis is perpendicular to the N_G–C_G^α–C'_G plane.[16] For the aliphatic carbons, it will be shown that the CSA interactions do not significantly affect simulated results. The ^{13}C and ^{15}N chemical shift parameters used for numerical simulations are collected in Table 1.

Figure 7 shows a ^{13}C COSY spectrum observed at $\nu_R = 17.5$ kHz under TPPM decoupling, presenting the connectivity between the observed eight signals (C_1–C_8) splitted by the

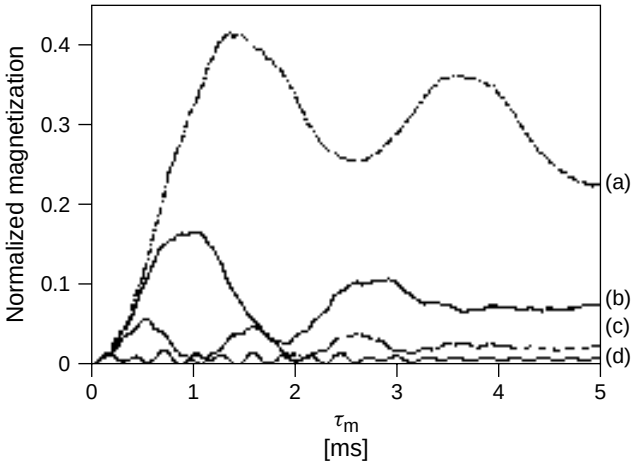

Figure 5 Simulated mixing-time dependence of the methine carbon magnetization under the same conditions as described in the caption of Figure 4, excluding the isotropic chemical shift of the methine carbon. The assumed chemical shift relative to the methyl carbon is: (a) 0 Hz, (b) 500 Hz, (c) 1000 Hz, and (d) 2340 Hz

^{13}C–^{13}C spin−spin couplings. From the connectivity and common knowledge of ^{13}C chemical shifts, all the signals can straightforwardly be assigned as $C_2 = C'_G$, $C_4 = C_G^\alpha$, $C_1 = C'_I$, $C_3 = C_I^\alpha$, $C_5 = C_I^\beta$, $C_6 = C_I^{\gamma 1}$, $C_7 = C_I^{\gamma 2}$, and $C_8 = C_I^\delta$. The observed isotropic chemical shifts are collected in Table 1.

Firstly, determination of the main-chain structure, which is described by dihedral angles conventionally named as ψ, ω, and ϕ (Figure 6), is discussed. ψ_G was determined by the selective-recoupling experiment of N_G and N_I. For the selective recoupling, an rf field with the intensity of 8300 Hz was applied on resonance to N_G, which satisfies a DQ condition under $\nu_R = 17.5$ kHz, and the recoupling-time dependence of the spin-locked magnetization of N_G was observed (Figure 8a). ψ_G was determined to be 180° from the root-mean-square deviation (RMSD) between the experimental data and the curves calculated for various ψ_G (Figure 8b). Let us examine to what extent the assumptions for the chemical shift tensors lead to error for determination of ψ_G. It was found that a deviation of 10° in the σ_{11} direction for N_I from the peptide bond direction to the N–C_α direction hardly changes the simulation curve. The deviation of 10° in the σ_{33} axis for N_G from the C_G^α–N_G bond direction does not change it either. The averages of the CSA parameters of the amide nitrogens[16] in $AcGlyGlyNH_2$, $AcGlyAlaNH_2$, $AcGlyTyrNH_2$, and GlyGly·HCl gives $(\delta, \eta) = (103.2\,\text{ppm}, 0.22)$, which are similar to the observed ones, leads to the same ψ_G value of 180° as above. It should be pointed out, however, that changing the observed CSA parameters of N_I to those for the amide nitrogen in $AcGlyTyrNH_2$ ($(\delta, \eta) = (96.4\,\text{ppm}, 0.26)$) or GlyGly·HCl ($(\delta, \eta) = (101.0\,\text{ppm}, 0.02)$)[16] results in the best-fit values of $\psi_G = \pm 154$ or $\pm 159°$, respectively. Such sensitivity of the recoupling-time dependence to the CSA parameters δ and η would be found particularly around $\psi = 180°$ at which the ^{15}N–^{15}N dipolar interaction becomes the weakest and thus insensitive to the dihedral angle. Nevertheless, the plot of $\Delta\chi^2$ shown in Figure 8(b) indicates that the 68% confidence interval ($\Delta\chi^2 < 1$) is still ±10°. For a better precision, it is desirable to measure the CSA parameters of amide nitrogens and use them in the simulations for determining ψ.

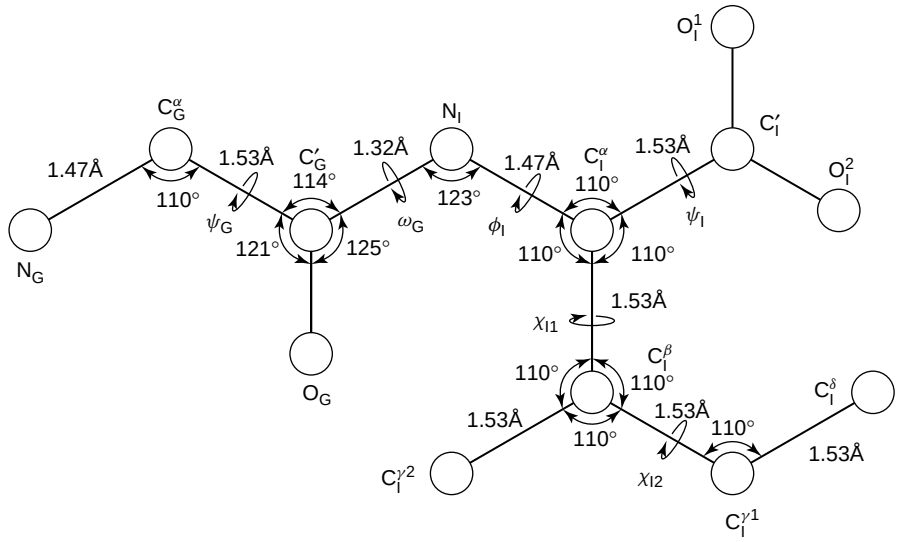

Figure 6 Schematic representation of a glycylisoleucine molecule. Typical values of the bond distances in Å and the bond angles in degrees are shown, which were used to simulate experimental results and construct the three dimensional structure of glycylisoleucine. The glycine carbonyl and C_α carbons are labeled as C'_G and C^α_G, and the isoleucine carboxyl, C_α, C_β, $C_{\gamma 1}$, $C_{\gamma 2}$, C_δ carbons are as C'_I, C^α_I, C^β_I, $C^{\gamma 1}_I$, $C^{\gamma 2}_I$, and C^δ_I, respectively. The glycine amine and the isoleucine amide nitrogens are labeled as N_G and N_I, respectively, and the glycine carbonyl oxygen as O_G, and the two isoleucine carboxyl oxygens as O^1_I and O^2_I. The dihedral angles ϕ_I, ω_G, ψ_G, ψ_I, χ_{I1}, and χ_{I2} are also shown. (Reproduced from Nomura et al.[13] with kind permission from Kluwer Academic Publishers)

Table 1 Chemical shift parameters used for the numerical simulations of the R2TR dipolar recoupling experiments in glycylisoleucine. (Reproduced by permission of Kluwer Academic Publishers from Nomura et al.[13])

	C'_I	C'_G	C^α_I	C^α_G	C^β_I	$C^{\gamma 1}_I$	$C^{\gamma 2}_I$	C^δ_I	N_I	N_G
δ_{iso}[a], ppm	178.9	169.3	64.0	40.3	36.3	26.7	17.0	12.4	120.9	23.1
δ[b], ppm	−71.0[c]	−79.3[d]	−19.7[e]	20.0[f]	6.67[g]	−12.3[h]	–	−13.9[i]	103.0[j]	19.5[j]
η[b]	0.84[c]	0.82[d]	0.44[e]	0.94[f]	0.60[g]	0.58[h]	–	0.32[i]	0.31[j]	0.68[j]

[a] ^{13}C and ^{15}N isotropic chemical shifts were obtained with respect to Me_4Si and liquid NH_3, respectively.
[b] The anisotropy δ and the asymmetry parameter η are defined as $\delta = \delta_{zz} - \delta_{iso}$ and $\eta = (\delta_{yy} - \delta_{xx})/\delta$, where δ_{iso} is the isotropic shift and $|\delta_{yy} - \delta_{iso}| \leq |\delta_{xx} - \delta_{iso}| \leq |\delta_{zz} - \delta_{iso}|$.
[c] Average of the values for the carboxyl carbons in glycine,[17] L-alanine,[18] L-serine,[19] L-threonine,[20] L-asparagine.[20]
[d] Average of the values for the carbonyl carbons in some peptides.[15]
[e] Values for the α carbon in L-alanine.[18]
[f] Values for the α carbon in glycine.[17]
[g] Values for the β carbon in isobutane.[22]
[h] Values for the α-methylene carbon in n-eicosane.[23]
[i] Values for the methyl carbon in n-eicosane.[23]
[j] Determined by the sideband analysis of a low-speed MAS spectrum.

To determine ϕ_I, the selective recoupling experiment was done for C'_G and C'_I, where an rf field with an intensity of 8500 Hz was applied on resonance to the C'_I carbon while spinning with $\nu_R = 17.054$ kHz. Figure 9(a) shows the observed recoupling-time dependence of the magnetization of C'_I. If only the dipolar interaction between C'_G and C'_I contributes to the result, only the absolute value of the dihedral angle ϕ_I can be determined from this experiment. In the present case, however, the large CSAs of both carbons and the relative orientations between the CSA tensors, and some dipolar tensors significantly affect the experimental result. Hence, there may be a good chance of determining not only ϕ_I but also ψ_I with the signs. Since peptide planes take the *trans* configuration except for cyclic peptides or peptides with proline, ω_G was assumed to be 180°. Therefore, the experimental curve was simulated, taking ϕ_I and ψ_I as adjustable parameters.

Figure 9(b) and (c) show the contour plots of RMSD between the experimental data and the curves calculated for various values of (ϕ_I, ψ_I) and $\Delta\chi^2$ around the global minimum of RMSD, respectively. These results provide the best-fit values of $(\phi_I, \psi_I) = (-76°, 147°)$ and the 68% confidence regions ($\Delta\chi^2 \sim 1$) of $(-1° \sim 1°)$ for ϕ_I and $(-9° \sim 6°)$ for ψ_I. Due to the imperfect selectivity of R2TR, C^α_G, C^α_I, and C^β_I in addition to C'_G and C'_I had to be included to best simulate the recoupling curve. This resolves the degeneracy for (ϕ_I, ψ_I) and $(-\phi_I, -\psi_I$ or $180 - \psi_I)$, which occurs if only C'_G and C'_I contribute to the recoupling curve. In fact, the $\Delta\chi^2$ value around $(\phi_I, \psi_I) = (76°, 33°)$ is relatively large (ca. 34). Hence, both ϕ_I and ψ_I could be uniquely determined. It should,

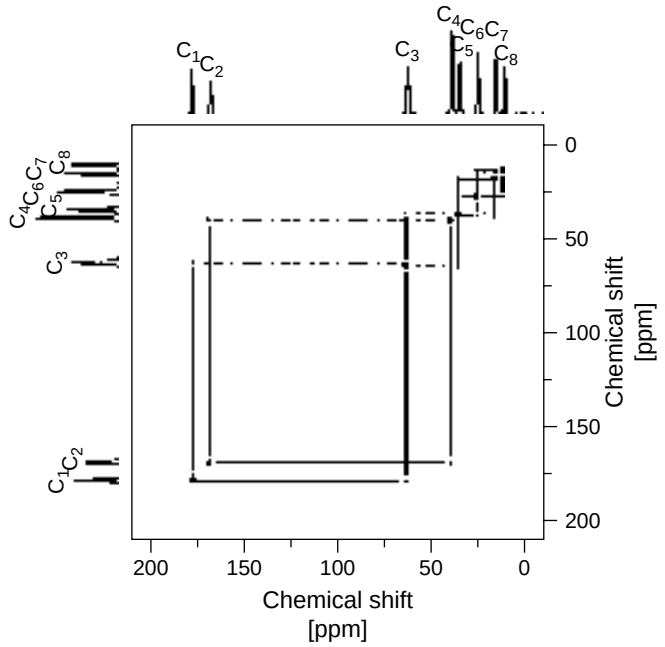

Figure 7 ^{13}C COSY spectrum of uniformly ^{13}C,^{15}N-labeled glycylisoleucine. It was obtained under the spinning speed of 17.5 kHz and TPPM decoupling. (Reproduced from Nomura et al.[13] with kind permission from Kluwer Academic Publishers)

however, be pointed out that ϕ_I is precisely determined but ψ_I is not. This is because the dipolar coupling directly contributes to the determination of ϕ_I, but ψ_I is obtained only through the relative orientation of the C'_I CSA tensor to the other tensors. Therefore, the validity of the use of the CSA tensors assumed for C'_G and C'_I in the above simulations should be examined.

First, as for C'_G, the experimental result was simulated using the CSA parameters and orientations determined for $AcGlyGlyNH_2$, $AcGlyAlaNH_2$, $AcGlyTyrNH_2$, and GlyGly·HCl.[15] The best-fit values of (ϕ_I, ψ_I) do not deviate significantly for the four sets of parameters ($-71° \sim -78°$, $139° \sim 148°$). As for the tensor orientation of C'_I, it was assumed that σ_{11} is parallel to the C^α_I–C'_I bond, while it may deviate from the bond direction by about 10°.[14] It was found that the 10° deviation leads to (ϕ_I, ψ_I) = ($-76°$, 138°). For the CSA parameters (δ, η), the values for glycine,[17] L-alanine,[18] L-serine,[19] L-threonine,[20] and L-asparagine[21] were used to find (ϕ_I, ψ_I) to be ($-75° \sim -76°$, $137° \sim 150°$).

These results show that the use of likely CSA tensors for C'_G and C'_I in the simulations causes only a small error in the determination of ϕ_I, but leads to a considerable error in ψ_I. This is also because the ϕ_I value is directly related to the distance, while the ψ_I value is related mainly to the relative orientations of the CSA tensors, being more sensitive to them. To obtain a more precise value for ψ_I, (δ, η) for C'_I should be measured by some method.

The present result of the recoupling experiment for C'_G and C'_I indicates that one dipolar recoupling experiment per amino acid residue is enough to determine dihedral angles (ψ, ω, ϕ) which provide the 3D backbone structure of a peptide. In the above, however, $\omega_G = 180°$ was assumed, while in cyclic peptides or peptides with proline, ω_G may be 0°. Hence, the possibility of determining whether $\omega_G = 0°$ or 180° was examined. The dotted line in Figure 9(a) shows

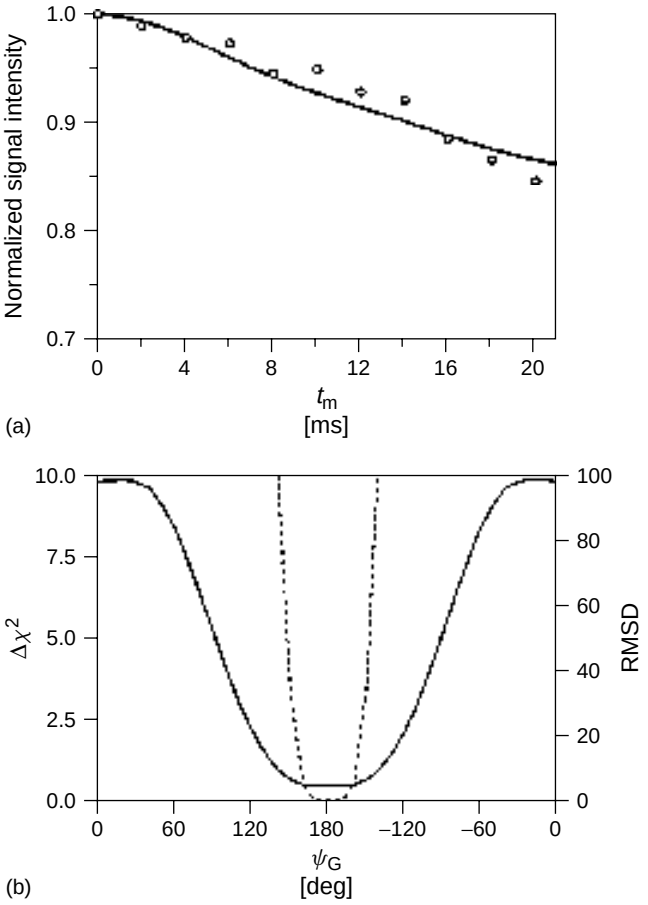

Figure 8 (a) Recoupling-time dependence of the normalized magnetization of N_G in 10% uniformly ^{13}C,^{15}N-labeled glycylisoleucine. The dipolar recoupling experiment was carried out using the pulse sequence in Figure 2(a) under a R2TR condition ($\nu_{eI} + \nu_{eS} = \nu_R$) satisfied for N_G and N_I by applying a rf field with the intensity of 8300 Hz on resonance to N_G under MAS with $\nu_R = 17.5$ kHz. Experimental points are shown by circles. The standard deviation for each point is ca. ±0.05. The curves are calculated for the dihedral angle ψ_G of 180°. $T_{1\rho}$ was determined to be 70 ms by an off-R2TR experiment, and used to remove the relaxation effect from the dipolar recoupling data. (b) Dihedral angle (ψ_G) dependence of RMSD (- - - - -) between the experimental (Figure 8a) and simulated data and of $\Delta\chi^2$ (———). (Reproduced from Nomura et al.[13] with kind permission from Kluwer Academic Publishers)

the curve simulated with $\omega_G = 0°$ and the best-fit values of (ϕ_I, ψ_I) = ($-86°$, 167°), showing that it is difficult to determine the difference between the two possibilities $\omega_G = 0°$ and $\omega_G = 180°$ by this experiment. Therefore, another recoupling experiment was made for C^α_G and C'_I, by applying an rf field with an intensity of 2800 Hz on resonance to the C'_I carbon which satisfies a DQ condition under spinning with $\nu_R = 17.03$ kHz. Figure 10 shows the recoupling-time dependence of the magnetization of C'_I together with the simulated curves obtained for the two sets of (ω_G, ϕ_I, ψ_I), namely, (180°, $-76°$, 147°) and (0°, $-86°$, 167°). Clearly, the former set reproduces the observation as expected. It indicates that even when one does not know whether $\omega = 0°$ or 180°, one can determine the three dihedral angles (ψ, ω, ϕ) by two dipolar recoupling experiments per amino acid residue.

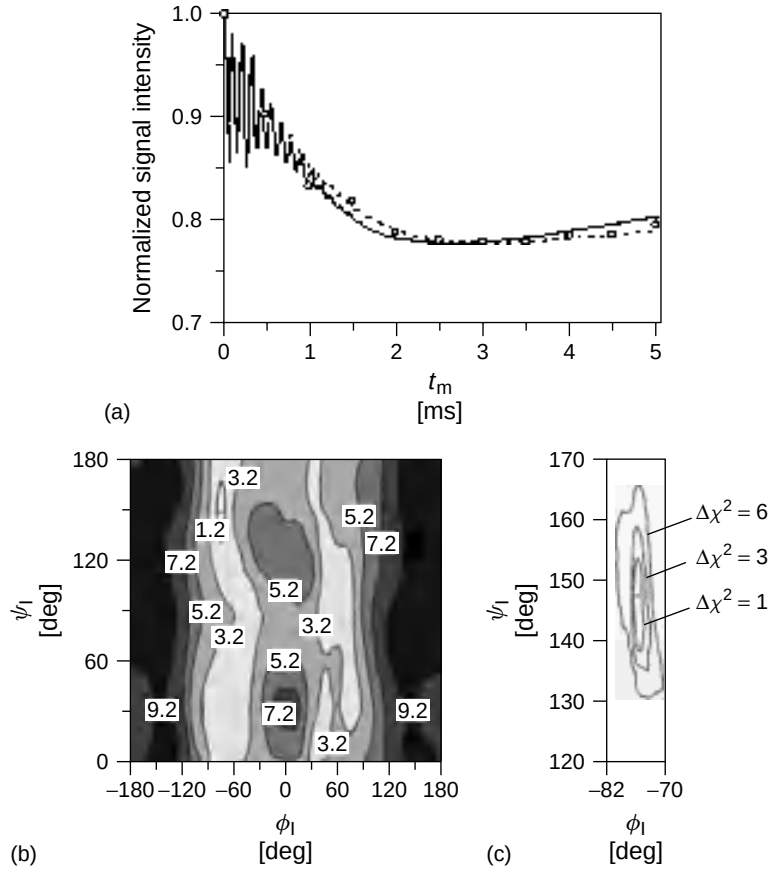

Figure 9 (a) Recoupling-time dependence of the normalized magnetization of C'_I in 10% uniformly ^{13}C,^{15}N-labeled glycylisoleucine. The dipolar recoupling experiment was carried out using the pulse sequence in Figure 2(a) under a R2TR condition ($\nu_{eI} + \nu_{eS} = \nu_R$) satisfied for C'_I and C'_G by applying a rf field with the intensity of 8500 Hz on resonance to the C'_I carbon under MAS with $\nu_R = 17.054$ kHz. Experimental points are shown by circles. The standard deviation for each point is ca. ± 0.03. The solid line is the curve calculated for the dihedral angles (ω_G, ϕ_I, ψ_I) = (180°, −76°, 147°), whereas the dotted line for (ω_G, ϕ_I, ψ_I) = (0°, −86°, 167°). $T_{1\rho}$ was determined to be 500 ms for C'_I in 10% uniformly ^{13}C,^{15}N-labeled glycylisoleucine, and used to correct the experimental data. (b) The contour plot of RMSD between the experimental spectrum (Figure 5a) and the simulations for various sets of (ϕ_I, ψ_I) and $\omega_G = 180°$. The global minimum is indicated by a dot. (c) Dihedral angles (ϕ_I and ψ_I) dependence of $\Delta\chi^2$ for $\omega_G = 180°$. (Reproduced from Nomura et al.[13] with kind permission from Kluwer Academic Publishers)

As exemplified here, the recoupling-time behavior in a general sp^2–sp^2 ^{13}C spin pair depends not only on the internuclear distance, but also on the relative orientations between the CSA tensors and the dipolar vector as well as the CSA parameters. Owing to the dependence caused by CSA, the magnitudes of not only ϕ but also ψ can be determined. Moreover, a few more carbons also contribute to the experimental result due to the incomplete selectivity; however, it provides the benefit of being able to determine the signs of ϕ and ψ. While the contribution of CSA tensors and other spins makes the simulation troublesome and somewhat reduces the accuracy in determination of dihedral angles, it provides information which cannot easily be obtained by other means.

As described above, the dihedral angles for the main chain were determined. The dihedral angles for the side chain in the isoleucine residue can also be determined in a similar manner. However, since their chemical-shift values are very similar to each other and moreover the atomic positions are close to each other, selective recoupling of one of these pairs is indeed difficult. In this sense, the isoleucine residue is one of the most demanding ones for the present approach.

The χ_{I1} angle was obtained by selective dipolar recoupling between C'_I and $C_I^{\gamma 1}$, which was attained by applying a rf field with the intensity of 2000 Hz on resonance to the C'_I carbon under MAS with $\nu_R = 17.46$ kHz. In the simulation, C_I^{α}, C_I^{β}, and C_I^{δ} besides C'_I and $C_I^{\gamma 1}$ were included, and χ_{I1} was determined to be 178°. The effect of the chemical shift tensors of C'_I on the χ_{I1} value were examined using the literature (δ, η) values of C′ in L-alanine, L-serine, L-threonine, and L-asparagine, and it was found that the best-fit values of χ_{I1} are virtually unaffected (175° ∼ 178°). Also, changing the CSA parameters for $C_I^{\gamma 1}$ to those determined for the α-methylene carbon of *n*-eicosane[23] provides essentially the same value of $\chi_{I1} = -176°$.

As exemplified by the present case, in a general sp^3–sp^2 ^{13}C spin pair, possible variations of the parameters and orientations of their CSA tensors barely affects the recoupling-time dependence. Thus, likely CSA parameters (δ, η) and tensor orientations for both carbons may be used safely.

To determine the χ_{I2} angle in the same way as above, it is necessary to selectively recouple C_I^{α} and C_I^{δ}, or $C_I^{\gamma 2}$ and C_I^{δ}. Due to the spectral congestion, it is difficult to find a R2TR

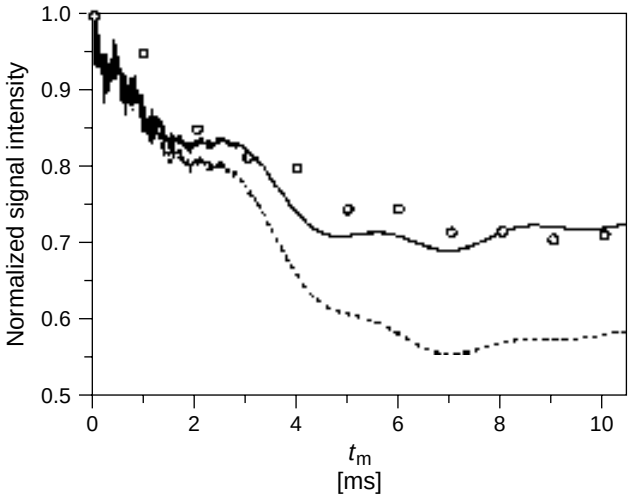

Figure 10 Recoupling-time dependence of the normalized magnetization of C'_I in 10% uniformly ^{13}C,^{15}N-labeled glycylisoleucine. The dipolar recoupling experiment was carried out using the pulse sequence in Figure 2(a) under a R2TR condition ($\nu_{eI} + \nu_{eS} = \nu_R$) satisfied for C'_I and C^{α}_G by applying a rf field with the intensity of 2800 Hz on resonance to the C'_I carbon under MAS with $\nu_R = 17.03$ kHz. Experimental points are shown by circles. The standard deviation for each point is ca. ± 0.04. The solid line is the curve calculated for the dihedral angles (ω_G, ϕ_I, ψ_I) = (180°, −76°, 147°), whereas the dotted line for (ω_G, ϕ_I, ψ_I) = (0°, −86°, 167°). $T_{1\rho}$ was determined to be 500 ms for C'_I in 10% ^{13}C,^{15}N-labeled glycylisoleucine, and used to correct the experimental data. (Reproduced from Nomura et al.[13] with kind permission from Kluwer Academic Publishers)

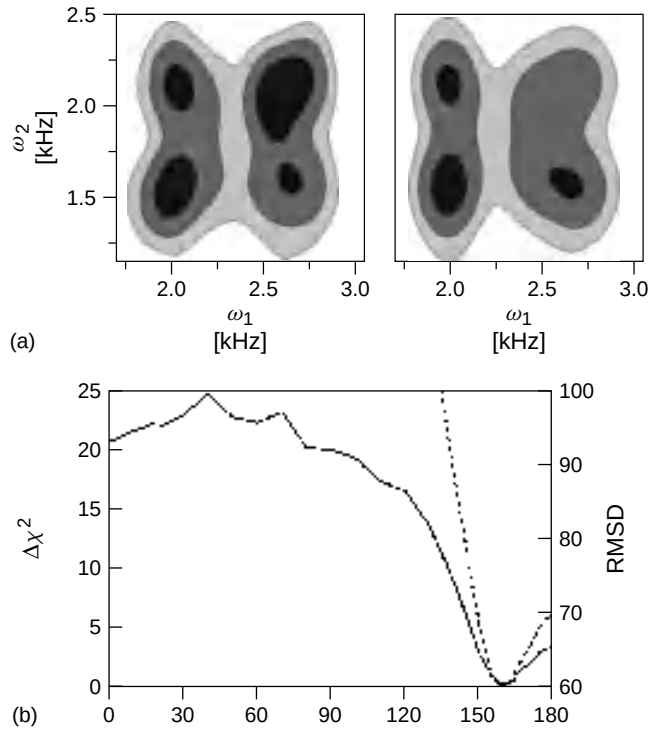

Figure 11 (a) The 2D C^{α}_I–C^{δ}_I/$C^{\gamma 2}_I$–C^{δ}_I dipolar correlation spectrum for uniformly ^{13}C,^{15}N-labeled glycylisoleucine. The experiment was performed using the pulse sequence in Figure 2(b). The spinning frequency ν_R is 5110 Hz. The ^{13}C rf-field intensities during the t_1 period, the mixing time, and the t_2 period are $\nu_1 = 2540$ (on resonance to the C^{δ}_I carbon), 0, and 1825 Hz (on resonance to the C^{α}_I carbon), respectively. (left) Experimental 2D spectrum. (right) Simulated 2D spectrum calculated for the $C^{\gamma 1}_I$–C^{δ}_I distance of 1.62 Å and the dihedral angle χ_{I2} of 160°. The contour lines are plotted at 65, 77, and 88% of the maximum intensity. (b) Dihedral angle (χ_{I2}) dependence of RMSD (- - - - -) between the experimental (Figure 11a) and simulated 2D dipolar correlation spectra and of $\Delta\chi^2$ (———). (Reproduced from Nomura et al.[13] with kind permission from Kluwer Academic Publishers)

condition suitable for these pairs. Therefore, a C^{α}_I–C^{β}_I/$C^{\gamma 1}_I$–C^{δ}_I dipolar correlation 2D powder pattern was observed using the sequence shown in Figure 2(b). In this experiment, a 100% uniformly labeled sample was used for obtaining a high signal-to-noise ratio. The use of the undiluted sample is justified, because the dipolar interactions recoupled in the t_1 and t_2 periods are of directly bonded ones, and thus much stronger than the intermolecular dipolar interactions.

The spinning speed ν_R was set to 5110 Hz, satisfying the R^2 condition for C^{δ}_I and C^{α}_I. In the t_1 period, a DQ condition is matched for $C^{\gamma 1}_I$ and C^{δ}_I by applying an rf field with an intensity of 2540 Hz on resonance to C^{δ}_I. During the mixing time t_m, the magnetization of C^{δ}_I is selectively transferred to C^{α}_I by R^2. In the t_2 period, a DQ condition is fulfilled for C^{α}_I and C^{β}_I by applying an rf field with an intensity of 1825 Hz on resonance to C^{α}_I. Figure 11(a) compares the experimental and the simulated 2D spectra, while Figure 11(b) shows the χ_{I2} dependence of RMSD between the experimental and calculated 2D spectra. Even though the agreement is not excellent, the $\Delta\chi^2$ plot in Figure 11(b) shows that the 68% confidence interval is ±5°, and χ_{I2} was determined to be 160°. The sign of χ_{I2} cannot be determined from this experiment. The dihedral angle ($C^{\gamma 2}_I$–C^{β}_I–$C^{\gamma 1}_I$–C^{δ}_I) was calculated to be 39° from $\chi_{I2} = -160°$, and to be 79° from $\chi_{I2} = 160°$; it suggests that the steric hindrance between the two methyl groups is smaller for the latter case. Therefore, the positive sign was preferred.

In the simulation, $C^{\gamma 2}_I$ in addition to C^{α}_I, C^{β}_I, $C^{\gamma 1}_I$, and C^{δ}_I were included, and a somewhat long $C^{\gamma 1}_I$–C^{δ}_I bond length of 1.62 Å had to be assumed for the best fitting. This unusual bond length was attributed to a thermal vibration of C^{δ}_I. It is worthy to be noted that with the existence of molecular motion, dihedral angles cannot be correctly determined from distance measurements. However, in a theoretical study of vibrational effects,[24] it has been proved that the dipolar 2D powder patterns provide correct dihedral angles even under the presence of molecular vibrations as long as the asymmetry of the vibration is negligible. It is a common problem for various methods of structure determination that we must pay attention to the presence of local motion.

In these simulations, chemical shift anisotropies are not included, but it was found that even if likely chemical shift tensors are included, the spectrum does not appreciably change, under the MAS frequency of ∼5 kHz. This is fortunate, because the CSA tensors of sp^3 carbons depend heavily on circumstances, so that it is very difficult to assume them appropriately for simulations. For a directly bonded sp^3–sp^3 ^{13}C spin pair, the effect of CSAs can indeed be neglected in comparison with the contribution of the dipolar coupling under MAS with a spinning speed a few times faster than $|\delta|$, according to

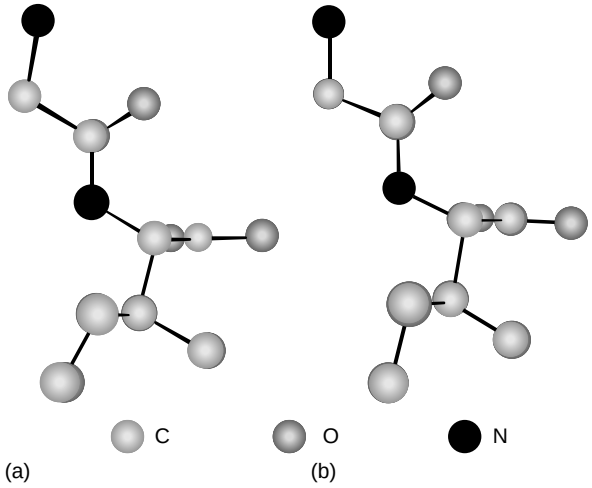

Figure 12 Three dimensional structure of glycylisoleucine. (a) NMR study; (b) X-ray crystallography. (Reproduced from Nomura et al.[13] with kind permission from Kluwer Academic Publishers)

our simulations. On the other hand, for a nonbonded, namely weakly dipolar coupled sp^3-sp^3 ^{13}C spin pair, the effect of the CSAs becomes more important than for a directly bonded pair. Therefore, the CSA effect must be reduced for accurate determination of dihedral angles by using a sufficiently fast spinning speed. Then large ν_1 is needed for satisfying a DQ recoupling condition, so that selectivity is declined. Therefore, when some other sp^3 carbons exist close to the relevant carbons, the dipolar recoupling experiment (Figure 2a) does not work well, and the 2D dipolar correlation experiment (Figure 2b) is recommended.

Figure 12 shows the 3D structure constructed from the dihedral angles determined by the R2TR experiments, and that determined by X-ray crystallography. The dihedral angles determined by NMR and X-ray are (ψ_G, ω_G, ϕ_I, ψ_I, χ_{I1}, χ_{I2}) = (180°, 180°, −76°, 147°, 178°, 160°) and (165°, 170°, −70°, 156°, 178°, 170°), respectively. Although of course the result by NMR includes errors, we note that the structure determined by X-ray diffraction is not very accurate either. Nevertheless, both structures are in good agreement, indicating that the present approach is useful for structure determination. Further, the X-ray diffraction showed that the thermal vibration parameters of C_I^{δ} are very large, agreeing with our observation by NMR.

5 CONCLUDING REMARKS

The complete 3D structure of a uniformly ^{13}C,^{15}N-labeled Gly-Ile molecule were determined using the R2TR method. All the dihedral angles were individually determined by selectively recoupling some dipolar interactions between three or four-bonds distant spins or observing a dipolar correlation 2D powder pattern. Choosing three adjustable parameters ν_1, ν_0, and ν_R properly, it was possible to find a R2TR condition suitable for selective recoupling of the pair of spins concerned. Furthermore, it is not always necessary that all resonances are resolved; it is possible to monitor the recoupling-time dependence if only one of the pair of the spins concerned is resolved well from the others.

The present approach can be applied to determine the 3D structure of a small molecule and also the structure of a restricted region important to the biological function of a large system using a sample in which the region is uniformly or multiply labeled. So far quantitative structural information obtained by solid state NMR has been almost limited to a single internuclear distance or dihedral angle. The present approach increases the obtainable quantity of structural information in a single powder sample.

6 REFERENCES

1. E. R. Andrew, S. Clough, L. F. Farnell, T. D. Gledhill, and I. Roberts, *Phys. Lett.*, 1966, **21**, 505.
2. D. P. Raleigh, G. S. Harbison, T. G. Neiss, J. E. Roberts, and R. G. Griffin, *Chem. Phys. Lett.*, 1987, **138**, 285.
3. B. H. Meier and W. L. Earl, *J. Am. Chem. Soc.*, 1987, **109**, 7937.
4. M. G. Colombo, B. H. Meier, and R. R. Ernst, *Chem. Phys. Lett.*, 1988, **146**, 189.
5. A. Kubo and C. A. McDowell, *J. Chem. Soc. Faraday Trans.*, 1988, **84**, 3713.
6. W. E. J. R. Maas and W. S. Veeman, *Chem. Phys. Lett.*, 1988, **149**, 170.
7. T. Nakai and C. A. McDowell, *J. Chem. Phys.*, 1992, **96**, 3452.
8. T. Nakai and C. A. McDowell, *Mol. Phys.*, 1996, **88**, 1263.
9. S. O. Smith, in 'Encyclopedia of NMR', eds D. M. Grant and R. K. Harris, Wiley: Chichester, 1996, Vol. 7, p. 4185.
10. K. Takegoshi, K. Nomura, and T. Terao, *Chem. Phys. Lett.*, 1995, **232**, 424.
11. K. Takegoshi, K. Nomura, and T. Terao, *J. Magn. Reson.*, 1997, **127**, 206.
12. K. Nomura, K. Takegoshi, T. Terao, K. Uchida, and M. Kaisnosho, *J. Am. Chem. Soc.*, 1999, **121**, 4064.
13. K. Nomura, K. Takegoshi, T. Terao, K. Uchida, and M. Kaisnosho, *J. Biol. NMR*, 2000, **17**, 111.
14. W. S. Veeman, *Prog. Nucl. Magn. Reson. Spectrosc.*, 1984, **16**, 193.
15. T. G. Oas, C. J. Hartzell, T. J. McMahon, G. P. Drobny, and F. W. Dahlquist, *J. Am. Chem. Soc.*, 1987, **109**, 5956.
16. T. G. Oas, C. J. Hartzell, F. W. Dahlquist, and G. P. Drobny, *J. Am. Chem. Soc.*, 1987, **109**, 5962.
17. R. A. Haberkorn, R. E. Stark, H. van Willigen, and R. G. Griffin, *J. Am. Chem. Soc.*, 1981, **103**, 2534.
18. A. Naito, S. Ganapathy, K. Akasaka, and C. A. McDowell, *J. Chem. Phys.*, 1981, **74**, 3190.
19. A. Naito, S. Ganapathy, P. Raghunathan, and C. A. McDowell, *J. Chem. Phys.*, 1983, **79**, 4173.
20. N. Janes, S. Ganapathy, and E. Oldfield, *J. Magn. Reson.*, 1983, **54**, 111.
21. A. Naito and C. A. McDowell, *J. Chem. Phys.*, 1984, **81**, 4795.
22. J. C. Facelli, A. M. Orendt, M. S. Solum, G. Depke, D. M. Grant, and J. Michl, *J. Am. Chem. Soc.*, 1986, **108**, 4268.
23. D. L. VanderHart, *J. Chem. Phys.*, 1976, **64**, 830.
24. Y. Ishii, T. Terao, and S. Hayashi, *J. Chem. Phys.*, 1997, **107**, 2760.

Biographical Sketches

K. Takegoshi, *b* 1956. B.Sc., 1979, Ph.D., 1984, Chemistry, Kyoto University, Japan. Postdoctoral Fellow at University of British Columbia (Canada) 1984–1986 and at University of California (Berkeley, USA) 1986–1987. Staff scientist at Foundation of Material Science and Technology of Japan 1987–1988. Assistant Professor at Hokkaido University 1988–1993. Associate Professor at Kyoto University 1993-present.

Takehiko Terao, *b* 1941. B.Sc., 1966, Ph.D., 1973, Physics, Kyoto University, Japan, where he was introduced to NMR by Tsuneo Hashi. Faculty of Science, Kyoto Sangyou University, 1971–75. Department of Chemistry, Graduate School of Science, Kyoto University, 1975-present. Research speciality: solid state NMR and its applications to chemistry and biology.

Through-Bond Experiments in Solids

Dimitris Sakellariou and Lyndon Emsley

Laboratoire de Stéréochimie et des Interactions Moléculaires, Ecole Normale Supérieure de Lyon, Lyon, France

1 Introduction 1
2 Using Homonuclear *J* Couplings 1
3 Using Heteronuclear *J* Couplings 6
4 Related Articles in Volumes 1–8 15
5 References 15

1 INTRODUCTION

In modern solid-state NMR, resolution and sensitivity can be enhanced by means of cross polarization (CP) (see **Cross Polarization in Solids,** Volume 3, **Cross Polarization in Rotating Solids: Spin-1/2 Nuclei,** Volume 3), spin decoupling (see **Line Narrowing Methods in Solids,** Volume 4) and magic angle spinning (MAS) (see **Magic Angle Spinning,** Volume 5). Spectra of either crystalline or amorphous samples can be recorded. The assignment of these spectra is usually performed on the basis of chemical shift considerations in conjunction with multidimensional correlation experiments relying mostly on the use of dipolar couplings.

Due to their large size, dipolar couplings are the obvious interaction to use in solid-state NMR in order to perform coherence transfer and thus correlate nuclei. Thus, a large number of methods have been developed in order to reintroduce heteronuclear or homonuclear dipolar couplings under magic angle spinning (see **Homonuclear Recoupling Schemes in MAS NMR,** Volume 4). Since dipolar coupling is a through-space interaction, these methods yield information about short and long range distances. In liquids, analogous experiments using the nuclear Overhauser effect (NOE) (see **Nuclear Overhauser Effect,** Volume 5) are the basic components for molecular structure determination (see **Protein Structures: Relaxation Matrix Refinement,** Volume 6).

In this entry we present an overview of techniques analogous in many respects to some liquid-state NMR techniques (see **Polarization Transfer Experiments via Scalar Coupling in Liquids,** Volume 6), which make use of *scalar* couplings in solid-state NMR. Until the end of the 1990s, only highly mobile solids, such as plastic crystals, yielded spectra with enough resolution to observe directly scalar couplings.[1,2] In such compounds, the dipolar couplings are partially averaged, and the *J* couplings are naturally resolved; thus, liquid-like sequences perform reasonably well. On the other hand, in more ordinary organic compounds, where motion is reduced, the strong dipolar couplings (say 20 kHz) hide the much smaller *J* couplings (say 100 Hz).

As we show in the following, improvements in magic angle spinning and spin decoupling techniques[3–6] have led to reduced intrinsic linewidths, thereby making it possible to resolve homonuclear and heteronuclear scalar couplings. Under such conditions, techniques using scalar couplings have great potential for unambiguous spectral assignment, since the coherence transfer is performed by means of a through-bond interaction, and not through-space. Indeed, as in liquid-state NMR,[7] an ideal approach to structure determination exploits the complementarity of through-space and through-bond interactions by using through-bond techniques to establish an unambiguous assignment of the NMR spectra before using through-space interactions to determine three-dimensional structure (see **Biological Macromolecules: Structure Determination in Solution,** Volume 2) and dynamics (see Figure 1).

2 USING HOMONUCLEAR *J* COUPLINGS

For the moment $^{1}H–^{1}H$ *J* couplings (∼10 Hz) are too small compared to residual linewidths (at best ∼100 Hz) to be exploited to obtain correlations. However, homonuclear *J* couplings of nuclei such as ^{13}C, ^{31}P and ^{29}Si are large enough to be observed, and in this section we discuss experiments which make use of them.

2.1 ^{13}C Homonuclear Scalar Couplings

Because of the low (1.1%) natural abundance of ^{13}C, sensitivity is the primary problem when trying to observe carbon–carbon *J* couplings. There are some examples where experiments were successfully performed on natural abundance samples, but in general the techniques discussed below are aimed at (partially or fully) carbon-13 enriched samples. The size of the ^{1}J coupling constants between directly bonded nuclei, which depends on the hybridization of the carbon orbitals and on the nature of the substituents, is usually found

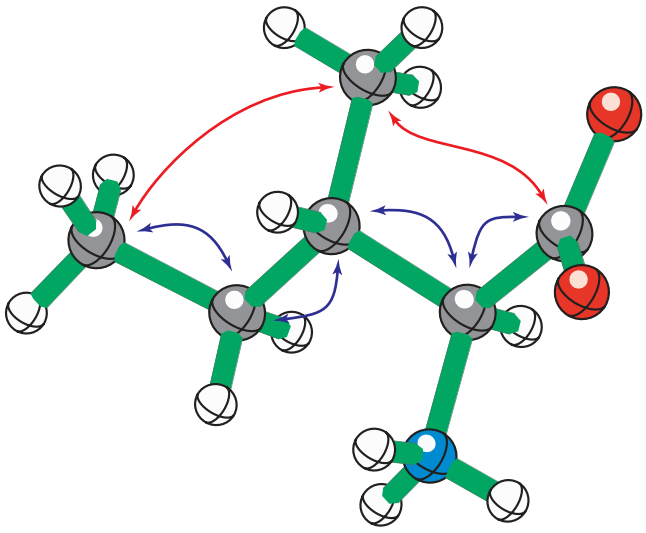

Figure 1 Through-bond correlations are necessary to assign the spectrum. Through-space correlations are used to establish the three-dimensional structure

between 35 and 75 Hz. ^2J and ^3J coupling constants are much smaller, typically between 0 and 5 Hz in liquids. The J coupling is thus usually approximately 40 times smaller than the dipolar coupling between two carbon nuclei (see **Dipolar & Indirect Coupling Tensors in Solids,** Volume 3).

2.1.1 *INADEQUATE*

The most straightforward approach to obtaining carbon–carbon through-bond connectivities is by using an INADEQUATE experiment adapted for solids. The liquid-state version of this experiment was first proposed by Bax, Freeman and co-workers[8,9] (see **INADEQUATE Experiment,** Volume 4). The INADEQUATE experiment selects only carbons that are directly bonded and filters any signals coming from isolated carbon nuclei (such as most of the natural abundance signal) The equivalent solid-state sequence is presented in Figure 2(a). Apart from the cross polarization period, and the fact that the sample is spinning at the magic angle, the experiment is completely analogous to its liquid-state cousin. After cross polarization from ^{1}H, the ^{13}C magnetization evolves during the delay 2τ under the homonuclear J coupling Hamiltonian

$$\mathcal{H} = \pi \sum_{i<j} J_{ij} 2I_{iz} I_{jz} \tag{1}$$

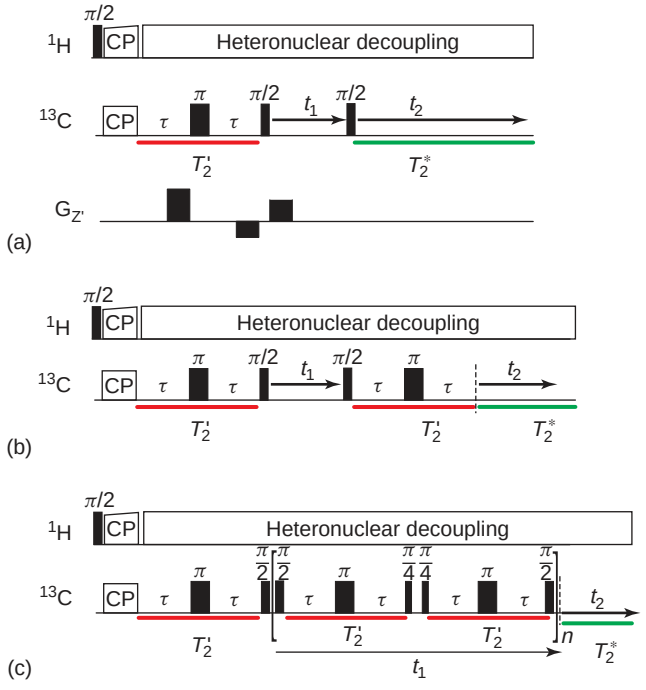

Figure 2 (a) The solid-state INADEQUATE pulse sequence. A 32 step phase cycle can be used, or alternatively the coherence transfer pathway can be selected using gradients. (b) Pulse sequence for solid-state refocused INADEQUATE. An extra Hahn echo period is added in order to refocus the signal after t_1. The τ delay should be synchronized to be an integral number of rotor periods. By T_2' and T_2^* we note the effective and the apparent damping time constants during the $\tau-\pi-\tau$ and the acquisition periods. (c) Pulse sequence for INADEQUATE-ce (see text for details)

Here we assumed that the chemical shift differences between the carbon nuclei are larger than the homonuclear J couplings, and thus only the truncated part of the Hamiltonian is effective. This is because the averaging of the chemical shift occurs over larger time scales than in the TOBSY scheme we analyze later.

The carbon–carbon homonuclear dipolar interactions, together with any anisotropies (chemical shift, or even J), are removed by fast MAS, and the isotropic chemical shift is refocused by the π pulse. The τ delay should be synchronized to be an integral number of rotor periods in order to average out completely the homonuclear carbon dipolar couplings. The heteronuclear dipolar and scalar interactions are averaged out by heteronuclear dipolar decoupling schemes, usually continuous wave (CW) decoupling, or the more efficient two-pulse phase modulation (TPPM) decoupling.[3] The solid-state INADEQUATE experiment is particularly simple to implement, and can be performed at high spinning frequencies.

The double quantum coherence created by the first carbon 90° pulse evolves during t_1, at a frequency which is the sum of the single-quantum frequencies of the two spins

$$\omega_{\mathrm{DQ}} = \omega_{\mathrm{SQ}}^A + \omega_{\mathrm{SQ}}^B \tag{2}$$

and is converted back into antiphase coherence by the last 90° pulse. This sequence leads to anti-phase lineshapes which were previously considered to be impractical in ordinary solids due to the residual linewidth. Nevertheless, such experiments were shown to be practical on plastic crystals[10,11] where the linewidth is only a few hertz, and, more recently, on *crystalline* organic compounds[12] where the linewidth in the one-dimensional carbon spectrum is comparable to the size of the scalar couplings.

The INADEQUATE experiment has been successfully applied to small molecules,[12] and an example of a two-dimensional spectrum is shown in Figure 3. Using fully labeled samples leads to a very good signal to noise ratio and, in this particular case, gradients were used to select the coherence transfer pathway in order to reduce the total experimental time (the spectrum was acquired with 10 mg of sample in 13 min). From the two-dimensional map, the atomic connectivity can be traced throughout the carbon skeleton in an unambiguous way. This experiment is sufficiently sensitive to obtain a spectrum of a powdered sample of *natural abundance* L-alanine with good signal to noise ratio over a weekend.[12]

Linewidths in *amorphous* solids can be much larger (hundreds of hertz) than those for the examples above and one might think that this would compromise the performance of the INADEQUATE experiment. However, the linewidth in solids arises from several different sources,[13] such as:

- the degree of crystallinity of the sample, which yields a more or less broad chemical shift distribution;
- the local magnetic field inhomogeneity (B_0 inhomogeneity, magnetic susceptibility effects . . .);
- dipolar couplings and higher order cross terms with chemical shift anisotropy (CSA) unaveraged by MAS;
- the incoherent effects of stochastically fluctuating local fields that yield T_2 relaxation.

These contributions can be divided into two categories depending on whether they are inhomogeneous or homogeneous.[14] Inhomogeneously broadened lineshapes, resulting from such

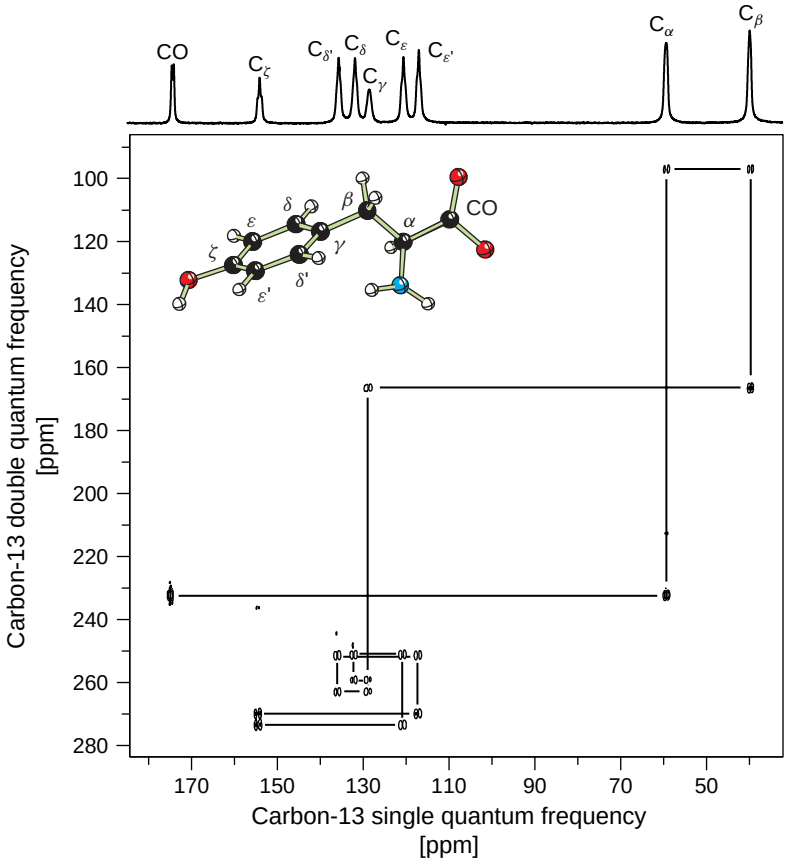

Figure 3 Two-dimensional INADEQUATE spectrum of a fully ^{13}C labeled sample of L-tyrosine hydrochloride. The one-dimensional carbon spectrum is also shown. The spinning frequency was 20 kHz and the decoupling radio-frequency field strength was 120 kHz. Starting from the carbonyl carbon, we can trace out the whole carbon skeleton of the molecule, yielding an unambiguous assignment of the carbon backbone of the molecule. This spectrum was obtained by Dr S. Steuernagel (Bruker Analytik Germany) and is reproduced from Ref.[50] with permission. A 10-mg sample was used and the coherence transfer pathway was selected using gradients (shown in Figure 2a) and led to an experimental time of 13 mins

mechanisms as chemical shift distributions or field inhomogeneity, consist of a continuum of independent lines that can be manipulated individually whereas homogeneously broadened lines due to multispin dipolar couplings or T_2 relaxation, react to pulses as an indivisible entity. The refocused INADEQUATE sequence in Figure 2(b) can be applied successfully to disordered samples since it leads to in-phase lineshapes due to the last $\tau - \pi - \tau$ refocusing period.[15] Assuming a short apparent relaxation time T_2^*, deduced from the linewidth, the efficiency of the refocused INADEQUATE experiment depends on the ratio T_2'/T_2^*, where T_2' is the transverse dephasing time measured in a spin echo experiment. We show where these respective damping constants are 'active' during the experiment in Figure 2. Another approach using composite refocusing (INADEQUATE-CR) was also introduced.[16] The magnetization in this experiment is channeled into one line of the J structure (α or β) and this leads to single absorptive peaks. The pulse sequence is shown in Figure 2(c). As in the refocused INADEQUATE experiment, in the case of broad peaks, the efficiency of INADEQUATE-CR depends on the ratio between the homogeneous and the inhomogeneous linewidth.

Figure 4 shows the refocused INADEQUATE spectrum of a sample of 10% randomly carbon-13 labeled purified cellulose recorded in a total experiment time of 16 h (250 mg of sample). As pointed out previously, in the two-dimensional map two directly bonded carbons share a common frequency in the double quantum dimension, and, provided that one carbon resonance can be identified a priori, assignment is quite straightforward. The cellulose spectrum contains resonances which have already been identified in previous studies, mainly by comparison with liquid spectra, and more recently by two-dimensional NMR.[17,18] The assignment shown in Figure 4 differs from the ones obtained using spin diffusion experiments, i.e., dipolar interactions, which underlines the fact that data from dipolar correlation techniques must be interpreted with caution as they may yield incorrect assignments.

2.1.2 TOBSY

The INADEQUATE experiment in solids can be considered to play the role of COSY in liquids, by establishing one-bond connectivities. In liquids, COSY is often complemented by TOCSY, which correlates all the spins in a coupled spin system with each other. Originally proposed in the liquid state by Braunschweiler and Ernst,[19] this experiment has been used extensively in liquids, together with COSY, INADEQUATE and NOESY, to provide assignment information for organic and biological molecules. Recently a solid-state version named TOBSY (for Total Through Bond Spectroscopy)

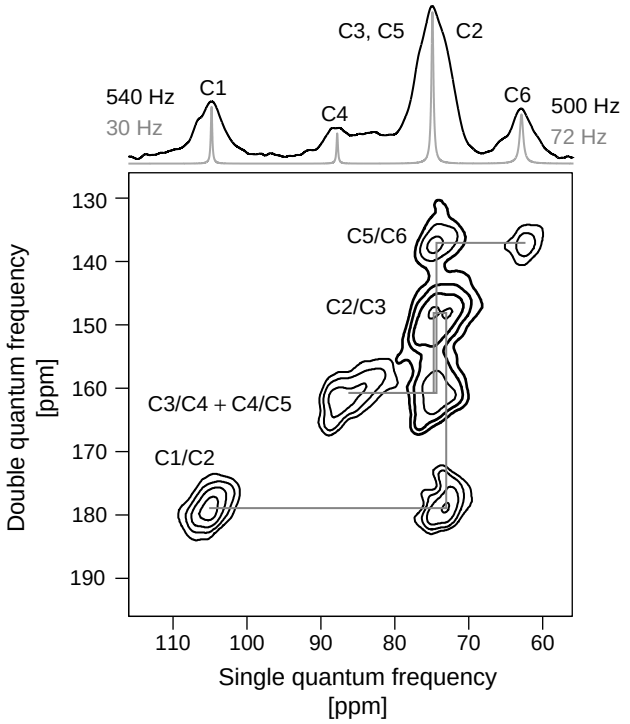

Figure 4 Two-dimensional refocused INADEQUATE spectrum of cellulose. The spectrum was obtained at 125 MHz on a Bruker DSX 500 spectrometer using a 7-mm double-tuned MAS probe. A total of 100 t_1 increments with 192 scans each were collected. The τ delay was set to 3 ms, and the contact time for cross polarization to 500 ms. The spinning speed was 6 kHz and the proton decoupling field strength was 100 kHz using continuous wave decoupling. The various connectivities between the directly bonded carbons are indicated by solid lines. The experimental one-dimensional spectrum is shown above the contour plot with a solid line. The homogeneous linewidth can be measured by a spin echo sequence, and from it we indicate the linewidths which are responsible for the damping during the two τ periods as a schematic spectrum as a thin line, for comparison, together with the measured linewidths. (Adapted from Lesage et al.[15] with permission, © 1999 American Chemical Society)

has been originally proposed by Baldus and Meier[20] and further improved.[21,22]

The correlation between nuclei is obtained by means of an isotropic Hamiltonian:

$$\mathcal{H} = 2\pi \sum_{i<j} J_{ij} \vec{I}_i \cdot \vec{I}_j \tag{3}$$

This Hamiltonian leads to a *net* polarization transfer as well as to antiphase signals[19] in the resulting two-dimensional spectra. The *net* polarization transfer $I_{1x} \rightarrow I_{2x}$ gives positive in-phase cross peaks while the anti-phase signals (originating from the transfer $I_{1x} \rightarrow I_{1y}I_{2z} - I_{1x}I_{2y}$) lead to dispersion signals in the detection period. These anti-phase components do not contribute to the signal at $t_2 = 0$, but evolve into observable coherences under the influence of the J interaction. In solids where the J interaction is not resolved, these anti-phase components are not observable, especially in the case of homogeneously broadened spectra. Under these conditions, the TOBSY experiment leads to pure absorption lineshapes in the two-dimensional spectrum.

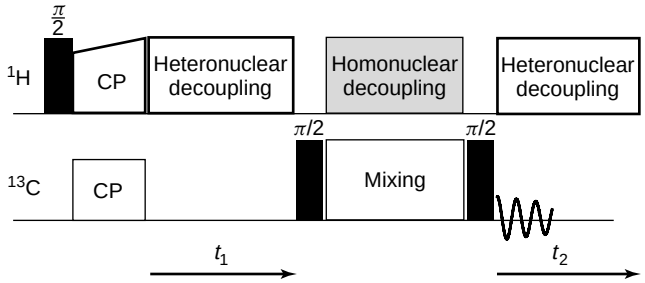

Figure 5 Two-dimensional TOBSY pulse scheme. During the t_1 evolution period, on-resonance high-power proton decoupling is used. The first 90° pulse on ^{13}C places magnetization along the z axis and then J-induced polarization transfer occurs during the mixing $\tau_{\text{mix}} = m\tau_{\text{MAS}}$ (where $m = 1, 2, 3, \ldots$) under simultaneous homonuclear proton decoupling. In the original TOBSY experiments[20] the mixing scheme $\text{R} = \overline{2}4\overline{2}3\overline{1}$, is applied such that $k = 4$ or $k = 8$ cycles cover one rotor period τ_{MAS}. For detection during t_2, high power on-resonance proton decoupling is applied. More recently the $\text{C}N_n^\nu$ schemes were proposed in order to perform the J-induced polarization transfer.[21,22] Usually cycles like WALTZ-4, POST-C7 and permuted WALTZ-4 can be used in order to improve the robustness of the pulse sequence with respect to rf field inhomogeneities. This pulse sequence can be easily adapted to cases where no proton nuclei are present (No proton channel in the above diagram)

To obtain an isotropic J mixing sequence (this means that the transfer does not depend on the initial condition of the magnetization), the Hamiltonian of equation (1) has to be crafted. The pulse sequence shown in Figure 5 achieves such an effective Hamiltonian. The philosophy of this pulse sequence is that MAS, together with rotor synchronized π pulses, can lead to a zeroth order average Hamiltonian that contains only the J couplings [see equation (3)]. The composite π pulses from the WALTZ decoupling scheme[23] have been used, and particular synchronization conditions have to be chosen in order to achieve pure J transfer.[20] The spin dynamics of rotor synchronized multiple pulse schemes is governed by the symmetry properties of the spin and space tensors of the interactions, and have been recently described at length using average Hamiltonian theory[24,25] (see **Symmetry-Based Pulse Sequences in Magic-Angle Spinning Solid-State NMR**). Introducing pulse sequences having the generic symmetry $\text{C}N_n^\nu$, where N cycles C_p with $p = 0, \ldots, N-1$, occupy n rotor periods, one can prove that appropriate choice of N, ν and n can be used to selectively average out given interactions. In fact the $\text{C}9_3^1$ symmetric class provides the basis for pure J magnetization transfer.[21] Studies using such symmetric pulse schemes have led to improved magnetization transfer efficiencies, and have allowed these experiments to perform well under faster MAS frequencies.[22] Heteronuclear dipolar decoupling of the protons is obtained using homonuclear proton decoupling in combination with MAS. We explain in detail how this works in the next section.

Experimental results using TOBSY are shown in Figure 6 for a powder sample of fully (^{13}C, ^{15}N)-labeled arginine. All one bond correlations are represented through cross peaks using a short mixing time, whereas long range connectivity coming from long-range and indirect couplings can be observed using a much longer mixing time.[20] The TOBSY spectrum of U–^{13}C, ^{15}N bacteriochlorophyll a is presented in Figure 7 as another example of the applicability of the

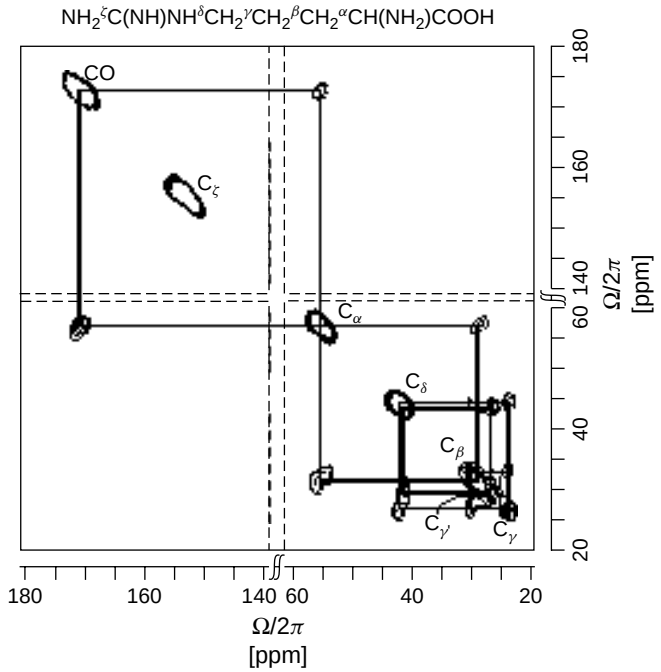

Figure 6 TOBSY initial-rate spectrum from a fully ^{13}C, ^{15}N-labeled arginine powder sample after a mixing time of 3 ms. Only the aromatic and aliphatic regions of the total two-dimensional spectrum are shown. All one-bond correlations are represented through cross-peaks. The spinning frequency was set to 8.5 kHz, and four R cycles per MAS period were used. A total of 256 t_1 experiments averaging eight transients in the t_2 was performed. Contour levels between 5 and 15 of the maximum signal intensity are shown. (Reproduced from Baldus and Meier,[20] © 1996, with permission from Academic Press)

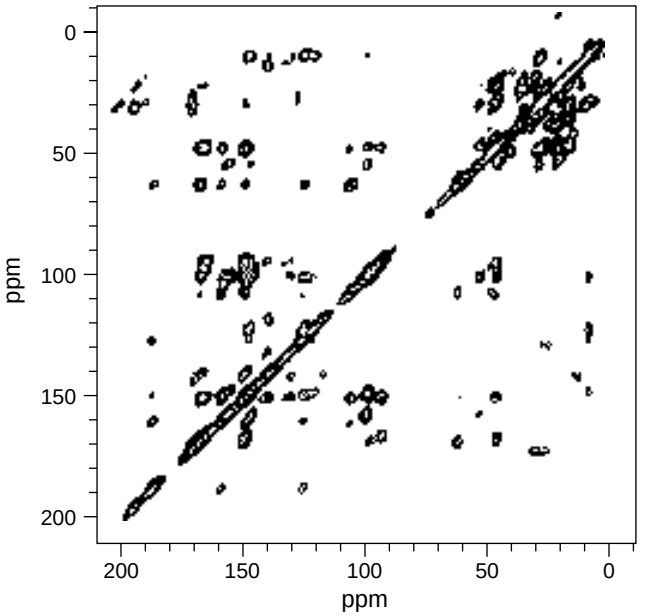

Figure 7 Part of a scalar correlation spectrum of U–^{13}C,^{15}N bacteriochlorophyll *a* recorded using POST-C9 as the isotropic mixing sequence at a MAS rate of 13 kHz, a mixing time of 9 ms, an rf amplitude for proton decoupling of 140 kHz, carbon rf amplitude of 78 kHz during POST-C9 and 113 kHz for the $\pi/2$ pulse, spectral width 30 kHz in each dimension, acquisition time 34 ms, 165 t_1 increments. Eight contour levels between 1% and 20% of the maximum positive spectra intensity are plotted. (Reproduced from Heindrichs et al.,[21] © 2001, with permission from Elsevier Science)

improved TOBSY sequences. Once again atomic connectivities along the carbon skeleton can be unambiguously determined.

2.2 Homonuclear Correlations for Other Nuclei

Up to now we have shown how homonuclear scalar couplings can be used for spectral assignment. Here we present an example in which *J* couplings can be used to probe geometric properties. In liquids, the well-known Karplus rule for the ^3J proton couplings is a useful tool for the determination of dihedral angles[7] (see **Vicinal Coupling Constants & Conformation of Biomolecules,** Volume 8). However, such couplings are not currently observable in solids. Homonuclear ^{31}P couplings have been used in order to determine bond angles in solid inorganic compounds.[26] The angle between two ^{31}P CSA tensors can be determined if polarization can be transferred between the two spins involved. By exploiting prior knowledge about the orientation of the CSA tensors relative to the molecular frame, bond angles can then be evaluated.

In many spin systems, such as SiP_2O_7, the evaluation of the experimental sideband patterns using dipolar techniques becomes difficult because cross-peaks between all resonances appear and greatly reduce the individual cross-peak intensities. The partial overlap of cross-peaks makes a quantitative analysis of the cross-peak intensity even more difficult. Therefore, the scalar *J* couplings are used as the polarization transfer mechanism, and only two ^{31}P spins within the P–O–P unit exchange polarization through the $^2J_{P-P}$ scalar coupling. Thus, the relative orientation of each unit can be measured selectively.

In Figure 8(a) the two-dimensional scalar correlation spectrum of a powder sample of the cubic phase of SiP_2O_7 is shown together with its one-dimensional spectrum. Only the centerband and the first sideband regions are shown. The intensity of the cross-peaks between different sidebands of chemically inequivalent spins contains information about the P–O–P angles, which can be obtained by numerical fitting. The results of such a fitting procedure are shown in Figure 8(b) and show that three pairs of P–O–P groups are bent, while one is linear.[26] These NMR data suggest that the "linear" pyrophosphate groups in SiP_2O_7 are in fact linear on the NMR time scale ($\sim$100 μs). A static disorder of 'normal' bent units, postulated previously, is clearly excluded.[26]

Other more exotic nuclei have also been investigated. One of the first examples of the application of INADEQUATE in the solid state was performed on the Sn nuclei.[11] ^{29}Si, whose natural abundance is 4.7%, has also been used to obtain scalar correlations. The ^1J couplings are of the order of 50 Hz and the ^2J couplings vary from 1 to 15 Hz. INADEQUATE helped find the correct structure of silanes in liquids. The technique was applied in the solid state by Benn et al.[27] to study very highly crystalline zeolites, where the linewidths are of the order of 1–20 Hz under proton decoupling. COSY-type experiments using J_{Si-Si} couplings have also been reported on glasses[28,29] (see **Silicon-29 NMR of Solid Silicates,** Volume 7).

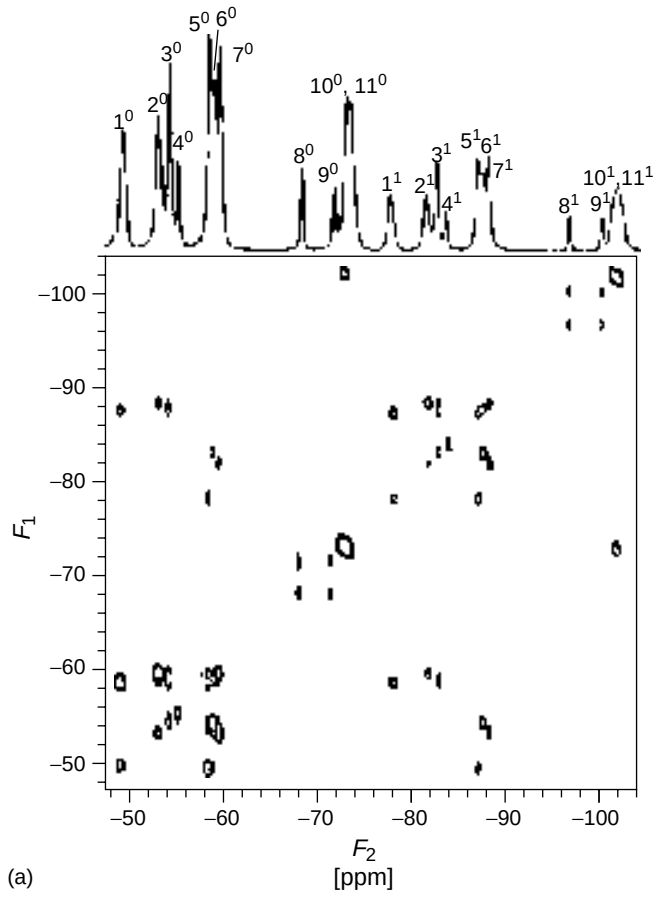

Figure 8 (a) Rotor-synchronized two-dimensional ^{31}P TOBSY spectrum of the cubic phase of SiP_2O_7 recorded with a MAS frequency of 4.63 kHz at a static field of 9.4 T. Only the region showing the centerband and the +1 sideband is reproduced. The pulse sequence from Figure 5 was used. The mixing time period was set to 21 ms at a rf field strength of 111 kHz. The ^{31}P chemical shift scale is referenced externally to phosphoric acid. (b) Normalized root-mean-square deviation between the experimental cross-peak intensities (taken into account were cross-peaks of order $n - m = 0, \pm 1, \pm 2$) as a function of the angle β for four sets of P–O–P units in SiP_2O_7. (Reproduced from Iulliucci and Meier[26] with permission, © 1998 American Chemical Society)

3 USING HETERONUCLEAR *J* COUPLINGS

The key step in characterizing and assigning *natural abundance* organic solids is through *heteronuclear* proton–carbon correlations. Until recently heteronuclear correlations in solids were obtained exclusively by dipolar correlations.[30–35] In the following, we review how heteronuclear coherence transfer can be obtained using scalar couplings leading to new sequences for spectral editing and heteronuclear *J* correlation.

3.1 How to Observe Heteronuclear Scalar Couplings: Homonuclear Proton Decoupling

The total Hamiltonian $\mathcal{H}$, under MAS and RF irradiation, is time dependent and can be written:

$$\mathcal{H}(t) = \mathcal{H}_I(t) + \mathcal{H}_S(t) + \mathcal{H}_{II}(t) + \mathcal{H}_{SS}(t) + \mathcal{H}_{IS}(t) + \mathcal{H}_{\mathrm{RF}}(t) \quad (4)$$

where $\mathcal{H}_X(t)$ accounts for the time dependent CSA interactions for the spin species X, $\mathcal{H}_{XY}$ for the dipolar and scalar coupling interactions between the spin species X and Y, and $\mathcal{H}_{\mathrm{RF}}(t)$ for the time dependent radio frequency fields that can be applied. In the following, we consider ordinary natural abundance organic solids (I refers to the ^{1}H nuclei and S refers to a rare nucleus such as ^{13}C or ^{15}N). Thus, it is reasonable to neglect the homonuclear Hamiltonian between rare spins $\mathcal{H}_{SS}(t)$.

To use the scalar couplings, one must first remove the dominant dipolar interactions (see **Average Hamiltonian Theory,** Volume 2, **Line Narrowing Methods in Solids,** Volume 4). Under homonuclear proton–proton decoupling (and assuming a fast radio-frequency averaging compared with the MAS time scale), the proton–proton dipolar interaction is, at least to first order, averaged to zero. The efficiency of the proton–proton decoupling depends on the decoupling sequence and many experimental parameters. Additionally, the proton chemical shift *and* the heteronuclear coupling interactions (dipolar and scalar) are scaled down by a scaling factor λ. In the absence of homonuclear interactions, the Hamiltonian becomes *inhomogeneous*[14,36,37] allowing for the averaging to zero, to first order, of the heteronuclear dipolar interactions and the CSA under MAS. The homonuclear scalar coupling terms between I spins, which are relatively small, are neglected. This leads to a considerable simplification of the effective Hamiltonian under homonuclear decoupling and MAS conditions. This effective Hamiltonian in the doubly rotating frame, can be written

$$\mathcal{H}_{\mathrm{eff}} = \lambda \sum_n \delta_n^I I_{nz} + \sum_m \delta_m^S S_{nz} + \lambda\pi \sum_{n,m} J_{nm}^{IS} 2 I_{nz} S_{mz} \quad (5)$$

and is very similar to the 'liquid state' NMR Hamiltonian that contains only the isotropic interactions.

In Figure 9(a) we show the carbon-13 spectrum of a powder sample of L-alanine recorded under proton-homonuclear decoupling and MAS. Figure 9(b) shows the methyl resonance of a powder sample of [2-^{13}C]sodium acetate recorded under the same conditions. Figure 9(c) shows the nitrogen-15 spectrum of a powder sample of glycine recorded under the same conditions. The frequency switched Lee–Goldburg (FSLG)[4,38] decoupling scheme was used with a rf decoupling amplitude of 100 kHz, and the MAS spinning frequency was set to 12 kHz. Splittings are observable in these spectra corresponding to

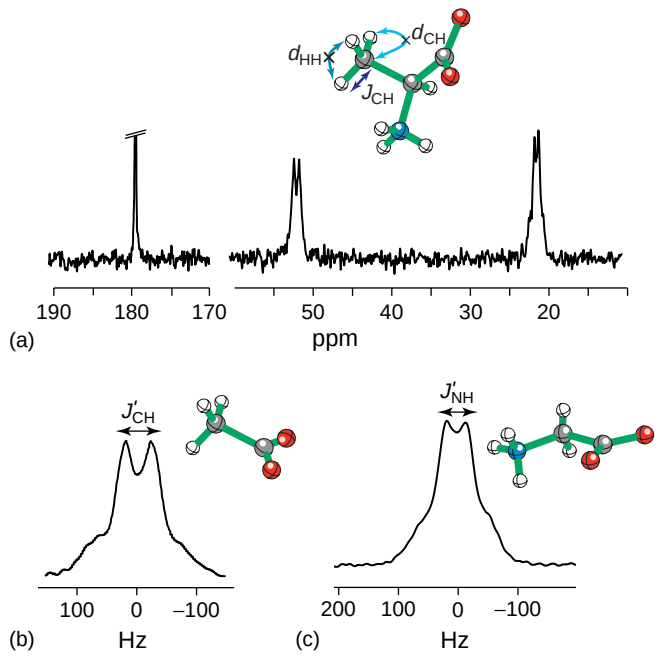

Figure 9 Carbon-13 (a,b) and nitrogen-15 (c) NMR spectra of powdered organic compounds under MAS and homonuclear proton dipolar decoupling. The homonuclear dipolar couplings are averaged by the rf sequence and the heteronuclear dipolar couplings by MAS, leaving only the heteronuclear scalar couplings. (a) In the carbon spectrum of L-alanine we can distinguish the doublet of the α carbon and the quartet of the methyl carbon. (b) Carbon spectrum of a sample of sodium acetate enriched at the methyl position. Only the methyl resonance is shown. A quartet is expected for the CH_3 group, which appears as a doublet in the spectrum because of the poor resolution of the outer transitions. (c) The same 'doublet' appears in the nitrogen-15 spectrum of glycine and hides the fine structure of the 1 : 3 : 3 : 1 quartet. Note that the heteronuclear proton–nitrogen couplings are smaller than the proton–carbon couplings. In all spectra the scalar couplings are scaled by the scaling factor of the decoupling sequence. In these experiments the FSLG decoupling sequence was used but other decoupling sequences can be used as well

the multiplet fine structure due to the heteronuclear J couplings. The α-carbon in L-alanine gives a doublet, while the methyl carbon in alanine and in sodium acetate gives a 'quartet', which is poorly resolved and appears in the spectrum as a doublet. Even though the proton–nitrogen J interactions are smaller (∼90 Hz) than the proton–carbon couplings (∼130 Hz), they can also be resolved, as we can see from the "quartet" present in the spectrum of glycine. It corresponds to the 1 : 3 : 3 : 1 fine structure of the NH_3^+ group.

3.2 Spectral Editing

One-dimensional spectral editing techniques such as INEPT, DEPT and APT, are very popular in the liquid state since they provide a quick and easy way of assigning carbon-13 resonances in many organic compounds (see **INEPT,** Volume 4, **Polarization Transfer Experiments via Scalar Coupling in Liquids,** Volume 6). They also constitute a first step towards the use of J couplings to perform heteronuclear correlation spectroscopy (see also **Heteronuclear Assignment Techniques,** Volume 4, **Spectral Editing Techniques: Hydrocarbon Solids,** Volume 7).

3.2.1 *Solid-State APT*

The attached proton test (APT) sequence is one of the simplest liquid-state spectral editing techniques,[39–41] and it has been modified and used for the solid state by Lesage et al.[42] The pulse sequence for the experiments is shown in Figure 10(a). Cross polarization is used to enhance the carbon polarization and homonuclear dipolar decoupling is introduced during the evolution periods to remove proton–proton dipolar couplings. As described above, under these conditions the inhomogeneous interactions, i.e., the chemical shift anisotropy and the heteronuclear dipolar couplings, are averaged out by rapid magic angle spinning, leaving only the isotropic chemical shift and the scalar J couplings. The π pulses applied simultaneously to proton and carbon in the center of the 2τ period, have the net effect of refocusing the carbon chemical shift evolution, while maintaining the evolution under the scaled scalar λJ_{IS} coupling. Thus, after cross polarization, carbon coherences evolve only under the effect of a scaled heteronuclear scalar coupling. The scaling factor λ varies according to the dipolar decoupling sequence that is used; for the FSLG sequence[4] the theoretical scaling factor is $1/\sqrt{3}$.

If the dynamics can be described by the simple Hamiltonian of equation (5), the theoretical evolution of carbon signals can easily be calculated using product operator algebra[43] since all terms in the Hamiltonian commute with each other. This formalism proves to be very useful since all of the following sequences can be calculated, to first order at least, as if they were liquid-state sequences. In the case of the APT sequence, since the carbon and the proton chemical shift evolution is refocused, the effective Hamiltonian during the 2τ period is

$$\mathcal{H}_{\text{eff}}^{\text{APT}} = \lambda\pi \sum_{n,m} J_{nm}^{IS} 2I_{nz}S_{mz} \tag{6}$$

and the observable signal intensity is

$$I_{I_nS}^{\text{APT}}(2\tau) = \cos^n(2\pi J'\tau)\exp\left(\frac{-2\tau}{T_2'^{I_nS}}\right) I_{I_nS}^0 \tag{7}$$

where I^0 is the signal intensity after cross polarization and T_2' is the transverse relaxation (dephasing) time during the period 2τ (equal to $1/\pi\Delta$). For each CH_n group ($n = 0$, 1, 2, 3), the intensities are shown in Figure 11(a) as functions of the delay τ. The calculations are shown for two different values of the linewidth Δ (1 Hz and 130 Hz, respectively, for the left and right panel) and J coupling (and 50 Hz and 70 Hz, respectively), corresponding to the 'ideal liquid state' case, and to the equivalent solid-state case. Note that the linewidth Δ indicated in the figures is the full linewidth at half-height of the signals evolving during 2τ (i.e., the linewidth for a single component of the fine structure of the multiplet), and is different from the overall linewidth of the signals observed during acquisition. The calculations were done in the ideal case where all protonated carbon groups have the same heteronuclear scalar couplings; 130 Hz is a typical value for a one-bond J_{CH} coupling for an aliphatic carbon, and the value of 70 Hz corresponds approximately to a scaling factor $\lambda = 1/\sqrt{3}$, due to the homonuclear proton decoupling. A τ value of $1/(2J)$ will produce a spectrum in which the C and CH_2 carbon peaks will be positive in sign, while the CH and CH_3 peaks will be inverted. Note that the sign of the

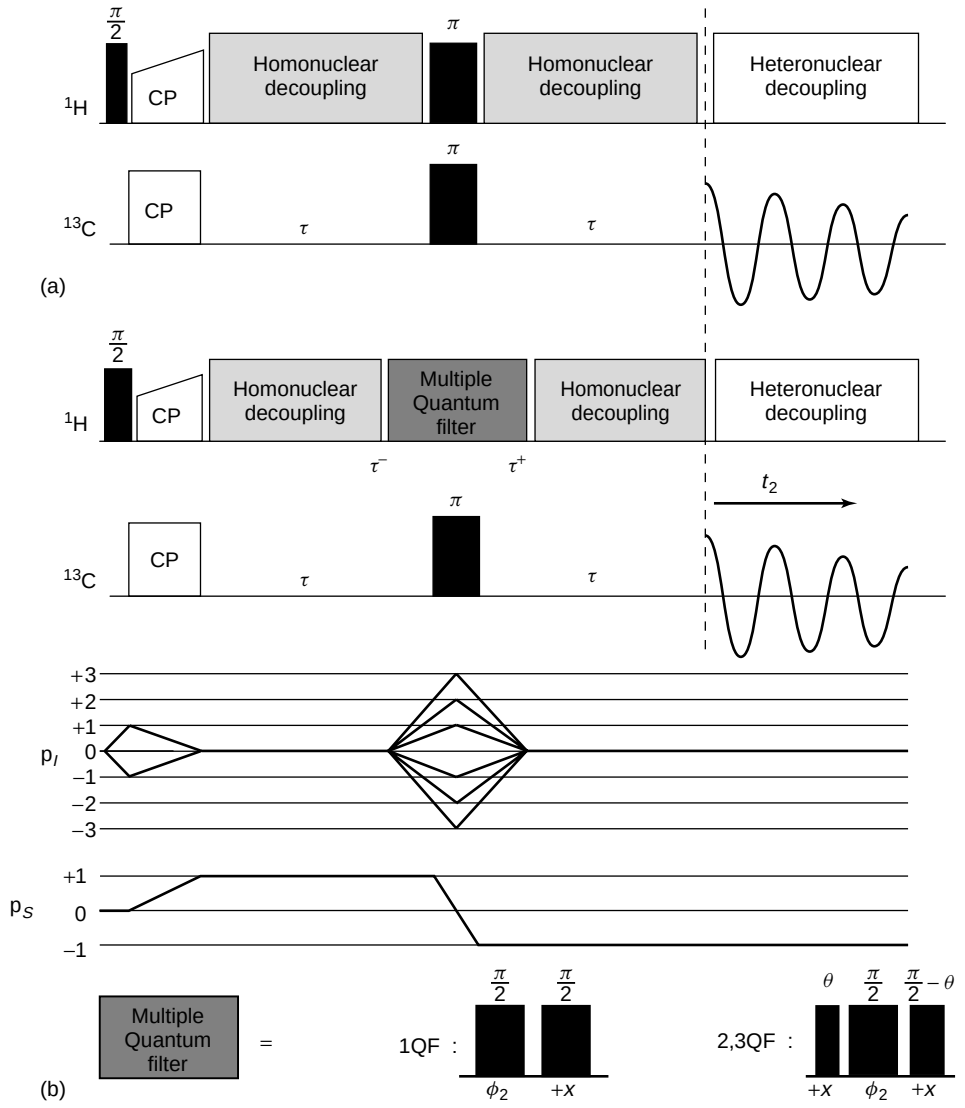

Figure 10 (a) The pulse sequence suitable for the solid-state APT and the corresponding coherence transfer pathway. (b) Pulse sequence and coherence transfer pathways for the J-MQ-Filter experiment. In the experiments presented in Figure 12 we used the FSLG sequence as the homonuclear proton decoupling scheme, thus θ is 54.7° pulse. Other homonuclear decoupling sequences can also be used instead of FSLG, by appropriately fixing θ. The MQ-Filter block is given at the bottom of the figure. (Detailed information about the implementation of these sequences is given in Refs.[42,44])

peaks is independent of the linewidth. Variations in linewidths will simply lead to a modulation of the amplitude of the signals but will not prevent discrimination between positive (CH_2) and negative (CH) signals. Note especially that, in cases where some groups are more flexible than others, partial averaging of the dipolar couplings through molecular motion will simply increase the signal amplitude (by decreasing the linewidth). Figure 11(b) shows a typical experimental example of this technique applied to L-histidine monohydrochloride monohydrate.

3.2.2 MAS-J-MQF

The APT sequence essentially serves as a parity test rather than removing resonances according to their multiplicity. An alternative sequence using the same principles but including a multiple-quantum filter block has been demonstrated to be capable of removing resonances from the spectrum according to their multiplicity.[44] The sequence is shown in Figure 10(b). Note that this experiment is applicable even when a carbon chemical shift distribution leads to inhomogeneous line broadening, since the π pulse on the carbon channel refocuses this effect. Thus, this technique (and the others considered in this section) should be applicable even in amorphous solids. Figure 12 shows an example of this approach applied to a protected tripeptide sample.

3.3 Two-dimensional Techniques

Multidimensional heteronuclear correlation spectroscopy is the cornerstone for assignment and structure determination in the liquid-state.[7] In analogy to liquid-state experiments (see **Two-Dimensional Carbon-Heteroelement Correlation,** Volume 8), the solid-state MAS-J-HMQC[45] and MAS-J-HSQC[46] sequences use heteronuclear multiple-quantum and heteronuclear single-quantum coherences, respectively, to

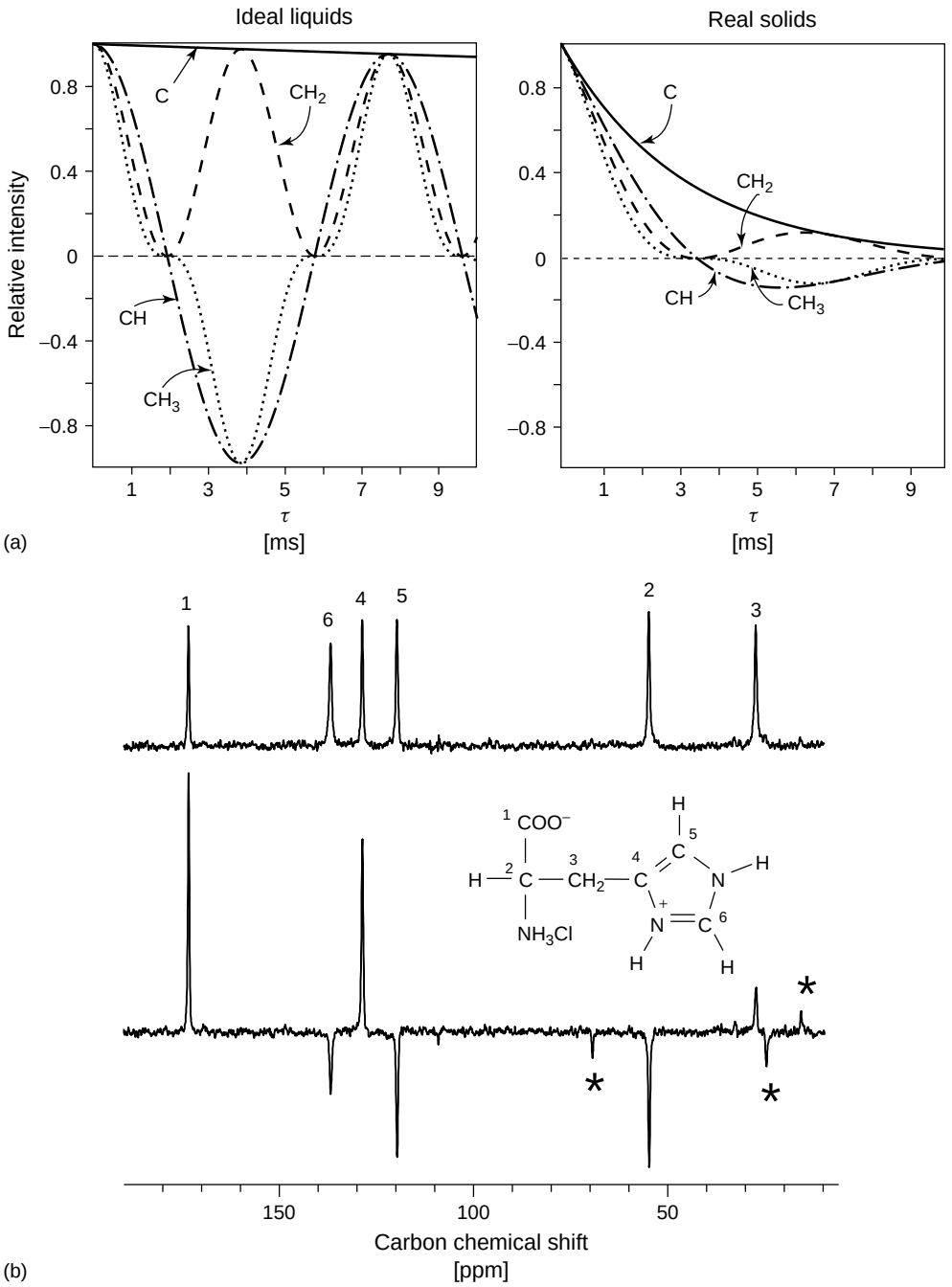

Figure 11 (a) Functional dependence of the observable signal as a function of the τ delay in the ATP sequence for the case of an ideal liquid and the solid-state. See text for details. A τ value of $1/(2J_{CH})$ will produce a spectrum in which the C and CH_2 carbon resonances will be positive in sign, while the CH and CH_3 resonances will be inverted. (b) One-dimensional CP/MAS spectrum (upper spectrum) and solid-state APT spectrum (lower spectrum) of L-histidine monohydrochloride monohydrate. A contact time of 1 ms was used and the spectra were recorded with 200 scans and 2048 scans, respectively. τ was set to 4 ms for the editing experiment. The spinning sidebands are marked with asterisks. (Reproduced from Lesage et al.[42] with permission, © 1998 American Chemical Society)

provide chemical-shift correlations between pairs of directly bonded nuclei in powder samples. Long range heteronuclear J couplings can also be used to probe multiple bond correlations, leading to the MAS-J-HMBC experiment.[47]

3.3.3 MAS-J-HMQC

This two-dimensional experiment is based on the polarization transfer techniques using scalar interactions that have been described in the spectral editing paragraph. The only difference is that a t_1 evolution time is included during which the multiple spin multiple quantum coherences evolve under the isotropic chemical shifts of the proton nuclei. The sequence is shown in Figure 13(a) and leads to two-dimensional spectra containing correlations between rare nuclei (carbons, nitrogens) along ω_2, and protons along ω_1 of the kind shown in Figure 14. The time τ is responsible for the polarization transfer, and it has been shown that for short τ evolutions only correlations from

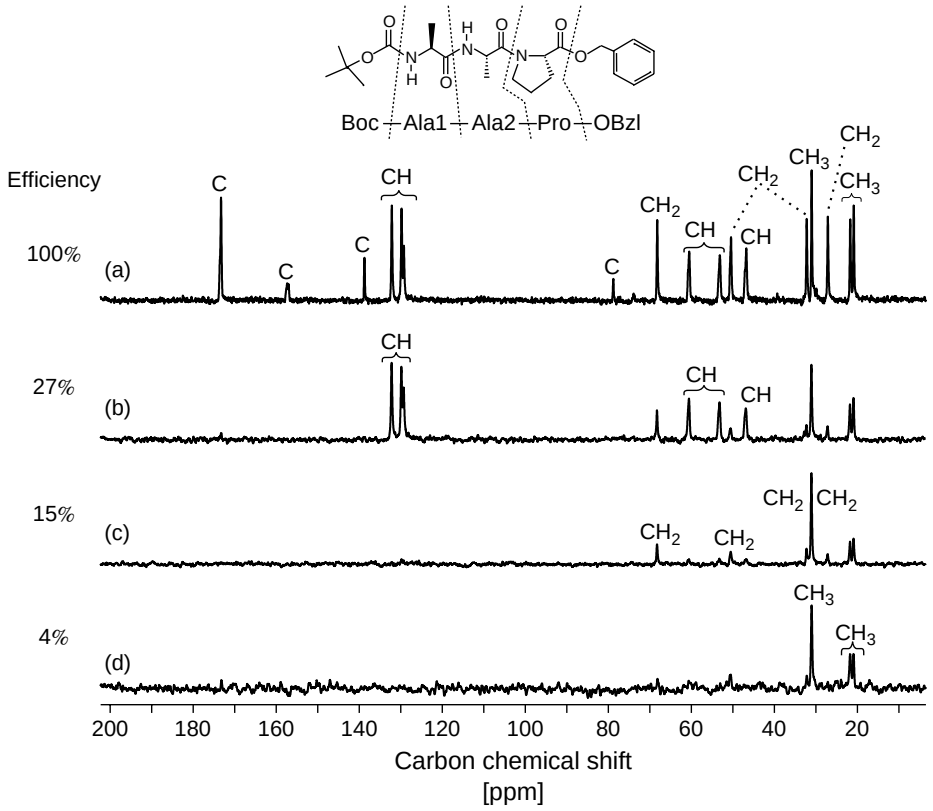

Figure 12 J-MQ-Filtered solid-state NMR spectra of the tripeptide Boc-Ala-Ala-Pro-O-Bzl. (a) Standard CP/MAS spectrum of 20 mg of a powder sample of the tripeptide. The spinning frequency was set to 12.5 kHz and a 1-ms cross polarization contact time was used. TPPM heteronuclear decoupling ($\omega_1/2\pi = 100$ kHz) was applied during acquisition; 64 scans were recorded. (b) 1Q-Filtered spectrum. As predicted, signals from the CH, CH_2 and CH_3 groups are present; 128 scans were recorded. (c) 2Q-Filtered spectrum. Only signals from the CH_2 and CH_3 groups are present; 2560 scans were recorded. (d) 3Q-Filtered spectrum. Only signals from the CH_3 groups are present; 4800 scans were recorded. The evolution time τ was set to 3.2 ms (synchronized with the MAS) for (b) and (c) and to 7.0 ms for (d) in order to enhance 3Q coherence creation. Spectra (c) and (d) were acquired within 2 and 4 h, respectively. The signal to noise ratio relative to the CP/MAS experiment, corrected for the number of scans, is given next to the spectrum for each experiment. (Reproduced by permission from Sakellariou et al.,[44] © 2001, with permission from Academic Press)

directly bonded nuclei are obtained. For longer τ periods, long range correlations are observed, and, in the case of camphor, fit well when ^2J and ^3J are included in spin Hamiltonian. Such correlations are thus exploited to explore long range connectivities like the HMBC experiment in liquids.[47] In what follows, we concentrate on the possibility of obtaining the full assignment of medium-size organic molecules using these correlation techniques.

3.3.4 Complete Assignment Using Multiple-Bond Correlations

For an approach to the complete assignment of the ^{13}C spectrum, we start with the one-bond (^1H, ^{13}C) correlations. This approach has yielded the complete assignment of the protected tripeptide shown in Figure 15, and here we demonstrate the assignment protocol only for one of the residues.

As mentioned above, for short values of the evolution period τ (typically 2 ms), the carbon–proton magnetization transfer is highly selective, i.e., it leads to only one-bond chemical shift correlations. Figure 15(a) shows the one-bond MAS-J-HMQC spectrum of the tripeptide Boc-Ala-Ala-Pro-O-Bzl (the three amino acids are referred to in the text as A1, A2 and P). Some resonance lines of the ^{13}C spectrum can be identified from this two-dimensional correlation map alone. We can readily identify the three carbon resonances at low field as well as the one around 77.3 ppm as quaternary carbons since they are not correlated with any proton in the ω_1 dimension. From carbon chemical shift considerations, the carbon resonance at 77.3 ppm can be assigned to the quaternary carbon of the ter-butyl group, and that at 137.3 ppm to the quaternary carbon of the benzyl group; the remaining two quaternary resonances must therefore correspond to the three amino acid carbonyl groups (171.9 ppm) and to the carbonyl carbon of the Boc group (155.7 ppm). The carbon peaks between 127 and 131 ppm yield correlations with protons at about 7 ppm, and are therefore likely to correspond to the protonated carbons of the benzyl group. From carbon peak intensity, the high-field resonance must correspond to the para carbon. A specific assignment of the two other aromatic resonances is not possible. In the high-field part of the spectrum, the three carbon resonances at 19.4, 20.3 and 29.6 ppm can be assigned to the three methyl groups since they correlate with protons around 1.5 ppm. Tentatively, from carbon chemical shifts and peak intensity, we assume that the peak at 29.6 ppm corresponds to the ter-butyl methyl groups,

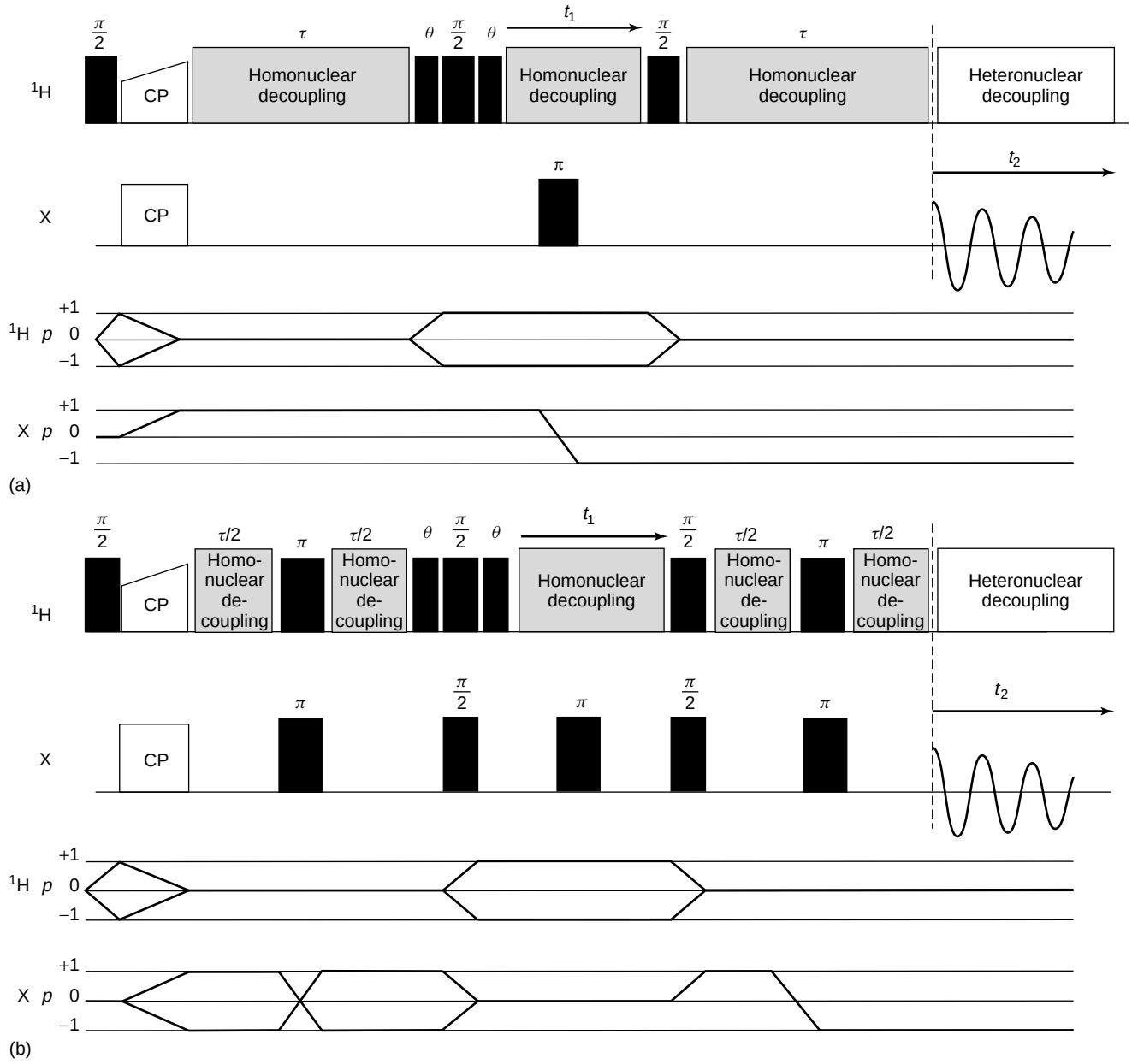

Figure 13 (a) Pulse sequence for the MAS-J-HMQC experiment. θ is a prepulse whose flip angle depends on the homonuclear decoupling scheme (for FSLG $\theta = \theta_m$, i.e., the magic angle). After cross polarization from ^{1}H (I spins), the magnetization of the rare S spins evolves during the delay τ only under an isotropic scaled heteronuclear J coupling Hamiltonian. For a pair of covalently bonded ^{1}H-S spins, the carbon magnetization evolves from in-phase (S_x) into antiphase ($2I_zS_y$) coherence with respect to the attached proton. A 90° pulse applied on protons transforms the antiphase carbon coherence into a multiple-quantum heteronuclear coherence which evolves during t_1 only under the effect of the proton chemical shift. At the end of the t_1 evolution period, the MQ coherence is converted back into an antiphase carbon coherence by the second 90° proton pulse. During the second τ period this coherence evolves to become an in-phase observable carbon coherence. (b) Pulse sequence for the MAS-J-HSQC experiment. During the t_1 evolution period only single quantum proton coherence evolves under the isotropic proton chemical shift

and the other two, to the Cβ of alanine residues. At this stage, however, it is not possible to determine to which alanine residue (A1 or A2) each methyl carbon resonance belongs. Of the remaining peaks, the two carbons at 25.7 and 30.8 ppm, which correlate with protons at around 2.5 ppm, are likely to correspond to the proline γ and β carbons, respectively. The remaining five peaks between 40 and 70 ppm therefore correspond to the proline α and δ carbons, to the two alanine α carbons, and to the O–CH_2 group.

Thus, multiple-bond proton–carbon correlations are required to lift this ambiguity. Geminal ^{13}C–^{1}H couplings ($^2J_{CH}$) and vicinal ^{13}C–^{1}H couplings ($^3J_{CH}$) are also active during the evolution periods, and thus contribute to the creation of heteronuclear multiple-quantum coherences. If the evolution periods τ are long enough, in theory of the order of $1/(2\,{}^nJ_{CH})$, multiple-bond couplings may yield significant correlations. Note that, in this case, the MAS-J-HMQC experiment should rather be compared to the liquid-state

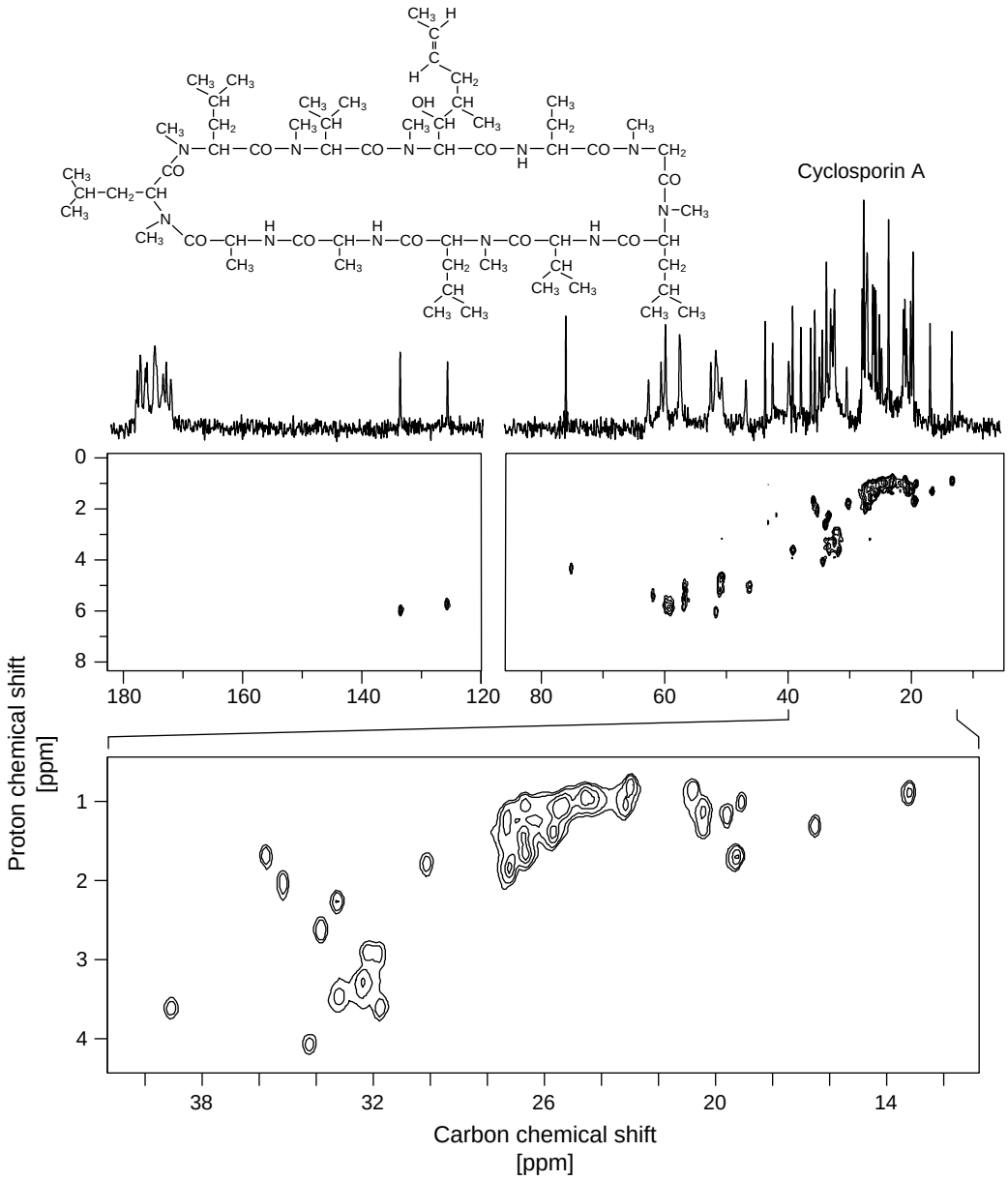

Figure 14 MAS-*J*-HMQC spectrum of Cyclosporin A. This spectrum was obtained at 500 MHz and shows one-bond carbon–proton correlations for the undecapeptide

heteronuclear multiple-bond correlation (HMBC) experiment. In organic compounds in the liquid-state, values between −10 and +66 Hz are usually found for $^{2}J_{CH}$ couplings, whereas the $^{3}J_{CH}$ couplings have values between 0 and 16 Hz.[48] In amino acids, the (CO–Hα) coupling constants range from −4 to −7 Hz while (CO–Hβ) coupling constants range from 2 to 6 Hz.

The apparent carbon linewidths under FSLG decoupling are obviously much larger than these multiple-bond scalar interactions. However, the dephasing time constant which is effective for the creation of the heteronuclear MQ coherences (τ periods) is related to the refocused linewidth (or the homogeneous linewidth), for which all the inhomogeneous broadening is removed by the carbon π pulse. It was recently shown that, under CW decoupling, the carbon line broadening for crystalline organic compounds is mainly inhomogeneous, and refocused linewidths as small as a few hertz on model organic samples have been measured.[15] Under homonuclear proton decoupling, the homogeneous linewidth increases for protonated carbons. However, it remains about the same for nonprotonated carbons, i.e., of the order of a few hertz, thus rendering the observation of multiple-bond correlations feasible for these nuclei. Figure 15(b) shows the MAS-*J*-HMQC spectrum of the tripeptide recorded with an evolution period τ equal to 16 ms. Besides the one-bond connectivity (except for those corresponding to CH_2 groups, all of them are present), many additional through-bond 'long-range' correlation peaks are observed. As expected, all the nonprotonated carbons (four resonance lines in the carbon spectrum) yield multiple-bond connectivity. For example, the carbonyl carbon of the Boc group at 155.7 ppm is expected to correlate with the amide proton of the N-terminal alanine residue (A1), and also with

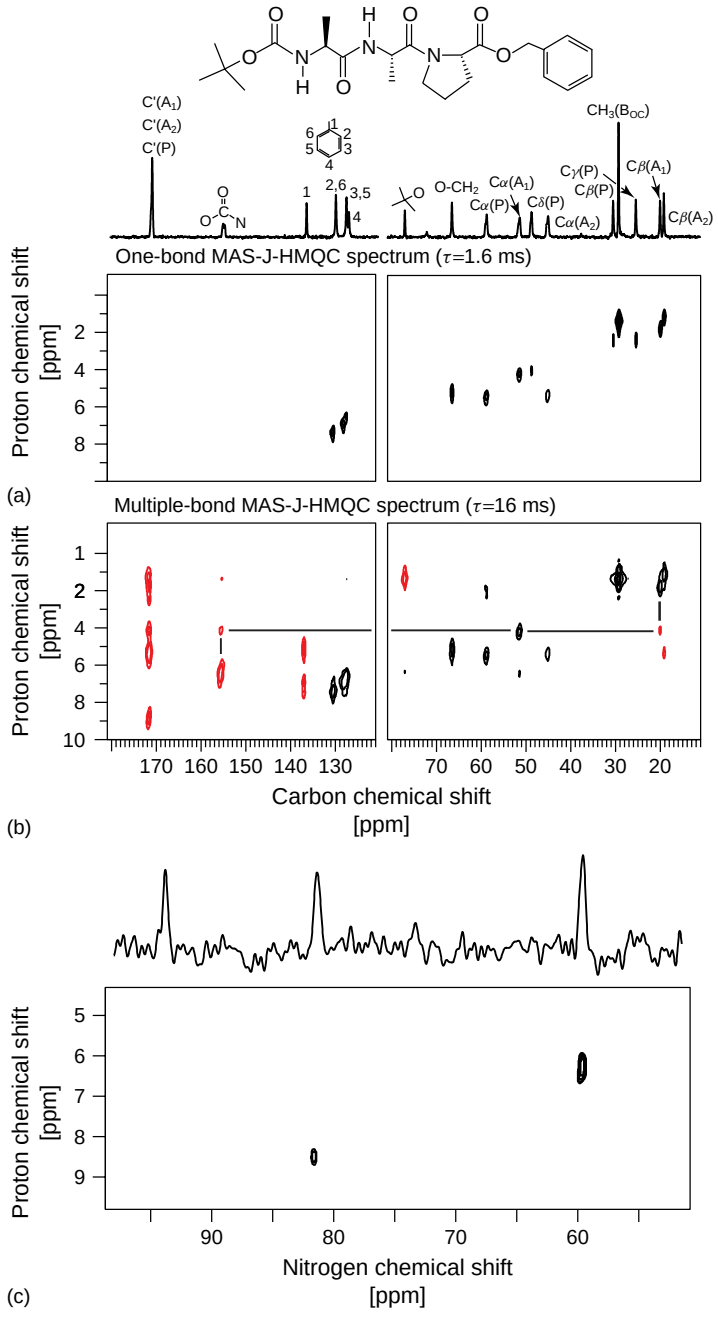

Figure 15 Carbon–proton two-dimensional MAS-*J*-HMQC spectra of the natural abundance tripeptide Boc-Ala-Ala-Pro-O-Bzl recorded with an evolution period (τ value) of (a) 1.6 ms, and (b) 16 ms. The one-dimensional CP/MAS ^{13}C spectrum is shown above the two-dimensional spectrum. The proton linewidths depend on the efficiency of the homonuclear decoupling scheme. Under our experimental conditions, we measured proton linewidths of about 200 Hz, 250 Hz and 400 Hz for the CH_3, CH and CH_2 groups, respectively. However, for CH_2 groups, the proton resonance may correspond to two magnetically nonequivalent protons. Note that, despite the long evolution periods (16 ms) which are required for the excitation of the long-range MQ coherences, the multiple-bond experiment remains quite sensitive since, as pointed out in the text, the effective time constants which characterize the decay of carbon magnetization during the τ delays, are 'refocused' time constants and thus, are longer than the apparent relaxation times. (c) ^{15}N-^{1}H two-dimensional MAS-*J*-HMQC spectra of the tripeptide. The spinning frequency was 12.5 kHz and τ was 4.32 ms. A total of 110 t_1 increments with 256 scans each were acquired. The other experimental conditions are the same as in (a) and (b). The one-dimensional CP/MAS ^{15}N spectrum is shown above the two-dimensional spectrum; 4 mm MAS probe ~20 mg, $\omega_{1H} = 100$ kHz. (Reproduced from Lesage et al.[47] with permission, © 2000 American Chemical Society)

the α proton of the same residue. Indeed, two cross-peaks, one very intense at 6.5 ppm and the other weaker at 4.25 ppm, are observed in the ω_1 dimension. From the proton chemical shifts, they must correspond respectively to the HN and Hα protons of A1. In the one-bond (^{1}H, ^{13}C) MAS-*J*-HMQC spectrum, the carbon resonance at 51.7 ppm is also correlated to the Hα(A1) proton, and can therefore be assigned to the Cα(A1). In addition to the quaternary carbons, the Cβ carbons of the alanine residues (methyl groups) yield weak multiple-bond correlations with the neighboring α protons. As the Hα(A1) proton

could be previously assigned at 4.25 ppm from its correlation with the carbonyl carbon of the Boc group (at 155.7 ppm), the assignment of the methyl carbons is now straightforward: the carbon resonance at 20.3 ppm corresponds to the Cβ(A1) and, by deduction, the resonance at 19.4 ppm to the Cβ(A2). By continuing in this way, all the proton, carbon and nitrogen resonances in the spectrum can be assigned (the nitrogen-15 assignment being obtained simply from the natural abundance proton–nitrogen HMQC experiment shown in Figure 15(c)).

MAS-*J*-HMQC experiments constitute a powerful tool for the characterization of the NMR spectra of solid-state natural abundance organic molecules. Despite the small size of multiple-bond scalar couplings, it has been shown experimentally[47] that it is possible to observe long-range connectivities that can be assigned to through-bond correlations, which is an important step towards complete assignment of ^{13}C CP/MAS spectra.

Note that it would be difficult to reliably identify multiple-through-bond correlations using dipolar based techniques, since, at long contact times, dipolar methods usually lead to a wide range of through-space interactions, often including inter-molecular contacts. In fact, long range dipolar and scalar experiments are complementary techniques, and differences in the correlation patterns could be very informative to identify, for example, effects such as hydrogen bonding in solids.

3.3.5 *MAS-J-HSQC*

The spin dynamics in the MAS-*J*-HMQC experiment can be very easily modified to have only a single quantum proton coherence evolution during the t_1, leading to the MAS-*J*-HSQC experiment. At first sight there should not be a significant difference between the two experiments. In fact, for natural abundance compounds, the MAS-*J*-HMQC and the MAS-*J*-HSQC experiments give about the same proton resolution in the indirect dimension, although the HSQC version is more prone to artifacts such as quadrature images or axial peaks, since there are more pulses in the sequence. On the other hand, for ^{13}C enriched materials, substantially narrower proton linewidths are obtained with the MAS-*J*-HSQC experiment, since homonuclear carbon–carbon couplings have no influence on the evolution of the single quantum proton coherence. The pulse sequence of the MAS-*J*-HSQC experiment is shown in Figure 13(b). The comparison between the two approaches is discussed in detail in Ref.[46]

3.3.6 *J-WISE*

The experiments discussed above are aimed at assigning complex spectra. However, controlled coherence transfer through scalar couplings can also be put to use in structural studies by comparing the results of polarization transfer using dipolar and scalar couplings. A striking example has recently been demonstrated for wideline proton (WISE) spectra in polymer systems to study hydration effects (see **Polymer Dynamics & Order from Multidimensional Solid State NMR,** Volume 6). Figure 16 shows a comparison between an 'ordinary' dipolar WISE spectrum,[49] recorded for a sample of partially rehydrated onion cell-wall material with a similar wideline spectrum where the proton–carbon correlation is obtained using a derivative of the MAS-*J*-HSQC experiment without applying decoupling during t_1 (dubbed *J*-WISE). Interestingly, all of the proton signals in the cell-wall material dipolar WISE spectra contain a broad signal split into spinning sidebands superimposed on a narrow component occurring at the centerband. By performing a *J*-WISE experiment, it was shown that the narrow line arises from water molecules close

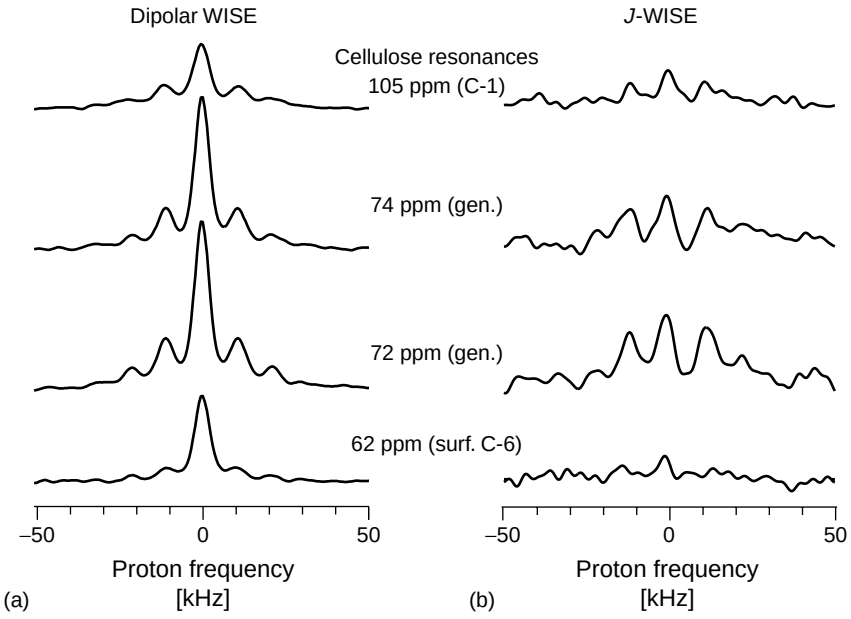

Figure 16 Comparative study of onion cell-wall material using the standard WISE and *J*-WISE experiments. Proton signals arising from immobile regions of the molecule give the broad signal split into sidebands onto which is clearly superimposed a narrow center component in the dipolar spectra (a). In the *J*-WISE spectra (b) this narrow component is absent, indicating that it belongs to 'bound water'. (Courtesy of Dr S. Hediger)

to the polysaccharides ('bound water'), since the narrow component disappears from the spectrum, indicating that there is no covalent connection between these protons and the carbon atoms of the polysaccharides. This is a particularly elegant demonstration of the complementarity between through-space and through-bond correlation techniques with which we conclude this entry.

4 RELATED ARTICLES IN VOLUMES 1–8

CRAMPS, Volume 3, Cross Polarization in Rotating Solids: Spin-1/2 Nuclei, Volume 3, Cross Polarization in Solids, Volume 3, Heteronuclear Assignment Techniques, Volume 4, Magic Angle Spinning, Volume 5, Rotating Solids, Volume 7, Spectral Editing Techniques: Hydrocarbon Solids, Volume 7.

5 REFERENCES

1. T. Terao, H. Miura, and A. Saika, *J. Chem. Phys.*, 1981, **75**, 1573.
2. K. W. Zilm and D. M. Grant, *J. Magn. Reson.*, 1982, **48**, 524.
3. A. E. Bennett, C. M. Rienstra, M. Auger, K. V. Lakshmi, and R. G. Griffin, *J. Chem. Phys.*, 1995, **103**, 6951.
4. A. Bielecki, A. C. Kolbert, and M. H. Levitt, *Chem. Phys. Lett.*, 1989, **155**, 341.
5. E. Vinogradov, P. K. Madhu, and S. Vega, *Chem. Phys. Lett.*, 1999, **314**, 443.
6. D. Sakellariou, A. Lesage, P. Hodgkinson, and L. Emsley, *Chem. Phys. Lett.*, 2000, **319**, 253.
7. K. Wüthrich, 'NMR of Proteins and Nucleic Acids', Wiley-Interscience: New York, 1986.
8. A. Bax, R. Freeman, and S. P. Kempsell, *J. Am. Chem. Soc.*, 1980, **102**, 4849.
9. A. Bax, R. Freeman, and T. A. Frenkiel, *J. Am. Chem. Soc.*, 1981, **103**, 2102.
10. T. A. Early, B. K. John, and L. F. Johnson, *J. Magn. Reson.*, 1987, **79**, 134.
11. I. D. Gay, C. H. Jones, and R. D. Sharma, *J. Magn. Reson.*, 1991, **91**, 186.
12. A. Lesage, C. Auger, S. Caldarelli, and L. Emsley, *J. Am. Chem. Soc.*, 1997, **119**, 7867.
13. D. L. VanderHart, W. L. Earl, and A. N. Garroway, *J. Magn. Reson.*, 1981, **44**, 361.
14. M. M. Maricq and J. S. Waugh, *J. Chem. Phys.*, 1979, **70**, 3300.
15. A. Lesage, M. Bardet, and L. Emsley, *J. Am. Chem. Soc.*, 1999, **121**, 10 987.
16. R. Verel, J. D. van Beek, and B. H. Meier, *J. Magn. Reson.*, 1999, **140**, 300.
17. M. Bardet, D. Gagnaire, R. Nardin, D. Robert, and M. Vincendon, *Holzforschung*, 1986, **40**, 17.
18. M. Bardet, L. Emsley, and M. Vincendon, *Solid State NMR*, 1997, **8**, 25.
19. L. Braunschweiler and R. R. Ernst, *J. Magn. Reson.*, 1983, **53**, 521.
20. M. Baldus and B. H. Meier, *J. Magn. Reson. A*, 1996, **121**, 65.
21. A. S. D. Heindrichs, H. Geen, C. Giordani, and J. J. Titman, *Chem. Phys. Lett.*, 2001, **335**, 89.
22. E. H. Hardy, R. Verel, and B. H. Meier, *J. Magn. Reson.*, 2001, **148**, 459.
23. A. J. Shaka, J. Keeler, T. Frenkiel, and R. Freeman, *J. Magn. Reson.*, 1983, **52**, 335.
24. M. Edén and M. H. Levitt, *J. Chem. Phys.*, 1999, **111**, 1511.
25. M. Carravetta, M. Edén, X. Zhao, A. Brinkmann, and M. H. Levitt, *Chem. Phys. Lett.*, 2000, **321**, 205.
26. R. J. Iuliucci and B. H. Meier, *J. Am. Chem. Soc.*, 1998, **120**, 9059.
27. R. Benn, H. Grondey, C. Brevard, and A. Pagelot, *J. Chem. Soc., Chem. Commun.*, 1988, **2**, 102.
28. C. A. Fyfe, H. Gies, and Y. Feng, *J. Chem. Soc., Chem. Commun.*, 1989, **17**, 1240.
29. C. T. G. Knight, R. J. Kirkpatrick, and E. Oldfield, *J. Noncryst. Solids*, 1990, **116**, 140.
30. P. Caravatti, G. Bodenhausen, and R. R. Ernst, *Chem. Phys. Lett.*, 1982, **89**, 363.
31. P. Caravatti, L. Braunschweiler, and R. R. Ernst, *Chem. Phys. Lett.*, 1983, **100**, 305.
32. J. E. Roberts, S. Vega, and R. G. Griffin, *J. Am. Chem. Soc.*, 1984, **106**, 2506.
33. C. H. Wu, A. Ramamoorthy, and S. J. Opella, *J. Magn. Reson. A*, 1994, **109**, 270.
34. Z. Gu, C. F. Ridenour, C. E. Bronnimann, T. Iwashita, and A. McDermott, *J. Am. Chem. Soc.*, 1996, **118**, 822.
35. B. J. Van Rossum, H. Forster, and H. J. M. De Groot, *J. Magn. Reson.*, 1997, **124**, 516.
36. R. K. Hester, J. L. Ackerman, B. L. Neff, and J. S. Waugh, *Phys. Rev. Lett.*, 1976, **36**, 1081.
37. T. Terao and S. Matshui, *Phys. Rev. B*, 1980, **21**, 3781.
38. A. Bielecki, A. C. Kolbert, H. J. M. De Groot, R. G. Griffin, and M. H. Levitt, *Adv. Magn. Reson.*, 1990, **14**, 111.
39. C. LeCocq and J.-Y. Lallemand, *J. Chem. Soc., Chem. Commun.*, 1981, **119**, 150.
40. F.-K. Pei and R. Freeman, *J. Magn. Reson.*, 1982, **48**, 318.
41. H. J. Jakobsen, O. W. Sørensen, W. S. Brey, and P. Kanya, *J. Magn. Reson.*, 1982, **48**, 328.
42. A. Lesage, S. Steuernagel, and L. Emsley, *J. Am. Chem. Soc.*, 1998, **120**, 7095.
43. O. W. Sørensen, G. W. Eich, M. H. Levitt, G. Bodenhausen, and R. R. Ernst, *Prog. NMR Spectrosc.*, 1983, **16**, 163.
44. D. Sakellariou, A. Lesage, and L. Emsley, *J. Magn. Reson.*, 2001, **151**, 40.
45. A. Lesage, D. Sakellariou, S. Steuernagel, and L. Emsley, *J. Am. Chem. Soc.*, 1998, **120**, 13 194.
46. A. Lesage and L. Emsley, *J. Magn. Reson.*, 2001, **148**, 449.
47. A. Lesage, P. Charmont, S. Steuernagel, and L. Emsley, *J. Am. Chem. Soc.*, 2000, **122**, 9739.
48. H. O. Kalinowski, S. Berger, and S. Braun, 'Carbon-13 NMR Spectroscopy', John Wiley & Sons: Chichester, 1988.
49. K. Schmidt-Rohr, J. Clauss, and H. W. Spiess, *Macromolecules*, 1992, **25**, 3273.
50. C. Auger, 'Une nouvelle technique de correlation deuterium-carbone pour l'attribution et la mesure des couplages quadrupolaires dans les materiaux orientes', Ph.D. thesis, ENS Lyon, 1998.

Acknowledgements

We would particularly like to acknowledge the invaluable contribution of Anne Lesage to the work we review here, we simply regret that she was not available to write this entry with us. We would like to dedicate this article to Alix. We would also like to thank Sabine Hediger, Paul Hodgkinson, Stefano Caldarelli, Celine Auger, Patrick Charmont, Stefan Steuernagel and all the other members of our group who have contributed to this work. We thank Jamie Walls, Malgorzata Marjanska and Steven P. Brown for helpful discussions and criticisms on this manuscript.

Biographical Sketches

Dimitris Sakellariou, *b* 1974. B.Sc. École Normale Supérieure de Lyon, 1996, Ph.D., École Normale Supérieure de Lyon, France, 2000 under the direction of Lyndon Emsley, Fellow of the Lawrence Berkeley National Laboratory, UC Berkeley, currently working with Alex Pines. Current research interests focus on NMR.

Lyndon Emsley, *b* 1964. B.Sc. Imperial College, London, 1986, Ph.D., Université de Lausanne, Switzerland, 1991 under the direction of Geoffrey Bodenhausen. Fellow of the Miller Institute for Basic Research in Science, UC Berkeley, 1991–1993 (collaboration with Alex Pines). Foreign member of the Institut Universitaire de France, 1994. Professor of Chemistry, École Normale Supérieure de Lyon 1995–present. Current research interests focus on fundamental aspects of NMR, with an emphasis on the solid state.

Two-Dimensional Powder Correlation Methods

Craig D. Hughes
Los Alamos National Laboratory, Los Alamos, NM, USA

1	Introduction	1
2	Experimental	1
3	Results	2
4	Simulations	4
5	Discussion	6
6	Related Articles	7
7	References	7

1 INTRODUCTION

There are two general motivations to measure the ^{13}C chemical shift tensor in a solid. The first is that it is sensitive to the electronic structure of the molecule in the vicinity of the nucleus, and therefore provides useful experimental data for testing theoretical models of molecular electronic structure. The second, more practical, motivation is analytic in nature; the chemical shift tensor is a sensitive and often unique tool for characterizing heterogeneous materials, and its orientational dependence can be exploited to help characterize partially oriented materials.

The measurement of the ^{13}C chemical shift tensor's principal values and its orientation with respect to the molecular coordinate system is often difficult. A common method is to rotate a single crystal of the sample in a magnetic field and map the relationship between the field direction and the resonance frequency for each magnetically equivalent carbon nucleus in the sample.[1] As the number of magnetically unique carbon nuclei in the crystal increases, correlated 2D exchange NMR spectroscopy is a powerful tool in resolving and correlating the peaks resulting from similar chemical shift tensors.[1,2]

When a good single crystal of the sample is not available, powder techniques must be used. In simple cases, the principal values may be measured from the breakpoints of a 1D powder pattern. The powder spectrum is then simulated with a chemical shift powder pattern for each unique carbon in the sample in order to measure the principal values. This technique is limited to relatively simple spectra, owing to the complexity of fitting multiple, overlapping 1D powder patterns. There are a number of alternate experimental approaches to solving this problem, many of which are reviewed elsewhere in this Encyclopedia.

A relatively simple 2D technique for measuring principal values of overlapping ^{13}C chemical shift tensor patterns in powders is the chemical shift–chemical shift correlation experiment developed for single crystal measurements.[2–4] The sample is rotated relative to the external magnetic field during the mixing time of a 2D exchange experiment, which correlates the powder patterns in the two different orientations. The resulting 2D powder patterns have a characteristic shape that depends on the angle of the rotation and the principal values of the chemical shift tensors in the sample. This method utilizes the additional resolution available in 2D spectroscopy, and is especially useful for sorting the principal values of chemical shift tensors in badly overlapped 1D powder patterns.

2 EXPERIMENTAL

The probe appropriate for the 2D powder correlation experiment is a double tuned, large-sample-volume system designed to allow ^{1}H decoupling and rapid 90° rotation of the sample about an axis perpendicular to the external magnetic field, as shown in Figure 1. The results reported here were obtained using a Bruker CXP-200 NMR spectrometer, with a resonance frequency of 50.3 MHz for ^{13}C.

The pulse sequence used in the experiment is shown in Figure 2. The first part of the pulse sequence is the common cross-polarization technique with Hartmann–Hahn matching and spin locking between the ^{1}H and ^{13}C spins. The remainder of the sequence is a chemical exchange experiment that correlates two different ^{13}C chemical shift evolutions. Here, v and w are the phases of the ^{1}H rf pulses, and x and Φ_i those of the ^{13}C pulses. In this experiment, the measured chemical shift is determined solely by the orientation of the crystallite in the magnetic field. The sample is rotated by 90° during the mixing time, so each crystallite in the powdered sample 'sees' two different magnetic field directions during t_1 and t_2, which results in two different evolution frequencies ω_1 and ω_2. The resulting 2D powder patterns contain information about all of the ^{13}C chemical shift tensors in the sample, and are characteristic of the 90° sample rotation.

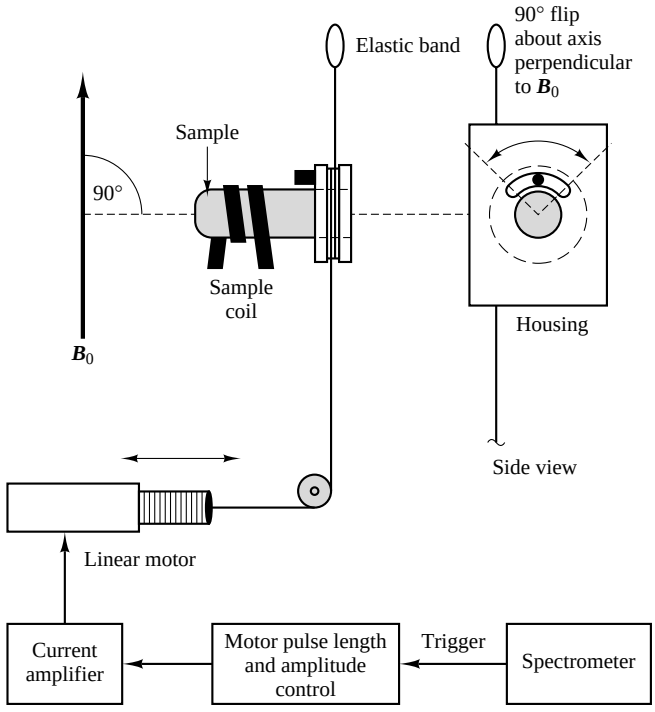

Figure 1 90° sample reorientation apparatus. The powdered sample is placed in a shortened 12 mm NMR tube, which is then epoxied into the sample pulley. The pulley is rotated inside a circular recess in the housing by pulling the attached string

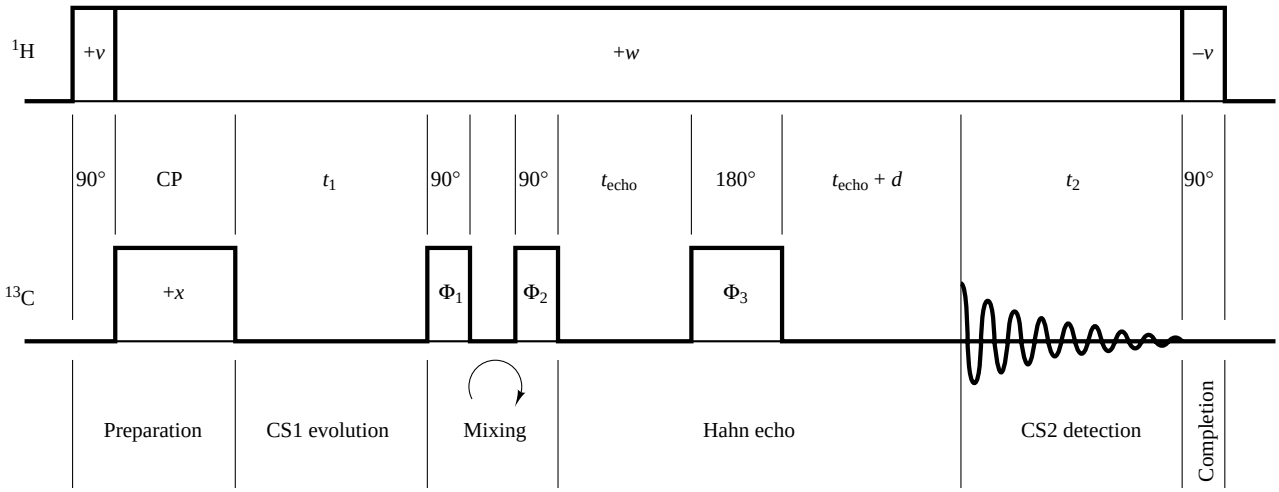

Figure 2 Chemical shift–chemical shift correlation pulse sequence. Phase cycling corrects for artifacts resulting from ^{13}C T_1 relaxation during the mixing time and cross polarization during the 180° echo pulse, and allows for quadrature detection during the evolution dimension. The mixing period is 35 ms long

The 2D data are gathered according to the prescription of States, Haberkorn, and Ruben,[5] which gives amplitude-modulated hypercomplex multidimensional data sets.

3 RESULTS

The spectrum in Figure 3 is a contour plot of the 2D chemical shift correlation spectrum of ferrocene, with the more familiar 1D projections of the spectrum shown at the sides. Ferrocene has an axially symmetric ^{13}C chemical shift tensor whose orientation is determined by its motion about the molecular rotational axis; $\delta_{\parallel}$ is the principal value of the chemical shift tensor when the field is parallel to ferrocene's rotational axis, and $\delta_{\perp}$ is the degenerate principal value when the field lies parallel to the ring plane. An axially symmetric 2D powder pattern has three large peaks connected by ridges forming a right isosceles triangular pattern with a deep basin in its interior. Comparing the features of the 2D spectrum with its 1D projections indicates that the peaks or cusps define the principal values of the chemical shift tensor.

The ferrocene spectrum is a simple example of a 2D chemical shift correlation pattern. The principal values could have been obtained equally well from a 1D powder spectrum. The 2D technique is significantly more useful when multiple overlapping bands in a 1D powder spectrum leave unresolvable ambiguities. The spectrum of coronene shown in Figure 4 illustrates how powerful the 2D correlation technique is. Coronene has three sets of unique carbons, and the molecule rapidly rotates about an axis perpendicular to its plane, averaging all of its chemical shift tensors to axial symmetry. The foremost challenge in measuring the principal values of the three coronene tensors from the 1D powder spectrum was to determine which pairs of the six breakpoints are grouped together as the principal values for each of the three different ^{13}C nuclei in the molecule. The spectrum in Figure 4 exhibits how these groupings were readily determined with the 2D chemical shift correlation experiment. The correlative properties of the powder pattern allows immediate connection of principal value pairs from each chemically distinct nucleus.

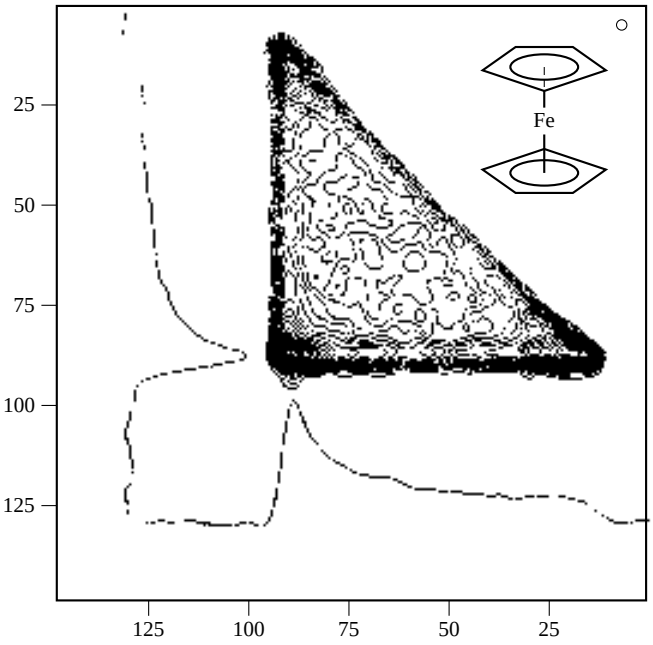

Figure 3 Equal-amplitude contour plot of the 2D ^{13}C chemical shift–chemical shift correlation experimental spectrum of ferrocene (dicyclopentadienyliron). The scales are in ppm from liquid TMS (positive values are to high frequency). ω_1 is the vertical dimension and ω_2 is the horizontal dimension. The diameter of the small circle plotted in the upper right-hand corner is the full width at halfheight of the Gaussian broadening ($\Delta\omega_G$) function that is convolved with the data. In this figure, $\Delta\omega_G$ = 3 ppm. The 1D powder projections are plotted on the vertical and horizontal axes

The 2D chemical shift correlation spectrum of isotactic polypropylene is shown in Figure 5. This spectrum indicates that the added correlation and resolution of two dimensions resolves three different chemical shift tensor patterns in a situation where the 1D powder pattern is intractable.

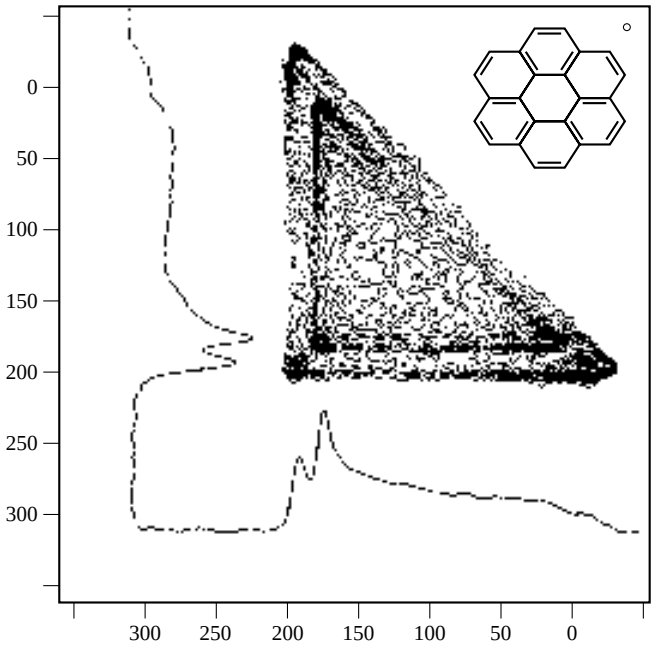

Figure 4 Contour plot of the spectrum of coronene (hexabenzobenzene). The Gaussian broadening in this figure is 3 ppm

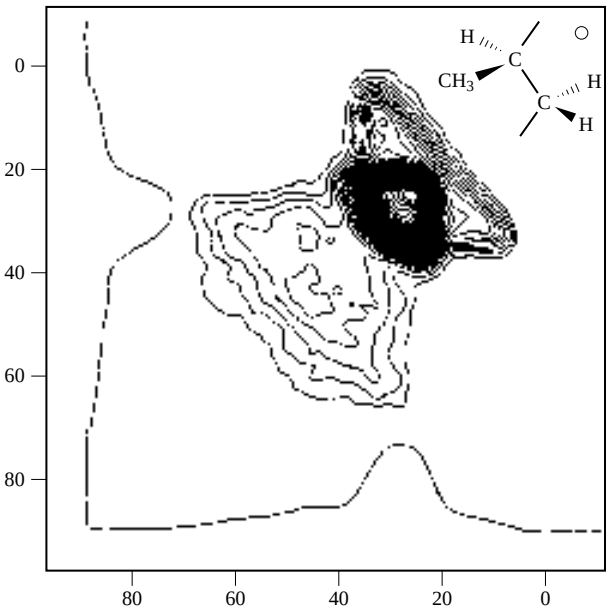

Figure 5 Contour plot of the spectrum of isotactic polypropylene. The Gaussian broadening in this figure is approximately 2.5 ppm

In an effort to determine the limits of resolution of this technique, a spectrum of methyl α-D-glucopyranoside was acquired (Figure 6). Methyl α-D-glucopyranoside has seven carbon types, whose severely overlapped ^{13}C chemical shift tensors have been measured in a single crystal, and therefore is an excellent candidate for comparison of techniques. The 1D powder spectrum is severely overlapped, with almost no distinguishable features to facilitate conventional fitting techniques. However, the 2D powder pattern does show a considerable improvement in resolution. At least four distinct powder patterns may be immediately recognized by the

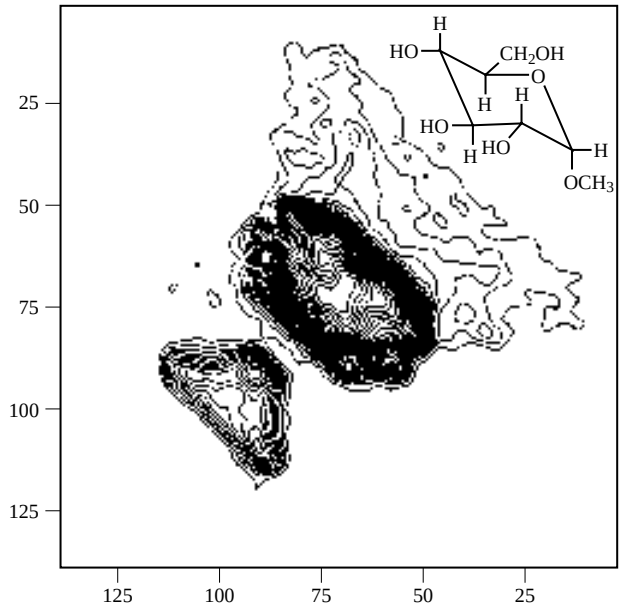

Figure 6 Contour plot of the spectrum of methyl α-D-glucopyranoside

outlines of the cliff-like features that form the boundaries of the patterns. This spectrum was simulated by successively subtracting out simulated components from the pattern and finding new component patterns in the residual spectrum. Prior knowledge of the tensor principal values was not used. The results of this fitting agree well with previous results,[6] as shown in Figure 7. Although this fitting technique left two possible shift tensors unresolved, one of the simulated component patterns has roughly twice the integrated amplitude of the remaining five patterns, indicating that the two unresolved tensor patterns have very similar principal values, which could not be reliably distinguished with this analysis technique.

The measurement of six of the seven ^{13}C chemical shift tensor principal values in methyl α-D-glucopyranoside represents a remarkable increase in resolution over 1D powder spectroscopy, and perhaps an upper limit on the number of overlapping powder patterns that can be successfully resolved with the 2D chemical shift correlation technique. The agreement between the single crystal data and the powder fitting data is very good.

The increased resolving power of the chemical shift correlation experiment has been applied to complex samples such as coals in order to measure the aromaticity of the sample. Figure 8 shows the spectrum of the Argonne premium coal, Pocahontas #3. This spectrum has a clear segregation of amplitude between two different regions. The small volume in the upper right-hand corner of the spectrum has a relatively narrow chemical shift anisotropy and an average chemical shift of approximately 25 ppm. These chemical shifts fall into a range expected from aliphatic carbon nuclei; therefore, this volume represents the aliphatic fraction of the sample. The triangular shaped volume in the lower left-hand corner of this spectrum has a broader chemical shift anisotropy, and an average chemical shift of approximately 130 ppm, and represents the aromatic fraction of the sample. The ratio of these two volumes gives an estimate of the sample's aromaticity:

$$\%\ \text{Aromaticity} = \frac{\text{Volume}_{\text{aromatic}}}{\text{Volume}_{\text{aromatic}} + \text{Volume}_{\text{aliphatic}}} \times 100\% \qquad (1)$$

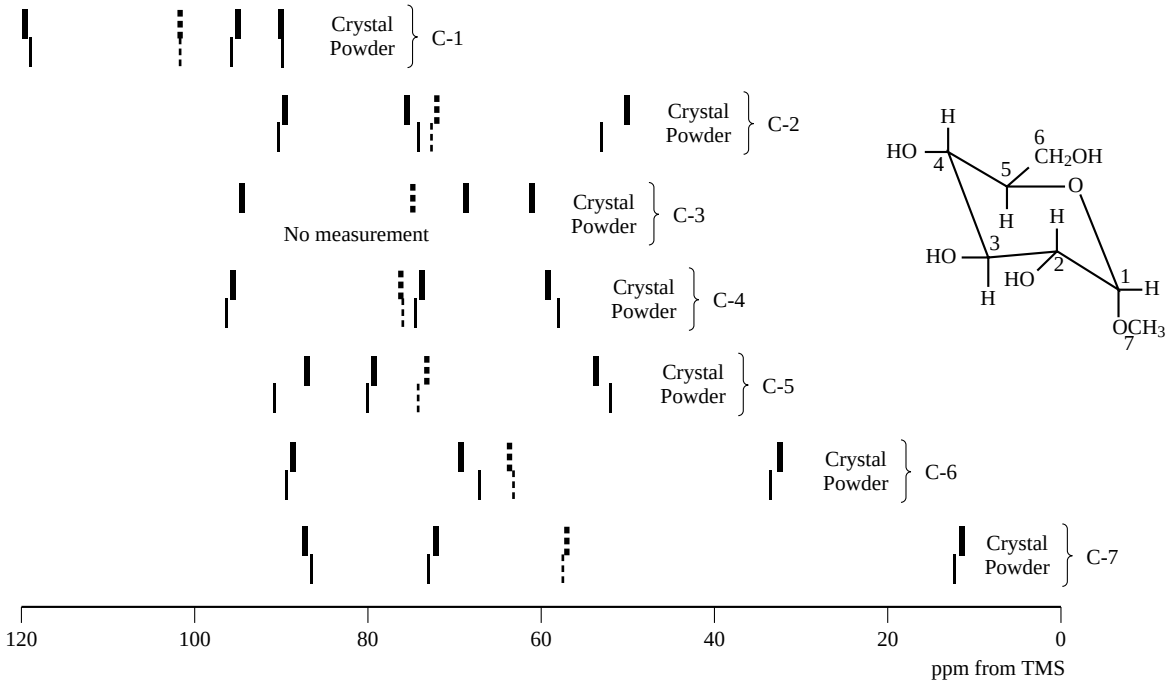

Figure 7 Chemical shift tensor principal values of methyl α-D-glucopyranoside. The bold lines indicate values measured in a single crystal experiment.[6] The lighter faced lines indicate values measured from fitting the 2D powder spectrum. The dashed lines indicate the values of the average chemical shift, i.e., $\delta_{\text{average}} = \frac{1}{3}(\delta_{11} + \delta_{22} + \delta_{33})$

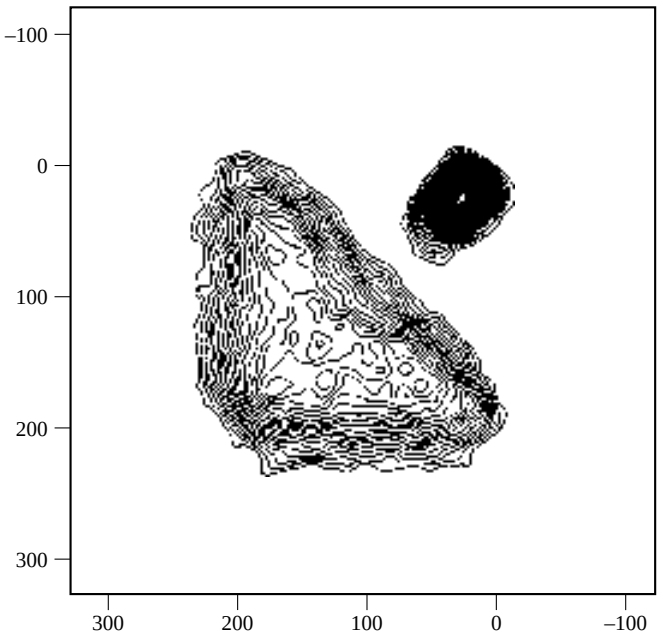

Figure 8 Contour plot of the spectrum of the Argonne premium coal, Pocahontas #3. The Gaussian broadening in this figure is approximately 20 ppm

This quantity has been measured from the spectrum in Figure 8, and the result is 87%. There is good agreement between the aromaticity measured from these data and the more conventional CP MAS result of 86%. An advantage of the chemical shift correlation technique is that it is less sensitive to the Hartmann–Hahn matching condition than is the CP MAS technique. This data also has the potential for testing theoretical models that attempt to correlate the components of the chemical structure of coals and related materials with the distributions of chemical shift anisotropy.

4 SIMULATIONS

In order briefly to establish the correspondence between the principal values of the chemical shift tensor and the features of 2D chemical shift correlation spectra, a series of computer simulations for the 90° sample rotation experiment representing the different classes of chemical shift tensors are shown in Figure 9. The general triangular or hexagonal shape of the simulations is a characteristic of the 90° sample rotation experiment. These simulations show the relationships between the ridges and peaks of this new type of 2D spectrum and the breakpoints in the 1D powder spectra, which are plotted as projections below the 2D simulations.

Often, the measurement of principal values from 1D powder patterns is seriously hindered by nonideal distribution of amplitude across the spectrum, especially when cross-polarization techniques are used. The ability to simulate this amplitude distortion in a 2D powder pattern would increase the accuracy of the measurement of principal values. The frequency and amplitude of the NMR signal from a particular nucleus in a given crystallite in a powdered sample is determined by the principal values of its chemical shift tensor and by that crystallite's orientation relative to the external magnetic field. Therefore, the simulation model is parameterized in terms of chemical shift tensor principal values and the three Euler orientation angles α, β, and γ that describe the relative orientation of the nuclear environment with the external magnetic field in a randomly oriented powder.

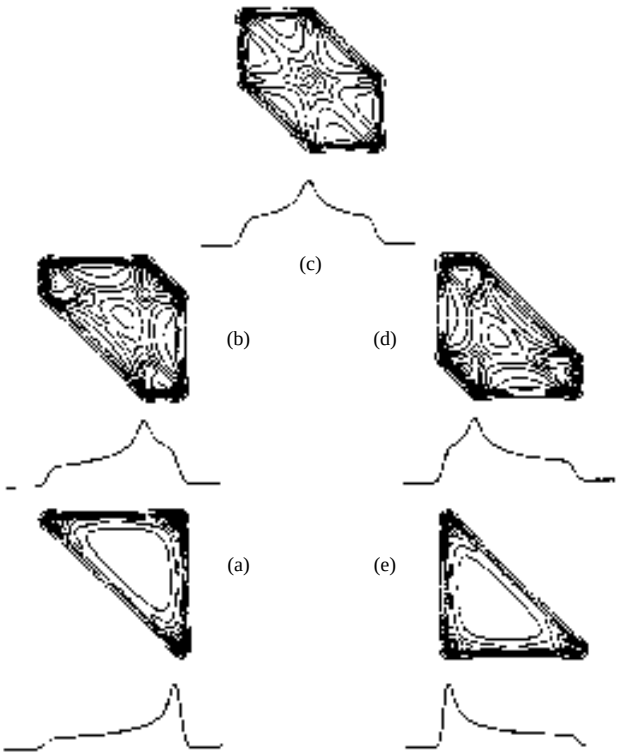

Figure 9 Contour plots of 2D 90° sample rotation simulations resulting from five different chemical shift tensors, showing the correspondence between the features in the 2D powder patterns and conventional 1D powder patterns: (a) axially symmetric chemical shift tensor with low-frequency (upfield) degenerate principal values; (b) general chemical shift tensor with $\delta_{11} - \delta_{22} = 3(\delta_{22} - \delta_{33})$; (c) general chemical shift tensor with $\delta_{11} - \delta_{22}=\delta_{22} - \delta_{33}$; (d) general chemical shift tensor with $3(\delta_{11} - \delta_{22}) = \delta_{22} - \delta_{33}$; (e) axially symmetric chemical shift tensor with high-frequency degenerate principal values

In this experiment, each nucleus in the sample has two resonance frequencies, which correspond to the two different orientations that the nucleus may have with the external field during t_1 and t_2. Assuming a random distribution of crystallite orientations, the simulated hypercomplex 2D FID from a single nucleus in an experiment where the external field is along the x sample axis during t_1 and along the y sample axis during t_2 can be written as

$$\begin{aligned} s_{\text{sim}}(t_1, t_2) = \frac{1}{8\pi^2} \int \mathrm{d}\alpha \sin\beta \, \mathrm{d}\beta \, \mathrm{d}\gamma \, A(\alpha, \beta, \gamma) \\ \times \left[\exp\{\mathrm{i}_1[\omega_x(\alpha, \beta, \gamma) - \omega_0]t_1\} \exp\left(-\frac{t_1^2 \Delta\omega_{\text{G1}}^2}{G^2}\right)\right] \\ \times \left[\exp\{\mathrm{i}_2[\omega_y(\alpha, \beta, \gamma) - \omega_0]t_2\} \exp\left(-\frac{t_2^2 \Delta\omega_{\text{G2}}^2}{G^2}\right)\right] \end{aligned} \quad (2)$$

where $A(\alpha, \beta, \gamma)$ is an amplitude weighting function that depends upon the crystallite orientation in the field. The frequency ω_0 is the spectrometer carrier frequency, and $\Delta\omega_{\text{G1}}$ and $\Delta\omega_{\text{G2}}$ are Gaussian broadenings in the t_1 and t_2 dimensions, respectively. G^2 is a constant equal to $4 \ln (2)/\pi^2$. The imaginary units i_1 and i_2 (with $\mathrm{i}_1^2 = \mathrm{i}_2^2 = -1$) distinguish the independent imaginary parts of the hypercomplex t_1 and t_2 data.[7] The resonance frequencies for the x and y field directions of a given crystallite with an α, β, γ orientation relative to the principal axis frame of the tensor are given by the matrix products

$$\left.\begin{aligned} \omega_x(\alpha, \beta, \gamma) = \boldsymbol{x}^{-1}\mathbf{R}^{-1}(\alpha, \beta, \gamma)\boldsymbol{\delta}\mathbf{R}(\alpha, \beta, \gamma)\boldsymbol{x} \\ \omega_y(\alpha, \beta, \gamma) = \boldsymbol{y}^{-1}\mathbf{R}^{-1}(\alpha, \beta, \gamma)\boldsymbol{\delta}\mathbf{R}(\alpha, \beta, \gamma)\boldsymbol{y} \end{aligned}\right\} \quad (3)$$

where $\boldsymbol{x}$ and $\boldsymbol{y}$ are unit column vectors in the x and y sample frame directions, respectively. The unitary rotation matrix $\mathbf{R}(\alpha, \beta, \gamma)$ rotates the chemical shift tensor $\boldsymbol{\delta}$ from its principal axis frame to the sample frame, and this tensor in the principal axis frame is

$$\boldsymbol{\delta} = \begin{bmatrix} \delta_{11} & 0 & 0 \\ 0 & \delta_{22} & 0 \\ 0 & 0 & \delta_{33} \end{bmatrix} \quad (4)$$

Nonideal amplitude distributions in powder spectra are primarily artifacts resulting from the orientational dependence of both cross polarization and spin relaxation. Functions of orientation described by the Euler angles α, β, and γ are conveniently expanded in the Wigner rotation matrices $\mathcal{D}^{(j)}_{m',m}(\alpha, \beta, \gamma)$, which form a complete, orthonormal basis set.[8,9] The three-dimensional amplitude weighting function that accounts for the polarization efficiency can be expanded as

$$A(\alpha, \beta, \gamma) = \sum_{j,m',m} a^{(j)}_{m',m} \mathcal{D}^{(j)}_{m',m}(\alpha, \beta, \gamma) \quad (5)$$

where the j sum is from 0 to ∞ and the m and m' sums run from $-j$ to $+j$. The expansion coefficients $a^{(j)}_{m',m}$ thus provide a complete description of the different amplitudes resulting from all possible crystallite orientations. The mathematical construct of Equation (5) can also be used to characterize ordering in partially oriented samples.

It can be shown that the simulated 2D FID may be expanded in a complete set of Wigner 2D subFIDs, where the linear coefficients $a^{(j)}_{m',m}$ are the weighting factors for each of the orthonormal Wigner subFIDs $s^{(j)}_{m',m}(t_1, t_2)$ in the basis set

$$s_{\text{sim}}(t_1, t_2) = \sum_{j,m',m} a^{(j)}_{m'm} s^{(j)}_{m',m}(t_1, t_2) \quad (6)$$

These functions can be used to determine any general amplitude distribution in the spectrum using standard linear fitting techniques.

Although all of the fitting is done in the time domain, the 2D Fourier transform of the 2D FID produces the more familiar simulated 2D spectra:[7]

$$\begin{aligned} S(\omega_1, \omega_2) = \int_{-\infty}^{+\infty} \mathrm{d}t_1 \exp(-\mathrm{i}_1\omega t_1) \\ \times \int_{-\infty}^{+\infty} \mathrm{d}t_2 \exp(-\mathrm{i}_2\omega t_2) s(t_1, t_2) \end{aligned} \quad (7)$$

Likewise, the Fourier transforms of the subFIDs give the subspectra:[10]

$$\begin{aligned} S^{(j)}_{m',m}(\omega_1, \omega_2) = \int_{-\infty}^{+\infty} \mathrm{d}t_1 \exp(-\mathrm{i}_1\omega t_1) \\ \times \int_{-\infty}^{+\infty} \mathrm{d}t_2 \exp(-\mathrm{i}_2\omega t_2) s^{(j)}_{m',m}(t_1, t_2) \end{aligned} \quad (8)$$

The first subspectrum in the series, $S^0_{0,0}$, is the 'ideal' powder spectrum. This subspectrum represents the case where each

spin in the sample contributes the same amplitude to the spectrum, and where every crystallite orientation is equally probable. This term is also the only member of the expansion whose integrated spectrum has a nonzero volume. The higher order subspectra in the series are positive in some areas and negative in others, so that they integrate to zero volume over the domain of the spectrum. These higher order subFIDs or subspectra describe modifications in the spectral amplitude that deviate from the 'ideal' powder response, and may be used to characterize the orientational dependence of the amplitude that results either from experimental artifacts or from macroscopically ordered samples. It has been found for most powder spectra that the number of terms necessary to simulate effectively all of the deficiencies in the spectrum is relatively small, indicating that $A(\alpha, \beta, \gamma)$ is a fairly smooth function in α, β, and γ. It has also been found for the 2D powder spectra presented here that the coefficient $a^0_{0,0}$ is much larger than the higher order coefficients, supporting the general observation that the amplitude distribution across a powder pattern is nearly ideal, with only relatively small nonideal contributions.

5 DISCUSSION

The chemical shift tensor principal values reported here result from fitting simulations calculated from Equation (6) to the data. The fitting is done in the time domain, where the fractional residual is taken as the figure of merit for any given simulation, and is minimized to find the 'best fit'. The fractional residual is defined as

$$\text{fractional residual} = \frac{\sum_{t_1,t_2} |s_{\text{data}}(t_1, t_2) - k s_{\text{sim}}(t_1, t_2)|^2}{\sum_{t_1,t_2} |s_{\text{data}}(t_1, t_2)|^2} \quad (9)$$

where $s_{\text{data}}(t_1, t_2)$ is the 2D hypercomplex data FID, and k is a scaling constant that adjusts for experimental factors in the acquisition and processing of the data.

The 'best fit' results for ferrocene, coronene, polyethylene, and polypropylene given in Table 1 are in excellent agreement with previous results.[11–14] The chemical shift principal values differ by 3 ppm or less from the values measured with other techniques, while the average chemical shifts i.e., $\delta_{\text{average}} = \frac{1}{3}(\delta_{11} + \delta_{22} + \delta_{33})$ differ from published CP MAS isotropic chemical shifts by 1 ppm or less.

This 2D technique has some distinct advantages over other methods for measuring ^{13}C shift tensor principal values in complex powdered solids. The inherent correlation and resolution advantage of 2D powder spectroscopy over conventional 1D techniques is evident in the spectra of coronene, polypropylene, methyl α-D-glucopyranoside, and coal. Powder patterns that overlap severely in 1D spectra can often be untangled with this 2D spectroscopy. Another powerful advantage of the technique is that the data can be simulated and fit with a high degree of fidelity using a straightforward physical model.

Another significant advantage of the technique is its simplicity. The sample does not spin at high speeds at the

Table 1 Chemical Shift Tensor Principal Values from Fits (ppm from External Liquid TMS)

	$\delta_\perp$		$\delta_\parallel$	δ_{average}	δ_{liquid}
Ferrocene:					
This work	94		17	68	
Previous results[11]	94		18	69	69.4
	$\delta_\perp$		$\delta_\parallel$	δ_{average}	δ_{CPMAS}
Coronene:					
(Protonated)					
This work	178		15	124	
Previous results[12]	175		15	122	123.5
(Bridging)					
This work	197		−15	126	
Previous results[12]	196		−16	125	126.0
(Inner)					
This work	193		−26	120	
Previous results[12]	191		−26	119	119.8
	δ_{11}	δ_{22}	δ_{33}	δ_{average}	δ_{CPMAS}
Polypropylene:					
(Methine)					
This work	37	22	22	27	26.5
Previous results	38[14]	21[14]	21[14]	27[14]	26.5[13]
(Methylene)					
This work	65	45	25	45	44.5
Previous results	65[14]	44[14]	26[14]	45[14]	44.5[13]
(Methyl)					
This work	32	32	5	23	22.5
Previous results	32[14]	32[14]	3[14]	22[14]	22.5[13]

magic angle; therefore, the probe can be designed to accept a larger volume sample inside a transverse solenoidal coil in order to optimize sensitivity. The 90° rotation of the sample is not difficult to accomplish accurately, both in terms of constructing and driving the mechanism. The sample is stationary during the cross-polarization time, which results in more effective Hartmann–Hahn matching. The principal values of the chemical shift are represented in frequencies measured from the spectrum, not from information encoded in spinning sideband amplitudes, as in slow spinning techniques. Furthermore, the frequencies of the principal values of the chemical shift tensors are measured directly from the spectra; there is no scaling factor relating the frequencies measured in the spectrum to the principal values of the chemical shift tensor.

6 RELATED ARTICLES

Chemical Shift Tensor Measurement in Solids; Chemical Shift Tensors; Chemical Shift Tensors in Single Crystals; Coal Structure from Solid State NMR; Double Resonance; Fossil Fuels; Magic Angle Turning and Hopping; Multidimensional Spectroscopy: Concepts; Polymer Dynamics and Order from Multidimensional Solid State NMR; Polymer Physics; Sideband Analysis in Magic Angle Spinning NMR of Solids; Variable Angle Sample Spinning.

7 REFERENCES

1. J. Jeener, B. H. Meier, P. Bachmann, and R. R. Ernst, *J. Chem Phys.*, 1979, **71**, 4546.
2. C. M. Carter, D. W. Alderman, and D. M. Grant, *J. Magn. Reson.*, 1985, **65**, 183.
3. P. M. Henrichs, *Macromolecules*, 1987, **20**, 2099.
4. C. D. Hughes, M. H. Sherwood, D. W. Alderman, and D. M. Grant, *J. Magn. Reson., Ser. A*, 1993, **102**, 58.
5. D. J. States, R. A. Haberkorn, and D. J. Ruben, *J. Magn. Reson.*, 1982, **36**, 286.
6. D. L. Sastry, K. Takegoshi, and C. A. McDowell, *Carbohydr. Res.*, 1987, **165**, 161.
7. R. R. Ernst, G. Bodenhausen, and A. Wokaun *Principles of Nuclear Magnetic Resonance in One and Two Dimensions*, Clarendon Press, Oxford, 1987, Chap. 6
8. A. R. Edmonds, *Angular Momentum in Quantum Mechanics*, Princeton University Press, Princeton, NJ, 1960, Chaps. 1 and 4.
9. M. E. Rose, *Elementary Theory of Angular Momentum*, Wiley, New York, 1957.
10. R. Hentschel, J. Schlitter, H. Sillescu, and H. W. Spiess, *J. Chem. Phys.*, 1978, **68**, 56.
11. D. E. Wemmer and A. Pines, *J. Am. Chem. Soc.*, 1980, **103**, 34.
12. H. A. Resing and D. L. VanderHart, *Z. Phys. Chem.*, 1987, **151**, 137.
13. A. Bunn, M. E. A. Cudby, R. K. Harris, K. J. Packer, and B. J. Say, *J. Chem. Soc., Chem. Commun.*, **1981**, 15.
14. T. Nakai, J. Ashida and T. Terao, *Magn. Reson. Chem.*, 1989, **27**, 666.

Biographical Sketch

Craig D. Hughes. *b* 1963. B.S., 1985, New Mexico Institute of Mining and Technology; Ph.D., University of Utah, 1992. Introduced to NMR by L. G. Werbelow and D. M. Grant. Research specialties; characterization of powdered, heterogeneous and oriented materials, catalytic zeolites, and imaging.

Ultraslow Motions in Solids

David C. Ailion

University of Utah, Salt Lake City, UT, USA

1	Introduction	1
2	Spin–Lattice Relaxation in the Rotating Frame ($T_{1\rho}$)	1
3	Dipolar Relaxation in the Laboratory Frame (T_{1D})	3
4	Dipolar Relaxation in the Rotating Frame ($T_{1D\rho}$)	5
5	Experimental Results using Ultraslow Motion Techniques	5
6	Conclusions	7
7	Related Articles	7
8	References	8

1 INTRODUCTION

The use of conventional NMR relaxation measurement techniques for studying moderately rapid atomic motions may result in observation of the following phenomena:

1. a decrease (or a minimum)[1] of the spin–lattice relation time T_1 in a plot of T_1 versus temperature;
2. motional narrowing of the resonance linewidth[2] (or motional lengthening of the free induction decay or the spin–spin relaxation time T_2);
3. a decrease[2] in the Hahn echo decay time compared to the Carr–Purcell–Meiboom–Gill (CPMG)[3] time constant (see ***Diffusion Measurements by Magnetic Field Gradient Methods***).

The term ultraslow motions[4] refers to motions that are observable by NMR but are sufficiently infrequent that they produce no motional narrowing of the resonance line and make no measurable contribution to the spin–lattice relaxation rate. Typical T_1 minima correspond to motions for which the mean atomic jump rate $1/\tau_c$ is of the order of the nuclear precession frequency Ω_0 ($\approx 10^8$ s^{-1}, typically).[1] Motions having jump frequencies one or two orders of magnitude higher or lower than that for the minimum usually still give measurable contributions to the relaxation rate. Since the condition for motional narrowing is that the atomic jump time τ_c be less than T_2, ultraslow motions are typically those for which $T_2 < \tau_c < T_1$.[4] A very wide range of atomic motions falls under this classification, since $T_2 \approx 10^{-4}$–10^{-5} s in solids, while T_1 can be as long as several seconds to hours in length.

It is clearly desirable to extend to lower frequencies the frequency range (and thus the temperature range) of motions that can be studied. One advantage of studying a wider range of atomic motions is that motions having slightly different activation energies may be distinguished if they are observed over a sufficiently wide temperature range. Also, motions associated with a particular phenomenon, like a phase transition, may occur only in a particular temperature region.

The basic idea of the ultraslow motion techniques can be understood by considering what happens to a T_1 minimum if the field B_0, and thus the resonant frequency, is greatly reduced. According to the Bloembergen, Purcell, and Pound (BPP) theory,[1] atomic diffusion or molecular reorientations will cause fluctuations in the dipolar interactions that can be treated as perturbations on the Zeeman levels, and, furthermore, these fluctuations can be described by an exponential correlation function. BPP derived for T_1 an expression of the form

$$\frac{1}{T_1} \approx \frac{\Omega_d^2 \tau_c}{1 + \Omega_0^2 \tau_c^2} \tag{1}$$

where Ω_0 is the Larmor angular frequency and Ω_d is the angular frequency corresponding to a typical dipolar splitting. (Actually, there are additional terms of similar form. For interactions involving identical spins, there is an extra term proportional to $1/(1 + 4\Omega_0^2\tau_0^2)$; for heteronuclear systems, there are also terms having $[1 + (\Omega_I - \Omega_S)^2\tau_c^2]$ and $[1 + (\Omega_I + \Omega_S)^2\tau_c^2]$ in the denominator.) Equation (1) predicts that, in a temperature plot of T_1, there will be a minimum value for T_1 at the temperature for which $\tau_c \approx \Omega_0^{-1}$, in agreement with the idea that the transition probability $1/T_1$ arises largely from frequency components in the perturbation that equal the energy level spacing divided by $\hbar$. If Ω_0 is reduced, the minimum will correspond to a longer value of τ_c, and thus to lower frequency motions. For a typical diffusion mechanism, atomic jumps become less frequent as the temperature is lowered. Thus the T_1 minimum in a low field will occur at a lower temperature than would the T_1 minimum at a higher field.

There are experimental problems associated with attempting to study relaxation in very weak fields where the NMR signal might be very small (see ***Zero Field NMR***). There are also theoretical difficulties, since the theory underlying equation (1) is a perturbation theory that treats the fluctuating dipolar Hamiltonian due to diffusion as a perturbation on the Zeeman Hamiltonian; such an assumption may not be valid in very weak applied fields. Solutions to both these problems will now be discussed. Ultraslow motion techniques have been reviewed by Ailion.[5–7]

2 SPIN–LATTICE RELAXATION IN THE ROTATING FRAME ($T_{1\rho}$)

One approach to studying relaxation in weak applied fields and yet having the strong signal strength for a large field is to use the field cycling method[8,9] (see ***Field Cycling Experiments***), in which the external magnetic field is reduced adiabatically to a small value and subsequently increased adiabatically back to the original value, where the signal is measured. If there are no irreversible processes, the entropy will be constant, and the full signal will be measured after the remagnetization. However, atomic diffusion constitutes an irreversible process, which will cause a loss of dipolar order. Thus, by plotting the signal strength versus time in the demagnetized state, the weak field relaxation can in principle be measured. One difficulty with this approach is that it may be difficult to satisfy the requirement that the demagnetization and remagnetization processes be sufficiently slow that the adiabatic condition is satisfied and yet be rapid compared with T_1.

An alternate approach is to measure $T_{1\rho}$, the spin–lattice relaxation time in the rotating frame of the rf field $\boldsymbol{B}_1$ (see ***Magnetization Transfer between Water and Macromolecules in Proton MRI***). According to Redfield,[10] a spin system

in an rf field strong enough to saturate the resonance line (i.e., $\gamma^2 B_1^2 T_1 T_2 \gg 1$) will form a canonical distribution among energy levels separated by γB_{eff} rather than γB_0, where the effective field $\boldsymbol{B}_{\text{eff}}$ in a frame rotating at angular frequency ω is given by

$$\boldsymbol{B}_{\text{eff}} = B_1 \boldsymbol{i} + (B_0 - \omega/\gamma)\boldsymbol{k} \tag{2}$$

In this case, the spins will, after equilibrium has been achieved, be characterized by a 'spin temperature in the rotating frame', which means that Curie's law will hold, but with $\boldsymbol{M}_{\text{eq}} = C\boldsymbol{H}_{\text{eff}}/T$. The significance is that, at exact resonance ($B_0 = \omega/\gamma$), the equilibrium magnetization $\boldsymbol{M}_{\text{eq}}$ will be parallel to $\boldsymbol{B}_1$ rather than to $\boldsymbol{B}_0$. The $T_{1\rho}$ minimum will then occur when $\gamma B_1 \tau_c \approx 1$, for B_0 at exact resonance. Since B_1 is typically of order 1–50 G, this minimum arises from much lower frequency motions than does the normal T_1 minimum. If B_1 is much larger than the magnetic dipolar or electric quadrupolar local fields, the dipolar and quadrupolar fluctuations can still be treated by perturbation theory (this approach is called the 'weak collision' theory).[11] If, on the other hand, B_1 is comparable to or less than the dipolar or quadrupolar local fields, perturbation theory fails, and a different theory, called the 'strong collision' theory,[12] must be used. In this article, we shall consider the case for a spin-$\frac{1}{2}$ nucleus or one in which quadrupolar interactions can be neglected; the inclusion of quadrupolar interactions in the strong collision theory has been described by Ailion.[5]

2.1 Weak Collision Theory

All of the weak collision calculations are applications of the BPP theory in which the fluctuating dipolar Hamiltonian is treated as a perturbation on the Zeeman system. The only important difference is that the basic laboratory frame Hamiltonian is replaced by a rotating frame Hamiltonian in which $\boldsymbol{B}_0$ is replaced by $\boldsymbol{B}_{\text{eff}}$, as given by equation (2). At exact resonance, this theory predicts that $T_{1\rho}$ should exhibit a low-frequency minimum of the form

$$\frac{1}{T_{1\rho}} = K \frac{\tau_c}{1 + 4\Omega_1^2 \tau_c^2} \tag{3}$$

where Ω_1 (= γB_1) is proportional to the energy level splitting in the rotating frame. Thus the $T_{1\rho}$ minimum occurs when $\tau_c \approx (2\Omega_1)^{-1}$, which may be several orders of magnitude longer than the value of τ_c at a typical T_1 minimum. Accordingly, a $T_{1\rho}$ minimum is deeper than a T_1 minimum, and corresponds to slower atomic motions occurring at lower temperatures, as shown in Figure 1.

2.2 Strong Collision Theory

In order to get even more effective relaxation so as to observe even lower frequency motions, B_1, and thus Ω_1 in equation (3), can be reduced to a value comparable to the local dipolar field, or even to zero (e.g., by adiabatic demagnetization in the rotating frame (ADRF),[13] which is discussed in Section 3.3). In this case, equation (3) would predict that the minimum would not occur unless τ_c were infinite. However, perturbation theories like BPP and the weak collision theory will not be valid, since the perturbation

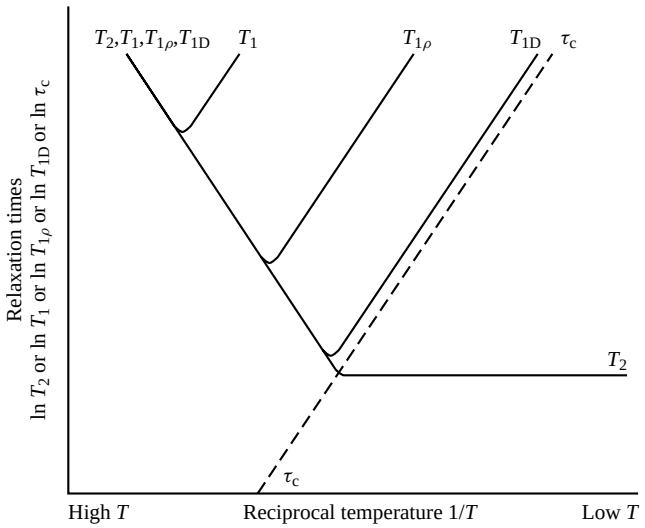

Figure 1 Temperature plot of relaxation times (T_2, T_1, $T_{1\rho}$, and T_{1D}) and atomic jump time τ_c. (Reproduced by permission of Academic Press from D. C. Ailion, in 'Methods of Experimental Physics', ed. J. N. Mundy, S. J. Rothman, M. J. Fluss, and L. C. Smedskjaer, Academic Press, Orlando, 1983, Vol. 21, Chap. 6)

(the dipolar Hamiltonian) in this case is comparable to or larger than the unperturbed Hamiltonian (the Zeeman Hamiltonian). Nevertheless, the condition for the relaxation time minimum in zero magnetic field can still be easily understood. The underlying physical basis for all relaxation time minima is that the most effective relaxation (and thus the minimum) occurs when the principal frequency components of the fluctuating Hamiltonian are comparable to the energy level splitting (in units of $\hbar$). We have seen, for Zeeman relaxation in the laboratory or rotating frames, that this requirement is equivalent to requiring that $1/\tau_c \approx \Omega_0$ or $1/\tau_c \approx \Omega_1$, respectively. For relaxation due to a fluctuating dipolar Hamiltonian in zero field, the energy level splittings $\hbar\Omega_d$ are determined by dipolar interactions. Thus the minimum in zero field occurs when $1/\tau_c \approx \Omega_d$ or $\tau_c \approx T_2$, which is at the onset of motional narrowing. The zero field relaxation time for the case in which quadrupolar interactions can be neglected is commonly called the dipolar relaxation time T_{1D},[14] and is also shown in Figure 1.

In order to study the dynamics of the atomic motions, it is desirable to obtain theoretical expressions that relate the measured relaxation time $T_{1\rho}$ or T_{1D} to the atomic jump time τ_c throughout the temperature range of observations. Experimental procedures for measuring these relaxation times are described in Sections 2.3 and 3.3, respectively. The strong collision theory, originally developed by Slichter and Ailion[12] for low-field relaxation, is not a perturbation theory, but is based on the assumption that sufficient time elapses between diffusion jumps to allow the dipolar and rotating frame Zeeman interactions to cross relax to a common spin temperature between each jump. This temperature is then disturbed by the sudden change in dipolar energy resulting from a jump, but reequilibrates in a time of order T_2 to a new value prior to the next jump. This spin temperature assumption is thus equivalent to requiring that $\tau_c \gg T_2$; hence the strong collision theory will be valid in the 'rigid lattice' below both the $T_{1\rho}$ minimum and the temperature for motional narrowing. If the

ADRF process is complete so that $\boldsymbol{B}_1$ is reduced to zero in the demagnetized state, the ADRF process will have transferred long-range Zeeman order due to spins aligned preferentially along $\boldsymbol{B}_{\text{eff}}$ to short-range dipolar order from spins aligned along their individual local fields. A single diffusion jump per spin will then have a major effect on the relaxation so that, in zero B_1, we should expect $T_{1\rho}$ (= $T_{1\text{D}}$ for zero field) to be of order τ_{c}. In the weak collision regime, much less of the order is dipolar and much more is Zeeman; accordingly, it will take many jumps to relax the magnetization, and $T_{1\rho}$ will be much larger than τ_{c}. Both these effects are shown in Figure 1.

The actual strong collision result[12] for $T_{1\rho}$ at exact resonance due to dipolar fluctuations of a homonuclear (i.e., having only one nuclear species) system in a field B_1 is

$$\frac{1}{T_{1\rho}} = \frac{1}{T_{1\text{D}}} \frac{B_{\text{D}}^2}{B_1^2 + B_{\text{D}}^2} \tag{4}$$

where B_{D} is the dipolar local field. We see that $T_{1\rho}$ reduces to $T_{1\text{D}}$ in the limit as B_1 approaches zero. Note that the local field B_{D} can be determined experimentally by measuring $T_{1\rho}$ versus B_1^2 for fixed $T_{1\text{D}}$ (i.e., at a fixed temperature).

2.3 Experimental Techniques for Measuring $T_{1\rho}$

Essentially all methods for measuring $T_{1\rho}$ start by tipping the magnetization from its original direction (the z direction) to a direction parallel to $\boldsymbol{B}_{\text{eff}}$ in the rotating frame, a procedure called spin locking. For exact resonance, the magnetization would then be aligned parallel to $\boldsymbol{B}_1$ (in contrast to the situation immediately after a $\frac{1}{2}\pi$ pulse, when the magnetization would be perpendicular to $\boldsymbol{B}_1$). $T_{1\rho}$ can then be determined by measuring the magnetization as a function of time τ in the aligned state, since $T_{1\rho}$ is given by

$$M_x = M_0 \exp(-\tau / T_{1\rho}) \tag{5}$$

where M_x is the height of the FID following the turn-off of the variable length B_1 pulse. Figure 2 shows several different pulse sequences for measuring $T_{1\rho}$.

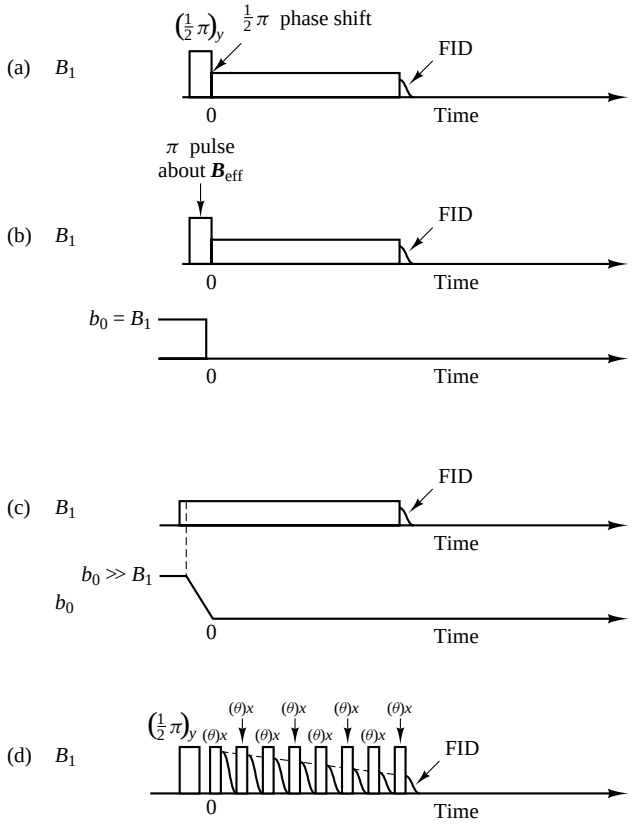

Figure 2 Pulse sequences for measuring $T_{1\rho}$. (a), (b), and (c) all have a spin locking sequence followed by a long rf pulse. The spin locking in (a) consists of a $\frac{1}{2}\pi$ pulse followed by a $\frac{1}{2}\pi$ phase shift. In (b), spin locking is achieved by a π pulse about $\boldsymbol{B}_{\text{eff}}$ (at an angle of 45° with respect to the z direction). In (c), $\boldsymbol{B}_1$ is turned on when the z field (or frequency) is far off resonance, and spin locking is achieved as a result of an adiabatic return to resonance. In (d), spin locking is achieved, as in (a), by a $\frac{1}{2}\pi$ pulse followed by a $\frac{1}{2}\pi$ phase shift; $T_{1\rho}$ is measured by monitoring the FID following short pulses of duration θ. (Reproduced with modifications by permission of Academic Press from D. C. Ailion, in 'Methods of Experimental Physics', ed. J. N. Mundy, S. J. Rothman, M. J. Fluss, and L. C. Smedskjaer, Academic Press, Orlando, 1983, Vol. 21, Chap. 6)

3 DIPOLAR RELAXATION IN THE LABORATORY FRAME ($T_{1\text{D}}$)

3.1 Homonuclear Systems

For homonuclear systems, $T_{1\text{D}}$ can be calculated by considering the fractional change in dipolar energy per jump for N jumping atoms with a time τ_{c} between jumps

$$\frac{1}{T_{1\text{D}}} = \frac{N}{\tau_{\text{c}}} \frac{E_{\text{Df}} - E_{\text{Di}}}{E_{\text{Di}}} = \frac{N}{\tau_{\text{c}}} \frac{\langle \hat{\mathcal{H}}_{\text{Df}}^{(0)} \rangle - \langle \hat{\mathcal{H}}_{\text{Di}}^{(0)} \rangle}{\langle \hat{\mathcal{H}}_{\text{Di}}^{(0)} \rangle} \tag{6}$$

where E_{Di} and E_{Df} are, respectively, the dipolar energies before and after a jump. $\hat{\mathcal{H}}_{\text{Di}}^{(0)}$ and $\hat{\mathcal{H}}_{\text{Df}}^{(0)}$ are, similarly, the secular parts of the dipolar Hamiltonian (i.e., those parts that commute with the Zeeman Hamiltonian), and the angle brackets indicate expectation values. If the system can be characterized by a spin temperature before each jump, the expectation values can be expressed as traces of the quantum mechanical operators, and the following expression is obtained in the high-temperature approximation:[2]

$$\frac{1}{T_{1\text{D}}} = \frac{N}{\tau_{\text{c}}} \frac{\text{Tr}(\hat{\mathcal{H}}_{\text{Di}}^{(0)})^2 - \text{Tr}(\hat{\mathcal{H}}_{\text{Di}}^{(0)} \hat{\mathcal{H}}_{\text{Df}}^{(0)})}{\text{Tr}(\hat{\mathcal{H}}_{\text{Di}}^{(0)})^2} \tag{7}$$

This equation can be rewritten as

$$\frac{1}{T_{1\text{D}}} = \frac{2(1-p)}{\tau_{\text{c}}} \tag{8}$$

where $1 - p$ is a calculable geometrical factor of order unity that characterizes the fractional change in energy resulting from a diffusion jump. Because of this factor, $T_{1\text{D}}$ shows a 10–20% dependence on the orientation of the field $\boldsymbol{B}_0$ relative to the crystal axes, and, furthermore, this anisotropy depends on diffusion mechanism.[15] We also note that $T_{1\text{D}}$ is of order τ_{c}, as we have seen intuitively. Diffusion can be studied by measuring either $T_{1\text{D}}$ or $T_{1\rho}$, provided the relaxation rate due to diffusion is greater than the relaxation rate due to other T_1

processes. The condition for observability of diffusion effects is then that $\tau_c < T_1$. Since T_1 values are typically 10^{-3}–10^3 s, this condition is much less stringent than the condition for motional narrowing ($\tau_c < T_2$).

We should note that the strong collision formula, equation (8), can be used to obtain τ_c from the measured relaxation time, assuming $\tau_c \gg T_2$. BPP-type theories can be used to determine τ_c in the motionally narrowed region where $\tau_c \ll T_2$. In the vicinity of the T_{1D} minimum, neither theory is valid.

3.2 Heteronuclear Systems

A problem arises in the interpretation of T_{1D} measurements for heteronuclear systems in which one nuclear species is diffusing and the others are stationary. For simplicity, consider a system containing two species of comparable abundance and gyromagnetic ratio, whose spin quantum numbers are labeled I and S. Assume further that the I and S spins are in strong contact. (A good example would be the alkali halide LiF, in which every lithium atom is surrounded by fluorines, and vice versa.) The problem is that if the I spins are irradiated and T_{1D} is measured, the result will be the same as when the S spins are irradiated and their T_{1D} measured, independent of which spin is actually diffusing.[16] Hence, from a T_{1D} measurement alone, it would not be possible in this case to determine which species is diffusing. This feature arises because there is normally strong coupling between parts of the dipolar interaction involving different species (i.e., the I–I and S–S dipolar terms are strongly coupled through the I–S interaction). So, if an S spin undergoes a jump, there will be rapid cross relaxation between I–I and S–S terms, which will result in the local heating being transferred rapidly to the entire spin system. Thus, in the strong collision limit, the entire dipolar reservoir is describable by a single temperature prior to a diffusion jump, but either spin species alone is not.

Fortunately, there is a way to determine in a T_{1D} experiment which spin species is diffusing for the case where the S spins are weakly magnetic (small γ_S) compared with the more strongly magnetic I spins (large γ_I). If the relaxation is due to the motion of S spins, T_{1D} will have an enormous anisotropy, whereas for diffusion of I spins the anisotropy will be very small [arising only from the $1 - p$ factor in equation (8)]. A more general strong collision theory,[17] appropriate for heteronuclear systems, shows that, for the case in which the strongly magnetic I spins are diffusing, only the I–I interaction terms need be kept. The resulting expression for $1/T_{1D}$ is similar to equation (8), only with p replaced by p_{II} and τ_c by τ_I:

$$\frac{1}{T_{1D}} = \frac{2(1 - p_{II})}{\tau_I} \tag{9}$$

However, if T_{1D} is due to the diffusion of weakly magnetic S spins then the diffusion produces significant changes in the I–S interaction, with the result that

$$\frac{1}{T_{1D}} = \frac{1 - p_{SI}}{\tau_S} \frac{B_{DIS}^2}{B_{DII}^2} \tag{10}$$

where B_{DIS} and B_{DII} are the I–S and I–I contributions to the dipolar local fields and τ_S is the time between jumps of the S spins. The precise definitions of these local fields and the parameters p_{II} and p_{SI} are given by Stokes and Ailion.[17] equation (10) predicts a strong anisotropy, arising from the factor B_{DIS}^2/B_{DII}^2, which is absent for motion by I atoms. The observation of this anisotropy would confirm that the diffusion arises from the motion of weakly magnetic spins. The experimental verification of this idea is shown in Figure 7 in Section 5 below.

3.3 Experimental Techniques for Measuring T_{1D}

There are basically two commonly used methods for measuring T_{1D}, and each involves transferring order to the dipolar system and then monitoring the decrease in dipolar order arising from dipolar relaxation. The first technique consists in following a spin locking sequence by an adiabatic demagnetization–remagnetization cycle of the rf field.[5] The second consists in creating a state of dipolar order by a pair of phase-shifted pulses and then using a third pulse to monitor the decrease in dipolar order due to the relaxation.[14] Both are shown in Figure 3.

3.3.1 Adiabatic Demagnetization in the Rotating Frame (ADRF)

This method, illustrated in Figure 3(a), is similar to the methods for measuring $T_{1\rho}$, shown in Figure 2(a)–(c), except that spin locking is now followed by an adiabatic demagnetization of B_1 to zero followed a variable time later by an adiabatic remagnetization, so that the NMR signal can be measured. The adiabatic demagnetization transfers order from Zeeman order in the rotating frame to dipolar order (in alignment of the spins along the local fields). The subsequent remagnetization converts the remaining dipolar order (not destroyed by the dipolar relaxation) back to Zeeman order, where it is observed in the form of an FID following the turn-off of the rf pulse. Dipolar relaxation results in a reduction in this FID.

One limitation of this technique arises from the conflicting requirements that the B_1 sweep be adiabatic yet that it also be

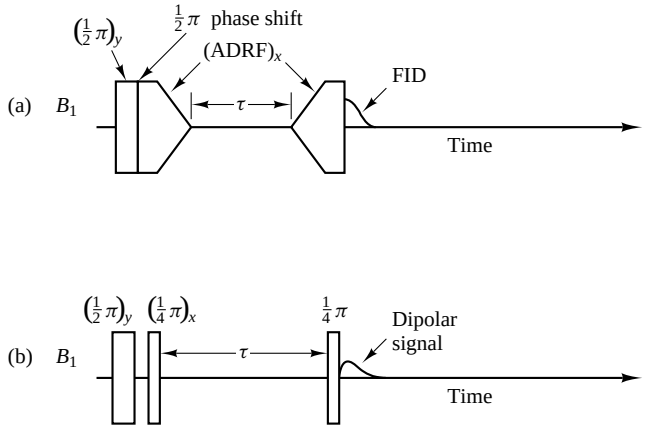

Figure 3 Pulse sequences for measuring T_{1D}. (a) The ADRF sequence showing demagnetization of B_1 following spin locking. (b) The phase-shifted pulse pair sequence. The first two pulses are separated by a time that is approximately T_2 for maximum signal. (Reproduced with modifications by permission of Academic Press from D. C. Ailion, in 'Methods of Experimental Physics', ed. J. N. Mundy, S. J. Rothman, M. J. Fluss, and L. C. Smedskjaer, Academic Press, Orlando, 1983, Vol. 21, Chap. 6)

completed in a time short compared with T_{1D}. This limitation makes it difficult to measure a T_{1D} less than about 0.1–1 ms.

3.3.2 *Phase-Shifted Pulse Pair*

This method, shown in Figure 3(b), avoids the difficulty in measuring a short T_{1D} inherent in ADRF. In this technique, a state of dipolar order is created by applying two closely spaced pulses that are 90° out of phase. The dipolar order is observed by applying a third pulse of arbitrary phase in the (x,y) plane. The dipolar signal that appears after the third pulse is proportional to the time derivative of the FID.

A major disadvantage of this technique is that the maximum efficiency for transfer of order is only about 56%, in contrast to the 100% efficiency theoretically obtainable with ADRF.

In summary, the ADRF technique is superior when measuring longer relaxation times or when $T_{1\rho}$ measurements are also desired, while the phase-shifted pulse pair method is better for very short T_{1D} measurement.

4 DIPOLAR RELAXATION IN THE ROTATING FRAME ($T_{1D\rho}$)

The last paragraph of Section 3.2 described the possibility of using a measurement of the anisotropy of T_{1D} in a single crystal to verify that a weakly magnetic spin species is diffusing. There are two disadvantages of this approach:

1. single crystals are not always available;
2. even though S spins are diffusing, they may not be dominating T_{1D} if they are sufficiently weakly magnetic or low in abundance.

This second feature can be seen in equation (10), since, for $B_{DIS} \ll B_{DII}$, we have $T_{1D} \gg \tau_S$ for weak (S) spin motion. In contrast, for strong (I) spin motion, $T_{1D} \approx \tau_I$. These results arise from the fact that the heat capacities of the terms involving S spins are much smaller than the I–I heat capacities. Accordingly, it may be very difficult, or even impossible, in many cases to study the diffusion of sufficiently weak S spins in a T_{1D} experiment.

In order to determine the diffusing species in a slow motion experiment, it is necessary to identify a parameter that is sensitive to which species is diffusing. If this parameter can be varied by the experimenter then the diffusing species can be identified and studied. Furthermore, for the case of diffusion by spins that are so weakly magnetic as to preclude their study through direct T_{1D} measurement, it is desirable to vary the parameter so as to enhance the temperature change of the entire system resulting from the weak spins' motions. A way to perform such experiments is to observe the dipolar relaxation in the rotating frame of one of the species, say, the I spins. In this frame, only part of the original dipolar Hamiltonian will be secular. The symbol $T_{1D\rho}$ is used for the relaxation time of this secular part of the rotating-frame Hamiltonian, in analogy to T_{1D}, which is the relaxation time for the secular part of the laboratory-frame dipolar Hamiltonian. $T_{1D\rho}$ may be considered to be the dipolar relaxation time in the rotating frame, whereas T_{1D} is the dipolar relaxation time in the laboratory frame. In contrast to T_{1D}, $T_{1D\rho}$ may depend on the angle θ_I between $\boldsymbol{B}_{\text{eff}}$ and $\boldsymbol{B}_0$ in the rotating reference frame. For diffusion by the strong I spins, $T_{1D\rho} = T_{1D}$ and is described by equation (9) for all θ_I except near the magic angle θ_m (defined by $\cos^2\theta_m = \frac{1}{3}$), where there is a small change.[17] However, for diffusion by weak S spins, the following expression is obtained for $T_{1D\rho}$:[17]

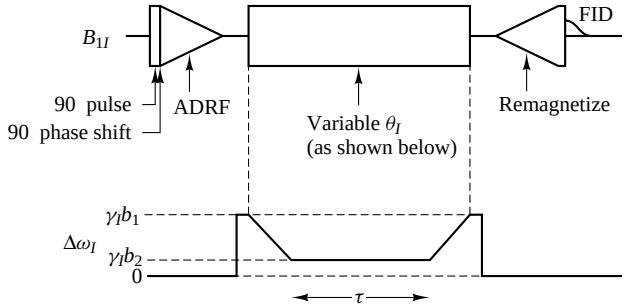

Figure 4 Pulse sequence for measuring $T_{1D\rho}$. The lower part of the figure shows the variation of $\Delta\omega_I = \gamma_I B_0 - \omega_I$, the off-resonance frequency of B_{1I}. (Reproduced with modifications by permission of the American Physical Society from H. T. Stokes and D. C. Ailion, *Phys. Rev. B*, 1978, **18**, 141)

$$\frac{1}{T_{1D\rho}(\theta_I)} = \frac{1}{\tau_S}\,\frac{\cos^2\theta_I B_{DIS}^2(1-p_{SI}) + 2B_{DSS}^2(1-p_{SS})}{[\frac{1}{2}(3\cos^2\theta_I - 1)^2]^2 B_{DII}^2 + \cos^2\theta_I B_{DIS}^2 + B_{DSS}^2} \quad (11)$$

where $1 - p_{SI}$ and $1 - p_{SS}$ are geometrical factors of order unity (analogous to p of the conventional strong collision theory). In contrast to the result obtained in the case of diffusion by the strong I spins, this expression predicts a very strong dependence of $T_{1D\rho}$ on θ_I, which can be observed experimentally, using the pulse sequence described in the next section.

4.1 Experimental Technique for Measuring $T_{1D\rho}$

Figure 4 shows a pulse sequence that can be used to measure $T_{1D\rho}$.[17] A spin locking sequence followed by an ADRF is applied on resonance to the I spins. This step transfers Zeeman order, which was originally along $\boldsymbol{B}_0$, to dipolar order. A large off-resonance pulse is then applied, which does not change the dipolar order but rather changes its reference frame from the laboratory frame to the rotating frame. After establishing a spin temperature in the rotating frame, the frequency of the rf pulse is then reduced adiabatically toward resonance, thereby reducing B_{eff} and changing θ_I. By reversing this sequence, the remaining order is transferred back to laboratory-frame Zeeman order, where it appears as an FID following the turn-off of the rf pulse. If one increases the time τ in the state at θ_I, the magnitude of the resulting FID will be reduced, owing to $T_{1D\rho}$ relaxation. A plot of magnetization versus τ on a semilogarithmic plot will yield a straight line of slope $-1/T_{1D\rho}(\theta_I)$. To vary θ_I, one merely needs to vary the frequency of the pulse (and thus b_2) in the variable time interval τ.

5 EXPERIMENTAL RESULTS USING ULTRASLOW MOTION TECHNIQUES

Ultraslow motions have been widely studied in the last 30 years, generally via $T_{1\rho}$ and T_{1D} measurements. It would be impossible in this article to summarize all the applications. Instead, just a few examples will be given to confirm various

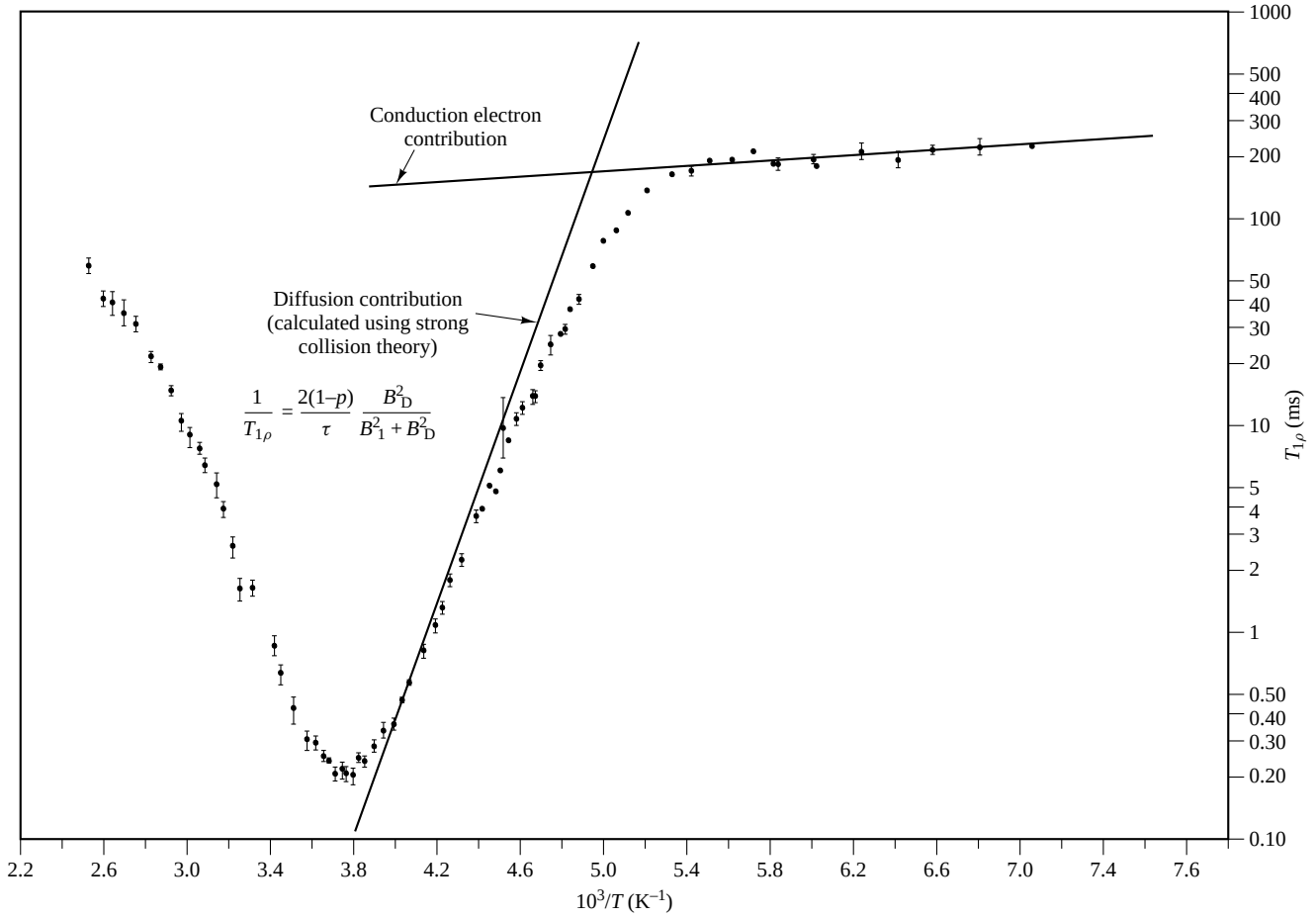

Figure 5 $T_{1\rho}$ versus reciprocal temperature in metallic lithium, with $B_1 = 1.3 \times 10^{-4}$ T. (Reproduced with modifications by permission of the American Physical Society from D. C. Ailion and, C. P. Slichter, *Phys. Rev.*, 1965, **137**, A235)

features of the previous discussion and illustrate the kinds of additional information that may be obtained from such measurements.

Figure 5 shows the original $T_{1\rho}$ data of Ailion and Slichter[18] in metallic lithium. The principal feature is that the $T_{1\rho}$ minimum is symmetric and occurs at the onset of motional narrowing. Furthermore, the minimum value of $T_{1\rho}$ is within an order of magnitude of T_2, as expected from the strong collision theory. Figure 6 shows a plot of the atomic jump time obtained from the experimental $T_{1\rho}$ values, using the strong collision theory. As can be seen, the data exhibit Arrhenius behavior over eight orders of magnitude, and correspond to extremely slow diffusion (of the order of one atomic jump per second) at the lowest temperatures.

Figure 7 shows the verification of the prediction of a very strong anisotropy in T_{1D} described in Section 3.2 for a system having diffusion dominated by weakly magnetic spins. These measurements were performed on a single crystal of KF doped with 0.1% CaF_2. In this case, mobile potassium vacancies are created to compensate for the extra charge of the Ca^{2+}. We thus have a case in which the diffusion of weak spins (potassium) dominates T_{1D} (of fluorine). The solid curve is the calculated anisotropy of the local field factor of equation (10).

Figure 8 shows experimental verification of the strong collision theory for $T_{1D\rho}$. The sample used in this experiment is the same KF:0.1% CaF_2 single crystal used for the data of Figure 7. The curve is calculated from equation (11). All the strong dependence of $T_{1D\rho}$ on θ_I (described earlier) appears, thereby indicating that the weak S spins (in this case, ^{39}K) are diffusing rather than the strong I spins (^{19}F here).

A possibly important potential application of this $T_{1D\rho}$ technique is the study of impurity diffusion. In this case, the S spins are weak because their concentration N_S is small (but γ_S may be large). As in the case of small γ_S, diffusion by the weak S spins should again be characterized by a sharp dip in $T_{1D\rho}$ at the magic angle. For this application to be fruitful, an abundant, easily observable I spin species must exist and be in good thermal contact with the S spins. However, it has been shown[19] that nonadiabatic effects will also give rise to a dip in $T_{1D\rho}$ at the magic angle, which could mask the effect of the S spins' diffusion. Nevertheless, by appropriately modifying the 'adiabatic' sweeps of Figure 4, these effects can be minimized.[19]

An interesting new application of ultraslow motion NMR has been developed[20] to study the ultraslow hopping of selenium atoms between two sites in crystalline Se having well-resolved separate NMR lines. By selective excitation, one of the lines is saturated. Then, as the ^{77}Se atoms jump between the two sites, the magnetization of the previously saturated site builds up and the magnetization of the previously unsaturated site decreases. By measuring the time constant for these decays, the jump time τ_c and the diffusion constant D can

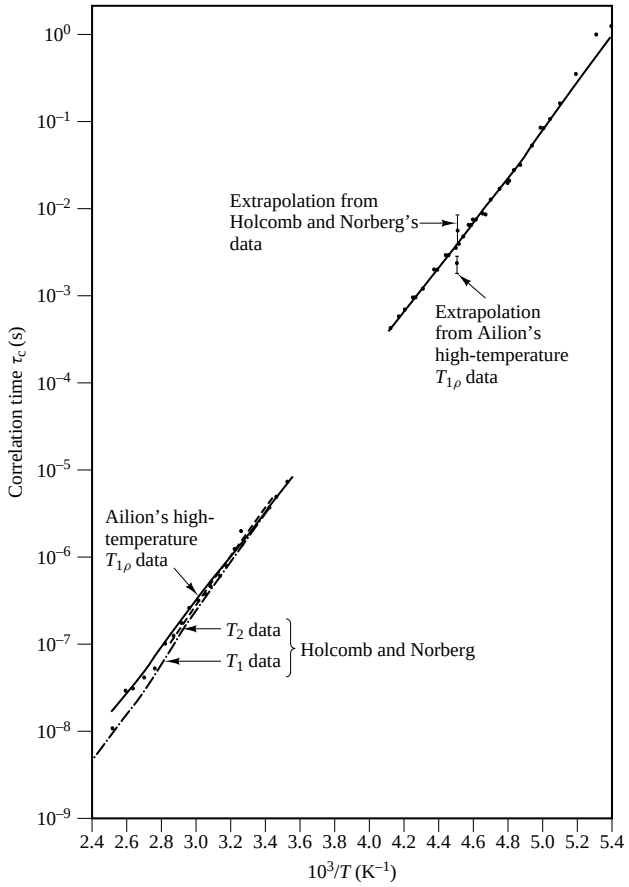

Figure 6 τ_c versus reciprocal temperature in metallic lithium. The experimental points were obtained from the data of Figure 5 using the strong collision theory in the low-temperature region and the weak collision theory in the high-temperature region. The 'gap' in the middle corresponds to the region around the $T_{1\rho}$ minimum where neither theory is valid. In the high temperature region, values of τ_c obtained from Holcomb and Norberg[21] were also plotted. (Reproduced with modifications by permission of the American Physical Society from D. C. Ailion and C. P. Slichter, *Phys. Rev.*, 1965, **137**, A235)

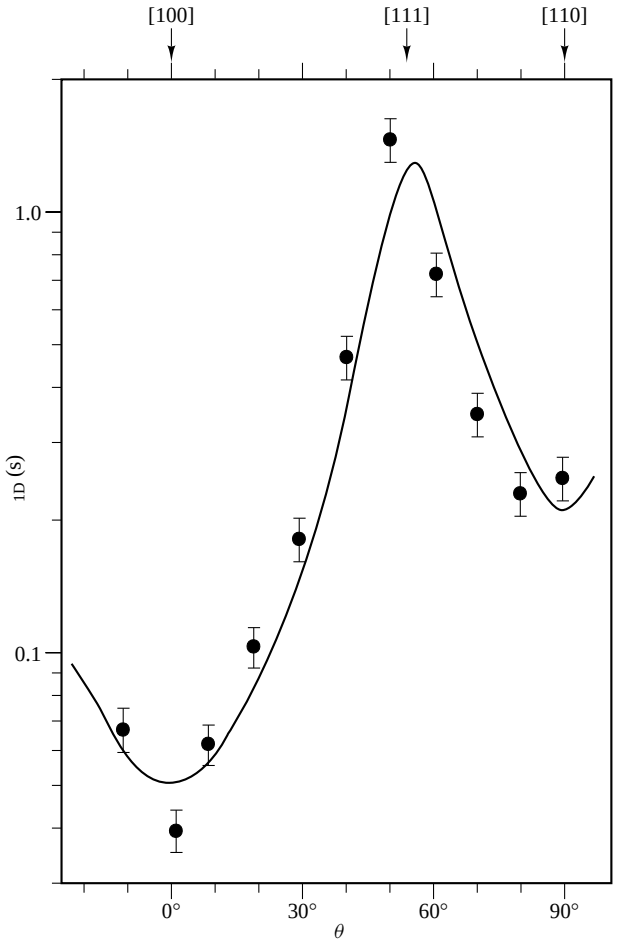

Figure 7 T_{1D} anisotropy in KF:0.1% CaF_2 at 227 °C. The crystal was rotated about its [110] axis. The curve is the calculated anisotropy of $B2/DII/B2/DIS$. (Reproduced by permission of the American Physical Society from H. T. Stokes and D. C. Ailion, *Phys. Rev. B*, 1978, **18**, 141)

both be directly determined. Excellent agreement was found between D measured by this NMR approach and D measured by radioactive tracers. As with the T_{1D} measurements, this technique will be able to observe jump times limited by T_1 for these specialized systems.

6 CONCLUSIONS

The most obvious advantage of the slow motion methods is to extend downward in temperature the range over which atomic diffusion can be studied. As a result, diffusion mechanisms occurring only at lower temperatures can be observed. Moreover, since the effect of diffusion on the dipolar relaxation time will be much greater than its effect on the spin–lattice relaxation time, going to zero field magnifies the relaxation effects, thereby making possible the observation of diffusion whose relaxation effects might otherwise be too weak to be observable. A measurement of the frequency dependence of the relaxation time can determine the relaxation mechanism and can check the validity of the theory used, such as the assumption of an exponential correlation function, underlying equation (1). $T_{1\rho}$ and T_{1D} measurements greatly increase the frequency range available, since they are effectively very low frequency measurements (of order 10^3 Hz), in contrast to typical T_1 measurements (of order 10^7 Hz). Finally, by having a wider temperature range available, it is possible to observe the onset of other diffusion mechanisms having different activation energies. $T_{1D\rho}$ measurements can be used to enhance the NMR effects arising from the ultraslow motions of weakly magnetic nuclei and, possibly, impurities.

7 RELATED ARTICLES

Brownian Motion and Correlation Times; Diffusion Measurements by Magnetic Field Gradient Methods; Diffusion in Rare Gas Solids; Diffusion in Solids; Double Resonance; Field Cycling Experiments; Low Spin Temperature NMR; Magnetization Transfer between Water and Macromolecules in Proton MRI; Relaxation Theory: Density Matrix Formulation; Rotating Frame Spin–Lattice Relaxation Off-Resonance; Slow and Ultraslow Motions in Biology; Zero Field NMR.

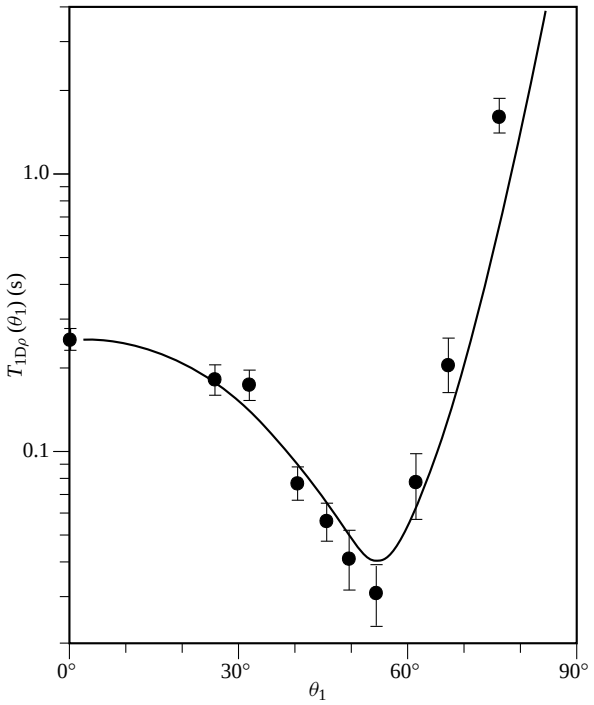

Figure 8 $T_{1D\rho}$ as a function of θ_I in KF:0.1% CaF_2 at 200 °C. The curve was calculated from equation (11). Note that the data point at $\theta_I = 0$ is T_{1D}. (Reproduced by permission of the American Physical Society from H. T. Stokes and D. C. Ailion, *Phys. Rev. B*, 1978, **18**, 141)

8 REFERENCES

1. N. Bloembergen. E. M. Purcell, and R. V. Pound, *Phys. Rev.*, 1948, **73**, 679.
2. C. P. Slichter, *Principles of Magnetic Resonance*, 3rd edn., Springer-Verlag, Berlin, 1990.
3. H. Y. Carr and E. M. Purcell, *Phys. Rev.*, 1954, **94**, 630; S. Meiboom and D. Gill, *Rev. Sci. Instrum.*, 1958, **29**, 6881.
4. D. C. Ailion and C. P. Slichter, *Phys. Rev. Lett.*, 1964, **12**, 168.
5. D. C. Ailion, in *Advances in Magnetic Resonance*, ed. J. S. Waugh, Academic Press, New York, 1971, Vol. 5, Chap. 4
6. D. C. Ailion, in *Methods of Experimental Physics*, ed. J. N. Mundy, S. J. Rothman, M. J. Fluss, and L. C. Smedskjaer, Academic Press, Orlando, 1983, Vol. 21, Chap. 6
7. D. C. Ailion, in *Proceedings of 10th Ampère Summer School and Symposium*, ed. R. Blinc, M. Vilfan, and J. Slak, J. Stefan Institute, Ljubljana, 1988, p. 47.
8. L. C. Hebel and C. P. Slichter, *Phys. Rev.*, 1959, **113**, 1504; A. G. Anderson and A. G. Redfield, *Phys. Rev.*, 1959, **116**, 583.
9. F. Noack, in *Progress in Nuclear Magnetic Resonance Spectroscopy*, ed. J. W. Emsley, J. Feeney, and L. H. Sutcliffe, Pergamon Press, Oxford, 1986, Vol. 18, p. 171.
10. A. G. Redfield, *Phys. Rev.*, 1955, **98**, 1787.
11. D. C. Look and I. J. Lowe, *J. Chem. Phys.*, 1966, **46**, 2995.
12. C. P. Slichter and D. C. Ailion, *Phys. Rev.*, 1964, **135**, A1099.
13. C. P. Slichter and W. C. Holton, *Phys. Rev.*, 1961, **122**, 1701.
14. J. Jeener and P. Broekaert, *Phys. Rev.*, 1967, **157**, 232.
15. D. C. Ailion and P. Ho, *Phys. Rev.*, 1968, **168**, 662.
16. H. T. Stokes and D. C. Ailion, *Phys. Rev. B*, 1977, **16**, 4746.
17. H. T. Stokes and D. C. Ailion, *Phys. Rev. B*, 1978, **18**, 141.
18. D. C. Ailion and C. P. Slichter, *Phys. Rev.*, 1965, **137**, A235.
19. B. Günther and D. C. Ailion, *J. Magn. Reson.*, 1985, **61**, 482.
20. B. Günther and O. Kanert, *Phys. Rev. B*, 1985, **31**, 20.
21. D. F. Holcomb and R. F. Norburg, *Phys. Rev.*, 1955, **98**, 1074.

Biographical Sketch

David C. Ailion. *b* 1937. A.B., 1956, M.S., 1958, Ph.D., 1964, Physics, University of Illinois, under supervision of C. P. Slichter. Faculty member (currently Professor of Physics) University of Utah, 1964–present. Fellow of American Physical Society, Humboldt Senior Research Award (1994–6), University of Utah Distinguished Research Award (1995), NIH Special Fellow (1971–2), Guest Member of AMPERE Committee. Approx. 130 publications. Current research specialties: magnetic resonance imaging of lungs, NMR of partially disordered systems (incommensurate insulators and glasses).

Variable Angle Sample Spinning

Naresh K. Sethi
Amoco Research Center, Naperville, IL, USA

1 Introduction 1
2 Background 1
3 Examples 2
4 Two-Dimensional (2D) Methods 3
5 Related Articles 4
6 References 4

1 INTRODUCTION

In polycrystalline solids, where the molecules have restricted mobility, tensorial NMR interactions such as chemical shift anisotropy (CSA) and dipolar couplings are manifested in broadening of resonance lines. Complete measure of these interactions provides valuable information on molecular geometry, bonding, and electronic structure. However, analysis of a solid state NMR spectrum to extract this information is often made very difficult by extensive overlap of broad lines from chemically different spins. Variable angle sample spinning (VASS) techniques are designed to unscramble overlapping solid state NMR spectral features from chemically different spins.

The resonance line-broadening effects of CSA and dipolar couplings can be removed by acquiring the NMR spectrum while spinning the sample at high speed along an axis inclined at the magic angle (54.74°) from the direction of the external magnetic field $\boldsymbol{B}_0$.[1,2] This technique of magic angle spinning (MAS) permits obtaining a 'liquid-like' spectrum for polycrystalline solids, which facilitates chemical analysis. However, this is accomplished at the expense of losing all the important information regarding the anisotropy of the interaction tensor. Of the various approaches that have been proposed to reintroduce the anisotropy information back into the NMR spectrum of spinning solids, VASS techniques are, conceptually, by far the simplest. In VASS, the anisotropy information is reintroduced in the NMR spectrum by simply spinning the sample at angles other than the magic angle.[3–5]

This article will discuss the basic principles behind VASS techniques, spectral features of the NMR signal when the sample spinning speed is slow or fast compared with the strength of the anisotropic interaction, and the use of two-dimensional (2D) techniques to overcome the limitations of one-dimensional (1D) VASS.

2 BACKGROUND

To illustrate VASS, we shall assume that CSA is the only NMR interaction affecting the spectral shape. The extension of these concepts to the case of dipolar couplings is fairly straightforward. Other articles in this Encyclopedia discuss the concept of chemical shift anisotropy. (Cross references to related articles are provided at the end of this one.) Also, a rigorous mathematical description of the NMR of spinning solids is beyond the scope of this article. Mathematical expressions relevant to the present discussion are used here in their final forms. Details may be found in the literature.[6–9]

The resonance frequency of a spin in the solid state depends upon the relative orientation of $\boldsymbol{B}_0$ and an axis system fixed to the crystallite geometry called the principal axis system (PAS) of the shielding tensor. In the case of polycrystalline or powdered solids, with no preferred crystallite orientation, all relative orientations of PAS and $\boldsymbol{B}_0$ are equally probable. The solid state NMR spectrum is therefore a superposition of resonance lines from all orientations. This results in a broad but very characteristic spectral pattern, called a powder pattern. The significant feature of the powder pattern is that it shows discontinuities or breakpoints at the three principal frequencies of the shielding tensor. These principal frequencies are precisely what we wish to be able to measure to characterize the tensor.

For a sample undergoing spinning motion, the relative orientation of the PAS and $\boldsymbol{B}_0$ acquires a periodic time dependence. The instantaneous resonance frequency of any spin therefore also changes periodically in time. The instantaneous resonance frequency of any given spin during the rotation period depends upon the initial orientation of the PAS and $\boldsymbol{B}_0$, the angle of spinning, and the strength of the anisotropic interaction. The dependence of the time evolution of the resonance frequency Ω of a given spin on the various variables that affect it is given by[6,9]

$$\Omega(\Theta, \Phi, \beta, t) = \Omega_0(\Theta, \Phi, \beta) + \Omega_a(\Theta, \Phi, \beta, t) \tag{1}$$

where

$$\Omega_0(\Theta, \Phi, \beta) = \sigma_i + \tfrac{1}{4}(3\cos^2\beta - 1)[(3\cos^2\Theta - 1)(\sigma_{33} - \sigma_i) + \sin^2\Theta\cos 2\Phi(\sigma_{11} - \sigma_{22})] \tag{2}$$

Here, Θ and Φ are the polar angles that define the relative orientation of the spinning axis direction in the PAS, and β is the angle between the sample spinning axis and $\boldsymbol{B}_0$. The three principal frequencies of the shielding tensor are given by σ_{11}, σ_{22}, and σ_{33}, with σ_i the isotropic frequency, which is the average of the three principal frequencies. The principal frequencies are defined such that $\sigma_{33} - \sigma_i \geq \sigma_{22} - \sigma_i \geq \sigma_{11} - \sigma_i$.

For the purposes of this article, equation (1) is written as the sum of two parts: a time-independent part Ω_0 and a time-dependent part Ω_a. This separation into two parts of the parametric dependence of the resonance frequency illustrates two essential features of the spectral response from spinning solids. The time-independent part determines the average frequency during a spinning period, and specifies the position of the main resonance line or the central line in the spectrum from a crystallite with given initial PAS orientation. The time-dependent part incorporates the explicit effect of periodic changes in the instantaneous resonance frequency on the spectral response. The exact form of Ω_a and methods adopted for solving it to calculate its effect on spectral response can be found in the literature.[6–9] For the purpose of discussion here, two significant properties of Ω_a are as follows:

$$\Omega_a(\Theta, \Phi, \beta, t) = \Omega_a(\Theta, \Phi, \beta, t \pm nt_r) \tag{3}$$

where t_r is the time of one rotation period and n = 1,2,3, . . . , and

$$\Omega_a(\Theta, \Phi, \beta, t) \propto \frac{\sigma_{33} - \sigma_i}{\omega_r} \quad (4)$$

where $\omega_r = 1/t_r$ is the spinning speed. Equation (3) illustrates the periodicity of Ω_a, i.e., after every rotation period, Ω_a returns to its original value. Since Ω_a from all crystallites return to their original values at the same instant, an echo is formed in the time domain NMR signal—the free induction decay (FID). The FID may contain multiple echoes spaced in time by t_r. The Fourier transform of the FID containing such an echo envelope shows the appearance of extra lines, called spinning sidebands, in the frequency domain NMR spectrum.[6] The spinning sidebands appear at intervals equal to ω_r from the centerband frequency, which is given by Ω_0. Equation (4) states that the effect of Ω_a diminishes with increasing ω_r or decreasing $\sigma_{33} - \sigma_i$. In reality, the effect of Ω_a on spectral response is negligible under the condition $\sigma_{33} - \sigma_i < \omega_r$, in which case the entire spectral shape is determined by Ω_0.

Figure 1 shows computer-calculated VASS powder patterns from a single spin under fast spinning conditions, i.e., $\sigma_{33} - \sigma_i < \omega_r$. The bottom trace is the nonspinning powder pattern. The three discontinuities in the powder pattern correspond to the three principal values of the shielding tensor. Under fast spinning VASS conditions, the shape of the powder pattern remains identical to that of the nonspinning pattern, except that the entire pattern is scaled by a factor of $\frac{1}{2}(3\cos^2\beta - 1)$ about σ_i. This scaling factor is 1 when $\beta = 0$, i.e., the same as the nonspinning case. As β is increased, the powder pattern is scaled by this factor, which at the magic angle ($\beta = 54.74^\circ$) is zero, and the entire powder pattern collapses into a single peak at σ_i. As β is moved past the magic angle, the scaling factor becomes negative, causing the entire powder pattern to be reflected about σ_i. The scaling factor has the maximum negative value of 0.5 at $\beta = 90^\circ$. As the powder pattern is scaled with changing β, so are the discontinuities in the powder pattern at the three principal values of the shielding tensor. The appearance of a discontinuity in the scaled powder pattern corresponding to any σ value is given by

$$\sigma = \sigma_i + \tfrac{1}{2}(3\cos^2\beta - 1)(\sigma - \sigma_i) \quad (5)$$

Figure 1 shows how the positions of discontinuities in the powder pattern change under fast spinning VASS conditions.

Figure 2 shows calculated VASS powder spectra under slow spinning conditions, i.e., $\sigma_{33} - \sigma_i > \omega_r$. For samples spinning at the magic angle, the entire pattern is broken up into a series of sharp peaks. The intensity distribution of spinning sidebands under slow magic angle spinning conditions is strongly dependent upon the principal frequencies of the shielding tensor.[7] Under VASS conditions, however, the sidebands take on a fascinating variety of shapes. Under slow spinning VASS conditions, the shapes of the centerband as well as the sidebands deviate significantly from the ideal powder pattern shown in Figure 1.[9,10]

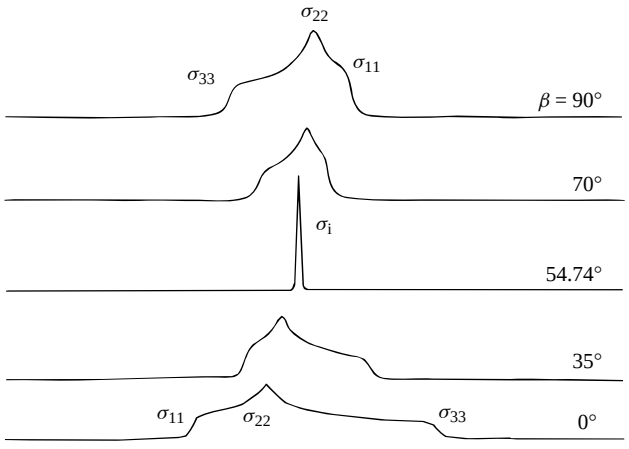

Figure 1 Effect of changing the angle of spinning β on powder patterns under fast spinning VASS conditions. Note that the positioning of all σs is reflected about σ_i for $\beta > 54.74^\circ$

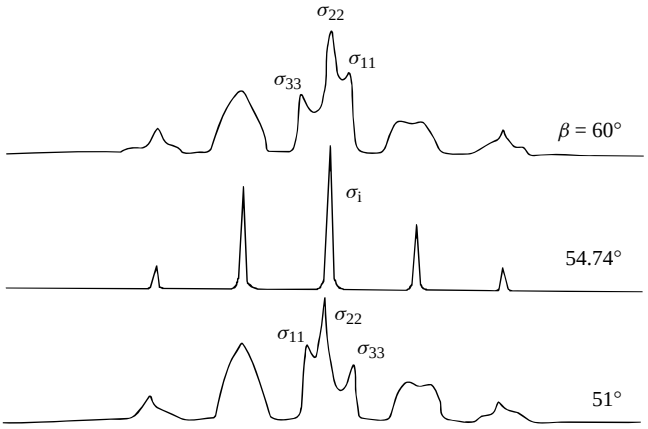

Figure 2 Distorted patterns under slow spinning VASS conditions. Note the cusps in the center band. (Reproduced with the permission of Taylor & Francis Ltd)

The shapes of slow spinning VASS spectral bands in Figure 2 can be understood by considering how the signal amplitude from any given crystallite is distributed between the centerband and the spinning sidebands. This distribution varies greatly amongst crystallites, depending upon the initial orientation of their PAS, i.e., two crystallites with different initial PAS orientations may not contribute the same signal amplitude to the centerband under slow spinning VASS conditions.[9] This results in the appearance of a distorted powder pattern, because the ideal powder pattern, shown in Figure 1, is predicated upon the fact that each crystallite, irrespective of its initial orientation, contributes the same amplitude to the pattern. This can only occur under nonspinning or fast spinning VASS conditions.

An interesting consequence of such a nonuniform distribution of signal amplitudes is that the centerband develops cusps at frequencies where the discontinuities from the principal frequencies of the shielding tensor are expected in the scaled powder pattern. This happens because those particular orientations of the crystallites with Ω_0 close to a scaled principal frequency, equation (5), contribute significantly more amplitude to the centerband than they do to the sidebands, while those having Ω_0 values in between any two principal frequencies contribute significantly more amplitude to the sidebands.[9] Consequently, the shapes of the bands become highly distorted, and the centerband develops cusps at the principal frequencies.

3 EXAMPLES

From a practical viewpoint, VASS exploits the fact that when spinning at angles other that the magic angle, NMR spectral patterns are influenced by the relationship between the three

principal frequencies and the isotropic frequency in a well-defined manner. This permits the design of experiments to measure the three principal frequencies in situations where the nonspinning spectrum has an overlap of different powder patterns to the extent that individual patterns cannot be identified.

We illustrate the applications of fast spinning VASS with an example. We wish to determine the principal values of CSA tensors for the three unique aromatic carbons in hexahydropyrene (HHP). Figure 3 shows the series of experimental and computer-calculated VASS spectra for HHP.[11] A broad pattern with few distinctive features is obtained in the nonspinning case (bottom trace, Figure 3), from which it is not possible to determine nine independent parameters, i.e., three σ values for three different types of aromatic carbons. Moreover, the σ_{33} values for all three aromatic carbons happen to be hidden under the uninteresting peaks from the methylene carbons, and therefore cannot even be detected. Figure 3 shows four fast spinning VASS spectra obtained at different β. Two immediate benefits of VASS are clear.

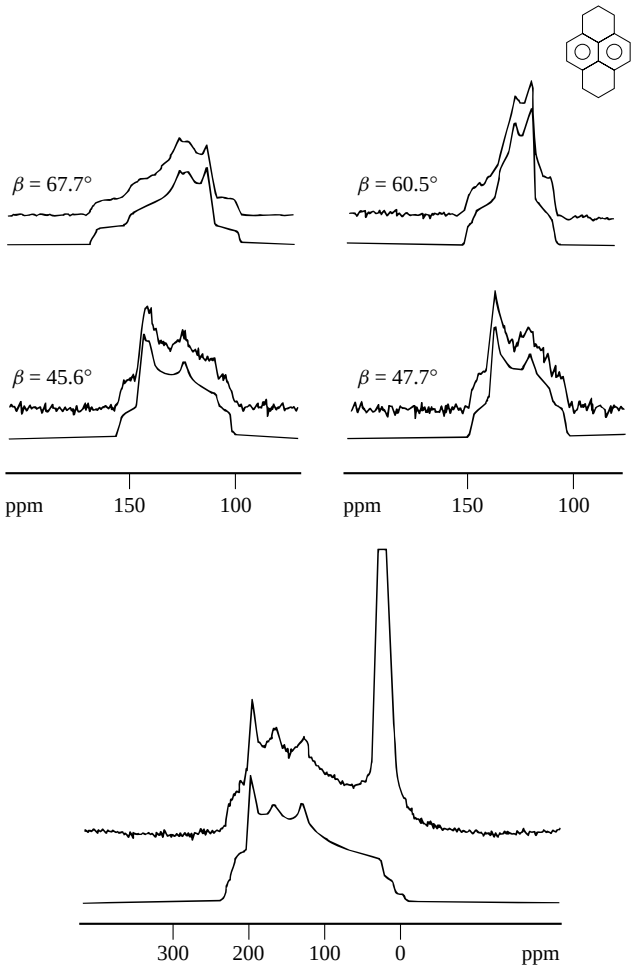

Figure 3 Experimental and computer calculated fast spinning VASS patterns from hexahydropyrene (HHP). The bottom trace shows the nonspinning spectrum and that calculated using parameters from VASS analysis. (Reproduced with the permission of the American Chemical Society)

1. Since the entire aromatic band has been scaled, the uninteresting methylene peaks can now be completely ignored for analysis.
2. More importantly, the aromatic bands at different β are not merely scaled versions of the nonspinning spectrum or of each other. This is a direct consequence of the fact that, although all three patterns are scaled by the same factor, the relative positioning of the three overlapping patterns changes as β is changed, because of the differences in their isotropic frequency.

The level of spectral information available to determine principal frequencies of shielding tensors is therefore augmented by obtaining VASS spectra at different β. The discontinuity in a pattern corresponding to some principal frequency may be clearly identified at a particular choice of β, which otherwise was indistinguishable because of overlap.[5,11]

All VASS spectra contain complementary information. Analysis of these spectra to determine principal frequencies of shielding tensors is best done by simultaneous computer fitting of all the spectra. The best values of principal frequencies are obtained when a single set of parameters is found to fit optimally all the VASS spectra. The results of such an analysis are plotted under each VASS spectrum in Figure 3. The parameters thus obtained can now be used to calculate the composite nonspinning spectra. This is shown at the bottom of Figure 3. Note that, while it may not have been possible to analyze unambiguously the nonspinning spectrum by itself, the data obtained from the analysis of multiple VASS spectra permitted characterizing it satisfactorily.

Figure 4 shows two experimental examples of slow spinning VASS. The bottom two traces are the experimental and computer-calculated spectra of carboxylic carbons of malonic acid. The shielding tensor for these carbons is known to be highly asymmetric.[12] The centerband, as expected, shows three spikes, corresponding to the three σ values, at positions given by equation (5). The top two traces in Figure 4 similarly show the experimental and calculated spectra of aromatic carbons of hexamethylbenzene (HMB). It is known that $\sigma_{11} = \sigma_{22}$ for HMB at room temperature.[13] Thus, only two spikes are seen in the centerband, indicating that two principal frequencies are sufficient to characterize this tensor. The simulations for both these examples are used to explain quantitatively the distorted lineshapes.[9]

Under optimum conditions, one could simply determine the principal frequencies by noting the frequencies of the cusps in the centerband for a given β, and using equation (5). For the examples shown in Figure 4, this procedure indeed yields satisfactory results for the principal frequencies of the shielding tensors.[9] However, it may not always be possible to resolve all the cusps from multiple patterns. Nevertheless, one should be aware of the phenomenon to avoid fortuitous misinterpretation of multiplicities of lines in solid state NMR spectrum when using MAS for chemical analysis, which can occur if β is not set precisely to the magic angle and the spinning speed is less than the anisotropy of the interaction tensor.

4 TWO-DIMENSIONAL (2D) METHODS

The VASS technique outlined above relies on obtaining a few VASS spectra individually, followed by computer analysis

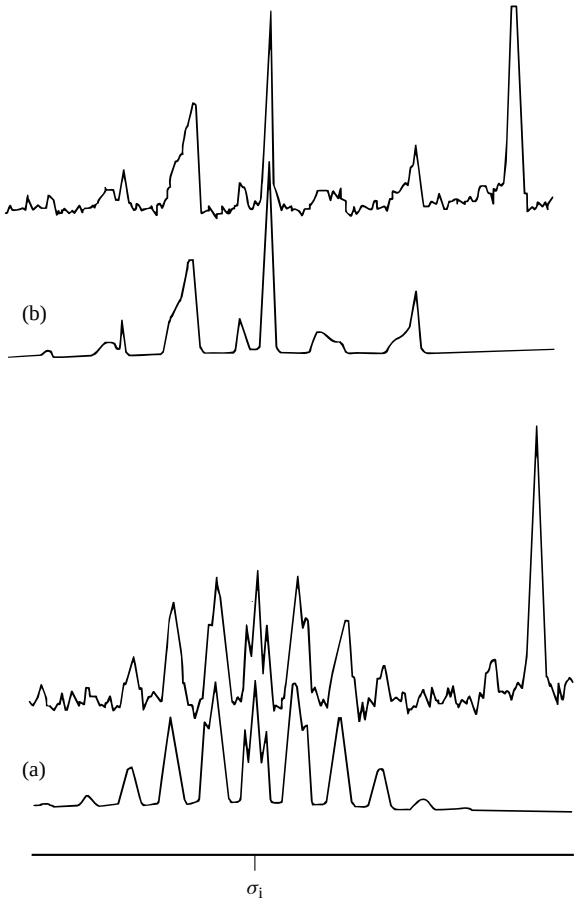

Figure 4 Experimental examples of slow spinning VASS, showing distorted band patterns from (a) malonic acid (with $\beta = 58.2^\circ$ and $\omega_r = 832$ Hz) and (b) hexamethylbenzene (with $\beta = 51.6^\circ$ and $\omega_r = 510$ Hz). In both cases, the intense peak on the right-hand side of the spectra is due to aliphatic carbons. (Reproduced with the permission of Taylor & Francis Ltd)

to determine principal frequencies of shielding tensors. All such 1D techniques are eventually limited by the resolution that they can afford. Two 2D methods are mentioned here that utilize the principles of VASS outlined above, but permit isolation of a VASS spectrum from each individual spin, thus allowing considerable simplification of analysis. The reader is also referred to other related NMR techniques: magic angle hopping (MAH),[14] stop and go (STAG),[15] shift scaling with rotation synchronized pulses,[16–19] and slow magic angle turning (MAT).[20]

In the switching angle sample spinning (SASS) (also called dynamic angle spinning, DAS) 2D technique, the isotropic chemical shift information is correlated with the VASS scaled anisotropic information.[21–23] During the preparation time of the SASS experiment, the scaled anisotropic information is encoded on the time domain NMR signal for a variable time t_1, while the sample spins at an angle far from the magic angle, say β_{t_1}. During the evolution time of a few milliseconds, β is mechanically switched to the magic angle. This is followed by the detection period, t_2, where a normal FID is collected. Since the FID is acquired under the MAS conditions, it only contains the isotropic frequency information, but each isotropic frequency had been modulated by the evolution during t_1 owing to scaled anisotropic information. A double Fourier transform of the data matrix generated with data acquired by systematically incrementing t_1 shows correlations between the isotropic peaks for each spin and its VASS spectrum for β_{t_1}. This allows VASS spectra for all spins to be isolated from each other, assuming their isotropic frequencies are sufficiently different, and analyzed individually.

The variable angle correlation spectroscopy (VACSY) 2D technique is a clever way to synthesize spectral information that is similar to SASS but without the need for any sudden mechanical switching of the spinning axis.[24,25] Instead, a series of 1D VASS spectra are obtained, one at a time, by systematically incrementing β. A 2D data matrix is then constructed, post hoc, by interpolating among all the 1D VASS data while exploiting the relationship between time evolution of the VASS NMR signal during data acquisition and the scaling factor $\frac{1}{2}(3\cos^2\beta - 1)$. Fourier analysis of these data permits isotropic versus full, i.e., unscaled, anisotropic information to be correlated.

The VACSY technique provides advantages over SASS/DAS in experimental simplicity, because it does not require switching β rapidly while the sample spins at high speed—a very demanding technical requirement. Also, the VACSY technique yields an unscaled powder pattern, thus providing somewhat superior resolution. However, a potential problem for the VACSY technique is that the scaling factor is bound within the limits 1.0 to -0.5. This causes incomplete data sampling in one dimension of the 2D experiment. Fourier analysis of incompletely sampled data results in baseline distortions that can complicate data analysis. In practice, though, this has not been found to be a serious drawback in the applicability of the VACSY technique.

The 2D techniques remove the limitations of the 1D VASS analysis, particularly for samples containing a large number of chemically different spins for which the 1D spectra are perhaps too complicated to permit an unambiguous analysis. This advantage, however, must be balanced against the technical difficulties and the time required to perform a full 2D experiment. Eventually, the experimenter must decide between the simplicity of the analysis from a complex 2D experiment and the complexity of analysis from a simple 1D spectrum—a ubiquitous dilemma in modern day NMR.

5 RELATED ARTICLES

Chemical Shift Tensor Measurement in Solids; Dynamic Angle Spinning; Line Narrowing Methods in Solids; Magic Angle Spinning; Magic Angle Turning and Hopping; Rotating Solids; Sideband Analysis in Magic Angle Spinning NMR of Solids.

6 REFERENCES

1. E. R. Andrew, A. Bradbury, and R. G. Eades, *Nature (London)*, 1959, **183**, 1802.
2. I. J. Lowe, *Phys. Rev. Lett.*, 1959, **2**, 285.
3. E. O. Stejskal, J. Schaefer, and R. A. McKay, *J. Magn. Reson.*, 1977, **25**, 569.
4. P. D. Murphy, and B. C. Gerstein, *J. Am. Chem. Soc.*, 1981, **103**, 3282.

5. N. K. Sethi, D. M. Grant, and R. J. Pugmire, *J. Magn. Reson.*, 1987, **71**, 476.
6. M. M. Maricq and J. S. Waugh, *J. Chem. Phys.*, 1979, **70**, 3300.
7. J. Herzfeld, and A. E. Burger, *J. Chem. Phys.*, 1980, **73**, 6021.
8. T. Tereo, H. Miura, and A. Saika, *J. Chem. Phys.*, 1986, **85**, 3816.
9. N. K. Sethi, D. W. Alderman, and D. M. Grant, *Mol. Phys.*, 1990, **71**, 217.
10. E. M. Merger, D. P. Raleigh, and R. G. Griffin, *J. Magn. Reson.*, 1985, **63**, 579.
11. A. M. Orendt, M. S. Solum, N. K. Sethi, C. D. Hughes, R. J. Pugmire, and D. M. Grant, in *Magnetic Resonance of Carbonaceous Solids*, ed. R. E. Botto and Y. Snada, *Advances in Chemistry Series 229*, American Chemical Society, Washington, DC, Chap. 22
12. J. Tegenfeldt, H. Feucht, G. Ruschitzka, and U. Haeberlen, *J. Magn. Reson.*, 1980, **39**, 509.
13. D. E. Wemmer, D. J. Ruben, and A. Pines, *J. Am. Chem. Soc.*, 1981, **103**, 28.
14. A. Bax, N. M. Szeverenyi, and G. E. Maciel, *J. Magn. Reson.*, 1983, **52**, 147.
15. R. C. Zeigler, R. A. Wind, and G. E. Maciel, *J. Magn. Reson.*, 1988, **79**, 299.
16. E. Lippma, M. Alla, and T. Tuherm, in *Proccedings of 19th Congrès Ampère, Heidelberg, 1976*, ed. H. Brunner, K. H. Hausser, and D. Schweiter, p. 113.
17. Y. Yarim-Agaev, P. N. Tutunjian, and J. S. Waugh, *J. Magn. Reson.*, 1982, **47**, 51.
18. A. Bax, N. M. Szeverenyi, and G. E. Maciel, *J. Magn. Reson.*, 1983, **51**, 400.
19. R. Tycho, G. Dabbagh, and P. A. Miura, *J. Magn. Reson.*, 1989, **85**, 265.
20. Z. Gan, *J. Am. Chem. Soc.*, 1992, **114**, 8307.
21. A. Bax, N. M. Szeverenyi, and G. E. Maciel, *J. Magn. Reson.*, 1983, **55**, 494.
22. G. E. Maciel, N. M. Szeverenyi, and M. Sardarshti, *J. Magn. Reson.*, 1985, **64**, 365.
23. T. Tereo, T. Fujji, T. Onodera, and A. Saika, *Chem. Phys. Lett.*, 1984, **107**, 145.
24. L. Frydman, G. C. Chingas, Y. K. Lee, P. J. Grandinetti, M. A. Eastman, G. A. Barrall, and A. Pines, *J. Chem. Phys.*, 1992, **97**, 4800.
25. L. Frydman, G. C. Chingas, Y. K. Lee, P. J. Grandinetti, M. A. Eastman, G. A. Barrall, and A. Pines, *Isr. J. Chem.*, 1992, **32**, 161.

Biographical Sketch

Naresh K. Sethi. *b* 1961. B.S., 1982, University of Delhi, India; Ph.D., 1988, University of Utah. Introduced to NMR by D. M. Grant. Analytical research scientist at Amoco Research Center, 1989–present. Research interests include: application of solid state and high resolution NMR for characterizing petroleum oils, polymers and catalysts, and the use of electron spectroscopy (XPS and Auger) for surface analysis.

Wide Lines for Nonquadrupolar Nuclei

Cecil Dybowski
University of Delaware, Newark, DE, USA
and
Günther Neue
Universität Dortmund, Dortmund, Germany

1	Introduction	1
2	CW Detection	1
3	Pointwise Detection by Spin Echoes	2
4	Excitation by Composite Pulses	2
5	Analyzing Broad Lines Using Transfer Functions	3
6	Related Articles	5
7	References	5

1 INTRODUCTION

Since the inception of NMR, one hallmark of its use has been the ability to analyze materials specifically by selectively detecting only resonances of certain nuclei in the material. Early on, the focus on protons by chemists resulted from the favorable NMR properties of this nucleus, but other spin-$\frac{1}{2}$ nuclei such as ^{13}C and ^{31}P have become routine targets because their spectroscopy addresses appropriate chemical problems with the same specificity as protons have for proton-containing organic materials.

An examination of the Periodic Table shows that approximately one-third of naturally occurring elements have at least one stable isotope with spin-$\frac{1}{2}$. Because the nuclear system of single spins $\frac{1}{2}$ has only two energy levels, these isotopes represent the simplest NMR spectroscopic systems. The proton occupies a unique position, being the spin-$\frac{1}{2}$ isotope of lowest atomic number. At the other extreme stands ^{207}Pb, the isotope of spin-$\frac{1}{2}$ having the highest atomic number. Thus, the NMR spectroscopy of this isotope logically represents the opposite extreme of NMR properties of spin-$\frac{1}{2}$ isotopes from the proton. Quite a few materials containing ^{207}Pb have been studied in solution, particularly the organolead compounds.[1] Despite its unique position, surprisingly little has been done to investigate the spectroscopy of ^{207}Pb in solid materials.

Figure 1 shows the shift ranges of several spin-$\frac{1}{2}$ nuclei. It is obvious that there is a loose correlation between the shift range of an isotope and its number of electrons. Elements with more electrons show a tendency to react more sensitively to their chemical environment than those with fewer electrons. It can be expected that similar arguments also hold for chemical shift anisotropies. The resulting broad spectra in noncubic environments lead to low signal-to-noise ratios and present problems for uniform excitation by pulses. The situation becomes even worse if the magnetogyric ratio is also low. Spin-$\frac{1}{2}$ nuclei of that type are sometimes nicknamed the 'Cinderella nuclei'.[2] Long T_1 values in solids may add to the problem.

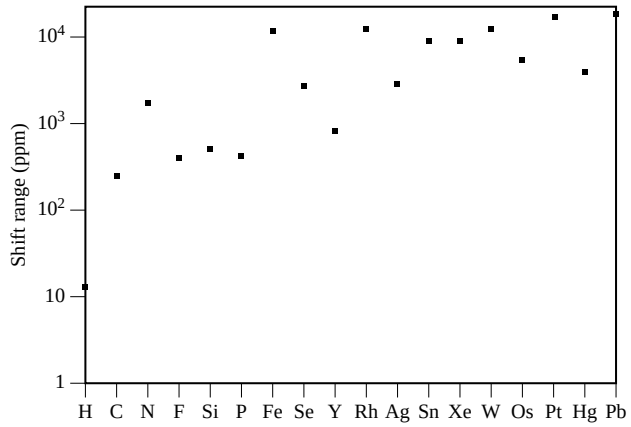

Figure 1 Shift ranges of some spin-$\frac{1}{2}$ nuclei ordered by increasing atomic number. The tendency of heavier nuclei to show larger shift ranges is clearly visible

Certainly, inherently difficult detection is a major reason for the comparatively fewer NMR studies of heavier isotopes. This article summarizes a few techniques for obtaining and analyzing spectra that consist of broad lines.

2 CW DETECTION

This old non-FT method scans a spectrum sequentially. The sensitivity is low, and therefore CW NMR has been replaced in most applications by the much more sensitive and more versatile pulse NMR. But this statement holds only for spectra consisting of narrow lines. Under such circumstances, a CW spectrometer scans detector noise of the baseline most of the time, while pulses excite all signals at once, as long as the pulse is strong enough. For liquids, the difference in the signal-to-noise ratio that can be obtained in a given time by both methods is striking (see e.g. Figure 4.3.4 on p. 157 of Ernst et al.[3]), and this characteristic boosted the development of FT NMR. However, this advantage becomes less important the broader the spectra are. For a faithful recording of very wide lines, CW spectrometers can be used. Swept CW detection always operates on resonance with a constant-amplitude rf signal. Among other things, this avoids offset effects and artifacts due to pulse imperfections. The detection of the ^{59}Co resonance in $KCoF_3$ gives an impression of what is possible with a CW wide line spectrometer.[4]

Essentially, there are two CW methods. The first is the slow passage experiment, which for a long time was the standard method for detecting NMR signals from liquids. Neglecting transient effects that result from noninfinitely slow scanning, the signal shape $g(\omega)$ depends on the amplitude of the rf field, B_1. For a Lorentzian peak with a linewidth described by T_2, one obtains[3]

$$g(\omega) \propto \gamma B_1 \frac{1/T_2}{(1+S)/T_2^2 + \omega^2} \tag{1}$$

where $S = (\gamma B_1)^2 T_1 T_2$ is called the saturation parameter. This quantity depends on both T_1 and T_2, as well as on B_1. It can be seen that there is a conflict. To maximize the

signal, B_1 has to be as big as possible, but to keep distortions low, B_1 has to be as small as possible. For solids with very long T_1 values, this may be a substantial problem. In such cases, a second CW method, the adiabatic fast passage through resonance, is useful.[5] This is based on the fact that, under certain circumstances, the nuclear magnetization always remains aligned with the effective field $\boldsymbol{B}_e = (B_1, 0, B_0 - \omega/\gamma)$ in the rotating frame. In solids, a signal can be observed if the B_1 field strength and the scanning rate $d|B_0|/dt$ fulfil the condition

$$\frac{1}{T_1} \ll \frac{1}{B_1}\frac{d|B_0|}{dt} \ll |\gamma B_1| \approx \frac{1}{T_2} \tag{2}$$

But, since the last relationship means that the nutation frequency $\omega_1 = \gamma B_1$ must be comparable to the linewidth, one has a restriction similar to that for pulse methods.

For details on both CW methods, the reader is referred to Abragam.[5] It should be noted, however, that it is becoming more and more difficult to find a commercially produced CW NMR spectrometer to use in such experiments.

3 POINTWISE DETECTION BY SPIN ECHOES

Spectra representing extremely broad shift distributions cannot be excited evenly over the whole shift range if pulses are used. Instead, only a region, which may be small compared with the total width of the spectrum, will be selected by the pulse. By using the basic idea of CW spectroscopy, sequential detection in different parts of the spectrum will outline the lineshape. In practice, one uses spin echoes to circumvent deadtime problems. The height of the echo is a direct measure of the intensity of the spectrum at the irradiation frequency. More precisely, it is a point on the true line smoothed with the excitation profile. Obviously, there are two possibilities to achieve the goal. Either the frequency or the field is changed from point to point. Field sweeps, if possible, are the better choice, because the tuning of the spectrometer can be kept constant.

With the limited availability of CW spectrometers, this method is becoming more and more the standard for observing extremely broad lines. It was, for example, extensively used for measuring the copper resonances in high-T_c superconductors.[6]

An instructive example to demonstrate the application and power of the spin echo technique is the study of the ^{195}Pt resonance of metallic Pt particles on an alumina-supported catalyst.[7,8]

Figure 2 shows a spin echo spectrum of such a catalyst with a Pt dispersion of 26% (= the percentage of surface atoms) covered by CO. The meaning of the structure of the spectrum is elucidated by a double resonance version of the spin echo experiment, where the ^{195}Pt resonance is observed while ^{13}C is irradiated. As only Pt atoms directly attached to CO can be observed, this method is surface-sensitive. By using this approach, it could be shown unambiguously that only the pronounced peak on the left side of the spectrum is due to surface atoms, while the right part belongs to resonances of ^{195}Pt atoms located within the small metal clusters.

4 EXCITATION BY COMPOSITE PULSES

To improve excitation over a wider range of frequencies, composite pulses have been used for many years.[9] The basic idea of this approach is to use a sequence of pulses that mimics the effect of a single pulse. The extra degrees of freedom in times (pulse durations, delays) and phases that are introduced by using several pulses are used to improve the properties of the equivalent pulse towards an ideal delta function pulse.

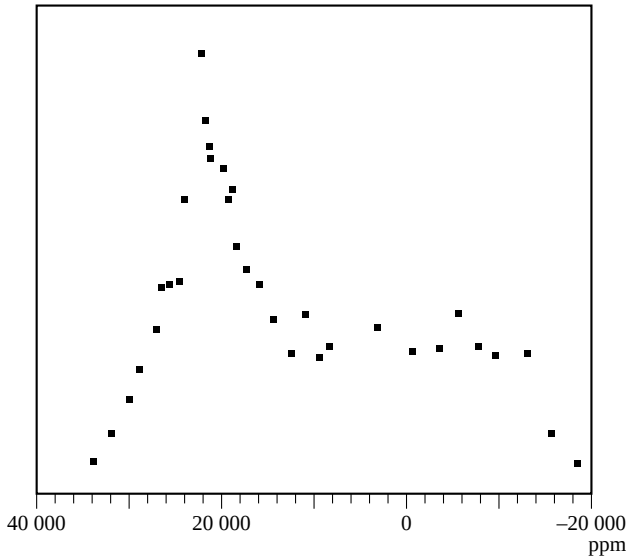

Figure 2 ^{195}Pt spin echo spectrum of small CO-covered Pt clusters on an alumina-supported catalyst. The data are taken from Makowka et al.[7]

There is a wide variety of suggestions for composite pulses. Usually, they are optimized to achieve a particular property. Many pulse sequences are designed to be tolerant to missettings of the pulse length to allow a more uniform excitation over a large sample volume with B_1 inhomogeneities.[10] Another area of successful application of composite pulses is spin decoupling.[11]

More important in the context of exciting wide lines is an optimization with respect to a minimal phase dispersion as a function of frequency offset. A well-known sequence with that property is the 'spin knotting' sequence[12]

$$(\phi_1)_{+x} - \tau_1 - (\phi_2)_{-x} - \tau_2 - (\phi_3)_{+x} \tag{3}$$

The rotation angles ϕ_i have to fulfil the condition $\phi_1 - \phi_2 + \phi_3 = 90^\circ$. The remaining four degrees of freedom can be used to optimize the performance of the sequence for each B_1 field strength by trial and error.[12] Figure 3 shows a simulated powder spectrum with shift anisotropy excited by a single $(\frac{1}{2}\pi)_{+x}$ pulse. The B_1 field strength was assumed to correspond to a nutation frequency of 10 kHz. Distortion of the lineshape is clearly visible. If the same spectrum is detected by applying the 'spin knotting' sequence with pulses of the same B_1 field strength, the result is an almost perfect powder pattern (Figure 4).

A more direct and general approach to the construction of sequences that approximate ideal pulses[13] predicts that a composite pulse

$$(385^\circ)_{+x}(320^\circ)_{-x}(25^\circ)_{+x} \tag{4}$$

is equivalent to a $(\frac{1}{2}\pi)_{+x}$ pulse with minimum phase dispersion. As this particular method uses a series expansion, higher order approximations can be found that consist of more

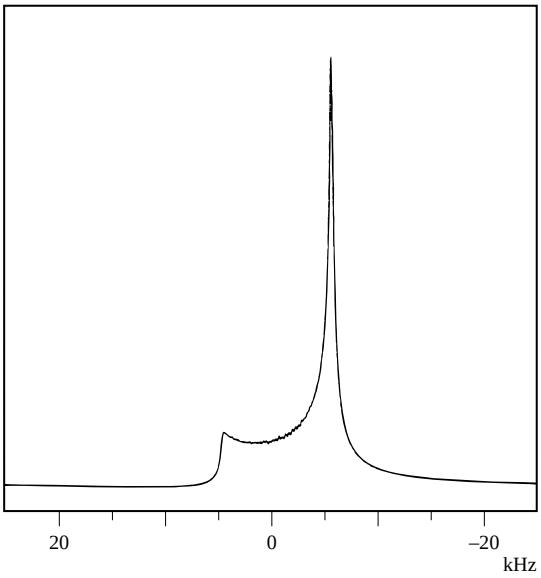

Figure 3 Simulation of a spectrum excited by a weak pulse and governed by chemical shift anisotropy. The rf pulse strength was assumed to correspond to a nutation frequency of 10 kHz

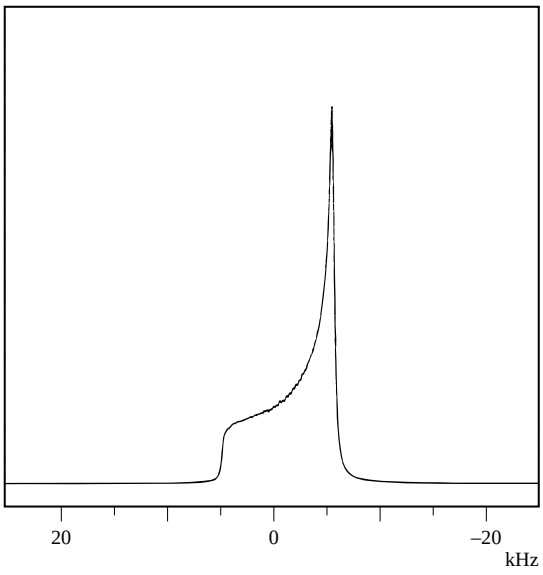

Figure 4 Simulation of the response of the same system as in Figure 3 to excitation by the spin knotting sequence with optimized parameters.[12] Again, the rf pulse strength was assumed to correspond to a nutation frequency of 10 kHz

and more pulses and that increase the spectral range over which the phases of the excitation are almost constant.

It may seem that cleverly designed composite pulses are the ultimate solution to the problem of exciting broad lines. But there are limitations. The power theorem of Fourier transforms,

$$\int_{-\infty}^{\infty} |p(t)|^2 \, \mathrm{d}t = \frac{1}{4\pi} \int_{-\infty}^{\infty} |P(\omega)|^2 \, \mathrm{d}\omega \tag{5}$$

relates the power in a pulse train as a function of time [amplitudes $p(t)$] to the power available in the spectrum as a function of the frequency [amplitudes $P(\omega)$]. In general, both amplitudes are complex functions, since one has to include the phases. By assuming a constant amplitude $|A|$ for the pulses and a flat spectrum of the pulse sequence with a constant amplitude $|B|$ (disregarding its practical realization), one obtains

$$|A|^2 \Delta t = \frac{1}{4\pi} |B|^2 \Delta\omega \tag{6}$$

where Δt is the total time during which the transmitter is on and $\Delta\omega$ is the bandwidth of the excitation. It is obvious that a larger frequency range $\Delta\omega$ can be obtained only by increasing the total lengths of the pulses, since the transmitter power $|A|^2$ is limited in practice. Note that the other quantity, $|B|$, is fixed by the condition to obtain a 90° pulse. Usually, in solids, there will be dipolar interactions that give rise to a T_2 decay of the order of a few tens of microseconds. On typical solids spectrometers $\frac{1}{2}\pi$ pulse lengths may be $5\,\mu$s. It should be observed that even simple composite pulse sequences such as those given above may last as long as typical decay times owing to dipolar interactions. Thus, in most solids, the bandwidth of ideal excitation cannot be increased much by more sophisticated and longer sequences than those given above. Similar bandwidth versus time arguments also hold for a newer development in the field of tailored excitation, namely, shaped pulses,[14] where extra degrees of freedom are obtained by modulating the amplitudes by analog signals rather than by pulses.

5 ANALYZING BROAD LINES USING TRANSFER FUNCTIONS

Despite the success of the methods described in the previous section, it might be inconvenient, difficult, or impractical to use them. Owing to the nonideal behavior of electronic circuits (finite rise times, power droop, etc.), one usually needs to adjust the pulses to optimize the operation of the sequence. Adjustments on the sample of interest may not be possible in cases of low intensities or long relaxation times. If one works with special probeheads that need insulation from the environment, like low- or high-temperature probes, then it may not be practical to substitute a calibration sample.

Very wide lines also present another problem. As discussed above, the possible bandwidth of excitation is subject to practical limitations like those imposed by relaxation. If the line extends over more than this range, application of the common composite pulse sequences destroys the wings of the line very efficiently. According to the power theorem, increasing the power in a given region of the spectrum means that, outside of that region, the excitation is reduced. In contrast to the almost rectangular excitation profile (transfer function) of a composite pulse, a simple single pulse spreads its energy over a much wider frequency range, though unevenly. This fact allows one to use another strategy for wide lines. As the transfer function is given by pulse timings, it can be calculated exactly and included in the data analysis. Under these circumstances, a simpler excitation has the advantage of giving a better signal-to-noise ratio far off resonance, allowing a better fit of data.[15] This is illustrated by Figure 5. It is clearly seen that if the lines are so broad that they cannot be covered by composite pulses, a simple pulse shows the singularities

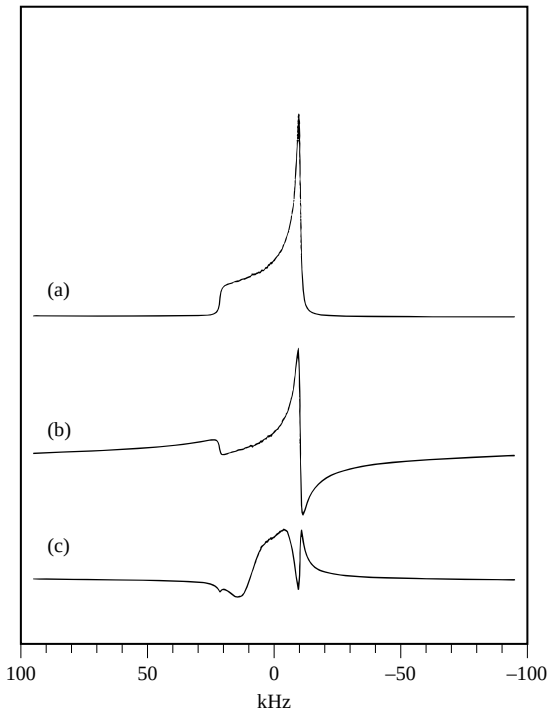

Figure 5 Simulation of the effects of different excitation methods on the appearance of spectra. (a) Ideal spectrum governed by chemical shift anisotropy. (b) Excitation by a single pulse. (c) Excitation by the spin knotting sequence. The rf pulse strength was always assumed to correspond to a nutation frequency of 10 kHz

and shoulders of powder spectra better, and the extraction of tensor elements consequently becomes more precise.

Because of receiver dead time, one cannot use a single pulse, but has to rely on spin echo techniques. Furthermore, the detection of weak signals very often suffers from acoustic ringing. A simple pulse sequence that produces a spin echo and removes acoustic ringing, as well as some other imperfections is

$$\begin{gathered}(\tfrac{1}{2}\pi)_{+x} - \tau - (\pi)_{+y} - \tau - (\mathrm{acq})_{+x} \\ (\pi)_{+x} - \tau_1 - (\tfrac{1}{2}\pi)_{+x} - \tau - (\pi)_{+y} - \tau - (\mathrm{acq})_{-x} \\ (\tfrac{1}{2}\pi)_{-x} - \tau - (\pi)_{-y} - \tau - (\mathrm{acq})_{-x} \\ (\pi)_{+x} - \tau_1 - (\tfrac{1}{2}\pi)_{-x} - \tau - (\pi)_{-y} - \tau - (\mathrm{acq})_{+x}\end{gathered} \tag{7}$$

where $(\theta)_\phi$ denotes a pulse with phase ϕ that produces a nutation by angle θ, and $(\mathrm{acq})_\phi$ stands for acquisition with receiver phase ϕ.

The effect of this sequence can be calculated by standard density matrix theory.[5,8,16] For signals governed by chemical shift anisotropy (CSA), we define the Hamiltonian in the rotating frame as

$$\hat{\mathcal{H}} = \begin{cases} -\Delta\omega_0 \hat{I}_z & \text{no pulse} \\ -\Delta\omega_0 \hat{I}_z \mp \omega_1 \hat{I}_{x,y} & \text{during pulses} \end{cases} \tag{8}$$

where $-\omega_1\hat{I}_x$ has to be used for a $(\theta)_x$ pulse, $+\omega_1\hat{I}_x$ for a $(\theta)_{-x}$ pulse, etc. As this Hamiltonian is a piecewise-constant function of time, the evolution of the density matrix $\hat{\rho}$ is given simply by[5]

$$\hat{\rho}(t) = \mathrm{e}^{-\mathrm{i}\hat{\mathcal{H}}_n t_n} \ldots \mathrm{e}^{-\mathrm{i}\hat{\mathcal{H}}_1 t_1}\, \hat{\rho}(0)\, \mathrm{e}^{\mathrm{i}\hat{\mathcal{H}}_1 t_1} \ldots \mathrm{e}^{\mathrm{i}\hat{\mathcal{H}}_n t_n} \tag{9}$$

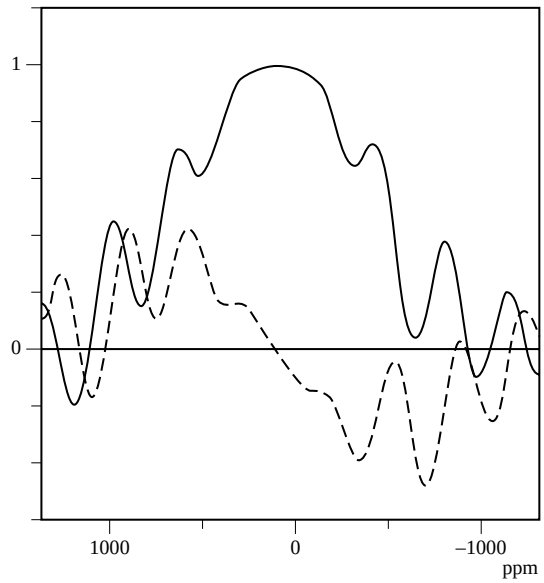

Figure 6 Complex transfer function for a pulse sequence using τ = 20 μs, $(\frac{1}{2}\pi)$ = 3.75 μs, and $\omega_0/2\pi$ = 62.60 MHz

where subscripts n label subsequent time intervals.

The numerical calculation of the evolution of the density matrix is fairly easy, since all operators of a spin-$\frac{1}{2}$ can be expressed by 2 × 2 matrices. Figure 6 shows a calculated transfer function for the excitation by the above sequence. The effect on both receiver channels of a quadrature detector was calculated. One sees the complicated distortions of amplitudes and phases as a function of offset frequency.

Least-squares fits become significantly more precise if the transfer function is included. It should be noted that no new fitting parameters are introduced, but the experiment with its

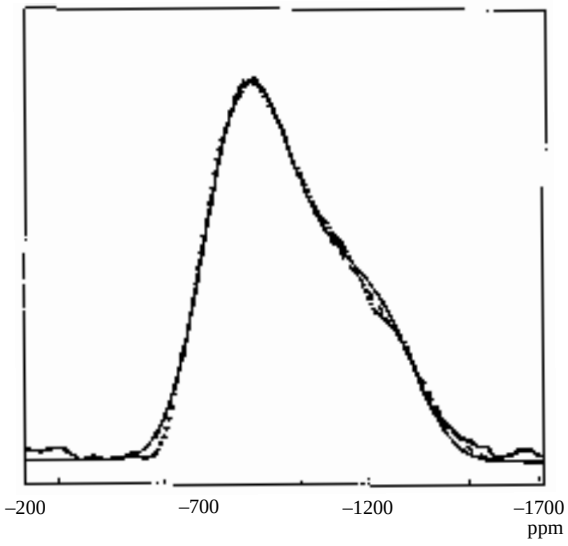

Figure 7 Experimental ^{207}Pb spectrum of $PbBr_2$ (squares) at 62.601 MHz. The rf pulse strength corresponds to a nutation frequency of 1000 ppm. The solid line represents a simple fit that assumes three shift tensor elements as well as a Gaussian broadening, while the dashed line is a best fit including the transfer function of the excitation. The ppm scale is referred to the chemical shift of $Pb(CH_3)_4$

timings of pulses and delays determines the transfer function completely.

The possible improvement is demonstrated by Figure 7. Though, at first sight, the differences seem to be small, application of the transfer function leads to a better reproduction of the almost triangular lineshape. The set of best-fit parameters changes from $\sigma_{11} = -710$ ppm, $\sigma_{22} = -849$ ppm, and $\sigma_{33} = -1350$ ppm without correction to $\sigma_{11} = -699$ ppm, $\sigma_{22} = -845$ ppm, and $\sigma_{33} = -1398$ ppm if the transfer function is included in the theoretical lineshape. The width of the line, $\sigma_{11} - \sigma_{33}$, changes by 10%, or 69 ppm, which is clearly outside the limit of statistical error. The mean-square deviation is also reduced by about 25%.

6 RELATED ARTICLES

Chemical Shift Tensor Measurement in Solids; Chemical Shift Tensors; Composite Pulses; Echoes in Solids; Fourier Transform and Linear Prediction Methods; Fourier Transform Spectroscopy; Magic Angle Turning and Hopping; Phase Cycling; Radiofrequency Pulses: Response of Nuclear Spins; Selective Pulses; Shaped Pulses; Shielding Tensor Calculations; Solid State Probe Design.

7 REFERENCES

1. B. Wrackmeyer and K. Horchler, in *Annual Reports on NMR Spectroscopy*, ed. G. A. Webb, Academic Press, London, 1990, Vol. 22, p. 249
2. B. E. Mann, in *Annual Reports on NMR Spectroscopy*, ed. G. A. Webb, Academic Press, London, 1991, p. 141.
3. R. R. Ernst, G. Bodenhausen, and A. Wokaun, *Principles of Nuclear Magnetic Resonance in One and Two Dimensions*, Oxford University Press, Oxford, 1987.
4. R. G. Shulman, *Phys. Rev. Lett.*, 1959, **2**, 459.
5. A. Abragam, *The Principles of Nuclear Magnetism*, Oxford University Press, Oxford, 1961.
6. T. Shimizu, H. Yasuoka, T. Imai, T. Tsuda, T. Takabatake, Y. Nakazawa, and M. Ishikawa , *J. Phys. Soc. Jpn.*, 1988, **57**, 2494.
7. C. D. Makowka, C. P. Slichter, and J. H. Sinfelt *Phys. Rev. Lett.*, 1982, **49**, 379; *Phys. Rev. B*, 1985, **31**, 5663.
8. C. P. Slichter, *Principles of Magnetic Resonance*, 3rd edn., Springer-Verlag, Berlin, 1990.
9. M. H. Levitt, and R. Freeman, *J. Magn. Reson.*, 1979, **33**, 473.
10. M. H. Levitt, *J. Magn. Reson.*, 1982, **48**, 234.
11. M. H. Levitt, R. Freeman, and T. Frenkiel, in *Advances in Magnetic Resonance*, ed. J. S. Waugh, Academic Press, New York, 1983, Vol. 11, p. 48.
12. R. Freeman, S. P. Kampsell, and M. H. Levitt, *J. Magn. Reson.*, 1980, **38**, 453.
13. R. Tycko, H. M. Cho, E. Schneider, and A. Pines, *J. Magn. Reson.*, 1985, **61**, 90.
14. L. Emsley and G. Bodenhausen, *J. Magn. Reson.*, 1990, **87**, 1.
15. G. Neue, C. Dybowski, M. L. Smith, and D. H. Barich, *Solid State NMR*, 1994, **3**, 115.
16. M. Mehring, *High Resolution NMR in Solids*, 2nd edn, Springer-Verlag, Berlin, 1982.

Acknowledgments

Simulations were performed using the program ANTIOPE, which was kindly provided by J. S. Waugh.

Biographical Sketches

Cecil Dybowski. *b* 1946. B.S., 1969, Ph.D., 1973, Texas. Faculty at the University of Delaware, 1976–present. Over 100 publications, including the book “Transient Techniques in the NMR of Solids” (with B. C. Gerstein). Research interests include all facets of NMR spectroscopy, the analysis of heterogeneous catalysis and catalytic processes, materials structure and function.

Günther Neue. *b* 1955. Dipl.-Chem., 1978, Dr.rer.nat., 1983, Priv.-Doz., 1988, Dortmund. Hochschuldozent, Universität Dortmund, 1988–present. Over 25 research publications. Research interests include development of analytical techniques in the fields of surface science and environmental chemistry.

Dynamics of Water in Biological Systems: Inferences from Relaxometry

Seymour H. Koenig
Relaxometry, Inc., Mahopac, NY, USA

1	Introduction to Relaxometry	1
2	Protein–Water Interfaces	2
3	Lipid–Water Interactions	6
4	Quantification of the Dynamics of Water on the Molecular Scale: Results from Magnetic Solutes	8
5	Water as a Viscous Vacuum	10
6	Concluding Remarks	10
7	Related Articles	11
8	References	11

1 INTRODUCTION TO RELAXOMETRY

The demonstration half a century ago of proton NMR in liquid water by Bloch et al.[1,2] and in solid paraffin by Purcell et al.[3] came one year after Rabi received the Nobel Prize (1944) 'for his discovery of a resonance method for recording the magnetic properties of atomic nuclei'; i.e., for discovering NMR. Rabi and his associates had worked with radiofrequency (rf) resonant transitions in atomic and molecular beams since the mid-1930s.[4,5] By the time of the discoveries of Bloch and Purcell, the proton g-value was known to six-figure accuracy,[6] the concept and language of rotating frames were in place,[7–9] and wartime technological advances were such that it was clear that a proton NMR signal could be seen in condensed matter well above noise at the then attainable fields 'provided that thermal equilibrium could be established in a reasonable time'.[3] The major unknown was the longitudinal relaxation time T_1 of protons, a parameter that has no relevance in beam measurements; early estimates for proton relaxation times for the condensed state were minutes to hours.[10] Bloch et al. used 'paramagnetic catalysts ... to accelerate the establishment of thermal equilibrium';[1] they added trace amounts of ferric nitrate to their water samples.[2] In addition they used the 'nuclear induction' signal generated by proton magnetization precessing in the transverse plane to help circumvent problems associated with a long T_1. Purcell et al. measured absorption using an rf bridge and a very low power level, such that 'the absorption would persist for hours regardless of the relaxation time, once thermal equilibrium had been established'.[3]

A fairly complete theory of proton relaxation in diamagnetic liquids, e.g. water and its mixtures with glycerol, and in solutions with trace millimolar amounts of small paramagnetic solutes was developed in short order.[11–14] The basic concept is that of 'motional narrowing' of the interaction ω_{int} (the intrinsic uncertainty width) that induces relaxation in liquid systems. The rapid Brownian motion of liquid molecules reduces the uncertainty width by the factor $\omega_{\text{int}}\tau_c \ll 1$, where τ_c is a correlation time that characterizes the timescale of the Brownian fluctuations. The result, in the limit of the external field B_0 approaching zero, is

$$1/T_1 = 1/T_2 \simeq 6\omega_{\text{int}}(\omega_{\text{int}}\tau_c) \quad (1)$$

for the interaction of two identical nuclei with spin of $\frac{1}{2}$. For protons of water the fluctuating interaction is a sum over the magnetic dipolar interaction of all pairs of protons (dominated by the intramolecular water proton–proton interaction of about 5 Oe). Where ω_{int} ($\sim 10^5$ s^{-1}) is the angular Larmor precession frequency ω_L of a proton in this interaction field and τ_c ($\sim 3 \times 10^{-12}$ s at 25 °C) is determined by the Brownian reorientational time of a water molecule since the magnetic interaction of two protons is a function of their spatial orientation. For water deuterons, the fluctuating interaction is that of the nuclear quadrupolar moment with the gradient of the electric field at the nucleus. For deuterons ω_{int} is three times larger than for protons, leading to intrinsic relaxation rates for deuterons that are ten times greater than for protons in analogous diamagnetic systems. The six-fold lower g-value of the deuteron makes magnetic interactions of deuterons, e.g. with proton and electronic moments, 40 times less than the analogous proton interactions and generally ignorable. However, for both protons and deuterons of solvent water, any diamagnetic solute (or other variable, such as temperature) that slows the motion of a water molecule, on average, reduces the effect of motional narrowing and thereby increases relaxation rates at low fields by comparable factors. Both $1/T_1$ and $1/T_2$ decrease with increasing B_0, with a Lorentzian dispersion centered near $\omega_L\tau_c = 1$. Hence there is a need for measurements of relaxation rates over a wide range of B_0 if relaxation mechanisms are to be studied effectively.

Early applications of proton NMR were directed towards an understanding of the molecular dynamics of water molecules in water solutions, i.e. the nature of microscopic viscosity, self-diffusion of solvent, Brownian motion of hydrated paramagnetic solutes and the lifetimes of solute–solvent complexes. The data were the relaxation rates of the majority solvent protons, as a function of temperature and, to the extent possible, as a function of the applied field B_0, since available NMR resolution and signal intensity were inadequate to resolve structure in the water line and certainly inadequate to detect solute nuclei. Hence the relaxation rates of solvent water nuclei served as indicators of solvent interactions with solute. With advances in magnet technology and electronics, 'higher resolution' NMR became possible, and research emphasis shifted to measurements of proton spectra in water solutions of relatively small solutes. Increasingly higher fields, superconducting magnets, signal averaging and Fourier transform methodologies have brought applications of high-resolution NMR to 600 MHz and beyond, with multidimensional high-field spectroscopy now routinely applied to solute polymers, polypeptides, and increasingly larger proteins.

As spectroscopy has advanced, so has 'relaxometry', the field—in analogy with spectroscopy—that includes the measurement and theory of, and instrumentation ('relaxometers') for, increasingly sophisticated investigations of relaxation rates

of (mainly) water nuclei in progressively more complex systems, both diamagnetic and paramagnetic. ('Relaxometry' and 'relaxometer' are terms coined by the author in 1983.) Initially, as noted, relaxometry was the approach of choice for the study of water dynamics in simple solute–solvent systems. When early improvements in resolution of NMR signals made possible the direct study of spectral lines of small solutes, relaxometry was applied, typically, to solutions of paramagnetic metalloproteins, including their complexes with small substrates and activators; the area now called 'bioinorganic chemistry.' With further improvements in NMR resolution, and the advent of proton spectroscopy of small protein solutes, relaxometry became the approach of choice for studying the dynamics of water in progressively more complex systems, including tissue. This was aided by the development of a field-cycling relaxometer,[15] based on the early ideas of Redfield,[16] that could record the dependence of $1/T_1$ on B_0 (called a nuclear magnetic relaxation dispersion (NMRD) profile) automatically, under computer control, over almost four decades of B_0. The discussion of the dynamics of water in biological systems presented here is based on NMRD data obtained with our field-cycling relaxometers.

In magnetic resonance imaging (MRI) in clinical diagnostic radiology, an increasingly important application of high-resolution NMR, the image generated is a three-dimensional spatial representation of tissue dependent relaxation rates of the volume of interest. Most tissues contain about the same amount of water, ostensibly for reasons of osmotic equilibrium, so MRI would be ineffectual unless signal intensity was weighted by some parameter other than (water) proton density. This has stimulated research on relaxation processes of water protons in complex systems, including several different tissues, and their model systems. We now have a relatively complete molecular theory of relaxation of water protons in tissue[17] (which is mostly water and immobile protein), as well as in solutions of proteins, both native and immobilized; the latter is an excellent model system for the relaxation behavior of water protons in most tissues. Much has been learned about the dynamics of water molecules in these macromolecular biological systems, particularly regarding the details of dynamic and magnetic protein–water interfacial interactions and, to a lesser extent, lipid–water interfacial interactions. Pertinent data, chosen to support the generalizations made here regarding water dynamics, are collected in this article. The theory and a short discussion of the instrumentation are given in another article in this Encyclopedia (***Relaxometry of Tissue***).

The emphasis throughout this article is on broad generalizations regarding the behavior of water in biological systems, concepts that have come from relaxometry investigations. In particular we argue for the view that water, even in complex tissues, is no more structured than is pure water, and that the water molecules in each have comparable mobility and diffusivity. In essence, solvent molecules, as regards their molecular dynamics—which in turn determines nuclear relaxation rates—really do not learn about the presence of small or macromolecular solute until solute and solvent molecules collide physically, essentially at their hard-core radii. The overall water dynamics are altered imperceptibly by these collisions and associations. However, relaxation rates are very sensitive to the details of these collisions—because of the possibility of massive, although momentary, lengthening of τ_c—and to the possibility of diffusion of proton magnetization in immobile macromolecules. The far-ranging result is a very rich set of phenomena that can be encompassed by a simple picture of water dynamics in biological systems.

2 PROTEIN–WATER INTERFACES

2.1 Water Deuteron $1/T_1$ NMRD Profiles in Systems of Immobile Protein

The data shown in Figure 1 are perhaps the most telling for the major generalization made here. They include $1/T_1$ NMRD profiles of deuterons in water–protein systems in which the protein is not free to rotate:[18] two samples of bovine serum albumin (BSA, 68 kDa) in water at relatively low concentrations, initially liquid, in which the solvent protein was immobilized by chemical cross linking; a third, otherwise identical sample, in which the macroscopic viscosity of the solvent was increased seven-fold by the addition of dextran before cross linking; and a sample of cross-linked bovine carbonic anhydrase (BCAB, 30 kDa), about one-half the molecular weight of BSA. (The solid curve is an empirical fit to the data for these four samples, for clarity.) A fifth sample was powder,[19] BSA hydrated to 50% by weight (corresponding to about four water hydration layers per BSA molecule). The profiles are all normalized to their low field values after

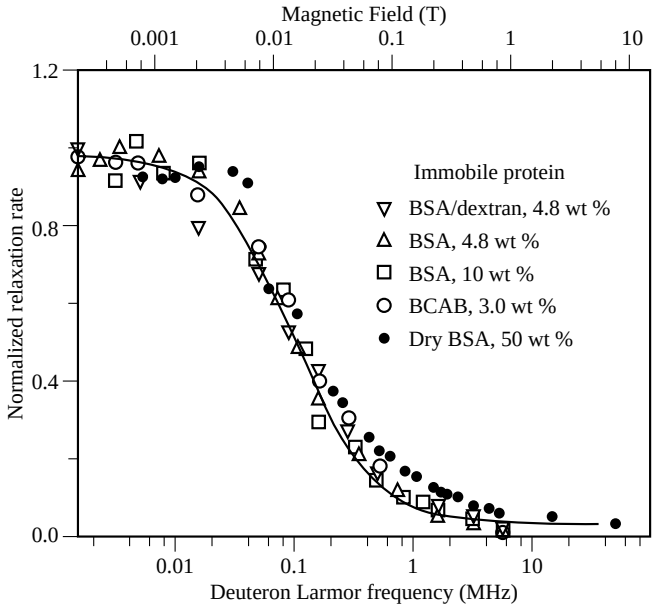

Figure 1 $1/T_1$ NMRD profiles of water deuterons for five samples of immobile proton, all normalized to the same vertical scale after subtraction of $1/T_1$ of solvent at each temperature. (∇,△) 4.8 wt %, chemically cross-linked BSA (68 kDa) at 35 °C, the first (∇) containing 70 mg ml^{-1} dextran, which increases the macroscopic solvent viscosity by a factor of 7.4. (□) As (△), but with 10% BSA. (○) 3 wt % BCAB (30 kDa) at 25 °C. The solid curve is an empirical fit to the profiles of these four samples, with ν_c = 0.097 MHz. The curve is for visual clarity, and has no theoretical importance in the present context. The low field rates, above the solvent background are, respectively, 42, 44, 75, and 24 s^{-1}. (●) Powder, dried BSA rehydrated to 50 wt % water, at 18 °C.[19] (Reproduced by permission from S. H. Koenig, R. D. Brown III, and R. Ugolini, *Biophys. J.*, 1988, **53**, 77)

subtraction of the background rate of pure water, to show that the normalized functional forms of the five profiles of these disparate samples are essentially the same. Deuterons were measured, rather than protons (although their signal is smaller than for protons and more difficult to obtain accurately), because their relaxation is predominantly electric quadrupolar. As a result, changes in their relaxation rates induced by solute arise only from (subtle) alterations of the molecular dynamics of the water solvent, uninfluenced by magnetic interactions. What do such data indicate?

The five samples all appear to be relatively solid, the cross-linking (in four of them) creating an extended network of immobile protein which entrains solvent water by capillarity. However, the proton NMR signals from the water deuterons in all the samples indicate that essentially all the water is highly liquid and mobile. That the normalized profiles of the 4.8 and 10% BSA samples have the same form, after correction for the uniform water background ($\sim 2\,s^{-1}$ at 35 °C, which is a significant fraction of the observed rates, particularly above ~ 0.5 MHz), means that the intrinsic $1/T_1$ contribution of the solvent water when not in interaction with the protein (i.e. τ_c, and therefore the Brownian rotation of the bulk water) is unaltered by the presence of solute protein. Similarly the presence of dextran in one sample, which increases solvent viscosity seven-fold, neither alters the form nor the magnitude of the NMRD profile. The correction for water background is essentially that for pure water, assumed to be unaltered by the large change in macroscopic viscosity. The data are similar for carbonic anhydrase, which shows that BSA is not unique in its surface properties. The most intriguing results are those for BSA hydrated powder. The very existence of a signal shows that most of the water in the four monolayers is highly mobile, i.e. the dynamics of a two-dimensional array of four monolayers of water molecules abutting a protein interface is very much like that of pure three-dimensional water.

The major question is what the inflection frequency ν_c (Figure 1) (at the half magnitude ~ 0.1 MHz) represents. It corresponds[20] to $\tau_c \simeq 1/11\nu_c$, or $\tau_c \simeq 1\,\mu$s because of factors of 2π and the contributions of both single- and double-quantum transitions to relaxation. We have only recently[17,18] been able to associate this correlation time with the lifetime of a class of water molecules held rigidly at two sites (rounded) per BSA molecule (one monolayer corresponds to 700 water molecules). It was argued that these two water molecules are bound in a very specific configuration by four hydrogen bonds, an accident of the geometry of protein surfaces. The conjecture is that one proton of a coordinated water binds symmetrically to the two oxygen atoms of a deprotonated surface carboxylate, attached by two hydrogen bonds. The other proton could bind similarly to a nearby carboxylate or, as found recently in a neutron diffraction study of myoglobin (B. Schoenborn, private communication), symmetrically between the deprotonated nitrogen atoms of two surface histidines. An estimate of the water lifetime, obtained from the energy required to break four such bonds (2.6 kcal mol^{-1} or ~ 5 kT each) and the infrared stretching frequency of such bonds ($\sim 3 \times 10^{12}$ s^{-1}), are consistent with the τ_c evident in Figure 1.

The foregoing leads directly to a 'two-site rapid exchange' view of relaxation in these systems, which we favor: water molecules bind at specific protein–water interfacial sites, at which the slowed motion increases their relaxation rates in situ. The resident lifetimes should be shorter than the interfacial T_1 values or the effect of binding will be limited by 'slow exchange'. Because of their quadrupolar relaxation, binding of deuterons will not alter the strength of the interaction that relaxes them, but will change the correlation time. The extent of this change for the samples (Figure 1) is known. Increases in τ_c from 3 ps in solution to $1\,\mu$s when bound leads to only two bound water molecules in rapid exchange being necessary to explain these data. It follows that all the other interfacial water molecules must have much shorter lifetimes. This view implicitly leads to an approach that readily allows—indeed requires—the various water molecules that hydrate protein to be grossly inequivalent. Some authors have taken exception to this in explaining water relaxation in protein and colloidal systems, noting without argument that the bound 'state comprises an unphysically small number of water molecules',[21] and have looked for mechanisms in which all interfacial water molecules behave identically at all interfacial locations, altered in their motion by the imposition of a very small order parameter with a long relaxation time, by unknown mechanisms. The data shown in Figure 1 and the discussion given in the next section make this view untenable; the small number of long-lived interfacial water molecules is indeed the physical reality.

2.2 Water Deuteron and Proton $1/T_1$ NMRD Profiles in Solutions of Mobile Protein

Figure 2 shows both deuteron and proton $1/T_1$ profiles of solutions of native (mobile) carbonic anhydrase for solvents of differing isotopic composition.[22] For deuterons the profiles are independent of whether water is partially or fully deuterated. This is as expected, since a deuteron is relaxed by very local interactions of its quadrupole moment with the local electric field gradient. A second point of note is that the quasi-Lorentzian form of the profile, although much like that of immobile carbonic anhydrase (Figure 1) has $\nu_c \simeq 4$ MHz, i.e. 40 times higher for mobile than immobile protein. It has been known for some time,[23,24] and demonstrated for almost three decades of molecular weight,[20] that ν_c for mobile proteins is determined in the main by the Brownian rotation of solute and is calculable from Stokes' law.

In contrast to the deuteron profiles, those for protons are dependent upon whether a water proton has another proton as its neighbor. However, this dependence is much less than the expected linear dependence on $1/T_1$ (including the solvent background) with proton dilution. This is the most direct evidence that interactions between solute and solvent protons ('cross relaxation'[22]) contribute to solvent proton relaxation. The extent of the contribution of cross relaxation to each sample can be inferred from the broken curves, which show the proton $1/T_1$ profiles predicted from the deuteron results, assuming no cross relaxation for protons. It is evident that cross relaxation and 'hydrodynamic' relaxation (for protons) are comparable for a protein of 30 kDa, even with undeuterated solvent.

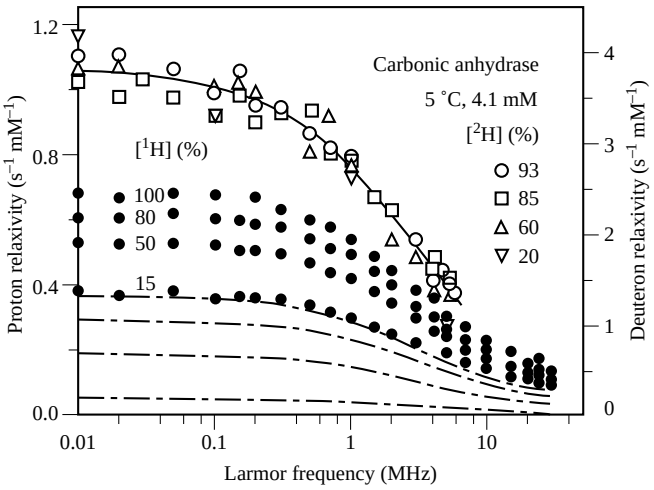

Figure 2 $1/T_1$ NMRD profiles of water deuterons (open symbols) and protons (filled symbols) for samples of 4.1 mM native (mobile) BCAB (30 kDa), at 5 °C. The data are expressed as relaxivity, the value of $1/T_1$, with the solvent contribution subtracted, per mM of solute protein. For the deuteron profiles, the water was 93% (○), 85% (□), 60% (△), and 20% (▽) deuterated. The solid curve is a fit to these profiles, which are seen to be independent of solvent isotopic composition. The broken curves are the profiles expected for protons, based on the deuteron results, taking into account only the different intrinsic relaxation rates of deuterons and protons in pure water. For the measured proton profiles, the water was 100, 80, 50, and 15% protonated. In each case, the relaxivities were significantly about the broken curves, indicating a significant contribution to the relaxivities arising from interactions between solute and solvent protons (cross relaxation). (Reproduced by permission from S. H. Koenig, R. G. Bryant, K. Hallenga, and G. S. Jacob, *Biochemistry*, 1978, **17**, 4348)

2.3 Conjectured Classes of Other Protein–Water Interfacial Binding Sites

We have argued for a class of interfacial binding sites with water molecules, held in place by four hydrogen bonds, having $\tau_M \simeq 1\,\mu$s. What then of three bonds, two bonds, etc? Table 1 gives our estimate of the interfacial lifetimes of these other configurations and the associated values of ν_c when protein rotation can be ignored. Each added bond is estimated to increase τ_M by a Boltzmann factor of about 50. What follows are data that support the table entries. The picture that emerges of the nature of the protein–water interface in solution is one of several (four) classes of water-binding site, each with a narrow and identifiable range of water lifetimes and increasing in number as the stereochemical requirements become less restrictive.

2.4 Influence of Protein Molecular Weight on Water Proton $1/T_1$ NMRD Profiles

Figure 3 shows proton $1/T_1$ profiles[24] for solutions of the same total protein content, but with molecular weights ranging from 14 to 450 kDa. For water molecules with $\tau_M \simeq 1\,\mu$s ($\nu_c \simeq 0.1$ MHz), this lifetime is sufficiently long to sense the protein rotation of all the proteins shown in the figure. It is only when the molecular weight becomes about 10 times greater than that of hemocyanin (∼5000 kDa) that Brownian

Table 1 Values of the Lifetime τ_M of a Water Molecule bound at a Protein–Water Interface when Held by n Hydrogen Bonds, Near 25°C[a]

n	τ_M	$\nu_c = \frac{1}{2}\pi(\sqrt{3})\tau_M$ (MHz)	B_0 (T)
4	1 μs	0.1	0.0024
3	20 ns	5	0.12
2	400 ps	250	6
1	8 ps	12500	300

[a]For immobile protein, τ_M becomes the correlation time for interfacial interactions, leading to an inflection in the NMRD profile at nuclear Larmor frequency ν_c, corresponding to a magnetic field B_0 for protons.

rotation is too slow to be sensed by these long-lived water molecules,[25] and so this is not a concern here. However, τ_M for three bonds was found[17] to be 23 ns in a particular case, which corresponds to $\nu_c \simeq 4$ MHz, a field well above the major dispersion of hemocyanin. A contribution from such shorter lived sites is clear in the hemocyanin data, shown here for proton profiles of a native mobile protein for the first time. The two solid lines represent true Lorentzian dispersive contributions to $1/T_1$, ostensibly the 1 μs and 20 ns sites, the latter with 5.2 times the population, and with values of ν_c of 0.4 and 4.0, respectively. For the lower field curve the dispersion relates to protein rotation, whereas for the higher field curve the dispersion arises from τ_M. The two curves sum to the open symbols (√), which clearly represent the data quite well.

The existence of three-bond sites has been argued for recently[17] (see ***Relaxometry of Tissue***), based mainly on extensive theoretical analysis of proton profiles of cross-linked BSA in highly deuterated solutions, to emphasize cross relaxation, but has also been deduced from analyses of data such as those shown in Figure 1. However, the density and lifetime of this three-bond class of sites are such that their contribution to relaxation can only be deduced with some certainty in special circumstances, including the high molecular weight hemocyanin (Figure 3), and then only if the existence of such sites is suspected.

The four- and three-bond sites still leave 97% of a hydrogen monolayer unaccounted for. Two-bond sites should have $\nu_c \simeq$ 250 MHz and $\tau_M \simeq 400$ ps, as in Table 1. Extensive arguments were given some time ago from the first NMRD profiles of protein solutions for sites with these characteristics:[23] they are ostensibly associated with water molecules surrounding polar groups at the protein–water interface, comprising about one-third of a hydration monolayer.[26] Quite recently, results of multidimensional NMR at 600 MHz were reported[27] for a very small protein (7 kDa), bovine pancreatic trypsin inhibitor—a protein too small to have any four-bond sites and few three-bond sites. The finding was that no water lifetimes were longer than about 300 ps, which is consistent with the foregoing discussion, although the fraction of interfacial water molecules that might exchange more rapidly was not determined.

The lifetime of a water molecule held by a single bond (Table 1) should be about 8 ps. This is only three times greater than the rotational relaxation time of a free water molecule at 25 °C. Even a monolayer of such bonds in a concentrated protein solution would contribute minimally to $1/T_1$, and be difficult to identify. It should be emphasized that it is very difficult to obtain an estimate of this value from the literature. An assiduous search was made earlier, when the relaxivity of

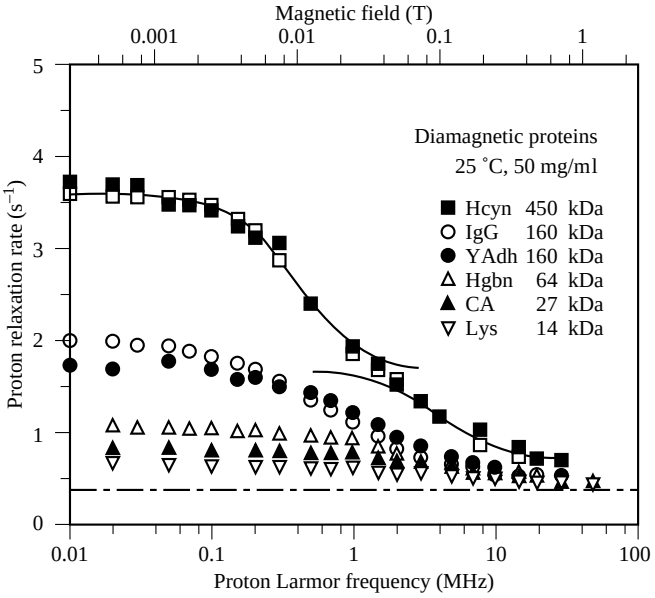

Figure 3 $1/T_1$ NMRD profiles of water protons in solutions of native proteins of various molecular weights, at a fixed concentration of 50 mg ml^{-1}, at 25 °C: (■) hemocyanin (450 kDa); (○) immunoglobulin G (160 kDa); (●) yeast alcohol dehydrogenase (160 kDa) (▲) bovine carbonic anhydrase (30 kDa); (▽) lysozyme (14 kDa). The broken horizontal line is the solvent background rate. The two solid curves associated with the hemocyanin data are Lorentzians, the sum of which (□) matches the data; they have ν_c values of 0.8 and 4.0 MHz. The lower field Lorentzian is, in our view, associated with exchange of water molecules bound at sites with lifetimes of about 1 μs, i.e. sufficiently long to sense the Brownian rotation of solute, and the higher field Lorentzian is associated with sites of lifetimes of about 20 ns, which is sufficiently short that the lifetime determines ν_c. (Reproduced by permission from K. Hallenga and S. H. Koenig, *Biochemistry*, 1976, **15**, 4255)

nitroxide radicals was studied in some detail.[28] There is clearly no formal inner coordination sphere for these solutes, but there was a question of whether they formed short-lived hydrogen-bonded complexes with solvent water. The conclusion was that any such complexes had to have lifetimes less than the rotational relaxation time of the nitroxide ($\lesssim$500 ps).

Relaxation of water deuterons by montmorillonite clays, which contain large lamellar particles with atomically smooth surfaces and oxygen atoms pointing to the water, were studied[29] in some detail to investigate interfacial interactions in these well-defined systems. Deuterons were measured to minimize artifactual contributions from possible paramagnetic impurities and interlamellar spacing was adjusted by dilution with solvent. The finding was a small contribution to $1/T_1$ that could be explained by a monolayer of water molecules being slowed in their rotation by a factor of about 5. We suggest that this could arise from the formation of a single hydrogen bond between each interfacial water proton with an uncharged surface oxygen atom. The major point is how little the motion of water is influenced by surfaces that have no special sites for enhancing solute–solvent interactions.

The power of computers and computing algorithms has advanced significantly during the last decade. Relevant interatomic and intermolecular interaction potentials are also well known, so that the molecular dynamics of water in relatively complex systems can be computed reliably to times approaching several hundred picoseconds. In a recent computation[30] of water interacting with myoglobin (15 kDa), the highly local self-diffusion constant of water was calculated near to the solute–solvent interface. The major result, as read by this author, is how little water is affected by the protein. Major questions would be whether the local diffusion constant is two- rather than three-fold different from its value in bulk water. There is no structure induced in the water, either temporal or spatial, other than that demanded by hard-sphere geometry, certainly to first order. Unfortunately, τ_M values for our three- and four-bond sites are far longer than the limits of such computations, although there are a few pockets of depressed diffusion that hint at the influence of these sites on local water dynamics.

2.5 Water Proton $1/T_1$ NMRD Profiles in Systems of Immobile Protein

The picture becomes complete when proton $1/T_1$ NMRD profiles of immobilized protein systems are also considered. Figure 4 shows[18] that, in contrast to deuterons, for protons the functional form of the profiles is dramatically altered by immobilization. Moreover, the profiles become like those of tissue, most of which have the same form but differ in magnitude.[20] Without going into details of theory and mechanism, which are covered elsewhere in this Encyclopedia (***Relaxometry of Tissue***), we note that—whether measured in a relaxometer or imager, or whether one measures $1/T_1$, $1/T_2$, or $1/T_{1\rho}$ at any field or temperature—it is not possible to

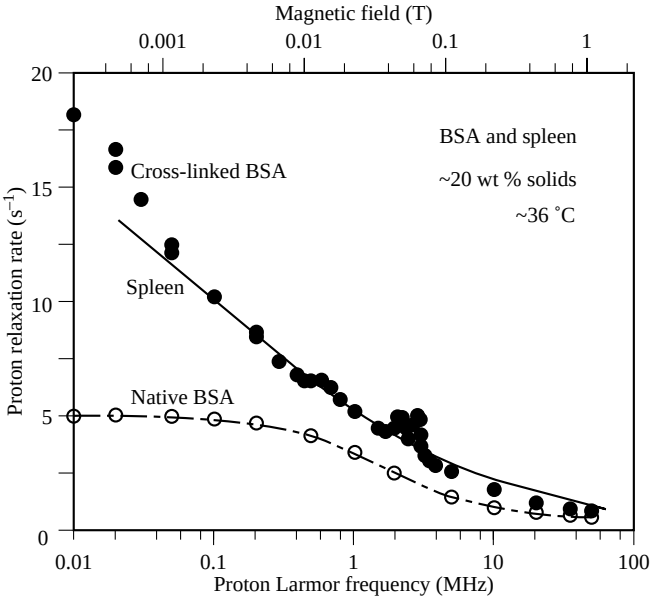

Figure 4 $1/T_1$ NMRD profiles of water protons of three samples with essentially the same (~20 wt %) solids content, at physiological temperature: human spleen (solid curve), native bovine serum albumin (○), and the same sample immobilized by chemical cross linking (●). Such cross-linked protein is an excellent model system for most tissue, so much so that the two cannot be distinguished by measurements in either a relaxometer or an imager[17] (Reproduced by permission from S. H. Koenig, R. D. Brown III, and R. Ugolini, *Magn. Reson. Med.*, 1993, **29**, 77)

distinguish a sample of, for example, cross-linked BSA from a typical tissue (exclusive of white matter and adipose tissues, both with different but significant lipid contributions). A ready inference is that water is not compartmentalized in tissue on a relaxation timescale, otherwise one would see tissue-specific effects. Most protein in tissue, which usually contains no more than protein and water, is also immobile.

The difference in functional form between proton and deuteron profiles in immobile systems (see Figures 1 and 4), but not mobile systems (Figure 2), must relate to the presence and absence, respectively, of cross relaxation for these two nuclei plus an increase in the importance of cross relaxation in immobilized systems. Briefly, the change relates to the mobility of proton magnetization in immobile systems, for which relaxation is like that in the solid state, and its absence in liquid state systems, where motional narrowing holds. For the solid state mutual spin flips of neighboring protons serve to transport Zeeman energy without loss of magnetization, since there are few fluctuations to relax the magnetization to the 'lattice'. Thus spin diffusion in the solute and chemical diffusion in the solvent generate a combined system that can be modeled as two Zeeman reservoirs. Each of these has spatially uniform magnetization which is coupled through interfacial interactions that transfer energy between the reservoirs. For protein–water systems the four-bond sites serve not only as the dominant sites for such transfer but, because of the relaxation that occurs at these sites, also serve as the major sites for relaxation of the total Zeeman energy with the thermal energy of the sample[17] (see also ***Relaxometry of Tissue***). For the liquid state, appropriate for mobile protein, the situation changes dramatically. Unlike the solid state case, for which mutual spin flips derive from the precession of a proton in the static interaction field, mutual spin flips arise from the zero quantum transitions generated by a fluctuating interaction field (ω_{int}). However these also generate single- and double-quantum transitions that relax the diffusing magnetization.[20] The net result is that the Zeeman energy of most of the solute is not in good contact with solvent and the potential amount of cross relaxation is reduced. In fact, as can be seen from Figure 2, the contributions of cross relaxation and hydrodynamic relaxation to $1/T_1$ of protons is comparable. That is, each proton of a water molecule bound at a $1\,\mu$s site is relaxed comparably by its intramolecular proton and protons of the protein. This conclusion was derived previously[17] by a quantitative analysis of the proton profile of cross-linked BSA in highly deuterated solvent. Put another way, Zeeman energy does not diffuse very far in liquids unless it is transported chemically.

2.6 Summary of the Dynamics of Water in Diamagnetic Protein–Water Systems

The picture presented so far, which derives from relaxometry measurements of deuteron and proton $1/T_1$ NMRD profiles of water in a range of protein–water systems of increasing complexity, models water as a slippery hard sphere. Despite the extended hydrogen bonding within the extended liquid, water can rotate substantially and move its own radius in times no longer than about 10 ps. These multiple bonds do not impede the rotational (or translational) motion of a water molecule; this time is 3 ps, not $1\,\mu$s. The reason for this is that rotation of a water molecule involves a concerted breaking and reforming of four bonds, which does not impose the energy requirements associated with removing a water molecule from an interfacial protein–water site, akin to evaporating it into the solvent. This is a major point, since the distinction amounts to more than six orders of magnitude difference in the relevant rate processes. (It is also not established theory, but an observation that is part of, and follows from, the larger picture of water mobility in biological systems, as discussed here.)

Macromolecular solutes (and small solutes) influence the molecular dynamics of water molecules only during physical collisions at solute–solvent interfaces. For proteins it was shown that four classes of interaction can be distinguished, corresponding to binding of water molecules to the protein by one, two, three, or four hydrogen bonds. For four bonds, the lifetime τ_{M} of the complex is about $1\,\mu$s; the lifetime is proportionately shorter for the other configurations (see Table 1). The relative densities of such sites appear to be similar for most proteins, including the proteins of most tissue, at least near physiological values of pH. The values of $1/T_1$ are very sensitive to the long values of τ_{M}, a $1\,\mu$s site generating an almost a million-fold enhancement of the magnitude of the perturbed water dynamics, making relaxometry relevant to MRI diagnostic radiology.

3 LIPID–WATER INTERACTIONS

Lipids, although minority constituents of tissue, are all important in that they form membranes which control the spatial organization of both macromolecules and small ions within and between cells. The interactions that concern us are interfacial, with the added feature that water can, and does, permeate membranes. The discussion in the earlier sections shows that, to first order, the presence of a plethora of membranes does not restrict the motion of water on a relaxation timescale (with the possible exception of organs designed to filter body fluids, such as kidney). The permeability to water of realistic biological membranes is often greater than in their analogs because of specialized pores that enhance water exchange. Nonetheless, exchange is also rapid in ideal systems, as expected from the generalizations presented above for water in protein and tissue and now extended below to water in lipid.

3.1 Myelin of White Matter

Myelin is the lipid of white matter, the membranes of specialized cells that generate a lipid–cytoplasm–lipid– ... 'jelly-roll' of electrical insulation and structural rigidity that surrounds the long axons which connect grey matter with other parts of the brain and beyond. About half the lipid includes a range of (unusual) phospholipids, with the polar and charged groups projecting into the intra- and extracellular spaces. Their contribution to the $1/T_1$ of white matter, as expected from the small contribution to the $1/T_1$ of the polar groups in the hydration layers of protein,[26] is too small to be resolved with any certainty in lipid systems[31] because of their limited solubility. On the other hand, half of the myelin lipid is cholesterol, a multiring alcohol that is highly insoluble in water and which adds to the stability of lipid–water systems by

dissolving in the lipid phase with the alcohol moiety projecting into the aqueous phases. This provides an extensive array of opportunities for interfacial hydrogen bonding. The presence of cholesterol also rigidifies the membrane, making it more like the solid state, and thereby increasing cross relaxation between water and lipid protons.[32] Studies of the NMRD profiles of white matter contain a contribution to $1/T_1$ from myelin that can be explained by assuming that each cholesterol has a hydrogen-bonded water with a lifetime of about 200 ps. (This corresponds to a continuous surface about 15 times more effective[31] at relaxing water than montmorillonite clay.[29]) From the data on interfacial interactions of water and protein (see Table 1) this suggests a geometry with two hydrogen bonds. The stereochemistry remains to be described, but the picture that emerges—particularly in the larger context—is quite satisfying. As an aside, the foregoing means that the widely known images of the adult brain in T_1-weighted MRI, in which white matter is much brighter than gray matter, is a map of the intact cholesterol-containing myelin of the white matter.[31] This relative brightness is not found in unmyelinated white matter of infants and it is altered in white matter disease by mechanisms that have yet to be quantified.

3.2 Permeability of Lipid Bilayer Membranes to Water

The water of myelin is about 15% of the water of white matter, so that unless it mixes with the majority (intra-axonal) water within the appropriate relaxation time (at physiological temperatures), myelin could not contribute to $1/T_1$ as generally measured. On a grander scale, white matter would not appear brighter than gray matter in MRI, since it is myelin that contains the needed relaxation sites. The question is what determines the permeability of lipid bilayers to water?

Here we elaborate the view that there is little that impedes the dynamics of a given water molecule in an extended solvent; water in water or water in lipid? Simply put, the molecular dynamics of water moving through an H_2O environment cannot be much different from water moving through an H_2C environment (the methylene groups that dominate lipid environments). The major difference between water and lipid environments arises from, on average, the four hydrogen bonds that a water molecule makes with its nearest water neighbors and which is absent for water in lipid.

A second difference between a water molecule in water and one in lipid is their different energies; water is highly polar (i.e. has a high dielectric constant), lipids are not. Call it image forces, electrostatics, or something more sophisticated, the extra electrostatic energy of a water molecule within a lipid reduces its probability of being there when it can be elsewhere—in particular when it can be in bulk water in contact with lipid. Thus the partition coefficient of water in water compared with water in lipid can be many orders of magnitude in favor of there being little water in the lipid. However, once there, given that the diffusion of water in lipid must be close in value to the self-diffusion of water, one can readily estimate that, for a water molecule somewhere within a (typical) 15 nm thick lipid membrane, water will escape in less than 50 ns. This view, based on the idea that it is in general very difficult to hold a water molecule chemically or physically, is the essence of the dissolve-and-diffuse theory of membrane permeability, which has been reviewed elsewhere.[33] Although not universally accepted, it is a simple and broadly applicable concept that follows from a larger picture of the dynamics of water in biological and related systems.

It is not simple to measure the permeability of bilipid layers either accurately or rapidly. An NMRD method was reported recently[34] which is rapid and accurate for those lipids that can be made to form unilamellar vesicles of relatively uniform size, something that is not too difficult to do in many instances. The technique is to entrain a chelated paramagnetic ion, of known NMRD profile, within the vesicles at a sufficiently high concentration such that $1/T_1$ within the vesicle is comparable to or less than the time it takes for a water molecule to 'escape' from the interior of the vesicle by permeation. The details are given elsewhere,[34] but typical results are shown in Figure 5. Here the influence of temperature and cholesterol on the permeability of POPC (1-palmitoyl-2-oleoyl-phosphatidylcholine) vesicles is shown for 100 nm diameter vesicles. The paramagnetic ion is Gd(DTPA) (diethylenetriaminepentaacetic acid), the relaxivity of which has been examined in great detail[20] given that it is used extensively as a contrast-enhancing agent in MRI. The accuracy or, at least the reproducibility, of the method can be gleaned from Figure 5. Data for one sample can be collected and analyzed in half a day. Interestingly, the escape time is of the order of milliseconds, which is shorter than the deadtime of earlier stopped-flow measurements that claim

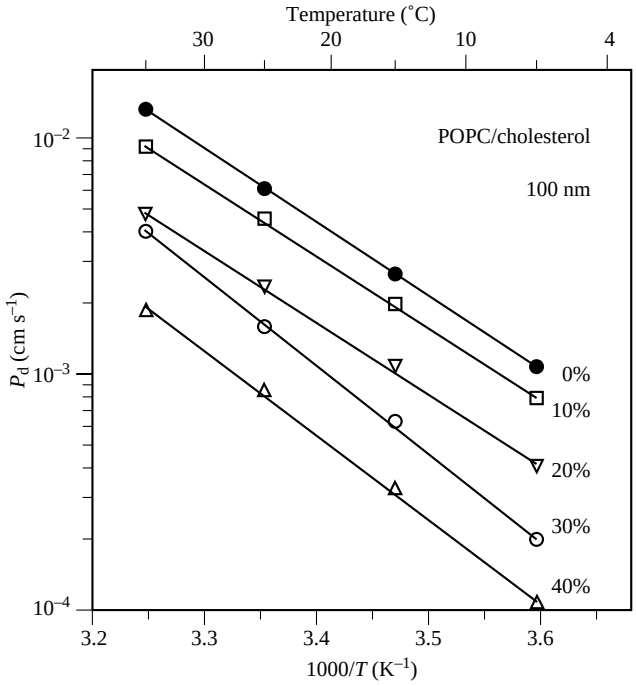

Figure 5 P_d, the permeability to water of bilayers of POPC unilamellar vesicles (100 nm diameter) as a function of temperature, for several values of cholesterol content. The vesicles, which occupy a small fraction of the total volume, contained sufficient paramagnetic ions (Gd(DTPA)) to make the $1/T_1$ of water protons within the vesicles comparable to the time required for water to 'escape' by permeation. The form of the $1/T_1$ NMRD profiles is then a function of the ratio of these two times, from which the permeability can then be calculated. (Reproduced by permission from S. H. Koenig, Q. F. Ankong, R. D. Brown III; M. Lafleur, M. Spiller, E. Unger, and C. Tilcock, *Magn. Reson. Med.*, 1992, **23**, 275)

to measure permeability by the swelling time of osmotically stressed vesicles.

3.3 Summary of the Dynamics of Water in Lipid–Water Systems

Lipid–water interfaces are quite different from their protein analogs. Unless the lipid contains components that have not only hydrophilic moieties but also, more specifically, OH (and possibly other) groups, and a surface geometry that favors extensive hydrogen bonding, the interfacial collisions are hard sphere collisions with no transient complex formation and little observable effect on $1/T_1$.

There is another major difference between lipid and protein interfaces. Proteins, because of their three-dimensional bonded structure, are not penetrable by water (on the timescales of interest here), whereas lipids have little lateral cohesion and water can readily penetrate, at least sterically. From the vesicle data (Figure 5), which gives an escape lifetime of the order of milliseconds and a transit time of about 50 ns, one can estimate that one encounter in 20 000 of a water molecule at a lipid bilayer interface will be successful in getting the water in. This makes it appropriate to consider these membranes as relatively impermeable. The kinetic factor (20 000) should (intuitively, according to the thinking here) relate directly to the equilibrium solubility of water in the lipid; in fact, it is a number that agrees well with the very low solubility of water in most lipids.[33] Nonetheless, the infrequent penetration of the membrane by water is generally sufficiently frequent to allow water to average out the intra- and extracellular environments of water within a relaxation time, thus making the NMRD profiles of tissue relatively insensitive to specific details of both the anatomical and histological morphologies of tissue, as can be observed.

4 QUANTIFICATION OF THE DYNAMICS OF WATER ON THE MOLECULAR SCALE: RESULTS FROM MAGNETIC SOLUTES

The emphasis above has been on the liquidity of water and how little its qualitative behavior is influenced by the presence of macromolecule–water interfaces and the specifics of the surface chemical composition. However, with the exception of the reference to results for clay[29] no quantitative results are presented that give values for the self-diffusion of water at this level (either translational or rotational) or the relative diffusion constants of molecular and macromolecular solute. A set of useful quantitative results can be obtained from the NMRD profiles of water protons in solutions of magnetic solutes. In the very early days of NMR such relaxometry data were used to learn about the structure of solutes,[14] with the assumptions about their influence (or lack thereof) on the solvent being left implicit. Due to the advent of MRI and the wide use of magnetic pharmaceuticals for altering contrast in MRI, enough is now known about the structure of many such solutes and the theory of their relaxivity that their presence can be used to probe the mobility of water in their vicinity. In essence, these particles produce magnetic fields that contribute to the relaxation of water protons out to a distance of about one solute diameter from the solute surface; this is called 'outer sphere' relaxation. In addition, the smaller agents (exemplified by Gd-DTPA) form a complex with a single water molecule coordinated directly to the metal ion which is in rapid exchange with solvent; this is 'inner sphere' relaxation.

4.1 Gd(DTPA)

About half of clinical MRI procedures involve magnetic agents, predominantly a commercial preparation of Gd(DTPA). Although this is often referred to as a paramagnetic agent [the magnetic susceptibility of solutions of Gd(DTPA) do exhibit classic Curie-law behavior], from the point of view of a mobile water molecule near a Gd(DTPA) solute molecule the water protons experience a fully magnetized S-state ion, spin of $\frac{7}{2}$, and a magnetic moment of 7 Bohr-magnetons from the parallel spins of the half-filled f shell. Thus, for our purposes, Gd(DTPA) can be considered as one of the smallest 'ferromagnetic' solute particles, with the seven spins of each particle permanently parallel.

Admittedly, particularly at low magnetic fields, the spatial orientation of the gadolinium moments fluctuates rapidly, corresponding to an electronic T_1 (τ_{1S}) of about 100 ps. However, this relaxation time, which affects both inner sphere and outer sphere relaxation, is field dependent[14,20] and, at typical imaging fields, τ_{1S} becomes much longer than the two other correlation times that contribute to the relaxivity of Gd(DTPA). These are τ_R, the reorientation time of the solute due to Brownian motion, which controls inner sphere relaxation and τ_D, a diffusional correlation time comparable to the time required for a water molecule to leave the solute environment, which controls outer sphere relaxation.

Figure 6 shows the measured proton $1/T_1$ NMRD profile of a solution of Gd(DTPA), together with two curves derived from theory (broken lines) for the (comparable) inner and outer sphere contributions to the relaxivity.[20] The inner sphere results assume one inner-coordinated water molecule in the usual geometry, with a lifetime of 1 ns, taken from that of the gadolinium aquoion. (Recent work has shown this time to be unexpectedly long,[35] about 250 ns, but this has little effect on the present discussion.) The zero field electronic relaxation time τ_{1S0} used is 85 ps, a correlation time τ_V of 20 ps characterizes its field dependence, and τ_R is 80 ps; this generates the inner sphere curve shown in Figure 6. Indeed, at high fields, τ_R is the only adjustable parameter that determines inner sphere relaxivity. For the outer sphere contribution, a τ_D of 41 ps and a (hard sphere) distance of closest approach a of 0.36 nm were used. Similarly, at high fields, the outer sphere contribution depends only (inversely) on a and the relative diffusion constant D of solute and solvent through the relation $\tau_D = a^2/D$. In turn, a must agree with the known crystallographic structure of Gd(DTPA). τ_R also depends on a and the applicability of Stokes' law at these molecular dimensions. Thus, there is little room to adjust the parameters that determine the relaxation at high fields. The high field data by themselves demand, in essence, that water behaves as a continuum fluid with fixed transport parameters even at solute dimensions, with a hard sphere interaction with the relatively small solute Gd(DTPA) molecules. In addition, since the inner and outer sphere contributions depend differently on field, fitting of the entire profile to theory fixes the relative amount

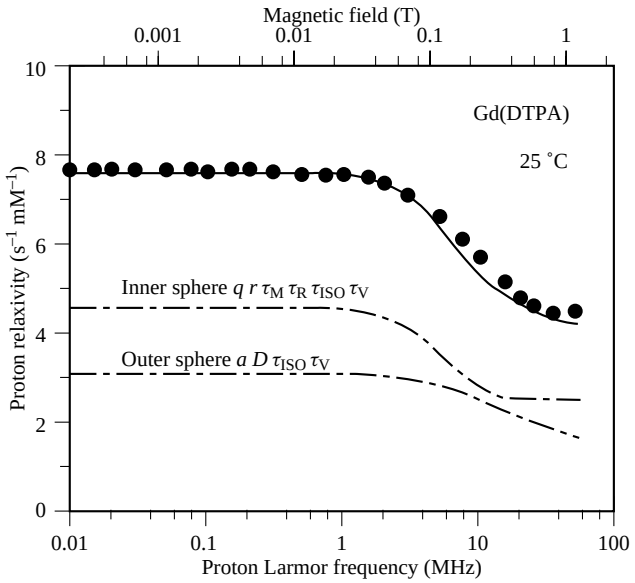

Figure 6 $1/T_1$ NMRD profile of water protons with solute Gd(DTPA) at 25 °C. The solid curve through the data is the sum of two contributions (broken lines): that of a single water molecule in rapid exchange from the inner coordination sphere of the gadolinium ion, and that of water molecules diffusing in the magnetic field of the gadolinium ion in the outer sphere environment of the chelate complex (see text). (Reproduced by permission from S. H. Koenig and R. D. Brown III, *Prog. NMR Spectrosc.*, 1990, **22**, 487)

of inner and outer sphere contributions, further constraining the values of the system parameters that describe the observed relaxivities. It is a fair estimate that small alterations (of the order of ±30%) of the parameters given would make a self-consistent fit of data and theory difficult.

4.2 Gd(DTPA) in Blood

In diagnostic radiology Gd(DTPA) is injected intravenously into the circulation where it mostly remains until excreted through the kidney. Its utility of course involves a balance of contrast enhancement versus toxicity, so that it is a realistic question as to whether NMRD data (Figure 6) can predict the behavior of Gd(DTPA) in clinical applications. Blood, like most tissues, is 20% solid, with one-third of its water in the dominant red cells. These contain the majority of blood protein (hemoglobin), although the extracellular space (plasma) contains an additional 30% of the total protein. The questions associated with Gd(DTPA) in blood are whether the agent attaches to, or enters, the cells and whether it binds to protein. Binding of small paramagnetic agents to macromolecules, which increases τ_R dramatically, can alter the NMRD profiles in the MRI field range in a particularly favorable way in a manner that is understood but not predictable.[15,20] From NMRD profiles of blood with and without added Gd(DTPA), and of the plasma that remains after the cells settle, it is readily demonstrated[36] that, from the water molecule's viewpoint, the partitioning of the blood by the cell membranes is irrelevant to relaxation, as the presence of macromolecules is to the relaxivity contribution of Gd(DTPA). All constituents—extracellular plasma protein, intracellular hemoglobin, and Gd(DTPA)—contribute independently to the NMRD profile of blood, with appropriate consideration given to excluded volume effects.

4.3 Superparamagnetic Particulates

Virus-size particles of iron oxide, predominantly magnetite, are becoming of increasing interest to the MRI community. Unlike smaller agents, these are removed from the circulation and deposited elsewhere in the body, apparently in ways that may prove useful for imaging liver, spleen, and marrow. These small 'nanoparticles,' typically in the range 5–10 nm diameter,[37] are generally protected from body fluids by attachments of polymeric sugars or starches designed to impede access of water as little as possible to the outer sphere environment of the iron oxide cores. They are termed 'superparamagnetic', a word that is ambiguous in that it can be properly applied to individual particles as well as to an ensemble of such particles in solution. In the latter case it means, as for Gd(DTPA), that the magnetic susceptibility of a solution obeys Curie's law, but now with a 'super' response. This is because the magnetic dipolar moment of each solute particle is very large and because the susceptibility of a solution containing a fixed total number of magnetic ions increases quadratically with the number of ions in each solute particle and only linearly in the total number of particles. Since a magnetite nanoparticle may contain about 5000 magnetite molecules,[38] susceptibility is enhanced by a factor of about 5000 over that of a solution of individual magnetite molecules. Ironically, the superparamagnetic aspects of the individual particles do not influence the behavior at imaging fields.[20]

Again, relaxometry studies of these particles, of which there are few—particularly on particles that are well-characterized chemically and magnetically—yield information on both solute and solvent. Here, outer sphere relaxation dominates, but the range is 10 times greater than for Gd(DTPA), which makes τ_D (which is proportional to the square of this range) very long and the intrinsic relaxivity of these particles very large. This is further enhanced because the relaxivity is also linearly proportional to the 'supersusceptibility' of the solute particles. Thus small total amounts of agent, far less on a molar basis of magnetic ion than for typical gadolinium chelate complexes, may prove adequate for diagnostic MRI. To this must be added that iron is an endogenous ion and questions of relative toxicity may favor iron over gadolinium. In any event, the increasing interest in such agents is making more relaxation data available and providing more knowledge of the behavior of water on a 10 nm scale. Again, 'water is water'. Initial results for particles with relatively narrow size distributions, measured by microscopy of one sort or another (X-ray, electron transmission, etc.) give contributions to $1/T_1$ at imaging fields[17] consistent with their size, using macroscopic values for the self-diffusion of water in microscopic environments.

4.4 Summary of Findings for Magnetic Solutes

There is a large body of literature on the influence of magnetic solutes, including metalloproteins, that has been discussed elsewhere.[15] The points considered here relate to the reality that the theory of relaxation of solvent protons

by magnetic solute has been improved remarkably within the past decade,[39] in part spurred by advances in clinical MRI and its incorporation of magnetic pharmaceuticals into its routine practice. Particularly as regards outer sphere relaxation in solutions of nanoparticles and larger particles (including paramagnetic red cells[40]), theory and data are in excellent agreement (even though the computations may be difficult). This agreement assumes the fluidity and mobility of water, often through organic binders and flagellate attachments[37] to the iron oxide cores of the nanoparticles.

There is one point that ought to be made for completeness, which relates to inhibition of inner sphere relaxation by protein-bound paramagnetic ions by the inhibition of protein function. Examples of this would be binding of sulfonamides to cobalt-substituted carbonic anhydrase and the reduction of cupric to cuprous ions in superoxide dismutase. The result is an NMRD profile like that of the diamagnetic protein, i.e., either demetalated or substituted with a diamagnetic metal ion. One might ask, on the basis of the extended diffusion of magnetization within immobilized protein considered in the sections above, whether in metalloproteins there is any contribution to the water proton relaxation by the magnetization diffusing through the protein to get around to the back of a paramagnetic ion for which water has been excluded by complex formation. The answer is that for mobile proteins no such effect has ever been reported, and for immobile proteins, that no pertinent data are available.

5 WATER AS A VISCOUS VACUUM

Important as the dynamics of water are for the proper functioning of biological systems, it is the behavior of the macromolecular solute, mainly protein, that underlies the functioning of these systems. Moreover, living systems typically contain about 20 wt % solids, mostly protein, a concentration far greater than the values of $<1\%$ that typify physico-chemical studies of protein in solution. There has been little emphasis on bridging this gap; understanding the behavior of protein at high concentration is often regarded as a hopeless activity. However, from our understanding of the dynamics of water in these systems, discussion of protein–protein interactions in solution at high concentration can be made simple. Several examples follow.

5.1 Rotational Relaxation of Solute Protein at High Concentration

For example, how free to rotate is the hemoglobin of red cells? The answer is known:[15] it is as free to rotate as in an infinite solution of hemoglobin at the same concentration, which is about 10 times slower than in the dilute limit. Is this reasonable: and what are the underlying physics? First, we remark that almost all soluble (globular) proteins have the same partial specific volume ($0.73\,\mathrm{cm}^3\,\mathrm{g}^{-1}$, with the exception of eye-lens protein, for reasons of lens transparency[25,41]), so that solute protein molecules can be regarded as relatively incompressible microsolids. As shown by Stokes in the middle of the last century, the rotational relaxation time of a sphere of radius r in an infinite viscous medium is proportional to its (macroscopic) viscosity η_0. Stokes also showed that if the sphere is at the center of a stationary larger sphere of radius R, its rotational relaxation time will increase as if the viscosity of the infinite medium were given by

$$\eta = \frac{\eta_0}{1 - [r/(R - r)]^3} \tag{2}$$

The increase in apparent viscosity is a geometric factor that is solely a function of the volume fraction occupied by the smaller sphere, i.e. the scale of the spheres is not germane (and of course should not be for a particle in a continuum fluid). For the protein–protein problem, let the outer sphere be an imaginary one defined as the largest sphere that excludes, on average, all protein neighbors of a given protein. If r is taken as the protein radius, and the radius of the imaginary sphere is taken as R in the Stokes example, then this simple model[26] affords an excellent description of the rotational mobility of hemoglobin as a function of protein concentration, up to the physiological concentrations in the red cell. Thus the interaction of proteins in solution is determined, in the main, by classical hydrodynamics, provided that there is no appreciable equilibrium association of solute.

5.2 Thermodynamics in a Viscous Vacuum

When considering the thermodynamics of an aqueous solution of protein at high concentration from the chemical viewpoint, it is usually handled as a two component system in equilibrium, with free energies being equal for the two components and for any other oligomeric forms in equilibrium with the monomer. From this viewpoint, it is difficult to address questions of, for example, osmotic pressure and possible phase separation. On the other hand, if one accepts the argument that the dynamics of water are little influenced by solute protein, then—realizing that equilibrium results derived from statistical mechanics of interacting particles are independent of the laws of motion of the particles—it becomes a powerful simplication to treat solute protein as a single system of interacting particles. The water may be considered as a vacuum in which Newton's laws are replaced by the response to a force typical of a viscous medium, and then ignored. The solute is then a hard sphere gas of identically charged particles that are weakly repulsive because of the high dielectric constant of water. Two extremely important results follow immediately, both of importance to the eye lens, in which the proteins reach uniquely high concentrations. One result is that the osmotic pressure of these proteins should be given by the results for hard spheres, as they are.[41] The second result is that, since a (three-dimensional) hard sphere gas with a repulsive interaction cannot have a first-order phase transition, the phase separation seen in one such protein, γ_{II}-crystallin, must be due to oligomerization and the creation of a multicomponent solute system.[42]

6 CONCLUDING REMARKS

Water in biological systems is in no sense innocuous. The polarity of its molecules (otherwise identical to neon) leads to a high dielectric constant, and thus water dissolves

and ionizes many salts. It also leads to extensive hydrogen bonding and the density minimum that keeps the oceans from freezing permanently. But once these effects are accounted for, which is done here by a 'renormalization' of attitude, then the molecular dynamic properties of water molecules can generally be ignored. Indeed, in order to use water in specialized ways in chemical reactions in biological systems, Nature has had to invent metalloproteins—with emphasis on the transition metals. In these compounds the water molecules can be maintained in desirable stereochemical orientations for times sufficient to allow enzymatic reactions to proceed, molecule by molecule. But this is another subject.

7 RELATED ARTICLES

Biological Macromolecules: Structure Determination in Solution; Brownian Motion and Correlation Times; Contrast Agents in MRI: Superparamagnetic Iron Oxide; Contrast Agents in Whole Body Magnetic Resonance: An Overview; Contrast Agents in Magnetic Resonance: Operating Mechanisms; Gadolinium Chelate Contrast Agents in MRI: Clinical Applications; Magnetization Transfer Contrast: Clinical Applications; Magnetization Transfer and Cross Relaxation in Tissue; Magnetization Transfer between Water and Macromolecules in Proton MRI; Molecular Motions: T_1 Frequency Dispersion in Biological Systems; Relaxometry of Tissue; Magnetic Resonance Imaging of White Matter Disease.

8 REFERENCES

1. F. Bloch, W. W. Hansen, and M. Packard, *Phys. Rev.*, 1946, **69**, 127.
2. F. Bloch, W. W. Hansen, and M. Packard, *Phys. Rev.*, 1946, **70**, 474.
3. E. M. Purcell, H. C. Torrey, and R. V. Pound, *Phys. Rev.*, 1946, **69**, 37.
4. I. I. Rabi, J. R. Zacharias, S. Millman, and P. Kusch, *Phys. Rev.*, 1938, **53**, 318.
5. I. I. Rabi, S. Millman, P. Kusch, and J. R. Zacharias, *Phys. Rev.*, 1939, **55**, 526.
6. J. M. B. Kellogg, I. I. Rabi, N. F. Ramsey, Jr., and J. R. Zacharias, *Phys. Rev.*, 1939, **56**, 728.
7. J. Schwinger, *Phys. Rev.*, 1937, **51**, 648.
8. I. I. Rabi, *Phys. Rev.*, 1937, **51**, 652.
9. F. Bloch and I. I. Rabi, *Rev. Mod. Phys.*, 1945, **17**, 237.
10. I. Waller, *Z. Phys.*, 1932, **79**, 370.
11. N. Bloembergen, E. M. Purcell, and R. V. Pound, *Phys. Rev.*, 1948, **73**, 679.
12. I. Solomon, *Phys. Rev.*, 1955, **99**, 559.
13. R. Kubo and K. Tomita, *J. Phys. Soc. Jpn*, 1954, **9**, 888.
14. N. Bloembergen and L. O. Morgan, *J. Chem. Phys.*, 1961, **34**, 842.
15. For a review and early references see: S. H. Koenig and R. D. Brown III, in *NMR Spectroscopy of Cells and Organisms*, ed. R. K. Gupta, CRC Press, Boca Raton, FL, 1987, Vol. 2.
16. A. G. Redfield, W. FiteII, and H. E. Bleich, *Rev. Sci. Instrum.*, 1968, **39**, 710.
17. S. H. Koenig and R. D. BrownIII, *Magn. Reson. Med.*, 1993, **30**, 685.
18. S. H. Koenig, R. D. BrownIII, and R. Ugolini, *Magn. Reson. Med.*, 1993, **29**, 77.
19. G. S. Schauer, R. Kimmich, and W. Nusser, *Biophys. J.*, 1988, **53**, 397.
20. S. H. Koenig and R. D. BrownIII, *Prog. NMR Spectrosc.*, 1990, **22**, 487.
21. L. Piculell and B. Halle, *J. Chem. Soc., Faraday Trans. 1*, 1986, **82**, 401.
22. S. H. Koenig, R. G. Bryant, K. Hallenga, and G. S. Jacob, *Biochemistry*, 1978, **17**, 4348.
23. S. H. Koenig and W. E. Schillinger, *J. Biol. Chem.*, 1969, **244**, 3283.
24. K. Hallenga and S. H. Koenig, *Biochemistry*, 1976, **15**, 4255.
25. S. H. Koenig, R. D. BrownIII, M. Spiller, B. Chakrabarti, and A. Pande, *Biophys. J.*, 1992, **61**, 776.
26. S. H. Koenig, in *Water in Polymers* (*ACS Symposium Series 127*), ed. S. P. Rowland, 1980, p. 23.
27. G. Otting, E. Liepinsh, and K. Wüthrich, *Science*, 1991, **254**, 974.
28. H. F. Bennett, R. D. BrownIII, S. H. Koenig, and H. M. Swartz, *Magn. Reson. Med.*, 1987, **4**, 93.
29. D. E. Woessner, *J. Magn. Reson.*, 1980, **39**, 297.
30. V. Lounnas, B. M. Pettitt, and G. N. Phillips, Jr, *Biophys. J.*, 1994, **66**, 601.
31. S. H. Koenig, R. D. BrownIII, M. Spiller, and N. Lundbom, *Magn. Reson. Med.*, 1990, **14**, 482.
32. T. A. Fralix, T. L. Ceckler, S. D. Wolff, S. A. Simon, and R. S. Balaban, *Magn. Reson. Med.*, 1991, **18**, 214.
33. A. Finkelstein, *Water Movement through Lipid Bilayers, Pores, and Plasma Membranes: Theory and Reality*, Wiley-Interscience, New York, 1987.
34. S. H. Koenig, Q. F. Ahkong, R. D. BrownIII, M. Lafleur, M. Spiller, E. Unger, and C. Tilcock, *Magn. Reson. Med.*, 1992, **23**, 275.
35. G. González, D. H. Powell, V. Tissières, and A. E. Merbach, *J. Phys. Chem.*, 1994, **98**, 53.
36. S. H. Koenig, M. Spiller, R. D. BrownIII, and G. L. Wolf, *Magn. Reson. Med.*, 1986, **3**, 791.
37. T. Shen, R. Weissleder, M. Papisov, A. Bogdanov, Jr, and T. J. Brady, *Magn. Reson. Med.*, 1993, **29**, 599.
38. S. H. Koenig, *Magn. Reson. Med.*, 1991, **22**, 183.
39. S. H. Koenig and K. Kellar, *Magn. Reson. Med.*, 1995, **34**, 227.
40. P. Gillis and S. H. Koenig, *Magn. Reson. Med.*, 1987, **5**, 323.
41. F. Vérétout, M. Delaye, and A. Tardieu, *J. Mol. Biol.*, 1989, **205**, 713.
42. S. H. Koenig, C. F. Beaulieu, R. D. BrownIII, and M. Spiller, *Biophys. J.*, 1990, **57**, 461.

Biographical Sketch

Seymour H. Koenig. *b* 1927. B.S., 1949, M.A., 1951, Ph.D., 1952, Physics, Columbia University, USA. IBM Research, 1952–93. Presently, Research Professor, Radiology, Dartmouth Medical School, Hanover, NH, USA and President, Relaxometry, Inc., Mahopac, NY, USA. Approximately 200 publications. Research specialties: atomic beams, solid state electrical transport, phonons and neutron scattering, laser-light scattering, and relaxometry, including protein structure and function, water proton relaxation in protein solutions and in tissue, and magnetic contrast-enhancing agents for MRI.

Field Cycling Experiments

Friedrich Noack

Universität Stuttgart, Physikalisches Institut, Stuttgart, Germany

1	Introduction	1
2	Basic FC Principles	1
3	Technical Problems and Instruments	3
4	Refinement and Extensions	6
5	Selected Examples	8
6	Related Articles	9
7	References	9

1 INTRODUCTION

In conventional NMR experiments the spin resonance is observed by irradiating selected nuclear magnetic spins of a sample material, which is exposed to a fixed high magnetic flux density $\boldsymbol{B}_0$ (Zeeman field, magnetic induction), with appropriate time-dependent rf fields $\boldsymbol{B}_1(t)$ tuned in resonance with the Larmor frequency $\nu \sum \omega/2\pi$ of the nuclei considered. This resonance frequency ν usually varies linearly with the magnitude of the Zeeman field $\boldsymbol{B}_0$ according to the Larmor condition $\nu = \gamma B_0/2\pi$, where γ is the characteristic magnetogyric ratio of the nuclear spin species; therefore, with decreasing field strength the standard procedures become more and more impracticable or even impossible for several reasons. The difficulties are primarily due to the related well known weakening of the NMR induction signal, which for a constant number of nuclei falls approximately as $B_0^{3/2}$, but serious problems also occur due to the tendency of the resonance to become broader at lower frequencies for a given linewidth. Hence it is not surprising that, generally, instruments operating at $\boldsymbol{B}_0$ fields or Larmor frequencies ν as high as possible are favored, and most endeavours in the past were concerned with ways to strengthen $\boldsymbol{B}_0$ to improve the signal quality. Presently, most spectrometers work under high-field conditions in the range between about 4 MHz up to 800 MHz for protons and up to 100 MHz for several spins with smaller γ, corresponding to a maximum Zeeman field of nearly 20 T. However, many good reasons can be given to support the less spectacular developments which oppose this familiar trend, that is, how to overcome the physical and technical barriers connected with NMR frequencies below the common megahertz range. The Earth's magnetic field $B_{\text{Earth}} \approx 5 \times 10^{-5}$ T can be easily compensated for to less than 1% of its value, allowing NMR spectroscopy with Larmor frequencies as low as, for example, 20 Hz for protons to be performed.

Numerous techniques have been successfully realized to solve the problems of NMR under low-field conditions below $\nu \approx 1$ MHz, ranging from simple enlargement of samples to sophisticated polarization transfer. One of these techniques, which is still relatively rarely used despite the great instrumental progress in recent years, is field cycling (FC) magnetic resonance or, more correctly, fast field cycling, where $\boldsymbol{B}_0$ is not fixed but periodically cycled. Several reviews on the subject have been published.[1–3] FC primarily makes it possible to extend the scope of frequency-dependent relaxation measurements from the megahertz regime to almost zero Larmor frequency. FC devices also, however, supplement or even replace presently used standard procedures, because once in operation the new approach is often less time-consuming than common practice: changes of the Larmor frequency do not require inconvenient retuning of electric circuits. Furthermore, the FC principle is very versatile, since cycling of both the strength and orientation of the Zeeman field $\boldsymbol{B}_0$, combined with special $\boldsymbol{B}_1(t)$ sequences, allows for possibilities which go far beyond the original intentions.[1,2] Typical subjects of FC studies are concerned with, for example, frequency-dependent relaxation times (relaxation dispersion), zero field spectra (resolution improvement), heteronuclear cross-relaxation effects (quadrupole dips), diffusion constants (magic angle averaging), and the angular dependence of these and related NMR parameters where lower Larmor frequencies introduce more favorable spectoscopic timescales than conventional magnetic resonance methods.

The origins of the FC technique go back to the early 1950s, when several groups started low-field work and searched for ways to improve the results. A simple yet slow mechanical field switch was first described in 1951 by Pound.[4] However, it took more than 10 years to develop instruments which allowed the FC principle to be applied to other than the most convenient cases. Essentially based on the pioneering concepts of Redfield et al.,[5] several laboratories succeeded in developing fast, versatile FC devices for measurements of fast relaxing signals of liquids and solids, and various prototypes of flexible, powerful machines have been described in the literature.[1–3,6–13] However, a commercial apparatus is not yet available. Due to the peculiar spin dynamics of some particularly ordered systems such as organic conductors[7] (spin waves) or anisotropic liquids[11] (order fluctuations), where as a rule a dramatic shortening of the longitutinal spin relaxation time occurs at low fields, studies of such materials require very fast cycling devices, which are difficult to construct. However, the presently available equipment will allow the application of FC NMR in most cases,

2 BASIC FC PRINCIPLES

2.1 Field Periods

FC requires the sample material to be in different Zeeman fields (two or more) at different times t. This implies that the normally constant external flux density $\boldsymbol{B}_0 \sum \mu \boldsymbol{H}_0$ or magnetic field $\boldsymbol{H}_0$ (μ is the permeability of the sample) has to be modulated periodically (cycled) in strength or direction (ideally both) in an adequately fast manner in a definite way (Figure 1). In the simplest case the nuclear spins are polarized and detected as usual by means of a field sufficiently high to yield a satisfactory signal quality. Unlike standard high-field NMR, however, between the period of polarization and the period of detection one inserts a period of evolution, during which the external field is decreased from the selected high value to an adjustable lower level. In this way any related Larmor frequency can be tuned easily over a broad range $\nu_{\min} < \nu < \nu_{\max}$, where the limits are mainly determined

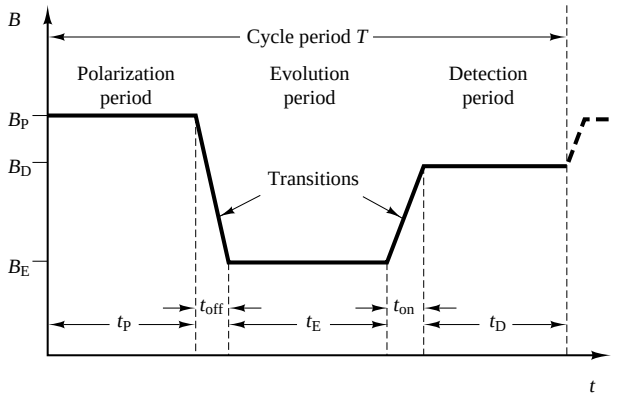

Figure 1 Typical $\boldsymbol{B}_0$ field cycle with polarization, evolution, and detection periods, and transition intervals from high to low and low to high

by the properties of the available magnet system and the exactness of the Earth's field compensation. As a consequence, features characteristic of the spins for frequencies between almost zero and an upper limit ν_{max}, at present typically 10–50 MHz, can be conveniently studied by well established high-field detection methods at a single fixed field. Obviously, the primary sensitivity problem is now transformed into the exacting task of switching an adequately high magnetic induction rapidly and reproducibly with sufficient accuracy. Sometimes it proves advantageous to use the highest accessible $\boldsymbol{B}_0$ not for the polarization and detection period, but only for the shorter evolution state, so that FC is a technique for both lowering and increasing the Larmor frequency compared with the fixed detection field.[3,11] During the different phases of the cycle the sample has to be irradiated by standard magnetic rf sequences $\boldsymbol{B}_1(t)$ to prepare and observe the nuclear magnetization or spin order, to determine the underlying frequency dependent spin parameters such as relaxation times, coupling constants, spectral shifts, jumping rates, etc.[1,2]

2.2 $\boldsymbol{B}_0$ Field Switches

To keep such experiments as flexible and transparent as possible, the cycle must fulfill several conditions on the level and speed of the field changes. It is obvious that both $\boldsymbol{B}_0$ and its time derivative $\mathrm{d}\boldsymbol{B}_0/\mathrm{d}t$ at the transitions should be made as large as is technically feasible to obtain good signals in the presence of fast magnetization decays. However, there are exceptions where it is necessary to slow down the switching to avoid effects on the spin order (see Section 2.4). Originally, the cycles were produced mechanically by moving or shooting the sample between a strong and a weak magnet[4] [Figure 2(a)]. This technique is relatively simple to realize, and is therefore still used,[14–16] taking advantage of strong cryomagnets for the high-field states, but it has some significant drawbacks. Above all, the switching times t_s (typically $t_{off} \approx t_{on} \geq 0.1\,s$) are generally too long for work on fast relaxing spins. The more powerful alternative[5] is to generate the transitions by quickly turning the current on or off through a magnet coil by means of an electronic switch [Figure 2(b)]. To understand the main problem of such a device one has to recall some elementary physics. If a voltage U is applied to a coil with inductance L and series resistance R_s, the current I through the coil, and

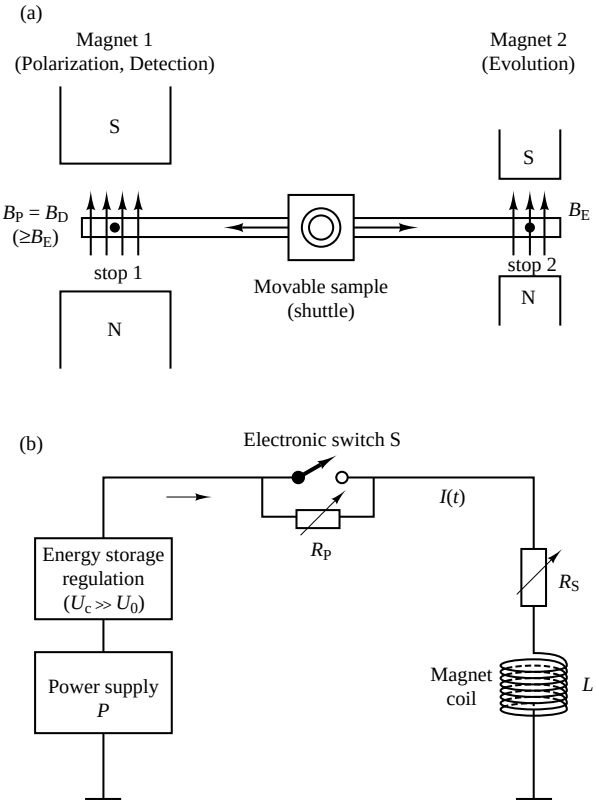

Figure 2 $\boldsymbol{B}_0$ field switch devices using either (a) a shuttle between two magnets (mechanical switch) or (b) a fast power supply control of the electric current I through a magnet coil (electronic switch)

hence the related field $\boldsymbol{B}_0$, increase exponentially with the time constant L/R_s. Owing to this increase, an equilibrium state is obtained more rapidly with a higher damping resistance, but this does not mean that the switching becomes faster by increasing R_s. Consideration of Faraday's induction law shows us that the fastest current change in the magnet is independent of R_s and determined by $(\mathrm{d}I/\mathrm{d}t)_{max} = U/L$; this maximum slope is maintained longer for a smaller R_s, and hence in principle a cryomagnet with $R_s = 0$ should give the best results. However, other features of cryomagnets, e.g. the maximum allowed current density, are less favorable. So to obtain fast field transitions one has to be concerned with high driving voltages U, and magnets with both low inductance L and low resistance R_s, i.e. with high-current air-cored coils instead of iron magnets. Since the highest electric power $P = UI$ is needed only for the (short) transition intervals, it is most effectively provided by an energy storage control which supplies a higher voltage (U_c) for the transition than for the steady states (U_0). All this was already known to Redfield,[5] but in 1968 adequate electronic components to build a powerful FC network were not available.

2.3 T_1 Cycle

A typical frequency-dependent FC measurement of the longitudinal relaxation time T_1 can be performed by combining a $\boldsymbol{B}_0$ cycle with standard $\boldsymbol{B}_1$ rf pulses as shown in Figure 3. When the Zeeman field is switched from its maximum value B_P to a selectable lower level B_R (in this case called the

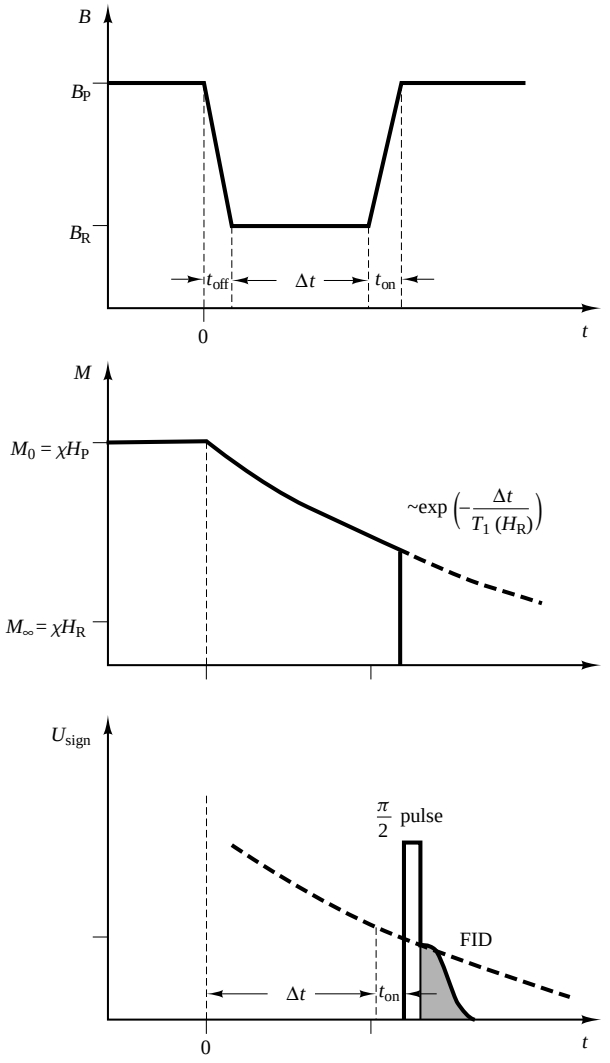

Figure 3 The FC principle for frequency- (or field-) dependent measurements of the longitudinal relaxation time $T_1(\nu)$ or $T_1(B)$. The diagram illustrates the $\boldsymbol{B}_0(t)$ cycle, the related magnetization decay $M(t)$ from M_0 to M_∞, and the FID signal $U_{sign}(t)$ after a $\pi/2$ $\boldsymbol{B}_1$ rf pulse

relaxation period), the initial longitudinal magnetization $\boldsymbol{M}_0 = \chi \boldsymbol{H}_0 = (\chi/\mu)\boldsymbol{B}_0$ along the external magnetic field $\boldsymbol{H}_0$ of, say, proton spins (χ is the nuclear spin susceptibility) decays exponentially with a time constant $T_1(H_R)$, characteristic of the Larmor frequency ν_R in the adjustable field H_R, to the new equilibrium $M_\infty = \chi H_R$. This decay is sampled as a function of the relaxation interval Δt by the FID amplitude after a $\pi/2$ rf pulse, applied in resonance with the Larmor frequency ν of the high detection field $B_D = B_P$, immediately after the transition to this detection state. Then the procedure is repeated over the available range of ν_Rs to give the full dispersion profile $T_1(\nu_R)$. If ν_R is near to ν_{max} and hence $M_0 - M_\infty$ becomes small, it is advantageous to precede the off switch by a π or $\pi/2$ rf pulse, which enhances the $M(t)$ change. The field switching times t_{off} and t_{on} must be shorter or at least comparable to the considered relaxation interval Δt and the observed T_1 value to get exact results. All these steps and the necessary data acquisition and processing, including the frequency changes, do not require hardware readjustments and can be conveniently made computer controlled. Frequency-dependent studies of other relaxation processes, e.g. transverse to $\boldsymbol{B}_0$ (T_2) or along the dipolar field $\boldsymbol{B}_d$ (T_{1d}), are less common in the literature and require more sophisticated cycles and different rf pulse sequences,[1–3] which are briefly commented on later in this article.

2.4 Adiabatic Condition

The main purpose of making the $\boldsymbol{B}_0$ field switches of a cycle fast is to avoid uncontrolled magnetization decay and hence signal losses by relaxation. For a T_1 cycle this essentially requires t_{off}, $t_{on} \leq T_1$. However, it is often overlooked that too fast transitions may also modify the magnetization or spin order undesirably in spite of negligible relaxation effects, namely by changing the angle of the magnetization $\boldsymbol{M}$ relative to the Zeeman field, and thus by inducing transitions between different Zeeman levels. Field changes preserving the initial angle during the transitions, which for normal FC T_1 measurements should be zero, for example, are called adiabatic, whereas nonadiabatic transitions perturb the angle.[1,2] Both types of switches are applied in FC experiments: standard relaxation studies demand adiabatic cycles;[1–3] nonadiabatic cycles[2,14,15] are mainly practised in zero field and Earth's field FC NMR, where rotations of $\boldsymbol{M}$ are necessary. The condition for adiabaticity requires that field variations perpendicular to the initial Zeeman field $\boldsymbol{B}_0$ must be slow compared with the effective Larmor frequency $\nu = \gamma B$ according to[1,2]

$$\frac{|\boldsymbol{B} \times \mathrm{d}\boldsymbol{B}/\mathrm{d}t|}{B^2} \ll \gamma B = 2\pi\nu \qquad (1)$$

which restricts the time derivative $\mathrm{d}\boldsymbol{B}/\mathrm{d}t$ if the direction is perpendicular to $\boldsymbol{B}$ because of the finite value of ν, particularly at low frequencies. Obviously, equation (1) is always valid, independent of the magnitude of $\mathrm{d}\boldsymbol{B}/\mathrm{d}t$, so long as the orientation of $\boldsymbol{B}$ is not changed. The condition becomes critical in the case of angular-dependent measurements, and in any case at low Larmor frequencies near $\nu \approx 10$ kHz, where for solids internal local field contributions $\boldsymbol{B}_{loc}$ are comparable in magnitude to the external field $\boldsymbol{B}$, and thus locally fast field rotations come into play. Similar effects may occur if the Earth's field is not properly compensated for or not correctly adjusted parallel to the Zeeman field of the spectrometer. Such problems have frequently been neglected and need more careful study. Adiabaticity sometimes requires that the cycle transition must be slowed down in the low-field range by appropriate current regulation, though such a step entails a dilemma between signal losses at transitions by either nonadiabaticity or by relaxation.

3 TECHNICAL PROBLEMS AND INSTRUMENTS

3.1 Magnet Switch Optimization

Magnets for fast FC NMR should provide the following from a given electric power P: (i) a magnetic flux density (induction) B or the related magnetic field $H = B/\mu$ as high as possible; (ii) the large flux variation rate $\mathrm{d}B/\mathrm{d}t$ needed for the cycle; and, in addition, (iii) a satisfactory field homogeneity

$B/\Delta B$ over the sample volume. These three requirements are strongly interrelated, and the problems of finding the most favorable switching network and coil geometry have still not been solved completely. This explains why many constructions described in the literature[5–13] are more or less based on semiempirical rules concerning the magnet system, though there are some sophisticated approaches. The basic aspect of the optimization problem is well demonstrated by considering estimations of B and dB/dt for a simple, long cylindrical coil with inductance L, resistance R_S, and field volume V in the solenoid approximation (length $\gg$ diameter), where the field is assumed to be constant over the whole coil volume, i.e. its inhomogeneity $\Delta B/B$ is neglected. If such a solenoid is driven by a power supply with maximum current I_{max} and maximum voltage U_{max} during the transitions, the greatest possible flux density and flux variation rate following from Maxwell's equations are determined by[1,2]

$$(B)_{max} = (\mu L/V)^{1/2} I_{max} = (\mu L/V)^{1/2}(U_0/R_S) \qquad (2)$$

$$(dB/dt)_{max} = (\mu/LV)^{1/2} U_{max} = (\mu/V)(P_{max}/B_{max}) \qquad (3)$$

with $P_{max} \sum I_{max}U_{max}$, $I_{max} \sum U_0/R_S$, and U_0 the steady state supply voltage. These relationships illustrate the intricate role of the magnet inductance L when trying to optimize the switch characteristics, i.e. to maximize both B and dB/dt, since the field strength increases with $L^{\frac{1}{2}}$, whereas dB/dt decreases with $1/L^{\frac{1}{2}}$. Essentially, equations (2) and (3) show the merits of high-current magnets in comparison with low-current coils, and also establish that the available electric power, the maximum field, and the field volume limit the switching or transition times t_{off}, t_{on} of the cycle. The time $t_S = (dt/dB)\ B$ for a transition from zero to B_{max}, or the inverse, becomes larger in the considered approximation ($\propto B_{max}^2$ and V), but smaller with higher power ($\propto 1/P_{max}$). Therefore the technical progress achieved in recent years is due to a great extent to the improved knowledge of handling smaller, yet still homogeneous magnet coils in combination with more powerful electric current supplies; advanced supplies typically should provide [11–13] an average power of 10–50 kW and a peak power of 100–500 kW to obtain fields of the order of 1–2 T, with switching times better than 1–10 ms and a homogeneity up to some 10^4 over 1 cm^3. One should note that equations (2) and (3) involve an interesting dependence on the permeability μ, which, however, has not been exploited in practice due to the technical problems of filling the coil volume around the sample with a magnetic material.

3.2 Energy Storage

Since the switching power $P_S = P_{max} = I_{max}U_{max}$ is only needed over the rather short field transition times, and both the power $P_0 = I_{max}U_0$ and voltage U_0 to maintain the stationary high-field states of the cycle are much lower than P_{max} and U_{max}, respectively (in the case of a superconducting magnet P_0 is zero!), it is advantageous to separate the driving networks for the transitions and for the steady states. This concept was first introduced by Redfield et al.,[5] but in a rather elementary way. Its main advantage comes from the fact that though P_S must be made extremely high (up to many hundreds of kilowatts) the related average energy $\langle E_S \rangle = P_S t_S$ is still relatively small because of the short switching time, typically of the order of milliseconds. Therefore, it is possible to take this switching energy and voltage from a precharged, sufficiently large high-voltage capacitor, C, which allows the collection and storage of the required energy over the whole cycle period from a comparably small auxiliary electric supply. Such a storage capacitor and suitable switching networks[6–13] can very effectively provide much higher driving voltages for the field transitions than the main lower-voltage current system, and thus achieve the fast current changes where desired. This is the well known energy storage principle of Redfield.[5] Since its original application the concept has been extended and refined in such a way that the magnetic energy of the coil is used to charge and recharge the storage capacitor during the field switch-off intervals instead of dissipating it in a damping resistor as in Redfield's work.[8,10,11] After the initial charging of the capacitor by the auxiliary supply, the switching device transforms magnetic coil energy to electric field energy and vice versa, so that the average additional power needed to generate the fast cycle transitions remains relatively low, typically less than a few percent of the main system. Essentially, only the ohmic losses of the circuits have to be compensated.

3.3 MOSFET–GTO Switching Networks

Figure 4 illustrates the basic components of an advanced fast FC network,[8–13] using high-voltage field effect transistors (MOSFETs) to regulate the magnet current for the stationary field states, and high-voltage gate turn-off thyristors (GTOs) to control the current paths of the energy storage during the transition periods. These and similar devices reported in the literature operate in general as follows. The current through the magnet coil, from a high-power low-voltage dc supply, is regulated by a MOSFET bank network, which tolerates the high-voltage peaks induced by the current switching of up to more than 1 kV without being damaged. To reduce the magnet current at the end of the polarization period, the gates of the MOSFETs are regulated to a selected level, and thus the decreasing current is partially driven by the storage capacitor, which is precharged by an additional high-voltage, low-current source up to the limits of the components, characteristically 1 kV. This auxiliary supply provides an adjustable voltage for the field transitions, so that the ratio U_C/L responsible for the slope of the current changes can be made considerably larger than the ratio U_0/L determined by the main current source, and consequently the transit from high to low becomes faster by a factor U_C/U_0. Similarly, to increase the current through the coil from a given lower level, the MOSFET gates are opened again, and simultaneously the high voltage of the storage capacitor is connected with the correct polarity to the coil by firing the GTO thyristor. In this way the current turn-off and turn-on can be driven by the same voltage $U_C \gg U_0$. Finally, as soon as the detection field level is reached, the GTO is switched off and the MOSFETs begin to stabilize the new detection state of the cycle. Figure 4 includes the different current paths for the four individual regulations of the switching network. In the high to low step the device transforms the magnetic coil energy to the electric field energy of the storage capacitor, and in the low to high step the process

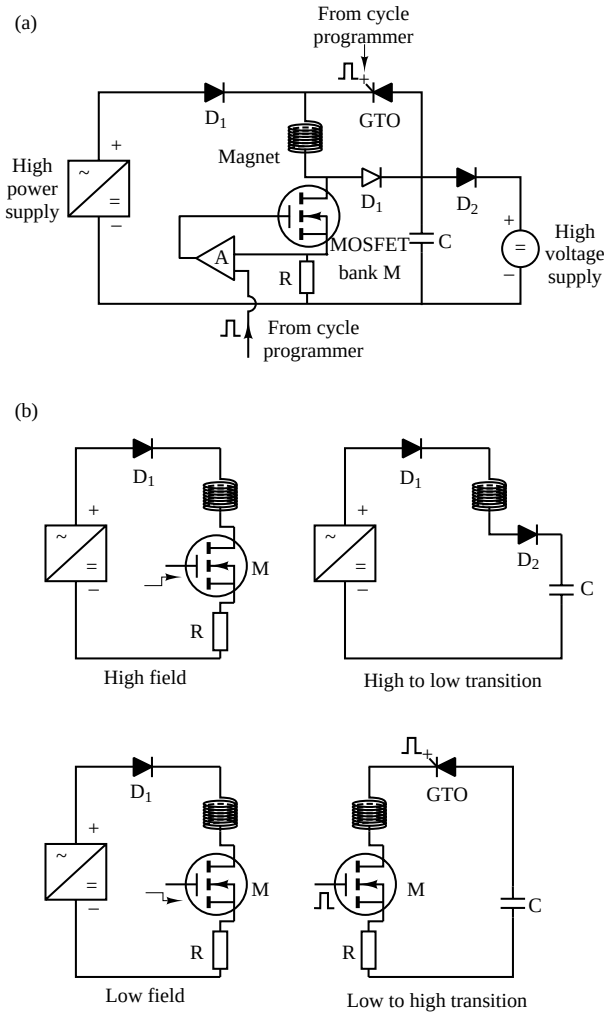

Figure 4 Basic components of a fast FC network with energy storage, making use of a MOSFET bank to regulate the current of the main power supply through the magnet coil, and a GTO to control the auxiliary high-voltage supply and the energy storage by the capacitor C. The figure illustrates (a) the basic network and (b) the four individual current paths for the transitions and steady states of the field cycle, timed by a cycle programmer

is inverted. By this means it has become possible to obtain maximum fields of more than 1 T with switching times of approximately 1 ms,[7–13] i.e. much more powerful and faster cycling instruments are possible than without energy storage. Unfortunately, commercial help for building such FC devices is still rather poor. Improvements to noncommercial switching networks, however, have become more and more facile by the availability of novel and less expensive semiconductor components such as POWER-MOSFET and POWER-IGBT (insulated gate bipolar transistor) packages,[17,18] which have properties similar to individual field effect transistors, but can handle higher currents without the need to connect an inconveniently large number of them in parallel.

3.4 Magnet Coil Geometries

Many different forms of air-cored coils have been considered and tried for FC spectrometers.[1,2] Originally, the Helmholtz ring pair arrangement was highly favored because of the well understood mathematics and the convenient radial access to the center of the magnet. However, the field at this center is markedly weakened relative to the strength near the inner surface of the conductor rings because of the wide air gap. Furthermore, even in the ideal case of negligible conductor cross section relative to the gap area, good homogeneity is confined to a rather small space around the midpoint region, and deviations from the ideal Helmholtz geometry are hard to correct. This circumstance, together with the poorer theoretical B/I ratio compared with cylindrical geometries, has made it evident that Helmholtz-type coils are not a good solution for FC magnets. Cylindrical coils can be designed that are superior to ring pairs with regard to many critical specifications such as maximum flux density, homogeneity, and total field volume, as was pointed out in the historic paper of Hak;[19] this result has long been overlooked. To take advantage of the cylinder geometry, however, one has to accept the inconvenience of having only axial access to the field center, which is why only later developments concentrated on such magnets. The ideal cylinder (solenoid, length $\gg$ diameter) theoretically gives a zero field gradient at its center, yet demands an unreasonable length and field volume, and hence it is necessary to look for short systems with suitable refinements of the field homogeneity. Various practicable ways exist to increase the current density at the ends of short cylindrical coils in order to diminish the field gradient over the central region by modifications to the conductor construction.[1,2,19–22] The most important of these modifications are shown in Figure 5, and are namely a linearly increasing number of conductor loops (linearly varied winding), a reduced number of loops (or even a gap) in the central part (outer notch), decreasing loop separations toward the coil ends (graduated current density), and conductor loops with a continuously variable cross section (optimized current

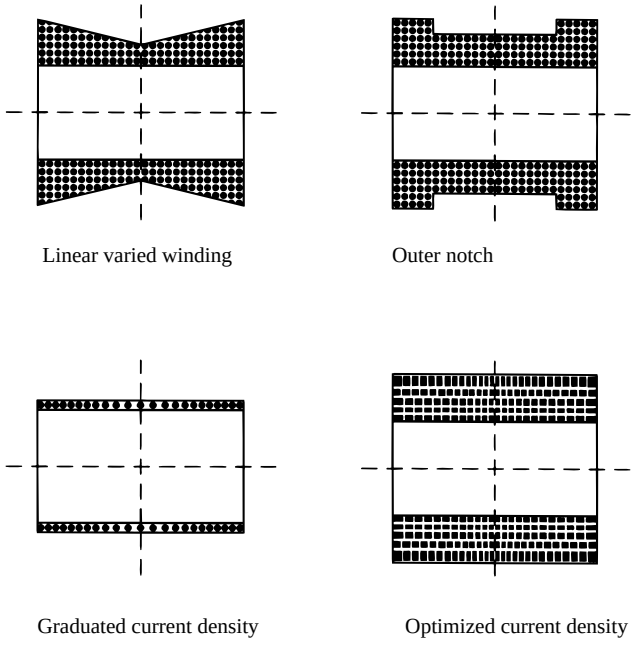

Figure 5 Cylindrical air core coil geometries to increase the field homogeneity of short FC magnets with small field volume

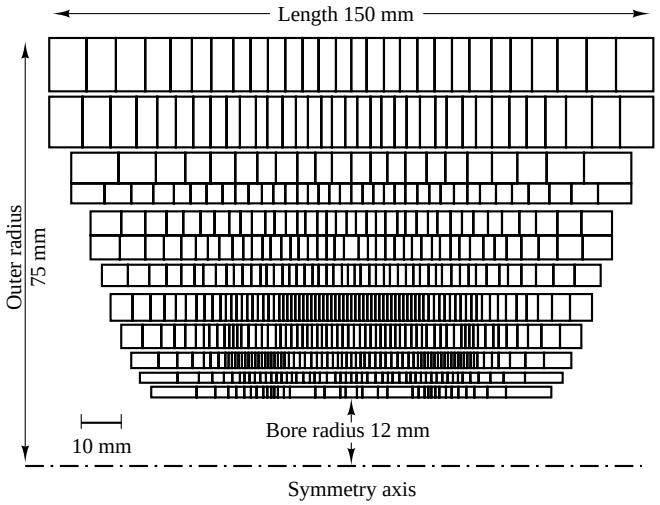

Figure 6 Conductor cross-section distribution (upper half) of a 2.4 T/50 kW FC magnet with optimized current density

density). By far the best results have been obtained using the last approach, which makes use of a novel Lagrange formalism[21] to calculate the most efficient coil and loop geometry under selectable constraints; i.e. it evaluates the conductor distribution that maximizes the field B for a given electric power P by simultaneously observing selectable target points (constraints) on the field homogeneity $B/\Delta B$ and the field volume V, i.e. indirectly on the inductance L. This Lagrange minimization procedure allows an inversion of the Biot–Savart law [$B(I)$ relationship] to a current–field law [$I(B)$ relationship] for conductor segments with an arbitrarily high number of adjustable coil parameters, and so gives an explicit (numeric) solution for the optimized current distribution. Several prototypes of such powerful FC magnets have been fabricated by cutting the calculated conductor rings from suitable copper and aluminum tubes. The cutting was performed either mechanically with isolating gaps as fine as 0.1 mm by means of a computer-controlled turning lathe,[11,21,22] or with less narrow gaps by computer-controlled spark erosion techniques.[12] Figure 6 represents the conductor cross sections of a 2.4 T/50 kW magnet manufactured in the author's laboratory.[22] The coil has 12 layers with about 20 000 parameters and an air bore of 24 mm diameter. The inner windings were cut from copper tubes, and the outer ones from aluminum tubes to lessen cutting problems.

4 REFINEMENT AND EXTENSIONS

FC is a particularly useful technique if the NMR properties to be investigated and the models involved depend on the Larmor frequency ν or the related magnetic energy splittings, and thus allow scaling of other frequencies, reorientation rates, coupling constants, and interaction energies of the spin system. Originally, FC was primarily used to study the frequency or field dependence of relaxation times in liquids, in order to analyze molecular motions by relaxation models; after numerous instrumental improvements, however, the technique can also be applied to quite different aims and problems. Though only relatively few laboratories have contributed systematically to instrumental developments, there has been a remarkable increase in the number of research groups working with FC, and numerous papers have now been published in this subject area.[1–16] Results are available for many types of materials, such as pure liquids, diamagnetic and paramagnetic solutions, liquid crystals, biological systems, molecular and ionic crystals, polymers, metals, alloys, and both classical and high-temperature superconductors. A large number of the earlier contributions have been summarized in several reviews[1–3] about both the technical concepts and physical findings of FC studies. Broadly, one can distinguish four types of applications, which require somewhat different spectrometers for suitable $\boldsymbol{B}_0$ cycles (Figure 7), rf pulse sequences $B_1(t)$, and data-processing methods. Some of these special FC subjects are described in related articles in this Encyclopedia.

4.1 Relaxation Dispersion

The main intention here is to study atomic or molecular motions by the frequency dependence of spin relaxation times[1–3] (relaxation spectroscopy, or relaxometry), commonly by $T_1(\nu)$ (longitudinal to $\boldsymbol{B}_0$, see Figure 3) and more rarely also by $T_2(\nu)$ (transverse to $\boldsymbol{B}_0$, see Figure 7). The interesting combination of FC with other spin relaxation processes such as $T_{1\rho}$ (rotating frame), $T_{1\mathrm{d}}$ (dipolar), or $T_{1\mathrm{q}}$ (quadrupolar), i.e. with more sophisticated spin preparation rf pulses, is still in its early stages.[23] In recent years, relaxation spectroscopy of solid-type signals has been extended from protons to other less sensitive but weaker coupled nuclei, e.g. deuterons, essentially to allow selective frequency-dependent measurements for different sites on a molecule by means of fast Fourier transform data processing.[11,24,25] The inclusion of this standard high-field NMR practice in fast electronic FC methods was an old but hard to realize challenge, and the experimental problems for this aim, which requires better magnet stability and homogeneity than previous nonselective work, have not yet been solved satisfactorily. Another fascinating recent development originated from the combination of relaxation spectroscopy with imaging procedures,[16] whereby using very inhomogeneous relaxation fields the T_1 dispersion over a broad range is spatially encoded in the sample; thus with adequate imaging rf pulses it is feasible to determine $T_1(\nu)$ in principle by one single B_R adjustment, i.e. by one single cycle. Obviously, these two refinements need almost opposite magnet specifications.

4.2 Zero Field NMR

In this case the original purpose was to enhance the spectral resolution[14,15,26] for polycrystalline or powdered samples through the phenomenon that in a zero magnetic field the Zeeman energy, and consequently also the line broadenings caused by the orientational distribution of dipolar or quadrupolar coupling tensors relative to the external Zeeman field $\boldsymbol{B}_0$, become irrelevant. In a zero field these interactions are made the dominant energy terms of the spin Hamiltonian, which can entail more favorable transition rules and thus simplify the NMR spectrum.[26] Almost all reported measurements were performed by mechanical FC

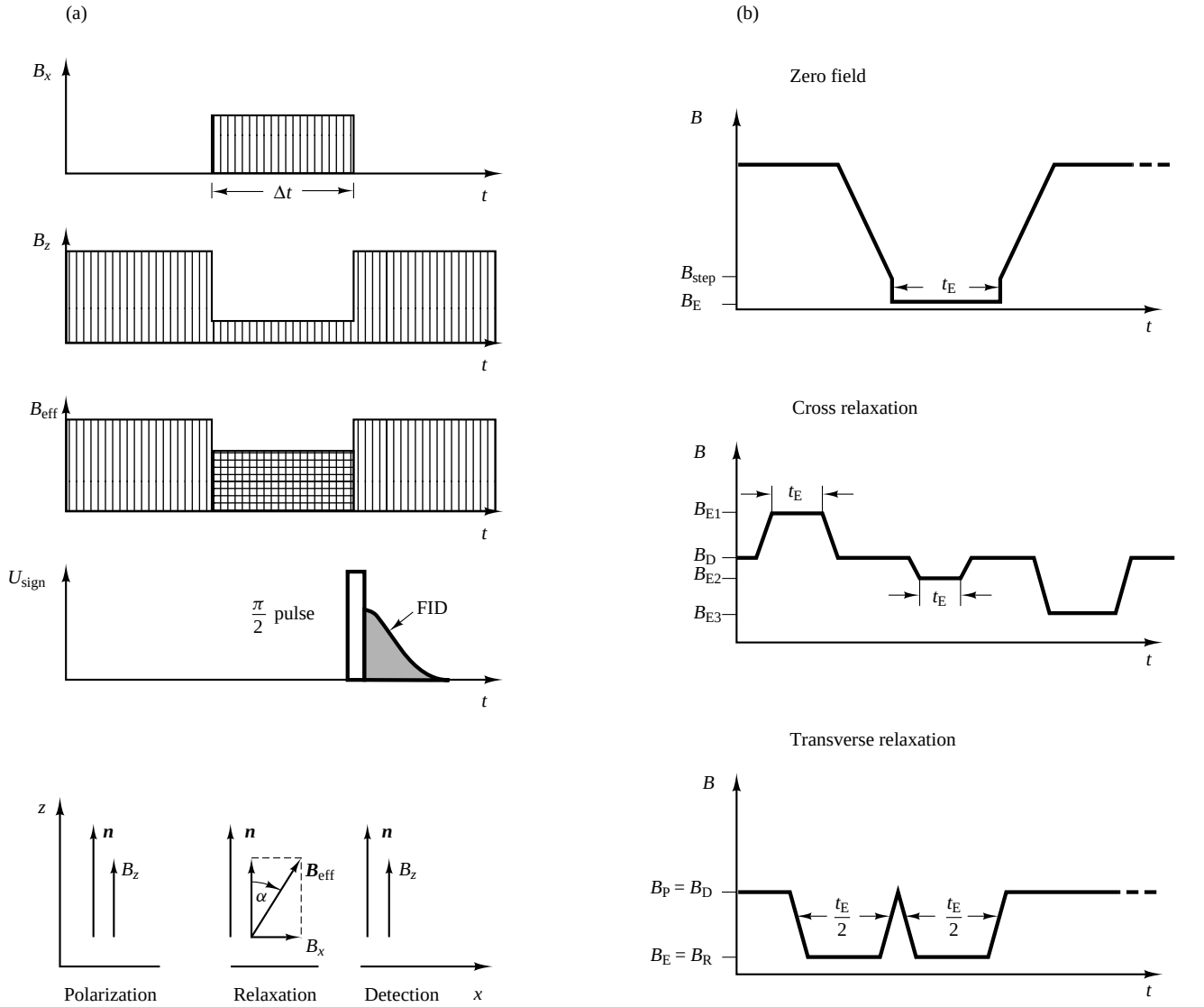

Figure 7 Advanced forms of $\boldsymbol{B}_0$ field cycles for (a) angular-dependent NMR measurements, making use of two perpendicular fields B_x, B_z, and (b) zero field, cross relaxation and transverse relaxation studies

instruments[14,15] and so are restricted to samples with long relaxation times T_1 ($\geq$0.1 s), which excludes, for example, biological membranes and liquid crystals. Unfortunately, the few experiments known so far for such samples with short T_1 s (millisecond range) in a zero field have proved rather disappointing,[27,28] because the expected resolution improvement could not be achieved; it seems to be hidden by the relaxation broadening and by experimental errors.

4.3 Cross-Relaxation Spectroscopy

Relaxation rates often involve a resonant increase in particular Zeeman fields where, as a function of $\boldsymbol{B}_0$, different energy levels of the spin system have a crossing point. The advantage of the FC method is to make use of such resonant exchange effects between dipolar, quadrupolar, Zeeman, and other (e.g. vibrational) splittings by properly adjusting the field to the resonance conditions[29–33] of multiple, different level crossing mechanisms. Using this method it has become possible to detect directly very small cross couplings between unlike spins or between like spins in different surroundings. These include interactions between protons and quadrupolar deuterons, nitrogens or chlorines,[2,29,30] between protons and vibrational modes in tunnel systems such as methyl groups,[9,31] or between quadrupolar spins in a highly symmetric crystal lattice and a less symmetric defect structure.[13,32,33] In the last case the technique is generally combined with selective irradiation of quadrupole transition frequencies at low fields to enhance the cross-coupling effects (nuclear quadrupole double resonance, NQDR). In addition to relaxation dispersion, several variants of NQRD belong to the most widely used FC applications.[13]

4.4 Angular Dependent FC

Originally, rotations of the field direction were introduced as a means of measuring relaxation times, which are angular dependent relative to special crystal axes,[2,34] for clearer

model discrimination, as illustrated in Figure 7. Later, the method initiated quite different types of work,[35–38] where fast electronic field switching is capable of extending considerably the previously used slower alternatives. For example, by changing the magnetic field direction relative to the symmetry axis (director) of liquid crystals, it becomes possible to study the short-time behavior of anisotropic flow processes, particularly the alignment of the director field parallel to $\boldsymbol{B}_0$, and thus the many anisotropic viscosities and elastic constants.[36] Similarly, one can reduce the dipolar coupling of spins by a fast magic angle orientation of $\boldsymbol{B}_0$ relative to the director and thus lengthen the effective transverse relaxation time T_2. In this way, the NMR pulsed field gradient (PFG) diffusion method has been successfully combined with FC for direct measurements of diffusion constants, even those that are angular-dependent, where normal solid-like FIDs are much too short to detect the contribution of the Fick's law signal decay more conventionally.[37,38]

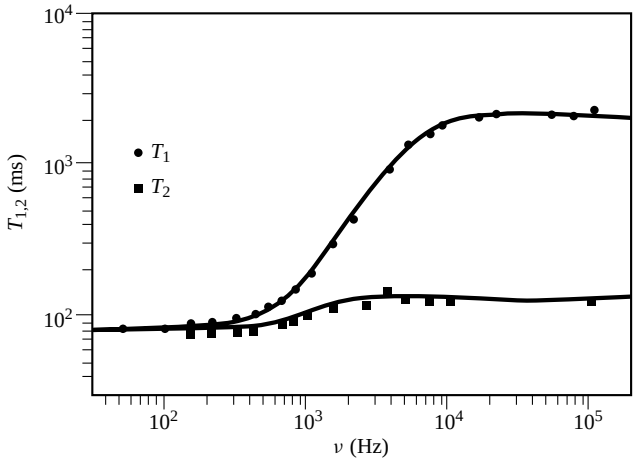

Figure 8 Proton spin relaxation dispersion of pure H_2O enriched with 4% ^{17}O (pH 7 and 26 °C) at low Larmor frequencies in the sub-Earth's field range. Lines are model fits[6,41]

5 SELECTED EXAMPLES

By far the most extensive applications of FC described in the literature are concerned with biological systems, polymers, and liquid crystals.[1–3] In these cases the usual NMR approach of determining molecular motions at a constant Larmor frequency by variation of the sample temperature suffers from limitations of the temperature ranges available without changing or degrading the phase of the materials. The following two examples were chosen from the numerous reported results because they required more sophisticated FC techniques than are commonly available.

5.1 Proton Relaxation Dispersion of Water

The mobilities of H_3O^+ and OH^- ions in pure H_2O are known to be considerably greater than those of any other univalent ions. This anomaly is understood to be a consequence of hydrogen bonds between water molecules and the ionic species under the premise that such links facilitate the rapid transfer of protons; for instance, one of the protons of an H_3O^+ ion can jump along the hydrogen bond to combine with an adjacent H_2O molecule faster than without the link. It was recognized by Meiboom as early as 1961[39] that the various time constants characteristic for the proton transfer reactions, in particular the mean proton exchange time τ_{ex} of a water molecule, can have a significant effect on the longitudinal and transverse spin relaxation times (T_1, T_2) of both the hydrogen (^1H) and oxygen (^{17}O) atoms (the more abundant isotopes ^{16}O and ^{18}O have no magnetic dipole moment). This additional relaxation rate is essentially due to a scalar magnetic coupling between neighboring ^1H and ^{17}O spins, which unlike the normal dipolar ^1H–^1H interaction is not averaged by the fast rotational and translational tumbling of H_2O molecules in the liquid state. According to standard relaxation models[40] the proton exchange statistically modulates the scalar coupling energy and leads to frequency-dependent proton relaxation times T_1 and T_2 at Larmor frequencies ν where $2\pi\nu\tau_{scal} \approx 1$. However, since the natural abundance of ^{17}O is only 0.037%, the dispersion step is extremely small in normal water (only ≈ 25%), but it could be observed[6,41] at low frequencies between 100 Hz and 2 kHz, i.e. for Zeeman fields below the Earth's magnetic field. By performing the measurements on ^{17}O-enriched samples, the scalar relaxation contribution is significantly increased, and more powerful FC instruments are needed to observe the full dispersion profiles at low fields. Figure 8 illustrates results for H_2O, enriched with 4% ^{17}O, at room temperature (26 °C) and pH 7. Note that near 100 Hz both T_1 and T_2 become shorter than 10 ms. The solid lines are fits of a two-spin relaxation model[40] with both dipolar ^1H–^1H and scalar ^1H–^{17}O couplings, and yield a correlation time τ_{scal} = 2.20 ms.[8,41] This is slightly shorter than literature data[39] for τ_{ex}, and indicates that the scalar interaction is also affected by mechanisms other than proton exchange, such as the ^{17}O spin relaxation. More details are given in the original papers.[6,8,41]

5.2 Proton and Deuteron Relaxation Dispersion of Liquid Crystals

Liquid crystalline mesophases have challenged NMR groups with FC equipment since the early 1970s, shortly after theoretical predictions became known that order director fluctuations (ODF, OF), i.e. collective thermal molecular excitations of the long-range orientational order (director field), may play an important role in nuclear spin relaxation. Unique to these materials, which contain rod-like or disk-like, i.e. anisotropic, molecules, it was predicted that such thermal fluctuations of the director should entail rather peculiar T_1 dispersion profiles. In the case of nematic order, they should produce a square root law frequency dependence of the longitudinal spin relaxation time, i.e. $T_1 \sim \nu^{1/2}$, which is a very unusual dispersion behavior[42,43] for low-viscosity liquids. Since the collective motions are superimposed on noncollective rotational and translational reorientation processes of individual molecules, it took a long time to separate the more common from the characteristic liquid crystalline phenomena. Controversies arose because the range of Larmor frequencies available to conventional spectrometers made the clear distinction of the different superimposed relaxation rates virtually impossible. With the development of fast T_1 FC devices capable of extending measurements of short T_1s to a regime where the

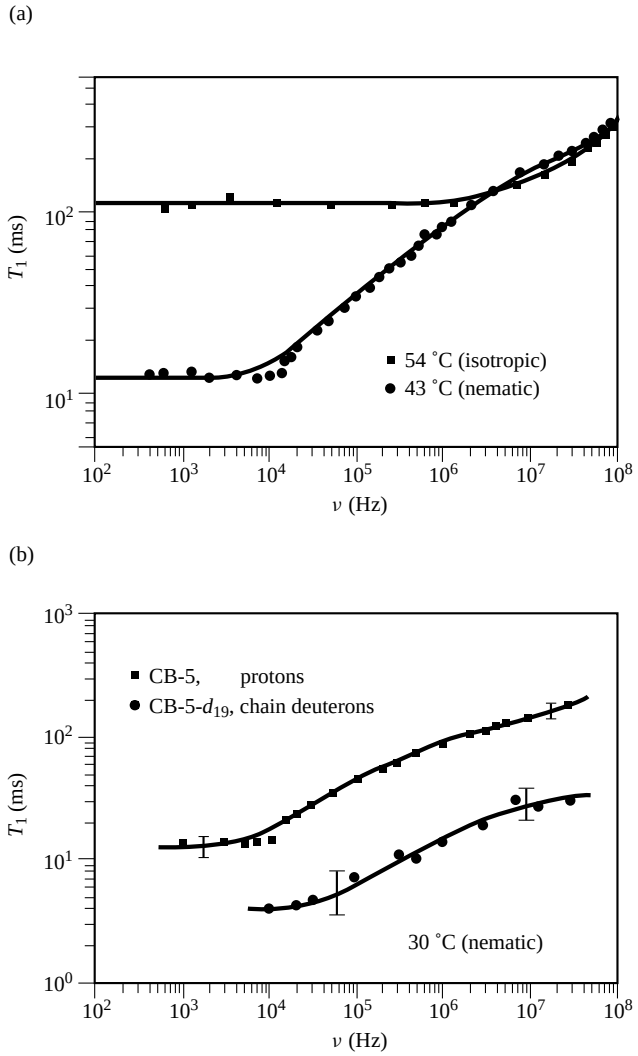

Figure 9 Proton and deuteron spin relaxation dispersion of nematogen liquid crystals. (a) Comparison of the proton T_1 for PCH-5 in the nematic and isotropic phase. (b) Comparison of the proton and chain deuteron T_1 values for normal and perdeuterated CB-5. Solid lines are model fits[11,24,25]

square root law dominates other competing terms (note that $T_1 \sim \nu^{1/2}$ gives $1/T_1 \to \infty$ for $\nu \to 0$), and which furthermore opened the way for angular-dependent studies under such conditions, a more reliable separation of the significant relaxation processes emerged. The results leave no doubt that the theoretical concept about relaxation by collective molecular fluctuations in liquid crystals at low ν values is basically correct. Figure 9 shows typical T_1 dispersion profiles[2,11,24,25] for two nematogen liquids: PCH-5 (pentyl**p**henyl**c**yclo**h**exane) and CB-5 (pentyl**c**yano**b**iphenyl). In both systems $T_1(\nu)$ exhibits at least three different frequency ranges where distinct mechanisms determine the total relaxation rate, in particular the broad square root law profile below the conventional Larmor frequency range. As expected, the $\nu^{1/2}$ contribution vanishes for the isotropic phase of the materials, and in deuterated molecules it is seen for both proton and deuteron spins. This idea allows acceptable theoretical fits[25,28] (solid lines in Figure 9) to the measured data. However, the detailed analysis of deuteron low-frequency results is only beginning, because of technical problems involved in selective deuteron FC experiments. The theoretical background of relaxation in liquid crystals and further experiments are discussed in other articles (***Amphiphilic Liquid Crystalline Samples: Nuclear Spin Relaxation***, ***Deuteron Relaxation Rates in Liquid Crystalline Samples: Experimental Methods***, and ***Liquid Crystalline Samples: Relaxation Mechanisms***).

6 RELATED ARTICLES

Amphiphilic Liquid Crystalline Samples: Nuclear Spin Relaxation; Brownian Motion and Correlation Times; Coupled Spin Relaxation in Polymers; Deuteron Relaxation Rates in Liquid Crystalline Samples: Experimental Methods; Diffusion Measurements by Magnetic Field Gradient Methods; Double Resonance; Dynamics of Water in Biological Systems: Inferences from Relaxometry; Fast Ion Conductors; Flow NMR; Liquid Crystalline Samples: Deuterium NMR; Liquid Crystalline Samples: Diffusion; Liquid Crystalline Samples: Relaxation Mechanisms; Paramagnetic Relaxation in Solution; Molecular Motions: T_1 Frequency Dispersion in Biological Systems; Polymer Dynamics and Order from Multidimensional Solid State NMR; Quantum Tunneling Spectroscopy; Relaxation Processes: Cross Correlation and Interference Terms; Relaxation Theory: Density Matrix Formulation; Relaxometry of Tissue; Slow and Ultraslow Motions in Biology; Zero Field NMR.

7 REFERENCES

1. R. Kimmich, *Bull. Magn. Reson.*, 1980, **1**, 195.
2. F. Noack, *Progr. Nucl. Magn. Reson. Spectrosc.*, 1986, **18**, 171.
3. S. H. Koenig and R. D. Brown, *Progr. Nucl. Magn. Reson. Spectrosc.*, 1990, **22**, 487.
4. R. Pound, *Phys. Rev.*, 1951, **81**, 156.
5. A. G. Redfield, W. Fite, and H. E. Bleich, *Rev. Sci. Instrum.*, 1968, **39**, 710.
6. S. P. Conti, Thesis, University of Geneva, 1984.
7. K. J. Glover, Thesis, University of California, Los Angeles, 1986.
8. E. Rommel, K. Mischker, G. Osswald, K.-H. Schweikert, and F. Noack, *J. Magn. Res.*, 1986, **70**, 219.
9. G. Vandemaele, P. Coppens, and L. van Gerven, *Proceedings of the 22nd Congress AMPERE, Zürich, 1984*, p. 398.
10. M. Blanz, G. Q. Chen, H. Birli, and R. Messer, *Proceedings of the 22nd Congress AMPERE, Zürich, 1984*, p. 596.
11. K. H. Schweikert, Thesis, Universität Stuttgart, 1991.
12. M. Blanz, T. J. Rayner, and J. A. S. Smith, *Meas. Sci. Technol.*, 1993, **4**, 48.
13. M. Notter, K. Konzelmann, G. Majer, and A. Seeger, *Z. Naturforsch., Teil A*, 1994, **49**.
14. D. B. Zax, A. Bielecki, K. W. Zilm, A. Pines, and D. P. Weitekamp, *J. Chem. Phys.*, 1985, **83**, 4877.
15. R. Kreis, A. Thomas, W. Studer, and R. R. Ernst, *J. Chem. Phys.*, 1988, **89**, 6623.
16. S. D. Swanson and S. D. Kennedy, *J. Magn. Res. A*, 1993, **102**, 375.
17. Harris Semiconductor, Product Selection Guide, 1992, Melbourne, USA.

18. Advanced Power Technology, Product Catalogue, 1992, Bend, USA.
19. J. Hak, *Arch. Elektrotech.*, 1936, **30**, 736.
20. G. Grössl, F. Winter, and R. Kimmich, *J. Phys. E.*, 1967, **18**, 358.
21. K. H. Schweikert, R. Krieg, and F. Noack, *J. Magn. Reson.*, 1988, **78**, 77.
22. St. Becker, K. H. Schweikert, and F. Noack, *Proceedings of the 25th Congress AMPERE, Stuttgart, 1990*, p. 458.
23. M. Reinöhl, Diploma Thesis, Universität Stuttgart, 1994.
24. K. H. Schweikert and F. Noack, *Mol. Cryst. Liq. Cryst.*, 1992, **212**, 33.
25. R. Köllner, K. H. Schweikert, F. Noack, and H. Zimmermann, *Liq. Cryst.*, 1993, **13**, 483.
26. J. W. Hennel, A. Birczyński, S. F. Sagnowski, M. Stachurowa, *Z. Phys. B*, 1985, **60**, 49.
27. E. Rommel, Thesis, Universität Sttutgart, 1988.
28. F. Noack, M. Notter, and W. Weiss, *Liq. Cryst.*, 1988, **3**, 907.
29. F. Winter and R. Kimmich, *Mol. Phys.*, 1982, **45**, 33.
30. D. J. Pusiol, R. Humpfer, and F. Noack, *Z. Naturforsch., Teil A*, 1992, **47**, 1105.
31. P. Coppens, L. van Gerven, S. Clough, and A. J. Horsewill, *J. Phys. C*, 1983, **16**, 567.
32. D. T Edmonds, *Phys. Rep.*, 1977, **29**, 233.
33. J. Seliger, *Proc. AMPERE Summer Institute on Advanced Techniques in Experimental Magnetic Resonance, Portorož, 1993*, p. 46.
34. J. Struppe and F. Noack, *22te Freiburger Arbeitstagung Flüssigkristalle, 1993*, p. 15.
35. A. F. Martins, P. Esnault, and F. Volino, *Phys. Rev. Lett.*, 1986, **57**, 1745.
36. H. Gotzig and F. Noack, *Abstracts of the 11th EENC, Lisbon 1992*, p. 88.
37. F. Noack, *Mol. Cryst. Liq. Cryst.*, 1984, **113**, 247.
38. J. Mager, Thesis, Universität Stuttgart, 1994.
39. S. Meiboom, *J. Chem. Phys.*, 1961, **34**, 375.
40. A. Abragam, *The Principles Of Nuclear Magnetism*, Oxford University Press, Oxford, 1961.
41. V. Graf, F. Noack, and G. J. Béné, *J. Chem. Phys.*, 1980, **72**, 861.
42. P. Pincus, *Solid State Commun.*, 1969, **7**, 415.
43. R. Blinc, D. L. Hogenboom, D. E. O'Reily, and E. M. Peterson, *Phys. Rev. Lett.*, 1969, **23**, 969.

Biographical Sketch

Friedrich Noack. *b* 1932. Ph.D., 1966, Physics, University of Stuttgart. Professor, 1978–present. Approx. 200 publications. Special interests are teaching of basic physics, developments of novel experimental NMR techniques such as field cycling, applications of NMR methods to investigate the molecular dynamics of liquid crystals and biological systems, and the critical analysis of scientific software.

Zero Field NMR

David B. Zax

Cornell University, Ithaca, NY, USA

1	Introduction	1
2	Why do High Field NMR?	1
3	Why do Zero Field NMR?	2
4	Making Low Field Detection Feasible	3
5	Frequency versus Time Domain	4
6	Other Approaches to Zero Field Results	9
7	Conclusions	11
8	Related Articles	11
9	References	11

1 INTRODUCTION

After 50 years of development, techniques for achieving high resolution in NMR are well developed for molecules in the liquid state, where subhertz linewidths are common. Achieving high resolution is a substantially different problem for materials in the solid state, where the 'natural' spectral linewidths (measured from the Fourier transform of the free induction decay following a single excitation pulse) are many kilohertz wide. Both theory and experiment have extensively demonstrated that manipulations of the spin degrees of freedom (using rf fields) and/or spatial degrees of freedom (typically via bulk sample rotation) make it possible to 'line-narrow'. In line-narrowing experiments, deterministic 'dynamics' imposed by the experimentalist efficiently substitute for Nature's chaotic efforts so as to eliminate those anisotropic interactions responsible for excess spectral breadth. What remains are the isotropic interactions only—a portion of the chemical shift tensor, some fraction of sufficiently large second-order interactions, and J couplings.

Where the molecular probes of greatest spectroscopic interest are the dipole–dipole or quadrupolar interactions (whose anisotropies are often responsible for the broad spectral lines observed in solids), techniques for achieving high resolution are substantially less well developed. Methods that focus on eliminating anisotropies are inappropriate, since in the limit of large applied magnetic fields, these interactions are entirely anisotropic. A fundamentally different approach is therefore required. Eliminating the anisotropy in the interaction is accomplished not by eliminating the interaction itself but by eliminating instead the laboratory-based, externally applied magnetic field. The resulting experiments are, therefore, zero field NMR experiments. In the absence of an applied field, NMR spectra of solids in their 'natural' spectroscopic state can be revealed.

In an era where research facilities rush to order spectrometers based on not yet operating superconducting magnets at newer and higher fields, it is far from obvious that some magnetic resonance experiments may be best executed in zero applied field. Yet zero field magnetic resonance has a long and important place in magnetic resonance, including experiments among the earliest[1] and of greatest impact.[2,3] Nonetheless, zero field NMR experiments occupy a relatively small niche in standard discussions of high resolution NMR in solids.[4] Thus one of the essential questions to be addressed below is the motivation for NMR experiments executed in low magnetic fields. A second question we shall address is how such experiments might be carried out without unacceptable sensitivity losses.

2 WHY DO HIGH FIELD NMR?

Why is NMR routinely performed in large applied magnetic fields? Two reasons come immediately to mind: the first is related to experimental sensitivity. Formulae for the signal amplitude in an NMR experiment predict an increase in that fundamental parameter by an amount that varies as the square of the transition frequency. This dependence can be traced directly to the Faraday law, which states that the electromotive force ϵ in a coil associated with a magnetic flux Φ is

$$|\varepsilon| \propto \frac{\mathrm{d}\Phi}{\mathrm{d}t} \propto \omega M_z \tag{1}$$

where ω is the transition frequency and M_z is the amplitude of the magnetization being detected. Experimentalists can control the transition frequency only where the Larmor interaction

$$\hat{\mathcal{H}}_\mathrm{L} = \gamma B_0 \hat{I}_z = \omega_\mathrm{L} \hat{I}_z \tag{2}$$

dominates the transition frequency so that $\omega \approx \omega_\mathrm{L}$. In the limit of high temperatures and Boltzmann statistics, the equilibrium magnetization M_z of equation (1) depends linearly on the same energy splitting ω. For most nuclei, and for all studies in liquid state NMR, the largest transition frequencies are found in the largest possible magnetic fields, and on combining equations (1) and (2) the signal amplitude is found to vary with ${B_0}^2$.

Large applied magnetic fields serve a second purpose. The chemical shift Hamiltonian can be written as a contraction

$$\hat{\mathcal{H}}_\mathrm{cs} = \gamma \hat{\boldsymbol{I}} \cdot \boldsymbol{\sigma} \cdot \hat{\boldsymbol{B}}_0 \tag{3}$$

and frequency shifts in equation (3) due to $\boldsymbol{\sigma}$ are proportional to B_0. Resolution of line shifts associated with two different chemical environments is therefore easiest in the largest available magnetic fields. Wherever chemical shift information is desired, the best measurements are made in the highest available fields.

In solids, the same considerations govern signal amplitudes, so that high field detection is always most sensitive. Chemical shifts scale in the same fashion in liquids and solids. But where the absorption spectrum is dominated by dipole–dipole couplings between spins (for abundant spin-$\frac{1}{2}$ nuclei, especially ^{1}H) and/or quadrupolar couplings (for spin-1 or higher nuclei), resolution is not necessarily improved in higher fields—in fact, the opposite is true.

The direct coupling between the magnetic dipole moments of pairs of spins A and B, is represented by the dipole–dipole Hamiltonian

$$\hat{\mathcal{H}}_\mathrm{D} = \hat{\boldsymbol{I}}_\mathrm{A} \cdot \boldsymbol{D} \cdot \hat{\boldsymbol{I}}_\mathrm{B} \tag{4}$$

where $D_{\alpha\beta} = \gamma_i \gamma_j \hbar {r_\mathrm{AB}}^{-3}(\delta_{\alpha\beta} - 3e_\alpha e_\beta)$ and e_α is the αth component of the unit vector along $\boldsymbol{r}_\mathrm{AB}$. For collections of dipolar-coupled spins, the total dipolar Hamiltonian is the

sum over all pairwise interactions. Typical dipole–dipole couplings are generally less than 50 kHz. (It is entirely possible that some of the dipole-like coupling between spins arises from anisotropic contributions to the J coupling tensor. As experiments provide little guidance as to how one might separate between the two, we shall ignore this possibility.)

The quadrupole Hamiltonian $\hat{\mathcal{H}}_{\mathrm{Q}}$ reflects the coupling between the nuclear electric quadrupole moment eQ (for $I \geq 1$ only; for $I = 0$ or $\frac{1}{2}$, the charge distribution in the nucleus is spherical and $eQ = 0$) and whatever local electric field gradients are found nearby, so that

$$\hat{\mathcal{H}}_{\mathrm{Q}} = \frac{eQ}{2I(2I-1)\hbar_i}\,\hat{\boldsymbol{I}}_i \cdot e\boldsymbol{q} \cdot \hat{\boldsymbol{I}}_i \tag{5}$$

where $\boldsymbol{q}$ is the field gradient tensor. Local field gradients reflect most strongly the distribution of electrons in valence orbitals, and somewhat less strongly the more distance ionic charges associated with a typical ionic lattice. Collectively, $\hat{\mathcal{H}}_{\mathrm{D}}$ and $\hat{\mathcal{H}}_{\mathrm{Q}}$ will be referred to as the local Hamiltonians.

Choosing the principal axis systems where these interactions are diagonal, the expanded version of the dipole–dipole Hamiltonian is

$$\hat{\mathcal{H}}_{\mathrm{D}} = \omega_{\mathrm{D}}(3\hat{I}_{z,i}\hat{I}_{z,\,j} - \hat{\boldsymbol{I}}_i \cdot \hat{\boldsymbol{I}}_j) \tag{6}$$

where $\omega_{\mathrm{D}} = \gamma_i\gamma_j\hbar/r_{ij}^3 = D_{xx}$. (In the absence of dynamics, the dipole–dipole Hamiltonian must satisfy $D_{zz} = -2D_{xx} = -2D_{yy}$.) The expanded version of the quadrupolar Hamiltonian is

$$\hat{\mathcal{H}}_{\mathrm{Q}} = \frac{\chi}{4I(2I-1)}[3\hat{I}_z^2 - I(I+1) + \tfrac{1}{2}\eta(\hat{I}_+^2 + \hat{I}_-^2)] \tag{7}$$

where q_{zz} is the largest principal value of $\boldsymbol{q}$ and $\chi = e^2q_{zz}Q/h$, with asymmetry parameter $\eta = (q_{yy} - q_{xx})/q_{zz}$. Typical values of χ range from 10 kHz to 100 MHz. Each of the interactions $\boldsymbol{D}$ and $\boldsymbol{q}$ is traceless, so that neither contributes to spectra of isotropically tumbling liquids.

Above, we have represented each of the local interactions $\hat{\mathcal{H}}_{\mathrm{D}}$ and $\hat{\mathcal{H}}_{\mathrm{Q}}$ in a locally defined reference frame. These interactions are often described (incorrectly) as field-independent because, unlike the chemical shift Hamiltonian of equation (3), the field appears nowhere in their description. This is a misnomer, which obscures the fact that these interactions may be best resolved in low applied fields. (In addition, second-order effects are largest in low fields. In DAS and DOR spectroscopy, for example, this leads to the surprising result that sensitivity to differing chemical environments may be best in low fields.[5])

The reference frames we have chosen are such that each of $\hat{\mathcal{H}}_{\mathrm{D}}$ and $\hat{\mathcal{H}}_{\mathrm{Q}}$ (or, collectively, $\hat{\mathcal{H}}_{\mathrm{loc}}$) is described in equations (6) and (7) in a consistent, molecule-based reference frame identical for both the spin vectors $\boldsymbol{I}$ and spatial interactions $\boldsymbol{D}$ or $\boldsymbol{q}$. A sufficiently large externally applied field $\boldsymbol{B}_0$ modifies the observable portions of $\hat{\mathcal{H}}_{\mathrm{loc}}$. Owing to the interaction of the field and spin moment of equation (2), the spin moment $\boldsymbol{I}$ is preferentially aligned parallel or antiparallel to the field. $\boldsymbol{D}$ and $\boldsymbol{q}$, however, are tied to their local frames of reference. Different orientations (with respect to the externally imposed field) of otherwise identical systems are differently affected. First-order perturbation theory predicts that the portions of $\hat{\mathcal{H}}_{\mathrm{loc}}$ observable in high field are

$$\hat{\mathcal{H}}'_{\mathrm{D}} = \tfrac{1}{2}\omega_{\mathrm{D}}(3\cos^2\theta - 1)(3\hat{I}_{z,i}\hat{I}_{z,j} - \hat{\boldsymbol{I}}_i \cdot \hat{\boldsymbol{I}}_j) \tag{8}$$

and

$$\hat{\mathcal{H}}'_{\mathrm{Q}} = \frac{\chi}{8I(2I-1)}(3\cos^2\theta - 1 + \eta\sin^2\theta\cos 2\phi)[3\hat{I}_z^2 - I(I+1)] \tag{9}$$

where the designation $\hat{\mathcal{H}}'$ in equations (8) and (9) indicates that these Hamiltonians are truncated by the external field, and $\hat{R}(\theta, \phi, 0)$ is the Euler transformation relating the molecular and laboratory frames. In $\hat{\mathcal{H}}'_{\mathrm{loc}}$, spectral energies depend explicitly on orientation, so that otherwise-equivalent local environments are spectroscopically distinguishable owing to the distribution of the angular parameters θ and ϕ. Where all orientations are equally probable, as in polycrystalline powders, this distribution manifests itself in 'powder pattern' lineshapes.[6] Where $\hat{\mathcal{H}}_{\mathrm{loc}}$ contains the information of greatest interest, $\hat{\mathcal{H}}'_{\mathrm{loc}}$ represents a more easily observed but lower resolution version of the original.

3 WHY DO ZERO FIELD NMR?

A deceptively simple answer to this simple question is that spectroscopy is performed in zero applied magnetic field because the information desired is less well observed in high magnetic fields. One of the first applications of zero field NMR techniques was to the measurement of the Earth's magnetic field, using the Larmor frequency of a suitably large sample of H_2O in zero applied field as the experimental observable.[7] Another early experiment suggested that the superior homogeneity of the Earth's field might yield longer-lived free induction decays than in available laboratory-generated fields, and this effect was demonstrated on a sample of fluorobenzene.[8] Nevertheless, applications focusing on liquid samples in low fields occupy a different scientific niche (see also ***Terrestrial Magnetic Field NMR***). Solid state applications of zero field spectroscopy most typically focus on measuring $\hat{\mathcal{H}}_{\mathrm{loc}}$, the low sensitivity spectrum, with high resolution so that all of the spectral information is available in its most readily interpreted form.

3.1 Relaxometry

In addition to revealing the interactions $\hat{\mathcal{H}}_{\mathrm{loc}}$ in their purest possible form, low field NMR experiments may reveal essential information inaccessible in high field experiments. A second application of low or zero field NMR is in the study of field-dependent spin–lattice relaxation times T_1 (see also ***Field Cycling Experiments***). Relaxation behavior depends sensitively on the spectral density functions $J(\omega)$, and the frequency dependence of dynamic processes may be best measured by varying the transition frequency of nuclear spin transitions over many orders of magnitude.[9] Low frequency fluctuations can be probed only at low Larmor frequencies.

In other systems, only the low field relaxation may be interesting. This is particularly true when a strong magnetic field changes the physical system in a fundamental, often undesireable, way. Early predictions that electron pairing at the metal-to-superconductor transition would lead to singularities in T_1 relaxation could only be verified by working in fields below the critical field strength where superconductivity

is suppressed. Zero field relaxation data provided one of the earliest confirmations of the Bardeen–Cooper–Schrieffer theory of superconductivity.[2,3]

3.2 Overcoming Selection Rules

Where the applied magnetic field aligns nuclear dipole moments, high field nuclear magnetic resonance is characterized by spectral selection rules that determine which transitions are observable. Much of modern multidimensional NMR focuses on overcoming these limiting selection rules. In very low magnetic fields, similar opportunities exist—for example, where the distinction between homonuclear and heteronuclear spins (characterized by no-longer-differing Larmor frequencies) is lost.[10]

Expanded selection rules provide a mechanism for probing other problems only poorly suited to study in high magnetic field. The high field selection rule $\Delta m = \pm 1$ may be overcome in high field multidimensional NMR via indirect detection of multiple quantum transitions. In zero or low fields, these selection rules are loosened, and absorption lines at multiples of the Larmor frequency,[11] or combinations of quadrupolar transition frequencies between pairs of inequivalent, dipolar-coupled sites, are directly observable.[12]

Quantum mechanical tunneling in methyl groups can be associated with a tunneling Hamiltonian and a tunneling splitting superposed on the normal spin Hamiltonian.[13] A measurement of these additional splittings provides an experimental probe of the tunneling rates. Within a given rotational manifold of the methyl group, these tunneling splittings are unobservable, and in high field NMR transitions are allowed only where the rotational state is unchanged. Transitions between differing rotational manifolds are allowed in low field, where the spin-only transitions are flanked by satellite lines offset by the tunneling splitting.[14]

4 MAKING LOW FIELD DETECTION FEASIBLE

4.1 The NQR Regime

Pure NQR has a history nearly as old as NMR. In many covalent bonds to halogen atoms, the electric field gradients $\boldsymbol{q}$ are sufficiently large that pure quadrupolar transitions are found at 30 MHz or higher. For these systems, the sensitivity of NQR is quite comparable to that of NMR in electromagnets. With limited modifications, similar techniques are appropriate in either case, and spectra might be accumulated by either transient or continuous wave methods. Aspects of pure NQR are reviewed in some detail in various classic texts.[15–17]

4.2 The Field Cycling Regime

Other than for the halogens and a select few other nuclei, the sensitivity of pure NQR is insufficient for routine use as a spectroscopic probe. Pure quadrupolar transitions are typically found at frequencies below 5 MHz for such common nuclear spins as ^{17}O, ^{14}N, ^{27}Al, and ^{2}H, and all the alkali metals. And these splittings are quite large when compared with the dipole–dipole couplings between nuclei, which are always substantially less than 1 MHz and too small to be probed directly except in extraordinary circumstances.[1] In such cases, an idea derived from early attempts to understand spin temperature in NMR, where the $\boldsymbol{B}_0$ field amplitude was understood to be an experimental variable, is key.[18] Nuclear spin–lattice relaxation times T_1 are often sufficiently long that the applied magnetic field might be changed (including reduced to very low values) without substantial loss of spin order. As the coupling between spins and the lattice is quite weak, the initially prepared high field magnetization may be stable for sufficiently long times in low field that the spins may be manipulated and returned to high field without debilitating signal loss due to reequilibration. Such experiments were exploited in a number of different applications in the first decades of NMR.[1–3,19]

Under these conditions, the polarization and detection periods (where the signal intensity depends on $\boldsymbol{B}_0$) are separated from the period during which the field-free experiment is performed, as is illustrated in Figure 1. The experimental probe during the low field time period can be as simple as waiting for the spins to relax back toward equilibrium with the lattice in low field; this is the regime of relaxometry experiments. Spectroscopy can be probed by the application of fields, either CW or pulsed, that probe the energy levels of the low field spin systems. Reviews covering experimental aspects of field cycling NMR, and many of its applications, are available elsewhere.[20]

Two different experimental approaches can be taken to executing a field cycling NMR experiment. In the first, the field at the sample is reduced by varying the current applied to an electromagnet. An electronic field sweep between about 1 T and an arbitrarily small value can be performed in 1–10 ms. Alternatively, the field can be cycled by physically removing the sample into the fringe field of the polarizing magnet,[21] where the residual field can be nulled with relatively small electromagnets or suitable magnetic shielding.[22] This method appears more feasible, although somewhat slower (about 100 ms), when working in a superconducting magnet. When the field cycle cannot be safely completed in a short time period, varying the temperature may lengthen T_1.

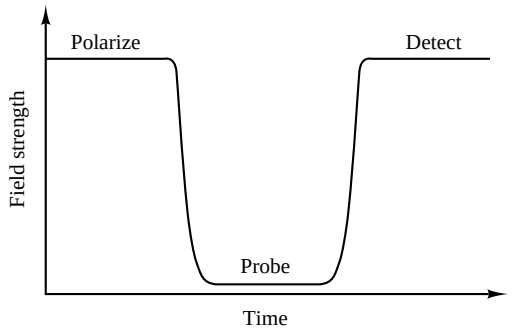

Figure 1 Generalized field cycling experiment. At the beginning of the field cycle, the sample sits in high field, so that an initially large spin polarization is prepared. In a time short compared with T_1, the field is reduced—either by draining current from an electromagnet or by removing the sample from the polarizing field. Features of the system in zero or low field are probed, and the sample returned to high field (often, but not necessarily, the same as the polarization field), where signal is detected

4.3 Demagnetization Cycles

The motivation for probing $\hat{\mathcal{H}}_{\text{loc}}$ in zero applied field has been described above. Where no preferred direction can be identified because there is no externally imposed field, all orientations contribute to precisely the same sets of transition frequencies. Field cycling makes it possible to detect zero field transitions with the sensitivity of high field NMR. Precisely what is observed, however, depends on precisely how the field cycle is executed and how the spins are manipulated once they are in the low field regime.

The influence of demagnetization rate on the final state achieved can be illustrated by analogy to the results of more familiar but entirely analogous rotating frame demagnetization experiments executed in high field.[23] Imagine a 90° pulse transforming longitudinal Zeeman polarization into transverse magnetization. A phase-shifted rf field of strength much greater than typical internal fields will spin lock transverse magnetization so that its decay is associated with a time constant $T_{1\rho}$ and not the much shorter time constant associated with the disappearance of the free induction decay. Demagnetization in the laboratory frame is accomplished by removing the static magnetic field along which longitudinal magnetization is 'locked'.

When the locking field is removed, the response of the spin system depends critically on the rate at which that field is turned off, and in particular on the rate of transition between where the locking fields are larger than the local fields, to where the locking fields are smaller. Where the transition is either very slow (adiabatic) or very rapid (sudden), the state achieved at the end of the demagnetization can be cleanly evaluated. (Necessary conditions for transitions to qualify as 'adiabatic' or 'sudden' are available in most textbooks on quantum mechanics; a particularly lucid presentation is given by Messiah.[24])

Where the field is reduced adiabatically (rotating frame or longitudinal) Zeeman spin order is preserved as spin order at each point during the field cycle, and when the demagnetization is complete, the original spin magnetization is fully transformed into nonevolving dipolar- or quadrupolar-ordered states. Where the field is reduced suddenly, rotating frame Zeeman order is left unchanged—but the associated locking field is absent. The no-longer-locked magnetization evolves at the natural frequencies of the system. Remagnetization, adiabatically or suddenly, reverses these processes.

5 FREQUENCY VERSUS TIME DOMAIN

5.1 Frequency Domain Zero Field NMR

The adiabatically demagnetized state preserves all of the polarization initially prepared in high field, stored as spin order with respect to the eigenstates of $\hat{\mathcal{H}}_{\text{loc}}$. Spin transitions in these nonevolving states can be probed directly by analogs to conventional absorption spectroscopy. Variable frequency irradiation will occasionally resonate with transitions of the spins in zero applied field. When the spin system is returned to high field, the saturation of the spins so effected in zero field is reflected by a decrease in the signal observed in high field, as illustrated in Figure 2.

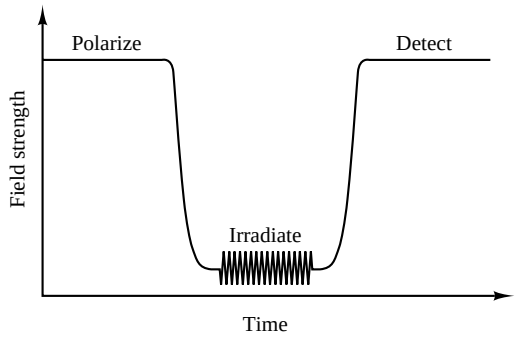

Figure 2 Frequency domain field cycling experiment. While the sample sits in zero applied field, it is irradiated with a low-frequency rf field. Where the frequency of the field matches a transition in the spin system, energy is absorbed until the transition is saturated. When the sample is returned to high field, this corresponds to a decrease in the detectable magnetization. A zero field spectrum is measured by repeating the experiment (polarization–demagnetization–irradiate–return to high field–probe the signal amplitude) with a continuously varied set of low field irradiation frequencies

Often, spin systems contain both rare, generally quadrupolar, nuclear spins S as well as more abundant high γ spin-$\frac{1}{2}$ nuclei. In such systems, substantially higher sensitivity is achieved if the 'interesting' S spins can be probed indirectly via polarization transfer to the easily observed abundant species.[23] As an example, assume the high γ nucleus is ^{1}H. In reasonably high magnetic fields, the ^{1}H Larmor frequency substantially exceeds the resonance frequency of all other spins. In low fields, where only the internal fields remain, the resonance frequencies of the ^{1}H spins are generally much lower than those associated with transitions in quadrupolar systems. At some intermediate field, the energy levels of the two spin systems (primarily determined by the Zeeman energies for the ^{1}H spins, and the quadrupolar energies for the S spins) must cross. When the level crossing field is traversed sufficiently slowly, dipole–dipole couplings transfer spin polarization from the more ordered ^{1}H spins to the less ordered S spins.

Once S spin order is destroyed via direct absorption in zero field, further ^{1}H spin order can be drained during the remagnetization process in the level crossing region. Zero field resonances of the S spins are observed as decreases in ^{1}H signal observed in high field. Where the S spins are rare, sensitivity can be substantially enhanced by repeated cycles through the level crossing region so that the contact between the S spins and the ^{1}H bath is established many times during a single high field polarization cycle.

This method has the substantial advantage of superior sensitivity to small numbers of S spins, and other modifications lead to yet greater signal-to-noise increases.[25,26] Its disadvantages are all those associated with absorption spectroscopy, namely, the trade-off between linewidths and sensitivity, decreasing sensitivity at low frequencies, and the inability to establish correlations of the sort common in high field multidimensional NMR.

5.2 Time Domain Zero Field NMR

An alternate approach that yields high resolution at very low frequencies is to perform the experiment entirely in the

time domain. The advantages of time domain experiments are comparable to the advantages of pulsed high field NMR as compared with the older continuous wave techniques. Amongst the most important is that the resolution and sensitivity are uncoupled, so that linewidths are limited in the time domain version to only those naturally associated with the experiment. Furthermore, the time domain experiment provides the possibility of performing correlation experiments of the sort that are routinely executed in high field, high-resolution NMR. These correlations may be between low field and high field parameters, or between low field and low field parameters. Furthermore, with some additional technical and theoretical effort, spin Hamiltonians can be selectively averaged in low as well as high field.

As in frequency domain zero field NMR experiments, the sample is polarized in high field, demagnetized, and once the zero field frequencies have been probed, returned to high field. As in time domain high field NMR, a time domain zero field NMR experiment begins when a field pulse disturbs a previously nonevolving spin system so as to establish coherence between eigenstates.

In zero field, these pulses can take a variety of forms—for instance, the sudden field transient described above and shown in Figure 3(a),[27] a broadband dc pulse at the nominal Larmor frequency of zero as shown in Figure 3(b),[28,29] or a resonant rf pulse tuned to one or more of the expected transition frequencies as shown in Figure 3(c).[22,30] The evolution period t_1 can be terminated at some later time in like fashion, and, as in multidimensional high field NMR experiments, the evolved signal is sampled indirectly once the the sample has been returned to high field. A complete zero field spectrum is evaluated by repeating the experiment for continuously incremented values of t_1, followed by Fourier transformation so as to reveal the zero field frequencies.

Only in a limited number of cases can an exact calculation of the expected signal be provided. The primary theoretical stumbling block is the difficulty of obtaining a detailed understanding of $\hat{\rho}$ at the end of an adiabatic field transition. Where the zero field spectrum is continuous, as is often the case for dense networks of spin-$\frac{1}{2}$ nuclei, the spin-temperature hypothesis may apply,[31] so that the demagnetized state satisfies $\hat{\rho}(0) \propto \hat{\mathcal{H}}_{\mathrm{D}}$. Where the zero field spectrum is discrete so that only a small number of well-separated lines are found, no similarly simple theory of the demagnetized state exists. An analysis of isolated spin-1 nuclei has suggested that the demagnetized state is nearly orientation-independent,[32] though dipole–dipole couplings to other nuclei may substantially complicate the situation. A numerical simulation is certainly possible, but accurate simulations require complete knowledge of all the parameters of all quadrupolar and dipolar Hamiltonians in the system—presumably the goal of the experimental effort. Furthermore, the results of such simulations will generally be orientation-dependent.

Theory can provide substantial guidance where evolution is initiated and terminated by field transients that take the spin system from high field to zero field and back 'suddenly', so that both the prepared and detected states are well defined. While the conditions for applicability of the sudden approximation are impossible to satisfy for typical polarizing fields of several tesla, practical experiments need only switch rapidly fields sufficiently large that $\hat{\mathcal{H}}_{\mathrm{L}} \gg \hat{\mathcal{H}}_{\mathrm{loc}}$. A practical scheme is illustrated in Figure 3(a). Under these conditions,

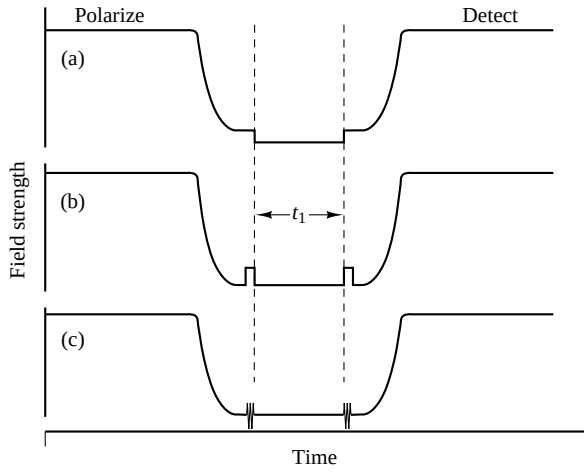

Figure 3 Time domain field cycling experiments. Polarization and detection occur in high magnetic fields. Low field evolution occurs during the time period t_1. A zero field interferogram is mapped out by repeating the experiment for regularly spaced increments in t_1. (a) Field cycling with sudden transients. The sample is partially demagnetized to an intermediate field strength where $\hat{\mathcal{H}}_{\mathrm{L}} \gg \hat{\mathcal{H}}_{\mathrm{loc}}$. Typical values of the intermediate field are 0.01–0.05 T. Fields of this magnitude can be turned off and on in 1–5 μs. The evolution period t_1 is initiated when the intermediate field is rapidly turned off, and ends when it is suddenly turned back on. In high field, the amplitude of the evolved ^{1}H magnetization is probed following a 90° pulse. (b) Field cycling with zero frequency pulses. The sample is demagnetized to zero field. Evolution is initiated and terminated with a short, strong zero frequency field pulse. (c) Field cycling with low-frequency pulses. The sample is demagnetized to zero field. Evolution is initiated and terminated with a short, low-frequency field pulse tuned to one or more of the spin system transition frequencies

a quantitative comparison between experiment and theory can be attempted.

In high magnetic field, the total system Hamiltonian is

$$\hat{\mathcal{H}}_{\mathrm{tot}} = \hat{\mathcal{H}}_{\mathrm{L}} + \hat{\mathcal{H}}'_{\mathrm{loc}} \tag{10}$$

where $\hat{\mathcal{H}}'_{\mathrm{loc}}$ represents whatever orientation-dependent local interactions exist, truncated as is appropriate for observation in high field. Any long-lived state prepared in high field must satisfy

$$[\hat{\rho}, \hat{\mathcal{H}}_{\mathrm{tot}}] = [\hat{\rho}, \hat{\mathcal{H}}_{\mathrm{L}}] = [\hat{\rho}, \hat{\mathcal{H}}'_{\mathrm{loc}}] = 0 \tag{11}$$

Equilibrium, which is the most easily prepared state satisfying equation (11), corresponds to $\hat{\rho}(0) \propto \hat{I}_z$.

In zero field, the total Hamiltonian is $\hat{\mathcal{H}}_{\mathrm{loc}}$. Assuming the field is turned off sufficiently rapidly, $\hat{\rho}$ is unchanged during the field transient. Other than in exceptional cases, $[\hat{\rho}(0), \hat{\mathcal{H}}_{\mathrm{loc}}] \neq 0$, and $\hat{\rho}$ evolves in time such that $\hat{\rho}(t) = \exp(-\mathrm{i}\hat{\mathcal{H}}_{\mathrm{loc}}t)\hat{\rho}(0)\exp(\mathrm{i}\hat{\mathcal{H}}_{\mathrm{loc}}t)$. At some arbitrary time t_1 later, evolution under $\hat{\mathcal{H}}_{\mathrm{loc}}$ can be interrupted by reapplying the field. Within a short time, the evolved density matrix again satisfies $[\hat{\rho}(t_1), \hat{\mathcal{H}}_{\mathrm{tot}}] = 0$.

In high field, a single rf pulse converts only longitudinal magnetization back to observable transverse magnetization, and, under most circumstances, only that portion of $\hat{\rho}(t_1)$ proportional to $\hat{I}_z$ is observable. The detectable signal is

therefore

$$\begin{aligned} S(t_1) &= \mathrm{Tr}[\hat{\rho}(t_1)\hat{I}_z] \\ &= \mathrm{Tr}[\exp(\mathrm{i}\hat{\mathcal{H}}_{\mathrm{loc}}t_1)\hat{\rho}(0)\exp(-\mathrm{i}\hat{\mathcal{H}}_{\mathrm{loc}}t_1)\hat{I}_z] \end{aligned} \tag{12}$$

A model calculation illustrates many of the features of spectral simulations in time domain zero field NMR initiated with sudden transients,[27,32,33] based on an evaluation of equation (12). We assume longitudinal magnetization is prepared and, ultimately, detected. In a laboratory frame of reference, $\hat{\rho}(0) = \hat{I}_{z,\mathrm{lab}}$, where, for simplicity, the proportionality constant has been arbitrarily set to one. The same density operator represents the system after the sudden field transient. While $\hat{\rho}(0)$ is most easily defined in the same laboratory frame, $\hat{\mathcal{H}}_{\mathrm{loc}}$ is most easily represented in a consistently chosen local frame of reference. Computational efficiency demands that all calculations be carried out in the local frame where $\hat{\mathcal{H}}_{\mathrm{loc}}$ is orientation-independent, so that $\hat{\rho}(0)$ must itself be transformed from its natural representation in the laboratory frame into the local frame. This precisely inverts the common 'high field' transformation through Euler angles θ and ϕ that takes $\hat{\mathcal{H}}_{\mathrm{loc}}$ from its natural frame of reference into the laboratory frame. Rotating via $-\phi$ and $-\theta$,

$$\begin{aligned} \hat{\rho}_{\mathrm{loc}}(0,\theta,\phi) &= \hat{R}(-\phi,-\theta,0)\hat{I}_{z,\mathrm{lab}}\hat{R}^{-1}(-\phi,-\theta,0) \\ &= \exp(\mathrm{i}\phi\hat{I}_{z,\mathrm{lab}})\exp(\mathrm{i}\theta\hat{I}_{y,\mathrm{lab}})\hat{I}_{z,\mathrm{lab}} \\ &\quad \times \exp(-\mathrm{i}\theta\hat{I}_{y,\mathrm{lab}})\exp(-\mathrm{i}\phi\hat{I}_{z,\mathrm{lab}}) \\ &= -\hat{I}_{x,\mathrm{loc}}\sin\theta\cos\phi + \hat{I}_{y,\mathrm{loc}}\sin\theta\sin\phi \\ &\quad + \hat{I}_{z,\mathrm{loc}}\cos\theta \end{aligned} \tag{13}$$

Any laboratory frame operator that might be prepared is transformed, in analogy to equation (13), via arbitrary angles θ and ϕ into all local frame operators of similar tensor rank.

After a period of free evolution, using the shorthand notation $\hat{I}_{j,\mathrm{loc}}(t_1) \equiv \exp(\mathrm{i}\hat{\mathcal{H}}_{\mathrm{loc}}t_1)\hat{I}_{j,\mathrm{loc}}\exp(-\mathrm{i}\hat{\mathcal{H}}_{\mathrm{loc}}t_1)$,

$$\begin{aligned} \hat{\rho}(t_1,\theta,\phi) &= -\hat{I}_{x,\mathrm{loc}}(t_1)\sin\theta\cos\phi \\ &\quad + \hat{I}_{y,\mathrm{loc}}(t_1)\sin\theta\sin\phi + \hat{I}_{z,\mathrm{loc}}(t_1)\cos\theta \end{aligned} \tag{14}$$

and the observable signal is

$$\begin{aligned} S(t_1,\theta,\phi) &= \mathrm{Tr}\{[-\hat{I}_{x,\mathrm{loc}}(t_1)\sin\theta\cos\phi \\ &\quad + \hat{I}_{y,\mathrm{loc}}(t_1)\sin\theta\sin\phi + \hat{I}_{z,\mathrm{loc}}(t_1)\cos\theta] \\ &\quad \times(-\hat{I}_{x,\mathrm{loc}}\sin\theta\cos\phi \\ &\quad + \hat{I}_{y,\mathrm{loc}}\sin\theta\sin\phi + \hat{I}_{z,\mathrm{loc}}\cos\theta)\} \end{aligned} \tag{15}$$

A complete evaluation of equations (14) and (15) requires a complete specification of the Hamiltonian governing evolution, as well as θ and ϕ. However, some general statements that substantially simplify calculations are possible.

Application of zero field NMR is largely restricted to disordered systems, so the observable signal is

$$S(t_1) = \int\int S(t_1,\theta,\phi)P(\theta,\phi)\,\mathrm{d}\theta\,\mathrm{d}\phi \tag{16}$$

In the common case where all orientations are equally probable (i.e., a polycrystalline powder), the distribution function of equation (16) is $P(\theta,\phi)\,\mathrm{d}\theta\,\mathrm{d}\phi = -(4\pi)^{-1}\,\mathrm{d}(\cos\theta)\,\mathrm{d}\phi$. Owing to the orthogonality relations between geometric factors (e.g., $\int\int\cos\theta\,\sin\theta\,\cos\phi\,\mathrm{d}(\cos\theta)\,\mathrm{d}\phi = 0$), only autocorrelations of the angular momentum functions yield observable signals, and, to within a proportionality constant,

$$S(t_1) = \tfrac{1}{3}\mathrm{Tr}[\hat{I}_{x,\mathrm{loc}}(t_1)\hat{I}_{x,\mathrm{loc}} + \hat{I}_{y,\mathrm{loc}}(t_1)\hat{I}_{y,\mathrm{loc}} + \hat{I}_{z,\mathrm{loc}}(t_1)\hat{I}_{z,\mathrm{loc}}] \tag{17}$$

or, in matrix form,

$$S(t_1) = \frac{1}{3}\sum_{l,k}\sum_{p=x,y,z}|\langle l|\hat{I}_{p,\mathrm{loc}}|k\rangle|^2\cos\omega_{kl}t_1 \tag{18}$$

where $|k\rangle$ and $|l\rangle$ are eigenstates of $\hat{\mathcal{H}}_{\mathrm{loc}}$ and ω_{kl} is the frequency difference between the eigenstates. As in all autocorrelations, equations (17) and (18) predict that $S(t_1)$ is a maximum at zero time, and all lines appear in phase. Furthermore, no quadrature information is available.

For spin 1, the fictitious spin-$\frac{1}{2}$ formalism[34] provides a particularly compact and elegant framework. In zero field and where $\eta \neq 0$, the three nondegenerate eigenstates are conventionally labeled $|x\rangle$, $|y\rangle$, and $|z\rangle$. Each of the operators $\hat{I}_j$ couples one of the three pairs of levels so that

$$\hat{I}_j(t) = \hat{I}_j\cos\omega_{kl}t - (\hat{I}_k\hat{I}_l + \hat{I}_l\hat{I}_k)\sin\omega_{kl}t \tag{19}$$

Equation (19) states that the initially prepared dipolar magnetization $\hat{I}_j$ oscillates between itself and a quadrupolar operator $\hat{I}_k\hat{I}_l + \hat{I}_l\hat{I}_k$ at a rate proportional to the quadrupolar transition frequencies $\omega_{xy} = \eta\pi\chi$, $\omega_{yz} = -\frac{1}{2}(3+\eta)\pi\chi$ and $\omega_{zx} = \frac{1}{2}(3-\eta)\pi\chi$. Owing to the orthogonality of the dipolar and quadrupolar operators [i.e., Tr $(\hat{I}_j\hat{I}_k\hat{I}_l) = 0$], the signal at the end of the time period t_1 is proportional to

$$\begin{aligned} S(t_1,\theta,\phi) &= \cos[\tfrac{1}{2}(3+\eta)\pi\chi t_1]\sin^2\theta\cos^2\phi \\ &\quad + \cos[\tfrac{1}{2}(3-\eta)\pi\chi t_1]\sin^2\theta\sin^2\phi \\ &\quad + \cos(\eta\pi\chi t_1)\cos^2\theta \end{aligned} \tag{20}$$

Equation (20) predicts that for any orientation of a spin-1 system in high field, one, two, or as many as three transitions might be observed, with varying intensities but well-defined frequencies simply related to the quadrupolar parameters χ and η. Differently oriented but otherwise equivalent systems have all spectral lines at identical zero field frequencies. Only the line intensities vary with orientation. In the common case where all orientations are equally probable, $\langle\sin^2\theta\cos^2\phi\rangle = \langle\sin^2\theta\sin^2\phi\rangle = \langle\cos^2\theta\rangle = \frac{1}{3}$, so that

$$\begin{aligned} S(t_1) &= \tfrac{1}{3}\{\cos[\tfrac{1}{2}(3+\eta)\pi\chi t_1] \\ &\quad + \cos[\tfrac{1}{2}(3-\eta)\pi\chi t_1] + \cos(\eta\pi\chi t_1)\} \end{aligned} \tag{21}$$

An experimental verification of the predictions of equation (21) is provided in Figure 4, showing the zero field interferogram and spectrum of perdeuterated dimethoxybenzene. What is perhaps most striking in this spectrum is that at each of the ^{2}H sites (two inequivalent sites on the ring and three equivalent sites on the $-C^2H_3$ group) η is substantial ($\approx$0.05 or larger), and is greatest at the methyl group sites. Differences in intensities between different chemical sites reflect the substantial differences in high field T_1 values, which can vary by several orders of magnitude. Intensity variations amongst the three lines associated with a single ^{2}H environment are much smaller, since the T_1 anisotropies associated with a given environment are substantially less.

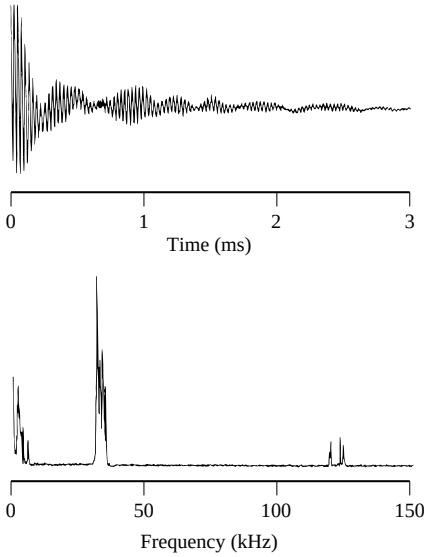

Figure 4 Zero field interferogram and associated zero field spectrum of perdeuterated 1,4-dimethoxybenzene, acquired with the field cycling sequence of Figure 3(a). The zero field spectrum reveals two inequivalent ring sites (with two lines each between 130 and 138 kHz, and one additional line each between 3 and 6 kHz) and two complex patterns (approx. 33–38 kHz and 1–3 kHz) associated with the dipole–dipole couplings within the $-C^2H_3$ groups. Intensity variations between the differing ^2H sites are due to vast differences in high field T_1 values. Reproduced by permission of D. B. Zax, A. Bielecki, K. W. Zilm, A. Pines, and D. P. Weitekamp, *J. Chem. Phys.*, 1985, **83**, 4877, © American Institute of Physics, 1985

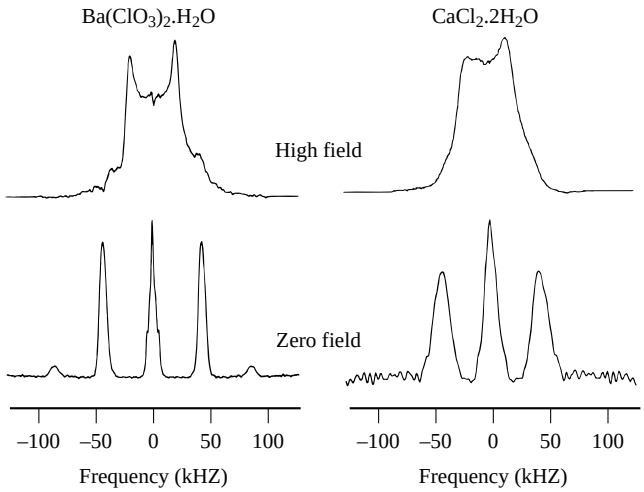

Figure 5 High field and zero field NMR spectra of crystalline H_2O molecules, in $CaCl_2{\cdot}2H_2O$ and $Ba(ClO_3)_2{\cdot}H_2O$. In each, a three-line dipolar spectrum is observed. The high-frequency lines evolve at $\pm\frac{3}{2}\omega_D$; one-third of the total spin magnetization prepared in high field is nonevolving in a two-level system. Reproduced by permission of A. Bielecki, © A. Bielecki, 1987

In homonuclear spin pairs, transitions between the singlet and triplet states for the nuclear spins are forbidden if $\hat{\rho}(0) = \hat{I}_{z,\mathrm{lab}}$. The three-level triplet system is formally identical to the three-level system of spin 1. Owing to the symmetry of the static dipole–dipole tensor, only a single nonzero evolution frequency ($\frac{3}{2}\omega_D$) is expected. Spectra of isolated water molecules, as are found in the crystalline forms of a number of inorganic salts, show the structure predicted from this two-spin model, and examples are shown in Figure 5. While the high field Pake doublet may be obscured by longer range dipole–dipole couplings and/or chemical shift anisotropies, the zero field spectrum is much better resolved, and clearly shows the dipole–dipole coupling frequency.

In many systems, dipolar resolution is limited because coupling networks are not well isolated from one another. More information can often be derived using isotopic dilution (e.g., replacing many of the ^1H nuclear spins with ^2H), so as to reduce longer range dipole–dipole couplings.[27,35] In the ^1H zero field spectrum of $Ba(ClO_3)_2{\cdot}H_2O$ (see Figure 5), the second moment of the line at $\frac{3}{2}\omega_D$ substantially exceeds calculated values[34] based on the known crystal structure. Figure 6 shows the zero field spectra as ^1H spins are successively replaced by increasing numbers of ^2H spins. At low ^1H pair densities, the dipolar spectrum shows sufficient resolution to reveal that the single line was actually a pair of lines due to dynamical averaging of the dipole–dipole coupling. The splitting between the two zero field frequencies is consistent with an effective asymmetry parameter $\eta \approx 0.05$.

Where local dynamics cause $\hat{\mathcal{H}}_{\mathrm{loc}}$ to be time-dependent, calculations of the zero field lineshapes are more involved. Dynamical averaging in zero field differs fundamentally from the same spectroscopic problem in high field. In pure dipole–dipole or quadrupolar spectroscopy, $\hat{\mathcal{H}}_{\mathrm{loc}}(t)$ is the main Hamiltonian rather than a perturbation. Furthermore, the averaging makes the orientation of $\boldsymbol{D}$ or $\boldsymbol{q}$ time-dependent, rather than its magnitude.[36–39]

5.2.1 Selection Rules?

What are the allowed nuclear spin transitions in time-domain zero field NMR? Equation (18) suggests that an equivalent question would be to ask which eigenstates are coupled by the initially prepared density operator. As in much of the theory of zero field NMR, somewhat different answers apply to half-integer quadrupolar nuclear spin states and integer spins (or, typically, collections of dipolar-coupled spin $\frac{1}{2}$ nuclei).

For half-integer quadrupolar nuclear spins, pairs of energy levels are always degenerate, and $\hat{I}_{z,\mathrm{loc}}$ is nearly a good quantum number. Under conditions where evolution is initiated by a sudden field transient, a portion of the initial magnetization is therefore nonevolving. Projections of $\hat{\rho}(0)$ corresponding to $\hat{I}_{x,\mathrm{loc}}$ and $\hat{I}_{y,\mathrm{loc}}$ couple transitions where $\Delta m = \pm 1$, and a series of $I - \frac{1}{2}$ zero field transitions will be observed. For nonzero η, additional transitions may be weakly allowed.[40]

Substantially different selection rules may be observed where field pulses generate and store coherence after adiabatic demagnetization. The demagnetized state satisfies $[\hat{\rho}, \hat{\mathcal{H}}_Q] = 0$. For half-integer quadrupolar spin systems, each of the operators that commute with $\hat{\mathcal{H}}_Q$ is proportional to $\hat{\mathcal{H}}_Q^n$, and $n_{\max} = I - \frac{1}{2}$. After a pulse initiates evolution, $\hat{\rho}$ contains operators that couple states with $\Delta m_{\max} = \pm(2I - 1)$, so new lines may appear at the sums of previously observed transition frequencies. These multiple quantum lines may prove helpful in making assignments in multisite systems.

Except in exceptional cases, no good quantum numbers are associated with $\hat{\mathcal{H}}_D$, or with $\hat{\mathcal{H}}_Q$ for integer-spin nuclei.

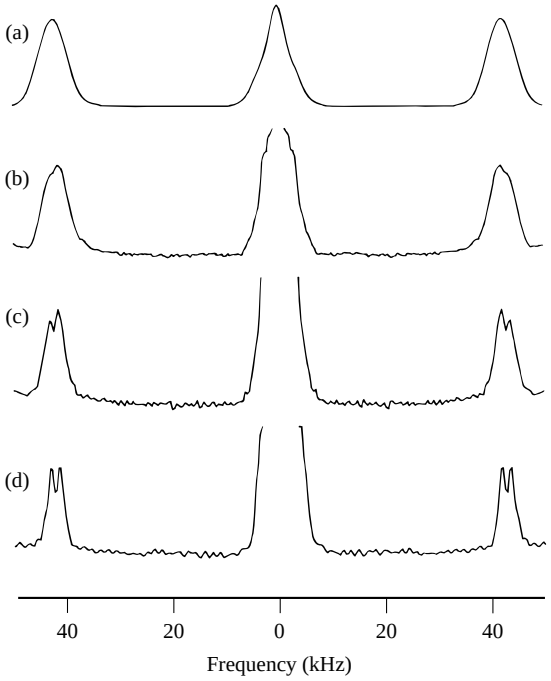

Figure 6 Zero field NMR spectra of progressively deuterated $Ba(ClO_3)_2{\cdot}H_2O$. (a) ^1H zero field NMR spectrum in $Ba(ClO_3)_2{\cdot}H_2O$, 100% ^1H. (b) ^1H zero field NMR spectrum in $Ba(ClO_3)_2{\cdot}H_2O/^1H^2HO/^2H_2O$, 60% ^1H. (c) ^1H zero field NMR spectrum in $Ba(ClO_3)_2{\cdot}H_2O/^1H^2HO/^2H_2O$, 31% ^1H. (d) ^1H zero field NMR spectrum in $Ba(ClO_3)_2{\cdot}H_2O/^1H^2HO/^2H_2O$, 10% ^1H. Progressive deuteration reduces the numbers of substantial dipole–dipole couplings. Pairs of ^1H nuclei in an ^1H_2O water molecule evolve primarily at the frequency of the intramolecular dipole–dipole coupling of approximately ± 42 kHz; ^1H nuclei in $^1H^2HO$ molecules evolve at very low frequencies associated with the weaker intermolecular couplings (and which overlap with the nonevolving magnetization from the spin pairs). As the magnitude and number of intramolecular couplings are decreased by replacement of ^1H by ^2H, sufficient additional resolution is achieved so as to observe a small motionally induced asymmetry parameter in the dipole–dipole tensor. Reproduced by permission of J. M. Millar, A. M. Thayer, D. B. Zax, and A. Pines, *J. Am. Chem. Soc.*, 1987, **91**, 2240, © American Chemical Society, 1987

(An exception is found where rapid motion in the molecular frame establishes a new quantization axis, as in rotating methyl groups.) Where dipole–dipole couplings dominate, essentially all eigenstates are coupled to all others; effectively, there are no selection rules. For N coupled spins, the number of transitions observable in zero field exceeds that found in a similarly sized spin system of specific orientation in high field. (Nevertheless, the absence of powder broadening generally ensures that the low field spectrum exhibits more structured features than the corresponding high field powder pattern.) Particularly when $N \leq 4$, experience shows that there is sufficient structure that a detailed analysis might be attempted.[27,41]

For $N \gg 4$, and where the dipolar fields are stationary, Gaussian and Markovian, the signal associated with $\hat{\mathcal{H}}_D$ is predicted to approach

$$S(t_1) = \tfrac{1}{3}[1 + 2(1 - \Delta^2 t_1^2)\exp(-\tfrac{1}{2}\Delta^2 t_1^2)] \qquad (22)$$

where Δ^2 is a mean square measure of the magnitude of local dipolar fields.[36] Alternate initial conditions are unlikely to be of substantial use in dipolar-coupled systems, since successful spectral analyses for $N \geq 3$ require that both frequencies and intensities be matched. Initial and final conditions derived from adiabatic de/remagnetization cycles are too poorly characterized to yield predictable line intensities. In analyzing quadrupolar spin systems, a knowledge of transition frequencies only is generally sufficient, and adiabatic cycles share the sensitivity advantages of polarization transfer and/or of indirect detection via abundant, high γ nuclei,[28] as in zero field NQR with level crossings.

5.2.2 Multipulse NMR Experiments in Zero Field

A distinct advantage of experiments executed in the time domain is the possibility that the information content of

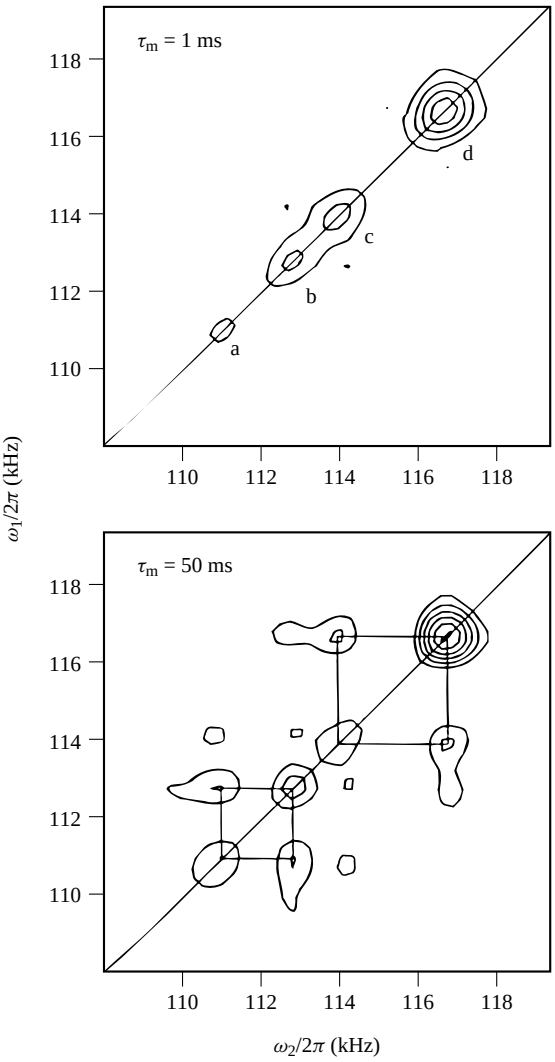

Figure 7 Two-dimensional zero field NMR experiment in diethyl terephthalate-d_4 (deuterated only at the methylene sites). The two time periods t_1 and t_2 are generated by short field pulses, in analogy to the one-dimensional experiment shown in Figure 3(b). The intervening mixing period τ_m allows for spin diffusion between deuterons. As can be seen, spin diffusion occurs on a timescale of a few milliseconds. Reproduced by permission of D. Suter, T. P. Jarvie, B. Sun, and A. Pines, *Phys. Rev. Lett.*, 1987, **59**, 106, © American Physical Society, 1987

the spectrum can be enhanced under the control of the experimentalist. In high field, rf pulses and/or sample rotation are the available tools. Qualitatively, it is a very different technical and theoretical problem to generate useful pulse sequences in zero field. Rapid sample rotation reintroduces powder broadening and is of limited value. In contrast to experience based on high field experiments, zero frequency pulses of different phases must be generated in physically orthogonal coils. As in traditional NQR experiments, pulse flip angles are only poorly defined, since the same pulse affects differently oriented molecular systems differently. Where the pulses are applied at nonzero frequencies, they must be carefully timed to maintain phase coherence between the spins and the rf field.[22,30]

Despite these complicating factors, substantial effort has been devoted to experiments using pulsed dc fields in zero field,[28,29] including composite pulses selective for specific nuclear spins[42] and multiple pulse NMR experiments in zero field.[43,44] Multidimensional zero field NMR experiments have demonstrated how correlations between multiple lines associated with a single site might be identified,[45] and how small dipole–dipole couplings between quadrupolar nuclear spins might be used to establish through-space connectivities in crystals.[46] An example of a two-dimensional zero field correlation experiment is shown in Figure 7. Two-dimensional zero field experiments with field cycling are, of course, three-dimensional NMR experiments, since the signal $S(t_1, t_2)$ can only be detected in a third, high field dimension (not shown in Figure 7).

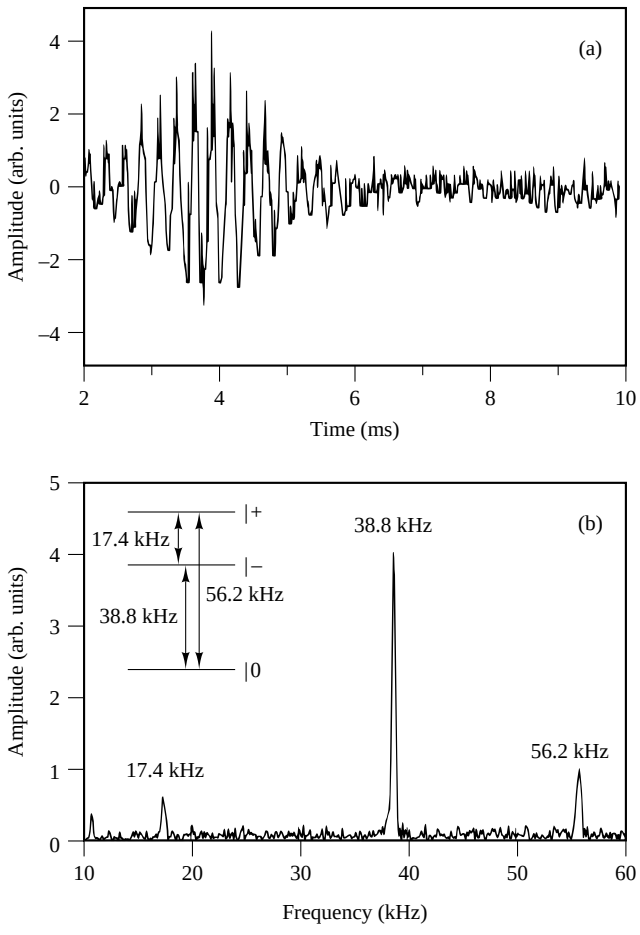

Figure 8 SQUID-detected zero field NQR in NH_4ClO_4 at 1.5 K. (a) Directly detected free induction decay and echo after two-pulse spin echo sequence (for purposes of display, demodulated with 35 kHz). (b) Fourier transform spectrum and energy levels in the three-level system corresponding to ^{14}N (I = 1). Reproduced by permission of N. Q. Fan and J. Clarke, *Rev. Sci. Instrum.*, 1991, **62**, 1453, © American Institute of Physics, 1991

6 OTHER APPROACHES TO ZERO FIELD RESULTS

Two promising new approaches to achieving high-resolution measurements of $\hat{\mathcal{H}}_{loc}$ have been demonstrated, and each has appealing advantages over the field cycling methods described above. The first relies on a new technical accomplishment that makes direct low-frequency detection with reasonable sensitivity feasible. The second relies, instead, on a tremendously original application of traditional multiple pulse NMR and average Hamiltonian theory working together so as to probe zero-field-like coupling patterns directly in high field.

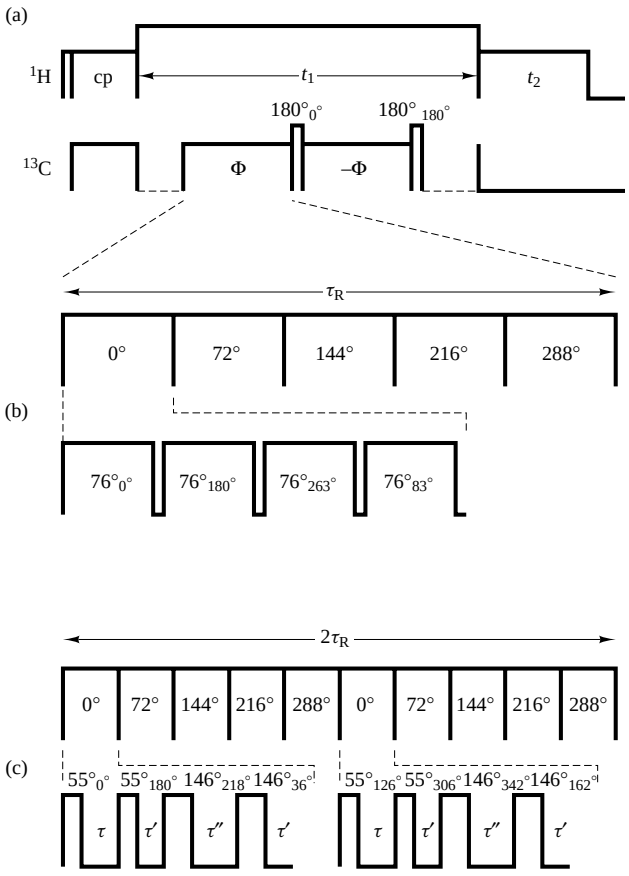

Figure 9 Two-dimensional pulse and rotation sequences for measuring zero-field-like spectra in high magnetic fields. Decoupling may be applied to abundant spins (i.e., ^{1}H) so as effectively to isolate small numbers of rare spin pairs. In sequence (b), the sample rotation axis is tilted by 64° with respect to the externally applied field; in sequence (c), the sample rotation axis is tilted by 66° with respect to the externally applied field. Angles such as 0°, 72°, etc. represent the relative phase of irradiation block, while θ_ϕ indicates a pulse with flip angle of θ and phase ϕ. Reproduced by permission of R. Tycko, G. Dabbagh, J. C. Duchamp, and K. W. Zilm, *J. Magn. Reson.*, 1990, **89**, 205, © Academic Press, 1990

6.1 Zero Field NMR with SQUID Detection

Superconducting Quantum Interference Devices (SQUIDs) are based on Josephson junction technology, and have long been an area of interest to low temperature physicists. Applications of SQUIDs have focused on their sensitivity to small amounts of magnetic flux. In low-frequency magnetic resonance, the advantage of a SQUID-based detector is that its output is proportional to the magnetic flux enclosed, and therefore directly monitors the nuclear spin magnetization (rather than its time derivative.) This removes one of the frequency-dependent factors in equation (1), and it is possible to monitor directly such slow processes as T_1-driven relaxation of longitudinal magnetization to equilibrium.[47]

Within the bandwidth limits of the associated circuitry, a SQUID detector is broadband, so that sensitivity is independent of frequency. Furthermore, the noise figure of a SQUID detector is substantially below that of typical room-temperature amplifiers. As a result, direct detection of zero field time domain signals is possible at arbitrarily low frequencies (see Figure 8), and an entire zero field free induction decay can be accumulated in a single experiment.[48] The ability continuously to detect evolving magnetization in real time is a substantial advance over point-by-point field cycling schemes.

6.2 Zero Field NMR in High Magnetic Fields

A remarkable experiment addressing the problem of 'zero field NMR in high magnetic field', has demonstrated that measurements of dipole–dipole couplings might be made with neither the complications associated with powder pattern lineshapes nor the technical difficulties associated with cycling the field strength at the sample. Instead, multiple pulse NMR combined with rapid sample spinning may be sufficient. While the frequencies found in the high field spectrum are orientation-dependent owing to the anisotropy of the spatial parameters in $\hat{\mathcal{H}}_{\text{loc}}$, where both spatial and spin parameters are time-dependent, a portion of the time-dependent Hamiltonian, which depends on the product of two anisotropic terms, is isotropic. Selective averaging based on average Hamiltonian theory can be used to predict which sequences, acting on both spaces, average away all orders of anisotropy so as to leave behind only the desired orientation-independent information. Neither bulk sample rotation nor rf pulses alone

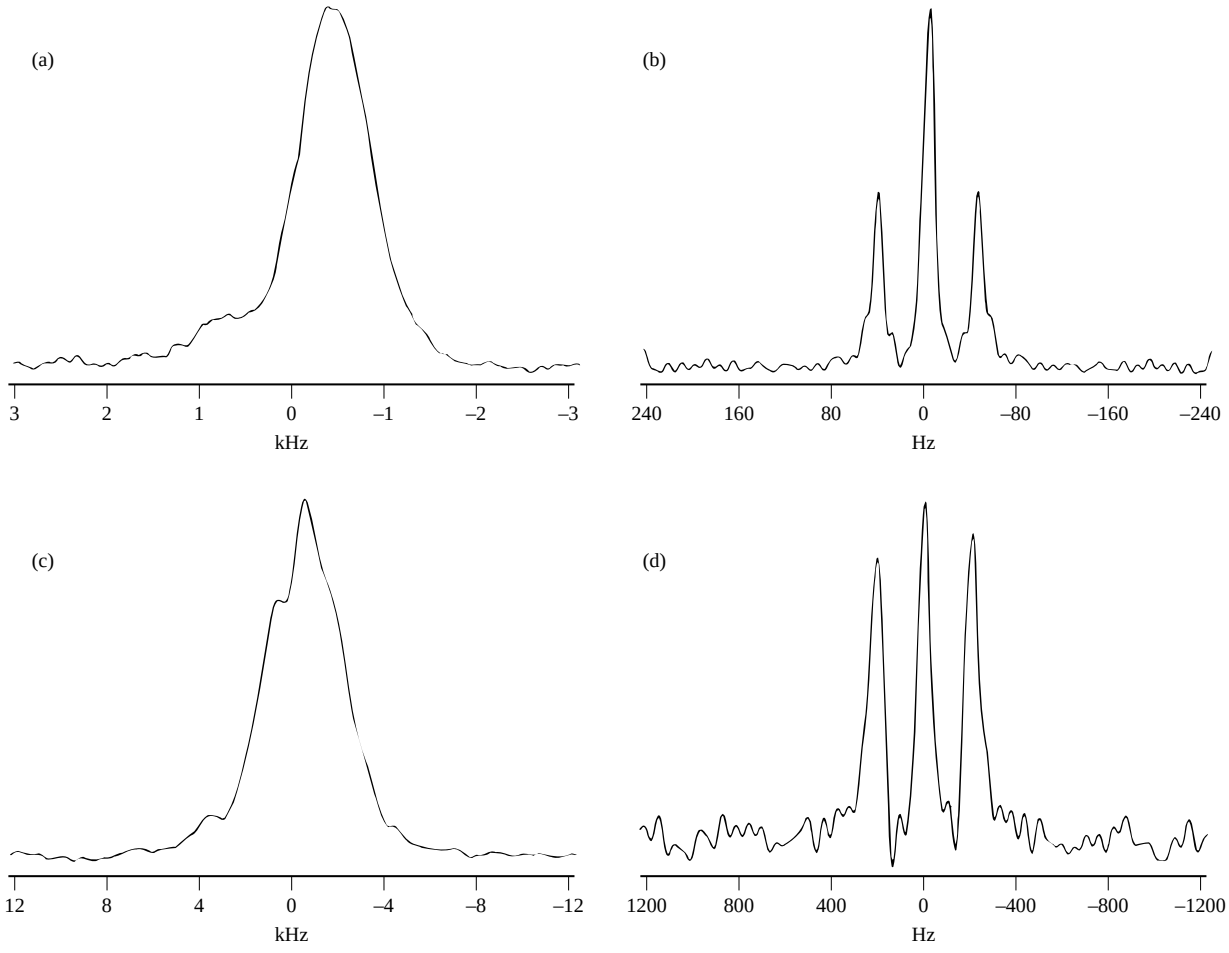

Figure 10 (a) and (b) High field ^{13}C spectra of the bisulfite adduct of acetone, with 5% of the molecules ^{13}C-labeled at both methyl carbons. (c) and (d) High field ^{13}C spectra of diammonium succinate, with 13% of the molecules labeled at both methylene carbons. (a) and (c) represent the normal high field powder pattern spectra, while (b) and (d) represent the spectra achieved using the zero field in high field sequences of Figure 9(c) and (a), respectively. Reproduced by permission of R. Tycko, G. Dabbagh, J. C. Duchamp, and K. W. Zilm, *J. Magn. Reson.*, 1990, **89**, 205, © Academic Press, 1990

can accomplish this. Instead, a clever combination of sample spinning correlated with multiple-pulse NMR and extensive phase cycling is required, as shown in Figure 9.[49] An example of a purely high field 'zero field spectrum' is shown in Figure 10. For two-spin systems, the same three-line spectrum is observed in high field NMR and in zero field NMR (see Figure 5), although in the high field version the splittings are scaled by a calculable scaling factor. While demonstrations have been limited to pairs of coupled spins, this is less of a limitation in high field than in low field, since spin decoupling can be applied where it is necessary to isolate experimentally specifically labeled spin pairs.

7 CONCLUSIONS

The realm of zero field NMR is the easy identification of structural features based on high resolution spectroscopy of anisotropic, traceless spin interactions. While amongst the oldest of NMR techniques, new technical, and theoretical advances have guaranteed that it is also amongst its youngest.

8 RELATED ARTICLES

Field Cycling Experiments; Internal Spin Interactions and Rotations in Solids; Line Narrowing Methods in Solids; Low Spin Temperature NMR; Molecular Motions: T_1 Frequency Dispersion in Biological Systems; Quadrupolar Nuclei in Solids; Quantum Tunneling Spectroscopy; Relaxometry of Tissue; SQUIDs; Terrestrial Magnetic Field NMR.

9 REFERENCES

1. F. Reif and E. M. Purcell, *Phys. Rev.*, 1953, **91**, 631.
2. L. C. Hebel and C. P. Slichter, *Phys. Rev.*, 1957, **107**, 901; 1959, **113**, 1504.
3. A. G. Redfield, *Phys. Rev. Lett.*, 1959, **3**, 85.
4. M. Mehring, *Principles of High Resolution NMR in Solids*, 2nd edn., Springer-Verlag, Berlin, 1983.
5. J. H. Baltisberger, S. L. Gann, E. W. Wooten, T. H. Chang, K. T. Mueller, and A. Pines, *J. Am. Chem. Soc.*, 1992, **114**, 7489.
6. N. Bloembergen and T. J. Rowland, *Acta Metall.*, 1953, **1**, 731.
7. M. Packard and R. Varian, *Phys. Rev.*, 1954, **93**, 941.
8. D. F. Elliott and R. T. Schumacher, *J. Chem. Phys.*, 1957, **26**, 1350.
9. R. Kimmich and H. W. Weber, *J. Chem. Phys.*, 1993, **98**, 5847.
10. D. B. Zax, A. Bielecki, K. W. Zilm, and A. Pines, *Chem. Phys. Lett.*, 1984, **106**, 550; A. M. Thayer, M. Luzar, and A. Pines, *J. Magn. Reson.*, 1987, **72**, 567.
11. A. Bielecki and A. Pines, *J. Magn. Reson.*, 1987, **74**, 381.
12. J. Koo and Y.-N. Hsieh, *Chem. Phys. Lett.*, 1971, **9**, 238.
13. F. Apaydin and S. Clough, *J. Phys. C*, 1968, **1**, 932.
14. K. J. Abed and S. Clough, *Chem. Phys. Lett.*, 1987, **142**, 209; K. J. Abed, S. Clough, A. J. Horsewill, and M. A. Mohammed, *Chem. Phys. Lett.*, 1988, **147**, 624.
15. M. H. Cohen and F. Reif, *Solid State Phys.*, 1957, **5**, 321.
16. T. P. Das and E. L. Hahn, *Solid State Phys. Suppl.*, 1958, **1**.
17. A. Abragam, *Principles of Nuclear Magnetism*, Oxford University Press, Oxford, 1961, Chap. 7
18. R. V. Pound, *Phys. Rev.*, 1951, **81**, 156; N. F. Ramsey and R. V. Pound, *Phys. Rev.*, 1951, **81**, 278; E. M. Purcell and R. V. Pound, *Phys. Rev.*, 1951, **81**, 279.
19. A. G. Andersen, *Phys. Rev.*, 1959, **115**, 863.
20. F. Noack, in *Progress in Nuclear Magnetic Resonance Spectroscopy*, eds. J. W. Emsley, J. Feeney, and L. N. Sutcliffe, Pergamon Press, Oxford, 1986, Vol. 18, p. 171; E. Rommel, K. Mischker, G. Osswald, K. H. Schweikert, and F. Noack, *J. Magn. Reson.*, 1986, **70**, 219.
21. A. Bielecki, D. B. Zax, K. W. Zilm, and A. Pines, *Rev. Sci. Instrum.*, 1986, **57**, 393.
22. R. Kreis, A. Thomas, W. Studer, and R. R. Ernst, *J. Chem. Phys.*, 1988, **89**, 6623.
23. A. G. Redfield, *Phys. Rev.*, 1963, **130**, 589.
24. A. Messiah, *Quantum Mechanics*, North-Holland, Amsterdam, 1961, Vol. 2, Chap. 17
25. R. Blinc, *Adv. Nucl. Quad. Reson.*, 1975, **2**, 71.
26. D. Edmonds, *Phys. Rep.*, 1977, **29**, 233; *Int. Rev. Phys. Chem.*, 1982, **2**, 103.
27. D. P. Weitekamp, A. Bielecki, D. B. Zax, K. W. Zilm, and A. Pines, *Phys. Rev. Lett.*, 1983, **50**, 1807; D. B. Zax, A. Bielecki, K. W. Zilm, A. Pines, and D. P. Weitekamp, *J. Chem. Phys.*, 1985, **83**, 4877.
28. J. M. Millar, A. M. Thayer, A. Bielecki, D. B. Zax, and A. Pines, *J. Chem. Phys.*, 1985, **83**, 934.
29. R. Kreis, D. Suter, and R. R. Ernst, *Chem. Phys. Lett.*, 1985, **118**, 120.
30. R. Kreis, D. Suter, and R. R. Ernst, *Chem. Phys. Lett.*, 1986, **123**, 154.
31. M. Goldman, *Spin Temperature and Nuclear Magnetic Resonance in Solids*, Clarendon Press, Oxford, 1970.
32. J. W. Hennel, A. Birczyński, S. F. Sagnowski, and M. Stachurowa, *Z. Phys. B*, 1984, **56**, 133.
33. Yu. A. Serebrennikov, *Chem. Phys.*, 1987, **112**, 253; *Chem. Phys. Lett.*, 1987, **137**, 183.
34. S. Vega, in *Advances in Magnetic Resonance*, ed. J. S. Waugh, Academic Press, New York, 1973, Vol. 6, p. 259; *J. Chem. Phys.*, 1975, **63**, 3769.
35. J. M. Millar, A. M. Thayer, D. B. Zax, and A. Pines, *J. Am. Chem. Soc.*, 1986, **108**, 5113; T. P. Jarvie, A. M. Thayer, J. M. Millar, and A. Pines, *J. Phys. Chem.*, 1987, **91**, 2240.
36. R. Kubo and T. Toyabe, in *Magnetic Resonance and Relaxation*, ed. R. Blinc, North-Holland, Amsterdam, 1967, p. 810; R. Kubo, T. Endo, S. Kamohara, M. Shimizu, M. Fujii, and H. Takano, *J. Phys. Soc. Jpn.*, 1987, **56**, 1172.
37. P. Jonsen, M. Luzar, A. Pines, and M. Mehring, *J. Chem. Phys.*, 1986, **85**, 4873.
38. J. W. Hennel, A. Birczyński, S. F. Sagnowski, and M. Stachurowa, *Z. Phys. B*, 1985, **60**, 49.
39. Yu. A. Serebrennikov, *Advances in Magnetic and Optical Resonance*, ed. W. S. Warren, Academic Press, New York, 1992, Vol. 17, p. 47.
40. M. H. Cohen, *Phys. Rev.*, 1954, **96**, 1278.
41. D. B. Zax, A. Bielecki, M. A. Kulzick, E. L. Muetterties, and A. Pines, *J. Phys. Chem.*, 1986, **90**, 1065.
42. A. M. Thayer and A. Pines, *J. Magn. Reson.*, 1986, **70**, 518.
43. C. J. Lee, D. Suter, and A. Pines, *J. Magn. Reson.*, 1987, **75**, 110.
44. A. Llor, Z. Olejniczak, J. Sachleben, and A. Pines, *Phys. Rev. Lett.*, 1991, **67**, 1989.
45. A. M. Thayer, J. M. Millar, and A. Pines, *Chem. Phys. Lett.*, 1986, **129**, 55.

46. D. Suter, T. P. Jarvie, B. Sun, and A. Pines, *Phys. Rev. Lett.*, 1987, **59**, 106.
47. C. Connor, J. Chang, and A. Pines, *J. Chem. Phys.*, 1990, **93**, 7639; *Rev. Sci. Instrum.*, 1990, **61**, 1059.
48. M. D. Hürlimann, C. H. Pennington, N. Q. Fan, J. Clarke, A. Pines, and E. L. Hahn, *Phys. Rev. Lett.*, 1992, **69**, 684.
49. R. Tycko, *Phys. Rev. Lett.*, 1988, **60**, 2734; *J. Chem. Phys.*, 1990, **92**, 5776; R. Tycko, G. Dabbagh, J. C. Duchamp, and K. W. Zilm, *J. Magn. Reson.*, 1990, **89**, 205.

Biographical Sketch

David B. Zax. *b* 1958. A.B., 1979, Harvard, USA; Ph.D., 1985, University of California at Berkeley, working with Professor A. Pines. Bantrell postdoctoral fellow with Professor S. Vega at the Weizmann Institute of Science, 1985–86. IBM Postdoctoral Fellow with Professor C. P. Slichter at the University of Illinois at Urbana–Champaign, 1986–87. Professor of Chemistry, Cornell, 1990–present. Approx. 40 publications in the field of magnetic resonance. Research interests include applications of solid state NMR to low-dimensional solids and confined solids, and of Floquet theory to problems in time-dependent quantum mechanics.

Gases at High Pressure

István T. Horváth and John M. Millar

Exxon Research & Engineering Company, Annandale, NJ, USA

1	Introduction	1
2	Apparatus for NMR Under High Gas Pressure	1
3	Applications of NMR Under High Gas Pressure	2
4	Related Articles	4
5	References	4

1 INTRODUCTION

Many chemical processes involving gases and liquids are carried out under high gas pressures to increase the concentration of gases in solution, leading to faster and more economical reaction rates or beneficial shifts in chemical equilibria. In addition, a large number of processes involve autogenic pressures which result from reactions performed at high temperatures in closed vessels. NMR has been adapted to study systems under gas pressures using various techniques, ranging from hydrostatic methods to glass and sapphire tubes.[1] Here, we shall *only* discuss applications of NMR to liquids under high (∼100 atm) gas pressure. Important studies which explore the use of extremely high hydrostatic pressures have recently been reviewed.[2]

IT SHOULD BE EMPHASIZED THAT SPECIAL PRECAUTIONS SHOULD BE TAKEN AT ALL STAGES OF ASSEMBLY, TESTING, AND USE OF ANY KIND OF HIGH-PRESSURE NMR APPARATUS BECAUSE OF THE HAZARDS INVOLVED.

2 APPARATUS FOR NMR UNDER HIGH GAS PRESSURE

2.1 High-Pressure Probes

The first high-pressure apparatus was developed for hydrostatic systems by Benedek and Purcell in the 1940s,[3] and was followed by many related designs, including some modifications for the examination of liquids under high gas pressure.[4]

2.2 High-Pressure Tubes

Glass tubes can be used conveniently even at relatively high pressures (∼20 atm).[5] Among their considerable advantages are that they contain no metal, do not require a dedicated probe, permit visual inspection of the contents, and can be used in routine instruments. Safety considerations, however, are of paramount importance in the use of these tubes.[7,8]

Sealed glass ampoules have been used at high pressures with the burst pressure limited by the ratio of the outer diameter to

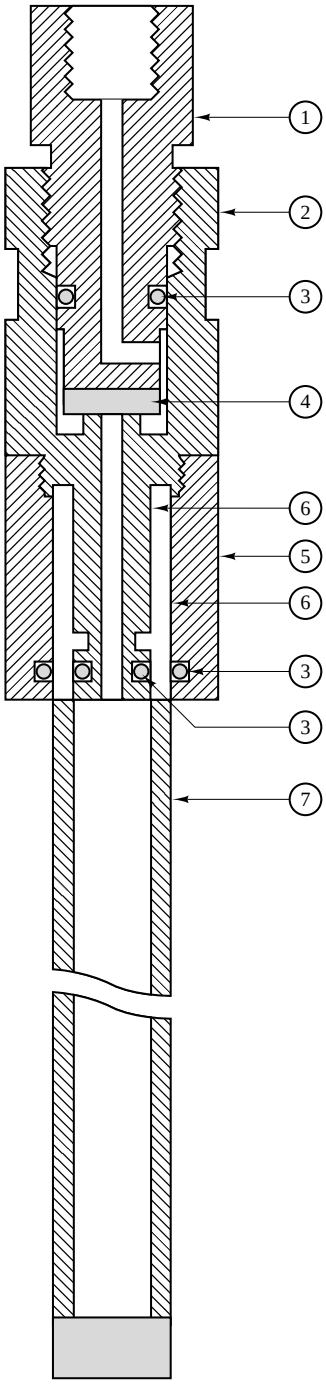

Figure 1 Schematic drawing of titanium valve and sapphire tube assembly by Horváth and Ponce:[8c] (1) valve stem, (2) valve body, (3) Viton O ring, (4) glass filled Teflon seat, (5) valve body end cap, (6) adhesive, and (7) sapphire tube

the inner diameter.[6] For glass tubes the burst pressure is given by

$$P_{max} = \sigma_T\{(R_o/R_i)^2 - 1\}/\{(R_o/R_i)^2 + 1\} \quad (1)$$

where R_o and R_i are the inside and outside diameters of the tube, and σ_T is the tensile strength of the glass in question. The tensile strengths of most ordinary glasses range from 10–100 MPa (ca. 100–1000 kg/cm^{-2}). In fact this theoretical result predicts a bursting pressure *many orders of magnitude higher than that found experimentally*.

Wayland has employed commercial heavy-walled 5 mm and 10 mm glass tubes up to 2.3 MPa (10 atm = 1 MPa) from −53 to 10 °C.[6e] Roe, using King's suggestion,[8a,b] developed a sapphire tube (5 mm o.d./3.4 mm i.d.) with a titanium alloy head to perform experiments up to about 13 MPa and from −100 to 150 °C.[7] The sapphire tubes are essentially chemically inert, but are sensitive to vibration. Horváth and Ponce's version uses a simple, lightweight valve system[8c] and the recent addition of two O rings isolates the reactants from the glue and improves the seal (Figure 1). The use of the 10 mm tube is recommended for an increased gas–liquid interface. Annealing the sapphire tube improves the strength of the tube.[9] Thick-walled Vespel tubes have been used by Merbach at pressures to about 100 MPa,[10a] and a modification spins a Vespel tube at temperatures up to 200 °C at 16 atm.[10b]

3 APPLICATIONS OF NMR UNDER HIGH GAS PRESSURE

High-pressure NMR can be used to follow overall reaction kinetics, investigate individual steps of multistep reactions, and determine concentrations of species at equilibrium.[1]

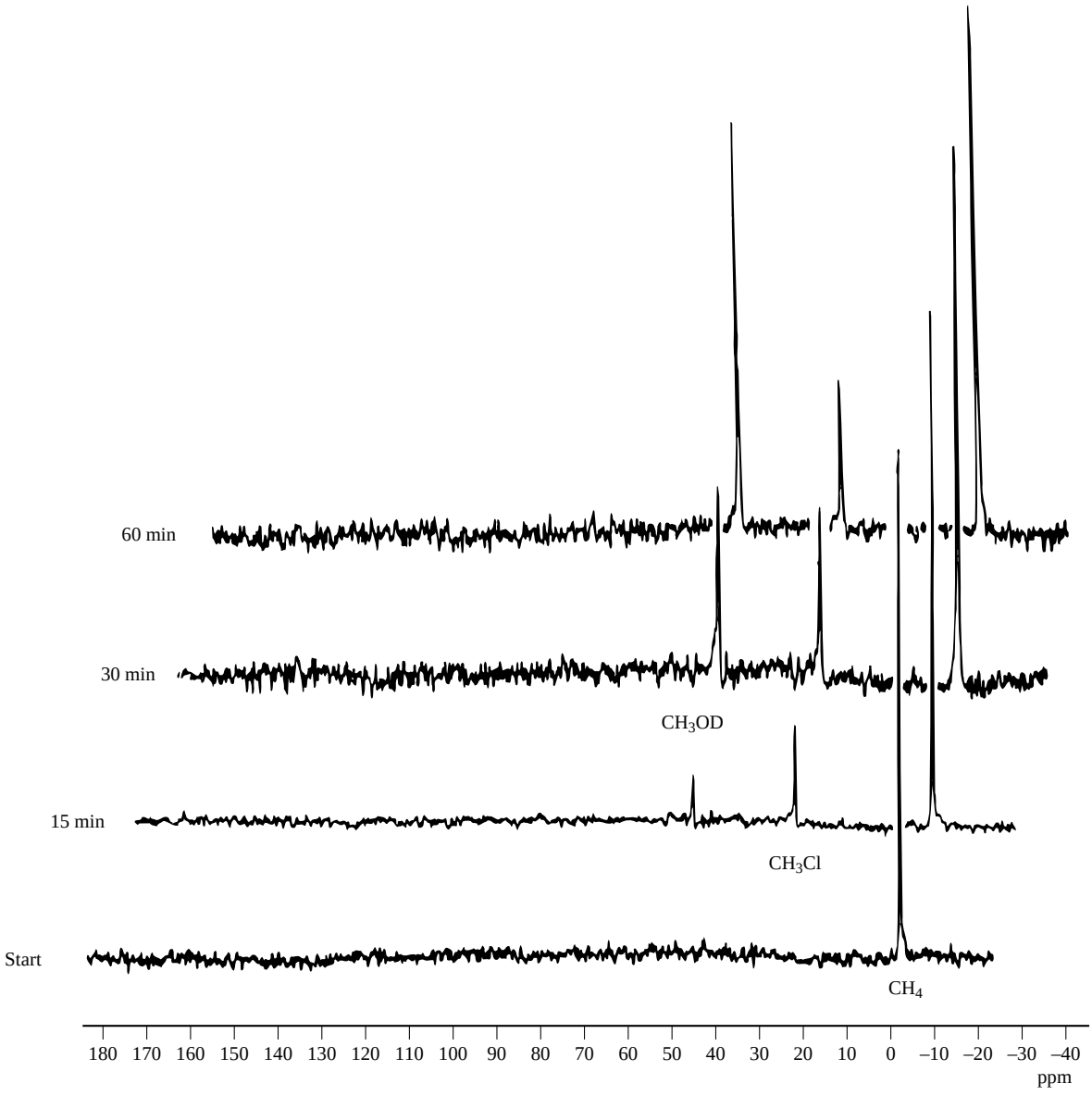

Figure 2 High-pressure ^{13}C NMR spectra of a solution containing 0.16 mmol of Na_2PtCl_4 and 1.2 mmol of Na_2PtCl_6 in 3 mL of D_2O after pressurization with 0.57 MPa of Cl_2 and 27.3 bar of $^{13}CH_4$ with heating to 125 °C for varied amounts of time[11]

3.1 In Situ Monitoring of Chemical Reactions

The essential feature of on-line monitoring is to follow either the concentration of the high-pressure gas itself or some component of the system as a function of time. A typical application is shown in Figure 2 for the platinum-assisted aqueous chlorination of methane to give methyl chloride and methanol.[10] Other applications involve the monitoring of autogenic or gas producing systems. The formation of formate ion intermediates during the reaction of low rank coals with carbon monoxide (4.7 MPa of CO at 25 °C) and water at 315 °C (about 15 MPa total pressure) was detected by NMR.[12] The formation of aromatic rings during the thermal degradation of poly(vinyl chloride) at 450 °C was established by variable temperature and pressure ^{1}H NMR.[13]

A new cobalt intermediate was detected during the investigation of a Co(III) polymerization catalyst.[14] When [(η^5-C_5Me_5)Co(CH_2CH_2-μ-H)(P($OMe)_3$)](BF_4) is treated with high-pressure ethylene at −70 °C, the ^{13}C NMR spectrum showed signals assigned to the ethylene carbons in [(η^5-C_5Me_5)Co(CH_2CH_3)(η^2-C_2H_4)(P($OMe)_3$)](BF_4).

Similar studies have been performed for reactions involving H_2[15a,b] and ethylene.[15c]

3.2 Investigations of Equilibrium Systems

Many important chemical systems consist of chemical equilibria involving gaseous species. High-pressure NMR can be used to determine the thermodynamic data of a given system at various temperatures and pressures. In addition, a unique feature of NMR is that experiments such as saturation transfer permit kinetic measurements under equilibrium conditions.

High-pressure NMR has been used extensively for mechanistic studies for both cobalt and rhodium catalyzed olefin hydroformylation [equation (2)].[16a] It is generally believed that the activation of molecular hydrogen in the cobalt catalyzed process occurs on a coordinatively unsaturated species {$RC(O)Co(CO)_3$},[16b] formed by the elimination of CO from $RC(O)Co(CO)_4$ [equation (3)]. The exchange of free CO and coordinated carbonyl ligands in $CH_3C(O)Co(CO)_4$ was studied at 80 °C up to 7.5 MPa of CO pressure (Figure 3).[7b] The results suggest that the loss of CO from $CH_3C(O)Co(CO)_4$ is accompanied by the formation of an {η^2-$CH_3C(O)Co(CO)_3$}[16c] intermediate. Similar studies have been performed for exchange reactions involving H_2,[17a] CO,[17b] CO/H_2,[17c,d] and CO_2.[17e]

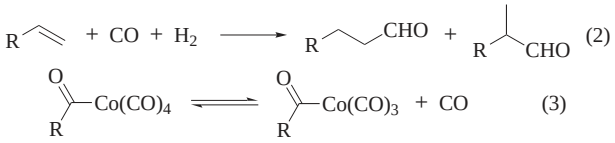

An example of obtaining kinetic data on an equilibrium system is provided by the study of a side-on H_2 complex. High-pressure NMR studies of the equilibrium [equation (4)] between 1 and 5.4 MPa of hydrogen revealed that the elimination of H_2 is a unimolecular process.[17a]

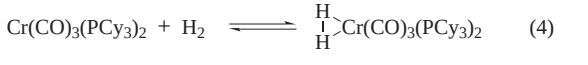

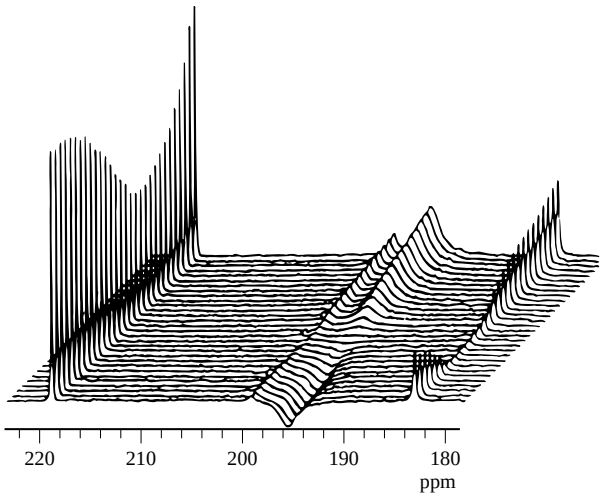

Figure 3 Observed ^{13}C NMR spectral response to selective inversion of the $Co(CO)_4$ signal (197.1 ppm) of $CH_3C(O)Co(CO)_4$ in methylcyclohexane-d_{14} at 70 °C[7b]

3.3 Utilization of Supercritical Fluids

The viscosities of supercritical fluids are 10 to 100 times less than conventional fluids, and can be of significant benefit in studying quadrupolar nuclei, since the linewidth is proportional to the correlation time.[9a,18a,b] Robert and Evilia have published a number of examples of the increase in resolution obtained with supercritical fluids, and these are shown in Figure 4.[18a] Linewidths in the supercritical

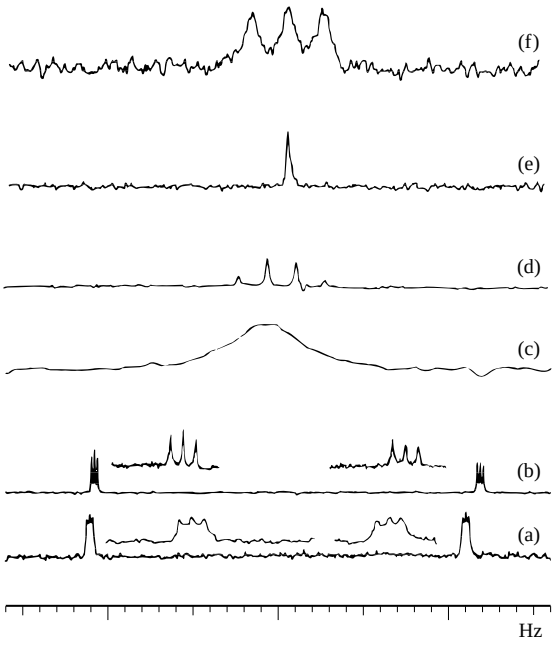

Figure 4 Natural abundance NMR spectra in super- and subcritical phases. All spectra are 800 Hz wide and each division is 25 Hz. (a) ^{14}N spectrum of hexane saturated with N_2O at 0.1 MPa and 28 °C, (b) ^{14}N spectrum of supercritical N_2O at 40 °C, (c) ^{14}N spectrum of 7 M aqueous NH_3, (d) ^{14}N spectrum of 0.5 M NH_3 in supercritical ethylene at 28 °C, (e) ^{17}O spectrum of subcritical CO_2 at 28 °C, (f) ^{17}O spectrum of subcritical N_2O at 28 °C[17a]

phases agreed well in all cases with those predicted from experimentally measured T_1 values. Jonas has shown line-narrowing factors ranging from 3 to 7 in ^{14}N, ^{33}S, and ^{55}Mn spectra using supercritical ethylene and CO_2.[19]

The relatively high diffusion coefficients found in supercritical fluids allow highly efficient chromatographic separation, and application of the NMR as a detector in liquid chromatography.[20]

Finally, the application of supercritical media in chemical reactions is an emerging area since the reaction is not affected by the usual liquid/gas mixing problems that can occur in conventional solvents, and its use to study the cobalt catalyzed hydroformylation of propylene has been demonstrated.[21]

4 RELATED ARTICLES

Analysis of High-Resolution Solution State Spectra; Gas Phase Studies of Intermolecular Interactions and Relaxation; Gas Phase Studies of Chemical Exchange Processes; High-Pressure NMR; Kinetics at High Pressure; Quadrupolar Nuclei in Liquid Samples.

5 REFERENCES

1. I. T. Horváth and J. M. Millar, *Chem. Rev.*, 1991, **91**, 1339.
2. (a) J. Jonas, *NMR Basic Principles and Progress*, Springer-Verlag, Berlin, 1991, Vol. 24; (b) R. van Eldik and J. Jonas, *High Pressure Chemistry and Biochemistry*, Reidel, Dordrecht, 1987.
3. G. B. Benedek and E. M. Purcell, *J. Chem. Phys.*, 1954, **22**, 2003.
4. (a) B. T. Heaton, J. Jonas, J. T. Eguchi, and G. A. Hoffman, *J. Chem. Soc., Chem. Commun.*, 1981, 331; (b) B. T. Heaton, L. Strona, J. Jonas, T. Eguchi, and G. A. Hoffman, *J. Chem. Soc., Dalton Trans.*, 1982, 1159; (c) D. G. Vander Velde and J. Jonas, *J. Magn. Reson.*, 1987, **71**, 480; (d) J. W. Rathke, *J. Magn. Reson.*, 1989, **85**, 150.
5. (a) S. Gordon and B. P. Dailey, *J. Chem. Phys.*, 1961, **34**, 1084; (b) W. T. Raynes, A. D. Buckingham, and H. J. Bernstein, *J. Chem. Phys.*, 1962, **36**, 3481; (c) A. K. Jameson, C. J. Jameson, and H. S. Gutowsky, *J. Chem. Phys.*, 1970, **53**, 2310; (d) C. J. Jameson, A. K. Jameson, and S. M. Cohen, *J. Chem. Phys.*, 1973, **59**, 4540; (e) V. L. Coffin, W. Brennen, and B. B. Wayland, *J. Am. Chem. Soc.*, 1988, **110**, 6063.
6. H. Yamada, Chapter 8, *High Pressure NMR*, *NMR, Basic Principles and Progress, 24*, Eds. P. Diehl, E. Fluck, H. Günther, R. Kosfeld, and J. Seelig, Springer-Verlag (1991) Berlin.
7. (a) D. C. Roe, *J. Magn. Reson.*, 1985, **63**, 388; (b) D. C. Roe, *Organometallics*, 1987, **6**, 942.
8. (a) See acknowledgement in Roe[7]a; (b) N. Nugara and A. D. King, Jr., *40th Southeast Regional Meeting of the ACS, Atlanta, GA, November 1988*; (c) I. T. Horváth and E. C. Ponce, *Rev. Sci. Instrum.*, 1991, **62**, 1104.
9. (a) J. M. Robert and R. F. Evilia, *Anal. Chem.*, 1988, 2035; (b) A. J. Mountvala and G. T. Murray, *J. Am. Chem. Soc.*, 1964, **86**, 237.
10. (a) H. Vanni, W. L. Earl, and A. E. Merbach, *J. Magn. Reson.*, 1987, **29**, 11; (b) S. D. Kinrade and T. W. Swaddle, *J. Magn. Reson.*, 1988, **77**, 569.
11. I. T. Horváth, R. A. Cook, J. M. Millar, and G. Kiss, *Organometallics*, 1993, **12**, 8.
12. I. T. Horváth and M. Siskin, *Energy Fuel*, 1991, **5**, 932.
13. S. Shimokawa, E. Yamada, and K. Makino, *Bull. Chem. Soc. Jpn.*, 1983, **56**, 412.
14. M. Brookhart, A. F. Volpe, Jr., D. M. Lincoln, I. T. Horváth, and J. M. Millar, *J. Am. Chem. Soc.*, 1990, **112**, 5634.
15. (a) P. J. Krusic, D. J. Jones, and D. C. Roe, *Organometallics*, 1986, **5**, 456; (b) R. Zoet, C. J. Elsevier, G. van Koten, P. Versloot, K. Vrieze, M. van Wijnkoop, C. A. Duineveld, K. Goubitz, D. Heijdenrijk, and C. H. Stam, *Organometallics*, 1989, **8**, 23; (c) T. B. Marder, D. C. Roe, and D. Milstein, *Organometallics*, 1988, **7**, 1451.
16. (a) J. Falbe, *Carbon Monoxide in Organic Synthesis*, Springer-Verlag, Berlin, 1970; (b) P. Pino, *Ann. N.Y. Acad. Sci.*, 1983, **415**, 111; (c) R. L. Sweany and F. N. Russell, *Organometallics*, 1988, **7**, 719.
17. (a) J. M. Millar, R. J. Kastrup, M. T. Melchior, I. T. Horváth, C. D. Hoff, and R. H. Crabtree, *J. Am. Chem. Soc.*, 1990, **112**, 9643; (b) J. M. Millar, R. V. Kastrup, S. Harris, and I. T. Horváth, *Angew. Chem., Int. Ed. Engl.*, 1990, **29**, 194; (c) D. T. Brown, T. Eguchi, B. T. Heaton, J. A. Iggo, and R. J. Whyman, *J. Chem. Soc., Dalton Trans.*, 1991, 677; (d) I. T. Horváth, R. V. Kastrup, A. A. Oswald, and E. J. Mozeleski, *Cat. Lett.*, 1989, **2**, 85; (e) D. J. Darensbourg, H. P. Wiegreffe, and P. W. Wiegreffe, *J. Am. Chem. Soc.*, 1990, **112**, 9252.
18. (a) J. M. Robert and R. F. Evilia, *J. Am. Chem. Soc.*, 1985, **107**, 3733; (b) D. Lamb, D. G. Vander Velde, and J. Jonas, *J. Magn. Reson.*, 1987, **73**, 345.
19. D. M. Lamb, S. T. Adamy, K. W. Woo, and J. Jonas, *J. Phys. Chem.*, 1989, **93**, 5002.
20. L. A. Allen, T. E. Glass, and H. C. Dorn, *Anal. Chem.*, 1988, **60**, 390.
21. J. W. Rathke, R. J. Klingler, and T. R. Krause, *Organometallics*, 1991, **10**, 1350.

Biographical Sketches

István T. Horváth. *b*. 1953. Diploma, 1977, Chemical Engineering, Ph.D., 1979, Chemistry, Veszprém University, Hungary. Approx. 60 publications. Research interests include homogeneous catalysis, organometallic chemistry, and the application of high-pressure spectroscopy.

John M. Millar. *b*. 1956. B.S., 1980, West Virginia University; Ph.D., 1986, University of California, Berkeley. Approx. 40 publications. Research interests include the development of NMR techniques and hardware and their applications to catalysis, colloids and organometallic chemistry.

High-Pressure NMR

Jiri Jonas

University of Illinois Urbana, Urbana, IL, USA

1	Introduction	1
2	Experimental Techniques	2
3	High-Pressure NMR Studies of Chemical Systems	4
4	High-Pressure NMR Studies of Biochemical Systems	6
5	Related Articles	10
6	References	10

1 INTRODUCTION

In recent years, there has been a major expansion of high-pressure research providing unique information about systems of interest to a wide range of scientific disciplines. Since NMR has been applied to a wide range of problems in chemistry, physics, and biochemistry, it is not surprising to find that techniques involving NMR at high pressures have also had many applications in these fields. Clearly, the wealth of information obtained from NMR experiments is enhanced by the ability to perform these experiments at high pressure.

The aim of a recent monograph[1] was to illustrate the wide range of problems of interest to physics, chemical physics, biochemistry, and chemical reaction kinetics, which can be successfully studied by high-pressure NMR. In many different ways, this monograph demonstrated the power of modern experimental and theoretical techniques to investigate very complex systems.

The use of pressure as an experimental variable in NMR spectroscopy leads to some added complexity in instrumentation; however, the unique information to be gained from this technique fully justifies its use. There are several fundamental reasons for performing experiments on liquids at high pressure:

1. It is important to realize that changing temperature at constant pressure affects molecular motions in two distinct ways: not only is the average kinetic energy of the molecule changed, but there is always an accompanying change in the average volume available for the motion of the molecule. Only by using both pressure and temperature as experimental variables can one separate the effects of density and temperature on molecular motions. Because of the close packing of molecules in a liquid, even a small change in density can produce a considerable change in the molecular dynamics of the system. Therefore, in order to test rigorously a theoretical model of a liquid or a model of a specific dynamic process in a liquid, one must perform isochoric, isothermal, and isobaric experiments.
2. Use of pressure allows one to extend the range of measurements above the boiling point and also permits the study of supercritical dense fluids.[2]
3. In an analogy to the concept of pressure tuning of energy levels in solids,[3] one can tune the intermolecular interactions in liquids by varying the pressure.[4]
4. Studies of reorientational motions and reaction dynamics require variation of the solvent shear viscosity η. In most studies η is changed by the use of different solvents, but in a high-pressure experiment η can be changed by changing pressure. Since introducing different solvents changes the solute–solvent intermolecular potential, the high pressure single solvent experiment represents a much cleaner experiment.

A large majority of NMR applications in chemistry and biochemistry deal with liquids in which the NMR lines are narrowed by motional averaging to a natural linewidth of the order of 0.1–1 Hz. High-resolution NMR spectra of complex molecules in the liquid phase usually exhibit a great deal of structure and yield a wealth of information about the molecule. Therefore, it is not surprising that the multinuclear high-resolution Fourier transform MR spectroscopy at high pressure represents the most promising technique in studies of the molecular dynamics in liquids. The information from the many advanced NMR techniques, including 2D NMR techniques such as NOESY, COSY, and ROESY, has yet to be fully explored at high pressures. Recent advances in superconducting magnets make it possible to attain a high homogeneity of the magnetic field over the sample volume so that even without sample spinning one can achieve high resolution. Achieving an NMR linewidth of 1.2 Hz for a sample diameter of 10 mm at the proton frequency of 300 MHz (B_0 = 7.05 T) is an impressive feat. The experimental capability of recording high-resolution NMR spectra on dilute spin systems opened an exciting new direction for high-pressure NMR spectroscopy dealing with pressure effects on biochemical systems.[5]

The rationale for using pressure as an experimental variable in studies of proteins and model membranes has been thoroughly discussed by a number of authors;[5] therefore, only the most important points are highlighted:

5. Because noncovalent interactions play a primary role in the stabilization of biochemical systems, the use of pressure allows one to change, in a controlled way, the intermolecular interactions without the major perturbations produced by changes in temperature and/or chemical composition.
6. Pressure affects chemical equilibria and reaction rates. The following standard equations define the reaction volume, ΔV, and the activation volume, $\Delta V^{\ddagger}$:

$$\Delta V = -\left[\frac{RT\,\partial\,\ln K}{\partial P}\right]_T, \Delta V^{\ddagger} = -\left[\frac{RT\,\partial\,\ln k}{\partial P}\right]_T \quad (1)$$

where K is the equilibrium constant, and k is the reaction rate. With the knowledge of ΔV and $\Delta V^{\ddagger}$ values, one can draw conclusions about the nature of the reaction and its mechanism.

7. Studies of simple liquids have indicated that volume (i.e. pressure) effects quite often determine the mechanism of a specific dynamic process, whereas temperature changes only the frequency of the motions without actually affecting the mechanism.
8. Although proteins are known to undergo pressure denaturation, few details are known about this important process or how it is related to thermal- or solvent-induced denaturation.

9. According to the high-pressure phase diagram of water, even at − 15 °C water is still a liquid. Therefore, protein solutions can be measured at subzero temperatures to investigate their cold-denaturation behavior.
10. Finally, the phase behavior and dynamics of phospholipid membranes can be explored more completely by carrying out experiments at high pressure. In fact, the lipid-phase transitions are influenced by pressure, and unique high-pressure gel phases are produced.

Pressures used to investigate liquids and biochemical systems range from 0.1 MPa to 1 GPa (0.1 MPa = 1 bar; 1 GPa = 10 kbar); such pressures change only intermolecular distances and affect conformations, but do not change covalent bond distances or bond angles. In fact, pressures in excess of 30 GPa are required to change the electronic structure of a molecule.[6]

Since the pioneering effort of Benedek and Purcell[7] in 1954, the research activity in studies of liquids by NMR at high pressure has been relatively low when compared with NMR at ambient pressure. The original NMR studies in solids, liquids, and gases at high pressure were reviewed by Benedek[8] in his monograph in 1963. For the last 25 years, our laboratory has been using NMR at high pressure to study the dynamic structure of liquids, supercritical fluids, polymers, disordered solids, and, more recently, biochemical systems. Several key reviews[1,9–11] summarize the results of our studies.

This contribution is organized as follows. Section 2 deals with experimental techniques for NMR at high pressures. Sections 3 and 4 give examples of high-pressure NMR studies of liquids, disordered solids, and biochemical systems. These specific examples will illustrate the unique information one obtains by carrying out the NMR experiment at high pressure.

2 EXPERIMENTAL TECHNIQUES

2.1 Pressure-Generating and Measuring Equipment

Nearly all the components such as hand pumps, high-pressure tubing and valves, intensifiers, and high-pressure separators necessary to build a high-pressure apparatus are currently available from several commercial sources. Pressures up to 2.8 kbar can be produced simply by a hand pump (e.g. Enerpac Model P-228, 40 000 psi) and the pressure measured by a Bourdon gauge. Another standard way of measuring the hydrostatic pressure is to measure the change in the resistance of a manganese alloy wire using the so-called manganin cell.

For hydrostatic pressures higher than 2.8 kbar, one has to use a pressure intensifier, which again is commercially available or can be built in any good machine shop. In our laboratory we use the high-pressure generating system depicted schematically in Figure 1. The system consists of Enerpac hand pumps, a pressure intensifier, a liquid separator, Heise Bourdon gauges, and high-pressure tubing and valves. Our system can generate hydrostatic pressures up to 10 kbar. Carbon disulfide was used as a pressure transmitting fluid for proton relaxation measurements at low temperatures, and tetrachloroethylene at higher temperatures. For other nuclei, a mixture of 50% SAE 10 W motor oil and 50% kerosene was used for temperatures up to 150 °C; at higher temperatures,

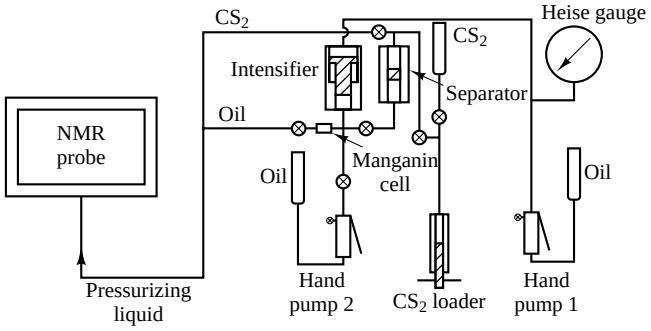

Figure 1 Schematic diagram of the high-pressure-generating equipment

above 300 °C, even the motor oil deteriorates rapidly, so silicone oils are recommended for temperatures up to 500 °C.

For low temperatures and temperatures higher than 500 °C, inert gases are the obvious choice for the pressure medium. However, gas systems are much harder to make leak free than are systems using a liquid pressure medium, and more attention must be paid to considerations involving safety.

2.2 High-Pressure, High-Resolution NMR Probes

Over the last 20 years, we have built a number of high-pressure NMR probes suitable for experiments on gases, liquids, and disordered solids. Their design and construction have been discussed in detail in earlier studies[12,13] covering the work of our laboratory. The very first multinuclear high-resolution FT magnetic resonance experiment[14] on liquids at high pressure was performed in our laboratory in 1971, using an electromagnet. However, the main applications were delayed until the availability of commercial high homogeneity superconducting magnets equipped with superconducting and room temperature shims. The early studies in other laboratories used the capillary techniques introduced by Yamada,[15] which have two inherent limitations for the investigation of biochemical systems: a limited pressure range (maximum pressures of 1.5–2 kbar) and a very small sample volume, usually a 1 mm wide sample cell. This, of course, markedly decreases the sensitivity and precludes the use of dilute biochemical samples, which are often necessary to prevent artifacts due to aggregation. We have succeeded only very recently in developing high-pressure NMR probes,[13] which allow high resolution and high sensitivity experiments on biochemical systems. This section discusses in a general way the design of the high-pressure, high-resolution NMR probe.

A schematic drawing of the high-pressure, high-resolution NMR probe is shown in Figure 2. The pressure vessel was made from a nonmagnetic titanium alloy (RMI 6Al–2Sn –4Zr–6Mo), which has a tensile strength of 0.012 kbar and excellent resistance to corrosion. In our earlier designs we used

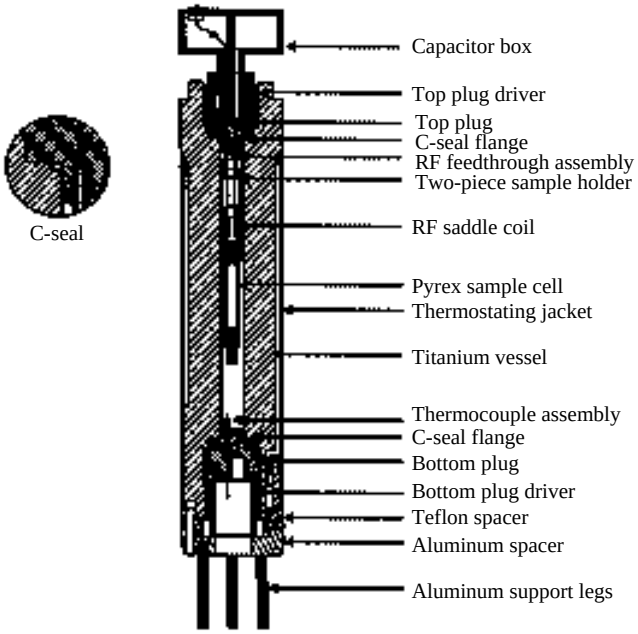

Figure 2 Schematic drawing of titanium-alloy high-pressure vessel used in the wide-bore 7.04 T superconducting magnet (maximum pressure 9.6 kbar). The C seal is shown in more detail in the inset

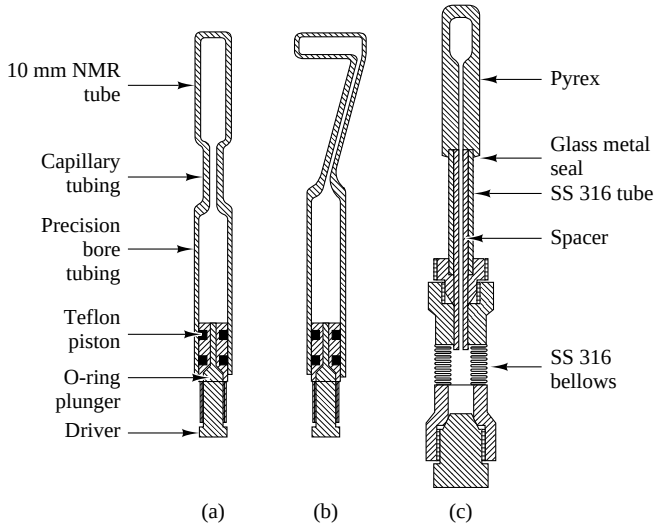

Figure 3 Types of sample cells used in the high-pressure NMR studies: (a) 10 mm, piston-type sample cell; (b) a sample cell used for ^{2}H NMR studies of model membranes; (c) an 8 mm sample cell with metallic bellows[13]

the classical Bridgman seal, but we found that the C seals (see insert in Figure 2) have many advantages for high-pressure NMR probes.

In this specific high-pressure, high-resolution NMR probe, we used the conventional design[12] of the high-pressure rf feedthroughs using SS316 cones soldered on copper wire; the plastic Vespel (SP-1 polyimide) was used as a sealing cone to provide electrical insulation from the plug body. This probe was used in the 7.05 T (300 MHz proton frequency) superconducting magnet (Oxford Instruments, Inc.), and the resolution for protons was 1 Hz for a 10 mm sample diameter. The sensitivity (signal-to-noise ratio) of this probe is comparable with ambient pressure commercial probes of the GN 300 NMR spectrometer (General Electric, Inc.).

In general, we use two types of high-pressure NMR sample cells, which differ in the way the pressure is transmitted to the sample. One is a piston-based design, while the other uses a bellows system. Both systems are shown in Figure 3. In the piston design, the part of the sample cell that is in the rf coil region is made of 10 mm NMR tube, which is then connected via capillary tubing to precision bore tubing that contains a piston made of Teflon, with a plunger pushed by a driver that allows for tighter contact with the glass surface. For a good seal in order to prevent contamination of the sample, two rubber O rings are used on the piston.

In the sample cell that uses bellows, a glass or quartz to metal seal connects the actual 10 mm glass sample chamber to the stainless steel. Stainless steel bellows accommodate the volume change of the liquid due to compression. A different shape of sample cell, shown in the center (b) of Figure 3 was used for our ^{2}H NMR studies in powder samples of pyridine-intercalated $CdPS_3$[16] and in membrane studies.[17] The pipelike sample cell, shown in Figure 3, allows the use of a solenoid coil, which has higher sensitivity than the saddle coil used in the other sample cells, a very important feature in ^{2}H NMR power studies where high-power, short pulses are required.

2.3 High-Pressure NMR Probes for Specialized Applications

In connection with our NMR studies[10] of transport and relaxation properties of water and heavy water, we became interested in the dynamic structure of compressed supercritical steam, which exhibits a number of unusual properties. These include its miscibility with nonpolar fluids in all proportions and its very high electric conductivity, which approaches that of fused alkali hydroxides. Since the high-temperature limit of our high-pressure NMR equipment[12] was 380 °C and the critical temperature of water is 374 °C, we had to develop a new NMR probe for work at high temperatures and high pressures.[18]

There were several basic design requirements for the high-pressure, high-temperature NMR probe. NMR measurements had to be carried out to at least 700 °C and 200 MPa pressure. It was highly desirable that the density of the sample could be easily changed over a wide range. As with any other NMR experiment, the sample could not be allowed to be contaminated by the container. Finally, the resolution, even at high temperatures, should be better than a part per million. This NMR probe[18] meets the above requirements and permits us to carry out NMR relaxation measurements in the temperature range 25–700 °C and at pressures from 0.1 to 200 MPa. Argon gas is used as a pressurizing medium.

A promising but little used application of high-pressure NMR spectroscopy lies in the study of homogeneous catalysts.[19] The use of NMR methods for structure determination and the large body of spectroscopic data of known organometallic compounds can be expected to extend considerably the mechanistic understanding of these systems. Initial experiments in our laboratory showed the need for a probe

specifically designed for such experiments. Important new features of the probe[20] are (1) a built-in stirring mechanism to mix catalyst solutions with reactive gases, necessary because diffusion across the gas/solution interface is otherwise extremely slow; and (2) much improved sensitivity, achieved by incorporating a commercial coaxial transmission line into the probe, making it possible to study dilute solutions by ^{13}C NMR.

A high-pressure sapphire tube suitable for studies of homogeneous catalysis has been described in the literature.[21] In comparison with the design discussed here, the sapphire insert has the advantages of simplicity and compatibility with conventional high-resolution probes. The pressure vessel based design has the advantages of a much larger sample volume (which could be further increased), a much better coil filling factor, and an increased safety margin for operation at pressures above those employed in this work or studies using the sapphire tube that have been published to date.

3 HIGH-PRESSURE NMR STUDIES OF CHEMICAL SYSTEMS

3.1 Dynamic Structure of Liquids

Both theoretical and experimental evidence indicate that many physical properties of liquids may be determined, to a large extent, by the size and shape of the constituent atoms or molecules. In particular, molecular dynamics studies by Alder et al.[22] have elucidated many aspects of the static and dynamic behavior of hard sphere fluids. This picture of fluids is based on the idea that when the liquid density is sufficiently high (approximately twice the critical density), the molecules are so closely packed that the forces between particles arise almost exclusively from the harsh short-range repulsive forces between nearest neighbors. The slowly varying attractive forces can be neglected.

On the basis of a successful prediction of the static properties of liquids, we thought it worthwhile to find the extent to which their dynamic properties can be explained in terms of hard sphere models. A major problem in this type of analysis, however, is determining which hard sphere system (that is, which hard sphere diameter) to associate with a particular liquid. Fortunately, this diameter can be determined from the density dependence of the self-diffusion coefficient under isothermal conditions. The purpose of our systematic studies[10,11] of diffusion in simple polyatomic molecular liquids such as $Si(CH_3)_4$, C_6H_6, SF_6, C_4F_8, and C_6H_{12} was to determine the hard sphere diameter, and then compare the experimental diffusion coefficients with those predicted theoretically with the rough hard sphere (RHS) model of liquids. The RHS model[23] takes into account the coupling between the rotational and translational motions of molecules, reflecting the fact that real molecules cannot be represented as smooth hard spheres. From the analysis of the experimental data in terms of the RHS model, we also determined the coupling between the rotational and translational motions of the molecules. We showed that the more pronounced the nonspherical shape of the molecules, the larger the coupling between rotational and translational motions. Our experiments established the limits of applicability of the RHS model and showed that, for simple molecular liquids composed of molecules approaching a spherical shape, this model describes their diffusion behavior well.

Since our experiments provided self-diffusion coefficients and shear viscosities of various liquids over a wide range of temperatures and densities, it was possible to test the validity of the hydrodynamic Stokes–Einstein equation on a molecular scale. This equation states that the product of the diffusion coefficient and the viscosity is a constant related to the diameter of the spherical particle moving through a fluid. Over a wide range of volumes and temperatures, the Stokes–Einstein equation is remarkably accurate.

In contrast to simple molecular liquids, the behavior of water is quite complex, so it is not surprising that the hard sphere picture is not applicable to this important liquid. During our studies of density effects on the dynamic structure of liquids, we observed that the most interesting behavior of various transport and relaxation properties for water and heavy water occurs at temperatures between -15 and $40\,^{\circ}C$. In normal fluids, compression and increased packing significantly slow down all motions. In water, on the other hand, the T_1, self-diffusion coefficients, and fluidity go through a maximum with initial compression, and only with further increases in pressure is motional freedom restricted. It is interesting to note that even the average residence time of a proton on a water molecule shows this anomalous behavior with compression at temperatures below $40\,^{\circ}C$.

The general effect of pressure and temperature on the dynamic properties of water is illustrated in Figure 4, which shows the effect of pressure on self-diffusion in liquid heavy water in the temperature range -15 to $200\,^{\circ}C$. Analogous plots can be drawn for any dynamic property of D_2O or H_2O. The anomalous motional behavior of water molecules with initial compression can be interpreted qualitatively in terms of a simple physical picture[24] based on changes in the random hydrogen bond network. The characteristic structural feature of liquid water is the local tetrahedral environment of each molecule, beyond which there is a randomized, imperfect space-filling network of hydrogen-bonded molecules. By compressing liquid water in the selected low-temperature range, we affect the hydrogen bond network and gradually go from optimal tetrahedral order toward a more compact packing arrangement. In water, the tendency of strongly directional forces to build an open, hydrogen bond network competes with the tendency for external pressure to pack the molecules together more efficiently. Since the process for self-diffusion, shear viscosity, and reorientation of the water molecules necessitates the breaking and reforming of hydrogen bonds, one can expect that it will be easier to break an already bent hydrogen bond that an undistorted one. Initial compression, therefore, increases motional freedom, and only further compression slows down all the dynamic processes because of a more compact packing of the water molecules. Under high compression, the repulsive hard-core interactions begin to compete strongly with the directional forces that are responsible for the open structure of water at low pressures and low temperatures.

3.2 Reaction Rates in Liquid Solutions

In view of its fundamental importance for understanding chemical reactions in solutions, not surprisingly the problem

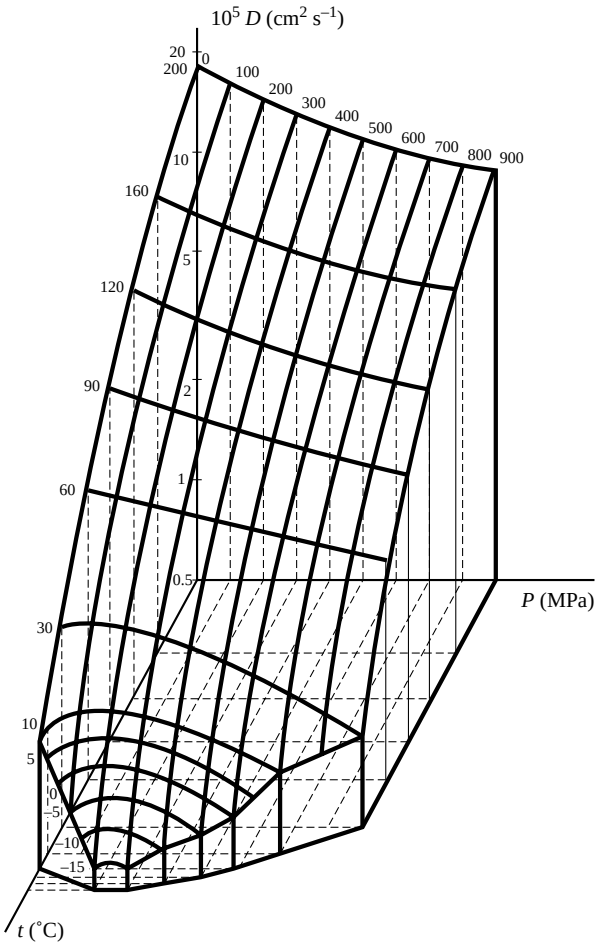

Figure 4 Self-diffusion as a function of temperature and pressure in liquid D_2O

of barrier crossing for chemical reaction in solutions has been investigated in many theoretical and experimental studies. One of the key issues is the observation of the so-called Kramers turnover for isomerization reactions in solutions. According to theoretical models[25] describing the dynamic effects of solvent on reaction rates in liquid solutions, the reaction coordinate is coupled to the solvent, enabling the system to gain sufficient energy to cross the barrier, lose energy, and become trapped into the product well. In the absence of electrostatic interactions, this coupling is produced by collisions between the solvent and solute molecules. In contrast to classical transition state theories for isomerization reactions, the stochastic models propose a dependence of the transmission coefficient κ upon the so-called 'collision frequency' α, which reflects the actual coupling of the reaction coordinate to the surrounding medium.

In all our studies[26] we used techniques of high-pressure, high-resolution NMR to investigate the dynamic solvent effects on the reaction rates in liquid solutions. It is appropriate to comment on the importance of using pressure as an experimental variable in the studies of dynamic solvent effects on reaction rates, because the collision frequency that reflects the coupling of the reaction coordinate to the medium can be related through simple hydrodynamic arguments to shear viscosity η. The collision frequency α in different solvents is given by the coefficient of friction ζ

$$\alpha = \zeta / m \tag{2}$$

and the molecular mass m of the solute. An estimate for ζ can be obtained by applying the Stokes law:

$$\zeta = c\pi\eta(\sigma/2) \tag{3}$$

where σ is the hard-core diameter and c is equal to 4 in the slipping boundary limit or 6 in the sticking boundary limit. Both theoretical and experimental studies show that the slipping boundary conditions are appropriate for cases discussed in our experiments. Therefore, the collision frequency is given by

$$\alpha = (2\pi/m)\eta\sigma \tag{4}$$

In most studies the shear viscosity η is changed by the use of different solvents, but in the high-pressure experiment, viscosity can be varied by changing pressure. One has to realize that viscosity represents only an approximate measure of the degree of coupling of the reaction coordinate to the reaction medium. Consequently, by changing solvents, one may influence the reaction rate by different molecular shape, size, or strength of the intermolecular interactions of the solvent molecule used. Therefore, different solvents of the same shear viscosity may not have the same effect on the reaction rate measured. Clearly, using the same solvent and changing its viscosity by pressure represents a much cleaner experiment.

Because most of the studies of simple isomerization reactions have utilized laser spectroscopy one should also comment on the relative merits of NMR. There are several advantages of using NMR to study isomerization and hindered rotation in liquid solutions. The system chosen can be very simple, and the molecule can be studied in its ground state. For example, the chair–chair isomerization of cyclohexane is a relatively simple process that can be characterized by two degrees of freedom.

However, there are some disadvantages connected with the use of the NMR lineshape technique to calculate the experimental rates. For this technique to be applicable, motions must fall within a narrow timescale, and the restricted range of measurable rates leads to a relatively large error in determined activation parameters. This inherent weakness of the use of NMR lineshape analysis has been overcome in our laboratory by using the NMR rotating frame technique[27] to measure rates. For example, for cyclohexane the highest measurable rate by the NMR lineshape technique is about 5×10^3 s^{-1}, whereas the NMR rotating frame method allows one to measure rates up to 5×10^5 s^{-1}.

Table 1 summarizes the results of our experimental high-pressure NMR studies[26] dealing with the dynamical solvent effects on reaction rates in dense liquid solvents.

3.3 Disordered Solids

As discussed in our earlier reviews,[28,29] the high-pressure NMR techniques used for studies of liquids are readily

Table 1 Summary of Experimental Results[26]

System	Process	Results[a]
Cyclohexane	Conformational isomerization	Kramers turnover
1,1-Difluorocyclohexane	Conformational isomerization	?
N,*N*-Dimethyltrichloroacetamide	Hindered rotation	Diffusive regime
π-Cyclopentadienyldiethylenerhodium	Ethylene rotation	Inertial regime
π-Cyclopentadienylethylenetetrafluoroethylenerhodium	Ethylene rotation	Kramers turnover

[a]For details, see Jonas and Peng.[26]

adaptable to experiments on disordered solids, which are relatively compressible even in the range 1 bar to 5 kbar. In this section, the main results of a high-pressure deuterium solid state study of the dynamics of pyridine-intercalated $CdPS_3$ are reviewed to illustrate the specific information content of such high-pressure NMR experiments.

Our earlier results on the dynamics of pyridine in several layered compounds provided motivation for the study[16] of the effects of pressure on the motion dynamics of pyridine-d_5 in $CdPS_3$. In the $CdPS_3$–pyridine system, the solid host layers are separated by 2D van der Waals (VDW) gaps. The pyridine is then intercalated into the gaps and the molecular reorientational motion can be determined through the analysis of the deuterium powder pattern lineshapes. Previously, our ^2H NMR temperature study on the polycrystalline pyridine–$CdPS_3$ system indicated that the pyridine experienced a large-amplitude reorientational diffusion about an in-plane axis perpendicular to the molecular C_2 symmetry axis in addition to small-amplitude librational motion (see Figure 5). We concluded that the molecule was oriented in the VDW gap so that the molecular plane was perpendicular to the host layers and the C_2 symmetry axis parallel to them. Both the dynamics and orientation of the pyridine in $CdPS_3$ host were very similar to those seen earlier for $(C_5H_5N)_3TaS_2$.

Because of the lamellar nature of the host material, $CdPS_3$ is compressible only along the *c* axis in the pressure range investigated. The application of pressure to the intercalation compound results in a decrease of the VDW gap dimension. In this study we examined the effect of compression on the reorientational motion of the intercalated molecule.

Pressure could affect the intercalated molecule in one of several ways. The compression could cause deintercalation of the pyridine, or the stage of the complex (number of host layers between occupied VDW gaps) could be altered and pressure could cause an increase in the stage of the potassium–graphite system without deintercalation. If this was the case in the pyridine–$CdPS_3$ system, the occupied gaps would have a higher density of pyridine after compression. This could conceivably alter the reorientational motion of the pyridine. Even in the absence of a change in staging, pressure might modify the mode of reorientational motion seen for the pyridine. Another possible result of the application of pressure to the compound would be lineshape changes similar to those obtained by decreasing the temperature.

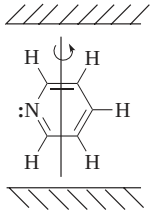

Figure 5 The orientation of the pyridine in the VDW gap of the $CdPS_3$ host materials and the rotational motion of the intercalated pyridine

In the high-pressure study of pyridine-intercalated $CdPS_3$, four isotherms were investigated: 270, 300, 330, and 360 K. At each temperature, powder pattern lineshapes were collected at pressures ranging from 1 to 4500 bar. A typical series of lineshapes obtained as a function of pressure is shown in Figure 6. At ambient pressure and 330 K, three motionally narrowed components and an isotropic pyridine component (0 Hz) are observed. The reorientational motion responsible for this powder pattern has been determined previously. The pyridine is undergoing a rapid rotational diffusion of threefold or higher symmetry about an in-plane axis perpendicular to the molecular C_2 symmetry axis. With increasing pressure, the three motionally narrowed components broaden and decrease in intensity. At 2.5 kbar low intensity indicates that the system is experiencing irreversible dephasing typically seen in an intermediate exchange regime. This behavior was observed previously for the pyridine–$CdPS_3$ system, and was reported in our temperature study on that system. At 3.0 kbar, the rigid component appears; by 4.0 kbar, no large amplitude reorientational motion remains.

The experimental results were analyzed in detail in our original study,[16] and we were able to conclude that the application of pressure does not change the reorientational dynamics of the intercalated molecule in this system. Instead, the motion is suppressed or hindered because of the compression of the host lattice. Also, there was no clear evidence for a change in the stage of the $CdPS_3$–pyridine complex. Increasing the pressure caused lineshape results very similar to those seen with a decrease in temperature. Although our results show similar effects for a pressure increase and temperature decrease, the two methods probe the system in different ways. High-pressure NMR techniques could be used in 'VDW gap tuning' experiments. The simulation of different host environments could be achieved through the application of pressure in order to study the effect of a variety of hosts on the dynamics of a particular intercalated molecule or ion.

4 HIGH-PRESSURE NMR STUDIES OF BIOCHEMICAL SYSTEMS

Even though NMR is one of the most important spectroscopic tools for the investigation of biochemical systems at

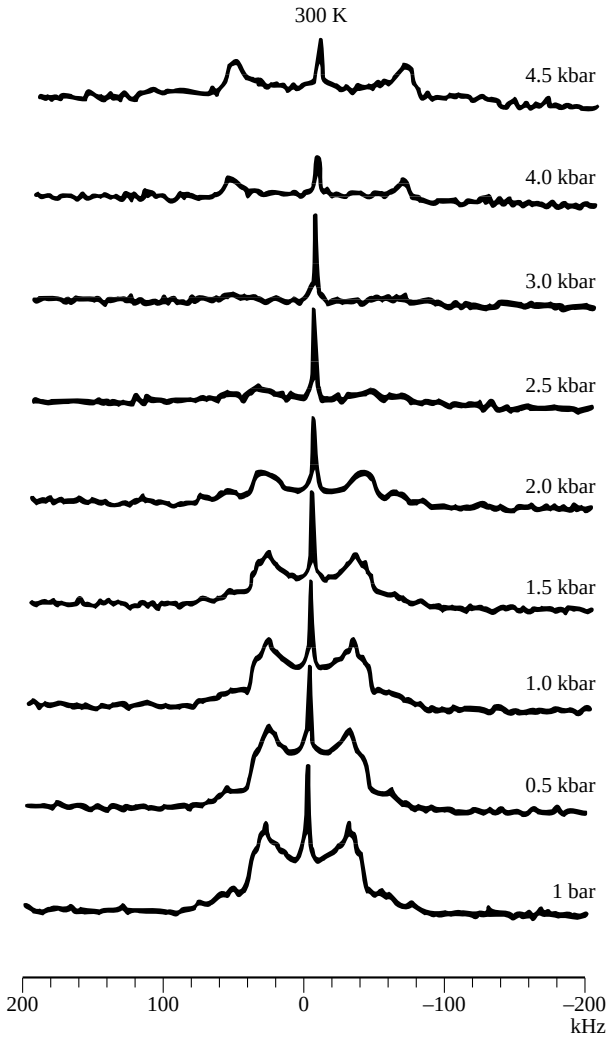

Figure 6 High-pressure deuterium solid state NMR lineshapes of $(C_5H_5N)_{0.41}CdPS_3$ obtained by using a solid echo sequence incorporating composite 90° pulses

ambient conditions, few high-pressure NMR studies[5] on biological molecules have been reported to date. Wagner[30] investigated the pressure effects on the rotation of the Tyr-35 and Phe-45 aromatic rings in bovine pancreatic trypsin inhibitor (BPTI); Williams et al.[31] studied the effect of pressure on the dynamics and α-helical structure in several homopolypeptides; and Morishima and co-workers[32] investigated the effects of pressure on heme proteins. Also, Ludemann and his co-workers[33] have studied the effects of pressure on the ionization of histidine and the rotation of amide groups in peptides.

The use of NMR to follow pressure-induced unfolding of proteins is, so far, limited to our work. Several recent studies illustrate the new information obtained by combining high-resolution NMR techniques with high pressure. In the study of pressure-induced reversible unfolding of lysozyme,[34] we followed the effects of pressure on the behavior of several amino acid residues located in different regions of this small protein. In the experiment on the cold-denaturation experiments[35] on ribonuclease A, we took advantage of the depression of the freezing point of water by high pressure to carry out experiments on the unfolding of this protein well below 0 °C. In addition, we observed the pressure dissociation of Arc repressor[35] and the formation of a compact unfolded state of its monomer. The study of the pressure dissociation of Arc repressor is discussed in more detail in the following section.

4.1 Pressure Dissociation of Arc Repressor

Our results on the high-resolution NMR studies of the pressure-induced dissociation and denaturation of Arc repressor illustrate the fact that pressure allows a more controlled, less drastic perturbation of proteins than does temperature or chemical denaturation. In fact, in these studies we show that pressure leads to 'compact denatured states' of Arc repressor, the term introduced by Dill and Shortle.[36] Arc repressor, a small DNA-binding protein of 53 amino acid residues (M_r = 13 000), is dimeric in solution. It has been reported that Arc, Mnt, and Met repressors belong to a new class of sequence-specific DNA-binding proteins that use a β-sheet as the DNA-binding motif in contrast to other structural motifs of DNA-binding proteins, such as the helix-turn-helix, zinc finger, and leucine-zipper. A tertiary structure model for Arc repressor has been proposed by Breg et al.[37] based on the homology between Arc repressor and *Escherichia coli* Met repressor and 2D NMR data. Silva et al.[38] have used high-pressure fluorescence techniques, and have established that the Arc repressor dimer reversibly dissociates into monomers by an increase of pressure at constant protein concentration, or by dilution at constant pressure. The dissociated monomer is compact and has properties characteristic of a molten globule.

Our studies[35,39] of Arc repressor had several goals. First, by using 1D and 2D NMR techniques we wanted to determine how different the pressure-dissociated Arc repressor monomer is from the monomer forms obtained by thermal or urea denaturation. Second, we wanted to provide experimental evidence for the existence of a pressure-induced predissociated state of Arc repressor, as was suggested by our preliminary NMR experiments. Third, we wanted to characterize partially the structure of the predissociated state and the molten globule monomer state of Arc repressor. Finally, we also wanted to show in a general way that pressure leads to a more easily controlled and less drastic perturbation of protein structure than does thermal or chemical denaturation.

The structure of Arc repressor, as shown by the NMR data, contains an intertwined dimer, in which residues 8–14 of each subunit participate in the formation of an antiparallel β-sheet. The two α-helices in each subunit also have substantial intersubunit interactions. It can be argued that the intersubunit interactions are as important as the intrasubunit interactions for the maintenance of the native conformation of Arc repressor. Therefore, it is conceivable that the monomers would lose most of their structure when separated from each other. Conformational changes in conjunction with the dissociation of Arc repressor were first observed on denaturation by guanidine. Large conformational changes were detected when the subunits were separated by hydrostatic pressure, but some residual structure remained.

More specific information that the pressure-dissociated monomer is different from the thermal or urea-denaturated states can be obtained by comparing the 2D NOESY spectra in the H-α–H-α region, where the NOE cross peaks in the β-sheet region (residues 8–14) are observed. Figure 7 compares

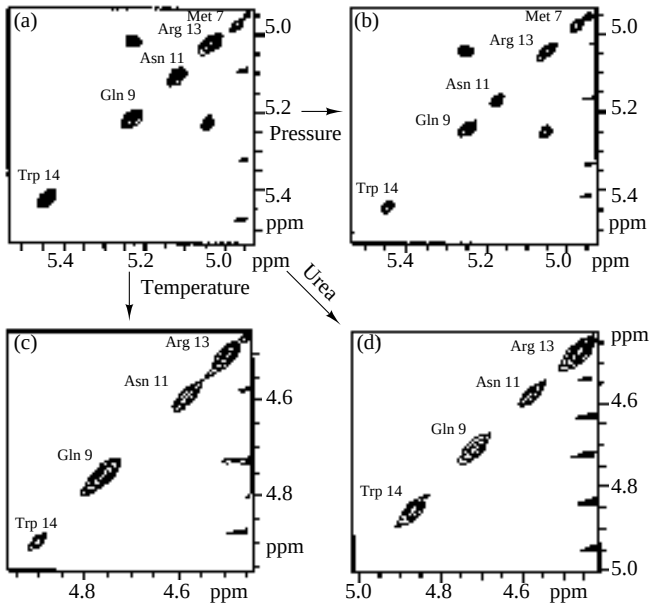

Figure 7 Comparison of an expanded region of NOESY spectra showing the H-α–H-α region in the β-sheet region of Arc repressor among the native state (a), pressure-induced molten globule state (b), thermally denatured state (c), and urea-denatured state (d)[40]

the NOESY spectra in the H-α–H-α region for the native state, the pressure-induced monomer state, the thermally denatured state, and the urea-denatured state. The most important finding is that NOE cross peaks between H-α of Glu-9 and Arg-13 occur even in the pressure-denatured form, indicating the proximity of these two residues.[40] By contrast, no NOEs are observed between the H-α protons of Glu-9 and Arg-13 in the NOESY spectra of Arc repressor at 70 °C, or in the presence of 7 M urea. This observation directly proves that Glu-9 and Arg-13 are no longer close to each other in the thermally or chemically denatured states. We observed changes in 1D NMR spectra prior to pressure dissociation of the Arc repressor dimer, a finding that suggested the existence of a predissociated state. Subsequently we carried out additional 2D NMR experiments in order to prove the existence of the predissociated state.

Conclusive experimental evidence[40] for the existence of a pressure-induced predissociated state of Arc repressor came from the 2D NOESY experiments in the H-α–H-α region of the β-sheet residues (residues 8–14) performed at high pressure. As expected, at 1 bar we observe a strong cross peak between Glu-9 and Arg-13, which indicates the presence of the intermonomer β-sheet in the Arc repressor dimer, as proposed by Breg et al.[37] The increase in pressure to 500 bar does not produce any significant changes in the NOESY spectra, but they change drastically at 1 kbar. At 1 kbar an additional cross peak appears between Glu-9 and Trp-14 and one between Met-7 and Glu-9. Essentially the same NOESY spectrum persists at 1.5 kbar, but at 2 kbar only the cross peak of Glu-9 and Arg-13 persists. This cross peak remains unchanged at pressures up to 5 kbar, i.e. in the pressure regime where Arc repressor dissociates into its molten globule monomers. This experimental evidence suggests that the conformation of the predissociated state could be intermediate between the antiparallel intermonomer β-sheet of native dimer and the intramolecular β-sheet of the molten globule monomer. Further increases in pressure cause the dissociation of the predissociated state into molten globule monomers.

4.2 Model Membranes

Our laboratory has combined NMR methods with high-pressure and variable temperature measurements to access diverse gel phases in phospholipid bilayers and to study the order and dynamics of phospholipids in bilayers as a function of volume changes. Eventually this will allow the testing of theoretical models for NMR relaxation times in the absence of confounding temperature effects. Table 2 lists the studies that have been performed in our laboratory[5,41] on phospholipid bilayers using high-pressure NMR methods.

As an illustrative example of a high-pressure NMR study of model membrane, I will discuss some of the results of our study[42] of pressure effects on the ^{31}P NMR lineshapes of pure dipalmitoylphosphatidylcholine (DPPC) bilayers and DPPC bilayers containing charged tetra-caged tetracaine (TTC) in the pressure range 1 bar to 5 kbar at 50 °C.

The goals of the study were as follows: (1) to determine the behavior of the headgroup in the liquid crystalline (LC) phase and the various gel phases accessible at high pressure; (2) to compare the pressure effects on pure DPPC bilayers with those observed for DPPC/TCC bilayers; (3) to determine whether the concept of molecular electrometer, as introduced by Seelig,[43] is also applicable to gel phases induced at high pressures.

The detailed analysis of the ^{31}P lineshapes was discussed in detail in the original reference; Figure 8 shows the effect of pressure on the measured chemical shift anistropy values $\Delta\sigma$ for both pure DPPC and DPPC/TTC bilayers. For pure DPPC the absolute value of $|\Delta\sigma|$ increases slightly with pressure in the LC phase in the pressure range from 1 to 500 bar. The transition from the LC phase to the Gel I phase is accompanied by a reduction of *gauche* isomer in the acyl chains affecting the available space for the headgroup motions and resulting in an increase of the absolute values of $|\Delta\sigma|$. The abrupt decrease of $|\Delta\sigma|$ that accompanied the Gel I/Gi phase transition provides supporting evidence for the existence of the interdigitated phase, Gi, in which the phospholipid headgroup has more available space and is thus less restricted. In this phase, the faster motion of the headgroup averages the chemical shift anisotropy leading to lower values. In contrast, in the Gel II phase, there is a further reduction of *gauche* conformers, and the two acyl chains are almost extended, making the chains tilt with respect to the bilayer normal. As a result, the available headgroup space decreases again, and the $|\Delta\sigma|$ value returns to higher values. In the Gel III phase, the headgroup motion is further restricted and the $|\Delta\sigma|$ value continues to increase with pressure. The phase change from the Gel III to the Gel X phase corresponds to a transformation to a rigid lattice spectrum, which shows a typical ^{31}P axially asymmetric powder pattern. However, in contrast to the deuterium lineshapes, there is no discontinuity in $\Delta\sigma$ at the phase transition pressures corresponding to Gel II/Gel III and Gel III/Gel X phase transitions, perhaps because the phase transitions are driven by the cooperative interactions between the DPPC fatty acid chain segments.

The increase in pressure in all phases is accompanied by an increase in the ^{31}P chemical shift anistropy $|\Delta\sigma|$, so as

Table 2 NMR Studies of Pressure Effects on Model Membranes[41a]

System	Experiment	Result
DPPC	Natural abundance ^{13}C, T_1, T_2	Phase transitions
DMPC		
POPC	^{1}H 2D NOESY	NOE buildup curves
DPPC-d_{62} (± TTC)	^{2}H lineshapes	Phase diagram, order parameters, pressure reversal of the effects of TTC
DPPC (± TTC)	^{31}P lineshapes, T_1	Structure and dynamics of the headgroup, phase diagram
DPPC-d_2 (2,2), (9,9), (13,13)	^{2}H lineshapes, T_1, T_2	Order parameters, chain motions
DPPC (± TTC)	^{1}H T_1, 2D NOESY	Dynamics, location of TTC, spin diffusion
DPPC-d_{62}-cholesterol	^{2}H lineshapes	Phase diagram
DPPC	^{1}H T_1	Lateral diffusion

[a]Pressure range from 0.1 to 500 MPa (1–5 kbar). Temperature range from 7 to 75 °C. High-resolution ^{1}H NMR (180 MHz).

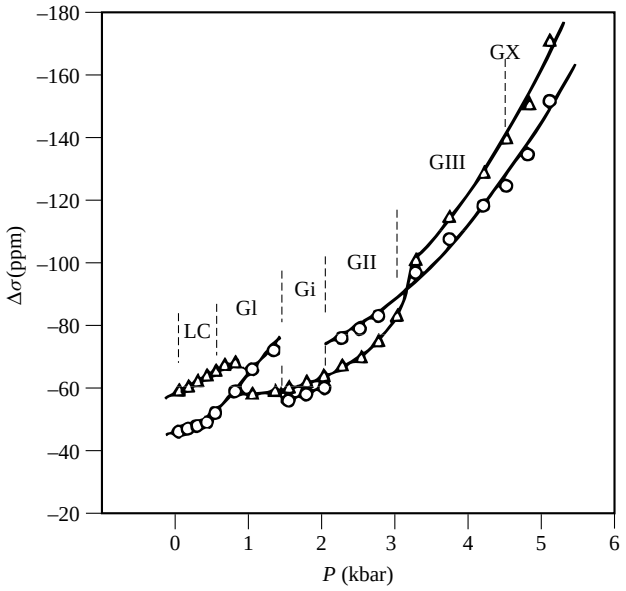

Figure 8 Pressure dependence of ^{31}P chemical shift anisotropy values for DPPC bilayers (○) and DPPC/TTC bilayers (Δ) at 50°C. The pressure ranges for different phases of pure DPPC are indicated[42]

headgroup motions are slowed down, the motional averaging is reduced. However, an alternative explanation should be considered for the $|\Delta\sigma|$ behavior in the LC phase. Increasing pressure causes a decrease in overall volume available for the DPPC molecules by 'squeezing' them together, with an increase in the overall interactions. Since there is an increase in the thickness of the bilayer with pressure, a decrease in the overall cross-sectional area of the phospholipid molecule is needed to explain the decreased volume. The average surface area per headgroup thus decreases. With pressure, the headgroup, which is normally oriented parallel to the bilayer surface, may change its orientation, thus contributing to the measured increase in bilayer thickness and leading to higher $|\Delta\sigma|$ values. In the gel phases this explanation is not applicable, because the bilayer thickness decreases with increasing pressure.[44] As is well documented in the literature,[45] the knowledge of the ^{31}P $\Delta\sigma$ value alone is not sufficient to determine the average orientation of the headgroup; therefore, we attribute the increase in $|\Delta\sigma|$ to pressure in the various phases of DPPC as a consequence of slower motions.

For the DPPC/TTC bilayers, the dependence of $\Delta\sigma$ upon pressure, as shown in Figure 8, can be divided into three regions. In the first region, between 1 bar and 0.8 kbar, which corresponds to the LC phase, the $|\Delta\sigma|$ values for the DPPC/TTC bilayers are greater than those for pure DPPC bilayers, as expected. The $\Delta\sigma$ change due to the charged form of tetracaine will be discussed in more detail later. The distance break that occurs at about 0.8 kbar represents the phase transition which is different from pure DPPC in three respects. First of all, the critical pressure of the main phase transition is shifted from $\sim$ 0.5 to 0.8 kbar. This increase in critical pressure upon addition of anesthetics has also been observed in the DPPC/TTC system by differential scanning calorimetry and small-angle neutron scattering.[44] Moreover, it is consistent with the depression of the main phase transition temperature at ambient pressure. Second, the phase transition is accompanied by an abrupt change in the $\Delta\sigma$ value, which is not observed in the pure DPPC bilayers. Finally, instead of the observed $|\Delta\sigma|$ increase for pure DPPC, the $|\Delta\sigma|$ value decreased significantly at the phase transition pressure. In the second region, from $\sim$0.8 to 3 kbar, the $|\Delta\sigma|$ values are significantly lower than those of pure DPPC bilayers in the Gel I and Gel II phases, but slightly higher than those in the interdigitated Gi gel phase. Thus, our results indicate that the addition of the charged form of TTC leads to the formation of the interdigitated gel Gi phase directly from the LC phase. In the Gi phase the $|\Delta\sigma|$ values increase with pressure and gradually approach the $\Delta\sigma$ values of pure DPPC in the Gel II and Gel III phases. In the third region, from about 3.1 to 5.1 kbar, the $|\Delta\sigma|$ values are greater than those observed for pure DPPC bilayers, similar to the situation for the LC phase. The question of the possible expulsion of anesthetic from the bilayer by high pressure cannot be answered by this study, but the fact remains that the $|\Delta\sigma|$ for the DPPC/TTC system is higher than the corresponding $\Delta\sigma$ values observed for the pure DPPC bilayers, even in the pressure range from 3.1 to 5.1 kbar.

One of the objectives of this study was to examine our data in the light of the results obtained by Scherer and Seelig[43] and MacDonald et al.,[46] who investigated the influence of membrane surface charges upon the conformation of the choline headgroup in various phosphatidylcholines. Our experimental results, discussed in detail in the original reference, provided supporting evidence for the proposal of MacDonald et al.[46] that the choline group of phosphatidylcholine responds to surface change effects even in gel-state liquid membranes.

5 RELATED ARTICLES

Gases at High Pressure; Kinetics at High Pressure.

6 REFERENCES

1. P. Diehl, E. Fluck, H. Gunther, R. Kosfeld, and J. Seelig (eds.), in *NMR Basic Principles and Progress*, guest ed. J. Jonas, Springer-Verlag, New York, 1991.
2. J. Jonas and D. M. Lamb, *ACS Symp. Ser.*, 1987, **329**, 15.
3. H. G. Drickamer, *NATO ASI Ser. C.*, 1987, **197**, 263.
4. W. Schindler, T. W. Zerda, and J. Jonas, *J. Chem. Phys.*, 1984, **81**, 4306.
5. J. Jonas and A. Jonas, *Annu. Rev. Biophys. Biomol. Struct.*, 1994, **23**, 287.
6. H. G. Drickamer and C. W. Frank, *Electronic Transition and the High Pressure Chemistry and Physics of Solids*, Chapman and Hall, London, 1973.
7. G. B. Benedek and E. M. Purcell, *J. Chem. Phys.*, 1954, **22**, 2003.
8. G. B. Benedek, *Magnetic Resonance at High Pressures*, Wiley-Interscience, New York, 1963.
9. J. Jonas, *Annu. Rev. Phys. Chem.*, 1975, **26**, 167.
10. J. Jonas, *Science*, 1982, **216**, 1179.
11. J. Jonas, *Acc. Chem. Res.*, 1984, **17**, 74.
12. J. Jonas, *Rev. Sci. Instrum.*, 1972, **42**, 643.
13. J. Jonas, P. Koziol, X. Peng, C. Reiner, and D. M. Campbell, *J. Magn. Reson.*, 1993, **102B**, 299.
14. D. J. Wilbur and J. Jonas, *J. Chem. Phys.*, 1971, **55**, 5840.
15. Y. Yamada, *Rev. Sci. Instrum.*, 1974, **45**, 640.
16. P. L. McDaniel, G. Liu, and J. Jonas, *Physica A*, 1989, **156**, 203.
17. D. A. Driscoll, S. Samarasinghe, S. Adamy, J. Jonas, and A. Jonas, *Biochemistry*, 1991, **30**, 3322.
18. T. H. DeFries and J. Jonas, *J. Magn. Reson.*, 1979, **35**, 111.
19. B. T. Heaton, J. Jonas, T. Eguchi, and G. A. Hoffman, *J. Chem. Soc., Chem. Commun.*, 1981, 331.
20. D. G. Vander Velde and J. Jonas, *J. Magn. Reson.*, 1987, **71**, 480.
21. D. C. Roe, *J. Magn. Reson.*, 1985, **63**, 388.
22. B. J. Alder, D. M. Gass, and T. E. Wainwright, *J. Chem. Phys.*, 1970, **53**, 3833.
23. D. Chandler, *J. Chem. Phys.*, 1974, **60**, 3500, 3508; 1975, **62**, 1358.
24. F. H. Stillinger and H. Rahman, *J. Chem. Phys.*, 1974, **61**, 4973; J. Jonas, *Comments Solid State Phys.*, 1977, 8129.
25. J. L. Skinner and P. G. Wolynes, *J. Chem. Phys.*, 1978, **69**, 2143; J. A. Montgomery, Jr., D. Chandler, and B. J. Berne, *J. Chem. Phys.*, 1979, **70**, 4056.
26. J. Jonas and X. Peng, *Ber. Bunsenges Phys. Chem.*, 1991, **95**, 243.
27. D. M. Campbell, M. Mackowiak, and J. Jonas, *J. Chem. Phys.*, 1992, **96**, 2717.
28. J. Jonas, *NATO ASI Ser. C*, 1978, **41**, 65.
29. J. Jonas, *NATO ASI Ser. C*, 1987, **197**, 193.
30. G. Wagner, *FEBS Lett.*, 1980, **112**, 280.
31. R. K. Williams, C. A. Fyfe, D. Bruck, and L. Van Veen, *Biopolymers*, 1979, **18**, 757.
32. I. Morishima in *Current Perspectives in High Pressure Biology*, ed. H. W. Janasch, R. E. Marquis, and A. M. Zimmerman, Academic Press, New York, 1987, p. 315.
33. H. Hauer, H. D. Ludemann, and R. Jaenicke, *Z. Naturforsch., C*, 1982, **37c**, 51.
34. S. Samarasinghe, D. M. Campbell, A. Jonas, and J. Jonas, *Biochemistry*, 1992, **31**, 7773.
35. X. Peng, J. Silva, J. Zhang, L. E. Ballard, A. Jonas, and J. Jonas, *Proceedings of the Steenbock Symposium on High Pressure Effects in Molecular Biophysics and Enzymology, University of Wisconsin, Madision, May 15–19, 1994*.
36. K. A. Dill and D. Shortle, *Annu. Rev. Biochem.*, 1991, **60**, 5082.
37. J. N. Breg, H. S. Van Opeusden, M. J. M. Burgering, R. Boelens, and R. Kaptein, *Nature*, 1990, **346**, 586.
38. J. L. Silva, C. F. Silveira, A. Correia, Jr., and L. Pontes, *J. Mol. Biol.*, 1992, **223**, 545.
39. X. Peng, J. Jonas, and J. Silva, *Proc. Natl. Acad. Sci. U.S.A.*, 1993, **90**, 1776.
40. X. Peng, J. Jonas, and J. Silva, *Biochemistry*, 1994, **33**, 8323.
41. A. Jonas, X. Peng, B.-S. Lee, S. Schwer, and J. Jonas, *Proceedings of the Steenbock Symposium on High Pressure Effects in Molecular Biophysics and Enzymology, University of Wisconsin, Madision, May 15–19, 1994*.
42. X. Peng and J. Jonas, *Biochemistry*, 1992, **31**, 6383.
43. P. G. Scherer and J. Seelig, *Biochemistry*, 1989, **27**, 7720.
44. R. Winter and W.-C. Pilgrim, *Ber. Bunsenges Phys. Chem.*, 1989, **93**, 708.
45. J. Seelig, *Biochim., Biophys. Acta*, 1978, **505**, 105.
46. P. M. McDonald, J. Leisen, and F. M. Marassi, *Biochemistry*, 1991, **30**, 3558.

Acknowledgments

This work was supported in part by the National Science Foundation under grant NSF CHE 90-17649, the Air Force Office of Scientific Research under grant F49620-93-1-0241, and the National Institutes of Health under grant PHS 5 R01 6M42452-05.

Biographical Sketch

Jiri Jonas. *b* 1932. B.Sc., 1956, Ph.D., 1960, Chemistry, Czech. Acad. Sci., Prague, Czechoslovakia. Postdoctoral work 1963–66 at the University of Illinois with Herb Gutowsky. Professor of Chemistry, University of Illinois, Urbana, IL, USA, 1966–present. Approx. 280 publications. Research specialties: NMR spectroscopy at high pressures; dynamic structure of liquids, biochemical systems and disordered solids.

Kinetics at High Pressure

D. Hugh Powell and André E. Merbach
University of Lausanne, Lausanne, Switzerland

1	Introduction	1
2	High-Pressure NMR Instrumentation and Methodology	2
3	Examples of Variable Pressure Kinetic Studies	3
4	Fields of Application of High-Pressure NMR in Chemical Kinetics	5
5	Related Articles	8
6	References	8

1 INTRODUCTION

In order to elucidate the mechanisms of chemical reactions, the kineticist studies the dependence of the reaction rate on a number of parameters, both chemical (reactant concentrations, pH, ionic strength, and solvent composition) and physical (normally temperature). The empirical rate law, the electronic and steric effects induced by changing the reactants, the variable temperature activation parameters (activation enthalpy, $\Delta H^{\#}$ and activation entropy, $\Delta S^{\#}$), and any other experimental or theoretical information available on the system are then used to assign a reaction mechanism. Such information may, however, be insufficient to distinguish clearly between alternative reaction mechanisms. Temperature is, however, not the only physical variable that can be varied in kinetic studies. Pressure can also affect the rate of a substitution reaction in solution, and variable pressure measurements yield an activation volume, $\Delta V^{\#}$, which is now widely used as a supplementary (and often decisive) parameter for mechanistic assignment.[1] Although the first high pressure kinetic study in inorganic chemistry was made over 30 years ago, the rapid development of the field has occurred in the last 20 years, since the adaptation for variable pressure studies of most fast reaction techniques: stopped flow, temperature jump, pressure jump, and, especially, NMR. This is illustrated by the number of recent reviews in the field, of which the reader is referred to the most recent.[2–4]

The pressure dependence of the rate of a chemical reaction is usually described by transition state theory. The activation volume, the difference between the partial molar volumes of the transition state and the reactants, at a temperature T is defined by

$$(\partial \ln k/\partial P)_T = -\Delta V^{\#}/RT \qquad (1)$$

where k is the rate constant. The activation volume may itself depend on pressure, and it is useful to define the compressibility coefficient of activation, $\Delta\beta^{\#}$, as

$$\Delta\beta^{\#} = -(\partial \Delta V^{\#}/\partial P)_T \qquad (2)$$

It is usual to assume that $(\partial^2\ \Delta V^{\#}/\partial P^2)_T = 0$, so that ln k has the quadratic form

$$\ln k = \ln k_0 - P\Delta V_0^{\#}/RT + P^2\Delta\beta^{\#}/2RT \qquad (3)$$

where $\Delta V_0{}^{\#}$ is the activation volume at zero pressure. It should be stressed that there is no physical justification for such a quadratic form. On the other hand, ln k is often found empirically to be approximately linear in pressure, and a simplified form of equation (3) with $\Delta\beta^{\#} = 0$ may be preferred.

Variable pressure NMR has most often been applied to ligand substitutions on metal ions as shown in equation (4), where X is the leaving ligand, Y the entering ligand, and L the nonreacting ligands on a metal M. The measured activation volume for such reactions is usually considered to be the sum of an intrinsic contribution, $\Delta V_{\text{int}}{}^{\#}$, due to changes in internuclear distances within the reactants on formation of the transition state and a solvent electrostrictive contribution, $\Delta V_{\text{elec}}{}^{\#}$. For substitution reactions involving charged species, $\Delta V^{\#}$ may be dominated by $\Delta V_{\text{elec}}{}^{\#}$, so that the sign of $\Delta V^{\#}$ may be different from $\Delta V_{\text{int}}{}^{\#}$. The power of the activation volume as a mechanistic indicator is particularly well illustrated by solvent exchange reactions [X = Y in equation (4)], which are of fundamental importance to all substitution reactions in inorganic chemistry. In this case, one cannot easily vary the concentrations of the reactants so that the mechanistic assignment must often be made on the basis of activation parameters alone. For these reactions there is no significant charge or dipole formation on going to the transition state, so that $\Delta V_{\text{elec}}{}^{\#}$ may be neglected. The sign of $\Delta V^{\#} \approx \Delta V_{\text{int}}{}^{\#}$ is then an immediate diagnostic of the activation step: dominant bond breaking results in a positive $\Delta V^{\#}$ while dominant bond making gives a negative $\Delta V^{\#}$.

$$L_nMX + Y \rightarrow L_nMY + X \qquad (4)$$

The classification of substitution reaction mechanisms originally proposed by Langford and Gray,[5] and widely used in coordination chemistry, is based on operational criteria. If kinetic tests show the presence of an intermediate of increased coordination number, an associative mechanism, A, is assigned. Conversely, if an intermediate of reduced coordination number is detected, a dissociative, D, mechanism is assigned. When no intermediate can be found, a concerted interchange, I, mechanism is assigned. This last category may be subdivided further, depending whether evidence is found for important incoming group influences (I_a) or not (I_d). Swaddle[6] has argued that this operational definition is too restrictive, and may be extended to include activation parameters as operational criteria. This is especially true for solvent exchange reactions, where few kinetic tests are applicable. The activation volume is of primary importance in this context. Microscopic reversibility for solvent exchange reactions means that the forward reaction path must be symmetrical to the reverse one. For an interchange process, with no true minimum along the reaction coordinate, the bond lengths to the entering and leaving solvent molecules must be equivalent at the transition state. Thus, for an I_a mechanism, the incoming and outgoing solvent molecules will both have relatively strong bonds, whereas for an I_d mechanism they will have relatively weak bonds. The difference between the two mechanisms will be manifested as a contraction or expansion at the transition state. If the bond distances between the central ion and nonexchanging solvent molecules are unaltered, $\Delta V^{\#}$ will be a direct measure of the degree of associativity or dissociativity

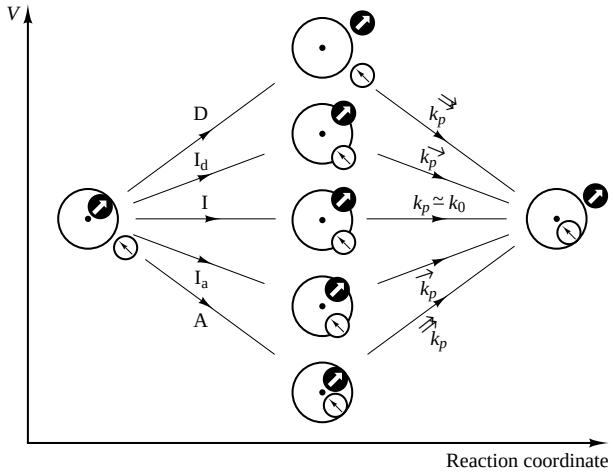

Figure 1 Volume profiles for solvent exchange mechanisms. (Reproduced by permission of Reidel from A. E. Merbach, in High Pressure Chemistry and Biochemistry, ed. R. van Eldik, 1987)

at the transition state. A continuous spectrum of transition states can thus be envisaged (Figure 1), ranging from limiting associative, A, with $\Delta V^{\#} = -|\Delta V_{\lim}{}^{\#}|$, via I_a and I_d to limiting dissociative, D, with $\Delta V^{\#} = +|\Delta V_{\lim}{}^{\#}|$. For interchange mechanisms characterized by $\Delta V^{\#} \approx 0$, the activation mode cannot be specified, and no subscript is assigned to the I mechanism.

We have established the primary importance of $\Delta V^{\#}$, and hence of variable pressure kinetic measurements, for the classification of reaction mechanisms. In Section 2 we will discuss the different approaches used to perform NMR measurements on liquids at high pressures. The rates of chemical reactions cover an enormous range of timescales: for example, water exchange rates at 298 K on metal cations vary from 10^{-8} s^{-1} for Rh^{3+} to almost 10^{10} s^{-1} for Cu^{2+}. A large battery of NMR techniques must be called on, therefore, to study these reactions. In Section 3 we draw on our work in Lausanne to illustrate some of the different techniques that are used and the importance of the activation volume in specific cases. Finally, in Section 4, we will give a brief review of the areas of chemical kinetics where high-pressure NMR has been applied, by our group and various others. In this section, we will give references only when the examples are drawn from recent research papers, otherwise the original references can be found in the aforementioned reviews.

2 HIGH-PRESSURE NMR INSTRUMENTATION AND METHODOLOGY

Two approaches have emerged for the measurement of NMR spectra at high pressure.[7,8] The simplest approach is to design a pressurizable thick-walled glass sample tube which can be placed directly in a standard spectrometer probe. Such systems work well, and sample spinning can be used, but there are certain disadvantages. If small pressure dependences (e.g. activation volumes) are to be measured with any precision, pressures of at least 1 kbar are required. This can be achieved with very thick-walled tubes where the sample is confined to a capillary, but the poor filling factor of these tubes results in low sensitivity. Furthermore, the temperature control of such tubes is not very good, and it cannot be emphasized too strongly that temperature has to be known as accurately as possible if the results of kinetic variable pressure measurements are to be meaningful.

The alternative approach is to manufacture a dedicated high-pressure probehead which will replace the ambient pressure commercial probehead. The probe is built around a high-pressure chamber provided with electrical lead-through contacts so that both the coil and sample are immersed in the high-pressure transmitting fluid. The coil can be wound on a support placed closely around the sample tube and so have a high filling factor. The pressure fluid is also a good heat transfer medium, and its heat capacity and that of the metallic bomb are such that temperature control can be more precise than is possible with the normal gas flow-type unit. The sample cannot be made to spin, or at least there are practical difficulties which preclude this, but using field lock and small diameter tubes (5 mm), good resolution can be obtained from the static sample. The signal-to-noise ratio does not suffer too much from this approach because of the good filling factor, and cryomagnets are capable of producing a remarkable magnetic field homogeneity over small volumes. In practice the static, specially built system has proved superior to the spinning pressure tube in all the factors outlined above, and especially for chemical kinetic studies.

For illustration we present a probe designed for a high-field spectrometer (Bruker AM-400).[9] Figure 2(a) is a schematic drawing of a probehead designed for a wide bore (87 mm diameter) superconducting magnet (9.4 T), which can be used up to 200 MPa and is made of a nonmagnetic beryllium–copper alloy. Three connectors are located at the bottom: one for the pressure transmitting liquid, and two for the inlet and outlet of the thermostating liquid. An upper aluminum support (not shown in Figure 3) contains the high-frequency cables, screwdrivers for the adjustment of the matching/tuning capacitors and the frequency adapter box. The adapter box contains a capacitive matching/tuning network that

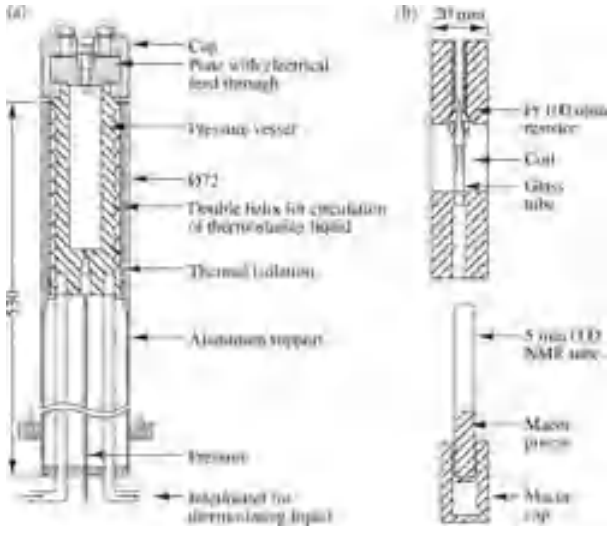

Figure 2 Schematic drawing of (a) a wide bore superconducting magnet multinuclear high-pressure bomb and (b) the internal component of the bomb made of Vespel (top) and the sample tube (bottom). (Reproduced by permission of Gordon and Breach from Frey et al.[9])

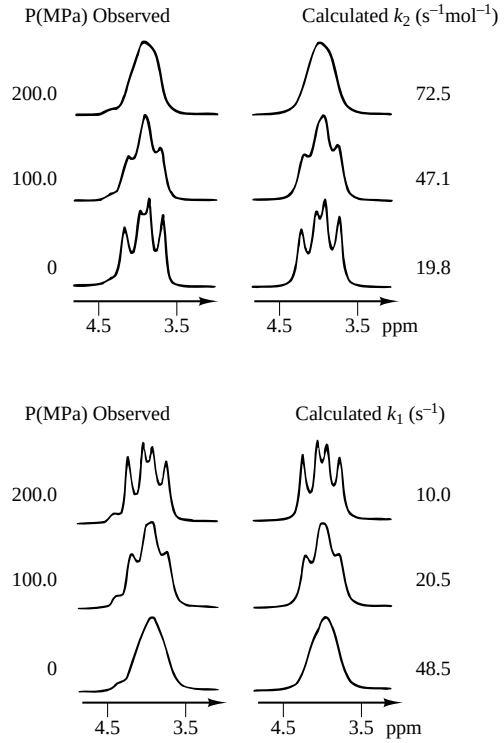

Figure 3 Observed and calculated 60 MHz ^{1}H NMR spectra of a solution of $M(TMPA)_6(ClO_4)_3$ dissolved in a mixture of TMPA and CD_3NO_2, recorded as a function of pressure. The top spectra are for M = In and the bottom spectra are for M = Al. (Reproduced by permission of Pergamon Press from Merbach[10])

is specific for a small frequency range and so must be changed in order to observe different nuclei. Provision is made for the use of a ^{2}H lock.

The internal components of the bomb and the sample tube are shown in Figure 2(b). The radiofrequency coil is wound in a saddle shaped form on 7 mm o.d. glass tubing to produce a radiofrequency field perpendicular to the vertical static magnetic field. The temperature is measured inside the bomb by a platinum resistor placed just above the sample tube. The temperature stability is better than ± 0.2 K and is not a limiting factor in the accuracy of measurements of activation volumes. The sample tube is a 5 mm o.d. NMR tube cut to the right length and closed with a movable seal, made of machinable glass, which allows pressure transmission to the sample. The sample tube was designed to minimize the volume (1 cm^3) to economize on expensive solvents such as ^{17}O enriched water. The surrounding pressure transmitting liquid is chosen so as not to contain the observed nucleus. The spectral resolution and magnetic field stability with this nonspinning high-pressure probe is better than 0.5 Hz at 400 MHz and routinely better than 1 Hz.

3 EXAMPLES OF VARIABLE PRESSURE KINETIC STUDIES

3.1 TMPA Exchange on Aluminum(III) and Indium(III)[10]

Here we describe the use of proton NMR to observe the way TMPA exchanges on two related metal ions, both of which form octahedral solvates with this ligand: $[M(TMPA)_6]^{3+}$, with M = Al and In. The ^{1}H spectrum of TMPA is a doublet due to spin–spin coupling to the phosphorus atom, and this doublet is maintained when the phosphate is complexed by a cation though it is shifted to high frequency. The spectrum of a solution of $[M(TMPA)_6]^{3+}$ with excess TMPA, using deuterated nitromethane (CD_3NO_2) as a diluent, is thus two doublets, provided exchange is sufficiently slow. Exchange between free and bound solvent will cause line broadening and eventual collapse of the doublets.

The use of an inert diluent gives reduced viscosity leading to better resolution and definition of the linewidths and also permits the free ligand concentration to be varied so that information can be obtained regarding the order of reaction. For TMPA exchange on Al^{3+} this is first order while for In^{3+} it is second order. The entropies of activation also have opposite signs so that the ambient pressure data indicate strongly that the activation mode for TMPA exchange is dissociative on Al^{3+} and associative on In^{3+}. The variable pressure kinetics (Figure 3) provide a very good visual proof that the mechanisms are indeed different. The ^{1}H NMR spectrum for the TMPA exchange on In^{3+} at ambient pressure shows a doublet at low frequency which is due to free TMPA and a doublet at high frequency due to the six TMPA molecules coordinated to In^{3+}. With increasing pressure, at constant temperature, one observes a coalescence of the signals. This means that the exchange rate is increasing and therefore the activation volume will be negative ($\Delta V^{\#} = -21.4\,cm^3\ mol^{-1}$). For $[Al(TMPA)_6]^{3+}$ the change in spectra with pressure is the contrary: the deceleration of the ligand exchange with pressure indicates a positive activation volume ($\Delta V^{\#} = +22.5\,cm^3\ mol^{-1}$). The difference in mechanistic behavior can be explained in terms of ionic radii. The large In^{3+} cation (r_i = 80 pm) can easily accommodate, at least partially, a seventh solvent molecule in forming the activated complex. The small Al^{3+} ion (r_i = 54 pm), on the other hand, is rather crowded, and has to expel a solvent molecule from the first coordination sphere at the transition state, before a new molecule can be accepted.

3.2 Water Exchange on the Lanthanide(III) Aqua Ions[11–14]

We now turn to aqueous solutions of the paramagnetic lanthanides, where the bound solvent signal is too broad to be observed and where the influence of the paramagnetic ion on the bulk solvent relaxation is given by the Swift and Connick equations (see ***Paramagnetic Relaxation in Solution***). Water exchange on the lanthanide(III) aqua ions is sufficiently rapid that the ^{17}O relaxation rates of aqueous lanthanide(III) perchlorate solutions are always in the fast exchange limit. In addition, for the paramagnetic lanthanide(III) ions Ce^{3+} to Yb^{3+} (except Gd^{3+}), the bound water relaxation is in the extreme narrowing limit, allowing one to use the approximate equation

$$\frac{1}{P_m}\left[\frac{1}{T_2} - \frac{1}{T_1}\right] = \frac{\Delta\omega_m^2}{k_{ex}} \qquad (5)$$

where P_m is the mole fraction of bound water. $\Delta\omega_m$, the difference in chemical shift between the bound water and the

bulk water (in the absence of paramagnetic interaction with the bulk water), can be determined from the chemical shift of the paramagnetic solution compared with a nonparamagnetic reference solution. Measurement of the longitudinal and transverse ^{17}O relaxation rates, $1/T_1$ and $1/T_2$, in the paramagnetic solution therefore allows the water exchange rate, k_{ex}, to be determined.

For the series Tb^{3+} to Yb^{3+} the relaxation rate difference, $1/T_2 - 1/T_1$, was observed at 4.7 T and 8.5 T to be proportional to the square of the magnetic field, confirming the approximations used in equation (5), and reliable parameters were obtained for this series. For the lighter lanthanides, Nd^{3+} and Eu^{3+}, the bound water chemical shift, $\Delta\omega_m$, was too small for the relaxation rate difference in equation (5) to be measurable. Variable pressure ^{17}O relaxation rate measurements were made in a high-pressure probe at 9.4 T.

As mentioned above, Gd^{3+} is a case apart. The relatively slow electronic relaxation rates lead to breakdown of the extreme narrowing approximation for bound water relaxation, and equation (5) cannot be used. In order to determine k_{ex} it is necessary to consider the microscopic origins of the relaxation of the bound water. The transverse ^{17}O relaxation rate in bound water, $1/T_{2m}$, is dominated by relaxation due to the scalar or contact interaction originating from the finite Gd^{3+} electron spin density at the ^{17}O nucleus and given in approximate form by

$$\frac{1}{T_{2m}} = \frac{1}{P_m}\left[\frac{1}{T_2} - \frac{1}{T_{2A}}\right] = \frac{S(S+1)}{3}\left(\frac{A}{\hbar}\right)^2\left[k_{ex} + \frac{1}{T_{1e}}\right]^{-1} \quad (6)$$

where $1/T_{2A}$ is the transverse relaxation rate in the nonparamagnetic reference, $S = \frac{7}{2}$ is the Gd^{3+} electron spin, and $1/T_{1e}$ is the longitudinal electronic relaxation rate. The scalar coupling constant, $A/\hbar$, is accessible from the chemical shift. Thus, ^{17}O NMR relaxation rate measurements allow one to determine k_{ex}, provided that $1/T_{1e}$ is known. It is therefore necessary to also make ESR measurements: the ESR linewidth is directly proportional to the transverse electronic relaxation rate, $1/T_{2e}$, which can be related to $1/T_{1e}$ using a theoretical model.

A combined ^{17}O NMR and EPR study of the Gd^{3+} aqua ion was first made in 1980, and has recently been improved by extension to a greater number of ESR and NMR magnetic fields. The calculated contribution of $1/T_{1e}$ to $1/T_{2m}$ decreases to less than 3% at 9.4 T, so that k_{ex} and the temperature and pressure activation parameters are determined well from these high-field measurements.

The water exchange parameters for the lanthanide(III) aqua ions Gd^{3+} to Yb^{3+} are shown in Figure 4. The water exchange rates decrease as one progresses along the series, as one might expect for a dissociative process (the energy required to remove a water molecule increasing with the lanthanide ion charge density). The negative $\Delta V^{\#}$, however, clearly indicate an associatively activated exchange mechanism. The coordination number of the lanthanide aqua ions is known from neutron diffraction experiments to change from nine for the larger aqua ions on the left of the series to eight for the smaller aqua ions on the right of the series. This coordination number change is manifested in the measured absolute partial molar volumes of the ions shown in Figure 4, which approach the calculated values for the ennea and octa aqua species for the lighter and heavier lanthanides respectively. The

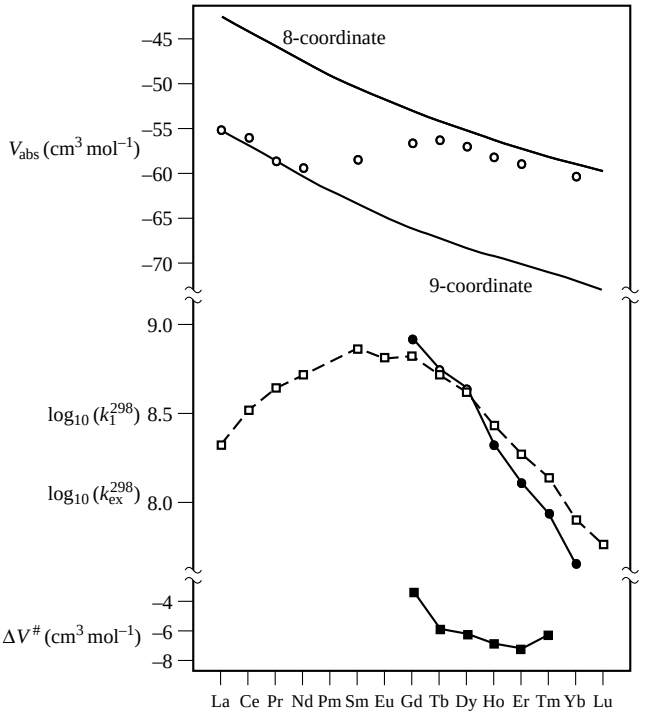

Figure 4 Absolute partial molar volumes, V_{abs}, of the Ln^{3+} aqua ions in $LnCl_3$ solutions, compared with calculated values for the octa and ennea aqua ions. □, interchange rate constants, k_I^{298} (s^{-1}), for complexation of the Ln^{3+} aqua ions with SO_4^{2-}; •, water exchange rates, k_{ex}^{298} (s^{-1}), and the corresponding activation volumes (■) for the Ln^{3+} aqua ions

water exchange mechanism on the lanthanide aqua ions can, therefore, be understood in terms of the reaction in equation (7). For the heavy lanthanides, the octa ion is the lowest energy species, and the ennea aqua ion is the intermediate (or transition state) in the associatively activated water exchange reaction. The activation volumes are, therefore, negative, and the water exchange rates increase toward the middle of the series, as less energy is required to reach the ennea aqua transition state. For the light lanthanides the ennea aqua ion is now the lowest energy species. One can expect, therefore, that the octa aqua ion will be the intermediate (or transition state) in the exchange process, which will proceed via a dissociative, D, or dissociative interchange, I_d, mechanism. For the mid-series lanthanides (Pm^{3+} to Eu^{3+} according to Figure 4), the octa and ennea aqua species are in equilibrium. The transition from one species to the other requires relatively little energy, so that these lanthanides should have the fastest water exchange rates for the series. This interpretation is supported by results from studies of complex formation on the lanthanide(III) aqua ions. The interchange rate, k_I^{298} (s^{-1}), of an inner sphere water molecule by a SO_4^{2-} ion already in an outer sphere complex is shown in Figure 4. The values are closely correlated with the rate of water exchange, and show a maximum in the middle of the series, which corresponds to the cross over in the absolute partial molar volumes of the aqua ions. If one could measure the water exchange rates on the light lanthanide ions, Ln^{3+} to Nd^{3+} (e.g. by using the very high NMR fields now available) one would, therefore, expect positive activation volumes for these aqua ions, and water exchange rates that decrease as one moves away from the middle of the series and more energy is

needed to reach the octa aqua transition state.

$$[\mathrm{Ln}\,(\mathrm{H_2O})_9]^{3+} \rightleftharpoons [\mathrm{Ln}\,(\mathrm{H_2O})_8]^{3+} + \mathrm{H_2O} \qquad (7)$$

3.3 TMPA Exchange on Tetrachlorobis(TMPA)zirconium(IV)[15]

The system discussed here involves a much more complex ligand exchange process. The two ligands, L, in $ZrCl_4 \cdot 2L$ can be either *cis* or *trans* with respect to one another so that there are three possible exchange reactions given by equations (8)–(10).

At 236 K, the ^{1}H NMR spectrum of a solution of $ZrCl_4 \cdot 2TMPA$ in chloroform with excess TMPA consists of three doublets due to the two forms of the complex and the free ligand, with $^3J(^{31}P,^1H)$ = 14.0 Hz for the latter and 11.7 and 11.8 Hz in the *cis* and *trans* complexes, respectively. As the temperature is raised, the doublets of the *cis* and *trans* isomers broaden and eventually coalesce, indicating that the *cis*/*trans* isomerization reaction occurs first. At a slightly higher temperature, the doublet of the free ligand also broadens and coalesces with the signal of the *cis*/*trans* isomers. The source of this second broadening could be due to a ligand exchange reaction between free ligand and the *cis* and/or *trans* isomer. In this case, NMR line-broadening simulation cannot easily be used to quantify the individual contribution of the three exchange reactions to the observed spectra.

$$cis\text{-}ZrCl_4 \cdot 2L + {}^*L \overset{k_c}{\rightleftharpoons} cis\text{-}ZrCl_4 \cdot L\,{}^*L + L \qquad (8)$$

$$trans\text{-}ZrCl_4 \cdot 2L + {}^*L \overset{k_t}{\rightleftharpoons} trans\text{-}ZrCl_4 \cdot L\,{}^*L + L \qquad (9)$$

$$cis\text{-}ZrCl_4 \cdot 2L \overset{k_i}{\rightleftharpoons} trans\text{-}ZrCl_4 \cdot 2L \qquad (10)$$

It has now been shown that this problem can be overcome by using the very powerful 2D NMR techniques. In the moderately slow exchange region where all the signals can be observed, a pulse sequence that is sensitive to exchange effects gives off-diagonal peaks where there is an exchange reaction. So, all the signals can be examined for exchange coupling and the individual exchange rate can be obtained. In addition, if a high-pressure probe is available for a suitable spectrometer, then it is possible to carry out a variable pressure 2D experiment without too much difficulty.

Proton (400 MHz) EXCSY spectra were recorded on a Bruker AM-400 spectrometer equipped with a home built high-pressure probe, using the pulse sequence $90^\circ(\Phi_1)-t_1-90^\circ(\Phi_2)-\tau_m-90^\circ(\Phi_3)-t_2$. A double Fourier transformation with respect to t_1 and t_2 gives a rectangular stacked spectrum plot (Figure 5) with the resonances of the normal spectrum displayed on a diagonal and any exchange is manifested by off-diagonal peaks at the intersection of the chemical shifts of the connected peaks in the two frequency directions. The relative intensities of the cross peaks is related to the relative rates of exchange and so these can be measured for all pathways and changes in both relative and absolute rates with pressure can be measured.

The length of the diagonal in Figure 5 is 0.50 ppm, and the doublet due to free ligand is at low frequency, to the right

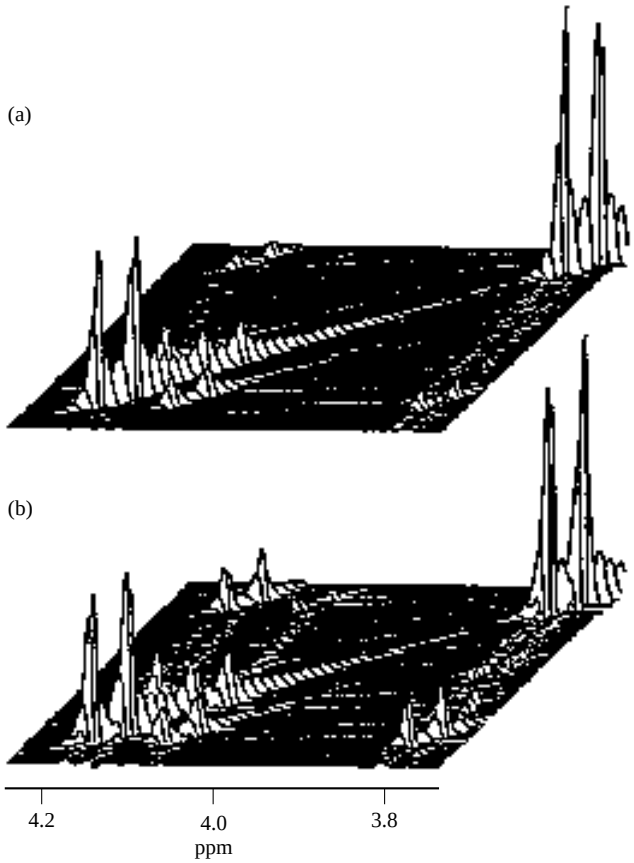

Figure 5 (400 MHz) 2D Proton EXCSY spectra of *cis*- and *trans*-$ZrCl_4 \cdot 2TMPA$ in the presence of excess TMPA, at two different pressures [(a) 0.1 MPa, (b) 198 MPa] demonstrating the effect of pressure on the intramolecular and intermolecular exchange pathways. (Reproduced by permission of Elsevier from Frey et al.[15])

of the plot. The doublet at the extreme opposite end of the diagonal is due to the *trans* isomer and the doublet of the *cis* isomer can be discerned a little to low frequency. At ambient pressure there are strong off-diagonal peaks connecting the resonances of the *cis* and *trans* isomers as would be expected (see above). Weaker off-diagonal peaks connect the free ligand with the *trans* isomer, and those connecting free ligand with the *cis* isomer are just discernible. An increase in the pressure produces a small increase in intensity of the off-diagonal peaks due to the *cis*/*trans* isomerisation reaction. This isomerization, with a small negative activation volume ($\Delta V_i^{\#} = -1.6 \pm 0.6\,\mathrm{cm^3\ mol^{-1}}$), is intramolecular and proceeds via a slightly contracted six-coordinate transition state. On the other hand, the intensities of the off-diagonal peaks due to the intermolecular ligand exchange on both *cis* and *trans* isomers increase strongly with pressure ($\Delta V_t^{\#} = -11.1 \pm 0.8\,\mathrm{cm^3\ mol^{-1}}$), showing that the ligand exchange reactions are both associative. This is in marked contrast to the similar reactions occurring with the analog with the smaller Ti^{4+} ion ($\Delta V^{\#}_c = +17.5\,\mathrm{cm^3\ mol^{-1}}$). Given that the reaction of the *trans* complex predominates, it is then possible to obtain activation parameters in the normal way and show, by changing the free ligand concentration, that the ligand exchange is second order, as required for an associative process.

4 FIELDS OF APPLICATION OF HIGH-PRESSURE NMR IN CHEMICAL KINETICS

4.1 Substitution Reactions and Solvent Exchange

The substitution reactions that have been most extensively studied by NMR are the solvent exchange reactions on divalent and trivalent first row transition metal ions. The measured activation volumes shown in Tables 1 and 2 clearly show a progressive change of activation mode from associative for the early elements to dissociative for the late elements. This change can be explained by the combined effect of the progressive filling of the d orbitals and the decrease in ionic radii across the series, both of which disfavor bonding processes. The only case where the mechanistic changeover is not clear cut is dimethylformamide (DMF) exchange on the divalent ions: the activation volumes are all positive, although very small for Mn^{2+}. This is presumably due to the relative bulkiness of DMF favoring a dissociative activation mode.

The effect of the size of the solvent molecules can be seen very clearly in studies of solvent exchange on tetravalently coordinated Be^{2+}. The measured activation volumes and assigned mechanisms are shown in Table 3. Solvent exchange takes place via associatively activated mechanisms (A or I_a) for H_2O, dimethyl sulfoxide (DMSO), and TMPA, but the greater bulk of the TMU and DMPU ligands prevents the incoming solvent molecule from entering the coordination sphere before the outgoing solvent molecule leaves, and the exchange mechanism is dissociative, D.

Another factor in determining solvent exchange mechanism is the effect of multidentate ligands on the exchange of remaining solvent molecules. This has been shown to be especially important for Gd^{3+} polyaminocarboxylates, where the rate of water exchange is important for their use as contrast agents in medical magnetic resonance imaging. Kinetic parameters for the Gd^{3+} octa aqua ion and the complexes with propylenediaminetetraacetate ($PDTA^{4-}$),[14] diethylenetriaminepentaacetate ($DTPA^{5-}$),[16] tetraazacyclododecanetetraacetate ($DOTA^{4-}$),[16] and diethylenetriaminepentaacetate bismethylamide ($DTPA\text{-}BMA^{3-}$)[17] are shown in Table 4. The exchange rates on the three contrast agents, $[Gd(DTPA)(H_2O)]^{2-}$, $[Gd(DOTA)(H_2O)]^{-}$, and $[Gd(DTPA\text{-}BMA)(H_2O)]$, are 200–2000 times lower than on the octa aqua ion. This rate decrease is accompanied by a change of sign of the activation volume, the large positive values for the three contrast agents indicating dissociatively, rather than associatively, activated water exchange. This is a consequence of the change of coordination number to nine for the contrast agents, which prevents the entry of a second water molecule into the coordination sphere. Without the participation of the incoming water molecule, more energy is required to break the bond between the outgoing water molecule and the highly charged Gd^{3+}, leading to the higher activation enthalpies and lower water exchange rates.

4.2 Redox Reactions

The effect of pressure on the classic outer sphere electron transfer reaction between the aqueous anions MnO_4^{2-} and MnO_4^{-} has been investigated by ^{55}Mn NMR line broadening. The reaction proceeds by two pathways: in one the cation facilitates the approach of the two anions whereas in the other the reaction is cation independent. The first pathway has a rather small activation volume, but for the second $\Delta V^{\#} \approx -21\,cm^3\ mol^{-1}$. This can be accommodated with current theory if it is assumed that the Mn–Mn distance in the

Table 1 Volumes of Activation ($cm^3\ mol^{-1}$) for Solvent S Exchange on MS_6^{2+} of the First Row Transition Metal Series by NMR[2]

M^{2+}	V	Mn	Fe	Co	Ni	Cu
r_i (pm)	79	83	78	74	69	(73)[a]
	t_{2g}^3	$t_{2g}^3e_g^2$	$t_{2g}^4e_g^2$	$t_{2g}^5e_g^2$	$t_{2g}^6e_g^2$	$t_{2g}^6e_g^3$
H_2O	−4.1	−5.4	+3.8	+6.1	+7.2	
MeOH		−5.0	+0.4	+8.9	+11.4	+8.3
MeCN		−7.0	+3.0	+8.1	+8.5	
DMF		+2.4	+8.5	+9.2	+9.1	
NH_3[b]					+5.9	

[a]Effective ionic radius.
[b]In 15 M aqueous NH_3.

Table 2 Volumes of Activation ($cm^3\ mol^{-1}$) for Solvent S Exchange on MS_6^{3+} of the First Row Transition Metal Series by NMR[a][2]

M^{3+}	Sc	Ti	V	Cr	Fe	Ga
r_i (pm)	75	67	64	61	64	62
	t_{2g}^0	t_{2g}^1	t_{2g}^2	t_{2g}^3	$t_{2g}^3e_g^2$	$t_{2g}^6e_g^4$
H_2O		−12.1	−8.9	−9.6	−5.4	+5.0
DMSO			−10.1	−11.3	−3.1	+13.1[b]
DMF				−6.3	−0.9	+7.9[b]
TMP	−21.3					+20.7[b]

[a]Except for Cr^{3+} by isotopic labeling.
[b]In CD_3NO_2 as the diluent.

Table 3 Activation Volumes and Assigned Mechanisms for Solvent S Exchange on BeS_4^{2+}[a]

	H_2O	DMSO	TMPA	TMU	DMPU
$\Delta V^{\#}$ (cm^3 mol^{-1})	−13.6	−2.5	−4.1	+10.5	+10.3
Mechanism	A	A, I[a]	A, I[a]	D	D

[a]In CD_3NO_2 as diluent by ^1H NMR, except for H_2O in neat water by ^{17}O NMR.
[b]TMU = tetramethylurea.
[c]DMPU = dimethylpropyleneurea.

Table 4 Water Exchange Kinetic Parameters Obtained for Different Gd^{3+} Complexes

	k_{ex}^{298} (s^{-1})	$\Delta H^{\#}$ (kJ mol^{-1})	$\Delta S^{\#}$ (J K^{-1} mol^{-1})	$\Delta V^{\#}$ (cm^3 mol^{-1})
$[Gd(H_2O)_8]^{3+}$	$(8.30 \pm 0.95) \times 10^8$	14.9 ± 1.3	−24.1 ± 4.1	−3.3 ± 0.2
$[Gd(PDTA)(H_2O)_2]^-$	$(1.02 \pm 0.10) \times 10^8$	11.0 ± 1.4	−54.6 ± 4.6	−1.5 ± 0.5
$[Gd(DTPA)H_2O]^{2-}$	$(4.1 \pm 0.3) \times 10^6$	52.0 ± 1.4	+56.2 ± 5	+12.5 ± 0.2
[Gd(DTPA-BMA)H_2O]	$(4.3 \pm 0.4) \times 10^5$	46.6 ± 1.3	+18.9 ± 4	+7.3 ± 0.2
$[Gd(DOTA)H_2O]^-$	$(4.8 \pm 0.4) \times 10^6$	48.8 ± 1.6	+46.6 ± 6	+10.5 ± 0.2

transition state ion pair is reduced as the pressure is increased, at a rate that allows the solvent cavity in which the ion pair is contained to compress to the same extent as the solvent. The outer sphere electron transfer between $[Mn(CNR)_6]^+$ and $[Mn(CNR)_6]^{2+}$ has also been studied using ^{55}Mn NMR with R = $CNBu^t$ and R = CNC_6H_{11} and in a series of solvents. The activation volumes range from −9 to −22 cm^3 mol^{-1}, and show evidence for ion pairing in the solvents of lower dielectric constant. The qualitative difference in the solvent dependence of the rate constant for R = $CNBu^t$ and R = CNC_6H_{11} is evidence for the significant influence of subtle differences in solvation on the molecular level that is not approximated by continuum models. Variable pressure NMR studies have also been made of electron transfer between the pairs Fe(II)/Fe(III), Cu(I)/Cu(II), and Ru(II)/Ru(III).

4.3 Spin Equilibria

Where Ni^{2+} is complexed by certain tetraaza macrocyclic ligands, an equilibrium exists between unsolvated planar diamagnetic and disolvated pseudooctahedral paramagnetic forms. The contact shift of the ligand protons can be used to measure the equilibrium between the forms, and a reaction volume for going from the planar to the pseudooctahedral form of -10.0 ± 0.1 cm^3 mol^{-1} was obtained in this way for the complex with the ligand 1,4,8,11-tetramethyl-1,4,8,11-tetraazacyclotetradecane in aqueous solution. This volume is much less than the molar volume of the two molecules that enter the first coordination sphere (36 cm^3 mol^{-1}). This is because the volume reduction is partially compensated by an expansion of the complex due to a change in the Ni−N distance on changing spin state.

4.4 Bioinorganic Chemistry

Variable pressure NMR has been used to study the kinetics of internal motions on proteins. For example, the reorientational motions of amino acid residues [phenylalanine (Phe45) and tyrosine (Tyr35)] buried in the interior of the basic pancreatic trypsin inhibitor were studied by ^1H NMR. The interior of this globular protein is quite compact, implying that internal fluctions of the protein backbone are necessary in order to permit reorientation within the residues. The motion of the aromatic rings had a similar activation volume for the two residues: 30 cm^3 mol^{-1} for Phe45 and 36 cm^3 mol^{-1} for Tyr35. These volumes correspond reasonably with the difference between the volume of a ring and the smallest volume that it can be regarded as sweeping out as it rotates. Alternatively, it was suggested that since the region around a ring contains a significant proportion of void space among the atoms hindering rotation, quite small adjustments to the positions of these atoms will provide free space to permit ring rotation.

4.5 Organometallic Chemistry and Catalysis

The study of organometallic catalytic processes under gas pressure is of great interest despite the hazards involved in using compressed gases. A striking recent example is the catalytic dimerisation of ethylene in aqueous Ru^{2+} solutions, which was studied by ^{17}O, ^{13}C, and ^1H NMR in pressurizable sapphire NMR tubes.[18] Three identical ^{17}O enriched aqueous solutions of $[Ru(H_2O)_6]^{2+}$ in 10 mm o.d. sapphire tubes were pressurized with ethylene at 6 MPa and mixed by shaking for different amounts of time. The NMR spectra showed the successive formation of $[Ru(CH_2{=}CH_2)(H_2O)_5]^{2+}$ and $[Ru(CH_2{=}CH_2)_2(H_2O)_4]^{2+}$. After shaking under ethylene pressure for 3 days, an organic phase formed above the solution. The ^{13}C spectra of this new organic phase, separated under pressure, show characteristic signals of butenes. This aqueous catalytic dimerization reaction is not stereoselective, and all the possible butenes are formed except 2-methylpropene. These results show the utility of NMR studies under gas pressure for the study of catalytic reactions in aqueous solution, which are increasingly attractive with respect to ecological considerations.

There is also interest in the measurement of activation volumes for reactions and internal processes in organometallic compounds. For instance, the ring inversion of cyclic thio ligands in *trans*-$PdBr_2(SCH_2CMe_2CH_2)_2$ was studied under pressure. The activation volume was essentially zero, indicating no association, dissociation, or solvent participation in the inversion process. The exchange processes in a mixture of dimeric $[Pd(2\text{-methylallyl})Cl]_2$ and monomeric Pd(2-methylallyl)Cl(PPh_3) was also studied by variable pressure ^1H NMR. The activation volume depends on temperature, indicating a change of mechanism. At 22 °C, $\Delta V^{\#}$ is essentially zero. The *syn*−*anti* exchange of the allyl hydrogen atoms occurs in the monomer, catalysed by association with

the dimer and the volume change due to this association is canceled by that due to cleavage of the dimer bridge. A 56 °C, $\Delta V^{\#} = +11 \pm 2\,\mathrm{cm^3\ mol^{-1}}$: methylallyl exchange now occurs by a process involving dimer cleavage followed by PPh_3 transfer, and it is the cleavage that produces the expansion.

4.6 Organic Chemistry

High-pressure NMR has been used to study a variety of reactions in organic chemistry. For instance, the volume profiles for the rearrangement of two norbornyl cations have been studied. For rearrangement of the 1,2-dimethoxy-2-norbornyl cation, $\Delta V^{\#} = +8.7 \pm 0.5\,\mathrm{cm^3\ mol^{-1}}$, expansion occurs because the transition state cation has a delocalized charge distribution that reduces interactions with the solvent. Rearrangement of the 7-methyl-7-norbornadienyl cation, on the other hand, takes place via an intermediate with increased charge localization, and one would expect a negative activation volume due to contraction around the transition state. In fact $\Delta V^{\#} \approx 0$, and this is explained by a cancellation of the contraction by an expansion due to bond rupture during the rearrangement.

In the thermolysis of acetyl benzoyl peroxide it was found that pressure retards the rate of peroxide cleavage and increases the ratio of cage product to escape product. The data yield the activation volume for the initiator decomposition ($4\,\mathrm{cm^3\ mol^{-1}}$) and the difference in activation volume for the formation of escape and cage products ($8\,\mathrm{cm^3\ mol^{-1}}$). The effect of pressure on the rates of sigmatropic shifts in 5-(trimethylsilyl)cyclopentadiene, 5-formylpentamethylcyclopentadiene, and bullavene has also been observed. The activation volumes for the silyl compound are negative and depend strongly on solvent, indicating that considerable charge separation occurs in the transition state in chloroform solution, but much less in benzene. The activation volume is much smaller for the formyl compound, indicating that no charge separation occurs, at least in benzene–Freon.

Two reactions that comprise equilibrium addition of a protic species to a carbonyl group have been studied. In the first case, the intramolecular hydroketone–hemiacetal interconversion, $\Delta V^{\#} = -3.2\,\mathrm{cm^3\ mol^{-1}}$, is interpreted as being the volume change necessary for bond formation in this necessarily associative process. The second reaction, the intramolecular addition of thiol to acetyl cyanide, has $\Delta V^{\#} = -13\,\mathrm{cm^3\ mol^{-1}}$. This much larger value is believed to comprise the volume change necessary for bond formation plus the larger volume contraction that occurs upon the simple association of two molecules.

4.7 Silicates

The initial stages of the sol–gel condensation process that occurs following hydrolysis of $Si(OMe)_4$ have been followed by variable pressure ^{29}Si NMR. Increased pressure increases markedly the rate of condensation without changing the mechanism, and it is possible that by carrying out such preparations at high pressure one can improve the properties of the glasses and ceramics that are the final objective of the process.

5 RELATED ARTICLES

Gadolinium Chelate Contrast Agents in MRI: Clinical Applications; Gadolinium Chelates: Chemistry, Safety and Behavior; High- Pressure NMR; Inorganic Chemistry Applications; Paramagnetic Relaxation in Solution; Probes for Special Purposes.

6 REFERENCES

1. R. van Eldik (ed.), *Inorganic High Pressure Chemistry: Kinetics and Mechanisms*, Elsevier, Amsterdam, 1986.
2. A. E. Merbach and J. W. Akitt, *NMR Basic Principles Progr.*, 1990, **24**, 189.
3. R. van Eldik and A. E. Merbach, *Comments Inorg. Chem.*, 1992, **12**, 341.
4. J. Jonas, *NMR Basic Principles Progr.*, 1990, **24**, 85.
5. C. H. Langford and H. B. Gray, *Ligand Substitution Processes*, Benjamin, New York, 1965.
6. T. W. Swaddle, *Adv. Inorg. Bioinorg. Mechanisms*, 1983, **2**, 95.
7. H. Vanni, W. L. Earl, and A. E. Merbach, *J. Magn. Reson.*, 1978, **29**, 11.
8. W. L. Earl, H. Vanni, and A. E. Merbach, *J. Magn. Reson.*, 1978, **30**, 571.
9. U. Frey, L. Helm, and A. E. Merbach, *High Press. Res.*, 1990, **2**, 237.
10. A. E. Merbach, *Pure Appl. Chem.*, 1982, **54**, 1479.
11. C. Cossy, L. Helm, and A. E. Merbach, *Inorg. Chem.*, 1988, **27**, 1973.
12. C. Cossy, L. Helm, and A. E. Merbach, *Inorg. Chem.*, 1989, **28**, 2699.
13. D. H. Powell, A. E. Merbach, G. González, E. Brücher, K. Micskei, M. F. Ottaviani, K. Köhler, A. von Zelewsky, O. Ya. Grinberg, and Ya. S. Lebedev, *Helv. Chim. Acta*, 1993, **76**, 2129.
14. K. Micskei, D. H. Powell, L. Helm, E. Brücher, and A. E. Merbach, *Magn. Res. Chem.*, 1993, **31**, 1011.
15. U. Frey, L. Helm, and A. E. Merbach, *Helv. Chim. Acta*, 1990, **73**, 199.
16. K. Micskei, L. Helm, E. Brücher, and A. E. Merbach, *Inorg. Chem.*, 1993, **32**, 3844.
17. G. González, D. H. Powell, V. Tissières, and A. E. Merbach, *J. Phys. Chem.*, 1994, **98**, 53.
18. G. Laurenczy and A. E. Merbach, *J. Chem. Soc., Chem. Commun.*, 1993, 187.

Acknowledgments

We wish to thank the large number of people who have contributed over the years to the work performed at Lausanne, as well as all those groups elsewhere with whom we have had fruitful collaborations. We also wish to thank the Swiss National Science Foundation for continued and generous support of our work.

Biographical Sketches

D. Hugh Powell. *b* 1965. B.Sc., 1986, Ph.D., 1989, Physics (supervisors G. W. Neilson and J. E. Enderby), University of Bristol, UK. Research Associate at the Institute of Inorganic and Analytical Chemistry of the University of Lausanne, Switzerland (with A. E. Merbach),

1989–1994, lecturer at the Dept. of Chemistry, University of Adelaide, 1995–present. Approx. 25 publications. Current research interests: multinuclear magnetic resonance, ESR and neutron diffraction studies of dynamics and structure in solution particularly of lanthanide based MRI contrast agents and related complexes.

André E. Merbach. *b* 1940. Diploma in Chemical Engineering, 1962 (EPUL), Ph.D., 1964, Chemistry, University of Lausanne, Switzerland. Postdoctoral work at the University of California at Berkeley, USA (with O. Redlich), 1964–65. Institute of Inorganic and Analytical Chemistry of the University of Lausanne, 1965–present. Full Professor of Chemistry, 1973–present. Approx. 200 publications. Research specialties: high pressure NMR, high-pressure kinetics, inorganic reaction mechanisms, metal ion solvation, MRI contrast agents, coordination chemistry.

Ortho–Para Hydrogen at Low Temperature

Neil S. Sullivan

University of Florida, Gainesville, FL, USA

1	Introduction	1
2	Orientational Parameters and NMR Spectra	1
3	Phase Diagram of Solid *Ortho–Para* Hydrogen Mixtures	4
4	Molecular Dynamics and Low Energy Excitations	5
5	Related Articles	6
6	References	6

1 INTRODUCTION

The solid hydrogens (H_2 and D_2) are the simplest molecular solids that exist in Nature, and a detailed understanding of their many body properties is of special interest because the rotational degrees of freedom are those of quantum rotors and their behavior at low temperatures can be understood from considerations of first principles. The interaction Hamiltonians are well known and studies of the ordering of the molecular orientations have revealed interesting new regimes of collective phenomena. NMR has provided one of the most sensitive tools for probing the orientational degrees of freedom of the quantum rotors because of the intimate relationship between the constraints on the molecular nuclear spin wave function and the rotational (or orbital) degrees of freedom that results in the existence of distinct molecular species: the *ortho* and *para* modifications.

All the homonuclear isotopes of molecular hydrogen (H_2, D_2, and T_2) have distinct molecular species;[1] i.e. *ortho* and *para* modifications, resulting from the requirements of symmetry considerations that apply to the molecular wave function. For H_2 and T_2, the nuclei are fermions with nuclear spin $I = \frac{1}{2}$, and the requirement that the total molecular wave function be antisymmetric can be satisfied in two ways: (1) *ortho*-H_2 (or T_2) for which the nuclear spin wave function for the molecule is symmetric with total nuclear spin $I_T = 1$ and for which the molecular orbital angular wave function is antisymmetric with orbital angular momentum J odd ($J = 1, 3, 5, \ldots$); and (2) *para*-H_2 (or T_2) for which the nuclear spin wave function is antisymmetric ($I_T = 0$) with J even ($J = 0, 2, 4, \ldots$). For D_2, the nuclei are bosons with nuclear spin $I = 1$, and the requirement that the total molecular wave function be symmetric can also be satisfied in two distinct ways: (1) *para*-D_2 with total nuclear spin $I_T = 1$ and orbital angular momentum J odd; (2) *ortho*-D_2 with the nuclear spin wave function symmetric ($I_T = 0$ or 2) and with orbital angular momentum J even. Table 1 summarizes the symmetry properties of these different molecular species.

The aspect of the molecular species of the hydrogens that make them unique compared with other (heavier) homonuclear diatomic molecules (such as N_2) is that the separation of the rotational energy levels is very large compared with the anisotropic interactions between the molecules. The rotational kinetic energies are given by $E_J = B_J J(J + 1)$ with $B_J = \hbar^2/(2mr^2)$, where r is the intermolecular separation and $B_J = 85.6\,\mathrm{K}$ for H_2 (43.2 K for D_2), and the $J = 1$ and $J = 2$ rotational states are 171 K and 510 K above the $J = 0$ ground state, respectively, for H_2 (and 86 K and 257 K, respectively, for D_2). We therefore only need to consider the lowest rotational states $J = 1$ and $J = 0$ in the solid hydrogens. Furthermore, the anisotropic interactions between the molecules that can admix different J states are very weak ($V_{\mathrm{aniso}} \simeq 1\,\mathrm{K}$). J is therefore a good quantum number to first order and we may consider the $J = 1$ species (*ortho*-H_2 (or T_2) and *para*-D_2) as quantum rotors.

The conversion of $J = 1$ molecular species to the ground state ($J = 0$) is very slow because it is doubly forbidden; two symmetries need to be broken simultaneously, the symmetry of the nuclear wave function and that of the orbital wave function, in order to convert a $J = 1$ *ortho* molecule into a $J = 0$ molecule. In the pure solid this conversion is induced by the intermolecular magnetic interactions, and leads to a bimolecular rate constant of 1.9% per hour for H_2 (and 0.06% per hour for D_2). This rate is sufficiently slow that we may consider the *ortho* species as stable on the timescale of ordinary experiments. On the other hand, over a few weeks or months, the experimenter may explore a wide range of *ortho* concentrations continuously, simply by allowing a sample to age at constant low pressure. Alternatively, samples of essentially pure $J = 0$ species or pure $J = 1$ species can be prepared by special techniques, and solid mixtures of the full range of *ortho*/*para* concentrations studied by mixing the appropriate amounts of $J = 0$ species and $J = 1$ species in the gaseous state and solidifying the mixture. Pure $J = 0$ species are prepared by conversion on paramagnetic surfaces[2] (e.g. zeolites saturated with chromic oxide), and $J = 1$ species by selective adsorption on alumina.[3]

The behavior of the $J = 1$ quantum rotors (*ortho*-H_2 and *para*-D_2) can be studied directly by NMR.[4,5] The total nuclear spin of these molecules is $I_T = 1$ and the intramolecular interactions do not average to zero if the molecules have a preferred orientation in space. A fine structure is observed in the absorption spectrum and this can be used to determine the quantum mechanical order parameters. Furthermore, the nuclear spin–lattice (T_1) and nuclear spin–spin (T_2) relaxation times depend on the fluctuation spectrum of the molecular orientations, and measurements of T_1 and T_2 can be used to determine the fundamental rotational excitations of the molecular rotors.

2 ORIENTATIONAL PARAMETERS AND NMR SPECTRA

The $J = 1$ molecules are not spherically symmetric; they have end-on symmetry and hence no permanent electric dipole moment, but they do have a small axial electric quadrupole moment Q. There is therefore a weak electrostatic quadrupole–quadrupole (EQQ) interaction between the molecules that depends on their relative orientations.[6] At high temperatures the molecules are free to rotate, but at low temperatures the $J = 1$ molecules adopt mutual orientations to minimize their EQQ interactions. The EQQ interaction is short

Table 1 Molecular Species of Hydrogen Isotopes[a]

	ortho-H_2 (or T_2)	(*para*-D_2)	*para*-H_2 (or T_2)	(*ortho*-D_2)
Angular momentum[b]	Odd $J = 1$	(Odd) ($J = 1$)	Even $J = 0$	(Even) ($J = 0$)
Total nuclear spin	Even $I_T = 1$	(Odd) ($I_T = 1$)	Odd $I_T = 0$	(Even) ($I_T = 0$ and 2)

[a]The terminology *ortho–para* refers to the total nuclear spin symmetry. The full molecular wave function must be odd (even) for molecular H_2 and T_2 (D_2), respectively. The total nuclear spin wave function: $|I_T m_T\rangle = \sum_{m_1 m_2} C^{I_1 I_2 I_T}_{m_1 m_2 m_T} |I_1 m_1\rangle\ |I_2 m_2\rangle$ where the $C^{I_1 I_2 I_T}_{m_1 m_2 m_T}$ are the Clebsch–Gordan coefficients, e.g. for *para*-H_2,$|\mathrm{OO}\rangle = 2^{-\frac{1}{2}}\{|\frac{1}{2}, \frac{1}{2}\rangle\ |\frac{1}{2}, -\frac{1}{2}\rangle - |\frac{1}{2}, -\frac{1}{2}\rangle\ |\frac{1}{2}, \frac{1}{2}\rangle\}$.
[b]Higher J states need not be considered for normal densities at low temperatures.

range and only nearest neighbor interactions need be considered. For an isolated pair the minimum energy configuration is a 'T' orientation (Figure 1) with the quadrupoles mutually perpendicular.

For a simple two-dimensional square lattice, a simple antiferro-orientational array is the minimum energy configuration [Figure 2(a)] and this is stable with respect to substitution by a spherical ($J = 0$) molecule. For other lattices, however, the molecules cannot all be oriented so that each neighboring pair is in the 'T' configuration. This is illustrated in Figure 2(b) for a triangular lattice for which the lowest total energy configuration is a herring-bone arrangement. This arrangement is not stable with respect to substitution by 'inert' $J = 0$ molecules. This topological incompatibility between the configuration of the lowest energy pair and the geometry of the crystal lattice structure is a particularly striking example of the phenomenon of 'frustration' that is a key feature of the spin glasses and many other glass formers. The effect of substitutional disorder on frustrated systems can be studied in depth using *ortho–para* mixtures because the substitution is close to ideal (a $J = 1$ molecular species being replaced by a $J = 0$ species, with no other change) and the order parameters and the molecular dynamics can be determined directly from NMR studies.

The distinction between the ordering in the familiar magnetic systems and the diatomic molecular systems is that for the former one needs in most cases to consider only the dipole moments $\langle S_x\rangle_k$, $\langle S_y\rangle_k$, and $\langle S_z\rangle_k$ of a spin S at lattice site k, whereas for the $J = 1$ rotors we need in general to specify the quadrupole moments $\langle J_\epsilon J_\phi\rangle_k$ as well as the vectorial moments $\langle J_\epsilon\rangle_k$. Only five of the quadrupole moments are independent variables; ϵ and ϕ represent one of the Cartesian components (x,y,z) of a local reference frame.

In the absence of any interactions that break time-reversal symmetry, the orbital angular momentum is quenched, i.e. the $\langle J_\epsilon\rangle_k$ vanish for all ϵ. Five parameters are needed to describe fully the rotational degrees of freedom, and the natural choice is to select as local reference axes (x, y, z) the principal axes

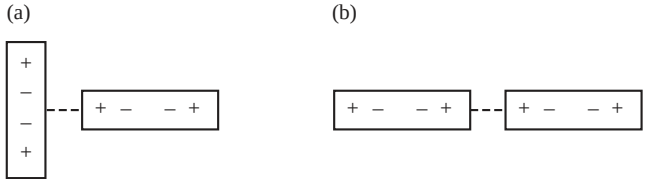

Figure 1 Configurations of a pair of interacting axial quadrupoles for (a) minimum, and (b) maximum energy

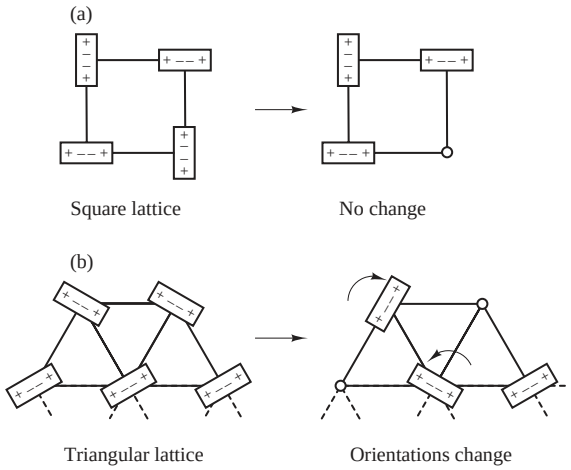

Figure 2 Schematic representation of the effect of substitutional disorder on quadrupolar arrays for (a) nonfrustrated, and (b) frustrated configurations

of the quadrupolar tensor with elements:

$$q_{\epsilon\phi} = \langle \tfrac{1}{2} J^2 \delta_{\epsilon\phi} - \tfrac{3}{4}(J_\epsilon J_\phi + J_\phi J_\epsilon)\rangle \tag{1}$$

In the local principal axes frame, the off-diagonal elements, $q_{xy} = q_{yz} = \ldots = q_{zx} = 0$, and the only intrinsic quadrupolar order parameters are: (1) the *alignment*

$$\sigma_k = Q_{zz} = \langle 1 - \tfrac{3}{2} J_z^2\rangle_k \tag{2}$$

and (2) the *eccentricity*

$$\eta_k = \langle J_x^2 - J_y^2\rangle_k \tag{3}$$

The five order parameters are the three local reference axes (specifying the direction of the molecular orientation), and the two quadrupolar order parameters σ and η (which describe the degree of alignment along those axes).

The strong positivity conditions on the single particle density matrix (i.e. that the eigenvalues be positive definite) limit the allowed values of σ and η to the bounds defined by

$$\tfrac{1}{3} + \tfrac{2}{3}\sigma \geq 0; \quad \tfrac{1}{3} - \tfrac{1}{3}\sigma \pm \tfrac{1}{2}\eta > 0 \tag{4}$$

Not all the allowed pairs (σ,η) in this range are physically distinguishable, however, since we are free to relabel the axes,

and by convention we choose axes such that $\sigma \geq \frac{1}{2}\eta > 0$. There are two single particle 'pure' states: ($\sigma = 1$, $\eta = 0$), corresponding to a ground state $|J_z = 0\rangle$ and ($\sigma = \frac{1}{2}$, $\eta = \pm 1$), corresponding to the ground state $|J_z = \pm 1\rangle$. States intermediate between these 'pure' states can be realized in the many-particle system; this feature was first observed in NMR studies of *ortho–para* hydrogen mixtures.[4,7]

The ability to study the orientational order parameters by NMR arises from the fact that the intramolecular nuclear dipole–dipole interaction $\hat{\mathcal{H}}_{\mathrm{DD}}$ between the two nuclei of a given molecule depends directly on the order parameters. This can be seen by expressing $\hat{\mathcal{H}}_{\mathrm{DD}}$ in terms of products of irreducible tensorial operators $\hat{T}_{LM}$ in the manifold $J = 1$ with the corresponding nuclear spin operators $\hat{N}_{LM}$ in the manifold $I = 1$:

$$\hat{\mathcal{H}}_{\mathrm{DD}} = \hbar D \sum_{M} \hat{T}_{LM} \hat{N}^{\dagger}_{2M} \tag{5}$$

The $\hat{T}_{LM}$ and $\hat{N}_{LM}$ transform in the same manner as the spherical harmonics Y_{LM} and are given in Table 2, with $D = 173.06\,\mathrm{kHz}$ for H_2 (2.74 kHz for D_2). [For D_2 there is an additional intramolecular term arising from the interaction of the nuclear electric quadrupole moment with the local electric field gradient. This interaction Hamiltonian transforms identically to the form given by equation (5) but with D replaced by $D_{\mathrm{Q}} = 22.50\,\mathrm{kHz}$.]

The dipolar interaction term given by equation (5) results in a small perturbation of the nuclear Zeeman energy levels. For high magnetic fields $\boldsymbol{B}_0$ lies along the z axis, and the nuclear Zeeman interaction

$$\hat{\mathcal{H}}_{\mathrm{Z}} = \gamma \hbar \hat{\boldsymbol{I}} \cdot \boldsymbol{B}_0 \tag{6}$$

results in three equally spaced Zeeman levels for $I_z = 1$, 0, -1 (Figure 3) with energy spacings $\Delta E_{10} = \Delta E_{-10} = \hbar\omega_{\mathrm{L}}$, where ω_{L} is the nuclear Larmor frequency. If $\hat{\mathcal{H}}_{\mathrm{DD}}$ is motionally averaged to zero (corresponding to isotropic molecular reorientation on a timescale that is short compared to D^{-1}), only a single NMR absorption line is observed at the Larmor frequency. If the molecule has a preferred orientation, $\hat{\mathcal{H}}_{\mathrm{DD}}$ does not average to zero and the transitions ΔE_{10} and ΔE_{-10} are no longer equal. $\hat{\mathcal{H}}_{\mathrm{DD}}$ is treated as a perturbation of

Table 2 Irreducible Angular Momentum Operators $\hat{T}_{LM}$ (in manifold $J = 1$) and Nuclear Spin Operators $\hat{N}_{LM}$ (in the manifold $I = 1$)[a]

	Tensorial operator, $\hat{T}_{LM}$	Tensorial operator, $\hat{N}_{LM}$
$L = 1$		
	$\hat{T}_{1,0} = 2^{-\frac{1}{2}}\hat{J}_z$	$\hat{N}_{1,0} = 2^{-\frac{1}{2}}\hat{I}_z$
	$\hat{T}_{1,\pm1} = \mp\frac{1}{2}(\hat{J}_x \pm \mathrm{i}\hat{J}_y)$	$\hat{N}_{1,\pm1} = \mp\frac{1}{2}(\hat{I}_x \pm \mathrm{i}\hat{I}_y)$
$L = 2$		
	$\hat{T}_{2,0} = 6^{-\frac{1}{2}}(3\hat{J}_z^2 - \hat{J}^2)$	$\hat{N}_{2,0} = 6^{-\frac{1}{2}}(3\hat{I}_z^2 - \hat{I}^2)$
	$\hat{T}_{2,\pm1} = \mp\frac{1}{2}(\hat{J}_\pm\hat{J}_z + \hat{J}_z\hat{J}_\pm)$	$\hat{N}_{2,\pm1} = \mp\frac{1}{2}(\hat{I}_\pm\hat{I}_z + \hat{I}_z\hat{I}_\pm)$
	$\hat{T}_{2,\pm2} = \frac{1}{2}(\hat{J}_\pm)^2$	$\hat{N}_{2,\pm2} = \frac{1}{2}(\hat{I}_\pm)^2$

[a] $\hat{T}_{LM} = (-)^M \hat{T}^{+}_{L,-M}$ and $\mathrm{Tr}(\hat{T}_{LM}\hat{T}^{+}_{L'M'}) = \delta_{LL'}\delta'_{MM}$; and similarly for the $\hat{N}_{LM}$.

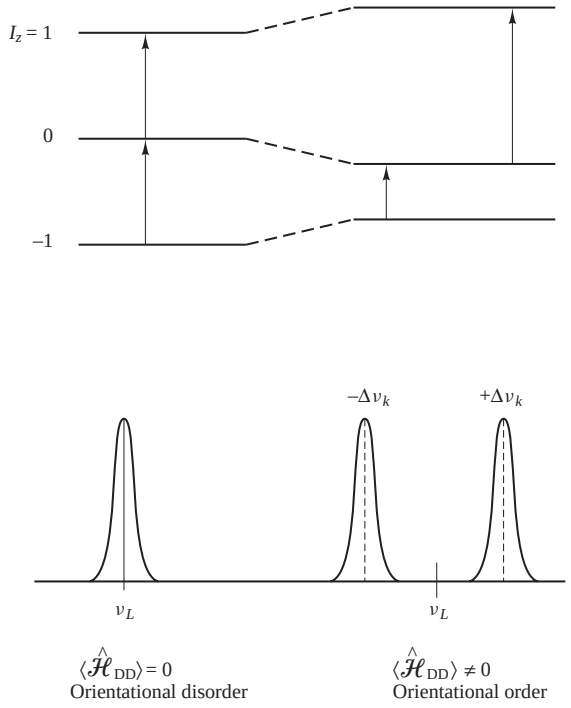

Figure 3 Splitting of the NMR absorption line at ν_L into a doublet with $|\Delta\nu_k| = D\langle 1 - \frac{3}{2}J_z^2\rangle_k$ for each molecule that is orientationally ordered

$\hat{\mathcal{H}}_z$ and each molecule now contributes a doublet to the NMR spectrum with components at frequencies

$$\Delta\nu_k = \mp D\langle 1 - \tfrac{3}{2}J_z^2\rangle_k \tag{7}$$

on either side of the Larmor frequency. Here, the brackets $\langle\ \rangle$ indicate averaging over all crystallite orientations with respect to the static field $\boldsymbol{B}$.

The average $\langle 1 - \frac{3}{2}J_z^2\rangle_k$ is valid for a timescale that is long compared with D^{-1}, and the expectation value is evaluated with respect to the magnetic field axis and not the local symmetry axis with respect to which the local molecular order parameters are defined. Transforming to the local molecular frame, we find that

$$\Delta\nu_k = \mp D[-\sigma_k P_2(\cos\alpha_k) + \tfrac{3}{4}\nu_k \sin 2\alpha_k \cos 2\beta_k] \tag{8}$$

where (α_k, β_k) are the polar angles defining the orientation of the applied magnetic field with respect to the local molecular axes. The analysis of the spectra has been carried out assuming local axial symmetry $\eta = 0$ for the molecular ordering, and while no inconsistency has been demonstrated for this assumption, it has not been established rigorously.

The majority of NMR experiments are carried out using powder samples, and the lineshapes calculated for a powder distribution with a fixed value of σ at each site yields the familiar Pake doublet lineshape (Figure 4). The intensities $I_{\pm1,0}$ for the transitions ΔE_{10} and ΔE_{-10} are given by

$$I_{\pm1,0}(\Delta\nu, \sigma) = \left[2\sqrt{3}D\sigma\left(1 \mp \frac{2\Delta\nu}{D\sigma}\right)^{1/2}\right]^{-1} \tag{9}$$

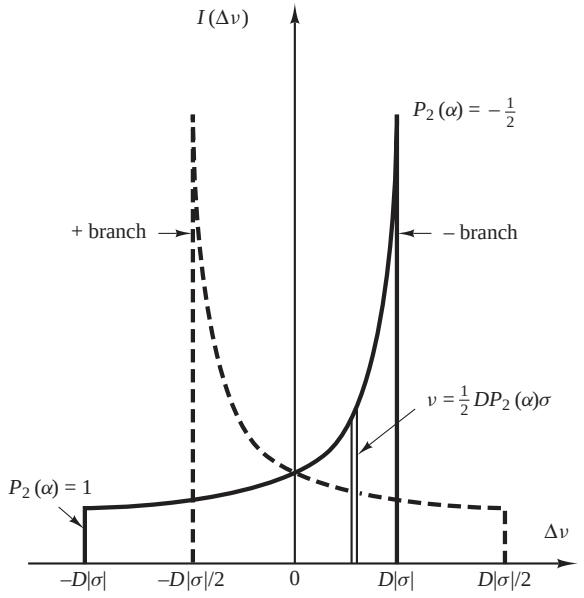

Figure 4 Pake doublet NMR absorption spectrum for the fixed value of molecular order parameter σ

The cusp singularities at $\Delta\nu = \mp \frac{1}{2}D\sigma$ correspond to molecules with $\alpha = \pi/2$, i.e. those molecules aligned in a plane normal to the applied magnetic field. The separation of the cusps provides a direct measure of the local molecular order parameters, and is thus used to study the collective ordering of the molecules as a function of temperature.

3 PHASE DIAGRAM OF SOLID *ORTHO–PARA* HYDROGEN MIXTURES

If the concentration of quadrupolar species ($J = 1$ molecules) is sufficiently high (>55% for H_2 and >59% for D_2), a long range periodic ordering of the molecular orientations is observed. At low temperatures the molecular alignments are ordered in a four-sublattice Pa_3 configuration on a fcc lattice (Figure 5), with the molecules aligned parallel to one of the four body diagonals in each sublattice. The local order parameters have the values $\sigma = 1$ at each site (when evaluated with respect to the local principal orientation axis in each sublattice). The transition to the ordered phase is first order (with a jump in the value of σ at the transition), and the transition triggers a lattice change from a hcp structure (the high-temperature phase) to a fcc lattice. Subsequent small thermal cycles above and below the transition temperature stabilize the cubic lattice, and one can observe the purely orientational order–disorder transitions on the fcc lattice. As the $J = 1$ concentration is lowered, the transition temperature is reduced, and the phase diagram calculated from first principles is in good qualitative agreement with experimental observations, but the theoretical values are consistently higher than the observed values by about 17%.[8,9]

Below the critical concentration of $J = 1$ species (approximately 55% for H_2 and 59% for D_2), the long-range periodic ordering is lost. At low concentrations a new quadrupolar glass structure is observed. Experimental observations (NMR studies and heat capacity measurements) all indicate that the molecules

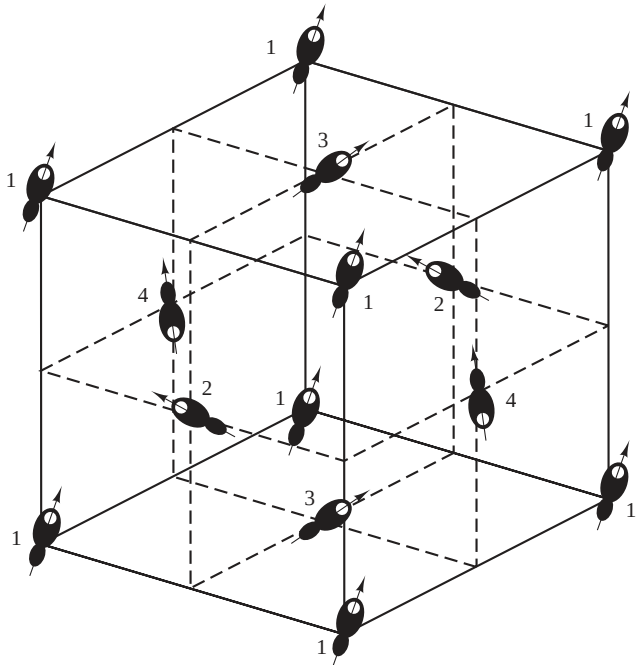

Figure 5 Pa_3 structure for molecular alignments in the fcc lattice

become frozen in a random configuration, with both the local molecular symmetry axes and the local alignments (the values of σ_k at each site) varying at random throughout the crystal. The tensorial order varies randomly from site to site in the glass state, as illustrated in Figure 6. The NMR spectra provide the strongest evidence for a glass phase from the appearance of a broad bell-shaped absorption line (Figure 7) rather than the Pake doublet lineshape which characterizes the periodic ordering.

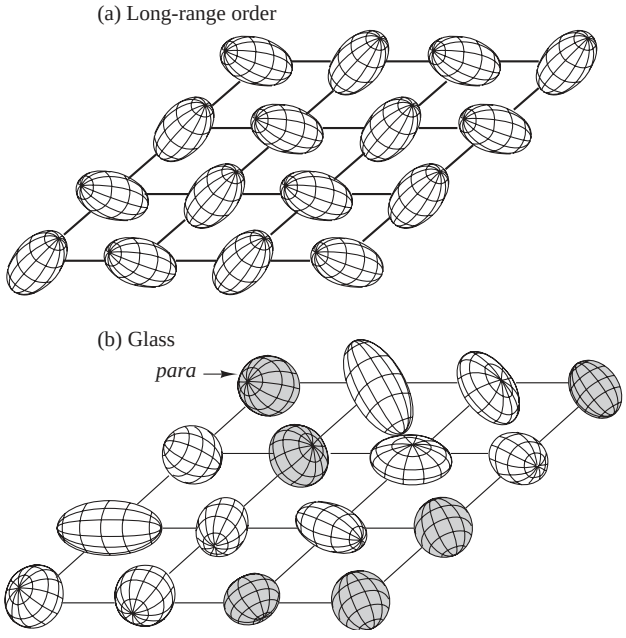

Figure 6 Schematic representation of molecular ordering for (a) a planar section of the Pa_3 structure, and (b) the quadrupolar glass phase

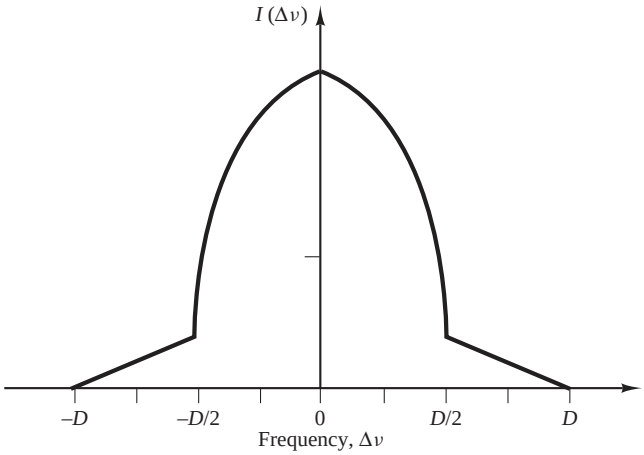

Figure 7 Bell-shaped NMR absorption line in the quadrupolar glass phase calculated for a linear distribution of order parameters

The loss of periodic order in the dilute *ortho–para* mixtures is attributed to the introduction of disorder in a highly frustrated system. The combined effects of frustration and disorder are believed to be universal features of magnetic spin glasses, and the quantum rotor glasses provide a particularly interesting example for probing the properties of these systems. The interactions are short range and well understood, the introduction of the disorder is especially clean, and the local order parameters and molecular dynamics can be studied directly by NMR.

The transitions from the high-temperature phase to the glass state are not abrupt. The molecular rotational fluctuations have been determined from measurements of the nuclear spin–lattice relaxation rates,[10–12] showing that the characteristic molecular fluctuation rates increase continuously but rapidly over a relatively small temperature range (Figure 8).

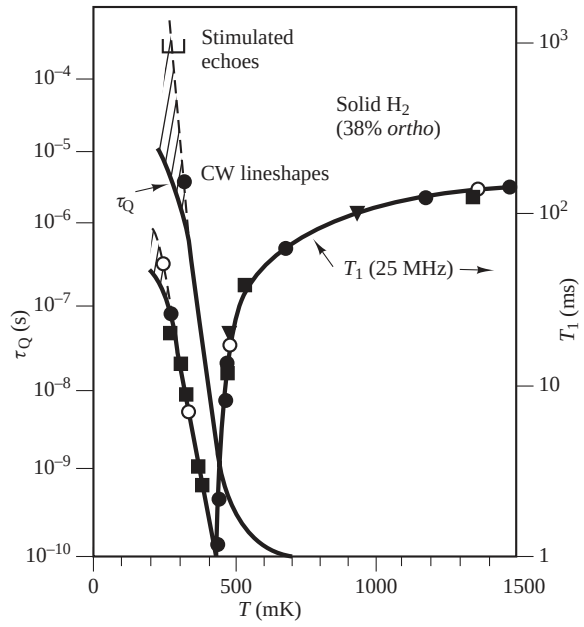

Figure 8 Temperature dependence of the nuclear spin–lattice relaxation times T_1 in the glass phase. τ_Q are the characteristic molecular reorientational times deduced from T_1

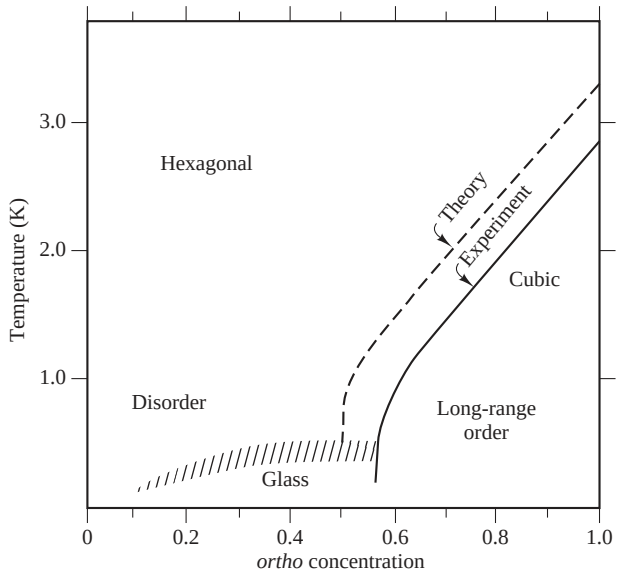

Figure 9 Phase diagram for orientationally ordered phases of solid hydrogen

The phase diagram for *ortho–para* H_2 mixtures deduced from NMR studies is shown in Figure 9. The solid and broken lines indicate first-order transitions to the periodic antiferro-orientational Pa_3 structure, and the hatched region corresponds to the continuous transition to the glass state. The behavior of the molecular orientations at very low temperatures below the percolation concentration (15%) has not been explored in detail. At very low $J = 1$ concentrations, indirect anisotropic long-range interactions are expected to dominate, and could lead to new behaviors.

4 MOLECULAR DYNAMICS AND LOW ENERGY EXCITATIONS

The molecular dynamics in the quadrupolar glass phase have been studied at low temperatures using stimulated echo techniques.[13–15] A preparatory two pulse sequence is used to store both nuclear polarizations $\langle I_z \rangle$ and nuclear spin alignments $\langle I_z^2 \rangle$ in a given initial state. After a waiting period, a third pulse is used to determine the changes in the molecular orientations during the waiting time. The intramolecular nuclear spin–spin interactions $\hat{\mathcal{H}}_{DD}$ determine the evolution during the waiting period, and because $\hat{\mathcal{H}}_{DD}$ depends directly on the order parameters σ_k, slowly varying changes in the molecular orientations can be detected using this method.

A logarithmic decay is observed for the stimulated echoes over a wide range of conditions, and this decay has been analyzed quantitatively in terms of a spectrum of low energy excitations corresponding to reorientations of clusters of molecules in the glass state. The spectrum of excitations deduced from the NMR measurements has been used to analyze the temperature dependence of the heat capacities determined from independent thermodynamic measurements.[16,17] An excellent fit to the thermodynamic data was obtained without any adjustable parameters, providing one of the most convincing demonstrations of the fundamental

nature of the glass state: a freezing of the molecular alignments in local short-range ordered clusters with a broad spectrum of collective excitations corresponding to molecular reorientations in the clusters.

The systematic NMR studies of solid *ortho*/*para* mixtures of hydrogen and deuterium have established the existence of a new quadrupolar glass state for dilute samples of quantum rotors. The local order parameters are tensorial rather than vectorial as in the conventional orientational glass and spin glass systems. The *ortho*/*para* mixtures have served as a test case for the study of glass formers in general because the interactions are well understood and the order parameters can be studied directly using NMR. Further studies on two-dimensional films and monolayers will provide new information about the effect of dimensionality on highly frustrated systems, and could reveal new collective behaviors for two-dimensional assemblies of quantum rotors at low temperatures.

5 RELATED ARTICLES

Amorphous Materials; Deuterium NMR in Solids; Hydrogen Molecules.

6 REFERENCES

1. A. Farkas, *Orthohydrogen, Parahydrogen and Heavy Hydrogen*, Cambridge University, Cambridge, 1935.
2. N. S. Sullivan, D. Zhou, and C. M. Edwards, *Cryogenics*, 1990, **30**, 734.
3. N. S. Sullivan, C. M. Edwards, M. Rall, and D. Zhou, *Cryogenics*, 1993, **33**, 1008.
4. A. B. Harris and H. Meyer, *Can. J. Phys.*, 1985, **63**, 3.
5. N. S. Sullivan, C. M. Edwards, Y. Lin, and D. Zhou, *Can. J. Phys.*, 1987, **65**, 1463.
6. A. B. Harris, *Phys. Rev. B*, 1970, **1**, 1881.
7. N. S. Sullivan, M. Devoret, B. P. Cowan, and C. Urbina, *Phys. Rev. B*, 1978, **17**, 5016.
8. J. C. Raich, *Phys. Rev.*, 1968, **168**, 425.
9. N. S. Sullivan, *J. Phys. Paris*, 1976, **37**, 981.
10. S. Washburn, M. Calkins, H. Meyer, and A. B. Harris, *J. Low Temp. Phys.*, 1982, **49**, 101.
11. W. T. Cochran, J. R. Gaines, R. P. McCall, P. E. Sokol, and B. R. Patton, *Phys. Rev. Lett.*, 1980, **45**, 1576.
12. N. S. Sullivan and D. Esteve, *Physica B*, 1981, **107**, 189.
13. I. Yu, S. Washburn, M. Calkins, and H. Meyer, *J. Low Temp. Phys.*, 1983, **51**, 401.
14. N. S. Sullivan, D. Esteve, and M. Devoret, *J. Phys. C*, 1982, **15**, 4895.
15. Y. Lin and N. S. Sullivan, *J. Magn. Reson.*, 1990, **86**, 319.
16. D. G. Haase, L. R. Perrell, and A. M. Saleh, *J. Low Temp. Phys.*, 1984, **55**, 283.
17. J. F. Jarvis, H. Meyer, and D. Ramm, *Phys. Rev.*, 1969, **178**, 1461.

Biographical Sketch

Neil Sullivan *b* 1942. B.Sc., 1964, M.Sc., 1965, Otago, New Zealand; Ph.D., 1972, Harvard, USA. Introduced to NMR by R. V. Pound. Staff physicist, C. E. N.-Saclay, 1972–82; Faculty in Physics, University of Florida, 1982–present; Chair Physics, University of Florida 1989–present. Approx. 180 publications. Research interests: NMR studies of quantum solids, ultralow temperature techniques, ultrahigh magnetic fields (coprincipal investigator at National High Magnetic Field Laboratory).

Supercritical Fluids

Craig M. V. Taylor and Gunilla B. Jacobson

Los Alamos National Laboratory, Los Alamos, NM, USA

1 Introduction to Supercritical Fluids 1
2 Supercritical Fluids 1
3 Instrument Requirements for High-Pressure NMR 7
4 Supercritical Fluid Applications 8
5 References 9

1 INTRODUCTION TO SUPERCRITICAL FLUIDS

While the existence of the supercritical 'phase' has been known for over 150 years it has been only in the last 20 years that the value of supercritical fluids (SCFs) as a medium for extraction, cleaning and synthesis has been recognized. It is now clear that SCF processes are often constrained to very narrow regions of economic feasibility due to the phase behavior of the solute-solvent system. As a result, there needs to be very tight controls over any industrial process employing SCFs. If the process parameters must be more exact, then so does the information required to generate the design parameters, which includes experimental measurements, theories, and the correlations that result in predictability in a given system. In an effort to expand the current understanding of SCFs and their applications, intensive studies are ongoing using nuclear magnetic resonance (NMR). In an effort to further explain the physical chemistry inherent to possible applications of SCFs, a brief introduction is given to this odd and often ignored 'phase' of substances. Following that is an introduction to NMR as it pertains to the study of SCF applications.

2 SUPERCRITICAL FLUIDS

2.1 General Properties

The supercritical state is defined by the critical pressure (P_c) and critical temperature (T_c). One of the most common phenomenological definitions describes critical pressure as the pressure above which, regardless of the applied temperature, a liquid cannot be made to boil. In a similar way, the critical temperature can be thought of as the temperature above which, regardless of the applied pressure, a gas cannot be converted into a liquid. Hence, above the critical point there is no longer a phase boundary between the liquid and the vapor. A liquid/vapor phase boundary represents a coexistence line so that material crossing it requires the expenditure of the latent heat of vaporization.

The concept of the supercritical state can be illustrated by a physical example. Consider a closed container of constant volume. Inside the container we start with some amount of pure liquid. The space above this pure liquid will be filled with pure vapor at the liquid's equilibrium vapor pressure. Now assume that we begin to heat up this container slowly and uniformly. The density of the liquid will begin to decrease through normal thermal expansion. Meanwhile, the density of the vapor phase begins to increase since more molecules are leaving the liquid to enter the vapor phase. Continued heating results in a further decrease of the liquid density and an increase in the vapor density. Eventually, at some temperature, T_c (and resulting, uniform pressure, P_c), the density of the liquid and vapor phases reach the same value, and the vapor and liquid 'phases' have identical compositions and identical densities.

Is this supercritical fluid phase to be considered a liquid or a gas? The answer is that a supercritical fluid reflects properties of both. Table 1 shows relative values of the density, diffusion coefficient, and viscosity for a typical liquid, gas, and supercritical fluid. These values indicate the mass transport properties (i.e., diffusivity) are similar to a gas, while the mechanical properties (viscosity and density) are similar to those of a liquid. This unique combination of properties makes supercritical fluids attractive for use as solvents. The high diffusivity and low viscosity allows the fluid to penetrate easily into matrices which are in the form of loose powders, compacted powders, or even fully cemented pre-forms. Further, the ability of a solvent to dissolve other liquids is, to a first approximation, related to the density of the solvent. The relatively high density of supercritical fluids, relative to gases, increases the useful levels of solubility that may be attained.

2.2 Supercritical CO_2

As a result of the law of corresponding states the physical properties of supercritical CO_2 apply to all fluids in the supercritical state. The critical values of temperature and pressure are unique for each gas/liquid and are determined by the type of intermolecular interactions occurring between

Table 1 Comparison of physico-chemical properties of a typical organic fluid in the liquid, gas, and supercritical fluid state

	Liquid	Supercritical fluid	Gas
Density ($g\,cm^{-3}$)	1	0.1–1	10^{-3}
Viscosity (Pa·s)	10^{-3}	10^{-4}–10^{-5}	10^{-5}
Diffusivity ($cm^2\,s^{-1}$)	10^{-5}	10^{-3}	10^{-1}

Table 2 Critical temperature, T_c, and Pressure, P_c, for some common fluids

Fluid	T_c (°C)	P_c (psi)
Neon, Ne	−229	400
Nitrogen, N_2	−147	492
Argon, Ar	−122	706
Xenon, Xe	17	858
Carbon dioxide, CO_2	31	1072
Sulfur hexafluoride, SF_6	46	545
Propane, C_3H_8	97	617
Ammonia, NH_3	133	1654
Water, H_2O	374	3209

the individual molecules. Table 2 gives the critical temperature and pressure of some common fluids. For example, the critical temperature and pressure required to transform water (H_2O) into a supercritical fluid are 374 °C and 218 atmospheres. These values are much higher than those for CO_2 because the water molecules exert an attractive force on each other, making the solid and liquid phases particularly stable. CO_2 molecules, on the other hand, have much weaker intermolecular attractive forces. It is important to note that, in the SCF region, attractive forces between molecules are minimized.

In the solid form CO_2 has a high density and a very high viscosity. Similarly, the liquid has a high density and a reasonably high viscosity, and the gas has a low density and low viscosity. Conversely, the supercritical fluid phase has a high density but a relatively low viscosity. The density of supercritical CO_2 can vary over a wide range from gas values, around 0.1 g cm^{-3}, to liquid values of about 2.0 g cm^{-3}. In other words, the density of supercritical CO_2 can be changed by over 2000% simply by varying the temperature and pressure within the supercritical region. A supercritical fluid is by definition both liquid and gas-like, and hence it is compressible. Thus, relatively small changes in temperature and/or pressure can significantly affect the density, as seen in Figure 1.

As the density of the CO_2 becomes more liquid-like, so do the solvent properties of the fluid. To a first approximation, the ability of a supercritical fluid to dissolve other fluids can be related to its density in the supercritical region. When operating in the supercritical region, therefore, both temperature and pressure can be used to vary the density, and therefore, the dissolving power of the fluid. It is this ability to alter the solvent power that makes supercritical CO_2 such an attractive solvent. To make the potential for SCFs even more promising, small additions of other components, called co-solvents or entrainers, often modify the observed phase equilibria dramatically. Again this special property affords the chemist the opportunity to *tailor* solvents to achieve a variety of goals, either in separations or reactions.

The viscosity of carbon dioxide is observed to change rapidly in the critical region, as is the case also for diffusivity. Even at high pressures of 300–400 atm it is still only about 0.09 centipoise, an order of magnitude below typical organic solvents. Because of these density and viscosity properties, supercritical CO_2 possesses certain other characteristics, which enhance its attractiveness as a solvent. In addition to possessing liquid-like densities over much of the temperature and pressure range of interest to industry, it exhibits the gas-like property of diffusivity with a zero value for the surface tension. These features alter the transport to allow for easy penetration of SCFs into nano-dimensional spaces.

The self-diffusion coefficient for carbon dioxide (which is approximately the same for similar sized molecules diffusing through carbon dioxide) is about one to two orders of magnitude higher than the diffusivities of comparable solutes in typical organic liquids.

2.3 NMR of Supercritical Fluids

The interactions of a nuclear moment with other nuclei and the electrons surrounding it provide a very sensitive site specific probe into the structure and dynamics in the solid, liquid, and gas phase. This work will concern itself with NMR in the supercritical fluid state of carbon dioxide. As mentioned above, these states exhibit properties of both the liquid and the gas phases. Thus, techniques and theory from work in both phases combine in these unique applications. Thorough reviews have been published on the unique information which can be obtained in the gas phase.[1,2] Other reviews have been published on experimental techniques and applications of high pressure NMR.[3,4] These reviews were published on or before

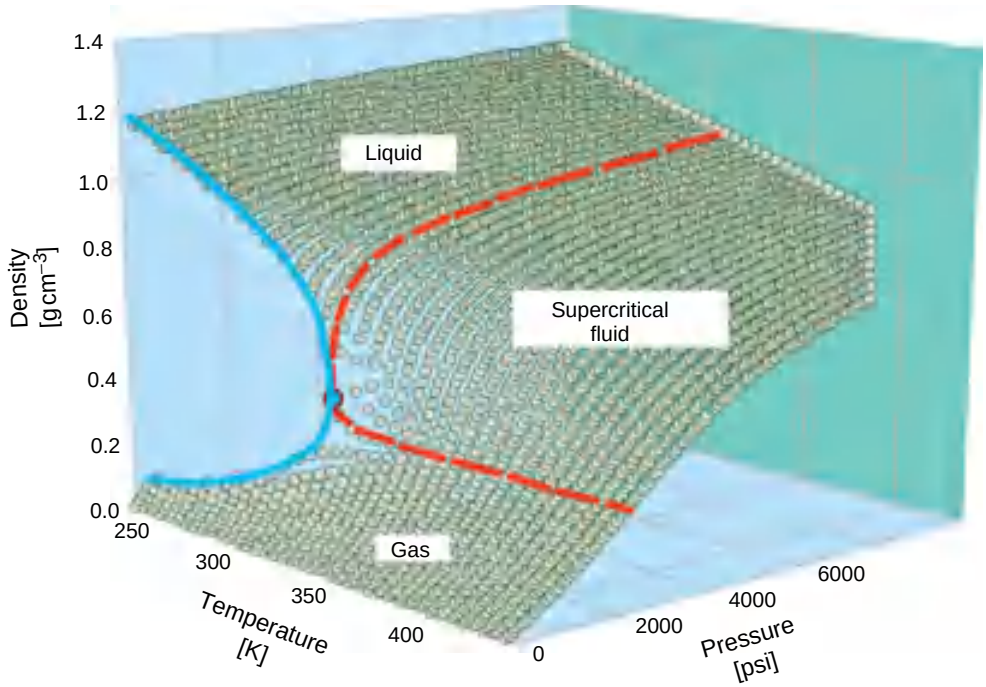

Figure 1 Pressure–temperature–density surface of pure CO_2

1991. We will discuss primarily studies published later, with information as it relates specifically to NMR determination of the dynamics and structure in the SCF state.

Although the application of high pressure NMR to simple fluids leads to some interesting additional complications, the information gained from the technique more than justifies its use. The pressure axis provides an additional dimension to the experimental matrix. For a liquid it is commonly known that temperature changes at constant pressure will effect the molecular motion via kinetic energy and molecular average volume collisional arguments. One can separate the effects of density and temperature on the molecular motion only if both the temperature and pressure are controlled variables in the NMR experiment. Increased pressure also allows for the experimental range to expand well above the normal boiling point and into the compressible supercritical fluid regime. Some examples of the usefulness of high pressure NMR will be given.

2.4 Introduction to the Basics of High-pressure NMR

The motions of molecules in liquids is accessible only through a large number of various models that depend upon phenomenological parameters such as the coefficient of rotational diffusion, the frequency of collisions, the time between jumps, etc. Three such theories: the random walk theory of Torrey,[5] the rotational diffusion theory of Abragam,[6] and the rotational Brownian motion of McConnell[7] form the basis upon which most NMR relaxation models in liquids are based. Other methods of studying molecular motion (optical, dielectric, neutron scattering, etc.) can in principal give additional detailed information. However, as a consequence of the many-particle effects present in these methods, the interpretation of the experimental results for liquids is often ambiguous. In NMR, the weak coupling of the spin system with the lattice allows one to focus better on isolated molecular motions to describe relaxation in liquids.[8] Information on the rotational motion of molecules in liquids of low viscosity, given by NMR, is obtained in the form of the integrals of the time correlation functions, i.e., the correlation times. This section will discuss the effects of dense gas and supercritical fluid states on the correlation times, and what this means to the NMR spectroscopist.

2.5 The Origin of Nuclear Spin Relaxation

Direct time dependant interactions have been shown to cause spin relaxation. However any static interaction can simply be treated as part of the normal spin Hamiltonian, altering the positions and intensities of the spectral lines. For example, a nuclear spin may experience a local magnetic field from the spins of other nuclei moving in its vicinity, from an unpaired electron, or from a variety of other mechanisms, such as the spin–rotation interaction in which the rotation of the molecular electrons generates a magnetic field at the nucleus. In general, rotational and diffusional motions are important sources of relaxation in fluids. Some mechanisms that make contributions to spin–lattice relaxation will be discussed.

2.5.1 Nuclear Spin Relaxation Mechanisms

There are a number of processes that provide the basis for nuclear spin relaxation. These include the nuclear magnetic dipole–dipole interactions (DD), the spin–rotation interactions (SR), the quadrupolar interactions (Q), and the chemical shift interactions, (CSA). The overall relaxation rate can be expressed as a sum of contributions from each mechanism.

2.5.2 Dipole–Dipole Interaction

The magnetic nuclei in molecules provide magnetic dipole fields that are proportional to the magnetic moments of the nuclei. These fields fluctuate in magnitude and direction as the molecule tumbles through space. When these random oscillating fields have magnetic field components at the Larmour frequency, the nuclear spin relaxes. This interaction depends upon the correlation time of the tumbling molecule as well as the distance between the interacting nuclei. The dipole interactions can be divided into intramolecular and intermolecular interactions. For both of these types of interactions there is a homo, and hetero-nuclear sub-interaction. These are reflected in the following equations

$$\text{For intra-homo:} \quad \frac{1}{T_1^{\mathrm{DD}}} = \frac{3\gamma_A^4\hbar^2\tau_c}{2r^6}$$

$$\text{For intra-hetero:} \quad \frac{1}{T_1^{\mathrm{DD}}} = \frac{\gamma_A^2\gamma_X^2\hbar^2\tau_c}{r^6} \tag{1}$$

$$\text{For inter-hetero:} \quad \frac{1}{T_1^{\mathrm{DD}}} = \frac{2N_x\gamma_A^2\gamma_X^2\hbar^2}{Da}$$

where r is the distance between the interacting nuclei, D is a mutual translational self-diffusion coefficient for the molecules containing A and X, and a is the distance of closest approach between A and X. τ_c is a rotational diffusion correlation time for molecular tumbling. This corresponds to the average time it takes for a molecule to rotate through one radian.

2.5.3 The Spin–Rotation (SR) Interaction

Spin–rotation relaxation of the nuclear magnetization in molecules is due to the intramolecular coupling of the individual nuclear spins to the molecular angular momentum. A fluctuating local magnetic field, which relaxes the nuclear spins, is the result of the collisional reorientation of the molecular rotational angular momentum. For linear molecules such as CO_2, the spin–rotation contribution to the total spin–lattice relaxation can be expressed as

$$\frac{1}{T_1^{\mathrm{SR}}} = \frac{4C_\perp^2 IkT\tau_j}{3\hbar^2} \tag{2}$$

$C_\perp$ is the spin–rotation constant and I is the moment of inertia. For a spherical top molecule, the relaxation rate has the form

$$\frac{1}{T_1^{\mathrm{SR}}} = \frac{2C_{\mathrm{eff}}^2 IkT\tau_j}{\hbar^2} \tag{3}$$

C_{eff} is the effective spin–rotation tensor. The τ_j is the correlation time for angular momentum transfer and therefore is closely related to the average time between collisions. The higher the temperature the faster the molecule reorients in accordance with the kT term. The result is that the spin–rotation contribution to the total spin–lattice relaxation

increases with temperature. This is quite the opposite in all other mechanisms examined in this work.

2.5.4 Quadrupolar Relaxation

Quadrupolar occurs when the nuclear electric quadrupole moment, interacts with electric field gradients to provide a very efficient nuclear relaxation process. The equation for these interactions is similar in form to that of the dipole interaction. The electric quadrupolar interaction between spin I and an electric field gradient can be written in the form given in equation (4).

$$\frac{1}{T_1^{\mathrm{Q}}} = \frac{3\pi^2(2I+3)\chi^2\tau_{\mathrm{c}}}{10[I^2(2I-1)]} \tag{4}$$

where χ is known as the nuclear quadrupolar coupling constant and is in units of frequency. The τ_{c} here is the rotational diffusion correlation time as it appeared in the dipolar equation. Because of its relative efficiency the quadrupolar interaction nearly dominates when quadrupolar nuclei are present.

2.5.5 Chemical Shift Anisotropy

Anisotropic shielding at the nucleus changes with the orientation of the molecule in a static field. Therefore the molecular tumbling modulates the local magnetic field resulting in relaxation. The spin–lattice relaxation rate due to this interaction is proportional to the square of the magnetic field:

$$\frac{1}{T_1^{\mathrm{CSA}}} = \frac{2}{15}\gamma_A^2 B^2 \Delta\sigma^2 \tau_{\mathrm{c}} \tag{5}$$

where Δ is the chemical shielding anisotropy of the nucleus and τ_{c} has the same meaning as before.

The spin–lattice relaxation can be measured and contributions from each of the mechanisms decoupled to yield dynamic and structural information pertaining to the species of interest. Each of the following sections will contain specific observation techniques and theoretical treatments used to provide insight into the often strange and unpredictable world of supercritical fluids.

Extensive studies have been performed on nuclear magnetic spin lattice relaxation and its dependence on molecular structure and dynamics. This is the subject of several review articles.[9–12] Decoupling techniques are often used to enhance the signal and to simplify the resulting spectrum. Such decoupling studies also yield the nuclear Overhauser enhancement (NOE), which allows the unique separation of the dipolar interaction from other relaxation interactions. However, decoupling also eliminates multiplet splittings from scalar couplings, thereby preventing direct measurement of some of the spectral features that are required to completely describe the relaxation of coupled nuclear spin systems.

Spin-coherent double-resonance experiments, which avoid this loss of information, and a general numerical method for analyzing the data obtained in relaxation studies of this type may be used.[13,14] Relaxation processes, described by a system of coupled linear differential equations, determine a variety of time-independent relaxation parameters that contain information on the molecular structure, and dynamic features of the motion. The relaxation parameters in the equations of motion can then be extracted from the experimental data using standard least squares methods.[13,14]

For polyatomic gases, nuclear spin relaxation proceeds primarily from the collisional modulation of the molecular rotational angular momentum coupled to the angular momentum of the nuclear spins. Reorientations of molecular angular momentum by collision then give rise to fluctuating internal magnetic fields, that effect the nuclear spins through intramolecular spin–rotation couplings. In addition to the spin–rotation mechanism molecular motional modulation of the chemical shift anisotropy, dipole-dipole and quadrupolar couplings also affect the relaxation rates.

In low-viscosity liquids and gases, spin–lattice relaxation may be treated as a temporal modulation associated with the thermal reorientation of the molecule. The study of spin lattice relaxation contributes to an understanding of molecular dynamics.[15] In dilute gaseous samples of small molecules where the interactions mediating spin relaxation are primarily intermolecular,[16,17] and the various interaction parameters are known accurately,[18–21] the study of relaxation reveals features of collisional processes responsible for reorientation of the molecules.[22–24]

2.6 Line Narrowing

All polyatomic gases possess more than one intramolecular relaxation mechanism. Even the molecule H_2, for instance, has two competing mechanisms: the spin–rotation and the direct dipole–dipole interaction. In condensed phase molecular hydrogen the contribution of the dipole–dipole mechanism is comparable to that of spin rotation because the distance between the protons is short enough for the dipole–dipole relaxation to be appreciable. In a gaseous system, however, spin rotation is normally the dominant relaxation mechanism. In such experiments high density carbon dioxide can be added to hydrogen isotopomers such as hydrogen deuteride, as suggested by Johnson and Waugh,[23] to shorten the rotational correlation times and thereby lengthen the spin–rotation relaxation time and narrow the resonances in the high-resolution spectra. The H_2 system is difficult to study because of the indistinguishability of the two particles. Thus research on the lower HD symmetry[18,19,21–23,25–28] provides more information from both the proton and deuteron resonances arising from indirect spin-spin couplings.

Supercritical fluids generally have viscosities 10–100 times lower than that of the normal liquid phase and self diffusion coefficients 10–100 times greater. To the NMR spectroscopist, these properties are of significant benefit in studying quadrupolar nuclei, since the quadrupolar linewidth is proportional to the rotational correlation time. The utility of NMR to study many quadrupolar nuclei has been somewhat limited. Quadrupolar relaxation can be very efficient, leading to broad lines and low sensitivities. In the extreme narrowing limit, the linewidth of these nuclei,$(1/\pi T_2)$ can be written as

$$\frac{1}{\pi T_2} = \frac{3}{8}\left(\frac{e^2qQ}{h}\right)^2\left(1+\frac{\eta^2}{3}\right)\tau \tag{6}$$

where e^2qQ/h is the quadrupolar coupling constant, τ is the rotational correlation time for the molecular motion, and η is the asymmetry parameter of the electric field gradient

tensor. Various studies have demonstrated the validity of the Stokes–Einstein–Debye equation.[29]

$$\tau = \frac{A\eta}{T + \tau_0} \tag{7}$$

in which τ is the rotational correlation time, η is the solvent viscosity, T is the temperature and τ_0 is the high temperature intercept. This equation predicts a linear relation between τ and η/T to a limiting value τ_0 attained in the limit as $\eta/T \rightarrow 0$. Comparisons with above equation show that NMR line widths should decrease with decreasing viscosity to a limiting value expected to be related to the free rotor correlation time given by

$$\tau_{\mathrm{FR}} = \left(\frac{2\pi I}{9kT}\right)^{1/2} \tag{8}$$

where I is the moment of inertia about the rotational axis.

2.7 NMR Determination of Structural Dynamics in High-Pressure Fluids

There have been direct spectroscopic probes of the local solvent structure around solutes in supercritical fluids. These include using the solvatochromic scales as in the ultraviolet-visible (UV) absorption of phenol blue in ethylene[30] and the fluorescence spectroscopy of pyrene in carbon dioxide.[31] The use of spectroscopic methods to study the local environment surrounding solute molecules in dilute supercritical fluid mixtures has been reviewed.[32] However the use of NMR to determine the local structure within supercritical fluids has thus far been sparse in the literature.

2.7.1 High Pressure NMR Studies of Hydrogen Bonded Liquids

An understanding of molecular interactions between solute and solvent molecules in supercritical fluids (SCF) is essential to an explanation of clustering phenomena, considered responsible for the unique SCF solvating characteristics compared to gases.[33–35] Although both theoretical[36–38] and experimental efforts[39–46] have been made to increase the understanding of these phenomena, a complete picture of clustering in SCFs is still evolving. The accumulation of experimental NMR relaxation data is expected to improve our physical picture of solvent clustering in SCF. Because the nuclear spin–lattice relaxation rates depend on the fluctuating molecular reorientation and molecular collision frequency, their measurement proves to be an effective method for studying such molecular interactions and dynamics in fluids.[47] One of the advantages of utilizing NMR relaxation data is that they provide not only information, similar to optical methods, on overall molecular motions but also site-specific information on intramolecular motions. The ^{13}C spin–lattice relaxation processes in CO_2 are dominated by spin–rotation interactions.[48–50] Nuclear spin–lattice relaxation rates have been measured under SCF conditions by Lamb et al.[51] and Etesse et al.[52–54] for various SCF mixtures. NMR chemical shift measurements[55] were also used to relate ^{129}Xe chemical shift data to the local solvent structures of SCF Xe. SCF fluid structures in pure methanol,[56] CO_2–methane,[39] CO_2–methanol,[40] and CO_2–decanol[40] mixtures have recently been made. The function of the hydroxyl group in solute-induced solvent clustering in SCF CO_2 appears to be especially important. Earlier developments in high pressure NMR studies of hydrogen bonded liquids may be found in a review article by Lang and Ludemann.[57]

Information on the nature and average rate of molecular motions may be obtained by determining the nuclear spin–lattice relaxation rates of nuclei in the molecules under investigation. The nuclear spin relaxation rate, $1/T_1$, depends on fluctuations in molecular reorientations as a consequence of molecular collisions, where T_1 is the time constant defining the exponential return of a perturbed nuclear spin to its equilibrium state. Many nuclear spin interaction mechanisms affect T_1 values. Among them, spin–rotation, quadrupolar and dipolar interactions are the most important ones at sub- and supercritical densities. Detailed descriptions of spin–rotation, quadrupolar and dipolar interactions may be found in the review articles by Grant et al.[58] and Jameson.[59] Briefly, determination of NMR nuclear relaxation rates provides the angular momentum[59] and rotational reorientation correlation times[58] from the spin–rotation and quadrupolar/dipolar interactions, respectively. Spin–rotation interactions are directly related to molecular collision frequencies and depend on macroscopic properties such as fluid density and temperature. Dipolar and quadrupolar interactions, however, are often related to fluid viscosity and temperature. Since the fluid viscosity may be treated as a function of local density in the compressible regions of CO_2, both correlation times may be considered as functions of local densities. Therefore, clustering phenomena in SCF resulting in fluctuations of local density may in principle be observed by NMR relaxation measurements.

The magnitude of the NOE effect is given by[60]

$$\mathrm{NOE}(A\{X\}) = \frac{I_A^*}{I_A^0} \tag{9}$$

where I_A^* is the integrated intensity of a decoupled spectrum with saturation of the nucleus X, and I_A^0 is the equilibrium intensity of A in the coupled spectrum. The maximum possible NOE of ^{13}C{^{1}H} occurs when ^{13}C and ^{1}H relax only by the dipolar mechanism given by[60] and is given by

$$\mathrm{NOE(max)} = 1 + \left(\frac{\gamma_{\mathrm{H}}}{2\gamma_{\mathrm{C}}}\right) = 2.988 \tag{10}$$

where γ_{H} and γ_{C} are the magnetogyric ratios for ^{1}H and ^{13}C, respectively. The NOE effect may be determined as a ratio of spectral intensities with proton decoupling to that of gated proton decoupling. Since the ^{13}C in CO_2 does not exhibit an NOE, its signal intensity may be used as a fiducial reference.

2.8 Significant Mechanism in Spin–Lattice Relaxation: Overall Rotational Motion

In general, the overall rotational motions of solute molecules depend on the intermolecular frictional forces between the solute and solvent molecules and, therefore, are dependent upon the solvent viscosity. The solvent viscoelastic response, in turn, is also dependent on various relaxation mechanisms of solvent molecules. Internal rotational motions including various local isomerization movements are driven by torsional forces.[61]

The rotational reorientation correlation time, τ_c, may be extracted from NMR spin–lattice relaxation time measurements, within the *extreme narrowing* limit, using the following expression[60]

$$T_{1,\mathrm{DD}}^{-1}(^{13}\mathrm{C}) = \frac{\upsilon\gamma_C^2\gamma_H^2\hbar^2\tau_c}{r^6} \tag{11}$$

where r is the bond distance between ^{1}H and ^{13}C (measured as 1.085 Å), and υ is the number of protons directly attached to the ^{13}C nucleus. The dipole–dipole relaxation rate, may be obtained from the standard relationship between the overall T_1 and NOE measurements:[60]

$$\mathrm{NOE} = 1 + \frac{\gamma_H}{2\gamma_C}\frac{T_{1,\mathrm{DD}}^{-1}(^{13}\mathrm{C})}{T_{1,\mathrm{Tot}}^{-1}(^{13}\mathrm{C})} \tag{12}$$

The reorientation correlation time obtained in this manner is an average assuming isotropic reorientation. This correlation time may be related to a rotational diffusion coefficient by assuming that each nuclear environment is roughly spherical and rotates randomly.[62]

$$\tau_c = \frac{1}{6D} \tag{13}$$

From the temperature dependence of rotational diffusion coefficients at fixed viscosity, one can determine effective rotational activation energies.

2.9 CO_2 Clustering

The rotational reorientation correlation time, τ_c, can be expressed by a modified Stokes–Einstein–Debye (SED) equation[63]

$$\tau_c = \frac{\eta V_p}{kT} f_{\mathrm{stick}} C + \tau_0 \tag{14}$$

where η is the fluid viscosity, V_p is the volume of solute molecule, f_{stick} is a well-defined shape parameter dependent only on the structure of solute molecules,[64] C is a boundary parameter dependent on the nature of the solute and solvent and upon their concentration, and finally τ_0 is the free-rotor correlation time. The success of this model strongly depends on the selection of parameters C and f_{stick}. Recently, Roy et al.[64] noted that the Dote, Kivelson, and Schwartz (DKS) model[63] is the best model for predicting reorientational correlation times for solutes with radii up to about 4.5 Å. Anderson and Kauffman[65] further modified the calculation of the smallest volume of free space per solvent molecule, ΔV, in the DKS model, and more recently, these two workers[66] related fluid viscosity and the parameter C in the SED model to the local density by introducing a radial distribution function into the hydrodynamic model. These modifications[65,66] by Anderson and Kauffman are referred to as the AK model.

In the AK model, the viscosity for a fluid is expressed as a function of local density ρ_{12}^1 by equation 4.7 described by Jossi et al.[67]

$$[(\eta - \eta_0)\xi_T^y + 1]^{1/4} = 1.023 + 0.23364\rho_r + 0.58533\rho_r^2 - 0.40758\rho_r^3 + 0.09324\rho_r^4 \tag{15}$$

where $\rho_r = \rho_{12}^1/\rho_c$ and $\xi_T = (T_c/M^3P_c^4)^{1/6}$. ρ_c, T_c, and P_c represent the critical density, temperature, and pressure, respectively. M is the molecular weight in the unit of g mol^{-1}. The local density of is related to the bulk density ρ by a radial distribution formalism

$$\rho_{12}^1 = \rho\{1 + F[g_{12}(r)]\} \tag{16}$$

where $F[g_{12}(r)]$ is an integral equation in the pair distribution function, $g_{12}(r)$, over the spatial coordinates and r is the distance between solvent and solute molecules. $F[g_{12}(r)]$ is a measure of the excess solvent density near the solute molecule and is treated as an adjustable parameter in the AK model. When $F[g_{12}(r)] = 0$, the local density equals the bulk density, and when $F[g_{12}(r)] = 1.0$, the local density is twice the bulk density.

In the AK model, the parameter $C(\rho_{12}^1)$ equivalent to C in the SED model, is also treated as a function of local density. According to the DKS model

$$C(\rho_{12}^1) = \frac{f_{\mathrm{slip}}V_p}{f_{\mathrm{slip}}V_p + \gamma V_p} \tag{17}$$

where f_{slip} is a factor for the slip boundary condition whose value estimated from f_{stick} by the method reported by Hu and Zwanzig[68] and γ is defined as

$$\gamma = \left(\frac{\Delta V}{V_p}\right)\left[4\left(\frac{V_p}{V_s}\right)^{\frac{2}{3}} + 1\right] \tag{18}$$

In equation (18), V_s is the solute molecular volume and ΔV is the free space volume for a solvent molecule. For supercritical fluids in their compressible regions, a large variation in the free space is expected, and ΔV is given by equation (19) relating molecular weight (MW) and local density:

$$\Delta V = \frac{\mathrm{MW}}{\rho_{12}^1} - V_s \tag{19}$$

Therefore, the parameter $C(\rho_{12}^1)$ is expressed as a function of local density ρ_{12}^1 though the free space volume ΔV.

Combining equations (18) and (19), the AK version of the SED equation may be expressed as[66]

$$\tau_c \equiv \frac{\eta(\rho_{12}^1)V_p}{kT} f_{\mathrm{stick}} C(\rho_{12}^1) + \tau_0 \tag{20}$$

Equation (20) relates the reorientation correlation time, τ_c, to the solvent local density at a given temperature. By performing a comparison experiment on *trans*,*trans*-1,4-diphenylbutadiene (DPB) solute in CO_2, Anderson and Kauffman[66] also observed that CO_2 solvent clustering only occurs in the vicinity of *trans*-4-(hydroxymethyl)stilbene (HMS) molecules. Because the extended π-electron systems existing in DPB and HMS are similar, Anderson and Kauffman concluded that the OH group in HMS is responsible for the association between the solute and solvent molecules. The one-to-one association between solute and solvent molecules may initiate further CO_2 clustering whenever strong many-body interactions affect the solvent structure in supercritical

fluids in the compressible density region. The CO_2 clustering gradients observed along the aliphatic chain of l-decanol molecules in the Bai et al.[39] study appear to support the observations by Anderson and Kauffman.

To verify further the importance of alcohol enhanced clustering, the same procedure was applied to a CO_2–methanol mixture,[69] where a specific association between CO_2 and CH_3OH has been observed also by the IR studies.[42] Such solvent-solute interactions may initiate CO_2 solvent clustering.[66] The low-pressure limit free-rotor correlation time can be calculated using the following expression[70]

$$\tau_0 = \frac{2\pi}{9}\left(\frac{I_\perp}{kT}\right)^{1/2} \tag{21}$$

where is the perpendicular component of the moment of inertia for methanol molecules. The calculated τ_0 from equation (21) is 0.20 ps, which agrees well with the 0.17 ps from fitting the low-density data.

2.10 More Evidence for the Formation of CO_2 Clusters in the Vicinity of Methanol

As stated above, NOE measurements allow the separation of the dipole–dipole contributions to spin–lattice relaxation rates from other mechanistic contributions. For methanol, the remaining relaxation contributions result essentially from the spin–rotation mechanisms described previously.[69] These spin–rotation relaxation rates allow one to calculate an angular momentum exchange correlation time, τ_J, which is strongly dependent on the fluid density. Methanol is a quasi-symmetric top molecule, but the relation between ρ, and spin–rotation relaxation rates for symmetric top molecules may be used as a good approximation for T_1^{SR}. The expression[71] is

$$\frac{1}{T_1^{SR}} = \frac{2\pi^2}{\alpha} C_{\text{eff}}{}^2 \tau_J \tag{22}$$

where pull down $\alpha = \hbar^2/(2kTI_\perp)$ and $I_\perp$ is the perpendicular part of the moment of inertia for methanol. The effective spin–rotation, C_{eff}, may be expressed as

$$C_{\text{eff}}{}^2 = k_1 C_a^2 + k_2 C_a C_d + k_3 C_d^2 \tag{23}$$

In equation (23), the structure parameters, k_i, only depend on molecular structure. C_a and C_d are the isotropic and anisotropic components of the spin–rotation tensor. Therefore, in principle, an experimental angular momentum correlation time, τ_J, may be estimated using equation (22). Since τ_J is linearly related to the time between molecular collisions, τ_{BC}, one may calculate τ_J using a gas kinetic theory. The slope of this linear relationship, called an effective collision number and referred to as Z,[72] provides the average number of collisions needed for an effective molecular angular momentum exchange. This number is found to be between 1.4 and 3.4 for many collision pairs (cf. Table 3 in Ref.[72]). In the use of a hard-sphere model (HSM) for calculating cross sections, choosing the effective collision number of two appeared to be a good approximation in the work of Maryott, Malmberg, and Gillen,[72] and therefore, this value is used in the following discussion. The expression for computing τ_J is given by[73]

$$\tau_J = \frac{Z}{\rho \overline{v} \sigma_K} \tag{24}$$

where ρ is fluid density, $\overline{v}$ is the average velocity of molecules, and ρ_K is the kinetic collisional cross section between solute and solvent molecules. Both $\overline{v}$ and σ_K may be estimated from molecular properties of the solute and solvent. If the density term, ρ, in equation (24) is replaced by a local density [cf. equation (16)], the estimated τ_J becomes a function of the excess solvent density parameter, $F[g_{12}(r)]$. In this case, equation (24) becomes

$$\tau_J = \frac{Z}{\rho\{1 + F[g_{12}(r)]\}\overline{v}\sigma_K} \tag{25}$$

There is good agreement between theoretical and experimental data when an increase in local density is employed in the predictions of τ_J. This provides additional evidence for the formation of SCF solvent clustering in the vicinity of hydrogen bonding solute molecules. Supposedly, these interactions are induced by the hydroxyl functional group present in alcohol molecules.

2.11 NMR Determination of Self-diffusion Coefficients in High-pressure Fluids

Many methods exist for measuring the diffusion coefficients of fluids. However, the experimental accuracy of many of these is quite limited.[74,75] Furthermore, methods that give reliable results in the low pressure regime are not always suitable at high pressures because the inverse dependence of the diffusion coefficient on pressure makes for experiments that take an inordinately long time. The most widely reported method for the measurement of diffusion coefficients in the SCF state is a gas chromatographic method based on Taylor dispersion, which has proven unreliable at lower pressures.[76–78]

The only other methods that can be utilized for this measurement in SCFs are photon correlation spectroscopy[79,80] and NMR.[81,82] They are not widely used at this time because the equipment is very expensive and their application to industrially important SCF's is still in its infancy. The use of the NMR technique has been confined to the measurement of self diffusion coefficients.[81,82]

3 INSTRUMENT REQUIREMENTS FOR HIGH-PRESSURE NMR

In order to perform NMR experiments under high pressure, it is necessary to devise a convenient means to control the pressure, temperature and sample concentration while it is inside the magnet. Two basic approaches to the design of high pressure NMR experiments have been reported: (1) construction of a probe which is capable of achieving the necessary pressures, referred to as the *high pressure probe technique*,[83] or (2) fabrication of a high pressure cell which can be used in a standard commercial NMR probe, referred to as the *high pressure cell technique*.

The very first high pressure NMR experiment was performed in 1954 by Benedek and Purcell.[84] They used a

hydrostatic high pressure probe capable of holding pressures up to 10 000 atm. For deformable samples the high pressure probe technique requires a sealed sample cell which incorporates a volume change mechanism such as bellows or a mercury column.[85] The cell is surrounded by a RF coil and is located inside a pressure vessel small enough to fit inside the NMR magnet. The high pressure probe technique usually offers higher sensitivity because of a better filling factor for the receiver coil. It also allows for higher pressures and is usually safer to work with. The disadvantages are that they require a more elaborate and expensive design and are therefore not suitable for a routine NMR laboratory. The approach to a high pressure probe has continually been developed by Jonas et al.[86] with improvements to pressure vessel design and electrical feed-throughs. The most recent advances to the probe design for studying supercritical fluids include the toroidal coil[87] and cavity[88] design by Rathke et al.

The high pressure cell technique allows the experiments to be performed in a commercial NMR probehead, thereby eliminating the need to alter the basic probe design. The earlier versions of high pressure cells experienced lower sensitivity and reduced working pressures. Yonker et al. designed a simple and safe method by coiling a fused silica capillary tube inside a commercial 5-mm NMR tube.[89] Newer cell designs have improved these limitations providing a more convenient and cost-effective means of carrying out high pressure NMR experiments. Roe et al.[90] designed the first cell made of single crystal sapphire and Horvath et al. later improved this design.[91,92] Pressure control while the cell is in the magnet is a major issue in the cell design. The previously reported designs of the sapphire NMR cells were unable to independently control both the sample temperature and pressure. In the Bai et al. design[93] a movable piston is used to control the sample pressure (see Figure 2). With this design it is possible to control temperature and pressure independently over a wide range of conditions while keeping the relative molar concentration ratios of the sample mixture intact. The sample volume must be restricted to the active coil in order to eliminate errors introduced through molecular diffusion between polarized and nonpolarized volume elements within the cell. Recently a high pressure cell constructed of high-performance polymers, such as poly(etherether ketone) (PEEK), was developed by Wallen et al.[94] with the purpose of simplifying the cell design to allow for more routine experiments on supercritical fluids.

The very first high pressure probe was made of a beryllium copper alloy (Berylco 25). This alloy was used due its strength and nonmagnetic properties, but does require special heat treatment and can have significant variations in the level of paramagnetic impurities. Berylco 25 is stable up to 10 000 atm and permits a temperature range of $-10\,^{\circ}\mathrm{C}$–$80\,^{\circ}\mathrm{C}$. Titanium alloys (IMI-680) are now more commonly used as they require no special heat treatment during machining and retain their strength up to 400 °C and 5000 atm. For even higher pressures, up to 100 kbar, the diamond anvil method can be used.[95] This method can only be used with very small samples so most studies concern sensitive nuclei, although a study on ^{13}C has been reported.

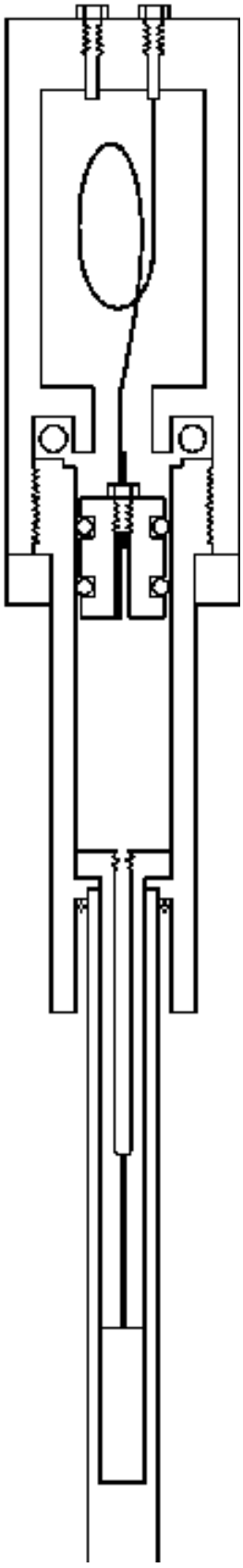

Figure 2 Schematic diagram of the high pressure piston NMR cell capable of independently controlling temperature, pressure and sample concentration

4 SUPERCRITICAL FLUID APPLICATIONS

Most of the high pressure NMR studies of supercritical fluids have involved measuring chemical shifts, such as ^{1}H,[96]

of both polar and nonpolar solute molecules in the dense phase fluid. Increased reaction rates of certain reactions in supercritical fluids has been attributed to specific solvent-solute and solute–solute interactions. By studying these specific interactions by NMR further insight into the variation of the surroundings of the solute molecules with the density of the supercritical fluid is obtained and can be compared to other experimental techniques, such as UV and vibrational spectroscopy.

Using a fused silica capillary cell an in situ photolysis study of organometallics in supercritical fluids was performed where the ligand exchange with the metal center was directly observed.[97] High pressure NMR was also used to determine the fundamental dynamic and electronic properties of the organometallic complexes in the SCF through the investigation of the spin–lattice relaxation times, T_1, and NMR magnetic shielding constants, σ.

Another interesting application of supercritical fluids is to use them as solvents for comprehensive NMR studies of large proteins. In conventional solvents large proteins (over 30 kDa) tumble too slowly and correspondingly the spin–spin relaxation times (T_2) become shorter, making some standard experiments unreliable. By encapsulating the protein in a reverse micelle dispersed in a low viscosity fluid, such as a supercritical fluid, the tumbling correlation time (τ_m) of the protein is reduced thereby increasing T_2.[98] This results in narrower lines in the spectrum.

High pressure NMR has also been used to investigate phase behavior of binary solvent systems in order to obtain vapor–liquid equilibrium (VLE) values. Usually VLE values of supercritical fluid solutions are obtained using variable volume view cells and off-line analysis techniques. By using NMR, this process can be simplified and made more efficient for numerous solvent systems. This technique is especially suitable for hydrocarbon containing solvent molecules as detection of solvent protons in both the liquid and vapor phase can be detected simultaneously.[99]

An advantage of using supercritical fluids as reaction media for chemical reactions is that gaseous reagents are completely miscible with the solvent. In catalytic reactions such as hydrogenations and hydroformylations where H_2 and CO are reactants this can have a significant impact on both the yield and selectivity of the desired products. Since only one phase is present in the supercritical system, stirring to achieve gas–liquid mixing is unnecessary. By studying these reactions in situ by NMR valuable information regarding the mechanism can be obtained.[100] In situ NMR was used to optimize the iridium catalyzed enantioselective hydrogenation of imines in supercritical CO_2. By studying the specific interactions between substrates and products with CO_2 conclusions about the different reactivities of structurally similar substrates were obtained.[101]

5 REFERENCES

1. C. J. Jameson, *Chem. Rev.*, 1991, **91**, 1375–1395.
2. R. L. Armstrong, *Magn. Reson. Rev.*, 1987, **12**, 91.
3. J. Jonas, ed, 'NMR Basic Principles and Progress', Springer Verlag: Berlin, 1991, Vol. 24 of High Pressure NMR.
4. I. T. Horvath and J. M. Millar, *Chem. Rev.*, 1991, **91**, 1339–1351.
5. H. C. Torrey, *Phys. Rev.*, 1953, **92**, 962.
6. A. Abragam, 'The Principals of Nuclear Magnetism', The Clarendon Press: Oxford, 1961.
7. J. McConnell, 'Rotational Brownian Motion and Dielectric Theory', Academic Press: London, 1980.
8. J. McConnell, 'The Theory of Nuclear Magnetic Resonance Relaxation in Liquids', Cambridge University Press: Cambridge, 1987.
9. S. W. Collins, T. D. Alger, D. M. Grant, K. F. Kuhlman, and J. C. Smith, *J. Phys. Chem.*, 1975, **79**, 2031.
10. C. L. Mayne, D. W. Alderman, and D. M. Grant, *J. Chem. Phys.*, 1975, **63**, 2514.
11. G. A. Gray and S. E. Cremer, *J. Magn. Reson.*, 1973, **12**, 5.
12. D. M. Grant, R. J. Pugmire, E. P. Black, and K. A. Christensen, *J. Phys. Chem.*, 1973, **95**, 8465.
13. D. M. Grant, C. L. Mayne, F. Liu, and T.-X. Xiang, *Chem. Rev.*, 1991, **91**, 1591–1624.
14. D. Canet, *Prog. NMR Spectrosc.*, 1989, **21**, 237.
15. D. M. Grant, C. L. Mayne, F. Liu, and T.-X. Xiang, *Chem. Rev.*, 1991, **91**, l591–1624.
16. N. Bloembergen, E. M. Purcell, and R. V. Pound, *Phys. Rev.*, 1948, **73**, 679.
17. A. Abragam, 'Principles of Nuclear Magnetism', Clarendon Press: Oxford, 1961, p. 1581.
18. N. F. Ramsey and H. R. Lewis, *Phys. Rev.*, 1957, **108**, 1246.
19. N. J. Harrick, R. G. Barnes, P. J. Bray, and N. F. Ramsey, *Phys. Rev.*, 1953, **90**, 260.
20. N. F. Ramsey, 'Molecular Beams', Clarendon Press: Oxford, 1956, p. 1454.
21. W. E. Quinn, J. M. Baker, J. T. LaTourrette, and N. F. Ramsey, *Phys. Rev.*, 1958, **112**, 1929.
22. J. R. Gains, P. C. Souers, E. M. Fearon, J. D. Sater, and E. R. Mapoles, *Phys. Rev. B*, 1989, **39**, 3943.
23. C. S. Johnson, Jr. and J. S. Waugh, *J. Chem. Phys.*, 1962, **36**, 2266.
24. P. R. McCourt, in 'NMR Basic Principles and Progress', eds P. Diehl, B. Fluck, and R. Kosfeld, Springer Verlag: Berlin, 1976, p. 56.
25. B. D. Nageswara Rao and L. R. Anders, *Phys. Rev.*, 1967, **140**, A112.
26. P. C. Souers, E. M. Fearon, J. D. Sater, E. R. Mapoles, J. R. Gaines, and P. A. Fedders, *J. Voc. Sci. Tec. A.*, 1991, **9**, 232.
27. R. S. Wagner, R. L. Armstrong, E. C. Bissonette, and F. R. W. McCourt, *J. Chem. Phys.*, 1990, **92**, 5907.
28. J. M. Deutch and I. Oppenheim, in 'Advances in Magnetic Resonance', ed J. S. Waugh, Academic Press: New York, 1966, p. 225.
29. R. B. Bird, W. E. Stewart, and L. N. Lightfoot, 'Transport Phenomena', Wiley: New York, 1960, Chapter 16.
30. S. Kim and K. P. Johnston, *Ind. Eng. Chem. Res.*, 1987, **26**, 1206.
31. J. F. Brennecke and C. A. Eckert, in *Proceedings of the International Symposium on Supercritical Fluids*, Nice, October, 1988.
32. K. P. Johnston, S. Kim, and J. Coombes, in 'Supercritical Fluid Science and Technology', eds K. P. Johnston and J. Penninger, ACS Symposium Series No. 406, American Chemical Society: Washington, DC, 1989.
33. P. G. Jessop, T. Ikariya, and R. Noyori, *Science*, 1995, **269**, 1065–1069.
34. T. J. Bruno and J. F. Ely, eds, 'Supercritical Fluid Technology – Reviews in Modern Theory and Applications', CRC Press: Boca Raton, FL, 1991.
35. E. Klesper, *Angew. Chem. Int. Ed. Engl.*, 1978, **17**, 738–746.
36. (a) J. W. Tom and P. G. Debenedetti, *Ind. Eng. Chem. Res.*, 1993, **32**, 2118–2128; (b) P. G. Debenedetti, *Chem. Eng. Sci.*, 1987, **42**, 2203–2212.
37. S. Kim and K. P. Johnston, *Ind. Eng. Chem. Res.*, 1987, **26**, 1206–1213.

38. (a) H. D. Cochran and L. L. Lee, in 'Supercritical Fluid Science and Technology – Reviews in Modern Theory and Applications', eds T. J. Bruno and J. F. Ely, CRC Press: Boca Raton, FL, 1991; (b) K. P. Johnston and J. Penninger, eds, 'Supercritical Fluid Science and Technology', ACS Symposium Series No. 406, American Chemical Society: Washington, DC, 1989, Chapter 3.
39. S. Bai, C. M. V. Taylor, F. Liu, C. L. Mayne, R. J. Pugmire, and D. M. Grant, *J. Phys. Chem. B*, 1997, **101**, 2923–2928.
40. C. M. V. Taylor, S. Bai, C. L. Mayne, and D. M. Grant, *J. Phys. Chem. B*, 1997, **101**, 5652–5658.
41. J. P. Blitz, C. R. Yonker, and R. D. Smith, *J. Phys. Chem.*, 1989, **93**, 6661–6665.
42. J. L. Fulton, G. G. Yee, and R. D. Smith, *J. Am. Chem. Soc.*, 1991, **113**, 8327–8334.
43. C. R. Yonker, S. L. Frye, D. R. Kalkwarf, and R. D. Smith, *J. Phys. Chem.*, 1986, **90**, 3022–3026.
44. C. R. Yonker and R. D. Smith, *J. Phys. Chem.*, 1988, **92**, 2374–2378.
45. J. Zagrobelny and F. V. Bright, *J. Am. Chem. Soc.*, 1993, **115**, 701–707.
46. T. A. Betts, J. Zagrobelny, and F. V. Bright, *J. Am. Chem. Soc.*, 1992, **114**, 8163–8171.
47. D. M. Grant, C. L. Mayne, F. Liu, and T. X. Xiang, *Chem. Rev.*, 1991, **91**, 1591–1624.
48. P. Etesse, J. A. Zega, and R. Kobayashi, *J. Chem. Phys.*, 1992, **97**, 2022–2029.
49. S. Bai, C. L. Mayne, R. J. Pugmire, and D. M. Grant, *J. Chem. Phys.*, 1997, **101**, 2923–2928.
50. C. J. Jameson, A. K. Jameson, N. C. Smith, and K. Jackowski, *J. Chem. Phys.*, 1987, **86**, 2717–2722.
51. D. M. Lamb, S. T. Adamy, K. W. Woo, and J. Jonas, *J. Phys. Chem.*, 1989, **93**, 5002–5005.
52. P. Etesse, J. A. Zega, and R. Kobayashi, *J. Chem. Phys.*, 1992, **97**, 2022–2029.
53. P. Etesse, A. M. Ward, and R. Kobayashi, *Physica B*, 1993, **183**, 45–52.
54. P. Etesse, W. G. Chapman, and R. Kobayashi, *Mol. Phys.*, 1993, **80**, 1145–1164.
55. D. M. Pfund, T. S. Zemanian, J. C. Linehan, J. L. Fulton, and C. R. Yonker, *J. Phys. Chem.*, 1994, **98**, 11 846–11 857.
56. S. Bai and C. R. Yonker, *J. Phys. Chem. A*, 1998, **102**, 8641–8647.
57. E. W. Lang and H. D. Ludemann, *Prog. NMR Spectrosc.*, 1993, **25**, 507.
58. D. M. Grant, C. L. Mayne, F. Liu, and T. X. Xiang, *Chem. Rev.*, 1991, **91**, 1591–1624.
59. C. J. Jameson, *Chem. Rev.*, 1991, **91**, 1375–1395.
60. R. K. Harris, 'Nuclear Magnetic Resonance Spectroscopy', The Bath Press: Avon, UK, 1986, Chapter 4.
61. F. Liu, W. J. Horton, C. L. Mayne, T. X. Xiang, and D. M. Grant, *J. Am. Chem. Soc.*, 1992, **114**, 5281–5294.
62. Y. J. Kim and J. Jonas, *J. Phys. Chem.*, 1995, **99**, 6777–6788.
63. J. L. Dote, D. Kivelson, and R. N. Schwartz, *J. Phys. Chem.*, 1981, **85**, 2169–2180.
64. M. Roy and S. Doraiswamy, *J. Chem. Phys.*, 1993, **98**, 3213–3223.
65. R. M. Anderson and J. F. Kauffman, *J. Phys. Chem.*, 1994, **98**, 12 117–12 124.
66. R. M. Anderson and J. F. Kauffman, *J. Phys. Chem.*, 1995, **99**, 13 759–13 762.
67. J. A. Jossi, L. I. Stiel, and G. Thodos, *AIChE J.*, 1961, **7**, 625.
68. C.-M. Hu and R. Zwanzig, *J. Chem. Phys.*, 1974, **60**, 4354–4357.
69. S. Bai, C. M. V. Taylor, F. Liu, C. L. Mayne, R. J. Pugmire, and D. M. Grant, *J. Phys. Chem. B.*, 1997, **101**, 2923–2928; C. M. V. Taylor, S. Bai, C. L. Mayne, and D. M. Grant, *J. Phys. Chem. B*, 1997, **101**, 5652–5658.
70. D. Ben-Amotz and T. W. Scott, *J. Chem. Phys.*, 1987, **87**, 3739.
71. B. L. Armstrong and J. Courtney, *Can. J. Phys.*, 1972, **50**, 1262–1272.
72. A. A. Maryott, M. S. Malmberg, and K. T. Gillen, *Chem. Phys. Lett.*, 1974, **25**, 169–174.
73. P. Etesse, J. A. Zega, and R. Kobayashi, *J. Chem. Phys.*, 1992, **97**, 2022–2029.
74. J. Kestin and W. A. Wakeham, in 'Transport Properties of Fluids: Thermal Conductivity, Viscosity and Diffusion Coefficients', CINDAS Data Series Material Properties, ed C. Y. Ho, Hemisphere Publishing: New York, 1988, Vol. 1.
75. T. R. Marrero and E. A. Mason, *J. Phys. Chem. Ref. Data*, 1972, **1**, 1.
76. I. Swaid and G. M. Schneider, *Ber. Bunsenges. Phys. Chem.*, 1979, **83**, 969.
77. R. Feist and G. M. Schneider, *Sep. Sci. Technol.*, 1980, **17**, 261.
78. Z. Balenovic, M. Myers, and J. C. Giddings, *J. Chem. Phys.*, 1970, **52**, 915.
79. H. Saad and E. Gulari, *Ber. Bunsenges. Phys. Chem.*, 1984, **88**, 834.
80. H. Saad and E. Gulari, *J. Phys. Chem.*, 1984, **88**, 136.
81. J. Jonas and D. M. Lamb, in 'ACS Symposium Series No. 329', eds T. G. Squires and M. E. Paulaitis, American Chemical Society: Washington, DC, 1987.
82. W. J. Lamb, G. A. Hoffmann, and J. Jonas, *J. Chem. Phys.*, 1981, **74**, 6875.
83. I. T. Horváth and J. M. Millar, *Chem. Rev.*, 1991, **91**, 1339–1351.
84. G. B. Benedek and E. M. Purcell, *J. Chem. Phys.*, 1954, **22**, 2003.
85. M. E. Smith and J. H. Strange, *Meas. Sci. Technol.*, 1997, **7**, 449–475.
86. B. Lance and J. Jonas, *Annu. Rep. NMR Spectrosc.*, 1997, **33**, 115–150.
87. J. W. Rathke, *J. Magn. Reson.*, 1989, **85**, 150–155.
88. K. Woelk, R. W. Rathke, and R. J. Klinger, *J. Magn. Reson. A*, 1994, **109**, 137–146.
89. C. R. Yonker, T. S. Zemanian, S. L. Wallen, J. C. Linehan, and J. A. Franz, *J. Magn. Reson. A*, 1995, **113**, 102.
90. D. C. Roe, *J. Magn. Reson.*, 1985, **63**, 388.
91. I. T. Horvath and E. C. Ponce, *Rev. Sci. Instrum.*, 1991, **62**, 1104.
92. I. T. Horvath and J. M. Millar, *Chem. Rev.*, 1991, **91**, 1339.
93. S. Bai, C. M. Taylor, C. L. Mayne, R. J. Pugmire, and D. M. Grant, *Rev. Sci. Instrum.*, 1996, **76**, 240–243.
94. S. L. Wallen, L. K. Schoenbachler, E. D. Dawson, and M. A. Blatchford, *Anal. Chem.*, 2000, **72**, 4230–4234.
95. R. Bertani, M. Mali, J. Roos, and D. Brinkmann, *Rev. Sci. Instrum.*, 1992, **63**, 3303.
96. M. Kanakubo, T. Aizawa, T. Kawakami, O. Sato, Y. Ikushima, K. Hatakeda, and N. Saito, *J. Phys. Chem. B*, 2000, **104**, 2749–2758.
97. J. C. Linehan, S. L. Wallen, C. R. Yonker, T. E. Bitterwolf, and J. T. Bays, *J. Am. Chem. Soc.*, 1997, **119**, 10 170–10 177.
98. M. R. Ehrhardt, P. F. Flynn, and A. J. Wand, *J. Biomol. NMR*, 1999, **14**, 75–78.
99. C. R. Yonker, J. C. Linehan, and J. L. Fulton, *J. Supercrit. Fluids*, 1998, **14**, 9–16.
100. J. W. Rathke, R. J. Klinger, R. E. Gerald II, K. W. Kramarz, and K. Woelk, *Prog. NMR Spectrosc.*, 1997, **30**, 209.
101. S. Kainz, A. Brinkmann, W. Leitner, and A. Pfalz, *J. Am. Chem. Soc.*, 1999, **121**, 6421–6429.

Biographical Sketches

Gunilla B. Jacobson, *b* 1969. Ph.D. 1996, Organic Chemistry, University of Uppsala, Sweden. Postdoctoral Research Associate with Keith P. Johnston, Univ. of Texas, Austin, 1997–1998. Research

Associate with William Tumas, Los Alamos National Laboratory, 1998–1999. Technical Staff Member, Los Alamos National Laboratory, 2000–present. Approx 30 publications. Current research interests: reactions, separations, and materials modifications using supercritical fluid technology.

Craig M. V. Taylor, *b* 1962. M.S., 1987 Organometallic Chemistry, New Mexico Institute of Mining and Technology, Ph.D. 1999, Physical Chemistry, University of Utah (supervisor David M. Grant) 1985–87 Research Associate on Supercritical Fluid Tertiary Oil Recovery, Petroleum Recovery Research Center Socorro New Mexico. 1987–94 Scientist Los Alamos National Laboratory (LANL). 1994–98 Principal Investigator Supercritical Fluids Facility, LANL. Leader of Applied Chemical Technologies Group, Chemistry Division, LANL 1998–present. Approx 25 publications. Current research interests: Supercritical Fluids Applications.

Thermometry

James F. Haw
Texas A&M University, College Station, TX, USA

1	Introduction to the Temperature Measurement Problem in MAS NMR	1
2	Phase Transition Thermometry	1
3	Chemical Shift Thermometry	2
4	Laser Heaters and Temperature Jumps	4
5	Related Articles	4
6	References	4

1 INTRODUCTION TO THE TEMPERATURE MEASUREMENT PROBLEM IN MAS NMR

Physical measurements of various sorts are performed as a function of temperature to characterize activated phenomena such as exchange or chemical reactions as well as variations in thermodynamic properties including phase changes. Variable temperature (VT) NMR measurements of solutions have long been regarded as routine; chemical applications of VT MAS NMR were first reviewed in 1982.[1] The most notable problem in temperature measurement and control for all NMR experiments is the necessity of locating electronic temperature sensors away from the coil (and hence sample) to avoid noise pickup. With the significant exception of MAS experiments, temperature measurement and control in solid state NMR experiments presents problems little different from those encountered in non-NMR studies in comparable temperature ranges.

The great majority of chemical applications of solid state NMR make use of MAS, and the design of spinning systems for this experiment presents formidable challenges for temperature measurement and control.[2] A number of such designs are currently in use, and a detailed critique of each would be unproductive, but it is appropriate to summarize the more common problems. The placement of the temperature sensor is either upstream or downstream of the spinning module, and appreciable temperature changes can occur between these points. These result not only from heat losses, but also from Joule–Thomson cooling of the spinning gas as it expands through the drive and bearing orifices. Most spinning systems use two to four gas streams running off of two regulated gas supplies to drive the rotor and stabilize it with several gas bearings. If these gas streams are also used to bathe the rotor then each, in principle, should be temperature regulated; in common practice only one stream is regulated. Other designs keep the drive and bearing gases near room temperature to simplify materials constraints and achieve VT operation by directing a separate gas stream onto the center of an elongated rotor. This approach intentionally creates a temperature gradient over the rotor but not over the sample, provided that mixture of the VT gas and bearing gas is avoided.

The very act of high-speed spinning is inimical to temperature regulation. Old-style Kel-F rotors readily developed a polished look due to frictional heating at the bearing surfaces. There were also reports that phase transitions near room temperature were accessible through changes in spinning speed,[3] although it was not always clear whether this reflected frictional heating or the effect of pressure. Another characteristic of many MAS experiments is the application of high-power radiofrequency pulses for dipolar decoupling or cross polarization. There were early anecdotal accounts of Kel-F rotors melting when lossy samples were pulsed with high duty cycles. The temperature accuracy issue was essentially ignored by most vendors before the late 1980s, and temperature errors of 20 K or more were typical. The situation has improved, but the user should still be skeptical of the indicated temperature until proven accurate.

There is no panacea for the problem of temperature measurement and control in MAS experiments, but attention to detail and application of some of the ideas presented below will greatly reduce the error, and useful data can be obtained over a wide temperature range. The first step is to bench-test the probe and VT unit using additional temperature sensors to characterize gradients across the spinning module. Many VT probes provide reasonable temperature accuracy with some gas flow settings but not others; a bench test is a good opportunity to explore this.

2 PHASE TRANSITION THERMOMETRY

Typical commercial MAS probes available at this time have recommended temperature ranges of approximately 123–173 K (low end) to 423–573 K (high end). The simplest way to begin the evaluation of a VT MAS probe is to observe a few phase transitions above room temperature. Melting transitions and solid–solid phase transitions have been reported for this purpose. Both also providing good

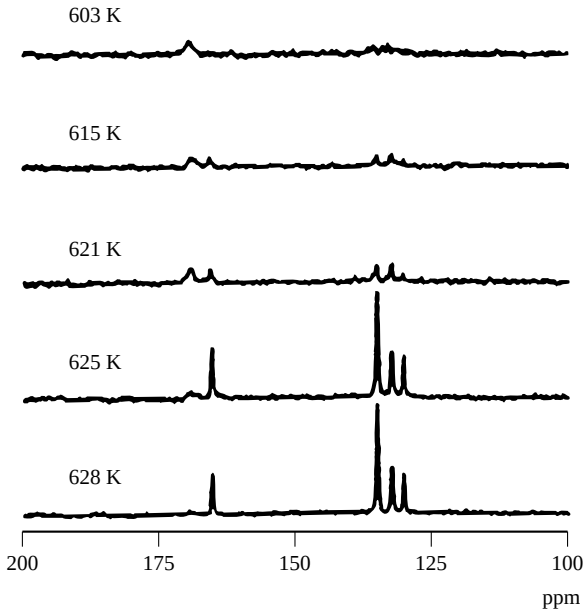

Figure 1 An example of a melting transition for thermometry. Carbon-13 MAS spectra of isophthalic acid were obtained as the sample was raised through its melting point (614 K). The pulse delay was such that only signals from the melt phase were observed

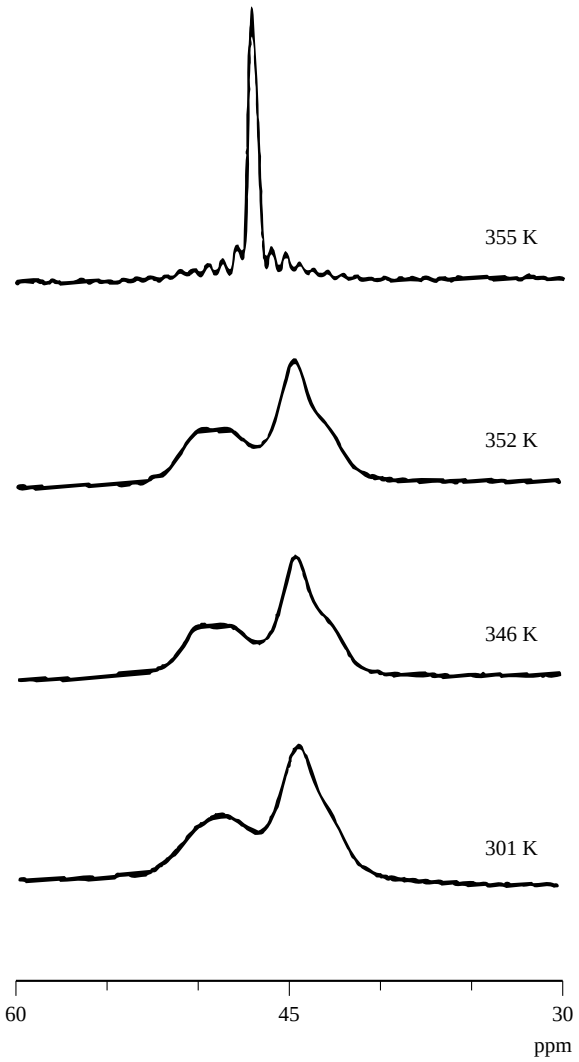

Figure 2 An example of a solid–solid phase transition for thermometry. Carbon-13 CP MAS spectra of 1,4-diazabicyclo-[2.2.2]octane were obtained in the vicinity of the transition

tests of spinning stability during changes in sample packing, and melting transitions are good tests of the integrity of rotor sealing; these are common challenges in VT MAS experiments. Figure 1 shows ^{13}C MAS spectra of a sample of isophthalic acid (m.p. 614 K) obtained as the indicated temperature of a prototype MAS probe was raised from 603 to 628 K.[4] The progress of melting as the temperature was slowly increased suggested the actual temperature was 5–10 K below that indicated and the temperature gradient was comparable. Caffeine and hexamethylbenzene work well at somewhat lower temperatures.

Figure 2 shows ^{13}C MAS spectra following the transition of 1,4-diazabicyclo[2.2.2]octane to the plastically crystalline state.[5] The onset of dynamics was reflected in lineshape changes due to averaging of the ^{13}C–^{14}N dipolar coupling. Similar transitions for camphor and adamantane have been used for low-temperature studies.

Although phase transitions are the easiest way to examine a new VT probe, they are not entirely perfect for temperature calibration. Supercooling may result when attempting to calibrate probes at lower temperatures using sealed ampoules of, for example, methanol. Solid–solid transitions can display hysteresis. Mass transport in melting samples could conceal a temperature gradient. But phase transitions are easy to observe, and they will immediately reveal a gross error in the indicated temperature. Regardless of the form of thermometry, the experience of our laboratory is that rather than apply a large temperature correction, it is preferable to adjust the gas flow rates or relocate the sensor to obtain a truer reading.

3 CHEMICAL SHIFT THERMOMETRY

The second form of thermometry reports continuous changes in temperature rather than the discrete temperatures supplied by phase transitions. The average sample temperature is reflected as a chemical shift, and the temperature gradient is mapped into the lineshape as in an imaging experiment. Chemical shift thermometry enjoys a long history in solution NMR. These methods employ well-characterized temperature dependences of isotropic shifts due to changes in hydrogen bonding or paramagnetism. Compartmentalized NMR tubes are sometimes used to piggy-back the thermometry experiment onto the sample of interest, and thus the sample temperature is known to a fraction of a degree. Sample filling factor and spinning stability have prevented the routine inclusion of a thermometer substance in VT MAS experiments, and thermometry is usually performed as a separate exercise.

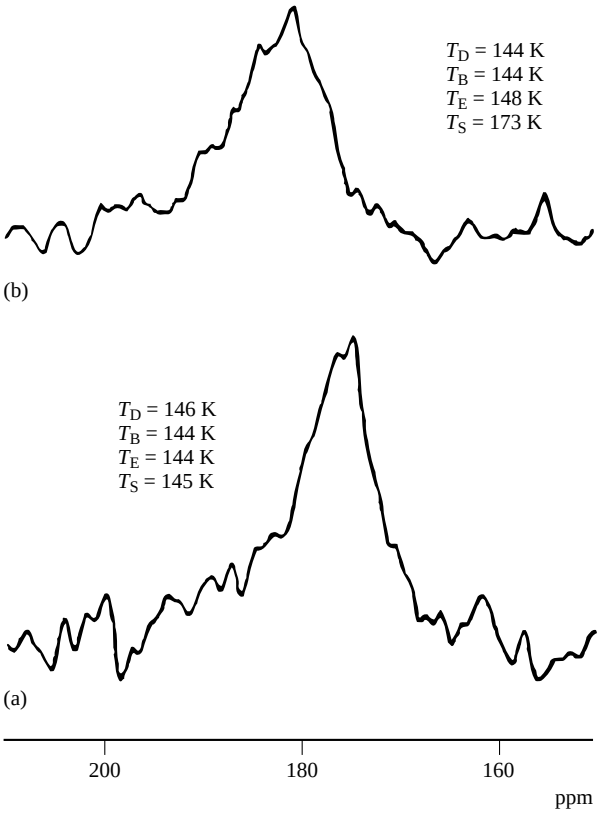

Figure 3 Carbon-13 CP MAS spectra of samarium acetate hydrate and graphite showing the effect of duty cycle on sample temperature as a result of rf heating. The gas temperature was 144 K in each case, but a high rf duty cycle heated the sample to 173 K as indicated by the chemical shift in the upper spectrum

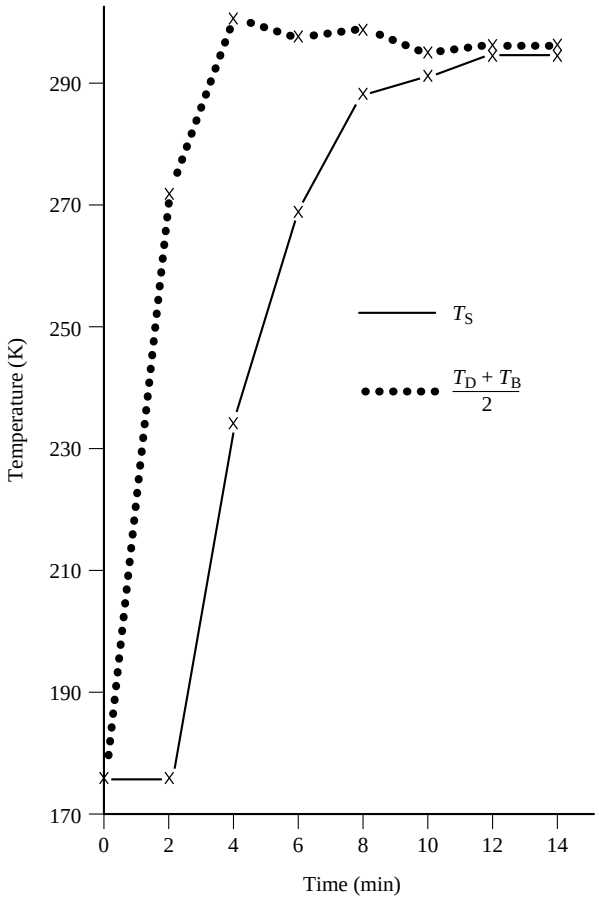

Figure 4 Demonstration of the use of samarium acetate thermometry to measure the equilibration time of sample temperature (solid line) following a near step change in gas temperature (dotted line)

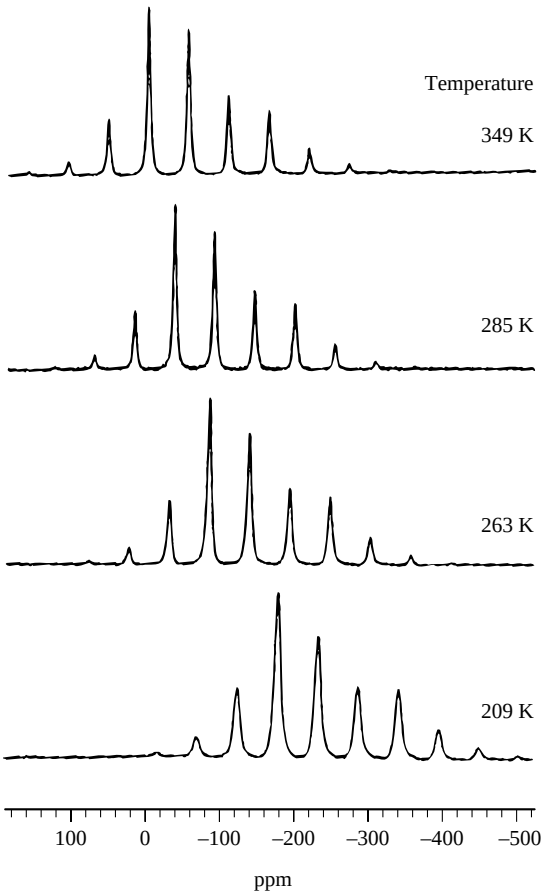

Figure 5 Tin-119 MAS spectra of $Sm_2Sn_2O_7$ at various temperatures. This compound is one of the better MAS thermometers yet found

In an early test of temperature accuracy in MAS experiments, English[6] loaded scaled ampoules of methanol or ethylene glycol into a rotor and characterized the temperature gradient by varying their position. Most subsequent work has employed solid chemical shift thermometers; one of these was based on chemical exchange,[7,8] but most have relied on paramagnetic compounds. Temperature-dependent paramagnetic shifts have been observed for a number of compounds: the single most important requirement for a suitable compound is that the ratio of $d\delta/dT$ to the linewidth be appreciable over the temperature range of interest, and many substances yield linewidths too broad for routine application.[9] Narrow linewidths require a small anisotropic magnetic susceptibility and thus, of the lanthanides, samarium compounds have been most studied. Paramagnetic broadening of the proton resonance complicates decoupling, and weak coupling or deuteration is desirable for a thermometer.

Most of the early MAS thermometry was based on the ^{13}C spectrum of samarium acetate hydrate.[2,10] The hydration state of this compound is somewhat variable, and this influences the exact temperature dependence of the resonances, but effects including rf heating and equilibration time were first explored with this standard. Figure 3 shows ^{13}C MAS spectra of a mixture of samarium acetate and graphite. The carbonyl chemical shift was strongly dependent upon ^{13}C and ^{1}H duty cycle, demonstrating that rf heating can produce 30 K or more of temperature error for lossy samples. A practical consideration in VT MAS experiments is how long should one wait for the sample to equilibrate after a step change in temperature. Figure 4 shows a measurement of equilibration time using samarium acetate thermometry. The gas temperature was abruptly changed from 173 to 303 K, and spectra of samarium acetate revealed that the sample temperature equilibrated to within 1 K of the final temperature after 8 min.

Recently, Grey et al. reinvigorated the practice of MAS chemical shift thermometry with the application of the ^{119}Sn shifts of $Sm_2Sn_2O_7$ and similar materials.[11] Figure 5 shows a representative result, and the temperature dependence of the isotropic shift was reported to be:

$$\delta = 223 - 9.53 \times 10^4 / T \quad (1)$$

from measurements at 14 temperatures. Using this class of thermometer, the authors established that friction heated the sample by several degrees when their spinning system was operated at higher rotation rates.

The lesson from thermometry studies is that temperature can be controlled in MAS experiments to perhaps ±2 K and certainly ±5 K over a fairly wide range if care is taken. One should fully characterize the probe and VT system on the bench, gain experience using standards including phase transitions and thermometers such as $Sm_2Sn_2O_7$, and minimize

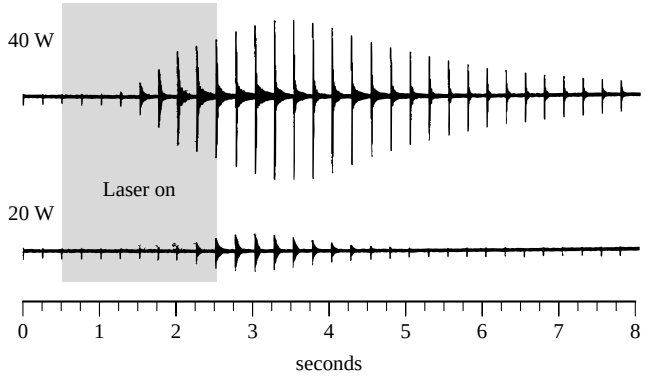

Figure 6 Proton FIDs obtained with small flip angles over the course of some fairly short experiments. The sample was hexamethylbenzene (m.p. 440 K) packed into a 5 mm quartz rotor. The spinning rotor was irradiated in the center with a CO_2 laser, and the progress of rapid heating and cooling was reflected in the signal intensity from the liquid phase. The shaded area denotes the duration of the laser pulse. This temperature-jump-and-quench experiment presents formidable obstacles to temperature measurement or modeling

rf and frictional heating using low duty cycles and moderate spinning speeds.

4 LASER HEATERS AND TEMPERATURE JUMPS

This section concludes with an example of an especially challenging problem in VT MAS temperature measurement. A CO_2 laser heater was constructed for very rapid sample heating through irradiation of the quartz MAS rotor. The intent of this experiment is very rapid temperature jumps followed by quenches possibly to trap chemical intermediates. Figure 6 shows series of ^{1}H FIDs acquired 200 ms apart for a spinning sample of hexamethylbenzene; the receiver delay was set to eliminate most of the signal from the solid component, and the formation and loss of signal intensity in the Figure corresponds to melting and refreezing of the sample over the short time course of the experiment. The very large spatial and temporal temperature gradients in this experiment will obviously be challenging to measure or model.

5 RELATED ARTICLES

Magic Angle Spinning.

6 REFERENCES

1. J. R. Lyerla, C. S. Yannoni, and C. A. Fyfe, *Acc. Chem. Res.*, 1982, **15**, 208.
2. J. F. Haw, G. C. Campbell, and R. C. Crosby, *Anal. Chem.*, 1986, **58**, 3172.
3. T. Bjorholm and H. J. Jakobsen, *J. Magn. Reson.*, 1989, **84**, 204.
4. F. G. Oliver, E. J. Munson, and J. F. Haw, *J. Phys. Chem.*, 1992, **96**, 8106.
5. J. F. Haw, R. A. Crook, and R. C. Crosby, *J. Magn. Reson.*, 1986, **66**, 551.
6. A. D. English, *J. Magn. Reson.*, 1984, **57**, 491.
7. B. Wehrle, F. Aguilar-Parrilla, and H.-H. Limbach, *J. Magn. Reson.*, 1990, **87**, 584.
8. F. Aguilar-Parrilla, B. Wehrle, H. Bräunling, and H.-H. Limbach, *J. Magn. Reson.*, 1990, **87**, 592.
9. H. Pan and B. C. Gerstein, *J. Magn. Reson.*, 1991, **92**, 618.
10. G. C. Campbell, R. C. Crosby, and J. F. Haw, *J. Magn. Reson.*, 1986, **69**, 191.
11. C. P. Grey, A. K. Cheetham, and C. M. Dobson, *J. Magn. Reson., Ser. A*, 1993, **101**, 299.

Biographical Sketch

James F. Haw. *b* 1954. B.S., Old Dominion University, 1977; M.S., North Carolina, 1979; Ph.D., Virginia Tech., 1982. Faculty in Chemistry, Texas A&M University, 1984–present. Approx. 100 publications. Research interests include the application of MAS NMR to the understanding of solid acidity and basicity, reaction mechanisms in heterogeneous catalysis, and other problems in materials science.

Bioreactors and Perfusion

Robert J. Gillies
University of Arizona Health Sciences Center, Tucson, AZ, USA

1	Introduction	1
2	Support System Design	1
3	Bioreactor Design Criteria	3
4	Is There an Optimal Design?	7
5	Related Articles	7
6	References	7

1 INTRODUCTION

1.1 Why Bioreactors?

NMR studies of living, cultured cells under physiologically relevant conditions require the application of bioreactors, i.e. specialized devices for growing and maintaining cultured cells in the steady state at the extremely high densities and within the well-defined geometries required by NMR. Any apparatus which satisfies these criteria is considered as a bioreactor. As discussed in this article, bioreactor systems are composed of two essential components: the bioreactor itself and the support system which maintains the steady state.

As discussed in other articles,[1] present cellular NMR studies have much in common with in vivo NMR studies. In some cases, they serve to complement in vivo MRS by examining the behavior of phenotypically homogeneous cells under defined conditions, as compared with the more heterogeneous conditions encountered in vivo. Thus, activities of particular metabolic pathways can be ascribed to particular cell types within organs. In other cases, cellular NMR provides a unique perspective to investigate metabolism and metabolic pathways in cells of diverse origins. As will be discussed, well-designed bioreactor systems provide a combination of spectral and temporal resolution which is unmatched by any other in vivo NMR approach.

1.2 Types of Cells Used

From an applications standpoint, there are essentially three types of cell: microorganisms (prokaryotic and eukaryotic), plant cells, and animal (mammalian) cells. Bioreactor systems should be uniquely designed for each cell type to be used. From a bioreactor design standpoint, however, all cells are the same, and exist on a multidimensional continuum of requirements.

There are a finite number of parameters common to all cells which need to be considered in the design of bioreactor systems, including cell metabolic rate, chemical substrates and growth factors, and requirements for attachment. By taking these parameters into account, bioreactor systems can be designed to support virtually any type of cell at extremely high densities for indefinite periods.

1.3 Bioreactor Technology

The design of bioreactor systems for individual applications occurs by taking the unique requirements of each system into account. This is a mature technology in the field of chemical engineering, where bioreactors are generally designed for the optimized production of cell-derived products with few spatial constraints. The major design criteria for NMR-compatible bioreactors are: (1) an extremely high cell density, (2) geometric constraints of high-field magnet systems, (3) magnetic permeability of construction materials, and (4) relatively large distances between the support system and the bioreactor itself. Thus, many of the specific designs extant in the biotechnology literature cannot be easily applied to NMR applications, and systems unique for NMR applications must be created.

2 SUPPORT SYSTEM DESIGN

In designing bioreactor systems, much attention is generally paid to the bioreactor itself. However, the support system is of equal or greater importance, since it is responsible for providing the high-density culture with an adequate, steady-state level of nutrients and a minimal, steady-state level of metabolic waste products. By analogy with metazoan systems, support circuits include the functions of cardiac, circulatory, renal, and pulmonary systems.

The number of parameters to be considered in designing a maintenance system are finite, and include medium delivery mode, medium composition, metabolic rates, temperature regulation, and specific requirements which are dictated by the experiment.

2.1 Medium Delivery Mode

All the bioreactors considered in this article are perfusion bioreactors. Thus, medium is pumped from a main reservoir through the bioreactor containing cells. This medium can either be (1) discarded, as in a one-pass system, or (2) returned to the medium vessel, as in a recirculation system. In recirculation systems, the medium in the main reservoir can either be (i) changed periodically, as in a step-change (i.e. a batch mode) system, or (ii) changed continuously, as in a bleed-and-feed system. These different approaches are illustrated in Figure 1.

The one-pass system is the simplest, containing only a main medium reservoir (Me), a pump (Pu), the bioreactor (BR), and a waste reservoir (Wa). For most applications, however, this approach is impractical, since it involves discarding medium which is still useful for cell growth. The step-change system is similar to the one-pass system, except that the main medium reservoir also acts as a waste reservoir. In this system, the medium is exchanged for fresh medium on a periodic basis (e.g. every 24 h). The major disadvantage of such a system is that the medium composition is never in a steady state. As medium is used, nutrients become depleted, waste products increase, and the pH changes. Although they suffer from this major disadvantage, such systems are often employed when cells are to be labeled (e.g. using ^{13}C) with a substrate which is either expensive or of limited availability, and cell physiology during the labeling period is not an important consideration.

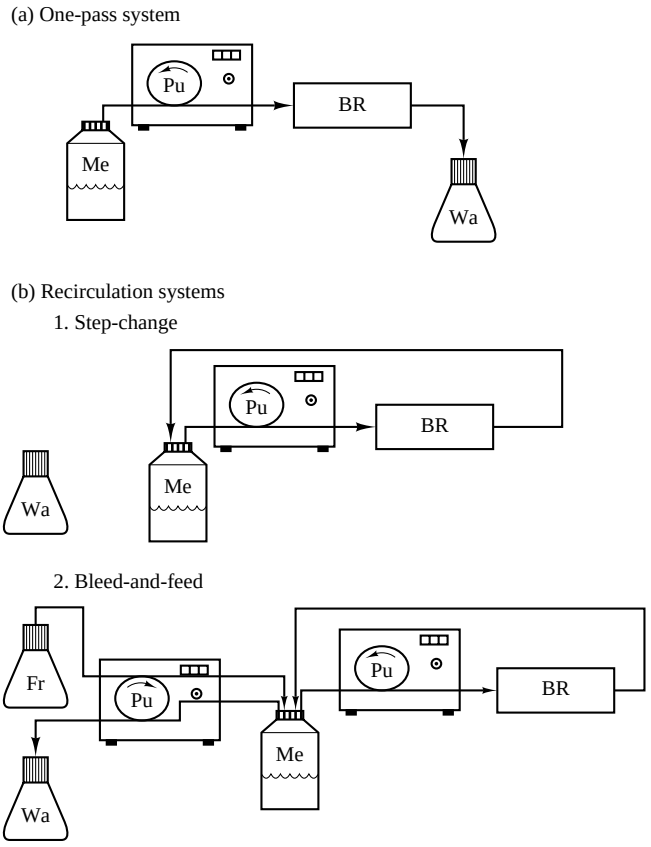

Figure 1 Types of medium delivery system. In a one-pass system, (a), fresh medium from the main medium reservoir (Me) is passed via a peristaltic pump (Pu) through the bioreactor (BR) and discarded into a waste receptacle (Wa). In recirculation systems (b) medium is recirculated back to the main medium reservoir (Me). In the step-change (or batch-mode) system (1), medium (Me) is changed periodically, whereas in the bleed-and-feed system (2), medium is continuously exchanged with an auxiliary pump connected to a fresh medium reservoir (Fr) and the waste reservoir

The system of choice is the bleed-and-feed system. This is more complex than the previous one in that an additional pump is required to add fresh medium (Fr) and remove spent medium (Wa) from the main medium reservoir. The total volume of the medium in the main reservoir is held in the steady state by placing the spent medium tube at a fixed height above the floor of the main medium reservoir and ensuring that this tubing, and hence the pump rate, is larger than that of the feed subcircuit. In such a system, the pumping rate is adjusted according to the total metabolic rate of the cells within the reactor such that the medium composition is held in the steady state. A sensitive measure of total cellular metabolic rate is reflected in the pH of the medium. The rate at which cells alter the medium pH is dependent on their total metabolic rate. Thus, adjusting the bleed-and-feed pump to maintain the medium reservoir pH constant ensures that the medium composition is in the steady state. Alternatively, the bleed-and-feed rate can be adjusted to maintain any medium constituent in the steady state. In systems with stringent nutrient requirements, the rate may be adjusted to keep a limiting nutrient well above its K_m for consumption. In systems with sensitivities to certain waste products, the bleed-and-feed rate may be adjusted to keep waste products at an acceptably low level.

With a bleed-and-feed circuit, the steady-state level of any nutrient is related to its consumption rate by the relationship:

$$dX_m/dt = (X_0R - X_mR - C)/V \quad (1)$$

where X_m is the concentration of component X in the medium (in mM), X_0 is the concentration of X in the fresh medium in the feed reservoir (in mM), R is the bleed-and-feed rate (in L min^{-1}), C is the consumption rate by the cells (in mmol min^{-1}), and V is the volume of the recirculating medium (in L). If we impose the boundary condition that $R > 0$, then X_m will reach a finite steady state and $(dX_m/dt)\ V = 0$. Under these conditions,

$$X_mR = X_0R - C \quad (2)$$

It can be seen that, if R becomes large with respect to C, then X_m approaches X_0. It should be noted that C is the product of the specific (i.e. per cell) consumption rate times the total number of cells in the reactor. If X_m is measured, all other parameters are known and C can be determined.

2.2 Medium Composition

It is generally true that medium which is used to grow cells in standard cell culture is not optimized for perfusion culture. For instance, when using a bleed-and-feed circuit, the rate of fresh medium addition is tied to one essential nutrient or waste product (see above). Thus, other nutrients may not have been utilized efficiently prior to discarding the spent medium.

This is a problem of practical as well as intellectual interest. For instance, mammalian cell culture requires growth factor supplements, usually provided by fetal bovine serum (FBS). Serum represents up to 80% of the cost of mammalian cell culture. Cells in perfused cultures have a much lower serum requirement than do cells in static cell cultures. Thus, for mammalian cell systems, serum can be reduced to concentrations as low as 2%, as compared with a concentration of 10% in static cell cultures. The serum requirement in perfused cultures is also a function of the cell density, with higher cell densities having a lower requirement. This apparent dichotomy is explained by the autocrine production of serum growth factors by many mammalian cells. Medium optimization is an iterative process and is probably not worthwhile for components other than those which are expensive or in limited supply, such as serum or isotopically labeled compounds.

2.3 Metabolism

A well-defined bioreactor system has to match delivery of nutrients to the cells at a rate which is equal to, or greater than, the total consumption rate. The most critical nutrient for optimization is oxygen (see below). Oxygen is generally supplied to the circuit by passing medium through a parallel set of gas-permeable fibers, such as silastic tubing. In order to ensure that an adequate amount of oxygen is reaching the cells, the desired concentration in the medium, C_0, must be determined using the models presented in Section 3. The mass transfer characteristics of the aerator must then be determined

at all flow rates. Although loss along the inlet tubes to the reactor can be eliminated by using gas-impermeable tubing (e.g. Teflon, glass), these are often too rigid to be of practical routine use. A relatively gas-impermeable tubing, such as neoprene, minimizes loss at low retention times (e.g. high flow rates or small inner diameters). In practice, the mass transfer loss of oxygen down the length of this tube can be significant and must be verified.[2] The appropriate C_0 can be iteratively maintained by increasing the partial pressure of O_2 in the gas mix as the culture grows (e.g. going from 20% O_2:5% CO_2:75% N_2 at inoculation to 60% O_2:5% CO_2:35% N_2 at maximum cell density). Concentrations of O_2 above 60% should not be used, since they can be cytotoxic.[3,4]

2.4 Temperature

In a well-defined bioreactor system, temperature must be tightly controlled. This is problematic in NMR-based perfusion systems since the sample is generally 7–8 m away from the main circuit. Temperature control using the spectrometer-supplied units is not sufficient, since the temperature of the bioreactor is primarily set by the temperature of the inflowing medium. In practice, the temperature of the'bioreactor is set by iteratively adjusting the temperature of the main circuit vessel to supraphysiological levels, and cladding the perfusion tubes within insulation. The temperature is monitored using temperature probes which insert into'the bioreactor itself. A number of such probes are available. Cost-efficient thermocouples are most often used, yet they interfere with NMR measurements and thus must be used offline.[2] In addition, more expensive fiber optic temperature monitors can be used continuously during experiments.[5]

3 BIOREACTOR DESIGN CRITERIA

The bioreactor itself must be designed to contain a maximum number of cells within a defined geometry. The most important criterion in designing a bioreactor is that all cells in the reactor must be maintained in similar environments.

3.1 Theoretical Considerations

The proper design of bioreactors and bioreactor systems must ensure that, throughout the reactor, all nutrient substrates are maintained well above their K_m for consumption, and that all waste products are maintained below their cytotoxic or cytostatic levels. There are numerous steady-state models which can be used to determine bioreactor geometries appropriate to meet these criteria.

3.1.1 Nutrients: Oxygen and Glucose

Due to its low solubility, O_2 is the most important limiting nutrient in bioreactor culture. Therefore, any design for bioreactors must ensure that all cells are adequately supplied with sufficient O_2. The problem of proper oxygenation is illustrated for a hollow fiber mammalian cell bioreactor in Figure 2. As shown in Figure 2(a) the O_2 concentration in the aqueous medium within the fiber at 37 °C is approximately

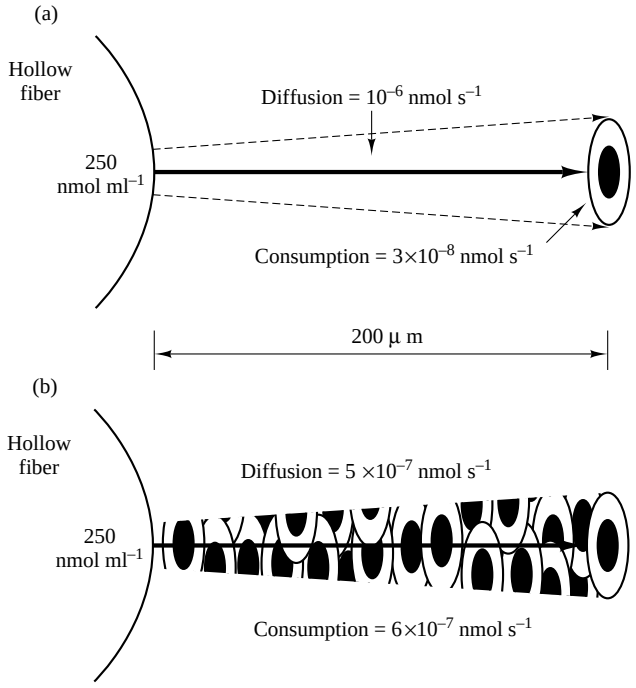

Figure 2 Illustration of oxygen limitation in bioreactor culture. (a) A single cell is placed 200 μm from a point source of medium oxygenated to air saturation (250 nmol ml^{-1}). The specific consumption rate for this cell (3×10^{-8} nmol s^{-1}) is easily supplied by diffusive flux in a column of medium with a diameter of 10 μm (one cell diameter). (b) If the culture is at tissue density, diffusive flux is reduced by a factor of 2, and consumption increases by a factor of 20. Thus, diffusion is only able to satisfy the requirements of approximately 16 cells within this column

250 μM. The diffusion coefficient for O_2 in aqueous media is 4.4×10^{-5} cm^2 s^{-1}, giving a diffusive flux of 10^{-6} nmol s^{-1} in a column of medium which is the width of a single, 10 μm diameter cell which is 200 μm away. Diffusive flux is sufficient, since this single cell requires only 3×10^{-8} nmol s^{-1} of O_2. However, as cell density increases, the diffusion coefficient for O_2 decreases, such that at tissue density the diffusion coefficient is 2 times less, or 5×10^{-7} nmol s^{-1}. This is enough to supply a little over 16 cells with adequate oxygen. Assuming a tissue density of 3×10^8 cells mL^{-1}, there will be approximately 20 cells between the fiber and a target cell 200 μm away, giving a total consumption of 6×10^{-7} cells mL^{-1}. As illustrated in this example, cells that are at tissue density and are more than 150 μm away from a source cannot be adequately supplied with O_2 via diffusive flux alone.

An analytical solution to the O_2 problem was first proposed by Krogh[6] and Erlang to define the concentration profile for oxygen in tissues and the following equation is adapted from their work:

$$C_0 - C_r = M/D\left[\frac{1}{2}r_t^2 \ln(r/r_c) - \frac{1}{4}(r^2 - r_c^2)\right] \qquad (3)$$

where, for a bioreactor, we are given the following:
Parameters

C_0 the concentration of O_2 in the capillary (*ca*. 250 nmol ml^{-1} at 1 atm)

r_c the radius of the capillary/hollow fiber (given, usually 50–200 μm)
M the O_2 consumption rate (*ca*. 10 nmol $s^{-1}cm^{-1}$ for mammalian cells at tissue density)
D the diffusion coefficient for O_2 in tissues (*ca*. 2.2 $\times 10^{-5}$ cm^2 s^{-1} at 37 °C

Variables

C_r the concentration of oxygen within the tissue at radius, *r* (variable)
r the radius from the center of a capillary (variable)
r_t the Krogh radius at which $dC/dX = 0$ (to be determined)

A plot of O_2 concentration at distances from the surface of a 100 μm diameter fiber is shown in Figure 3. Isobars for O_2 concentrations at different consumption rates are presented to illustrate the observation that steady-state O_2 levels are extremely sensitive to cell density. At 50% maximal cell density, the culture consumes O_2 at a rate of 5 nmol s^{-1} cm^{-3}, and cells 300 μm away from the fiber wall can be oxygenated adequately. At tissue density, when the consumption rate, M, is 10 nmol s^{-1} cm^{-3}, the O_2 is exhausted 125 μm away from the fiber wall. In order to determine the maximum interfiber distance, we can design a special case, where the Krogh radius is maximal, i.e. $C = 0$ when $r = r_t$. Equation (3) can then be rewritten as:

$$C_0 = M/D\left[\frac{1}{2}r_t^2 \ln(r_t/r_c) - \frac{1}{4}(r_t^2 - r_c^2)\right] \qquad (4)$$

It can be seen that the Krogh radius is related to the capillary radius by both scalar ($r_t{}^2 - r_c{}^2$) and relative (r_t/r_c) terms. I asked my mathematician friend, Tim Secomb, for his assistance and he provided the following. If we define a dimensionless quantity, X, as $(4DC_0)/(Mr_c{}^2)$, then substituting into equation (4) yields:

$$X = (4DC_0)/(Mr_c^2) = 2[(r_t/r_c)^2 \ln(r_t/r_c)] - (r_t/r_c)^2 + 1 \qquad (5)$$

The quantity X can be defined with known parameters and used to relate r_t (the maximum distance from the center of the fiber that a cell can be oxygenated) to r_c, the radius of the fiber. A plot of X as a function of r_t/r_c is shown in Figure 4. In this figure, horizontal arrows are positioned at values of X at different consumption rates. Note that, for a fiber with a diameter of 50 μm, the Krogh radius is 185 μm. Since the Krogh radius is measured from the center of the fiber, this places the point of O_2 depletion at 135 μm from the fiber wall, which is in good agreement with data presented in Figure 3.

Similar analyses have been numerically and analytically solved for mammalian cells and microorganisms in bioreactor culture.[7,8] All analyses have arrived at similar conclusions: if O_2 is required by a cell, then it will be the limiting substrate for growth and maintenance.

The above analyses are general, i.e. they can be used for virtually any substrate and for any bioreactor configuration. Therefore, to determine the extent of glucose limitation, one simply needs to put in values for the glucose diffusion coefficient (ca. 0.5×10^{-5} cm^2 s^{-1}), the glucose consumption rate (ca. 100 nmol s^{-1} cm^{-3} at tissue density), and the concentration of glucose in the medium (2–23 mM). In the case of glucose and other nutrients, a further adjustment is also necessary to account for the fact that the K_m for consumption is not zero. Since O_2 is taken up with extremely high affinity, the consumption is near V_{max} at all levels. In the case of glucose, various glucose transporters have different affinities, ranging from < 100 μM to > 5 mM.[9] Thus, the K_m for consumption must be determined for each system, and the concentration at r_t must be held at 5 times this K_m value to

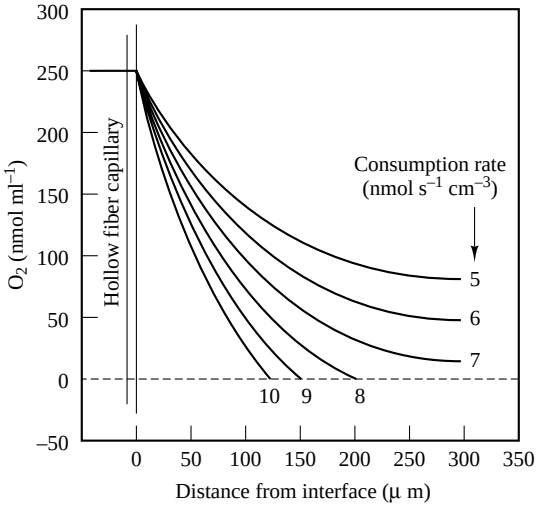

Figure 3 The modified Krogh function (equation (3)) showing dissolved O_2 concentration as a function of distance from an interface at different oxygen-consumption rates. This was calculated for a hollow fiber capillary with a radius of 50 μm. Most cultured mammalian cells at tissue density will consume oxygen at a rate approaching 10 $nmol^{-1}$ cm^{-3}. At this density, oxygen will be depleted 135 μm from the capillary wall

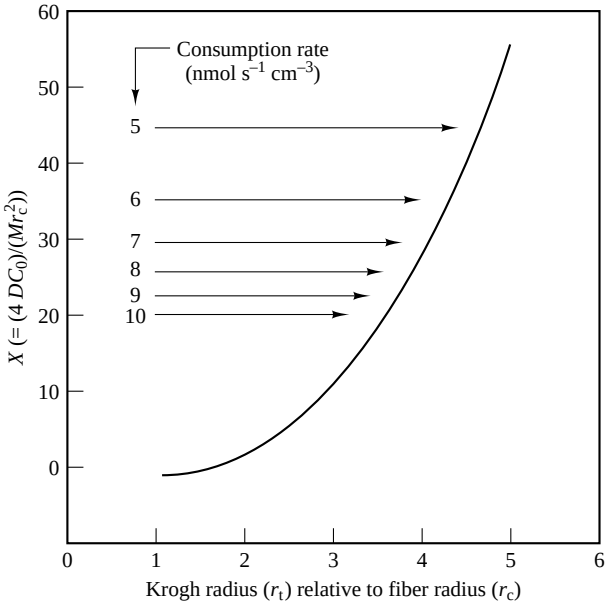

Figure 4 Isobar plot illustrating the relationship (equation (5)) between the dimensionless quantity, X, and the ratio of the Krogh radius to the radius of the hollow fiber capillary. X embodies terms for measurable parameters. The Krogh radius in this relationship relates to the special case where the concentration of O_2 is zero. The dotted lines indicate the values of X at consumption rates of s–10 nmol s^{-1} cm^{-3}

ensure a V_{max} consumption rate. If cells are immobilized in beads or threads, the above equations can be applied mutatis mutandis with respect to the geometric differences.

3.1.2 Waste Products

An often overlooked parameter in bioreactor design is the cytostatic effects of accumulated waste products, such as ammonium and lactate. Both of these metabolic byproducts can build up to supraphysiological levels (e.g. >5 mM) and exert significant cytostatic effects.[8,10] In order to maintain these waste products below acceptable levels, a derivation of equation (3) can be applied, using the boundary condition that $C = C_{max}$ at $r = r_t$, and M is now a production rate, P, with opposite sign:

$$C_0 = C_{max} + P/D\left[\frac{1}{2}r_t^2 \ln(r_t/r_c) - \frac{1}{4}(r_t^2 - r_c^2)\right] \quad (6)$$

Given the production rate, diffusivity, fiber radius (r_c) and interfiber distance (r_t), one can thus determine the maximum allowable concentration of waste products within the circulating medium which will maintain the C_{max} at acceptable levels at all points within the reactor. In practice, lactate and ammonium levels are carefully monitored in the perfusate, and the bleed-and-feed rate is adjusted to maintain them below this determined value of C_0.

3.2 Practical Considerations

3.2.1 Substrata

By definition, all microorganisms are free-living and thus are not immobilized in their physiological state. In contrast, while some mammalian cells, such as blood cells and some tumor cells, can be cultured in suspension, most mammalian cells have a substrate-attachment requirement for growth and physiological function. This is often an area of consternation, since it adds a level of complexity to the proper design of culture systems. In perfusion systems, however, cell immobilization can relieve some constraints on bioreactor design.

For any perfusion system, the cells must be supplied with fresh medium while being maintained within a defined geometry. Thus, the cells must be trapped within the NMR sample chamber. This can be accomplished by physically separating the cells from the perfusing medium, as in a hollow fiber reactor. In this type of reactor, cells in suspension are separated from the perfusate by a wall which is impermeable to cells. Trapping can also be accomplished by immobilization within a matrix which is either inert (e.g. agarose, alginate) or biologically active (e.g. Matrigel, collagen). In these reactors the medium is superfused over and around the immobilization matrix. In addition, hollow fiber reactors can be adapted to house cells immobilized within matrixes. Care should be taken in the choice of immobilizing gel, since it is well known that the identity of the extracellular matrix (ECM) can have profound effects on cell physiology and function. It is clear that cells entrapped in different matrices can exhibit different NMR spectra and physiological responses.[11,12]

3.2.2 Gradients

From a biotechnological perspective, an ideal bioreactor would be *gradientless* in that all cells within the culture would exist within a homogeneous microenvironment. From a biological perspective, however, it is unclear whether a lack of gradients is necessary to understand complex phenomena, since gradients are an essential component of tissues. This is a point of some controversy since, in practice, gradientless operation is impossible to achieve. Bioreactors can be adapted to yield robust biological data if the gradients are minimized and well characterized. Gradients can be characterized using derivations of the Krogh models described above. The effects of gradients can be minimized if all nutrients are maintained well above their K_m for consumption and all waste products are maintained at minimum levels.

The above argument refers to bioreactors which are not only well-designed, but are also well built. Unfortunately, the mass construction of bioreactors has lagged far behind their design. For instance, hollow fibers are often manufactured such that fiber distribution is heterogeneous. This can lead to significant heterogeneities in perfusion and cell distribution.[13] Superfusion (or trickle-bed) reactors, which employ cells immobilized in beads, are prone to 'channeling' of perfusate at intermediate flow rates. Since this channeling is not controlled, the degree of heterogeneity will vary from experiment to experiment. At high flow rates in trickle-bed reactors the beads are extremely well mixed and the reactor approaches gradientless operation. However, under these conditions the density of cells is drastically decreased and loss of signal occurs.

3.2.3 Size

Practically speaking, bioreactor size is most often adjusted to fit the available probes and magnet. This is not necessarily optimal, however. The optimum diameter for bioreactors is a product of experimental considerations and the design of the coil. From signal-to-noise (S/N) considerations alone, Alecci et al.[14] have modeled the sensitivity of a conductive sample in a Helmholtz coil. According to their calculations the optimum sample diameter of a 150 mM salt sample is 12–15 mm. By the time the sample radius is 25 mm, the sensitivity factor, ηQ, has dropped five-fold. The loss of sensitivity in conductive samples is due mainly to capacitive coupling between the coil and the sample.[15] A strategy to reduce this lossy coupling is to reduce the amount of the coil that is in close apposition to the sample, by using a 'birdcage' coil design.

Experimental considerations can override the need for an optimum S/N ratio. For instance, if cells are to be labeled with a substrate of limited availability, then smaller sample sizes might be preferred. Hollow fiber reactors as small as 5 mm diameter have been successfully constructed, with reasonable S/N ratios (K. A. McGovern, personal communication).

3.2.4 Cell Density

Bioreactors for NMR should immobilize and support cells at the maximum possible density within the coil volume.

There are two volumes to consider in bioreactor design: (1) the perfusion volume, which is dedicated to the perfusing media; and (2) the nonperfusion volume, which is dedicated to cells and interstitial fluid. Thus NMR-based reactors have two opposing design criteria: (1) to minimize gradients and ensure that cells are not deprived of oxygen, the perfusion volume must be as large as possible; and (2) to ensure that the global cell density is maximal, the perfusion volume should be as small as possible. In tissues, the perfusion (capillary) volume is 6–8%.[19] In hollow fiber and trickle-bed bioreactors this volume is nearer 35%. Thus 65% of the total volume is available for cells. Within this volume of a well-designed reactor, cell density can approach a tight pack. Thus global cell densities can approach 50%. With ^{31}P the cell density in bioreactors can be measured using dimethyl methylphosphonate (DMMP) which undergoes a chemical shift upon entering cells.[20]

3.3 Types of Reactor

As discussed in Section 1, there are many types of bioreactor available for use in NMR. The choice of system depends first on availability and second on design. At this point, commercial bioreactors designed for NMR use are not commercially available. Therefore, systems must be either homemade, or adapted from commercial designs. In the following an iteration of reactor types is given, together with a discussion of their advantages and disadvantages. It must be remembered, though, that the mass transfer characteristics of all reactors follow the same basic rules, outlined by equations (3)–(5).

3.3.1 Gel Embedding

The simplest reactor that one can construct is a perfusion system wherein cells are immobilized in threads or beads of bioactive or inert gels. These cell–gel matrices are placed within a modified NMR tube and superfused with fresh medium [Figure 5(a)]. As shown in Figure 5(a), perfusate is pushed to the bottom of the NMR tube, where it percolates up through the cell–gel matrix and, into an aft chamber, where it is aspirated out of the system back to the main reservoir.

An advantage of this system is its simplicity. It is easily constructed and can be made inhouse with little cost. Multiple samples can be prepared from stock cultures, and many experiments can be run per day, if needed. A further advantage is that the Teflon plugs can be easily modified to fit reactors with a variety of diameters. Disadvantages of this system are the abovementioned heterogeneity of flow (channeling), and an often-observed heterogeneity in the bead or fiber diameter, which can have important consequences for diffusion-mediated nutrient delivery or waste-product removal. These systems are also difficult to sterilize. Thus, experiments are often limited to a few hours. This is problematic, since preparation of the gel often involves unphysiological conditions, such as dramatic alterations in temperature, pH and Ca^{2+} concentration. After these treatments, cells require a recovery period to reach steady state (up to 24 h). Nonetheless, if care is taken to prepare the sample under sterile conditions, these systems can be used to maintain cultures for days or weeks. Under some conditions, cultures can be demonstrated to increase in cell density during this incubation time.[16]

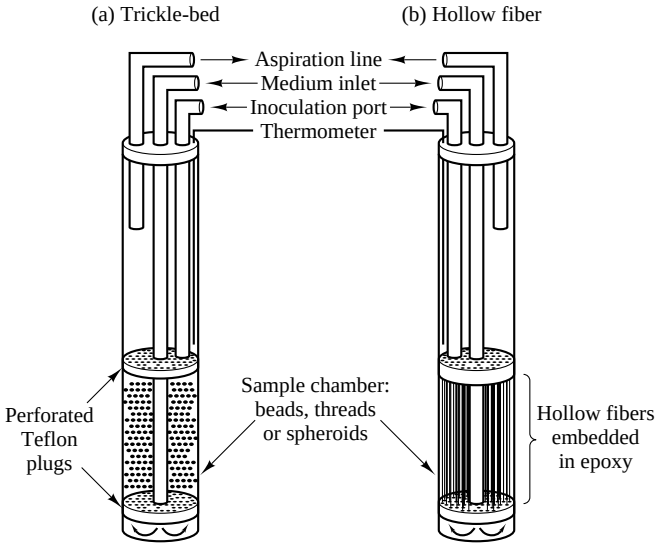

Figure 5 Two major types of bioreactor. In the trickle-bed perfusion reactor (a) cells are embedded in semisolid matrices (beads or gels) of inert or bioactive gels. These matrices are immobilized between two porous plates and medium is perfused (i.e. superfused) over the gels. The medium channels between the beads via undefined routes. The hollow fiber reactor (b) is similar, except that cells are immobilized within the extracapillary space by exclusion, and the medium perfuses through the sample within (theoretically) well-defined geometries

3.3.2 Hollow Fibers

Hollow fiber reactors have been used to maintain cells under NMR conditions for some time.[17] A typical hollow fiber setup is illustrated in Figure 5(b). Medium is pushed to the bottom of the sample tube and percolates up through isotropically spaced hollow fibers. Cells, either in suspension or immobilized, exist in the interfiber spaces. Generally, reactors which are employed are modifications of commercially available hollow fiber reactors designed for dialysis, ion exchange, etc. Recently, hollow fibers have been designed and constructed specifically for NMR applications.[2] Such reactors are not commercially available and must be constructed ad hoc, generally with a limited amount of diameters. Thus hollow fiber reactors suffer from limited availability. In operation, hollow fibers are difficult to set up. Although they are easily sterilized by auto claving or ethylene oxide, hollow fiber reactors are optimally designed for long-term operation. Thus, each experimental setup usually operates for many weeks. This is also an advantage of hollow fiber reactors, since they can be used to investigate long-term adaptations.

Hollow fiber reactors can also be used to perfuse cells embedded in beads.[2] Thus, under these conditions, substratum-requiring cells can be cultured in hollow fiber reactors. In this case, the system is identical to a trickle-bed reactor, except that 'channeling' is limited to the lumens of the hollow fibers themselves. Thus channeling has the potential to be well controlled and homogeneous.

Sample spectra from cells cultured in a 25-mm diameter hollow fiber reactor are shown in Figure 6. This spectrum was acquired in 5 min with optimum (Ernst angle) pulsing, and

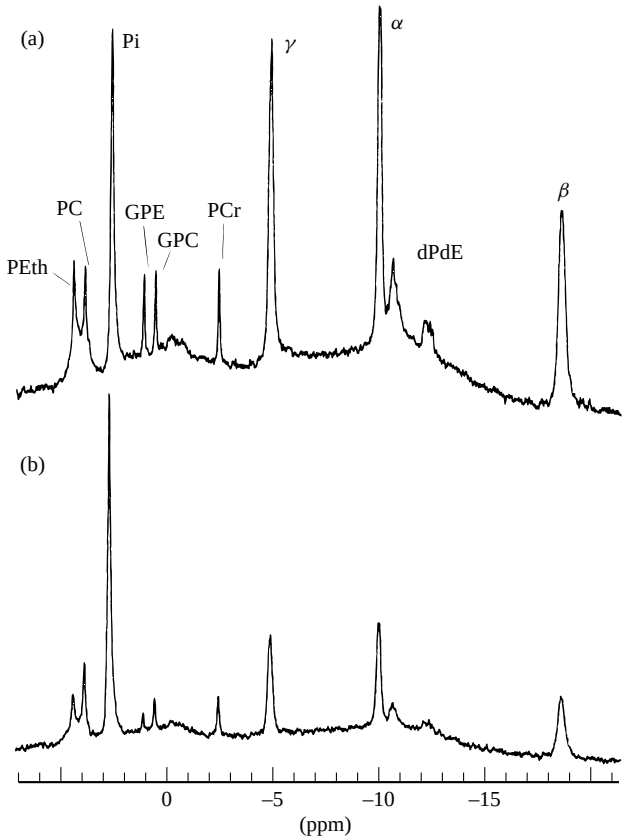

Figure 6 ^{31}P spectra (5 min) of C6 glioma cells grown in a 25-mm hollow fiber bioreactor. Spectra were obtained at 352 h (a) and 5 h (b) postinoculation. Spectra were acquired with 300 transients induced with 22 μs (30°) pulses every 1.0 s. FID data were processed using 5 Hz exponential line broadening. Abbreviations: PEth, phosphorylethanolamine; PC, phosphorylcholine; Pi, inorganic phosphate; GPE, glycerolphosphorylethanolamine; GPC, glycerolphosphorylcholine; PCr, phosphocreatine; γ, terminal phosphates of nucleoside tri- and diphosphates (i.e. NTP/NDP); α, primary phosphate of NTP/NDP; dPdE, diphosphodiesters [e.g. uridine diphosphorylglucose/galactose, nicotinamide adenine dinucleotide (phosphate)]; β, middle phosphate of NTP

illustrates the excellent S/N ratio available from high-density samples. The data were processed with 5 Hz line broadening and illustrate the excellent spectral resolution that is available from these samples.

3.3.3 Spheroids

Spheroids occur when tumor cells which require substrate attachment are cultured at high density.[18] They usually start out as a ball of cells 0.05–0.1 mm in diameter and can grow as large as 2 mm diameter. From the standpoint of bioreactor design, they are similar to bead-embedded cells, except for the added complexity that the bead/spheroid diameter increases with time.

4 IS THERE AN OPTIMAL DESIGN?

Bioreactor systems have two components: the maintenance circuit and the bioreactor itself. For physiologically relevant experiments, it is essential that the conditions in the bioreactor are in the steady state for the duration of the experiment, so that any experimental perturbation of the steady-state can be compared with a well-defined control. Therefore, the maintenance circuit must include a bleed-and-feed subcircuit. The rate of bleed-and-feed transfer will establish the steady-state levels of all medium components (see equation (1) and equation (2)) and this rate must be well established prior to the experimental perturbation and maintained throughout the data-acquisition period. This is not a trivial point, since the rate of medium replacement must be decided well in advance of experiments, and it subsequently establishes the experimental conditions, cost of labeled materials, amount of medium used, etc.

Therefore there is a single appropriate design for maintenance systems. In contrast, there are numerous specific bioreactor designs available. Topologically, however, they are all similar [see Figure 5(a) and (b)] in that they immobilize cells within the coil volume while perfusing or superfusing medium through the cell matrix. This can be achieved in many appropriate ways, from embedding cells in threads, to immobilizing them in the extracapillary space of a hollow fiber reactor. The rational choice of bioreactor model can therefore be system-dependent, depending on the size of the magnet, requirement of cells for attachment to substrata, etc.

All NMR-based bioreactors are faced with opposing design criteria. On the one hand they should provide maximal volume for the cells to populate and hence generate a maximal S/N ratio. On the other hand, the more volume that is provided for the cells implies less volume for perfusing medium and hence a greater probability of diffusional limitation. With current technology, a minimum of 33% volume should be reserved for the perfusing medium. By contrast, the volume fraction reserved for perfusion in tissues can approach 6–8%.[19] Any design is appropriate, as long as it demonstrably satisfies the criteria outlined by equation (3) and equation (4) and for O_2 and other essential nutrients.

5 RELATED ARTICLES

Cell Suspensions; Cells and Cell Systems MRS

6 REFERENCES

1. (a) B. S. Szwergold, *Annu. Rev. Physiol.*, 1992, **54**, 775. (b) K. A. McGovern, *NMR in Physiology and Biomedicine*, ed. R. J. Gillies, Academic Press, London, 1994. (c) R. J. Gillies, B. E. Dale, D. D. Drury, and T. J. Chresand, *Rev. Magn. Reson. Med.*, 1987, **1**, 155. (d) C. S. Ho and D. I. C. Wang, *Animal Cell Bioreactors*, Butterworth-Heinemann, Oxford, 1991. (e) S. F. Shedd and L. D. Spicer, *NMR Biomed.*, 1991, **4**, 246.
2. R. J. Gillies, J. P. Galons, K. A. McGovern, P. G. Scherer, Y. H. Lien, C. Job, R. Ratcliff, F. Chapa, S. Cerdan, and B. E. Dale, *NMR Biomed.*, 1993, **6**, 95.
3. W. M. Miller, C. R. Wilke, and H. W. Blanch, *J. Cell. Physiol.*, 1987, **132**, 524.
4. J. P. Freyer, E. Tustanoff, A. J. Franko, and R. M. Sutherland, *J. Cell. Physiol.*, 1984, **118**, 53.
5. C. T. Ng, K. A. McGovern, J. P. Wehrle, and J. D. Glickson, *Magn. Reson. Med.*, 1992, **27**, 296.

6. A. Krogh, *J. Physiol. (London)*, 1919, **52**, 409.
7. I. A. Webster and M. L. Shuler, *Biotechnol. Bioeng.*, 1978, **20**, 1541; 1979, **21**, 1725.
8. T. J. Chresand, R. J. Gillies, and B. E. Dale, *Biotechnol. Bioeng.*, 1988, **32**, 983, 1029.
9. C. F. Burant, W. I. Sivitz, H. Fukumoto, T. Kayano, S. Nagamatsu, S. Senio, J. E. Pessin, and G. J. Bell, *Recent Progr. Horm. Res.*, 1991, **47**, 349.
10. (a) M. W. Glacken, *Bio/Technology*, 1988, **6**, 1041. (b) M. W. Glacken, R. J. Fleishaker, and A. J. Sinskey, *Biotechnol. Bioeng.*, 1985, **27**, 1375.
11. D. L. Foxall and J. S. Cohen, *J. Magn. Reson.*, 1983, **52**, 346.
12. (a) N. R. Aiken, K. A. McGovern, C. E. Ng, J. P. Wehrle, and J. D. Glickson, *Magn. Reson. Med.*, 1994, **31**, 241. (b) N. Suzuki, I. L. Kwee, L. B. Tamas and T. Nakada, *Magn. Reson. Med.*, 1991, **19**, 422.
13. B. Callies and K. A. Brindle, *Bio/Technology*, 1994.
14. M. Alecci, G. Gualtieri, and A. Sotgiu, *J. Phys. E*, 1989, **22**, 354.
15. R. W. Dykstra, *J. Magn. Reson.*, 1989, **84**, 388.
16. B. S. Szwergold, T. R. Brown, and J. Freed, *J. Cell Physiol.*, 1989, **138**, 227.
17. P. M. Gullino and R. A. Knazek, *Methods Enzymol. Cell Cult*, 1979, **58**, 178.
18. (a) J. P. Freyer and R. M. Sutherland, *Cancer Res.*, 1986, **46**, 3504, 3513. (b) J. P. Freyer, P. L. Schor, K. A. Jarrett, M. Neeman, and L. O. Sillerud, *Cancer Res.*, 1991, **51**, 3831.
19. E. M. Renkin, in *Textbook of Physiology*, H. D. Patton, A. F. Fuchs, B. Hille, A. M. Scher, and R. Steiner, Saunders, Philadelphia, 1989, pp. 860–878.
20. J. A. Barry, K. A. McGovern, Y.-H. H. Lien, B. Ashmore, and R. J. Gillies, *Biochemistry*, 1993, **32**, 4665.

Biographical Sketches

Robert J. Gillies. *b* 1953. B.S., 1974; University of California, Irvine, Ph.D., 1979, University of California, Davis. Introduced to NMR by R. G. Shulman, Bell Laboratories, 1978–1979; Postdoctoral associate with R. G. Shulman, Yale University, 1979–1982; Faculty Department of Biochemistry, Colorado State University, 1982–1988; Faculty Departments of Biochemistry, Physiology and Radiology, University of Arizona, 1988–present. Approximately 60 publications, including 'Magnetic Resonance in Physiology and Biomedicine', Academic Press, 1994. Research interest: cell physiology of carcinogenesis, and cell pH regulation.